广西南海珊瑚礁研究重点实验室
年度报告
（2025年）

2025 Annual Report on Guangxi Laboratory on the Study of Coral Reefs in the South China Sea

广西南海珊瑚礁研究重点实验室 编辑
2026年01月



目录

一、基本信息 2
（一）实验室简介 3
（二）实验室定位 5
（三）实验室的研究方向 5
（四）实验室平台与设施 5
（五）实验室组成框架 9
二、年度主要进展 21
（一）科研项目立项 21
（二）奖励与荣誉 27
（三）论文发表 30
（四）代表性成果 31
（五）学术交流 51
（六）出海科考 52
（七）人才引进 53
（八）人才培养 58
（九）硬件设施建设 67
三、论著列表 71
（一）南海珊瑚礁生物与生态方向 71
（二）南海珊瑚礁地质与环境方向 77
（三）南海珊瑚礁环境与化学方向 80
（四）南海珊瑚礁遥感与监测方向 90
四、在研基金项目列表 92
（一）纵向科研基金项目 92
（二）横向科研基金项目 100
五、授权/公开专利列表 103
六、学术交流 105
（一）会议交流 105
（二）学者讲学 119
七、开放课题和自主课题 122
八、科普与宣传 124
九、其他社会服务活动 128
十、运营管理 129
（一）现有主要仪器设备 129
（二）三十万元以上设备的年度使用情况 132
十一、附录：年度论文集 136

一、基本信息

实验室名称：

中文：广西南海珊瑚礁研究重点实验室

英文：Guangxi Laboratory on the Study of Coral Reefs in the South China Sea

依托单位：广西大学

实验室学术委员会主任：焦念志

实验室主任：余克服

通讯地址：广西南宁市西乡塘区大学东路 100 号

联系人：黄荣永

联系电话：15277103086

EMail：coralreefs@gxu.edu.cn

网　址　：https://shj.gxu.edu.cn

学科与学位点：

	学科	
学科分类	名称	代码
本科专业	海洋科学	0707
硕士点	海洋科学	0707
博士点	生物学	0710
博士后站	生物学/生态学	0710/0713
研究性质	■ 基础研究 ■应用基础研究 □社会公益性研究 □高技术研发	
归口领域	□化学 □数理 ■地学 □生命科学 □医学科学 □信息 □材料 □工程	
注：学科名称与代码参考国务院学位委员会、教育部印发的《研究生教育学科专业目录（2022 年）》（http://www.moe.gov.cn/srcsite/A22/moe_833/202209/t20220914_660828.html）。		

（一）实验室简介

广西南海珊瑚礁研究重点实验室（以下简称“实验室”）于 2016 年获批成立，是广西 2016 年唯一无需培育而直接认定的省级重点实验室，也是我国迄今唯一聚焦珊瑚礁研究的省部级重点实验室，已连续在三轮全区重点实验室三年评估（2015-2017 年、2018-2020 年、2021-2023 年）中获评优秀等级。

目前，实验室是广西唯一的“本-硕-博”一体化的海洋科学人才培养基地，拥有“海洋科学”本科专业、“海洋科学”一级学科硕士学位授权点，以及“海洋生物资源与环境保护”二级学科博士学位授权点。“海洋科学”作为广西大学土木工程与先进材料学科群的核心学科于 2017 年入选“世界一流建设学科”。

从珊瑚礁研究的角度，实验室拥有国内场地最大、设备最齐全的珊瑚礁研究设施，拥有国内专业方向最齐全、人数最多的珊瑚礁研究队伍。实验室面积为 17310 m^2，科研仪器设备总值 8995 万元；固定科研人员 45 人，技术人员 3 人，管理人员 8 人。固定科研人员有 71%不超过 40 岁，有 91%不超过 50 岁；全部拥有博士学位（均为中国科学院、“985”高校或双一流高校的博士学位），包含国家重大人才工程计划项目、国家杰出青年科学基金获得者、国家重大科学研究计划项目（“973”项目）首席科学家、国务院政府特殊津贴获得者等。

实验室与三沙航迹珊瑚礁保护研究所建立了长期、稳定和密切的合作关系，合作共建有联合研究中心和三沙永乐龙洞保护站；建有潜水培训中心和“蓝色梦想”珊瑚礁科考团队，先后出海考察 107 航次，参与 527 人次，累计 1769 天，总航程 71299 海里，范围覆盖整个中国南海、华南沿岸、西太平洋、东印度洋和南印度洋等。以考察采集获得的数据与样本为基础，实验室已建成国内样本数量最丰富、种类最齐全、覆盖范围最广的南海珊瑚礁样品库。其中，既有钻穿西沙群岛琛航岛珊瑚礁的岩芯（琛科 2 井，928.75 m，平均取芯率 70%），又有广西大学历史首次南海深潜获得的深海冷水珊瑚和深海沉积物等珍贵样品。

实验室拥有涠洲岛珊瑚馆、岛礁生态修复实验室、海洋科教馆、广西涠洲岛珊瑚礁国家级海洋公园管理站和广西大学海洋科学广西院士工作站等平台，形成了集研究、教学、实践、服务于一体的珊瑚礁系统科学研究与人才培养基地，迄今被授予中国科协涠洲岛珊瑚馆科普教育基地、广西科普基地、广西海洋科普与意识教育基地和广西科普教育基地等。

依托以上条件，实验室自成立以来：

1. 已获得国家自然科学基金重大研究计划重点支持项目、国家自然科学基金重点项目和国家自然科学基金重大项目课题等 255 项基金项目（经费 20237 万元）。

2. 获得了一系列新的科学发现、提出了一系列新的学术观点，形成了珊瑚礁系统科学理论的基本框架，共计发表学术论文 758 篇（含 SCI 检索 502 篇），出版学术著作 3 部，其中《珊瑚礁科学概论》是我国迄今唯一关于珊瑚礁的综合性学术著作与教材。此外，本年度在编的《南海珊瑚礁与环境》已获国家科学技术学术专著出版基金优先资助。

3. 以珊瑚礁系统科学理论为基础，构建了能够避免传统“拆东墙补西墙”问题的“珊瑚选种、育苗、选址、移植、维护、可视化监控”的全链条珊瑚礁生态修复新技术体系，建成了涠洲岛自然海区珊瑚礁生态修复示范区（国内目前唯一对公众开放、可随时参观的珊瑚礁生态修复示范区），获批了涠洲岛 200 亩专门用于珊瑚生态修复实验的科研用海（迄今涠洲岛唯一对外批复的科研用海项目），并实施了 6992 万中央海洋生态保护修复资金项目（修复涠洲岛 30 公顷的受损珊瑚礁），成效已入选 2025 年全国。

4. 申请专利 97 项（发明专利 77 项、实用新型专利 20 项），其中已获得授权 38 项（发明专利 18 项、实用新型专利 20 项）。

5. 培养硕士研究生 488 人（已获硕士学位 251 人）、博士研究生 57 人（已获博士学位 28人）、本科生 764 人（已获学士学位 442 人，参与发表学术论文 44 篇，其中 SCI 检索 12 篇、北大中文核心论文 19 篇）；骨干教师拥有国家杰出青年科学基金获得者和国家重大人才工程计划项目等人才称号 31 人次，担任教育部科技委学部委员、中国第四纪科学研究会常务理事和中国海洋湖沼协会地质学分会副理事长等重要学术组织职务 57 人次和 *Marine Environmental Research* 主编、《海洋学研究》副主编和《海洋学报》（中英文版）编委等 30 本重要期刊职务，入选全球最具影响力气候领域科学家等学术排名榜单 13 人次。

6. 免费向社会开放涠洲岛珊瑚馆、岛礁生态修复实验室和海洋科教馆，至今累计参观 40 万人次，开展大型科普与宣传公益活动 88 场次，中央电视台、中国日报和新华社等权威媒体报道近 180 次，有效地向社会普及了海洋和珊瑚礁知识，提高了民众南海领土主权和生态环境保护意识，曾入选广西科学家精神宣讲团名单、中国青少年宫协会会员单位，并获国家自然科学基金科学传播类专项项目、中国科协全国科普日优秀活动、“八桂科普大行动”优秀特色活动、“八桂科普大行动”先进个人、广西“十佳优秀科普教育基地”和广西“十佳优秀科学传播活动”等科普奖。

实验室基于研究成果完成的一份报告被海军有关部门评价为“为南海岛礁工程规划选址和施工过程中的生态环境保护提供了重要科学依据”；参与完成的关于南海岛礁工程维护与后续建设的另一份报告，得到了国家最高领导人的亲自批示；参与编制的《黄岩岛海域生态环境状况调查评估报告》被评价“为服务国家政治外交大局提供了支撑保障”。

总而言之，实验室形成了理论研究、技术研发和应用服务等多学科集成的珊瑚礁系统科学研究框架，并奠定了我国珊瑚礁系统科学专业人才培养的基础，因而获得了广西自然科学奖一等奖、二等奖，广西高等教育自治区级教学成果一等奖，广西创新争先奖和广西工人先锋号等。

（二）实验室定位

实验室以珊瑚礁系统科学研究为特色，以建设代表中国最高水平的珊瑚礁研究和人才培养基地为目标，致力于建成集探索科学前沿和服务国家需求于一体的科学研究、人才培养机构，服务于我国珊瑚礁学科的发展与人才培养。

（三）实验室的研究方向

实验室面向国家重大需求和学科发展前沿，瞄准我国南海珊瑚礁研究和应用所面临的关键科学问题，例如，在全球变暖、海洋酸化、富营养化等多重环境压力的背景下，珊瑚礁对未来环境变化的适应潜力以及响应方式等，通过多学科交叉的方式，围绕南海珊瑚礁的生物、生态、地质、资源与环境等开展系统的科学研究，揭示珊瑚礁学科的规律，服务于我国南海珊瑚礁开发利用的长远规划与可持续发展、南海珊瑚礁生态系统的修复、以及南海岛礁工程建设与长期维护等。具体研究方向包括：1. 南海珊瑚礁生物与生态；2. 南海珊瑚礁地质与环境；3. 南海珊瑚礁环境与化学；4. 南海珊瑚礁遥感与监测。

（四）实验室平台与设施

实验室总面积 17310 m^2，科研仪器设备总值 8995 万元，其中价值超过 50 万元的大型仪器设备 36 台（套），总值 4850 万元。实验室典型的基地/平台设施举例如下：

1.广西大学海洋科学广西院士工作站

广西大学海洋科学广西院士工作站是实验室与武汉大学遥感信息工程学院摄影测量与遥感学家张祖勋院士为贯彻落实向海图强战略而组建的科研平台。其目标是融合武汉大学遥感信息工程学院世界一流遥感学科的优势与实验室珊瑚礁系统科学研究的特色，拓展实验室的研究领域，促进实验室的学科建设，完善实验室的人才培养体系，从而提高实验室

的科学研究水平与综合影响力，提升实验室的人才培养与服务国家重大需求的能力。该平台在 2025 年度广西院士工作站绩效评价中获得优秀。

2.南海珊瑚礁样品库

截至 2025 年 12 月，实验室组织赴南海、西太平洋、东印度洋、孟加拉湾、赤道印度洋和南印度洋等开展科学考察共计 527 人次，累积 1769 天，航程达 71299 海里。科学考察采集了大量关于珊瑚礁地质、地貌、生态与环境等方面的关键数据和样本，形成了国内样本数量最多、种类最齐全、覆盖范围最广的南海珊瑚礁样品库。目前存储生物样品 26498 个、沉积物及珊瑚砂 691 袋、海水水样 3472 份。其中含有珊瑚样品 11428 个（包括鹿角珊瑚、滨珊瑚、盔形珊瑚、蔷薇珊瑚等 25 属 136 种）、长棘海星样品 14200 个，其他样品（包括鱼类样品、藻类样品、螺类样品等）870 个。南海珊瑚礁样品库为评估南海珊瑚礁的生态状况提供了第一手的素材，为南海珊瑚岛礁的开发、建设与维护，以及珊瑚礁生态系统的保护、修复与可持续发展积累了丰富的数据，为深入揭示印太交汇区代表性物种的生物多样性演变及其生态功能提供了关键的材料，为实验室高质量完成国家与广西的重大科学研究项目奠定了基础。

3.岛礁生态修复实验室

岛礁生态修复实验室占地 120 m^2，拥有 31 套珊瑚养殖系统和 1 套珊瑚有性繁殖系统，设有 4 m×0.6 m×0.6 m 的珊瑚礁生态展示缸 1 个、4 m×0.8 m×0.4 m 的珊瑚断肢繁殖缸 1 个和实验模拟缸 22 个。目前养殖珊瑚 36 种，共 5000 余株。岛礁生态修复实验室是实验室研究珊瑚对温度、营养盐、环境污染物等非生物胁迫响应和珊瑚抗病机制的重要平台，能为南海珊瑚礁的保护与修复提供科学的理论依据和实践材料。该室功能以服务科研教学为主，辅以珊瑚礁科普展览展示，旨在为实验室师生提供安全可靠的珊瑚礁研究场地和设备。2025 年，该室累计承接模拟实验 35 人次，供应珊瑚实验样品 100 余个；接待外来参观 99 批次，累计接待人数 4840 人，科研支撑与科普传播成效显著。

4.涠洲岛珊瑚礁野外生态修复实验基地

实验室研发了从人工繁殖、水族箱养殖和维护、海区苗圃、珊瑚移植等一体化的珊瑚礁生态修复技术。该技术在涠洲岛自然海区的应用形成了面积 2000 m2 的自然海区珊瑚礁生态修复示范区，是国内迄今唯一可随时供人参观的珊瑚礁生态修复示范区。以此为基础，实验室获批涠洲岛 200 亩的科研用海（迄今涠洲岛唯一对外批复的科研用海项目），用于珊瑚礁生态系统修复实验。该基地的珊瑚礁生态修复模式，奠定了未来南海珊瑚礁生态修

复的基础，为南海珊瑚礁的保护和科学利用提供了重要的技术支撑，并为全球珊瑚礁退化治理贡献了“中国智慧”。2025 年，以该基地为基础的珊瑚礁生态修复成果入选了 2025 年全国海洋生态保护修复典型案例；而相关的《北部湾珊瑚礁生态修复技术与示范项目》和《智筑珊海——珊瑚礁生态修复科技创新实践》则在首届联合国“海洋十年”海洋生态保护修复大赛中分别获得了“海洋十年”中国行动国际合作种子基金重点项目和重大项目。

5.涠洲岛珊瑚馆

与北海市涠洲岛管理委员会合作共建的珊瑚馆，总面积约 500 m^2，拥有 1 个 10 米大型生态缸、1 个 4 米珊瑚礁生态展示缸、2 个 4 米大型繁殖缸，养殖水体 90 m^3。该基地建设探索出了科研、科普、旅游三位一体的珊瑚礁保护与修复新模式：直接建设在涠洲岛上，能为实验室进行野外珊瑚礁保护和修复实验研究提供保障；面向全社会开放，向社会宣传和普及珊瑚礁生态与保护的知识，增强社会民众的海洋意识和环保意识，是迄今全国最大的珊瑚礁公益科普馆。至今已被授予中国科协涠洲岛珊瑚馆科普教育基地、广西科普基地、广西海洋科普与意识教育基地和广西科普教育基地等。本年度接待参观 7.59 万人次，媒体参访与报道 6 次，组织大型科普活动 2 场次，开展大型公益讲解 119 次。

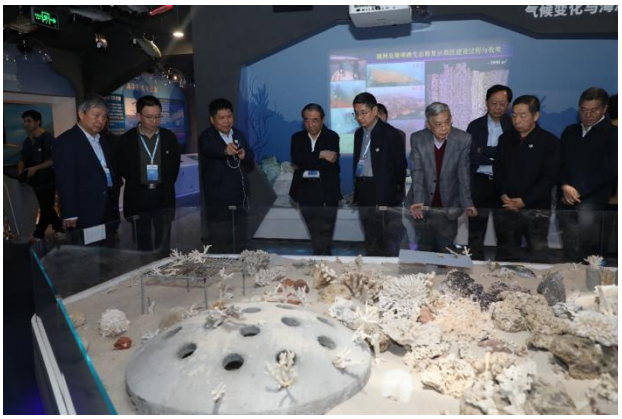
6.三沙航迹珊瑚礁保护研究所联合研究中心与三沙市永乐龙洞保护站

实验室与三沙航迹珊瑚礁保护研究所于 2019 年签订合作协议共建联合研究中心，旨在促进我国珊瑚礁领域的人才培养和科学探索，为南海生态环境保护建言献策，服务于国家海洋强国战略和海上丝绸之路建设。该联合研究中心成立至今，已围绕南海珊瑚礁生态环境保护等科学问题，联合开展南海珊瑚礁科学考察 23 次（今年 3 次）。之后，在三沙市政府相关部门的大力支持下，实验室在 2024 年与国家海洋环境监测中心、三沙航迹珊瑚礁保护研究所联合建成三沙市永乐龙洞保护站。本年度依托该站开展相关科研工作的师生人数达到 40 人次。2025 年 9 月 15-16 日，实验室主办三沙市永乐龙洞保护站工作研讨会，对保护站建站以来的科研平台建设现状与成效、存在问题及不足等进行了深入讨论，并研讨敲定了保护站未来工作重点和发展方向。实验室通过三沙市永乐龙洞保护站实现了对西沙晋卿岛龙洞及周边珊瑚礁海域的全天候长期定点监测，以及关于珊瑚礁生物生态、环境化学和地质地貌等多学科交叉的系统性综合实验与研究。

7.海洋科教馆

海洋科教馆位于广西大学综合实验大楼 1 楼，面积 1400 m^2，主要功能是为珊瑚礁系统科学研究提供人才培养（专业课、校选课和第二课堂）、学术交流、成果展示和科学传播

等的平台。该馆迄今已被授予广西海洋科普与意识教育基地、广西科普教育基地。本年度接待参观 204 场次，共 1.85 万人次，包括中国科学院领导、中国科协 2025 年高层次人才国情考察活动（广西）院士专家团、面向东盟蓝色经济合作发展论坛专家代表团、香港特区政府驻广西联络处主任王卓然等。2025 年 3 月，海洋科教馆入选中国青少年宫协会会员单位。2025 年 4 月，广西大学海洋科教馆科学家精神宣讲工作室入围第三批广西科学家精神宣讲团名单。这标志着海洋科教馆已成为弘扬科学家精神、传播科学思想领域的重要阵地。





海洋科教馆人才培养、科学研究与科学传播一体化得到国内知名专家学者的高度肯定

左：中国科协 2025 年高层次人才国情考察活动（广西）院士专家团；右：王景全院士与郑皆连院士。

（五）实验室组成框架

（1）学术委员会

学术委员会主任

焦念志	教授、中国科学院院士	厦门大学

学术委员会副主任

陈发虎	教授、中国科学院院士	中国科学院青藏高原研究所

学术委员会委员（按姓名拼音字母的字典顺序排序）

戴民汉	教授、中国科学院院士	厦门大学
葛全胜	研究员	中国科学院地理科学与资源研究所
郭正堂	研究员、中国科学院院士	中国科学院大学
翦知湣	教授、中国科学院院士	同济大学
林　间	教授、欧洲科学院院士	南方科技大学
刘丛强	研究员、中国科学院院士	天津大学
李铁刚	研究员	自然资源部第一海洋研究所
祁士华	教授	中国地质大学（武汉）
余克服	教授	广西大学
王英辉	教授	广西大学
韦刚健	研究员	中国科学院广州地化所

学术委员会顾问（按姓名拼音字母的字典顺序排序）

黄鼎成	研究员	中国科学院地质与地球物理研究所
汪　稔	研究员	中国科学院武汉岩土力学研究所
王苏民	研究员	中国科学院南京地理与湖泊研究所
张祖勋	教授、中国工程院院士	武汉大学遥感信息工程学院

（2）固定人员信息

实验室主任：余克服

实验室副主任：黄荣永（常务）、黄雯

实验室秘书：姜伟、苏宏飞、张瑞杰、雍阳阳、李艳丹

1.固定人员列表

序号	姓名	性别	出生年月	学位	职称	专业方向	类型
1	余克服	男	1969.03	博士	教授	地球化学	研究
2	徐向荣	女	1973.06	博士	教授	环境科学	研究
3	王英辉	女	1970.01	博士	教授	环境工程	研究
4	姜伟	男	1989.12	博士	教授	地球化学	研究
5	刘珊	女	1986.06	博士	教授	环境科学	研究
6	王丽伟	女	1986.05	博士	副教授	无机化学	研究
7	梁甲元	男	1986.11	博士	副教授	微生物学	研究
8	王广华	男	1981.04	博士	副教授	海洋生物学	研究
9	黄雯	男	1988.01	博士	副教授	水产养殖学	研究
10	苏宏飞	男	1984.09	博士	副教授	海洋生物学	研究
11	巩三强	男	1986.06	博士	副教授	生物学	研究
12	陈飚	男	1992.11	博士	副教授	海洋生物学	研究
13	王瑞	男	1983.03	博士	副教授	地质学	研究
14	张瑜	男	1985.04	博士	副教授	地质学	研究
15	张瑞杰	男	1982.01	博士	副教授	环境科学	研究
16	张媛媛	女	1981.07	博士	副教授	环境工程	研究

17	裴继影	女	1989.06	博士	副教授	分析化学	研究
18	潘长桂	男	1985.07	博士	副教授	环境工程	研究
19	陈小燕	女	1974.07	博士	副教授	环境工程	研究
20	姚作芳	女	1982.08	博士	副教授	环境科学	研究
21	黄荣永	男	1985.10	博士	副教授	摄影测量与遥感	研究
22	陈正华	女	1980.01	博士	副教授	地理学	研究
23	左秀玲	女	1986.03	博士	副教授	地图学与地理信息	研究
24	雍阳阳	女	1987.06	博士	副教授	气象学	研究
25	邓珊珊	女	1993.09	博士	副教授	自然地理学	研究
26	黄爱国	男	1991.09	博士	副教授	水生生物学	研究
27	韦芬	女	1986.01	博士	讲师	水产养殖学	研究
28	覃祯俊	男	1991.03	博士	讲师	海洋生物学	研究
29	张曼	女	1986.12	博士	讲师	海洋生物学	研究
30	范天来	男	1984.06	博士	讲师	自然地理学	研究
31	吴司琪	女	1993.09	博士	讲师	古生物学	研究
32	乐远福	男	1982.07	博士	讲师	地质学	研究
33	宋宜	女	1991.11	博士	讲师	地质学	研究
34	宁志铭	男	1988.12	博士	讲师	海洋化学	研究
35	唐兴颖	男	1986.08	博士	讲师	动力工程与工程热物理	研究
36	梁作栋	男	1992.08	博士	讲师	海洋工程	研究
37	俞小鹏	男	1992.11	博士	讲师	海洋生物学	研究

38	江红蕾	男	1992.11	博士	讲师	生态学	研究
39	江蕾蕾	女	1995.02	博士	讲师	生物学	研究
40	黄钦	男	1994.08	博士	讲师	海洋地质学	研究
41	郭泽军	男	1994.10	博士	讲师	生态学	研究
42	韩民伟	男	1992.05	博士	讲师	生物学	研究
43	王刘炜	男	1997.10	博士	讲师	环境科学与工程	研究
44	李正浩	男	1996.01	博士	讲师	地理学	研究
45	黄硕文	男	1997.06	博士	讲师	资源与环境	研究
46	韦朝帅	男	1989.05	硕士	实验师	环境科学	技术
47	张俊	男	1988.06	硕士	实验师	环境科学与工程	技术
48	张威	男	1988.12	博士	助理实验师	环境科学与工程	技术
49	秦华东	男	1978.12	博士	副研究员	作物栽培学与耕作学	管理
50	黄学勇	男	1986.03	硕士	讲师	生态学	管理
51	刘旗扬	女	1974.12	硕士	高级工程师	行政管理学	管理
52	李周佳	男	1982.01	硕士	讲师	音乐学	管理
53	周剑	男	1986.04	硕士	助理研究员	新闻与传播	管理
54	林玉华	女	1979.01	硕士	助理研究员	公共管理	管理
55	龙海华	女	1974.03	硕士	讲师	英语	管理
56	梁琪	女	1993.10	硕士	助理研究员	农村与区域发展	管理

2.研究单元

序号	研究组	带头人	其他成员
1	珊瑚礁生物与生态	巩三强	黄　雯、梁甲元、苏宏飞、王广华、陈　飚、俞小鹏、黄爱国、韦　芬、覃祯俊、张　曼、郭泽军
2	珊瑚礁地质与环境	余克服	姜　伟、王　瑞、范天来、吴司琪、乐远福、张　瑜、宋　宜、黄　钦
3	珊瑚礁环境与化学	徐向荣	王英辉、刘　珊、张瑞杰、张媛媛、裴继影、王丽伟、潘长桂、宁志铭、唐兴颖、韩民伟、王刘炜
4	珊瑚礁遥感与监测	黄荣永	左秀玲、陈正华、陈小燕、雍阳阳、姚作芳、梁作栋、邓珊珊、江红蕾、江蕾蕾、李正浩、黄硕文

说明：研究队伍人员全部拥有博士学位，年龄有 71%不超过 40 岁，有 91%不超过 50 岁。

3.人才称号

序号	姓名	荣誉称号	年份
1	余克服	国家重大人才工程计划项目	2016
2	余克服	国家重大人才工程计划项目	2016
3	余克服	政府特殊津贴获得者	2015
4	余克服	广西 B 层次人才	2019
5	余克服	广西八桂学者	2014
6	余克服	国家百千万人才工程	2013
7	余克服	国家重大科学研究项目（“973”项目）首席科学家	2012
8	余克服	国家杰出青年科学基金获得者	2010
9	余克服	青年科技创新领军人才	2014
10	余克服	广西人才小高地	2025

11	王英辉	第九批自治区优秀专家	2018
12	王英辉	广西五一巾帼标兵	2016
13	王英辉	“广西新世纪十百千人才工程”第二层次人选	2013
14	王英辉	全区教育系统“巾帼标兵”	2013
15	徐向荣	中国科学院“引进国外杰出人才”（百人计划）	2011
16	黄雯	广西“最美科技工作者”	2024
17	黄雯	八桂科普大行动先进个人	2022
18	姜伟	自治区重大人才项目	2024
19	左秀玲	自治区重大人才项目	2025
20	王丽伟	自治区重大人才项目	2025
21	刘珊	自治区重大人才项目	2025
22	陈飚	自治区重大人才项目	2025
23	巩三强	自治区重大人才项目	2025
24	王英辉	广西 D 层次人才	2025
25	姜伟	广西 D 层次人才	2025
26	徐向荣	南宁市 A 层次人才	2025
27	黄雯	南宁市 B 层次人才	2025
28	陈飚	南宁市 D 层次人才	2024
29	黄爱国	南宁市 D 层次人才	2024

30	俞小鹏	南宁市 D 层次人才	2025
31	郭泽军	南宁市 D 层次人才	2025
32	吴司琪	南宁市 D 层次人才	2025

4.学术组织任职

序号	姓名	学术组织	职务	时间
1	余克服	教育部科技委学部	委员	2016.01-2020.12 2021.01-2025.12
2	余克服	中国第四纪科学研究会	常务理事	2012.01-2015.12 2016.01-2019.12 2020.01-2023.12 2024.01-2027.12
3	余克服	中国海洋湖沼协会地质学分会	副理事长	2022.10-2027.09
4	余克服	中国第四纪科学研究会海岸与海洋专业委员会	副主任	2021.01-2024.12 2025.01-2028.12
5	余克服	中国海洋学会海洋生态资源保护与修复分会	副主任委员	2022.09-至今
6	余克服	海南南沙珊瑚礁生态系统国家野外科学观测研究站学术委员会	副主任	2021.12-至今
7	余克服	教育部 2011 计划“中国南海研究协同创新中心”	特约研究员	2012.07-至今
8	余克服	北部湾海洋生态环境广西野外观测研究站学术委员会	副主任委员	2024.09-2027.09
9	余克服	中国古生物学会生物沉积学分会	理事	2024.01-至今
10	余克服	海底科学与探测技术教育部重点实验室(中国海洋大学)第四届学术委员会	委员	2025.01-2030.01
11	徐向荣	中国土壤学会环境微塑料工作组工作委员会	副主任	2024.12-2028.11
12	徐向荣	中国海洋湖沼学会化学分会	理事	2022.11-2027.10
13	徐向荣	中国海洋发展研究会	理事	2024.12-2028.12

14	王英辉	广西近海海洋环境科学重点实验室学术委员会	副主任	2023.12-2026.12
15	王英辉	广西绿色低碳产业技术协会第一届理事会	秘书长	2023.08-2028.08
16	王英辉	广西产研院绿色低碳技术研究所有限公司	执行董事	2023.08-2028.08
17	黄雯	广西海洋学会	副理事长	2024.12-2028.12
18	黄荣永	广西地理学会	常务理事	2024.11-至今
19	左秀玲	广西遥感学会	常务理事	2025.07-2029.07
20	黄雯	北海市全民科学素质工作领岛小组办公室	北海市科学传播海洋生态首席专家	2022.09-2025.09
21	黄雯	广西海洋产业专家咨询委员会	顾问	2020.11-至今
22	雍阳阳	广西气象学会	理事	2021.01-2026.01
23	雍阳阳	广西气候变化与防灾减灾研究会	理事	2023.05-2028.04
24	雍阳阳	广西海洋学会	理事	2024.12-2028.12
25	左秀玲	中国太平洋学会海洋电子信息科学与技术分会	理事	2025.10-2028.10
26	王瑞	广西海洋学会	理事	2024.12-2028.12
27	雍阳阳	钦州市气象局	钦州市精细化气象预报服务创新团队导师	2023.07-至今
28	余克服	南方海洋科学与工程广东省实验室（珠海）--深海生命与生态过程团队	首席科学家	2022.11-至今
29	余克服	北部湾环境演变与资源利用教育部重点实验室学术委员会	委员	2021.01-2025.12
30	徐向荣	海南三亚海洋生态系统国家野外科学观测研究站学术委员会	委员	2024.12-2027.12
31	徐向荣	巴塞尔公约亚太区域中心化学品和废物环境管理智	专家	2023.11-2028.11

		库		
32	徐向荣	海洋化学与应用技术福建省高校重点实验室（厦门大学）学术委员会	委员	2024.12-2027.12
33	徐向荣	中国合成树脂协会塑料循环利用分会海洋塑料防治技术委员会	委员	2021.04-2025.04
34	徐向荣	中国海洋与湖沼学会海岸带可持续发展委员会	委员	2021.04-2025.04
35	徐向荣	中国生态学会	会员	2023.10-2028.10
36	徐向荣	广东省新污染物治理专家委员会	委员	2023.10-2028.10
37	徐向荣	广西北部湾海洋环境变化与灾害研究重点实验室学术委员会	委员	2024.01-2026.12
38	徐向荣	广东省应急管理专家委员会	委员	2022.01-2025.01
39	余克服、陈飚、徐向荣、韩民伟、张瑞杰、覃祯俊、江蕾蕾、黄荣永、姜伟、陈小燕、俞小鹏、左秀玲、王刘炜、李周佳、江红蕾、黄雯	国际海洋碳负排放组织	创始会员	2025.10-至今
40	梁甲元	中国海洋学会大洋深潜分会	委员	2024.08-2027.08
41	左秀玲	国际数字地球学会中国国家委员会数字海岸带专业委员会	委员	2024.05-2029.05
42	徐向荣、陈飚、巩三强、韩民伟、黄钦、黄荣永、梁甲元、宁志铭、潘长桂、裴继影、王丽伟、姜伟、俞小鹏、张瑞杰、张媛媛、左秀玲、张威、江红蕾	广西海洋学会	会员	2024.12-2028.12
43	左秀玲	国际数字地球学会中国国家委员会青年科学家工作	委员	2025.04-2029.04

		委员会		
44	王丽伟	学术桥论文辅导专家库	成员	2025.03-2028.03
45	江蕾蕾	中国第四纪科学研究会专业委员会-历史时期气候变化专业委员会	委员	2025.01-2028.01
46	海洋科教馆	中国青少年宫协会	会员	2025.03-至今
47	梁甲元	中国生态学学会第六届海洋生态专业委员会	委员	2022.01-2027.01
48	梁甲元	中国太平洋学会海洋测绘研究分会	理事	2023.01-2028.01
49	徐向荣	中国生产力促进中心协会海洋分会	主任委员	2026.01-2028.01
50	徐向荣	中国生态学学会生态毒理学专委会	委员	2025.10-2028.10
51	徐向荣	中国颗粒学会微塑料专委会	委员	2026.01-至今

5.学术期刊任职

序号	姓名	学术期刊名称	职务	时间
1	余克服	《海洋学研究》	副主编	2022.12-至今
2	余克服	《中国科学：地球科学》和《SCIENCE CHINA: Earth Sciences》	编委	2018.01-2027.12
3	余克服	《第四纪研究》	编委	2020.01-至今
4	余克服	《海洋学报》和《Acta Oceanologica Sinica》	编委	2017.01-至今
5	余克服	《海洋科学进展》	编委	2023.01-至今
6	余克服	《Anthropocene Coasts》	编委	2022.01-至今
7	余克服	《海洋与湖沼》	编委	2025.04-2030.04
8	徐向荣	《Marine Environmental Research》	主编	2021.12-2025.11
9	徐向荣	《生态毒理学报》	编委	2023.09-2028.09
10	徐向荣	《Watershed Ecology and the Environment》	编委	2023.01-2027.12
11	徐向荣	《Journal of Environmental Exposure Assessment》	编委	2024.04-2026.04
12	徐向荣	《环境生态学》	编委	2019.01-2023.01 2023.01-2027.01
13	徐向荣	《海洋环境科学》	编委	2022.12-2026.12
14	徐向荣	《Water Emerging Contaminants & Nanoplastics》	副主编	2025.07-2027.07
15	雍阳阳	《气象研究与应用》	编委	2019.01-至今
16	左秀玲	《地理科学》	青年编委	2025.05-至今
17	刘珊	《Fishes》	编委	2024.10-2026.10

18	刘珊	《Water Emerging Contaminants & Nanoplastics》	编委	2024.06-2026.06
19	刘珊	《Journal of Environmental Exposure Assessment》	编委	2024.12-2026.12
20	王刘炜	《Environmental Geochemistry and Health》	副主编	2025.07-2027.07
21	王刘炜	《Soil Use and Management》	副主编	2025.08-至今
22	姜伟	《Frontiers in Marine Science》	副编辑	2021.02-至今
23	姜伟	《Scientific Reports》	编委	2025.03-至今
24	潘长桂	《Toxics》	编委	2023.01-至今
25	潘长桂	《Journal of Environmental Exposure Assessment》	编委	2024.05-2025.05
26	潘长桂	《Emerging Contaminants and Environmental Health》	编委	2024.01-至今
27	唐兴颖	《Energy & Environment Nexus》	编委	2025.11-2029.11

二、年度主要进展

（一）科研项目立项

本年度科研项目立项 50 项（合计经费 1221.54 万元），其中国家自然科学基金 9 项（合计经费 302 万元），广西自然科学基金/广西科技基地与人才专项/广西重点研发计划项目 25 项（合计经费 802 万元），其他项目 16 项（合计经费 117.54 万元）。

序号	来源/类型	名称	编号	起始年份	结束年份	经费（万元）	负责人
1	国家自然科学基金委/国家自然科学基金面上项目	基于物理信息扩散模型高精度重建陆-海水质量迁移过程及区域质量海平面预算闭合	42571043	2026 年	2029 年	46	邓珊珊
2	国家自然科学基金委/国家自然科学基金面上项目	流体饱和状态对西沙群岛晚中新世白云岩结构的调控机制	42572123	2026 年	2029 年	47	王瑞
3	国家自然科学基金委/国家自然科学基金面上项目	北部湾近岸海域典型阻燃剂的源汇格局及其风险调控机制研究	42576143	2026 年	2029 年	50	徐向荣
4	国家自然科学基金委/国家自然科学基金地区科学基金项目	强还原活性物种对海水病原微生物的灭活及消毒副产物协同控制效应与机制研究	52560001	2026 年	2029 年	33	张媛媛
5	国家自然科学基金委/国家自然科学基金地区科学基金项目	机器学习驱动电化学生物传感技术对珊瑚致病菌的快速检测及健康评估研究	22564003	2026 年	2029 年	31	王丽伟
6	国家自然科学基金委/国家自然科学基金青年基金项目	海岸带景观格局和气候变化对生态系统服务供需的影响机制与优化调控	42501364	2026 年	2029 年	30	江红蕾

7	国家自然科学基金委/国家自然科学基金青年基金项目	南海北部珊瑚记录的 5.5 ka BP 事件期间 ENSO 活动及其对太阳辐照度的响应	42502176	2026 年	2029 年	30	江蕾蕾
8	国家自然科学基金委/国家自然科学基金青年基金项目	造礁石珊瑚对多环芳烃及其衍生物的兴奋效应及其分子机制	42506130	2026 年	2029 年	30	韩民伟
9	国家自然科学基金委/国家自然科学基金专项项目	科学传播类：基于珊瑚礁特色的广西海洋教育小学示范校科普活动分层分级实施	42542038	2026 年	2029 年	5	徐向荣
10	广西壮族自治区科技厅/广西自然科学基金广西重点研发计划	面向海洋中小尺寸塑料垃圾的无人船智能监测技术研发与应用示范	2025FN9619929	2026 年	2029 年	96	徐向荣
11	广西壮族自治区科技厅/广西自然科学基金广西科技成果转化计划	基于碳点传感检测的分级氧化-吸附协同全量化处理垃圾渗滤液关键技术研发及应用	2025ZG0312057	2026 年	2029 年	0	唐兴颖
12	广西壮族自治区科技厅/广西自然科学基金面上项目	细胞穿膜肽介导 VP28 特异性纳米抗体抗对虾 WSSV 作用机制研究	2025JJA130007	2026 年	2029 年	10	黄爱国
13	广西壮族自治区科技厅/广西自然科学基金面上项目	全球变暖与平陆运河悬浮物增加叠加对北部湾珊瑚礁生态影响与适应潜力研究	2025JJA150187	2026 年	2029 年	10	俞小鹏
14	广西壮族自治区科技厅/广西自然科学基金面上项目	高温实验模拟珊瑚白云石化过程中稀土元素的迁移机制	2025JJA150010	2026 年	2029 年	10	王瑞

15	广西壮族自治区科技厅/广西自然科学基金青年基金项目	桂西南地区下雷锰矿成矿环境和富集机制研究	2025JJB150038	2026 年	2029 年	8	黄钦
16	广西壮族自治区科技厅/广西自然科学基金青年基金项目	典型热带岛礁土壤微塑料赋存特征与老化机制研究	2025JJB150027	2026 年	2029 年	8	王刘炜
17	广西壮族自治区科技厅/广西自然科学基金青年基金项目	涠洲珊瑚礁区波致海底埋管动力灾变机理与分析方法	2025JJB160006	2026 年	2029 年	8	梁作栋
18	广西壮族自治区科技厅/广西自然科学基金广西科技基地和人才专项	广西南海珊瑚礁研究重点实验室科技创新能力建设	桂科 AD25069075	2025 年	2028 年	400	余克服
19	广西壮族自治区科技厅/广西自然科学基金广西重点研发计划	广西北部湾海漂垃圾溯源追踪技术研究及应用示范	桂科 AB25069113	2025 年	2027 年	74	徐向荣
20	广西壮族自治区科技厅/广西自然科学基金面上项目	滨珊瑚的海平面指示意义及在南海北部全新世海平面重建中的应用	2025GXNSFAA069160	2025 年	2028 年	10	乐远福
21	广西壮族自治区科技厅/广西自然科学基金面上项目	紫外光催化双酮高级氧化还原体系对海水有害微生物的灭活及副产物协同控制研究	2025GXNSFAA0691008	2025 年	2028 年	10	张媛媛
22	广西壮族自治区科技厅/广西自然科学基金面上项目	南海造礁石珊瑚骨骼及珊瑚砂中黑碳的赋存/埋藏特征及其碳汇能力初探	2025GXNSFAA069701	2025 年	2028 年	10	张瑞杰

23	广西壮族自治区科技厅/广西自然科学基金面上项目	虫黄藻 Cladocopium goreaui 的热驯化及其对涠洲岛苗圃区珊瑚耐热性的作用研究	2025GXNSFAA069187	2025 年	2028 年	10	覃祯俊
24	广西壮族自治区科技厅/广西自然科学基金面上项目	桂东南大瑶山燕山早期高 Sr/Y 花岗岩类成因及其深部动力学意义	2025GXNSFAA069324	2025 年	2028 年	10	张瑜
25	广西壮族自治区科技厅/广西自然科学基金面上项目	超临界水中磷化腐蚀膜抑制晶界扩散行为对镍基合金晶间腐蚀的影响机制研究	2025GXNSFAA069823	2025 年	2028 年	10	唐兴颖
26	广西壮族自治区科技厅/广西自然科学基金面上项目	近岸礁区有孔虫分布特征及其对生态环境的指示意义——以广西涠洲岛为例	2025GXNSFAA069592	2025 年	2028 年	10	孟敏
27	广西壮族自治区科技厅/广西自然科学基金青年基金项目	不同温度条件下造礁石珊瑚的脂类组成变化及其指示意义	2025GXNSFBA069092	2025 年	2028 年	8	宋宜
28	广西壮族自治区科技厅/广西自然科学基金青年基金项目	造礁石珊瑚应对多环芳烃污染的响应与适应机理研究	2024JJB150202	2025 年	2028 年	8	韩民伟
29	广西壮族自治区科技厅/广西自然科学基金青年基金项目	涠洲岛造礁珊瑚对平陆运河工程低盐水输入适应机制研究	2025GXNSFBA069587	2025 年	2028 年	8	俞小鹏
30	广西壮族自治区科技厅/广西自然科学基金青年基金项目	南海北部季节性海表温度和盐度对东亚季风降雨预报的可靠性与机制研究	2025GXNSFBA069398	2025 年	2028 年	8	江蕾蕾

31	广西壮族自治区科技厅/广西自然科学基金青年基金项目	红树植物白骨壤耐盐相关基因的筛选及功能研究	2025GXNSFBA069196	2025 年	2028 年	8	郭泽军
32	广西壮族自治区科技厅/广西自然科学基金青年基金项目	广西平陆运河流域生态系统服务多尺度权衡/协同关系、影响因素与优化管理策略研究	2024JJB150108	2025 年	2028 年	8	江红蕾
33	广西壮族自治区人力资源和社会保障厅，广西壮族自治区财政厅/青苗人才补助	桂西南地区沉积锰矿富集机制与成矿规律研究	202502325	2025 年	2030 年	30	黄钦
34	广西壮族自治区人力资源和社会保障厅，广西壮族自治区财政厅/青苗人才补助	单宁在红树植物镉耐受中的作用机制研究	202502322	2025 年	2030 年	30	郭泽军
35	中国科学院南海海洋研究所	海洋样品类固醇激素测试服务	202500606	2025 年	2026 年	4	潘长桂
36	三亚海洋生态环境工程研究院	海南河口海域微塑料测试服务	202501010	2025 年	2025 年	9.13	潘长桂
37	国家海洋环境监测中心	小公鱼、球形棕囊藻传感器构建数据资料	202500125	2025 年	2025 年	6	张曼
38	中国科学院南海海洋研究所研究所	海洋沉积物和水体样品抗生素检测和数据分析	202501984	2025 年	2026 年	3.92	刘珊
39	三沙航迹珊瑚礁保护研究所	2025 年度龙洞生态环境监测服务和报告撰写	202501912	2025 年	2026 年	25.12	韩民伟
40	中国科学院南海海洋研究所研究所	塑料样品检测与数据分析	202501893	2025 年	2026 年	3.8	刘珊
41	国家海洋环境监测中心	三沙永乐龙洞周边海域珊瑚礁生态、水文和沉积物通量历史监测数据分析和报告撰写服务项目	202501691	2025 年	2025 年	19.91	陈飚

42	生态环境部华南环境科学研究所	2025 年度南海海域生态环境监测服务项目	202501660	2025 年	2025 年	149.8	俞小鹏
43	中国科学院南海海洋研究所研究所	南海北部边缘造礁珊瑚对高温与高浑浊度双重胁迫的适应机制研究	202501391	2025 年	2027 年	4.0	俞小鹏
44	广西汇康能环保科技有限公司	塑料废弃物裂解炭黑的纯化与功能材料制备技术研究	202501244	2025 年	2026 年	6.5	唐兴颖
45	中国科学院南海海洋研究所	海洋沉积物样品环境参数测试服务	202501186	2025 年	2026 年	4.95	刘珊
46	中国检验认证集团广西有限公司	城市垃圾填埋场渗滤液中污染物识别及关键技术研究服务	202501039	2025 年	2026 年	5.0	唐兴颖
47	广西产研院绿色低碳技术研究所	水热酸解甘蔗渣制备 C5/C6 糖水解液研究技术服务	202502130	2025 年	2025 年	9.38	张威
48	广西青辉环保技术有限责任公司	再生混凝土微观孔结构调控与多场景性能提升改性研究	202502508	2025 年	2025 年	31	王英辉
49	广西青辉环保技术有限责任公司	再生混凝土微观孔结构优化与有害元素控制改性研究	202502474	2025 年	2025 年	30	王英辉
50	中国科学院南海海洋研究所	红树林沉积物环境参数分析服务	202502590	2025 年	2026 年	4.32	刘珊

（二）奖励与荣誉

2025 年新增重要奖励与荣誉 18 项，含第四届广西创新争先奖、广西工人先锋号、福建省科技进步奖二等奖、中国国际大学生创新大赛广西赛区金奖、国家级一流本科课程和 2025 年全国海洋生态保护修复典型案例等。

序号	姓名	项目名称	奖项名称与等级	授予单位
1	余克服、吴志强、王瑞、梁甲元、黄荣永、姜伟、苏宏飞、黄雯、张瑞杰、左秀玲、裴继影、王丽伟、王少鹏、陈 飚、俞小鹏、宁志铭	南海珊瑚岛礁保护与科学利用团队	第四届广西创新争先奖	广西壮族自治区科学技术协会、广西壮族自治区科学技术厅、广西壮族自治区工业和信息化厅、广西壮族自治区人力资源和社会保障厅、广西壮族自治区人民政府国有资产监督管理委员会
2	余克服、左秀玲、覃祯俊	课程《珊瑚礁科学概论》	国家级一流本科课程	中华人民共和国教育部
3	“蓝色梦想”海洋科考队	广西工人先锋号	广西工人先锋号	广西壮族自治区总工会
4	蔡明刚、徐向荣、夏斌、孙承君、施华宏、李锐龙、李恒翔	海洋环境微塑料的全链条分析体系构建与关键技术研发及应用	福建省科技进步二等奖	福建省人民政府
5	广西南海珊瑚礁研究重点实验室珊瑚礁生态保护与修复团队（余克服、黄雯、陈飚和俞小鹏等）	科技赋能珊瑚海，共谱人鲸和美新乐章——广西北海市涠洲岛珊瑚礁生态保护修复案例	全国海洋生态保护修复典型案例	自然资源部国土空间生态修复司
6	张媛媛	课程名称《海洋科学导论》	第五届全国高校教师教学创新大赛广西赛区新工科组二等奖	广西高等教育学会

7	李正浩	基于遥感的海洋浮游植物对环境气候变化响应研究	中国遥感优秀成果二等奖	中国遥感委员会
8	左秀玲	南海珊瑚礁遥感监测与预警研究	第二十七届生态环境遥感论坛优秀青年学术报告一等奖	中国遥感应用协会
9	余克服、梁甲元、黄荣永、徐向荣、黄 雯、姜 伟、左秀玲、苏宏飞、张瑞杰、雍阳阳、王 瑞、俞小鹏、陈飚、王丽伟、裴继影、江红蕾、黄学勇、周 剑	基于南海岛礁特色的海洋科学研究生培养体系的构建与实现路径	广西大学高等教育（研究生）教学成果特等奖	广西大学
10	广西大学海洋学院	第二届(2025 年)全国海洋学教学大赛	全国海洋学教学大赛优秀组织奖	教育部高等学校海洋科学类专业教学指导委员会
11	黄雯	海洋科学导论（说课）开启蓝色科学之旅	全国海洋学教学大赛二等奖	教育部高等学校海洋科学类专业教学指导委员会
12	裴继影、宁志铭、江蕾蕾	海洋科学导论说课及教学	全国海洋学教学大赛优秀奖（3 项）	教育部高等学校海洋科学类专业教学指导委员会
13	张睿、刘扶真、浦诚书、何小方、仇旭华、梁嘉裕、樊孝荣、梁腾（指导老师：袁功林, 张振荣, 王少鹏, 王丽伟, 杨天山, 香赵政, 曾凡辉）	探海智测--海洋环境多维度智能监测技术领跑者	中国国际大学生创新大赛“建行杯”广西赛区选拔赛金奖	广西壮族自治区教育厅

14	康亚茹、谢婷、吴博、李昌恒、方贵瑾、林子业、赖秋月、刘缘、于尚科、彭梦娇、陆晔、何煜、劳子彤等（指导老师：黄学勇、黄雯、巩三强、余克服、徐向荣、王瑞、秦华东、张媛媛、黄荣永、刘旗扬、王刘炜、李周佳、周剑、林玉华、梁琪等）	蓝色梦想·珊海同行——专注于珊瑚礁保护的公益服务先锋卫士	中国国际大学生创新大赛“建行杯”广西赛区选拔赛铜奖	广西壮族自治区教育厅
15	黄雯,余克服,黄学勇,梁作栋,苏宏飞,徐向荣,巩三强,黄荣永,陈小燕,王明威,彭梦娇,刘书萌,谭何勇	北部湾珊瑚礁生态修复技术与示范项目	联合国“海洋十年”中国行动国际合作种子基金重点项目	中国海洋大学、“每洋十年”国际合作中心、全球青年创新预袖共同体促进会
16	谭何勇、彭梦娇、王明威、刘书萌、许辉、陆晔、徐烨、劳子彤、徐明培、周榆鹏、王永刚（指导老师：黄学勇,黄雯,梁作栋）	智筑珊海——珊瑚礁生态修复科技创新实践	联合国“海洋十年”中国行动国际合作种子基金重大项目	中国海洋大学、“每洋十年”国际合作中心、全球青年创新预袖共同体促进会
17	高德硕（指导老师：裴继影）	基于 3D 打印-SPME 牙签喷雾质谱快速检测复杂基质中的有机紫外吸收剂	第七届高校大学生海洋与化学科技实践论坛口头报告一等奖	教育部高等学校海洋科学类专业教学指分委员会
18	王秋婷（指导老师：张瑞杰）	珊瑚砂和珊瑚骨骼中黑碳赋存特点及其碳封存意义	第七届高校大学生海洋与化学科技实践论坛口头报告二等奖	教育部高等学校海洋科学类专业教学指分委员会

（三）论文发表

本年度以第一或通讯作者发表学术论文 113 篇，其中 SCI 检索 75 篇（中国科学院一区和二区 50 篇，JCR Q1 和 Q2 区 69篇），中国科协高质量科技期刊 T1 级 39 篇、T2 级 19 篇、T3 级 26 篇，如下表所示：

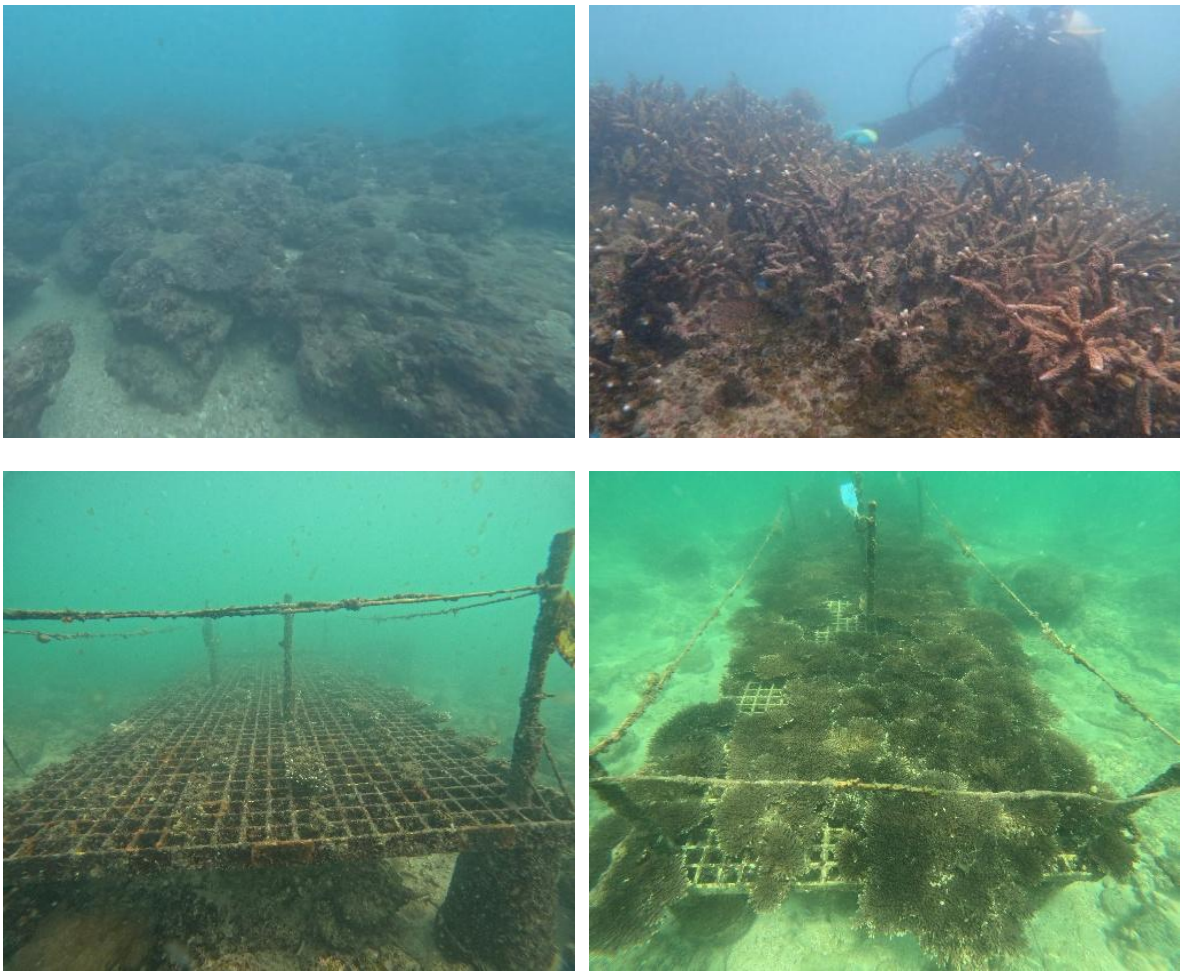
年份	中国科协高质量科技期刊分级			中国科学院分区				JCR 分区				SCI	论文总数
	T1	T2	T3	一区	二区	三区	四区	Q1	Q2	Q3	Q4		
2014	1	1	3	0	5	1	3	6	1	2	0	9	11
2015	5	7	1	4	4	10	3	8	6	2	3	21	28
2016	8	10	15	3	6	7	9	9	4	6	5	25	49
2017	9	6	9	2	10	6	4	10	5	4	2	22	43
2018	14	9	9	3	12	6	6	17	4	2	4	27	48
2019	16	5	14	7	14	17	1	26	9	2	2	39	47
2020	29	17	9	16	9	22	3	30	11	5	4	50	68
2021	32	9	9	15	24	5	0	38	3	3	0	44	58
2022	36	20	20	14	20	17	2	39	13	0	1	53	94
2023	43	13	11	17	23	13	4	43	9	5	0	57	88
2024	48	20	18	25	28	21	6	58	14	3	5	80	111
2025	**39**	**19**	**26**	**20**	**30**	**23**	**2**	**59**	**10**	**4**	**2**	**75**	**113**
合计	**280**	**136**	**144**	**126**	**185**	**148**	**43**	**343**	**89**	**38**	**28**	**502**	**758**

（四）代表性成果

※**《2025年黄岩岛海域生态环境状况调查评估报告》：**继去年参与对黄岩岛的首次摸底调查并编制《黄岩岛海域生态环境状况调查评估报告》（被评价“为服务国家政治外交大局提供了支撑保障”）之后，团队在本年度再次参与了生态环境部对黄岩岛海域生态环境状况的系统调查。与去年相比，这次调查更具系统性与针对性、更具科学性与先进性、更注重多源数据资料融合。而基于现场调查、卫星遥感和历史调查研究等资料，我们系统评估了黄岩岛海域环境质量状况和珊瑚礁生态系统状况，分析了面临的主要压力和生态风险，进而编制并发布了《2025年黄岩岛海域生态环境状况调查评估报告》。结果再次表明，黄岩岛海域环境质量优，自然生态系统多样性、稳定性、持续性好，可以为南海海洋生物提供重要栖息地和庇护所，具有重要的生态价值、资源价值和科研价值。换而言之，该成果为黄岩岛珊瑚礁未来的科学研究与深化保护指明了方向，为推动黄岩岛自然生态系统健康状况持续向好发展奠定了基础，因而被生态环境部评价为“系统展示了我国南海海洋生态环境保护成效，为服务国家政治外交大局提供了有力支撑”。

※ **国家级海洋生态保护修复典型案例**: 实验室牵头实施的涠洲岛北部珊瑚礁修复项目，针对热带北缘珊瑚礁修复效率低、稳定性不足和技术体系缺失等关键问题，系统构建了“选址—选种—育苗—移植—管护”一体化的全链条修复技术体系，实现了由单点修复向生态系统重建的转变。该项目在珊瑚扩繁、抗逆性提升与智能化管护方面取得多项突破：1）建立了陆海协同的珊瑚育苗体系，海区育苗规模达10万株，鹿角珊瑚年生长速率超过15厘米，修复成活率稳定在80%以上；2）首次在人工环境中实现鹿角杯型珊瑚有性繁殖，能有效维护本地珊瑚遗传多样性；3）通过热驯化技术，使珊瑚耐热阈值提升2–3°C，显著增强修复群落对气候变暖的适应能力。在工程实践方面，项目于涠洲岛北部修复了30公顷受损珊瑚礁，成为北部湾规模最大、集成度最高的珊瑚礁生态修复工程，而且是国内迄今唯一随时可参观的珊瑚礁生态修复项目。依托多功能人工礁体和物联网监测平台，项目还实现了修复环境的实时感知与智能管护。迄今修复区活珊瑚覆盖率已由5.1%提升至19.7%，且

鱼类和大型底栖生物数量显著增长，布氏鲸等大型海洋生物稳定回归，生态系统功能持续恢复。该项目探索了“科研—教学—科普—旅游”一体化融合的发展模式，促进了渔民转产就业与区域绿色发展，打造了珊瑚岛礁生态系统修复的“中国样板”。2025年，该项目入选国家级海洋生态保护修复典型案例，为全球珊瑚礁退化治理提供了可复制、可推广的中国经验。

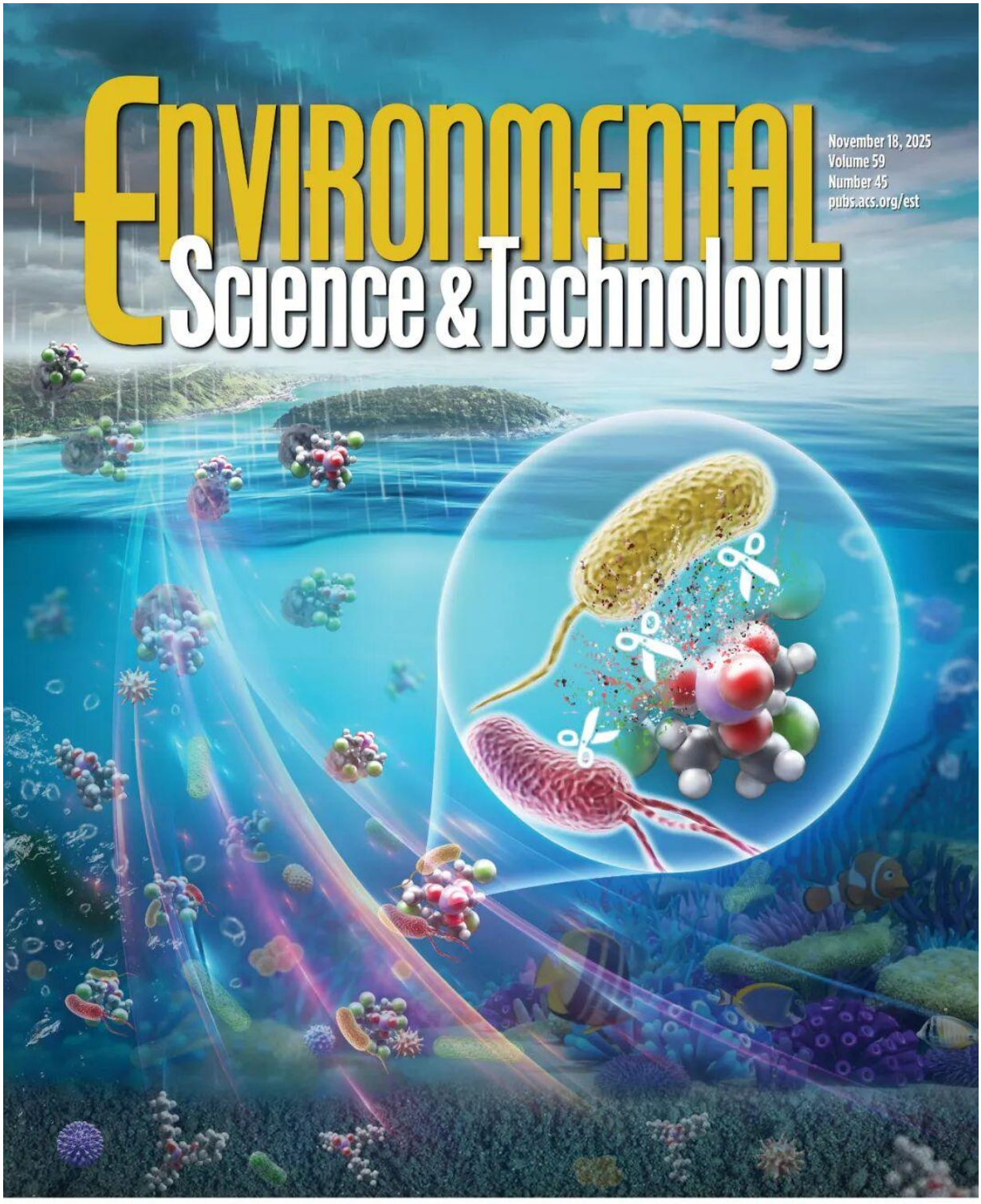


涠洲岛珊瑚礁生态系统修复前后的对比效果

左：珊瑚礁生态系统前的状况；右：珊瑚礁生态系统后的状况

※**《Environmental Science & Technology》（副封面报道）：**有机磷酸酯（OPEs）作为全球消费量巨大的阻燃剂、塑化剂和消泡剂添加剂，已在全球海洋环境（包括南大洋、极地等偏远海域）中普遍检出，其高亲脂性促进在海洋生物体内的累积和食物链传递，对生态系统和人类健康构成潜在威胁。然而，OPEs在海洋环境中的迁移机制、归趋过程及生态效应仍不明确。西北南海（WSCS）地处热带，拥有丰富的珊瑚礁生态系统，但持续遭受陆源污染、航运排放和河流输入（珠江、湄公河）的多重压力，加上印度支那半岛和吕宋岛等陆源污染物通过大气长距离传输的输入，使其成为研究陆源新兴污染物向远洋传输及其生态影响的理想天然实验室。在全球变暖与海洋酸化背景下，OPEs对珊瑚礁等敏感生态系统的毒性效应愈发凸显，但其在深海系统中的垂直传输机制以及生物地球化学循环过程尚不清楚，亟需系统研究以揭示其环境行为与生态风险。本研究系统揭示了西北南海OPEs的污染现状、迁移机制与生态风险，证实大气沉降是OPEs进入海洋的主导途径，颗粒物介导的垂直传输是驱动OPEs在深海富集的关键物理过程，而微生物群落通过生态位分化和降解酶上调在OPEs归趋中发挥重要生物调控作用。OPEs的长期上升趋势对南海珊瑚礁和深海生态系统构成潜在威胁，其通过食物链传递和微生物群落扰动可能引发连锁生态效应。研究强调需加强对区域工业、航运和电子垃圾拆解等排放源的监管，特别是控制颗粒物相关排放；同时提出保护海洋健康需从"大气-表层水-深海"连续统视角制定管理策略。该研究为理解颗粒反应性新兴污染物的海洋生物地球化学循环提供了范式，凸显了物理输运与生物转化耦合作用在决定污染物环境影响中的核心地位，对全球海洋新兴污染物风险防控具有重要借鉴意义。

论文信息：Minwei Han, Kefu Yu*, Ruijie Zhang, Biao Chen, Mei Xiong, Yaru Kang, Xiaopeng Yu, Zhenjun Qin, Xiangrong Xu, Organophosphate Ester Migration Mechanisms and Environmental Impacts in the Western South China Sea, *Environmental Science & Technology*, 2025, 59(45):24538–24552. https://doi.org/10.1021/acs.est.5c09148.


ENVIRONMENTAL
Science & Technology
November 18, 2025
Volume 59
Number 45
pubs.acs.org/est
ACS Publications
Most Trusted. Most Cited. Most Read.
www.acs.org

※ **《Environmental Chemistry and Ecotoxicology》：**作为我国水产养殖的“明星品种”，珍珠龙胆石斑鱼产量占全国石斑鱼总产量的 70%，2022 年产量已达 20.58 万吨，在水产养殖产业中具有重要地位。然而，全球每年超 4 亿吨塑料生产带来的污染问题，让这一 “水产优等生” 面临严峻挑战 —— 约 90% 的塑料垃圾未能有效回收，最终渗入土壤或进入海洋，降解形成粒径小于 5 毫米的微塑料和小于 100 纳米的纳米塑料。这些 “海洋隐形杀手” 能吸附重金属和有毒有机污染物，通过食物链传递危害生物健康。而珍珠龙胆石斑鱼在越冬期（10–15℃）不仅要抵御低温，还要应对微纳塑料的 “隐性攻击”，此前科学界对这种双重胁迫的影响知之甚少。聚焦这一关键科学问题，团队通过系统研究取得多项重要发现：在富集规律上，微纳塑料在鱼体内的分布呈现明显 “尺寸偏好”：纳米塑料主要靶向富集于肝脏，湿组织中含量最高达 22.94 μg/g，成为肝脏内的微型 “破坏者”；微塑料则更倾向于分布在消化器官，悄悄干扰消化功能。组织病理学观察显示，石斑鱼肝脏在微纳塑料暴露下出现肝细胞肿胀、炎症、空泡变性等损伤，原本储存能量的脂滴数量显著减少，且损伤程度随塑料颗粒尺寸减小而加剧，证实纳米塑料的毒性显著强于微塑料。在代谢层面，微纳塑料引发了一系列 “连锁危机”：氧化应激升级，SOD 与 CAT 等 “抗氧化卫士” 活性下降，MDA 与 GSH 等 “氧化损伤标志物” 含量升高；脂质代谢失衡，甘油三酯（TG）减少，总胆固醇（T-CHO）和低密度脂蛋白胆固醇（LDL-C）升高，机体被迫加速分解脂肪供能；397-499 个差异表达基因被激活，其中 PNPLA2、MGLL 等脂肪分解相关基因异常活跃，低温条件下更为显著，导致能量稳态失衡。研究进一步明确，微纳塑料通过三重途径威胁石斑鱼越冬生存：激活免疫反应增加能量需求、直接调控脂肪分解基因加速脂滴消耗、干扰甘油三酯分解与转运，三者共同作用导致低温下石斑鱼能量储备快速耗尽，死亡风险大幅上升。该研究首次系统阐明了微纳塑料与低温双重胁迫对珍珠龙胆石斑鱼的毒性机制，构建了“环境胁迫 - 基因 - 代谢” 的完整作用模型，不仅为塑料污染对水生生物的影响研究提供了创新思路，更为推动可持续水产养殖、保障食品安全和生态安全提供了重要理论支撑。

论文信息：Julong Wang, Yan Gao, Shanshan Yao, Lang Lin*, Hengxiang Li, Shan Liu, Rui Hou, Zhijian Jiang, Xiangrong Xu*, Emerging microplastic and nanoplastic

threats: Decoding winter survival mechanisms in hybrid groupers through hepatic metabolic disruption, *Environmental Chemistry and Ecotoxicology*, 2025, 7：2544-2555. https://doi.org/10.1016/j.enceco.2025.07.021.

※ **《Microbial Ecology》**：受气候变化和人类活动的双重干扰，全球珊瑚礁生态系统急剧退化，需要对珊瑚的高温适应机制进行深入探究。珊瑚体内存在大量的光合细菌，在部分珊瑚物种或个体中光合细菌可占到总细菌相对丰度的50%以上。然而，此类细菌是否对高温条件下虫黄藻的光合作用具有补偿效应尚不清楚。在本研究中，我们以北部湾涠洲岛珊瑚礁区一种典型的块状珊瑚—十字牡丹珊瑚（Pavona decussata）为研究对象：首先，通过固定样的方式进行四个季度连续监测其共生虫黄藻和光合细菌的群落结构动态变化，特别是光合细菌在夏季高温条件下的动态；其次，在室内实验室离体培养下验证光合细菌对虫黄藻光合作用的补偿效应。研究结果发现，四个季节中虫黄藻群落组成稳定，主要以Cladocopium goreaui为主导（81.63%~82.33%），但虫黄藻的密度和叶绿素a的含量则变化显著。夏季高温期虫黄藻的密度和叶绿素a的含量分别为$0.51 \pm 0.17 \times 106$ cells cm^{-2}和5.71 ± 0.18 μg • cm^{-2}，显著低于其他季节（$p < 0.05$）。更值得关注的是，夏季高温期细菌群落结构与其它季节显著不同（$p < 0.05$），其中，第一主导属为视紫质细菌（BD1-7_clade），相对丰度占总细菌的50.59%；而Synechococcus_CC9902和Cyanobium_PCC-6307则分别占蓝细菌总数的61.85%和31.48%，这3种光合细菌的丰度在夏季高温期显著高于其他季节（$p < 0.05$）。由此推测，这种此消彼长的动态变化可能在维持珊瑚共生功能体的光合能量供给方面起着重要作用。进一步从P. decussata中成功分离了虫黄藻主导系群C. goreaui和光合细菌Cyanobium_PCC-6307，在离体培养的情况下，模拟高温胁迫时在生长率和Fv/Fm方面的变化，发现Cyanobium_PCC-6307对C. goreaui均具有显著的补偿效应。本研究探究了珊瑚共生虫黄藻和光合细菌之间潜在的协同效应，揭示了这些动态关系在帮助珊瑚抵御环境压力方面发挥重要作用。

论文信息：Xu Yongqian, Liang Jiayuan, Qin Liangyun, Niu Tianyi, Liang Zhuqing, Li Zhicong, Chen Biao, Zhou Jin, Yu Kefu, The Dynamics of Symbiodiniaceae and

Photosynthetic Bacteria Under High Temperature Conditions. Microbial Ecology, *Microbial Ecology*,2025, 87, 169. https://doi.org/10.1007/s00248-024-02470-4.

※ **《Environmental Research》：**随着人类社会的发展，微塑料污染正威胁着地球的各个角落。生物多样性以及初级生产力都非常高的珊瑚礁生态系统受到的威胁程度也不容忽视，更需要关注。在珊瑚礁生态系统中，虫黄藻是造礁石珊瑚最重要的共生伙伴之一，它能为珊瑚共生功能体提供约90%的光合能量。然而虫黄藻对微塑料的生理响应以及受影响程度目前还知之甚少。本研究使用聚苯乙烯材质的微塑料（PS-MPs）对一种广布型的珊瑚共生虫黄藻（Cladocopium goreaui）所产生的毒性危害进行了探究。结果表明，微米级别的PS比纳米级别的对C. goreaui毒害作用更大，粒径10 μm浓度为20 mg/L的PS-MPs对C. goreaui的生长抑制率高达62.9% - 86%，几乎完全抑制了细胞增殖。暴露于10 μm的PS-MPs显著增加了细胞损伤。例如，细胞外聚合物和丙二醛的浓度在暴露第10天至20天分别增加了161.6%、184.4% 和 261.8%、896%。此外，当C. goreaui受到PS-MPs胁迫抑制时，它可以通过提高细胞色素的含量来维持光合功能的稳定，并且受抑制程度越强烈色素含量的提高越显著。然而，暴露于10 μm的PS-MPs可能会损害C. goreaui的叶绿体，导致光合色素的合成能力下降，进而引起光合作用能力降低。C. goreaui的形态和基因活性表明，PS-MPs主要引起细胞皱缩变形，以及细胞核和叶绿体溶解性损伤，同时较多的基因表达被抑制，主要涉及琥珀酸脱氢酶、四吡咯结合、血红素结合和离子运输相关功能，以及与氧化还原等有关的活动。这项研究探究了PS-MPs对珊瑚关键共生伙伴（虫黄藻）的毒害作用以及藻细胞做出的积极响应，从而揭示了微塑料对珊瑚礁生态系统的影响。

论文信息：Liang Jiayuan, Niu Tianyi, Zhang Li, Yang Yating, Li Zhicong, Liang Zhuqing, Yu Kefu, Gong Sanqiang, Polystyrene microplastics exhibit toxic effects on the widespread coral symbiotic Cladocopium goreaui, *Environmental Research*,2025, 268, 120750. https://authors.elsevier.com/sd/article/S0013-9351(25)00001-5.

※ **《IEEE Journal of Selected Topics in Applied Earth Observations and Remote Sensing》：**水深是表征珊瑚礁环境的重要地形要素。由于珊瑚礁底质和地形具有高 度的空间异质性，目前的遥感水深反演方法在获取珊瑚礁区大范围浅水水深时精度仍较低。本研究以我国南海西沙群岛的11个珊瑚礁（海域面积607 km2）为研究区，结合目前在轨的星载激光雷达ICESat-2水深数据以及中分辨率的高分一号（GF-1）和高分辨率的WorldView-2/3（WV-2/3）多光谱卫星影像，构建了一种基于地貌分区的多参数模型组合水深反演方法（PMCGS）。该方法使用ICESat-2数据和多光谱卫星影像在每个地貌带构建5个参数模型，然后组合每个地貌带的最优模型进行水深反演，并将其外推应用至其他珊瑚礁进行大范围水深反演。实验结果表明，礁坪、浅潟湖和点礁地貌带的最优参数模型为多波段比值模型，礁坡和深潟湖地貌带的最优模型为二项式模型。经大量实测水深数据和少部分ICESat-2数据验证，当PMCGS方法外推应用反演大范围珊瑚礁区的水深时，GF-1影像反演的水深均方根误差（RMSE）为0.91 m，WV-2/3反演的水深RMSE为0.70–0.88 m，该精度均高于未分地貌建模的水深反演方法。与前人研究相比，该方法反演0–10 m和15–25 m处的水深精度更高，尤其是在礁坪和浅潟湖这类浅水珊瑚礁区。本研究提出的PMCGS水深反演方法显著提高了中高分辨率影像的水深反演精度，在获取珊瑚礁区大范围水深数据方面具有很大的应用潜力，可辅助应用于珊瑚礁生境的评估、保护和恢复。

论文信息： Xiuling Zuo, Juncan Teng, Fenzhen Su, Zhengxian Duan and Kefu Yu. Multimodel combination bathymetry inversion approach based on geomorphic segmentation in coral reef habitats using ICESat-2 and multispectral satellite images. *IEEE Journal of Selected Topics in Applied Earth Observations and Remote Sensing*, 2025.18：3267-3280. https://doi.org/10.1109/JSTARS.2024.3523296.

※ **《Paleoceanography and Paleoclimatology》：**珊瑚礁作为地球生物多样性最丰富的生态系统之一，对气候变化和环境波动极为敏感，是记录古环境信息的天然档案。但珊瑚礁区广泛分布的底栖有孔虫，其环境指示意义的研究还非常有限，极少用于古环境重建研究。该研究对采集自南海黄岩岛、羚羊礁表层沉积物中的底

栖有孔虫进行了全壳碳氧同位素分析。结果表明，研究区底栖有孔虫表现出显著种间差异，大型底栖有孔虫碳氧同位素结果偏离平衡方解石估算值。同时，大部分物种的碳氧同位素值也表现出显著的种内差异，只有部分物种种内稳定性较高。结合所研究的每种有孔虫的生态特征，发现礁区底栖有孔虫壳体碳氧同位素指标主要受镁元素含量、共生藻类型、钙化方式及个体发育等因素影响。此外，该研究还发现，基于大型底栖有孔虫物种Sorites orbiculus和 Neorotalia calcar的碳氧同位素值反演的表层海水温度及生产力水平，总体上与两处研究区域的实际环境条件吻合，证实了礁区有孔虫特定物种碳氧同位素作为古环境指标的潜力。

论文信息： Siqi Wu, Risheng Liang, Kefu Yu*, The Potential of Benthic Foraminifera Carbon and Oxygen Isotopic Proxies as Environmental Indicators in Coral Reef Regions.*Paleoceanography and Paleoclimatology*,2025,40(5), e2024PA005080. https://doi.org/10.1029/2024PA005080.

※ **《BMC Genomics》：**由于全球气候变化，珊瑚礁正面临日益严重的威胁，然而，一些生活在边缘环境中的珊瑚却表现出很强的耐受性。为了进一步了解珊瑚应对环境变化的分子机制，本研究结合生理学和多组学技术，揭示了涠洲岛十字牡丹珊瑚经历不同季节陆上暴露后的转录调控特征。结果表明，与未经历陆上暴露的珊瑚相比，有季节性陆上暴露史的珊瑚在能量代谢和防御机制方面发生了全面的变化。在夏季，经历陆上暴露的珊瑚可能通过增加T-SOD和CAT酶的活性来增强抗氧化防御；珊瑚共附生细菌中优势类群主要来自α-变形菌纲，可能有助于珊瑚抵抗环境压力；珊瑚宿主TCA循环转录水平的下降和鸟氨酸代谢物含量的增加可能指示了能量代谢途径的改变。在冬季，经历陆上暴露后的珊瑚Chl a含量较高，且珊瑚共附生细菌中优势类群转变为γ-变形菌纲，可能指示了珊瑚具有更高的能量储备；珊瑚宿主TGF-beta信号通路的激活和代谢产物白三烯D4的积累可能表明珊瑚具有更高的抗炎需求，并通过先天免疫进行调节。本研究揭示了涠洲岛十字牡丹珊瑚适应季节性环境波动的分子特征，为珊瑚分子生物学和珊瑚礁生态保护提供了进一步的理论依据。

论文信息：Man Zhang, Shan Huang, Li Luo, Kefu Yu. Environmental acclimatization

of the relatively high latitude scleractinian coral Pavona decussata: integrative perspectives on seasonal subaerial exposure and temperature fluctuations. *BMC Genomics*, 2025,26: 483. https://doi.org/10.1186/s12864-025-11660-4.

※ **《Journal of Marine Science and Engineering》：**人工珊瑚礁在生态修复与海岸防护方面具有双重效益，然而其在珊瑚礁生境中的波浪衰减效能尚未得到充分评估。为此，本研究创新性地融合了现场实测地形与人工礁体数据，构建了二维数值波浪水槽，模拟了包含礁前斜坡与礁坪的典型岸礁剖面，系统分析了波浪在跨礁传播过程中的波高衰减、增水效应以及反射与透射特性。研究主要结论包括：（1）礁坪水深对波浪演化过程具有主导调控作用。低潮时的最大波高与增水幅度较高潮时分别提升45.7%与78.5%。水深变化通过调节波浪破碎过程显著影响反射系数与透射系数的分布，是决定波浪传播形态的关键因子。（2）潮位状态显著影响人工礁体结构参数对波浪耗散的作用机制。低潮时礁体间距对波浪反射影响显著，而礁体行数的影响相对有限；高潮时增大礁体间距可使峰值波高降低2.1%，峰值增水减小2.4%；而增加礁体行数则使峰值波高上升5.2%，同时波增水下降10.5%。（3）对于部署于外礁坪的现有礁体结构，其在调控波浪透射方面效果有限。在不同潮位、行数与间距组合下，所引起的透射系数变化均低于5%。结果表明，需通过结构优化，如增加礁体高度或将礁体铺设于礁前斜坡，以提升整体波浪衰减性能。该研究首次将北部湾涠洲岛现场地形与人工礁体参数相结合，定量评估了现有人工礁体在规则波作用下的波浪耗散效能，为珊瑚礁生态修复与海岸防护工程设计提供了理论依据与结构优化方向。

论文信息：Liang Zuodong, Huang Guangxian, Huang Wen, Chen Hailun, Yu Kefu, Jeng Dong-Sheng. Numerical Modeling of Wave Hydrodynamics Around Submerged Artificial Reefs on Fringing Reefs in Weizhou Island of Northern South China Sea. *Journal of Marine Science and Engineering*, 2025, 13(11), 2031. https://doi.org/10.3390/jmse13112031.

※ **《Analytical Methods》、《Marine Environmental Research》：**作为全球已知最深的海洋蓝洞，西沙永乐蓝洞拥有独特的垂直分层水环境，从表层有氧区、中间

化学跃层到深层缺氧区，形成了鲜明的氧化还原梯度和生态位分化，为研究极端环境下DOM的循环机制提供了天然实验室。DOM作为海洋碳循环的核心载体，其组成与动态变化直接影响全球碳储存效率与营养盐循环平衡，是解开海洋生物地球化学谜题的关键。在发表于Analytical Methods的工作中，研究团队系统对比了质谱正负电喷雾电离（ESI+与ESI−）两种模式对DOM的检测效能。研究发现，ESI+模式可捕获比ESI−模式更多的DOM，尤其擅长检测含氮化合物（CHN、CHON、CHONS）及多肽、多酚类物质；而ESI−模式在富硫化合物（CHOS）检测中表现更优，在缺氧层的检测灵敏度尤为突出。两种模式虽能共同识别碳水化合物、富羧基脂环分子（CRAM）等核心组分，但在高不饱和化合物检测效率上存在显著差异，证实单一电离模式易导致DOM解读偏差，双模式联用可实现DOM信息的全方位捕获，为后续研究提供了标准化检测方案。在此技术基础上，团队在Marine Environmental Research发表的研究中，进一步整合非靶代谢组学与宏基因组学技术，深入解析了蓝洞不同水层中DOM与微生物群落的互作调控机制。研究揭示，蓝洞 DOM 呈现显著的垂直分层特征：缺氧层溶解有机硫（DOS）浓度显著高于表层，而化学跃层溶解有机氮（DON）含量最低，这种分布差异与微生物代谢活动密切相关——缺氧层中脱硫杆菌目等厌氧菌富集，通过硫酸盐还原作用生成硫化氢，进而促进DOS积累；化学跃层则因硝化菌与反硝化菌的耦合作用，通过“DON→氨→硝酸盐→气态氮”的转化路径，加速DON矿化流失。同时，微生物还通过精准调节脂质、氨基酸、异戊酰肉碱等代谢物的生成，适应不同的氧化还原环境。这两项研究层层深入，电离检测技术为精准解析DOM组成提供了关键工具支撑。研究通过构建蓝洞DOM的完整分子图谱，系统揭示了微生物代谢活动对DOM生物地球化学循环中的核心调控作用。该成果不仅弥补了极端海洋环境DOM系统研究的不足，更为全球海洋碳循环方法学优化及极端生态系统保护提供了重要科学依据。

论文信息： 1.Pei Jiying, Chen Shiguo, Zhang Jiayu, Yu Wenfeng, Qin Weijie, Yu Kefu. Comparative evaluation of positive and negative LC-MS modes for DOM profiling. *Analytical Methods*, 2025,17: 6598 — 6608. https://doi.org/10.1039/d5ay00679a.

2. Pei Jiying, Chen Shiguo, Yu Kefu, Liang Jiayuan, Zhang Ruijie, Li Penghui, Hou Zhuanghao, Fu Liang, Ma Honglin. Microbial regulation of dissolved organic matter revealed by integrated metabolomics and metagenomics in the World's deepest blue hole. *Marine Environmental Research*, 2025, 210: 107354. https://doi.org/10.1016/j.marenvres.2025.107354.

※ **《Talanta》**：OUVs广泛应用于防晒霜、化妆品及塑料制品中，在紫外线防护和材料抗老化方面发挥重要作用。然而，这类化合物通过生活污水排放、休闲娱乐活动等途径大量进入水体环境，已被证实会对海洋生物造成珊瑚白化、幼体发育受阻等毒性效应，部分OUVs还具有潜在内分泌干扰风险，对生态系统和人类健康构成双重威胁。传统液相色谱-质谱（LC-MS）、气相色谱-质谱（GC-MS）等检测方法虽灵敏度高，但存在样品前处理繁琐、分析周期长、有机溶剂消耗量大、仪器成本高等局限，难以满足现场快速检测和高通量筛查需求。为此，研究团队提出模块化集成创新方案：以C_{18}修饰的牙签作为固相微萃取探针，借助木材表面羟基富集目标物；通过3D打印定制化接口装置调控离子源与质谱仪相对位置，提升检测稳定性与可重复性；将萃取探针与常压质谱联用，无需复杂预处理即可快速分析。该技术平台表现出优异性能，检测限低至0.23-8.17 μg/L，超纯水和洁面后冲洗液中回收率达81.3%-119.6%，人工海水中回收率保持50.9%-83.0%，分析时间缩短至分钟级，且无需昂贵色谱柱和大量有机溶剂，显著降低检测成本与环境负担。实际应用中，该方法检测8款商用防晒霜的结果与产品标注完全吻合，可实现防晒品质量控制；证实表面活性剂辅助清洁能使皮肤残留OUVs释放量提升1.58-2.31倍，为评估个人卫生习惯对环境排放的影响提供数据支撑；同时在游泳池水及马来西亚仙本那珊瑚礁海域成功检出BP-1、EHMC、ODPABA等典型OUVs，其中珊瑚礁水域EHMC浓度最高达55.59 μg/L，揭示了旅游密集区域的OUVs污染现状，为珊瑚礁生态保护提供警示。该研究成功实现3D打印、固相微萃取与牙签喷雾常压质谱的一体化集成，有效突破传统色谱-质谱技术在现场快速检测中的应用瓶颈，构建了“富集-电离-检测”一体化高效分析流程。该技术平台兼具低成本与便携性优势，在提升环境监测效率、强化污染风险预警等方面

展现出重要潜在应用价值，为复杂基质中目标污染物的快速筛查提供了创新技术方案。

论文信息： Yingyuan Zhang, Deshuo Gao, Kefu Yu, Ruijie Zhang, Jiayu Zhang, Wenfeng Yu, Shiguo Chen, Jiying Pei. 3D-printed SPME-based wooden-tip mass spectrometry for rapid detection of organic ultraviolet absorbers in complex matrices. *Talanta*, 2025, 297: 128692. https://doi.org/10.1016/j.talanta.2025.128692.

※ **《Acta Oceanologica Sinica》：**西沙群岛位于南海北部陆缘，长期以来被厚层新生代沉积物覆盖，岩浆岩样品难以通过钻探获取，导致该区域在地幔源区岩浆活动与构造演化方面的研究相对有限。其中，西沙地区新生代岩浆活动是否与海南地幔柱有关，一直是学界争议的焦点，这一问题的解答直接影响对南海北部陆缘伸展过程及区域构造—岩浆演化规律的认识。本研究基于CK-2井基底玄武质火山碎屑岩的矿物化学和全岩地球化学数据，系统揭示了其地幔源区性质及原生岩浆特征。结果表明，西沙新生代岩浆活动的地幔源区中存在辉石岩组分，该组分很可能由再循环洋壳与地幔橄榄岩反应形成。通过橄榄石—熔体Mg-Fe交换温度计估算，地幔潜在温度介于1502–1756℃之间，与典型地幔柱相关的洋岛玄武岩温度范围一致。此外，样品具有较低的H_2O含量（0.01–1.47 wt.%），显著低于典型大型火成岩省原生岩浆的含水量。综合以上证据，研究提出西沙群岛玄武质火山碎屑岩来源于一个贫挥发分的地幔柱源区。该成果不仅为南海新生代玄武岩成因机制提供了新的约束，也对认识南海形成的地球动力学背景具有重要科学意义。

论文信息： Zhang Yu, Yuan Yaqi, Yu Kefu. Geochemical characteristics and petrogenesis of the basaltic pyroclastic rocks from the Xisha Islands, Northwestern South China Sea. *Acta Oceanologica Sinica*, 2025. 44(9): 81 – 94. https://doi.org/10.1007/s13131-025-2511-3.

※ **《The ISME Journal》：**开创性地以“同一个星球，同一个健康（One Planet, One Health）”为研究视角，对涵盖无脊椎动物至人类的13个类群生物的肠道微生物群对490多种环境污染物的转化能力。所涉及的污染物类型广泛，包括持久

性有机污染物、重金属、药品和个人护理品、工业添加剂等。此外，论文还明确揭示了肠道微生物群在污染物转化过程中的普遍作用机制，深入探讨了该转化过程对污染物生物利用度、毒性水平及环境归趋的影响。在此基础上，研究团队进一步提出“污染物—肠道微生物群—宿主”相互作用的系统化研究方向，并倡导将肠道微生物的转化能力纳入跨学科研究范式，为相关领域研究提供全新思路。

论文信息：Rui Hou, Xiaowei Jin, Jingchun Feng*, Jingchuan Xue, Chengzhi Chen, Yuanqiang Zou, Xiangrong Xu*, Kefu Yu, Peiyuan Qian, Wei Zhang, Jizhong Zhou, Si Zhang, Zhifeng Yang, Deciphering the Universal Role of Gut Microbiota in Pollutant Transformation, *The ISME Journal*, 2025, 19(1): wraf215. https://doi.org/10.1093/ismejo/wraf215.

※ **《Marine Pollution Bulletin》：**随着微塑料在海洋环境中的累积，其对珊瑚礁等生态系统的威胁日益凸显。虫黄藻作为造礁珊瑚的关键共生藻类，其生理状态直接影响珊瑚的健康与存活。然而，不同颜色微塑料对虫黄藻的毒性效应及其内在机制尚不明确。本研究以常见造礁石珊瑚的共生虫黄藻——Cladocopium goreaui为研究对象，系统评估了红、黄、绿、蓝、白五种颜色聚苯乙烯微塑料（粒径5 μm，浓度20 mg/L）对其生长、光合生理、氧化应激及基因表达的影响。研究发现：1. 显著抑制藻细胞生长：所有颜色PS-MPs均对C. goreaui生长产生抑制作用（$P<0.05$），其中蓝色与白色PS-MPs的抑制效应最强，藻细胞生长率最高下降约36%。2. 光合生理响应与能量重新分配：尽管藻细胞通过上调光合色素含量（如蓝色PS-MPs暴露组中叶绿素a、叶绿素c和类胡萝卜素含量在第20天分别增加39%、108%和38%）以应对微塑料遮光效应，但光合产能被大量用于抵抗氧化胁迫，导致藻体生长受限。3. 关键代谢通路基因表达下调：转录组分析表明，PS-MPs显著抑制了与生物合成、氮同化、脂代谢等关键代谢通路相关的基因表达。其中，蓝色与白色PS-MPs对脂肪酸代谢和核糖体功能相关基因的抑制尤为明显（$P<0.05$）。4. 颜色差异调控毒性强度：微塑料的颜色差异通过影响其颗粒聚集行为及光吸收与反射特性，进而调控毒性效应的强弱。该研究首次系统阐明微塑料颜色差异在调控其对珊瑚共生虫黄藻毒性效应中的作用，从生理响应与

基因表达层面揭示了不同颜色微塑料的生态风险差异，为评估微塑料污染对珊瑚礁生态系统的潜在影响提供了新的科学依据。

论文信息：Tianyi Niu, Yating Yang, Sanqiang Gong, Kefu Yu, Jiayuan Liang* Color disparity enhances the toxic effects of polystyrene microplastics on Cladocopium goreaui. *Marine Pollution Bulletin*, 2025，222 (Part 2) : 118815. https://doi.org/10.1016/j.marpolbul.2025.118815.

※ **《Quaternary Science Reviews》：**该研究以贵州西部娘娘山湿地泥炭岩芯为载体，建立了中国黔西地区MIS3晚期和早全新世以来的植被演化序列，通过与临近的草海记录对比，探讨了地形特征与沉积环境对西南地区古植被重建的影响作用，为全球山地生态系统对气候与人类活动的响应等相关研究提供了新的参考模式。受印度夏季风（ISM）影响的中国西南地区，因其复杂的高山峡谷与喀斯特地貌格局，成为全球生物多样性热点区与重要冰川避难所，是揭示古植被—气候互动机制的理想区域。然而，该区域植被重建研究仍存在不确定性，其中一个重要原因是忽略了受地形特征和沉积环境影响的孢粉来源等相关问题。本研究选取云贵高原黔西娘娘山湿地（26°34′40″–26°36′38″N、104°45′29″–104°48′45″E，海拔 2050 米）为研究对象，其独特的湿地沉积环境可捕获局地植被信号，为修正传统记录偏差提供了较为理想载体。研究结果表明，末次冰期以来研究点周围植被类型发生了明显变化，MIS3晚期以落叶栎、桦木科为主，早全新世柯/栲属、青冈属主导群落，常绿阔叶林广泛分布。通过对比娘娘山湿地（局地花粉来源）与临近的草海湖泊（广域花粉来源）的记录发现，西南传统湖泊记录可能高估了常绿硬叶栎林（ESQF）的扩张范围，实际LGM时期ESQF可能仅垂直下移500-800米。在驱动机制方面，本研究在传统影响因素之外，强调了AMOC对西南植被演替的影响作用。

论文信息：Xiao Zhang, Yuanfu Yue*, Ziyan Zhang, Liuying He, Xinmeng Yuan, Xintian Yu, Qiuchi Wan, Cong Chen, Yongjie Tang, Zhuo Zheng, Kangyou Huang, The topographic features and sedimentary environment potentially influenced the vegetation reconstruction in southwestern China since the MIS3. *Quaternary Science*

Reviews,2025.369, 109636. https://doi.org/10.1016/j.quascirev. 2025. 109636.

※ **《Remote Sensing》**：海洋热浪（Marine Heatwaves）和冷浪（Marine Cold-spells）往往会对暖水珊瑚造成严重威胁。然而，全球珊瑚礁区海洋热浪与冷浪的历史与未来时空格局、驱动机制及其对珊瑚礁生态系统的影响研究仍然缺乏。鉴于此，本研究基于OISST v2.1与CMIP6数据，系统分析了1982–2022年及2023–2070年期间全球海洋热浪和冷浪的时空演化特征；结合四种机器学习方法与可解释性工具SHAP（SHapley Additive exPlanations）识别了全球海洋热浪的关键驱动因子，分析了其与全球十大珊瑚礁区平均活珊瑚覆盖度之间的相关关系。结果表明：1.过去40年间，全球海洋热浪的平均强度和极端性均增强，而海洋冷浪则呈下降趋势。其中，红海、波斯湾和南太平洋群岛等海域的热浪事件天数增幅最高，可达每十年增加28天。2.高纬度珊瑚礁区的海洋热浪增幅显著高于赤道区域，这可能会削弱高纬度区域作为“珊瑚避难所”的潜在功能。3.根据高排放情景（SSP5-8.5）的预测，到2070年，几乎全年为海洋热浪状态；低排放情景（SSP2-4.5）下，海洋热浪的发生面积约为海洋冷浪的100倍，而高排放情景下则高达196倍。4.年均温度的变异系数、年海洋热含量的变异系数以及月均温度的变异系数被识别为驱动海洋热浪强度变化的三大关键因素。因此，在海洋热浪预测与评估中应更加关注气候指标的变异性，而不仅仅是平均值。5.活珊瑚覆盖度与热浪事件显著负相关（$r=-0.54$，$p<0.01$），与冷浪事件显著正相关（$r=0.60$，$p<0.01$）。其中，太平洋海域的活珊瑚覆盖度对海洋热浪最为敏感；在经历海洋热浪事件后，珊瑚群落呈现明显的死亡后衰退（post mortality）与滞后恢复（lag recovery）过程。本研究揭示了海洋热浪与冷浪的历史与未来时空格局、驱动机制及其对珊瑚礁生态系统的影响，凸显了在气候变化压力日益加剧的背景下，提升珊瑚礁生态韧性与适应性的紧迫性

论文信息：Jiang Honglei, Ren Tianfei, Huang Rongyong, Yu Kefu*. Marine Heatwaves and Cold Spells in Global Coral Reef Regions (1982–2070): Characteristics, Drivers, and Impacts. *Remote Sensing*. 2025, 17, 2881. https://doi.org/10.3390/rs17162881.

※ **《Algal Research》：**虫黄藻（Symbiodiniaceae）作为造礁珊瑚的核心共生伙伴，为珊瑚宿主提供90%以上的光合能量。然而，异常温度胁迫会破坏珊瑚与虫黄藻的共生关系，导致珊瑚白化。不同种属的虫黄藻生理功能各异，对珊瑚的环境适应性，特别是高温/低温耐受性，具有重要影响。本研究探究了两种虫黄藻——高温敏感型*Cladocopium goreaui (C. goreaui)*与高温耐受型*Durusdinium trenchii*（*D. trenchii*）——在异常高温（34℃）和低温（16℃）胁迫下的响应策略。结果表明：1.*C. goreaui*对高温极为敏感，细胞密度显著下降（$P<0.05$），比生长率从0.119降至-0.125 day^{-1}，光系统II（PSII）最大光量子产率（*Fv/Fm*）从0.66降至0（胁迫14天），叶绿素a骤降90.22%，电镜观察显示叶绿体严重解体，各项生化指标均指示其遭受强烈的氧化胁迫；与之相反，*D. trenchii*则表现出较强的高温耐受性，比生长率仅从0.10降至0.066 day^{-1}（$P>0.05$），*Fv/Fm*仅下降10%，细胞结构完整。蛋白质组学显示其通过上调热休克蛋白（HSP70）和泛素介导的蛋白降解通路维持稳态。2.在低温胁迫下，两种虫黄藻均呈现适度的生理变化。*C. goreaui*激活三羧酸循环（TCA循环）和谷胱甘肽抗氧化通路，叶绿素a仅下降27.16%，*Fv/Fm*降幅（11.5%）显著低于*D. trenchii*（47%），表明其增强了耐寒性。*D. trenchii*则依赖RNA剪接通路（剪接体相关蛋白富集度最高）进行转录后调控，但光合损伤更严重，提示其存在一种适应性的转录后调控机制。本研究阐明了虫黄藻不同物种间独特的温度响应策略，为理解其在气候胁迫下物种特异性的适应力提供了新见解。

论文信息： Jiayuan Liang, Liangyun Qin, Li Zhang, Yongqian Xu, Tianyi Niu, Zhicong Li, Yating Yang, Zhuqing Liang, Kefu Yu*, Sanqiang Gong. The stress response strategies of two typical coral Symbiodiniaceae (Cladocopium goreaui and Durusdinium trenchii) under abnormal temperatures. *Algal Research*, 2025,91:104187. https://doi.org/10.1016/j.algal.2025.104187.

※ **《Marine Pollution Bulletin》：**类固醇激素作为典型内分泌干扰物，其环境行为与生态风险已成为国际研究热点。九龙江口长期受到流域内城市化、农业面源和

工业排放的复合污染压力，污染物负荷显著。但针对该区域类固醇激素污染的系统性风险评估和管理措施仍存在空白，亟需开展其时空分布特征解析及优先管控污染物识别等研究。徐向荣教授团队于2014年11月（枯水期）和2015年6月（丰水期）对九龙江口水体及沉积物中22种类固醇激素的污染特征进行了系统研究，首次揭示该区域类固醇激素的时空分布规律，并建立了优先管控污染物清单。研究表明，水体中检出7种类固醇激素（浓度范围0.2-51 ng L^{-1}），沉积物中检出10种类固醇激素（浓度范围ND-12 ng g^{-1}）；在不同季节，天然激素在水和沉积物中均呈现显著优势；类固醇激素在水-沉积物系统中的分布受疏水性及温度、盐度、pH、叶绿素-a和总有机碳含量等多种环境因子的影响；沉积物中赋存的类固醇激素占总量的90%以上，证实其作为重要储存库的关键作用。此外，基于多标准综合评价体系，研究确定九龙江口枯水期需优先管控黄体酮和睾酮，丰水期则以黄体酮为核心管控对象。该研究通过多介质环境行为解析与风险源精准识别，为河口环境风险管控与“蓝色海湾”生态保护提供科学依据，对区域生态安全屏障构建具有重要实践价值。

论文信息：Ru Xu, Niannian Wu, Shan Liu, Hui Chen, Qinwei Hao, Yongxia Hu, Bing Hong, Shen Yu, Xiangrong Xu*, Spatiotemporal distribution and priority assessment of steroids in the estuarine environment: Implications for environmental risk management. *Marine Pollution Bulletin*, 2025, 216:117980. https://doi.org/10.1016/j.marpolbul.2025.117980.

※ **《Ecological Informatics》：**全球变化背景下，微生物组对造礁石珊瑚的气候适应性与恢复力至关重要。然而，晚分化珊瑚家系微生物组对多尺度环境的响应和适应模式仍不清楚。本研究聚焦南海西沙群岛、南沙群岛跨越6个纬度的8个热带珊瑚礁，以石芝珊瑚科（Fungiidae）较晚分化的鳞状石叶珊瑚（*Lithophyllon scabra*；分化于13.5969Ma）为研究对象，解析其共生虫黄藻（Symbiodiniaceae）与共生附生细菌群落对不同纬度、岛礁以及地貌带的多尺度环境响应模式及其生态功能。结果显示：1.鳞状石叶珊瑚在大空间尺度上与压力耐受型虫黄藻C27亚系群建立特异性共生关系，其相对丰度介于59.73-67.61%，指示该珊瑚物种采用

与抗逆型虫黄藻特异性共生的方式适应多尺度环境变化；2.鳞状石叶珊瑚共生虫黄藻群落构建过程主要由稀有共生体所驱动，并在差异空间尺度上存在显著差异。共生虫黄藻群落构建的确定性过程在纬度尺度上与营养盐浓度下降相关，而在岛礁尺度和地貌带潟湖相上则分别受气候因子与高温、高盐、高溶解氧调控。此外，共生虫黄藻群落构建的随机性过程则主要受水体交换水平与扩散能力驱动。3.鳞状石叶珊瑚共附生细菌群落具有极高的灵活性，其群落构建过程在纬度、岛礁及地貌带间完全由确定性过程占据主导。在纬度与岛礁尺度上，多尺度环境因子对鳞状石叶珊瑚细菌群落结构的影响模式符合“皮尔·卡丹准则”（Pierre Cardin Principle；PCP），即环境因子独立作用对细菌群落结构的生态影响要显著高于耦合作用。而鳞状石叶珊瑚细菌群落对环境压力的响应模式则符合“安娜·卡列尼娜准则”（Anna Karenina Principle；AKP）；4.鳞状石叶珊瑚共附生细菌群落功能特征在外礁坡与潟湖之间存在显著差异。潟湖中的珊瑚共附生细菌群落具备更强的氮代谢（氮代谢、反硝化作用）与光合自养能力，而外礁坡则呈现出更高丰度的异养营养（化能异养、有氧化能异养）与抗菌潜能，指示鳞状石叶珊瑚可通过调节共附生细菌群落营养模式与功能组成以适应地貌带环境变化。本研究揭示了南海鳞状石叶珊瑚微生物组对纬度、岛礁以及地貌带的多尺度环境响应模式，为深入理解晚分化珊瑚家系微生物组的生态互作机制及其对气候适应策略提供了新的见解。

论文信息：Biao Chen, Lin Liang, Kefu Yu*, Yuxin Wei, Xinyue Liang, Zeming Bao, Zhiheng Liao, Xiaopeng Yu, Zhenjun Qin, Lijia Xu, Yongzhi Wang, Yaru Kang, Microbiome dynamics and multiscale environmental response patterns of later-diverging coral clade across latitudes, reefs and geomorphological zones in the South China Sea. *Ecological Informatics*. 2025,90, 103244. doi: 10.1016/j.ecoinf.2025.103244.

※ **《Global and Planetary Change》：**厄尔尼诺—南方涛动（El Niño–Southern Oscillation，ENSO）是全球年际气候变率的主导模态，对自然环境与人类社会产生深远影响。然而，对ENSO在全新世时期的演变特征的认识仍存在较大的缺陷，

限制了对其长期机制的理解。本研究以南海北部采集的113段化石滨珊瑚和1段现代滨珊瑚（*Porites lutea*）为研究材料，基于铀系测年和X射线影像揭示的珊瑚年生长纹层信息，构建了一条覆盖5829–2643 a BP时间跨度达2203年的年分辨率珊瑚生长率序列，并据此定量重建了该时段的年平均海表温度（Sea Surface Temperature，SST）及ENSO变率。研究结果表明，重建的年均SST在24.2–27.5℃范围内波动，其均值为25.6 ± 0.4℃，比1982–2023年的实测SST低～0.7℃。在此期间（5829–2643 a B），至少出现了14个暖期与18个冷期，其中冷期的演变呈现出～200年的准周期性特征；ENSO变率表现出多尺度波动，从中全新世（~5800–4200 a BP）整体弱于现代（1994–2023年）的类La Niña态转变为晚全新世（~4200–2600 a BP）强于现代的类El Niño态。进一步分析表明，气候系统内部动力学（特别是海洋—大气相互作用）在驱动中晚全新世ENSO变率非线性演化过程中发挥主导作用。

论文信息：Huang Dahua, Yu Kefu, Jiang Leilei, Jiang Wei. ENSO variations during the mid- to late Holocene: Evidence from coral growth rates spanning 2203 years in the northern South China Sea. *Global and Planetary Change*, 2025, 257: 105259. https://doi.org/10.1016/j.gloplacha.2025.105259.

※ **《Global and Planetary Change》：**晚全新世（~4200 cal yr BP 至今）是地球系统从自然主导转向人类活动强化影响的关键转型期，火活动作为重要生态驱动因子，通过森林砍伐、刀耕火种农业等人类活动深刻改变全球生态系统。中国云贵高原位于印度夏季风与东亚夏季风交汇区，地形复杂（喀斯特地貌为主）、生物多样性丰富，是研究古气候-植被-人类互动的天然实验室。该区域晚全新世火活动与生态系统变化已被部分研究关注，但存在明显局限：一是地理覆盖不均，贵州西部相较于云南等地研究薄弱，限制了区域规律的认知；二是对气候变率与人类活动的相对贡献量化不足，尤其是人类活动成为主导驱动的时间节点不明确；三是生物多样性对复合驱动因素的响应模式尚未厘清。贵州西部娘娘山湿地作为贵州西部最大的泥炭沼泽湿地，具备连续沉积、高分辨率的优势，为填补上述空白提供了理想的天然档案。该研究以贵州西部娘娘山湿地泥炭岩芯为载体，通过

高分辨率花粉、炭屑、粒度等多指标分析，辅以 PCA 主成分分析与稀疏度生物多样性量化，重建了过去 3400 年植被演化、火活动历史与人类-环境互动过程，揭示了亚热带季风区生态系统对气候变率和人类活动的响应机制。研究明确中全新世适宜期在该区域持续至~3200 cal yr BP，地形对季风减弱的缓冲作用使常绿林存续更久，明清时期人类活动成为生态系统转型的关键阈值，打破了自然气候的调控作用。科学上，该研究填补了贵州西部晚全新世高分辨率古生态研究空白，建立了亚热带季风区 “气候-植被-火-人类” 互动范式，完善了多指标古环境重建方法；现实意义上，揭示的长期生态系统响应规律，为西南喀斯特地区植被恢复、生物多样性保护提供了历史参照，也为未来气候波动下的生态韧性预测和可持续管理提供了科学依据。

论文信息： Yuanfu Yue, Shixiong Yang*, Liuying He, Zhuo Zheng, Xiao Zhang, Cong Chen, Qiuchi Wan, Yongjie Tang, Kangyou Huang, Fang Gu. Vegetation ecosystem responses to climate-human interactions since the Late Holocene from peat record of Niangniang Mountain, western Guizhou. *Global and Planetary Change*, 2025, 257: 105238. https://doi. org/10. 1016/j. gloplacha. 2025. 105238.

（五）学术交流

实验室本年度参加学术会议交流 39 场次（284 人次），其中国内会议 34 场次（227 人次）、国际会议 5 场次（57 人次）；合计开展会议报告 183 人次（国际会议 46 人次），其中特邀报告 9 人次（国际会议 3 人次），口头报告 145 人次（国际会议 19 人次），展板报告 38 人次（国际会议 27 人次）。

实验室本年度邀请国内知名专家学者讲学 14 场次（18 人次），包括美国亚利桑那州立大学终身教授、生命科学与可持续发展学院杰出教授邬建国，中国科学院海洋研究所所长、中国科学院大学海洋学院院长王凡，广西壮族自治区海洋局党组成员、副局长宁向军，三沙航迹珊瑚礁保护研究所所长傅亮等。

此外，实验室本年度主办/承办/协办学术会议 8 场次，包括第八届地球系统科学大会、国家重点研发计划“地球系统与全球变化”重点专项“热带西太平洋全新世高分辨率气候

变化重建、集成和同化研究”项目 2025 年度进展暨学术研讨会、国家自然科学基金重大项目“印太交汇区物质能量汇聚中心海洋环境与生态过程的耦合作用和生态效应”2024 年度总结暨学术交流会、三沙市永乐龙洞保护站工作研讨会等。

（六）出海科考

本年度实验室“蓝色梦想”科考团队共组织赴南海东北部、西沙群岛、南沙群岛、中沙群岛、吕宋海峡、菲律宾海和密克罗尼西亚南部等地科考共计 6 航次（含基金委 2025 年西太平洋共享航次，NORC2024-09），累计 132 天、11 人次，总航程 13050 海里（24169 公里），累计完成礁区生态调查、表层海水和沉积物采集站位 159 站，布设生态调查样线 251 条，共计拍摄了样线录像 2065 分钟、样方照片 11725 张、底栖特写照片 4701 张，采集造礁石珊瑚样本 67 种 5408 份、礁栖生物样本 102 份、礁区海水滤膜样本 211 份、礁区表层沉积物样本 88 份，极大地丰富了实验室南海珊瑚礁样品库的样本和数据，为开展珊瑚礁生态系统对全球变化的响应与适应机制提供了新的研究材料。同时，珊瑚礁科考强化了实验室与生态环境部、国家海洋环境监测中心、生态环境部华南环境科学研究所、三沙市海洋和渔业局、三沙市海洋保护区管局和三沙航迹珊瑚礁保护研究所等单位的合作研究与协同创新。







实验室“蓝色梦想”科考团队 2025 年的珊瑚礁科学考察

左上：实验室 2015 年第一次登上黄岩岛开展科学考察；右上：实验室 2025 年再次登上黄岩岛开展科学考察；左中：基金委西太平洋共享航次（NORC2024-09）；右中：西沙群岛晋卿岛永乐龙洞海域综合科学考察；左下、右下：南海珊瑚礁水下考察。

（七）人才引进

本年度引进刘珊教授、王刘炜博士、李正浩博士和黄硕文博士等 4 名教师：

（1）刘珊

刘珊，博士毕业于中国科学院大学，理学博士，主要围绕河口、海湾、珊瑚礁等典型海洋生态系统，结合野外调查、室内模拟、模型估算等手段，基于靶向和非靶向分析方法，构建快速精准的新污染物（类固醇激素、橡胶添加剂、抗生素、微塑料等）的定量分析技术，甄别其关键组分，开展典型新污染物的环境地球化学行为和生态风险评估等研究工作。曾主持或参与国家自然科学基金、科技基础资源调查专项、国家重点研发计划课题和国家高端智库重点研究项目等 10 余项科研项目。以第一作者/通讯作者在 Environmental Science & Technology，Water Research，Journal of Hazardous Materials 等期刊发表 SCI 论

文 20 余篇，迄今总被引 6000 余次；参与编写英文专著 2 部、中文专著 1 部。担任 Fishes、Water Emerging Contaminants & Nanoplastics 和 Journal of Environmental Exposure Assessment 期刊编委。

代表论文：

[1] Li-Jun Zhou, Shan Liu*, Man Wang, Nian-Nian Wu, Ru Xu, Li-Ni Wei, Xiang-Rong Xu, Jian-Liang Zhao, Peng Xing, Huabing Li, Jin Zeng, Qinglong L. Wu*. Nationwide occurrence and prioritization of tire additives and their transformation products in lake sediments of China. *Environment International*, 2024, 193, 109139.

[2] Li-Ni Wei#, Nian-Nian Wu#, Ru Xu, Shan Liu*, Heng-Xiang Li, Lang Lin, Rui Hou, Xiang-Rong Xu, Jian-Liang Zhao*, Guang-Guo Ying. First Evidence of the Bioaccumulation and Trophic Transfer of Tire Additives and Their Transformation Products in an Estuarine Food Web. *Environmental Science & Technology*, 2024, 58, 6370-6380.

[3] Yuan Liu, Nian-Nian Wu, Ru Xu, Zhi-Hua Li*, Xiang-Rong Xu, Shan Liu*. Phthalates released from microplastics can't be ignored: Sources, fate, ecological risks, and human exposure risks. TrAC Trends in Analytical Chemistry, 2024, 179, 117870.

[4] Nian-Nian Wu, Shan Liu*, Ru Xu, Qian-Yi Huang, Yun-Feng Pan, Heng-Xiang Li, Lang Lin, Rui Hou, Yuan-Yue Cheng, Xiang-Rong Xu*. New insight into the bioaccumulation and trophic transfer of free and conjugated antibiotics in an estuarine food web based on multimedia fate and model simulation. *Journal of Hazardous Materials*, 2024, 465, 133088.

[5] Ru Xu, Shan Liu*, Yun-Feng Pan, Nian-Nian Wu, Qian-Yi Huang, Heng-Xiang Li, Lang Lin, Rui Hou, Xiang-Rong Xu*, Yuan-Yue Cheng. Steroid metabolites as overlooked emerging contaminants: Insights from multimedia partitioning and source–sink simulation in an estuarine environment. *Journal of Hazardous Materials*, 2024, 461, 132673.

[6] Ru Xu, Shan Liu*, Hui Chen, Qin-Wei Hao, Yong-Xia Hu, Heng-Xiang Li, Lang Lin, Rui Hou, Bing Hong, Shen Yu, Xiang-Rong Xu. An effective tool for tracking steroids and their metabolites at the watershed level: Combining fugacity modeling and a chemical indicator. *Environmental Pollution*, 2023, 326, 121499.

[7] Shan Liu, Ru Xu, Yun-Feng Pan, Qian-Yi Huang, Nian-Nian Wu, Heng-Xiang Li, Lang

Lin, Rui Hou, Xiang-Rong Xu*. Free and conjugated forms of metabolites are indispensable components of steroids: The first evidence from an estuarine food web. *Water Research*, 2023, 235, 119913.

[8] Shan Liu, Fei Tian, Yun-Feng Pan, Heng-Xiang Li, Lang Lin, Rui Hou, Lin-Bao Zhang, Zhe Zhang, Shuang-Shuang Liu, Xiang-Rong Xu, Yuan-Yue Cheng, Hai-Gang Chen*. Contamination and ecological risks of steroid metabolites require more attention in the environment: Evidence from the fishing ports. *Science of the Total Environment*, 2022, 807, 150814.

[9] Shan Liu, Yun-Feng Pan, Heng-Xiang Li, Lang Lin, Rui Hou, Zhen Yuan, Peng Huang, Ming-Gang Cai, Xiang-Rong Xu*. Microplastic pollution in the surface seawater in Zhongsha Atoll, South China Sea. *Science of the Total Environment,* 2022, 822, 153604.

[10] Shan Liu, Haochang Su, Heng-Xiang Li, Jin-Jun Liu, Lang Lin, Xiang-Rong Xu*, Lin-Zi Zuo, Jian-Liang Zhao*. Uptake, Elimination, and Biotransformation Potential of a Progestagen (Cyproterone Acetate) in Tilapia Exposed at an Environmental Concentration. *Environmental Science & Technology*, 2019, 53, 6804-6813

（2）王刘炜

王刘炜，博士毕业于清华大学，理学博士，主要从事水土环境污染的老化机制、迁移归趋与长效风险管控相关研究，近 5 年以第一作者在 Environmental Science &Technology、Water Research 等期刊发表学术论文 24 篇，含 5 篇 Nature Index 期刊论文，其中有 2 篇 Environmental Science &Technology 封面论文、1 篇 Environmental Science &Technology 年度最佳论文、8 篇入选 ESI 高被引论文（引用量前 1%）、3 篇入选 ESI 热点论文（引用量前 0.1%）。迄今论文总被引 3811 次。相关成果被 Nature、《中国科学报》、中央人民广播电台、美国《新闻周刊》（Newsweek）等国内外百余家知名媒体报道。至今获授权发明专利 7 项（完成成果转化 2 项）并取得软件著作权 3 项。迄今多次入选斯坦福大学全球前 2%顶尖科学家榜单，曾获黑龙江省水利科学技术奖一等奖和日内瓦国际发明展银奖。

代表论文：

[1] Liuwei Wang, Caide Huang, Junhao Cao, Pingfan Zhou, Siqi Han, Guangyu Qu, Michael S.

Bank, Deyi Hou*. Polymer type, oxidation, size, and abundance of microplastics in subsoils versus topsoils with varying land use in Beijing, China. *Environmental Science & Technology*, 2025,59, 12933-12946.

[2] LiuweiWang, JingGao, WeiminWu, JianLuo, MichaelS.Bank, AlbertA.Koelmans, JohnJ.Boland, DeyiHou*. Rapid generation of microplastics and plastic-derived dissolved organic matter from food packaging films under simulated aging conditions. *Environmental Science & Technology*, 2024, 58, 20147-20159.

[3] WLiuweiWang, MichaelS.Bank, JörgRinklebe, DeyiHou*. Plastic-rock complexes as hotspots for microplastic generation. *Environmental Science & Technology*, 2023,57, 7009-7017.

[4] LiuweiWang, PengfeiLi, QiZhang, WeiminWu, JianLuo, DeyiHou*. Modeling the conditional fragmentation-induced microplastic distribution. *Environmental Science & Technology*, 2021,55, 6012-6021.

[5] Liuwei Wang, David O'Connor, Jörg Rinklebe, Yong Sik Ok, Daniel C.W. Tsang, Zhengtao Shen, Deyi Hou*. Biochar aging: Mechanisms, physicochemical changes, assessment, and implications for field applications. *Environmental Science & Technology*, 2020.54, 14797-14814.

[6] Liuwei Wang, Jiameng Guo, Huixia Wang, Jian Luo, Deyi Hou*. Stimulated leaching of metalloids along 3D-printed fractured rock vadose zone. *Water Research*, 2022,226, 119224.

[7] Jing Gao, Liuwei Wang, Yong Sik Ok, Michael S. Bank, Jian Luo, Weimin Wu, Deyi Hou*. Nanoplastic stimulates metalloid leaching from historically contaminated soil via indirect displacement. *Water Research*,2022, 218, 118468.

[8] Liuwei Wang, Deyi Hou*. Plastistone: An emerging type of sedimentary rock. *Earth-Science Reviews*, 2023,247, 104620.

[9] Liuwei Wang, Jing Guo, Michael S. Bank, Lukas Van Zwieten, Nanthi S. Bolan, Weimin Wu, Deyi Hou*. Organo-mineral interaction between plastic film and sedimentary rock induced by UV irradiation. *Chemical Geology*, 2024,662, 122240.

[10] Liuwei Wang, Jiameng Guo, Daniel C.W. Tsan, Deyi Hou *. Cadmium isotope fractionation during sorption to soil minerals: Lab evidence and field implication. *Chemical Geology*, 2023,634, 121607.

（3）李正浩

博士毕业于南京信息工程大学，理学博士，主要从事海洋光学、海洋水色遥感和海洋生态环境监测等相关领域研究。研究兴趣包括海洋浮游植物群落结构和初级生产力卫星遥感、海洋水体光学特征机理、海岸带水质环境监测等。近五年在国内外权威期刊先后发表论文 17 篇，其中以第一作者在 Science Advances 发表论文 2 篇（2024、2025 年），Global Change Biology 发表论文 1 篇。获得授权发明专利 1 项。目前担任 Earth's Future 等国内外权威期刊审稿专家。曾获得中国遥感优秀成果奖一等奖（2023 年）、二等奖（2025 年），上海海洋科学技术奖二等奖，江苏省海洋学会科学技术奖一等奖等奖励。

代表论文：

[1] Zhenghao Li, Deyong Sun*, Shengqiang Wang, Yu Huan, Hailong Zhang, Yibo Yuan, Yijun He.. Satellites reveal hotspots of ocean changes in the early 21st century. *Science Advances*, 2025,11 (23), eads0307

[2] Zhenghao Li, Deyong Sun*, Shengqiang Wang, Yu Huan, Hailong Zhang, Yibo Yuan, Yijun He. Ocean-scale patterns of environment and climate changes driving global marine phytoplankton biomass dynamics. *Science Advances,* 2024,10 (45), eadm7556

[3] Zhenghao Li, Deyong Sun*, Shengqiang Wang, Yu Huan, Hailong Zhang, Yibo Yuan,, Jianqiang Liu, Yijun He. A global satellite observation of phytoplankton taxonomic groups over the past two decades. *Global Change Biology*, 2023,29, 4511-4529

[4] 李正浩, 陈志钊, 王力彦, 孙德勇, 赵彬如, 和王胜强. 结合GOCI数据反演近海浮游植物叶绿素和类胡萝卜素浓度. 光学学报, 2021,41, 7-17

（4）黄硕文

黄硕文，博士毕业于武汉大学，工程博士，毕业于武汉大学遥感信息工程学院，主要从事人工智能遥感数据处理方法、海洋三维重建和遥感监测、测绘装备研发等相关领域研究。近5年发表学术论文12篇，其中第一或通讯作者8篇（中国科学院一区2篇）。担任Automation in Construction和IEEE Geoscience and Remote Sensing Letters等国际期刊审稿专家。曾参与国家重点研发计划专项、国家自然科学基金和社会科学基金等项目。作为核心成员参与相关机载激光雷达、手持扫描仪等装备的软硬件研发，产品出口德国、美国等国家，累计销售千余套，产生经济效益超千万元。

代表论文：

[1] Shuowen Huang, Qingwu Hu*, Pengcheng Zhao, Mingyao Ai, Wenwu Ou, Jiayuan Li, Shaohua Wang. Dynamic street scene 3D reconstruction with self-supervised Gaussian Splatting using spatiotemporal deformation field. *Big Earth Data*, 2025.2595830.

[2] Shuowen Huang, Qingwu Hu*, Pengcheng Zhao, Mingyao Ai, Xujie Zhang, Wenwu Ou, Linze Li. 3D reconstruction for unconstrained image collections using Gaussian Splatting with foundation model. *Geo-spatial Information Science*, 2025: 1-14

[3] Yunqiang Li, Shuowen Huang#, Ying Chen, Yong Ding, Pengcheng Zhao, Qingwu Hu*, Xujie Zhang. RGBTSDF: an efficient and simple method for color truncated signed distance field (TSDF) volume fusion based on RGB-D images. *Remote Sensing*, 2024, 16(17): 3188.

[4] Yunqiang Li, Shuowen Huang#, Ying Chen, Yong Ding, Pengcheng Zhao, Qingwu Hu*, Xujie Zhang. RGBTSDF: an efficient and simple method for color truncated signed distance field (TSDF) volume fusion based on RGB-D images. *Remote Sensing*, 2024, 16(17): 3188.

[5] Shuowen Huang, Qingwu Hu*, Pengcheng Zhao, Jiayuan Li, Mingyao Ai, Shaohua Wang. ALS point cloud semantic segmentation based on graph convolution and transformer with elevation attention. *IEEE Journal of Selected Topics in Applied Earth Observations and Remote Sensing*, 2023, 17: 2877-2889.

[6] Jian Li, Shuowen Huang*, Hao Cui, Yurong Ma, Xiaolong Chen. Automatic point cloud registration for large outdoor scenes using a priori semantic information. *Remote Sensing*, 2021, 13(17): 3474.

（八）人才培养

1.骨干教师培养

本年度新增人才称号 12 人次、学术组织任职 12 人次和学术期刊任职 14 本。其中，余克服教授入选广西人才小高地；刘珊博士、王丽伟博士、左秀玲博士、陈飚博士和巩三强博士入选自治区重大人才项目；徐向荣入选南宁市 A 层次人才，黄雯入选南宁市 B层次人才，俞小鹏博士、郭泽军博士、吴琪博士入选南宁市 D 层次人才；新增王丽伟博士晋升教授，邓珊珊博士和黄爱国博士晋升副教授；新增王刘炜博士担任 *Soil Use and Management* 和 *Environmental Geochemistry and Health* 期刊副主编，刘珊博士担任 *Water*

Emerging Contaminants & Nanoplastics 、 *Fishe*s 和 *Journal of Environmental Exposure Assessment* 期刊编委；新增徐向荣教授担任中国生产力促进中心协会海洋分会主任委员，江蕾蕾博士担任中国第四纪科学研究会专业委员会-历史时期气候变化专业委员会委员，左秀玲博士担任广西遥感学会常务理事等。

此外，余克服教授、徐向荣教授和王丽伟博士入选了美国斯坦福大学和国际权威学术出版社爱思唯尔共同发布的全球前 2%顶尖科学家榜单“年度科学影响力排行榜”。其中，余克服教授和徐向荣教授同时入选“终身科学影响力排行榜”，且还双双入选爱思唯尔“中国高被引学者年度榜单”。

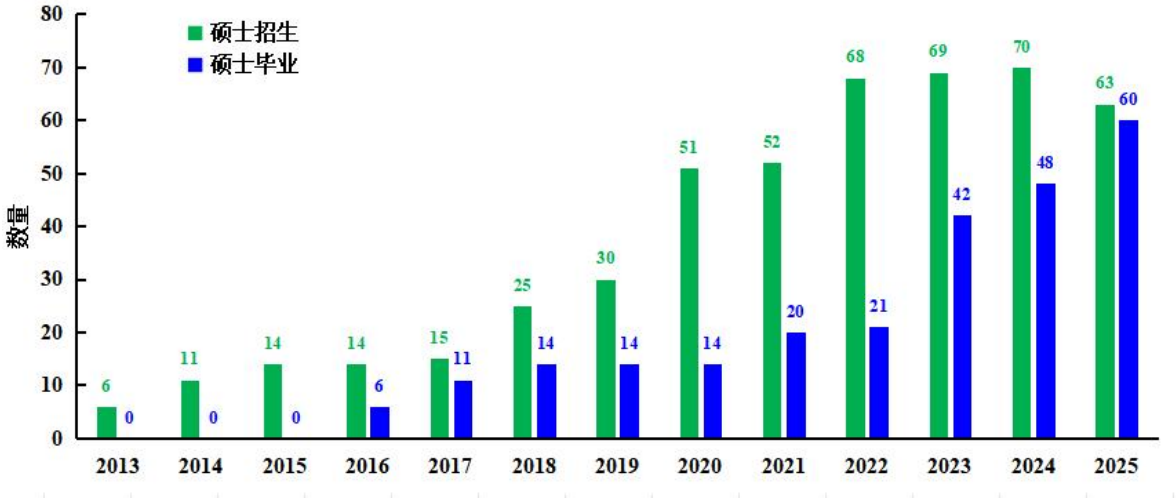
2.研究生培养

实验室 2025 年招收硕士研究生 63 人（海洋科学 44 人、环境工程 19 人），招收博士研究生 11 人（海洋生物资源与环境保护），招收博士后 1 人。毕业硕士学位研究生 61 人（海洋科学 39 人、环境工程 22 人），毕业博士学位研究生 4 人（海洋生物资源与环境保护）。

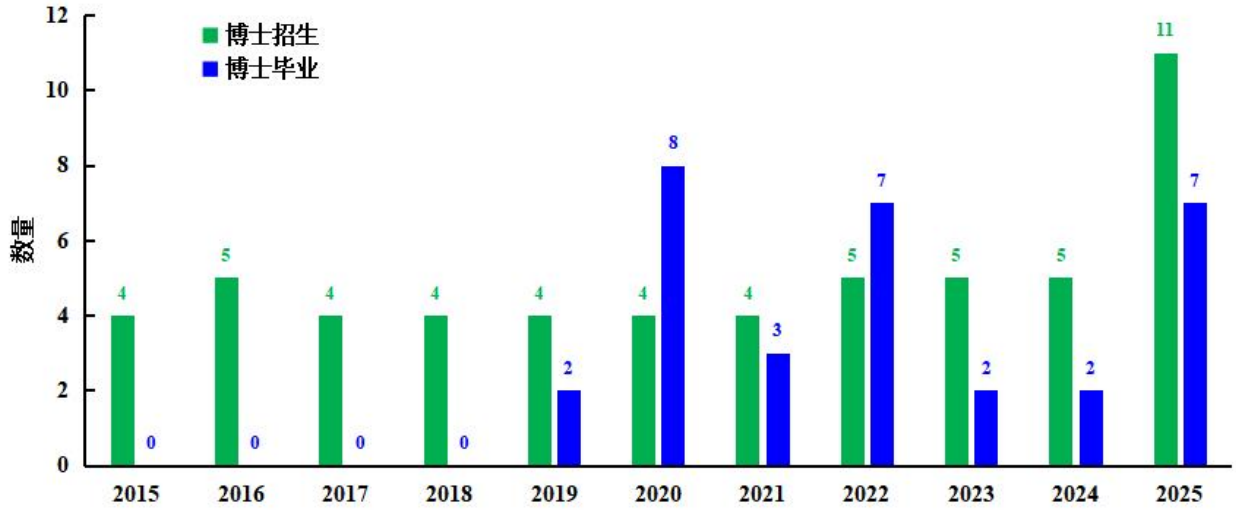
毕业研究生中，获得优秀博士学位论文 2 篇（南海珊瑚礁区有机磷酸酯的时空分布、环境行为及对珊瑚的毒性效应，康亚茹；基于 qPCR 技术的钦州湾球形棕囊藻游离单细胞分布及其控制因子研究，王佳乐）和优秀硕士论文 4 篇（三氯生对澄黄滨珊瑚的毒理效应及机制研究，梁浩；南海典型珊瑚礁区海水和沉积物磷的赋存形态、分配行为和吸附解吸特征，刘志金；多尺度系统对中国夏季大气河的影响及其极端降雨效应，杨凯；西沙群岛琛科 2 井晚中新世-早上新世脂类分布特征及其古海洋环境响应，黄建容）；获得区级优秀毕业生 1 人（博士 1 人：康亚茹）、校级优秀毕业生 5 人（博士 2 人：康亚茹、陈健；硕士 3 人：罗兰、黄思宇、包泽铭）；获得校长奖学金 1 人（博士 1 人：康亚茹）。获得首届联合国“海洋十年”海洋生态保护修复大赛“海洋十年”中国行动国际合作种子重大项目 1 项（谭何勇、彭梦娇、王明威、刘书萌、许辉、陆晔、徐烨、劳子彤、徐明培、周榆鹏、王永刚）。

研究生参加国内外学术会议交流约 70 人次，典型包括：第八届地球系统科学大会，40 多名研究生积极参加（黄达华获“优秀学生展板”奖）；第六届“未来科学家”全国研究生“海洋与气候”学术论坛，共 2 名学生积极参加（研究生梁馨月获“最佳墙报奖”

奖和“优秀口头报告三等奖”，李炫霖获“优秀墙报”奖）；第三届海岸带大会，共有 6 名师生积极参加（余芷丽获“优秀报告”奖）。



历年硕士研究生培养情况



历年博士研究生培养情况

实验室研究生培养充分利用珊瑚礁系统科学研究特色，采用理论与实践相结合的理念，成效显著，因而在本年度获得广西大学高等教育（研究生）教学成果特等奖。目前，该成果正在参加广西高等教育（研究生）教学成果奖的评定。



广西大学高等教育（研究生）教学成果等次

证　书

为表彰2025年广西大学高等教育（研究生）教学成果等次的获得者，特颁发此证书。

成 果 名 称：基于南海岛礁特色的海洋科学研究生培养体系的构建与实现路径

主要完成人：余克服、梁甲元、黄荣永、徐向荣、黄　雯、姜　伟、左秀玲、苏宏飞、张瑞杰、雍阳阳、王　瑞、俞小鹏、陈　飚、王丽伟、裴继影、江红蕾、黄学勇、周　剑

主要完成单位：海洋学院

等　　次：特等

证 书 编 号：GXU-Y-T-2025006

广西大学

2025年6月12日

广西大学高等教育（研究生）教学成果特等奖

3.储备人才培养

实验室基于“科教融合、师生互惠”的理念，将科研资源转化为教学资源，让本科生在导师指导下 100%参与导师的科研项目、100%进实验室、100%参与创新实践活动，取得了显著成效：

（1）《珊瑚礁科学概论》入选**国家级一流本科课程**；

（2）本科生读研率达到 41.6%，获得区级优秀毕业生 1 人（赖秋月）、校级优秀毕业生 7 人（赖秋月、于尚科、黄旗旗、宋紫文、刘缘、蒋孟芸、秦子阳），获得校长奖学金 1 人（赖秋月）；

（3）本科生结题“大学生创新创业训练项目”13 项（含优秀结题 4 项），新增“大学生创新创业训练项目”项目 14 项（国家级 5 项、自治区级 9 项）；

（4）本科生获得第八届地球系统科学大会优秀展板 1 项（张佳宇）、2025 年中国国际大学生创新大赛省级铜奖 1 项，并获得第七届高校大学生海洋与化学科技实践论坛口头报告一等奖和二等奖各 1 项（高德硕、王秋婷）；

（5）本科生参与发表学术论文 8 篇（本科生一作 3 篇），申请发明专利 1 项、实用新型专利 1 项、软件著作权 1 项；

（6）承办第二届全国海洋学教学大赛，吸引全国涉海高校 100 多名代表参加，实验室成员获二等奖 1 项、优秀奖 3 项。

此外，实验室根据《关于资助优秀本科生参加高水平学术会议和出海科学考察的规定》（https://shj.gxu.edu.cn/info/1068/3514.htm），本年度择优资助了 1 名本科生（张佳宇）参加第八届地球系统科学大会并获“优秀学生展板”奖。

4.在读研究生列表

序号	导师姓名	硕士生	博士生
1	乐远福	张博、袁欣萌、黄代钊	无
2	任幸	路霄杰	无
3	余克服	黄俞文、罗伟霖、韦競、彭梦娇、谭荣华、王健雄、钟云清、李炫霖、张楚卉、周煦、方心怡、何燃、林雪姣、马洪林、苏琥、王若谷	向柯宇、夏荣林、崔梦瑶、马静、滕君灿、高洁、李雨箫、黄达华、肖竣友
4	俞小鹏	马玉玲、郑月、杨兰、陆安馨、覃至辉	无
5	关瑶	黄曼玉	无
6	刘珊	张廷超	何佳利
7	吴司琪	李玫、李钰涵、黄雨洁	无
8	唐兴颖	覃祖安、张莹莹、解贵元、黄琳程、冯一茗、李科、吴雨萌、卢恺富、王玉婷、林玉升、何海锋、蒋林海、刘文静	无
9	喻达辉	无	桑秀秀
10	姚作芳	覃正宇、潘袁乐、田顺鑫	无
11	姜伟	刘彩凤、杜思琦、杨婷、孙瑞朋、曾洋、江昱燕、石宇辰、欧阳慧	郭宁、顾庭舞
12	宋宜	王佳宝、覃齐、廖书昕	无
13	左秀玲	罗盛、黎蔚琪、梁宏业、余芷丽、元剑南、钟莹莹、李帅	蓝斐芜、李志文
14	巩三强	黄蕾蕾、庞骁、曾璐佳、曾峻森	邢清淦
15	张媛媛	李旭东、薛鹏飞、韦泽福、卓儀俐、梁芳雨、程元勋	无

16	张瑜	原雅琪、俞欣甜、张振涛	无
17	张瑞杰	刘环鑫、杨昕谕、莫立伟、秦贵帮、孙卓珑、段永辉、纪哲鸿、韦盼、叶全发、伊喆	无
18	徐向荣	韦益善、杨欣、李昊天、赵梓睿	甘品、梁翠珠
19	林武辉	王一潼、刘晨	无
20	梁作栋	陈海伦、刘大军、覃河融、梁钦皓	无
21	梁甲元	胡思雨、梁祝清、卢铭垚、蔡圣海、冯宜合、石文杰、卢毅	无
22	江红蕾	任天飞、朱桂涛、郭裕、郭宝彤	无
23	江蕾蕾	赵佰玲、黄紫云	无
24	潘长桂	陈济迅、谢镇桐、梁译、廖彪、韦柳亦、罗丽媛、吴晓君、赵宇航	胡俊杰
25	王丽伟	朱振宇、吴可欣、万仕伟、许辉	无
26	王广华	王辰燕、黄金生、丁夏芬	李蜜
27	王瑞	吴松烨、花绘、邓筱晟	无
28	王英辉	何伟豪、谢凌君、黄成立、麦旭志、韦雪敏、罗松林、韦顺强、王梓睿、徐丹丹、徐伟峰、方世伟、李树、黄泽涛	王文欢、邓淞文、何建乔、黄佳升、吴文乾
29	苏宏飞	陈凡、秦晓、孙非龙、汪韦辉、邹杰、刘名定	无
30	范天来	吴观生、马晓玲	无
31	裴继影	余文峰、李童、谢铭轶、苏琼、徐德泽、农春妮、贤爱华	无
32	覃祯俊	韦丽菲、阳琪芝、张毓琳、罗涛	无
33	邓珊珊	胡安戈、赵治文、晏安钦	无

34	郭泽军	李展泓、张逸轩、陈喜、黄骞	无
35	陈小燕	闫兆千、黄世龙、武茁、熊志祥、杨艳彬	刘珂、吴艳柳
36	陈飚	梁林、梁馨月、黄堉杰	无
37	雍阳阳	蓝弋朝、杨诗语、吴子同、张虞	无
38	韦芬	玉颢瑜、唐柳格、莫云杰	无
39	马笑晚	黄云帆、张志鹏	无
40	黄爱国	韦炎钦、马振涛、易楚顺、曾繁晟、韦婷玉、黄家龙、陈国豪	无
41	黄荣永	鲁宇贤、曾仕卿、杨享运、陈兆年	无
42	黄钦	赵凌楠、余松易	无
43	黄雯	王明威、谭何勇、徐烨、黄光贤、宛强、刘书萌、周兴旺、何玉洋	无
44	黄鹄	无	周姣娣
45	宁志铭	周志恒	无
46	陈正华	曾俊杰	无
47	张曼	温倍华	无

5.毕业研究生列表

序号	导师姓名	硕士生	博士生
1	余克服	伍锐	康亚茹、陈健
2	俞小鹏	陈俊伶	无
3	吴司琪	黄晓婷	无
4	唐兴颖	朱日广、陈积权、王智洁、薛宇阳	无

5	姜伟	肖玉雯、张兆琳	无
6	宁志铭	刘志金	无
7	宋宜	黄建容	无
8	左秀玲	段晓鹏、邱妮珊	无
9	张媛媛	甘品、罗兰	无
10	张瑜	周宇	无
11	张瑞杰	谢松霖、沈红双、王镜宇、王馨怡	无
12	林武辉	黄思宇、罗柱、张翊邦	无
13	梁甲元	李志聪、杨雅婷、张丽	无
14	潘长桂	周超洋、梁浩、刘珍珠	无
15	王丽伟	何雅怡、刘雅玲、张涛、张毅博	无
16	王广华	卢锟	无
17	王瑞	刘春彤	无
18	王英辉	王志燊、李尚泽、魏怡华	王佳乐、王少鹏
19	苏宏飞	何旭聪、陈祺琦	无
20	范天来	张明望	无
21	裴继影	陈仕国、张樱元	无
22	覃祯俊	蓝梦玲	无
23	邓珊珊	张雯茜	无
24	陈小燕	蒿若星、张文倩、彭润乾、吴秋昀、杜宇豪、余清	无
25	陈振华	陈旭	无
26	陈正华	李华德	无

27	陈飚	包泽铭	无
28	雍阳阳	杨凯	无
29	韦芬	潘晓媛	无
30	黄荣永	李泽琛、尹迦南	无
31	黄雯	陈锦连、黄智华、徐明培、周榆鹏	无

（九）硬件设施建设

硬件设施建设方面，本年度投入 228.5 万元用于仪器设备购置以及平台维护与升级。其中，新增设备 88 台（套），总值 220.1 万元，详情如下表所示：

序号	资产名称	型号	品牌	单价（元）
1	水肺潜水装备	定制	Mares.S.p.A	28700.00
2	水肺潜水装备	定制	Mares.S.p.A	28700.00
3	水肺潜水装备	定制	Mares.S.p.A	28700.00
4	水肺潜水装备	定制	Mares.S.p.A	28700.00
5	水肺潜水装备	定制	Mares.S.p.A	28700.00
6	无人机监测系统	大疆 350、大疆 P1、大疆 L2、华测导航 Coprocess	DJI 大疆	199260.00
7	智能无线超低温冷链监控系统	ML-4TU	中科美菱	1580.00
8	智能无线超低温冷链监控系统	ML-4TU	中科美菱	1580.00
9	智能无线超低温冷链监控系统	ML-4TU	中科美菱	1580.00
10	智能无线超低温冷链监控系统	ML-4TU	中科美菱	1580.00
11	智能无线超低温冷链监控系统	ML-4TU	中科美菱	1580.00
12	智能无线超低温冷链监控系统	ML-4TU	中科美菱	1580.00
13	智能无线超低温冷链监控系统	ML-4TU	中科美菱	1580.00
14	智能无线冷链监控系统	ML-4TH	中科美菱	1480.00
15	智能无线冷链监控系统	ML-4TH	中科美菱	1480.00
16	智能无线冷链监控系统	ML-4TH	中科美菱	1480.00

17	智能无线冷链监控系统	ML-4TH	中科美菱	1480.00
18	智能无线冷链监控系统	ML-4TH	中科美菱	1480.00
19	智能无线冷链监控系统	ML-4TH	中科美菱	1480.00
20	智能无线冷链监控系统	ML-4TH	中科美菱	1480.00
21	智能无线冷链监控系统	ML-4TH	中科美菱	1480.00
22	智能无线冷链监控系统	ML-4TH	中科美菱	1480.00
23	智能无线冷链监控系统	ML-4TH	中科美菱	1480.00
24	智能无线冷链监控系统	ML-4TH	中科美菱	1480.00
25	智能无线冷链监控系统	ML-4TH	中科美菱	1480.00
26	智能无线冷链监控系统	ML-4TH	中科美菱	1480.00
27	智能无线冷链监控系统	ML-4TH	中科美菱	1480.00
28	智能无线冷链监控系统	ML-4TH	中科美菱	1480.00
29	智能无线冷链监控系统	ML-4TH	中科美菱	1480.00
30	智能无线冷链监控系统	ML-4TH	中科美菱	1480.00
31	智能无线冷链监控系统	ML-4TH	中科美菱	1480.00
32	智能无线冷链监控系统	ML-4TH	中科美菱	1480.00
33	智能无线冷链监控系统	ML-4TH	中科美菱	1480.00
34	智能无线冷链监控系统	ML-4TH	中科美菱	1480.00
35	智能无线冷链监控系统	ML-4TH	中科美菱	1480.00
36	智能无线冷链监控系统	ML-4TH	中科美菱	1480.00
37	智能无线冷链监控系统	ML-4TH	中科美菱	1480.00
38	智能无线冷链监控系统	ML-4TH	中科美菱	1480.00
39	智能无线冷链监控系统	ML-4TH	中科美菱	1480.00
40	智能无线冷链监控系统	ML-4TH	中科美菱	1480.00
41	智能无线冷链监控系统	ML-4TH	中科美菱	1480.00
42	智能无线冷链监控系统	ML-4TH	中科美菱	1480.00
43	激光打印机	Huawei PixLab B5	华为	1900.00
44	显示器	Redmi G Pro 27U	小米	3000.00

45	笔记本电脑	MacBook Pro	苹果/Apple	34800.00
46	工作站	Precision T3680	戴尔	38549.00
47	图型工作站	T7920	戴尔	97200.00
48	备用发电机组	XM-300	扬州鑫明	399937.18
49	除湿机	DY-8220C	宁波德业	5520.83
50	双电源自动切换配电柜	定制	民尚电力	12094.60
51	灭火器	GQQ70/2.5	江苏共安	3550.12
52	灭火器	GQQ70/2.5	江苏共安	3550.12
53	配电箱	定制	民尚电力	1067.17
54	配电箱	定制	民尚电力	1067.17
55	配电柜	定制	民尚电力	4980.13
56	全波长酶标仪	Epoch	安捷伦	99000.00
57	叶绿素荧光仪	AquaPen AP110-C	PSI	28000.00
58	万分之一天平	BCE224-1CCN	赛多利斯	10500.00
59	冻干机	CTFD-18S-U	永合创信	55000.00
60	高速冷冻离心机	3K15	SIGMA	89000.00
61	不间断供电电源系统	3C3HD-300K	山特/santak	418800.00
62	空调	RF12WPdQ/NhA-N3JY01	格力	14000.00
63	不间断电源	3C3 HD-20K	山特/SANTAK	47600.00
64	不间断电源	3C15KS	山特/SANTAK	28560.00
65	笔记本电脑	MateBook 14	华为	9000.00
66	笔记本电脑	MateBook 14	华为	9000.00
67	笔记本电脑	YOGA Pro 14s 1MH9	联想	8500.00
68	笔记本电脑	Y9000P	联想	12500.00
69	笔记本电脑	ThinkBook 16+	联想	8990.00
70	笔记本电脑	ThinkBook 16+	联想	8990.00
71	LED 显示屏	C1.8PRO	超想电子	51800.00
72	超低温冰箱	DW-HL680	中科美菱	69800.00

73	超低温冰箱	DW-HL680	中科美菱	69800.00
74	冰柜	BCD-301DTECGS	中科美菱	1770.00
75	冰柜	BCD-301DTECGS	中科美菱	1770.00
76	冰柜	BCD-301DTECGS	中科美菱	1770.00
77	冰柜	BCD-301DTECGS	中科美菱	1770.00
78	冰柜	BCD-301DTECGS	中科美菱	1770.00
79	冰柜	BC/BD-408DTE	中科美菱	2170.00
80	冰柜	BC/BD-408DTE	中科美菱	2170.00
81	冰柜	BC/BD-408DTE	中科美菱	2170.00
82	冰柜	BC/BD-408DTE	中科美菱	2170.00
83	冰柜	BC/BD-408DTE	中科美菱	2170.00
84	智能人工气候箱	RDN-600B	宁波东南	17000.00
85	智能人工气候箱	RDN-600B	宁波东南	17000.00
86	旋转蒸发仪	R-300EL	瑞士 BUCHI	101000.00
87	监控电视录像机	DS-7732N-K4		1820.00
88	监控电视录像机	DS-7732N-K4		1820.00
		合计		2201136.32

三、论著列表

本年度以第一或通讯作者发表学术论文 113 篇，其中 SCI 检索 75 篇，含 JCR Q1 区 59 篇。此外，本年度正在编撰的《南海珊瑚礁与环境》已获得国家科学技术学术专著出版基金优先资助。

（一）南海珊瑚礁生物与生态方向

序号	作者	论文题目	期刊名称	级别	影响因子	JCR分区	中国科学院分区	中国科协期刊分级	是否TOP期刊
1	Zejun Guo, Siyao Liao, Chaoqun Xu, Mingyue Wei, Lingyu Song, Hezi Huang, Zhanhong Li, Xi Chen, Lei Jiang, Hailei Zheng*	Silicon enhances potassium uptake and leaf growth in Avicennia marina, asilicon-accumulating mangrove plant with silicon transporters	Industrial Crops and Products	SCI	5.6	1	1	T1	是
2	Tingyu Wei, Xuemin Wei, Jialong Huang, Songlin Luo, Aiguo Huang*	Nitrite-induced intestinal injury mechanisms and multi-organ toxicity in Tilapia: Insights from integrated multi-omics analysis	Aquaculture	SCI	3.8	2	2	T2	否
3	Biao Chen, Lin Liang, Kefu Yu*, Yuxin Wei, Xinyue Liang, Zeming Bao, Zhiheng Liao, Xiaopeng Yu, Zhenjun Qin, Lijia Xu, Yongzhi Wang, Yaru Kang	Microbiome dynamics and multiscale environmental response patterns of later-diverging coral clade across latitudes, reefs and geomorphological zones in the South China Sea	Ecological Informatics	SCI	7.3	1	2	T2	否

4	Yongqian Xu, Jiayuan Liang*, Liangyun Qin, Tianyi Niu, Zhuqing Liang, Zhicong Li, Biao Chen, Jin Zhou, Kefu Yu*	The Dynamics of Symbiodiniaceae and Photosynthetic Bacteria Under High-Temperature Conditions	Microbial Ecology	SCI	3.3	1	3	T2	否
5	Aiguo Huang, Yanqin Wei, Jialong Huang, Songlin Luo, Tingyu Wei, Jing Guo, Fali Zhang*, Yinghui Wang*	Effects of Natural Ingredient Xanthohumol on the Intestinal Microbiota, Metabolic Profiles and Disease Resistance to Streptococcus agalactiae in Tilapia Oreochromis niloticus	Microorganisms	SCI	4.1	2	2	/	否
6	Linqing Meng , Ronghua Tan, Zunyong Xiao, Jinlian Chen, Zhihua Huang, Yonggang Wang, Enguang Yang, Yupeng Zhou, Mingpei Xu, Kefu Yu, Wen Huang*	Antioxidant capacity is a key factor in the difference in thermal tolerance between massive Porites lutea and branching Acropora formosa	Marine Pollution Bulletin	SCI	5.3	1	3	T3	否
7	Tianyi Niu, Yating Yang, Sanqiang Gong, Kefu Yu, Jiayuan Liang*	Color disparity enhances the toxic effects of polystyrene microplastics on Cladocopium goreaui	Marine Pollution Bulletin	SCI	5.3	1	3	T3	否
8	Jiayuan Liang*, Liangyun Qin, Li Zhang, Yongqian Xu, Tianyi Niu, Zhicong Li, Yating Yang, Zhuqing Liang, Kefu Yu*, Sanqiang Gong	The stress response strategies of two typical coral Symbiodiniaceae (Cladocopium goreaui and Durusdinium trenchii) under abnormal temperatures	Algal Research-Biomass Biofuels and Bioproducts	SCI	4.5	1	2	/	否

9	Lifei Wei, Shuchang Chen, Zhenjun Qin*, Nengbin Pan, Mengling Lan, Tingchao Zhang, Ran He, Hongye Liang, Wenzhi Deng, Changhao Mo, Kefu Yu*	Responses of the Coral Symbiont Cladocopium goreaui to Extreme Temperature Stress in Relatively High-Latitude Reefs, South China Sea	Microbial Ecology	SCI	3.3	1	3	T2	否
10	Man Zhang, Shan Huang, Li Luo, Kefu Yu*	Environmental acclimatization of the relatively high latitude scleractinian coral Pavona decussata: integrative perspectives on seasonal subaerial exposure and temperature fluctuations	BMC Genomics	SCI	3.5	2	2	T2	否
11	Qiqi Chen, Lin Wang, Jie Li, Qiqi Li, Hongfei Su*, Zhimao Mai*	Characteristics of Carbonatogenic Bacteria and Their Role in Enhancing the Stability of Biocrusts in Tropical Coral Islands	Microorganisms	SCI	4.1	2	2	/	否
12	Zhenjun Qin*, Mengling Lan, Nengbin Pan, Kefu Yu*, Lifei Wei, Qizhi Yang, Tingchao Zhang, Ran He	Coral polyp and skeletal microbiome in tropical and subtropical reefs in the South China Sea: spatial variation and implications for coral environmental adaptability	Acta Oceanologica Sinica	SCI	1.7	3	3	T1	否
13	Mengling Lan, Kaixiang Gao, Zhenjun Qin*, Zhanhong Li, Ru Meng, Lifei Wei, Biao	Coral microbiome in estuary coral community of Pearl River Estuary insights into variation in coral holobiont	Bmc Microbiology	SCI	4	2	2	/	否

	Chen, Xiaopeng Yu, Lijia Xu, Yongzhi Wang, Kefu Yu*	adaptability to low-salinity conditions							
14	Ziyang Xian, Yayi He, Chaoxin Zhang, Hao Fu, Yaling Liu, Tao Zhang, Shaopeng Wang, Shan Lu, Man Zhang*, Liwei Wang*	Sensitive detection of early growth of Skeletonema costatum using a gold-doped carbon sphere-gold nanoparticle electrochemical biosensor	New Journal of Chemistry	SCI	2.5	3	3	/	否
15	Siyu Hu, Kun Lu, Chenyan Wang, Mi Li, Jinsheng Huang, Guanghua Wang*	Carbonatibacter coralli gen. nov., sp. nov., a carbonate-producing and vitamin B12-sharing bacterium isolated from coral Porites lutea, reclassification of Kiloniellaceae and proposal of Aestuariispiraceae fam. nov.	International Journal of Systematic and Evolutionary Microbiology	SCI	2	4	3	无	否
16	Jiayuan Liang*, Tianyi Niu, Li Zhang, Yating Yang, Zhicong Li, Zhuqing Liang, Kefu Yu*, Sanqiang Gong	Polystyrene microplastics exhibit toxic effects on the widespread coral symbiotic Cladocopium goreaui	Environmental Research	SCI	7.7	1	2	T1	是
17	Wen Huang*, Jinlian Chen, Enguang Yang, Linqing Meng, Yi Feng, Yinmin Chen, Zhihua Huang, Ronghua Tan, Zunyong Xiao, Yupeng Zhou, Mingpei Xu, Kefu Yu*	Heat-tolerant subtropical Porites lutea may be better adapted to future climate change than tropical one in the South China Sea	Science of the Total Environment	SCI	8.2	1	1	T1	是

18	张廷超，潘能斌，唐媛媛，何燃，蓝梦玲，韦丽菲，覃祯俊*	虫黄藻（Effreniumvoratum）对高温胁迫的生理响应	海南热带海洋学院学报	/	0.645	/	/	/	/
19	马玉玲，俞小鹏*，余克服*，陈俊伶，郑月，陈健	造礁珊瑚热适应相关功能基因的研究进展	海洋学报	北大核心,CSCD	1.329	/	/	T1	/
20	徐明培，黄雯*，陈锦连，黄智华，周榆鹏，宛强，李雨箫，余克服	涠洲岛四种造礁石珊瑚耐热阈值测定及其差异性对比	海洋湖沼通报	北大核心,CSCD	1.265	/	/	T3	/
21	周榆鹏，肖遵勇，陈锦连，黄智华，徐明培，谭荣华，蒙林庆，王永刚，余克服，黄雯*	美丽鹿角珊瑚(Acropora muricata)与风信子鹿角珊瑚 (Acropora hyacinthus)的耐热性差异研究	海洋学报	北大核心,CSCD	1.329	/	/	T1	/
22	苏宏飞，梁甲元，余克服*	海洋生物学进展研究生课程个性化教学改革探索与实践	科教导刊 - 电子版	/	0.297	/	/	/	/
23	何燃,高楷翔,潘能斌,李展泓,张廷超,梁宏业,卢晓燕,蓝梦玲,覃祯俊*	虫黄藻对低盐胁迫的生理响应	热带生物学报	/	1.618	/	/	/	/
24	张丽,李志聪,杨雅婷,梁祝清,冯宜合,卢铭垚,胡思雨,余克服,梁甲元*	两种环境敏感性不同的虫黄藻(Cladocopium goreaui 和 Durusdinium trenchii)的脂质代谢对热胁迫的响应模式	海洋学报	北大核心,CSCD	1.329	/	/	T1	/
25	陈凡,韦冬冬,谢瑾琨,余庆,高艳侠,黄静,何金钊,施金谷,赵明明,	两株海洋来源贝莱斯芽孢杆菌的筛选、分离鉴定及益生特性	广东海洋大学学报	北大核心,CSCD	1.765	/	/	T3	/

	覃向谋,苏宏飞*,李鹏飞*								
26	邹杰,王琳,陈祺琦,何旭聪,黄金梅,孙天奕,苏宏飞*	珊瑚源噬虫嗪降解菌的分离、鉴定及其降解特性研究	广东农业科学	/	2.159	/	/	T3	/
27	黄菲菲,崔梦瑶,韦芬*,杨溪月,潘晓媛,玉颢瑜	室内养殖条件下两种造礁石珊瑚的性腺发育研究	广西科学	北大核心	1.252	/	/	/	/
28	刘名定,蔡永超,李洁,刘青,张健,吕丽娜,苏宏飞*	一株珊瑚来源二苯甲酮-3 降解菌 Sphingopyxis terrae SCSIO 90395 的分离鉴定及基因组特征	热带海洋学报	北大核心,CSCD	1.38	/	/	T2	/
29	崔梦瑶,韦芬*,余克服*	造礁珊瑚有性繁殖的研究进展	海洋学报	北大核心,CSCD	1.329	/	/	T1	/
30	陈俊伶,马玉玲,郑月,余克服*,俞小鹏*	基于转录组学的造礁石珊瑚环境胁迫响应机制研究进展	广西科学	北大核心	1.252	/	/	/	/
31	李志聪,胡思雨,梁祝清,杨雅婷,卢铭垚,余克服,梁甲元*,张丽,冯宜合	珊瑚共生蓝藻 Synechococcus sp.GXU01 对两种典型虫黄藻的代谢协调作用	广西科学	北大核心	1.252	/	/	/	/
32	汪婷婷,周兴旺,谭何勇,肖遵勇,黄雯,胡庭俊*	涠洲岛海域 7 种造礁石珊瑚的生长差异研究	广西科学	北大核心	1.252	/	/	/	/
33	曾心茹,韦芬*,崔梦瑶,玉颢瑜,潘晓媛,余克服	基于环境 DNA 技术的造礁石珊瑚物种多样性分析 ——以涠洲岛珊瑚礁区为例	海洋环境科学	北大核心,CSCD	1.646	/	/	T2	/

（二）南海珊瑚礁地质与环境方向

序号	作者	论文题目	期刊名称	级别	影响因子	JCR分区	中国科学院分区	中国科协期刊分级	是否TOP期刊
1	Yinqiang Li, Kefu Yu*, Lizeng Bian, Baoqing Hu, Zhiheng Liao, Shengmin Huang, Zhiguang Song, Weihua Liao	Dominance of coralline algae in the South China Sea: Insights into their responses to paleoceanographic events over the last 20 million years	Palaeogeography Palaeoclimatology Palaeoecology	SCI	2.6	1	2	T2	是
2	Wei Jiang, Yuwen Xiao, Kefu Yu*, Rui Wang, Shendong Xu, Ning Guo, Tingwu Gu	Holocene coral reef carbonate REY geochemistry during the neomorphism from aragonite to calcite: A case study in the South China Sea	Palaeogeography Palaeoclimatology Palaeoecology	SCI	2.6	1	2	T2	是
3	Tingwu Gu, Wei Jiang*, Yansong Han, Chunmei Feng, Ning Guo, Caifeng Liu, Yu Zhang, Kefu Yu	High-Resolution Coral Records of Rare Earth Elements and Yttrium in Seawater Driven by Submarine Groundwater Discharge in a Basalt Island: A Case Study in the Northern South China Sea	journal of geophysical research-earth surface	SCI	3.5	1	2	T2	否
4	Siqi Wu, Risheng Liang, Kefu Yu*	The Potential of Benthic Foraminifera Carbon and Oxygen Isotopic Proxies as Environmental Indicators in Coral Reef Regions	Paleoceanography and Paleoclimatology	SCI	3.2	1	2	T1	否
5	Yu Zhang, Yaqi Yuan, Kefu Yu*	Geochemical characteristics and petrogenesis of the basaltic pyroclastic rocks from the Xisha Islands, northwestern South China Sea	Acta Oceanologica Sinica	SCI	1.7	3	3	T1	否

6	Guo Ning, Jiang Wei *, Li Yueer, Yu Kefu	Geochemical behavior of redox sensitive trace metals in marine environment and their applications as paleoredox proxies	Palaeogeography Palaeoclimatology Palaeoecology	SCI	2.6	1	2	T2	是
7	Yi Song, Thomas J. Algeo, Carlton Brett, Zhanhong Liu, Shucheng Xie*	Molecular indicators of microbial community change linked to salinity variation and terrestrial inputs during the Ordovician-Silurian transition (East-Central USA)	Chemical Geology	SCI	3.6	1	2	T1	否
8	Xiao Zhang, Yuanfu Yue*, Ziyan Zhang, Liuying He, Xinmeng Yuan, Xintian Yu, Qiuchi Wan, Cong Chen, Yongjie Tang, Zhuo Zheng, Kangyou Huang	The topographic features and sedimentary environment potentially influenced the vegetation reconstruction in southwestern China since the MIS3	Quaternary Science Reviews	SCI	3.2	1	1	T1	是
9	Lingnan Zhao, Qin Huang*, Daohui Pi, Yi Zhang, Daqing Ding, Sasmaz Ahmet	Microbially-mediated supergene dissolution and oxidization of solid manganese carbonate in the Malkantu manganese ore deposit in West Kunlun, Northwest China	Ore Geology Reviews	SCI	3.2	1	2	T1	否
10	Shendong Xu*, Hongyan Mo, Kefu Yu*, Jie Gao, Zheng Men	Seasonal Variations in Coral Lipids and Their Significance for Energy Maintenance in the South China Sea	Journal of Geophysical Research-Oceans	SCI	3.4	1	2	T1	否
11	Dahua Huang, Kefu Yu*, Leilei Jiang, Wei Jiang	ENSO variations during the mid- to late Holocene: Evidence from coralgrowth rates spanning 2203 years in the northern South China Sea	Global and Planetary Change	SCI	4	1	1	T1	是

12	Yuanfu Yue, Shixiong Yang*, Liuying He, Zhuo Zheng, Xiao Zhang, Cong Chen, Qiuchi Wan, Yongjie Tang, Kangyou Huang, Fang Gu	Vegetation ecosystem responses to climate-human interactions since the Late Holocene from peat record of Niangniang Mountain, western Guizhou	Global and Planetary Change	SCI	4	1	1	T1	是
13	臧明思,王佳宝,宋宜*,黄雯,余克服	珊瑚脂类生物标志物组成及对环境的响应：研究进展与问题	地球环境学报	CSCD	2.126	/	/	T2	/
14	乐远福*,赵毅恒,唐立超,张博,熊海仙,张雅泽	南海北部滨珊瑚微环礁的海平面指示意义及其反映的中全新世海平面历史	地球科学	北大核心,EI,CSCD	4.582	/	/	T1	/
15	陈裕月，姜伟*，杨浩丹，余克服	近 30 年来涠洲岛海域海水磷含量变化及其影响因素——来自高分辨率珊瑚记录的证据	热带海洋学报	北大核心,CSCD	1.38	/	/	T2	/
16	姜伟，梁甲元，黄荣永，余克服*	互联网在海洋科学研究生教育中的应用：现状、挑战与应对	中国多媒体与网络教学学报	/	0.176	/	/	/	/
17	王瑞,刘春彤,吴松烨,花绘	海相碳酸盐硼同位素反演古海水 pH 值模型及其应用	石油与天然气地质	北大核心,EI,CSCD	7.149	/	/	T1	/
18	黄晓婷,李玫,吴司琪*	南海礁区大型底栖有孔虫 Mg/Ca 值微区分布及其应用潜力	微体古生物学报(中英文)	北大核心,CSCD	0.656	/	/	T2	/

19	余骄洋,俞小鹏,余克服*,马玉玲	西沙群岛太阳长棘海星（Acanthaster solaris）幽门盲囊细菌多样性及群落组成研究	热带地理	北大核心,CSCD	3.364	/	/	T3	/

（三）南海珊瑚礁环境与化学方向

序号	作者	论文题目	期刊名称	级别	影响因子	JCR 分区	中国科学院分区	中国科协期刊分级	是否 TOP 期刊
1	Minwei Han, Kefu Yu*, Ruijie Zhang, Biao Chen, Mei Xiong, Yaru Kang, Xiaopeng Yu, Zhenjun Qin, Xiangrong Xu	Organophosphate Ester Migration Mechanisms and Environmental Impacts in the Western South China Sea	Environmental Science & Technology	SCI	11.3	1	1	T1	是
2	Qianyi Huang, Rui Hou*, Yuchen Wang, Lang Lin, Hengxiang Li, Shan Liu, Xiangrong Xu*, Kefu Yu, Xiaoping Huang	Emerging and legacy organophosphate flame retardants in the tropical estuarine food web: Do they exhibit similar bioaccumulation patterns, trophic partitioning and dietary exposure?	Water Research	SCI	11.4	1	1	T1	是
3	Junjie Hu, Changgui Pan*, Xiangrong Xu*, Fengjiao Peng, Shan Liu, Jiying Pei, Zhenzhu Liu, Hao Liang, Kefu Yu	Cytochrome P450-mediated biotransformation of octocrylene in Tetradesmus obliquus Integrative insights from transcriptomics, proteomics, molecular docking, and density functional theory calculation	Journal of Hazardous Materials	SCI	12.2	1	1	T1	是

4	Liuwei Wang, Caide Huang, Junhao Cao, Pingfan Zhou, Siqi Han, Guangyu Qu, Michael S. Bank, Deyi Hou*	Polymer Type, Oxidation, Size, and Abundance of Microplastics in Subsoils versus Topsoils with Varying Land Use in Beijing, China	Environmental Science & Technology	SCI	11.3	1	1	T1	是
5	Junjie Hu, changgui Pan*, Fengjiao Peng*, Hao Liang, Zhenzhu Liu, Kefu Yu	An integrated multi-omics approach reveals octocrylene disrupts Tetradesmus obliquus growth by triggering a cascade of photosynthetic inhibition and metabolic dysregulation	Journal of Hazardous Materials	SCI	12.2	1	1	T1	是
6	Yuan Liu, Jiaming Zhou, Niannian Wu, Shan Liu*, Xiaoliang Liao, Haijiang Wu, Lin Zhu, Hengxiang Li, Lang Lin, Rui Hou, Zhihua Li, Xiangrong Xu, Zhifeng Chen*, Zongwei Cai	Targeted and non-targeted analyses reveal trophic biomagnification of rubber-derived chemicalin an estuarine food web near China's largest rubber production region	Journal of Hazardous Materials	SCI	12.2	1	1	T1	是
7	Lini Wei, Niannian Wu, Ru Xu, Yuan Liu, Shan Liu*, Haiyan Zhang, Zitong Li, Yuehong Liu, Xiangrong Xu, Jianliang Zhao*, Guangguo Ying	Rainfall, seasonal variation, and stream type governing the multi-media fate and ecological risks of tire additives and their transformation products in mega-urban streams	Water Research	SCI	11.4	1	1	T1	是
8	Jiying Pei, Qiong Su, Shuiyuan Jiang, Jianxiu Li*, Nengzhong Xie*	Exploring the structural diversity and spatiotemporal dynamics of mogrosides in Siraitia grosvenorii	Food Chemistry	SCI	9.8	1	1	T1	是

9	Julong Wang, Yan Gao, Shanshan Yao, Lang Lin*, Hengxiang Li, Shan Liu, Rui Hou, Zhijian Jiang, Xiangrong Xu*	Emerging microplastic and nanoplastic threats: Decoding winter survival mechanisms in hybrid groupers through hepatic metabolic disruption	Environmental Chemistry and Ecotoxicology	SCI	8.2	1	1	/	是
10	Rui Hou, Xiaowei Jin, Jingchun Feng*, Jingchuan Xue, Chengzhi Chen, Yuanqiang Zou, Xiangrong Xu*, Kefu Yu, Peiyuan Qian, Wei Zhang, Jizhong Zhou, Si Zhang, Zhifeng Yang	Deciphering the Universal Role of Gut Microbiota in Pollutant Transformation	The ISME Journal	SCI	10	1	1	T1	是
11	Shan Liu, Qinge Zhou, Yuan Liu, Biao Li, Huabing Li, Jixun Chen, Niannian Wu, Man Wang, Xiangrong Xu, Lijun Zhou*, Qinglong L. Wu*	Nationwide occurrence, distribution drivers, and source apportionment of steroids in China's coastal wetlands: An urgent priority for 4-andro\u0002stene-3,17-dione and progesterone	Environmental Chemistry and Ecotoxicology	SCI	8.2	1	1	/	是
12	Qiqi Huang, Jiqiao Zhang, Ziwen Song, Xianwang Deng, Songlin Luo, Weizhi Yua, Xiaofang He, Pengfei Zheng, Shaopeng Wang*, Liwei Wang*	Construction of S-type CdS@ZnIn2S4 heterojunctions with core-shell hollow nanosphere and their application in visible light photocatalytic degradation of antibiotics	Journal of Alloys and Compounds	SCI	5.8	1	2	T1	否
13	Liwei Wang, Liping Gao*, Hongjie Liu*, Qian Zhang, Hao Fu, Zhelin Liu	Constructing of Bi2O3-In2O3 nanofibers for sensitive detection of freshness gas markers in aquatic products	Journal of Alloys and Compounds	SCI	5.8	1	2	T1	否

14	Yaling Liu, Yibo Zhang, Changrui Ye, Yayi He, Shaopeng Wang, Man Zhang, Hao Fu, Shan Lu*, Liwei Wang*	Electrochemical biosensor based on strand displacement reaction for on-site detection of Skeletonema costatum	Microchimica Acta	SCI	5.4	1	2	/	否
15	Xuan Chen, Pin Gan, Kunling Huang, Fangyu Liang, Tianhao Wu, Xudong Li, Yuanyuan Zhang*	Comparison of UV based advanced oxidation processes (UV/H2O2, UV/NaClO, and UV/Na2S2O8) for inactivating Uronema marinum inmarine water	Journal of Water Process Engineering	SCI	6.3	1	3	T3	否
16	Junjie Hu, Shangke Yu, Chao Yin, Fengjiao Peng, Shuangshuang Liu, Changgui Pan*, Kefu Yu	Sorption and mechanisms of legacy and emerging per- and polyfluoroalkyl substances (PFASs) on different particle size fractions of marine sediments	Environmental Research	SCI	7.7	1	2	T1	是
17	Beihua Wen, Zhenyu Zhu, Junjie Zeng, Shiwei Wan, Chaoxin Zhang, Yingzhan Chen, Liwei Wang*, Man Zhang*, Kefu Yu	A ratiometric electrochemical DNA biosensor for the detection of crown-of-thorns starfish eDNA	Bioelectrochemistry	SCI	4.8	1	2	T2	否
18	Xiangrong Xu*, Zhen Yuan, Yanxu Zhang, Hengxiang Li, Lang Lin, Shan Liu, Rui Hou, Eddy Y. Zeng	Atmospheric transport of microplastics from land to sea is inefficient: Evidence from multimedia observations	Journal of Hazardous Materials	SCI	12.2	1	1	T1	是
19	Ru Xu, Niannian Wu, Shan Liu, Hui Chen, Qinwei Hao, Yongxia Hu, Bing Hong, Shen Yu, Xiangrong Xu*	Spatiotemporal distribution and priority assessment of steroids in the estuarine environment: Implications for environmental risk management	Marine Pollution Bulletin	SCI	5.3	1	3	T3	否

20	Yiming Feng, Xueling Hu, Yuyang Xue, Xingying Tang*, Donghai Xu, Yingying Zhang, Yumeng Wu	Hydrothermal carbonization of model compounds of municipal sludge: Effects of reaction conditions and aqueous phase recirculation	Journal of Environmental Chemical Engineering	SCI	7.2	1	2	/	否
21	Ke Li, Jiquan Chen, Guiyuan Xie, Xingying Tang*, Donghai Xu, Jianqiao Yang	A novel phosphorus segregation–driven chromium depletion mechanism for intergranular corrosion of inconel 625 in SCWO–HyMoS environments	Corrosion Science	SCI	8.5	1	1	T1	是
22	Sisi Chen, Xingying Tang*, Jiquan Chen, Yuyang Xue, Yinghui Wang, Donghai Xu	Regulation of slow-release performance of high-sugar biomass waste filter mud and sugarcane bagasse by co-hydrothermal carbonization and potential evaluation of hydrochar-based slow-release fertilizers	Biomass & Bioenergy	SCI	5.8	1	2	T3	否
23	Yumeng Wu, Jianjun Cai*, Xingying Tang*, Shubin Wang, Mingkang Fang, Shengfeng Yao, Jiafeng Zhang	Efficient and selective recovery of lithium from spent lithium-ion batteries by biomass single-component regulated pyrolysis with synergistic water leaching approach	Journal of Environmental Chemical Engineering	SCI	7.2	1	2	/	否
24	Fengjiao Peng, Ronggui Zhu, Changgui Pan*, Chaoyang Zhou, Junjie Hu, Sen Li, Xingjun Feng, Kefu Yu	Parabens and Their Metabolites in Surface Sediment from Estuaries to the Sea: Occurrence, Spatial Distribution, and Potential Sources	Acs Es&T Water	SCI	4.3	1	3	T3	否

25	Jingyu Wang, Ruijie Zhang*, Jingzhen Wang*, Liwei Mo, Zhehong Ji, Pan Wei, Chaoshuai Wei, Kefu Yu	Occurrence, spatiotemporal distribution and environmental behavior of dissolved, particulate, and sedimentary black carbon in a subtropical coastal environment: Differences between semi-enclosed and open estuaries.	Marine Pollution Bulletin	SCI	5.3	1	3	T3	否
26	Zhiming Ning, Zhijin Liu, Kefu Yu, Ronglin Xia, Wei Jiang, Bin Yang, Guodong Song*	Further increasing nitrogen concentration does not enhance the denitri cation and DNRA potentials in eutrophic reefs: Insights from the differences in benthic categories	Limnology And Oceanography	SCI	3.7	1	2	T1	否
27	Yingyuan Zhang, Deshuo Gao, Kefu Yu, Ruijie Zhang, Jiayu Zhang, Wenfeng Yu, Shiguo Chen, Jiying Pei*	3D-printed SPME-based wooden-tip mass spectrometry for rapid detection of organic ultraviolet absorbers in complex matrices	Talanta	SCI	5.6	1	1	/	是
28	Jiying Pei, Shiguo Chen, Jiayu Zhang, Wenfeng Yu, Weijie Qin, Kefu Yu*	Comparative evaluation of positive and negative LC-MS modes for DOM profiling	Analytical Methods	SCI	2.7	1	3	T2	否
29	Jiying Pei*, Shiguo Chen, Kefu Yu*, Jiayuan Liang*, Ruijie Zhang, Penghui Li, Zhuanghao Hou, Liang Fu, Honglin Ma	Microbial regulation of dissolved organic matter revealed by integrated metabolomics and metagenomics in the World's deepest blue hole	Marine Environmental Research	SCI	3	1	3	T3	否

30	Dandan Xu, Rui Xue, Mengyuan Luo, Wenhuan Wang, Wei Zhang*, Yinghui Wang*	Advances in Dissolved Organic Carbon Remote Sensing Inversion in Inland Waters: Methodologies, Challenges, and Future Directions	Sustainability	SCI	3.3	2	3	T3	否
31	Xuzhi Mai, Quan Li, Weifeng Xu, Songwen Deng, Wenhuan Wang, Wenqian Wu, Wei Zhang*, Yinghui Wang	Estimation of Mangrove Aboveground Carbon Using Integrated UAV-LiDAR and Satellite Data	Sustainability	SCI	3.3	2	3	T3	否
32	Hongshuang Shen, Fang Liu, Ruijie Zhang*, Annan Yan, Yaru Kang, Jingyu Wang, Kefu Yu	Influence of Air, Water, Light, and Salinity on Release of Plasticizers, Flame Retardants, and Ultraviolet Absorbents from Polystyrene Plastic.	Bulletin of Environmental Contamination and Toxicology	SCI	2.2	3	4	/	否
33	Fangyu Liang, Yuanyuan Zhang*	Research progress on fungi and their spore inactivation in different water bodies	Desalination and Water Treatment	SCI	1	4	4	/	否
34	Riguang Zhu, Guiyuan Xie, Zu-an Qin, Xingying Tang*, Jianjun Cai, Jianqiao Yang	Effects of dissolved oxygen accelerated P. aeruginosa on the corrosion mechanism of X70 steel in simulated marine environments	Materials Chemistry and Physics	SCI	4.7	2	3	T2	否
35	Jiquan Chen, Zitao Lin, Xingying Tang*, Ke Li, Riguang Zhu, Jianqiao Yang	Comparative study of the corrosion behavior of Inconel 625 in supercritical water containing dissolved and molten phosphates	Journal of Supercritical Fluids	SCI	4.4	2	3	/	否

36	Bin Chen, Yang Zhou, Kazi Belayet Hossain, Yixin Chen, Xiaoshan Zhu, Hengxiang Li, Xiangrong Xu*, Minggang Cai*	Microplastic in tropical island estuaries in China: Source identification and management framework development	Marine Environmental Research	SCI	3	1	3	T3	否
37	Zhishen Wang, Huiling Wu, Weihao He, Shunqiang Wei, Xuemin Wei, Chaoshuai Wei, Yinghui Wang*, Aiguo Huang	Protective Effect of Nanobodies Targeting Sip Protein Against Streptococcus agalactiae Infection in Tilapia (Oreochromis niloticus)	Animals	SCI	2.7	1	2	/	否
38	Weifeng Xu, Xuzhi Mai, Songwen Deng, Wenhuan Wang, Wenqian Wu, Wei Zhang*, Yinghui Wang	High-Resolution Mapping and Impact Assessment of Forest Aboveground Carbon Stock in the Pinglu Canal Basin: A Multi-Sensor and Multi-Model Machine Learning Approach	Forests	SCI	2.4	1	3	T3	否
39	Songwen Deng, Mengyuan Luo, Wenhuan Wang, Sixiang Lan, Weifeng Xu, Xuzhi Mai, Wei Zhang*	Assessment of biodiversity and landscape changes during the Pinglu Canal construction and the benefits of ecological restoration based on Rao's Q index	Ecological Engineering	SCI	4.1	1	2	T3	否
40	Geng Yang, Xingying Tang*, Xingtao Wang, You Wu, Hui Ma, Shengyan Pu	Synergistic hydrothermal carbonization and wet oxidation for sustainable sewage sludge valorization and process waters toxicity mitigation	Biomass & Bioenergy	SCI	5.8	1	2	T3	否
41	Yibo Zhang, Hongjie Liu, Shaopeng Wang*, Hao Fu, Yuanyu Xie, Chaoxin Zhang, Man Zhang, Jie Lu, Liwei	Advancements of the Vibrio coralliilyticus eDNA detection based on Co-Fe PBA-assisted biosensors for the rapid coral-disease warning	Biochemical Engineering Journal	SCI	3.7	2	3	/	否

	Wang*, Kefu Yu								
42	Weifeng Xu, Yaofei Cheng, Mengyuan Luo, Xuzhi Mai, Wenhuan Wang, Wei Zhang*, Yinghui Wang*,	Progress and Limitations in Forest Carbon Stock Estimation Using Remote Sensing Technologies: A Comprehensive Review	Forests	SCI	2.4	1	3	T3	否
43	张佳宇,陈仕国,余克服,梁甲元,侯壮豪,裴继影*	基于单细胞质谱组学研究珊瑚共生虫黄藻的化学多样性	质谱学报	北大核心, CSCD	1.35	/	/	T1	/
44	陈思思,薛宇阳,唐兴颖*,王智洁,张莹莹,钱黎黎,李尚泽,王英辉	液相循环对制糖固废共水热碳化影响机制研究	中国环境科学	北大核心,EI,CSCD	3.419	/	/	T1	/
45	邢 政，王佳乐，赖俊翔*，王英辉*，李 杰	氮磷限制条件下球形棕囊藻生理生化响应及转录组学研究	广西科学	北大核心	1.252	/	/	/	/
46	韦丽妮,刘珊*,赵建亮,吴念念,徐茹,刘源	不同类型城市受纳河涌大型底栖动物多样性及其对水环境因子的响应	生态毒理学报	北大核心,CSCD	1.648	/	/	T3	/
47	黄思宇,林武辉*,何贤文,林晓东	大气中 7Be 和 210Pb 时空分布特征差异和机制解析	核技术	北大核心,CSCD	0.99	/	/	T2	/

48	秦贵帮,张瑞杰*,王煜轩,康亚茹,史敬,王辰燕,韩民伟,余克服	涠洲岛珊瑚礁区有机氯农药的污染水平、来源和生物富集特征研究	上海海洋大学学报	北大核心,CSCD	2.289	/	/	T3	/
49	裴继影*, 张樱元, 余克服, 余文峰, 张瑞杰, 王瑞	基于科教融合人才培养模式的“化学海洋学”教学改革与实践	科技风	/	/	/	/	/	
50	康亚茹, 张瑞杰*, 余克服, 曾维斌, 王瑞轩	广西北部湾典型水产品中有机磷酸酯的生物富集特征和食用风险评估	上海海洋大学学报	北大核心,CSCD	2.289	/	/	T3	

（四）南海珊瑚礁遥感与监测方向

序号	作者	论文题目	期刊名称	级别	影响因子	JCR分区	中国科学院分区	中国科协期刊分级	是否TOP期刊
1	Honglei Jiang, Tianfei Ren, Rongyong Huang, Kefu Yu*	Marine Heatwaves and Cold Spells in Global Coral Reef Regions (1982–2070): Characteristics, Drivers, and Impacts	Remote Sensing	SCI	4.2	1	2	T3	否
2	Huade Li, Jinshui Zhang, Zhenghua Chen, Mingwei Zhang	A new remote sensing index of mildew for winter wheat disaster area extraction	International Journal of Digital Earth	SCI	4.9	1	2	T1	否
3	Zuodong Liang, Guangxian Huang, Wen Huang, Hailun Chen, Kefu Yu*, Dongsheng Jeng	Numerical Modeling of Wave Hydrodynamics Around Submerged Artificial Reefs on Fringing Reefs in Weizhou Island of Northern South China Sea	Journal of Marine Science and Engineering	SCI	2.7	1	3	T2	否
4	Yanliu Wu, Xiaoyan Chen*, Yuhao Du, Zhenhua Chen, Zhaoqian Yan, Hongfei Su, Zhenjun Qin, Zhiming Ning, Yuxiao Li, Kefu Yu*	Metabolism of wildfire-derived methoxyphenol in Acropora formosa: Metabolite identification, toxicity prediction, and impact on coral health	Journal of Hazardous Materials	SCI	12.2	1	1	T1	是
5	陈正华,兰思香,张锦水,张威,李华德,赵丽芳	城市黑臭水体遥感监测的研究现状与展望	遥感技术与应用	北大核心,CSCD	2.403	/	/	T3	/

6	滕君灿,余克服,左秀玲*,李志文,黄学勇,段正贤,蓝斐芳	相对高纬度珊瑚礁的有限弹性：气候变化和人类影响下的结构复杂度退化	中国科学:地球科学	北大核心,CSCD	4.032	/	/	T1	/
7	江蕾蕾，黄达华，赵佰玲，余克服*	珊瑚骨骼荧光记录环境变化的研究进展	海洋学报	北大核心,CSCD	1.38	/	/	T1	/
8	左秀玲,梁甲元,余克服*,苏宏飞,梁作栋	珊瑚礁领域研究生课程教学模式创新探索	中国多媒体与网络教学学报	/	0.245	/	/	/	/

四、在研基金项目列表

本年度在研各类科研基金 94 项，合同经费 10186.17 万元，其中国家自然科学基金 28 项（合计经费 1612 万元；含国家自然科学基金重点项目和国家自然科学基金重大课题项目各 1 项，经费分别为 305 万元和 400 万元）、广西自然科学基金/广西科技基地与人才专项/广西重点研发计划项目 44 项（合计经费 1215 万元）、中央海洋生态保护修复资金 1 项（经费 6992.14 万元）。

（一）纵向科研基金项目

本年度在研纵向科研项目 72 项，总经费 2827 万元，其中国家自然科学基金 28 项（合计经费 1162 万元）、广西自然科学基金/广西科技基地与人才专项/广西重点研发计划项目 44 项（合计经费 11215 万元）。国家自然科学基金中包含国家自然科学基金重点项目和国家自然科学基金重大课题项目各 1 项，经费分别为 305 万元和 400 万元。

序号	来源	类型	名称	编号	起止时间	经费（万元）	负责人
1	国家自然科学基金委	国家自然科学基金重大研究计划项目	印太交汇区代表性物种的生物多样性演变及其生态功能	42090041	2021.01-2025.12	400	余克服
2	国家自然科学基金委	国家自然科学基金重点项目	全新世南海珊瑚礁发育的时-空差异及其对全球变暖的适应机制	42030502	2021.01-2025.12	305	余克服
3	国家自然科学基金委	国家自然科学基金面上项目	基于物理信息扩散模型高精度重建陆-海水质量迁移过程及区域质量海平面预算闭合	42571043	2026.01-2029.12	46	邓珊珊

4	国家自然科学基金委	国家自然科学基金面上项目	流体饱和状态对西沙群岛晚中新世白云岩结构的调控机制	42572123	2026.01-2029.12	47	王瑞
5	国家自然科学基金委	国家自然科学基金面上项目	北部湾近岸海域典型阻燃剂的源汇格局及其风险调控机制研究	42576143	2026.01-2029.12	50	徐向荣
6	国家自然科学基金委	国家自然科学基金面上项目	基于 ^{40}K 重建多时间尺度的涠洲岛珊瑚岸礁生长发育历史	42276044	2023.01-2026.12	56	林武辉
7	国家自然科学基金委	国家自然科学基金面上项目	珊瑚礁碳酸钙产量大尺度分布遥感综合估算研究	42276182	2023.01-2026.12	55	左秀玲
8	国家自然科学基金委	国家自然科学基金面上项目	隐花色素介导蓝光调控珊瑚-虫黄藻共生体热白化耐受性的机理	42476137	2025.01-2028.12	48	巩三强
9	国家自然科学基金委	国家自然科学基金面上项目	河口环境孕激素及其代谢产物的赋存特征与降解转化机制	42177388	2022.01-2025.12	39.90824	刘珊
10	国家自然科学基金委	国家自然科学基金地区科学基金项目	强还原活性物种对海水病原微生物的灭活及消毒副产物协同控制效应与机制研究	52560001	2026.01-2029.12	33	张媛媛
11	国家自然科学基金委	国家自然科学基金地区科学基金项目	机器学习驱动电化学生物传感技术对珊瑚致病菌的快速检测及健康评估研究	22564003	2026.01-2029.12	31	王丽伟
12	国家自然科学基金委	国家自然科学基金地区科学基金项目	全新世以来南海北部“高纬度珊瑚礁”对全球变化的响应及演化趋势预测	42466003	2025.01-2028.12	30	范天来
13	国家自然科学基金委	国家自然科学基金地区科学基金项目	海南岛珊瑚礁全新世发育过程和海平面重建及气候变化响应研究	42366002	2024.01-2027.12	32	乐远福

14	国家自然科学基金委	国家自然科学基金地区科学基金项目	基于南海珊瑚数据再利用和机器学习技术重建近两百年台风历史记录	42265007	2023.01-2026.12	33	雍阳阳
15	国家自然科学基金委	国家自然科学基金地区科学基金项目	南海西沙新生代玄武质火山碎屑岩地球化学特征及成因研究	42166003	2022.01-2025.12	35	张瑜
16	国家自然科学基金委	国家自然科学基金地区科学基金项目	基于非靶代谢组学及分子网络探究珊瑚对高温胁迫的代谢应答机制	22264003	2023.01-2026.12	33	裴继影
17	国家自然科学基金委	国家自然科学基金地区科学基金项目	原位可视化定量研究全尺寸微塑料在北部湾典型红树林区植物根系的时空分布特征	22266005	2023.01-2026.12	33	李锐龙
18	国家自然科学基金委	国家自然科学基金青年科学基金项目	海岸带景观格局和气候变化对生态系统服务供需的影响机制与优化调控	42501364	2026.01-2028.12	30	江红蕾
19	国家自然科学基金委	国家自然科学基金青年科学基金项目	南海北部珊瑚记录的 5.5 ka BP 事件期间 ENSO 活动及其对太阳辐照度的响应	42502176	2026.01-2028.12	30	江蕾蕾
20	国家自然科学基金委	国家自然科学基金青年科学基金项目	造礁石珊瑚对多环芳烃及其衍生物的兴奋效应及其分子机制	42506130	2026.01-2028.12	30	韩民伟
21	国家自然科学基金委	国家自然科学基金青年科学基金项目	南海珊瑚礁区大型底栖有孔虫碳氧同位素的影响因素及古环境意义	42402007	2025.01-2027.12	30	吴司琪
22	国家自然科学基金委	国家自然科学基金青年科学基金项目	高温促进红树植物白骨壤盐腺泌盐的机制研究	42406121	2025.01-2027.12	30	郭泽军
23	国家自然科学基金委	国家自然科学基金青年科学基金项目	氮代谢调整在温度波动驯化提高珊瑚耐热性的作用机制	42406143	2025.01-2027.12	30	俞小鹏

24	国家自然科学基金委	国家自然科学基金青年科学基金项目	地质脂类记录的阿巴拉契盆地晚泥盆世海洋微生物组成对生态危机事件的响应	42302348	2024.01-2026.12	30	宋宜
25	国家自然科学基金委	国家自然科学基金青年科学基金项目	造礁石珊瑚病毒群落对急性低盐胁迫的响应模式研究	42306165	2024.01-2026.12	30	陈飚
26	国家自然科学基金委	国家自然科学基金青年科学基金项目	基于地极移动的陆地水储量及相应海平面长期演化特征与机理研究	42201024	2023.01-2025.12	30	邓珊珊
27	国家自然科学基金委	国家自然科学基金青年科学基金项目	入侵型和土著型虫黄藻-珊瑚共生体对高温胁迫响应的差异性研究	42206157	2023.01-2025.12	30	覃祯俊
28	国家自然科学基金委	国家自然科学基金专项项目	科学传播类：基于珊瑚礁特色的广西海洋教育小学示范校科普活动分层分级实施	42542038	2025.08-2026.12	5	徐向荣
29	广西壮族自治区科技厅	广西自然科学基金广西科技基地和人才专项	广西南海珊瑚礁研究重点实验室科技创新能力建设	桂科AD25069075	2025.03-2028.02	400	余克服
30	广西壮族自治区科技厅	广西自然科学基金广西重点研发计划	广西北部湾海漂垃圾溯源追踪技术研究及应用示范	桂科AB25069113	2025.03-2027.02	74	徐向荣
31	广西壮族自治区科技厅	广西自然科学基金广西重点研发计划	面向海洋中小尺寸塑料垃圾的无人船智能监测技术研发与应用示范	2025FN9619929	2026.01-2029.12	96	徐向荣
32	广西壮族自治区科技厅	广西自然科学基金广西科技成果转化计划	基于碳点传感检测的分级氧化-吸附协同全量化处理垃圾渗滤液关键技术研发及应用	2025ZG0312057	2026.01-2029.12	0	唐兴颖
33	广西壮族自治区科技厅	广西自然科学基金面上项目	细胞穿膜肽介导 VP28 特异性纳米抗体抗对虾 WSSV 作用机制研究	2025JJA130007	2026.01-2029.12	10	黄爱国

34	广西壮族自治区科技厅	广西自然科学基金面上项目	全球变暖与平陆运河悬浮物增加叠加对北部湾珊瑚礁生态影响与适应潜力研究	2025JJA150187	2026.01-2029.12	10	俞小鹏
35	广西壮族自治区科技厅	广西自然科学基金面上项目	高温实验模拟珊瑚白云石化过程中稀土元素的迁移机制	2025JJA150010	2026.01-2029.12	10	王瑞
36	广西壮族自治区科技厅	广西自然科学基金青年科学基金项目	桂西南地区下雷锰矿成矿环境和富集机制研究	2025JJB150038	2026.01-2029.12	8	黄钦
37	广西壮族自治区科技厅	广西自然科学基金青年科学基金项目	典型热带岛礁土壤微塑料赋存特征与老化机制研究	2025JJB150027	2026.01-2029.12	8	王刘炜
38	广西壮族自治区科技厅	广西自然科学基金青年科学基金项目	涠洲珊瑚礁区波致海底埋管动力灾变机理与分析方法	2025JJB160006	2026.01-2029.12	8	梁作栋
39	广西壮族自治区科技厅	广西自然科学基金广西重点研发计划项目	陶瓷膜-光催化耦合降解消杀技术及一体化装备研发与应用示范	桂科AB24010117	2024.05-2027.04	150	姚作芳
40	广西壮族自治区科技厅	广西自然科学基金广西科技基地和人才专项	气候变化背景下陆-海水质量迁移的时空特征及机理研究	桂科AD23026069	2023.06-2026.05	10	邓珊珊
41	广西壮族自治区科技厅	广西自然科学基金面上项目	滨珊瑚的海平面指示意义及在南海北部全新世海平面重建中的应用	2025GXNSFAA069160	2025.03-2028.02	10	乐远福
42	广西壮族自治区科技厅	广西自然科学基金面上项目	紫外光催化双酮高级氧化还原体系对海水有害微生物的灭活及副产物协同控制研究	2025GXNSFAA0691008	2025.03-2028.02	10	张媛媛
43	广西壮族自治区科技厅	广西自然科学基金面上项目	南海造礁石珊瑚骨骼及珊瑚砂中黑碳的赋存/埋藏特征及其碳汇能力初探	2025GXNSFAA069701	2025.03-2028.02	10	张瑞杰

44	广西壮族自治区科技厅	广西自然科学基金面上项目	虫黄藻 Cladocopium goreaui 的热驯化及其对涠洲岛苗圃区珊瑚耐热性的作用研究	2025GXNSFAA069187	2025.03-2028.02	10	覃祯俊
45	广西壮族自治区科技厅	广西自然科学基金面上项目	桂东南大瑶山燕山早期高 Sr/Y 花岗岩类成因及其深部动力学意义	2025GXNSFAA069324	2025.03-2028.02	10	张瑜
46	广西壮族自治区科技厅	广西自然科学基金面上项目	超临界水中磷化腐蚀膜抑制晶界扩散行为对镍基合金晶间腐蚀的影响机制研究	2025GXNSFAA069823	2025.03-2028.02	10	唐兴颖
47	广西壮族自治区科技厅	广西自然科学基金面上项目	近岸礁区有孔虫分布特征及其对生态环境的指示意义——以广西涠洲岛为例	2025GXNSFAA069592	2025.03-2028.02	10	孟敏
48	广西壮族自治区科技厅	广西自然科学基金面上项目	粤桂地区滨海核电站周边大气γ剂量率变异机制与跨省输运研究	2024GXNSFAA010449	2024.05-2027.04	10	林武辉
49	广西壮族自治区科技厅	广西自然科学基金面上项目	海洋环境中有机紫外吸收剂的常压质谱分析方法学研究与应用	2023GXNSFAA026488	2023.06-2026.05	10	裴继影
50	广西壮族自治区科技厅	广西自然科学基金面上项目	南海澄黄滨珊瑚共生虫黄藻 C15 及其宿主的遗传多样性分布及关键驱动因子分析	2023GXNSFAA026510	2023.06-2026.05	10	黄雯
51	广西壮族自治区科技厅	广西自然科学基金面上项目	种间珊瑚微生物组移植的抗病作用及机制研究	2023GXNSFAA026388	2023.06-2026.05	10	苏宏飞
52	广西壮族自治区科技厅	广西自然科学基金面上项目	基于高分辨率遥感的涠洲岛珊瑚礁碳酸钙产量分布精确估算方法研究	2022GXNSFAA035548	2022.04-2025.03	10	左秀玲
53	广西壮族自治区科技厅	广西自然科学基金面上项目	厄尔尼诺-南方涛动与准两年振荡对广西夏季极端降水的协同影响	2022GXNSFAA035441	2022.04-2025.03	10	雍阳阳

54	广西壮族自治区科技厅	广西自然科学基金面上项目	基于 MOS p-n 异质结的水分子诱导效应及气敏机理研究	2022GXNSFAA035565	2022.04-2025.03	10	王丽伟
55	广西壮族自治区科技厅	广西自然科学基金青年科学基金项目	不同温度条件下造礁石珊瑚的脂类组成变化及其指示意义	2025GXNSFBA069092	2025.03-2028.02	8	宋宜
56	广西壮族自治区科技厅	广西自然科学基金青年科学基金项目	造礁石珊瑚应对多环芳烃污染的响应与适应机理研究	2024JJB150202	2025.03-2028.02	8	韩民伟
57	广西壮族自治区科技厅	广西自然科学基金青年科学基金项目	涠洲岛造礁珊瑚对平陆运河工程低盐水输入适应机制研究	2025GXNSFBA069587	2025.03-2028.02	8	俞小鹏
58	广西壮族自治区科技厅	广西自然科学基金青年科学基金项目	南海北部季节性海表温度和盐度对东亚季风降雨预报的可靠性与机制研究	2025GXNSFBA069398	2025.03-2028.02	8	江蕾蕾
59	广西壮族自治区科技厅	广西自然科学基金青年科学基金项目	红树植物白骨壤耐盐相关基因的筛选及功能研究	2025GXNSFBA069196	2025.03-2028.02	8	郭泽军
60	广西壮族自治区科技厅	广西自然科学基金青年科学基金项目	广西平陆运河流域生态系统服务多尺度权衡/协同关系、影响因素与优化管理策略研究	2024JJB150108	2025.03-2028.02	8	江红蕾
61	广西壮族自治区科技厅	广西自然科学基金青年科学基金项目	造礁石珊瑚共附生微生物对潮间带波动生境的响应模式	2024GXNSFBA010307	2024.05-2027.04	8	陈飚
62	广西壮族自治区科技厅	广西自然科学基金青年科学基金项目	利用南海珊瑚礁区底栖有孔虫碳氧同位素指标重建古海洋环境的可靠性评估	2024GXNSFBA010231	2024.05-2027.04	8	吴司琪
63	广西壮族自治区科技厅	广西自然科学基金青年科学基金项目	基于 GRACE/GFO 重力卫星数据的全球海水质量变化特征与归因研究	2024GXNSFBA010158	2024.05-2027.04	8	邓珊珊

64	广西壮族自治区科技厅	广西自然科学基金青年科学基金项目	涠洲岛珊瑚共生虫黄藻季节性变化规律及共生虫黄藻对高温/低温胁迫的响应研究	2022GXNSFBA035449	2022.04-2025.03	8	覃祯俊
65	广西壮族自治区教育厅	广西壮族自治区教育厅	海洋科学专业导师制课程实施模式研究——以本科生和研究生团队合作为基础	2023JGB111	2023.06-2026.05	1	张媛媛
66	广西壮族自治区人力资源和社会保障厅，广西壮族自治区财政厅	青苗人才补助（科研启动经费）	桂西南地区沉积锰矿富集机制与成矿规律研究	202502325	2025.09-2030.12	30	黄钦
67	广西壮族自治区人力资源和社会保障厅，广西壮族自治区财政厅	青苗人才补助（科研启动经费）	单宁在红树植物镉耐受中的作用机制研究	202502322	2025.09-2030.12	30	郭泽军
68	广西壮族自治区人力资源和社会保障厅，广西壮族自治区财政厅	青苗人才补助（科研启动经费）	景观格局和气候变化对平陆运河流域生态系统服务的影响研究	202402024	2024.12-2029.12	30	江红蕾
69	广西壮族自治区人力资源和社会保障厅，广西壮族自治区财政厅	青苗人才补助（科研启动经费）	潮间带微观尺度造礁珊瑚耐热性差异调控机制研究	202402021	2024.12-2029.12	30	俞小鹏
70	广西壮族自治区人力资源和社会保障厅，广西壮族自治区财政厅	青苗人才补助（科研启动经费）	极端波流耦合荷载下珊瑚岛礁场地回填管线上浮失稳机理与预测研究	202402020	2024.12-2029.12	30	梁作栋

71	广西壮族自治区人力资源和社会保障厅，广西壮族自治区财政厅	青苗人才补助（科研启动经费）	南海北部季节性海表温度和盐度对东亚季风降雨预报的可靠性与机制	202401998	2024.12-2029.12	30	江蕾蕾
72	广西壮族自治区人力资源和社会保障厅，广西壮族自治区财政厅	青苗人才补助（科研启动经费）	南海珊瑚礁区大型底栖有孔虫镁钙比值的影响因素及古环境意义	202401977	2024.12-2029.12	30	吴司琪

（二）横向科研基金项目

本年度在研横向基金项目 22 项，总经费 7298.27 万元，含中央海洋生态保护修复资金 1 项，经费 6992.14 万元。

序号	项目来源	项目名称	项目编号	起止时间	经费（万元）	负责人
1	中央海洋生态保护修复资金	广西北海市涠洲岛北部珊瑚礁生态修复项目	KLBH2022-G2-0003	2022.11.30-2026.12.30	6992.14	黄雯
2	生态环境部华南环境科学研究所	2025 年度南海海域生态环境监测服务项目	202501660	2023.07-2025.06	149.8	俞小鹏
3	三沙航迹珊瑚礁保护研究所	2025 年度龙洞生态环境监测服务和报告撰写	202501912	2025.09-2026.09	25.12	韩民伟
4	中国科学院南海海洋研究所研究所	海洋沉积物和水体样品抗生素检测和数据分析	202501984	2025.08-2026.08	3.92	刘珊

5	中国科学院南海海洋研究所研究所	塑料样品检测与数据分析	202501893	2025.09-2027.08	3.8	刘珊
6	中国科学院南海海洋研究所研究所	南海北部边缘造礁珊瑚对高温与高浑浊度双重胁迫的适应机制研究	202501391	2025.03-2026.03	4.0	俞小鹏
7	中国科学院南海海洋研究所	海洋样品类固醇激素测试服务	202500606	2025.06-2026.06	4	潘长桂
8	中国科学院南海海洋研究所	海洋沉积物样品环境参数测试服务	202501186	2025.05-2026.12	4.95	刘珊
9	中国检验认证集团广西有限公司	城市垃圾填埋场渗滤液中污染物识别及关键技术研究服务	202501039	2025.08-2025.12	5.0	唐兴颖
10	三亚海洋生态环境工程研究院	海南河口海域微塑料测试服务	202501010	2025.04-2025.07	9.13	潘长桂
11	国家海洋环境监测中心	小公鱼、球形棕囊藻传感器构建数据资料	202500125	2025.09-2026.06	6	张曼
12	国家海洋环境监测中心	三沙永乐龙洞周边海域珊瑚礁生态、水文和沉积物通量历史监测数据分析和报告撰写服务项目	202501691	2025.03-2025.12	19.91	陈飚
13	国家海洋环境监测中心	滨海核电冷源取水区两种毛虾的特异性 DNA 探针设计及性能评价	202500119	2025.09-2025.10	4.8	张曼
14	自然资源部第四海洋研究所	MOF@微生物协同可见光光催化降解海产养殖废水中 TCH 机制研究	MRESD-2023C05	2024.11-2025.08	3	王少鹏

15	广西汇康能环保科技有限公司	塑料废弃物裂解炭黑的纯化与功能材料制备技术研究	202501244	2025.07-2026.07	6.5	唐兴颖
16	广西大学	基于环境 DNA 耦合电化学生物传感技术的珊瑚致病菌快速检测研究	2023BZRC025	2023.06-2025.05	10	王丽伟
17	广西大学	基于空间尺度上推的珊瑚礁结构复杂度指数遥感反演研究	2023BZRC019	2023.06-2025.05	10	左秀玲
18	广西产研院绿色低碳技术研究所	水热酸解甘蔗渣制备 C5/C6 糖水解液研究技术服务	202502130	2025.09-2025.10	9.38	张威
19	广西产研院绿色低碳技术研究所	再生混凝土样品理化性质测试分析	202402084	2024.12-2025.01	22.5	张威
20	广西青辉环保技术有限责任公司	再生混凝土微观孔结构调控与多场景性能提升改性研究	202502508	2025.09-2025.12	31	王英辉
21	广西青辉环保技术有限责任公司	再生混凝土微观孔结构优化与有害元素控制改性研究	202502474	2025.08-2025.11	30	王英辉
22	中国科学院南海海洋研究所	红树林沉积物环境参数分析服务	202502590	2025.12-2026.12	4.32	刘珊

五、授权/公开专利列表

本年度获授权专利 6 项（含发明专利 2 项、实用新型专利 4 项）、公开发明专利 9 项。

序号	名称	专利号	发明人	申请日期	授权/公开日期	类型	状态
1	一种可调刀距的岩石薄板自动切割机	CN119748657A	江蕾蕾,赵佰玲,黄达华,姜伟	2025.02.24	2025.09.23	发明	授权
2	一种混凝土用再生骨料及其全再生混凝土的制备方法	CN119349911A	程耀飞,郑建安,何建乔,肖建庄,蒙秋江,吴海乐,应敬伟,王纪云,王文欢,王英辉,陈润成	2024.08.01	2025.11.07	发明	授权
3	一种适用于珊瑚岛礁动力环境监测的分段式海床基	CN223192370U	梁作栋,刘大军,余克服,黄雯,陈海伦	2024.10.12	2025.08.05	实用新型	授权
4	一种适用于珊瑚礁海岸动力环境的沉积物捕获器	CN223192635U	梁作栋,陈海伦,余克服,黄雯	2024.09.11	2025.08.05	实用新型	授权
5	一种便携式珊瑚礁场地沉积物通量监测装置	CN223192374U	梁作栋,覃河融,余克服,黄雯,黄光贤	2025.05.27	2025.08.05	实用新型	授权
6	一种用于珊瑚礁生态修复的梯形玻璃钢礁体	CN223391831U	彭梦娇,周榆鹏,劳子彤,黄雯,余克服,徐明培,黄智华,黄学勇	2024.10.10	2025.09.30	实用新型	授权
7	基于夜光遥感序列的人类活动对珊瑚礁生态健康评估方法	CN119251695A	李泽琛，黄荣永	2024.08.27	2025.01.03	发明	公开

8	一种基于 Landsat 影像的珊瑚礁区表层海水叶绿素 a 浓度反演方法	CN120217721A	张威,王英辉,邓淞文,徐伟峰,麦旭志	2025.05.26	2025.06.27	发明	公开
9	珊瑚物种语义样本智能自动化生成系统及方法	CN120673412A	左秀玲,蓝斐芜,滕君灿	2025.06.09	2025.09.19	发明	公开
10	基于 DEM 和 Geomorphons 方法的岛礁微观地貌遥感分类方法	CN119649092A	左秀玲,余芷丽	2024.11.18	2025.03.18	发明	公开
11	一种基于固相微萃取和常压质谱检测紫外线吸收剂的装置及检测方法	CN120558682A	裴继影,张樱元,高德硕	2025.05.28	2025.08.29	发明	公开
12	基于多源遥感技术的森林碳储量与碳汇监测评估方法	CN120833559A	王文欢,吴文乾,兰思香,王英辉,张威	2025.07.08	2025.10.24	发明	公开
13	功能性生物有机复合肥及其制备方法	CN119707585A	王英辉,李尚泽,唐兴颖,黄爱国,邱书维	2024.10.30	2025.03.28	发明	公开
14	一种再生微粉水泥基灌浆料及其制备方法	CN119683941A	韦庭丛,肖建庄,王英辉,杨海峰	2024.12.27	2025.03.25	发明	公开
15	一种靶向无乳链球菌 SIP 蛋白的纳米抗体制备及其应用	CN119552244A	王英辉,黄爱国,何建乔,王志燊,张发利,姜晓玉	2024.08.21	2025.03.04	发明	公开

六、学术交流

（一）会议交流

实验室本年度参加学术会议交流 39 场次（284 人次），其中国内会议 34 场次（227 人次）、国际会议 5 场次（57 人次）；合计开展会议报告 183 人次（国际会议 46 人次），其中特邀报告 9 人次（国际会议 3 人次），口头报告 145 人次（国际会议 19 人次），展板报告 38 人次（国际会议 27 人次）。

序号	会议名称	时间	地点	国际/国内	参会人数	报告题目（姓名）	报告类型
1	第三届“空间、大气、海洋与环境光学”学术会议	2025.04.18-04.20	武汉	国内	1	南海珊瑚岛“地貌-生态”演变过程的遥感分析(黄荣永)	口头报告
2	印太交汇区物质能量汇聚中心海洋环境与生物过程的耦合作用和生态效应 2024 年度总结及学术交流会	2025.05.19-05.20	南宁	国内	20	重大项目课题 1 进展汇报(余克服)	口头报告
						印太交汇区珊瑚礁的生态特征及其热适应模式(陈小燕)	口头报告
						印太交汇区共生-游离态虫黄藻的空间分布及其生态效应(陈 飚)	口头报告
3	第三届中山大学海洋系统科学开放年会	2025.10.17-10.20	珠海	国内	2	广东近岸造礁珊瑚对高温和低盐胁迫的适应性研(俞小鹏)	口头报告
						西沙群岛珊瑚礁的发育演化历史及其古环境记录——以琛科 2 井为例(王瑞)	特邀报告
4	2025 第二届环境科学与环境材料学术会议	2025.04.25-04.27	南京	国内	1	潮间带微观尺度造礁珊瑚耐热性差异调控机制研究(俞小鹏)	口头报告
5	2025 年中国环境科学学会科学技术年会	2025.07.20	南京	国内	1	南海长棘海星快速示踪及暴发预警研究(王丽伟)	口头报告
6	第十届地学青年论坛		合肥	国内	10	南海灰沙岛与沙洲地貌近 30 年演变及其环境驱动因素的遥感分析(黄荣永)	邀请报告

						中国沿海地区植被 NPP 的突变时空格局和驱动机制(江红蕾)	口头报告
						Escalating MarineHeatwaves and DecliningCold-spells in Coral Reefs:Spatiotemporal Trends andFuture Projections(任天飞)	口头报告
						南海珊瑚礁生态系统健康状况的多光谱卫星遥感分析(肖竣友)	口头报告
						亚热带海岸环境中不同形态黑碳的时空变化及环境行为：半封闭海湾和开放河口的差异(王镜宇)	展板报告
						南海北部珊瑚生长率记录的中-晚全新世共 2203 年的 SST 及 ENSO 变化(黄达华)	展板报告
						珊瑚骨骼 P/Ca 示踪南海北部边缘礁表层海水磷含量变化(郭宁)	展板报告
						台湾恒春珊瑚礁对热带气旋的响应与记录(石宇辰)	展板报告
						热带气旋对河流入海沉积物的影响及其珊瑚记录一以海南岛为例(刘彩凤)	展板报告
						南海北部表层海水稀土元素的珊瑚记录及其环境气候意义(顾庭舞)	展板报告
						涠洲岛沙质海岸侵蚀及其与珊瑚礁退化的关系研究(黄荣永)	特邀报告
						全新世南海珊瑚礁发育的南北差异及相对高纬度避难所意义(江蕾蕾)	特邀报告
7	第八届地球系统科学大会	2025.07.02-07.05	上海	国际	50	塑岩理化性质与形成原因的初步探索(王刘炜)	口头报告
						潮间带微观尺度造礁珊瑚耐热性差异调控机制研究(俞小鹏)	口头报告
						基于单细胞质谱组学研究珊瑚共生虫黄藻的化学多样性(张佳宇)	口头报告

南海珊瑚礁不同地貌带沉积物中有机碳含量、组成及来源的空间异质性(高洁)	展板报告
珊瑚骨骼 P/Ca 示踪南海北部边缘礁表层海水磷含量变化(郭宁)	展板报告
基于地貌分区建模的珊瑚礁遥感水深反演方法(滕君灿)	口头报告
西沙群岛珊瑚礁区的尿素分布特征及其来源分析(夏荣林)	口头报告
南海北部涠洲岛珊瑚岸礁波浪破碎与增水特性数值模拟研究(陈海伦)	展板报告
南海北部表层海水稀土元素的珊瑚记录及其环境气候意义(顾庭舞)	展板报告
西沙群岛晚中新世宣德组沉积相对白云石晶体发育演化的控制作用(花绘)	展板报告
南海北部珊瑚生长率记录的中－晚全新世共 2203 年的 SST 及 ENSO 变化(黄达华)	展板报告
南海西沙群岛羚羊礁底栖有孔虫群落特征差异性分析(李玫)	展板报告
南海第四纪珊瑚礁生态系统演化中海胆的调控作用(李钰涵)	展板报告
造礁石珊瑚病毒群落对急性低盐胁迫的响应模式研究(梁林)	展板报告
靶向接种：潜在益生菌为热胁迫下珊瑚白化 “降温”(梁祝清)	展板报告
热带气旋对河流入海沉积物的影响及其珊瑚记录—以海南岛为例(刘彩凤)	展板报告
近 40 年来大亚湾造礁石珊瑚群落结构的演变分析(卢锟)	展板报告
益生菌 Bacillus firmus GXU-Z9 的珊瑚抗病作用与机制研究(秦晓)	展板报告

珊瑚礁区海洋热浪加剧与冷浪衰减：时空演变及未来趋势(任天飞)	展板报告
Ammonia removal mitigates white plague type II in the coral Pocillopora damicornis(孙非龙)	展板报告
琛科 2 井晚中新世-早上新世脂类分布特征及其古海洋环境变化的响应(王佳宝)	口头报告
珊瑚砂和珊瑚骨骼中黑碳赋存特点及其碳封存意义——基于 BPCA 分子标志物法的证据(王镜宇)	口头报告
广西涠洲岛珊瑚来源虫黄藻 Cladocopium goreaui 的热驯化及高温响应机制(韦丽菲)	口头报告
高温实验模拟文石质珊瑚白云石化过程中稀土元素的变化特征(吴松烨)	展板报告
基于多光谱卫星的活珊瑚覆盖度反演方法研究(肖竣友)	口头报告
葡萄糖和五氯酚暴露下澄黄滨珊瑚的代谢和生理破坏：珊瑚碳循环的意义(薛鹏飞)	口头报告
南海北部边缘珊瑚礁区珊瑚-虫黄藻共生体对急性/慢性温度胁迫的响应机制(阳琪芝)	展板报告
联合转录组与蛋白质组学技术解析丛生盔形珊瑚热应激的分子响应机制(余文峰)	展板报告
北部湾海域涠洲岛晚全新世气候定量重建及珊瑚礁响应(袁欣萌)	展板报告
过去 2000 年南海北部冬季海表温度预报东亚季风区降雨的可靠性验证(张楚卉)	展板报告

						过去 2000 年南海北部春季海表盐度对东亚季风降雨的预报(赵佰玲)	展板报告
						上新世-更新世东亚季风演化：来自南海珊瑚礁碳酸盐岩 Nd 同位素特征的证据(赵凌楠)	展板报告
						海洋热浪引发的适应性机制提升霜鹿角珊瑚（Acropora pruinosa）热耐受性(郑月)	展板报告
						公元 700 年 ENSO 引发南海北部海表盐度显著变化(周煦)	展板报告
						热驯化提高珊瑚耐热阈值的分子机制研究(马玉玲)	展板报告
						南海全新世珊瑚砂对泻湖填充的碳汇效应(杜思琦)	展板报告
						澄黄滨珊瑚共生绿藻 Trebouxiophyceae sp.的分离鉴定与系统发育分析(卢铭垚)	展板报告
						基于多时相遥感影像的南海珊瑚礁面积估算(黄荣永)	口头报告
						黄岩岛环礁地貌近 40 年变化的遥感分析(黄荣永)	口头报告
						涠洲岛沙质岸线侵蚀与珊瑚礁退化的关系：珊瑚礁退化削弱沙质岸线稳定(黄荣永)	口头报告
8	珊瑚岛礁系统科学发展战略研讨会	2025.10.15-10.19	南宁	国内	13	南海珊瑚记录之全新世高分辨率气候进展(江蕾蕾)	口头报告
						全新世南海珊瑚礁发育的空间差异及相对高纬度避难所意义(江蕾蕾)	口头报告
						南海珊瑚礁的发育演化及其环境记录——以西沙群岛琛科 2 井为例(王瑞)	口头报告
						大空间尺度南海珊瑚礁的生态现状与动态过程(陈小燕)	口头报告
						南海珊瑚礁环境压力大尺度分布遥感	口头报告

						研究(左秀玲)	
						南海珊瑚礁区新污染物研究：进展与展望(张瑞杰)	口头报告
						广西涠洲岛珊瑚礁生态修复实践与岛礁修复思路探讨(黄雯)	口头报告
						南海珊瑚礁敌害生物快速示踪及预警新方法研究(王丽伟)	口头报告
						水动力作用下珊瑚礁区沉积物响应机制与分析方法(梁作栋)	口头报告
						无机防晒剂对涠洲岛造礁珊瑚的毒性效应及影响评估研究(陈健)	口头报告
9	第六届“未来科学家”全国研究生“海洋与气候”学术论坛	2025.10.25	青岛	国内	3	礁石珊瑚共附生微生物对潮间带波动生境的响应模式(梁馨月)	展板报告
						礁石珊瑚共附生微生物对潮间带波动生境的响应模式(梁馨月)	口头报告
						南海珊瑚共附生微生物对极端海洋热浪事件的响应模式(李炫霖)	展板报告
						方法学挑战物质环境危害评估——微纳塑料专场(徐向荣)	专场主持人、学术委员会成员
						轮胎添加剂及其转化产物在河口环境的时空分布特征及生物富集规律(刘珊)	主旨报告
10	第十届全国生态毒理学大会	2025.04.20-04.22	嘉兴	国内	10	斜生四链藻中细胞色素 P450 介导的奥克立林生物转化：转录组学、蛋白质组学、分子对接和密度泛函理论计算(胡俊杰)	口头报告
						三氯生与热胁迫对澄黄滨珊瑚的协同毒性效应：从生理响应到分子机制(潘长桂)	口头报告
						潮间带微观尺度造礁珊瑚耐热性差异调控机制研究(俞小鹏)	口头报告

						八放珊瑚对高温、镉胁迫以及微塑料胁迫的响应机制(马玉玲)	口头报告
						多组学揭示亚硝酸盐暴露对罗非鱼的免疫毒性机制(韦婷玉)	口头报告
						热应激影响下造礁石珊瑚对 PAHs 的响应与适应策略(韩民伟)	展板报告
						珠江口万山群岛鹿角杯形珊瑚对“南方暴雨”寻致低盐事件差异响应机制的研究(俞小鹏)	展板报告
						磺胺甲噁唑暴露对罗非鱼多组织的损伤(韦雪敏)	展板报告
						/(裴继影)	仅参会，未作报告
						/(张瑞杰)	仅参会，未作报告
11	第七届高校大学生海洋与化学科技实践论坛	2025.11.07-11.10	汕头	国内	6	珊瑚砂和珊瑚骨骼中黑碳赋存特点及其碳封存意义(王秋婷)	口头报告
						基于 3D 打印-SPME 牙签喷雾质谱快速检测复杂基质中的有机紫外吸收剂(高德硕)	口头报告
						海上石油污染对发泡聚苯乙烯泡沫和聚乙烯膜塑料中添加剂释放的影响及作用机制研究(蔡晓莉)	口头报告
						基于质谱非靶代谢组学研究 BP-3 对珊瑚的毒理效应(张佳宇)	口头报告
						2025 年西沙群岛珊瑚礁及永乐龙洞综合科学考察工作汇报(陈 飚)	口头报告
						龙洞浮游植物群落变化特征(陈小燕)	口头报告
12	2025 年三沙市永乐龙洞保护站工作研讨会	2025.09.15-09.16	南宁	国内	22	珊瑚礁生态遥感及其在龙洞监测中的应用(黄荣永)	口头报告
						长棘海星全生命周期监测预警(王丽伟)	口头报告
						全球变暖对棘冠海星爆发的影响(向柯	口头报告

						宇)	
						塑岩理化性质与形成原因的初步探索(王刘炜)	口头报告
						广西涠洲岛珊瑚礁区典型新污染物的污染特征及其对珊瑚健康的生态风险(张瑞杰)	口头报告
13	第九届全国环境地球化学大会	2025.10.31-11.02	广州	国内	5	中南海山山坡和山脚处沉积柱黑碳的埋藏历史及其环境意义(韦盼)	口头报告
						基于北部湾沉积物岩心焦炭与烟炱黑碳记录的燃烧模式转变追踪：埋藏通量控制与碳汇功能评估(莫立伟)	口头报告
						Source-Dependent Transformation and Sequestration of Black Carbon in Shelf and Slope Sediments of the Northern South China Sea(纪哲鸿)	口头报告
						大数据支持珊瑚礁可持续发展(左秀玲)	特邀报告
						涠洲岛沙质海岸侵蚀及其与珊瑚礁退化的关系(黄荣永)	专题报告
						全球珊瑚礁区海洋热浪/冷浪(1982-2070)：特征、机制和影响(江红蕾)	专题报告
14	2025 第三届海岸带大会	2025.07.28-07.30	烟台	国内	6	中国海陆过渡带植被恢复力并非随着植被变绿而持续增强(郭裕)	口头报告
						南海西沙群岛宏观地形分析与珊瑚分布空间格局研究(余芷丽)	口头报告
						基千时间序列多光谱卫星影像的珊瑚与藻类指数构建及其在珊瑚礁生态状况评估中的应用(肖竣友)	口头报告
						轮胎添加剂及其转化产物在河口环境的时空分布特征及生物富集规律(刘珊)	口头报告
15	2025 年《中国环境科学》青年学术会议	2025.08.15-08.16	长沙	国内	3	斜生四链藻对环境浓度奥克立林的胁迫响应及生物转化机制(潘长桂)	口头报告
						差异化营养水平下珊瑚礁关键氮转化	口头报告

						过程的 分配变异与调控(宁志铭)	
16	第十二届中国红树林学术研讨会暨中国生态学学会红树林生态专业委员会 2025 年年会	2025.11.14-11.17	海口	国内	3	红树植物秋茄和白骨的水通道蛋白在其适应海岸潮间带环境中发挥的作用(郭泽军) /(李展泓) /(陈喜)	口头报告 仅参会，未作报告 仅参会，未作报告
17	2025 年中国质谱学术大会	2025.09.19-09.23	郑州	国内	1	紫外吸收剂在南海珊瑚礁区的分布及其分析方法构建(裴继影)	口头报告
18	第二届 Carbon Research 大会	2025.11.07-11.09	绍兴	国际	1	塑岩理化性质与形成原因的初步探索(王刘炜)	口头报告
19	2025 海南蓝碳论坛新兴海洋碳汇机制与潜力分论坛	2025.07.17-07.20	陵水	国内	1	广西涠洲岛珊瑚礁生态修复的技术与进展(黄雯)	口头报告
20	Xiamen Symposium on Marine Environmental Sciences--Transformative Science and Technology for a Sustainable 0cean	2025.01.14-01.17	厦门	国际	4	Atmospheric transport of microplastics from land to sea is inefficient: Evidence from multimedia observations(徐向荣) Monitoring and early alerting of coral reef environment in the South China Sea basedon remote sensing integrated technologies(左秀玲) Coral nutritional strategies in response to wildfire ash deposition(刘珂) Dual impact of extreme wildfires and tropical cyclones on phytoplankton in coral reef regions(吴秋云)	邀请报告 口头报告 口头报告 口头报告
21	14th international Symposium on Digital Earth--Theme: Digital Earth Facilitating Sustainable Development Goals	2025.04.21-04.25	重庆	国际	1	Satellite Monitoring and Early Alerting of Coral Reefs in the South China Sea(左秀玲)	口头报告
22	The 5th International Forum on Big Data for Sustainable	2025.09.06-09.08	北京	国际	1	Big data supports the sustainable development of coral reefs(左秀玲)	口头报告

	Development Goals						
23	第二十七届生态环境遥感论坛暨第十五届桂粤闽赣遥感科技大会	2025.09.25-09.27	桂林	国内	1	南海珊瑚礁遥感监测与预警研究(左秀玲)	口头报告
24	国际数字地球学会中国国家委员会第一届青年科学家工作委员会第一次会议暨学术交流会	2025.07.18	昆明	国内	1	/(左秀玲)	仅参会，未作报告
25	中国太平洋学会海洋电子信息科学与技术分会第一届理事会第一次会议	2025.10.28	深圳	国内	1	/(左秀玲)	仅参会，未作报告
26	中国海洋学会海洋化学分会 2025 年度学术研讨会	2025.11.21-11.23	杭州	国内	1	/(余克服)	学术委员会
27	国家自然科学基金委员会地球科学部变化中的河口-海湾生态环境：多米诺与蝴蝶效应	2025.12.4-12.6	钦州	国内	1	河口海湾新型替代阻燃剂的食物链传递机制—挑战与应对(徐向荣)	口头报告
28	2025 年海洋生态环境保护及监测技术研讨会	2025.11.02-11.03	杭州	国内	2	南海相对高纬度礁区珊瑚共生虫黄藻 C.goreaui 对极端高/ 低温胁迫的响应(韦丽菲) 南海边缘礁区珊瑚- 共生虫黄藻对急性/慢性温度胁迫的响应机制(阳琪芝)	口头报告 口头报告
29	中国科学院大学 2025 年研究生海洋科学学术论坛暨第 9 届“青年与海洋科学”学术论坛	2025.11.27	广州	国内	2	造礁石珊瑚共附生微生物对潮间带波动生境的响应模式(梁馨月) 南海珊瑚微生物组对极端海洋热浪事件的响应模式(李炫霖)	口头报告 口头报告
30	2025 年有益微生物资源与生物产业发展论坛	2025.11.22-11.23	防城港	国内	2	第三代高通量测序引导下珊瑚共附生细菌的富集培养技术研究(王辰燕) 从体外抗菌到体内益生：一株珊瑚黏液相关细菌可缓解热应激诱导的珊瑚白化(梁祝清)	口头报告 口头报告
31	广西南海珊瑚礁研究重点实	2025.12.09	南宁	国内	20	北部湾沉积柱黑碳埋藏记录及其环境	口头报告

	验室 2025 年度学术委员会会议暨学术年会活动之海洋环境与化学研究生学术论坛					指示意义(叶全发)	
						类固醇激素在全国滨海湿地的赋存特征、来源贡献与优控污染物的筛选(周沁歌)	口头报告
						考洲洋红树林生态系统中类固醇激素的分布与积累特征(陈济迅)	口头报告
						海洋环境中塑料衍生溶解性有机质的赋存特征与潜在生态效应(何燃)	口头报告
						四种有机物胁迫下橙黄滨珊瑚碳源汇效应改变及机制研究(薛鹏飞)	口头报告
						基于质谱代谢组学研究 BP-3 对珊瑚的毒理效应(张佳宇)	口头报告
						藻质生物炭协同微生物对模拟虾塘废水中磺胺甲恶唑的吸附降解效应与机制研究(钟文轩)	口头报告
						基于物理感知与多尺度特征解耦的复杂海况海漂垃圾精准监测研究(曾峻森)	口头报告
						茅尾海海漂垃圾轨迹分布及溯源数值模拟(韦益善)	口头报告
						CRISPR-DNA 水凝胶比色传感器用于中国毛虾的现场快速智能检测(万仕伟)	口头报告
						全球海洋典型浮游植物类群卫星遥感及气候变化响应研究(李正浩)	口头报告
						蒸气压亏缺导致中国沿海植被绿度与生态系统恢复力解耦(郭裕)	口头报告
32	广西南海珊瑚礁研究重点实验室 2025 年度学术委员会会议暨学术年会活动之物理海洋与遥感研究生学术论坛	2025.12.19	南宁	国内	22	印度-太平洋交汇区野火活动特征及其环境影响研究(闫兆千)	口头报告
						时间复合型东亚大气河的特征(杨诗语)	口头报告
						南海北部珊瑚 Sr/Ca 记录 3.8 ka BP 较强的 ENSO 活动(赵佰玲)	口头报告
						利用 GRACE（-FO）重力卫星数据与 ConvLSTM 模型反演珠江流域高分辨	口头报告

						率水储量异常(胡安戈)	
						莫雷阿岛珊瑚礁对海洋热浪的响应：地貌、水深与群落动态的时空异质性(黎蔚琪)	口头报告
						基于 ICESat-2 和多光谱影像珊瑚礁地貌分类的深度学习水深反演方法(罗盛)	口头报告
						海南岛椰林湾砂质岸线近 40 年对珊瑚礁人为毁坏响应的遥感影像记录(曾仕卿)	口头报告
						广西北部湾沿岸海洋冷却效应量化及其驱动机制研究(覃正宇)	口头报告
						基于无人机激光雷达与卫星数据融合的红树林地上碳储量估算研究(麦旭志)	口头报告
						北部湾涠洲岛岸礁区域人工礁体周围波浪水动力特性数值模拟研究(黄光贤)	口头报告
						非线性波流荷载作用下沟槽管道周围钙质海床动力响应试验研究(刘大军)	口头报告
						南海陆缘岩石圈伸展破裂过程的构造-地层记录(高圆圆)	口头报告
						热带气旋对海南岛山区河流输送水和悬浮沉积物的影响(刘彩凤)	口头报告
						黄岩岛潟湖沉积记录的近~1100 年来的风暴信息(钟云清)	口头报告
33	广西南海珊瑚礁研究重点实验室 2025 年度学术委员会会议暨学术年会活动之海洋地质与环境研究生学术论坛	2025.12.24	南宁	国内	18	南海珊瑚礁区底栖有孔虫群落特征、壳体尺寸及碳氧同位素的环境指示意义(李玫)	口头报告
						高温实验模拟文石质珊瑚白云石化过程中稀土元素的迁移机制(吴松烨)	口头报告
						大西洋年代际振荡和太阳辐射对热带气旋的调控—来自台湾南部珊瑚百年尺度的记录(石宇辰)	口头报告
						U–Pb zircon, geochemical and Sr–Nd–Hf	口头报告

						isotopic constraints on age and origin of Mid-Late Jurassic granites from Dayaoshan in Guangxi, South China: Indication of paleo-Pacific subduction(原雅琪)	
34	广西南海珊瑚礁研究重点实验室 2025 年度学术委员会会议暨学术年会活动之海洋生物与生态研究生学术论坛	2025.12.26	南宁	国内	28	广西涠洲岛滨珊瑚营养方式的季节性差异对其骨骼碳同位素的影响(韦競)	口头报告
						南海北部表层海水锌含量年际变化的珊瑚记录(王健雄)	口头报告
						人为压力导致营养物质对珊瑚生长效应的转变：来自南海北部的证据(曾洋)	口头报告
						野火源甲氧基酚在鹿角珊瑚中的代谢转化及其介导的白化机制(吴艳柳)	口头报告
						澄黄滨珊瑚对热胁迫的记忆效应：共生功能体耐热性提升的分子基础(马玉玲)	口头报告
						同质化驯养对不同纬度澄黄滨珊瑚耐热性影响研究(谭荣华)	口头报告
						不同光质驯化对涠洲岛美丽鹿角珊瑚热耐受性的影响研究(宛强)	口头报告
						广西涠洲岛珊瑚来源虫黄藻 Cladocopium goreaui 的热驯化及高温响应机制(韦丽菲)	口头报告
						造礁石珊瑚病毒群落对急性低盐胁迫的响应模式研究(梁林)	口头报告
						一株珊瑚礁区新属蓝藻的形态鉴定与功能分析(石文杰)	口头报告
						广西涠洲岛珊瑚礁生态修复效果评估(彭梦娇)	口头报告
						广西涠洲岛造礁石珊瑚与人工礁体生长适配性研究(王明威)	口头报告
						中国鲎胚胎期抗菌肽的活性功能研究(黄云帆)	口头报告

						海洋益生菌筛选及其增强石斑鱼抗病能力研究(陈凡)	口头报告
						纳米抗体 Nb24 抗白斑综合征病毒作用研究(韦雪敏)	口头报告
						凡纳滨对虾通过调节自噬和凋亡增强亚硝氮耐受性(马振涛)	口头报告
						亚硝酸盐与吡虫啉联合暴露下凡纳滨对虾组织的差异性基因表达及代谢组学响应(黄成立)	口头报告
						亚硝酸盐诱导的罗非鱼肠道损伤机制和多器官毒性：综合多组学分析的见解(韦婷玉)	口头报告
						珊瑚来源二苯甲酮-3 降解菌的分离、鉴定及基因组特征(刘名定)	口头报告
						第三代高通量测序引导下珊瑚共附生细菌的富集培养技术研究(王辰燕)	口头报告
						饲料中添加姜黄素对金鲳鱼养殖的影响效果(路霄杰)	口头报告
35	第四届渔业生态环境大会	2025.12.12-12.14	北海	国内	2	海洋环境微塑料生态风险评估：关键挑战与应对策略(徐向荣)	主旨报告
						专题 3 污染物的渔业生物效应与风险防控(余克服)	专题主席
36	第六届全国环境微塑料污染与管控学术研讨会	2025.04.28-04.30	咸阳	国内	1	环境微塑料的生态风险评估研究挑战(徐向荣)	特邀报告
37	2025 全国污染生态学学术研讨会	2025.08.29-08.31	天津	国内	1	南珊瑚礁生态系统中多环芳烃的环境行为、来源及生态风险(韩民伟)	口头报告
						热带玄武岩岛屿化学风化与地下水排泄驱动的表层海水稀土元素参数变化：来自珊瑚的证据(姜伟)	口头报告
38	国家重点研发计划项目《热带西太平洋全新世高分辨率气候变化重建、集成和同化研究》（2023YFF0804800）2025 年度学术研讨会	2025.12.19-12.21	国内	南宁	15	珊瑚记录的中晚全新世 ENSO 活动及其对南海珊瑚礁发育的影响机制(江蕾蕾)	口头报告

						南海北部滨珊瑚生长率记录的中晚全新世共 2203 年的 SST 及 ENSO 变化(黄达华)	口头报告
39	第十二届海洋强国战略论坛	2025.11.16	国内	杭州	1	蓝色国土:南海珊瑚礁地貌与生态演变的遥感研究与应用(黄荣永)	口头报告

（二）学者讲学

实验室 2025 年度邀请国内知名学者讲学 14 场次（18 人次）。

序号	报告题目/内容	学者	单位	时间	地点
1	LSS-Integrating Ecology, Geography, and Design for Sustainability（景观可持续科学-整合生态学、地理学与设计以实现可持续性）	邬建国教授	美国亚利桑那州立大学、生命科学与可持续发展学院	2025.3.21	海洋学院 215 会议室
2	多孔隙介质中水气两相驱替过程探索 海洋碳酸盐台地研究展望——来自科学钻探目标	陆钊副研究员 吴时国教授	浙江大学海南研究院 海南热带海洋学院海洋科学技术学院、中国科学院深海科学与工程研究所	2025.4.15	海洋学院 215 会议室

3	多尺度海洋生态动力学建模与应用	马莜沣博士	海南大学生态学院	2025.4.21	海洋学院 215 会议室
4	塑岩理化性质与形成原因的初步探索	王刘炜博士	清华大学	2025.4.30	海洋学院 1104 会议室
5	深海多圈层相互作用新认知及其对气候变化、宜居地球、生命起源的启示 Aapplcations in the reconstructionofmut-scae ocean structure	王凡研究员 杜岩研究员	中国科学院海洋研究所 中国科学院海洋研究所	2025.5.18	广西大学君武馆第二会议室
6.	野外科学观测台站内涵与定位、发展历程、成效和展望	周文能教授，南方海洋科学与工程广东省实验室（广州）副主任	南方海洋科学与工程广东省实验室	2025.6.16	海洋学院 1104 会议室
7	强化海洋意识，发展海洋经济，建设海洋强区	宁向军，广西壮族自治区海洋局党组成员、副局长	广西壮族自治区海洋局	2025.4.30	海洋学院 1104 会议室
8	基于表型组学的环境风险物质识别与评估	张琨副教授	上海交通大学	2025.6.30	海洋学院 1104 会议室
9	波澜万丈的海底构造与板块构造理论诞生	赵明辉研究员	中国科学院南海海洋研究所	2025.9.11	海洋学院 215 会议室

	滨海城市可持续发展海洋解决方案工具包（COAST）介绍	赵杰臣，联合国“海洋十年”海洋与气候协作中心（DCC-OCC）项目官员			
	联合国“海洋十年”：进展与未来	管松副研究员，联合国“海洋十年”海洋与气候协作中心（DCC-OCC）高级项目主管	自然资源部第一海洋研究所		
10	海洋藻毒素的生物合成与化学生态学研究	李爱峰教授，中国海洋大学近海环境污染与生态健康研究所所长	中国海洋大学	2025.9.18	海洋学院 215 会议室
11	湛蓝海平面下的另一个世界——谈谈用潜水调查法开展海洋研究工作	傅亮，三沙航迹珊瑚礁保护研究所所长	三沙航迹珊瑚礁保护研究所	2025.9.17	广西大学君武馆玉林厅
12	海洋生态环境效应与大数据分析	胡献刚教授，南开大学碳中和交叉科学中心副主任、环境污染过程与基准教育部重点实验室副主任	南开大学	2025.11.12	海洋学院 1104 会议室
13	强化海洋意识，发展海洋经济，建设海洋强区	宁向军，广西壮族自治区海洋局党组成员、副局长	广西壮族自治区海洋局	2025.12.09	海洋学院 215 会议室
14	高通量单细胞和单细胞细菌 RNA 测序技术的开发和应用	王永成研究员	浙江大学	2026.1.7	海洋学院 1104 会议室

七、开放课题和自主课题

本年度申请结题开放/自主课题 7 项、申请延期开放课题/自主课题 4 项，具体情况如下表所示：

序号	课题名称（项目编号）	类型	负责人	单位	起止时间	经费（万元）	状态	成果
1	南海西沙海域甘泉海台锶同位素年代学研究（GXLSCRSCS2019001）	开放课题	张江勇	广州海洋地质调查局	2019.12-2025.12	7	申请延期	国际会议报告 2 次。
2	北部湾涠洲岛珊瑚礁区果胞藻属的时-空变化规律及其碳酸钙储量研究（GXLSCRSCS2021001）	开放课题	廖芝衡	南宁师范大学	2021.12-2025.12	25	申请延期	参加学术会议 3 次。
3	造礁珊瑚摄食对其骨骼 $\delta^{13}C$ 的影响研究（GXLSCRSCS2022001）	开放课题	许慎栋	南方海洋科学与工程广东省实验室（广州）	2022.12-2025.12	25	申请结题	发表 SCI 检索论文 2 篇。
4	钙化藻中诱导棘冠海星幼虫附着的活性物质研究（GXLSCRSCS2022002）	开放课题	姚秋翠	南宁师范大学	2022.12-2025.12	20	申请延期	正在撰写 SCI 检索论文 1 篇。
5	限制粤东珊瑚群落恢复的机制研究——以大亚湾为例（GXLSCRSCS2022003）	开放课题	陈天然	中国科学院南海海洋研究所	2022.12-2025.12	5	申请结题	已提交图书章节“大亚湾石珊瑚群落的长期演变”；发表 SCI 检索论文 1 篇；参与学术会议 1 次。
6	南海现代热白化珊瑚地球化学	开放	王浩	信阳师范	2023.12-	15	申请	正在撰写 SCI 检索论文 1 篇；参

	指标特征研究（GXLSCRSCS2023001）	课题		大学	2025.12		延期	加学术会议 1 次。
7	中新世以来南海北部珊瑚礁岩的风化作用特征和成因模式（GXLSCRSCS2023002）	开放课题	杨洋	桂林理工大学	2023.12 - 2025.12	15	申请结题	发表 SCI 检索论文 2 篇；参与学术会议 4 次。
8	南海珊瑚礁中多核素联合重建人类核活动历史与核污染溯源（GXLSCRSCS2023003）	开放课题	林武辉	集美大学	2023.12 - 2025.12	20	申请结题	发表 EI 检索论文 3 篇、中文核心论文 2 篇；获中国辐射防护学会潘自强青年科学家奖和中国海洋发展研究中心优秀论文各 1 项；获《科学通报》2024 年度地球与环境科学最佳论文；参与学术会议 2 次。
9	基于完全替换策略探究南海 D1 型虫黄藻（*Durusdinium*）在珊瑚宿主中的生物学功能（GXLSCRSCS2023101）	自主课题	梁甲元	广西大学	2023.12 - 2025.12	30	申请结题	发表 SCI 检索论文 4 篇。
10	南海长棘海星快速示踪及暴发预警研究（GXLSCRSCS2023102）	自主课题	王丽伟	广西大学	2023.12 - 2025.12	30	申请结题	入选全球 Top 2%顶尖科学家“年度科学影响力排行榜；发表 SCI 检索论文 6 篇；获授权专利 1 项；参与学术会议 4 次；获奖 2 项。
11	美丽鹿角珊瑚配子发育相关基因的功能研究（GXLSCRSCS2023103）	自主课题	韦芬	广西大学	2023.12 - 2025.12	30	申请结题	发表 SCI 检索论文 1 篇、中文核心论文 4 篇。

八、科普与宣传

除了实验室主页（https://shj.gxu.edu.cn/）之外，科普与宣传活动主要依托于涠洲岛珊瑚馆、海洋科教馆、岛礁生态修复实验室和国内相关媒体。本年度涠洲岛珊瑚馆、海洋科教馆和岛礁生态修复实验室接待参观 444 场次，学生志愿参与科普与宣传讲解 214 人次。详细的年度科普与宣传统计信息如下表所示：

序号	参观人数（人次）	媒体参访与报道（次）	大型科普活动（场）
涠洲岛珊瑚馆	75873	6	2
海洋科教馆	18481	6	27
岛礁生态修复实验室	5102	6	27
合计	99456	18	29

鉴于实验室科学传播活动的显著成效，海洋科教馆于 2025 年 3 月入选中国青少年宫协会会员单位；广西大学海洋科教馆科学家精神宣讲工作室于 2025 年 4 月入围第三批广西科学家精神宣讲团名单。这标志着海洋科教馆已成为弘扬科学家精神、传播科学思想领域的重要阵地。

需要特别指出的是，实验室本年度第一次获得国家自然科学基金专项项目——科学传播类：基于珊瑚礁特色的广西海洋教育小学示范校科普活动分层分级实施（项目编号：42542038）。依托该项目，实验室本年度已 7 次走进南宁市金阳路小学开展“国家自然科学基金科普项目首入广西小学系列课堂”。

以下进一步列举实验室在本年度的代表性科普宣传/媒体报道活动：

序号	主题	时间	场地	备注
1	2024 广西最美科技工作者丨黄雯：屡赴深蓝，守护岛礁绚烂新生态	2025.01.08	海洋学院	• 广西日报（https://apph5.cloudgx.cn/article/sync1876932462610083840）
2	涠洲岛上，听“珊瑚奶爸”讲珊瑚	2025.01.17	涠洲岛	• 科普时报社（https://digitalpaper.stdaily.com/http_www.kjrb.com/kjwzb/html/2025-01/17/node_125.htm）
3	《逐梦珊海》，一曲海洋生态文明的赞歌	2025.01.15	海洋学院	• 广西日报（https://ssw.gxrb.com.cn/json/interface/epaper/api.php?name=gxrb&date=2025-01-14&code=021&xuhao=4）
4	在海底种出鲜花	2025.03.25	涠洲岛	• 广西日报（https://apph5.cloudgx.cn/article/sync1904196746046197760） • 广西新闻网（http://edu.gxnews.com.cn/staticpages/20250324/newgx67e17d02-21773449.shtml） • 广西壮族自治区科学技术厅网站（http://kjt.gxzf.gov.cn/dtxx_59340/kjdt/t19751272.shtml）
5	奋斗在一线 广西 “珊瑚奶爸”：在海底播种希望	2025.05.03	涠洲岛	• 央视新闻（CCTV 13）（https://tv.cctv.com/2025/05/03/VIDEApYcAdy6mUj8bGHreoyp250503.shtml）
6	海底“种”珊瑚是怎样一种体验？跟“珊瑚奶爸”一探究竟	2025.05.03	涠洲岛	• 中国新闻网（https://www.chinanews.com.cn/sh/2025/05-03/10410001.shtml）

7	[中国三农报道]五四青年节 广西北海 修复珊瑚礁 在海底播种希望	2025.05.04	涠洲岛	• 央视新闻（CCTV 17）（https://tv.cctv.com/2025/05/04/VIDEaZiyyuiCoz5EAAslaRfA250504.shtml）
8	世界孤独症关注日·守护“星星的孩子”	2025.04.02	海洋科教馆	• 央视新闻（CCTV 1）（https://tv.cctv.com/2025/04/02/VIDEXsxyyEOIcfnqxwVwhpJG250402.shtml?spm=C31267.PvNPVPq0jA22.EhdUNGSvFP7C.24）
9	“文明校园”系列节目——《我是接班人》	2025.05.05	涠洲岛	• 广西卫视（https://h5.gxtv.cn/html/live/tvLive.html?dataSource=2&objId=415a7b5e4194438a8be0480741a12342）
10	请查收这份来自 2025 年八桂青年的投稿	2025.05.04	海洋学院	• 广西日报视频号（https://haokan.baidu.com/v?vid=4414975172161435223） • 广西大学（https://www.gxu.edu.cn/info/1004/38161.htm） • 广西新闻网微博（https://www.weibo.com/1986954045/Pqj5xt5sq?s=6cm7D0&type=repost）
11	AI 长卷|那一片向海的深蓝里，有专注、坚守和奋斗	2025.04.25	涠洲岛	• 学习强国（https://article.xuexi.cn/articles/index.html?art_id=8158470817465685731&item_id=8158470817465685731&to_audit_timestamp=2025-04-24+15%3A50%3A50&study_style_id=feeds_default&pid=&ptype=-1&source=share&share_to=wx_single）
12	青春在志愿服务中闪闪发光 ——广西大学学生广泛参与志愿服务的火热实践	2025.03.12	海洋学院	• 人民网（http://gx.people.com.cn/n2/2025/0312/c390645-41161772.html）
13	开放的大门——首批沿海城市开放 40 年大型全媒体行动北海行	2025.03.18	涠洲岛珊瑚馆	• 广西广播电视台（https://h5.gxtv.cn/html/live/tvLive.html?dataSource=2&objId=4322f89de24e46bebaa7e206ac16f298） • 海洋学院（https://ma.gxu.edu.cn/info/1031/6234.htm）

14	守护好这片“海底雨林”（山水间的财富密码④	2025.08.25	涠洲岛	人民日报（https://mk.haiwainet.cn/n/2025/119/013EN2025082530099138.html?id=E_N_20250825_30099138&contentType=CT001#/）
15	点燃蓝色梦想！广西海洋日系列活动丰富多彩	2025.06.10	海洋学院	广西新闻网（https://www.gxnews.com.cn/staticpages/20250610/newgx684820c9-21808511.shtml）
16	从“种珊瑚”到“育珊瑚” 海底“造林”有了新进展	2025.06.08	涠洲岛	新华社客户端（https://h.xinhuaxmt.com/vh512/share/12580385?docid=12580385&newstype=1001&d=134fff0&channel=weixin&time=1749374905553）
17	广西大学海洋学院亮相全国科普月，展现珊瑚礁保护新作为	2025.9.19	海洋学院	央视频（https://www.yangshipin.cn/video/home?vid=h0000448c3z） 广西大学海洋学院（https://ma.gxu.edu.cn/info/1031/6446.htm）

九、其他社会服务活动

※ 参与编制《2025 年黄岩岛海域生态环境状况调查评估报告》，服务我国在南海的生态安全；

※ 实施中央海洋生态保护修复资金项目，修复涠洲岛 30 公顷受损珊瑚礁，入选全国 2025 年海洋生态保护修复典型案例，打造了岛礁生态系统修复的“中国样板”，在首届联合国“海洋十年”海洋生态保护修复大赛中获“海洋十年”中国行动国际合作种子基金重点项目和重大项目；

※ 对海南省生态环境监测中心在海口召开的《珊瑚礁生态质量监测技术体系》专家咨询会进行指导，并参与海南省生态环境监测中心行业标准《珊瑚礁生态监测技术规范》预研究与方案编制；

※ 为海口无境深蓝海洋生态保护中心提供的技术咨询服务，支撑“珊瑚礁人工繁育修复”与“珊瑚礁普查”等两门科学课程通过 PADI（专业潜水教练协会，全球最大的潜水培训和认证机构）保育专长课；

※ 涠洲岛珊瑚馆、海洋科教馆和岛礁生态修复实验室组织大型科普活动 29 场、媒体参访 18 次，累计接待 9.95 万人次，撰写的《打造南海珊瑚礁国家旅游名片助力海洋强国建设》社情民意信息被自治区政协教科卫体委员会报送至全国政协教科委卫体委员会和广西政协，而广西大学海洋科教馆科学家精神宣讲工作室则入围第三批广西科学家精神宣讲团名单；

※ 帮助桂林市森林公安局对 190 个珊瑚礁生物进行物种鉴定，打击了珊瑚礁生物的非法贸易，从而服务了珊瑚礁生物的保护。

十、运营管理

（一）现有主要仪器设备

1.海上探测平台

（1）地球物理探测系统

序号	设备名称	型号	厂家
1	多功能回声探测仪	DT-X	美国 Biosonics 公司
2	工业级大范围侧扫声呐	4200-MP	美国 EdgeTech 公司
3	水下高光谱剖面仪	Profiler Ⅱ	加拿大 satlantic
5	便携式高分辨率侧扫声呐	4125	美国 EdgeTech 公司
6	双频测深仪	EA400	康士伯海事公司
7	声学多普勒海流剖面仪	WHS-1200	美国 TRDI 公司
9	全数字双变频测深仪	HD-380	广州市中海达测绘仪器有限公司
10	浅地层剖面仪	3100P	美国 EdgeTech 公司
11	便携式地物光谱仪	HH2325-1075	美国 LICA INTERNATIONAL GROUP LIMIT
12	无人机监测系统	大疆 350、大疆 P1、大疆 L2、华测导航 Coprocess	DJI 大疆创新科技有限公司
13	标准型波潮仪	virtuoso3D|wave16	青岛亚必锐海洋仪器设备有限公司

（2）定位与通信系统

序号	设备名称	型号	厂家
1	卫星接收系统	GS15	徕卡测量系统贸易（北京）有限公司

2	智能型 GPS RTK 接收机	IRTK2	广州中海达测绘仪器有限公司

（3）样品数据采集系统

序号	设备名称	型号	厂家
1	浮游植物流式细胞仪	cytosense	荷兰 cytobuoy 公司
2	水下原位营养盐分析仪	EcolABII	GreenEyes 公司
3	连续监测荧光仪	MONITORING-PAM	德国 WALZ
4	温盐深仪	SBE19PlusV2	美国 SeaBird 公司
5	便携式地物光谱仪	HH2325-1075	LICA INTERNATIONAL GROUP LIMIT
6	多参数水质仪	YSI ProDSS	美国 YSI（赛莱默）分析仪器公司
7	水质多参数原位检测系统	LBF-SZDC3.5	青岛罗博飞海洋技术有限公司
8	珊瑚智能化监控平台	LBF-I0T002CR	青岛罗博飞海洋技术有限公司
9	水下调制叶绿素荧光仪	DIVING-PAM-II	德国 WALZ
10	珊瑚原位呼吸代谢测量仪	CISME	加拿大 Qubit Systems
11	CTD 采水器	MISS	意大利 IDRONAUT

2.实验分析平台

序号	设备名称	型号	厂家
1	电子探针显微分析仪	JXA-8230	日本 JEOL 公司
2	岩芯综合测试系统	MSCL-S	英国 GEOTEK 公司
3	稳定同位素质谱仪	MAT 253	赛默飞世尔科技有限公司
4	发射扫描电子显微镜	SU5000	日本 HITACHI 公司
5	超高效液相色谱-三重四级杆质谱联用仪	AGILENT 1290/6460	安捷伦科技有限公司

6	显微激光共焦拉曼光谱仪	invia	英国雷尼绍公司
7	气质联用仪	Agilent 7890B/7000C	美国 AGILENT TECHNOLOGIES
8	电感耦合等离子体质谱仪	ICAPQC	赛默飞世尔科技有限公司
9	电感耦合等离子体质谱仪	Plasma Quant MS	德国耶拿分析仪器股份有限公司
10	离子阱质谱仪	LTQ XL	美国赛默飞世尔科技有限公司
11	X 射线粉末衍射仪	Ultima IV	日本朱式会社理学
12	高纯锗γ谱仪	GWL-120-15-LB-AWT	美国 AMETEK 公司
13	电感耦合发射光谱仪	ICAP7400	赛默飞世尔科技有限公司
14	微生物鉴定系统	GEN III MicroStation	美国 BIOLOG 公司
15	元素分析仪	VARIO MACRO CUBE	德国 ANALYSENSYSTEME GMBH
16	高效液相色谱仪	ULTIMATE 3000	赛默飞世尔科技
17	全自动气体吸附分析仪	AUTOSORB-IQ-MP	唐塔公司
18	总溶解性无机碳分析仪	AS-C6	美国 Apollo Scitech
19	荧光定量 PCR 仪	7500Fast	美国 ABI 公司
20	气相色谱仪	AGILENT 7890B	安捷伦科技有限公司
21	总碱度分析仪	AS-ALK2	美国 Apollo Scitech
22	紫外可见分光光度计	LAMBDA 1050	英国 PERKIN ELMER 公司
23	多功能酶标仪	Varioskan LUX	美国赛默飞世尔科技有限公司
24	偏光显微镜	LV100NPOL	日本尼康株式会社
25	电动摄影生物显微镜	Ni-E	日本尼康公司
26	三维建模可视化系统	EVS	美国 C TECH 公司
27	原子荧光光度计	AFS-9230	北京吉天仪器有限公司

28	多功能生物分子成像仪	ImageQuant LAS500	美国 GE 公司
29	超纯水系统	Milli-Q Integral 10	默克密理博有限公司
30	紫外分光光度计	UV-2700	日本岛津公司
31	珊瑚养殖系统	定制	广西南宁市铭嘉水产养殖有限公司
32	金相显微镜	LV150N	日本尼康公司
33	颚式破碎仪	JC6	北京格瑞德曼仪器设备有限公司
34	磁控离子溅射仪	MSP-2S	美国 IXRF 公司
35	叶绿素荧光测定仪	Trilogy	美国纳特，YURNER DESIGNS
36	磁化率仪	MS2	Bartington Instruments Ltd
37	体式显微镜	SZX16	奥林巴斯（中国）有限公司
38	微波消解萃取仪	MDS15	上海新仪
39	热循环仪	LabCycler	德国 SENSOQUEST（圣欧）有限责任公司
40	超微量分光光度计	DS-11FX+	美国 DeNovix Inc 公司
41	电化学工作站	Zennium XC	德国 Zahner 公司
42	研究级正置荧光显微镜	DM2000LED	德国徕卡公司
43	全波长酶标仪 Epoch 安捷伦科技有限公司	全波长酶标仪 Epoch 安捷伦科技有限公司	全波长酶标仪 Epoch 安捷伦科技有限公司

（二）三十万元以上设备的年度使用情况

序号	设备名称	型号	购买时间	价格（万元）	使用时间（小时）
1	高纯锗γ谱仪	GWL-120-15-LB-AWT	2018.04	103.9	0
2	电动摄影生物显微镜	Ni-E	2019.05	31.5	150

3	卫星接收系统	GS15	2017.05	39.0	80
4	浮游植物流式细胞仪	cytosense	2016.09	229.9	380
5	高效液相色谱仪	ULTIMATE 3000	2019.04	59.9	45
6	岩芯综合测试系统	MSCL-S	2017.12	419.7	50
7	三维建模可视化系统	EVS	2019.03	31.0	200
8	温盐深仪	SBE19PlusV2	2016.09	34.9	80
9	连续液流仪器分析仪	San++	2016.06	84.9	800
10	全自动营养盐分析仪	QuAAtro	2016.06	67.9	50
11	便携式高分辨率侧扫声呐	4125	2016.09	54.9	85
12	工业级大范围侧扫声呐	4200-MP	2016.09	84.8	20
13	多功能回声探测仪	DT-X	2016.09	84.9	500
14	双频测深仪	EA400	2016.11	39.9	70
15	电子探针显微分析仪	JXA-8230	2018.05	463.6	81
16	显微激光共焦拉曼光谱仪	invia	2019.11	220.9	80
17	水下高光谱剖面仪	Profiler Ⅱ	2017.03	79.8	75
18	声学多普勒海流剖面仪	WHS-1200	2017.03	33.3	80
19	稳定同位素质谱仪	MAT 253	2015.03	369.3	8541
20	元素分析仪	VARIO MACRO CUBE	2015.11	82.1	357
21	连续监测荧光仪	MONITORING-PAM	2016.09	56.7	821
22	水下原位营养盐分析仪	EcolABII	2016.09	75.5	60
23	X 射线粉末衍射仪	Ultima IV	2016.09	139.9	50

24	珊瑚原位呼吸代谢测量仪	CISME	2023.03	51.8	400
25	全自动气体吸附分析仪	AUTOSORB-IQ-MP	2016.06	50.0	500
26	超高效液相色谱仪	H-CLASS	2016.06	76.8	461
27	超高效液相色谱-三重四级杆质谱联用仪	AGILENT 1290/6460	2015.12	250.2	500
28	气质联用仪	Agilent 7890B/7000C	2016.09	193.6	2021
29	电感耦合等离子体质谱仪	Plasma Quant MS	2016.09	174.9	200
30	离子阱质谱仪	LTQ XL	2016.11	162.9	277
31	电感耦合等离子体质谱仪	ICAPQC	2015.03	169.5	230
32	多功能酶标仪	Varioskan LUX	2016.11	39.8	400
33	微生物鉴定系统	GEN III MicroStation	2016.09	87.9	30
34	荧光定量 PCR 仪	7500Fast	2016.06	47.9	40
35	偏光显微镜	LV100NPOL	2015.10	34.9	140
36	原子吸收光谱仪	ZEEnit700P	2015.11	65.1	515
37	电感耦合发射光谱仪	ICAP7400	2015.03	103.1	870
38	傅立叶变换红外光谱仪	IRTrace-100	2016.06	36.0	90
39	发射扫描电子显微镜	SU5000	2016.09	279.9	259
40	水下调制叶绿素荧光仪	DIVING-PAM-II	2023.03	58.8	350
41	气相色谱仪	AGILENT 7890B	2015.12	47.0	20
42	珊瑚智能化监控平台	LBF-I0T002CR	2021.04	54.7	8760
43	CTD 采水器	MISS	2020.07	49.7	20

44	温湿度控制-气液配气系统	DGL-III	2018.12	73.55	744
45	光电综合测试平台	CGS-MT	2019.05	39.78	150
46	总碱度分析仪	AS-ALK2	2020.07	31.95	75
47	总溶解性无机碳分析仪	AS-C6	2020.07	84.95	20
48	紫外可见分光光度计	LAMBDA 1050	2020.07	54.95	20
49	手持式矿石分析仪	XL3t 950	2020.12	39.68	135
50	研究级正置荧光显微镜	DM2000LED	2022.06	33.94	265
51	藻类自动在线监测系统	CytoBST3942	2022.12	99.55	0
52	水质多参数原位检测系统	LBF-SZDC3.5	2023.06	39.27	8760

十一、附录：年度论文集

实验室 2025 年论文集索引表：

方向 1　南海珊瑚礁生物与生态

序号	题目（作者）	期刊	页码
1	Silicon enhances potassium uptake and leaf growth in Avicennia marina, asilicon-accumulating mangrove plant with silicon transporters (Zejun Guo, Siyao Liao, Chaoqun Xu, Mingyue Wei, Lingyu Song, Hezi Huang, Zhanhong Li, Xi Chen, Lei Jiang, Hailei Zheng*)	Industrial Crops and Products	146
2	Nitrite-induced intestinal injury mechanisms and multi-organ toxicity in Tilapia: Insights from integrated multi-omics analysis (Tingyu Wei, Xuemin Wei, Jialong Huang, Songlin Luo, Aiguo Huang*)	Aquaculture	162
3	Microbiome dynamics and multiscale environmental response patterns of later-diverging coral clade across latitudes, reefs and geomorphological zones in the South China Sea (Biao Chen, Lin Liang, Kefu Yu*, Yuxin Wei, Xinyue Liang, Zeming Bao, Zhiheng Liao, Xiaopeng Yu, Zhenjun Qin, Lijia Xu, Yongzhi Wang, Yaru Kang)	Ecological Informatics	173
4	The Dynamics of Symbiodiniaceae and Photosynthetic Bacteria Under High- Temperature Conditions (Yongqian Xu, Jiayuan Liang*, Liangyun Qin, Tianyi Niu, Zhuqing Liang, Zhicong Li, Biao Chen, Jin Zhou, Kefu Yu*)	Microbial Ecology	193
5	Effects of Natural Ingredient Xanthohumol on the Intestinal Microbiota, Metabolic Profiles and Disease Resistance to Streptococcus agalactiae in Tilapia Oreochromis niloticus (Aiguo Huang, Yanqin Wei, Jialong Huang, Songlin Luo, Tingyu Wei, Jing Guo, Fali Zhang*, Yinghui Wang*)	Microorganisms	206
6	Antioxidant capacity is a key factor in the difference in thermal tolerance between massive Porites lutea and branching Acropora Formosa (Linqing Meng , Ronghua Tan, Zunyong Xiao, Jinlian Chen, Zhihua Huang, Yonggang Wang, Enguang Yang, Yupeng Zhou, Mingpei Xu, Kefu Yu, Wen Huang*)	Marine Pollution Bulletin	224
7	Color disparity enhances the toxic effects of polystyrene microplastics on Cladocopium goreaui (Tianyi Niu, Yating Yang, Sanqiang Gong, Kefu Yu, Jiayuan Liang*)	Marine Pollution Bulletin	235

8	The stress response strategies of two typical coral Symbiodiniaceae (Cladocopium goreaui and Durusdinium trenchii) under abnormal temperatures (Jiayuan Liang*, Liangyun Qin, Li Zhang, Yongqian Xu, Tianyi Niu, Zhicong Li, Yating Yang, Zhuqing Liang, Kefu Yu*, Sanqiang Gong)	Algal Research-Biomass Biofuels and Bioproducts	248
9	Responses of the Coral Symbiont Cladocopium goreaui to Extreme Temperature Stress in Relatively High- Latitude Reefs, South China Sea (Lifei Wei, Shuchang Chen, Zhenjun Qin*, Nengbin Pan, Mengling Lan, Tingchao Zhang, Ran He, Hongye Liang, Wenzhi Deng, Changhao Mo, Kefu Yu*)	Microbial Ecology	260
10	Environmental acclimatization of the relatively high latitude scleractinian coral Pavona decussata: integrative perspectives on seasonal subaerial exposure and temperature fluctuations (Man Zhang, Shan Huang, Li Luo, Kefu Yu*)	BMC Genomics	273
11	Characteristics of Carbonatogenic Bacteria and Their Role in Enhancing the Stability of Biocrusts in Tropical Coral Islands (Qiqi Chen, Lin Wang, Jie Li, Qiqi Li, Hongfei Su*, Zhimao Mai*)	Microorganisms	290
12	Coral polyp and skeletal microbiome in tropical and subtropical reefs in the South China Sea: spatial variation and implications for coral environmental adaptability (Zhenjun Qin*, Mengling Lan, Nengbin Pan, Kefu Yu*, Lifei Wei, Qizhi Yang, Tingchao Zhang, Ran He)	Acta Oceanologica Sinica	303
13	Coral microbiome in estuary coral community of Pearl River Estuary insights into variation in coral holobiont adaptability to low-salinity conditions (Mengling Lan, Kaixiang Gao, Zhenjun Qin*, Zhanhong Li, Ru Meng, Lifei Wei, Biao Chen, Xiaopeng Yu, Lijia Xu, Yongzhi Wang, Kefu Yu*)	Bmc Microbiology	323
14	Sensitive detection of early growth of Skeletonema costatum using a gold-doped carbon sphere-gold nanoparticle electrochemical biosensor (Ziyang Xian, Yayi He, Chaoxin Zhang, Hao Fu, Yaling Liu, Tao Zhang, Shaopeng Wang, Shan Lu, Man Zhang*, Liwei Wang*)	New Journal of Chemistry	340
15	Carbonatibacter coralli gen. nov., sp. nov., a carbonate-producing and vitamin B12-sharing bacterium isolated from coral Porites lutea, reclassification of Kiloniellaceae and proposal of Aestuariispiraceae fam. nov. (Siyu Hu, Kun Lu, Chenyan Wang, Mi Li, Jinsheng Huang, Guanghua Wang*)	International Journal of Systematic and Evolutionary Microbiology	350
16	Polystyrene microplastics exhibit toxic effects on the widespread coral symbiotic Cladocopium goreaui (Jiayuan Liang*, Tianyi Niu, Li Zhang, Yating Yang, Zhicong Li, Zhuqing Liang, Kefu Yu*, Sanqiang Gong)	Environmental Research	359
17	Heat-tolerant subtropical Porites lutea may be better adapted to future climate change than tropical one in the South China Sea (Wen Huang*, Jinlian Chen, Enguang Yang, Linqing Meng, Yi Feng, Yinmin Chen, Zhihua Huang, Ronghua Tan, Zunyong Xiao,	Science of the Total Environment	371

	Yupeng Zhou, Mingpei Xu, Kefu Yu*)		
18	虫黄藻（Effreniumvoratum）对高温胁迫的生理响应(张廷超，潘能斌，唐媛媛，何 燃，蓝梦玲，韦丽菲，覃祯俊*)	海南热带海洋学院学报	383
19	造礁珊瑚热适应相关功能基因的研究进展(马玉玲，俞小鹏*，余克服*，陈俊伶，郑月，陈健)	海洋学报	393
20	涠洲岛四种造礁石珊瑚耐热阈值测定及其差异性对比(徐明培，黄雯*，陈锦连，黄智华，周榆鹏，宛强，李雨箫，余克服)	海洋湖沼通报	413
21	美丽鹿角珊瑚(Acropora muricata)与风信子鹿角珊瑚(Acropora hyacinthus)的耐热性差异研究(周榆鹏，肖遵勇，陈锦连，黄智华，徐明培，谭荣华，蒙林庆，王永刚，余克服，黄雯*)	海洋学报	425
22	海洋生物学进展研究生课程个性化教学改革探索与实践(苏宏飞，梁甲元，余克服*)	科教导刊 - 电子版	436
23	虫黄藻对低盐胁迫的生理响应(何燃,高楷翔,潘能斌,李展泓,张廷超,梁宏业,卢晓燕,蓝梦玲,覃祯俊*)	热带生物学报	439
24	两种环境敏感性不同的虫黄藻(Cladocopium goreaui 和 Durusdinium trenchii)的脂质代谢对热胁迫的响应模式(张丽,李志聪,杨雅婷,梁祝清,冯宜合,卢铭垚,胡思雨,余克服,梁甲元*)	海洋学报	447
25	两株海洋来源贝莱斯芽孢杆菌的筛选、分离鉴定及益生特性(陈凡,韦冬冬,谢瑾琨,余庆,高艳侠,黄静,何金钊,施金谷,赵明明,覃向谋,苏宏飞*,李鹏飞*)	广东海洋大学学报	461
26	珊瑚源噻虫嗪降解菌的分离、鉴定及其降解特性研究(邹杰,王琳,陈祺琦,何旭聪,黄金梅,孙天奕,苏宏飞*)	广东农业科学	472
27	室内养殖条件下两种造礁石珊瑚的性腺发育研究(黄菲菲,崔梦瑶,韦芬*,杨溪月,潘晓媛,玉颢瑜)	广西科学	486
28	一株珊瑚来源二苯甲酮-3 降解菌 Sphingopyxis terrae SCSIO 90395 的分离鉴定及基因组特征(刘名定,蔡永超,李洁,刘青,张健,吕丽娜,苏宏飞*)	热带海洋学报	494
29	造礁珊瑚有性繁殖的研究进展(崔梦瑶,韦芬*,余克服*)	海洋学报	505
30	基于转录组学的造礁石珊瑚环境胁迫响应机制研究进展(陈俊伶,马玉玲,郑月,余克服*,俞小鹏*)	广西科学	519
31	珊瑚共生蓝藻 Synechococcus sp.GXU01 对两种典型虫黄藻的代谢协调作用(李志聪,胡思雨,梁祝清,杨雅婷,卢铭垚,余克服,梁甲元*,张丽,冯宜合)	广西科学	539
32	涠洲岛海域 7 种造礁石珊瑚的生长差异研究(汪婷婷,周兴旺,谭何勇,肖遵勇,黄雯,胡庭俊*)	广西科学	550

33	基于环境 DNA 技术的造礁石珊瑚物种多样性分析 ——以涠洲岛珊瑚礁区为例(曾心茹,韦芬*,崔梦瑶,玉颢瑜,潘晓媛,余克服)	海洋环境科学	558

方向 2　南海珊瑚礁地质与环境

序号	题目（作者）	期刊	页码
34	Dominance of coralline algae in the South China Sea: Insights into their responses to paleoceanographic events over the last 20 million years (Yinqiang Li, Kefu Yu*, Lizeng Bian, Baoqing Hu, Zhiheng Liao, Shengmin Huang, Zhiguang Song, Weihua Liao)	Palaeogeography Palaeoclimatology Palaeoecology	568
35	Holocene coral reef carbonate REY geochemistry during the neomorphism from aragonite to calcite: A case study in the South China Sea (Wei Jiang, Yuwen Xiao, Kefu Yu*, Rui Wang, Shendong Xu, Ning Guo, Tingwu Gu)	Palaeogeography Palaeoclimatology Palaeoecology	580
36	High-Resolution Coral Records of Rare Earth Elements and Yttrium in Seawater Driven by Submarine Groundwater Discharge in a Basalt Island: A Case Study in the Northern South China Sea (Tingwu Gu, Wei Jiang*, Yansong Han, Chunmei Feng, Ning Guo, Caifeng Liu, Yu Zhang, Kefu Yu)	journal of geophysical research-earth surface	590
37	The Potential of Benthic Foraminifera Carbon and Oxygen Isotopic Proxies as Environmental Indicators in Coral Reef Regions (Siqi Wu, Risheng Liang, Kefu Yu*)	Paleoceanography and Paleoclimatology	605
38	Geochemical characteristics and petrogenesis of the basaltic pyroclastic rocks from the Xisha Islands, northwestern South China Sea (Yu Zhang, Yaqi Yuan, Kefu Yu*)	Acta Oceanologica Sinica	622
39	Geochemical behavior of redox sensitive trace metals in marine environment and their applications as paleoredox proxies (Guo Ning, Jiang Wei *, Li Yueer, Yu Kefu)	Palaeogeography Palaeoclimatology Palaeoecology	636
40	Molecular indicators of microbial community change linked to salinity variation and terrestrial inputs during the Ordovician-Silurian transition (East-Central USA) (Yi Song, Thomas J. Algeo, Carlton Brett, Zhanhong Liu, Shucheng Xie*)	Chemical Geology	660
41	The topographic features and sedimentary environment potentially influenced the vegetation reconstruction in southwestern China since the MIS3(Xiao Zhang, Yuanfu Yue*, Ziyan Zhang, Liuying He, Xinmeng Yuan, Xintian Yu, Qiuchi Wan, Cong Chen, Yongjie Tang, Zhuo Zheng, Kangyou Huang)	Quaternary Science Reviews	675
42	Microbially-mediated supergene dissolution and oxidization of solid manganese carbonate in the Malkantu manganese ore deposit in West Kunlun, Northwest China (Lingnan Zhao, Qin Huang*, Daohui Pi, Yi Zhang, Daqing Ding, Sasmaz Ahmet)	Ore Geology Reviews	689
43	Seasonal Variations in Coral Lipids and Their Significance for Energy Maintenance in the South China Sea (Shendong Xu*, Hongyan Mo, Kefu Yu*, Jie Gao, Zheng Men)	Journal of Geophysical Research-Oceans	699

44	ENSO variations during the mid- to late Holocene: Evidence from coralgrowth rates spanning 2203 years in the northern South China Sea (Dahua Huang, Kefu Yu*, Leilei Jiang, Wei Jiang)	Global and Planetary Change	712
45	Vegetation ecosystem responses to climate-human interactions since the Late Holocene from peat record of Niangniang Mountain, western Guizhou（Yuanfu Yue,Shixiong Yang*,Liuying He,Zhuo Zheng,Xiao Zhang,Cong Chen,Qiuchi Wan,Yongjie Tang,Kangyou Huang,Fang Gu）	Global and Planetary Change	725
46	珊瑚脂类生物标志物组成及对环境的响应：研究进展与问题(臧明思,王佳宝,宋宜*,黄雯,余克服)	地球环境学报	740
47	南海北部滨珊瑚微环礁的海平面指示意义及其反映的中全新世海平面历史(乐远福*,赵毅恒,唐立超,张博,熊海仙,张雅泽)	地球科学	752
48	近 30 年来涠洲岛海域海水磷含量变化及其影响因素——来自高分辨率珊瑚记录的证据(陈裕月，姜伟*，杨浩丹，余克服)	热带海洋学报	766
49	互联网在海洋科学研究生教育中的应用：现状、挑战与应对(姜伟，梁甲元，黄荣永，余克服*)	中国多媒体与网络教学学报	777
50	海相碳酸盐硼同位素反演古海水 pH 值模型及其应用(王瑞,刘春彤,吴松烨,花绘)	石油与天然气地质	781
51	南海礁区大型底栖有孔虫 Mg/Ca 值微区分布及其应用潜力(黄晓婷,李玫,吴司琪*)	微体古生物学报(中英文)	794
52	西沙群岛太阳长棘海星（Acanthaster solaris）幽门盲囊细菌多样性及群落组成研究(余骄洋,俞小鹏,余克服*,马玉玲)	热带地理	807

方向 3　南海珊瑚礁环境与化学

序号	题目（作者）	期刊	页码
53	Organophosphate Ester Migration Mechanisms and Environmental Impacts in the Western South China Sea (Minwei Han, Kefu Yu*, Ruijie Zhang, Biao Chen, Mei Xiong, Yaru Kang, Xiaopeng Yu, Zhenjun Qin, Xiangrong Xu)	Environmental Science & Technology	821
54	Emerging and legacy organophosphate flame retardants in the tropical estuarine food web: Do they exhibit similar bioaccumulation patterns, trophic partitioning and dietary exposure? (Qianyi Huang,Rui Hou*,Yuchen Wang,Lang Lin,Hengxiang Li,Shan Liu,Xiangrong Xu*,Kefu Yu,Xiaoping Huang)	Water Research	836
55	Cytochrome P450-mediated biotransformation of octocrylene in Tetradesmus obliquus Integrative insights from transcriptomics, proteomics, molecular docking, and density	Journal of Hazardous Materials	847

	functional theory calculation (Junjie Hu, Changgui Pan*, Xiangrong Xu*, Fengjiao Peng, Shan Liu, Jiying Pei, Zhenzhu Liu, Hao Liang, Kefu Yu)		
56	Polymer Type, Oxidation, Size, and Abundance of Microplastics in Subsoils versus Topsoils with Varying Land Use in Beijing, China (Liuwei Wang, Caide Huang, Junhao Cao, Pingfan Zhou, Siqi Han, Guangyu Qu, Michael S. Bank, Deyi Hou*)	Environmental Science & Technology	858
57	An integrated multi-omics approach reveals octocrylene disrupts Tetradesmus obliquus growth by triggering a cascade of photosynthetic inhibition and metabolic dysregulation (Junjie Hu, changgui Pan*, Fengjiao Peng*, Hao Liang, Zhenzhu Liu, Kefu Yu)	Journal of Hazardous Materials	872
58	Targeted and non-targeted analyses reveal trophic biomagnification of rubber-derived chemicalin an estuarine food web near China's largest rubber production region (Yuan Liu, Jiaming Zhou, Niannian Wu, Shan Liu*, Xiaoliang Liao, Haijiang Wu, Lin Zhu, Hengxiang Li, Lang Lin, Rui Hou, Zhihua Li, Xiangrong Xu, Zhifeng Chen*, Zongwei Cai)	Journal of Hazardous Materials	885
59	Rainfall, seasonal variation, and stream type governing the multi-media fate and ecological risks of tire additives and their transformation products in mega-urban streams (Lini Wei, Niannian Wu, Ru Xu, Yuan Liu, Shan Liu*, Haiyan Zhang, Zitong Li, Yuehong Liu, Xiangrong Xu, Jianliang Zhao*, Guangguo Ying)	Water Research	896
60	Exploring the structural diversity and spatiotemporal dynamics of mogrosides in Siraitia grosvenorii (Jiying Pei, Qiong Su, Shuiyuan Jiang, Jianxiu Li*, Nengzhong Xie*)	Food Chemistry	908
61	Emerging microplastic and nanoplastic threats: Decoding winter survival mechanisms in hybrid groupers through hepatic metabolic disruption (Julong Wang, Yan Gao, Shanshan Yao, Lang Lin*, Hengxiang Li, Shan Liu, Rui Hou, Zhijian Jiang, Xiangrong Xu*)	Environmental Chemistry and Ecotoxicology	920
62	Deciphering the Universal Role of Gut Microbiota in Pollutant Transformation (Rui Hou, Xiaowei Jin, Jingchun Feng*, Jingchuan Xue, Chengzhi Chen, Yuanqiang Zou, Xiangrong Xu*, Kefu Yu, Peiyuan Qian, Wei Zhang, Jizhong Zhou, Si Zhang, Zhifeng Yang)	The ISME Journal	932
63	Nationwide occurrence, distribution drivers, and source apportionment of steroids in China's coastal wetlands: An urgent priority for 4-andro\u0002stene-3,17-dione and progesterone (Shan Liu, Qinge Zhou, Yuan Liu, Biao Li, Huabing Li, Jixun Chen, Niannian Wu, Man Wang, Xiangrong Xu, Lijun Zhou*, Qinglong L. Wu*)	Environmental Chemistry and Ecotoxicology	954
64	Construction of S-type CdS@ZnIn2S4 heterojunctions with core-shell hollow nanosphere and their application in visible light photocatalytic degradation of antibiotics (Qiqi Huang, Jiqiao Zhang, Ziwen Song, Xianwang Deng, Songlin Luo,	Journal of Alloys and Compounds	966

	Weizhi Yua, Xiaofang He, Pengfei Zheng, Shaopeng Wang*, Liwei Wang*)		
65	Constructing of Bi2O3-In2O3 nanofibers for sensitive detection of freshness gas markers in aquatic products (Liwei Wang, Liping Gao*, Hongjie Liu*, Qian Zhang, Hao Fu, Zhelin Liu)	Journal of Alloys and Compounds	976
66	Electrochemical biosensor based on strand displacement reaction for on- site detection of Skeletonema costatum (Yaling Liu, Yibo Zhang, Changrui Ye, Yayi He, Shaopeng Wang, Man Zhang, Hao Fu, Shan Lu*, Liwei Wang*)	Microchimica Acta	985
67	Comparison of UV based advanced oxidation processes (UV/H2O2, UV/NaClO, and UV/Na2S2O8) for inactivating Uronema marinum inmarine water (Xuan Chen, Pin Gan, Kunling Huang, Fangyu Liang, Tianhao Wu, Xudong Li, Yuanyuan Zhang*)	Journal of Water Process Engineering	998
68	Sorption and mechanisms of legacy and emerging per- and polyfluoroalkyl substances (PFASs) on different particle size fractions of marine sediments (Junjie Hu, Shangke Yu, Chao Yin, Fengjiao Peng, Shuangshuang Liu, Changgui Pan*, Kefu Yu)	Environmental Research	1010
69	A ratiometric electrochemical DNA biosensor for the detection of crown-of-thorns starfish eDNA (Beihua Wen, Zhenyu Zhu, Junjie Zeng, Shiwei Wan, Chaoxin Zhang, Yingzhan Chen, Liwei Wang*, Man Zhang*, Kefu Yu)	Bioelectrochemistry	1022
70	Atmospheric transport of microplastics from land to sea is inefficient: Evidence from multimedia observations (Xiangrong Xu*, Zhen Yuan, Yanxu Zhang, Hengxiang Li, Lang Lin, Shan Liu, Rui Hou, Eddy Y. Zeng)	Journal of Hazardous Materials	1032
71	Spatiotemporal distribution and priority assessment of steroids in the estuarine environment: Implications for environmental risk management (Ru Xu, Niannian Wu, Shan Liu, Hui Chen, Qinwei Hao, Yongxia Hu, Bing Hong, Shen Yu, Xiangrong Xu*)	Marine Pollution Bulletin	1042
72	Hydrothermal carbonization of model compounds of municipal sludge: Effects of reaction conditions and aqueous phase recirculation (Yiming Feng, Xueling Hu, Yuyang Xue, Xingying Tang*, Donghai Xu, Yingying Zhang, Yumeng Wu)	Journal of Environmental Chemical Engineering	1053
73	A novel phosphorus segregation–driven chromium depletion mechanism for intergranular corrosion of inconel 625 in SCWO–HyMoS environments (Ke Li, Jiquan Chen, Guiyuan Xie, Xingying Tang*, Donghai Xu, Jianqiao Yang)	Corrosion Science	1064
74	Regulation of slow-release performance of high-sugar biomass waste filter mud and sugarcane bagasse by co-hydrothermal carbonization and potential evaluation of hydrochar-based slow-release fertilizers (Sisi Chen, Xingying Tang*, Jiquan Chen, Yuyang Xue, Yinghui Wang, Donghai Xu)	Biomass & Bioenergy	1076
75	Efficient and selective recovery of lithium from spent lithium-ion batteries by biomass single-component regulated pyrolysis with synergistic water leaching approach	Journal of Environmental Chemical Engineering	1090

	(Yumeng Wu, Jianjun Cai*, Xingying Tang*, Shubin Wang, Mingkang Fang, Shengfeng Yao, Jiafeng Zhang)		
76	Parabens and Their Metabolites in Surface Sediment from Estuaries to the Sea: Occurrence, Spatial Distribution, and Potential Sources (Fengjiao Peng, Ronggui Zhu, Changgui Pan*, Chaoyang Zhou, Junjie Hu, Sen Li, Xingjun Feng, Kefu Yu)	Acs Es&T Water	1101
77	Occurrence, spatiotemporal distribution and environmental behavior of dissolved, particulate, and sedimentary black carbon in a subtropical coastal environment: Differences between semi-enclosed and open estuaries. (Jingyu Wang,Ruijie Zhang*,Jingzhen Wang*,Liwei Mo,Zhehong Ji,Pan Wei,Chaoshuai Wei,Kefu Yu)	Marine Pollution Bulletin	1111
78	Further increasing nitrogen concentration does not enhance the denitri cation and DNRA potentials in eutrophic reefs: Insights from the differences in benthic categories (Zhiming Ning, Zhijin Liu, Kefu Yu, Ronglin Xia, Wei Jiang, Bin Yang, Guodong Song*)	Limnology and Oceanography	1122
79	3D-printed SPME-based wooden-tip mass spectrometry for rapid detection of organic ultraviolet absorbers in complex matrices (Yingyuan Zhang, Deshuo Gao, Kefu Yu, Ruijie Zhang, Jiayu Zhang, Wenfeng Yu, Shiguo Chen, Jiying Pei*)	Talanta	1137
80	Comparative evaluation of positive and negative LC-MS modes for DOM profiling (Jiying Pei, Shiguo Chen, Jiayu Zhang, Wenfeng Yu, Weijie Qin, Kefu Yu*)	Analytical Methods	1146
81	Microbial regulation of dissolved organic matter revealed by integrated metabolomics and metagenomics in the World's deepest blue hole (Jiying Pei*, Shiguo Chen, Kefu Yu*, Jiayuan Liang*, Ruijie Zhang, Penghui Li, Zhuanghao Hou, Liang Fu, Honglin Ma)	Marine Environmental Research	1157
82	Advances in Dissolved Organic Carbon Remote Sensing Inversion in Inland Waters: Methodologies, Challenges, and Future Directions (Dandan Xu, Rui Xue, Mengyuan Luo, Wenhuan Wang, Wei Zhang*, Yinghui Wang*)	Sustainability	1167
83	Estimation of Mangrove Aboveground Carbon Using Integrated UAV-LiDAR and Satellite Data (Xuzhi Mai, Quan Li, Weifeng Xu, Songwen Deng, Wenhuan Wang, Wenqian Wu, Wei Zhang*, Yinghui Wang)	Sustainability	1202
84	Influence of Air, Water, Light, and Salinity on Release of Plasticizers, Flame Retardants, and Ultraviolet Absorbents from Polystyrene Plastic. (Hongshuang Shen,Fang Liu,Ruijie Zhang*,Annan Yan,Yaru Kang,Jingyu Wang,Kefu Yu)	Bulletin of Environmental Contamination and Toxicology	1231
85	Research progress on fungi and their spore inactivation in different water bodies (Fangyu Liang, Yuanyuan Zhang*)	Desalination and Water Treatment	1240
86	Effects of dissolved oxygen accelerated P. aeruginosa on the corrosion mechanism of X70 steel in simulated marine environments (Riguang Zhu, Guiyuan Xie, Zu-an Qin, Xingying Tang*, Jianjun Cai, Jianqiao Yang)	Materials Chemistry and Physics	1250

87	Comparative study of the corrosion behavior of Inconel 625 in supercritical water containing dissolved and molten phosphates (Jiquan Chen, Zitao Lin, Xingying Tang*, Ke Li, Riguang Zhu, Jianqiao Yang)	Journal of Supercritical Fluids	1266
88	Microplastic in tropical island estuaries in China: Source identification and management framework development (Bin Chen, Yang Zhou, Kazi Belayet Hossain, Yixin Chen, Xiaoshan Zhu, Hengxiang Li, Xiangrong Xu*, Minggang Cai*)	Marine Environmental Research	1278
89	Protective Effect of Nanobodies Targeting Sip Protein Against Streptococcus agalactiae Infection in Tilapia (Oreochromis niloticus) (Zhishen Wang, Huiling Wu, Weihao He, Shunqiang Wei, Xuemin Wei, Chaoshuai Wei, Yinghui Wang*, Aiguo Huang)	Animals	1290
90	High-Resolution Mapping and Impact Assessment of Forest Aboveground Carbon Stock in the Pinglu Canal Basin: A Multi-Sensor and Multi-Model Machine Learning Approach (Weifeng Xu, Xuzhi Mai, Songwen Deng, Wenhuan Wang, Wenqian Wu, Wei Zhang*, Yinghui Wang)	Forests	1305
91	Assessment of biodiversity and landscape changes during the Pinglu Canal construction and the benefits of ecological restoration based on Rao's Q index (Songwen Deng, Mengyuan Luo, Wenhuan Wang, Sixiang Lan, Weifeng Xu, Xuzhi Mai, Wei Zhang*)	Ecological Engineering	1330
92	Synergistic hydrothermal carbonization and wet oxidation for sustainable sewage sludge valorization and process waters toxicity mitigation (Geng Yang, Xingying Tang*, Xingtao Wang, You Wu, Hui Ma, Shengyan Pu)	Biomass & Bioenergy	1343
93	Advancements of the Vibrio coralliilyticus eDNA detection based on Co-Fe PBA-assisted biosensors for the rapid coral-disease warning (Yibo Zhang, Hongjie Liu, Shaopeng Wang*, Hao Fu, Yuanyu Xie, Chaoxin Zhang, Man Zhang, Jie Lu, Liwei Wang*, Kefu Yu)	Biochemical Engineering Journal	1354
94	Progress and Limitations in Forest Carbon Stock Estimation Using Remote Sensing Technologies: A Comprehensive Review (Weifeng Xu, Yaofei Cheng, Mengyuan Luo, Xuzhi Mai, Wenhuan Wang, Wei Zhang*, Yinghui Wang*,)	Forests	1363
95	基于单细胞质谱组学研究珊瑚共生虫黄藻的化学多样性(张佳宇,陈仕国,余克服,梁甲元,侯壮豪,裴继影*)	质谱学报	1399
96	液相循环对制糖固废共水热碳化影响机制研究(陈思思,薛宇阳,唐兴颖*,王智洁,张莹莹,钱黎黎,李尚泽,王英辉)	中国环境科学	1413
97	氮磷限制条件下球形棕囊藻生理生化响应及转录组学研究 (邢 政，王佳乐，赖俊翔*，王英辉*，李 杰)	广西科学	1424
98	不同类型城市受纳河涌大型底栖动物多样性及其对水环境因子的响应(韦丽妮,刘	生态毒理学报	1442

	珊*,赵建亮,吴念念,徐茹,刘源)		
99	大气中 7Be 和 210Pb 时空分布特征差异和机制解析(黄思宇,林武辉*,何贤文,林晓东)	核技术	1455
100	涠洲岛珊瑚礁区有机氯农药的污染水平、来源和生物富集特征研究(秦贵帮,张瑞杰*,王煜轩,康亚茹,史敬,王辰燕,韩民伟,余克服)	上海海洋大学学报	1470
101	基于科教融合人才培养模式的“化学海洋学”教学改革与实践（裴继影*,张樱元,余克服,余文峰,张瑞杰,王瑞）	科技风	1479
102	广西北部湾典型水产品中有机磷酸酯的生物富集特征和食用风险评估（康亚茹,张瑞杰*,余克服,曾维斌,王瑞轩）	上海海洋大学学报	1482

方向 4　南海珊瑚礁遥感与监测

序号	题目（作者）	期刊	页码
103	Marine Heatwaves and Cold Spells in Global Coral Reef Regions (1982–2070): Characteristics, Drivers, and Impacts (Honglei Jiang, Tianfei Ren, Rongyong Huang, Kefu Yu*)	Remote Sensing	1501
104	A new remote sensing index of mildew for winter wheat disaster area extraction (Huade Li, Jinshui Zhang, Zhenghua Chen, Mingwei Zhang)	International Journal of Digital Earth	1532
105	Numerical Modeling of Wave Hydrodynamics Around Submerged Artificial Reefs on Fringing Reefs in Weizhou Island of Northern South China Sea (Zuodong Liang, Guangxian Huang, Wen Huang, Hailun Chen, Kefu Yu*, Dongsheng Jeng)	Journal of Marine Science and Engineering	1554
106	Metabolism of wildfire-derived methoxyphenol in Acropora formosa: Metabolite identification, toxicity prediction, and impact on coral health (Yanliu Wu, Xiaoyan Chen*, Yuhao Du, Zhenhua Chen, Zhaoqian Yan, Hongfei Su, Zhenjun Qin, Zhiming Ning, Yuxiao Li, Kefu Yu*)	Journal of Hazardous Materials	1575
107	城市黑臭水体遥感监测的研究现状与展望(陈正华,兰思香,张锦水,张威,李华德,赵丽芳)	遥感技术与应用	1589
108	相对高纬度珊瑚礁的有限弹性：气候变化和人类影响下的结构复杂度退化(滕君灿,余克服,左秀玲*,李志文,黄学勇,段正贤,蓝斐芳)	中国科学:地球科学	1603
109	珊瑚骨骼荧光记录环境变化的研究进展(江蕾蕾，黄达华，赵佰玲，余克服*)	海洋学报	1615
110	珊瑚礁领域研究生课程教学模式创新探索(左秀玲,梁甲元,余克服*,苏宏飞,梁作栋)	中国多媒体与网络教学学报	1627

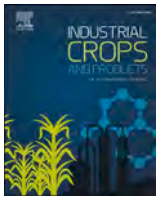
Industrial Crops & Products 228 (2025) 120876



Contents lists available at ScienceDirect

Industrial Crops & Products

journal homepage: www.elsevier.com/locate/indcrop





Silicon enhances potassium uptake and leaf growth in *Avicennia marina*, a silicon-accumulating mangrove plant with silicon transporters

Zejun Guo [a,b,1], Siyao Liao [a], Chaoqun Xu [b], Mingyue Wei [c], Lingyu Song [b], Hezi Huang [b], Zhanhong Li [a], Xi Chen [a], Lei Jiang [a], Hai-Lei Zheng [b,2,*]

[a] *Guangxi Laboratory on the Study of Coral Reefs in the South China Sea, Coral Reef Research Center of China, School of Marine Sciences, Guangxi University, Nanning 530004, China*
[b] *Key Laboratory of the Ministry of Education for Coastal and Wetland Ecosystems, College of the Environment and Ecology, Xiamen University, Xiamen 361102, China*
[c] *College of Ecology, Resources and Environment, DeZhou University, DeZhou, Shandong 253000, China*

ARTICLE INFO

Keywords:
Mangrove
Silicon accumulation
Silicon transporter
Lsi1
SIET4
Potassium uptake

ABSTRACT

Silicon (Si) is an essential fertilizer that enhances plant growth and stress resilience. Mangroves thrive in high-salinity, oxygen-deficient soils with high productivity, rapid decomposition, and fast elemental cycling. However, the physiological effects of Si on mangrove plants, as well as their mechanisms for Si uptake, transport, and function, remain unclear. In this study, we identified *Avicennia marina* as a Si-accumulating mangrove species and elucidated its Si transport pathways and associated physiological benefits. Through bioinformatics and heterologous expression in yeast, we demonstrated that the Si transporters AmLsi1 and AmSIET4 are localized to cellular membranes and mediate Si transport. RT-qPCR and RNA-seq analyses revealed that AmLsi1 and AmSIET4 are predominantly expressed in roots and leaves, respectively, with comparable expression levels. Both genes showed similar responses to salt, flooding, and Si treatments, indicating their coordinated roles in Si transport. AmLsi1 acts as a bidirectional transporter of Si and As(III) in roots, also facilitating H_2O and H_2O_2 transport, while AmSIET4 functions as an efflux transporter for Si and As(III) in leaves. Si absorption by roots and secretion through salt glands were further confirmed using SEM-EDX and ICP-MS. Si treatment enhanced leaf area, upregulated K^+ channel gene expression, enhanced K^+ uptake, and reduced Na^+ concentration in the roots, improving the K^+/Na^+ ratio and restoring F_v/F_m under saline conditions. This study provides new insights into Si uptake, transport, and its physiological significance in mangroves, deepening our understanding of Si's role in *A. marina* and its contribution to mangrove ecosystem productivity.

1. Introduction

Silicon (Si) is the second most abundant element in the Earth's crust and is a beneficial element for many plant species (Yamaji and Ma, 2021). Most plants absorb Si in the form of monosilicic acid ($Si(OH)_4$) through their roots (Takahashi and Hino, 1978). $Si(OH)_4$ is a soluble form of Si that is present in soil solution, produced by the weathering of silicate minerals in the soil. The uptake of Si by rice is facilitated by Lsi1, a aquaporin (AQP) protein expressed in the roots that acts as a bi-directional Si transporter (Mitani et al., 2008). The absorbed Si in the form of $Si(OH)_4$ permeates through Lsi1 into the plant roots, and is then transported to the aboveground parts through transpiration stream and eventually deposited as amorphous Si ($nSiO_2$-nH_2O) in leaves or other tissues (Ma and Takahashi, 2002). The Si concentration in plants is usually highest in the leaves, ranges from 0.1 % to 10 % of their dry weight (Deshmukh et al., 2020; Ma and Takahashi, 2002).

Lsi1 was first identified as a Si transporter in rice, is polarly localized on the plasma membrane of the distal side of both endodermis and exodermis of root and is essential for Si accumulation. It belongs to the NIPIII subfamily of AQP proteins, which share the general features of AQPs, including six transmembrane domains, two complete NPA motifs, and a specific aromatic/Arginine (ar/R) selectivity filter, with four amino acid residues at G-S-G-R positions (Saitoh et al., 2021). In addition to Si transport, Lsi1 has been identified to transport As(III) (Saitoh

* Corresponding author.
E-mail address: zhenghl@xmu.edu.cn (H.-L. Zheng).
[1] 0000-0002-7747-7304
[2] 0000-0001-8588-1529

https://doi.org/10.1016/j.indcrop.2025.120876
Received 24 December 2024; Received in revised form 14 March 2025; Accepted 16 March 2025
Available online 22 March 2025
0926-6690/© 2025 The Author(s). Published by Elsevier B.V. This is an open access article under the CC BY license (http://creativecommons.org/licenses/by/4.0/).

et al., 2021). Later, its homolog, Lsi6, was found to also transport Si, responsible for unloading Si from the xylem to the leaf in rice (Yamaji et al., 2015).

Lsi2, Lsi3, and SIET4 are homologous genes but are not homologous to Lsi1. Initially identified as Si efflux transporters in rice, these genes are characterized by their distinct tissue localizations. Lsi2 is polarly localized on the proximal side of the plasma membrane in the same cells as Lsi1 in the roots, where they work together to facilitate Si transport through the Casparian strips into the xylem (Ma et al., 2007). Lsi3 is localized in the root pericycle, where it is responsible for loading Si into the xylem (Huang et al., 2022). SIET4 is polarly localized on the distal side of epidermal cells and the cells surrounding bulliform cells in the leaf blade, playing a crucial role in exporting Si from leaf cells to the surface. This ensures proper Si accumulation, contributing to the healthy growth of rice on land (Mitani-Ueno et al., 2023).

Functional homologs of the Si transporters Lsi1 or Lsi2/SIET4 have been identified in various plants beyond rice, including monocots like barley (*Hordeum vulgare*) (Chiba et al., 2009) and maize (*Zea mays*) (Mitani et al., 2009a; Mitani et al., 2009b), as well as dicots such as soybean (*Glycine max*) (Deshmukh et al., 2013), cucumber (*Cucumis sativus*) (Sun et al., 2018; Sun et al., 2017), pumpkin (*Cucurbita moschata*) (Mitani-Ueno et al., 2011a), grapevine (*Vitis vinifera*) (Noronha et al., 2020), poplar (*Populus trichocarpa*) (Deshmukh et al., 2015), date palm (*Phoenix dactylifera*) (Bokor et al., 2019), and the fern horsetail (*Equisetum arvense*) (Grégoire et al., 2012; Vivancos et al., 2016). Plants with the *Lsi1* gene typically accumulate more Si, and the presence of *Lsi1* can be used to predict the potential for Si uptake (Deshmukh et al., 2020).

Si has been proven to have positive effects on plant growth, particularly in monocotyledonous plants such as rice and sorghum. Absorption of Si can enhance cell wall strength, providing mechanical strength to plants (Lux et al., 2003; Ma and Takahashi, 2002). Additionally, Si has been shown to increase photosynthetic activity and improve rice yield (Lavinsky et al., 2016). Si absorption has also been demonstrated to enhance plant resistance to biotic and abiotic stressors. For example, accumulation of Si in plant tissues can prevent herbivores and pathogens (Ma and Yamaji, 2006). Si also plays an important role in alleviating the negative impacts of abiotic stress factors such as drought, salinity, and heavy metal toxicity (Debona et al., 2017).

Mangroves are highly productive, which makes them an important player in tropical Si cycling (Elizondo et al., 2021). The uptake of Si by mangroves can have significant impacts on the Si cycling in the coastal wetland ecosystem, affecting the flux of Si between sediments and water. It has been reported that biogenic silica in sediments dissolves 7–20 times faster than mineral silicates (Cornelis et al., 2011). Additionally, the accumulation of Si in mangrove sediments may impact the productivity of mangroves and the functions of the larger estuarine and coastal ecosystems they support, through its effects on nutrient uptake by mangrove plants. As an important member of mangroves, the transport and role of Si in *Avicennia marina* is still unclear.

In this study, we inferred the Si uptake capacity of three mangrove plants by comparing their Si concentrations and verified it through identification and functional analysis of Si transporters. We systematically analyzed the absorption, transportation, and effects of Si on the growth and physiology such as the uptake of potassium (K) of the Si accumulator *A. marina*. Our findings provide a deeper understanding of Si transport in mangrove plants and clarify the role of Si in the growth and physiological processes of *A. marina*.

2. Materials and methods

2.1. Bioinformatics analysis

Homologous genes for silicon transporters Lsi1 and Lsi2 were identified by searching the genomes of three mangrove species: *Avicennia marina* (Ma et al., 2022), *Aegiceras corniculatum* (Ma et al., 2021), *Kandelia obovata* (Qiao et al., 2024). The protein sequences used for the phylogenetic analysis of the NIP subfamily, to which Lsi1 belongs, were obtained from our previously published *A. marina* AQP information (Guo et al., 2024) and *K. obovata* AQP information (Guo et al., 2022). NIPs from model plants, including Arabidopsis AQPs (Johanson et al., 2001) and *Populus trichocarpa* AQPs (Gupta and Sankararamakrishnan, 2009), were also included. The sequences of OsLsi1 (NP_001403822.1) and OsLsi6 (NP_001389719.1) were downloaded from NCBI Protein. Full-length NIP protein sequences were aligned using the ClustalW tool, and a phylogenetic tree was generated using the neighbor-joining method with 1000 bootstrap replicates in MEGA X software (Kumar et al., 2018).

In the multi-species phylogenetic analysis and sequence alignment analysis, the following sequences were used: GmNIP2–2 (NP_001240190.1), CsLsi1 (ACU29603.1), SlLsi1 (NP_001274283.1), VvNIP2–1 (RVW31404.1), PtLsi1 (XP_002324057.1), PdNIP2–1 (XP_008802606.1), ZmLsi1 (NP_001105637.1), OsLsi2 (NP_001388947.1), ZmLsi2 (NP_001183945.1), CsLsi2 (APT69295.1), CmLsi2–1 (AB551951) and CmLsi2–2 (AB551952), all of which were obtained from the NCBI Protein database. The sequence for EaLsi2–1 was obtained from the study by Coskun et al. (2021). The sequence information for AmLsi1 and AmSIET4 was provided in Table S3. Sequences alignment was performed using the Clustal Omega tools (https://www.ebi.ac.uk/Tools/msa/clustalo/), and the resulting alignment was visualized using GeneDoc software.

Subcellular localization of the proteins was predicted using the WoLF PSORT tool, 3D protein structure modeling was performed with the AlphaFold 3 server, and channel pore analysis was conducted using PoreWalker.

2.2. Cloning and transformation of Si transporter genes in yeast

The methods for gene cloning and yeast transformation were performed as previously described (Guo et al., 2022). Total RNA was extracted from mixed root and leaf samples of *A. marina* using the Plant Total RNA Isolation Kit (Vazyme, China) following the manufacturer's instructions. The first-strand cDNA synthesis was performed using the 1st Strand cDNA Synthesis Kit (Vazyme, China) with 1 μg of total RNA in a 20 μL reaction volume. The resulting cDNA was used as a template for PCR amplification of *AmLsi1* and *AmSIET4* coding sequences (CDS), using primers for Si transporter genes cloning listed in Table S1 and DNA Polymerase (TransGen Biotech, China). The amplified DNA fragments were then cloned into the pYES2-GFP vector using the *pEASY*®-Basic Seamless Cloning and Assembly Kit (TransGen Biotech, China). The resulting plasmids, along with the empty plasmid, were transformed into *Saccharomyces cerevisiae* strain INVSc1 via the lithium acetate method. Following transformation, the yeast cells were cultured for three days at 29°C on SD-URA screening medium containing 2 % (w/v) glucose.

2.3. Subcellular localization, and permeability of water and substrates

For the substrate sensitivity assay as previously described (Guo et al., 2022), yeast cells were first cultured in YNB liquid medium at 29°C for 24 h. The yeast culture was then diluted with sterile water to an OD 600 value of 1.0, followed by 10-fold serial dilutions for 5 times. Next, 10 μL of each diluted yeast culture was spotted on YNB solid medium containing 2 % (w/v) galactose and 1 % (w/v) raffinose, with or without 3 mM H_2O_2, 5 mM H_3BO_3, or 2 mM $NaAsO_2$, and cultured at 29°C for 4 d.

For yeast subcellular localization and cell volume observation, as previously described (Guo et al., 2022), yeast cells cultured for 24 h in liquid medium were directly aspirated and imaged through the GFP channel, using a Zeiss LSM900 laser confocal microscope. The lengths of the long and short axes of yeast cells with GFP signals were measured using ZEN 3.1 software, and the volume was calculated based on the spheroid volume formula.

2.4. RNA-seq data collection

RNA-seq data from unpublished work were used to investigate the expression patterns of *AmLsi1* and *AmSIET4* genes in seedlings of *A. marina* subjected to salt and simulated tidal flooding treatments. Seedlings at 3 months of age were divided into three salt treatment groups: 0, 250 and 500 mM NaCl. The 500 mM NaCl treatment was gradually increased, following a one-week acclimation period at 250 mM NaCl. For the simulated tidal flooding treatment, the water was maintained at 250 mM NaCl, with tidal flooding from 8:00–16:00 by a daily cycle. After two weeks of treatment, roots and leaves were harvested from seedlings subjected to salt treatment, 8 hours of tidal flooding (TF), and 16 hours of aerial exposure after tidal flooding (ATF). Total RNA was extracted from these tissues and used for transcriptome sequencing.

2.5. Plant materials and treatments

The mature and healthy leaves of three mangrove species, *A. marina*, *A. corniculatum*, and *K. obovata*, were used to compare their Si accumulation. The plant materials were collected from a small area within the same natural habitat of mangroves located in the Zhangjiang River Estuary Mangrove National Natural Reserve (23°55'N, 117°26'E), Fujian, China.

For indoor seedling treatment experiments, plants were cultured from propagules obtained from the Zhangjiang River Estuary, following previously described methods (Guo et al., 2023). Four healthy and similarly sized propagules were planted in a plastic pot (diameter 9 cm, height 9 cm, bottom with holes) filled with clean sand. Twelve plastic pots were placed in a large plastic container (40 ×30 ×8 cm). The small pots were immersed in 1/2 Hoagland nutrient solution without being submerged. The nutrient solution was changed once a week, and fresh water was added every day to compensate for evaporation losses. The seedlings were grown in a greenhouse with a temperature of 26 ± 2℃, a light period of 14 hours/10 hours (light/dark), and photosynthetically active radiation (PAR) about 150 μmol m^{-2} s^{-1}. After 3 months of growth, seedlings with consistent height were selected and divided into seven groups: CK, 200 mM NaCl, 500 mM NaCl, 0.5 mM Na_2SiO_3, 1.5 mM Na_2SiO_3, 200 mM NaCl + 0.5 mM Na_2SiO_3, and 500 mM NaCl + 1.5 mM Na_2SiO_3 treatments. The 1.5 mM Na_2SiO_3 is designated as the high-Si treatment, while 0.5 mM Na_2SiO_3 is deemed a more suitable (moderate) Si concentration for *A. marina* based on our pilot experiment. The treatment solutions contained 1/2 Hoagland nutrient solution concentration, and the nutrient solution was changed weekly. After 3 months of treatment, the plants were subjected to SEM-EDX detection for Si localization, physiological measurement, RT-qPCR analysis, ICP-MS measurement for ion concentration, and NMT measurement for potassium ion (K^+) flux. For physiological measurements, plant water content was calculated as (fresh weight - dry weight) / fresh weight. The chlorophyll fluorescence F_v/F_m ratio was measured using a LI-6800 Portable Photosynthesis System (LI-COR, USA) in the dark.

2.6. Real-time quantitative PCR (RT-qPCR) analysis

The method for extracting total RNA from plant samples and synthesizing first-strand cDNA was consistent with the description in the Materials and Methods section of the gene cloning part. The synthesized cDNA was used for RT-qPCR analysis, which was performed with SYBR qPCR Master Mix (Vazyme) using a Real-Time PCR Detection System (Bio-Rad, USA). RT-qRCR primers for Si transporter and K^+ channel genes were listed in Table S2. *18 s rRNA* was used as internal control. Relative expression levels of genes were calculated by the $2^{-\Delta\Delta CT}$ method.

2.7. Scanning electron microscopy (SEM) and energy-dispersive X-ray spectroscopy (EDX)

The localization and relative concentration of Si in different tissues of *A. marina* were determined using SEM combined with EDX as previously described (Guo et al., 2023). All plant tissue samples were cut into small pieces and freeze-dried, and then fixed onto carbon tape with the observation side facing upwards, followed by sputter coating using a Quorum 550x sputter coater. The metal-coated samples were photographed using a scanning electron microscope (Phenom Pharos G2 Desktop FEG-SEM, Netherlands) at an acceleration voltage of 15 kV. The Si concentration and localization of the displayed sample area were analyzed using an EDX detector. Five randomly captured images of fixed sizes were taken for each sample, and the most representative one was selected for display.

2.8. Elemental concentration determination

For plant samples, all samples used for measurements were freshly collected, cleaned of surface impurities, and surface ions were removed using ultrapure water. The samples were then dried in an oven at 80°C until a constant weight was achieved and ground into a powder.

For yeast samples, they were cultured in YNB liquid medium containing either 0.5 mM Na_2SiO_3 or 0.5 mM $NaAsO_2$ for approximately 24 h at 29°C. When the yeast cell density reached an OD600 value of 1, the cells were collected by centrifugation and washed four times with ultrapure water. The yeast cells were then dried at 80°C and prepared for subsequent sample digestion.

Sample preparation for ICP-MS analysis followed previously described methods (Guo et al., 2023). Then, 50 mg of the sample was mixed with 3 mL of 65 % concentrated nitric acid in a digestion tube, and digested using a microwave digestion system (CEM MARS6, USA). The temperature was raised to 180°C within 15 min and held at 180°C for 15 min to digest the sample into ions. After cooling, the digestion tube was opened and the excess nitric acid was evaporated by heating to 150°C using an electric furnace, leaving approximately 500 μL of liquid. The digestion solution was then diluted to 50 mL with ultrapure water for measurement of Na^+, K^+, As and Si concentration. For measurement of Si concentration in plant tissues, the digestion method followed the protocol described by Haysom and Ostatek-Boczynski (2006). After digestion with concentrated nitric acid and evaporation of excess nitric acid, 2.5 mL of 10 % NaOH (w/v) was added to the digestion tube, and the sample was subjected to microwave digestion again at 180°C for 15 min. The sample was then titrated to neutrality using 2 M nitric acid, with phenolphthalein as an indicator. The resulting solution was diluted with ultrapure water to a final volume of 50 mL for measurement. The concentration of Na^+, K^+, Si and As in the test solution was measured using inductively coupled plasma mass spectrometry (ICP-MS) (Agilent 7500ce, USA).

2.9. Measurement of the net K^+ flux from the root of A. marina

Plants were uprooted, cleaned and a 1 cm long segment with the root tip was cut and placed in test solution (0.1 mM $CaCl_2$, 0.1 mM KCl, 0.1 mM $MgCl_2$, 0.2 mM Na_2SO_4, 0.5 mM NaCl, 0.3 mM MES, pH 6.0) for 2 h. The root samples were then transferred to a culture dish containing 5 mL of fresh test solution. Non-invasive micro-test technology (NMT) (Xuyue Science and Technology, China) was used to measure the net K^+ flux from the root tip of *A. marina*, following the method previously described (Guo et al., 2023). According to the manufacturer's instructions, commercial microsensors and liquid ion-exchange cocktail (K^+ LIX, Xuyue, China) were used to make ion-selective electrodes. The ion-selective electrode was mounted on a three-dimensional micro-manipulator and calibrated with 0.05, 0.1 and 0.5 mM KCl before measuring ion flux. The tip of the ion-selective electrode was located at two positions near the root and 30 microns away from the root in the

X-axis direction, moving back and forth every 6 sec. The NMT system calculated the net ion flux by measuring the electrochemical potential difference between the two positions of the microelectrode and converting it to an ion concentration difference using the calibrated slope. Six samples were measured for each treatment group, with each sample being measured for 10 min. The average of six samples was used for evaluation.

2.10. Statistical analysis

The data reported in this study are presented as means ± SD, with a minimum of three sample replicates ($n \geq 3$). Statistical analysis was conducted using either Student's *t*-test or one-way ANOVA, and post-hoc comparisons were performed using Fisher's least significant difference (LSD) test with a significance level of $p < 0.05$.

3. Results

3.1. A. marina is an accumulator of Si and As in mangrove ecosystems

To investigate Si accumulation in coexisting mangrove species, we quantified the Si concentration in the leaves of *A. marina*, *A. corniculatum*, and *K. obovata* using ICP-MS. Our study found that *A. marina* leaves had the highest Si concentration, followed by *A. corniculatum* and *K. obovata* (Fig. 1a). We also quantified the concentration of another metalloid, arsenic (As), and observed a consistent trend of Si and As accumulation across the three mangrove species (Fig. 1b). These results demonstrate that *A. marina* is an accumulator of both Si and As in mangrove ecosystems.

3.2. A. marina has putative Si transporters AmLsi1

Given the difference in Si accumulation levels among three mangrove species in the same habitat, we further identified whether they have a Si transporter Lsi1. Phylogenetic analysis of the NIP subfamily genes of *A. marina*, *A. corniculatum*, *K. obovata* as well as two model plants, Arabidopsis and poplar, was conducted with rice OsLsi1 as a reference for known functionality. Results showed that each of *A. marina* and *A. corniculatum* had a putative Lsi1, while *K. obovata* did not (Fig. 2a). Among them, AmLsi1 had the highest similarity to PtNIP2;1, which was also identified as a Si transporter.

To further verify whether AmLsi1 has Si transporter characteristics, sequence alignment analysis was performed with previously identified Si transporters Lsi1 from species *Glycine max*, *Cucumis sativus*, *Solanum lycopersicum*, *Vitis vinifera*, *Populus trichocarpa*, *Phoenix dactylifera*, *Oryza sativa*, and *Zea mays*. The AmLsi1 sequence showed high similarity with the identified Si transporter Lsi1 sequences (Fig. 3a). The highest similarity was with VvLsi1 at 83 %, followed by SlLsi1 at 80 %, and OsLsi1 at 71 %. AmLsi1 also had the typical features of AQP with six transmembrane domains (Fig. 3a). Four residues of the ar/R selectivity filter of AmLsi1 were consistent with those of Lsi1 of other species and were the Si-specific filters G-S-G-R (Fig. 3a) (Mitani-Ueno et al., 2011b). The other two Si-selective filters located at Thr65 and Thr181 of OsLsi1 (Saitoh et al., 2021) were also present in AmLsi1 at the corresponding positions, with both being Thr residues (Fig. 3a). Furthermore, the two NPA motifs of AmLsi1 are separated by 108 amino acids (Fig. 3a), which is a characteristic feature of Si transporters, where there is a strict 108 amino acid spacing between the two NPA motifs of Lsi1 (Deshmukh et al., 2015). On the other hand, AcLsi1 from *A. corniculatum*, had a missing amino acid sequence at the N-terminus, and its sequence similarity with other Lsi1 sequences was low, with the highest similarity being 48 % with SlLsi1. Furthermore, the selective filter residue at the position corresponding to OsLsi1 Thr181 was mutated to C in AcLsi1 and the two NPA intervals were separated by 113 amino acids (Fig. 3a). In summary, the sequence analysis suggests that AmLsi1 has the characteristics of a typical Si transporter Lsi1 and is considered a candidate Si transporter. In contrast, AcLsi1 does not possess these characteristics and therefore is not a Si transporter.

3.3. A. marina has putative Si efflux transporter AmSIET4

To investigate the presence of Si efflux transporters, specifically Lsi2, in three mangrove species, we conducted a genome-wide BLAST analysis. Lsi2 homologs were identified exclusively in *A. marina*. Our results revealed two homologous proteins of OsLsi2 in *A. marina*, Am09079 and Am09078, both of which are more closely related to OsSIET4 than to OsLsi2 (Fig. 2b). Among these, Am09079 is expressed in the leaves, while Am09078 shows no detectable expression in either roots or leaves, suggesting it may be a pseudogene (Fig. S1). Due to its potential functional role in the leaves, we designated Am09079 as AmSIET4.

Next, a phylogenetic analysis was conducted to compare AmSIET4 with Lsi2/SIET4 transporters known for Si efflux functions in *Cucumis*

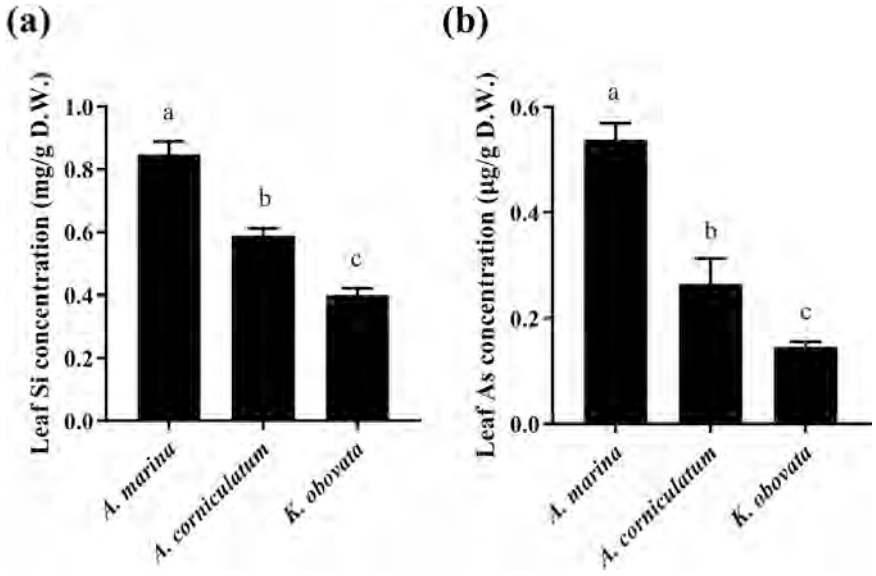


Fig. 1. Si and As concentrations in the leaves of three mangrove species in the same habitat. Si (a) and As (b) concentration were measured using ICP-MS. Values are means ± SD of four biological replicates. Different letters indicate significant differences ($p < 0.05$).

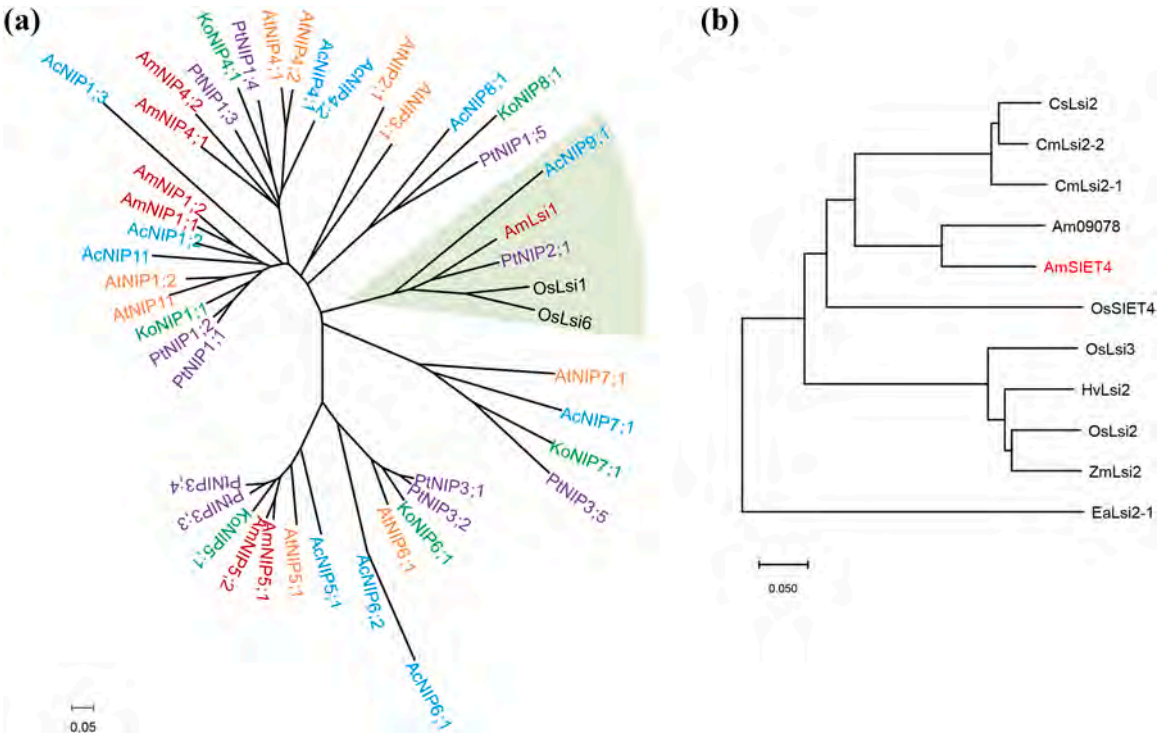


Fig. 2. Phylogenetic tree of homologous genes of Si transporters AmLsi1 and AmSIET4. (a) Identification of Lsi1 in three mangrove plants. The phylogenetic tree shows homologs of Lsi1 in the NIP subfamily of three mangrove plants (*A. marina*, *A. corniculatum*, and *K. obovata*) and model plants (*A. thaliana* and *P. trichocarpa*), using OsLsi1 and OsLsi6 from *Oryza sativa* as references. (b) Phylogenetic relationship of AmSIET4 with other known Si efflux transporters, SIET4/Lsi2. The homologous genes are from species including *C. sativus*, *C. moschata*, *O. sativa*, *H. vulgare*, *Z. mays*, and *E. arvense*. Phylogenetic trees were constructed using MEGA-X.

sativus, *Cucurbita moschata*, *Oryza sativa*, *Hordeum vulgare*, *Zea mays*, and *Equisetum arvense*. The analysis showed that AmSIET4 is a homologous gene to these transporters and is more closely related to OsSIET4 (Fig. 2b). Furthermore, amino acid sequence alignment was performed between AmSIET4 and its homologs, including OsLsi2, OsLsi3, and OsSIET4 from *O. sativa* and CsLsi2 from *C. sativus*. The alignment revealed that AmSIET4 shares high sequence similarity with these homologs and contains 11 transmembrane domains. The highest sequence similarity was found between AmSIET4 and CsLsi2, with a similarity of 79 %, followed by OsSIET4 at 75 %, and OsLsi2 at 63 % (Fig. 3b). This sequence analysis suggests that AmSIET4 is a putative Si efflux transporter.

3.4. Subcellular localization and water transport activity of AmLsi1 and AmSIET4

Subcellular localization predictions, 3D structural modeling, and pore analysis all demonstrate that AmLsi1 and AmSIET4 are plasma membrane channel proteins (Fig. S2). To further validate this result experimentally, we heterologously expressed GFP-tagged AmLsi1 and AmSIET4 in yeast cells. Laser confocal microscopy revealed that AmLsi1 and AmSIET4 were located on the membrane system of the yeast cells, whereas the fluorescence signal of the control (GFP) was uniformly distributed in the cytoplasm (Fig. 4a). Additionally, when observing the cell morphology, we found that the yeast cells expressing AmLsi1 expanded in volume to twice that of the control cells, which was caused by the water transport activity of AmLsi1 that allows the cells to absorb water and swell. In contrast, there was no change in the volume of the yeast cells expressing AmSIET4 (Fig. 4b). These results indicate that AmLsi1 and AmSIET4 are both membrane proteins, with AmLsi1 having the function of transporting water.

3.5. Substrates transported by AmLsi1 and AmSIET4

To further investigate the functions of AmLsi1 and AmSIET4, a yeast system was employed to identify their substrate permeability. Four substrates, namely H_2O_2, H_3BO_3, As(III), and Si, were used for testing. Given the cytotoxicity of H_2O_2, H_3BO_3, and As(III), substrate sensitivity assays were conducted to determine the permeability of AmLsi1 and AmSIET4 towards these substrates. The results showed that AmLsi1 was sensitive to H_2O_2 and As(III), but not to H_3BO_3, indicating that AmLsi1 has inward permeability to H_2O_2 and As(III) (Fig. 5a). AmSIET4 was insensitive to H_2O_2 and H_3BO_3 but had low sensitivity to As(III), suggesting that AmSIET4 has outward transport for As(III) (Fig. 5a). Additionally, since Si is non-toxic to cells, the transport of Si by transporter proteins was assessed by measuring Si concentration in yeast cells grown under Si-containing liquid medium. The results showed that both AmLsi1 and AmSIET4 transformed yeast had lower levels of Si compared to the control, with AmLsi1 showing the lowest Si concentration (Fig. 5b). At this point, both AmLsi1 and AmSIET4 exhibited Si efflux. As (III), as an analogue of Si, showed a similar pattern of enrichment in AmLsi1 and AmSIET4 transformed yeast (Fig. 5b, c). These results indicate that AmLsi1 has bidirectional permeability towards Si and As (III), while AmSIET4 has an outward transport function for Si and As (III).

3.6. Effects of salinity, tidal flooding and Si on the expression of AmLsi1 and AmSIET4

After confirming the Si transport activity of *AmLsi1* and *AmSIET4*, we aimed to further investigate their tissue-specific expression and response to intertidal environment in *A. marina*. Firstly, we retrieved the expression information of *AmLsi1* and *AmSIET4* from our previous RNA-Seq data. The data showed that *AmLsi1* was predominantly expressed in roots, and its expression was significantly reduced under high salinity (500 mM NaCl) and tidal flooding (Fig. 6a). In contrast, *AmSIET4* was

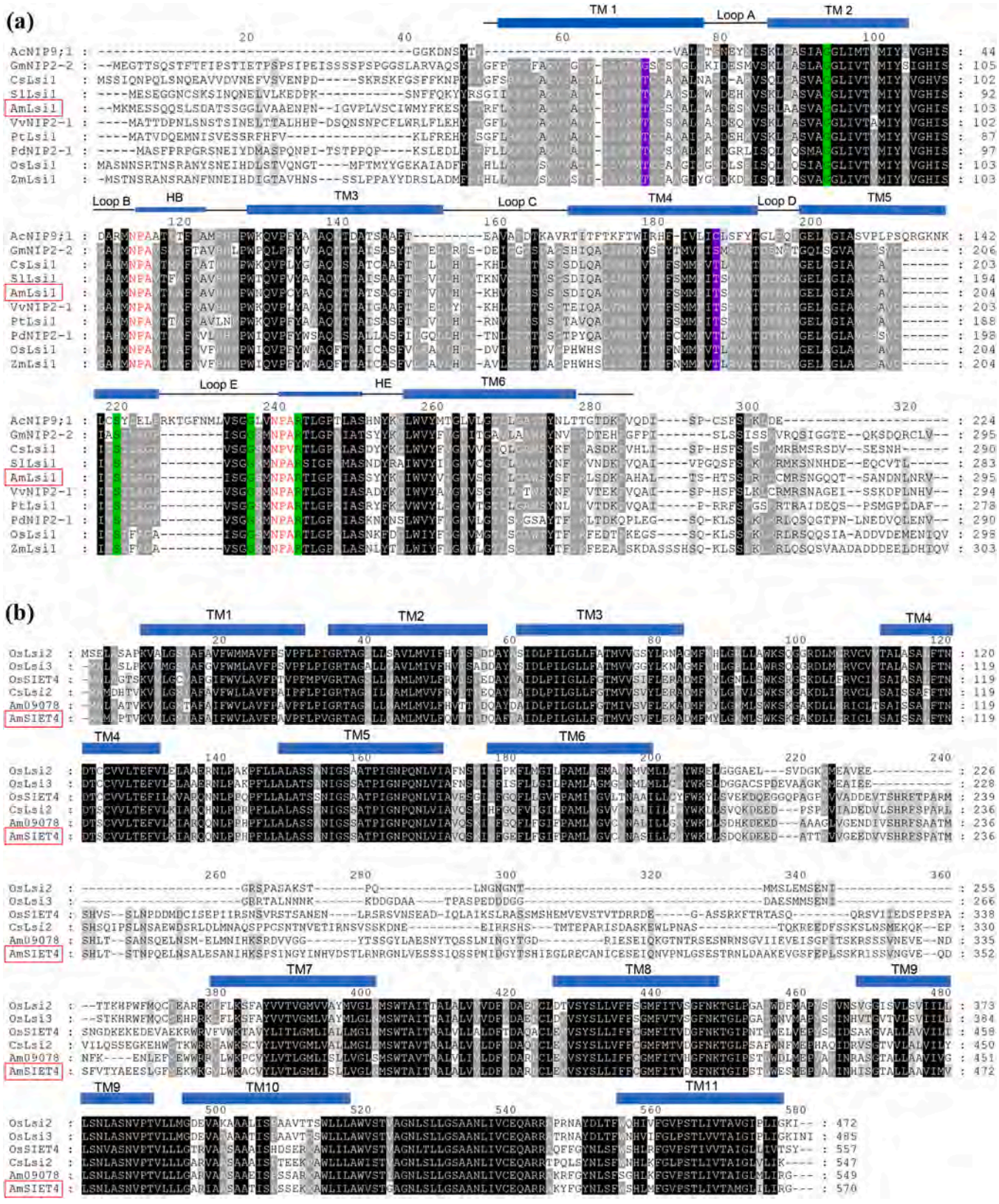


Fig. 3. Sequence alignment analysis of Si transporter proteins Lsi1 and SIET4 from various species. (a) Sequence alignment of putative *A. marina* and *A. corniculatum* Lsi1 with known Lsi1 from *G. max*, *C. sativus*, *S. lycopersicum*, *V. vinifera*, *P. trichocarpa*, *P. dactylifera*, *O. sativa* and *Z. mays*. The NPA motif is highlighted in red font, and the G-S-G-R amino acid residues, which is the ar/R selectivity filter, is highlighted in green background. The other two Si selectivity filters, located at Thr65 and Thr181 on OsLsi1, are highlighted in purple background. (b) Sequence alignment of putative AmSIET4 with identified Si efflux transporter SIET4/Lsi2 from *O. sativa* and *C. sativus*.

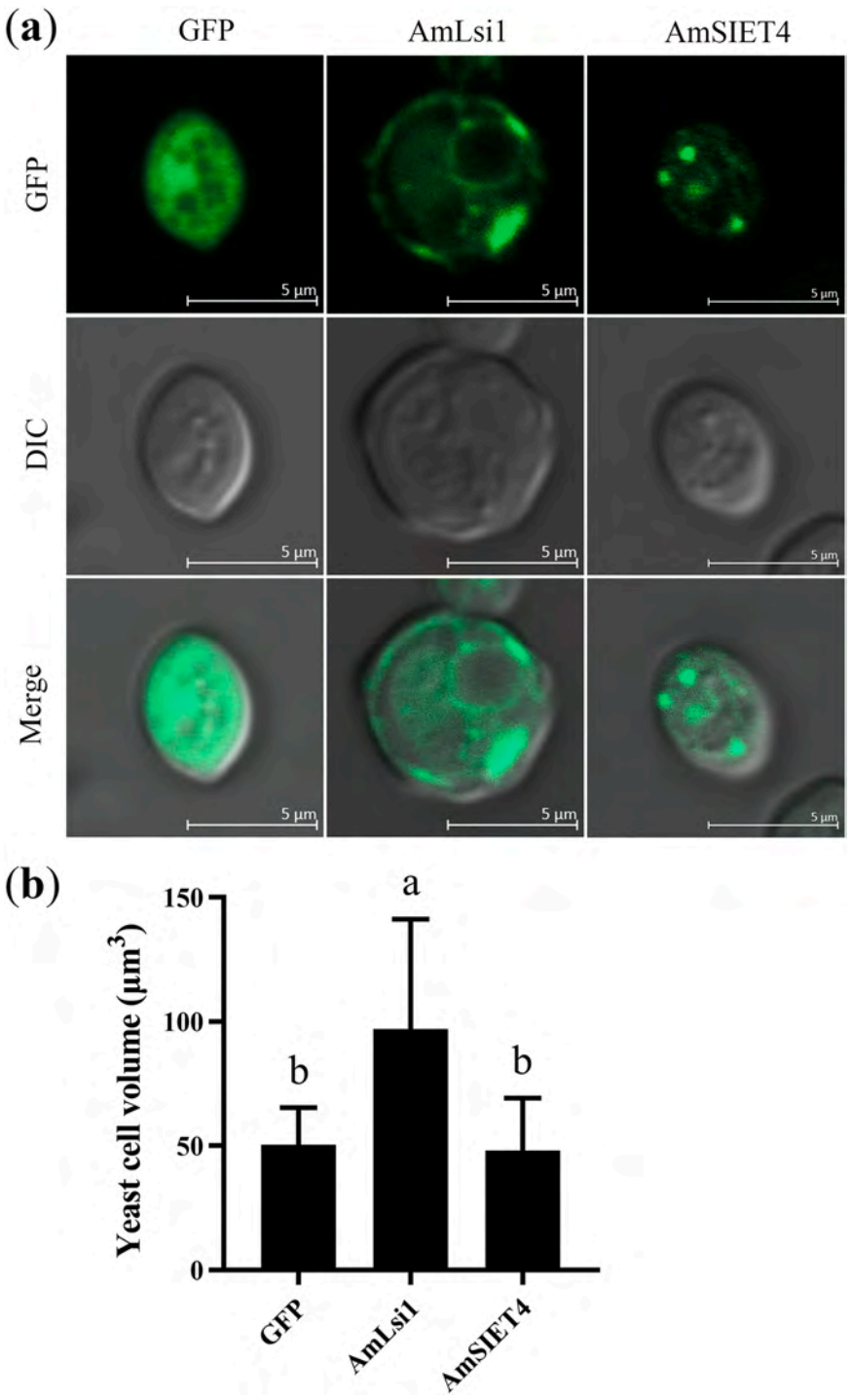


Fig. 4. The subcellular localization and cell volume in AmLsi1 and AmSIET4 transformed yeasts. (a) AmLsi1 and AmSIET4 were expressed in yeast cells. GFP channel shows the fluorescence signals and the differential interference contrast (DIC) channel shows cell morphology. Scale bar = 5 μm. (b) Cell volume measurement of AmLsi1 and AmSIET4 transformed yeasts. GFP transformed yeast as a control. Values are means ± SD (n = 30). Different letters indicate significant differences ($p < 0.05$).

highly expressed in leaves, and its expression was also downregulated under high salinity (Fig. 6b). Interestingly, they showed comparable expression levels in roots and leaves, with FPKM values of around 40 (Fig. 6a, b), which was confirmed by subsequent RT-qPCR analysis (Fig. 6c).

Moreover, to investigate the response of *AmLsi1* and *AmSIET4* to Si and salt, we performed RT-qPCR analysis on *A. marina* seedlings subjected to Si, salt, and combined treatments. The results showed that their expression levels were reduced under salt treatment, and significantly downregulated under high salinity, which was consistent with the RNA-Seq data (Fig. 6d, e). Comparing their expression levels under low Si (0.5 mM Na_2SiO_3) and high Si (1.5 mM Na_2SiO_3) treatments, high Si significantly inhibited their expression (Fig. 6d, e). Under the combined treatment of low Si and low salt, there was no significant change in expression levels, while under the combined treatment of high Si and high salt, both genes were significantly inhibited (Fig. 6d, e).

Taken together, these results suggest that *AmLsi1* is expressed in roots, while *AmSIET4* is expressed in leaves, and both genes exhibit

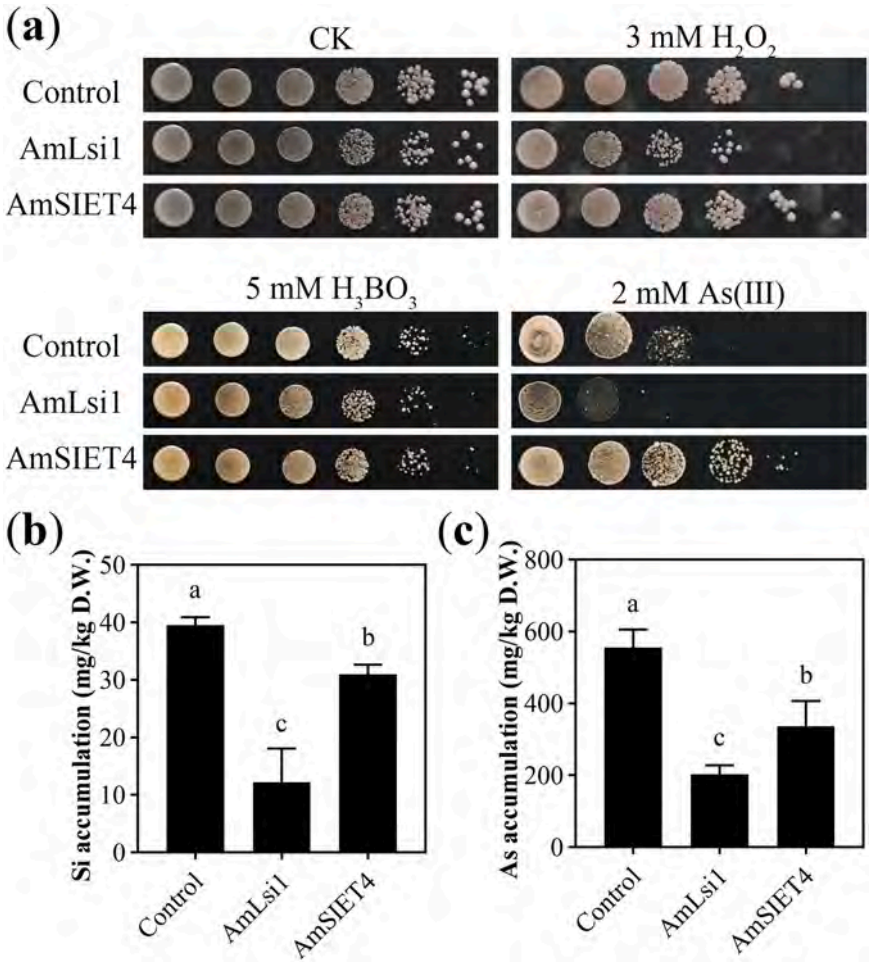


Fig. 5. Identification of substrate transported by AmLsi1 and AmSIET4 using a yeast model. (a) Toxicity of externally applied H_2O_2, H_3BO_3 and As(III) on yeast cells expressing AmLsi1 and AmSIET4. Yeast cells Control (empty vector pYES2) and expressing AmLsi1, AmSIET4 were ten-fold diluted and spotted on solid induction medium containing H_2O_2, H_3BO_3 or As(III). The cells were incubated at 29°C for 4 d. Accumulation of Si (b) and As (c) in control and AmLsi1 and AmSIET4 transformed yeast exposed to 0.5 mM Na_2SiO_3 or 0.5 mM As(III). The yeast cells were incubated in liquid YNB induction medium at 29°C for 24 h. The data represent the mean ± SD (n = 4). Different letters indicate significant differences ($p < 0.05$).

similar responses to salt and Si.

3.7. Si accumulation at salt glands on the adaxial surface of A. marina leaves

To gain further insight into the distribution of Si in different tissues of *A. marina*, we utilized scanning electron microscopy (SEM) combined with energy dispersive X-ray spectroscopy (EDX) to examine various plant tissues. Our results showed that Si was evenly distributed in the cross-section of the root, with a weight percentage of 0.08 % (Fig. 7a). No Si was detected in the stem (Fig. 7b). In the leaf, cross-section scans revealed a Si concentration of 0.05 %, mainly concentrated on the adaxial surface (Fig. 7c). The Si concentration on the surface of non-glandular hair on the abaxial side of the leaf was 0.06 % (Fig. 7d). The Si concentration on the adaxial surface of the leaf was 0.26 %, and Si was found to be concentrated at the salt gland (Fig. 7e). Further scanning of the salt gland showed that Si was deposited above the gland, with a high concentration of 7.6 %. The localization of Si overlapped with oxygen (O), and the only other elements with high concentration in this region were carbon (C), as shown by the spectrum (Fig. 7f-i). Moreover, the fact that this material was insoluble in water after washing the leaf surface also supports the identification of the deposited material as SiO_2. In summary, the highest Si concentration in *A. marina* was found in the leaf, mainly deposited on the surface of the salt gland, in the form of SiO_2.

3.8. Effect of Si on the growth of A. marina

To gain deeper insights into the effects of Si on *A. marina*, we treated *A. marina* seedlings with 0.5 mM Na_2SiO_3, 200 mM NaCl, and a combination of both for three months to observe their growth. Statistical analyses of the growth parameters revealed that either Si alone or salt alone significantly increased plant height, dry weight, fresh weight, and leaf area compared with the control (Fig. 8). Under salt conditions, Si treatment did not affect plant height, dry weight, or fresh weight, but significantly increased leaf area (Fig. 8). Moreover, Si, salt, and their combination all reduced plant water content while increasing the proportion of dry matter (Fig. 8g). Notably, Si alleviated the salt-induced decline in maximum quantum yield of primary photochemistry (F_v/F_m) (Fig. 8i). These results indicate that Si enhances leaf expansion in *A. marina* and has a more pronounced growth-promoting effect under low salinity, while under saline conditions, Si may help restore light energy utilization efficiency.

3.9. Si promotes potassium uptake in A. marina seedlings

In order to further investigate the roles of Si uptake in *A. marina*, we utilized ICP-MS to measure the elemental concentration of *A. marina* seedling tissue treated with 0.5 mM Na_2SiO_3, 200 mM NaCl, and a combination of both. The results indicated that the individual Si treatment significantly increased the Si concentration in both roots and

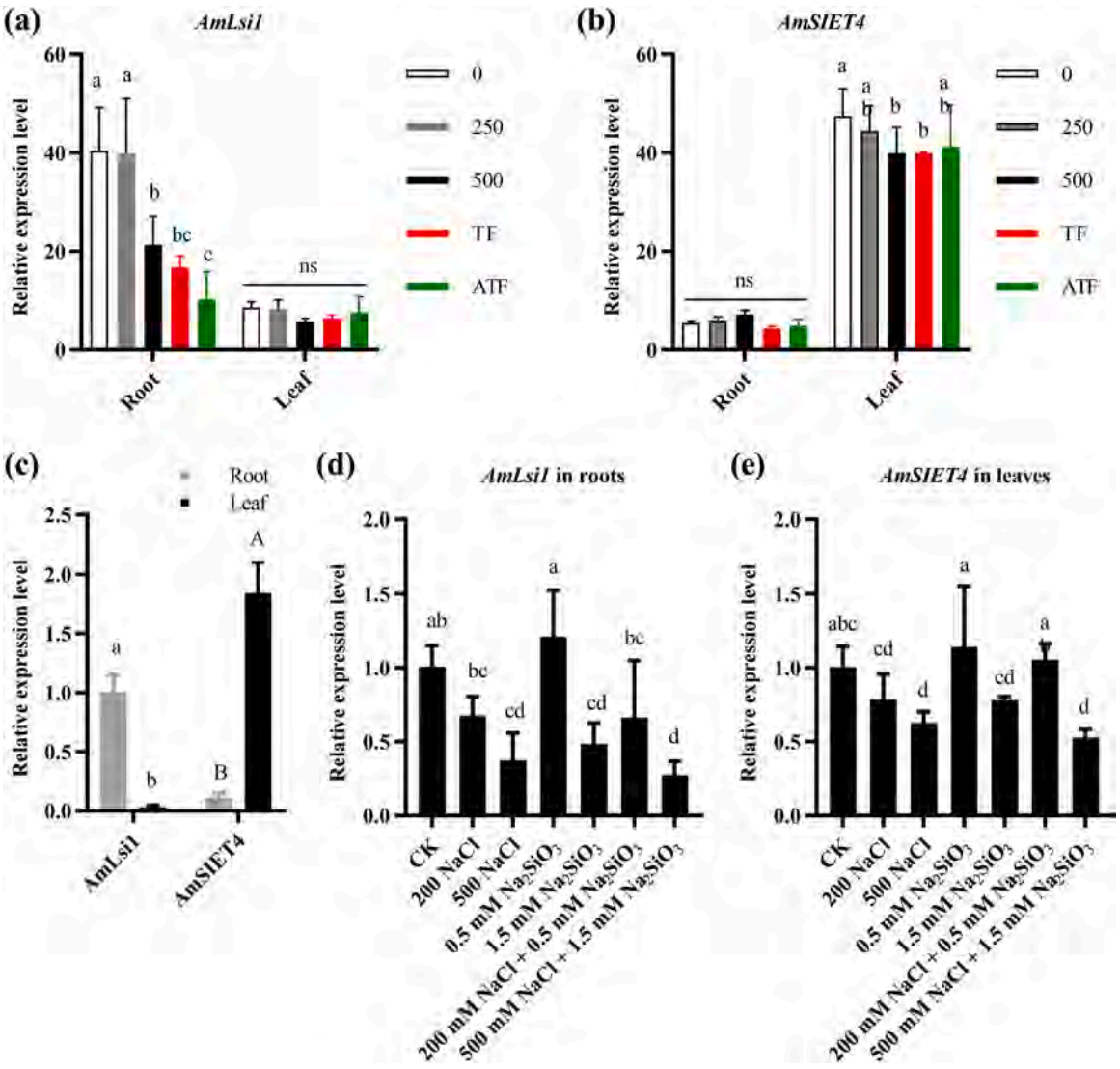


Fig. 6. Tissue-specific expression of *AmLsi1* and *AmSIET4* and their response to salt, tidal flooding and silicate in *A. marina*. Expression of *AmLsi1* (a) and *AmSIET4* (b) in roots and leaves of *A. marina* at salinity of 0, 250 and 500 mM NaCl and at TF and ATF during simulated tidal flooding treatments. (c) RT-qRCR analysis of *AmLsi1* and *AmSIET4* expression in roots and leaves, respectively. RT-qPCR analysis of the response of *AmLsi1* in roots (d) and *AmSIET4* in leaves (e) to different salt concentrations (200 or 500 mM NaCl), different concentrations of silicate (0.5 or 1.5 mM Na_2SiO_3), and their combined treatments. The data represent the mean ± SD (n = 3). Different letters within the same group indicate significant differences ($p < 0.05$), as determined by one-way ANOVA.

leaves. However, Si treatment under saline conditions did not increase the Si concentration in roots and leaves (Fig. 9a). Additionally, compared to the control group, the individual Si treatment increased the K concentration in roots, stems, and leaves, while the individual salt treatment reduced the K concentration in these tissues. When salt treatment was combined with Si treatment, the K concentration in roots was significantly enriched, but in leaves was reduced (Fig. 9b). The 0.5 mM Na_2SiO_3 treatment had no effect on the Na concentration in roots and stems, but slightly increased the Na concentration in leaves due to the enrichment effect of Na in *A. marina* leaves. The salt treatment increased the Na concentration in roots, stems, and leaves, while the combined Si treatment reduced the Na concentration in roots (Fig. 9c). Furthermore, the K/Na ratio in roots increased after Si treatment (Fig. 9d). In summary, salt inhibited the absorption of Si, while Si promoted the uptake of K in the roots and inhibited the uptake of Na.

3.10. Si promotes the inward flow of K^+ into the roots of A. marina

To further investigate the K^+ uptake in *A. marina* roots, non-invasive micro-test technology (NMT) was used to measure the K^+ flux at a distance of 400 μm from the root tip (Fig. 10a). The results showed that Si treatment, under both saline and non-saline conditions, significantly reduced K^+ efflux, indicating a relative increase in K^+ influx by approximately 200 pmol cm^{-2} s^{-1} (Fig. 10b, c). These findings provide further evidence that Si promotes K^+ uptake in *A. marina* roots.

3.11. Si promotes the expression of K^+ channel genes in the roots of A. marina

In light of the fact that Si promotes K^+ uptake in *A. marina* roots, further investigation was conducted to verify whether this effect is attributed to the regulation of K^+ channel gene expression. RT-qPCR analysis was used to identify the expression of K^+ channel genes in the roots of *A. marina* seedlings treated with 0.5 mM Na_2SiO_3, 200 mM NaCl, and a combination of both. The results showed that Si treatment under non-saline conditions increased the expression of the high-affinity K^+ transporter (*HAK5*), inward-rectifier K^+ channel (*AKT1*) and the outwardly-rectifying K^+ channel *GORK1* and *GORK2*. Si treatment under saline conditions increased the expression of *HAK5* and *GORK2* genes (Fig. 11). These results indicate that Si treatment increases the

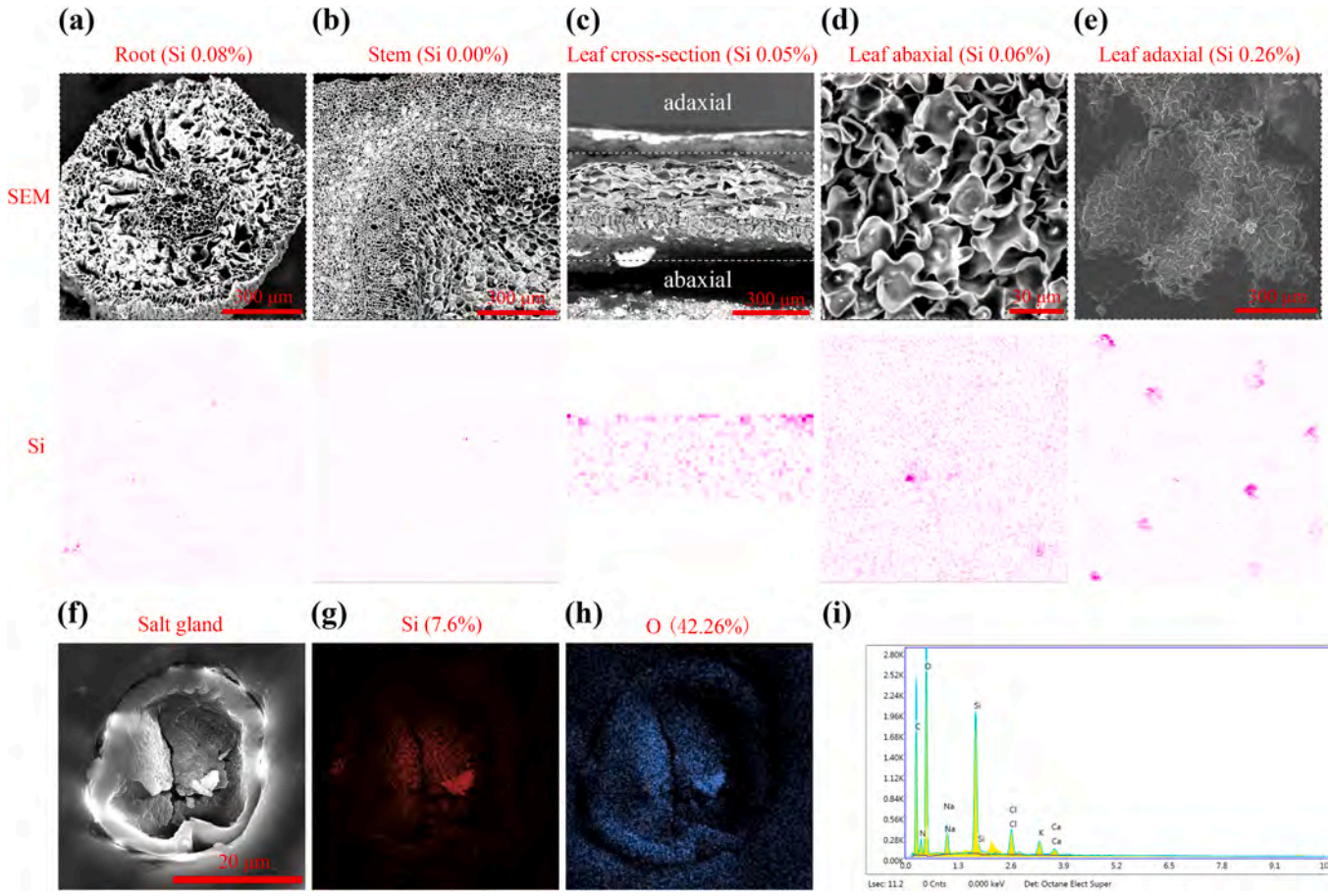


Fig. 7. Si localization in tissues of *A. marina*. SEM and EDX analysis of Si enrichment in the root (a), stem (b), leaf cross-section (c), abaxial leaf surface (d), adaxial leaf surface (e), and salt gland of the adaxial leaf surface (f-h) of *A. marina*. The upper panels in (a-e) show SEM images of the tissues, while the lower panels show the mapping of Si localization in the tissues with pink dots using EDX analysis. EDX analysis was also used to map the localization of Si (g) and O (h) elements on the surface of the salt gland. (i) Elemental spectrum of the salt gland scan. The labels above the image indicate the weight percentage content of the elements.

transcriptional levels of K^+ channel genes in *A. marina* roots.

4. Discussion

4.1. Relationship between plant Si concentration and Si transporters in A. marina

Study on the transport and function of Si in plants has mainly focused on monocotyledonous plants, as they often accumulate large amounts of Si in their bodies. For example, the Si concentration in rice leaves can reach 10 % of the plant dry weight (Ma and Takahashi, 2002). In contrast, the Si concentration accumulated in dicotyledonous plants under natural conditions is relatively low, such as around 1 % in the leaves of bottle gourd (Kumawat et al., 2021), approximately 0.5 % in the aboveground parts of grapes (Noronha et al., 2020), 0.3 % in soybean leaves (Deshmukh et al., 2013), and 0.2 % in strawberry leaves (Ouellette et al., 2017). The presence of the Si transporter *Lsi1* has been identified in these dicotyledonous plants, which have relatively high Si concentration. Some dicotyledonous plants have a Si concentration of less than 0.1 %, such as cruciferous plants, which do not have the *Lsi1* (Deshmukh et al., 2020). The Si concentration is also closely related to the number of Si transporters, such as in rice where there are two homologous genes, *Lsi1* and *Lsi6* (Ma et al., 2011). *Helianthus annuus* has seven *Lsi1* genes, and the leaf Si concentration can reach up to 3.7 % under Si treatment (Deshmukh et al., 2020), indicating that the number of *Lsi1* genes also affects the potential for Si absorption.

In our study, the Si concentration of three plant species in mangroves was less than 0.1 %, but relative to the other two species, the Si concentration in *A. marina* leaves was the highest (Fig. 1). When we identified their Si transporters, we found that only *A. marina* has a functional Si transporter, Lsi1 (Figs. 2 and 3). In addition to the presence of Si transporters, the Si concentration in plants is also related to the concentration of soluble $Si(OH)_4$ in the soil. Most soluble Si in soils ranges from 100 to 500 μM (Sommer et al., 2006), and we measured the soluble Si concentration in the Zhangjiang Estuary mangroves as 140 μM, which may be the reason for the low Si concentration in *A. marina*. After treatment with 0.5 mM Na_2SiO_3, the Si concentration in *A. marina* leaves increased by 50 % (Fig. 9). These results indicate that the Si concentration in plants is related to the presence and quantity of *Lsi1* genes and the Si concentration in the soil.

4.2. Structure and function of AmLsi1 and AmSIET4

Si transporter Lsi1 is a type of AQP protein belonging to the NIPIII subfamily and is located in the plasma membrane. Unlike other AQPs, it has a unique Si-selective filter, with four amino acids at positions ar/R selectivity filter being G-S-G-R (Mitani-Ueno et al., 2011b), and two residues, Thr65 and Thr181, also having selectivity for Si (Saitoh et al., 2021). In addition, the amino acid spacing between the two NPA motifs is considered important for Si permeation, typically being 108 amino acids (Deshmukh et al., 2015). AmLsi1 exhibits all of these characteristics and is highly similar in sequence identity to other Si transporter Lsi1 proteins (Fig. 3). Subcellular localization analysis also indicates that AmLsi1 is located in the plasma membrane (Fig. 4). *Lsi1* from multiple

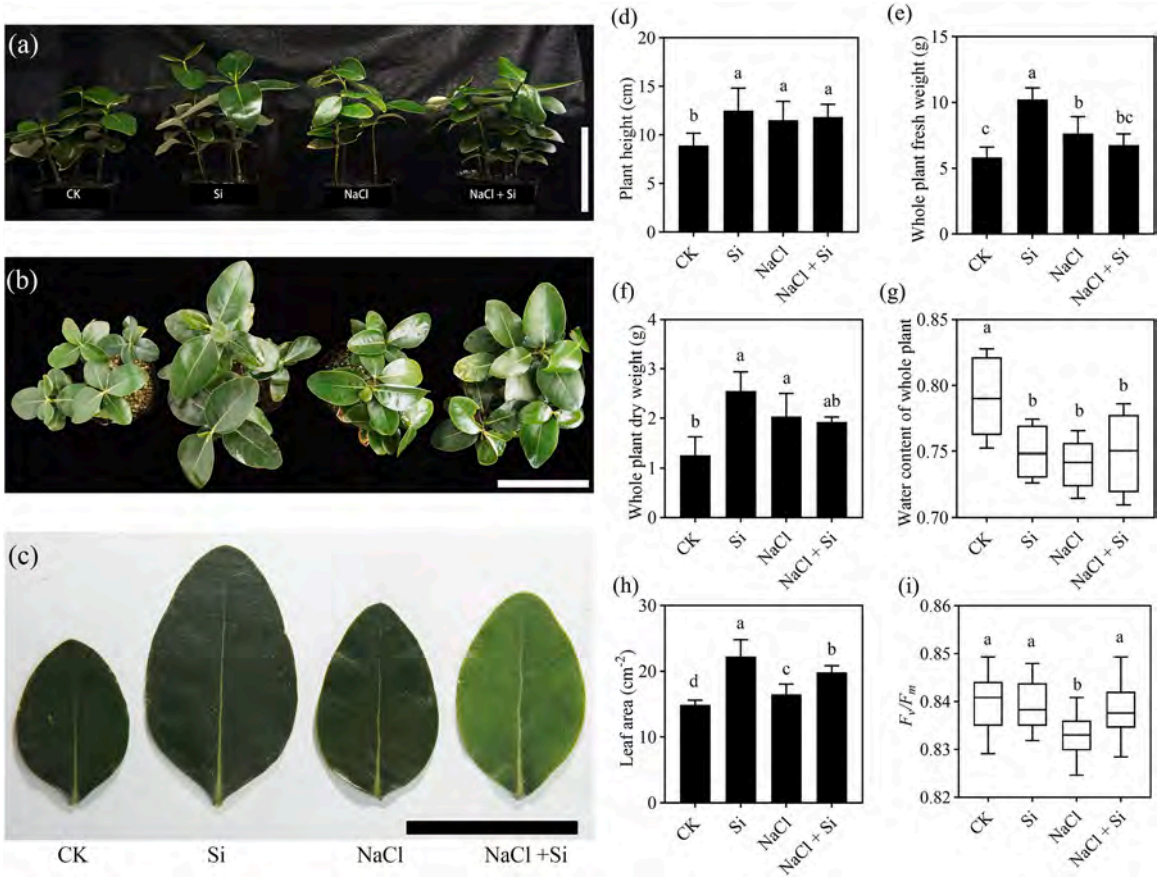


Fig. 8. Effect of Si and salt treatments on *A. marina* phenotype. (a-c) display the frontal, aerial, and leaf morphology of *A. marina* seedlings treated with a combination of 0.5 mM Na_2SiO_3, 200 mM NaCl or a combination of both, respectively. Plant height (d), whole plant fresh weight (e), whole plant dry weight (f), whole plant water content (g), leaf area (h), and F_v/F_m (i) were measured and statistically analyzed. Data are presented as the mean ± SD (d-f, h) or min to max (g and i) (n = 10, 5, 5, 5, 10, 22 for a-i, respectively). Different letters indicate significant differences ($p < 0.05$).

species, such as rice (Ma et al., 2006), grape (Noronha et al., 2020), and cucumber (Wang et al., 2014), all show high expression in the roots. Our gene expression pattern analysis also indicates high expression of *AmLsi1* in the roots of *A. marina* (Fig. 6).

AmSIET4 is a homolog of Lsi2, a family of Si efflux transporters. The Si efflux function of various Lsi2 genes has been identified in several plants, including rice (*OsLsi2*, *OsLsi3*, *OsSIET4*) (Huang et al., 2022; Ma et al., 2007; Mitani-Ueno et al., 2023), maize (*ZmLsi2*), barley (*HvLsi2*) (Mitani et al., 2009a), cucumber (*CsLsi2*) (Sun et al., 2018) and pumpkin (*CmLsi2*) (Mitani-Ueno et al., 2011a). However, their tissue localization varies. For example, *OsLsi3*, *ZmLsi2*, and *HvLsi2*, which belong to the same evolutionary clade as *OsLsi2* (Fig. 2b), are expressed in the roots and function in loading Si into the xylem. In contrast, *OsSIET4*, *CmLsi2–1*, and *CmLsi2–2*, which cluster in the same evolutionary clade as *AmSIET4* (Fig. 2b), are highly expressed in the shoots or leaves. Notably, *OsSIET4* plays a crucial role in the correct deposition of Si in the leaves and the export of Si to the leaf surface, which is essential for the healthy growth of rice (Mitani-Ueno et al., 2023). In our study, *AmSIET4* is exclusively expressed in the leaves (Fig. 6), where it mediates Si efflux (Fig. 5). Additionally, Si deposition was observed on the salt glands of the leaf surface, suggesting that *AmSIET4* may facilitate Si efflux in the leaves of *A. marina*, leading to Si deposition on the salt glands.

The Si transport function of rice Lsi1 and Lsi2 has been validated by expression in *Xenopus* oocytes. Lsi1 mediates bidirectional Si permeation that is independent of energy consumption, whereas Lsi2 only exhibits efflux activity for Si and relies on a proton gradient-driven process that requires energy consumption (Ma et al., 2007; Mitani et al., 2008). The Si transport function of other species' Si transporters has also been verified in *Xenopus* oocytes, such as grape (Noronha et al., 2020) and tomato (Sun et al., 2020). In our study, we used yeast cells to validate the permeability of AmLsi1 and AmSIET4 to Si (Fig. 5). This method is feasible and relatively easier to operate. In addition to their Si transport function, the Si transporters Lsi1 and Lsi2 also exhibit permeability to germanium (Ge) and As(III) (Ma et al., 2008; Noronha et al., 2020; Saitoh et al., 2021). Ge is a Si analogue that cannot be distinguished from Si by plant roots. It can be used to identify Si permeability (Ma et al., 2007). Similarly, As(III) is also a Si analogue. Our results indicate that AmLsi1 and AmSIET4 exhibit similar trends in their permeability to Si and As(III) (Fig. 5b, c). Combined with the substrate sensitivity assay for As(III) (Fig. 5a), it suggests that AmLsi1 is capable of bidirectional permeation of both Si and As(III), while AmSIET4 exhibits efflux activity (Fig. 5).

4.3. Response of AmLsi1 and AmSIET4 to Si and other environmental factors

In our study, both *AmLsi1* and *AmSIET4* showed similar trends in response to Si, salt, and tidal flooding, with downregulation observed at high concentrations of Si and salt as well as under tidal flooding conditions (Fig. 6). Similar downregulation of *Lsi1* expression under Si supply has been reported in rice (Ma et al., 2006; Ma et al., 2007) and other species such as ryegrass (Pontigo et al., 2021), soybean (Deshmukh et al., 2013), date palm (Bokor et al., 2019), and pigeonpea (Mandlik et al., 2022). This feedback mechanism maintains the Si concentration within a certain range, as appropriate Si levels are beneficial for plants (dos Santos Sarah et al., 2021). Dehydration stress and abscisic

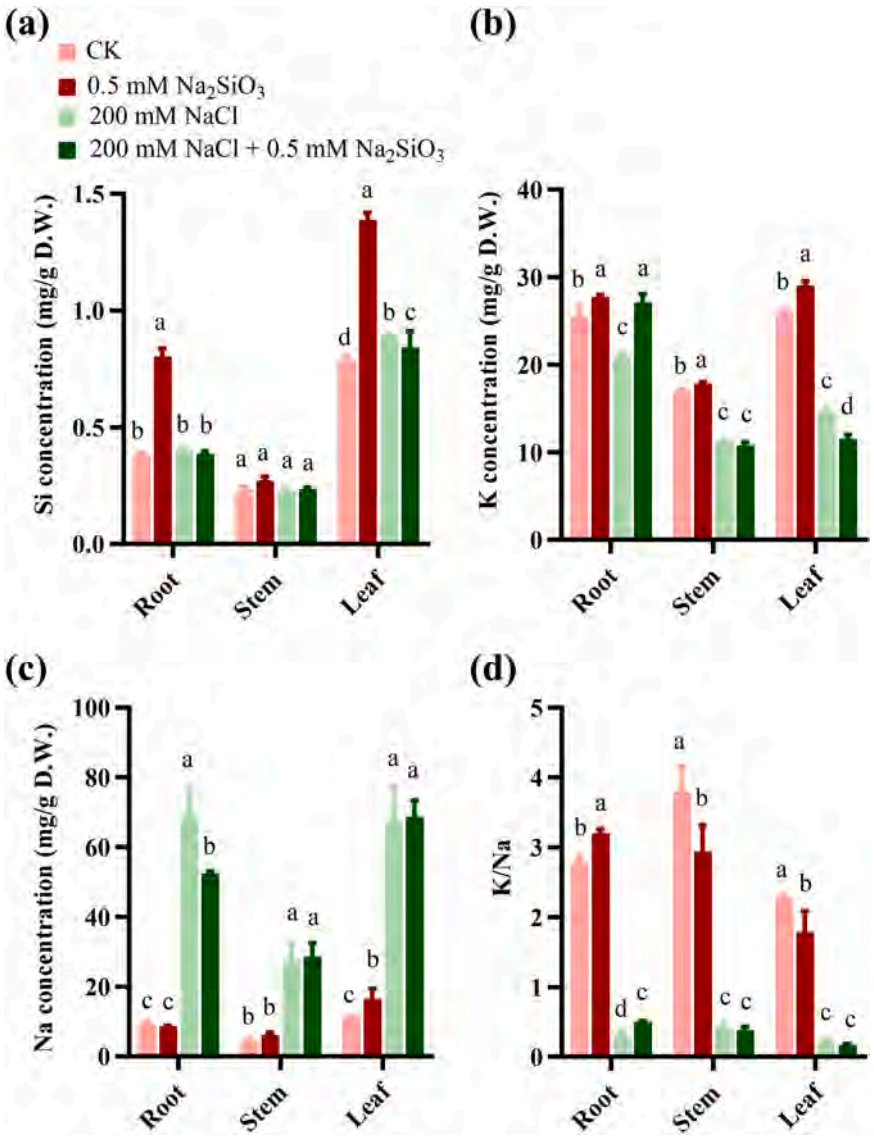


Fig. 9. Effect of Si and salt treatments on element accumulation in *A. marina* tissues. Si, Na, and K element concentrations (measured by ICP-MS) in the roots, stems, and leaves of *A. marina* treated with silicate (0.5 mM Na_2SiO_3), salt (200 mM NaCl), or a combination of both are shown in (a), (b), and (c), respectively. (d) Presents the K/Na ratio. Values are expressed as means ± SD (n = 4). Different letters within the same group indicate significant differences ($p < 0.05$), as determined by one-way ANOVA.

acid (ABA) treatment can rapidly suppress the expression of *Lsi1* and *Lsi2* in rice and reduce Si uptake (Yamaji and Ma, 2007, 2011). Drought and salinity significantly downregulate the expression of rice *Lsi1* and *Lsi6* (Nguyen et al., 2013). In our results, the combination of Si and salinity treatment further intensified the downregulation of *AmLsi1* and *AmSIET4* genes, and interestingly, the addition of Si under salinity conditions did not increase the Si concentration in the leaves, but instead led to a slight reduction (Figs. 6 and 9). This suggests that *A. marina* reduces Si uptake when accumulating salt, possibly to optimize energy allocation. These findings indicate that osmotic stress leads to downregulation of Si transporter genes and a consequent reduction in Si uptake.

Si in *A. marina* mainly accumulates in leaves, and we observed the phenomenon of salt gland secretion of Si, even under non-saline conditions (Figs. 7 and 9). Similar deposition of Si has also been found in salt glands of other species such as *Tamarix* (Storey and Thomson, 1994) and Plumbaginaceae (Faraday and Thomson, 1986). The plants do not appear to intercept Si as it is excreted through the salt glands with secreted sap. Based on the tissue-specific expression of *AmSIET4* in leaves and the identification of *AmSIET4* expression in the transcriptome of salt glands by laser capture microdissection (unpublished data), we propose that Si secretion in salt glands is regulated by AmSIET4. The transport of Si by AmSIET4 requires energy, and under saline conditions, *AmSIET4* has lower expression levels with energy mainly allocated to salt secretion.

4.4. Insights into the role of silicon in A. marina

Previous studies have mainly focused on the beneficial effects of Si uptake in plants on enhancing plant strength and rigidity, as well as resisting biotic and abiotic stresses (Ma and Yamaji, 2006). For example, Si has been shown to restore the photosynthetic capacity of okra under salt stress (Abbas et al., 2015). Similarly, in our study, we found that Si restored chlorophyll fluorescence (F_v/F_m) under salt treatment, thereby enhancing photosynthetic potential and stress resistance in *A. marina* seedlings. Since F_v/F_m reflects the efficiency of electron transport in the photosynthetic process and the overall health of the plant (Maxwell and Johnson, 2000), these findings underscore the positive impact of Si on

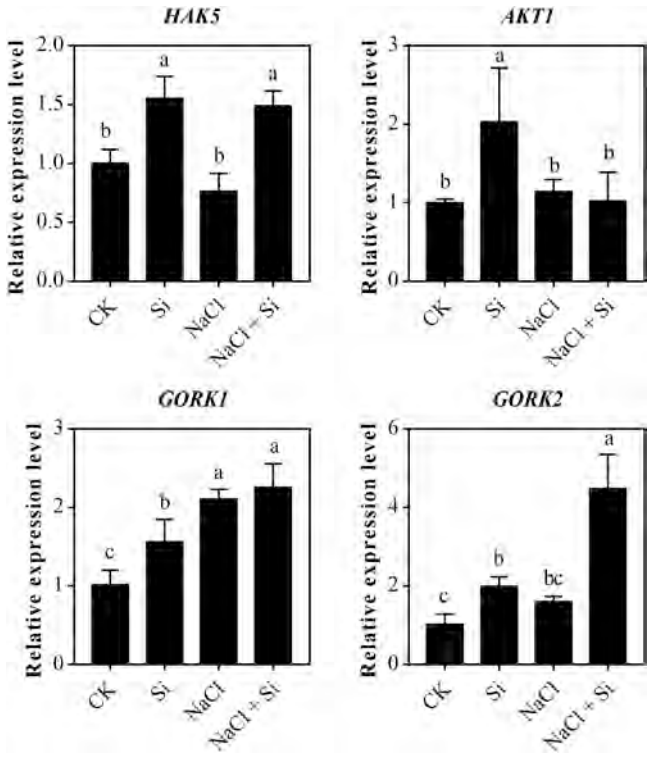


Fig. 10. Effect of Si and salt treatments on K^+ flux in *A. marina* roots. Non-invasive micro-test technology (NMT) was used to measure the K^+ flux in the roots of *A. marina* treated with 0.5 mM Na_2SiO_3, 200 mM NaCl, or a combination of both. (a) shows the probe measuring at a distance of 400 μm from the root tip. The real-time flux of K^+ over 5 min (b) and the average flux rate (c) are presented. The data are presented as means ± SD (n = 6). Different letters indicate significant differences ($p < 0.05$).

photosynthetic function under salinity. Growth measurements further indicated that Si application promoted biomass accumulation, reduced water content, and enhanced dry matter accumulation (Fig. 8), all of which may contribute to stress resistance. More notably, Si significantly increased leaf area and promoted seedling growth (Fig. 8). Subsequent measurements of ion concentration and flux indicated that Si facilitated K^+ uptake in the root of *A. marina* (Figs. 9 and 10), and RT-qPCR analysis revealed that K^+ channel genes were upregulated in response to Si treatment (Fig. 11). These findings are consistent with previous reports in other plant species. For instance, exogenous Si application has been shown to promote K^+ absorption and increase leaf area in common beans (dos Santos Sarah et al., 2021), improve K^+ uptake and transport in rice under salt stress (Yan et al., 2021), and alleviate K^+ deficiency symptoms in peanuts by enhancing K^+ uptake through the roots (Patel et al., 2022). In soybean, Si rescues plants from K^+ deficiency stress and increasing K^+ concentration (Miao et al., 2010) and, under salt stress, decreases Na^+ concentration while increasing K^+ concentration and leaf area (Peña-Calzada et al., 2023). Consistent with these observations, our study demonstrated that Si treatment also reduced the Na^+ concentration in the roots under salt conditions (Fig. 9c). Taken together, in *A. marina*, Si regulates the K^+/Na^+ balance and enhances photosynthetic efficiency, ultimately promoting growth and salt tolerance.

In this study, we observed significant Si deposition on the salt gland surfaces of *A. marina*. However, it is unclear whether this Si is actively secreted by the glands or part of their cell wall structure. Similar findings in *Tamarix aphylla* suggested that Si might be secreted by salt glands (Storey and Thomson, 1994). Si has been reported to strengthen cell walls, reduce transpiration, and improve water retention, inhibition of electrolyte leakage and resistance to osmotic or salt stress (Agarie et al., 1998; Sheng et al., 2018; Souri et al., 2021). Silica layers may reinforce salt gland integrity, maintaining functionality under high salinity and preventing salt backflow. Alternatively, Si might influence ion transport or excretion by modulating gland cell permeability or stability. These possibilities remain speculative. Future research with high-resolution Si localization and experiments on Si's effects on salt secretion will be key to clarifying its role in salt gland functionality.

5. Conclusions

In this study, we investigated the Si concentration and transporters in three mangrove species and confirmed that *A. marina* is a Si accumulator in the mangrove ecosystem. Sequence analysis revealed that AmLsi1 and AmSIET4 are putative Si transporters, and heterologous expression in yeast confirmed that AmLsi1 is a bidirectional transporter for Si, with additional transport activity for H_2O, H_2O_2, and As(III), while AmSIET4 is an efflux transporter for Si and As(III). Gene expression analysis indicated that *AmLsi1* functions in the roots, while *AmSIET4* functions in the leaves, and both are negatively regulated by Si and salt stress. We described the process from Si uptake in the roots to Si secretion from the salt glands of leaf (Fig. 12). Si treatment increased the plant's Si concentration and promoted expression of K^+ channel genes, enhancing root uptake of K^+ and ultimately increasing leaf area (Fig. 12). Additionally, Si reduced Na^+ accumulation in the roots, improved the K^+/Na^+ ratio, and preserved photosynthetic potential. Overall, this study reveals the critical role of Si transporters in facilitating Si uptake and transport in mangrove plants, with a particular emphasis on their physiological benefits in *A. marina*. These findings deepen our understanding of how Si enhances growth and stress resilience in mangroves, underscoring its importance in these unique ecosystems.

CRediT authorship contribution statement

Guo Zejun: Writing – original draft, Visualization, Validation, Project administration, Methodology, Investigation, Funding acquisition, Formal analysis, Data curation, Conceptualization. **Zheng Hai-Lei:**

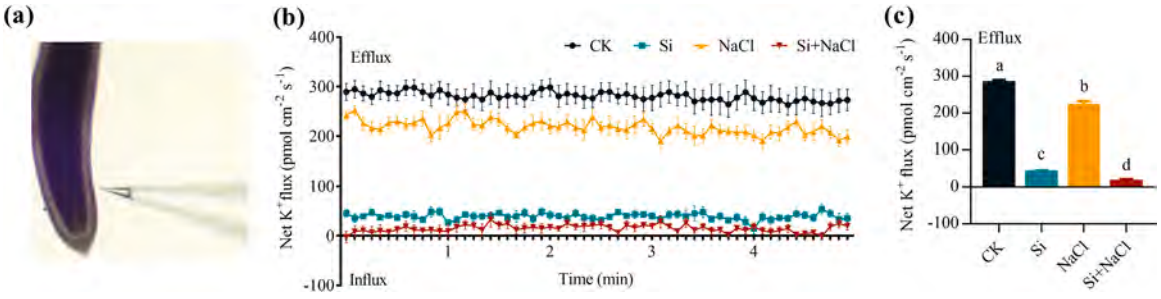


Fig. 11. Effect of Si and salt treatments on K^+ channel genes expression in *A. marina* roots. The expression levels of the inward K^+ channels *HAK5*, *AKT1* and the two outward K^+ channels *GORK* in the roots of *A. marina* treated with 0.5 mM Na_2SiO_3, 200 mM NaCl, or a combination of both are shown. The data are presented as means ± SD (n = 4). Different letters indicate significant differences ($p < 0.05$).

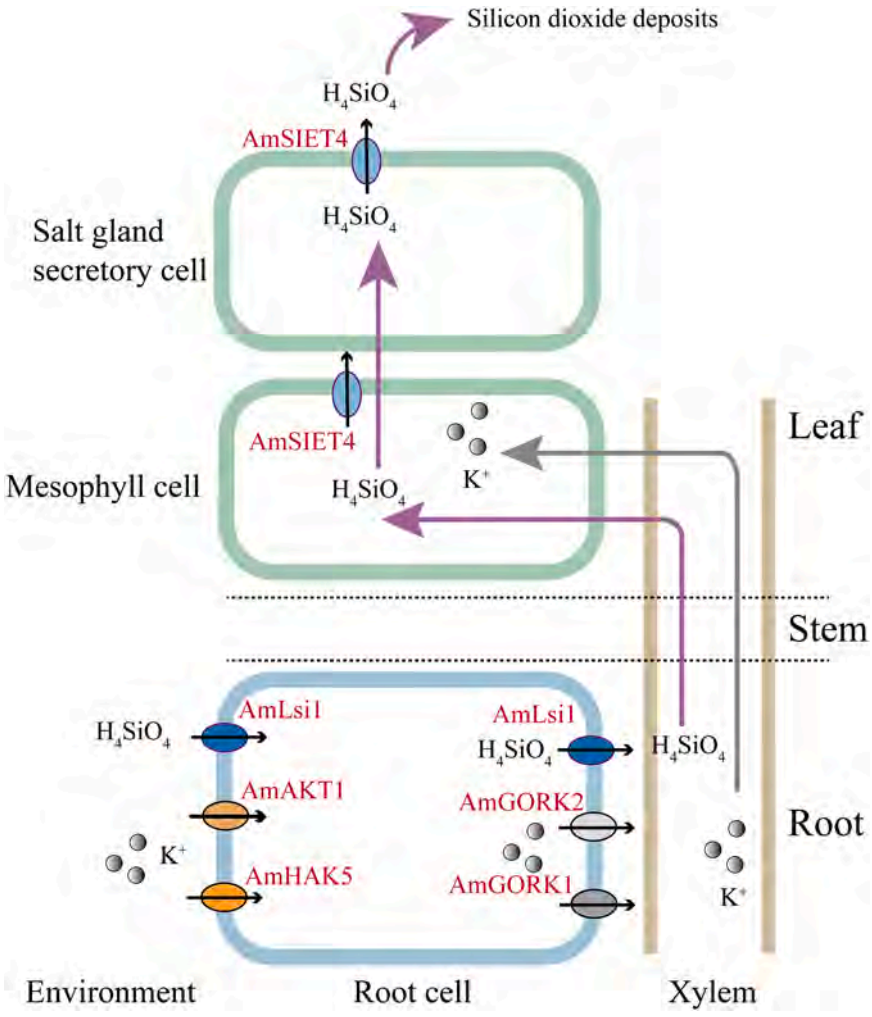


Fig. 12. The diagram illustrates the Si transport and potassium uptake promotion mechanism in *A. marina*. Initially, $Si(OH)_4$ in the environment enters the root through the Si transporter AmLsi1, and then unloads into the xylem and is transported to the leaves via the vascular system. Subsequently, silicic acid is released into the salt gland through the Si efflux protein AmSIET4 in the leaf, and eventually excreted from the salt gland, where it forms silica deposition on the surface. On the other hand, high Si concentration in the environment promotes the expression of K^+ channels, where the highly expressed inward potassium transporter *AmAKT1* and *AmHAK5*, as well as two highly expressed outward K^+ channels *AmGORK1* and *AmGORK2*, work together to promote potassium uptake and enhance the growth of *A. marina* under the saline environment.

Writing – review & editing, Supervision, Project administration, Funding acquisition, Conceptualization. **Wei Mingyue:** Methodology. **Song Lingyu:** Methodology. **Liao Siyao:** Methodology. **Xu Chaoqun:** Data curation. **Chen Xi:** Methodology. **Jiang Lei:** Methodology. **Huang Hezi:** Methodology. **Li Zhanhong:** Methodology.

Declaration of Competing Interest

The authors declare that they have no known competing financial interests or personal relationships that could have appeared to influence the work reported in this paper.

Acknowledgements

This work was financially supported by the Natural Science Foundation of China (NSFC) (42406121, 32171740) and Improvement Program of Young and Middle-aged Teachers in Guangxi Universities (2024KY0015). We appreciate anonymous reviewers and the editor for the insightful comments and valuable suggestions.

Appendix A. Supporting information

Supplementary data associated with this article can be found in the online version at doi:10.1016/j.indcrop.2025.120876.

Data availability

Data will be made available on request.

References

Abbas, T., Balal, R.M., Shahid, M.A., Pervez, M.A., Ayyub, C.M., Aqueel, M.A., Javaid, M. M., 2015. Silicon-induced alleviation of NaCl toxicity in okra (*Abelmoschus esculentus*) is associated with enhanced photosynthesis, osmoprotectants and antioxidant metabolism. Acta Physiol. Plant 37, 6. https://doi.org/10.1007/s11738-014-1768-5.

Agarie, S., Uchida, H., Agata, W., Kubota, F., Kaufman, P.B., 1998. Effects of silicon on transpiration and leaf conductance in rice plants (*Oryza sativa* L.). Plant Prod. Sci. 1, 89–95. https://doi.org/10.1626/pps.1.89.

Bokor, B., Soukup, M., Vaculík, M., Vď ačný, P., Weidinger, M., Lichtscheidl, I., Vávrová, S., Šoltys, K., Sonah, H., Deshmukh, R., Bélanger, R.R., White, P.J., El-Serehy, H.A., Lux, A., 2019. Silicon uptake and localisation in date palm (*Phoenix dactylifera*) – a unique association with sclerenchyma. Front. Plant Sci. 10, 988. https://doi.org/10.3389/fpls.2019.00988.

Chiba, Y., Mitani, N., Yamaji, N., Ma, J.F., 2009. HvLsi1 is a silicon influx transporter in barley. Plant J. 57, 810–818. https://doi.org/10.1111/j.1365-313X.2008.03728.x.

Cornelis, J.T., Delvaux, B., Georg, R.B., Lucas, Y., Ranger, J., Opfergelt, S., 2011. Tracing the origin of dissolved silicon transferred from various soil-plant systems towards rivers: a review. Biogeosciences 8, 89–112. https://doi.org/10.5194/bg-8-89-2011.

Coskun, D., Deshmukh, R., Shivaraj, S.M., Isenring, P., Bélanger, R.R., 2021. Lsi2: a black box in plant silicon transport. Plant Soil 466, 1–20. https://doi.org/10.1007/s11104-021-05061-1.

Debona, D., Rodrigues, F.A., Datnoff, L.E., 2017. Silicon's role in abiotic and biotic plant stresses. Annu. Rev. Phytopathol. 55, 85–107. https://doi.org/10.1146/annurev-phyto-080516-035312.

Deshmukh, R., Sonah, H., Belanger, R.R., 2020. New evidence defining the evolutionary path of aquaporins regulating silicon uptake in land plants. J. Exp. Bot. 71, 6775–6788. https://doi.org/10.1093/jxb/eraa342.

Deshmukh, R.K., Vivancos, J., Guérin, V., Sonah, H., Labbé, C., Belzile, F., Bélanger, R.R., 2013. Identification and functional characterization of silicon transporters in soybean using comparative genomics of major intrinsic proteins in Arabidopsis and rice. Plant Mol. Biol. 83, 303–315. https://doi.org/10.1007/s11103-013-0087-3.

Deshmukh, R.K., Vivancos, J., Ramakrishnan, G., Guerin, V., Carpentier, G., Sonah, H., Labbe, C., Isenring, P., Belzile, F.J., Belanger, R.R., 2015. A precise spacing between the NPA domains of aquaporins is essential for silicon permeability in plants. Plant J. 83, 489–500. https://doi.org/10.1111/tpj.12904.

Elizondo, E.B., Carey, J.C., Al-Haj, A.N., Lugo, A.E., Fulweiler, R.W., 2021. High productivity makes mangroves potentially important players in the tropical silicon cycle. Front. Mar. Sci. 8, 652615. https://doi.org/10.3389/fmars.2021.652615.

Faraday, C.D., Thomson, W.W., 1986. Functional aspects of the salt glands of the Plumbaginaceae. J. Exp. Bot. 37, 1129–1135. https://doi.org/10.1093/jxb/37.8.1129.

Grégoire, C., Rémus-Borel, W., Vivancos, J., Labbé, C., Belzile, F., Bélanger, R.R., 2012. Discovery of a multigene family of aquaporin silicon transporters in the primitive plant *Equisetum arvense*. Plant J. 72, 320–330. https://doi.org/10.1111/j.1365-313X.2012.05082.x.

Guo, Z., Ma, D., Li, J., Wei, M., Zhang, L., Zhou, L., Zhou, X., He, S., Wang, L., Shen, Y., Li, Q.Q., Zheng, H.-L., 2022. Genome-wide identification and characterization of aquaporins in mangrove plant *Kandelia obovata* and its role in response to the intertidal environment. Plant Cell Environ. 45, 1698–1718. https://doi.org/10.1111/pce.14286.

Guo, Z., Wei, M.-Y., Zhong, Y.-H., Wu, X., Chi, B.-J., Li, J., Li, H., Zhang, L.-D., Wang, X.-X., Zhu, X.-Y., Zheng, H.-L., 2023. Leaf sodium homeostasis controlled by salt gland is associated with salt tolerance in mangrove plant *Avicennia marina*. Tree Physiol. 43, 817–831. https://doi.org/10.1093/treephys/tpad002.

Guo, Z., Wei, M., Xu, C., Wang, L., Li, J., Liu, J., Zhong, Y., Chi, B., Song, S., Zhang, L., Song, L., Ma, D., Zheng, H.-L., 2024. Genome-wide identification of *Avicennia marina* aquaporins reveals their role in adaptation to intertidal habitats and their relevance to salt secretion and vivipary. Plant Cell Environ. 47, 832–853. https://doi.org/10.1111/pce.14769.

Gupta, A.B., Sankararamakrishnan, R., 2009. Genome-wide analysis of major intrinsic proteins in the tree plant *Populus trichocarpa*: characterization of XIP subfamily of aquaporins from evolutionary perspective. BMC Plant Biol. 9, 134. https://doi.org/10.1186/1471-2229-9-134.

Haysom, M.B., Ostatek-Boczynski, Z.A., 2006. Rapid, wet oxidation procedure for the estimation of silicon in plant tissue. Commun. Soil Sci. Plant Anal. 37, 2299–2306. https://doi.org/10.1080/00103620600819420.

Huang, S., Yamaji, N., Sakurai, G., Mitani-Ueno, N., Konishi, N., Ma, J.F., 2022. A pericycle-localized silicon transporter for efficient xylem loading in rice. N. Phytol. 234, 197–208. https://doi.org/10.1111/nph.17959.

Johanson, U., Karlsson, M., Johansson, I., Gustavsson, S., Sjövall, S., Fraysse, L., Weig, A. R., Kjellbom, P., 2001. The complete set of genes encoding major intrinsic proteins in Arabidopsis provides a framework for a new nomenclature for major intrinsic proteins in plants. Plant Physiol. 126, 1358–1369. https://doi.org/10.1104/pp.126.4.1358.

Kumar, S., Stecher, G., Li, M., Knyaz, C., Tamura, K., 2018. MEGA X: molecular evolutionary genetics analysis across computing platforms. Mol. Biol. Evol. 35, 1547–1549. https://doi.org/10.1093/molbev/msy096.

Kumawat, S., Khatri, P., Ahmed, A., Vats, S., Kumar, V., Jaswal, R., Wang, Y., Xu, P., Mandlik, R., Shivaraj, S.M., Deokar, A., Sonah, H., Sharma, T.R., Deshmukh, R., 2021. Understanding aquaporin transport system, silicon and other metalloids uptake and deposition in bottle gourd (*Lagenaria siceraria*). J. Hazard. Mater. 409, 124598. https://doi.org/10.1016/j.jhazmat.2020.124598.

Lavinsky, A.O., Detmann, K.C., Reis, J.V., Ávila, R.T., Sanglard, M.L., Pereira, L.F., Sanglard, L.M.V.P., Rodrigues, F.A., Araújo, W.L., DaMatta, F.M., 2016. Silicon improves rice grain yield and photosynthesis specifically when supplied during the reproductive growth stage. J. Plant Physiol. 206, 125–132. https://doi.org/10.1016/j.jplph.2016.09.010.

Lux, A., Luxová, M., Abe, J., Tanimoto, E., Hattori, T., Inanaga, S., 2003. The dynamics of silicon deposition in the sorghum root endodermis. N. Phytol. 158, 437–441. https://doi.org/10.1046/j.1469-8137.2003.00764.x.

Ma, D., Guo, Z., Ding, Q., Zhao, Z., Shen, Z., Wei, M., Gao, C., Zhang, L., Li, H., Zhang, S., Li, J., Zhu, X., Zheng, H.-L., 2021. Chromosome-level assembly of the mangrove plant *Aegiceras corniculatum* genome generated through Illumina, PacBio and Hi-C sequencing technologies. Mol. Ecol. Resour. 21, 1593–1607. https://doi.org/10.1111/1755-0998.13347.

Ma, D., Ding, Q., Guo, Z., Xu, C., Liang, P., Zhao, Z., Song, S., Zheng, H.-L., 2022. The genome of a mangrove plant, *Avicennia marina*, provides insights into adaptation to coastal intertidal habitats. Planta 256, 6. https://doi.org/10.1007/s00425-022-03916-0.

Ma, J.F., Takahashi, E., 2002. Soil, fertilizer, and plant silicon research in Japan. Elsevier, Dordrecht, the Netherlands.

Ma, J.F., Yamaji, N., 2006. Silicon uptake and accumulation in higher plants. Trends Plant Sci. 11, 392–397. https://doi.org/10.1016/j.tplants.2006.06.007.

Ma, J.F., Tamai, K., Yamaji, N., Mitani, N., Konishi, S., Katsuhara, M., Ishiguro, M., Murata, Y., Yano, M., 2006. A silicon transporter in rice. Nature 440, 688–691. https://doi.org/10.1038/nature04590.

Ma, J.F., Yamaji, N., Mitani, N., Tamai, K., Konishi, S., Fujiwara, T., Katsuhara, M., Yano, M., 2007. An efflux transporter of silicon in rice. Nature 448, 209–212. https://doi.org/10.1038/nature05964.

Ma, J.F., Yamaji, N., Mitani, N., Xu, X.-Y., Su, Y.-H., McGrath, S.P., Zhao, F.-J., 2008. Transporters of arsenite in rice and their role in arsenic accumulation in rice grain. Proc. Natl. Acad. Sci. USA 105, 9931–9935. https://doi.org/10.1073/pnas.0802361105.

Ma, J.F., Yamaji, N., Mitani-Ueno, N., 2011. Transport of silicon from roots to panicles in plants. P. Jpn. Acad. B-Phys. 87, 377–385. https://doi.org/10.2183/pjab.87.377.

Mandlik, R., Singla, P., Kumawat, S., Khatri, P., Ansari, W., Singh, A., Sharma, Y., Singh, A., Solanke, A., Nadaf, A., Sonah, H., Deshmukh, R., 2022. Understanding aquaporin regulation defining silicon uptake and role in arsenic, antimony and germanium stress in pigeonpea (*Cajanus cajan*). Environ. Pollut. 294, 118606. https://doi.org/10.1016/j.envpol.2021.118606.

Maxwell, K., Johnson, G.N., 2000. Chlorophyll fluorescence—a practical guide. J. Exp. Bot. 51, 659–668. https://doi.org/10.1093/jexbot/51.345.659.

Miao, B.-H., Han, X.-G., Zhang, W.-H., 2010. The ameliorative effect of silicon on soybean seedlings grown in potassium-deficient medium. Ann. Bot. 105, 967–973. https://doi.org/10.1093/aob/mcq063.

Mitani, N., Yamaji, N., Ma, J.F., 2008. Characterization of substrate specificity of a rice silicon transporter, Lsi1. Pflug. Arch. Eur. J. Phy. 456, 679–686. https://doi.org/10.1007/s00424-007-0408-y.

Mitani, N., Chiba, Y., Yamaji, N., Ma, J.F., 2009a. Identification and characterization of maize and barley Lsi2-like silicon efflux transporters reveals a distinct silicon uptake system from that in rice. Plant Cell 21, 2133–2142. https://doi.org/10.1105/tpc.109.067884.

Mitani, N., Yamaji, N., Ma, J.F., 2009b. Identification of maize silicon influx transporters. Plant Cell Physiol. 50, 5–12. https://doi.org/10.1093/pcp/pcn110.

Mitani-Ueno, N., Yamaji, N., Zhao, F.-J., Ma, J.F., 2011b. The aromatic/arginine selectivity filter of NIP aquaporins plays a critical role in substrate selectivity for silicon, boron, and arsenic. J. Exp. Bot. 62, 4391–4398. https://doi.org/10.1093/jxb/err158.

Mitani-Ueno, N., Yamaji, N., Ma, J.F., 2011a. Silicon efflux transporters isolated from two pumpkin cultivars contrasting in Si uptake. Plant Signal. Behav. 6, 991–994. https://doi.org/10.4161/psb.6.7.15462.

Mitani-Ueno, N., Yamaji, N., Huang, S., Yoshioka, Y., Miyaji, T., Ma, J.F., 2023. A silicon transporter gene required for healthy growth of rice on land. Nat. Commun. 14, 6522. https://doi.org/10.1038/s41467-023-42180-y.

Nguyen, M.X., Moon, S., Jung, K.-H., 2013. Genome-wide expression analysis of rice aquaporin genes and development of a functional gene network mediated by aquaporin expression in roots. Planta 238, 669–681. https://doi.org/10.1007/s00425-013-1918-9.

Noronha, H., Silva, A., Mitani-Ueno, N., Conde, C., Sabir, F., Prista, C., Soveral, G., Isenring, P., Ma, J.F., Bélanger, R.R., Gerós, H., 2020. The grapevine NIP2;1 aquaporin is a silicon channel. J. Exp. Bot. 71, 6789–6798. https://doi.org/10.1093/jxb/eraa294.

Ouellette, S., Goyette, M.-H., Labbé, C., Laur, J., Gaudreau, L., Gosselin, A., Dorais, M., Deshmukh, R.K., Bélanger, R.R., 2017. Silicon transporters and effects of silicon amendments in strawberry under high tunnel and field conditions. Front. Plant Sci. 8, 949. https://doi.org/10.3389/fpls.2017.00949.

Patel, M., Fatnani, D., Parida, A.K., 2022. Potassium deficiency stress tolerance in peanut (*Arachis hypogaea*) through ion homeostasis, activation of antioxidant defense, and metabolic dynamics: alleviatory role of silicon supplementation. Plant Physiol. Biochem 182, 55–75. https://doi.org/10.1016/j.plaphy.2022.04.013.

Peña-Calzada, K., Olivera-Viciedo, D., Calero-Hurtado, A., de Mello Prado, R., Habermann, E., Lata Tenesaca, L.F., Ajila, G., de Oliveira, R., Rodríguez, J.C., Lupino Gratão, P., 2023. Silicon mitigates the negative impacts of salt stress in soybean plants. J. Sci. Food Agric. 103, 4360–4370. https://doi.org/10.1002/jsfa.12503.

Pontigo, S., Larama, G., Parra-Almuna, L., Nunes-Nesi, A., Mora, MdlL., Cartes, P., 2021. Physiological and molecular insights involved in silicon uptake and transport in ryegrass. Plant Physiol. Biochem 163, 308–316. https://doi.org/10.1016/j.plaphy.2021.04.013.

Qiao, H., Zhou, X., Yi, Y., Wei, L., Xu, X., Jin, P., Su, W., Weng, Y., Yu, D., He, S., Fu, M., Hou, C., Pan, X., Wang, W., Zhang, Y.-Y., Ming, R., Ye, C., Li, Q.Q., Shen, Y., 2024. Molecular mechanism of vivipary as revealed by the genomes of viviparous mangroves and non-viviparous relatives. e3707 Curr. Biol. 34, 3707–3721. https://doi.org/10.1016/j.cub.2024.07.010.

Saitoh, Y., Mitani-Ueno, N., Saito, K., Matsuki, K., Huang, S., Yang, L., Yamaji, N., Ishikita, H., Shen, J.-R., Ma, J.F., Suga, M., 2021. Structural basis for high selectivity of a rice silicon channel Lsi1. Nat. Commun. 12, 6236. https://doi.org/10.1038/s41467-021-26535-x.

dos Santos Sarah, M.M., de Mello Prado, R., de Souza Júnior, J.P., Teixeira, G.C.M., dos Santos Duarte, J.C., de Medeiros, R.L.S., 2021. Silicon supplied via foliar application and root to attenuate potassium deficiency in common bean plants. Sci. Rep. 11, 19690. https://doi.org/10.1038/s41598-021-99194-z.

Sheng, H., Ma, J., Pu, J., Wang, L., 2018. Cell wall-bound silicon optimizes ammonium uptake and metabolism in rice cells. Ann. Bot. 122, 303–313. https://doi.org/10.1093/aob/mcy068.

Sommer, M., Kaczorek, D., Kuzyakov, Y., Breuer, J., 2006. Silicon pools and fluxes in soils and landscapes—a review. J. Plant Nutr. Soil Sci. 169, 310–329. https://doi.org/10.1002/jpln.200690016.

Souri, Z., Khanna, K., Karimi, N., Ahmad, P., 2021. Silicon and plants: Current knowledge and future prospects. J. Plant Growth Regul. 40, 906–925. https://doi.org/10.1007/s00344-020-10172-7.

Storey, R., Thomson, W.W., 1994. An X-ray microanalysis study of the salt glands and intracellular calcium crystals of *Tamarix*. Ann. Bot. 73, 307–313. https://doi.org/10.1006/anbo.1994.1036.

Sun, H., Guo, J., Duan, Y., Zhang, T., Huo, H., Gong, H., 2017. Isolation and functional characterization of *CsLsi1*, a silicon transporter gene in *Cucumis sativus*. Physiol. Plant 159, 201–214. https://doi.org/10.1111/ppl.12515.

Sun, H., Duan, Y., Qi, X., Zhang, L., Huo, H., Gong, H., 2018. Isolation and functional characterization of *CsLsi2*, a cucumber silicon efflux transporter gene. Ann. Bot. 122, 641–648. https://doi.org/10.1093/aob/mcy103.

Sun, H., Duan, Y., Mitani-Ueno, N., Che, J., Jia, J., Liu, J., Guo, J., Ma, J.F., Gong, H., 2020. Tomato roots have a functional silicon influx transporter but not a functional silicon efflux transporter. Plant Cell Environ. 43, 732–744. https://doi.org/10.1111/pce.13679.

Takahashi, E., Hino, K., 1978. Silica uptake by rice plant with special reference to the forms of dissolved silica. J. Sci. Soil Manure (Jpn. 49, 357–360. https://doi.org/10.20710/dojo.49.5_357.

Vivancos, J., Deshmukh, R., Grégoire, C., Rémus-Borel, W., Belzile, F., Bélanger, R.R., 2016. Identification and characterization of silicon efflux transporters in horsetail (*Equisetum arvense*). J. Plant Physiol. 200, 82–89. https://doi.org/10.1016/j.jplph.2016.06.011.

Wang, H.-S., Yu, C., Fan, P.-P., Bao, B.-F., Li, T., Zhu, Z.-J., 2014. Identification of two cucumber putative silicon transporter genes in *Cucumis sativus*. J. Plant Growth Regul. 34, 332–338. https://doi.org/10.1007/s00344-014-9466-5.

Yamaji, N., Ma, J.F., 2007. Spatial distribution and temporal variation of the rice silicon transporter Lsi1. Plant Physiol. 143, 1306–1313. https://doi.org/10.1104/pp.106.093005.

Yamaji, N., Ma, J.F., 2011. Further characterization of a rice silicon efflux transporter, Lsi2. Soil Sci. Plant Nutr. 57, 259–264. https://doi.org/10.1080/00380768.2011.565480.

Yamaji, N., Ma, J.F., 2021. Metalloid transporters and their regulation in plants. Plant Physiol. 187, 1929–1939. https://doi.org/10.1093/plphys/kiab326.

Yamaji, N., Sakurai, G., Mitani-Ueno, N., Ma, J.F., 2015. Orchestration of three transporters and distinct vascular structures in node for intervascular transfer of silicon in rice. Proc. Natl. Acad. Sci. USA 112, 11401–11406. https://doi.org/10.1073/pnas.1508987112.

Yan, G., Fan, X., Zheng, W., Gao, Z., Yin, C., Li, T., Liang, Y., 2021. Silicon alleviates salt stress-induced potassium deficiency by promoting potassium uptake and translocation in rice (Oryza sativa L.). J. Plant Physiol. 258-259, 153379. https://doi.org/10.1016/j.jplph.2021.153379.

Aquaculture 609 (2025) 742961



Contents lists available at ScienceDirect

Aquaculture

journal homepage: www.elsevier.com/locate/aquaculture





Nitrite-induced intestinal injury mechanisms and multi-organ toxicity in Tilapia: Insights from integrated multi-omics analysis

Tingyu Wei [a], Xuemin Wei [b], Jialong Huang [a], Songlin Luo [b], Aiguo Huang [b,*]

[a] School of Resources, Environment and Materials, Guangxi University, Nanning 530004, China
[b] Guangxi Laboratory on the Study of Coral Reefs in the South China Sea, Coral Reef Research Center of China, School of Marine Sciences, Guangxi University, Nanning 530004, China

ARTICLE INFO

Keywords:
Nitrite
Tilapia
Intestinal microbiota
Inflammatory response
Conjoint analysis

ABSTRACT

The rapid accumulation of nitrite in aquaculture systems, primarily caused by high-protein feed utilization and fecal waste buildup, has become a significant environmental concern. In this study, we investigated the mechanisms underlying nitrite-induced intestinal injury and multi-organ injury in tilapia (*Oreochromis niloticus*). Under nitrite exposure, *Mycobacterium* and *Peptostreptococcaceae* in the intestine of tilapia increased by 1.44- and 6.28-fold, while *Romboutsia* decreased by 0.65-fold and *Neochlamydia* decreased by 22.20-fold. Exposure to nitrite not only disrupted intestinal microbiota homeostasis, but also led to aberrant activation of DNA damage repair pathways. Based on topological overlap matrix (TOM) analysis, the screened intestinal microbe ASV489 may modulate tilapia's intestinal barrier function, affecting physiological functions. The changes in the tissue sections of the liver and spleen, the increased activity of SOD, CAT and PO, as well as the upregulation of *MyD88* and *C-TLZ* in multiple tissues, jointly indicated significant oxidative damage and inflammatory response in these tissues. These perturbations induced systemic oxidative stress and inflammatory response, culminating in multi-organ dysfunction. By integrating multi-omics analyses of intestinal microbiota, this study provided a more comprehensive understanding of the adverse effects of nitrite on fish health.

1. Introduction

Nitrite, a traditional contaminant naturally pervasive in aquatic ecosystems (Ciji and Akhtar, 2020), jeopardizes aquaculture sustainability and aquatic organism health (Camargo and Alonso, 2006; Romano and Zeng, 2013; Zhang et al., 2025). In conventional extensive aquaculture practices, nitrite concentrations rarely surpass the 1 mg/L threshold considered tolerable for aquatic species (Ciji and Akhtar, 2020). In recent years, due to the economic benefits brought by intensive breeding, excessive feeding of high-protein feed (van Vuuren et al., 2015), and the accumulation of large amounts of aquaculture feces (Dauda et al., 2019), the nitrite content in the aquaculture water has sharply increased. The nitrite content could even surge to as high as 50 mg/L (Ciji and Akhtar, 2020). This could pose health risks to aquatic organisms, including reproductive and developmental toxicity (Bian et al., 2025; Keshari et al., 2016), metabolic disorders (Yan et al., 2024; Yang et al., 2024), and immunosuppression (Jia et al., 2016; Li et al., 2025a). The intestine, as a target organ for nutrient absorption, immune defense (Qin et al., 2010), and the bioaccumulation of nitrite, plays a critical role in maintaining overall health. (Liang et al., 2022; Wang et al., 2024). Previous studies have revealed the injury caused by nitrite to the intestinal barrier of shrimp species such as crayfish and prawns (Guo et al., 2020; Yildiz and Benli, 2004; Yu et al., 2019), as well as its impact of intestinal antioxidant capacity, The intestinal immunity, and energy metabolism (Bian et al., 2024; Hou et al., 2024). The toxicity of nitrite in fish varies in different tissues, including blood (Gao et al., 2020), gills (Li et al., 2022), liver (Lin et al., 2018b), brain (Beaver et al., 2020) and muscle (Xu et al., 2022). The highest accumulation of nitrite is found in fish blood, where the nitrite concentration may be up to 60 times higher than that in the surrounding water (Fontenot et al., 1999), leading to methemoglobinemia (Lewis Jr. and Morris, 1986). It caused physiological abnormalities and even death in fish (Brown and McLeay, 1975; Maestre et al., 2009). However, there is limited research on the interaction between intestinal microbes and systemic organs.

The tilapia (*Oreochromis niloticus*), due to its rapid growth and strong adaptability to various environmental conditions, has rapidly become one of the most widely farmed fish species globally (Getnet et al., 2024). Studies have shown that the 96-h 50 % Lethal Concentration (LC_{50}) of

* Corresponding author.
E-mail address: aiguo_200891@126.com (A. Huang).

https://doi.org/10.1016/j.aquaculture.2025.742961
Received 3 June 2025; Received in revised form 11 July 2025; Accepted 15 July 2025
Available online 16 July 2025
0044-8486/© 2025 Elsevier B.V. All rights are reserved, including those for text and data mining, AI training, and similar technologies.

nitrite for small Nile tilapia (4.40 ± 1.50 g) was 81 mg/L, while for large Nile tilapia (90.70 ± 16.43 g) was 8 mg/L, indicating that small tilapia is more resistant to nitrite (Atwood et al., 2001). Nitrite not only induced hypoxic responses of tilapia (Obirikorang et al., 2020), suppressing nonspecific immune enzymes and immunoglobulin activity (Xu et al., 2016), but also reduced the cell vitality of leukocytes and increased susceptibility to *Streptococcus agalactiae* (Zhao et al., 2020). This response was further exacerbated in the presence of *Lactococcus lactis* (Tan et al., 2022). Current research has mainly focused on the effects of probiotics, such as *Clostridium butyricum* (Zhang et al., 2021), *Pediococcus acidilactici* (Ferguson et al., 2010), on the antioxidant capacity, immune response, and intestinal microbiota of tilapia. However, the impact of pathogenic bacteria presented in the intestine on the tilapia remains unclear, especially when nitrite concentrations in the aquaculture environment sharply increase.

Based on the above background, our study leverages 16S ribosomal RNA (16S rRNA), eukaryotic transcriptome, histopathological observations, as well as quantitative Real-time PCR (RT-qPCR) to:(1) investigate the mechanisms of nitrite-induced intestinal damage using multi-omics approaches and analyzing multiple tissues; (2) map the intestinal-derived damage to various tissues, providing a more comprehensive understanding of the adverse effects of nitrite on fish health.

2. Materials and methods

2.1. Chemicals and animals

Sodium Nitrite ($NaNO_2$, CAS: 7632-00-0, purity: 95 %) was purchased from Chuandong Chemical Group (Chongqing, China) and dissolved in ultrapure water to prepare stock solutions of 1 mg/L and 10 mg/L, which were stored in the dark at 4 °C. Tilapia (initial body weight: 8.5 ± 0.5 g; total length: 8.5 ± 0.5 cm) were obtained from the Pengqian Aquaculture Base (Nanning, Guangxi, China). Prior to the experiment, fish were acclimated for 7 days in a laboratory recirculating water system (28 ± 1 °C; dissolved oxygen >6 mg/L) at a stocking density of 400 fish/200 L water. Fish were fed once daily at 12:00 with Xiamen Jiakang commercial feed, and fasting was implemented 24 h before the experiment. All animal experimental protocols were approved by the Experimental Animal Welfare Ethics Committee of Guangxi University.

2.2. Experimental design

Acclimated Tilapia were randomly divided into three groups, each containing 15 fish. Based on previous studies, the safe concentration of nitrite during tilapia aquaculture was determined to be 0.1 mg/L, and the 96-h median lethal concentration (96 h-LC_{50}) was 28.18 mg/L (Yanbo et al., 2006). Experimental concentrations were set accordingly. The experimental groups were designated as follows: Control group (CK) – no nitrite exposure (0 mg/L), and nitrite exposure groups (NS1, NS10) – low concentration (1 mg/L) and high concentration (10 mg/L) nitrite exposure. The experimental conditions were maintained at a temperature of 28 ± 1 °C, with a 12:12 h light-dark cycle, pH 7.9 ± 0.2, and dissolved oxygen above 6 mg/L. Water was exchanged every 24 h to maintain experimental conditions. After 7 days of exposure, three fish were randomly selected from each group, and their liver, spleen, brain, gills, and intestines were dissected (each tissue weighed approximately 50 ± 10 mg) and stored in 1.5 mL centrifuge tubes at −80 °C for subsequent analysis.

2.3. Tissue sections

Liver and spleen tissues from tilapia exposed to different concentrations were collected and fully immersed in 4 % paraformaldehyde fixative (pH 7.0–7.5) at 25 °C for preservation. After fixation, the tissues were dehydrated, cleared, and embedded in paraffin using specific embedding molds. The paraffin blocks were sectioned, dewaxed to water, and the frozen sections were re-warmed and fixed. Following pretreatment, hematoxylin and eosin staining was performed, and the sections were dehydrated, mounted, and examined under a microscope.

2.4. Biochemical testing

Liver, spleen, brain, and gill tissues were collected for the assessment of superoxide dismutase (SOD), catalase (CAT), and phenoloxidase (PO) activities. The activity assays were performed using commercial kits provided by Nanjing Jiancheng Bioengineering Institute. Simply, 100 mg of tissues were weighed and placed in a sterile centrifuge tube containing physiological saline, homogenized in an ice water bath, centrifuged at 4 °C 4000 r/min for 10 min, and finally the supernatants were taken for detection. The 96 well microplates were used and the wells were added the test samples, distilled water, enzyme working solution, enzyme dilution solution, and substrate application solution, respectively. The tests were contained control wells, control blank wells, test wells, and test blank wells. The microplates were gently shaken to mix solutions, and incubated at 37 °C for 20 min. Finally, the microplates were tested at 450 nm using an enzyme detector, and the results were calculated using the formula.

$$\mathrm{SOD}_{\text{inhibition rate}}\ (\%) = \frac{(A1 - A2) - (A3 - A4)}{(A1 - A2)} \times 100\% \quad (1)$$

$$\text{SOD Activity}\ (\mathrm{U/mg\ prot}) = \mathrm{SOD}_{\text{inhibition rate}} \div 50\% \times \frac{B}{C} \times \left(\frac{0.24\mathrm{mL}}{0.02\mathrm{mL}}\right) \div D \quad (2)$$

A_1 —— control wells.
A_2 —— control blank wells
A_3 —— test wells
A_4 —— test blank wells
B —— 240 μL reaction system
C —— 100-fold dilution factor
D —— the concentration of the sample protein to be tested , mg prot/mL

$$\text{CAT Activity}\ (\mathrm{U/mg\ prot}) = \triangle A \times 271 \div V_{\mathrm{Sample}} \div T \div C_{pr} \quad (3)$$

$\triangle A$ —— $A_{control} - A_{test}$ at 405 nm
V_{Sample} —— 100 μL sample volume
T —— 60-s reaction time
C_{pr} —— protein concentration of the homogenate solution

$$\text{PO Activity}\ (\Delta \mathrm{OD490/min/g}) = \Delta A \div (W \times V1 \div V) \div 0.001 \div T = 333.3 \times \Delta A \div W \quad (4)$$

V —— add the volume of the extracted liquid, 1 mL
T —— reaction time, 30 min
V_1 —— add sample volume, 0.1 mL
W —— sample quality, 0.1 g
$\Delta A = A_2 - A_1$
A_1 —— absorbance at 490 nm
A_2 —— absorbance at 490 nm after incubation at 35 °C for 30 min

2.5. RT-qPCR

Total RNA was extracted from liver, spleen, brain, and gill tissues using Trizol reagent. RNA quality was assessed via agarose gel electrophoresis, followed by cDNA synthesis using the RNA Reverse Transcription Kit (Kangwei Century, China) according to the manufacturer's instructions. The synthesized cDNA was then subjected to RT-qPCR analysis, and relative gene expression levels were calculated using the $2^{-\Delta\Delta Ct}$ method. Quantitative PCR was performed using the ABI FAST 7500 Real-Time PCR System. The primers for quantification targeted the cfb gene, and Ultra SYBR Mixture (CWBIO, China) was used for the PCR

assays. The target genes analyzed in tilapia included inflammation-related genes (*IL-1β, IL-8, IL-10*), antioxidant stress-related gene (*Cat*), and immune-related genes (*C-TLZ, MyD88*), with *β-Actin* as the internal reference gene.

2.6. Microbial diversity analysis

Microbial community DNA was extracted from the intestinal contents of tilapia and assessed for quality and concentration using 1 % agarose gel electrophoresis and NanoDrop2000. The 16S rRNA gene V3-V4 region was PCR amplified using the 338F and 806R primers, and the amplicons were purified and used for sequencing library construction with the NEXTFLEX Rapid DNA-Seq Kit. Sequencing was performed on the Illumina Nextseq2000 platform. Raw sequencing data were quality controlled and merged using fastp and FLASH software, followed by DADA2 denoising in Qiime2 to generate amplicon sequence variants (ASVs) for species classification. Alpha diversity indices and inter-group differences were analyzed using mothur and Wilcoxon test, while microbial community structure differences were assessed via PCoA and PERMANOVA. LEfSe was used to identify bacterial taxa with significant differential abundance, and Spearman correlation analysis was employed to construct species correlation networks.

2.7. Transcriptome analysis

Each group included three biological replicates ($n = 3$). RNA purification, reverse transcription, library construction and sequencing were performed at Shanghai Majorbio Bio-pharm Biotechnology Co., Ltd. (Shanghai, China) according to the manufacturer's instructions. RNA quality was assessed using NanoDrop (Thermo Fisher Scientific, America) and Agilent 5300 (Agilent, America) spectrophotometers. High-quality RNA (OD260/280 = 1.8–2.2, RQN > 6.5) meeting the required criteria was used for library construction. The tilapia intestinal contents RNA-seg transcriptome library was prepared following llumina® Stranded mRNA Prep, Ligation (San Diego, CA) using 1 μg of total RNA. High-throughput sequencing was performed on the NovaSeq XPlus platform.

Raw sequencing data from each group were processed for quality control and filtering to obtain clean reads, which were then aligned to the reference genome (HiSat2, version 2.2.1). Transcript abundance was quantified using RSEM (version 1.2.8), and differentially expressed genes (DEGs) were identified using DESeq2, with a threshold of *fold change* ≥ 2 and *FDR* < 0.05. Gene Ontology (GO) annotation and Kyoto Encyclopedia of Genes and Genomes (KEGG) pathway analysis were performed using the ClusterProfiler package, with significant GO terms and KEGG pathways identified at *p-value* ≤ 0.05.

2.8. Statistical analyses

All experimental data are presented as the mean ± standard error of the mean (SEM), with each experiment repeated at least three times. Statistical analysis was performed using SPSS 27 and MATLAB R2023a, with data visualization done via R 4.4.1, OriginPro 2023 and Cytoscape 3.10.3. *t*-tests and ANOVA were used for statistical assessment, with significance levels indicated as $*p < 0.05$, $**p < 0.01$, and $***p < 0.001$.

3. Results and discussion

3.1. Intestinal microbial structural changes under nitrite exposure

The intestinal microbiome, as a critical interface between environmental stressors and host physiology, exhibited pronounced structural and functional alterations following nitrite exposure in tilapia (*Oreochromis niloticus*). 16S rRNA sequencing analysis identified 42 differentially abundant ASVs from 406 total ASVs ($|Log_2FC| > 1, p < 0.05$). Rank abundance analysis (Fig. S1a), alpha diversity indices (Fig. 1a), and beta diversity indices collectively revealed significant restructuring of microbial community (Fig. 1b). LEfSe analysis demonstrated the decrease of order level variety after exposure (Fig. 1c), identifying 48 unique genera in the NS10 compared with 46 in the CK (Fig. 1d). Integrated analysis of the community heatmap and Circos network (Fig. S1c-d) revealed distinct divergence in dominant bacterial communities between the NS10 and CK, demonstrating nitrite-induced restructuring of core microbiota.

The main components of the intestinal microflora of tilapia were *Firmicutes, Actinobacteria, Chlamydiae*, *Fusobacteria* and *Verrucomicrobia.* The four dominant microbial genera exhibited restructured intestinal microbiota profiles under nitrite exposure (Fig. 1e). NS10 exhibited differential microbial abundance compared to CK. Compared with CK, *Peptostreptococcaceae* increased by 6.28 times, *Mycobacteria* increased by 1.44 times, *Romboutsia* decreased by 0.65 times, while *Neochlamydia* decreased significantly by 22.2 times. Specifically, *Mycobacterium*, which is a major pathogen in aquaculture, can cause liver and spleen inflammation and damaging phenomena upon infection (Delghandi et al., 2020; Talwani et al., 2011). Histopathological analysis of tissue sections suggested that the inflammatory infiltrate observed in the liver and spleen organs was linked to the pathogenic path caused by *Mycobacterium* (Fig. S4a-b). When tilapia was infected with *Mycobacterium*, the area of melanomacrophage centers will increase, causing organ damage and even death (Gauthier and Rhodes, 2009; Manrique et al., 2019). The depletion of *Romboutsia*, which produces butyrate and has anti-inflammatory properties, exacerbated intestinal barrier dysfunction, consistent with findings in zebrafish (López Nadal et al., 2023). Notably, *Peptostreptococcaceae*, which is an opportunistic pathogen, formed a stable co-occurrence module with the *Clostridiaceae* family, playing a central role in the intestinal microbiota of cichlid fish and this genus was also linked to human intestinal inflammation and rectal cancer (Riera and Baldo, 2020). Additionally, *Microbacteriaceae* and *Clostridiaceae* exhibited significant increases in the NS10. *Microbacteriaceae,* a group of Gram-positive bacteria commonly found in aquatic ecosystems and the intestinal tracts of fish, may enhance their proliferation under nitrite stress through metabolic pathways that convert nitrite into ammonia or other low-toxicity compounds (Shan et al., 2024). Meanwhile, nitrite-induced intestinal hypoxia could favor the growth of *Clostridiaceae,* as these obligate anaerobes exhibit a competitive edge under oxygen-deprived conditions.

The changes in the composition of intestinal microorganisms indicated that exposure to nitrite might have caused immune-mediated inflammatory response in tilapia. Collectively, nitrite exposure induced marked restructuring of the intestinal microbiota in tilapia, which may promote adverse outcomes including immune dysregulation, inflammatory responses, and multi-tissue injury (Barbosa and Rescigno, 2010; Clavel and Haller, 2007; Gaudino and Kumar, 2019). To delineate the microbiota-host interplay, we performed transcriptomic profiling of the microbial community and quantified tissue-specific immune/inflammatory biomarkers to systematically unravel the intestinal toxicity mechanisms in tilapia.

3.2. Transcriptome analysis of tilapia intestinal tissue under nitrite exposure

A total of 800 DEGs were identified ($|Log_2FC| > 1$, $p < 0.05$), including 455 upregulated and 345 downregulated genes. Principal component analysis (cumulative variance explained 50.12 %) revealed significant separation between the NS10 and the CK (Fig. 2a), confirming biological significance. Notably, transmembrane serine protease 15 (*TMPRSS15*) showed the most significant upregulation ($Log_2FC = 11.16$) (Fig. 2b). *TMPRSS15* was closely associated with the activation of gastrointestinal digestive enzymes and immune regulation, serving as a critical molecular target in the study of gastrointestinal physiology and pathology (Bildstein et al., 2024; Fraser et al., 2022; Li et al., 2025b).

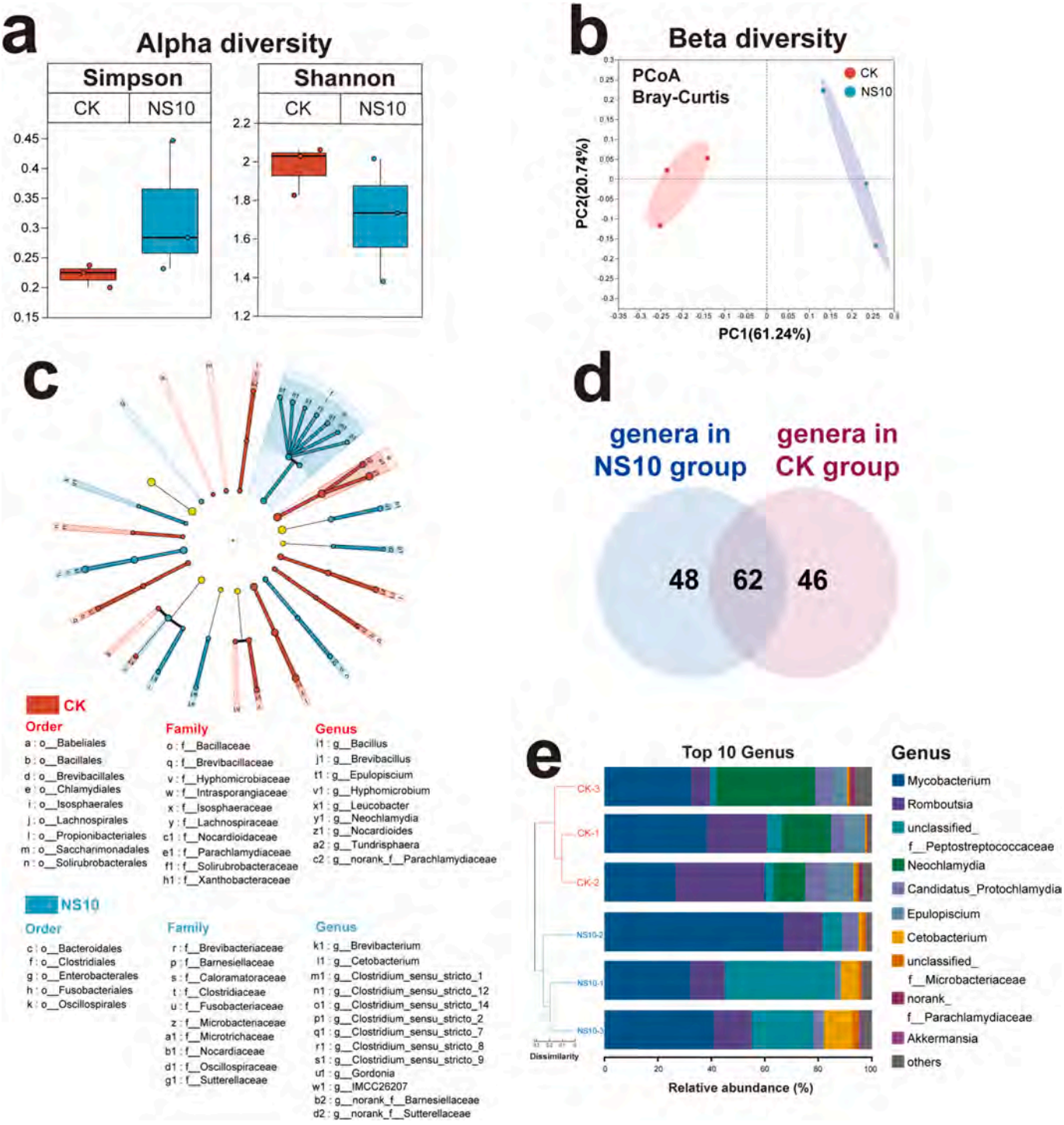


Fig. 1. Intestinal microbial structural changes under nitrite exposure.
a. CK and NS10 alpha diversity (Simpson and Shannon indices). **b.** CK and NS10 beta diversity (PCoA analysis), based on Bray-Curtis distance algorithm. **c.** LEfSe analysis (from outer to inner circles; LDA score threshold >3.34; only clearly classified taxa are shown). **d.** The Venn diagram of CK and NS10 genera. **e.** Relative abundance of the top 10 bacterial genera from CK and NS10.

The upregulation of *TMPRSS15* indicated impaired intestinal digestion and nutrient absorption. The Random Forest algorithm identified 49 key genes (29 upregulated; 20 downregulated) (Fig. 2c), with the top-ranked genes *DLGAP5* ($Log_2FC = -1.27$) (Pan et al., 2024; Zhou et al., 2024), *WEE1* ($Log_2FC = -1.08$) (Guo et al., 2022), and *RAG1* ($Log_2FC = 1.84$) (Delmonte et al., 2018) linked to immune regulation (Hewit et al., 2018).

Based on the topological parameters (Degree, Closeness, and Betweenness), a protein-protein interaction (PPI) network was constructed to analyze DEGs (Fig. 2d). The highlighted key hub genes *kif11* ($Log_2FC = 1.30$), *ccna2* ($Log_2FC = 1.19$), and *cdc6* ($Log_2FC = 1.36$), primarily associated with cell cycle regulation and cell division (Calzada et al., 2001; Malvezzi et al., 2018; Venere et al., 2015; Xu et al., 2019). Functional enrichment analysis revealed significant activation of the ubiquitination regulatory system and highlighted α-linolenic acid metabolism and DNA mismatch repair as core perturbation pathways

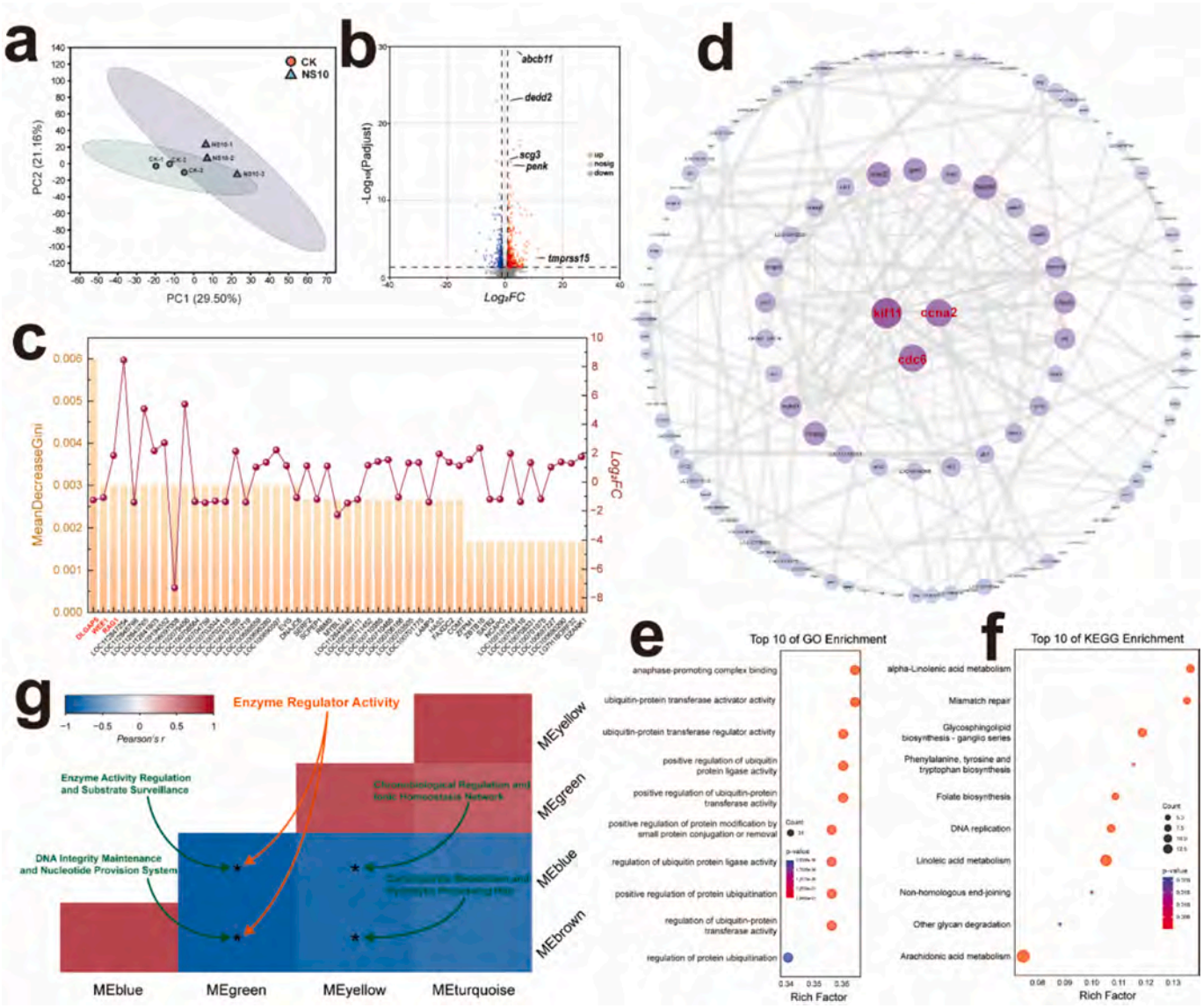


Fig. 2. Transcriptome analysis of tilapia intestinal tissue under nitrite exposure.
a. PCA of CK and NS10. **b.** Volcano plot. **c.** Random forest-based identification of key DEGs. **d.** PPI network of DEGs. **e-f.** Functional enrichment of DEGs. The color gradient represents the *p-value*, thus indicating the significance of the KEGG term enrichment, whereas the size of the dots reflects the count of genes associated with each term (the Rich Factor). **g.** WGCNA co-expression network.

(Fig. 2e-f). Dysregulation of the ubiquitin-proteasome system may lead to excessive degradation of repair proteins, thereby exacerbating intestinal barrier dysfunction (Chen et al., 2022; Cleynen et al., 2014). Ubiquitination played a crucial role in various DNA-driven processes. Specific E3 ligases can recognize and ubiquitinate tight junction proteins, promoting the degradation by the proteasome. In the DNA damage response, ubiquitinated proteins recruited and activated factors involved in DNA damage recognition and repair, ensuring the stability of cellular genetic information (Li et al., 2025c). Abnormal enrichment of the ubiquitin pathway following nitrite exposure, the proteasome triggered stress and directly induces apoptosis of epithelial cells, ultimately undermined intestinal health.

A more in-depth analysis of the results, using WGCNA co-expression network analysis, demonstrated significant negative interactions among the Green, Yellow, Blue, and Brown modules (Fig. 2g). Enrichment analysis was conducted on each module. The results showed that the differentially expressed genes were closely related to the regulation of enzyme activity and the maintenance of DNA integrity. Nitrite might disrupt the active hubs of key enzymes in the intestine. Impairment of enzymatic activity may disrupt oxidative stress regulation and inflammatory response modulation, thereby compromising immune homeostasis maintenance in tilapia. Further integrated analysis was needed to investigate the intestinal injury and concomitant microbiome changes in tilapia.

3.3. *Microbiome and transcriptome synergistic analysis of tilapia intestinal tissue under nitrite exposure*

To describe the interaction between microorganisms and host gene regulation, we identified the top ten hub genes within each co-expression module based on topological overlap matrix (TOM) analysis, as well as the TOM of intestinal microbiota and key genes in tilapia (Fig. 3a-b). ASV489 (Log_2FC = 4.20; *Actinobacteriota/ g_unclassified_f_Microbacteriaceae*) was identified as a core node in the blue module. In addition, epidermal development-related gene *evpl* and calcium ion transport regulator gene *sln* (*kWithin* > 0.96) (Huang et al., 2022; Robinson et al., 2024) also played important roles in this module. This module was functionally enriched in peptide transmembrane

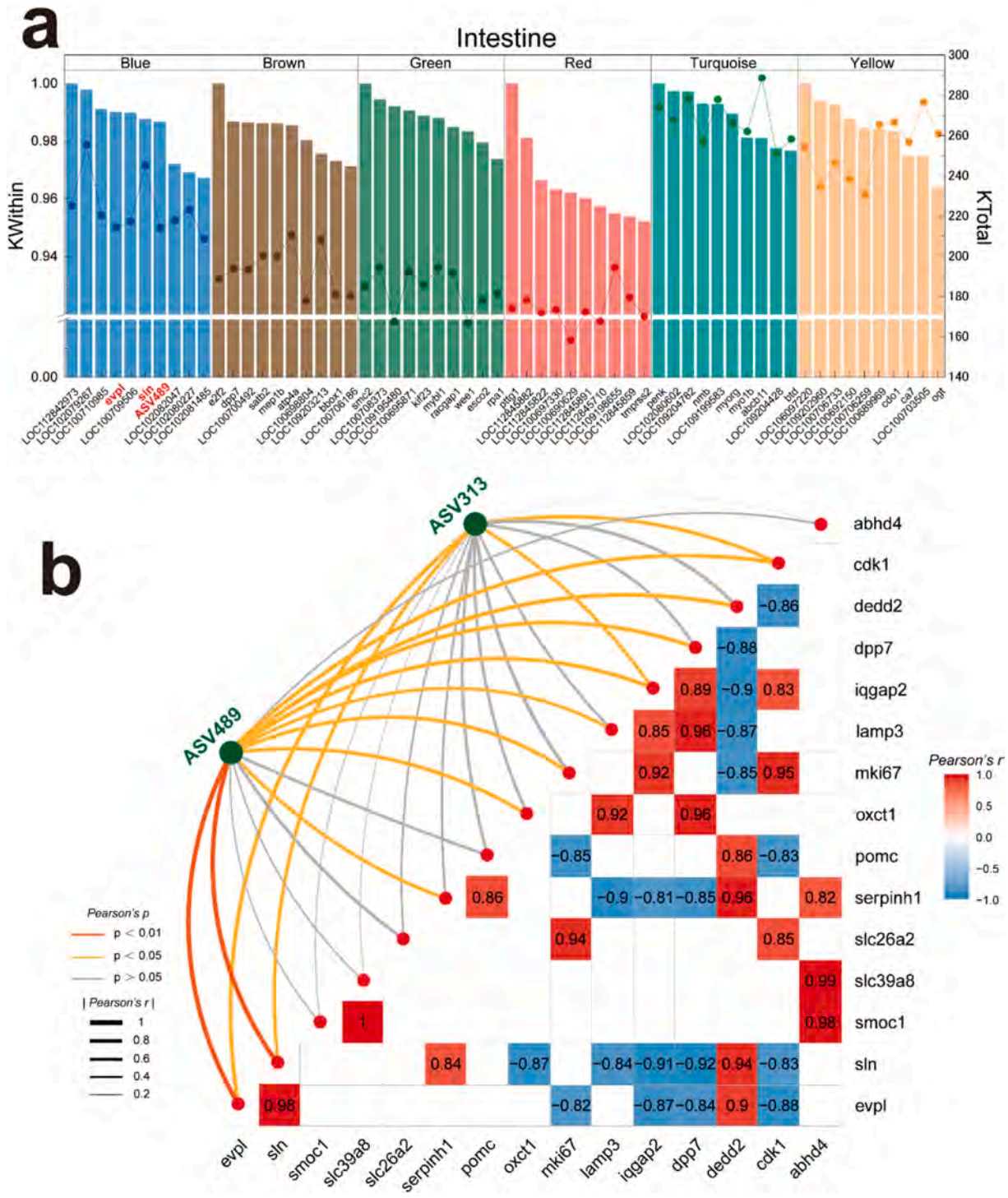


Fig. 3. Microbiome and transcriptome synergistic analysis of tilapia intestinal tissue under nitrite exposure
a. Top ten hub genes within each co-expression module based on TOM analysis. **b.** Strain-Gene Interaction Network Analysis.

transport and DNA damage repair pathways. ASV313 (Log_2FC = 5.43; *Firmicutes/g_Clostridium_sensu_stricto_13*) was selected as a core strain through random forest-based multi-omics modeling. At the same time, the 51 key genes were involved in redox homeostasis regulation, lipid metabolism balance, and programmed cell death. Previous studies have shown that *Clostridium* can regulate the balance of the microbial community, enhance the immune response and produce short-chain fatty acids (Meng et al., 2021), thereby promoting the intestinal health of fish (Poolsawat et al., 2020). *Microbacteriaceae* plays a role in assisting the host's immune response (Li et al., 2024). In tilapia, *Clostridium* may enhance intestinal barrier integrity and disease resistance through butyrate-mediated anti-inflammatory pathways (Salvi and Cowles, 2021), while *Microbacteriaceae* likely contributes to nutrient metabolism and pathogen inhibition (Chen et al., 2023), collectively synergizing to optimize intestinal homeostasis under environmental stressors. Strain-gene interaction network analysis showed that ASV489 exhibited stronger correlations with oxidative stress and inflammation response-associated genes compared to ASV313. Furthermore, ASV489 exhibited co-expression with genes such as *smoc1* (cell adhesion regulation) (Awwad et al., 2015; Gao et al., 2019), *slc39a8* (zinc transport) (Lin

et al., 2018a), and *dpp7* (peptidase activity) (Zhang et al., 2023). The co-expression of ASV489 with *smoc1* suggested their potential synergistic role in modulating the tissue repair microenvironment, while its co-expression with *slc39a8* may indicate regulation of metal ion homeostasis in the local microenvironment, potentially influencing host immune cell tolerance to oxidative stress. Furthermore, ASV489- *dpp7* co-expression could implicate involvement in immune-metabolic axis regulation. These co-expression results suggested that this *Actinobacteria* strain may influence host physiological status by modulating epidermal barrier function, ion homeostasis, and protein metabolism networks. The correlation between ASV489 and epidermal barrier-related genes suggested that *Actinobacteriota* expansion may potentially through microbial metabolite-mediated inhibition of epithelial repair.

3.4. Nitrite exposure-affected physiological functions in liver, spleen, brain and gill tissues

Biochemical analysis revealed dose-dependent changes in the activities of superoxide dismutase (SOD), catalase (CAT), and phenol oxidase (PO) in liver, spleen, brain, and gill tissues (Fig. S2a-c). NS1 could induce a mild upregulation of enzyme activities, while NS10 significantly enhanced enzyme activity in liver and gill tissues. Thess results revealed that high-concentration exposure alleviates oxidative stress by activating the antioxidant system (Ilderbayev et al., 2022). RT-qPCR analysis (Fig. S2d-i) revealed that NS1 significantly upregulated the expression of oxidative gene *Cat* and various inflammatory (*IL-1β, IL-8, IL-10)* and immune (*MyD88, C-TLZ*) genes across all tissues. Although NS10 sustained elevated expression of inflammatory and immune genes, *Cat* expression was suppressed in the liver and spleen, while it remained upregulated in the brain and gill. This biphasic regulation suggested that low concentration nitrite activates oxidative defense and immune responses, inducing compensatory protection. However, high nitrite concentrations induce liver and spleen damage, consistent with histopathological alterations observed in our analysis (Fig. S5a-b). Specifically, 7 days of nitrite exposure induced dose-dependent histopathological damage in tilapia liver and spleen tissues. Liver tissue sections (Fig. 4a) showed that CK exhibited intact hepatic sinusoids and closely arranged hepatocytes. In the NS1, early oxidative damage was observed with widened intercellular spaces and nuclear swelling. In the NS10, significant disruption of liver cord structure accompanied by inflammatory cell infiltration was noted. Spleen damage exhibited a concentration-dependent pattern (Fig. 4b). The NS1 showed white pulp atrophy and apoptotic body formation, while the NS10 displayed abnormal macrophage activation. Nitrite exposure caused injury to the tilapia intestinal, which subsequently affected physiological functions in liver, spleen, brain and gill tissues. The mechanism of intestinal toxicity induced by nitrite and the resulting multi-organ injury deserve further exploration and research.

3.5. The multi-organ injury caused by the intestinal toxicity mechanism induced by nitrite

Core members of the blue module (ASV489*, evpl, sln*) demonstrated significant correlations with SOD, CAT, and PO activities across multiple tilapia tissues (Fig. 5a-b). These results further suggested that nitrite may regulate multiorgan enzyme activities through gut microbiota modulation, consequently inducing systemic oxidative stress responses. Module-biomarker correlation analysis further demonstrated strong positive associations between yellow/blue/turquoise modules and liver/brain enzyme activities (*Pearson's* $r = 0.530–0.776$; $p < 0.01$). The above-mentioned modules were mainly enriched with calcium ion homeostasis regulation, pH regulation, and anion transmembrane transport pathways. These results suggested that intestinal microbial imbalance may trigger oxidative damage in the liver and brain tissues by disrupting the ionic dynamic balance. Conversely, green and brown modules showed negative correlations with liver/brain enzymatic

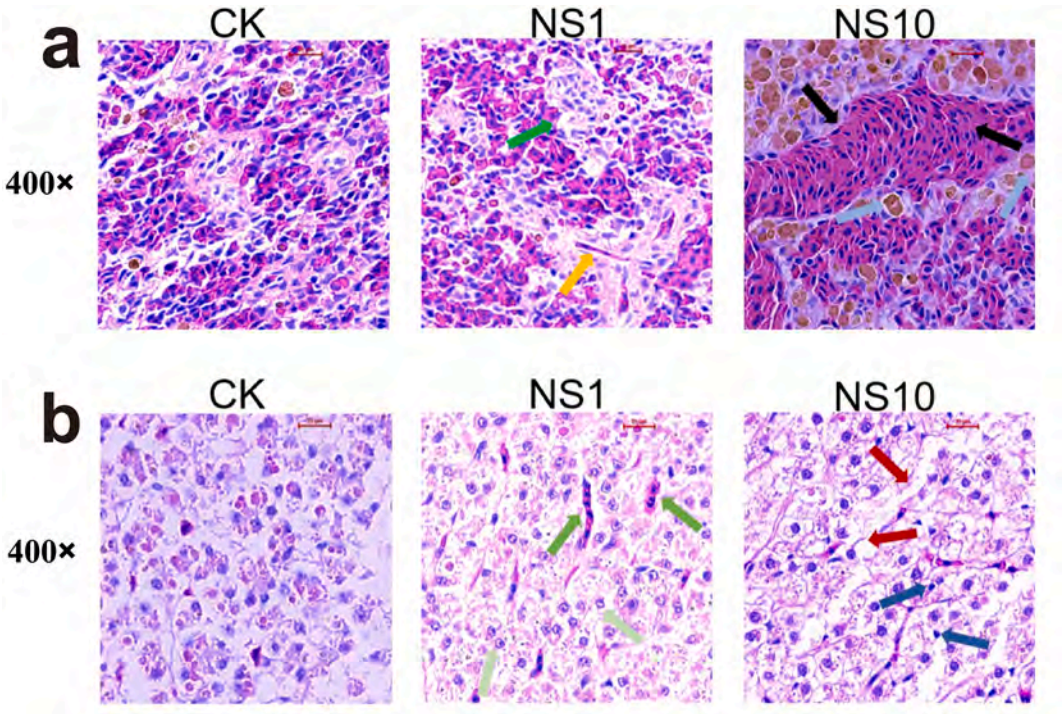


Fig. 4. Effects of nitrite exposure on liver and spleen tissues.
a. H&*E*-stained liver tissue sections from tilapia, obtained from CK, NS1 and NS10. Green arrows indicate hepatocyte vacuolization, yellow arrows point to cellular infiltration zones, black arrows show sinusoids dilation, and blue arrows represent fatty degeneration. b. H&E-stained spleen tissue sections. Green arrows indicate fibrotic trabeculae, light green arrows point to macrophage aggregation, red arrows indicate cellular vacuolization, and blue arrows represent congestion of red pulp. (For interpretation of the references to color in this figure legend, the reader is referred to the web version of this article.)

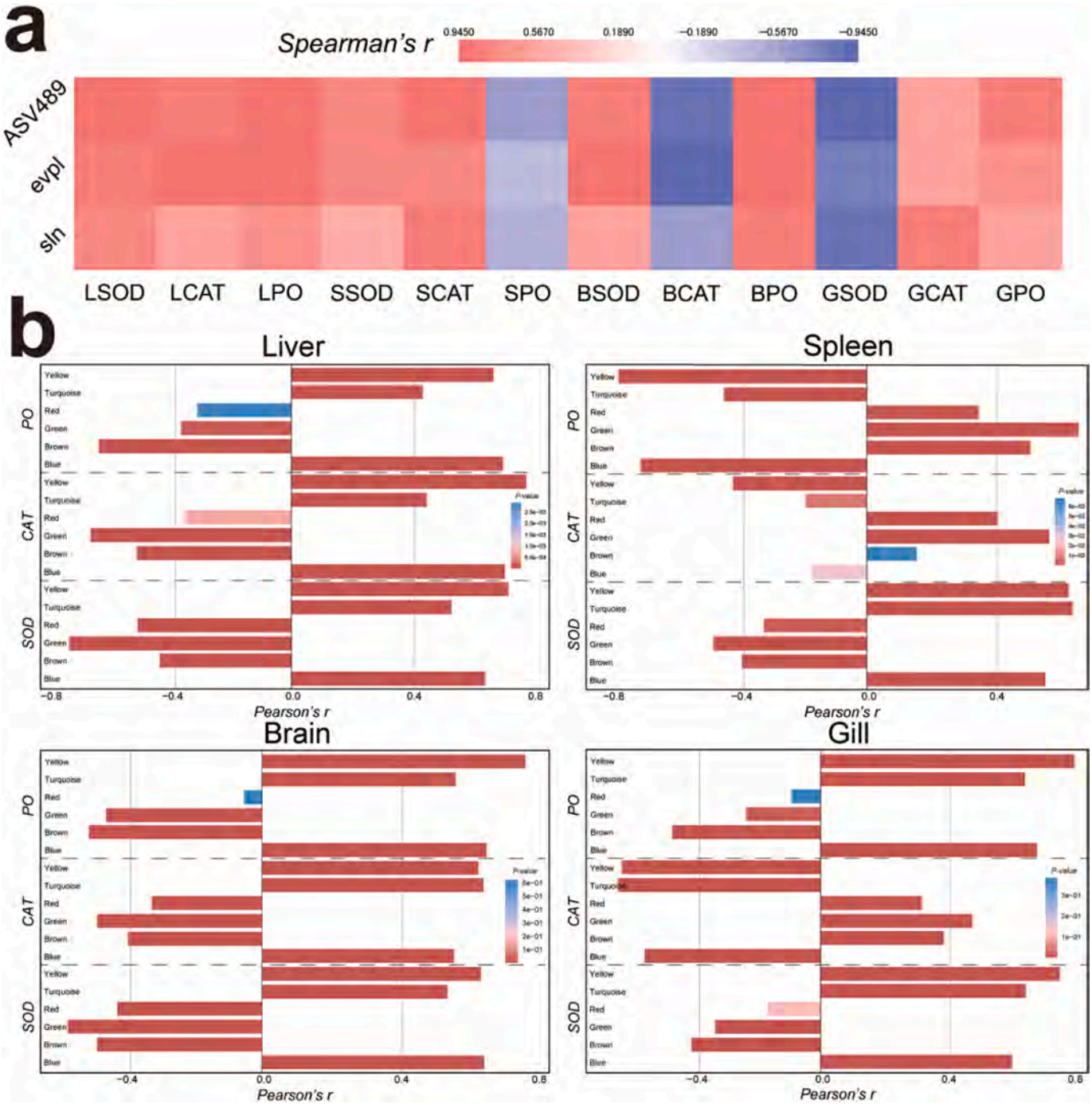


Fig. 5. Multi-omics topological overlap matrix (TOM) construction and correlation analysis with biomarks.
a. Spearman correlations between *ASV489, evpl* and *sln* with oxidative stress biomarkers across tissues. **b.** Modules-biomarkers association analysis.

indices (*Pearson's* $r = -0.733 \sim -0.362$; $p < 0.01$). Mechanistically, the pivotal regulatory gene *e2f2* might attenuate lipid peroxidation through coordinated suppression of macrophage pro-inflammatory responses coupled with modulation of amino acid metabolic pathways (Timmers et al., 2007). The tissue-specific analysis revealed that the enzyme activities in the spleen and gill tissues exhibited a bidirectional regulatory feature with the Yellow/Blue/Turquoise module. The results may be related to the tissue-specific distribution of microbial metabolites and their interaction with the local microenvironment. The Green and Brown modules also exhibited similar regulatory heterogeneity in the spleen and gill tissues. These results suggested that the oxidative stress effect was finely regulated by organ-specific signaling pathways.

4. Conclusion

This study employed tilapia (*Oreochromis niloticus*) as a model organism to systematically evaluate nitrite induced intestinal injury mechanisms through integrated multi-omics analyses of intestinal microbiota dynamics, transcriptomics, and multi-tissue physiological assessments. The results showed that nitrite exposure markedly altered intestinal microbial diversity. It promoted *Mycobacterium* proliferation while depleting beneficial microbiota like *Romboutsia*. The TOM identified ASV489(*Actinobacteriota/g_unclassified_f_Microbacteriaceae*) and ASV313(*Firmicutes/g_Clostridium_sensu_stricto_13*) as keystone microbiota biomarkers. These microorganisms strongly correlated with key

dysregulated genes, indicating microbiota-host interplay in nitrite toxicity. Transcriptomics revealed nitrite -triggered overactivation of ubiquitin-dependent proteolysis and DNA repair pathways. WGCNA further linked co-expressed gene modules to enzymatic regulation and genome stability. Notably, Actinobacteria-associated ASV489 showed close relationship with epidermal barrier disruption, ion imbalance, and proteomic dysregulation, suggesting its role in systemic toxicity amplification. The enrichment of Actinobacteria (e.g., ASV489) may activate the TLR4/MyD88 pathway through the secretion of lipopolysaccharide (LPS), thereby inducing the expression of E3 ligases and accelerating the degradation of barrier proteins.

Mechanistically, nitrite exposure not only disrupted intestinal microbiota homeostasis in tilapia, but also led to aberrant activation of DNA damage repair pathways. These perturbations propagate systemic oxidative stress and inflammatory response, culminating in multi-organ injury. By integrating multi-omics analyses of intestinal microbiota and differentially expressed genes, this study investigated the ecotoxicological of nitrite. The identification of microbiota-gene network hubs offered novel biomarkers and provided a more comprehensive understanding of the adverse effects of nitrite on fish health.

CRediT authorship contribution statement

Tingyu Wei: Writing – original draft, Software, Methodology, Data curation, Conceptualization. **Xuemin Wei:** Writing – review & editing, Methodology. **Jialong Huang:** Writing – review & editing. **Songlin Luo:** Supervision. **Aiguo Huang:** Writing – review & editing, Supervision, Project administration, Funding acquisition.

Declaration of competing interest

The authors declare that they have no known competing financial interests or personal relationships that could have appeared to influence the work reported in this paper.

Acknowledgements

This work was supported by Natural Science Foundation of Guangxi (2021GXNSFBA075008), Guangxi Science and Technology Program (No. AD22080029) and National Natural Science Foundation of China (No. 42106133).

Appendix A. Supplementary data

Supplementary data to this article can be found online at https://doi.org/10.1016/j.aquaculture.2025.742961.

Data availability

Data will be made available on request.

References

Atwood, H., Fontenot, Q., Tomasso, J., Isely, J., 2001. Toxicity of nitrite to Nile tilapia: effect of fish size and environmental chloride. N. Am. J. Aquac. 63 (1), 49–51. https://doi.org/10.1577/1548-8454(2001)063<0049:TONTNT>2.0.CO;2.

Awwad, K., Hu, J., Shi, L., Mangels, N., Abdel Malik, R., Zippel, N., Fisslthaler, B., Eble, J. A., Pfeilschifter, J., Popp, R., 2015. Role of secreted modular calcium-binding protein 1 (SMOC1) in transforming growth factor β signalling and angiogenesis. Cardiovasc. Res. 106 (2), 284–294. https://doi.org/10.1016/j.cbpa.2023.111534.

Barbosa, T., Rescigno, M., 2010. Host-bacteria interactions in the intestine: homeostasis to chronic inflammation. Mech. Dis. 2 (1), 80–97. https://doi.org/10.1002/wsbm.48.

Beaver, L., García-Jaramillo, M., Truong, L., Axton, E., Keller, R., Prater, M., Magnusson, K., Tanguay, R., Stevens, J., Hord, N., 2020. Nitrate and nitrite treatment affect zebrafish behavior and brain metabolomic profile. Curr. Dev. Nutr. 4. https://doi.org/10.1093/cdn/nzaa057_006 nzaa057_006.

Bian, D.-D., Shi, Y.-X., Zhu, X.-R., Sun, X.-L., Xu, X., Ding, L., Zhang, D.-Z., Liu, Q.-N., Tang, B.-P., Zhu, B.-J., 2024. Effects of nitrite exposure on the oxidative stress, immune response and intestine microbiota of Procambarus clarkii. Aquaculture 593, 741331. https://doi.org/10.1016/j.aquaculture.2024.741331.

Bian, D.-D., Liu, X., Jiang, J.-J., Sun, X.-L., Shi, Y.-X., Zhu, X.-R., Zhang, D.-Z., Liu, Q.-N., Tang, B.-P., Zhu, B.-J., 2025. An insight into nitrite-induced reproductive toxicity and the alleviation of injury by selenomethionine through activation of the Keap1/Nrf2 pathway in Procambarus clarkii. Int. J. Biol. Macromol. 306, 141616. https://doi.org/10.1016/j.ijbiomac.2025.141616.

Bildstein, T., Charbit-Henrion, F., Azabdaftari, A., Cerf-Bensussan, N., Uhlig, H.H., 2024. Cellular and molecular basis of proximal small intestine disorders. Nat. Rev. Gastroenterol. Hepatol. 21 (10), 687–709. https://doi.org/10.1038/s41575-024-00962-9.

Brown, D., McLeay, D., 1975. Effect of nitrite on methemoglobin and total hemoglobin of juvenile rainbow trout. N. Am. J. Aquac. 37 (1), 36–38. https://doi.org/10.1577/1548-8659(1975)37[36:EONOMA]2.0.CO;2.

Calzada, A., Sacristán, M., Sánchez, E., Bueno, A., 2001. Cdc6 cooperates with Sic1 and Hct1 to inactivate mitotic cyclin-dependent kinases. Nature 412 (6844), 355–358. https://doi.org/10.1038/35085610.

Camargo, J.A., Alonso, Á., 2006. Ecological and toxicological effects of inorganic nitrogen pollution in aquatic ecosystems: a global assessment. Environ. Int. 32 (6), 831–849. https://doi.org/10.1016/j.envint.2006.05.002.

Chen, R., Pang, X., Li, L., Zeng, Z., Chen, M., Zhang, S., 2022. Ubiquitin-specific proteases in inflammatory bowel disease-related signalling pathway regulation. Cell Death Dis. 13 (2), 139. https://doi.org/10.1038/s41419-022-04566-6.

Chen, J., Ke, Y., Zhu, Y., Chen, X., Xie, S., 2023. Deciphering of sulfonamide biodegradation mechanism in wetland sediments: from microbial community and individual populations to pathway and functional genes. Water Res. 240, 120132. https://doi.org/10.1016/j.watres.2023.120132.

Ciji, A., Akhtar, M.S., 2020. Nitrite implications and its management strategies in aquaculture: a review. Rev. Aquac. 12 (2), 878–908. https://doi.org/10.1111/raq.12354.

Clavel, T., Haller, D., 2007. Bacteria- and host-derived mechanisms to control intestinal epithelial cell homeostasis: implications for chronic inflammation. Inflamm. Bowel Dis. 13 (9), 1153–1164. https://doi.org/10.1002/ibd.20174.

Cleynen, I., Vazeille, E., Artieda, M., Verspaget, H.W., Szczypiorska, M., Bringer, M.-A., Lakatos, P.L., Seibold, F., Parnell, K., Weersma, R.K., Mahachie John, J.M., Morgan-Walsh, R., Staelens, D., Arijs, I., De Hertogh, G., Müller, S., Tordai, A., Hommes, D. W., Ahmad, T., Wijmenga, C., Pender, S., Rutgeerts, P., Van Steen, K., Lottaz, D., Vermeire, S., Darfeuille-Michaud, A., 2014. Genetic and microbial factors modulating the ubiquitin proteasome system in inflammatory bowel disease. GUT 63 (8), 1265–1274. https://doi.org/10.1136/gutjnl-2012-303205 %J Gut.

Dauda, A.B., Ajadi, A., Tola-Fabunmi, A.S., Akinwole, A.O., 2019. Waste production in aquaculture: sources, components and managements in different culture systems. Aquac. Fish. 4 (3), 81–88. https://doi.org/10.1016/j.aaf.2018.10.002.

Delghandi, M.R., El-Matbouli, M., Menanteau-Ledouble, S., 2020. Mycobacteriosis and infections with non-tuberculous mycobacteria in aquatic organisms: a review, 8 (9), 1368. https://doi.org/10.3390/microorganisms8091368.

Delmonte, O.M., Schuetz, C., Notarangelo, L.D., 2018. RAG deficiency: two genes, many diseases. J. Clin. Immunol. 38 (6), 646–655. https://doi.org/10.1007/s10875-018-0537-4.

Ferguson, R.M.W., Merrifield, D.L., Harper, G.M., Rawling, M.D., Mustafa, S., Picchietti, S., Balcázar, J.L., Davies, S.J., 2010. The effect of Pediococcus acidilactici on the gut microbiota and immune status of on-growing red tilapia (Oreochromis niloticus). J. Appl. Microbiol. 109 (3), 851–862. https://doi.org/10.1111/j.1365-2672.2010.04713.x.

Fontenot, Q., Isely, J.J., Tomasso, J.J., 1999. Characterization and inhibition of nitrite uptake in shortnose sturgeon fingerlings. Aquatic Anim. Health 11 (1), 76–80. https://doi.org/10.1577/1548-8667(1999)011<0076:CAIONU>2.0.CO;2.

Fraser, B.J., Beldar, S., Seitova, A., Hutchinson, A., Mannar, D., Li, Y., Kwon, D., Tan, R., Wilson, R.P., Leopold, K., Subramaniam, S., Halabelian, L., Arrowsmith, C.H., Bénard, F., 2022. Structure and activity of human TMPRSS2 protease implicated in SARS-CoV-2 activation. Nat. Chem. Biol. 18 (9), 963–971. https://doi.org/10.1038/s41589-022-01059-7.

Gao, Q., Mok, H.-P., Zhuang, J., 2019. Secreted modular calcium-binding proteins in pathophysiological processes and embryonic development. Chin. Med. J. 132 (20), 2476–2484. https://doi.org/10.1097/CM9.0000000000000472.

Gao, X.-Q., Fei, F., Huo, H.H., Huang, B., Meng, X.S., Zhang, T., Liu, B.-L., 2020. Impact of nitrite exposure on plasma biochemical parameters and immune-related responses in Takifugu rubripes. Aquat. Toxicol. 218, 105362. https://doi.org/10.1016/j.aquatox.2019.105362.

Gaudino, S.J., Kumar, P., 2019. Cross-talk between antigen presenting cells and T cells impacts intestinal homeostasis, bacterial infections, and tumorigenesis. Front. Immunol. 10, 360. https://doi.org/10.3389/fimmu.2019.00360.

Gauthier, D.T., Rhodes, M.W., 2009. Mycobacteriosis in fishes: A review. Vet. J. 180 (1), 33–47. https://doi.org/10.1016/j.tvjl.2008.05.012.

Getnet, M.A., Mekonnen, M.Y., Yimam, H.M., Berihun, A.M., Malede, B.A., 2024. Histopathology based study of Nile tilapia fish (Oreochromis niloticus) as a biomarker for water pollution evaluation in the southern gulf of Lake Tana, Ethiopia. BMC Vet. Res. 20 (1), 409. https://doi.org/10.1186/s12917-024-04230-5.

Guo, K., Ruan, G., Fan, W., Fang, L., Wang, Q., Luo, M., Yi, T., 2020. The effect of nitrite and sulfide on the antioxidant capacity and microbial composition of the intestines of red swamp crayfish, Procambarus clarkii. Fish Shellfish Immunol. 96, 290–296. https://doi.org/10.1016/j.fsi.2019.11.052.

Guo, E., Xiao, R., Wu, Y., Lu, F., Liu, C., Yang, B., Li, X., Fu, Y., Wang, Z., Li, Y., Huang, Y., Li, F., Wu, X., You, L., Qin, T., Lu, Y., Huang, X., Ma, D., Mills, G.B., Sun, C., Chen, G., 2022. WEE1 inhibition induces anti-tumor immunity by activating

ERV and the dsRNA pathway. J. Exp. Med. 219 (1). https://doi.org/10.1084/jem.20210789.
Hewit, K., Sandilands, E., Martinez, R.S., James, D., Leung, H.Y., Bryant, D.M., Shanks, E., Markert, E.K., 2018. A functional genomics screen reveals a strong synergistic effect between docetaxel and the mitotic gene DLGAP5 that is mediated by the androgen receptor. Cell Death Dis. 9 (11), 1069. https://doi.org/10.1038/s41419-018-1115-7.
Hou, D., Li, H., Wang, S., Weng, S., He, J., 2024. Nitrite nitrogen stress disrupts the intestine bacterial community by altering host-community interactions in shrimp. Sci. Total Environ. 925, 171536. https://doi.org/10.1016/j.scitotenv.2024.171536.
Huang, P., Tang, L., Zhang, L., Ren, Y., Peng, H., Xiao, Y., Xu, J., Mao, D., Liu, L., Liu, L., 2022. Identification of biomarkers associated with CD4+ T-cell infiltration with gene coexpression network in dermatomyositis. Front. Immunol. 13, 854848. https://doi.org/10.3389/fimmu.2022.854848.
Ilderbayev, O., Okassova, A., Rakhyzhanova, S., Ilderbayeva, G., Zhazykbayeva, L., 2022. The levels of oxidative stress in a combination of stress factors. J. Med. Life 15 (8), 927–931. https://doi.org/10.25122/jml-2021-0060.
Jia, R., Liu, B.-L., Han, C., Huang, B., Lei, J.-L., 2016. The physiological performance and immune response of juvenile turbot (Scophthalmus maximus) to nitrite exposure. Comp. Biochem. Physiol., Part C: Toxicol. Pharmacol. 181-182, 40–46. https://doi.org/10.1016/j.cbpc.2016.01.002.
Keshari, V., Adeeb, B., Simmons, A.E., Simmons, T.W., Diep, C.Q., 2016. Zebrafish as a Model to Assess the Teratogenic Potential of Nitrite, 1940-087X. https://doi.org/10.3791/53615.
Lewis Jr., W.M., Morris, D.P., 1986. Toxicity of nitrite to fish: a review. Trans. Am. Fish. Soc. 115 (2), 183–195. https://doi.org/10.1577/1548-8659(1986)115<183:TONTF>2.0.CO;2 %J Transactions of the American Fisheries Society.
Li, Q., Liu, Y., Li, S., Guo, X., Fu, Y., He, N., Ruan, G., Wang, Q., Gao, W., Fang, L., 2022. Impact of nitrite exposure on oxidative stress and antioxidative-related genes responses in the gills of Procambarus clarkii. Fish Shellfish Immunol. 131, 624–630. https://doi.org/10.1016/j.fsi.2022.10.053.
Li, Q., Sun, L.-H., Yang, B.-C., Jiang, J.-H., Chen, J.-M., Zheng, G., Gao, L.-M., Peng, J., Guo, J.-L., 2024. Effectiveness of a novel compound microbial agent for water quality and the gut microbiota of Micropterus salmoides. Front. Mar. Sci. 11, 1379711. https://doi.org/10.3389/fmars.2024.1379711.
Li, Y., Guo, H., Ge, H., Sha, H., Wu, Y., Zou, G., Liang, H., 2025a. A time-dependent interactive effect of nitrite and ammonia on inflammatory and immune response in the head kidney of silver carp (Hypophthalmichthys molitrix). Comp. Biochem. Physiol. Part C Toxicol. Pharmacol. 288, 110078. https://doi.org/10.1016/j.cbpc.2024.110078.
Li, Y., Li, R., Pan, Y., Zhou, W., Wang, X., Dong, L., Liu, X., Zhang, H., 2025b. Enterokinase deficiency associated with novel TMPRSS15 gene mutations: a case report. Front. Pediatr. 13, 1484208. https://doi.org/10.3389/fped.2025.1484208.
Li, Z., Zhu, T., Wu, Y., Yu, Y., Zang, Y., Yu, L., Zhang, Z., 2025c. Functions and mechanisms of non-histone post-translational modifications in cancer progression. Cell Death Dis. 11 (1), 125. https://doi.org/10.1038/s41420-025-02410-2.
Liang, X., Wang, Y., Liu, L., Zhang, X., Li, L., Tang, R., Li, D., 2022. Acute nitrite exposure interferes with intestinal thyroid hormone homeostasis in grass carp (Ctenopharyngodon idellus). Ecotoxicol. Environ. Saf. 237, 113510. https://doi.org/10.1016/j.ecoenv.2022.113510.
Lin, W., Li, D., Cheng, L., Li, L., Liu, F., Hand, N.J., Epstein, J.A., Rader, D.J., 2018a. Zinc transporter Slc39a8 is essential for cardiac ventricular compaction. J. Clin. Invest. 128 (2), 826–833. https://doi.org/10.1172/JCI96993.
Lin, Y., Miao, L.-H., Pan, W.-J., Huang, X., Dengu, J.M., Zhang, W.-X., Ge, X.-P., Liu, B., Ren, M.-C., Zhou, Q.-L., 2018b. Effect of nitrite exposure on the antioxidant enzymes and glutathione system in the liver of bighead carp, Aristichthys nobilis. Fish Shellfish Immunol. 76, 126–132. https://doi.org/10.1016/j.fsi.2018.02.015.
López Nadal, A., Boekhorst, J., Lute, C., van den Berg, F., Schorn, M.A., Bergen Eriksen, T., Peggs, D., McGurk, C., Sipkema, D., Kleerebezem, M., Wiegertjes, G.F., Brugman, S., 2023. Omics and imaging combinatorial approach reveals butyrate-induced inflammatory effects in the zebrafish gut. Anim. Microbiome 5 (1), 15. https://doi.org/10.1186/s42523-023-00230-2.
Maestre, R., Pazos, M., Medina, I., 2009. Involvement of methemoglobin (MetHb) formation and hemin loss in the pro-oxidant activity of fish hemoglobins. J. Agric. Food Chem. 57 (15), 7013–7021. https://doi.org/10.1021/jf9006664.
Malvezzi, J.V.M., Magalhaes I, H., S Costa, S., Otto, P.A., Rosenberg, C., Bertola, D.R., Lm Fernandes, W., Vianna-Morgante, A.M., Krepischi, A.C.V., 2018. KIF11 microdeletion is associated with microcephaly, chorioretinopathy and intellectual disability. Human Genome Variation 5 (1), 18010. https://doi.org/10.1038/hgv.2018.10.
Manrique, W.G., Pereira Figueiredo, M.A., Charlie-Silva, I., de Andrade, Antonio, Belo, M., Dib, C.C., 2019. Spleen melanomacrophage centers response of Nile tilapia during Aeromanas hydrophila and Mycobacterium marinum infections. Fish Shellfish Immunol. 95, 514–518. https://doi.org/10.1016/j.fsi.2019.10.071.
Meng, X., Wu, S., Hu, W., Zhu, Z., Yang, G., Zhang, Y., Qin, C., Yang, L., Nie, G., 2021. Clostridium butyricum improves immune responses and remodels the intestinal microbiota of common carp (Cyprinus carpio L.). Aquaculture 530, 735753. https://doi.org/10.1016/j.aquaculture.2020.735753.
Obirikorang, K.A., Acheampong, J.N., Duodu, C.P., Skov, P.V., 2020. Growth, metabolism and respiration in Nile tilapia (Oreochromis niloticus) exposed to chronic or periodic hypoxia. Comp. Biochem. Physiol. A Mol. Integr. Physiol. 248, 110768. https://doi.org/10.1016/j.cbpa.2020.110768.
Pan, Q., Ma, D., Xiao, Y., Ji, K., Wu, J., 2024. Transcriptional regulation of DLGAP5 by AR suppresses p53 signaling and inhibits CD8(+)T cell infiltration in triple-negative breast cancer. Transl. Oncol. 49, 102081. https://doi.org/10.1016/j.tranon.2024.102081.
Poolsawat, L., Li, X., He, M., Ji, D., Leng, X.J.A.N., 2020. Clostridium butyricum as probiotic for promoting growth performance, feed utilization, gut health and microbiota community of tilapia (Oreochromis niloticus× O. aureus). Aquac. Nutr. 26 (3), 657–670. https://doi.org/10.1111/anu.13025.
Qin, J., Li, R., Raes, J., Arumugam, M., Burgdorf, K.S., Manichanh, C., Nielsen, T., Pons, N., Levenez, F., Yamada, T., Mende, D.R., Li, J., Xu, J., Li, S., Li, D., Cao, J., Wang, B., Liang, H., Zheng, H., Xie, Y., Tap, J., Lepage, P., Bertalan, M., Batto, J.-M., Hansen, T., Le Paslier, D., Linneberg, A., Nielsen, H.B., Pelletier, E., Renault, P., Sicheritz-Ponten, T., Turner, K., Zhu, H., Yu, C., Li, S., Jian, M., Zhou, Y., Li, Y., Zhang, X., Li, S., Qin, N., Yang, H., Wang, J., Brunak, S., Doré, J., Guarner, F., Kristiansen, K., Pedersen, O., Parkhill, J., Weissenbach, J., Antolin, M., Artiguenave, F., Blottiere, H., Borruel, N., Bruls, T., Casellas, F., Chervaux, C., Cultrone, A., Delorme, C., Denariaz, G., Dervyn, R., Forte, M., Friss, C., van de Guchte, M., Guedon, E., Haimet, F., Jamet, A., Juste, C., Kaci, G., Kleerebezem, M., Knol, J., Kristensen, M., Layec, S., Le Roux, K., Leclerc, M., Maguin, E., Melo Minardi, R., Oozeer, R., Rescigno, M., Sanchez, N., Tims, S., Torrejon, T., Varela, E., de Vos, W., Winogradsky, Y., Zoetendal, E., Bork, P., Ehrlich, S.D., Wang, J., Meta, H. I.T.C., 2010. A human gut microbial gene catalogue established by metagenomic sequencing. Nature 464 (7285), 59–65. https://doi.org/10.1038/nature08821.
Riera, J.L., Baldo, L., 2020. Microbial co-occurrence networks of gut microbiota reveal community conservation and diet-associated shifts in cichlid fishes. Anim. Microbiome 2 (1), 36. https://doi.org/10.1186/s42523-020-00054-4.
Robinson, S., Hechter, D., Almoumen, F., Franck, J.P., 2024. Sarcolipin (sln) and sarcoplasmic reticulum calcium ATPase pump (serca1) expression increase in Japanese medaka (Oryzias latipes) skeletal muscle tissue following cold challenge. Comp. Biochem. Physiol. A Mol. Integr. Physiol. 287, 111534. https://doi.org/10.1016/j.cbpa.2023.111534.
Romano, N., Zeng, C., 2013. Toxic effects of ammonia, nitrite, and nitrate to decapod crustaceans: a review on factors influencing their toxicity, physiological consequences, and coping mechanisms. Rev. Fish. Sci. 21 (1), 1–21. https://doi.org/10.1080/10641262.2012.753404.
Salvi, P.S., Cowles, R.A., 2021. Butyrate and the intestinal epithelium: modulation of proliferation and inflammation in homeostasis and disease. Cells 10 (7), 1775. https://doi.org/10.3390/cells10071775.
Shan, H., Du, Y., Li, T., Wang, F., Li, H., Wang, H., 2024. Bacterial community characteristics and roles in nitrogen transformation in industrial farming Systems of Litopenaeus vannamei. J Mar Sci Eng 12 (5), 787. https://doi.org/10.3390/jmse12050787.
Talwani, R., Gilliam, B.L., Howell, C., 2011. Infectious diseases and the liver. Clin. Liver Dis. 15 (1), 111–130. https://doi.org/10.1016/j.cld.2010.09.002.
Tan, C., Li, Q., Yang, X., Chen, J., Zhang, Q., Deng, X., 2022. Lactococcus lactis' effect on the intestinal microbiota of Streptococcus agalactiae-infected zebrafish (Danio rerio). Microbiol. Spectr. 10 (5). https://doi.org/10.1128/spectrum.01128-22 e01128–01122.
Timmers, C., Nidhi, S., Rene, O., Baidehi, M., Lizhao, W., Juan, W., Daniel, O., Prashant, T., Saavedra, H.I., Leone, G., 2007. E2f1, E2f2, and E2f3 control E2F target expression and cellular proliferation via a p53-dependent negative feedback loop. Mol. Cell. Biol. 27 (1), 65–78. https://doi.org/10.1128/MCB.02147-05.
van Vuuren, A.M., Pineiro, C., van der Hoek, K.W., Oenema, O., 2015. In: Reis, S., Howard, C., Sutton, M.A. (Eds.), Costs of Ammonia Abatement and the Climate co-Benefits. Springer, Netherlands, Dordrecht, pp. 35–51.
Venere, M., Horbinski, C., Crish, J.F., Jin, X., Vasanji, A., Major, J., Burrows, A.C., Chang, C., Prokop, J., Wu, Q., 2015. The mitotic kinesin KIF11 is a driver of invasion, proliferation, and self-renewal in glioblastoma. Sci. Transl. Med. 7 (304). https://doi.org/10.1126/scitranslmed.aac6762, 304ra143-304ra143.
Wang, Y., Shu, Y., Sun, Y., Zeng, Q., Zhang, W., Bao, Z., Ding, W., 2024. Acute nitrite exposure causes gut microbiota dysbacteriosis and proliferation of pathogenic Photobacterium in shrimp. Ecotoxicol. Environ. Saf. 283, 116829. https://doi.org/10.1016/j.ecoenv.2024.116829.
Xu, Z., Li, E., Xu, C., Gan, L., Qin, J.G., Chen, L., 2016. Response of AMP-activated protein kinase and energy metabolism to acute nitrite exposure in the Nile tilapia Oreochromis niloticus. Aquat. Toxicol. 177, 86–97. https://doi.org/10.1016/j.aquatox.2016.05.020.
Xu, S., Wu, W., Huang, H., Huang, R., Xie, L., Su, A., Liu, S., Zheng, R., Yuan, Y., Zheng, H.L., 2019. The p53/miRNAs/Ccna2 pathway serves as a novel regulator of cellular senescence: complement of the canonical p53/p21 pathway. Aging Cell 18 (3), e12918. https://doi.org/10.1111/acel.12918.
Xu, Z., Zhang, H., Guo, M., Fang, D., Mei, J., Xie, J., 2022. Analysis of acute nitrite exposure on physiological stress response, oxidative stress, gill tissue morphology and immune response of large yellow croaker (Larimichthys crocea). Animals 12 (14), 1791. https://doi.org/10.3390/ani12141791.
Yan, H., Zhao, Z., Li, W., 2024. Nitrite exposure leads to glycolipid metabolic disorder via the heme-HO pathway in teleost. Ecotoxicol. Environ. Saf. 281, 116653. https://doi.org/10.1016/j.ecoenv.2024.116653.
Yanbo, W., Wenju, Z., Weifen, L., Zirong, X., 2006. Acute toxicity of nitrite on tilapia (Oreochromis niloticus) at different external chloride concentrations. Fish Physiol. Biochem. 32, 49–54. https://doi.org/10.1007/s10695-005-5744-2.
Yang, H., Ou-Yang, K., He, Y., Wang, X., Wang, L., Yang, Q., Li, D., Li, L., 2024. Nitrite induces hepatic glucose and lipid metabolism disorders in zebrafish through mitochondrial dysfunction and ERs response. Aquat. Toxicol. 273, 107015. https://doi.org/10.1016/j.aquatox.2024.107015.
Yildiz, H.Y., Benli, A.C.K., 2004. Nitrite toxicity to crayfish, Astacus leptodactylus, the effects of sublethal nitrite exposure on hemolymph nitrite, total hemocyte counts, and hemolymph glucose. Ecotoxicol. Environ. Saf. 59 (3), 370–375. https://doi.org/10.1016/j.ecoenv.2003.07.007.

Yu, J., Ji, X., Wang, X., Li, T., Wang, H., Zeng, Q., 2019. Identification and characterization of differentially expressed genes in hepatopancreas of oriental river prawn Macrobrachium nipponense under nitrite stress. Fish Shellfish Immunol. 87, 144–154. https://doi.org/10.1016/j.fsi.2018.12.075.

Zhang, M., Dong, B., Lai, X., Chen, Z., Hou, L., Shu, R., Huang, Y., Shu, H., 2021. Effects of Clostridium butyricum on growth, digestive enzyme activity, antioxidant capacity and gut microbiota in farmed tilapia (Oreochromis niloticus). Aquac. Res. 52 (4), 1573–1584. https://doi.org/10.1111/are.15009.

Zhang, W., Wang, H., Wang, H., Xu, C., Zhao, R., Yao, J., Zhai, C., Han, W., Pan, H., Sheng, J., 2023. Integrated analysis identifies DPP7 as a prognostic biomarker in colorectal cancer. Cancers 15 (15), 3954. https://doi.org/10.3390/cancers15153954.

Zhang, K., Ye, Z., Qi, M., Cai, W., Saraiva, J.L., Wen, Y., Liu, G., Zhu, Z., Zhu, S., Zhao, J., 2025. Water quality impact on fish behavior: a review from an aquaculture perspective. Rev. Aquac. 17 (1), e12985. https://doi.org/10.1111/raq.12985.

Zhao, Z., Sun, C., Chen, L., Qin, J., Yuan, X., Li, W., 2020. Inorganic nitrite increases the susceptibility of tilapia (Oreochromis niloticus) leucocytes to Streptococcus agalactiae. Fish Shellfish Immunol. 97, 1–11. https://doi.org/10.1016/j.fsi.2019.12.039.

Zhou, F., Deng, Z., Shen, D., Lu, M., Li, M., Yu, J., Xiao, Y., Wang, G., Qian, K., Ju, L., Wang, X., 2024. DLGAP5 triggers proliferation and metastasis of bladder cancer by stabilizing E2F1 via USP11. Oncogene 43 (8), 594–607. https://doi.org/10.1038/s41388-023-02932-y.

Ecological Informatics 90 (2025) 103244



Contents lists available at ScienceDirect

Ecological Informatics

journal homepage: www.elsevier.com/locate/ecolinf



Microbiome dynamics and multiscale environmental response patterns of later-diverging coral clade across latitudes, reefs and geomorphological zones in the South China Sea

Biao Chen [a], Lin Liang [a], Kefu Yu [a,b,*], Yuxin Wei [a], Xinyue Liang [a], Zeming Bao [a], Zhiheng Liao [c], Xiaopeng Yu [a], Zhenjun Qin [a], Lijia Xu [d], Yongzhi Wang [d], Yaru Kang [a]

[a] Guangxi Laboratory on the Study of Coral Reefs in the South China Sea; Coral Reef Research Center of China; School of Marine Sciences, Guangxi University, Nanning, China
[b] Southern Marine Science and Engineering Guangdong Laboratory (Guangzhou), Guangzhou, China
[c] Key Laboratory of Environmental Change and Resource Use in Beibu Gulf, Ministry of Education, Nanning Normal University, Nanning, China
[d] South China Institute of Environmental Sciences, MEE, China

ARTICLE INFO

Keywords:
Microbiome dynamics
Multiscale environmental response
Adaptive strategy
Later-diverging coral
South China Sea

ABSTRACT

The climatic adaptability and resilience of coral-associated microbiomes are pivotal under the global change. However, the environmental responses and acclimation patterns of microbiome within corals from the latest clades across multiple spatial scales remain unclear. This study analyzed the community and function characteristics of Symbiodiniaceae and bacteria in *Lithophyllon scabra* (latest-diverging clade of Fungiidae) across latitudes, reefs and geomorphological zones in the South China Sea. The results showed that *L.scabra* acclimated to environmental variation at multiple spatial scales by establishing specific symbioses with C27 sub-clade. The deterministic assembly of Symbiodiniaceae was associated with nutrient declines at latitudinal scales, while at reefal and geomorphological scales, it is driven by climatic factors and their interactions with local effects, respectively. However, the stochastic process of Symbiodiniaceae was shaped by symbionts dispersal across multiple spatial scales. Notably, environment filtration entirely governed the bacterial assembly process. At latitudinal and reefal scales, the environmental effects and responses pattern of bacterial community aligned with "Pierre Cardin principle" and "Anna Karenina principle", respectively. Interestingly, bacterial community was enriched with nitrogen-metabolizing taxa and photoautotrophic functions in the lagoon, while exhibiting a higher abundance of heterotrophic functions and antibacterial taxa on the reef slope, which suggests that changes in nutritional patterns and composition of the bacterial community were crucial for the acclimation of *L. scabra* to distinct geomorphological zones. These results provide novel insights into the environmental interactions and adaptive strategies of the microbiome associated with younger clades of coral across multiple spatial scales in the context of climate change.

1. Introduction

Coral reefs are one of ecosystems with the most biodiversity and symbiotic diversity of in the earth, which are hailed as "tropical rainforest of the ocean" (Blackall et al., 2015; Galand et al., 2023; Reaka-Kudla et al., 1997). However, over the past two decades, coral reefs have experienced substantial degradation primarily driven by climate change (Spalding and Brown, 2015; Hughes et al., 2017a; Hughes et al., 2018a, 2018b; Sully et al., 2019; Lin et al., 2023; Voolstra et al., 2025). This has resulted in a dramatic global decline in live coral cover, estimated to range from 50% to 80% (Silverstein et al., 2015). Between 1977 and 2001, Caribbean reefs experienced a significant decline in live coral cover, dropping from approximately 50% to around 10% (Gardner et al., 2003; Pittman et al., 2018; Yu, 2012). Similarly, in the Indo-Pacific region, coral cover decreased from 42.5% in the early 1980s to 22.1% by 2003 (Bruno and Selig, 2007; Tkachenko, 2017). The third global coral bleaching event (2014–2017) had profoundly negative impacts on biodiversity and ecosystem health of 74% of coral reef in worldwide

* Corresponding author at: Guangxi Laboratory on the Study of Coral Reefs in the South China Sea; Coral Reef Research Center of China; School of Marine Sciences, Guangxi University, Nanning, China.
E-mail address: kefuyu@scsio.ac.cn (K. Yu).

https://doi.org/10.1016/j.ecoinf.2025.103244
Received 25 January 2025; Received in revised form 28 May 2025; Accepted 28 May 2025
Available online 2 June 2025
1574-9541/© 2025 The Authors. Published by Elsevier B.V. This is an open access article under the CC BY-NC-ND license (http://creativecommons.org/licenses/by-nc-nd/4.0/).

(Eakin et al., 2019; Hughes et al., 2017b; Hughes et al., 2018a, 2018b; Perry and Morgan, 2017). This event resulted in catastrophic die-offs of staghorn and tabular corals, transforming the three-dimensional structure and ecological functionality of 29% of the 3,863 reefs in the Great Barrier Reef (GBR), and approximately 35% of global reefs experienced significant coral mortality (Eakin et al., 2022; Hughes et al., 2018a, 2018b). The recent study by Reimer et al. (2024) indicates that the fourth global coral bleaching event, which began in October 2023, has led to extensive coral mortality and reef degradation across multiple regions, including Kenya (Watamu), Australia (Capricorn Bunkers in the Southern Great Barrier Reef), Panama (Bocas del Toro), and Brazil (Costa dos Corais). The interval between global bleaching events, driven by extreme climate change, is now less than six years, providing insufficient time for damaged coral reefs to recover to their original state (Hughes et al., 2018a, 2018b). Notably, the bleaching susceptibility and mortality of coral exhibited spatial heterogeneity. Importantly, coral bleaching susceptibility and mortality exhibit significant spatial heterogeneity. For instance, while northern GBR reefs experienced extremely high sea surface temperatures (SST) during the 2016 bleaching event, some northern reefs displayed significantly lower damage levels compared to reefs in the central and southern GBR (Hughes et al., 2017b; Stuart-Smith et al., 2018). This spatial variability in the decline of live coral cover across the GBR is closely linked to the independent or combined effects of climatic, local, and nutrient factors (e.g., cyclones, upwelling) across multiple scales (Beger et al., 2014; Stuart-Smith et al., 2018; Thirukanthan et al., 2025). It is worth noting that the highest level of coral bleaching risk and frequency occur at tropical intermediated latitudes regions that spanning 15-20° north and south latitude based on the field observations of coral bleaching at 3351 sites in 81 countries from 1998-2017 (Sully et al., 2019). Also, the Persian/Arabian Gulf and Coral Triangle are the warmest regions in the earth (Hume et al., 2016; Smith et al., 2022; Zhang et al., 2023), yet the most abundant coral reefs developed in these region (Veron et al., 2015). These findings suggest that coral thermal bleaching susceptibility and stress tolerance exhibit spatial heterogeneity and variation across multiple scales. However, while spatial heterogeneity in coral degradation and mortality can be partially explained by global and local stressors (Veron et al., 2015), the environmental impact on corals and their response pattern in multiple spatial scale among latitudes, reefs and geomorphological zones remain unclear.

Coral reefs are recognized as hotspots of microbiome diversity in the ocean, exhibiting exceptional genetic and symbiotic diversity on Earth (Galand et al., 2023). Corals exhibit the biological characteristics of a holobiont, consisting of coral hosts and their associated microbiomes, including endosymbiotic Symbiodiniaceae, bacteria, fungi, viruses, and archaea (Bourne et al., 2016; Osman et al., 2020; Voolstra et al., 2024). Studies have shown that coral-associated microbiota play an important role in stress adaptability and environment resistance of coral in multiple scales (Gantt et al., 2024; Hernandez-Agreda et al., 2017; Tran, 2022; van Oppen and Blackall, 2019), thereby significantly shaping the coral holobiont's response to environmental changes (Santoro et al., 2025). Within the coral holobiont, Symbiodiniaceae and bacterial communities exhibit distinct ecological dynamics and functional roles due to their non-overlapping ecological niches (Robbins et al., 2019; Voolstra et al., 2021). Symbiodiniaceae are widely distributed in the open ocean and coral reef regions (Armstrong et al., 2023; Decelle et al., 2018; Million et al., 2025), exhibiting a high level diversity within coral microhabitats and reef niches (Million et al., 2025). Symbiodiniaceae and corals share a co-evolutionary history spanning approximately 140–200 million years, characterized by long-term stable symbiotic relationships (Lajeunesse et al., 2018). As the primary photosynthetic symbionts, Symbiodiniaceae supply up to 95% of the coral host's energy requirements through photosynthesis (Falkowski et al., 1984; Muscatine et al., 1984), which will assist coral to acclimate environmental regimes through community shifts or establishment of specific symbioses in multiple scales (Grottoli et al., 2014; Voolstra et al., 2021). Shifts in Symbiodiniaceae community composition are widely documented across extensive spatial and latitudinal gradients. For instance, *Pocillopora damicornis* in Taiwan and New Caledonia is primarily dominated by *Cladocopium* (C1 subclade), whereas in Djibouti and French Polynesia, the community shifts to *Durusdinium* (D1 subclade) dominance (Brener-Raffalli et al., 2018). This ecological process is largely driven by long-term environmental and geographic factors and has been documented across various coral species in the Persian/Arabian Gulf and the South China Sea (SCS) along latitudinal gradients (Chen et al., 2019; Chen et al., 2020; Hume et al., 2016; Reimer et al., 2017; Ziegler et al., 2017a). In addition, certain coral species exhibit higher symbiotic stability and rely on specific Symbiodiniaceae subclades to cope with environmental and stress-induced changes on a latitudinal scale, such as *Porites*-C15 subclade (Chen et al., 2019; Osman et al., 2020; Terraneo et al., 2019), *Pocillopora meandrina-Cladocopium latusorum* (L5) and SSH5_Pver-*Cladocopium goreaui* (L1) (Armstrong et al., 2023). In reefs scale, it has been found that coral recovery under elevated temperatures was driven by a tenfold increase in the relative abundance of *Durusdinium* within the Symbiodiniaceae community. This phenomenon was observed in Kiritimati, located in the equatorial Pacific Ocean, during the 2015–2016 heatwave, providing enhanced heat tolerance crucial for the long-term persistence of corals (Claar et al., 2020). Also, distinct coral species exhibited different environmental response patterns in their Symbiodiniaceae communities at the reefal scale (Chankong et al., 2020; Lee et al., 2022; Pratomo et al., 2022). For instance, the Symbiodiniaceae community structures in *Diploastrea heliopora* exhibited relative stability across ten reef sites along the coasts of the Malay Peninsula (Ong et al., 2022). In contrast, *Pachyseris speciosa* showed strong associations with both *Cladocopium* and *Durusdinium*, while *Pocillopora acuta* and *D. heliopora* were predominantly dominated by *Durusdinium*, which has closely associations with climatic (temperature, salinity) and local (calcite centration, cloud fraction, primary productivity and phosphate concentration) environment regimes among reefs (Ong et al., 2022). However, the restructure and shift of coral-Symbiodiniaceae symbioses seems to be unstable, which mediated by repeated coral bleaching and can not transfer to filial generation of corals (Boulotte et al., 2016a; Quigley et al., 2022). Moreover, climate change also results in sharp increase of environmental stress in small spatial scale, which will lead to more extreme environment and lower habitat availability in lagoon and tidal zone that has higher level of stress than reef slope (Camp et al., 2017; Hughes et al., 2017b). However, the switching and shuffling of dominated Symbiodiniaceae in corals across geomorphological zones was rare (Alessi, 2024; Qin et al., 2021). In addition, the evolutionary divergence, functional diversity, and symbiotic strategies of Symbiodiniaceae can influence the environmental tolerance of the coral holobiont (Chen et al., 2024; Lajeunesse et al., 2010; Lajeunesse et al., 2018), yet these factors have not been sufficiently considered across multiple spatial scales. Thus, the contribution of specific symbioses and background symbionts to adaptability and stress response patterns of coral holobiont at small-scale still largely unknown.

Bacterial communities play essential roles in the coral holobiont by contributing to nutrient metabolism (Kimes et al., 2010; Wegley et al., 2007; Ainsworth et al., 2015; Hochart et al., 2023), producing antibiotics (Ritchie, 2006; van Oppen and Blackall, 2019), maintaining metal homeostasis (Zhang et al., 2015), and facilitating the remediation of organic compounds (Santoro et al., 2025; Zhang et al., 2015). These communities exhibit remarkable flexibility in responding to environmental stresses and changes across diverse biogeographic scales. In latitudinal scales, coral-associated bacteria community responded to environment variation and climatic event by increasing abundance of potential beneficial bacteria (Chen et al., 2021; Osman et al., 2020), altering the core bacterial microbiota (Chen et al., 2021), modulating bacterial richness and diversity (Mcdevitt-Irwin et al., 2017; van Oppen and Blackall, 2019; Zaneveld et al., 2017). For instance, based on the 16S rRNA barcoding analysis of 681 coral samples collected from 21 sites in Australia, the coral-associated bacterial communities exhibited

high levels of community dispersion and a notable abundance of environmental resistance genes (Sessa et al., 2022). Also, the bacteria community of *Pocillopora* exhibited huge diversity and flexibility to respond to the environmental and geographic regimes across Indo-Pacific regions, which not only regulated by global or local stress levels, but also shaped by historical process and habitat heterogeneity (Brener-Raffalli et al., 2018; Galand et al., 2023; Osman et al., 2020). *Pocillopora* corals possess the capacity to regulate the relative abundance and genetic composition of beneficial Endozoicomonadaceae bacteria, enabling them to acclimate to environmental variations across latitudinal and longitudinal gradients (Chen et al., 2021; Hochart et al., 2023). Similar patterns of bacterial community adaptation have been observed across reef scales (Qin et al., 2020; Zaneveld et al., 2016; Ziegler et al., 2017b; Ziegler et al., 2019), depth gradients (Hernandez-Agreda et al., 2016; Qin et al., 2024), geomorphological zones (Lima et al., 2020; Qin et al., 2021). However, the assembly process, functions change and the independent or combined effects of environmental factors on coral-associated bacteria communities across multiple spatial scales remain unclear. This has led to the complexity and instability of environmental influence patterns and the response strategies of coral-associated bacteria, as observed in previous studies.

The SCS is located northwest of the Coral Triangle region that is the diversity center of the world from Indo-Pacific convergence (Veron et al., 2015). The degradation trend of coral reefs in the SCS mirrors the global pattern observed under climate change, with approximately 50–70% of coral cover lost since the 1960s (Yu, 2012). Although many coral reefs in the northern and central SCS experienced severe thermal bleaching and mass mortality during the 2020 marine heatwave event (Baum et al., 2023; Feng et al., 2022; Lin et al., 2023; Liu et al., 2021; Szereday et al., 2024), the percentage and susceptibility of coral thermal bleaching exhibited significant interspecific differences (Chen et al., 2024; Yu et al., 2021). Notably, members of the Fungiidae family exhibited remarkable heat tolerance and bleaching resistance, with an exceptionally low 2.0% thermal bleaching rate observed during the extreme warming event of 2020 (Chen et al., 2024). Previous studies have also shown that Fungiidae can thrive in stressful habitats characterized by temperature fluctuations, low light, and high turbidity, without experiencing significant mortality (Bongaerts et al., 2012; Hoeksema, 1991; Hughes et al., 2017b; Loya and Sakai, 2008; Qin et al., 2021; Wei et al., 2024), which suggest that Fungiidae employs a uniquely ecological strategy to respond and acclimate to diverse environmental regimes. *Lithophyllon scabra* is one of the most recently diverged species in the family Fungiidae (Wei et al., 2024). In long-term warm habitats, it demonstrates a greater capacity for microbiome regulation and enhanced community stability within its holobiont compared to other members of this family (Wei et al., 2024), which implied that *L. scabra* holobiont may has stronger stress tolerance and resistance in the SCS. However, the environmental impact and response pattern of *L. scabra*-associated microbiome across multi-spatial scales remain unclear, which impede the spatial evaluation of coral community evolutionary patterns and their differentiated microbial adaptive strategies in the context of climate change. Therefore, the diverse environmental conditions and coral habitats types spanning 19 latitudes in the SCS create a natural laboratory for investigating the environmental impacts and response patterns of the *L. scabra*-associated microbiome across multiple spatial scales (Liao et al., 2021; Wang and Li, 2009; Yu, 2012).

This study aimed to investigate, for the first time, the diversity and community structure of Symbiodiniaceae and bacterial communities associated with *L. scabra* across four latitudinal regions, eight reefs, and two geomorphological zones in the tropical SCS, and it evaluated the stability and adaptability of these microbial communities across multiple spatial scales. Additionally, the assembly processes of the microbial community are analyzed to determine the relative contributions of deterministic and stochastic process in shaping the Symbiodiniaceae and bacterial communities across different latitudes, reefs, and geomorphological zones. Moreover, a correlation analysis between microbial community variation and environmental factors will be conducted to elucidate the environmental response patterns of the *L. scabra*-associated microbiome. Variation Partitioning Analysis (VPA) will be employed to identify the environmental impact pattern of the Symbiodiniaceae and bacterial communities of *L. scabra*. Furthermore, community composition analysis and functional traits prediction will be used to assess the stress response and acclimation strategies of the microbial community across multiple spatial scales. The findings of this study will deepen our understanding of the dynamics and assembly processes of coral holobiont microbiomes across diverse habitats and environmental regimes. They will also offer valuable insights into the unique environmental response patterns of coral-associated microbiomes at multiple spatial scales, particularly in the context of climate change.

2. Materials and methods

2.1. Sample collection and environmental parameter measurements

Using SCUBA diving at a depth range of 2-15 m, a total of 55 samples of *L.scabra* were collected from eight reefs, include Zhaoshu Island (ZS), Shiyu (SY), Longdong patch reef (LD), Ganquan Island (GQ), Jinqing Island (JQ), Lingyang Reef (LY), Huaguang Reef (HG) and Sanjiao Reef (SJ), spanning four latitudinal regions (ZS, Yongle atoll [YL], HG and SJ) in the SCS (Fig. 1; Table.1). The morphologically distinct colonies of *L. scabra* were collected at least 10 m apart, and eight sampling sites were separated by as much as 5 km, which will avoid duplicate sampling and collection of fragments from asexually reproducing colonies. The samples were transferred to the ship and cleaned with artificial sterile seawater (salinity: 35‰) to remove the interference from free-living Symbiodiniaceae and bacteria in in the seawater. All coral samples were transferred to 15 mL cryotubes (Jet Biofil, Guangzhou, China), and 20% dimethyl sulfoxide (DMSO) buffer or 95% ethanol was added. After the above operation, the cryotubes were stored at -20°C until DNA extraction.

In situ coral reef water samples (5L/sample) were collected from study sites for environmental parameters determining, and the sea surface temperature (SST; °C), salinity (PSU), dissolved oxygen (DO; mg/L), pH and turbidity (FNU) were test by ProDSS Multiparameter Digital Water Quality Mater (YSI, USA) at the same time as that of *L. scabra* samples collection. Consequently, the seawater samples were stored at -80°C for nutrient measured, and SiO_3^{2-} (μmol/L), PO_4^{3-} (μmol/L), NH_4^+ (μmol/L), NO^{2-} (μmol/L) and NO^{3-} (μmol/L) were measured using an QuAAtro auto-continuous flow analyzer (SEAL, Germany) in the scientific expedition vessel.

2.2. Total DNA extraction, PCR amplification and next-generation sequencing

Total microbiome DNA of *L.scabra* was extracted using TIANamp Marine Animals DNA Kit (Tiangen, Beijing, China), and extraction strategy is performed according to the manufacturer's instructions. The concentration and purity of the microbiome DNA were assessed using a NanoDrop 2000 ultraviolet spectrophotometer (Thermo Fisher Scientific, MA, USA), and only high-quality DNA samples were selected as templates for PCR amplification. The Symbiodiniaceae rDNA ITS2 gene was amplified with ITSintfor2 (5'-GATTGCAGAACTCCGTG-3') (Lajeunesse and Trench, 2000) and ITS2-reverse (5'-GGGATCCATATGCTTAAGTTCAGCGGGT-3') (Coleman et al., 1994). Meanwhile, 338F (5'-ACTCCTACGGGAGGCAGCAG-3') and 806R (5'-GGACTACHVGGGTWTCTAAT-3') were used to amplify the highly variable V3-V4 region of the 16S rRNA bacterial gene (Mori et al., 2014). PCR was performed with ~10ng of DNA, 1.6μL (5μM) prime, 0.4 μL Trans Start Fastplu DNA Polymerase, 4μL 5×FastPfu Buffer, 0.2μL BSA, 2μL 2.5mM dNTPs, and ddH_2O at a total volume of 20 μL. PCR amplification

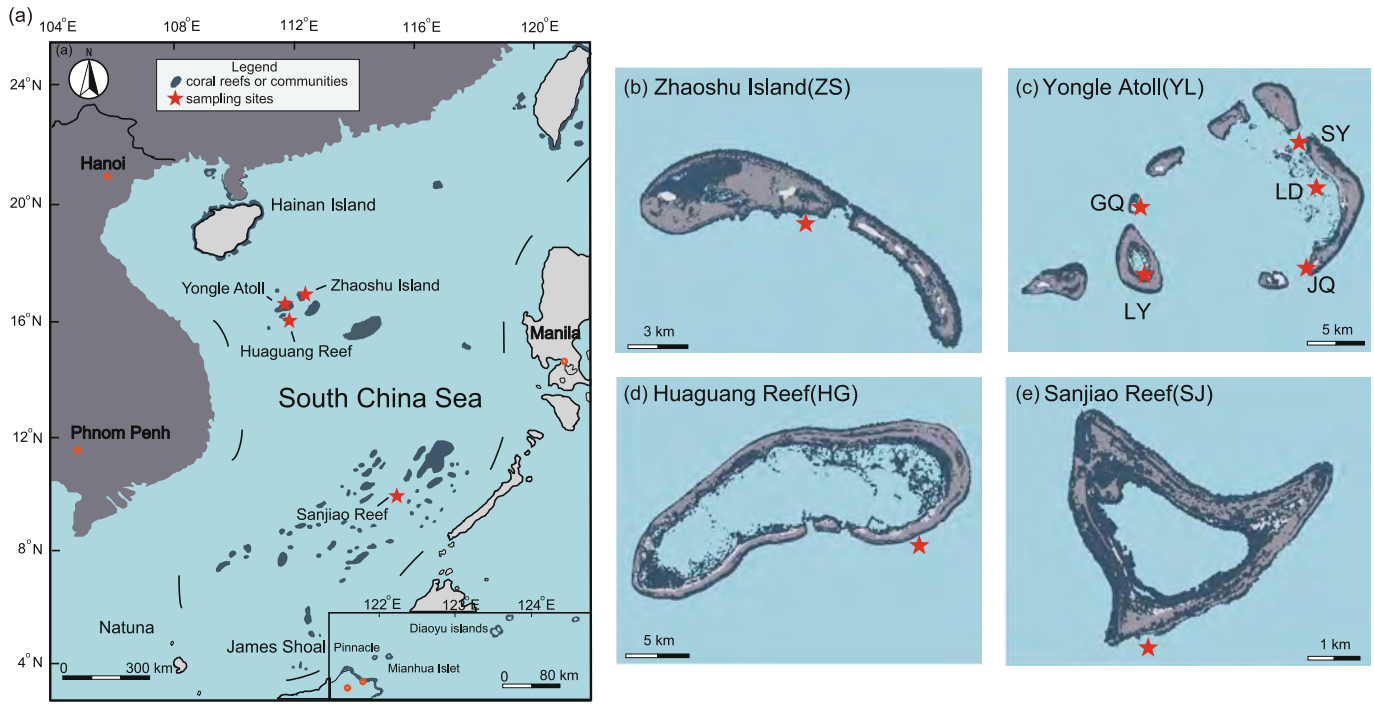


Fig. 1. Overview of the study areas. (a) The dark blue areas represent the distribution of coral reefs in the South China Sea (SCS). The red star marks the sampled areas of *Lithophyllon scabra*. (b) Zhaoshu Island (ZS). (c) Yongle Atoll (YL): Shiyu (SY), Longdong point reef (LD), Ganquan Island (GQ), Jinqing Island (JQ), Lingyang Reef (LY); (d) Huaguang Reef (HG); (e) Sanjiao Reef (SJ).

Table 1
Details of the sampling of *Lithophyllon scabra* conducted in this study. Nb denotes the number of *Lithophyllon scabra* sampled at each reefs.

Reefs	Region	Geomorphological zones	Longitude	Latitude	Nb
Zhaoshu Island (ZS)	Yongle Atoll	reef slope	N 16.9658	E 112.2755	8
Shiyu (SY)			N 16.5466	E 111.7335	6
Longdong patch reef (LD)		lagoon	N 16.5227	E 111.7508	6
Ganquan Island (GQ)		reef slope	N 16.5025	E 111.5808	8
Jinqing Island (JQ)		lagoon	N 16.4703	E 111.7380	8
Lingyang Reef (LY)		lagoon	N 16.4523	E 111.5977	7
Huaguang Reef (HG)			N 16.2199	E 111.7755	6
Sanjiao Reef (SJ)			N 10.1746	E 115.2748	6

was conducted on an ABI GeneAmp® 9700 thermocycle controller with the following program: 3min at 95°C, followed by 35 cycles of 95°C for 30 s, 55°C for 30 s, 72°C for 45 s, and a final extension at 72°C for 10 min. The PCR products were purified using the QIAquick Gel Extraction Kit (Qiagen, Hilden, Germany), which were pair-end sequenced on an Illumina Miseq platform (Majorbio, Shanghai, China) using 2 × 300 bp mode based on standard protocols after entry quality control and adapter ligation. The raw read dataset of ITS2 and 16S rRNA amplicons have been submitted into the NCBI Sequence Read Archive database (Accession Number: PRJNA1063379 and PRJNA1063386).

2.3. Bioinformatics processing and microbial sequences identification

Microbiome sequences were processed based on Quantitative Insights Into Microbial Ecology 2 (Bokulich et al., 2018). The low-quality reads and concatenate the bacterial and Symbiodiniaceae reads have been removed using the DADA2 pipeline in R statistical software (Callahan et al., 2016), and qualified reads were rarefied to an equal sequencing depth. After quality control and filtration, Symbiodiniaceae and bacterial reads were clustered into amplicon sequence variant (ASVs) using the DADA2 algorithm (Callahan et al., 2016). However, the Symbiodiniaceae ITS2 region is a multicopy molecular marker, and intragenomic variation as well as pseudogenes can lead to overestimation of Symbiodiniaceae α and β diversity (Stat et al., 2011; Thornhill et al., 2007). Thus, ITS2 read alignment and ASV analyses were applied to enhance the reliability of the results regarding Symbiodiniaceae community dynamics together (Ziegler et al., 2017a, 2017b; Chen et al., 2019). The quality-filtered ITS2 reads were aligned to the local Symbiodiniaceae database using BLASTN (Supplementary Material Dataset S1 and Code S1), and the alignment scheme was executed following the pipeline detailed in previous studies (Chen et al., 2019; Chen et al., 2023; Chen et al., 2024). The presence of Symbiodiniaceae ITS2 reads at a minimum cut-off >5% in at least one sample were identified as dominant Symbiodiniaceae sub-clades (Chen et al., 2019; Chen et al., 2020; Ziegler et al., 2017a; Supplementary Table S1), which was applied to Symbiodiniaceae community composition analysis. In addition, the Symbiodiniaceae ASVs was used to evaluate α and β diversity of Symbiodiniaceae by reducing the proportion of ITS2 variants rather than relying on the taxonomy (Chen et al., 2024; Wei et al., 2024). However, not all ASVs that were clustered by ITS2 reads belonged to Symbiodiniaceae, because the significance of individual base pair differences within the Symbiodiniaceae ITS2 sequence was ambiguous (Cunning et al., 2018; Howe-Kerr et al., 2020). Therefore, after removing chimeras using DADA2 pipeline, the representative sequences of ASVs were also aligned with the duplication-free ITS2 database based on local BLASTN to remove non-Symbiodiniaceae ASVs (Supplementary Material Dataset S1 and Code S1; Chen et al., 2019).

The high-confidence Symbiodiniaceae ASVs were utilized for downstream analysis. For bacterial ASVs, the classification sklearn (naïve Bayes) method based on the SILVA 132 database was used for alignment with a confidence threshold of 0.7 (Bokulich et al., 2018; Caporaso et al., 2010; Yilmaz et al., 2014). The ASVs of the chloroplasts, mitochondria, and other nonbacterial cells were removed.

2.4. Statistical analyses of microbial ecological indices

The α diversity (Chao1 richness and Shannon diversity indices) of Symbiodiniaceae and bacterial communities in *L. scabra* was performed using the Vegan package in R (Oksanen et al., 2015). Kruskal-Wallis test was conducted to assess differences of Symbiodiniaceae and bacterial communities α diversity among latitudinal and reefal scales, and Student-Newman-Keuls (SNK) test was used for post-hoc multiple comparisons of significant result. The Welch t-test was used for comparisons on Symbiodiniaceae and bacterial communities α diversity between geomorphological zones, and the false discovery rate (FDR) was used for two-tailed testing. These significance tests were conducted using GraphPad Prism 8. Also, the significant differences of Symbiodiniaceae and bacteria community structure in *L. scabra* were test by permutational multivariate analysis of variance (PERMANOVA) with 9,999 permutation-based Bary-Curtis dissimilarity matrix. The results of PERMANOVA were visualized by the principal coordinate analysis (PCoA) based on the Bray-Curtis distance in the Vegan package in R (Oksanen et al., 2015). The community assembly process of Symbiodiniaceae and bacteria in *L. scabra* among distinct scales were evaluated by neutral community model (NCM) using R (Burns et al., 2016), and R^2>0.5 was as the threshold for assessing better goodness fit. The normalized stochasticity ratio (NST) was used to quantify the importance of deterministic and stochastic processes in the assembly of Symbiodiniaceae and bacteria communities that has the better goodness fit of NCM. The 50% was set as threshold for identifying the predominance of stochastic or deterministic processes (Ning et al., 2019). Canonical correspondence analysis (CCA) and redundancy analysis (RDA) were used to establish the relationship among environmental factors, multi-scale sampling regions and relative abundance of ASV of Symbiodiniaceae and bacteria. CCA/RDA were performed in R using the Vegan package, and significance levels were based on 1,000 Monte Carlo permutations. A VPA was conducted to quantify the contributions of climate (SST and salinity), nutrient (SiO_3^{2-}, PO_4^{3-}, NH_4^+, NO^{2-} and NO^{3-}) and local factors (turbidity, pH, DO) on microbial community structure among multi-scale habitats using the varpart function of the Vegan package in R (Oksanen et al., 2015). The environmental variables redundancy was conducted by varclus in Hmisc R package (Harrell, 2008), and co-linearity effects have been limited. Moreover, the annotation of prokaryotic taxa (FAPROTAX) was used to predict the ecological functional profiles of bacterial communities (Louca et al., 2016), and the top 10 functional profiles in terms of abundance are used for subsequent analysis. Wilconxon rank-sum test was applied to determine the significant differences of functional profiles of bacterial communities between geomorphological zones, and post-hoc test was conducted by FDR. Above all, p-values below 0.05 was considered indicative of significant differences for all statistical test.

3. Results

3.1. Diversity and community structure of Symbiodiniaceae in multiple spatial-scale

For the Symbiodiniaceae ITS2 reads analysis, *Cladocopium*, *Durusdinium*, and *Gerakladium* were identified in *L. scabra* from the SCS after quality control. At the sub-clade level, 177 Symbiodiniaceae sub-clades were aligned, belonging to *Cladocopium* (n = 162), *Durusdinium* (n = 13), *Fugacium* (n = 1), and *Gerakladium* (n = 1). The results of the Symbiodiniaceae ASV analyses showed that 626 valid Symbiodiniaceae ASVs from *L. scabra* were obtained after subsampling (n = 22,289; Supplementary Table S2) and filtering, which were then used for α diversity analyses of Symbiodiniaceae (Chao richness and Shannon diversity indices). However, no significant differences were observed in the Chao richness index of the Symbiodiniaceae community in *L. scabra* across latitudes (Kruskal-Wallis H test, $p = 0.1172 > 0.05$; Fig. 2a), reefs (Kruskal-Wallis H test, $p = 0.1616 > 0.05$; Fig. 2b), or geomorphological zones (Welch's t-test, $p = 0.1709 > 0.05$; Fig. 2c). It is also noteworthy that the Shannon diversity index of the Symbiodiniaceae community in *L. scabra* exhibited the same pattern, with no significant differences across latitudes (Kruskal-Wallis H test, $p = 0.1463 > 0.05$; Fig. 2d), reefs (Kruskal-Wallis H test, $p = 0.071 > 0.05$; Fig. 2e), or geomorphological zones (Welch's t-test, $p = 0.1150 > 0.05$; Fig. 2f).

For Symbiodiniaceae community composition, *L. scabra* in the SCS was dominated by *Cladocopium* (88.97%) and *Durusdinium* (10.88%). Gerakladium was rare in the *L. scabra* holobionts, with a relative abundance of 0.15%. In addition, eight predominant Symbiodiniaceae sub-clades were identified in *L. scabra* from the SCS (relative abundance > 5% in at least one sample; Supplementary Table S1), all belonging to *Cladocopium* (C27, C1, Cspc, C3d, C1ca, C1# and C93) and *Durusdinium* (D1; Fig. 3). The C27 sub-clade dominated the Symbiodiniaceae communities across latitudes (relative abundance: 67.61±8.32%; Fig. 3a), reefs (relative abundance: 59.73±15.50%; Fig. 3b), and geomorphological zones (relative abundance: 60.63±4.33%; Fig. 3c), showing strong, stable symbiosis with *L. scabra* in the SCS. The C1 sub-clade was the subdominant Symbiodiniaceae sub-clade in *L. scabra* across latitudinal (relative abundance: 12.56±8.81%; Fig. 3a), reef (relative abundance: 21.22±14.61%; Fig. 3b), and geomorphological zone scales (relative abundance: 20.24±4.22%; Fig. 3c). Notably, the heat-tolerant D1 sub-clade also appeared in the Symbiodiniaceae community composition across different habitat scales (latitudes: 0.56±0.62%; reefs: 1.15±1.48%; geomorphological zones: 1.31±1.59%; Fig. 3).

Nevertheless, the results of PCoA and PERMANOVA showed no significant differences in the Symbiodiniaceae community structure of *L. scabra* across latitudes (PERMANOVA, $F = 1.461$, $R^2 = 0.0792$, $p = 0.1999 > 0.05$; Fig. 3d), reefs (PERMANOVA, $F = 1.940$, $R^2 = 0.2055$, $p = 0.0992 > 0.05$; Fig. 3e), or geomorphological zones (PERMANOVA, $F = 0.799$, $R^2 = 0.0237$, $p = 0.3829 > 0.05$; Fig. 3f). Therefore, the α diversity and community structure of the Symbiodiniaceae communities of *L. scabra* exhibited homogenization characteristics across multiple spatial scales in the SCS.

3.2. Diversity and community structure of bacteria in multiple spatial-scale

After quality control of the 16S rRNA reads and subsampling (n = 19,209), 7,528 valid bacterial ASVs were obtained. A total of 43 phyla, 107 classes, 270 orders, 466 families, 969 genera, and 1,715 species were identified in the bacterial communities of *L. scabra* in the SCS (Supplementary Table S3). The results of α diversity analyses showed significant differences in the Chao richness index of the bacterial community of *L. scabra* across latitudes (Kruskal-Wallis H test, $p = 0.0117 < 0.05$; Fig. 4a), reefs (Kruskal-Wallis H test, $p = 0.0001 < 0.05$; Fig. 4b), and geomorphological zones (Welch's t-test, $p = 0.0175 < 0.05$; Fig. 4c). The patterns of the Shannon diversity index were consistent with those of the Chao richness index, with significant differences also observed across latitudes (Kruskal-Wallis H test, $p = 0.0201 < 0.05$; Fig. 4d), reefs (Kruskal-Wallis H test, $p = 0.0085 > 0.05$; Fig. 4e), and geomorphological zones (Welch's t-test, $p = 0.0421 < 0.05$; Fig. 4f). At the latitudinal scale, the Chao richness index of the bacterial community of *L. scabra* in HG was significantly higher than in ZS (Fig. 4a), and the Shannon diversity index of the bacterial community of *L. scabra* in HG was also lower than in ZS and YL (Fig. 4d). At the reefal scale, the Chao richness and Shannon diversity indices of the bacterial community in GQ were significantly lower than those in other reefs (SY, LD, and JQ) except LY (Fig. 4c and d). At the geomorphological zone scale, the

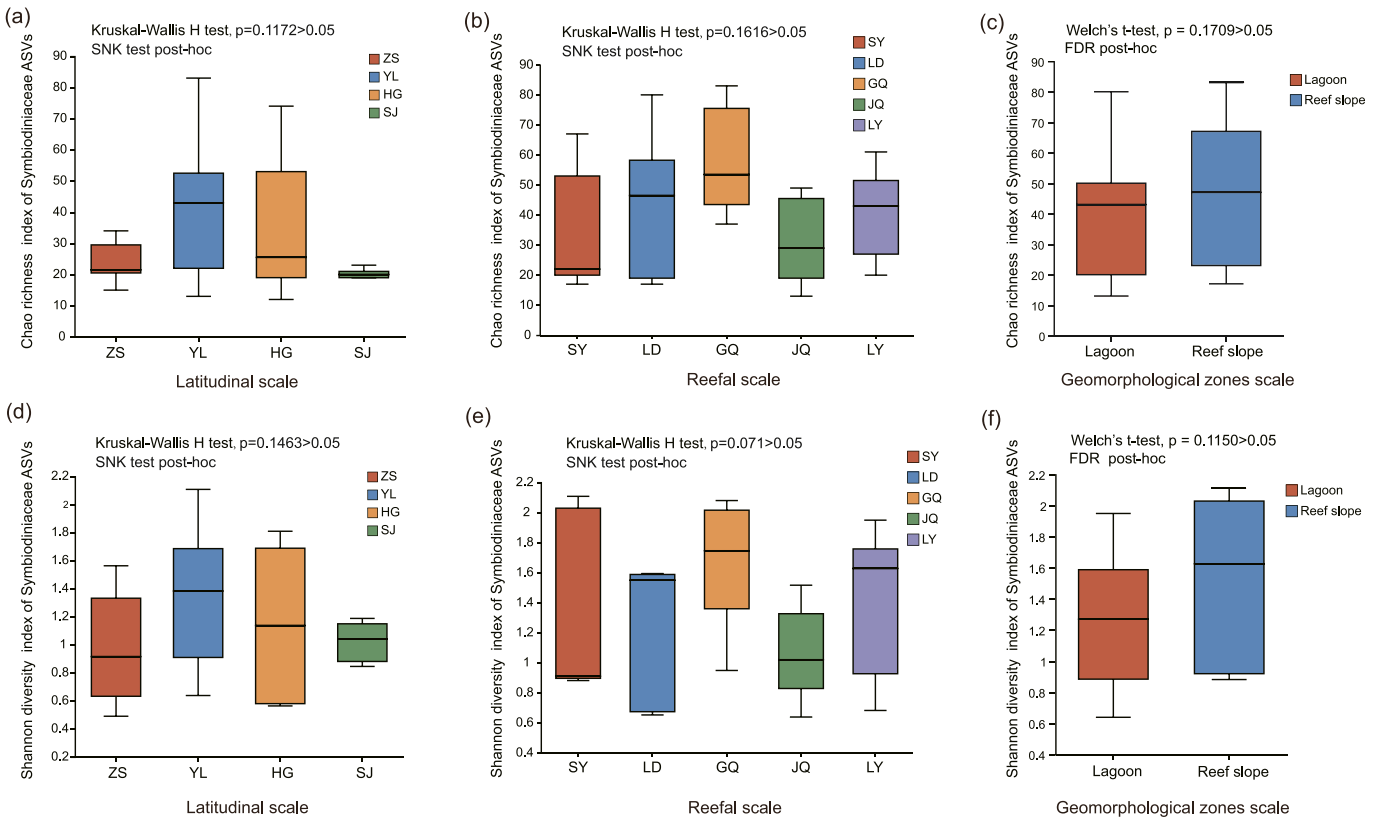


Fig. 2. The α diversity of Symbiodiniaceae communities of *Lithophyllon scabra* at ASV level at multiple spatial scales in the South China Sea (SCS). (a-c) Chao richness index of Symbiodiniaceae communities in *L. scabra* across latitudes, reefs and geomorphological zones in the SCS; (d-f) Shannon diversity index of Symbiodiniaceaea communities in *L. scabra* among latitudes, reefs and geomorphological zones in the SCS.

changes in the Chao richness index of coral-associated bacterial communities were consistent with those of the Shannon diversity index, and the α diversity of the bacterial community of *L. scabra* in the lagoon was significantly higher than in the reef slope (Fig. 4e and f).

At the class level, the bacterial community of *L. scabra* across all latitudes in the SCS was dominated by α-proteobacteria (52.48 ±20.18%), γ-proteobacteria (37.66±23.49%), Bacilli (3.94±5.92%), and Bacteroidia (1.94±0.86%; Fig. 5a). At the genus level, 24 genera had relative abundances greater than 1% (Fig. 5b). At the latitudinal scale, it is worth noting that Terasakiellaceae dominated the *L. scabra* associated-bacterial community at different latitudes (ZS, 40.33%; YL, 26.66%; HG, 75.15%; SJ, 40.30%). *Vibrio* exhibited the highest relative abundance in the bacterial community of *L. scabra* in ZS (24.36%) compared to other latitudinal regions (YL: 6.07%; HG: 0.00%; SJ: 7.10%; Fig. 5b), while the BD1-7 clade also showed a high relative abundance in L. scabra in SJ (8.27%; Fig. 5b). Additionally, *Pseudoalteromonas* (20.79%) and *Shewanella* (9.07%) dominated the bacterial community of *L. scabra* at YL (Fig. 5b). The results of PERMANOVA and PCoA showed significant differences in the bacterial community structure of *L. scabra* across latitudes (PERMANOVA, $F = 3.970$, $R^2 = 0.1894$; $p = 0.0001 < 0.05$; Fig. 5c). At the reef scale, α-proteobacteria (34.52±24.75%), γ-proteobacteria (55.43±29.70%), Bacteroidia (2.88 ±1.74%), and Bacilli (2.05±2.58%) also dominated the bacterial communities of *L. scabra* in SY, LD, GQ, JQ, and LY (Fig. 5d). Notably, at the genus level, the bacterial community of *L. scabra* from LD had a higher abundance of *Shewanella* (52.80%), whereas the GQ community was dominated by *Pseudoalteromonas* (78.58%; Fig. 5e). Furthermore, there were significant differences in the bacterial community of L. scabra among reefs (PERMANOVA, $F = 10.217$, $R^2 = 0.5767$; $p = 0.0001 < 0.05$; Fig. 5f). Interestingly, the relative abundance of predominant bacterial classes and genera in *L. scabra* was distinct between the lagoon and reef slope (Fig. 6). The γ-proteobacteria had a high relative abundance in the bacterial community of *L. scabra* from the reef slope (77.64%), while α-proteobacteria (47.70%) dominated those from the lagoon (Fig. 6a). At the genus level, 14 bacterial genera were identified as predominant taxa, including *Pseudoalteromonas*, unclassified Terasakiellaceae, *Shewanella*, *Vibrio*, *Dyella*, *Cobetia*, *Alteromonas*, *Halomonas*, unclassified α-proteobacteria, unclassified γ-proteobacteria, unclassified Thalassobaculales, Photobacterium, BD1-7 clade, and unclassified Rhodobacteraceae (Fig. 6b). The results of PCoA and PERMANOVA found a significant difference in the bacterial community structure of L. scabra between the lagoon and reef slope (PERMANOVA, $F = 7.979$, $R^2 = 0.1947$, $p = 0.0001 < 0.05$; Fig. 6c). Additionally, some bacterial genera of *L. scabra* showed significantly distinct enrichment between the lagoon and reef slope (Fig. 6d). The bacterial community of *L. scabra* in the lagoon had a higher abundance of Terasakiellaceae (lagoon: 35.92%; reef slope: 12.79%; Welch's t-test, $p = 0.0036 < 0.01$) and *Shewanella* (lagoon: 15.11%; reef slope: 0.02%; $p = 0.0417 < 0.05$) than in the reef slope. In contrast, *Vibrio* (lagoon: 2.49%; reef slope: 11.42%; Welch's t-test, $p = 0.0221 < 0.01$) and *Pseudoalteromonas* (lagoon: 2.34%; reef slope: 48.48%; Welch's t-test, $p < 0.0001$) were more enriched in the bacterial community of *L. scabra* in the reef slope than in the lagoon.

3.3. Community assembly of Symbiodiniaceae and bacteria in multiple spatial-scale

The results of the NCM showed that the Symbiodiniaceae communities across latitudes ($R^2 = 0.6685$), reefs ($R^2 = 0.6580$), and geomorphological zones (lagoon: $R^2 = 0.5356$; reef slope: $R^2 = 0.6211$) were better fitted to an NCM (Fig. 7a-d). The migration rate of the Symbiodiniaceae community in the reef slope ($m = 0.0026$; Fig. 7c) was

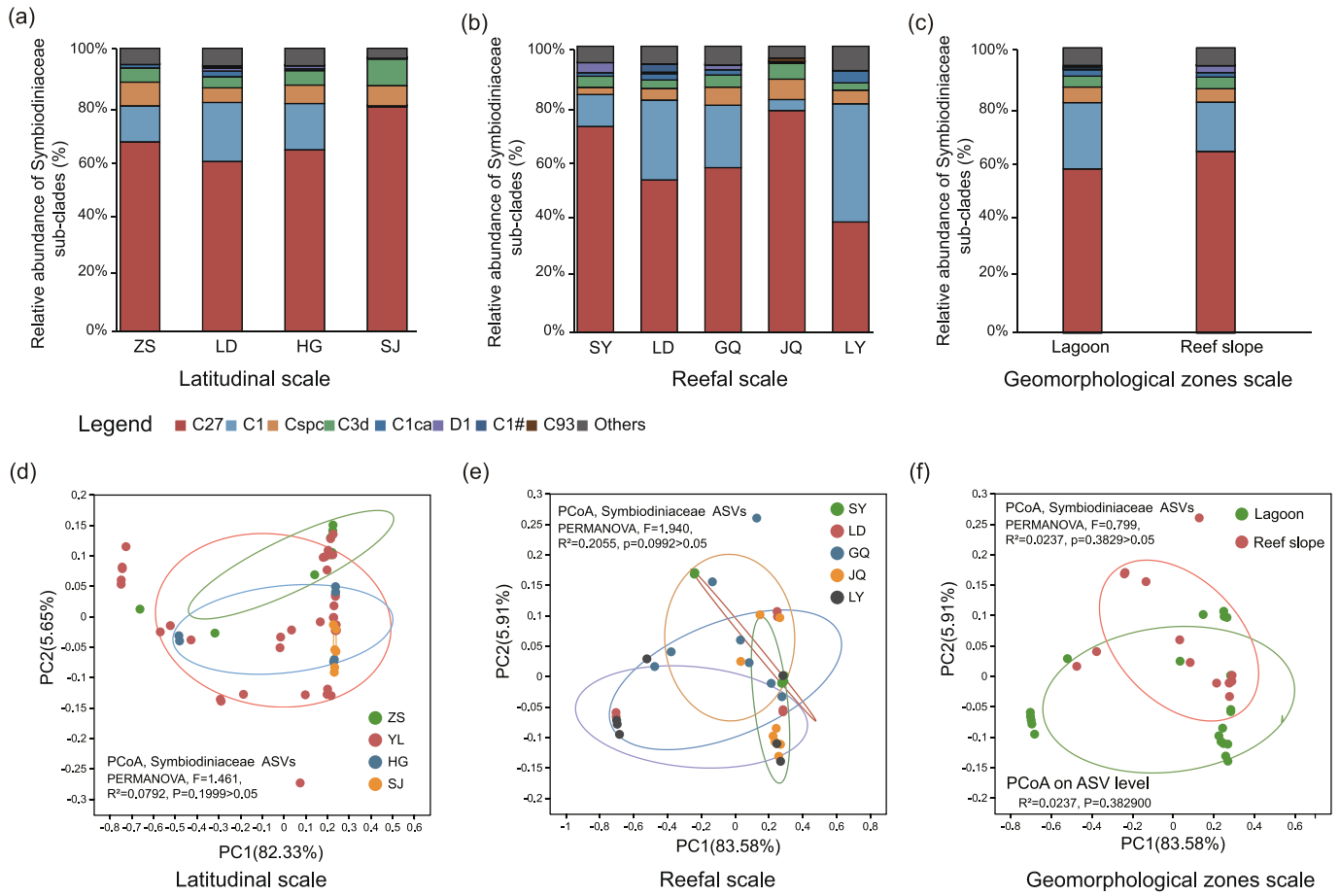


Fig. 3. Symbiodiniaceae community composition and structure of *Lithophyllon scabra* at multiple spatial scales of the South China Sea (SCS). (a-c) Community composition of Symbiodiniaceae in *L. scabra* at the sub-clade level across latitudinal, reef, and geomorphological zone scales in the SCS. (d-f) Principal Coordinates Analysis (PCoA) of Bray-Curtis distances for ASVs of *L. scabra* across latitudinal, reef, and geomorphological zones in the SCS. Ellipses represent significant differences in Symbiodiniaceae community structure of *L. scabra* across multiple spatial scales, as determined by Permutational Multivariate Analysis of Variance (PERMANOVA).

greater than that in the lagoon (Fig. 7d), which was also higher than that in the latitudinal and reef scales. However, the migration rate of the Symbiodiniaceae community of *L. scabra* was relatively low across all spatial scales, indicating that the Symbiodiniaceae communities were influenced by restricted dispersal. The NST analysis suggested that the community assembly of Symbiodiniaceae in *L. scabra* was mainly dominated by deterministic processes at the latitudinal scale, with the NST of the Symbiodiniaceae community in SJ (5.3±0.9%) being significantly lower than that in other islands or reefs at higher latitudes (ZS: 36.7±22.1%; YL: 51.8±7.9%; HG: 31.7±14.4%; FDR, $p < 0.001$). Additionally, the community assembly process of Symbiodiniaceae in *L. scabra* showed heterogeneity at the reef scale. It was dominated by stochastic processes in GQ (80.6±15.3%) and SY (58.7±22.9%), while the deterministic process contributed more to the assembly of Symbiodiniaceae communities in LD (10.3±4.2%), JQ (27.1±8.0%), and LY (37.9±20.7%; FDR, $p < 0.001$). It is worth noting that the NST value of Symbiodiniaceae community assembly in the reef slope was significantly higher than that in the lagoon (FDR, $p < 0.001$). Stochastic processes dominated the assembly of the Symbiodiniaceae community in the reef slope (71.1±15.8%), while deterministic processes dominated in the lagoon (29.9±6.0%).

In addition, the bacterial community assembly pattern of *L. scabra* did not fit the NCM across all spatial scales, as the goodness-of-fit values for the bacterial community were less than 50% (latitudinal scale: 0.0689; reefal scale: 0.2019; lagoon: 0.0822; reef slope: 0.4860; Fig. 7e-f). Therefore, the bacterial community assembly of *L. scabra* was almost completely controlled by deterministic processes across latitudes, reefs, and geomorphological zones, which differs from the Symbiodiniaceae community assembly process.

3.4. *Effects of environmental factors on the microbial communities in multi-scale environment*

In the latitudinal scale, the Symbiodiniaceae community of *L. scabra* in ZS, HG, and SJ was influenced by environmental factors (Fig. 8a). The relative abundance of Symbiodiniaceae ASVs in ZS, with higher latitudes, was positively correlated with higher levels of NH_4^+, SiO_3^{2-}, and pH, but negatively correlated with salinity. However, the relative abundance of Symbiodiniaceae ASVs in SJ, with lower latitudes, showed a positive correlation with salinity and a negative correlation with higher levels of NH_4^+, SiO_3^{2-}, and pH. The relative abundance of Symbiodiniaceae ASVs in HG, at intermediate latitudes, was primarily positively correlated with higher temperature and turbidity, but negatively correlated with lower DO. For the bacterial community of *L. scabra*, the relative abundance of bacterial ASVs in ZS, HG, and SJ was also positively correlated with higher levels of SiO_3^{2-}, turbidity, and pH, and negatively correlated with salinity (Fig. 8b). It is worth noting that the correlations between the community structure of Symbiodiniaceae and bacteria and environmental factors were weak in YL. VPA was used to further assess the contribution of climate (SST and salinity), local factors (turbidity, pH, DO), and nutrients (SiO_3^{2-}, PO_4^{3-}, NH_4^+, NO_2^-, and NO_3^-) to the Symbiodiniaceae and bacterial community structures

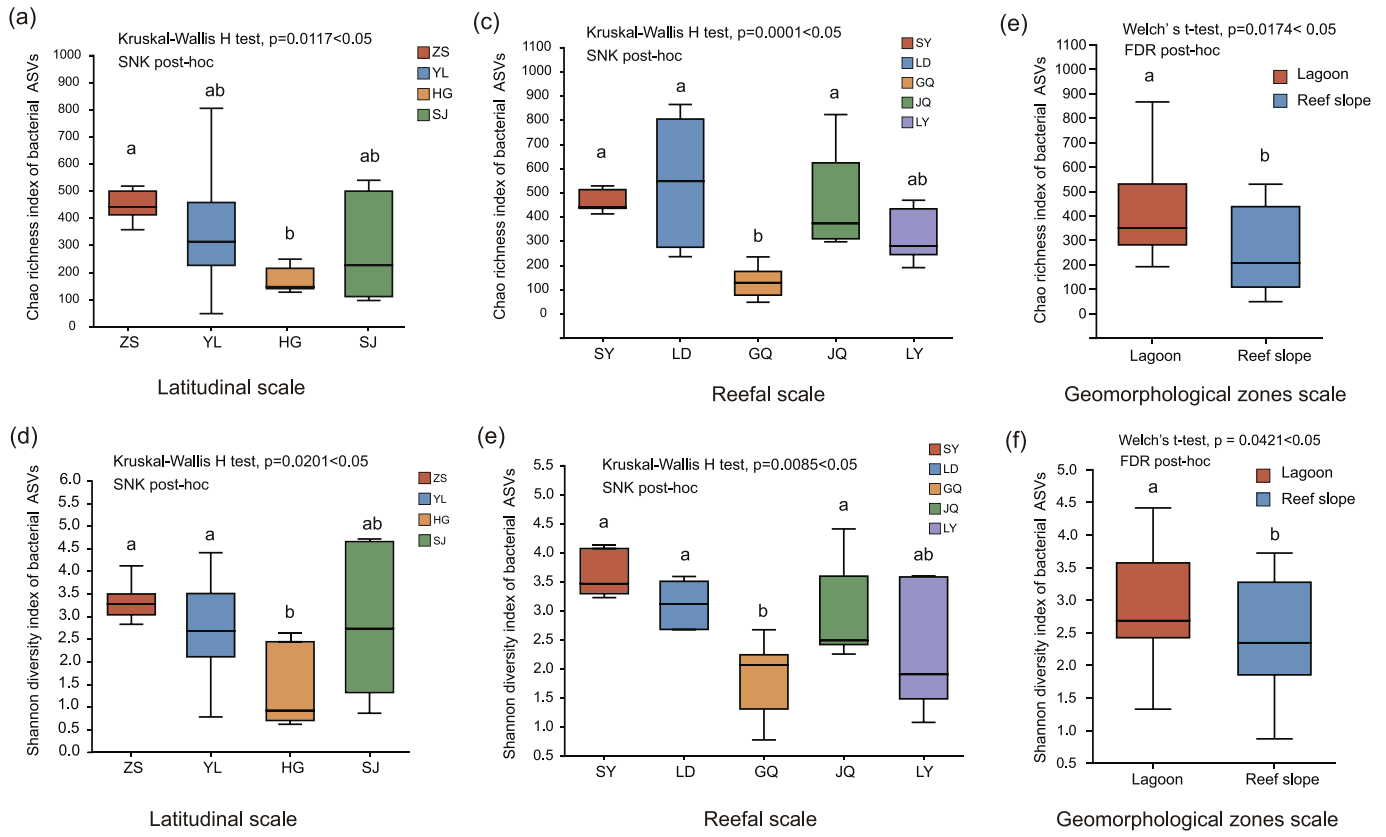


Fig. 4. The α diversity of bacterial communities of *Lithophyllon scabra* at ASV level at multiple spatial scales in the South China Sea (SCS). (a-c) Chao richness index of bacterial communities in *L. scabra* across latitudes, reefs, and geomorphological zones in the SCS; (d-f) Shannon diversity index of bacterial communities in *L. scabra* among latitudes, reefs and geomorphological zones in the SCS.

(Fig. 8a-b). The independent effect of nutrient factors contributed the highest percentage of variation (14.56%) to the Symbiodiniaceae community structure of *L. scabra* across latitudes (Fig. 8a), and the bacterial community variation of *L. scabra* was also shaped by the independent effects of climate (14.62%), local factors (15.42%), and nutrients (8.98%; Fig. 8b).

At the reef scale, the Symbiodiniaceae and bacterial communities of *L. scabra* were primarily influenced by temperature, DO, pH, and salinity, which are climate and local factors (Fig. 8c-d). The relative abundance of Symbiodiniaceae ASVs in JQ was mainly positively correlated with high salinity, but negatively correlated with temperature (Fig. 8c). Meanwhile, the Symbiodiniaceae community in LD and SY was positively correlated with low DO and pH. In addition, the relative abundance of bacterial ASVs of *L. scabra* in GQ and LD was positively correlated with temperature (Fig. 8d). However, the bacterial community in GQ showed negative associations with salinity, pH, and DO, while those in LD were positively correlated with these environmental factors. Moreover, the results of VPA suggest that the independent effect of climate contributed the highest level of variation in the Symbiodiniaceae community of *L. scabra* at the reef scale, explaining 14.52% of the community shift (Fig. 8c). Although the combined effect of climate and local factors explained 16.03% of the bacterial community variation of *L. scabra* at the reef scale, the independent effects of climate and local factors contributed 19.46% and 19.47% to bacterial community changes, respectively (Fig. 8d).

At the geomorphological scale, the results of the Mantel test showed no significant associations between environmental factors and the Symbiodiniaceae community (Fig. 8e). The Symbiodiniaceae communities in the lagoon had a weak positive association with climatic (temperature: Mantel'r = 0.0397, p = 0.239 > 0.05; salinity: Mantel'r = 0.0400, p = 0.223 < 0.05) and local factors (pH: Mantel'r = 0.0967, p = 0.094 > 0.05; DO: Mantel'r = 0.0598, p = 0.162 > 0.05), while the communities in the reef slope showed a weak negative correlation with climatic (temperature: Mantel'r = -0.0386, p = 0.570 > 0.05; salinity: Mantel'r = -0.0385, p = 0.564 > 0.05) and local factors (pH: Mantel'r = -0.0387, p = 0.489 > 0.05; DO: Mantel'r = -0.0405, p = 0.577 > 0.05). However, these potential correlations were not significant. The results of AVD analysis also showed that the variation and stability of the Symbiodiniaceae community of *L. scabra* in the lagoon (AVD: 0.540) were similar to those in the reef slope (AVD: 0.542; Fig. 8e). However, the bacterial community of *L. scabra* showed a significantly positive correlation with climatic (temperature: Mantel'r = 0.4565, p = 0.002 < 0.05; salinity: Mantel'r = 0.5514, p = 0.001 < 0.05) and local factors (pH: Mantel'r = 0.2720, p = 0.009 < 0.05; DO: Mantel'r = 0.2180, p = 0.011 < 0.05) in the lagoon (Fig. 8f). It is worth noting that the bacterial communities of *L. scabra* also had a significantly positive association with climatic (temperature: Mantel'r = 0.7693, p = 0.001 < 0.05; salinity: Mantel'r = 0.7655, p = 0.002 < 0.05) and local factors (pH: Mantel'r = 0.7470, p = 0.001 < 0.05; DO: Mantel'r = 0.2180, p = 0.011 < 0.05) in the reef slope. The AVD value of the bacterial community of *L. scabra* in the reef slope (AVD: 0.585) was higher than that in the lagoon (AVD: 0.491; Fig. 8f).

3.5. Functional profile prediction of bacterial communities in multiple spatial-scale

The results of the FAPROTAX analysis showed that the top 10 functional profiles in terms of abundance are associated with the nutrient pattern and nitrogen metabolism of the bacterial community in *L. scabra* (Fig. 9a). However, there were no significant differences or variations in the functional profiles of the bacterial community of *L. scabra* among latitudes (Kruskal-Wallis H test, p > 0.05). It is worth

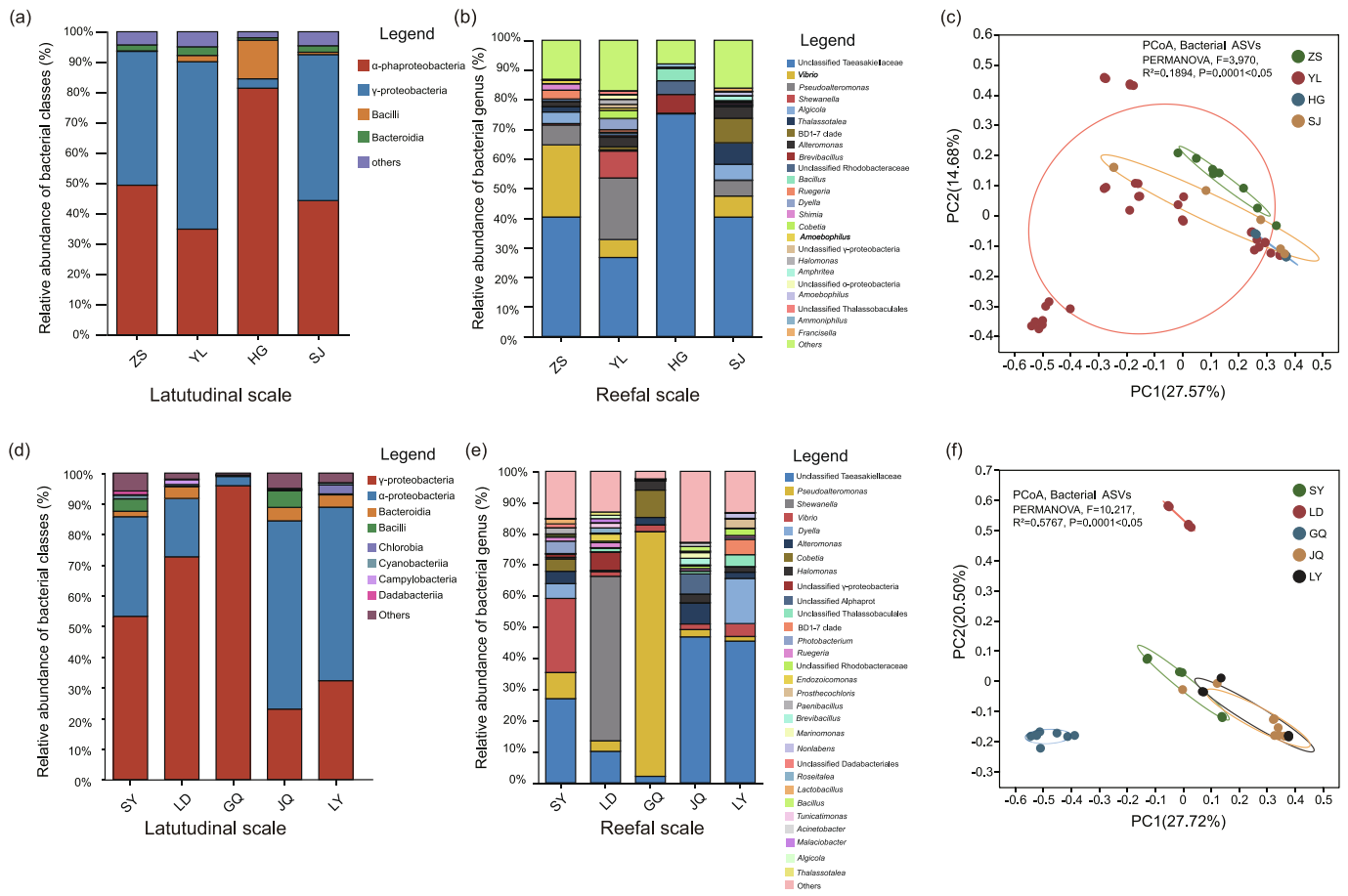


Fig. 5. The bacterial community composition and structure of *Lithophyllon scabra* at latitudinal and reefal scales in the South China Sea (SCS). The bacterial community composition associated with *L. scabra* at (a) the class and (b) genus levels at latitudinal scales in the SCS. (c) Principal Coordinates Analysis (PCoA) of Bray-Curtis distances of bacterial ASV composition in *L. scabra* at latitudinal scales. Ellipses represent significant differences in bacterial ASV communities among Zhaoshu Island (ZS), Yongle Atoll (YL), Huaguang Reef (HG), and Sanjiao Reef (SJ), as determined by Permutational Multivariate Analysis of Variance (PERMANOVA). (d-e) Bacterial community composition at (d) the class and (e) genus levels of *L. scabra* at reefal scales in the SCS. (f) PCoA of Bray-Curtis distances of bacterial ASV communities in *L. scabra* across five reefs in the SCS. Ellipses denote significant differences in bacterial ASV communities among Shiyu (SY), Longdong Point Reef (LD), Ganquan Island (GQ), Jinqing Island (JQ), and Lingyang Reef (LY), based on PERMANOVA.

noting that there were significant differences in the potential ecological functions of the bacterial community of *L. scabra* within YL among reefs (Fig. 9b). The relative abundance of chemoheterotrophy (Kruskal-Wallis H test, $p < 0.001$) and aerobic chemoheterotrophy (Kruskal-Wallis H test, $p < 0.001$) in the bacterial community of *L. scabra* in GQ was higher than in the other reefs, while phototrophy (Kruskal-Wallis H test, $p < 0.001$), photoautotrophy (Kruskal-Wallis H test, $p < 0.001$), anoxygenic photoautotrophy (Kruskal-Wallis H test, $p = 0.002 < 0.05$), anoxygenic photoautotrophy S oxidizing (Kruskal-Wallis H test, $p = 0.039 < 0.05$), cyanobacteria (Kruskal-Wallis H test, $p = 0.003 < 0.05$), and oxygenic photoautotrophy (Kruskal-Wallis H test, $p = 0.003 < 0.05$) in the bacterial community of *L. scabra* from LY had higher relative abundance. In addition, the nitrogen metabolism (Kruskal-Wallis H test, $p < 0.001$) and nitrate respiration (Kruskal-Wallis H test, $p < 0.001$) of the bacterial community of *L. scabra* in LD were stronger than in SY, GQ, JQ, and LY. Therefore, the nutrient pattern and nitrogen metabolism of the bacterial community in *L. scabra* exhibited spatial heterogeneity at the reef scale.

Interestingly, the relative abundance of functional profiles related to chemoheterotrophy (FDR, $p = 0.002 < 0.05$) and aerobic chemoheterotrophy (FDR, $p = 0.001 < 0.05$) showed an enrichment pattern in the *L. scabra*-associated bacterial community in the reef slope, which was significantly higher than in the lagoon at the geomorphological scale (Fig. 9c). However, the relative abundance of phototrophy (Wilcoxon rank-sum test, $p = 0.004 < 0.05$), photoautotrophy (Wilcoxon rank-sum test, $p = 0.006 < 0.05$), anoxygenic photoautotrophy (Wilcoxon rank-sum test, $p = 0.005 < 0.05$), anoxygenic photoautotrophy S oxidizing (Wilcoxon rank-sum test, $p = 0.019 < 0.05$), cyanobacteria (Wilcoxon rank-sum test, $p = 0.021 < 0.05$), and oxygenic photoautotrophy (Wilcoxon rank-sum test, $p = 0.0208 < 0.05$) in the bacterial community of *L. scabra* in the lagoon were significantly higher than those in the reef slope. Therefore, there were clear differences in the nutrient patterns of the bacterial community of *L. scabra* between the reef slope and lagoon. The nutrient pattern of the bacterial community of *L. scabra* in the reef slope was dominated by chemoheterotrophy, whereas the bacterial community of *L. scabra* in the lagoon was controlled by photoautotrophy. Additionally, the relative abundance of nitrogen metabolism (Wilcoxon rank-sum test, $p < 0.01$) and nitrate respiration (Wilcoxon rank-sum test, $p < 0.01$) functional profiles in the bacterial community of *L. scabra* in the lagoon was significantly higher than in the reef slope.

4. Discussion

4.1. Multi-scale environmental response pattern of L. cabra-associated Symbiodiniaceae was regulated by specific symbiosis

The results of the α diversity indices showed no significant differences in Chao richness and Shannon diversity in the Symbiodiniaceae communities of *L. scabra* across latitudes, reefs, and geomorphological zones (Fig. 2a-c). Additionally, the community structure of

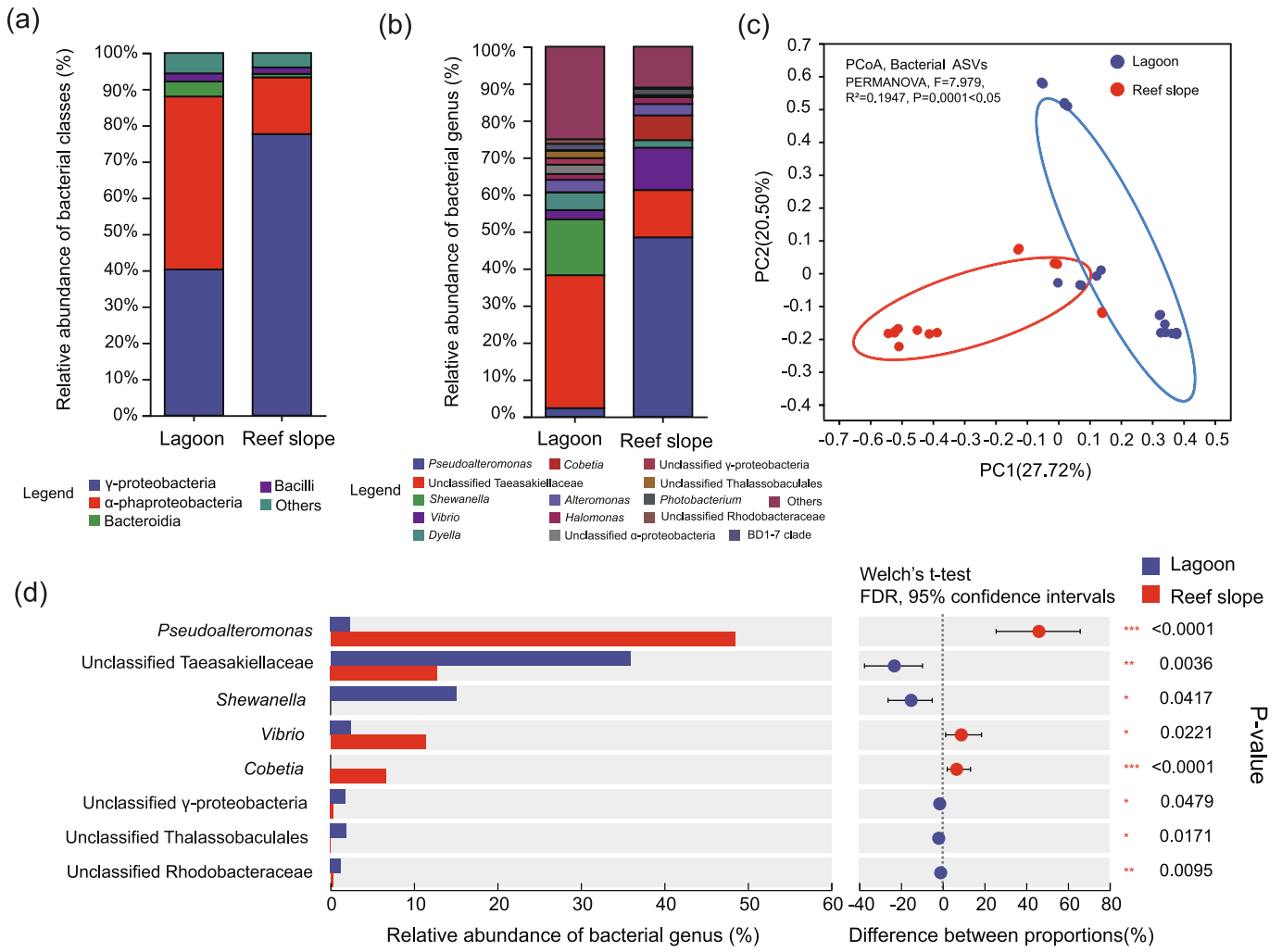


Fig. 6. The bacterial community composition, structure and enrichment characteristics of *Lithophyllon scabra* between geomorphological zones in the South China Sea. The bacterial community composition associated with *L. scabra* at (a) the class and (b) genus levels between reef slope and lagoon in the SCS. (c) Principal Coordinates Analysis (PCoA) of Bray-Curtis distances of bacterial ASV communities in L. scabra between reef slope and lagoon in the SCS. (d) Enrichment characteristics of bacterial genera between reef slope and lagoon in the SCS.

Symbiodiniaceae in *L. scabra* exhibited no significant variation across multiple spatial scales (Fig. 3d-f). However, the Symbiodiniaceae communities in *L. scabra* were predominantly dominated by the C27 subclade across distinct latitudes, reefs, and geomorphological zones. This finding suggests that the *L. scabra* holobiont responds to multi-scale environmental variation by establishing a specific symbiosis with the C27 sub-clade, which does not rely on shifts in the overall Symbiodiniaceae community composition. Previous studies have recognized shifts in Symbiodiniaceae communities, including shuffling and switching, as essential adaptive strategies that enable corals to respond to climate and environmental changes across spatial scales, thereby enhancing their stress tolerance and resilience. (Apprill and Gates, 2007; Berkelmans and van Oppen, 2006; Cunning et al., 2015; Ladner et al., 2012; Quigley et al., 2022). For instance, in the northern Red Sea, the Symbiodiniaceae community of *Pocillopora damicornis* shifted from being dominated by the A1, A1c, and C1h sub-clades in high latitudes to being dominated by the A1 variant in intermediate latitudes, a pattern closely linked to thermal response and acclimation in latitudinal gradients (Osman et al., 2020). A comparable shift in symbiont composition has been documented in the SCS, where coral communities and reef assemblages at higher latitudes are predominantly associated with the C1 subclade. In contrast, reefs at intermediate and lower latitudes exhibit an increased relative abundance of stress-tolerant symbiont types (e.g., C15, D1, and C3u), likely reflecting coral adaptive responses to environmental variability (Chen et al., 2019; Chen et al., 2021). In addition, in the Andaman Sea and Zanzibar in the Indian Ocean, the Symbiodiniaceae communities of seven coral genera with horizontal transmission of symbionts shifted from being dominated by C3u in offshore regions to D1-4 inshore, where higher turbidity is found (Lajeunesse et al., 2010). However, the reconstruction and shift of Symbiodiniaceae community composition in coral holobionts seem opportunistic and unreliable across multiple spatial scales. Symbiont switching in coral holobionts has been shown to be limited by Symbiodiniaceae transmission patterns and repeated bleaching events (Boulotte et al., 2016). Evidence from 1,643 symbiont communities of corals across approximately 900 kilometers of the GBR indicates that although Symbiodiniaceae community turnover and redistribution occurred after the 2016 mass bleaching event, the increase in diversity and abundance of heat-tolerant symbionts was only observed in certain environments and coral species across latitudinal scales (Quigley et al., 2022). Moreover, the inheritance of changed Symbiodiniaceae community composition in corals is rare (Quigley et al., 2018; Voolstra et al., 2021), occurring only in cases of strong specificity (Howells et al., 2020; Hume et al., 2020; Lajeunesse et al., 2018). Thus, while shifts in Symbiodiniaceae community composition may enhance the environmental resilience and acclimation capacity of the parental coral generation, this

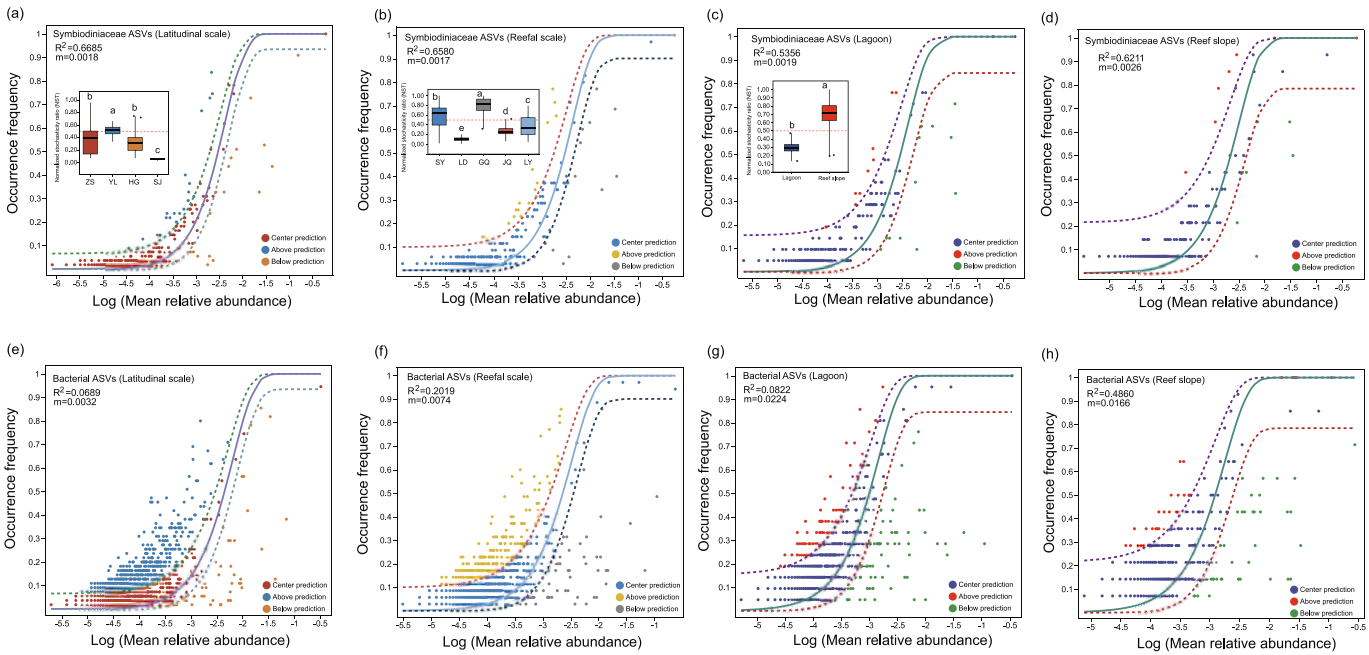


Fig. 7. Fit of the neutral community model (NCM) of Symbiodiniaceae and bacteria community assembly of *Lithophyllon scabra* in multiple spatial scales in the South China Sea. The predicted occurrence frequencies for Symbiodiniaceae communities of *L. scabra* at (a) latitudinal scale, (b) reef scale, (c) lagoon and (d) reef slope. The predicted occurrence frequencies of *L. scabra*-associated bacterial communities at (e) latitudes, (f) reefs, (g) lagoon habitat and (h) reef slope habitat. The green lines represent the best fit to the NCM, while the deep blue and red lines indicate the 95% confidence intervals for model predictions. ASVs of Symbiodiniaceae and bacteria that occur more or less frequently than predicted by the NCM are shown in red and green, respectively. The variable m denotes the community size multiplied by the immigration rate of Symbiodiniaceae and bacteria in *L. scabra*, and R^2 represents the goodness of fit to the NCM.

strategy remains limited in ensuring the long-term adaptive potential of their offspring. However, for *L. scabra*, establishing a specific symbiosis with the stress-tolerant C27 sub-clade could be an effective and stable strategy for responding to multi-scale environmental changes, avoiding the negative consequences of non-heritable shifts in Symbiodiniaceae communities. It has been shown that *L. scabra* diverged relatively recently in the Fungiidae family (81.73 Ma; Wei et al., 2024), and its close relatives have maintained stable, specific symbioses with the C27 sub-clade across various habitats with distinct environmental stresses (e.g., long-term high temperatures and high coral bleaching risk; Chen et al., 2024; Wei et al., 2024). Qin et al. (2021) also reported a strongly stable, specific symbiosis between a close relative of *L. scabra* and the C27 sub-clade across reef slopes and lagoons in the Panshiyu of the Xisha Islands, following the global coral bleaching event. Notably, the C27 sub-clade is closely related to the C3 sub-clade, which is a living ancestor of *Cladocopium* and exhibits greater adaptability to high SST, photosynthetically active radiation (PAR), and salinity (Chen et al., 2019; Lajeunesse, 2005). Therefore, the specific symbiosis between *L. scabra* and the C27 sub-clade represents an ecologically robust strategy for responding to multi-scale environmental stress in the context of climate change. This pattern has also been observed in other coral species, such as *Galaxea fascicularis* with *Durusdinium trenchii* (Chen et al., 2020), *Porites* with the C15 sub-clade (Chen et al., 2019; Chen et al., 2021; Lajeunesse et al., 2010; Osman et al., 2020), and *Stylophora* with the A1 sub-clade (Ziegler et al., 2017a), all of which exhibit lower bleaching susceptibility than other coral species.

Accordingly, *L. scabra* responds to multi-scale environmental stress by establishing a specific symbiosis with the potentially stress-tolerant C27 sub-clade, which represents a potentially useful and stable strategy for coral holobionts to adapt to climate change. Future research should focus on the distribution and abundance of the C27 sub-clade at the micro scale within individual coral holobionts, as these factors likely play a crucial role in shaping the ecological adaptability and resilience of coral-Symbiodiniaceae symbioses (Turnham et al., 2025; van Oppen and Raina, 2023). In addition, employing higher-resolution markers such as the chloroplast psbA^{ncr} or flanking sequences of microsatellite loci to resolve the roles of different Symbiodiniaceae species and genotypes within the C27 sub-clade in shaping coral-Symbiodiniaceae specificity and their multi-scale environmental response patterns would offer valuable insights into information of symbionts community variation and ecological process at micro scale within the coral holobiont (Hume et al., 2015; Hume et al., 2016; Reimer et al., 2017).

4.2. *Symbiodiniaceae dynamic in L. cabra was driven by rare taxa, environment variation and dispersal capacity*

There was a stable, specific symbiosis between *L. cabra* and the C27 sub-clade, but the results of community assembly were also influenced by both deterministic and stochastic processes (Fig. 7a-d). RDA and VPA indicated that the dynamics of the Symbiodiniaceae community were shaped by multiple environmental factors across latitudes, reefs, and geomorphological zones (Fig. 8a, c, e). These findings suggest that the variation in the Symbiodiniaceae community of *L. cabra* was primarily driven by sub-dominant Symbiodiniaceae sub-clades and a rare symbiont biosphere. It has been shown that these background symbionts play an important role in maintaining the stability of the Symbiodiniaceae community structure and in enhancing the resilience of coral-Symbiodiniaceae symbiosis (Boulotte et al., 2016; Lee et al., 2016; Wei et al., 2024; Ziegler et al., 2018). At low latitudes (SJ), the deterministic processes shaping the Symbiodiniaceae communities of *L. cabra* were more pronounced than those observed at intermediate latitudes within the SCS (Fig. 7a). This may be primarily driven by a decrease in nutrient concentration, particularly $NH4^+$. The independent effect of nutrients contributed the most to the variation in the Symbiodiniaceae community across latitudes (Fig. 8a). While high sea surface temperature (SST) and salinity are crucial in shaping coral-Symbiodiniaceae symbiosis at low latitudes (Chen et al., 2021; Claar et al., 2020; Hume et al., 2016), background symbiont communities in corals are also associated with low nutrient concentrations (Morris et al., 2019). Warm, eutrophic conditions promote Symbiodiniaceae to sequester more

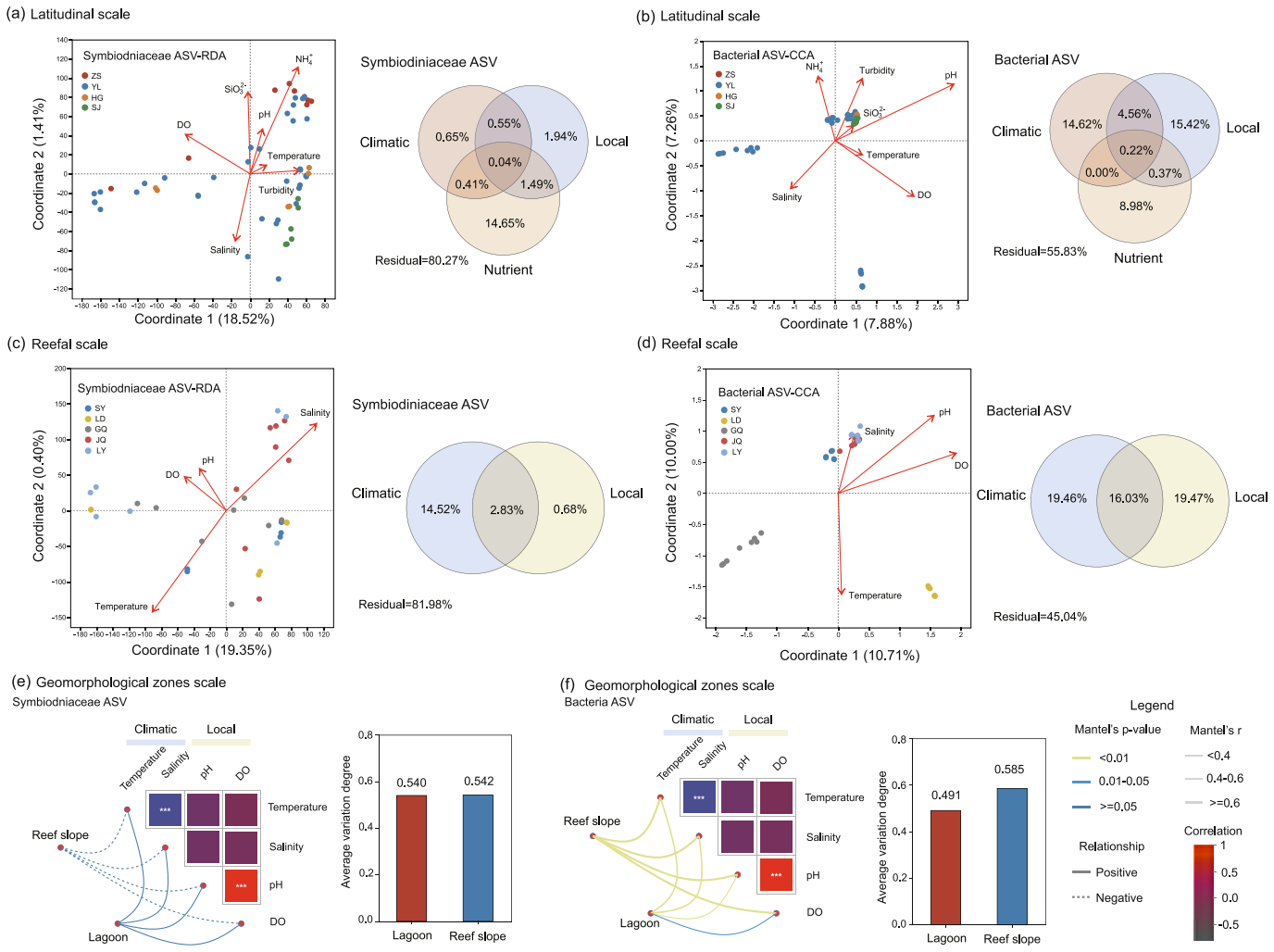


Fig. 8. Correlations between environmental factors and microbial community variation of *Lithophyllon scabra* in multiple spatial scales in the South China Sea. The Canonical Correspondence Analysis (CCA) and Redundancy Analysis (RDA) indicated that climatic, local, and nutrient factors influence the Symbiodiniaceae and bacterial communities of *L. scabra* at (a, b) latitudinal and (c, d) reefal scales in the SCS. Variation Partitioning Analysis (VPA) was used to assess the relative contributions of climatic, local, and nutrient variables to the variation in the Symbiodiniaceae and bacterial community structure. The metal-test heatmaps for (e) *Symbiodiniaceae* and (f) bacterial ASVs of *L. scabra* in relation to environmental factors. Edge width corresponds to Mantel's r statistic for the distance correlations, while edge color indicates statistical significance. Pairwise comparisons of environmental factors are shown, with a color gradient representing Pearson's correlation coefficient. The average variation degree of Symbiodiniaceae and bacterial communities of *L. scabra* between lagoon and reef slope zones is also shown.

resources and energy for growth (Marubini and Davies, 1996; Morris et al., 2019), which can lead to a shift from symbiotic to parasitic or opportunistic states (Baker et al., 2018; Lee et al., 2016). Therefore, a decrease in nutrient concentrations may play a crucial role in maintaining the stability of the *L. cabra*-C3u sub-clade symbiosis and the background symbiont community, driving deterministic processes in the assembly of the Symbiodiniaceae community across latitudes. In addition, at the reef scale, the Symbiodiniaceae communities of *L. cabra* in YL were predominantly controlled by stochastic processes, especially in reefs with strong hydrodynamic forces (Fig. 7b). It has been observed that GQ, located in the western part of YL, experiences stronger seawater exchange and tidal activity (Wang, 2001). SY, located in the northeastern water exchange channel of YL, has the highest average wave energy (0.9 kW/m) and wave direction frequency (20%) in the eastern and northeastern regions of YL (Qiu et al., 2024). These hydrological characteristics may influence the stochastic processes of Symbiodiniaceae community assembly, particularly dispersal and horizontal transmission. Approximately 75% of reef-building corals acquire their Symbiodiniaceae via horizontal transmission from the environment (Baird et al., 2009; Decelle et al., 2018), which is closely related to the homogenized or heterogeneous dispersal of Symbiodiniaceae. Nevertheless, climatic factor played an important role in the deterministic processes of Symbiodiniaceae assembly in LD, JQ and LY at the reefal scale. Moreover, the assembly of the Symbiodiniaceae community of *L. cabra* in lagoons was predominantly driven by deterministic processes, while stochastic processes dominated in the reef slope. In the lagoon, the variation in Symbiodiniaceae community structure was positively correlated with climatic and local factors (Fig. 8e), suggesting that high temperature, salinity, pH, and dissolved oxygen (DO) levels may shape the community variation and assembly of the Symbiodiniaceae community. In contrast, the stronger water exchange and weaker environmental filtration in the reef slope led to a dominance of stochastic processes in the assembly of the Symbiodiniaceae community. It has been found that the reef slope has the highest wave height (1.8 m) and energy (7.8 kW/m), whereas the wave height and energy in the lagoon are much lower (0.6 m and 0.7 kW/m, respectively) (Qiu et al., 2024). Additionally, the migration rate of the Symbiodiniaceae community in the reef slope ($m = 0.0026$) was higher than that in the lagoon ($m = 0.0019$; Fig. 7c-d). These suggestions may provide the bases for dispersal and stochastic assembly of Symbiodiniaceae community of *L. cabra* in reef slope.

Accordingly, the assembly process of the Symbiodiniaceae

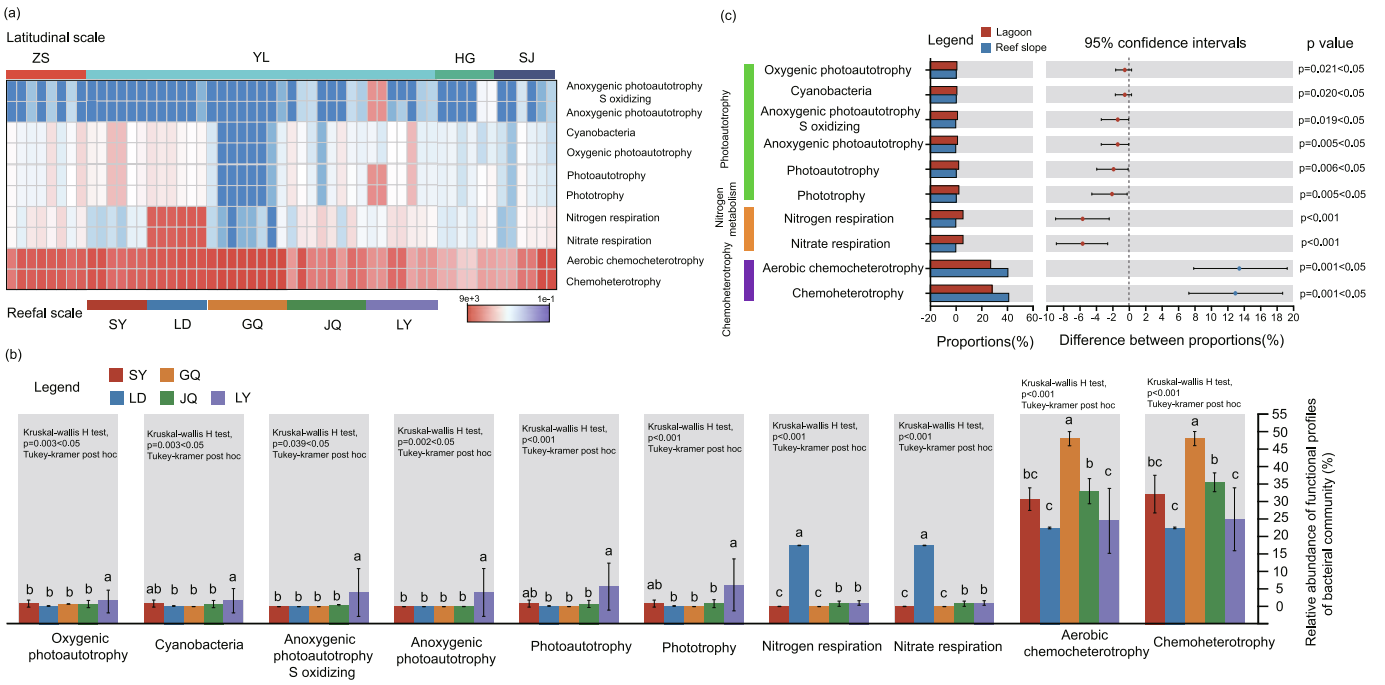


Fig. 9. The top 10 of predicted functional traits of bacterial communities of *Lithophyllon scabra* in multiple spatial scales in the South China Sea (SCS). The heatmap shows the top 10 bacterial functional traits of *L. scabra* at (a) latitudinal and reefal scales. Significant differences in chemoheterotrophy, nitrogen metabolism, and photoautotrophy were observed among *L. scabra*-associated bacterial communities across (b) five reefs and (c) two geomorphological zones (reef slope and lagoon) in the SCS.

community was influenced by background symbionts. The deterministic processes driving Symbiodiniaceae community assembly appeared to be closely associated with a decrease in nutrient concentrations across latitudinal scales, climatic factors at the reef scale, and high levels of temperature, salinity, pH, and DO in the lagoon. In contrast, the stochastic processes governing Symbiodiniaceae community assembly were likely regulated by water exchange levels and the dispersal of symbionts at multiple spatial scales. Therefore, this investigation lays the groundwork for establishing a comprehensive understanding of the relationship between Symbiodiniaceae community dynamics and ecological factors in later-diverging coral species. Nevertheless, future studies should elucidate the temporal dynamics and coral hosts interspecific differences of assembly process of Symbiodiniaceae community. Given that the assembly of Symbiodiniaceae communities is closely influenced by factors such as life history stage (Thornhill et al., 2017), the identity of symbiotic host species (Lin et al., 2024), and prevailing external environmental conditions (Li et al., 2025), it is imperative that these key ecological factors are explicitly considered in subsequent investigations.

4.3. Multi-scale environmental effect and response on bacterial community of L. scabra respective consist with "Pierre Cardin principle" and "Anna Karenina principle"

The bacterial community assembly process of *L. scabra* deviates from the neutral community model, indicating that the bacterial community is predominantly shaped by environmental filtration across multiple scales (Fig. 7e-h). The results of the VPA revealed that the independent effects of climatic, local, and nutrient factors explained a greater proportion of the variation in the *L. scabra* bacterial community compared to the combined effects of these environmental factors at the latitudinal scale (Fig. 8b-d). A similar trend was observed in the bacterial community of *L. scabra* at the reefal scale. These results indicated that the multi-scale environmental effect on bacterial community of *L.scabra* consist with "Pierre Cardin principle" (PCP; one plus one may not equal two, and the effect of ineffective combination stacking can even equal zero). It has been found that coral bacterial communities exhibit significant flexibility in response to environmental stress across both temporal and spatial scales (Chen et al., 2021; Mcdevitt-Irwin et al., 2017; Qin et al., 2021; van Oppen and Blackall, 2019). However, previous studies focus on the impact of single environmental stressors on coral-associated bacterial communities. For example, heat stress has been shown to drive shifts in coral-associated bacterial communities, transitioning from a dominance of beneficial bacteria (e.g., *Endozoicomonas*) to an increase in pathogenic (e.g., *Vibrio*) or opportunistic bacteria (e.g., *Rhodobacterales*) (Bourne et al., 2008; Tout et al., 2015; Mcdevitt-Irwin et al., 2017; Pootakham et al., 2019; Teeling et al., 2012; Welsh et al., 2016). Similarly, a decrease in seawater pH alters the bacterial community structure in *Acropora millepora*, reducing the relative abundance of beneficial *Endozoicomonas* by more than 50% in volcanic CO_2 seep areas (Morrow et al., 2015). Some studies have also addressed the combined effects of multiple stressors on coral-associated bacterial communities, highlighting that the influence of combined stressors is often stronger than that of individual factors (Zaneveld et al., 2016; Zhu et al., 2023). For instance, the combined effects of parrotfish predation and nutrient enrichment significantly increased the relative abundance of pathogenic Proteobacteria in *Porites*, a trend that was more pronounced than the effect of either stressor alone (Zaneveld et al., 2016). However, environmental factors are interconnected, influenced, and constrained by each other and may affect the environmental adaptations of coral holobionts in complex ways (Pendleton et al., 2016). The combined effect of external environmental stressors may reduce their overall impact on coral and their bacterial community, which is consistent with the PCP. It has been found that the combined effects of nutrients, predation, and temperature on bacterial community structure in *Pocillopora meandrina* were weaker than the impact of individual factors (Maher et al., 2019). Similarly, in *Pocillopora verrucosa* across tropical and biogeographical transition zones in the SCS, the independent effects of environmental factors (temperature, nutrients, and turbidity; 38.5%) explained more variation in bacterial community composition than the combined effects of environmental and geographical factors (latitude and longitude; 11.0%; Chen et al., 2021).

Thus, the environmental influences on the bacterial community of *L. scabra* align closely with the PCP across multiple scales. This suggests that the combined effects of climatic, nutrient, and local factors may mitigate the impact of individual environmental stressors on certain coral-bacteria symbioses in the context of climate change. These findings offer new insights into how multiple environmental stressors shape coral-bacteria symbioses and drive the succession of dominant coral species across various scales, particularly spanning ocean basins, climate zones, and latitudinal gradients (Brener-Raffalli et al., 2018; Chen et al., 2021; Galand et al., 2023; Osman et al., 2020), as well as at regional scales including islands, reefs, river deltas, upwelling zones, and marginal reefs (Hernandez-Agreda et al., 2016; Lima et al., 2020; Zhu et al., 2023). However, significant interspecific differences exist regarding the effects of multiple environmental stressors on the bacterial communities of coral holobionts (Hochart et al., 2023; Lan et al., 2025; Qin et al., 2020; Sessa et al., 2022). Therefore, the ecological applicability of PCP to the bacterial communities of different coral species, as well as its effectiveness under extreme climatic and local events, requires further investigation.

Interestingly, the bacterial community of *L.scabra* showed lower α and β diversity in HG than those in the other latitudinal regions (Fig. 4d, Fig. 5c). These results indicated the *L.scabra* in HG has greater bacterial community stability and environmental resistance. It has been found that the α and β diversity of coral holobiont bacterial communities generally increase under local and global stressors (Gantt et al., 2024; Mcdevitt-Irwin et al., 2017), which is associated with destabilized microbiota and immune responses of coral holobionts (van Oppen and Blackall, 2019). This increase in diversity is primarily driven by pathogenic and opportunistic bacteria, such as Flavobacteriales, Rhodobacterales and Alteromonadales (Gignoux-Wolfsohn and Vollmer, 2015; Mcdevitt-Irwin et al., 2017; van Oppen and Blackall, 2019). These bacteria have been identified under various environmental stress condition, including thermal stress (Bourne et al., 2008), ocean acidification (Meron et al., 2011; Morrow et al., 2012; Morrow et al., 2015), overfishing (Zaneveld et al., 2016), eutrophication (Jessen et al., 2013), and exposure to algal contact environments (Vega Thurber et al., 2012). Therefore, the environment response pattern of bacterial microbiota of coral holobiont consist with "Anna Karenina principle" (AKP) across diverse habitats (Mcdevitt-Irwin et al., 2017; Zaneveld et al., 2017). The *L. scabra* in HG showed low level of α and β diversity of bacteria community, and pathogenic *Vibrio* has not been identified (Fig. 5b), which suggest this there were weaker environmental stress, stronger bacterial community stability and resistance on *L.scabra* holobiont in HG. However, the variation of bacterial communities of *L.scabra* has spatial heterogeneity at latitudinal scales, because the change trend of the α and β diversity of bacterial community in *L.scabra* not associated with the shift of latitudes. In addition, at reefal scale, the bacterial community of *L. scabra* showed the lowest level of α, β diversity (Fig. 4e and Fig. 5f) and has the highest relative abundance of *Pseudoalteromonas* (78.58%; Fig. 5e) in GQ from YL. The bacterial community of *L.scabra* in GQ has negatively correlations with pH, DO and salinity (Fig. 7d). These results suggest that the *L. scabra* holobiont can acclimate to reef environments characterized by acidification, hypoxia, and hyposmolality by maintaining bacterial community stability and promoting the abundance of beneficial bacteria. The evidence from Hawaiian coral reefs has shown that short-term hyposalinity stress increases infections by *Vibrio coralliilyticus* and *Vibrio owensii*, pathogens responsible for white syndrome in corals (Shore-Maggio et al., 2018). Furthermore, hypoxia has been shown to alter bacterial community composition and increase the relative abundance of potential pathogens (e.g., *Halodesulfovibrio*, *Vibrio*) in coral reefs, which in turn leads to increased disease and mortality in coral holobionts (Doyle et al., 2022). Low pH environments are also known to result in the loss of beneficial symbionts in corals (Ge et al., 2021; Morrow et al., 2015; Webster et al., 2016). However, it has been found that *Pseudoalteromonas* has strong antimicrobial activity in coral holobiont (Kvennefors et al., 2012), and it's metabolites played important roles in algal removal, antifouling and biofilm activities of corals (Delgadillo-Ordoñez et al., 2024; Jessen et al., 2013; Shnit-Orland et al., 2012). Additionally, the bacterial community of *L.scabra* in GQ showed enrichment characteristics of aerobic chemocheterotrophy and chemoheterotrophy (Fig. 9b). Therefore, *L.scabra* in GQ may acclimate to acidification, hypoxia and hyposmolality by enhancing the abundance of beneficial *Pseudoalteromonas*, inhibiting the activity of potentially pathogenic bacteria and improving the heterotrophy intensity of bacterial community, thereby maintaining the stability of bacterial community. The environmental response pattern of *L.scabra*-associated bacterial community consist with AKP at reefal scale.

Accordingly, the environmental influence on the *L. scabra* bacterial community aligns with the PCP at both latitudinal and reefal scales, while the multi-scale stress response pattern of bacterial community adheres to AKP. However, the acclimatization and adaptive strategy of *L.scabra*-associated bacteria community exhibit spatial heterogeneity and flexibility across latitudes and reefs.

4.4. Bacterial nutritional shifts underlying L. scabra's habitat acclimation across geomorphological zones

The results of this study showed that the α diversity of the *L. scabra*-associated bacteria community in lagoon was higher than those in the reef slope (Fig. 4f), while the AVD variation of *L. scabra*-associated bacteria community exhibited the opposite trend between lagoon and reef slope (Fig. 7f). The bacterial community variation in *L. scabra* from reef slope was greater than that in lagoon, suggesting that *L. scabra* holobionts on the reef slope experience stronger environmental stress than those in the lagoon, in line with AKP (Mcdevitt-Irwin et al., 2017; Zaneveld et al., 2017). Previous studies have indicated that lagoons are less favorable for coral growth due to weaker seawater exchange (Burt et al., 2020; Guo et al., 2019; Qin et al., 2022), greater temperature fluctuations (Lima et al., 2020; Tkachenko, 2014; Tkachenko and Soong, 2017), and reduced pH and DO levels (Camp et al., 2017; Manzello et al., 2012). In addition, *L. scabra* and coral species from the Fungiidae family show a preference for reef slope habitats, a phenomenon observed in the Spermonde Islands, Indonesia (Hoeksema, 2012), and the northern Red Sea (Goffredo and Chadwick, 2000; Goffredo and Chadwick-Furman, 2003). However, members of Fungiidae family have exhibited remarkable adaptive capabilities and aggregation behavior in the lagoon of the SCS (Qin et al., 2021; Wei et al., 2022), and *L. scabra* is also well known for its thermal tolerance and bleaching resistance in the tropical SCS (Chen et al., 2024; Wei et al., 2024). These results suggest that lagoon habitats may be more adaptive for *L. scabra* holobionts in the SCS than reef slopes. Interestingly, the potentially beneficial Terasakiellaceae (35.92%) and *Shewanella* (15.11%) of *L. scabra* exhibited enrichment characteristic in the lagoon, which has closed associations with nitrogen metabolism processes in coral holobionts (He et al., 2021; Weiler et al., 2018). It has been found that members of Terasakiellaceae may become nitrogen-fixing agents that participate in nitrogen metabolism in coral holobiont under limited food supply conditions (Quintanilla et al., 2022; Weiler et al., 2018). In addition, *Shewanella* has capacity to denitrify nitrate or nitrite (Van Spanning et al., 2005), and a nearly complete nitrogen metabolism network has been identified in *Shewanella* within cnidarian (He et al., 2021). In oligotrophic coral reef ecosystems, nitrogen is often a limiting nutrient (Falkowski, 1997; Tyrrell, 1999), and the photosynthetic performance of Symbiodiniaceae is closely dependent on nitrogen availability (Cook and D'Elia, 1987; Mcauley, 1987; Radecker et al., 2015; Tyrrell, 1999). Thus, the enrichment of potentially beneficial bacteria with nitrogen metabolism capabilities likely facilitates *L. scabra* holobionts' occupation of broader ecological niches within lagoon habitats. The results of ecological functions prediction also showed that the relative abundance of nitrogen and nitrate respiration profiles in the bacterial community of *L. scabra* in the lagoon was higher than that in the reef slope (Fig. 9c), suggesting that the *L. scabra*–bacteria symbiosis in the lagoon exhibits stronger nitrogen

metabolism activity. However, the bacteria community of *L. scabra* showed the higher relative abundance of potentially pathogenic *Vibrio* (11.42%) and antimicrobial *Pseudoalteromonas* (48.48%) in reef slope than those in the lagoon (Fig. 6b and 6d). This evidence suggests that the stronger environmental stress on the reef slope increases the likelihood of pathogen infection and β diversity in the bacterial community of *L. scabra*. It has been found that *Vibrio* will increase more than 20-40% of relative abundance in coral holobiont in the environmental stress condition and bleaching event (Liu et al., 2016; Mcdevitt-Irwin et al., 2017; Rosenberg et al., 2009), and the expression of virulence factor-related genes significantly increases (Nelson et al., 2013; van Oppen and Blackall, 2019). Interestingly, the potentially beneficial and antibacterial *Pseudoalteromonas* dominated in the bacterial community of *L. scabra* in reef slope, which imply that *L. scabra* may inhibit the pathogenic *Vibrio* by increasing the relative abundance of beneficial *Pseudoalteromonas*. A similar strategy has been observed in other coral species; for example, *Vibrio fortis*, *Vibrio chagsiii*, and *Vibrio harveyi* dominate the bacterial community of *P. verrucosa* in a biogeographical transition zone, but this coral can increase the relative abundance of antimicrobial *Endozoicomonas* to suppress the activity of pathogenic *Vibrio* (Chen et al., 2021).

Notably, the bacterial community nutritional pattern of *L. scabra* shifted from photoautotrophy in the lagoon to chemoheterotrophy on the reef slope (Fig. 9c), suggesting that changes in the bacterial community's nutritional strategies play a crucial role in helping *L. scabra* acclimate to environmental stress variations across geomorphological zones. Previous studies have shown that photosynthetic bacteria, such as *Erythrobacter* sp. (29%), dominate the bacterial communities of six coral species in thermally stressed environments, such as at Wadi El Gemal (the warmest site in the southern Red Sea; Osman et al., 2020). The abundance of these bacteria increases with a decrease in the latitudinal gradient of the Red Sea (Osman et al., 2020). Additionally, Symbiodiniaceae provide 70-90% of energy requirement for coral respiration through solar energy utilization and photosynthesis (Davy et al., 2012), and photosynthetic autotrophic capacity of Symbiodiniaceae will be inhibited in the stress condition and bleaching event (Huang et al., 2011; Leal and Ferrier-Pages, 2016). However, the density and chlorophyll b content of photosynthetic bacteria, such as cyanobacteria, increase by 55% and 50%, respectively, and exhibit faster recovery compared to Symbiodiniaceae during the coral recovery phase after short-term heat stress (Liang et al., 2021). Therefore, it is inferred that the abundance of photoautotrophic functional profiles in the bacterial community of *L. scabra* may provide additional energy and photosynthates to the coral-Symbiodiniaceae symbiosis, thereby enhancing the adaptability and stability of both *L. scabra* and its associated microbiota in the lagoon. However, *L. scabra* holobiont faced stronger competition stress of light and habitat in reef slope that those in lagoon in the SCS, which may lead to the enrichment of chemoheterotrophy traits in the bacterial community of *L. scabra*. It has been observed that the average cover of turf algae and macroalgae on the reef slope was 28.4±3.46% and 12.2 ±2.89%, respectively, significantly higher than in the lagoon (turf: 10.7 ±4.69%; macroalgae: 5.3±5.3%) in the study area (Lei, 2024). Previously studies have been found that increases in turf algae and macroalgae cover lead to coral bleaching, mortality, and a decline in coral larval settlement (Haas et al., 2010; Hughes et al., 2007; Zaneveld et al., 2016). These flourishing algal communities compete with corals for space in already crowded reef habitats (Mccook et al., 2001) and reduce the photosynthetic efficiency and growth rate of coral holobionts by shading sunlight (Lirman, 2001; Titlyanov et al., 2007), exerting negative ecological effects on coral reef ecosystems (Adjeroud et al., 2018; Graham et al., 2015; Liao et al., 2021). Fungiidae prefer to live in the sheltered habitat in reef slope (depth< 20m), because there is low level of reef species competition, sedimentation rate and predation in this habitat (Goffredo and Chadwick, 2000; Sammarco, 1991). However, light limitation in these habitats reduces the photosynthesis of *L. scabra* and other Fungiidae species, requiring these corals to rely more on heterotrophy to meet their nutritional and energy demands for holobiont growth and survival. It has been found that heterotrophy is an crucial strategy for coral holobiont in environmental stress, which can assist coral to survival in thermal or disturbed habitats by compensating for the lack of energy supply for photosynthesis (Baumann et al., 2014; Hoogenboom et al., 2010; Palardy et al., 2008; Xu et al., 2021). Therefore, high abundance of chemoheterotrophy traits in bacterial community may played an important role in energy supply in heterotrophy pattern of *L. scabra* holobont in the reef slope with weaker light and stronger algae competition.

In summary, significant differences were observed in the dynamics and acclimation strategies of the *L. scabra* holobiont bacterial community between lagoon and reef slope habitats. In lagoons, *L. scabra* enriched nitrogen-metabolizing bacteria, thus expanding its ecological niche, whereas on reef slopes, the increased abundance of antibacterial bacteria likely suppressed pathogens. Additionally, the enrichment of photoautotrophic functions in the lagoon bacterial community may provide additional photosynthates, enhancing *L. scabra*'s adaptability. In contrast, the bacterial community on the reef slope exhibited higher heterotrophic activity, which likely supports *L. scabra* by supplying energy and nutrients in the face of low light and intense algal competition. These findings suggest that *L. scabra* may adapt to geomorphological variations by adjusting its bacterial community composition and nutritional strategies.

5. Conclusions

The *L. scabra* holobiont adapts to multi-scale environmental conditions by forming a specific symbiotic relationship with the C27 subclade. This partnership may help mitigate the negative impacts of opportunistic Symbiodiniaceae and the limited long-term adaptability of coral offspring during the reconstruction and transition of the Symbiodiniaceae community. In addition, The Symbiodiniaceae assembly process was influenced by background symbionts, with deterministic assembly closely linked to decreasing nutrient concentrations at a latitudinal scale. At the reef scale and across geomorphological zones, deterministic assembly is primarily driven by climatic factors and their interactions with local environmental conditions. However, the stochastic process of Symbiodiniaceae community was regulated by symbionts dispersal in multi-scale. Also, the bacterial community assembly of *L. scabra* was primarily governed by deterministic processes. At multiple scales, the independent effects of climatic, nutrient, and local factors outweighed their combined influence on bacterial community variation. This suggests that the multi-scale environmental effects on the *L. scabra*-associated bacterial community align with the PCP. Nevertheless, the multi-scale stress response pattern of the *L. scabra*-associated bacterial community aligns with the AKP model. The community's acclimatization and adaptive strategies demonstrate spatial heterogeneity and flexibility across different latitudes and reef environments. Moreover, according to the AKP, *L. scabra* holobionts on reef slopes experience greater environmental stress compared to those in lagoons, as evidenced by the higher AVD of their associated bacterial community. It was worth noting that the *L. scabra*-associated bacterial community displayed distinct dynamic patterns and response strategies between lagoon and reef slope habitats. In lagoons, the bacterial community was enriched with nitrogen-metabolizing bacteria and photoautotrophic functions, enhancing photosynthate supply and improving the holobiont's adaptability. In contrast, on reef slopes, the bacterial community exhibited a higher abundance of heterotrophic functions and antibacterial taxa, supporting *L. scabra* holobionts by providing additional nutrients and inhibiting pathogens under conditions of low light and intense algal competition. This study highlights the environmental impacts and response patterns of the *L. scabra* microbiome across multiple spatial scales, including latitudes, reefs, and geomorphological zones. These findings offer new insights into the microbial-ecological processes and adaptive strategies of later-diverging coral holobionts in

the face of climate change. Furthermore, a comprehensive understanding of the temporal and micro-scale dynamics of microbial communities associated with later-diverging corals is crucial for developing robust ecological models that predict coral holobiont responses to climate change.

Supplementary data to this article can be found online at https://doi.org/10.1016/j.ecoinf.2025.103244.

CRediT authorship contribution statement

Biao Chen: Writing – original draft, Visualization, Validation, Resources, Methodology, Data curation, Conceptualization. **Lin Liang:** Writing – review & editing, Visualization, Validation, Resources, Data curation. **Kefu Yu:** Writing – review & editing, Visualization, Resources, Project administration, Methodology, Funding acquisition, Conceptualization. **Yuxin Wei:** Validation, Methodology, Investigation. **Xinyue Liang:** Validation, Methodology, Investigation. **Zeming Bao:** Validation, Methodology, Investigation. **Zhiheng Liao:** Validation, Methodology, Investigation. **Xiaopeng Yu:** Resources, Methodology, Investigation. **Zhenjun Qin:** Resources, Methodology, Investigation. **Lijia Xu:** Supervision, Resources, Funding acquisition. **Yongzhi Wang:** Resources, Investigation. **Yaru Kang:** Writing – review & editing, Investigation.

Declaration of competing interest

The authors declare that they have no competing interests.

Acknowledgements

This work was supported by the National Natural Science Foundation of China [Nos. 42090041, 42306165 and 42030502]; the Guangxi Natural Science Foundation [No. 2024GXNSFBA010307]; the Central Public-Interest Scientific Institution Basal Research Fund [No. PM-zx703-202408-288]; Guangdong S&T programme [No. 2024B1212050012]; the Innovation Project of Guangxi Graduate Education [No. YCBZ2023032].

Data availability

The raw sequencing datasets of ITS2 and 16S rRNA amplicons have been deposited in the NCBI Sequence Read Archive (Symbiodiniaceae ITS2: PRJNA1063379; Bacterial 16S rDNA: PRJNA1063386). Quality control and filtering of the next-generation amplicon sequences were performed using the pipeline described by Callahan et al. (2016). A deduplicated Symbiodiniaceae ITS2 dataset and the local BLASTN workflow are provided in the Supplementary Materials as Dataset S1 and Code S1, respectively. The analysis of Symbiodiniaceae ITS2 and bacterial 16S rRNA ASVs was conducted following the methods detailed by Chen et al. (2019), Chen et al. (2023) and Chen et al. (2024).

Reference

Adjeroud, M., Kayal, M., Iborra-Cantonnet, C., Vercelloni, J., Bosserelle, P., Liao, V., et al., 2018. Recovery of coral assemblages despite acute and recurrent disturbances on a south central pacific reef. Sci. Rep. 8, 9680. https://doi.org/10.1038/s41598-018-27891-3.

Ainsworth, T.D., Krause, L., Bridge, T., Torda, G., Raina, J., Zakrzewski, M., et al., 2015. The coral core microbiome identifies rare bacterial taxa as ubiquitous endosymbionts. ISME J. 9 (10), 2261–2274. https://doi.org/10.1038/ismej.2015.39.

Alessi, C.A.L.H., 2024. Algal symbiont diversity in *Acropora muricata* from the extreme reef of Bouraké associated with resistance to coral bleaching. PLoS One 19 (2), e0296902. https://doi.org/10.1371/journal.pone.0296902.

Apprill, A.M., Gates, R.D., 2007. Recognizing diversity in coral symbiotic dinoflagellate communities. Mol. Ecol. 16 (6), 1127–1134. https://doi.org/10.1111/j.1365-294X.2006.03214.x.

Armstrong, E.J., Le-Hoang, J., Carradec, Q., Aury, J., Noel, B., Hume, B.C.C., et al., 2023. Host transcriptomic plasticity and photosymbiotic fidelity underpin *Pocillopora* acclimatization across thermal regimes in the Pacific Ocean. Nat. Commun. 14 (1), 3056. https://doi.org/10.1038/s41467-023-38610-6.

Baird, A.H., Guest, J.R., Willis, B.L., 2009. Systematic and biogeographical patterns in the reproductive biology of scleractinian corals. Annu. Rev. Ecol. Evol. Syst. 40, 551–571. https://doi.org/10.1146/annurev.ecolsys.110308.120220.

Baker, D.M., Freeman, C.J., Wong, J.C.Y., Fogel, M.L., Knowlton, N., 2018. Climate change promotes parasitism in a coral symbiosis. ISME J. 12 (3), 921–930. https://doi.org/10.1038/s41396-018-0046-8.

Baum, J.K., Claar, D.C., Tietjen, K.L., Magel, J.M.T., Maucieri, D.G., Cobb, K.M., et al., 2023. Transformation of coral communities subjected to an unprecedented heatwave is modulated by local disturbance. Sci. Adv. 9 (14), eabq5615. https://doi.org/10.1126/sciadv.abq5615.

Baumann, J., Grottoli, A.G., Hughes, A.D., Matsui, Y., 2014. Photoautotrophic and heterotrophic carbon in bleached and non-bleached coral lipid acquisition and storage. J. Exp. Mar. Biol. Ecol. 461, 469–478. https://doi.org/10.1016/j.jembe.2014.09.017.

Beger, M., Sommer, B., Harrison, P.L., Smith, S.D.A., Pandolfi, J.M., 2014. Conserving potential coral reef refuges at high latitudes. Divers. Distrib. 20 (3), 245–257. https://doi.org/10.1111/ddi.12140.

Berkelmans, R., van Oppen, M.J.H., 2006. The role of zooxanthellae in the thermal tolerance of corals: a 'nugget of hope' for coral reefs in an era of climate change. Proc. Biol. Sci. 273 (1599), 2305–2312. https://doi.org/10.1098/rspb.2006.3567.

Blackall, L.L., Wilson, B., van Oppen, M.J.H., 2015. Coral-the world's most diverse symbiotic ecosystem. Mol. Ecol. 24 (21), 5330–5347. https://doi.org/10.1111/mec.13400.

Bokulich, N.A., Kaehler, B.D., Rideout, J.R., Dillon, M., Bolyen, E., Knight, R., et al., 2018. Optimizing taxonomic classification of marker-gene amplicon sequences with QIIME 2's q2-feature-classifier plugin. Microbiome 6, 90. https://doi.org/10.1186/s40168-018-0470-z.

Bongaerts, P., Hoeksema, B.W., Hay, K.B., Hoegh-Guldberg, O., 2012. Mushroom corals overcome live burial through pulsed inflation. Coral Reefs 31 (2), 399. https://doi.org/10.1007/s00338-011-0862-z.

Boulotte, N.M., Dalton, S.J., Carroll, A.G., Harrison, P.L., Putnam, H.M., Peplow, L.M., et al., 2016. Exploring the *Symbiodinium* rare biosphere provides evidence for symbiont switching in reef-building corals. ISME J. 10 (11), 2693–2701. https://doi.org/10.1038/ismej.2016.54.

Bourne, D., Iida, Y., Uthicke, S., Smith-Keune, C., 2008. Changes in coral-associated microbial communities during a bleaching event. ISME J. 2 (4), 350–363. https://doi.org/10.1038/ismej.2007.112.

Bourne, D.G., Morrow, K.M., Webster, N.S., 2016. Insights into the coral microbiome: underpinning the health and resilience of reef ecosystems. Ann. Rev. Microbiol. 70 (1), 317–340. https://doi.org/10.1146/annurev-micro-102215-095440.

Brener-Raffalli, K., Clerissi, C., Vidal-Dupiol, J., Adjeroud, M., Bonhomme, F., Pratlong, M., et al., 2018. Thermal regime and host clade, rather than geography, drive *Symbiodinium* and bacterial assemblages in the scleractinian coral *Pocillopora damicornis sensu lato*. Microbiome 6, 39. https://doi.org/10.1186/s40168-018-0423-6.

Bruno, J.F., Selig, E.R., 2007. Regional decline of coral cover in the Indo-Pacific: timing, extent, and subregional comparisons. PLoS One 2 (8), e711. https://doi.org/10.1371/journal.pone.0000711.

Burns, A.R., Stephens, W.Z., Stagaman, K., Wong, S., Rawls, J.F., Guillemin, K., et al., 2016. Contribution of neutral processes to the assembly of gut microbial communities in the zebrafish over host development. ISME J. 10 (3), 655–664. https://doi.org/10.1038/ismej.2015.142.

Burt, J.A., Camp, E.F., Enochs, I.C., Johansen, J.L., Morgan, K.M., Riegl, B., et al., 2020. Insights from extreme coral reefs in a changing world. Coral Reefs 39 (3), 495–507. https://doi.org/10.1007/s00338-020-01966-y.

Callahan, B.J., Mcmurdie, P.J., Rosen, M.J., Han, A.W., Johnson, A.J.A., Holmes, S.P., 2016. DADA2: High-resolution sample inference from Illumina amplicon data. Nat. Methods 13 (7), 581–583. https://doi.org/10.1038/nmeth.3869.

Camp, E.F., Nitschke, M.R., Rodolfo-Metalpa, R., Houlbreque, F., Gardner, S.G., Smith, D. J., et al., 2017. Reef-building corals thrive within hot-acidified and deoxygenated waters. Sci. Rep. 7, 2434. https://doi.org/10.1038/s41598-017-02383-y.

Caporaso, J.G., Kuczynski, J., Stombaugh, J., Bittinger, K., Bushman, F.D., Costello, E.K., et al., 2010. QIIME allows analysis of high-throughput community sequencing data. Nat. Methods 7 (5), 335–336. https://doi.org/10.1038/nmeth.f.303.

Chankong, A., Kongjandtre, N., Senanan, W., Manthachitra, V., 2020. Community composition of Symbiodiniaceae among four scleractinian corals in the eastern Gulf of Thailand. Reg. Stud. Mar. Sci. 33, 100918. https://doi.org/10.1016/j.rsma.2019.100918.

Chen, B., Yu, K., Liang, J., Huang, W., Wang, G., Su, H., et al., 2019. Latitudinal variation in the molecular diversity and community composition of Symbiodiniaceae in coral from the South China Sea. Front. Microbiol. 10, 1278. https://doi.org/10.3389/fmicb.2019.01278.

Chen, B., Yu, K., Qin, Z., Liang, J., Wang, G., Huang, X., et al., 2020. Dispersal, genetic variation, and symbiont interaction network of heat-tolerant endosymbiont *Durusdinium trenchii* : Insights into the adaptive potential of coral to climate change. Sci. Total Environ. 723, 138026. https://doi.org/10.1016/j.scitotenv.2020.138026.

Chen, B., Yu, K., Liao, Z., Yu, X., Qin, Z., Liang, J., et al., 2021. Microbiome community and complexity indicate environmental gradient acclimatisation and potential microbial interaction of endemic coral holobionts in the South China Sea. Sci. Total Environ. 765, 142690. https://doi.org/10.1016/j.scitotenv.2020.142690.

Chen, B., Yu, K., Fu, L., Wei, Y., Liang, J., Liao, Z., et al., 2023. The diversity, community dynamics, and interactions of the microbiome in the world's deepest blue hole: insights into extreme environmental response patterns and tolerance of marine

microorganisms. Microbiol. Spectr. 11, e0053123. https://doi.org/10.1128/spectrum.00531-23.
Chen, B., Wei, Y., Yu, K., Liang, Y., Yu, X., Liao, Z., et al., 2024. The microbiome dynamics and interaction of endosymbiotic Symbiodiniaceae and fungi are associated with thermal bleaching susceptibility of coral holobionts. Appl. Environ. Microbiol. 90 (4). https://doi.org/10.1128/aem.01939-23 e01939-23.
Claar, D.C., Starko, S., Tietjen, K.L., Epstein, H.E., Cunning, R., Cobb, K.M., et al., 2020. Dynamic symbioses reveal pathways to coral survival through prolonged heatwaves. Nat. Commun. 11 (1), 6097. https://doi.org/10.1038/s41467-020-19169-y.
Coleman, A.W., Suarez, A., Goff, L.J., 1994. Molecular delineation of species and syngens in Volvocacean green algae (Chlorophyta) 1. J. Phycol. 30 (1), 80–90. https://doi.org/10.1111/j.0022-3646.1994.00080.x.
Cook, C.B., D'Elia, C.F., 1987. Are natural populations of zooxanthellae ever nutrient-limited? Symbiosis 4, 199–211.
Cunning, R., Vaughan, N., Gillette, P., Capo, T.R., Mate, J.L., Baker, A.C., 2015. Dynamic regulation of partner abundance mediates response of reef coral symbioses to environmental change. Ecology 96 (5), 1411–1420. https://doi.org/10.1890/14-0449.1.
Cunning, R., Bay, R.A., Gillette, P., Baker, A.C., Traylor-Knowles, N., 2018. Comparative analysis of the *Pocillopora damicornis* genome highlights role of immune system in coral evolution. Sci. Rep. 8 (1), 16134. https://doi.org/10.1038/s41598-018-34459-8.
Davy, S.K., Allemand, D., Weis, V.M., 2012. Cell biology of cnidarian-dinoflagellate symbiosis. Microbiol. Mol. Biol. Rev. 76 (2), 229–261. https://doi.org/10.1128/mmbr.05014-11.
Decelle, J., Carradec, Q., Pochon, X., Henry, N., Romac, S., Mahe, F., et al., 2018. Worldwide occurrence and activity of the reef-building coral symbiont Symbiodinium in the Open Ocean. Curr. Biol. 28 (22), 3625–3633. https://doi.org/10.1016/j.cub.2018.09.024.
Delgadillo-Ordoñez, N., Garcias-Bonet, N., Raimundo, I., García, F.C., Villela, H., Osman, E.O., Santoro, E.P., Curdia, J., Rosado, J.G.D., Cardoso, P., Alsaggaf, A., Barno, A., Antony, C.P., Bocanegra, C., Berumen, M.L., Voolstra, C.R., Benzoni, F., Carvalho, S., Peixoto, R.S., 2024. Probiotics reshape the coral microbiome in situ without detectable off-target effects in the surrounding environment. Commun. Biol. 7. https://doi.org/10.1038/s42003-024-06135-3.
Doyle, S.M., Self, M.J., Hayes, J., Shamberger, K.E.F., Correa, A.M.S., Davies, S.W., et al., 2022. Microbial community dynamics provide evidence for hypoxia during a coral reef mortality event. Appl. Environ. Microbiol. 88 (9), e322–e347. https://doi.org/10.1128/aem.00347-22.
Eakin, C.M., Sweatman, H.P.A., Brainard, R.E., 2019. The 2014-2017 global-scale coral bleaching event: insights and impacts. Coral Reefs 38 (4), 539–545. https://doi.org/10.1007/s00338-019-01844-2.
Eakin, C.M., Devotta, D., Heron, S., Connolly, S., Liu, G., et al., 2022. The 2014–17 global coral bleaching event: the most severe and widespread coral reef destruction. Res. Sq. 1555992. https://doi.org/10.21203/rs.3.rs-1555992/v1.
Falkowski, P.G., 1997. Evolution of the nitrogen cycle and its influence on the biological sequestration of CO_2 in the ocean. Nature 387 (6630), 272–275. https://doi.org/10.1038/387272a0.
Falkowski, P.G., Dubinsky, Z., Muscatine, L., Porter, J.W., 1984. Light and the bioenergetics of a symbiotic coral. Bioscience 34 (11), 705–709. https://doi.org/10.2307/1309663.
Feng, Y., Bethel, B.J., Dong, C., Zhao, H., Yao, Y., Yu, Y., 2022. Marine heatwave events near Weizhou Island, Beibu Gulf in 2020 and their possible relations to coral bleaching. Sci. Total Environ. 823, 153414. https://doi.org/10.1016/j.scitotenv.2022.153414.
Galand, P.E., Ruscheweyh, H., Salazar, G., Hochart, C., Henry, N., Hume, B.C.C., et al., 2023. Diversity of the Pacific Ocean coral reef microbiome. Nat. Commun. 14 (1), 3039. https://doi.org/10.1038/s41467-023-38500-x.
Gantt, S.E., Kemp, K.M., Colin, P.L., Hoadley, K.D., LaJeunesse, T.C., Warner, M.E., Kemp, D.W., 2024. Influence of reef habitat on coral microbial associations. Environ. Microbiol. Rep. 16. https://doi.org/10.1111/1758-2229.70051.
Gardner, T.A., Côté, I.M., Gill, J.A., Grant, A., Watkinson, A.R., 2003. Long-term region-wide declines in Caribbean corals. Science 301 (5635), 958–960. https://doi.org/10.1126/science.1086050.
Ge, R., Liang, J., Yu, K., Chen, B., Yu, X., Deng, C., et al., 2021. Regulation of the coral-associated bacteria and Symbiodiniaceae in *Acropora valida* under ocean acidification. Front. Microbiol. 12, 767174. https://doi.org/10.3389/fmicb.2021.767174.
Gignoux-Wolfsohn, S.A., Vollmer, S.V., 2015. Correction: identification of candidate coral pathogens on white band disease-infected staghorn coral. PLoS One 10 (11), e142760. https://doi.org/10.1371/journal.pone.0142760.
Goffredo, S., Chadwick, N., 2000. Abundance and distribution of mushroom corals (Scleractinia: Fungidae) on a coral reef at Eilat, northern Red Sea. Bull. Mar. Sci. 66 (1), 241–254.
Goffredo, S., Chadwick-Furman, N.E., 2003. Comparative demography of mushroom corals (Scleractinia: Fungiidae) at Eilat, northern Red Sea. Mar. Biol. 142 (3), 411–418. https://doi.org/10.1007/s00227-002-0980-9.
Graham, N.A.J., Jennings, S., Macneil, M.A., Mouillot, D., Wilson, S.K., 2015. Predicting climate-driven regime shifts versus rebound potential in coral reefs. Nature 518 (7537), 94–97. https://doi.org/10.1038/nature14140.
Grottoli, A.G., Warner, M.E., Levas, S.J., Aschaffenburg, M.D., Schoepf, V., Mcginley, M., et al., 2014. The cumulative impact of annual coral bleaching can turn some coral species winners into losers. Glob. Chang. Biol. 20 (12), 3823–3833. https://doi.org/10.1111/gcb.12658.
Guo, J., Yu, K., Wang, Y., Zhang, R., Huang, X., Qin, Z., 2019. Potential impacts of anthropogenic nutrient enrichment on coral reefs in the South China Sea: evidence from nutrient and chlorophyll a levels in seawater. Environ. Sci. Process Impacts 21 (10), 1745–1753. https://doi.org/10.1039/c9em00331b.
Haas, A., El-Zibdah, M., Wild, C., 2010. Seasonal monitoring of coral-algae interactions in fringing reefs of the Gulf of Aqaba, northern Red Sea. Coral Reefs 29 (1), 93–103. https://doi.org/10.1007/s00338-009-0556-y.
Harrell, F.E.J., 2008. Hmisc: harrell miscellaneous. R Pack. Vers. 3, 4.
He, L.M., Karlep, L., Li, Z.Y., 2021. The nitrogen - cycling network of bacterial symbionts in the sponge S*pheciospongia vesparium*. J. Ocean Univ. 20 (4), 999–1012. https://doi.org/10.1007/s11802-021-4530-9.
Hernandez-Agreda, A., Leggat, W., Bongaerts, P., Ainsworth, T.D., 2016. The microbial signature provides insight into the mechanistic basis of coral success across reef habitats. mBio 7. https://doi.org/10.1128/mBio.00560-16.
Hernandez-Agreda, A., Gates, R.D., Ainsworth, T.D., 2017. Defining the core microbiome in corals' microbial soup. Trends Microbiol. 25 (2), 125–140. https://doi.org/10.1016/j.tim.2016.11.003.
Hochart, C., Paoli, L., Ruscheweyh, H., Salazar, G., Boissin, E., Romac, S., et al., 2023. Ecology of *Endozoicomonadaceae* in three coral genera across the Pacific Ocean. Nat. Commun. 14 (1), 3037. https://doi.org/10.1038/s41467-023-38502-9.
Hoeksema, B., 1991. Control of bleaching in mushroom coral populations (Scleractinia: Fungiidae) in the Java Sea: Stress tolerance and interference by life history strategy. Mar. Ecol. Prog. Ser. 74, 225–237. https://doi.org/10.3354/meps075225.
Hoeksema, B.W., 2012. Distribution patterns of mushroom corals (Scleractinia: Fungiidae) across the Spermonde Shelf, south Sulawesi. Raffles Bull. Zool. 60 (1), 183–212.
Hoogenboom, M., Rodolfo-Metalpa, R., Ferrier-Pages, C., 2010. Co - variation between autotrophy and heterotrophy in the Mediterranean coral *Cladocora caespitosa*. J. Exp. Biol. 213 (14), 2399–2409. https://doi.org/10.1242/jeb.040147.
Howe-Kerr, L.I., Bachelot, B., Wright, R.M., Kenkel, C.D., Bay, L.K., Correa, A.M.S., 2020. Symbiont community diversity is more variable in corals that respond poorly to stress. Glob. Chang. Biol. 26 (4), 2220–2234. https://doi.org/10.1111/gcb.14999.
Howells, E.J., Bauman, A.G., Vaughan, G.O., Hume, B.C.C., Voolstra, C.R., Burt, J.A., 2020. Corals in the hottest reefs in the world exhibit symbiont fidelity not flexibility. Mol. Ecol. 29 (5), 899–911. https://doi.org/10.1111/mec.15372.
Huang, L., Yu, K., Shi, Q., Zhao, M., Chen, T., Yan, H., 2011. Diurnal variations of photosynthetic efficiency of symbiotic algae of reef-building corals in a Sanya fringing reef. J. Trop. Oceanogr. 2 (30), 46–50. https://doi.org/10.11978/j.issn.1009-5470.2011.02.046.
Hughes, T.P., Rodrigues, M.J., Bellwood, D.R., Ceccarelli, D., Hoegh-Guldberg, O., Mccook, L., et al., 2007. Phase shifts, herbivory, and the resilience of coral reefs to climate change. Curr. Biol. 17 (4), 360–365. https://doi.org/10.1016/j.cub.2006.12.049.
Hughes, T.P., Barnes, M.L., Bellwood, D.R., Cinner, J.E., Cumming, G.S., Jackson, J.B.C., et al., 2017a. Coral reefs in the Anthropocene. Nature 546 (7656), 82–90. https://doi.org/10.1038/nature22901.
Hughes, T.P., Kerry, J.T., Alvarez-Noriega, M., Alvarez-Romero, J.G., Anderson, K.D., Baird, A.H., et al., 2017b. Global warming and recurrent mass bleaching of corals. Nature 543 (7645), 373. https://doi.org/10.1038/nature21707.
Hughes, T.P., Anderson, K.D., Connolly, S.R., Heron, S.F., Kerry, J.T., Lough, J.M., et al., 2018a. Spatial and temporal patterns of mass bleaching of corals in the Anthropocene. Science 359 (6371), 80. https://doi.org/10.1126/science.aan8048.
Hughes, T.P., Kerry, J.T., Baird, A.H., Connolly, S.R., Dietzel, A., Eakin, C.M., et al., 2018b. Global warming transforms coral reef assemblages. Nature 556 (7702), 492–496. https://doi.org/10.1038/s41586-018-0041-2.
Hume, B.C.C., D'Angelo, C., Smith, E.G., Stevens, J.R., Burt, J., Wiedenmann, J., 2015. *Symbiodinium thermophilum* sp. nov., a thermotolerant symbiotic alga prevalent in corals of the world's hottest sea, the Persian/Arabian Gulf. Sci. Rep. 5. https://doi.org/10.1038/srep08562.
Hume, B.C.C., Voolstra, C.R., Arif, C., D'Angelo, C., Burt, J.A., Eyal, G., et al., 2016. Ancestral genetic diversity associated with the rapid spread of stress-tolerant coral symbionts in response to Holocene climate change. Proc. Natl. Acad. Sci. USA 113 (16), 4416–4421. https://doi.org/10.1073/pnas.1601910113.
Hume, B.C.C., Mejia-Restrepo, A., Voolstra, C.R., Berumen, M.L., 2020. Fine-scale delineation of Symbiodiniaceae genotypes on a previously bleached central Red Sea reef system demonstrates a prevalence of coral host-specific associations. Coral Reefs 39 (3), 583–601. https://doi.org/10.1007/s00338-020-01917-7.
Jessen, C., Villa Lizcano, J.F., Bayer, T., Roder, C., Aranda, M., Wild, C., et al., 2013. In-situ effects of eutrophication and overfishing on physiology and bacterial diversity of the red sea coral *Acropora hemprichii*. PLoS One 8 (4), e62091.
Kimes, N.E., Van Nostrand, J.D., Weil, E., Zhou, J., Morris, P.J., 2010. Microbial functional structure of *Montastraea faveolata*, an important Caribbean reef-building coral, differs between healthy and yellow-band diseased colonies. Environ. Microbiol. 12 (2), 541–556. https://doi.org/10.1111/j.1462-2920.2009.02113.x.
Kvennefors, E.C.E., Sampayo, E., Kerr, C., Vieira, G., Roff, G., Barnes, A.C., 2012. Regulation of bacterial communities through antimicrobial activity by the coral holobiont. Microb. Ecol. 63 (3), 605–618. https://doi.org/10.1007/s00248-011-9946-0.
Ladner, J.T., Barshis, D.J., Palumbi, S.R., 2012. Protein evolution in two co-occurring types of *Symbiodinium* : an exploration into the genetic basis of thermal tolerance in *Symbiodinium clade D*. BMC Evol. Biol. 12, 217. https://doi.org/10.1186/1471-2148-12-217.
Lajeunesse, T.C., 2005. "Species" radiations of symbiotic dinoflagellates in the Atlantic and Indo-Pacific since the Miocene-Pliocene transition. Mol. Biol. Evol. 22 (3), 570–581. https://doi.org/10.1093/molbev/msi042.
Lajeunesse, T.C., Trench, R.K., 2000. Biogeography of two species of Symbiodinium (Freudenthal) inhabiting the intertidal sea anemone Anthopleura elegantissima (Brandt). Biol. Bull. 199 (2), 126–134. https://doi.org/10.2307/1542872.

Lajeunesse, T.C., Pettay, D.T., Sampayo, E.M., Phongsuwan, N., Brown, B., Obura, D.O., et al., 2010. Long-standing environmental conditions, geographic isolation and host-symbiont specificity influence the relative ecological dominance and genetic diversification of coral endosymbionts in the genus Symbiodinium. J. Biogeogr. 37 (5), 785–800. https://doi.org/10.1111/j.1365-2699.2010.02273.x.

Lajeunesse, T.C., Parkinson, J.E., Gabrielson, P.W., Jeong, H.J., Reimer, J.D., Voolstra, C. R., et al., 2018. Systematic revision of Symbiodiniaceae highlights the antiquity and diversity of coral endosymbionts. Curr. Biol. 28 (16), 2570–2580. https://doi.org/10.1016/j.cub.2018.07.008.

Lan, M., Gao, K., Qin, Z., Li, Z., Meng, R., Wei, L., Chen, B., Yu, X., Xu, L., Wang, Y., Yu, K., 2025. Coral microbiome in estuary coral community of Pearl River Estuary: insights into variation in coral holobiont adaptability to low-salinity conditions. BMC Microbiol. 25, 278. https://doi.org/10.1186/s12866-025-04013-4.

Leal, M.C., Ferrier-Pages, C., 2016. Molecular trophic markers in marine food webs and their potential use for coral ecology. Mar. Genomics 29, 1–7. https://doi.org/10.1016/j.margen.2016.02.003.

Lee, M.J., Jeong, H.J., Jang, S.H., Lee, S.Y., Kang, N.S., Lee, K.H., et al., 2016. Most low-abundance "background" Symbiodinium spp. are transitory and have minimal functional significance for symbiotic corals. Microb. Ecol. 71 (3), 771–783. https://doi.org/10.1007/s00248-015-0724-2.

Lee, L.K., Leaw, C.P., Lee, L.C., Lim, Z.F., Hii, K.S., Chan, A.A., et al., 2022. Molecular diversity and assemblages of coral symbionts (Symbiodiniaceae) in diverse scleractinian coral species. Mar. Environ. Res. 179, 13. https://doi.org/10.1016/j.marenvres.2022.105706.

Lei, M., 2024. Study on the Rapid Ecological Degradation of Coral Reefs and Its Impact on Fish in Yongle Atoll, Xisha Island in 2021 and 2023. Guangxi University, Nanning.

Li, J., Shao, Z., Cheng, K., Yang, Q., Ju, H., Tang, X., Zhang, S., Li, J., 2025. Coral-associated Symbiodiniaceae exhibit host specificity but lack phylosymbiosis, with *Cladocopium* and *Durusdinium* showing different cophylogenetic patterns. New Phytol. https://doi.org/10.1111/nph.70184.

Liang, J., Deng, C., Yu, K., Ge, R., Xu, Y., Qin, Z., et al., 2021. Cross-linked regulation of coral-associated dinoflagellates and bacteria in *Pocillopora sp.* during high-temperature stress and recovery. Microorganisms 9 (9), 1972. https://doi.org/10.3390/microorganisms9091972.

Liao, Z., Yu, K., Chen, B., Huang, X., Qin, Z., Yu, X., 2021. Spatial distribution of benthic algae in the South China Sea: Responses to gradually changing environmental factors and ecological impacts on coral communities. Divers. Distrib. 27 (5), 929–943. https://doi.org/10.1111/ddi.13243.

Lima, L.F.O., Weissman, M., Reed, M., Papudeshi, B., Alker, A.T., Morris, M.M., et al., 2020. Modeling of the coral microbiome: the influence of temperature and microbial network. mBio 11 (2), 10–1128. https://doi.org/10.1128/mbio.02691-19.

Lin, Y., Feng, S., Lai, C., Tseng, H., Huang, C., 2023. Applying deep learning to predict SST variation and tropical cyclone patterns that influence coral bleaching. Ecol. Inform. 77, 102261. https://doi.org/10.1016/j.ecoinf.2023.102261.

Lin, S., Li, L., Zhou, Z., Yuan, H., Saad, O.S., Tang, J., Cai, W., Yu, K., Lin, S., 2024. Higher genotypic diversity and distinct assembly mechanism of free-living Symbiodiniaceae assemblages than sympatric coral-endosymbiotic assemblages in a tropical coral reef. Microbiol. Spectr. 12. https://doi.org/10.1128/spectrum.00514-24 e00514-24.

Lirman, D., 2001. Competition between macroalgae and corals: effects of herbivore exclusion and increased algal biomass on coral survivorship and growth. Coral Reefs 19 (4), 392–399. https://doi.org/10.1007/s003380000125.

Liu, Z., Chen, C., Gao, L., Zhang, Y., Pei, J., Ren, C., et al., 2016. Differences in microbial communities between healthy and bleached coral *Acropora solitaryensis* from Xisha Islands, South China Sea. Mar. Biol. Res. 12 (10), 1101–1108. https://doi.org/10.1080/17451000.2016.1236201.

Liu, B., Guan, L., Chen, H., 2021. Detecting 2020 coral bleaching event in the northwest Hainan Island using CoralTemp SST and Sentinel-2B MSI imagery. Remote Sens. 13 (23), 4948. https://doi.org/10.3390/rs13234948.

Louca, S., Parfrey, L.W., Doebeli, M., 2016. Decoupling function and taxonomy in the global ocean microbiome. Science 353 (6305), 1272–1277. https://doi.org/10.1126/science.aaf4507.

Loya, Y., Sakai, K., 2008. Bidirectional sex change in mushroom stony corals. Proc. Biol. Sci. 275 (1649), 2335–2343. https://doi.org/10.1098/rspb.2008.0675.

Maher, R.L., Rice, M.M., Mcminds, R., Burkepile, D.E., Thurber, R.V., 2019. Multiple stressors interact primarily through antagonism to drive changes in the coral microbiome. Sci. Rep. 9, 6834. https://doi.org/10.1038/s41598-019-43274-8.

Manzello, D.P., Enochs, I.C., Melo, N., Gledhill, D.K., Johns, E.M., 2012. Ocean acidification refugia of the Forida Reef Tract. PLoS One 7 (7), e41715. https://doi.org/10.1371/journal.pone.0041715.

Marubini, F., Davies, P.S., 1996. Nitrate increases zooxanthellae population density and reduces skeletogenesis in corals. Mar. Biol. 127 (2), 319–328. https://doi.org/10.1007/BF00942117.

Mcauley, P.J., 1987. Nitrogen limitation and amino-acid metabolism of *Chlorella symbiotic* with green hydra. Planta 171 (4), 532–538. https://doi.org/10.1007/BF00392303.

Mccook, L.J., Jompa, J., Diaz-Pulido, G., 2001. Competition between corals and algae on coral reefs: a review of evidence and mechanisms. Coral Reefs 19 (4), 400–417. https://doi.org/10.1007/s003380000129.

Mcdevitt-Irwin, J.M., Baum, J.K., Garren, M., Thurber, R.L.V., 2017. Responses of coral-associated bacterial communities to local and global stressors. Front. Mar. Sci. 4, 262. https://doi.org/10.3389/fmars.2017.00262.

Meron, D., Atias, E., Kruh, L.I., Elifantz, H., Minz, D., Fine, M., et al., 2011. The impact of reduced pH on the microbial community of the coral *Acropora eurystoma*. ISME J. 5 (1), 51–60. https://doi.org/10.1038/ismej.2010.102.

Million, W.C., Voolstra, C.R., Perna, G., Puntin, G., Rowe, K., Ziegler, M., 2025. Resolving symbiodiniaceae diversity across coral microhabitats and Reef Niches. Environ. Microbiol. 27, e70065. https://doi.org/10.1111/1462-2920.70065.

Mori, H., Maruyama, F., Kato, H., Toyoda, A., Dozono, A., Ohtsubo, Y., et al., 2014. Design and experimental application of a novel non-degenerate universal primer set that amplifies prokaryotic 16S rRNA genes with a low possibility to amplify eukaryotic rRNA genes. DNA Res. 21 (2), 217–227. https://doi.org/10.1093/dnares/dst052.

Morris, L.A., Voolstra, C.R., Quigley, K.M., Bourne, D.G., Bay, L.K., 2019. Nutrient availability and metabolism affect the stability of Coral-Symbiodiniaceae symbioses. Trends Microbiol. 27 (8), 678–689. https://doi.org/10.1016/j.tim.2019.03.004.

Morrow, K.M., Moss, A.G., Chadwick, N.E., Liles, M.R., 2012. Bacterial associates of two caribbean coral species reveal species-specific distribution and geographic variability. Appl. Environ. Microbiol. 78 (18), 6438–6449. https://doi.org/10.1128/aem.01162-12.

Morrow, K.M., Bourne, D.G., Humphrey, C., Botte, E.S., Laffy, P., Zaneveld, J., et al., 2015. Natural volcanic CO_2 seeps reveal future trajectories for host-microbial associations in corals and sponges. ISME J. 9 (4), 894–908. https://doi.org/10.1038/ismej.2014.188.

Muscatine, L., Falkowski, P.G., Porter, J.W., Dubinsky, Z., 1984. Fate of photosynthetic fixed carbon in light- and shade-adapted colonies of the symbiotic coral *Stylophora pistillata*. Proc. Roy. Soc. Lond. Ser. B Biol. Sci. 222, 181–202. https://doi.org/10.1098/rspb.1984.0058.

Nelson, C.E., Goldberg, S.J., Kelly, L.W., Haas, A.F., Smith, J.E., Rohwer, F., et al., 2013. Coral and macroalgal exudates vary in neutral sugar composition and differentially enrich reef bacterioplankton lineages. ISME J. 7 (5), 962–979. https://doi.org/10.1038/ismej.2012.161.

Ning, D., Deng, Y., Tiedje, J.M., Zhou, J., 2019. A general framework for quantitatively assessing ecological stochasticity. Proc. Natl. Acad. Sci. USA 116 (34), 16892–16898. https://doi.org/10.1073/pnas.1904623116.

Oksanen, J., Blanchet, F.G., Kindt, R., Legendre, P., Minchin, P., O'Hara, B., et al., 2015. Vegan: community ecology package. R Pack. Vers. 2.3-0. https://CRAN.R-project.org/package=vegan.

Ong, J.H., Wainwright, B.J., Jain, S.S., Afiq-Rosli, L., Lee, J.N., Huang, D., 2022. Species and spatio-environmental effects on coral endosymbiont communities in Southeast Asia. Coral Reefs 41 (4), 1131–1145. https://doi.org/10.1007/s00338-022-02254-7.

Osman, E.O., Suggett, D.J., Voolstra, C.R., Pettay, D.T., Clark, D.R., Pogoreutz, C., et al., 2020. Coral microbiome composition along the northern Red Sea suggests high plasticity of bacterial and specificity of endosymbiotic dinoflagellate communities. Microbiome 8 (1), 8. https://doi.org/10.1186/s40168-019-0776-5.

Palardy, J.E., Rodrigues, L.J., Grottoli, A.G., 2008. The importance of zooplankton to the daily metabolic carbon requirements of healthy and bleached corals at two depths. J. Exp. Mar. Biol. Ecol. 367 (2), 180–188. https://doi.org/10.1016/j.jembe.2008.09.015.

Pendleton, L.H., Hoegh-Guldberg, O., Langdon, C., Comte, A., 2016. Multiple stressors and ecological complexity require a new approach to coral reef research. Front. Mar. Sci. 3, 36. https://doi.org/10.3389/fmars.2016.00036.

Perry, C.T., Morgan, K.M., 2017. Bleaching drives collapse in reef carbonate budgets and reef growth potential on southern Maldives reefs. Sci. Rep. 7, 40581. https://doi.org/10.1038/srep40581.

Pittman, S.J., Poti, M., Jeffrey, C.F.G., Kracker, L.M., Mabrouk, A., 2018. Decision support framework for the prioritization of coral reefs in the U.S. Virgin Islands. Ecol. Inform. 47, 26–34. https://doi.org/10.1016/j.ecoinf.2017.09.008.

Pootakham, W., Mhuantong, W., Yoocha, T., Putchim, L., Jomchai, N., Sonthirod, C., et al., 2019. Heat - induced shift in coral microbiome reveals several members of the Rhodobacteraceae family as indicator species for thermal stress in *Porites lutea*. Microbiologyopen 8 (12), e935. https://doi.org/10.1002/mbo3.935.

Pratomo, A., Bengen, D.G., Zamani, N.P., Lane, C., Humphries, A.T., Borbee, E., et al., 2022. Diversity and distribution of Symbiodiniaceae detected on coral reefs of Lombok, Indonesia using environmental DNA metabarcoding. PeerJ 10, e14006. https://doi.org/10.7717/peerj.14006.

Qin, Z., Yu, K., Liang, J., Yao, Q., Chen, B., 2020. Significant changes in microbial communities associated with reef corals in the Southern South China Sea during the 2015/2016 global-scale coral bleaching event. J. Geophys. Res. Oceans 125, e2019JC015579. https://doi.org/10.1029/2019JC015579.

Qin, Z., Yu, K., Chen, S., Chen, B., Liang, J., Yao, Q., et al., 2021. Microbiome of juvenile corals in the outer reef slope and lagoon of the South China Sea: insight into coral acclimatization to extreme thermal environments. Environ. Microbiol. 23 (8), 4389–4404. https://doi.org/10.1111/1462-2920.15624.

Qin, Z., Chen, S., Yu, K., Chen, B., Pan, N., Wei, X., 2022. Lagoon coral microbiomes and their potential relationship with adaptation of coral holobionts to extreme high-temperature environments. Mar. Ecol. Prog. Ser. 699, 19–32. https://doi.org/10.3354/meps14173.

Qin, Z., Pan, N., Yu, K., Chen, S., Wei, X., Chen, B., et al., 2024. Depth distribution and depth adaptation of microbiomes in juvenile and adult scleractinian corals (*Pocillopora verrucosa*) in the central South China Sea. Coral Reefs 43 (3), 587–600. https://doi.org/10.1007/s00338-024-02485-w.

Qiu, N., Yao, Z., Zuo, X., Luo, S., 2024. Numerical simulation and spatiotemporal analysis of waves at Yongle Atoll, Xisha Islands based on SWAN modeling. Prog. Geogr. 43 (09), 1811–1825. https://doi.org/10.18306/dlkxjz.2024.09.010.

Quigley, K.M., Bay, L.K., Willis, B.L., 2018. Leveraging new knowledge of *Symbiodinium* community regulation in corals for conservation and reef restoration. Mar. Ecol. Prog. Ser. 600, 245–253. https://doi.org/10.3354/meps12652.

Quigley, K.M., Ramsby, B., Laffy, P., Harris, J., Mocellin, V.J.L., Bay, L.K., 2022. Symbioses are restructured by repeated mass coral bleaching. Sci. Adv. 8 (49), eabq8349. https://doi.org/10.1126/sciadv.abq8349.

Quintanilla, E., Rodrigues, C.F., Henriques, I., Hilario, A., 2022. Microbial associations of abyssal gorgonians and anemones (>4,000 m depth) at the clarion-clipperton fracture zone. Front. Microbiol. 13, 828469. https://doi.org/10.3389/fmicb.2022.828469.

Radecker, N., Pogoreutz, C., Voolstra, C.R., Wiedenmann, J., Wild, C., 2015. Nitrogen cycling in corals: the key to understanding holobiont functioning? Trends Microbiol. 23 (8), 490–497. https://doi.org/10.1016/j.tim.2015.03.008.

Reaka-Kudla, M.L., Wilson, D.E., Wilson, E., 1997. Biodiversity II: Understanding & Protecting Our Biological Resources. Joseph Henry Press, Washington DC.

Reimer, J.D., Herrera, M., Gatins, R., Roberts, M.B., Parkinson, J.E., Berumen, M.L., 2017. Latitudinal variation in the symbiotic dinoflagellate *Symbiodinium* of the common reef zoantharian *Palythoa tuberculosa* on the Saudi Arabian coast of the Red Sea. J. Biogeogr. 44 (3), 661–673. https://doi.org/10.1111/jbi.12795.

Reimer, J.D., Peixoto, R.S., Davies, S.W., Traylor-Knowles, N., Short, M.L., Cabral-Tena, R.A., et al., 2024. The fourth global coral bleaching event: where do we go from here? Coral Reefs 43 (4), 1121–1125. https://doi.org/10.1007/s00338-024-02504-w.

Ritchie, K.B., 2006. Regulation of microbial populations by coral surface mucus and mucus-associated bacteria. Mar. Ecol. Prog. Ser. 322, 1–14. https://doi.org/10.3354/meps322001.

Robbins, S.J., Singleton, C.M., Chan, C.X., Messer, L.F., Geers, A.U., Ying, H., et al., 2019. A genomic view of the reef-building coral *Porites lutea* and its microbial symbionts. Nat. Microbiol. 4 (12), 2090–2100. https://doi.org/10.1038/s41564-019-0532-4.

Rosenberg, E., Kushmaro, A., Kramarsky-Winter, E., Banin, E., Yossi, L., 2009. The role of microorganisms in coral bleaching. ISME J. 3 (2), 139–146. https://doi.org/10.1038/ismej.2008.104.

Sammarco, P.W., 1991. Geographically specific recruitment and postsettlement mortality as influences on coral communities: The cross-continental shelf transplant experiment. Limnol. Oceanogr. 36 (3), 496–514. https://doi.org/10.4319/lo.1991.36.3.0496.

Santoro, E.P., Cardenas, A., Villela, H., Vilela, C., Ghizelini, A.M., Duarte, G., Perna, G., Saraiva, J.P., Thomas, T., Voolstra, C.R., Peixoto, R.S., 2025. Inherent differential microbial assemblages and functions associated with corals exhibiting different thermal phenotypes. Sci. Adv. 11, eadq2583. https://doi.org/10.1126/sciadv.adq2583.

Sessa, J., Syed, D., Zainab, A., Al-Ghushami, A.H., Ahmed, M., 2022. Towards heat tolerant metagenome functional prediction, coral microbial community composition, and enrichment analysis. Ecol. Inform. 69, 101635. https://doi.org/10.1016/j.ecoinf.2022.101635.

Shnit-Orland, M., Sivan, A., Kushmaro, A., 2012. Antibacterial activity of *Pseudoalteromonas* in the coral holobiont. Microb. Ecol. 64 (4), 851–859. https://doi.org/10.1007/s00248-012-0086-y.

Shore-Maggio, A., Aeby, G.S., Callahan, S.M., 2018. Influence of salinity and sedimentation on *Vibrio* infection of the Hawaiian coral *Montipora capitata*. Dis. Aquat. Org. 128 (1), 63–71. https://doi.org/10.3354/dao03213.

Silverstein, R.N., Cunning, R., Baker, A.C., 2015. Change in algal symbiont communities after bleaching, not prior heat exposure, increases heat tolerance of reef corals. Glob. Chang. Biol. 21 (1), 236–249. https://doi.org/10.1111/gcb.12706.

Smith, E.G., Hazzouri, K.M., Choi, J.Y., Delaney, P., Al-Kharafi, M., Howells, E.J., et al., 2022. Signatures of selection underpinning rapid coral adaptation to the world's warmest reefs. Sci. Adv. 8 (2), eabl7287. https://doi.org/10.1126/sciadv.abl7287.

Spalding, M.D., Brown, B.E., 2015. Warm-water coral reefs and climate change. Science 350 (6262), 769–771. https://doi.org/10.1126/science.aad0349.

Stat, M., Bird, C.E., Pochon, X., Chasqui, L., Chauka, L.J., Concepcion, G.T., Logan, D., Takabayashi, M., Toonen, R.J., Gates, R.D., 2011. Variation in Symbiodinium ITS2 sequence assemblages among coral colonies. PLoS One 6, e15854. https://doi.org/10.1371/journal.pone.0015854.

Stuart-Smith, R.D., Brown, C.J., Ceccarelli, D.M., Edgar, G.J., 2018. Ecosystem restructuring along the Great Barrier Reef following mass coral bleaching. Nature 560 (7716), 92–96. https://doi.org/10.1038/s41586-018-0359-9.

Sully, S., Burkepile, D.E., Donovan, M.K., Hodgson, G., van Woesik, R., 2019. A global analysis of coral bleaching over the past two decades. Nat. Commun. 10, 1264. https://doi.org/10.1038/s41467-019-09238-2.

Szereday, S., Voolstra, C.R., Amri, A.Y., 2024. Back-to-back bleaching events in Peninsular Malaysia (2019–2020) selectively affect hard coral taxa across- and within-reef scales. Mar. Biol. 171. https://doi.org/10.1007/s00227-024-04495-2.

Teeling, H., Fuchs, B.M., Becher, D., Klockow, C., Gardebrecht, A., Bennke, C.M., et al., 2012. Substrate-controlled succession of marine bacterioplankton populations induced by a phytoplankton bloom. Science 336 (6081), 608–611. https://doi.org/10.1126/science.1218344.

Terraneo, T., Fusi, M., Hume, B.C.C., Arrigoni, R., Voolstra, C.R., Benzoni, F., et al., 2019. Environmental latitudinal gradients and host-specificity shape Symbiodiniaceae distribution in *Red Sea Porites* corals. J. Biogeogr. 46 (10), 2323–2335. https://doi.org/10.1111/jbi.13672.

Thirukanthan, C.S., Kallem, P., Pratama, I.S., Lananan, F., Wei, L.S., Kari, Z.A., Gao, H., Azra, M.N., Talaat, W.I.A.W., 2025. Marine protected area and climate change: a mapping review. Ecol. Inform. 86, 103042. https://doi.org/10.1016/j.ecoinf.2025.103042.

Thornhill, D.J., Lajeunesse, T.C., Santos, S.R., 2007. Measuring rDNA diversity in eukaryotic microbial systems: how intragenomic variation, pseudogenes, and PCR artifacts confound biodiversity estimates. Mol. Ecol. 16, 5326–5340. https://doi.org/10.1111/j.1365-294X.2007.03576.x.

Thornhill, D.J., Howells, E.J., Wham, D.C., Steury, T.D., Santos, S.R., 2017. Population genetics of reef coral endosymbionts (*Symbiodinium*, Dinophyceae). Mol. Ecol. 26, 2640–2659. https://doi.org/10.1111/mec.14055.

Thurber, R.V., Burkepile, D.E., Correa, A.M.S., Thurber, A.R., Shantz, A.A., Welsh, R., et al., 2012. Macroalgae decrease growth and alter microbial community structure of the reef - building coral, *Porites astreoides*. PLoS One 7 (9), e44246. https://doi.org/10.1371/journal.pone.0044246.

Titlyanov, E.A., Yakovleva, I.M., Titlyanova, T.V., 2007. Interaction between benthic algae (*Lyngbya bouillonii, Dictyota dichotoma*) and scleractinian coral *Porites lutea* in direct contact. J. Exp. Mar. Biol. Ecol. 342 (2), 282–291. https://doi.org/10.1016/j.jembe.2006.11.007.

Tkachenko, K.S., 2014. The influence of repetitive thermal stresses on the dominance of reef-building *Acropora* spp. (Scleractinia) on coral reefs of the maldive islands. Russ. J. Mar. Biol. 40 (4), 286–294. https://doi.org/10.1134/S1063074014040105.

Tkachenko, K.S., 2017. Coral reefs in the face of ecological threats of the 21st century. Biol. Bull. Rev. 7 (1), 64–83. https://doi.org/10.1134/S2079086416050091.

Tkachenko, K.S., Soong, K., 2017. Dongsha Atoll: a potential thermal refuge for reef-building corals in the South China Sea. Mar. Environ. Res. 127, 112–125. https://doi.org/10.1016/j.marenvres.2017.04.003.

Tout, J., Jeffries, T.C., Petrou, K., Tyson, G.W., Webster, N.S., Garren, M., et al., 2015. Chemotaxis by natural populations of coral reef bacteria. ISME J. 9 (8), 1764–1777. https://doi.org/10.1038/ismej.2014.261.

Tran, C., 2022. Coral-microbe interactions: their importance to reef function and survival. Emerg. Top. Life Sci. 6 (1), 33–44. https://doi.org/10.1042/etls20210229.

Turnham, K.E., Lewis, A.M., Kemp, D.W., Warner, M.E., Wham, D.F., Smith, R.T., Hoadley, K., Colin, P.L., Golbuu, Y., LaJeunesse, T.C., 2025. Limited persistence of the heat-tolerant zooxanthella, Durusdinium trenchii, in corals transplanted to a barrier reef where it is rare among natal colonies. Coral Reefs. https://doi.org/10.1007/s00338-025-02625-w.

Tyrrell, T., 1999. The relative influences of nitrogen and phosphorus on oceanic primary production. Nature 400 (6744), 525–531. https://doi.org/10.1038/22941.

van Oppen, M.J.H., Blackall, L.L., 2019. Coral microbiome dynamics, functions and design in a changing world. Nat. Rev. Microbiol. 17 (9), 557–567. https://doi.org/10.1038/s41579-019-0223-4.

van Oppen, M.J.H., Raina, J.B., 2023. Coral holobiont research needs spatial analyses at the microbial scale. Environ. Microbiol. 25, 179–183. https://doi.org/10.1111/1462-2920.16237.

Van Spanning, R.J.M., Delgado, M.J., Richardson, D.J., 2005. The nitrogen cycle: Denitrification and its relationship to N_2 fixation. In: Werner, D., Newton, W.E. (Eds.), Nitrogen Fixation in Agriculture, Forestry, Ecology, and the Environment, 4. Springer Netherlands, Dordrecht, pp. 277–342. https://doi.org/10.1007/1-4020-3544-6_13.

Veron, J., Stafford-Smith, M., Devantier, L., Turak, E., 2015. Overview of distribution patterns of zooxanthellate Scleractinia. Front. Mar. Sci. 1, 81. https://doi.org/10.3389/fmars.2014.00081.

Voolstra, C.R., Suggett, D.J., Peixoto, R.S., Parkinson, J.E., Quigley, K.M., Silveira, C.B., et al., 2021. Extending the natural adaptive capacity of coral holobionts. Nat. Rev. Earth Environ. 2 (11), 747–762. https://doi.org/10.1038/s43017-021-00214-3.

Voolstra, C.R., Raina, J., Dörr, M., Cárdenas, A., Pogoreutz, C., Silveira, C.B., Mohamed, A.R., Bourne, D.G., Luo, H., Amin, S.A., Peixoto, R.S., 2024. The coral microbiome in sickness, in health and in a changing world. Nat. Rev. Microbiol. 22, 460–475. https://doi.org/10.1038/s41579-024-01015-3.

Voolstra, C.R., Alderdice, R., Colin, L., Staab, S., Apprill, A., Raina, J.B., 2025. Standardized methods to assess the impacts of thermal stress on Coral Reef marine life. Annu. Rev. Mar. Sci. 17, 193–226. https://doi.org/10.1146/annurev-marine-032223-024511.

Wang, G., 2001. Sedimentology of coral reef areas in the South China Sea. China Ocean Press, Beijing.

Wang, P., Li, Q., 2009. The South China Sea : Paleoceanography and Sedimentology. Springer.

Webster, N.S., Negri, A.P., Botte, E.S., Laffy, P.W., Flores, F., Noonan, S., et al., 2016. Host-associated coral reef microbes respond to the cumulative pressures of ocean warming and ocean acidification. Sci. Rep. 6, 19324. https://doi.org/10.1038/srep19324.

Wegley, L., Edwards, R., Rodriguez-Brito, B., Liu, H., Rohwer, F., 2007. Metagenomic analysis of the microbial community associated with the coral *Porites astreoides*. Environ. Microbiol. 9 (11), 2707–2719. https://doi.org/10.1111/j.1462-2920.2007.01383.x.

Wei, Y., Yu, K., Chen, B., 2022. Fungiidae classification, life history, and biogeographic research progress. Trop. Geogr. 42 (11), 1783–1796. https://doi.org/10.13284/j.cnki.rddl.003587.

Wei, Y., Chen, B., Yu, K., Liao, Z., Yu, X., Qin, Z., et al., 2024. Evolutionary radiation and microbial community dynamics shape the thermal tolerance of Fungiidae in the southern South China Sea. Microbiol. Spectr. 12 (2), e243623. https://doi.org/10.1128/spectrum.02436-23.

Weiler, B.A., Verhoeven, J.T.P., Dufour, S.C., 2018. Bacterial communities in tissues and surficial mucus of the cold - water coral *Paragorgia arborea*. Front. Mar. Sci. 5, 378. https://doi.org/10.3389/fmars.2018.00378.

Welsh, R.M., Zaneveld, J.R., Rosales, S.M., Payet, J.P., Burkepile, D.E., Thurber, R.V., 2016. Bacterial predation in a marine host-associated microbiome. ISME J. 10 (6), 1540–1544. https://doi.org/10.1038/ismej.2015.219.

Xu, S., Zhang, Z., Yu, K., Huang, X., Chen, H., Qin, Z., et al., 2021. Spatial variations in the trophic status of *Favia palauensis* corals in the South China Sea: Insights into their different adaptabilities under contrasting environmental conditions. Sci. China Earth Sci. 64 (6), 839–852. https://doi.org/10.1007/s11430-020-9774-0.

Yilmaz, P., Parfrey, L.W., Yarza, P., Gerken, J., Pruesse, E., Quast, C., et al., 2014. The SILVA and "All-species Living Tree Project (LTP)" taxonomic frameworks. Nucleic Acids Res. 42 (D1), D643–D648. https://doi.org/10.1093/nar/gkt1209.

Yu, K.F., 2012. Coral reefs in the South China Sea: their response to and records on past environmental changes. Sci. China Earth Sci. 55 (8), 1217–1229. https://doi.org/10.1007/s11430-012-4449-5.

Yu, X., Yu, K., Chen, B., Liao, Z., Liang, J., Yao, Q., et al., 2021. Different responses of scleractinian coral *Acropora pruinosa* from Weizhou Island during extreme high temperature events. Coral Reefs 40 (6), 1697–1711. https://doi.org/10.1007/s00338-021-02182-y.

Zaneveld, J.R., Burkepile, D.E., Shantz, A.A., Pritchard, C.E., Mcminds, R., Payet, J.P., et al., 2016. Overfishing and nutrient pollution interact with temperature to disrupt coral reefs down to microbial scales. Nat. Commun. 7, 11833. https://doi.org/10.1038/ncomms11833.

Zaneveld, J.R., Mcminds, R., Thurber, R.V., 2017. Stress and stability: applying the Anna Karenina principle to animal microbiomes. Nat. Microbiol. 2 (9), 17121. https://doi.org/10.1038/nmicrobiol.2017.121.

Zhang, Y., Ling, J., Yang, Q., Wen, C., Yan, Q., Sun, H., et al., 2015. The functional gene composition and metabolic potential of coral-associated microbial communities. Sci. Rep. 5, 16191. https://doi.org/10.1038/srep16191.

Zhang, Y., Xu, J., Li, G., Lu, Z., Jiang, Z., Zhang, W., et al., 2023. ENSO-like evolution of the tropical Pacific climate mean state and its potential causes since 300ka. Quat. Sci. Rev. 315, 108241. https://doi.org/10.1016/j.quascirev.2023.108241.

Zhu, W., Liu, X., Zhu, M., Xia, J., Chen, R., Li, X., 2023. Coastal upwelling under anthropogenic influence drives the community change, assembly process, and co-occurrence pattern of coral associated microorganisms. J. Geophys. Res. Oceans 128 (2), 19. https://doi.org/10.1029/2022JC019307.

Ziegler, M., Arif, C., Burt, J.A., Dobretsov, S., Roder, C., Lajeunesse, T.C., et al., 2017a. Biogeography and molecular diversity of coral symbionts in the genus *Symbiodinium* around the Arabian Peninsula. J. Biogeogr. 44 (3), 674–686. https://doi.org/10.1111/jbi.12913.

Ziegler, M., Seneca, F.O., Yum, L.K., Palumbi, S.R., Voolstra, C.R., 2017b. Bacterial community dynamics are linked to patterns of coral heat tolerance. Nat. Commun. 8, 14213. https://doi.org/10.1038/ncomms14213.

Ziegler, M., Eguiluz, V.M., Duarte, C.M., Voolstra, C.R., 2018. Rare symbionts may contribute to the resilience of coral-algal assemblages. ISME J. 12 (1), 161–172. https://doi.org/10.1038/ismej.2017.151.

Ziegler, M., Grupstra, C.G.B., Barreto, M.M., Eaton, M., Baomar, J., Zubier, K., et al., 2019. Coral bacterial community structure responds to environmental change in a host-specific manner. Nat. Commun. 10, 3092. https://doi.org/10.1038/s41467-019-10969-5.

Microbial Ecology (2024) 87:169
https://doi.org/10.1007/s00248-024-02470-4

RESEARCH

The Dynamics of Symbiodiniaceae and Photosynthetic Bacteria Under High-Temperature Conditions

Yongqian Xu[1,2] · Jiayuan Liang[1] · Liangyun Qin[1] · Tianyi Niu[1] · Zhuqing Liang[1] · Zhicong Li[1] · Biao Chen[1] · Jin Zhou[3] · Kefu Yu[1,4]

Received: 24 December 2023 / Accepted: 25 November 2024
© The Author(s) 2024

Abstract

Coral thermal tolerance is intimately linked to their symbiotic relationships with photosynthetic microorganisms. However, the potential compensatory role of symbiotic photosynthetic bacteria in supporting Symbiodiniaceae photosynthesis under extreme summer temperatures remains largely unexplored. Here, we examined the seasonal variations in Symbiodiniaceae and photosynthetic bacterial community structures in *Pavona decussata* corals from Weizhou Island, Beibu Gulf, China, with particular emphasis on the role of photosynthetic bacteria under elevated temperature conditions. Our results revealed that Symbiodiniaceae density and Chlorophyll *a* concentration were lowest during the summer and highest in the winter. Notably, the summer bacterial community was predominately composed of the proteorhodopsin bacterium BD 1–7 _clade, alongside a significant increase in Cyanobacteria, particularly *Synechococcus*_CC9902 and *Cyanobium*_PCC-6307, which represented 61.85% and 31.48% of the total Cyanobacterial community, respectively. In vitro experiments demonstrated that Cyanobacteria significantly enhanced Symbiodiniaceae photosynthetic efficiency under high-temperature conditions. These findings suggest that the increased abundance of photosynthetic bacteria during summer may mitigate the adverse physiological effects of reduced Symbiodiniaceae density, thereby contributing to coral stability. Our study highlights a potential synergistic interaction between Symbiodiniaceae and photosynthetic bacteria, emphasizing the importance of understanding these dynamic interactions in sustaining coral resilience against environmental stress, although further research is necessary to establish their role in preventing coral bleaching.

Keywords Coral reef · Photosynthetic symbionts · Synergistic effect · Seasonal variation

Introduction

Coral reefs are complex ecosystems composed of coral hosts and a diverse community of associated microorganisms, including Symbiodiniaceae, bacteria, archaea, fungi, protists, viruses, and others [1]. These microorganisms play crucial and intricate roles in the coral's response to thermal stress [2]. Among these symbiotic partners, photosynthetic microorganisms are essential components of coral holobionts, contributing significantly to coral growth, development, and the intricate ecological interactions within coral reef ecosystems [3]. For instance, Symbiodiniaceae, as faithful partners of corals, transfer most photosynthetic products to corals, providing energy for coral calcification [4]. Cyanobacteria, as the predominant photosynthetic bacterial group within corals [5], actively participate in carbon and nitrogen cycling, potentially aiding corals in maintaining homeostasis under environmental stress [6].

Yongqian Xu and Jiayuan Liang contributed to the work equally and should be regarded as co-sharing first authors.

✉ Jiayuan Liang
jyliang@gxu.edu.cn

✉ Kefu Yu
kefuyu@scsio.ac.cn

1 Guangxi Laboratory on the Study of Coral Reefs in the South China Sea, Coral Reef Research Center of China, School of Marine Sciences, Guangxi University, Nanning 530004, China

2 Shenzhen Key Laboratory of Marine Archaea Geo-Omics, Department of Ocean Science and Engineering, Southern University of Science and Technology, Shenzhen 518055, China

3 Institute for Ocean Engineering, Shenzhen International Graduate School, Tsinghua University, Shenzhen 518000, China

4 Southern Marine Science and Engineering Guangdong Laboratory (Guangzhou), Guangzhou 510030, China

Published online: 09 January 2025

Despite the well-studied relationship between corals and Symbiodiniaceae, the roles of the photosynthetic bacteria within corals remain largely unexplored[7, 8]. The breakdown of coral-Symbiodiniaceae symbiosis due to rising sea surface temperature has led to global coral reef degradation [9, 10]. Within coral holobionts, Symbiodiniaceae and bacteria engage in metabolic exchanges essential for element cycling [11]. For instance, Symbiodiniaceae growth is enhanced through metabolic interactions with associated bacteria[12]. The co-localization of bacteria and Symbiodiniaceae within coral tissues suggests a mutualistic relationship suggests a mutualistic relationship, essential for metabolic cycling [13]. Cyanobacteria were observed adjacent to Symbiodiniaceae and are often in high densities throughout the gastrodermal tissues[6, 14]. Given this close association, it is likely that Symbiodiniaceae preferentially uptake the products from Cyanobacteria over those from host tissues [15].

Understanding the interactions between Symbiodiniaceae and photosynthetic bacteria is critical for advancing coral reef recovery efforts [16]. Photosynthetic bacteria may compensate for the photosynthesis of Symbiodiniaceae, and there may be synergistic effects between them, which were impacted by variations in temperature [17], light [18], pH [19], or other environmental stresses [20]. However, mechanisms for such synergistic effects' environmental impact were poorly understood. To gain a deeper understanding of the role of photosynthetic bacteria in coral adaptation to seasonal environmental fluctuations, especially in the context of high-temperature conditions during the summer, we focused on *Pavona decussata* in Weizhou Island, Beibu Gulf. Weizhou Island exhibits clear seasonality, particularly during the summer when the maximum sea water temperature exceeds 32 °C [21].

We aimed to verify the auxiliary role of photosynthetic bacteria in supporting the photosynthesis of Symbiodiniaceae under high-temperature conditions. The results initially revealed the compensatory effect of symbiotic photosynthetic bacteria on algae photosynthetic efficiency, which should help us better understand the ecological resilience and survival strategies of coral holobionts.

Material and Methods

Coral Sample Collection and Environmental Data

Coral samples of *P. decussata* were collected on Weizhou Island (21°N8.27′, 109°E12.6′) in July and October 2019 and in January and April 2020, respectively (Fig. 1a). A total of 20 samples were collected across four seasons, with 5 coral fragments collected in each season. Sampling was conducted at a depth range of 6—7 m. To avoid duplicate sampling and the collection of individuals involved in coral asexual reproduction, the distance between sampling points for the same specimen exceeded 6 m [22]. To minimize contamination by exogenous microorganisms, each coral fragment was thoroughly rinsed three times with sterile seawater immediately after retrieval. Subsequently, the coral samples were immediately placed in sterile, airtight bags, flash-frozen in liquid nitrogen, and then transported back to the laboratory for further experimentation.

Remote sensing data for the Weizhou Island coral reef area from July 2019 to July 2020 were obtained using the Giovanni Ocean Color tool (https://giovanni.gsfc.nasa.gov/giovanni). The data included Sea Surface Temperature (SST; °C), Photosynthetically Active Radiation (PAR; E m^{-2} d^{-1}), Chlorophyll *a* concentration (mg m^{-3}), 490 nm diffuse attenuation coefficient (Kd490; Kd m^{-1}), and Particulate Organic Carbon (POC; mg m^{-3}).

Determination of Symbiodiniaceae Density and Chlorophyll a Concentration

The determination of Symbiodiniaceae density followed the standard procedure [23]. To separate Symbiodiniaceae from coral skeletons and tissues, we utilized a high-pressure water jet (WaterPik irrigator) powered by sterile filtered seawater. All rinse water was collected and measured. A 1 mL of rinse water was centrifuged at 4000 × g for 10 min, and the supernatant was discarded. The remaining cells were resuspended in 1 mL of 4% formaldehyde fixative. This suspension was placed on a hemocytometer, covered with a glass slide, and counted under the optical microscope (Nikon, DS-Ri2). The washed coral skeletons were dried in an oven at 60 °C for 72 h to remove moisture. Each coral skeleton fragment was fully wrapped in aluminum foil. A 5 cm × 5 cm piece of aluminum foil was weighed to determine the coral surface area based on the weight-to-area ratio [24]. The density of Symbiodiniaceae per unit area of coral was calculated as described in the previous study [25]. To determine Chlorophyll *a* concentration, coral fragments were soaked in 90% acetone and extracted in the dark at 4 °C for 24 h. The absorbance of 664 nm, 647 nm, and 630 nm was measured using a spectrophotometer (Thermo Fisher), and the concentration was calculated using the equations recommended by Jeffery and Humphrey [26].

DNA Extraction, High Throughout Sequencing and Bioinformatics Analysis

A fragment weighing about 90 mg, including calcium carbonate skeleton, tissue, and mucous components, was taken from each coral sample to extract genomic DNA. DNA extraction was performed using the Marine Animal Genomic DNA Extraction Kit (TIANGEN, DP324), following the

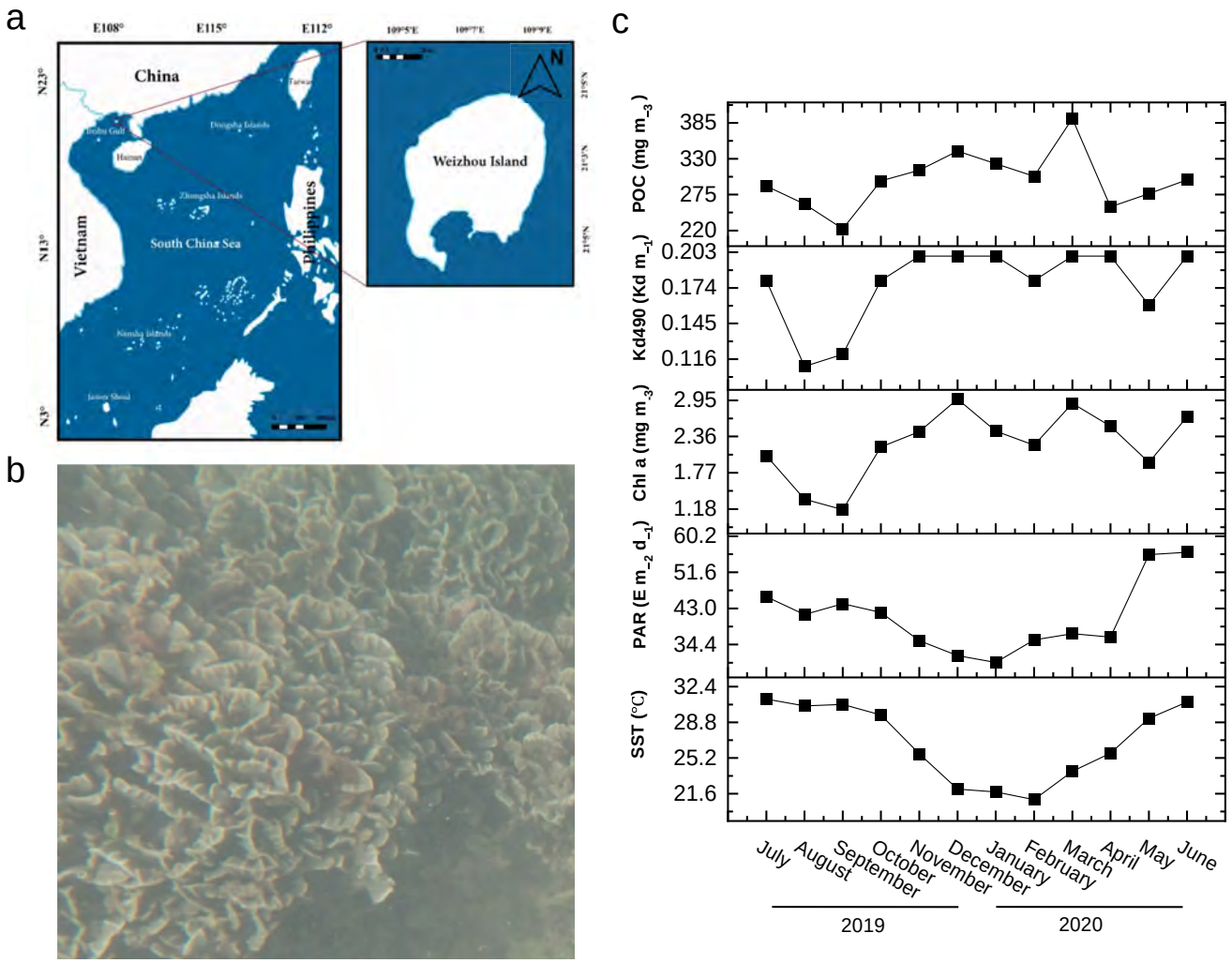


Fig. 1 The collection of coral samples and environmental data. (**a**) Sampling site in the coral reef area of Weizhou Island; (**b**) State of *P. decussata* in summer; (**c**) Environmental parameters of Weizhou Island coral reef area each month from 2019 to 2020

manufacturer's instructions. After extraction, DNA quality was checked using agarose gel electrophoresis and UV A260/A280 absorbance measurements to ensure it met the required standards. Using high-quality DNA as a template, the ITS2 region of Symbiodiniaceae and the V3-V4 region of the bacterial 16S gene were amplified separately. The PCR reactions were set up, and conditions followed as described [17]. Qualified PCR products were sent on dry ice to Shanghai Meiji Biomedical Technology Co., Ltd. for MiSeq library construction and high-throughput sequencing.

To ensure the quality of the sequencing data, raw reads from the Illumina MiSeq Platform were processed using Trimmonmatic to filter out low-quality bases. High-quality reads were assembled and trimmed using PEAR, and chimeras were detected and removed through MOTHUR. Primer sequences were trimmed using CUTADAPT. The data were cleaned using DADA2 and Deblur to correct sequencing errors, remove chimeric sequences, filter out low-quality reads, and trim potential contaminants. This process produced accurate ASV representative sequences and abundance tables.

To analyze Symbiodiniaceae community composition, we used a refined, non-duplicate ITS2 database to avoid replicate sequences. This database was created by compiling several published datasets and processing them with the CD-HIT Suite at a 100% sequence identity cut-off, as described in our previous study [27]. This method allowed us to accurately identify representative sequences and generate abundance tables for Symbiodiniaceae subclades.

Isolation and Cultivation of Coral-Associated Photosynthetic Microorganisms

To facilitate the subsequent isolation of photosynthetic microorganisms, the collected *P. decussata* were transported to the Coral Reef Research Center at Guangxi University and placed in an aquarium with stable conditions: 600 mm × 600 mm × 600 mm (length × width × height), water flow at 6,500 L/h, color temperature at 15,000 K (12 h of light daily from 6:00 to 18:00), salinity of 35 g/L, pH between 7.5–8.0, Ca^{2+} concentration of 380–450 ppm, Mg^{2+} concentration of 1,200–1,320 ppm, and water temperature at 25 °C.

All subsequent microbial isolations were from *P. decussata*. Once the coral's tentacles had fully extended, a healthy 2 cm × 2 cm fragment was excised and placed in sterile cryovials. The fragment was rinsed three times with sterile seawater to remove contaminants, then transferred to a sterile shaker with grinding beads (Shanghai Jingxin, JXFSTPRP-24) and 3 mL of sterile seawater. The shaker was set to 50 Hz for 1 min to disrupt the coral polyps and release the Symbiodiniaceae cells.

The cultivation of Symbiodiniaceae was as previously described [28]. Briefly, the Symbiodiniaceae were isolated from coral fragments using micro-strainer filtration and density gradient centrifugation, then cultured in 96-well plates with L1 medium. Single cells were isolated by dilution to extinction, and species and phylogenetic relationships were identified using ITS2 sequences. Culturing was conducted in a light incubator (Yanghui Instruments, RDN-500D-CO2) under the following conditions: 25 °C, 45 ± 5 µmol photons m^{-2} s^{-1}, and a 14:10 h light–dark cycle for two weeks.

Cyanobacteria were released and isolated similarly. Cyanobacteria were cultured on BG-11 plates under the same conditions as the Symbiodiniaceae. Colonies with significant morphological differences were selected for isolation and purification. Morphological characteristics were observed using optical and scanning electron microscopes, as described previously [29].

Temperature Experiment of Coral-Associated Photosynthetic Microorganisms

The temperature stress experiments were designed based on remote sensing data from the Weizhou Island coral reef area. High, ambient, and low temperatures were set at 32 °C, 25 °C, and 20 °C, respectively, representing the highest summer SST, the average spring and autumn SST, and the lowest winter SST (Fig. 1c).

The experiments included four parts: individual cultivations of *Cladocopium* C1 and *Cyanobium*_PCC-6307 and co-cultivation with a density ratio 100:1. Photosynthetic microorganisms were synchronously cultured under different temperature conditions for 7 days. The temperature experiment used isoclonal cultures, with three biological replicates for each condition, and each biological replicate included at least three technical replicates. After the temperature experiment, the following photosynthetic physiological parameters were measured. (1) Fv/Fm measurement: Fv/Fm was measured using Pulse-Amplitude Modulation (Walz Heinz GmbH, Effeltrich, Germany) to determine the PSII photochemical efficiency of photosynthetic microorganisms 20 min after turning off the light. (2) Density measurement: Symbiodiniaceae density was counted using a hemocytometer under an optical microscope [30]. The density of individually cultured cyanobacteria was measured by reading the absorbance value at 730 nm to estimate the number of cells [31]. The density of cyanobacteria in co-cultures was measured using Real-Time Quantitative PCRs. (3) Chlorophyll *a* measurement: Chlorophyll *a* was extracted using 90% acetone at 4 °C in the dark for 24 h. Absorbance values were measured at 664 nm, 647 nm, and 630 nm using a spectrophotometer (Varioskan LUX, Thermos Fisher Scientific, USA), and the concentration was calculated using the equations by Jeffery and Humphrey [26]. (4) Reducing sugar measurement: Reducing sugar content was determined using the phenol–sulfuric acid method[32].

Real-Time Quantitative PCR

To quantify changes in Cyanobacterial abundance in the co-culture experiment, the primers BD16SF (5' CACACT GGGACTGAGACAC −3') and BD16SR (5' CTGCTGGCA CGGAGTTAG −3') were selected as Cyanobacteria-specific primers for real-time quantitative PCR [33]. The reactions mixture, with a total volume of 10 µL, consisted of 5 µL SYBR Premix EX Taq™, 0.2 µL of each primer (10 pmol/µL), 1 µL DNA template, and 3.6 µL ddH_2O. The reactions were run on the QuantStudio™ 5 Real-Time PCR Instrument (Thermos Fisher Scientific, USA), with the following conditions: an initial denaturation at 95 °C for 30 s, followed by 35 cycles of 95 °C for 30 s, 56 °C for 30 s, 72 °C for 45 s, with a final extension at 72 °C for 10 min.

Statistical Analysis and Data Visualization

For data following a normal distribution, a one-way analysis of variance (ANOVA) was conducted to assess significant differences, followed by Tukey's Honestly Significant Difference (HSD) post-hoc test for pairwise comparisons. The non-parametric Kruskal–Wallis test was applied for data not following a normal distribution, followed by pairwise comparisons with the Bonferroni-Dunn adjustment for multiple comparisons. Statistical analyses were performed using

SPSS 27.0. Data visualization was carried out using Origin Pro 2023 and R 4.3.3.

Results

Seasonal Variation of Environmental Parameters at Weizhou Island

The environmental parameters in the Weizhou Island coral reef area show significant seasonal fluctuations, with the most extreme values occurring in either summer or winter. SST and PAR follow similar trends, with their lowest values in winter and highest in summer and late spring. During the sampling period, the highest values for SST and PAR were 31.15 °C and 45.78 E m^{-2} d^{-1}, respectively, occurring in summer (July 2019). The lowest values were 20.99 °C and 30.15 E m^{-2} d^{-1}, respectively, in winter (July 2019, February, and January 2020). The two parameters have a strong positive correlation (Pearson correlation coefficient, $r = 0.789$, $P < 0.01$, Table S1) and exhibit consistent, gradual seasonal changes.

Chl *a* Kd490, and POC exhibit extreme values in either summer or winter. The highest values for Chl *a*, Kd490, and POC were 2.9 mg m^{-3}, 0.201 Kd m^{-1}, 391.783 mg m^{-3}, respectively, in the summer (July 2019). The lowest values were 1.17 mg m^{-3}, 0.116 Kd m^{-1}, 222.738 mg m^{-3} in autumn (December 2019) and winter (March 2020). These three environmental parameters do not show a strong correlation with seasonal changes. Overall, within the sampling time frame, Weizhou Island exhibits experienced high temperatures and strong sunlight in summer, as well as low temperatures and weak sunlight in winter. Notably, *P. decussata* showed no signs of bleaching (Fig. 1b).

Seasonal Variation of Coral-Associated Photosynthetic Physiological State

The density of Symbiodiniaceae varied across the four seasons, ranging from 0.32×10^6 cells·cm^{-2} to 1.47×10^6 cells·cm^{-2} (Fig. 2a). The lowest density was in summer (0.51×10^6 cells·cm^{-2}), followed by spring and autumn. The highest was in winter (0.84×10^6 cells·cm^{-2}), about 1.64 times higher than in summer. Chlorophyll *a* concentration ranged from 3.48 μg·cm^{-2} to 12.45 μg·cm^{-2} (Fig. 2b). Similar to Symbiodiniaceae density, Chlorophyll *a* concentration was lowest in summer (5.20 ± 0.38 μg·cm^{-2}), and highest in winter (8.93 ± 1.79 μg·cm^{-2}), approximately 1.72 times that of summer. Statistic analysis showed that Symbiodiniaceae density and Chlorophyll *a* concentration were significantly higher in winter than in summer.

Molecular marker analysis based on ITS2 was performed on *P. decussata* samples. After quality control and filtering, 117 ASVs were detected. All identified Symbiodiniaceae belonged to the genus *Cladocopium*, with 115 subclade sequences. At the subclade level, the Symbiodiniaceae community composition showed no significant variation across the seasons. The dominant subclade was consistently C1, with relative abundances ranging from 81.63% to 82.33%. Other subclades, such as C1ca, C1p, C72, and Cspc, had relative abundances ranging from 2.57% to 3.06%, 3.30% to 3.11%, 2.45% to 2.77%, and 1.98% to 2.18%, respectively. Overall, the Symbiodiniaceae community remained stable throughout the four seasons.

Seasonal Variation of Coral-Associated *Bacteria*

At the phylum level, Proteobacteria and Bacteroidota dominated the bacterial communities across all four seasons. Proteobacteria had the highest relative abundance, ranging from 65.21% to 88.52%. Bacteroidota was the second most abundant phylum, with relative abundances from 1.48% to 21.07% (Fig. 3a). At the genus level, the dominant genera were the BD1-7_clade and *Endozoicomonas* of the phylum Proteobacteria. BD1-7_clade had relative abundances of 50.59%, 45.70%, 34.67%, and 21.25% in summer, autumn, winter, and spring, respectively. *Endozoicomonas* had relative abundances of 34.76%, 28.16%, and 24.84% in autumn, winter, and spring but dropped to 0.13% in summer (Fig. 3b).

Principal Coordinates Analysis (PCoA) based on the Bray–Curtis algorithm at the ASV level showed significant differences in the bacterial community structure among the seasons (PERMANOVA, $R^2 = 0.26$, $P < 0.05$, Fig. 3c). While there was some overlap in the bacterial communities across all seasons, the structure in summer was significantly different from the others. The relative abundance of the photosynthetic bacterium BD1-7_clade peaked in summer at 50.59%, compared to 21.25%—45.70% in other seasons. In contrast, the relative abundance of *Endozoicomonas* in summer dropped to 0.13% (Fig. 3b), much lower than that in the other three seasons (24.84%—34.76%). This shift indicates that BD1-7_clade dominates the bacterial community composition in summer, while in other seasons, both BD1-7_clade and *Endozoicomonas* co-dominate.

Seasonal Variation of Coral-Associated Photosynthetic *Bacteria*

Among the top 20 species at the genus level by relative abundance, we identified three photosynthetic bacteria: the proteorhodopsin bacterium BD1-7_clade, *Synechococcus*_CC9902, and *Cyanobium*_PCC-6307. The relative abundance of all three photosynthetic bacteria peaked in the summer. BD1-7_clade, the dominant genus in all four seasons, had a relative abundance of 50.59% in summer, 45.70%

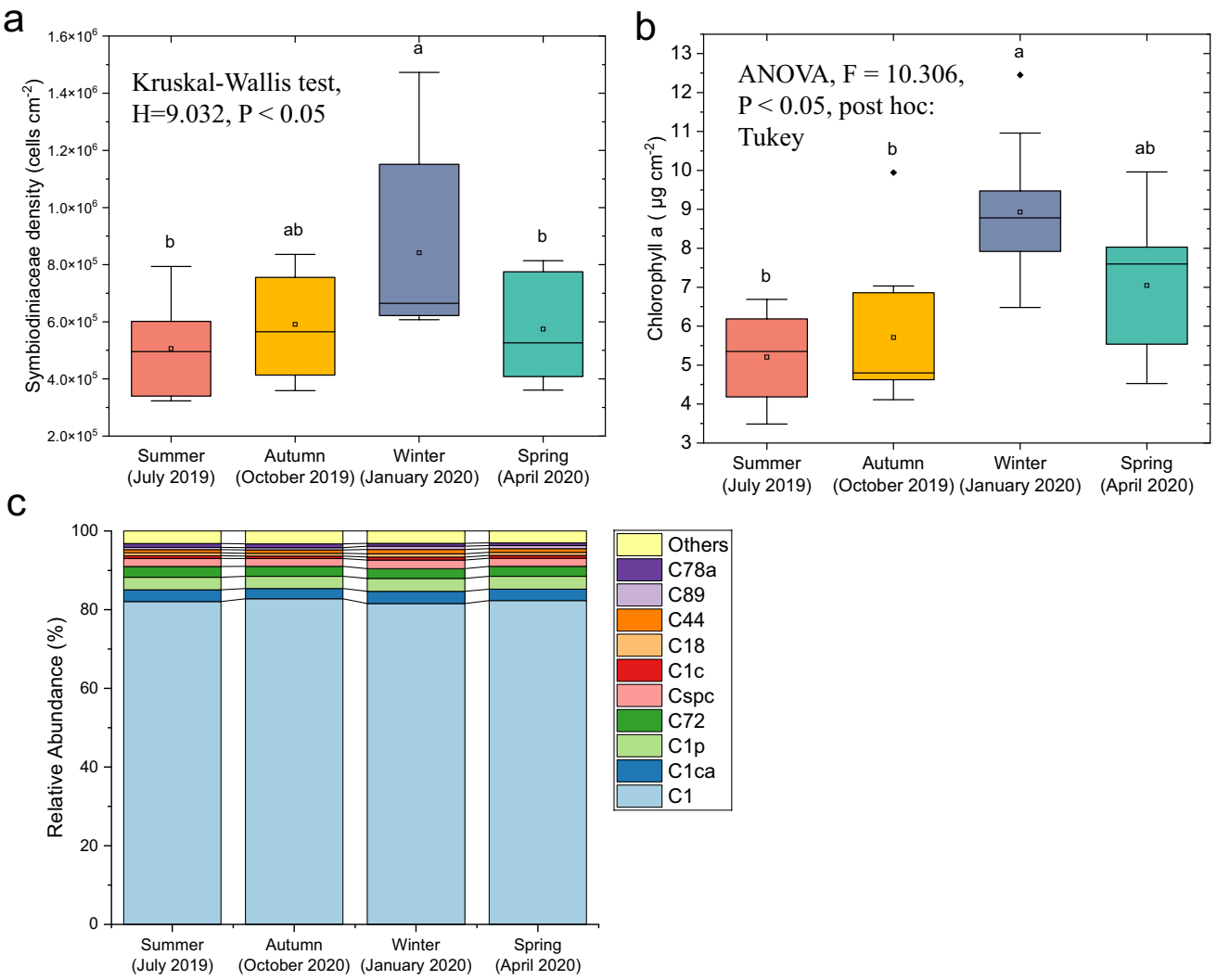


Fig. 2 Seasonal variation differences in the photosynthetic physiological state of *P. decussata*. (a) Seasonal variation differences in Symbiodiniaceae density of *P. decussata*; (b) Seasonal variation differences in Chlorophyll *a* concentration of *P. decussata*. (c) Seasonal variation differences in Symbiodiniaceae community composition of *P. decussata*. Data in Fig. 2c are mean values, and the number of samples for each season is 5

in autumn, 34.67% in winter, and 21.25% in spring. Despite showing no significant seasonal differences in relative abundance, BD1-7_clade reached its highest levels in summer (Figs. 3b and 4c). The relative abundance of *Synechococcus*_CC9902 was 1.08% in summer, 0.60% in autumn, 0.05% in winter, and 0.27% in spring, showing significant differences across the seasons. Similarly, the relative abundance of *Cyanobium_PCC-6307* was 0.55% in summer, 0.17% in autumn, 0.009% in winter, and 0.01% in spring, demonstrating significant seasonal variation (Fig. 4a).

Based on 16S amplicon sequencing data, the community composition and ASVs of Cyanobacteria at the phylum level were obtained for each sample. 381 Cyanobacteria ASVs were detected across the coral samples in all four seasons, belonging to 3 orders, 11 families, 21 genera, and 36 species (Table S2). In summer and autumn, *Synechococcus*_CC9902 and *Cyanobium*_PCC-6307 were dominant, with their relative abundance peaking in summer, at 61.85% and 31.48%, respectively (Fig. 4b).

Effect of High Temperatures on Coral-Associated Photosynthetic Microorganisms

We successfully isolated *Cladocopium* C1 and *Cyanobium*_PCC-6307 from *P. decussata,* but could not isolate BD1-7_clade and *Synechococcus*_CC9902. Symbiodiniaceae cultures are known to harbor their own microbiomes, which may include *Synechococcus* and *Cyanobium* [34]. To account for this, we sequenced the in vitro microbiomes of the isolated *Cladocopium* C1 cultures. The results showed

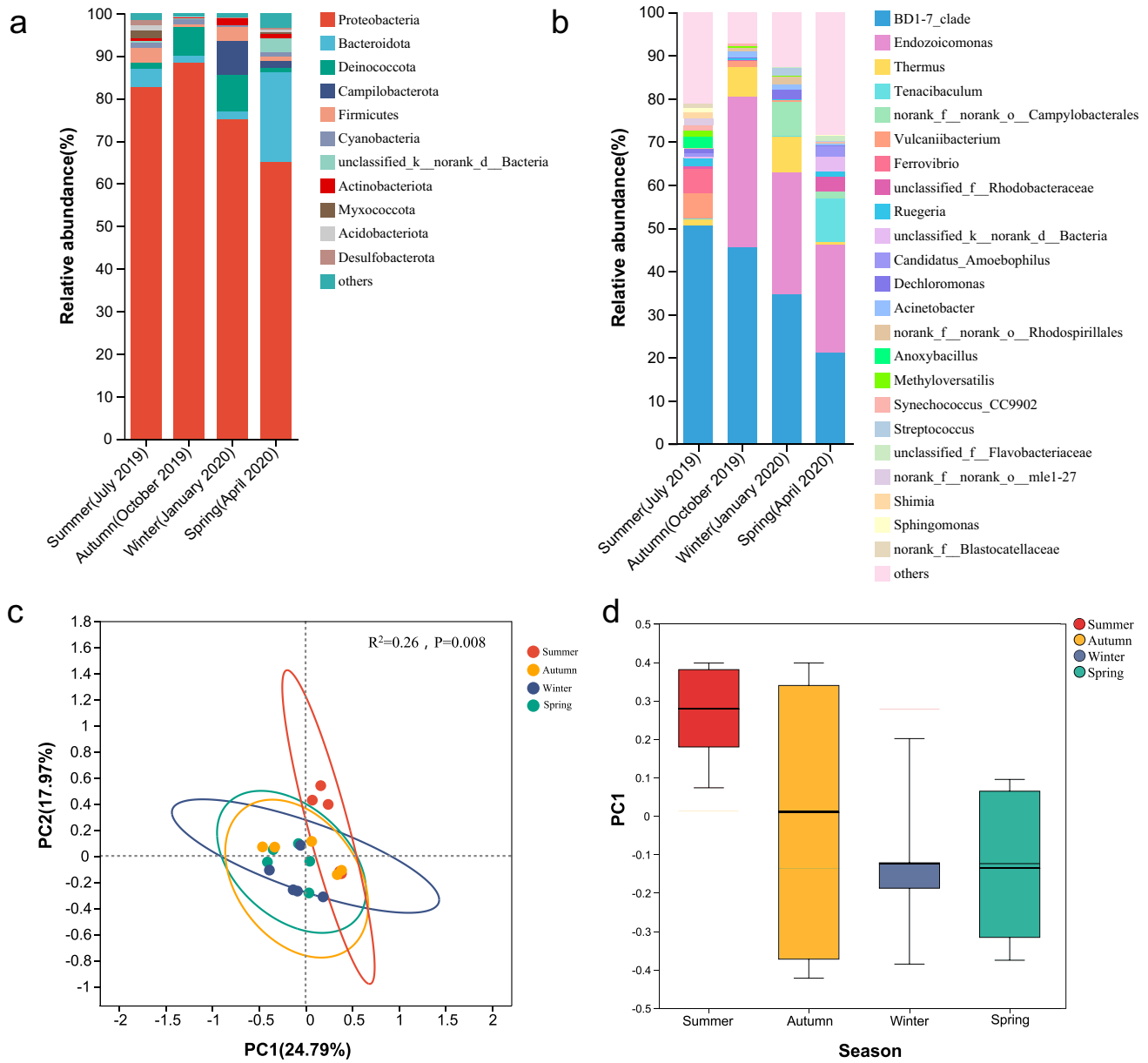


Fig. 3 Seasonal variation differences in the bacterial community of *P. decussata*. (a) The bacterial community composition at the phylum level; (b) The bacterial community composition at the genus level; (c) Principal Coordinates Analysis (PCoA) of the bray–curtis distance matrix representing differences in community structure at the ASV level; (d) The distribution dispersion of samples on the PC1 axis under different seasons. Data in the Fig. 3 are mean values, and the number of samples for each season is 5

that the associated bacterial community of *Cladocopium* C1 did not contain any Cyanobacteria (Table S3 and Fig. S2).

Under different temperature conditions, the photosynthetic physiological indicators of *Cladocopium* C1 changed significantly. At 20 °C, 25 °C, and 32 °C, the Symbiodiniaceae density was $(1.20 \pm 0.05) \times 10^6$ cells cm^2, $(3.25 \pm 0.22) \times 10^6$ cells cm^2, and $(1.15 \pm 0.12) \times 10^6$ cells cm^2, respectively (Fig. 5c). At 20 °C, 25 °C, and 32 °C, the Fv/Fm was 0.57 ± 0.05, 0.68 ± 0.04, and 0.46 ± 0.03, respectively (Fig. 5d). The Chlorophyll *a* concentrations at 20 °C, 25 °C and 32 °C were 0.50 ± 0.04 μg/mL, 1.33 ± 0.23 μg/mL, and 0.42 ± 0.03 μg/mL, respectively (Fig. 5e). Statistic analysis showed that both high and low temperatures led to a significant decrease in cell density, Fv/Fm, and Chlorophyll *a* concentration, with a more pronounced reduction at high temperatures.

In contrast, the photosynthetic physiological indicators of the *Cyanobium*_PCC-6307 improved with increasing temperature. At 32 °C, OD_{730} was 1.36 ± 0.07, representing a significant increase of 25.93% and 49.45% compared to 25 °C and

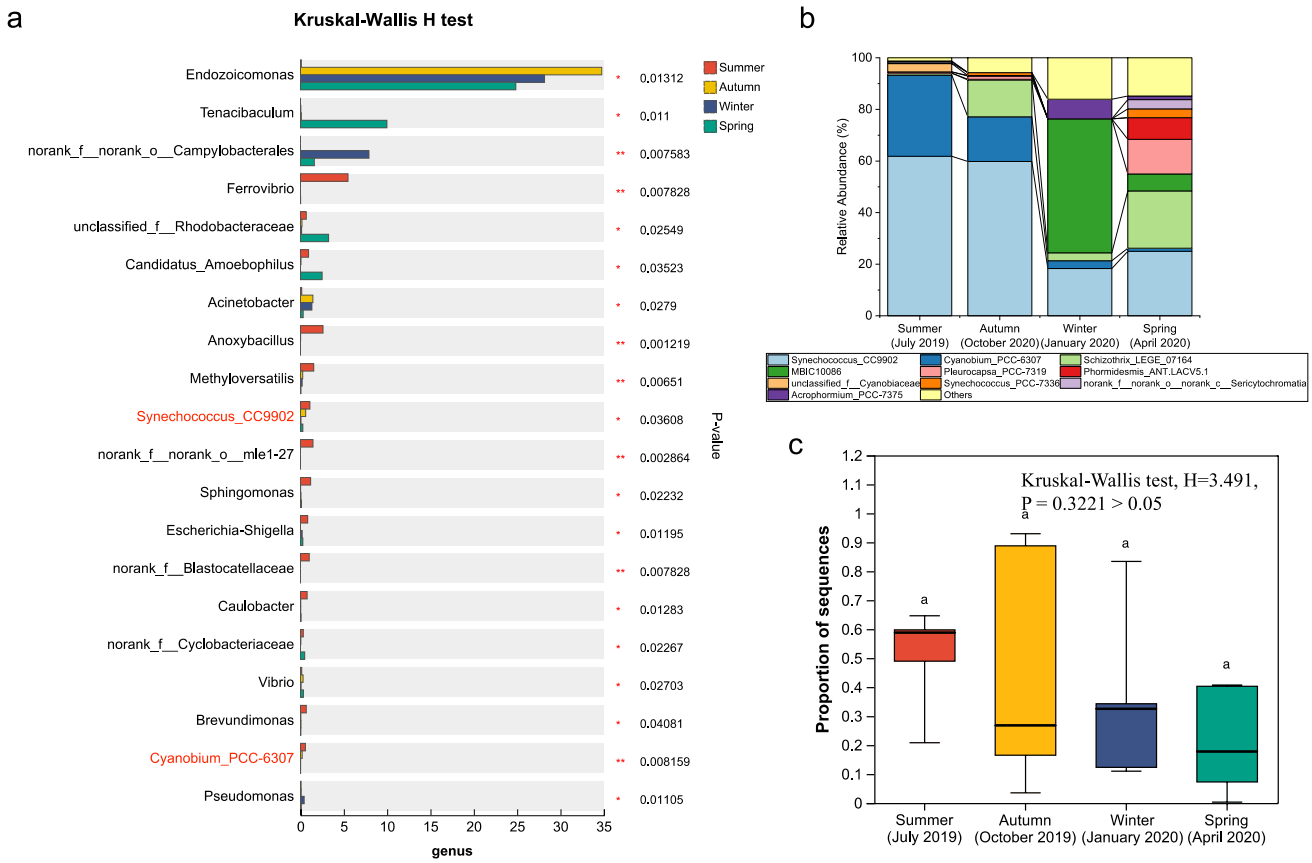


Fig. 4 Changes of photosynthetic bacteria in different seasons. (**a**) Multiple comparisons of the top 20 species with significant differences in relative abundance at the genus level. * $0.01 < P \leq 0.05$, ** $0.001 < P \leq 0.01$, *** $P \leq 0.001$. (**b**) Seasonal variation differences in Cyanobacteria community composition of *P. decussata* on genus level (**c**) The proportion of BD 1–7 clade in four seasons. Data in the Fig. 4 are mean values, and the number of samples for each season is five

20 °C, respectively (Fig. 5h). Similarly, at 32 °C, Fv/Fm was 0.52 ± 0.15, showing a significant increase of 10.64% and 44.44% compared to 25 °C and 20 °C, respectively (Fig. 5i).

The photosynthetic indicators exhibited distinct patterns under different temperature conditions in *Cladocopium* C1 and *Cyanobium*_PCC-6307 co-culture. The density of *Cladocopium* C1 and *Cyanobium*_PCC-6307 at 25 °C were significantly higher than at 20 °C and 32 °C (Figs. 6a and 6b). The density of *Cladocopium* C1 at 25 °C was $(8.39 \pm 2.22) \times 10^5$ cells/mL. At 20 °C and 32 °C, it decreased to $(4.61 \pm 1.19) \times 10^5$ cells/mL and $(4.78 \pm 1.33) \times 10^5$ cells/mL, respectively. The density of *Cyanobium*_PCC-6307 at 25 °C was $(1.53 \pm 0.39) \times 10^7$ copies/mL. At 20 °C and 32 °C, it decreased to $(1.06 \pm 0.43) \times 10^7$ copies/mL and $(0.65 \pm 0.54) \times 10^7$ copies/mL. However, Fv/Fm increased significantly with rising temperature, reaching 0.64 ± 0.02, 0.70 ± 0.02, 0.72 ± 0.03 at 20 °C, 25 °C, and 32 °C, respectively (Fig. 6c). Additionally, the concentration of reducing sugar and Chlorophyll *a* did not show significant differences with temperature changes. The reducing sugar concentration at 20 °C, 25 °C, and 32 °C were 0.81 ± 0.07 μg/mL, 0.81 ± 0.03 μg/mL, and 0.79 ± 0.04 μg/mL, respectively. The Chlorophyll *a* concentration at 20 °C, 25 °C, and 32 °C were 0.42 ± 0.06 μg/mL, 0.43 ± 0.05 μg/mL, and 0.39 ± 0.02 μg/mL, respectively.

Discussion

Seasonal Variation Pattern of Coral-Associated Photosynthetic Physiological State

Symbiodiniaceae plays a crucial role in the health and resilience of corals, with its density and community composition commonly used to characterize coral photosynthetic performance and assess environmental adaptability [35]. Higher Symbiodiniaceae density is generally associated with better stress resistance in corals [23]. Corals can also adjust the relative abundance of symbiotic Symbiodiniaceae or acquire new types from the environment through processes known as reshuffling or replacement to adapt to changing environmental conditions [36].

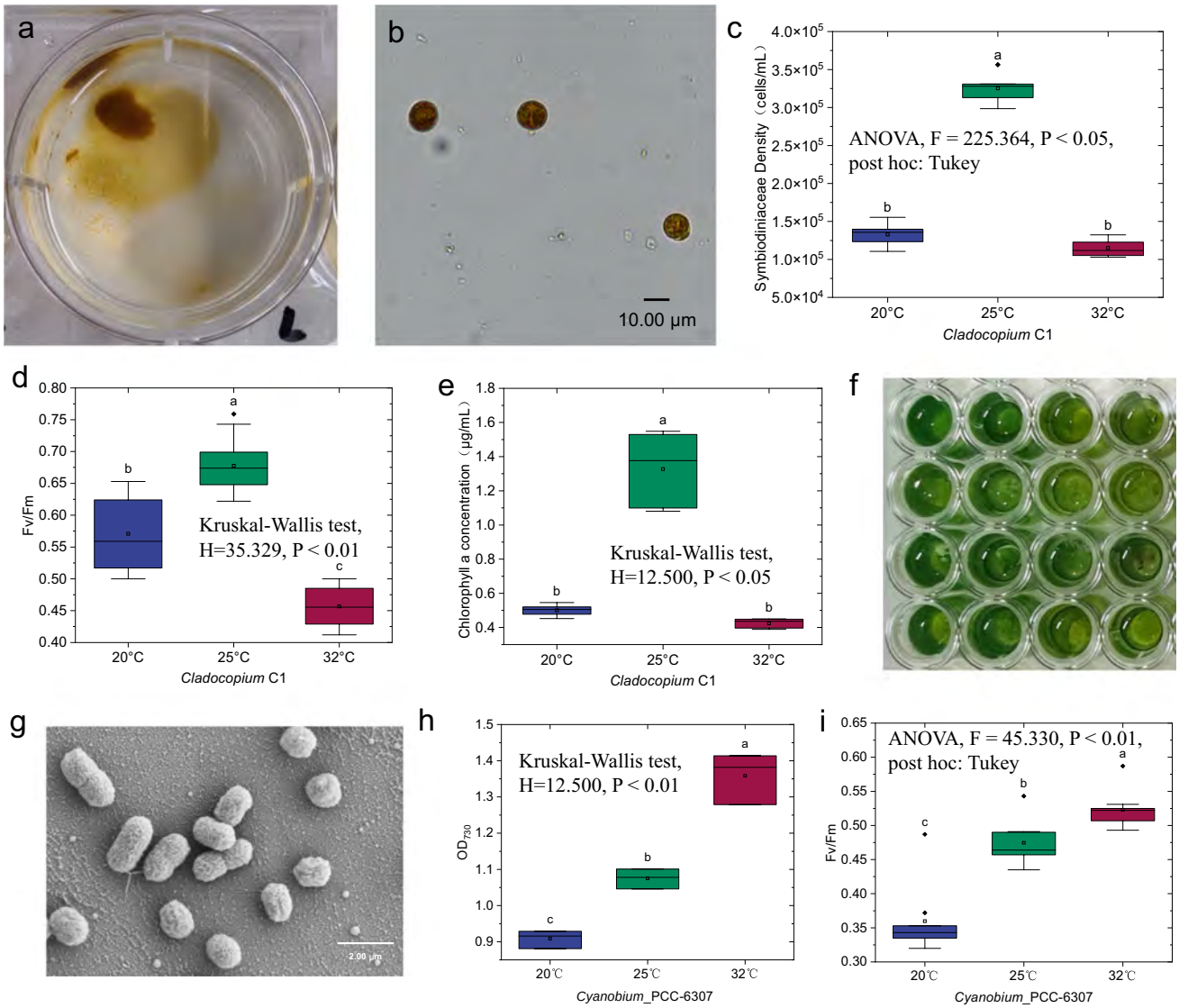


Fig. 5 The photophysical status of coral-associated photosynthetic microorganisms under different temperature conditions. (**a**) L1 medium showing growth of *Cladocopium* C1. (**b**) Morphological characteristic of *Cladocopium* C1 in vitro under optical microscopy. (**c**) The density of *Cladocopium* C1 under different temperatures. (**d**) The Fv/Fm of *Cladocopium* C1 under different temperatures. (**e**) The Chlorophyll *a* concentration of *Cladocopium* C1 under different temperatures. (**f**) BG-11 medium showing growth of *Cyanobium*_PCC-6307. (**g**) Morphological characteristic of *Cyanobium*_PCC-6307 in vitro under scanning electron microscopy. (**h**) Changes in OD_{730} of *Cyanobium*_PCC-6307 under different temperatures. (**i**) Changes in Fv/Fm of *Cyanobium*_PCC-6307 under different temperatures

Our results showed that *Cladocopium* C1 stably symbioses with *P. decussata*, remaining the dominant species (81.63%~82.33%), with a stable Symbiodiniaceae community composition (Fig. 2c). The Symbiodiniaceae density and Chlorophyll *a* concentration followed a seasonal pattern, being lowest in summer and highest in winter (Figs. 2a and 2b), consistent with previous studies [37]. In summer, high temperatures and intense light can damage the photosystem II of Symbiodiniaceae chloroplasts [38], reducing photosynthetic efficiency, generating excess electrons, leading to the overproduction of reactive oxygen species, which can damage coral tissue and DNA, ultimately causing Symbiodiniaceae cell death or expulsion from the coral host [39]. Consequently, in the high-temperature, intense-light environment of summer, Symbiodiniaceae density and Chlorophyll *a* concentration significantly decrease, photosynthetic efficiency drops, and the ability to fix carbon may decrease [40], leading to a significant reduction in organic carbon transferred to the coral host. This suggests that the energy supply of *P. decussata* may be compromised. However, field observations in summer showed that *P. decussata* on Weizhou Island did not exhibit apparent bleaching (Fig. 1b), indicating that other microorganisms may help maintain the stability of *P. decussata*.

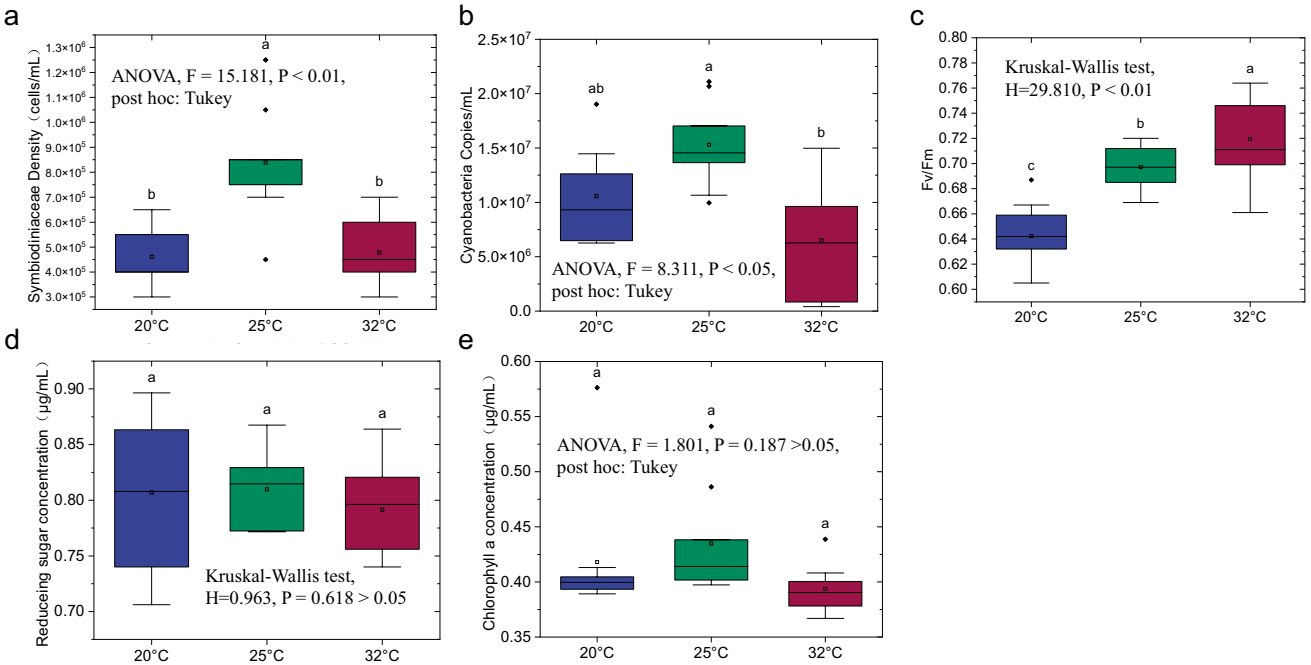


Fig. 6 The photophysical status of *Cladocopium* C1 and *Cyanobium*_PCC-6307 co-cultured under different temperatures. (**a**) The density of co-cultured *Cladocopium* C1 under different temperatures. (**b**) The copies of co-cultured *Cyanobium*_PCC-6307 under different temperatures. (**c**) The Fv/Fm of *Cladocopium* C1 and *Cyanobium*_PCC-6307 co-cultured under different temperatures. (**d**) The reducing sugar concentration of *Cladocopium* C1 and *Cyanobium*_PCC-6307 co-cultured under different temperatures. (**e**) The Chlorophyll *a* concentration of *Cladocopium* C1 and *Cyanobium*_PCC-6307, was co-cultured under different temperatures

Seasonal Variation Pattern of Coral-Associated Photosynthetic Microorganisms

Symbiotic bacteria are integral to coral adaptation to environmental changes, playing critical roles in nutrient cycling, energy provision, and immune responses [41]. Our results showed that the bacterial structure during the summer significantly differed from other seasons, shifting from the co-dominance of BD1-7_clade and *Endozoicomonas* to the sole dominance of BD1-7_clade. Additionally, the relative abundance of *Synechococcus*_CC9902 and *Cyanobium*_PCC-6307 peaked during the summer.

BD1-7_clade is an oligotrophic bacteria adapted to extreme carbon source limitation and nutrient depletion conditions [42]. Its genome contains genes encoding rhodopsin, carotenoids, and polyketide synthase, allowing it to perform photosynthesis via proteorhodopsin even in environments with low organic matter [43]. This reduces the energy demands on *P. decussata* and likely explains the peak abundance of BD1-7_clade in summer. BD1-7_clade's ability to perform photoheterotrophy through rhodopsins may also help mitigate the impact of high light conditions on *P. decussata* and offset the reduced photosynthesis by Symbiodiniaceae.

Similarly, Cyanobacteria displayed a comparable seasonal variation pattern. *Synechococcus*_CC9902 and *Cyanobium*_PCC-6307 had the highest abundance in summer under high temperatures and intense light, while they were lowest in winter under low temperatures and weak light (Fig. 4b). These Cyanobacteria are small, distributed in marine environments globally [44], and have evolved highly efficient photosynthetic apparatuses [45]. They also tolerate high temperatures and can uptake nutrients at low concentrations [46, 47]. For instance, *Synechococcus*_WH7803 prefers high temperatures, with an optimal growth temperature of up to 33 °C, and maintains high photosynthetic efficiency even at elevated temperatures [48, 49]. Synechococcales are well adapted to oligotrophic environments, with cyanobacterial densities reaching up to 4×10^5 cells/mL [50]. Given their high photosynthetic efficiency under low nutrient concentration, *Synechococcus*_CC9902 and *Cyanobium*_PCC-6307 may potentially supply photosynthetic products to Symbiodiniaceae during summer.

Response Pattern of Cultured Coral-Associated Photosynthetic Microorganisms to High-temperature Conditions

The in vitro cultivation of coral-associated microorganisms is crucial for understanding how coral responds to

environmental changes [51]. To explore whether photosynthetic bacteria can compensate for the decreased photosynthetic efficiency of Symbiodiniaceae under high-temperature conditions, we studied *Cladocopium* C1 and *Cyanobium*_PCC-6307, both individually and in co-culture, under different temperature conditions.

After 7 days of single culturing, the physiological indicators of *Cladocopium* C1 declined under high and low temperatures. Fv/Fm and Chlorophyll *a* concentration, which reflect the photosynthetic efficiency of Symbiodiniaceae[52], showed significant decreases. This suggests that extreme temperatures, particularly high temperatures, impair the photosynthetic efficiency of Symbiodiniaceae, supporting previous research indicating that *Cladocopium* C1 is thermally sensitive [53]. Abnormal temperatures can lead to the accumulation of reactive oxygen species (ROS) [54], damaging to the photosystem that absorbs excitation energy [55]. In contrast, *Cyanobium*_PCC-6307 demonstrated strong adaptability to high temperatures. After 7 days of 32℃, the Fv/Fm of and OD_{730} of *Cyanobium*_PCC-6307 significantly increased compared to routine and low-temperature conditions (Figs. 5h and 5i), indicating enhanced photosynthetic efficiency under high-temperature conditions. This is consistent with previous reports that certain Cyanobacterial strains prefer high temperatures, showing maximal growth rates, cell density, and Fv/Fm [48].

After 7 days of co-culturing, Fv/Fm increased significantly with rising temperature, reaching the highest value at 32 °C, which was higher than that observed in the single cultures of *Cladocopium* C1 and *Cyanobium*_PCC-6307, reflecting a synergistic effect. However, further studies are needed to quantify the individual contributions to overall photosynthetic performance. The concentrations of reducing sugar and Chlorophyll *a* were unaffected by temperature, showing no significant differences across the temperature gradients. Surprisingly, *Cladocopium* C1 and *Cyanobium*_PCC-6307 exhibited the same responses to temperature changes. The Symbiodiniaceae density in the co-culture system was highest at 25 °C and significantly decreased at 20 °C and 32 °C, consistent with the results from the single cultures. However, the Cyanobacteria copies were lowest at 32 °C, contrary to the results observed in the single cultures. This discrepancy may be due to interactions between the symbiotic bacterial community of Symbiodiniaceae and Cyanobacteria [16]. Despite this, the Cyanobacteria density still reached 10^6 copies/mL, sufficient to maintain the photosynthesis efficiency of the co-culture system. Results from the co-culture experiment indicated that high temperatures had minimal impact on the photosynthesis efficiency of *Cladocopium* C1 and *Cyanobium*_PCC-6307 co-culture system. Previous research has shown that Symbiodiniaceae can benefit from metabolic exchanges with bacteria. For example, the co-culture of Symbiodiniaceae and *Ruegeria* sp. thrives in nitrogen-free conditions, with ^{15}N-stable isotope probing-single cell Raman spectroscopy verifying *Ruegeria* sp.'s role as a nitrogen supplier to Symbiodiniaceae [56]. Furthermore, *Labrenzia alexandrii* and *Marinobacter* sp. synthesize indole-3-acetic acid (IAA), a phytohormone that enhances the growth of Symbiodiniaceae [12].

Our results show that *Cyanobium*_PCC-6307 can help Symbiodiniaceae improve photosynthetic efficiency and may offer metabolic benefits under high-temperature conditions. Further research is needed to establish a direct link between these findings and the prevention of coral bleaching *in hospite*. Overall, our results highlight the significant role of photosynthetic bacteria, particularly *Cyanobium*_PCC-6307, in enhancing the photosynthetic efficiency of Symbiodiniaceae under high-temperature conditions. By boosting Symbiodiniaceae photosynthesis, *Cyanobium*_PCC-6307 indirectly contributes to maintaining coral health and aiding adaptation to environmental changes. This knowledge provides new insights into the potential role of photosynthetic bacteria within the coral holobiont and is essential for developing strategies to protect and restore coral reefs.

Conclusion

We employed a comprehensive approach utilizing amplicon sequencing, microbiological isolation, and cultivation to analyze the dynamic changes in symbiotic Symbiodiniaceae and photosynthetic bacteria in *P. decussata* across four seasons on Weizhou Island. Additionally, we examined the physiological states of *Cladocopium* C1, *Cyanobium_PCC-6307*, and their co-culture under varying temperature conditions in the laboratory. Our findings suggest that symbiotic Symbiodiniaceae and photosynthetic bacteria may collectively contribute to the energy supply of *P. decussata* symbiotic consortia in response to seasonal changes. Furthermore, the results indicate a potential compensatory effect of photosynthetic bacteria on the photosynthesis of Symbiodiniaceae under high-temperature conditions. However, while our results highlight the possible synergistic interaction between photosynthetic microorganisms in maintaining coral photosynthetic physiology under high-temperature conditions, the direct impact of these interactions on the coral host, particularly in maintaining healthy photosynthate translocation, requires further investigation. These findings underscore the potential role of photosynthetic bacteria in supporting coral adaptation to high-temperature environments, particularly during the summer. It provides valuable insights into the environmental adaptability of coral symbiotic consortia.

Supplementary Information The online version contains supplementary material available at https://doi.org/10.1007/s00248-024-02470-4.

Acknowledgements Professor Guanghua Wang and Xiaopeng Yu from the School of Marine Sciences at Guangxi University provided assistance in samples collection and paper editing. And Professor Hong Ji from the College of Science at Guangdong University of Petrochemical Technology provided assistance in the aspect of paper editing. We would like to express our gratitude for their help.

Author Contributions Yongqian Xu: Conceptualization, Methodology, Resources, Data curation, Visualization, Validation, Writing – review & editing. Jiayuan Liang: Conceptualization, Resources, Validation, Writing – review & editing, Project administration, Funding acquisition. Liangyun Qin: Methodology, Resources, Investigation. Tianyi Ni: Methodology, Data curation. Zhicong Li and Zhuqing Liang: Data curation, Formal analysis Biao Chen: Software, Writing – review & editing Jin Zhou: Writing – review &editing. Kefu Yu: Project administration, Funding acquisition, review &editing.

Funding This work was supported by the National Natural Science Foundation of China (42030502 and 42090041), the Self-Topic Project of Guangxi Laboratory on the Study of Coral Reefs in the South China Sea (GXLSCRSCS2023101), and the Project of Shenzhen Science and Technology Innovation Committee (KCXFZ20211020165547011).

Data Availability Sequence data supporting this study's findings have been deposited in the NCBI SRA database (Accession number: PRJNA880748).

Declarations

Competing interests The authors declare no competing interests.

Open Access This article is licensed under a Creative Commons Attribution-NonCommercial-NoDerivatives 4.0 International License, which permits any non-commercial use, sharing, distribution and reproduction in any medium or format, as long as you give appropriate credit to the original author(s) and the source, provide a link to the Creative Commons licence, and indicate if you modified the licensed material. You do not have permission under this licence to share adapted material derived from this article or parts of it. The images or other third party material in this article are included in the article's Creative Commons licence, unless indicated otherwise in a credit line to the material. If material is not included in the article's Creative Commons licence and your intended use is not permitted by statutory regulation or exceeds the permitted use, you will need to obtain permission directly from the copyright holder. To view a copy of this licence, visit http://creativecommons.org/licenses/by-nc-nd/4.0/.

References

1. Voolstra CR, Suggett DJ, Peixoto RS et al (2021) Extending the natural adaptive capacity of coral holobionts. Nat Rev Earth Environ 2:747–762. https://doi.org/10.1038/s43017-021-00214-3
2. Voolstra CR, Raina J-B, Dörr M et al (2024) The coral microbiome in sickness, in health and in a changing world. Nat Rev Microbiol 1–16. https://doi.org/10.1038/s41579-024-01015-3
3. van Oppen MJH, Blackall LL (2019) Coral microbiome dynamics, functions and design in a changing world. Nat Rev Microbiol 17:557–567. https://doi.org/10.1038/s41579-019-0223-4
4. Jacobovitz MR, Hambleton EA, Guse A (2023) Unlocking the Complex Cell Biology of Coral-Dinoflagellate Symbiosis: A Model Systems Approach. Annu Rev Genet 57:411–434. https://doi.org/10.1146/annurev-genet-072320-125436
5. Huggett MJ, Apprill A (2019) Coral microbiome database: Integration of sequences reveals high diversity and relatedness of coral-associated microbes. Environ Microbiol Rep 11:372–385. https://doi.org/10.1111/1758-2229.12686
6. Lesser MP, Mazel CH, Gorbunov MY, Falkowski PG (2004) Discovery of symbiotic nitrogen-fixing cyanobacteria in corals. Science 305:997–1000. https://doi.org/10.1126/science.1099128
7. Ainsworth TD, Fordyce AJ, Camp EF (2017) The Other Microeukaryotes of the Coral Reef Microbiome. Trends Microbiol 25:980–991. https://doi.org/10.1016/j.tim.2017.06.007
8. Davy SK, Allemand D, Weis VM (2012) Cell Biology of Cnidarian-Dinoflagellate Symbiosis. Microbiol Mol Biol Rev 76:229–261. https://doi.org/10.1128/MMBR.05014-11
9. Yu K (2012) Coral reefs in the South China Sea: Their response to and records on past environmental changes. Sci China Earth Sci 55:1217–1229. https://doi.org/10.1007/s11430-012-4449-5
10. Morris LA, Voolstra CR, Quigley KM et al (2019) Nutrient Availability and Metabolism Affect the Stability of Coral-Symbiodiniaceae Symbioses. Trends Microbiol 27:678–689. https://doi.org/10.1016/j.tim.2019.03.004
11. Matthews JL, Raina J-B, Kahlke T et al (2020) Symbiodiniaceae-bacteria interactions: rethinking metabolite exchange in reef-building corals as multi-partner metabolic networks. Environ Microbiol 22:1675–1687. https://doi.org/10.1111/1462-2920.14918
12. Matthews JL, Khalil A, Siboni N et al (2023) Coral endosymbiont growth is enhanced by metabolic interactions with bacteria. Nat Commun 14:6864. https://doi.org/10.1038/s41467-023-42663-y
13. Ainsworth TD, Krause L, Bridge T et al (2015) The coral core microbiome identifies rare bacterial taxa as ubiquitous endosymbionts. ISME J 9:2261–2274. https://doi.org/10.1038/ismej.2015.39
14. Kvennefors E, Roff G (2009) Evidence of cyanobacteria-like endosymbionts in Acroporid corals from the Great Barrier Reef. Coral Reefs 28:547–547. https://doi.org/10.1007/s00338-009-0473-0
15. Lesser MP, Falcón LI, Rodríguez-Román A et al (2007) Nitrogen fixation by symbiotic cyanobacteria provides a source of nitrogen for the scleractinian coral Montastraea cavernosa. Mar Ecol Prog Ser 346:143–152. https://doi.org/10.3354/meps07008
16. Camp EF, Kahlke T, Nitschke MR et al (2020) Revealing changes in the microbiome of Symbiodiniaceae under thermal stress. Environ Microbiol 22:1294–1309. https://doi.org/10.1111/1462-2920.14935
17. Liang J, Deng C, Yu K et al (2021) Cross-Linked Regulation of Coral-Associated Dinoflagellates and Bacteria in Pocillopora sp. during High-Temperature Stress and Recovery. Microorganisms 9:1972. https://doi.org/10.3390/microorganisms9091972
18. Matthews JL, Hoch L, Raina J-B et al (2023) Symbiodiniaceae photophysiology and stress resilience is enhanced by microbial associations. Sci Rep 13:20724. https://doi.org/10.1038/s41598-023-48020-9
19. Ge R, Liang J, Yu K et al (2021) Regulation of the Coral-Associated Bacteria and Symbiodiniaceae in Acropora valida Under Ocean Acidification. Front Microbiol 12:3745. https://doi.org/10.3389/fmicb.2021.767174
20. Claar DC, McDevitt-Irwin JM, Garren M et al (2020) Increased diversity and concordant shifts in community structure of coral-associated Symbiodiniaceae and bacteria subjected to chronic human disturbance. Mol Ecol 29:2477–2491. https://doi.org/10.1111/mec.15494
21. Yu X, Yu K, Liao Z et al (2021) Seasonal fluctuations in symbiotic bacteria and their role in environmental adaptation of the scleractinian coral Acropora pruinosa in high-latitude coral reef area of the South China Sea. Sci Total Environ 792:148438. https://doi.org/10.1016/j.scitotenv.2021.148438
22. Pettay DT, LaJeunesse TC (2013) Long-Range Dispersal and High-Latitude Environments Influence the Population Structure

of a "Stress-Tolerant" Dinoflagellate Endosymbiont. PLoS ONE 8:e79208. https://doi.org/10.1371/journal.pone.0079208
23. Qin Z, Yu K, Wang Y et al (2019) Spatial and intergeneric variation in physiological indicators of corals in the south china sea: insights into their current state and their adaptability to environmental stress. J Geophys Res: Oceans 124:3317–3332. https://doi.org/10.1029/2018JC014648
24. Shu LI, Kefu YU, Tianran C et al (2011) Seasonal patterns of densities of symbiotic zooxanthellae in scleractinian corals from Daya Bay, northern South China Sea, and relation to coral bleaching. J Trop Oceanogr 30:39–45. https://doi.org/10.11978/j.issn.1009-5470.2011.02.039
25. Xu L, Yu K, Li S et al (2017) Interseasonal and interspecies diversities of Symbiodinium density and effective photochemical efficiency in five dominant reef coral species from Luhuitou fringing reef, northern South China Sea. Coral Reefs 36:477–487. https://doi.org/10.1007/s00338-016-1532-y
26. Jeffrey SW, Humphrey GF (1975) New spectrophotometric equations for determining chlorophylls a, b, c1 and c2 in higher plants, algae and natural phytoplankton. Biochem Physiol Pflanz 167:191–194. https://doi.org/10.1016/S0015-3796(17)30778-3
27. Chen B, Yu K, Liang J et al (2019) Latitudinal Variation in the Molecular Diversity and Community Composition of Symbiodiniaceae in Coral From the South China Sea. Front Microbiol 10:1278. https://doi.org/10.3389/fmicb.2019.01278
28. Qin L, Xu Y, Chen J et al (2023) Optimization of in vitro culture method for zooxanthellae associated with reef-building corals. Acta Microbiologica Sinica 63:1658–1671. https://doi.org/10.13343/j.cnki.wsxb.20220656
29. Lyndby NH, Rädecker N, Bessette S et al (2020) Amoebocytes facilitate efficient carbon and nitrogen assimilation in the Cassiopea-Symbiodiniaceae symbiosis. Proceed Royal Soc B: Biol Scie 287:20202393. https://doi.org/10.1098/rspb.2020.2393
30. Liang Y, Yu K, Pan Z et al (2021) Intergeneric and geomorphological variations in Symbiodiniaceae densities of reef-building corals in an isolated atoll, central South China Sea. Mar Pollut Bull 163:111946. https://doi.org/10.1016/j.marpolbul.2020.111946
31. Korosh TC, Dutcher A, Pfleger BF, McMahon KD (2018) Inhibition of Cyanobacterial Growth on a Municipal Wastewater Sidestream Is Impacted by Temperature. mSphere 3:https://doi.org/10.1128/msphere.00538-17
32. Nielsen SS (2010) Phenol-Sulfuric Acid Method for Total Carbohydrates. In: Nielsen SS (ed) Food Analysis Laboratory Manual. Springer, US, Boston, MA, pp 47–53
33. Pinto F, Pacheco CC, Ferreira D et al (2012) Selection of Suitable Reference Genes for RT-qPCR Analyses in Cyanobacteria. PLoS ONE 7:e34983. https://doi.org/10.1371/journal.pone.0034983
34. Maire J, Girvan SK, Barkla SE et al (2021) Intracellular bacteria are common and taxonomically diverse in cultured and in hospite algal endosymbionts of coral reefs. ISME J 15:2028–2042. https://doi.org/10.1038/s41396-021-00902-4
35. Hinrichs S, Patten NL, Waite AM (2013) Temporal Variations in Metabolic and Autotrophic Indices for Acropora digitifera and Acropora spicifera – Implications for Monitoring Projects. PLoS ONE 8:e63693. https://doi.org/10.1371/journal.pone.0063693
36. Baker AC (2003) Flexibility and Specificity in Coral-Algal Symbiosis: Diversity, Ecology, and Biogeography of Symbiodinium. Annu Rev Ecol Evol Syst 34:661–689. https://doi.org/10.1146/annurev.ecolsys.34.011802.132417
37. Xu Y, Chen B, Qin L et al (2023) Seasonal Variation Characteristics of the Symbiodiniaceae Community Associated with Acropora pruinosa from Weizhou Island. Guangdong Agric Sci 50:164–172. https://doi.org/10.16768/j.issn.1004-874X.2023.07.017
38. Warner ME, Fitt WK, Schmidt GW (1999) Damage to photosystem II in symbiotic dinoflagellates: A determinant of coral bleaching. PNAS 96:8007–8012. https://doi.org/10.1073/pnas.96.14.8007
39. Lesser MP (1997) Oxidative stress causes coral bleaching during exposure to elevated temperatures. Coral Reefs 16:187–192. https://doi.org/10.1007/s003380050073
40. Grottoli AG, Rodrigues LJ, Palardy JE (2006) Heterotrophic plasticity and resilience in bleached corals. Nature 440:1186–1189. https://doi.org/10.1038/nature04565
41. Rosenberg E, Koren O, Reshef L et al (2007) The role of microorganisms in coral health, disease and evolution. Nat Rev Microbiol 5:355–362. https://doi.org/10.1038/nrmicro1635
42. Cho J-C, Giovannoni SJ (2004) Cultivation and Growth Characteristics of a Diverse Group of Oligotrophic Marine Gammaproteobacteria. Appl Environ Microbiol 70:432–440. https://doi.org/10.1128/AEM.70.1.432-440.2004
43. Oh H-M, Kang I, Ferriera S et al (2010) Genome Sequence of the Oligotrophic Marine Gammaproteobacterium HTCC2143, Isolated from the Oregon Coast. J Bacteriol 192:4530–4531. https://doi.org/10.1128/JB.00683-10
44. Waterbury JB, Watson SW, Guillard RRL, Brand LE (1979) Widespread occurrence of a unicellular, marine, planktonic, cyanobacterium. Nature 277:293–294. https://doi.org/10.1038/277293a0
45. Huokko T, Ni T, Dykes GF et al (2021) Probing the biogenesis pathway and dynamics of thylakoid membranes. Nat Commun 12:3475. https://doi.org/10.1038/s41467-021-23680-1
46. Agawin NSR, Duarte CM, Agustí S (2000) Nutrient and temperature control of the contribution of picoplankton to phytoplankton biomass and production. Limnol Oceanogr 45:591–600. https://doi.org/10.4319/lo.2000.45.3.0591
47. Otero-Ferrer JL, Cermeño P, Bode A et al (2018) Factors controlling the community structure of picoplankton in contrasting marine environments. Biogeosciences 15:6199–6220. https://doi.org/10.5194/bg-15-6199-2018
48. Pittera J, Humily F, Thorel M et al (2014) Connecting thermal physiology and latitudinal niche partitioning in marine Synechococcus. ISME J 8:1221–1236. https://doi.org/10.1038/ismej.2013.228
49. Pittera J, Jouhet J, Breton S et al (2018) Thermoacclimation and genome adaptation of the membrane lipidome in marine Synechococcus. Environ Microbiol 20:612–631. https://doi.org/10.1111/1462-2920.13985
50. Latasa M, Scharek R, Morán XAG et al (2022) Dynamics of phytoplankton groups in three contrasting situations of the open NW Mediterranean Sea revealed by pigment, microscopy, and flow cytometry analyses. Prog Oceanogr 201:102737. https://doi.org/10.1016/j.pocean.2021.102737
51. Schultz J, Modolon F, Rosado AS, et al (2022) Methods and strategies to uncover coral-associated microbial dark matter. mSystems 7:e00367-22. https://doi.org/10.1128/msystems.00367-22
52. Xiao L, Johansson S, Rughöft S et al (2022) Photophysiological response of Symbiodiniaceae single cells to temperature stress. ISME J 1–5. https://doi.org/10.1038/s41396-022-01243-6
53. LaJeunesse TC, Parkinson JE, Gabrielson PW et al (2018) Systematic Revision of symbiodiniaceae highlights the antiquity and diversity of coral endosymbionts. Current Biology 28:2570-+. https://doi.org/10.1016/j.cub.2018.07.008
54. Lesser MP (1996) Elevated temperatures and ultraviolet radiation cause oxidative stress and inhibit photosynthesis in symbiotic dinoflagellates. Limnol Oceanogr 41:271–283. https://doi.org/10.4319/lo.1996.41.2.0271
55. Takahashi S, Whitney S, Itoh S et al (2008) Heat stress causes inhibition of the de novo synthesis of antenna proteins and photobleaching in cultured Symbiodinium. PNAS 105:4203–4208. https://doi.org/10.1073/pnas.0708554105
56. Liu Y, Wu H, Shu Y et al (2024) Symbiodiniaceae and Ruegeria sp. Co-Cultivation to Enhance Nutrient Exchanges in Coral Holobiont. Microorganisms 12:1217. https://doi.org/10.3390/microorganisms12061217

microorganisms

MDPI

Article

Effects of Natural Ingredient Xanthohumol on the Intestinal Microbiota, Metabolic Profiles and Disease Resistance to *Streptococcus agalactiae* in Tilapia *Oreochromis niloticus*

Aiguo Huang [1], Yanqin Wei [1], Jialong Huang [1,2], Songlin Luo [1], Tingyu Wei [1,2], Jing Guo [3], Fali Zhang [1,4,*] and Yinghui Wang [1,4,*]

[1] Guangxi Laboratory on the Study of Coral Reefs in the South China Sea, Coral Reef Research Center of China, School of Marine Sciences, Guangxi University, Nanning 530004, China; aiguo_200891@126.com (A.H.); weiyanqin113@163.com (Y.W.); m13471931176@163.com (J.H.); luosonglin0528@163.com (S.L.); weitingyu0323@163.com (T.W.)
[2] School of Resources, Environment and Materials, Guangxi University, Nanning 530004, China
[3] Key Laboratory of Environment Change and Resources Use in Beibu Gulf, Ministry of Education, Nanning Normal University, Nanning 530001, China; guojing8925@126.com
[4] Institute of Green and Low Carbon Technology, Guangxi Institute of Industrial Technology, Nanning 530000, China
* Correspondence: 2027301033@st.gxu.edu.cn (F.Z.); wyh@gxu.edu.cn (Y.W.)

Abstract

Streptococcus agalactiae (SA) is a severe prevalent pathogen, resulting in high morbidity and mortality in the global tilapia industry. With increasing bacterial resistance to antibiotics, alternative strategies are urgently needed. This study aims to investigate the antibacterial activity and the underlying mechanisms of the natural product xanthohumol (XN) against SA infection in tilapia (*Oreochromis niloticus*). The results showed that XN could significantly reduce the bacterial loads of SA in different tissues (liver, spleen and brain) after treatment with different tested concentrations of XN (12.5, 25.0 and 50.0 mg/kg). Moreover, XN could improve the survival rate of SA-infected tilapia. 16S rRNA gene sequencing demonstrated that the alpha-diversity index (Chao1 and Shannon_e) was significantly increased in the XN-treated group (MX group) compared to the SA-infected group (CG group) ($p < 0.05$), and the Simpson diversity index significantly decreased. The Bray–Curtis similarity analysis of non-metric multidimensional scaling (NMDS) and principal coordinate analysis (PCA) showed that there were significant differences in microbial composition among groups. At the phylum level, the relative abundance of the phyla Actinobacteria, Proteobacteria and Bacteroidetes decreased in the MX group compared to the CG group, while the relative abundance of the phyla Fusobacteria, Firmicutes and Verrucomicrobia increased. Differences were also observed at the genus level; the relative abundance of *Mycobacterium* decreased in the MX group, but the abundance of *Cetobacterium* and *Clostridium_sensu_stricto_1* increased. Metabolomics analysis revealed that XN changed the metabolic profile of the liver and significantly enriched aspartate metabolism, glycine and serine metabolism, phosphatidylcholine biosynthesis, arginine and proline metabolism, glutamate metabolism, urea cycle, purine metabolism, methionine metabolism, betaine metabolism, and carnitine synthesis. Correlation analysis indicated an association between the intestinal microbiota and metabolites. In conclusion, XN may be a potential drug for the prevention and treatment of SA infection in tilapia, and its mechanism of action may be related to the regulation of the intestinal microbiota and liver metabolism.

check for updates

Academic Editors: Konstantinos A. Kormas and Anca Zanfirescu

Received: 5 June 2025
Revised: 5 July 2025
Accepted: 14 July 2025
Published: 20 July 2025

Citation: Huang, A.; Wei, Y.; Huang, J.; Luo, S.; Wei, T.; Guo, J.; Zhang, F.; Wang, Y. Effects of Natural Ingredient Xanthohumol on the Intestinal Microbiota, Metabolic Profiles and Disease Resistance to *Streptococcus agalactiae* in Tilapia *Oreochromis niloticus*. *Microorganisms* **2025**, *13*, 1699. https://doi.org/10.3390/microorganisms13071699

Copyright: © 2025 by the authors. Licensee MDPI, Basel, Switzerland. This article is an open access article distributed under the terms and conditions of the Creative Commons Attribution (CC BY) license (https://creativecommons.org/licenses/by/4.0/).

Keywords: *Streptococcus agalactiae*; tilapia; xanthohumol; antibacterial activity; intestinal microbiota; metabolomics

1. Introduction

Tilapia is one of the largest fish species globally, and its production is increasing every year. However, the emergence of pathogens has become a major limiting factor for the production and supply of tilapia. Among pathogens, *Streptococcus agalactiae* (SA) is the main bacterial pathogen in tilapia farms. SA infection can result in high mortality rates of up to 30–90% for tilapia, causing severe economic losses for the tilapia aquaculture industry [1]. Antibiotics are used to control SA infection to some extent [2]. However, the abuse of antibiotics leads to the emergence of drug-resistant microbes and antibiotic residues in foods [3]. Thus, it is urgent to identify new prevention and therapy agents against SA infection in tilapia aquaculture.

Medicinal plants and their chemical composition are considered potential candidates for antimicrobial drugs. Many studies have demonstrated that medicinal plants have notable anti-SA activity in tilapia, such as *Aristolochia debilis*, *Panax ginseng*, *Spatholobus suberectus, Scutellaria baicalensis* and *Sophora flavescens* [4–6]. Some plant extracts can also regulate the intestinal microbiota and hepatic metabolism of tilapia. Guava and Star gooseberry leaf extracts, whether used alone or in combination, can enhance the intestinal microbial diversity of tilapia infected with *Aeromonas hydrophila*, increase the abundance of probiotics, and combat Aeromonas hydrophila infection [7]. *Bidens pilosa* can regulate the composition of the intestinal microbiota in tilapia, thereby affecting various metabolic pathways in the liver, such as amino acid metabolism, carbohydrate metabolism and lipid metabolism, and promoting growth through the gut–liver axis [8]. Interestingly, the chemical composition of medicinal plants also exhibits antibacterial activity. For instance, baicalin is the main component of *Scutellaria baicalensis*, and it has significant antibacterial activity against SA infection in tilapia by attenuating SA virulence [9]. Xanthohumol (XN), an isoprenylated flavonoid component in *Sophora flavescens*, can regulate inflammation- and apoptosis-related innate immunity and exert multi-directional pro-healing properties on damaged hair cells in zebrafish embryos [10]. Furthermore, XN has a safe concentration in tilapia exceeding 100 mg/kg and can significantly inhibit GBS infection in tilapia [6]. However, previous research only confirmed that XN possesses antibacterial activity, while the underlying mechanisms of its antibacterial activity and its potential associations with intestinal microbiota and hepatic metabolism remain insufficiently studied.

In this study, the antibacterial activity and potential mechanism of XN against SA infection were evaluated in tilapia (GIFT, *Oreochromis niloticus*). The anti-SA activity of XN in tilapia was investigated by quantifying the bacterial loads using quantitative real-time PCR (qPCR) and evaluating the mortality rates of SA-infected tilapia. Furthermore, we employed 16S rRNA sequencing and untargeted metabolomics to identify the changes in intestinal microbiota and liver metabolites, respectively. This study will provide a comprehensive understanding of the regulatory roles of XN in tilapia.

2. Materials and Methods

2.1. Fish, Bacteria and Chemicals

Tilapia *Oreochromis niloticus* (body weight: 8.85 ± 0.11 g) was purchased from a fish farm in Nanning, Guangxi, China. Fish were acclimatized for 14 days in 200 L aquariums at 30 °C and fed with a commercial pellet diet twice daily. The animal use protocol was approved by the Animal Care and Welfare Committee of Guangxi University (GXU-2023-

0531). SA strain GXYL7, originally isolated from tilapia suffering from bacterial disease, was used in our study [11]. Natural compound XN (CAS No. 6754-58-1) was purchased from Aladdin Biochemical Technology Co., Ltd. (Shanghai, China).

2.2. SA Quantification

SA quantification was performed using qPCR, as in our previous study [12]. Simply, the *cfb* gene, which encoded the CAMP factor, was selected as the target gene. It was cloned using the primers cfb-F (5′-TAGCTTAGTTATCCCAAATCCC-3′) and cfb-R (5′-TAAAGACTTCATTGCGTGCC-3′) into the pMD19-T simple vector (Takara, Shanghai, China) for the target amplicon. The copy numbers of the target amplicon were quantified by measuring the concentration using a NanoDrop spectrophotometer (NanoDrop Technologies Inc., Wilmington, DE, USA). The target amplicon was diluted and used as the template for qPCR. The qPCR was performed using UltraSYBR Mixture (CWBIO, Taizhou, China) in the ABI 7500 Fast Real-Time PCR System. The PCR cycling conditions were as follows: 95 °C for 10 min, then 40 cycles at 95 °C denaturation for 15 s, followed by annealing at 60 °C for 1 min. To verify the amplification of a single product, a melt curve analysis of 5 s per step from 65 to 95 °C was performed at the end of each PCR thermal profile. Regression of the log of *cfb* gene copy numbers and the corresponding cycle threshold (Ct) value was used as a standard curve to determine the copy numbers of SA.

2.3. Experimental Design and Sampling

The anti-SA activity of XN was evaluated in SA-infected tilapia, as in a previous study [6]. The experimental tilapia were grouped using a random number table method and assigned to the control group, infection group, and XN treatment group. We further evaluated the anti-SA activity of XN in tilapia. Tilapia were divided into the control group and XN experimental groups (12.5, 25.0 and 50.0 mg/kg). The control groups were injected with SA only, and the experimental groups were injected with SA suspensions and different concentrations of XN. Each fish was injected with 100 μL suspensions. The final concentration of SA bacterial suspensions was 1×10^8 cfu/mL. The liver, spleen, brain or intestinal tissues were sampled and stored at −80 °C for analysis.

To investigate the preventive and control effects of XN, a 14-day experiment was conducted on tilapia. For the XN-treated groups, tilapia were intraperitoneally injected with a premixed solution of SA and XN, resulting in XN concentrations in tilapia reaching 12.5, 25, and 50 mg/kg (drug weight: fish weight), which were designated as the 12.5 mg/kg XN group (LX), 25 mg/kg XN group (MX), and 50 mg/kg XN group (HX), respectively. The infected group (CG) was injected with SA bacterial solution alone, while the healthy group was injected with PBS solution (CP). Each group was set with 3 replicates, with 15 fish in each replicate. Each fish was injected with 100 μL of the treatment solution, and the final concentration of GBS bacterial solution was 1×10^8 cfu/mL. Mortality was recorded daily.

2.4. DNA Extraction and Absolute Quantification of the Copy Numbers of SA Genomic DNA

The 15 mg tissue samples were taken for DNA extraction, and all tissues were triturated using a tissue homogenizer (Sangon Biotech, Shanghai, China). Total genomic DNA was extracted using the TIANamp Bacteria DNA Kit (Tiangen, Sichuan, China) following the manufacturer's instructions. Extracted DNA was subjected to quantification via NanoDrop spectrophotometer (NanoDrop Technologies Inc., Wilmington, DE, USA). Then, the DNA was used to quantify the copy numbers of SA genomic DNA via qPCR.

2.5. 16S rRNA Gene Sequencing for the Intestinal Microbiota Analysis

The genomic DNA of different samples was extracted according to the E.Z.N.A. ®Stool DNA Kit (Omega, Inc., Dewitt, NY, USA). PCR amplification was performed in a 25 μL reaction mixture to obtain the V3–V4 regions of 16S rRNA gene using the primers 338F (5′-ACTCCTACGGGAGGCAGCA-3′) and 806R (5′-GGACTACHVGGGTWTCTAAT-3′). The 5′ ends of the primers were tagged with specific barcodes for each sample and were sequenced with universal primers. The PCR condition consisted of an initial denaturation at 94 °C for 5 min; 30 cycles of denaturation at 94 °C for 30 s, annealing at 52 °C for 30 s, and extension at 72 °C for 30 s; and then final extension at 72 °C for 10 min. The PCR product was confirmed using 1% agarose gel electrophoresis. Following the standard protocol of the ALFA-SEQ DNA Library Prep Kit (Ark Biosafety Technology (Guangzhou) Co., Ltd., Guangzhou, China), the library construction is carried out. Subsequently, the size of the library fragments is evaluated on the Qsep400 High-Throughput Nucleic Acid and Protein Analysis System (Hangzhou Houze Biotech Co., Ltd., Hangzhou, China), and the concentration of the library is measured using the Qubit 4.0 Fluorometer (Thermo Fisher Scientific, Waltham, MA, USA). The library was sequenced on the Illumina NovaSeq 6000 platform, and 250 bp paired-end (PE) reads were generated (Guangdong Magigene Biotechnology Co. Ltd., Guangdong, China).

2.6. LC-MS Conditions for Metabolomics Analysis

The metabolomics analysis of the liver sample was conducted using an ultra-performance liquid chromatography (UPLC) system (Vanquish, Thermo Fisher Scientific, Waltham, MA, USA). An ACQUITY UPLC BEH Amide column (50 mm × 2.1 mm, 1.7 μm, Waters, UK) was used for the separation. The mobile phase A of liquid chromatography is an aqueous phase containing 25 mmol/L ammonium acetate and 25 mmol/L ammonia water, while mobile phase B is acetonitrile. Sample tray temperature is 4 °C, and injection volume is 2 μL. The Orbitrap Exploris 120 mass spectrometer (Thermo Fisher Scientific, Waltham, MA, USA) was used to detect the eluted metabolites. The Orbitrap Exploris 120 mass spectrometer was operated in both positive and negative ion modes. Sheath gas flow rate was 50 Arb, Aux gas flow rate was 15 Arb, capillary temperature was 320 °C, full MS resolution was 60,000, MS/MS resolution was 15,000, collision energy was SNCE 20/30/40, spray voltage was 3.8 kV (positive) or −3.4 kV (negative), respectively. During the entire acquisition period, the mass accuracy was calibrated after every 20 samples. Furthermore, a quality control (QC) sample was analyzed after every 10 samples to evaluate the stability of LC-MS during the whole acquisition (for relevant details, refer to Supplementary Materials).

2.7. 16S rRNA Data Analysis

Paired-end (PE) reads were assigned to individual samples based on their unique barcode sequences, which were subsequently truncated to remove the barcode and primer sequences. The resulting reads were merged using the FLASH v1.2.11 software. Quality filtering was performed under stringent conditions using the fastp (v0.14.1) to obtain high-quality clean tags (For QC, refer to Supplementary Materials Table S2). Chimeric sequences were identified and removed using the Usearch software (v10.0.240). DADA2 was employed for dereplication, resulting in a feature table and sequence data. Feature abundance was normalized relative to each sample's total abundance based on the SILVA (release 132) classifier. Operational taxonomic units (OTUs) were analyzed at a 97% sequence similarity threshold using the Usearch (v10.0.240). Alpha-diversity indices, including ACE, coverage, Simpson, Chao1, and Shannon_e, were calculated using the QIIME2 2023.5 to evaluate species complexity. Beta diversity was assessed through principal coordinate analysis

(PCoA) and non-metric multidimensional scaling (NMDS) based on bray_curtis, also using QIIME2. Differential intestinal microbiota between groups were detected, and their species composition was analyzed at the phylum and genus levels. Linear discriminant analysis effect size (LEfSe) analysis was performed to identify differential microbiota taxa. Linear discriminant analysis effect size (LEfSe) was performed based on the OTU annotation results, and multiple testing correction was conducted using Benjamini–Hochberg FDR ($p < 0.05$) to identify species with significant differences in abundance between groups. Differential species analysis was conducted using the non-parametric Kruskal–Wallis rank-sum test and Wilcoxon rank-sum test. Bacterial genera with linear discriminant analysis (LDA) score greater than 3 and *p*-values less than 0.05 were selected for further analysis, aiming to discover the differential biomarker species among the intestinal microbiota of tilapia under different treatments. All statistical analyses were conducted using R version 4.3.3 and different R packages (phyloseq v1.42.0, DESeq2 v1.38.3, vegan v2.6.2 and ggplot2 v3.3.6).

2.8. Metabolomics Data Processing

The raw data were converted to the mzXML format using ProteoWizard 3.0.7414 and processed with an in-house program, which was developed using R and based on XCMS, for peak detection, extraction, alignment, and integration. Then, the MS2 database was applied to metabolite annotation. The cutoff for annotation was set at 0.3. Using the R package stats (v4.0.3), principal component analysis (PCA) is conducted. For Orthogonal Projections to Latent Structures–Discriminant Analysis (OPLS-DA), the R language package ropls (v1.22.0) is employed. Variable Importance in the Projection (VIP) scores > 1, along with absolute Fold Change (FC) values > 2 or <0.5, and $p < 0.05$, are applied as criteria for screening differential metabolites. The selected differential metabolites are then annotated, classified, clustered, and analyzed using the proprietary database established by Guangdong Magigene Biotechnology Co., Ltd. Venn diagrams are generated using Metware Cloud 2024.1.26 (https://cloud.metware.cn; accessed on 24 March 2024) for visualizing and comparing sets of differential metabolites or pathways across different experimental conditions or analyses. Metabolic pathway analysis is performed via MetaboAnalyst 6.0 (https://genap.metaboanalyst.ca/; accessed on 26 March 2024), with statistical significance set at $p < 0.05$. Metabolic pathways with an impact value > 0.1 are considered significantly relevant to the study conditions, indicating that these pathways are the most pertinent ones associated with the experimental conditions. The correlation heatmap was drawn using the OmicStudio tools 3.6 at https://www.omicstudio.cn/tool (accessed on 8 October 2024).

2.9. Statistical Analysis

All data are presented as means ± SD. The statistical analysis was carried out with SPSS 18.0 statistical software (SPSS Inc., Chicago, IL, USA). $p \leq 0.05$ was considered significant. Spearman's correlation analysis was conducted to analyze the correlation relationship between the microbiota and metabolite using the data of significantly differential genus-level microbiota and differential secondary metabolites. A scaled heatmap was constructed for the correlation matrix using the default clustering method.

3. Results

3.1. Xanthohumol Inhibits SA Replication in Tilapia

As shown in Figure 1A–C, XN could significantly inhibit SA infection in different tissues of tilapia after treatment with different concentrations of XN for 24 h. Compared with the control groups, the copy numbers of SA in the liver, spleen, and brain tissues of tilapia in the XN groups reduced by 6.45-fold, 5.96-fold and 7.73-fold, respectively.

Furthermore, XN could also significantly inhibit SA infection in the liver tissues of tilapia after treatment with different concentrations of XN for 24, 48 and 72 h (Figure 1D–F).

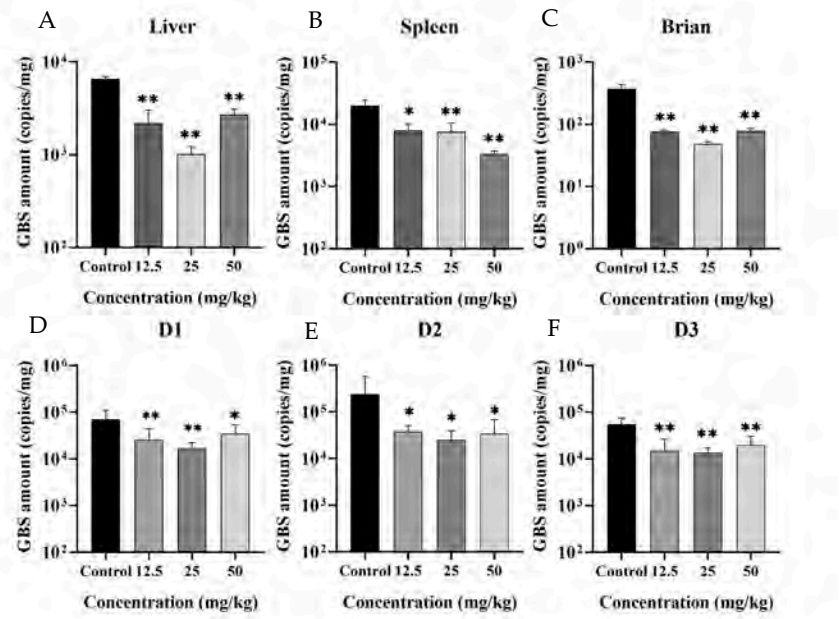


Figure 1. Xanthohumol (XN) inhibited the proliferation of Streptococcus agalactiae (SA) in tilapia. Bacterial loads in the (**A**) liver, (**B**) spleen and (**C**) brain of SA-infected tilapia treated with different concentrations of XN for 24 h. Bacterial loads in the liver of SA-infected tilapia treated with different concentrations of XN for (**D**) 24 h, (**E**) 48 h and (**F**) 72 h. Asterisks mark the significant difference between experimental data and control data (* $p < 0.05$, ** $p < 0.01$).

3.2. Xanthohumol Improves the Survival Rate of SA-Infected Tilapia

To explore the therapeutic effect of XN, SA-infected tilapia was treated with XN (12.5, 25, and 50 mg/kg) and observed for 14 days. As shown in Figure 2, the survival rate of tilapia was significantly different between the treatment and control groups. The cumulative survival rate of tilapia in the CP groups (treated with PBS only) was 100%, while it was only 20% in the CG groups (treated with SA only). Interestingly, the cumulative survival rates of SA-infected tilapia after treatment with 12.5 mg/kg (LX groups), 25 mg/kg (MX groups) and 50 mg/kg (HX groups) XN for 14 d were increased to 40%, 80% and 40%, respectively.

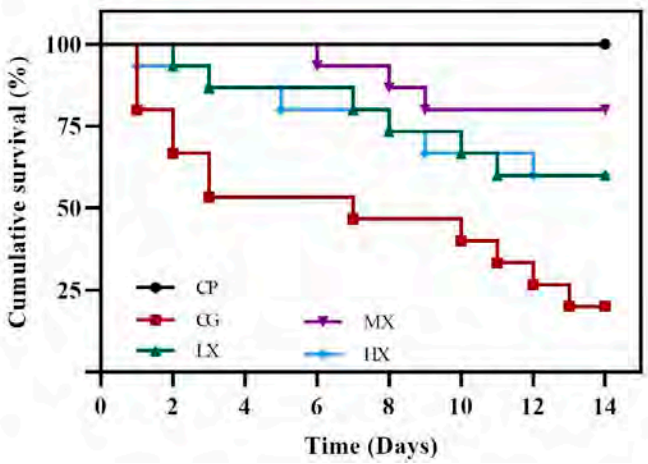


Figure 2. XN improved the survival rate of tilapia infected with SA. The CP groups were injected with PBS solution only; the CG groups were injected with SA bacterial solution only; the LX (12.5 mg/kg XN), MX (25 mg/kg), and HX (50 mg/kg XN) groups were injected with a mixture of XN and SA bacterial solution. The mortality of each group (n = 45) was continuously detected for 14 days. Survival Rate = (Number of Survivors/Initial Number) × 100%.

3.3. Effects of Xanthohumol on the Intestinal Microbial Diversity

As shown in Table 1, there were no significant differences in ACE and coverage indices among the MX groups, CP groups and CG groups ($p > 0.05$), but the ACE index in the MX groups was higher than that in the CG groups, and the MX groups were lower than that in the CP groups. There were significant differences in Simpson, Chao1, and Shannon_e indices between both the MX group and CG groups, as well as between the CP group and CG groups ($p < 0.05$). The results of the α-diversity indices indicated that XN could regulate the α-diversity of intestinal microbial communities in tilapia. In addition, the Bray–Curtis similarity analysis of NMDS and PCoA among different groups showed that there were significant differences in microbial composition among groups (Figure 3).

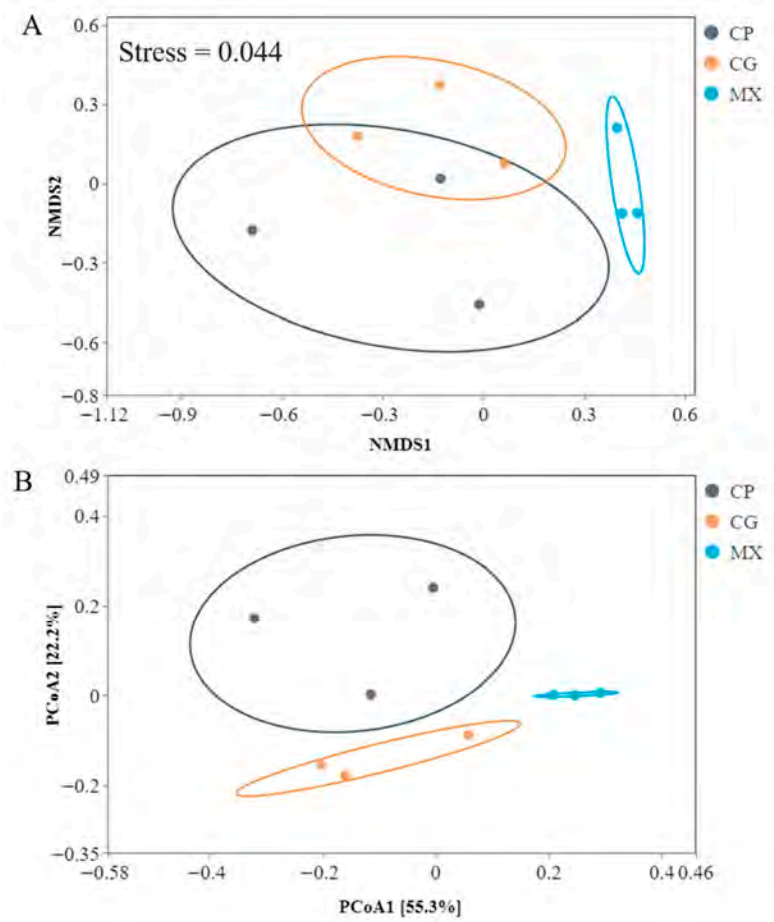


Figure 3. The β-diversity of intestinal microbiota of tilapia in different groups. (**A**) NMDS analysis. Stress = 0.044 indicates that NMDS can accurately reflect changes in the community between samples; (**B**) PCoA analysis. PCoA scatter plot of OTUs. The gray, yellow and blue circles represent the CP group, CG group and MX group, respectively.

Table 1. The α-diversity analyses of intestinal microbiota in the three groups.

Index	CG	CP	MX
ACE	430.88 ± 17.10	473.79 ± 25.22	464.80 ± 15.92
Coverage	1.00 ± 0.00	1.00 ± 0.00	1.00 ± 0.00
Simpson	0.26 ± 0.02 ^{a}	0.18 ± 0.01 ^{b}	0.15 ± 0.01 ^{c}
Chao1	265.63 ± 14.25 ^{b}	321.63 ± 21.47 ^{a}	346.20 ± 10.85 ^{a}
Shannon_e	2.08 ± 0.08 ^{b}	2.40 ± 0.07 ^{ab}	2.55 ± 0.06 ^{a}

Different letters in the same row indicate the significant differences between various groups ($p < 0.05$).

3.4. Effects of Xanthohumol on Intestinal Microbial Composition

As shown in Figure 4, the intestinal microbial composition of the dominant microbiota was essentially the same but with changes in abundance. At the phylum level, the relative abundance of the phyla Actinobacteria, Proteobacteria and Bacteroidetes decreased in the MX compared to the CG, while the relative abundance of the phyla Fusobacteria, Firmicutes and Verrucomicrobia increased (Figure 4A). Compared with the CP group, the relative abundance of Proteobacteria, Bacteroidetes, and Firmicutes in the CG group was decreased, while the relative abundance of Fusobacteria, Actinobacteria, and Verrucomicrobia was increased (Figure 4A). Differences were also observed at the genus level; the relative abundance of *Mycobacterium* decreased in the MX, but the abundance of *Cetobacterium* and *Clostridium_sensu_stricto_1* increased (Figure 4B). Compared with the CP group, the relative abundance of Cetobacterium and Clostridium_sensu_stricto_1 in the CG group was decreased, while the abundance of Mycobacterium was increased (Figure 4B).

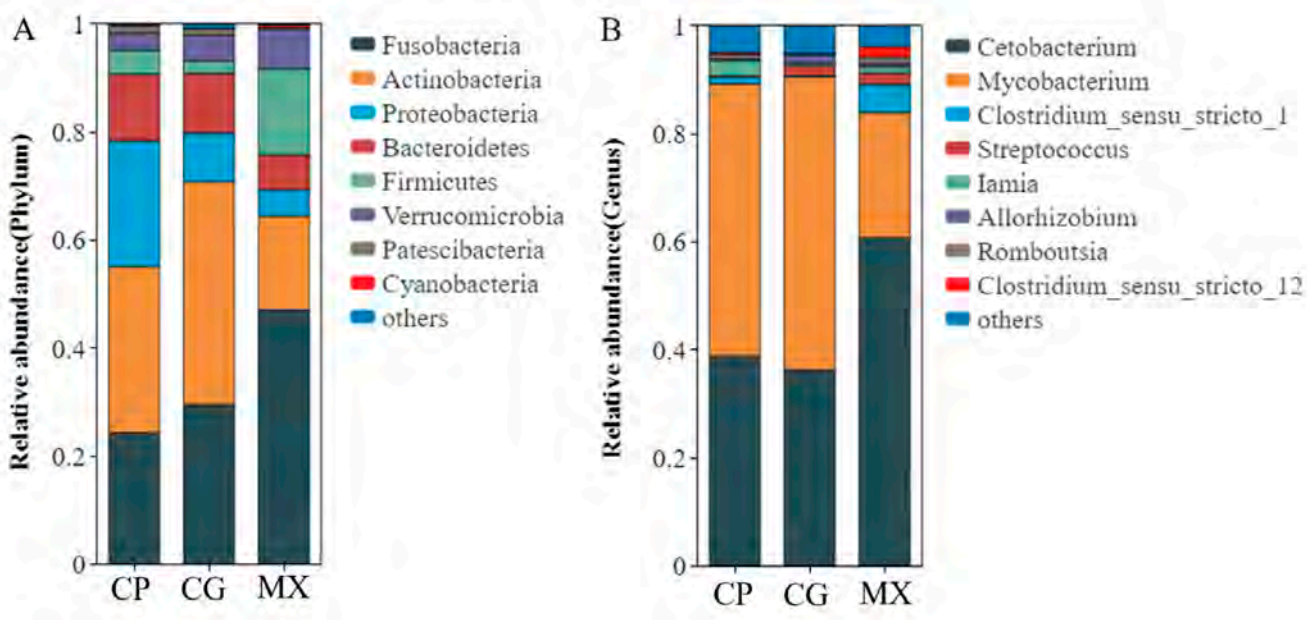


Figure 4. The relative abundance of intestinal microbiota in different groups at the phylum (**A**) and genus (**B**) taxonomic level.

3.5. Identification of Potential Intestinal Microbial Biomarkers

To evaluate the potential biomarker taxa in tilapia, we compared the intestinal microbial communities between the CG and CP groups and the CG and MX groups using the linear discriminant analysis effect size (LEfSe, Table 2). LEfSe analysis was performed based on the LDA effect size and could be used to compare between groups for the identification of biomarker taxa with the most significant differences in abundance. Between the CG and CP groups, the CP groups had four taxa with significantly enriched abundance, while three taxa were upregulated in the CG groups. In addition, the MX groups had 17 taxa with significantly enriched abundance compared to the CG groups, and 5 taxa were upregulated in the CG groups. In CG vs. MX, the biomarkers recognized for the MX group were *g_Cetobacterium* and *g_Clostridium_sensu_stricto_1*, while *g_Mycobacterium* was identified as biomarkers in the CG group.

Table 2. LEfSe analysis of group CP, group CG and group MX at the genus level.

	Group	Biomarker ID	LDA	*p*-Value
CG vs. CP	CG	*g. Allorhizobium*	3.654	0.0495
		g. Streptococcus	3.552	0.0495
		g. Brevinema	3.219	0.0495
	CP	*g. Iamia*	3.789	0.0495
		g. Clostridium_sensu_stricto_1	3.424	0.0495
		g. Romboutsia	3.207	0.0495
		g. Anaerobacterium	3.092	0.0463
CG vs. MX	CG	*g. Deinococcus*	3.990	0.0369
		g. Anoxybacillus	3.879	0.0463
		g. Methylobacterium	3.388	0.0495
		g. Mycobacterium	3.042	0.0369
		g. Xanthobacter	3.004	0.0463
	MX	*g. Cetobacterium*	4.806	0.0495
		g. Clostridium_sensu_stricto_1	4.129	0.0495
		g. Lachnoclostridium	4.090	0.0369
		g. Massilia	3.961	0.0369
		g. Clostridium_sensu_stricto_2	3.895	0.0463
		g. Ruminococcaceae_UCG	3.762	0.0495
		g. Caproiciproducens	3.650	0.0369
		g. Clostridium_sensu_stricto_12	3.646	0.0495
		g. Akkermansia	3.422	0.0495
		g. Cellulosilyticum	3.401	0.0369
		g. Romboutsia	3.396	0.0495
		g. Anaerobacterium	3.333	0.0463
		g. Clostridium_sensu_stricto_7	3.295	0.0463
		g. Clostridium_sensu_stricto_13	3.270	0.0495
		g. Epulopiscium	3.215	0.0495
		g. Clostridium_sensu_stricto_18	3.164	0.0463
		g. Iamia	3.144	0.0495

The linear discriminant analysis (LDA) effect size (LEfSe) was used to compare the differences in gut microbial community composition in different groups. LDA score > 3.

3.6. Effect of Xanthohumol on Metabolomic Alterations

The results of PCA analysis showed that there was no overlap between CP3 and CG3 and CG3 and MX3 (Figure 5A). Figure 5B–E show scatter plots of the OPLS-DA model between the CG and CP groups and CG and MX groups. The farther the distance between the points, the greater the difference between their physiological and pathological states. It can be seen from Figure 5B,D that the main components of the CG3 group and CP3 group and the CG3 group and MX3 group are separated and do not overlap; thus, there is a significant difference between the CG3 group and CP3 group and the CG3 group and MX3 group. Meanwhile, we use the OPLS-DA model to calculate the VIP through the control group to assess the contribution of metabolites to the differences between groups. To assess the model, an alignment test is performed. An alignment verification chart is shown in Figure 5. As shown in Figure 5C,E, the original model has a good fit and there is no overfitting.

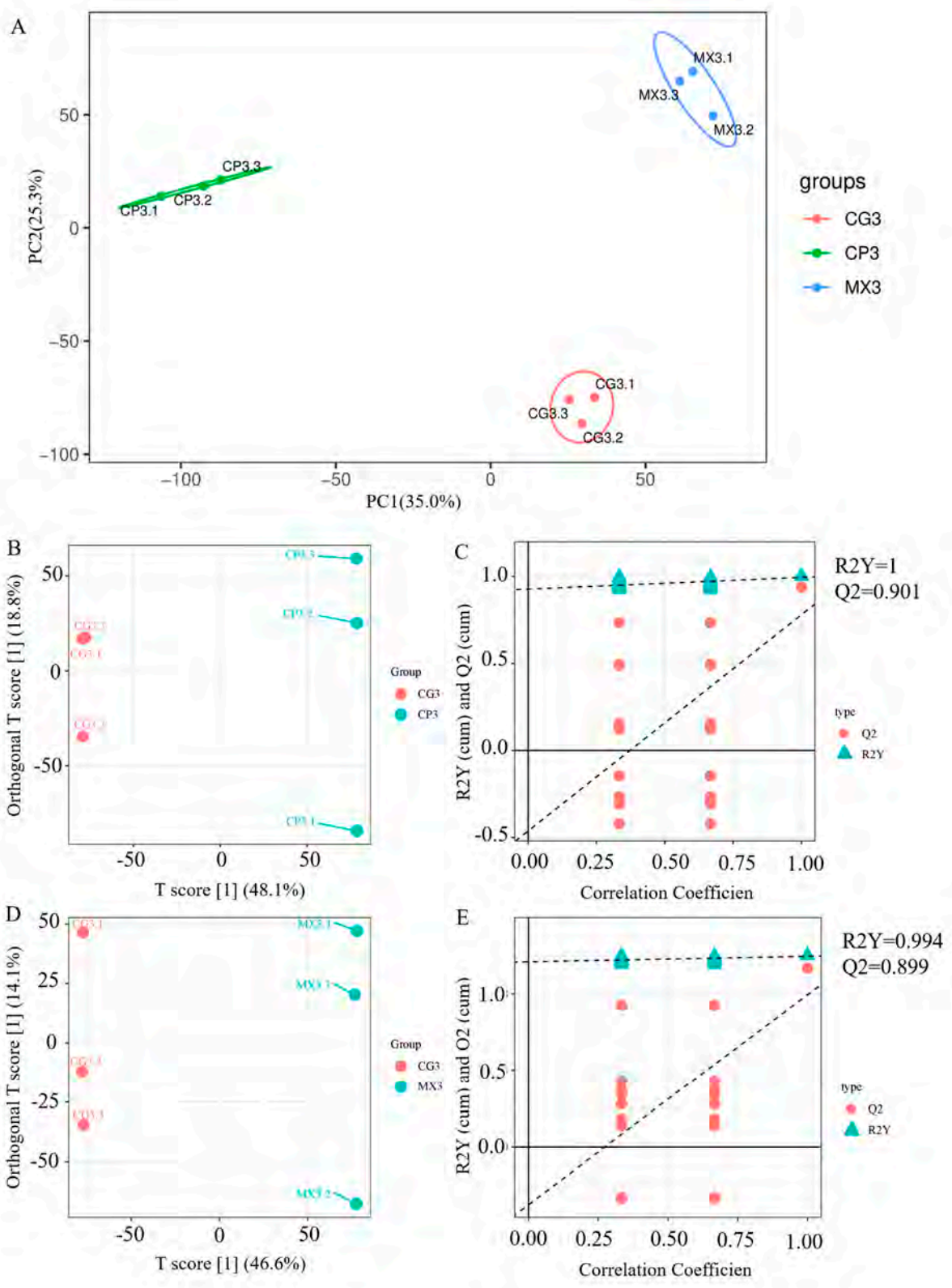


Figure 5. The PCA and OPLS-DA analysis of liver metabolites of tilapia in different groups. (**A**) PCA analysis. The yellow, green and blue circles represent the CG3 group, CP3 group and MX3 group, respectively; (**B**) score scatter plot and (**C**) permutation test result plot of OPLS-DA model in CG3 vs. CP3; (**D**) score scatter plot and (**E**) permutation test result plot of OPLS-DA model in MX3 vs. CG3.

3.7. Differential Metabolic Pathways and Differential Metabolites

Compared with the CP3 group, there were 211 downregulated and 103 upregulated metabolites in the CG3 group (Figure 6A). Compared with the CG3 group, the number of downregulated and upregulated metabolites in the MX3 group was 124 and 230 (Figure 6B), respectively.

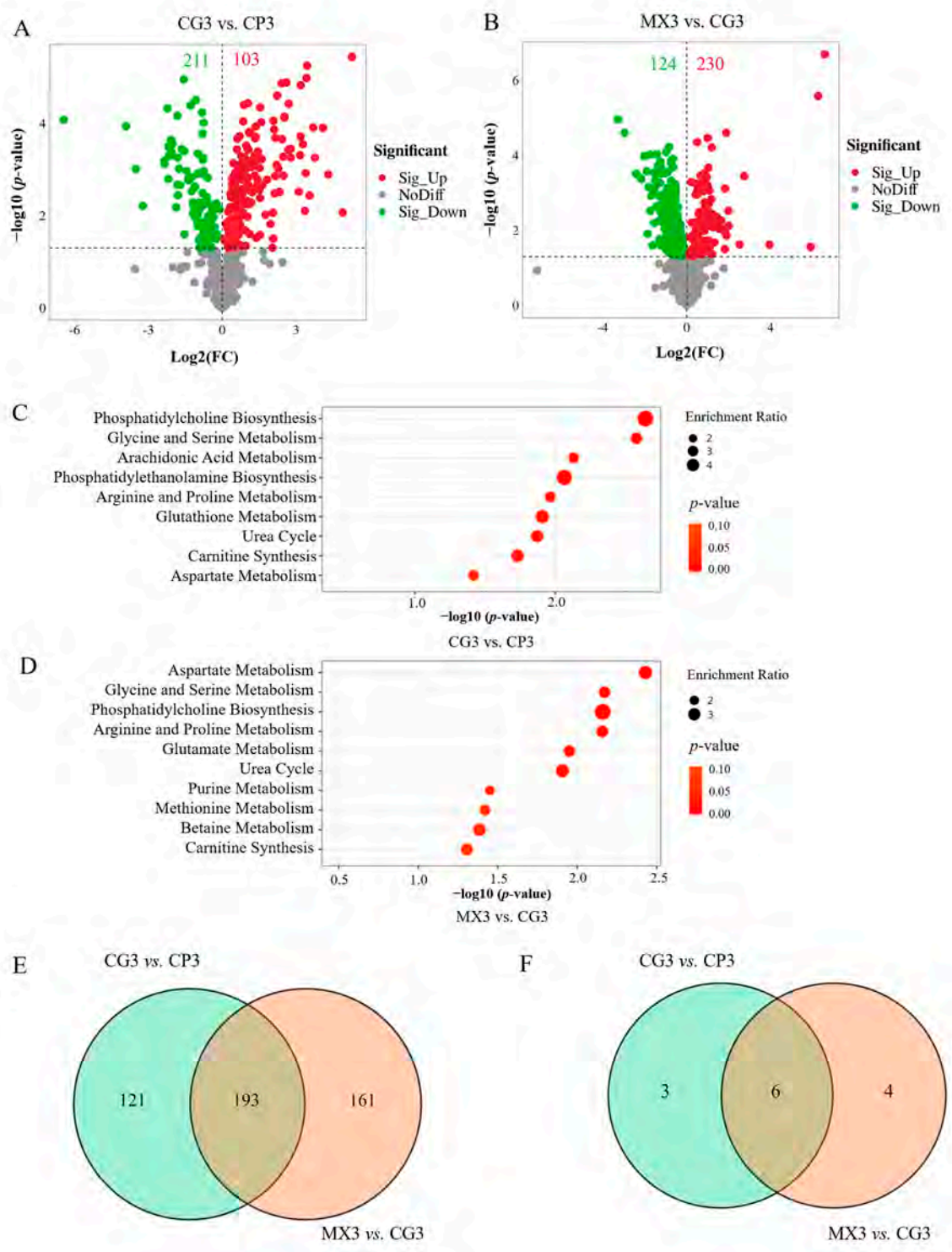


Figure 6. The analysis of DEMs and differential metabolic pathways in different groups. The volcano plot of DEMs in CG3 vs. CP3 (**A**) and in MX3 vs. CG3 (**B**); the pairwise comparison of differential metabolic pathways in CG3 vs. CP3 (**C**) and MX3 vs. CG3 (**D**); the Venn diagram of DEMs (**E**) and differential metabolic pathways (**F**) in different groups.

Differential metabolites were imported into the Metaboanalyst 6.0 database for metabolic pathway analysis. The results of the differential metabolic pathways indicated that, in CG3 vs. CP3, the metabolic pathways of phosphatidylcholine biosynthesis, glycine and serine metabolism, arachidonic acid metabolism, phosphatidylethanolamine biosynthesis, arginine and proline metabolism, glutathione metabolism, urea cycle, carnitine synthesis, aspartate metabolism in the CG3 group were mainly enriched (Figure 6C). In MX3 vs. CG3, the metabolic pathways of aspartate metabolism, glycine and serine metabolism, phosphatidylcholine biosynthesis, arginine and proline metabolism, glutamate metabolism, urea cycle, purine metabolism, methionine metabolism, betaine metabolism, carnitine synthesis in the MX3 group were mainly enriched (Figure 6D).

The Venn diagram analysis revealed an overlap of 193 differentially expressed metabolites (DEMs) and 6 differential metabolic pathways shared between the two comparison groups (Figure 6E,F). Additionally, exclusive to the CG3 versus CP3 comparison, there were 121 unique DEMs and 3 distinct metabolic pathways, whereas the MX3 versus CG3 comparison exhibited 161 exclusive DEMs and 4 unique metabolic pathways.

3.8. Association Between the Intestinal Microbiota and Metabolites

The correlation analysis of 16S sequencing and metabolomics was performed to explore the relationship between the intestinal microbiota and host metabolism using the data of differential genus-level microbiota and differential secondary metabolites using Pearson's correlation analysis (Figure 7). According to the genus-level microbial species analysis, compared with the other two groups, the relative abundance of *cetobacterium* and *Clostridium_sensu_stricto_1* in the MX group was higher, while the relative abundance of *Mycobacterium* was lower. As shown in Figure 7A, Spearman's correlation analysis revealed that in the comparison between CG3 and CP3, *Clostridium_sensu_stricto_1* exhibited a significant positive correlation with saikosaponin B1. In contrast, prostaglandin F2a, 4-guanidinobutyric acid, Yucalexin B20, arecaidine, alpha-ketoisovaleric acid, methylsuccinic acid, and prostaglandin A1 showed significant negative correlations with *Clostridium_sensu_stricto_1*. Moreover, *Streptococcus* had a significant positive correlation with arecaidine and 2,3,4,5-tetrahydropyridine-2-carboxylate, while kinsenoside and S-Adenosyl-L-homocysteine showed significant negative correlations with *Streptococcus*. As shown in Figure 7B, in the comparison between MX3 and CG3, *Clostridium_sensu_stricto_1* demonstrated a significant positive correlation with sphingosine. *Mycobacterium* showed a significant positive correlation with bisosthenon B, galanthamine N-Oxide, 2-Biphenylol, and 2-Hydroxyethanesulfonic acid. *Cetobacterium* also had a significant positive correlation with galanthamine N-Oxide, 2-Biphenylol, and 2-hydroxyethanesulfonic acid, whereas N-Acetyl-L-arginine showed a significant negative correlation with *Cetobacterium*. However, the correlation analysis in this study only reveals statistical associations between variables, and causal relationships cannot be inferred at this stage.

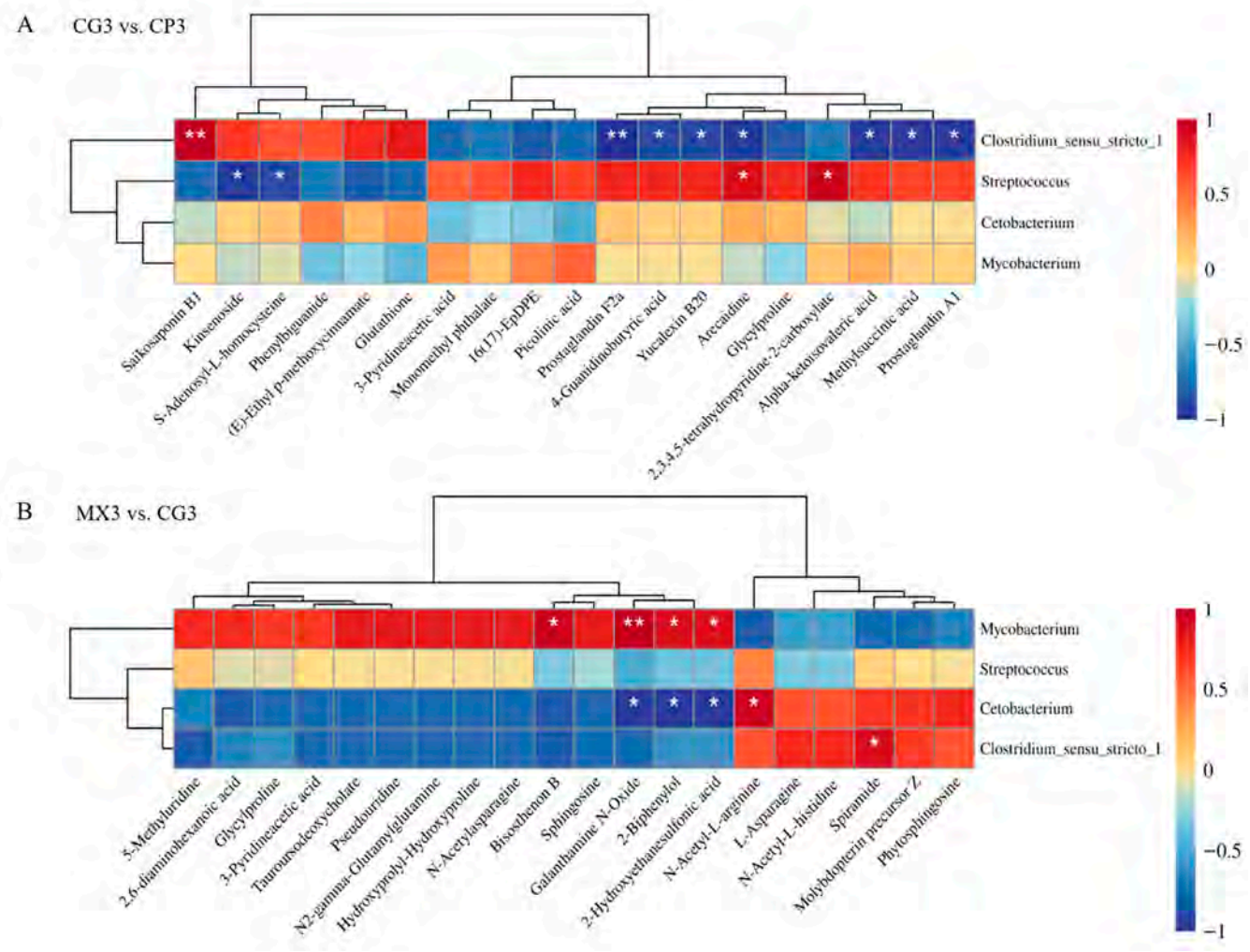


Figure 7. The combination analysis of differential microbiota and differential metabolites in pairwise comparison of the three groups. (**A**) CG3 vs. CP3, (**B**) MX3 vs. CG3 (* $p < 0.05$, ** $p < 0.01$).

4. Discussion

In the present study, we utilized qPCR to assess the variation in SA loads in the tissues of tilapia following SA infection and subsequent treatment with XN. This approach was employed to quantify the drug's anti-SA efficacy and to evaluate its potential as an anti-SA agent. In disease treatment, the effectiveness of a drug depends on the dosage, and many phytochemicals exhibit hormetic effects. This is a biphasic dose–response model, usually showing a "J"-shaped or inverted "U"-shaped curve, which is characterized by "stimulation at low doses and inhibition at high doses" [13]. In our study, different concentrations of XN all showed significant protective effects on tilapia, among which the 25 mg/kg concentration exhibited the best efficacy. This is highly consistent with the hormetic effect model. Furthermore, our survival rate results were similar to the anti-SA effects, where the 25 mg/kg XN exhibited the optimal protective effect, further supporting that xanthohumol may possess a hormetic effect. In other studies, 5 mg/L XN can alleviate DNA damage caused by oxidative stress in *Saccharomyces cerevisiae*, while concentrations higher than 5 mg/L lead to a reduced growth rate and aggravated DNA damage [14]. In summary, XN may exhibit a hormetic effect and has a good anti-SA effect in tilapia, indicating that XN has great therapeutic potential for SA infection.

The integrity of gut microbiota structure and function is intricately linked to microbial diversity [15], which, in turn, is correlated with the health status of fish [16]. In alignment

with previous findings, SA infection significantly diminishes the richness and diversity of the zebrafish gut microbiota while concurrently increasing the prevalence of pathogenic bacteria, thus aggravating the zebrafish condition [17]. The diversity resistance hypothesis posits that microbial communities with greater diversity are more likely to contain species capable of resisting invaders or pathogens [18]. Treatment with XN has been shown to elevate the ACE, Chao, and Shannon indices of the tilapia gut microbiota and to decrease the Simpson index, suggesting an enhancement in α-diversity. The reason for this phenomenon may be that, although XN has antibacterial activity, it mainly targets and inhibits pathogenic bacteria while having little impact on beneficial bacteria in the intestine. In addition, XN may promote the proliferation of beneficial bacteria by regulating intestinal composition and improving the intestinal environment, thereby increasing the overall diversity of microbiota. This mechanism is different from that of traditional broad-spectrum antibiotics, reflecting the specific advantages of XN. This implies that XN may bolster resistance to SA invasion through the promotion of gut microbial α-diversity.

The bacterial community composition in the XN-treated group diverged from that of the infected group, suggesting that both XN and SA are capable of modulating the tilapia gut microbiota structure. Donoso et al. [19] observed that XN can alter the abundance of specific gut microbial genera and significantly affect the β-diversity in a rat maternal separation model. Logan et al. [20] discovered through 16S rRNA gene sequencing of fecal samples from obese mice that XN supplementation can modify the microbial composition and substantially alter the predicted functional capabilities of the gut microbiota. Additionally, dietary garlic supplementation has been shown to regulate the gut microbial community in tilapia, influencing bacterial counts, diversity indices, and community structure, thereby countering *Streptococcus iniae* infection [21]. These findings collectively suggest that XN may alter the tilapia gut microbiota structure, potentially conferring protection against SA infection.

In the XN-treated group, the relative abundance of *Cetobacterium* and *Clostridium_sensu_stricto_1* was significantly higher compared to the infected group, whereas *Mycobacterium* was significantly less abundant. Li Ming et al. [22] noted significant shifts in the gut microbiota composition and diversity of tilapia following oral SA infection, with an increase in pathogenic genera such as *Edwardsiella* and *Pseudomonas* and a decrease in beneficial genera like *Cetobacterium*, *Lactococcus*, and *Propionibacterium*. Zhao et al. [23] reported a marked increase in the relative abundance of the pathogen *Campylobacter* in the gut of SA-infected tilapia under high-temperature conditions, potentially compromising the fish's immune defenses. *Mycobacterium* is a genus known to pose significant threats to fish, with several species inducing severe and often fatal diseases across a broad spectrum of fish species globally [24,25]. *Cetobacterium*, an anaerobic bacterium native to the guts of many freshwater fish, has been shown to produce butyrate through the fermentation of peptides and carbohydrates, thereby inhibiting the growth of potential pathogens [26]. Recent studies have highlighted *Cetobacterium*'s ability to produce vitamin B12, which fortifies intra-microbiota interactions and enhances the host's resistance to pathogenic infections [27]. Consistent with our observations, Radix Rehmanniae Preparata polysaccharides have also been reported to increase the abundance of *Cetobacterium* in the perch gut [28]. *Clostridium_sensu_stricto_1*, capable of metabolizing proteins and carbohydrates to produce small organic acids and hydrogen, is regarded as a beneficial bacterial genus in the context of bacterial infections due to its butyrate production [29]. XN can specifically enrich *Clostridium_sensu_stricto_1* and *Cetobacterium* (which are capable of producing short-chain fatty acids) in the intestines of tilapia, whereas other plant extracts (such as allicin) mainly exert their effects directly by inhibiting pathogenic bacteria [30,31]. This unique mode of action may be an important reason for the in vivo antibacterial activity of XN. This indicates

that XN may counteract SA infection by increasing the proportion of beneficial bacteria, such as *Cetobacterium* and *Clostridium_sensu_stricto_1*. However, regarding the impact of XN on the intestinal microbiota of tilapia, due to taxonomic limitations, further verification of its role in the tilapia intestine through metagenomics or single-bacterium isolation and culture experiments will be required in the future.

Bacterial infections are a significant cause of metabolic disorders in fish. Current research indicates that a variety of bacteria, including *Vibrio vulnificus*, *Vibrio alginolyticus*, *Aeromonas hydrophila*, *Edwardsiella tarda*, and SA, can alter the host's metabolic pathways [32–36]. The findings suggest that the metabolic state of aquatic animals is closely related to their infection resistance. For instance, studies have shown that *crucian carp* can regulate their metabolism to resist *Edwardsiella tarda* infection at 30 °C [37]. Existing research indicates that XN can ameliorate the dysfunctional glucose and lipid metabolism in diet-induced obese mouse models [20]. Our results indicated that, compared with the CG3 group, the number of downregulated and upregulated metabolites in the MX3 group was 124 and 230. Moreover, many metabolic pathways, including the aspartate metabolism, glycine and serine metabolism and phosphatidylcholine biosynthesis, were enriched in the MX3 group, indicating that XN changed the tilapia metabolic profiles. Aspartate was found to enhance the defense capability of zebrafish against antibiotic-sensitive and -resistant *Edwardsiella tarda* by promoting the biosynthesis of nitric oxide (NO) [38]. Exogenous aspartate could protect zebrafish from infection, and similarly, exogenous aspartate could enable *Cyprinus carpio* to combat *Aeromonas hydrophila* infection by promoting the release of NO [35]. Furthermore, aspartate metabolism also promotes the secretion of interleukin-1β (IL-1β) in inflammatory macrophages [39], indicating that aspartate metabolism also plays a key role in regulating macrophage function and inflammatory responses. Glycine and serine are two non-essential amino acids that play significant roles in the growth, health, and immune systems of aquatic animals. Glycine is involved in the construction of the antioxidant system and can stimulate the immune system [40]. In *Cyprinus carpio*, dietary supplementation with glycine can significantly improve growth performance, red blood cell stability, and humoral and mucosal immunity [40]. The regulation of serine metabolism can promote the survival of Nile tilapia after infection with *Edwardsiella tarda* [36].

The gut microbiota plays a key role both in the digestion and absorption of amino acids and in the breakdown and fermentation of amino acids in the intestine [41]. The intestinal microbiota of tilapia is rich in species participating in amino acid metabolism [42], especially, *Cetobacterium* and *Clostridium_sensu_stricto_1* [30]. The Spearman correlation analysis indicates a positive correlation between *Cetobacterium* and *Clostridium_sensu_stricto_1* with N-Acetyl-L-arginine, L-Asparagine, and N-Acetyl-L-histidine. Thus, XN may have enhanced the number of microorganisms capable of producing metabolically produced amino acids to facilitate immunopotentiation in the host.

XN shows promise as a preventive and therapeutic agent against SA infection in tilapia, with its mechanism of action likely involving the regulation of intestinal microbiota and liver metabolism (Figure 8). This study provides a foundation for the application of natural products in aquaculture to combat bacterial infections.

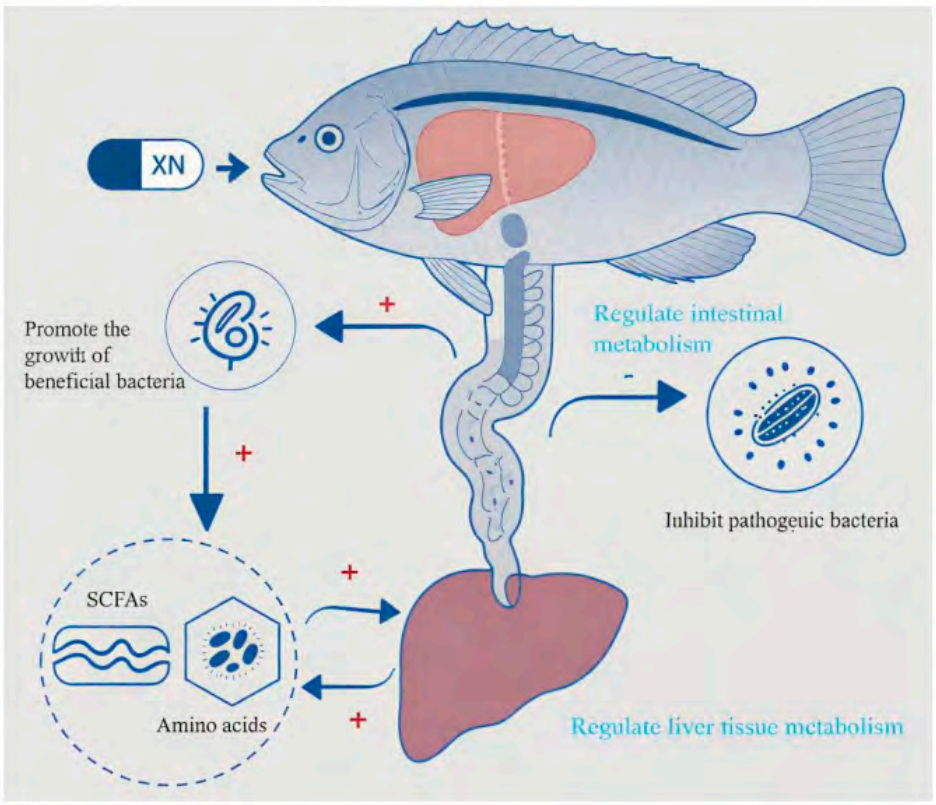


Figure 8. XN-mediated modulation of microbiota and liver metabolism in preventing SA infection. "+" represents promotion, and "−" represents inhibition.

Supplementary Materials: The following supporting information can be downloaded at: https://www.mdpi.com/article/10.3390/microorganisms13071699/s1, Figure S1: Total Ion Chromatogram (TIC) of QC samples detected by UHPLC-OE-MS in positive ion mode; Figure S2: Total Ion Chromatogram (TIC) of QC samples detected by UHPLC-OE-MS in negative ion mode; Figure S3: Extracted Ion Chromatogram (EIC) of internal standards in all QC samples (positive ion mode); Figure S4: Extracted Ion Chromatogram (EIC) of internal standards in all QC samples (negative ion mode); Figure S5: EIC of internal standards in blank and QC samples (positive ion mode); Figure S6: EIC of internal standards in blank and QC samples (negative ion mode); Figure S7: PCA score plot. Green dots represent QC samples, blue dots represent experimental samples; Figure S8: One-dimensional PCA-X distribution of QC samples; Figure S9: Correlation analysis of QC samples; Table S1: Stability of internal standard responses in QC samples; Table S2: QC report on clean tags of 16S rRNA data.

Author Contributions: Methodology, A.H., Y.W. (Yanqin Wei), J.H., S.L., T.W., J.G., F.Z. and Y.W. (Yinghui Wang); validation, Y.W. (Yanqin Wei), J.H., S.L. and F.Z.; investigation, A.H.; data curation, T.W. and F.Z.; writing—original draft, A.H., F.Z. and Y.W. (Yinghui Wang); writing—review and editing, A.H. and Y.W. (Yinghui Wang); funding acquisition, A.H. All authors have read and agreed to the published version of the manuscript.

Funding: This work was supported by the Guangxi Science and Technology Program (AD22080029), Natural Science Foundation of Guangxi (2021GXNSFBA075008), National Natural Science Foundation of China (42106133), Institute of Green and Low Carbon Technology, and Green and Low Carbon Technology Program of Guangxi Institute of Industrial Technology (DTS-202305001, DTS-202503001).

Institutional Review Board Statement: The animal use protocol was approved by the Animal Care and Welfare Committee of Guangxi University on 5 January 2023 (GXU-2023-0531). SA strain GXYL7, originally isolated from tilapia suffering from bacterial disease, was used in our study [11]. Natural compound XN (CAS No. 6754-58-1) was purchased from Aladdin Biochemical Technology Co., Ltd.

Informed Consent Statement: Not applicable.

Data Availability Statement: The original contributions presented in this study are included in the article/Supplementary Material. Further inquiries can be directed to the corresponding authors.

Conflicts of Interest: The authors declare no conflicts of interest.

References

1. Chen, M.; Li, L.-P.; Wang, R.; Liang, W.-W.; Huang, Y.; Li, J.; Lei, A.-Y.; Huang, W.-Y.; Gan, X. PCR detection and PFGE genotype analyses of streptococcal clinical isolates from tilapia in China. *Vet. Microbiol.* **2012**, *159*, 526–530. [CrossRef] [PubMed]
2. Dong, J.; Zhang, L.; Xu, N.; Zhou, S.; Song, Y.; Yang, Q.; Liu, Y.; Yang, Y.; Ai, X. Rutin reduces the pathogenicity of *Streptococcus agalactiae* to tilapia by inhibiting the activity of sortase A. *Aquaculture* **2021**, *530*, 735743. [CrossRef]
3. Zhang, D.; Liu, Z.; Ren, Y.; Wang, Y.; Pan, H.; Liang, D.; Bei, W.; Chang, O.; Wang, Q.; Shi, C. Epidemiological characteristics of *Streptococcus agalactiae* in tilapia in China from 2006 to 2020. *Aquaculture* **2022**, *549*, 737724. [CrossRef]
4. Ding, Z.-H.; Hong, J.-M.; Guo, W.-L.; Li, G.-H.; Zhao, Z.-C.; Zhou, Y.; Wang, S.-F.; Sun, Y.; Li, J.-L.; Zhang, D.-D.; et al. The screen herbal immunopotentiator and research on its effect on the innate immune system and disease resistance of Nile tilapia (*Oreochromis niloticus*) against *Streptococcus agalactiae*. *Aquaculture* **2021**, *541*, 736778. [CrossRef]
5. Guo, W.-L.; Deng, H.-W.; Wang, F.; Wang, S.-F.; Zhong, Z.-H.; Sun, Y.; Chen, X.-F.; Wang, J.-H.; Zhou, Y.-C. In vitro and in vivo screening of herbal extracts against *Streptococcus agalactiae* in Nile tilapia (*Oreochromis niloticus*). *Aquaculture* **2019**, *503*, 412–421. [CrossRef]
6. Zhang, F.-L.; Yang, L.; He, W.-H.; Xie, L.-J.; Yang, F.; Wang, Y.-H.; Huang, A.-G. In vivo antibacterial activity of medicinal plant *Sophora flavescens* against *Streptococcus agalactiae* infection. *J. Fish Dis.* **2023**, *46*, 977–986. [CrossRef] [PubMed]
7. Kamble, M.T.; Chaiyapechara, S.; Salin, K.R.; Bunphimpapha, P.; Chavan, B.R.; Bhujel, R.C.; Medhe, S.V.; Kettawan, A.; Thiyajai, P.; Thompson, K.D.; et al. Guava and Star gooseberry leaf extracts improve growth performance, innate immunity, intestinal microbial community, and disease resistance in Nile tilapia (*Oreochromis niloticus*) against *Aeromonas hydrophila*. *Aquac. Rep.* **2024**, *35*, 101947. [CrossRef]
8. Chen, C.-C.; Lin, C.-Y.; Lu, H.-Y.; Liou, C.-H.; Ho, Y.-N.; Huang, C.-W.; Zhang, Z.-F.; Kao, C.-H.; Yang, W.-C.; Gong, H.-Y. Transcriptomics and gut microbiome analysis of the edible herb *Bidens pilosa* as a functional feed additive to promote growth and metabolism in tilapia (*Oreochromis* spp.). *BMC Genom.* **2024**, *25*, 785. [CrossRef] [PubMed]
9. Wang, F.; Xian, X.-R.; Guo, W.-L.; Zhong, Z.-H.; Wang, S.-F.; Cai, Y.; Sun, Y.; Chen, X.-f.; Wang, Y.-q.; Zhou, Y.-C. Baicalin attenuates *Streptococcus agalactiae* virulence and protects tilapia (*Oreochromis niloticus*) from group B streptococcal infection. *Aquaculture* **2020**, *516*, 734645. [CrossRef]
10. Kasica, N.; Kaleczyc, J. Xanthohumol, a prenylated flavonoid from hops (*Humulus lupulus* L.) exerts multidirectional pro-healing properties towards damaged zebrafish hair cells by regulating the innate immune response. *Toxicol. Appl. Pharmacol.* **2024**, *483*, 116809. [CrossRef] [PubMed]
11. Huang, A.-G.; Su, L.-J.; He, W.-H.; Zhang, F.-L.; Wei, C.-S.; Wang, Y.-H. Natural component plumbagin as a potential antibacterial agent against *Streptococcus agalactiae* infection. *J. Fish Dis.* **2022**, *45*, 815–823. [CrossRef] [PubMed]
12. Huang, A.-G.; He, W.-H.; Su, L.-J.; Zhang, F.-L.; Wang, Y.-H. Identification of a camelid-derived nanobody as a potential therapeutic agent against *Streptococcus agalactiae* infection. *Aquaculture* **2022**, *561*, 738725. [CrossRef]
13. Wang, D.; Calabrese, E.J.; Lian, B.; Lin, Z.; Calabrese, V. Hormesis as a mechanistic approach to understanding herbal treatments in traditional Chinese medicine. *Pharmacol. Ther.* **2018**, *184*, 42–50. [CrossRef] [PubMed]
14. Carvalho, D.O.; Oliveira, R.; Johansson, B.; Guido, L.F. Dose-Dependent Protective and Inductive Effects of Xanthohumol on Oxidative DNA Damage in *Saccharomyces cerevisiae*. *Food Technol. Biotechnol.* **2016**, *54*, 60–69. [CrossRef] [PubMed]
15. Li, T.; Li, H.; Gatesoupe, F.-J.; She, R.; Lin, Q.; Yan, X.; Li, J.; Li, X. Bacterial Signatures of "Red-Operculum" Disease in the Gut of Crucian Carp (*Carassius auratus*). *Microb. Ecol.* **2017**, *74*, 510–521. [CrossRef] [PubMed]
16. She, R.; Li, T.-T.; Luo, D.; Li, J.-B.; Yin, L.-Y.; Li, H.; Liu, Y.-M.; Li, X.-Z.; Yan, Q.-g. Changes in the Intestinal Microbiota of Gibel Carp (*Carassius gibelio*) Associated with *Cyprinid herpesvirus* 2 (CyHV-2) Infection. *Curr. Microbiol.* **2017**, *74*, 1130–1136. [CrossRef] [PubMed]
17. Zhang, Q.-L.; Li, H.-W.; Wu, W.; Zhang, M.; Guo, J.; Deng, X.-Y.; Wang, F.; Lin, L.-B. The Response of Microbiota Community to *Streptococcus agalactiae* Infection in Zebrafish Intestine. *Front. Microbiol.* **2019**, *10*, 2848. [CrossRef] [PubMed]
18. Fargione, J.E.; Tilman, D. Diversity decreases invasion via both sampling and complementarity effects. *Ecol. Lett.* **2005**, *8*, 604–611. [CrossRef]
19. Donoso, F.; Egerton, S.; Bastiaanssen, T.F.S.; Fitzgerald, P.; Gite, S.; Fouhy, F.; Ross, R.P.; Stanton, C.; Dinan, T.G.; Cryan, J.F. Polyphenols selectively reverse early-life stress-induced behavioural, neurochemical and microbiota changes in the rat. *Psychoneuroendocrinology* **2020**, *116*, 104673. [CrossRef] [PubMed]

20. Logan, I.E.; Shulzhenko, N.; Sharpton, T.J.; Bobe, G.; Liu, K.; Nuss, S.; Jones, M.L.; Miranda, C.L.; Vasquez-Perez, S.; Pennington, J.M.; et al. Xanthohumol Requires the Intestinal Microbiota to Improve Glucose Metabolism in Diet-Induced Obese Mice. *Mol. Nutr. Food Res.* **2021**, *65*, e2100389. [CrossRef] [PubMed]
21. Foysal, M.J.; Alam, M.; Momtaz, F.; Chaklader, M.R.; Siddik, M.A.B.; Cole, A.; Fotedar, R.; Rahman, M.M. Dietary supplementation of garlic (*Allium sativum*) modulates gut microbiota and health status of tilapia (*Oreochromis niloticus*) against *Streptococcus iniae* infection. *Aquac. Res.* **2019**, *50*, 2107–2116. [CrossRef]
22. Li, M.; Ma, C.-X.; Li, J.-B.; Lei, A.-Y.; Li, L.-P.; Li, D.-L.; Chen, F.-Y.; Chen, M. Effects of *Streptococcus agalactiae* on intestinal flora of tilapia. *J. South. Agric.* **2019**, *50*, 1647–1656.
23. Zhao, Z.; Zou, Q.; Han, S.; Shi, J.; Yan, H.; Hu, D.; Yi, Y. Omics analysis revealed the possible mechanism of streptococcus disease outbreak in tilapia under high temperature. *Fish Shellfish. Immunol.* **2023**, *134*, 108639. [CrossRef] [PubMed]
24. Jacobs, J.M.; Stine, C.B.; Baya, A.M.; Kent, M.L. A review of mycobacteriosis in marine fish. *J. Fish Dis.* **2009**, *32*, 119–130. [CrossRef] [PubMed]
25. Davidovich, N.; Morick, D.; Carella, F. Mycobacteriosis in Aquatic Invertebrates: A Review of Its Emergence. *Microorganisms* **2020**, *8*, 1249. [CrossRef] [PubMed]
26. Tsuchiya, C.; Sakata, T.; Sugita, H. Novel ecological niche of *Cetobacterium somerae*, an anaerobic bacterium in the intestinal tracts of freshwater fish. *Lett. Appl. Microbiol.* **2008**, *46*, 43–48. [CrossRef] [PubMed]
27. Qi, X.; Zhang, Y.; Zhang, Y.; Luo, F.; Song, K.; Wang, G.; Ling, F. Vitamin B_{12} produced by *Cetobacterium somerae* improves host resistance against pathogen infection through strengthening the interactions within gut microbiota. *Microbiome* **2023**, *11*, 135. [CrossRef] [PubMed]
28. Wu, C.; Shan, J.; Feng, J.; Wang, J.; Qin, C.; Nie, G.; Ding, C. Effects of dietary *Radix Rehmanniae Preparata* polysaccharides on the digestive enzymes, morphology, microbial communities and mucosal barrier function of the intestine of *Luciobarbus capito*. *Aquac. Res.* **2020**, *51*, 1026–1037. [CrossRef]
29. Ma, X.; Yu, M.; Yang, M.; Zhang, S.; Gao, M.; Wu, C.; Wang, Q. Effect of liquid digestate recirculation on the ethanol-type two-phase semicontinuous anaerobic digestion system of food waste. *Bioresour. Technol.* **2020**, *313*, 123534. [CrossRef] [PubMed]
30. Zhu, H.; Qiang, J.; Li, Q.; Nie, Z.; Gao, J.; Sun, Y.; Xu, G. Multi-kingdom microbiota and functions changes associated with culture mode in genetically improved farmed tilapia (*Oreochromis niloticus*). *Front. Physiol.* **2022**, *13*, 974398. [CrossRef] [PubMed]
31. Tao, Z.; Geng, D.; Tao, J.; Wang, J.; Liu, S.; Wang, Q.; Xu, F.; Xiao, S.; Wang, R. Synergistic Antibacterial Effect and Mechanism of Allicin and an Enterobacter cloacae Bacteriophage. *Microbiol. Spectr.* **2023**, *11*, e0315522. [CrossRef] [PubMed]
32. Zhao, X.-l.; Han, Y.; Ren, S.-t.; Ma, Y.-m.; Li, H.; Peng, X.-x. L-proline increases survival of tilapias infected by *Streptococcus agalactiae* in higher water temperature. *Fish Shellfish. Immunol.* **2015**, *44*, 33–42. [CrossRef] [PubMed]
33. Gong, Q.-y.; Yang, M.-j.; Yang, L.-f.; Chen, Z.-g.; Jiang, M.; Peng, B. Metabolic modulation of redox state confounds fish survival against *Vibrio alginolyticus* infection. *Microb. Biotechnol.* **2020**, *13*, 796–812. [CrossRef] [PubMed]
34. Nurdalila, A.w.A.; Natnan, M.E.; Baharum, S.N. The effects of amino acids and fatty acids on the disease resistance of *Epinephelus fuscoguttatus* in response to *Vibrio vulnificus* infection. *3 Biotech* **2020**, *10*, 544. [CrossRef] [PubMed]
35. Zhao, X.; Yang, Y.; Wang, L.; Chen, H.; Zhu, L.; Li, L.; Kong, X. Aspartate induces metabolic changes and improves the host's ability to fight against *Aeromonas hydrophila* infection in *Cyprinus carpio*. *Aquac. Res.* **2022**, *53*, 1050–1061. [CrossRef]
36. Yang, D.-X.; Yang, M.-J.; Yin, Y.; Kou, T.-S.; Peng, L.-T.; Chen, Z.-G.; Zheng, J.; Peng, B. Serine Metabolism Tunes Immune Responses To Promote *Oreochromis niloticus* Survival upon *Edwardsiella tarda* Infection. *Msystems* **2021**, *6*, e0042621. [CrossRef] [PubMed]
37. Jiang, M.; Chen, Z.-g.; Zheng, J.; Peng, B. Metabolites-Enabled Survival of Crucian Carps Infected by *Edwardsiella tarda* in High Water Temperature. *Front. Immunol.* **2019**, *10*, 01991. [CrossRef] [PubMed]
38. Xiang, J.; Li, M.-y.; Li, H. Aspartate metabolic flux promotes nitric oxide to eliminate both antibiotic-sensitive and -resistant *Edwardsiella tarda* in zebrafish. *Front. Immunol.* **2023**, *14*, 1277281. [CrossRef] [PubMed]
39. Wang, H.; Zheng, X.; Liu, B.; Xia, Y.; Xin, Z.; Deng, B.; He, L.; Deng, J.; Ren, W. Aspartate Metabolism Facilitates IL-1β Production in Inflammatory Macrophages. *Front. Immunol.* **2021**, *12*, 753092. [CrossRef] [PubMed]
40. Abbasi, M.; Mirghaed, A.T.; Hoseini, S.M.; Rajabiesterabadi, H.; Hoseinifar, S.H.; Van Doan, H. Effects of Dietary Glycine Supplementation on Growth Performance, Immunological, and Erythrocyte Antioxidant Parameters in Common Carp, *Cyprinus carpio*. *Animals* **2023**, *13*, 412. [CrossRef] [PubMed]
41. Galley, J.D.; Chen, H.J.; Antonson, A.M.; Gur, T.L. Prenatal stress-induced disruptions in microbial and host tryptophan metabolism and transport. *Behav. Brain Res.* **2021**, *414*, 113471. [CrossRef] [PubMed]
42. Wu, Z.; Wang, S.; Zhang, Q.; Hao, J.; Lin, Y.; Zhang, J.; Li, A. Assessing the intestinal bacterial community of farmed Nile tilapia (*Oreochromis niloticus*) by high-throughput absolute abundance quantification. *Aquaculture* **2020**, *529*, 735688. [CrossRef]

Disclaimer/Publisher's Note: The statements, opinions and data contained in all publications are solely those of the individual author(s) and contributor(s) and not of MDPI and/or the editor(s). MDPI and/or the editor(s) disclaim responsibility for any injury to people or property resulting from any ideas, methods, instructions or products referred to in the content.

Marine Pollution Bulletin 221 (2025) 118556

Contents lists available at ScienceDirect

Marine Pollution Bulletin

journal homepage: www.elsevier.com/locate/marpolbul

Antioxidant capacity is a key factor in the difference in thermal tolerance between massive *Porites lutea* and branching *Acropora formosa*

Linqing Meng [a,b], Ronghua Tan [a], Zunyong Xiao [c], Jinlian Chen [a], Zhihua Huang [a], Yonggang Wang [a], Enguang Yang [a], Yupeng Zhou [c], Mingpei Xu [c], Kefu Yu [a,d], Wen Huang [a,*]

[a] Guangxi Laboratory on the Study of Coral Reefs in the South China Sea, Coral Reef Research Center of China, School of Marine Sciences, Guangxi University, Nanning 530004, China
[b] College of Ocean and Earth Sciences, Xiamen University, Xiamen 361005, China
[c] School of Resources, Environment and Materials, Guangxi University, Nanning 530004, China
[d] Southern Marine Science and Engineering Guangdong Laboratory, Zhuhai 519080, China

ARTICLE INFO

Keywords:
Coral holobionts
Heat stress
Antioxidant
Heat tolerance
Reef restoration

ABSTRACT

Identifying the reasons behind differences in thermal tolerance among reef-building corals is pivotal to projecting their ability to withstand increasing seawater temperatures. Antioxidant responses are common in marine organisms and are strongly linked with coral thermotolerance. However, the mechanism by which the antioxidant response affects the thermotolerance of coral holobionts remains unclear. In this study, heat stress experiments were performed on massive *Porites lutea* and branching *Acropora formosa* from Weizhou Island in the northern South China Sea and analyzed for physiological indices, antioxidant levels, and high-throughput sequencing. Following heat stress, *A. formosa* exhibited more severe physiological bleaching and significantly lower Symbiodiniaceae density, Fv/Fm, and antioxidant levels than *P. lutea*. Moreover, *P. lutea* host and its Symbiodiniaceae (*Cladocopium* C15) downregulated fewer antioxidant-related genes than *A. formosa* at 34 °C. Specifically, *P. lutea* host had a more complex antioxidant regulatory capacity and mainly regulated glutathione (GSH). *Cladocopium* C15 enhanced the regulation of GSH, peroxisome, and ascorbate-related genes, thereby boosting antioxidant capacity. *P. lutea* also had more antioxidant-functional coral-associated bacteria than *A. formosa* at high temperatures, including *Endozoicomonas*, *Ruegeria*, and *Dinoroseobacter*. Overall, the superior antioxidant capacity of the coral holobionts plays a key role in the greater thermotolerance of *P. lutea*. These findings suggest that antioxidants can potentially be used as biomarkers for coral reef management. Our research deepens the understanding of high-temperature adaptation strategies for thermotolerant corals and provides a theoretical basis for their selection and reef restoration.

1. Introduction

Coral reefs are biodiversity hotspots that provide ecosystem services to millions of individuals (Eddy et al., 2021). However, recent studies show that global warming has tripled the number of annual marine heatwave days (Marcos et al., 2025), leading to widespread coral bleaching and reef degradation (Hughes et al., 2017; Pockley, 2000). Coral bleaching events have occurred more frequently recently, such as in 2023–2024, which is recognized as the fourth global coral bleaching event year (Reimer et al., 2024). The survival of reef-building corals during bleaching events depends on their thermal tolerance—once seawater temperatures exceed this threshold, corals experience thermal stress (Lachs et al., 2023). Numerous field and laboratory studies have shown that corals with different morphologies exhibit varying levels of thermal tolerance. For example, massive corals (e.g., *Poritidae*, *Faviidae*, *Fungiidae*) tend to be more thermotolerant than branching corals (e.g., *Acropora*, *Pocilloporidae*, *Milleporidae*) (Harithsa et al., 2005; Liang et al., 2017; Marshall and Baird, 2000; Muir et al., 2021). The underlying

Abbreviations: Fv/Fm, the maximum photochemical efficiency of photosystem II; GSH, glutathione; SOD, superoxide dismutase; CAT, catalase; POD, peroxidase; ROS, reactive oxygen species; H_2O_2, hydrogen peroxide; $^1O_2$, singlet oxygen; O_2^-, superoxide radical; ASVs, amplicon sequence variants; PCoA, principal coordinate analysis; LEfSe, linear discriminant analysis effect size; KEGG, Kyoto encyclopedia of genes and genomes; GO, gene ontology; TPM, transcripts per million reads; DEGs, differentially expressed genes; ANOVA, analysis of variance; SD, standard deviation; DMS, dimethylsulfide; DMSP, dimethylsulfoniopropionate.

* Corresponding author.
E-mail address: wenhuang@gxu.edu.cn (W. Huang).

https://doi.org/10.1016/j.marpolbul.2025.118556
Received 20 May 2025; Received in revised form 23 July 2025; Accepted 6 August 2025
0025-326X/© 2025 Elsevier Ltd. All rights are reserved, including those for text and data mining, AI training, and similar technologies.

mechanisms driving thermotolerance variation are complex, involving genetic influences, the coral host, associated endosymbiotic algae, and microbial communities, but they are not fully understood (Putnam, 2021; Strand et al., 2024). Therefore, exploring the factors underlying thermotolerance in massive and branching corals is important and urgent, as it enhances our understanding of reef-building coral survival strategies and supports coral reef restoration.

The antioxidant response, widely observed in coral reef ecosystems, involves a series of antioxidants (e.g., superoxide dismutase, SOD; catalase, CAT) that scavenge excess reactive oxygen species (ROS) to prevent cellular damage, and is closely linked to coral thermotolerance (Halliwell, 2006; Lesser, 2006; Morris et al., 2022). For example, at heat stress and higher irradiances, ROS production in symbiotic Symbiodiiaceae is a major stressor leading to programmed cell death (Downs et al., 2002; Lesser, 2024). As key components of the coral holobionts, the coral host and its associated microbiome also produce ROS, especially in response to environmental stressors (Suggett and Smith, 2020). This suggests that the ability of corals to effectively scavenge the high ROS accumulated (i.e., antioxidant capacity) determines their ability to withstand high temperatures and regulate coral health (Cziesielski et al., 2019; Weis, 2008). It is evident that antioxidant capacity may influence the thermal tolerance of corals with different morphologies. For example, previous studies have shown that, due to differences in antioxidant capacity, the massive *Galaxea fascicularis* and *Platygyra verweyi* exhibit greater thermotolerance than the branching *Pocillopora damicornis* and *Isopora palifera* (Dias et al., 2019; Wang et al., 2022). These studies have enhanced our understanding of thermotolerance and antioxidant responses in corals to some extent, but they have primarily explored the issue from a single perspective—such as physiological indicators or the coral host—leaving many underlying mechanisms still unclear. A more comprehensive understanding of the mechanisms underlying the differences in antioxidant response and thermotolerance between massive and branching corals is required through the integrated response of their hosts, Symbiodiniaceae, and coral-associated bacteria (Avila-Magaña et al., 2021; Huang et al., 2024). Unfortunately, relatively less research has been conducted on this topic.

As an important component of the antioxidant system, SOD disproportionates superoxide to hydrogen peroxide (H_2O_2), and CAT inactivates H_2O_2 to generate water and oxygen to avoid oxidative damage in the organism (Lesser, 2006). GSH also quenches harmful ROS, such as H_2O_2, singlet oxygen ($^1O_2$), and superoxide radical (O_2^-), and plays an important defense mechanism (Fernández-Checa et al., 1997; Lesser, 2006). In addition, peroxidase (POD), ascorbate, carotenoids, tocopherol, and small-molecule antioxidants, such as uric acid, dimethylsulfide, and mycosporine-like amino acids, also play important roles (Halliwell, 2006; Lesser, 2006). Previous studies have found differences in SOD and CAT activities under heat stress in coral hosts and Symbiodiniaceae (Doering et al., 2023; Yakovleva et al., 2004). This suggests that the proportion and contribution of these antioxidants may vary between corals and their symbiotic partners. Therefore, molecular-level analyses of antioxidant expression in massive and branching coral holobionts are crucial for elucidating the mechanisms by which corals respond to heat stress.

Acropora formosa and *Porites lutea* are well-known typical branching and massive corals, respectively, and the genomes of their host and symbiotic algae have recently been revealed (Robbins et al., 2019; Shinzato et al., 2021). Although thermotolerance of the two corals have been studied previously, they mainly focused on the physiological indictors and Symbiodiniaceae (Fisher et al., 2012; Harithsa et al., 2005). A comprehensive study on antioxidant response of the two coral holobionts is lacking. In the present study, we comprehensively analyzed the differences in thermal tolerance between the two corals using physiological indicators, antioxidant levels, and high-throughput sequencing. The main objectives were to (1) explore the effect of the antioxidant response on the difference in thermotolerance between massive *P. lutea* and branching *A. formosa*; (2) further analyze the antioxidant differences between the two corals in their host, Symbiodiniaceae, and coral-associated bacteria; (3) explore the potential of antioxidants as biomarkers for application in coral reef restoration. These findings provide new insights into the adaptation mechanism of thermotolerant corals to future warming seawater and provide theoretical support for the restoration and protection of severely degraded coral reefs.

2. Materials and methods

2.1. Sample collection and experimental design

Massive *P. lutea* and branching *A. formosa* were collected in November 2021 from Weizhou Island in the northern South China Sea (21°00′–21°10′ N, 109°00′–109°15′ E). Five colonies for both coral species were sampled using SCUBA at depths of 4–6 m and water temperatures of approximately 25 °C (Huang et al., 2024). Sampling distance was at least 5 m to minimize the possibility of sampling clonal genotypes (Baums et al., 2006). All colonies were transported within 1 h to the laboratory at the Weizhou Island Coral Museum of Guangxi University and placed in 400 L aquarium tanks with pumps to maintain water flow. Circulating seawater was filtered using live rock and protein skimmers. Each colony was divided into two uniformly sized ramets (~4 cm) for experimental sampling at 26 °C and 34 °C, respectively. These ramets were acclimated at 26 °C for 15 d before the formal experiments began.

Heat-stress experiments are effective for examining differences in coral thermotolerance ability (Voolstra et al., 2020). The temperature of 26 °C is suitable for coral growth, while 34 °C simulates future ocean warming (Huang et al., 2024). Therefore, two temperature conditions were applied: 26 °C as the control (normal temperature) and 34 °C as the experimental treatment (extreme high temperature) (Fig. 1A). The experimental tank seawater was raised from 26 °C by 1 °C daily to simulate warming. Given that the average summer seawater temperature around Weizhou Island is 30 °C, seawater in the tank was maintained at 30 °C for 2 d to acclimate the coral ramets to the anticipated heat stress. The temperature was then increased to 34 °C at the same rate, maintained for 2 d, and followed by sampling. The control tank had been maintained at a seawater temperature of 26 °C and sampled at the end of the experiment (i.e., 26 °C for 11 d). Here, only two tanks were used in the experiment. Although multiple replicate tanks would improve statistical reliability, resource constraints limited their feasibility (Huang et al., 2024).

Both tanks were exposed to natural light with an average daily intensity of ~180 μmol m^{-2} s^{-1}. Tank temperatures were controlled using aquarium heaters and chillers, with 20 % of the water volume replaced daily with filtered natural seawater. Water quality parameters were tested and maintained within natural seawater ranges, and corals were not fed. Temperature and light levels were recorded using HOBO thermometers, with measurement ranges of −20 to 50 °C and 0 to 167,731 lx, respectively (Onset Corporation, Bourne, MA, USA). According to the manufacturer's reference, 1 μmol m^{-2} s^{-1} equaled 54 lx under sunlight. All conditions were identical between the tanks, except for temperature. To facilitate subsequent data analysis, four groups were established: 26 °C-treated *P. lutea* (CP), 34 °C-treated *P. lutea* (HP), 26 °C-treated *A. formosa* (CA), and 34 °C-treated *A. formosa* (HA).

2.2. Phenotype, physiological indicators, and antioxidant indicators

The ramet health status was observed and photographed daily using an Olympus Tough TG-6 camera. The Fv/Fm values were measured daily using a DIVING-PAM after 30 min in the dark to allow the corals to adapt. Dark-adapted Fv/Fm provides a good approximation for the maximum photochemical efficiency of photosystem II (Huang et al., 2022; Warner et al., 1999). To minimize variations in the Fv/Fm values, all measurements were taken perpendicular to the coral tissue at a distance of 1 cm (Putnam and Edmunds, 2011).

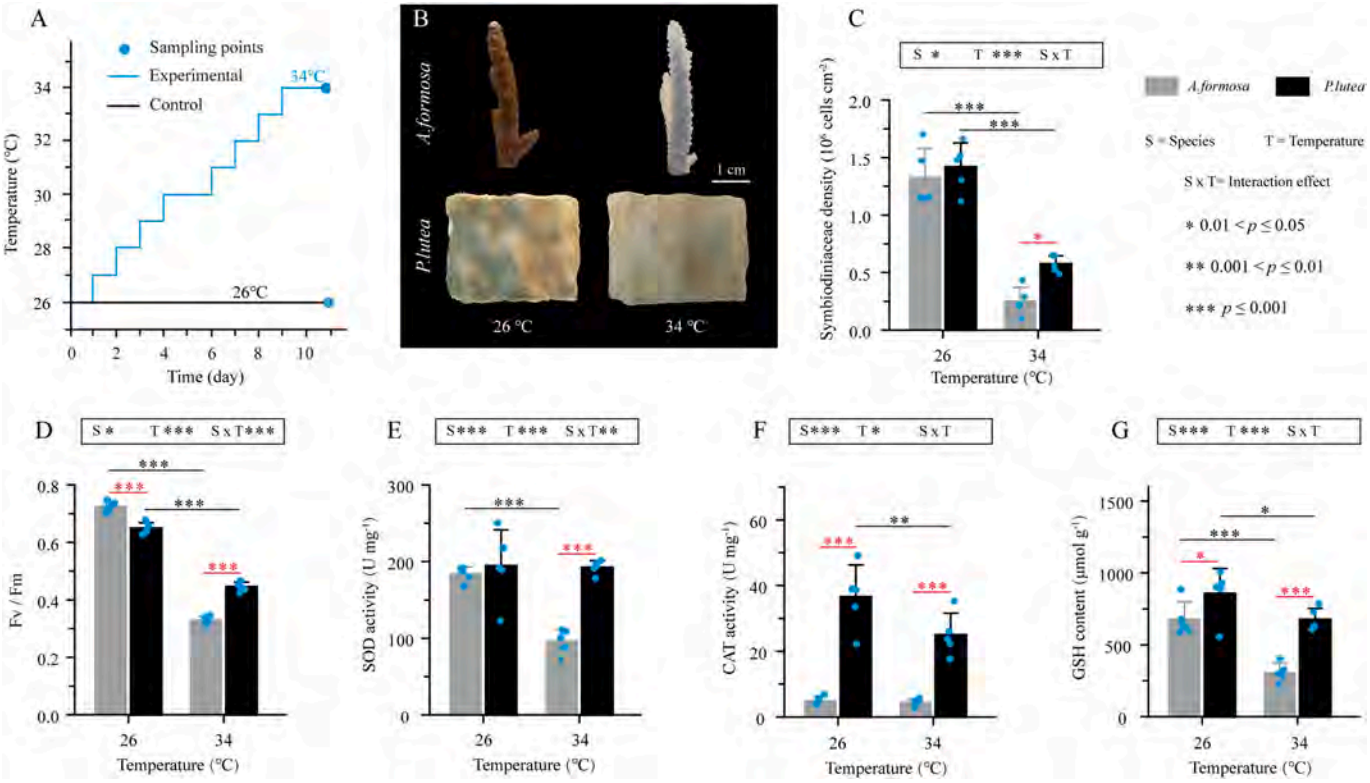


Fig. 1. Experiment design, Physiology indicators, and antioxidant indicators. (A) Heat-stress experiment design. (B) Coral phenotype. (C) Symbiodiniaceae density. (D) Fv/Fm. (E) Superoxide dismutase, SOD. (F) Catalase, CAT. (G) Glutathione, GSH. Significant differences in two-way ANOVA for species, temperature, and their interaction effects are boxed. In pairwise comparisons, black asterisks indicate significant differences between temperature treatments within the same species, while red asterisks denote significant differences between species at a given temperature. (For interpretation of the references to color in this figure legend, the reader is referred to the web version of this article.)

At each sampling point, tissue samples (~4–6 cm^2) were collected for DNA and RNA analysis, while the remaining tissue (~10–12 cm^2) was immediately used for physiological and antioxidant activity assessments.

Symbiodiniaceae density was measured as described previously (Huang et al., 2024; Qin et al., 2019). Briefly, coral tissue was rinsed by a Waterpik with 0.22-μm filtered seawater. Fifty milliliters of the initial slurry measured with a graduated cylinder was centrifuged at 4 °C, 3000*g* for 10 min, and the supernatant was discarded. After resuspension in 10 mL of filtered seawater and centrifugation of a 1 mL aliquot, the supernatant was removed, and the algae were preserved in 1 mL of 5 % formaldehyde at 6 °C for 2–4 h. Symbiodiniaceae numbers were calculated by the hemocytometer counts (8 replicates). Coral surface area was determined using the aluminum foil method (Johannes et al., 1970), with 8–10 replicates to reduce error, particularly for branching corals.

The high-concentration tissue homogenate (<10 mL) was centrifuged at 4 °C, 6000*g* for 15 min, and the supernatant was used to determine antioxidant indicators. SOD and CAT activities, along with GSH concentration, were measured using commercial kits (Nanjing Jiancheng Bioengineering Institute, Nanjing, China) according to the manufacturer's instructions (Huang et al., 2022; Zhou et al., 2018). To normalize the total level of each antioxidant, coral homogenates were assayed for protein concentration using the BCA Protein Assay Kit (Sangon Biotech, Shanghai, China). All antioxidant indicators were measured from coral tissue homogenate and thus are values for coral holobionts (Huang et al., 2024).

2.3. Composition analysis of Symbiodiniaceae clade type

DNA was extracted using a DNeasy Plant Mini Kit (QIAGEN, Hilden, Germany) according to the manufacturer's instructions. PCR amplification of the ITS2 region of Symbiodiniaceae rDNA was performed using quality-checked DNA (n = 6) as a template (Chen et al., 2019), ITSintfor2 (5′-GAATTGCAGA ACTCCGTG-3′) and ITS-reverse (5′-GGGATCCATA TGCTTAAGTT CAGCGGGT-3′) as primers (Coleman et al., 1994; LaJeunesse and Trench, 2000). All qualified purified amplicons were combined in equimolar amounts following the manufacturer's instructions and paired-end sequenced on an Illumina MiSeq platform (2 × 300). Sequencing was performed by Majorbio Biopharm Technology Co., Ltd. (Shanghai, China). Sequencing data were analyzed with reference to previous methods (Chen et al., 2019; Huang et al., 2024).

2.4. 16S rRNA sequencing analysis

DNA was extracted using the TIANamp Marine Animals DNA Kit (Tiangen Biotech, Beijing, China). DNA (n = 12) was selected after quality testing, bacterial 16S rRNA V3V4 was amplified by PCR using previously reported cycling conditions and primers 338F (5′-ACTCCTACGGGGAGGCAGCAG-3′) and 806R (5′-GGACTACHVGGGTWTCTAAT-3′) (Liu et al., 2016). Amplicons were purified, polymerized at equimolar concentrations, and sequenced at Majorbio Biopharm Technology Co., Ltd. using the Illumina MiSeq platform following standard protocols (Huang et al., 2024).

The raw sequences were quality controlled using Fastp software (version 0.20.0) (Chen et al., 2018). Splicing was performed using FLASH software (version 1.2.7) (Magoč and Salzberg, 2011) and the splicing standard was described previously (Yu et al., 2020). After QC splicing, the optimized sequences were denoised using the DADA2 plugin in Qiime2 to obtain amplicon sequence variants (ASVs) (Callahan et al., 2016). All samples annotated as chloroplast and mitochondrial sequences were removed and flattened using a minimum number of

sequences (Huang et al., 2024). The species taxonomy of the ASVs was based on the silva138/16s_bacteria gene database using the Naïve Bayes classifier in Qiime2. Alpha diversity was calculated using Mothur software (Schloss et al., 2009), and principal coordinate analysis (PCoA) based on the Bray-Curtis distance algorithm was used to test the similarity of the coral-associated microbial community structure. The microbial species composition of each sample and its relative abundance were determined at different taxonomic levels using R software (version 3.3.1). Linear discriminant analysis Effect Size (LEfSe, LDA > 3, $p < 0.05$) was used to identify bacterial taxa with significant differences in abundance from the phylum to the genus levels between groups (Huang et al., 2024). Based on Spearman's correlation ($|r| > 0.6$, $p < 0.05$), co-occurrence network analyses were performed using R to analyze the correlations between the top 50 coral-associated bacteria (at the genus level) in total abundance and antioxidant activities in different groups (Sweet et al., 2019; Zhang et al., 2021).

2.5. RNA-seq analysis

Total RNA was extracted from coral tissue using Trizol reagent (Life Technologies, USA) by strictly following the product instructions as detailed in Huang et al. (2024). High-quality RNA samples (OD260/280 = 1.8–2.2, OD260/230 $\geq$ 1.0, RIN $\geq$ 8.0, $>$ 1 μg) were selected to construct a total of cDNA libraries (n = 12). Libraries were constructed following conventional processes, such as oligo dT enrichment of mRNA, fragmentation of mRNA, reverse synthesis of cDNA, ligation of the adaptor, fragment screening, and PCR amplification (Huang et al., 2024). Paired-end RNA-sequencing libraries were quantified using TBS380 and sequenced on an Illumina NovaSeq 6000 sequencer (2 × 150 bp read length).

Raw paired-end reads were trimmed and quality controlled using Fastp with default parameters to obtain high-quality sequencing data (i.e., clean reads) (Chen et al., 2018). The clean reads of each sample were compared to the reference genome using HISAT2 software (Kim et al., 2015). The *P. lutea* hosts and their Symbiodiniaceae (*Cladocopium* C15) reference genome (http://plut.reefgenomics.org/) were obtained from Robbins et al. (2019). *A. formosa* hosts were compared to the reference genome of *Acropora* spp. (https://marinegenomics.oist.jp/ahya/viewer/info?project_id=91) (Shinzato et al., 2021), and their Symbiodiniaceae were compared to the reference genome of *Cladocopium* C1 (http://symbs.reefgenomics.org/download/). The clean reads of each sample were first compared with those of the host genome, and the remaining data were compared with those of Symbiodiniaceae. The successfully matched genes were annotated using BLAST in six databases (Kyoto Encyclopedia of Genes and Genomes (KEGG), Gene Ontology (GO), Clusters of Orthologous Groups, Swiss-Prot, Pfam, and Non-redundant). The read counts for each sample gene were obtained using RSEM (Li and Dewey, 2011) and normalized to Transcripts Per Million reads (TPM).

Antioxidant-related genes were searched in the annotated gene sets to explore coral antioxidant expression in the different groups. These antioxidants are common in marine organisms (Halliwell, 2006; Lesser, 2006), and include SOD, CAT, GSH, POD, ascorbate/ascorbic acid, tocopherol, carotenoid, urate/uric acid, dimethylsulfide, and mycosporine-like amino acids. The TPM values of these antioxidant-related genes were counted and summarized individually. Finally, the results were plotted as histograms, and the selected antioxidants with high expression levels were plotted as heatmaps.

Differential expression analysis was performed using DESeq2 software (Love et al., 2014), and genes were considered as differentially expressed genes (DEGs) when Padjust < 0.05, $|\log2FC| \geq 2$. GO term and KEGG pathway analysis of the DEGs were performed using Goatools and KOBAS, and the terms or pathways were considered to be significantly enriched when Padjust < 0.05. To compare the antioxidant capacities of the two corals at high temperatures, we normalized the GO and KEGG pathways of the upregulated and downregulated DEGs in each group (HP vs. CP_up, HP vs. CP_down, HA vs. CA_up, and HA vs. CA_down). Briefly, the number of antioxidant-related terms or pathways (N_{ant}) and the total number of terms or pathways (N_{total}) were counted separately according to the description of the GO term or KEGG pathway for each group. The ratios of the antioxidant-related terms or pathways in each group were obtained using N_{ant}/N_{total} and compared as the net change ratio.

2.6. Statistical analysis

Physiological indices and antioxidant activities were assessed using a two-way analysis of variance (ANOVA) with species and temperature treatments as fixed factors after a normal distribution and homogeneity of variance test. When ANOVA detected a significant main effect ($p < 0.05$), post hoc pairwise comparisons of marginal estimated means were conducted to assess the differences between species within each temperature treatment (Voolstra et al., 2020). In addition, pairwise comparisons were used to test the significance of data from different temperature treatments in the same species. All data are expressed as mean ± standard deviation (SD).

For 16S rRNA data analysis, the Kruskal-Wallis H test was used for between-group differences in alpha diversity, and the ANOSIM method was used for the between-group difference test of PCoA. The Kruskal-Wallis sum-rank test and Wilcoxon rank-sum test were used to obtain significantly different bacterial taxa for LEfSe.

3. Results

3.1. Changes in phenotype and physiology of coral

P. lutea and *A. formosa* in the control group remained in good condition, with fully stretched tentacles, throughout the experiment. In the experimental group, both corals remained healthy at 26 °C, but *A. formosa* was darker in color. When the temperature was increased further to 34 °C, *A. formosa* clearly lost tissue, exposed white skeletons, and showed severe bleaching. *P. lutea* was also affected by heat stress and began tentacle contraction but did not show clear bleaching and was in a significantly better condition than *A. formosa* (Fig. 1B).

Symbiodiniaceae density and Fv/Fm were significantly affected by species and temperature, and the latter was also affected by temperature × habitat (two-way ANOVA, $p \leq 0.01$) (Fig. 1C–D). These indicators were significantly decreased in both corals during the temperature increase from 26 °C to 34 °C (pairwise comparisons, $p \leq 0.01$). This was consistent with the phenotypic changes, suggesting that high temperatures severely damaged both corals. The Symbiodiniaceae density of *P. lutea* was higher than *A. formosa* at any temperature, with a significant difference at 34 °C (pairwise test, $p \leq 0.01$). The Fv/Fm of *A. formosa* was significantly higher than *P. lutea* at 26 °C (pairwise test, $p \leq 0.001$), but higher values were observed for *P. lutea* at 34 °C (pairwise test, $p \leq 0.001$). These results indicate that *P. lutea* has better physiological performance than *A. formosa* at high temperatures.

3.2. Antioxidant responses of coral holobionts

Two-way ANOVA showed that SOD, CAT activity, and GSH concentration were significantly affected by species and temperature ($p \leq 0.05$), whereas SOD activity were also significantly affected by temperature × habitat ($p \leq 0.01$) (Fig. 1E–G). As the temperature increased from 26 °C to 34 °C, all three antioxidant indicators of *P. lutea* decreased, with CAT activity and GSH content showing significant differences (pairwise comparison, $p \leq 0.05$). Between 26 °C and 34 °C, SOD activity and GSH concentration in *A. formosa* significantly decreased (pairwise comparison, $p \leq 0.01$), while CAT activity remained unchanged with increasing temperature (Fig. 1F).

GSH concentration (pairwise test, $0.01 < p \leq 0.05$) and SOD activity (pairwise test, $p > 0.05$) of *P. lutea* were slightly higher than *A. formosa* at 26 °C. However, these enzyme activities of *P. lutea* were significantly

higher than *A. formosa* at 34 °C (pairwise test, $p \leq 0.001$) (Fig. 1E, G). Notably, CAT activity in *P. lutea* was consistently significantly higher than that in *A. formosa* during warming (pairwise test, $p \leq 0.001$) and reached an order of magnitude difference (Fig. 1F). These results suggest that massive *P. lutea* have higher antioxidant levels at high temperatures.

3.3. Antioxidant transcriptional response in the coral host

Twelve cDNA libraries were constructed for the heat stress experiment, with three biological replicates per group (CP, HP, CA, and HA). Sequencing data for each sample met the requirements for transcriptome analysis (Table S1).

The results showed that *P. lutea* mainly expressed GSH, SOD, and POD-related genes at 26 °C; when at 34 °C, the expression of GSH-related genes was significantly increased, followed by ascorbate, SOD, and POD (Fig. 2A). Similarly, *A. formosa* mainly expressed GSH, POD, and ascorbate-related genes at 26 °C, and POD, GSH, POD, and CAT-related genes at 34 °C (Fig. 2B). The heatmap shows that the expression of GSH-related genes decreased and the expression of SOD, CAT, POD, and ascorbate-related genes increased in *A. formosa* after high-temperature stress (Fig. 2B). However, the expression of all these genes increased in *P. lutea* after high-temperature stress (Fig. 2A). Gene expression includes upregulation and down-regulation. Therefore, to clarify the up- and down-regulation of these antioxidant-related genes, we identified DEGs in *P. lutea* (HP vs. CP) and *A. formosa* (HA vs. CA) after high-temperature treatment (Fig. 2C). The upregulated and downregulated DEGs were analyzed for GO and KEGG enrichment, respectively.

Table 1 showed that the ROS-related GO terms were not found in the upregulated DEGs of *P. lutea* after high-temperature stress, whereas the downregulated DEGs had less than 0.01 % of related GO terms. *A. formosa* upregulated DEGs were found to be 0.09 % ROS-related GO terms, whereas no downregulated related terms were found. This suggests that *A. formosa* lacks the ability to regulate ROS compared to *P. lutea*. Among the antioxidant-related terms, *P. lutea* was upregulated by 0.05 % and downregulated by 3.34 %, for a net change of down-regulation of 3.29 %, while *A. formosa* was upregulated by 3.05 % and downregulated by 10.76 %, for a net change of downregulation of 7.71 %. In contrast, *P. lutea* responded to heat stress by reducing the decline in its antioxidant terms. Unexpectedly, among the significantly enriched antioxidant-related GO terms (Padjust < 0.05), *A. formosa* was more

Table 1
Summary of GO terms for up- and down-regulated DEGs in two coral hosts at 34 °C. "Ratio" represents the number of GO terms for each category in each group divided by the total number of GO terms in the group. "–" means that there are no relevant GO terms. Data details and calculation process were given in Table S2.

Category	Group		Ratio	Net change ratio
Related to ROS	HP vs. CP	Up	–	<0.01 % (down)
		Down	<0.01 %	
	HA vs. CA	Up	0.09 %	0.09 % (up)
		Down	–	
Related to antioxidants	HP vs. CP	Up	0.05 %	3.29 % (down)
		Down	3.34 %	
	HA vs. CA	Up	3.05 %	7.71 % (down)
		Down	10.76 %	

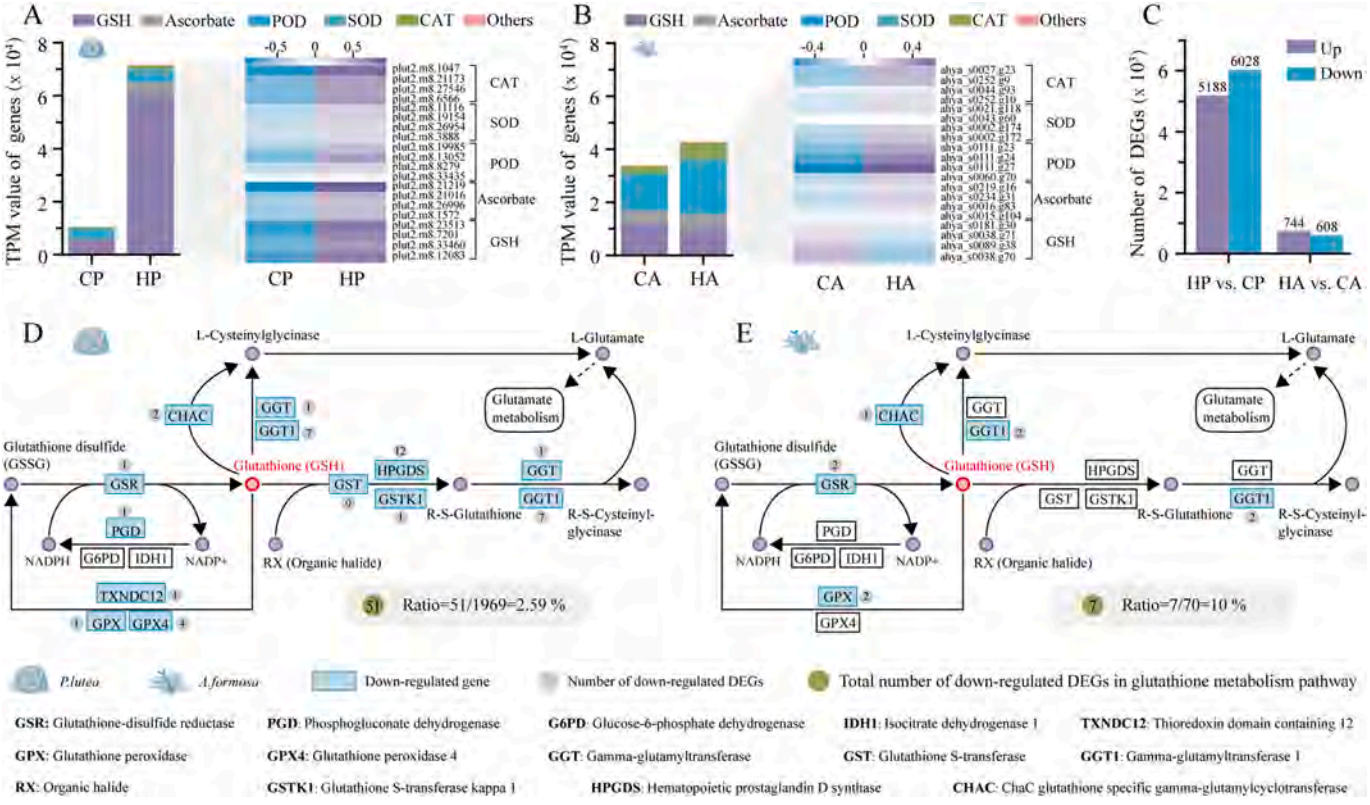


Fig. 2. Coral host gene expression responses. Expression of antioxidant-related genes in (A) *P. lutea* and (B) *A. formosa*, as indicated by the TPM values. The left panel shows the TPM values of various antioxidants, including GSH, ascorbate, POD, SOD, CAT, and "Others". "Others" represents antioxidants with low TPM values, including tocopherol, carotenoid, uric acid/urate, dimethylsulfide, and mycosporine-like amino acids. The right panel displays the gene expression levels of major antioxidants (excluding "Others"), with blue indicating low expression and purple indicating high expression. (C) Host up- and downregulated DEGs under high-temperature stress. The GSH metabolism pathway of downregulated DEGs obtained based on KEGG enrichment analyses in (D) *P. lutea* and (E) *A. formosa*. "Ratio" represents the gene numbers of GSH metabolism pathway divided by the gene numbers of all pathways in the down-regulated DEGs. (For interpretation of the references to color in this figure legend, the reader is referred to the web version of this article.)

frequently upregulated, and *P. lutea* was more frequently downregulated (Table S2).

KEGG enrichment results showed that both corals did not show upregulated antioxidant-related pathways and downregulated only one of related GO terms (GSH metabolism) after high-temperature stress. Although the number of downregulated DEGs was higher in *P. lutea*, the percentage of downregulated genes was 2.59 % in *P. lutea* and 10 % in *A. formosa* (Fig. 2D, E). Further analysis showed that *P. lutea* downregulated fewer genes that form GSH (e.g., the process by which GSH is formed from glutathione disulfide) and downregulated more genes that consume GSH (e.g., the process by which GSH forms R-S-Glutathione or L-Cysteinylglycinase) than *A. formosa*. This may have allowed *P. lutea* to contain more GSH for ROS removal.

3.4. Community composition and antioxidant-related gene expression of Symbiodiniaceae

Symbiodiniaceae in all *P. lutea* samples were dominated by the subclade *Cladocopium* C15, whereas *A. formosa* were dominated by *Cladocopium* C1 (Fig. 3A). Therefore, the genomes of both subclades were used as reference genomes for Symbiodiniaceae RNA-seq analysis. *Cladocopium* C15 expressed more GSH, ascorbate, and POD-related genes at 26 °C; when the temperature is 34 °C, the expression of these genes was clearly increased (Fig. 3B). *Cladocopium* C1 mainly expressed

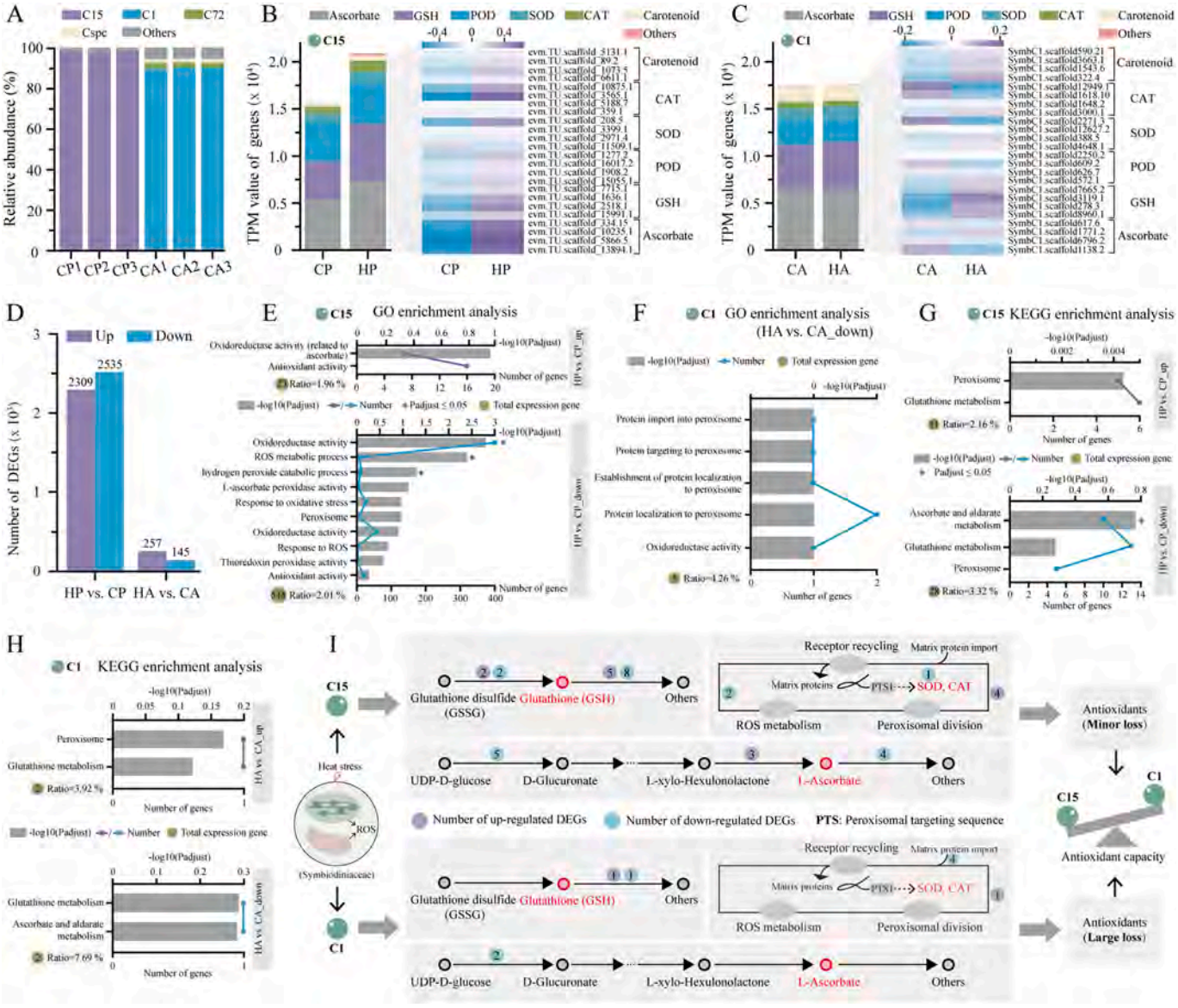


Fig. 3. Community composition and antioxidant-related gene expression of Symbiodiniaceae. (A) Relative abundances of different Symbiodiniaceae subclades in coral samples. "Others" represents subclades with an abundance of <1 %. Expression of antioxidant-related genes in (B) *Cladocopium* C15 and (C) *Cladocopium* C1, as indicated by TPM values. The left panel shows the TPM values of various antioxidants, including ascorbate, GSH, POD, SOD, CAT, carotenoid, and "Others". "Others" represents antioxidants with low TPM values, including tocopherol, uric acid/urate, dimethylsulfide, and mycosporine-like amino acids. The right panel displays the gene expression levels of major antioxidants (excluding "Others"), with blue indicating low expression and purple indicating high expression. (D) Symbiodiniaceae up- and downregulated DEGs under high-temperature stress. GO enrichment analysis of up- and downregulated DEGs in (E) *Cladocopium* C15 and (F) *Cladocopium* C1 at high temperatures. KEGG enrichment analysis of up- and downregulated DEGs in (G) *Cladocopium* C15 and (H) *Cladocopium* C1 at high temperatures. "Ratio" represents the DEGs numbers of antioxidant-related terms/pathways divided by the DEGs numbers of all terms/pathways. (I) Schematic depicting *Cladocopium* C15 with greater antioxidant capacity. The diagram summarizes the KEGG-enriched pathways, including "Glutathione metabolism," "Peroxisome," and "Ascorbate and aldarate metabolism." (For interpretation of the references to color in this figure legend, the reader is referred to the web version of this article.)

ascorbate, GSH, POD, and carotenoid-related genes at 26 °C and 34 °C, but most of these genes were reduced at 34 °C (Fig. 3C).

Similar to the coral host, *Cladocopium* C15 had more DEGs than *Cladocopium* C1 at high temperatures (Fig. 3D). GO enrichment results showed that *Cladocopium* C15 was upregulated by 1.96 % and downregulated by 2.01 % of antioxidant-related terms under heat stress, with a net change in downregulation of 0.05 % (Fig. 3E). *Cladocopium* C1 did not show upregulated antioxidant-related terms and downregulated 4.26 % of related GO terms (Fig. 3F). KEGG enrichment analysis also showed that *Cladocopium* C15 had a net downregulation of 1.16 % antioxidant-related pathways (2.16 % upregulation and 3.32 % downregulation; Fig. 3G), whereas *Cladocopium* C1 had a net downregulation of 3.77 % related pathways (3.92 % upregulation and 7.69 % downregulation; Fig. 3H). Both Symbiodiniaceae subclades mainly regulated the GSH, peroxisome, ascorbate, and aldarate metabolism pathways. Overall, in these pathways, *Cladocopium* C15 regulated more DEGs but had a lower ratio than *Cladocopium* C1 to minimize the loss of antioxidant activity, which may help the *P. lutea* holobiont maintain its antioxidant capacity against heat stress (Fig. 3I).

3.5. Sequencing analysis of coral-associated bacteria

The Chao and Shannon indices showed that the species richness and diversity of both coral-associated bacteria increased under heat stress, and these indices were higher for *P. lutea* than for *A. formosa* at 34 °C, but were not significant (Fig. 4A–B). The PCoA result indicated that the associated bacterial community structure of *P. lutea* showed more obvious changes after high-temperature stress (Fig. 4C). The coral-associated bacterial communities were similar in composition at the phylum level in different groups, with *Proteobacteria*, *Firmicutes*, and *Bacteroidota* being the dominant taxa (Fig. 4D). Significant differences were observed at the genus level (Fig. 4E). Specifically, *P. lutea* associated bacteria were dominated by *Endozoicomonas* (>50 %) and *Ruegeria* at 26 °C. As the temperature rose to 34 °C, they remained the dominant genera, while the abundances of *Vulcaniibacterium*, *Comamonadaceae*, *Thermus*, *Acinetobacter*, and *Rhodobacteraceae* increased. *A. formosa* associated bacteria were dominated by *Alphaproteobacteria*, *Comamonadaceae*, and *Vulcaniibacterium* at different temperatures. The *Ruegeria* decreased sharply and the relative abundance of *Thermus*, *Vibrio*, and *Brevibacillus* were increased at 34 °C.

LEfSe analysis showed that *P. lutea* had significantly different

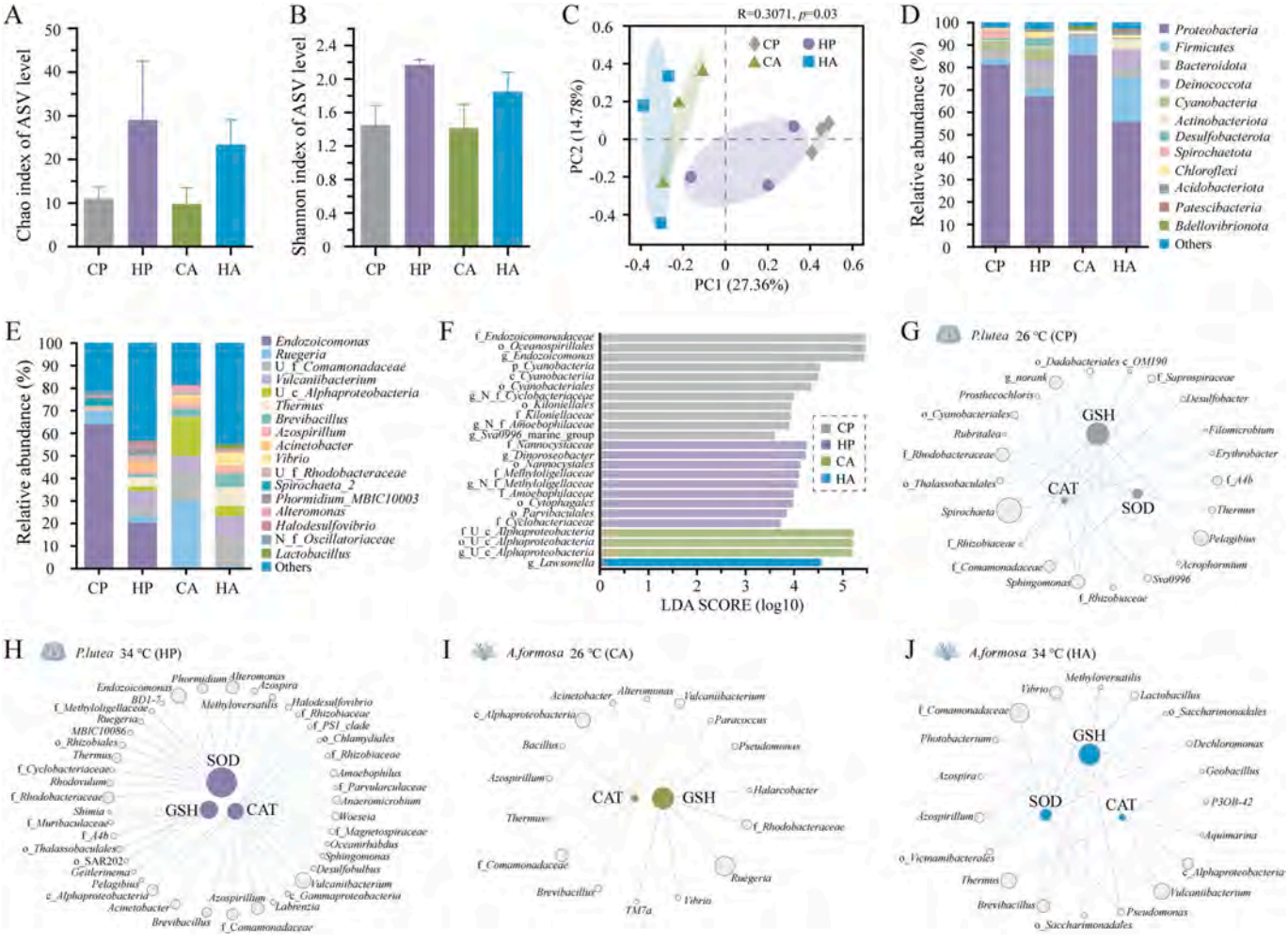


Fig. 4. Coral-associated bacterial community composition and structure. Chao index (A), Shannon index (B), and PCoA (C) of ASV levels. (D) Bacterial community composition on the phylum level, bacteria with a relative abundance of <1 % were classified as "Others". (E) Bacterial community composition on the genus level, bacteria with a relative abundance of <2 % were classified as "Others". (F) LEfSe analysis from the phylum to genus level, LDA > 3, $p < 0.05$. Co-occurrence network analysis was conducted on data from the CP (G), HP (H), CA (I), and HA (J) groups. Each connection indicates a significant correlation (Spearman, $p < 0.05$), and the color represents the correlation (purple is positive, blue is negative). Node size was correlated with the relative abundance of bacterial taxa and antioxidant activity. Here, U stands for unclassified, and N represents the norank. (For interpretation of the references to color in this figure legend, the reader is referred to the web version of this article.)

bacterial taxa from *A. formosa* at different temperatures (Fig. 4F). Eleven significantly different taxa of *P. lutea* associated bacteria at 26 °C, mainly *Endozoicomonas*, *Oceanospirillales*, *Cyanobacteriia*, and *Kiloniellaceae*. Nine significantly different taxa were recorded when the temperature rose to 34 °C, including *Nannocystaceae*, *Dinoroseobacter*, *Methyloligellaceae*, *Amoebophilaceae*, and *Cytophagales*. In contrast, the number of significantly different taxa of *A. formosa* were clearly lower, with *Alphaproteobacteria* at 26 °C and *Lawsonella* at 34 °C. Network analysis showed that the number of bacteria (i.e., the degree of nodes) connected to CAT, GSH, and SOD in *P. lutea* at 26 °C was 18, 19, and 5, respectively (Fig. 4G). As the temperature rose to 34 °C, the degrees of the three enzymes were 22, 6, and 14, respectively (Fig. 4H). The degrees of CAT and GSH in *A. formosa* at 26 °C were 9 and 7, respectively, and no bacteria were significantly correlated with SOD (Fig. 4I). The degrees of CAT, GSH, and SOD at 34 °C were 15, 15, and 4, respectively (Fig. 4J).

4. Discussion

Reef-building corals are increasingly exposed to frequent marine heatwaves (Marcos et al., 2025), as exemplified by the recently confirmed Fourth Global Coral Bleaching Event in 2023–2024 (Reimer et al., 2024). Massive and branching reef-building corals exhibit different survival rates under marine heatwaves, which may be attributed to their varying antioxidant capacities. Heat stress causes coral holobionts to produce high levels of ROS (Cziesielski et al., 2019), and the antioxidant capacity plays an important role in their ability to survive (Halliwell, 2006; Helgoe et al., 2024). However, it remains unclear how antioxidant responses contribute to the differences in thermal tolerance between massive and branching corals. Here, we performed heat stress experiments on the massive *P. lutea* and branching *A. formosa*. The results indicated that *P. lutea* performed better against bleaching. Symbiodiniaceae density was not significantly different between the two corals, and the Fv/Fm of *P. lutea* was significantly lower than *A. formosa* at 26 °C. However, *P. lutea* had significantly higher values of these parameters at 34 °C. The coral phenotype, Symbiodiniaceae density, and Fv/Fm are useful indicators of health status (Huang et al., 2024; Voolstra et al., 2020). These results strongly suggest that *P. lutea* is more thermotolerant than *A. formosa*, which is consistent with previous findings (Fisher et al., 2012; Harithsa et al., 2005).

High-temperature stress increases ROS levels in coral holobionts, thereby activating antioxidant systems (Cziesielski et al., 2019; Doering et al., 2023; Weis, 2008). Under heat stress, antioxidant levels in *P. lutea* and *A. formosa* declined continuously. However, *P. lutea* maintained higher antioxidant levels than *A. formosa* throughout the warming process, particularly at 34 °C. This may be due to more severe thermal damage in *A. formosa*, which have impaired the production of antioxidant enzymes. Some studies believe that high antioxidant level is indicative of coral heat-sensitivity (Yakovleva et al., 2004; Yu et al., 2020), but coral antioxidant level has species-specific differences (Roberty et al., 2016) as well as being closely related to health status (Martignago et al., 2024). Our previous studies have shown that healthy *P. lutea* produces higher antioxidant levels to enhance resistance to temperature stress (Huang et al., 2024; Huang et al., 2022). Similarly, a series of studies have indicated that corals with higher antioxidant levels have better thermotolerance (Dias et al., 2019; Martignago et al., 2024; Wang et al., 2022). Therefore, by combining this with the coral phenotype, we suggest that the greater thermotolerance of *P. lutea* is associated with its higher antioxidant levels. Next, we explored the differences in the antioxidant responses of the two corals in their hosts, Symbiodiniaceae, and coral-associated bacteria.

GSH, ascorbate, and POD are important antioxidants that scavenge harmful ROS, such as H_2O_2, $^1O_2$, and O_2^- (Halliwell, 2006; Lesser, 2006). Both coral hosts downregulated the expression of these antioxidant-related genes due to high temperatures, whereas *P. lutea* host had a smaller downregulation ratio (Table 1, Fig. 2D–E). In addition, *A. formosa* hosts upregulated ROS-related genes. This suggests that *P. lutea* hosts maintain their health and withstand high temperatures by retaining more antioxidant activities (Wang et al., 2022), a strategy lacking in *A. formosa* hosts. Unexpectedly, the significantly enriched antioxidant-related GO terms of hosts were downregulated in *P. lutea* and upregulated in *A. formosa* (Table S2). The possible reasons for this are as follows: (1) *P. lutea* hosts maintain their health at high temperatures through the regulation of metabolism, immunity, apoptosis, and disease resistance (Huang et al., 2024). They may indirectly maintain their antioxidant capacity in these ways, even if antioxidant genes are downregulated. Although *A. formosa* hosts upregulated antioxidant genes, they failed to produce high levels of antioxidants because of the low number of DEGs expressed and severe tissue damage. This may be caused by species-specific differences in constitutive antioxidant activity (Roberty et al., 2016). (2) GSH is the main regulated antioxidant gene in *P. lutea* host, and the downregulation of GSH metabolism may lead to the downregulation of glutamate metabolism, which in turn enhances cellular energy availability and maintains the host's ability to cope with oxidative stress (Radecker et al., 2021). This reflected the strong and complex antioxidant regulatory capacity of *P. lutea* host. In addition, GSH not only scavenges various types of ROS and participates in various regulatory pathways but is also an essential substrate for glutathione peroxidase (Lesser, 2006). This also explains why it was the main antioxidant gene expressed in both coral host (especially *P. lutea*).

Similar to the host, the expression of antioxidant-related genes was downregulated in both Symbiodiniaceae at 34 °C, but in a simpler and more direct manner. Compared to *Cladocopium* C1, *Cladocopium* C15 slowed the decrease in antioxidant levels and thus enhanced antioxidant capacity by regulating the GSH, peroxisome, and ascorbate metabolism pathways (Fig. 3I). This bestows *Cladocopium* C15 with greater heat resistance, which in turn benefits its host *P. lutea* against high temperatures (Huang et al., 2024). Previous studies have shown that different Symbiodiniaceae types influence coral thermotolerance (Al-Hammady et al., 2022; Rowan, 2004), whereas thermotolerant Symbiodiniaceae have a stronger antioxidant capacity (Krueger et al., 2014; McGinty et al., 2012; Roberty et al., 2016; Xiao et al., 2024). Combined with the findings of the present study, we suggest that thermotolerance in Symbiodiniaceae is positively correlated with antioxidant level.

Heat stress can cause coral diseases (Bruno et al., 2007), and potentially pathogenic bacteria were found at high temperatures in both corals. For example, *Acinetobacter* and *Phormidium* were found in *P. lutea* at 34 °C; while *A. formosa* increased the relative abundance of *Vibrio* and *Brevibacillus*, and the differential bacterium *Lawsonella* was also found. These bacteria were considered as potential pathogens in most reports (Escapa et al., 2018; Forsgren, 2010; Qin et al., 2021; Richardson and Kuta, 2003; Rosado et al., 2019). However, *A. formosa* showed greater occupancy by pathogenic bacteria, which may be more damaging to its health. Notably, in both corals, their associated bacteria with antioxidant functions adjusted to respond to high temperatures. *P. lutea* had higher relative abundance of *Endozoicomonas*, *Comamonadaceae*, *Rhodobacteraceae*, and *Ruegeria* at 34 °C. *Endozoicomonas* encodes a dimethylsulfoxide reductase that catalyzes the conversion to dimethylsulfide (DMS), providing an effective pathway for ROS removal (Robbins et al., 2019; Sunda et al., 2002). *Variovorax terrae*, a member of *Comamonadaceae*, has potential antioxidant activity (Woo and Kim, 2022). *Ruegeria* belongs to *Rhodobacteraceae*, and one of its members (*Ruegeria pomeroyi*) degrades DMSP to DMS and has an antioxidant capacity (Reisch et al., 2013; Sunda et al., 2002). For different bacteria in *P. lutea*, *Dinoroseobacter* can detoxify ROS (Tomasch et al., 2011), and a member of the *Cytophagales* can produce carotenoids to improve antioxidant capacity (Irschik and Reichenbach, 1978). In contrast, the high percentage of antioxidant-functioning bacteria in *A. formosa* was only *Comamonadaceae* at 34 °C, indicating a severe lack of the antioxidant capacity to cope with high temperatures.

Indeed, many bacteria are opportunistic, and their functions vary depending on the coral host and environment, such as *Acinetobacter* (Qin et al., 2021), *Rhodobacteraceae* (Pootakham et al., 2019). Although

analyzing the antioxidant function of coral-associated bacteria through metagenomic sequencing would make our conclusions more robust, funding and resource limitations prevent this. Therefore, we further proved our hypothesis using a co-occurrence network analysis between antioxidant activity and bacteria (Sweet et al., 2019; Zhang et al., 2021). At high temperatures, the number of bacteria associated with antioxidants was significantly higher in *P. lutea* than in *A. formosa*. This may be due to the higher bacterial diversity and abundance of *P. lutea*, which increases the probability of functional antioxidant bacteria (Huang et al., 2024). Previous studies have also shown that increasing the diversity of coral-associated bacteria is beneficial for thermotolerance (Liang et al., 2017; Yu et al., 2020). The high number of CAT-associated bacteria in *P. lutea* may indicate that it produces more CAT, which seems to explain the unusual phenomenon of an order of magnitude difference in CAT activity between the two coral holobionts (Fig. 1F). In summary, our results suggest that *P. lutea* has more antioxidant-functional bacteria than *A. formosa* and thus improves the antioxidant capacity against pathogenic bacteria and heat stress.

However, this study was limited by the insufficient number of coral species, which may have weakened the universality of the conclusions. In the future, more thermotolerance comparisons between massive and branching corals should be conducted to further clarify the role of antioxidant capacity using multiomics approaches. In particular, the size contribution of the coral host, Symbiodiniaceae, and coral-associated bacteria to antioxidant capacity. We believe that these findings will be confirmed in future studies, which will benefit coral reef management. Specifically, antioxidants can be used as biomarkers indicative of coral thermotolerance and reef degradation monitoring (Downs et al., 2000; Marangoni et al., 2019). A study of Great Barrier Reef corals across 12 latitudes found that antioxidant capacity can be also used as a genetic marker to select stress-resistant corals (Jin et al., 2016). Corals with tolerant genotypes can facilitate the high-quality restoration of damaged reefs through selective breeding or even assisted evolution (Jin et al., 2016; van Oppen et al., 2015). Here, we suggest that thermotolerant corals can be identified based on the antioxidant level after short-term acute heat stress assays (Voolstra et al., 2020) and transplanted for restoration, which provides a novel coral reef management approach. However, the realization of rescue measures is based on the reduction of threats to marine ecosystems and effective management approaches (Bay et al., 2023).

5. Conclusion

In the present study, massive and branching corals were tested for thermotolerance. The results showed that massive *P. lutea* exhibited greater thermotolerance than branching *A. formosa*, closely related to its higher GSH concentration and elevated SOD and CAT activities. High-throughput sequencing analysis showed that compared with *A. formosa*, *P. lutea* host had more complex antioxidant regulatory mechanisms at 34 °C, mainly through slowing down the downregulation of GSH-related genes to maintain the antioxidant capacity. *Cladocopium* C15 enhanced the regulation of GSH, peroxisome, and ascorbate-related genes, giving *P. lutea* a greater antioxidant capacity. *P. lutea* also had greater coral-associated bacterial diversity than *A. formosa*, reduced the proportion of potentially pathogenic bacteria, and increased the number of bacteria with antioxidant functions, including *Endozoicomonas*, *Ruegeria*, and *Dinoroseobacter*. Overall, we found that the heat resistance of *P. lutea* and *A. formosa* was positively correlated with their antioxidant levels. This study provides new insights into the high-temperature coping mechanisms of thermotolerant corals and the reef ecosystem restoration.

Supplementary data to this article can be found online at https://doi.org/10.1016/j.marpolbul.2025.118556.

CRediT authorship contribution statement

Linqing Meng: Writing – review & editing, Writing – original draft, Visualization, Validation, Software, Resources, Methodology, Formal analysis, Data curation, Conceptualization. **Ronghua Tan:** Methodology, Data curation. **Zunyong Xiao:** Resources, Data curation, Conceptualization. **Jinlian Chen:** Methodology, Formal analysis. **Zhihua Huang:** Resources, Methodology. **Yonggang Wang:** Software, Formal analysis. **Enguang Yang:** Software, Methodology. **Yupeng Zhou:** Resources, Investigation. **Mingpei Xu:** Resources, Investigation. **Kefu Yu:** Resources, Project administration, Funding acquisition. **Wen Huang:** Writing – review & editing, Validation, Resources, Project administration, Methodology, Funding acquisition, Conceptualization.

Declaration of competing interest

All authors have no known competing financial interests or personal relationships that could have appeared to influence the work reported in this paper.

Acknowledgements

This work was financially supported by the National Natural Science Foundation of China [#42090041 and 42030502] and the Guangxi Natural Science Foundation [#2023GXNSFAA026510]. We thank the staff of the Weizhou Island Coral Museum of Guangxi University for their assistance with this study. We thank laboratory members for their continuous technical advice and helpful discussions. We would like to thank Editage (www. edita.org.cn) for the English language editing.

Data availability

Raw ITS2, 16S rRNA, and RNA-seq data were submitted to the NCBI Sequence Read Archive database (accession numbers: PRJNA1128349, PRJNA1128360, and PRJNA1128399, respectively). Data on physiological and antioxidant indicators are provided in the supplementary files.

References

Al-Hammady, M.A.M.M., Silva, T.F., Hussein, H.N.M., Saxena, G., Modolo, L.V., Belasy, M.B.I., Farag, M.A., 2022. How do algae endosymbionts mediate for their coral host fitness under heat stress? A comprehensive mechanistic overview. Algal Res. 67, 102850. https://doi.org/10.1016/j.algal.2022.102850.

Avila-Magaña, V., Kamel, B., DeSalvo, M., Gómez-Campo, K., Enríquez, S., Kitano, H., Rohlfs, R.V., Iglesias-Prieto, R., Medina, M., 2021. Elucidating gene expression adaptation of phylogenetically divergent coral holobionts under heat stress. Nat. Commun. 12, 5731. https://doi.org/10.1038/s41467-021-25950-4.

Baums, I.B., Miller, M.W., Hellberg, M.E., 2006. Geographic variation in clonal structure in a reef-building Caribbean coral, *Acropora palmata*. Ecol. Monogr. 76, 503–519. https://doi.org/10.1890/0012-9615(2006)076[0503:Gvicsi]2.0.Co;2.

Bay, L.K., Gilmour, J., Muir, B., Hardisty, P.E., 2023. Management approaches to conserve Australia's marine ecosystem under climate change. Science 381, 631–636. https://doi.org/10.1126/science.adi3023.

Bruno, J.F., Selig, E.R., Casey, K.S., Page, C.A., Willis, B.L., Harvell, C.D., Sweatman, H., Melendy, A.M., 2007. Thermal stress and coral cover as drivers of coral disease outbreaks. PLoS Biol. 5, e124. https://doi.org/10.1371/journal.pbio.0050124.

Callahan, B.J., McMurdie, P.J., Rosen, M.J., Han, A.W., Johnson, A.J.A., Holmes, S.P., 2016. DADA2: high-resolution sample inference from Illumina amplicon data. Nat. Methods 13, 581–583. https://doi.org/10.1038/nmeth.3869.

Chen, S.F., Zhou, Y.Q., Chen, Y.R., Gu, J., 2018. fastp: an ultra-fast all-in-one FASTQ preprocessor. Bioinformatics 34, 884–890. https://doi.org/10.1093/bioinformatics/bty560.

Chen, B., Yu, K.F., Liang, J.Y., Huang, W., Wang, G.H., Su, H.F., Qin, Z.J., Huang, X.Y., Pan, Z.L., Luo, W.W., et al., 2019. Latitudinal variation in the molecular diversity and community composition of Symbiodiniaceae in coral from the South China Sea. Front. Microbiol. 10, 1278. https://doi.org/10.3389/fmicb.2019.01278.

Coleman, A.W., Suarez, A., Goff, L.J., 1994. Molecular delineation of species and syngens in Volvocacean green algae (Chlorophyta). J. Phycol. 30, 80–90. https://doi.org/10.1111/j.0022-3646.1994.00080.x.

Cziesielski, M.J., Schmidt-Roach, S., Aranda, M., 2019. The past, present, and future of coral heat stress studies. Ecol. Evol. 9, 10055–10066. https://doi.org/10.1002/ece3.5576.

Dias, M., Ferreira, A., Gouveia, R., Madeira, C., Jogee, N., Cabral, H., Diniz, M., Vinagre, C., 2019. Long-term exposure to increasing temperatures on scleractinian coral fragments reveals oxidative stress. Mar. Environ. Res. 150, 104758. https://doi.org/10.1016/j.marenvres.2019.104758.

Doering, T., Maire, J., Chan, W.Y., Perez-Gonzalez, A., Meyers, L., Sakamoto, R., Buthgamuwa, I., Blackall, L.L., van Oppen, M.J.H., 2023. Comparing the role of ROS and RNS in the thermal stress response of two cnidarian models, *Exaiptasia diaphana* and *Galaxea fascicularis*. Antioxidants 12, 1057. https://doi.org/10.3390/antiox12051057.

Downs, C.A., Mueller, E., Phillips, S., Fauth, J.E., Woodley, C.M., 2000. A molecular biomarker system for assessing the health of coral (*Montastraea faveolata*) during heat stress. Mar. Biotechnol. 2, 533–544. https://doi.org/10.1007/s101260000038.

Downs, C.A., Fauth, J.E., Halas, J.C., Dustan, P., Bemiss, J., Woodley, C.M., 2002. Oxidative stress and seasonal coral bleaching. Free Radic. Biol. Med. 33, 533–543. https://doi.org/10.1016/s0891-5849(02)00907-3.

Eddy, T.D., Lam, V.W.Y., Reygondeau, G., Cisneros-Montemayor, A.M., Greer, K., Palomares, M.L.D., Bruno, J.F., Ota, Y., Cheung, W.W.L., 2021. Global decline in capacity of coral reefs to provide ecosystem services. One Earth 4, 1278–1285. https://doi.org/10.1016/j.oneear.2021.08.016.

Escapa, I.F., Chen, T., Huang, Y., Gajare, P., Dewhirst, F.E., Lemon, K.P., 2018. New insights into human nostril microbiome from the Expanded Human Oral Microbiome Database (eHOMD): a resource for the microbiome of the human aerodigestive tract. mSystems 3. https://doi.org/10.1128/mSystems.00187-18.

Fernández-Checa, J.C., Kaplowitz, N., García-Ruiz, C., Colell, A., Miranda, M., Marí, M., Ardite, E., Morales, A., 1997. GSH transport in mitochondria: defense against TNF-induced oxidative stress and alcohol-induced defect. Am. J. Physiol. Gastrointest. Liver Physiol. 273, G7–G17. https://doi.org/10.1152/ajpgi.1997.273.1.G7.

Fisher, P.L., Malme, M.K., Dove, S., 2012. The effect of temperature stress on coral-*Symbiodinium* associations containing distinct symbiont types. Coral Reefs 31, 473–485. https://doi.org/10.1007/s00338-011-0853-0.

Forsgren, E., 2010. European foulbrood in honey bees. J. Invertebr. Pathol. 103, S5–S9. https://doi.org/10.1016/j.jip.2009.06.016.

Halliwell, B., 2006. Reactive species and antioxidants. Redox biology is a fundamental theme of aerobic life. Plant Physiol. 141, 312–322. https://doi.org/10.1104/pp.106.077073.

Harithsa, S., Raghukumar, C., Dalal, S.G., 2005. Stress response of two coral species in the Kavaratti Atoll of the Lakshadweep archipelago, India. Coral Reefs 24, 463–474. https://doi.org/10.1007/s00338-005-0008-2.

Helgoe, J., Davy, S.K., Weis, V.M., Rodriguez-Lanetty, M., 2024. Triggers, cascades, and endpoints: connecting the dots of coral bleaching mechanisms. Biol. Rev. 99, 715–752. https://doi.org/10.1111/brv.13042.

Huang, W., Yang, E.G., Yu, K.F., Meng, L.Q., Wang, Y.G., Liang, J.Y., Huang, X.Y., Wang, G.H., 2022. Lower cold tolerance of tropical *Porites lutea* is possibly detrimental to its migration to relatively high latitude refuges in the South China Sea. Mol. Ecol. 31, 5339–5355. https://doi.org/10.1111/mec.16662.

Huang, W., Meng, L.Q., Xiao, Z.Y., Tan, R.H., Yang, E.G., Wang, Y.G., Huang, X.Y., Yu, K.F., 2024. Heat-tolerant intertidal rock pool coral *Porites lutea* can potentially adapt to future warming. Mol. Ecol. 33, e17273. https://doi.org/10.1111/mec.17273.

Hughes, T.P., Kerry, J.T., Álvarez-Noriega, M., Álvarez-Romero, J.G., Anderson, K.D., Baird, A.H., Babcock, R.C., Beger, M., Bellwood, D.R., Berkelmans, R., et al., 2017. Global warming and recurrent mass bleaching of corals. Nature 543, 373–377. https://doi.org/10.1038/nature21707.

Irschik, H., Reichenbach, H., 1978. Intracellular location of flexirubins in *Flexibacter elegans* (Cytophagales). Biochim. Biophys. Acta 510, 1–10. https://doi.org/10.1016/0005-2736(78)90125-6.

Jin, Y.K., Lundgren, P., Lutz, A., Raina, J.B., Howells, E.J., Paley, A.S., Willis, B.L., van Oppen, M.J.H., 2016. Genetic markers for antioxidant capacity in a reef-building coral. Sci. Adv. 2, e1500842. https://doi.org/10.1126/sciadv.1500842.

Johannes, R.E., Coles, S.L., Kuenzel, N.T., 1970. The role of zooplankton in the nutrition of some scleractinian corals. Limnol. Oceanogr. 15, 579–586. https://doi.org/10.4319/lo.1970.15.4.0579.

Kim, D., Landmead, B., Salzberg, S.L., 2015. HISAT: a fast spliced aligner with low memory requirements. Nat. Methods 12. https://doi.org/10.1038/nmeth.3317, 357-U121.

Krueger, T., Becker, S., Pontasch, S., Dove, S., Hoegh-Guldberg, O., Leggat, W., Fisher, P.L., Davy, S.K., 2014. Antioxidant plasticity and thermal sensitivity in four types of *Symbiodinium* sp. J. Phycol. 50, 1035–1047. https://doi.org/10.1111/jpy.12232.

Lachs, L., Donner, S.D., Mumby, P.J., Bythell, J.C., Humanes, A., East, H.K., Guest, J.R., 2023. Emergent increase in coral thermal tolerance reduces mass bleaching under climate change. Nat. Commun. 14, 4939. https://doi.org/10.1038/s41467-023-40601-6.

LaJeunesse, T.C., Trench, R.K., 2000. Biogeography of two species of *Symbiodinium* (Freudenthal) inhabiting the intertidal sea anemone *Anthopleura elegantissima* (Brandt). Biol. Bull. 199, 126–134. https://doi.org/10.2307/1542872.

Lesser, M.P., 2006. Oxidative stress in marine environments: biochemistry and physiological ecology. Annu. Rev. Physiol. 68, 253–278. https://doi.org/10.1146/annurev.physiol.68.040104.110001.

Lesser, M.P., 2024. Irradiance dependency of oxidative stress and coral bleaching. Coral Reefs 43, 1393–1403. https://doi.org/10.1007/s00338-024-02545-1.

Li, B., Dewey, C.N., 2011. RSEM: accurate transcript quantification from RNA-Seq data with or without a reference genome. BMC Bioinf. 12, 323. https://doi.org/10.1186/1471-2105-12-323.

Liang, J.Y., Yu, K.F., Wang, Y.H., Huang, X.Y., Huang, W., Qin, Z.J., Pan, Z.L., Yao, Q.C., Wang, W.H., Wu, Z.C., 2017. Distinct bacterial communities associated with massive and branching scleractinian corals and potential linkages to coral susceptibility to thermal or cold stress. Front. Microbiol. 8, 979. https://doi.org/10.3389/fmicb.2017.00979.

Liu, C.S., Zhao, D.F., Ma, W.J., Guo, Y.D., Wang, A.J., Wang, Q.L., Lee, D.J., 2016. Denitrifying sulfide removal process on high-salinity wastewaters in the presence of *Halomonas* sp. Appl. Microbiol. Biotechnol. 100, 1421–1426. https://doi.org/10.1007/s00253-015-7039-6.

Love, M.I., Huber, W., Anders, S., 2014. Moderated estimation of fold change and dispersion for RNA-seq data with DESeq2. Genome Biol. 15, 550. https://doi.org/10.1186/s13059-014-0550-8.

Magoč, T., Salzberg, S.L., 2011. FLASH: fast length adjustment of short reads to improve genome assemblies. Bioinformatics 27, 2957–2963. https://doi.org/10.1093/bioinformatics/btr507.

Marangoni, L.F.D., Dalmolin, C., Marques, J.A., Klein, R.D., Abrantes, D.P., Pereira, C.M., Calderon, E.N., Castro, C.B.E., Bianchini, A., 2019. Oxidative stress biomarkers as potential tools in reef degradation monitoring: a study case in a South Atlantic reef under influence of the 2015–2016 El Niño/southern oscillation (ENSO). Ecol. Indic. 106, 105533. https://doi.org/10.1016/j.ecolind.2019.105533.

Marcos, M., Amores, A., Agulles, M., Robson, J., Feng, X.B., 2025. Global warming drives a threefold increase in persistence and 1 °C rise in intensity of marine heatwaves. Proc. Natl. Acad. Sci. USA 122, e2413505122. https://doi.org/10.1073/pnas.2413505122.

Marshall, P.A., Baird, A.H., 2000. Bleaching of corals on the Great Barrier Reef: differential susceptibilities among taxa. Coral Reefs 19, 155–163. https://doi.org/10.1007/s003380000086.

Martignago, D.C., Godoy, L., Amaral, A.P., Oliveira, G.T., 2024. Establishment of oxidative stress biomarkers in oocytes from healthy and bleached scleractinian corals. J. Exp. Mar. Biol. Ecol. 570, 151963. https://doi.org/10.1016/j.jembe.2023.151963.

McGinty, E.S., Pieczonka, J., Mydlarz, L.D., 2012. Variations in reactive oxygen release and antioxidant activity in multiple *Symbiodinium* types in response to elevated temperature. Microb. Ecol. 64, 1000–1007. https://doi.org/10.1007/s00248-012-0085-z.

Morris, J.J., Rose, A.L., Lu, Z.Y., 2022. Reactive oxygen species in the world ocean and their impacts on marine ecosystems. Redox Biol. 52, 102285. https://doi.org/10.1016/j.redox.2022.102285.

Muir, P.R., Done, T., Aguirre, J.D., 2021. High regional and intrageneric variation in susceptibility to mass bleaching in Indo-Pacific coral species. Glob. Ecol. Biogeogr. 30, 1889–1898. https://doi.org/10.1111/geb.13353.

Pockley, P., 2000. Global warming identified as main threat to coral reefs. Nature 407, 932. https://doi.org/10.1038/35039690.

Pootakham, W., Mhuantong, W., Yoocha, T., Putchim, L., Jomchai, N., Sonthirod, C., Naktang, C., Kongkachana, W., Tangphatsornruang, S., 2019. Heat-induced shift in coral microbiome reveals several members of the Rhodobacteraceae family as indicator species for thermal stress in *Porites lutea*. Microbiologyopen 8, e935. https://doi.org/10.1002/mbo3.935.

Putnam, H.M., 2021. Avenues of reef-building coral acclimatization in response to rapid environmental change. J. Exp. Biol. 224, jeb239319. https://doi.org/10.1242/jeb.239319.

Putnam, H.M., Edmunds, P.J., 2011. The physiological response of reef corals to diel fluctuations in seawater temperature. J. Exp. Mar. Biol. Ecol. 396, 216–223. https://doi.org/10.1016/j.jembe.2010.10.026.

Qin, Z.J., Yu, K.F., Wang, Y.H., Xu, L.J., Huang, X.Y., Chen, B., Li, Y., Wang, W.H., Pan, Z.L., 2019. Spatial and intergeneric variation in physiological indicators of corals in the South China Sea: insights into their current state and their adaptability to environmental stress. J. Geophys. Res. Oceans 124, 3317–3332. https://doi.org/10.1029/2018jc014648.

Qin, J.Y., Feng, Y., Lü, X.J., Zong, Z.Y., 2021. Precise species identification for *Acinetobacter*: a genome-based study with description of two novel *Acinetobacter* species. mSystems 6, e0023721. https://doi.org/10.1128/mSystems.00237-21.

Radecker, N., Pogoreutz, C., Gegner, H.M., Cardenas, A., Roth, F., Bougoure, J., Guagliardo, P., Wild, C., Pernice, M., Raina, J.B., et al., 2021. Heat stress destabilizes symbiotic nutrient cycling in corals. Proc. Natl. Acad. Sci. USA 118, e2022653118. https://doi.org/10.1073/pnas.2022653118.

Reimer, J.D., Peixoto, R.S., Davies, S.W., Traylor-Knowles, N., Short, M.L., Cabral-Tena, R.A., Burt, J.A., Pessoa, I., Banaszak, A.T., Winters, R.S., et al., 2024. The fourth global coral bleaching event: where do we go from here? Coral Reefs 43, 1121–1125. https://doi.org/10.1007/s00338-024-02504-w.

Reisch, C.R., Crabb, W.M., Gifford, S.M., Teng, Q., Stoudemayer, M.J., Moran, M.A., Whitman, W.B., 2013. Metabolism of dimethylsulphoniopropionate by *Ruegeria pomeroyi* DSS-3. Mol. Microbiol. 89, 774–791. https://doi.org/10.1111/mmi.12314.

Richardson, L.L., Kuta, K.G., 2003. Ecological physiology of the black band disease cyanobacterium *Phormidium corallyticum*. FEMS Microbiol. Ecol. 43, 287–298. https://doi.org/10.1016/s0168-6496(03)00025-4.

Robbins, S.J., Singleton, C.M., Chan, C.X., Messer, L.F., Geers, A.U., Ying, H., Baker, A., Bell, S.C., Morrow, K.M., Ragan, M.A., et al., 2019. A genomic view of the reef-building coral *Porites lutea* and its microbial symbionts. Nat. Microbiol. 4, 2090–2100. https://doi.org/10.1038/s41564-019-0532-4.

Roberty, S., Furla, P., Plumier, J.C., 2016. Differential antioxidant response between two *Symbiodinium* species from contrasting environments. Plant Cell Environ. 39, 2713–2724. https://doi.org/10.1111/pce.12825.

Rosado, P.M., Leite, D.C.A., Duarte, G.A.S., Chaloub, R.M., Jospin, G., da Rocha, U.N., Saraiva, J.P., Dini-Andreote, F., Eisen, J.A., Bourne, D.G., et al., 2019. Marine probiotics: increasing coral resistance to bleaching through microbiome manipulation. ISME J. 13, 921–936. https://doi.org/10.1038/s41396-018-0323-6.

Rowan, R., 2004. Coral bleaching - thermal adaptation in reef coral symbionts. Nature 430, 742. https://doi.org/10.1038/430742a.

Schloss, P.D., Westcott, S.L., Ryabin, T., Hall, J.R., Hartmann, M., Hollister, E.B., Lesniewski, R.A., Oakley, B.B., Parks, D.H., Robinson, C.J., et al., 2009. Introducing mothur: open-source, platform-independent, community-supported software for describing and comparing microbial communities. Appl. Environ. Microbiol. 75, 7537–7541. https://doi.org/10.1128/aem.01541-09.

Shinzato, C., Khalturin, K., Inoue, J., Zayasu, Y., Kanda, M., Kawamitsu, M., Yoshioka, Y., Yamashita, H., Suzuki, G., Satoh, N., 2021. Eighteen coral genomes reveal the evolutionary origin of *Acropora* strategies to accommodate environmental changes. Mol. Biol. Evol. 38, 16–30. https://doi.org/10.1093/molbev/msaa216.

Strand, E.L., Wong, K.H., Farrai, A., Gray, S., McMenamin, A., Putnam, H.M., 2024. Coral species-specific loss and physiological legacy effects are elicited by an extended marine heatwave. J. Exp. Biol. 227, jeb246812. https://doi.org/10.1242/jeb.246812.

Suggett, D.J., Smith, D.J., 2020. Coral bleaching patterns are the outcome of complex biological and environmental networking. Glob. Chang. Biol. 26, 68–79. https://doi.org/10.1111/gcb.14871.

Sunda, W., Kieber, D.J., Kiene, R.P., Huntsman, S., 2002. An antioxidant function for DMSP and DMS in marine algae. Nature 418, 317–320. https://doi.org/10.1038/nature00851.

Sweet, M., Burian, A., Fifer, J., Bulling, M., Elliott, D., Raymundo, L., 2019. Compositional homogeneity in the pathobiome of a new, slow-spreading coral disease. Microbiome 7, 139. https://doi.org/10.1186/s40168-019-0759-6.

Tomasch, J., Gohl, R., Bunk, B., Diez, M.S., Wagner-Döbler, I., 2011. Transcriptional response of the photoheterotrophic marine bacterium *Dinoroseobacter shibae* to changing light regimes. ISME J. 5, 1957–1968. https://doi.org/10.1038/ismej.2011.68.

van Oppen, M.J.H., Oliver, J.K., Putnam, H.M., Gates, R.D., 2015. Building coral reef resilience through assisted evolution. Proc. Natl. Acad. Sci. USA 112, 2307–2313. https://doi.org/10.1073/pnas.1422301112.

Voolstra, C.R., Buitrago-López, C., Perna, G., Cárdenas, A., Hume, B.C.C., Rädecker, N., Barshis, D.J., 2020. Standardized short-term acute heat stress assays resolve historical differences in coral thermotolerance across microhabitat reef sites. Glob. Chang. Biol. 26, 4328–4343. https://doi.org/10.1111/gcb.15148.

Wang, J.T., Wang, Y.T., Chen, C.A., Meng, P.J., Tew, K.S., Chiang, P.W., Tang, S.L., 2022. Extra high superoxide dismutase in host tissue is associated with improving bleaching resistance in "thermal adapted" and *Durusdinium trenchii*-associating coral. PeerJ 10, e12746. https://doi.org/10.7717/peerj.12746.

Warner, M.E., Fitt, W.K., Schmidt, G.W., 1999. Damage to photosystem II in symbiotic dinoflagellates: a determinant of coral bleaching. Proc. Natl. Acad. Sci. USA 96, 8007–8012. https://doi.org/10.1073/pnas.96.14.8007.

Weis, V.M., 2008. Cellular mechanisms of cnidarian bleaching: stress causes the collapse of symbiosis. J. Exp. Biol. 211, 3059–3066. https://doi.org/10.1242/jeb.009597.

Woo, C.Y., Kim, J., 2022. *Variovorax terrae* sp. nov. isolated from soil with potential antioxidant activity. J. Microbiol. Biotechnol. 32, 855–861. https://doi.org/10.4014/jmb.2205.05018.

Xiao, Y.L., Gao, L.Y., Li, Z.Y., 2024. Unique high-temperature tolerance mechanisms of zoochlorellae *Symbiochlorum hainanensis* derived from scleractinian coral *Porites lutea*. mBio 15, e0278023. https://doi.org/10.1128/mbio.02780-23.

Yakovleva, I., Bhagooli, R., Takemura, A., Hidaka, M., 2004. Differential susceptibility to oxidative stress of two scleractinian corals: antioxidant functioning of mycosporine-glycine. Comp. Biochem. Physiol. B Biochem. Mol. Biol. 139, 721–730. https://doi.org/10.1016/j.cbpc.2004.08.016.

Yu, X.P., Yu, K.F., Huang, W., Liang, J.Y., Qin, Z.J., Chen, B., Yao, Q.C., Liao, Z.H., 2020. Thermal acclimation increases heat tolerance of the scleractinian coral *Acropora pruinosa*. Sci. Total Environ. 733, 139319. https://doi.org/10.1016/j.scitotenv.2020.139319.

Zhang, Y., Yang, Q.S., Ling, J., Long, L.J., Huang, H., Yin, J.P., Wu, M.L., Tang, X.Y., Lin, X.C., Zhang, Y.Y., et al., 2021. Shifting the microbiome of a coral holobiont and improving host physiology by inoculation with a potentially beneficial bacterial consortium. BMC Microbiol. 21, 130. https://doi.org/10.1186/s12866-021-02167-5.

Zhou, Z., Yu, X.P., Tang, J., Wu, Y.B., Wang, L.G., Huang, B., 2018. Systemic response of the stony coral *Pocillopora damicornis* against acute cadmium stress. Aquat. Toxicol. 194, 132–139. https://doi.org/10.1016/j.aquatox.2017.11.013.

Marine Pollution Bulletin 222 (2026) 118815



Contents lists available at ScienceDirect

Marine Pollution Bulletin

journal homepage: www.elsevier.com/locate/marpolbul



Color disparity enhances the toxic effects of polystyrene microplastics on *Cladocopium goreaui*

Tianyi Niu [a,c,d], Yating Yang [a], Sanqiang Gong [a], Kefu Yu [a,b], Jiayuan Liang [a,*]

[a] Guangxi Laboratory on the Study of Coral Reefs in the South China Sea, School of Marine Sciences, Guangxi University, Nanning, 530004, China
[b] Southern Marine Science and Engineering Guangdong Laboratory (Guangzhou), Guangzhou, 510030, China
[c] State Key Laboratory of Urban and Regional Ecology, Research Center for Eco-Environmental Sciences, Chinese Academy of Sciences, Beijing, 100085, China
[d] University of Chinese Academy of Sciences, Beijing, 100049, China

ARTICLE INFO

Keywords:
Coral reef ecosystems
Symbiodiniaceae
Microplastic color disparity
Biosynthesis inhibition
Metabolic disruption

ABSTRACT

Coral reef ecosystems are increasingly threatened by environmental stressors, with microplastics (MPs) emerging as a pervasive and harmful contaminant. As essential symbionts of reef-building corals, *Symbiodiniaceae* are vital to coral health; however, their physiological responses to MPs remain largely unexplored. This study investigates the toxic effects of polystyrene microplastics (PS-MPs) of five distinct colors (red, yellow, green, blue, and white) on *Cladocopium goreaui*, a dominant coral symbiont. Exposure to 5 μm PS-MPs at 20 mg/L significantly inhibited algal growth, with blue and white PS-MPs exhibiting the strongest suppression. Growth rates decreased by up to approximately 36.0 % compared to controls over a 20-day exposure period. Although *C. goreaui* upregulated photosynthetic pigment content to compensate for reduced light availability due to MP aggregation, a substantial portion of the generated energy was diverted to mitigate oxidative stress. Transcriptomic analysis revealed that PS-MPs exposure downregulated key genes involved in biosynthetic pathways (e.g., peptide/amide formation) and primary metabolism (e.g., nitrogen assimilation, lipid metabolism). The pronounced toxicity of blue and white PS-MPs was attributed to their strong suppression of fatty acid metabolism and ribosomal function. These findings highlight the role of color disparity in modulating MP toxicity and offer new insight into the physiological and molecular responses of coral symbionts to MP pollution, with implications for coral reef health and resilience.

1. Introduction

Most coral reefs are distributed in tropical and subtropical oligotrophic shallow waters. Despite covering only approximately 0.25 % of the global ocean area, these ecosystems hold immense ecological and economic significance for humanity. Renowned as the "tropical rainforests of the sea", coral reefs support extraordinary biodiversity and functional diversity while providing critical habitat for nearly 30 % of marine species. Their unique combination of ecological value, aesthetic appeal, and ecosystem services makes them indispensable to marine environments and human societies alike (Reaka-Kudla, 1997; Yu, 2018; Jones et al., 2022). The unique morphological structure of coral reefs enables them to function as natural hydraulic barriers These ecosystems serve three critical coastal protection roles: (1) replenishing beach sand through biogenic sediment production, (2) filtering and trapping suspended sediments, and (3) significantly mitigating shoreline erosion through wave energy dissipation (Smith, 1978; Fisher et al., 2015; Peixoto et al., 2019; Woodhead et al., 2019). Coral holobionts comprise the coral host's mucus, ambient seawater, and sediment-associated benthic microbial communities (Pogoreutz et al., 2020). The composition and structure of microbial communities within coral holobionts are highly responsive to environmental fluctuations (e.g., temperature, light availability) and stressors (e.g., toxic substances) (Ursell et al., 2012; Webster and Thomas, 2016). The symbiotic relationship between *Symbiodiniaceae* and reef-building corals forms the foundation of coral reef ecosystems, with the photosynthates (e.g., amino acids, glucose, glycerol) provided by the algae satisfying up to 90 % of the coral hosts' energy requirements (Houlbrèque and Ferrier-Pagès, 2009; González-Pech et al., 2019). *C. goreaui* forms widespread symbiotic relationships with corals across the Indo-Pacific region, exhibiting high photosynthetic efficiency that enhances host coral tolerance to seasonal low temperatures and elevated nutrient conditions (Baker et al., 2013).

* Corresponding author.
E-mail address: jyliang@gxu.edu.cn (J. Liang).

https://doi.org/10.1016/j.marpolbul.2025.118815
Received 16 July 2025; Received in revised form 31 August 2025; Accepted 5 October 2025
Available online 8 October 2025
0025-326X/© 2025 Published by Elsevier Ltd.

Subject to escalating pressures from global warming, overfishing, and environmental pollution, coral reef ecosystems are experiencing accelerating degradation (Hughes et al., 2003; van Woesik and Kratochwill, 2022). Coral bleaching has emerged as the predominant driver of large-scale reef degradation worldwide. The dazzling colors of corals come from *Symbiodiniaceae* living in their tissues and when corals lose these *Symbiodiniaceae* or the *Symbiodiniaceae* loss of pigmentation, the corals turn white—a process called bleaching (Guibert, 2024; Mellin et al., 2024). Mortality occurs in bleached corals when *Symbiodiniaceae* repopulation does not achieve threshold densities within species-specific recovery windows.

Given the ecological fragility of coral reefs and their dependence on *Symbiodiniaceae*, it is crucial to understand emerging anthropogenic stressors that may exacerbate reef degradation. Among these, plastic pollution and particularly MPs have attracted increasing global attention. Anthropogenic development has made plastics and their additives a major emerging threat to Earth's ecosystems (Jambeck et al., 2015; Sendra et al., 2021). Under environmental stressors including photodegradation (UV exposure), oxidative weathering, and microbial degradation, plastics undergo progressive fragmentation into microscale particles (Thompson et al., 2004; Lambert et al., 2013; Jambeck et al., 2015; Auta et al., 2017). MPs are globally pervasive, found in rivers, soils, oceans, and air (Li et al., 2021a; Zhou et al., 2021). Each year, over 100,000 tons of plastic enter the oceans through various pathways, where they are carried by ocean currents, widely dispersed, and pose serious threats to marine ecosystems across entire food webs (Liu et al., 2022; Xia et al., 2023; Zhang et al., 2024; Kazancı et al., 2025). MP ingestion by marine organisms has become ubiquitous, raising significant concerns about ecosystem stability (Kühn and Van Franeker, 2020; Lu et al., 2025). These MPs cause severe physiological impacts, including gastrointestinal obstruction, organ damage, and growth impairment (Wright et al., 2013; Huang et al., 2019). A MP analysis of 1381 fish specimens revealed contamination in 42.4 % of samples, comprising fibers, microbeads, and fragments (Peters et al., 2017). Importantly, the ecological risks of MPs are not limited to higher trophic levels such as fish, but also extend to primary producers like marine algae, which play key roles in sustaining coral reef ecosystems. MPs pose significant threats to marine algae, causing both direct physical damage and photosynthetic inhibition (Ding et al., 2019b). Elevated MP concentrations inhibit algal growth, induce oxidative stress, and enhance the release of algal proteins and polysaccharides (Li et al., 2020). These MPs can form aggregates with the secreted biomolecules, which subsequently persist in the water column or settle into benthic sediments (Lagarde et al., 2016; Zhang et al., 2017; Li et al., 2020; Li et al., 2021b).

Building on this, recent studies have suggested that not only the presence of MPs but also their physical characteristics—such as size, shape, and particularly color—can further modulate their ecological impacts. In natural environments, coloration is an evolutionarily adaptive trait that enhances survival through predator avoidance or light capture optimization (Croce and Van Amerongen, 2014; Karpestam et al., 2014). Color is a functional trait in both natural and synthetic systems. Plastics are manufactured in various colors to fulfill specific industrial purposes, with color influencing their environmental interactions (Shtykova et al., 2006; Greenway and Gerstenberger, 2010). Colored MPs dominate aquatic plastic debris, with black, white, red, yellow, green, and blue being most common (Shaw and Day, 1994; Su et al., 2016; Wang et al., 2017; Zhang et al., 2018). A global survey of oceanic floating plastic fragments revealed that white and transparent/sem-transparent MPs are the most abundant, accounting for up to 47 % of particles collected, highlighting the environmental relevance of chromatic variation in MPs (Zhao et al., 2022). The plastisphere refers to the unique ecological niche formed by microbial communities adhering to and colonizing MP surfaces (Zettler et al., 2013). Blue polyethylene MPs (2.76–2.88 mm) uniquely enhance microbial diversity and select for distinct taxa in aquaculture pond plastispheres compared to yellow/transparent counterparts (Wen et al., 2020), possibly because different colors alter surface energy and adsorption properties, thereby shaping microbial colonization dynamics. Exposure to 5 μm PS-MPs of varying colors (white, green, orange, red) significantly inhibited growth in the freshwater microalga *Scenedesmus obliquus*, with the least suppression observed in green PS-MPs that closely matched the algal cell's pigmentation (Chen et al., 2020). This pattern suggests that color-dependent light absorbance and reflectance can influence photosynthetically active radiation, thereby modulating algal physiological responses. In addition, recent studies have demonstrated that marine and freshwater organisms, including fish and crustaceans, exhibit selective ingestion based on MP color, suggesting ecological relevance of plastic color in exposure dynamics and potential toxicity (Horie et al., 2024). Such feeding selectivity may reflect visual perception biases, where certain colors mimic natural prey or contrast strongly with the surrounding environment, thereby altering ingestion risk. These findings indicate color-mediated differential ecological risks of MPs, though the mechanistic basis of chromatic toxicity is poorly understood.

Reef-building corals serve as the ecological foundation of coral reef ecosystems, predominantly establishing symbiotic relationships with *Symbiodiniaceae* through horizontal transmission. This coral-algal symbiosis represents a critical biological partnership, where the physiological status of the symbionts directly determines holobiont stability. In recent years, escalating inputs of MPs into marine environments have emerged as a significant threat to *Symbiodiniaceae* survival, consequently compromising the functionality of coral reef ecosystems. PS-MPs, due to their persistence and bioavailability, exhibit high mobility in the environment, can accumulate through food chains, and induce multiple biological toxic effects such as cytotoxicity and oxidative stress, thereby posing a serious threat to ecosystems (Wang et al., 2024; Wang et al., 2025).

To elucidate the color-dependent mechanisms of MP toxicity in *Symbiodiniaceae*, we investigated the responses of the globally widespread coral symbiont *C. goreaui* to five color-annotated PS-MPs (red, yellow, green, blue, and white; 20 mg/L; 5 μm). By systematically assessing algal growth rate, photosynthetic efficiency, oxidative stress responses, and transcriptomic alterations, this study reveals color-specific impacts of PS-MPs on cellular physiology and gene expression. Our findings demonstrate that PS-MPs of different colors exert distinct levels of toxicity on *Symbiodiniaceae*, highlight the molecular mechanisms driving these divergent responses, and provide a basis for more accurate risk assessment of color-dependent MP impacts on coral–algal symbioses and reef conservation.

2. Materials and methods

2.1. Materials and experimental design

The strain of *C. goreaui* used in this study was isolated by our laboratory from *Acropora pruinosa* collected in Weizhou Island, Beibu Gulf, South China Sea (Qin et al., 2023). The cultures were maintained in L1 seawater medium under controlled conditions: salinity 35 ‰, temperature 25 ± 1 °C, light intensity 90 μmol photons m^{-2} s^{-1}, with a 14:10 h light: dark photoperiod (Guillard and Hargraves, 1993). L1 medium components were sourced from Guangyu Biotechnology Co., Ltd. (Shanghai, China). Monodisperse colored latex PS microspheres were obtained from Beisile Technology Research Center (Tianjin, China). These particles were synthesized by incorporating chromophores via surface coatings. The microspheres exhibit spherical morphology with smooth surfaces, high purity (>99 %), and narrow size distribution (5 μm ± 0.2 μm). In 250 mL conical flasks, *C. goreaui* was cultured in a 150 mL system until reaching a cell density of 1.0×10^5 cells/mL, after which PS-MPs stock solution was added to achieve a final concentration of 20 mg/L (Higher concentrations facilitate the observation of significant changes within a short period, enabling an effective assessment of the toxic effects arising from color differences in PS-MPs). In the control

group, an equal volume of ultrapure water (the solvent for the microplastics) was added. Six experimental treatments were established: red, yellow, green, blue, and white PS-MPs, along with a control group, each group with three biological replicates. All sampling procedures were conducted in a clean bench, and the experiment was maintained for 20 days.

2.2. Indicator measurement

2.2.1. growth ratios

At days 0, 5, 10, and 20 of the experiment, 1 mL aliquots were collected and fixed with 100 μL formaldehyde at 4 °C in the dark for 24 h. algal cells were then enumerated using a hemocytometer under an optical microscope. Cell density (cells/mL) and growth ratios were calculated from the recorded data. The specific growth rate (μ, day^{-1}) was determined as: $\mu = [\ln(N_2/N_1)] / (t_2 - t_1)$, where: N_1 and N_2 = cell densities (cells/mL) at time points t_1 and t_2, respectively.

2.2.2. Maximum photochemical efficiency Fv/fm and photosynthetic pigment content

Fv/fm was measured after 30-min dark adaptation using a PAM fluorometer (Walz, Germany) at four timepoints (days 0, 5, 10, 20). Measurements followed established protocols with 3 biological replicates (Schreiber et al., 1986; Sun, 2020). At each sampling timepoint (days 0, 5, 10, 20), 2 mL aliquots were centrifuged (5000 ×*g*, 5 min, 4 °C). The supernatant was discarded, and the pellet was resuspended in 1 mL methanol. After vortex mixing, samples were wrapped in aluminum foil and dark-incubated at 4 °C for 24 h to extract pigments. Following subsequent centrifugation (5000 ×*g*, 5 min, 4 °C), the supernatant was analyzed spectrophotometrically for optical density (OD) at 480, 510, 630, 664, and 750 nm wavelengths using a microplate reader (Ritchie, 2006). Light-protected protocols were strictly maintained throughout. Pigment contents were normalized to per-cell values and calculated as:

$$\text{Chlorophyll a } (\mu g/mL) = 13.6849 \times (OD_{664} - OD_{750}) - 3.4551 \times (OD_{630} - OD_{750})$$

$$\text{Chlorophyll c } (\mu g/mL) = -7.014 \times (OD_{664} - OD_{750}) + 32.9371 \times (OD_{630} - OD_{750})$$

$$\text{Carotenoids } (\mu g/mL) = 7.6 \times (OD_{480} - OD_{750}) - 1.49 \times (OD_{510} - OD_{750})$$

2.2.3. Extracellular polymeric substances content

Since the primary component of extracellular Polymeric Substances (EPS) is polysaccharides, EPS content was estimated by quantifying polysaccharide levels using the phenol-sulfuric acid (H_2SO_4) method (Li et al., 2020; Cao et al., 2022b; Yue et al., 2022). At days 0, 10, and 20 of the experiment, 5 mL of algal culture was heated at 80 °C for 30 min, followed by centrifugation at 8000 ×*g* and 4 °C for 10 min to collect the supernatant. Heat-extracted supernatants (80 °C, 30 min) were reacted with phenol/H_2SO_4 under controlled thermal conditions (100 °C × 20 min → 0 °C × 10 min). Absorbance at 490 nm was calibrated against glucose standards (0–90 μg/mL, $R^2 > 0.99$).

2.2.4. Soluble protein content, MDA level, and SOD activity

For cell lysis, at days 0, 10, and 20 of the experiment, 20 mL algal suspensions were pelleted (3000 ×g, 10 min, 4 °C), resuspended in PBS, and subjected to bead-beating (0.5 mm ZrO_2 beads; 10 s ON/30 s OFF ×6 cycles) in a pre-chilled homogenizer. Lysates were cleared by centrifugation (3000 ×*g*, 10 min, 4 °C). Total protein concentration in the supernatant was determined using a BCA microprotein assay kit (Sangon Biotech, Shanghai, China). Malondialdehyde (MDA) content was quantified with a commercial MDA assay kit (A003, Jiancheng Bioengineering, Nanjing, China). Superoxide dismutase (SOD) activity was measured using an SOD detection kit (A001, Jiancheng Bioengineering). All measurements were normalized to per-cell values.

2.3. Transcriptome sequencing

At the experimental endpoint (day 20), algal cells from 100 mL cultures were harvested by centrifugation (5000 ×*g*, 10 min, 4 °C). Following PBS washing (3 × 20 mL) and final pelleting, samples were snap-frozen in liquid nitrogen (30 min) prior to RNA-seq analysis (Illumina NovaSeq X Plus; Majorbio, Shanghai). Datasets were analyzed on the online platform of Majorbio Cloud Platform (https://cloud.majorbio.com/) (Han et al., 2024). The detailed steps are provided in the supplementary materials.

2.4. Statistical analysis

All statistical tests were implemented in SPSS. All data were tested for normality (Shapiro-Wilk test) and homogeneity of variances (Levene's test) prior to ANOVA. When these assumptions were satisfied, Tukey's HSD was applied for multiple comparisons ($p < 0.05$). Graphical representations were created in Origin, and all values expressed as mean ± SEM (n = X).

3. Results

3.1. PS-MPs exposure significantly inhibited the growth of C. goreaui

The decline in growth ratios directly reflected cellular damage in *C. goreaui*. All colored PS-MPs exposure significantly inhibited algal growth ($p < 0.05$), but the inhibition was less severe in color-matched groups (yellow and green) than in spectrally distinct groups (red, blue, and white) (Fig. 1A). Specifically, yellow and green PS-MPs caused transient growth inhibition during days 0–10, while red, blue, and white PS-MPs induced sustained suppression throughout the experiment. The most pronounced inhibition occurred in the blue and white groups, with growth rates decreasing by 33.6 % and 36 % (day 5), 32.5 % and 34.7 % (day 10), and 32.1 % and 35.4 % (day 20) compared to the control, respectively.

The photosynthesis of *Symbiodiniaceae* plays a very important role in symbiotic functional organisms. Throughout the experimental period, no significant changes in *Fv/fm* were observed across all treatment groups (Fig. 1B). As photosynthetic pigments are critical for maintaining photosynthetic function, exposure to 20 mg/L of 5 μm PS-MPs of different colors resulted in significantly increased chlorophyll *a* (Chl-a) content in the red, green, and blue groups compared to the control, except for the yellow and white groups (Fig. 1C). The red group exhibited the most pronounced increase in Chl-a at days 5–10 ($p < 0.001$). No significant difference in Chl-a content was detected between the yellow group and the control, while the white group showed a transient increase at day 5 ($p < 0.05$) followed by a significant decline at days 10–20 ($p < 0.05$). For chlorophyll *c* (Chl-c), the blue group demonstrated a highly significant increase ($p < 0.001$), whereas the yellow group showed a reduction at day 5 ($p < 0.05$) and the red group displayed elevated levels at days 10–20 ($p < 0.05$). The white group exhibited similar trends in Chl-c as in Chl-a (Fig. 1D). From days 5–20, carotenoid content significantly increased in the red and green groups ($p < 0.0001$), with the blue group showing a delayed response (significant only at day 20, $p < 0.001$). No significant change was observed in the yellow group, while the white group mirrored the Chl-a pattern (Fig. 1E).

3.2. PS-MPs exposure induced cellular damage in C. goreaui

EPS play a protective role against toxicant penetration into cells. Upon exposure to 20 mg/L of 5 μm color-differentiated PS-MPs, all groups exhibited significantly elevated EPS production by day 10 ($p <$

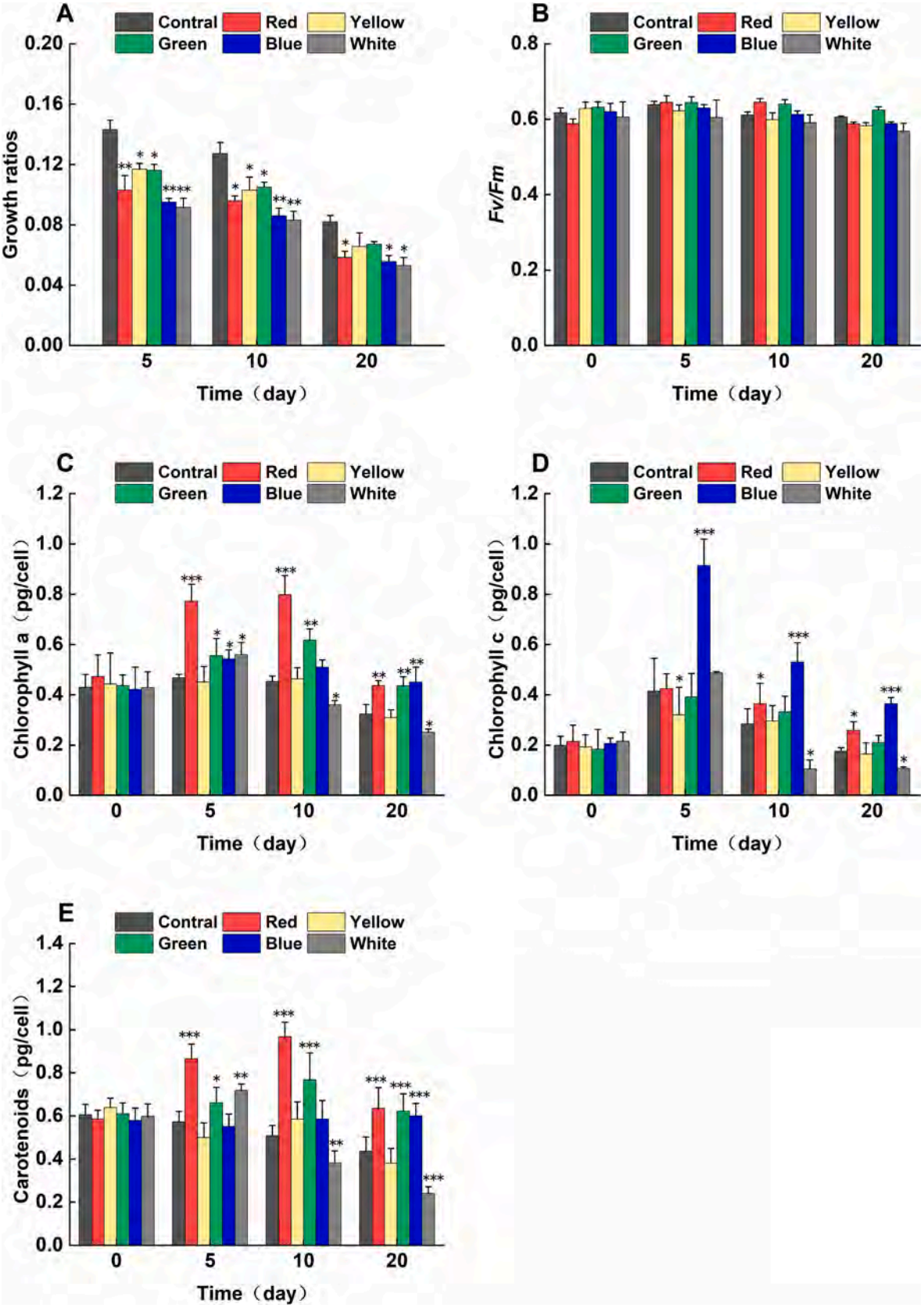


Fig. 1. The growth and photosynthetic indicators of *C. goreaui* after exposure to PS-MPs. (A) Growth ratios. (B) *Fv/fm*. (C) Chl-a content. (D) Chl-c content. (E) Carotenoids content. The bar shapes represent the mean ± the standard error (three biological replicates). The significance between the experimental group and the control group is indicated by asterisks (*: $p < 0.05$, **: $p < 0.01$, ***: $p < 0.001$).

0.001), with yellow and green groups (similar in color to algal cells) showing less pronounced increases than spectrally distinct red, blue, and white groups (Fig. 2A). The blue and white PS-MPs induced maximal EPS secretion, reaching 127 % and 139.9 % above control levels at day 10, and maintaining 83.7 % and 93.8 % increases at day 20, respectively.

Soluble proteins, serving as essential nutrients and osmoregulators, exhibited concentration patterns analogous to EPS following exposure to 20 mg/L of 5 μm color-variant PS-MPs. Consistent with EPS dynamics, yellow and green groups (spectrally similar to algal cells) demonstrated lower protein accumulation than red, blue, and white groups (Fig. 2B). All treatments showed significant increases in soluble protein content ($p < 0.05$), except the yellow group at day 10. Notably, blue and white PS-MPs triggered extreme upregulation ($p < 0.001$), elevating protein levels by 56.4 % and 82.3 % (day 10), and 114.1 % and 145.2 % (day 20) relative to controls, respectively.

MP toxicity induced substantial reactive oxygen species (ROS) generation in algal cells, where excessive ROS accumulation triggered membrane lipid peroxidation and elevated malondialdehyde (MDA) production. Superoxide dismutase (SOD) activity, as a critical ROS scavenger, showed coordinated patterns with MDA, extracellular polymeric substances (EPS), and soluble protein levels under 20 mg/L of 5 μm color-differentiated PS-MPs exposure (Figs. 2C, D). All treatments exhibited significant increases in both SOD activity and MDA content ($p < 0.05$), with yellow and green groups (spectrally matched to algal cells) displaying less pronounced responses than red, blue, and white groups. Specifically, blue and white PS-MPs induced the most severe oxidative stress: SOD activity surged to 58.3 % and 61.7 % above controls at day 10, and 113.7 % and 106 % at day 20, while MDA levels escalated by 94.6 % and 118.1 % (day 10), and 290.5 % and 313.1 % (day 20), respectively.

3.3. PS-MPs exposure suppressed biosynthesis and energy metabolism in *C. goreaui*

3.3.1. Gene expression and gene set level

Cluster analysis was performed using Pearson correlation coefficients with complete linkage clustering and Euclidean distance metrics, applying log10 transformation to group-averaged values. The results demonstrated high reproducibility across all biological replicates, with inter-sample correlation coefficients exceeding 0.97 (Fig. 3A). Principal component analysis (PCA) revealed distinct separation between blue/white PS-MPs groups and controls in terms of differentially expressed genes (DEGs) patterns (Fig. 3B). Raw counts were directly analyzed using DESeq2 based on the negative binomial distribution. Differentially expressed genes between groups were identified following standard normalization and filtering procedures, with default thresholds set at Padjust <0.05 and $|\log_2 FC| \geq 1$. Analysis of DEGs in *C. goreaui* following PS-MPs exposure showed that red, yellow, and green groups shared similar upregulated DEG profiles, whereas blue and white groups exhibited more extensive alterations, particularly the white group showing the greatest number of upregulated genes (Fig. 3C). For downregulated DEGs, the yellow group displayed the most substantial changes, followed by white, blue, green, and red groups in descending order.

Venn analysis of differentially expressed genes (DEGs) in *C. goreaui* following PS-MPs exposure revealed only 8 common DEGs across all five color groups, demonstrating distinct transcriptomic responses to different MP colors (Fig. 4A). Notably, blue and white PS-MPs, which showed the strongest growth inhibition, shared 465 overlapping DEGs. GO functional annotation (level 4) of these DEGs identified significant terms across three categories: Biological Process (BP), Cellular Component (CC), and Molecular Function (MF) (Fig. 4B). The most affected

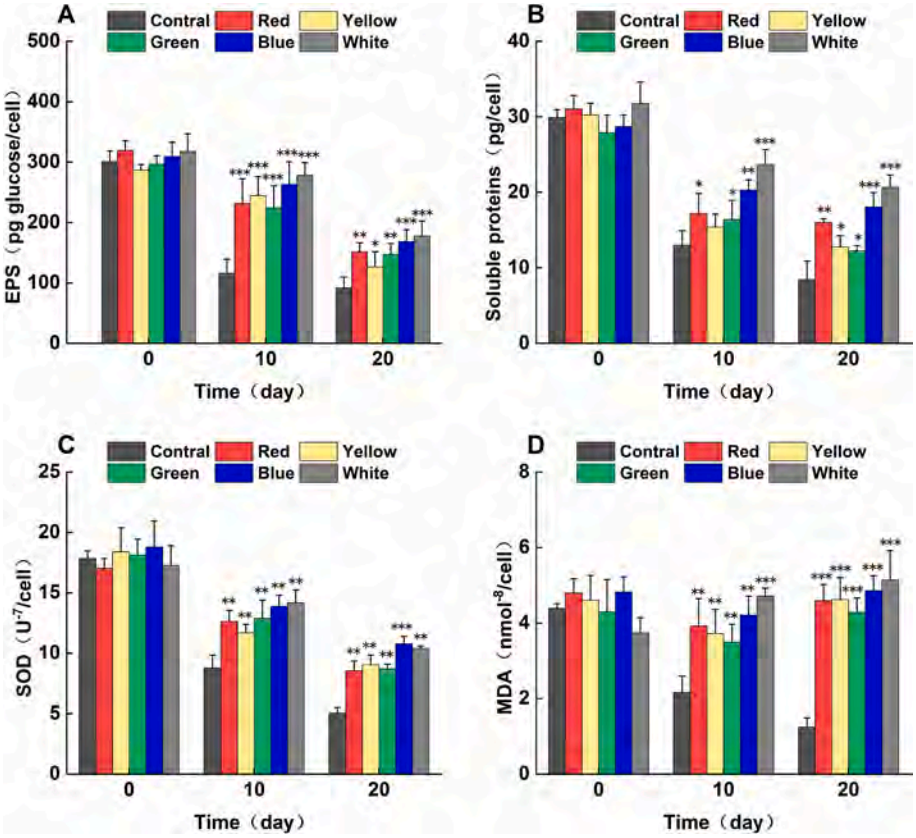


Fig. 2. The cellular defense and oxidative stress indicators of *C. goreaui* after exposure to PS-MPs. (A) EPS content. (B) soluble proteins content. (C) SOD activity. (D) MDA content. The bar shapes represent the mean ± the standard error (three biological replicates). The significance between the experimental group and the control group is indicated by asterisks (*: $p < 0.05$, **: $p < 0.01$, ***: $p < 0.001$).

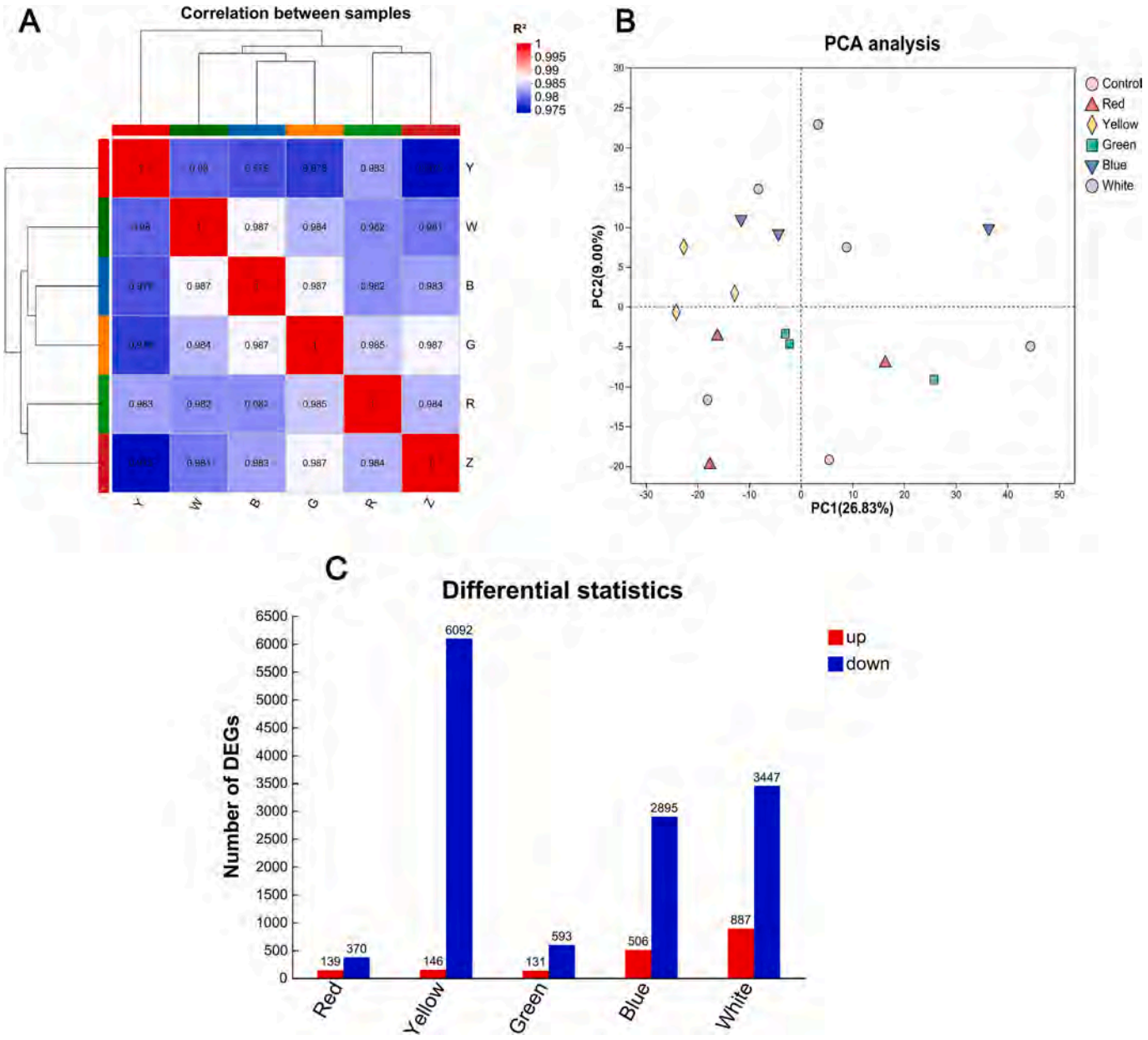


Fig. 3. Expression level analysis of genes in each group after exposure to PS-MPs. (A) Cluster analysis between samples. Z: Control; R: Red; Y: Yellow; G: Green; B: Blue; W: White. (B) PCA analysis between samples. (C) Differential expression statistics. Three biological replicates. (For interpretation of the references to color in this figure legend, the reader is referred to the web version of this article.)

molecular functions included ion binding, nucleotide binding, and ATP binding, while cellular processes were primarily associated with macromolecular metabolism and nitrogen/phosphorus metabolic pathways.

3.3.2. *Functional enrichment*

Protein-protein interaction (PPI) network analysis was conducted for the white PS-MPs group (showing strongest toxicity), from which 21 functionally pivotal genes were selected for cluster analysis, with results visualized in a heatmap (Fig. 5). These genes predominantly encode ribosomal proteins involved in large and small subunit assembly. Striking expression divergence was observed between the white group and controls, exhibiting inverse transcriptional patterns. Subsequent GO and KEGG enrichment analyses of differentially expressed genes (DEGs) across all groups were performed, with results displayed as the union of the top 10 most significantly enriched GO terms and KEGG pathways per group (Fig. 6).

GO enrichment analysis of DEGs revealed a spectral transition pattern following the color sequence from red to blue to white (Fig. 6A). Functional overlaps were observed specifically between white and blue groups, while blue groups additionally shared some terms with yellow groups. Red groups showed distinct GO profiles from all other treatments. Notably, the most growth-inhibitory groups (blue and white) exhibited significant suppression of ribosome-related functions, particularly cytoplasmic large ribosomal subunit assembly, protein-RNA complex organization, and protein-RNA complex assembly. Concurrently, blue and yellow groups showed impaired biosynthesis and metabolism of amides and peptides. Photosynthesis-related terms were downregulated in green groups, whereas red groups displayed reduced signal reception capacity for proteases.

Pathway analysis revealed consistent perturbations across multiple treatment groups in essential metabolic pathways including ribosome

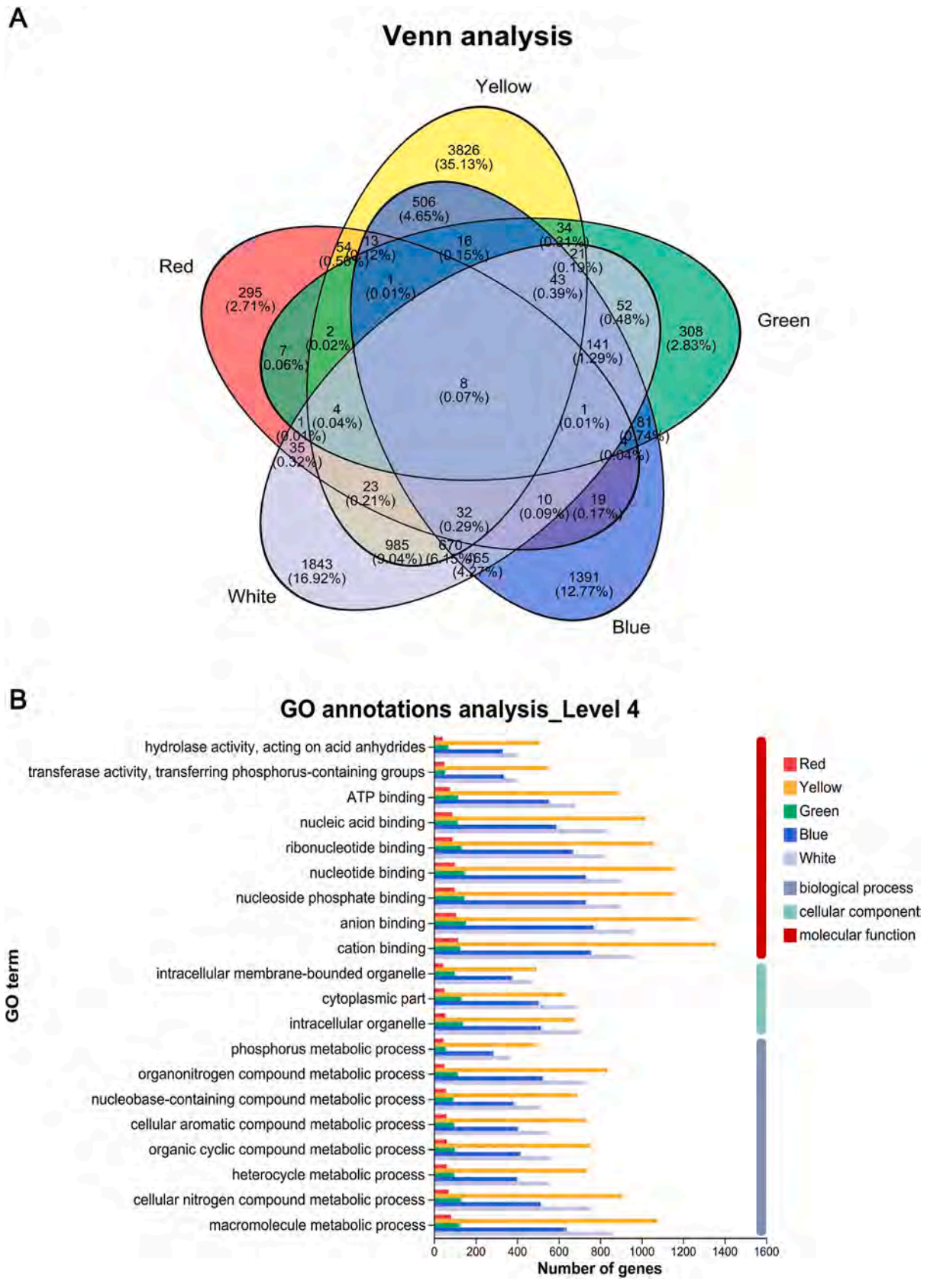


Fig. 4. Gene set analysis of DEGs in each group after exposure to PS-MPs. (A) Venn analysis of DEGs in each group. (B) GO functional annotation analysis. Three biological replicates.

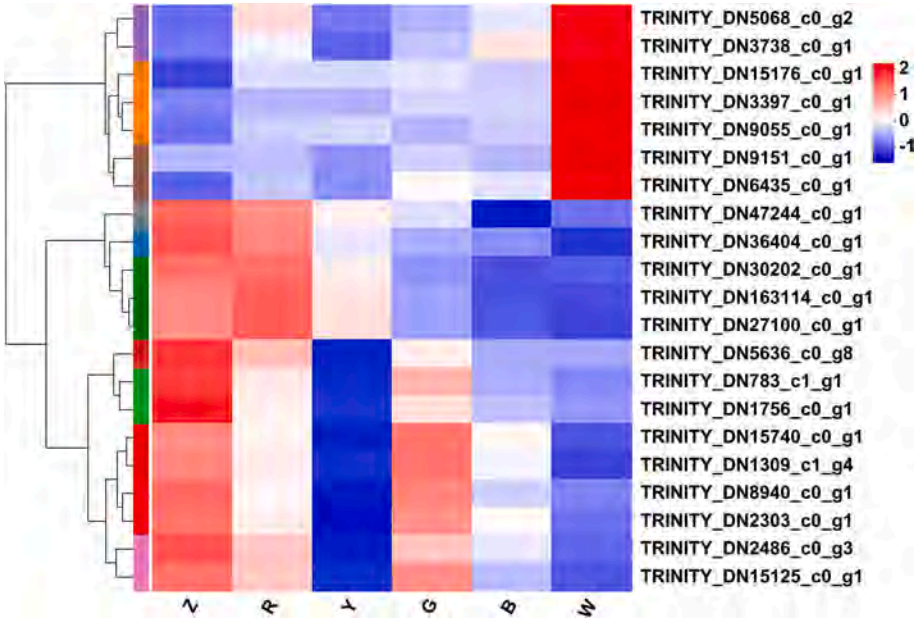


Fig. 5. DEGs clustering heatmap with strong importance after exposure to white PS-MPs. Z: Control; R: Red; Y: Yellow; G: Green; B: Blue; W: White. Three biological replicates. (For interpretation of the references to color in this figure legend, the reader is referred to the web version of this article.)

function, unsaturated fatty acid biosynthesis, TCA cycle, and lipoic acid metabolism (Fig. 6B) - all critical for cellular growth and proliferation in *C. goreaui*. The white group showed additional suppression of peroxisome and fatty acid degradation pathways, while the blue group exhibited impaired proteasome activity and endoplasmic reticulum protein processing. These findings indicate: (1) compromised energy metabolism and (2) attenuated proteolytic signaling in these high-toxicity groups. Furthermore, yellow groups displayed inhibited carbohydrate/alcohol biosynthesis and photosynthetic pathways, whereas red groups showed downregulation of sugar metabolism and disease resistance mechanisms - collectively suggesting severe impairment of energy production and stress defense capacities.

4. Discussion

4.1. PS-MPs exposure exerted detrimental effects on the growth of C. goreaui

The increasing severity of global coral reef degradation and the pivotal role of *Symbiodiniaceae* in reef ecosystems have driven growing research focus on their stress response mechanisms, with particular attention to MP toxicity as pollution escalates. Exposure to 1 μm PS-MPs at 5 mg/L concentration inhibited detoxification activity and assimilatory metabolism in *C. goreaui*, while activating ion transport mechanisms and elevating apoptosis levels, collectively suppressing algal growth (Su et al., 2020). In this study, 5 μm PS-MPs at 20 mg/L similarly reduced the growth ratios of *C. goreaui*, with greater growth inhibition observed in red, blue, and white groups that exhibited larger chromatic differences from algal cells compared to the spectrally similar yellow and green groups showing relatively milder suppression. This color-dependent toxicity likely reflects combined effects of optical shading and differential aggregation influencing cellular stress and transcriptional responses. Darker or more reflective colors may alter particle-cell adhesion rates, influencing aggregate formation and light penetration. This pattern was corroborated in parallel experiments with *Scenedesmus obliquus* exposed to 5 μm PS-MPs of different colors (red, orange, green, white), where the green PS-MPs (color-matched to chloroplasts) induced less toxicity than chromatic-mismatched groups, as further evidenced by irregular and slower algal cell motility in red, orange, and white treatments relative to green PS-MPs (Chen et al., 2020). Faster-moving algal cells can acquire greater light exposure, thereby generating higher biomass, suggesting potential color discrimination capabilities and chromatic preferences in these organisms. Previous studies have demonstrated that ultrastructural observations reveal adverse effects of MPs exposure on algal cells, including surface shrinkage and thylakoid distortion (Jiang et al., 2025; Liang et al., 2025). Furthermore, ribosomal function was severely impaired in all groups except the red treatment. Such ribosomal dysfunction may result from color-dependent aggregation and chemical interactions, as reflected in transcriptomic downregulation of ribosomal genes in blue and white groups (Ni and Buszczak, 2023). Ribosomal dysfunction induced by PS-MPs concurrently diminishes both antioxidant capacity (via enzyme activity reduction) and immune protease function, ultimately severely compromising *C. goreaui* growth, with the white group's uniquely elevated toxicity attributable to specific dysregulation of ribosomal subunit genes (60S/40S) (Ford et al., 2025).

For colors, Wen et al. demonstrated through biofilm cultivation experiments in aquaculture pond water systems with different colored MPs (blue, yellow, transparent) that plastisphere communities exhibited enhanced diversity and evenness, particularly in blue MP groups which harbored more unique species, indicating a color-driven selection mechanism among plastisphere microbiota (Wen et al., 2020). This finding is particularly relevant given that *Symbiodiniaceae* survival depends critically on symbiotic bacteria for essential nutrients like nitrogen and phosphorus. Previous studies have documented that PS-MPs tend to form large aggregates with *C. goreaui*, with these aggregates encapsulating significant populations of symbiotic bacteria within the plastisphere (Liang et al., 2025). Therefore, color-dependent aggregation may modulate light availability and bacterial interactions, potentially contributing to the observed growth variations and transcriptomic changes. Exposure to differently colored PS-MPs may induce distinct bacterial community shifts in the microalgal-bacterial symbiotic system, potentially contributing to the observed growth variations in *C. goreaui* across experimental groups. The chromatic properties of plastic microbeads, determined by wavelength-specific absorption and reflection patterns of surface dyes, critically influence light availability for photosynthesis. White PS-MPs, exhibiting poor light reflectivity, significantly reduced light energy acquisition in *C. goreaui*, leading to

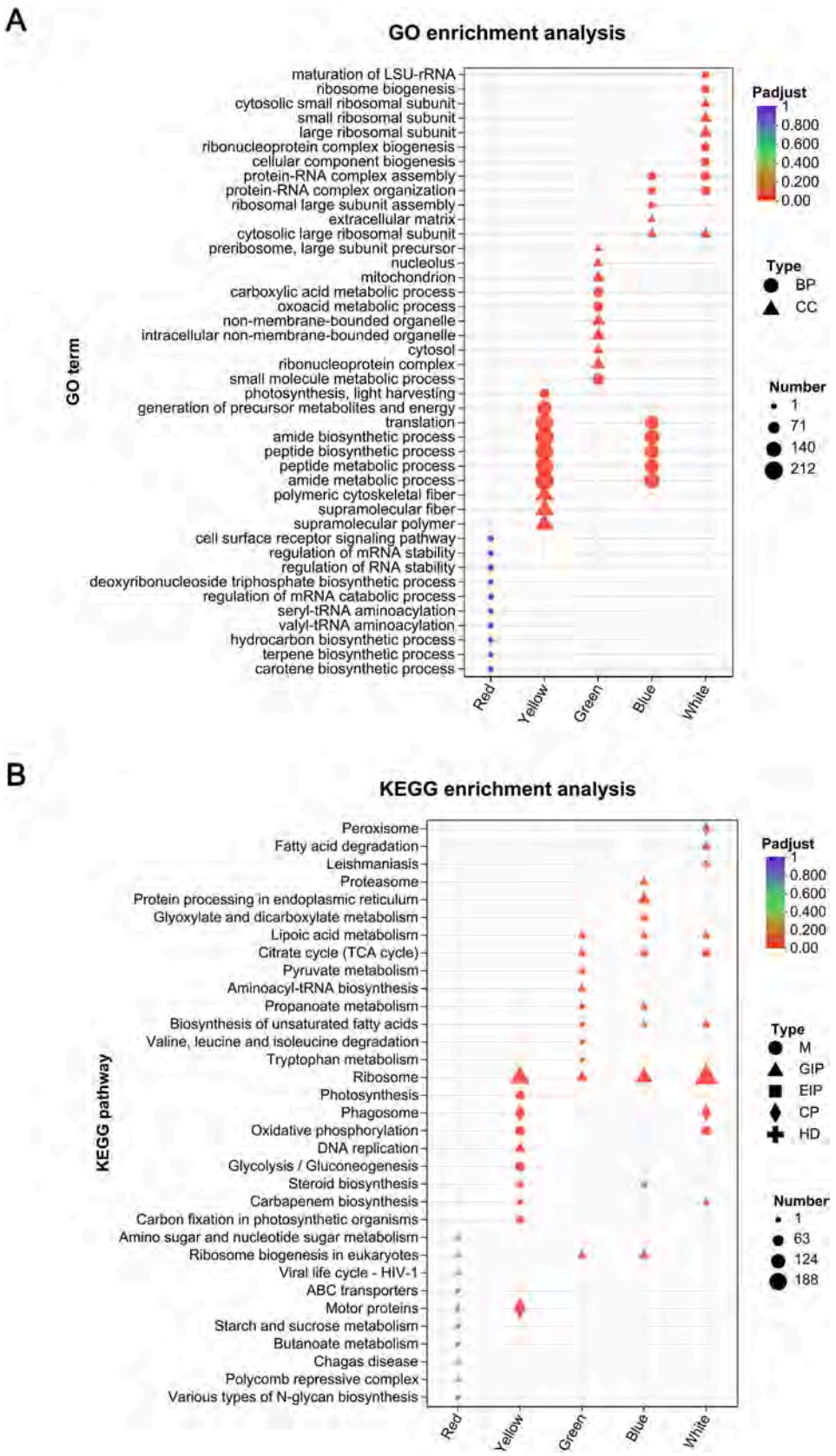


Fig. 6. Functional enrichment analysis of DEGs in each group after exposure to PS-MPs. (A) Bubble chart of multi-gene set GO enrichment analysis. (B) Bubble chart of multi-gene set KEGG enrichment analysis. Three biological replicates.

impaired growth and energy synthesis. This energy limitation was further exacerbated by PS-MPs-induced downregulation of key metabolic pathways, as demonstrated by transcriptomic data showing suppressed DEGs in lipoic acid metabolism, unsaturated fatty acid biosynthesis, and TCA cycle-all essential for energy transduction (Zhao et al., 2023; Cheng et al., 2024). Functional annotation revealed severe macromolecular metabolic deficiencies in blue and white groups, particularly in nitrogen/phosphorus assimilation, correlating with their maximal growth inhibition. Specifically, the combined effects of inhibited fatty acid degradation in white groups and disrupted protein processing in blue groups created synergistic bottlenecks in both energy supply and anabolic capacity, explaining their pronounced growth suppression (Zheng et al., 2025). Moreover, the color variations of plastic products in the environment often result from manufacturers using different types of dyes. In this sense, the distinct effects of these dyes on *Symbiodiniaceae* may be considered one of the factors contributing to the observed differences in the toxicity of microplastics of different colors. This is because microplastics of varying colors are unlikely to incorporate dyes with identical chemical compositions. In this study, all differently colored PS-MPs were obtained from the same manufacturer and product line, with identical particle size and polymer grade. Based on the supplier's specifications and previous studies (e.g., Chen et al., 2020), we assumed in our experimental design that these PS-MPs were consistent in material composition and additives, differing only in color. However, as FTIR or Raman spectroscopy was not performed in this work to directly verify this assumption, a degree of uncertainty remains. Future studies should employ spectroscopic characterization to further confirm the chemical consistency of differently colored PS-MPs.

4.2. Regulatory mechanisms for photosynthetic homeostasis in *C. goreaui* under PS-MPs exposure

EPS production constitutes an adaptive strategy in algae, where environmentally induced secretion of these polysaccharide-protein complexes mediates both proliferation and stress defense (Li et al., 2020). However, excessive EPS promotes aggregation with MPs, causing color-dependent shading that attenuates light availability and alters transcription of photosynthesis-related genes, as demonstrated by 1 μm PS-MPs forming dense EPS-MP complexes on *Chlorella pyrenoidosa* surfaces that critically impair light-harvesting capacity (Cao et al., 2022b). Under light-limiting conditions, the algal cells upregulated chlorophyll biosynthesis to enhance photosynthetic efficiency, thereby maintaining photostasis (Falkowski and Owens, 1980). The *Symbiodiniaceae* within corals transition from a monolayer to a multilayer configuration during winter months with lower temperature and light intensity to enhance light capture efficiency, whereas under summer conditions of elevated temperature and irradiance, both their density and photosynthetic pigment content decrease (Venn et al., 2008). These seasonal adaptations demonstrate the algal symbionts' capacity to modulate their photopigmentation to maintain photosynthetic homeostasis. In this study, the red and blue PS-MPs treatment groups exhibited a significant increase in photosynthetic pigment content compared to the control, while *Fv/fm* values remained unchanged. This indicates that, despite color-dependent shading and aggregation stress, *C. goreaui* maintained photosynthetic performance via compensatory upregulation of pigment-synthesis genes, consistent with transcriptomic evidence. Similarly, Su et al. (2020) reported that chl-a content in *C. goreaui* significantly increased on day 7 following exposure to 1 μm PS-MPs at a concentration of 5 mg/L, while photochemical efficiency remained unchanged throughout the exposure period. However, due to the necessity of counteracting toxic and/or oxidative stress, the photosynthetically derived energy was largely diverted from growth-related processes. This pattern may reflect the limited light availability caused by the poor reflectivity of white PS-MPs, which constrained photosynthetic input and ultimately led to pigment reduction. Moreover, spectral differences among coral reef substrates have been reported to influence light absorption and, consequently, chlorophyll content in *Symbiodiniaceae* (Xu et al., 2019). In this study, the significant differences in photosynthetic pigment content across treatment groups may be explained by the distinct spectral absorption and reflection characteristics of the surface dyes on PS-MPs, which likely altered the wavelengths of light reaching algal cells. Although the majority of differentially expressed genes related to photosynthesis and light-harvesting were downregulated in the yellow group, photosynthetic pigment levels and *Fv/fm* remained largely unaffected. This phenomenon may be attributed to the efficient absorption of yellow light by *C. goreaui*, likely owing to the spectral similarity between the yellow PS-MPs and the intrinsic pigmentation of the algal cells.

4.3. Defensive mechanisms and oxidative damage of *C. goreaui* following exposure to PS-MPs

Higher EPS content leads to increased attachment of particulate matter, enhancing co-aggregation and further elevating EPS levels, which in turn causes severe oxidative damage to the cells (Chen et al., 2012). The higher the EPS content, the more severe the cellular exposure to toxic substances, resulting in greater oxidative damage to the cells. Soluble proteins, as key nutrients and osmotic regulators, enhance cellular water retention and protect vital cellular components and biological membranes, making them commonly used as indicators for screening cellular resistance (Guzmán-Murillo et al., 2007; Qian et al., 2008). Our investigation showed that EPS and soluble protein levels in the red, blue, and white groups increased significantly, with higher increases compared to the yellow and green groups. These color-dependent increases suggest that greater aggregation and shading by chromatically mismatched PS-MPs enhance stress signaling, consistent with transcriptomic activation of EPS and stress-response genes.

Algal cells possess mechanisms for both the production and removal of reactive oxygen species (ROS), maintaining a dynamic equilibrium. However, excessive ROS, including superoxide radicals (O^{2-}), hydroxyl radicals (•OH), and hydrogen peroxide (H_2O_2), are generated upon exposure to toxic pollutants (Cao et al., 2022a; Jin et al., 2024). When ROS cause severe damage to the cell membrane and organelles, cells activate their immune system to produce antioxidant enzymes such as CAT, SOD, and POD to mitigate the negative effects of ROS (Cao et al., 2015). In the present work, SOD activity significantly increased in all experimental groups, with the red, blue, and white groups showing greater increases than the yellow and green groups. This pattern reflects higher ROS production induced by color-dependent aggregation and shading, consistent with transcriptomic activation of oxidative stress pathways.

MDA, a product of membrane lipid peroxidation, serves as an indicator of oxidative damage in algal cells. Excessive ROS promotes lipid peroxidation of the cell membrane, thereby increasing MDA levels (Qian et al., 2008; Cao et al., 2022a; Cao et al., 2022b). All experimental groups showed a significant increase in MDA levels, indicating that PS-MPs exposure causes severe oxidative damage to *C. goreaui*. The red, blue, and white groups, which exhibit greater color differences from the algal cells, generated higher ROS levels and exhibited higher MDA content, resulting in more extensive cellular damage. Carotenoids, as antioxidants in living organisms, play a crucial role in scavenging lipid peroxidation free radicals, and the increase in carotenoid levels is closely linked to the cellular capacity to eliminate reactive oxygen species (Kaur et al., 2024; Sanniyasi et al., 2024). Following PS-MPs exposure, carotenoid content significantly increased in all groups except the yellow group, suggesting a compensatory defense response coordinated with transcriptional regulation of antioxidant pathways. The decline in functions related to cytosolic large ribosomal subunits, protein-RNA complex assembly, and protein-RNA complex organization in the blue and white groups, as observed in transcriptomic results, could be one of the key reasons for the severe cellular damage in these

groups. The reduction in ribosomal function slows down metabolic processes, leading to severe ROS accumulation, while the impaired function of protein receptors responsible for antioxidant enzyme production prevents timely ROS clearance, exacerbating cellular damage. Moreover, the downregulation of peroxisomal pathways in the white group weakens its ability to eliminate ROS, resulting in the most severe lipid peroxidation, which may explain the highest MDA levels observed in this group.

4.4. Ecological implications: Symbiosis disruption and coral reef risk assessment

The symbiotic relationship between reef-building corals and *Symbiodiniaceae* underpins the ecological stability and productivity of coral reef ecosystems (Matthews et al., 2020). *Symbiodiniaceae* supply up to 90 % of the energy required by their coral hosts through photosynthetic carbon translocation (Ros et al., 2020). Our findings reveal that MPs exposure, particularly from blue and white PS-MPs, induces severe physiological stress, oxidative damage, and metabolic suppression in *C. goreaui*, which could reduce its contribution to the host's energy budget. The enhanced immune response of symbiotic algae to their host also induces metabolic trade-offs, deplete energy reserves and consequently reduces photoprotective capacity (Tang et al., 2025). Through quantitative analytical reasoning, if algal photosynthate translocation decreases by ~90 %, key coral functions such as calcification (potentially reduced by 50–70 %), protein synthesis (reduced by ~40 %), reproduction (reduced by 30–50 %), and stress resilience (reduced thermal tolerance by 1–2 °C) are likely to be compromised (Dufault et al., 2013; Schoepf et al., 2013; Hughes et al., 2018). Impaired algal function compromises the translocation of essential photosynthates to corals, reducing host energy reserves and exacerbating susceptibility to bleaching and mortality under environmental stress (Suggett et al., 2017). Moreover, previous studies have shown that oxidative imbalance and metabolic reprogramming in *Symbiodiniaceae* are key early events preceding symbiosis breakdown (Wang et al., 2020). Therefore, the physiological impairments observed in this study could initiate or intensify coral bleaching phenomena, particularly under combined stressors such as warming or eutrophication.

It should be noted that the experimental MP concentrations used here (20 mg/L) are higher than the typical background levels in coral reef waters (~0.1–10 mg/L), but fall within reported hotspots of local pollution (John et al., 2022; Yu and Singh, 2023). This comparison suggests that even moderate environmental MPs may pose cumulative risks to algal symbionts and consequently the coral energy supply. Given the increasing ubiquity of MPs in coral reef habitats (Ding et al., 2019a; Kaandorp et al., 2023; Lin et al., 2024), our results underscore the urgent need to incorporate MP-induced symbiosis disruption into coral reef health assessments and risk models. This study provides critical mechanistic evidence linking MP pollution to coral-algal symbiosis destabilization, offering a novel dimension to the ecological risk framework for coral reefs. Future conservation strategies should thus prioritize mitigating MP contamination alongside addressing climate-induced stressors to safeguard reef ecosystem resilience.

5. Conclusion

This study shows that PS-MP toxicity to *C. goreaui* is strongly color-dependent, with blue and white particles—most divergent from algal pigmentation—causing the greatest physiological and molecular disruptions. Although photosynthesis was maintained via increased pigment content, much energy was diverted to counter oxidative stress, impairing growth and cellular homeostasis. Transcriptomic analysis revealed suppression of genes in key biosynthetic, metabolic, and energy pathways, especially fatty acid metabolism and ribosomal function. These findings shed light on the mechanisms by which microplastics compromise the health of *Symbiodiniaceae*, potentially destabilizing coral-algal mutualisms and reef resilience, highlighting the urgent need to mitigate MP contamination.

CRediT authorship contribution statement

Tianyi Niu: Writing – review & editing, Writing – original draft, Visualization, Validation, Software, Methodology, Investigation, Formal analysis, Data curation, Conceptualization. **Yating Yang:** Writing – review & editing, Validation, Software, Investigation. **Sanqiang Gong:** Writing – review & editing, Supervision, Methodology, Formal analysis, Conceptualization. **Kefu Yu:** Supervision, Resources, Project administration, Funding acquisition, Data curation. **Jiayuan Liang:** Writing – review & editing, Supervision, Resources, Project administration, Methodology, Funding acquisition, Formal analysis, Data curation, Conceptualization.

Declaration of competing interest

The authors declare that they have no known competing financial interests or personal relationships that could have appeared to influence the work reported in this paper.

Acknowledgements

This work was supported by the National Natural Science Foundation of China (42030502 and 42090041), the Self-Topic Project of Guangxi Laboratory on the Study of Coral Reefs in the South China Sea (GXLSCRSCS2023101), and the Science and Technology Project of Guangxi (Nos. AD17129063 and AA17204074).

Appendix A. Supplementary data

Supplementary data to this article can be found online at https://doi.org/10.1016/j.marpolbul.2025.118815.

Data availability

The data generated as part of this study are available upon request. The raw sequence data (a total of 18 RNA sequencing libraries) produced in this study were deposited in the Sequence Read Archive (PRJNA1255781) of the NCBI (https://www.ncbi.nlm.nih.gov/bioproject/PRJNA1255781).

References

Auta, H., Emenike, C., Fauziah, S., 2017. Screening of *Bacillus* strains isolated from mangrove ecosystems in peninsular Malaysia for microplastic degradation. Environ. Pollut. 231, 1552–1559.
Baker, D.M., Andras, J.P., Jordán-Garza, A.G., Fogel, M.L., 2013. Nitrate competition in a coral symbiosis varies with temperature among *Symbiodinium* clades. ISME J. 7 (6), 1248–1251.
Cao, D.-j., Shi, X.-d., Li, H., Xie, P.-p., Zhang, H.-m., Deng, J.-w., Liang, Y.-G., 2015. Effects of lead on tolerance, bioaccumulation, and antioxidative defense system of green algae, Cladophora. Ecotoxicol. Environ. Saf. 112, 231–237.
Cao, Q., Jiang, Y., Yang, H., Zhang, Y., Wei, W., 2022a. Comprehensive toxic effects of povidone iodine on microalgae Chlorella pyrenoidosa under different concentrations. Aquac. Res. 53 (5), 1833–1841.
Cao, Q., Sun, W., Yang, T., Zhu, Z., Jiang, Y., Hu, W., Wei, W., Zhang, Y., Yang, H., 2022b. The toxic effects of polystyrene microplastics on freshwater algae Chlorella pyrenoidosa depends on the different size of polystyrene microplastics. Chemosphere 308, 136135.
Chen, P., Powell, B.A., Mortimer, M., Ke, P.C., 2012. Adaptive interactions between zinc oxide nanoparticles and Chlorella sp. Environ. Sci. Technol. 46 (21), 12178–12185.
Chen, Q., Li, Y., Li, B., 2020. Is color a matter of concern during microplastic exposure to Scenedesmus obliquus and Daphnia magna? J. Hazard. Mater. 383, 121224.
Cheng, S., Keang, K., Cross, J.S., 2024. Evidence that microplastics at environmentally relevant concentration and size interfere with energy metabolism of microalgal community. J. Hazard. Mater. 476, 134995.
Croce, R., Van Amerongen, H., 2014. Natural strategies for photosynthetic light harvesting. Nat. Chem. Biol. 10 (7), 492–501.

Ding, J., Jiang, F., Li, J., Wang, Z., Sun, C., Wang, Z., Fu, L., Ding, N.X., He, C., 2019a. Microplastics in the coral reef systems from Xisha Islands of South China Sea. Environ. Sci. Technol. 53 (14), 8036–8046.
Ding, J., Li, J., Sun, C., Jiang, F., Ju, P., Qu, L., Zheng, Y., He, C., 2019b. Detection of microplastics in local marine organisms using a multi-technology system. Anal. Methods 11 (1), 78–87.
Dufault, A.M., Ninokawa, A., Bramanti, L., Cumbo, V.R., Fan, T.-Y., Edmunds, P.J., 2013. The role of light in mediating the effects of ocean acidification on coral calcification. J. Exp. Biol. 216 (9), 1570–1577.
Falkowski, P.G., Owens, T.G., 1980. Light—shade adaptation: two strategies in marine phytoplankton. Plant Physiol. 66 (4), 592–595.
Fisher, R., O'Leary, R.A., Low-Choy, S., Mengersen, K., Knowlton, N., Brainard, R.E., Caley, M.J., 2015. Species richness on coral reefs and the pursuit of convergent global estimates. Curr. Biol. 25 (4), 500–505.
Ford, P.W., Garshott, D.M., Narasimhan, M., Ge, X., Jordahl, E.M., Subramanya, S., Bennett, E.J., 2025. RNF10 and RIOK3 facilitate 40S ribosomal subunit degradation upon 60S biogenesis disruption or amino acid starvation. Cell Rep. 44 (3).
González-Pech, R.A., Bhattacharya, D., Ragan, M.A., Chan, C.X., 2019. Genome evolution of coral reef symbionts as intracellular residents. Trends Ecol. Evol. 34 (9), 799–806.
Greenway, J.A., Gerstenberger, S., 2010. An evaluation of lead contamination in plastic toys collected from day care centers in the Las Vegas Valley, Nevada, USA. Bull. Environ. Contam. Toxicol. 85, 363–366.
Guibert, I., 2024. Assisted evolution of algal symbionts to enhance coral reef bleaching tolerance: a success story. Glob. Chang. Biol. 30 (1), e17150.
Guillard, R., Hargraves, P., 1993. Stichochrysis immobilis is a diatom, not a chrysophyte. Phycologia 32 (3), 234–236.
Guzmán-Murillo, M.A., López-Bolaños, C.C., Ledesma-Verdejo, T., Roldan-Libenson, G., Cadena-Roa, M.A., Ascencio, F., 2007. Effects of fertilizer-based culture media on the production of exocellular polysaccharides and cellular superoxide dismutase by Phaeodactylum tricornutum (Bohlin). J. Appl. Phycol. 19, 33–41.
Han, C., Shi, C., Liu, L., Han, J., Yang, Q., Wang, Y., Li, X., Fu, W., Gao, H., Huang, H., 2024. Majorbio cloud 2024: update single-cell and multiomics workflows. Imeta 3 (4), e217.
Horie, Y., Mitsunaga, K., Yamaji, K., Hirokawa, S., Uaciquete, D., Ríos, J., Yap, C., Okamura, H., 2024. Variability in microplastic color preference and intake among selected marine and freshwater fish and crustaceans. Discov. Oceans. 1, 5.
Houlbrèque, F., Ferrier-Pagès, C., 2009. Heterotrophy in tropical scleractinian corals. Biol. Rev. 84 (1), 1–17.
Huang, Y., Yan, M., Xu, K., Nie, H., Gong, H., Wang, J., 2019. Distribution characteristics of microplastics in Zhubi reef from South China Sea. Environ. Pollut. 255, 113133.
Hughes, T.P., Baird, A.H., Bellwood, D.R., Card, M., Connolly, S.R., Folke, C., Grosberg, R., Hoegh-Guldberg, O., Jackson, J.B., Kleypas, J., 2003. Climate change, human impacts, and the resilience of coral reefs. science 301 (5635), 929–933.
Hughes, T.P., Kerry, J.T., Baird, A.H., Connolly, S.R., Dietzel, A., Eakin, C.M., Heron, S. F., Hoey, A.S., Hoogenboom, M.O., Liu, G., 2018. Global warming transforms coral reef assemblages. Nature 556 (7702), 492–496.
Jambeck, J.R., Geyer, R., Wilcox, C., Siegler, T.R., Perryman, M., Andrady, A., Narayan, R., Law, K.L., 2015. Plastic waste inputs from land into the ocean. Science 347 (6223), 768–771.
Jiang, S., Lu, H., Xie, Y., Zhou, T., Dai, Z., Sun, R., He, L., Li, C., 2025. Toxicity of microplastics and nano-plastics to coral-symbiotic alga (Dinophyceae Symbiodinium): evidence from alga physiology, ultrastructure. OJIP kinetics and multi-omics. Water Research 273, 123002.
Jin, W., Zhang, W., Tang, H., Wang, P., Zhang, Y., Liu, S., Qiu, J., Chen, H., Wang, L., Wang, R., 2024. Microplastics exposure causes the senescence of human lung epithelial cells and mouse lungs by inducing ROS signaling. Environ. Int. 185, 108489.
John, J., Nandhini, A., Velayudhaperumal Chellam, P., Sillanpää, M., 2022. Microplastics in mangroves and coral reef ecosystems: a review. Environ. Chem. Lett. 20 (1), 397–416.
Jones, L.A., Mannion, P.D., Farnsworth, A., Bragg, F., Lunt, D.J., 2022. Climatic and tectonic drivers shaped the tropical distribution of coral reefs. Nat. Commun. 13 (1), 3120.
Kaandorp, M., Lobelle, D., Kehl, C., Dijkstra, H., Van Sebille, E., 2023. Global mass of buoyant marine plastics dominated by large long-lived debris. Nat. Geosci. 16, 689–694.
Karpestam, E., Merilaita, S., Forsman, A., 2014. Natural levels of colour polymorphism reduce performance of visual predators searching for camouflaged prey. Biol. J. Linn. Soc. 112 (3), 546–555.
Kaur, J., Khan, S., Taleuzzaman, M., 2024. Carotenoids' neuroprotective effects via a free radical scavenging pathway, and they are being characterized, and evaluated as food additives. In: Microbial Vitamins and Carotenoids in Food Biotechnology. Elsevier, pp. 401–426.
Kazancı, Y., Alyürük, N., Alpergün, C., Kara, N., Baycan, N., Gündüz, O., 2025. Analysis of microplastic flux from the Gediz River to the Aegean Sea: a modeling study for environmental management. J. Environ. Manag. 391, 126412.
Kühn, S., Van Franeker, J.A., 2020. Quantitative overview of marine debris ingested by marine megafauna. Mar. Pollut. Bull. 151, 110858.
Lagarde, F., Olivier, O., Zanella, M., Daniel, P., Hiard, S., Caruso, A., 2016. Microplastic interactions with freshwater microalgae: hetero-aggregation and changes in plastic density appear strongly dependent on polymer type. Environ. Pollut. 215, 331–339.
Lambert, S., Sinclair, C.J., Bradley, E.L., Boxall, A.B., 2013. Effects of environmental conditions on latex degradation in aquatic systems. Sci. Total Environ. 447, 225–234.
Li, C., Wang, X., Liu, K., Zhu, L., Wei, N., Zong, C., Li, D., 2021a. Pelagic microplastics in surface water of the eastern Indian Ocean during monsoon transition period: abundance, distribution, and characteristics. Sci. Total Environ. 755, 142629.
Li, J., Ouyang, Z., Liu, P., Zhao, X., Wu, R., Zhang, C., Lin, C., Li, Y., Guo, X., 2021b. Distribution and characteristics of microplastics in the basin of Chishui River in Renhuai, China. Sci. Total Environ. 773, 145591.
Li, S., Wang, P., Zhang, C., Zhou, X., Yin, Z., Hu, T., Hu, D., Liu, C., Zhu, L., 2020. Influence of polystyrene microplastics on the growth, photosynthetic efficiency and aggregation of freshwater microalgae Chlamydomonas reinhardtii. Sci. Total Environ. 714, 136767.
Liang, J., Niu, T., Zhang, L., Yang, Y., Li, Z., Liang, Z., Yu, K., Gong, S., 2025. Polystyrene microplastics exhibit toxic effects on the widespread coral symbiotic Cladocopium goreaui. Environ. Res. 268, 120750.
Lin, J., Zhao, Y.-M., Zhan, Z.-G., Zheng, J.-Y., Zhou, Q.-Z., Peng, J., Li, Y., Xiao, X., Wang, J.-H., 2024. Microplastics in remote coral reef environments of the Xisha Islands in the South China Sea: source, accumulation and potential risk. J. Hazard. Mater. 469, 133872.
Liu, D., Guo, Z.-F., Xu, Y.-Y., Chan, F.K.S., Xu, Y.-Y., Johnson, M., Zhu, Y.-G., 2022. Widespread occurrence of microplastics in marine bays with diverse drivers and environmental risk. Environ. Int. 168, 107483.
Lu, H., Ni, Z., Wang, Y., Ye, S., 2025. Deposition characteristics of microplastics in coral reef fish with different feeding habits from the Xisha Islands waters, South China Sea. J. Environ. Manag. 378, 124736.
Matthews, J.L., Raina, J.B., Kahlke, T., Seymour, J.R., van Oppen, M.J., Suggett, D.J., 2020. Symbiodiniaceae-bacteria interactions: rethinking metabolite exchange in reef-building corals as multi-partner metabolic networks. Environ. Microbiol. 22 (5), 1675–1687.
Mellin, C., Brown, S., Cantin, N., Klein-Salas, E., Mouillot, D., Heron, S.F., Fordham, D.A., 2024. Cumulative risk of future bleaching for the world's coral reefs. Science. Advances 10 (26), eadn9660.
Ni, C., Buszczak, M., 2023. The homeostatic regulation of ribosome biogenesis. In: Seminars in cell & developmental biology. Elsevier, pp. 13–26.
Peixoto, R.S., Sweet, M., Bourne, D.G., 2019. Customized medicine for corals. Frontiers Media SA.
Peters, C.A., Thomas, P.A., Rieper, K.B., Bratton, S.P., 2017. Foraging preferences influence microplastic ingestion by six marine fish species from the Texas Gulf Coast. Mar. Pollut. Bull. 124 (1), 82–88.
Pogoreutz, C., Voolstra, C.R., Rädecker, N., Weis, V., Cardenas, A., Raina, J.-B., 2020. The coral holobiont highlights the dependence of cnidarian animal hosts on their associated microbes. In: Cellular Dialogues in the Holobiont. CRC Press, pp. 91–118.
Qian, H., Chen, W., Sheng, G.D., Xu, X., Liu, W., Fu, Z., 2008. Effects of glufosinate on antioxidant enzymes, subcellular structure, and gene expression in the unicellular green alga Chlorella vulgaris. Aquat. Toxicol. 88 (4), 301–307.
Qin, L., Xu, Y., Chen, J., Niu, T., Yu, K., Liang, J., 2023. Optimization of in vitro culture method for zooxanthellae associated with reef-building corals. Acta Microbiol Sin. 63 (04), 1658–1671. https://doi.org/10.13343/j.cnki.wsxb.20220656.
Reaka-Kudla, M.L., 1997. The global biodiversity of coral reefs: a comparison with rain forests. Biodiversity II: Understanding and protecting our biological resources 2, 551.
Ritchie, R.J., 2006. Consistent sets of spectrophotometric chlorophyll equations for acetone, methanol and ethanol solvents. Photosynth. Res. 89, 27–41.
Ros, M., Camp, E.F., Hughes, D.J., Crosswell, J.R., Warner, M.E., Leggat, W.P., Suggett, D.J., 2020. Unlocking the black-box of inorganic carbon-uptake and utilization strategies among coral endosymbionts (Symbiodiniaceae). Limnol. Oceanogr. 65 (8), 1747–1763.
Sanniyasi, E., Gopal, R.K., Raj, P.P., Kalaiselvi, R., Chandhinipriya, S., 2024. Extraction, characterization and the antioxidant activity of carotenoid pigment canthaxanthin from an aero-terrestrial and filamentous green microalga Trentepohlia sp. Bioresource Technology Reports 25, 101803.
Schoepf, V., Grottoli, A.G., Warner, M.E., Cai, W.-J., Melman, T.F., Hoadley, K.D., Pettay, D.T., Hu, X., Li, Q., Xu, H., 2013. Coral energy reserves and calcification in a high-CO2 world at two temperatures. PLoS One 8 (10), e75049.
Schreiber, U., Schliwa, U., Bilger, W., 1986. Continuous recording of photochemical and non-photochemical chlorophyll fluorescence quenching with a new type of modulation fluorometer. Photosynth. Res. 10, 51–62.
Sendra, M., Pereiro, P., Yeste, M.P., Mercado, L., Figueras, A., Novoa, B., 2021. Size matters: zebrafish (Danio rerio) as a model to study toxicity of nanoplastics from cells to the whole organism. Environ. Pollut. 268, 115769.
Shaw, D.G., Day, R.H., 1994. Colour-and form-dependent loss of plastic micro-debris from the North Pacific Ocean. Mar. Pollut. Bull. 28 (1), 39–43.
Shtykova, L., Ostrovskii, D., Jacobsson, P., Nydén, M., 2006. Interaction between medetomidine and alkyd resins: NMR and FTIR investigation of antifouling marine paint model systems. J. Appl. Polym. Sci. 99 (5), 2797–2809.
Smith, S., 1978. Coral-reef area and the contributions of reefs to processes and resources of the world's oceans. Nature 273 (5659), 225–226.
Su, L., Xue, Y., Li, L., Yang, D., Kolandhasamy, P., Li, D., Shi, H., 2016. Microplastics in taihu lake, China. Environ. Pollut. 216, 711–719.
Su, Y., Zhang, K., Zhou, Z., Wang, J., Yang, X., Tang, J., Li, H., Lin, S., 2020. Microplastic exposure represses the growth of endosymbiotic dinoflagellate Cladocopium goreaui in culture through affecting its apoptosis and metabolism. Chemosphere 244, 125485.
Suggett, D.J., Warner, M.E., Leggat, W., 2017. Symbiotic dinoflagellate functional diversity mediates coral survival under ecological crisis. Trends Ecol. Evol. 32 (10), 735–745.

Sun, Y., 2020. Studies on Physiological Response and Omics Analysis of Early Development of Tow Reff Corals to Ocean Warming and Acidification. University of Chinese Academy of Sciences, Doctor.
Tang, C.-H., Lin, C.-Y., Li, H.-H., 2025. Coral incorporating microplastics leads to a health-risking immunometabolic shift. Chemosphere 374, 144245.
Thompson, R.C., Olsen, Y., Mitchell, R.P., Davis, A., Rowland, S.J., John, A.W., McGonigle, D., Russell, A.E., 2004. Lost at sea: where is all the plastic? Science 304 (5672), 838.
Ursell, L.K., Metcalf, J.L., Parfrey, L.W., Knight, R., 2012. Defining the human microbiome. Nutr. Rev. 70 (suppl_1), S38–S44.
van Woesik, R., Kratochwill, C., 2022. A global coral-bleaching database, 1980–2020. Sci Data 9 (1), 20.
Venn, A.A., Loram, J.E., Douglas, A.E., 2008. Photosynthetic symbioses in animals. J. Exp. Bot. 59 (5), 1069–1080.
Wang, S., Chen, H., Zhou, X., Tian, Y., Lin, C., Wang, W., Zhou, K., Zhang, Y., Lin, H., 2020. Microplastic abundance, distribution and composition in the mid-West Pacific Ocean. Environ. Pollut. 264, 114125.
Wang, S., Feng, R., Hu, K., Hu, X., Qu, Q., Mu, L., Wen, J., Ma, C., 2024. Polystyrene microplastics facilitate formation of refractory dissolved organic matter and reduce CO2 emissions. Environ. Int. 190, 108809.
Wang, W., Ndungu, A.W., Li, Z., Wang, J., 2017. Microplastics pollution in inland freshwaters of China: a case study in urban surface waters of Wuhan, China. Sci. Total Environ. 575, 1369–1374.
Wang, Z., He, Y., Luo, M., Liu, S., Hou, J., Cao, B., An, X., 2025. Transfer toxicity of polystyrene microplastics in vivo: multi-organ crosstalk. Environ. Int. 109604.
Webster, N.S., Thomas, T., 2016. The sponge hologenome. MBio 7 (2). https://doi.org/10.1128/mbio. 00135-00116.
Wen, B., Liu, J.-H., Zhang, Y., Zhang, H.-R., Gao, J.-Z., Chen, Z.-Z., 2020. Community structure and functional diversity of the plastisphere in aquaculture waters: does plastic color matter? Sci. Total Environ. 740, 140082.
Woodhead, A.J., Hicks, C.C., Norström, A.V., Williams, G.J., Graham, N.A., 2019. Coral reef ecosystem services in the Anthropocene. Funct. Ecol. 33 (6), 1023–1034.
Wright, S.L., Thompson, R.C., Galloway, T.S., 2013. The physical impacts of microplastics on marine organisms: a review. Environ. Pollut. 178, 483–492.
Xia, F., Tan, Q., Qin, H., Wang, D., Cai, Y., Zhang, J., 2023. Sequestration and export of microplastics in urban river sediments. Environ. Int. 181, 108265.
Xu, J., Li, f., Meng, Q., Wang, F., 2019. The analysis of spectral Separability of different coral reef benthos and influence of pigments on coral spectra based on in situ data. Spectrosc. Spectr. Anal. 39 (08), 2462–2469.
Yu, K., 2018. Introduction to the Science of Coral Reefs, 1st ed. Science Press, Beijing.
Yu, R.-S., Singh, S., 2023. Microplastic pollution: threats and impacts on global marine ecosystems. Sustainability 15 (17), 13252.
Yue, F., Zhang, J., Xu, J., Niu, T., Lü, X., Liu, M., 2022. Effects of monosaccharide composition on quantitative analysis of total sugar content by phenol-sulfuric acid method. Front. Nutr. 9, 963318.
Zettler, E.R., Mincer, T.J., Amaral-Zettler, L.A., 2013. Life in the "plastisphere": microbial communities on plastic marine debris. Environ. Sci. Technol. 47 (13), 7137–7146.
Zhang, C., Chen, X., Wang, J., Tan, L., 2017. Toxic effects of microplastic on marine microalgae Skeletonema costatum: interactions between microplastic and algae. Environ. Pollut. 220, 1282–1288.
Zhang, J., Choi, C.E., Gao, F., 2024. Effects of microplastics on the rheological properties of sediment slurries in aquatic environments. Environ. Int. 193, 109095.
Zhang, K., Shi, H., Peng, J., Wang, Y., Xiong, X., Wu, C., Lam, P.K., 2018. Microplastic pollution in China's inland water systems: a review of findings, methods, characteristics, effects, and management. Sci. Total Environ. 630, 1641–1653.
Zhao, T., Tan, L., Han, X., Ma, X., Lin, K., Wang, J., 2023. Energy metabolism response induced by microplastic for marine dinoflagellate Karenia mikimotoi. Sci. Total Environ. 866, 161267.
Zhao, X., Wang, J., Yee Leung, K.M., Wu, F., 2022. Color: an important but overlooked factor for plastic photoaging and microplastic formation. Environ. Sci. Technol. 56 (13), 9161–9163.
Zheng, Y., Li, J., Zhu, H., Hu, J., Sun, Y., Xu, G., 2025. Endocytosis, endoplasmic reticulum, actin cytoskeleton affected in tilapia liver under polystyrene microplastics and BDE153 acute co-exposure. Comp. Biochem. Physiol., Part C: Toxicol. Pharmacol. 289, 110117.
Zhou, Z., Zhang, P., Zhang, G., Wang, S., Cai, Y., Wang, H., 2021. Vertical microplastic distribution in sediments of Fuhe River estuary to Baiyangdian wetland in northern China. Chemosphere 280, 130800.

Algal Research 91 (2025) 104187



Contents lists available at ScienceDirect

Algal Research

journal homepage: www.elsevier.com/locate/algal





The stress response strategies of two typical coral Symbiodiniaceae (*Cladocopium goreaui* and *Durusdinium trenchii*) under abnormal temperatures

Jiayuan Liang [a,*,1], Liangyun Qin [a,1], Li Zhang [c,1], Yongqian Xu [a], Tianyi Niu [a], Zhicong Li [a], Yating Yang [a], Zhuqing Liang [a], Kefu Yu [a,b,*], Sanqiang Gong [d]

[a] *Guangxi Laboratory on the Study of Coral Reefs in the South China Sea, School of Marine Sciences, Guangxi University, Nanning 530004, China*
[b] *Southern Marine Science and Engineering Guangdong Laboratory (Guangzhou), Guangzhou 510030, China*
[c] *School of Resources, Environment and Materials, Guangxi University, Nanning 530004, China*
[d] *Key Laboratory of Tropical Marine Bio-resources and Ecology & Guangdong Provincial Key Laboratory of Applied Marine Biology, South China Sea Institute of Oceanology, Chinese Academy of Sciences, Guangzhou 510301, China*

ARTICLE INFO

Keywords:
Coral reefs
Symbiodiniaceae
Environmental adaptability
Global change
South China Sea

ABSTRACT

Temperature stress disrupts the coral–Symbiodiniaceae symbiosis and contributes to coral bleaching. Symbiodiniaceae, essential symbionts for reef-building corals, provide over 90 % of the coral holobionts photosynthetic energy. This study examined the thermal response strategies of two Symbiodiniaceae types, *Cladocopium goreaui* (*C. goreaui*) and *Durusdinium trenchii* (*D. trenchii*), at high (34 °C) and low (16 °C) temperatures. *C. goreaui* exhibited heat sensitivity, with reduced cell density, impaired photochemical efficiency of photosystem II (PSII) (*Fv/Fm*), pigment loss, and chloroplast degradation. In contrast, *D. trenchii* maintained photosynthetic performance and upregulated proteins related to heat shock response, antioxidant defense, and membrane stability. Under cold stress, both species showed moderate physiological changes. *C. goreaui* activated pathways associated with redox homeostasis and the TCA cycle, indicating enhanced cold tolerance. *D. trenchii* primarily responded by upregulating RNA splicing-related pathways, suggesting an adaptive post-transcriptional regulation mechanism. These results highlight distinct thermal response strategies and provide insight into species-specific resilience among Symbiodiniaceae under climate stress.

1. Introduction

The cornerstone of coral reef ecosystems is the "holobiont" composed of coral polyps and their associated microorganisms, which include Symbiodiniaceae, bacteria, fungi, and protists. Among these, Symbiodiniaceae contribute >95 % of the photosynthetic products (e.g., amino acids, glucose, glycerol) to the "holobiont" [1,2]. Simultaneously, they acquire the essential carbon dioxide and nutrients (such as ammonia and phosphate) necessary for their survival and for photosynthesis from the coral host [3]. The stable symbiosis between coral hosts and Symbiodiniaceae is crucial for the health of coral reef ecosystems [4]. When the surrounding environment undergoes abnormal changes, the stability of the "holobiont" is compromised, leading to coral bleaching and, ultimately, death. Among the various stresses, abnormal seawater temperature is a primary factor affecting the stability of the "holobiont". However, extensive field survey data indicate that not all coral species undergo bleaching and death in the face of extreme temperature stress. Some species exhibit resilience to high-temperature and survive under such conditions [5,6]. These temperature resistance characteristics are closely related to both the coral host and the specific Symbiodiniaceae species involved [7–11].

LaJeunesse et al. [12] proposed that the Symbiodiniaceae clades actually represent up to 15 distinct species in morphologically or phylogenetically. Physiological characteristics and environmental tolerances vary significantly among different species of Symbiodiniaceae, aiding coral hosts in resisting external environmental stressors. Recent research generally suggests that some species within the genus *Durusdinium* (clade D), such as *D. trenchii* in the D1and D1a/D1–4 clades, are

* Corresponding authors.
E-mail addresses: jyliang@gxu.edu.cn (J. Liang), kefuyu@scsio.ac.cn (K. Yu).
[1] These authors contributed to the work equally and should be regarded as co-first authors.

https://doi.org/10.1016/j.algal.2025.104187
Received 16 January 2025; Received in revised form 15 June 2025; Accepted 2 July 2025
Available online 17 July 2025
2211-9264/© 2025 Elsevier B.V. All rights are reserved, including those for text and data mining, AI training, and similar technologies.

evolved to thrive in extremely high temperatures and high-turbidity environments [13]. When establishing symbiotic relationships with cnidarians (corals and anemones), these species can resist the breakdown of the symbiotic system induced by stress from abnormal environmental conditions, known as coral bleaching [14]. Research by Manzello et al. [15] demonstrated that *D. trenchii* improves the thermal resilience of the coral *Orbicella faveolata*, enabling this species to persist through extensive thermal bleaching episodes in the Florida Keys. *Durusdinium* are widely distributed in the Indo-Pacific and are also found in coral reefs in the South China Sea at mid to low latitudes [16]. On the other hand, *Cladocopium* (clade C) is one of the most diverse genera of Symbiodiniaceae, with different subclades exhibiting distinct physiological characteristics. Subclade C1 contains several species that form symbiotic relationships with corals in the Indo-Pacific region, often displaying high photochemical efficiency of PSII (*Fv/Fm*) and helping coral hosts tolerate seasonally low temperatures and high-nutrient conditions [17]. Species within the C15 subclade mainly form stable symbiotic relationships with corals in the genus *Porites*, which tolerate high temperatures and turbidity [18].

In various coral reef regions in the South China Sea at different latitudes, including the Nansha Islands, Xisha Islands, Luhuitou in Sanya, Leizhou Peninsula, Weizhou Island, Daya Bay, and Dongshan Island, the dominant Symbiodiniaceae genera associated with reef-building corals are *Cladocopium* (Clade C) and *Durusdinium* (Clade D) [16]. At the subclade level, there are significant differences in the composition of Symbiodiniaceae communities among coral species in coral reef regions at different latitudes [19]. Specifically, in relatively high-latitude reef-building corals in the South China Sea, the Symbiodiniaceae community is predominantly composed of the C1 subclade [20]. In contrast, in mid- to low-latitude reef-building corals, the Symbiodiniaceae community is dominated by diverse subclade types, including the C50, Cspc, C15, C1, and D1 subclades [18,20,21]. Overall, the community composition of Symbiodiniaceae in South China Sea corals shows a spatial distribution pattern transitioning from the dominance of the C1 subclade at higher latitudes to the codominance of heat-tolerant Symbiodiniaceae such as C15, C3u, and D1 at mid- to low latitudes [16].

The evidence above indicates that the unique identity of Symbiodiniaceae influences the adaptability of corals to their environment [22]. However, the specific biological functions of different species of Symbiodiniaceae, especially their response strategies under temperature changes, have not been fully elucidated. Due to the unique symbiotic relationship between Symbiodiniaceae and corals, very few species can be cultured outside their host organisms for an extended period. Ahles et al. [23] conducted in vitro cultivation studies on Symbiodiniaceae from 70 different hosts and reported that <25 % could survive briefly in ASP-8A medium. Using f/2 medium, Kinzie [24] also reported that only a few species of Symbiodiniaceae survived in vitro cultivation. Additionally, K medium [24] and ISM medium [25] have been applied for in vitro cultivation of Symbiodiniaceae but with suboptimal results.

In the preliminary stages of our research, two Symbiodiniaceae strains, were isolated and cultured: a *Cladocopium* species (C1 type) from *Acropora pruinosa* in the relatively high-latitude coral reef areas of Weizhou Island; and a *Durusdinium* species (D1 type) from *Galaxea fascicularis* in the low-latitude coral reef area of the Xisha Islands in the South China Sea [26]. This study focused on these species, aiming to explore their response strategies under abnormal temperatures of 34 °C and 16 °C. The goal of this study was to gain a deeper understanding of the mechanisms of environmental adaptation in coral reefs and future evolutionary trends from the perspective of these key symbiotic partners.

2. Materials and methods

2.1. Cultivation of and experimental design for C. goreaui and D. trenchii

The Symbiodiniaceae strains used in this study were isolated and cultured from coral reefs in the South China Sea in the preliminary phase of the project. The species were identified as *Cladocopium goreaui* (*C. goreaui*) (100 %) and *Durusdinium trenchii* (*D. trenchii*) (100 %) through ITS and LSU sequence determination and homology search [26], respectively. Prior to the experiments, Symbiodiniaceae strains were cultured in L1 medium at 25 °C under a light intensity of 90 μmol photons m^{-2} s^{-1}, the Symbiodiniaceae were cultivated to the mid-logarithmic phase to ensure optimal growth conditions. For the temperature stress experiments, mid-logarithmic *C. goreaui* and *D. trenchii* cultures were centrifuged at 800 ×*g* for 5 min, the supernatant was removed, and the cells were transferred to 500 mL conical flasks containing 300 mL of L1 medium. The initial cell concentration was adjusted to 1.0×10^5 cells/mL, and the cultures were maintained for 1 day before the temperature stress experiment was initiated. The lowest monthly mean sea surface temperature (SST) was 17.3 °C between 1960 and 2001 [27]. SST below 18 °C in winter was found to severely affect corals [28]. By analysing satellite SST data from 1985 to 2019 (https://coralreefwatch.noaa.gov), we found that the SST at Weizhou Island is generally around 30 °C in summer and 19 °C in winter. The SST around Weizhou Island has been increasing at a rate of 0.33 °C/10 yr over the past decades [27]. Different temperature conditions were used, including a normal cultivation temperature of 25 °C (control group), an abnormally high temperature of 34 °C (to simulate possible future seawater temperatures [29]), and an abnormally low temperature of 16 °C (to simulate seawater temperatures under extreme cold conditions in winter). On day 0, cultures of both *C. goreaui* and *D. trenchii* were transferred into conical flasks. For the high- and low-temperature groups, the temperature was adjusted from 25 °C by increasing or decreasing 1 °C every 8 h until the target temperature was reached, followed by a 10-day temperature stress period. Each group included three biological replicates. Measurements of cell density, *Fv/Fm*, and chlorophyll content were conducted at 12:00 PM on days 1, 4, 7, 10, and 14.

2.2. Cell density and growth rate determination

A 1 mL aliquot of algal culture was fixed by adding 100 μL of formaldehyde reagent. Cell counting for Symbiodiniaceae was performed using a plankton counting chamber under an upright optical microscope (Nikon, ECLIPSE Ni-E). The data were recorded, and cell density was calculated. The growth rate (μ) was determined using the formula $\mu = \ln(N2/N1)/(t2\text{-}t1)$, where μ is the growth rate, N2 and N1 are the cell densities at times t2 and t1, respectively, which are calculated by the stress temperature arrival time t1, that is, the initial density under stress conditions on day 4.

2.3. Determination of the photochemical efficiency of PSII (Fv/Fm)

The *Fv/Fm* value can indicate the energy conversion efficiency of PSII in photosynthetic organisms. According to the methods of Guo et al. [30], *Fv/Fm* was measured during dark adaptation for 30 min with a Moni-DA Plant Monitoring PAM (WALZ, Germany), the maximum fluorescence value (*Fm*) was determined by a 0.6 s saturation pulse (approximately 8000 μmol $m^{-2}{\cdot}s^{-1}$).

2.4. Determination of photosynthetic pigment levels

Ten milliliters of algal culture was centrifuged at 5000 ×*g* for 5 min, after which the supernatant was removed. Then, 1 mL of 100 % methanol solution was added, followed by vortexing and shaking. The mixture was stored in the dark at 4 °C for 24 h. After extraction, the absorbance at 480 nm, 510 nm, 630 nm, 664 nm, and 750 nm was measured using a spectrophotometer (Thermal). The concentrations of chlorophyll *a* (Chl a) and carotenoids (CARs) in the Symbiodiniaceae were calculated using the formulas provided by Ritchie et al. [31].

$$\text{Chlorophyll a}(\mu g/ml) = 13.6849 \times (A_{664} - A_{750}) - 3.4551 \times (A_{630} - A_{750})$$

$$\text{Carotenoids}(\mu g/ml) = 7.6 \times (A_{480} - A_{750}) - 1.49 \times (A_{510} - A_{750})$$

2.5. Transmission electron microscopy (TEM)

On the 14th day, *C. goreaui* and *D. trenchii* cells under different temperature stress were collected for transmission electron microscopy (TEM) analysis. Thirty milliliters of algal culture was centrifuged using a Sigma horizontal-rotor centrifuge at 800 ×*g* for 10 min to collect the cells. The cells were washed twice with 0.1 mol/L phosphate-buffered saline (PBS) (pH = 7.4) for 10 min each time. Then, the cells were fixed in a solution of glutaraldehyde-polyformaldehyde (2.5 %–2 %) (P1116; Beijing Solebao Technology Co., Ltd.) at room temperature in the dark for 2 h and stored at 4 °C. The fixed cells were rinsed three times with PBS for 15 min each time. Subsequently, the cells were fixed in 1 % osmium tetroxide prepared in PBS at room temperature in the dark for 2 h, followed by centrifugation and washing with PBS three times for 15 min each time. The samples were dehydrated in an ethanol gradient (30 %, 50 %, 70 %, 80 %, 95 %, and twice in 100 %, each for 20 min) and embedded in 812 embedding resin (SPI, US). The embedding blocks were sectioned using an EM UC7 ultramicrotome (Leica), stained with uranyl acetate and lead citrate, and observed and photographed using an HT7800 transmission electron microscope (Hitachi). Images were processed using ImageJ software to calculate the proportion of chloroplast area within the cells, with five cells analyzed for statistical purposes.

2.6. Proteomic analysis

Due to the complete bleaching of *C. goreaui* algal cells under heat stress in the later stages of the experiment, making it impossible to obtain sufficient quantity for proteomic analysis, we opted to conduct proteomic analysis on *C. goreaui* under cold stress and normal temperature, as well as on *D. trenchii* algal cells under all three cultivation conditions. Approximately 120 mL of algal culture was centrifuged at 3000 ×*g* for 5 min at 4 °C using a horizontal rotor. The pellet was washed twice with 0.1 mol/L PBS (pH = 7.4) at 4 °C for 5 min each time. After freezing in liquid nitrogen for half an hour, the samples were stored at −80 °C.

The samples were subsequently transported on dry ice to Shanghai Meiji Biomedical Technology Co., Ltd., for label-free quantitative proteomic analysis. Frozen samples were transferred into MP shaker tubes, supplemented with 1 % polyvinylpolypyrrolidone (PVPP) and an appropriate volume of BPP buffer. Samples were homogenized three times (40 s each) using a high-throughput tissue grinder. The homogenate was centrifuged at 12,000 ×*g* for 20 min at 4 °C, and the supernatant was collected. The supernatant was mixed with an equal volume of Tris-saturated phenol and vortexed at 4 °C for 10 min. After centrifugation (12,000 ×*g*, 20 min, 4 °C), the phenol phase was retained and re-extracted with an equal volume of BPP buffer. The mixture was vortexed again for 10 min and centrifuged under the same conditions. The phenol phase was then mixed with five volumes of pre-chilled ammonium acetate in methanol and incubated overnight at −20 °C to precipitate proteins. The next day, samples were centrifuged, and the supernatant was discarded. The protein pellet was washed twice with 90 % pre-chilled acetone, with centrifugation after each wash (12,000 ×*g*, 20 min, 4 °C). The final pellet was dissolved in lysis buffer (8 M urea, 1 % SDS, with protease inhibitor cocktail), sonicated on ice for 2 min, and centrifuged. The protein-containing supernatant was collected, quantified using the BCA assay, and assessed by SDS-PAGE.

After reducing, alkylating, and enzymatic digesting the protein samples, peptide desalting and quantification were performed. According to the quantification results of peptides, peptides with a concentration of 0.1 μg/μL were dissolved in mass spectrometry loading buffer (2 % acetonitrile, 0.1 % formic acid) for mass spectrometry analysis. The chromatographic separation was performed using a mobile phase system gradient composed of 2 % acetonitrile and 0.1 % formic acid (solvent A) and 80 % acetonitrile and 0.1 % formic acid (solvent B). The gradient elution of solvent B increased from 3 % at 0 min to 28 % at 45 min, then increased to 44 % at 50 min, further increased to 90 % at 55 min, and finally ended the program at 60 min, with a total chromatographic separation time of 60 min. The post-separation samples were analyzed by timsTOF Pro2 mass spectrometer (Brucker) for DDA mass spectrometry analysis. The detection mode was positive ion, with the ion source voltage set at 1.5 kV, and both MS and MS/MS were detected and analyzed using TOF. The mass spectrometry scan range was set to 100–1700 *m/z*. The data acquisition mode adopted Parallel Accumulation Serial Fragmentation (PASEF) mode.

The data analysis was performed using MaxQuant software (version 2.0.3.1). The search was based on trypsin/P digestion, with methylation of cysteine as a fixed modification, N-terminal acetylation and methionine oxidation as variable modifications, and a maximum missed cleavage value of 2. The global false discovery rate (FDR) for peptide identification was set to 0.01. The annotations of proteins from the *C. goreaui* and *D. trenchii* genome databases were used for proteomic analysis of Symbiodiniaceae. Differentially expressed proteins (DEPs) were identified based on a fold change (FC) > 1.2 for upregulated proteins and FC < 0.83 for downregulated proteins (default for label-free items). The statistical analysis of protein samples was performed using independent sample *t*-tests, with a *p* value threshold of <0.05 (default value for proteomics). R software was used to analyze the relationship between the differential expression of proteins and quantity and to generate PCA plots. For the proteins in the experimental samples, Blast2GO (2.5.0) software was used for Gene Ontology (GO) functional annotation, KOBAS (2.1.1) was used for Kyoto Encyclopedia of Genes and Genomes (KEGG) pathway functional annotation, hmmsca was used for Pfam functional annotation (identifying protein domains), Diamond (V0.8.3.37.99) was used for Clusters of Orthologous Groups of proteins (EggNOG) and Non-Redundant Protein Sequence Database (NR) functional annotation, and MultiLoc2 was used for Subcellular Localization (Subloc) prediction.

Enrichment analysis of the DEPs was performed for GO and KEGG pathways using Goatools for GO enrichment. Fisher's exact test was used, and the *p* values were corrected based on the Benjamini–Hochberg method. GO functions were considered significantly enriched if the corrected p value (FDR) was <0.05. Python-based analysis was used for KEGG pathway enrichment, with Fisher's exact test and Benjamini–Hochberg correction applied and a threshold of 0.05 for corrected p values.

2.7. Data statistics and analysis

The data obtained from the experiments, including the photochemical efficiency of PSII (*Fv/Fm*) and Symbiodiniaceae growth rate, were processed using Microsoft Excel. The results are presented as the mean ± standard deviation (mean ± SD). The statistical analysis was performed using SPSS 24.0 software, employing the Mann–Whitney *U* test for nonparametric analysis, with the significance level set at 0.05. Graphs were generated using Origin 2023.

3. Results

3.1. Analysis of the algal cell density and growth rate

When subjected to abnormal high-temperature stress at 34 °C, the density of the *C. goreaui* strain exhibited an overall decreasing trend, and after day 10, its value was significantly lower than the initial density ($P < 0.05$). In contrast, under normal temperature conditions (25 °C), the algal cell density increased (Supporting Information Fig. S1A). Under abnormal high-temperature stress, the density of *D. trenchii* increased, even surpassing the growth observed under normal temperature

condition (Supporting Information Fig. S1B); which also increased the growth rate analysis showed that the growth rate of *C. goreaui* decreased from 0.119 (25 °C) to −0.125 (34 °C), while that of *D. trenchii* decreased from 0.10 ± 0.01 (25 °C) to 0.066 ± 0.008 (34 °C), though the latter change was not significant ($P > 0.05$) (Fig. 1A). However, when subjected to abnormal low-temperature stress at 16 °C, the cell density of *C. goreaui* remained unchanged compared to 25 °C (Supporting Information Fig. S1A), and the growth rate was essentially 0. *D. trenchii* still exhibited slow growth, with a growth rate of 0.055 ± 0.010 (Supporting Information Fig. S1B). From the perspective of algal cell growth, *D. trenchii* was more resistant to both abnormal high- and low-temperature stress than *C. goreaui* was.

3.2. Analysis of the Fv/Fm value and photosynthetic pigments

Under high-temperature stress at 34 °C, the *Fv/Fm* values of *C. goreaui* gradually decreased. When the stress temperature reached 34 °C on the 4th day, the *Fv/Fm* value decreased from 0.66 ± 0.03 to 0.63 ± 0.02 and dropped to 0 on the 14th day. (Fig. 1B). However, under low-temperature stress at 16 °C, the *Fv/Fm* value of *C. goreaui* decrease during the initial 4 days of cooling from 0.61 to 0.55 but then remained mostly stable, reaching 0.54 ± 0.04 by the 14th day (Fig. 1B). Compared to *C. goreaui*, *D. trenchii* showed no significant inhibition of *Fv/Fm* under 34 °C high-temperature stress, with the value declining from 0.65 ± 0.01 to 0.58 ± 0.02 from the 1st day to the 14th day (a decrease of approximately 10 %) (Fig. 1C). However, under 16 °C low-temperature stress, the *Fv/Fm* value was significantly reduced, showing a continuous downward trend from 0.62 ± 0.01 on the 1st day to 0.32 ± 0.03 on the 14th day (a decrease of 47 %) (Fig. 1C).

When *C. goreaui* was subjected to high-temperature stress, the Chl a concentration gradually decreased, and the CAR concentration showed an overall decreasing trend. On the 14th day of 34 °C high-temperature stress, the Chl a concentration suddenly decreased by 90.22 % (Fig. 2A), while the CAR concentration decreased by only 29.56 % (0.22 ± 0.08) (Fig. 2B). However, under 16 °C low-temperature stress, the Chl a concentration exhibited an overall decreasing trend, reaching 0.42 ± 0.03 on the 14th day (a decrease of 27.16 %) (Fig. 2A). However, the CAR concentration showed an overall increasing trend, with an increase of 62.42 % (0.37 ± 0.01) on the 10th day (Fig. 2B). Compared to *C. goreaui*, *D. trenchii* showed no significant decrease in Chl a and CAR concentrations under 34 °C high-temperature stress compared to the control group; instead, both pigments showed a marked increase during the initial phase of the experiment. However, under 16 °C low-temperature stress, both Chl a and CAR concentrations gradually decreased, reaching 0.51 ± 0.05 (a decrease of 25.92 %) (Fig. 2C) and 0.42 ± 0.06 (a decrease of 6.49 %) (Fig. 2D) on the 14th day. Therefore, changes in photosynthetic pigments and *Fv/Fm* values indicate that *D. trenchii* has a tolerance to high temperature, while *C. goreaui* has a tolerance to low temperature.

3.3. Intracellular structure analysis of Symbiodiniaceae

The integrity of the cell structure is crucial for normal growth and reproduction. After 10 days of exposure to 34 °C high-temperature stress, *C. goreaui* exhibited morphological deformities, including shrinkage, invagination, separation of the cell wall, and disintegration of chloroplasts and chromatin, ultimately leading to cell death (Fig. 3A). However, when subjected to 16 °C low-temperature stress for 10 days, *C. goreaui* maintained an intact cell morphology, and the accumulation of lipids was observed within the cells (Fig. 3A). Due to severe cell necrosis and chloroplast disintegration caused by abnormally high temperatures, it was not possible to analyze the proportion of the chloroplast area in *C. goreaui* cells. However, under low-temperature stress conditions, the proportion of the chloroplast area in *C. goreaui* cells significantly decreased compared to that in the control group ($P < 0.05$), dropping from the normal state of 16.8 ± 3.6 % to 8.3 ± 2.0 %. In contrast to *C. goreaui*, *D. trenchii* maintained good integrity with no severe deformities after 10 days of exposure to 34 °C high-temperature stress (Fig. 3B). However, low-temperature stress resulted in cell deformities and sparse chloroplasts in *D. trenchii*. Analysis of the proportion of the chloroplast area inside the cells revealed a significant decrease under abnormal temperature stress (from 41.8 ± 2.2 % to 36.3 ± 3.0 % in the high-temperature group and from 41.8 ± 2.2 % to 30.7 ± 3.6 % in the low-temperature group). Importantly, no lipid accumulation was observed within the algal cells under these conditions (Fig. 3B). Thus, lipid accumulation inside algal cells may constitute an adaptive strategy employed by *C. goreaui* in response to abnormal low-temperature stress. At present, our results primarily reflect changes in chloroplast morphology rather than direct evidence of functional impairment. These morphological alterations may be associated with changes in photosynthetic performance.

3.4. Proteomic analysis

Based on the response of the two types of Symbiodiniaceae, *C. goreaui* and *D. trenchii*, to abnormal temperatures (in terms of growth rate, *Fv/Fm*, photosynthetic pigment concentration, and intracellular structural changes), it was found that the former could not maintain integrity under continuous high-temperature stress for 13 days, with severe disintegration of intracellular structures observed; in contrast, the latter exhibited greater tolerance under high-temperature stress. Additionally, after 13 days of low-temperature stress at 16 °C, both *C. goreaui* and *D. trenchii* could maintain structural integrity but showed different response patterns. Therefore, to explore the protein molecular response mechanisms of *C. goreaui* under low-temperature stress and *D. trenchii* under high/low-temperature stress, cells of *C. goreaui* subjected to low-temperature stress and normal temperature culture on the 14th day, as well as cells of *D. trenchii* subjected to high/low-temperature stress and normal temperature culture, were collected simultaneously for proteomic analysis.

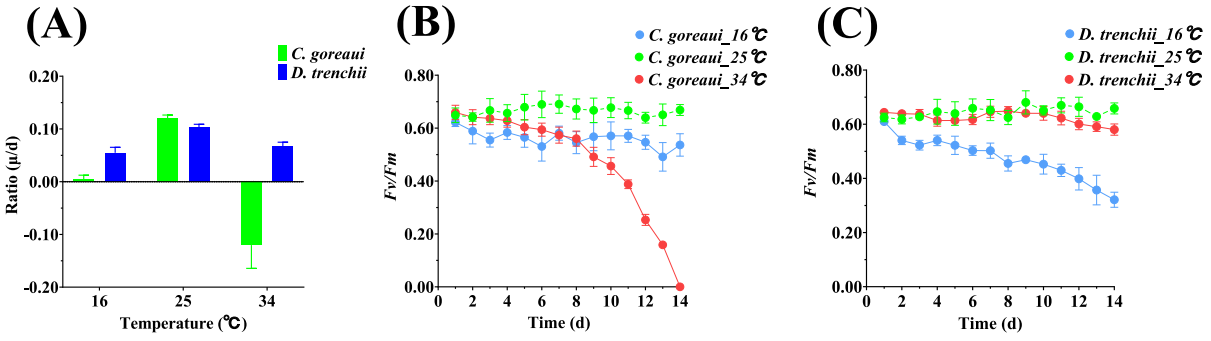


Fig. 1. Impact of temperature stress on the growth rate (μ) and the *Fv/Fm* value of Symbiodiniaceae. (A) Impact of temperature stress on the growth rate (μ) of *C. goreaui* and *D. trenchii*. (B) Influence of temperature stress on the *Fv/Fm* value of *C. goreaui*. (C) Influence of temperature stress on the *Fv/Fm* value of *D. trenchii*.

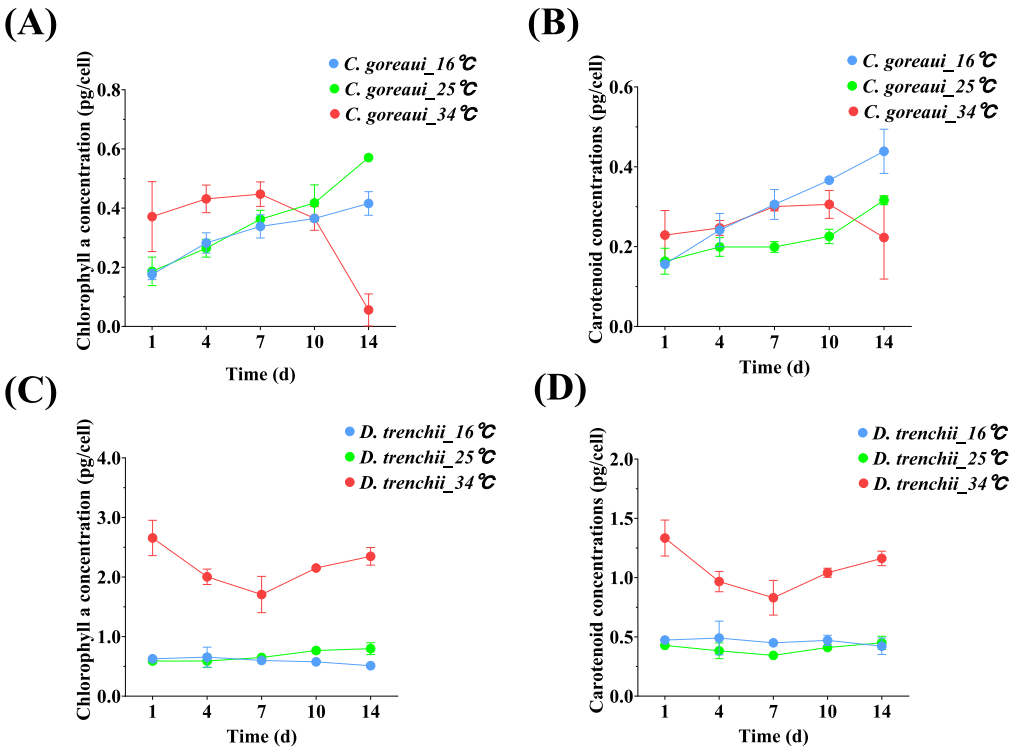


Fig. 2. Changes in the photosynthetic pigments of Symbiodiniaceae under high/low-temperature stress. (A) Changes in the Chl a Concentration of *C. goreaui* under High- and Low-Temperature Stress. (B) Changes in the CAR Concentration of *C. goreaui* under High- and Low-Temperature Stress. (C) Changes in the Chl a Concentration of *D. trenchii* under High- and Low-Temperature Stress. (D) Changes in the CAR Concentration of *D. trenchii* under High and Low-Temperature Stress.

With MaxQuant software used for database search analysis, a total of 15 samples yielded 32,461 spectra, with 31,339 unique spectra matching 4782 peptides and 1336 proteins. The number of proteins assembled into different protein groups in all the samples was 1030 (Supporting Information Fig. S2A). Among all the detected proteins, 893 were annotated by EggNOG, 856 by GO, 746 by KEGG, 883 by Pfam, and 1030 by subcellular localization (Subloc) (Supporting Information Fig. S2B). Specific functional annotations of all proteins are provided in Supporting Information Figs. S3-S7. Among the detected proteins, significant DEPs were recovered under low-temperature stress in *C. goreaui* compared to the control group, low-temperature stress in *D. trenchii* compared to the control group, and high-temperature stress in *D. trenchii* compared to the control group; the numbers of uniquely expressed proteins were 95, 183, and 179, and the total numbers of significant DEPs were 237, 267, and 268, respectively (Fig. 4A, B, C). The results for the upregulated and downregulated proteins are shown in Fig. 4D. PCA indicated that the effect of species identity (PC1 45.5 %) was greater than the effect of abnormal temperature (PC2 14.5 %) on these species (Fig. 4E). Similarly, within the same species, high/low-temperature stresses did not affect them to the same extent (Supporting Information Fig. S8).

3.4.1. GO enrichment analysis

We conducted enrichment analysis of DEPs in three major GO categories: Biological Processes (BP), Cellular Components (CC), and Molecular Functions (MF). The results revealed that under low-temperature stress, the top 10 significantly enriched GO terms for DEPs in *C. goreaui* were (Fig. 5): purine-containing compound biosynthetic process; phosphoric ester hydrolase activity; IMP metabolic process; 4 iron, 4 sulfur cluster binding; cellular metabolic compound salvage; metal ion binding; metal cluster binding; iron–sulfur cluster binding; ribonucleotide biosynthetic process; ribose phosphate biosynthetic process.

Under low-temperature stress, the top 10 significantly enriched GO terms for DEPs in *D. trenchii* were (Fig. 5): nuclear protein-containing complex; spliceosomal snRNP complex; small nuclear ribonucleoprotein complex; Sm-like protein family complex; U2 snRNP; ribonucleoprotein complex subunit organization; ribonucleoprotein complex assembly; RNA binding; spliceosomal complex assembly; protein–containing complex assembly.

Under high-temperature stress, the top 10 significantly enriched GO terms for DEPs in *D. trenchii* were (Fig. 5): ubiquitin-like protein transferase activity; response to inorganic substance; sulfur compound metabolic process; thioester biosynthetic process; purine nucleoside bisphosphate biosynthetic process; nucleoside bisphosphate biosynthetic process; acyl–CoA biosynthetic process; ribonucleoside bisphosphate biosynthetic process; organic hydroxy compound biosynthetic process; response to metal ion.

3.4.2. KEGG enrichment analysis

Likewise, to further understand the impact of abnormal temperature stress on Symbiodiniaceae cells and their related pathways, pathway enrichment analysis was conducted for the top 10 most significantly enriched KEGG pathways. An adjusted *P* value (*P*adjust) <0.05 was considered to indicate a significantly enriched KEGG pathway function. The results indicated that under abnormal low-temperature stress, the DEPs were significantly enriched in *C. goreaui* were (Fig. 6): Citrate cycle (TCA cycle); ribosome; inositol phosphate metabolism; oxidative phosphorylation; spliceosome; purine metabolism; butanoate metabolism; nitrogen metabolism; valine, leucine and isoleucine degradation; glutathione metabolism.

When subjected to abnormal low-temperature stress, *D. trenchii* exhibited significant enrichment of DEPs in pathways such as Spliceosome; ribosome biogenesis in eukaryotes; peroxisome; proteasome; plant–pathogen interaction; nicotinate and nicotinamide metabolism; glycerophospholipid metabolism; biosynthesis of cofactors; arginine biosynthesis; propanoate metabolism (Fig. 6).

For *D. trenchii* under abnormally high-temperature stress, the DEPs were significantly enriched in RNA degradation; pantothenate and CoA

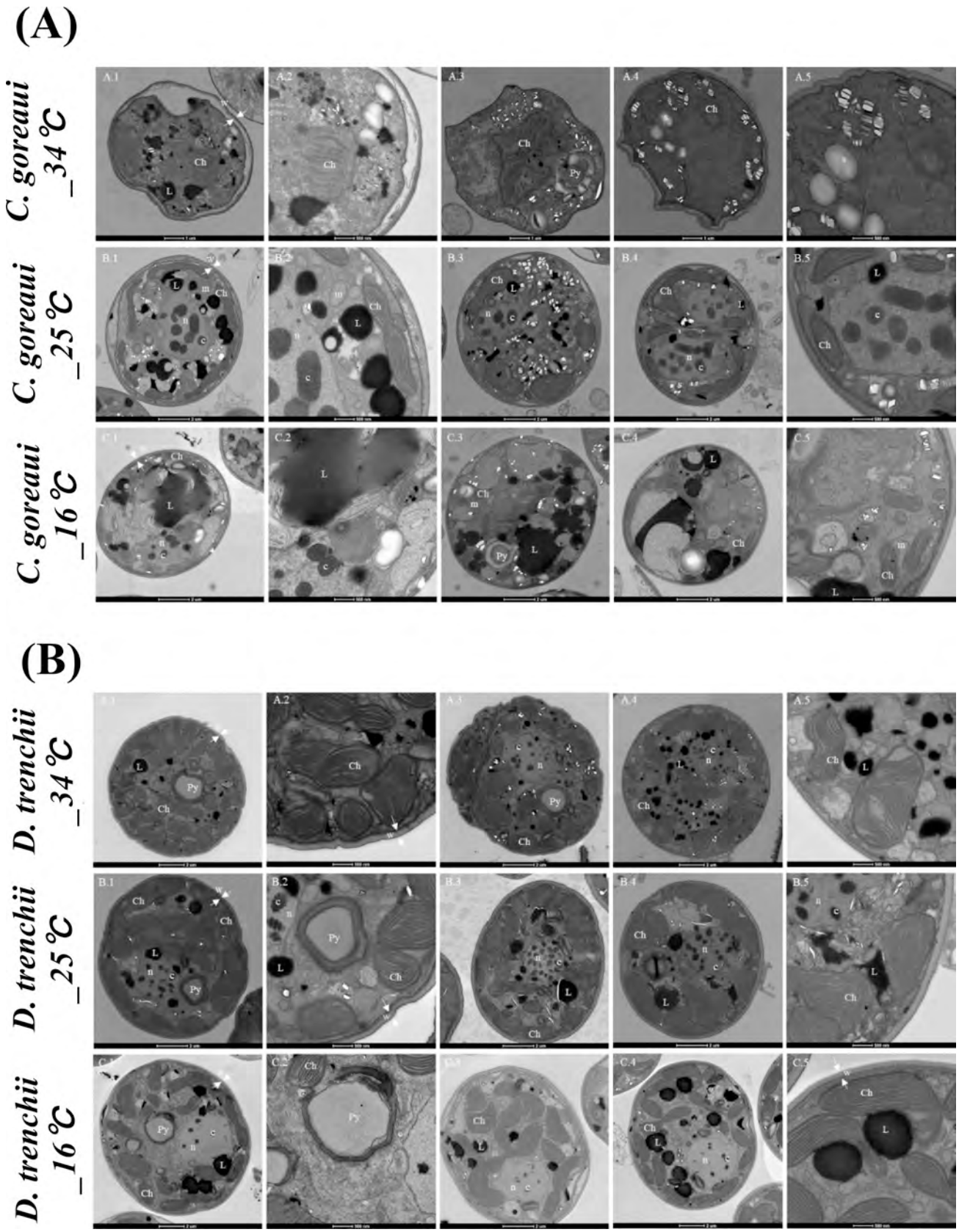


Fig. 3. (A). Ultrastructure of *C. goreaui*; (B). Ultrastructure of *D. trenchii* n: nucleus; c: chromosome; Ch: chloroplast; Py: pyrenoid; m: mitochondrion; s: starch; a: accumulation body; w: cell wall (paired arrows indicate cell wall thickness); v: vacuole.

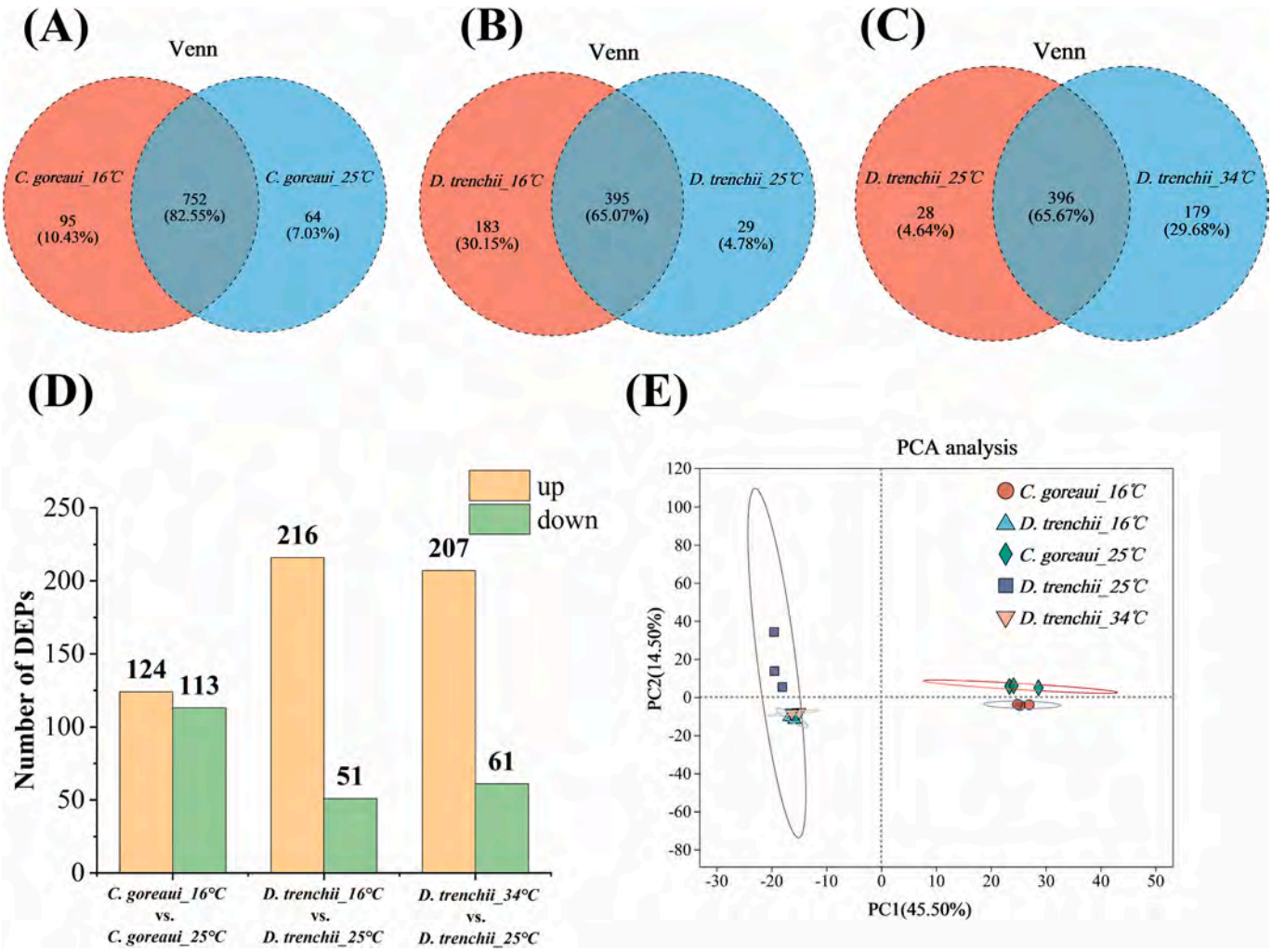


Fig. 4. (A) Specific protein expression in *C. goreaui* induced by abnormal low-temperature stress. (B) Specific protein expression in *D. trenchii* induced by abnormal low-temperature stress (C) Specific protein expression in *D. trenchii* induced by abnormal high-temperature stress. (D) Differential protein expression under different conditions. (E) PCA.

biosynthesis; thiamine metabolism; fatty acid biosynthesis; fatty acid degradation; alanine, aspartate and glutamate metabolism; fructose and mannose metabolism; nucleotide metabolism; porphyrin metabolism; glycerophospholipid metabolism (Fig. 6).

4. Discussion

The molecular basis of the physiological response of coral-Symbiodiniaceae symbiosis to environmental stress has been investigated mainly through transcriptomics and metabolomics. Various gene expression methods have been utilized to assess the genetic responses of corals to stress. Although these studies have made significant progress in enhancing our understanding of the molecular responses of coral hosts, symbiotic microorganisms, and the entire system under environmental stress, they do not necessarily represent the true phenotypes at the protein level in these cells. The proteome provides a more accurate reflection of biological functions since proteins typically have higher abundances than transcripts and have longer half-lives inside cells [32]. The presence of Symbiodiniaceae plays a crucial role in the survival of coral hosts, and temperature fluctuations can lead to changes in algal density, photosynthetic pigment concentration, photochemical efficiency of PSII, photosynthetic capacity, and the xanthophyll cycle [33]. It is well established that both thermal and cold anomalies can drive coral bleaching (i.e., loss of symbionts) and increase mortality rates [34–36]. Heat stress and cold stress primarily exert adverse effects on photosynthesis but can induce enhanced photoprotective mechanisms, thereby mitigating the impact of transient exposure on photosynthetic processes [33]. However, these temperature extremes affect distinct physiological processes and may involve trade-offs in stress tolerance [37]. In this study, the physiological characteristics and molecular stress response mechanisms of *C. goreaui* and *D. trenchii* were investigated under abnormally high/low temperatures during the same period. Both cold and heat stress had negative effects on Symbiodiniaceae, this research contributes to elucidating the adaptive strategies of different species of Symbiodiniaceae to different temperatures: for *C. goreaui*, high-temperature stress had a greater impact than low-temperature stress, while the opposite was observed for *D. trenchii* under stress.

4.1. Physiological and proteomic responses of two Symbiodiniaceae species to high temperature stress

Elevated temperatures are known to cause PSII photoinhibition and impair photodamage repair mechanisms in Symbiodiniaceae [38]. These impairments suppress metabolic performance and represent a primary driver of thermal bleaching in corals [38–41]. Previous studies have reported damage to coral hosts under prolonged exposure to 34 °C (12h) or extended periods of extreme temperature stress at 36 °C, leading to apoptosis or necrosis in Symbiodiniaceae cells, which are

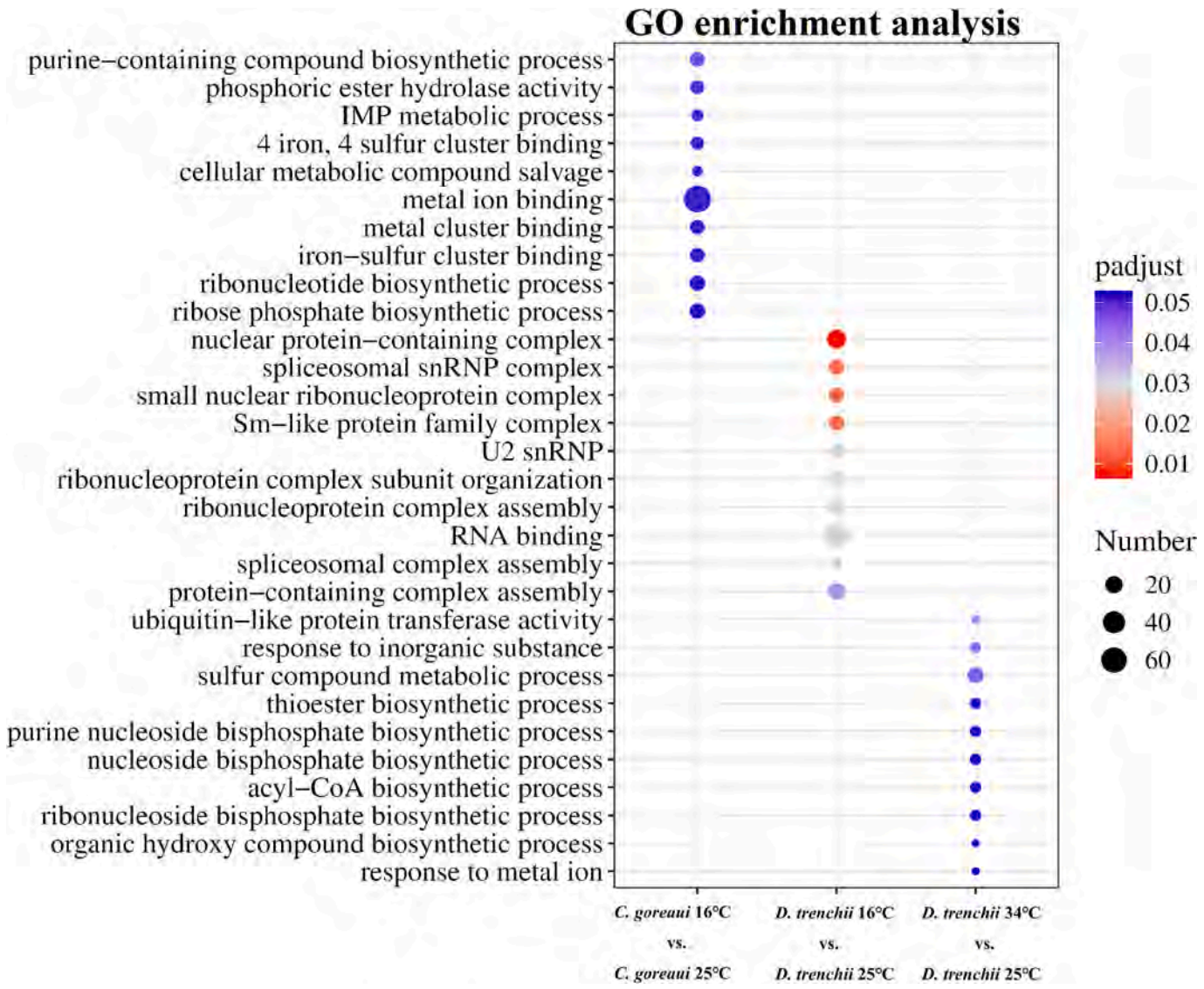


Fig. 5. GO enrichment analysis of DEPs in Symbiodiniaceae under abnormal temperature stress. (The x-axis represents different groups, the y-axis represents the GO term, and the size of the bubbles is proportional to the number of proteins enriched in this GO term.)

subsequently expelled [42,43].

Under high-temperature stress (34 °C), *Cladocopium goreaui* exhibited typical thermosensitive characteristics [9], including a significant decline in cell density (Supporting Information S1A), negative growth rate ($\mu < 0$) (Fig. 1A), a sharp reduction in the *Fv/Fm* value (Fig. 1B), and fluctuating levels of Chl a and CARs (initial increase followed by decrease; Fig. 2A, B). Moreover, its cellular structure was severely damaged, with disintegration of chloroplast morphology (Fig. 3A), indicating a pronounced impairment of photosynthesis [44]. These physiological deteriorations are consistent with previously described heat-induced photosynthetic inhibition and oxidative stress damage [45–48]. Heat stress suppresses D1 protein repair and destabilizes PSII reaction centers, contributing to the observed *Fv/Fm* decline [49,50]. Additionally, pigment degradation is a known photoprotective strategy that limits Reactive oxygen species (ROS) accumulation [51,52]. Chloroplast structures are disrupted prior to widespread oxidative damage under thermal stress, and diminished photosynthesis forces Symbiodiniaceae chloroplasts to reroute electrons via the Mehler reaction [53].

In contrast, *Durusdinium trenchii* demonstrated higher thermal tolerance under the same stress conditions [54,55]. Although its growth rate was reduced compared to the control (Fig. 1A), cell density increased (Supporting Information S1B), *Fv/Fm* showed only a modest decline (Fig. 1B), pigment concentrations remained relatively high (Fig. 2C, D), and cell structures, including chloroplasts, remained intact (Fig. 3B), indicating a more stable photosynthetic and metabolic function under heat stress. Proteomic analysis supported these findings. GO enrichment revealed significant upregulation of ATP-dependent protein-folding chaperones such as *HSP70* (Fig. 5), suggesting enhanced proteostasis mechanisms to counteract heat-induced protein denaturation [56–58]. KEGG pathway analysis also showed strong activation of endocytosis and ubiquitin-mediated proteolysis pathways (Fig. 6), indicating an enhanced cellular response to misfolded proteins [48,59,60]. Meanwhile, protein expression associated with photosystem I (PSI), the Calvin cycle, and pigment biosynthesis was downregulated (Figs. 5, 6), implying reduced light absorption and electron transport, which may lower the synthesis of photosynthetic products [61]. Proteins involved in chloroplast lipid biosynthesis, such as acetyl-CoA carboxylase (ACC) and ω-6 fatty acid desaturase (FAD6), were upregulated (Fig. 5). ACC catalyzes the carboxylation of acetyl-CoA in the rate-limiting step of fatty acid biosynthesis, potentially increasing unsaturated fatty acid content to enhance membrane fluidity and chloroplast stability [62]. High expression of proteins such as 4-hydroxyphenylpyruvate dioxygenase (HPPD) and 2-methyl-6-phytyl-1,4-hydroquinone methyltransferase (MPBQ-MT) was observed in the biosynthesis of

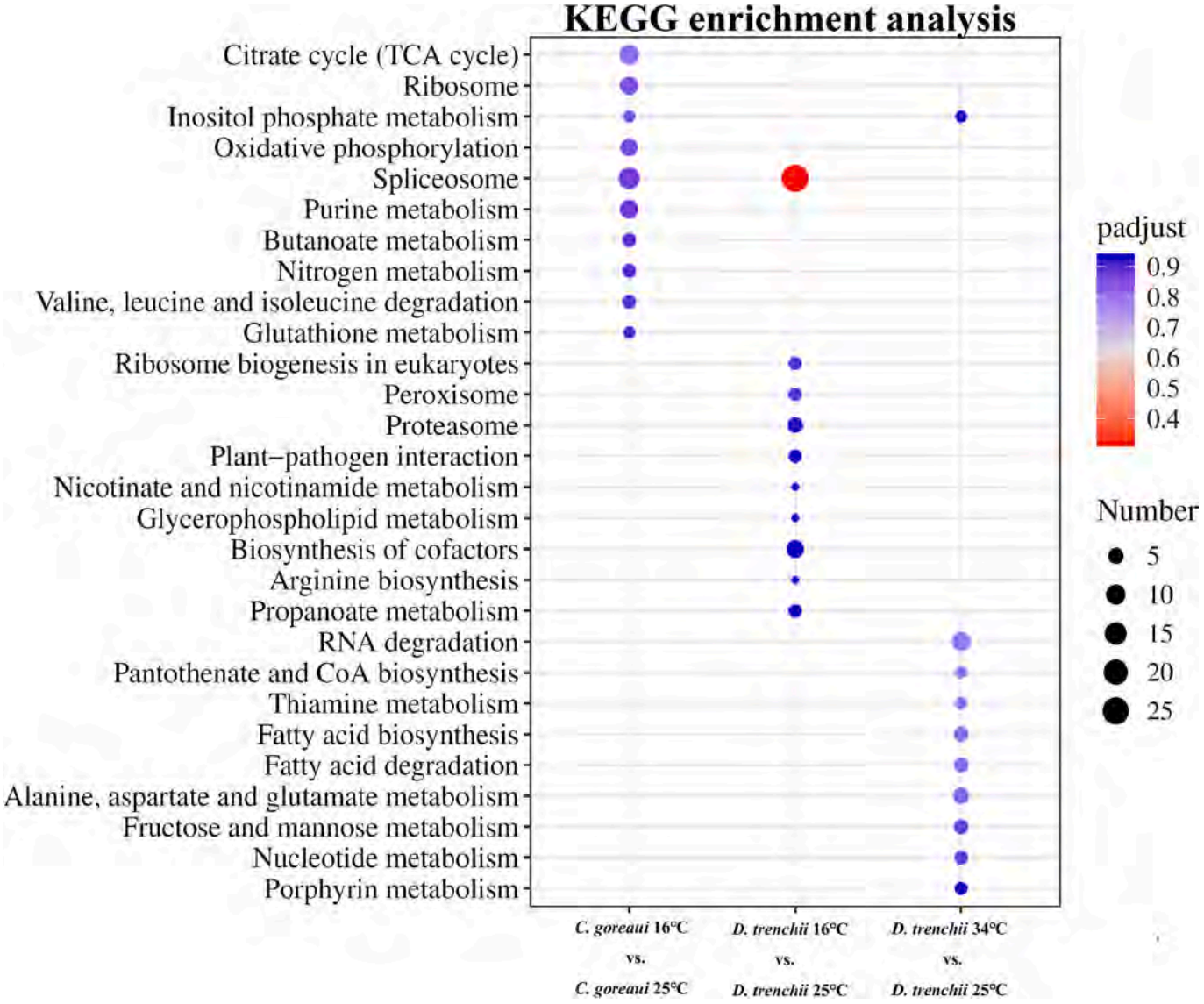


Fig. 6. KEGG pathway analysis of DEPs in Symbiodiniaceae under abnormal temperature stress. (The x-axis represents different groups, the y-axis represents the KEGG pathway, and the size of the bubbles indicates the number of proteins enriched in the KEGG pathway.)

plastoquinones and other terpenoid quinones under heat stress (Figs. 5, 6). These pathways are critical for α-tocopherol (vitamin E) synthesis, a lipid-soluble antioxidant that scavenges singlet oxygen within chloroplasts, protects membrane lipids from peroxidation, and stabilizes photosynthetic complexes. The quinone form of α-tocopherol also integrates into the thylakoid electron transport chain, providing additional photoprotection [63]. In addition, biosynthetic pathways for macromolecules and organic compounds were downregulated, possibly reflecting a strategic reallocation of resources toward stress response mechanisms [64].

In summary, *C. goreaui* exhibited extreme sensitivity to heat stress, displaying a characteristic "photoinhibition–cell collapse" pattern, while *D. trenchii* showed strong thermal adaptation through enhanced chaperone activity, protein degradation systems, and pigment stability. These differential responses are consistent with previous studies on the evolutionary thermal tolerance and species-specific adaptation of Symbiodiniaceae [10,65–69].

4.2. Physiological and proteomic responses of two Symbiodiniaceae species to low temperature stress

Both high and low temperatures have been shown to accelerate photoinhibition (fixing CO_2 by severely limiting photosynthesis) [70–72]. The structural integrity of symbiont chloroplasts is essential for maintaining photosynthetic capacity under thermal stress. Similarly, exposure to cold stress also reduces the *Fv/Fm* in Symbiodiniaceae, potentially leading to photoinhibition and photodamage [36,61]. It negatively affects photosynthesis by reducing chlorophyll fluorescence quantum yield, weakening the activity of carbon fixation enzymes [33,36,61,73], and lowering membrane fluidity [61].

Under low temperature stress (16 °C), neither species exhibited severe physiological damage. Although cell density growth slowed during the later stages of the experiment, the overall μ values remained positive (Fig. 1A). Cellular structures remained intact (Fig. 3), and concentrations of Chl a and CARs showed no significant differences from the control group ($P > 0.05$; Fig. 2), suggesting a degree of cold tolerance in both species. However, both experienced declines in the *Fv/Fm* value, with a more pronounced decrease in *D. trenchii* than in *C. goreaui* (Fig. 1B), indicating that despite stable pigment content, PSII function

was impaired in both, and *C. goreaui* may be better adapted to cold stress [9]. Proteomic analysis further revealed the molecular basis of this adaptation. In *C. goreaui*, GO-enriched pathways upregulated under cold stress included metal ion transport, glutathione biosynthesis, and α-ketoglutarate dehydrogenase activity, indicating the activation of redox homeostasis and mitochondrial TCA cycle pathways [74,75]. Glutathione synthesis can help scavenge cold-induced ROS and maintain intracellular redox balance [76]. KEGG analysis also showed significant downregulation of fatty acid, pyruvate, and nicotinamide metabolism, supporting a strategy of metabolic suppression [77].

In *D. trenchii*, cold stress predominantly triggered extensive upregulation of RNA splicing-related pathways, including the spliceosome, snRNP complexes, and mRNA splicing (significant in both GO and KEGG enrichment), suggesting active post-transcriptional regulation and rapid adjustment to temperature changes via splicing machinery [78–80]. Concurrently, pathways related to carbohydrate biosynthesis and the electron transport chain were downregulated, indicating reduced energy metabolism under cold conditions [81]. NAD^+-dependent GPD1 was upregulated in *C. goreaui*, and FAD-dependent GPD2 was upregulated in *D. trenchii*. Both enzymes catalyze the conversion of dihydroxyacetone phosphate (DHAP) to glycerol-3-phosphate (G3P), providing the glycerol backbone for triacylglycerol (TAG) synthesis [82]. The fatty acid β-oxidation enzyme ACAA1 was also upregulated in *D. trenchii*, which is associated with reduced lipid synthesis and decreased TAG accumulation, indicating a metabolic shift from lipid storage to utilization [83].

In conclusion, *C. goreaui* demonstrated a degree of cold tolerance by activating antioxidant and metabolic homeostasis mechanisms, while *D. trenchii*, despite being more photosynthetically sensitive, showed active post-transcriptional regulation through enhanced spliceosome-related protein expression. These strategic differences reflect distinct priorities in resource allocation and regulatory focus in response to cold stress.

5. Conclusion

Many ecological studies on coral reefs have shown that the density of Symbiodiniaceae *in hospite* is lower in warmer summers and higher in winters [84]. This patterns may be explained by the impact of low temperatures on Symbiodiniaceae, with the weaken photosynthesis and decrease nutrient supply to corals [36,61,85]. However, the relationship between the density of Symbiodiniaceae and metabolism are nuanced [86]. For instance, an increase in nutrients within a certain range may lead to an increase in the density of Symbiodiniaceae [87]. But, when the nutrient level exceeds a certain threshold, the density of Symbiodiniaceae may actually decrease [87]. Recent transcriptomics and metabolomics studies demonstrate the importance of nutrients in host-symbiont interactions [58,88–91], they can provide insights into the molecular mechanisms underlying the changes in Symbiodiniaceae density and metabolism.

This study elucidates the distinct stress-response strategies of two Symbiodiniaceae species, *Cladocopium goreaui* and *Durusdinium trenchii*, under extreme temperature conditions. At elevated temperatures (34 °C), *C. goreaui* exhibited marked reductions in growth, photosynthetic efficiency, and cellular integrity, indicating pronounced thermal sensitivity. In contrast, *D. trenchii* maintained relatively stable physiological functions while activating multiple protective mechanisms, including chaperone-mediated protein folding and antioxidant biosynthesis. Under cold stress (16 °C), both species displayed minimal physiological impairment; however, *C. goreaui* appeared more cold-tolerant through modulation of redox homeostasis and TCA cycle activity, whereas *D. trenchii* responded via enhanced post-transcriptional regulation involving spliceosome-related pathways. These results highlight species-specific thermal adaptation mechanisms and provide new insights into the resilience of coral-algal symbioses in the context of climate change.

CRediT authorship contribution statement

Jiayuan Liang: Writing – review & editing, Writing – original draft. **Liangyun Qin:** Writing – review & editing, Writing – original draft, Methodology, Investigation, Formal analysis, Data curation. **Li Zhang:** Writing – review & editing, Writing – original draft, Investigation, Data curation. **Yongqian Xu:** Methodology, Investigation. **Tianyi Niu:** Methodology, Investigation. **Zhicong Li:** Methodology, Investigation. **Yating Yang:** Methodology, Investigation. **Zhuqing Liang:** Methodology, Investigation. **Kefu Yu:** Funding acquisition. **Sanqiang Gong:** Data curation.

Declaration of competing interest

All authors declare no conflict of interest.

Acknowledgements

This work was supported by the National Natural Science Foundation of China (42030502 and 42090041), and the Self-Topic Project of Guangxi Laboratory on the Study of Coral Reefs in the South China Sea (GXLSCRSCS2023101).

Appendix A. Supplementary data

Supplementary data to this article can be found online at https://doi.org/10.1016/j.algal.2025.104187.

Data availability

Data will be made available on request.

References

[1] L. Muscatine, L.R. McCloskey, R.E. Marian, Estimating the daily contribution of carbon from zooxanthellae to coral animal respiration, Limnol. Oceanogr. 26 (1981) 601–611.
[2] P.G. Falkowski, Z. Dubinsky, L. Muscatine, J.W. Porter, Light and the bioenergetics of a symbiotic coral, BioScience 34 (1984) 705–709.
[3] M.S. Roth, The engine of the reef: photobiology of the coral-algal symbiosis, Front. Microbiol. 5 (2014).
[4] D.G. Bourne, K.M. Morrow, N.S. Webster, Insights into the coral microbiome: underpinning the health and resilience of reef ecosystems, in: S. Gottesman (Ed.), Annual Review of Microbiology Vol 70, 2016, pp. 317-+.
[5] S.L. Coles, Reef corals occurring in a highly fluctuating temperature environment at Fahal Island, Gulf of Oman (Indian Ocean), Coral Reefs 16 (1997) 269–272.
[6] P. Craig, C. Birkeland, S. Belliveau, High temperatures tolerated by a diverse assemblage of shallow-water corals in American Samoa, Coral Reefs 20 (2001) 185–189.
[7] N.M. Boulotte, S.J. Dalton, A.G. Carroll, P.L. Harrison, H.M. Putnam, L.M. Peplow, M.J.H. van Oppen, Exploring the *Symbiodinium* rare biosphere provides evidence for symbiont switching in reef-building corals, ISME J. 10 (2016) 2693–2701.
[8] T.A. Oliver, S.R. Palumbi, Many corals host thermally resistant symbionts in high-temperature habitat, Coral Reefs 30 (2011) 241–250.
[9] R. Rowan, Coral bleaching: thermal adaptation in reef coral symbionts, Nature 430 (2004) 742.
[10] R. Berkelmans, M.J.H. van Oppen, The role of zooxanthellae in the thermal tolerance of corals: a 'nugget of hope' for coral reefs in an era of climate change, Proc. R. Soc. B Biol. Sci. 273 (2006) 2305–2312.
[11] D. Abrego, K.E. Ulstrup, B.L. Willis, M.J.H. van Oppen, Species–specific interactions between algal endosymbionts and coral hosts define their bleaching response to heat and light stress, Proc. R. Soc. B Biol. Sci. 275 (2008) 2273–2282.
[12] T.C. LaJeunesse, J.E. Parkinson, P.W. Gabrielson, H.J. Jeong, J.D. Reimer, C. R. Voolstra, S.R. Santos, Systematic revision of Symbiodiniaceae highlights the antiquity and diversity of coral endosymbionts, Curr. Biol. 28 (2018) 2570.
[13] T.C. LaJeunesse, D.T. Pettay, E.M. Sampayo, N. Phongsuwan, B. Brown, D. O. Obura, O. Hoegh-Guldberg, W.K. Fitt, Long-standing environmental conditions, geographic isolation and host–symbiont specificity influence the relative ecological dominance and genetic diversification of coral endosymbionts in the genus *Symbiodinium*, J. Biogeogr. 37 (2010) 785–800.
[14] T.C. LaJeunesse, R. Smith, M. Walther, J. Pinzon, D.T. Pettay, M. McGinley, M. Aschaffenburg, P. Medina-Rosas, A.L. Cupul-Magana, A. Lopez Perez, H. Reyes-Bonilla, M.E. Warner, Host-symbiont recombination versus natural selection in the response of coral-dinoflagellate symbioses to environmental disturbance, Proc. R. Soc. B Biol. Sci. 277 (2010) 2925–2934.

[15] D.P. Manzello, M.V. Matz, I.C. Enochs, L. Valentino, R.D. Carlton, G. Kolodziej, X. Serrano, E.K. Towle, M. Jankulak, Role of host genetics and heat-tolerant algal symbionts in sustaining populations of the endangered coral *Orbicella faveolata* in the Florida keys with ocean warming, Glob. Chang. Biol. 25 (2019) 1016–1031.
[16] B. Chen, Spatial Changes of Coral Miceobiome and Environmental Adaption Mechanism in the South Chine Sea, Guangxi University, 2021.
[17] D.M. Baker, J.P. Andras, A.G. Jordán-Garza, M.L. Fogel, Nitrate competition in a coral symbiosis varies with temperature among *Symbiodinium* clades, ISME J. 7 (2013) 1248–1251.
[18] K.D. Hoadley, D.T. Pettay, A. Lewis, D. Wham, C. Grasso, R. Smith, D.W. Kemp, T. LaJeunesse, M.E. Warner, Different functional traits among closely related algal symbionts dictate stress endurance for vital Indo-Pacific reef-building corals, Glob. Chang. Biol. 27 (2021) 5295–5309.
[19] B. Chen, K. Yu, J. Liang, W. Huang, G. Wang, H. Su, Z. Qin, X. Huang, Z. Pan, W. Luo, Y. Luo, Y. Wang, Latitudinal variation in the molecular diversity and community composition of Symbiodiniaceae in coral from the South China Sea, Front. Microbiol. 10 (2019).
[20] S. Keshavmurthy, K.-H. Tang, C.-M. Hsu, C.-H. Gan, C.-Y. Kuo, K. Soong, H.-N. Chou, C.A. Chen, *Symbiodinium* spp. associated with scleractinian corals from Dongsha Atoll (Pratas), Taiwan, in the South China Sea, PeerJ 5 (2017) e2871.
[21] B. Chen, K. Yu, J. Liang, W. Huang, G. Wang, H. Su, Z. Qin, X. Huang, Z. Pan, W. Luo, Y. Luo, Y. Wang, Latitudinal variation in the molecular diversity and community composition of Symbiodiniaceae in coral from the South China Sea, Front. Microbiol. 10 (2019) 1278.
[22] E.M. Sampayo, T. Ridgway, P. Bongaerts, O. Hoegh-Guldberg, Bleaching susceptibility and mortality of corals are determined by fine-scale differences in symbiont type, Proc. Natl. Acad. Sci. USA 105 (2008) 10444–10449.
[23] M.D. Ahles, Some Aspects of the Morphology and Physiology of *Symbiodinium microadriaticum*, Fordham University, 1967.
[24] R.A. Kinzie, P.L. Jokiel, R. York, Effects of light of altered spectral composition on coral zooxanthellae associations and on zooxanthellae *in vitro*, Mar. Biol. 78 (1984) 239–248.
[25] J.J. Lee, M.E. McEnery, J.R. Garrison, Experimental studies of larger foraminifera and their symbionts from the Gulf of Elat on the Red Sea, J. Foraminifer. Res. 10 (1980) 31–47.
[26] L. Qin, Y. Xu, J. Chen, T. Niu, K. Yu, J. Liang, Optimization of in vitro culture method for zooxanthellae associated with reef-building corals, Acta Microbiol Sin. 63 (2023) 1658–1671.
[27] Y.U. Kefu, J. Mingxing, C. Zhiqiang, C. Tegu, Latest forty two years' sea surface temperature change of Weizhou Island and its influence on coral reef ecosystem, Chin. J. Appl. Ecol. (2004) 506–510.
[28] J.E.N. Veron, P.R. Minchin, Correlations between sea surface temperature, circulation patterns and the distribution of hermatypic corals of Japan, Cont. Shelf Res. 12 (1992) 835–857.
[29] W. Huang, L. Meng, Z. Xiao, R. Tan, E. Yang, Y. Wang, X. Huang, K. Yu, Heat-tolerant intertidal rock pool coral *Porites lutea* can potentially adapt to future warming, Mol. Ecol. 33 (2024) e17273.
[30] Y.P. Guo, D.P. Guo, H.F. Zhou, M.J. Hu, Y.G. Shen, Photoinhibition and xanthophyll cycle activity in bayberry (*Myrica rubra*) leaves induced by high irradiance, Photosynthetica 44 (2006) 439–446.
[31] R.J. Ritchie, Consistent sets of spectrophotometric chlorophyll equations for acetone, methanol and ethanol solvents, Photosynth. Res. 89 (2006) 27–41.
[32] A.J. Weston, W.C. Dunlap, J.M. Shick, A. Klueter, K. Iglic, A. Vukelic, A. Starcevic, M. Ward, M.L. Wells, C.G. Trick, P.F. Long, A profile of an endosymbiont-enriched fraction of the coral *Stylophora pistillata* reveals proteins relevant to microbial-host interactions, Mol. Cell. Proteomics 11 (2012).
[33] M.S. Roth, R. Goericke, D.D. Deheyn, Cold induces acute stress but heat is ultimately more deleterious for the reef-building coral *Acropora yongei*, Sci. Rep. 2 (2012).
[34] P.L. Jokiel, S.L. Coles, Response of Hawaiian and other Indo-Pacific reef corals to elevated temperature, Coral Reefs 8 (1990) 155–162.
[35] T.C. LaJeunesse, H. Reyes-Bonilla, M.E. Warner, Spring "bleaching" among *Pocillopora* in the Sea of Cortez, Eastern Pacific, Coral Reefs 26 (2007) 265–270.
[36] T. Saxby, W.C. Dennison, O. Hoegh-Guldberg, Photosynthetic responses of the coral *Montipora digitata* to cold temperature stress, Mar. Ecol. Prog. Ser. 248 (2003) 85–97.
[37] M.S. Roth, D.D. Deheyn, Effects of cold stress and heat stress on coral fluorescence in reef-building corals, Sci. Rep. 3 (2013) 1421.
[38] M.E. Warner, W.K. Fitt, G.W. Schmidt, Damage to photosystem II in symbiotic dinoflagellates: a determinant of coral bleaching, Proc. Natl. Acad. Sci. 96 (1999) 8007–8012.
[39] S. Takahashi, T. Nakamura, M. Sakamizu, R.v. Woesik, H. Yamasaki, Repair machinery of symbiotic photosynthesis as the primary target of heat stress for reef-building corals, Plant Cell Physiol. 45 (2004) 251–255.
[40] S. Takahashi, S. Whitney, S. Itoh, T. Maruyama, M. Badger, Heat stress causes inhibition of the *de novo* synthesis of antenna proteins and photobleaching in cultured *Symbiodinium*, Proc. Natl. Acad. Sci. USA 105 (2008) 4203–4208.
[41] D.J. Smith, D.J. Suggett, N.R. Baker, Is photoinhibition of zooxanthellae photosynthesis the primary cause of thermal bleaching in corals? Glob. Chang. Biol. 11 (2004) 1–11.
[42] P.W. Sammarco, K.B. Strychar, Responses to high seawater temperatures in zooxanthellate octocorals, PLoS One 8 (2013).
[43] K.B. Strychar, P.W. Sammarco, Exaptation in corals to high seawater temperatures: low concentrations of apoptotic and necrotic cells in host coral tissue under bleaching conditions, J. Exp. Mar. Biol. Ecol. 369 (2009) 31–42.
[44] C. Ferrier-Pagès, C. Rottier, E. Beraud, O. Levy, Experimental assessment of the feeding effort of three scleractinian coral species during a thermal stress: effect on the rates of photosynthesis, J. Exp. Mar. Biol. Ecol. 390 (2010) 118–124.
[45] M.P. Lesser, Experimental biology of coral reef ecosystems, J. Exp. Mar. Biol. Ecol. 300 (2004) 217–252.
[46] D. Tchernov, M.Y. Gorbunov, C. de Vargas, S. Narayan Yadav, A.J. Milligan, M. Häggblom, P.G. Falkowski, Membrane lipids of symbiotic algae are diagnostic of sensitivity to thermal bleaching in corals, Proc. Natl. Acad. Sci. 101 (2004) 13531–13535.
[47] T. Krueger, T.D. Hawkins, S. Becker, S. Pontasch, S. Dove, O. Hoegh-Guldberg, W. Leggat, P.L. Fisher, S.K. Davy, Differential coral bleaching-contrasting the activity and response of enzymatic antioxidants in symbiotic partners under thermal stress, Comp. Biochem. Physiol. A Mol. Integr. Physiol. 190 (2015) 15–25.
[48] C.A. Oakley, M.F. Ameismeier, L. Peng, V.M. Weis, A.R. Grossman, S.K. Davy, Symbiosis induces widespread changes in the proteome of the model cnidarian *Aiptasia*, Cell. Microbiol. 18 (2016) 1009–1023.
[49] S. Takahashi, N. Murata, How do environmental stresses accelerate photoinhibition? Trends Plant Sci. 13 (2008) 178–182.
[50] R.J. Jones, O. Hoegh-Guldberg, A.W.D. Larkum, U. Schreiber, Temperature-induced bleaching of corals begins with impairment of the CO_2 fixation mechanism in zooxanthellae, Plant Cell Environ. 21 (1998) 1219–1230.
[51] E.S. McGinty, J. Pieczonka, L.D. Mydlarz, Variations in reactive oxygen release and antioxidant activity in multiple *Symbiodinium* types in response to elevated temperature, Microb. Ecol. 64 (2012) 1000–1007.
[52] O. Ladrière, P. Compère, D. Nicole, P. Vandewalle, M. Poulicek, Morphological alterations of zooxanthellae in bleached cnidarian hosts, Cah. Biol. Mar. 49 (2008) 215–227.
[53] C.A. Downs, K.E. McDougall, C.M. Woodley, J.E. Fauth, R.H. Richmond, A. Kushmaro, S.W. Gibb, Y. Loya, G.K. Ostrander, E. Kramarsky-Winter, Heat-stress and light-stress induce different cellular pathologies in the symbiotic dinoflagellate during coral bleaching, PLoS One 8 (2013).
[54] R.N. Silverstein, R. Cunning, A.C. Baker, Tenacious D: *Symbiodinium* in clade D remain in reef corals at both high and low temperature extremes despite impairment, J. Exp. Biol. 220 (2017) 1192–1196.
[55] A.C. Baker, C.J. Starger, T.R. McClanahan, P.W. Glynn, Corals' adaptive response to climate change, Nature 430 (2004), 741-741.
[56] M.E. Feder, G.E. Hofmann, Heat-shock proteins, molecular chaperones, and the stress response: evolutionary and ecological physiology, Annu. Rev. Physiol. 61 (1999) 243–282.
[57] R. Rosenzweig, N.B. Nillegoda, M.P. Mayer, B. Bukau, The Hsp70 chaperone network, Nat. Rev. Mol. Cell Biol. 20 (2019) 665–680.
[58] T. Li, X. Lin, L. Yu, S. Lin, I.B. Rodriguez, T.-Y. Ho, RNA-seq profiling of *Fugacium kawagutii* reveals strong responses in metabolic processes and symbiosis potential to deficiencies of iron and other trace metals, Sci. Total Environ. 705 (2020) 135767.
[59] M.H. Glickman, A. Ciechanover, The ubiquitin-proteasome proteolytic pathway: destruction for the sake of construction, Physiol. Rev. 82 (2002) 373–428.
[60] L. Zhang, J. Xing, J. Lin, At the intersection of exocytosis and endocytosis in plants, New Phytol. 224 (2019) 1479–1489.
[61] D.J. Thornhill, D.W. Kemp, B.U. Bruns, W.K. Fitt, G.W. Schmidt, Correspondence between cold tolerance and temperate biogeography in a Western Atlantic *Symbiodinium* (Dinophyta) lineage[1], J. Phycol. 44 (2008) 1126–1135.
[62] E. Diaz-Almeyda, P.E. Thome, M. El Hafidi, R. Iglesias-Prieto, Differential stability of photosynthetic membranes and fatty acid composition at elevated temperature in *Symbiodinium*, Coral Reefs 30 (2011) 217–225.
[63] S. Munné-Bosch, L. Alegre, The function of tocopherols and tocotrienols in plants, Crit. Rev. Plant Sci. 21 (2002) 31–57.
[64] D.J. Barshis, J.T. Ladner, T.A. Oliver, F.O. Seneca, N. Traylor-Knowles, S. R. Palumbi, Genomic basis for coral resilience to climate change, Proc. Natl. Acad. Sci. 110 (2013) 1387–1392.
[65] T.C. LaJeunesse, J.E. Parkinson, P.W. Gabrielson, H.J. Jeong, J.D. Reimer, C. R. Voolstra, S.R. Santos, Systematic revision of Symbiodiniaceae highlights the antiquity and diversity of coral endosymbionts, Curr. Biol. 28 (2018), 2570-2580. e2576.
[66] E.J. Howells, V.H. Beltran, N.W. Larsen, L.K. Bay, B.L. Willis, M.J.H. van Oppen, Coral thermal tolerance shaped by local adaptation of photosymbionts, Nat. Clim. Chang. 2 (2012) 116–120.
[67] L.J. Chakravarti, V.H. Beltran, M.J.H. van Oppen, Rapid thermal adaptation in photosymbionts of reef-building corals, Glob. Chang. Biol. 23 (2017) 4675–4688.
[68] A.F. Little, M.J.H. van Oppen, B.L. Willis, Flexibility in algal endosymbioses shapes growth in reef corals, Science 304 (2004) 1492–1494.
[69] A.C. Baker, Reef corals bleach to survive change, Nature 411 (2001) 765–766.
[70] S.B. Powles, Photoinhibition of photosynthesis induced by visible light, Annu. Rev. Plant Biol. 35 (1984) 15–44.
[71] B. Demmig-Adams, W.W. Adams, Photoprotection and other responses of plants to high light stress, Annu. Rev. Plant Biol. 43 (1992) 599–626.
[72] N. Murata, S. Takahashi, Y. Nishiyama, S.I. Allakhverdiev, Photoinhibition of photosystem II under environmental stress, Biochim. Biophys. Acta Bioenerg. 1767 (2007) 414–421.
[73] C.A. Oakley, G.W. Schmidt, B.M. Hopkinson, Thermal responses of *Symbiodinium* photosynthetic carbon assimilation, Coral Reefs 33 (2014) 501–512.
[74] K. Yonekura-Sakakibara, Y. Higashi, R. Nakabayashi, The origin and evolution of plant flavonoid metabolism, Front. Plant Sci. 10 - 2019 (2019).
[75] P. da Fonseca-Pereira, D.M. Daloso, J. Gago, F.M. de Oliveira Silva, J.A. Condori-Apfata, I. Florez-Sarasa, T. Tohge, J.-P. Reichheld, A. Nunes-Nesi, A.R. Fernie, W. L. Araújo, The mitochondrial thioredoxin system contributes to the metabolic

responses under drought episodes in Arabidopsis, Plant Cell Physiol. 60 (2018) 213–229.
[76] K. Apel, H. Hirt, Reactive oxygen species: metabolism, oxidative stress, and signal transduction, Annu. Rev. Plant Biol. 55 (2004) 373–399.
[77] D.A. Los, N. Murata, Membrane fluidity and its roles in the perception of environmental signals, Biochim. Biophys. Acta Biomembr. 1666 (2004) 142–157.
[78] V. Chinnusamy, J. Zhu, J.-K. Zhu, Cold stress regulation of gene expression in plants, Trends Plant Sci. 12 (2007) 444–451.
[79] S.G. Palusa, G.S. Ali, A.S.N. Reddy, Alternative splicing of pre-mRNAs of Arabidopsis serine/arginine-rich proteins: regulation by hormones and stresses, Plant J. 49 (2007) 1091–1107.
[80] J. Zhu, C.-H. Dong, J.-K. Zhu, Interplay between cold-responsive gene regulation, metabolism and RNA processing during plant cold acclimation, Curr. Opin. Plant Biol. 10 (2007) 290–295.
[81] H. Shin, S.-J. Hong, C. Yoo, M.-A. Han, H. Lee, H.-K. Choi, S. Cho, C.-G. Lee, B.-K. Cho, Genome-wide transcriptome analysis revealed organelle specific responses to temperature variations in algae, Sci. Rep. 6 (2016) 37770.
[82] M.-H. Liang, J.-G. Jiang, Advancing oleaginous microorganisms to produce lipid via metabolic engineering technology, Prog. Lipid Res. 52 (2013) 395–408.
[83] C. Liu, Y. Zhang, L. Huang, X. Yu, Y. Luo, L. Jiang, Y. Sun, S. Liu, H. Huang, Differences in fatty acids and lipids of massive and branching reef-building corals and response to environmental changes, Front. Mar. Sci. 9 (2022).
[84] S. Jandang, V. Viyakarn, Y. Yoshioka, C. Shinzato, S. Chavanich, The seasonal investigation of Symbiodiniaceae in broadcast spawning, *Aropora humilis* and brooding, *Pocillopora* cf. d*amicornis* corals, PeerJ 10 (2022).
[85] J. Helgoe, S.K. Davy, V.M. Weis, M. Rodriguez-Lanetty, Triggers, cascades, and endpoints: connecting the dots of coral bleaching mechanisms, Biol. Rev. 99 (2024) 715–752.
[86] L.A. Morris, C.R. Voolstra, K.M. Quigley, D.G. Bourne, L.K. Bay, Nutrient availability and metabolism affect the stability of coral–Symbiodiniaceae symbioses, Trends Microbiol. 27 (2019) 678–689.
[87] S.E. McIlroy, C.P. terHorst, M. Teece, M.A. Coffroth, Nutrient dynamics in coral symbiosis depend on both the relative and absolute abundance of Symbiodiniaceae species, Microbiome 10 (2022) 192.
[88] G. Cui, Y.J. Liew, Y. Li, N. Kharbatia, N.I. Zahran, A.-H. Emwas, V.M. Eguiluz, M. Aranda, Host-dependent nitrogen recycling as a mechanism of symbiont control in *Aiptasia*, PLoS Genet. 15 (2019) e1008189.
[89] G. Cui, Y.J. Liew, M.K. Konciute, Y. Zhan, S.-H. Hung, J. Thistle, L. Gastoldi, S. Schmidt-Roach, J. Dekker, M. Aranda, Nutritional control regulates symbiont proliferation and life history in coral-dinoflagellate symbiosis, BMC Biol. 20 (2022) 103.
[90] T. Krueger, N. Horwitz, J. Bodin, M.E. Giovani, S. Escrig, M. Fine, A. Meibom, Intracellular competition for nitrogen controls dinoflagellate population density in corals, Proc. Biol. Sci. 287 (2020) 20200049.
[91] S. Lin, L. Yu, H. Zhang, Transcriptomic responses to thermal stress and varied phosphorus conditions in *Fugacium kawagutii*, Microorganisms 7 (2019) 96.

Microbial Ecology (2025) 88:88
https://doi.org/10.1007/s00248-025-02587-0

RESEARCH

Responses of the Coral Symbiont *Cladocopium goreaui* to Extreme Temperature Stress in Relatively High-Latitude Reefs, South China Sea

Lifei Wei[1] · Shuchang Chen[1] · Zhenjun Qin[1] · Nengbin Pan[1] · Mengling Lan[1] · Tingchao Zhang[1] · Ran He[1] · Hongye Liang[1] · Wenzhi Deng[1] · Changhao Mo[1] · Kefu Yu[1,2]

Received: 10 April 2025 / Accepted: 25 July 2025
© The Author(s) 2025

Abstract
Global climate change has led to frequent extreme temperature events in oceans. Corals are susceptible to extreme high-temperature stress in summer and extreme low-temperature stress in winter in the relatively high-latitude reef areas of the South China Sea (SCS). The most abundant symbiotic coral Symbiodiniaceae in the higher-latitude reefs of the SCS is *Cladocopium goreaui*, predominantly associating with dominant coral hosts such as *Acropora* and *Porites*. However, to date, relatively few studies have focused on the response and mechanism of *C. goreaui* to the extreme high- and low-temperature stress. In this study, the responses and regulatory mechanisms of the dominant *C. goreaui* to extreme high- and low-temperature stress were investigated based on physiological indexes, transmission electron microscopy (TEM), and transcriptome analysis. The results showed that (1) under 34 °C heat stress, the disintegration of thylakoids triggered photosynthetic collapse in *C. goreaui*; survival is enabled through metabolic reprogramming that upregulates five protective pathways and redirects energy via pentose/glucuronate shunting to sustain ATP homeostasis, revealing a trade-off between damage containment and precision energy governance under thermal extremes. (2) Low temperature exposure induced suppression of maximum quantum yield (F_v/F_m), compounded by glutathione pathway inhibition, crippling ROS scavenging. The transcriptome results revealed that C. goreaui prioritizes gene fidelity maintenance under low temperature stress. These findings reveal that energy allocation trade-offs constitute the core strategy of *C. goreaui* temperature response: prioritizing energy maintenance under high-temperature stress, while safeguarding genetic fidelity at the expense of antioxidant defense under low-temperature stress.

Keyword *Cladocopium goreaui* · Extreme high and low temperature · F_v/F_m; Transcriptome

Introduction

The coral holobiont comprises the coral host, symbiotic microalgae (Symbiodiniaceae), and a diverse microbiota including bacteria, archaea, fungi, and viruses, which collectively drive nutrient cycling and stress resilience [1]. One of the most important symbiotic relationships is that between the coral host and Symbiodiniaceae, which is a family of symbiotic dinoflagellates that form mutualistic associations with corals and other marine invertebrates [2]. However, this symbiotic partnership is highly vulnerable to environmental stressors, particularly temperature fluctuations that trigger coral bleaching—a phenomenon now imperiling the survival of coral reefs worldwide [3, 4].

Thermal sensitivity varies markedly among Symbiodiniaceae [2]. The *Cladocopium* genus is particularly sensitive to even moderate temperature increases. Such increases disrupt the structure of Photosystem II (PSII) and chloroplast-like vesicle membranes [5]. These changes limit CO_2 fixation and affect Symbiodiniaceae growth [6]. Under thermal stress, excessive production of reactive oxygen species (ROS) in chloroplasts leads to DNA, protein, and lipid damage [7]. ROS further impairs photosynthetic activity by inhibiting PSII repair mechanisms and disrupting photosynthetic membranes [6]. Excessive ROS

✉ Zhenjun Qin
qzj_gxu@163.com

✉ Kefu Yu
kefuyu@scsio.ac.cn

[1] Guangxi Laboratory On the Study of Coral Reefs in the South China Sea, Coral Reef Research Center of China, School of Marine Sciences, Guangxi University, Nanning 530004, China

[2] Southern Marine Science and Engineering Guangdong Laboratory (Guangzhou), Guangzhou, China

Published online: 12 August 2025

can cause coral tissue damage and discharge of symbiotic Symbiodiniaceae, leading to coral bleaching and death [8, 9]. In contrast to the extensively studied thermal stress, cold stress as another potential threat remains significantly under-researched. Sudden low temperatures caused by regional extreme low-temperature events such as oceanic cold currents can lead to extensive coral bleaching, death, and coral reef degradation [10]. Under marine cold-spells, Symbiodiniaceae exhibit cold-induced photoinhibition through impaired PSII function, characterized by decline in maximal photosynthetic efficiency, which triggers ROS accumulation and subsequent photodamage to thylakoid membranes. This results in the accumulation of ROS in tissues, coral bleaching, and death [8, 11, 12]. In the context of global warming, coral reefs at higher latitudes are gaining ecological prominence as potential climate refugia due to their cooler waters, which may offer thermal respite for sensitive coral species [13, 14]. However, their role as refugia is complicated by winter low-temperature stress, which itself poses a significant physiological challenge to coral survival [15].

High-latitude coral reefs occur in temperate regions and are characterized by seasonal temperature fluctuations and lower mean temperatures compared to tropical reefs [14]. High-latitude coral reefs are distributed worldwide, including locations such as Western Australia, South Africa, and Japan [14, 16, 17]. The South China Sea (SCS), with a relatively high latitude, belongs to the relatively high-latitude reef region. Relatively high-latitude coral reef areas in the SCS include the Weizhou Island (Guangxi), Daya Bay (Guangdong), Hong Kong, Dongshan (Fujian), and Taiwan [18–20]. The SST of the Weizhou Island (WI) waters can be as high as 32 °C at extremely high temperatures and as low as 12.3 °C at extremely low temperatures [21, 22]. In summer, marine heatwaves cause corals to undergo thermal bleaching in these regions. Meanwhile, marine cold-spells may cause cold bleaching in winter. Although Symbiodiniaceae heat responses are well-studied, their autonomous cold acclimation mechanisms in high-latitude SCS reefs remain elusive, with most research focusing on holobiont level responses [23–26]. *Cladocopium* dominates the Symbiodiniaceae community composition in SCS high-latitude coral reefs, with its prevalence exhibiting a positive latitudinal gradient correlated with seasonal temperature variability [27]. The mechanisms of how *C. goreaui* responds to extremely high and low temperatures remain unclear.

This study systematically investigates *C. goreaui*'s extreme temperature responses (34 °C heat stress/14 °C cold stress vs 26 °C control) using three complementary approaches: (1) F_v/F_m as a biomarker for photosystem impairment; (2) transmission electron microscopy (TEM) revealing ultrastructural changes; and (3) transcriptomics identifying DEGs in energy metabolism, protein folding, and stress signaling. These collectively address how high-latitude populations reconfigure gene networks to withstand thermal fluctuations.

Materials and Methods

Experimental Subjects and Design

C. goreaui was isolated from *Acropora formosa* colonies collected from Weizhou Island reef flats (21°N, 109°E; 2–4 m depth) in August 2022. Coral fragments (5–10 cm) were harvested by underwater chiseling, transported in seawater, and air-brushed to extract tissues. During sampling, surface seawater conditions were as follows: temperature = 28.5 ± 0.5 °C, salinity = 35 ± 1.5‰, and pH = 8.2 ± 0.1. Measurements were conducted using the protocols of Qin et al. [28]. Symbiodiniaceae were purified using a discontinuous Percoll density gradient (40%, 60%, and 80% in sterile seawater) followed by centrifugation at 4000 × g for 10 min. The algal layer at the 60–80% interface was collected. The prepared algal suspension was aseptically transferred to 96-well plates containing L1 medium (Supplementary Table 1) and cultured in LED climate chambers (RDN-500D-CO_2) under controlled conditions (50 µmol photons·m^{-2}·s^{-1}, 26 ± 0.5 °C, 12 h:12 h light:dark cycle). The Symbiodiniaceae cultures were subcultured every 2 weeks using a 1:10 dilution method (culture: medium ratio). Weekly growth monitoring was performed using inverted microscopy. Following morphological confirmation as Symbiodiniaceae, Sanger sequencing was conducted to verify their identity as Symbiodiniaceae. To verify the purification efficiency of Symbiodiniaceae, a second round of high-throughput sequencing was performed after 2 months of culture following the initial high-throughput sequencing. The results demonstrated that the relative abundance of *C. goreaui* exceeded 90% in both sequencing runs. Detailed sequencing metrics are provided in Supplementary Table 2.

Cell density of *C. goreaui* was counted using a hemocytometer (Marienfeld Superior). The cell density of each experimental group was adjusted to 1.1×10^5 cells/mL by adding sterile seawater. Figure 1B and C show the microscopic examination of *C. goreaui* under an optical microscope (Nikon, ECLIPSE Ni-E) at × 400 magnification. The experimental temperature gradients were set as follows: high temperature group (26 °C, 29 °C, 32 °C, and 34 °C) and low temperature group (26 °C, 20 °C, and 14 °C), with an initial temperature of 26 °C, each containing three technical replicates. The temperatures are in reference to the extreme temperatures in WI [29]. Technical replicates were defined as triplicate subcultures derived from the same parent *C. goreaui* population and maintained in three identical under synchronized conditions. Daily verification was performed

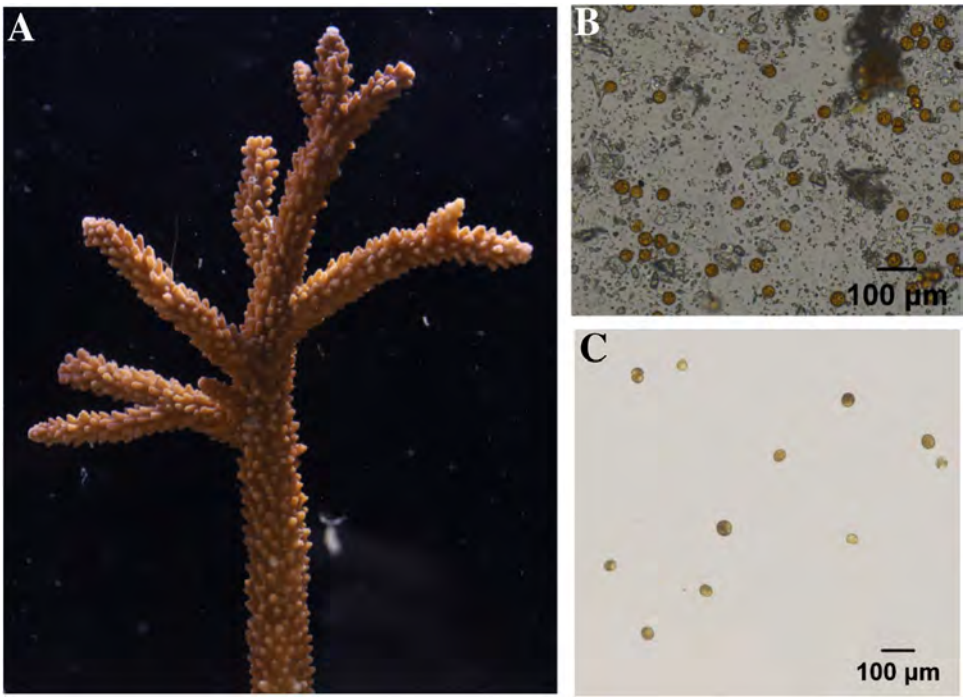


Fig. 1 Cultured *Cladocopium goreaui* were observed under an optical microscope. **A** The *Acropora formosa* symbiotic with *C. goreaui*. **B** Initial isolation of *C. goreaui* from *Acropora formosa*. **C** *C. goreaui* after purification culture

using Traceable® ISO 17025-certified thermometers (± 0.1 °C accuracy). Control samples (ambient temperature, 26 °C) were collected at the experiment's initiation. Temperature adjustments were applied weekly in stepwise increments (Fig. 2). Environmental parameters excluding temperature were standardized across all incubators to eliminate confounding variables. The light intensity of the incubators was uniformly adjusted to 50 μmol photons·m^{-2}·s^{-1}, the humidity was adjusted to 60% RH, and the CO_2 concentration was adjusted to 500 ppm.

Maximum Quantum Yield (F_v/F_m) and Transmission Electron Microscopy (TEM)

In this study, the F_v/F_m in *C. goreaui* was quantified at all sampling timepoints using a DIVING-PAM Submersible Fluorometer (WalzHeinaGmbh, Effeltrich, Germany). Prior to measurement, symbiont cultures were dark-adapted for > 2 h in lighted incubator. F_m was the maximum chlorophyll fluorescence of dark-adapted cells in the presence of a saturating blue light pulse (3000 μmol photons m^{-2} s^{-1}, 1 s). F_O was the minimum fluorescence in the presence of a weakly modulated measured light. F_v/F_m [30] was calculated as follows:

$$\frac{F_V}{F_m} = \frac{F_m - F_o}{F_m}$$

Samples of *C. goreaui* were post-fixed in 1% OsO4/0.1 M phosphate buffer (pH 7.4) for 2 h at RT (dark), rinsed 3 × 15 min with the same buffer, then dehydrated through an ethanol series (30% → 50% → 70% → 80% → 95% → 100%, 20 min each) and acetone (2 × 15 min). Infiltration with EMBed 812 resin followed sequential mixtures: acetone:resin (1:1, 2–4 h; 1:2, overnight) and pure resin (5–8 h) at 37 °C. After embedding and polymerization (37 °C overnight → 60 °C, 48 h), ultrathin Sects. (60–80 nm) were mounted on 150-mesh copper grids. Double staining with 2% uranyl acetate (8 min, dark) and 2.6% lead citrate (8 min, CO_2-free) was performed, with rinses in 70% ethanol and ultrapure water. Grids were air-dried overnight and imaged via TEM (Hitachi HT-7800, 80 kV).

Transcriptome Sequencing and Bioinformatics Analysis

C. goreaui samples from the control group (26 °C), high temperature group (34 °C), and low temperature group (14 °C) were collected for transcriptomic sequencing following temperature treatment. The culture solution containing *C. goreaui* cells was dispensed into 50-mL sterile and enzyme-free centrifuge tubes, vortexed and mixed, and centrifuged using a high-speed cryocentrifuge at 500 × *g* for 10 min at 4 °C. The supernatant was aspirated, the cells were washed with PBS two to three times, and the cells were removed from the centrifuge. After removing phosphate-buffered saline by aspiration, pelleted *C. goreaui* cells were transferred to 2-mL cryogenic vials (CORNING, MEX), snap-frozen in liquid nitrogen, and stored at − 80 °C until RNA extraction.

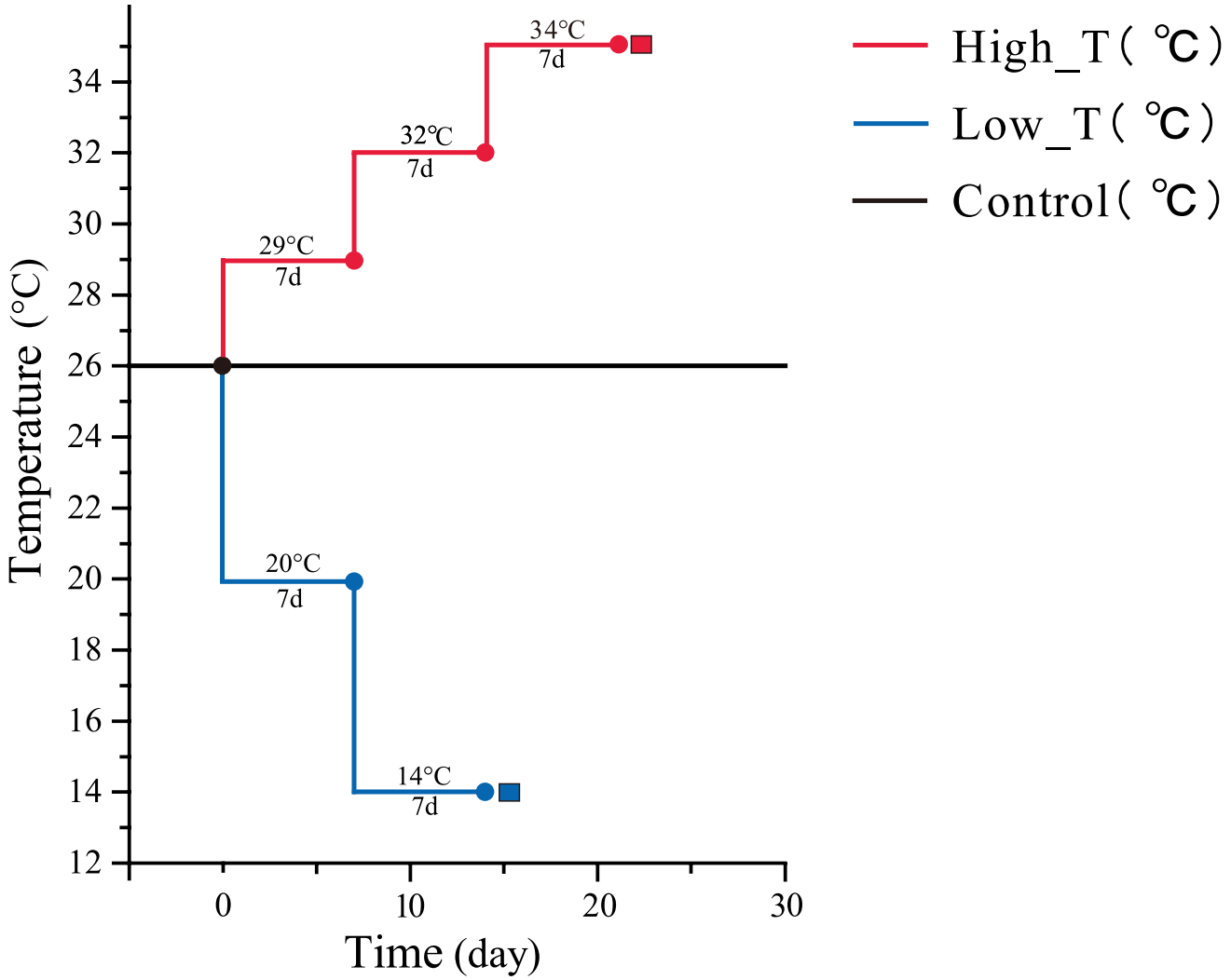


Fig. 2 Experimental temperature settings. Red line represents the high-temperature group (26 °C → 29 °C → 32 °C → 34 °C), black line indicates the control group (constant 26 °C), and blue line denotes the low-temperature group (26 °C → 20 °C → 14 °C). Circles mark sampling points for maximum quantum yield of Photosystem II (F_v/F_m). Squares indicate transcriptomic sampling and transmission electron microscopy (TEM) analyses timepoints

Total RNA was extracted from *C. goreaui* samples using TRIzol® Reagent (QIAzol Lysis Reagent, Qiagen), with quality control parameters rigorously validated: RNA purity (A260/A280 = 1.8–2.2; A260/A230 ≥ 2.0) was assessed via NanoDrop ND-2000, while RNA integrity (RQN ≥ 6.5) and ribosomal ratios (28S:18S ≥ 1.0) were confirmed using Agilent 5300 Bioanalyzer (RNA ScreenTape Assay). Poly(A) + mRNA was enriched from 1 μg high-quality RNA and fragmented to 300 ± 50 bp using NEBNext Magnesium RNA Fragmentation Module (94 °C, 8 min). Stranded RNA-seq libraries were constructed with Illumina Stranded mRNA Prep Kit (Cat. 20,040,534), including cDNA synthesis (SuperScript IV Reverse Transcriptase, Invitrogen), end repair, A-tailing, and adapter ligation. Final libraries were validated via Agilent 4200 TapeStation (DNA HS D1000, insert size 320 ± 25 bp) and sequenced on Illumina NovaSeq X Plus (2 × 150 bp paired-end) at Majorbio Bio-pharm Biotechnology Co., Ltd.

The raw paired end reads were trimmed and quality controlled by fastp [31] with default parameters. Then, clean reads were separately aligned to reference genome with orientation mode using HISAT2 [32] (http://ccb.jhu.edu/software/hisat2/index.shtml) software. The specific filtering procedures are detailed as follows: Adapter sequences were removed from reads, and reads without inserted fragments (e.g., due to adapter self-ligation) were discarded. Low-quality bases (quality score < 20) at the 3′ end were trimmed. If any base with a quality score below 10 remained after trimming, the entire read was discarded; otherwise, it was retained. Reads containing > 10% undetermined bases (N) were eliminated.

Post-trimming reads shorter than 20 bp were excluded. After quality control, filtered data underwent re-evaluation including base error rate distribution analysis and nucleotide content distribution statistics. The filtered clean data were compared with the reference genome *C. goreaui* (http://symbs.reefgenomics.org/download/) [33], and the mapped data were used for transcript assembly and expression calculation. The mapped reads of each sample were assembled by StringTie [34] in a reference-based approach. To identify DEGs (differential expression genes) between two different samples, the expression level of each transcript was calculated according to the transcripts per million reads (TPM) method [35]. RSEM [36] was used to quantify gene abundances. Differential expression analysis was performed using the DESeq2 (http://bioconductor.org/packages/stats/bioc/DESeq2/). DEGs with |log2FC|≧1 and FDR < 0.05(DESeq2) or FDR < 0.001(DEGseq) [37] were considered to be significantly different expressed genes. In addition, functional-enrichment analysis including KEGG was performed to identify which DEGs were significantly enriched in metabolic pathways at Bonferroni-corrected *P*-value < 0.05 compared with the whole-transcriptome background. *C. goreaui* differentially expressed genes were categorized into biological pathways or functional hierarchies using the KEGG Orthology (KO) system via Blast KOALA [38] annotation (sequence-based KO assignment), followed by KEGG Mapper's Reconstruct tool to map K numbers to organism-specific pathways, and enrichment analysis of DEGs through the KEGG PATHWAY database [39]. The KEGG pathway enrichment analysis was performed using the Python SciPy package [40]. To control for the calculation of the false-positive rate, multiple tests were performed using the BH (FDR) method. The corrected *P*-value was thresholded at 0.05 using Fisher's exact test; the corrected *P*-value was thresholded and KEGG pathways meeting this condition were defined as those that were significantly enriched in differentially expressed genes [41].

Statistical Analysis

All data are presented as the mean ± standard deviation of at least three independent technical replicates. Statistical analyses were performed using IBM SPSS Statistics 26 (IBM Corp., Armonk, NY, USA). Differences between groups were assessed by one-way ANOVA using the nonparametric Kruskal–Wallis test, with a *P*-value < 0.05 considered statistically significant.

Results

Physiological Changes in *C. goreaui* Under Extreme High/Low-Temperature Stress

Kruskal–Wallis analysis showed (Fig. 3) that the *C. goreaui* under ambient temperature (26 °C) exhibited the highest F_v/F_m, indicating intact photosystem II (PSII) function. In contrast, the low-temperature groups (at 20 °C and 14 °C) showed a significant reduction in F_v/F_m ($P = 0.000$), suggesting direct structural damage to PSII. Notably, the high temperature group at 29 °C maintained an F_v/F_m level comparable to that of the ambient temperature (26 °C) ($P = 0.146$), while the groups at 32 °C presented marked declines in F_v/F_m ($P = 0.002$). F_v/F_m became undetectable when the temperature reached 34 °C. The raw F_v/F_m data and statistical analysis results can be found in Supplementary Material 3.

Ultrastructure of *C. goreaui* Under Extreme High/Low-Temperature Stress

In Fig. 4, TEM revealed that under the ambient temperature (26 °C), *C. goreaui* cells (8–13 μm) exhibited intact ultrastructure with pyrenoid-containing chloroplasts surrounded by starch granules. *C. goreaui* in the low temperature group

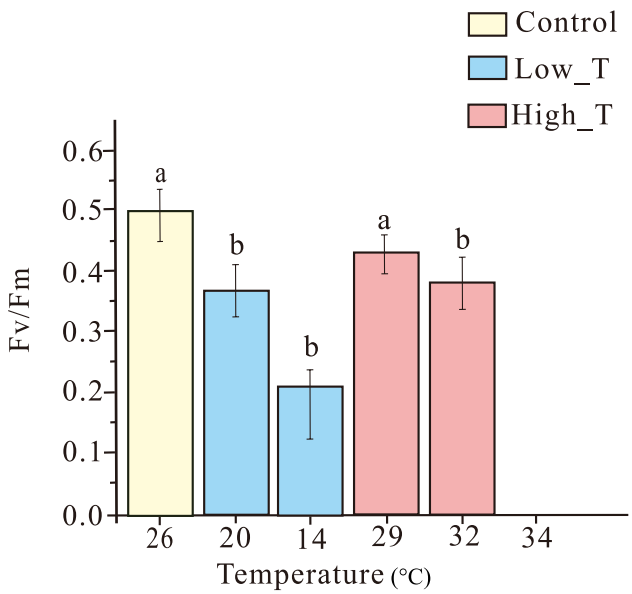


Fig. 3 F_v/F_m activity in *C. goreaui* under experimental treatments. Control (maintained at 26 °C), Low_T (exposed to 14 °C and 20 °C for 7 days), and High_T (exposed to 29 °C, 32 °C and 34 °C for 7 days) are represented by yellow, blue, and red, respectively. Different lowercase letters (a, b) above the bars indicate statistically significant differences. F_v/F_m values could not be detected due to severe disruption of thylakoid membranes within chloroplasts at 34 °C

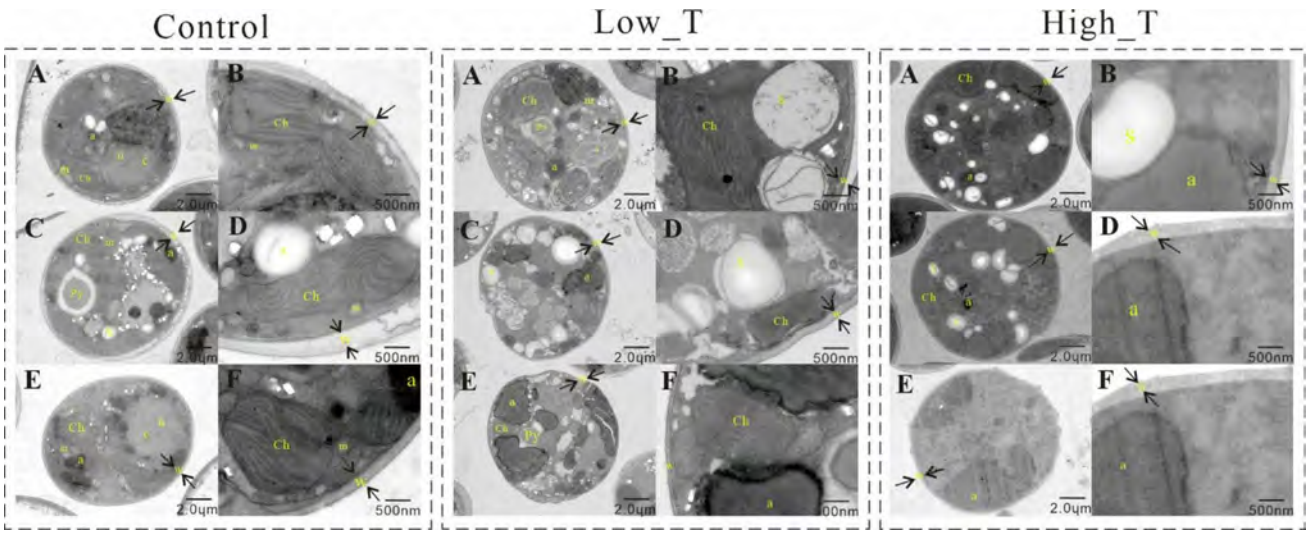


Fig. 4 TEM results of *C. goreaui* under different experimental treatment groups. The experimental groups included: Control (maintained at 26 °C), High-T (exposed to 34 °C for 7 days), and Low-T (exposed to 14 °C for 7 days). "n," nucleus; "Ch," chloroplast; "m," mitochondrion; "s," starch; "a," accumulation body; "w," cell wall; "Py," pyrenoid; "v," chromosome

(14 °C) initially showed stress responses. Although the cell wall still existed, the spatial relationship between the cell and the cell wall might have undergone subtle changes, such as a slight trend of plasmolysis. The internal structure of the chloroplast gradually became disordered, and the arrangement of thylakoids was distorted, which seriously threatened the progress of the light-dependent reaction in photosynthesis. *C. goreaui* in the high temperature group (34 °C) suffered more severe damage. Apoptotic characteristics were significant, and the physiological functions of the cells were on the verge of collapse. The abnormal accumulation of starch revealed the blockage of the pathway for the conversion and utilization of photosynthesis products. A large number of thylakoids in chloroplasts were lost, and photosynthesis was basically paralyzed. The spatial changes between the cell wall and the cells were exacerbated, and the cell morphology was severely distorted.

Transcriptome Analysis of *C. goreaui* Under Extreme High/Low-Temperature Stress

RNA-seq generated 74.13 Gb clean data (> 7.4 Gb per group), with Q30 scores > 92.18% indicating > 99.9% base-call accuracy. The percentage of clean reads mapped to the designated reference genome ranged from 75.86% to 78.0% across samples (Supplementary Table 4).

The Venn diagram (Fig. 5A) identified 21,400 shared genes among control group (26 °C), high temperature group (34 °C), and low temperature group (14 °C) with 67, 342, and 243 group specific genes, respectively, indicating overlapping and unique temperature responses to guide KEGG analysis. PCA (Fig. 5B) revealed PC1 (43.6%) and PC2 (31.82%) collectively explained 75.42% of variance, visualizing major expression differences and separating experimental groups most distinctly high temperature group (34 °C) vs control group (26 °C) confirming significant temperature impacts on *C. goreaui*. Tight intra-group clustering in PCA demonstrated strong technical reproducibility. Correlation heatmap (Fig. 5C) further validated replicate consistency (intra-group $R^2 > 0.98$, dark red), excluding technical artifacts. Table 1 summarizes DEGs under temperature stress. The High-T group exhibited 2831 DEGs ($P < 0.05$, $|\log_2 FC| \geq 1$), comprising 2364 upregulated and 467 downregulated genes. The Low-T group showed 2774 DEGs, with 1498 significantly upregulated and 1249 downregulated genes. Complete datasets are provided in Supplementary Tables 5 and 6.

KEGG analysis revealed temperature-dependent pathway shifts: at 34 °C, upregulation biosynthesis of various plant secondary metabolites, arginine and proline metabolism, nucleocytoplasmic transport, fatty acid biosynthesis, propanoate metabolism, and tryptophan metabolism pathway (Fig. 6A), while downregulation protein processing in endoplasmic reticulum, ascorbate and aldarate metabolism, ribosomes, pentose and glucuronate interconversions, phagosome, and porphyrin metabolism pathway (Fig. 6B) (P value < 0.05). Among these, the differentially expressed genes UGT/DHx38 were significantly downregulated in the ascorbate and aldarate metabolism pathway, while HSP90A and HSP90B were significantly downregulated in the protein processing in endoplasmic reticulum pathway. At 14 °C, spliceosome, mRNA surveillance, nucleocytoplasmic transport, and ribosome biogenesis in eukaryotes pathway were upregulated (Fig. 6C), but glutathione

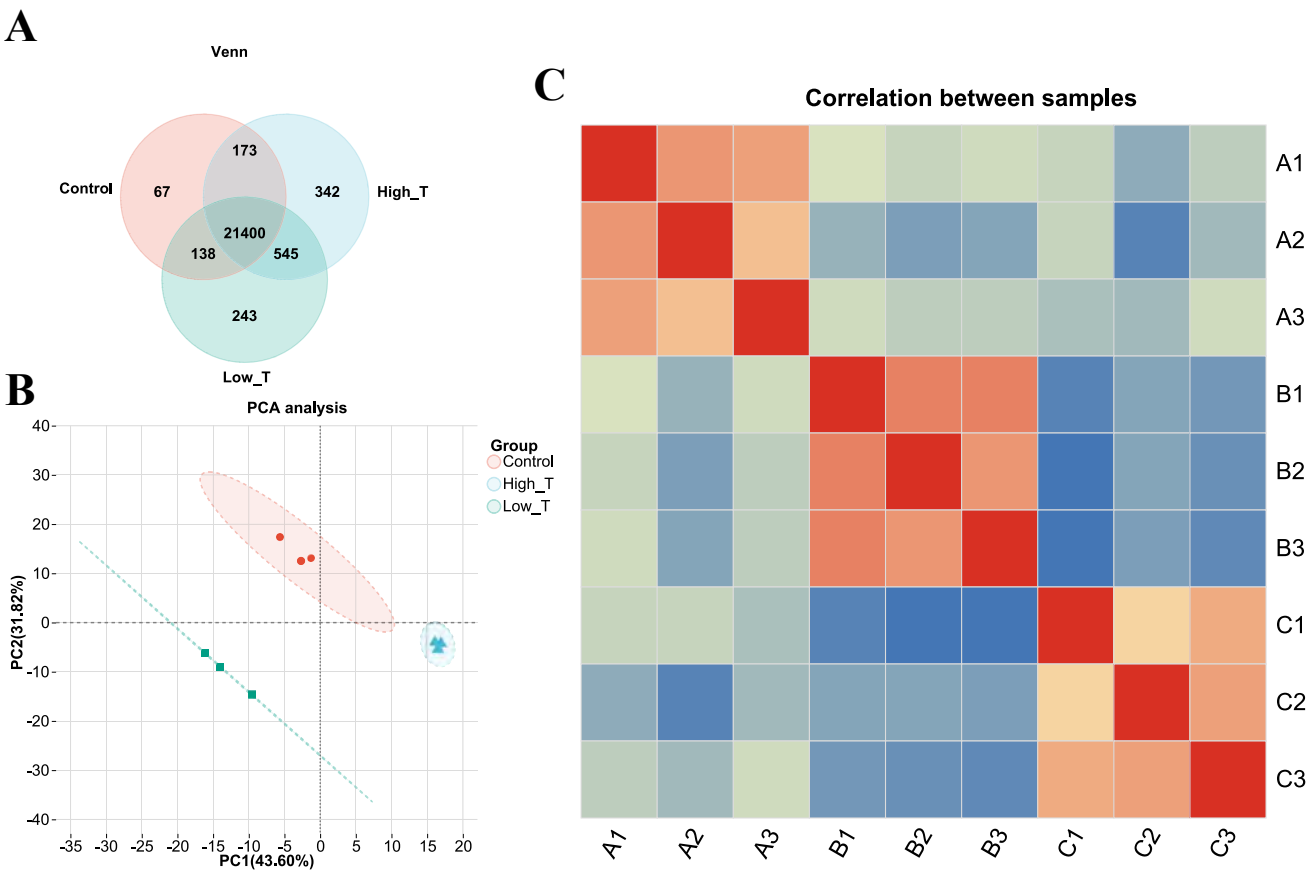


Fig. 5 Correlation and differentially expressed gene analysis of the expression level of *C. goreaui* transcriptome under high/low-temperature stress. **A** Venn diagram of the number of *C. goreaui* specific and shared genes in different experimental groups. **B** PCA analysis of the expression levels of *C. goreaui* transcriptomes in different experimental groups. **C** Graph of correlation analysis between different experimental groups based on the *C. goreaui*'s transcriptomes. Control (maintained at 26 °C), High-T (exposed to 34 °C for 7 days), and Low-T (exposed to 14 °C for 7 days)

Table 1 Different expression gene numbers among groups of *C. goreaui* under extreme high/low-temperature stress

Group	Significantly differentially expressed genes	Upregulated DEGs	Downregulated DEGs
High_T_vs_Control	2831	2364	467
Low_T_vs_Control	2747	1498	1249

metabolism and protein processing in endoplasmic reticulum pathway downregulated (Fig. 6D) (P value < 0.05). Among these, the differentially expressed gene GST was significantly downregulated in the glutathione metabolism pathways, while HSP90B and HSPBP1 were significantly downregulated in the protein processing in endoplasmic reticulum pathway. Supplementary Table 7 includes KEGG pathway analysis of differentially expressed genes (DEGs) under difference stress.

Discussion

Multidimensional Response Mechanisms of Photosynthetic Function and Metabolic Pathways in *C. goreaui* Under High Temperature Stress

Temperature stress affects the physiological state of Symbiodiniaceae. Elevated temperatures perhaps disrupt electron transfer in the photosynthetic system, reducing the F_v/F_m and ultimately impairing photosynthetic efficiency [42]. As shown in Fig. 3A, F_v/F_m at 29 °C showed no significant difference from the control group (26 °C). After 32 °C, F_v/F_m decreased sharply, identifying 32 °C as the critical threshold for PSII heat damage, and at 34 °C, F_v/F_m was undetectable. Howells et al. (2011) demonstrated that Symbiodinium C1 shows no stress at 32 °C after 11 days, with F_v/F_m 16% higher than controls (27 °C), and a follow-up study confirmed stable photosynthetic performance and exROS levels after 15 days at 32 °C [26]. The F_v/F_m of *C. goreaui* remains stable at 29 °C, likely reflecting its short-term

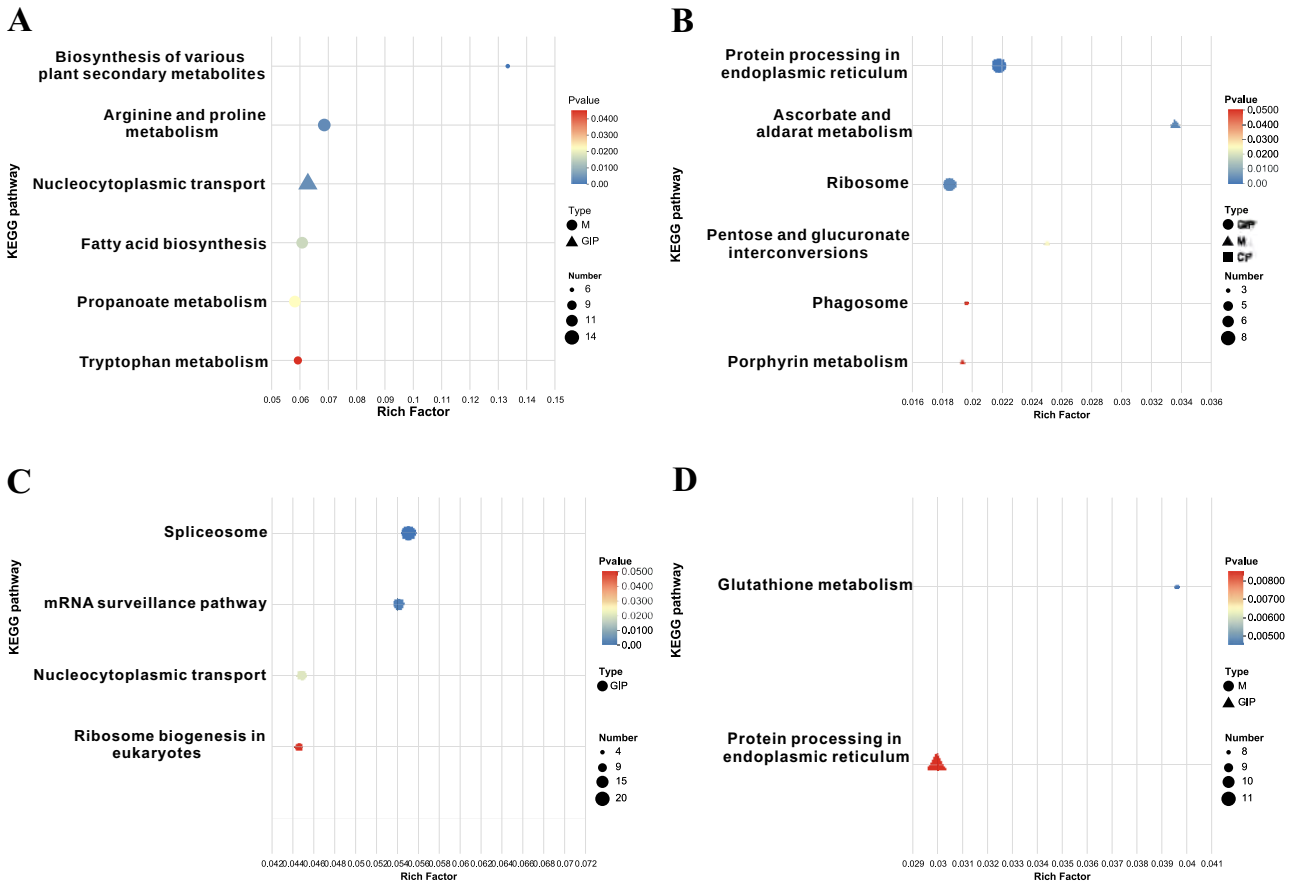


Fig. 6 KEGG enrichment analysis plot of differentially expressed genes. **A** Enrichment results of significantly upregulated genes in the high-temperature group. **B** Enrichment results of significantly downregulated genes in the high-temperature group. **C** Enrichment results of significantly upregulated genes in the low-temperature group. **D** Enrichment results of significantly downregulated genes in the low-temperature group. The y-axis displays pathway names, while the x-axis represents the Rich factor (defined as the ratio of enriched genes in the pathway to the annotated background genes). Larger Rich factors indicate stronger enrichment. The size of each point corresponds to the number of genes in the pathway, and the color denotes different ranges of adjusted *p*-values. M, metabolism; GIP, genetic information processing; CP, cellular process

thermal acclimation capacity, which is consistent with the performance of corals in high-latitude regions. There, seasonal temperature fluctuations have selected for physiological plasticity in coral responses to temperature stress within marginal coral communities [43]. In contrast, Symbiodinium C1 can enhance F_v/F_m at 32 °C, suggesting that tropical symbionts may have evolved constitutive heat tolerance to persist in stable, warm environments [26]. The divergence between *C. goreaui* and Symbiodinium C1 also underscores the potential for "symbiont shuffling" in high-latitude corals. If warming exceeds *C. goreaui*'s threshold, corals may switch to more heat-tolerant symbionts (e.g., *Durusdinium*), as observed in tropical systems [26, 44]. Structurally, thylakoid membranes—embedded in the chloroplast stroma and densely distributed around the pyrenoid—are central to light energy capture [45]. TEM images of the high temperature group (Fig. 4) revealed *C. goreaui* thylakoid membrane disintegration and loss of light energy capture efficiency. This structural collapse likely explains the undetectable F_v/F_m at 34 °C [46].

High temperature stress increases the concentration of ROS in Symbiodiniaceae cells [47]. High concentration ROS interacts with components involved in mitochondrial apoptosis, which promotes cell apoptosis [48]. In eukaryotic cells, superoxide dismutase (SOD) is one of the important antioxidant pathways, providing the first line of defense against O_2^- and H_2O_2 and alleviating the damage caused by ROS to cells [49]. KEGG enrichment analysis revealed a significant upregulation of arginine and proline metabolism pathways in the high-temperature group. These two nitrogen-containing compounds are not only important osmoregulators but also can indirectly enhance ROS scavenging capacity by participating in the glutathione cycle [50]. Polyamines derived from arginine can stabilize thylakoid membrane structures, while proline directly scavenges hydroxyl radicals (·OH) and assists SOD in coping with the explosive accumulation of

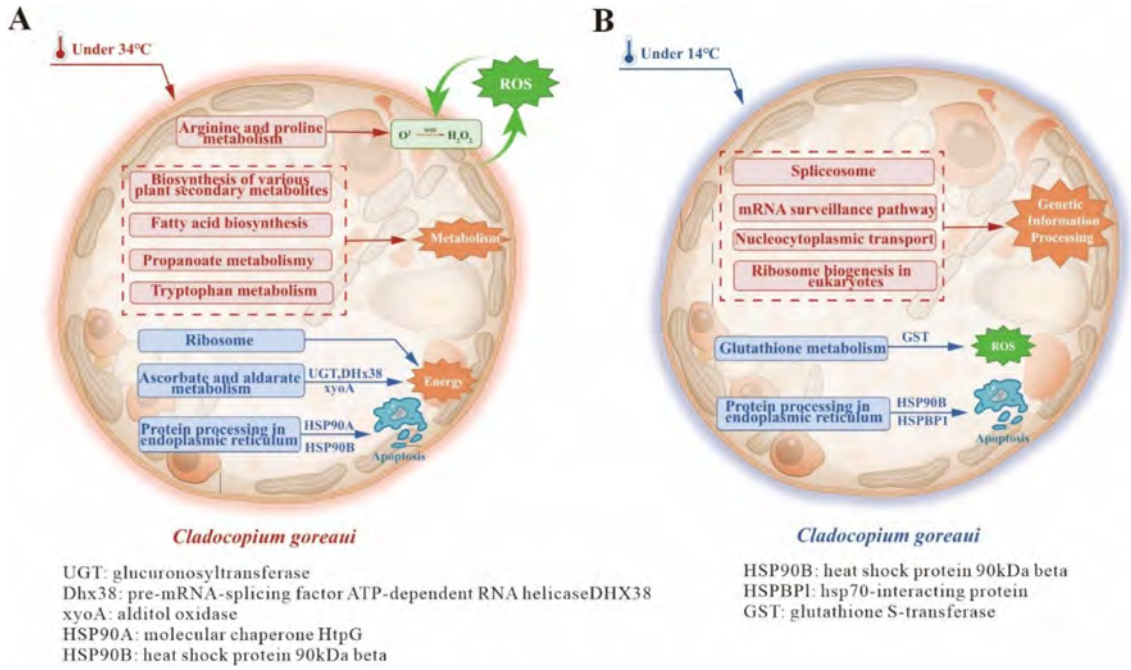


Fig. 7 Response mechanisms of *C. goreaui* at different temperatures. **A** High temperature at 34 °C. **B** Low temperature at 14 °C. Color types indicate *C. goreaui* upregulated (red) and downregulated (blue) expression

O_2^- and H_2O_2, thereby delaying the vicious cycle of oxidative damage → photosynthetic collapse [51].

High temperature may induce apoptosis in *C. goreaui* cells [52]. KEGG enrichment analysis shows that the protein processing in endoplasmic reticulum pathway in dinoflagellate symbionts was significantly downregulated, indicating that the cells were reducing protein synthesis [53]. Within the ER protein processing pathway, the significant downregulation of HSP90A and HSP90B represents a critical tipping point for apoptosis in *C. goreaui*. HSP90 is a conserved molecular chaperone with dual roles: maintaining the stability of client proteins (e.g., signaling kinases, transcription factors) and directly inhibiting apoptotic signaling [54]. Studies have shown differential expression patterns of HSP70 and HSP90 in coral hosts and their algal symbionts under heat stress. In *Acropora aspera*, coral HSP90 and HSP70 were significantly upregulated during bleaching, while symbiont HSP90 decreased [55]. Similarly, in Symbiodinium, moderate heat stress increased HSP70 expression, but extreme stress reduced it, while HSP90 expression decreased under all heat stress conditions [54]. In coral symbionts, HSP90 upregulation is typically associated with thermal tolerance—for example, tropical *Durusdinium* strains upregulate HSP90 to protect photosynthetic machinery under heat stress [56]. In this study, downregulation of heat shock proteins may lead to apoptosis in *C. goreaui* [57].

High-temperature stress critically disrupts *C. goreaui* metabolism and survival, triggering upregulation of five protective metabolic pathways—biosynthesis of plant secondary metabolites, fatty acid biosynthesis, propanoate metabolism, arginine and proline metabolism, and tryptophan metabolism—which enhance osmoprotection, membrane integrity, and antioxidant capacity as observed in analogous heat-stressed phototrophs like seaweed *Pyropia haitanensis* [58]. Concurrently, *C. goreaui* counteracts energy metabolism disorder [59] by downregulating energy-intensive processes (e.g., ribosome biogenesis and ascorbate/aldarate metabolism) [60], while redirecting carbon flux through UGT/xyoA-catalyzed pentose/glucuronate interconversions to optimize TCA cycle efficiency for ATP homeostasis. This dual strategy of protective metabolite induction and precision energy governance, aligned with proteomic-documented prioritization of photosynthesis and defense over protein synthesis [61], sustains cellular function under thermal extremes. For high-latitude coral reefs dominated by *C. goreaui*, this metabolic flexibility provides partial buffering against climate change. Upregulation of stress pathways may extend survival during transient heatwaves, consistent with predictions that temperate reefs could serve as climate refugia [62]. Notably, this metabolic profile contrasts sharply with tropical symbionts (e.g., *Durusdinium*), which typically upregulate energy-intensive pathways such as oxidative phosphorylation to enhance antioxidant defenses [56]. This divergence likely reflects adaptation to distinct thermal regimes: tropical symbionts prioritize sustained defense in stable, warm environments, whereas high-latitude *C. goreaui*

prioritizes plastic energy conservation to survive seasonal fluctuations (Fig. 7).

Energy Reallocation in Cold-Stressed *C. goreaui*: Prioritize Genetic Fidelity

Low-temperature stress, as a non-negligible abiotic disturbance factor in the marine environment, exerts a remarkable remodeling effect on the physiological homeostasis of coral symbiotic Symbiodiniaceae [63]. Figure 3 shows that the F_v/F_m in the 20 °C and 14 °C groups was significantly lower than that in the control group, reflecting the blockage of the photosynthetic electron transport chain [64]. The phenomenon of thylakoid disintegration was observed from the TEM results, which may be the reason for the significant decrease in F_v/F_m [46]. In addition to photosynthetic damage, low temperature stress may also inhibit the antioxidant defense capacity of *C. goreaui*, rendering cells vulnerable to the accumulation of ROS [65]. KEGG enrichment analysis shows that the glutathione metabolic pathway was significantly downregulated, and the gene GST related to the glutathione metabolic pathway was also significantly downregulated. Glutathione plays a crucial role in the cellular antioxidant system. GST is a key enzyme in glutathione metabolism, which can accelerate glutathione synthesis, and reduced glutathione can counteract ROS [66]. This indicates that *C. goreaui* may have defects in the enzymatic antioxidant pathway. This stands in sharp contrast to *C. goreaui*'s response to heat stress, where arginine/proline metabolism is upregulated to enhance ROS scavenging.

Low-temperature stress poses unique challenges to cellular integrity, affecting various aspects of genetic information transfer. Cold denaturation can alter protein structure at quaternary, tertiary, and secondary levels, leading to cellular injuries [67]. Eukaryotic cells respond to hypothermia through various regulatory mechanisms, including alterations in gene expression, attenuated protein synthesis, and changes in lipid composition, to preserve energy and prolong cell survival [68]. In our study, KEGG enrichment analysis revealed that *C. goreaui* significantly upregulated four pathways related to genetic information processing: the spliceosome pathway, mRNA surveillance pathway, nucleocytoplasmic transport, and ribosome biogenesis in eukaryotes. While downregulating the endoplasmic reticulum protein processing pathway. The spliceosome repairs pre-mRNA splicing errors to ensure the correct expression of cold-responsive genes [69]. The mRNA surveillance pathway degrades abnormal mRNA, thereby maintaining transcriptome quality [70]. Nucleocytoplasmic transport accelerates the nuclear import of stress factors and the export of mature mRNA, safeguarding the continuity of gene expression [71]. Ribosome biogenesis in eukaryotes optimizes ribosome assembly to support the translation of key proteins [72]. Collectively, the upregulation of these pathways indicates that *C. goreaui* prioritizes ensuring the fidelity of genetic information flow over protein-dependent repair mechanisms (e.g., heat shock proteins) under cold stress. This emphasis on genetic repair stands in sharp contrast to *C. goreaui*'s response to heat stress, where protein-dependent defenses are prioritized.

ER stress may trigger cell death [73]. Under cold stress, *C. goreaui* exhibits ER stress characterized by downregulation of protein processing pathways within the ER [74]—a critical system for cellular protein synthesis and modification. Specifically, key heat shock protein (HSP) genes (HSP90B and HSPBP1) in this pathway are significantly suppressed. Notably, HSPs play essential roles in stabilizing protein folding, preventing aggregation, and facilitating stress response under abiotic challenges including cold [75]. This coordinated downregulation likely reflects *C. goreaui*'s adaptive resource reallocation strategy: redirecting energy from protein processing toward cold adaptation mechanisms. While this prioritization may temporarily sustain cellular function, it carries trade-offs—insufficient chaperone activity that may trigger apoptotic pathways under extreme cold stress [76]. High-latitude coral reefs experience seasonal cold snaps but return to optimal temperatures annually [77]. Under cold stress, *C. goreaui* regulates genetic information processing while suppressing ER protein processing, demonstrating its resource allocation strategy under energy-limited conditions. By prioritizing the fidelity of genetic information flow, it ensures survival during cold exposure (Fig. 7).

Conclusion

Temperature stress significantly impacts the physiological state of *C. goreaui*, disrupting photosynthetic electron transfer and reducing F_v/F_m, thereby impairing photosynthetic efficiency. At 29 °C, F_v/F_m remains comparable to the control (26 °C), but beyond 32 °C—a critical threshold for PSII damage—it declines sharply, becoming undetectable at 34 °C. While Symbiodinium C1 exhibits thermal tolerance at 32 °C, *C. goreaui* demonstrates short-term acclimation at 29 °C, reflecting adaptations to seasonal fluctuations in high-latitude reefs. Structural damage to thylakoid membranes at high temperatures explains the photosynthetic collapse. Concurrently, heat stress elevates ROS levels, triggering apoptosis, though antioxidant pathways (e.g., arginine/proline metabolism) and metabolic adjustments (e.g., downregulation of energy-intensive processes) partially mitigate damage. In contrast, cold stress (14–20 °C) impairs photosynthesis and antioxidant capacity (e.g., glutathione downregulation), while *C. goreaui*

prioritizes genetic fidelity via upregulated spliceosome and mRNA surveillance pathways, sacrificing protein repair mechanisms. This divergence in stress responses underscores *C. goreaui*'s adaptive strategies: metabolic flexibility for heat and genetic preservation for cold, aligning with its niche in thermally variable reefs.

Supplementary Information The online version contains supplementary material available at https://doi.org/10.1007/s00248-025-02587-0.

Acknowledgements This research was supported by the National Natural Science Foundation of China (42206157, 42030502, 42090041), the Natural Science Foundation of Guangxi Province (2025GXNSFAA069187). The authors declare that the research was conducted in the absence of any commercial or financial relationships that could be construed as a potential conflict of interest. The raw data were deposited in the NCBI Sequence Read Archive (SRA) database (https://www.ncbi.nlm.nih.gov/, PRJNA1245310).

Author Contribution Author Contributions Statement LFW (First Author): Conceptualization, Methodology, Formal Analysis, Writing—Original Draft; SCC: Data Curation, Software, Validation; ZJQ(Corresponding Author): Methodology, Formal Analysis, Visualization;Writing—Review & Editing, Funding Acquisition; NBP: Formal Analysis, Writing—Review & Editing; MLL: Software Development, Data Visualization; TCZ: Formal Analysis, Supervision; RH: Methodology, Validation, Writing—Review & Editing; HYL: Data Collection, Visualization; WZD: Supervision, Writing—Review & Editing; CHM: Formal Analysis, Statistical Analysis; KFY (Corresponding Author): Conceptualization, Funding Acquisition, Supervision, Writing—Review & Editing, Project Administration. All authors have reviewed and approved the final version of the manuscript.

Funding This research was supported by the National Natural Science Foundation of China (42206157, 42030502, 42090041), the Natural Science Foundation of Guangxi Province (2025GXNSFAA069187).

Data Availability The raw data were deposited in the NCBI Sequence Read Archive (SRA) database (https://www.ncbi.nlm.nih.gov/, PRJNA1245310).

Declarations

Competing Interests The authors declare no competing interests.

Open Access This article is licensed under a Creative Commons Attribution-NonCommercial-NoDerivatives 4.0 International License, which permits any non-commercial use, sharing, distribution and reproduction in any medium or format, as long as you give appropriate credit to the original author(s) and the source, provide a link to the Creative Commons licence, and indicate if you modified the licensed material. You do not have permission under this licence to share adapted material derived from this article or parts of it. The images or other third party material in this article are included in the article's Creative Commons licence, unless indicated otherwise in a credit line to the material. If material is not included in the article's Creative Commons licence and your intended use is not permitted by statutory regulation or exceeds the permitted use, you will need to obtain permission directly from the copyright holder. To view a copy of this licence, visit http://creativecommons.org/licenses/by-nc-nd/4.0/.

References

1. Voolstra CR, Suggettd DJ, Peixoto RS et al (2021) Extending the natural adaptive capacity of coral holobionts. Nat Rev Earth Environ 2(11):747–762. https://doi.org/10.1038/s43017-021-00214-3
2. Lajeunesse TC, Everett PJ, Gabrielson PW et al (2018) Systematic revision of Symbiodiniaceae highlights the antiquity and diversity of coral endosymbionts. Curr Biol 28:2570–2580. https://doi.org/10.1016/j.cub.2018.07.008
3. Zhang M, Huang S, Luo L (2015) Environmental acclimatization of the relatively high latitude scleractinian coral Pavona decussata: integrative perspectives on seasonal subaerial exposure and temperature fluctuations. BMC Genomics 26(1):483. https://doi.org/10.1186/s12864-025-11660-4
4. Hughes Terry P, Kerry James T, Álvarez-Noriega M et al (2017) Global warming and recurrent mass bleaching of corals. Nature 543(7645):373–377. https://doi.org/10.1038/nature21707
5. Chakravarti LJ, Beltran VH, Van Oppen MJH (2017) Rapid thermal adaptation in photosymbionts of reef-building corals. Glob Change Biol 10:40. https://doi.org/10.1111/gcb.13702
6. Muratan N, Takahashi S, Nishiyama Y et al (2007) Photoinhibition of photosystem II under environmental stress. Biochimica et Biophysica Acta (BBA)-Bioenergetics 1767(6):414–421. https://doi.org/10.1016/j.bbabio.2006.11.019
7. Wang Q L, Chen J H, He N Y (2018) Metabolic reprogramming in chloroplasts under heat stress in plants. Int J Mol Sci 2018. 19(3). https://doi.org/10.3390/ijms19030849
8. Marangoni L F D B, C Rottier, C Ferrier-Pagès (2021) Symbiont regulation in Stylophora pistillata during cold stress: an acclimation mechanism against oxidative stress and severe bleaching. J Experimental Biol 224(Pt 3). https://doi.org/10.1242/jeb.235275
9. Solayan A (2016) Biomonitoring of coral bleaching - a glimpse on biomarkers for the early detection of oxidative damages in corals, in Invertebrates - experimental models in toxicity screening, M.L. Larramendy and S. Soloneski, Editors. 2016, IntechOpen: Rijeka. https://doi.org/10.5772/61831
10. Yao Y, Wang C (2022) Marine heatwaves and cold-spells in global coral reef zones. Prog Oceanogr. https://doi.org/10.1016/j.pocean.2022.102920
11. Thornhill Daniel J, Kemp Dustin W, Bruns Brigitte U et al (2010) Correspondence between cold tolerance and temperate biogeography in a western Atlantic Symbiodinium (Dinophyta) Lineage1. J Phycol 44(5):1126–1135. https://doi.org/10.1111/j.1529-8817.2008.00567.x
12. Smith D, Suggett D, Baker N (2005) Is photoinhibition of zooxanthellae photosynthesis the primary cause of thermal bleaching in corals? Global Change Biol. Global Change Biol 11:1–11. https://doi.org/10.1111/j.1529-8817.2003.00895.x
13. Shaohua Mo, Tianran C, Zesheng C et al (2022) Marine heatwaves impair the thermal refugia potential of marginal reefs in the northern South China Sea. Sci Total Environ 825:154100. https://doi.org/10.1016/j.scitotenv.2022.154100
14. Tom B, Legorreta F, Mitch RB et al (2014) Variable responses of benthic communities to anomalously warm sea temperatures on a high-latitude coral reef. PLoS One 9:e113079. https://doi.org/10.1371/journal.pone.0113079
15. Wei X, Yu K, Qin Z et al (2024) The acute and chronic low-temperature stress responses in Porites lutea from a relatively high-latitude coral reef of the South China Seahttps://doi.org/10.3389/fmars.2024.1321865
16. Schleyer Michael H, Laing FC, Stuart CS et al (2018) What can South African reefs tell us about the future of high-latitude coral systems? Mar Pollut Bull 136:491–507. https://doi.org/10.1016/j.marpolbul.2018.09.014

17. Denis V, Mezaki T, Tanaka K et al (2013) Coverage, diversity, and functionality of a high-latitude coral community (Tatsukushi, Shikoku Island, Japan). PLoS One 8(1):e54330. https://doi.org/10.1371/journal.pone.0054330
18. Chen Tianran, Yu Kefu (2014) Responses and high-resolution records for marine environment changes in the relatively high-latitude corals from the South China Sea[J]. Quaternary Sciences, 34(6): 1288-1295https://doi.org/10.3969/j.issn.1001-7410.2014.06.18
19. Wang Y, Yu K, Chen X et al (2020) An approach for assessing ecosystem-based adaptation in coral reefs at relatively high latitudes to climate change and human pressure. Environ Monit Assess 192:579. https://doi.org/10.1007/s10661-020-08534-5
20. Huang W, Yang E, Yu K et al (2022) Lower cold tolerance of tropical Porites lutea is possibly detrimental to its migration to relatively high latitude refuges in the South China Sea. Mol Ecol 31(20):5339–5355. https://doi.org/10.1111/mec.16662
21. YU Kefu, Jiang Mingxing, Cheng Zhiqiang et al (2004) Latest forty two years' sea surface temperature change of Weizhou Island and its influence on coral reef ecosysten. 15(3): 506–510. https://www.cjae.net/EN/Y2004/V/I3/506
22. Yu K (2012) Coral reefs in the South China Sea: their response to and records on past environmental changes. Sci China Earth Sci. https://doi.org/10.1007/s11430-012-4449-5
23. Nunn Brook L, Tanya B, Emma T-S et al (2025) Protein signatures predict coral resilience and survival to thermal bleaching events. Commun Earth Environ 6(1):191. https://doi.org/10.1038/s43247-025-02167-7
24. Levin RA, Beltran VH, Hill R et al (2016) Sex, scavengers, and chaperones: transcriptome secrets of divergent Symbiodinium thermal tolerances. Mol Biol Evol 33(9):2201–2215. https://doi.org/10.1093/molbev/msw119
25. McGinty ES, Pieczonka J, Mydlarz LD (2012) Variations in reactive oxygen release and antioxidant activity in multiple Symbiodinium types in response to elevated temperature. Microb Ecol 64(4):1000–1007. https://doi.org/10.1007/s00248-012-0085-z
26. Howells E J Beltran, V H Larsen N W et al (2012) Coral thermal tolerance shaped by local adaptation of photosymbionts. Nat Climate Change 2(2): 116-120https://doi.org/10.1038/nclimate1330
27. Chen B, Yu K, Liang J et al (2019) Latitudinal variation in the molecular diversity and community composition of Symbiodiniaceae in coral from the South China Sea. Front Microbiol 10. https://doi.org/10.3389/fmicb.2019.01278
28. Qin, Zhenjun, Yu, Kefu, Liang, Jiayuan et al (2020) Significant changes in microbial communities associated with reef corals in the southern South China Sea during the 2015/2016 global-scale coral bleaching event. J Geophysical Res Oceans 125. https://doi.org/10.1029/2019JC015579
29. Feng Y, Bethel BJ, Dong C et al (2022) Marine heatwave events near Weizhou Island, Beibu Gulf in 2020 and their possible relations to coral bleaching. Sci Total Environ 823:153414. https://doi.org/10.1016/j.scitotenv.2022.153414
30. Van KO, Snel JF (1990) The use of chlorophyll fluorescence nomenclature in plant stress physiology. Photosynth Res 25(3):147–150. https://doi.org/10.1007/bf00033156
31. Chen S, Zhou Y, Chen Y et al (2018) fastp: an ultra-fast all-in-one FASTQ preprocessor. Bioinformatics 34(17):i884–i890. https://doi.org/10.1093/bioinformatics/bty560
32. Kim D, Paggi J, M Park C et al (2019) Graph-based genome alignment and genotyping with HISAT2 and HISAT-genotype. Nat Biotechnol 37(8): 907-915https://doi.org/10.1038/s41587-019-0201-4
33. Liew Y J, M Aranda, and C R Voolstra (2016) Reefgenomics.Org - a repository for marine genomics data. Database J Biological Databases Curation. https://doi.org/10.1093/database/baw152
34. Pertea M, Pertea G, Antonescu C et al (2015) Stringtie enables improved reconstruction of a transcriptome from RNA-seq reads. Nat Biotechnol 33:290–295. https://doi.org/10.1038/nbt.3122
35. In H L Y, and R Pincket (2022)Transcripts per million ratio: applying distribution-aware normalisation over the popular TPM method. https://doi.org/10.48550/arXiv.2205.02844
36. Li B, Dewey CN (2011) RSEM: accurate transcript quantification from RNA-Seq data with or without a reference genome. BMC Bioinformatics 12(1):323. https://doi.org/10.1186/1471-2105-12-323
37. Love MI, Huber W, Anders S (2014) Moderated estimation of fold change and dispersion for RNA-seq data with DESeq2. Genome Biol 15(12):550. https://doi.org/10.1186/s13059-014-0550-8
38. Kanehisa M, Sato Y, Morishima K (2016) BlastKOALA and GhostKOALA: KEGG tools for functional characterization of genome and metagenome sequences. J Mol Biol 428(4):726–731. https://doi.org/10.1016/j.jmb.2015.11.006
39. Kanehisa M, Goto S (2000) KEGG: Kyoto Encyclopedia of Genes and Genomes. Nucleic Acids Res 28(1):27–30. https://doi.org/10.1093/nar/gkw1092
40. Virtanen P, Gommers R, Oliphant TE et al (2020) SciPy 1.0: fundamental algorithms for scientific computing in Python. Nat Methods 17:261–272. https://doi.org/10.1038/s41592-019-0686-2
41. Chen Xie 1, Xizeng Mao, Jiaju Huang et al (2011) KOBAS 2.0: a web server for annotation and identification of enriched pathways and diseases. Nucleic Acids Research. 39(Web Server issue) 316–22. https://doi.org/10.1093/nar/gkr483
42. Warner ME, Fitt WK, Schmidt GW (1996) The effects of elevated temperature on the photosynthetic efficiency of zooxanthellae in hospite from four different species of reef coral: a novel approach. Plant Cell Environ 19:291–299. https://doi.org/10.1111/j.1365-3040.1996.tb00251.x
43. Keshavmurthy S, Beals M, Hsieh HJ et al (2021) Physiological plasticity of corals to temperature stress in marginal coral communities. Sci Total Environ 758:143628. https://doi.org/10.1016/j.scitotenv.2020.143628
44. Abbott E, Dixon G, Matz M (2021) Shuffling between Cladocopium and Durusdinium extensively modifies the physiology of each symbiont without stressing the coral host. Mol Ecol 30(24):6585–6595. https://doi.org/10.1111/mec.16190
45. Zhao LS, Huokko T, Wilson S et al (2020) Structural variability, coordination and adaptation of a native photosynthetic machinery. Nat Plants 6:869–882. https://doi.org/10.1038/s41477-020-0694-3
46. Koji Y, Michio K, Mitsutaka T et al (2008) Correlation between chloroplast ultrastructure and chlorophyll fluorescence characteristics in the leaves of rice (Oryza sativa L.) grown under salinity. Plant Prod Sci 11(1):139–145. https://doi.org/10.1626/pps.11.139
47. Amario M, Villela LB, Jardim-Messeder D et al (2023) Physiological response of *Symbiodiniaceae* to thermal stress: reactive oxygen species, photosynthesis, and relative cell size. PLoS One 18(8):e0284717. https://doi.org/10.1371/journal.pone.0284717
48. Hawkins TD, Bradley BJ, Davy SK (2013) Nitric oxide mediates coral bleaching through an apoptotic-like cell death pathway: evidence from a model sea anemone-dinoflagellate symbiosis. FASEB J 27(12):4790–4798. https://doi.org/10.1096/fj.13-235051
49. Cziesielski MJ, Schmidt-Roach S, Aranda M (2019) The past, present, and future of coral heat stress studies. Ecol Evol 9(17):10055–10066. https://doi.org/10.1002/ece3.5576
50. You J, Hu H, Xiong L (2012) An ornithine δ-aminotransferase gene OsOAT confers drought and oxidative stress tolerance in rice. Plant Sci 197:59–69. https://doi.org/10.1016/j.plantsci.2012.09.002
51. Shaghef Ejaz, Shah Fahad, Muhammad Akbar Anjum et al (2020). Role of osmolytes in the mechanisms of antioxidant defense of plants. In: Lichtfouse, E. (eds) Sustainable agriculture reviews 39.

Sustainable Agriculture Reviews, 39. Springer, Cham. https://doi.org/10.1007/978-3-030-38881-2_4
52. Zhi Zhou, Kaidian Zhang, Lingui Wang et al (2021) *N*itrogen availability improves the physiological resilience of coral endosymbiont Cladocopium goreaui to high temperature. J Phycology 57. https://doi.org/10.1111/jpy.13156
53. DuRose JB, Scheuner D, Kaufman RJ et al (2009) Phosphorylation of eukaryotic translation initiation factor 2α coordinates rRNA transcription and translation inhibition during endoplasmic reticulum stress. Mol Cell Biol 29(15):4295–4307. https://doi.org/10.1128/MCB.00260-09
54. Rosic NN, Pernice M, Dove S et al (2011) Gene expression profiles of cytosolic heat shock proteins Hsp70 and Hsp90 from symbiotic dinoflagellates in response to thermal stress: possible implications for coral bleaching. Cell Stress Chaperones 16(1):69–80. https://doi.org/10.1007/s12192-010-0222-x
55. Leggat W P, Seneca F, Wasmund K et al (2011). Differential responses of the coral host and their algal symbiont to thermal stress. PLoS ONE, 6. https://doi.org/10.1371/journal.pone.0026687
56. Cunning R, Baker AC (2020) Thermotolerant coral symbionts modulate heat stress-responsive genes in their hosts. Mol Ecol 29(15):2940–2950. https://doi.org/10.1111/mec.15526
57. Pinzón JH, Kamel B, Burge CA et al (2015) Whole transcriptome analysis reveals changes in expression of immune-related genes during and after bleaching in a reef-building coral. Royal Soc Open Sci 2(4):140214. https://doi.org/10.1098/rsos.140214
58. Zeb A, Khan Y, Yang X et al (2024) Impact of temperature stress on Pyropia yezoensis and its inhabitant microbiota to promote aquaculture. Environ Adv 16:100532. https://doi.org/10.1016/j.envadv.2024.100532
59. Sun Y, Jiang L, Gong S et al (2022) Changes in physiological performance and protein expression in the larvae of the coral Pocillopora damicornis and their symbionts in response to elevated temperature and acidification. Sci Total Environ 807:151251. https://doi.org/10.1016/j.scitotenv.2021.151251
60. Kos-Braun IC, Jung I, Koš M et al (2017) Tor1 and CK2 kinases control a switch between alternative ribosome biogenesis pathways in a growth-dependent manner. PLoS Biol 15(3):e2000245. https://doi.org/10.1371/journal.pbio.2000245
61. Shi J, Chen Y, Xu Y et al (2017) Differential proteomic analysis by iTRAQ reveals the mechanism of *Pyropia haitanensis* responding to high temperature stress. Sci Rep 7:44734. https://doi.org/10.1038/srep44734
62. González-Pech RA, Hughes DJ, Strudwick P et al (2022) Physiological factors facilitating the persistence of Pocillopora aliciae and Plesiastrea versipora in temperate reefs of south-eastern Australia under ocean warming. Coral Reefs 41:1239–1253. https://doi.org/10.1007/s00338-022-02277-0
63. Roth M, Goericke R, Deheyn D (2012) Cold induces acute stress but heat is ultimately more deleterious for the reef-building coral *Acropora yongei*. Sci Rep 2:240. https://doi.org/10.1038/srep00240
64. Krause GH, Somersalo S (1989) Fluorescence as a tool in photosynthesis research: application in studies of photoinhibition, cold acclimation and freezing stress [and Discussion]. Philos Trans R Soc B Biol Sci 323(1216):281–293. https://doi.org/10.1098/rstb.1989.0010
65. Rezayian M, Niknam V, Ebrahimzadeh H (2019) Oxidative damage and antioxidative system in algae. Toxicol Rep 6:1309–1313. https://doi.org/10.1016/j.toxrep.2019.10.001
66. Allocati N, Masulli M, Di Ilio C et al (2018) Glutathione transferases: substrates, inihibitors and pro-drugs in cancer and neurodegenerative diseases. Oncogenesis 7:8. https://doi.org/10.1038/s41389-017-0025-3
67. Gulevsky AK, Relina LI (2013) Molecular and genetic aspects of protein cold denaturation. Cryo Letters 34(1):62–82
68. Adjirackor N A, K E Harvey, and S C (2020) Harvey, Eukaryotic response to hypothermia in relation to integrated stress responses. Cell Stress Chaperones. 25(6): p. 833-846https://doi.org/10.1007/s12192-020-01135-8
69. Chung-An Lu, Huang C-K, Huang W-S et al (2020) DEAD-box RNA helicase 42 plays a critical role in pre-mRNA splicing under cold stress. Plant Physiol 182(1):255–271. https://doi.org/10.1104/pp.19.00832
70. Wagner E, Lykke-Andersen J (2002) mRNA surveillance: the perfect persist. J Cell Sci 115(Pt 15):3033–3038. https://doi.org/10.1242/jcs.115.15.3033
71. Kose S, Imamoto N (1840) Nucleocytoplasmic transport under stress conditions and its role in HSP70 chaperone systems. Biochimica et Biophysica Acta (BBA) - General Subjects 1840(9):2953–2960. https://doi.org/10.1016/j.bbagen.2014.04.022
72. Biedka S, Wu S, LaPeruta AJ et al (2017) Insights into remodeling events during eukaryotic large ribosomal subunit assembly provided by high resolution cryo-EM structures. RNA Biol 14(10):1306–1313. https://doi.org/10.1080/15476286.2017.1297914
73. Gorman AM, Healy SJM, Jäger R et al (2012) Stress management at the ER: regulators of ER stress-induced apoptosis. Pharmacol Ther 134(3):306–316. https://doi.org/10.1016/j.pharmthera.2012.02.003
74. Perinur Bozaykut, Nesrin Kartal Ozer, Betul Karademir et al (2014) Regulation of protein turnover by heat shock proteins. Free Radical Biol Med 77. https://doi.org/10.1016/j.freeradbiomed.2014.08.012
75. Ha JS, Lee JW, Seo SH et al (2019) Optimized cryopreservation of *Ettlia* sp. using short cold acclimation and controlled freezing procedure. J Appl Phycol 31:2277–2287. https://doi.org/10.1007/s10811-019-1743-z
76. Duprey Y, Bhagooli R, Daniels C (2017) Gene expression biomarkers of heat stress in scleractinian corals: promises and limitations. Comp Biochem Physiol Part C: Toxicol Pharmacol 191:63–77. https://doi.org/10.1016/j.cbpc.2016.08.007
77. Tuckett CA, Thomas W (2018) High latitude corals tolerate severe cold spell. Front Marine ence 5:14. https://doi.org/10.3389/fmars.2018.00014

Publisher's Note Springer Nature remains neutral with regard to jurisdictional claims in published maps and institutional affiliations.

BMC Genomics

RESEARCH Open Access

Environmental acclimatization of the relatively high latitude scleractinian coral *Pavona decussata*: integrative perspectives on seasonal subaerial exposure and temperature fluctuations

Man Zhang[1], Shan Huang[1], Li Luo[1] and Kefu Yu[1,2*]

Abstract

Background Coral reefs are being increasingly threatened due to global climate change. However, some coral species have shown strong tolerance despite living in marginal environments. The species *Pavona decussata* from Weizhou Island in the South China Sea experiences subaerial exposure in summer and winter due to extreme low tides, and their environmental acclimatization to this aerial exposure remains unexplored.

Results Here we aimed to explore the molecular mechanism of *P. decussata* under season or subaerial exposure background through physiological and multi-omics integrative analyses. Specifically, corals with a history of seasonal air exposure underwent comprehensive changes in energy metabolism and defense mechanisms compared to permanently submerged corals. In summer, corals experiencing subaerial exposure enhanced antioxidant defense by increasing the activities of the enzymes T-SOD and CAT, and the coral-associated bacterial community shifted toward the class Alphaproteobacteria that may have provided corals with resistance to environmental stresses. Moreover, the decrease in the transcript levels of the TCA cycle and the increase in metabolite content of ornithine suggested an alteration in energy metabolic pathways. Corals with an air-exposed background may have enhanced energy reserves in winter, as indicated by a higher content of Chl *a* and a rebound in coral-associated bacterial community toward the class Gammaproteobacteria. Furthermore, accumulation of the metabolite leukotriene D4 and activation of the TGF-beta signaling pathway suggested higher anti-inflammatory requirements and positive regulation by innate immunity.

Conclusions This study provides insights into the acclimatization of *P. decussata* to seasonal environmental fluctuations and demonstrates that relatively high-latitude corals possess the plasticity and acclimatory capacity to adapt to marginal environments.

*Correspondence:
Kefu Yu
kefuyu@scsio.ac.cn

Full list of author information is available at the end of the article

© The Author(s) 2025. **Open Access** This article is licensed under a Creative Commons Attribution-NonCommercial-NoDerivatives 4.0 International License, which permits any non-commercial use, sharing, distribution and reproduction in any medium or format, as long as you give appropriate credit to the original author(s) and the source, provide a link to the Creative Commons licence, and indicate if you modified the licensed material. You do not have permission under this licence to share adapted material derived from this article or parts of it. The images or other third party material in this article are included in the article's Creative Commons licence, unless indicated otherwise in a credit line to the material. If material is not included in the article's Creative Commons licence and your intended use is not permitted by statutory regulation or exceeds the permitted use, you will need to obtain permission directly from the copyright holder. To view a copy of this licence, visit http://creativecommons.org/licenses/by-nc-nd/4.0/.

Keywords Scleractinian coral, *Pavona decussate*, Seasonal environmental fluctuations, Subaerial exposure, Temperature variation, Acclimatization

Background

The biodiversity of coral reefs provides diverse ecosystem services [1]. Scleractinian corals are the main frame-builders of coral reef ecosystems, comprising a mutually beneficial symbiosis with microorganisms such as zooxanthellae and bacteria [2]. Due to the complexity of coral holobionts, changes in environmental factors may lead to imbalances in the symbioses [3, 4], and the corals are then bleached or even threatened with death [5–7]. Therefore, in the context of coral habitat expansion driven by global warming [3], exploring the adaptive mechanisms by which corals survive under abiotic stress is critical to predicting their continued viability in changing environments.

Corals that survive in marginal marine habitats have attracted increasing attention as representing an alternative developmental state for corals in the face of environmental change [8]. In Hong Kong, the massive coral *Oulastrea crispata* is widely distributed along the highly urbanized coastline where there are vastly contrasting water quality conditions; yet, the coral showed continued environmental robustness [9]. Similarly, in the western fringing reef at Pulau Satumu, shallow reef communities surviving in highly turbid waters recovered quickly from acute thermal bleaching [10]. In Honolulu Harbor, the massive *Porites* corals living in shallow waters also exhibited greater bleaching resilience during several thermal stress events [11]. Furthermore, corals living in the intertidal and subtidal zones where environmental changes are more intense have been the focus of research in recent years. As sessile benthic organisms, corals are unable to move to seek shelter during tidal changes. Therefore, corals in intertidal and subtidal zones are often exposed at extreme low tides that exposes the corals to hypoxia, desiccation and UV stress and experience changes in temperature, salinity, and other environmental factors [12]. Such natural phenomena are commonly found in lower latitudes, for example, on Gorgona Island [13], Madura Island [14], Guam [15], Shell Island [16, 17], and the Pelorous and Orpheus Islands [18]. Corals in these habitats appear to be uniquely adapted to local environmental fluctuations. Similar to thermal bleaching, the branching coral genus *Acropora* and the family Pocilloporidae are susceptible to air exposure, while massive corals are the least affected [18]. An in situ simulation experiment on Gorgona Island in the tropical eastern Pacific demonstrated that extreme low tides were not lethal to the branching coral *Pocillopora damicornis* [13]. Thus, in the long term, studying how corals acclimate to air exposure may be able to provide insights into the future survival of corals in a changing climate.

Theoretically, under the effects of climate-induced stress, corals may migrate to higher latitudes where the range of seasonal temperature fluctuations is greater compared to tropical regions [19]. This serves to buffer the stress of abnormal environmental temperatures on corals, but also poses a new survival challenge for corals—how to cope with low winter temperatures. Further, air exposure and low winter temperatures can bring a double threat to corals. Hoegh-Guldberg et al. [20] reported that *Acropora aspera* from the Great Barrier Reef were exposed to unusually cold and dry air during subaerial exposure and suffered bleaching and mortality. This implies that the survival of corals under such marginal environmental conditions will depend on their ability to tolerate dynamic environments with more intense disturbances [21]. Therefore, understanding how relatively high-latitude corals acclimate to air exposure in wintry weather is essential for predicting the fate of corals. In general, acclimatization is achieved by a combination of differential gene expression by the coral host and the flexible composition of symbiotic microorganisms. Differential regulation of innate immunity and energy metabolism in coral hosts may reflect the results of acclimatization to distinct environments [22]. The coral-associated bacterial community may likewise be altered by the acclimatization process [23, 24]. Moreover, the metabolite profiles of corals after experiencing environmental changes could be used as signatures to reveal their adaptive history, and this would apply to an extended period following stress [25]. Studies that combine these characteristics will help provide insight into the acclimatization of corals to seasonal subaerial exposure.

Located in the relatively high latitude of the South China Sea, Weizhou Island has abundant coral resources, especially in the northern subtidal zone where there are large areas of *Pavona decussata*. Compared to tropical coral reef areas, Weizhou Island has a greater range of temperature variation, with a difference of up to 13.6 °C throughout the year [26], and the corals may thus be more tolerant to large temperature fluctuations [26]. Moreover, the subtidal *P. decussata* is periodically exposed to air due to extreme low tides in summer and winter. These corals may be acclimated to long-term seasonal environmental fluctuations. It is conceivable that the environmentally susceptible coral-associated bacteria and coral host gene regulation would allow *P. decussata* to survive under seasonal environmental fluctuations and that this would leave an associated metabolic history

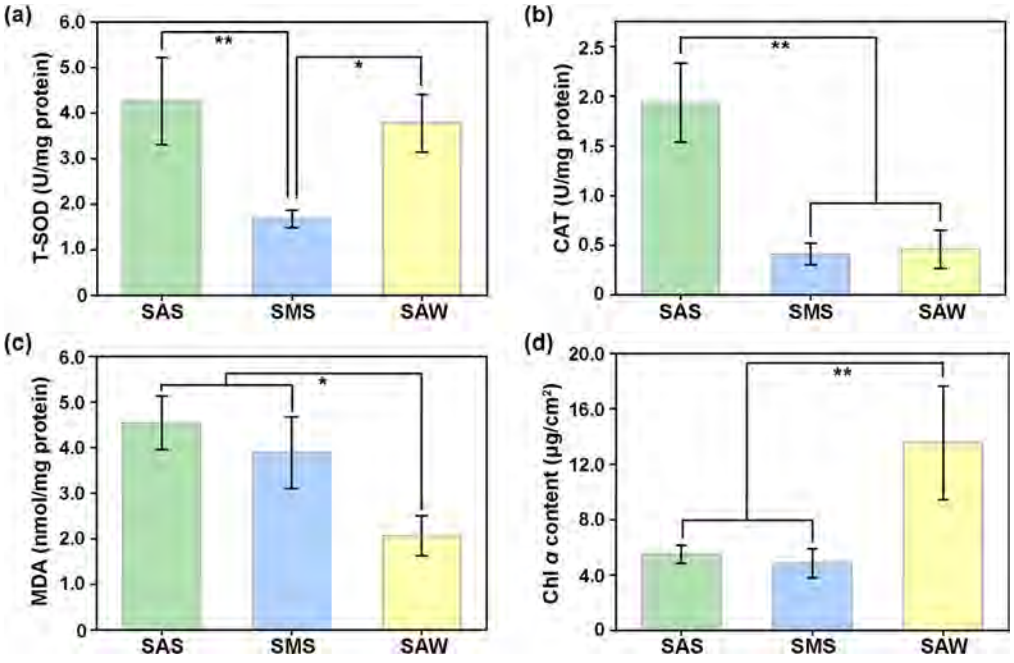


Fig. 1 The quantification of antioxidant capacity and Chl *a* content. (**a**) T-SOD, total superoxide dismutase. (**b**) CAT, catalase. (**c**) MDA, malondialdehyde. (**d**) Chl *a* content. Data are expressed as mean ± standard deviation (SD; $n = 4$). U should be Unit. Significant differences were analyzed between groups (*$p < 0.05$, **$p < 0.01$)

Table 1 Alpha diversity statistics of coral-associated bacterial community

Estimators	SAS-Mean	SAS-SD	SMS-Mean	SMS-SD	SAW-Mean	SAW-SD	*p* value (SAS vs. SMS)	*p* value (SAW vs. SAS)
Ace	324.1	222.5	194.5	123.3	659.8	201.9	NS	**
Chao	319.1	219.6	192.2	121.1	657.1	200.7	NS	**
Sobs	316.6	217.7	191.4	120	651.6	199.1	NS	**
Shannon	3.64	1.38	1.58	1	4.01	1.04	**	NS
Simpson	0.15	0.12	0.53	0.3	0.14	0.15	**	NS

Note: Mean represented 'mean value', and the SD represented 'standard deviation'. NS represented 'non-significance', **$p < 0.01$

during long-term survival. Therefore, the research design incorporated: (1) quantification of antioxidant capacity and Chlorophyll *a* (Chl *a*) content; and (2) coral-associated bacterial diversity assessment, transcriptomic analysis, and metabolomic analysis. Assessing the survivability of *P. decussata* in seasonal environmental fluctuations is essential for understanding the plasticity of adaptive capacity under global climate change. This research will also enhance our understanding of coral stress tolerance at relatively high latitudes and provide a theoretical basis for future marginal reef conservation.

Results

Analysis of coral physiological indicators

The quantification of antioxidant capacity and Chl *a* content between different groups are shown in Fig. 1. In the experienced subaerial exposure in summer (SAS) group, the total superoxide dismutase (T-SOD) activity was significantly higher than that in the permanently submerged corals (SMS) group (Fig. 1a; $p < 0.01$), with an increase of 155%. Similarly, the activity of the antioxidant enzyme catalase (CAT) in the SAS group was significantly higher from those in the SMS and SAW groups (Fig. 1b, $p < 0.01$). Compared to the SMS group, the SAS group had a significant increase in CAT of about four times. The SAW group in winter had a significant 76% decrease compared to the SAS group in summer. In relative terms, the malondialdehyde (MDA) content of the SAW group was significantly lower than SAS group (Fig. 1c, $p < 0.05$), with a decrease of 55%. Conversely, the Chl *a* content in the SAW group was significantly 147% higher than that in SAS group (Fig. 1d, $p < 0.01$).

Dynamics of coral-associated bacterial communities

After 16S rRNA sequencing of 15 samples from the SAS, SMS, and SAW groups, 1,045,350 processed bacterial sequences were assigned to 12,306 amplicon sequence variants (ASVs), and the sequence details are presented in Additional file 2: Table S1. The statistics for alpha diversity are presented in Table 1. The Ace, Chao, and Sobs indices suggested no significant difference in community richness between the SAS and SMS groups, while

the richness of the SAW group was significantly higher than that of the SAS group ($p < 0.01$). In addition, the Shannon index reflecting community diversity was significantly higher for the SAS group than for the SMS group but was not significantly different from that of the SAW group. The Simpson index is inversely proportional to the Shannon index, and this indicated that the lowest diversity of coral-associated bacterial communities was in the SMS group. Overall, the SMS group had the lowest alpha diversity.

Based on the Bray-Curtis dissimilarity, principal coordinate analysis (PCoA) was used for demonstrating the variable characteristics of the coral-associated bacteria, with all samples being clustered and differentiated by groups (Fig. 2a). SMS group could be clearly distinguished from SAS and SAW groups on the PC2 axis. The dominant bacterial taxa in all three groups were similar, but their abundances were altered. At the phylum level, the main constituents of all three groups were Proteobacteria, Firmicutes, and Actinobacteriota (Fig. 2b). At the genus level, the top genera in relative abundance included BD1-7_clade, *Rhodopseudomonas*, and unclassified_k__norank_d__Bacteria in three groups (Fig. 2c). Moreover, linear discriminant analysis effect size (LEfSe) analysis identified differential microbial communities between groups, with alterations of the phylum Proteobacteria being mainly responsible for the differences in both SAS vs. SMS and SAW vs. SAS. Specifically, the SAS group has different compositions of the classes Alphaproteobacteria and Gammaproteobacteria

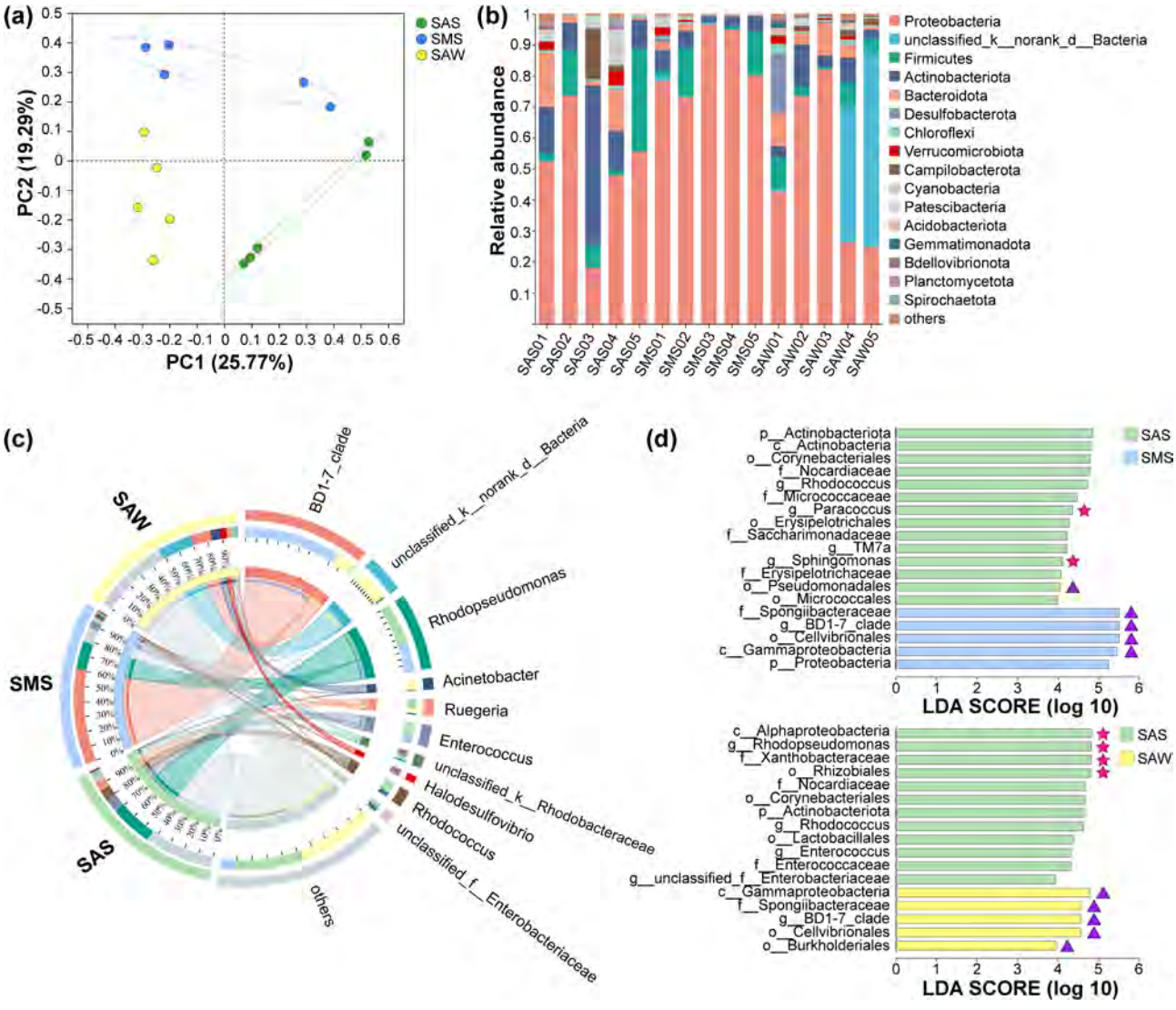
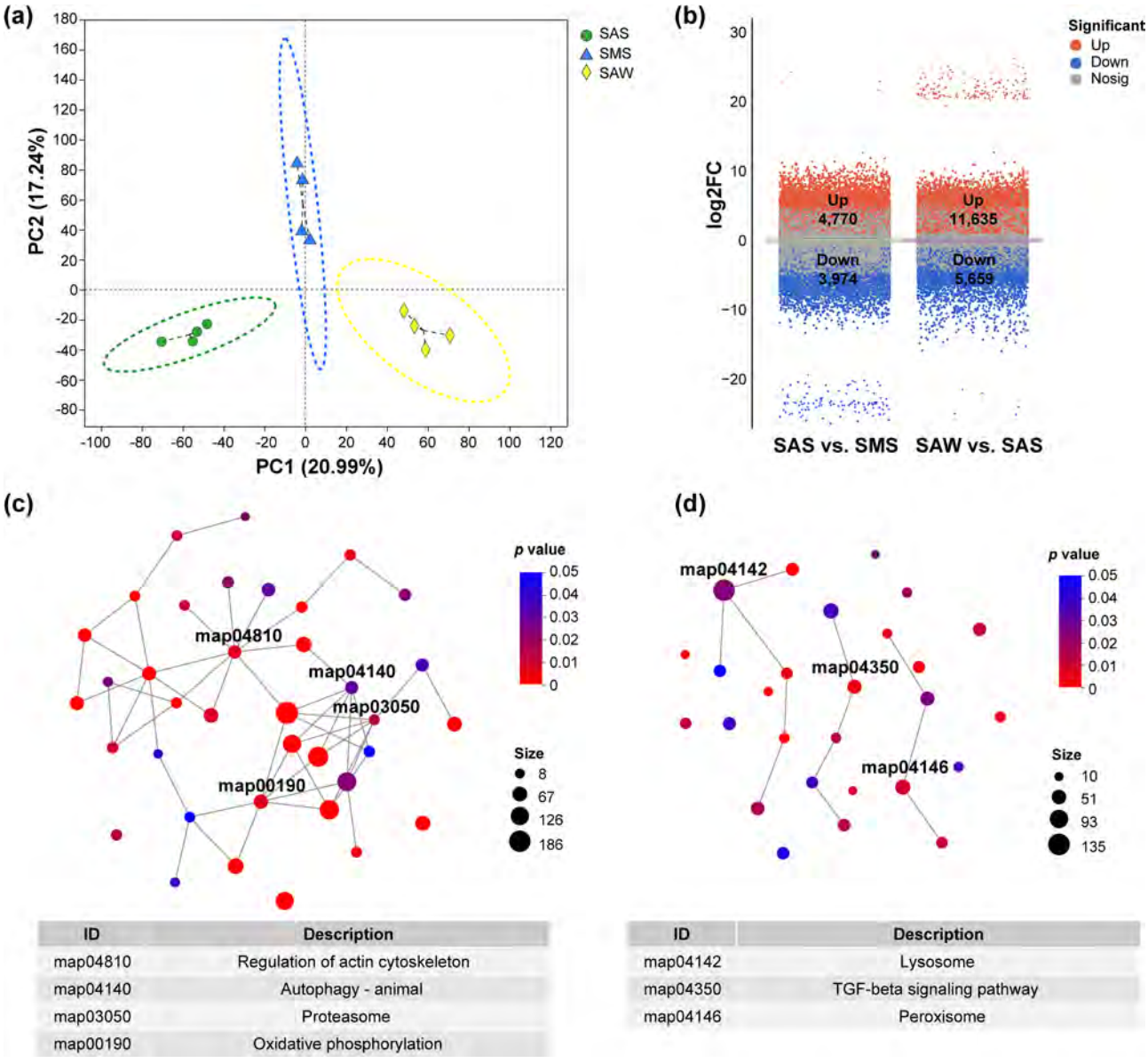


Fig. 2 The microbial beta diversity and community composition statistics. (**a**) PCoA analysis. (**b**) Microbial community composition at the phylum level. (**c**) Microbial community composition at the genus level between groups. (**d**) Statistics of taxa constituting differences between groups. The pink pentagrams marked taxa belonging to the class Alphaproteobacteria, and the purple triangles marked the counterparts of the class Gammaproteobacteria

compared to SAW and SMS groups (Fig. 2d). Relative to the SMS group, the relative abundance of the genus BD1-7 clade was lower in the SAS group, while the relative abundance of the genera *Paracoccus* and *Sphingomonas* was higher. Compared to SAS group, the relative abundance of the genus BD1-7 clade was elevated in the SAW group.

Different transcriptional responses of coral hosts

To determine the molecular mechanisms underlying the acclimatization of coral hosts to annual environmental changes, 12 samples from the SAS, SMS, and SAW groups were employed for RNA sequencing. In total, 583,925,222 clean reads were produced based on 592,968,090 raw reads, which were then assembled into 267,502 unigenes. The sequencing results are detailed in Additional file 3: Table S2. The analysis of molecular variance (AMOVA) results for single nucleotide polymorphism (SNP) loci are presented in Additional file 4: Table S3. There was minimal genetic differentiation between the groups (F_{ST} < 0.05, p < 0.05). Principal component analysis (PCA) plots revealed differences in expression



ID	Description
map04810	Regulation of actin cytoskeleton
map04140	Autophagy - animal
map03050	Proteasome
map00190	Oxidative phosphorylation

ID	Description
map04142	Lysosome
map04350	TGF-beta signaling pathway
map04146	Peroxisome

Fig. 3 Characterization and comparison of the transcriptional profiles. (**a**) PCA plot. (**b**) Scatter diagram demonstrating the DEGs for two different comparison schemes (SAS vs. SMS and SAW vs. SAS, the latter is considered the reference group). The FDR < 0.01 is indicated in red, while the FDR ≥ 0.01 is indicated in blue. The networks showed the core pathways of (**c**) SAS vs. SMS and (**d**) SAW vs. SAS. Each dot represented a pathway, and only the significant pathways are shown. The more DEGs enriched within the pathway, the larger the dot. Also, the color of the dot reflected the *p*-value. Only the names and map IDs of critical pathways are shown in the map

between the SAS and SMS groups, as well as between the SAW and SAS groups (Fig. 3a), with replicates showing higher correlation within groups and a clear separation between groups. Subsequently, unigenes with significant differential expression between groups were identified. There were 8,744 differentially expressed unigenes (DEGs) in the SAS group relative to the SMS group. In addition, compared to the SAS group, 17,294 DEGs were identified in the SAW group (Fig. 3b).

Gene Ontology (GO) annotation analysis indicated that these two sets of DEGs had similar functional classification. Among these, "cellular process" and "metabolic process" were the dominant subcategories in biological process. The "cell part" had the highest proportion in cellular component, while "binding" and "catalytic activity" were the most important in molecular function (Additional file 1: Fig. S2). The GO functions of these DEGs were enriched, and the top 20 significantly enriched ($p < 0.05$) GO terms in biological process reflected certain changes. Compared to the SMS group, the SAS group was significantly enriched in the subcategories of "cellular process" and "metabolic process", with the upregulation of terms belonging to "cellular process" such as "cilium movement (GO: 0003341)" and "cellular component assembly (GO: 0022607)" and the downregulation of terms belonging to "metabolic process" such as "respiratory electron transport chain (GO: 0022904)" and "peptide biosynthetic process (GO: 0043043)" (Additional file 1: Fig. S3a). Meanwhile, the SAW group was significantly enriched in "biological regulation" and "metabolic process" subcategories, and both showed upregulation compared to the SAS group; for example, this included "proteasomal protein catabolic process (GO: 0010498)", "organonitrogen compound catabolic process (GO: 1901565)", and "regulation of biosynthetic process (GO: 0009889)" (Additional file 1: Fig. S3b).

In the Kyoto Encyclopedia of Genes and Genomes (KEGG) pathway enrichment analysis, the DEG set of SAS vs. SMS was significantly enriched ($p < 0.05$) in 42 pathways, including "citrate cycle (TCA cycle) (map00020)" and "steroid biosynthesis (map00100)" (Additional file 5: Table S4). Figure 3c shows that four pathways, "regulation of actin cytoskeleton (map04810)", "oxidative phosphorylation (map00190)", "autophagy-animal (map04140)", and "proteasome (map03050)", had strong associations with other pathways. In contrast, the DEG set of SAW vs. SAS was significantly enriched in 27 pathways, including "biosynthesis of unsaturated fatty acids (map01040)" (Additional file 5: Table S4), with three pathways showing associations with other pathways, namely "lysosome (map04142)", "TGF-beta signaling pathway (map04350)", and "peroxisome (map04146)" (Fig. 3d).

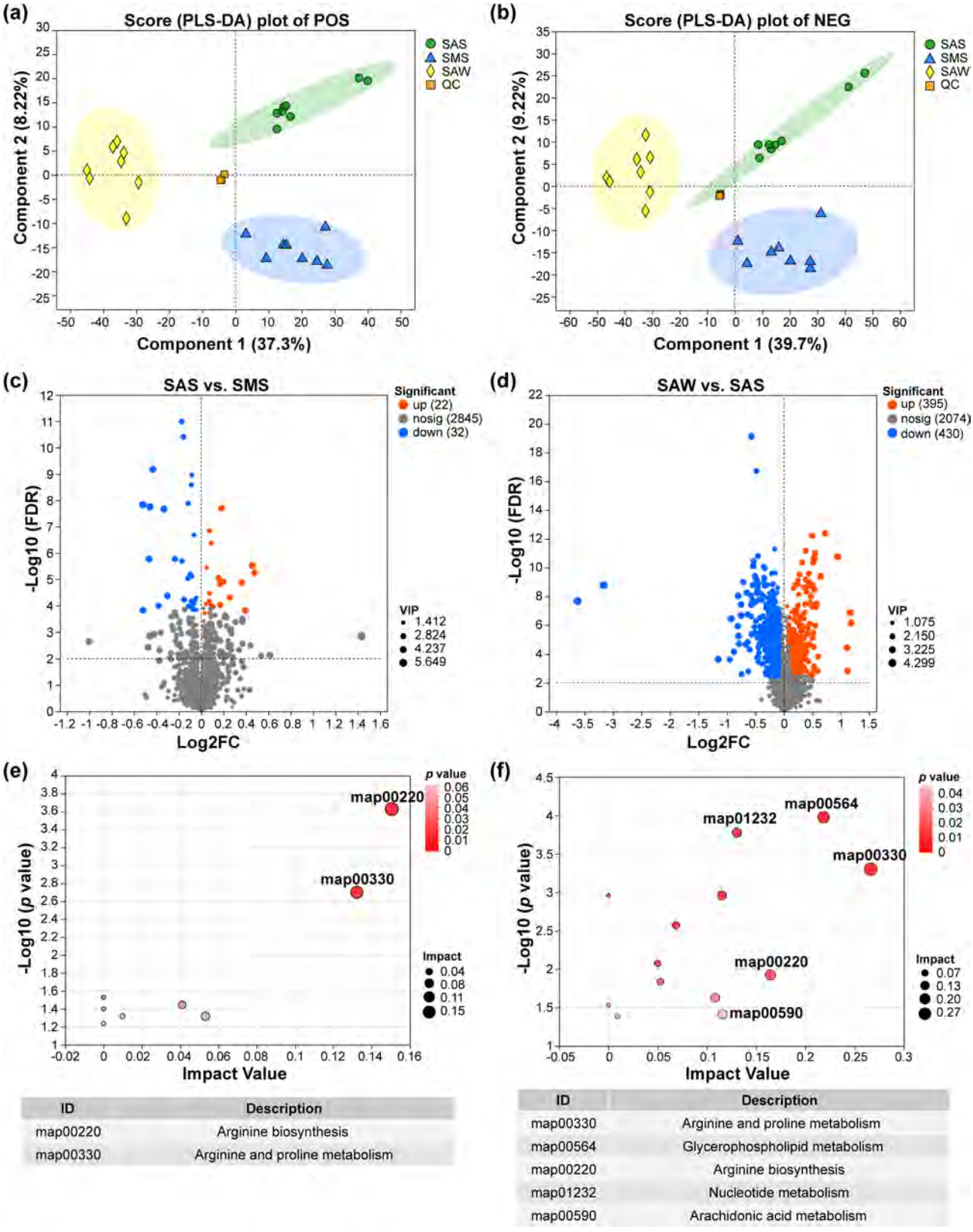
Metabolomic profiling of *P. decussata*

The changes in the metabolome of *P. decussata* under different environmental conditions were analyzed using LC-MS. After forming the data matrix, a total of 1,889 variables were identified in positive (POS) ionization mode and 1,248 in negative (NEG) mode, which were preprocessed to obtain metabolite quantities. A total of 1,741 metabolites were identified in POS mode and 1,152 metabolites in NEG for all samples. The number of metabolites identified accounted for 92.17% and 92.31% of the number of variables in the POS and NEG models, respectively. After data processing, the partial least squares discriminant analysis (PLS-DA) score plot showed significant differences in metabolites in both POS and NEG modes (Fig. 4a and b). Subsequently, an orthogonal partial least squares discriminant analysis (OPLS-DA) model was used to discriminate the significantly different metabolites (DMs). In both POS and NEG modes, 54 DMs were obtained for SAS vs. SMS (Fig. 4c), and 825 DMs were obtained for SAW vs. SAS (Fig. 4d).

Upon analyzing the KEGG metabolic pathway information for these DMs (Additional file 6: Table S5), the majority in both groups were involved in two categories of energy supply pathways, "amino acid metabolism" and "lipid metabolism" (Additional file 1: Fig. S4). A topological pathway analysis identified two significantly enriched pathways in SAS vs. SMS, namely "arginine biosynthesis (map00220)" and "arginine and proline metabolism (map00330)" (Fig. 4e). Both pathways contained the upregulated metabolite ornithine (Additional file 1: Fig. S5a) associated with amino acid metabolism. In SAW vs. SAS, five significantly enriched pathways were identified, namely "arginine and proline metabolism (map00330)", "glycerophospholipid metabolism (map00564)", "arginine biosynthesis (map00220)", "nucleotide metabolism (map01232)", and "arachidonic acid metabolism (map00590)" (Fig. 4f). In contrast, the abundance of metabolite ornithine decreased in SAW group compared to SAS group. The metabolite leukotriene D4 of "arachidonic acid metabolism (map00590)" associated with lipid metabolism was upregulated in SAW vs. SAS (Additional file 1: Fig. S5b).

Association analyses of transcriptome and metabolome

The O2PLS model was fitted to the DEGs and DMs of SAS vs. SMS and SAW vs. SAS. The contributions of each part showed that both SAS vs. SMS and SAW vs. SAS had high contributions of their "Joint part", ranging from 86.55 to 100.00% of "Joint part and Orthogonal part" individually (Additional file 7: Table S6), indicating that the model could be used to explain the joint variation in the transcriptome and metabolome. Furthermore, the joint loadings plot showed the extent to which each



ID	Description
map00220	Arginine biosynthesis
map00330	Arginine and proline metabolism

ID	Description
map00330	Arginine and proline metabolism
map00564	Glycerophospholipid metabolism
map00220	Arginine biosynthesis
map01232	Nucleotide metabolism
map00590	Arachidonic acid metabolism

Fig. 4 Characterization and comparison of the metabolite profiles. PLS-DA analysis of individual samples in (**a**) POS mode and (**b**) NEG mode. The volcano plots showed the DMs of (**c**) SAS vs. SMS and (**d**) SAW vs. SAS. The key pathways in (**e**) SAS vs. SMS and (**f**) SAW vs. SAS were shown. The key pathways are labelled in terms of impact value. The larger the impact value, the more important the pathway. Only the top five pathways in (**f**) are labelled

variable in one omics approach was associated with the other omics in two dimensions, with larger absolute values indicating stronger associations. In this study, both SAS vs. SMS (Additional file 1: Fig. S6a and Fig. S6b) and SAW vs. SAS (Additional file 1: Fig. S6d and Fig. S6e) had strong correlations between almost all the variables among muti-omics.

To further explore the main mechanisms of transcriptional and metabolic regulation in the corals with a seasonal air-exposed background, the pathways concerning energy metabolism and innate immunity were selected from the above enrichment results for correlation analysis (Additional file 8: Table S7). The strong correlations between gene expression and metabolite abundances in these pathways are shown in Additional file 1: Fig. S7. In the SAS vs. SMS comparison, ornithine was an important metabolite based on the above omics analyses, and it was significantly negatively correlated with the rate-limiting enzymes citrate synthase (*CS*) and isocitrate dehydrogenase (*IDH*), which were downregulated in "citrate cycle (TCA cycle) (map00020)" (Fig. 5a). In the SAW vs. SAS comparison, leukotriene D4 was enriched as a key metabolite, and it was significantly positively correlated with genes related to "arachidonic acid metabolism (map00590)" and with bone morphogenetic protein receptor, type I (*BMPRI*), bone morphogenetic protein (*BMP*) and SMAD family member 4 (*SMAD4*), which were upregulated in "TGF-beta signaling pathway (map04350)" (Fig. 5b).

Discussion

Physiological plasticity of *P. decussata* in response to variable environmental stress

P. decussata has shown strong tolerance to environmental stress [7, 26], and this may be reflected at the physiological level in the present study. The potential of *P. decussata* to acclimatize to air exposure included stronger activities of the antioxidant enzymes T-SOD and CAT (Fig. 1a and b), acclimatization that may be beneficial in eliminating reactive oxygen species (ROS) generated by dramatic environmental changes [27, 28]. Moreover, free radicals react with lipids to form MDA [29], and thus the lower MDA content may be indicative of a decreased oxidative response in *P. decussata* that experienced air exposure in winter. Meanwhile, the higher Chl *a* content in the SAW group (Fig. 1d) could also provide stronger photoprotection through the xanthophyll cycle of zooxanthellae [30], resulting in a reduction of potential existential threats during the winter months.

Coral-associated bacterial communities may be involved in the acclimatization

Coral-associated bacterial communities play key roles in coral health, disease, and evolution due to the fact that their habitats are closely linked to host tissue structures [31–34]. Thus, coral-associated bacteria are vulnerable to environmental variation, and the corresponding changes in their composition may in turn affect the coral hosts [35]. Previous studies have shown that the alpha diversity of coral-associated bacteria increases to a certain

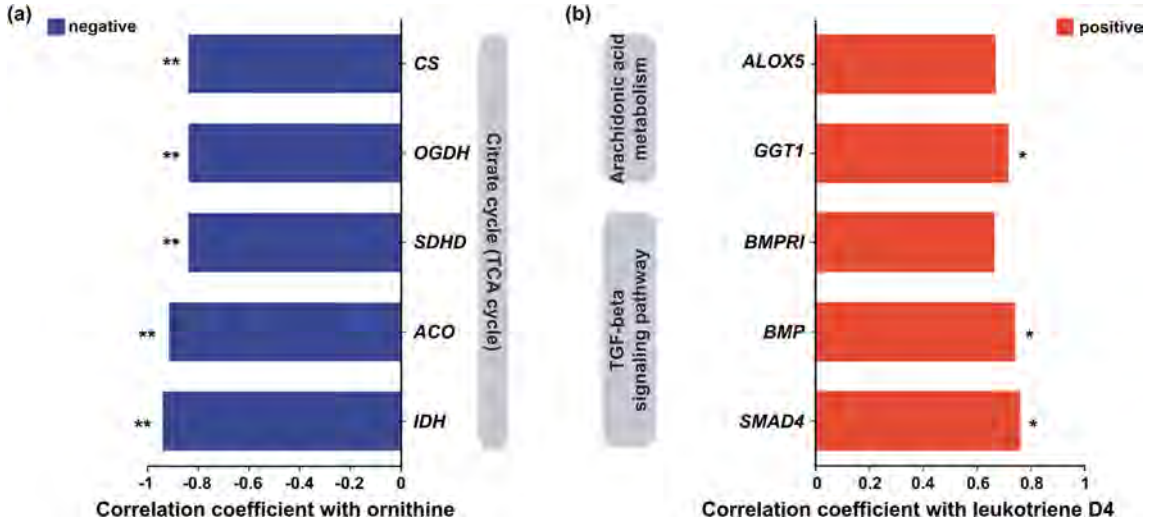


Fig. 5 The correlation plot between the expression of key genes and the abundances of core metabolites. The left chart reflected the correlation between metabolite ornithine and genes associated with the citrate cycle (TCA cycle) in (**a**) SAS vs. SMS, and the right chart represented the correlation between metabolite leukotriene D4 and genes related to the arachidonic acid metabolism and TGF-beta signaling pathway in (**b**) SAW vs. SAS. The blue bars represented negative correlations and red represented positive. The horizontal coordinate showed the correlation coefficient. Significance of differences was indicated by $*p < 0.05$ and $**p < 0.01$. *CS*, citrate synthase; *OGDH*, oxoglutarate dehydrogenase; *SDHD*, succinate dehydrogenase complex subunit D; *ACO*, aconitate hydratase; *IDH*, isocitrate dehydrogenase; *ALOX5*, arachidonate 5-lipoxygenase; *GGT1*, leukotriene-C4 hydrolase; *BMPRI*, bone morphogenetic protein receptor, type I; *BMP*, bone morphogenetic protein; *SMAD4*, SMAD family member 4

extent under external stresses [36, 37], contributing to the symbiont's resistance to infections and the maintenance of essential functions of the microbiota [26]. In our research, both the SAS and SAW groups that experienced subaerial exposure showed higher alpha diversity of coral-associated bacteria than the always-submerged SMS group (Table 1). The sensitive changes in coral-associated bacterial community diversity may indicate that the disturbance from air exposure is a potential stressor for *P. decussata* both in summer and winter. Interestingly, the community richness indices Ace, Chao, and Sobs were significantly higher in the SAW group compared to the SAS group, in contrast to previous findings on *P. decussata* [26]. This indicated that *P. decussata* may be also highly tolerant to air exposure in winter. Additionally, our results showed that the microbial communities of the samples that were influenced by extremely low tides showed intercolonial variability, and the degree of variability varied between samples from different seasons (Fig. 2a). This implied that despite having the same coral host, there were effects of different environments on the microbiomes.

In this study, *P. decussata* experiencing subaerial exposure showed a decrease in the relative abundance of class Gammaproteobacteria and an increase in class Alphaproteobacteria in the SAS group relative to the SMS group (Fig. 2d). Unsurprisingly, the current study suggested that most bacteria that confer benefit to the symbiont belonged to the classes Gammaproteobacteria and Alphaproteobacteria [38], and the shift in these classes in coral-associated bacteria may be based on environmental acclimatization. The BD1-7 clade that carries out carotenoid biosynthesis [39] has been detected in corals and other marine organisms [26, 40]. The biosynthetic process is crucial for symbiont health [41]. *Paracoccus* sp. was demonstrated to be able to kill harmful bloom-forming algae [42], showing the potential for application in regulating environmentally harmful factors. Moreover, it has been shown that *P. marcusii* can produce ROS-reactive pigments to help detoxify free radicals and ROS [43]. In addition, a metabolic characteristic of the genus *Sphingomonas* is the capacity for xenobiotic degradation, an ability that may play an essential role in adaptation to oligotrophic marine environments [44]. Therefore, the switch from class Gammaproteobacteria (genus BD1-7 clade), which may favor the maintenance of a stable healthy state of the coral host, to class Alphaproteobacteria (genera *Paracoccus* and *Sphingomonas*) that are resistant to exogenous stresses may be microbiological evidence that *P. decussata* was affected by air exposure and acclimatized to this stress. In addition, compared to SAS group, the relative abundances of some bacteria from the class Gammaproteobacteria was elevated after air exposure in winter (Fig. 2d). The genus BD1-7 clade played a key role in energy utilization [26]. This suggested that coral-associated bacterial communities may assist *P. decussata* in acclimatizing to environmental fluctuations during winter by shifting to structures that favored symbiont energy reserves.

Overall, changes in the diversity of coral-associated bacterial communities, along with differences in bacterial taxa, allowed the coral host to cope with stresses in different conditions, suggesting that *P. decussata* may be resistant to external pressures due to the presence of the symbiont.

Coral hosts responded to environmental stresses through flexible gene regulation

Extensive studies on scleractinian corals have shown that energy metabolism and homeostasis are closely linked under exogenous stresses [4, 45, 46]. The citrate acid cycle, also known as the TCA cycle, was a conserved primitive metabolic pathway typically serving as the organism's energy engine [47]. We noted that the "citrate cycle (TCA cycle) (map00020)" pathway was significantly enriched in SAS vs. SMS. In this pathway, *CS* and *IDH* were both downregulated in the SAS group, suggesting that air exposure limited the TCA cycle and affected the efficiency of energy utilization in the coral host. The result was consistent with that of previous studies on the response of coral hosts to exogenous stresses [4, 48]. Moreover, the "peroxisome (map04146)" pathway was enriched in the SAW vs. SAS comparison (Fig. 3d), possibly dominating more abundant amino or fatty acid metabolism and regulating the level of ROS [49]. This may be a survival advantage for *P. decussata* in response to extremely low tides in winter.

P. decussata has demonstrated remarkable resilience to thermal stress, as evidenced by having flexible regulation of the antioxidant response and innate immunity [7]. Specifically, proteasomes are protease complexes that selectively degrade short-lived regulatory or damaged proteins [50]. To maintain homeostasis during oxidative stress in the organism, ubiquitinated proteins are degraded by the proteasome as a general damage signature [51]. In this study, the "proteasome (map03050)" pathway were enriched in the SAS group relative to the SMS group (Fig. 3c). Moreover, autophagy is an essential component of cellular response to stress [52] as a type of programmed cell death pathway [53] and can be activated by oxidative stress [54]. In the SAS vs. SMS comparison, the "autophagy-animal (map04140)" pathway (Fig. 3c) may reveal plasticity in gene expression after stimulation by subaerial exposure. Additionally, in the SAW group, the activated "lysosome (map04142)" pathway (Fig. 3d) may have been used to control oxidative stress [28], similar to the activated "peroxisome (map04146)" pathway. Therefore, we hypothesized that *P. decussata*

experiencing seasonal subaerial exposure may respond to oxidative stress in different ways. In summer, individuals that were consistently submerged may maintain cellular homeostasis through ubiquitinated protein degradation by proteasomes, whereas their counterparts that experienced subaerial exposure may protect cells through enhanced antioxidant T-SOD and CAT enzyme activities and activation of autophagy. In winter, *P. decussata* that experienced air exposure maintained high antioxidant enzyme (T-SOD) activity and may further cope with oxidative stress through lysosomes. Ultimately, there was no significant difference in the extent of oxidative damage between SAS and SMS groups (Fig. 1c), reflecting the effectiveness of gene regulation in *P. decussata* with subaerial exposure in summer. In addition, the corals in winter may have a significant reduction in the degree of oxidative damage (Fig. 1c) due to the combined action of their antioxidant enzymes and organelles.

Innate immunity seems to play an essential role in the response of *P. decussata* to air exposure. As a form of innate immunity [55], autophagy could be activated when the coral host is stressed and challenged, as shown in the SAS group. Similar results have been observed in tolerant *Porites* species [56]. In addition, *BMPRI*, *BMP* and *SMAD4* in "TGF-beta signaling pathway (map04350)" was upregulated in the SAW group relative to the SAS group. It is known that the TGF-beta signaling pathway can act as an innate immune pathway as an enforcer of immune tolerance and an inhibitor of inflammation [57]. In *P. decussata*, the anti-inflammatory effect of the TGF-beta signaling pathway may be beneficial for maintaining organismal health during air exposure in winter. It follows that *P. decussata* defends against threats from subaerial exposure by regulating the innate immune-related pathways, both in summer and winter; this may be a clue to its resilience.

In summary, the flexible gene regulation capacity of *P. decussata* may be a necessary asset for its survival in changing environmental conditions, which either directly or indirectly impacted its basic physiological processes.

Altered metabolic profiles may reflect the stress history of *P. decussata*

The metabolome results for both SAS vs. SMS and SAW vs. SAS showed that the enriched KEGG pathways contained "arginine biosynthesis (map00220)" and "arginine and proline metabolism (map00330)" on amino acid metabolism (Fig. 4e and f). This implied that the changes in amino acid metabolism may be a sensitive reflection of coral responses to environmental changes, and the same results were also found in the metabolic profiles of corals undergoing thermal stress [58]. Scleractinian corals absorb and utilize nitrogen for growth and development under stable conditions, including their most representative calcification. Previous studies have demonstrated that urea may be an important source of nitrogen for corals [59–61] and that the urea cycle is also involved in calcification in scleractinian corals [62]. In this study, the changes in the above two pathways focused on ornithine, an intermediate molecule in the urea cycle that is also an essential substrate for proline synthesis [63]. Compared to the SMS and SAW groups, the upregulation of ornithine in the SAS group (Additional file 1: Fig. S5) predicted a stronger material basis for the urea cycle. Additionally, *P. decussata* that experienced air exposure may have a stronger capacity for calcification in summer, consistent with the findings from other reef-building corals [64–67], suggesting that subaerial exposure may not affect classic seasonal patterns of coral calcification.

In the present study, changes in lipid metabolism such as "glycerophospholipid metabolism (map00564)" and "arachidonic acid metabolism (map00590)" were observed in the SAW vs. SAS comparison (Fig. 4f). Two types of metabolites phosphatidylcholine (PC) and phosphatidylserine (PS) in "glycerophospholipid metabolism (map00564)", which usually serve as typical cnidarian lipids [68], were upregulated in SAW vs. SAS (Additional file 1: Fig. S5b). These lipids comprise the major lipid structures in eukaryotic cell membranes, suggesting that *P. decussata* with a history of air exposure ultimately may acclimat to winter by improving membrane fluidity to help maintain cellular function [69]. Similarly, arachidonic acid, which can be used as an indicator to evaluate coral health [70], indicated physiological changes in *P. decussata* experiencing subaerial exposure and low temperatures during winter. In "arachidonic acid metabolism (map00590)" pathway, the downstream catabolic product leukotriene acts as an inflammatory mediator to trigger or participate in inflammatory responses [71]. In our metabolome results, leukotriene D4 was upregulated in the SAW group relative to the SAS group (Additional file 1: Fig. S5b), suggesting that *P. decussata* experiencing air exposure may have a higher risk of inflammation in winter.

Taken together, the changes in amino acid and lipid metabolism may be historical signatures of seasonal environmental fluctuations experienced by *P. decussata* and may further reveal the variation in biological processes in different seasons. These findings were essential for our comprehensive assessment of the acclimatization of *P. decussata*.

Integrated evaluation of the acclimatization and survival potential of *P. decussata* to marginal environments

The future of coral reefs depends on the ability of reef-building corals to respond to rapid environmental changes [72]. In this study, in addition to the flexible

coral-associated bacterial communities, *P. decussata* with a history of seasonal air exposure had apparent physiological advantages in antioxidant and photosynthetic capacity (Fig. 6). Subsequent O2PLS models successfully fitted transcriptomic and metabolomic data and revealed strong correlations (Additional file 1: Fig. S6), implying a link between gene regulation and metabolite abundances. Further analyses found that similar to other scleractinian corals [4, 54], *P. decussata* from Weizhou Island located in a subtropical marginal coral reef responded to stress through alterations in energy metabolism and innate immunity. Thus, these changes could be used to assess the acclimatization and survival potential of *P. decussata* under varied environmental conditions.

In general, coral-associated microbes have shorter generation times compared to coral hosts, implying that they may acclimatize more rapidly and provide corresponding adaptive capacity to the corals [72]. Thus, changes in bacterial community structure and diversity under different conditions [24, 73] have been evaluated in previous studies of coral acclimatization and adaptation [72]. Similar to our findings, the coral-associated bacterial community was altered at the genus level on Madura Island reefs where cyclical subaerial exposure also occurred, although Proteobacteria was still the dominant phylum [13]. Both at low and relatively high latitudes, these results demonstrated the involvement of coral-associated bacteria in the ongoing effects caused by subaerial exposure. Their specific alterations may contribute to coral stress resistance and energy reserves (Fig. 6), although the exact mechanism of bacteria in the acclimatization of corals to seasonal environmental fluctuations remains unclear. For coral hosts, the degree of genetic differentiation among populations can be assessed to evaluate the impacts of environmental fluctuations. In this study, the low yet statistically significant level of genetic differentiation among populations may suggest adaptation of the *P. decussata* coral host to tidal-induced environmental fluctuations at Weizhou Island. However, due to the small sample size and the limitations of RNA-seq, the interpretation of F_{ST} value may lack comprehensiveness, necessitating further validation.

Additionally, the level of energy metabolism in the coral host is closely linked to the stress response process. In previous studies, energy allocation by corals was the basis for acclimatization [12, 74]. In this research, compared to the SMS group, the TCA cycle pathway in the SAS group was downregulated, while the activities of antioxidant enzymes T-SOD and CAT, proteins containing a large number of amino acid residues [75], were significantly increased (Fig. 6). These phenomena may indicate that *P. decussata* with a subaerial exposure history may reduce the efficiency of energy utilization and allocate energy to the antioxidant system in summer. In contrast, the negative correlation between the abundance of the metabolite ornithine in the urea cycle and the gene expression of *CS* and *IDH* in the TCA cycle (Fig. 5a) may point to some degree of substance flow between the two pathways. Theoretically, the urea cycle and the TCA cycle are connected by aspartic acid and fumarate, i.e.,

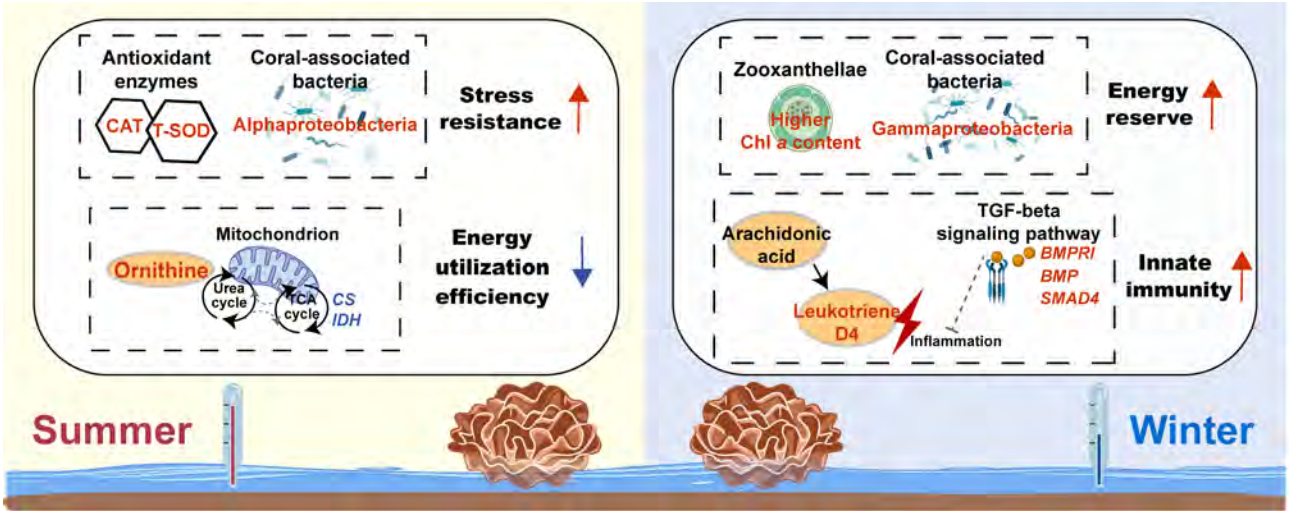


Fig. 6 Overview of the subtidal *P. decussata* acclimatization to seasonal subaerial exposure and temperature fluctuations. The left half of it depicted changes in corals with an exposure history during the summer relative to those without exposure backgrounds, and the right half detailed the variations of corals which experienced subaerial exposure under cold temperature conditions in winter. Characters in italics represented genes, and characters on the orange oval and white hexagonal icons represented substances. Red font and arrows indicated up-regulation or increase, while blue font and arrows indicated down-regulation or decrease. The black arrows denoted the direction of the response and the dotted lines signified presumptions. CAT, catalase; T-SOD, total superoxide dismutase; *CS*, citrate synthase; *IDH*, isocitrate dehydrogenase; *BMPRI*, bone morphogenetic protein receptor, type I; *BMP*, bone morphogenetic protein; *SMAD4*, SMAD family member 4

oxaloacetate from the TCA cycle synthesizes aspartic acid and then participates in the urea cycle, while fumarate produced by the urea cycle enters the TCA cycle [76, 77]. In our metabolome data, the active urea cycle indicated by ornithine may be a surrogate program for the TCA cycle due to the reduction of energy utilization efficiency (Fig. 6), although neither aspartic acid nor fumarate was detected, possibly due to detection errors. Thus, *P. decussata*, similar to other corals that experience subaerial exposure [12], has certain energy adjustment strategies to cope with high temperatures and air exposure in summer, and such advantages may allow the corals to survive.

Higher Chl *a* content favored coral photosynthesis, in turn facilitating resistance to environmental stress [78]. In this research, *P. decussata* with an air-exposed background possessed a higher Chl *a* content in winter, indicating the resistance to marginal environments at relatively high latitudes and an energy advantage (Fig. 6). At low temperatures, innate immunity is thought to benefit corals to adapt to environmental stresses [26, 54], and the same result was obtained in our study. *P. decussata* emerged from the sea surface for hours and then became submerged in cold seawater, and this may cause abnormalities in lipid metabolism such as an increase in leukotriene D4 indicative of the high risk of inflammation. In addition, the abundance of leukotriene D4 was positively correlated with the expression of *BMPRI*, *BMP* and *SMAD4* related to the TGF-beta signaling pathway (Fig. 5b), demonstrating that innate immunity functions in *P. decussata* to prevent inflammatory responses and maintain homeostasis in winter (Fig. 6).

In general, the adaptive capacity of corals to extreme environments has been closely linked to taxa [79], similar to thermal bleaching events [80, 81]. The leaf coral *P. decussata*, an intermediate between branching and massive corals, may have innate tolerant and adaptive advantages. Additionally, due to the geographical advantage of relatively high latitudes, similar to north-western Australia and in Reunion Island [82, 83], most air exposure on Weizhou Island occurs at sunrise or sunset, a factor that may have protected *P. decussata* from prolonged exposure to the sun and the threat of high temperatures, allowing this species to continue to survive after the seasonal subaerial exposure. Overall, biotic and abiotic factors have allowed *P. decussata* to successfully acclimatize to seasonal environmental fluctuations in Weizhou Island.

Conclusions

Scleractinian coral possess the potential to survive in marginal environments. Multi-omic analyses highlighted that coral-associated bacterial community structure and diversity of *P. decussata* on Weizhou Island changed in a direction that favored coral survival under seasonal subaerial exposure and temperature fluctuations. In addition, dynamic changes in energy metabolism and innate immunity were beneficial for maintaining coral homeostasis. To conclude, our analysis has contributed to a deeper comprehension of coral persistence in environmental fluctuations and provides a theoretical basis for future acclimation of relatively high-latitude corals.

Methods

Sample collection

The study site was located at Weizhou Island on the northern edge of the South China Sea (Fig. 7a). Field surveys in the northern part of Weizhou Island found that *P. decussata* surviving in the Blue Bridge area (21°4.16′N, 109°5.79′E) were exposed to recurrent extreme low tides (http://global-tide.nmdis.org.cn/default.html) in summer (June–August) and winter (December–February next year), similar to subtidal corals in other areas [16]. Such extreme low tides typically occurred around sunrise and lasted almost 3 h in summer. In winter, such tides occurred around sunset and lasted for about 3 h (Additional file 1: Fig. S1; Fig. 7b). These events usually occurred in succession, and at least three consecutive occurrences were observed during most of the summer and winter months. The sampling began at approximately 2 weeks after the end of consecutive extreme low tide events. We collected samples from corals that experienced subaerial exposure (SAS) by scuba diving on 28 August 2022. The seawater had a temperature of 30.3 °C and a salinity of 34.2 PSU, while the air had a temperature of 33.8 °C and a relative humidity of 57.6%. At the same time, we collected samples of permanently submerged corals (SMS) in water depths of approximately 3 m located at the same sampling sites. Similarly, we collected coral samples with a subaerial exposure background in winter (SAW) at the same sampling site on 3 March 2023. The seawater was recorded with a temperature of 20.4 °C and a salinity of 33.0 PSU, and the air conditions were noted as 21.0 °C in temperature and 52% in relative humidity. The distance between the SAS/SAW and SMS groups is approximately 10 m. Samples from eight different colonies were taken as 2–4 cm patches using hammers and chisels and as far away as possible to ensure that more comprehensive biological information was obtained. The samples were then rinsed with 0.22-μm filtered seawater to prevent contamination. Ultimately, all samples were quickly frozen in liquid nitrogen and stored at − 80 °C.

Physiological measurements

A total of 12 samples (four samples of each group) were used for quantifying the antioxidant capacity and

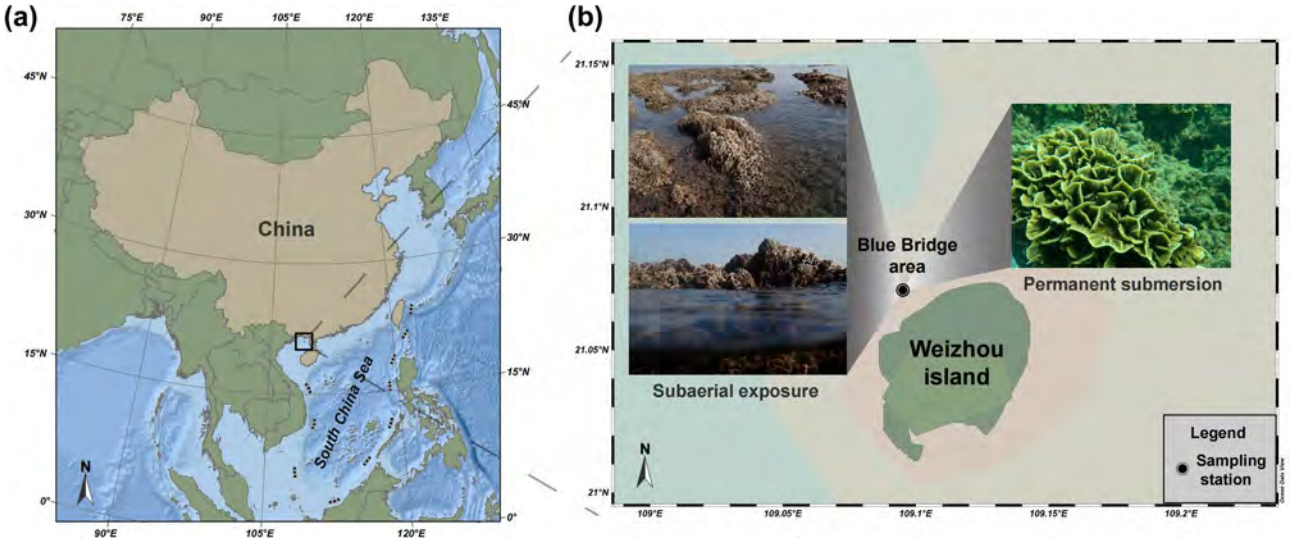


Fig. 7 The location map of sampling sites. (**a**) Weizhou Island in the South China Sea. (**b**) The image on the left showed that *P. decussata* in Blue Bridge area experienced subaerial exposure during extreme low tide event on 5 January 2022, and the image on the right showed their permanently submerged counterparts

Chl *a* contents of the corals. As previously described, a WaterPik® Ultra Water Jet (Water Pik, USA) filled with 0.22-μm filtered seawater was used to remove the coral tissue from the skeleton [84]. After obtaining coral tissue homogenates, three subsamples were taken from each replication. Then, the coral tissue homogenate supernatant was used to analyze the antioxidative indicators. The activities of total superoxide dismutase (T-SOD) and catalase (CAT) and the content of malondialdehyde (MDA) were assayed using commercial kits (Nanjing Jiancheng Bioengineering Institute, China). The total protein was measured using a quantitative assay kit (Nanjing Jiancheng Bioengineering Institute, China), and all data for antioxidative indicators were normalized to the total protein content. Meanwhile, 100% acetone was used for extracting Chl *a* in a 24-hour dark period at − 20 °C according to the method of Zhang et al. [7]. The homogenate was centrifuged using Sigma 3-18KS freezing centrifuge (Sigma Laborzentrifugen GmbH, Germany) at 4,000 rpm for 10 min; the supernatant was collected, and the absorbance was measured at OD630 and OD663 using a UV-2700 spectrophotometer (SHIMADZU, Japan). The chlorophyll content was computed using the equations in Jeffrey and Humphrey [85]. The coral antioxidant-related indices and the Chl *a* content were analyzed. Pairwise group comparisons were performed using t-tests, and *p*-values were adjusted for multiple testing via Bonferroni correction, with $p < 0.05$ representing a significant difference and $p < 0.01$ representing a highly significant difference.

DNA extraction, 16S rRNA gene amplicon sequencing, and data analysis

Small amounts (2–4 g) of each coral sample were crushed with a mortar and pestle, and DNA was extracted using the TIANamp Marine Animals DNA Kit (Tiangen, China). Finally, the high-quality DNA of 15 samples from three groups was extracted. PCR amplification was performed using the primers 338 F (5′-ACTCCTACGGGAGGCAGCAG-3′) and 806R (5′-GGACTACHVGGGTWTCTAAT-3′) for the V3V4 variable region of bacterial 16S rRNA with an ABI GeneAmp 9700 thermal cycler (Thermo Fisher Scientific, USA), followed by detection and quantification of the PCR products. A TruSeq™ DNA Sample Prep Kit (Illumina, USA) was used to prepare Illumina libraries, which were then sequenced on an Illumina MiSeq platform following standard protocols.

The raw data were split according to the samples and then quality-filtered and merged using the Trimmomatic read trimming tool and FLASH [84]. The resulting high-quality reads were denoised using Qiime2 (Version 2023.5.0) via the DADA2 plugin to obtain amplicon sequence variants (ASVs) [86]. All sequences annotated as being from chloroplasts and mitochondria were removed to ensure the purity of the data, and the remaining sequences were normalized by the lowest number of sequences. To quantify fluctuations in bacterial species, the values of alpha diversity indices (Ace, Chao, Sobs, Shannon, and Simpson) were calculated using Mothur (https://mothur.org/), and the data were analyzed using the Kruskal-Wallis H test [87]. Sample spacing of beta diversity was calculated using principal coordinate analysis (PCoA) based on the weighted

Bray-Curtis algorithm in order to visualize the community structure between samples. Linear discriminant analysis effect size (LEfSe; http://huttenhower.sph.harvard.edu/galaxy/root?tool_id=lefse_upload) was used to profile the species characteristics that explained most of the differences between groups with a linear discriminant analysis (LDA) threshold of 4 and a p-value < 0.05. The data were analyzed through the free online platform of majorbio cloud platform (http://cloud.majorbio.com) [88].

RNA extraction, transcriptome sequencing, and data analysis

The coral total RNA was extracted from four samples per group using a TRIzol™ Plus RNA Purification Kit (Thermo Fisher Scientific, USA) according to the manufacturer's instructions. Oligo (dT) magnetic beads were used to enrich the mRNA. An Illumina Stranded mRNA Prep Ligation Kit (Illumina, USA) was then used to construct a library. Sequencing was performed using an Illumina NovaSeq 6000 according to standard protocols.

Clean reads were obtained after adapter removal, pruning, and filtering of raw reads via Fastp (https://github.com/OpenGene/fastp) [89]. All clean reads were assembled *de novo* by Trinity (https://github.com/trinityrnaseq/trinityrnaseq/wiki) [26]. BLASTx was used to obtain the sequences from the coral hosts, according to Yu et al. [6]. The sequences were annotated using non-redundant (Nr; Version 2022.10), Gene Ontology (GO; Version 2022.0915), and Kyoto Encyclopedia of Genes and Genomes (KEGG; Version 2022.10) databases. To measure the transcription and gene expression levels, RSEM (version 1.3.3) was used and the transcripts per million (TPM) was applied. To further determine whether the groups had genetic differences, the AMOVA analysis of the SNP sites in the transcript data was performed using Arlequin (Version 3.5.2.2). The samples were clustered based on the expression of unigenes by principal component analysis (PCA), followed by the identification of differentially expressed unigenes (DEGs) using DESeq2 (Version 1.24.0) with a false discovery rate (FDR) < 0.01 and an absolute value of $\log_2$FC ≥ 1. To further explore the DEGs, information regarding function and pathways was obtained by GO and KEGG annotation. The KEGG enrichment analyses was carried out using majorbio cloud platform [88] with Python package scipy, and used Fisher's exact test and $p < 0.05$ as the criteria for significant judgment. To avoid result narrowing due to overcorrection, no multiple testing correction was applied to enrichment analyses, but the FDR values, corrected using the Benjamini-Hochberg method, are still provided in Additional File 5 for the reader's reference. Enrichment network analysis was performed based on the relationship between significant KEGG pathways to obtain the major pathways, and then key DEGs were screened by the most dominant and representative pathway mechanism.

Extraction and identification of metabolites

A total of 24 samples (eight samples per group) were employed to extract the metabolites. First, a small amount of each coral sample (100 ± 5 mg) was added to a mortar, and metabolite extraction was performed using 400 µL of methanol-water extraction solution (4:1, v/v) containing 0.02 mg/mL of internal standard (L-2-chlorophenylalanine). Samples were ground by the Wonbio-96c frozen tissue grinder (Shanghai wanbo biotechnology, China) for 6 min at − 10 °C, followed by low-temperature ultrasonic extraction for 30 min at 5 °C. The samples were then allowed to left at − 20 °C for 30 min, and centrifuged using Centrifuge 5430R (Eppendorf, Germany) at 11,500 rpm for 10 min. Finally, the supernatant was collected. Equal volumes of all sample supernatant were taken and mixed to prepare quality control samples (QC), and a QC was included in every eight samples during instrumental analysis. All supernatant were analyzed by LC-MS using a UHPLC-Q Exactive HF-X system (Thermo Fisher Scientific, USA) with the following conditions. An ACQUITY UPLC HSS T3 column (100 mm × 2.1 mm i.d., 1.8 µm; Waters, USA) was used for extraction. Mobile phase A consisted of 95% water and 5% acetonitrile (with 0.1% formic acid), and mobile phase B consisted of 47.5% acetonitrile, 47.5% isopropanol, and 5% water (with 0.1% formic acid). The injection volume was 3 µL, and the column temperature was 40 °C. The samples were ionized by electrospray, the specific parameters of the mass spectra were as follows. Sheath gas flow rate was set to 50 arb and aux gas flow rate was 13 arb. Spray voltage was 3,500 in positive mode and 3,500 in negative mode. Normalized collision energy was 20 eV, 40 eV, 60 eV. Full MS resolution was 60,000, and MS/MS resolution was 7500. Scan type was 70–1050 m/z. The mass spectral signals were collected in positive (POS) and negative (NEG) ion scanning modes. Then, the raw data were imported into Progenesis QI (Waters, USA) for baseline filtering, peak identification, integration, retention time correction, and peak alignment. Finally, a data matrix of retention time, mass-to-charge ratio, and peak intensity was obtained, which was then matched according to the HMDB (https://hmdb.ca/) and Metlin (https://metlin.scripps.edu/) databases.

Before analyzing the data, the data matrix was preprocessed by removing and filling in missing values. Specifically, only those metabolic features with non-zero values in at least 80% of the samples in any set were preserved. The empty values are then filled using the smallest value in the original matrix. The mass spectrometry peak intensities corresponding to all metabolic features were normalized using the sum normalization method.

Variables with a relative standard deviation > 30% in QC were removed, and the remaining variables were log transformed. Partial least squares discriminant analysis (PLS-DA) was used to examine group differences. The Ropls package in R (Version 1.6.2) was used to perform the OPLS-DA. Further, metabolites from POS and NEG modes were combined for significantly different metabolite (DM) identification and further analysis. DMs were identified based on the value of variable importance in the projection (VIP) obtained from the orthogonal partial least squares discriminant analysis (OPLS-DA) model and FDR from Student's *t*-test. Metabolites with FDR < 0.01 and VIP > 1 were defined as DMs. DMs were matched to the KEGG database and analyzed for enrichment using the Python package scipy.stats, and the *p*-values were obtained by Fisher's exact test. Similar to the transcriptomic analysis, to prevent the narrowing of results from overcorrection, multiple testing correction was not applied to the enrichment analyses. KEGG pathway analysis was performed based on the relative-betweenness centrality of the topology. The metabolomics data analysis was performed using the free online platform of majorbio cloud platform (http://cloud.majorbio.com) [88].

Association analyses and statistics

To determine whether gene expression levels and metabolite abundances were correlated, a credible O2PLS model was applied to fit two omics datasets [90, 91] according to the description in Bouhaddani et al. [92]. The DEGs were designated as the X dataset, and the DMs were defined as the Y dataset. For assessing the explanatory ability of the two datasets, the contribution values (R^2X and R^2Y) were output separately. Significantly enriched KEGG pathways were screened in both transcriptomics and metabolomics. First, pathways were selected with first category as metabolism. Then, among the pathways in the first category of cellular processes, the innate immune pathways that have been reported in corals [55] were selected. Finally, DEGs from these pathways and DM were correlated. Spearman correlation coefficients and the significance of gene expression and metabolite abundances were calculated based on the overall determination of the correlation between the two omics with the O2PLS model. The integrative model diagram was created by BioRender (https://biorender.com) and Adobe Illustrator 2020 (Adobe, USA).

Supplementary Information

The online version contains supplementary material available at https://doi.org/10.1186/s12864-025-11660-4.

Supplementary Material 1

Supplementary Material 2

Supplementary Material 3

Supplementary Material 4

Supplementary Material 5

Supplementary Material 6

Supplementary Material 7

Supplementary Material 8

Supplementary Material 9

Supplementary Material 10

Acknowledgements
We thank the staff of the Weizhou Island Coral Museum of Guangxi University for their assistance and support in this study. We thank the experts who edited and reviewed this paper for publication.

Author contributions
Study conception: MZ; Field work: LL; Lab work: SH; Data Curation: MZ, SH; Writing-Original Draft: MZ, SH; Writing-Review & Editing: MZ, SH, KY; Visualization: SH; Supervision: MZ; Project Administration: MZ; Funding Acquisition: KY.

Funding
This work was supported by National Natural Science Foundation of China (No. 42030502), Guangxi Science and Technology Program (No. AD25069075), National Natural Science Foundation of China (No. 42090041).

Data availability
The raw 16S rRNA gene amplicon sequencing data have been submitted to the NCBI Sequence Read Archive (SRA) database (BioProject ID: PRJNA1049633). The raw data generated from RNA sequencing could be found in the BioProject (PRJNA1041081) at the NCBI SRA database. The data matrix of metabolomics has been uploaded to MetaboLights (MTBLS8982).

Declarations

Ethics approval and consent to participate
The animal trial was carried out at the Guangxi Laboratory on the Study of Coral Reefs in the South China Sea and approved by the ethical review committee for animal project in Guangxi University.

Consent for publication
Not applicable.

Competing interests
The authors declare no competing interests.

Author details
[1]Guangxi Laboratory on the Study of Coral Reefs in the South China Sea, Coral Reef Research Center of China, School of Marine Sciences, Guangxi University, Nanning 530004, PR China
[2]Southern Marine Science and Engineering Guangdong Laboratory (Guangzhou), Guangzhou 511458, PR China

Received: 14 August 2024 / Accepted: 30 April 2025
Published online: 14 May 2025

References

1. Spalding M, Burke L, Wood SA, Ashpole J, Hutchison J. zu Ermgassen P. Mapping the global value and distribution of coral reef tourism. Mar Policy. 2017;82:104–13.
2. Bourne DG, Morrow KM, Webster NS. Insights into the coral microbiome: underpinning the health and resilience of reef ecosystems. Annu Rev Microbiol. 2016;70:317–40.

3. Huang W, Yang E, Yu K, Meng L, Wang Y, Liang J, et al. Lower cold tolerance of tropical *Porites lutea* is possibly detrimental to its migration to relatively high latitude refuges in the South China sea. Mol Ecol. 2022;31:5339–55.
4. Rädecker N, Pogoreutz C, Gegner HM, Cardenas A, Roth F, Bougoure J, et al. Heat stress destabilizes symbiotic nutrient cycling in corals. Proc Natl Acad Sci USA. 2021;118:e2022653118.
5. Sully S, Burkepile DE, Donovan MK, Hodgson G, van Woesik R. A global analysis of coral bleaching over the past two decades. Nat Commun. 2019;10:1264.
6. Yu X, Yu K, Chen B, Liao Z, Liang J, Yao Q, et al. Different responses of scleractinian coral *Acropora pruinosa* from Weizhou Island during extreme high temperature events. Coral Reefs. 2021;40:1697–711.
7. Zhang Y, Ip JC, Xie JY, Yeung YH, Sun Y, Qiu JW. Host-symbiont transcriptomic changes during natural bleaching and recovery in the leaf coral *Pavona decussata*. Sci Total Environ. 2022;806:150656.
8. Perry CT, Larcombe P. Marginal and non-reef-building coral environments. Coral Reefs. 2003;22:427–32.
9. Röthig T, Bravo H, Corley A, Prigge T-L, Chung A, Yu V, et al. Environmental flexibility in *Oulastrea crispata* in a highly urbanised environment: a microbial perspective. Coral Reefs. 2020;39:649–62.
10. Guest JR, Low J, Tun K, Wilson B, Ng C, Raingeard D, et al. Coral community response to bleaching on a highly disturbed reef. Sci Rep. 2016;6:20717.
11. Brown NP, Forsman ZH, Tisthammer KT, Richmond RH. A resilient brooding coral in the broadcast spawning *Porites lobata* species complex: a new endemic, introduced species, mutant, or new adaptive potential? Coral Reefs. 2020;39:809–18.
12. Barros Y, Lucas CC, Soares MO. An urban intertidal reef is dominated by fleshy macroalgae, sediment, and bleaching of a resilient coral (*Siderastrea stellata*). Mar Pollut Bull. 2021;173:112967.
13. Castrillón-Cifuentes AL, Lozano-Cortés DF, Zapata FA. Effect of short-term subaerial exposure on the cauliflower coral, *Pocillopora damicornis*, during a simulated extreme low-tide event. Coral Reefs. 2017;36:401–14.
14. Alina DN, Rachmawati R, Zamani NP, Madduppa H. Exposure at low tide leads to a different microbial abundance of intertidal coral *Acropora pulchra*. Mar Biol Res. 2022;18:520–30.
15. Raymundo LJ, Burdick D, Lapacek VA, Miller R, Brown V. Anomalous temperatures and extreme tides: Guam Staghorn *Acropora* succumb to a double threat. Mar Ecol Prog Ser. 2017;564:47–55.
16. Speelman PE, Parger M, Schoepf V. Divergent recovery trajectories of intertidal and subtidal coral communities highlight habitat-specific recovery dynamics following bleaching in an extreme macrotidal reef environment. PeerJ. 2023;11:e15987.
17. Jung EMU, Stat M, Thomas L, Koziol A, Schoepf V. Coral host physiology and symbiont dynamics associated with differential recovery from mass bleaching in an extreme, macro-tidal reef environment in Northwest Australia. Coral Reefs. 2021;40:893–905.
18. Anthony KRN, Kerswell AP. Coral mortality following extreme low tides and high solar radiation. Mar Biol. 2007;151:1623–31.
19. Pandolfi JM, Kiessling W. Gaining insights from past reefs to inform Understanding of coral reef response to global climate change. Curr Opin Env Sust. 2014;7:52–8.
20. Hoegh-Guldberg O, Fine M, Skirving W, Johnstone R, Dove S, Strong A. Coral bleaching following wintry weather. Limnol Oceanogr. 2005;50:265–71.
21. Modys AB, Oleinik AE, Toth LT, Precht WF, Mortlock RA. Modern coral range expansion off Southeast Florida falls short of late holocene baseline. Commun Earth Environ. 2024;5:119.
22. Huang W, Meng L, Xiao Z, Tan R, Yang E, Wang Y, et al. Heat-tolerant intertidal rock pool coral *Porites lutea* can potentially adapt to future warming. Mol Ecol. 2024;33:e17273.
23. Shiu J-H, Keshavmurthy S, Chiang P-W, Chen H-J, Lou S-P, Tseng C-H, et al. Dynamics of coral-associated bacterial communities acclimated to temperature stress based on recent thermal history. Sci Rep. 2017;7:14933.
24. Ziegler M, Seneca FO, Yum LK, Palumbi SR, Voolstra CR. Bacterial community dynamics are linked to patterns of coral heat tolerance. Nat Commun. 2017;8:14213.
25. Roach TNF, Dilworth J, Jones HCM, Quinn AD, Drury RA. Metabolomic signatures of coral bleaching history. Nat Ecol Evol. 2021;5:495–503.
26. Yu X, Yu K, Liao Z, Chen B, Qin Z, Liang J, et al. Adaptation strategies of relatively high-latitude marginal reef corals in response to severe temperature fluctuations. Sci Total Environ. 2023;903:166439.
27. Cheng CM, Cheng YR, Ding DS, Chen YT, Sun WT, Pan CH. Effects of ciliate infection on the activities of two antioxidant enzymes (SOD and CAT) in captive coral (*Goniopora columna*) and evaluation of drug therapy. Biol. 2021;10:1216.
28. Zhang Y, Chen RW, Liu X, Zhu M, Li Z, Wang A, et al. Oxidative stress, apoptosis, and transcriptional responses in *Acropora microphthalma* under simulated diving activities. Mar Pollut Bull. 2022;183:114084.
29. Chen YT, Ding DS, Lim YC, Singhania RR, Hsieh S, Chen CW, et al. Impact of polyethylene microplastics on coral *Goniopora columna* causing oxidative stress and histopathology damages. Sci Total Environ. 2022;828:154234.
30. Stambler N, Dubinsky Z. Stress effects on metabolism and photosynthesis of hermatypic corals. In: Rosenberg E, Loya Y, editors. Coral health and disease. Berlin, Heidelberg: Springer Berlin Heidelberg; 2004. pp. 195–215.
31. Rosenberg E, Koren O, Reshef L, Efrony R, Zilber-Rosenberg I. The role of microorganisms in coral health, disease and evolution. Nat Rev Microbiol. 2007;5:355–62.
32. Patel NP, Shimpi GG, Haldar S. A comparative account of resistance and antagonistic activity of healthy and bleached coral-associated bacteria as an indicator of coral health status. Ecol Indic. 2021;120:106886.
33. Han S, Cheng X, Wang T, Li X, Cai Z, Zheng H, et al. AI-2 quorum sensing signal disrupts coral symbiotic homeostasis and induces host bleaching. Environ Int. 2024;188:108768.
34. Hsieh YE, Lu C-Y, Liu P-Y, Kao J-M, Yang S-Y, Wu C-Y, et al. Successive responses of three coral holobiont components (coral hosts, symbiotic algae, and bacteria) to daily temperature fluctuations. Ecol Indic. 2024;158:111515.
35. Hernandez-Agreda A, Gates RD, Ainsworth TD. Defining the core Microbiome in corals' microbial soup. Trends Microbiol. 2017;25:125–40.
36. Röthig T, Ochsenkühn MA, Roik A, van der Merwe R, Voolstra CR. Long-term salinity tolerance is accompanied by major restructuring of the coral bacterial Microbiome. Mol Ecol. 2016;25:1308–23.
37. Ahmed HI, Herrera M, Liew YJ, Aranda M. Long-term temperature stress in the coral model *Aiptasia* supports the Anna karenina principle for bacterial microbiomes. Front Microbiol. 2019;10:975.
38. Mohamed AR, Ochsenkühn MA, Kazlak AM, Moustafa A, Amin SA. The coral microbiome: towards an Understanding of the molecular mechanisms of coral-microbiota interactions. FEMS Microbiol Rev. 2023;47:fuad005.
39. Oh HM, Kang I, Ferriera S, Giovannoni SJ, Cho JC. Genome sequence of the oligotrophic marine gammaproteobacterium HTCC2143, isolated from the Oregon Coast. J Bacteriol. 2010;192:4530–1.
40. Hu X, Su H, Zhang P, Chen Z, Xu Y, Xu W, et al. Microbial community structure and metabolic characteristics of intestine and gills of dwarf-form populations of *Sthenoteuthis oualaniensis* in South China sea. Fishes. 2022;7:191.
41. van de Water JAJM, Voolstra CR, Rottier C, Cocito S, Peirano A, Allemand D, et al. Seasonal stability in the microbiomes of temperate gorgonians and the red coral *Corallium rubrum* across the mediterranean sea. Microb Ecol. 2017;75:274–88.
42. Zheng N, Ding N, Gao P, Han M, Liu X, Wang J, et al. Diverse algicidal bacteria associated with harmful bloom-forming *Karenia Mikimotoi* in estuarine soil and seawater. Sci Total Environ. 2018;631–2:1415–20.
43. Varasteh T, Hamerski L, Tschoeke D, Lima AS, Garcia G, Cosenza CAN, et al. Conserved pigment profiles in phylogenetically diverse symbiotic bacteria associated with the corals *Montastraea cavernosa* and *Mussismilia braziliensis*. Microb Ecol. 2020;81:267–77.
44. García-Romero I, Pérez-Pulido AJ, González-Flores YE, Reyes-Ramírez F, Santero E, Floriano B. Genomic analysis of the nitrate-respiring *Sphingopyxis granuli* (formerly *Sphingomonas macrogoltabida*) strain TFA. BMC Genomics. 2016;17:93.
45. Huang S, Luo L, Wen B, Liu X, Yu K, Zhang M. Metabolic signatures of two scleractinian corals from the Northern South China sea in response to extreme high temperature events. Mar Environ Res. 2024;198:106490.
46. Zhang M, Huang S, Luo L, Yu X, Wang H, Yu K, et al. Insights into the molecular mechanisms underlying the different heat tolerance of the scleractinian coral *Pavona decussata*. Coral Reefs. 2024;43:429–42.
47. MacLean A, Legendre F, Appanna VD. The Tricarboxylic acid (TCA) cycle: a malleable metabolic network to counter cellular stress. Crit Rev Biochem. 2023;58:81–97.
48. da Silva Fonseca J, de Barros Marangoni LF, Marques JA, Bianchini A. Energy metabolism enzymes Inhibition by the combined effects of increasing temperature and copper exposure in the coral *Mussismilia harttii*. Chemosphere. 2019;236:124420.
49. Yang D, Tang Y, Zhu B, Pang H, Rong X, Gao Y, et al. Engineering cell membrane-cloaked catalysts as multifaceted artificial peroxisomes for biomedical applications. Adv Sci. 2023;10:2206181.

50. Kapetanou M, Athanasopoulou S, Gonos ES. Transcriptional regulatory networks of the proteasome in mammalian systems. IUBMB Life. 2021;74:41–52.
51. Porro B, Zamoum T, Forcioli D, Gilson E, Poquet A, Di Franco E, et al. Different environmental response strategies in sympatric corals from Pacific Islands. Commun Earth Environ. 2023;4:311.
52. Maiuri MC, Zalckvar E, Kimchi A, Kroemer G. Self-eating and self-killing: crosstalk between autophagy and apoptosis. Nat Rev Mol Cell Biol. 2007;8:741–52.
53. Majerova E, Carey FC, Drury C, Gates RD. Preconditioning improves bleaching tolerance in the reef-building coral *Pocillopora acuta* through modulations in the programmed cell death pathways. Mol Ecol. 2021;30:3560–74.
54. Filomeni G, De Zio D, Cecconi F. Oxidative stress and autophagy: the clash between damage and metabolic needs. Cell Death Differ. 2015;22:377–88.
55. Mansfield KM, Gilmore TD. Innate immunity and cnidarian-Symbiodiniaceae mutualism. Dev Comp Immunol. 2019;90:199–209.
56. Fuess LE, Pinzón CJH, Weil E, Grinshpon RD, Mydlarz LD. Life or death: disease-tolerant coral species activate autophagy following immune challenge. Proc R Soc B. 2017;284:20170771.
57. Massagué J, Sheppard D. TGF-β signaling in health and disease. Cell. 2023;186:4007–37.
58. Pei JY, Yu WF, Zhang JJ, Kuo TH, Chung HH, Hu JJ, et al. Mass spectrometry-based metabolomic signatures of coral bleaching under thermal stress. Anal Bioanal Chem. 2022;414:7635–46.
59. Biscéré T, Ferrier-Pagès C, Grover R, Gilbert A, Rottier C, Wright A, et al. Enhancement of coral calcification via the interplay of nickel and urease. Aquat Toxicol. 2018;200:247–56.
60. Crandall JB, Teece MA. Urea is a dynamic pool of bioavailable nitrogen in coral reefs. Coral Reefs. 2011;31:207–14.
61. Grover R, Maguer JF, Allemand D, Ferrier-Pagès C. Urea uptake by the scleractinian coral *Stylophora pistillata*. J Exp Mar Biol Ecol. 2006;332:216–25.
62. Crossland CJ, Barnes DJ. The role of metabolic nitrogen in coral calcification. Mar Biol. 1974;28:325–32.
63. Muthukumaran S, Jaidev J, Umashankar V, Sulochana KN. Ornithine and its role in metabolic diseases: an appraisal. Biomed Pharmacother. 2017;86:185–94.
64. Courtney TA, Lebrato M, Bates NR, Collins A, de Putron SJ, Garley R, et al. Environmental controls on modern scleractinian coral and reef-scale calcification. Sci Adv. 2017;3:e1701356.
65. Vajed Samiei J, Saleh A, Mehdinia A, Shirvani A, Kayal M. Photosynthetic response of Persian Gulf acroporid corals to summer versus winter temperature deviations. PeerJ. 2015;3:e1062.
66. Kuffner IB, Hickey TD, Morrison JM. Calcification rates of the massive coral *Siderastrea siderea* and crustose coralline algae along the Florida keys (USA) outer-reef tract. Coral Reefs. 2013;32:987–97.
67. Marshall AT, Clode P. Calcification rate and the effect of temperature in a zooxanthellate and an azooxanthellate scleractinian reef coral. Coral Reefs. 2004;23:218–24.
68. Sikorskaya TV. Coral lipidome: molecular species of phospholipids, glycolipids, betaine lipids, and sphingophosphonolipids. Mar Drugs. 2023;21:335.
69. Imbs AB, Dang LTP. Seasonal dynamics of fatty acid biomarkers in the soft coral *Sinularia flexibilis*, a common species of Indo-Pacific coral reefs. Biochem Syst Ecol. 2021;96:104246.
70. Rocker MM, Francis DS, Fabricius KE, Willis BL, Bay LK. Temporal and Spatial variation in fatty acid composition in *Acropora tenuis* corals along water quality gradients on the great barrier reef, Australia. Coral Reefs. 2019;38:215–28.
71. Wei J, Chen S, Guo W, Feng B, Yang S, Huang C, et al. Leukotriene D4 induces cellular senescence in osteoblasts. Int Immunopharmacol. 2018;58:154–9.
72. Torda G, Donelson JM, Aranda M, Barshis DJ, Bay L, Berumen ML, et al. Rapid adaptive responses to climate change in corals. Nat Clim Change. 2017;7:627–36.
73. Hernandez-Agreda A, Leggat W, Bongaerts P, Ainsworth TD. The microbial signature provides insight into the mechanistic basis of coral success across reef habitats. mBio. 2016;7:e00560–16.
74. Yu X, Yu K, Chen B, Liao Z, Huang W. Nanopore long-read RNAseq reveals regulatory mechanisms of thermally variable reef environments promoting heat tolerance of scleractinian coral *Pocillopora damicornis*. Environ Res. 2021;195:110782.
75. Sáez GT, Están-Capell N. Antioxidant enzymes. In: Schwab M, editor. Encyclopedia of Cancer. Berlin, Heidelberg: Springer; 2014.
76. Ginguay A, Cynober LA. Amino acids| amino acid metabolism. In: Jez J, editor. Encyclopedia of biological chemistry III (Third Edition). Oxford: Elsevier; 2021. pp. 2–9.
77. Cohen GN. The aspartic acid family of amino acids. Biosynthesis. Microbial biochemistry. Dordrecht: Springer; 2004.
78. Keighan R, van Woesik R, Yalon A, Nam J, Houk P. Moderate chlorophyll-*a* environments reduce coral bleaching during thermal stress in Yap, Micronesia. Sci Rep. 2023;13:9338.
79. Dandan SS, Falter JL, Lowe RJ, McCulloch MT. Resilience of coral calcification to extreme temperature variations in the Kimberley region, Northwest Australia. Coral Reefs. 2015;34:1151–63.
80. Marshall PA, Baird AH. Bleaching of corals on the great barrier reef: differential susceptibilities among taxa. Coral Reefs. 2000;19:155–63.
81. Loya Y, Sakai K, Yamazato K, Nakano Y, Sambali H, van Woesik R. Coral bleaching: the winners and the losers. Ecol Lett. 2001;4:122–31.
82. Buckee J, Hetzel Y, Edge W, Verduin J, Pattiaratchi C. Daily timing of low tide drives seasonality in intertidal emersion mortality risk. Front Mar Sci. 2022;9:904191.
83. Hoarau L, Mouquet P, Ropert M, Cuvillier A, Massé L, Bonhommeau S, et al. Negative sea level anomalies with extreme low tides in the South-West Indian ocean shape reunion Island's fringing coral reef flats. Ecol Indic. 2023;154:110508.
84. Yu X, Yu K, Huang W, Liang J, Qin Z, Chen B, et al. Thermal acclimation increases heat tolerance of the scleractinian coral *Acropora pruinosa*. Sci Total Environ. 2020;733:139319.
85. Jeffrey SW, Humphrey GF. New spectrophotometric equations for determining chlorophylls *a*, *b*, c_1 and c_2 in higher plants, algae and natural phytoplankton. Biochemie Und Physiologie Der Pflanzen. 1975;167:191–4.
86. Bolyen E, Rideout JR, Dillon MR, Bokulich NA, Abnet CC, Al-Ghalith GA, et al. Reproducible, interactive, scalable and extensible Microbiome data science using QIIME 2. Nat Biotechnol. 2019;37:852–7.
87. Kruskal WH, Wallis WA. Use of ranks in one-criterion variance analysis. J Am Stat Assoc. 1952;47:583–621.
88. Ren Y, Guo Y, Shi C, Liu L, Guo Q, Han C, et al. Majorbio cloud: A one-stop, comprehensive bioinformatic platform for multiomics analyses. iMeta. 2022;1:e12.
89. Chen S, Zhou Y, Chen Y, Gu J. Fastp: an ultra-fast all-in-one FASTQ preprocessor. Bioinform. 2018;34:i884–90.
90. Bouhaddani SE, Houwing-Duistermaat J, Salo P, Perola M, Jongbloed G, Uh H-W. Evaluation of O2PLS in omics data integration. BMC Bioinform. 2016;17:S11.
91. Trygg J, Wold S. O2-PLS, a two-block (X-Y) latent variable regression (LVR) method with an integral OSC filter. J Chemom. 2003;17:53–64.
92. Bouhaddani SE, Uh H-W, Jongbloed G, Hayward C, Klarić L, Kiełbasa SM, et al. Integrating omics datasets with the OmicsPLS package. BMC Bioinform. 2018;19:371.

Publisher's note

Springer Nature remains neutral with regard to jurisdictional claims in published maps and institutional affiliations.

microorganisms

MDPI

Article

Characteristics of Carbonatogenic Bacteria and Their Role in Enhancing the Stability of Biocrusts in Tropical Coral Islands

Qiqi Chen [1,2,†], Lin Wang [2,†], Jie Li [2], Qiqi Li [2], Hongfei Su [1,*] and Zhimao Mai [2,*]

[1] School of Resources, Environment and Materials, School of Marine Sciences, Guangxi University, Nanning 530004, China
[2] CAS Key Laboratory of Tropical Marine Bio-Resources and Ecology, South China Sea Institute of Oceanology, Chinese Academy of Sciences, Guangzhou 510301, China
* Correspondence: shf2016@gxu.edu.cn (H.S.); maizhimao@scsio.ac.cn (Z.M.)
† These authors contributed equally to this work.

Abstract: Soil erosion is a serious environmental problem that leads to land degradation and ecological imbalance, thereby eliciting extensive and profound worldwide concern. Biological soil crusts (biocrusts) play a crucial role in soil stabilization; however, the underlying microbial enzymatic mechanisms remain poorly understood. The present study aimed to characterize carbonatogenic bacteria and investigate the role of their carbonic anhydrase-induced carbonate crystals in promoting soil shear strength within biocrusts. The results demonstrated a significant increase in the activity of carbonic anhydrase during biocrust formation and development ($p < 0.05$). A total of 35 strains exhibiting carbonic anhydrase activity were isolated from biocrusts, belonging to Actinomycetota, Bacillota, Pseudomonadota and Cyanobacteriota. The subsequent investigation revealed a positive correlation between the carbonic anhydrase activities of the strains and the shear strength during sand consolidation. Specifically, strain SCSIO19859, a type of cyanophyta, exhibited the highest carbonic anhydrase activity, of 1.50 U/mL. It produced 0.70 g/day of calcium carbonate and demonstrated a shear strength that was 6.09 times greater than that of the control group after sand consolidation for seven days of incubation under optimal conditions. X-ray diffraction and scanning electron microscope analysis revealed that SCSIO19859 produced calcite and vaterite carbonates, which significantly increased the shear strength of the sand grains ($p < 0.05$). This study provides evidence for the ecological function of biocrusts in promoting soil erosion resistance from the perspective of carbonatogenic bacteria-derived carbonic anhydrase. The functional strains with carbonic anhydrase obtained from this study have significant potential applications in enhancing soil erosion resistance.

Keywords: biocrusts; carbonic anhydrase; shear strength; sand consolidation

check for updates

Academic Editor: Mohamed Hijri

Received: 22 January 2025
Revised: 21 February 2025
Accepted: 25 February 2025
Published: 27 February 2025

Citation: Chen, Q.; Wang, L.; Li, J.; Li, Q.; Su, H.; Mai, Z. Characteristics of Carbonatogenic Bacteria and Their Role in Enhancing the Stability of Biocrusts in Tropical Coral Islands. *Microorganisms* **2025**, *13*, 523. https://doi.org/10.3390/microorganisms13030523

Copyright: © 2025 by the authors. Licensee MDPI, Basel, Switzerland. This article is an open access article distributed under the terms and conditions of the Creative Commons Attribution (CC BY) license (https://creativecommons.org/licenses/by/4.0/).

1. Introduction

Soil erosion, resulting from both natural factors (wind or water erosion) and human activities that remove soil from the surface, is a widespread form of land degradation, affecting 84% of degraded lands [1,2]. Soil erosion leads to several severe issues, including the loss of soil organic carbon [3], a reduction in biodiversity [4] and an increase in the occurrence of natural disasters such as landslides and dust storms [5,6]. Globally, wind and water erosion affect more than 1.5 billion hectares of land, whereas in China, the area of water and soil loss exceeds 26 million hectares, primarily occurring in desert regions, plateaus, grasslands and islands [7–9]. Particularly on tropical coral islands, nutrient

availability is limited within the coral sand matrix, resulting in sparse vegetation cover. Moreover, these coral islands are exposed to extreme environmental conditions such as intense rainfall events and frequent storms that significantly increase the vulnerability of loose coral sand to erosion [10]. Hence, it is imperative to implement measures for mitigating soil erosion in these regions.

Biological soil crusts (biocrusts) are intricate composites formed through the adhesion of microorganisms such as bacteria, fungi and algae (including cyanobacteria and algae), as well as cryptogamic plants such as mosses, along with their mycelia and secretions, to soil particles [11]. These pioneer organisms can thrive in extreme environments characterized by high temperatures, intense light exposure and limited water availability; therefore, they are vital for restoring desert ecosystems [12]. Biocrusts are essential in providing soil ecosystem services, including accelerating soil respiration, enhancing photosynthesis, improving fertility, regulating water flow and facilitating weathering processes [13–16]. More importantly, biocrusts can mitigate wind and water erosion effectively, thereby enhancing soil stability [17]. Consequently, they have been extensively utilized in desert and plateau regions to ameliorate soil stability and diminish erosion [18,19]. The involvement of microorganisms is crucial in the process of sand stabilization in biocrusts. The intertwining of microbial hyphae with soil particles results in the formation of aggregates that increase soil stability [20]. Moreover, microbial secretion of extracellular polymeric substances contributes to promoting soil structural stability by adhering to soil particles [21,22]. Additionally, these substances contain diverse active components, including microbial enzymes [23]. However, few studies have investigated the mechanisms through which microbial enzymes increase the erosion resistance of biocrusts.

Carbonic anhydrase is a zinc-containing metalloenzyme that can catalyze the hydration reaction of carbon dioxide, thereby facilitating the formation of carbonates. This enzyme is widely distributed among living organisms and is characterized by its remarkable catalytic efficiency [24]. Current research suggests that carbonic anhydrase has extensive applications in soil stabilization, enhancing the performance of concrete materials and restoring damaged buildings and cultural relics [25,26]. The findings from our previous research indicate a positive correlation between erosion resistance and microbial carbonic anhydrase activity in biocrusts [27]. The result indicated that biocrusts may harbor carbonatogenic bacteria with elevated carbonic anhydrase activity, which could play a pivotal role in promoting sand stabilization. The further isolation and screening of carbonic anhydrase strains from biocrusts, along with the elucidation of the role of carbonates in sand consolidation, hold significant importance for future applications.

Therefore, cyanobacterial biocrusts at different developmental stages were selected. The purposes of this study were to (1) elucidate the variations in carbonic anhydrase activity during biocrust formation and development, (2) isolate microbial strains with carbonic anhydrase activity and (3) identify the characteristics of carbonates induced by carbonic anhydrase and illustrate their role in sand consolidation.

2. Materials

2.1. Sampling Methods

This study was conducted on a tropical coral island in the South China Sea characterized by a tropical oceanic monsoon climate. The annual average temperature on the island is 27.4 °C, coupled with an annual mean humidity of 83% and a mean wind speed of 3.4 m/s [28]. The soil composition of tropical coral islands is rich in calcium carbonate, with a fragile and morphologically diverse substrate that is particularly prone to erosion [29]. The vegetation cover on the island is sparsely distributed, with a low extent of coverage.

Cyanobacteria-dominated biocrusts account for approximately 6.25% of the total land area [30].

In July 2024, three sample types (bare soil, light biocrusts and dark biocrusts) were collected from the unvegetated soil surface (0–2 cm). Chlorophyll-*a* was used to assess the photosynthetic potential, which serves as an index for the developmental stage of biocrusts. Light biocrusts represent the initial three years of growth, whereas dark biocrusts indicate later stages of more than five years [13,31]. Eight 1 m × 1 m quadrats spaced more than 20 m apart were set up, and five samples were collected from each quadrat. All the samples were stored at 4 °C for enzyme activity tests and bacterial cultivation.

2.2. Determination of Chlorophyll-a and Carbonic Anhydrase Activity

The samples were dried at 25 °C and passed through a 35-mesh sieve to remove coarse particles. Chlorophyll-*a* was determined by ethanol spectrophotometry [32]. In the dark environment, 1 g of biocrusts was added to 5 mL of 95% ethanol solution, boiled at 95 °C for 5 min and allowed to cool for 30 min. The absorbance was immediately measured at 665 nm. The carbonic anhydrase activity of biocrusts was determined according to a previous report [33]. The biocrust samples were ground, and then 1 g of each sample was taken and placed into a 15 mL centrifuge tube, after which 1 mL of deionized water was added. The mixture was vortexed for 5 min and centrifuged at 3000× *g* for 5 min at 4 °C. The supernatant was collected for assessment of soil carbonic anhydrase activity. The enzyme activity was measured by the rate of pH reduction by one unit at a temperature of 4 °C. The assay mixture comprised 5 mL of phosphate buffer (20 mmol/L, pH = 8.3), 0.5 mL of either boiled or unboiled sample and 4.5 mL of CO_2-saturated water. Carbonic anhydrase activity was calculated by the formula U = 10(To/Te − 1). To and Te denote the time of one-unit decrease in pH of boiled or unboiled samples.

2.3. Microbiological Analysis

2.3.1. Isolation of Carbonatogenic Bacteria

One gram of soil sample was added to 9 mL of sterile deionized water. After vortexing and standing for 30 min, the sample was diluted and the supernatant was coated onto blue–green 11 (BG-11) and tryptose soybean agar (TSA) medium plates and incubated aerobically at 30 °C. After a period of incubation, single colonies were collected and cultured at 30 °C in sterilized BG-11 or TSB medium. The carbonic anhydrase activity of the strains was determined according to the standard procedure. The strains with carbonic anhydrase activity were stored at −80 °C with 30% (*w/v*) sterilized glycerin.

2.3.2. Bacterial Identification

Bacterial DNA was extracted using EasyPure Bacterial Genomic DNA Kit. The universal primers 27F and 1492R were used to amplify 16S rRNA gene by polymerase chain reaction (PCR). Reaction conditions were as follows: predenaturation at 95 °C for 5 min, 95 °C for 3 min, 57 °C for 30 s and 72 °C for 1 min, for 30 cycles; and a final cycle of 10 min at 70 °C. The PCR products were sequenced using the Sanger method and compared on EZBioCloud website (www.ezbiocloud.net) (accessed on 1 September 2024) to determine the closely related species of the isolated strain. The 16S rRNA gene sequences with the highest similarity in database were taken as references, and the Clustal W method in MEGA-11 (version 11.0) software was used for multiple sequence comparison [34]. Phylogenetic trees depicting the relationships among the related bacteria were constructed using the neighbor-joining method [35].

2.4. Sand Consolidation

The strains with high carbonic anhydrase activity were selected, and the method of sand consolidation refers to our previous study [27]. In total, 10 mL of bacterial culture solution, 10 mL of 1 mol/L $CaCl_2$ solution and 10 mL of 1 mol/L $NaHCO_3$ solution were added to 300 g of quartz sand (with Ca^{2+} removed by 1 mol/L HCl solution and dried early) for seven consecutive days, after the quartz sand was dried. Sterile water was used instead of bacterial solution as the control group (CK). Shear strength was measured using a soil shear testing device (Eijkelkamp, Giesbeek, The Netherlands).

2.5. Optimization of Carbonate Formation Conditions

The OD values of bacterial cultures were measured at various temperatures and pH levels to determine the optimal conditions for growth. The concentration of the carbon source ($NaHCO_3$) utilized for analyzing carbonic anhydrase-induced carbonate formation ranged from 0.5 to 1.25 mol/L, with an incremental step of 0.25 mol/L. The $CaCl_2$ and $Ca(C_2H_3O_2)_2$ were selected to test for the optimal calcium source for carbonic anhydrase-induced carbonate formation. The production of carbonic anhydrase-induced calcium carbonate was measured under the optimal condition.

2.6. Analysis of the Morphology of Carbonate Crystals

Five grams of particles were scraped from the surface of the consolidated sand for X-ray diffraction (XRD) and scanning electron microscopy (SEM) analysis. The crystal profile of the crystal was analyzed by an X-ray crystal diffractometer (D8 ADVANCE, Berlin, Germany) with CuKα radiation (λ = 0.154 nm), a diffraction angle of 2θ and scanning speeds of 10–80° and 10°/min. The consolidated sand was subjected to ion beam sputtering (ISC150 T, SuPro, Shenzhen, China) and sprayed with gold metal for 60 s. SEM (S-3400 N, Hitachi, Tokyo, Japan) was subsequently used to observe and photograph the cementation effect of carbonate precipitation induced by carbonic anhydrase on sand.

2.7. Statistical Analysis

SPSS (version 26.0) was utilized to perform a univariate ANOVA (employing the Tukey HSD test) to assess significant differences in parameter variances. The Clustal W method in MRGA-11 (version 11.0) software was used for multisequence comparison, the predictive tree building model was Tamura-Nei and the neighbor-joining method was adopted for clustering analysis.

3. Results

3.1. Carbonic Anhydrase Activity and Chlorophyll-a Contents of Biocrusts

The carbonic anhydrase activities of the three sample types are illustrated in Figure 1A. The carbonic anhydrase activity of the dark biocrusts was 1.20 U/g dry soil, which was significantly higher than those of the light biocrusts and bare soil ($p < 0.05$). The chlorophyll-*a* content in the dark biocrusts was 25.22 mg/kg, which was significantly higher than those of the light biocrusts and bare soil ($p < 0.05$), and that of the dark biocrusts was 2.77 times higher than that of the light biocrusts (Figure 1B). Chlorophyll-*a* serves as an indicator of biocrust development and exhibits a positive correlation with carbonic anhydrase activity (Figure 1C).

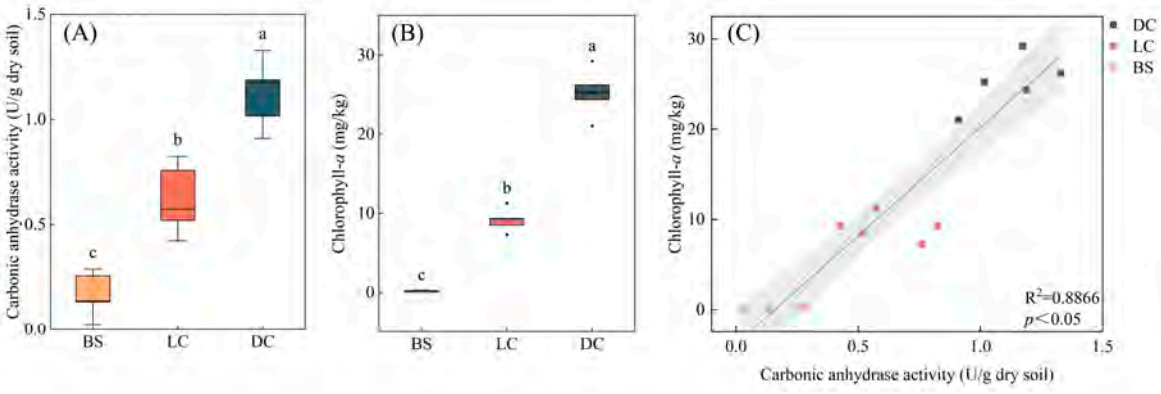


Figure 1. The carbonic anhydrase activity, chlorophyll-*a* content and their correlation. (**A**) Carbonic anhydrase activities of the three sample types. (**B**) Chlorophyll-*a* content in the three sample types. (**C**) Correlation between carbonic anhydrase activity and chlorophyll-*a* content ($y = 24.0379x - 3.8156$, $R^2 = 0.8866$, $p < 0.05$). The presence of distinct letters (a, b, and c) indicates noteworthy variances between groups, with a significance level below $p < 0.05$. The scattered solid shapes depict the specimens obtained from various sites, with yellow, red and blue scatters symbolizing samples collected from bare soil (BS), light biocrusts (LCs) and dark biocrusts (DCs), respectively.

3.2. Characteristics of Carbonatogenic Bacteria and Their Carbonic Anhydrase Activity

In this study, 35 bacterial strains with carbonic anhydrase activity, which belong to four phyla and eight genera, were isolated from biocrusts (Figure 2A,B). The carbonic anhydrase activity of the isolated strains ranged from 0.09 to 1.26 U/mL (Table S1). The correlation between the carbonic anhydrase activity of the strains and the shear strength of the sand consolidation is illustrated in Figure 3A,B. The strain SCSIO19859, which exhibits the highest carbonic anhydrase activity, demonstrated the greatest shear strength in sand consolidation. A significant positive correlation was observed between the microbial carbonic anhydrase activity and the shear strength during sand consolidation ($p < 0.05$) (Figure 3C). Given that strain SCSIO19859 exhibited the highest carbonic anhydrase activity and demonstrated the greatest shear strength in sand consolidation, it was selected for further investigation. The SEM and optical microscope analyses revealed that strain SCSIO19859 exhibited a globular filamentous morphology (Figure 4A,B). Furthermore, the phylogenetic tree analysis indicated that SCSIO19859 could be preliminarily identified as *Nostoc calcicola* (Figure 4C).

In this study, 35 bacterial strains with carbonic anhydrase activity, which belong to four phyla and eight genera, were isolated from biocrusts (Figure 2A,B). The carbonic anhydrase activity of the isolated strains ranged from 0.09 to 1.26 U/mL (Table S1). The correlation between the carbonic anhydrase activity of the strains and the shear strength of the sand consolidation is illustrated in Figure 3A,B. The strain SCSIO19859, which exhibits the highest carbonic anhydrase activity, demonstrated the greatest shear strength in sand consolidation. A significant positive correlation was observed between the microbial carbonic anhydrase activity and the shear strength during sand consolidation ($p < 0.05$) (Figure 3C). Given that strain SCSIO19859 exhibited the highest carbonic anhydrase activity and demonstrated the greatest shear strength in sand consolidation, it was selected for further investigation. The SEM and optical microscope analyses revealed that strain SCSIO19859 exhibited a globular filamentous morphology (Figure 4A,B). Furthermore, the phylogenetic tree analysis indicated that SCSIO19859 could be preliminarily identified as *Nostoc calcicola* (Figure 4C).

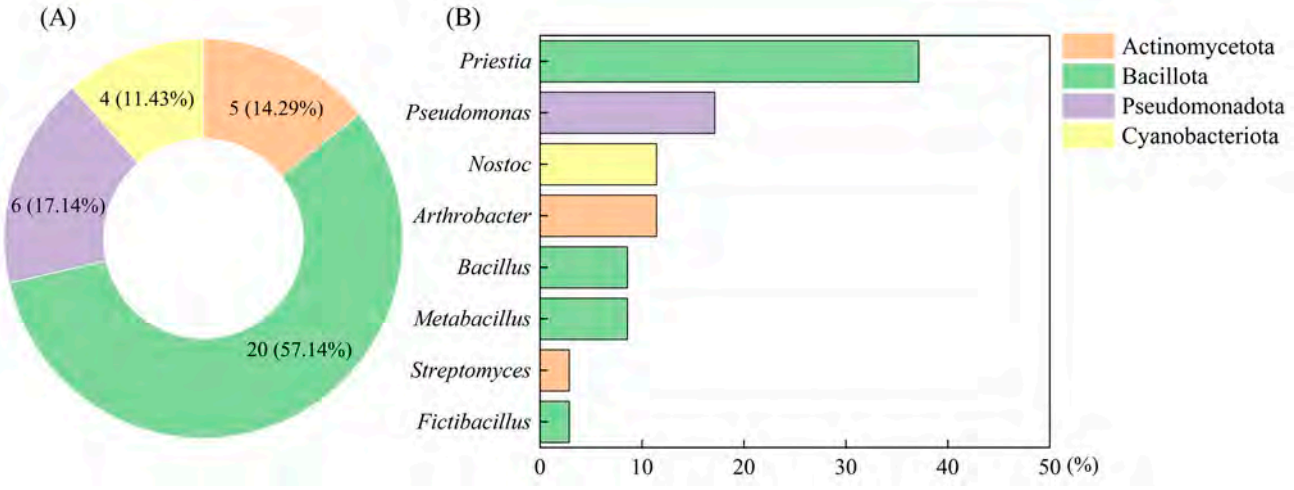


Figure 2. The composition of carbonatogenic bacteria. (**A**) Classification of strains at phylum level. (**B**) Classification of strains at genus level.

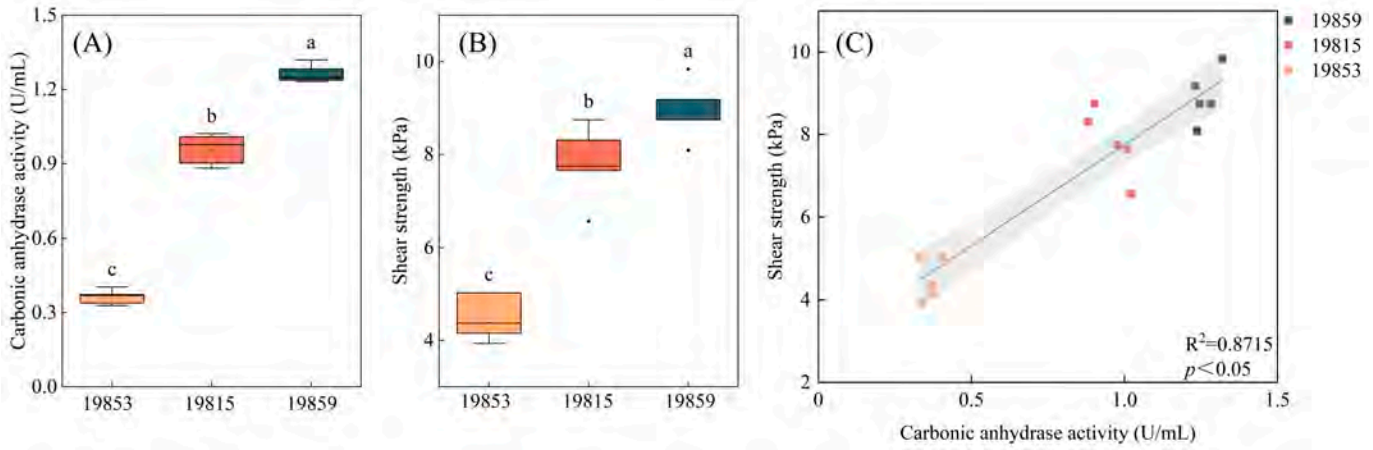


Figure 3. Correlation between carbonic anhydrase activity and shear strength in sand consolidation treated with isolated strains. (**A**) Carbonic anhydrase activity of strain SCSIO19853, SCSIO19815 and SCSIO19859. (**B**) The shear strength in sand consolidation treated with strain SCSIO19853, SCSIO19815, and SCSIO19859. (**C**) Correlation between carbonic anhydrase activity and shear strength in sand consolidation ($y = 4.8812x + 2.8698$, $R^2 = 0.8715$, $p < 0.05$). The presence of distinct letters (a, b, and c) indicates noteworthy variances between groups, with a significance level below $p < 0.05$.

Figure 3. Correlation between carbonic anhydrase activity and shear strength in sand consolidation treated with isolated strains. (**A**) Carbonic anhydrase activity of strain SCSIO19853, SCSIO19815 and SCSIO19859. (**B**) The shear strength in sand consolidation treated with strain SCSIO19853, SCSIO19815, and SCSIO19859. (**C**) Correlation between carbonic anhydrase activity and shear strength in sand consolidation ($y = 4.8812x + 2.8698$, $R^2 = 0.8715$, $p < 0.05$). The presence of distinct letters (a, b, and c) indicates noteworthy variances between groups, with a significance level below $p < 0.05$.

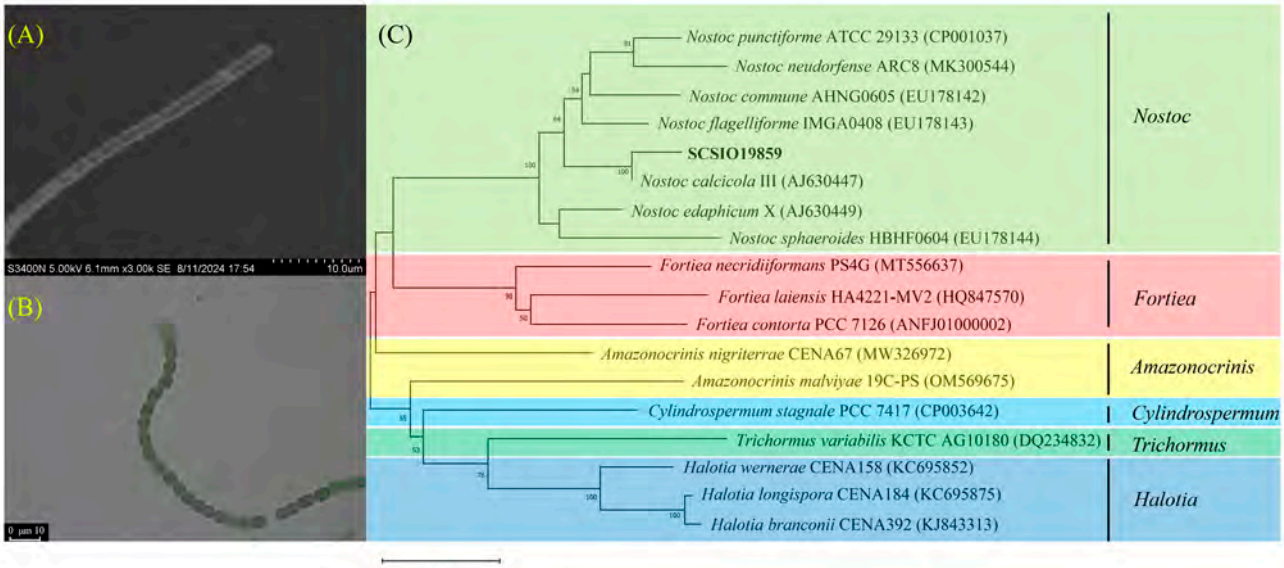


Figure 4. Morphological and phylogenetic tree analyses of strain SCSIO19859. (**A**) Scanning electron microscopy analysis of SCSIO19859. (**B**) Optical microscope analysis of SCSIO19859. (**C**) Phylogenetic tree analysis of SCSIO19859.

Figure 4. Morphological and phylogenetic tree analyses of strain SCSIO19859. (**A**) Scanning electron microscopy analysis of SCSIO19859. (**B**) Optical microscope analysis of SCSIO19859. (**C**) Phylogenetic tree analysis of SCSIO19859.

3.3. Optimal Conditions for Carbonate Formation

As illustrated in Figure 5A,B, the optimal conditions for the growth of strain SCSIO19859 are a temperature of 25 °C and a pH of 7. Under these conditions, strain SCSIO19859 exhibited maximal calcium carbonate production in a 1.5 mol/L $NaHCO_3$ solution (Figure 5C). Furthermore, strain SCSIO19859 induced greater calcium carbonate precipitation when $CaCl_2$ was used as the calcium source compared to $Ca(C_2H_3O_2)_2$ (Figure 5D). Under optimal conditions, strain SCSIO198597 can produce 0.70 g/day of $CaCO_3$, a rate that surpasses both that obtained in non-optimized conditions and that of the control group (Figure 6A). Additionally, a significantly positive correlation was observed between $CaCO_3$ content and shear strength in sand consolidation ($p < 0.05$) (Figure 7B).

3.3. Optimal Conditions for Carbonate Formation

As illustrated in Figure 5A,B, the optimal conditions for the growth of strain SCSIO19859 are a temperature of 25 °C and a pH of 7. Under these conditions, strain SCSIO19859 exhibited maximal calcium carbonate production in a 1.5 mol/L $NaHCO_3$ solution (Figure 5C). Furthermore, strain SCSIO19859 induced greater calcium carbonate precipitation when $CaCl_2$ was used as the calcium source compared to $Ca(C_2H_3O_2)_2$ (Figure 5D). Under optimal conditions, strain SCSIO198597 can produce 0.70 g/day of $CaCO_3$, a rate that surpasses both that obtained in non-optimized conditions and that of the control group (Figure 6A). Additionally, a significantly positive correlation was observed between $CaCO_3$ content and shear strength in sand consolidation ($p < 0.05$) (Figure 7B).

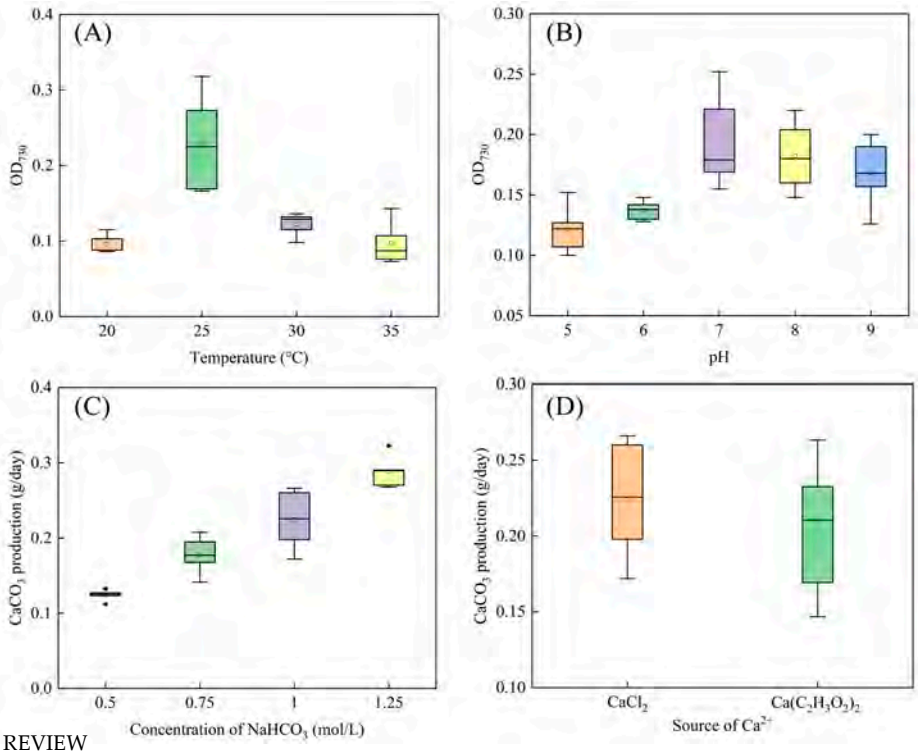


Figure 5. Optimization of carbonate formation conditions of SCSIO19859. (**A**) The optimal temperature for SCSIO19859 growth. (**B**) The optimal pH for SCSIO19859 growth. (**C**) The optimal $NaHCO_3$ concentration for $CaCO_3$ production. (**D**) The optimal Ca^{2+} source for $CaCO_3$ production.

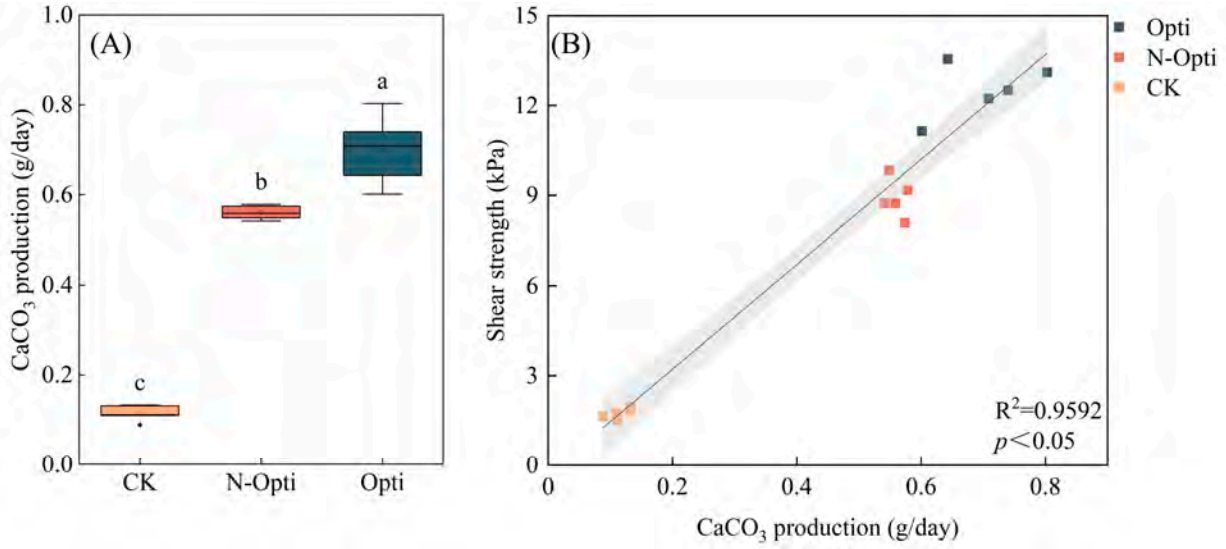


Figure 6. Correlation between $CaCO_3$ production and shear strength in sand consolidation obtained through treatment with strain SCSIO19859. (**A**) $CaCO_3$ production for optimized (Opti) and non-optimized (N-Opti) conditions, as well as control group (CK). (**B**) Correlation between $CaCO_3$ production and shear strength ($y = 1.7478x - 0.2793$, $R^2 = 0.9592$, $p < 0.05$). The presence of distinct letters (a, b, and c) indicates noteworthy variances between groups, with a significance level below $p < 0.05$.

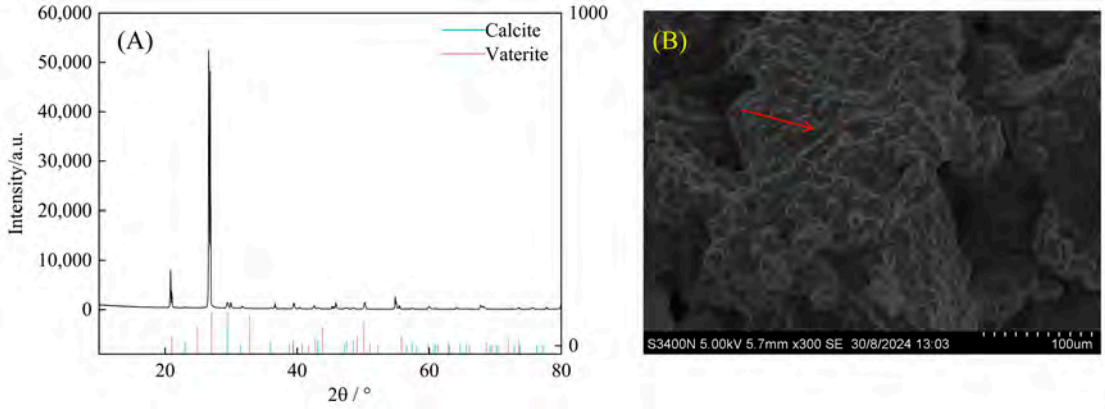


Figure 7. XRD and SEM analyses of calcium carbonate in sand consolidation for treatment with strain SCSIO19859. (**A**) XRD analysis of CaCO$_3$ crystals during sand consolidation. The horizontal coordinate in the XRD analysis is twice the incidence angle of the X-ray (2θ), and the vertical coordinate indicates the diffraction intensity. (**B**) SEM analysis of CaCO$_3$ crystal during sand consolidation at 300× magnification. The red arrow indicates the presence of calcium carbonate crystals on the surface and within the interstices of sand particles.

3.4. Characteristics of Carbonate Induced by Carbonic Anhydrase

As illustrated in Figure 7A, the XRD analysis revealed that the calcium carbonate particles induced by strain SCSIO19859 primarily consisted of calcite and vaterite. The SEM analysis revealed a significant formation of calcium carbonate crystals produced during the sand consolidation process with the treatment with strain SCSIO19859. These crystals were observed both on the surface and within the interstices between the sand particles (Figure 7B).

4. Discussion

4.1. Biocrusts Development Promotes the Activity of Microbial Carbonic Anhydrase

The results revealed variations in carbonic anhydrase activity among the different sample types, demonstrating a significant increase concurrent with biocrust formation and development ($p < 0.05$) (Figure 1A). Investigations in karst ecosystems have also revealed variations in the activity of carbonic anhydrase due to distinct karst characteristics, vegetation types, and coverage [36]. Similarly, in marine environments, the enzyme's activity is influenced by variations across different circulation zones and depths [37]. Moreover, soil type also exerts a notable impact on carbonic anhydrase activity, with forests exhibiting the highest levels, followed by Mediterranean ecosystems and deserts, while agricultural soils display the lowest activity [38]. The increase in carbonic anhydrase activity may be attributed to the formation and development of biocrusts. In this study, carbonic anhydrase content was observed to increase with the development of biocrusts (Figure 1B). Consistent with our findings, previous studies have also reported a substantial increase in chlorophyll content with biocrust development [39,40]. Biocrust development [39,40]. Biocrusts, rich in cyanobacteria and algae, exhibit relatively high levels of photosynthetic capacity, thereby potentially contributing to soil organic matter [41]. An increase in soil fertility can provide a greater abundance of resources for microorganisms, thereby facilitating microbial proliferation and, consequently, enhancing the activity of soil enzymes [12,41,42]. Moreover, previous studies have also indicated that the development of biocrusts can also enhance the proliferation of specific microbial communities associated with carbonic anhydrase secretion [27]. The development of biocrusts can also enhance soil physical and chemical properties, including pH, salinity and moisture, thereby promoting an increase in carbonic anhydrase activity [43,44].

Increases in soil carbonic anhydrase activity may contribute to the soil stabilization capabilities of biocrusts. The findings of our previous research indicate a positive correlation between the activity of carbonic anhydrase in biocrusts and their resistance to soil erosion [27]. The strains obtained in this study also revealed a positive correlation between high carbonic anhydrase activity and increased sand-fixation strength (Figure 3C). Previous research has demonstrated that the application of carbonic anhydrase biostimulation significantly enhances the shear strength of soil, resulting in a six-fold increase compared to soil without biostimulation [45]. The compressive strength of concrete treated with carbonic anhydrase-producing bacteria was significantly enhanced [46]. In this study, biocrusts exhibiting well-developed characteristics demonstrated higher carbonic anhydrase activity (Figure 1A), indicating their potential for stronger sand-fixing capabilities. This finding highlights the significance of promoting the development of biocrusts and enhancing carbonic anhydrase activity to improve their ability to stabilize soil for future cultivation and management.

4.2. Carbonatogenic Bacteria and Their Role in Sand Consolidation

A total of 35 strains capable of secreting carbonic anhydrase were isolated from biocrusts (Table S1). These strains are classified under the phyla Cyanobacteriota, Actinomycetota, Bacillota and Pseudomonadota (Figure 2A). The findings from our previous investigations demonstrated that these microorganisms constitute the predominant bacterial assemblage within biocrusts [27,30]. The bacteria isolated from biocrusts are also primarily Chloroflexota, Pseudomonadota, Bacteroidota, Actinomycetota and Acidobacteriota [47,48]. It was reported that cyanobacteria possess the ability not only to perform photosynthesis for organic matter synthesis, but also to harbor genes responsible for carbonic anhydrase secretion and regulation, which holds significant potential for calcification [49]. Firmicutes, such as Bacillus, are well known for their high levels of carbonic anhydrase and possess significant potential applications in soil stabilization. Bacillus strains possess the ability to form biofilms, thereby enhancing bacterial colonization, nutrient acquisition and interactions with other microorganisms. Moreover, these strains can produce extracellular polymeric substances, which consist of proteins that facilitate the formation of mineralized products with diverse crystal morphologies, leading to increased inter-particle friction [50,51]. Similarly, Actinomycetota and Pseudomonadota bacteria are also capable of producing carbonic anhydrase, which facilitates CO_2 sequestration and carbonate generation [52,53]. The carbonic anhydrase activity of the strains obtained in this study ranged from 0.03 to 1.26 U/mL. Among these strains, strain SCSIO19859 demonstrated the highest degree of carbonic anhydrase activity, which is higher than that of the strain *Chryseobacterium gambrini* from the developed karst area of Yunnan Province, but lower than that of the strain *Bacillus* from mine sediment [21,54].

Microbial carbonic anhydrase facilitates the catalysis of carbonate formation, thereby promoting soil stability. The strain SCSIO19859 exhibited enhanced calcium carbonate precipitation when 1.25 mol/L $NaHCO_3$ and $CaCl_2$ were utilized as substrates (Figure 5). Consistent with other studies, the calcium carbonate particles produced by microbial carbonic anhydrase using calcium chloride as a substrate exhibited higher levels compared to those from other sources of calcium. This can be attributed to the high solubility of the calcium chloride solution and high surface energy [55]. The production of $CaCO_3$ was substantially enhanced under optimized conditions compared to non-optimized conditions ($p < 0.05$) (Figure 6A). Moreover, the quantity of $CaCO_3$ exhibited a positive correlation with shear strength during the sand consolidation process (Figure 6B). A study conducted along coastlines to induce microbial carbonate precipitation for mitigating coastal erosion also revealed a clear linear relationship between calcium carbonate content and erosion

resistance [56]. The XRD analysis revealed that the $CaCO_3$ crystals induced by strain SCSIO19859 were predominantly composed of calcite and vaterite (Figure 7A). Carbonic anhydrase is an effective enzyme that catalyzes the formation of calcite, aragonite and precipitates [57]. This process guides newly formed particles into existing calcium spiral structures to facilitate the growth of larger crystals [58]. The stability of calcite crystals derived from calcium carbonate has been reported to be higher than that of aragonite crystals formed by alternative sources of calcium [59]. The strain SCSIO19859 in this study was found to induce calcite production, which could potentially account for the increased formation of calcium carbonate and enhanced sand-fixation strength. The SEM analysis further revealed that calcium carbonate crystals, mediated by carbonic anhydrase, were tightly wrapped around the sand grains (Figure 7B). The process of sand and gravel bonding can be enhanced by the presence of calcium carbonate crystals, which contribute to increased soil density and improved stability [60]. Furthermore, carbonic anhydride crystals can enhance the roughness and friction characteristics of the sand surface, thereby increasing its stability [61]. More crucially, calcium carbonate crystals facilitate robust adhesion among sand particles, thereby enhancing the mechanical stability of the sand [62,63]. In addition to microbial carbonic anhydrase, there may be other factors, including the adsorption of extracellular polymeric substances, the accumulation of organic matter and soil fine particles, or the entanglement of mycelia, which can also enhance soil stability [64–66]. Consequently, it is an even greater challenge to explore additional pathways to maintain soil stability during biocrust formation and development.

The present study characterizes the carbonic anhydrase activity of isolated carbonate-producing bacteria and elucidates their role in enhancing soil shear strength during biocrust development. It is plausible that other uncultivated strains also possess carbonic anhydrase activity, which warrants further investigation. Therefore, future research should focus on the isolation and characterization of additional carbonatogenic bacteria. Moreover, efforts should be directed toward optimizing the application of known carbonatogenic bacteria, such as SCSIO19859, to promote biocrust development and enhance soil shear strength under field conditions. Additionally, incorporating an evaluation of the long-term stability of calcium carbonate crystals and exploring potential synergies with other soil stabilization techniques would be of significant importance.

5. Conclusions

The present study provides evidence for a link between the carbonic anhydrase activity of carbonatogenic bacteria and the stability of biocrusts. The results demonstrate a significant enhancement in carbonic anhydrase activity with biocrust development ($p < 0.05$). A total of 35 strains capable of secreting carbonic anhydrase were isolated from the biocrusts. The data further revealed a positive correlation between the carbonic anhydrase activity and the shear strength during sand consolidation under these strains. The strain SCSIO19859, which exhibits high carbonic anhydrase activity, can induce the stable formation of calcite and vaterite under optimized conditions. The calcium carbonate crystals can efficiently bind the sand particles, thereby enhancing the shear strength of the sand. This study offers a novel insight into the erosion resistance of biocrusts from the perspective of culturable carbonatogenic bacteria and their carbonic anhydrase. Furthermore, this investigation also highlights the significance of these strains in enhancing soil stability.

Supplementary Materials: The following supporting information can be downloaded at: https://www.mdpi.com/article/10.3390/microorganisms13030523/s1, Table S1: The carbonic anhydrase activity and closely related species of isolated strains.

Author Contributions: Conceptualization, Z.M.; methodology, Q.C. and Q.L.; software, Q.C.; validation, Q.C. and H.S.; formal analysis, Q.C. and Q.L.; investigation, Q.C. and L.W.; writing—original draft preparation, Q.C. and Z.M.; writing—review and editing, Z.M. and H.S.; supervision, Z.M. and J.L.; project administration, Z.M.; funding acquisition, J.L. and Z.M. All authors have read and agreed to the published version of the manuscript.

Funding: This work was supported by the National Key R&D Program of China (Key Special Project for Marine Environmental Security and Sustainable Development of Coral Reefs 2022-103), the Natural Science Foundation of Guangdong Province (grant number 2024A1515011389), the Natural Science Foundation of Guangxi Province (2023GXNSFAA026388) and the National Natural Science Foundation of China (grant number 42206155).

Institutional Review Board Statement: Not applicable.

Informed Consent Statement: Not applicable.

Data Availability Statement: Data is contained within the article or supplementary material. The original contributions presented in this study are included in the article/supplementary material. Further inquiries can be directed to the corresponding author.

Conflicts of Interest: The authors declare no conflict of interest.

References

1. Ma, X.; Zhao, C.; Zhu, J. Aggravated risk of soil erosion with global warming—A global meta-analysis. *Catena* **2021**, *200*, 105129. [CrossRef]
2. Li, P.; Mu, X.; Holden, J.; Wu, Y.; Irvine, B.; Wang, F.; Gao, P.; Zhao, G.; Sun, W. Comparison of soil erosion models used to study the Chinese Loess Plateau. *Earth-Sci. Rev.* **2017**, *170*, 17–30. [CrossRef]
3. Olson, K.R.; Al-Kaisi, M.; Lal, R.; Cihacek, L. Impact of soil erosion on soil organic carbon stocks. *J. Soil Water Conserv.* **2016**, *71*, 61A–67A. [CrossRef]
4. Hancock, G.R.; Ovenden, M.; Sharma, K.; Rowlands, W.; Gibson, A.; Wells, T. Soil erosion—The impact of grazing and regrowth trees. *Geoderma* **2020**, *361*, 114102. [CrossRef]
5. Senanayake, S.; Pradhan, B.; Huete, A.; Brennan, J. Spatial modeling of soil erosion hazards and crop diversity change with rainfall variation in the Central Highlands of Sri Lanka. *Sci. Total Environ.* **2022**, *806*, 150405. [CrossRef] [PubMed]
6. Middleton, N.J. Desert dust hazards: A global review. *Aeolian Res.* **2017**, *24*, 53–63. [CrossRef]
7. Lal, R. Soil erosion and the global carbon budget. *Environ. Int.* **2003**, *29*, 437–450. [CrossRef]
8. Zhang, B.-J.; Zhang, G.-H.; Yang, H.-Y.; Zhu, P.-Z. Temporal variation in soil erosion resistance of steep slopes restored with different vegetation communities on the Chinese Loess Plateau. *Catena* **2019**, *182*, 104170. [CrossRef]
9. Wang, L.; Huang, Y.; Yang, Q.; Mai, Z.; Xie, F.; Lyu, L.; Zhang, S.; Li, J. Biocrust reduces the soil erodibility of coral calcareous sand by regulating microbial community and extracellular polymeric substances on tropical coral island, South China Sea. *Front. Microbiol.* **2023**, *14*, 1283073. [CrossRef] [PubMed]
10. Han, S.; Liu, S.; Hu, S.; Song, X.; Mo, X. Evapotranspiration on Natural and Reclaimed Coral Islands in the South China Sea. *Remote Sens.* **2021**, *13*, 1110. [CrossRef]
11. Belnap, J.; Weber, B.; Büdel, B. Biological Soil Crusts as an Organizing Principle in Drylands. In *Biological Soil Crusts: An Organizing Principle in Drylands*; Weber, B., Büdel, B., Belnap, J., Eds.; Springer International Publishing: Cham, Switzerland, 2016; pp. 3–13.
12. Belnap, J. The world at your feet: Desert biological soil crusts. *Front. Ecol. Environ.* **2003**, *1*, 181–189. [CrossRef]
13. Zaady, E.; Kuhn, U.; Wilske, B.; Sandoval-Soto, L.; Kesselmeier, J. Patterns of CO_2 exchange in biological soil crusts of successional age. *Soil Biol. Biochem.* **2000**, *32*, 959–966. [CrossRef]
14. Chamizo, S.; Mugnai, G.; Rossi, F.; Certini, G.; De Philippis, R. Cyanobacteria Inoculation Improves Soil Stability and Fertility on Different Textured Soils: Gaining Insights for Applicability in Soil Restoration. *Front. Environ. Sci.* **2018**, *6*, 49. [CrossRef]
15. Li, S.; Bowker, M.A.; Xiao, B. Biocrust impacts on dryland soil water balance: A path toward the whole picture. *Glob. Change Biol.* **2022**, *28*, 6462–6481. [CrossRef]
16. Li, Z.; Chen, C.; Gao, Y.; Wang, B.; Wang, D.; Du, Y.; Liu, L.; Wu, Z.; Cai, D. Synergistic effect of cyanobacteria and nano-sand-stabilizer on biocrust formation and sand fixation. *J. Environ. Chem. Eng.* **2021**, *9*, 104887. [CrossRef]
17. Gao, L.; Sun, H.; Xu, M.; Zhao, Y. Biocrusts resist runoff erosion through direct physical protection and indirect modification of soil properties. *J. Soils Sediments* **2020**, *20*, 133–142. [CrossRef]
18. Chiquoine, L.P.; Abella, S.R.; Bowker, M.A. Rapidly restoring biological soil crusts and ecosystem functions in a severely disturbed desert ecosystem. *Ecol. Appl.* **2016**, *26*, 1260–1272. [CrossRef]

19. Xie, Y.; Wen, X.; Tu, Y.; He, Y.; Wang, Y.; Luo, S.; Ge, H.; Zhang, D. Mechanisms of artificial biological soil crusts development for anti-desertification engineering on the Qinghai-Tibetan Plateau. *Environ. Technol. Innov.* **2024**, *33*, 103542. [CrossRef]
20. Chock, T.; Antoninka, A.J.; Faist, A.M.; Bowker, M.A.; Belnap, J.; Barger, N.N. Responses of biological soil crusts to rehabilitation strategies. *J. Arid. Environ.* **2019**, *163*, 77–85. [CrossRef]
21. Zhu, J.; Sun, J.; Pang, C.; Li, Q.; Yang, Z.; Li, G. Isolation, Identification, and Carbonate Mineralization Characteristics of a Newly Carbonic Anhydrase–Producing Strain. *Appl. Biochem. Biotechnol.* **2024**, *196*, 8009–8025. [CrossRef]
22. Yu, X.; Xiao, B.; Cao, Y.; Kidron, G.J. Microbial-induced extracellular polymers are fundamentally responsible for the mechanical stability of biocrusts in drylands. *CATENA* **2024**, *245*, 108349. [CrossRef]
23. de Caire, G.Z.; de Cano, M.S.; Palma, R.M.; de Mulé, C.Z. Changes in soil enzyme activities following additions of cyanobacterial biomass and exopolysaccharide. *Soil Biol. Biochem.* **2000**, *32*, 1985–1987. [CrossRef]
24. Chang, S.; He, Y.; Li, Y.; Cui, X. Study on the immobilization of carbonic anhydrases on geopolymer microspheres for CO_2 capture. *J. Clean. Prod.* **2021**, *316*, 128163. [CrossRef]
25. Li, Z.; Liu, A.; Sun, C.; Li, H.; Kong, Z.; Zhai, H. Biomineralization Process of $CaCO_3$ Precipitation Induced by Bacillus mucilaginous and Its Potential Application in Microbial Self-healing Concrete. *Appl. Biochem. Biotechnol.* **2024**, *196*, 1896–1920. [CrossRef] [PubMed]
26. Ma, X.; Liu, L.; Tang, K. Carbon Dioxide Sequestration by Microbial Carbonic Anhydrases from Submarine Hydrothermal Systems. *Front. Mar. Sci.* **2022**, *9*, 908818. [CrossRef]
27. Mai, Z.; Chen, Q.; Wang, L.; Zhang, J.; Cheng, H.; Su, H.; Zhang, S.; Li, J. Bacterial carbonic anhydrase-induced carbonates mitigate soil erosion in biological soil crusts. *J. Environ. Manag.* **2024**, *352*, 120085. [CrossRef] [PubMed]
28. Huang, Y.; Ren, H.; Wang, J.; Liu, N.; Jian, S.; Cai, H.; Hui, D.; Guo, Q. Relationships between vegetation and soil seed banks along a center-to-edge gradient on a tropical coral island. *Ecol. Indic.* **2020**, *117*, 106689. [CrossRef]
29. Yang, J.; Xu, D.; Shen, J.; Wei, H.; Wang, R.; Xiao, X. Effect of coral sand powders and seawater salinity on the impact mechanical properties of cemented coral sand. *Soils Found.* **2022**, *62*, 101206. [CrossRef]
30. Wang, L.; Li, J.; Zhang, S. A comprehensive network integrating signature microbes and crucial soil properties during early biological soil crust formation on Tropical Reef Islands. *Front. Microbiol.* **2022**, *13*, 831710. [CrossRef] [PubMed]
31. Gabay, T.; Rotem, G.; Gillor, O.; Ziv, Y. Understanding changes in biocrust communities following phosphate mining in the Negev Desert. *Environ. Res.* **2022**, *207*, 112200. [CrossRef] [PubMed]
32. Castle, S.C.; Morrison, C.D.; Barger, N.N. Extraction of chlorophyll a from biological soil crusts: A comparison of solvents for spectrophotometric determination. *Soil Biol. Biochem.* **2011**, *43*, 853–856. [CrossRef]
33. Li, W.; Yu, L.-J.; He, Q.-F.; Wu, Y.; Yuan, D.-X.; Cao, J.-H. Effects of microbes and their carbonic anhydrase on Ca2+ and Mg2+ migration in column-built leached soil-limestone karst systems. *Appl. Soil Ecol.* **2005**, *29*, 274–281. [CrossRef]
34. Kumar, S.; Stecher, G.; Li, M.; Knyaz, C.; Tamura, K. MEGA X: Molecular Evolutionary Genetics Analysis across Computing Platforms. *Mol. Biol. Evol.* **2018**, *35*, 1547–1549. [CrossRef]
35. Saitou, N.; Nei, M. The neighbor-joining method: A new method for reconstructing phylogenetic trees. *Mol. Biol. Evol.* **1987**, *4*, 406–425. [CrossRef]
36. Li, W.; Yu, L.-j.; Yuan, D.-x.; Wu, Y.; Zeng, X.-d. A study of the activity and ecological significance of carbonic anhydrase from soil and its microbes from different karst ecosystems of Southwest China. *Plant Soil* **2005**, *272*, 133–141. [CrossRef]
37. Subhas, A.V.; Adkins, J.F.; Dong, S.; Rollins, N.E.; Berelson, W.M. The carbonic anhydrase activity of sinking and suspended particles in the North Pacific Ocean. *Limnol. Oceanogr.* **2020**, *65*, 637–651. [CrossRef]
38. Meredith, L.K.; Ogée, J.; Boye, K.; Singer, E.; Wingate, L.; von Sperber, C.; Sengupta, A.; Whelan, M.; Pang, E.; Keiluweit, M.; et al. Soil exchange rates of COS and $CO^{18}O$ differ with the diversity of microbial communities and their carbonic anhydrase enzymes. *ISME J.* **2019**, *13*, 290–300. [CrossRef] [PubMed]
39. Gypser, S.; Herppich, W.B.; Fischer, T.; Lange, P.; Veste, M. Photosynthetic characteristics and their spatial variance on biological soil crusts covering initial soils of post-mining sites in Lower Lusatia, NE Germany. *Flora—Morphol. Distrib. Funct. Ecol. Plants* **2016**, *220*, 103–116. [CrossRef]
40. Ye, C.-R.; Tao, Y.; Zhang, Y.-R.; Cao, J.; Ke, T.; Wei, S.-J.; De Philippis, R.; Chen, L.-Z. Monosaccharide composition of primary cell wall polysaccharides as a developmental level indicator of biological soil crusts. *Catena* **2020**, *195*, 104782. [CrossRef]
41. Liu, Y.; Yang, H.; Li, X.; Xing, Z. Effects of biological soil crusts on soil enzyme activities in revegetated areas of the Tengger Desert, China. *Appl. Soil Ecol.* **2014**, *80*, 6–14. [CrossRef]
42. Wang, C.; Li, W.; Shen, T.; Cheng, W.; Yan, Z.; Yu, L. Influence of soil bacteria and carbonic anhydrase on karstification intensity and regulatory factors in a typical karst area. *Geoderma* **2018**, *313*, 17–24. [CrossRef]
43. Niu, J.; Yang, K.; Tang, Z.; Wang, Y. Relationships between Soil Crust Development and Soil Properties in the Desert Region of North China. *Sustainability* **2017**, *9*, 725. [CrossRef]
44. Stark, J.M.; Firestone, M.K. Mechanisms for soil moisture effects on activity of nitrifying bacteria. *Appl. Environ. Microbiol.* **1995**, *61*, 218–221. [CrossRef]

45. Mwandira, W.; Mavroulidou, M.; Satheesh, A.; Gunn, M.J.; Gray, C.; Purchase, D.; Garelick, J. An electrokinetic-biocementation study for clay stabilisation using carbonic anhydrase-producing bacteria. *Environ. Sci. Pollut. Res.* **2023**, *30*, 104916–104931. [CrossRef] [PubMed]
46. Oyewole, O.A.; Maddela, N.R.; Ibrahim, O.H.; Adebayo-Anwo, I.; Adejumo, T.E.; Agbese, E.O.; Egwim, E.C.; Prasad, R. Leveraging the concretes calcification with carbonic anhydrase produced by Alcaligenes faecalis GA(B) (Mn847724.1). *Bioresour. Technol. Rep.* **2023**, *22*, 101434. [CrossRef]
47. Becerra-Absalón, I.; Muñoz-Martín, M.Á.; Montejano, G.; Mateo, P. Differences in the Cyanobacterial Community Composition of Biocrusts from the Drylands of Central Mexico. Are There Endemic Species? *Front. Microbiol.* **2019**, *10*, 937. [CrossRef]
48. Sommer, V.; Mikhailyuk, T.; Glaser, K.; Karsten, U. Uncovering Unique Green Algae and Cyanobacteria Isolated from Biocrusts in Highly Saline Potash Tailing Pile Habitats, Using an Integrative Approach. *Microorganisms* **2020**, *8*, 1667. [CrossRef] [PubMed]
49. Yang, Z.-N.; Li, X.-M.; Umar, A.; Fan, W.-H.; Wang, Y. Insight into calcification of *Synechocystis* sp. enhanced by extracellular carbonic anhydrase. *RSC Adv.* **2016**, *6*, 29811–29817. [CrossRef]
50. Dhami, N.K.; Reddy, M.S.; Mukherjee, A. Bacillus megaterium mediated mineralization of calcium carbonate as biogenic surface treatment of green building materials. *World J. Microbiol. Biotechnol.* **2013**, *29*, 2397–2406. [CrossRef]
51. Chinnappa, B.; Thirupathi, B.; Sundaram, T.; Pongen, Y.L.; Vinayagam, S.; Gnanasekaran, L.; Rajput, V.D.; Durairaj, T. Unveiling halophilic microbial communities in calcite fossil sedimentary rocks and their implications for biomineralization. *Appl. Soil Ecol.* **2025**, *206*, 105835. [CrossRef]
52. Sangeetha, M.; Sivarajan, A.; Radhakrishnan, M.; Siddharthan, N.; Balagurunathan, R. Biosequestration of carbon dioxide using carbonic anhydrase from novel Streptomyces kunmingensis. *Arch. Microbiol.* **2022**, *204*, 270. [CrossRef]
53. Srivastava, S.; Bharti, R.K.; Verma, P.K.; Thakur, I.s. Cloning and expression of gamma carbonic anhydrase from *Serratia* sp. ISTD04 for sequestration of carbon dioxide and formation of calcite. *Bioresour. Technol.* **2015**, *188*, 209–213. [CrossRef]
54. Sundaram, S.; Thakur, I.S. Induction of calcite precipitation through heightened production of extracellular carbonic anhydrase by CO_2 sequestering bacteria. *Bioresour. Technol.* **2018**, *253*, 368–371. [CrossRef] [PubMed]
55. Moon, D.H.; Eu, J.; Lee, W.; Kim, Y.E.; Park, K.T.; Ko, Y.N.; Jeong, S.K.; Youn, M.H. Comparison of reactions with different calcium sources for $CaCO_3$ production using carbonic anhydrase. *Greenh. Gases: Sci. Technol.* **2020**, *10*, 898–906. [CrossRef]
56. Li, Y.; Guo, Z.; Wang, L.; Zhu, Y.; Rui, S. Field implementation to resist coastal erosion of sandy slope by eco-friendly methods. *Coast. Eng.* **2024**, *189*, 104489. [CrossRef]
57. Krause, S.; Liebetrau, V.; Löscher, C.R.; Böhm, F.; Gorb, S.; Eisenhauer, A.; Treude, T. Marine ammonification and carbonic anhydrase activity induce rapid calcium carbonate precipitation. *Geochim. Cosmochim. Acta* **2018**, *243*, 116–132. [CrossRef]
58. Müller, W.E.G.; Schlossmacher, U.; Schröder, H.C.; Lieberwirth, I.; Glasser, G.; Korzhev, M.; Neufurth, M.; Wang, X. Enzyme-accelerated and structure-guided crystallization of calcium carbonate: Role of the carbonic anhydrase in the homologous system. *Acta Biomater.* **2014**, *10*, 450–462. [CrossRef]
59. Hao, Z.; Su, Y.; Liu, S.; Zhang, X. Roles of bacteria and extracellular polymeric substance in calcium carbonate formation: Insights from the effects of calcium source and deposition rate on nucleation. *Biochem. Eng. J.* **2024**, *202*, 109160. [CrossRef]
60. De Muynck, W.; De Belie, N.; Verstraete, W. Microbial carbonate precipitation in construction materials: A review. *Ecol. Eng.* **2010**, *36*, 118–136. [CrossRef]
61. Wang, Y.-K.; Guo, L.; Gao, Y.-F.; Qiu, Y.; Hu, X.-Q.; Zhang, Y. Anisotropic Drained Deformation Behavior and Shear Strength of Natural Soft Marine Clay. *Mar. Georesources Geotechnol.* **2016**, *34*, 493–502. [CrossRef]
62. Al-Salloum, Y.; Hadi, S.; Abbas, H.; Almusallam, T.; Moslem, M.A. Bio-induction and bioremediation of cementitious composites using microbial mineral precipitation—A review. *Constr. Build. Mater.* **2017**, *154*, 857–876. [CrossRef]
63. Wang, Z.; Zhang, N.; Cai, G.; Jin, Y.; Ding, N.; Shen, D. Review of ground improvement using microbial induced carbonate precipitation (MICP). *Mar. Georesources Geotechnol.* **2017**, *35*, 1135–1146. [CrossRef]
64. Lan, S.; Wu, L.; Zhang, D.; Hu, C. Successional stages of biological soil crusts and their microstructure variability in Shapotou region (China). *Environ. Earth Sci.* **2012**, *65*, 77–88. [CrossRef]
65. Felde, V.J.M.N.L.; Chamizo, S.; Felix-Henningsen, P.; Drahorad, S.L. What stabilizes biological soil crusts in the Negev Desert? *Plant Soil* **2018**, *429*, 9–18. [CrossRef]
66. Bao, T.; Zhao, Y.; Gao, L.; Yang, Q.; Yang, K. Moss-dominated biocrusts improve the structural diversity of underlying soil microbial communities by increasing soil stability and fertility in the Loess Plateau region of China. *Eur. J. Soil Biol.* **2019**, *95*, 103120. [CrossRef]

Disclaimer/Publisher's Note: The statements, opinions and data contained in all publications are solely those of the individual author(s) and contributor(s) and not of MDPI and/or the editor(s). MDPI and/or the editor(s) disclaim responsibility for any injury to people or property resulting from any ideas, methods, instructions or products referred to in the content.

Acta Oceanol. Sin., 2025, Vol. 44, No. 8, P. 1–20
https://doi.org/10.1007/s13131-025-2495-z

Coral polyp and skeletal microbiome in tropical and subtropical reefs in the South China Sea: spatial variation and implications for coral environmental adaptability

Zhenjun Qin[1*], Mengling Lan[1], Nengbin Pan[1], Kefu Yu[1, 2*], Lifei Wei[1], Qizhi Yang[1], Tingchao Zhang[1], Ran He[1]

[1] Coral Reef Research Center of China, Guangxi Laboratory on the Study of Coral Reefs in the South China Sea, School of Marine Sciences, Guangxi University, Nanning 530004, China

[2] Southern Marine Science and Engineering Guangdong Laboratory (Guangzhou), Guangzhou 510000, China

Received 27 November 2024; accepted 20 February 2025

© Chinese Society for Oceanography and Springer-Verlag GmbH Germany, part of Springer Nature 2025

Abstract

The environments of tropical and subtropical coral reef regions (CRR) differ from each other; however, it is not known if these environmental differences influence coral polyp and skeleton microbiome composition. In this study, *Coelastrea palauensis* corals were collected from tropical and subtropical CRR in the South China Sea, and bacterial, archaeal, and fungal communities in polyps and skeletons were analyzed. Results showed that the microbial diversity and composition of *C. palauensis* significantly differed between the polyps and skeletons, and between the tropical and subtropical CRR. Regarding bacteria associated with corals, *C. palauensis* was mainly associated with bacteria closely related to the nitrogen cycle in the subtropical CRR. The relative abundances of Terasakiellaceae and *Chlorobium* in both coral polyps and skeletons in the subtropical CRR were higher than those in the tropical CRR. In the tropical CRR, *C. palauensis* was mainly associated with opportunistic pathogenic bacteria. The relative abundances of *Tenacibaculum* and *Vibrio* in coral polyps and skeletons in the tropical CRR were higher than those in the subtropical CRR. Regarding archaea associated with corals, polyps and skeletons of *C. palauensis* in both tropical and subtropical reef areas were dominated by n_Woesearchaeales, and the relative abundance of n_Woesearchaeales in skeletons is significantly higher than that in polyps. In addition, the relative abundances of n_Woesearchaeales in polyps and skeletons in the subtropical CRR were significantly higher than those in the tropical CRR. Regarding fungi associated with corals, Ascomycota was dominant in polyps and skeletons in the subtropical CRR, while Sordariomycetes, *Periconia*, *Cladosporium*, and *Aspergillus* were dominant in polyps and skeletons in the tropical CRR. Besides, the diversity differences of coral-associated microorganisms were related to environmental factors such as nutrients and temperature that may affect the survival of coral-associated microorganisms. These results implied that corals may adjust the composition of microorganisms, conducive the coral holobiont to better adapting the environment. Our research will be beneficial in understanding the differences and adaptations of coral polyp and skeletal microbiome.

Key words coral microbiome, polyp microbiome, skeleton microbiome, microbial diversity, environmental adaptability

Citation Qin Zhenjun, Lan Mengling, Pan Nengbin, Yu Kefu, Wei Lifei, Yang Qizhi, Zhang Tingchao, He Ran. 2025. Coral polyp and skeletal microbiome in tropical and subtropical reefs in the South China Sea: spatial variation and implications for coral environmental adaptability. Acta Oceanologica Sinica, 44(8): 1–20, doi: 10.1007/s13131-025-2495-z

Foundation item: The National Natural Science Foundation of China under contract Nos 42206157, 42030502, and 42090041; the Natural Science Foundation of Guangxi Province under contract No. 2022GXNSFBA035449; the Self-Topic Project of Guangxi Laboratory on the Study of Coral Reefs in the South China Sea under contract No. GXLSCRSCS2022103.

*Corresponding author, E-mail: qzj_gxu@163.com; kefuyu@scsio.ac.cn

http://www.aosocean.com
E-mail: ocean2@hyxb.org.cn

1 Introduction

Reef-building corals are the main constructors of coral reef ecosystems, and are composed of a large number of porous voluminous calcium carbonate skeletons and polyps (Levy et al., 2021). Coral polyps and skeletons are associated with various microorganisms, including Symbiodiniaceae, bacteria, fungi, archaea, viruses, and protozoa (Bourne et al., 2016). Coral polyps include the mucus and tissue layers. In the mucus layer, the microbial community play an important role in nutrient cycling and prevention of pathogen invasion (Kemp et al., 2015). In the tissue layer, the microbial community is usually stable, and some microorganisms form cell-associated microbial aggregates (Sweet et al., 2011; Work and Aeby, 2014; Bourne et al., 2016). Bacteria play important roles in coral polyps, such as in the nitrogen cycle (Lesser et al., 2004; Lema et al., 2012), carbon cycle (Kimes et al., 2010), sulfur cycle (Raina et al., 2009), and antibiotic secretion (Ritchie, 2006).

The coral polyp microbiome is typically dominated by Proteobacteria (especially Gammaproteobacteria and Alphaproteobacteria), Actinobacteria, Bacteroidetes, Firmicutes and Cyanobacteria (Blackall et al., 2015; Huggett and Apprill, 2019). The coral skeletal microhabitat clearly differs from that of coral polyps (Luo et al., 2021). The coral skeleton is composed of aragonite crystals, and its loose and porous structure provides a good habitat for the survival of microorganisms (Meibom et al., 2008). Skeletal microbes survive in low light and low oxygen content, and the pH of coral skeletons fluctuates significantly due to some microorganisms in the coral perform light deterioration during the day and respiration at night carry out photosynthesis during the day and respiration at night (Shashar and Stambler, 1992; Ricci et al., 2019; Pernice et al., 2020). The difference of microhabitat strongly affects the composition of the skeletal microbial communities (Ainsworth et al., 2010). Microbes in coral skeletons usually exhibit high biodiversity and mainly include Proteobacteria, Bacteroides, Firmicutes, Actinomyces, Phytococca, Acidobacter and Chlorophyta (Li et al., 2014; Williams et al., 2015; Marcelino and Verbruggen, 2016; Yang et al., 2019; Chen et al., 2021; Ricci et al., 2021). These skeletal microbes contribute to material circulation and energy exchanges of microbial communities to hosts, such as the nitrogen and carbon cycles (Sangsawang et al., 2017; Yang et al., 2019). Coral polyps and skeletons have different microbial associations and respond differently to environmental stress, which may influence the microbial communities (Sweet et al., 2011; Luo et al., 2021). In addition, it has been reported that the composition and diversity of bacterial communities in coral skeletons can be driven by biogeographical or local environmental factors, resulting in regional differences (Liu et al., 2022; Yang et al., 2016, 2019, 2020; Ricci et al., 2021). However, few studies have focused on the diversity and composition differences in coral skeletal bacteria in tropical and subtropical coral reef regions (CRR) as well as differences from coral polyps' bacteria.

Similarly, few studies have focused on the differences of archaea and fungi between coral polyps and skeletons. Previous studies have indicated that members of Euryarchaeota and Thaumarchaeota are associated with corals and that some archaea members play key roles in ammonia oxidation, affecting the nitrogen cycle in corals (Francis et al., 2007; Huggett and Apprill, 2019). Most fungi in corals belong to *Ascomycota*, followed by Basidiomycota and Chytridiomycota (Wegley et al., 2007; Raghukumar and Ravindran, 2012). Fungi are generally considered opportunistic pathogens in corals under environmental stress but may also be non-pathogenic invasive microorganisms (Le Campion-Alsumard et al., 1995b; Ainsworth et al., 2017). In addition, some fungi play important roles in coral mineralization (Le Campion-Alsumard et al., 1995b) and antibacterial activity (Xu et al., 2018; Wang et al., 2011). However, the differences between skeletal archaea and fungi of corals in tropical and subtropical CRR as well as the differences in coral polyps are not well studied.

The massive *Coelastrea* corals are stress tolerant, and are the dominant coral populations in Indo-Pacific coral reefs (Darling et al., 2012). *Coelastrea* corals are distributed in coral reefs in different regions of the South China Sea (SCS), with a high abundance in tropical CRR (such as Xisha Islands and Nansha Islands) and subtropical CRR (such as Weizhou Island and Daya Bay) (Liao et al., 2021). In these regions, *Coelastrea palauensis* is the common species of *Coelastrea* genus (Zou, 2001; He and Huang, 2019). The specific skeletal structure and distribution of *Coelastrea* corals affect the composition and function of associated microorganisms in response to environmental fluctuations (Torda et al., 2017). However, the spatial variation of *Coelastrea* skeletal and polyp microorganisms in different climate zones and between coral skeletons and polyps remains unclear. These differences are important for studying the interaction of coral microorganisms and their relationship with environmental stress adaptation.

In this study, we examined *C. palauensis* in tropical and subtropical CRR. Based on the composition and diversity of *C. palauensis* polyp and skeleton bacteria, archaea, and fungi, and environmental parameters of the two CRR, two scientific problems were investigated: (1) the differences in the composition and diversity of *C. palauensis* polyp and skeletal bacteria, archaea, and fungi in tropical and subtropical CRR; and (2) the potential relationship of bacteria, archaea, and fungi in *C. palauensis* skeletons and polyps with coral environmental adaptability. Regarding this, two scientific hypotheses were proposed: (1) there is a difference between the composition and diversity of *C. palauensis* polyp and skeletal bacteria, archaea, and fungi in tropical and subtropical CRR; and

(2) the differences in the composition of bacteria, archaea, and fungi in the polyp and skeletons of *C. palauensis* corals correlate with the coral environments. The composition and diversity of bacteria, archaea and fungi in coral polyp and skeletons from the subtropics and tropics CRR in the SCS were investigated to test our hypotheses in relation to *in situ* aquatic environmental parameters in the study area. Our research will be beneficial in understanding the differences and adaptations of coral polyp and skeletal microbiome.

2 Materials and methods

2.1 *Study area*

The study areas (Fig. 1) in this study spanned two climate zones in the SCS, the Bombay Reef (16°03′N, 112°33′E) in the tropical CRR and Weizhou Island (21°00′N, 109°00′E) in the subtropical CRR. The annual average sea surface temperature (SST) of the Xisha Islands is 27.5℃. The lowest SST was 24.8℃, which occurred between December and February, while the highest average SST was 29.9℃, which occurred between May and September (Zhang et al., 2014). An ecological survey suggested that the average live coral cover (LCC) of the Bombay Reef in the tropical reef area was 11% (Chen et al., 2019).

The annual average SST of Weizhou Island in the subtropical reef area is 24.6℃. Low SST was observed during winter, with an average of 17.5–19.8℃, while high SST was observed during summer, with an average of 29.0–30.3℃ (Wang et al., 2016; Yu et al., 2019). The coral reefs on Weizhou Island have suffered from serious degradation due to destructive human activities, with the average LCC decreasing from about 42% in 1984 to about 10% in 2015 (Yu et al., 2019).

2.2 *Coral sample collection and seawater parameter measurement*

A total of 34 *C. palauensis* nubbins were sampled from the Bombay Reef and Weizhou Island in August 2021. All the coral samples were collected in 5–6 m depths at the outer reef slope both of Bombay Reef and Weizhou Island. To remove attached microorganisms, coral samples were washed with sterile seawater. After quick freezing with liquid nitrogen, the samples were stored at –20℃, and transported to the laboratory for subsequent sample treatment. In the laboratory, surface polyps of each coral sample were obtained by sterile scissor in 2 mL sterile centrifuge tube on sterile console. After the polyp on the coral surface was removed, the coral sample was thoroughly washed using a Waterpik containing sterile seawater to remove the residual tissue of coral polyps. The coral skeleton was then split, and the skeleton sample was cut using sterile forceps, the skeleton piece which does not directly contact the tissue layer was carefully separated. The coral polyp and skeleton fragments were stored 15 mL freezing tubes in a –80℃ freezer.

Environmental parameters were measured including water temperature, salinity, dissolved oxygen (DO), pH, transparency, turbidity, dissolved inorganic nitrogen (DIN), and soluble reactive phosphorus (SRP). Water temperature, salinity, and DO were assessed with a YSI water quality analyzer (YSI Inc., Yellow Springs, OH,

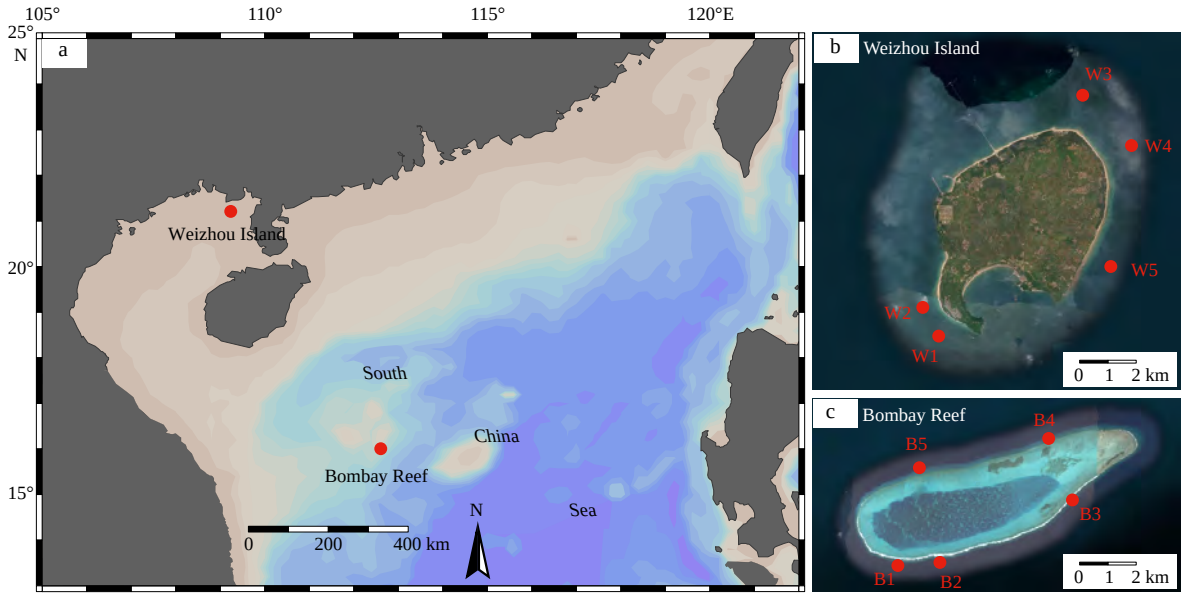


Fig. 1. Location map of coral reef sampling sites in the Bombay Reef and Weizhou Island. *Coelastrea palauensis* nubbins were sampled in B1–B2 from the Bombay Reef and W1–W2 from the Weizhou Island. Environmental parameters were measured and water samples were collected in B1–B5 from the Bombay Reef and W1–W5 from the Weizhou Island.

USA). Seawater samples were collected and immediately filtered (Whatman GF/F; GE Healthcare, Chicago, IL, USA). The pH was measured with separate portable meters (PHB-4). Turbidity was measured by a portable turbidity meter (WGZ-20B, 0–20 NTU). Transparency was measured with a Secchi disc (SD 30). Nitrate and SRP were measured using a continuous flow analyzer (SEAL QuAAtro; SEAL Analytical Shanghai, Shanghai, China). In this study, environmental parameters were measured at five sites in the Bombay Reef or Weizhou Island, and each site was measured once (Fig. 1, Table S1). Since no significant difference in these environmental parameters among five sites on a same island, these parameters on a same island were served as a set of data. The Wilcoxon rank-sum test was used to analyze the differences between the Bombay Reef and Weizhou Island, and the Mann-Whitney test was used to perform post hoc tests. The statistical results of these environmental parameters were expressed using mean ± standard deviation (SD), and the significant level threshold was defined as 0.05 ($p < 0.05$).

2.3 *DNA extraction, PCR and sequencing*

Total DNA was extracted from *C. palauensis* polyp or skeleton samples using the TIANamp Marine Animals DNA Kit (Tiangen Biotech, Beijing, China) according to the manufacturer's instructions. After extraction, 1 μL of DNA was used to determine the concentration and purity using a NanoDrop2000 trace UV spectrophotometer (Thermo Fisher Scientific, Waltham, MA, USA). After quality and purity testing, the extracted DNA sample was used as a PCR template. Primers were used to amplify the following regions: V3−V4 region of the 16S rRNA gene in bacteria (338F:5'-ACTCCTACGGAGGCAGCAGCAG-3', 806R: 5'-GGACTACHVGGGTWTCTAAT-3') (Mori et al., 2014, Xu et al., 2016); V4−V5 region of the 16S rRNA gene in archaea (524F10extF:5'-TGYCAGCGCCGCGGTAA-3', Arch958RmodR:5'-YCCGCGGTTGAVTCCAATT-3') (Liu et al., 2016); and Internal Transcribed Spacer 2 (ITS2) region in fungi (ITS3F:5'-GCATCGATGAAGAACGCAGC-3' and ITS4R:5'-TCCTCGCTTATTGATGC-3') (Toju et al., 2012).

Each sample had a unique barcode, and PCR amplification was performed in a 50-μL reaction volume containing approximately 50 ng of DNA, 25 μL of 2X Taq platinum polymerase chain reaction stock solution (Tiangen Biotech, Beijing, China), 200 nmol/L of each primer, and double-distilled H_2O to make up the final volume. Using an ABI GeneAmp system with a 9 700 Thermal Cycler (Applied Biosystems, Waltham, MA, USA), the reaction was allowed to proceed for 5 min at 94℃; 35 cycles were subsequently carried out at 94℃, 51℃, and 72℃ for 30 s each, and, finally, the temperature was maintained at 72℃ for 5 min (Sun et al., 2014). 3 μL PCR product was collected per sample and tested product integrity using 2% agarose gel electrophoresis (115 V, 45 min) to ensure that the amplicon was in the size of 301–340 bp. An AxyPrep DNA gel extraction kit (Axygen Biosciences Inc. Union City, CA, USA) and a QuantiFluor ST fluorescence quantification system (Promega, Madison, WI, USA) were used to purify and quantify the amplicon.

After quality inspection, the amplified samples were subjected to paired-end sequencing on an Illumina MiSeq platform (Majorbio Bio-pharm Technology, Shanghai, China). The raw sequences were deposited in the National Center for Biotechnology Information (NCBI) Sequence Read Archive (SRA) database (accession number: fungi: PRJNA923503; bacteria: PRJNA923743; archaea: PRJNA923739).

2.4 *Bioinformatics and statistical analysis*

The original bacterial and archaea data from *C. palauensis* samples were derived from the raw sequences obtained using Illumina MiSeq sequencing. PEAR (v.0.9.8) was used to assemble the paired reads of the bacterial 16S rRNA gene produced by the Illumina MiSeq platform to generate the complete V3−V4 region sequence of the 16S rRNA gene, and archaea 16S rRNA gene produced by the Illumina MiSeq platform to generate the complete V4−V5 region sequence of the 16S rRNA gene, with a maximum allowed mismatch ratio of 0.2 (Zhang et al., 2014). The valid sequences of the samples were then identified based on the sequence primer sequences and barcodes, and the sequence orientation was adjusted (barcode quality control threshold: mismatch number 0; maximum primer mismatch number 2). Non-repetitive sequences were extracted from the optimized sequences using Uparse (version 7.1), while removing single sequences without repeats and chimeras. The SILVA 138.1/16S_Bacteria and SILVA 138.1/16S_Archaea were used to identify and classify the bacteria, archaea, respectively, and clustering them into groups of amplicon sequence variants (ASV) (Callahan et al., 2016; Savary et al., 2021). Based on ASV clustering and rarefied, Mothur (version 1.30.1) was used to calculate α diversity indices, including the Shannon–Wiener, Simpson, Sobs, and Ace indices (Schloss et al. 2011).

The raw fungal ITS2 sequences were screened, and the unqualified sequences were deleted using the Mothur (version 1.30.1) platform (Caporaso et al., 2010; Zhang et al., 2014). According to the next generation sequencing data quality control standards, the "trim.seqs" function was used to remove low-quality reads, including barcode sequences, up-stream primers, homopolymers (>6 bp), and short length sequences (<250 bp) (Schloss et al., 2009). Chimeras were removed from the sequence using UCHIME. NT_v20200327/ITS was used to identify and classify the fungi, and clustering them into groups of ASV (Nilsson et al., 2019). Based on ASV clustering and rarefied, Mothur (version 1.30.1) was used to calculate fungal α diversity indices, including the Shannon-Wiener (H′), Simpson, Sobs, and Ace indices (Schloss et al.,

2011).

The Wilcoxon rank sum test was used to compare the differences in α diversity and microbial composition between the skeletons and polyps of *C. palauensis* in the Bombay Reef and Weizhou Island, and the Mann-Whitney test was used to perform post hoc tests. The Circos (version 0.67-7, http://circos.ca/) was used to analyze the composition of dominant bacteria, archaea, and fungi, and the proportion of dominant microbial members between the skeletons and polyps. Venn diagram analysis at ASV level was conducted using VennDiagram package. Principal coordinates analysis (PCoA) at the ASV level was used to conduct a β-diversity analysis of the coral associated bacteria, archaea, and fungi. They were used to visualize the results of Permutational Multivariate Analysis of Variance (PERMANOVA) generated by the Bray Curtis distance to reveal the microbial community structure of the different groups of coral skeletons and polyps in the Bombay Reef and Weizhou Island. All multi-dimensional statistical analysis was performed using R version 3.1.2 and the Vegan package (Oksanen et al., 2015). In this study, because of Detrended Correspondence Analysis (DCA) < 3, a redundancy analysis (RDA) was performed in Canoco 4.5 software to examine the correlation among environmental factors, sampling areas, and ASV of bacteria, archaea, and fungi. Statistical results of this study were expressed using mean ± SD in this study, and the significance level threshold was defined as 0.05 (p < 0.05). The data of environmental parameters, diversity community bacteria, archaea and fungus from coral polyp and skeleton in tropical and subtropical CRR can be available from the Dryad (https://datadryad.org. DOI: 10.5061/dryad.c59zw3rh8).

3 Results

3.1 *Environmental parameters*

The DIN and SRP in the subtropical CRR were higher than those in the tropical CRR (Table S1, Wilcoxon rank sum test, p = 0.008). In contrast, the SST, salinity, and transparency of the tropical CRR were higher than those of the subtropical CRR (Wilcoxon rank sum test, p = 0.008). No significant differences were found in DO and pH between the subtropical and tropical CRR (Wilcoxon rank sum test, p > 0.05). These data show that the seawater of the subtropical CRR is characterized by a relatively high nutrient content and high turbidity while that of the tropical CRR is characterized by high water temperature, high transparency, and low nutrient content.

3.2 *The bacterial community of coral polyp and skeleton in tropical and subtropical CRR*

After quality filtering, 18 571 ASV were obtained using Illumina MiSeq platform. α-diversity index was measured using the Sobs, Ace, Shannon-Wiener, and Simpson indices (Table S2, Figs 2 and S1). In the tropical CRR, the Shannon-Wiener (Wilcoxon rank sum test, p = 0.185) and Simpson (Wilcoxon rank sum test, p = 0.181) indices of skeletal bacteria in *C. palauensis* were not significant different from those of polyp bacteria. In the subtropical CRR, the Ace and Sob indices of skeletal bacteria in *C. palauensis* were significantly higher than those of polyp bacteria (Wilcoxon rank sum test, Ace, p < 0.001; Sob, p = 0.001). Besides, this study showed that the Shannon-Wiener index of coral polyp bacteria in tropical CRR was significantly higher than that in subtropical CRR (Wilcoxon rank sum test, p = 0.014), while the Simpson diversity index coral polyp bacteria in tropical CRR was significantly lower than that in subtropical CRR (Wilcoxon rank sum test, p < 0.001). The Ace and Sob indices of the coral skeletal bacteria in the subtropical CRR were significantly higher than those indices in the tropical CRR (Wilcoxon rank sum test, Ace index, p = 0.002; Sob, p = 0.003).

Total taxonomic composition of bacteria in the analyzed samples included 52 phyla, 156 classes, 390 orders, 643 families, and 1 273 genera. At the class level, 17 classes of bacteria in *C. palauensis* had an abundance greater than 1% (Table S3). In the tropical CRR, the relative abundance of Bacteroidia in coral polyps was significantly higher than those in the skeletons (Wilcoxon rank sum test, p = 0.047), but the relative abundance of Gammaproteobacteria in coral polyps was significantly lower than those in the skeletons (Wilcoxon rank sum test, p = 0.001). In the subtropical CRR, the relative abundance of Alphaproteobacteria in coral polyps was significantly higher than those in the skeletons (Wilcoxon rank sum test, p = 0.001), but the relative abundance of Gammaproteobacteria in coral polyps was significantly lower than those in the skeletons (Wilcoxon rank sum test, p = 0.001). Besides, the relative abundance of Gammaproteobacteria and Bacteroidia of the coral polyps in the tropical CRR was significantly higher than that in subtropical CRR (Wilcoxon rank sum test, p < 0.001 and p = 0.015, respectively), but significantly lower in the relative abundance of Alphaproteobacteria (p = 0.006). Meanwhile, the coral skeletal bacteria were dominated by Gammaproteobacteria and Alphaproteobacteria in the subtropical and tropical CCRs, but there was no significant difference (Wilcoxon rank sum test, p = 0.423 and p = 0.815, respectively). In the subtropical CRR, higher abundance of Chlorobia was found in the coral skeletons, whereas was barely detected in tropical CCR (<0.1%). The percentage of Anaerolineae of the coral skeletons in the tropical was significantly higher than that in the subtropical (Wilcoxon rank sum test, p = 0.000).

At the bacterial genus level, the composition of associated bacterial communities significantly differed among *C. palauensis* samples in the tropical and subtropical CRR (Table S4, Fig. 3a). For polyp bacteria, high relative abundances of Terasakiellaceae (Wilcoxon rank sum test, p < 0.001), *Blastocatella* (p = 0.002) and *Chlorobium* (p <

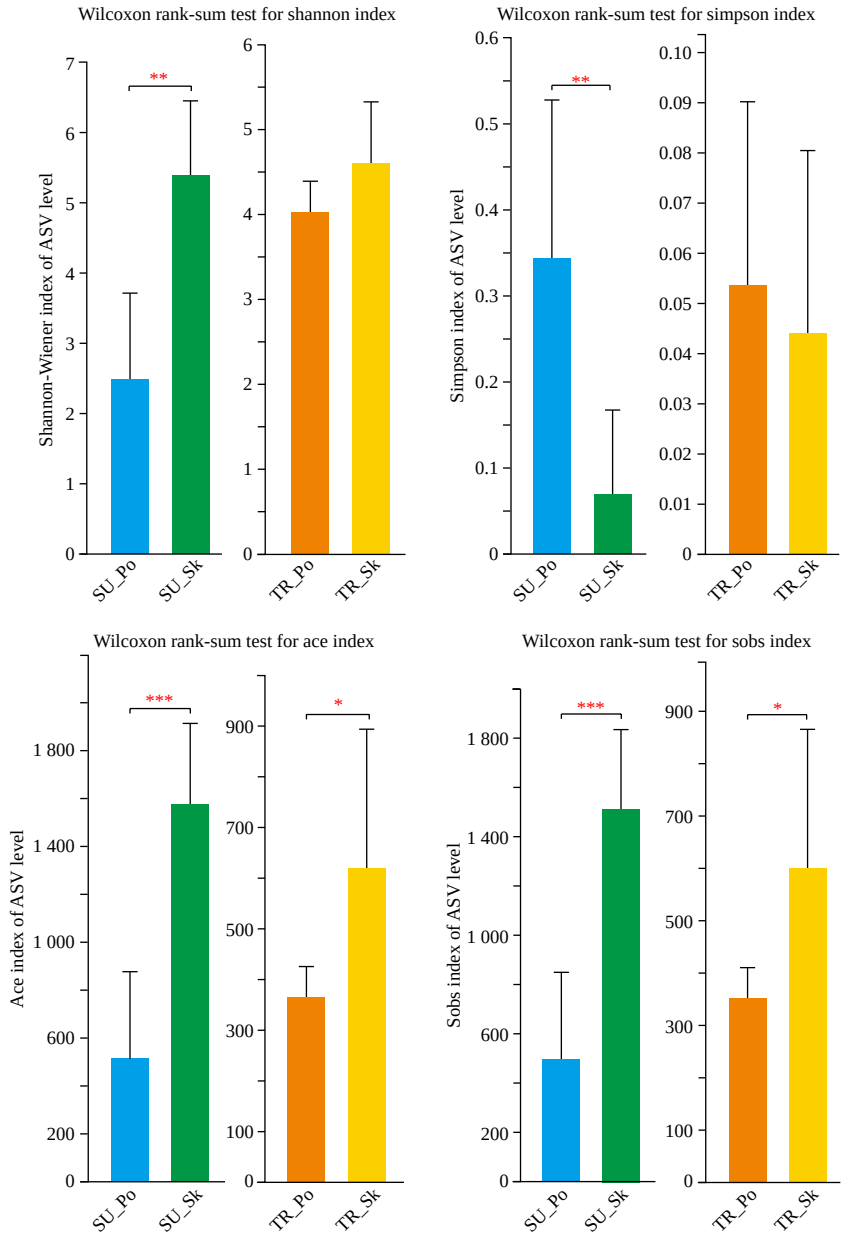


Fig. 2. The Ace, Sobs, Shannon-Wiener, and Simpson diversity indices of associated bacteria based on ASV level in coral polyp and skeleton in the tropical and subtropical coral reef regions (CRR) in the South China Sea (SCS). The "SU_Po" "SU_Sk" "TR_Po" "TR_Sk" represent "coral polyp in subtropical CRR" "coral skeleton in subtropical CRR" "coral polyp in tropical CRR" "coral skeleton in tropical CRR", respectively. The red asterisks "*" "**" and "***" represent "$0.01 < p < 0.05$" "$0.001 < p < 0.01$" and "$p < 0.001$", respectively.

0.001) was detected in the subtropical CRR than in the tropical CRR, as shown in Fig. 4. In contrast, high relative abundances of Rhodobacteraceae ($p < 0.001$), *Pseudoalteromonas* (Wilcoxon rank sum test, $p < 0.001$), and *Vibrio* (Wilcoxon rank sum test, $p < 0.001$) was suggested in the tropical CRR. For skeletal bacteria, high relative abundances of Terasakiellaceae (Wilcoxon rank sum test, $p < 0.001$) and *Chlorobium* ($p = 0.001$) was detected in subtropical CRR. In contrast, the relative abundances of *Cyclobacilluscaeae* (Wilcoxon rank sum test, $p < 0.001$) and A4b (Wilcoxon rank sum test, $p = 0.002$) were low in the subtropical CRR.

Some bacterial taxa differed significantly between polyps and skeletons of *C. palauensis*. For example, in the subtropical CRR, the relative abundances of Terasakiellaceae (Wilcoxon rank sum test, $p < 0.001$) and *Blastocatella* (Wilcoxon rank sum test, $p = 0.004$) in coral polyps were significantly higher than those in skeletons, but those of *Ruegeria* and *Woeseia* (Wilcoxon rank sum test, $p = 0.002$) in skeletons were significantly higher than those in polyps (Wilcoxon rank sum test, $p = 0.024$). In the tropical CRR, the relative abundances of Rhodobacteraceae (Wilcoxon rank sum test, $p = 0.017$), *Pseudoalteromonas* (Wilcoxon rank sum test, $p < 0.001$), *Vibrio* ($p = 0.002$), A4b ($p < 0.001$), and SAR202_clade ($p < 0.001$) differed significantly between polyps and skeletons.

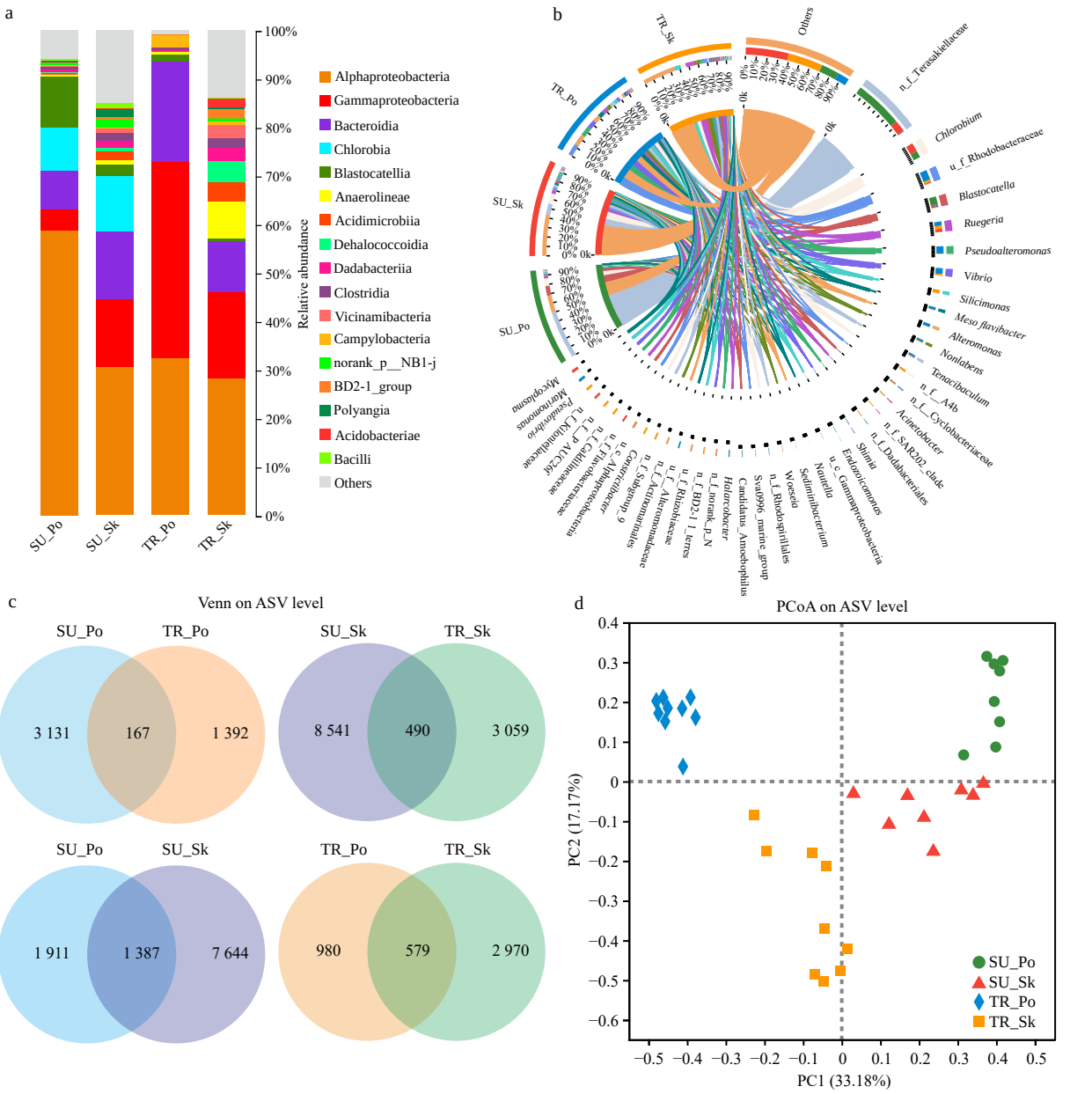


Fig. 3. Relative abundances of coral-associated bacterial communities at class level in polyp and skeletal of *C. palauensis* in the tropical and subtropical CRR in the SCS. a. The relative abundance of coral-associated bacteria at class level. b. The relative abundance of coral-associated bacteria at genus level. c. Venn, Venn analysis was based on ASV level. d. Principal co-ordinates analysis (PCoA). PC1 and PC2 explained 33.17% and 17.17% of total variation, respectively.

Venn diagram analysis revealed common and specific bacterial ASV in different polyps and skeletons of *C. palauensis* (Fig. 3c). The results showed that ASV found in coral skeletons were higher than in coral polyps, and ASV found in the subtropical CRR were higher than in the tropical CRR. PCoA showed that the coral samples of coral polyps in subtropical CRR, coral skeletons in subtropical CRR, coral polyps in tropical CRR, and coral skeleton in tropical CRR were divided into four independent groups (Fig. 3d, PERMANOVA, df = 3, F = 11.09, p = 0.001). PCoA and Venn analyses showed that the associated bacterial communities were different between the skeletons and polyps of *C. palauensis*, as well as between different climate zones. According to the RDA analysis (Fig. S4a), SST, DIN, SRP and transparency were the main factors affecting bacterial ASV of polyps and skeleton. Coral polyp and skeletal bacterial ASV were significantly negatively correlated with DIN and positively correlated with transparency and SST.

3.3 *The archaeal community of coral polyp and skeleton in tropical and subtropical CRR*

After quality filtering, 1 268 effective ASV were obtained using the Illumina MiSeq platform. α-diversity was measured using the Sobs, Ace, Shannon–Wiener, and Simpson indices (Table S5, Figs 5 and S2). The Sobs and

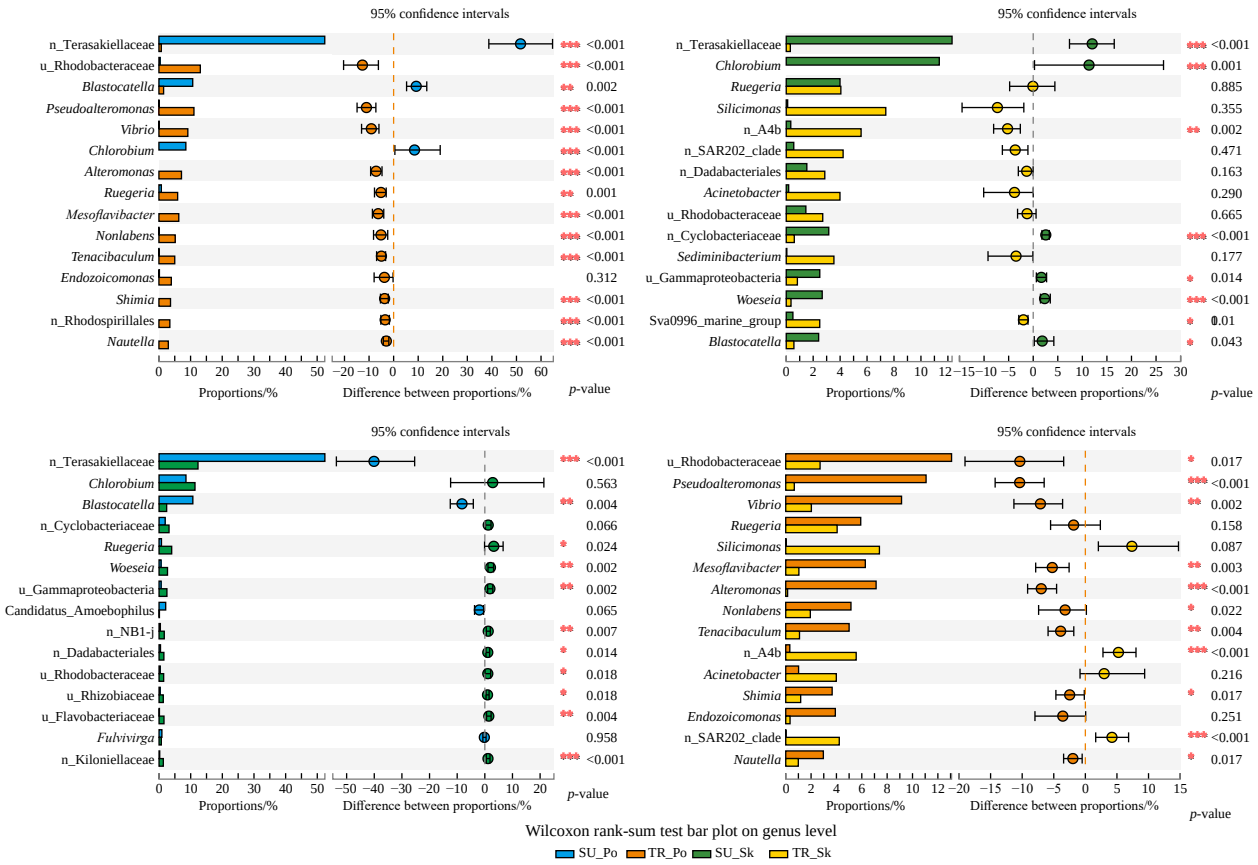


Fig. 4. Wilcoxon rank-sum test bar plot of associated bacterial communities at genus level in coral polyp and skeleton in the tropical and subtropical CRR in the SCS. Some of microbes such as n_Terasakiellaceae, u_Rhodobacteraceae represent norank coral-associated microbial genera of Terasakiellaceae and unclassified coral-associated microbial genera of Rhodobacteraceae, respectively. The red asterisks "*" "**" and "***" represent "$0.01 < p < 0.05$" "$0.001 < p < 0.01$" and "$p < 0.001$", respectively.

Ace indices of *C. palauensis* polyp archaea were significantly higher in the subtropical CRR than in the tropical CRR (Wilcoxon rank sum test, Sobs $p = 0.012$, Ace $p = 0.016$), while the Ace index of skeletal archaea was significantly higher in the tropical CRR than in the subtropical CRR (Wilcoxon rank sum test, $p = 0.046$). Meanwhile, the Shannon and Simpson indices of polyp archaea were significantly higher in the subtropical CRR than in the tropical CRR (Wilcoxon rank sum test, Shannon $p = 0.001$; Simpson $p = 0.002$).

The total taxonomic composition of archaea in the analyzed samples included five phyla, seven classes, eight orders, nine families, and nine genera. At the class level, unclassified_Archaea [(11 ± 4)%–(69 ± 18)%] and Nanoarchaeia [(31 ± 18)%–(89 ± 4)%] were detected (Table S6, Fig. 6a). At the genus level, Woesearchaeales [(64 ± 4)%–(88 ± 4)%] were dominant in the coral polyps in subtropical CRR, coral skeletons in subtropical CRR and coral polyps in tropical CRR groups. In the coral polyps in tropical CRR groups, Woesearchaeales [(31 ± 18)%] were also dominant archaea (Fig. 6a).

Common and unique archaeal ASV (Fig. 6c) were detected in the polyps and skeletons in the tropical and subtropical CRR. In the tropical CRR, the ASV found in coral skeletons were higher than in coral polyps. In the subtropical CRR, the ASV found in coral polyps were higher than in coral skeletons. Besides, in coral polyps, the ASV found in the subtropical CRR were higher than in the tropical CRR. For coral skeletons, the ASV found in the tropical CRR were higher than in the subtropical CRR. PCoA showed that the coral samples of coral polyps in subtropical CRR, coral skeletons in subtropical CRR, coral polyps in tropical CRR, and coral skeletons in tropical CRR were divided into four independent groups (Fig. 6d, PERMANOVA, df = 3, $F = 55.54$, $p = 0.001$). PCoA and Venn diagram analysis showed that the associated archaeal communities were different between tropical and subtropical CRR as well as between polyps and skeletons.

For polyp archaea, the relative abundance of archaea was significantly higher in the subtropical CRR than in tropical CRR (Table S7, Wilcoxon rank sum test, $p < 0.001$), while that of Woesearchaeales showed the opposite trend (Wilcoxon rank sum test, $p < 0.001$), as shown in Fig. 7. For skeletal archaea, the relative abundance of Woesearchaeales was significantly higher in the subtropical CRR than in the tropical CRR (Wilcoxon rank sum test, $p < 0.001$). Moreover, some archaea of *C. palauensis*

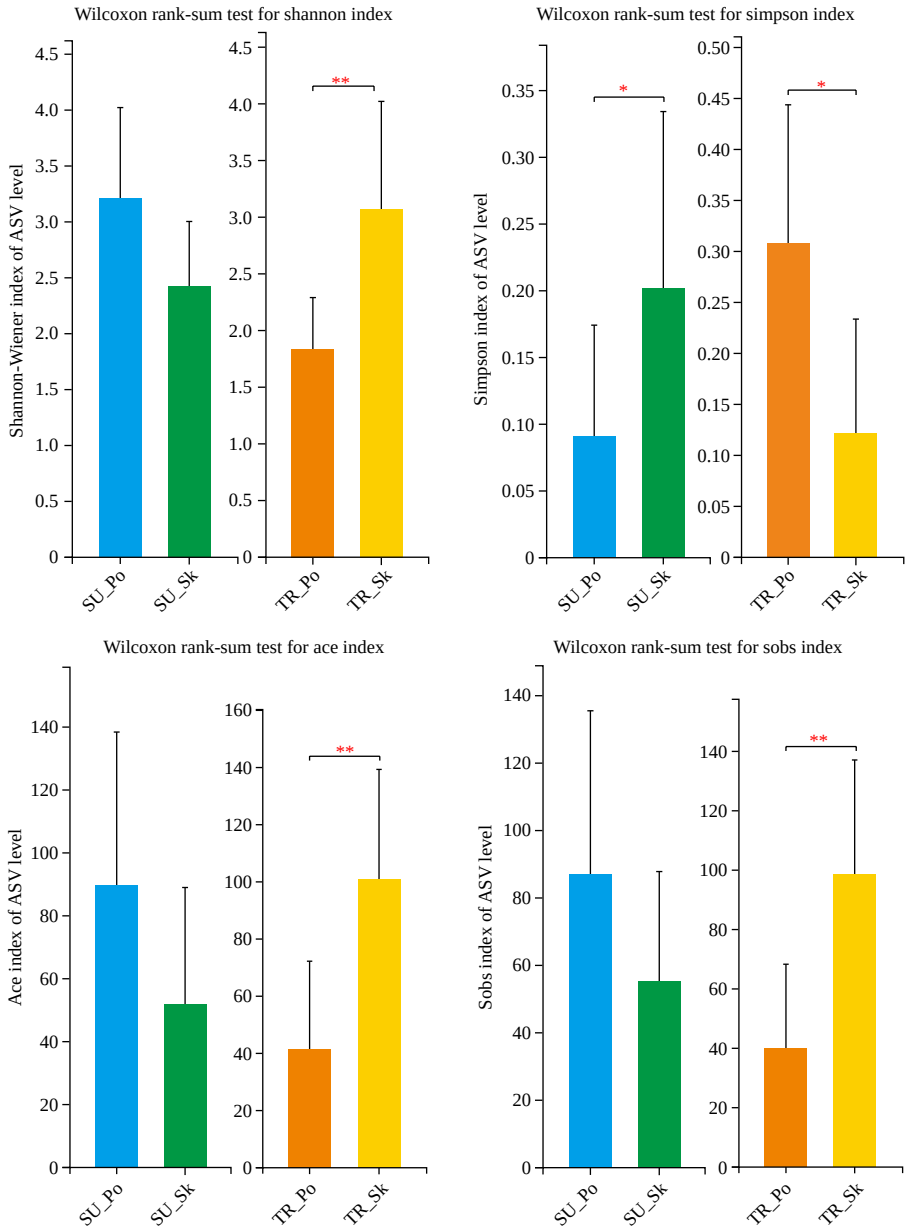


Fig. 5. The Ace, Sobs, Shannon-Wiener, and Simpson diversity indices of coral-associated archaea in coral polyp and skeleton in the tropical and subtropical CRR in the SCS. The red asterisks "*" "**" and "***" represent "$0.01 < p < 0.05$" "$0.001 < p < 0.01$" and "$p < 0.001$", respectively.

differed significantly between the polyps and skeletons. In the subtropical CRR, the relative abundance of Woesearchaeales was significantly higher in the skeletons than in the polyps (Wilcoxon rank sum test, $p < 0.001$). In the tropical CRR, the relative abundance of unclassified_Archaea was significantly higher in the polyps than in the skeletons (Wilcoxon rank sum test, $p < 0.001$), while that of Woesearchaeales was significantly higher than in the skeletons than in the polyps (Wilcoxon rank sum test, $p < 0.001$). According to the RDA analysis (Fig. S4b), SST, DIN, SRP and transparency were the main factors affecting archaeal ASV of polyps and skeleton. Coral polyp and skeletal bacterial ASV were significantly negatively correlated with DIN and positively correlated with transparency and SST.

3.4 *The fungal community of coral polyp and skeleton in tropical and subtropical CRR*

After quality filtering, 857 valid fungal ASV were obtained using an Illumina MiSeq platform. α-diversity was measured using the Sobs, Ace, Shannon-Wiener, and Simpson indices. In the subtropical CRR, the Sobs, Ace, Shannon-Wiener, and Simpson indices of skeletal fungi were significantly higher than those of polyp fungi (Table S8, Wilcoxon rank sum test, Sobs, $p = 0.001$; Ace, $p = 0.008$; Shannon-Wiener, $p = 0.025$; Simpson, $p = 0.01$; Figs 8 and S3). Meanwhile, the Sobs and Ace indices of polyp fungi were significantly higher in the tropical CRR than in the subtropical CRR (Sobs $p = 0.001$, Ace $p = 0.042$).

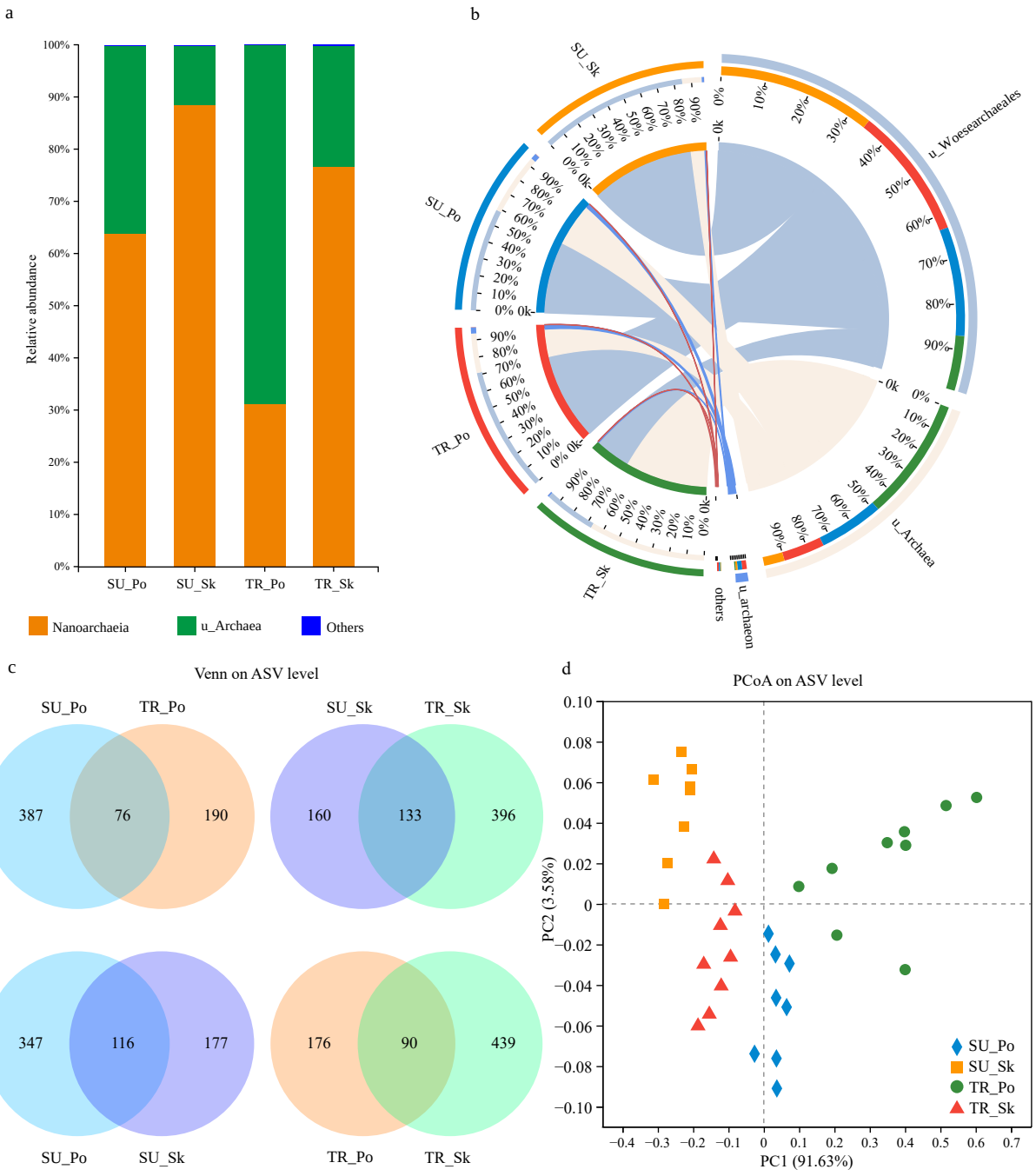


Fig. 6. Relative abundances of associated archaea communities at class level in coral polyp and skeleton in the tropical and subtropical CRR in the SCS. a. The relative abundance of coral-associated bacteria at class level. b. The relative abundance of coral-associated bacteria at genus level. c. Venn, Venn analysis based on ASV level. d. PcoA. PC1 and PC2 explained 91.63% and 3.58% of total variation, respectively.

At the genus level, *Ascomycota* (99%–100%) was dominant in the subtropical CRR, while *Ascomycota* [(41 ± 19)%–(81 ± 7)%] and *Sordariomycetes* [(2 ± 3)%–(32 ± 21)%] were dominant in the tropical CRR (Fig. 9a). Comparison of the sequences of fungi revealed unique ASV in the polyps and skeletons of *C. palauensis* corals in the tropical and subtropical CRR (Fig. 9c). In coral skeletons, the ASV were found higher than in coral polyps. And in the subtropical CRR, the ASV were found higher than in the tropical CRR. PCoA analysis showed that coral samples were divided into four independent groups (Fig. 9d, PERMANOVA, df = 3, F = 13.61, p = 0.001). PCoA and Venn diagram analysis showed that the coral-associated fungal communities were different between coral polyps and skeletons as well as between coral locations.

The fungal composition of *C. palauensis* corals varies regionally in the tropical and subtropical CRR (Table S9 and S10, Fig. 10). In coral polyps, the relative abundance of *Ascomycota* was high in the subtropical CRR (Wilcoxon rank sum test, p < 0.001), while that of Sordariomycetes was significantly higher in the tropical CRR



Fig. 7. Wilcoxon rank-sum test bar plot of associated archaea communities at genus level in coral polyp and skeleton in the tropical and subtropical CRR in the SCS. The red asterisks "*" "**" and "***" represent "$0.01 < p < 0.05$" "$0.001 < p < 0.01$" and "$p < 0.001$", respectively.

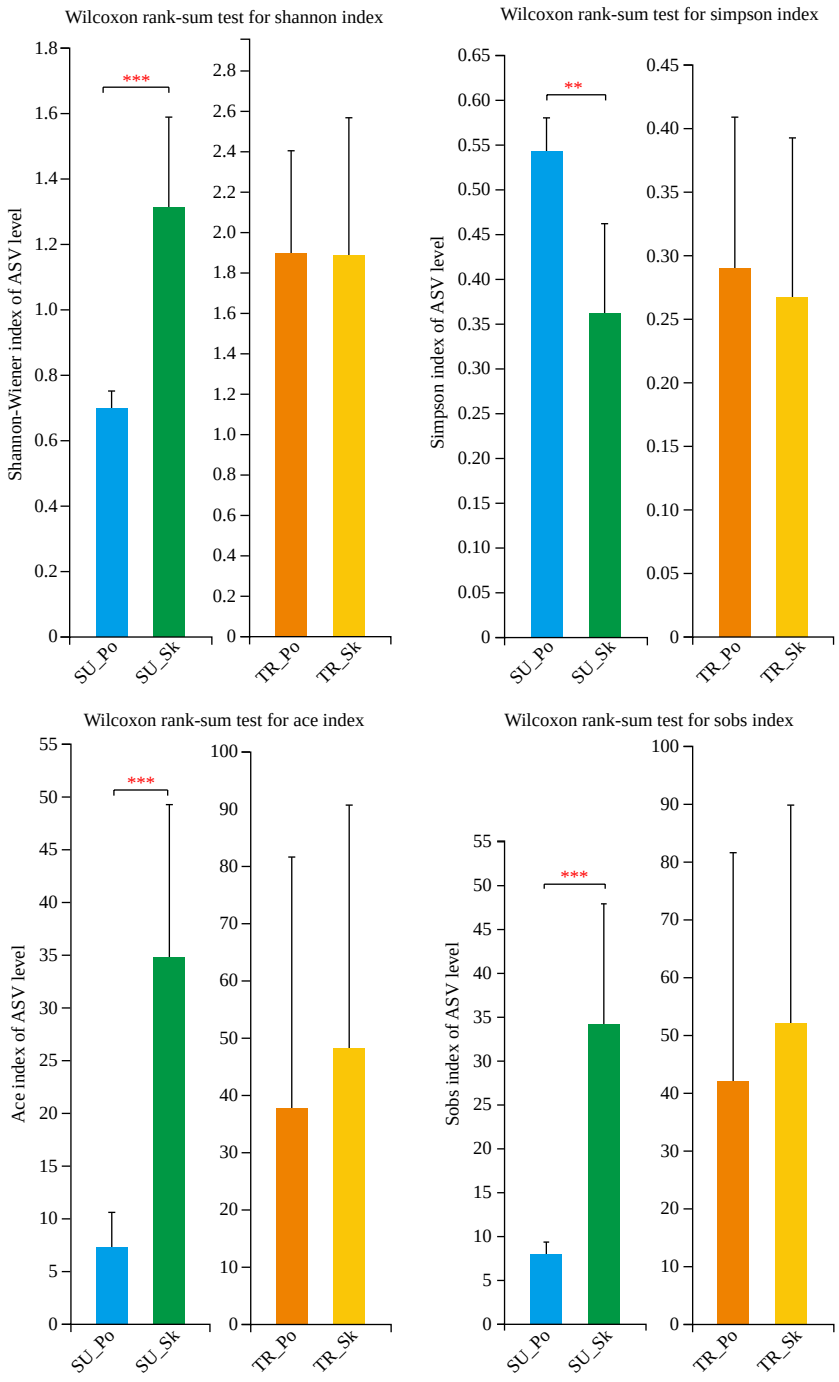


Fig. 8. The Ace, Sobs, Shannon-Wiener, and Simpson diversity indices of associated fungi communities in coral polyp and skeleton in the tropical and subtropical CRR in the SCS. The red asterisks "**" and "***" represent "$0.001 < p < 0.01$" and "$p < 0.001$", respectively.

(Wilcoxon rank sum test, $p = 0.020$). Similarly, in coral skeletons, the relative abundance of *Ascomycota* was significantly higher in the subtropical CRR than in the tropical CRR (Wilcoxon rank sum test, $p < 0.001$), while that of *Sordariomycetes* showed the opposite trend (Wilcoxon rank sum test, $p < 0.001$). According to RDA analysis (Fig. S4c), SST, DIN, SRP and transparency were the main factors affecting fungal ASV of polyps and skeleton. Coral polyp and skeletal bacterial ASV were significantly negatively correlated with DIN and positively correlated with transparency and SST.

4 Discussion

4.1 *Differences and influencing factors in the polyp and skeletal bacterial communities of corals in tropical and subtropical CCRs*

In this study, the community compositions of bacteria in coral polyps and skeletons were significantly different between tropical and subtropical CRR. Environmental stresses such as high temperature (Santos et al., 2014; Bourne et al., 2008), eutrophication (Jessen et al., 2013),

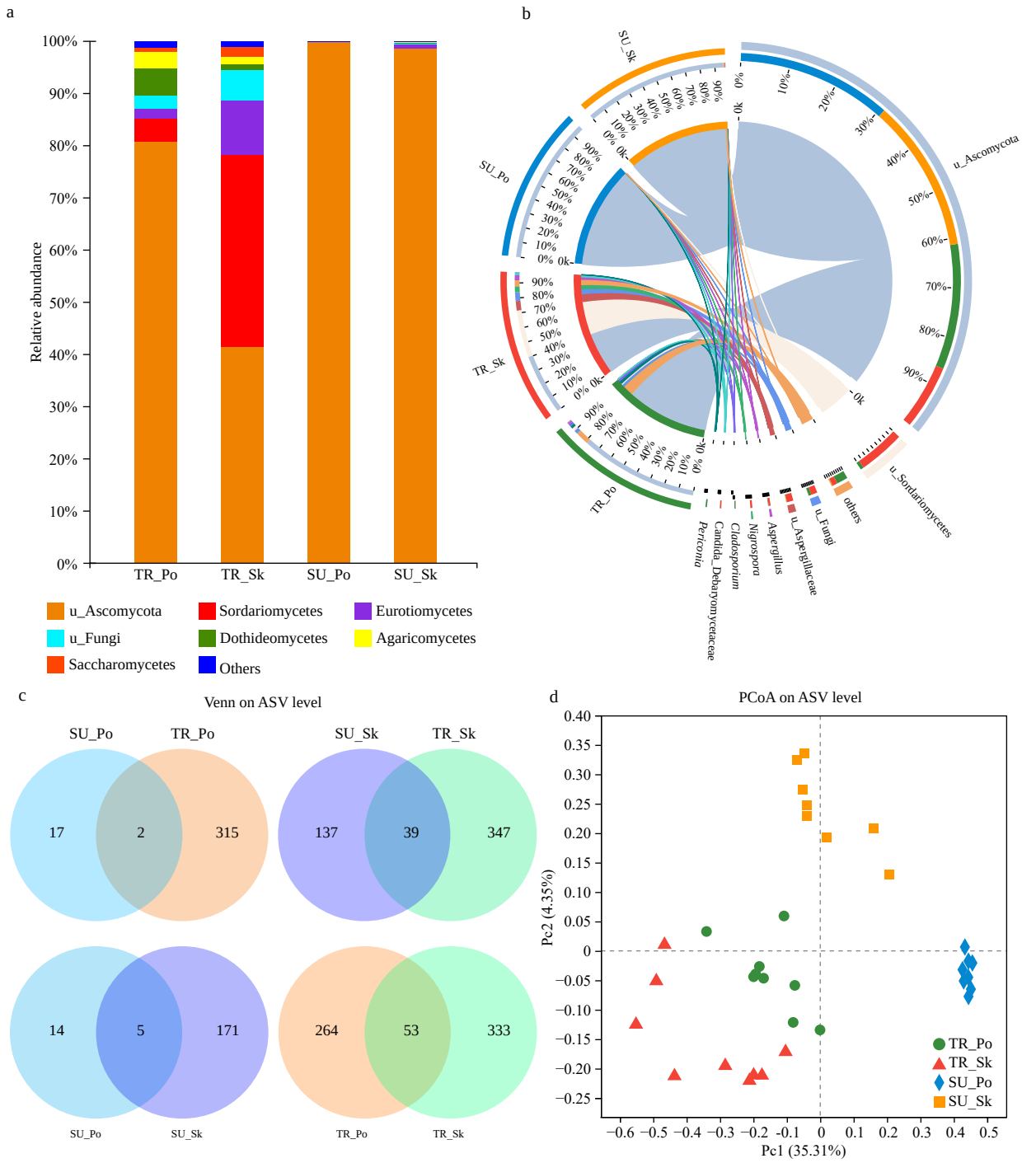


Fig. 9. Relative abundances of associated fungi communities at class level in coral polyp and skeleton in the tropical and subtropical CRR in the SCS. a. The relative abundance of coral-associated bacteria at class level. b. The relative abundance of coral-associated bacteria at genus level. c. Venn, Venn analysis based on ASV level. d. PcoA. PC1 and PC2 explained 35.31% and 4.35% of total variation, respectively.

and water pollution (Ziegler et al., 2016) reduce the ability of the coral host or its microbiome to regulate community composition, which could affect the α-diversity of bacterial community (Zaneveld et al., 2017; McDevitt-Irwin et al., 2017). In this study, coral-associated bacteria may have been influenced by different environmental stresses between tropical and subtropical CRR. High SST and salinity may influence corals in the tropical CRR, while relative high eutrophication and turbidity may influence corals in the subtropical CRR. RDA analyses showed that DIN, SST and transparency were the main environmental influences in coral polyps and skeletal bacteria (Fig. S4a). The different responses of coral polyp and skeletal bacteria to these environmental stresses may be the main reason for the regional differences in Sobs, Ace, Shannon-Wiener, and Simpson indices.

In the subtropical CRR of the SCS, coral polyps and skeletons contain a high relative abundance of bacteria

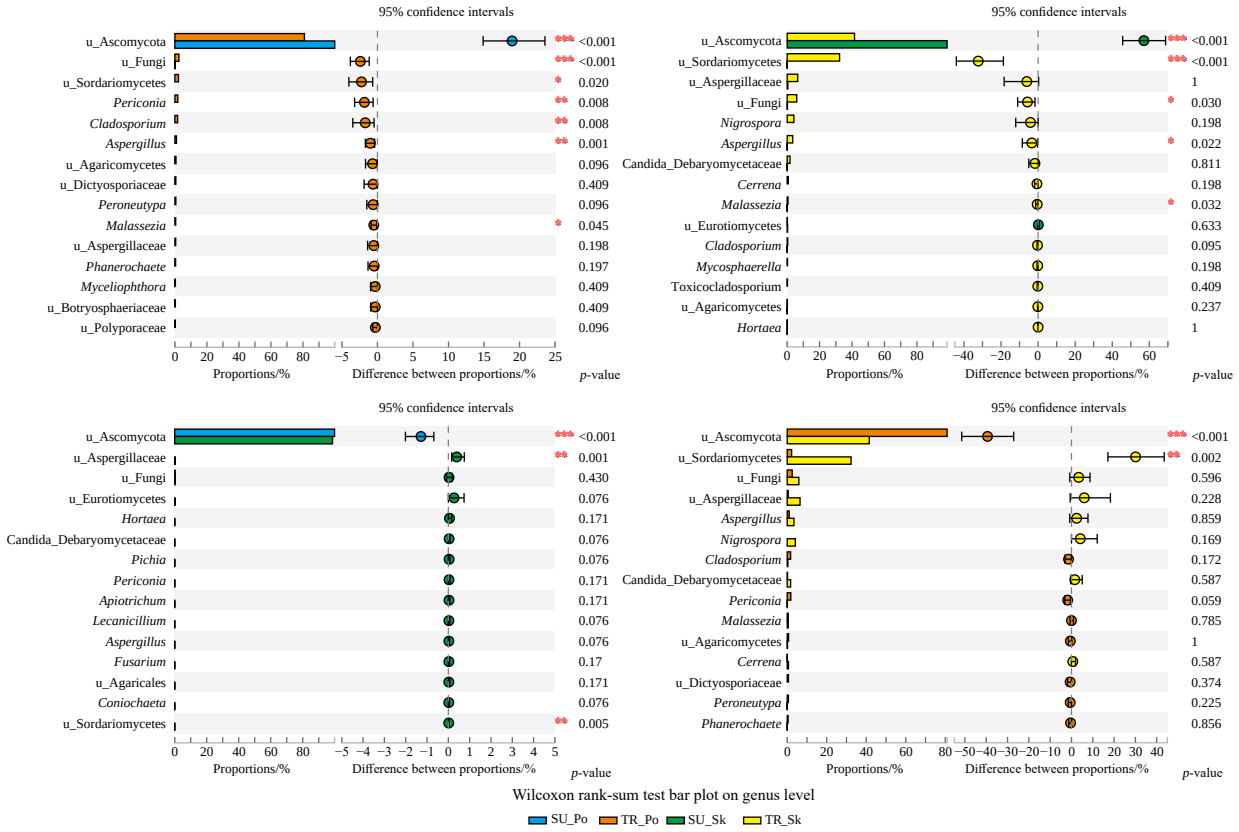


Fig. 10. Wilcoxon rank-sum test bar plot of associated fungi communities at genus level in coral polyp and skeleton in the tropical and subtropical CRR in the SCS.

that are related to the nitrogen cycle and local environment adaptation. A high abundance of Terasakiellaceae was detected in coral polyps in the subtropical CRR, which may contribute to nitrogen cycling of coral holobionts, especially in habitats where nutrients are limited (Weiler et al., 2018; Quintanilla et al., 2022). The Terasakiellaceae were documented to be nitrogen fixed and may be important for the nitrogen metabolism (Tiedje, 1988). It may be a biomarker for organisms involved in the nitrogen cycle (Weiler et al., 2018). The azotobacter *Chlorobium*, which usually survives in hypoxic aquatic environments (Frigaard and Bryant, 2004), was also the dominant bacteria in coral polyps and skeletons in the subtropical CRR. The RDA analysis showed that DIN was the main factor influencing in the subtropical CRR, which may be a factor resulting in high abundance of *Chlorobium* in coral skeletons and polyps. Some members of *Chlorobium* belong to the nitrogen-fixing bacteria, which are related with the nitrogen cycle and may be high abundance in high nutrient environment (Frigaard and Bryant, 2004; Fan et al., 2021). In addition, *Cyclobacilluscaeae* which can assimilate ammonia nitrogen (Fan et al., 2021), Woeseia (Mußmann et al., 2017; Zhang et al., 2020), which is capable of dissimilatory sulfur oxidation and denitrification, and Blastocatalla (Huang et al., 2017), which can remove nitrogen, phosphorus, and organic matter, were also highly abundant in the *C. palauensis* coral in the subtropical CRR in the SCS.

In the tropical CRR, a relatively high relative abundances of opportunistic, pathogenic, and antibacterial bacteria were detected in coral polyps of *C. palauensis*. High SST influences the dynamic balance between invasion and resistance of opportunistic and pathogenic coral bacteria (Qin et al., 2020). In this study, some members of Rhodobacteraceae were dominant in coral polyps, some of which were fast-growing opportunistic bacteria that significantly increased in abundance in stressed corals that found in previous studies (Teeling et al., 2012; Meron et al., 2011; Sharp et al., 2012). In addition, some potential pathogens, namely *Tenacibaculum*, *Nonlabens*, *Mesoflavibacter*, and *Vibrio,* also had relatively high abundances in coral polyps. *Tenacibaculum*, *Nonlabens*, and *Mesoflavibacter* belong to the family Flavobacteriaceae, which is related to coral bleaching (Gignoux-Wolfsohn and Vollmer, 2015). The abundance of pathogenic bacteria will significantly increase when coral holobionts suffer from thermal stress and coral diseases, causing an increase in gene expression related to virulence factors (McDevitt-Irwin et al., 2017; van Oppen and Blackall, 2019). However, high relative abundances of the *Pseudoalteromonas* and *Alteromonas* were also detected in coral polyps. Some members of *Pseudoalteromonas* have antibacterial activity against coral bacteria (Shnit-Orland et al., 2012; Tang et al., 2020), and some members of *Alteromonas* can participate in the coral nitrogen and sulfur cycle (Raina et al., 2009; Ceh et al., 2013). In addition,

20% of the members of coral-associated bacteria *Photobacterium* and *Alteromonas* can secrete antibiotics to resist the invasion of coral pathogens (Ritchie, 2006). Therefore, coral polyps in the tropical CRR may be associated with potential probiotics to resist the negative effects of a high abundance of pathogenic bacteria.

In the coral skeletons in the tropical CRR, a high relative abundance of A4b was detected. The bacteria of A4b belong to the Anaerolineae, which is related to carbohydrate decomposition during anaerobic digestion of organic substances (Ni et al., 2022). Sangsawang et al. (2017) found that coral skeleton bacteria have a high primary productivity and can be transferred to coral polyps. Therefore, coral skeleton bacteria may be important for the survival and recovery of corals.

4.2 *Differences and influencing factors in the polyp and skeletal archaeal communities of corals in tropical and subtropical CRR*

In this study, Nanoarchaeota and unclassified Archaea were the dominate archaea in corals in the tropical and subtropical CRR. Woesearchaeales and unclassified Archaea accounted for approximately 99% of the relative abundance of archaea. Recent research has revealed the potential role of Woesearchaeales in anaerobic biogeochemical cycles of carbon, nitrogen, and sulfur (Liu et al., 2021). Liu et al. (2018) reported that various Woesearchaeales were distributed in different biological communities and were mainly concentrated in anoxic environments. Most Woesearchaeales are anaerobes or facultative anaerobes, and the environmental oxygen content is one of the key factors affecting the Woesearchaeales community (Kühl et al., 2008). In deeper parts of coral skeleton below the endolithic algal layer, oxygen content decreases rapidly, creating a hypoxic or anaerobic environment (Kühl et al., 2008; Ricci et al., 2019) that is conducive to the survival of the Woesearchaeales community. Our study showed that the relative abundance of Woesearchaeales in coral skeletons was significantly higher than that in coral polyps. RDA analysis showed that DIN, SRP, SST and Transparency were the main environmental influences on coral polyp and skeletal archaeal ASV. DIN and SRP were positively correlated, while SST and transparency were negatively correlated. DO was positively correlated with archaeal ASV. The significant difference in Woesearchaeales may be due to the combined effects of DO content, elevated nutrients due to water pollution, and SST.

4.3 *Differences and influencing factors in the polyp and skeletal fungal communities of corals in tropical and subtropical CRR*

The α-diversity of coral-associated fungi showed regional differences. Generally, SST is an important environmental factor that drives the richness and community of fungi in seawater with a positive correlation (Li et al., 2019). A high SST could result in an increase in fungal community diversity in corals (Thurber et al., 2009). Our results showed a high α-diversity of fungal community of coral skeletons and polyps in the tropical CRR with higher SST. Although invasion from the polyps to the skeleton triggers the defense mechanism, fungi with strong drilling capacity can successfully break through coral skeleton structures under the influence of high SST (Golubic et al., 1975, 2005; Bentis et al., 2000). The relatively high abundance of fungi in the tropical CRR causes intense competition in the skeletons, resulting in the survival of some fungi in coral polyps. Besides, high abundances of Sordariomycetes, Periconia, Cladosporium, and Aspergillus were detected in the tropical CRR. A higher SST could be the driving factor for these fungal abundances. Most members of Sordariomycetes are classified as Halosphaeriales and Lulworthiales. Halosphaeriales are adaptable to extremely high temperatures (Zhang et al., 2006). Meanwhile, combined with the RDA, the results showed that SST was the main environmental influencing factor for the fungal communities in coral skeletons and polyps. This could explain why Sordariomycetes were the dominant fungi in coral polyps and skeletons in the tropical CRR, which had relatively high SST.

In this study, *Ascomycota* was the dominant fungus in coral skeletons and polyps in tropical and subtropical CRR. Several studies have reported a relatively high abundance of *Ascomycota* in corals from coral reefs including the SCS (Xu et al., 2018), Bocas del Toro (Wegley et al., 2007), Florida (Bonthond et al., 2018), Ofu Island in USA (Amend et al., 2012), the Great Barrier Reef (Littman et al., 2011), and Hawaii (Thurber et al., 2009). In addition, microscopic observations of coral skeletons suggested that *Ascomycota* are common fungi in healthy coral skeletons (Wegley et al., 2007; Góes-Neto et al., 2020). These *Ascomycota* associate with coral early in life and grow with the carbonate skeleton to maintain their position just under the coral polyps (Le Campion-Alsumard et al., 1995a; Wegley et al., 2007). The abundance of *Ascomycota* is closely related to the organic matter and chemical composition of coral skeletons and polyps (Paulino et al., 2017, 2020). Some *Ascomycota* can degrade organic carbon and sugars, and thereby promoting their growth (Suh et al., 2006). The mucus in coral polyps is mainly composed of glucose, galactose, lipids, and other monosaccharides (Ducklow and Mitchell, 1979; Glasl et al., 2016), whereas the coral skeleton is mainly composed of calcium carbonate, resulting in a higher abundance of *Ascomycota* in the polyps than in the skeletons. Some Ascomycetes can participate in multiple carbon nitrogen coupled cycles, such as carbon fixation, ammonia assimilation, and ammoniation, and bioactive substances can participate in immune regulation and antibacterial activity (Gleason et al., 2017, Wegley et al., 2007). *Ascomycota* is the dominant fungal phylum in the honeycomb corals in the tropical and subtropical CRR, and some of

them have positive effects. It is possible to conduct in-depth research on how to utilize these beneficial fungi to maintain the ecology of coral reefs.

5 Conclusions

In this study, coral-microbial assemblages in coral polyps and skeletons varied at tropical and subtropical reefs in the SCS. In the subtropical CRR of Weizhou Island, the nitrogen-fixing bacterium *Chlorobium* was the dominant bacterium in the polyps and skeletons of *C. palauensis*. The *Woeseia*, which is capable of sulfur oxidation and denitrification, as well as high abundance of *Blastocatella*, which could remove high nitrogen, phosphorus, and organic particulate matter were detected in the *C. palauensis* polyps or skeletons. In addition, the relative abundance of Woesearchaeales was significantly higher than that of corals from the tropical CRR. This may be due to anthropogenic activities impacts such as high nutrients and turbidity. Relatively high abundance of opportunistic, pathogenic and antimicrobial bacteria was detected in *C. palauensis* polyps in the tropical CRR. The potentially pathogenic fungi such as *Periconia*, *Cladosporium*, and *Aspergillus* were significantly higher in polyp and skeleton from the tropical CRR than the subtropical CRR. Suffered from high thermal stress in summer, corals in the tropical CRR may be threatened by potential bacterial or fungal diseases, and are susceptible to coral bleaching under the thermal stress. Therefore, in the subtropical CRR, anthropogenic activities should be reduced, which is conducive to corals' health. In the tropical CRR, it is advised to enhance monitoring for abnormally high temperatures, which will be conducive to early detection the threat of abnormally high thermal to the corals.

References

Ainsworth T D, Fordyce A J, Camp E F. 2017. The other microeukaryotes of the coral reef microbiome. Trends in Microbiology, 25(12): 980–991, doi: 10.1016/j.tim.2017.06.007

Ainsworth T D, Thurber R V, Gates R D. 2010. The future of coral reefs: a microbial perspective. Trends in Ecology & Evolution, 25(4): 233–240, doi: 10.1016/j.tree.2009.11.001

Amend A S, Barshis D J, Oliver T A. 2012. Coral-associated marine fungi form novel lineages and heterogeneous assemblages. The ISME Journal, 6(7): 1291–1301, doi: 10.1038/ismej.2011.193

Bentis C J, Kaufman L, Golubic S. 2000. Endolithic fungi in reef-building corals (Order: Scleractinia) are common, cosmopolitan, and potentially pathogenic. The Biological Bulletin, 198(2): 254–260, doi: 10.2307/1542528

Blackall L L, Wilson B, van Oppen M J H. 2015. Coral-the world's most diverse symbiotic ecosystem. Molecular Ecology, 24(21): 5330–5347, doi: 10.1111/mec.13400

Bonthond G, Merselis D G, Dougan K E, et al. 2018. Inter-domain microbial diversity within the coral holobiont *Siderastrea siderea* from two depth habitats. PeerJ, 6: e4323, doi: 10.7717/peerj.4323

Bourne D, Iida Y, Uthicke S, et al. 2008. Changes in coral-associated microbial communities during a bleaching event. The ISME Journal, 2(4): 350–363, doi: 10.1038/ismej.2007.112

Bourne D G, Morrow K M, Webster N S. 2016. Insights into the coral microbiome: underpinning the health and resilience of reef ecosystems. Annual Review of Microbiology, 70: 317–340, doi: 10.1146/annurev-micro-102215-095440

Callahan B J, Mcmurdie P J, Rosen M J, et al. 2016. DADA2: high-resolution sample inference from illumina amplicon data. Nature Methods, 13(7): 581–583, doi: 10.1038/nmeth.3869

Caporaso J G, Kuczynski J, Stombaugh J, et al. 2010. QIIME allows analysis of high-throughput community sequencing data. Nature Methods, 7(5): 335–336, doi: 10.1038/nmeth.f.303

Ceh J, Kilburn M R, Cliff J B, et al. 2013. Nutrient cycling in early coral life stages: *Pocillopora damicornis* larvae provide their algal symbiont (*Symbiodinium*) with nitrogen acquired from bacterial associates. Ecology and Evolution, 3(8): 2393–2400, doi: 10.1002/ece3.642

Chen Yu-Hsiang, Yang Shan-Hua, Tandon Kshitij, et al. 2021. Potential syntrophic relationship between coral-associated *Prosthecochloris* and its companion sulfate-reducing bacterium unveiled by genomic analysis. Microbial Genomics, 7(5): 000574, doi: 10.1099/mgen.0.000574

Chen Xiaoyan, Yu Kefu, Huang Xueyong, et al. 2019. Atmospheric nitrogen deposition increases the possibility of macroalgal dominance on remote coral reefs. Journal of Geophysical Research: Biogeosciences, 124(5): 1355–1369, doi: 10.1029/2019JG005074

Darling E S, Alvarez-Filip L, Oliver T A, et al. 2012. Evaluating life-history strategies of reef corals from species traits. Ecology Letters, 15(12): 1378–1386, doi: 10.1111/j.1461-0248.2012.01861.x

Ducklow H W, Mitchell R. 1979. Composition of mucus released by coral reef coelenterates 1. Limnology and Oceanography, 24(4): 706–714, doi: 10.4319/lo.1979.24.4.0706

Fan Siqi, Ji Bin, Abu Hasan H, et al. 2021. Microalgal–bacterial granular sludge process for non-aerated aquaculture wastewater treatment. Bioprocess and Biosystems Engineering, 44(8): 1733–1739, doi: 10.1007/s00449-021-02556-0

Fine M, Roff G, Ainsworth T D, et al. 2006. Phototrophic microendoliths bloom during coral "white syndrome". Coral Reefs, 25(4): 577–581, doi: 10.1007/s00338-006-0143-4

Francis C A, Beman J M, Kuypers M M M. 2007. New processes and players in the nitrogen cycle: the microbial ecology of anaerobic and archaeal ammonia oxidation. The ISME Journal, 1(1): 19–27, doi: 10.1038/ismej.2007.8

Frigaard N U, Bryant D A. 2004. Seeing green bacteria in a new

light: genomics-enabled studies of the photosynthetic apparatus in green sulfur bacteria and filamentous anoxygenic phototrophic bacteria. Archives of Microbiology, 182(4): 265–276, doi: 10.1007/s00203-004-0718-9

Gignoux-Wolfsohn S A, Vollmer S V. 2015. Identification of candidate coral pathogens on white band disease-infected staghorn coral. PLoS ONE, 10(8): e0134416, doi: 10.1371/journal.pone.0134416

Glasl B, Herndl G J, Frade P R. 2016. The microbiome of coral surface mucus has a key role in mediating holobiont health and survival upon disturbance. The ISME Journal, 10(9): 2280–2292, doi: 10.1038/ismej.2016.9

Gleason F H, Gadd G M, Pitt J I, et al. 2017. The roles of endolithic fungi in bioerosion and disease in marine ecosystems. Ⅱ. Potential facultatively parasitic anamorphic ascomycetes can cause disease in corals and molluscs. Mycology, 8(3): 216–227, doi: 10.1080/21501203.2017.1371802

Góes-Neto A, Marcelino V R, Verbruggen H, et al. 2020. Biodiversity of endolithic fungi in coral skeletons and other reef substrates revealed with 18S rDNA metabarcoding. Coral Reefs, 39(1): 229–238, doi: 10.1007/s00338-019-01880-y

Golubic S, Perkins R D, Lukas K J. 1975. Boring microorganisms and microborings in carbonate substrates. In: Frey R W, ed. The Study of Trace Fossils: A Synthesis of Principles, Problems, and Procedures in Ichnology. Berlin, Heidelberg: Springer, 229–259

Golubic S, Radtke G, Le Campion-Alsumard T. 2005. Endolithic fungi in marine ecosystems. Trends in Microbiology, 13(5): 229–235, doi: 10.1016/j.tim.2005.03.007

He Jingke, Huang Zhenpeng. 2019. The distribution of corals in Weizhou Island, Guangxi. Ocean Development and Management (in Chinese), 36(1): 57–62

Huang Xiao, Dong Wenyi, Wang Hongjie, et al. 2017. Biological nutrient removal and molecular biological characteristics in an anaerobic-multistage anaerobic/oxic (A-MAO) process to treat municipal wastewater. Bioresource Technology, 241: 969–978, doi: 10.1016/j.biortech.2017.05.161

Huggett M J, Apprill A. 2019. Coral microbiome database: integration of sequences reveals high diversity and relatedness of coral-associated microbes. Environmental Microbiology Reports, 11(3): 372–385, doi: 10.1111/1758-2229.12686

Jessen C, Villa Lizcano J F, Bayer T, et al. 2013. *In-situ* effects of eutrophication and overfishing on physiology and bacterial diversity of the Red Sea coral *Acropora hemprichii*. PLoS ONE, 8(4): e62091, doi: 10.1371/journal.pone.0062091

Kemp D W, Rivers A R, Kemp K M, et al. 2015. Spatial homogeneity of bacterial communities associated with the surface mucus layer of the reef-building coral *Acropora palmata*. PLoS ONE, 10(12): e0143790, doi: 10.1371/journal.pone.0143790

Kimes N E, Van Nostrand J D, Weil E, et al. 2010. Microbial functional structure of *Montastraea faveolata*, an important Caribbean reef-building coral, differs between healthy and yellow-band diseased colonies. Environmental Microbiology, 12(2): 541–556, doi: 10.1111/j.1462-2920.2009.02113.x

Kühl M, Holst G, Larkum A W D, et al. 2008. Imaging of oxygen dynamics within the endolithic algal community of the massive coral *Porites lobata*. Journal of Phycology, 44(3): 541–550, doi: 10.1111/j.1529-8817.2008.00506.x

Le Campion-Alsumard T, Golubic S, Hutchings P. 1995a. Microbial endoliths in skeletons of live and dead corals: *Porites lobata* (Moorea, French Polynesia). Marine Ecology Progress Series, 117: 149–157, doi: 10.3354/meps117149

Le Campion-Alsumard T, Golubic S, Priess K. 1995b. Fungi in corals: symbiosis or disease? Interaction between polyps and fungi causes pearl-like skeleton biomineralization. Marine Ecology Progress Series, 117: 137–147, doi: 10.3354/meps117137

Lema K A, Willis B L, Bourne D G. 2012. Corals form characteristic associations with symbiotic nitrogen-fixing bacteria. Applied and Environmental Microbiology, 78(9): 3136–3144, doi: 10.1128/AEM.07800-11

Lesser M P, Mazel C H, Gorbunov M Y, et al. 2004. Discovery of symbiotic nitrogen-fixing cyanobacteria in corals. Science, 305(5686): 997–1000, doi: 10.1126/science.1099128

Levy S, Elek A, Grau-Bové X, et al. 2021. A stony coral cell atlas illuminates the molecular and cellular basis of coral symbiosis, calcification, and immunity. Cell, 184(11): 2973–2987. e18, doi: 10.1016/j.cell.2021.04.005

Li Jie, Chen Qi, Long Lijuan, et al. 2014. Bacterial dynamics within the mucus, tissue and skeleton of the coral *Porites lutea* during different seasons. Scientific Reports, 4: 7320, doi: 10.1038/srep07320

Li Wei, Wang Mengmeng, Burgaud G, et al. 2019. Fungal community composition and potential depth-related driving factors impacting distribution pattern and trophic modes from Epi- to abyssopelagic zones of the Western Pacific Ocean. Microbial Ecology, 78(4): 820–831, doi: 10.1007/s00248-019-01374-y

Liao Zhiheng, Yu Kefu, Chen Biao, et al. 2021. Spatial distribution of benthic algae in the South China Sea: responses to gradually changing environmental factors and ecological impacts on coral communities. Diversity and Distributions, 27(5): 929–943, doi: 10.1111/ddi.13243

Littman R, Willis B L, Bourne D G. 2011. Metagenomic analysis of the coral holobiont during a natural bleaching event on the Great Barrier Reef. Environmental Microbiology Reports, 3(6): 651–660, doi: 10.1111/j.1758-2229.2010.00234.x

Liu Xiaobo, Li Meng, Castelle C J, et al. 2018. Insights into the ecology, evolution, and metabolism of the widespread Woesearchaeotal lineages. Microbiome, 6(1): 102, doi: 10.1186/s40168-018-0488-2

Liu Can, Li Huan, Zhang Yuyao, et al. 2016. Evolution of microbial community along with increasing solid concentration during high-solids anaerobic digestion of sewage

sludge. Bioresource Technology, 216: 87–94, doi: 10.1016/j.biortech.2016.05.048

Liu Xiaobo, Wang Yali, Gu Jidong. 2021. Ecological distribution and potential roles of Woesearchaeota in anaerobic biogeochemical cycling unveiled by genomic analysis. Computational and Structural Biotechnology Journal, 19: 794–800, doi: 10.1016/j.csbj.2021.01.013

Liu Po-Yu, Yang Sung-Yin, Lu Chih-Ying, et al. 2022. Ocean currents may influence the endolithic bacterial composition in coral skeletons. Frontiers in Marine Science, 9: 850984, doi: 10.3389/fmars.2022.850984

Luo Danli, Wang Xiaojun, Feng Xiaoyuan, et al. 2021. Population differentiation of Rhodobacteraceae along with coral compartments. The ISME Journal, 15(11): 3286–3302, doi: 10.1038/s41396-021-01009-6

Marcelino V R, Verbruggen H. 2016. Multi-marker metabarcoding of coral skeletons reveals a rich microbiome and diverse evolutionary origins of endolithic algae. Scientific Reports, 6(1): 31508, doi: 10.1038/srep31508

Mcdevitt-Irwin J M, Baum J K, Garren M, et al. 2017. Responses of Coral-Associated bacterial communities to local and global stressors. Frontiers in Marine Science, 4: 262, doi: 10.3389/fmars.2017.00262

Meibom A, Cuif J P, Houlbreque F, et al. 2008. Compositional variations at ultra-structure length scales in coral skeleton. Geochimica et Cosmochimica Acta, 72(6): 1555–1569, doi: 10.1016/j.gca.2008.01.009

Meron D, Atias E, Iasur Kruh L, et al. 2011. The impact of reduced pH on the microbial community of the coral *Acropora eurystoma*. The ISME Journal, 5(1): 51–60, doi: 10.1038/ismej.2010.102

Mori H, Maruyama F, Kato H, et al. 2014. Design and experimental application of a novel non-degenerate universal primer set that amplifies prokaryotic 16S rRNA genes with a low possibility to amplify eukaryotic rRNA genes. DNA Research, 21(2): 217–227, doi: 10.1093/dnares/dst052

Mußmann M, Pjevac P, Krüger K, et al. 2017. Genomic repertoire of the *Woeseiaceae*/JTB255, cosmopolitan and abundant core members of microbial communities in marine sediments. The ISME Journal, 11(5): 1276–1281, doi: 10.1038/ismej.2016.185

Ni Jialing, Ji Jiayuan, Li Yuyou, et al. 2022. Microbial characteristics in anaerobic membrane bioreactor treating domestic sewage: effects of HRT and process performance. Journal of Environmental Sciences, 111: 392–399, doi: 10.1016/j.jes.2021.04.022

Nilsson R H, Larsson K H, Taylor A F S, et al. 2019. The UNITE database for molecular identification of fungi: handling dark taxa and parallel taxonomic classifications. Nucleic Acids Research, 47(D1): D259–D264, doi: 10.1093/nar/gky1022

Oksanen J, Blanchet FG, Kindt R, et al. 2015. Vegan: community ecology package. R Package Version 2:3

Paulino G V B, Félix C R, Broetto L, et al. 2017. Diversity of culturable yeasts associated with zoanthids from Brazilian reef and its relation with anthropogenic disturbance. Marine Pollution Bulletin, 123(1-2): 253–260, doi: 10.1016/j.marpolbul.2017.08.050

Paulino G V B, Félix C R, Landell M F. 2020. Diversity of filamentous fungi associated with coral and sponges in coastal reefs of northeast Brazil. Journal of Basic Microbiology, 60(2): 103–111, doi: 10.1002/jobm.201900394

Pernice M, Raina J B, Rädecker N, et al. 2020. Down to the bone: the role of overlooked endolithic microbiomes in reef coral health. The ISME Journal, 14(2): 325–334, doi: 10.1038/s41396-019-0548-z

Qin Zhenjun, Yu Kefu, Liang Jiayuan, et al. 2020. Significant changes in microbial communities associated with reef corals in the southern South China Sea during the 2015/2016 global-scale coral bleaching event. Journal of Geophysical Research: Oceans, 125(7): e2019JC015579, doi: 10.1029/2019JC015579

Quintanilla E, Rodrigues C F, Henriques I, et al. 2022. Microbial associations of abyssal gorgonians and anemones (>4,000 m Depth) at the Clarion-Clipperton Fracture Zone. Frontiers in Microbiology, 13: 828469, doi: 10.3389/fmicb.2022.828469

Raghukumar C, Ravindran J. 2012. Fungi and their role in corals and coral reef ecosystems. In: Raghukumar C, ed. Biology of Marine Fungi. Berlin, Heidelberg: Springer, 89–113

Raina J B, Tapiolas D, Willis B L, et al. 2009. Coral-associated bacteria and their role in the biogeochemical cycling of sulfur. Applied and Environmental Microbiology, 75(11): 3492–3501, doi: 10.1128/AEM.02567-08

Ricci F, Fordyce A, Leggat W, et al. 2021. Multiple techniques point to oxygenic phototrophs dominating the *Isopora palifera* skeletal microbiome. Coral Reefs, 40(2): 275–282, doi: 10.1007/s00338-021-02068-z

Ricci F, Rossetto Marcelino V, Blackall L L, et al. 2019. Beneath the surface: community assembly and functions of the coral skeleton microbiome. Microbiome, 7(1): 159, doi: 10.1186/s40168-019-0762-y

Ritchie K B. 2006. Regulation of microbial populations by coral surface mucus and mucus-associated bacteria. Marine Ecology Progress Series, 322: 1–14, doi: 10.3354/meps322001

Sangsawang L, Casareto B E, Ohba H, et al. 2017. ^{13}C and ^{15}N assimilation and organic matter translocation by the endolithic community in the massive coral *Porites lutea*. Royal Society Open Science, 4(12): 171201, doi: 10.1098/rsos.171201

Santos H F, Carmo F L, Duarte G, et al. 2014. Climate change affects key nitrogen-fixing bacterial populations on coral reefs. The ISME Journal, 8(11): 2272–2279, doi: 10.1038/ismej.2014.70

Savary R, Barshis D J, Voolstra C R, et al. 2021. Fast and pervasive transcriptomic resilience and acclimation of extremely heat-tolerant coral holobionts from the northern Red Sea. Proc Natl Acad Sci USA, 118(19): e2023298118, doi: 10.1073/pnas.2023298118

Schloss P D. 2009. A high-throughput DNA sequence aligner for microbial ecology studies. PLoS ONE, 4(12): e8230, doi: 10.1371/journal.pone.0008230

Schloss P D, Gevers D, Westcott S L. 2011. Reducing the effects of PCR amplification and sequencing artifacts on 16S rRNA-based studies. PLoS ONE, 6(12): e27310, doi: 10.1371/journal.pone.0027310

Sharp K H, Distel D, Paul V J. 2012. Diversity and dynamics of bacterial communities in early life stages of the Caribbean coral *Porites astreoides*. The ISME Journal, 6(4): 790–801, doi: 10.1038/ismej.2011.144

Shashar N, Stambler N. 1992. Endolithic algae within corals - life in an extreme environment. Journal of Experimental Marine Biology and Ecology, 163(2): 277–286, doi: 10.1016/0022-0981(92)90055-F

Shnit-Orland M, Sivan A, Kushmaro A. 2012. Antibacterial activity of *Pseudoalteromonas* in the coral holobiont. Microbial Ecology, 64(4): 851–859, doi: 10.1007/s00248-012-0086-y

Suh S O, Blackwell M, Kurtzman C P, et al. 2006. Phylogenetics of Saccharomycetales, the ascomycete yeasts. Mycologia, 98(6): 1006–1017, doi: 10.1080/15572536.2006.11832629

Sun Zhen, Li Guoping, Wang Chengwei, et al. 2014. Community dynamics of prokaryotic and eukaryotic microbes in an estuary reservoir. Scientific Reports, 4(1): 6966, doi: 10.1038/srep06966

Sweet M J, Croquer A, Bythell J C. 2011. Bacterial assemblages differ between compartments within the coral holobiont. Coral Reefs, 30(1): 39–52, doi: 10.1007/s00338-010-0695-1

Tang Kaihao, Zhan Waner, Zhou Yiqing, et al. 2020. Antagonism between coral pathogen *Vibrio coralliilyticus* and other bacteria in the gastric cavity of scleractinian coral *Galaxea fascicularis*. Science China Earth Sciences, 63(1): 157–166, doi: 10.1007/s11430-019-9388-3

Teeling H, Fuchs B M, Becher D, et al. 2012. Substrate-controlled succession of marine bacterioplankton populations induced by a phytoplankton bloom. Science, 336(6081): 608–611, doi: 10.1126/science.1218344

Thurber R V, Willner-Hall D, Rodriguez-Mueller B, et al. 2009. Metagenomic analysis of stressed coral holobionts. Environmental Microbiology, 11(8): 2148–2163, doi: 10.1111/j.1462-2920.2009.01935.x

Tiedje J M. 1988. Ecology of denitrification and dissimilatory nitrate reduction to ammonium. In: Zehnder AJB, ed. Biology of Anaerobic Microorganisms. New York, NY: John Wiley and Sons, 179–244

Toju H, Tanabe A S, Yamamoto S, et al. 2012. High-coverage ITS primers for the DNA-based identification of ascomycetes and basidiomycetes in environmental samples. PLoS ONE, 7(7): e40863, doi: 10.1371/journal.pone.0040863

Torda G, Donelson J M, Aranda M, et al. 2017. Rapid adaptive responses to climate change in corals. Nature Climate Change, 7(9): 627–636, doi: 10.1038/nclimate3374

Van Oppen M J H, Blackall L L. 2019. Coral microbiome dynamics, functions and design in a changing world. Nature Reviews Microbiology, 17(9): 557–567, doi: 10.1038/s41579-019-0223-4

Wang Yanan, Shao Changlun, Zheng Caijuan, et al. 2011. Diversity and antibacterial activities of fungi derived from the gorgonian *Echinogorgia rebekka* from the South China Sea. Marine Drugs, 9(8): 1379–1390, doi: 10.3390/md9081379

Wang Wenhuan, Yu Kefu, Wang Yinghui. 2016. A review on the research of coral reefs in the Weizhou Island, Beibu Gulf. Tropical Geography (in Chinese), 36(1): 72–79, doi: 10.13284/j.cnki.rddl.002806

Wegley L, Edwards R, Rodriguez-Brito B, et al. 2007. Metagenomic analysis of the microbial community associated with the coral *Porites astreoides*. Environmental Microbiology, 9(11): 2707–2719, doi: 10.1111/j.1462-2920.2007.01383.x

Weiler B A, Verhoeven J T P, Dufour S C. 2018. Bacterial communities in tissues and surficial mucus of the cold-water coral *Paragorgia arborea*. Frontiers in Marine Science, 5: 378, doi: 10.3389/fmars.2018.00378

Williams A D, Brown B E, Putchim L, et al. 2015. Age-related shifts in bacterial diversity in a reef coral. PLoS ONE, 10(12): e0144902, doi: 10.1371/journal.pone.0144902

Work T M, Aeby G S. 2014. Microbial aggregates within tissues infect a diversity of corals throughout the Indo-Pacific. Marine Ecology Progress Series, 500: 1–9, doi: 10.3354/meps10698

Xu Nan, Tan Guangcai, Wang Hongyuan, et al. 2016. Effect of biochar additions to soil on nitrogen leaching, microbial biomass and bacterial community structure. European Journal of Soil Biology, 74: 1–8, doi: 10.1016/j.ejsobi.2016.02.004

Xu Wei, Guo Shuangshuang, Gong Linfeng, et al. 2018. Phylogenetic survey and antimicrobial activity of cultivable fungi associated with five scleractinian coral species in the South China Sea. Botanica Marina, 61(1): 75–84, doi: 10.1515/bot-2017-0005

Yang Shan-Hua, Lee S T M, Huang Chang-Rung, et al. 2016. Prevalence of potential nitrogen-fixing, green sulfur bacteria in the skeleton of reef-building coral *Isopora palifera*. Limnology and Oceanography, 61(3): 1078–1086, doi: 10.1002/lno.10277

Yang Sung-Yin, Lu Chih-Ying, Tang Sen-Lin, et al. 2020. Effects of ocean acidification on coral endolithic bacterial communities in *Isopora palifera* and *Porites lobata*. Frontiers in Marine Science, 7: 603293, doi: 10.3389/fmars.2020.603293

Yang Shan-Hua, Tandon Kshitij, Lu Chih-Ying, et al. 2019. Metagenomic, phylogenetic, and functional characterization of predominant endolithic green sulfur bacteria in the coral *Isopora palifera*. Microbiome, 7(1): 3, doi: 10.1186/s40168-018-0616-z

Yu Wanjun, Wang Wenhuan, Yu Kefu, et al. 2019. Rapid decline of a relatively high latitude coral assemblage at

Weizhou Island, northern South China Sea. Biodiversity and Conservation, 28(14): 3925–3949, doi: 10.1007/s10531-019-01858-w

Zaneveld J R, Mcminds R, Vega Thurber R. 2017. Stress and stability: applying the Anna Karenina principle to animal microbiomes. Nature Microbiology, 2(9): 17121, doi: 10.1038/nmicrobiol.2017.121

Zhang Ning, Castlebury L A, Miller A N, et al. 2006. An overview of the systematics of the Sordariomycetes based on a four-gene phylogeny. Mycologia, 98(6): 1076–1087, doi: 10.1080/15572536.2006.11832635

Zhang Xuwang, Ji Zhe, Shao Yating, et al. 2020. Seasonal variations of soil bacterial communities in *Suaeda* wetland of Shuangtaizi River estuary, Northeast China. Journal of Environmental Sciences, 97: 45–53, doi: 10.1016/j.jes.2020.04.012

Zhang Huiling, Yu kefu, Shi Qi, et al. 2014. Sea surface temperature variations during the Mid-Late Holocene reconstructed by Porites coral growth rates in the Xisha Islands. Quaternary Sciences (in Chinese), 34(6): 1296–1305, doi: 10.3969/j.issn.1001-7410.2014.06.19

Ziegler M, Roik A, Porter A, et al. 2016. Coral microbial community dynamics in response to anthropogenic impacts near a major city in the central Red Sea. Marine Pollution Bulletin, 105(2): 629–640, doi: 10.1016/j.marpolbul.2015.12.045

Zou Renlin. 2001. Fauna Sinica-Hermatypic coral (in Chinese). Beijing: Science Press

Supplementary information:

Figure S1. The Ace, Sobs, Shannon-Wiener, and Simpson diversity indices of associated bacteria based on ASV level in coral polyp and skeleton between the Bombay Reef and Weizhou Island in the South China Sea (SCS). The “SU_Po” “SU_Sk” “TR_Po” “TR_Sk” represent “coral polyp in subtropical CRR” “coral skeleton in subtropical CRR” “coral polyp in tropical CRR” “coral skeleton in tropical CRR”, respectively. The red asterisks “*” “**” and “***” represent “$0.01 < p < 0.05$” “$0.001 < p < 0.01$” and “$p < 0.001$”, respectively.

Figure S2. The Ace, Sobs, Shannon-Wiener, and Simpson diversity indices of associated archaea based on ASV level in coral polyp and skeleton between the Bombay Reef and Weizhou Island in the SCS.

Figure S3. The Ace, Sobs, Shannon-Wiener, and Simpson diversity indices of associated fungi based on ASV level in coral polyp and skeleton between the Bombay Reef and Weizhou Island in the SCS.

Figure S4. The correlation among environmental factors, sampling areas, and ASV of coral associated bacteria, archaea, and fungi based on redundancy analysis (RDA). a. bacteria-ASV, b. archaea-ASV, c. fungi-ASV.

Table S1. Data of seawater temperature, DIN, SRP, DO, pH, salinity, and transparency in the Bombay Reef and Weizhou Island.

Table S2. Sample information of associated bacteria including number of sequences and diversity indicated by the Shannon-Wiener, Simpson, Ace and Chao indices of Coelastrea palauensis corals in the Bombay Reef and Weizhou Island.

Table S3. The relative abundance of coral-associated bacterial community of Coelastrea palauensis corals on class level in the Bombay Reef and Weizhou Island.

Table S4. The relative abundance of coral-associated bacterial community of Coelastrea palauensis corals on genus level in the Bombay Reef and Weizhou Island.

Table S5. Sample information of associated archaea including number of sequences and diversity indicated by the Shannon-Wiener, Simpson, Ace and Chao indices of Coelastrea palauensis corals in the Bombay Reef and Weizhou Island.

Table S6. The relative abundance of coral-associated archaeal community of Coelastrea palauensis corals on class level in the Bombay Reef and Weizhou Island.

Table S7. The relative abundance of coral-associated archaeal community of Coelastrea palauensis corals on genus level in the Bombay Reef and Weizhou Island.

Table S8. Sample information of associated fungi including number of sequences and diversity indicated by the Shannon-Wiener, Simpson, Ace and Chao indices of Coelastrea palauensis corals in the Bombay Reef and Weizhou Island.

Table S9. The relative abundance of coral-associated fungal community of Coelastrea palauensis corals on class level in the Bombay Reef and Weizhou Island.

Table S10. The relative abundance of coral-associated fungal community of Coelastrea palauensis corals on genus level in the Bombay Reef and Weizhou Island.

The supplementary information is available online at https://doi.org/10.1007/s13131-025-2495-z and http://www.aosocean.com/. The supplementary information is published as submitted, without typesetting or editing. The responsibility for scientificaccuracy and content remains entirely with the authors

BMC Microbiology

RESEARCH Open Access

Coral microbiome in estuary coral community of Pearl River Estuary: insights into variation in coral holobiont adaptability to low-salinity conditions

Mengling Lan[1†], Kaixiang Gao[1†], Zhenjun Qin[1*], Zhanhong Li[1], Ru Meng[1], Lifei Wei[1], Biao Chen[1], Xiaopeng Yu[1], Lijia Xu[3], Yongzhi Wang[3] and Kefu Yu[1,2*]

Abstract

Background Low salinity is a crucial environmental stressor that affects estuarine coral ecosystems considerably. However, few studies have focused on the effects of low-salinity conditions on coral-associated microorganisms and the adaptability of coral holobionts.

Methods We explored the community structure of coral symbiotic Symbiodiniaceae and associated bacteria in low-salinity conditions using samples of six coral species from the Pearl River Estuary and analyzed the adaptability of coral holobionts in estuaries.

Results The symbiotic Symbiodiniaceae of all six studied coral species were dominated by *Cladocopium,* but, the Symbiodiniaceae subclades differed among these coral species. Some coral species (e.g., *Acropora solitaryensis*) had a high diversity of symbiotic Symbiodiniaceae but low Symbiodiniaceae density, with different adaptability to low-salinity stress in the Pearl River Estuary. Other coral species (e.g., *Plesiastrea versipora*) potentially increased their resistance by associating with specific Symbiodiniaceae subclades and with high Symbiodiniaceae density under low-salinity stress. The microbiome associated with the coral species were dominated by *Proteobacteria*, *Chloroflexi*, and *Bacteroidetes*; however, its diversity and composition varied among coral species. Some coral species (e.g., *Acropora solitaryensis*) had a high diversity of associated bacteria, with different adaptability owing to low-salinity stress. Other coral species (e.g., *Plesiastrea versipora*) potentially increased their resistance by having minority bacterial dominance under low-salinity stress.

Conclusions High Symbiodiniaceae density and high bacterial diversity may be conducive to increase the tolerance of coral holobiont to low-salinity environments. Different coral species have distinct ways of adapting to low-salinity stress, and this difference is mainly through the dynamic regulation of the coral microbiome by corals.

Keywords Coral holobionts, Associated bacteria, Symbiotic Symbiodiniaceae, Low-salinity stress, Microbial community variation

[†]Mengling Lan and Kaixiang Gao contributed equally to this work.

*Correspondence:
Zhenjun Qin
qzj_gxu@163.com
Kefu Yu
kefuyu@scsio.cn
Full list of author information is available at the end of the article

© The Author(s) 2025. **Open Access** This article is licensed under a Creative Commons Attribution-NonCommercial-NoDerivatives 4.0 International License, which permits any non-commercial use, sharing, distribution and reproduction in any medium or format, as long as you give appropriate credit to the original author(s) and the source, provide a link to the Creative Commons licence, and indicate if you modified the licensed material. You do not have permission under this licence to share adapted material derived from this article or parts of it. The images or other third party material in this article are included in the article's Creative Commons licence, unless indicated otherwise in a credit line to the material. If material is not included in the article's Creative Commons licence and your intended use is not permitted by statutory regulation or exceeds the permitted use, you will need to obtain permission directly from the copyright holder. To view a copy of this licence, visit http://creativecommons.org/licenses/by-nc-nd/4.0/.

Introduction

Coral reefs, known as the "rainforests of the ocean," are distributed in 110 countries and regions worldwide, accounting for approximately 0.17–0.5% of the global ocean and providing habitat for approximately 30% of marine organisms [1, 2]. The association between coral hosts and their microbiome is the basis for coral growth and reef development [3]. Coral holobionts include cnidarian polyps, bacteria, Symbiodiniaceae, archaea, fungi, and other microorganisms [4, 5]. Symbiodiniaceae are critical microorganisms in coral holobionts that use light energy for photosynthesis and provide fixed organic carbon to the coral host [6]. Symbiodiniaceae can utilize the metabolic waste produced by the coral host to replenish its nitrogen, phosphorus, and other vital nutrients [7]. Community-associated bacterial communities play key roles in coral holobionts, including nitrogen [8, 9], carbon [10], sulfur [11, 12], phosphorus fixation [13], intrametallic homeostasis [13], tissue repair [13], and antibiotic production [14]. Many coral-associated bacteria also protect corals from invasion by pathogens and other exogenous bacteria by secreting antibiotics [14, 15].

Corals are generally considered stenohaline, with limited ability to regulate osmotic pressure and adapt to or survive salinity changes [16]. Salinity is a critical environmental factor affecting their growth and distribution, and the suitable salinity range for growth is generally 32–40‰ [17]. Changes in salinity due to climate change may affect the physiology and metabolism of corals [18–20]. The corals have poor ability to regulate cellular osmotic pressure [21]. A short-term decline in salinity leads to significant changes in cellular respiration and photosynthesis in the coral symbiont Symbiodiniaceae [22]. Freshwater runoff is a major cause of coral mortality in estuarine coral reefs, particularly in those close to major river systems [22].

Environmental changes caused by global warming and destructive anthropogenic activity exacerbate damage to coral reef ecosystems and predispose coral holobionts to dysbiosis [23, 24], leading to high susceptibility to infections by opportunistic pathogens and coral mortality. Estuarine ecosystems are characterized by complex and variable environments, high biodiversity and productivity, and a high degree of human disturbance [25]. Global climate change has led to an unusual increase in extreme rainfall events in multiple regions [26–28], resulting in marine organisms frequently experiencing low-salinity stress in estuarine regions. Low salinity is one of the causes of coral bleaching. Many studies have explored the effects of low salinity on the physiological performance of the early stages of coral; for example, low salinity decreases coral larval recruitment and growth rates [29–31]. Low salinity may affect the physiological and biochemical processes, cellular changes, microbiome alterations, as well as the reproductive and survival capabilities of corals [32–34]. Low salinity stress can disrupt the symbiotic relationship within the coral holobiont, influencing the adaptability and stability of the coral holobiont [22]. In conclusion, Low-salinity stress can severely impact the growth, reproduction, photosynthesis, and respiration of corals, impair the normal functions of cells, and pose a serious threat to the health of corals [22, 35].

The sea section of the Pearl River Estuary in Guangdong represents the estuary of the Pearl River, the second largest river in China in annual runoff. Facing the South China Sea, the Pearl River Estuary is a typhoon-prone area and is susceptible to storm surges and flooding outbreaks, resulting in a large influx of freshwater into the estuary [36]. Corals in the Pearl River Estuary are affected by the year-round influx of freshwater. In the summer of 2022, record-breaking pre-flood rainfall in South China was lasted from May to June, resulting in a severe coral bleaching event in the coral communities of the Wanshan Islands in the Pearl River Estuary [37]. However, the effects of low-salinity stress on coral holobionts in the Wanshan Islands, and corals' adaptability to low-salinity environments, are not well studied.

In this study, we aimed to answer two fundamental questions: are there differences in coral microorganisms in the coral communities of the Pearl River Estuary, and how well are the coral holobionts adapted to low salinity. We tested two hypotheses: (1) the compositions of coral microorganisms in the coral communities of the Pearl River Estuary vary in low-salinity conditions when compared with high salinity conditions, and (2) the physiological parameters of corals influence coral adaptability to low-salinity. To answer the two questions, we collected local water quality parameters and the coral symbiotic Symbiodiniaceae density, chlorophyll a (Chl a) content, and microbial diversity throughout the Pearl River Estuary. The findings of this study enhance the understanding of changes in estuarine coral reef communities and facilitate the conservation of estuarine corals and further research.

Experimental procedures

Study area and coral sample collection

The study area was located in the Wanshan Islands, Pearl River Estuary, China (Fig. 1). The Pearl River is the largest river in southern China and comprises Lingdingyang, Jidianmen, Mudianmen, and Huangmaohai. A large amount of freshwater from the Pearl River flows into the South China Sea, resulting in the salinity of seawater in the Pearl River Estuary being lower than the average salinity of seawater. Furthermore, rainstorms decrease seawater salinity in the Pearl River Estuary. In this study, after the

rainstorm, two islands, Pingzhou and Miaowan, from the Pearl River Estuary were used for coral sample collection (Fig. 1). Water parameters, including the seawater surface temperature (SST; °C), surface water dissolved oxygen content (DO; mg/L), and salinity (Sal), were measured around the two islands.

In the Wanshan Islands, the dominant coral genera are, for example, *Plesiastrea*, *Platygyra*, *Porites*, *Montipora*, and *Acropora* [38]. In this study, 36 samples of six representative coral species, *Platygyra daedalea*, *Plesiastrea versipora*, *Acropora solitaryensis*, *Montipora peltiformis*, *Echinophyllia aspera*, and *Galaxea fascicularis*, were collected from around the two islands at water depths of 3–6 m. Among these samples, there are six samples for each coral species. The coral samples were obtained by scuba divers using hammers and chisels. The coral samples were cleaned using artificial sterile seawater (salinity: 35‰) to ensure they were not disturbed by free-living Symbiodiniaceae and fungi. A portion of the coral samples were 20–50 cm^{-2} in size, and Symbiodiniaceae density and chlorophyll a (Chl a) content were determined. The remaining coral samples were cut and placed in 5 mL freezing tubes, immediately snap-frozen, and stored in liquid nitrogen for subsequent experiments. The data related to corals in normal salinity were extracted from existing studies and reanalyzed [39–46]. Relevant data comprised Symbiodiniaceae density, Chl a content, symbiotic Symbiodiniaceae and coral-associated bacteria composition, and diversity of coral-associated bacteria. The data from under normal salinity were compared with those from low-salinity conditions, and their differences were observed.

Coral symbiotic Symbiodiniaceae

Measurement of coral symbiotic Symbiodiniaceae density and Chl a content

Coral tissue was removed using a Waterpik™ (3–5 kgf cm^{-2}) containing 0.22 μm filtered seawater, and the volume of the initial slurry was measured in a graduated cylinder. The slurry was homogenized and resampled into four 3 mL aliquots. The slurry samples were centrifuged for 5 min (6,500 $r{\cdot}min^{-1}$). After discarding the supernatant, the Symbiodiniaceae at the bottom were preserved in 1 mL 5% formaldehyde at 6 °C for 2–4 h before proceeding to the next step of the analysis. Repeated counts of Symbiodiniaceae densities were performed using hemocytometry ($n = 8–12$). The coral surface area was determined based on the correlation between the weight of the aluminum foil and the surface area [47, 48]. In detail, the aluminum foil was pressed to cover the surface of the coral skeleton, and the foil from the covered area was cut and weighted. A 10 × 10 cm piece of aluminum foil was used to confirm the weight of the foil per square centimeter. The surface area of the coral skeleton was calculated using the weight of the foil covering the surface of the coral skeleton and the weight of the foil per square centimeter. Next, 2 mL of the algal solutions were collected thrice from the same sample bottle in 2 mL centrifuge tubes and centrifuged for 5 min (4,000 $r{\cdot}min^{-1}$). The supernatant was slowly removed, 1.5 mL acetone solution was added to the precipitate, and these samples were stored at 4 ℃ for 24 h. The extracted solutions were centrifuged for 5 min (4,000 $r{\cdot}min^{-1}$), and 200 μL of the supernatant was collected to determine the absorbance

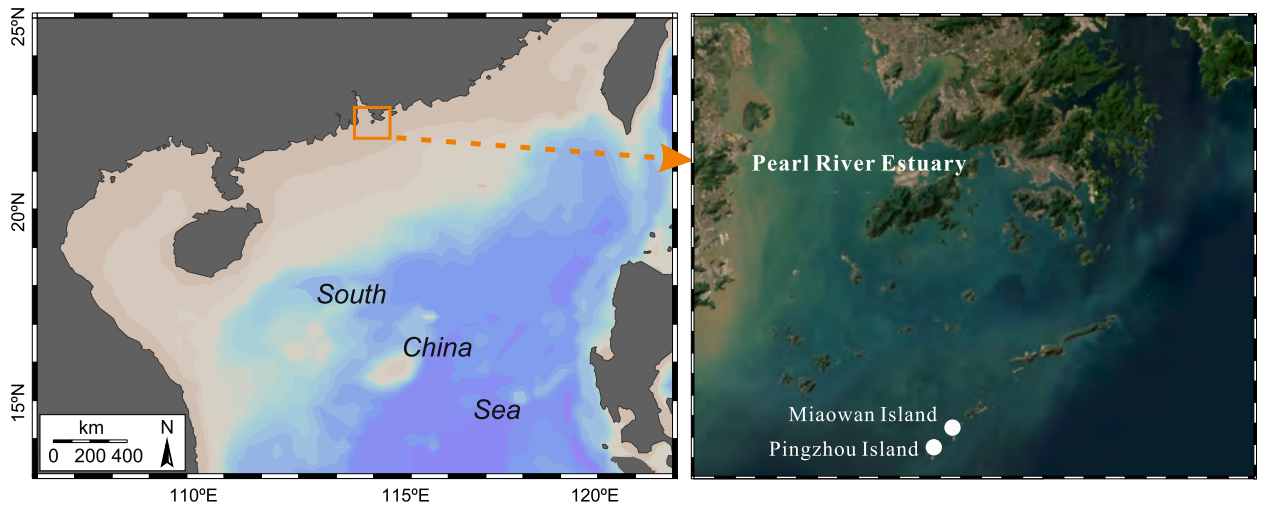


Fig. 1 Sampling site information. Coral samples and local water environmental parameters were collected in two islands of Pingzhou and Miaowan, from the Wanshan Islands, Pearl River Estuary, China

by using a spectrophotometer at wavelengths of 750, 664, 647, and 663 nm. The Mann–Whitney U test was used to analyze the significance of differences between groups ($p < 0.05$).

Total DNA extraction, Polymerase Chain Reaction (PCR) amplification, and Illumina MiSeq sequencing of coral symbiotic Symbiodiniaceae

The total DNA of coral holobionts was extracted as follows: ~ 50 mg of coral tissue and mucus was sampled, and genomic DNA was extracted using the DNeasy® Plant Kit per the manufacturer's instructions. The extracted DNA samples were used as PCR templates after the examination of quality and purity. The quality and concentration of DNA were determined using 1.0% agarose gel electrophoresis and a NanoDrop2000 spectrophotometer (Thermo Scientific, United States) and stored at −80 ℃ for further use. PCR amplification of the Symbiodiniaceae ITS2 region of rDNA was performed using the primers F:5′-GAATTGCAGAACTCCGTG-3′ and R:5′-GGGATCCATATATGCTTAAGTTCAGCGGGGT-3′, with a six-nucleotide barcode unique to each sample [49, 50], and a 50 μL reaction volume PCR amplification was performed. The reaction volume contained ~ 50 ng DNA, 25 μL 2 × Taq Platinum Polymerase Chain Reaction Master Mix (Tiangen, China), 200 nM of each primer, and ddH2O added to achieve the final volume. The reaction was conducted for 5 min at 94 °C, 35 cycles of 30 s at 94 °C, 30 s at 51 °C, and 30 s at 72 °C, with a final extension for 5 min at 72 °C, using an ABI GeneAmp® 9700 thermal cycler [51]. Triplicate PCR products were collected from each sample, purified, and quantified using the AxyPrep DNA Gel Extraction Kit and QuantiFluor™ ST Fluorescence Quantification System for sizes between 301 and 340 bp. Purified amplicons were pooled in equimolar amounts and subjected to paired-end sequencing on an Illumina MiSeq platform according to standard protocols (2 × 300).

Analysis of α-diversity and community composition of coral symbiotic Symbiodiniaceae

Strict quality control and sequence filtering were performed to ensure the accuracy of the results. After short and low-quality sequences were removed by the sequencing company, full-length ITS2 rDNA fragments were obtained by applying the paired-end-sequence amalgamation (PEAR) tool to merge overlapping PE reads to generate ITS2 sequences [52]. After identifying a unique sequence, ITS2 tags were demultiplexed into all samples using the QIIME 2 platform [53]. BLASTn was used to compare all ASV sequences with the ITS2 database [54, 55]. The resulting symbiont ITS2 Symbiodiniaceae subclade counts were combined for downstream statistical analyses. The symbiotic Symbiodiniaceae H′ diversity index was calculated using the R software environment (version 4.2.3) and Bray–Curtis to assess the α-diversity in the symbiotic Symbiodiniaceae composition among coral species. Kruskal–Wallis analysis was performed on the α-diversity data based on different corals. A phylogenetic tree of the Symbiodiniaceae was constructed in MEGA 6 by using the maximum likelihood method (based on the Kimura 2-parameter model) [44, 56]. Raw reads were deposited into the NCBI Sequence Read Archive database (Accession Number: PRJNA1086834).

Coral-associated bacteria

Total DNA extraction, PCR amplification, and Illumina MiSeq sequencing of coral-associated bacteria

Approximately 50 mg of coral tissue and mucus was cut with scissors, and the total genomic DNA was extracted from the coral samples by using the TIANamp Marine Animal DNA Kit per the manufacturer's instructions. The quality and concentration of DNA were determined using 1.0% agarose gel electrophoresis and a NanoDrop2000 spectrophotometer (Thermo Scientific, United States) and stored at −80 ℃ for further use. The total genomic DNA that fulfilled the conditions 1.8 < 260/280 < 2.0 and 260/230 > 2.0 was used as a template. Upstream primers carrying Barcode sequences 338F (5'-ACTCCTACGGGG AGGCAGCAG-3') and 806R (5'-GGACTACHVGGG TWTCTAAT-3') were used with the ABI GeneAmp® 9700 Thermal Cycler for the PCR amplification of the V3–V4 region of the bacterial 16S rRNA gene [48, 57]. An ABI GeneAmp 9700 thermal cycler (Thermo Fisher Scientific, Waltham, MA, United States) was used as a PCR reaction system, and the reactions were conducted under the following conditions: 3 min at 95°C, followed by 35 cycles of 95°C for 30 s, 55°C for 30 s, 72°C for 45 s, and a final extension at 72°C for 10 min. PCRs were run in triplicate per sample, which were conducted using a 20 μL reaction volume of TransGen AP221-02 (TransGen Biotech, Beijing, China) containing: 4 μL 5 × FastPfu Buffer (TransGen Biotech, Beijing, China), 2 μL 2.5 mM dNTPs, 0.8 μL (5 μm) forward primer, 0.8 μL (5 μm) reverse primer, 0.4 μL FastPfu DNA Polymerase (TransGen Biotech, Beijing, China), 0.2 μL BSA and 10 ng template DNA; the final volume was adjusted to 20 μL using ddH_2O [55]. Next, 2 μL amplified product was collected, and product integrity was determined using 2% agarose gel electrophoresis at a voltage of 115 V for 45 min to confirm whether the fragment size was between 420 and 460 bp. PCR products were purified using PCR Clean-up Kit according to the manufacturer's instructions (Yuhua, China), and Qubit 4.0 (Thermo Fisher Scientific, USA) was used

to detect and quantify the recovered products. The purified PCR products were constructed using NEXTFLEX ® Rapid DNA-SeqKit: (1) split-link (2) Use magnetic bead screening to remove split-self-connected segments; (3) Enrichment of library templates by PCR amplification; (4) The PCR products were recovered by magnetic beads to obtain the final library. Sequencing was performed using the umimaNextseq2000 platform (Majorbio Biopharm Technology Company, Shanghai, China). Raw reads were deposited into the NCBI Sequence Read Archive database (Accession Number: PRJNA1086806).

Analysis of α-diversity and community composition of associated bacteria

Paired reads of the bacterial 16S rRNA gene output from the Illumina MiSeq platform were merged with overlapping PE reads by using PEAR software to obtain the complete 16S rRNA gene V3–V4 region sequence, which allowed for a maximum mismatch ratio of 0.2. The complete 16S rRNA gene V3–V4 region was homogenized to remove average quality scores of < 20 and bases of < 50 bp. Sequence orientation was based on primer sequences with valid sequences from barcode-identified samples. Non-repetitive sequences were extracted using Uparse. Single sequences and chimeras without repeats were removed, and based on the valid ASV data, they were processed and denoised. Next, species were classified to obtain the ASVs of bacterial samples for the assessment and statistical analysis of bacterial diversity and community composition. The SILVA v138 database was used for the identification of bacterial species. Rarefaction curves construction as well as alpha diversity indices were calculated on rarified data set (30,000 sequences for bacteria) using the Mothur (v1.30.2). Alpha diversity indices were compared with Kruskal Wallis test using the stats package in R (v3.3.1). The bacterial community composition was visualized by NMDS based on Bray–Curtis distance, using the Vegan package in R software (version 4.2.3). PERMANOVA was conducted to test for statistically significant differences in community composition among groups [58].

Results

Water parameters of Wanshan Islands, Pearl River Estuary

The water parameters of the Wanshan Islands in the Pearl River Estuary showed that in July 2022, the SST ranged from 29.44 ± 0.07 °C to 29.72 ± 0.08 °C, DO ranged from 6.65 ± 1.46 to 7.84 ± 0.56 mg/L, and salinity ranged from 23.26 ± 0.05‰ to 24.83 ± 1.03‰. Owing to heavy rainfall in the upper reaches of the Pearl River over several days, a large amount of freshwater was imported into the Pearl River Estuary, resulting in low-salinity conditions. In this study, the average salinity of the sampling sites was 24.4 ± 1.1‰, which is much lower than the normal salinity level (30.61–32.39‰) in the Pearl River Estuary [59], indicating that corals are subjected to low-salinity conditions in the Wanshan Islands.

Coral symbiotic Symbiodiniaceae in Wanshan Islands, Pearl River Estuary

Density and Chl a content of coral symbiotic Symbiodiniaceae

The Symbiodiniaceae density significantly differed among the six coral species (Fig. 2A, $p < 0.05$, Table S1). The symbiotic Symbiodiniaceae density assessment results showed that *P. daedalea* had the highest Symbiodiniaceae density ($6.91 \pm 2.07 \times 10^6$ cells/cm^2), and *E. aspera* had the lowest density ($3.31 \pm 0.88 \times 10^6$ cells/cm^2). Thus, the densities of other Symbiodiniaceae coral species were between those of *P. daedalea* and *E. aspera*.

Moreover, there was a significant difference in Chl a content among these coral species ($p < 0.05$). *G. fasciculatis* exhibited the highest Chl a content (14.88 ± 2.19 μg/cm^2), which was much higher than those of the other coral species (Fig. 2B). The lowest Chl a content was 4.55 ± 1.56 μg/cm^2 for *A. solitaryensis*, *M. peltiformis*, *P. versipora*, *P. daedalea*, and *E. aspera*. The Chl a content of *E. aspera* was between that of *A. solitaryensis* and *G. fascicularis*.

Diversity of coral symbiotic Symbiodiniaceae

In this study, 1,535,930 Symbiodiniaceae ITS2 reads were obtained in low-salinity conditions to fulfill the analysis criteria after rigorous screening and quality control. Of the Symbiodiniaceae ASVs, 1,070 valid ASVs were obtained for diversity and community analyses.

The Ace, Chao, Shannon, and Simpson indices for the symbiotic coral Symbiodiniaceae are shown in Fig. 3 and Table S2. The symbiotic Symbiodiniaceae of *E. aspera* had the highest Shannon index (2.09 ± 0.05), and that of *P. daedalea* was the lowest (1.27 ± 0.22). Overall, significant differences were observed in the diversity indices among the six coral species ($p < 0.05$).

Composition of coral symbiotic Symbiodiniaceae

As shown in the composition diagram (Fig. 4), *Cladocopium* was the dominant Symbiodiniaceae among the six coral species (relative abundance > 97%, Table S3). Among them, *A. solitaryensis*, *P. daedalea*, and *G. fascicularis* had similar compositions to Symbiodiniaceae, and the abundance of the dominant *Cladocopium* C1 ranged from 80.4% to 84.5%. The compositions of *P. versipora*, *E. aspera*, and *M. peltiformis* differed from those of *A. solitaryensis*, *P. daedalea*, and *G. fascicularis*. *P.*

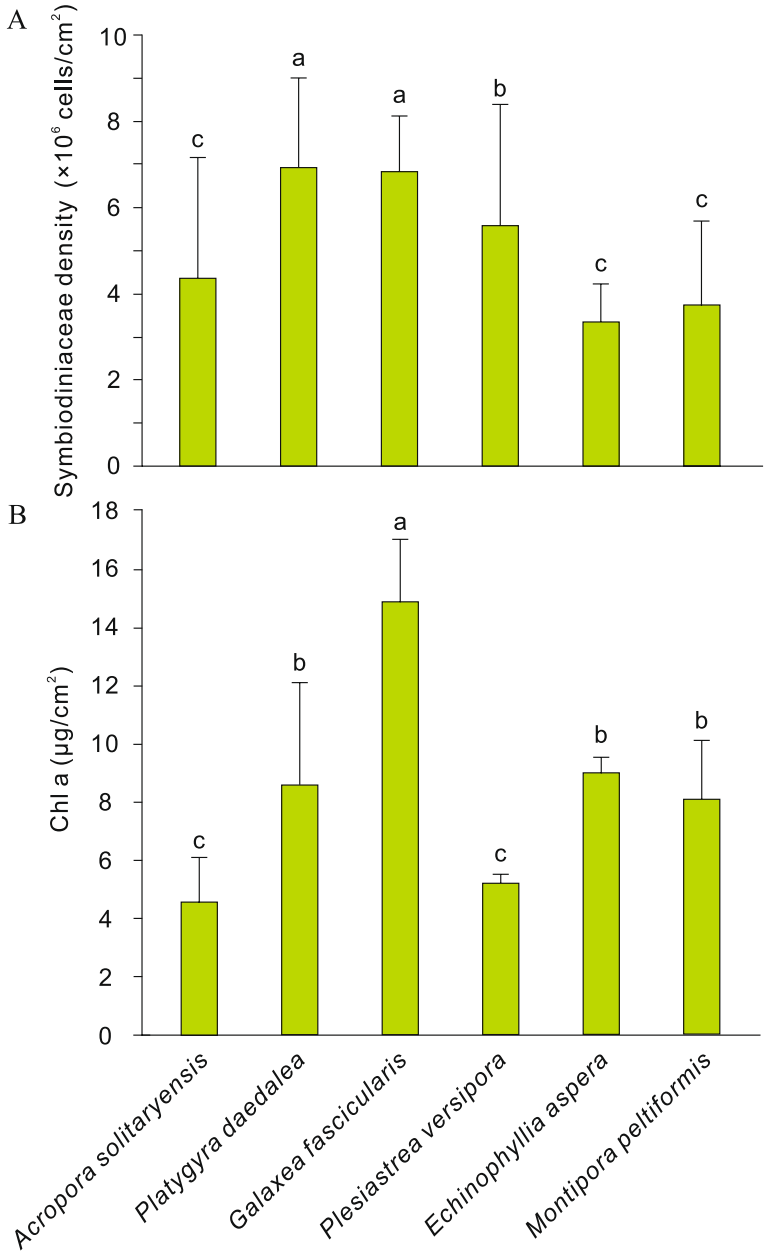


Fig. 2 Symbiodiniaceae density (**a**) and Chl a content (**b**) of six coral species from the Wanshan Islands, Pearl River Estuary. 'a', 'b' and 'c' represent the differences between different corals in Symbiodiniaceae density and Chl a conten, respectively (Mann–Whitney U test, $P < 0.05$)

versipora had the highest percentage of *Cladocopium* C1, and the abundance of *Cladocopium* C1 was lower than that of *A. solitaryensis*, *P. daedalea*, and *G. fascicularis*. *Cladocopium* Cspc, *Cladocopium* C44, and *Cladocopium* C1p were highly abundant (> 5%). The symbiotic Symbiodiniaceae of *E. aspera* had the highest abundance of *Cladocopium* C18 (49.7%), followed by *Cladocopium* C1 (26.4%) and *Cladocopium* C1p, *Cladocopium* C16 (> 5%). *Cladocopium* C3d was dominant in *M. peltiformis* (79.8%). *Cladocopium* C21.11 and *Cladocopium* Cspc also showed a high abundance (> 5%).

A phylogenetic tree of the dominant Symbiodiniaceae subclades in low-salinity conditions was constructed (Fig. 5). Three major groups were suggested for the development of the symbiotic Symbiodiniaceae in six coral species from the Pearl River Estuary. *Cladocopium* C16, *Cladocopium* C21.11, and *Cladocopium* Cspc had close phylogenetic relationships, and the phylogenetic

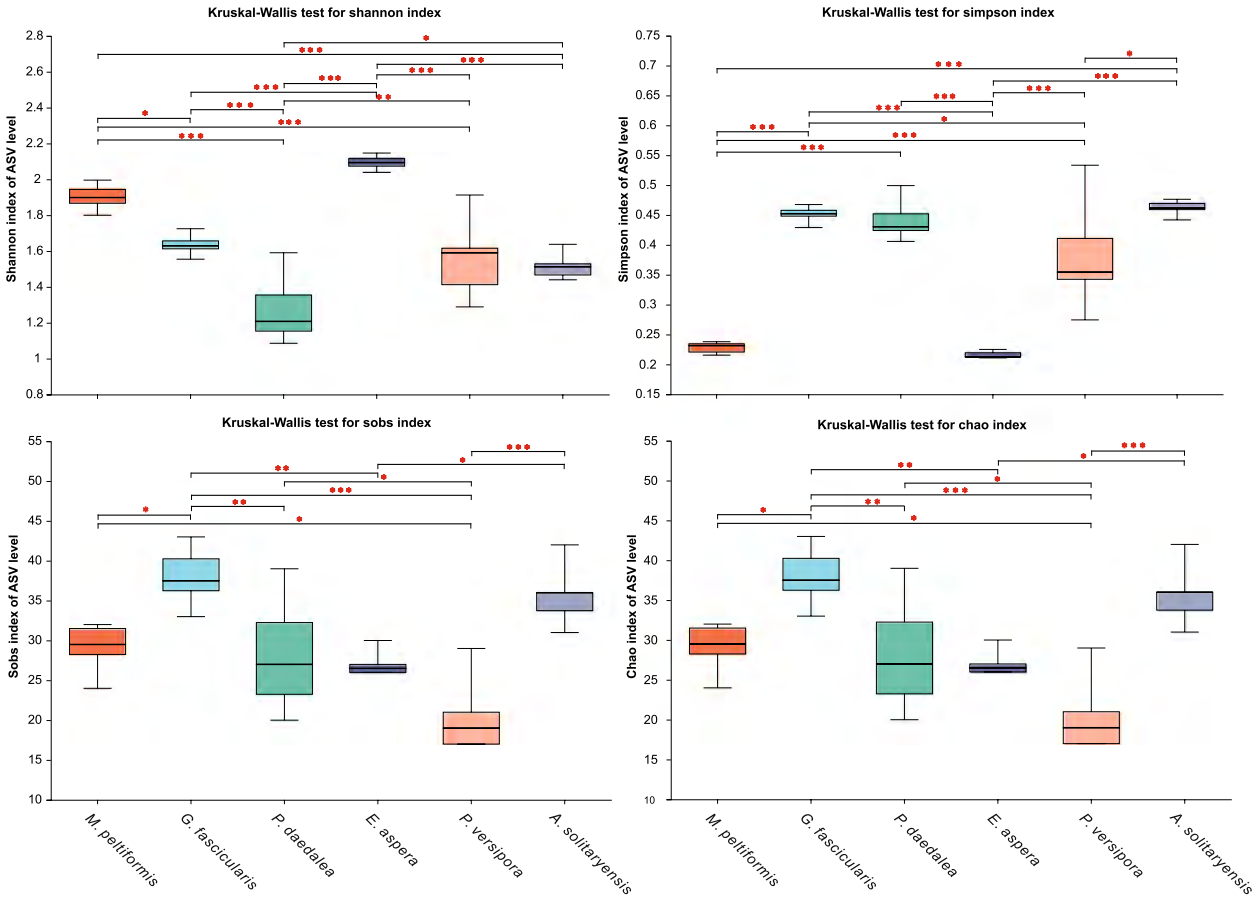


Fig. 3 Diversity indices of coral symbiotic Symbiodiniaceae of six coral species from the Wanshan Islands, Pearl River Estuary. The statistical differences were calculated by the Kruskal–Wallis H Test followed by pairwise testing using the Mann–Whitney U test (*: $0.01 < p < 0.05$; **: $0.001 < p < 0.05$; ***: $p < 0.001$)

relationships of *Cladocopium* C65a, *Cladocopium* C1p, and *Cladocopium* C72 were closer than those of *Cladocopium* C44, *Cladocopium* C1ca, and *Cladocopium* C1. The symbiotic Symbiodiniaceae composition of *M. peltiformis*, including *Cladocopium* C3.14, *Cladocopium* C21.11, *Cladocopium* Cspc, and *Cladocopium* C3d, showed closer phylogenetic relationships. The symbiotic Symbiodiniaceae composition of *A. solitaryensis*, including *Cladocopium* Cspc, *Cladocopium* C72, *Cladocopium* C1p, *Cladocopium* C1p.C45, *Cladocopium* C1ca, *Cladocopium* C1, and *Cladocopium* C78a, showed closer phylogenetic relationships.

Diversity and composition of coral-associated bacteria in Wanshan Islands, Pearl River Estuary

Diversity of coral-associated bacteria

In this study, 1,425,904 reads were obtained from the six coral species after rigorous screening and quality control (Table S4). After excluding archaea, chloroplasts, and mitochondrial sequences, in total, 16,112 valid bacterial ASVs were identified. Per these bacterial ASVs, the Shannon index showed that *A. solitaryensis* had a relatively low level of associated bacterial diversity and that *P. versipora* and *G. fascicularis* had higher levels of associated bacterial diversity (Fig. 6). The Shannon index also showed a significant difference in bacterial community diversity between *P. versipora* and *A. solitaryensis* ($p < 0.001$). The bacterial community diversity of *P. versipora* and *M. peltiformis* also significantly differed ($p < 0.05$). The Simpson diversity index was the opposite of that of the Shannon diversity index. The Ace index statistics showed that *P. versipora* and *G. fascicularis* had the highest levels of total ASVs (Fig. 6), and *A. solitaryensis* had the lowest levels of total bacterial species, which differed from those of *P. versipora* ($p < 0.05$). In normal salinity, the Sobs index and Shannon index of *M. peltiformis* and *Platygyra* were lower than in low-salt conditions. Furthermore, at normal salinity, the Simpson index of *M. peltiformis* and *Platygyra* was higher than that of

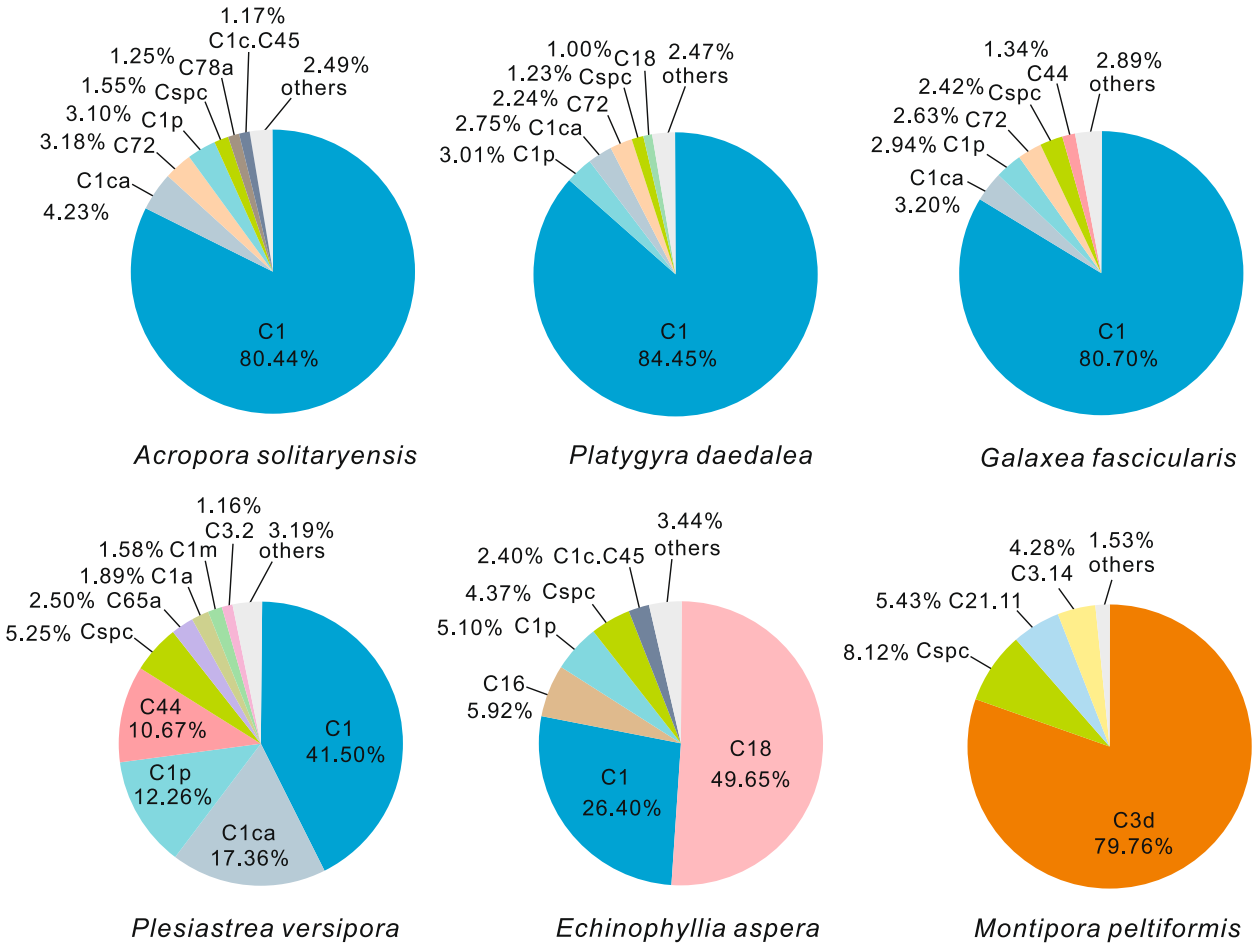


Fig. 4 Composition of symbiotic Symbiodiniaceae in six coral species from the Wanshan Islands, Pearl River Estuary. The Symbiodiniaceae subclades such as C1, C44, and Cspc,were be classified as the *Cladocopium*

low-salinity conditions. These results indicated increased bacterial diversity in corals in low-salinity conditions.

According to the NMDS analysis (Fig. 7), the community composition of the bacteria associated with the six coral species suggested that *E. aspera* differed significantly ($p<0.05$) from the other coral species in associated bacterial community composition. The NMDS analysis also suggested that the associated bacteria community of *P. versipora* differed significantly from those of the other coral species ($p<0.05$). *A. solitaryensis*, *M. peltiformis*, *P. daedalea*, and *G. fascicularis* had similar bacterial communities.

Composition of coral-associated bacteria

At the phylum level, the bacteria associated with *A. solitaryensis* and *P. daedalea* were dominated by Proteobacteria (Fig. 8, Table S5). For *P. versipora* and *E. aspera*, Chloroflexi were the dominant bacteria; other bacteria, such as Proteobacteria, Bacteroidota, and Actinomycetota, also had relatively high abundances. In the cases of *G. fascicularis* and *M. peltiformis*, the dominant bacteria were Proteobacteria, Bacteroidota, and Firmicutes. The bacterial composition of corals in normal salinity differs from that in low-salinity conditions. The bacteria associated with *M. peltiformis* were dominated by Cyanobacteria, with relative abundances of 92.15% at normal salinity. In normal conditions, the relative abundances of γ-proteobacteria (20%), α-proteobacteria (12%), and Cyanobacteria (39%) in the associated bacteria community of *G. fascicularis* were relatively high. The dominant bacteria in both low-salt conditions is Proteobacteria, and the dominant bacteria in normal salinity is Cyanobacteria. For *Platygyra*, Proteobacteria was the dominant phylum, with 71.87% in normal salinity, followed by Firmicutes. This suggests that different corals are affected by low salinity to different degrees and that low-salinity conditions affect the composition of some coral symbiotic bacteria.



Fig. 5 Phylogenetic tree of coral symbiotic Symbiodiniaceae of six coral species from the Wanshan Islands, Pearl River Estuary

At the genus level, we selected the top 30 bacteria in terms of total abundance for plotting. Among these six coral species had high abundances of *Vibrio* (relative abundance: 4.2 ± 4.8%) and Rhodobacteraceae (relative abundance: 3.9 ± 2.6%, Fig. 9, Table S6). *G. fascicularis* had high abundances of *Pseudomonas* (relative abundance: 4.6 ± 2.4%), *Photobacterium* (relative abundance: 4.5 ± 2.4%), and *Pseudoalteromonas* (relative abundance: 4.5 ± 2.4%). *Ruegeria* was observed in *P. daedalea* and *M. peltiformis*, with relative abundances of 2.9 ± 1.9% and 1.0 ± 1.2%, respectively. At the genus level, in normal salinity, the bacteria associated with *M. peltiformis* were dominated by *Synechococcus* CC9902 (89.16%). The dominant genus in *Platygyra* was *Endozoicomonas* (52.30%). The results demonstrated that the dominant genus composition of corals differed significantly between normal salinity and low-salinity conditions (Mann–Whitney U test, $p < 0.05$).

Discussion

Adaptation of coral-Symbiodiniaceae holobionts to the low-salinity in the Pearl River Estuary

Owing to the influences of short-term rainstorms and massive freshwater input, low-salinity conditions endure in the Pearl River Estuary. Low-salinity conditions have significant negative impacts on coral-Symbiodiniaceae holobionts, and coral symbiotic Symbiodiniaceae density decreases in low salinity [22, 60]. The symbiotic Symbiodiniaceae density reflects differences in the adaptability of coral species in low-salinity conditions. For example, *G. fascicularis* can normally survive more than 60 d when exposed to 20‰ salinity [61]; however, the growth rate of *Platygyra acuta* slows when the salinity is < 26‰ and stops at salinities < 22‰ [30]. In low-salinity conditions, Liu et al. [60] found that the Symbiodiniaceae density and Chl a content of *Porites lutea* decreased significantly when the surrounding seawater salinity was < 30‰, and

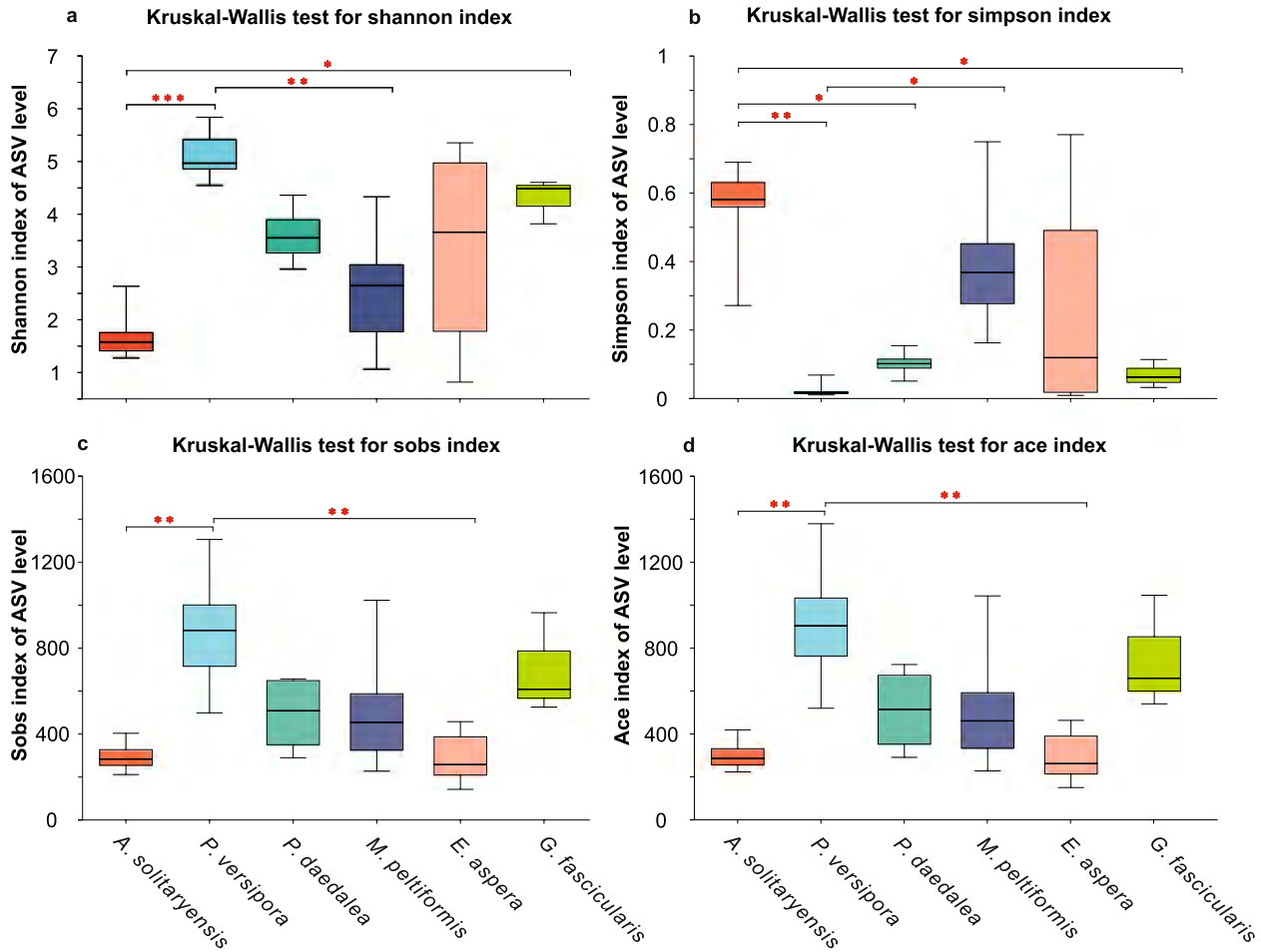


Fig. 6 Diversity indices of coral-associated bacteria of six coral species from the Wanshan Islands, Pearl River Estuary. The statistical differences were calculated by the Kruskal–Wallis H Test followed by pairwise testing using the Mann–Whitney U test (*: $0.01 < p < 0.05$; **: $0.001 < p < 0.05$; ***: $p < 0.001$)

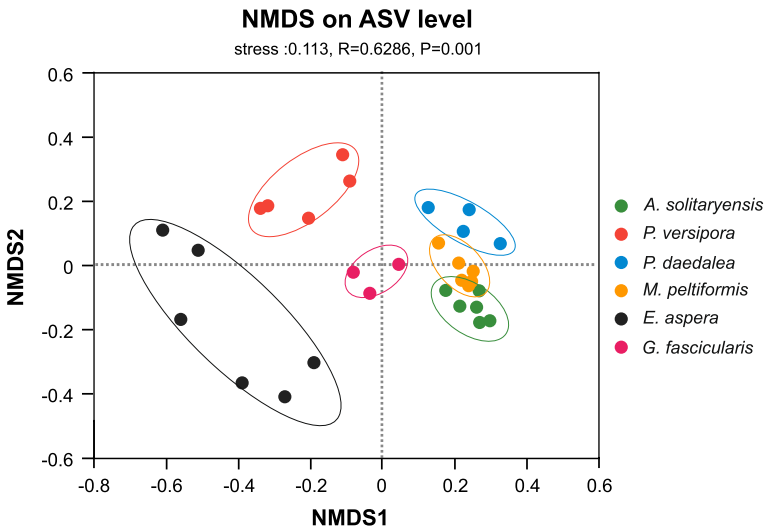


Fig. 7 NMDS analysis of associated bacteria of six coral species from the Wanshan Islands, Pearl River Estuary

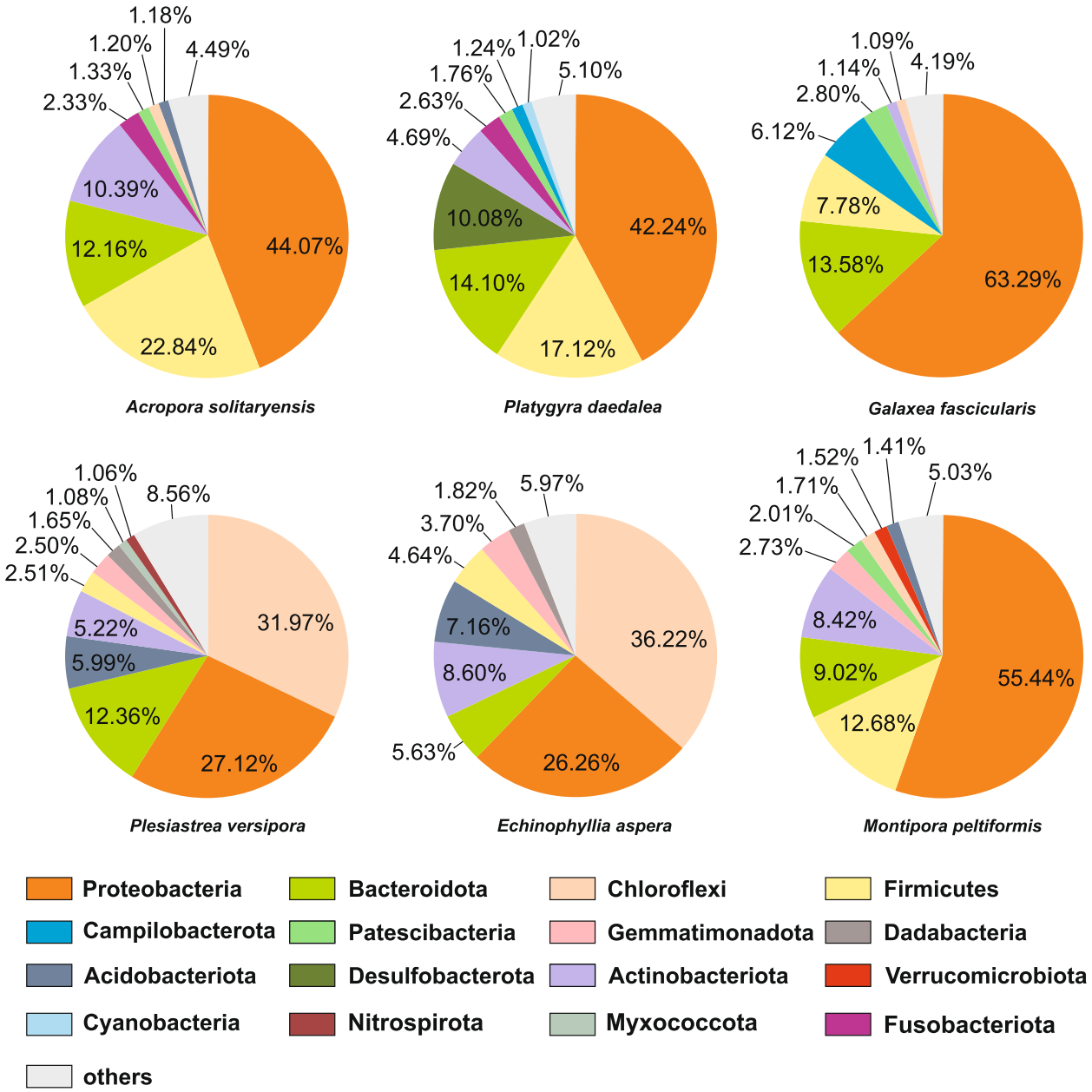


Fig. 8 Composition of coral-associated bacteria at the phylum level in the Wanshan Islands, Pearl River Estuary

the Symbiodiniaceae density and Chl a content decreased dramatically when the salinity decreased from 30‰ to 20‰ until the corals bleached. Similarly, in this study, the density and Chl a content of coral symbiotic Symbiodiniaceae differed significantly in the low-salinity conditions of the estuary, with some corals showing high Symbiodiniaceae densities and Chl a content, such as *G. fascicularis*; other corals showed low Symbiodiniaceae densities, such as *E. aspera*. The Symbiodiniaceae density of *P. versipora* was 6.8×10^6 cells/cm^2 [39], and that of *M. peltiformis* was 4×10^6 cells/cm^2 at normal salinity [40]. Both corals exhibited a decrease in Symbiodiniaceae density in low-salinity conditions. The Chl a content of *A. solitaryensis* was 15.21 μg/cm^2, and that of *M. peltiformis* was approximately 11 μg/cm^2 at normal salinity [41, 42]. In this study, the Chl a content of *A. solitaryensis* was 2.43 μg/cm^2, and that of *M. peltiformis* was 8.09 μg/cm^2 in low-salinity conditions. Both corals showed decreases in Chl a content. These findings suggest that low-salinity conditions affect Symbiodiniaceae density and Chl a

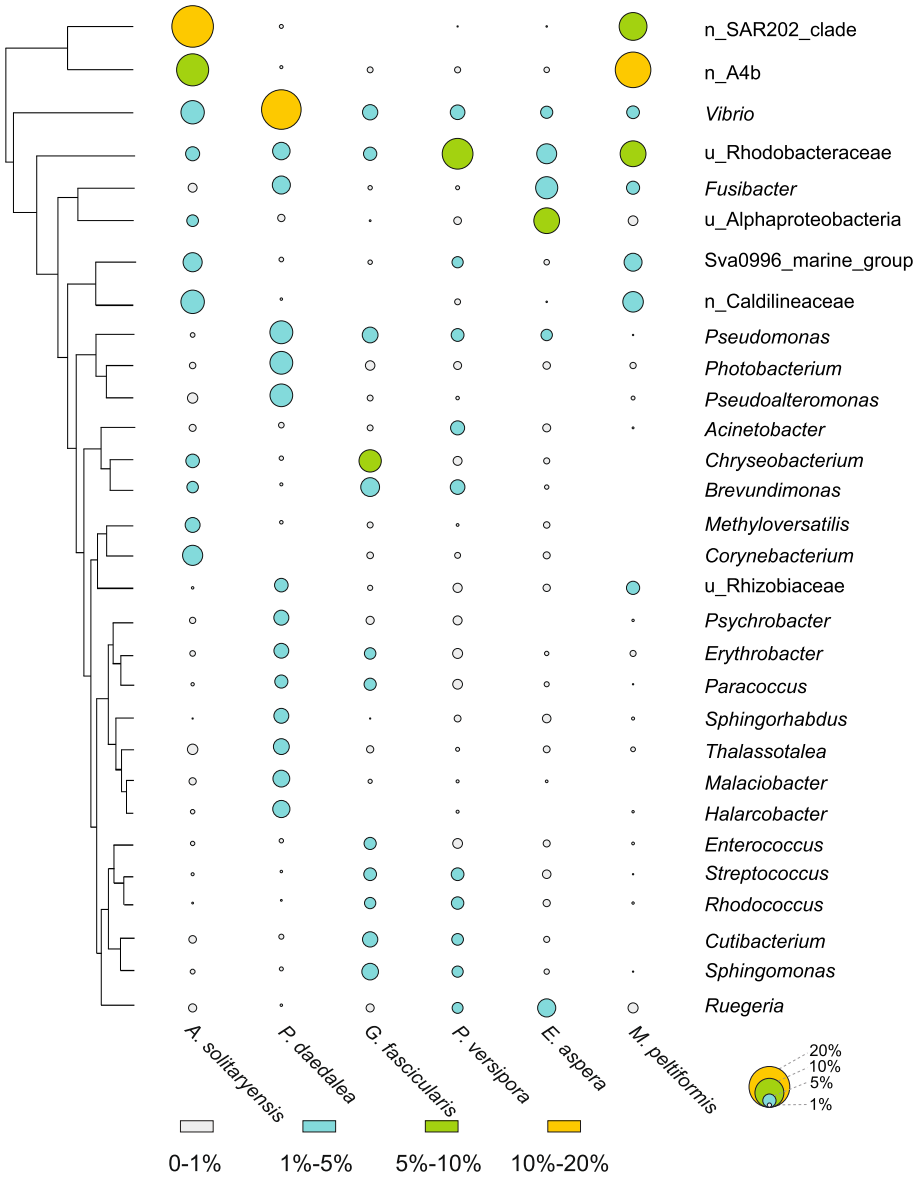


Fig. 9 Associated bacterial composition at the genus level of six coral species in the Wanshan Islands, Pearl River Estuary

content, and differences in Symbiodiniaceae density and Chl a content could be responsible for the different adaptations of corals to low-salinity conditions.

Environmental factors drive various types of and different environmental influences in Symbiodiniaceae coral holobionts [62, 63]. Studies have found that the dominant symbiotic Symbiodiniaceae is closely related to the tolerance of coral-Symbiodiniaceae holobionts to environmental stress [64–66]. Symbiodiniaceae subclades confer different physiological characteristics and environmental tolerances to coral holobionts [65, 67, 68]. In this study, the dominant symbiotic Symbiodiniaceae subclades in all corals were *Cladocopium* C1, excluding *M. peltiformis* and *E. aspera*. Some corals with *Cladocopium* C1-dominant species had a lower percentage of *Cladocopium* C1 than corals in normal salinity conditions, for example, *P. versipora* with 75% in normal salinity and 41.5% in this experiment [43], and some coral *Cladocopium* C1 percentage gaps do not vary much, for example, *G. fascicularis*, with approximately 80% in normal and low-salinity conditions [43]. *Cladocopium* C1 is a subclade of Symbiodiniaceae with high photosynthetic efficiency [69]. Under the low-salinity stress, corals may establish a symbiotic relationship with highly photosynthetically

efficient Symbiodiniaceae to maintain the functioning of the calcium carbonate secretion-storage system [70]. However, some of the dominant symbiotic Symbiodiniaceae subclades change from corals between the normal salinity and low-salinity conditions. In normal conditions, for example, the dominant symbiotic Symbiodiniaceae subclades of the *M. peltiformis* were *Cladocopium* C3d, followed by *Cladocopium* C2r [44]. In low-salinity conditions, the dominant symbiotic Symbiodiniaceae subclades were *Cladocopium* C3d, followed by *Cladocopium* Cspc. Notably, some corals were symbiotic with different symbiotic Symbiodiniaceae subclades when experienced low-salinity stress. For example, *Cladocopium* Cspc and C3d were detected from *M. peltiformis* in low salinity conditions, but *Cladocopium* C3d and C2r were detected in normal salinity conditions. Research has observed that *M. peltiformis* has high susceptibility to environmental influences [45]. The flexible changes in the composition of symbiotic Symbiodiniaceae subclades may be conducive *M. peltiformis* to survive and adapt to low-salinity stress.

Coral symbiotic Symbiodiniaceae types are typically determined by environmental selection and co-evolution [71]. The results of this study showed that among the six coral species, some of them differed significantly in their Symbiodiniaceae diversity and composition. Coral holobionts can regulate physiological and ecological characteristics (e.g., coral host stress, Symbiodiniaceae densities, Symbiodiniaceae subclades, and bacterial communities) to adapt to external environmental changes [72, 73]. The results suggest that different corals adapt to low salinity by regulating their symbiotic relationship with Symbiodiniaceae. Based on the phylogenetic tree of Symbiodiniaceae, two typical symbiotic Symbiodiniaceae species selected by corals survived in low-salinity conditions. For example, the Symbiodiniaceae subclades of *M. peltiformis* belong to similar branches of the phylogenetic tree, and those of *A. solitaryensis* are distributed throughout the phylogenetic tree. This suggests that symbiotic Symbiodiniaceae may be regulated by corals in low-salinity conditions. Some coral species establish symbiotic relationships with specific Symbiodiniaceae subclades (e.g., *Cladocopium* C1) to increase their photosynthetic rate, and other coral species establish symbiotic relationships with multiple Symbiodiniaceae subclades to enhance their Symbiodiniaceae diversity and tolerance to low-salinity conditions.

Adaptation of coral-bacterial holobionts to low-salinity Pearl River Estuary condition

Salinity is a key factor influencing the diversity and composition of bacterial communities in coastal corals [74, 75]. Microbiome dynamics are linked to coral environmental tolerance [76]. And a high diversity of the bacterial community may contribute to niche complementation and/or functional redundancy [23, 77]. In our study, six studied coral species suggested that the bacterial communities associated with each of them showed significant differences in diversity and composition. Specifically, relatively high bacterial diversity was detected in the *P. versipora*, while relatively low bacterial diversity in the *A. solitaryensis*.

Compared with normal salinity environment, bacterial composition of different corals widely changed in low-salinity environment [45, 46]. For example, *M. peltiformis* showed distinct changes in bacterial composition. At the phylum level, the bacteria associated with *M. peltiformis* were dominated by Cyanobacteria, with relative abundances of 92.15% in normal salinity environment. At the genus level, the bacteria associated with *M. peltiformis* were dominated by *Synechococcus* CC9902 (89.16%) [45]. However, in low-salinity conditions, the dominant ASVs were Proteobacteria at the phylum level. At the genus level, u_Rhodobacteraceae were the dominant bacteria. *Synechococcus* spp. is conducive coral holobiont to nitrogen fixation [78] and photosynthesis [79], indicating their potential roles in the hologenomic nutrient cycling of corals and the health state of coral hosts. Rhodobacteraceae may also enhance the resilience of corals by absorbing DMSP from Symbiodiniaceae and producing antibacterial compounds against pathogens [80]. Evidently, low salinity can affect changes in the bacterial composition of corals, which further impacts the health of coral holobionts [45]. In contrast, the bacterial composition of *G. fascicularis* was relatively in stable. Under normal-salinity conditions, the relative abundances of γ-Proteobacteria, α-Proteobacteria, and Cyanobacteria of *G. fascicularis* were 20%, 12%, and 39% respectively, remaining at a relatively high level [46]. Under low-salinity environment, Proteobacteria becomes were also the dominant bacteria, which is similar to the bacterial composition under normal conditions. This indicates a potential variation between the stability of the microbiome and the susceptibility to bleaching among coral species. The bacterial diversity might be important factors in coral adaptability to low-salinity conditions. Some coral species may survive better than others in low-salinity conditions by maintaining a high level of bacterial diversity. Coral microbiome with high diversity may have high physiological and ecological acclimatization to low-salinity conditions [81].

Community-associated bacterial communities have high flexibility and diverse functions and are closely related to the health of coral symbiotic functionaries. For

example, Proteobacteria and Bacteroidetes have a high tolerance to salinity stress [82]. In this study, bacteria from Proteobacteria and Bacteroidetes tended to dominate the coral-associated communities, and their insensitivity to salinity allowed these bacteria to survive better than other bacteria in low-salinity conditions. Rhodobacteraceae were highly abundant in all six coral species, and their ability to grow through photosynthesis, metabolize CO_2, and fix nitrogen plays an important role in the carbon and nitrogen cycles of marine ecosystems [83].

In this study, additional differences were observed in the relative abundances of bacterial phyla and genera, reflecting varying adaptability among coral species in low-salinity conditions. Coral-associated bacteria may be related to coral growth, nutrient metabolism, the immune system, antioxidant capacity, resilience, and tolerance [84, 85]. In our study, the coral microbial communities in low-salinity areas revealed that *Pseudoalteromonas* was extremely abundant in some corals, such as *P. daedalea*. *Pseudoalteromonas* has been shown to have significant antagonistic effects on various pathogens [86]. In this study, *Pseudoalteromonas* and *Vibrio* were detected in the composition of coral-associated bacteria. *Pseudoalteromonas* may be conducive to inhibit the growth and reproduction of *Vibrio* via antagonism, potentially decreasing the risk of disease in corals [87]. Furthermore, a high abundance of *Ruegeria* was found in *P. daedalea* and *M. peltiformis*. *Ruegeria* is a potential probiotic coral that produces antibiotics that can inhibit the growth of *Vibrio* [88]. High abundance of *Vibrio* in low-salinity conditions may interfere with the associated relationship between corals and bacteria [89, 90]; the antagonistic effect of *Pseudoalteromonas* and the antibiotics produced by *Ruegeria* could be conducive to inhibiting the growth of *Vibrio*, maintaining the stability of the relationship and the mutual cooperation between corals and bacteria. Under low-salinity stress, the increased abundance of specific bacterial taxa may contribute to the health and survival of corals [91, 92].

Conclusions

Different coral species have different adaptations to low-salinity stress by regulating the diversity and composition of Symbiodiniaceae and bacteria. Some coral species improved their adaptation to low-salinity stress in the Pearl River Estuary based on a high diversity of symbiotic Symbiodiniaceae and associated bacteria. In contrast, some other coral species may increase their resistance by associating with specific Symbiodiniaceae subclades, with high Symbiodiniaceae density, or minority bacterial dominance under low-salinity stress.

Supplementary Information

The online version contains supplementary material available at https://doi.org/10.1186/s12866-025-04013-4.

Supplementary Material 1.
Supplementary Material 2.
Supplementary Material 3.
Supplementary Material 4.
Supplementary Material 5.
Supplementary Material 6.

Acknowledgements
This research was supported by the National Natural Science Foundation of China (42030502, 42090041, 42206157), the Natural Science Foundation of Guangxi Province (2022GXNSFBA035449), and the Self-Topic Project of Guangxi Laboratory on the Study of Coral Reefs in the South China Sea (GXLSCRSCS2022103), and the Central Public-Interest Scientific Institution Basal Research Fund (PM-zx703-202004-143 and PM-zx703-202105-176). The authors declare that the research was conducted in the absence of any commercial or financial relationships that could be construed as a potential conflict of interest. The data used in this paper are available from supporting information (SI), and the raw sequences were deposited in the NCBI Sequence Read Archive (SRA) database (https://www.ncbi.nlm.nih.gov/, accession number: Symbiodiniaceae: PRJNA1086834; bacteria: PRJNA1086806).

Authors' contributions
We have taken appropriate measures to ensure the accuracy and reliability of the data and have followed the principles of scientific integrity in data analysis and result presentation. Z.Q. and K.Y. conceived the research; Z.Q., B.C., X.Y. and Y.Z. contributed the materials; M.L., K.G., Z.L. and R.M. performed all experiments; L.W. and L.X. identified coral species; M.L., K.G., Z.Q., and K.Y. wrote the manuscript; all authors edited and approved the manuscript. The authors declare that they have no conflict of interest.

Funding
This research was supported by the National Natural Science Foundation of China (42030502, 42090041, 42206157), the Natural Science Foundation of Guangxi Province (2022GXNSFBA035449), and the Self-Topic Project of Guangxi Laboratory on the Study of Coral Reefs in the South China Sea (GXLSCRSCS2022103), and the Central Public-Interest Scientific Institution Basal Research Fund (PM-zx703-202004–143 and PM-zx703-202105–176).

Data availability
The data used in this paper are available from supporting information (SI), and the raw sequences were deposited in the NCBI Sequence Read Archive (SRA) database (https://www.ncbi.nlm.nih.gov/, accession number: Symbiodiniaceae: PRJNA1086834; bacteria: PRJNA1086806).

Declarations

Ethics approval and consent to participate
Not applicable.

Consent for publication
Not applicable.

Competing interests
The authors declare no competing interests.

Author details
[1]Guangxi Laboratory On the Study of Coral Reefs in the South China SeaCoral Reef Research Center of ChinaSchool of Marine Sciences, Guangxi University, Nanning, China. [2]Southern Marine Science and Engineering Guangdong Laboratory (Guangzhou), Guangzhou, China. [3]South China Institute of Environmental Sciences, MEE, Guangzhou, China.

Received: 2 December 2024 Accepted: 30 April 2025
Published online: 08 May 2025

References

1. Bellwood DR, Hughes TP, Folke C, Nystrom M. Confronting the coral reef crisis. Nature. 2004;429:827–33. https://doi.org/10.1038/nature02691.
2. Yu KF. Coral reefs in the South China Sea: Their response to and records on past environmental changes. Science China-Earth Science. 2015;55:1217–29. https://doi.org/10.1007/s11430-012-4449-5.
3. van Oppen MJH, Blackall LL. Coral microbiome dynamics, functions and design in a changing world. Nat Rev Microbiol. 2019;17:557–656. https://doi.org/10.1038/s41579-019-0223-4.
4. Rohwer F, Seguritan V, Azam F, Knowlton N. Diversity and distribution of coral-associated bacteria. Mar Ecol Prog Ser. 2002;243:1–10. https://doi.org/10.3354/meps243001.
5. Garrido AG, Machado LF, Zilberberg C, Leite DCD. Insights into 'Symbiodiniaceae phycosphere' in a coral holobiont. Symbiosis. 2021;83:25–39. https://doi.org/10.1007/s13199-020-00735-3.
6. Brodersen KE, Lichtenberg M, Ralph PJ, Kühl M, Wangpraseurt D. Radiative energy budget reveals high photosynthetic efficiency in symbiont-bearing corals. J R Soc Interface. 2014;11:20130997. https://doi.org/10.1098/rsif.2013.0997.
7. Falkowski PG, Dubinsky Z, Muscatine L, Poter JW. Light and the Bioenergetics of a Symbiotic Coral. Bioscience. 1984;34:705–9. https://doi.org/10.2307/1309663.
8. Lema KA, Willis BL, Bourne DG. Corals Form Characteristic Associations with Symbiotic Nitrogen-Fixing Bacteria. Appl Environ Microbiol. 2012;78:3136–44. https://doi.org/10.1128/AEM.07800-11.
9. Lesser MP, Mazel CH, Gorbunov MY, Falkowski PG. Discovery of Symbiotic Nitrogen-Fixing Cyanobacteria in Corals. Science. 2004;305:997–1000. https://doi.org/10.1126/science.1099128.
10. Kimes NE, Van Nostrand JD, Weil E, Zhou J, Morris PJ. Microbial functional structure of Montastraea faveolata, an important Caribbean reef-building coral, differs between healthy and yellow-band diseased colonies. Environ Microbiol. 2010;12:541–56. https://doi.org/10.1111/j.1462-2920.2009.02113.x.
11. Raina J-B, Tapiolas D, Willis BL, Bourne DG. Coral-Associated Bacteria and Their Role in the Biogeochemical Cycling of Sulfur. Appl Environ Microbiol. 2009;75:3492–501. https://doi.org/10.1128/AEM.02567-08.
12. Wegley L, Edwards R, Rodriguez-Brito B, Liu H, Rohwer F. Metagenomic analysis of the microbial community associated with the coral Porites astreoides. Environ Microbiol. 2007;9:2707–19. https://doi.org/10.1111/j.1462-2920.2007.01383.x.
13. Zhang YY, Ling J, Yang QS, Wen CQ, Yan QY, Sun HY, Van Nostrand JD, Shi Z, Zhou JZ, Dong JD. The functional gene composition and metabolic potential of coral-associated microbial communities. Sci Rep. 2015;5:16191. https://doi.org/10.1038/srep16191.
14. Ritchie KB. Regulation of microbial populations by coral surface mucus and mucus-associated bacteria. Mar Ecol Prog Ser. 2006;322:1–14. https://doi.org/10.3354/meps322001.
15. Rypien KL, Ward JR, Azam F. Antagonistic interactions among coral-associated bacteria. Environ Microbiol. 2010;12:28–39. https://doi.org/10.1111/j.1462-2920.2009.02027.x.
16. Seveso D, Montano S, Strona G, Orlandi I, Galli P, Vai M. Exploring the effect of salinity changes on the levels of Hsp60 in the tropical coral Seriatopora caliendrum. Mar Environ Res. 2013;90:96–103. https://doi.org/10.1016/j.marenvres.2013.06.002.
17. Ding DS, Patel AK, Singhania RR, Chen CW, Dong CD. Effects of Temperature and Salinity on Growth, Metabolism and Digestive Enzymes Synthesis of Goniopora columna. Biology. 2022;11:436. https://doi.org/10.3390/biology11030436.
18. Blaxter JHS. 1 Pattern and Variety in Development. Fish Physiology. 1998;11:1–58. https://doi.org/10.1016/S1546-5098(08)60198-3.
19. Rombough PJ. The effects of temperature on embryonic and larval development. In: Wood CM, McDonald DG, editors. Global Warming: Implications for Freshwater and Marine Fish. Cambridge University Press: Society for Experimental Biology Seminar Series; 1997. p. 177–224.
20. Hoegh-Guldberg O, Smith GJ. The effect of sudden changes in temperature, light and salinity on the population density and export of Symbiodiniaceae from the reef corals Stylophora pistillata Esper and Seriatopora hystrix Dana. J Exp Mar Biol Ecol. 1989;129:279–303. https://doi.org/10.1016/0022-0981(89)90109-3.
21. Mayfield AB, Gates RD. Osmoregulation in anthozoan-dinoflagellate symbiosis. Comparative biochemistry and physiology. Part A, Molecular & integrative physiology. 2007;147:1–10. https://doi.org/10.1016/j.cbpa.2006.12.042.
22. Kuanui P, Chavanich S, Viyakarn V, Omori M, Lin C. Effects of temperature and salinity on survival rate of cultured corals and photosynthetic efficiency of zooxanthellae in coral tissues. Ocean Science Journal. 2015;50:263–8. https://doi.org/10.1007/s12601-015-0023-3.
23. Bourne DG, Morrow KM, Webster NS. Insights into the Coral Microbiome: Underpinning the Health and Resilience of Reef Ecosystems. Annu Rev Microbiol. 2016;70:317–40. https://doi.org/10.1146/annurev-micro-102215-095440.
24. Thurber RV, Willner-Hall D, Rodriguez-Mueller B, Desnues C, Edwards RA, Angly F, Dinsdale E, Kelly L, Rohwer F. Metagenomic analysis of stressed coral holobionts. Environ Microbiol. 2009;11:2148–63. https://doi.org/10.1111/j.1462-2920.2009.01935.x.
25. Mei S, Yu K, Chen B. Salinity Influencing the Formation of Special Niches of Bacterioplankton in Pearl River Estuary, China (in Chinese). Acta Scientiarum Naturalium Universitatis Pekinensis. 2021;57:903–915. https://doi.org/10.13209/j.0479-8023.2021.067
26. Lee T, Chan K, Chan H, Kok M. Projections of extreme rainfall in Hong Kong in the 21st century. Acta Meteor Sin. 2011;25:691–709. https://doi.org/10.1007/s13351-011-0601-y.
27. IPCC. 2013. Climate change. The Physical Science Basis. In T. F. Stocker, D. Qin, G. K. Plattner, M. Tignor, S. K. Allen, J. Boschung, et al Contribution of Working Group I to the Fifth Assessment Report. Working Group I to the Fifth Assessment Report of the Intergovernmental Panel on Climate Change (UK and New York, NY, USA.: Cambridge University Press). 2013. https://doi.org/10.1101/gr.120618.111
28. Knutson TR, Sirutis JJ, Zhao M, Tuleya RE, Bender M, Vecchi GA, Villarini G, Chavas D. Global projections of intense tropical cyclone activity for the late twenty-first century from dynamical downscaling of CMIP5/RCP4.5 scenarios. J Clim. 2015;28:7203–24. https://doi.org/10.1175/JCLI-D-15-0129.1.
29. Hoegh-Guldberg O. Climate change, coral bleaching and the future of the world's coral reefs. Marine And Freshwater Research. 1999;50:839–66. https://doi.org/10.1071/mf99078.
30. Chui APY, Ang PO. Elevated temperature enhances normal early embryonic development in the coral Platygyra acuta under low salinity conditions. Coral Reefs. 2015;34:461–9. https://doi.org/10.1007/s00338-014-1247-x.
31. Hedouin L, Pilon R, Puisay A. Hyposalinity stress compromises the fertilization of gametes more than the survival of coral larvae. Mar Environ Res. 2015;104:1–9. https://doi.org/10.1016/j.marenvres.2014.12.001.
32. Kregting LT, Gibbs MT. Salinity controls the upper depth limit of black corals in Doubtful Sound, New Zealand. NZ J Mar Freshwat Res. 2006;40:43–52. https://doi.org/10.1080/00288330.2006.9517402.
33. Scott A, Harrison PL, Brooks LO. Reduced salinity decreases the fertilization success and larval survival of two scleractinian coral species. Mar Environ Res. 2013;92:10–4. https://doi.org/10.1016/j.marenvres.2013.08.001.
34. Röthig T, Ochsenkühn MA, Roik A, van der Merwe R, Voolstra CR. Long-term salinity tolerance is accompanied by major restructuring of the coral bacterial microbiome. Mol Ecol. 2016;25:1308–23. https://doi.org/10.1111/mec.13567.
35. Moberg F, Nyström M, Kautsky N, Tedengren M, Jarayabhand P. Effects of reduced salinity on the rates of photosynthesis and respiration in the hermatypic corals Porites lutea and Pocillopora damicornis. Mar Ecol Prog Ser. 1997;157:53–9. https://doi.org/10.3354/MEPS157053.
36. Chen P, Zhang Z, Song Z, Zhang W, Ye R, Li Y. Simulation of storm surge and analysis of the factors around Lingdingyang Bay, Pearl River Estuary: Take typhoon Mangkhut as an example. Marine Sci Bullet. 2023;42:645–657. https://doi.org/10.11840/j.issn.1001-6392.2023.06.004
37. Liu B, Zhu C, Xu K, Ma S, Lu M, Han X, Hua L. Record-breaking pre-flood rainfall over South China in 2022: role of historic warming over the Northeast Pacific and Maritime Continent. Clim Dyn. 2023;61:3147–63. https://doi.org/10.1007/s00382-023-06734-6.

38. Huang H, You F, Lian J, Zhang C, Yang J, Li X, Yuan T, Zhang Y, Zhou G. Status and conservation strategies of the scleractinian coral community in the Wanshan Islands at Pearl River Estuary. Marine Sci Bullet. 2012;31:189–197. https://doi.org/10.11840/j.issn.1001-6392.2012.2.010
39. Li S, Yu KF, Shi Q, Chen TR, Zhao MX, Zhao JX. Interspecific and spatial differences in the coral symbiotic Symbiodiniaceae density and its effect on coral reef bleaching in the northern part of the South China Sea. Chin Sci Bull. 2007;52:2655–62. https://doi.org/10.1360/csb2007-52-22-2655.
40. Ip JC, Zhang Y, Xie JY, Yeung YH, Qiu JW. Comparative transcriptomics of two coral holobionts collected during the 2017 El Niño heat wave reveal differential stress response mechanisms. Mar Pollut Bull. 2022;182:114017. https://doi.org/10.1016/j.marpolbul.2022.114017.
41. Li S, Yu KF, Chen TR, Shi Q, Chen TG. Seasonal patterns of densities of symbiotic zooxanthellae in scleractinian corals from Daya Bay, northern South China Sea, and relation to coral bleaching. J Trop Oceanogr. 2011;02:39–45. https://doi.org/10.3969/j.issn.1009-5470.2011.02.006.
42. Qin Z, Yu K, Wang Y, Xu L, Huang X, Chen B, Li Y, Wang W, Pan Z. Spatial and intergeneric variation in physiological indicators of corals in the South China Sea: Insights into their current state and their adaptability to environmental stress. J Geophys Res Oceans. 2019;124:3317–32. https://doi.org/10.1029/2018JC014648.
43. Chen B, Yu K, Qin Z, Liang J, Wang G, Huang X, Wu Q, Jiang L. Dispersal, genetic variation, and symbiont interaction network of heat-tolerant endosymbiont Durusdinium trenchii: Insights into the adaptive potential of coral to climate change. The Science of the total environment. 2020;723:138026. https://doi.org/10.1016/j.scitotenv.2020.138026.
44. Tong H, Cai L, Zhou G, Yuan T, Zhang W, Tian R, Huang H, Qian PY. Temperature shapes coral-algal symbiosis in the South China Sea. Sci Rep. 2017;7:40118. https://doi.org/10.1038/srep40118.
45. Zou Y, Ip JC, Xie JY, Yeung YH, Wei L, Guo Z, Zhang Y, Qiu JW. Dynamic changes in bacterial communities in three species of corals during the 2017 bleaching event in subtropical Hong Kong waters. Mar Pollut Bull. 2024;199:116002. https://doi.org/10.1016/j.marpolbul.2023.116002.
46. Chen B, Yu K, Liao Z, Yu X, Qin Z, Liang J, Wang G, Wu Q, Jiang L. Microbiome community and complexity indicate environmental gradient acclimatisation and potential microbial interaction of endemic coral holobionts in the South China Sea. Sci Total Environ. 2021;765. https://doi.org/10.1016/j.scitotenv.2020.142690.
47. Li S, Yu K, Shi Q, Chen TR, Zhao MX, Zhao JX. Interspecies and spatial diversity in the symbiotic zooxanthellae density in corals from northern South China Sea and its relationship to coral reef bleaching. Chin Sci Bull. 2008;53:295–303. https://doi.org/10.1007/s11434-007-0514-4.
48. Xu LJ, Yu KF, Li S, Liu GH, Tao SC, Shi Q, Chen TR, Zhang HL. Interseasonal and interspecies diversities of Symbiodinium density and effective photochemical efficiency in five dominant reef coral species from Luhuitou fringing reef, northern South China Sea. Coral Reefs. 2017;36:477–87. https://doi.org/10.1007/s00338-016-1532-y.
49. Lajeunesse TC, Trench RK. Biogeography of two species of Symbiodinium (Freudenthal) inhabiting the intertidal sea anemone Anthopleura elegantissima (Brandt). Biol Bull. 2000;199:126–34. https://doi.org/10.2307/1542872.
50. Lajeunesse TC, Loh WKW, van Woesik R, Hoegh-Guldberg O, Schmidt GW, Fitt WK. Low symbiont diversity in southern Great Barrier Reef corals, relative to those of the Caribbean. Limnol Oceanogr. 2003;48:2046–54. https://doi.org/10.4319/lo.2003.48.5.2046.
51. Sun Z, Li GP, Wang CW, Jing YH, Zhu YP, Zhang SM, Liu Y. Community dynamics of prokaryotic and eukaryotic microbes in an estuary reservoir. Sci Rep. 2014;4:6966. https://doi.org/10.1038/srep06966.
52. Zhang JJ, Kobert K, Flouri T, Stamatakis A. PEAR: A fast and accurate Illumina Paired-End reAd mergeR. Bioinformatics. 2014;30:614–20. https://doi.org/10.1093/bioinformatics/btt593.
53. Caporaso JG, Kuczynski J, Stombaugh J, Bittinger K, Bushman FD, Costello EK, Fierer N, Peña AG, Goodrich JK, Gordo. QIIME allows analysis of high-throughput community sequencing data. Nat Methods. 2010;7:335–6. https://doi.org/10.1038/nmeth.f.303.
54. Altschul SF, Gish W, Miller W, Myers EW, Lipman DJ. Basic local alignment search tool. J Mol Biol. 1990;215:403–10. https://doi.org/10.1016/S0022-2836(05)80360-2.
55. Chen B, Yu K, Liang J, Huang W, Wang G, Su H, Qin Z, Huang X, Pan Z, Luo W, Luo Y, Wang Y. Latitudinal Variation in the Molecular Diversity and Community Composition of Symbiodiniaceae in Coral From the South China Sea. Front Microbiol. 2019;10. https://doi.org/10.3389/fmicb.2019.01278
56. Ronquist F, Teslenko M, van der Mark P, Ayres DL, Darling A, Höhna S, Larget B, Liu L, Suchard MA, Huelsenbeck JP. MrBayes 3.2: efficient bayesian phylogenetic inference and model choice across a large model space. Syst Biol. 2012;61:539–42. https://doi.org/10.1093/sysbio/sys029.
57. Mori H, Maruyama F, Kato H, Toyoda A, Dozono A, Ohtsubo Y, Nagata A, Fujiyama A, Tsuda M, Kurokawa K. Design and experimental application of a novel non-degenerate universal primer set that amplifies prokaryotic 16S rRNA genes with a low possibility to amplify eukaryotic rRNA genes. DNA Res. 2013;21:217–27. https://doi.org/10.1093/dnares/dst052.
58. Kim DR, Jeon CW, Cho G, Thomashow LS, Weller DM, Paik M, Lee YB, Kwak YS. Glutamic acid reshapes the plant microbiota to protect plants against pathogens. Microbiome. 2021;9:244. https://doi.org/10.1186/s40168-021-01186-8.
59. Ma Y, Zhang W, Li R,Zhu P, Mou J, Liu C, Zhang J, Su X, Liang Y, Zeng F. The spatiotemporal variations of nutrients and its ecological response in the Pearl River Estuary and its adjacent sea areas under the influence of El Niño. Acta Scientiae Circumstantiae. 2023;43:36–46. https://doi.org/10.13671/j.hjkxxb.2022.0358
60. Li L, Li Z, Shen Y, Yang X. Study of stress of four environmental factors on *Porites lutea* and *Goniopora stutchburyi* (in Chinese). J Trop Oceanogr. 2013;32:72–7. https://doi.org/10.3969/j.issn.1009-5470.2013.03.011.
61. Dias M, Ferreira A, Gouveia R, Vinagre C. Synergistic effects of warming and lower salinity on the asexual reproduction of reef-forming corals. Ecol Ind. 2019;98:334–48. https://doi.org/10.1016/j.ecolind.2018.11.011.
62. Stat M, Carter D, Hoegh-Guldberg O. The evolutionary history of Symbiodinium and scleractinian hosts-Symbiosis, diversity, and the effect of climate change. Perspectives in Plant Ecology Evolution and Systematics. 2006;8:23–43. https://doi.org/10.1016/j.ppees.2006.04.001.
63. Cantin NE, van Oppen MJH, Willis BL, Mieog JC, Negri AP. Juvenile corals can acquire more carbon from high-performance algal symbionts. Coral Reefs. 2009;28:405–14. https://doi.org/10.1007/s00338-009-0478-8.
64. Ortiz JC, González-Rivero M, Mumby PJ. Can a thermally tolerant symbiont improve the future of Caribbean coral reefs? Glob Change Biol. 2013;19:273–81. https://doi.org/10.1111/gcb.12027.
65. Hume BCC, D'Angelo C, Smith EG, Stevens JR, Burt J, Wiedenmann J. Symbiodinium thermophilum sp. nov., a thermotolerant symbiotic alga prevalent in corals of the world's hottest sea, the Persian/Arabian Gulf. Sci Rep. 2015;5:8562. https://doi.org/10.1038/srep08562
66. Silverstein RN, Cunning R, Baker AC. Change in algal symbiont communities after bleaching, not prior heat exposure, increases heat tolerance of reef corals. Glob Change Biol. 2015;21:236–49. https://doi.org/10.1111/gcb.12706.
67. Brading P, Warner ME, Davey PA, Smith DJ, Achterberg EP, Suggett DJ. Differential effects of ocean acidification on growth and photosynthesis among phylotypes of Symbiodinium (Dinophyceae). Limnol Oceanogr. 2011;57:1255. https://doi.org/10.4319/lo.2012.57.4.1255.
68. Hume BCC, Voolstra CR, Arif C, D'Angelo C, Burt JA, Eyal G, Loya Y, Wiedenmann J. Ancestral genetic diversity associated with the rapid spread of stress-tolerant coral symbionts in response to Holocene climate change. Proc Natl Acad Sci. 2016;113:4416–21. https://doi.org/10.1073/pnas.1601910113.
69. Baker DM, Andras JP, Jordán-Garza AG, Fogel ML. Nitrate competition in a coral symbiosis varies with temperature among Symbiodinium clades. ISME J. 2013;7:1248–51. https://doi.org/10.1038/ismej.2013.12.
70. Palmas SD, Denis V, Ribas-Deulofeu L, Loubeyres M, Woo S, Hwang SJ, Song JI, Chen CA. *Symbiodinium* spp. associated with high-latitude scleractinian corals from Jeju Island. South Korea Coral Reefs. 2015;34:919–25. https://doi.org/10.1007/s00338-015-1286-y.
71. Lesser MP, Falcón LI, Rodríguez-Román A, Enríquez S, Hoegh-Guldberg O, Iglesias-Prieto R. Nitrogen fixation by symbiotic cyanobacteria provides a source of nitrogen for the scleractinian coral Montastraea cavernosa. Mar Ecol Prog Ser. 2007;346:143–52. https://doi.org/10.3354/meps07008.
72. D'Angelo C, Hume BCC, Burt J, Smith EG, Achterberg EP, Wiedenmann J. Local adaptation constrains the distribution potential of heat-tolerant Symbiodinium from the Persian/Arabian Gulf. ISME J. 2015;9:2551–60. https://doi.org/10.1038/ismej.2015.80.
73. Boulotte NM, Dalton SJ, Carroll AG, Harrison PL, Putnam HM, Peplow LM, van Oppen MJH. Exploring the Symbiodinium rare biosphere

provides evidence for symbiont switching in reef-building corals. ISME J. 2016;10:2693–701. https://doi.org/10.1038/ismej.2016.54.
74. Campbell BJ, Kirchman DL. Bacterial diversity, community structure and potential growth rates along an estuarine salinity gradient. ISME J. 2013;7:210–20. https://doi.org/10.1038/ismej.2012.93.
75. Kirchman DL, Cottrel MT, DiTullio GR. Shaping of bacterial community composition and diversity by phytoplankton and salinity in the Delaware Estuary, USA. Aquat Microb Ecol. 2017;78:93–106. https://doi.org/10.3354/ame01805.
76. Ziegler M, Seneca FO, Yum LK, Palumbi SR, Voolstra CR. Bacterial community dynamics are linked to patterns of coral heat tolerance. Nat Commun. 2017;8:14213. https://doi.org/10.1038/ncomms14213.
77. Shade A, Peter H, Allison SD, Baho DL, Berga M, Bürgmann H, Huber DH, Langenheder S, Lennon JT, Martiny JB, Matulich KL, Schmidt TM, Handelsman J. Fundamentals of microbial community resistance and resilience. Front Microbiol. 2012;3:417. https://doi.org/10.3389/fmicb.2012.00417.
78. Teoh F, Shah B, Ostrowski M, Paulsen I. Comparative membrane proteomics reveal contrasting adaptation strategies for coastal and oceanic marine *Synechococcus* cyanobacteria. Environ Microbiol. 2020;22:1816–28. https://doi.org/10.1111/1462-2920.14876.
79. Kim Y, Jeon J, Kwak MS, Kim GH, Koh I, Rho M. Photosynthetic functions of *Synechococcus* in the ocean microbiomes of diverse salinity and seasons. PLoS ONE. 2018;13: e0190266. https://doi.org/10.1371/journal.pone.0190266.
80. Reisch CR, Moran MA, Whitman WB. Bacterial Catabolism of Dimethylsulfoniopropionate (DMSP). Front Microbiol. 2011;2:172. https://doi.org/10.3389/fmicb.2011.00172.
81. Alsharif SM, Waznah MS, Ismaeil M, El-Sayed WS. 16S rDNA-based diversity analysis of bacterial communities associated with soft corals of the Red Sea, Al Rayyis, White Head, KSA. J Taibah Univ Sci. 2023;17. https://doi.org/10.1080/16583655.2022.2156762
82. Zhang L. Intermittent aerated membrane bioreactor for high salinity wastewater treatment and microbial community structure analysis. Membrane Science and Technology (in Chinese). Membrane Sci Technol. 2020;40:101–110. https://doi.org/10.16159/j.cnki.issn1007-8924.2020.05.014
83. Bai J, Li H, Zhao Y. Bacterial distribution at different stations in the Northern Yellow Sea (in Chinese). Acta Microbiologica Sinica. 2009;49:343–350. https://doi.org/10.13343/j.cnki.wsxb.2009.03.005
84. Shnit-Orland M, Kushmaro A. Coral mucus-associated bacteria: a possible first line of defense. FEMS Microbiol Ecol. 2009;67:371–80. https://doi.org/10.1111/j.1574-6941.2008.00644.x.
85. Lima LFO, Alker AT, Papudeshi B, Morris MM, Edwards RA, de Putron SJ, Dinsdale EA. Coral and Seawater Metagenomes Reveal Key Microbial Functions to Coral Health and Ecosystem Functioning Shaped at Reef Scale. Microb Ecol. 2023;86:392–407. https://doi.org/10.1007/s00248-022-02094-6.
86. Yang H, Zhang X, Long H, Li Y, Feng YQ, Xie ZY. Antagonistic Mechanism of Pseudoalteromonas sp. against *Vibrio harveyi*. Fisheries Sci. 2019;38:833–838. https://doi.org/10.16378/j.cnki.1003-1111.2019.06.013
87. Tang K, Zhan W, Zhou Y, Xu T, Chen X, Wang W, Zeng Z, Wang Y, Wang X. Antagonism between coral pathogen Vibrio coralliilyticus and other bacteria in the gastric cavity of scleractinian coral Galaxea fascicularis. Sci China Earth Sci. 2020;63:157–66. https://doi.org/10.1007/s11430-019-9388-3.
88. Chen J, Liang J, Yu K, Yu X, Ge R, Qin L, Xu Y. Diversity of potential heat-tolerant bacteria associated with two species of scleractinian corals in Weizhou Island (in Chinese). Microbiol China. 2023;50:909—923. https://doi.org/10.1007/s11430-019-9388-3
89. Munn CB. The Role of Vibrios in Diseases of Corals. Microbiol Spectr. 2015;3. https://doi.org/10.1128/microbiolspec.VE-0006-2014
90. Sun X, Li Y, Yang Q, Zhang H, Xu N, Tang Z, Wu S, Jiang Y, Mohamed HF, Ou D, Zheng X. Identification of quorum sensing-regulated Vibrio fortis as potential pathogenic bacteria for coral bleaching and the effects on the microbial shift. Front Microbiol. 2023;14:1116737. https://doi.org/10.3389/fmicb.2023.1116737.
91. McDevitt-Irwin JM, Baum JK, Garren M, Vega Thurber RL. Responses of Coral-Associated Bacterial Communities to Local and Global Stressors. Front Marine Sci. 2017;4. https://doi.org/10.3389/fmars.2017.00262
92. Hussein EI, Juhmani AF, Jacob JH, Telfah MA, Abd Al-razaq MA, Al-Horani FA, Al Zoubi MS, Malkawi HI. Effect of Various Local Anthropogenic Impacts on the Diversity of Coral Mucus-Associated Bacterial Communities. Journal of Marine Science and Engineering. 2022;10:863. https://doi.org/10.3390/jmse10070863.

Publisher's Note

Springer Nature remains neutral with regard to jurisdictional claims in published maps and institutional affiliations.

NJC

ROYAL SOCIETY OF CHEMISTRY

PAPER

View Article Online
View Journal

Check for updates

Cite this: DOI: 10.1039/d5nj02636a

Sensitive detection of early growth of *Skeletonema costatum* using a gold-doped carbon sphere-gold nanoparticle electrochemical biosensor

Ziyang Xian, †[a] Yayi He,†[a] Chaoxin Zhang,[b] Hao Fu,[b] Yaling Liu,[a] Tao Zhang,[b] Shaopeng Wang,[a] Shan Lu,[c] Man Zhang*[a] and Liwei Wang *[ab]

Received 26th June 2025,
Accepted 4th September 2025

DOI: 10.1039/d5nj02636a

rsc.li/njc

The red tide caused by *Skeletonema costatum* (*S. costatum*), which greatly harms the ecosystem, makes the accurate, sensitive, and quick detection of *S. costatum* a challenge within the field, despite early warning being conducive to intervening and managing its occurrence. This paper proposes an electrochemical biosensor composed of gold-doped carbon spheres (CBAu) and gold nanoparticles to detect its early growth. CBAu has excellent conductivity and provides an effective channel for the transmission of electrical signals in the biosensor. At the same time, the unique characteristics of gold nanoparticles can effectively enrich ferrocene-labeled DNA (FcDNA). Therefore, this biosensor displays excellent detection performance, including a low detection limit (LOD = 51.28 fg μL^{-1}), a low limit of quantitation (LOQ = 137.85 fg μL^{-1}), and a wide linear range (100 fg μL^{-1}–10 pg μL^{-1}). A linear relationship has been established between the algal density and current value, with the calculated LOD being 2672 cells per L and LOQ 4575 cells per L. Both of these values are far below the algal bloom threshold of 10^7 cells per L. The reliability and accuracy of the biosensor are further verified by comparison with optical microscopy and droplet digital PCR (ddPCR). In addition, the applicability of the biosensor is re-verified in the field test in the Beibu Gulf.

Published on 19 September 2025. Downloaded by Guangxi University on 9/20/2025 2:29:51 PM.

1. Introduction

Skeletonema costatum (*S. costatum*) is one of the high red tide algae and a perennial dominant species in the world's coastal waters.[1] It can reproduce rapidly under adequate nutrient salinity and relatively stable hydrological and meteorological conditions, and it can cause seawater discoloration and produce reactive aldehydes, which hurt copepod hatching.[2] Besides endangering aquatic ecosystems, high algae densities lead to massive fish kills and economic losses.[3] The technical specification for red tide monitoring issued by the Chinese Ocean Disaster Monitoring and Early Warning Technology Laboratory defines red tide as a condition when the density of *S. costatum* is more than 10^7 cells per L. According to China's ocean disaster report statistics, *S. costatum* red tide occurred almost every year from 2002 to 2022 and fluctuated. Up to 2022, 44 red tides caused by *S. costatum* occurred, with a cumulative area of more than 17 906 km^2, which cause frequent outbreaks and a wide range of impacts. Red tide is a natural phenomenon that cannot practically be eliminated, but an effective detection program can provide early warning of red tide and mitigate its adverse environmental impacts. Currently, the identification and counting of *S. costatum* mainly rely on light microscopes.[4,5] This method is time-consuming and prone to human errors. By contrast, emerging molecular detection techniques can identify and quantify it more quickly and accurately. Polymerase chain reaction (PCR) and quantitative polymerase chain reaction (qPCR) have been widely used in microalgae detection.[6–9] However, they require professional personnel and laboratories, and thus they can't meet the practical needs for rapid and efficient detection of *S. costatum*, further hindering the development of related technologies. Therefore, it is urgent to develop rapid on-site analysis methods. Electrochemical biosensors have recently drawn public attention. They respond quickly with high sensitivity and relatively low costs and support on-site instant analysis.[10,11] An increasing number of research reports focus on using such sensors to detect microalgae.[12–14] For example, Yoseph

[a] *Guangxi Laboratory on the Study of Coral Reefs in the South China Sea, Coral Reef Research Center of China, School of Marine Sciences, Guangxi University, Nanning, 530004, China. E-mail: sdyczm@163.com, wangliwei0427@163.com*
[b] *School of Resources, Environment and Materials, School of Chemistry and Chemical Engineering, State Key Laboratory for Conservation and Utilization of Subtropical Agro-Bioresources, College of Agriculture, Guangxi University, Nanning, 530004, China*
[c] *Beibu Gulf Marine Ecological Environment Field Observation and Research Station of Guangxi, Marine Environmental Monitoring Centre of Guangxi, Beihai, 536000, China*
† These authors contributed equally to this study.

Published on 19 September 2025. Downloaded by Guangxi University on 9/20/2025 2:29:51 PM.

Seo *et al.* developed a rapid and sensitive electrochemical biosensor for detecting harmful cyanobacteria based on species–specific DNA primers.[15] Emma Izzati Zakariah *et al.* developed an electrochemical DNA biosensor that uses AQMS as a redox marker to detect the DNA of *Alexandrium minutum*.[16] These biosensors are characterized by strong specificity and easy miniaturization. However, they still face challenges in terms of sensitivity and reliability, which, to some extent, limit their practical application in fields such as marine organism monitoring and early warning. However, these biosensors still face challenges in accuracy, sensitivity, and reliability, which, to some extent, limit their practical application in fields such as marine biological monitoring and early warning.

Carbon nanomaterials have recently become the focus of research to address the above challenge due to their significant advantages, such as high mechanical strength, large specific surface area, and facilitation of electron transfer.[17] Their highly adjustable surface characteristics enable carbon nanomaterials to sensitively recognize signal molecules, further enhancing their sensitivity and selectivity as judgment tools.[18,19] In addition, gold nanoparticles have attracted increasing attention in the field of sensing due to their unique properties, such as excellent conductivity, low toxicity, and high compatibility.[20] When applied to electrochemical biosensors, gold nanoparticles can play two roles. One is an efficient conductive mediator in detecting biomolecules or chemical substances; the rapid electron transfer enables the biosensor to generate an apparent electrical signal response to target substances at extremely low concentrations.[21–23] Another is that signal probes can be combined with gold nanoparticles through physical adsorption[24] and chemical bonding,[25] thereby achieving highly enriched signal probes. This enrichment effect can amplify the detection signal significantly, enabling even trace amounts of target substances to produce detectable signal responses.[26,27] Therefore, gold nanoparticles can significantly improve accurate target identification.

Here, a biosensor was developed for detecting the DNA of *S. costatum* by using electrode modification materials (gold-doped carbon balls, marked as CBAu) and gold nanoparticles (Au NPs) that can enrich signaling molecules (DNA labeled with ferrocene, marked as FcDNA). Due to the excellent conductivity of CBAu and the amplification of current signals achieved by the enrichment of signal molecules through gold nanoparticles, this biosensor shows excellent sensitivity and specificity. In addition, its satisfactory accuracy in detecting *S. costatum* was confirmed by comparing it with droplet digital polymerase chain reaction (ddPCR) and microscopic detection methods. Moreover, its applicability was also verified through the analysis of actual samples from the Beibu Gulf. Therefore, we believe that this work provides a new perspective for the on-site quantitative analysis of *S. costatum* and lays a foundation for the early warning of its outbreak.

2. Materials and methods

2.1. Preparation of the material

CB was synthesized as previously described in the literature,[28] with slight modifications. First, 70 mL of ethanol, 10 mL of distilled water, and 3 mL of concentrated ammonia were mixed into a solution and stirred for 15 min, and then 0.4 g of resorcinol and 0.56 mL of formaldehyde solution were added to the mixed solution and stirred for 24 h. After the reaction, the sample was washed three times with water and three times with ethanol, respectively, and the resulting precipitates were placed in a vacuum-drying oven and dried at 60 °C for 12 h. After the sample was completely dried and ground, it was calcined in a tube furnace protected by a nitrogen atmosphere at 700 °C for 5 h, and the temperature increase rate was set at 5 °C min^{-1}. The carbon spheres produced were doped with gold using a chemical reduction method to obtain CBAu.[29] The reagents and instruments used in the experiment are in SI S1.1.

2.2. Primer and probe design

Design primer and probe sequences in the internal transcribed spacer region 2 (ITS2) gene sequence. The specific experimental details of DNA extraction and PCR amplification are in SI S1.2. The preliminary screening of specific primers after PCR amplification is shown in Fig. S1A. Table S1 shows the gene sequences of specific primers and targets of *S. costatum*, where *S. costatum* DNA was used as a template. The specific primers were amplified by PCR, and the amplified length was 214 bp. Red tide high-prevalence algae were selected as the interfering species, including *Prorocentrum donghaiense*, *Akashiwo sanguinea*, *Prorocentrum minimum*, and *Heterosigma akashiwo*. The specificity of the selected primers was verified by PCR amplification (SI Fig. S1B).

2.3. Fabrication of an electrochemical biosensor

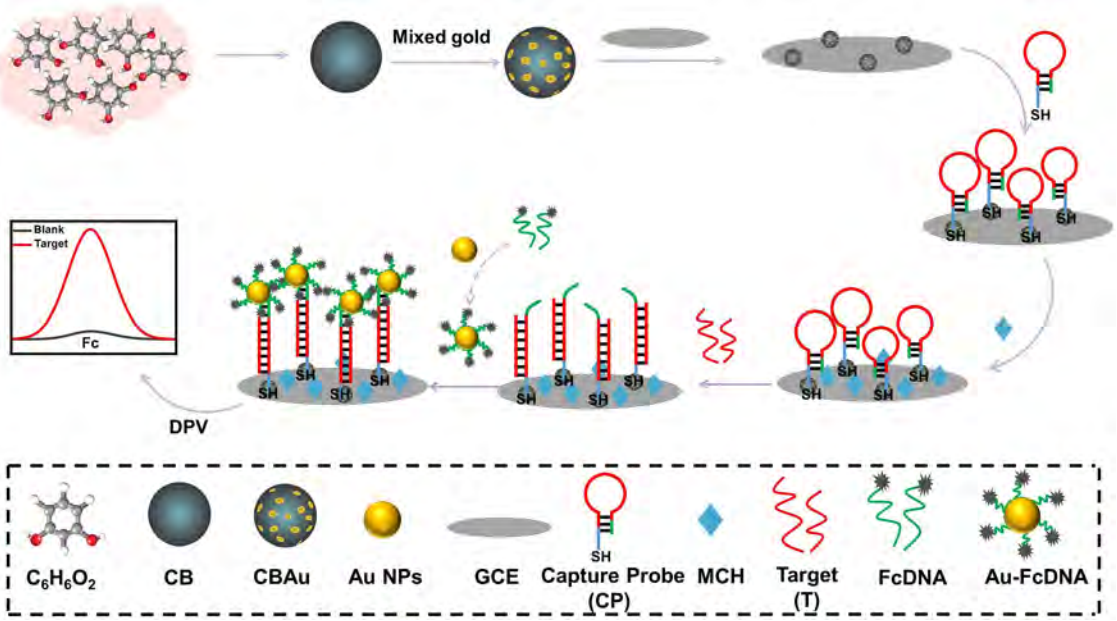
In Scheme 1 of this paper, the stepwise modification process of the electrochemical biosensor is described. Specifically, the GCE electrode was polished with 0.5 μm and 0.05 μm alumina powders and sonicated in ultrapure water. 4 mg of CBAu was dispersed in 1 mL of 0.2% chitosan acetic acid solution (CS), and 10 μL of the mixed suspension was added dropwise onto the bare glass electrode and dried at room temperature. CP/CBAu/GCE was prepared by adding 10 μL of diluted capture probe (CP) solution dropwise onto the prepared CBAu/GCE, and incubated for 2 h before being dried at room temperature. The preparation method of the CP is in SI S1.3. 10 μL of 5 mM MCH was added and incubated for 2 h for non-specific confinement of the electrode surface, and MCH/CP/CBAu/GCE was prepared. After that, 10 μL of the target (T) was added and reacted with CP for 2 h to form T/MCH/CP/CBAu/GCE, and finally, 10 μL Au-FcDNA was added and incubated for 2 h to complete the preparation of the Au-FcDNA/T/MCH/CP/CBAu/GCE electrode. The electrochemical test conditions are in SI S1.4.

2.4. Actual sample analysis

The Beibu Gulf of Guangxi is the target area of this study. In recent years, red tides of *S. costatum* have been frequently reported in this area. Based on the locations of red tides, nine sampling points, namely P1–9, are set up in the study area. The information on these sampling points is shown in Table S2.

 This journal is © The Royal Society of Chemistry and the Centre National de la Recherche Scientifique 2025

Published on 19 September 2025. Downloaded by Guangxi University on 9/20/2025 2:29:51 PM.



Scheme 1 Schematic diagram of the DNA biosensor for the detection of *S. costatum* DNA.

Briefly, after collecting 1 L of seawater samples at each sampling point, filtration is carried out, and the DNA in the seawater samples is extracted and stored at −80 °C for subsequent experiments. At the same time, the enriched DNA samples are analyzed on-site by portable electrochemical biosensors. For the DNA enrichment of actual samples, please refer to SI S1.5.

3. Results and discussion

3.1. Material characterization

The morphology of the prepared electrode material, CBAu was characterized by scanning electron microscopy (SEM) and transmission electron microscopy (TEM). As can be seen from Fig. 1A, the synthesized carbon balls have a regular spherical structure with uniform carbon ball sizes, and the diameters are about 381 nm (Fig. S2A). This uniformity in size provides a stable substrate structure for biosensors, and the even distribution of carbon spheres ensures consistency in the modification of the electrode surfaces, preventing signal fluctuations caused by differences in material morphology, thereby effectively guaranteeing the repeatability of sensor detection from a hardware perspective. In addition, the presence of C, N, O, and Au elements can be observed from the energy dispersive spectroscopy diagrams (Fig. S2B and C). In Fig. S2D, the particle size of Au NPs before incorporation into the CBAu material was 6.83 nm, which decreased to 4.44 nm after incorporation (Fig. S2E). This phenomenon is attributed to interfacial charge transfer and other interactions between the AuNPs and carbon materials, which alter the electronic structure and surface energy of the gold particles. These interactions enhance the thermodynamic stability of smaller nanoparticles, inhibit the Ostwald ripening process, reduce the dissolution of small particles and mass migration to larger particles, ultimately stabilizing the AuNP size at a smaller dimension, which initially proves the successful synthesis of the CBAu composite material.[30] The introduction of Au elements not only significantly enhances the conductivity of the material, but also provides precise binding sites for the immobilisation of CP through surface Au active sites, laying a solid foundation for subsequent specific recognition of target DNA with high loading capacity.[31]

The X-ray diffraction (XRD) patterns of CB and CBAu are consistent with the standard card in the energy spectrum diagram in Fig. 1B, indicating the successful synthesis of the material. Among them, CBAu has two strong diffraction peaks related to graphite carbon (002) and (101), indicating that carbon atoms form an orderly arranged large π bond system through sp^2 hybridisation, and this structure is the core source of the high electrical conductivity of CBAu.[32] This result is also confirmed by the Raman spectrum in Fig. 1C. This may be caused by the interaction between the incorporated gold and the defects in the carbon material and the filling of some defect sites. After calculation, the ratio of the D band to the G band of CB decreases to 0.71 after gold doping.[33,34] This may be caused by the interaction between the incorporated gold and the defects in the carbon material and the filling of some defect sites.[35] The above results suggest that CBAu has a degree of graphitization. The existence of graphitized carbon allows the electrons in the π bond system to move relatively freely, thereby endowing the material with excellent conductivity and improving the detection ability of the biosensor.[36]

In order to reveal the chemical valence state of the elements in the material and the modified functional groups, X-ray photoelectron spectroscopy (XPS) tests were performed in Fig. S2F. The O element in CBAu and CB comes from the phenolic resin precursor and exists in C–O, C═O, and O–C═O chemical bonds[37] (Fig. 1D and E). Among them, the C–O bond and the C═O bond mainly exist in the defects of the

Published on 19 September 2025. Downloaded by Guangxi University on 9/20/2025 2:29:51 PM.

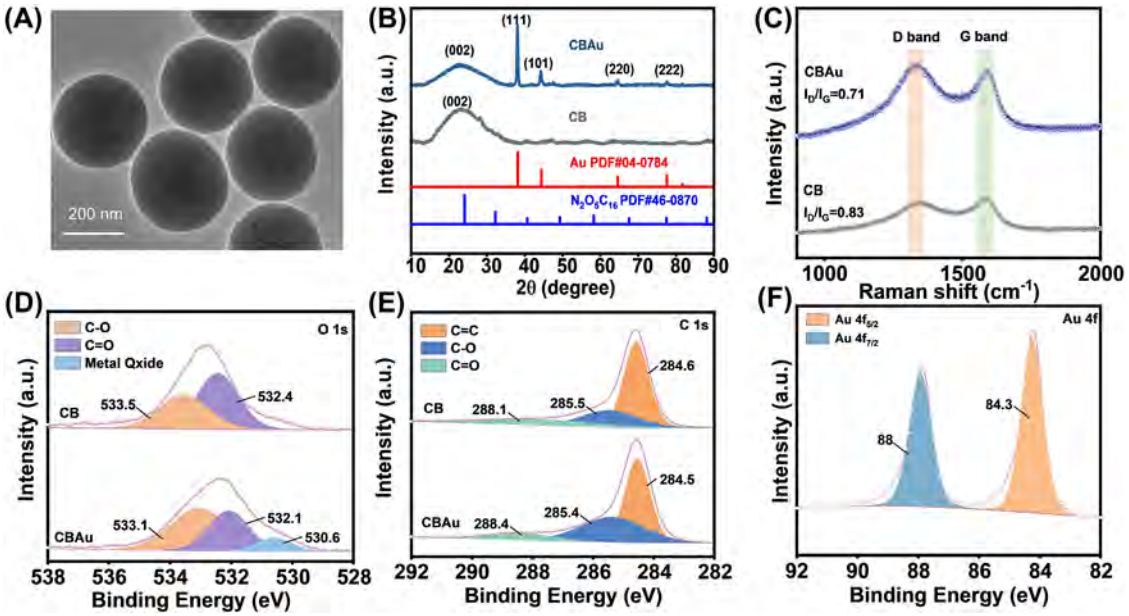


Fig. 1 Characterization of material CBAu. (A) TEM image of CBAu, (B) XRD pattern of CB and CBAu, (C) Raman spectra of CBAu, (D) XPS spectra survey spectrum of CB and CBAu C 1s, (E) O 1s and (F) Au 4f.

graphite lattice,[38] and the two can react with Au to form an Au–O bond (Fig. 1F).[39] Compared with CB, the characteristic peak of O 1s of CBAu shifts in the direction of decreasing binding energy. This may be caused by the electronic structure of gold affecting the electron cloud density around oxygen atoms and causing changes in the electron binding energy of oxygen. This further optimises the interfacial charge distribution of the material and enhances the efficiency of electrical signal conduction.[40] These results further illustrate the successful doping of Au.

Fig. S3A and B show the Brunauer–Emmett–Teller (BET) plots of CB and CBAu, respectively. The specific surface area of the carbon material is 375.41 $m^2\ g^{-1}$, while that of CBAu is 11.79 $m^2\ g^{-1}$. During the gold doping process, the micropores of the carbon material are occupied by gold, which significantly reduces the internal surface area available for gas adsorption, thus leading to a decrease in the BET-specific surface area. Au NPs successfully fill the microporous structure of the carbon material, which reduces the internal surface area for gas adsorption, yet constructs a large number of Au active sites on the material surface. These sites provide a dedicated binding platform for the covalent anchoring of CP. As shown in Fig. S3C, cyclic voltammetry (CV) is employed for electrochemical characterization of the material. Fig. S3D is the linear fitting curve of scan rate and peak current. According to the Randles–Sevcik equation[41] (SI; eqn (S1)), the effective electrochemically active surface area of CBAu is 0.25 cm^2. This indicates that CBAu has active sites that participate in electrochemical reactions. Therefore, based on the above discussion, CBAu composites can be used as electrode materials to further construct high-performance electrochemical DNA biosensors.

3.2. Characterization of the electrochemical biosensor

The current signal level of biosensors is not only directly related to the concentration of the target substance T but also depends on the precise design of the DNA probe. The "switch" characteristic of CP, combined with the signal amplification ability of Au-FcDNA, together constitute the core advantages of the sensor's high specificity and high sensitivity. The sensing principle is shown in Fig. 2A. When the T exists on the electrode surface, CP will open and combine with T to form a double strand, and the conformational changes of the returning probe have strict target selectivity, responding only to the target sequence. At this time, the addition of Au-FcDNA will bind with the double strand, and the large amount of Fc will have a redox reaction on the surface of the electrode to produce a high signal, realizing the sensitive detection of the trace T. If there is no T on the electrode surface, the CP will not be turned on, and the weak current signal generated by the non-specific adsorption of Au-FcDNA on the electrode surface, which belongs to the background signal current value. In addition, the formation of Au-FcDNA was verified by UV-vis spectroscopy. As shown in Fig. S4A, the absorption peak of bare Au NPs is about 522 nm. After modification with FcDNA, the DNA shows a sharp characteristic peak at 260 nm due to the formation of Au-FcDNA.[42] At the same time, the absorption peak of Au NPs shifts from 522 nm to 524 nm. It indicates that FcDNA is stably modified on the surface of Au NPs through Au–S bonds. This stable covalent binding not only prevents signal drift caused by probe detachment but also enhances the electron transfer efficiency between Fc and the electrode surface through the nanoscale effect of Au NPs. The density of DNA probes on CBAu was calculated using chronocoulometric (CC) measurements, as shown in Fig. S4B. According to eqn (S2) and (S3), the DNA density was calculated to be 2.276 $\times$1013 molecules cm^{-2}, which provides sites for subsequent reactions.[43,44] Fig. 2B shows the validation of the biosensor probe strategy using polyacrylamide gel electrophoresis, where the molecular weight size affects its migration rate on the gel. Lanes 1, 2, and 3 are CP, T, and FcDNA, respectively; their molecular weight

 This journal is © The Royal Society of Chemistry and the Centre National de la Recherche Scientifique 2025

Published on 19 September 2025. Downloaded by Guangxi University on 9/20/2025 2:29:51 PM.

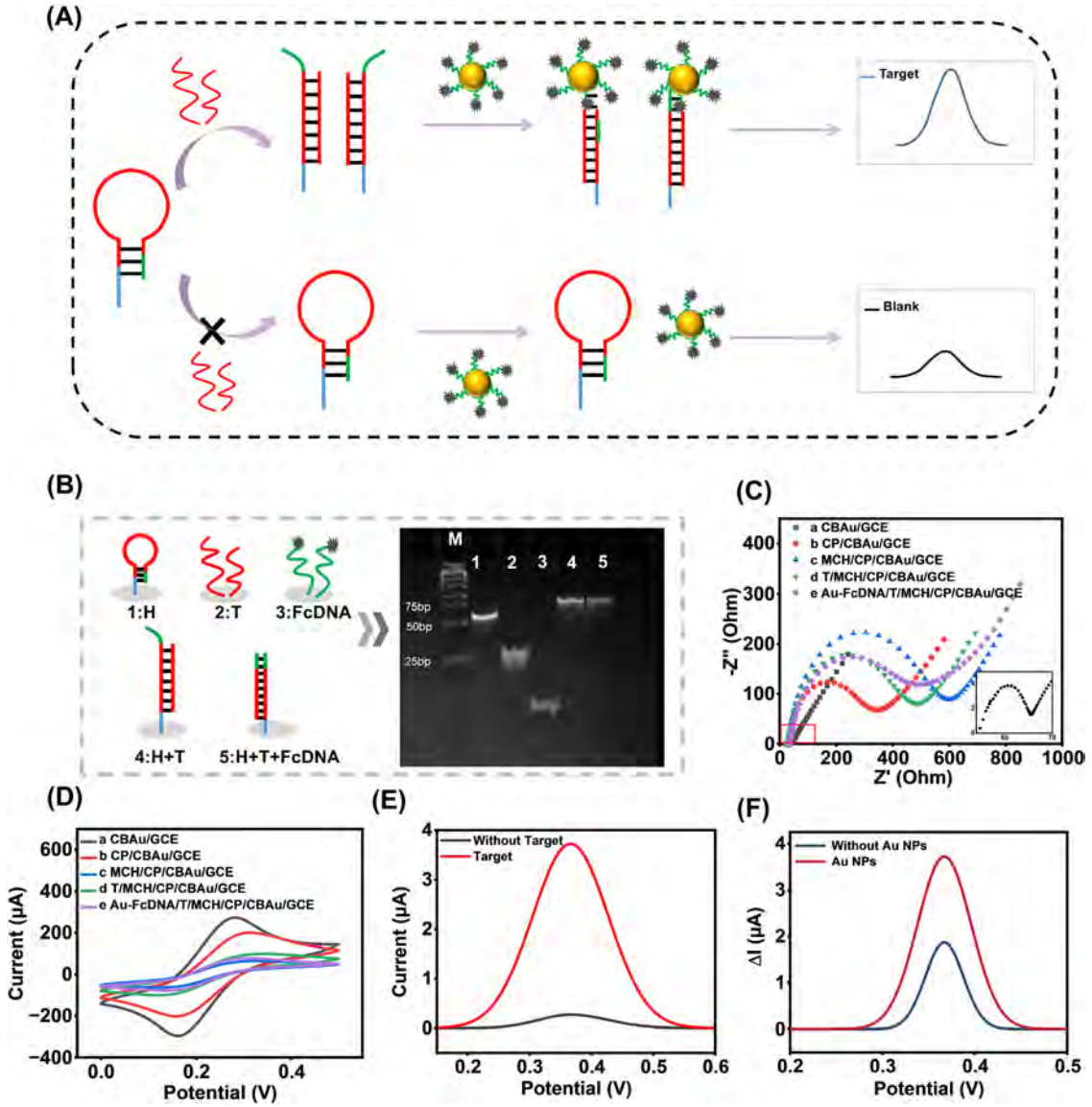


Fig. 2 Feasibility verification of the electrochemical biosensor detection strategy. (A) Schematic diagram of the detection strategy. (B) The programmed detection strategy was characterized by using 20% polyacrylamide gel. (C) Different modified steps of electrodes by CV and (D) EIS measurements with the Nyquist plots in 5 mM of $K_3[Fe(CN)_6]/K_4[Fe(CN)_6]$ solution containing 0.1 M of KCl. (E) and (F) DPV responses of the electrochemical biosensor.

sizes are 58 bp, 28 bp, and 8 bp. From the electrophoretic bands, it can be seen that the migration rate slows down with the increase of molecular weight. Lane 4 is the product of the combination of CP and T, and due to the increase in molecular weight, the movement of CP–T is slower than that of the previous three lanes. Lane 5 is the product of the combination of CP, T, and FcDNA, Due to the small molecular weight of FcDNA, its electrophoretic band is similar to lane 4. Lane 5 is the product of the combination of CP, T, and FcDNA; due to the small molecular weight of FcDNA, its electrophoretic band is similar to lane 4.

Fig. 2C and D show the step-by-step construction process of the biosensor characterized by electrochemical impedance spectroscopy (EIS) and CV. The EIS high-frequency semicircular cross-section corresponds to the charge-transfer confinement process, where an increase in the semicircular diameter indicates an increase in the interfacial charge-transfer resistance (R_{ct}). The semicircle diameter is the impedance of CBAu/GCE (R_{ct} = 11 Ω, Fig. 2C, curve a), which has a faster charge transfer process at this point due to the excellent electrical conductivity of the material itself. The attachment of CP generates a spatial potential resistance on the electrode surface, affecting the electron transfer rate and decreasing the redox current.[45] Therefore, the R_{ct} value of CP/CBAu/GCE increases to approximately 313 Ω compared with that of CBAu/GCE (Fig. 2C, curve b). Passivating the surface with MCH further leads to a significant increase in the R_{ct} value (about 573 Ω, Fig. 2C, curve c), because MCH can form a film with a thickness of several molecular layers on the electrode surface, which completely seals the Au on the electrode surface and hinders the charge transfer between potassium ferricyanide and the electrode surface.[46] Hybridization of the T with CP decreases the spatial potential resistance

Published on 19 September 2025. Downloaded by Guangxi University on 9/20/2025 2:29:51 PM.

of the electrode surface, and the CP opens to form a double strand (about 460 Ω, Fig. 2C, curve d). The Au-FcDNA hybridizes to the open double strand, and the increase in the surface material of the electrode level after hybridization increases the impedance. Still, since gold nanoparticles increase the electrical conductivity of the electrode surface, they also improve the electron transfer rate (about 465 Ω, Fig. 2C, curve e). The results obtained by cyclic voltammetry (CV) are consistent with those of EIS, both of which prove the successful construction of the biosensor.

Differential pulse voltammetry (DPV) was used to test the current's magnitude, indicating the target's presence or absence (Fig. 2E). A relatively large current value will be generated when the T exists in the reaction system (red line). At this time, T will open CP on the electrode surface and connect with Au-FcDNA, and Fc will undergo redox reactions on the electrode surface. When T is absent, the current signal is only generated by non-specific adsorption (black line); the current signal is relatively weak. Subsequent DPV tests verified the effect of FcDNA enrichment on gold nanoparticles by comparing the current response in Fig. 2F. The results show that the current signal of Au-FcDNA is twice that of FcDNA, indicating that the enrichment effect of gold nanoparticles has enhanced the detection ability of the biosensor. The above results further prove the successful construction of the biosensor.

3.3. Performance testing of the biosensor

To improve the detection ability of the biosensor, the experimental parameters (incubation time of CP and T, concentration of CP, and volume ratio (μL) of Au NPs to FcDNA) were optimized (Fig. S5, ΔI is the difference in current before and after the biosensor detects T). According to the experimental results, optimal experimental conditions were obtained when the incubation time of T was 90 min, the incubation time of CP was 120 min, the concentration of CP was 0.8 μM, and the volume ratio (μL) of Au NPs to FcDNA was 5/40. A standard curve was constructed according to the above experimental conditions.

The constructed biosensors were incubated with different concentrations of T, and the current signal changes are observed using a DPV test (Fig. 3A). The peak current of Fc increased with the increase in *S. costatum* DNA concentration. The linear range is 100 fM–10 nM, and a relationship is established between ΔI and the logarithm of *S. costatum* DNA concentration. The fitting formula is:

$$\Delta I = 0.72 + 5.60 \lg C \quad (1)$$

ΔI represents the signal value, μA; C represents the concentration of target DNA, μM. R^2 = 0.96 (Fig. 3B). The limit of detection (LOD) and limit of quantification (LOQ) were calculated using eqn (S4) and (S5). The LOD was calculated as 29.47 fM and the LOQ as 90.47 fM according to the above formula.

For selectivity, excluding potential interference from other algae in the marine environment is an essential indicator of *S. costatum* DNA sensing. Therefore, highly incident red tide algae (*P. donghaiense*, *A. sanguinea*, *P. minimum*, and *H. akashiwo*) were selected as interferons for the selectivity test, in which the concentration of interferons was nM, the concentration of the

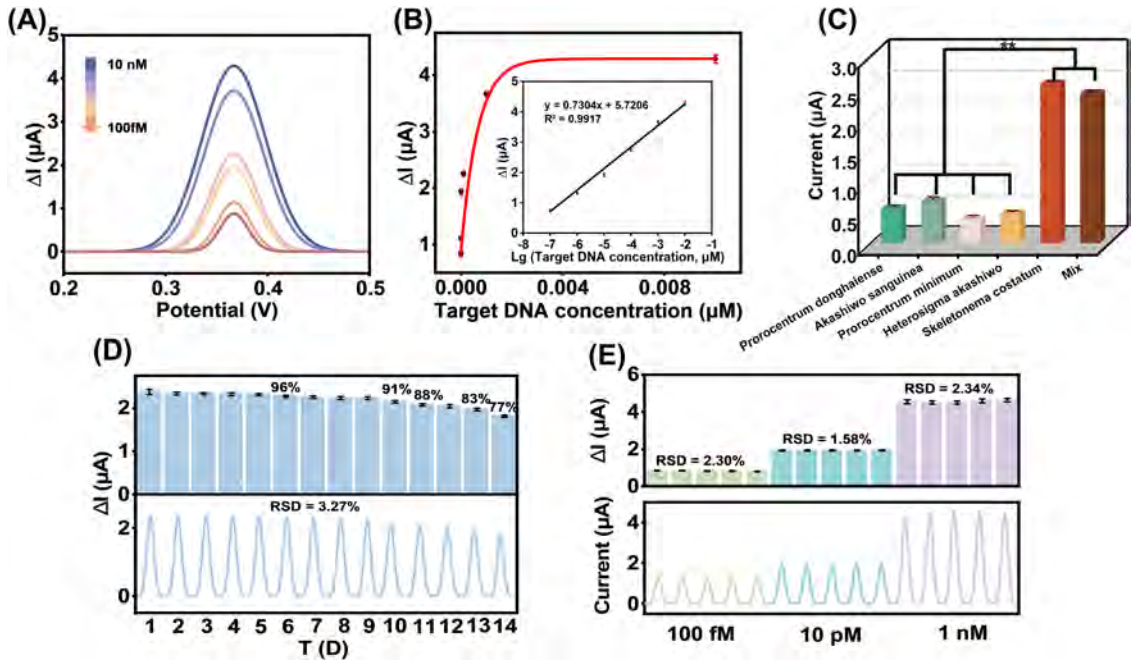


Fig. 3 Electrochemical biosensor performance testing. (A) Current response values of targets at different concentrations (100 fM, 1 pM, 10 pM, 100 pM, 1 nM, and 10 nM) and (B) the corresponding calibration curve. (C) Selectivity of the biosensor. (D) Stability of current response values for detecting targets after storage at 4 °C for 1–14 days. (E) Reproducibility of the biosensor (targets at 100 fM, 10 pM, and 1 nM, respectively). The error bars represent the standard deviations (n = 5). $^{**}P \leq 0.01$.

 This journal is © The Royal Society of Chemistry and the Centre National de la Recherche Scientifique 2025

Published on 19 September 2025. Downloaded by Guangxi University on 9/20/2025 2:29:51 PM.

target was 100 pM, and the mixtures contained the target and interferons with concentrations of 100 pM and 1 nM, respectively. As shown in Fig. 3C, the current response of the target is nearly 4 times higher than that of the interferon, and the current response of the interferon is almost equal to the blank. In addition, even for a mixture with a concentration ratio of 10, the current response is very close to that of the target alone. Subsequent significance analyses of the current values for each group show $P \leq 0.01$ indicating that 1 nM (10 fold) of interferons have no significant effect on the target signal. This arises from two aspects of advantage: on one hand, the hairpin structure of the CP achieves precise recognition through base complementary pairing, opening its conformation only for the specific sequence of *S. costatum*, while maintaining closure for the non-complementary sequences of interfering algae, thereby blocking non-specific binding at the molecular level; on the other hand, the uniform spherical structure of the CBAu material and the ordered distribution of surface Au sites ensure that the probe is fixed at a uniform density, reducing non-specific adsorption caused by differences in material morphology, thus further enhancing the selective barrier.

The stability and reproducibility of the biosensor were tested as shown in Fig. 3D and E. The prepared biosensor was tested after being stored at room temperature for 1–14 days, respectively, to evaluate the stability of the sensing system. The DPV response shows that the current peak's relative standard deviation (RSD) within fourteen days is 3.27% when the T concentration is 100 pM. The highly graphitized structure of CBAu endows the material with excellent chemical stability. Furthermore, the DNA probes stably bind to the gold sites on the surface of CBAu through Au–S bonds. Combined with the passivation effect of MCH, this forms a dense probe-sealing agent bilayer structure, significantly reducing the risk of probe detachment. In addition, the biosensor was tested for

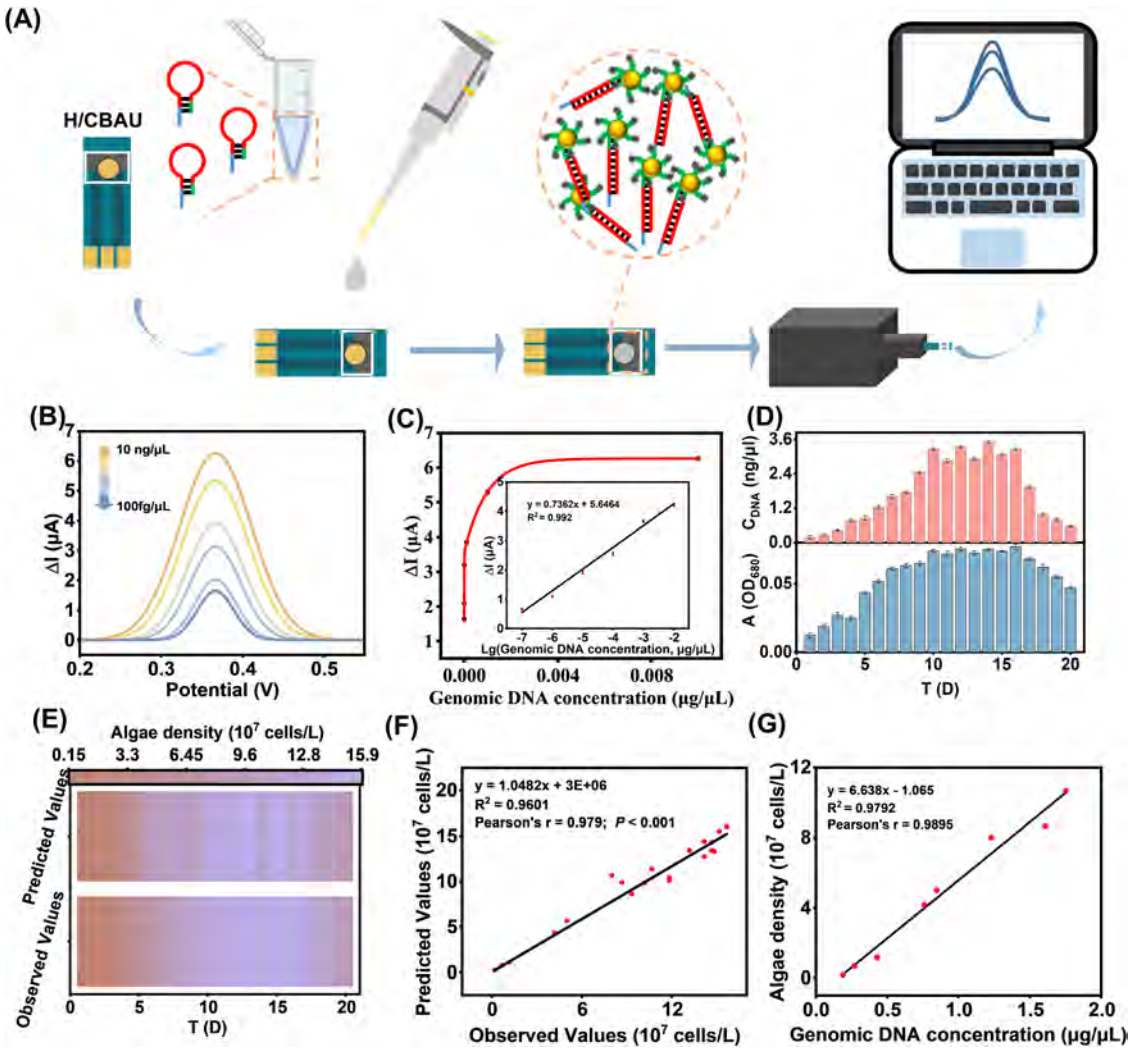


Fig. 4 Schematic diagram of portable biosensor detection. (A) Schematic diagram of the process of on-site detection by a portable biosensor. (B) Current response values at different concentrations (100 fg μl^{-1}, 1 pg μl^{-1}, 10 pg μl^{-1}, 100 pg μl^{-1}, 1 pg μl^{-1} and 10 pg μl^{-1}) and (C) the corresponding calibration curve. (D) DNA concentration and absorbance at 680 nm during the growth cycle of *S. costatum*. (E) Observed and predicted values of *S. costatum* algae density and (F) linear relationship. (G) A linear relationship between algae density and genomic DNA concentration.

Published on 19 September 2025. Downloaded by Guangxi University on 9/20/2025 2:29:51 PM.

reproducibility with target substances at 100 fM, 10 pM, and 1 nM, respectively. The results show the relative standard deviations of the current peak T, which are2.30%, 1.58% and 2.34% respectively, all within the acceptable range. Spiked recovery experiments were performed for different concentrations to assess the accuracy and applicability of the biosensor. As shown in Table S3, the recovery rates obtained for different concentrations of T (5×10^{-3}, 5×10^{-4}, 5×10^{-5} and 5×10^{-6} μM) are 102.98%, 104.30%, 94.46% and 96.96%, respectively, which is a desirable recovery for the biosensor. The satisfactory stability and reproducibility of the biosensor are attributed to the material having stable chemical properties, which ensures the biosensor's ability to test in complex testing environments.

3.4. Verification of accuracy

A portable biosensor based on screen-printed carbon electrode (SPCE) is used to further explore the applicability of electrochemical biosensors (Fig. 4A). The working curve of the portable biosensor for detecting target genomic DNA is constructed in the laboratory. As the concentration of the target increases, ΔI increases. A relationship is established between ΔI and the logarithm of the target genomic DNA concentration ranges from 100 fg μL^{-1} to 10 ng μL^{-1}. The fitting formula is:

$$\Delta I = 0.88 + 7.77 \lg C \quad (2)$$

ΔI represent the signal value, μA; C represents the concentration of genomic DNA, μg μL^{-1} and $R^2 = 0.98$ (Fig. 4B and C). The LOD and LOQ were calculated by eqn (S4) and (S5). The LOD was calculated as 51.28 fg μL^{-1} and the LOQ as 137.85 fg μL^{-1} according to the above formula. The higher sensitivity and broader linear range indicate that this biosensor can detect the target sensitively. The biosensor is also compared with assays used to identify and quantify other algae, and the results show that the detection ability of this biosensor is acceptable and competitive (Table S4).

Algae density and DNA concentration were analyzed using an electrochemical biosensor and optical microscope to construct a quadratic polynomial regression model. Subsequently, *S. costatum* was cultured in the laboratory for 20 days to observe its growth, and algal growth curves (Fig. 4D and Fig. S6A), density (Fig. 4E and Fig. S6B), and the corresponding DNA concentrations (Fig. 4D and Fig. S6C) were tested. The specific experimental details are shown in SI S1.6 and S1.7. They can be used for subsequent evaluation of biosensor suitability. A linear analysis is conducted on the algal density of *S. costatum* cultured for 20 days and the predicted algal density values (Fig. 4F). There is a significantly correlated relationship between the algal density detected by the biosensor and the observed algal density ($r = 0.98$; $P < 0.001$), showing a relatively linear relationship. Additionally, a relationship between genomic DNA and algal density was established, which also showed a good linear relationship ($R^2 = 0.9792$, Pearson's $r = 0.9895$, Fig. 4G). On one hand, the rich Au active sites on the surface of CBAu ensure a high density of DNA probes, with sufficient recognition sites ensuring that the DNA of algal cells at different concentrations can be fully captured, thus avoiding signal saturation caused by insufficient probes; on the other hand, the signal amplification mechanism of Au-FcDNA significantly enhances the signal distinguishability of low-concentration algal cells, allowing for quantifiable current responses even during the late logarithmic growth phase when algal density is relatively low, thereby extending the linear detection range. In order to verify the accuracy of the biosensor, the densities of different gradients of algal sap are selected to do a linear analysis with the corresponding current values (Fig. S6D). As the density of *S. costatum* algae increased, ΔI increased, and a relationship is established between. ΔI and the logarithm of the density of *S. costatum* algae. The fitting formula is:

$$\Delta I = 0.90 + 1.60 \lg C \quad (3)$$

ΔI represents the signal value, μA; C represents the concentration of cells, cells per L. $R^2 = 0.96$, based on the calculation of eqn (S4) and (S5), LOD = 2672 cells per L, LOQ = 4575 cells per L. This linear relationship can be helpful for the application of subsequent field tests.

3.5. Analysis of environmental samples

Fig. 5A is a flowchart of actual sample testing in the field. A portable biosensor was used to detect the DNA of *S. costatum* at five sampling sites in the Beibu Gulf, China. Fig. 5B shows the geographical location of each sampling site and indicates the algal density by color. The algal densities of P1 and P2 are 1.97×10^5 and 2.92×10^4 cells per L, well below the outbreak threshold. Fig. 5C shows the *S. costatum* DNA concentration level of positive samples obtained by the portable biosensor, consistent with the results measured by ddPCR ($P > 0.05$; Table S5). The strong electrochemical signals detected at P1 and P2 indicate a high target concentration. In contrast, the biosensor can only detect current signals equivalent to the background at P3, P4, P5, P6, P7, P8 and P9. (Fig. 5D). The experimental results are consistent with the situation of the ecological survey at that time. These results prove that the portable electrochemical biosensor can be used for field detection.

4. Conclusion

In this work, the detection of *S. costatum* was realized by enriching FcDNA using Au NPs and introducing nanomaterial CBAu, which performed well in amplifying the detection signal. Firstly, the nanomaterials have excellent electrical conductivity, indicating a high electron transport rate, which can improve the detection ability of the biosensor. Secondly, the hairpin probe has stability and selectivity as a capture probe, which improves the specific detection of the target; finally, the current signal is amplified by enriching FcDNA with Au NPs to realize the detection of the trace target. This biosensor has excellent sensitivity, with the LOD and LOQ calculated as 51.28 fg μL^{-1} and 137.85 fg μL^{-1}. Moreover, this biosensor's satisfactory applicability and accuracy were demonstrated during the on-site detection of *S. costatum* in the Beibu Gulf. The *S. costatum*

 This journal is © The Royal Society of Chemistry and the Centre National de la Recherche Scientifique 2025

Published on 19 September 2025. Downloaded by Guangxi University on 9/20/2025 2:29:51 PM.

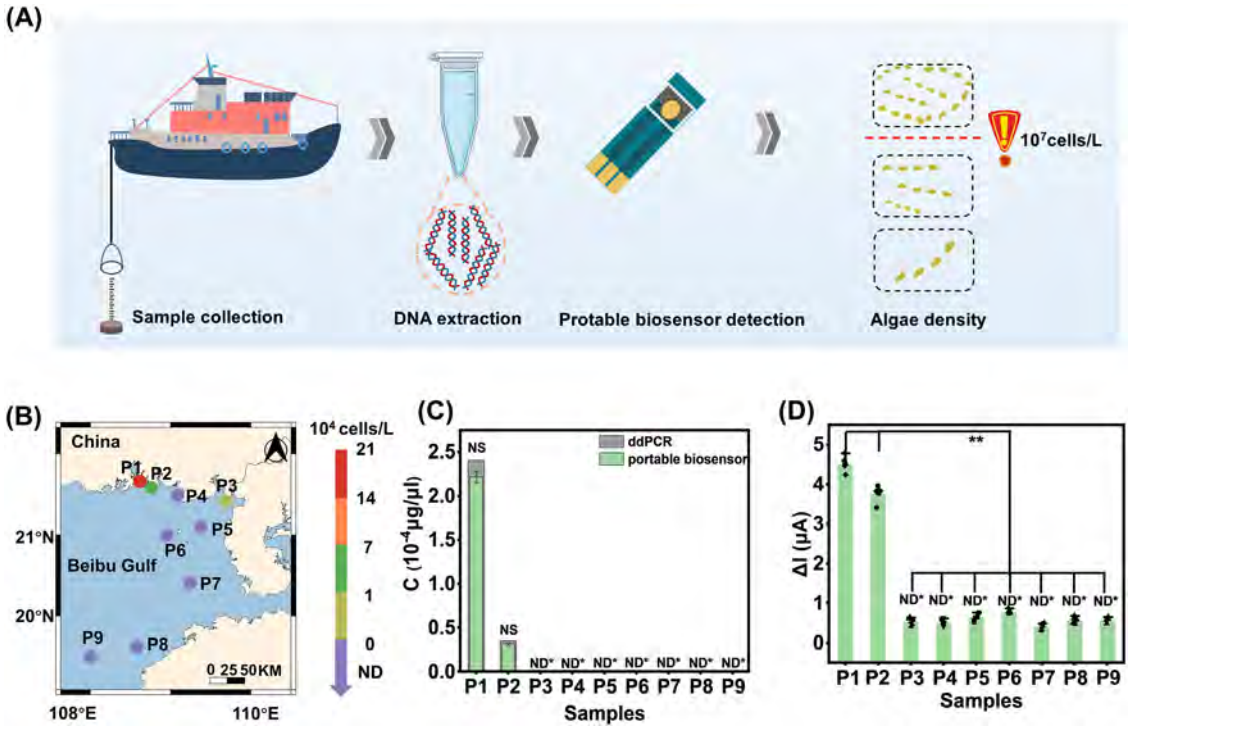


Fig. 5 Schematic diagram of offshore detention. (A) Schematic diagram of on-site sampling and testing. (B) Distribution of sampling sites in Beibu Gulf and colors represent the density of algae at different sites. (C) DNA concentration was provided by the portable biosensor, and those obtained by ddPCR were in all examined on-site samples. (D) The value of the station current. ND*: non-detectable, NS: *$P > 0.05$ and **$P \leq 0.01$.

DNA concentration obtained in this area by the biosensor is consistent with that of ddPCR ($P > 0.05$). This biosensor can mainly be attributed to the ultrasensitive detection of trace amounts of *S. costatum* DNA in three aspects. Firstly, the excellent electrical conductivity of CBAu enhances the interfacial transfer rate of electrons, enabling the biosensor to respond sensitively to the electron transfer in the redox reaction of FcDNA. Secondly, the stability and selectivity of the hairpin probe, acting as a capture probe, improve the specific recognition ability of the target. Thirdly, the current signal is amplified by enriching FcDNA with Au NPs, achieving the detection of trace targets. However, the biosensor for detecting *S. costatum* should undergo further validation and address some issues, such as the ease of DNA enrichment. Nevertheless, it offers excellent potential for subsequent integration into miniaturized devices, bringing it closer to field detection. Thus, this work is a breakthrough for the rapid and straightforward detection of *S. costatum* in the field.

Author contributions

Ziyang Xian and Yayi He: writing – original draft, validation, methodology, data curation, and conceptualization. Chaoxin Zhang, Hao Fu, Yaling Liu and Tao Zhang: investigation and data curation. Shaopeng Wang and Shan Lu: funding acquisition. Man Zhang: writing – review & editing and supervision. Liwei Wang: writing – review & editing.

Conflicts of interest

There are no conflicts to declare.

Data availability

The datasets used and/or analysed during the current study are available from the corresponding author on reasonable request.

All data generated or analysed during this study are included in this published article and its SI. Supplementary information: Experimental processes and images of primer screening, feasibility verification, and condition optimization in the construction process of electrochemical biosensors, as well as the experiments and images of laboratory-cultured algae samples. See DOI: **https://doi.org/10.1039/d5nj02636a**.

Acknowledgements

This work was supported by the Guangxi Major Talent Project (Bagui Young Elite Talents), the Self-Topic Project of Guangxi Laboratory on the Study of Coral Reefs in the South China Sea, Nanning, China (No. GXLSCRSCS2023102), the National General Innovation Training Program of Guangxi University (No. 202410593444), the Natural Science and Technology Innovation and Doubling Plan Project, University Development Guangxi (No. 2022BZRC025 and 2024BZRC009).

Published on 19 September 2025. Downloaded by Guangxi University on 9/20/2025 2:29:51 PM.

Notes and references

1 H. J. Jeong, H. C. Kang, A. S. Lim, S. H. Jang, K. Lee, S. Y. Lee, J. H. Ok, J. H. You, J. H. Kim, K. H. Lee, S. A. Park, S. H. Eom, Y. D. Yoo and K. Y. Kim, *Sci. Adv.*, 2021, **7**, eabe4214.

2 A. Miralto, G. Barone, G. Romano, S. A. Poulet, A. Ianora, G. L. Russo, I. Buttino, G. Mazzarella, M. Laabir, M. Cabrini and M. G. Giacobbe, *Nature*, 1999, **402**, 173–176.

3 S. Alvarez, C. E. Brown, M. Garcia Diaz, H. O'Leary and D. Solís, *J. Environ. Manage.*, 2024, **351**, 119811.

4 Z. Ni, L. Tan, J. Wang, Y. Chen, N. Zhang, F. Meng and J. Wang, *Sci. Total Environ*, 2023, **857**, 159614.

5 V. Giussani, V. Asnaghi, A. Pedroncini and M. Chiantore, *Harmful Algae*, 2017, **68**, 97–104.

6 J. Wei, X. Xie, F. Huang, L. Xiang, Y. Wang, T. Han, I. Y. Massey, G. Liang, Y. Pu and F. Yang, *Environ. Pollut.*, 2020, **256**, 113444.

7 J. Li, X. Xian, X. Xiao, S. Li and X. Yu, *Environ. Pollut.*, 2023, **335**, 122256.

8 A. Srivastava, G.-G. Choi, C.-Y. Ahn, H.-M. Oh, A. K. Ravi and R. K. Asthana, *Water Res.*, 2012, **46**, 817–827.

9 M. Vassalli, A. Penna, F. Sbrana, S. Casabianca, N. Gjeci, S. Capellacci, V. Asnaghi, E. Ottaviani, V. Giussani, L. Pugliese, C. Jauzein, R. Lemée, M. A. Hachani, S. Turki, L. Açaf, M. A.-A. Saab, A. Fricke, L. Mangialajo, R. Bertolotto, C. Totti, S. Accoroni, E. Berdalet, M. Vila and M. Chiantore, *Ecol. Indic.*, 2018, **85**, 1092–1100.

10 X. Hai, Y. Li, C. Zhu, W. Song, J. Cao and S. Bi, *TrAC, Trends Anal. Chem.*, 2020, **133**, 116098.

11 M. Negahdary and L. Angnes, *Coord. Chem. Rev.*, 2022, **464**, 214565.

12 D. N. Roxby, H. Rivy, C. Gong, X. Gong, Z. Yuan, G.-E. Chang and Y.-C. Chen, *Biosens. Bioelectron.*, 2020, **165**, 112420.

13 S. Oloketuyi, E. Mazzega, J. Zavašnik, K. Pungjunun, K. Kalcher, A. de Marco and E. Mehmeti, *Biosens. Bioelectron.*, 2020, **154**, 112052.

14 S. R. Bickman, K. Campbell, C. Elliott, C. Murphy, R. O'Kennedy, P. Papst and M. J. Lochhead, *Environ. Sci. Technol.*, 2018, **52**, 11691–11698.

15 Y. Seo, Y. Yoon, M. Lee, M. Jang, T.-H. Kim, Y. Kim, H. Y. Yoo, J. Min and T. Lee, *Colloids Surf., B*, 2023, **225**, 113218.

16 E. I. Zakariah, E. Y. Ariffin, D. Nokarajoo, M. A. Mohamed Akbar, Y. H. Lee and S. A. Hasbullah, *Microchem. J.*, 2024, **199**, 109997.

17 R. Eivazzadeh-Keihan, E. Bahojb Noruzi, E. Chidar, M. Jafari, F. Davoodi, A. Kashtiaray, M. Ghafori Gorab, S. Masoud Hashemi, S. Javanshir, R. Ahangari Cohan, A. Maleki and M. Mahdavi, *Chem. Eng. J.*, 2022, **442**, 136183.

18 Y. Yang, X. Yang, Y. Yang and Q. Yuan, *Carbon*, 2018, **129**, 380–395.

19 J. Wen, Y. Xu, H. Li, A. Lu and S. Sun, *Chem. Commun.*, 2015, **51**, 11346–11358.

20 Z. Hua, T. Yu, D. Liu and Y. Xianyu, *Biosens. Bioelectron.*, 2021, **179**, 113076.

21 H.-B. Wang, H.-D. Zhang, Y.-H. Zhang, H. Chen, L.-L. Xu, K.-J. Huang and Y.-M. Liu, *J. Electrochem. Soc.*, 2015, **162**, B173.

22 H. Zhang, Z. Xing, M. Pan, H.-B. Wang and Y.-M. Liu, *J. Electrochem. Soc.*, 2020, **167**, 126504.

23 Z. Liu, J. Tao, Z. Zhu, Y. Zhang, H. Wang, P. Pang, H. Wang and W. Yang, *J. Electrochem. Soc.*, 2022, **169**, 027504.

24 P. Vorobjev, A. Epanchintseva, A. Lomzov, A. Tupikin, M. Kabilov, I. Pyshnaya and D. Pyshnyi, *Langmuir*, 2019, **35**, 7916–7928.

25 Y. Zhang, G. M. Zeng, L. Tang, J. Chen, Y. Zhu, X. X. He and Y. He, *Anal. Chem.*, 2015, **87**, 989–996.

26 H. Peng, X.-F. Li, H. Zhang and X. C. Le, *Nat. Commun.*, 2017, **8**, 14378.

27 X. Yang, Y. Tang, S. D. Mason, J. Chen and F. Li, *ACS Nano*, 2016, **10**, 2324–2330.

28 Y. Cheng, H. Zhao, Y. Zhao, J. Cao, J. Zheng and G. Ji, *Carbon*, 2020, **161**, 870–879.

29 Y. Tan, Y. Liu, L. Kong, L. Kang and F. Ran, *J. Power Sources*, 2017, **363**, 1–8.

30 Y. Dong, D. Zhang, D. Li, H. Jia and W. Qin, *Sci. China Mater.*, 2023, **66**, 1249–1255.

31 H. Zhang, S. Yao, X. Song, K. Xu, J. Wang, J. Li, C. Zhao and M. Jin, *Talanta*, 2021, **232**, 122448.

32 G. Shen, Y. Xu, B. Liu, P. Du, Y. Li, J. Zhu and D. Zhang, *J. Alloys Compd.*, 2016, **680**, 553–559.

33 Y. Wang, W. Wang, J. Sun, C. Sun, Y. Feng and Z. Li, *Carbon*, 2018, **135**, 1–11.

34 S. Li, Y. Huang, D. Ling, N. Zhang, M. Zong, X. Qin and P. Liu, *J. Colloid Interface Sci.*, 2019, **544**, 188–197.

35 J. Zhu and S. Mu, *Adv. Funct. Mater.*, 2020, **30**, 2001097.

36 L. Liu, W. Zhang, B. Lu, Z. Cheng, H. Cao, J. Li, Z. Fan and X. An, *Biomass Bioenergy*, 2024, **186**, 107265.

37 J.-F. Veyan, E. de Obaldia, J. J. Alcantar-Peña, J. Montes-Gutierrez, M. J. Arellano-Jimenez, M. José Yacaman and O. Auciello, *Carbon*, 2018, **134**, 29–36.

38 Y. Zhang, X. Li, P. Dong, G. Wu, J. Xiao, X. Zeng, Y. Zhang and X. Sun, *ACS Appl. Mater. Interfaces*, 2018, **10**, 42796–42803.

39 A. I. M. Rabee, D. Zhao, S. Cisneros, C. R. Kreyenschulte, V. Kondratenko, S. Bartling, C. Kubis, E. V. Kondratenko, A. Brückner and J. Rabeah, *Appl. Catal., B*, 2023, **321**, 122083.

40 F. Liao, Y. Shi, Q. Dang, H. Yang, H. Huang, Z. Kang and M. Shao, *J. Colloid Interface Sci.*, 2022, **606**, 1274–1283.

41 Y. Ma, Y. Wang, D. Xie, Y. Gu, X. Zhu, H. Zhang, G. Wang, Y. Zhang and H. Zhao, *Chem. Eng. J.*, 2018, **347**, 953–962.

42 X.-J. Yang, K. Zhang, T.-T. Zhang, J.-J. Xu and H.-Y. Chen, *Anal. Chem.*, 2017, **89**, 4216–4222.

43 F. Jia, D. Liu, N. Dong, Y. Li, S. Meng and T. You, *Biosens. Bioelectron.*, 2021, **182**, 113169.

44 J. Zhu, H. Gan, J. Wu and H. Ju, *Anal. Chem.*, 2018, **90**, 5503–5508.

45 W. Zhang, M. B. Dixon, C. Saint, K. S. Teng and H. Furumai, *ACS Sens.*, 2018, **3**, 1233–1245.

46 H. Shen, J. Yang, Z. Chen, X. Chen, L. Wang, J. Hu, F. Ji, G. Xie and W. Feng, *Biosens. Bioelectron.*, 2016, **81**, 495–502.

 This journal is © The Royal Society of Chemistry and the Centre National de la Recherche Scientifique 2025

INTERNATIONAL JOURNAL OF SYSTEMATIC AND EVOLUTIONARY MICROBIOLOGY

RESEARCH ARTICLE

Hu *et al.*, *Int. J. Syst. Evol. Microbiol.* 2025;75:006928

DOI 10.1099/ijsem.0.006928

MICROBIOLOGY SOCIETY

Carbonatibacter coralli gen. nov., sp. nov., a carbonate-producing and vitamin B_{12}-sharing bacterium isolated from coral *Porites lutea*, reclassification of *Kiloniellaceae* and proposal of *Aestuariispiraceae* fam. nov.

Siyu Hu[1], Kun Lu[1], Chenyan Wang[1], Mi Li[1], Jinsheng Huang[1] and Guanghua Wang[2,*]

Abstract

A Gram-stain-negative, non-spore-forming, carbonate-producing, vitamin B_{12}-sharing, aerobic rod, designated strain GXU_MW_B19^T, was isolated from coral *Porites lutea*. Cells grew at 20–40 °C, pH 6.5–10 and no more than 5% NaCl (w/v). Global alignment based on 16S rRNA gene sequence indicated that the new isolate is most close to members of the genus *Kiloniella* with identities of 92.9–94.1%, while sharing no more than 91.7% similarity with other type strains. The maximum average nucleotide identity and average amino acid identity to closely related species were 69.5 and 62.8%, respectively. Phylogenetic analysis based on both 16S rRNA gene sequences and the whole-genome sequences indicated that strain GXU_MW_B19^T forms a stable cluster with genus *Kiloniella* in the order *Rhodospirillales*. The genome G+C content was 54.5 mol%. The dominant cellular fatty acids (≥10%) included iso-$C_{10:0}$2OH, $C_{12:1}$, $C_{14:1}$ ω5c and iso-$C_{17:0}$3OH. The major polar lipids comprised phosphatidylethanolamine, diphosphatidylglycerol, unidentified ninhydrin-positive lipid and three unidentified lipids. Alpha-1,6-glucosidase, alkaline phosphatase, isochorismate-related enzymes and P2-like prophage-related proteins were encoded in the new isolate, all of which were absent in closely related species. Based on these distinct phylogenetic, genomic and chemotaxonomic characteristics, the new isolate is suggested to represent a new species in a new genus, for which the name *Carbonatibacter coralli* gen. nov., sp. nov. is proposed. The type strain is GXU_MW_B19^T (=KCTC 8092^T=MCCC 1K08794^T). Finally, phylogenetic analyses led to the reclassification of the *Kiloniellaceae* and the proposal of *Aestuariispiraceae* fam. nov.

INTRODUCTION

Kiloniellaceae, a family within the phylum *Pseudomonadota*, was proposed by Wiese *et al.* based on the genus *Kiloniella* [1] and revised by Hördt *et al.* [2]. However, the classification range of *Kiloniellaceae* remains controversial. At the time of writing, the genera *Kiloniella* and *Aestuariispira* have been assigned to this family [2]. Additionally, three other genera, namely, *Thalassocola*, *Marivibrio* and *Curvivirga*, have been tentatively assigned to this family due to lack of genomic data or based on *stare decisis* [2, 3]. Meanwhile, the Genome Taxonomy Database (GTDB, https://gtdb.ecogenomic.org/) indicates that this family contains 5 subclades and at least 15 genera.

Members of *Kiloniellaceae* are usually marine organisms associated, such as sponges [4, 5], corals [5–8], lobster guts [9], crabs and clams [10], shrimp [11], fish [12] and macroalgae [1], in addition to seawater [13, 14] and sediments [15]. Especially, some *Kiloniellaceae* bacteria were closely associated with coral *Symbiodiniaceae* algae (could not be separated from algae by filtration) [16]. Cells are typically rod-, spiral- or vibrio-shaped; mesophilic; chemoheterotrophic; and moderately halotolerant [1–3, 17–19]. However, the function of these bacteria is still unclear.

Marine microbial carbon sink has become a research hotspot due to global warming caused by excess emissions of carbon dioxide [20], and calcium carbonate precipitation from algae–bacteria consortium is believed to be one of the important microbial carbon

Author affiliations: [1]Guangxi Laboratory on the Study of Coral Reefs in the South China Sea, Nanning 530004, PR China; [2]School of Marine Sciences, Guangxi University, Nanning 530004, PR China.
***Correspondence:** Guanghua Wang, wgh@gxu.edu.cn
Keywords: carbonate; *Carbonatibacter coralli*; vitamin B_{12}.
Abbreviations: AAI, average amino acid identity; ANI, average nucleotide identity; GTDB, Genome Taxonomy Database; JCM, Japan Collection of Microorganisms; Q-10, ubiquinone 10.
The 16S rRNA gene and whole-genome sequence were deposited in GenBank under PP719616 and JBBUTJ000000000, respectively.
Six supplementary figures and three supplementary tables are available with the online version of this article.

006928 © 2025 The Authors

sink channels [21]. Meanwhile, vitamin B_{12} is vital to animals, most of the algae and bacteria, but can only be synthesized *de novo* by a few bacteria or archaea [22, 23]. In this study, a carbonate-producing and vitamin B_{12}-sharing *Kiloniellaceae* strain, designated GXU_MW_B19^T, was isolated from *Porites lutea* and characterized by polyphasic identification.

HABITAT AND ISOLATION

Strain GXU_MW_B19^T was isolated from *P. lutea* from Weizhou Island, China (21° 03′ 42″ N 109° 08′ 35″ E). The coral tissue and bones were ground in a mortar and diluted with sterile seawater. The homogenate was serially diluted (10^{-1} fold) and spread on one-tenth strength of R2A+2216E agar medium (HaiBo, China) for 2 weeks of incubation at 25 °C. A white and transparent colony, designated strain GXU_MW_B19^T, was picked, purified and stored with 25% glycerol at −80 °C. Strain GXU_MW_B19^T grows well on 2216E agar medium. Type strains *Kiloniella laminariae* DSM 19542^T and *Kiloniella spongiae* JCM 19930^T, obtained from the German Collection of Microorganisms and Cell Cultures (DSM) and Japan Collection of Microorganisms (JCM), respectively, were used as references.

CULTURAL, MORPHOLOGICAL AND PHYSIOLOGICAL FEATURES

Morphology of cells was determined using transmission electron microscope (Hitachi HT-7700) after incubation for 3 days in 2216E liquid medium at 25 °C. Catalase activity was determined by observing bubble production in a 3% (v/v) hydrogen peroxide solution, and oxidase activity was determined using oxidase test strips (Huankai, China). Endospore formation was examined as described by Dong and Cai [24]. Gram-staining analysis was carried out using the Gram-staining kit (Huankai 029010) according to the manufacturer's instructions. The mobility of strain GXU_MW_B19^T was determined using the hanging drop technique [25]. Anaerobic growth was tested using the AnaeroPack system according to its instructions. Optimal growth temperature was determined at 4, 10, 15, 20, 25, 30, 37, 40, 45 and 50 °C using 2216E agar medium. NaCl tolerance was tested in 1/5 strength R2A liquid medium (dissolved in ultrapure water) at 25 °C for 7 days with different NaCl concentrations [0, 0.5, 1, 1.5, 2, 2.5, 3, 4, 5, 6, 7, 8, 9, 10 and 12% (w/v)]. The pH range was tested in 2216E liquid medium at 25 °C for 7 days (pH 4, 5, 5.5, 6, 6.5, 7, 7.5, 8, 8.5, 9, 10 and 11). Metabolic ability was tested by using API 20NE, API ZYM strips (bioMérieux) and the Biolog Gen III MicroPlate according to the manufacturers' protocols. Anaerobic fermentation was determined using API 50CH strips according to the manufacturer's protocol with yeast extract amended artificial seawater (0.1%, w/v). Carbonate in the plate was checked by visual observation (sand-like particles) and determined by observing bubble production in 1% HCl.

The detailed morphological, physiological and biochemical characteristics of GXU_MW_B19^T were provided in Table 1 and the species description. Cells of strain GXU_MW_B19^T are Gram-stain-negative, aerobic rods, motile by a single polar flagellum (Fig. S1A, available in the online Supplementary Material). Strain GXU_MW_B19^T can grow at 20–40 °C, pH 6.5–10 and in 0–5% NaCl (w/v), and the optimal conditions were at 30–37 °C, pH 8 and in 0.5–1% NaCl (w/v). The highest temperature for growth is consistent with that of genus *Pelagibius*, but higher than those of *Kiloniella* and *Denitrobaculum*, and lower than those of *Thalassocola*, *Curvivirga* and *Marivibrio* (Table 1). Tests for oxidase, catalase and nitrate reduction were positive. In the API ZYM assay, strain GXU_MW_B19^T was negative for chymotrypsin, *α*-galactosidase, *β*-galactosidase, *β*-glucuronidase, *α*-glucosidase, *β*-glucosidase, *N*-acetyl-*β*-glucosidase and *α*-mannosidase, and this profile was consistent with those of genera *Curvivirga*, *Marivibrio*, and *Aestuariispira*, but opposite to those of *K. laminariae* DSM 19542^T, *K. spongiae* JCM 19930^T and *D. tricleocarpae* R148^T (Table 1). Carbonate deposition was detected in the solid media of strain GXU_MW_B19^T, *K. laminariae* DSM 19542^T and *K. spongiae* JCM 19930^T (Fig. S2).

GENOMIC CHARACTERIZATION AND PHYLOGENY

The 16S rRNA gene of strain GXU_MW_B19^T was obtained by using PCR amplification with the universal bacterial primers 27F and 1492R [26] and sequenced using the Sanger method with the same primers. Whole-genome sequencing was performed on the Illumina HiSeq PE150 platforms at the Beijing Novogene Bioinformatics Technology Co., Ltd. Genome information was extracted according to Riesco and Trujillo [27]. Determination of the 16S rRNA gene sequence similarities was performed in the EzBioCloud [28] and the NCBI database. Alignment of 16S rRNA gene sequences was performed using online SINA [29]. Phylogenetic trees were reconstructed using the maximum-likelihood [30], the neighbour-joining [31] and the maximum-parsimony [32] algorithms in the software MEGA11 [33]. The phylogenetic distance matrices were estimated by the Kimura two-parameter model [34]. The topology of the phylogenetic tree was evaluated by using the bootstrap resampling method of Felsenstein [35] with 1,000 replicates. The phylogenomic tree was reconstructed using FastTreeMP [36] on the basis of the GTDB concatenated proteins for 120 marker genes [37], then edited using iTOL [38].

Genome assembly of strain GXU_MW_B19^T yielded 23 scaffolds with a total size of 3.63 Mbp and a digital G+C content of 54.5 mol%. The genome annotation revealed 3,240 protein-coding genes, along with 53 tRNA genes, four 5S rRNA genes, one 16S rRNA gene and one 23S rRNA gene. The complete 16S rRNA gene sequence (1,482 bp) derived from the whole-genome sequence is identical to the Sanger sequencing result (1,355 bp).

Table 1. Morphological, physiological and chemotaxonomic characteristics of strain GXU_MW_B19^T and related type strains or genera

Strains: 1, GXU_MW_B19^T; 2, *K. laminariae* DSM 19542^T; 3, *K. spongiae* JCM 19930^T; 4, *Kiloniella* [1, 5, 10, 11, 14]; 5, *Denitrobaculum* [56]; 6, *Pelagibius* [57, 58]; 7, *Thalassocola* [17]; 8, *Curvivirga* [3]; 9, *Marivibrio* [18]; 10, *Aestuariispira* [13, 19].

Characteristics	1	2	3	4	5	6	7	8	9	10
Source	Coral	Macroalga†	Sponge‡	Algae, sponge, spider crab, clam	Coralline algae	Seawater, sediment	Seawater	Marine sponge	Salt mine	Tidal flat, seawater
Cell morphology	Curved rod	Spiral or rod†	Rod‡	Rod or spirals	Rod	Curved rod or rod	Rod	Curved-to-spiral rod	Spiral or curved rod	Curved-to-spiral rod
Temperature (optimal) (°C)	20–40 (30–37)	20–30 (25)	20–30 (25)	0–37	15–37 (25)	10–40	20–45 (30)	15–45 (30–37)	10–50	15–45
pH (optimal)	6.5–10 (8)	6–10 (9)	5–10 (8)	4–10	8–9	6–11	5–9	6–8 (6–7)	6–10	5–9.5
NaCl content (optimal) (%, w/v)	0–5 (0.5–1)	0–4 (2)	0–3 (1.5–2)	0.5–7	0.5–5 (0.5)	0–10	0–6 (3)	0.5–10 (2–3)	2–15	1–12
Beta-galactosidase	–	+	+	v	+	v	–	–	–	–
Alpha-glucosidase	–	+	+	v	+	–	+	–	–	–
Major quinone	Q-9	Q-9	Q-9	Q-9	Q-10	Q-10	Q-10	Q10, Q-9	Q-10	Q-10
Genome size (Mb)	3.63	4.44	4.48	4.31–4.48	6.44	5.44–6.03	un	3.56	4.18	4.36–4.82
Protein-coding genes	3240	4066	4148	3991–4148	5853	5065–5583	un	3373	3769	4051–4471
DNA G+C content (mol%)	54.5	51.5	45	45–51.5	59.5	62.5–66.5	61.2	42	66	55.5–57
16S rRNA gene identity to strain GXU_MW_B19^T (%)	100	93.9	94.1	92.9–94.1	91.7	91.2–91.4	89.8	90.5	89	90.2–90.6
ANI to strain GXU_MW_B19^T (%)	100	69.5	68.4	68.4–69.5	68.7	68.1–68.6	un	66	66.7	66.9–67.5
AAI to strain GXU_MW_B19^T (%)	100	62.6	62.4	62.4–62.8	58.5	58–58.6	un	55.4	55.2	55.4–56
The dominant fatty acids (>10%)	$C_{10:0}$ 2OH, $C_{12:1}$, $C_{14:1}$ ω5c	anteiso-$C_{19:0}$, iso $C_{11:0}$ 3OH	$C_{11:0}$ 3OH, iso-$C_{10:0}$, iso$C_{17:0}$ 3OH, iso$C_{11:0}$ 3OH, $C_{11:0}$,	$C_{18:1}$ ω6c/$_{C18:1}$ ω7c, $C_{16:1}$ ω6c/$_{C16:1}$ ω7c	$C_{18:1}$ ω7c, $C_{16:1}$ ω7c, $C_{19:0}$cyclo 9, 10 DMA	$C_{18:1}$ ω7c/$C_{18:1}$ ω6c, $C_{18:1}$ 2-OH, $C_{18:0}$ 3-OH, $C_{19:0}$ cyclo ω8c	$C_{18:1}$ ω7c/$C_{18:1}$ ω6c	$C_{18:1}$ ω7c/$C_{18:1}$ ω6c, $C_{16:0}$	$C_{19:0}$ cyclo ω8c, $C_{16:0}$	$C_{18:1}$ ω7c/$C_{18:1}$ ω6c, $C_{16:0}$
The major polar lipid*	PE, DPG, NL, Ls	PE, PG, DPG	PE, PG, DPG, NLs	PE, PG, DPG, NL, PL, L	PME, PE, PG, DPG, NL	PG, PE, PME, NL	DPG, PG, NL	PG, PE	PE, PG, DPG, NL	PE, PG, PL, NL

*PE, phosphatidylethanolamine; PG, phosphatidylglycerol; DPG, diphosphatidylglycerol; NL, unidentified ninhydrin-positive lipid; PL, unidentified phospholipid; L, unidentified lipid.
†Data from literature [1].
‡Data from literature [5].
+, positive; –, negative; v, variable; un, data unavailable.

Global alignment of 16S rRNA gene sequences revealed that strain GXU_MW_B19^T clustered with members of the genus *Kiloniella* (92.9–94.1%), showing the highest similarity (94.1%) to *K. spongiae* JCM 19930^T. And the following genera were *Denitrobaculum* (91.7%) and *Pelagibius* (91.2–91.4%). These similarity values (<95%) indicate that strain GXU_MW_B19^T may represent a new genus [39].

Phylogenetic analysis using maximum-likelihood and neighbour-joining algorithms indicated that strain GXU_MW_B19^T forms a stable clade with members of the genus *Kiloniella* within a large clade under the order *Rhodospirillales*, though with low bootstrap support (Figs 1, S3 and S4). The large clade comprises members of the families *Kiloniellaceae*, *Rhodovibrionaceae* (*Aquibaculum*, *Fodinicurvata*, *Limibacillus*, *Limimonas*, *Pelagibius*, *Rhodovibrio* and *Tistlia*) [2] and *Rhodospirillaceae* (namely, *Algihabitans*, *Denitrobaculum*, *Ferruginivarius*, *Hwanghaeella* and 'Pacificispira'). Consistent support across phylogenetic algorithms was observed for four monophyletic subclades: subclade I (*Aestuariispira*, *Curvivirga*, *Hwanghaeella*, *Marivibrio* and 'Pacificispira'), subclade II (*Fodinicurvata*, *Aquibaculum* and *Algihabitans*), subclade III (*Rhodovibrio*, *Ferruginivarius* and *Limimonas*) and subclade IV (the new isolate and *Kiloniella*). Subclades II and III represent the core of the family *Rhodovibrionaceae* [2], yet the monophyly of this family was unstable across algorithms due to the phylogenetic positions of genera *Pelagibius*, *Denitrobaculum* and *Limibacillus* (Figs S3 and S4). However, in the maximum-parsimony tree, subclade I was separated from the large clade of the maximum-likelihood and neighbour-joining trees by other species of the family *Rhodospirillales* (Fig. S5). These results suggest that the family assignment of genera *Aestuariispira*, *Curvivirga* and *Marivibrio* should be reassigned.

Phylogenomic analysis based on the concatenated amino sequences from 120 marker genes also supported the large clade identified in phylogenetic analysis with high bootstrap values (>0.9) (Fig. 2). The monophyly of the four subclades was also supported with high bootstrap values. The main difference between phylogenomic and phylogenetic analysis was that subclades II and III formed a distinct branch with high bootstrap support, while genera *Pelagibius*, *Denitrobaculum* and *Limibacillus* and subclade IV members formed another separate branch with high bootstrap support. These results indicated that the taxonomic ranges of

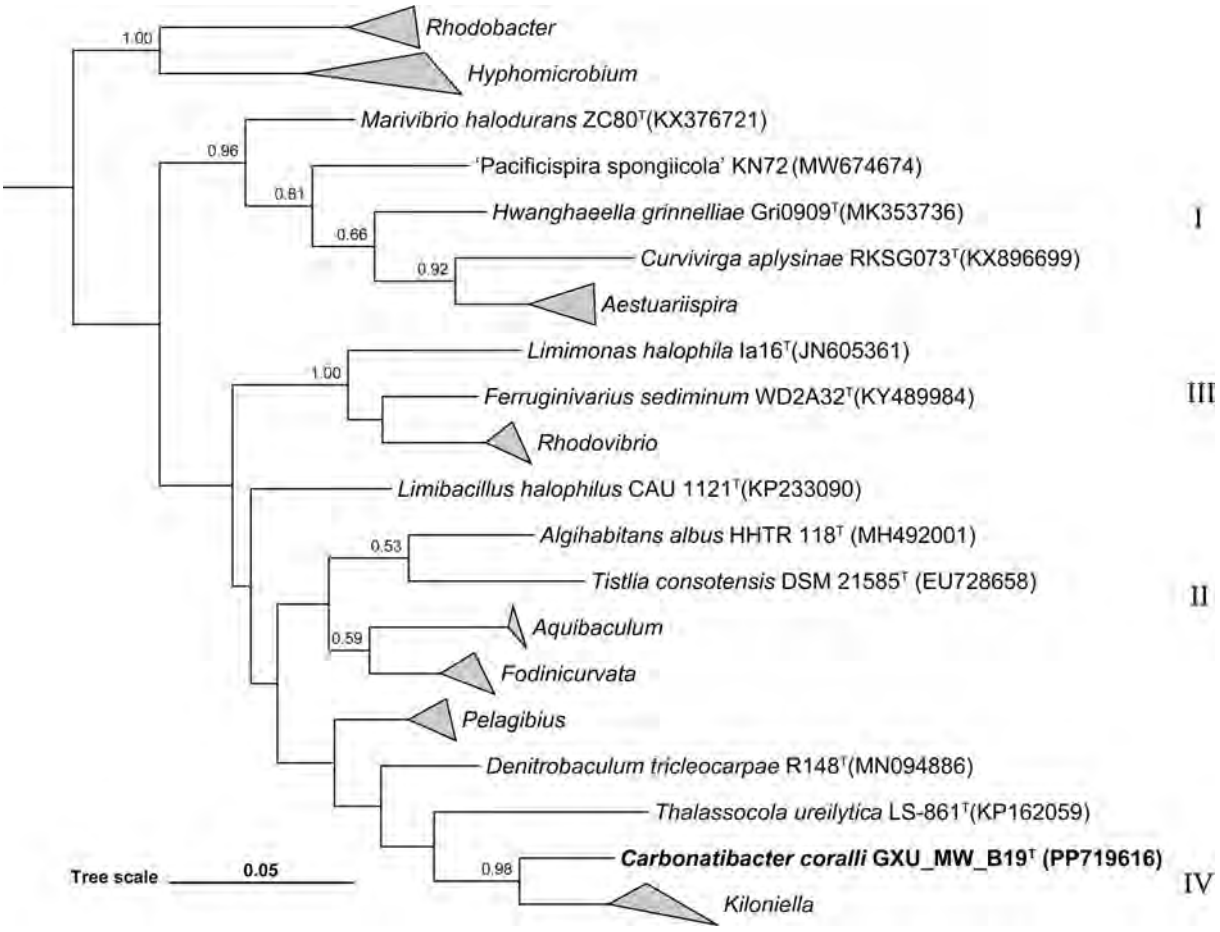


Fig. 1. Subtree of the family *Rhodospirillales* based on 16S rRNA gene sequences using the maximum-likelihood algorithm. Numbers at nodes indicate percentages of 1,000 bootstrap resamplings; only values above 0.5 are shown. Bar, 0.05 substitutions per nucleotide position.

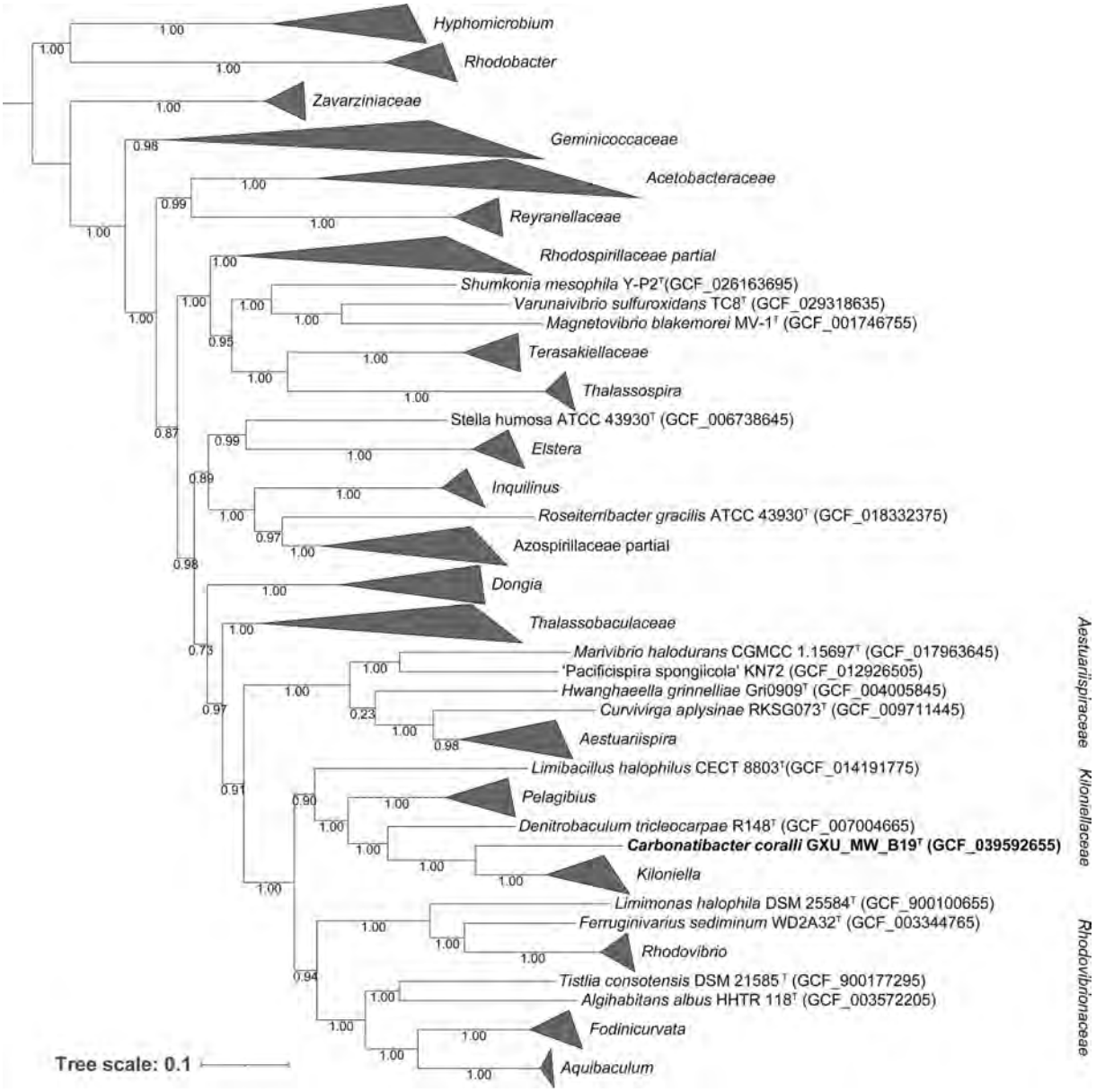


Fig. 2. Phylogenomic tree inferred using FastTree based on GTDB-Tk alignment (concatenated amino acid sequence of 120 core genes). Support indices are given at branching points. Bar, 0.1 substitutions per position.

families *Kiloniellaceae* and *Rhodovibrionaceae* need further adjustment and that a third family encompassing genera *Aestuariispira*, *Curvivirga*, *Hwanghaeella*, *Marivibrio* and 'Pacificispira' should be additionally proposed. The family *Rhodovibrionaceae* should contain the genera *Algihabitans*, *Ferruginivarius* and *Aquibaculum* along with *Fodinicurvata*, *Limimonas*, *Rhodovibrio* and *Tistlia*. The family *Kiloniellaceae* should contain genus *Kiloniella* and the new isolate as core members and tentatively include the genera *Denitrobaculum*, *Pelagibius* and *Limibacillus*.

COMPARATIVE GENOMICS

Average nucleotide identity (ANI) was calculated using the web service in the EzBioCloud [40]. The average amino acid identity (AAI) was calculated using the CompareM software. Clusters of Orthologous Groups of proteins were annotated using the eggNOG-mapper [41].

The genome size of strain GXU_MW_B19^T is 3.63 Mb, lower than those of the closely related type strains except *Curvivirga aplysinae* RKSG073^T (3.56 Mb) (Table 1). Its genome encodes 3,240 proteins, the lowest count among closely related type strains

(ranging from 3,373 to 5,853) (Table 1). The maximum ANI of strain GXU_MW_B19^T to validly published species was 69.5% (against *K. laminariae* DSM 19542^T), indicating that this new isolate does not belong to any existing species [27]. Additionally, AAI values between strain GXU_MW_B19^T and closely related species were ≤62.8% (Table S1), suggesting that it may represent a new genus (the genus threshold for AAI is 45–65%) [42, 43]. The range of AAI values among the clades is as follows: 54.07–57.22% between subclade I and *Rhodovibrionaceae*, 54.37–57.78% between subclade I and subclade IV and 55.74–60.86% between *Rhodovibrionaceae* and subclade IV (Table S1).

EggNOG annotation of 25 genomes indicated that the genome of strain GXU_MW_B19^T encodes alpha-1,6-glucosidase, alkaline phosphatase, isochorismate-related enzymes and P2-like prophage-related proteins, all of which are absent in closely related species (Table S2). Capsule-related proteins were identified in its genome, consistent with Transmission electron microscope observations of capsule structures (Fig. S1B). Notably, most phylogenetically related species or genera (including GXU_MW_B19^T, genera *Kiloniella*, *Pelagibius*, *Denitrobaculum*, *Tistlia*, *Fodinicurvata*, *Rhodovibrio* and *Algihabitans*) encode vitamin B_{12} *de novo* biosynthesis genes (Table S2). Additionally, ankyrin-repeat domains associated with symbiosis were detected in genomes of strain GXU_MW_B19^T and its relatives.

CHEMOTAXONOMY

Biomass for the analysis of quinones and polar lipids was obtained from 2216E liquid medium after 4 days of incubation at 25 °C. Respiratory quinones were extracted as described by Collins [44] and analysed using reversed-phase HPLC [45]. The isoprenoid quinones were eluted by a mixture of methanol-2-propanol (2:1, v/v) at a flow rate of 1 ml min^{-1} at room temperature and detected by UV absorbance at 270 nm. Polar lipids were extracted as described by Kamekura [46] and identified by spraying with ethanolic molybdophosphoric acid, molybdenum blue and ninhydrin after two-dimensional TLC [47]. Biomass for cellular fatty acid analysis was obtained by scraping the colonies from the fourth quadrant of 2216E agar medium, which was incubated at 25 °C for 3 days. Cellular fatty acids were examined by GC (Agilent G6890N) and determined via the Sherlock Microbial Identification System version 6.0 following its standard MIDI (Microbial Identification System) protocol [48]. Vitamin B_{12} production employed the medium described by Sultana *et al.* [23], and detection was performed using *Lactobacillus delbrueckii* subsp. *lactis* CICC 6077 (=ATCC 7830) [49].

The major respiratory quinone of strain GXU_MW_B19^T was Q-9, consistent with *K. laminariae* DSM 19542^T and *K. spongiae* JCM 19930^T. In contrast, *C. aplysinae* RKSG073^T contains both Q-10 (ubiquinone 10) and Q-9 [3], while *Rhodovibrio* strains possess Q-10 and MK-10 (menaquinones) [50]. Other genera phylogenetically related to strain GXU_MW_B19^T predominantly contain Q-10 [51–54] (Table 1). The major cellular fatty acids (>5%) of strain GXU_MW_B19^T were iso-$C_{10:0}$2OH (18.7%), $C_{12:1}$ (15.4%), $C_{14:1}$ ω5c (11.8%), iso-$C_{17:0}$3OH (10%), $C_{18:2}$ ω6,9c/ante-$C_{18:0}$ (8.5%), $C_{19:0}$ cyclo ω8c (8.3%), iso-$C_{15:1}$H/$_{C13:0}$3OH (7.8%), $C_{16:1}$ ω6c/ω7c (7.6%), $C_{10:0}$ (6.7%) and anteiso- $C_{17:0}$ (5.3%) (Table S3). This profile markedly differed from those of *K. laminariae* DSM 19542^T (dominant fatty acid is anteiso-$C_{19:0}$, 12.2%) and *K. spongiae* JCM 19930^T (dominant fatty acid is $C_{11:0}$3OH, 18.8%) (Tables 1 and S3). In contrast, the dominant fatty acids (>10%) of genera *Denitrobaculum*, *Pelagibius*, *Thalassocola*, *Curvivirga* and *Aestuariispira* are usually long-chain C_{19}, C_{18} and C_{16} fatty acids (Table 1). The major polar lipids of GXU_MW_B19^T comprised phosphatidylethanolamine, diphosphatidylglycerol, unidentified ninhydrin-positive lipid and three unidentified lipids (Fig. S6). In contrast, *K. laminariae* DSM 19542^T contained phosphatidylethanolamine, phosphatidylglycerol and diphosphatidylglycerol, while *K. spongiae* JCM 19930^T exhibited phosphatidylethanolamine, phosphatidylglycerol, diphosphatidylglycerol and two unidentified ninhydrin-positive lipids (Fig. S6). Other related genera also contain phosphatidylglycerol as a major polar lipid (Table 1). Vitamin B_{12} was detected in the broth of all three strains (GXU_MW_B19^T, *K. laminariae* DSM 19542^T and *K. spongiae* JCM 19930^T), indicating their capacity to provide VB_{12} to other organisms [23].

DISCUSSION AND CONCLUSION

Morphological analysis (produces capsule), physiological characteristics (absence of chymotrypsin, *α*-galactosidase, *β*-galactosidase, *β*-glucuronidase, *α*-glucosidase, *β*-glucosidase, *N*-acetyl-*β*-glucosidase and *α*-mannosidase), chemotaxonomic data (dominant fatty acid is iso-$C_{10:0}$2OH), comparative genomics (maximum 16S rRNA gene identity to validly published species<95%, maximum ANI<95% and maximum AAI<65%) (Table 1) and phylogenetic analysis (robust clustering with genus *Kiloniella*) collectively indicate that strain represents a new species in a new genus in the *Kiloniellaceae*, for which the name *Carbonatibacter coralli* gen. nov., sp. nov. is proposed.

Genera *Kiloniella*, *Carbonatibacter*, *Denitrobaculum*, *Pelagibius* and *Limibacillus* formed a distinct branch in phylogenomic analysis with high bootstrap support (≥0.9) (Fig. 2), suggesting that these genera may belong to the existing family *Kiloniellaceae*. The observation of high AAI (≥58%) among genera within this branch (except *Limibacillus*) compared to genera outside this branch (Table S1) also supports the assignment of these genera into one family. While the genera *Kiloniella* and *Carbonatibacter* possess Q-9 as the major respiratory quinone, in contrast to Q-10 found in other genera (Table 1), this biochemical distinction solidifies the close relationship of *Kiloniella* to *Carbonatibacter*. Therefore, the genera *Kiloniella* and *Carbonatibacter* are proposed

as the core of the family *Kiloniellaceae*, and genera *Denitrobaculum*, *Pelagibius* and *Limibacillus* are tentatively assigned to this family. As the genome of *Thalassocola* is still unavailable, its phylogenetic position leads to its tentatively being assigned to this family as well.

The monophyly of subclade I (comprising genera *Aestuariispira*, *Curvivirga*, *Hwanghaeella*, *Marivibrio* and 'Pacificispira') suggests that this subclade should be assigned to a new family within the order *Rhodospirillales*, despite its members being originally classified under families *Kiloniellaceae* and *Rhodospirillaceae*. The AAI values among these genera (≥58%) further support their close phylogenetic relationship (Table S1). Thus, the new family *Aestuariispiraceae* fam. nov. is proposed to accommodate all genera of subclade I.

Phylogenomic analysis revealed that genera of the family *Rhodovibrionaceae* formed two distinct subclades with strong bootstrap support (0.94; Fig. 2). This separation was more evident in phylogenetic analyses (Figs 1 and S3–S5), supporting the proposal of *Fodinicurvataceae* fam. nov. in 2023 [55]. The AAI values among *Rhodovibrionaceae* genera (58.01–66.03%) remain comparable to those observed in *Kiloniellaceae* (57.33–63.31%) and *Aestuariispiraceae* (58.32–66.54%) (Table S1), supporting the tentative retention of *Rhodovibrionaceae*. Additionally, the genera *Algihabitans* and *Ferruginivarius* should be reclassified into *Rhodovibrionaceae* from *Rhodospirillaceae* based on high bootstrap support in phylogenomic analysis (Fig. 2).

DESCRIPTION OF *CARBONATIBACTER* GEN. NOV.

Carbonatibacter (Car.bo.na.ti.bac'ter. N.L. masc. n. *carbonas*, carbonate; N.L. masc. n. *bacter*, rod; N.L. masc. n. *Carbonatibacter*, carbonate-producing rod).

Cells are Gram-stain-negative, aerobic rods, motile by a single polar flagellum. Catalase and oxidase are positive. The only detected respiratory quinone is Q-9. The dominant fatty acids are iso-$C_{10:0}$2OH, $C_{12:1}$, $C_{14:1}$ ω5c and iso-$C_{17:0}$3OH. The major polar lipids are phosphatidylethanolamine, diphosphatidylglycerol, unidentified ninhydrin-positive lipid and three unidentified lipids. This genus phylogenetically belongs to *Kiloniellaceae*.

The type species is *Carbonatibacter coralli*.

DESCRIPTION OF *CARBONATIBACTER CORALLI* SP. NOV.

Carbonatibacter coralli (co.ral'li. L. gen. n. *coralli*, of coral).

The features are as described in the genus description with the following additions. Cells are usually 0.36–0.58 µm wide and 1.0–2.1 µm long. Cells grow at 20–40 °C, pH 6.5–10 and 0–5% NaCl (w/v), and the optimal conditions were 30–37 °C, pH 8 and 0.5–1% NaCl (w/v). Colonies of strain GXU_MW_B19^T are white, transparent, round, convex, and smooth on 1/10 strength R2A+2216E agar medium after 3 days of incubation at 25 °C. Nitrate reduction is positive. Capsule and carbonate are produced. Vitamin B_{12} was produced and shared. In the API ZYM assay, alkaline phosphatases, butyrate esterase, caprylate esterase-lipase, myristate lipase, leucine aminopeptidases, valine aminopeptidases, cystine aminopeptidases, trypsin, acid phosphatases and phosphoamidase are positive. In the Biolog Gen III microplate, D-maltose, D-trehalose, D-cellobiose, sucrose, *β*-methyl-D-glucoside, D-salicin, *N*-acetyl-D-glucosamine, *α*-D-glucose, D-fructose, D-galactose, inosine, myo-inositol, glycerol, D-glucose-6-PO_4, D-fructose-6-PO_4, D-serine, L-histidine, pectin, methyl pyruvate, D-lactic acid methyl ester, L-lactic acid, citric acid, *α*-keto-glutaric acid, D-malic acid, L-malic acid, bromo-succinic acid, *γ*-amino-butyric acid, *α*-hydroxy-butyric acid, *β*-hydroxy-D,L-butyric acid, *α*-keto-butyric acid, propionic acid, acetic acid and formic acid are positive. The major fatty acids also include $C_{18:2}$ ω6,9c/ante-$C_{18:0}$, $C_{19:0}$ cyclo ω8c, iso-$C_{15:1}$ H/$_{C13:0}$3OH, $C_{16:1}$ ω6c/ω7c, $C_{10:0}$ and anteiso-$C_{17:0}$.

The type strain, GXU_MW_B19^T (=KCTC 8092^T=MCCC 1K08794^T), was isolated from *P. lutea*. The genome DNA G+C content is 54.5 mol%. The 16S rRNA gene and whole-genome sequence was deposited in GenBank under PP719616 and JBBUTJ000000000, respectively.

EMENDED DESCRIPTION OF *KILONIELLACEAE* WIESE *ET AL*. 2009 EMEND. HÖRDT *ET AL*. 2020

The description is as given before [1, 2] with the following modification. The family houses *Kiloniella* (the type genus) and *Carbonatibacter. Thalassocola*, *Denitrobaculum*, *Pelagibius* and *Limibacillus* are tentatively assigned to this family as well.

EMENDED DESCRIPTION OF *RHODOVIBRIONACEAE* HÖRDT *ET AL*. 2020

The description is as given before [2] with the following modification. *Algihabitans* and *Ferruginivarius* are phylogenetically assigned to this family.

DESCRIPTION OF *AESTUARIISPIRACEAE* FAM. NOV.

Aestuariispiraceae (Aes.tu.a.ri.i.spi.ra'ce.ae. N.L. fem. n. *Aestuariispira*, name of a bacterial genus; L. fem. pl. n. suff. *-aceae*, ending to denote a family; N.L. fem. pl. n. *Aestuariispiraceae*, the *Aestuariispira* family)

Cells are Gram-negative, usually curved-to-spiral rod, motile, aerobic or facultatively anaerobic and heterotrophic. The major isoprenoid quinone is Q-10. Major fatty acids are $C_{18:1}$ ω7c/ω6c, $C_{16:0}$ or $C_{19:0}$ cyclo ω8c. The major polar lipids are phosphatidylglycerol and phosphatidylethanolamine. The genomic G+C content is 55.5–66 mol%. This family has been separated from other families based on phylogenetic analyses of genome and 16S rRNA gene sequences. The family contains *Aestuariispira*, *Curvivirga*, *Hwanghaeella*, *Marivibrio* and 'Pacificispira'.

The type genus is *Aestuariispira*.

Funding information
This research was supported by the Guangdong Basic and Applied Basic Research Foundation (2020B1515420002) and the National Natural Science Foundation of China (41866004).

Conflicts of interest
The authors declare that there are no conflicts of interest.

References

1. Wiese J, Thiel V, Gärtner A, Schmaljohann R, Imhoff JF. *Kiloniella laminariae* gen. nov., sp. nov., an alphaproteobacterium from the marine macroalga *Laminaria saccharina*. *Int J Syst Evol Microbiol* 2009;59:350–356.
2. Hördt A, López MG, Meier-Kolthoff JP, Schleuning M, Weinhold L-M, *et al*. Analysis of 1,000+ type-strain genomes substantially improves taxonomic classification of Alphaproteobacteria. *Front Microbiol* 2020;11:468.
3. Goldberg SR, Haltli BA, Correa H, Kerr RG. *Curvivirga aplysinae* gen. nov., sp. nov., a marine bacterium isolated from the sea sponge *Aplysina fistularis*. *Int J Syst Evol Microbiol* 2021;71:004873.
4. Margassery LM, Kennedy J, O'Gara F, Dobson AD, Morrissey JP. Diversity and antibacterial activity of bacteria isolated from the coastal marine sponges *Amphilectus fucorum* and *Eurypon major*. *Lett Appl Microbiol* 2012;55:2–8.
5. Yang S-H, Seo H-S, Lee J-H, Kim S-J, Kwon KK. *Kiloniella spongiae* sp. nov., isolated from a marine sponge and emended description of the genus *Kiloniella* Wiese *et al*. 2009 and *Kiloniella laminariae*. *Int J Syst Evol Microbiol* 2015;65:230–234.
6. Meron D, Atias E, Iasur Kruh L, Elifantz H, Minz D, *et al*. The impact of reduced pH on the microbial community of the coral *Acropora eurystoma*. *ISME J* 2011;5:51–60.
7. Sharp KH, Distel D, Paul VJ. Diversity and dynamics of bacterial communities in early life stages of the Caribbean coral *Porites astreoides*. *ISME J* 2012;6:790–801.
8. Séré MG, Tortosa P, Chabanet P, Turquet J, Quod J-P, *et al*. Bacterial communities associated with *Porites* white patch syndrome (PWPS) on three western Indian Ocean (WIO) coral reefs. *PLoS One* 2013;8:e83746.
9. Meziti A, Mente E, Kormas KA. Gut bacteria associated with different diets in reared *Nephrops norvegicus*. *Syst Appl Microbiol* 2012;35:473–482.
10. Gerpe D, Buján N, Diéguez AL, Lasa A, Romalde JL. *Kiloniella majae* sp. nov., isolated from spider crab (*Maja brachydactyla*) and pullet carpet shell clam (*Venerupis pullastra*). *Syst Appl Microbiol* 2017;40:274–279.
11. Wang L, Li X, Lai Q, Shao Z. *Kiloniella litopenaei* sp. nov., isolated from the gut microflora of Pacific white shrimp, *Litopenaeus vannamei*. *Antonie van Leeuwenhoek* 2015;108:1293–1299.
12. Martin-Antonio B, Manchado M, Infante C, Zerolo R, Labella A, *et al*. Intestinal microbiota variation in Senegalese sole (*Solea senegalensis*) under different feeding regimes. *Aquaculture Res* 2007;38:1213–1222.
13. Park S, Park J-M, Kang C-H, Yoon J-H. *Aestuariispira insulae* gen. nov., sp. nov., a lipolytic bacterium isolated from a tidal flat. *Int J Syst Evol Microbiol* 2014;64:1841–1846.
14. Si O-J, Yang H-Y, Hwang CY, Kim S-J, Choi S-B, *et al*. *Kiloniella antarctica* sp. nov., isolated from a polynya of Amundsen Sea in western Antarctic Sea. *Int J Syst Evol Microbiol* 2017;67:2397–2402.
15. Bowman JP, McCammon SA, Gibson JAE, Robertson L, Nichols PD. Prokaryotic metabolic activity and community structure in Antarctic continental shelf sediments. *Appl Environ Microbiol* 2003;69:2448–2462.
16. Maire J, Girvan SK, Barkla SE, Perez-Gonzalez A, Suggett DJ, *et al*. Intracellular bacteria are common and taxonomically diverse in cultured and in hospite algal endosymbionts of coral reefs. *ISME J* 2021;15:2028–2042.
17. Lin S-Y, Hameed A, Young C-C, Liu Y-C, Hsu Y-H, *et al*. *Thalassocola ureilytica* gen. nov., sp. nov., of the family *Phyllobacteriaceae* isolated from seawater. *Int J Syst Evol Microbiol* 2015;65:4100–4106.
18. Chen S, Xu Y, Zheng C, Ke LX. *Marivibrio halodurans* gen. nov., sp. nov., a marine bacterium in the family *Rhodospirillaceae* isolated from underground rock salt. *Int J Syst Evol Microbiol* 2017;67:4266–4271.
19. Kang JY, Lee B, Kim JA, Kim MS, Kim CH. Identification and characterization of an ectoine biosynthesis gene cluster from *Aestuariispira ectoiniformans* sp. nov., isolated from seawater. *Microbiol Res* 2022;254:126898.
20. Jiao N, Luo T, Chen Q, Zhao Z, Xiao X, *et al*. The microbial carbon pump and climate change. *Nat Rev Microbiol* 2024;22:408–419.
21. Gu W, Wu S, Liu X, Wang L, Wang X, *et al*. Algal-bacterial consortium promotes carbon sink formation in saline environment. *J Adv Res* 2024;60:111–125.
22. Croft MT, Lawrence AD, Raux-Deery E, Warren MJ, Smith AG. Algae acquire vitamin B12 through a symbiotic relationship with bacteria. *Nature* 2005;438:90–93.
23. Sultana S, Bruns S, Wilkes H, Simon M, Wienhausen G. Vitamin B_{12} is not shared by all marine prototrophic bacteria with their environment. *ISME J* 2023;17:836–845.
24. Dong X, Cai M. *Determinative Manual for Routine Bacteriology*. Beijing: Scientific Press; 2001.
25. Bernardet J-F, Nakagawa Y, Holmes B. Proposed minimal standards for describing new taxa of the family *Flavobacteriaceae* and emended description of the family. *Int J Syst Evol Microbiol* 2002;52:1049–1070.
26. Barry T, Colleran G, Glennon M, Dunican LK, Gannon F. The 16s/23s ribosomal spacer region as a target for DNA probes to identify eubacteria. *Genome Res* 1991;1:51–56.

27. Riesco R, Trujillo ME. Update on the proposed minimal standards for the use of genome data for the taxonomy of prokaryotes. *Int J Syst Evol Microbiol* 2024;74:006300.
28. Yoon S-H, Ha S-M, Kwon S, Lim J, Kim Y, *et al*. Introducing EzBioCloud: a taxonomically united database of 16S rRNA gene sequences and whole-genome assemblies. *Int J Syst Evol Microbiol* 2017;67:1613–1617.
29. Pruesse E, Peplies J, Glöckner FO. SINA: accurate high-throughput multiple sequence alignment of ribosomal RNA genes. *Bioinformatics* 2012;28:1823–1829.
30. Felsenstein J. Evolutionary trees from DNA sequences: a maximum likelihood approach. *J Mol Evol* 1981;17:368–376.
31. Trees RP. The neighbor-joining method: a new method for reconstructing phylogenetic trees. *Mol Biol Evol* 1987;4:406–425.
32. Fitch WM. Toward defining the course of evolution: minimum change for a specific tree topology. *Syst Biol* 1971;20:406–416.
33. Tamura K, Stecher G, Kumar S. MEGA11: molecular evolutionary genetics analysis version 11. *Mol Biol Evol* 2021;38:3022–3027.
34. Kimura M. A simple method for estimating evolutionary rates of base substitutions through comparative studies of nucleotide sequences. *J Mol Evol* 1980;16:111–120.
35. Felsenstein J. Confidence limits on phylogenies: an approach using the bootstrap. *Evolution* 1985;39:783–791.
36. Price MN, Dehal PS, Arkin AP. FastTree 2--approximately maximum-likelihood trees for large alignments. *PLoS One* 2010;5:e9490.
37. Chaumeil PA, Mussig AJ, Hugenholtz P, Parks DH. GTDB-Tk: a toolkit to classify genomes with the Genome Taxonomy Database. *Bioinformatics* 2019;36:1925–1927.
38. Letunic I, Bork P. Interactive Tree of Life (iTOL) v6: recent updates to the phylogenetic tree display and annotation tool. *Nucleic Acids Res* 2024;52:W78–W82.
39. Yarza P, Yilmaz P, Pruesse E, Glöckner FO, Ludwig W, *et al*. Uniting the classification of cultured and uncultured bacteria and archaea using 16S rRNA gene sequences. *Nat Rev Microbiol* 2014;12:635–645.
40. Yoon SH, Ha SM, Lim J, Kwon S, Chun J. A large-scale evaluation of algorithms to calculate average nucleotide identity. *Antonie van Leeuwenhoek* 2017;110:1281–1286.
41. Cantalapiedra CP, Hernández-Plaza A, Letunic I, Bork P, Huerta-Cepas J. eggNOG-mapper v2: functional annotation, orthology assignments, and domain prediction at the metagenomic scale. *Mol Biol Evol* 2021;38:5825–5829.
42. Konstantinidis KT, Rosselló-Móra R, Amann R. Uncultivated microbes in need of their own taxonomy. *ISME J* 2017;11:2399–2406.
43. Park M-J, Kim YJ, Park M, Yu J, Namirimu T, *et al*. Establishment of genome-based criteria for classification of the family *Desulfovibrionaceae* and proposal of two novel genera, *Alkalidesulfovibrio* gen. nov. and *Salidesulfovibrio* gen. nov. *Front Microbiol* 2022;13:738205.
44. Collins MD. Analysis of isoprenoid quinones. In: *Methods in Microbiology*, vol. 18. Academic Press, 1985. pp. 329–366.
45. Komagata K, Suzuki KI. Lipid and cell-wall analysis in bacterial systematics. *Methods Microbiol* 1988;19:161–207.
46. Kamekura M. Lipids of extreme halophiles. In: Vreeland RH and Hoch-stein LI (eds). *The Biology of Halophilic Bacteria*. Boca Raton: CRC Press; 1993. pp. 135–161.
47. Tindall B. Lipid composition of *Halobacterium lacusprofundi*. *FEMS Microbiol Lett* 1990;66:199–202.
48. Sasser M. Identification of bacteria by gas chromatography of cellular fatty acids. In: *MIDI Technical Note 101*, vol. 101. Newark, DE: MIDI, 1990
49. Chamlagain B, Edelmann M, Kariluoto S, Ollilainen V, Piironen V. Ultra-high performance liquid chromatographic and mass spectrometric analysis of active vitamin B12 in cells of *Propionibacterium* and fermented cereal matrices. *Food Chem* 2015;166:630–638.
50. Imhoff JF, Petri R, Süling J. Reclassification of species of the spiral-shaped phototrophic purple non-sulfur bacteria of the alpha-Proteobacteria: description of the new genera *Phaeospirillum* gen. nov., *Rhodovibrio* gen. nov., *Rhodothalassium* gen. nov. and *Roseospira* gen. nov. as well as transfer of *Rhodospirillum fulvum* to *Phaeospirillum fulvum* comb. nov., of *Rhodospirillum molischianum* to *Phaeospirillum molischianum* comb. nov., of *Rhodospirillum salinarum* to *Rhodovibrio salexigens*. *Int J Syst Bacteriol* 1998;48:793–798.
51. Ahn S, Choi DH-S, Weerawongwiwat V, Kim J-H, Sukhoom A, *et al*. *Aquibaculum arenosum* gen. nov., sp. nov., a novel member of the family *Rhodovibrionaceae*, isolated from sea sand. *Int J Syst Evol Microbiol* 2024;74:006458.
52. He W, Li Y, Zhang D. *Pacificispira spongiicola* gen. nov., sp. nov., a nitrate-reducing bacterium isolated from tropical western Pacific. *Antonie van Leeuwenhoek* 2021;114:2083–2090.
53. Wang Z, Zhang Z, Li C, Zhang M, Zhao D, *et al*. *Algihabitans albus* gen. nov., sp. nov., isolated from a culture of the green alga Ulva prolifera. *Int J Syst Bacteriol* 2019;69:828–832.
54. Wang S, Ye ZH, Wang NN, Mu DS, Du ZJ. *Ferruginivarius sediminum* gen. nov., sp. nov., isolated from a marine solar saltern. *Int J Syst Bacteriol* 2019;69:3056–3061.
55. Koziaeva VV, Sorokin DY, Kolganova TV, Grouzdev DS. *Magnetospirillum sulfuroxidans* sp. nov., capable of sulfur-dependent lithoautotrophy and a taxonomic reevaluation of the order *Rhodospirillales*. *Syst Appl Microbiol* 2023;46:126406.
56. Wang G, Tang D, Li G, Xu S, Dang G, *et al*. *Denitrobaculum tricleocarpae* gen. nov., sp. nov., a marine bacterium from coralline algae *Tricleocarpa* sp. *Int J Syst Evol Microbiol* 2020;70:3335–3339.
57. Choi DH, Hwang CY, Cho BC. *Pelagibius litoralis* gen. nov., sp. nov., a marine bacterium in the family *Rhodospirillaceae* isolated from coastal seawater. *Int J Syst Evol Microbiol* 2009;59:818–823.
58. Yang C, Zhu S, Sun C, Ding L, Jung D, *et al*. *Pelagibius marinus* sp. nov., a novel bacterium isolated from marine sediment, and emended description of the genus *Pelagibius*. *Int J Syst Evol Microbiol* 2022;72:005325.

The Microbiology Society is a membership charity and not-for-profit publisher.

Your submissions to our titles support the community – ensuring that we continue to provide events, grants and professional development for microbiologists at all career stages.

Find out more and submit your article at microbiologyresearch.org

Environmental Research 268 (2025) 120750

Contents lists available at ScienceDirect

Environmental Research

journal homepage: www.elsevier.com/locate/envres

Polystyrene microplastics exhibit toxic effects on the widespread coral symbiotic *Cladocopium goreaui*

Jiayuan Liang [a,*,1], Tianyi Niu [a,d,1], Li Zhang [c], Yating Yang [a], Zhicong Li [a], Zhuqing Liang [a], Kefu Yu [a,b,**], Sanqiang Gong [a]

[a] Guangxi Laboratory on the Study of Coral Reefs in the South China Sea, School of Marine Sciences, Guangxi University, Nanning, 530004, China
[b] Southern Marine Science and Engineering Guangdong Laboratory (Guangzhou), Guangzhou, 510030, China
[c] School of Resources, Environment and Materials, Guangxi University, Nanning, 530004, China
[d] State Key Laboratory of Urban and Regional Ecology, Research Center for Eco-Environmental Sciences, Chinese Academy of Sciences, Beijing, 100085, China

ARTICLE INFO

Keywords:
Microplastics
Coral reef ecosystem
Symbiodiniaceae
Photosynthesis
Energy metabolism

ABSTRACT

Within the coral reef habitat, members of the Symbiodiniaceae family stand as pivotal symbionts for reef-building corals. However, the physiological response of Symbiodiniaceae on microplastics are still poorly understood. Research conducted in this investigation assessed the harmful impact of polystyrene microparticles (PS-MPs) on *Cladocopium goreaui*, a Symbiodiniaceae species with a broad distribution. The results showed that micrometre-sized PS-MPs had a greater toxic effect on *C. goreaui* than nanometre-sized PS-MPs, and the growth inhibition rate of a concentration of 20 mg/L with 10 μm-sized PS-MPs on *C. goreaui* was as high as 62.9%–86%, which almost completely inhibited cell proliferation. Exposure to 10 μm PS-MPs significantly increased cell damage, for instance, the concentration of extracellular polymeric substance and malondialdehyde have increased by 161.6%–184.4% and 261.8%–896% on days 10–20 respectively. Furthermore, When PS-MPs inhibited the photosynthesis of *C. goreaui*, it could ensure their typical photosynthetic activity maintained by increasing their chlorophyll levels, and the increase in chlorophyll concentration is proportional to the level of inhibition experienced. However, Exposure to 10 μm PS-MPs could damage the chloroplasts of *C. goreaui*, leading to a decrease in the ability to synthesize photosynthetic pigments and subsequently resulting in a reduction in photosynthetic capacity. The morphology and genetic activity of *C. goreaui* suggest that PS-MPs primarily induce cellular shrinkage and distortion, as well as the disintegration and impairment of nuclear and chloroplastic structures, concurrently eliciting a greater number of suppressed genes, predominantly those associated with the function of succinate dehydrogenase, the attachment to tetrapyrroles, the binding of haem, and the handling of iron ions, including activities related to oxidoreduction. The investigation examined the adverse impacts of PS-MPs on a crucial coral symbiont (Symbiodiniaceae) and the beneficial reaction of these algal organisms, enhancing comprehension of how microplastic pollution affects the coral reef ecosystem.

1. Introduction

Coral reefs showcase significant levels of primary productivity alongside a rich variety of biodiversity (Mooney et al., 2009; Hoegh--Guldberg, 2011). Although coral reefs occupy only approximately 0.25% of the global marine area, they provide habitat for nearly 30% of marine organisms and are known as "tropical rainforests of the sea" (Reaka-Kudla and L, 1997; Yu, 2018). The continuous decline in the health of coral reef habitats is intensifying as a result of issues including climate change, excessive fishing practices, and the contamination of the natural environment (Hughes et al., 2003; Yu, 2012). With societal development, plastic pollution and that of its additives have become serious threats to Earth's ecosystems (Jambeck et al., 2015; Sendra et al., 2021). In the natural environment, plastic waste is gradually decomposed into small particles through physical, chemical, and biological processes, forming microplastics (MPs) with diameters less than 5 mm

* Corresponding author.
** Corresponding author. Guangxi Laboratory on the Study of Coral Reefs in the South China Sea, School of Marine Sciences, Guangxi University, Nanning, 530004, China.
E-mail addresses: jyliang@gxu.edu.cn (J. Liang), kefuyu@scsio.ac.cn (K. Yu).
[1] These authors contributed to the work equally and should be regarded as co-first authors.

https://doi.org/10.1016/j.envres.2025.120750
Received 5 November 2024; Received in revised form 22 December 2024; Accepted 1 January 2025
Available online 2 January 2025
0013-9351/© 2025 Elsevier Inc. All rights are reserved, including those for text and data mining, AI training, and similar technologies.

(Thompson et al., 2004; Lambert et al., 2013; Auta et al., 2017; Yang et al., 2020). And after secondary decomposition, nanoplastics with particle size less than 100 nm can be formed (Sana et al., 2020). MPs are widely distributed, including in rivers, soil, oceans, and even the air (Li et al., 2021a, b; Zhou et al., 2021). It is estimated that more than 8 million tons of plastic waste enter the ocean from land each year and are dispersed to every corner of the ocean by ocean currents (Schwarz et al., 2019; Van Sebille et al., 2020). This has led to the ubiquitous threat of MPs pollution in coral reefs. MPs have been detected in coral reef areas such as the Great Barrier Reef in Australia (Jensen et al., 2019), the Maldives archipelago (Imhof et al., 2017; Saliu et al., 2018), and numerous islands in the South China Sea (Ding et al., 2019a; Huang et al., 2019). MPs in coral reef ecosystems can be ingested by reef-dwelling organisms in different ways, thereby entering the food chain cycle and being difficult to degrade (Wright et al., 2013; Ivleva et al., 2017). Rotjan et al. (2019) analysed different coral species on Rhode Island and detected many MPs in each polyp, with an average content of more than 100. Simultaneously, in indoor experiments, it was found that when polyethylene MPs (107.5–230.8 μm) and brine shrimp eggs of similar size coexisted, the coral *Astrangia poculata* preferred to ingest MPs and exhibited a certain resistance response to brine shrimp eggs, indicating that corals would inhibit their intake of other foods after ingesting MPs. Tang et al. (2018) have found that short-term contact with PS-MPs provokes a stress reaction within the scleractinian coral species *Pocillopora damicornis*, which activates the JNK and ERK signalling pathways. This activation impairs the coral's fungal detoxification and defense mechanisms, consequently diminishing its ability to resist stress and compromising its immune function.

Reef-building corals are typical symbiotic organisms that are composed of coral polyps and various microorganisms, such as Symbiodiniaceae, bacteria, fungi, viruses, and protozoa, that form a "holobiont" in a mutualistic symbiotic relationship (Wegley et al., 2007; Robbins et al., 2019). In tropical and subtropical coral reef environments, Symbiodiniaceae constitute the predominant group of symbiotic phototrophs (Su et al., 2020). The partnership between these microorganisms and reef-building corals forms the foundation of coral reef ecosystems, due to the fact that the energy produced through photosynthesis by Symbiodiniaceae fulfills up to 95% of the nutritional needs of the corals they inhabit (Houlbrèque and Ferrier-Pagès, 2009; González-Pech et al., 2019).The family Symbiodiniaceae comprises several distinct clades, such as *Symbiodinium* (Clade A), *Breviolum* (Clade B), *Cladocopium* (Clade C), *Durusdinium* (Clade D), and *Fugacium* (Clade F) (LaJeunesse et al., 2018). As identified by Gong et al. (2021) with *Cladocopium* and *Durusdinium* being dominant in tropical Indo-Pacific corals. The Cladocopium genus is the most diverse genus of Symbiodiniaceae, and *C. goreaui* is the most representative species. It has high photosynthetic efficiency, which can help coral hosts tolerate seasonal low temperature and high nutrient environments (Baker et al., 2013). Symbiotic dinoflagellates play a key role in coral bleaching, therefore, they are often used as important indicators of coral health. MPs not only inhibit the photosynthesis of phytoplankton but also cause direct physical damage to algae (Ding et al., 2019b). Microparticle contaminants in marine environments vary in dimension from several nanometers to hundreds of micrometers, with their harmful impacts being intimately linked to the scale of the particles. Chen et al. (2020) found that after exposure to MPs of different sizes at the micrometre level for 72 h, *Scenedesmus quadricauda* and *Platymonas helgolandica* var. *tsingtaoensis*, two types of microalgae, contained 1–2 μm diameter MPs in some cells, with a significant decrease in microalgal density and inhibition of photosynthesis; however, MPs with a diameter of 3–5 μm were not found inside the cells. Moreover, Xiao et al. (2020) reported that at a concentration of 10 mg/L, the toxicity of 5 μm diameter MPs to the freshwater microalga *Euglena gracilis* was greater than that of 0.1 μm diameter MPs. These MPs not only inhibited algal cell growth but also reduced the content of photosynthetic pigments and increased SOD activity. In the study by Cao et al. (2022b),1 μm MP had a significantly greater inhibitory effect on the growth of the freshwater alga *Chlorella pyrenoidosa* than 5 μm MP did, also significantly reducing the content of photosynthetic pigments, inducing an oxidative stress response in cells, and damaging the integrity of cell membranes. The varied outcomes demonstrate that analyses of MPs' influence on microalgae should encompass not just the adverse impacts of uniform-sized particles but also the collective toxicity stemming from a range of MPs sizes. Regarding the toxicity of MPs to Symbiodiniaceae, Marangoni et al. (2022) reported that 20 nm PS-MPs reduced the maximum electron transfer rate and total antioxidant capacity of *Symbiodinium* (Clade A) and increased lipid peroxidation. Ripken et al. (2020)'s study indicated that exposure to nanoscale MPs (42 nm) resulted in the upregulation of genes associated with *Cladocopium* sp.(clade C) involvement in motor protein movement and the downregulation of genes related to photosynthesis, mitosis, and intracellular degradation, with more genes being downregulated than upregulated. Research by Su et al. (2020) showed that exposure to 1 μm MP at 5 mg/L suppressed the detoxification activity, nutrient absorption, and photosynthesis of *C. goreaui* observed that elevated oxidative stress and enhanced cellular apoptosis by stimulating ion transport. At present, studies concerning the impact of MPs on Symbiodiniaceae have predominantly focused on minute fragments (20 nm, 42 nm, and 1 μm), while the toxicological consequences of MPs varying in particle size and concentration remain unexplored.

The initiation of the symbiotic partnership termed "coral-Symbiodiniaceae symbiosis" occurs via horizontal transmission for most species that construct coral reefs, according to Ali et al. (2019). Planktonic larvae are important during the early development of corals, and they must absorb free-living Symbiodiniaceae from the environment to form a "coral-Symbiodiniaceae" symbiont (Ng et al., 2019). The peril that MPs pose to Symbiodiniaceae has a direct impact on the wellbeing and equilibrium of the whole coral reef ecosystem. In order to further investigate the toxic mechanism of MPs on Symbiodiniaceae, this study conducted a short-term indoor acute exposure experiment to MPs to study the physiological and biochemical changes and transcription products of *C. goreaui*. Some research had shown that the main types of MPs in the western Pacific Ocean are PP, PVC, PS, and PE (Cui et al., 2022); The main types of MPs in the eastern Indian Ocean are PP, PE, PVC, PS, and PET (Li et al., 2021a, b); The main types of MPs in the Persian Gulf waters are PE, PS, PP (Kor and Mehdinia, 2020). So, this research delved into how various amounts and dimensions (microplastic grade) of polystyrene—among the most prevalent commercial plastics globally—affect the Symbiodiniaceae family detrimentally, examining the underlying processes. Insights garnered from this investigation are anticipated to enhance comprehension of how pivotal coral-associated microbes react to MPs pressures and the implications of these interactions for coral reef environments and further evaluate the potential impact of microplastic pollution on the entire coral reef ecosystem.

2. Materials and methods

2.1. Cultivation of the C. goreaui strain and experimental reagents

The *C. goreaui* strain used in this study was isolated and cultured from Acropora pruinosa on Wuzhou Island, northern South China Sea (Qin et al., 2023). *C. goreaui* was grown in L1 marine water mixture, featuring a 35 parts per thousand saline content, ambient warmth of 25 °C with a 1-degree margin, 90 μmol per square meter per second of luminance, and a photoperiod of 14 h illuminated to 10 h unlit. Using artificial plastic microbeads to simulate the environment can better control experimental conditions, observe the impact characteristics of MPs under different conditions, and more accurately evaluate their potential impact on coral reef environments. In addition, it also can help researchers understand the response patterns of MPs under specific environmental conditions, providing scientific basis for environmental protection and risk assessment. PS-MPs were procured from Tianjin Besttech Research Center, located in Tianjin, China, and were preserved

in suspension form at a concentration of 2.5% by weight to volume in a 10-mL solution. PS-MPs were uniformly dispersed in water and did not precipitate or accumulate during the cultivation experiments.

2.2. MPs exposure experiment

Owing to the steady breakdown and diminishment of plastic within nature, it becomes undetectable when it falls below a specific threshold. So this study selected a wide range of concentrations of MPs from 0 to 50 mg/L and a size range of MPs from 100 nm to 10 μm. *C. goreaui* was cultured to a density of 1.0×10^5 cells/mL. Six groups were set up with different concentrations of 1 μm PS-MPs, 0 mg/L, 2 mg/L, 5 mg/L, 10 mg/L, 20 mg/L, and 50 mg/L, with three replicates per group. The concentration of PS-MPs was fixed at 20 mg/L, and five experimental groups with different particle sizes of 0.1 μm, 0.4 μm, 1 μm, 5 μm, and 10 μm were set up, with three replicates per group. This study selected a particle size range of 0.1–10 μm, ranging from small particle size to particle size similar to *C. goreaui* cells (9.8 ± 1.3 μm) (Qin et al., 2023), to comprehensively explore the toxic effects of microplastic particle size on *C. goreaui*. The particle size was set to 1 μm (the middle value of the particle size range) to investigate the toxicity of MPs at different concentrations, and had good radiation effect on both extreme values on both sides. Setting up a high concentration simulation environment is beneficial for better controlling experimental conditions, observing the impact characteristics of MPs under different conditions, and thus more accurately evaluating their potential impact on coral reef environments. In addition, a high concentration simulated environment helps to enhance the cumulative effect of convex MPs and assists researchers in understanding the response patterns of MPs under specific environmental conditions, providing scientific basis for environmental protection and risk assessment. Therefore, set the concentration range to 0–50 mg/L, and when exploring the toxic effects of MPs with different particle sizes, set the concentration to 20 mg/L. The cultivation conditions were the same as those mentioned above.

2.3. Sample processing and data analysis

2.3.1. C. goreaui growth rate analysis

Samples were taken at 0, 5, 10, and 20 days of culture for analysis and testing. One millilitre of sample solution was removed and fixed with 100 μL of formaldehyde reagent. Cell quantification was performed with a haemocytometer while utilizing a Nikon ECLIPSE Ni-E upright light microscope. Subsequently, the recordings of this data enabled the determination of both cell concentration and proliferation velocity. To compute these parameters, the equation utilized was: Proliferation velocity (μ) = ln(N2/N1)/(t2-t1), wherein μ represents the proliferation velocity (per day), and N2 and N1 signify the respective cellular concentrations (cells/mL) at the distinct time points t2 and t1.

2.3.2. Determination of the photosynthetic pigment content and photobiological efficiency of C. goreaui

Samples were taken at 0, 2, 5, 10, and 20 days of culture for analysis and testing. A 5 mL aliquot of the test liquid was pipetted into a centrifuge tube, then spun at a temperature of 4 °C and a force of 5000×*g* for a duration of 5 min. Following this, the clear liquid above the sediment was discarded, and the residue was treated with 1 mL of methanol. The sample was thoroughly mixed with a vortex mixer, covered in aluminum foil, and stashed away from light at a temperature of 4° Celsius for a full day to allow for the extraction of the photosynthetic pigments. A Varioskan™ LUX multifunctional microplate reader (Thermo Scientific) was used to measure optical density (OD) at 480, 510, 630, 664, and 750 nm wavelengths (Ritchie, 2006; Sun, 2020) in the dark. The photosynthetic pigment content was normalized to the single-cell content (pg/cell). The formulas for determining Chl a, Chl c, and carotenoid levels are as follows:

$$\text{Chlorophyll a } (\mu g/ml) = 13.6849 \times (OD_{664} - OD_{750}) - 3.4551 \times (OD_{630} - OD_{750})$$

$$\text{Chlorophyll c } (\mu g/ml) = -7.014 \times (OD_{664} - OD_{750}) + 32.9371 \times (OD_{630} - OD_{750})$$

$$\text{Carotenoids } (\mu g/ml) = 7.6 \times (OD_{480} - OD_{750}) - 1.49 \times (OD_{510} - OD_{750})$$

The *C. goreaui* cells were incubated in a dark setting for half an hour before their photosystem II (PS II) peak photochemical efficiency, denoted as Fv/Fm, was quantified using a WALZ brand PAM device from Germany.

2.3.3. Determination of extracellular polymeric substance content

Samples were taken at 0, 10, and 20 days of culture for analysis and testing. The quantity of extracellular polymeric substance (EPS) (The main component is exopolysaccharide) was determined through the phenol-sulfuric acid technique as described by Li et al. (2022) and Yue et al. (2022). For this process, the specimen underwent a thermal phase of 80° Celsius lasting 30 min prior to being spun at a force of 8000×*g* for a duration of 10 min at a temperature of 4 °C. From the clarified liquid, a volume of 2 mL was extracted, to which was then introduced 1 mL of phenol at a 6% concentration within a chilled environment. Subsequently, a measured 5 mL of sulfuric acid was incrementally dispensed, taking care to minimize or eliminate thermal emission. Subsequent to the initial procedure, the concoction underwent a boiling process within a water bath for a duration of 20 min, followed by a chilling period in an ice bath spanning 10 min. The OD was then ascertained at a 490 nm wavelength. For calibration purposes, a glucose solution served as the reference. A series of ten varying concentrations (0, 10, 20, 30, 40, 50, 60, 70, 80, and 90 μg/mL) were systematically prepared to establish a concentration gradient. From each level of this gradient, a volume of 2 mL was sampled, and the OD for each was gauged at a 490 nm wavelength, adhering to the procedures previously described.A calibration curve, showing concentration along the horizontal axis and OD vertically, was used to determine the sample's EPS levels, which were then adjusted based on individual cell quantities.

2.3.4. Evaluation of dissolved protein levels, malondialdehyde quantities and superoxide dismutase functionality

Samples were taken at 0, 10, and 20 days of culture for analysis and testing. A volume of 20 mL of the test fluid underwent centrifugation at a temperature of 4 °C and a force of 3000×*g* for a duration of 10 min. Following the extraction of the clear fluid above the sediment, the precipitate was reconstituted with 1.5 mL of Phosphate Buffered Saline and then relocated into a centrifuge tube with a capacity of 2 mL. Then,100 μL of 0.5 mm zirconia grinding beads was added. A mechanical device for tissue homogenization (manufactured by Shanghai Jingxin) facilitated the pulverization process, operating in cycles of 10 s on, 30 s off, totalling six cycles, with the apparatus's adapter precooled in a freezer set to minus 20 °C prior to its application. Following homogenization, the samples were spun at a force of 3000×*g* and a temperature of 4 °C for a duration of 10 min, subsequent to which the clear liquid above the settled particles was extracted. To quantify the amount of dissolvable protein present, an assay kit specifically designed for bicinchoninic acid (BCA) protein analysis (procured from Shanghai Shenggong, China) was employed. The enzymatic function of Superoxide dismutase (SOD) was quantified with the employment of a specific SOD detection kit (A001, Nanjing Jiancheng, China), while the level of malondialdehyde (MDA) was ascertained utilizing a corresponding MDA measurement kit (A003, Nanjing Jiancheng, China). The results were normalized to the single-cell content.

2.3.5. Ultrastructural analysis

Three particle size groups with significant differences, namely 0.1 μm, 1 μm, and 10 μm, were selected for ultrastructural analysis.

2.3.5.1. SEM analysis. Twenty days into the experiment, a 50 mL sample of *C. goreaui* cells was harvested and subjected to centrifugation at 4 °C and at a force of 5000×*g* for a duration of 10 min, subsequently discarding the supernatant. The cells were then rinsed thrice using PBS (0.1 M, excluding NaCl). A 2.5–3% solution of glutaraldehyde, chilled to 4 °C, was introduced to the cells for fixation over a period of 4 h at the same temperature. Following fixation, the preserving agent was eliminated, and the samples underwent a quintuple wash with PBS (0.1 M, NaCl omitted) for 15 min per wash. Subsequent to the attachment of the specimens to the slides, a sequential dehydration was conducted using a range of ascending alcohol concentrations (30%, 50%, 70%, 80%, 90%, 95%, 100%). The alcohol solution was added once for 15 min each, after which the samples were thoroughly dehydrated with 100% alcohol twice for 10 min each. Subsequently, a critical point dryer (Leica EM CPD300) was used for drying treatment. Finally, an ion sputtering coating instrument (Leica EM ACE200) was used to vacuum spray the samples, which were observed through scanning electron microscopy (SEM; HITACHI SU-8010).

2.3.5.2. TEM analysis. On experiment day Twenty, a 50 mL sample of the algal population was harvested, followed by a centrifugation process at 5000×*g* for a duration of 10 min at a temperature of 4 °C. Subsequently, the overlaying liquid was discarded. The collected cells were then stabilized using glutaraldehyde. After being submerged in 0.1M phosphate-buffered saline, the stabilized algal cells were subjected to a triple rinse. The samples were again centrifuged under the same conditions to eliminate any remaining supernatant, with each rinse lasting 20 min. The cells were then treated with 1% osmic acid while maintained at a cool 4 °C, solidified at this temperature for a period between 2 and 3 h, and finally, they were washed with 0.1M PBS three times, allotting 20 min for each washing session. After dehydration with a series of gradient alcohols (30%, 50%, 70%, 80%, 85%, 90%, 95%, 100%), each concentration of alcohol was used once for 15 min each time, after which the samples were thoroughly dehydrated with 100% alcohol twice for 10 min each. Subsequently, used the penetrant to infiltrate, and the penetrant is a mixture of 2 times acetone and 1 time epoxy resin, a mixture of acetone and epoxy resin in equal proportions, and epoxy resin, each at 37 °C overnight in an incubator. Ultimately, the permeated specimen was positioned within a compact container, followed by the incorporation of an embedding medium of epoxy resin, after which the specimen underwent a curing process at a temperature of 60 °C for a duration of 48 h. After curing, the sample was trimmed to a suitable size and shape and sliced on an ultrathin sectioning machine (EM UC7) with a thickness of approximately 60–100 nm. Following the application of lead and uranium as contrasting agents, the specimens underwent examination using a Tecnai G220 TWIN transmission electron microscope (TEM).

2.4. Extraction and sequencing of transcription products

The transcription products were analysed for experimental samples with significant physiological index effects. On day 20 of the stress trial, we gathered and preserved the *C. goreaui* cells from test cohort of control, 1 μm-10 mg/L, 1 μm-20 mg/L, 1 μm-50 mg/L, and 10 μm-20 mg/L by immersing them in liquid nitrogen for a duration of 30 min. The samples were subsequently sent to Shanghai Meiji Biomedical Technology Co., Ltd., for transcriptome sequencing analysis (see Supplementary File S1 for specific methods).

2.5. Statistical analysis

Statistical evaluation was conducted through the application of SPSS, with p-values below 0.05 marking the threshold for statistical relevance. Subsequent examinations of datasets exhibiting notable disparities were carried out utilizing Tukey's post hoc analysis. Figures were generated employing Origin software. Data representation took the form of the mean ± the standard error.

3. Results

3.1. Physiological effects of PS-MPs exposure on C. goreaui

3.1.1. Growth ratios

Fig. 1 illustrates how varying amounts and sizes of PS-MPs particles influence *C. goreaui* cell's development. The particle diameter of PS-MPs was a stronger deterrent to the proliferation rate of *C. goreaui* compared to the quantity. *C. goreaui* cell's expansion was not notably impacted by PS-MPs particles measuring 1 μm C. *goreaui* at different concentrations (0–50 mg/L). However, at a concentration of 20 mg/L, PS-MPs particles 5 μm and 10 μm in size more significantly inhibited the growth of *C. goreaui*. On the 5th, 10th, and 20th days, compared with those in the control group, the growth rates of *C. goreaui* exposed to 5 μm PS-MPs decreased by 22.9%, 22.8%, and 28.8% in these three days respectively. And the growth rates of *C. goreaui* exposed to 10 μm PS-MPs decreased by 62.9%, 86%, and 81.9% in these three days respectively. In particular, PS-MPs with a particle size of 10 μm almost completely inhibited the growth of the cells.

3.1.2. Photosynthesis

During experiments involving various concentrations and sizes of PS-MPs particles, the photochemical efficiency (Fv/Fm) of *C. goreaui* remained stable, except for that of the 10 μm-20 mg/L exposure group, which showed significant inhibition starting from the 5th day (19.5% decrease compared to the control group); moreover, no Fv/Fm values were detected starting from the 10th day (Fig. 2A and B). Photosynthetic pigments are crucial for maintaining photosynthesis. After exposure to different concentrations of PS-MPs with a particle size of 1 μm, a positive correlation was observed on the Chl a content of *C. goreaui*, and in the 1 μm-50 mg/L group, the Chl a content significantly increased beginning on the 5th day (Fig. 2C). When exposed to PS-MPs at size of 5 μm and 10 μm at a concentration of 20 mg/L, the Chl a content of *C. goreaui* significantly increased beginning on the 2nd day and then noticeably decreased on the 10th day (Fig. 2D). When exposed to PS-MPs at particle sizes of 0.1 μm, 0.4 μm, and 1 μm at a concentration of 20 mg/L, the Chl a content of *C. goreaui* significantly increased only on the 20th day ($p < 0.05$). The changes in the Chl c and carotenoid contents were similar to those in the Chl a content (Fig. 2E, F, G, H). The 0.1 μm, 0.4 μm, and 1 μm particles at concentrations of 10–20 mg/L had significantly greater carotenoid contents on the 5th day than did the control group (Fig. 2G and H).

3.2. Impacts of PS-MPs interaction on antioxidant response and cellular protection mechanisms within C. goreaui cells

Following interaction with PS-MPs, there was a direct correlation between the PS-MPs' quantities and dimensions and the amounts of EPS, soluble protein, and MDA, as well as the enzymatic action of SOD in *C. goreaui* cells (Fig. 3). When exposed to PS-MPs at a particle size of 1 μm, the experimental treatment with a concentration lower than 20 mg/L had no significant impact on the EPS content in *C. goreaui* cells, while the experimental treatment with a concentration higher than 20 mg/L had a significant increase in EPS content on days 10–20 compared to that of the control group (Fig. 3A). When exposed to PS-MPs at a concentration of 20 mg/L and different particle sizes, the EPS content in *C. goreaui* cells was significantly greater on days 10–20 than that in the

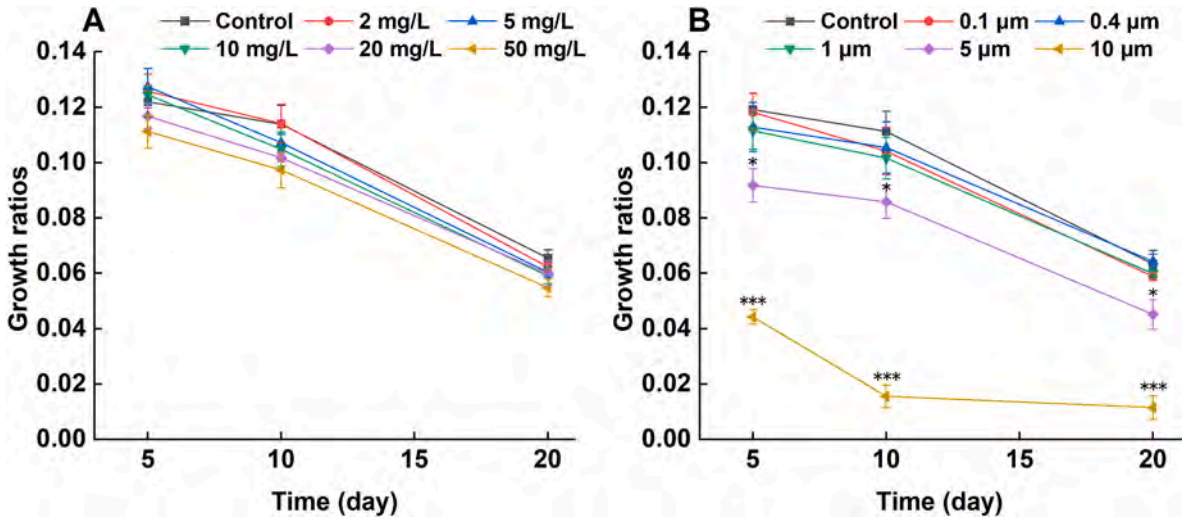


Fig. 1. The influence of PS-MPs exposure on the growth rate of *C. goreaui*. (A) Exposure to PS-MPs with different concentrations of particles with a diameter of 1 μm. (B) Exposure to PS-MPs with a concentration of 20 mg/L and different particle sizes. The data points and bars represent the mean ± the standard error (three biological replicates). The significance between the experimental group and the control group is indicated by asterisks (*: $p < 0.05$, **: $p < 0.01$, ***: $p < 0.001$).

control group (Fig. 3B), and the degree of significance was in the following order: 10 μm > 5 μm > 1 μm ≈ 0.4 μm ≈ 0.1 μm. Among the groups, the experimental group exposed to 10 μm PS-MPs had the highest degree of significance, with increases in EPS of 161.6% and 184.4% on days 10 and 20, respectively.

Upon exposure to PS-MPs with either a 20 mg/L concentration and particle sizes of 5 μm or 10 μm, or a 50 mg/L concentration with 1 μm particles, there was an alteration in the soluble protein levels in *C. goreaui* cells significantly increased on days 10–20, while the other groups showed no significant differences (Fig. 3C and D). The experimental group exposed to 10 μm PS-MPs exhibited the highest degree of significance, with increases in soluble protein of 151.6% and 190.3% on days 10 and 20, respectively.

Upon encountering PS-MPs, the alterations observed in SOD activity closely paralleled those in soluble protein levels found in *C. goreaui* cells (Fig. 3E and F). The experimental group exposed to 10 μm PS-MPs exhibited the highest degree of significance, with increases in SOD activity of 147% and 169% on days 10 and 20, respectively.

Subjecting *C. goreaui* cells to varying levels and sizes of PS-MPs particles led to a marked elevation in its MDA levels on days 10–20 of the experiment (Fig. 3G and H). Relative to the control group, the levels of MDA in the various experimental groups rose over time and exhibited a direct relationship with both the concentration and the size of the particles. Among the groups, the experimental group exposed to 10 μm PS-MPs had the greatest degree of significance, with increases in the MDA content of 261.8% and 896% on days 10 and 20, respectively.

3.3. Effects of PS-MPs exposure on the structure of C. goreaui cells

SEM analysis clearly revealed the interaction between the algal cells and the PS-MPs. When *C. goreaui* cells were exposed to PS-MPs, a large amount of PS-MPs aggregated with extracellular polysaccharides to form EPS (Fig. 4E, F, G). In the control group, the associated bacteria were in a free state and did not aggregate with *C. goreaui* (Fig. 4D), while in the experimental group, most of the associated bacteria aggregated in the EPS (Fig. 4E, F, G). Even PS-MPs with a particle size of 10 μm and a concentration of 20 mg/L caused severe wrinkling and deformation of the algal cells (Fig. 4G).

TEM observation of the damage in algal cells revealed that exposure to PS-MPs at a particle size of 10 μm and a concentration of 20 mg/L had detrimental effects on the growth of *C. goreaui*, causing cell wrinkling, dissolution of accumulations (preliminarily judged as lipids), separation of the plasma membrane, sparse fractures of the thylakoid layer, disintegration of chloroplasts, and nuclear disintegration (Fig. 5D). Furthermore, compared to those in the control group, the volume of chloroplasts in the *C. goreaui* experimental group exposed to 10 μm PS-MPs at a concentration of 20 mg/L significantly increased.

3.4. Effects of PS-MPs exposure on the transcription products of C. goreaui cells

3.4.1. Analysis of variable gene expression and Gene Ontology functional annotation in C. goreaui

Subsequent to being subjected to varying sizes and concentrations of polystyrene particles (1 μm at 10, 20, and 50 mg/L, and 10 μm at 20 mg/L), there was an observed association between the volume of upregulated genes exhibiting differential expression and the amount of PS-MPs present. In contrast, the quantity of genes showing decreased expression levels was linked to both the amount and size of the PS-MPs particles (Fig. 6A). As the concentration of PS-MPs heightened, there was an uptick in the number of downregulated differentially expressed genes, whereas the count of upregulated genes initially rose before it went on a decline. Increasing the particle size of the PS-MPs resulted in an increase in the number of downregulated differentially expressed genes (DEGs).

GO functional annotation analysis of the DEGs revealed that the effects of PS-MPs exposure on *C. goreaui* were mainly about the functions of predominantly encompassed enzyme catalysis, molecular binding, components of cells, membrane segments, metabolic functions, and cellular operations, as depicted in Fig. 6B. The impact of PS-MPs exposure on these biochemical functions was mainly manifested by the greater influence of larger particle sizes and higher concentrations (in order of significance: 10 μm-20 mg/L, 1 μm-50 mg/L, 1 μm-20 mg/L, and 1 μm-10 mg/L).

3.4.2. GO functional enrichment analysis

A further examination was carried out on the ten most markedly enhanced Gene Ontology(GO) terms associated with differentially expressed genes found within the GO enrichment analysis, as depicted in Fig. 6C. Following interaction with various particle sizes and PS-MPs concentrations, the expression of DEGs in the cohort subjected to 1 μm particles at a 20 mg/L concentration underwent upregulation. Conversely, in cohorts subjected to particle parameters of 1 μm–10 mg/L, 1 μm-50 mg/L, and 10 μm-20 mg/L, there was a predominance of downregulation in DEG numbers compared to those experiencing

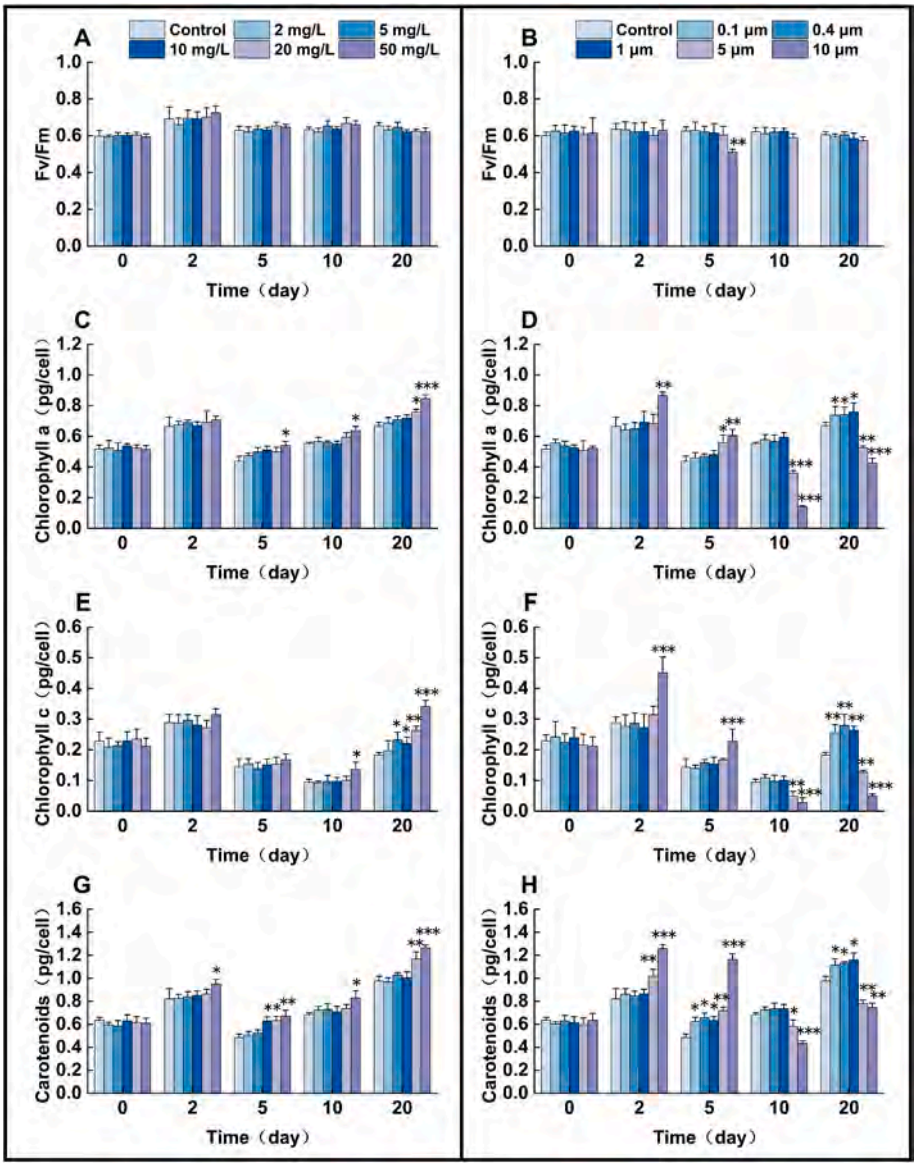


Fig. 2. Effects of PS-MPs exposure on the photosynthetic efficiency and pigment content of *C. goreaui*. (A) Exposure to PS-MPs with different concentrations of particles with a diameter of 1 μm on the Fv/Fm ratio. (B) Exposure to PS-MPs with a concentration of 20 mg/L and different particle sizes on the Fv/Fm. (C) Exposure to PS-MPs with different concentrations of particles with a diameter of 1 μm on the chlorophyll *a* concentration. (D) Exposure to PS-MPs with a concentration of 20 mg/L and different particle sizes on the chlorophyll *a* content. (E) Exposure to PS-MPs with different concentrations of particles with a diameter of 1 μm on the chlorophyll *c* content. (F) Exposure to PS-MPs with a concentration of 20 mg/L and different particle sizes on the chlorophyll *c* content. (G) Exposure to PS-MPs with different concentrations of particles with a diameter of 1 μm on the carotenoid content. (H) Exposure to PS-MPs with a concentration of 20 mg/L and different particle sizes on the carotenoid content. The bar shapes represent the mean ± the standard error (three biological replicates). The significance between the experimental group and the control group is indicated by asterisks (*: $p < 0.05$, **: $p < 0.01$, ***: $p < 0.001$).

upregulation. Among them, the experimental group exposed to a particle size of 10 μm had the highest number of downregulated DEGs, which were associated with functions such as succinate dehydrogenase activity, tetrapyrrole binding, haem binding, ionic binding, and the thylakoid lumen. Patterns of gene expression pertaining to these roles (with certain DEGs showing enrichment across various GO categories) were examined and depicted as a heatmap (refer to Fig. S1). Genes (SymbC1.scaffold2946.4) implicated in light capture and counteracting photo-oxidative stress exhibited a marked increase in expression within the experimental cohorts subjected to particle concentrations spanning 1 μm to 50 mg/L and 10 μm to 20 mg/L. Nevertheless, within the test group subjected to a particle size and a concentration of 10 μm–20 mg/L, there was also a notable elevation in the relative gene expression levels associated with the production of fatty acids (SymbC1.scaffold1086.4) and malonyl-CoA synthesis (SymbC1.scaffold6029.2, SymbC1.For scaffold5219.1, whose genes have a close association with the TCA cycle, the expression levels of the other genes were reduced.

3.4.3. KEGG pathway enrichment analysis

Fig. S2 presents the foremost 10 KEGG pathways that were markedly enriched among differentially expressed genes (DEGs) as identified by the KEGG pathway enrichment analysis. The findings suggest that the pathways most affected by various concentrations and sizes of PS-MPs pertain predominantly to metabolic functions, biosynthetic activities, and the processing of genetic information, exhibiting different degrees of involvement. Within these pathways, there was a mix of genes with increased and decreased expression levels; however, with the exception of DEGs in the group exposed to 1 μm-50 mg/L PS-MPs, the majority of DEGs exhibited decreased expression. The number of enriched DEGs in the 10 μm-20 mg/L and 1 μm-50 mg/L groups was relatively high.The

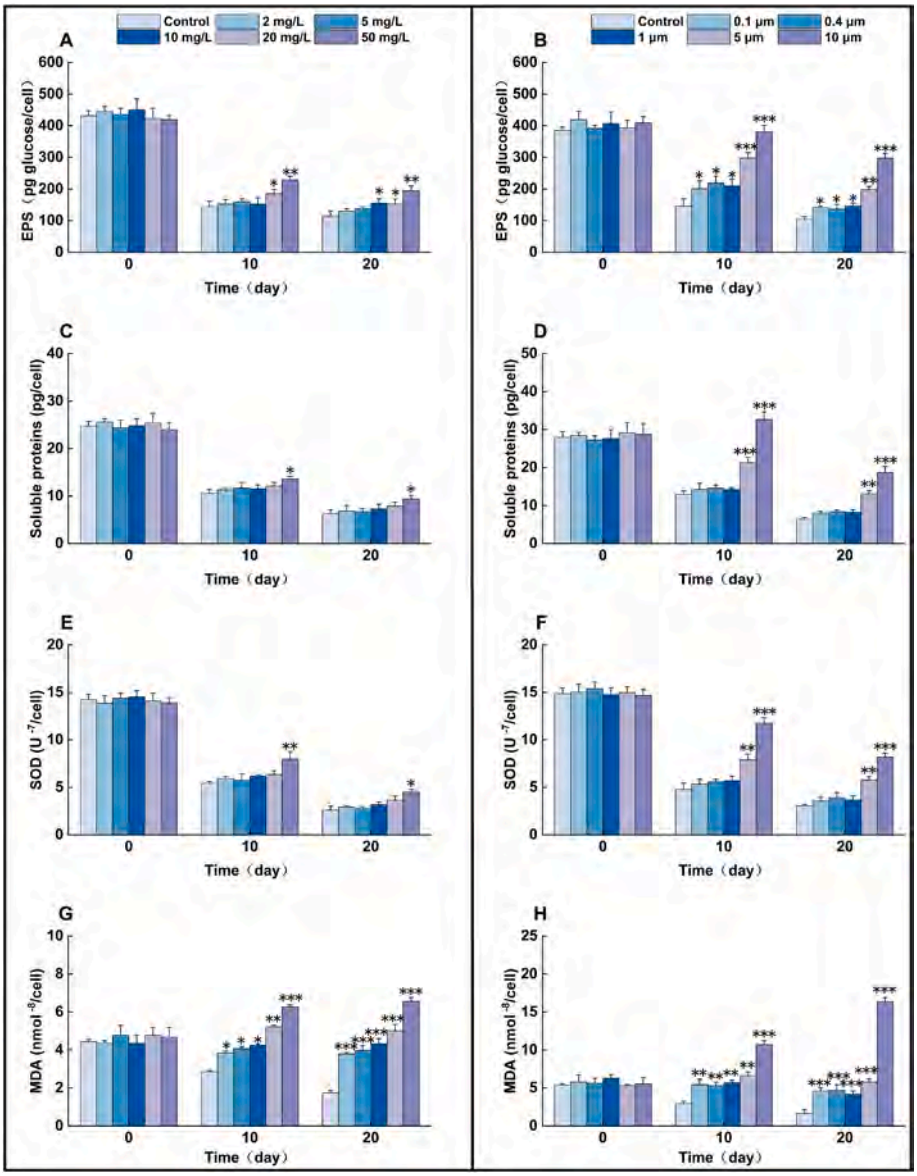


Fig. 3. Effects of PS-MPs exposure on important metabolites in *C. goreaui* cells. (A) Exposure to PS-MPs with different concentrations of particles with a diameter of 1 μm on EPS. (B) Exposure to PS-MPs with a concentration of 20 mg/L and different particle sizes on EPS. (C) Exposure to PS-MPs with different concentrations of particles with a diameter of 1 μm on soluble proteins. (D) Exposure to PS-MPs with a concentration of 20 mg/L and different particle sizes on soluble proteins. (E) Exposure to PS-MPs with different concentrations of particles with a diameter of 1 μm on SOD activity. (F) Exposure to PS-MPs with a concentration of 20 mg/L and different particle sizes on SOD activity. (G) Exposure to PS-MPs with different concentrations of particles with a diameter of 1 μm on MDA levels. (H) Exposure to PS-MPs with a concentration of 20 mg/L and different particle sizes on the MDA concentration. The bar shapes represent the mean ± the standard error (three biological replicates). The significance between the experimental group and the control group is indicated by asterisks (*: $p < 0.05$, **: $p < 0.01$, ***: $p < 0.001$).

distribution of particular gene expression within these networks (with certain differentially expressed genes being prevalent in a number of KEGG pathways) was examined and is depicted as a heatmap (refer to Fig. S3).

4. Discussion

4.1. The effect of various concentrations and sizes of PS-MPs particles on the suppression of C. goreaui growth

Although the research indicated an absence of noteworthy disparity in the growth rate of *C. goreaui* cells exposed to PS-MPs at a particle size of 1 μm or at different concentrations (0–50 mg/L), upon exposure to PS-MPs with a density of 20 mg per liter, featuring particles measuring 5 μm and 10 μm, there was a marked suppression in the proliferation of *C. goreaui*. With the most pronounced effect observed in the subset subjected to the 10-μm particles, which had decreased 62.9%–86% of the growth rate compared to the control group, nearly halted growth entirely. This indicated that larger PS-MPs particle sizes have a greater impact on the growth of *C. goreaui*. Similarly, Liu et al. (2019) reported that when *Scenedesmus obliquus* was exposed to PS-MPs at a concentration of 75 mg/L, the inhibitory effect on growth was significantly greater for 0.5 μm particles than for 0.1 μm particles. Xiao et al. (2020) also reported that at a concentration of 10 mg/L, the toxicity of 5 μm particles on *Euglena gracilis* growth was greater than that of 0.1 μm particles. In addition, through SEM, this study revealed that PS-MPs of different sizes all aggregated with *C. goreaui* to form EPS, and the larger particle size group formed more EPS than the smaller particle size group. The group of 10 μm–20 mg/L caused cell shrinkage and deformation. However, Cao et al. (2022b) reported that smaller PS-MPs (1 μm) were

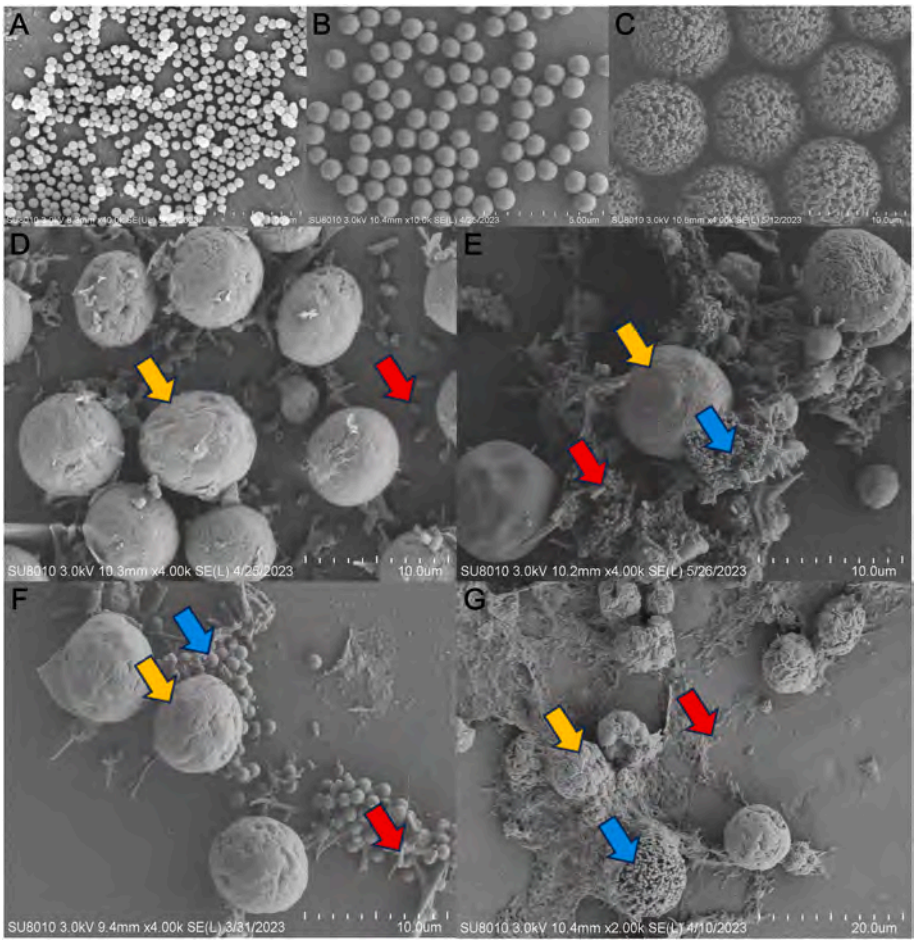


Fig. 4. Effects of PS-MPs exposure on the surface structure of *C. goreaui* cells. (A) PS-MPs with a particle size of 0.1 μm. (B) PS-MPs with a particle size of 1 μm. (C) PS-MPs with a particle size of 10 μm. (D) Control group. (E) Exposure group with a particle size of 0.1 μm and a concentration of 20 mg/L. (F) Exposure group with a particle size of 1 μm and a concentration of 20 mg/L. (G) Exposure group with a particle size of 10 μm and a concentration of 20 mg/L. Yellow arrows point to *C. goreaui* cells, red arrows point to associated bacteria, and blue arrows point to PS-MPs. (For interpretation of the references to colour in this figure legend, the reader is referred to the Web version of this article.)

more likely to interact with *C. pyrenoidosa* and form EPS on the cell surface, while PS-MPs particles with a size of 5 μm did not aggregate with *C. pyrenoidosa* cells to form EPS. This indicates that the impact of PS-MPs on marine microalgae is species specific. Therefore, when exploring the toxic effects of MPs on marine microalgae, it is necessary to carefully consider the differences in response of different microalgae species to MPs. Algal cells excrete EPS into their surrounding milieu, which are crucial for their development and intrinsic defense mechanisms (Li et al., 2020). When PS-MPs aggregate with algal cells to form a large amount of EPS, they can block light and affect the photosynthesis of algal cells, causing severe oxidative damage to the cells (Chen et al., 2012). Furthermore, this study revealed that the increase in EPS caused by PS-MPs exposure also affected the growth of bacteria associated with *C. goreaui*, thereby impacting the growth of *C. goreaui*.

4.2. Stress regulation of photosynthetic pigments in C. goreaui after PS-MPs exposure

When the available light energy for cells decreases, the chlorophyll content increases to maintain photosynthesis (Falkowski and Owens, 1980). During the chill of winter, the symbiotic algae housed within corals transition from a simple layer structure to a more complex, stratified configuration, enhancing their ability to absorb light, which consequently raises both the concentration and the chlorophyll concentration in these algae, as reported by (Venn et al., 2008). Conversely, in the summer months, characterized by greater warmth and more intense sunlight, there is a reduction in both the concentration and chlorophyll levels of the symbiotic algae. These findings indicate that symbiotic algae regulate their own chlorophyll content to maintain stable photosynthesis. During the PS-MPs exposure experiments, *C. goreaui* also employed similar stress strategies. The chlorophyll *a* content in *C. goreaui* cells significantly increased on the 7th day of exposure to PS-MPs at a particle size and concentration ranging from 1 μm to 5 mg/L, while the photochemical efficiency remained stable throughout the exposure experiment (Su et al., 2020). This study revealed that, during the initial stage of PS-MPs exposure, *C. goreaui* cells adjust their content of photosynthetic pigments to maintain stable photosynthesis. In the experimental groups exposed to larger particles (5 μm-20 mg/L and 10 μm-20 mg/L), the contents of pigment in *C. goreaui* cells significantly increased in the early stage of exposure (0–5 days), indicating a positive response from the algal cells. However, due to the stronger damaging effect of larger PS-MPs on *C. goreaui*, following the fifth day, there was a notable reduction in the pigment concentration within the algal cells. Thus it can be seen that when the particle size of PS-MPs exceeds 5 μm, the chloroplast function of *C. goreaui* is impaired. Furthermore, cell structure analysis also revealed that *C. goreaui* cells exhibited severe damage, such as cell contraction and chloroplast disintegration, in the exposure experiment at a particle size and concentration of 10 μm–20 mg/L, leading to weakened photosynthesis. The synthesis of photosynthetic pigments is directly related to tetrapyrrole

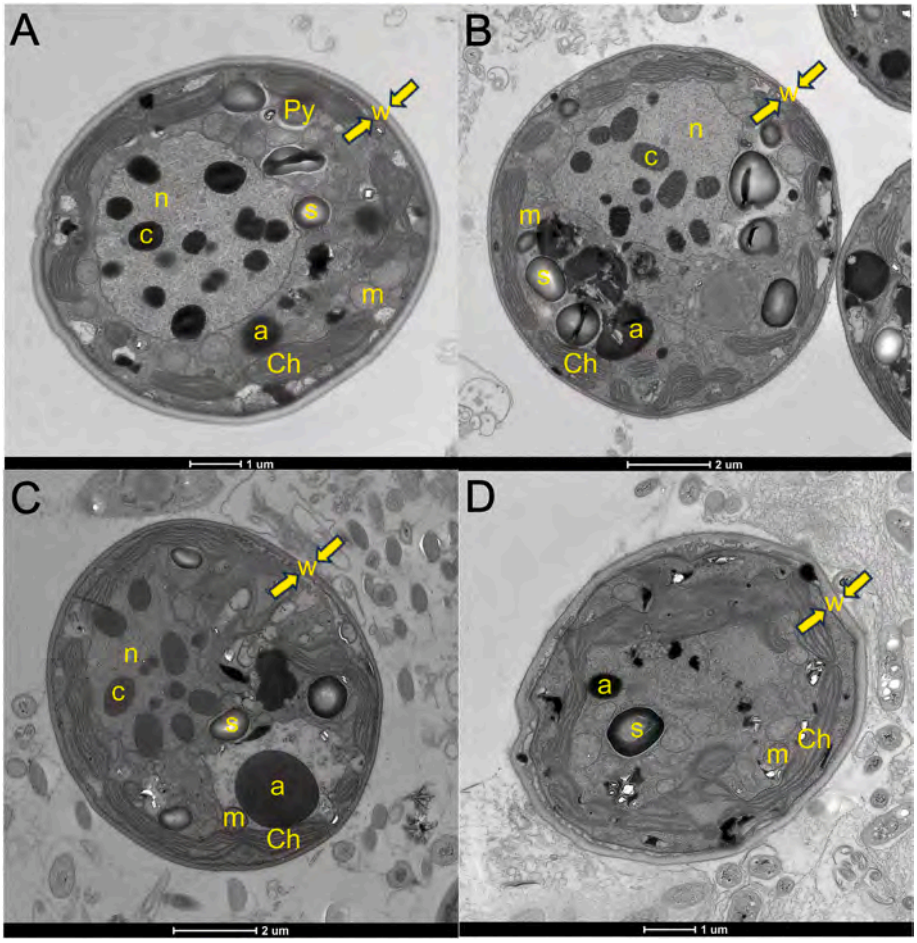


Fig. 5. Effects of PS-MPs exposure on the internal structure of *C. goreaui* cells. (A) Control group. (B) Exposure group with a particle size of 0.1 μm and a concentration of 20 mg/L. (C) Exposure group with a particle size of 1 μm and a concentration of 20 mg/L. (D) Exposure group with a particle size of 10 μm and a concentration of 20 mg/L "n": nucleus; "c": chromosome; "Ch": chloroplast; "Py": pyrenoid; "m": mitochondrion; "s": starch; "a": accumulation body; "w": cell wall.

binding and haem binding (Ikeuchi and Ishizuka, 2008; Xiao et al., 2023), and these dual functions are based on ionic binding. During the experiment involving exposure to PS-MPs, genomic investigation demonstrated a notable decrease in the expression of genes associated with these activities within the group subjected to particles varying in size from 10 μm and having a concentration up to 20 mg/L, suggesting a diminished synthesis of photosynthetic pigments followed by a reduction in the ability to perform photosynthesis. And the significant downregulation of gene expression related to chloroplast thylakoid lumina indicates that chloroplast function is inhibited.

4.3. Exposure to PS-MPs induces oxidative stress and incurs oxidative damage in C. goreaui

Succinate dehydrogenase is one of the key components connecting oxidative phosphorylation and electron transfer, providing electrons for aerobic respiration and energy production in eukaryotic mitochondria and various prokaryotic cells (Lussey-Lepoutre et al., 2015). Haem binding also plays an important role in cellular respiration and energy metabolism (Khan and Quigley, 2011; Xiao et al., 2023). In the PS-MPs exposure experiment, transcriptomic analysis revealed significant downregulation of gene expression related to Succinate dehydrogenase activity, haem, and ionic binding in the experimental group with particle size and concentration of 10 μm–20 mg/L (Fig. 6C), indicating insufficient energy supply and inhibited metabolism. During this process, *C. goreaui* cell growth is restricted, and metabolism is disrupted. Due to its photosynthetic autotrophic nature, *C. goreaui* accumulated energy substances such as sugars and proteins through photosynthesis during cultivation. And the MDA produced by oxidation reaction will also increase with the increase of cell number. As the exposure days increased, the total metabolite content in the control group gradually accumulated, however, as the number of cells increases, their single-cell content gradually decreases, which is consistent with the results of other researchers (Li et al., 2020; Cao et al., 2022b).

Soluble proteins are important nutrients and osmoregulatory substances in cells that not only contribute to the improvement of cell water-holding capacity but also protect biomacromolecules and biomembranes in cells (Guzmán-Murillo et al., 2007; Qian et al., 2008). When exposed to relatively high concentrations (1 μm-50 mg/L) and large particle sizes (5 μm-20 mg/L and 10 μm-20 mg/L) of PS-MPs, the markedly higher presence of the content of soluble proteins in *C. goreaui* cells compared to the control group could be associated with the algae's innate self-repair and defense capabilities. The content of soluble proteins in *C. goreaui* cells increased with increasing PS-MPs particle size, indicating that larger PS-MPs particles (5 μm and 10 μm) cause more severe damage to algal cells and produce stronger stress responses.

When PS-MPs exposure leads to the inhibition of photosynthesis and insufficient energy supply in *C. goreaui*, the electron transfer rate decreases, resulting in electron accumulation and increased generation of reactive oxygen species (ROS) (Cao et al., 2022a). Upon suffering extensive harm to their cellular structures and internal components due to ROS, cells activate their innate defense mechanisms to synthesize protective enzymes like catalase (CAT), superoxide dismutase (SOD), and peroxidase (POD), with the objective of mitigating the detrimental

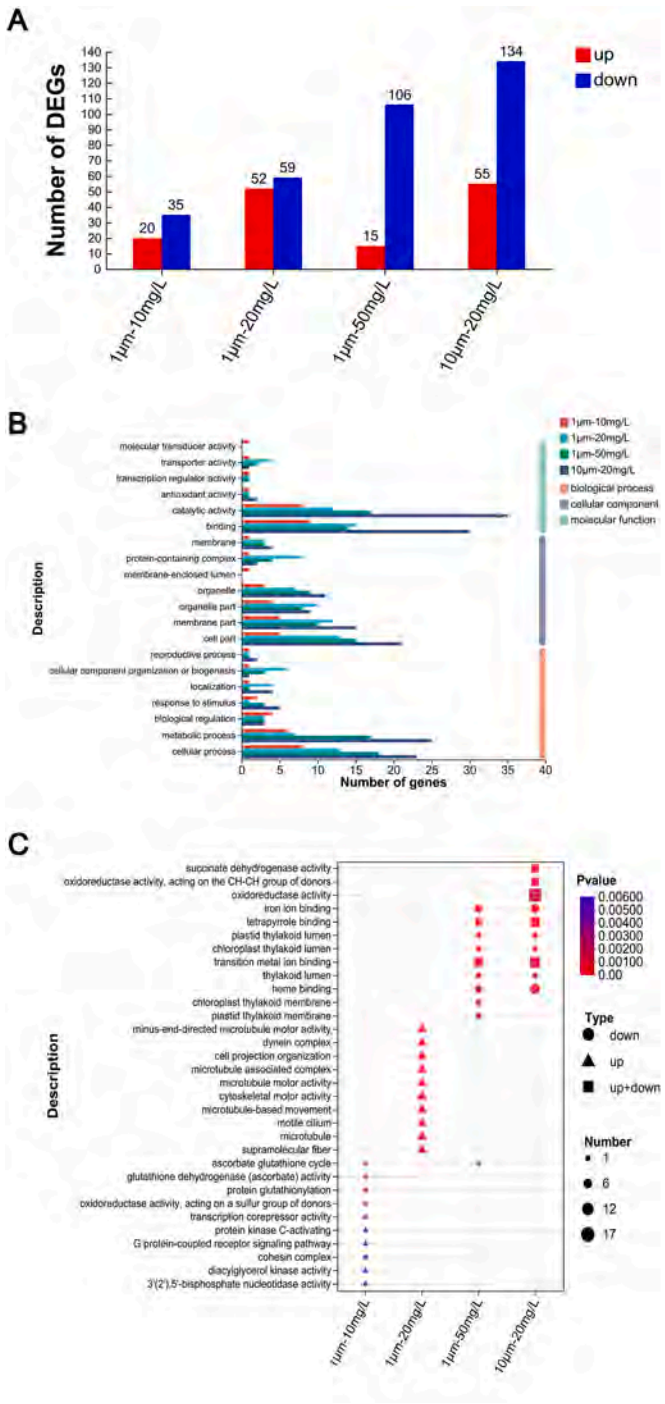


Fig. 6. Effects of PS-MPs exposure on the transcription products. (A) Difference statistics for the Number of total DEGs. (B) GO functional annotation analysis. (C) Bubble chart of multi-gene set GO enrichment analysis.

impact of these reactive molecules (Cao et al., 2015). In the present study, when different-sized PS-MPs (1 μm at 50 mg/L, 5 μm at 20 mg/L, and 10 μm at 20 mg/L) were administered to the *C. goreaui*, resulting in a marked elevation in the SOD activity within the algal cells compared to the control group. This suggests an increase in ROS generation in the cells, with the SOD activity showing a direct relationship to the PS-MPs particle size. These findings suggested that larger PS-MPs particles have stronger toxic effects on *C. goreaui*, leading to the production of more ROS in the cells.

The substance MDA, which results from the peroxidation of membrane lipids, serves as an indicator of the extent of oxidative harm (Qian et al., 2008; Melegari et al., 2012). Excessive ROS exacerbates cell membrane lipid peroxidation, resulting in the production of a large amount of MDA (Melegari et al., 2012; Xiao et al., 2020). Upon subjecting *C. goreaui* cells to various levels and sizes of PS-MPs, there was a notable increase in MDA levels compared to the control group. Additionally, it was observed that an upsurge in both the amount and dimensions of the particles led to an enhanced accumulation of MDA, signifying intensified oxidative harm.

4.4. Considerations on the use of higher concentrations of MPs in experimental design

In marine environments, the toxicological effects of MPs are a prolonged process. In this study, we employed higher concentrations of MPs to investigate their impact on key symbiotic microorganisms of corals, with the aim of exploring the potential threats posed by MPs to coral reef ecosystems. As indicated by similar studies, utilizing higher concentrations of MPs in short-term acute exposure experiments provides clearer insights into their potential impacts (Mao et al., 2018; Li et al., 2020; Cui et al., 2022; Khatiwada et al., 2023). It is undeniable that using higher concentrations of MPs to explore their toxicological effects has certain limitations. However, due to the current inadequacies in detection methods for microplastic concentrations at micron and nanoscale levels in natural environments, the measured values may be lower than the actual values. Moreover, the global production and discharge of plastic products are still increasing, and large particles of plastic are further decomposed into small particle size MPs (Thompson et al., 2004; Lambert et al., 2013; Auta et al., 2017; Yang et al., 2020). As such, the experimental findings of this study provide valuable insights into the impacts of MPs on coral reef ecosystems to some extent.

5. Conclusion

This research indicated harmful impacts of PS-MPs on *C. goreaui*, and the impacts are closely related to particle size, with larger particles exhibiting greater toxicity. Specifically, PS-MPs aggregate with *C. goreaui* cells to form a large amount of EPS, which blocks light and inhibits photosynthesis, significantly increases the ROS content, and causes structural damage to *C. goreaui* cells. In addition, PS-MPs inhibited the expression of genes related to photosynthesis and cellular metabolism in *C. goreaui* cells. Overall, based on the toxic effects of PS-MPs on the common coral symbiont Symbiodiniaceae (*C. goreaui*) and the importance of Symbiodiniaceae to coral, MPs pollution is presumed to pose a potential threat to coral reef ecosystems. Due to the difficulty of degrading MPs in the natural environment and the continuous increase in plastic waste emissions, if not controlled, future plastic pollution will inevitably severely damage coral reef ecosystems.

CRediT authorship contribution statement

Jiayuan Liang: Writing – review & editing, Writing – original draft, Validation, Resources, Project administration, Methodology, Investigation, Formal analysis, Data curation, Conceptualization. **Tianyi Niu:** Writing – review & editing, Writing – original draft, Visualization, Validation, Software, Methodology, Investigation, Data curation. **Li Zhang:** Writing – review & editing, Supervision, Formal analysis. **Yating Yang:** Software, Methodology. **Zhicong Li:** Visualization, Validation, Supervision. **Zhuqing Liang:** Writing – review & editing, Validation, Investigation. **Kefu Yu:** Writing – review & editing, Supervision, Resources, Project administration, Funding acquisition, Conceptualization. **Sanqiang Gong:** Visualization, Software, Methodology.

Data availability

The data generated as part of this study are available upon request.

The raw sequence data (a total of 15 RNA sequencing libraries) produced in this study were deposited in the Sequence Read Archive (PRJNA1056117) of the NCBI (https://blast.ncbi.nlm.nih.gov).

Declaration of competing interest

The authors declare the following financial interests/personal relationships which may be considered as potential competing interests: Jiayuan Liang reports financial support was provided by the National Natural Science Foundation of China. If there are other authors, they declare that they have no known competing financial interests or personal relationships that could have appeared to influence the work reported in this paper.

Acknowledgements

This work was supported by the National Natural Science Foundation of China (42030502 and 42090041), the Self-Topic Project of Guangxi Laboratory on the Study of Coral Reefs in the South China Sea (GXLSCRSCS2023101), and the Science and Technology Project of Guangxi (Nos. AD17129063 and AA17204074).

Appendix A. Supplementary data

Supplementary data to this article can be found online at https://doi.org/10.1016/j.envres.2025.120750.

Data availability

Data will be made available on request.

References

Ali, A., Kriefall, N.G., Emery, L.E., Kenkel, C.D., Matz, M.V., Davies, S.W., 2019. Recruit symbiosis establishment and Symbiodiniaceae composition influenced by adult corals and reef sediment. Coral Reefs 38, 405–415.

Auta, H., Emenike, C., Fauziah, S., 2017. Screening of Bacillus strains isolated from mangrove ecosystems in Peninsular Malaysia for microplastic degradation. Environ. Pollut. 231, 1552–1559.

Baker, D.M., Andras, J.P., Jordán-Garza, A.G., Fogel, M.L., 2013. Nitrate competition in a coral symbiosis varies with temperature among Symbiodinium clades. ISME J. 7 (6), 1248–1251.

Cao, D.-j., Shi, X.-d., Li, H., Xie, P.-p., Zhang, H.-m., Deng, J.-w., Liang, Y.-g., 2015. Effects of lead on tolerance, bioaccumulation, and antioxidative defense system of green algae, Cladophora. Ecotoxicol. Environ. Saf. 112, 231–237.

Cao, Q., Jiang, Y., Yang, H., Zhang, Y., Wei, W., 2022a. Comprehensive toxic effects of povidone iodine on microalgae *Chlorella pyrenoidosa* under different concentrations. Aquacult. Res. 53 (5), 1833–1841.

Cao, Q., Sun, W., Yang, T., Zhu, Z., Jiang, Y., Hu, W., Wei, W., Zhang, Y., Yang, H., 2022b. The toxic effects of polystyrene microplastics on freshwater algae *Chlorella pyrenoidosa* depends on the different size of polystyrene microplastics. Chemosphere 308, 136135.

Chen, P., Powell, B.A., Mortimer, M., Ke, P.C., 2012. Adaptive interactions between zinc oxide nanoparticles and *Chlorella sp.* Environ. Sci. Technol. 46 (21), 12178–12185.

Chen, Y., Ling, Y., Li, X., Hu, J., Cao, C., He, D., 2020. Size-dependent cellular internalization and effects of polystyrene microplastics in microalgae *P. helgolandica var. tsingtaoensis* and *S. quadricauda*. J. Hazard Mater. 399, 123092.

Cui, Y., Liu, M., Selvam, S., Ding, Y., Wu, Q., Pitchaimani, V.S., Huang, P., Ke, H., Zheng, H., Liu, F., 2022. Microplastics in the surface waters of the South China sea and the western Pacific Ocean: different size classes reflecting various sources and transport. Chemosphere 299, 134456.

Ding, J., Jiang, F., Li, J., Wang, Z., Sun, C., Wang, Z., Fu, L., Ding, N.X., He, C., 2019a. Microplastics in the coral reef systems from xisha islands of South China sea. Environ. Sci. Technol. 53 (14), 8036–8046.

Ding, J., Li, J., Sun, C., Jiang, F., Ju, P., Qu, L., Zheng, Y., He, C., 2019b. Detection of microplastics in local marine organisms using a multi-technology system. Anal. Methods 11 (1), 78–87.

Falkowski, P.G., Owens, T.G., 1980. Light—shade adaptation: two strategies in marine phytoplankton. Plant Physiol. 66 (4), 592–595.

Gong, S., Chai, G., Sun, W., Zhang, F., Yu, K., Li, Z., 2021. Global-scale diversity and distribution characteristics of reef-associated symbiodiniaceae via the cluster-based parsimony of internal transcribed spacer 2 sequences. J. Ocean Univ. China 20, 296–306.

González-Pech, R.A., Bhattacharya, D., Ragan, M.A., Chan, C.X., 2019. Genome evolution of coral reef symbionts as intracellular residents. Trends Ecol. Evol. 34 (9), 799–806.

Guzmán-Murillo, M.A., López-Bolaños, C.C., Ledesma-Verdejo, T., Roldan-Libenson, G., Cadena-Roa, M.A., Ascencio, F., 2007. Effects of fertilizer-based culture media on the production of exocellular polysaccharides and cellular superoxide dismutase by Phaeodactylum tricornutum (Bohlin). J. Appl. Phycol. 19, 33–41.

Hoegh-Guldberg, O., 2011. Coral reef ecosystems and anthropogenic climate change. Reg. Environ. Change 11, 215–227.

Houlbrèque, F., Ferrier-Pagès, C., 2009. Heterotrophy in tropical scleractinian corals. Biol. Rev. 84 (1), 1–17.

Huang, Y., Yan, M., Xu, K., Nie, H., Gong, H., Wang, J., 2019. Distribution characteristics of microplastics in zhubi reef from South China sea. Environ. Pollut. 255, 113133.

Hughes, T.P., Baird, A.H., Bellwood, D.R., Card, M., Connolly, S.R., Folke, C., Grosberg, R., Hoegh-Guldberg, O., Jackson, J.B., Kleypas, J., 2003. Climate change, human impacts, and the resilience of coral reefs. Science 301 (5635), 929–933.

Ikeuchi, M., Ishizuka, T., 2008. Cyanobacteriochromes: a new superfamily of tetrapyrrole-binding photoreceptors in cyanobacteria. Photochem. Photobiol. Sci. 7 (10), 1159–1167.

Imhof, H.K., Sigl, R., Brauer, E., Feyl, S., Giesemann, P., Klink, S., Leupolz, K., Löder, M. G., Löschel, L.A., Missun, J., 2017. Spatial and temporal variation of macro-, meso- and microplastic abundance on a remote coral island of the Maldives, Indian Ocean. Mar. Pollut. Bull. 116 (1–2), 340–347.

Ivleva, N.P., Wiesheu, A.C., Niessner, R., 2017. Microplastic in aquatic ecosystems. Angew. Chem. Int. Ed. 56 (7), 1720–1739.

Jambeck, J.R., Geyer, R., Wilcox, C., Siegler, T.R., Perryman, M., Andrady, A., Narayan, R., Law, K.L., 2015. Plastic waste inputs from land into the ocean. Science 347 (6223), 768–771.

Jensen, L.H., Motti, C.A., Garm, A.L., Tonin, H., Kroon, F.J., 2019. Sources, distribution and fate of microfibres on the Great barrier reef, Australia. Sci. Rep. 9 (1), 9021.

Khan, A.A., Quigley, J.G., 2011. Control of intracellular heme levels: heme transporters and heme oxygenases. Biochim. Biophys. Acta Mol. Cell Res. 1813 (5), 668–682.

Khatiwada, J.R., Madsen, C., Warwick, C., Shrestha, S., Chio, C., Qin, W., 2023. Interaction between polyethylene terephthalate (PET) microplastic and microalgae (Scenedesmus spp.): effect on the growth, chlorophyll content, and hetero-aggregation. Environ. Adv. 13, 100399.

Kor, K., Mehdinia, A., 2020. Neustonic microplastic pollution in the Persian Gulf. Mar. Pollut. Bull. 150, 110665.

LaJeunesse, T.C., Parkinson, J.E., Gabrielson, P.W., Jeong, H.J., Reimer, J.D., Voolstra, C.R., Santos, S.R., 2018. Systematic revision of Symbiodiniaceae highlights the antiquity and diversity of coral endosymbionts. Curr. Biol. 28 (16), 2570, 2580. e2576.

Lambert, S., Sinclair, C.J., Bradley, E.L., Boxall, A.B., 2013. Effects of environmental conditions on latex degradation in aquatic systems. Sci. Total Environ. 447, 225–234.

Li, C., Wang, X., Liu, K., Zhu, L., Wei, N., Zong, C., Li, D., 2021a. Pelagic microplastics in surface water of the Eastern Indian Ocean during monsoon transition period: abundance, distribution, and characteristics. Sci. Total Environ. 755, 142629.

Li, J., Ouyang, Z., Liu, P., Zhao, X., Wu, R., Zhang, C., Lin, C., Li, Y., Guo, X., 2021b. Distribution and characteristics of microplastics in the basin of Chishui river in Renhuai, China. Sci. Total Environ. 773, 145591.

Li, S., Wang, P., Zhang, C., Zhou, X., Yin, Z., Hu, T., Hu, D., Liu, C., Zhu, L., 2020. Influence of polystyrene microplastics on the growth, photosynthetic efficiency and aggregation of freshwater microalgae Chlamydomonas reinhardtii. Sci. Total Environ. 714, 136767.

Liu, G., Jiang, R., You, J., Muir, D.C., Zeng, E.Y., 2019. Microplastic impacts on microalgae growth: effects of size and humic acid. Environ. Sci. Technol. 54 (3), 1782–1789.

Lussey-Lepoutre, C., Hollinshead, K.E., Ludwig, C., Menara, M., Morin, A., Castro-Vega, L.-J., Parker, S.J., Janin, M., Martinelli, C., Ottolenghi, C., 2015. Loss of succinate dehydrogenase activity results in dependency on pyruvate carboxylation for cellular anabolism. Nat. Commun. 6 (1), 8784.

Mao, Y., Ai, H., Chen, Y., Zhang, Z., Zeng, P., Kang, L., Li, W., Gu, W., He, Q., Li, H., 2018. Phytoplankton response to polystyrene microplastics: perspective from an entire growth period. Chemosphere 208, 59–68.

Marangoni, L.F., Beraud, E., Ferrier-Pagès, C., 2022. Polystyrene nanoplastics impair the photosynthetic capacities of Symbiodiniaceae and promote coral bleaching. Sci. Total Environ. 815, 152136.

Melegari, S.P., Perreault, F., Moukha, S., Popovic, R., Creppy, E.E., Matias, W.G., 2012. Induction to oxidative stress by saxitoxin investigated through lipid peroxidation in Neuro 2A cells and Chlamydomonas reinhardtii alga. Chemosphere 89 (1), 38–43.

Mooney, H., Larigauderie, A., Cesario, M., Elmquist, T., Hoegh-Guldberg, O., Lavorel, S., Mace, G.M., Palmer, M., Scholes, R., Yahara, T., 2009. Biodiversity, climate change, and ecosystem services. Curr. Opin. Environ. Sustain. 1 (1), 46–54.

Ng, T.Y., Chui, A.P.Y., Ang, P., 2019. Onset of symbiosis in planula larvae of scleractinian corals. Hydrobiologia 842 (1), 113–126.

Qian, H., Chen, W., Sheng, G.D., Xu, X., Liu, W., Fu, Z., 2008. Effects of glufosinate on antioxidant enzymes, subcellular structure, and gene expression in the unicellular green alga Chlorella vulgaris. Aquat. Toxicol. 88 (4), 301–307.

Qin, L., Xu, Y., Chen, J., Niu, T., Yu, K., Liang, J., 2023. Optimization of in vitro culture method for zooxanthellae associated with reef-building corals. Acta Microbiol. Sin. 63 (4), 1658–1671. https://doi.org/10.13343/j.cnki.wsxb.20220656.

Reaka-Kudla, L, M., 1997. The global biodiversity of coral reefs: a comparison with rain forests. Biodiversity II: Understanding and protecting our biological resources 2, 551.

Ripken, C., Khalturin, K., Shoguchi, E., 2020. Response of coral reef dinoflagellates to nanoplastics under experimental conditions. bioRxiv 2020, 2009. 2023.310847.

Ritchie, R.J., 2006. Consistent sets of spectrophotometric chlorophyll equations for acetone, methanol and ethanol solvents. Photosynth. Res. 89, 27–41.

Robbins, S.J., Singleton, C.M., Chan, C.X., Messer, L.F., Geers, A.U., Ying, H., Baker, A., Bell, S.C., Morrow, K.M., Ragan, M.A., 2019. A genomic view of the reef-building coral Porites lutea and its microbial symbionts. Nat Microbiol 4, 2090–2100.
Rotjan, R.D., Sharp, K.H., Gauthier, A.E., Yelton, R., Lopez, E.M.B., Carilli, J., Kagan, J. C., Urban-Rich, J., 2019. Patterns, dynamics and consequences of microplastic ingestion by the temperate coral, Astrangia poculata. Proceedings of the Royal Society B 286 (1905), 20190726.
Saliu, F., Montano, S., Garavaglia, M.G., Lasagni, M., Seveso, D., Galli, P., 2018. Microplastic and charred microplastic in the Faafu Atoll, Maldives. Mar. Pollut. Bull. 136, 464–471.
Sana, S.S., Dogiparthi, L.K., Gangadhar, L., Chakravorty, A., Abhishek, N., 2020. Effects of microplastics and nanoplastics on marine environment and human health. Environ. Sci. Pollut. Control Ser. 27, 44743–44756.
Schwarz, A., Ligthart, T., Boukris, E., Van Harmelen, T., 2019. Sources, transport, and accumulation of different types of plastic litter in aquatic environments: a review study. Mar. Pollut. Bull. 143, 92–100.
Sendra, M., Pereiro, P., Yeste, M.P., Mercado, L., Figueras, A., Novoa, B., 2021. Size matters: Zebrafish (Danio rerio) as a model to study toxicity of nanoplastics from cells to the whole organism. Environ. Pollut. 268, 115769.
Su, Y., Zhang, K., Zhou, Z., Wang, J., Yang, X., Tang, J., Li, H., Lin, S., 2020. Microplastic exposure represses the growth of endosymbiotic dinoflagellate *Cladocopium goreaui* in culture through affecting its apoptosis and metabolism. Chemosphere 244, 125485.
Sun, Y., 2020. Studies on Physiological Response and Omics Analysis of Early Development of Tow Reff Corals to Ocean Warming and Acidification. University of Chinese Academy of Sciences, Doctor.
Tang, J., Ni, X., Zhou, Z., Wang, L., Lin, S., 2018. Acute microplastic exposure raises stress response and suppresses detoxification and immune capacities in the scleractinian coral Pocillopora damicornis. Environ. Pollut. 243, 66–74.
Thompson, R.C., Olsen, Y., Mitchell, R.P., Davis, A., Rowland, S.J., John, A.W., McGonigle, D., Russell, A.E., 2004. Lost at sea: where is all the plastic? Science 304 (5672), 838-838.
Van Sebille, E., Aliani, S., Law, K.L., Maximenko, N., Alsina, J.M., Bagaev, A., Bergmann, M., Chapron, B., Chubarenko, I., Cózar, A., 2020. The physical oceanography of the transport of floating marine debris. Environ. Res. Lett. 15 (2), 023003.
Venn, A.A., Loram, J.E., Douglas, A.E., 2008. Photosynthetic symbioses in animals. J. Exp. Bot. 59 (5), 1069–1080.
Wegley, L., Edwards, R., Rodriguez-Brito, B., Liu, H., Rohwer, F., 2007. Metagenomic analysis of the microbial community associated with the coral Porites astreoides. Environ. Microbiol. 9 (11), 2707–2719.
Wright, S.L., Thompson, R.C., Galloway, T.S., 2013. The physical impacts of microplastics on marine organisms: a review. Environ. Pollut. 178, 483–492.
Xiao, X., Li, W., Li, S., Zuo, X., Liu, J., Guo, L., Lu, X., Zhang, L., 2023. The growth inhibition of polyethylene nanoplastics on the bait-microalgae isochrysis galbana based on the transcriptome analysis. Microorganisms 11 (5), 1108.
Xiao, Y., Jiang, X., Liao, Y., Zhao, W., Zhao, P., Li, M., 2020. Adverse physiological and molecular level effects of polystyrene microplastics on freshwater microalgae. Chemosphere 255, 126914.
Yang, H., Xiong, H., Mi, K., Xue, W., Wei, W., Zhang, Y., 2020. Toxicity comparison of nano-sized and micron-sized microplastics to Goldfish Carassius auratus Larvae. J. Hazard Mater. 388, 122058.
Yu, K., 2012. Coral reefs in the South China Sea: their response to and records on past environmental changes. Sci. China Earth Sci. 42 (8), 1160–1172.
Yu, K., 2018. Introduction to the Science of Coral Reefs, first ed. Science Press, Beijing.
Yue, F., Zhang, J., Xu, J., Niu, T., Lü, X., Liu, M., 2022. Effects of monosaccharide composition on quantitative analysis of total sugar content by phenol-sulfuric acid method. Front. Nutr. 9, 963318.
Zhou, Z., Zhang, P., Zhang, G., Wang, S., Cai, Y., Wang, H., 2021. Vertical microplastic distribution in sediments of Fuhe river estuary to Baiyangdian Wetland in northern China. Chemosphere 280, 130800.

Science of the Total Environment 962 (2025) 178381

Contents lists available at ScienceDirect

Science of the Total Environment

journal homepage: www.elsevier.com/locate/scitotenv

Heat-tolerant subtropical *Porites lutea* may be better adapted to future climate change than tropical one in the South China Sea

Wen Huang [a,*], Jinlian Chen [a], Enguang Yang [a], Linqing Meng [a], Yi Feng [a], Yinmin Chen [a], Zhihua Huang [a], Ronghua Tan [a], Zunyong Xiao [c], Yupeng Zhou [c], Mingpei Xu [c], Kefu Yu [a,b,**]

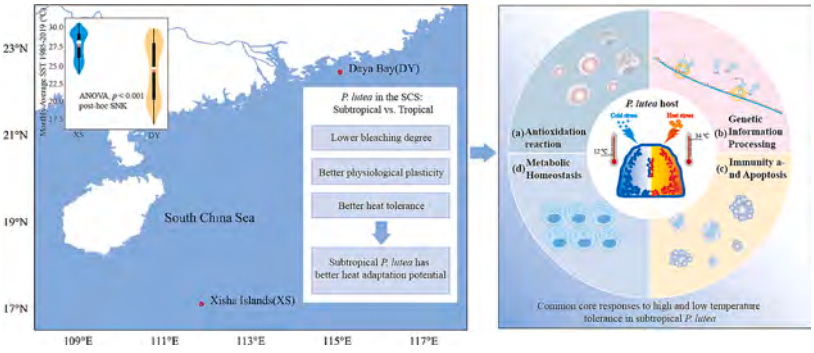
[a] Guangxi Laboratory on the Study of Coral Reefs in the South China Sea, Coral Reef Research Center of China, School of Marine Sciences, Guangxi University, Nanning 530004, China
[b] Southern Marine Science and Engineering Guangdong Laboratory (Guangzhou), Guangzhou 511458, China
[c] School of Resources, Environment and Materials, Guangxi University, Nanning 530004, China

HIGHLIGHTS

- The heat resistance of *Porites lutea* varies at different latitudes in the SCS.
- Subtropical *P. lutea* has a stronger heat tolerance.
- Better heat tolerance associated with a negative feedback transcription mechanism
- Subtropical *P. lutea* in the SCS may adapt to future climate change.

GRAPHICAL ABSTRACT

***P. lutea* sample collection locations. (a) Violin plots of sampling locations and monthly mean sea temperature in the two regions. (b) Monthly mean and standard deviation of sea temperature at the sampling location. (c) Temperature design of the heat stress experiment.**



ARTICLE INFO

Editor: Sergi Diez Salvador

Keywords:
Porites lutea
Latitude
Heat stress
Heat resistance
Climate change

ABSTRACT

Coral reefs are degrading at an accelerating rate owing to climate change. Understanding the heat stress tolerance of corals is vital for their sustainability. However, this tolerance varies substantially geographically, and information regarding coral responses across latitudes is lacking. In this study, we conducted a high temperature (34 °C) stress experiment on *Porites lutea* from tropical Xisha Islands (XS) and subtropical Daya Bay (DY) in the South China Sea (SCS). We compared physiological levels, antioxidant activities, and transcriptome sequencing to explore heat tolerance mechanisms and adaptive potential. At 34 °C, both XS and DY corals experienced significant bleaching and the physiological/biochemical index decreased, with XS corals exhibiting greater changes than DY corals. Transcriptome analysis revealed that coral hosts respond to heat stress mainly by boosting metabolic activity. The subtle transcriptional responses of zooxanthellae C15 underscored the host's pivotal role in thermal stress responses. DY coral hosts showed lower bleaching, stronger physiological plasticity,

* Corresponding author.
** Correspondence to: K. Yu, Southern Marine Science and Engineering Guangdong Laboratory (Guangzhou), Guangzhou 511458, China.
E-mail addresses: wenhuang@gxu.edu.cn (W. Huang), kefuyu@scsio.ac.cn (K. Yu).

https://doi.org/10.1016/j.scitotenv.2025.178381
Received 9 July 2024; Received in revised form 28 November 2024; Accepted 2 January 2025
Available online 11 January 2025
0048-9697/© 2025 Elsevier B.V. All rights are reserved, including those for text and data mining, AI training, and similar technologies.

and higher temperature tolerance thresholds than XS, indicating superior heat tolerance. This superiority is linked to negative feedback transcriptional regulation strategies, including active environmental stress response and genetic information damage repair. The differences in thermal adaptability between tropical and subtropical *P. lutea* in the SCS may be attributed to their genetic differences and native habitat environments, suggesting that subtropical *P. lutea* may have the potential to adapt to future climate change. This study provides novel insights for predicting the fate of corals at different latitudes in terms of global warming and provides instructive guidance for coral reef ecological restoration.

1. Introduction

Climate change and anthropogenic factors have driven coral reef degradation (HughesTP et al., 2003; Hughes et al., 2017). High sea surface temperatures (SST) owing to global warming have led to severe thermal bleaching events, posing a serious threat to coral reef survival (Ainsworth et al., 2016; HughesTP et al., 2003). As climate warming persists, these bleaching events are expected to become more frequent and intense (Sully et al., 2019). Therefore, under current climate scenarios, corals must adapt in order to survive over the long term. However, the extent of their adaptability to thermal changes (Mumby and van Woesik, 2014) and the mechanisms by which naturally resilient corals might enhance their tolerance to climate change remains unclear (Langlais et al., 2017; Sully et al., 2019). Therefore, understanding these factors is crucial for assessing the future viability of coral ecosystems.

Temperature fluctuations of 1–2 °C above or below normal levels can prove fatal for narrowly temperate corals (Hoegh-Guldberg, 1999), although these thresholds vary across regions (Langlais et al., 2017; Sully et al., 2019). In addition, coral thermal tolerance thresholds are also related to factors such as coral holobionts genetic adaptation (Howells et al., 2016; Manzello et al., 2019), recent thermal history (Voolstra et al., 2020), latitude (Dixon et al., 2015), depth (Tavakoli-Kolour et al., 2023), and species (Marzonie et al., 2022). Recent fieldwork suggests that, in some locations, reef-building corals can tolerate heat stress at temperatures that exceed the global average (Masoudi and Asrari, 2023), particularly in habitats with thermal extremes (e.g., corals in the Persian–Arabian Gulf can tolerate water temperatures of 36 °C) (Coles and Riegl, 2013; D'Angelo et al., 2015), and thermal hypervariability (e.g., corals in the American Samoan back reef tanks of Ofu Island at 35 °C) (Palumbi et al., 2014). However, these findings are mostly limited to specific regions, and widespread spatial heterogeneity exists in the thermal tolerance of corals (Langlais et al., 2017; Sully et al., 2019). Moreover, a clear understanding of the thermal tolerance responses and adaptive potential of corals across latitudinal temperature gradients is lacking.

Ecological studies have shown that coral species occupying a wide range of ecological niches span strong environmental temperature gradients and often vary phenotypically (Bruno and Edmunds, 1997; Rowan et al., 2021). Examples include Red Sea corals (Osman et al., 2017) and Australian Great Barrier Reef corals (Barfield et al., 2018). Further studies suggest that this phenotypic variation is related to local adaptation to the thermal regime of the host (Savary et al., 2021; Voolstra et al., 2021) as well as short-term physiological acclimation (Voolstra et al., 2021). Coral populations are undergoing strong regional selection for tolerance and exhibit significant individual genetic variability in response to rapid climate change (Barker, 2018; Quigley, 2023), offering potential for genetic rescue-assisted evolution to enhance their thermal resilience (Selmoni et al., 2024). Therefore, identifying temperature-tolerant coral populations at similar spatial acale ranges is required to restore coral reef ecosystems.

South China Sea (SCS) coral reefs, with their large latitudinal spans and notable temperature gradients, provide a unique natural laboratory for exploring intra- and intercommunity coral responses to climate change (Yu, 2012). Agglomerated *Porites lutea* is considered a highly resistant coral species widely distributed in the Indo-Pacific reef zone in tropical and subtropical regions (Huang et al., 2015, 2012). *P. lutea* is an ideal research species for studying various stress responses and coral physiology, and is a dominant species in SCS coral reefs (Li et al., 2013). Robbins et al. (2019) revealed the genome of *P. lutea*, including its symbiotic dinoflagellate *Cladocopium* C15 and associated microorganisms, providing a foundational resource for molecular studies. Preliminary studies on *P. lutea* in the SCS have been conducted. For example, Huang et al. (2018) reported high genetic diversity and low genetic differentiation levels in *P. lutea* populations from different geographic locations in the SCS. Luo et al. (2022) demonstrated a close correlation between genetic differentiation, genetic variation levels, and latitudinal SST. Additionally, Huang et al. (2022) used metatranscriptome sequencing methods to explore the differences in the cold tolerance of *P. lutea* at different latitudes in the SCS. However, regarding global warming, the heat resistance response of *P. lutea* at different latitudes in the SCS is not yet fully understood, and the underlying molecular mechanisms remain lacking.

In this study, we used physiological and metatranscriptome sequencing to explore the response and underlying adaptation mechanisms of *P. lutea* to thermal stress at different latitudes in the SCS. Additionally, we conducted association analyses by combining previous findings on cold stress and population genetics to explore understanding of the survival status and environmental stress adaptability of *P. lutea* to climate change. By shedding light on the adaptability of corals at diverse latitudes amid ongoing climate warming, this research offers instructive guidance for conserving and ecologically rehabilitating coral reefs.

2. Materials and methods

2.1. Sample collection and experimental design

P. lutea samples were collected from two latitudes in the South China Sea, namely the tropical Xisha XS North Reef (111°51′E, 17°06′N) and subtropical Daya Bay DY Sanmen Island (114°64′E, 22°27′N), with a latitudinal span of approximately 5° (see Fig. 1a for sampling point details). The 5 km daily mean SST data were obtained from NOAA's Coral Reef Watch (http://coralreefwatch.noaa.gov). The monthly mean SSTs at different sampling locations (Fig. 1b) was obtained from a previous study (Huang et al., 2022). Colonies were collected at approximately the same depth (~5 m) at each sampling location using a scuba diving device with a hammer and tongs. Colonies were sampled >5 m apart to avoid gene cloning. After sampling, the live coral samples were quickly transported to the 300 L aquarium tanks of the China Coral Reef Research Center of Guangxi University and temporarily restored at 26 °C. Five *P. lutea* were randomly selected from each sampling point for study. Three fragments (~16 cm^2 each) were removed from each coral using a small cutter to serve as three independent sampling points (26, 30, and 34 °C), i.e., each sampling point had five biological replicates, and one location had 15 fragments. All fragments were restored at 26 °C for 15 days before the formal experiment.

The heat stress experiment used three temperature treatments: 26 °C for the control group (optimal temperature for coral growth), 30 °C (normal temperature in summer) and 34 °C (extremely high temperature) for the experimental group, with consistent temperature intervals between the sampling points (Fig. 1c). Owing to resource limitations, only two tanks were used in this experiment, namely the control (26 °C treatment, 5 fragments × 2 locations = 10) and the experimental (30 °C

and 34 °C treatments, 5 fragments × 2 locations × 2 treatments = 20) tanks. To simulate marine environment warming, the experimental tank was heated by 1 °C every 24 h starting at 26 °C. After reaching 30 °C, the temperature was maintained for three days, and samples were taken. The temperature was then further increased and samples were taken after three days at 34 °C. The heat stress experiment cycle was 12 days. Simultaneously, the control tank was maintained at 26 °C for 12 days and samples were collected.

All aquariums were illuminated using metal halide (250 W) and four T5HO lamps to simulate natural light in a 12 h:12 h light-dark cycle. Preheated and filtered seawater (20 %) was replaced daily to maintain the following water conditions: salinity 34–35 ppt, carbonate hardness (dKH) 7.3–7.5, c(Ca^{2+}) 380–400 ppm, and c(Mg^{2+}) 1200–1300 ppm. The aquarium temperature was controlled using 600 W aquarium heating rods and chillers, and continuously monitored and recorded with a HOBO thermometer (±0.1 °C accuracy). The corals were not fed during the experiment. The experimental and control tanks were maintained under the same conditions, except for the temperature difference.

2.2. Sample handling and measurement

2.2.1. Phenotypic and physiological index determination

The coral samples were photographed and recorded daily using an underwater camera. The black-and-white tape was used as a reference background for image intensity calibration, and the degree of coral bleaching was analyzed using the computerized photo analysis software Image Pro Plus (version 6.0) (Chow et al., 2016; Huang et al., 2022). Specifically, the original photo was converted to an 8-bit grayscale image with a gray of 0 for pure black dots and a gray of 255 for pure white dots and then calibrated for color intensity using black and white reference points around the optical quadrant. After obtaining the actual intensity of the reference points, the intensity readings of 0 to 255 (8-bit) were reset, with the lowest intensity reading representing black being set to 0 and the highest intensity reading being set to 255 representing white. Finally, the gray value of the calibrated coral surface was measured, and the degree of bleaching of the entire coral surface was calculated using a defined black-and-white reference. In this study, the coral was considered "healthy" at 26 °C, and its bleaching degree was 0. The gray value at this time = K, and the gray values at other temperatures were defined as X. The formula was calculated as follows:

$$\text{Coral bleaching degree} = (X - K)/(255 - K) \times 100\%$$

The maximum quantum yield (*Fv/Fm*) of *P. lutea* was measured daily using Diving-PAM (Heinz Walz GmbH, Effeltrich, Germany) fluorometer. To ensure adequate relaxation time for the corals, *Fv/Fm* was measured 30 min after the dark adaptation period, as this parameter closely approximates the maximum photochemical efficiency of photosystem II (PSII) (Bilger et al., 1995; Huang et al., 2022; Warner et al., 1999). During measurements, the fiber optic cable of fluorometer was maintained approximately 1 cm above the coral surface. To ensure the authenticity of *Fv/Fm* values, all measurements were performed randomly five times at different locations in the fragments.

Symbiodiniaceae density was determined as previously described (Chow et al., 2016; Qin et al., 2019), using a recirculating Waterpik filled with filtered seawater (0.45 μm) to rinse the coral surfaces, and quantifying the total volume of tissue homogenate using a measuring cylinder. Subsequently, 50 mL of homogenate was centrifuged (3000 ×*g* for 10 min at 4 °C), the supernatant was removed, 20 mL of filtered seawater was centrifuged, and de-supernatant was added (repeated thrice) to quantify the cell density. The collected algae-containing cell pellets were fixed in 4 % formaldehyde solution and counted using a hemocytometer. Symbiodiniaceae density (cells cm^{-2}) was calculated by normalizing the number of symbionts with respect to the surface area of stony corals derived from the aluminum foil method (Johannes et al., 1970).

The chlorophyll *a* content was determined using the absorbance method. Homogenate (15 mL) was placed in a sterile centrifuge tube and centrifuged at 4000 $rmin^{-1}$ for 5 min at 4 °C. The supernatant was removed, precipitate fixed with 10 mL 90 % acetone, and extracted at 4 °C in the absence of light for 24 h. The solution was then centrifuged and resuspended and the supernatant was subjected to optical density measurements at wavelengths of 630 nm, 647 nm, 664 nm, and 750 nm using a microplate reader (Varioskan LUX). The chlorophyll *a* content (μg/mL) was calculated using the published method (Jeffrey and Humphrey, 1975). Finally, the chlorophyll *a* content per unit area of coral (ug/cm^2) was obtained by converting the surface area of the coral.

2.2.2. Enzyme activity assay

The catalase (CAT), superoxide dismutase (SOD), peroxidase (POD), and glutathione (GSH) activities in the coral symbionts measured in this study were determined using commercial kits (Nanjing Jiancheng Bioengineering Institute, Nanjing, China) in strict accordance with the manufacturer's recommendations. We used a bicinchoninic acid (BCA) protein analysis kit (Shanghai Bioengineering Co., Ltd., Shanghai, China) to determine the concentration of total supernatant protein

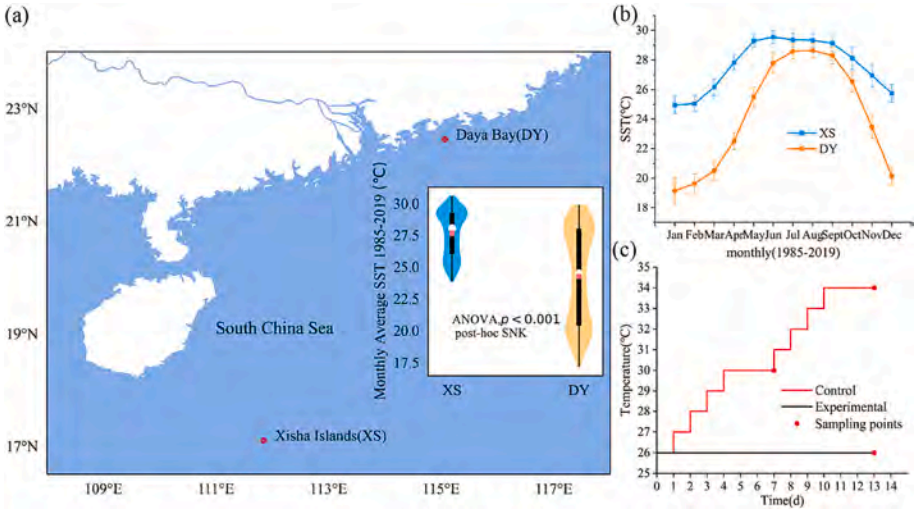


Fig. 1. *P. lutea* sample collection locations. (a) Violin plots of sampling locations and monthly mean sea temperature in the two regions. (b) Monthly mean and standard deviation of sea temperature at the sampling location. (c) Temperature design of the heat stress experiment.

according to the manufacturer's recommendations (Dodd and Drickamer, 2001). The enzyme activity in the sample supernatants was expressed as the ratio of total enzyme activity units to total protein (U/mg protein).

All data of physiological indices and enzyme activities were expressed as the mean ± standard deviation (SD). Two-way analysis of variance (ANOVA) was used to analyze the main effects and interactions of the fixed factors (coral location and temperature). When main or interaction effects were significant ($P \leq 0.05$), post hoc pairwise comparisons of variable means were conducted to determine if differences between coral locations in each temperature treatment were statistically significant (Lenth et al., 2019). Meanwhile, post-hoc multiple comparisons (Duncan's test) were used to determine the significance of data treated with different temperatures in the same coral location.

2.3. Symbiotic zooxanthellae identification

Genomic DNA was extracted from coral symbionts using the DNeasy Plant Mini Kit (QIAGEN, Hilden, Germany) according to the manufacturer's instructions. The ITS2 region of the symbiotic zooxanthellae rDNA was PCR amplified using ITS intfor2 (5′-GAATTGCAGA ACTCCGTG-3′) (Lajeunesse and Trench, 2000) and ITS2-Reverse (5′-GGGATCCATA TGCTTAAGTT CAGCGGGT-3′) (Coleman et al., 1994) primers (Chen et al., 2019). All qualified amplification products were mixed in equimolar amounts and subjected to nucleic acid sequencing using an Illumina MiSeq instrument in 2 × 300 bp paired-end mode, according to the manufacturer's instructions. All sequencing was completed by Majorbio Biopharm Technology Co., Ltd. (Shanghai, China). The remainder of the analyses followed the method described by Chen et al. (2019). All the sequencing data were submitted to the NCBI for inclusion in the Biotechnology Information Sequence Read Archive database (accession no. PRJNA810338).

2.4. Transcriptome sequencing

2.4.1. P. lutea RNA extraction

Following our established procedure, coral samples were carefully dissected, with a portion of coral tissue from each experimental sampling point placed individually into 2 mL sterile, enzyme-free centrifuge tube using RNA-removing enzyme-enzymatic forceps. Subsequently, the samples were rapidly frozen in liquid nitrogen for a minimum of 15 min, then transferred and stored in a −80 °C freezer for subsequent RNA extraction (Huang et al., 2022). Total RNA was extracted from each coral tissue sample using TRIzol (Life Technologies, USA), according to the manufacturer's instructions and product datasheet. RNA was purified using the MicroElute® RNA Clean Up Kit (Omega Biotech, Guangzhou, China) to remove contaminants, such as proteins, pigments, and polysaccharides, from the mixtures. The total RNA purity and concentration were measured using a NanoDrop 2000 UV–vis spectrophotometer (Thermo Fisher Scientific, Wilmington, VA, USA) (Desjardins and Conklin, 2010). RNA integrity was measured using the Agilent Bioanalyzer 2100 system (Agilent Technologies, Santa Clara, CA, USA).

Total RNA quality was assessed using 1 % agarose gel electrophoresis, and high-quality nucleic acid solutions were stored at −80 °C to prevent degradation from repeated freezing and thawing cycles.

2.4.2. RNA-Seq analysis

RNA sequencing was performed using the Illumina TruseqTM RNA Sample Prep Kit, and 12 cDNA libraries were constructed from tissue samples that met the requirements for library construction (total RNA > 1 μg, concentration > 35 ng/μL, OD260/280 > 1.8, OD260/230 > 1.0). A total of 12 cDNA libraries were constructed. Briefly, mRNA was enriched using magnetic beads with oligo (dT) for A-T base pairing with the poly A tails at their 3′ ends. A fragmentation buffer was added to fragment the mRNA, and small fragments of approximately 300 bp were separated via magnetic bead screening. Subsequently, using a reverse transcriptase, six-base random primers (random hexamers) and mRNA templates were reverse-transcribed to form a double-stranded structure with stable sticky ends. The paired-end RNA-seq library was sequenced using the Illumina NovaSeq 6000 platform (2 × 150 bp read length) by forming adaptor junctions and performing cDNA target fragment screening, amplification, and quantification. All the sequencing data were submitted to the NCBI for inclusion into the Biotechnology Information Sequence Read Archive database (accession no. PRJNA994659).

2.4.3. Bioinformatics analysis

To ensure the accuracy of subsequent bioinformatics analysis, we removed the adapter sequences and incorrectly self-connected reads in the reads and trimmed the low-quality (quality value <30) bases at the end (3'end) of the sequence. Reads with an N-ratio of >10 % were removed, and finally, the adapter and sequences with a length of <50 bp after quality trimming were discarded to obtain clean reads. The clean reads of each sample were then aligned to the *P. lutea* host and *Cladocopium* C15 reference genomes (Robbins et al., 2019) (http://plut.reefgenomics.org/) using TopHat2 (Version 2.1.0) (Kim et al., 2013). Reads that matched the coral host genes were not further aligned to *Cladocopium* C15. BLAST alignment was performed using six databases: Non-redundant (NR), Swiss-prot, Pfam, Clusters of Orthologous Groups (COG), Gene Ontology (GO) and the Kyoto Encyclopedia of Genes and Genomes (KEGG). Successfully matched genes were annotated and the number of reads was mapped to each gene and counted using RMSE (Version 1.3.3) (Li and Dewey, 2011). Finally, gene expression levels were normalized using the transcripts per million (TPM) method. The normalized expressions of all 12 samples were hierarchically clustered using Spearman correlation, and the obtained numerical matrix was visually displayed using a Heatmap diagram. Differential expression analysis was performed using DESeq2 (Version 1.24.0) (Love et al., 2014), and genes with $|\log2(\text{Fold Change})| \geq 1$ and $P_{adjust} < 0.05$ were classified as differentially expressed genes (DEGs). Genes with important functions were searched in the annotations of the DEG sets, and the expression changes were visualized. To study the biological functions of DEG functions, we used the KEGG database to enrich and analyze the various metabolic pathways. We evaluated the degree of enrichment of KEGG based on the rich factor, corrected P_{adjust}, and number of genes. When $P_{adjust} < 0.05$, the pathway was considered significantly enriched. To visualize the protein interaction network of the DEGs, we used String (version 11.5) and the homologous species, *Pocillopora damicornis*. The results were imported into Cytoscape (version 3.9.1) to map some of the gene networks using the top integrated values, and the Maximal Clique Centrality (MCC) algorithm in the software's built-in Cytohubba plugin was used to identify the top 10 hub genes of corals responding to high-temperature stress (Jeong et al., 2001). Because of the limited number of DEGs in zooxanthellae, we conducted expression change analysis for the entire gene set using Gene Set Enrichment Analysis (GSEA) to overcome the limitations of DEGs enrichment analysis.

3. Results

3.1. Physiological and biochemical indicator analysis of P. lutea under heat stress

3.1.1. Phenotypic and physiological indicators

The differences in coral thermal bleaching phenotypes are related to heat resistance, thus the phenotypic variation plot showed that DY *P. lutea* had better heat resistance than XS (Fig. S1). In addition, consistent with the phenotypic changes, DY *P. lutea* had a lower bleaching degree and higher retention of maximum light quantum yield (*Fv/Fm*) than XS. In this high temperature stress experiment, the bleaching degree and *Fv/Fm* were significantly affected by coral geographical location, temperature, and location × temperature (two-way ANOVA, $P \leq 0.001$) (Fig. 2a, b). The severity of coral bleaching

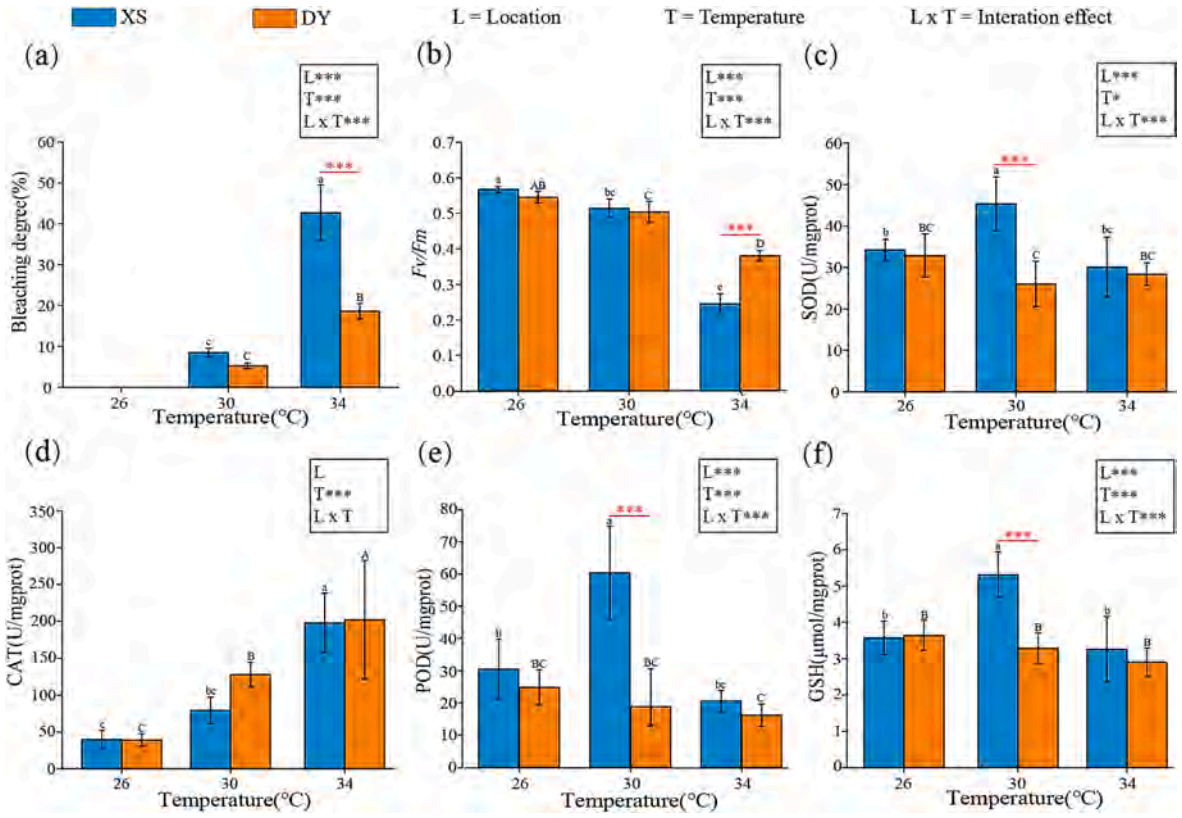


Fig. 2. Physiological and enzyme activity changes of coral samples. (a) bleaching degree. (b) Fv/Fm. (c) Superoxide dismutase, SOD. (d) catalase, CAT. (e) peroxidase, POD. (f) glutathione, GSH. Error bars represent SD of the mean obtained using multiple replicates. Error bars represent the standard deviation of the mean (SD, n = 5) obtained using multiple replicates. Two-way ANOVA testing of coral location, temperature, and their interaction was framed (*$P \leq 0.05$, **$P \leq 0.01$, ***$P \leq 0.001$). Different lowercase or uppercase letters indicate that the parameters were significantly different between the temperature treatments (Duncan's test, $P < 0.05$), respectively. Red asterisks indicate significant differences between two coral geographic locations at a given temperature (*$P \leq 0.05$, **$P \leq 0.01$, ***$P \leq 0.001$).

increased with increasing temperature (Fig. 2a). At 34 °C, the bleaching degree of corals at the two latitudes differed significantly with XS *P. lutea* being significantly more bleached than DY corals (pairwise test, $P \leq 0.001$). In contrast, *Fv/Fm* decreased with increasing temperature, only decreasing significantly at 34 °C (Duncan's test, $P > 0.05$) and differing significantly between the two latitude corals (paired test, $P \leq 0.05$), indicating its significantly higher *Fv/Fm* in DY *P. lutea* than that in XS *P. lutea.*

3.1.2. Enzyme activity biochemical indicators

Two-way ANOVA results showed that SOD, CAT, GSH, and POD enzyme activities were significantly affected by temperature ($P \leq 0.05$). Except for CAT, other enzyme activities were significantly affected by coral location and coral location × temperature ($P \leq 0.001$) (Fig. 2c–f).

Throughout the temperature-raising experiment, the levels of SOD, POD, and GSH in XS *P. lutea* initially increased and then decreased significantly ($P < 0.05$). Among the antioxidants of DY *P. lutea*, SOD, POD and GSH all decreased slightly, but the changes were not significant ($P > 0.05$). CAT activity was significantly increased in corals in both locations ($P < 0.05$), and the CAT activity of DY *P. lutea* was higher than that of XS *P. lutea*, although not significantly ($P \geq 0.05$) at each temperature. In corals from both latitudes, all enzyme activities, except that of CAT, differed significantly only at 30 °C, and the level of enzyme activity was significantly higher in XS *P. lutea.* In addition, at 34 °C, except for the CAT activity of the two groups of corals which was higher than that at 26 °C, the other antioxidant enzyme activities were lower than those at 26 °C, although not significantly ($P > 0.05$).

3.2. RNA sequencing data and alignment rate

Twelve cDNA libraries were constructed, comprising samples from *P. lutea* hosts in XS and DY at 26 °C (C_XS, C_DY) and 34 °C (H_XS, H_DY). Transcriptome sequencing analysis of 12 coral host samples was completed, and a total of 80.42 Gb of clean data was obtained. The clean data of each sample reached >5.53 Gb, the Q30 base percentage was >93.86 %, and the GC content was between 42.11 and 46.44 %. The clean reads of each sample were aligned with the specified reference genome, with alignment rates between 40.08 and 69.72 %. In addition, transcriptome sequencing of the symbiotic zooxanthellae C15 obtained 30.89 Gb of clean data. Clean data for each sample exceeded 1.32 GB, with a Q30 base percentage exceeding 92.82 % and GC content ranging between 41.42 and 50.69 %. The alignment rate ranged from 0.63 and 34.45 %. The sequence information is provided in Table S1.

3.3. P. lutea host heat stress response

3.3.1. Host gene expression analysis

In the sample correlation analysis, most of the *P. lutea* samples were clearly clustered into the control group at 26 °C and the high-temperature group at 34 °C (Fig. 3a). However, the XS3 sample deviated somewhat, and considering the slight differences between coral individuals, we retained all samples for subsequent analysis. At 34 °C, the expression level of the caspase-3 gene in coral hosts increased significantly, with the expression level in DY hosts being the highest. The expression levels of SOD-related functional genes at both latitudes increased slightly, whereas those of CAT- and GSH-related functional genes decreased; the decrease in expression in XS corals was lower than

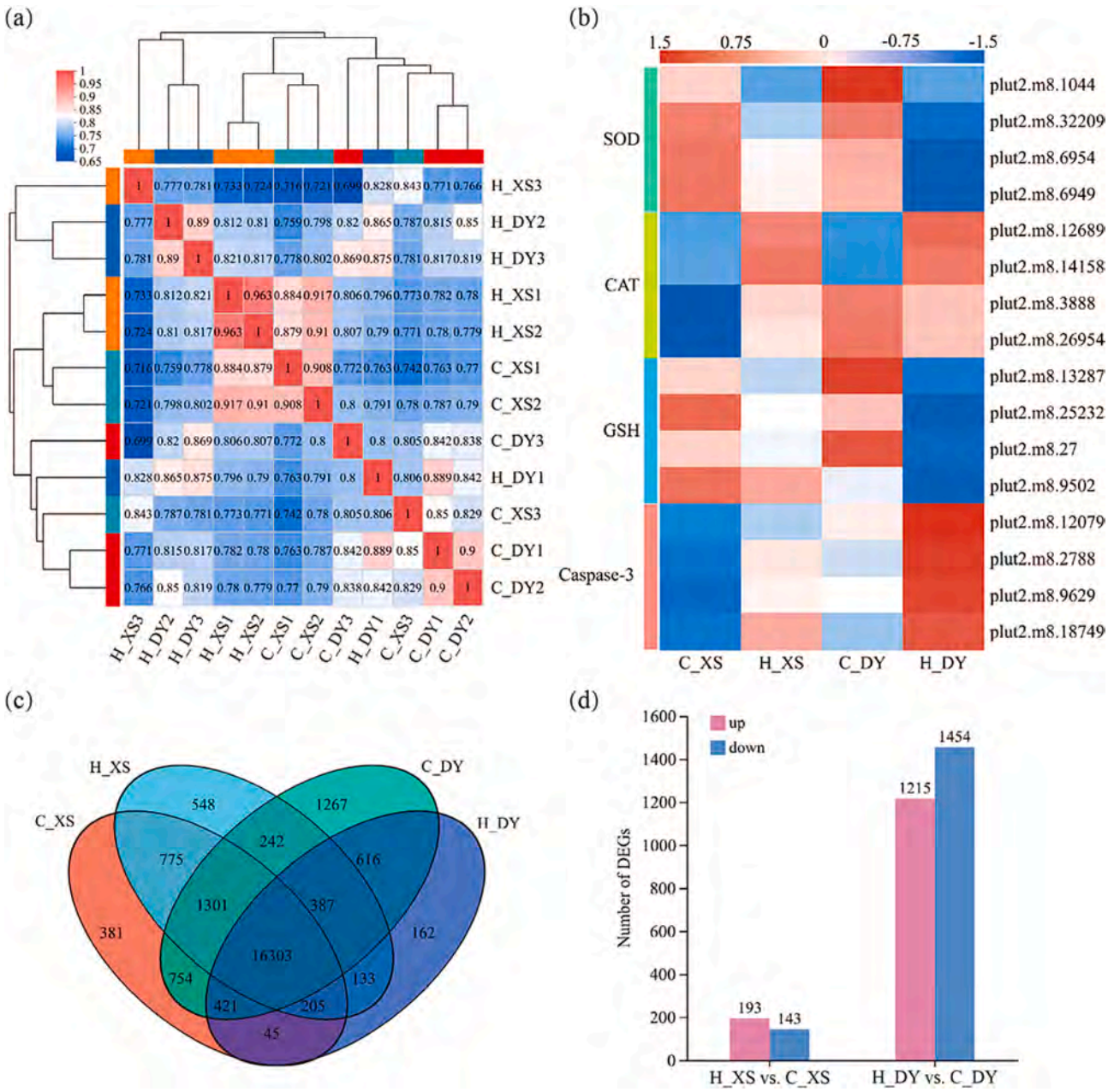


Fig. 3. Correlation between host genes and samples. (a) Heatmap showing changes in expression levels of functional genes during high-temperature stress. (b) Sample correlation clustering heat map (the numbers in the rectangles represent the correlation coefficients between samples). (c) Venn diagram of sequencing samples. (d) Number of DEGs in hosts (C: 26℃, H: 34℃).

that in DY corals (Fig. 3b). The number of common unigenes in all samples sequenced from *P. lutea* hosts (XS and DY) was 16,303. At 26 °C, the number of genes specific to XS and DY was 381 and 1267, respectively. At 34 °C, the number of genes unique to XS and DY was 548 and 162, respectively, indicating large differences in gene expression between XS and DY coral hosts (Fig. 3c).

3.3.2. *Differential expression and enrichment analysis*

The screening criteria were set as fold change ≥2 and false discovery rate value ≤0.05, and differential expression analysis was performed on H_XS vs. C_XS and H_DY vs. C_DY. The results revealed 336 DEGs in XS *P. lutea* hosts at 34 °C compared to 26 °C, comprising 193 upregulated genes and 143 downregulated genes. A total of 2669 DEGs were identified in the DY coral host, of which 1215 were upregulated and 1454 were downregulated (Fig. 3d). The number of DEGs in the relatively high-latitude DY coral hosts under heat stress was significantly higher than that in the XS coral hosts. Among the DEGs between the two groups of corals, 113 genes were upregulated (Hot_two up) and 90 genes were downregulated (Hot_two down) of the DEGs, 127 were XS-specific (Hot_XS diff) and 2460 were DY-specific (Hot_DY diff). KEGG enrichment analysis was performed for each of these gene sets, and the results are displayed in terms of the top 20 KEGG pathways (Fig. 4a–d).

KEGG enrichment analysis showed that compared with the control group (26 °C), the common upregulated DEGs of the two groups of coral hosts were significantly enriched in pathways related to metabolism, immune system, information processing, and disease infection. These pathways included Herpes simplex virus 1 infection, RIG-I-like receptor signaling pathway, cytosolic DNA-sensing pathway, shigellosis, influenza A, measles, glyoxylate and dicarboxylate metabolism, retinol metabolism, *Vibrio cholerae* infection, pathogenic *Escherichia coli*

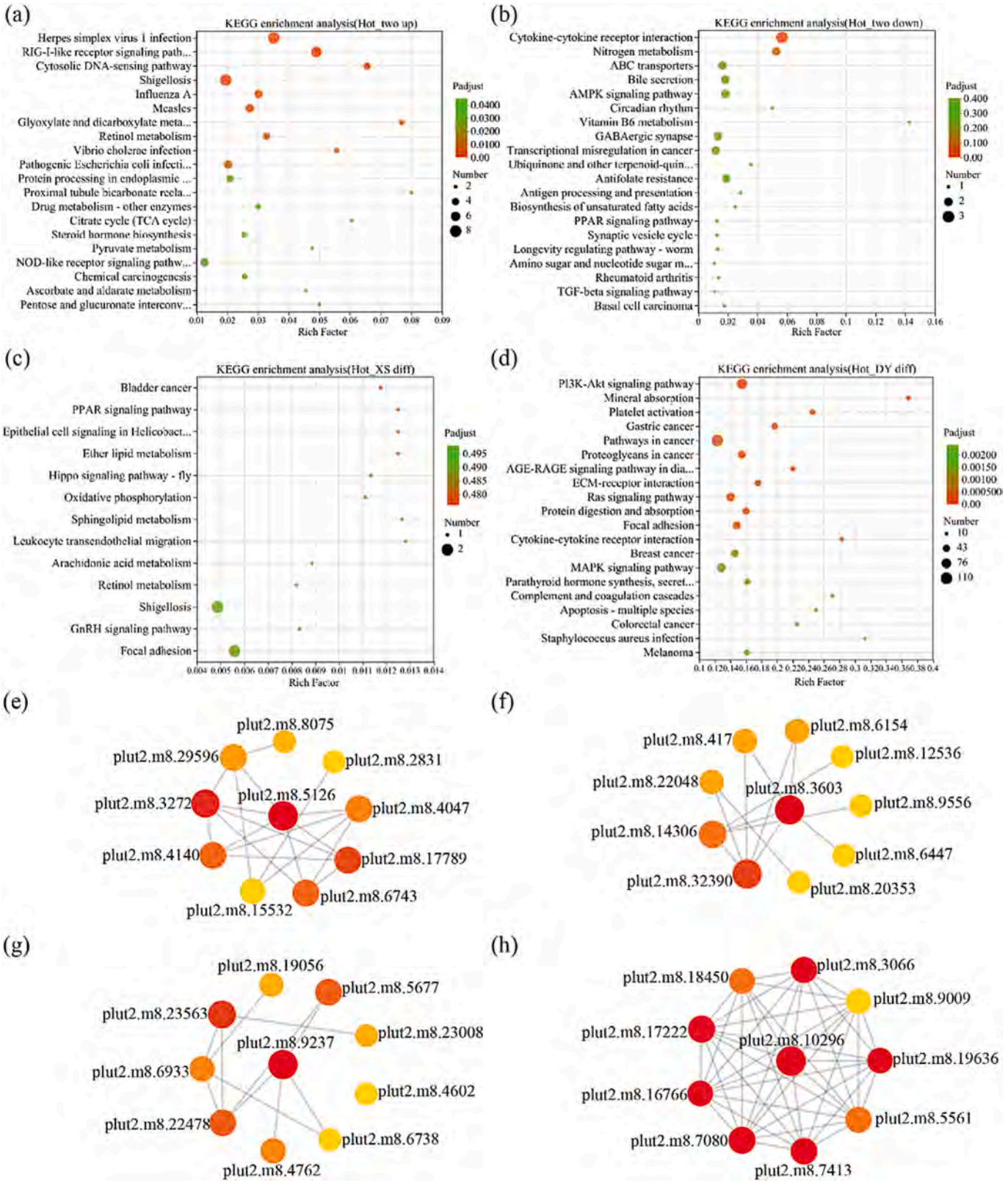


Fig. 4. KEGG pathway enrichment analysis and PPI network modules of host DEGs. KEGG enrichment analysis analyzed (a) significantly upregulated genes and (b) significantly downregulated genes in P. lutea samples from two regions. (c) XS-specific DEGs. (d) DY-specific DEGs. PPI network modules of (e) Hot_two up; (f) Hot_two down; (g) Hot_XS diff; (h) Hot_DY diff. Node color represents MCC score (The redder the color, the higher the score).

infection, protein processing in endoplasmic reticulum, proximal tubule bicarbonate reclamation, drug metabolism - other enzyme, TCA cycle, steroid hormone biosynthesis, pyruvate metabolism, NOD-like receptor signaling pathway, chemical carcinogenesis, ascorbate and aldarate metabolism, and pentose and glucuronate interconversions ($P_{adjust} < 0.05$) (Fig. 4a). The common downregulated DEGs were only significantly enriched in the cytokine–cytokine receptor interaction pathway during environmental information processing ($P_{adjust} < 0.05$) (Fig. 4b). Notably, XS-specific DEGs were not significantly enriched in any metabolic pathway ($P_{adjust} > 0.05$) (Fig. 4c). However, DY-specific DEGs were significantly enriched in metabolic pathways related to environmental information processing, organic systems, and cellular processes. These pathways included the PI3K-Akt signaling pathway, mineral absorption, platelet activation, ECM-receptor interaction, Ras signaling pathway, protein digestion and absorption, focal adhesion, cytokine–cytokine receptor interaction, MAPK signaling pathway, arathyroid hormone synthesis, secretion and action, complement and coagulation cascades, and apoptosis-multiple species ($P_{adjust} < 0.05$) (Fig. 4d).

3.3.3. DEGs protein–protein interaction (PPI) network module construction and hub gene screening

The XS and DY common DEGs, as well as the Hot_XS diff and Hot_DY diff gene set nodes, were ranked using the MCC score of the CytoHubba plugin. The top 10 genes with the highest scores were selected as hub genes for the PPI network module (Fig. 4e–h). We predicted that these hub genes have important biological relevance in the coral hosts to heat stress.

The top 10 hub genes in each of the four PPI network modules were analyzed for KEGG functional enrichment. Module (e) exhibited significant enrichment in pathways related to cellular energy metabolism, such as the citrate cycle (TCA cycle), pyruvate metabolism, proximal tubule bicarbonate reclamation, and longevity-regulating pathway-multiple species ($P_{adjust} < 0.05$). Notably, heat shock protein genes (HSP) expression was upregulated in this pathway. Module (f) was significantly enriched in cytokine–cytokine receptor interactions, AMPK signaling pathway, and vitamin B6 metabolism ($P_{adjust} < 0.05$). Module (g) was enriched in the chemical carcinogenesis and bile secretion pathways, albeit not significantly ($P_{adjust} > 0.05$). Finally, module (h) was significantly enriched in the cell cycle ($P_{adjust} < 0.05$), with upregulation of serine/threonine protein kinase genes CHK1,2, and cell division control protein genes CDC6 and CDC45.

3.4. Response of P. lutea algal symbionts to heat stress

3.4.1. Composition of symbiotic zooxanthellae in P. lutea

The dominant genus of symbiotic zooxanthellae across all coral samples was *Cladocopium*, and the dominant species was subclade C15 (Fig. S2a). Therefore, the community structure of symbiotic zooxanthellae in *P. lutea* at the two latitudes in this study was similar in composition and relative abundance, all dominated by the C15 subclade.

3.4.2. Analysis of gene expression and enrichment of algal symbiont C15

Consistent with the host analysis criteria, C15 zooxanthellae symbiotic with corals in XS and DY were analyzed. The results showed that C15 contained 11,934 common unigenes at different temperatures. At 26 °C, DY coral C15-specific unigenes outnumbered XS coral-specific unigenes, at 687 and 350, respectively (Fig. S2b). At 34 °C, XS coral-specific unigenes decreased to 107, while DY coral-specific unigenes slightly decreased to 149. Notably, the number of DEGs in C15 under high-temperature stress was minimal, while XS exhibited a total of 20 DEGs, including 11 upregulated and 9 downregulated genes (Fig. S2c). Nine DEGs were identified in the DY group, including seven upregulated and two downregulated genes. All possible pathways of XS and DY C15 were enriched using GSEA (Table S2). GSEA analysis showed that genes enriched for protein output were significantly downregulated in the XS and DY C15 groups compared with those in the control group. Additionally, XS C15 significantly downregulated genes expression related to RNA polymerase, whereas DY C15 significantly downregulated genes expression related to proteasomes and spliceosomes.

4. Discussion

4.1. Response of P. lutea population to high-temperature stress in the SCS

During the heat stress process, the bleaching degree of the two groups of corals increased significantly with the change in temperature, and the density of zooxanthellae, *Fv/Fm*, and chlorophyll *a* content gradually decreased. These results suggest that rising temperatures can lead to coral bleaching, photodamage to photosynthetic system II, and disruption of the symbiotic relationship between the host and zooxanthellae (Evensen et al., 2021; Hazraty-Kari et al., 2023, 2024). Heat stress triggers the antioxidant mechanisms of corals and increases ROS levels in corals (DeSalvo et al., 2008). However, the coral–algae symbiosis can also effectively remove ROS via antioxidant systems, including POD, GSH, SOD and CAT (Anithajothi et al., 2014; Pei et al., 2022). Changes in the activity levels of these antioxidant enzymes and their genes expression, as well as the significant upregulation of the caspase-3 gene associated with cellular immune apoptosis, indicated that the corals have oxidative stress and apoptosis responses (Figs. 2, 3b).

Transcriptome sequencing results showed that high-temperature stress mainly activated pathways related to cell metabolism and apoptosis, inhibiting the expression of cytokine genes related to immune signaling (Fig. 4a, b). High-energy metabolic demands may suggest that the coral host is energy-limited and responds to cellular demands for energy balance by enhancing metabolism (Anthony et al., 2009). However, the KEGG enrichment analysis results of the DEGs upregulated by both were also significantly enriched in disease pathways related to viral or bacterial infections, indicating that extreme temperatures can significantly increase the risk of coral disease (Yu et al., 2023). In addition, the gene expression profile of zooxanthellae C15 was similar to that of *P. lutea* under low-temperature stress at different latitudes (Huang et al., 2022) with few significant DEGs in both groups (Fig. 5c). The GSEA of symbiotic zooxanthellae C15 showed that both XS and DY C15 significantly downregulated protein export-related genes at high temperatures. Protein export may be related to the activity of antioxidant-related proteins in symbiotic algae (Anithajothi et al., 2014; Buerger et al., 2020). The consistent downregulation of protein export-related genes alongside the substantial decrease in zooxanthellae density suggests that the high temperature of 34 °C may have damaged the organelles responsible for secreting antioxidants, leading to a significant loss of zooxanthellae, underscoring the decline in antioxidant enzyme content (Fig. 3f–i). In summary, the thermal tolerance of *P. lutea* mainly depends on the host itself (Huang et al., 2024; Yu et al., 2023). Furthermore, high-energy metabolism and antioxidant capacity are strategies for corals to avoid high-temperature threats and reduce oxidative damage.

4.2. Differences in heat tolerance between tropical XS and subtropical DY P. lutea in the SCS

Following exposure to heat stress at 34 °C, tropical *P. lutea* exhibited more severe bleaching than subtropical *P. lutea* and displayed a poorer physiological state characterized by lower zooxanthellae density, chlorophyll *a* content, and *Fv/Fm*. Therefore, we speculated that subtropical *P. lutea* is more heat-tolerant than tropical *P. lutea*. Notably, poor physiological status does not necessarily imply that XS *P. lutea* is completely incapable of regulating heat stress. We observed that during the entire heat stress process, the antioxidant enzyme activities of XS *P. lutea* changed significantly compared with DY coral, and the enzyme activity level was slightly higher at 34 °C. This finding suggested that tropical XS corals have a stronger antioxidant response to heat stress

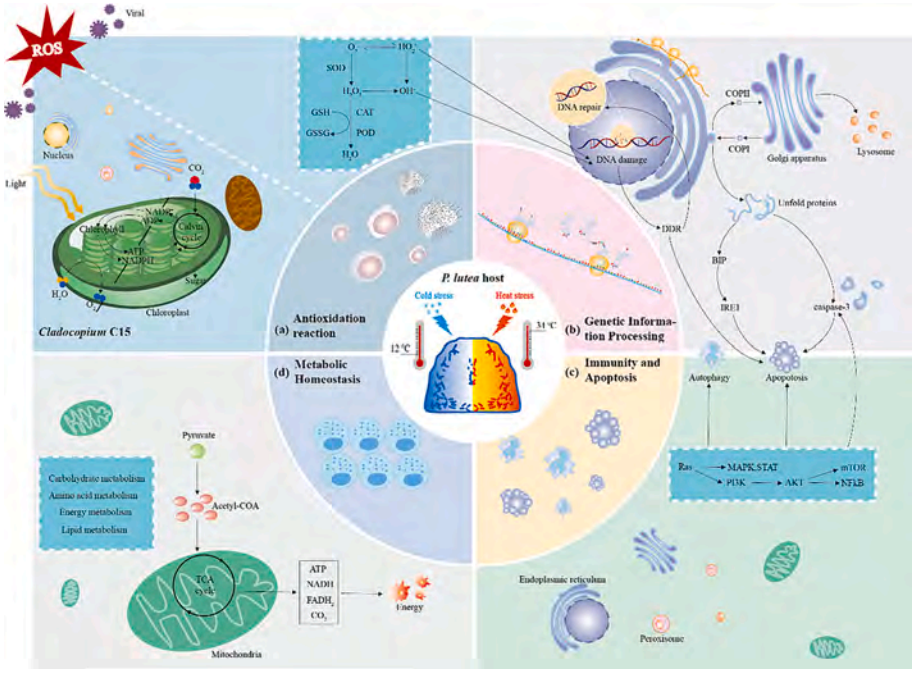


Fig. 5. Common core stress responses of *P. lutea* that are more tolerant to temperature stress. Genes and pathways related to (a) antioxidation reaction, (b) genetic information processing, (c) immunity and apoptosis, and (d) metabolic homeostasis are shown.

than subtropical DY corals, probably because XS *P. lutea* survives for a long period in waters with higher SSTs and can respond rapidly to heat stress by regulating enzyme activities (Dias et al., 2020). Regardless, our physiological results support the fact that subtropical *P. lutea* has good heat tolerance properties, mainly in terms of its resistance to bleaching and symbiotic algal retention under heat stress (Brown et al., 1999; Hoadley et al., 2021; Keshavmurthy et al., 2021).

DEGs can, to some extent, clarify the differences in resistance molecules among coral hosts (Maor-Landaw et al., 2017; Voolstra et al., 2021). Under heat stress, the DEGs of the DY coral hosts were much higher than those of XS coral hosts, and their unique DEGs were significantly enriched in pathways related to environmental information processing and cellular processes, whereas XS corals were not significantly enriched in any pathway (Fig. 4c, d). This finding indicates that the transcriptional response of subtropical corals to high temperatures is stronger and more complex, while the response of tropical corals is simpler and more rapid, which may be the main reason for the differences in phenotypes and physiology between the two groups of corals (Ip et al., 2022). In addition, temperatures triggered the DNA damage response (DDR) of DY *P. lutea* and activated the upstream factors ATM/ATR. ATM/ATR is a member of the PI3 family of serine-threonine kinases that plays a role in protecting cells from DNA damage (Maréchal and Zou, 2013). In this pathway, ATM/ATR phosphorylates CHK1 and CHK2 kinases, respectively, initiating a series of reactions that ultimately trigger the cell repair pathway. The genetic material of DY *P. lutea* hosts may be damaged, potentially due to excessive ROS production (Schwarz et al., 2012). However, DY *P. lutea* can actively participate in DNA damage repair to maintain the integrity of cell chromosomes during the process of resisting high-temperature stress, which may enhance its heat tolerance (Downs et al., 2002). However, compared to DY *P. lutea,* the DEGs of XS *P. lutea* were only enriched in pathways related to disease infection, although not significantly (Fig. 4c). This suggests that XS *P. lutea* may be susceptible to infections at extremely high temperatures. Proteasomes can degrade proteins through ubiquitination and play a key role in maintaining cellular protein homeostasis and stress responses (Basler and Groettrup, 2021). Proteasome expression in DY C15 cells may lead to the accumulation of misfolded and damaged proteins, affecting cellular protein homeostasis (Basler and Groettrup, 2021; Pei et al., 2022). However, proteasome inhibition may indirectly activate the expression of HSP expression to enhance cellular thermotolerance and trigger the unfolded protein response to reduce misfolded protein aggregation (Schubert et al., 2000; Seveso et al., 2019). While these perspectives may appear contradictory, further research is necessary to comprehend the intricacies of coral-symbiont relationships and the associated trade-offs. Another study has reported a functional link between the ubiquitin-like (UBL) family and pre-mRNA splicing processes (Chanarat and Mishra, 2018). Thus, the co-downregulated expression of spliceosomes and proteasomes in DY C15 cells may further illustrate their relationship and their potential impact on thermotolerance. RNA polymerase is related to the transcription of genetic information of gene DNA in organisms and its expression was downregulated in XS C15 cells, indicating restricted transcription.

In general, at 34 °C, DY *P. lutea* suffered less stress and DNA oxidative damage than XS corals and could actively mediate heat stress. For XS *P. lutea*, this temperature may have exceeded its maximum tolerance temperature critical point, resulting in a higher degree of bleaching than that observed in DY *P. lutea*. Therefore, our results suggest that subtropical *P. lutea* in the SCS has a higher thermal tolerance and adaptive potential than tropical *P. lutea*. This result is also supplemented by the expansion of previous data. Previous studies have shown that the high level of genetic differentiation between subtropical DY *P. lutea* populations in the SCS and other geographical populations of *P. lutea* (Huang et al., 2018) may have enabled it to adapt to cold winter sea temperatures at the genetic level and show enhanced cold tolerance (Huang et al., 2022). This further illustrates that the wide range of phenotypic differences in thermal tolerance among corals in the SCS at different latitudes may be attributed to geographical distance and different temperature histories, benefiting from limited gene flow. This, under the synergistic effect of genetic drift and natural selection, promotes phenotypic variation and adaptation to local thermal conditions of *P. lutea* populations at different spatial scales in the SCS (Marzonie et al., 2022; Pinsky et al., 2023). Therefore, we posit that the greater heat resistance of DY *P. lutea* and its symbionts at the transcriptional level (genes related to genetic information, spliceosomes, and proteasomes) may be the result of genetic differentiation, and may have

generated inherent genetic variation during long-term natural selection.

4.3. Potential temperature tolerance mechanisms in subtropical P. lutea in the SCS

Notably, previous studies on cold stress in tropical XS and subtropical DY *P. lutea* populations in the SCS used samples from the same batch of isolates as the experimental corals used in the present study to avoid potential individual variation and genetic background effects (Huang et al., 2022). Combined with the previous results of cold stress studies, it is evident that subtropical DY *P. lutea* in the SCS exhibits a stronger temperature tolerance and adaptability potential than tropical XS *P. lutea*. Therefore, by comparing the results of this study with those in a previous study by Huang et al. (2022) on cold stress in XS and DY *P. lutea*, we found that various transcriptional regulatory pathways participated in both cold and heat stress in DY *P. lutea* (Fig. 5 and Table S3). Continuous exposure to heat or cold can cause severe oxidative stress in coral hosts and symbionts, resulting in immune damage, damage to nucleotides and algal photosynthetic systems, and energy dissipation (Hernández Elizárraga et al., 2023). Corals and their algae activate antioxidant systems to clear excess ROS and reduce damage. Corals also change their metabolism to meet their energy distribution and supply needs for immunity and repair (Yu et al., 2023). In the process of removing active oxygen and oxygen free radicals, CAT degrades H_2O_2 generated by O_2^- (catalyzed by SOD), and converts it into H_2O and O_2 (Anithajothi et al., 2014). Similarly, ROS can be removed by antioxidants, such as POD and GSH, to reduce damage to lipids and DNA (M. K. DeSalvo et al., 2008). Our results found that ROS signaling also triggers NFkB-mediated cellular inflammation, apoptosis, and innate immune responses (DeSalvo et al., 2010; Souter et al., 2011). During this process, corals alleviate ROS-induced stress ROS by regulating the signal transduction systems related to cell proliferation (such as PI3K-AKT, MAPK, and mTOR) to maintain their immune balance, which is particularly important for maintaining cell homeostasis and adapting to the environment (Ocampo et al., 2015; Voss et al., 2023). Notably, the thermotolerance transcriptional regulatory pathways discovered in this study were identical to the transcriptional responses of thermotolerant *P. lutea* to high-temperature stress in intertidal rock pools (Huang et al., 2024). Therefore, we inferred that these stress transcriptional regulatory strategies may be the common and core transcriptomes mediating *P. lutea* tolerance to higher/lower temperature stress and that these common response modes, once activated, can effectively help *P. lutea* reduce the threat posed by temperature stress. Therefore, the molecular mechanisms discovered in this study provide strong theoretical guidance for evaluating the response of tolerant reef-building corals to global climate change.

Coral reef ecosystems are severely degraded worldwide owing to global warming (Hughes et al., 2017). Identifying highly resistant coral species and introducing meaningful adaptive variation through genetic rescue or relocated selective breeding may offer a strategy to mitigate the impact of climate change on stony corals (Dixon et al., 2015; Quigley, 2023). Our results suggest that *P. lutea* in the subtropical DY of the SCS exhibits strong physiological plasticity, temperature tolerance, and adaptive potential and may have adapted to the seasonally fluctuating, wide range (14–28 °C) SST environment at the genetic level, and may be a potential candidate population to withstand future climate disturbances. Therefore, we posit that other relatively high-latitude coral populations, such as DY *P. lutea* in the subtropics of the SCS, may exhibit comparable temperature tolerance, and these corals may serve as resilient parents for sexual reproduction to promote heat-tolerant genotypes in their offspring (Bay et al., 2017; Dixon et al., 2015; Quigley et al., 2020). In particular, attention should be paid to the importance of susceptible branching corals in helping to restore coral reef communities, owing to their rapid growth and good domestication potential. This requires more work in the future to conduct similar research and verification on severely degraded branching corals to promote coral reef recovery.

Notably, our results also highlight the importance of protecting coral reef habitats. Although some coral species (such as DY *P. lutea*) have the ability to tolerate a wide range of temperature changes (12–34 °C), climatic conditions are unfavorable for most coral species in high latitudes (Kim et al., 2019). Corals in marginal areas have limited resilience to the ongoing impacts of climate change (including exposure to harsh environments and human activities) (HughesTP et al., 2003; Hughes et al., 2017). Thus, their temperature plasticity may be lost within decades without appropriate conservation and management strategies (Pandolfi et al., 2011; Pinsky et al., 2023).

5. Conclusion

In this study, we explored and analyzed the heat stress response of tropical XS and subtropical DY *P. lutea* populations in the SCS, and found that *P. lutea* mediates heat stress mainly by enhancing host metabolism levels to increase energy supply as a survival strategy. We also found considerable differences in heat tolerance among *P. lutea* at different latitudes in the SCS, with subtropical *P. lutea* showing greater resistance to heat stress than tropical *P. lutea*. The main manifestations are DY corals (1) have good physiological conditions under high-temperature environment, with low bleaching degree, high zooxanthellae density, *Fv/Fm* value, and chlorophyll *a* content, although XS corals have high enzyme activity; (2) live in seasonally fluctuating seawater temperatures (14–28 °C) year-round, with a wide range of temperature tolerance; and (3) have a negative-feedback transcriptional regulation strategy, namely, active environmental stress response and repair of genetic information damage. Simultaneously, combined with previous cold stress and population genetics studies, we posit *P. lutea* in the subtropical SCS has stronger temperature tolerance and adaptability potential than those in the tropical SCS, which may mediate their adaption to climate change.

CRediT authorship contribution statement

Wen Huang: Writing – review & editing, Validation, Resources, Project administration, Methodology, Funding acquisition, Conceptualization. **Jinlian Chen:** Writing – original draft, Visualization, Validation, Methodology, Data curation. **Enguang Yang:** Resources, Methodology, Investigation, Data curation. **Linqing Meng:** Methodology, Data curation. **Yi Feng:** Visualization, Software. **Yinmin Chen:** Visualization, Software. **Zhihua Huang:** Validation, Methodology. **Ronghua Tan:** Validation, Methodology. **Zunyong Xiao:** Software, Formal analysis. **Yupeng Zhou:** Software, Formal analysis. **Mingpei Xu:** Software, Formal analysis. **Kefu Yu:** Writing – review & editing, Resources, Project administration, Funding acquisition, Conceptualization.

Declaration of competing interest

The author declares no conflict of interest.

Acknowledgements

We thank Sansha Track Ocean Coral Reef Protection Institute for collecting specimens in Xisha. We would like to thank Editage (www.editage.cn) for English language editing. This study was financially supported by the National Natural Science Foundation of China (grant nos. 42030502 and 42090041) and Guangxi Natural Science Foundation (grant nos. 2023GXNSFAA026510).

Appendix A. Supplementary data

Supplementary data to this article can be found online at https://doi.org/10.1016/j.scitotenv.2025.178381.

Data availability

The 5 km daily average sea surface temperature data for the tropical Xisha and subtropical Daya Bay areas of the South China Sea can be obtained from NOAA's Coral Reef Watch (https://coralreefwatch.noaa.gov). The raw read data have been deposited in the Sequence Read Archive (SRA) database at NCBI under Bioproject IDs PRJNA994659 and PRJNA810338.

References

Ainsworth, T.D., Heron, S.F., Ortiz, J.C., Mumby, P.J., Grech, A., Ogawa, D., Eakin, C.M., Leggat, W., 2016. Climate change disables coral bleaching protection on the Great Barrier Reef. Science 352, 338–342. https://doi.org/10.1126/science.aac7125.

Anithajothi, R., Duraikannu, K., Umagowsalya, G., Ramakritinan, C.M., 2014. The presence of biomarker enzymes of selected scleractinian corals of Palk Bay, southeast coast of India. Biomed. Res. Int. 2014. https://doi.org/10.1155/2014/684874.

Anthony, K.R.N., Hoogenboom, M.O., Maynard, J.A., Grottoli, A.G., Middlebrook, R., 2009. Energetics approach to predicting mortality risk from environmental stress: a case study of coral bleaching. Funct. Ecol. 23, 539–550. https://doi.org/10.1111/j.1365-2435.2008.01531.x.

Barfield, S.J., Aglyamova, G.V., Bay, L.K., Matz, M.V., 2018. Contrasting effects of *Symbiodinium* identity on coral host transcriptional profiles across latitudes. Mol. Ecol. 27, 3103–3115. https://doi.org/10.1111/mec.14774.

Barker, V., 2018. Exceptional thermal tolerance of coral reefs in American Samoa. Curr. Clim. Chang. Rep. 4, 417–427. https://doi.org/10.1007/s40641-018-0112-3.

Basler, M., Groettrup, M., 2021. On the role of the immunoproteasome in protein homeostasis. Cells 10. https://doi.org/10.3390/cells10113216.

Bay, R.A., Rose, N.H., Logan, C.A., Palumbi, S.R., 2017. Genomic models predict successful coral adaptation if future ocean warming rates are reduced. Sci. Adv. 3. https://doi.org/10.1126/sciadv.1701413.

Bilger, W., Schreiber, U., Bock, M., 1995. Determination of the quantum efficiency of photosystem II and of non-photochemical quenching of chlorophyll fluorescence in the field. Oecologia 102, 425–432. https://doi.org/10.1007/bf00341354.

Brown, B.E., Dunne, R.P., Ambarsari, I., Le Tissier, M.D.A., Satapoomin, U., 1999. Seasonal fluctuations in environmental factors and variations in symbiotic algae and chlorophyll pigments in four Indo-Pacific coral species. Mar. Ecol. Prog. Ser. 191, 53–69. https://doi.org/10.3354/meps191053.

Bruno, J.F., Edmunds, P.J., 1997. Clonal variation for phenotypic plasticity in the coralmadracis mirabilis. Ecology 78, 2177–2190. https://doi.org/10.1890/0012-9658(1997)078[2177:cvfppi]2.0.co;2.

Buerger, P., Alvarez-Roa, C., Coppin, C.W., Pearce, S.L., Chakravarti, L.J., Oakeshott, J. G., Edwards, O.R., van Oppen, M.J.H., 2020. Heat-evolved microalgal symbionts increase coral bleaching tolerance. Sci. Adv. 6. https://doi.org/10.1126/sciadv.aba2498.

Chanarat, S., Mishra, S.K., 2018. Emerging roles of ubiquitin-like proteins in pre-mRNA splicing. Trends Biochem. Sci. 43, 896–907. https://doi.org/10.1016/j.tibs.2018.09.001.

Chen, B., Yu, K., Liang, J., Huang, W., Wang, G., Su, H., Wang, Y., 2019. Latitudinal variation in the molecular diversity and community composition of symbiodiniaceae in coral from the South China Sea. Front. Microbiol. 10. https://doi.org/10.3389/fmicb.2019.01278.

Chow, M.H., Tsang, R.H.L., Lam, E.K.Y., Ang, P., 2016. Quantifying the degree of coral bleaching using digital photographic technique. J. Exp. Mar. Bio. Ecol. 479, 60–68. https://doi.org/10.1016/j.jembe.2016.03.003.

Coleman, A.W., Suarez, A., Goff, L.J., 1994. Molecular delineation of species and syngens in volvocacean green algae (chlorophyta) 1. J. Phycol. 30 (1), 80–90. https://doi.org/10.1111/j.0022-3646.1994.00080.x.

Coles, S.L., Riegl, B.M., 2013. Thermal tolerances of reef corals in the Gulf: a review of the potential for increasing coral survival and adaptation to climate change through assisted translocation. Mar. Pollut. Bull. 72 (2), 323–332. https://doi.org/10.1016/j.marpolbul.2012.09.006.

D'Angelo, C., Hume, B.C., Burt, J., Smith, E.G., Achterberg, E.P., Wiedenmann, J., 2015. Local adaptation constrains the distribution potential of heat-tolerant *Symbiodinium* from the Persian/Arabian Gulf. ISME J. 9 (12), 2551–2560. https://doi.org/10.1038/ismej.2015.80.

DeSalvo, M.K., Voolstra, C.R., Sunagawa, S., Schwarz, J.A., Stillman, J.H., Coffroth, M. A., Szmant, A.M., Medina, M., 2008. Differential gene expression during thermal stress and bleaching in the Caribbean coral *Montastraea faveolata*. Mol. Ecol. 17, 3952–3971. https://doi.org/10.1111/j.1365-294x.2008.03879.x.

DeSalvo, M.K., Sunagawa, S., Voolstra, C.R., Medina, M., 2010. Transcriptomic responses to heat stress and bleaching in the Elkhorn coral *Acropora palmata*. Mar. Ecol. Prog. Ser. 402, 97–113. https://doi.org/10.3354/meps08372.

Desjardins, P., Conklin, D., 2010. NanoDrop microvolume quantitation of nucleic acids. Jove-J. Vis. Exp. 93. https://doi.org/10.3791/2565.

Dias, M., Madeira, C., Jogee, N., Ferreira, A., Gouveia, R., Cabral, H., Diniz, M., Vinagre, C., 2020. Integrative indices for health assessment in reef corals under thermal stress. Ecol. Indic. 113. https://doi.org/10.1016/j.ecolind.2020.106230.

Dixon, G.B., Davies, S.W., Aglyamova, G.V., Meyer, E., Bay, L.K., Matz, M.V., 2015. Genomic determinants of coral heat tolerance across latitudes. Science 348, 1460–1462. https://doi.org/10.1126/science.1261224.

Dodd, R.B., Drickamer, K., 2001. Lectin-like proteins in model organisms: implications for evolution of carbohydrate-binding activity. Glycobiology 11, 71R–79R. https://doi.org/10.1093/glycob/11.5.71r.

Downs, C.A., Fauth, J.E., Halas, J.C., Dustan, P., Bemiss, J., Woodley, C.M., 2002. Oxidative stress and seasonal coral bleaching. Free Radical Bio. Med. 33, 533–543. https://doi.org/10.1016/s0891-5849(02)00907-3.

Evensen, N.R., Fine, M., Perna, G., Voolstra, C.R., Barshis, D.J., 2021. Remarkably high and consistent tolerance of a Red Sea coral to acute and chronic thermal stress exposures. Limnol. Oceanogr. 66 (5), 1718–1729. https://doi.org/10.1002/lno.11715.

Hazraty-Kari, S., Morita, M., Tavakoli-Kolour, P., Nakamura, T., Harii, S., 2023. Reactions of juvenile coral to three years of consecutive thermal stress. Sci. Total Environ. 863, 161227. https://doi.org/10.1016/j. scitotenv.2022.161227.

Hazraty-Kari, S., Tavakoli-Kolour, P., Nakamura, T., Morita, M., 2024. Susceptibility of *Acropora tenuis* to consecutive thermal stress. Coral Reefs 43 (4), 1097–1107. https://doi.org/10.1007/s00338-024-02530-8.

Hernández Elizárraga, V.H., Olguín-López, N., Hernández-Matehuala, R., Caballero-Pérez, J., Ibarra-Alvarado, C., Rojas-Molina, A., 2023. Transcriptomic differences between bleached and unbleached hydrozoan *Millepora complanata* following the 2015-2016 ENSO in the Mexican Caribbean. PeerJ 11. https://doi.org/10.7717/peerj.14626.

Hoadley, K.D., Pettay, D.T., Lewis, A., Wham, D., Grasso, C., Smith, R., Warner, M.E., 2021. Different functional traits among closely related algal symbionts dictate stress endurance for vital Indo-Pacific reef-building corals. Glob. Chang. Biol. 27 (20), 5295–5309. https://doi.org/10.1111/gcb.15799.

Hoegh-Guldberg, O., 1999. Climate change, coral bleaching and the future of the world's coral reefs. Mar. Freshw. Res. 50, 839–866. https://doi.org/10.1071/mf99078.

Howells, E.J., Abrego, D., Meyer, E., Kirk, N.L., Burt, J.A., 2016. Host adaptation and unexpected symbiont partners enable reef-building corals to tolerate extreme temperatures. Glob. Chang. Biol. 22, 1702–2714. https://doi.org/10.1111/gcb.13250.

Huang, D., Licuanan, W.Y., Hoeksema, B.W., Chen, C.A., Ang, P.O., Huang, H., Chou, L. M., 2015. Extraordinary diversity of reef corals in the South China Sea. Mar. Biodivers. 45, 157–168. https://doi.org/10.1007/s12526-014-0236-1.

Huang, H., Zhang, C.L., Yang, J.H., You, F., Lian, J.S., Tan, Y.H., 2012. Scleractinian coral community characteristics in Zhubi reef sea area of Nansha Islands. J Oceanogr Taiwan St 31, 79–84. https://doi.org/10.3969/J.ISSN.1000-8160.2012.01.012.

Huang, W., Li, M., Yu, K., Wang, Y., Li, J., Liang, J., Wei, F., 2018. Genetic diversity and large-scale connectivity of the scleractinian coral *Porites lutea* in the South China Sea. Coral Reefs 37, 1259–1271. https://doi.org/10.1007/s00338-018-1724-8.

Huang, W., Yang, E., Yu, K., Meng, L., Wang, Y., Liang, J., Huang, X., Wang, G., 2022. Lower cold tolerance of tropical *Porites lutea* is possibly detrimental to its migration to relatively high latitude refuges in the South China Sea. Mol. Ecol. 31, 5339–5355. https://doi.org/10.1111/mec.16662.

Huang, W., Meng, L., Xiao, Z., Tan, R., Yang, E., Wang, Y., Huang, X., Yu, K., 2024. Heat-tolerant intertidal rock pool coral *Porites lutea* can potentially adapt to future warming. Mol. Ecol. 33. https://doi.org/10.1111/mec.17273.

Hughes, T.P., Barnes, M.L., Bellwood, D.R., Cinner, J.E., Cumming, G.S., Jackson, J.B., Scheffer, M., 2017. Coral reefs in the Anthropocene. Nature 546 (7656), 82–90. https://doi.org/10.1038/nature22901.

HughesTP, B., BellwoodDR, C., ConnollySR, F., GrosbergR, H.G., JacksonJB, K., Lough, J. M., RosenB, R., 2003. Climate change, human impacts, and the resilience of coral reefs. Science 301, 929–933. https://doi.org/10.1126/science.1085046.

Ip, J.C.-H., Zhang, Y., Xie, J.Y., Yeung, Y.H., Qiu, J.-W., 2022. Comparative transcriptomics of two coral holobionts collected during the 2017 El Niño heat wave reveal differential stress response mechanisms. Mar. Pollut. Bull. 411, 41–42. https://doi.org/10.1016/j.marpolbul.2022.114017.

Jeffrey, S.T., Humphrey, G.F., 1975. New spectrophotometric equations for determining chlorophylls a, b, c1 and c2 in higher plants, algae and natural phytoplankton. Biochem. Physiol. Pflanzen 167 (2), 191–194. https://doi.org/10.1016/S0015-3796(17)30778-3.

Jeong, H., Mason, S.P., Barabási, A.L., Oltvai, Z.N., 2001. Lethality and centrality in protein networks. Nature 411, 41–42. https://doi.org/10.1038/35075138.

Johannes, R.E., Coles, S.L., Kuenzel, N.T., 1970. The role of zooplankton in the nutrition of some Scleractinian corals 1. Limnol. Oceanogr. 15 (4), 579–586. https://doi.org/10.4319/lo.1970.15.4.0579.

Keshavmurthy, S., Beals, M., Hsieh, H.J., Choi, K.S., Chen, C.A., 2021. Physiological plasticity of corals to temperature stress in marginal coral communities. Sci. Total Environ. 758, 143628. https://doi.org/10.1016/j.scitotenv.2020.143628.

Kim, D., Pertea, G., Trapnell, C., Pimentel, H., Kelley, R., Salzberg, S.L., 2013. TopHat2: accurate alignment of transcriptomes in the presence of insertions, deletions and gene fusions. Genome Biol. 14. https://doi.org/10.1186/gb-2013-14-4-r36.

Kim, S.W., Sampayo, E.M., Sommer, B., Sims, C.A., Gómez-Cabrera, M.D.C., Dalton, S.J., Pandolfi, J.M., 2019. Refugia under threat: mass bleaching of coral assemblages in high-latitude eastern Australia. Glob. Chang. Biol. 25, 3918–3931. https://doi.org/10.1111/gcb.14772.

Lajeunesse, T.C., Trench, R.K., 2000. Biogeography of two species of *Symbiodinium* (Freudenthal) inhabiting the intertidal sea anemone Anthopleura elegantissima (Brandt). Biol. Bull. 199, 126–134. https://doi.org/10.2307/1542872.

Langlais, C.E., Lenton, A., Heron, S.F., Evenhuis, C., Sen Gupta, A., Brown, J.N., Kuchinke, M., 2017. Coral bleaching pathways under the control of regional temperature variability. Nat. Clim. Chang. 7 (7(11)), 839–844. https://doi.org/10.1038/nclimate3399.

Lenth, R., Singmann, H., Love, J., Buerkner, P., Herve, M., 2019. emmeans: estimated marginal means, aka least-squares means. R package version 1.4.5. https://cran.r-project.org/web/packages/emmeans/index.html.

Li, B., Dewey, C.N., 2011. RSEM: accurate transcript quantification from RNA-Seq data with or without a reference genome. BMC Bioinform. 12. https://doi.org/10.1186/1471-2105-12-323.

Li, J., Chen, Q., Zhang, S., Huang, H., Yang, J., Tian, X.-P., Long, L.-J., 2013. Highly heterogeneous bacterial communities associated with the South China Sea reef corals *Porites lutea*, *Galaxea fascicularis* and *Acropora millepora*. PloS One 8. https://doi.org/10.1371/journal.pone.0071301.

Love, M.I., Huber, W., Anders, S., 2014. Moderated estimation of fold change and dispersion for RNA-seq data with DESeq2. Genome Biol. 15. https://doi.org/10.1186/s13059-014-0550-8.

Luo, Y., Huang, W., Yu, K., Li, M., Chen, B., Huang, X., Qin, Z., 2022. Genetic diversity and structure of tropical *Porites lutea* populations highlight their high adaptive potential to environmental changes in the South China Sea. Front. Mar. Sci. 9. https://doi.org/10.3389/fmars.2022.791149.

Manzello, D.P., Matz, M.V., Enochs, I.C., Valentino, L., Carlton, R.D., Kolodziej, G., Jankulak, M., 2019. Role of host genetics and heat-tolerant algal symbionts in sustaining populations of the endangered coral *Orbicella faveolata* in the Florida Keys with ocean warming. Glob. Chang. Biol. 25, 1016–1031. https://doi.org/10.1111/gcb.14545.

Maor-Landaw, K., et al., 2017. Mediterranean versus Red Sea corals facing climate change, a transcriptome analysis. Sci. Rep. 7. https://doi.org/10.1038/srep42405.

Maréchal, A., Zou, L., 2013. DNA damage sensing by the ATM and ATR kinases. Csh. Perspect. Biol. 5. https://doi.org/10.1101/cshperspect.a012716.

Marzonie, M.R., Bay, L.K., Bourne, D.G., Hoey, A.S., Matthews, S., Nielsen, J.J.V., Harrison, H.B., 2022. The effects of marine heatwaves on acute heat tolerance in corals. Glob. Chang. Biol. 29, 404–416. https://doi.org/10.1111/gcb.16473.

Masoudi, M., Asrari, E., 2023. Hazard assessment of global warming around the world using GIS. Environ. Monit. Assess. 195 (9), 1025. https://doi.org/10.1007/s10661-023-11464-7.

Mumby, Peter J., van Woesik, R., 2014. Consequences of ecological, evolutionary and biogeochemical uncertainty for coral reef responses to climatic stress. Curr. Biol. 24, R413–R423. https://doi.org/10.1016/j.cub.2014.04.029.

Ocampo, I.D., Zárate-Potes, A., Pizarro, V., Rojas, C.A., Vera, N.E., Cadavid, L.F., 2015. The immunotranscriptome of the Caribbean reef-building coral *Pseudodiploria strigosa*. Immunogenetics 67, 515–530. https://doi.org/10.1007/s00251-015-0854-1.

Osman, E.O., Smith, D.J., Ziegler, M., Kürten, B., Conrad, C., El-Haddad, K.M., Voolstra, C.R., Suggett, D.J., 2017. Thermal refugia against coral bleaching throughout the northern Red Sea. Glob. Chang. Biol. 24. https://doi.org/10.1111/gcb.13895.

Palumbi, S.R., Barshis, D.J., Traylor-Knowles, N., Bay, R.A., 2014. Mechanisms of reef coral resistance to future climate change. Science 344 (6186), 895–898. https://doi.org/10.1126/science.1251336.

Pandolfi, J.M., Connolly, S.R., Marshall, D.J., Cohen, A.L., 2011. Projecting coral reef futures under global warming and ocean acidification. Science 333, 418–422. https://doi.org/10.1126/science.1204794.

Pei, Y., Chen, S., Diao, X., Wang, X., Zhou, H., Li, Y., Li, Z., 2022. Deciphering the disturbance mechanism of BaP on the symbiosis of *Montipora digitata* via 4D-proteomics approach. Chemosphere 312. https://doi.org/10.1016/j.chemosphere.2022.137223.

Pinsky, M.L., Clark, R.D., Bos, J.T., 2023. Coral reef population genomics in an age of global change. Annu. Rev. Genet. 57, 87–115. https://doi.org/10.1146/annurev-genet-022123-102748.

Qin, Z., Yu, K., Chen, B., Wang, Y., Liang, J., Luo, W., Xu, L., Huang, X., 2019. Diversity of Symbiodiniaceae in 15 coral species from the Southern South China Sea: potential relationship with coral thermal adaptability. Front. Microbiol. 10. https://doi.org/10.3389/fmicb.2019.02343.

Quigley, K.M., 2023. Breeding and selecting corals resilient to global warming. Annu. Rev. Anim. Biosci. 12, 209–232. https://doi.org/10.1146/annurev-animal-021122-093315.

Quigley, K.M., Bay, L.K., van Oppen, M.J.H., 2020. Genome-wide SNP analysis reveals an increase in adaptive genetic variation through selective breeding of coral. Mol. Ecol. 29, 2176–2188. https://doi.org/10.1111/mec.15482.

Robbins, S.J., Singleton, C.M., Chan, C.X., Messer, L.F., Geers, A.U., Ying, H., Bourne, D. G., 2019. A genomic view of the reef-building coral *Porites lutea* and its microbial symbionts. Nat. Microbiol. 4, 2090–2100. https://doi.org/10.1038/s41564-019-0532-4.

Rowan, H.M., James, T.P., Agustí, M.-G., Noah, L.W., Christopher, P.J., Robert, J.T., Andréa, G.G., 2021. Environmental gradients drive physiological variation in Hawaiian corals. Coral Reefs 40, 1505–1523. https://doi.org/10.1007/s00338-021-02140-8.

Savary, R., Barshis, D.J., Voolstra, C.R., Cárdenas, A., Evensen, N.R., Banc-Prandi, G., Fine, M., Meibom, A., 2021. Fast and pervasive transcriptomic resilience and acclimation of extremely heat-tolerant coral holobionts from the northern Red Sea. Proc. Natl. Acad. Sci. 118. https://doi.org/10.1073/pnas.2023298118.

Schubert, U., Antón, L.C., Gibbs, J., Norbury, C.C., Yewdell, J.W., Bennink, J.R., 2000. Rapid degradation of a large fraction of newly synthesized proteins by proteasomes. Nature 404, 770–774. https://doi.org/10.1038/35008096.

Schwarz, J.A., Mitchelmore, C.L., Jones, R., O'Dea, A., Seymour, S., 2012. Exposure to copper induces oxidative and stress responses and DNA damage in the coral *Montastraea franksi*. Comp. Biochem. Phys. C. 157, 272–279. https://doi.org/10.1016/j.cbpc.2012.12.003.

Selmoni, O., Bay, L.K., Exposito-Alonso, M., Cleves, P.A., 2024. Finding genes and pathways that underlie coral adaptation. Trends Genet. 40, 213–227. https://doi.org/10.1016/j.tig.2024.01.003.

Seveso, D., Arrigoni, R., Montano, S., Maggioni, D., Orlandi, I., Berumen, M.L., Galli, P., Vai, M., 2019. Investigating the heat shock protein response involved in coral bleaching across scleractinian species in the central Red Sea. Coral Reefs 39, 85–98. https://doi.org/10.1007/s00338-019-01878-6.

Souter, P., Bay, L., Andreakis, N., Csaszar, N., Seneca, F., Van Oppen, M., 2011. A multilocus, temperature stress-related gene expression profile assay in *Acropora millepora*, a dominant reef-building coral. Mol. Ecol. Resour. 11 (2), 328–334. https://doi.org/10.1111/j.1755-0998.2010.02923.x.

Sully, S., Burkepile, D.E., Donovan, M.K., Hodgson, G., van Woesik, R., 2019. A global analysis of coral bleaching over the past two decades. Nat. Commun. 10. https://doi.org/10.1038/s41467-019-09238-2.

Tavakoli-Kolour, P., Sinniger, F., Morita, M., Nakamura, T., Harii, S., 2023. Variability in thermal stress thresholds of corals across depths. Front. Mar. Sci. 10, 1210662. https://doi.org/10.3389/fmars.2023.1210662.

Voolstra, C.R., Buitrago-Lopez, C., Perna, G., Cardenas, A., Hume, B.C.C., Raedecker, N., Barshis, D.J., 2020. Standardized short-term acute heat stress assays resolve historical differences in coral thermotolerance across microhabitat reef sites. Glob. Chang. Biol. 26 (8), 4328–4343. https://doi.org/10.1111/gcb.15148.

Voolstra, C.R., Valenzuela, J.J., Turkarslan, S., Cárdenas, A., Hume, B.C., Perna, G., Barshis, D.J., 2021. Contrasting heat stress response patterns of coral holobionts across the Red Sea suggest distinct mechanisms of thermal tolerance. Mol. Ecol. 30, 4466–4480. https://doi.org/10.1111/mec.16064.

Voss, P.A., Gornik, S.G., Jacobovitz, M.R., Rupp, S., Dörr, M., Maegele, I., Guse, A., 2023. Host nutrient sensing is mediated by mTOR signaling in cnidarian-dinoflagellate symbiosis. Curr. Biol. 33. https://doi.org/10.1016/j.cub.2023.07.038.

Warner, M.E., Fitt, W.K., Schmidt, G.W., 1999. Damage to photosystem II in symbiotic dinoflagellates: a determinant of coral bleaching. Proc. Natl. Acad. Sci. 98, 8007–8012. https://doi.org/10.1073/pnas.96.14.8007.

Yu, K., 2012. Coral reefs in the South China Sea: their response to and records on past environmental changes. Sci. China Earth Sci. 55, 1217–1229. https://doi.org/10.1007/s11430-012-4449-5.

Yu, X., Yu, K., Liao, Z., Chen, B., Qin, Z., Liang, J., Gao, X., 2023. Adaptation strategies of relatively high-latitude marginal reef corals in response to severe temperature fluctuations. Sci. Total Environ. 903. https://doi.org/10.1016/j.scitotenv.2023.166439.

虫黄藻(*Effrenium voratum*)对高温胁迫的生理响应

张廷超[a],潘能斌[a],唐媛媛[a],何 燃[a],蓝梦玲[a],韦丽菲[a],覃祯俊[a,b,c]
(广西大学 a. 海洋学院;b. 广西南海珊瑚礁研究重点实验室;c. 珊瑚礁研究中心,南宁 530004)

摘要:全球气候变暖对珊瑚的生存带来极大威胁,近年来珊瑚白化事件频发,珊瑚共生虫黄藻的死亡或损失是珊瑚发生白化的主要因素,而虫黄藻对高温胁迫的耐受性是决定珊瑚白化阈值的关键。以离体培养的虫黄藻(*Effrenium voratum*)为研究对象,首先对其进行分子鉴定,然后开展高温胁迫试验。将对照组的环境温度设置为26 ℃恒温,将处理组的环境温度分别设置为29 ℃和32 ℃,以此研究在全球气候变暖的背景下,海水升温对虫黄藻*E. voratum*的生长状况、叶绿素a(Chl a)质量浓度、超氧化物歧化酶(SOD)和过氧化氢酶(CAT)活性的生理影响。高通量测序结果显示,离体培养藻液中*E. voratum*的相对丰度为(99.971±0.032)%。高温胁迫试验结果显示,29 ℃下,*E. voratum*的生长受到抑制,但仍能保持密度上升的趋势,Chl a浓度在短时间内上升并维持相对较高水平,SOD与CAT活性呈持续上升趋势;32 ℃下,虫黄藻密度呈负增长,Chl a浓度先上升后下降至低于对照组水平,SOD活性呈先升后降的趋势,CAT活性呈持续上升的趋势。因此,*E. voratum*在26~29 ℃温度范围内可能具备一定的适应潜力,而在32 ℃时,高温胁迫将导致虫黄藻出现细胞损伤甚至死亡。

关键词:虫黄藻;*Effrenium voratum*;高温胁迫;生理响应;离体培养;高通量测序
中图分类号:Q949.2 **文献标志码**:A **文章编号**:2096-3122(2025)02-0001-10
DOI:10.13307/j.issn.2096-3122.2025.02.01

0 引言

珊瑚礁生态系统是具有全球最高生态多样性和初级生产力的生态系统,被喻为海底热带雨林,具有生境功能、产出功能、调节功能和信息功能等[1]。然而,人类生产引起前所未有的气候变化,让珊瑚面临巨大的威胁,尤其是全球气候变暖导致了大规模珊瑚白化事件发生越来越频繁,如1998、2010、2015—2017年的全球珊瑚白化事件[2]。据联合国政府间气候变化专门委员会(Intergovernmental Panel on Climate Change,IPCC)预计,相对工业化前水平,温度升高1.5 ℃时珊瑚礁会减少70%~90%,温度升高2 ℃时会造成珊瑚礁损失超过99%[3]。珊瑚作为窄温性动物,受到热应激所引起的珊瑚白化,主要是由于其体内共生虫黄藻与珊瑚之间的共生关系破裂,即虫黄藻从各自珊瑚宿主的组织中排出的过程,这一过程会对珊瑚造成压力进而导致珊瑚死亡[4]。研究表明,海水温度上升也被认为是虫黄藻的主要压力事件[5-6],高温对虫黄藻的生长产生极大影响[7],甚至发现大多数虫黄藻在高温试验结束前就已经死亡[8],同时,在高温胁迫下,虫黄藻密度、最大光量子产量(F_v/F_m)和叶绿素a(Chl a)质量浓度明显降低。温度的升高可能导致虫黄藻光合系统电子转移受阻[9],也可能会破坏虫黄藻的光合作用,出现光抑制现象,最终导致虫黄藻死亡[10]。有研究指出,虫黄藻对温度升高的适应力因物种而异[11-13],某些虫黄藻物种可能通过补偿机制具有一定的高温耐受性的能力[14-17]。然而,离体培养的虫黄藻对高温胁迫下的生理响应研究较少,且虫黄藻具有上百种不同的类群,不同类群的虫黄藻无论是在生活方式,还是对珊瑚虫的相互作用方面,都具有各自不同的生理特征。虫黄藻与珊瑚的共生关系是全球热带与亚热带珊瑚礁生态系统存在的基础,在珊

收稿日期:2024-11-10
基金项目:广西自然科学基金青年基金项目(2022GXNSFBA035449);国家自然科学基金项目(42206157);大学生创新创业训练计划项目(202310593497)
通信作者:覃祯俊,男,广西桂平人,讲师,博士,研究方向为珊瑚共生体微生态。

中国知网 https://www.cnki.net

瑚礁系统的建立中起着重要作用。目前,离体培养的虫黄藻类群对高温胁迫的响应机制研究还相对较少,极大程度地限制了人们对全球气候变暖趋势下虫黄藻—珊瑚共生关系的基本理解[18]。

共生虫黄藻主要分为*Symbiodinium*、*Breviolum*、*Cladocopium*、*Durusdinium*、*Effrenium*、*Fugacium*、*Gerakladium*、*Clade* H和*Clade* I 9个属,其中*Effrenium*属目前只包含*E. voratum*[19]。*E. voratum*广泛分布于温带和亚热带水域,如太平洋、大西洋和地中海地区,因其得益于在各种海洋环境中的生存条件,该物种具有宽温度范围、高光强度的耐受性以及混养能力[20],但研究指出的宽温度范围耐受性仅局限于对低温的耐受,而对高温响应的相关研究还较少[21-24],在面对高温时的响应在很大程度上还是未知。因此,本研究以高温作为环境压力源,将*E. voratum*在26、29、32 ℃温度下,测定*E. voratum*的生长状况、Chl a质量浓度、超氧化物歧化酶(SOD)和过氧化氢酶(CAT)活力等生理生化指标,以此研究全球气候变暖的背景下虫黄藻对海水升温的响应过程。本研究结果将为虫黄藻种群的高温响应与适应机制以及构建可适应高温环境的虫黄藻物种提供基础数据和参考。

1 材料与方法

1.1 材料

虫黄藻从试验室已有的*E. voratum*母液中转接获取,在装有L1-Si培养基的250 mL锥形瓶中保存,置于室内恒温光照培养箱中培养,温度为26 ℃,光照强度为5 000 lx,光/暗周期为12 h/12 h。每隔1周用显微镜(奥克巴斯-BX53)观察转接的*E. voratum*生长情况,对其进行形态学鉴定。为了确定培养的共生虫黄藻的纯度,对转接后培养的虫黄藻*E. voratum*进行DNA提取处理,将提取的DNA样品经过质量和纯度检测后送至上海美吉生物医药科技有限公司进行高通量测序。

1.2 方法

1.2.1 试验设计

试验设置3个不同的温度条件处理:26 ℃(室温,对照)、29 ℃、32 ℃。待细胞进入指数增长期后,首先将母液转接到1 L的大培养瓶中,转接后大培养瓶内虫黄藻的数量为1×10^6个,然后均匀分配至各个容量为500 mL的小培养瓶中,每瓶200 mL,分别进行编号。随机抽取锥形瓶并分为对照组和处理组,将处理组分别移至温度为29 ℃和32 ℃的培养箱进行处理,其他条件保持一致,并在试验开始后的4、24、48 h取出相应的试验样品进行生理生化指标测定。

1.2.2 生理指标测定

用微量移液器取每份100 μL的3份均匀藻液于2 mL离心管内,加入900 μL无菌海水稀释,将稀释后的虫黄藻溶液用漩涡混匀器充分混匀。然后,移取100 μL稀释后的藻液到浮游生物计数框中(覆盖盖玻片),在显微镜下观察并进行虫黄藻计数(n=10),最后将统计结果换算成总体积溶液内所含虫黄藻的数量,即虫黄藻密度(D,单位:个·mL^{-1})。

充分混合均匀锥形瓶中的藻液,取出每份2 mL的3份溶液,分别加入离心管中,使用台式高速冷冻离心机(Sigma-3K15)进行离心分离。4 000 r·min^{-1},离心5 min后,去除上清液,在沉淀物中加入1.5 mL 100%的丙酮,4 ℃条件下萃取24 h;再次进行离心分离,4 000 r·min^{-1},离心5 min,取上清液200 μL。用分光光度计分别测试波长750、664、647、630 nm处的吸光度,利用公式(1)计算Chl a质量浓度。

$$C_a=11.85\times(A_{664}-A_{750})-1.54\times(A_{647}-A_{750})-0.08\times(A_{630}-A_{750}), \quad (1)$$

式中,C_a为Chl a质量浓度,单位:mg·L^{-1};A为吸光度。

1.2.3 生化指标测定

使用商用试剂盒(货号A001-3、A007-2-1,南京建成生物工程研究所有限公司)参照测定试剂盒使用说明书,具体操作步骤参照刘旭[25]的方法,分别测定藻液中SOD、F_v/F_m和CAT总活性。

1.2.4 数据处理

所有数据均记录为至少3个独立生物重复试验的平均值±标准偏差。使用非参数检验Kruskal-Wallis

中国知网 https://www.cnki.net

单因素ANOVA分析对试验数据作显著性分析。使用SPSS Statistics软件进行结果分析和可视化处理。

2 结果与分析

2.1 虫黄藻的分子鉴定结果分析

本研究对3个离体培养的藻液样品(E_{01}、E_{02}、E_{03})进行高通量测序,以检测藻液的虫黄藻组成(表1)(原始数据上传至NCBI数据库https://www.ncbi.nlm.nih.gov/,SRA:PRJNA1000185)。测序结果表明,本研究中离体培养的藻样中*E. voratum*的纯度达到99.93%~99.99%,可以确定本研究藻种为虫黄藻*E. voratum*,能够开展后续研究。本研究建立了*E. voratum*与其他虫黄藻系群的系统发育树(图1),结果表明*E. voratum*与其他虫黄藻系群在系统发育树中分布紧密,相对于Clade C而言,*E. voratum*与Clade A的*Symbiodinium microadriaticum*、A15a,与Clade D的*Durusdiniuum trenchii*的系统发育关系更为密切。

表1　虫黄藻藻液样品高通量测序结果

虫黄藻类群	相对丰度/%			
	E_{01}	E_{02}	E_{03}	平均值±标准偏差
Effrenium voratum	99.988	99.934	99.991	99.971±0.032
Cladocopium goreaui	0	0.052	0.005	—
Cladocopium Clp	0.002	0	0	—
Cladocopium Cl5a	0.002	0	0	—
Durusdiniuum trenchii	0	0	0.002	—
其他	0.007	0.014	0.002	—

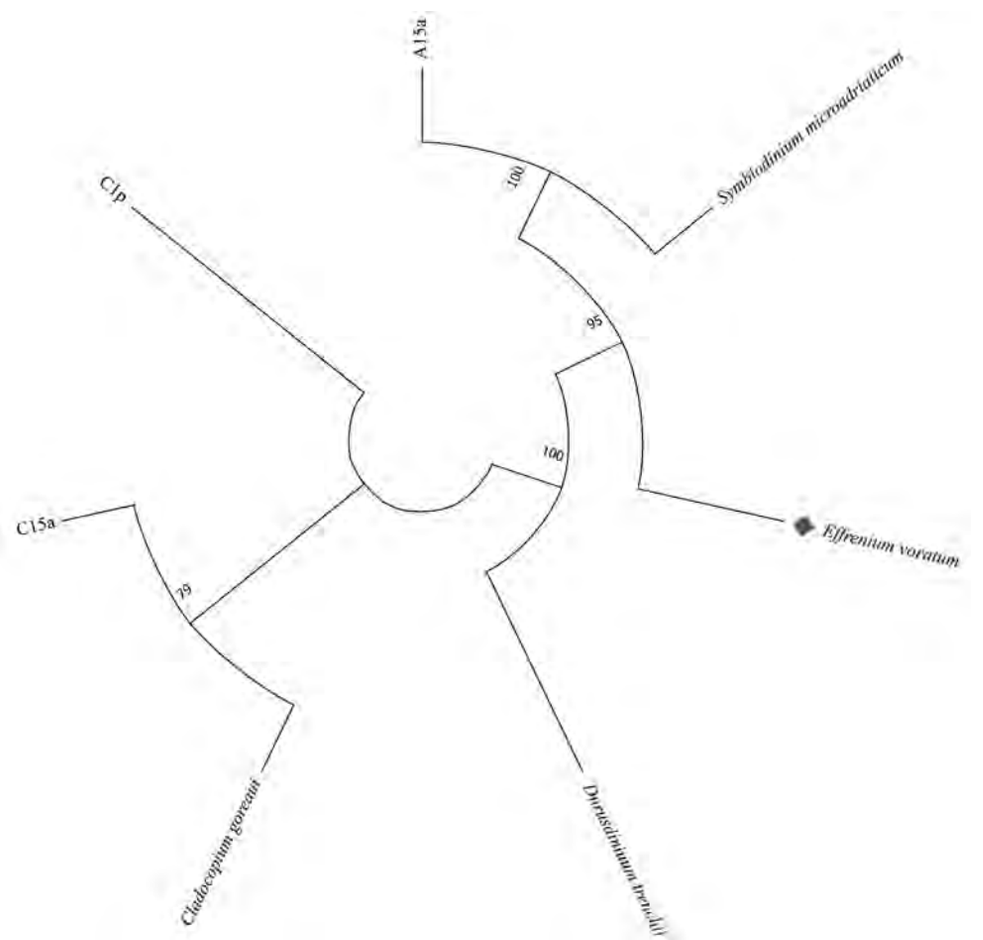
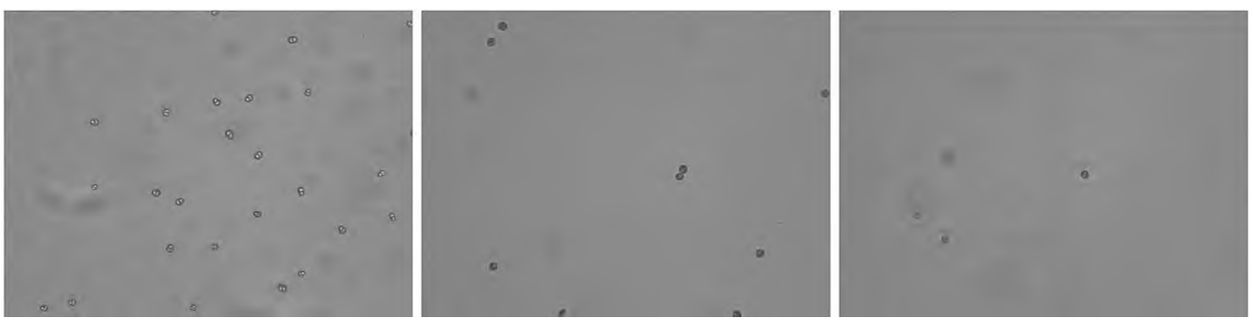


图1　虫黄藻系群的系统发育树

中国知网　https://www.cnki.net

2.2 虫黄藻*E. voratum*在高温胁迫下的生长曲线变化

在显微镜下，观察不同温度条件下藻液中虫黄藻*E. voratum*的密度差异（图2），进一步处理分析，结果如图3所示。在转接后并平均分至500 mL锥形瓶胁迫4 h时，对照组与29 ℃、32 ℃处理组的虫黄藻密度相近。24 h温度胁迫后，处理组与对照组的*E. voratum*细胞能保持生长，密度均有所上升，对照组虫黄藻密度的上升幅度稍微大于处理组，但差异不显著。高温胁迫48 h后，对照组的虫黄藻密度大幅上升，29 ℃处理组的密度也有上升，但远小于对照组，而32 ℃处理组的虫黄藻密度则转而下降，与对照组差异显著（$P < 0.05$）。



（a）26 ℃　　（b）29 ℃　　（c）32 ℃

图2　不同温度下虫黄藻*E. voratum*的镜像观察

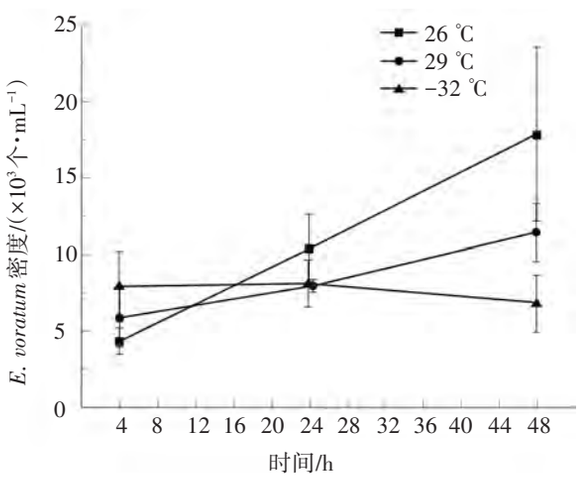


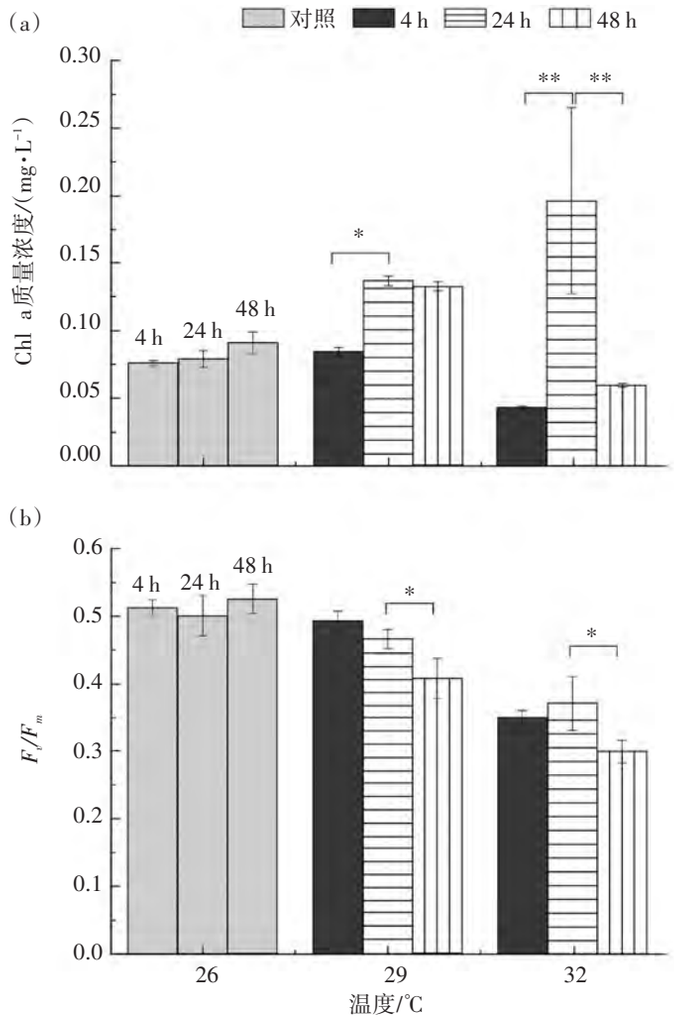
图3　不同温度下虫黄藻*E. voratum*密度随胁迫时间的变化

2.3 虫黄藻*E. voratum*在高温胁迫下Chl a质量浓度和F_v/F_m的变化

虫黄藻*E. voratum*在高温胁迫下Chl a质量浓度的变化结果[图4(a)]显示，29 ℃处理组的Chl a质量浓度在4 h时与对照组的差异不显著，而在24 h出现显著上升（$P<0.05$），48 h的Chl a质量浓度与24 h的差异不显著。32 ℃处理组的Chl a质量浓度在4 h较对照组的下降，但差异不显著，在24 h时极显著上升（$P<0.01$），48 h较24 h的Chl a质量浓度极显著下降（$P<0.01$）。

虫黄藻*E. voratum*的最大光量子产量（F_v/F_m）值的变化结果[图4(b)]显示，29 ℃处理组的F_v/F_m值在4 h时与对照组的差异不显著，而在24 h时稍有下降，但差异不显著，48 h的F_v/F_m值再次下降，与24 h的差异显著（$P<0.05$）。32 ℃处理组的F_v/F_m值在4 h时较对照组的下降，但差异不显著，而在24 h的F_v/F_m值较在4 h的上升，差异不显著，但低于对照组在24 h的F_v/F_m值；32 ℃处理组在48 h的F_v/F_m值较在24 h的显著下降（$P<0.05$），并低于29 ℃处理组在48 h的F_v/F_m值，较对照组在48 h的显著下降（$P<0.05$）。

中国知网　https://www.cnki.net



*表示处理间差异显著（$P<0.05$）；**表示处理间差异极显著（$P<0.01$）。

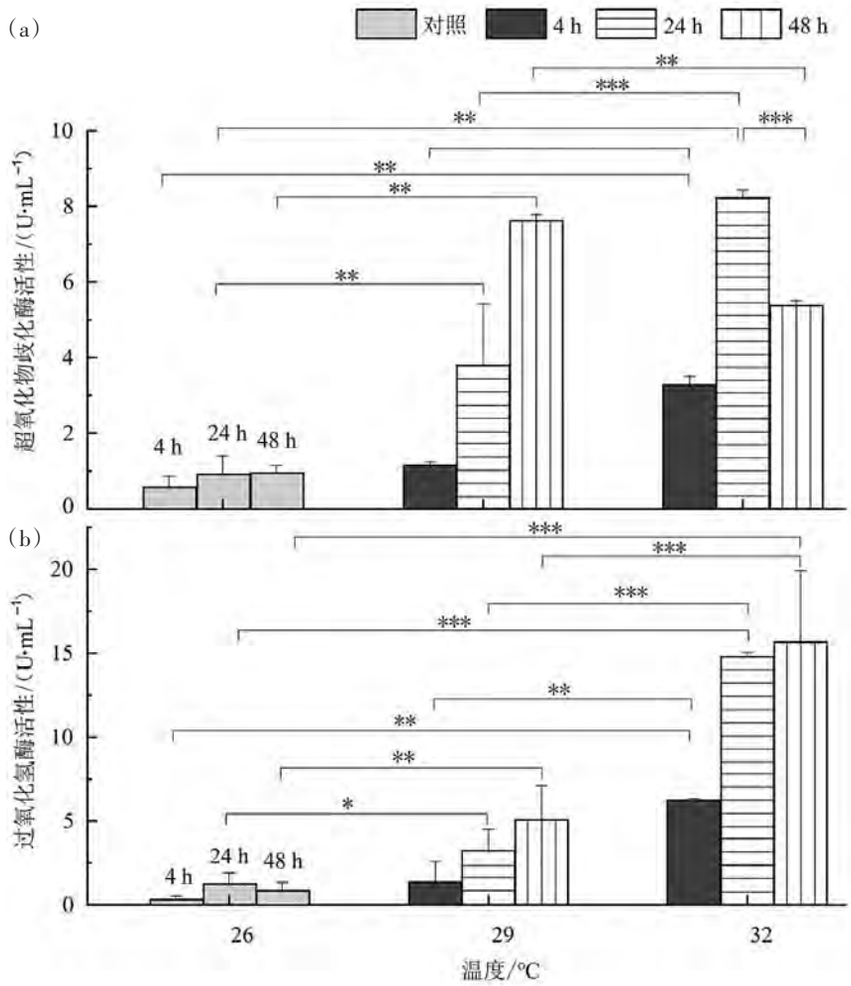
图4　不同温度下虫黄藻*E. voratum*的Chl a质量浓度和F_v/F_m随胁迫时间的变化

2.4 虫黄藻*E. voratum*在高温胁迫下SOD与CAT的活性变化

虫黄藻*E. voratum*的超氧化物歧化酶(SOD)活性结果[图5(a)]显示,对照组的SOD活性较低;29 ℃处理组在4 h的SOD活性较对照组差异不显著,而在24 h与48 h的均出现显著上升($P<0.01$)。32 ℃处理组在4 h的SOD活性较对照组的显著上升($P<0.01$),在24 h的进一步显著上升($P<0.01$),在48 h的较32 ℃处理组24 h的SOD活性出现极显著下降($P<0.01$),并显著低于29 ℃处理组48 h的SOD活性($P<0.01$),较对照组48 h的显著上升($P<0.05$)。

虫黄藻*E. voratum*的过氧化氢酶(CAT)活性结果[图5(b)]显示,对照组的CAT活性较低;29 ℃处理组在4 h的CAT活性较对照组的上升,但差异不显著,在24 h的显著上升($P<0.05$),48 h时继续显著上升($P<0.01$)。32 ℃处理组在4 h的CAT活性较对照组的显著上升($P<0.01$),在24、48 h的均出现极显著上升($P<0.001$)。32 ℃处理组的CAT活性较29 ℃处理组4 h的显著($P<0.001$)和24 h、48 h的极显著($P<0.001$)。

中国知网　https://www.cnki.net



*表示处理间差异显著（P<0.05）；**，***表示处理间差异极显著（P<0.01，P<0.001）。

图5　不同温度下虫黄藻*E. voratum*的超氧化物歧化酶SOD(a)、过氧化氢酶CAT(b)活性随胁迫时间的变化

3 讨论

本研究虫黄藻*E. voratum*样品的相对丰度达到(99.971±0.032)%，纯度较高，可以很好地作为高温胁迫的试验材料。对照组的虫黄藻*E. voratum*细胞在48 h内一直保持着生长，而高温胁迫中相对长时间(大于24 h)的*E. voratum*生长则遭到抑制，过高温度(32 ℃)甚至出现负增长。实际上，32 ℃及以上的温度已经超过了*E. voratum*对温度耐受的阈值，32 ℃的高温胁迫下*E. voratum*参与减数分裂的相关基因表达相比对照组显著下调，导致细胞分裂遭到限制，甚至出现细胞死亡[22-34]。而*E. voratum*似乎可以适应26~29 ℃的温度范围，尽管在29 ℃处理下的虫黄藻密度增长小于对照组，但仍能维持细胞生长，保持着虫黄藻密度上升的趋势。虫黄藻的Chl a质量浓度和F_v/F_m值与虫黄藻密度存在着紧密联系[8]，同时也是评估藻类对海洋变暖敏感性的快速可用指标[22]。此外，高温会导致虫黄藻出现光抑制现象，从而降低光合作用能力[35-36]，Chl a和F_v/F_m值作为光能的捕获器，其质量浓度也作为评估高温胁迫下虫黄藻光合效率和适应能力的指标。本研究中，24 h时，相较于对照组*E. voratum*的Chl a质量浓度，高温胁迫组显著上升，而在一定范围内适度提高生长温度被证实有助于虫黄藻进行光合作用[37]。48 h时，32 ℃处理组的*E. voratum*的Chl a质量浓度出现大幅下降，结合前人的研究，本研究中32 ℃处理组在24 h后，*E. voratum*的Chl a可能由于受到压力，活性氧大量积累进而使Chl a与活性氧反应导致的色素降解[38-39]；也可能由于参与叶绿素降解的相关基因表达上调[33]，最终导致Chl a色素降解。相较于对照组的*E. voratum*，29 ℃和32 ℃处理组F_v/F_m均出现整体下降趋势，虽然32 ℃处理组F_v/F_m在24 h时较4 h时出现了小幅上升，但在48 h时出现更大的降幅，表现为整体下降。当虫黄藻受到高温胁迫时，光合作用系统II(PSII)的功能会受到影响，F_v/F_m

中国知网　https://www.cnki.net

值会降低。

活性氧分子(ROS)是光合作用和细胞呼吸的常见副产物[40-41]。通常,为了控制细胞水平的毒性,保护细胞免受氧化损伤,细胞内的抗氧化机制也会被触发[8,42],其中包括酶与非酶的抗氧化剂,比如SOD、CAT、POD,以及一些小分子,如维生素C和硫醇类抗氧化剂[34,43-44],SOD与CAT则作为其中的2种抗氧化剂在这一过程中起到重要作用。SOD通过催化$O_2^{\cdot-}$转化成水和H_2O_2提供了抗氧化的第一道防线[45],CAT则会将H_2O_2还原成水和氧气[46]。因此,SOD与CAT的活性作为氧化应激参数已被广泛用作高温胁迫下细胞应激的生物学指标[21,47],通过氧化酶活性的测定,能够反映取样时刻细胞内ROS和抗氧化机制之间的平衡状态。但在高温胁迫条件下,虫黄藻会加速产生具有破坏性的ROS,比如H_2O_2、OH^-、$O_2^{\cdot-}$等有害自由基[34,48-49],前人的研究表明,这一反应机制是由于虫黄藻光合作用能力受到抑制,阻碍电子转移的过程,导致PSII上的D1蛋白损伤,并且损伤的速度远低于修复的速度,平衡循环受到破坏[25]。而Gong等[33]在*E. voratum*的高温胁迫试验中发现*E. voratum*细胞内光合作用的相关基因(编码PSII中的PsbB、PsbC、PsbD、PsbO、FCPA、LHC与PSII中的PsaA、PsaC以及叶绿素ATP酶中的ATPF1B和ATPF1A的基因)和抗氧化活性相关的基因(编码HSP70、SOD和CAT的基因)均在高温条件下相比对照组显著上调,其研究结论也同样认为可能是由于通过抗氧化相关系统的修复机制与光合作用相关蛋白的失活速率不匹配导致*E. voratum*的光抑制。PSII的生理功能不能继续进行,导致传递链断开,分子氧增加,使得活性氧增多[25]。当细胞内的ROS质量浓度累积到超过阈值,则会引起细胞氧化损伤和细胞死亡[34]。在本研究中,29 ℃处理的SOD与CAT活性随着时间的变化趋势一致,表现为4 h时其活性高于对照组,并且随着时间的推移,活性不断升高;32 ℃处理的SOD与CAT活性随着时间变化的趋势存在差异,4 h时,SOD与CAT活性均表现出高于对照组,在24 h时均呈持续升高,48 h时CAT活性依旧呈上升趋势而SOD活性则呈下降趋势,并且除48 h的SOD活性外,相同时间下,32 ℃处理的SOD、CAT活性均显著高于29 ℃处理。刘旭[25]和杨晓红[34]的研究结果显示,SOD和CAT酶活性在短时间内高温胁迫均显著增加,本试验稍有不同,在较长时间的高温胁迫下SOD酶活性出现先上升后下降的现象。抗氧化酶的上升说明温度升高激活了*E. voratum*细胞的氧化应激反应,并且2个温度的酶活性差异说明温度越高反应越剧烈,抗氧化能力的显著增加也同时从侧面揭示了温度胁迫下*E. voratum*的ROS产量增加。

通过试验观察到温度胁迫下,SOD活性先上升后下降存在几种可能性,首先是影响细胞抗氧化机制的ROS,杨晓红[34]的研究表明,高温胁迫下*E. voratum*的ROS处于先上升后下降的趋势。短期的高温处理能够刺激ROS的增加[50-51],但随着时间的推移,可能会由于细胞抗氧化机制的作用或者产生ROS的通路代谢从高水平恢复至正常水平,也可能由于高温条件下,细胞受损严重且活性丧失,细胞内产生的ROS通路机制严重损坏,从而导致ROS水平下降[34];其次是负责清除ROS的抗氧化机制中也存在多种抗氧化物发挥作用[43],可能由于在ROS上升期间,富集的ROS超过了可控的阈值,即ROS的降解速度远远小于其生成速度,大量的ROS富集会对虫黄藻生理功能造成损伤,即有可能导致产生SOD通路遭到损坏,导致SOD活性下降,同时,在不同的温度和时间下,其他的抗氧化物可能承担了受损或者未受损通路产生SOD的部分功能,这也解释了在29 ℃与32 ℃温度下同种抗氧化酶活性的波动幅度不一致的原因。综合来看,*E. voratum*应对温度升高存在2种结果:1) *E. voratum*无法适应该程度下的高温胁迫,其生理功能受到严重损伤;2) *E. voratum*适应了该程度下的高温胁迫,表现出其在进化过程中所形成的抗逆性。在本研究中,*E. voratum*能够适应29 ℃而无法适应32 ℃的温度胁迫,尽管在抗氧化酶活性上,2个温度胁迫试验在前期均呈相似的变化趋势,但在试验后期,32 ℃处理的SOD活性降低,而29 ℃处理的SOD活性还在升高,因此不大可能是由于32 ℃下细胞抗氧化机制的作用导致ROS水平下降,进而导致SOD活性水平的下降,结合虫黄藻密度与Chl a质量浓度的变化,32 ℃下的*E. voratum*已经出现细胞死亡与色素分解现象,该温度下*E. voratum*氧化与抗氧化机制可能已经被严重损坏。

4 结论

本文研究了高温作为环境压力源下虫黄藻*E. voratum*的生理生化反应。在高温(29 ℃、32 ℃)胁迫下,

中国知网　https://www.cnki.net

*E. voratum*均表现出生长受到抑制和短时间内Chl a的质量浓度上升，以及短时间内抗氧化酶SOD和CAT活性的上升，说明2组温度胁迫下的*E. voratum*具有类似的高温响应机制。但是，长时间下32 ℃处理组的虫黄藻密度出现负增长、Chl a质量浓度与SOD活性大幅下降，而29 ℃处理的*E. voratum*生长抑制效果和色素降解程度更低，仍能保持着虫黄藻密度上升的趋势及长时间其体内高水平的Chl a质量浓度。研究结果表明，*E. voratum*能适应26~29 ℃的温度，具有一定的耐热性和适应性，但无法适应过高的温度(32 ℃)，一旦超过阈值，将会导致细胞损伤甚至死亡。本研究结果为虫黄藻种群的高温响应与适应机制以及构建可适应高温环境的虫黄藻物种提供了基础数据和参考。

参考文献：

[1] 李宇亮，高宇，郑新庆，等.珊瑚礁生态系统功能产生机制及评价方法[J].应用海洋学学报，2022(3)：475.

[2] BOTTÉ E S，CANTIN N E，MOCELLIN V J L，et al.Reef location has a greater impact than coral bleaching severity on the microbiome of *Pocillopora acuta*[J].Coral reefs，2022(1)：63.

[3] HOEGH-GULDBERG O，JACOB D，BINDI M，et al.Impacts of 1.5 C global warming on natural and human systems[R].Global warming of 15 C an IPCC special report，2018：1.

[4] CURRAN A，BARNARD S.What is the role of *zooxanthellae* during coral bleaching? Review of zooxanthellae and their response to environmental stress[J].South African journal of science，2021，117：1.

[5] HUGHES T P，BARNES M L，BELLWOOD D R，et al.Coral reefs in the anthropocene[J].Nature，2017(7656)：82.

[6] HUGHES T P，KERRY J T，BAIRD A H，et al.Global warming transforms *Coral reef* assemblages[J].Nature，2018(7702)：492.

[7] PATTHANASIRI K，LIRTWITAYAPRASIT T，YEEMIN T，et al.Comparative growth rates of cultured *Zooxanthellae* and the effects of temperature and salinity[J].Journal of fisheries and environment，2022(2)：136.

[8] 蒙林庆，黄雯，阳恩广，等.高温白化事件可提高涠洲岛澄黄滨珊瑚(*Porites lutea*)的耐热性[J].海洋学报，2022(8)：87.

[9] MOYA A，SAKAMAKI K，MASON B M，et al.Functional conservation of the apoptotic machinery from coral to man：the diverse and complex Bcl-2 and caspase repertoires of *Acropora millepora*[J].BMC genomics，2016(1)：62.

[10] TCHERNOV D，GORBUNOV M Y，DE VARGAS C，et al.Membrane lipids of *symbiotic algae* are diagnostic of sensitivity to thermal bleaching in corals[J].Proceedings of the national academy of sciences，2004(37)：13531.

[11] AIHARA Y，TAKAHASHI S，MINAGAWA J.Heat induction of cyclic electron flow around photosystem I in the symbiotic *dinoflagellate Symbiodinium*[J].Plant physiology，2016(1)：522.

[12] DÍAZ-ALMEYDA E M，PRADA C，OHDERA A H，et al.Intraspecific and interspecific variation in thermotolerance and photoacclimation in *Symbiodinium dinoflagellates*[J].Proceedings of the royal society B：biological sciences，2017(1868)：1767.

[13] SILVERSTEIN R N，CUNNING R，BAKER A C.Change in algal symbiont communities after bleaching，not prior heat exposure，increases heat tolerance of reef corals[J].Global change biology，2015(1)：236.

[14] BERKELMANS R，VAN OPPEN M J H.The role of zooxanthellae in the thermal tolerance of corals：a ‘nugget of hope’ for coral reefs in an era of climate change[J].Proceedings of the Royal Society B：biological sciences，2006(1599)：2305.

[15] LAJEUNESSE T C，SMITH R，WALTHER M，et al.Host-symbiont recombination versus natural selection in the response of coral-dinoflagellate symbioses to environmental disturbance[J].Proceedings of the Royal Society B：biological sciences，2010(1696)：2925.

[16] ROWAN R.Thermal adaptation in reef coral symbionts[J].Nature，2004(7001)：742.

[17] WHAM D C，NING G，LAJEUNESSE T C.*Symbiodinium glynnii* sp. nov.，a species of stress-tolerant symbiotic dinoflagellates from pocilloporid and montiporid corals in the Pacific Ocean[J].Phycologia，2017(4)：396.

[18] 龙超，罗肇河，韦章良，等.海南三亚鹿回头虫黄藻(*Effrenium voratum*)的形态学和系统发育学研究[J].热带海洋学报，2021(4)：35.

[19] LAJEUNESSE T C，PARKINSON J E，GABRIELSON P W，et al.Systematic revision of *Symbiodiniaceae* highlights the antiquity and diversity of coral endosymbionts[J].Current biology，2018(16)：2570.

中国知网 https://www.cnki.net

[20] KANG N S,KIM E S,LEE J A,et al. First report of the dinoflagellate genus *Effrenium* in the east sea of Korea: morphological,genetic,and fatty acid characteristics[J].Sustainability,2020(9):3928.

[21] MCGINTY E S,PIECZONKA J,MYDLARZ L D.Variations in reactive oxygen release and antioxidant activity in multiple *Symbiodinium* types in response to elevated temperature[J].Microbial ecology,2012(4):1000.

[22] YANG F,WEI Z,LONG L.Response mechanisms to ocean warming exposure in *Effrenium voratum* (*Symbiodiniaceae*)[J]. Marine pollution bulletin,2022, 82:114032.

[23] PIERANGELINI M,THIRY M,CARDOL P.Different levels of energetic coupling between photosynthesis and respiration do not determine the occurrence of adaptive responses of *Symbiodiniaceae* to global warming[J].New phytologist, 2020(3):855.

[24] ROS M,CAMP E F,HUGHES D J,et al.Unlocking the black-box of inorganic carbon-uptake and utilization strategies among *coral endosymbionts* (Symbiodiniaceae)[J].Limnology and oceanography,2020(8):1747.

[25] 刘旭.造礁石珊瑚对温度胁迫的响应机制研究[D].南宁:广西大学,2020.

[26] FRANKLIN E C,STAT M,POCHON X,et al.GeoSymbio:a hybrid,cloud-based web application of global geospatial bioinformatics and ecoinformatics for *Symbiodinium*-host symbioses[J].Molecular ecology resources,2012(2):369.

[27] ARIF C,DANIELS C,BAYER T,et al.Assessing *Symbiodinium* diversity in scleractinian corals via next-generation sequencing-based genotyping of the ITS2 rDNA region[J].Molecular ecology,2014(17):4418.

[28] CHEN X,YU K,HUANG X,et al.Atmospheric nitrogen deposition increases the possibility of macroalgal dominance on remote coral reefs[J].Journal of geophysical research: biogeosciences,2019(5):1355.

[29] ALTSCHUL S F,GISH W,MILLER W,et al.Basic local alignment search tool[J].Journal of molecular biology,1990 (3):403.

[30] RONQUIST F,TESLENKO M,VAN DER MARK P,et al.MrBayes 3.2:efficient bayesian phylogenetic inference and model choice across a large model space[J].Systematic biology,2012(3):539.

[31] TONG H,CAI L,ZHOU G,et al.Temperature shapes coral-algal symbiosis in the South China Sea[J].Scientific reports,2017(1):40118.

[32] QIN Z,YU K,CHEN B,et al.Diversity of *Symbiodiniaceae* in 15 coral species from the southern South China Sea: potential relationship with coral thermal adaptability[J].Frontiers in microbiology,2019,10:2343.

[33] GONG S,LI G,JIN X,et al.Photobleaching and recovery of *Symbiodiniaceae Effrenium voratum* SCS01 reveals life form transformation under thermal stress[J].Frontiers in marine science,2021,8:740416.

[34] 杨晓红.高温及营养缺乏诱导虫黄藻氧化胁迫的初步研究[D].厦门:厦门大学,2020.

[35] BHAGOOLI R,HIDAKA M.Photoinhibition,bleaching susceptibility and mortality in two scleractinian corals,*Platygyra ryukyuensis* and *Stylophora pistillata*,in response to thermal and light stresses[J].Comparative biochemistry and physiology part a:molecular & integrative physiology,2004(3):547.

[36] LESSER M P.Elevated temperatures and ultraviolet radiation cause oxidative stress and inhibit photosynthesis in *Symbiotic dinoflagellates*[J].Limnology and oceanography,1996(2):271.

[37] TANAKA Y,NISHIYAMA Y,MURATA N.Acclimation of the photosynthetic machinery to high temperature in *Chlamydomonas reinhardtii* requires synthesis de novo of proteins encoded by the nuclear and chloroplast genomes1[J]. Plant physiology,2000(1):441.

[38] XU Z,JIANG Y,ZHOU G.Response and adaptation of photosynthesis,respiration,and antioxidant systems to elevated CO_2 with environmental stress in plants[J].Frontiers in plant science,2015,6:701.

[39] MCCOY S J,KAMENOS N A.*Coralline algae* (Rhodophyta) in a changing world:integrating ecological,physiological, and geochemical responses to global change[J].Journal of phycology,2015(1):6.

[40] ASADA K.The water-water cycle in chloroplasts:scavenging of active oxygens and dissipation of excess photons[J]. Annual review of plant physiology and plant molecular biology,1999(1):601.

[41] BYCZKOWSKI J Z,GESSNER T.Biological role of superoxide ion-radical[J].International journal of biochemistry, 1988(6):569.

[42] CZIESIELSKI M J,SCHMIDT-ROACH S,ARANDA M.The past,present,and future of coral heat stress studies[J]. Ecology and evolution,2019(17):10055.

中国知网 https://www.cnki.net

[43] MISHRA S,IMLAY J.Why do bacteria use so many enzymes to scavenge hydrogen peroxide?[J].Archives of biochemistry and biophysics,2012(2):145.
[44] VANAPORN M,WAND M,MICHELL S L,et al.Superoxide dismutase C is required for intracellular survival and virulence of *Burkholderia pseudomallei*[J].Microbiology,2011(8):2392.
[45] FRIDOVICH I.Superoxide radical and superoxide dismutases[J].Annual review of biochemistry,1995(1):97.
[46] VENN A A,LORAM J E,DOUGLAS A E.Photosynthetic symbioses in animals[J].Journal of experimental botany,2008(5):1069.
[47] DIAS M,MADEIRA C,JOGEE N,et al. Oxidative stress on *Scleractinian coral* fragments following exposure to high temperature and low salinity[J].Ecological indicators,2019,107:105586.
[48] LESSER M P.Oxidative stress in marine environments:biochemistry and physiological ecology[J].Annual review of physiology,2006(1):253.
[49] DOWNS C A,FAUTH J E,HALAS J C,et al.Oxidative stress and seasonal coral bleaching[J].Free radical biology and medicine,2002(4):533.
[50] WAHID A,GELANI S,ASHRAF M,et al.Heat tolerance in plants:an overview[J].Environmental and experimental botany,2007(3):199.
[51] PUCCIARIELLO C,BANTI V,PERATA P.ROS signaling as common element in low oxygen and heat stresses[J].Plant physiology and biochemistry,2012,59:3.

(责任编辑:白 净)

Physiological Response of *Effrenium voratum* to High-temperature Stress

ZHANG Tingchao[a], PAN Nengbin[a], TANG Yuanyuan[a], HE Ran[a],
LAN Mengling[a],WEI Lifei[a], QIN Zhenjun[a,b,c]
(a. School of Marine Sciences;b. Guangxi Laboratory on the Study of Coral Reefs in the South China Sea;
c. Coral Reef Research Center of China, Guangxi University, Nanning 530004, China)

Abstract: Global warming poses a great threat to the survival of corals. In recent years, coral bleaching events have occurred frequently, and the death or loss of the coral symbiotic zooxanthellae is the major factor of coral bleaching. The tolerance of coral zooxanthellae to high-temperature stress is the key to determining the threshold of coral bleaching. Using the isolated cultured *Effrenium voratum* as the research object, the molecular characterization of coral zooxanthellae was first carried out, and followed by the high-temperature stress experiment. The ambient temperature of the control group was set at a constant temperature of 26 ℃, and that of the experimental group was set at 29 ℃ and 32 ℃, respectively, to study the physiological effects of seawater warming on the growth, Chl a concentration, superoxide dismutase (SOD) and catalase (CAT) activity of *E. voratum* under the background of global warming. The high-throughput sequencing results showed that the relative abundance of *E. voratum* in the isolated culture algal solution was (99.971±0.032)%. The results of high-temperature stress experiments showed that the growth of *E. voratum* was inhibited when exposed to 29 ℃. Still, they managed to maintain the trend of increasing density, Chl a increased and maintained a relatively high level within a short period, and the activities of the antioxidant enzymes SOD and CAT exhibited a continuous upward trend. When *E. voratum* was exposed to 32 ℃, the density of *E. voratum* showed a negative increase, Chl a showed a rise and then decreased to a level lower than that of the control group, SOD activity showed a rise and then decreasing trend, and CAT activity showed a trend of continuous increase. Therefore, *E. voratum* may have certain adaptation potential at the temperature range of 26~29 ℃, while at 32 ℃, high temperature stress will lead to cell damage or even death of *E. voratum*.

Keywords: coral zooxanthellae; *Effrenium voratum*; high temperature stress; physiological response; in vitro culture; high throughput sequencing

中国知网 https://www.cnki.net

马玉玲, 俞小鹏, 余克服, 等. 造礁珊瑚热适应相关功能基因的研究进展[J]. 海洋学报, 2025, 47(9): 23–42, doi:10.12284/hyxb2025108
Ma Yuling, Yu Xiaopeng, Yu Kefu, et al. Research progress on functional genes related to coral thermal adaptation[J]. Haiyang Xuebao, 2025, 47(9): 23–42, doi:10.12284/hyxb2025108

造礁珊瑚热适应相关功能基因的研究进展

马玉玲[1], 俞小鹏[1*], 余克服[1, 2*], 陈俊伶[1], 郑月[1], 陈健[1]

(1. 广西大学 广西南海珊瑚礁研究重点实验室/珊瑚礁研究中心/海洋学院, 广西 南宁 530004; 2. 南方海洋科学与工程广东省实验室(广州), 广东 广州 511458)

摘要: 全球变暖和极端高温事件导致了珊瑚大规模白化, 引起全球珊瑚礁生态系统的快速退化。识别热适应相关的功能基因有助于进一步揭示珊瑚对全球变暖的响应及适应策略, 科学预测珊瑚礁生态系统的发育趋势。但目前对珊瑚共生功能体热适应分子机制的认识非常不足。因此, 本文综述了珊瑚热适应相关功能基因的研究进展。热适应相关基因在珊瑚受到热胁迫后会产生一系列的连锁反应。首先, Toll 受体等识别受体识别到热胁迫后参与信号通路激活进而启动免疫响应过程, 主要包括: 热休克蛋白基因上调使变性多肽重新折叠; 抗氧化蛋白基因上调避免活性氧损伤; 细胞凋亡与细胞焦亡基因清除“有害”细胞。随着热胁迫加剧, 珊瑚会启动一系列复杂过程共同维持细胞稳态, 包括: 光保护蛋白基因快速修复虫黄藻光系统、宿主荧光蛋白基因维持氧化平衡; 钙离子通道蛋白基因维持细胞内 Ca^{2+} 水平稳定; 代谢基因保持代谢平衡以确保营养供给; 细胞周期调控基因抑制细胞复制以保存能量; 细胞骨架基因维持珊瑚骨架的完整性; 泛素相关基因调节蛋白质的去泛素化等。此外, 反复出现的热胁迫对珊瑚具有驯化作用, 可能通过减缓珊瑚宿主代谢、减少热胁迫相关蛋白质的损伤、提高抗氧化物和铵同化酶等活性等提高珊瑚耐热性。

关键词: 全球变暖; 造礁珊瑚; 热适应; 功能基因; 热驯化

中图分类号: Q178.53 **文献标志码:** A **文章编号:** 0253−4193(2025)09−0023−20

1 引言

珊瑚礁生态系统具有极高的生物多样性, 给将近 30% 的海洋动物提供了栖息地以及食物能源[1]。但珊瑚礁生态系统也是最脆弱的海洋生态系统之一, 在全球变暖和海洋热浪加剧背景下, 珊瑚礁生态系统会遭遇严重的白化威胁[2−4]。平均水温仅超过夏季正常温度 2℃ 就会导致珊瑚共生功能体共生关系崩溃进而导致珊瑚白化和死亡[5−6], 这是珊瑚退化死亡的重要原因。然而, 科学家们发现, 在高温下, 一些珊瑚群落几乎不受影响, 而另一些则完全白化。即使是同一物种的珊瑚, 在不同地点的耐热性也各不相同[7]。并且部分地区珊瑚遭受二次热胁迫时白化程度没有预期的严重, 珊瑚总覆盖率也没有显著下降[8], 这表明珊瑚的热适应性在抵御热胁迫方面发挥了重要作用[9]。了解珊瑚的耐热性差异对于制定有效的保护和管理策略至关重要。天然耐热珊瑚的存在为大规模珊瑚礁恢复和保护工作提供了目标。通过深入研究这些差异, 可以更好地理解珊瑚如何适应气候变暖, 从而制定出更有效的保护措施。

收稿日期: 2025−01−12; **修订日期:** 2025−05−07。

基金项目: 国家自然科学基金重大项目(42030502); 广西科技基地与人才专项(桂科 AD25069075); 国家自然科学基金重点项目 (42090041); 国家自然科学基金(42406143); 广西研究生教育创新计划资助项目(YCBZ2024045)。

作者简介: 马玉玲(2001—), 女, 广西壮族自治区崇左市人, 主要研究方向为海洋生物与生态。E-mail: 2327301017@st.gxu.edu.cn

*** 通信作者:** 俞小鹏, 助理教授, 主要从事南海珊瑚生态与环境适应机制研究工作。E-mail: yuxiaopeng100@foxmail.com; 余克服, 教授, 主要从事南海珊瑚礁地质和生态环境方面的研究工作。E-mail: kefuyu@scsio.ac.cn

中国知网 https://www.cnki.net

20 世纪 30 年代,“珊瑚白化”被首次报道,21 世纪初开始研究珊瑚功能基因表达模式[10]。尽管进行了 20 多年的研究,但功能基因在珊瑚共生功能体响应热胁迫过程中的表达模式及作用机制仍不够明确[11]。而且共生体中参与微生物活动、竞争和应激反应的基因还未完全找出[12]。研究热适应性相关功能基因有助于揭示珊瑚共生功能体对环境变化和疾病的适应潜力,对珊瑚的未来有着极其重要意义[13]。

目前国内关于珊瑚相关功能基因的综述文章主要聚焦于经典热应激基因(如 Hsp、抗氧化蛋白基因、钙调素等钙离子通道蛋白相关基因等),且仅追溯到 2013 年[14]与 2018 年[15];国际上主要有对已知的热应激、海洋酸化和营养污染对珊瑚免疫系统的影响[16],以及综述热应激的基因表达生物标志物(热休克蛋白基因、代谢基因、抗氧化蛋白基因、免疫反应基因等)[11],且仅追溯到 2017 年。近年来,随着生物技术体系的迭代更新和分子生物学研究方法的革新性突破,早期文献在时效性和技术适配性方面难以满足现代研究需求。本文利用美国科学信息研究所(Institute for Scientife Information, ISl)的 Web of Science 核心合集的 SCIE 数据库,以及中国知网(China National Knowledge Infrastructure, CNKI)数据库为检索源,选择已发表的国内外期刊论文作为研究对象。对于珊瑚功能基因,英文以“coral ” “heat stress ” “gene” “ RNA-seq”为检索关键词;中文以“珊瑚” “热胁迫” “基因” “转录组”等为检索主题词,运用计算机检索语言将各个检索词进行联结,来源类别以 SCI 来源期刊、EI 来源期刊、中文核心期刊、硕博论文为来源库。检索 1982–2025 年珊瑚功能基因的期刊,为后续的研究提供参考。本文介绍了功能基因相关研究手段,重点综述了珊瑚白化与热适应的关系、热适应相关基因表达模式及潜在功能以及驯化提高耐热性的研究进展,系统提升了珊瑚热适应功能基因综述的全面性与前瞻性,进而阐述珊瑚白化与驯化之间的关系,明确热驯化可以提高珊瑚耐热性,推动该领域的发展,为进一步、全方位研究珊瑚热适应机制提供参考和指导。

2 珊瑚白化与热适应的关系

过去 30 年珊瑚白化事件呈现快速增加的趋势[17]。在全球变暖加剧背景下,预计这一趋势仍将延续,2050 年,珊瑚白化将使活珊瑚覆盖率减小 50%~75%; 2100 年,全球珊瑚礁栖息地丧失将达到 60%[18]。但最近的研究发现,在 2010 年至 2013 年期间,Pulau Layang-Layang 岛珊瑚覆盖率下降 5.2%,直到 2019 年有所恢复,珊瑚面积增加了 10.3%,约 27.1 hm^2[19];太平洋珊瑚礁系统中珊瑚群落的耐热值以 0.1°C/10 年的速度增加[20],使白化的影响并没有预期严重。珊瑚覆盖度的恢复均得利于珊瑚的适应性、白化后的恢复力以及群落结构的变化等多因素的调控[21]。尽管目前已经发现了珊瑚对热胁迫的潜在适应性,但其耐热性是否能跟上变暖的速度以及是否能够干预具体的适应机制仍不得而知。为了适应全球变暖,珊瑚需要忍受越来越严峻的高温,其应对方法主要有[21]:(1)其分布向中层水深、中光层和相对高纬度“避难所”迁移;(2)珊瑚−虫黄藻及细菌等微生物组共生关系重组;(3)通过调节相关功能基因表达来提高热适应性。归其根本,热适应过程是珊瑚共生功能体各组分共同作用的复杂分子过程。热应激增加了宿主代谢中的能量需求以及氮可用性,并导致虫黄藻的光合和线粒体膜会受到损伤从而产生活性氧(ROS)并触发宿主免疫反应[22],进而导致共生关系分解[23]。但无论温度或者热应激时间长短如何,虫黄藻主导系群不会发生变化[8]。但目前大多研究主要聚焦于虫黄藻密度以及系群组成的变化[24];共生细菌主要通过细菌群落多样性组成变化以及核心系群的切换来应对热胁迫;对于宿主来说,主要是研究其相关基因的变化,通过差异基因找出热适应相关分子机制。例如珊瑚面临白化时,共生功能体一方面可能会减少光合作用、呼吸、生长和代谢等生理活动[25],另一方面其氧化应激、钙离子稳态、热休克、免疫、代谢、DNA 修复、细胞凋亡和细胞焦亡等相关基因的表达也发生变化[7, 26],通过抑制高温导致的不良生理反应从而避免白化。珊瑚功能基因的研究揭示了分子应激反应的初步反应,并为生物标志物的进一步开发奠定了基础。因此聚焦于功能基因的研究能够更好地找出珊瑚面对热胁迫后产生的一系列热适应分子过程。热胁迫后相关功能基因变化的适应机制如图 1 所示。

此外,有研究发现经历过白化事件之后的珊瑚会进行一系列的自我修复,能够适应更高的温度,这被称为“环境记忆”现象。“环境记忆”现象类似于免疫系统中的免疫记忆(即机体首次遇到某种抗原物质时,会对该物质产生记忆,当再次遇到同种抗原物质时,会迅速做出反应,维持机体稳定)[27]。热驯化是珊瑚拥有“环境记忆”的一个重要手段。目前已有大量室内模拟实验对珊瑚进行热驯化以增加珊瑚耐热性从而达到驯化的效果。“环境记忆”是珊瑚应对多变气候的重要机制,拥有“环境记忆”的珊瑚耐热性会更高。然而,目前对“环境记忆”分子层面(主要是热适

中国知网 https://www.cnki.net

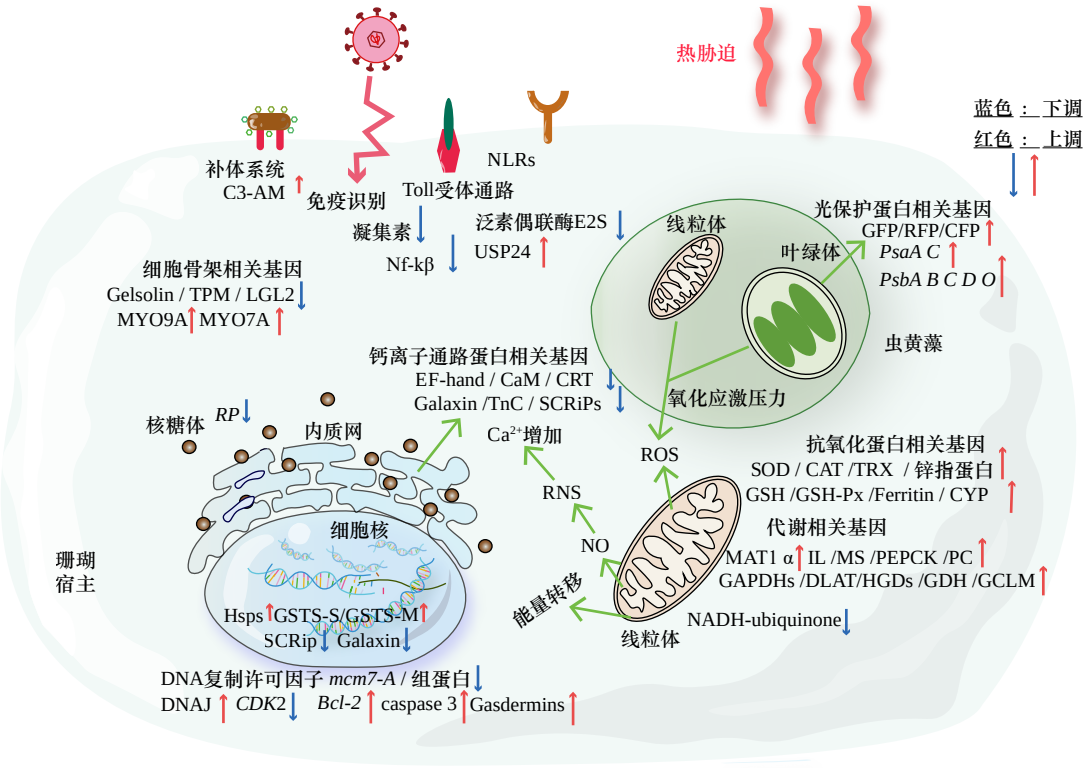


图 1　热适应相关功能基因变化示意图

Fig. 1　Schematic diagram of changes in functional genes related to thermal adaptation

应基因发挥作用)尚未得到明确的描述。因此，提高对珊瑚热适应相关基因的研究能够更好地预测珊瑚对未来气候变化的反应，从而更有针对性地保护珊瑚礁生态系统。

3　珊瑚功能基因研究方法与进展

基因功能的研究已经成为后“基因组时代”的一个重要课题。首先，在研究一个基因的功能前，要先对基因的时空表达谱(包括 mRNA 和蛋白质两个水平上的基因表达谱分析)进行分析[28]。珊瑚功能基因的时空表达谱主要技术是 21 世纪后出现的转录测序技术(RNA-Seq)，它通过捕获热胁迫下珊瑚的全转录本信息，快速筛选差异表达基因，成为解析珊瑚热适应机制的主要技术手段，促进了生物学研究的发展[29]。其次，需要通过实验来进行研究和验证基因功能，如基因敲除技术、RNA 干扰(RNAi)、基因过表达技术、微阵列分析等，这些方法被广泛运用于植物、动物、细菌等生物群中[30]。其中，传统基因敲除(如同源重组、T-DNA 插入)与新兴 CRISPR-Cas9 等定点编辑技术已在其他生物中广泛应用，但在珊瑚中的实践仍有限，目前仅见 van Oppen 和 Oakeshott 对珊瑚幼虫的 HSF1 基因使用 CRISPR-Cas9 基因敲除技术[31]；RNA 干扰(RNAi)是一种高效、特异、新兴的基因阻断技术[32]。该技术早些年在海葵[33–34]、水螅[35]研究中成功应用，但目前只有 Yuyama 等用来测定珊瑚幼体的 TRX 和 GFP 基因[36]。目前，珊瑚主要利用 cDNA 微阵列和 RNA-Seq 两种手段来研究热适应功能基因[37–39]。2005 年 cDNA 微阵列方法被首次大规模应用于珊瑚功能基因的研究中[40]，这是珊瑚转录组学研究的先驱。转录组学高通量测序(RNA-Seq)是目前研究珊瑚热适应基因主要研究手段[10]，能够全面快速地获取热胁迫下珊瑚几乎所有的转录本[41]。

随着技术的进步，一些新兴技术开始在珊瑚中应用。例如 Li 等使用单细胞转录组技术来分析珊瑚的共生关系[42]；日本的研究人员已经在培养皿中培养出珊瑚(*Acropora tenuis*)的可持续细胞系[43]。尽管技术进步显著，但技术适配性不足、模型系统局限及基因–表型关联薄弱仍是主要挑战。因此，需要加强珊瑚对热适应相关基因的研究，对构建健康稳定的珊瑚礁生态系统具有重要作用。

4　热适应相关功能基因的研究

在造礁珊瑚中，热适应相关功能基因是珊瑚耐受高温的分子基础。目前对珊瑚热适应相关功能基因的研究主要涉及免疫相关基因(热休克蛋白相关基因、抗氧化蛋白相关基因、细胞凋亡与细胞焦亡相关

中国知网　https://www.cnki.net

基因、其他免疫蛋白基因)、代谢相关基因、光保护蛋白相关基因、钙离子通道蛋白相关基因、细胞生长调控相关基因等(表 1)。

4.1 免疫相关基因

免疫系统响应分为 3 个阶段:(1)识别威胁,即免疫识别系统(PRR);(2)信号通路激活;(3)免疫效应阶段,负责消除威胁。珊瑚受到热胁迫后免疫系统发挥作用。

首先,第一阶段的免疫受体(主要是 Toll 样受体)发挥作用,开始识别病原体。Toll 受体包括 NLRs

表 1 珊瑚热适应相关功能基因列表

Table 1 List of functional genes related to coral's thermal adaptation

	研究对象	采用技术	GenBank Acc.	基因(蛋白)	已开展研究珊瑚物种	研究区域	潜在功能	热胁迫响应过程	参考文献
免疫相关基因	珊瑚宿主	RNA-Seq; cDNA微阵列分析	NW018149896	Nf-kβ1	*Acropora millepora*、*Acropora aspera*	大堡礁	DNA修复,染色质稳定相关	温度升高表达量降低	van de Water等[44] van de Water等[45]
			NW018149776	Nf-kβ2					
			NW018148758	补体因子c3样蛋白(C3-Am)	*Montastraea faveolata*; *Acropora millepora*、*Acropora aspera*	加勒比海; 大堡礁	免疫相关; 病原体的直接杀伤	温度升高表达量升高	Desalvo等[46] van de Water等[44] van de Water等[45]
	珊瑚宿主; 虫黄藻	RNA-Seq; cDNA微阵列分析	XM020776963	C型凝集素	*Montastraea faveolata*; *Acropora millepora*、*Pocillopora damicornis*	加勒比海; 南海	识别病原菌达到免疫作用	温度升高表达量降低	吴逸波[47] Wu等[48] Desalvo等[38]
			NW018150402	半乳糖凝集素(galectin)					
	珊瑚宿主	RNA-Seq; cDNA微阵列分析	—	HSP16	*Porites astreoides*	墨西哥湾	抗氧化作用; 抗凋亡	温度升高表达量升高	Kenkel等[49]
			—	HSP32	*Pocillopora damicornis*	琉球群岛			Thummasan等[50]
			GAL06223	HSP60	*Pocillopora damicornis*; *Seriatopora caliendrum*; *Montastraea faveolata*	琉球群岛; 地中海; 加勒比海	促进新合成蛋白的折叠阻止细胞凋亡		Thummasan等[50] Seveso等[51] Desalvo等[38]
			DR987088	TCP-1					
	珊瑚宿主; 虫黄藻		NW018148923	HSP70	*Acropora tenuis*、*Acropora muricata*; *Goniopora djiboutiensis*; *Porites lutea*	印度洋; 缅甸海; 南海	抑制细胞凋亡; 变性蛋白重折叠		Louis等[52] Li等[53] Xiao等[54] Sharp等[55]
			DR988373	HSP90	*Montastraea faveolata*; *Acropora tenuis*	加勒比海; 琉球群岛	负责新合成多肽的构象成熟和变性蛋白的再成熟		Desalvo等[38] 张懿丹等[56] Yuyama等[26]
	珊瑚宿主		—	HSP100	*Pocillopora damicornis*	南海	水解酶活性; 降解变性多肽聚合体		张懿丹等[56]
	珊瑚宿主; 虫黄藻	RNA-Seq; cDNA微阵列分析	DR987062	Glutathione S-transferasesigma(GST-S)	*Montastraea faveolata*; *Favia favus*; *Mussismilia* sp. *Siderastrea* sp.; *Porites* sp.、*Acropora* sp.; *Porites lutea* *Acropora pruinosa*	加勒比海; 红海; 南大西洋; 大加纳利岛; 南海	免疫作用	温度升高表达量升高	黄晖等[14] Desalvo等[38] Levy等[57] Martignago等[58] Camilo等[59] Vilas等[60] 蒙林庆等[61] Yu等[8]
			DR988371	Glutathione S-tranferaseMu(GST-M)			细胞防御相关	温度升高表达量降低	
			NW018149119	谷胱甘肽过氧化物酶(GSH-Px)			ECM固结, 过氧化物酶活性; 增强细胞抗氧化能力; 增强免疫力	温度升高表达量升高	
			NW018150375	超氧化物歧化酶(SOD)					
			DR987689	过氧化氢酶(CAT)					
			DR988170	锌指蛋白基因(Zn^{2+}-metallo-protease)	*Montastraea faveolata*; *Acropora millepora*; *Porites lutea*	加勒比海; 大堡礁; 南海	锌离子结合转录因子	温度升高表达量升高	Desalvo等[38] Császár等[62] 许昌有等[63]
			FE039547	Ferritin			铁离子结合; 平衡铁浓度	温度升高表达量升高	
			CAON1879	细胞色素(p450)	*Montastraea faveolata*; *Pocillopora damicornis*; *Acropora aspera*	加勒比海; 南海; 大堡礁	参与细胞解毒; 抗氧化	温度升高表达量升高	Louis等[11] Liu等[64] Rosic等[65]

中国知网 https://www.cnki.net

续表 1

	研究对象	采用技术	GenBank Acc.	基因（蛋白）	已开展研究珊瑚物种	研究区域	潜在功能	热胁迫响应过程	参考文献
免疫相关基因	珊瑚宿主; 虫黄藻	RNA-Seq; RNAi; cDNA微阵列分析	—	TRX	*Acropora tenuis*; *Diploria strigosa*; *Acropora cervicornis*、*Montastraea faveolata*	琉球群岛; 百慕大群岛; 佛罗里达群岛	螯合活性氧	温度升高表达量升高	Morgan等[66] Yuyama等[36] Edge等[66]
			FE040110	NADH-ubiquinone	*Montastraea faveolata*; *Galaxea facicularis*; *Acropora* sp.	琉球群岛	线粒体电子传递; 建立合成ATP所需的跨膜质子梯度	温度升高表达量降低	Voolstra等[67]
	珊瑚宿主; 虫黄藻	RNA-Seq	NW018150375	Bcl-2	*Acropora aspera*、*Acropora millepora*	大堡礁	调控凋亡	温度升高表达量升高	T.D.A等[68] Pernice等[69]
			NW018150269	caspase 3	*Acropora millepora*; *Pocillopora damicornis*; *Orbicella faveolata* 、*Porites Astreoides*;	大堡礁; 琉球群岛、南海; 加勒比海	细胞凋亡指示剂		Pernice等[69] Thummasan等[50] Yu等[70] Shrestha等[71]
			—	Gasdermins	*Pocillopora damicornis*	南海	引发细胞焦亡		Jiang等[72]
	珊瑚宿主	RNA-Seq; cDNA微阵列分析	NW018148758	补体因子c3样蛋白(C3-Am)	*Montastraea faveolata*; *Acropora millepora*、*Acropora aspera*	加勒比海; 大堡礁	免疫相关; 病原体的直接杀伤	温度升高表达量升高	Desalvo等[38] van de Water等[44] van de Water等[45]
			DR988012	组蛋白(H3)	*Montastraea faveolata*; *Acropora formosa*	加勒比海、墨西哥湾; 大堡礁	核小体组装	温度升高表达量降低	Desalvo等[38] Miller等[73] Voolstra等[74]
			DR988033	组蛋白(H2A)					
			DR987246	H2A家族					
代谢相关基因	珊瑚宿主	RNA-Seq; cDNA微阵列分析	FE040151	MAT 1α	*Montastraea faveolata*; *Galaxea facicularis*; *Acropora* sp.	加勒比海、西大西洋	S-腺苷甲硫氨酸生物合成	温度升高表达量升高	Desalvo等[38, 46] Watanabe等[74] Voolstra等[67]
		RNA-Seq	—	异柠檬酸裂解酶（IL）	*Acropora millepora*; *Pocillopora astreoides*; *Pocillopora woodjonesi*、*Pocillopora kelleheri*、*Pocillopora verrucose*	大堡礁	从脂质β-氧化产物中合成碳水化合物	温度升高表达量升高	Rocker等[75] Kenkel等[76] Sun等[7]
			—	苹果酸合酶（MS）		墨西哥湾			
			—	丙酮酸羧激酶（PEPCK）		南海	促进糖异生增强	温度升高表达量升高	
			—	丙酮酸羧化酶（PC）					
			—	甘油醛-3-磷酸脱氢酶（GAPDHs）	*Pavona decussata*	南海;	参与糖降解, 维持珊瑚能量代谢平衡	温度升高表达量升高	Zhang等[77]
			—	丙酮酸脱氢酶复合物（DLATs）					
			—	匀浆 1,2 双加氧酶(HGDs)					
			—	谷氨酸脱氢酶（GDHs）	*Pavona decussata*、*Stylophora pistillata*	南海; 红海	分解代谢谷氨酸以推动TCA 循环	温度升高表达量升高	Zhang等[77] Rädecker等[78]
			—	谷氨酰胺合成酶(GS)	*Stylophora pistillata*	红海		温度升高表达量降低	Rädecker等[78]
			—	谷氨酸合酶(GOGAT)					
	共生微生物	宏基因组测序	—	糖基转移酶（GT）	*Favites* sp.	南海	合成多糖/糖蛋白	温度升高表达量升高	Sun等[79]
			—	糖苷水解酶（GH）			降解和转化碳水化合物	温度升高表达量降低	
			代谢相关基因	共生微生物					
		宏基因组测序	—	碳水化合物酯酶(CE)	*Favites* sp.	南海	降解和转化碳水化合物	温度升高表达量降低	Sun F等[79]

中国知网 https://www.cnki.net

续表 1

	研究对象	采用技术	GenBank Acc.	基因（蛋白）	已开展研究珊瑚物种	研究区域	潜在功能	热胁迫响应过程	参考文献
光保护蛋白相关基因	虫黄藻	RNA-Seq	—	PsaA	*Pocillopora woodjones*、*Pocillopora kelleheri*、*Pocillopora verrucose*、*Galaxea astreata*、*Acropora tenuis*	南海	修复虫黄藻光系统结构; 增强光合能力	温度升高表达量升高	Sun等[80] 沈城等[80] Gong等[81]
				PsaC					
			—	PsbA					
				PsbB					
				PsbC					
				PsbD					
				PsbO					
	珊瑚宿主	RNA-Seq; RNAi; cDNA微阵列分析	DR987865	GFP	*Montastraea faveolata*; *Acropora yongei*; *Acropora millepora*、*Acropora digitifera*、*Montipora digitata*; *Goniopora lobata*、*Goniopora norfolkensis*	加勒比海; 西太平洋; 大堡礁; 南海	能量传递受体; 光保护; 抗氧化与珊瑚颜色相关	随光照的增加减少而快速变化; 温度升高表达量降低	Desalvo等[38] Roth等[82] Smith-Keune等[83] Conaco等[84] 黄文靖[85]
		RNA-Seq; cDNA微阵列分析	—	RFP	*Acropora digitifera*、*Montipora digitata*、*Favites colemani*、*Seriatopora caliendrum*; *Goniopora lobata*、*Goniopora norfolkensis*	大堡礁; 南海			Conaco等[84] 黄文靖[85]
			—	CFP					
钙离子通道蛋白相关基因	珊瑚宿主	RNA-Seq; cDNA微阵列分析	DR987851	Similar to EF-hand domain protein	*Montastraea faveolata*	加勒比海	Ca^{2+} 结合区域	温度升高表达量降低	Desalvo等[38]
			DR987178	CaM	*Montastraea faveolata*; *Galaxea astreata*、*Acropora muricata*	加勒比海; 南海	视紫红素介导的信号调节; 维持 Ca^{2+} 平衡	高温下表达量降低	Desalvo等[38] Huang等[86] 黄元佳[87] Chiou等[88]
			NW018149378	CRT	*Montastraea faveolata*; *Galaxea astreata*; *Acropora tenuis*	加勒比海、墨西哥湾; 南海; 琉球群岛	维持 Ca^{2+} 稳态; 内质网 ER Ca^{2+} 容量的调节	温度升高表达量降低	Desalvo等[38] 黄元佳[87] Huang等[89] Voolstra等[74] Yuyama等[26]
			DR987943	Galaxin	*Montastraea faveolata*、*Galaxea fascicularis*	加勒比海	有机基质可溶性蛋白; 作为分子伴侣协助维持细胞内 Ca^{2+} 稳态水平		Desalvo等[38]
			NW018148627	TnC	*Acropora muricata*	南海、东大西洋			Chiou等[88] Weston等[90]
			DR987097	SCRiP3A	*Montastraea faveolata*	加勒比海、墨西哥湾	分泌肽; 细胞凋亡相关		黄晖等[14] Desalvo等[38] Reyes-Bermudez等[91]
			DR987884	SCRiP5					
			DR987486	SCRiP8					
			DR987831	SCRiP1					
			DR987097	SCRiP2					
			DR987965	SCRiP7					
细胞生长调控基因	珊瑚宿主	RNA-Seq; cDNA微阵列分析	NW018148815	DNA replication licensing factor mcm7-A	*Montastraea faveolata*、*Acropora tenuis*	加勒比海、墨西哥湾; 琉球群岛	DNA 复制许可因子	温度升高表达量降低	Desalvo等[38] Yuyama等[26] Voolstra等[74]
			NW018150375	DNAJ（Hsp40）			参与内质网未折叠蛋白反应	温度升高表达量升高	
			DR986717	RPL3	*Montastraea faveolata*; *Acropora pruinosa*、*Acropora nasuta*	加勒比海; 南海	蛋白质合成; 核糖体的结构成分	温度升高表达量升高	Desalvo等[38] Tian 和 Niu[92]
			DR986615	RPL9					

中国知网 https://www.cnki.net

续表 1

	研究对象	采用技术	GenBank Acc.	基因（蛋白）	已开展研究珊瑚物种	研究区域	潜在功能	热胁迫响应过程	参考文献
细胞生长调控基因	珊瑚宿主	RNA-Seq; cDNA微阵列分析	DR988078	RPL14	*Montastraea faveolata*; *Acropora pruinosa*、*Acropora nasuta*	加勒比海; 南海	蛋白质合成; 核糖体的结构成分	温度升高表达量升高	Desalvo等[38] Tian 和 Niu[92]
			AXP85384	RPL16					
			DR987703	RPL23					
			DR987703	RPL26					
			DR986615	RPS2					
			DR988446	RP S3					
			DR988446	RP S5					
			DR988266	RPS7					
			DR986825	RPS25					
			NW018148536	细胞周期基因（CDK2）	*Montastraea faveolata*	加勒比海、墨西哥湾	调控G1/S期	温度升高表达量降低	Desalvo等[38] Voolstra等[74]
其他基因	珊瑚宿主	RNA-Seq; cDNA微阵列	DR988150	凝胶素 Gelsolin（GSN）	*Montastraea faveolata*; *Pocillopora astreoides*、*Acropora cervicornis*	加勒比海; 西大西洋	钙调节的肌动蛋白切断蛋白	温度升高表达量降低	Desalvo等[38] Vollmer等[93] Kenkel等[94]
			DR986355	原肌球蛋白（TPM）			肌动蛋白结合细胞骨架成分		
			FE039783	Lethal giant larvae homologue 2（LGL2）			细胞骨架组织; 半桥体组装		
			DR988233	肌球蛋白 9A（MYO9A）			肌动蛋白依赖性ATP酶活性	温度升高表达量升高	
			DR987650	肌球蛋白 7A（MYO7A）					
	珊瑚宿主	RNA-Seq; cDNA微阵列	DR986515	泛素偶联酶 E2S	*Montastraea faveolata*; *Galaxea fascicularis*、*Montipora capricornis*	加勒比海; 东大西洋	蛋白质的去泛素化; 膜转运	温度升高表达量降低	Desalvo等[38] Yohann等[95]
			DR987159	泛素特异性蛋白酶 24（USP24）			蛋白质的去泛素化	温度升高表达量升高	

注:“—”表示无GenBank登录号。

（NOD-like receptors）、RLR（RIG-like receptor）和 MDA5（Melanoma differentiation-associated gene 5）以及 C 型凝集素[96]。在 Toll 样受体中 TLRs 是高度保守的跨膜蛋白, 主要表达在细胞或内噬体表面[97]; NLRs 能够检测细菌和毒力因子[98]; C 型凝集素家族可识别特定的碳水化合物并凝集各种类型的动物细胞, 在细胞和分子水平上发挥识别作用[99]。珊瑚主要研究 C 型凝集素家族（C-type lectin_family), 它分为甘露糖结合 C 型凝集素、半乳糖凝集素（galectin）等。高温诱导珊瑚 Hsp 的表达, 导致甘露糖结合 C 型凝集素下调。凝集素的下降不仅会抑制珊瑚 C 型凝集素对虫黄藻的识别效果[100], 还导致珊瑚对致病菌的识别能力下降[47], 最终使得珊瑚−虫黄藻共生的平衡以及相关免疫系统被破坏。

其次, 第二阶段是信号通路的激活。受体识别抗原后信号通路被激活, 如 Caspase-1 和 NF-kβ、MAPK 信号途径。这些信号通路的激活会促进促炎因子的产生, 从而启动免疫。Caspase-1 能够促进感染细胞凋亡, NF-kβ 和 MAPK 通路能够与 TLR 配体协同提高促炎因子和其他抗菌因子的产生, 从而能够提高机体对病原微生物的抵抗能力[96]。其中 Nf-kβ 基因在信号通路激活中发挥着重要作用。Nf-kβ 家族主要是 Nf-kβ1 和 Nf-kβ2, 它是参与调节免疫应答的主要转录因子, 参与信号传导、细胞凋亡、免疫和细胞周期调控等过程[15]。Nf-kβ（Nf-kβ1, Nf-kβ2）的表达量在热胁迫后可增加 1～2 倍[101]。

最后, 第三阶段是免疫效应阶段（主要是免疫相关基因), 主要负责消除威胁。其表现为热休克相关基因上调、抗氧化基因大部分上调和转录相关基因上调, 具体如下:

中国知网　https://www.cnki.net

4.1.1 热休克蛋白相关基因

热休克蛋白基因(Hsp)是珊瑚热适应性研究最多的基因[49, 102−103],也是第一个被确定的生物标志物。热休克蛋白是一类蛋白质,在热胁迫中起修复缓解作用,参与珊瑚热白化和冷白化过程以及变性蛋白重折叠过程[80]。热休克蛋白在胞内环境中与多肽链非特异性结合,调控多肽的折叠、装配、转运,热胁迫能使 Hsp 的胞内浓度升高,能在几分钟内增加 20 倍,以抑制不良反应[104],将错误折叠蛋白选择性降解或正确折叠,避免蛋白质聚集等[105]。但 Hsp 的上调是短暂的,长期的热胁迫会显示下调[106]。根据分子量可将珊瑚的热休克蛋白分为 Hsp100、Hsp90、Hsp70、Hsp60、小分子蛋白(Hsp16 和 Hsp32)[107]。

小分子蛋白协助其他休克蛋白一起表达,共同阻止蛋白质聚合,让变性多肽重新折叠[94]。其中,Hsp16(～16 kDa)是迄今为止对热胁迫反应最灵敏的基因之一,但热胁迫期间 Hsp16 的表达尚未在共生虫黄藻中进行研究[11]。另外,Hsp32(～32 kDa)是一种血红素加氧酶 1(HO-1),可保护细胞免受氧化应激。Hsp32 能将有毒血红素降解为游离铁,并去除细胞质中的一氧化碳(CO)和胆绿素[50]。在长时间热胁迫下 Hsp32 作为抗凋亡伴侣,发挥重要作用[50]。

Hsp60 是调节正常或应激条件下珊瑚蛋白结构的伴侣蛋白。Hsp60 蛋白由线粒体合成并运输,它能够促进新合成蛋白的折叠,其上调程度由热胁迫的严重程度决定[51]。Hsp60 家族成员还有重要的 T 复合体多肽(Tcp-1),它在其他热休克蛋白(Hsp90、Hsp70 等)表达后才上调[108]。

Hsp70 家族是一个多基因、多结构的家族[109],大部分蛋白质结构较为稳定,主要位于细胞质中。Hsp70 不但可以保护细胞免受多种凋亡刺激[110−112],还能阻止 caspase3 酶的激活,其丰度能够反映出机体对应激的反应的剧烈程度。目前研究发现 Hsp 存在一定的特异性。在 *Acropora* 属中珊瑚宿主 Hsp70 显著上调发挥关键作用[52],而在 *Porites* 属中虫黄藻 Hsp70 上调,证明虫黄藻正在保持其蛋白质稳态[54]。

Hsp90 是热休克蛋白中最丰富的一类,负责多肽的合成、构象与成熟并调节珊瑚变性蛋白的成熟。Hsp90 在受到热胁迫后基因呈现上调的趋势[113]。尽管近年来在 Hsp90 基因的研究取得了一些进展,但 Hsp70 的抗凋亡机制仍存在争议。

Hsp100 是一种大分子伴侣蛋白,它由 Hsp70 激活[114],与 Hsp70 一同溶解蛋白聚集体。随后,变性蛋白重新折叠并降解变性多肽聚合体。Hsp100 在高温下呈现上调的趋势并增加珊瑚耐热性[115]。

4.1.2 抗氧化蛋白相关基因

珊瑚白化受到各种环境因素的影响。然而,无论受到何种环境因素的影响,珊瑚应激产生的活性氧(ROS)都是导致珊瑚白化的关键因素之一[116]。海水温度升高会引起光抑制,共生虫黄藻光合作用的能力受到损伤导致 ROS 积累[117]。过量的 ROS 自由基会造成脂质过氧化、细胞膜损伤、酶失活和 DNA 链断裂等损伤[117]。ROS 对细胞具有高度的破坏性,会使蛋白质变性并破坏核酸[81]。珊瑚抗氧化蛋白基因包括抗氧化相关酶(GST-S、GST-M、SOD、CAT、GSH-Px)、锌指蛋白(Zn^{2+}-metalloprotease)、铁蛋白基因(ferritin)、细胞色素 P450(CYP)、硫氧还蛋白(TRX)、泛醌氧化还原酶(NADH-ubiquinone)。

抗氧化相关酶包括超氧化物歧化酶(SOD)、过氧化氢酶(CAT)和谷胱甘肽过氧化物酶(GSH-Px)、谷胱甘肽酶(GST-S 与 GST-M)、谷胱甘肽过氧化物酶(GSH-Px)。温度升高,除了调控谷胱甘肽 S-转染酶(GST-M)的基因表达量降低外[26],其他抗氧化蛋白基因表达量升高以清除 ROS。蒙林庆等对南海澄黄滨珊瑚的研究表明超氧化物歧化酶活性、过氧化氢酶活性、还原型谷胱甘肽含量都是先升高后降低[61]。虽然有抗氧化蛋白基因的调节,但逐渐积累的 ROS 将激活核转录因子(NF-kβ),进而使宿主产生 NO,最终导致细胞被破坏、酶活性下降[118−119]。此外,Levin 等表明[120],在热胁迫下不同共生虫黄藻系群的抗氧化基因存在不同的变化。

锌指蛋白是一种金属蛋白酶基因,能够降解细胞外基质(ECM)。锌指蛋白与 Zn^{2+} 结合可激活蛋白水解酶的活性。金属蛋白酶基因与抗氧化酶基因是机体抗氧化的重要功能基因,这些基因在珊瑚白化过程中的作用值得继续深入探索[15]。

铁蛋白基因编码的铁蛋白在多孔鹿角珊瑚中覆盖率为 100%[63],该蛋白能够减少自由基的合成从而降低细胞的氧化压力[14, 121]。在长时间的热胁迫下,珊瑚中的铁蛋白会持续上调。

细胞色素 P450 由一大组血红素蛋白组成[122],可催化多种反应,参与细胞解毒,能够减缓氧化应激。细胞色素 P450 通过掺入单个氧原子来氧化底物,参与生物体化学防御的第一线[65]。珊瑚受到热胁迫后体内的细胞色素 P450 表达量升高。

硫氧还蛋白(TRX)是一种氧化还原调节蛋白,可作为生物体氧化应激的指标,螯合活性氧达到抗氧化作用[66]。TRX 作为单线态氧淬灭剂和羟基自由基清

中国知网 https://www.cnki.net

除剂, 维持真核细胞内的氧化还原平衡[66]。在高温环境中, 珊瑚的 TRX 基因表达量升高[36]。

泛醌氧化还原酶(NADH-ubiquinone)是线粒体中活性氧的主要来源, 也是细胞氧化应激的重要促成因素。泛醌氧化还原酶不仅能催化电子与质子跨膜易位偶联, 还有助于建立合成 ATP 所需的跨膜质子梯度[123−124]。高温下珊瑚的线粒体功能损伤导致相关基因表达下调, 从而抑制细胞呼吸活性并降低细胞 ATP 水平。

4.1.3　细胞凋亡与细胞焦亡相关基因

珊瑚细胞的凋亡和组织层的减少发生在热胁迫反应早期, 它在受到严重损伤后会大量坏死[125]。调节细胞凋亡是珊瑚热应激后的重要组成部分, 其中半胱天冬酶发挥重要作用。半胱天冬酶的激活已被用作评估珊瑚细胞凋亡的标志, 它可以通过外源性(细胞表面死亡受体)途径或内源性途径启动[69]。其中, caspase3 是细胞凋亡中的主要执行基因, 热胁迫导致 ROS 的过剩并激活 caspase-3 介导的细胞凋亡[126]。热胁迫下珊瑚 caspase-3 呈现上调[70]。此外, 细胞凋亡后 Bcl-2 基因会过表达, 开始延迟保护反应。开始细胞死亡时, caspase 家族中的蛋白质相互作用, 控制细胞色素 C 的释放以及线粒体外膜和细胞器膜的通透性[68], 从而调控细胞凋亡。

细胞焦亡是一种程序性坏死细胞死亡, 其特征是细胞快速肿胀、膜破坏和大量胞浆内容释放[127]。细胞焦亡是由 caspase3 基因裂解并激活成孔的 gasdermin 家族蛋白, 从而介导细胞内容物释放, 随后引发焦亡[72]。目前仅有 Jiang 等对珊瑚进行研究并发现 gasdermin 是炎症性细胞死亡的一种形式, 发生在病原体感染的过程中。

4.1.4　其他免疫蛋白基因

补体系统指参与直接消除入侵微生物的另一种效应机制, 主要通过促进吞噬作用和诱导膜攻击复合物的形成[45]。其中, 补体因子 C3 样蛋白(C3-Am)是先天免疫的另一个关键参与者。补体 C3 样蛋白的表达在短期高温下没有显著变化, 但长期下表达量会升高[44, 128], 表明热胁迫下补体因子正在引导相关能源以保护珊瑚共生体, 它是补体系统的关键[44]。

组蛋白基因负责核小体的组装, 在热胁迫下表达量降低。其中组蛋白 H3 编码基因具有 3′-发夹结构, 在非多聚腺苷酸化组蛋白 mRNA 中为终止或加工信号[73], 在转录翻译上发挥作用。

4.2　**代谢相关基因**

高温会对珊瑚新陈代谢造成负面影响。高温下大多数代谢基因呈上调的趋势[128], 从而保持珊瑚的代谢平衡。受到热胁迫的珊瑚其碳水化合物代谢、氮代谢等许多分子过程变得更加活跃, 但代谢需求会降低[129]。代谢相关基因包括乙醛酸循环酶(IL、MS)、蛋氨酸腺苷转移酶(MAT)、能量代谢相关基因(PEP-CK、PC、GAPDHs、DLATs、HGDs、GDH、GS、GOGAT)以及细菌碳水化合物活性酶(GT、GH、CE)。

珊瑚细胞通过乙醛酸循环可将脂肪酸氧化分解为乙酰 CoA, 生成琥珀酸、乙醛酸和苹果酸, 对珊瑚合成碳水化合物有重要生理意义[129]。其中, 参与乙醛酸循环的酶有异柠檬酸裂解酶(IL)和苹果酸合酶(MS)。IL 和 MS 能够从脂质 β-氧化产物中合成碳水化合物, 该过程被认为是乙醛酸循环的特征, 具有特异性[76]。

热胁迫下珊瑚的蛋氨酸代谢受到影响, 为保持蛋氨酸含量的平衡, 蛋氨酸腺苷转移酶表达量升高[108]。其中的蛋氨酸腺苷转移酶 1α(MAT 1α)在多个水平上抑制细胞色素的表达, 增加转硫途径的通量[130], 增强抗氧化剂谷胱甘肽(GSH)的产生来调节线粒体功能[131]。

珊瑚能量代谢相关基因有助于缓解珊瑚共生体的热胁迫反应, 进一步加速热胁迫下珊瑚宿主的新陈代谢[132]。珊瑚遭受热胁迫后可以通过糖酵解将一些非碳水化合物底物(如丙酮酸、生糖氨基酸等)转化为糖类从而参与三羧酸途径为宿主提供能量[133]。涉及糖酵解相关的基因(蛋白)有磷酸烯醇丙酮酸羧激酶(PEPCK)、丙酮酸羧化酶(PC)、甘油醛-3-磷酸脱氢酶(GAPDHs)、丙酮酸脱氢酶复合物(DLATs)和匀浆 1, 2 双加氧酶(HGDs)。这些糖酵解相关基因(蛋白)均在热胁迫下呈现上调的趋势这是为了加快合成葡萄糖和谷氨酸等以维持能量平衡。PEPCK 是糖异生中的限速酶, 在 PC 催化丙酮酸转化为草酰乙酸后才进行催化[134]。此外, GAPDHs 是参与糖酵解的关键酶, DLATs 能够催化糖酵解产物丙酮酸转化为乙酰辅酶 A, HGDs 催化酪氨酸降解以保持热胁迫期间珊瑚健康的[77]。

珊瑚遭受热胁迫后也通过三羧酸循环积极利用氨基酸从而保持能量平衡, 它是珊瑚细胞代谢产能的主要途径。其中, GDH 促进谷氨酸的代谢合成以及谷氨酸的代谢降解, 以推动 TCA 循环[135]。此外, 谷氨酰胺合成酶(GS)和谷氨酸合酶(GOGAT)在氮代谢过程中起着关键作用。谷氨酰胺合成酶通过催化谷氨酸和氨的缩合形成谷氨酰胺, 在氮的代谢中起着至关重要的作用[136]。GS 和 GOGAT 共同参与氨同化的调控, GOGAT 以 NADH 为电子供体, 催化谷氨酰

中国知网　https://www.cnki.net

胺的氨基转移到 α-酮戊二酸形成两分子的谷氨酸，随后 GS 催化谷氨酸形成谷氨酰胺，进行氮的储存和转换。热胁迫下，GS 和 GOGAT 这两个关键珊瑚宿主基因在谷氨酸生物合成中的表达下调[78]。其中 GS 具有解毒代谢的作用，其活性降低可能导致体内过多的氨和谷氨酸积累，从而破坏氮代谢平衡[137]；GOGAT 活性的降低可能导致对氮同化和循环过程的干扰，并影响氨基酸和蛋白质等含氮化合物的合成[138]。

此外，共生细菌在热胁迫下发挥作用，主要参与碳代谢相关过程。这得利于细菌碳水化合物活性酶（CAZymes）降解和转化碳水化合物。CAZymes 包括糖基转移酶（GT）、糖苷水解酶（GH）以及碳水化合物酯酶（CE），异养微生物利用这些酶进行多糖和复合糖的组装、分解和修饰[139]。其中，GT 是负责合成多糖或糖蛋白的蛋白质[140]；GH 构成一组参与多糖代谢的酶，多糖包括淀粉、纤维素、半纤维素和甲壳素[141]；CE 家族可以将这些复杂的碳水化合物分解成更简单的形式，助力珊瑚更高效地获取能量。白化珊瑚中 GT 的含量大幅增加，而 GH、CE 的含量明显下降。这说明热胁增加了能够合成多糖的异养细菌丰度，且降低了细菌群落水解碳水化合物的能力[79]。

4.3 光保护蛋白相关基因

珊瑚共生虫黄藻体内的光合器官叶绿体在高温下会受到损伤，导致光合作用受到抑制，抑制 PSⅡ的修复，光系统基因积极转录，表达量均升高[81]。虫黄藻叶绿体中的光合系统Ⅰ（PSⅠ）主要有 *psaA* 与 *psaC*；光合系统Ⅱ的基因包括 *psbA*、*psbB*、*psbC*、*psbD* 和 *psbO*[81]。其中，*psaA* 基因编码 P_{700} 蛋白，也是 ABC 运输过程中 Mn^{2+} 的最初受体[142]。*psbA* 上调[80]，这是由于 *psbA* 基因编码 PSⅡ反应中心的核心蛋白 D1 蛋白。在光照条件下 D1 蛋白会快速降解，且降解速度与光照强度成正比，需要不断地合成 D1 蛋白来维持其正常的生理需求[143]。在热胁迫下，D1 蛋白的降解速率超过了合成速率，这将造成 D1 蛋白含量缺失，从而使 PSⅡ反应中心的结构遭受破坏，最终导致光合作用受到抑制。

荧光蛋白作为光保护剂和抗氧化剂，在热胁迫下能够将较短波长的光转换为较长波长的光，从而保护珊瑚免受有害波长的影响，并增强共生虫黄藻的可用光[144]。荧光蛋白的表达量在热胁迫期间会降低[38]。珊瑚的颜色主要是绿色（GFP）、蓝绿色（CFP）和红色（RFP）以及非荧光色蛋白共同作用的结果。其中绿色荧光蛋白是最为常见的一种荧光蛋白，也是所有荧光蛋白种类中最鲜艳的一种[85]。绿色荧光蛋白的浓度会随着光照水平的增加或减少而快速变化。高能蓝光会直接损害 PSⅡ，并通过产生活性氧抑制 PSⅡ的修复[145]。而绿色荧光蛋白不仅能吸收高能蓝光，还具有光保护作用。

4.4 钙离子通道蛋白相关基因

在全球变暖的背景下，钙离子通道蛋白相关基因通过维持钙稳态、调节共生关系，帮助珊瑚应对热胁迫，对于珊瑚礁保护和气候变化响应具有重要意义。细胞内的钙离子（Ca^{2+}）作为普遍存在的细胞信使，参与珊瑚的钙化生长，它们的调节会受到热胁迫的影响[38]。珊瑚钙化生长是钙离子与碳酸盐在珊瑚组织基质和骨架之间的钙化中心中结合形成碳酸钙骨骼[146]。珊瑚钙化时 Ca^{2+} 泵密集地向上皮细胞中泵入 Ca^{2+}，而活性氧簇（ROS）、活性氮簇（RNS）和钙调素 CaM 失活会减弱 Ca^{2+} 泵的活性导致细胞 Ca^{2+} 失衡，钙化率下降[14]。这些过程在热胁迫下受到影响，这主要取决于钙离子浓度的变化，因此研究钙离子通道蛋白相关基因尤为重要。钙离子通道蛋白相关基因主要有 EF-hand 超家族、钙调素（calmodulin, CaM）、钙网蛋白（calreticulin, CRT）、生物矿化蛋白（Galaxin）、肌钙蛋白 C 和富含半胱氨酸的小蛋白质（SCRiPs）。

EF-hand 超家族蛋白是一种负责编码 Ca^{2+} 结合区域的蛋白，温度升高导致钙离子结合蛋白表达量降低，如钙调蛋白和 EF-hand 蛋白[38]。

钙调素（CaM）是真核细胞中普遍存在的钙传感蛋白，一种多功能钙代谢调节剂，介导许多重要的信号通路并参与视紫红素介导的信号调节通路[87]。CaM 在热胁迫下表达量降低。其中，钙调素中的钙调蛋白（CaLP）是多功能钙敏感元件，它在钙信号传导中起重要作用[86]。因此，温度应激影响信号传导的同时也会影响 CaLP 的表达。Huang 等表明[86]，热胁迫下的珊瑚能量供应会减少，从而导致蛋白质合成减少[26]。

钙网蛋白（CRT）是内质网主要的 Ca^{2+} 结合蛋白，通过协助蛋白质正确折叠、维持细胞 Ca^{2+} 稳态、调节内质网（ER）Ca^{2+} 容量来调节基因表达和自身免疫等[147−148]。CRT 属于热激蛋白家族[149]，它在细胞经受急性热胁迫后增加内质网腔的 Ca^{2+} 储存能力，在热胁迫下表达量降低[74]。

生物矿化蛋白（Galaxin）位于有机基质中，在珊瑚钙化中尤为重要。它作为内质网的膜结合凝集素，可瞬时与新合成的糖蛋白结合并参与有机基质的合成[38]。该蛋白最先在丛生盔形珊瑚中发现[150]。高温下珊瑚中的虫黄藻流失从而影响有机基质的组成，最终导致 *Galaxin* 基因下调。

中国知网 https://www.cnki.net

肌钙蛋白 C 是肌钙蛋白复合物中的结合亚基, 充当各种信号通路的第二信使。在维持细胞内 Ca^{2+} 稳态水平、维持信号级联和细胞稳态中肌钙蛋白 C 是必不可少的[151]。在受到热胁迫后肌钙蛋白 C 表达上调, 在细胞胞吐过程中起到重要作用[90]。

Sunagawa 等发现的富含半胱氨酸的小蛋白质(SCRiPs)与珊瑚钙化或钙离子平衡相关且具有分泌肽[150]。SCRiPs 有细胞凋亡相关的功能, 在高温下表达量下降[14]。

4.5　细胞生长调控相关基因

细胞周期调控相关基因在珊瑚中会使用大量的能量来调节细胞生长、分裂分化、衰老凋亡等过程, 在热胁迫下, 珊瑚会为了保存能量从而抑制细胞周期调控基因的表达。相关基因包括 DNA replication licensing factor *mcm7-A*、DNAJ、核糖体基因(RPG)、细胞周期基因和转录调控基因。

DNA 复制许可因子 *mcm7-A*(DNA replication licensing factor *mcm7-A*)是 MCM 复合物(MCM2-7)六聚体的一部分, 在真核细胞 DNA 复制中起核心作用, 高温导致 DNA 在 S 期异常复制, 随后激活 DNA 损伤反应(DDR)使细胞周期停止[152]。DNAJ(也称 Hsp40)在高温下表达量升高, 热胁迫下参与内质网未折叠蛋白的反应[153], 它作为 Hsp70 的特异性调节因子能够调节 Hsp70 的伴侣功能[154]。

核糖体基因(*RP*)是核糖体的重要组成部分, 是核糖体生物合成和蛋白质翻译的关键基因, 对细胞生长有重要作用[155]。高温下珊瑚 *RP* 呈上调趋势[156]。细胞周期素依赖性激酶 2(*CDK2*)是一种细胞周期基因, 主要调控 G1/S 期[157], 在未白化珊瑚中检测不出, 在高温下白化珊瑚的 *CDK2* 表达量升高[74]。

4.6　其他基因

珊瑚在高温下会产生热休克、氧化应激、钙化减少、新陈代谢下降、细胞生长受到限制、细胞凋亡等反应。除此之外还有一些基因也参与到珊瑚共生体内一系列热适应过程中, 例如细胞骨架相关基因和泛素相关基因等。

珊瑚细胞骨架对高温极其敏感, 主要是 5 个肌动蛋白基因的差异表达[46]。其中 Gelsolin、原肌球蛋白(TPM)和 Lethal giant larvae homologue 2(LGL2)在热胁迫下调, 而肌球蛋白 7A(MYO7A)和 9A(MYO9A)略有上调[26]。Gelsolin 是肌动蛋白结合蛋白, 可切断肌动蛋白, 覆盖肌动蛋白丝的倒钩末端并促进肌动蛋白聚合的成核[158]。原肌球蛋白(TPM)的存在可以增加肌动蛋白细丝的刚性、降低 TPM 对解聚因子的敏感性来增强细丝。LGL2 是细胞骨架组织, 参与半桥体组装。肌球蛋白 7A 和 9A 控制肌动蛋白依赖性 ATP 酶活性。

在细胞膜转运和 DNA 修复和信号传导方面还有重要的细胞泛素−蛋白酶系统发挥作用, 它还参与了蛋白质的去泛素化, 是细胞内蛋白质降解的主要途径[101]。细胞泛素−蛋白酶系统包含 USP24 Ubiquitin-conjugating enzyme E2S 和泛素特异性蛋白酶 24(USP24)。泛素偶联酶 E2S 是泛素−蛋白酶体通路通过泛素连接酶将活化的泛素连接到靶蛋白所需的酶, 决定了泛素链的连接类型, 调节底物蛋白的稳定性和活性。泛素特异性蛋白酶 24(USP24)是真核生物体内的一种去泛素化酶, 它通过去泛素化调控靶蛋白的降解从而参与细胞凋亡及细胞周期生长, 还能参与 DNA 损伤修复途径[159]。

4.7　热适应过程中的关键基因

近年来, 珊瑚热适应功能基因的研究已成为海洋生物学领域的重要课题。研究表明, 尽管已鉴定出多个与热适应相关的功能基因, 但研究焦点主要集中于少数高频出现的核心基因上。并且这些高频的核心基因已经被广泛认可和验证。大量研究认为珊瑚相关识别受体(主要为 Toll 样受体)识别到热胁迫后激活一系列免疫作用(Hsp、抗氧化蛋白基因、caepase3 等免疫相关基因上调), 此外代谢基因保持代谢平衡以确保营养供给(GS/GDH 推动三羧酸循环、PEPCK/PC 促进糖异生增强); 光保护蛋白基因快速修复虫黄藻光系统(*Psa*/*Psb* 上调)、宿主荧光蛋白基因维持氧化平衡(GFP 下调); 钙离子通道蛋白基因维持细胞内 Ca^{2+} 水平稳定(钙调素/钙网蛋白/肌钙蛋白下调), 进而提高了珊瑚的耐热能力(图 2)。

5　热驯化提高珊瑚耐热性

在全球变暖的大背景下, 珊瑚白化事件频发。但幸运的是, 珊瑚可以通过提高耐热阈值来适应更高强度的高温[160]。目前许多研究从珊瑚功能基因入手, 并且发现适当的热胁迫存在一定的驯化效果。热驯化是基于珊瑚适应性差异功能基因的应用, 对全球持续变暖背景下珊瑚未来具有重要意义, 是人为干预提高珊瑚适应性的过程。生物体耐热能力往往具有一定的可塑性, 珊瑚也不例外。这种耐热性可以通过热驯化(生物体改变生长机制)或适应(繁殖体更适合改变的条件)来获得[160]。关于珊瑚热驯化已经开展了实验室模拟实验和自然海域对比研究[161]。在自然环境中, 波动的温度环境会提高珊瑚的耐热性。例如, 受潮汐影响的珊瑚比在稳定环境中的同种珊瑚表现

中国知网　https://www.cnki.net

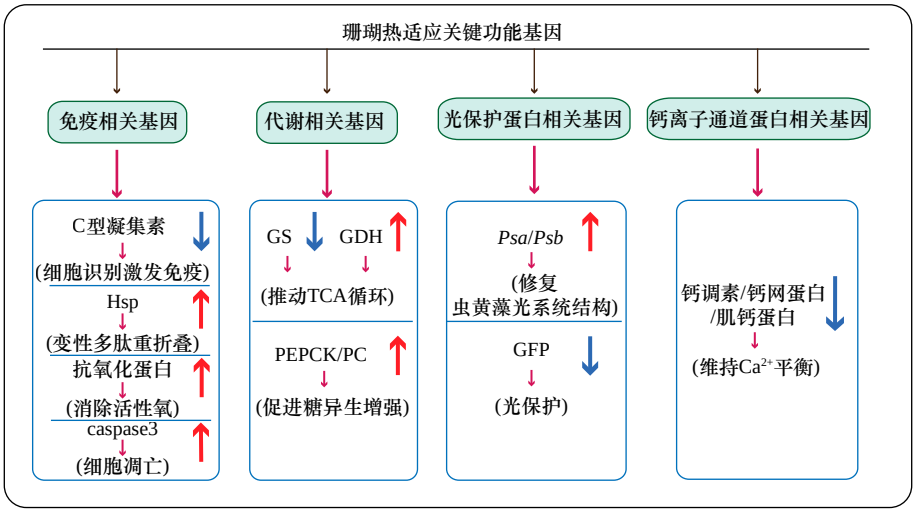


图 2 热胁迫后造礁珊瑚关键热适应基因变化(蓝色为下调,红色为上调)

Fig. 2 Key heat adaptation gene changes in corals after heat stress (blue is downregulated and upregulated in red)

出更高的耐热性[162]、浅层的珊瑚比中层的珊瑚耐热性更高[163]。在实验室热驯化中,Evensen 等发现珊瑚对急性热胁迫和更长时间的热暴露的反应具有一定的一致性[164]、Yu 等发现热驯化可以通过减缓宿主代谢、改变优势细菌种群和增加细菌多样性来增加珊瑚的热耐受性[8]、Takahashi 等发现热驯化有助于提高共生虫黄藻 PS Ⅱ 的耐热性[165]、刘旭等人发现适度的热胁迫对珊瑚会有一定的驯化作用[166]且不同种珊瑚的驯化效果不同[167]、Jiang 等[168]发现珊瑚成体驯化后可以改变珊瑚幼虫的热耐受性。这些都表明驯化能提高珊瑚耐热性与气候适应能力,但这种耐热性中具体的分子机制知之甚少。

同时,不同珊瑚个体热驯化后产生的热适应能力存在差异[161]。其主要是分子层面上的不同即热适应基因表达的差异性。珊瑚共生功能体参与热驯化过程中的分子机制是相互依赖的[169]。热驯化期间各种细胞和分子发生反应以增强珊瑚耐热性,例如:脂质组成、新陈代谢和蛋白质表达的变化;热休克蛋白作用于重新折叠变性的细胞和结构蛋白[105];机体产生使有害氧自由基失活的氧化酶[59]以及抗光强的色素[144]等。热驯化可以通过减缓珊瑚宿主代谢[8]、减少热胁迫相关蛋白质的损伤[170]、提高抗氧化物和铵同化酶活性[61]等来增加珊瑚耐热性。

总之,热驯化帮助造礁珊瑚在升温的未来环境中生存。然而,其带来的耐热能力能否抵挡未来高频高温袭击还有待确定。因此,侧重于评估珊瑚体内热适应功能基因的潜在影响,有助于了解珊瑚潜在功能基因对适应未来高温环境做出的贡献,对全球变暖下珊瑚耐热性的进化具有重要意义。

6 问题与展望

气候变化对海洋生物圈产生深远影响,影响范围从生物个体到生态系统的各个组织层面[171]。预计在最乐观的温室气体排放量下,未来仍有 70% 至 90% 的珊瑚面临白化死亡[172−173]。保护珊瑚礁是一个全球性的环境问题。珊瑚耐热能力取决于体内复杂的分子反应和适应机制,因此研究珊瑚热适应基因对保护珊瑚有重要意义。然而,对于珊瑚热适应相关基因的研究目前还存在许多难题。国内外关于珊瑚热适应相关基因的研究尚处于初步阶段,热适应基因的表达特征以及介导其他应激反应的分子机制在很大程度上仍未被探索[174]。目前关于珊瑚热适应功能基因方面的研究还存在以下不足:

(1)珊瑚热适应基因在共生功能体(珊瑚宿主、虫黄藻、共生菌)中的相互作用机制的研究不足。

相比于其他腔肠动物,珊瑚在个体细胞组织等层面上研究较少。有研究发现在相同的高温条件下,同种珊瑚的不同个体存在耐热性差异[7]。在同一块珊瑚中白化部分和未白化部分之间,有许多生物和分子过程显著富集,白化以全面的方式影响珊瑚共生体[7]。归其根本,珊瑚白化是一个大规模发生的单细胞过程[175]。在单细胞水平上研究珊瑚白化可以减少整体研究导致的偏差。因此,未来可以从单细胞方面研究,更加精准区分珊瑚共生体中珊瑚宿主、共生虫黄藻、共附生细菌、共生真菌或古菌之间的相互作用。因此,在全球变暖的大背景下我们迫切需要对共生功能体之间的热适应基因进行大量研究,以更好地了解每个组分在热胁迫中发挥的分子机制。

中国知网 https://www.cnki.net

(2)多组学和基因功能验证技术在珊瑚热适应的研究中存在局限。

高通量测序技术可以区分珊瑚宿主以及虫黄藻的基因, 并筛选出重要潜在基因进行更深入的分析, 从而挖掘出热适应关键基因和通路。组学技术的研究成果是相互印证的, 单一的组学分析技术已无法满足当前的研究需求。不同类型组学数据的关联分析有助于揭示不同类型的分子和生化反应的复杂调控机制, 将来我们可以借助多组学分析手段, 深入阐释珊瑚响应热胁迫的分子机理。目前珊瑚基因主要从表达水平上(qPCR)和基因功能验证(基因克隆、RNAi)上进行验证, 但高质量的热适应相关基因组资源不够丰富[176]。

(3)未来研究方向。

未来随着基因验证技术的不断优化和发展, 可以尝试使用其他功能基因的研究手段, 如 ZFN、TALEN 和 CRISPR-Cas9 等基因敲除技术。采用更多基因功能验证技术来验证珊瑚热适应基因有利于解决高质量热适应相关基因组资源不够丰富这一难题, 为后续珊瑚热适应基因的研究提供便利。目前, 日本的研究人员已经在培养皿中培养出珊瑚(*Acropora tenuis*)的可持续细胞系[38]。这些细胞系是通过从珊瑚幼虫中分离出细胞, 然后发展成 8 种不同的细胞类型而形成的。8 种细胞类型中的 7 种是稳定的, 可以无限期地生长, 甚至在冷冻后仍可保持活力。使用这些细胞系进行未来研究的意义是深远的。基于珊瑚细胞系开展相关研究, 有助于实时观察活珊瑚组织中发生的详细变化, 例如钙化、白化以及珊瑚/生体相互作用进行详细的分子分析。

参考文献:

[1] Plaisance L, Caley M J, Brainard R E, et al. The diversity of coral reefs: what are we missing?[J]. PloS one, 2011, 6(10): e25026.

[2] Cannon S E, Aram E, Beiateuea T, et al. Coral reefs in the gilbert islands of kiribati: resistance, resilience, and recovery after more than a decade of multiple stressors[J]. PLoS One, 2021, 16(8): e0255304.

[3] Head C E I, Bayley D T I, Rowlands G, et al. Coral bleaching impacts from back-to-back 2015-2016 thermal anomalies in the remote central Indian ocean[J]. Coral Reefs, 2019, 38(4): 605−618.

[4] Zuo Xiuling, Qin Binni, Teng Juncan, et al. Optimized spatial and temporal pattern for coral bleaching heat stress alerts for China's coral reefs[J]. Marine Environmental Research, 2023, 191: 106152.

[5] Lee I H, Fan T Y, Fu K H, et al. Temporal variation in daily temperature minima in coral reefs of Nanwan Bay, Southern Taiwan[J]. Scientific Reports, 2020, 10(1): 8656.

[6] Hsieh Y E, Lu C Y, Liu Poyu, et al. Successive responses of three coral holobiont components (coral hosts, symbiotic algae, and bacteria) to daily temperature fluctuations[J]. Ecological Indicators, 2024, 158: 111515.

[7] Sun Fulin, Yang Hongqiang, Zhang Xiyang, et al. Metabolic and metatranscriptional characteristics of corals bleaching induced by the most severe marine heatwaves in the South China Sea[J]. Science of the Total Environment, 2023, 858: 160019.

[8] Yu Xiaopeng, Yu Kefu, Huang Wen, et al. Thermal acclimation increases heat tolerance of the scleractinian coral *Acropora pruinosa*[J]. Science of the Total Environment, 2020, 733: 139319.

[9] Lyu Yihua, Zhou Zihua, Zhang Yangmei, et al. The mass coral bleaching event of inshore corals form South China Sea witnessed in 2020: insight into the causes, process and consequence[J]. Coral Reefs, 2022, 41(5): 1351−1364.

[10] Cziesielski M J, Schmidt-Roach S, Aranda M. The past, present, and future of coral heat stress studies[J]. Ecology and Evolution, 2019, 9(17): 10055−10066.

[11] Louis Y D, Bhagooli R, Kenkel C D, et al. Gene expression biomarkers of heat stress in scleractinian corals: promises and limitations[J]. Comparative Biochemistry and Physiology Part C: Toxicology & Pharmacology, 2017, 191: 63−77.

[12] Lima L F O, Alker A T, Papudeshi B, et al. Coral and seawater metagenomes reveal key microbial functions to coral health and ecosystem functioning shaped at reef scale[J]. Microbial Ecology, 2023, 86(1): 392−407.

[13] Fuller Z L, Mocellin V J L, Morris L A, et al. Population genetics of the coral *Acropora millepora*: toward genomic prediction of bleaching[J]. Science, 2020, 369(6501): eaba4674.

[14] 黄晖, 许昌有, 袁涛. 造礁石珊瑚白化相关功能基因的研究进展[J]. 热带海洋学报, 2013, 32(4): 43−50.
Huang Hui, Xu Changyou, Yuan Tao. Research progress on functional genes involved in coral bleaching[J]. Journal of Tropical Oceanography, 2013, 32(4): 43−50.

[15] 袁吉贵, 刘丽, 张艳苹. 珊瑚白化及温度相关基因的研究进展[J]. 基因组学与应用生物学, 2018, 37(9): 3810−3816.
Yuan Jigui, Liu Li, Zhang Yanping. Research progress on coral bleaching and temperature related genes[J]. Genomics and Applied Biology, 2018, 37(9): 3810−3816.

[16] Traylor-Knowles N, Connelly M T. What is currently known about the effects of climate change on the coral immune response[J]. Current Climate Change Reports, 2017, 3(4): 252−260.

[17] Cornet V J, Cantin N E, Joyce K E, et al. Enhancing coral bleaching predictive tools through integrating sensitivity to heat exposure[J]. Biological Conservation, 2025, 302: 110958.

中国知网　https://www.cnki.net

[18] Dutra L X C, Haywood M D E, Singh S, et al. Synergies between local and climate-driven impacts on coral reefs in the Tropical Pacific: a review of issues and adaptation opportunities[J]. Marine Pollution Bulletin, 2021, 164: 111922.
[19] Han D H T, James D, Waheed Z, et al. THREE-DECADE changes of reef cover in pulau layang-layang, malaysia using multitemporal landsat images[J]. Marine Environmental Research, 2024, 197: 106454.
[20] Lachs L, Donner S D, Mumby P J, et al. Emergent increase in coral thermal tolerance reduces mass bleaching under climate change[J]. Nature Communications, 2023, 14(1): 4939.
[21] 马静, 余克服. 大规模白化对珊瑚礁生态系统的影响研究进展[J]. 生态学杂志, 2023, 42(9): 2227−2240.
Ma Jing, Yu Kefu. Effects of mass bleaching events on coral reef ecosystems[J]. Chinese Journal of Ecology, 2023, 42(9): 2227−2240.
[22] Marangon E, Rädecker N, Li J Y Q, et al. Destabilization of mutualistic interactions shapes the early heat stress response of the coral holobiont[J]. Microbiome, 2025, 13(1): 31.
[23] Tanaka Y, Inoue M, Nakamura T, et al. Loss of zooxanthellae in a coral under high seawater temperature and nutrient enrichment[J]. Journal of Experimental Marine Biology and Ecology, 2014, 457: 220−225.
[24] 舒杨. 珊瑚、虫黄藻及微生物组的多组学分析: 全共生体生长, 胁迫, 驯化及重构[D]. 海口: 海南大学, 2022.
Shu Yang. Multi-omic analysis of coral, Symbiodinium and microbiota: growth, stress, acclimation and reconstruction of coral holobiont[D]. Haikou: Hainan University, 2022.
[25] Hazraty-Kari S, Tavakoli-Kolour P, Kitanobo S, et al. Adaptations by the coral *Acropora tenuis* confer resilience to future thermal stress[J]. Communications Biology, 2022, 5(1): 1371.
[26] Yuyama I, Ito Y, Watanabe T, et al. Differential gene expression in juvenile polyps of the coral acropora tenuis exposed to thermal and chemical stresses[J]. Journal of Experimental Marine Biology and Ecology, 2012, 430-431: 17−24.
[27] Hackerott S, Martell H A, Eirin-Lopez J M. Coral environmental memory: causes, mechanisms, and consequences for future reefs[J]. Trends in Ecology & Evolution, 2021, 36(11): 1011−1023.
[28] 杜玉梅, 左正宏. 基因功能研究方法的新进展[J]. 生命科学, 2008, 20(4): 589−592.
Du Yumei, Zuo Zhenghong. Advances in research methods for gene function[J]. Chinese Bulletin of Life Sciences, 2008, 20(4): 589−592.
[29] Jiang Hui, Wong W H. Statistical inferences for isoform expression in RNA-seq[J]. Bioinformatics, 2009, 25(8): 1026−1032.
[30] 雷华, 赵广展, 林志艺. 基因功能验证方法及研究进展[J]. 四川农业科技, 2023(9): 83−86.
Lei Hua, Zhao Guangzhan, Lin Zhiyi. Methods and research progress in gene function verification[J]. Sichuan Agricultural Science and Technology, 2023(9): 83−86.
[31] van Oppen M J H, Oakeshott J G. A breakthrough in understanding the molecular basis of coral heat tolerance[J]. Proceedings of the National Academy of Sciences of the United States of America, 2020, 117(46): 28546−28548.
[32] 赵文君. 应用 RNAi 技术验证灰树花 AAP 基因功能[D]. 牡丹江: 牡丹江师范学院, 2023.
Zhao Wenjun. Application of RNAi technology to verify the function of AAPgene in Grifola frondosa[D]. Mudanjiang: Mudanjiang Normal University, 2023.
[33] Dunn S R, Phillips W S, Green D R, et al. Knockdown of actin and caspase gene expression by RNA interference in the symbiotic anemone *Aiptasia pallida*[J]. The Biological Bulletin, 2007, 212(3): 250−258.
[34] Technau U, Genikhovich G. Evolution: directives from sea anemone *Hox* genes[J]. Current Biology, 2018, 28(22): R1303−R1305.
[35] Galliot B, Miljkovic-Licina M, Ghila L, et al. RNAi gene silencing affects cell and developmental plasticity in hydra[J]. Comptes Rendus Biologies, 2007, 330(6/7): 491−497.
[36] Yuyama I, Higuchi T, Hidaka M. Application of RNA interference technology to acroporid juvenile corals[J]. Frontiers in Marine Science, 2021, 8: 688876.
[37] Zhou Zhi, Zhang Guoqing, Chen Guangmei, et al. Elevated ammonium reduces the negative effect of heat stress on the stony coral *Pocillopora damicornis*[J]. Marine Pollution Bulletin, 2017, 118(1/2): 319−327.
[38] Desalvo M K, Voolstra C R, Sunagawa S, et al. Differential gene expression during thermal stress and bleaching in the Caribbean coral *Montastraea faveolata*[J]. Molecular Ecology, 2008, 17(17): 3952−3971.
[39] 郭卓君. 造礁珊瑚全长转录组的测序和分析[D]. 南京: 东南大学, 2022.
Guo Zhuojun. Sequencing and analysis of full-length transcriptomes of reef-building corals[D]. Nanjing: Southeast University, 2022.
[40] Morgan M B, Edge S E, Snell T W. Profiling differential gene expression of corals along a transect of waters adjacent to the bermuda municipal dump[J]. Marine Pollution Bulletin, 2005, 51(5/7): 524−533.
[41] 韩霞, 方佳丽, 孟沈坤儿, 等. 高通量测序技术在药用植物微生物多样性研究中的应用进展[J]. 浙江农业科学, 2024, 65(2): 329−334.
Han Xia, Fang Jiali, Meng Shenkuner, et al. Application of high-throughput sequencing technology in the study of microbial diversity of medicinal plants[J]. Journal of Zhejiang Agricultural Sciences, 2024, 65(2): 329−334.
[42] Li Minli, Liu Hongde, Guo Yunxia, et al. Single symbiotic cell transcriptome sequencing of coral[J]. Genomics, 2020, 112(6): 5305−5312.
[43] Shikina S, Lin T C, Chu Yiling, et al. Culturing reef-building corals on a laboratory dish: a simple experimental platform for stony cor-

中国知网 https://www.cnki.net

als[J]. Frontiers in Marine Science, 2023, 10: 1149495.
[44] van de Water J A J M, Leggat W, Bourne D G, et al. Elevated seawater temperatures have a limited impact on the coral immune response following physical damage[J]. Hydrobiologia, 2015, 759(1): 201−214.
[45] van de Water J A J M, Lamb J B, van Oppen M J H, et al. Comparative immune responses of corals to stressors associated with offshore reef-based tourist platforms[J]. Conservation Physiology, 2015, 3(1): cov032.
[46] Desalvo M K, Sunagawa S, Fisher P L, et al. Coral host transcriptomic states are correlated with *Symbiodinium* genotypes[J]. Molecular Ecology, 2010, 19(6): 1174−1186.
[47] 吴逸波. 鹿角杯形珊瑚半乳糖凝集素识别虫黄藻和病原菌的活性特征研究[D]. 海口: 海南大学; 2019.
Wu Yibo. The recognition activities of a galectin to pathogen and symbiont in the scleractinian coral *Pocillopora damicornis*[D]. Haikou: Hainan University; 2019.
[48] Wu Yibo, Zhou Zhi, Wang Jun, et al. Temperature regulates the recognition activities of a galectin to pathogen and symbiont in the scleractinian coral *Pocillopora damicornis*[J]. Developmental & Comparative Immunology, 2019, 96: 103−110.
[49] Kenkel C D, Aglyamova G, Alamaru A, et al. Development of gene expression markers of acute heat-light stress in reef-building corals of the genus *Porites*[J]. PLoS One, 2011, 6(10): e26914.
[50] Thummasan M, Casareto B E, Ramphul C, et al. Physiological responses (Hsps 60 and 32, caspase 3, H_2O_2 scavenging, and photosynthetic activity) of the coral *Pocillopora damicornis* under thermal and high nitrate stresses[J]. Marine Pollution Bulletin, 2021, 171: 112737.
[51] Seveso D, Montano S, Strona G, et al. Exploring the effect of salinity changes on the levels of Hsp60 in the tropical coral *Seriatopora caliendrum*[J]. Marine Environmental Research, 2013, 90: 96−103.
[52] Louis Y D, Bhagooli R, Seveso D, et al. Local acclimatisation-driven differential gene and protein expression patterns of Hsp70 in *Acropora muricata*: implications for coral tolerance to bleaching[J]. Molecular Ecology, 2020, 29(22): 4382−4394.
[53] Li Chunying, Lee J S, Ko Y G, et al. Heat shock protein 70 inhibits apoptosis downstream of cytochrome c release and upstream of caspase-3 activation[J]. Journal of Biological Chemistry, 2000, 275(33): 25665−25671.
[54] Xiao Yilin, Gao Luyao, Li Zhiyong. Unique high-temperature tolerance mechanisms of zoochlorellae *Symbiochlorum hainanensis* derived from scleractinian coral porites lutea[J]. mBio, 2024, 15(3): e02780−23.
[55] Sharp V A, Brown B E, Miller D. Heat shock protein (hsp 70) expression in the tropical reef coral *Goniopora djiboutiensis*[J]. Journal of Thermal Biology, 1997, 22(1): 11−19.
[56] 张懿丹. 热胁迫下鹿角杯形珊蝴 HSP70 的基因表达与活性分析[D]. 海口: 海南大学, 2016.
Zhang Yidan. Gene expression and activity analysis of *Pocillopora damicornis* HSP70 under heat stress[D]. Haikou: Hainan University, 2016.
[57] Levy O, Achituv Y, Yacobi Y Z, et al. The impact of spectral composition and light periodicity on the activity of two antioxidant enzymes (SOD and CAT) in the coral *Favia favus*[J]. Journal of Experimental Marine Biology and Ecology, 2006, 328(1): 35−46.
[58] Martignago D C, Godoy L, Amaral A P, et al. Establishment of oxidative stress biomarkers in oocytes from healthy and bleached scleractinian corals[J]. Journal of Experimental Marine Biology and Ecology, 2024, 570: 151963.
[59] Camilo J P G, Nunes V F C, Miranda R J, et al. Management strategy influences coral oxidative stress responses in a marine protected area in the Southwestern Atlantic[J]. Marine Pollution Bulletin, 2024, 198: 115832.
[60] Vilas Bhagwat P, Ravindran C, Irudayarajan L. Characterization of the defense properties of healthy and diseased coral mucus[J]. Journal of Invertebrate Pathology, 2023, 201: 108001.
[61] 蒙林庆, 黄雯, 阳恩广, 等. 高温白化事件可提高涠洲岛澄黄滨珊瑚 (*Porites lutea*) 的耐热性[J]. 海洋学报, 2022, 44(8): 87−96.
Meng Linqing, Huang Wen, Yang Enguang, et al. High temperature bleaching events can increase thermal tolerance of *Porites lutea* in the Weizhou Island[J]. Haiyang Xuebao, 2022, 44(8): 87−96.
[62] Császár N B M, Seneca F O, van Oppen M J H. Variation in antioxidant gene expression in the scleractinian coral *Acropora millepora* under laboratory thermal stress[J]. Marine Ecology Progress Series, 2009, 392: 93−102.
[63] 许昌有, 黄晖, 练健生, 等. 澄黄滨珊瑚 *ferritin* 基因部分 cDNA 序列的获得及分析[J]. 科学能报, 2013, 58(17): 1590−1595.
Xu Changyou, Huang Hui, Lian Jiansheng, et al. A partial cDNA sequence of the *ferritin* gene in *Porites lutea*[J]. Chinese Science Bulletin, 2013, 58(17): 1590−1595.
[64] Liu Zhaoqun, An Mingxun, Geng Xinxing, et al. The scleractinian coral *Pocillopora damicornis* relies on neuroendocrine regulation to cope with polycyclic aromatic hydrocarbons under heat stress[J]. Environmental Pollution, 2023, 316: 120565.
[65] Rosic N N, Pernice M, Dunn S, et al. Differential regulation by heat stress of novel cytochrome P450 genes from the dinoflagellate symbionts of reef-building corals[J]. Applied and Environmental Microbiology, 2010, 76(9): 2823−2829.
[66] Edge S E, Morgan M B, Gleason D F, et al. Development of a coral cDNA array to examine gene expression profiles in *Montastraea faveolata* exposed to environmental stress[J]. Marine Pollution Bulletin, 2005, 51(5/7): 507−523.
[67] Voolstra C R, Schnetzer J, Peshkin L, et al. Effects of temperature on gene expression in embryos of the coral *Montastraea faveolata*[J]. BMC Genomics, 2009, 10(1): 627.
[68] Ainsworth T D, Wasmund K, Ukani L, et al. Defining the tipping point. A complex cellular life/death balance in corals in response to

中国知网　https://www.cnki.net

stress[J]. Scientific Reports, 2011, 1(1): 160.

[69] Pernice M, Dunn S R, Miard T, et al. Regulation of apoptotic mediators reveals dynamic responses to thermal stress in the reef building coral *Acropora millepora*[J]. PLoS One, 2011, 6(1): e16095.

[70] Yu Qiuyu, He Chunlong, Wang Yi, et al. The differential physiological responses to heat stress in the scleractinian coral *Pocillopora damicornis* are affected by its energy reserve[J]. Marine Environmental Research, 2025, 204: 106966.

[71] Shrestha S, Tung J, Grinshpon R D, et al. Caspases from scleractinian coral show unique regulatory features[J]. Journal of Biological Chemistry, 2020, 295(43): 14578−14591.

[72] Jiang Shuai, Zhou Zhi, Sun Yuanyuan, et al. Coral gasdermin triggers pyroptosis[J]. Science Immunology, 2020, 5(54): eabd2591.

[73] Miller D J, McMillan J, Miles A, et al. Nucleotide sequence of the histone H3-encoding gene from the scleractinian coral *Acropora formosa* (cnidaria: scleractinia)[J]. Gene, 1990, 93(2): 319−320.

[74] Watanabe T, Nishida M, Watanabe K, et al. Polymorphism in nucleotide sequence of mitochondrial intergenic region in scleractinian coral (*Galaxea fascicularis*)[J]. Marine Biotechnology, 2005, 7(1): 33−39.

[75] Rocker M M, Noonan S, Humphrey C, et al. Expression of calcification and metabolism-related genes in response to elevated pCO_2 and temperature in the reef-building coral *Acropora millepora*[J]. Marine Genomics, 2015, 24: 313−318.

[76] Kenkel C D, Meyer E, Matz M V. Gene expression under chronic heat stress in populations of the mustard hill coral (*Porites astreoides*) from different thermal environments[J]. Molecular Ecology, 2013, 22(16): 4322−4334.

[77] Zhang Man, Huang Shan, Luo Li, et al. Insights into the molecular mechanisms underlying the different heat tolerance of the scleractinian coral *Pavona decussata*[J]. Coral Reefs, 2024, 43(2): 429−442.

[78] Rädecker N, Pogoreutz C, Gegner H M, et al. Heat stress destabilizes symbiotic nutrient cycling in corals[J]. Proceedings of the National Academy of Sciences of the United States of America, 2021, 118(5): e2022653118.

[79] Sun Fulin, Yang Hongqiang, Zhang Xiyang, et al. Significant response of coral-associated bacteria and their carbohydrate-active enzymes diversity to coral bleaching[J]. Marine Environmental Research, 2024, 201: 106694.

[80] 沈城, 刘楚吾, 刘丽. 温度胁迫及恢复初期稀杯盔形珊瑚共生虫黄藻 *Hsp70*、*Hsp90*、*psaA*、*psbA* 基因表达分析[J]. 热带海洋学报, 2016, 35(3): 72−78.
Shen Cheng, Liu Chuwu, Liu Li. Heat-induced stress genes *Hsp70, Hsp90* and chloroplast *psaA* and *psbA* gene expressions of *Galaxea astreata* endosymbiotic zooxanthella revealing the ability of tolerance and recovery[J]. Journal of Tropical Oceanography, 2016, 35(3): 72−78.

[81] Gong Sanqaing, Liang Jiayuan, Xu Lijia, et al. Blue light increases thermal bleaching tolerance of coral via remodeling host-Symbiodiniaceae symbiosis[J]. Ecological Indicators, 2023, 155: 111020.

[82] Roth M S, Latz M I, Goericke R, et al. Green fluorescent protein regulation in the coral *Acropora yongei* during photoacclimation[J]. Journal of Experimental Biology, 2010, 213(21): 3644−3655.

[83] Smith-Keune C, Dove S. Gene expression of a green fluorescent protein homolog as a host-specific biomarker of heat stress within a reef-building coral[J]. Marine Biotechnology, 2008, 10(2): 166−180.

[84] Dizon E G S, Da-Anoy J P, Roth M S, et al. Fluorescent protein expression in temperature tolerant and susceptible reef-building corals[J]. Journal of the Marine Biological Association of the United Kingdom, 2021, 101(1): 71−80.

[85] 黄文靖. 角孔珊瑚属 3 种珊瑚的物种鉴定及其进化关系研究[D]. 湛江: 广东海洋大学, 2023.
Huang Wenjing. A morphology classification and phylogenetic analysis of three species of the scleractinian coral genus *Goniopora*[D]. Zhanjiang: Guangdong Ocean University, 2023.

[86] Huang Yuanjia, Yuan Jigui, Zhang Yanping, et al. Molecular cloning and characterization of calmodulin-like protein CaLP from the Scleractinian coral *Galaxea astreata*[J]. Cell Stress and Chaperones, 2018, 23(6): 1329−1335.

[87] 黄元佳. 稀杯盔形珊瑚钙调素类似蛋白、钙网蛋白、碳酸酐酶基因的克隆及表达分析[D]. 湛江: 广东海洋大学, 2019.
Huang Yuanjia. Cloning and expression analysis of calmodulin-like protein, calreticulin and carbonic anhydrase in *Galaxea astreata*[D]. Zhanjiang: Guangdong Ocean University, 2019.

[88] Chiou C Y, Chen I P, Chen C, et al. Analysis of *Acropora muricata* calmodulin (*CaM*) indicates that scleractinian corals possess the ancestral exon/intron organization of the eumetazoan *CaM* gene[J]. Journal of Molecular Evolution, 2008, 66(4): 317−324.

[89] Huang Yuanjia, Zhang Yanping, Peng Huipai, et al. Cloning and functional analysis of the calreticulin gene from the scleractinian coral *Galaxea astreata*[J]. Acta Oceanologica Sinica, 2020, 39(6): 58−64.

[90] Weston A J, Dunlap W C, Beltran V H, et al. Proteomics links the redox state to calcium signaling during bleaching of the scleractinian coral *Acropora microphthalma* on exposure to high solar irradiance and thermal stress[J]. Molecular & Cellular Proteomics, 2015, 14(3): 585−595.

[91] Reyes-Bermudez A, DeSalvo M K, Voolstra C R, et al. Gene expression microarray analysis encompassing metamorphosis and the onset of calcification in the scleractinian coral *Montastraea faveolata*[J]. Marine Genomics, 2009, 2(3/4): 149−159.

[92] Tian Peng, Niu Wentao. The complete mitochondrial genome of the *Acropora pruinosa*[J]. Mitochondrial DNA Part B, 2017, 2(2): 652−653.

[93] Vollmer S V, Selwyn J D, Despard B A, et al. Genomic signatures of disease resistance in endangered staghorn corals[J]. Science, 2023,

中国知网 https://www.cnki.net

381(6665): 1451−1454.
[94] Kenkel C D, Sheridan C, Leal M C, et al. Diagnostic gene expression biomarkers of coral thermal stress[J]. Molecular Ecology Resources, 2014, 14(4): 667−678.
[95] Guedes A F, Sargento L, Braz-Nogueira J, et al. Translational Research and Innovation in Human and Health Science[J]. Annals of Medicine, 2018, 50(sup1): S1−S9.
[96] 马金柱, 王北艳, 崔玉东, 等. NLRs 蛋白家族的研究进展[J]. 中国免疫学杂志, 2011, 27(3): 281−284.
Ma Jinzhu, Wang Beiyan, Chui Yudong, et al. Research progress on the NLRs protein family[J]. Chinese Journal of Immunology, 2011, 27(3): 281−284.
[97] Williams L M, Fuess L E, Brennan J J, et al. A conserved toll-like receptor-to-NF-κB signaling pathway in the endangered coral *Orbicella faveolata*[J]. Developmental & Comparative Immunology, 2018, 79: 128−136.
[98] Dimos B A, Butler C C, Ricci C A, et al. Responding to threats both foreign and domestic: NOD-like receptors in corals[J]. Integrative and Comparative Biology, 2019, 59(4): 819−829.
[99] Brudner M, Karpel M, Lear C, et al. Lectin-dependent enhancement of ebola virus infection via soluble and transmembrane C-type lectin receptors[J]. PLoS One, 2013, 8(4): e60838.
[100] Zhou Zhi, Zhao Shuimiao, Ni Junyi, et al. Effects of environmental factors on C-type lectin recognition to zooxanthellae in the stony coral *Pocillopora damicornis*[J]. Fish & Shellfish Immunology, 2018, 79: 228−233.
[101] Souter P, Bay L K, Andreakis N, et al. A multilocus, temperature stress-related gene expression profile assay in *Acropora millepora*, a dominant reef-building coral[J]. Molecular Ecology Resources, 2011, 11(2): 328−334.
[102] Rosic N N, Pernice M, Dove S, et al. Gene expression profiles of cytosolic heat shock proteins Hsp70 and Hsp90 from symbiotic dinoflagellates in response to thermal stress: possible implications for coral bleaching[J]. Cell Stress and Chaperones, 2011, 16(1): 69−80.
[103] Meyer E, Aglyamova G V, Matz M V. Profiling gene expression responses of coral larvae (*Acropora millepora*) to elevated temperature and settlement inducers using a novel RNA-seq procedure[J]. Molecular Ecology, 2011, 20(17): 3599−3616.
[104] Chowdhury S, White R, Ewell A, et al. Abstract 2204 subcellular expression of heat-shock protein in the coral holobiont[J]. Journal of Biological Chemistry, 2024, 300(3): 107064.
[105] Llorente L, Aquilino M, Herrero Ó, et al. Characterization and expression of heat shock and immune genes in natural populations of *Prodiamesa olivacea* (Diptera) exposed to thermal stress[J]. Ecotoxicology and Environmental Safety, 2023, 263: 115359.
[106] Cleves P A, Krediet C J, Lehnert E M, et al. Insights into coral bleaching under heat stress from analysis of gene expression in a sea anemone model system[J]. Proceedings of the National Academy of Sciences of the United States of America, 2020, 117(46): 28906−28917.
[107] Tkáčová J, Angelovičová M. Heat shock proteins (HSPs): a review[J]. Lucrări Ştiinţifice Zootehnie şi Biotehnologii, 2012, 45(1): 349−353.
[108] Rodriguez-Lanetty M, Harii S, Hoegh-Guldberg O. Early molecular responses of coral larvae to hyperthermal stress[J]. Molecular Ecology, 2009, 18(24): 5101−5114.
[109] 陈曦. 6 种模式生物热休克蛋白 70 家族的进化分析[J]. 安徽农业科学, 2011, 39(2): 701−702.
Chen Xi. Evolutionary analysis on heat shock protein 70 family from ascidian and other 5 model organisms[J]. Journal of Anhui Agricultural Sciences, 2011, 39(2): 701−702.
[110] Beere H M, Green D R. Stress management–heat shock protein-70 and the regulation of apoptosis[J]. Trends in Cell Biology, 2001, 11(1): 6−10.
[111] Arya R, Mallik M, Lakhotia S C. Heat shock genes-integrating cell survival and death[J]. Journal of Biosciences, 2007, 32(3): 595−610.
[112] Trautinger F, Kindås-Mügge I, Knobler R M, et al. Stress proteins in the cellular response to ultraviolet radiation[J]. Journal of Photochemistry and Photobiology B: Biology, 1996, 35(3): 141−148.
[113] Prodromou C. Mechanisms of Hsp90 regulation[J]. Biochemical Journal, 2016, 473(16): 2439−2452.
[114] Mogk A, Bukau B, Kampinga H H. Cellular handling of protein aggregates by disaggregation machines[J]. Molecular Cell, 2018, 69(2): 214−226.
[115] Okuda M, Niwa T, Taguchi H. Single-molecule analyses of the dynamics of heat shock protein 104 (Hsp104) and protein aggregates[J]. Journal of Biological Chemistry, 2015, 290(12): 7833−7840.
[116] Motone K, Takagi T, Aburaya S, et al. Protection of coral larvae from thermally induced oxidative stress by redox nanoparticles[J]. Marine Biotechnology, 2018, 20(4): 542−548.
[117] 王兰英, 韩丹丹, 邓恒, 等. 蜂巢珊瑚共生真菌的分离、鉴定及其抗氧化活性[J]. 西北农业学报, 2019, 28(3): 459−465.
Wang Lanying, Han Dandan, Deng Heng, et al. Isolation, identification and antioxidant activity of epiphytic fungi from *Favia speciosa*[J]. Acta Agriculturae Boreali-Occidentalis Sinica, 2019, 28(3): 459−465.
[118] Perez S, Weis V. Nitric oxide and cnidarian bleaching: an eviction notice mediates breakdown of a symbiosis[J]. Journal of Experimental Biology, 2006, 209(14): 2804−2810.
[119] Hoegh-Guldberg O. Climate change, coral bleaching and the future of the world's coral reefs[J]. Marine and Freshwater Research, 1999, 50(8): 839−866.

中国知网　https://www.cnki.net

[120] Levin R A, Beltran V H, Hill R, et al. Sex, scavengers, and chaperones: transcriptome secrets of divergent *Symbiodinium* thermal tolerances[J]. Molecular Biology and Evolution, 2016, 33(9): 2201−2215.

[121] Sudarev V V, Gette M S, Bazhenov S V, et al. Ferritin-based fusion protein shows octameric deadlock state of self-assembly[J]. Biochemical and Biophysical Research Communications, 2024, 690: 149276.

[122] Pankov K V, McArthur A G, Gold D A, et al. The cytochrome P450 (CYP) superfamily in cnidarians[J]. Scientific Reports, 2021, 11(1): 9834.

[123] Hatefi Y. The mitochondrial electron transport and oxidative phosphorylation system[J]. Annual Review of Biochemistry, 1985, 54: 1015−1069.

[124] Hegde R. The 24-kDa subunit of the bovine mitochondrial NADH: ubiquinone oxidoreductase is a G protein[J]. Biochemical and Biophysical Research Communications, 1998, 244(3): 620−629.

[125] Ainsworth T D, Hoegh-Guldberg O, Heron S F, et al. Early cellular changes are indicators of pre-bleaching thermal stress in the coral host[J]. Journal of Experimental Marine Biology and Ecology, 2008, 364(2): 63−71.

[126] Yu Xiaopeng, Huang Bo, Zhou Zhi, et al. Involvement of caspase3 in the acute stress response to high temperature and elevated ammonium in stony coral *Pocillopora damicornis*[J]. Gene, 2017, 637: 108−114.

[127] Shi Jianjin, Gao Wenqing, Shao Feng. Pyroptosis: gasdermin-mediated programmed necrotic cell death[J]. Trends in Biochemical Sciences, 2017, 42(4): 245−254.

[128] Jiang Lei, Sun Youfang, Zhou Guowei, et al. Ocean acidification elicits differential bleaching and gene expression patterns in larval reef coral *Pocillopora damicornis* under heat stress[J]. Science of the Total Environment, 2022, 842: 156851.

[129] 安华. 两株异养硝化菌的脱氮性能及乙醛酸循环的研究[D]. 太原: 太原理工大学, 2014.
An Hua. Study on nitrification efficiency and glyoxylate cycle by heterotrophic nitrication bacteria[D]. Taiyuan: Taiyuan University of Technology, 2014.

[130] Coleman D N, Totakul P, Onjai-uea N, et al. Rumen-protected methionine during heat stress alters mTOR, insulin signaling, and 1-carbon metabolism protein abundance in liver, and whole-blood transsulfuration pathway genes in holstein cows[J]. Journal of Dairy Science, 2022, 105(9): 7787−7804.

[131] Murray B, Peng H, Barbier-Torres L, et al. Methionine adenosyltransferase α1 is targeted to the mitochondrial matrix and interacts with cytochrome P450 2E1 to lower its expression[J]. Hepatology, 2019, 70(6): 2018−2034.

[132] Zhang Jingjing, Huang Zanhui, Li Yuanchao, et al. Synergistic/antagonistic effects of nitrate/ammonium enrichment on fatty acid biosynthesis and translocation in coral under heat stress[J]. Science of the Total Environment, 2023, 876: 162834.

[133] 胡文心, 杨杰. 糖异生相关通路的研究进展及中药的改善作用[J]. 云南中医中药杂志, 2023, 44(12): 83−87.
Hu Wenxin, Yang Jie. Research advances in gluconeogenesis-related pathways and the regulatory effects of traditional Chinese medicine[J]. Yunnan Journal of Traditional Chinese Medicine and Materia Medica, 2023, 44(12): 83−87.

[134] Jitrapakdee S, Wallace J C. Structure, function and regulation of pyruvate carboxylase[J]. Biochemical Journal, 1999, 340(1): 1−16.

[135] Meister A. Metabolism and function of glutathione: an overview[J]. Biochemical Society Transactions, 1982, 10(2): 78−79.

[136] Su Yilu, Zhou Zhi, Yu Xiaopeng. Possible roles of glutamine synthetase in responding to environmental changes in a scleractinian coral[J]. Molecular Biology Reports, 2018, 45(6): 2115−2124.

[137] 俞小鹏. Caspase3 和谷氨酰胺合成酶在鹿角杯形珊瑚环境应激中的功能研究[D]. 海口: 海南大学, 2018.
Yu Xiaopeng. Functional study of Caspase3 and glutamine synthetase in the environmental stress of *Pocillopora damicornis*[D]. Haikou: Hainan University, 2018.

[138] Chen Jian, Yu Kefu, Yu Xiaopeng, et al. Transcriptomic and physiological analyses reveal the toxic effects of inorganic filters (nZnO and nTiO_2) on scleractinian coral *Galaxea fascicularis*[J]. Environmental Research, 2025, 267: 120663.

[139] Mühlenbruch M, Grossart H, Eigemann F, et al. Mini-review: phytoplankton-derived polysaccharides in the marine environment and their interactions with heterotrophic bacteria[J]. Environmental Microbiology, 2018, 20(8): 2671−2685.

[140] Upreti R K, Kumar M, Shankar V. Bacterial glycoproteins: functions, biosynthesis and applications[J]. Proteomics, 2003, 3(4): 363−379.

[141] Stewart R D, Auffret M D, Warr A, et al. Assembly of 913 microbial genomes from metagenomic sequencing of the cow rumen[J]. Nature Communications, 2018, 9(1): 870.

[142] 佘大为, 张海波, 王月, 等. 坛紫菜叶绿体 *psaA* 基因片段的序列分析[J]. 水产科学, 2007, 26(5): 289−291.
She Dawei, Zhang Haibo, Wang Yue, et al. Sequence analyses of chloroplastic *psaA* gene fragment from *Porphyra haitanensis*[J]. Fisheries Science, 2007, 26(5): 289−291.

[143] 汤紫依, 吴倩, 田盛野, 等. 华顶杜鹃叶绿体 *psbA-trnH* 序列的克隆与分析[J]. 台州学院学报, 2022, 44(3): 81−86,92.
Tang Ziyi, Wu Qian, Tian Shengye, et al. Isolation and sequence analysis of chloroplast *psbA-trnH* from *Rhododendron huadingense*[J]. Journal of Taizhou University, 2022, 44(3): 81−86,92.

[144] Shinzato C, Shoguchi E, Tanaka M, et al. Fluorescent protein candidate genes in the coral *Acropora digitifera* genome[J]. Zoological Science, 2012, 29(4): 260−264.

[145] Yuyama I, Harii S, Hidaka M. Algal symbiont type affects gene expression in juveniles of the coral *Acropora tenuis* exposed to thermal

中国知网 https://www.cnki.net

stress[J]. Marine Environmental Research, 2012, 76: 41−47.

[146] 袁翔城, 梁宇娴, 宋严, 等. CO_2 升高对风信子鹿角珊瑚 (*Acropora hyacinthus*) 钙化速率和基因表达的影响[J]. 热带海洋学报, 2024, 43(3): 40−48.
Yuan Xiangcheng, Liang Yuxian, Song Yan, et al. Effects of ocean acidification on the calcification and gene expression in coral *Acropora hyacinthus*[J]. Journal of Tropical Oceanography, 2024, 43(3): 40−48.

[147] 徐菲菲, 刘秀华. 钙网蛋白的生理及病理生理学作用[J]. 生理科学进展, 2006, 37(3): 216−220.
Xu Feifei, Liu Xiuhua. Research on physiological and pathophysiological functions of calreticulin[J]. Progress in Physiological Sciences, 2006, 37(3): 216−220.

[148] Saito Y, Ihara Y, Leach M R, et al. Calreticulin functions *in vitro* as a molecular chaperone for both glycosylated and non-glycosylated proteins[J]. The EMBO Journal, 1999, 18(23): 6718−6729.

[149] Conway E M, Liu Lili, Nowakowski B, et al. Heat shock-sensitive expression of calreticulin: *in vitro* and *in vivo* up-regulation[J]. Journal of Biological Chemistry, 1995, 270(28): 17011−17016.

[150] Sunagawa S, DeSalvo M K, Voolstra C R, et al. Identification and gene expression analysis of a taxonomically restricted cysteine-rich protein family in reef-building corals[J]. PLoS One, 2009, 4(3): e4865.

[151] Umasuthan N, Elvitigala D A S, Saranya Revathy K, et al. Identification and *in silico* analysis of a novel *troponin C* like gene from *Ruditapes philippinarum* (Bivalvia: Veneridae) and its transcriptional response for calcium challenge[J]. Gene, 2013, 519(1): 194−201.

[152] Liang Zheyong, Li Wenjie, Liu Jie, et al. Simvastatin suppresses the DNA replication licensing factor MCM7 and inhibits the growth of tamoxifen-resistant breast cancer cells[J]. Scientific Reports, 2017, 7(1): 41776.

[153] Maor-Landaw K, Levy O. Gene expression profiles during short-term heat stress; branching *vs*. massive Scleractinian corals of the red sea[J]. PeerJ, 2016, 4: e1814.

[154] Cyr D M, Langer T, Douglas M G. DnaJ-like proteins: molecular chaperones and specific regulators of Hsp70[J]. Trends in Biochemical Sciences, 1994, 19(4): 176−181.

[155] 钟芳芳, 江海燕, 张俊平. 核糖体蛋白及其在疾病中的作用[J]. 药学实践与服务, 2023, 41(9): 519−523,556.
Zhong Fangfang, Jiang Haiyan, Zhang Junping. Research progress on ribosomal proteins and their functions in diseases[J]. Journal of Pharmaceutical Practice and Service, 2023, 41(9): 519−523,556.

[156] 袁吉贵. 稀杯盔形珊瑚 *Gagalaxin* 基因的功能分析[D]. 湛江: 广东海洋大学, 2019.
Yuan Jigui. Analysis on *Gagalaxin* function of *Galaxea astreata*[D]. Zhanjiang: Guangdong Ocean University, 2019.

[157] 张静, 彭靖淇. 微小 RNA-K1-5p 调控 G1/S 期相关基因的表达影响内皮细胞周期[J]. 安徽医药, 2023, 27(1): 108−112.
Zhang Jing, Peng Jingqi. Effect of miR-K1-5p on the cycle of endothelial cells by regulating G1/S phase related gene expressions[J]. Anhui Medical and Pharmaceutical Journal, 2023, 27(1): 108−112.

[158] Khaitlina S, Fitz H, Hinssen H. The interaction of gelsolin with tropomyosin modulates actin dynamics[J]. The FEBS Journal, 2013, 280(18): 4600−4611.

[159] 孙绽, 王筱寅, 应奕雯, 等. 泛素特异性蛋白酶 24 的研究进展[J]. 生命的化学, 2020, 40(10): 1792−1799.
Sun Zhan, Wang Xiaoyin, Ying Yiwen, et al. Recent advances in the studies of ubiquitin-specific protease 24[J]. Chemistry of Life, 2020, 40(10): 1792−1799.

[160] Middlebrook R, Hoegh-Guldberg O, Leggat W. The effect of thermal history on the susceptibility of reef-building corals to thermal stress[J]. Journal of Experimental Biology, 2008, 211(7): 1050−1056.

[161] Bay R A, Palumbi S R. Rapid acclimation ability mediated by transcriptome changes in reef-building corals[J]. Genome Biology and Evolution, 2015, 7(6): 1602−1612.

[162] Castillo K D, Helmuth B S T. Influence of thermal history on the response of *Montastraea annularis* to short-term temperature exposure[J]. Marine Biology, 2005, 148(2): 261−270.

[163] Yu Xiaopeng, Yu Kefu, Chen Biao, et al. Metabolic and immune costs balance during natural acclimation of corals in fluctuating environments[J]. Marine Environmental Research, 2024, 193: 106284.

[164] Evensen N R, Fine M, Perna G, et al. Remarkably high and consistent tolerance of a red sea coral to acute and chronic thermal stress exposures[J]. Limnology and Oceanography, 2021, 66(5): 1718−1729.

[165] Takahashi S, Yoshioka-Nishimura M, Nanba D, et al. Thermal acclimation of the symbiotic alga *Symbiodinium* spp. Alleviates photobleaching under heat stress[J]. Plant Physiology, 2013, 161(1): 477−485.

[166] 刘旭, 黄雯, 俞小鹏, 等. 适度热胁迫对造礁石珊瑚热耐受性影响的研究[J]. 海洋湖沼通报, 2022, 44(1): 99−105.
Liu Xu, Huang Wen, Yu Xiaopeng, et al. Studies on the effect of moderate heat stress on the heat tolerance of scleractinian coral[J]. Transactions of Oceanology and Limnology, 2022, 44(1): 99−105.

[167] 刘旭. 造礁石珊瑚对温度胁迫的响应机制研究[D]. 南宁: 广西大学, 2020.
Liu Xu. Responsive mechanism of reef-building coral rocks to temperature stress[D]. Nanning: Guangxi University, 2020.

[168] Jiang L, Liu C Y, Cui G, et al. Rapid shifts in thermal reaction norms and tolerance of brooded coral larvae following parental heat acclimation[J]. Molecular Ecology, 2023, 32(5): 1098−1116.

[169] 俞小鹏. 南海北部造礁珊瑚对高温胁迫的响应及适应性研究[D]. 南宁: 广西大学, 2022.

中国知网　https://www.cnki.net

Yu Xiaopeng. Response and adaptation of scleractinian coral to high temperature stress in the northern South China Sea[D]. Nanning: Guangxi University, 2022.
[170] Gibbin E M, Krueger T, Putnam H M, et al. Short-term thermal acclimation modifies the metabolic condition of the coral holobiont[J]. Frontiers in Marine Science, 2018, 5: 10.
[171] Smith E G, Hazzouri K M, Choi J Y, et al. Signatures of selection underpinning rapid coral adaptation to the world's warmest reefs[J]. Science Advances, 2022, 8(2): eabl7287.
[172] Kovalchuk A, Driessen A J M. Phylogenetic analysis of fungal ABC transporters[J]. BMC Genomics, 2010, 11(1): 177.
[173] Howells E J, Abrego D, Liew Y J, et al. Enhancing the heat tolerance of reef-building corals to future warming[J]. Science Advances, 2021, 7(34): eabg6070.
[174] Rivera H E, Tramonte C A, Samaroo J, et al. Heat challenge elicits stronger physiological and gene expression responses than starvation in symbiotic *Oculina arbuscula*[J]. Journal of Heredity, 2023, 114(4): 312−325.
[175] Nielsen D A, Petrou K, Gates R D. Coral bleaching from a single cell perspective[J]. The ISME Journal, 2018, 12(6): 1558−1567.
[176] Bay R A, Guerrero L. Can genomes predict coral bleaching?[J]. Science, 2020, 369(6501): 249−250.

Research progress on functional genes related to coral thermal adaptation

Ma Yuling[1], Yu Xiaopeng[1], Yu Kefu[1,2], Chen Junling[1], Zheng Yue[1], Chen Jian[1]

(1. *Guangxi Laboratory on the Study of Coral Reefs in the South China Sea/Coral Reef Research Center of China/School of Marine Sciences*, *Guangxi University*, *Nanning* 530004, *China*; 2. *Southern Marine Science and Engineering Guangdong Laboratory*, *Guangzhou* 511458, *China*)

Abstract: Global warming and extreme thermal events have induced widespread coral bleaching, leading to the rapid degradation of coral reef ecosystems across the globe. Identifying functional genes associated with thermotolerance is crucial for elucidating coral adaptation mechanisms to climate warming and enabling scientific predictions regarding coral reef ecosystem trajectories. However, the current understanding of the molecular mechanism of coral holobiont in response to heat stress is very insufficient. Therefore, this paper reviews the research progress of functional genes related to coral thermal adaptation. Initially, pattern recognition receptors (PRRs), including Toll-like receptors (TLRs), play a crucial role in detecting heat stress and activating downstream signaling cascades, thereby initiating the immune response process. These responses primarily involve: upregulation of heat shock proteins (HSPs) to facilitate the refolding of denatured polypeptides; induction of antioxidant protein genes to mitigate oxidative damage caused by reactive oxygen species (ROS); genes associated with apoptosis and pyroptosis play a crucial role in eliminating “harmful” cells. As thermal stress intensifies, corals initiate a sophisticated network of cellular processes to maintain. As heat stress intensifies, corals initiate a series of complex processes to jointly maintain cellular homeostasis. This includes: rapid activation of photoprotective protein genes to repair the photosynthetic apparatus of Symbiodiniaceae; expression of host fluorescent proteins to maintain redox balance; calcium channel proteins maintain the stability of intracellular Ca^{2+} levels; modulation of metabolic pathways to ensure adequate nutrient supply; inhibition of cell cycle progression to conserve energy; maintenance of cytoskeletal integrity to preserve structural stability; and regulation of ubiquitin-proteasome system for protein quality control. Furthermore, recurrent thermal stress events can induce acclimatization in corals, potentially enhancing their thermal tolerance through multiple mechanisms: downregulation of host metabolic rate, protection of heat-sensitive proteins, and upregulation of antioxidant enzymes and ammonium assimilation pathways.

Key words: global warming; coral reef; thermal adaptation; functional genes; thermal acclimation

中国知网 https://www.cnki.net



海洋湖沼通报(中英文)
Transactions of Oceanology and Limnology
ISSN 1003-6482,CN 37-1141/P

《海洋湖沼通报(中英文)》网络首发论文

题目：涠洲岛四种造礁石珊瑚耐热阈值测定及其差异性对比
作者：徐明培，黄雯，陈锦连，黄智华，周榆鹏，宛强，李雨箫，余克服
收稿日期：2025-04-11
网络首发日期：2025-06-16
引用格式：徐明培，黄雯，陈锦连，黄智华，周榆鹏，宛强，李雨箫，余克服．涠洲岛四种造礁石珊瑚耐热阈值测定及其差异性对比[J/OL]．海洋湖沼通报(中英文).https://link.cnki.net/urlid/37.1141.P.20250613.1720.004

网络首发：在编辑部工作流程中，稿件从录用到出版要经历录用定稿、排版定稿、整期汇编定稿等阶段。录用定稿指内容已经确定，且通过同行评议、主编终审同意刊用的稿件。排版定稿指录用定稿按照期刊特定版式（包括网络呈现版式）排版后的稿件，可暂不确定出版年、卷、期和页码。整期汇编定稿指出版年、卷、期、页码均已确定的印刷或数字出版的整期汇编稿件。录用定稿网络首发稿件内容必须符合《出版管理条例》和《期刊出版管理规定》的有关规定；学术研究成果具有创新性、科学性和先进性，符合编辑部对刊文的录用要求，不存在学术不端行为及其他侵权行为；稿件内容应基本符合国家有关书刊编辑、出版的技术标准，正确使用和统一规范语言文字、符号、数字、外文字母、法定计量单位及地图标注等。为确保录用定稿网络首发的严肃性，录用定稿一经发布，不得修改论文题目、作者、机构名称和学术内容，只可基于编辑规范进行少量文字的修改。

出版确认：纸质期刊编辑部通过与《中国学术期刊（光盘版）》电子杂志社有限公司签约，在《中国学术期刊（网络版）》出版传播平台上创办与纸质期刊内容一致的网络版，以单篇或整期出版形式，在印刷出版之前刊发论文的录用定稿、排版定稿、整期汇编定稿。因为《中国学术期刊（网络版）》是国家新闻出版广电总局批准的网络连续型出版物（ISSN 2096-4188，CN 11-6037/Z），所以签约期刊的网络版上网络首发论文视为正式出版。

网络首发时间：2025-06-16 09:40:58　网络首发地址：https://link.cnki.net/urlid/37.1141.P.20250613.1720.004

涠洲岛四种造礁石珊瑚耐热阈值测定及其差异性对比

徐明培[1,2]，黄雯[2*]，陈锦连[2]，黄智华[2]，周榆鹏[1,2]，宛强[1,2]，李雨箫[2]，余克服[2,3]

（1.广西大学 资源环境与材料学院，广西 南宁，530004；2.广西大学 海洋学院，珊瑚礁研究中心，广西南海珊瑚礁研究重点实验室，广西 南宁，530004；3.南方海洋科学与工程广东省实验室(广州)，广东 广州，511458）

摘要：全球变暖大背景下，海水温度上升导致大规模珊瑚白化事件频发，严重威胁了珊瑚礁生态系统的健康。为比较不同形态珊瑚的耐热性差异，向珊瑚礁生态修复工作提供科学依据。本研究引入 CBASS（Coral Bleaching Automated Stress System）方法，对涠洲岛 2024 年夏季极端高温时期四种石珊瑚的耐热阈值进行测定，同时分析其生理生化指标。结果显示：（1）珊瑚耐热阈值与生理生化指标反映一致，鹿角珊瑚耐热性最低，四种珊瑚耐热阈值分别为：风信子鹿角珊瑚（*Acropora hyacinthus*）37.55℃，美丽鹿角珊瑚（*Acropora muricata*）36.84℃，十字牡丹珊瑚（*Pavona decussata*）39.40℃，澄黄滨珊瑚（*Porites lutea*）39.50℃；（2）由耐热性差异表明面对高温压力时鹿角珊瑚将最先退化，其在珊瑚礁生态修复工作中应被优先关注；（3）涠洲岛当地珊瑚并未受到环境温度带来的致命威胁。这意味着涠洲岛仍具有作为相对高纬度珊瑚避难所的巨大潜力。

关键词：涠洲岛；全球变暖；珊瑚礁生态修复；珊瑚耐热性；珊瑚避难所

中图分类号:Q-1　　**文献标识码：A**

引　言

在地球大环境变化下，尤其是全球气候变暖和海洋酸化，被认为对珊瑚礁生态系统的影响是巨大的，有学者预计在本世纪末会出现大规模的珊瑚礁消失及退化，并伴随着物种的灭绝[1-3]。在珊瑚礁生存环境恶化之前，相对高纬度海域的水体环境更为动荡，且受多种自然与人为因素的叠加影响，这类区域被称为珊瑚礁生存的“边缘”[4]。这些“边缘”环境通常在冬季会有大幅度的降温并不适宜珊瑚生存。全球变暖驱使下，热带低纬度的珊瑚生存环境温度超过了其承受极限，造成大部分珊瑚的退化，例如大堡礁、安达曼海域[5-6]。理论上，全球变暖提高了“边缘”的海水温度，夏季提高的温度对珊瑚礁而言并不致命，但冬季温度的提升使原本不适宜珊瑚礁生存的环境得到改善[7]，所以相对高纬度地区可能是理想的珊瑚避难所[8]。

与此同时，由于不同珊瑚对环境变化的耐受度不同，珊瑚礁生态系统单一化的问题也日趋严重，多样性减少的问题也必须重视。当然，并不排除珊瑚在环境压力下有进化并适应的发展可能性，但这一进程是缓慢的，就珊瑚礁对地球生态系统以及人类社会的巨大贡献而言，我们不能将希望都寄托于自然演化。综合而言，如何在全球海水升温背景下快速构建一个结构稳定，功能强大的珊瑚群落去遏制珊瑚礁生态系统的退化是迫在眉睫的问题。人为介入，帮助珊瑚礁生态系统修复是有必要且行之有效的方法，并已取得诸多成效[9-10]。

CBASS（Coral Bleaching Automated Stress System，珊瑚白化自动应激系统）方法，是一种便捷的珊瑚白化阈值测定方法，可以实现精确控制水温、光照等环境参数，模拟不同海洋环境条件，并同时进行多个实验，实时监测与评估珊瑚的生理状态，通过对比不同温度条件下的珊瑚反应来分析珊瑚的耐受性与适应性。此方法对于测定石珊瑚的耐热上限具有巨大潜力。Evensen[11]等的研究证明该方法在急性与慢性处理下，具有相似的结果，可以作为快速测定珊瑚阈值的技术。同时他们用此技术测定了红海四种造礁石珊瑚的耐热阈值[12]，相比于传统的根据白化程度来测定珊瑚耐热极限，更为科学量化。

基金项目：广西自然科学基金(2023GXNSFAA026510)；国家自然科学基金(42090041、42030502)

作者简介：徐明培（1999—），男，在读研究生，主要从事珊瑚礁生态修复研究。E-mail: 1005342113@qq.com

通信作者：黄雯（1988—），男，博士，副教授，硕士生导师，主要从事珊瑚礁生态修复和珊瑚群体遗传学研究工作。E-mail：wenhuang@gxu.edu.cn

收稿日期：2025-04-11

Alderdice[13]等在澳大利亚大堡礁区域运用此技术评估在原位苗圃框架上繁殖前后的珊瑚耐热阈值，帮助他们筛选出具有耐热优势的珊瑚进行培育。

本实验利用 CBASS 方法测定涠洲岛当地 2024 年夏季极端高温时期四种造礁石珊瑚的耐热阈值，结合生理生化指标分析，旨在对涠洲岛当地四种不同形态的造礁石珊瑚耐热性进行对比，为珊瑚礁生态修复的选种工作提供科学依据。同时对地处“边缘”的涠洲岛是否适合珊瑚避难所的定位提出新的看法，为保护和管理涠洲岛当地珊瑚礁生态提供理论基础。

1 材料与方法

1.1 研究区域与材料

本实验所使用的四种活体珊瑚（风信子鹿角珊瑚、美丽鹿角珊瑚、十字牡丹珊瑚及澄黄滨珊瑚）均采集于广西北海涠洲岛西北近岸海域（经纬度：21° 00′ ～21° 10′ N， 109° 00′ ～109° 15′ E），水深为 4~6 m。所有珊瑚样本同时采集于 2024 年 8 月中旬，此时正值涠洲岛海域海水高温时期（采集时海水温度为 32 ℃）。此批样本为抵御高温侵袭后的健康样本，每种珊瑚各采集 5 株，共 20 株珊瑚。

1.2 实验设计

所有珊瑚采集上岸后均迅速带水运输至广西大学涠洲岛珊瑚馆内进行分样处理。风信子鹿角珊瑚与美丽鹿角珊瑚分割为 5 cm 左右长的断枝，十字牡丹珊瑚与澄黄滨珊瑚用小型切割机切割成表面积大约为 16 cm^2 的小块。分样完成后将所有珊瑚样本放入海水养殖缸内以 26 ℃暂养恢复 14 d，待珊瑚触手自然伸展，消除所有应激反应后，每种珊瑚选取 20 株，共 80 株样本进行实验。

本次正式实验共使用 4 个相同规格为 900 mm× 600 mm× 800 mm（长×宽×高）的循环海水养殖缸，单个养殖缸的储水量约为 450 L。为还原珊瑚生长的真实环境，实验室采用通过透明阳光棚的自然光线作为光源，每个养殖缸单独配备一台水冷机（温控区间 18 ~32 ℃）维持温度稳定，暂养期间定期更换自然海水，并对水体定期检测，保持水体稳定在盐度 33‰ ~35‰、KH 7~7.5、pH 8.1~ 8.3、Ca^{2+} 浓度 380-420 ppm、Mg^{2+}浓度 1 230~1 380 ppm、NH^{3+}＜ 0.15 ppm、NO^{3-}＜ 0.1 ppm。本实验使用的各个养殖缸串联于一体，共用一个系统过滤池，保持水流速度和水质营养盐条件完全一致。

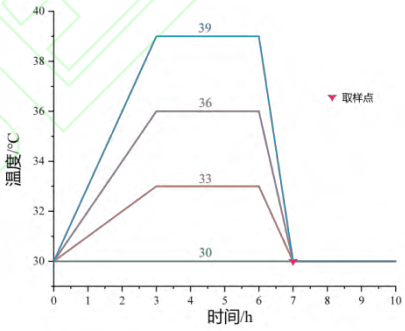


图 1 CBASS 实验步骤示意图

Fig. 1 CBASS experimental steps

本实验共设置 4 个实验温度梯度，分别为基准线温度 30 ℃（参考涠洲岛当地往年最大月平均海水温度，数据来自本实验室于涠洲岛海域安放的 HOBO 水下温度计），轻度应激温度 33 ℃，中度应激温度 36 ℃，极度应激温度 39 ℃。实验所用珊瑚采样时为涠洲岛夏季极端高温时期，珊瑚自然生存环境温度已到达本实验所设置的基准线温度（30 ℃），珊瑚并未白化死亡，故而认为实验待测珊瑚耐热阈值大于 30 ℃，因此并未设置正常温度水平的对照组。实验过程中，每个实验缸除了升温上限不同，其余处理均保持一致。将选取的珊瑚样本随机分放至实验缸中。每个实验缸放入四种珊瑚样本，每种 5 株，即每个实验缸中拥有 20 株珊瑚，实验缸初始温度为 30 ℃。考虑到实验时涠洲岛当地日落时间以及取样时珊瑚至少经历 45 min 以上的暗反应时间，本实验从下午 13 时开始，于自然光照条件下进行。利用

水族缸加热棒进行调控温度。下午 13 时，四个实验缸同时开始升温 3 h，到达设定温度后维持 3 h 后移除所有加热设备（由于加热设备的精确度关系，本实验各实验缸实际最高温度为 30 ℃、33.1 ℃、36.2 ℃、39.1 ℃），1 h 降温至基准线温度（30 ℃）。降温完成后，利用脉冲振幅调制荧光仪（DIVING-PAM-Ⅱ，Walz，德国）检测各珊瑚样本最大光量子产量（*Fv/Fm*）。随即用液氮急速冷冻珊瑚，放入-80 ℃环境保存，而后将珊瑚样本带回广西大学海洋学院生物实验室进行虫黄藻密度、叶绿素 *a* 含量、超氧化物歧化酶（SOD）活性、过氧化氢酶（CAT）活性等生理生化指标测量。

1.3 生理生化指标测量

1.3.1 生理指标测量

使用洗牙器（WP-70EC，Water pik，美国）盛装过滤海水（孔径为 0.45 μm 滤膜过滤）冲洗珊瑚样本，得到珊瑚组织匀浆冲洗液和珊瑚骨骼，测量冲洗液总体积后，取 2 mL 冲洗液以 5 000 重力加速度（g）于 4 ℃离心 10 min，去上清液，用纯水定容为 4 mL 后使用流式细胞仪测量单位虫黄藻密度（C，单位：cells/ mL），用铝箔技术法测得珊瑚表面积，最后根据以下公式得到共生虫黄藻密度（D，单位：cells/ cm^2）[14]。

$$D = C \times 2 \times V /（M/G） \quad (1)$$

式中,*V* 为冲洗液的总体积（单位：mL）；*M* 为贴合包裹珊瑚骨骼表面的铝箔纸质量（单位：g）；*G* 为铝箔纸单位面积质量（单位：g/ cm^2）[14]。

共生虫黄藻叶绿素 *a* 含量参照 Jeffrey 和 Humphrey 的方法[15]计算，结合珊瑚表面积进一步换算可以得到单位面积叶绿素 *a* 含量。从总冲洗液中取 15 mL 以 4 000 重力加速度（g）于 4 ℃离心 7 min，缓慢去除上清液，于沉淀物中加入 5 mL 90 %丙酮，然后在 4 ℃冷藏条件下萃取 24 h。将萃取 24 h 后的溶液再次离心（离心参数不变），取上清液用分光光度计分别测试波长为 750 nm、664 nm、647 nm 和 630 nm 处的吸光度，带入下列公式得到叶绿素 *a* 含量（Chl *a*，单位：μg / mL）：

$$\text{Chl } a = 11.85 \times (A664-A750) - 1.54 \times (A647-A750) - 0.08 \times (A630-A750) \quad (2)$$

式中，A750、A664、A637、A630 分别代表波长为 750 nm、664 nm、647 nm、和 630 nm 处的吸光度值。再结合总冲洗液体积（单位：mL）和珊瑚骨骼样本表面积（单位：cm^2）计算可得叶绿素 *a* 含量（单位：μg / cm^2）。

1.3.2 生化指标测量

取 2 mL 珊瑚匀浆于低温高速离心机（3-18KS，SIGMA，德国）中 4 ℃、5 000 g 下离心 10 min 后取上清液，-80 ℃保存，用于各生化指标测量[16]。使用商用试剂盒分别测定超氧化物歧化酶（SOD）活性和过氧化氢酶（CAT）活性。所有试剂盒均购自南京建成生物工程研究所，货号分别为 A001 和 A007，具体操作步骤见文献[14]。并使用 BCA 蛋白分析试剂盒（上海生工生物工程股份有限公司）测得所得上清液蛋白质浓度，以此对上清液为基础样品的各生化指标总活性进行统一标准化，得到各特定生化指标活性[17]。

1.4 实验数据处理

所有实验数据均采用 IBM SPSS Statistics27 进行双因素(two-way ANOVA)方差分析对固定因子（珊瑚种类和实验温度）进行主效应和交互效应分析，当主效应或交互效应显著（$P \leqslant 0.05$）时，对变量进行事后配对比较，用以确定每个温度处理下的不同种类珊瑚之间的差异是否具有统计学意义[18]。同时，进行多重比较（邓肯检验）以用于比较同种珊瑚不同温度处理下数据的显著性。不同温度处理后的各珊瑚样本最大光量子产量（*Fv/Fm*）数据利用 R 软件 version 4.4.0 处理，使用 drc 包分别拟合每种珊瑚的温度-光合效率曲线。

2 实验结果

2.1 通过 *Fv/Fm* 分析四种珊瑚耐热阈值

如图 2 所示，整个实验过程中不同种珊瑚的最大光量子产量（*Fv/Fm*）在面对温度上升的实验环境下都表现出一致的变化模式，总体都是随温度上升而下降。具体来说，最大光量子产量（*Fv/Fm*）均受

到珊瑚种类、实验温度和珊瑚种类×实验温度的显著影响（双向方差分析，$P \leq 0.01$）。从同温度下来看，在 30 ℃和 33 ℃处理下，仅在十字牡丹珊瑚与澄黄滨珊瑚之间存在显著差异（成对检验，$P \leq 0.05$）；当升温到 36 ℃后，澄黄滨珊瑚与其余珊瑚之间均存在显著差异，并且美丽鹿角珊瑚与十字牡丹珊瑚之间也存在显著差异（成对检验，$P \leq 0.05$）； 39 ℃处理下，所有珊瑚之间均存在显著差异（成对检验，$P \leq 0.05$,）。另外，从不同珊瑚种类来看，风信子鹿角珊瑚和十字牡丹珊瑚在 30 ℃、33 ℃和 36℃处理下，最大光量子产量（*Fv/Fm*）均无显著差异（邓肯检验，$P \leq 0.05$）；美丽鹿角珊瑚是 36℃处理下与 33 ℃之间出现显著差异（邓肯检验，$P \leq 0.05$）；澄黄滨珊瑚则是此温度处理下，与前两个处理温度均出现显著差异（邓肯检验，$P \leq 0.05$）；并且四种珊瑚均在 39 ℃与其他温度处理出现显著差异（邓肯检验，$P \leq 0.05$）。整个实验过程中，风信子鹿角珊瑚和美丽鹿角珊瑚最大光量子产量（*Fv/Fm*）降幅最大，十字牡丹珊瑚和澄黄滨珊瑚相比基准线温度也降低了 50%左右，二者的最大光量子产量（*Fv/Fm*）明显优于前两者。

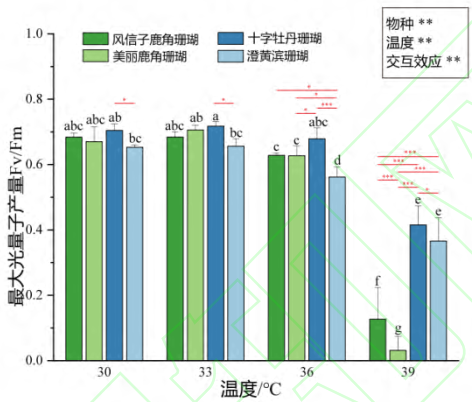


图 2　CBASS 实验中四种造礁石珊瑚最大光量子产量（*Fv/Fm*）变化

Fig. 2: Changes in maximum photon production (*Fv/Fm*) of four reef building coral species in the CBASS experiment

数据拟合后，最终我们得到了以下曲线以及各珊瑚的 Ed50 值（median effective dose, ED50，此处解释为最大光量子半数损失剂量）来代表珊瑚的耐热阈值。在 CBASS 系统实验条件下，美丽鹿角珊瑚的 Ed50 为 36.84± 0.238 ℃，风信子鹿角珊瑚的 Ed50 为 37.55± 0.253 ℃，十字牡丹珊瑚的 Ed50 为 39.40± 0.138 ℃，澄黄滨珊瑚的 Ed50 为 39.50± 0.245 ℃。且通过 R 语言包进行似然比检验结果表明，光合效率的变化具有显著的温度效应（$p < 0.01$）。

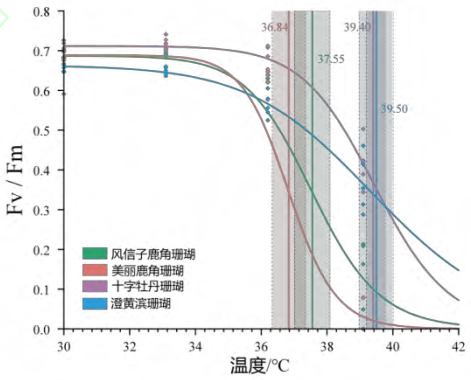


图 3 温度-光合效率拟合曲线

Fig. 3 Temperature photosynthetic efficiency fitting curve

注：散点代表实验中实际测得的各珊瑚最大光量子产量（*Fv/Fm*）值，曲线为 R 软件语言包拟合的温度-光合效率拟合曲线，竖线代表各珊瑚的 Ed50 值，阴影部分为各值的 95 %置信区间

2.2 生理生化指标变化

2.2.1 生理指标变化

如图 4（a，b）所示，整个实验过程中，四种珊瑚的虫黄藻密度，叶绿素 *a* 含量变化模式一致，总体趋势都是随温度升高而先升后降。与此同时，两个生理指标均受到珊瑚种类，实验温度和珊瑚种类×实验温度的显著影响（双向方差分析，$P \leqslant 0.01$）。虫黄藻密度结果显示，30 ℃处理下，澄黄滨珊瑚与其他三种珊瑚均存在显著差异（成对检验，$P \leqslant 0.001$），33 ℃处理下，除风信子鹿角珊瑚与美丽鹿角珊瑚之间外，其余珊瑚之间均存在显著差异（成对检验，$P \leqslant 0.05$）；36 ℃处理下，除美丽鹿角珊瑚与十字牡丹珊瑚之间外，其余珊瑚之间均存在显著差异（成对检验，$P \leqslant 0.05$）；39 ℃处理下，澄黄滨珊瑚与其余三种珊瑚均存在显著差异，同时风信子鹿角珊瑚与美丽鹿角珊瑚之间也存在显著差异（成对检验，$P \leqslant 0.05$）。四种石珊瑚的虫黄藻密度从总体趋势来看，风信子鹿角珊瑚、美丽鹿角珊瑚及澄黄滨珊瑚呈现先增加后减少的趋势，十字牡丹珊瑚则是先减少后回升，再减少的趋势。对比两种鹿角珊瑚，风信子鹿角珊瑚在 36 ℃和 39 ℃之间没有明显差异，美丽鹿角则存在（邓肯检验，$P \leqslant 0.05$），说明风信子鹿角珊瑚在高温环境下更能保持虫黄藻密度的稳定，从而保证整个共生体的主要能量来源。十字牡丹珊瑚则是在前三个温度之间都相对稳定，仅在 39 ℃处理下显著下跌（邓肯检验，$P \leqslant 0.05$）。澄黄滨珊瑚全程都是数值最高的珊瑚，且是最高温和基准线温度相比损失唯一不超过 50%的珊瑚，其稳定性为四种珊瑚中最高。

叶绿素 *a* 含量结果显示，30 ℃处理下，仅在十字牡丹珊瑚与风信子鹿角珊瑚、澄黄滨珊瑚之间存在显著差异（成对检验，$P \leqslant 0.05$）；33 ℃处理下，除风信子鹿角珊瑚与美丽鹿角珊瑚之间外，其余珊瑚之间均存在显著差异（成对检验，$P \leqslant 0.01$）；36 ℃处理下，澄黄滨珊瑚与其余三种珊瑚均存在显著差异，并且风信子鹿角珊瑚与十字牡丹珊瑚之间也存在显著差异（成对检验，$P \leqslant 0.05$）；最后在 39 ℃处理下，仅有澄黄滨珊瑚与其余三种珊瑚之间均存在显著差异（成对检验，$P \leqslant 0.01$）。总体来看，四种珊瑚叶绿素 *a* 含量均呈现先增后减的变化趋势。与虫黄藻密度变化情况基本相同，美丽鹿角珊瑚在 36℃相比于风信子鹿角珊瑚数值更高，但 36℃与 39℃之间存在显著差异，风信子则不存在，说明风信子鹿角珊瑚稳定性还是略胜一筹（邓肯检验，$P \leqslant 0.05$）。十字牡丹珊瑚前三个温度同样稳定，在 39 ℃处理下显著下跌（邓肯检验，$P \leqslant 0.05$）。澄黄滨珊瑚在全程数值最高，同样的，其最高温和基准线温度相比损失是四种珊瑚中唯一不超过 50%的。

2.2.2 生化指标变化

如图 4（c，d）所示，整个实验过程中，CAT 和 SOD 两个生化指标均受到珊瑚种类、实验温度和珊瑚种类×实验温度的显著影响（双向方差分析，$P \leqslant 0.01$）。从 CAT 结果分析，30 ℃和 39 ℃处理下，仅在澄黄滨珊瑚与其余三种珊瑚之间存在显著差异（成对检验，$P \leqslant 0.001$）；33 ℃处理下，除风信子鹿角珊瑚与美丽鹿角珊瑚之间外，其余珊瑚之间均存在显著差异（成对检验，$P \leqslant 0.05$）；36 ℃处理下除风信子鹿角珊瑚与十字牡丹珊瑚之间外，其余珊瑚之间均存在显著差异（成对检验，$P \leqslant 0.01$）。单从珊瑚种类分析，美丽鹿角珊瑚在整个实验过程中 CAT 变化均无明显差异（邓肯检验，$P \leqslant 0.05$）；风信子鹿角珊瑚仅在 30 ℃和 36 ℃之间存在显著差异（邓肯检验，$P \leqslant 0.05$）；十字牡丹珊瑚仅在 30 ℃与其余三个温度之间存在显著差异（邓肯检验，$P \leqslant 0.05$）；澄黄滨珊瑚在 33 ℃与其余三个温度之间以及基准线温度（30 ℃）和 39℃之间存在显著差异（邓肯检验，$P \leqslant 0.05$）。就各珊瑚 CAT 含量变化趋势而言，两种鹿角珊瑚在 39℃处理下，CAT 含量基本持平，但前三个处理温度风信子鹿角珊瑚始终高于美丽鹿角珊瑚，说明其抗氧化应激反应更加积极。十字牡丹珊瑚和澄黄滨珊瑚二者相比于鹿角珊瑚，高温处理下数值高，变化小（邓肯检验，$P \leqslant 0.05$），说明二者对高温的响应更积极，且以澄黄滨珊瑚为最高。

从 SOD 结果分析，30 ℃处理下十字牡丹珊瑚与其余三种珊瑚之间存在显著差异（成对检验，$P \leqslant 0.01$），以及美丽鹿角珊瑚与澄黄滨珊瑚之间存在显著差异（成对检验，$P \leqslant 0.01$）；33 ℃处理下，除美丽鹿角珊瑚与十字牡丹珊瑚之间外，其余珊瑚之间均存在显著差异（成对检验，$P \leqslant 0.001$）；36 ℃处理下，除风信子鹿角珊瑚与澄黄滨珊瑚之间外，其余珊瑚之间均存在显著差异（成对检验，$P \leqslant 0.001$）；

39 ℃处理下，仅在十字牡丹珊瑚与其余珊瑚之间存在显著差异（成对检验，$P \leqslant 0.001$）。四种珊瑚的 SOD 含量显示，风信子鹿角珊瑚在前三个温度均高于美丽鹿角珊瑚，且较为稳定，在三个处理温度下均不存在显著差异（邓肯检验，$P \leqslant 0.05$）。美丽鹿角珊瑚虽然数值不如风信子鹿角珊瑚高，但也比较稳定，仅在 39℃下 SOD 含量升高（邓肯检验，$P \leqslant 0.05$），相比而言，其抗氧化积极性不如风信子鹿角珊瑚。十字牡丹珊瑚与澄黄滨珊瑚则是先升后降，且和风信子鹿角珊瑚一样，都在 39℃处理下和基准线温度之间并无明显差异，这种情况或许说明此三种珊瑚对高温环境适应性更强，反观美丽鹿角珊瑚均在 39℃和 30℃存在显著差异（邓肯检验，$P \leqslant 0.05$），说明其在高温下调整自身的能力不如其他三种珊瑚。

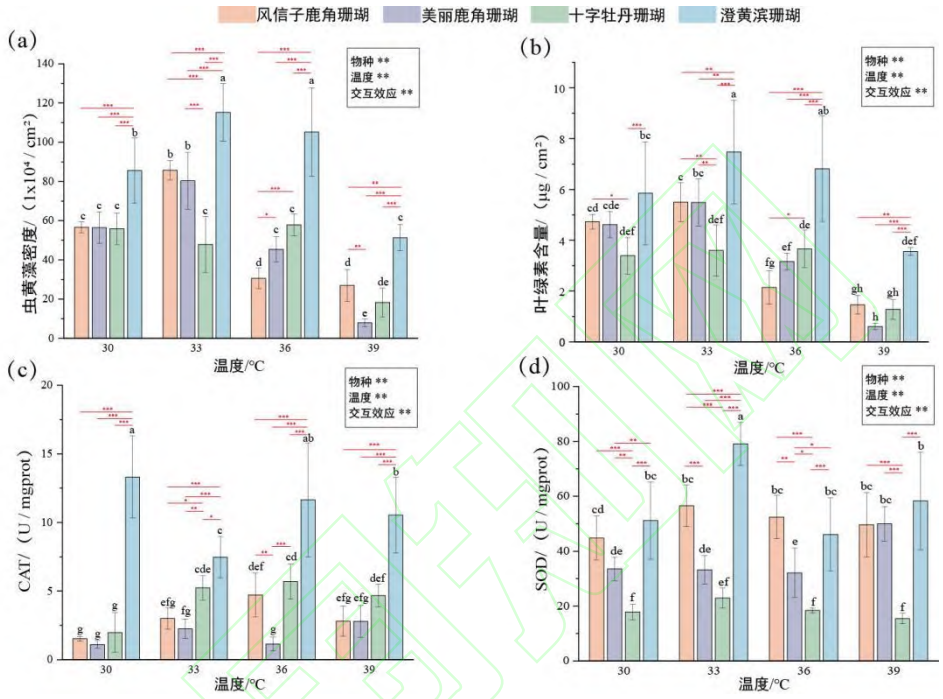


图 4　CBASS 系统实验条件下四种珊瑚生理生化指标的变化

Fig. 4 Changes in physiological and biochemical indicators of four corals under experimental conditions of CBASS system

3　讨论

3.1 涠洲岛四种造礁石珊瑚耐热性差异分析

虫黄藻密度、叶绿素 *a* 含量和最大光量子产量等光合作用特征被视为珊瑚重要的自养指标，也是评估珊瑚共生体系健康程度的重要指标[19-20]。本实验中两种鹿角珊瑚及澄黄滨珊瑚的虫黄藻密度、叶绿素 *a* 含量和最大光量子产量三个指标均呈现先升后降的趋势，而十字牡丹珊瑚则为先降再升又降趋势。结合 CBASS 方法测得珊瑚耐热阈值来看，在环境温度接近阈值之前，温度上升可能对珊瑚具有一些正面效应。有研究表明，温度上升会增强珊瑚的光合效应，为珊瑚共生体的日常生理活动及恢复提供帮助以调控自身来适应当前环境[21]。但当环境温度逼近甚至超过珊瑚耐热阈值时，其阈值前后生理指标均存在显著差异，比如美丽鹿角珊瑚耐热阈值为 36.8 ℃，在 33 ℃处理下和 36 ℃处理下之间，三个生理指标均存在显著差异。后续降低是因为环境温度超过其耐热阈值导致珊瑚−虫黄藻共生体系发生崩溃，使虫黄藻分离导致密度降低[22]，高温环境还会使虫黄藻光合系统电子转移受阻，所以最大光量子产量也会降低[23]，这可能会导致虫黄藻出现光抑制现象，导致光合作用能力降低[24]。

CAT 与 SOD 作为抗氧化酶可以反映珊瑚的防御机制，即在不利的环境变化中生物有机体将产生有害的活性氧，此时珊瑚的应激反应会促进抗氧化酶的分泌以应对环境压力[20]。风信子鹿角珊瑚在环境温度逼近其耐热阈值时两种抗氧化酶均存在显著高于基准线温度（30 ℃），但其余三种珊瑚并不明显。两种鹿角珊瑚对比，风信子鹿角珊瑚表现出更强烈的抗氧化反应以维持共生体的稳定，所以我们认为风信

子鹿角珊瑚可能有着更好的耐热性潜力，这也与 CBASS 方法测出风信子鹿角珊瑚有着更高耐热阈值的结果一致。

十字牡丹珊瑚和澄黄滨珊瑚的抗氧化酶则并没有统一趋势变化。结合 CBASS 结果，二者相对较高的耐热阈值来看，可能是因为环境温度对它们的威胁没有对鹿角珊瑚的那么巨大，其抗氧化酶的起伏趋势随温度呈现先升后降的波浪形或许说明这两种珊瑚对高温环境有更高的适应性。此二者珊瑚在环境改变之初也会积极进行抗氧化反应，但随着温度上升，共生体逐渐适应环境改变，抗氧化水平回落。之后再上升下降是珊瑚共生体在重复对环境温度改变应激与适应的过程。这可能就是一些研究证据中，澄黄滨珊瑚等珊瑚白化率及死亡率都低于鹿角珊瑚[25-27]的原因。并且，大量的研究表明造成不同形态珊瑚耐热性差异的原因是多样的。分枝状的鹿角珊瑚表面积与体积比相比块状及片状珊瑚更高，与周围水体热量交换更迅速，故而更容易受到热应力影响[28]；不同形态珊瑚的共生虫黄藻多样性不同，这也导致了其珊瑚-虫黄藻共生体对高温的耐受性差异[29]；从能量储备而言，块状珊瑚通常具有更厚的组织，能量储备更充足，可以在高温条件下维持相对更长的时间[30]；此外，块状珊瑚可能更擅长激活热休克蛋白（HSPs）和其他保护基因以应对高温压力[31]。根据 CBASS 方法的耐热阈值结果以及本实验中，当实验温度超过不同珊瑚各自的耐热阈值时的各项生理生化指标，我们认为涠洲岛四种造礁石珊瑚中，鹿角珊瑚的耐热性低于其余两种珊瑚，且风信子鹿角珊瑚优于美丽鹿角珊瑚。

3.2 鹿角珊瑚是珊瑚礁生态修复工作优先关注的种群并应将其作为主要修复品种

多项研究表明，与大块状珊瑚相比，分枝状的鹿角珊瑚耐热性较低，这可能与珊瑚形态、生长速度、虫黄藻组成以及细菌组成有关[32-35]，并且鹿角珊瑚往往成片聚集生长，其群体高整合性导致鹿角群落会对温度异常有更大反应[36]。换言之，即一个健康的珊瑚礁生态系统在面临环境恶化时，鹿角珊瑚可能是最先退化甚至消失的。鹿角珊瑚的消失又会导致整个珊瑚礁生态系统多样性减少，系统抗性下降，进而整个生态系统面临更大的退化风险。所以在人为进行珊瑚礁生态修复工作时，我们应当首先关注鹿角珊瑚的退化程度。结合本实验结果，虽然十字牡丹珊瑚与澄黄滨珊瑚有更高的耐热阈值，但考虑到此两种珊瑚生长缓慢，且形态多样性低，并不适合作为珊瑚礁生态修复工程的主要品种。所以，我们将目光锁定至鹿角珊瑚。鹿角珊瑚具有生长迅速和形态多样性丰富等优势，并且，考虑到未来可能持续恶化的珊瑚礁生存环境，风信子鹿角珊瑚具有更高的耐热阈值及耐热潜力，风信子鹿角珊瑚是更为理想的珊瑚礁生态修复品种。

基于此，以风信子鹿角珊瑚为主要品种，辅以多种珊瑚共同进行珊瑚礁生态修复，可以达到快速构建珊瑚礁生态系统的同时又保证此生态系统内部多样性，增强其抵御外界环境变化能力的效果。这为实施珊瑚礁生态修复和可持续发展提供重要参考和相关依据。

3.3 涠洲岛海域仍具有作为相对高纬度珊瑚避难所的巨大潜力

本实验采样地点涠洲岛地处热带北缘，从地理条件、纬度和气候来看涠洲岛都满足珊瑚避难所假说，但相关的文献记载以及当地珊瑚礁历史演变[37-39]结合涠洲岛现状来看似乎又并没有达到珊瑚避难所假说的预期。但无法忽略的是涠洲岛作为热门的海岛旅游地，其人为因素对珊瑚礁生存环境的影响已经超出了珊瑚礁生存“边缘”的界定。

本实验考虑珊瑚的自然生长，利用 CBASS 系统方法测定了四种当地造礁石珊瑚的耐热阈值，所得结果均大于当地最高海水温度（33 ℃，数据来源于本实验室投放的 HOBO 温度计）。实验珊瑚在 33 ℃处理下，相比基准线温度（30 ℃）其生理指标略微上升表明珊瑚-虫黄藻共生系统并未受到太大影响，甚至略有正面效应。生化指标变化也较小，说明其抗氧化应激反应并不强烈，其耐热阈值超过 33℃是可信的。本实验所得到的珊瑚耐热阈值横向对比其余海域的类似实验中的同种珊瑚较高[12,40-41]，首先或许是因为所使用的珊瑚样品是采集于 8 月的健康珊瑚，涠洲岛海域环境温度相对其他研究区域更高，且珊瑚本身在面临了至少一轮（2024 年当年）海水高温中保持健康，可能受到自然高温驯化增强了其热耐受性[42-44]，并时处夏季，就以往的研究经验，不同季节（主要区别是珊瑚生存海水温度），同种珊瑚耐热阈值也不尽相同。此外，本实验反映的是此四种石珊瑚在短期急性应激环境所预测的耐热阈值，所以其阈值结果高过许多长期胁迫研究所得结论，是因为本实验所得珊瑚耐热阈值并不代表珊瑚可以长

期生存在此高温中，而更倾向于进行不同珊瑚或同种珊瑚不同季节中耐热性的对比，并非作为长期珊瑚胁迫评估的依据。

本实验所测的四种珊瑚耐热阈值说明当地四种珊瑚在高温季节有着超过生存环境的耐热阈值，在涠洲岛水域这一相对高纬度地区的珊瑚或许已经逐渐适应了环境改变，高纬度地区水温较冷不适合珊瑚生长这一问题正在被珊瑚自身逐步克服，这也满足相关研究所推断的珊瑚礁分布范围正在向高纬度地区扩展[45]。

综上所述，涠洲岛当地造礁石珊瑚并未受到来自环境温度上升带来的致命威胁，并且在一些近岸水域，还发现了以较为脆弱的鹿角珊瑚为主的新珊瑚群落生长[46]，总体而言，涠洲岛海域从其地理位置以及当地珊瑚所具备的高纬度珊瑚礁的生态特征[47]来看，具有较高可待发掘的作为珊瑚避难所的潜力。其珊瑚礁生长现状未达到预期的原因可能更多是来自人类活动的干扰[48]，如过度捕捞、物理损伤（船锚拖底、渔网纠缠）、多种排放物造成的沉积物覆盖、盗采珊瑚等，所以在保护、修复涠洲岛珊瑚礁的同时，加强监管维护，规范渔业行为或许能更大程度上减轻涠洲岛珊瑚礁生存压力。

参考文献

[1] CARPENTER K E, ABRAR M, AEBY G, et al. One-third of reef-building corals face elevated extinction risk from climate change and local impacts [J]. Science, 2008, 321(5888): 560-563.

[2] HOEGH-GULDBERG O, MUMBY P J, HOOTEN A J, et al. Coral reefs under rapid climate change and ocean acidification [J]. Science, 2007, 318(5857): 1737-1742.

[3] HUGHES T P, KERRY J T, ÁLVAREZ-NORIEGA M, et al. Global warming and recurrent mass bleaching of corals [J]. Nature, 2017, 543(7645): 373-377.

[4] KLEYPAS J A, MCMANUS J W, MEÑEZ L A B. Environmental limits to coral reef development: Where do we draw the line? [J]. American Zoologist, 1999, 39.

[5] COOPER T F, DE'ATH G, FABRICIUS K E, et al. Declining coral calcification in massive *Porites* in two nearshore regions of the northern Great Barrier Reef [J]. Global Change Biology, 2008, 14(3): 529-538.

[6] TANZIL J T I, BROWN B E, TUDHOPE A W, et al. Decline in skeletal growth of the coral *Porites lutea* from the Andaman Sea, south Thailand between 1984 and 2005 [J]. Coral Reefs, 2009, 28(2): 519-528.

[7] DENIS V, MEZAKI T, TANAKA K, et al. Coverage, diversity, and functionality of a high-latitude coral community (Tatsukushi, Shikoku Island, Japan) [J]. Plos One, 2013, 8(1): e54330.

[8] RIEGL B, PILLER W E. Possible refugia for reefs in times of environmental stress [J]. International Journal of Earth Sciences, 2003, 92(4): 520-531.

[9] 王欣, 高霆炜, 陈骁, 等. 涠洲岛园艺式珊瑚苗圃的架设与移植 [J]. 广西科学, 2017, 024(005): 462-467.

[10] 蓝军南, 杨艳华, 王欣, 等. 涠洲岛珊瑚礁生态恢复可行性评估及其恢复策略 [J]. 应用海洋学学报, 2023, 42(2): 235-245.

[11] EVENSEN N R, FINE M, PERNA G, et al. Remarkably high and consistent tolerance of a Red Sea coral to acute and chronic thermal stress exposures [J]. Limnology & Oceanography, 2021, 66(5): 1718-1729.

[12] EVENSEN N R, VOOLSTRA C R, FINE M, et al. Empirically derived thermal thresholds of four coral species along the Red Sea using a portable and standardized experimental approach [J]. Coral reefs, 2022, 41: 239-252.

[13] ALDERDICE R, VOOLSTRA C R, LENDO C I N, et al. Loss of coral thermotolerance following year-long in situ nursery propagation with a consecutively high summer heat-load [J]. Coral Reefs, 2024, 43(4): 919-933.

[14] 刘旭. 造礁石珊瑚对温度胁迫的响应机制研究 [D]. 南宁：广西大学, 2020.

[15] JEFFREY S W, HUMPHREY G F. New spectrophotometric equations for determining chlorophylls a, b, c1, and c2 in higher plants, algae and natural phytoplankton [J]. Plant Physiology and Biochemistry, 1975, 8: 53-59.

[16] TANG J, NI X, ZHOU Z, et al. Acute microplastic exposure raises stress response and suppresses detoxification and immune capacities in the scleractinian coral *Pocillopora damicornis* [J]. Environ Pollut, 2018, 243(Pt A): 66-74.

[17] ZHOU Z, NI X, WU Z, TANG J. Physiological and transcriptomic analyses reveal the threat of herbicides glufosinate

and glyphosate to the scleractinian coral *Pocillopora damicornis* [J]. Ecotoxicology and Environmental Safety, 2022, 229: 113074.

[18] VOOLSTRA C R, BUITRAGO MMóPEZ C, PERNA G, et al. Standardized short-term acute heat stress assays resolve historical differences in coral thermotolerance across microhabitat reef sites [J]. Global Change Biology, 2020, 26(8): 4328-4343.

[19] SASKIA H, PATTEN N L, WAITE A M, et al. Temporal variations in metabolic and autotrophic indices for *Acropora digitifera* and *Acropora spicifera* – implications for monitoring projects [J]. Plos one, 2013, 8(5): e63693.

[20] 张海洋，赵美霞，钟瑜，等. 南海北部造礁石珊瑚共生体光合作用特征季节性监测 [J]. 海洋地质前沿, 2021, 37(06): 84-91.

[21] HOEGH-GULDBERG O. Climate change, coral bleaching and the future of the world's coral reefs [J]. Marine and Freshwater Research, 1999, 50(8): 839-866.

[22] MOYA A, SAKAMAKI K, MASON B M, et al. Functional conservation of the apoptotic machinery from coral to man: The diverse and complex bcl-2 and caspase repertoires of *Acropora millepora* [J]. BMC Genomics, 2016, 17(1): 62.

[23] BHAGOOLI R, HIDAKA M. Photoinhibition, bleaching susceptibility and mortality in two scleractinian corals, *platygyra ryukyuensis* and *stylophora pistillata*, in response to thermal and light stresses [J]. Comparative Biochemistry and Physiology part A: Molecular & Integrative Physiology, 2004, 137(3): 547-555.

[24] MCCORD J M. Oxygen-derived free radicals in postischemic tissue injury [J]. New England Journal of Medicine, 1985, 312(3): 159-163.

[25] XU H, FENG B, XIE M, et al. Physiological characteristics and environment adaptability of reef-building corals at the Wuzhizhou Island of South China Sea [J]. Frontiers in Physiology, 2020, 11.

[26] MADEIRA C, DIAS M, FERREIRA A, et al. Does predation exacerbate the risk of endosymbiont loss in heat stressed hermatypic corals? Molecular cues provide insights into species-specific health outcomes in a multi-stressor ocean [J]. Frontiers in Physiology, 2022, 13.

[27] CANNON S, ARAM E, BEIATEUEA T, et al. Coral reefs in the Gilbert Islands of Kiribati: Resistance, resilience, and recovery after more than a decade of multiple stressors [J]. Plos one, 2021, 16(8): e0255304.

[28] LOYA Y, SAKAI K, YAMAZATO K, et al. Coral bleaching: The winners and the losers [J]. Ecology Letters, 2001, 4(2): 122-131.

[29] DOUMA S, VAN LAAR T, ZEVENHOVEN J, et al. Suppression of anoikis and induction of metastasis by the neurotrophic receptor trkb [J]. Nature, 2004, 430(7003): 1034-1039.

[30] ANTHONY K R N, HOOGENBOOM M O, CONNOLLY S R. Adaptive variation in coral geometry and the optimization of internal colony light climates [J]. Functional Ecology, 2005, 19(1): 17-26.

[31] MAYFIELD A B, CHAN P-H, PUTNAM H M, et al. The effects of a variable temperature regime on the physiology of the reef-building coral seriatopora hystrix: Results from a laboratory-based reciprocal transplant [J]. Journal of Experimental Biology, 2012, 215(23): 4183-95.

[32] BARKER V. Exceptional thermal tolerance of coral reefs in American Samoa: A review [J]. Current Climate Change Reports, 2018, 4(4): 417-427.

[33] MCCLANAHAN T R, BAIRD A H, MARSHALL P A, et al. Comparing bleaching and mortality responses of hard corals between southern Kenya and the Great Barrier Reef, Australia [J]. Marine Pollution Bulletin, 2004, 48(3): 327-335.

[34] ONG R H，KING A J C，KAANDROP J A, et al. The effect of allometric scaling in coral thermal microenvironments [J]. Plos one, 2017, 12(10): e0184214.

[35] XU M, CHENG K, XIAO B, et al. Bacterial communities vary from different scleractinian coral species and between bleached and non-bleached corals [J]. Microbiology Spectrum, 2023, 11(3): e04910-22.

[36] BAIRD A H, MARSHALL P A. Mortality, growth and reproduction in scleractinian corals following bleaching on the Great Barrier Reef [J]. Marine Ecology Progress Series, 2002, 237: 133-141.

[37] CHEN T, LI S, YU K, et al. Increasing temperature anomalies reduce coral growth in the Weizhou Island, northern South China Sea [J]. Estuarine, Coastal and Shelf Science, 2013, 130(3): 121-126.

[38] WANG W，YU K，WANG Y. A review on the research of coral reefs in the Weizhou Island, Beibu Gulf [J]. Tropical Geography, 2016, 36(1): 72-79.

[39] 周浩郎，葛文标. 北部湾石珊瑚多样性 [J]. 广西科学院学报, 2024, 40(3): 310-330.

[40] ANDERSON K D, CANTIN N E, CASEY J M, et al. Independent effects of ocean warming versus acidification on the growth, survivorship and physiology of two *Acropora* corals [J]. Coral Reefs, 2019, 38(6): 1225-1240.

[41] MARSHALL P A, BAIRDA H. Bleaching of corals on the Great Barrier Reef: differential susceptibilities among taxa [J]. Coral Reefs, 2000, 19(2): 155-163.

[42] HARRISON H B, ÁLVAREZ-NORIEGA M, BAIRD A H, et al. Back-to-back coral bleaching events on isolated atolls in the Coral Sea [J]. Coral Reefs, 2019, 38(4): 713-719.

[43] MIDDLEBROOK R, HOEGH-GULDBERG O, LEGGAT W. The effect of thermal history on the susceptibility of reef-building corals to thermal stress [J]. Journal of Experimental Biology, 2008, 211(7): 1050-1056.

[44] 蒙林庆，黄雯，阳恩广，等. 高温白化事件可提高涠洲岛澄黄滨珊瑚（*Porites lutea*）的耐热性 [J]. 海洋学报, 2022, 44(08): 87-96.

[45] YAMANO H, SUGIHARA K, NOMURA K. Rapid poleward range expansion of tropical reef corals in response to rising sea surface temperatures [J]. Geophysical Research Letters, 2011, 38(4): L04601.

[46] 史海燕. 广西北海涠洲岛珊瑚礁海域生态环境监测与评价 [D]. 青岛：中国海洋大学, 2012.

[47] BEGER M, SOMMER B, HARRISON P L, et al. Conserving potential coral reef refuges at high latitudes [J]. Diversity and Distributions, 2014, 20(3): 245-257.

[48] HUGHES T P, BARNES M L, BELLWOOD D R, et al. Coral reefs in the anthropocene [J]. Nature, 2017, 546(7656): 82-90.

Determination and comparative analysis of thermal tolerance thresholds and the differences for four species of reef-building corals around Weizhou Island

XU Mingpei[1,2]，HUANG Wen[2*]，CHEN Jinlian[2]，HUANG Zhihua[2]，
ZHOU Yupeng[1,2]，WAN Qiang[1,2]，LI Yuxiao[2]，YU Kefu[2,3]

（1.School of Resources, Environment and Materials, Guangxi University, Nanning 530004, China; 2. Guangxi Laboratory on the Study of Coral Reefs in the South China Sea, Coral Reef Research Center of China, School of Marine Sciences, Guangxi University, Nanning 530004, China;3. Southern Marine Science and Engineering Guangdong Laboratory (Guangzhou), Guangzhou 511458, China）

Abstract: Against the background of global warming, rising sea temperatures have led to frequent large-scale coral bleaching events, severely threatening the health of coral reef ecosystems. To compare the differences in thermal tolerance among different coral morphologies and provide a scientific basis for coral reef restoration efforts, this study introduced the CBASS (Coral Bleaching Automated Stress System) method to determine the thermal thresholds of four species of stony corals during the extreme high-temperature period in the summer of 2024 on Weizhou Island, while analyzing their physiological and biochemical indicators. The results showed: (1) The thermal thresholds of the corals were consistent with their physiological and biochemical indicators, with *Acropora* exhibiting the lowest thermal tolerance. The thermal thresholds of the four coral species were as follows: *Acropora hyacinthus* 37.55℃, *Acropora muricata* 36.84℃, *Pavona decussata* 39.40℃, and *Porites lutea* 39.50℃; (2) The differences in thermal tolerance indicate that *Acropora* will degrade first under high-

temperature stress, and thus should be prioritized in coral reef restoration efforts; (3) The local corals on Weizhou Island were not subjected to lethal threats from environmental temperatures. This suggests that Weizhou Island still holds significant potential as a relatively high-latitude coral refuge.
Key words: Weizhou Island; global warming; coral reef ecological restoration；coral heat resistance; coral refuge

周榆鹏, 肖遵勇, 陈锦连, 等. 美丽鹿角珊瑚(*Acropora muricata*)与风信子鹿角珊瑚(*Acropora hyacinthus*)的耐热性差异研究[J]. 海洋学报, 2025, 47(7): 1–11, doi:10.12284/hyxb2025078
Zhou Yupeng, Xiao Zunyong, Chen Jinlian, et al. The difference in thermal tolerance between *Acropora muricata* and *Acropora hyacinthus*[J]. Haiyang Xuebao, 2025, 47(7): 1–11, doi:10.12284/hyxb2025078

美丽鹿角珊瑚（*Acropora muricata*）与风信子鹿角珊瑚（*Acropora hyacinthus*）的耐热性差异研究

周榆鹏[1,2]，肖遵勇[1,2]，陈锦连[2]，黄智华[2]，徐明培[1,2]，谭荣华[2]，蒙林庆[2]，王永刚[2]，余克服[2,3]，黄雯[2*]

(1. 广西大学 资源环境与材料学院, 广西 南宁 530004; 2. 广西大学 海洋学院, 珊瑚礁研究中心, 广西南海珊瑚礁研究重点实验室, 广西 南宁 530004; 3. 南方海洋科学与工程广东省实验室(广州), 广东 广州 511458)

摘要: 全球变暖导致珊瑚大规模白化事件频发, 珊瑚礁生态系统加速退化。国际上通常采用珊瑚移植的方式来修复退化的珊瑚礁, 其中移植的珊瑚中鹿角珊瑚（*Acropora*）占大部分。然而, 快速生长的枝状鹿角珊瑚对热更敏感, 影响其在日益变暖的海洋环境中的修复效果。为了了解鹿角珊瑚的高温响应模式以及耐热性差异, 本研究对广西涠洲岛美丽鹿角珊瑚（*Acropora muricata*）和风信子鹿角珊瑚（*Acropora hyacinthus*）进行了高温胁迫实验。通过生理生化指标分析, 高温胁迫后, 美丽鹿角珊瑚触手收缩、颜色变淡, 抗氧化物（超氧化物歧化酶、还原型谷胱甘肽、过氧化氢酶）、铵同化酶（谷氨酰胺合成酶）以及半胱氨酸天冬氨酸蛋白酶 3（caspase-3）的活性（含量）水平表现为先升后降的趋势, 风信子鹿角珊瑚的响应模式也几乎保持一致（除超氧化物歧化酶和谷氨酰胺合成酶外）。在 34℃ 下, 风信子鹿角珊瑚的生理指标表现更佳, 超氧化物歧化酶、铵同化酶和 caspase-3 始终保持高活性及灵敏反应, 意味着风信子鹿角珊瑚通过提高这些蛋白酶活性来抵抗高温环境, 其比美丽鹿角珊瑚更具耐热性。本研究揭示了两种鹿角珊瑚高温胁迫下的生理响应模式, 并比较了两者之间的耐热性差异, 为耐热珊瑚挑选和珊瑚礁生态修复提供理论依据。

关键词: 涠洲岛; 鹿角珊瑚; 高温胁迫; 耐热性; 珊瑚礁修复

中图分类号:　　**文献标志码:** A　　**文章编号:** 0253−4193(2025)07−0001−11

1　引言

作为地球上最具生产力的海洋生态系统之一, 珊瑚礁生态系统在生物资源保护、环境调节、海岸保护、休闲娱乐等方面起着重要的作用[1−2]。然而, 近年来由于气候变暖, 导致了珊瑚大规模白化事件频发[3−4], 过去 30 a 已发生 4 次全球珊瑚白化事件[5], 并且第二次事件(2010 年)与第三次事件(2014−2017 年)之间仅仅间隔 4 a[6]。全球珊瑚礁生态系统正在快速退化, 预计到 21 世纪中叶珊瑚覆盖度将减少 70%～90%, 全球变暖是主要的原因之一[7−8]。除非迅速减少碳排放, 否则到本世纪末, 世界上所有的珊瑚礁可能都将白化[9]。因此, 对珊瑚抵抗高温能力的研究尤为重要且紧迫。

珊瑚的耐热性与体内一些蛋白酶活性密切相关, 如抗氧化酶、谷氨酰胺合成酶(Glutamine Synthetase, GS)及 caspase-3 等[10]。不同种珊瑚高温胁迫实验也

收稿日期: 2025−01−03; **修订日期:** 2025−03−20。
基金项目: 广西自然科学基金 (2023GXNSFAA026510); 国家自然科学基金 (42090041, 42030502)。
作者简介: 周榆鹏(1999—), 男, 广西壮族自治区桂林市人, 主要从事珊瑚礁生态修复研究。E-mail: 19997971546@163.com
*** 通信作者:** 黄雯, 副教授, 硕士生导师, 主要从事珊瑚礁生态修复和珊瑚群体遗传学研究工作。E-mail: wenhuang@gxu.edu.cn

发现，耐热性差异与抗氧化酶活性高低有关[11−12]。对大堡礁跨越 12 个纬度珊瑚的遗传标记研究认为，抗氧化能力可以作为标记来选择耐受性珊瑚用于珊瑚礁管理[13]。因此，探索不同种珊瑚在热应激下的抗氧化酶等蛋白酶活性变化，有利于了解不同种珊瑚之间耐热性的反应及其差异，这对于当前退化严重的珊瑚礁生态系统的恢复至关重要。

不同形态珊瑚的耐热性存在差异，通常来说，块状＞片状＞枝状[14−15]。枝状珊瑚尤其是鹿角珊瑚作为珊瑚礁生态修复的功能性物种，在珊瑚移植工作中被广泛使用[16−18]。值得注意的是，移植的枝状珊瑚之间存活率存在差异，耐热性高低可能是原因之一。有研究发现，在没有干扰的情况下，移植到人工基底上的鹿角珊瑚的死亡率比杯形珊瑚（*Pocillopora*）低 37%；在海洋热浪期间，鹿角珊瑚的死亡率反而比杯形珊瑚高[19]。因此，了解枝状珊瑚之间耐热性的差异，筛选出耐热性较强的枝状珊瑚，对珊瑚礁管理和珊瑚礁生态修复有重要意义。

美丽鹿角珊瑚和风信子鹿角珊瑚在国内外的珊瑚礁修复工作中均有移植[16, 17, 20]。在广西北海涠洲岛海域，美丽鹿角珊瑚（*Acropora muricata*）和风信子鹿角珊瑚（*Acropora hyacinthus*）是枝状珊瑚中的优势种，也是涠洲岛珊瑚礁生态修复工作中首选的枝状珊瑚物种[21]。尽管先前有对这两种鹿角珊瑚的耐热性研究，但主要集中在生理和共生藻层面[22−23]，抗氧化酶方面的讨论较少。在涠洲岛海域，有对澄黄滨珊瑚（*Porites lutea*）[11]、十字牡丹珊瑚（*Pavona decussata*）[10]和霜鹿角珊瑚（*Acropora pruinosa*）[24]等珊瑚的耐热性研究，但尚未见有对该海域的美丽鹿角珊瑚和风信子鹿角珊瑚在这方面的报道。为了了解这两种鹿角珊瑚的耐热性差异及其热应激反应，本研究以涠洲岛采集的美丽鹿角珊瑚和风信子鹿角珊瑚活体样本，进行高温胁迫实验，通过对比虫黄藻密度、叶绿素 *a* 含量等生理指标变化以及超氧化物歧化酶（Superoxide Dismutase, SOD）、过氧化氢酶（Catalase , CAT）、还原型谷胱甘肽（Glutathione, GSH）、GS 和 caspase-3 活性（含量）高低，探索这两种鹿角珊瑚面对高温的响应模式以及耐热性差异，为珊瑚礁修复中移植种类的选择和决策提供理论依据。

2 材料与方法

2.1 研究区域与材料

本实验所使用的美丽鹿角珊瑚和风信子鹿角珊瑚活体样品均采集于广西北海市涠洲岛（20°54′～21°10′N，109°00′～109°15′E）北部的珊瑚苗圃区（图 1A），水深 2～5 m，采集时间为 2023 年 8 月。

2.2 实验设计

本次实验采集两种鹿角珊瑚样品各 5 株，采样完成后使用带水水箱打包运送至广西大学涠洲岛珊瑚馆，放入循环海水珊瑚养殖缸以 26℃ 海水进行暂养。待珊瑚触手自然伸展，生长状态良好时，即可进行下一步实验。使用斜嘴钳从每株鹿角珊瑚样品中剪切下 3 个长约为 10 cm 的珊瑚分枝，将其中 1 个珊瑚分支放于对照缸（用于 26℃ 对照与取样），剩余 2 个珊瑚分枝放于实验缸（分别用于 30℃ 和 34℃ 取样），以此方法处理完所有的珊瑚样品。最后，将缸里的珊瑚分枝暂养至健康状况恢复良好。本次实验使用的对照缸和实验缸均为循环海水养殖缸，规格为 900 mm×600 mm×800 mm（长×宽×高），整个养殖系统的储水量约为 450 L。采用通过透明阳光棚的自然太阳光作为光源，使用加热棒和水冷机维持水温稳定，定期更换自然海水，并定期检测水质，保持水体指标稳定在盐度 33～35、KH7.0～7.3、pH8.1～8.3、Ca^{2+}质量浓度为 340×10^{-6}～380×10^{-6}、Mg^{2+}浓度 $1\,330\times10^{-6}$～$1\,370\times10^{-6}$、$NH^{+}_{4}<0.15\times10^{-6}$、$NO^{-}_{3}<0.1\times10^{-6}$、PO3- 4＜$0.1\times10^{-6}$，即在自然海水参数范围内。对照缸与实验缸除水温不一样外，其他条件均保持一致。

根据涠洲岛自然海域温度情况（图 1B），本实验设置 3 个取样点（图 1C），分别为 26℃（适宜水温）、30℃（夏季正常水温）和 34℃（极端高温）。实验缸水温从 26℃ 开始，每天晚上 20: 00 调节加热棒和水冷机，按照 1℃/d 的升温幅度进行升温，在水温 30℃ 停留 3 d 后取样，使珊瑚机体有充分的时间来应对环境温度的变化，随后以同样的方式升温，在水温 34℃ 持续 3 d 后取样。对照缸水体温度保持 26℃ 不变，直至实验结束后取样，本次实验周期为 13 d。取样时迅速把样品装入无菌无酶的样品袋，做上标记并立刻用液氮进行急冻 15 min 处理。随后把收集好的珊瑚样品用干冰保存运输到广西大学珊瑚礁研究中心的实验室，迅速放入−80℃ 冰箱保存，用于后续生理生化指标的检测。

2.3 生理生化指标测量

2.3.1 生理指标测量

珊瑚表型：实验过程中，每天观察珊瑚样品的表观形态，如触手伸展情况、颜色变化、黏液分泌、组织脱落等情况，并使用 Olympus Tough TG-6（Olympus, OM Digital Solutions Corporation, Tokyo, Japan）对各个珊瑚分枝样品拍照记录。

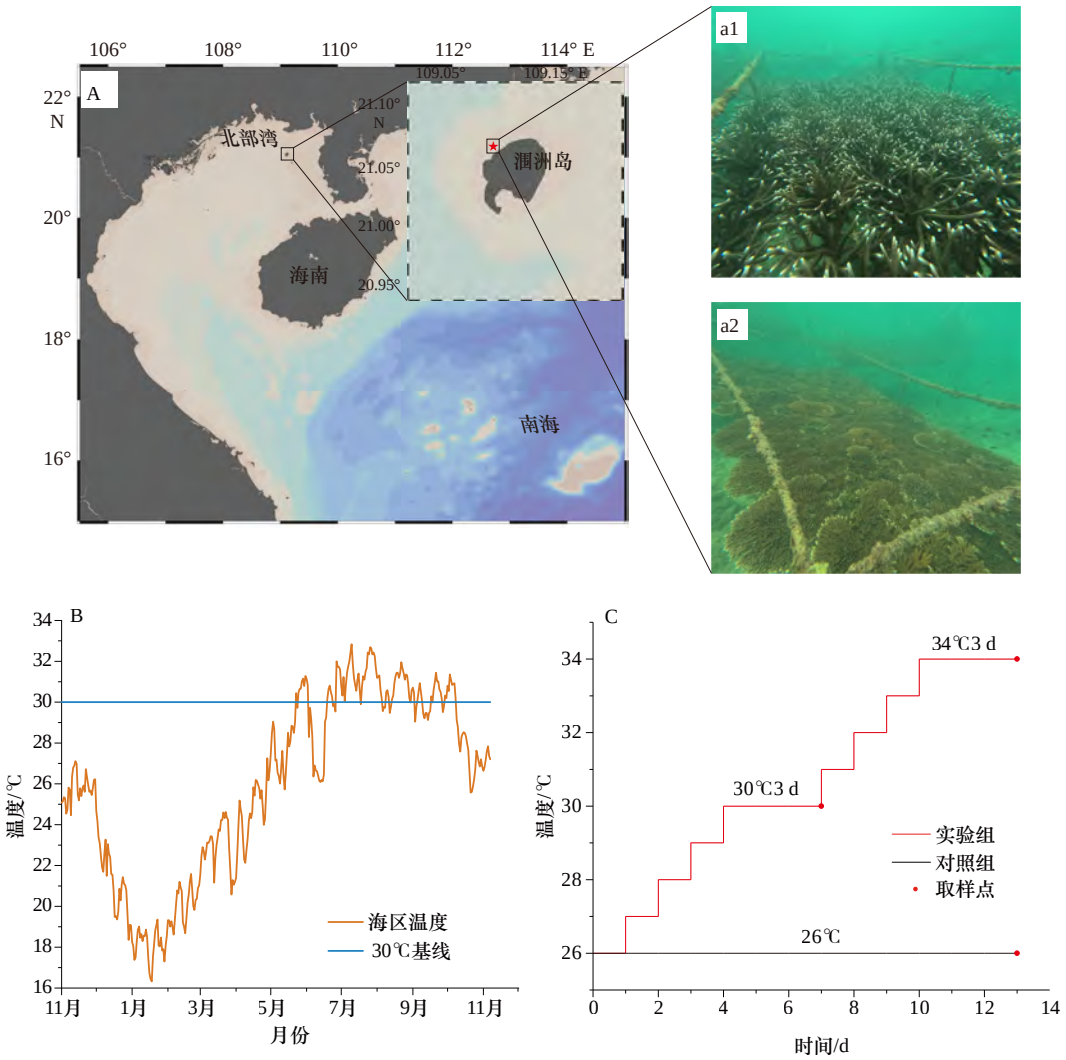


图 1　采样区域和实验方法

Fig. 1　Sampling locations and experimental method

A. 红色星形为具体采样海域, a1 为美丽鹿角珊瑚苗圃, a2 为风信子鹿角珊瑚苗圃; B. 2022 年 11 月至 2023 年 11 月自然海区温度, 采用 HOBO 水下温度计(Onset 公司, 美国)实测; C. 高温胁迫实验设计方法

Fig.1 A. The red star is the sampling area, a1 is the *Acropora muricata* nursery, a2 is the *Acropora hyacinthus* nursery; B. The natural sea temperature from November 2022 to November 2023 was measured by the HOBO underwater thermometer (Onset, USA); C. Method of heat-stress experiment design

虫黄藻密度测定: 用装有无菌过滤海水(滤膜孔径 0.45 μm)的洗牙器(Waterpik, 美国)冲洗珊瑚样品, 得到珊瑚组织冲洗液和珊瑚骨骼, 测量冲洗液总体积(V, 单位: mL)后, 取 50 mL 冲洗液在 3 000 g、4℃ 条件下离心 10 min, 弃上清液, 再加 20 mL 过滤海水继续离心, 重复 2～3 次后, 弃上清液, 加入 10 mL 过滤海水摇匀后进行镜检, 通过镜检后再次摇匀并取其中 1 mL 液体离心, 弃上清液, 加入 1 mL 4% 甲醛溶液固定, 使用血球计数板法(重复 8 次)测得虫黄藻浓度(C, 单位: cells/mL)。珊瑚骨骼置于 35℃ 烘箱干燥后, 采用铝箔法测量表面积[25]。根据以下公式计算得出虫黄藻密度(D, 单位: cells/cm^{-2})。

$$D = C \times V/(M/G), \qquad (1)$$

式中: M 为包裹珊瑚骨骼表面的铝箔纸质量(单位: g); G 为铝箔纸单位面积质量(单位: g/cm^2)。

叶绿素 a 测定: 从冲洗液中取 15 mL 以 4 000 r/min 离心 5 min, 缓慢去除上清液, 将 10 mL 90% 丙酮加入剩余沉淀物中, 在 4℃ 条件下萃取 24 h。将萃取后的溶液再次以相同条件离心, 用酶标仪分别测试波长为 750 nm、664 nm、647 nm 和 630 nm 处的吸光度, 参照 Jeffrey 和 Humphrey[26] 的方法, 代入下列公式得到叶绿素 a(Chl a, 单位: μg/mL)。

$$\text{Chl } a = 11.85 \times (A_{664} - A_{750}) - 1.54 \times (A_{647} - A_{750}) - 0.08 \times (A_{630} - A_{750}) \qquad (2)$$

式中: A_{750}、A_{664}、A_{647}、A_{630} 分别代表波长为 750 nm、664 nm、647 nm 和 630 nm 处的吸光度值。进一步计

算得到总体积冲洗液叶绿素 *a* 质量(单位: μg), 再除以珊瑚骨骼表面积即可得到单位面积叶绿素 *a* 含量(单位: μg/cm^2)。

2.3.2 生化指标测量

同样用洗牙器冲洗珊瑚样品组织得到高浓度组织匀浆(<10 mL), 取 2 mL 在 4℃、6 000 g 条件下离心 15 min, 取 1 mL 上清液, 用于生化指标测量。本实验使用商用试剂盒(南京建成生物工程研究所)进行各生化指标的测量, 根据试剂盒使用说明, 分别测量上清液中 SOD、CAT、GS、caspase-3 总活性和 GSH 含量, 具体操作步骤见文献[10]。随后使用 BCA 蛋白质分析试剂盒(上海生工生物工程股份有限公司)测得上清液蛋白质浓度, 最后依据试剂盒说明书的计算公式得到各生化指标活性和含量[27]。

2.4 实验数据处理

本实验使用 Ocean Data View 软件绘制研究区域地图, 使用 Photoshop 软件处理实验过程中拍摄的珊瑚样品照片。对于生理生化数据, 采用 IBM SPSS Statistics 27 软件检验各组数据均符合正态分布和方差齐性后, 以温度和珊瑚物种处理为固定因素, 进行双因素方差分析。当方差分析中存在显著的主效应($p < 0.05$)时, 对边际估计均值进行事后两两比较(Pairwise test), 以确定每种温度处理下珊瑚物种之间的差异是否具有统计学意义。此外, 事后多重比较(Duncan's multiple comparison)用来检验同一珊瑚物种中不同温度下数据的显著性。所有数据都是以均数±标准差(SD)表示。使用 Origin 2024 将实验结果绘制成图, 所有图像的整理、排版均在 Adobe Illustrator 2025 软件中进行。

3 实验结果

3.1 两种鹿角珊瑚的生理指标变化

3.1.1 表观形态变化

如图 2 所示, 在高温胁迫过程中, 两种鹿角珊瑚表观形态均表现为: 26℃ 时, 触手自然伸出, 颜色正常, 整体状态良好; 30℃ 时, 触手依旧伸展, 颜色没有明显变化; 34℃ 时, 触手收缩, 颜色明显变淡, 并有黏液分泌。除此以外, 在 34℃ 第 3 天时, 美丽鹿角珊瑚的颜色明显比风信子鹿角珊瑚淡, 更趋向于白化。

3.1.2 共生藻生理指标变化

如图 3 所示, 双因素方差分析结果表明, 两种鹿角珊瑚的虫黄藻密度均受温度显著影响($p<0.001$), 除此之外, 还受到温度×珊瑚物种显著影响($p<0.001$); 而两种鹿角珊瑚的叶绿素 *a* 含量还受到珊瑚物种的显著影响($p<0.001$)。在整个实验过程中, 除风信子鹿角珊瑚的虫黄藻密度在 26℃ 至 30℃ 时变



图 2 两种鹿角珊瑚在高温胁迫过程中表型变化

Fig. 2 Phenotypic changes of two species of staghorn corals under heat-stress

A1−A3.美丽鹿角珊瑚; B1−B3.风信子鹿角珊瑚

A1−A3. *Acropora muricata* ; B1−B3. *Acropora hyacinthus*

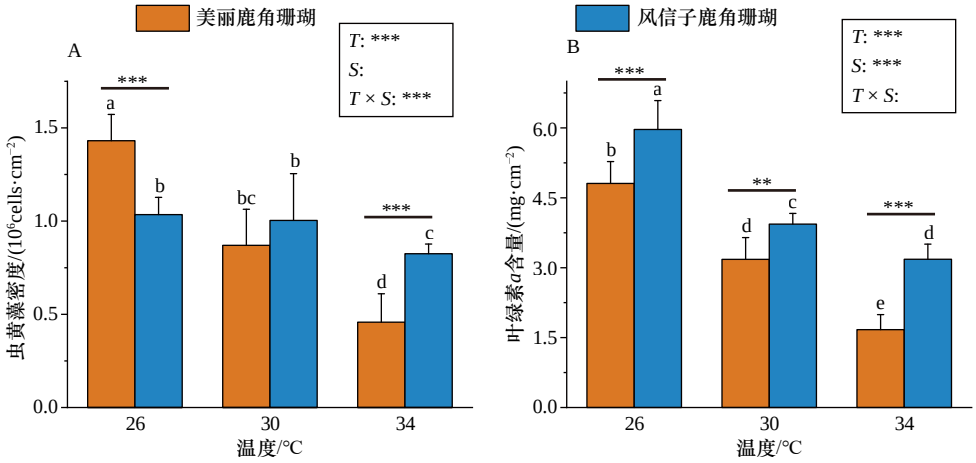


图 3　两种鹿角珊瑚高温胁迫过程中生理指标变化误差线表示多次重复所得平均值的标准误差。方框里为双因素 ANOVA 方差分析温度(*T*)、珊瑚物种(*S*)及其交互关系(*T* × *S*)(**p*<0.05, ***p*<0.01, ****p*<0.001)。不同小写字母表示温度处理之间的参数存在显著差异(*p*<0.05)。横线上的星号表示在同一温度下两种珊瑚之间存在显著差异(**p*<0.05, ***p*<0.01, ****p*<0.001)

Fig. 3　Changes of physiological indexes under heat-stress in two species of staghorn corals In the box are two-way ANOVA for temperature (*T*), coral species (*S*) and their interaction (*T* × *S*) (**p*<0.05, ***p*<0.01, ****p*<0.001). Different lowercase letters indicate significant differences in parameters between temperature treatments(*p*<0.05). The asterisk on the line indicates a significant difference between the two corals at the same temperature(**p*<0.05, ***p*<0.01, ****p*<0.001)

化不大之外, 两种珊瑚的虫黄藻密度、叶绿素 *a* 含量均随温度的升高而显著降低(*p*<0.05)。在 26℃ 时美丽鹿角珊瑚的虫黄藻密度显著高于风信子鹿角珊瑚(*p*<0.05); 然而, 随着温度升高(30℃ 和 34℃ 下), 风信子鹿角珊瑚的虫黄藻密度始终高于美丽鹿角珊瑚, 在 34℃ 时尤为显著(*p*<0.05)。在整个升温过程中, 风信子鹿角珊瑚的叶绿素 *a* 含量均显著高于美丽鹿角珊瑚(*p*<0.05)。

3.2　生化指标变化

如图 4 所示, 双因素方差分析结果表明, SOD、GS 活性和 GSH 含量均与温度、珊瑚物种和温度×珊瑚物种三者显著相关(*p*<0.05), 而 CAT 活性与这三者均没有显著相关性(*p*>0.05), caspase-3 只受到温度的显著影响(*p*<0.001)。美丽鹿角珊瑚的 CAT、SOD、GS、caspase-3 活性以及 GSH 含量均随温度升高表现出先升后降的趋势, 且除 CAT 活性外, 其他指标变化显著(*p*<0.05); 风信子鹿角珊瑚的 CAT、caspase-3 和 GSH 含量也呈现先升后降的趋势, 而 SOD 和 GS 酶活性随温度升高呈上升趋势。整个实验过程中, 风信子鹿角珊瑚的 SOD 和 GS 酶活性均高于美丽鹿角, 且在 34℃ 时具有极显著性(*p*<0.001); 美丽鹿角珊瑚的 CAT 活性和 GSH 含量高于风信子鹿角珊瑚, 但在 34℃ 时均没有显著差异(*p*>0.05); 风信子鹿角珊瑚的 caspase-3 活性在 26℃ 和 30℃ 时低于美丽鹿角珊瑚, 而在 34℃ 时风信子鹿角珊瑚更高但没有显著性(*p*>0.05)。这些结果表明, 风信子鹿角珊瑚在 34℃ 极端温度条件下相比美丽鹿角珊瑚有着更高的抗氧化能力和铵清除能力来抵抗高温胁迫。

4　讨论

4.1　两种鹿角珊瑚对高温胁迫的响应模式

海水温度升高, 珊瑚会发生热应激响应, 导致珊瑚体内活性氧(Reactive Oxygen Species, ROS)浓度增加。ROS 的过量产生和毒性积累可能会对珊瑚宿主和共生虫黄藻的细胞器造成永久性损伤[28]。因此, 当体内 ROS 浓度过高时, 会触发珊瑚-虫黄藻共生体的抗氧化机制, 释放出抗氧化物来处理过剩的 ROS, 如通过 SOD 催化 O- 2 生成 H_2O_2, CAT 和 GSH 则参与 H_2O_2 的降解, 以此来保护细胞免受氧化损伤[10, 28–30]。两种鹿角珊瑚体内的抗氧化酶活性(含量)随着温度的升高而表现出上升的趋势(图 4), 说明珊瑚-虫黄藻共生体正分泌出更多的抗氧化物处理过量的 ROS, 这与先前其他研究结果类似[31]。然而, 随着温度继续上升, 珊瑚的抗氧化酶活性(风信子鹿角珊瑚的 SOD 除外)有下降的趋势(图 4), 这可能是珊瑚-虫黄藻共生体产生的 ROS 比体内抗氧化物能处理的更多[28, 32], 逐渐累积的 ROS 可能造成了细胞损伤, 开始出现毒害作用, 珊瑚的抗氧化能力也因此变弱。

GS 负责生物体内的铵同化, 可通过调节氨氮含量水平起到一定的解毒代谢效果[10]。两种鹿角珊瑚

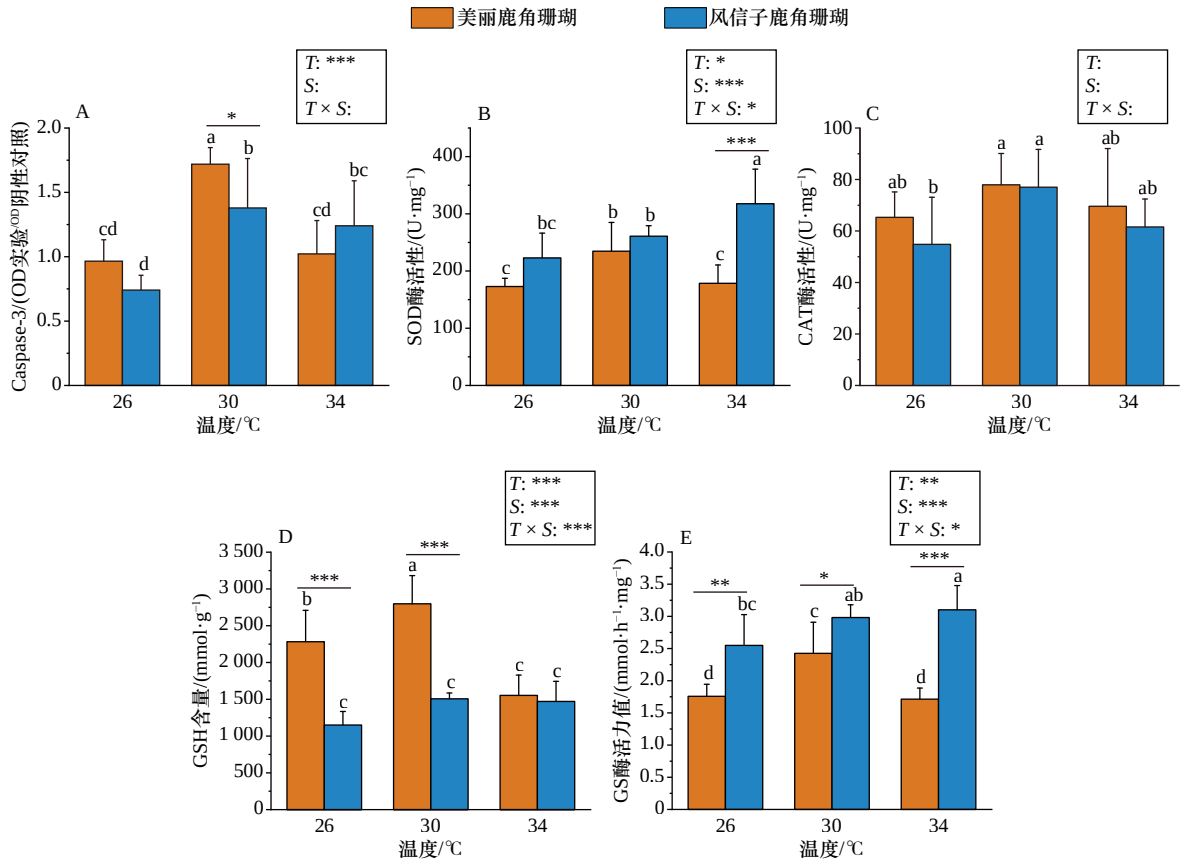


图 4 两种鹿角珊瑚高温胁迫过程中生化指标变化误差线表示多次重复所得平均值的标准误差。方框里为双因素 ANOVA 方差分析温度(T)、珊瑚物种(S)及其交互关系($T \times S$)(*p<0.05, **p<0.01, ***p<0.001)。不同小写字母表示温度处理之间的参数存在显著差异(p<0.05)。横线上的星号表示在同一温度下两种珊瑚之间存在显著差异(*p<0.05, **p<0.01, ***p<0.001)

Fig. 4 Changes of biochemical indexes under heat-stress in two types of staghorn corals in the box are two-way ANOVA for temperature (T), coral species (S) and their interaction ($T \times S$) (*p<0.05, **p<0.01, ***p<0.001). Different lowercase letters indicate significant differences in parameters between temperature treatments(p<0.05). The asterisk on the line indicates a significant difference between the two corals at the same temperature(*p<0.05, **p<0.01, ***p<0.001)

的 GS 随温度变化的趋势与 SOD 一致(图 4),在对鹿角杯形珊瑚(*Pocillopora damicornis*)急性热胁迫的研究中也发现 GS 活性增加[33],这可能是在维持机体健康。随着温度继续上升,持续的高温会抑制 GS 在转录和蛋白质水平上的催化能力,而且高温也会使得珊瑚细胞受到损伤,进而导致 GS 的基因表达下降[11, 34]。因此,相较于 30℃,珊瑚(风信子鹿角珊瑚除外)在 34℃ 时的 GS 活性表现出下降的趋势(图 4E)。

caspase-3 是细胞凋亡的关键效应蛋白酶,属于一种执行蛋白[10]。高温胁迫引起珊瑚-虫黄藻共生体产生过量的 ROS,激活肿瘤坏死因子(TNF)介导的信号通路,引起 caspase-3 活性上调,使得珊瑚-虫黄藻共生体细胞凋亡,进一步导致共生虫黄藻的减少和珊瑚白化[35−36]。与 Huang 等[12] 的研究结果类似,在升温过程中,两种鹿角珊瑚受到高温影响,caspase-3 活性有显著提高(图 4),表明共生体内 ROS 过量,细胞受到损伤。随着高温的持续,共生体细胞凋亡越来越多,细胞数量减少 caspase-3 合成也随之减少,这可能是 34℃ 时 caspase-3 活性下降的原因。

综上所述,两种鹿角珊瑚面对高温胁迫的响应机制如图 5 所示。

4.2 两种鹿角珊瑚抵抗高温能力的差异性

多项研究发现,块状珊瑚的耐热性大于片状的和枝状的[12, 35, 37],但是同一形状珊瑚之间的耐热性探讨较少。珊瑚的耐热性高低与抗氧化能力强弱有关[13],而抗氧化能力与抗氧化酶活性密切相关[11, 38]。高温胁迫后两种鹿角珊瑚的生理和生化指标有所不同,意味着它们之间的耐热性存在差异。

随着温度升高,两种鹿角珊瑚出现触手逐渐收缩,颜色逐步变淡,有黏液分泌的现象(图 2),这与李淑等[37] 研究结果一致。珊瑚的黏液具有物质传输、能量传递和保护珊瑚共生体等多种生物学功能[10, 37],

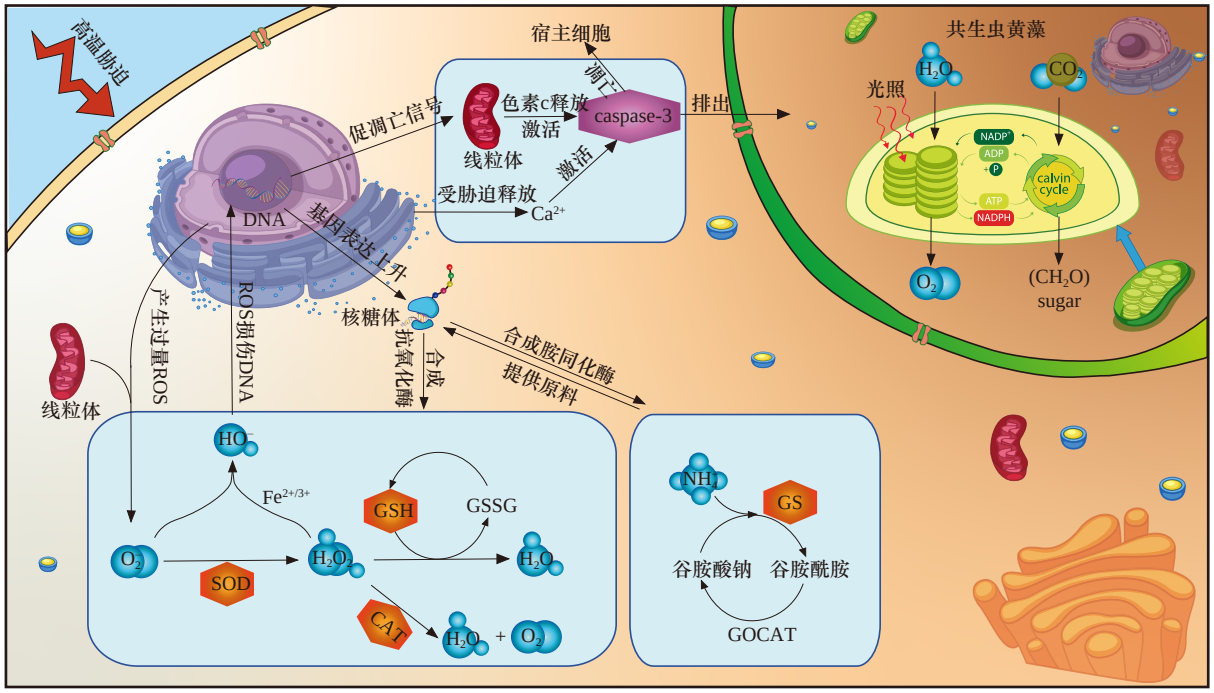


图 5　两种鹿角珊瑚高温响应机制图

Fig. 5　Diagram of the heat response mechanism of two types of staghorn corals

由此可见, 这是珊瑚面对高温胁迫时的自我保护机制之一。虫黄藻密度、叶绿素 *a* 含量等光合作用特征被视为珊瑚的自养指数, 是评估珊瑚共生体健康状况的重要指标[39−40], 会因为外界环境影响而发生变化[41−42]。在高温胁迫过程中, 珊瑚共生虫黄藻会通过原位分解、胞外分泌、细胞凋亡等方式损失, 使得珊瑚体内虫黄藻密度下降, 并且温度越高虫黄藻丧失越多[37], 进而导致叶绿素 *a* 浓度降低。另一方面, 高温也会导致虫黄藻出现光抑制现象, 光合作用能力下降, 从而与光合作用相关的蛋白合成减少, 最终也会导致叶绿素 *a* 浓度下降[43]。从珊瑚表观形态来看, 表现为颜色变淡甚至白化。在 34℃ 高温胁迫 3 d 后, 美丽鹿角珊瑚表现出趋向于白化的现象而风信子鹿角珊瑚却没有(图 3), 且风信子鹿角珊瑚的虫黄藻密度和叶绿素 *a* 含量显著高于美丽鹿角珊瑚(图 4), 这表明风信子鹿角珊瑚可能具有更好的耐热性。

高温会激发珊瑚-虫黄藻共生体抗氧化系统保护细胞避免受到损伤。与澄黄滨珊瑚的高温胁迫实验结果类似[11], 即两种珊瑚的抗氧化酶活性随温度升高而呈现先升后降的趋势(风信子鹿角珊瑚 SOD 除外), 是 ROS 逐渐积累, 氧化与抗氧化达到动态平衡, 机体自我保护的体现[44−45]。风信子鹿角珊瑚在 34℃ 时体内 SOD 活性没有表现出下降的趋势(图 4), 说明面对环境因素胁迫时, 不同种类珊瑚抗氧化酶活性下降临界点会有所不同, 这可能与胁迫强度、胁迫时间以及耐受性有关。其他研究也有此类发现, 即使在 34℃ 高温胁迫 3 d, 澄黄滨珊瑚 SOD、CAT 和 caspase-3 活性也没有降低的趋势[10]。以往的研究发现, 具有更高抗氧化酶活性的珊瑚耐热性更好[11, 12, 45]。风信子鹿角珊瑚 SOD 活性要显著高于美丽鹿角珊瑚, 尽管其 CAT 活性相对低于美丽鹿角珊瑚, 但不显著(图 4B), 这说明风信子鹿角珊瑚可能比美丽鹿角珊瑚更具有抵抗高温的能力。除此之外, 风信子鹿角珊瑚 GS 活性在 3 个温度条件下均显著高于美丽鹿角珊瑚(图 4E)。而 GS 在珊瑚体内负责铵的同化以降低毒性, 其分泌增多旨在增强自我保护能力[11, 34]。这也意味着风信子鹿角珊瑚比美丽鹿角珊瑚具有更强的耐热性。综上所述, 结合表观形态和生理指标来看, 拥有更高抗氧化酶(SOD)和铵同化酶(GS)活性的风信子鹿角珊瑚可能具有比美丽鹿角珊瑚更强的抵抗高温的能力。

共生虫黄藻作为珊瑚宿主的合作伙伴, 在维持共生体健康和响应环境变化中发挥重要作用。有研究表明, 涠洲岛鹿角珊瑚属的共生虫黄藻以 C1 亚系群为主导[46], 在对涠洲岛海域的霜鹿角珊瑚[47]、美丽鹿角珊瑚[48]和浪花鹿角珊瑚(*Acropora cytherea*)[49]等珊瑚的共生虫黄藻的研究进一步证明了这一观点。因此, 我们推测风信子鹿角珊瑚的共生虫黄藻可能也是以 C1 亚系群为主导。以往的研究表明, 不同共生藻类型影响着珊瑚的耐热性[50−51], 而风信子鹿角珊瑚的

共生虫黄藻主导系群可能与美丽鹿角珊瑚一致，这意味着这两种鹿角珊瑚的耐热性差异主要是由虫黄藻密度、叶绿素 *a* 含量等生理指标以及抗氧化酶活性的不同导致的。

4.3 耐热性强的鹿角珊瑚更适合用于珊瑚礁修复

在气候变暖加剧的背景下，全球珊瑚礁持续退化，自然恢复的窗口越来越窄，这使得需要采用积极的人为干预方式促进珊瑚礁恢复。世界范围内，有不少国家开展了珊瑚礁修复工作。例如，印度尼西亚在 2 hm^2 退化的珊瑚礁上投放了大约 11, 000 个人工礁，活珊瑚覆盖率由最初的不足 10% 增加到超过 60%[17]；张浴阳等[16]在海南三亚市蜈支洲岛一共移植了 6 000 株造礁石珊瑚，经过 3 a 的生长，修复区域造礁石珊瑚平均覆盖率从 9.3% 提升到 35.3%。上述珊瑚礁生态修复工作移植的珊瑚中鹿角珊瑚占绝大部分，其中的原因之一是鹿角珊瑚具有生长速度快、驯化潜力好的特点，可以帮助受损珊瑚礁快速恢复。本研究通过两种鹿角珊瑚的高温胁迫实验发现，风信子鹿角珊瑚具有比美丽鹿角珊瑚更高的耐热性。因此，我们认为风信子鹿角珊瑚可能是珊瑚礁生态修复的重要功能性物种，这为未来珊瑚礁生态修复项目对移植珊瑚种类的选取提供了一定的借鉴意义。

在未来，应结合共生体微生物、分子生物学以及基因表达等方面，进行多层次、全方位的分析，更全面地了解广西涠洲岛造礁石珊瑚的高温响应机制。同时，可对涠洲岛热敏性珊瑚进行人工热驯化，增强其耐热性，并将驯化珊瑚用于珊瑚礁生态修复工作，提高珊瑚在海水温度过高时的存活率，进而提升长期的修复效果。

参考文献：

[1] Spalding M, Ravilious C, Green E P. World atlas of coral reefs[M]. Bethesda: University of California Press, 2003.

[2] Bellwood D R, Streit R P, Brandl S J, et al. The meaning of the term ‘function’ in ecology: a coral reef perspective[J]. Functional Ecology, 2019, 33(6): 948−961.

[3] Reaser J K, Pomerance R, Thomas P O. Coral bleaching and global climate change: scientitic findings and policy recommendations[J]. Conservation Biology, 2000, 14(5): 1500−1511.

[4] Hughes T P, Kerry J T, Álvarez-Noriega M, et al. Global warming and recurrent mass bleaching of corals[J]. Nature, 2017, 543(7645): 373−377.

[5] Reimer J D, Peixoto R S, Davies S W, et al. The fourth global coral bleaching event: where do we go from here?[J]. Coral Reefs, 2024, 43(4): 1121−1125.

[6] Eakin C M, Sweatman H P A, Brainard R E. The 2014-2017 global-scale coral bleaching event: insights and impacts[J]. Coral Reefs, 2019, 38: 539−545.

[7] Hoegh-Guldberg O, Kennedy E V, Beyer H L, et al. Securing a long-term future for coral reefs[J]. Trends in Ecology & Evolution, 2018, 33(12): 936−944.

[8] Hughes T P, Anderson K D, Connolly S R, et al. Spatial and temporal patterns of mass bleaching of corals in the Anthropocene[J]. Science, 2018, 359(6371): 80−83.

[9] Hooidonk R V, Maynard J, Grimsditch G, et al. Projections of future coral bleaching conditions using IPCC CMIP6 models: climate policy implications, management applications, and regional seas summaries[R]. Nairobi, Kenya: United Nations Environment Programme, 2020.

[10] 刘旭. 造礁石珊瑚对温度胁迫的响应机制研究[D]. 南宁: 广西大学, 2020.
Liu Xu. Responsive mechanism of reef-building coral rocks to temperature stress[D]. Nanning: Guangxi University, 2020.

[11] 蒙林庆, 黄雯, 阳恩广, 等. 高温白化事件可提高涠洲岛澄黄滨珊瑚 (*Porites Lutea*) 的耐热性[J]. 海洋学报, 2022, 44(8): 87−96.
Meng Linqing, Huang Wen, Yang Enguang, et al. High temperature bleaching events can increase thermal tolerance of *Porites lutea* in the Weizhou Island[J]. Haiyang Xuebao, 2022, 44(8): 87−96.

[12] Huang Wen, Xiao Zunyong, Liu Xu, et al. Short-term thermal acclimation improved the thermal tolerance of three species of scleractinian corals in the South China Sea[J]. Journal of Sea Research, 2024, 199: 102505.

[13] Jin Y K, Lundgren P, Lutz A, et al. Genetic markers for antioxidant capacity in a reef-building coral[J]. Science Advances, 2016, 2(5): e1500842.

[14] Marshall P A, Baird A H. Bleaching of corals on the Great Barrier Reef: differential susceptibilities among taxa[J]. Coral Reefs, 2000, 19(2): 155−163.

[15] Muir P R, Done T, Aguirre J D. High regional and intrageneric variation in susceptibility to mass bleaching in Indo-Pacific coral species[J]. Global Ecology and Biogeography, 2021, 30(9): 1889−1898.

[16] 张浴阳, 刘骋跃, 王丰国, 等. 典型近岸退化珊瑚礁的成功修复案例——蜈支洲珊瑚覆盖率的恢复[J]. 应用海洋学学报, 2021, 40(1): 26−33.
Zhang Yuyang, Liu Chengyue, Wang Fengguo, et al. Successful restoration of typical degraded coastal coral reefs — a restoration of cor-

al coverage at Wuzhizhou Island[J]. Journal of Applied Oceanography, 2021, 40(1): 26−33.

[17] Williams S L, Sur C, Janetski N, et al. Large-scale coral reef rehabilitation after blast fishing in Indonesia[J]. Restoration Ecology, 2019, 27(2): 447−456.

[18] Bayraktarov E, Banaszak A T, Maya P M, et al. Coral reef restoration efforts in Latin American countries and territories[J]. PLoS One, 2020, 15(8): e0228477.

[19] Morand G, Dixon S, Le Berre T. Identifying key factors for coral survival in reef restoration projects using deep learning[J]. Aquatic Conservation: Marine and Freshwater Ecosystems, 2022, 32(11): 1758−1773.

[20] Okubo N. Insights into coral restoration projects in Japan[J]. Ocean & Coastal Management, 2023, 232: 106371.

[21] 王欣, 高霆炜, 陈骁, 等. 涠洲岛园艺式珊瑚苗圃的架设与移植[J]. 广西科学, 2017, 24(5): 462−467.
Wang Xin, Gao Tingwei, Chen Xiao, et al. The construction and transplantation of coral gardening nursery in Weizhou Island[J]. Guangxi Sciences, 2017, 24(5): 462−467.

[22] Harithsa S, Raghukumar C, Dalal S G. Stress response of two coral species in the Kavaratti atoll of the Lakshadweep Archipelago, India[J]. Coral Reefs, 2005, 24: 463−474.

[23] 李淑, 余克服, 陈天然, 等. 在细胞水平上对高温珊瑚白化的初步研究[J]. 热带海洋学报, 2011, 30(2): 33−38.
Li Shu, Yu Kefu, Chen Tianran, et al. Preliminary study of coral bleaching at cellular level under thermal stress[J]. Journal of Tropical Oceanography, 2011, 30(2): 33−38.

[24] 俞小鹏. 南海北部造礁珊瑚对高温胁迫的响应及适应性研究[D]. 南宁: 广西大学, 2022.
Yu Xiaopeng. Response and adaptation of scleractinian coral to high temperature stress in the Northern South China Sea[D]. Nanning: Guangxi University, 2022.

[25] E Johannes R, L Coles S, L Kuenzel N T J, et al. The role of coolants in the nutrition of some scarlatina corals[J]. Limnology and Oceanography, 1970, 15(4): 5799−5586. (**查阅网上资料, 未找到本条文献信息, 请确认**)

[26] Jeffrey Dr S W, Humphrey G F. New spectrophotometric equations for determining chlorophylls a, b, c_1 and c_2 in higher plants, algae and natural phytoplankton[J]. Biochemie Und Physiologie Der Pflanzen, 1975, 167(2): 191−194.

[27] Zhou Zhi, Ni Xingzhen, Wu Zhongjie, et al. Physiological and transcriptomic analyses reveal the threat of herbicides glufosinate and glyphosate to the scleractinian coral *Pocillopora damicornis*[J]. Ecotoxicology and Environmental Safety, 2022, 229: 113074.

[28] Tang Xiaoyu, Yang Qingsong, Zhang Ying, et al. Validating the use of ROS-scavenging bacteria as probiotics to increase coral resilience to thermal stress[J]. Journal of Oceanology and Limnology, 2024, 42(4): 1242−1260.

[29] Ighodaro O M, Akinloye O A. First line defence antioxidants-superoxide dismutase (SOD), catalase (CAT) and glutathione peroxidase (GPX): their fundamental role in the entire antioxidant defence grid[J]. Alexandria Journal of Medicine, 2018, 54(4): 287−293.

[30] Nimse S B, Pal D. Free radicals, natural antioxidants, and their reaction mechanisms[J]. RSC Advances, 2015, 5(35): 27986−28006.

[31] Dias M, Ferreira A, Gouveia R, et al. Long-term exposure to increasing temperatures on scleractinian coral fragments reveals oxidative stress[J]. Marine Environmental Research, 2019, 150: 104758.

[32] Lesser M P. Oxidative stress in marine environments: biochemistry and physiological ecology[J]. Annual Review of Physiology, 2006, 68: 253−278.

[33] Tang Jia, Ni Xingzhen, Wen Jianqing, et al. Increased ammonium assimilation activity in the scleractinian coral *Pocillopora damicornis* but not its symbiont after acute heat stress[J]. Frontiers in Marine Science, 2020, 7: 565068.

[34] Su Yilu, Zhou Zhi, Yu Xiaopeng. Possible roles of glutamine synthetase in responding to environmental changes in a scleractinian coral[J]. Molecular Biology Reports, 2018, 45(6): 2115−2124.

[35] 刘旭, 黄雯, 俞小鹏, 等. 适度热胁迫对造礁石珊瑚热耐受性影响的研究[J]. 海洋湖沼通报, 2022, 44(1): 99−105.
Liu Xu, Huang Wen, Yu Xiaopeng, et al. Studies on the effect of moderate heat stress on the heat tolerance of scleractinian coral[J]. Transactions of Oceanology and Limnology, 2022, 44(1): 99−105.

[36] Yu Xiaopeng, Huang Bo, Zhou Zhi, et al. Involvement of caspase3 in the acute stress response to high temperature and elevated ammonium in stony coral *Pocillopora damicornis*[J]. Gene, 2017, 637: 108−114.

[37] 李淑, 余克服, 施祺, 等. 海南岛鹿回头石珊瑚对高温响应行为的实验研究[J]. 热带地理, 2008, 28(6): 534−539.
Li Shu, Yu Kefu, Shi Qi, et al. Experimental study of stony coral response to the high temperature in Luhuitou of Hainan Island[J]. Tropical Geography, 2008, 28(6): 534−539.

[38] Huang Wen, Meng Linqing, Xiao Zunyong, et al. Heat - tolerant intertidal rock pool coral *Porites lutea* can potentially adapt to future warming[J]. Molecular Ecology, 2024, 33(5): e17273.

[39] Hinrichs S, Patten N L, Waite A M. Temporal variations in metabolic and autotrophic indices for *acropora digitifera* and *acropora spicifera* - implications for monitoring projects[J]. PLoS One, 2013, 8(5): e63693.

[40] 张海洋, 赵美霞, 钟瑜, 等. 南海北部造礁石珊瑚共生体光合作用特征季节性监测[J]. 海洋地质前沿, 2021, 37(6): 84−91.
Zhang Haiyang, Zhao Meixia, Zhong Yu, et al. Seasonal monitoring of photosynthesis characteristics of scleractinian corals in the Northern South China Sea[J]. Marine Geology Frontiers, 2021, 37(6): 84−91.

[41] Stimson J. The annual cycle of density of zooxanthellae in the tissues of field and laboratory-held *Pocillopora damicornis* (Linnaeus)[J]. Journal of Experimental Marine Biology and Ecology, 1997, 214(1-2): 35−48.

[42] Brown B E, Dunne R P, Ambarsari I, et al. Seasonal fluctuations in environmental factors and variations in symbiotic algae and chlorophyll pigments in four Indo-Pacific coral species[J]. Marine Ecology Progress Series, 1999, 191: 53−69.
[43] Bhagooli R, Hidaka M. Photoinhibition, bleaching susceptibility and mortality in two scleractinian corals, *Platygyra ryukyuensis* and *Stylophora pistillata*, in response to thermal and light stresses[J]. Comparative Biochemistry and Physiology Part A: Molecular & Integrative Physiology, 2004, 137(3): 547−555.
[44] Cziesielski M J, Schmidt-Roach S, Aranda M. The past, present, and future of coral heat stress studies[J]. Ecology and Evolution, 2019, 9(17): 10055−10066.
[45] Weis V M. Cellular mechanisms of Cnidarian bleaching: stress causes the collapse of symbiosis[J]. Journal of Experimental Biology, 2008, 211(19): 3059−3066.
[46] 邓传奇. 南海环境敏感型造礁珊瑚共生微生物应对温度改变的生态过程[D]. 南宁: 广西大学, 2021.
Deng Chuanqi. Ecological process of symbiotic microorganisms in environmentally sensitive reef-building corals in the South China Sea in response to temperature changes[J]. Nanning: Guangxi University, 2021.
[47] 许勇前, 陈飚, 覃良云, 等. 涠洲岛霜鹿角珊瑚共生虫黄藻群落的季节变化特征[J]. 广东农业科学, 2023, 50(7): 164−172.
Xu Yongqian, Chen Biao, Qin Liangyun, et al. Seasonal variation characteristics of the symbiodiniaceae community associated with *Acropora pruinosa* from Weizhou Island[J]. Guangdong Agricultural Sciences, 2023, 50(7): 164−172.
[48] 韦雪露. 涠洲岛珊瑚共生功能体对季节性温度波动及极端温度胁迫的响应[D]. 南宁: 广西大学, 2024.
Wei Xuelu. The response of coral holobionts to seasonal temperature fluctuations and extreme temperature stress in Weizhou Island[D]. Nanning: Guangxi University, 2024.
[49] 骆雯雯. 涠洲岛造礁石珊瑚共生体系对异常温度胁迫响应的实验研究[D]. 南宁: 广西大学, 2019.
Luo Wenwen. Experimental response of reef-building coral symbiotic system in Weizhou Island to abnormalous temperature stress[D]. Nanning: Guangxi University, 2019.
[50] Rowan R. Coral bleaching: thermal adaptation in reef coral symbionts[J]. Nature, 2004, 430(7001): 742.
[51] Al-Hammady M A M M, Silva T F, Hussein H N M, et al. How do algae endosymbionts mediate for their coral host fitness under heat stress? A comprehensive mechanistic overview[J]. Algal Research, 2022, 67: 102850.

The difference in thermal tolerance between *Acropora muricata* and *Acropora hyacinthus*

Zhou Yupeng[1, 2], Xiao Zunyong[1, 2], Chen Jinlian[2], Huang Zhihua[2], Xu Mingpei[1, 2], Tan Ronghua[2], Meng Linqing[2], Wang Yonggang[2], Yu Kefu[2, 3], Huang Wen[2]

(1. *School of Resources*, *Environment and Materials*, *Guangxi University*, *Nanning* 530004, *China*; 2. *Guangxi Laboratory on the Study of Coral Reefs in the South China Sea*, *Coral Reef Research Center of China*, *School of Marine Sciences*, *Guangxi University*, *Nanning* 530004, *China*; 3. *Southern Marine Science and Engineering Guangdong Laboratory* (*Guangzhou*), *Guangzhou* 511458, *China*)

Abstract: Global warming has led to frequent large-scale coral bleaching events, accelerating the degradation of coral reef ecosystems. Internationally, coral transplantation is commonly employed as a method to restore degraded coral reefs, with *Acropora* species constituting the majority of the transplanted corals. However, fast-growing branching *Acropora* corals are more sensitive to heat, which affects their restoration efficacy in the increasingly warming marine environment. To understand the thermal response patterns and thermal tolerance differences of *Acropora*, this study conducted high-temperature stress experiments on *Acropora muricata* and *Acropora hyacinthus* from Weizhou Island, Guangxi. Through the analysis of physiological and biochemical indicators, it was observed that after high-temperature stress, *A. muricata* exhibited tentacle retraction and color fading, and the activity levels of antioxidants (superoxide dismutase, glutathione, catalase), ammonium assimilation enzyme (glutamine synthetase), and cysteinyl aspartate specific proteinase-3 (caspase-3) showed a trend of initially increasing and then decreasing. *A. hyacinthus* showed a similar response pattern, except for superoxide dismutase and glutamine synthetase. At 34℃, *A. hyacinthus* performed better in physiological indicators, with superoxide dismutase, ammonium assimilation enzyme, and caspase-3 maintained high activity and sensitive response, indicating that *A. hy-*

acinthus resists high-temperature environments by increasing the activity of these proteases, and it is more heat-tolerant than *A. muricata*. This study revealed the physiological response patterns of the two *Acropora* species under high-temperature stress and compared their thermal tolerance differences, providing a theoretical basis for the selection of heat-tolerant corals and the ecological restoration of coral reefs.

Key words: Weizhou Island; *Acropora*; high-temperature stress; thermal tolerance; coral reef restoration

海洋生物学进展研究生课程个性化教学改革探索与实践

苏宏飞，梁甲元，余克服*

（广西大学海洋学院/珊瑚礁研究中心/广西南海珊瑚礁研究重点实验室，广西 南宁 530004）

摘 要 海洋生物学进展是海洋科学硕士研究生培养的核心课程，其教学效果直接影响到学生的专业素养和创新能力。但是，传统教学模式往往过于注重知识灌输，导致学生学习兴趣不高进而创新能力受限。文章基于个性化教学理念，对课程进行了全面的教学改革和探索实践。通过制定个性化教学策略、实施多样化教学方法、改革教学效果评价体系等措施，有效提升了学生的学习兴趣、创新能力和实践能力。研究结果表明，个性化教学策略能够显著提高学生的学习成绩和课程满意度，为海洋生物学进展课程的教学提供改革新思路与创新方法。

关键词 海洋生物学进展；个性化教学；教学改革；创新能力；实践能力

中图分类号：G643 **文献标识码**：A

0 引言

海洋生物学进展是一门前沿和综合性的学科，其教学改革对国内学位与研究生教育的发展具有深远的意义。然而，传统教学模式过于注重知识的传授，往往忽略学生的个体差异与学习需求，导致学生学习兴趣不高进而导致学生创新能力受限。因此，进行课程个性化教学改革显得尤为重要。个性化教学是指根据学生的学习背景、兴趣、需求和能力，制定个性化的教学策略和方法，达到学生的个性化学习效果，从而推动学生全面发展。目前，国内外关于课程的个性化教学改革已经取得可喜的研究进展。

在国外，Tomlinson等[1]根据不同学生的学科水平和兴趣，提供不同难度和内容的学习材料，发现个性化的教学模式可以显著提高学生的学科理解能力，同时显著提升学生整体的学科成绩。Verma等[2]在课程中引入了项目式教学，加入了与海洋科技相关的实际研究项目，显著提高了学生的应用创新能力、实际问题解决能力和团队合作水平。Tetzlaff 等[3]制订了个性化学习计划，学生可依自己的学科需求和兴趣针对性地选择不同的学习模块，提高了学生的学习自主性，激发了学习兴趣，提升了教学成效。

国内也逐渐进行海洋生物学进展课程的个性化教学研究和实践。杨舜然等[4]以程序语言设计课程为例进行个性化学习模型的应用与个性化学习实践，围绕学生的学科水平和兴趣设定了不同的学习目标和任务，提高了学生的学科兴趣和参与度。李玉蓉等[5]通过引入实践项目让学生参与海洋生物学研究的实际任务，既帮助学生培养实际动手能力和科研意识，同时又提高了学生整体的学科素养。张婷等[6]在教学中采用了差异化教学策略，灵活地提高了理论难度与学生认知水平之间的适配度，有效调动了学生的学习积极性，同时加深了学生对学科理论知识的理解。余克服等[7]借助特色教学实践基地进行海洋个性化教学，对学科理论进行有效拓展，帮助学生通过见习、观察、思考等方式快速掌握理论知识，同时培养学生的科研兴趣与实践能力。苏宏飞等[8]探索了课程知识点模块化等个性化教学策略、“教”“研”相结合等教学内容改革，加深了学生对学科理论知识的认知和理解，提升了理论知识的应用创新水平。

个性化教学强调以学生为中心，注重调动学生的学习兴趣和积极性，培养学生的创新能力和实践能力。本文将基于个性化教学理念，对海洋生物学进展课程进行教学改革探索与实践，注重学生个体差异的基础上提供丰富的个性化课程内容，以满足所有硕士研究生个体实现个性的差异化发展，以期为海洋生物学进展课程的教学改革提供参考。

1 个性化教学策略的制定

1.1 明确学生背景和需求

首先了解学生的背景，包括研究生的生源地、学历背景、专业基础、兴趣爱好以及职业发展规划。通过访谈、问卷调查等方式，统计分析学生的基本信息与学习需求，为后续个性化教学策略的制定提供依据。例如，首先对于来自不同生源地的学生，可能存在地域文化差异和学术背景差异，制定更加贴近其实际需求的课程内容和学习方式。其次，针对不同专业背景的学生，根据其已有的知识体系和学习习惯，调整教学内容和难度，确保每位学生都能在课程中有所收获。最后，了解学生未来的职业方向和发展目标，帮助教师更好地把握教学重点，为学生提供更加有针对性的指导和帮助。

万方数据

1.2 学习计划个性化与学习模块定制化

教师需了解学生的学习期望和目标。通过一对一的交流或小组讨论等,更全面地了解每个学生的学习能力和目标需求,为制定个性化的学习计划提供依据。充分考虑学生的个性化学习需求和能力水平。对于基础薄弱的学生,提供更加基础的学习内容和辅导;对于具有较强学习能力的学生,则可布置更高层次和富有挑战性的学习任务。同时,根据学生的兴趣和职业规划定制个性化的学习模块,以满足其特定领域的学习需求。例如,对于希望从事海洋生物资源开发利用的学生,可以增加海洋生物资源评估与管理等相关内容;对于希望从事海洋生态保护的学生,则可以增加海洋生态系统保护与修复等方面的知识。设计个性化的学习模块,可更好地调动学生的学习兴趣和动力,持续促进学生全面发展。

1.3 教学内容的模块化、教学大纲和计划编制

模块化教学将课程内容划分成相对独立的学习模块,每个模块包含特定的知识点和技能点。编写教学大纲和计划时,充分考虑学生的学习需求和目标。根据教学大纲的要求和学生的学习背景,确定每个模块的教学主要目标、教学重点内容、教学创新方法和差异化评估方式等。同时,需要合理安排教学进度和时间表,确保学生能够按照计划顺利完成学习任务。还需注重教学内容的时效性和前沿性,不断更新教学模块内容,确保学生能掌握最新的海洋生物学知识和技术。

1.4 组建匹配的教学团队

组建专业知识深厚和教学经验丰富的教学团队,充分考虑教师专业特长、教研经验和教学水平,同时将学生的学习模块和教师的专业能力进行匹配,确保每位学生都能得到精准的指导和帮助。如海洋生物分类学模块,选择分类学知识和经验丰富的教师进行授课;海洋生态学模块,则选择具有生态学背景和研究经验的教师。通过精准匹配充分利用教师的专业优势与科研经历,提高教学效果和质量。此外,定期开展教研活动和教学经验分享,促进团队成员之间的互相学习和进步。同时,邀请校外专家举办讲座或指导,为学生创造开阔学术视野的机会。

2 个性化教学策略的实施

2.1 问题驱动教学:提出研究问题,建立解决方案小组

问题驱动教学是一种以问题为导向的教学方法,旨在通过引导学生解决实际问题来培养其创新思维和实践能力。首先,教师整理与课程内容相关的研究问题,可以是来自实际科研项目的难题,也可以是海洋生物学领域的热点问题。通过引导学生关注和思考,提高其学习兴趣和探索欲望。其次,建立问题解决小组,每组负责一个或几个问题。小组成员需要共同讨论来制定解决方案,然后通过查阅资料、进行实验等方式来验证方案的可行性。最后,进行阶段性报告和讨论,定期向全班汇报小组的研究进展和遇到的问题,大家提出问题和建议。通过互动交流促进学生的思考和反思,提高解决实际问题和团队协同合作能力。教师给予适当的指导和帮助,保证学生顺利完成任务。

2.2 案例教学法:制定案例教学计划,选择前沿案例

案例教学法通过分析和讨论实践案例来培养学生分析、解决问题的能力。首先,确定案例来教学计划。教师根据课程内容和学生需求选择合适的案例,可来自科研论文、新闻报道或实际项目的实例,通过引导学生分析和讨论,帮助他们掌握相关的理论知识和实践技能。其次,保持课程的前沿性和时效性。教师需要更新和选择最新的海洋生物学案例,可源于海洋生态系统保护、海洋生物资源开发等方面的热点问题,引发学生关注和思考,调动其学习兴趣和探索欲望。最后,组织案例分析和小组讨论。教师提供相关的背景资料和问题引导,学生互相交流和分享自己的观点和认识。同时,教师提供指导意见和改进建议,帮助学生快速掌握学科知识和研究技能。

2.3 实践基地建设和实践性教学:配备实验仪器,制订更新计划

通过实践基地开展教学,培养学生的动手操作能力与其创新协调能力。首先,准备实验基地设备。根据课程内容和实践需求,教师提前准备相关的实验设备和材料。如显微镜、离心机、PCR仪等常用的分子生物学实验设备,或者用于海洋生态调查和样品采集的专用仪器,为学生提供良好的学习实践环境与条件。其次,确定实验基地设备的更新计划。教师定期检查和评估实验设备的性能和状态,及时更换老旧或损坏的设备,确保学生能够使用到最新、最先进的实验设备和技术。最后,组织学生进行实践基地建设和实践性教学活动。教师带领学生参观实验基地,介绍和演示实验设备和仪器的操作和注意事项。同时,安排学生进行实验操作和实践技能训练,提高他们的实操能力和实验技巧。此外,鼓励学生参与实践基地的研究项目建设,为他们提供更多的实践机会。

2.4 团队协作与讨论:设立"1对1课程导师"团队合作项目

通过设立"1对1课程导师"团队合作项目设计和讨论来促进学生的团队协作和交流。首先,设立"1对1课程导师"制度。每位导师负责指导一定数量的学生,与他们进行定期的交流和讨论。通过"1对1课程导师"制度,导师更加深入地了解学生的学习状态和需求,为他们提供更加个性化的指导和帮助。同时,学生可通过与导师的交流和讨论,

万方数据

加深对课程内容的理解和认识。其次，组织团队合作项目设计和讨论。教师可以根据课程内容和学生需求设计一系列团队合作项目，鼓励学生组成跨学科、跨年级的团队，共同设计和开展团队合作项目。项目可以是关于海洋生态系统保护、海洋生物资源开发、海洋环境污染治理等方面的实际问题。通过团队合作项目的设计和实施，学生可以培养团队协作能力和沟通协调能力，同时加深对海洋生物学领域的认识和理解。最后，定期组织跨团队项目展示与交流。学生可了解其他团队的研究进展和成果，相互学习和借鉴，促进不同团队之间的合作与交流，增进彼此之间的了解和友谊。

3 教学效果评价改革

通过学习成果统计、成绩对比分析以及课程满意度调查，全面、深入地开展学生的学习成果评价与教学成效评估。首先，重视对学生成果的整理与表现的分析。包括对学生提交的研究报告、论文发表以及专利申请等学术成果的细致梳理，仔细审阅每一份报告和论文，评估其内容的深度、广度以及创新性，关注学生在研究过程中展现出的批判性思维、问题解决能力和团队协作精神。对于专利申请，则着重考察其技术方案的可行性、创新点以及市场应用潜力。其次，成绩对比分析。通过对比个性化教学方法与传统教学方法下学生的学科成绩，直观地了解两种教学策略下学生学业成绩的表现。评估个性化教学下的学生成绩学习积极性和自主学习能力方面的优势。最后，开展学生满意度调查。通过问卷调查、座谈会等形式，面向学生征集个性化教学的意见和建议，帮助团队及时发现并解决教学问题，更为持续改进教学策略、提升教学质量提供了参考。

4 结论与展望

通过个性化教学策略探索与实践，建立改革教学效果评价体系，有效提升海洋生物学进展课程的教学质量。个性化教学激发了学生的学习兴趣，增强了其解决现实问题的能力，还提高了学生自主学习与思维创新能力。多元化、全过程的教学效果评价体系则提供了全面、客观的评估依据，促进了教学体系的持续改进。今后的研究，还可引入在线学习平台，为学生提供更加灵活、丰富、便利的学习方式；也可利用虚拟现实技术，模拟海洋生态环境，使学生能够在虚拟环境中反复练习实践操作，提高实践技术水平。另外，加强与行业、企业、兄弟院校的合作，整合实践平台资源，拓宽实践渠道，为学生提供综合实习实训机会，增强研究生的就业竞争力。通过持续创新与实践，培养出更多富有实践能力和创新精神的海洋科学人才，为我国海洋科学事业的发展壮大贡献应有力量。

*通信作者：余克服

★基金项目：2024年广西大学研究生教育教学改革倍增计划项目“个性化教学策略在研究生海洋生物学进展课程的运用”。

参考文献

[1] Tomlinson C A. How to differentiate instruction in mixed-ability classrooms[M]. Ascd, 2001.

[2] Verma A K, Dickerson D, McKinney S. Engaging students in STEM careers with project-based learning—MarineTech project[J]. Technology and engineering teacher, 2011, 71(1):25-31.

[3] Tetzlaff L, Schmiedek F, Brod G. Developing personalized education: A dynamic framework[J]. Educational Psychology Review, 2021, 33: 863-882.

[4] 杨舜然.基于聚类集成的大学生个性化学习的研究——以《程序语言设计》课程为例[D].黑龙江:哈尔滨师范大学,2019.

[5] 李玉蓉,尹诗白,陈中普.项目式学习在“数据库原理及应用”课程差异化教学中的应用效果研究[J].教学学术,2023(1):44-54.

[6] 张婷.差异化专业基础课混合教学设计与实践[J].辽宁警察学院学报,2023,25(2):123-128.

[7] 余克服,黄荣永,林武辉,等.海洋遥感本科生导师制教学模式探索与实践[J].高教学刊,2023(9):98-101.

[8] 苏宏飞,何旭聪,林武辉,等.“海洋生物学基础”课程教学改革探索[J].大众科技,2023(25):148-151.

万方数据

·全健康·

DOI: 10.15886/j.cnki.rdswxb.20240202

主持人: 韩　谦, 刘萌萌

Open Access

虫黄藻对低盐胁迫的生理响应

何　燃[1#], 高楷翔[1], 潘能斌[1], 李展泓[1], 张廷超[1], 梁宏业[1], 卢晓燕[1], 蓝梦玲[1], 覃祯俊[1,2,3*]

(1. 广西大学 海洋学院, 广西 南宁 530004 中国; 2. 广西大学 南海珊瑚礁研究重点实验室, 广西 南宁 530004 中国; 3. 广西大学 珊瑚礁研究中心, 广西 南宁 530004 中国)

摘　要: 为了探究虫黄藻(*Effrenium voratum*)在低盐胁迫条件下的生理变化, 以离体培养的虫黄藻为对象, 对虫黄藻进行高通量测序获得其相对丰度, 开展低盐胁迫实验, 研究低盐环境对 *E. voratum* 的生长状况、单个虫黄藻 Chl a 浓度、超氧化物歧化酶(SOD)和过氧化氢酶(CAT)活力的生理影响。结果显示: 1)35 盐度下, *E. voratum* 的细胞密度稳定增长, 表明其生长状态良好; 25 的低盐胁迫下, 其生长受抑制但仍能维持生存。15 的低盐胁迫下, 其细胞密度在 48 h 后显著下降, 呈负增长趋势, 表明其生长受到严重抑制。2)15 的低盐胁迫下, *E. voratum* 的单个虫黄藻叶绿素 a 浓度在 4 h 后持续下降, 表明其光合作用能力受到显著抑制, 趋势明显。3)25 和 15 的低盐胁迫下, *E. voratum* 的 SOD 活性和 CAT 活性在 4 h 内有所上升, 但在 24 h 后持续下降, 表明其抗氧化能力初期有所增强, 但随胁迫时间的延长, 抗氧化能力逐渐减弱。

关键词: 虫黄藻; 低盐胁迫; 生理响应; 高通量测序

中图分类号: Q949.2　　**文献标志码:** A　　**文章编号:** 1674 − 7054(2025)06 − 0890 − 08

何燃, 高楷翔, 潘能斌, 等. 虫黄藻对低盐胁迫的生理响应 [J]. 热带生物学报, 2025, 16(6): 890−897. doi: 10.15886/j.cnki.rdswxb.20240202

珊瑚礁生态系统具有全球最高生态多样性和初级生产力, 被誉为海底热带雨林,具有生境功能、产出功能、调节功能和信息功能等[1]。受人类活动和全球气候变化的影响, 全球珊瑚礁正在遭受众多危机, 珊瑚白化等问题日渐严重, 目前, 大约有三分之一的珊瑚物种面临灭绝的风险[2]。在当前珊瑚生存面临严重威胁的背景下, 相比于全球变暖、海洋酸化而言, 盐度是影响珊瑚生长发育的重要环境因子, 但其在珊瑚低盐胁迫响应中的研究仍较缺乏。主要的原因可能是海洋中盐度的变化通常较为稳定, 其次珊瑚正常生长的盐度范围较为广泛, 一般是 27 ~ 40 盐度, 且具有一定的抗高盐特性[3]。但珊瑚在面对低盐环境时的表现却较为敏感[4 − 5], 海水变暖期间暴露于低盐度的近岸珊瑚比离岸珊瑚经历了更多的白化[6], 且珊瑚自身缺乏渗透压调节能力[7], 因此, 在低盐环境下, 珊瑚白化的风险极高。除此之外, 在热带地区, 尤其是入海口区域, 极端强降雨时沿岸陆地径流骤增可能会导致海水盐度降低超过 10[8], 部分珊瑚被迫生活在盐度低于 15 的环境中, 珊瑚很容易白化甚至死亡[3,9]。

珊瑚白化是指珊瑚体内的虫黄藻(*Effrenium voratum*)与珊瑚的共生关系被破坏从而导致珊瑚变白的现象。虫黄藻在珊瑚的生长发育过程中扮演着极为重要的角色, 虫黄藻的光合作用产物是珊瑚宿主的主要能量来源[10]。以往的研究将盐度的变化导致珊瑚白化归因于盐度对虫黄藻的影响, 导致转移到珊瑚的能量减少[11 − 13]。低盐环境下的渗透压使虫黄藻细胞体积增加、膨胀, 导致离子和有机溶质的流失以及膜和细胞器的损伤, 最

收稿日期: 2024 − 12 − 30　　**修回日期:** 2025 − 05 − 07

基金项目: 国家自然科学基金项目资助 (42206157); 广西自然科学基金青年基金项目 (2022GXNSFBA035449)

#**第一作者:** 何燃(2002—), 男, 广西大学海洋学院 2021 级海洋科学专业本科生。E-mail: 2473737673@qq.com

*通信作者: 覃祯俊 (1991—), 博士, 讲师。研究方向: 珊瑚共附生微生物生态学。E-mail: qinzhenjun@gxu.edu.cn

中国知网　https://www.cnki.net

终可能导致酶系统受到抑制, 破坏新陈代谢功能, 甚至细胞破裂[14−15]。Downs 等[16]的研究揭示了低盐胁迫会诱导虫黄藻产生氧化应激反应。而 Sakami[17]的研究也证实, 低盐条件下, 会对离体虫黄藻光合作用带来直接的负面影响。然而, 虫黄藻含有上百种不同的类群, 不同类群的虫黄藻无论是在生活方式还是对珊瑚虫的相互作用方面, 都有各自的生理特征。只有通过对不同类群的虫黄藻进行分离培养, 收集与分析环境胁迫下虫黄藻的响应数据, 才能更好地揭示虫黄藻在珊瑚-虫黄藻共生体关系构建、维持、破坏和重建中的作用[18]。目前, 离体培养的虫黄藻对低盐胁迫的响应机制研究相对较少, 一定程度限制了人们对当前虫黄藻−珊瑚共生关系的基本理解[19]。近期的研究者将共生虫黄藻主要分为 *Symbiodinium*、*Breviolum*、*Cladocopium*、*Durusdinium*、*Effrenium*、*Fugacium*、*Gerakladium*、*Clade H* 和 *Clade I*, 其中, 虫黄藻 *Effrenium* 属目前只包含 *Effrenium voratum*[20]。*E. voratum* 广泛分布于温带和亚热带水域, 如太平洋、大西洋和地中海地区, 得益于其在世界各地的各种海洋环境中的生存, 近期研究发现, 该物种具有宽温度范围、高光强度的耐受性及混养能力[21]。*E. voratum* 虫黄藻不仅可以与珊瑚宿主共生, 还可以在珊瑚礁生态系统中浮游生存。研究低盐胁迫下离体培养 *E. voratum* 的响应机制, 有助于初步了解虫黄藻对盐度变化的生理耐受性。然而, 离体状态与共生状态下的胁迫响应可能存在显著差异。在共生状态下, 虫黄藻位于珊瑚细胞内, 受到宿主的渗透调节和保护, 而离体培养的虫黄藻直接暴露于低盐环境, 可能表现出更强的敏感性。因此, 未来研究需结合共生体系, 进一步探究低盐胁迫对虫黄藻−珊瑚共生关系的影响。因此, 本研究以低盐作为环境压力源, 将 *E. voratum* 在不同盐度环境下进行培养, 测定 *E. voratum* 的生理生化指标包括生长状况、单个虫黄藻 Chl a 浓度、超氧化物歧化酶(SOD)和过氧化氢酶(CAT)活力, 研究在低盐环境下虫黄藻 *E. voratum* 的响应过程, 旨在为虫黄藻种群的耐盐性研究提供了基础数据。

1　材料与方法

1.1　研究材料　虫黄藻(*E. voratum*)从实验室已有的 *E. voratum* 母液中转接获取, 在 250 mL 的装有 L1-Si 培养基的锥形瓶中保存, 置于室内恒温光照培养箱中培养, 温度为 26 ℃, 光照强度为 90 μmol·m^{-2}·s^{-1}, 光暗周期为 L(光): D(暗)=12 h: 12 h, 盐度条件为 35、25、15。每隔 1 周用显微镜(奥克巴斯−BX53)观察转接的虫黄藻生长情况, 并对其进行形态学鉴定。

1.2　虫黄藻的分子鉴定　为了确定培养的共生虫黄藻的纯度, 对转接后培养的虫黄藻进行了 DNA 提取, 使用 DNeasy®植物试剂盒(Qiagen, Hilden, Germany)按说明书步骤提取基因组 DNA。然后, 将提取的 DNA 样品送至上海美吉生物有限公司进行高通量测序。利用引物 F: 5′−GAATTGCAGAACTCCGTG−3'和 R: 5′−GGGATCCATATGCTTAAGTTCAGCGGGT−3′对虫黄藻 rDNA 的 ITS2 区进行了 PCR 扩增。使用 AxyPrep DNA 凝胶提取试剂盒(Axygen Biosciences)和 QuantiFluorTM ST 荧光定量系统(Promega)将最后的 PCR 产物纯化和定量在 301 ~ 340 bp。纯化的扩增子以等摩尔量汇集, 然后, 根据制造商标准使用协议在 Illumina Mi Seq 测序平台进行测序。

1.3　低盐胁迫实验设计　本实验使用 L1-Si 培养基, 利用虫黄藻细胞作为实验对象开展实验研究。设定 3 个不同的盐度条件, 分别为正常的 35 盐度对照组和低盐的 25、15 盐度实验组。每个盐度条件设置至少 3 个独立的生物学重复, 每个重复包含 200 mL 培养基, 初始细胞密度为 1×10^4 cells·mL^{-1}。待细胞进入指数增长期后, 重新接种于灭菌后盐度分别为 35、25、15 的 L1-Si 培养基中, 所有培养瓶在恒温光照培养箱中随机排列, 在 26 ℃, L(光): D(暗)=12 h: 12 h 光周期等其他培养条件相同的环境下胁迫 48 h。在 0、4、24、48、72 h 收集样品, 每个时间点的样品均进行 3 次重复测定, 以测定细胞密度、单个虫黄藻 Chl a 含量、酶活性等生理指标。

1.4　生理生化指标测量

1.4.1　生理指标测定　用微量移液器取一式 3 份, 每份 100 μL 均匀藻液于 2 mL 离心管内, 加入 900 μL 无菌海水稀释, 将稀释后的虫黄藻溶液用旋涡混匀器充分混合均匀。然后, 用微量移液器移取 100 μL 稀释后的藻液到浮游生物计数框中(覆盖盖玻片), 在显微镜(奥克巴斯−BX53)下进行虫黄藻的计数(n=10), 最后将统计结果换算成总

中国知网　https://www.cnki.net

体积溶液内所含虫黄藻的数量，即虫黄藻密度（D，单位：cells·mL^{-1}）。

在充分混合均匀锥形瓶中的藻液之后，从中取出一定量的溶液，每份为 2 mL，共取 3 份。将这些溶液分别加入离心管中，使用台式高速冷冻离心机（Sigma−15）进行离心分离（设定 4 000 r·min^{-1} 的速度，离心 5 min）。之后，慢慢地倾倒去除上清液，留下的沉淀物再加入 1.5 mL φ＝100% 的丙酮，在 4 ℃ 条件下进行 24 h 的萃取。在萃取了 24 h 后，将溶液再次进行离心分离（设定 4 000 r·min^{-1} 的速度，离心 5 min），然后取其上清液（200 μL），用分光光度计分别测试波长 750、664、647 和 630 nm 处的吸光度，代入公式（1）计算 Chl a 质量浓度：

$$Ca = 11.85\times(A_{664}-A_{750}) - 1.54\times(A_{647}-A_{750}) - 0.08\times(A_{630}-A_{750}), \quad (1)$$

式中，Ca 代表 Chl a 浓度 (mg·L^{-1})。

再换算成实验总体积的藻液内 Chl a 质量浓度。最后，使用根据单位体检虫黄藻密度和 Chl a 质量浓度，用公式（2）计算出单个虫黄藻 Chl a 含量：

$$\text{单个细胞的 Chla 含量} = (\text{Chla质量浓度}\times 10^{9})/\text{细胞密度}, \quad (2)$$

式中，单个虫黄藻 Chl a 含量的单位为 pg·cell^{-1}；Chl a 质量浓度的单位为 mg·mL^{-1}；细胞密度的单位为 cells·mL^{-1}。

1.4.2 生化指标测定及数据分析 使用商用试剂盒（货号 A001−3，A007−2−1）分别测定藻液中超氧化物歧化酶（SOD）与过氧化氢酶（CAT）总活性，所有试剂盒购买自南京建成生物工程研究所，使用方法参照测定试剂盒的操作方法，具体操作步骤见文献 [22]。

所有数据均记录为至少 3 个独立生物重复实验的平均值 ± 标准偏差。使用非参数检验 Kruskal-Wallis 对实验数据作显著性分析，并将 P<0.05 视为具有显著差异，P>0.05 视为差异不显著。对于同一盐度组内不同时间点的数据，不同盐度组在同一时间点的数据，均采用 Kruskal-Wallis 检验进行组间比较。所有结果的分析使用软件 SPSS Statistics 进行，可视化使用软件 Origin2021 进行。

2 结果与分析

2.1 虫黄藻的分子鉴定结果 本实验对离体培养的藻液样品进行高通量测序，以检测藻液的虫黄藻组成（原始数据上传至 NCBI 数据库 https://www.ncbi.nlm.nih.gov/，SRA：PRJNA1000185）。测序结果（表 1）表明，本研究中离体培养的藻样中虫黄藻（*E. voratum*）的纯度达到（99.971±0.032）%，可以确定本次实验藻种为虫黄藻（*E. voratum*），这些虫黄藻可以用于开展后续实验。

表 1 离体培养虫黄藻 *E. voratum* 藻液样品高通量测序结果

Tab. 1 High-throughput sequencing of the algal liquid of the dinoflagellate *E. voratum* cultured *in vitro* %

虫黄藻物种 Taxon	样本1相对丰度 Sample1 Relative abundance	样本2相对丰度 Sample2 Relative abundance	样本3相对丰度 Sample3 Relative abundance	均值 Mean	*SD*
Effrenium voratum	99.988	99.934	99.991	99.971	0.032
Others	0.011	0.066	0.009		

2.2 低盐胁迫下虫黄藻的生长曲线 本实验将正常条件培养盐度为 35 的虫黄藻作为对照组，盐度条件改变为 25、15 培养的虫黄藻作为胁迫实验组。虫黄藻的初始理论接种浓度控制在 1×10^{4} cells·mL^{-1}。从图 1 可知，盐度 35 正常条件培养下的虫黄藻密度在 72 h 内有较为稳定的上升趋势但不显著，25 的低盐胁迫下在 72 h 内虫黄藻密度变化不显著，而 15 的低盐胁迫下虫黄藻密度变化呈现不断下降趋势且在第 48 h 已显著低于的初始阶段（P = 0.045）。在 48 h 时，25 与 15 盐度下的虫黄藻密度均已显著低于 35 盐度下的虫黄藻密度（P < 0.05）。

2.3 低盐胁迫下单个虫黄藻的 Chl a 含量变化 如图 2 所示，3 个盐度梯度（35、25、15）下，单个虫黄藻细胞的 Chl a 初始含量分别为（10.55 ± 0.76）、（10.66 ± 1.57）和（10.43 ± 0.69）pg·cell^{-1}，4 h 时单个虫黄藻细胞的 Chl a 含量与初始含量无显著差异（P > 0.05）。在盐度 35 培养条件下，单个虫黄藻细

中国知网 https://www.cnki.net

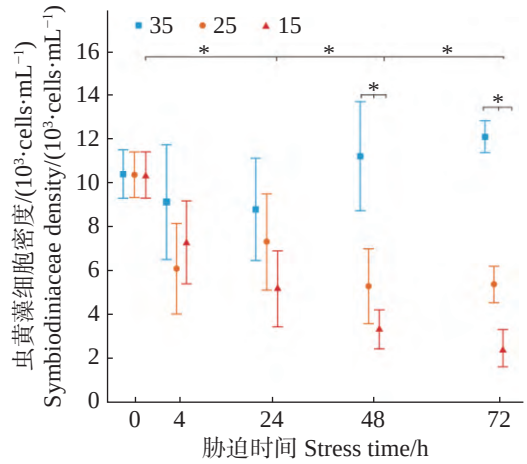


图 1　不同盐度条件下虫黄藻密度随胁迫时间的变化

Fig. 1　Changes in Symbiodiniaceae density under different salinity conditions over stress time

*表示 $P<0.05$。下同。

*means $P<0.05$. similarly hereinafter

胞的 Chl a 的含量在 48 h 内有上升趋势并在 72 h 后有所下降, 但仍比初始含量高。在 25 盐度的培养条件下, 单个虫黄藻细胞的 Chl a 的含量在 24 h 内保持稳定, 在 24 h 后略有下降, 但差异不显著($P>0.05$)。而 15 盐度培养下, 从4 h 开始的单个虫黄藻细胞的 Chl a 含量出现连续下降趋势, 48、72 h 时单个虫黄藻细胞的 Chl a 含量显著低于初始含量($P<0.05$)。

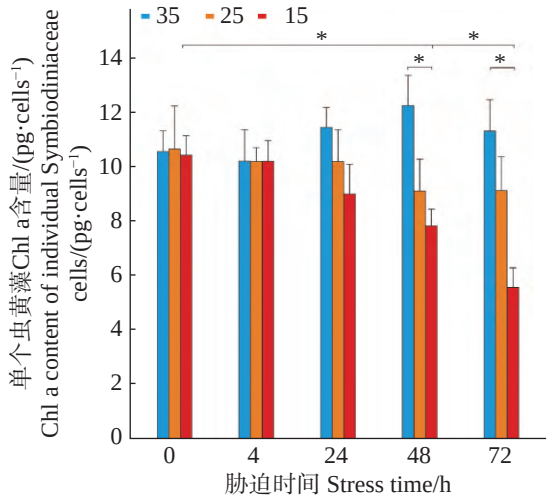


图 2　不同盐度条件下单个虫黄藻的 Chl a 含量随胁迫时间的变化

Fig. 2　Changes in Chl a content of individual Symbiodiniaceae cells under different salinity conditions over stress time

2.4　低盐胁迫下虫黄藻的超氧化物歧化酶（SOD）的活性变化　如图 3 所示, 3 个盐度梯度(35、25、15)的虫黄藻 SOD 初始活力分别为(12.57±1.83)、(14.68±1.39)、(10.74±1.59)U·mL^{-1}, 低盐胁迫实验组的平均值在 4 h 时要高于对照组但两者的差异性并不显著。在随后的 24 h 与 48 h, 低盐胁迫实验组呈现不断下降趋势; 盐度 25 实验组在 72 h 时与 48 h 持平, 而盐度 15 实验组则仍在下降。在胁迫 48、72 h 时胁迫实验组中盐度 25 和 15 的 SOD 活力均小于初始阶段的虫黄藻的 SOD 活力($P<0.05$), 且均小于对照组中盐度 35 的 SOD 在胁迫了 48、72 h 的虫黄藻 SOD 活力。

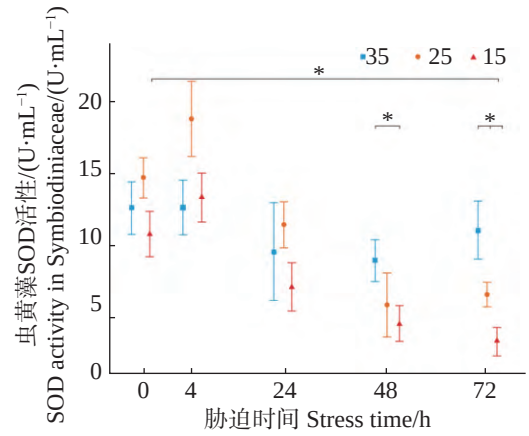


图 3　不同盐度条件下虫黄藻超氧化物歧化酶 SOD 活力随胁迫时间的变化

Fig. 3　Changes in SOD activity in Symbiodiniaceae under different salinity conditions over stress time.

2.5　低盐胁迫下虫黄藻（*E. voratum*）的过氧化氢酶（CAT）的活性变化　如图 4 所示, 3 个盐度梯度(35、25、15)的虫黄藻 CAT 初始活力分别为(0.24±0.02)、(0.23±0.04)、(0.21±0.02)U·mL^{-1}, 低盐胁迫实验组的平均值在 4 h 要高于对照组, 但两者的差异不显著。在随后的 24 与 48 h, 低盐胁迫实验组则呈现不断下降趋势。在 72 h 时, 25

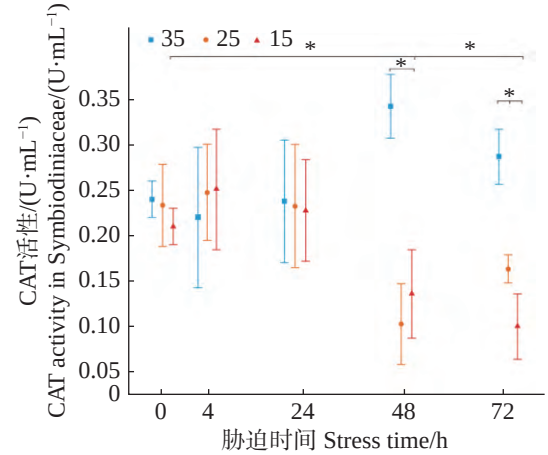


图 4　不同盐度条件下虫黄藻过氧化氢酶 CAT 活力随胁迫时间的变化

Fig. 4　Changes in CAT activity of Symbiodiniaceae under varying salinity conditions over stress time

中国知网　https://www.cnki.net

盐度实验组 CAT 活性略有上升，而盐度 15 实验组仍在下降。在胁迫 48、72 h 时，胁迫实验组中盐度 25 和 15 的 CAT 活力均显著小于正常培养盐度 35 条件下对照组虫黄藻的 CAT 活力（$P < 0.05$）。

3 讨 论

本研究结果表明，低盐胁迫显著抑制了虫黄藻的生长并导致其抗氧化系统崩溃，15 的盐度环境已超过其耐受阈值。具体而言，在 15 盐度下，*E. voratum* 的细胞密度在 48 h 后呈现显著负增长，同时伴随单个虫黄藻细胞的叶绿素 a 浓度持续下降，表明低盐环境严重抑制了其光合作用能力，这与 Sakami[17] 的研究一致，即在高温加低盐胁迫条件下会显著抑制虫黄藻的光合作用，结合本研究中单个虫黄藻细胞 Chl a 浓度的下降，推测其机制可能涉及光合系统Ⅱ的损伤。此外，Chl a 的降解可能与 ROS 诱导的脂质过氧化有关[23]，低盐胁迫下细胞膜透性增加，加速了叶绿体结构的破坏，这进一步解释了光合能力下降的机制。且 SOD 与 CAT 活性大幅降低（$P < 0.05$），说明低盐胁迫引发的渗透压失衡导致虫黄藻细胞内 ROS 过量积累，而抗氧化系统（如 SOD 和 CAT）的活性下降进一步削弱了 ROS 清除能力，最终加剧细胞损伤。值得注意的是，在 25 盐度下，尽管 SOD 与 CAT 活性初期短暂升高（4 h），但随着胁迫时间延长（24 h 后），酶活性仍持续下降，表明虫黄藻的短期应激机制不足以应对长期低盐压力。这些发现首次明确了 *E. voratum* 的盐度耐受下限为 15，并提出了其抗氧化系统的“双阶段响应”模式，短期激活与长期失效的共存。这一机制不仅解释了低盐环境下珊瑚白化的关键驱动因素（虫黄藻功能崩溃先于宿主损伤），也暗示非优势虫黄藻类群（如 *E. voratum*）可能在极端盐度波动区域中通过快速响应策略维持局部生态功能，为珊瑚礁适应性研究提供了新视角。

以往的研究将盐度胁迫下珊瑚产生白化主要归因于盐度对其体内的虫黄藻光合作用的影响[11－13]。在本研究中，观察到 15 盐度条件下单个虫黄藻细胞 Chla 的降低趋势且差异显著（$P<0.05$）。结合以往的研究，导致 *E. voratum* 的 Chl a 浓度下降的主要原因可以分为外在因素与内在因素。首先是外在因素，珊瑚受到盐度胁迫时，会发生水螅体回缩的行为，从而减少组织与周围海水接触的表面积，可能会导致到达虫黄藻的有效光合辐射大大减少，进而影响虫黄藻的 Chl a 浓度[11－12]；其次是内在因素，可能是 *E. voratum* 受到压力，活性氧大量积累进而加速了色素降解[23－24]，也可能是低盐环境导致细胞器产生损伤甚至细胞凋亡[14－15]。

虫黄藻在低盐压力胁迫下会产生氧化应激反应，加速产生具有破坏性的活性氧分子（ROS），比如过氧化氢（H_2O_2）、羟基自由基（OH^-）、超氧阴离子自由基（$O_2^{\bullet-}$）等[16,25－27]，其次是光合作用和细胞呼吸的常见副产物[28－29]，但当细胞内的 ROS 浓度累积到超过阈值则会引起细胞氧化损伤和细胞死亡[27]。与此同时，为了控制细胞水平的毒性，保护细胞免受氧化损伤，细胞内的抗氧化机制也会被触发[30－31]，包括酶与非酶的抗氧化剂，比如超氧化物歧化酶（SOD）、过氧化氢酶（CAT）、过氧化物酶（POD），以及一些小分子，如维生素 C 和硫醇类抗氧化剂[27,32－33]，其中的 SOD 与 CAT 则作为其中的 2 种抗氧化剂在这一过程中起到重要作用。SOD 通过催化 $O_2^{\bullet-}$ 转化成水和 H_2O_2 提供了抗氧化的第一道防线[34]，CAT 则会将 H_2O_2 还原成水和氧气[35]。因此，SOD 与 CAT 的活性作为氧化应激参数已被广泛用作低盐胁迫下细胞应激的生物学指标[36－37]，通过对氧化酶活性的测定，能够反映取样时刻细胞内 ROS 和抗氧化机制之间的平衡状态。在本研究中，25 与 15 的低盐度实验组 *E. voratum* 的 SOD 与 CAT 活性随着时间变化趋势一致，表现为初始阶段均高于 35 盐度对照组活性水平，并且随着时间的推移，活性均不断下降至低于对照组活性水平。初始阶段抗氧化酶的上升可能是由于渗透调节的需求导致代谢率升高进而导致虫黄藻体内 ROS 的增加所导致的[38]，即盐度下降激活了 *E. voratum* 细胞的氧化应激反应。而随后的酶活下降可能是低盐条件下，细胞受损严重且活性丧失，细胞内产生的 ROS 通路机制严重损坏，从而导致 ROS 水平下降[27]，或是在 ROS 上升期间，产生抗氧化酶的通路受损，又或是其他的抗氧化物可能承担了受损或者未受损通路产生的抗氧化酶的部分功能[32]。综合来看，25 与 15 的盐度胁迫下的 *E. voratum* 氧化或者抗氧化机制可能已经被严重破坏。

综上所述，面对低盐胁迫，*E. voratum* 的响应模式如图 5 所示。低盐胁迫下，虫黄藻 *E. voratum*

中国知网 https://www.cnki.net

的生长受到抑制, 光合作用减弱, 产生氧化应激反应, 出现活性氧分子等有害自由基积累, 抗氧化酶 SOD 与 CAT 活性初期升高, 增强了虫黄藻的抗氧化能力, 后期抗氧化机制被破坏。极端低盐环境下, 细胞受损, 酶活性下降, ROS 通路受损, 导致抗氧化机制被破坏。

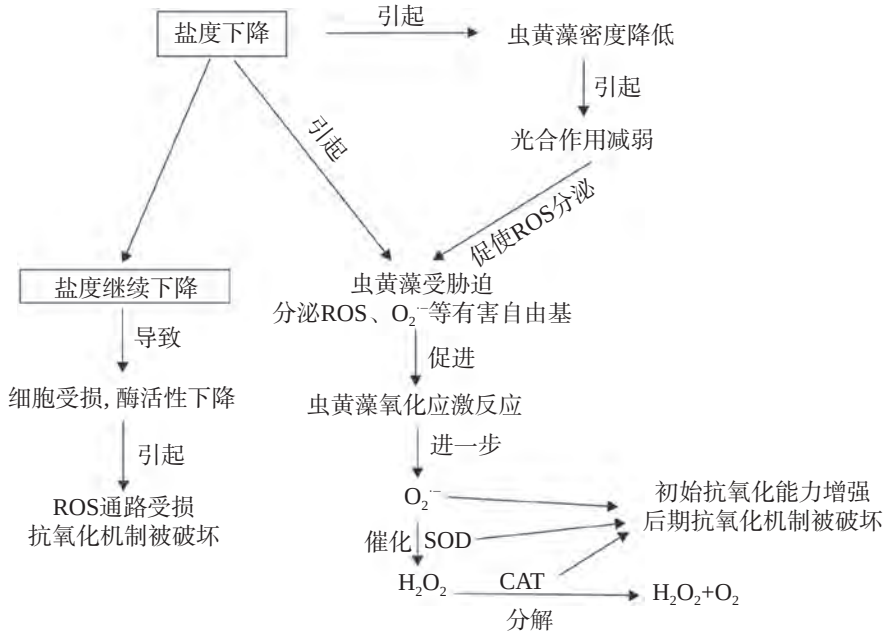


图 5　*E. voratum* 对低盐胁迫的响应模式

Fig. 5　Response patterns of *E. voratum* to low-salt stress

因此, 低盐胁迫对离体虫黄藻造成的负面影响, 包括虫黄藻密度降低、单个虫黄藻细胞 Chl a 浓度减少和关键抗氧化酶活性下降等, 其他虫黄藻系群和共生藻类也可能会表现出类似的反应, 因为盐度、Chl a 浓度和抗氧化酶活性在虫黄藻生长中起着基本的生理作用。已有研究证明, 低盐胁迫对紫色巴里沙软珊瑚共生虫黄藻的超氧化物歧化酶和过氧化氢酶具有抑制作用[39], 但不同种类的虫黄藻对盐度变化可能表现出不同的耐受性, 然而目前对虫黄藻低盐胁迫响应机制的研究较少, 具体不同系群虫黄藻对低盐胁迫的响应机制有待进一步研究。本研究为理解虫黄藻种群对低盐胁迫的响应和适应机制提供了数据支持, 有助于深入探究虫黄藻在低盐条件下的生理变化, 为未来构建和培育适应低盐环境的虫黄藻物种提供了参考依据。本研究首次揭示了离体虫黄藻的低盐响应机制, 但仍存在以下局限: 1)离体与共生状态下虫黄藻的胁迫响应差异需通过共培养实验进一步验证; 2)不同虫黄藻属(如 *Cladocopium*、*Durusdinium*)对低盐的响应可能存在差异, 需扩展比较研究以完善理论框架。希望下一步开展对 *Breviolum*、*Cladocopium*、*Durusdinium* 等不同属虫黄藻的低盐胁迫研究, 完善低盐条件对具体虫黄藻系群的影响及其不同的响应机制。

4　结　论

本研究以低盐作为环境压力源, 研究了低盐胁迫下虫黄藻(*E. voratum*)的生理生化反应。基于高通量测序, 本研究进行实验的虫黄藻样品中 *E. voratum* 的相对丰度达到(99.971±0.032)%。盐度为 25 与 15 的低盐胁迫下, *E. voratum* 均表现出生长受到抑制出现负增长趋势, 抗氧化酶 SOD 和 CAT 活性的下降。15 的盐度条件下已经限制了细胞分裂, 甚至出现细胞死亡, 表明这些盐度条件已经超过了 *E. voratum* 对盐度耐受的阈值。本研究通过离体培养实验, 初步揭示了 *E. voratum* 对低盐胁迫的生理响应机制, 为虫黄藻种群的耐盐性研究提供了基础数据。然而, 离体状态与共生状态下的胁迫响应可能存在显著差异, 未来研究需结合共生体系, 进一步探究低盐胁迫对虫黄藻–珊瑚共生关系的综合影响, 为珊瑚礁生态系统的保护与修复提供更全面的科学依据。

参考文献:

[1] 李宇亮, 高宇, 郑新庆, 等. 珊瑚礁生态系统功能产生机制及评价方法[J]. 应用海洋学学报, 2022, 41(3): 475 –

中国知网　https://www.cnki.net

482.
[2] CARPENTER K E, ABRAR M, AEBY G, et al. One-third of reef-building corals face elevated extinction risk from climate change and local impacts[J]. Science, 2008, 321(5888): 560 − 563.
[3] 陈燕, 李成才, 晁飞飞, 等. 环境因子对造礁石珊瑚白化影响的研究进展及思考[J]. 黑龙江科技信息, 2016(2): 129 − 130.
[4] MOBERG F, NYSTRÖM M, KAUTSKY N, et al. Effects of reduced salinity on the rates of photosynthesis and respiration in the hermatypic corals *Porites lutea* and *Pocillopora damicornis*[J]. Marine Ecology Progress Series, 1997, 157: 53 − 59.
[5] HOEGH-GULDBERG O. Climate change, coral bleaching and the future of the world's coral reefs[J]. Marine and Freshwater Research, 1999, 50(8): 839 − 866.
[6] BERKELMANS R, OLIVER J K. Large-scale bleaching of corals on the great barrier reef[J]. Coral Reefs, 1999, 18(1): 55 − 60.
[7] HOEGH-GULDBERG O, SMITH G J. The effect of sudden changes in temperature, light and salinity on the population density and export of zooxanthellae from the reef corals *Stylophora pistillata* Esper and *Seriatopora hystrix* Dana[J]. Journal of Experimental Marine Biology and Ecology, 1989, 129(3): 279 − 303.
[8] HAAPKYLÄ J, UNSWORTH R K F, FLAVELL M, et al. Seasonal rainfall and runoff promote coral disease on an inshore reef[J]. PLoS One, 2011, 6(2): e16893.
[9] 李泽鹏. 主要环境因子对滨珊瑚的胁迫作用研究[D]. 湛江: 广东海洋大学, 2012. doi:10.7666/d.Y2215224
[10] FALKOWSKI P G, DUBINSKY Z, MUSCATINE L, et al. Light and the bioenergetics of a symbiotic coral[J]. BioScience, 1984, 34(11): 705 − 709.
[11] MUTHIGA N A, SZMANT A M. The effects of salinity stress on the rates of aerobic respiration and photosynthesis in the hermatypic coral *Siderastrea siderea*[J]. The Biological Bulletin, 1987, 173(3): 539 − 551.
[12] MANZELLO D, LIRMAN D. The photosynthetic resilience of *Porites furcata* to salinity disturbance[J]. Coral Reefs, 2003, 22(4): 537 − 540.
[13] KUANUI P, CHAVANICH S, VIYAKARN V, et al. Effects of temperature and salinity on survival rate of cultured corals and photosynthetic efficiency of zooxanthellae in coral tissues[J]. Ocean Science Journal, 2015, 50(2): 263 − 268.
[14] LOBBAN C S, HARRISON P J. Seaweed Ecology and Physiology[M]. Cambridge: Cambridge University Press, 1994: 210−240.
[15] KERSWELL A P, JONES R J. Effects of hypo-osmosis on the coral *Stylophora pistillata*: nature and cause of 'low-salinity bleaching'[J]. Marine Ecology Progress Series, 2003, 253: 145 − 154.
[16] DOWNS C A, KRAMARSKY-WINTER E, WOODLEY C M, et al. Cellular pathology and histopathology of hypo-salinity exposure on the coral *Stylophora pistillata*[J]. Science of the Total Environment, 2009, 407(17): 4838 − 4851.
[17] SAKAMI T. Effects of temperature, irradiance, salinity and inorganic nitrogen concentration on coral zooxanthellae in culture[J]. Fisheries Science, 2000, 66(6): 1006 − 1013.
[18] WANG J, CHEN J Q, WANG S Y, et al. Monoclonal culture and characterization of Symbiodiniaceae C1 strain from the scleractinian coral *Galaxea fascicularis* [J]. Frontiers in Physiology, 2021, 11: 621111.
[19] 龙超, 罗肇河, 韦章良, 等. 海南三亚鹿回头虫黄藻 (*Effrenium voratum*) 的形态学和系统发育学研究[J]. 热带海洋学报, 2021, 40(4): 35 − 43.
[20] LAJEUNESSE T C, PARKINSON J E, GABRIELSON P W, et al. Systematic revision of Symbiodiniaceae highlights the antiquity and diversity of coral endosymbionts[J]. Current Biology, 2018, 28(16): 2570-2580. e6. doi:10.1016/j.cub.2018.07.008
[21] KANG N S, KIM E S, LEE J A, et al. First report of the dinoflagellate genus *Effrenium* in the East Sea of Korea: morphological, genetic, and fatty acid characteristics[J]. Sustainability, 2020, 12(9): 3928.
[22] 刘旭. 造礁石珊瑚对温度胁迫的响应机制研究[D]. 南宁: 广西大学, 2020. doi:10.27034/d.cnki.ggxiu.2020.001544
[23] XU Z Z, JIANG Y L, ZHOU G S. Response and adaptation of photosynthesis, respiration, and antioxidant systems to elevated CO_2 with environmental stress in plants[J]. Frontiers in Plant Science, 2015, 6: 701.
[24] MCCOY S J, KAMENOS N A. Coralline algae (Rhodophyta) in a changing world: integrating ecological, physiological, and geochemical responses to global change[J]. Journal of Phycology, 2015, 51(1): 6 − 24.
[25] LESSER M P. OXIDATIVE STRESS IN MARINE ENVIRONMENTS: biochemistry and physiological ecology [J]. Annual Review of Physiology, 2006, 68: 253 − 278.
[26] DOWNS C A, FAUTH J E, HALAS J C, et al. Oxidative stress and seasonal coral bleaching[J]. Free Radical Biology and Medicine, 2002, 33(4): 533 − 543.
[27] 杨晓红. 高温及营养缺乏诱导虫黄藻氧化胁迫的初步研究[D]. 厦门: 厦门大学, 2020. doi:10.27424/d.cnki.gxmdu.2020.000447
[28] ASADA K. THE WATER-WATER CYCLE IN CHLOROPLASTS: scavenging of active oxygens and dissipation of excess photons[J]. Annual Review of Plant Physiology and Plant Molecular Biology, 1999, 50: 601 − 639.
[29] BYCZKOWSKI J Z, GESSNER T. Biological role of superoxide ion-radical[J]. International Journal of Biochemistry, 1988, 20(6): 569 − 580.
[30] CZIESIELSKI M J, SCHMIDT-ROACH S, ARANDA M. The past, present, and future of coral heat stress studies[J]. Ecology and Evolution, 2019, 9(17): 10055 − 10066.
[31] 蒙林庆, 黄雯, 阳恩广, 等. 高温白化事件可提高涠洲

中国知网 https://www.cnki.net

岛澄黄滨珊瑚 (*Porites lutea*) 的耐热性[J]. 海洋学报, 2022, 44(8): 87 − 96.
[32] MISHRA S, IMLAY J. Why do bacteria use so many enzymes to scavenge hydrogen peroxide?[J]. Archives of Biochemistry and Biophysics, 2012, 525(2): 145 − 160.
[33] VANAPORN M, WAND M, MICHELL S L, et al. Superoxide dismutase C is required for intracellular survival and virulence of *Burkholderia pseudomallei*[J]. Microbiology, 2011, 157(Pt 8): 2392 − 2400. doi:10.1099/mic.0.050823-0
[34] FRIDOVICH I. Superoxide radical and superoxide dismutases[M]//GILBERT D L. Oxygen and living processes. New York, NY: Springer, 1981: 250 − 272. doi:10.1007/978-1-4612-5890-2_13
[35] VENN A A, LORAM J E, DOUGLAS A E. Photosynthetic symbioses in animals[J]. Journal of Experimental Botany, 2008, 59(5): 1069 − 1080.
[36] MCGINTY E S, PIECZONKA J, MYDLARZ L D. Variations in reactive oxygen release and antioxidant activity in multiple *Symbiodinium* types in response to elevated temperature[J]. Microbial Ecology, 2012, 64(4): 1000 − 1007.
[37] DIAS M, MADEIRA C, JOGEE N, et al. Oxidative stress on scleractinian coral fragments following exposure to high temperature and low salinity[J]. Ecological Indicators, 2019, 107: 105586.
[38] FREIRE C A, WELKER A F, STOREY J M, et al. Oxidative stress in estuarine and intertidal environments (temperate and tropical)[M]//ABELE D, VÁZQUEZ-MEDINA J P, ZENTENO-SAVIN T. Oxidative stress in aquatic ecosystems. Chichester: Wiley-Blackwell, 2011: 41-57. doi:10.1002/9781444345988.ch3
[39] DING D S, WANG S H, SUN W T, et al. The effect of feeding on *Briareum violacea* growth, survival and larval development under temperature and salinity stress[J]. Biology, 2022, 11(3): 410.

Physiological response of coral Symbiodiniaceae to low-salt stress

HE Ran[1#], GAO Kaixiang[1], PAN Nengbin[1], LI Zhanhong[1], ZHANG Tingchao[1], LIANG Hongye[1], LU Xiaoyan[1], LAN Mengling[1], QIN Zhenjun[1,2,3*]

(1. School of Marine Sciences, Guangxi University, Nanning, Guangxi 530004, China; 2. Guangxi Laboratory on the Study of Coral Reefs in the South China Sea, Guangxi University, Nanning, Guangxi 530004, China; 3. Coral Reef Research Center of China, Guangxi University, Nanning, Guangxi 530004, China)

Abstract: To investigate the physiological responses of Symbiodiniaceae under low-salinity stress, high-throughput sequencing was conducted on isolated culture of *Effrenium voratum* to obtain its relative abundance, and low-salinity stress experiments were performed on *E. voratum* for systematical analysis of the effects of low-salinity environments on the growth status, chlorophyll a (Chl a) concentration per symbiodiniaceae, superoxide dismutase (SOD) and catalase (CAT) activities of *E. voratum*. The results demonstrated that the cell density of *E. voratum* cultured under 35 salinity showed stable growth, indicating favorable growth at this level of salinity. At 25 salinity, *E. voratum* was inhibited in growth but could maintain survival. Severe growth inhibition occurred at 15 salinity, with cell density significantly declining after 48 hours, exhibiting a negative growth trend. Under 15 salinity stress, the Chl a concentration per *symbiodiniaceae* progressively decreased after 4 hours, suggesting significant suppression of photosynthetic capacity. Both SOD and CAT activities of *E. voratum* initially increased within 4 hours under 25 and 15 salinity stresses, but showed a continuous decline after 24 hours, revealing transient enhancement of antioxidant capacity at the early stages followed by progressive weakening with prolonged stress exposure.

Keywords: *Effrenium voratum*; low-salt stress; physiological response; next-generation sequencing

(责任编辑:潘学峰)

中国知网 https://www.cnki.net

张丽, 李志聪, 杨雅婷, 等. 两种环境敏感性不同的虫黄藻 (*Cladocopium goreaui* 和 *Durusdinium trenchii*) 的脂质代谢对热胁迫的响应模式[J]. 海洋学报, 2025, 47(9): 101–114, doi:10.12284/hyxb2025100

Zhang Li, Li Zhicong, Yang Yating, et al. Lipid metabolic response patterns to heat stress in two Symbiodiniaceae species with different environmental sensitivities (*Cladocopium goreaui* and *Durusdinium trenchii*)[J]. Haiyang Xuebao, 2025, 47(9): 101–114, doi:10.12284/hyxb2025100

两种环境敏感性不同的虫黄藻 (*Cladocopium goreaui* 和 *Durusdinium trenchii*) 的脂质代谢对热胁迫的响应模式

张丽[1], 李志聪[2], 杨雅婷[2], 梁祝清[2], 冯宜合[1], 卢铭垚[2], 胡思雨[2], 余克服[2,3], 梁甲元[2,3*]

(1. 广西大学 资源环境与材料学院, 广西 南宁 530004; 2. 广西大学 海洋学院, 广西 南宁 530004; 3. 广西大学 广西南海珊瑚礁研究重点实验室, 广西 南宁 530004)

摘要: 虫黄藻是珊瑚共生体系中不可或缺的伙伴, 不同种类的虫黄藻对环境胁迫的敏感性不同, 从而影响珊瑚宿主的环境适应能力。本研究从脂质代谢角度, 探讨了广泛分布的两种珊瑚共生虫黄藻——环境敏感型 *Cladocopium goreaui* 和环境耐受型 *Durusdinium trenchii* 在热胁迫下的应激模式。研究发现, 热胁迫显著影响两者的生长密度、光合色素含量、称为光系统Ⅱ (PSⅡ) 的光化学效率 (F_v/F_m) 及抗氧化活性, 且差异均具有统计学意义 ($P<0.05$)。脂质组学显示, *C. goreaui* 和 *D. trenchii* 在应对热胁迫时, 磷脂酰胆碱、甘油三酯、磷脂酰乙醇胺和溶血磷脂酰胆碱等脂质差异代谢物显著富集于甘油磷脂代谢、甘油酯代谢及多不饱和脂肪酸相关代谢通路。值得注意的是, 两者在鞘脂代谢方面存在显著差异: *D. trenchii* 通过下调神经酰胺水平减少细胞氧化应激损伤, 调控自噬过程, 并适应膜流动性的变化; 而 *C. goreaui* 主要通过上调富含多不饱和脂肪酸的脂质分子, 以维持膜稳定性和调控信号传导。深入解析不同环境敏感性虫黄藻在热胁迫下的脂质代谢应激机制, 有助于从共生伙伴的角度, 为提升珊瑚对环境变化的适应能力提供新的见解。

关键词: 热胁迫; 虫黄藻; 鞘脂代谢; 脂质组学; 氧化应激

中图分类号: Q178.53 **文献标志码:** A **文章编号:** 0253−4193(2025)09−0101−14

1 引言

虫黄藻属于甲藻门的单细胞藻类, 是珊瑚、海葵等海洋无脊椎动物和一些原生生物的内共生生物[1]。在虫黄藻与刺胞动物的共生过程中, 前者利用太阳光能和二氧化碳产生糖、氨基酸、酯、醇和脂类等各种代谢物转移到宿主体内[2−4], 后者则为前者提供无机营养物质[4−5]。早期研究者确定了 9 个不同的虫黄藻 (共生藻属: *Symbiodinium*) 系群 (Clade A-I)[6], 最新的研究依据系统发育学、形态学、生物地理学等特点将共生藻属 (*Symbiodinium*) 提升为共生藻科 (Symbiodiniaceae), 并且分为 *Symbiodinium*、*Breviolum*、*Cladocopium*、*Durusdinium*、*Effrenium*、*Fugacium*、*Gerakladium*、*Halluxium*、*Freudenthalidium*、*Miliolidum*、*Philozoon* 等

收稿日期: 2024−12−13; **修订日期:** 2025−04−25。

基金项目: 科技基础资源调查专项 (2023FY100804)。

作者简介: 张丽 (1998—), 女, 福建省龙岩市人, 研究方向为海洋微生物资源开发与应用。E-mail: lingjunluo@outlook.com

*** 通信作者:** 梁甲元, 副教授, 硕士生导师, 研究方向为珊瑚礁微生物生理、海洋微生物资源开发与应用。E-mail: jyliang@gxu.edu.cn

中国知网 https://www.cnki.net

11个属[7–9]。其中，*Cladocopium* 和 *Durusdinium* 属是与印度洋–太平洋珊瑚共生的主要属[10–12]，后者通常被归类为耐热型共生藻[12–13]，前者则被认为对温度更敏感[14]。研究发现，热胁迫会导致虫黄藻产生过量的活性氧（Reactive oxygen species, ROS），导致光系统损伤、脂质过氧化及细胞凋亡[15]。在相同高温条件下，*Cladocopium* 产生较高水平的丙二醛（Malonaldehyde, MDA），表明膜脂过氧化较严重，而 *Durusdinium* 具有更高的超氧化物歧化酶（Superoxide Dismutase, SOD）活性，可有效清除ROS，减轻细胞损伤[16]。

虫黄藻和珊瑚的不同组合对环境的适应存在差异，有证据表明虫黄藻类型会影响珊瑚的生长速度[17]及其应对急性胁迫的能力[18]。与具有 *Cladocopium* 属共生体的同种珊瑚相比，具有 *Durusdinium* 属共生体的珊瑚对热应力的抵抗力更强[14, 19–20]，而且一些多次发生白化现象的珊瑚礁中 *Durusdinium* 属共生体的比例更高[13]。例如，以 *Durusdinium* 属为主导的“洗牌”可提高耐热性，使珊瑚能快速提高其适应能力[21–22]。据报道，当珊瑚 *Acropora millepora* 中的共生虫黄藻系群 Clade C(*Cladocopium*) 被 Cladde D (*Durusdinium*) 取代时，其耐热性会提高 1～1.5℃[11]。珊瑚–虫黄藻共生关系的建立和维持受到温度的强烈影响，近年来严重的珊瑚白化现象主要是由热胁迫引起的[23–25]。对珊瑚共生体受到热损伤提出了多种与共生藻有关的原因，包括PSⅡ的D1蛋白功能障碍[26]、D1的修复机制[27]、核酮糖-1, 5-二磷酸羧化酶/氧化酶（Ribulose-1, 5-bisphosphate carboxylase/oxygenase）[28]、碳浓缩机制[28]和采光复合物[29]。总而言之，对虫黄藻的热损伤会导致ROS的产生，而这些ROS被认为会损害虫黄藻及其珊瑚宿主[30]，并通过多种细胞机制之一导致共生关系的崩解[31]。事实上，虫黄藻与宿主细胞的比率可能是有用的代用指标，可反映虫黄藻密度与宿主组织生物量的关系[32]。研究表明，除了视觉上的色素沉着差异外，检测白化早期迹象最广泛使用的方法之一是使用PAM仪，该仪器可测量PSⅡ的光合能力[33]。

细胞膜由大量生物大分子组成，包括脂质、糖蛋白和糖脂[34]。脂质在生物体内普遍存在，大多数脂质是脂肪酸和醇形成的酯类及其衍生物。与健康珊瑚中共生的虫黄藻的中性脂质相比，白化珊瑚中的虫黄藻中性脂质的积累增加[35]，且脂质组成的不同会对不同种类的虫黄藻适应环境变化的能力产生不同的影响[4]。脂质不仅是维持细胞膜结构和控制细胞功能的基本成分[4]，而且也是氧自由基等ROS攻击的主要目标[36]。甘油磷脂（Glycerophospholipids）、甘油酯（Glycerolipids）和鞘脂（Sphingolipids）等属于细胞膜脂质的组成部分，在能量储存、信号转导、细胞增殖和细胞凋亡等多种生理过程中发挥着重要作用[37–38]，也是自由基攻击的主要目标[36]。脂肪酸（Fatty acid）一直被用作确认海洋环境关系的定性标记[39]，根据不饱和度可划分为：饱和脂肪酸（Saturated fatty acyls）、单不饱和脂肪酸（Monounsaturated fatty acyls）、多不饱和脂肪酸（Polyunsaturated fatty acyls）和奇数脂肪酸（Odd-numbered fatty acyls），其中多不饱和脂肪酸的膜更容易被ROS（尤其是自由基）氧化[36, 40]，高温下，较高的多不饱和脂肪酸可能会导致膜的流动性过高，进而导致膜的不稳定性[20]。

由于脂质是细胞代谢产物的一部分，因此脂质组学属于更广泛的“代谢组学”领域[41]。事实上，大多数代谢组学研究都会涉及某些类别的脂质分析，或在一定程度上扩展脂质的分析范围[42]。然而，与大多数水溶性细胞代谢物相比，脂质具有特殊的物理和化学特性，使脂质组学成为区别于一般代谢组学的一个独立学科。但无论是单个脂质分子种类的含量还是整个脂质类别的含量都无法提供有关进出代谢节点的通量信息，因此，与一般代谢组学相比，脂质组学对代谢的理解要复杂得多[41]。以往关于脂质的研究主要集中在脂质的来源、合成途径、成分分析等[43–44]，且更多集中在“刺胞动物–虫黄藻”整体[45–47]，而对于热胁迫导致虫黄藻的脂质产生变化的报道较少。因此，对虫黄藻进行脂质组学分析也成为了新的切入点。共生虫黄藻的离体培养自20世纪以来就有研究，研究者采取多种培养方法成功实现了不同种属虫黄藻的离体培养[48–50]，并成功证实了虫黄藻对珊瑚共生体环境耐受性的影响[51]。

综上所述，*Cladocopium* 和 *Durusdinium* 在耐热机制上存在显著差异，特别是在ROS清除和膜脂调控方面。然而，相较于基因组学、转录组学和蛋白质组学研究，目前对不同虫黄藻脂质代谢响应高温的差异机制尚不清晰。因此，在本研究中，以离体培养的两种典型虫黄藻 *Cladocopium goreaui* 和 *Durusdinium trenchii* 为实验对象，研究两者在常温（25℃）和热胁迫（32℃）培养条件下的生理生化和脂质代谢变化，分别对比热胁迫下与常温培养的同一系群虫黄藻和同一温度条件下不同系群虫黄藻在密度、光合色素含量、SOD活力、MDA含量和脂质代谢物变化情况，通过深入分析两种环境敏感性不同的虫黄藻在热胁迫下的应激机制，可以从共生伙伴的视角为珊瑚应对全

中国知网 https://www.cnki.net

球变暖提供新的见解。

2　材料与方法

2.1　虫黄藻的离体培养

虫黄藻 *C. goreaui* 和 *D. trenchii* 由本课题组分离自涠洲岛(21°54′～21°10′N, 109°00′～109°15′E)的霜鹿角珊瑚 (*Acropora pruinose*) 和西沙群岛(15°46′～17°08′N, 111°11′～112°54′)的丛生盔形珊瑚 (*Galaxea fascicularis*), 培养方案参照覃良云等[52]的描述: 将虫黄藻 *C. goreaui* 和 *D. trenchii* 培养至生长对数中期后(对数生长期内, 生长速率与初始密度无关[53]; 且在此期间营养供给充足时, 比生长率主要受环境因子调控[54]), 转移至 500 mL 锥形瓶中在 L1 培养基、盐度 35、光照强度 90 μmol/(m^2·s)、明暗周期 14 h∶10 h 的环境条件下培养。温度根据 Waheed 和 Hoeksema[55] 的研究设置 2 个温度 25℃、32℃, 其中 25℃ 作为对照组。每组 3 个重复(C_C 组 = *C. goreaui* 25℃ 对照组; C_T 组 = *C. goreaui* 32℃ 实验组; D_C 组 = *D. trenchii* 25℃ 对照组; D_T 组 = *D. trenchii* 32℃ 实验组)。

2.2　生理生化分析

2.2.1　生长速率测定

吸取 1 mL 藻液加入终浓度为 5% 的戊二醛进行固定, 使用血球计数板(0.10 mm, 1/400 mm^2)在光学显微镜下计数得出细胞密度, 3 个重复取均值后计算生长率 (μ): $\mu = \ln(N_2/N_1)/(t_2 - t_1)$。其中, μ 为比生长速率 (d^{-1}), N_2、N_1 分别为 t_2、t_1 时刻的细胞密度 (cells/mL)。

2.2.2　光合色素含量和 PSⅡ 的最大量子产率(F_v/F_m)的测定

吸取 2 mL 藻液离心 (12 000 r/min, 5 min, 4℃) 后去除上清液并在沉淀物中加入纯甲醇, 于 4℃ 避光条件下萃取 24 h。萃取完成后将溶液再次离心 (12 000 r/min, 5 min, 4℃), 离心后取其上清液用酶标仪(Thermo)读取测定吸光值。叶绿素 *a*(chlorophyll *a*)、叶绿素 *c*(chlorophyll *c*)和类胡萝卜素(carotenoids)的测定基于 Strychar 和 Sammarco[56] 及 Ritchie[57] 的方程。对 PSⅡ 最大光量子产率(F_v/F_m), 将藻液避光黑暗处理 30 min 后, 使用 monitoring PAM 仪对虫黄藻细胞进行检测。

2.2.3　可溶性蛋白、SOD 活力和 MDA 含量测定

取 15 mL 藻液至离心管中在 4℃、4 000 r/min 条件下离心 15 min, 去上清后加入 1 mL PBS 溶液重悬, 移入 1.5 mL 离心管中, 加入 0.3 mm 氧化锆研磨珠 100 μL, 使用全自动样品快速研磨仪(上海净信)进行研磨, 运行 30 s, 暂停 10 s, 共运行 10 次(使用前将适配器放入 −20℃ 冰箱中预冷)。随后在 4℃、12 000 r/min 条件下离心 5 min, 收集上清液。分别采用 BCA 法微量蛋白质浓度测定试剂盒(上海生工, 中国)、SOD 试剂盒(A001, 南京建成, 中国)和 MDA 测定试剂盒(A003, 南京建成, 中国)测定可溶性蛋白的浓度、SOD 活力和 MDA 含量。

2.2.4　统计分析

使用软件 GraphPad Prism 9.5 进行数据分析, $P < 0.05$ 认为差异有统计学意义。采用 Tukey 事后检验对有显著差异的数据进行随访检验。实验数据均归一化到单位细胞内(该单位换算方法在藻类抗氧化研究中已被广泛验证[58]), 采用“平均值 ± 标准误差”(Mean ± SEM)表示($n = 3$)。

2.3　脂质组学分析

2.3.1　样品处理

为探究热胁迫对两种虫黄藻脂质变化的影响, 收集对照组和实验组培养至第 15 天的虫黄藻细胞(离体培养的虫黄藻经离心纯化后, 显微镜检查确认无宿主细胞残留, 确保脂质组学分析仅针对虫黄藻)。精确称取(50 ± 5) mg 样品至 2 mL 离心管中, 加入一颗直径 6 mm 的研磨珠; 加入 280 μL 提取液(甲醇∶水 = 2∶5), 再加入 400 μL MTBE; 冷冻组织研磨仪研磨 6 min (−10℃, 50 Hz); 低温超声提取 30 min(5℃, 40 kHz), 将样品静置于−20℃, 30 min; 离心 15 min(13 000 g, 4℃), 取 350 μL 上清液于 EP 管中, 氮气吹干; 加入 100 μL 提取液(异丙醇∶乙腈 = 1∶1)复溶; 涡旋 30 s, 低温超声萃取 5 min(5℃, 40 kHz); 离心 10 min(13 000 g, 4℃), 移取上清液至带内插管的进样小瓶中上机分析; 另外, 每个样本分别移取 20 μL 上清液混合后作为质控样本。

2.3.2　LC-MS 分析

本次 LC-MS 分析的仪器平台为赛默飞公司的超高效液相色谱串联傅里叶变换质谱 UHPLC -Q Exactive HF-X 系统。

色谱条件: 色谱柱为 Accucore C30 柱(100 mm × 2.1 mm i.d., 2.6 μm; Thermo); 流动相 A 为 50% 乙腈水溶液(含 0.1% 甲酸, 10 mmol/L 乙酸铵), 流动相 B 为乙腈/异丙醇/水(10/88/2)(含 0.02% 甲酸, 2 mmol/L 乙酸铵), 进样量为 5 μL, 柱温为 40℃, 洗脱流速为 0.4 mL/min。流动相洗脱梯度为: 65%A、35%B(0 min); 40%A、60%B (4 min); 15%A、85%B(12 min); 100%B (15～17 min); 65%A、35%B(18～20 min)。

质谱条件: 样品质谱信号采集采用正、负离子扫描模式, 质量扫描范围 *m/z*: 200～2 000。正模式离子

中国知网　https://www.cnki.net

喷雾电压为 3 000 V, 负模式离子喷雾电压为−3 000 V, 鞘气 60 psi, 辅助加热气 20 psi, 离子源加热温度 370℃, 20−40−60 V 循环碰撞能, 采用 DDA 模式采集数据。

2.3.3 质控

质控样本(quality control, QC)由所有样本的提取液等体积混合制备而成, 每个 QC 的体积与样本相同, 用与分析样本相同的方法处理和检测, 在仪器分析的过程中, 每 5～15 个分析样本中插入一个 QC 样本, 以考察整个检测过程的稳定性。

2.3.4 数据分析

2.3.4.1 数据预处理和搜库

原始数据导入脂质组学处理软件 Lipidsearch (Thermo Fisher, USA)进行基线过滤、峰识别、积分、保留时间校正、峰对齐等, 最终得到含保留时间、质荷比和峰强度等信息的数据矩阵。其后采用该软件进行特征峰搜库鉴定, 将 MS 和 MS/MS 质谱信息与代谢数据库进行匹配, MS 质量误差设置为小于 10×10^{-6}, 同时根据二级质谱匹配得分鉴定代谢物。

搜库后的矩阵数据上传至美吉生物云平台(https://cloud.majorbio.com)进行数据分析, 首先进行数据预处理, 数据矩阵用 20% 规则来去除缺失值, 即保留至少一组样品中非零值 80% 以上的变量, 在进行填补空缺值(原始矩阵中极小值填补空缺值), 为减小样品制备及仪器不稳定带来的误差, 用总和归一化法对样本质谱峰的响应强度进行归一化, 得到归一化后的数据矩阵, 同时删除 QC 样本对标准偏差(RSD)大于 30% 的变量, 并进行 lg 对数化处理, 得到最终用于后续分析的数据矩阵。

2.3.4.2 差异代谢物分析

对与处理后的矩阵文件进行差异分析。R 软件包 ropls(Version1.6.2)进行主成分分析(Principal component analysis, PCA)和正交最小偏二乘判别分析(Orthogonal partial least squares discriminant analysis, OPLS-DA), 并使用 7 次循环交互验证来评估模型的稳定性。此外, 进行 student's *t* 检验和差异倍数分析。差异代谢物分析默认使用单变量统计分析(*t* 检验)联合多元统计分析(OPLS-DA)以及倍数变化值(FC)共同筛选差异代谢物, 默认筛选条件为 $P<0.05$ 且 VIP > 1 且(FC < 1 或 FC > 1)。

差异代谢物通过 KEGG 数据库(https://www.kegg.jp/kegg/pathway.html)进行的代谢通路注释, 获得差异代谢物参与的通路, Python 软件包 scipy.stats 进行通路富集分析, 并通过 Fisher 精确检验获得与实验处理最相关的生物学途径。

3 结果

3.1 生理生化指标

3.1.1 生长速率

在整体实验周期中, C_T 组与 C_C 组的生长密度、D_C 组与 D_T 的生长密度均无显著差异($P>0.05$)(图 1a); 前者的 μ 表现出显著差异($P<0.05$), 后者的 μ 未表现出显著差异($P>0.05$)(图 1b)。培养至第 11、13、15 天时, C_T 组的 μ 与 C_C 组的 μ 对比分别下降了 84.00%、86.83% 和 93.88%, 同样条件下, D_T 组的 μ 仅下降了 32.01%、32.96% 和 26.85%(图 1b)。高温下 C_T 组的 μ 波动较大, 除在第 7 天时 μ 为正值, 其余均为负值, 表明细胞在高温下受到抑制; 而 D_T 组相较于 D_C 组, 尽管在早期(第 1 天)高温对其有抑制, 但后期(第 7～15 天)的 μ 有所回升, 这说明 *D. trenchii* 对高温的耐受性较好(图 1b)。

3.1.2 光合色素含量和 PSⅡ的最大量子产率(F_v/F_m)

光合色素的存在是虫黄藻进行光合作用的关键。不同温度下的 *D. trenchii* 的叶绿素 *a*、叶绿素 *c* 和类胡萝卜素的浓度均表现出与生长密度正相关, 而 *C. goreaui* 的叶绿素 *a*、叶绿素 *c* 和类胡萝卜素浓度从第 9 天起 C_T 组与 C_C 组与生长密度的关系表现为负相关。其中, 从第 7 天开始, C_T 组的叶绿素 *a* 浓度[(1.085 3 ± 0.03) pg/cell] 相较于 C_C 组[(2.182 7 ± 0.034) pg/cell] 而言显著下降($P<0.05$)(图 1c); 叶绿素 *c* 浓度从第 5 天[C_C 组:(5.300 5 ± 0.08) pg/cell, C_T 组:(8.374 3 ± 0.24) pg/cell] 显著提升($P<0.05$), 并且在第 11 天出现进一步提升[C_C 组:(2.641 9 ± 0.35) pg/cell, C_T 组:(16.281 2 ± 0.26) pg/cell](图 1e); 类胡萝卜素浓度的趋势从第 11 天起持续走高(图 1d)。由于 *D. trenchii* 对高温的耐受性, 其 D_T 组的叶绿素 *a*、叶绿素 *c* 和类胡萝卜素浓度与 D_C 组相比, 虽同为表现为增长趋势, 但到实验后期(第 7～15 天), 两组的光合色素含量无显著差异($P<0.05$)(图 1c、1d、1e)。D_C 组和 D_T 组的 F_v/F_m 值基本保持稳定, 除了第 1、3 和 5 天出现稳步提升的现象。C_C 组同样在实验周期基本保持稳定, 而 C_T 组(0.55 ± 0.02)在第 11 天显著下降(与对 C_C 组(0.669 ± 0.01)相比, F_v/F_m 值下降了 17.81%, 图 1f)($P<0.05$)。

3.1.3 可溶性蛋白、SOD 和 MDA 含量

在实验周期中, C_C 组、D_C 组和 D_T 组可溶性蛋白含量整体呈现平稳趋势, 而 C_T 组则稳步上升(图 2a)。1～15 天中, C_T 组的可溶性蛋白含量(957.740 3 pg/cell)相比 C_C 组(491.140 5 pg/cell)具有显著差异($P<0.05$),

中国知网 https://www.cnki.net

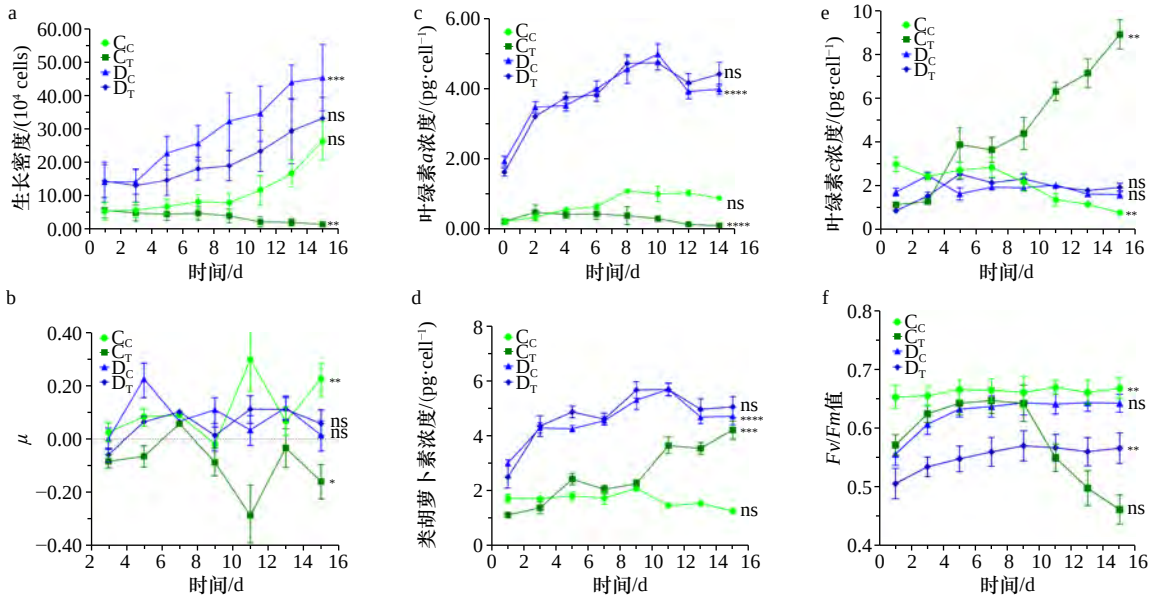


图 1　热胁迫下两种虫黄藻的生理指标变化

Fig. 1　Physiological parameter changes of two Symbiodiniaceae species under heat stress

a. C_C 组、C_T 组、D_C 组和 D_T 组的生长密度; b. C_C 组、C_T 组、D_C 组和 D_T 组的生长速率(μ); c. C_C 组、C_T 组、D_C 组和 D_T 组的叶绿素 c 含量变化; d. C_C 组、C_T 组、D_C 组和 D_T 组的类胡萝卜素含量变化; e. C_C 组、C_T 组、D_C 组和 D_T 组的叶绿素 *c* 含量变化; f. C_C 组、C_T 组、D_C 组和 D_T 组的 F_v/F_m 值变化。误差棒表示 SEM(3 个生物学重复), 实验组和对照组之间的显著性用星号表示(*: $P<0.05$; **: $P<0.01$; ***: $P<0.001$; ****: $P<0.0001$)

a. Growth density of C_C, C_T, D_C, and D_T groups; b. Growth rate (μ) of C_C, C_T, D_C, and D_T groups; c. Changes in chlorophyll *a* content in C_C, C_T, D_C, and D_T groups; d. Changes in carotenoid content in C_C, C_T, D_C, and D_T groups; e. Changes in chlorophyll *c* content in C_C, C_T, D_C, and D_T groups; f. Changes in F_v/F_m values in C_C, C_T, D_C, and D_T groups. Error bars represent SEM (n = 3 biological replicates), statistical significance between experimental and control groups is indicated by asterisks (*: $P<0.05$; **: $P<0.01$; ***: $P<0.001$; ****: $P<0.0001$)

而 D_T 组(672.546 2 pg/cell)与 D_C 组(722.623 1 pg/cell)无显著差异($P>0.05$)。如图 2b, C_C 组的 SOD 活力随时间下降[第 1 天(148.444 6 ± 6.02) U^{-7}/cell, 第 15 天(6.007 9 ± 0.73) U^{-7}/cell], 而 C_T 组的 SOD 活力下降至最低点(第 7 天 44.546 8 U^{-7}/cell)后迅速上升, 并在第 15 天[(172.195 2 ± 33.27) U^{-7}/cell] 显著高于 C_C 组($P<0.05$); 而 D_C 组和 D_T 组的 SOD 活力较低, 且随时间无明显变化。C_C 组、C_T 组、D_C 组和 D_T 组的 MDA 含量整体均随时间下降(图 2c)。其中, CT 组的 MDA 含量在第 9 天[(557.267 9 ± 40.91) $nmol^{-7}$/cell] 开始有所回升, 至第 13 天升到顶点[(911.385 1 ± 75.34) $nmol^{-7}$/cell] 后又下降, 并在第 15 天显著高于 C_C 组($P<0.05$); 而 D_C 组和 D_T 组的 MDA 含量相对较低, 随时间缓慢下降, 差异不显著($P>0.05$)。

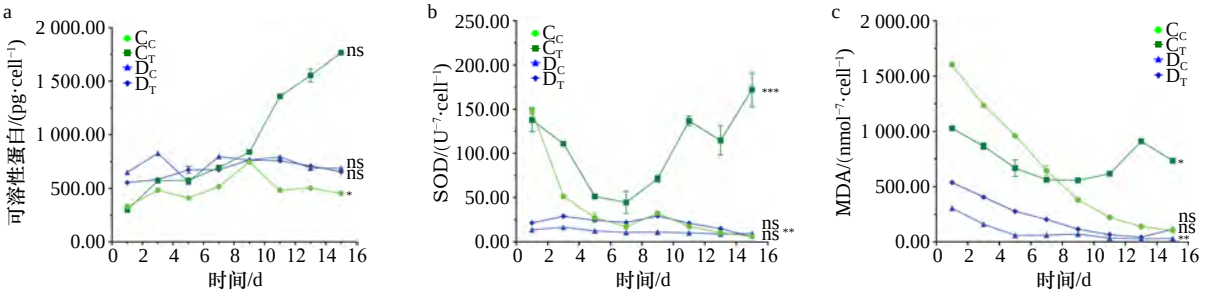


图 2　热胁迫下两种虫黄藻抗氧化物活性(含量)变化

Fig. 2　Changes in antioxidant activity (content) of two Symbiodiniaceae species under heat stress

a. C_C 组、C_T 组、D_C 组和 D_T 组的可溶性蛋白浓度的变化; b. C_C 组、C_T 组、D_C 组和 D_T 组的 SOD 活力的变化; c. C_C 组、C_T 组、D_C 组和 D_T 组的 MDA 含量的变化。误差棒表示 SEM(3 个生物学重复), 实验组和对照组之间的显著性用星号表示(*: $P<0.05$; **: $P<0.01$; ***: $P<0.001$)

a. Changes in soluble protein concentration in C_C, C_T, D_C, and D_T groups; b. Changes in SOD activity in C_C, C_T, D_C, and D_T groups; c. Changes in MDA content in C_C, C_T, D_C, and D_T groups. Error bars represent SEM (n = 3 biological replicates), statistical significance between experimental and control groups is indicated by asterisks (*: $P<0.05$; **: $P<0.01$; ***: $P<0.001$)

中国知网　https://www.cnki.net

3.2 脂质代谢分析

3.2.1 脂质变化

两种虫黄藻共检测到 1 886 种不同的脂质种类(图 3a), 包括 64 种脂肪酸, 1 204 种甘油酯, 320 种甘油磷脂, 236 种鞘脂和 62 种固醇脂(Sterol Lipids)。根据脂质链不饱和度分类统计如图 3b 所示: 单不饱和脂肪酸 96 种(13.77%), 奇数脂肪酸 159 种(22.81%), 多不饱和脂肪酸 245 种(35.15%), 饱和脂肪酸 142 种(20.37%), 其余 55 种(7.89%)。其中, 多不饱和脂肪酸占比最大, 表明虫黄藻的脂质中它是主要的脂肪酸类型。分别对 C_C 组、C_T 组、D_C 组和 D_T 组的脂质亚类进行分析(图 3c), 脂质分子数量排名前 5 的脂质亚类是甘油三酯(Triglyceride)、甘油二酯(Diglyceride)、单半乳糖二酰甘油酯(Monogalactosyldiacylglycerol)、神经酰胺(Ceramides)和心磷脂(Cardiolipin)。

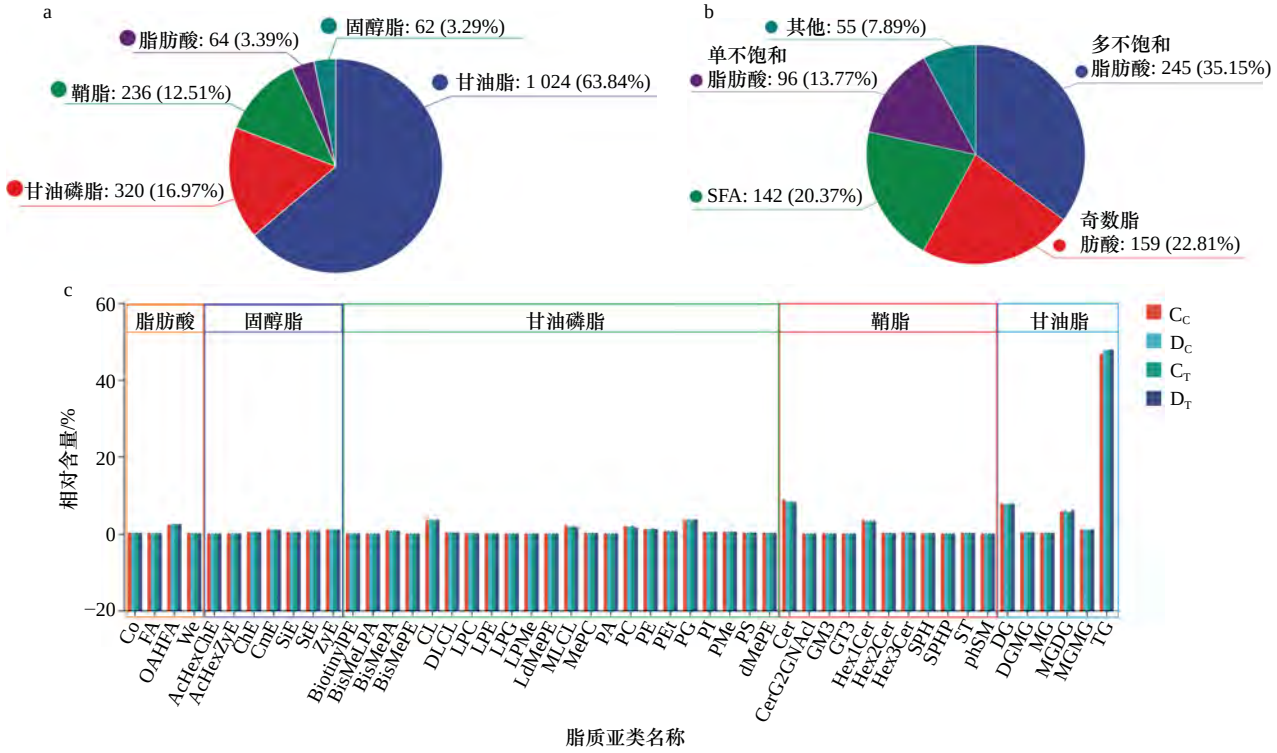


图 3 热胁迫下两种虫黄藻脂质变化注释图

Fig. 3 Annotated diagram of lipid changes in two types of Symbiodiniaceae species under heat stress

a. 虫黄藻全脂质分类统计图; b. 虫黄藻脂质链不饱和度分类统计图; c. C_C 组、C_T 组、D_C 组和 D_T 组的脂质分类统计图。误差棒表示 SEM(6 个生物学重复)

a. Total lipid classification chart for Symbiodiniaceae; b. Lipid chain unsaturation classification chart for Symbiodiniaceae; c. Lipid classification chart for the C_C, C_T, D_C, and D_T groups. Error bars represent SEM (n = 6 biological replicates)

3.2.2 多元统计分析

本实验通过脂质组学探究高温下虫黄藻 *C. goreaui* 和 *D. trenchii* 脂代谢相关的脂质分子的变化, 反映高温对虫黄藻 *C. goreaui* 和 *D. trenchii* 脂代谢水平的影响。对鉴定到的脂质分子在正、负离子模式下进行主成分分析(PCA), 对照组和实验组在两种模式下的 PCA 得分图(图 4a 和 4b)上均有不同的聚类趋势, 同一组内重复样品相似度最高, 说明在高温下两种虫黄藻的脂质代谢物存在差异。

为更直观反映实验组和对照组之间的差异, 进行有监督模式的正交偏最小二乘法判别分析(OPLS-DA), OPLS-DA 得分图(图 4c–f)显示, 两种虫黄藻的脂质代谢成分具有良好的区分度, 对构建的 OPLS-DA 模型(表 1)的重复性和可靠性进行验证得到: 所有构建的模型均不存在过拟合现象, 具备良好的稳定性和预测能力。

3.2.3 差异代谢物分析

C_C 组和 C_T 组鉴定到的差异代谢物共 695 个(图 5a), 其中 402 个上调, 293 个下调; 鉴定到 D_C 组和 D_T 组之间的差异代谢物共 619 个(图 5b), 其中 243 个上调, 376 个下调; C_C 组和 D_C 组鉴定到的差异代谢物共 683 个(图 5c), 其中 373 个上调, 310 个下调; 鉴定到 C_T 组和 D_T 组之间的差异代谢物共 695 个(图 5d), 其中 315 个上调, 380 个下调。这意味着在

中国知网 https://www.cnki.net

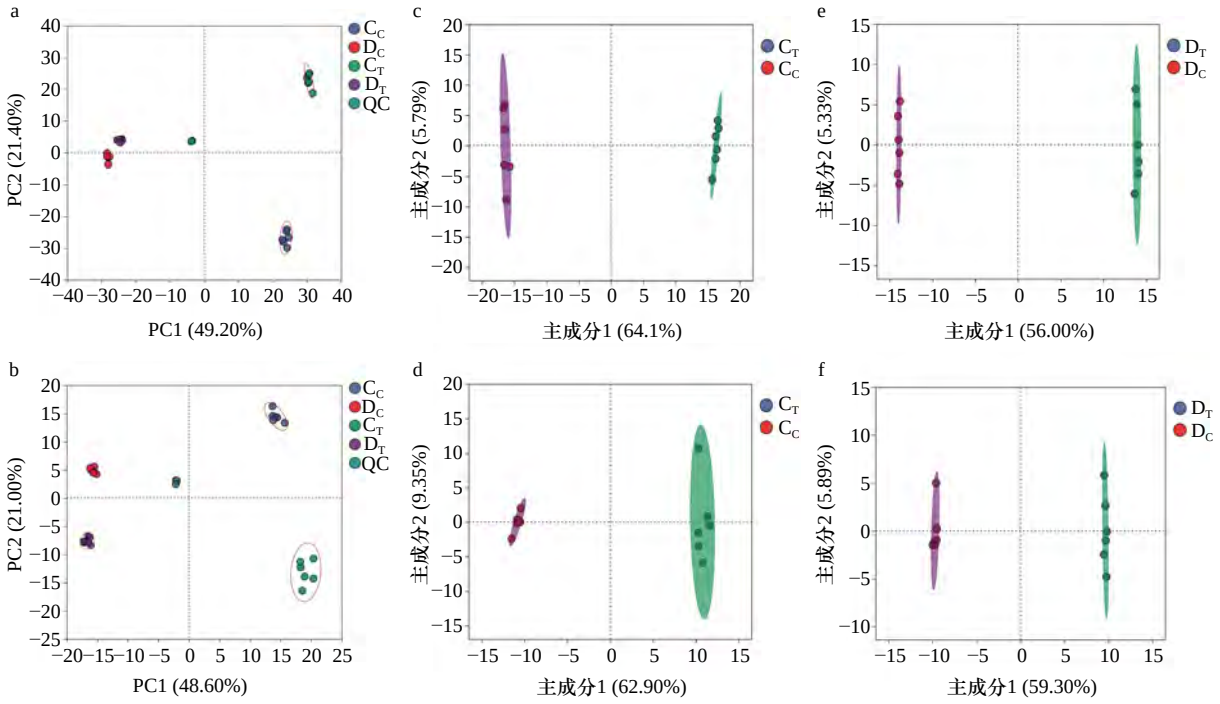


图 4　热胁迫下两种虫黄藻的 PCA 得分图和 OPLS-DA 得分图

Fig. 4　PCA score plot and OPLS-DA score plot of two types of Symbiodiniaceae species under heat stress

a、b.正、负离子模式 C_C 组、C_T 组、D_C 组、D_T 组的 PCA 得分图; c、d.正、负离子模式下 C_C 组、C_T 组的 OPLS-DA 得分图; e、f.正、负离子模式下 D_C 组、D_T 组的 OPLS-DA 得分图

a, b. PCA score plots for the C_C, C_T, D_C, and D_T groups in positive and negative ion modes; c, d. OPLS-DA score plots for the C_C and C_T groups in positive and negative ion modes; e, f. OPLS-DA score plots for the D_C and D_T groups in positive and negative ion modes

表 1　OPLS-DA 模型

Table 1　OPLS-DA modles

模型	R^2X(cum)	R^2Y(cum)	Q^2(cum)
C_C vs C_T	0.641	0.992	0.987
C_C vs C_T *	0.629	0.993	0.988
D_C vs D_T	0.560	0.998	0.990
D_C vs D_T *	0.593	0.997	0.991

注: *代表负离子模式。

高温条件下, C_T 组有更大的代谢上调反应, 表明 *C. goreaui* 可能更积极地调整自身的代谢以应对高温压力; 相比之下, D_T 组更多代谢物下调, 表明 *D. trenchii* 可能更多地通过抑制代谢活动来应对高温环境。

采用单因素方差(scheffe > 0.95)分析 C_C 组、C_T 组、D_C 组和 D_T 组的脂质谱, 差异 test bar plot 分析结果如图 6 所示。由图可知, 两种虫黄藻在高温条件下筛选出 *P* 值排名前 10 的代谢物, 磷脂酰肌醇(Phosphatidylinositol, PI)、甘油三酯、甘油二酯、神经酰胺和单半乳糖单酰甘油酯(Monogalactosylmonoacylglycerol, MGMG)等脂类代谢物出现说明高温对这几类脂类的代谢产生了显著影响($P < 0.001$)。这些代谢物与细胞膜的稳定性、信号转导和能量储存密切相关, 可能是高温应激响应的关键调节因子。其中, 甘油三酯作为储存能量的主要形式, 可能通过脂质堆积或降解响应温度变化, 以提供细胞所需的能量或调节脂质稳态。

3.2.4　脂质代谢物 KEGG 通路分析

为了解虫黄藻细胞受到热胁迫时对其相关通路的影响情况, 本研究对上述差异脂质代谢物进行了 KEGG 通路分析。当经过校正的 *P* 值($P_{adjust} < 0.05$)时, 认为此 KEGG PATHWAY 功能存在显著富集情况。结果显示, C_T 组的差异代谢物相较于 C_C 组主要富集在细胞过程(Cell Processes, CP)和代谢(Metabolism, M)通路(图 7a)上: 上调差异代谢物[PE(16∶1/18∶1)、PE(16∶0/16∶0) 和 PE(15∶0/15∶0)] 显著富集到自噬−其他和和糖基磷脂酰肌醇(GPI)−锚的生物合成通路; 上调差异代谢物[TG(16∶0/16∶1/20∶4)、TG(16∶0/16∶0/16∶1) 和 TG(20∶0/16∶0/16∶0)] 和下调差异代谢物[TG(16∶1/18∶1/18∶1)] 显著富集到甘油脂代谢通路; 上调差异代谢物[PC(16∶0/20∶5)、PC(18∶4/16∶0)、PC(20∶3/20∶3)、PC(15∶0/14∶0) 和 PC(16∶0/16∶0)] 显著富集到亚油酸、α-亚麻酸代谢和花生四烯酸代谢通路; 上调差异代谢物[PE(16∶1/18∶1)、PC(16∶0/20∶5)、PC(18∶

中国知网　https://www.cnki.net

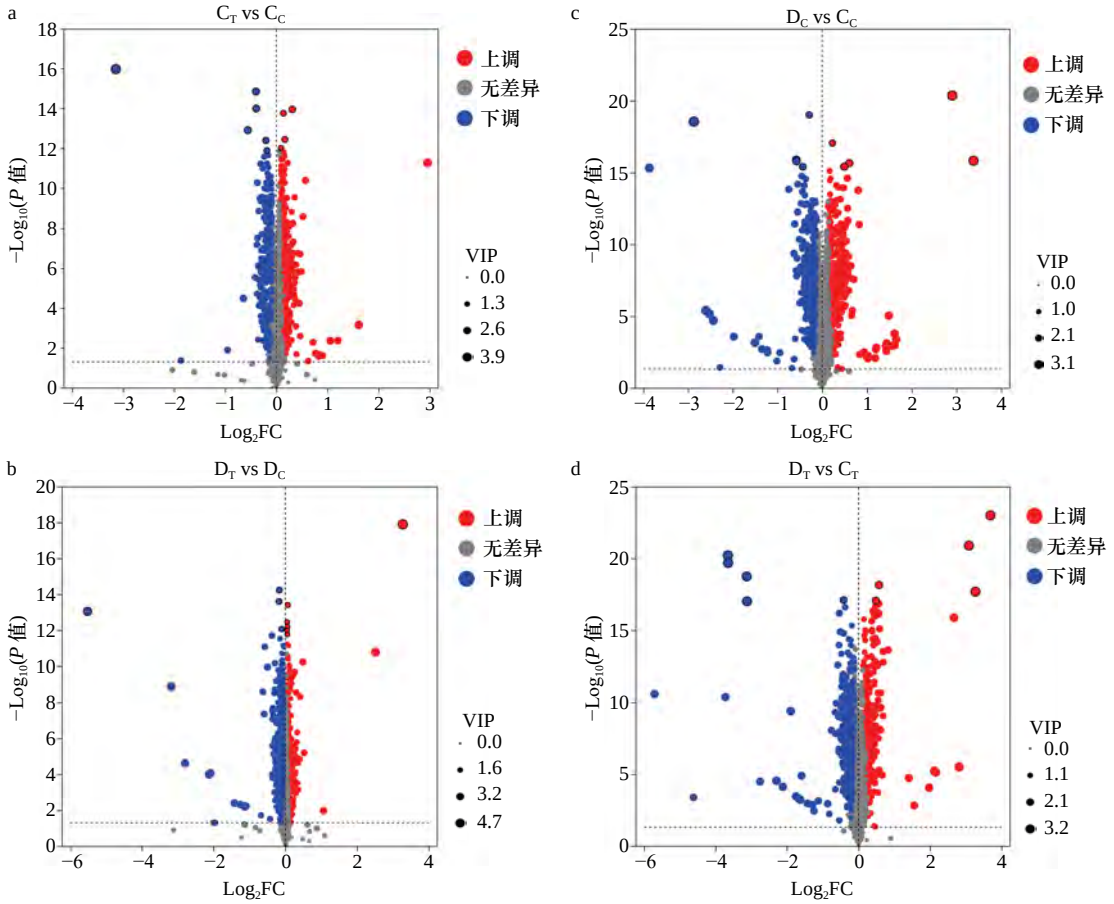


图 5 热胁迫下两种虫黄藻的显著差异代谢物火山图

Fig. 5 Volcano plot of significant different metabolites in two Symbiodiniaceae species under heat stress

a. C_C vs C_T 显著差异代谢物火山图; b. D_C vs D_T 显著差异代谢物火山图; c. C_C vs D_C 显著差异代谢物火山图; d. C_T vs D_T 显著差异代谢物火山图。以 *P* 值取前 10 的代谢物进行标记, *P* 值越小越显著

a. Volcano plot of significant different metabolites in C_C vs C_T; b. Volcano plot of significant different metabolites in D_C vs D_T; c. Volcano plot of significant different metabolites in C_C vs D_C; d. Volcano plot of significant different metabolites in C_T vs D_T. Mark the top 10 metabolites by *P*-value, with lower *P*-values indicating greater significance

4/16∶0)、PE(16∶0/16∶0)、PC(20∶3/20∶3)、PE(15∶0/15∶0)、PC(15∶0/14∶0) 和 PC(16∶0/16∶0)] 和下调差异代谢物(LPC(16∶0))显著富集到甘油磷脂代谢通路。

D_T 组相较于 D_C 组的差异代谢物主要富集在细胞过程和代谢通路(图 7b)上: 下调差异代谢物(Cer(d18∶1/16∶0))显著富集到鞘脂代谢通路; 上调差异代谢物[PC(22∶6/22∶6)] 和下调差异代谢物[PC(15∶0/14∶0)] 显著富集到亚油酸、α-亚麻酸代谢和花生四烯酸代谢通路; 上调差异代谢物[PE(15∶0/16∶0)、PE(15∶0/15∶0) 和 PE(14∶0/22∶2)] 显著富集到糖基磷脂酰肌醇(GPI)−锚的生物合成和自噬−其他通路; 上调差异代谢物[TG(16∶0/18∶1/18∶2) 和 TG(16∶0/16∶1/18∶2)] 和下调差异代谢物[TG(12∶0/12∶0/12∶0) 和 TG(10∶0/12∶0/13∶0)] 显著富集到甘油脂代谢通路; 上调差异代谢物[PE(15∶0/16∶0)、PE(15∶0/15∶0)、PC(15∶0/14∶0) 和 PE(14∶0/22∶2)) 和下调差异代谢物(PC(22∶6/22∶6)、LPC(22∶6) 和 LPC(16∶0)] 显著富集到甘油磷脂代谢通路。

在同一温度条件下, 对两种虫黄藻分别进行分析, D_C 组相较于 C_C 组的差异代谢物主要富集在细胞过程和代谢通路(图 7c)上: PE(16∶1/18∶1) 在糖基磷脂酰肌醇(GPI)−锚的生物合成和自噬-其他通路显著下调; PC(22∶5/22∶6) 在亚油酸、α-亚麻酸代谢和花生四烯酸代谢通路显著下调; 下调差异代谢物[PE(16∶1/18∶1) 和 PC(22∶5/22∶6)] 和上调差异代谢物[LPC(16∶0)] 显著富集到甘油磷脂代谢通路; 下调差异代谢物[TG(16∶1/18∶1/18∶1)] 和上调差异代谢物[TG(16∶0/18∶1/20∶4)、TG(12∶0/12∶0/12∶0) 和 TG(10∶0/12∶0/13∶0)] 显著富集到甘油脂代谢通路。D_T 组相较于 C_T 组的差异代谢物主要富集在细胞过程和代谢通路(图 7d)上: TG(12∶0/12∶0/12∶0) 在甘油脂代谢通路显著上调; PC(22∶6/22∶6)、PC

中国知网 https://www.cnki.net

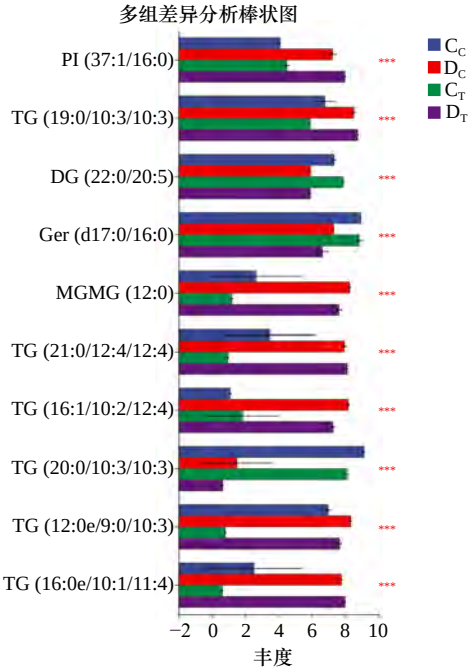


图 6　热胁迫下两种虫黄藻的单因素方差分析棒状图

Fig. 6　One-way ANOVA histogram of two Symbiodiniaceae species under heat stress

图中纵坐标轴表示代谢物名称, 横坐标表示表示代谢物在不同分组中平均相对丰度, 不同颜色的柱子表示不同分组; 误差棒表示 SEM(6 个生物学重复)。星号为显著性为 P 值(*: $0.01 < P \leqslant 0.05$, **: $0.001 < P \leqslant 0.01$, ***: $P \leqslant 0.001$)

The y-axis of the chart represents metabolite names, while the x-axis represents the average relative abundance of metabolites in different groups. Bars of different colors correspond to different groups. Error bars represent SEM (n = 6 biological replicates). Asterisks indicate significance levels of P-values (*: $0.01 < P \leqslant 0.05$, **: $0.001 < P \leqslant 0.01$, ***: $P \leqslant 0.001$)

(18∶4/16∶0)、PC(20∶3/20∶3) 和 PC(22∶5/22∶6) 在亚油酸、α-亚麻酸代谢和花生四烯酸代谢通路显著下调; 上调差异代谢物 [PE(15∶0/16∶0) 和 PE(14∶0/22∶2)] 和下调差异代谢物[PE(16∶1/18∶1)、PE(16∶0/16∶0) 和 PE(15∶0/15∶0)] 显著富集在糖基磷脂酰肌醇(GPI)−锚的生物合成和自噬−其他通路; 上调差异代谢物(PE(15∶0/16∶0) 和 PE(14∶0/22∶2)) 和下调差异代谢物 [PC(22∶6/22∶6)、PE(16∶1/18∶1)、PC(18∶4/16∶0)、PE(16∶0/16∶0)、PC(20∶3/20∶3)、PE(15∶0/15∶0)、LPC(22∶6)、LPC(16∶0) 和 PC(22∶5/22∶6)] 显著富集在甘油磷脂代谢通路。

4　讨论

4.1　两种虫黄藻应对热胁迫的生理生化响应策略

Cladocopium goreaui 和 *D. trenchii* 是两种典型的环境敏感性不同的虫黄藻。目前的证据表明, 温度的升高会加剧可利用光能大量过剩条件导致的虫黄藻共生关系破坏[59], 从而减少光合作用中可利用的光能。虫黄藻的碳固定速率、氧进化速率、叶绿素含量和生长速率均会低于其最适温度[60−62], 所观察到的影响程度取决于虫黄藻的支系型。本实验中, 热胁迫下 *C. goreaui* 的密度、叶绿素 *a* 含量和 F_v/F_m 值均在中后期显著下降($P < 0.05$)(图 1a、c、f), 而叶绿素 *c* 含量和类胡萝卜素含量则呈现上升趋势(图 1d 和 e); 但 *D. trenchii* 的各项数值均与常温培养趋势一致, 且胁迫结束两者未表现出显著差异性($P > 0.05$)(图 1a−f), 与之前内共生虫黄藻的报道一致[63]。有研究表明, 光合色素吸收的过量光能是通过抑制光损伤 PSⅡ的修复而不是通过加速 PSⅡ的光损伤来加速光抑制的[64−65]。叶绿素 *a* 是主要的光能捕获色素, 而叶绿素 *c* 和类胡萝卜素则在保护细胞和补充光合作用方面起到辅助作用。F_v/F_m 值的下降表明了 *C. goreaui* 受到了压力[10], 而 *D. trenchii* 的 F_v/F_m 值整体变化并不明显, 也较为直观的表明了其热耐受性(图 1f)。由此看来, 热胁迫下, 虫黄藻密度降低必然使得光合作用减弱从而导致 F_v/F_m 值和叶绿素 *a* 含量降低, 三者存在正相关的关系, 而叶绿素 *c* 和类胡萝卜素则在叶绿素 *a* 含量下降无法抑制 PSⅡ的光损伤修复时发挥作用。

高温可能通过抑制关键酶来限制光合作用, 它们可能会限制光合作用所需的 CO_2 供应, 最终 ROS 生成增加[66], 光合作用随之受损[26]。ROS 可以通过还原性谷胱甘肽和过氧化物酶等抗氧化物实现清除。MDA 是脂质过氧化的产物[67], 主要来源于多不饱和脂肪酸被 ROS 氧化后分解生成, 是氧化应激程度和膜损伤的重要标志物。SOD 是一种重要的抗氧化酶, 能够将能将超氧自由基(O-2)转化为过氧化氢(H_2O_2)和氧气(O_2)[63, 68], 减少 ROS 对细胞的损害, 是生物体抗氧化系统的第一道防线。热胁迫下, *C. goreaui* 的可溶性蛋白显著上升(图 2a), 同时 SOD(图 2b)和 MDA(图 2c)呈现先降后升的波动趋势, 表明其通过快速合成热休克蛋白(如 HSPs)和动态调节抗氧化系统以应对氧化损伤, 但伴随阶段性代谢失衡[69]; 而 *D. trenchii* 的上述指标在常温和高温下均保持稳定或缓慢下降(图 2a、b、c), 反映其依赖预存的耐热机制(如结构性抗氧化能力或代谢抑制)维持内稳态, 减少能量消耗[70]。这种差异揭示了两种虫黄藻应对高温的两种策略: *C. goreaui* 的“主动响应”适合短期波动环境, 而 *D. trenchii* 的“稳态耐受”更适应长期热胁迫, 可能影响其在珊瑚共生体系中的竞争优势及宿主适应气候变化的潜力。

中国知网　https://www.cnki.net

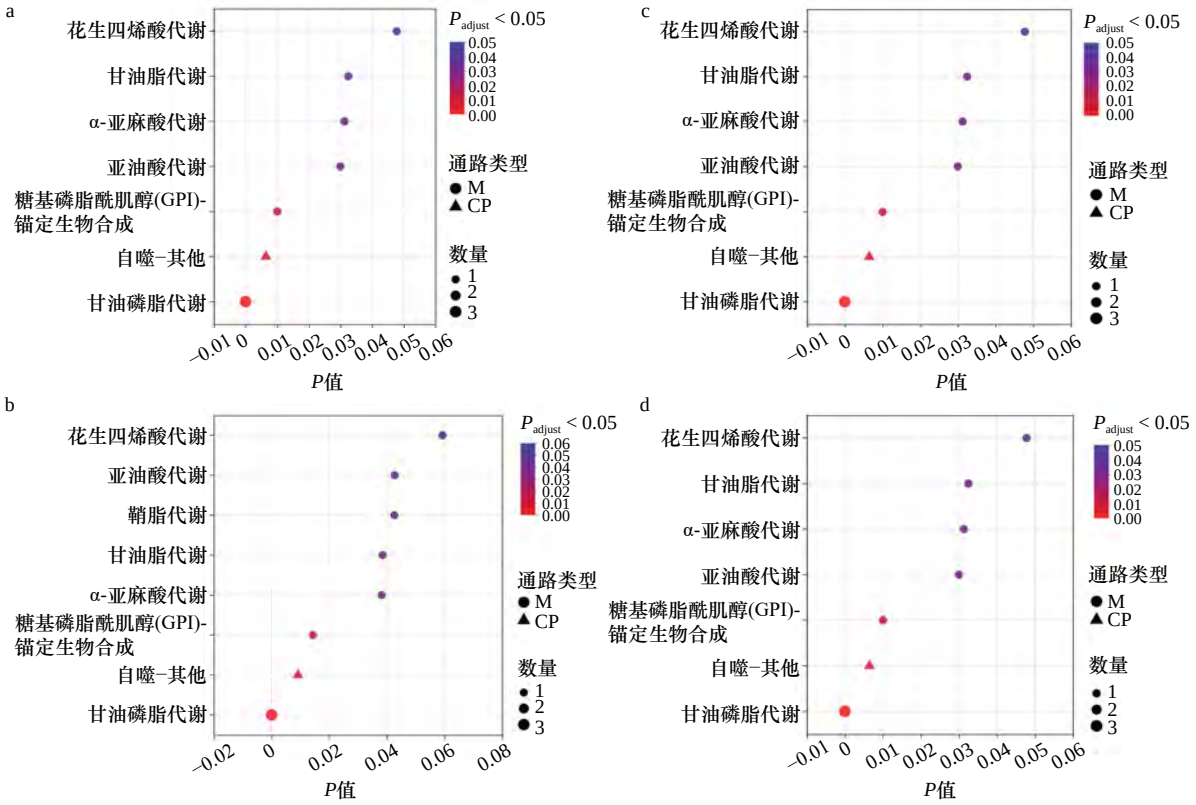


图 7 热胁迫下两种虫黄藻差异代谢物的 KEGG 富集气泡图

Fig. 7 KEGG enrichment bubble plot of different metabolites in two Symbiodiniaceae species under heat stress

a. C_C vs C_T 的差异代谢物的 KEGG 富集分析通路图; b. D_C vs D_T 的差异代谢物的 KEGG 富集分析通路图; c. C_C vs D_C 的差异代谢物的 KEGG 富集分析通路图; d. C_T vs D_T 的差异代谢物的 KEGG 富集分析通路图。横坐标为富集显著性 *P* 值, *P* 值越小, 在统计学上就越有显著意义, 一般 $P < 0.05$ 认为该功能为显著富集项; 纵坐标为 KEGG 通路。图中气泡的颜色代表该通路富集显著性, 气泡的大小代表该通路中富集到代谢集中代谢物的数量

a. KEGG pathway enrichment analysis of different metabolites of C_C vs C_T; b. KEGG pathway enrichment analysis of different metabolites of D_C vs D_T; c. KEGG pathway enrichment analysis of different metabolites of C_C vs D_C; d. KEGG pathway enrichment analysis of different metabolites of C_T vs D_T. The x-axis represents the enrichment significance *P*-value, where smaller *P*-values indicate higher statistical significance. Generally, pathways with $P < 0.05$ are considered significantly enriched. The y-axis represents KEGG pathways. In the chart, the color of the bubbles indicates the enrichment significance of the pathway, while the size of the bubbles represents the number of metabolites enriched in the corresponding pathway

4.2 两种虫黄藻应对热胁迫的脂质代谢分析

在热胁迫结束时, *C. goreaui* 和 *D. trenchii* 在脂质代谢的脂质亚类类别并无明显差异(图 3c)($P > 0.05$)。藻类中的主要脂质类别是膜脂和储存脂质[71], 甘油三酯和胆固醇酯在细胞中的积累可能会激活细胞凋亡[72]并改变浮游植物的膜完整性和光合活性[73]。虫黄藻的热敏性会影响甘油磷脂等的分布, 除主要的结构功能外, 几类极性脂质(包括磷脂酰乙醇胺和磷脂酰胆碱)还可参与各种细胞过程。脂质不仅构成细胞膜的基质, 而且直接参与膜的运输、调节膜蛋白、细胞结构, 并在膜中形成有助于细胞功能的特定亚区[74]。

热胁迫下的 *C. goreaui* 和 *D. trenchii* 的 KEGG 通路富集分析均发现磷脂酰乙醇胺、磷脂酰胆碱、溶血磷脂酰胆碱和甘油三酯的变化。磷脂酰胆碱是自噬体膜的主要成分[75], 自噬过程是细胞面对高温应激时的一种重要自我保护机制[76]。糖基磷脂酰肌醇(GPI)-锚的生物合成与细胞膜的重塑和信号传导有关[77], 这可能是 *C. goreaui* 在应对外部胁迫时的关键适应策略。甘油三酯的增加(图 7a)表明 *C. goreaui* 可能通过储存更多的中性脂质来适应高温引起的能量需求和膜流动性的变化。亚油酸和 α-亚麻酸是重要的多不饱和脂肪酸, 它们在维持膜流动性、抗氧化防御和信号传导中扮演关键角色。花生四烯酸代谢与细胞的抗炎反应和信号转导密切相关。*Cladocopium goreaui* 通过上调这些磷脂酰胆碱可能在应对热胁迫的过程中增加膜的流动性, 减少膜脂质的过氧化, 保持细胞膜功能的稳定性。多不饱和脂肪酸代谢的变化说明 *C. goreaui* 在应对热胁迫时依赖这些脂质分子调节膜流动性及其他细胞功能, 脂质代谢的重塑可能是对抗外界压力的关键机制。

鞘脂类在细胞膜稳定性和信号传导中具有重要

中国知网 https://www.cnki.net

作用[78], 尤其在应对外界压力时可能调控细胞凋亡和存活。神经酰胺因为各种应激刺激(如缺氧、热应激和辐射)通过增加细胞内神经酰胺来启动凋亡信号传导, 从而引起细胞凋亡[79], 还可通过激活内质网应激或线粒体功能障碍信号(如 ROS 积累), 诱导自噬相关通路的激活。然而, D_T 组中神经酰胺的下调(图 7b)可能削弱了这种应激信号的传递[80], 转而通过其他脂质代谢物(如磷脂酰乙醇胺和磷脂酰胆碱的异常富集)触发代偿性自噬通路(如"自噬−其他"通路上调)[81]。在热胁迫下, 上调的甘油三酯可能表明 *D. trenchii* 通过积累特定的中性脂质来适应胁迫环境, 而下调的甘油三酯可能反映了代谢的重新分配或某些特定脂肪酸的消耗。热胁迫下, *D. trenchii* 可能通过上调磷脂酰乙醇胺和磷脂酰胆碱类脂质来稳定细胞膜, 而溶血磷脂酰胆碱的下调可能与其氧化活性、膜破裂和修复过程有关[82]。

5　结论

本研究通过比较 *C. goreaui* 和 *D. trenchii* 在热胁迫(32℃)下的生理响应和脂质代谢变化, 揭示了两种虫黄藻在耐热性方面的差异。前者在热胁迫下生长速率下降显著, 光合色素含量减少, PSⅡ光系统(F_v/F_m 值)损伤严重; MDA 含量显著上升, 表明受到更严重的氧化损伤; 脂质代谢调整能力较弱, 可能导致其细胞膜在高温环境下更易受损, 从而影响其生存能力。后者在热胁迫下维持较稳定的生长速率和较高的 F_v/F_m 值, 表现出更强的耐热能力; 通过更有效的抗氧化机制(如 SOD 活性调节)减少了氧化损伤; 通过调节脂质代谢(如增加耐热性脂质的比例), 提高了细胞膜的稳定性和适应性, 使其在高温环境下表现出更强的适应能力。

综上, *D. trenchii* 通过优化生理状态和脂质代谢策略, 在高温环境下具有更强的适应性, 而 *C. goreaui* 的耐热能力较低, 容易受到热胁迫的负面影响。这些发现为理解珊瑚共生藻的热耐受机制提供了新的见解, 并有助于预测珊瑚生态系统在气候变化下的响应趋势。

参考文献:

[1] Trench R K. Microalgalinvertebrate symbioses: a review[J]. Endocytobiosis and Cell Research, 1993, 9(2/3): 135−175.

[2] Von Holt C, Von Holt M. Transfer of photosynthetic products from zooxanthellae to coelenterate hosts[J]. Comparative Biochemistry and Physiology, 1968, 24(1): 73−81.

[3] Cernichiari E, Muscatine L, Smith D C. Maltose excretion by the symbiotic algae of *Hydra viridis*[J]. Proceedings of the Royal Society of London Series B, Biological Sciences, 1969, 173(1033): 557−576.

[4] Gordon B R, Leggat W. *Symbiodinium*-Invertebrate symbioses and the role of metabolomics[J]. Marine Drugs, 2010, 8(10): 2546−2568.

[5] Yellowlees D, Rees T A V, Leggat W. Metabolic interactions between algal symbionts and invertebrate hosts[J]. Plant Cell Environ, 2008, 31(5): 679−694.

[6] Pochon X, Gates R D. A new *Symbiodinium* clade (dinophyceae) from soritid foraminifera in Hawai'i[J]. Molecular Phylogenetics and Evolution, 2010, 56(1): 492−497.

[7] Pochon X, Lajeunesse T C. *Miliolidium* n. gen, a new symbiodiniacean genus whose members associate with soritid foraminifera or are free-living[J]. Eukaryotic Microbiology, 2021, 68(4): e12856.

[8] Nitschke M R, Craveiro S C, Brandão C, et al. Description of *Freudenthalidium* gen. nov. and *Halluxium* gen. nov. to formally recognize clades Fr3 and H as genera in the family symbiodiniaceae (dinophyceae)[J]. Journal of Phycology, 2020, 56(4): 923−940.

[9] Lajeunesse T C, Parkinson J E, Gabrielson P W, et al. Systematic revision of symbiodiniaceae highlights the antiquity and diversity of coral endosymbionts[J]. Current Biology, 2018, 28(16): 2570−2580. e6.

[10] Abrego D, Ulstrup K E, Willis B L, et al. Species–specific interactions between algal endosymbionts and coral hosts define their bleaching response to heat and light stress[J]. Proceedings of the Royal Society B: Biological Sciences, 2008, 275(1648): 2273−2282.

[11] Berkelmans R, Van Oppen M J H. The role of zooxanthellae in the thermal tolerance of corals: a 'nugget of hope' for coral reefs in an era of climate change[J]. Proceedings of the Royal Society B: Biological Sciences, 2006, 273(1599): 2305−2312.

[12] Silverstein R N, Cunning R, Baker A C. Tenacious D: *Symbiodinium* in clade D remain in reef corals at both high and low temperature extremes despite impairment[J]. Journal of Experimental Biology, 2017, 220(7): 1192−1196.

[13] Baker A C, Starger C J, Mcclanahan T R, et al. Coral reefs: corals' adaptive response to climate change[J]. Nature, 2004, 430(7001): 741.

[14] Rowan R. Thermal adaptation in reef coral symbionts[J]. Nature, 2004, 430(7001): 742.

[15] Krueger T, Hawkins T D, Becker S, et al. Differential coral bleaching-contrasting the activity and response of enzymatic antioxidants in symbiotic partners under thermal stress[J]. Comparative Biochemistry and Physiology Part: A Molecular & Integrative Physiology, 2015, 190: 15−25.

[16] Baker D M, Freeman C J, Wong J C Y, et al. Climate change promotes parasitism in a coral symbiosis[J]. The ISME Journal, 2018, 12(3): 921−930.

[17] Little A F, Van Oppen M J H, Willis B L. Flexibility in algal endosymbioses shapes growth in reef corals[J]. Science, 2004, 304(5676):

中国知网　https://www.cnki.net

1492−1494.
[18] Baker A C. Reef corals bleach to survive change[J]. Nature, 2001, 411(6839): 765−766.
[19] Glynn P W, MatéJ, Baker A C, et al. Coral bleaching and mortality in panamá and ecuador during the 1997-1998 El niño-southern oscillation event: spatial/temporal patterns and comparisons with the 1982-1983 event[J]. Bulletin of Marine Science, 2001, 69(1): 79−109.
[20] Tchernov D, Gorbunov M Y, De Vargas C, et al. Membrane lipids of symbiotic algae are diagnostic of sensitivity to thermal bleaching in corals[J]. Proceedings of the National Academy of Sciences of the United States of America, 2004, 101(37): 13531−13535.
[21] Huang Yayi, Carballo-Bolaños R, Kuo Chaoyang, et al. *Leptoria phrygia* in southern taiwan shuffles and switches symbionts to resist thermal-induced bleaching[J]. Scientific Reports, 2020, 10(1): 7808.
[22] Fay S A, Weber M X. The occurrence of mixed infections of *symbiodinium* (dinoflagellata) within individual hosts[J]. Journal of Phycology, 2012, 48(6): 1306−1316.
[23] Abrego D, Van Oppen M J H, Willis B L. Onset of algal endosymbiont specificity varies among closely related species of *Acropora* corals during early ontogeny[J]. Molecular Ecology, 2009, 18(16): 3532−3543.
[24] Klepac C N, Barshis D J. Reduced thermal tolerance of massive coral species in a highly variable environment[J]. Proceedings of the Royal Society B: Biological Sciences, 2020, 287(1933): 20201379.
[25] Stat M, Gates R D. Clade d *symbiodinium* in scleractinian corals: a “nugget” of hope, a selfish opportunist, an ominous sign, or all of the above?[J]. Journal of Marine Sciences, 2011, 2011(2011): 1−9.
[26] Warner M E, Fitt W K, Schmidt G W. Damage to photosystem II in symbiotic dinoflagellates: a determinant of coral bleaching[J]. Proceedings of the National Academy of Sciences of the United States of America, 1999, 96(14): 8007−8012.
[27] Takahashi S, Nakamura T, Sakamizu M, et al. Repair machinery of symbiotic photosynthesis as the primary target of heat stress for reef-building corals[J]. Plant and Cell Physiology, 2004, 45(2): 251−255.
[28] Jones R J, Hoegh-Guldberg O, Larkum A W D, et al. Temperature-induced bleaching of corals begins with impairment of the CO_2 fixation mechanism in zooxanthellae[J]. Plant, Cell & Environment, 1998, 21(12): 1219−1230
[29] Takahashi S, Whitney S, Itoh S, et al. Heat stress causes inhibition of the *de novo* synthesis of antenna proteins and photobleaching in cultured *symbiodinium*[J]. Proceedings of the National Academy of Sciences of the United States of America, 2008, 105(11): 4203−4208.
[30] Weis V M. Cellular mechanisms of Cnidarian bleaching: stress causes the collapse of symbiosis[J]. Journal of Experimental Biology, 2008, 211(19): 3059−3066.
[31] Gates R D, Baghdasarian G, Muscatine L. Temperature stress causes host cell detachment in symbiotic cnidarians: implications for coral bleaching[J]. The Biological Bulletin, 1992, 182(3): 324−332.
[32] Cunning R, Baker A C. Not just who, but how many: the importance of partner abundance in reef coral symbioses[J]. Frontiers in Microbiology, 2014, 5: 400.
[33] Fitt W K, Brown B E, Warner M E, et al. Coral bleaching: interpretation of thermal tolerance limits and thermal thresholds in tropical corals[J]. Coral Reefs, 2001, 20: 51−65.
[34] Wu Di, Tang Haiping, Qiu Xingyu, et al. Native MS-guided lipidomics to define endogenous lipid microenvironments of eukaryotic receptors and transporters[J]. Nature Protocols, 2025, 20(1): 1−25.
[35] Luo Y J, Wang L H, Chen W N U, et al. Ratiometric imaging of gastrodermal lipid bodies in coral–dinoflagellate endosymbiosis[J]. Coral Reefs, 2009, 28(1): 289−301.
[36] Yin Huiyong, Xu Libin, Porter N A. Free radical lipid peroxidation: mechanisms and analysis[J]. Chemical Reviews, 2011, 111(10): 5944−5972.
[37] Han Xianlin. Lipidomics for studying metabolism[J]. Nature Reviews Endocrinology, 2016, 12(11): 668−679.
[38] Endle H, Horta G, Stutz B, et al. AgRP neurons control feeding behaviour at cortical synapses via peripherally derived lysophospholipids[J]. Nature Metabolism, 2022, 4(6): 683−692.
[39] Sikorskaya T V, Ermolenko E V, Efimova K V. Lipids of Indo-Pacific gorgonian corals are modified under the influence of microbial associations[J]. Coral Reefs, 2022, 41: 277−291.
[40] Greenberg M E, Li Xinmin, Gugiu B G, et al. The lipid whisker model of the structure of oxidized cell membranes[J]. Journal of Biological Chemistry, 2008, 283(4): 2385−2396.
[41] Han Xianlin, Gross R W. The foundations and development of lipidomics[J]. Journal of Lipid Research, 2022, 63(2): 100164.
[42] Domenick T M, Gill E L, Vedam-Mai V, et al. Mass spectrometry-based cellular metabolomics: current approaches, applications, and future directions[J]. Analytical Chemistry, 2021, 93(1): 546−566.
[43] Imbs A B, Latyshev N A, Dautova T, et al. Distribution of lipids and fatty acids in corals by their taxonomic position and presence of zooxanthellae[J]. Marine Ecology Progress Series, 2010, 409: 65−75.
[44] Baumann J, Grottoli A G, Hughes A D, et al. Photoautotrophic and heterotrophic carbon in bleached and non-bleached coral lipid acquisition and storage[J]. Journal of Experimental Marine Biology and Ecology, 2014, 461: 469−478.
[45] Chen Hungkai, Wang L H, Chen W N U, et al. Coral lipid bodies as the relay center interconnecting diel-dependent lipidomic changes in different cellular compartments[J]. Scientific Reports, 2017, 7: 3244.
[46] Revel J, Massi L, Mehiri M, et al. Differential distribution of lipids in epidermis, gastrodermis and hosted *Symbiodinium* in the sea

中国知网 https://www.cnki.net

anemone *Anemonia viridis*[J]. Comparative Biochemistry and Physiology Part A: Molecular & Integrative Physiology, 2016, 191: 140−151

[47] Pasaribu B, Lin I P, Tzen J T C, et al. SLDP: a novel protein related to caleosin is associated with the endosymbiotic *symbiodinium* lipid droplets from *euphyllia glabrescens*[J]. Marine Biotechnology, 2014, 16(5): 560−571.

[48] Fitt W K. Chemosensory responses of the symbiotic dinoflagellate *Symbiodinium microadriaticum* (dinophyceae)[J]. Journal of Phycology, 1985, 21(1): 62−67.

[49] Ishikura M, Hagiwara K, Takishita K, et al. Isolation of new symbiodinium strains from tridacnid giant clam (*Tridacna crocea*) and sea slug (*Pteraeolidia ianthina*) using culture medium containing giant clam tissue homogenate[J]. Marine Biotechnology, 2004, 6(4): 378−385.

[50] Krueger T, Gates R D. Cultivating endosymbionts — host environmental mimics support the survival of *symbiodinium* C15 *ex hospite*[J]. Journal of Experimental Marine Biology and Ecology, 2012, 413: 169−176.

[51] Buerger P, Alvarez-ROA C, Coppin C W, et al. Heat-evolved microalgal symbionts increase coral bleaching tolerance[J]. Science Advances, 2020, 6(20): eaba2498.

[52] 覃良云, 许勇前, 陈金妮, 等. 造礁石珊瑚共生虫黄藻离体培养方法的优化[J]. 微生物学报, 2023, 63(4): 1658−1671.
Qin Liangyun, Xu Yongqian, Chen Jinni, et al. Optimization of *in vitro* culture method for zooxanthellae associated with reef-building corals[J]. Acta Microbiologica Sinica, 2023, 63(4): 1658−1671.

[53] Andersen R A. Algal Culturing Techniques[M]. New York: Academic Press, 2005.

[54] Goldman J C, Mccarthy J J. Steady state growth and ammonium uptake of a fast-growing marine diatom[J]. Limnology and Oceanography, 1978, 23(4): 695−703.

[55] Waheed Z, Hoeksema B. Diversity patterns of scleractinian corals at Kota Kinabalu, Malaysia, in relation to exposure and depth[J]. The Raffles Bulletin of Zoology, 2014, 62: 66−82.

[56] Strychar K, Sammarco P. Effects of heat stress on phytopigments of zooxanthellae (*Symbiodinium* spp.) symbiotic with the corals acropora hyacinthus, *Porites solida*, and *Favites complanata*[J]. International Journal of Biology, 2012, 4(1).

[57] Ritchie R J. Consistent sets of spectrophotometric chlorophyll equations for acetone, methanol and ethanol solvents[J]. Photosynthesis Research, 2006, 89(1): 27−41.

[58] Rijstenbil J W. Assessment of oxidative stress in the planktonic diatom *Thalassiosira pseudonana* in response to UVA and UVB radiation[J]. Journal of Plankton Research, 2002, 24(12): 1277−1288.

[59] Lesser M P, Farrell J H. Exposure to solar radiation increases damage to both host tissues and algal symbionts of corals during thermal stress[J]. Coral Reefs, 2004, 23: 367−377.

[60] Buck B H, Rosenthal H, Saint-Paul U. Effect of increased irradiance and thermal stress on the symbiosis of *Symbiodinium microadriaticum* and *Tridacna gigas*[J]. Aquatic Living Resources, 2002, 15(2): 107−117.

[61] Goulet T L, Cook C B, Goulet D. Effect of short - term exposure to elevated temperatures and light levels on photosynthesis of different host-symbiont combinations in the *Aiptasia pallida*/*Symbiodinium* symbiosis[J]. Limnology and Oceanography, 2005, 50(5): 1490−1498.

[62] Muller-Parker G, Pierce-Cravens J, Bingham B L. Broad thermal tolerance of the symbiotic dinoflagellate *symbiodinium muscatinei* (dinophyta) in the sea anemone *Anthopleura elegantissima* (cnidaria) from northern latitudes[J]. Journal of Phycology, 2007, 43(1): 25−31.

[63] 刘旭. 造礁石珊瑚对温度胁迫的响应机制研究[D]. 南宁: 广西大学, 2020.
Liu Xu. Responsive mechanism of reef-building coral rocks to temperature stress[D]. Nanning: Guangxi University, 2020.

[64] Murata N, Takahashi S, Nishiyama Y, et al. Photoinhibition of photosystem II under environmental stress[J]. Biochimica et Biophysica Acta (BBA) - Bioenergetics, 2007, 1767(6): 414−421.

[65] Nishiyama Y, Allakhverdiev S I, Murata N. A new paradigm for the action of reactive oxygen species in the photoinhibition of photosystem II[J]. Biochimica Et Biophysica Acta(BBA)-Bioenergetics, 2006, 1757(7): 742−749.

[66] Venn A A, Loram J E, Douglas A E. Photosynthetic symbioses in animals[J]. Journal of Experimental Botany, 2008, 59(5): 1069−1080.

[67] Del Rio D, Stewart A J, Pellegrini N. A review of recent studies on malondialdehyde as toxic molecule and biological marker of oxidative stress[J]. Nutrition, Metabolism and Cardiovascular Diseases, 2005, 15(4): 316−328.

[68] Fridovich I. Superoxide anion radical ($O^{\cdot-}_2$), superoxide dismutases, and related matters[J]. Journal of Biological Chemistry, 1997, 272(30): 18515−18517.

[69] Barshis D J, Ladner J T, Oliver T A, et al. Lineage-Specific transcriptional profiles of *symbiodinium* spp. unaltered by heat stress in a coral host[J]. Molecular Biology and Evolution, 2014, 31(6): 1343−1352.

[70] Rosic N N, Pernice M, Dove S, et al. Gene expression profiles of cytosolic heat shock proteins Hsp70 and Hsp90 from symbiotic dinoflagellates in response to thermal stress: possible implications for coral bleaching[J]. Cell Stress and Chaperones, 2011, 16(1): 69−80.

[71] Li-Beisson Y, Thelen J J, Fedosejevs E, et al. The lipid biochemistry of eukaryotic algae[J]. Progress in Lipid Research, 2019, 74: 31−68.

[72] Maxfield F R, Tabas I. Role of cholesterol and lipid organization in disease[J]. Nature, 2005, 438(7068): 612−621.

[73] Veldhuis M, Gijsbert K, Timmermans K. Cell death in phytoplankton: correlation between changes in membrane permeability, photosynthetic activity, pigmentation and growth[J]. European Journal of Phycology, 2001, 36(2): 167−177.

中国知网　https://www.cnki.net

［74］ Shevchenko A, Simons K. Lipidomics: coming to grips with lipid diversity[J]. Nature Reviews Molecular Cell Biology, 2010, 11(8): 593−598.
［75］ Li F Q, Vierstra R D. Autophagy: a multifaceted intracellular system for bulk and selective recycling[J]. Trends in plant science, 2012, 17(9): 526−537.
［76］ Singh R, Kaushik S, Wang Y Q, et al. Autophagy regulates lipid metabolism[J]. Nature, 2009, 458(7242): 1131−1135.
［77］ Hou Q C, Ufer G, Bartels D. Lipid signalling in plant responses to abiotic stress[J]. Plant, Cell & Environment, 2016, 39(5): 1029−1048
［78］ Berkowitz L, Cabrera-Reyes F, Salazar C, et al. Sphingolipid profiling: a promising tool for stratifying the metabolic syndrome-associated risk[J]. Frontiers in Cardiovascular Medicine, 2022, 8: 785124.
［79］ Huang W C, Chen C L, Lin Y S, et al. Apoptotic sphingolipid ceramide in cancer therapy[J]. Journal of Lipids, 2011, 2011: 565316.
［80］ Sun X F, Li Y, Du J, et al. Targeting ceramide transfer protein sensitizes AML to FLT3 inhibitors via a GRP78-ATF6-CHOP axis[J]. Nature Communications, 2025, 16(1): 1358.
［81］ Li Y Z, Wang L C, Wang H M, et al. Polysaccharides from *Eucommia ulmoides* Oliv. leaves alleviates alcohol-induced mouse brain injury and BV-2 microglial dysfunction[J]. International Journal of Biological Macromolecules, 2024, 273: 132887.
［82］ Zhang M, Su R N, Corazzin M, et al. Lipid transformation during postmortem chilled aging in Mongolian sheep using lipidomics[J]. Food Chemistry, 2023, 405: 134882.

Lipid metabolic response patterns to heat stress in two Symbiodiniaceae species with different environmental sensitivities (*Cladocopium goreaui* and *Durusdinium trenchii*)

Zhang Li[1], Li Zhicong[2], Yang Yating[2], Liang Zhuqing[2], Feng Yihe[1], Lu Mingyao[2], Hu Siyu[2], Yu Kefu[2,3], Liang Jiayuan[2,3]

(1. *School of Resources*, *Environment and Materials*, *Guangxi University*, *Nanning* 530004, *China*; 2. *School of Marine Sciences*, *Guangxi University*, *Nanning* 530004, *China*; 3. *Southern Marine Science and Engineering Guangxi Laboratory*, *Nanning* 530004, *China*)

Abstract: Symbiodiniaceae are indispensable partners in the coral symbiotic system, and different species exhibit varying sensitivities to environmental stress, thereby influencing the environmental adaptability of their coral hosts. This study investigates the stress response patterns of two widely distributed coral symbiotic Symbiodiniaceae species—environmentally sensitive *Cladocopium goreaui* and environmentally tolerant *Durusdinium trenchii*—under heat stress from the perspective of lipid metabolism. The results showed that heat stress significantly affected their cell density, photosynthetic pigment content, photochemical efficiency of photosystem Ⅱ (F_v/F_m), and antioxidant activity, with statistically significant differences ($P < 0.05$). Lipidomics revealed that lipid-differentiated metabolites such as phosphatidylcholine, triglycerides, phosphatidylethanolamine and lysophosphatidylcholine were significantly enriched in glycerophospholipid metabolism, triglyceride metabolism, and polyunsaturated fatty acid-related metabolic pathways in response to heat stress in *C. goreaui* and *D. trenchii*. Notably, the two species exhibited significant differences in sphingolipid metabolism: *D. trenchii* downregulated ceramide levels to reduce oxidative stress damage, regulate autophagy, and adapt to changes in membrane fluidity, whereas *C. goreaui* primarily upregulated lipid molecules rich in polyunsaturated fatty acids to maintain membrane stability and regulate signal transduction. A deeper understanding of the lipid metabolic stress response mechanisms of Symbiodiniaceae with different environmental sensitivities under heat stress provides new insights into enhancing coral adaptability to environmental changes from a symbiotic partner perspective.

Key words: heat stress; symbiodiniaceae; sphingolipid metabolism; lipidomics; oxidative stress

中国知网 https://www.cnki.net

陈凡, 韦冬冬, 谢瑾琨, 等. 两株海洋来源贝莱斯芽孢杆菌的筛选、分离鉴定及益生特性[J]. 广东海洋大学学报, 2025, 45(4): 138-148.

两株海洋来源贝莱斯芽孢杆菌的筛选、分离鉴定及益生特性

陈　凡[1,2], 韦冬冬[2], 谢瑾琨[2], 余　庆[2], 高艳侠[2], 黄　静[2], 何金钊[3], 施金谷[3], 赵明明[2], 覃向谋[2], 苏宏飞[1], 李鹏飞[1,2]

（1. 广西大学海洋学院,广西 南宁 530004;2. 广西海洋科学院 / 广西科学院 / 广西水产生物技术与现代生态养殖重点实验室 / 广西渔业重大疫病防控与高效健康养殖产业技术工程研究中心,广西 南宁 530007;
3. 广西壮族自治区水产技术推广站,广西 南宁 530199）

摘　要:【目的】分离筛选海洋环境来源耐高温芽孢杆菌(*Bacillus* sp.),评估其潜在益生性能,为开发海水养殖微生态制剂提供理论基础。【方法】通过热处理角蜂巢珊瑚(*Favites flexuosa*)组织匀浆以及珍珠龙胆石斑鱼(*Epinephelus fuscoguttatus*♀×*Epinephelus lanceolatus*♂)体表黏液,筛选潜在耐热型芽孢杆菌,结合形态学观察、生理生化鉴定以及16S rRNA基因序列分析鉴定目标菌株。通过体外实验评估菌株耐胆盐、耐酸、广谱抑菌活性及产酶能力,并对2株菌潜在安全性进行评估。【结果】通过分离鉴定,得到2株形态不同且具有生长优势的贝莱斯芽孢杆菌(*Bacillus velezensis*)SH39和TG1,2株菌在Luria-Bertani培养基中生长性能相似,均能耐受高盐以及强酸性环境,其中SH39在添加质量分数0.4%胆盐的LB培养液中存活率(60%)极显著高于TG1(20%)($P < 0.01$)。抑菌实验结果显示,SH39与TG1具有广谱抑菌活性,显著抑制嗜水气单胞菌(*Aeromonas hydrophila*)、哈维氏弧菌(*Vibrio harveyi*)等14种细菌性病原生长($P < 0.05$)。此外,2株菌均具有蛋白酶、淀粉酶和纤维素酶活性,其中SH39蛋白酶活性(酶活性指数1.81 ± 0.03)显著高于TG1(1.35 ± 0.23)($P < 0.05$)。安全性实验表明,2株菌对恩诺沙星、氟苯尼考等9种常见抗生素敏感,无溶血活性,石斑鱼在1×10^8 CFU/mL腹腔注射后未见死亡或发病症状。【结论】SH39和TG1具有优良环境耐受性、广谱抑菌活性、产酶能力以及安全性,可作为水产养殖益生菌候选菌株。

关键词: 海洋益生菌; 贝莱斯芽孢杆菌; 抑菌活性; 酶活性; 水产养殖
中图分类号: S816.3　　**文献标志码:** A　　**文章编号:** 1673-9159(2025)04-0138-11
doi: 10.3969/j.issn.1673-9159.2025.04.015

Screening, Isolation, Identification, and Probiotic Characterization of Two Marine-Derived *Bacillus velezensis* Strains

CHEN Fan[1,2], WEI Dongdong[2], XIE Jinkun[2], YU Qing[2], GAO Yanxia[2], HUANG Jing[2], HE Jinzhao[3], SHI Jingu[3], ZHAO Mingming[2], QIN Xiangmou[2], SU Hongfei[1], LI Pengfei[1,2]

(1. *School of Marine Sciences, Guangxi University, Nanning* 530004, *China*; 2. *Guangxi Academy of Marine Sciences / Guangxi Academy of Sciences / Guangxi Key Laboratory of Aquatic Biotechnology and Modern Ecological Aquaculture / Guangxi Engineering Research Center for Fishery Major Diseases Control and Efficient Healthy Breeding Industrial Technology, Nanning* 530007, *China*; 3. *Guangxi Fisheries Technology Extension Station, Nanning* 530199, *China*)

收稿日期: 2025-07-07
基金项目: 广西自然科学基金(2024GXNSFFA010017, AD23026171);广西科技项目(GUIKEFA〔2024〕102-2);国家现代农业产业技术体系广西创新团队项目(nycytxgxcxtd-2021-08-02);来宾科技计划(Laikechan 241519)
第一作者: 陈凡(1999—),男,硕士研究生,主要从事海洋微生物资源开发利用研究。E-mail: 1324013054@qq.com
通信作者: 李鹏飞(1988—),男,博士,研究员,主要从事水产种苗高效繁育与生态健康养殖技术研究。E-mail: pfli2014@126.com
苏宏飞(1985—),男,博士,副教授,主要从事海洋生物资源多样性与功能化利用研究工作。E-mail: shf2016@gxu.edu.cn

中国知网 https://www.cnki.net

Abstract:【Objective】This study aimed to isolate and screen thermotolerant *Bacillus* strains from marine environments, evaluate their potential probiotic properties, and provide a theoretical foundation for developing microbial ecological agents in mariculture.【Methods】Thermotolerant *Bacillus* strains were preliminarily screened from heat-treated tissue homogenates of *Favites flexuosa* and epidermal mucus of *Epinephelus fuscoguttatus*♀×*Epinephelus lanceolatus*♂. The isolates were identified by morphological characterization, physiological-biochemical tests, and 16S rRNA gene sequencing. In vitro experiments were conducted to evaluate the bacterial strains' bile salt tolerance, acid resistance, broad-spectrum antimicrobial activity, and enzyme production capacity. Additionally, the potential safety of the two strains were assessed.【Results】Two *Bacillus velezensis* strains (SH39 and TG1) with distinct morphology and competitive growth advantages were isolated and identified. The growth performance of the two strains in Luria-Bertani medium was similar, both of which could tolerate high salt and strong acidic environments. Notably, SH39 showed significantly higher survival (60% vs 20%, $P < 0.01$) in LB broth supplemented with a mass fraction of 0.4% bile salts than TG1. Antimicrobial assays revealed broad-spectrum inhibitory activity, significantly inhibiting the growth of 14 bacterial pathogens, such as *Aeromonas hydrophila* and *Vibrio harveyi* ($P < 0.05$). Both strains displayed protease, amylase, and cellulase activities, and SH39 exhibited significantly higher protease activity than TG1 (enzyme activity index: 1.81 ± 0.03 vs 1.35 ± 0.23, $P < 0.05$). Safety evaluation demonstrated that both strains were sensitive to nine common antibiotics (including enrofloxacin and florfenicol), showed no hemolytic activity, and caused no mortality or clinical symptoms in groupers after intraperitoneal injection at bacterial concentration of 1×10^8 CFU/mL.【Conclusion】The strains SH39 and TG1 demonstrated excellent environmental tolerance, broad-spectrum antimicrobial activity, enzyme production capacity, and safety, making them promising probiotic candidates for aquaculture.

Key words: marine probiotics; *Bacillus velezensis*; bacteriostatic activity; enzymatic activity; aquaculture

长期以来,传统水产病害防控主要依赖抗生素和化学消毒剂,过度使用抗生素不仅导致病原体耐药性增强,更造成养殖生态环境污染和药物残留问题,最终对人类健康构成潜在威胁[1−2]。益生菌的研制和应用被视为绿色、有效的水产养殖病害防控新工具[3]。在众多益生菌中,芽孢杆菌(*Bacillus* sp.)能够有效帮助宿主抵抗病原菌[4]、病毒[5]、寄生虫[6]等水生病原,被认为是水产饲料理想添加剂之一。大部分肠道益生菌具有高度宿主特异性,其分离和产业化较为困难[7],而环境来源益生菌不仅宿主特异性低,而且能够通过定植在水产动物体表,占据肠道生态位对宿主产生益生作用[8−9]。目前海洋环境水产益生菌的研究与应用仍较为匮乏。石斑鱼(*Epinephelus* sp.)为海洋底栖性鱼类,其成鱼主要栖息于珊瑚礁及近岸岩礁区域,本研究于角蜂巢珊瑚(*Favites flexuosa*)以及珍珠龙胆石斑鱼(*Epinephelus fuscoguttatus*♀×*Epinephelus lanceolatus*♂)两种典型海洋生物中筛选芽孢杆菌,从产酶特性、抑菌谱、环境适应性等方面解析其益生潜力,为开发兼具高效性和生态安全性的新型渔用微生态制剂提供依据。

1　材料和方法

1.1　材料

珍珠龙胆石斑鱼购自广西壮族自治区南宁市某海鲜市场。角蜂巢珊瑚采集自三亚市鹿回头半岛三亚湾(109°28′E, 18°13′N),暂养于广西南海珊瑚礁研究重点实验室。实验中使用的维氏气单胞菌(*Aeromonas veronii*)、嗜水气单胞菌(*Aeromonas hydrophila*)、金黄色葡萄球菌(*Staphylococcus aureus*)、霍乱弧菌(*Vibrio cholerae*)、大肠埃希菌(*Escherichia coli*)、美人鱼发光杆菌(*Photobacterium damselae*)、弗氏柠檬酸杆菌(*Citrobacter freundii*)、摩氏摩根氏菌(*Morganella morganii*)、溶藻弧菌(*Vibrio alginolyticus*)、副溶血弧菌(*Vibrio parahaemolyticus*)、哈维氏弧菌(*Vibrio harveyi*)、河流弧菌(*V. fluvialis*)、轮虫弧菌(*Vibrio rotiferianus*)、欧文斯氏弧菌(*Vibrio owensii*)、创伤弧菌(*Vibrio vulnificus*)、地中海弧菌(*Vibrio*

中国知网 https://www.cnki.net

mediterranei)均由广西水产生物技术与现代生态养殖重点实验室分离并保存。

1.2 主要仪器与试剂

酵母提取物、琼脂粉、牛胆盐、脱脂奶粉、蛋白胨,北京索莱宝科技有限公司;可溶性淀粉培养基、胰蛋白胨,海博生物技术有限公司;哥伦比亚CNA血琼脂平板,广西南宁康维生物科技有限公司;羧甲基纤维素钠,生工生物工程(上海)股份有限公司;刚果红、磷酸二氢钾,天津市大茂化学试剂厂;氯化钠、硫酸镁,成都金山化学试剂有限公司;革兰染色试剂盒,北京兰杰柯科技有限公司;药敏纸片,杭州天和微生物试剂有限公司;IF-A接种液、Biolog GEN III微孔板为美国BIOLOG公司产品;多功能酶标仪,赛默飞世尔科技公司;分析天平,梅特勒-托利多仪器(上海)有限公司;PCR仪,德国艾本德股份公司;平场相差显微镜,尼康株式会社。16S rRNA引物序列由武汉奥科鼎盛生物科技有限公司合成,PCR产物由该公司进行测序。

1.3 方法

1.3.1 *样品采集与处理* 选取健康状态良好、体表无明显病理特征的珍珠龙胆石斑鱼,在无菌条件下刮取体表黏液于离心管中,获得黏液样本;同时取采集自近海的角蜂巢珊瑚样本,用无菌牙刷刷洗其表面,制备珊瑚组织匀浆。取200 μL上述体表黏液及组织匀浆,样品在70 ℃下水浴20 min[10],分别接种于20 mL LB液体培养基中,37 ℃、220 r/min振荡培养约12 h。随后对样品进行划线分离,筛选出形态均一的优势菌落。通过初步拮抗病原菌筛选实验,获得抑菌活性良好的2株优势菌。优势菌经多次分离纯化后获得单克隆菌株,以体积分数25%的甘油作为保护剂于−80 ℃超低温保存备用。

1.3.2 *益生菌形态学鉴定* 将2株优势菌分别划线接种于LB固体培养基,37 ℃培养24 h后观察菌落形态及生长特性。挑取单菌落进行LB液体培养,制备菌悬液涂片,通过革兰染色后在油镜下观察并记录菌体形态学特征。

1.3.3 *菌株的生理生化特性鉴定* 参考Biolog GEN III微孔板使用说明书的操作步骤,使用无菌棉签轻柔刮取适量菌落悬浮于IF-A接种液。接种液涡旋震荡2 min,以100 μL/孔剂量接种至GEN III微孔板。微孔板于37 ℃培养12 h后,在590 nm下测定光密度(D_{590}),分析菌株生理生化特性。

1.3.4 *益生菌分子生物学鉴定* 采用Chelex-100法提取细菌基因组DNA,并以其为模板,使用16S rRNA通用引物27F:5′–AGAGTTTGATCCTGGCTCAG–3′和1492R:5′–TACGACTTAACCCCAATCGC–3′对基因组进行扩增[11]。PCR反应体系:2 × Taq Master Mix 25 μL,ddH_2O 22 μL,上、下游引物各1 μL,DNA模板1 μL。PCR反应条件:94 ℃预变性5 min;94 ℃变性30 s,55 ℃退火45 s,72 ℃延伸90 s,共35个循环,72 ℃最终延伸10 min。扩增产物经琼脂糖凝胶电泳验证,送至武汉奥科鼎盛生物科技有限公司进行测序。测序结果在美国国家生物技术信息中心数据库中进行比对,使用MEGA 11.0软件的邻接法(Neighbor-Joining)构建16S系统发育树,以确定菌株分类地位及其与相关菌株亲缘关系。

1.3.5 *益生菌产酶能力测定* 为评估益生菌产酶能力,参考林淑华等[12]方法分别测定蛋白酶、淀粉酶和纤维素酶的活性。蛋白酶活性测定:将菌株接种于LB液体培养基中,37 ℃、220 r/min培养24 h,取1 μL发酵液,点接于含质量分数1.5%脱脂奶粉的LB固体培养基表面,37 ℃恒温培养约12 h。通过观察菌落周围是否形成透明水解圈来评估蛋白酶活性,测量菌落直径($d_{菌落}$)及水解圈直径($d_{水解圈}$),计算蛋白酶活性指数($I_p = d_{水解圈}/d_{菌落}$)。淀粉酶活性测定:将1 μL发酵液点接于可溶性淀粉培养基表面,37 ℃培养24 h后,均匀喷施Lugol's碘液,观察并测量菌落直径($d_{菌落}$)及水解圈直径($d_{水解圈}$),计算淀粉酶活性指数($I_a = d_{水解圈}/d_{菌落}$)。纤维素酶活性测定:纤维素酶活性由纤维素酶培养基评估,将1 μL发酵液点接于纤维素培养基表面,37 ℃培养48 h。依次用1 mmol/L NaCl溶液处理10 min和1 g/L刚果红溶液染色30 min。观察菌落周围是否形成透明圈,测量菌落直径($d_{菌落}$)以及水解圈直径($d_{水解圈}$),计算纤维素酶活性指数($I_c = d_{水解圈}/d_{菌落}$)。实验设置3个平行。

1.3.6 *益生菌成膜能力测定* 采用结晶紫染色测定菌株生物膜形成能力[13]。取对数生长期的菌液,5 000 *g*离心10 min收集菌体,使用无菌磷酸缓冲盐溶液PBS(pH 7.4,0.01 mol/L)洗涤2次后将菌体重悬于LB培养基并调整D_{600}至0.8。取200 μL菌悬液于96孔板,37 ℃密封静置24 h后,弃去培养基并使用PBS洗涤3次。每孔加入200 μL质量分数0.1%的结晶紫溶液染色15 min,无菌水漂洗3次后,加入200 μL体积分数95%乙醇解吸附生物膜结合的结晶紫,通过测定D_{570}分析菌株生物膜形成能力,实验设置3个重复。

1.3.7 *生长曲线及回归方程的建立* 将活化菌株以体积分数2%接种量接种于100 mL LB液体培养基,37 ℃、220 r/min振荡培养72 h,以无菌LB培养

中国知网 https://www.cnki.net

基作为空白对照测定不同时间点D_{600}值,绘制菌株生长曲线。采用平板计数法构建标准曲线:取对数期菌悬液进行梯度稀释,同步测定各稀释度D_{600}值,并将稀释菌液涂布LB平板,实验设置3个重复。培养24 h后,筛选菌浓度(Colony forming unit, CFU)在30 ~ 300之间的平板计数,绘制标准曲线,并通过线性回归分析建立两者间的定量关系方程。

1.3.8 *益生菌耐受能力评估*　参考文献[4]并稍作修改。pH耐受实验:使用2 mol/L的HCl和NaOH溶液将LB液体培养基的pH分别调整为2.0、4.0、6.0、7.0、8.0、10.0和12.0,灭菌后备用。将对数生长期的菌液按体积分数10%接种量接种于不同pH培养基,37 ℃、220 r/min培养4 h后测定D_{600},实验设置3个重复。NaCl耐受实验:制备盐度为10、20、30、40的LB液体培养基,取对数期菌液以体积分数10%接种量接种,37 ℃、220 r/min培养4 h后测定D_{600},实验设置3个重复。胆盐耐受实验:制备含有质量分数0.4%牛胆盐的LB液体培养基,以体积分数10%接种量接入对数期菌液,取初始菌液以及37 ℃、220 r/min培养2、4 h时菌液分别涂板,计算存活率,实验设置3个重复。

1.3.9 *益生菌体外抑菌能力评估*　采用打孔法检测两株潜在益生菌对水产行业中常见致病菌的抑制效果,实验选维氏气单胞菌、嗜水气单胞菌等16种病原作为指示菌,所有指示菌经3次活化后接种于LB液体培养基中,37 ℃培养至对数生长期。使用PBS缓冲液将病原菌浓度调整至1×10^7 CFU/mL,取200 μL稀释液均匀涂布于LB平板,使用无菌打孔器在涂布病原菌的平板上打孔,每孔加入60 μL益生菌发酵液,37 ℃培养24 h,观察加样孔周围抑菌圈形成情况,并使用游标卡尺测量抑菌圈直径(mm),评估分离株抑菌能力。

1.3.10 *溶血性测定*　参考文献[14]方法,取1 μL细菌发酵液点种至哥伦比亚CNA血琼脂平板,37 ℃恒温培养24 h,观察菌株溶血特征,以初步评估其潜在安全性。

1.3.11 *抗生素敏感性测定*　采用纸片琼脂扩散法(K-B法)检测潜在益生菌对抗菌药物敏感性。实验选用恩诺沙星、氟苯尼考、磺胺甲恶唑、新霉素、多西环素、环丙沙星、磺胺间甲氧嘧啶、甲砜霉素和氟甲喹等9种常见抗生素进行药敏试验。将待测菌液稀释至1×10^8 CFU/mL,吸取200 μL均匀涂布于LB琼脂平板表面,将药敏纸片轻贴于平板表面,37 ℃培养24 h后,使用游标卡尺测量抑菌圈直径,根据抑菌圈大小判断菌株药物敏感性。

1.3.12 *活体安全性验证*　挑取体长为(4.31 ± 0.47)cm健康石斑鱼进行安全性评价,实验设置3个组别,各组腹腔分别注射50 μL无菌PBS、50 μL TG1(1×10^8 CFU/mL)、50 μL SH39(1×10^8 CFU/mL),每组3个平行各10尾。注射后连续观察1周,观察各组石斑鱼生长及死亡情况。

2　结果与分析

2.1　SH39与TG1的分离鉴定

分别从角蜂巢珊瑚组织匀浆液和珍珠龙胆石斑鱼体表黏液中筛选一株有拮抗活性的耐热型芽孢杆菌,命名为SH39和TG1。分离株SH39在LB固体平板上形成的菌落呈近圆形,表面粗糙、中部凸起,湿润且黏稠(图1(A))。取对数生长期的细胞进行革兰染色,显微镜下观察显示呈蓝紫色,为革兰阳性菌(图1(C))。分离株TG1的菌落形态边缘不规则、菌落扁平,干燥且无光泽(图1(B))。油镜下观察细胞呈短棒状(图1(D)),革兰染色结果为阳性。

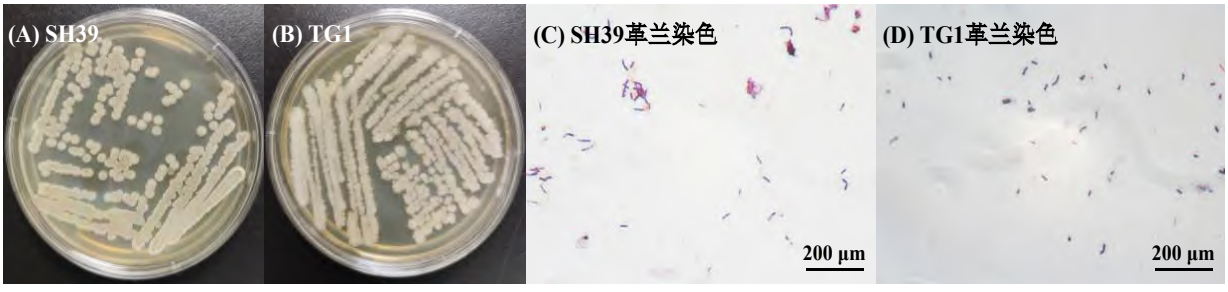


图1　分离株SH39和TG1形态学表征

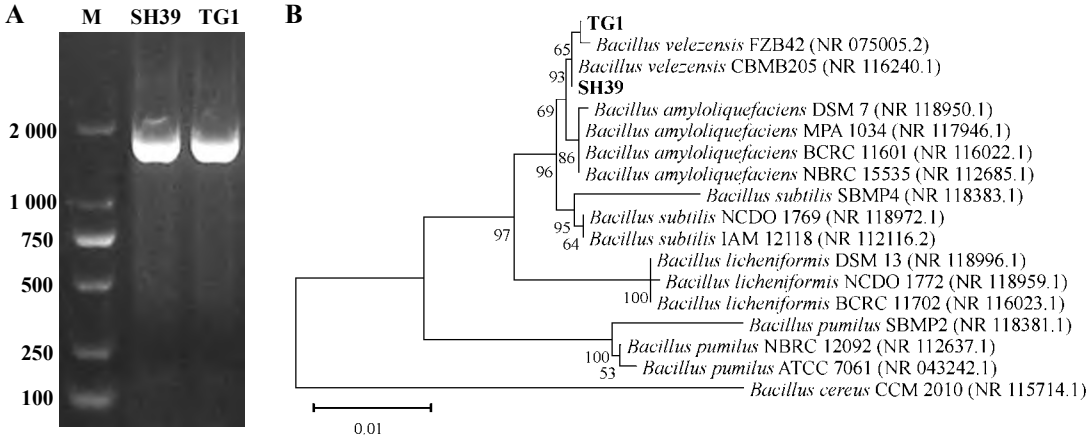
Fig. 1　Morphological characterization of isolates SH39 and TG1

2.2　SH39与TG1的16S rRNA测序结果

SH39和TG1的DNA凝胶电泳条带单一、完整、明亮(图2(A)),经16S rRNA通用引物扩增的片段长度分别为1 472和1 466 bp。系统发育树

中国知网　https://www.cnki.net

(图2(B))表明,分离株SH39与TG1与贝莱斯芽孢杆菌(*Bacillus velezensis*)FZB42和CBMB205聚为一支。综合形态学以及分子生物学鉴定结果,最终确定SH39和TG1为贝莱斯芽孢杆菌。



M,DL2000 DNA marker

图2 SH39与TG1 16S分子生物学鉴定

Fig. 2 16S molecular biology identification of SH39 and TG1

2.3 SH39与TG1的产酶性能

由表1可知,通过蛋白酶培养基测定,SH39的蛋白酶指数为1.81 ± 0.03,显著高于TG1的1.35 ± 0.23($P < 0.05$)。纤维素酶活性测定结果显示,SH39和TG1均表现出一定纤维素酶活性,其指数分别为2.25 ± 0.30和1.91 ± 0.20。尽管SH39的纤维素酶活性略高于TG1,但两者之间差异不显著($P > 0.05$)。在可溶性淀粉培养基中,SH39的淀粉酶活性指数为2.36 ± 0.27之间,显著高于TG1的1.92 ± 0.15($P < 0.05$)。由图3可知,SH39和TG1均表现出一定的消化酶活性,但SH39在蛋白酶和淀粉酶活性方面显著优于TG1。在培养24 h条件下,SH39表现出更高产酶潜力。

表1 SH39与TG1消化酶活性指数比较

Table 1 Comparison of SH39 and TG1 digestive enzyme activity indexes

菌株编号 Strain number	蛋白酶活性指数 Protease enzyme activity index	纤维素酶活性指数 Cellulase enzyme activity index	淀粉酶活性指数 Amylase enzyme activity index
SH39	1.81 ± 0.03*	2.25 ± 0.30	2.36 ± 0.27*
TG1	1.35 ± 0.23	1.91 ± 0.20	1.92 ± 0.15

注:以平均值 ± 标准差表示,同列数据含*表示数据间差异显著($P < 0.05$)。

Note: The data are expressed as mean ± standard deviation, and asterisks (*) within the same column indicate significant differences between the data($P < 0.05$).

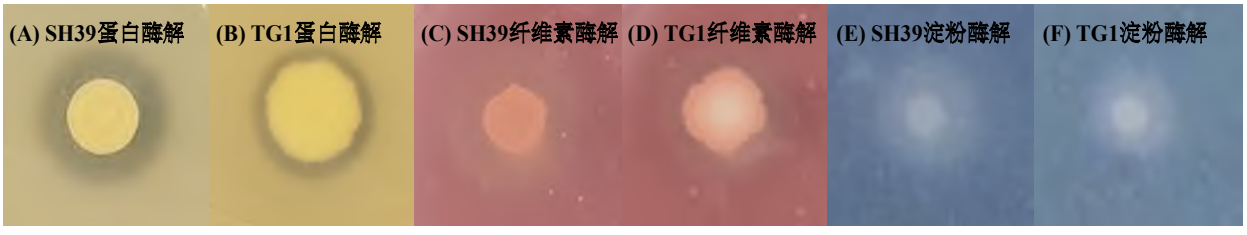


图3 SH39与TG1消化酶活性能力验证

Fig. 3 SH39 and TG1 digestive enzyme activity verification

2.4 SH39与TG1生长曲线测定及回归方程

由图4 (A–B)可知,SH39与TG1均呈典型的微生物生长规律,且生长迟缓期均较短。培养4 h后,两株菌迅速增长,进入对数生长期,细胞数量呈指数增长。培养24 h左右时,生长曲线趋于平稳,进入稳定期。培养30 h后,两株菌的D_{600}均略有下降。为确定光密度与菌浓度之间数量关系,选取不同光密度的菌液进行平板涂布,构建光密度与菌浓度之间的标准曲线,由图4 (C–D)可知,SH39与TG1的线性回归方程分别是$\hat{y} = 1.377\ 3 \times 10^9 x - 7.523\ 5 \times 10^7$($R^2 = 0.991\ 6$)和$\hat{y} = 1.388\ 6 \times 10^9 x - 1.464\ 0 \times 10^7$($R^2 = 0.997\ 2$),回归方程可用于后续通过测定菌液的$D_{600}$计算菌液浓度。

2.5 SH39与TG1体外抑菌活性

基于打孔法对分离株SH39和TG1的广谱抑菌活性进行测定。由表2可知,除河流弧菌与创伤弧

中国知网 https://www.cnki.net

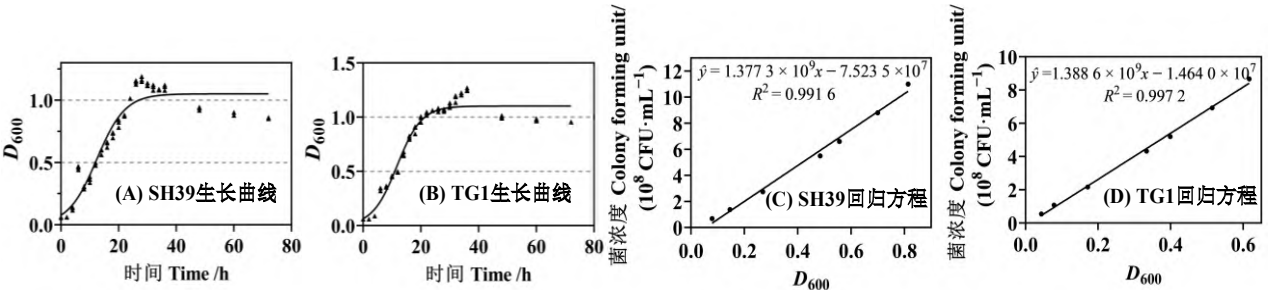


图4　SH39与TG1的生长曲线与回归方程

Fig. 4　Growth curves and regression equations of SH39 and TG1

菌之外,SH39与TG1对维氏气单胞菌、嗜水气单胞等14种病原均表现出一定抑菌活性,但对金黄色葡萄球菌、霍乱弧菌、溶藻弧菌、哈维氏弧菌、轮虫弧菌以及欧文斯氏弧菌的抑菌能力差异显著(P < 0.05),其中SH39与TG1对欧文斯氏弧菌的抑菌效果最佳[抑菌圈直径分别为(21.77 ± 0.42)、(24.26 ± 0.40)mm],表明SH39和TG1具有广谱抑菌特性。

表2　SH39和TG1广谱抑菌活性比较

Table 2　Comparison of broad-spectrum antibacterial activity of SH39 and TG1

病原 Pathogens	抑菌圈直径 Diameter of inhibition circle/mm		病原 Pathogens	抑菌圈直径 Diameter of inhibition circle/mm	
	SH39	TG1		SH39	TG1
维氏气单胞菌(*Aeromonas veronii*)	19.63 ± 0.15	21.10 ± 0.66	嗜水气单胞菌(*Aeromonas hydrophila*)	16.47 ± 2.43	17.13 ± 1.79
金黄色葡萄球菌(*Staphylococcus aureus*)	15.47 ± 1.60	18.00 ± 0.26*	霍乱弧菌(*Vibrio cholerae*)	12.80 ± 0.10	14.33 ± 0.86*
大肠埃希菌(*Escherichia coli*)	14.17 ± 1.12	14.53 ± 1.81	美人鱼发光杆菌(*Photobacterium damselae*)	13.77 ± 0.40	11.77 ± 0.49
弗氏柠檬酸杆菌(*Citrobacter freundii*)	13.90 ± 2.00	14.40 ± 0.89	摩氏摩根菌(*Morganella morganii*)	12.23 ± 0.32	12.80 ± 0.44
溶藻弧菌(*Vibrio alginolyticus*)	16.60 ± 0.66*	13.43 ± 0.84	副溶血弧菌(*Vibrio parahaemolyticus*)	12.80 ± 0.70	11.77 ± 0.15
哈维氏弧菌(*Vibrio harveyi*)	12.63 ± 1.10	17.67 ± 0.42*	河流弧菌(*Vibrio fluvialis*)	0	0
轮虫弧菌(*Vibrio rotiferianus*)	13.46 ± 0.40*	11.77 ± 0.74	欧文斯氏弧菌(*Vibrio owensii*)	21.77 ± 0.42	24.26 ± 0.40*
创伤弧菌(*Vibrio vulnificus*)	0	0	地中海弧菌(*Vibrio mediterranei*)	12.80 ± 0.10	12.17 ± 0.40

注:打孔器直径7 mm。抑菌圈直径以平均值 ± 标准差表示。同行数据含*表示数据间差异显著(P < 0.05)。

Note: The diameter of the perforator is 7 mm. The diameter of the inhibition circle is expressed as mean ± standard deviation, and the data in the same row containing * indicate significant differences between the data (P < 0.05).

2.6　SH39与TG1生理生化指标

实验使用GEN III微孔板对分离株SH39和TG1的碳源代谢及化学敏感性进行测定。由表3和表4可知,SH39对N-乙酰-D-半乳糖胺、L-焦谷氨酸等24种碳源代谢呈阴性,对D-丝氨酸、萘啶酮酸等11种化学物质反应呈阴性;TG1对α-D-乳糖、N-乙酰神经氨酸等18种碳源代谢呈阴性,对梭链孢酸、醋竹桃霉素等8种化学物质反应呈阴性。

2.7　SH39与TG1成膜能力

SH39与TG1在LB中的成膜能力使用结晶紫染色法测定。由图5可知,TG1成膜能力显著高于SH39(P < 0.05),表明TG1可能具有更强定植能力。

2.8　SH39与TG1耐受能力

由图6 (A–B)可知,SH39的生长随培养基中盐度增加受到轻微抑制,尽管如此,当盐度达40时,SH39仍保持相对较好生长活性,表明SH39对高盐环境具有一定耐受性。TG1在不同盐度LB培养基中表现出一定嗜盐性,统计分析可知,其在盐度20的培养基中长势最佳(P < 0.05)。在不同pH值的LB培养基培养4 h后,两株分离菌在pH为6 ~ 8时生长良好,在低pH环境中仍保持一定存活率。

由图7可知,随分离菌在胆盐培养基中培养时间延长,两株菌存活率均有一定程度下降,4 h时,SH39与TG1存活率分别为60%与20%,SH39胆盐耐受力显著高于TG1(P < 0.01)。

2.9　SH39与TG1安全性

由图8 (A–B)可知,分离株SH39和TG1在哥伦比亚CNA血琼脂平板上生长时周围均未出现溶血圈,鉴定为非溶血性菌株。

中国知网　https://www.cnki.net

表3 SH39与TG1碳源代谢验证

Table 3 Carbon source metabolism verification of SH39 and TG1

测试项目 Test items	TG1	SH39	测试项目 Test items	TG1	SH39
糊精(Dextrin)	+	+	氨基乙酰-L-脯氨酸(Glycyl-L-Proline)	+	+
D-麦芽(D-Maltose)	+	+	L-丙氨酸(L-Alanine)	+	+
D-海藻糖(D-Trehalose)	+	+	L-精氨酸(L-Arginine)	+	+
D-纤维二糖(D-Cellobiose)	+	+	L-天冬氨酸(L-Aspartic acid)	+	+
龙胆二糖(Gentiobiose)	+	+	L-谷氨酸(L-Glutamic acid)	+	+
蔗糖(Sucrose)	+	+	L-组胺(L-Histidine)	+	+
D-松二糖(D-Turanose)	+	+	L-焦谷氨酸(L-Pyroglutamic acid)	+	–
水苏糖(Stachyose)	+	+	L-丝氨酸(L-Serine)	+	–
蜜三糖(D-Raffinose)	+	+	果胶(Pectin)	+	+
α-D-乳糖(α-D-Lactose)	–	+	D-半乳糖醛酸(D-Galacturonic acid)	+	+
蜜二糖(D-Melibiose)	+	+	L-半乳糖醛酸内酯(L-Galactonic acid lactone)	+	+
β-甲酰-D-葡糖苷(β-Methyl-D-Glucoside)	+	+	D-葡糖酸(D-Gluconic acid)	+	+
D-水杨苷(D-Salicin)	+	+	D-葡糖醛酸(D-Glucuronic acid)	+	+
N-乙酰-D-葡糖胺(N-Acetyl-D-Glucosamine)	+	+	葡糖醛酰胺(Glucuronamide)	–	–
N-乙酰-β-D-甘露糖胺(N-Acetyl-β-DMannosamine)	+	+	黏酸(Mucic acid)	–	–
N-乙酰-D-半乳糖胺(N-Acetyl-D-Galactosamine)	+	–	奎宁酸(Quinic acid)	+	–
N-乙酰神经氨酸(N-Acetyl neuraminic acid)	–	–	糖质酸(D-Saccharic acid)	–	–
α-D-葡糖(α-D-Glucose)	+	+	p-羟基-苯乙酸(p-Hydroxy- Phenylacetic acid)	–	–
D-甘露糖(D-Mannose)	+	+	丙酮酸甲酯(Methyl pyruvate)	+	+
D-果糖(D-Fructose)	+	+	D-乳酸甲酯(D-Lactic acid methyl ester)	+	–
D-半乳糖(D-Galactose)	+	+	L-乳酸(L-Lactic acid)	+	+
3-甲酰葡糖(3-Methyl glucose)	–	–	柠檬酸(Citric acid)	+	+
D-岩藻糖(D-Fucose)	–	–	α-酮-戊二酸(α-Keto-Glutaric acid)	–	–
L-岩藻糖(L-Fucose)	–	–	D-苹果酸(D-Malic acid)	–	–
L-鼠李糖(L-Rhamnose)	–	–	L-苹果酸(L-Malic acid)	+	+
肌苷(Inosine)	+	–	溴-丁二酸(Bromo-Succinic acid)	+	+
D-山梨醇(D-Sorbitol)	+	+	吐温40(Tween 40)	+	+
D-甘露醇(D-Mannitol)	+	+	γ-氨基-丁酸(γ-Amino-Butryric acid)	–	–
D-阿拉伯醇(D-Arabitol)	–	–	α-羟基-丁酸(α-Hydroxy-Butyric acid)	–	–
肌醇(myo-Inositol)	+	+	β-羟基-D,L 丁酸(β-Hydroxy-D, L Butyric acid)	+	+
甘油(Glycerol)	+	+	α-酮-丁酸(α-Keto-Butyric acid)	–	–
D-葡糖-6-磷酸(D-Glucose-6-PO4)	–	–	乙酰乙酸(Acetoacetic acid)	+	+
D-果糖-6-磷酸(D-Fructose-6-PO4)	+	+	丙酸(Propionic acid)	+	–
D-天冬氨酸(D-Aspartic acid)	+	+	乙酸(Acetic acid)	+	+
D-丝氨酸(D-Serine)	–	–	甲酸(Formic acid)	+	+
明胶(Gelatin)	+	+			

注:“+”,阳性反应;“–”阴性反应。Note: “+”, positive reaction; “–” negative reaction.

采用纸片扩散法测试了分离株SH39和TG1对恩诺沙星、氟苯尼考等9种抗菌药物的药物敏感性。由表5可知,SH39与TG1对所测试9种抗生素均表现为敏感。

分别向石斑鱼腹腔注射50 μL无菌PBS、1 × 10^8 CFU/mL的TG1、SH39后观察7 d,石斑鱼进食良好,无发病和死亡现象。

中国知网 https://www.cnki.net

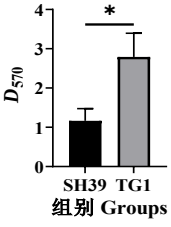
表4　SH39与TG1化学敏感性验证

Table 4　Chemical sensitivity verification of SH39 and TG1

测试项目 Test items	TG1	SH39	测试项目 Test items	TG1	SH39
pH 6	+	+	盐酸胍	+	+
pH 5	+	+	硫酸四癸钠	−	−
质量分数1% NaCl	+	+	万古霉素	−	−
质量分数4% NaCl	+	+	四唑紫	−	−
质量分数8% NaCl	+	+	四唑蓝	−	−
质量分数1%乳酸钠	+	+	萘啶酮酸	+	−
梭链孢酸	−	−	氯化锂	+	+
D-丝氨酸	+	−	亚碲酸钾	+	+
醋竹桃霉	−	−	氨曲南	+	+
利福霉素SV	+	+	丁酸钠	+	+
二甲胺四环	−	−	溴酸钠	−	−
林肯霉	+	−			

注:“+”,阳性反应;“−”阴性反应。

Note: “+”, positive reaction; “−” negative reaction.

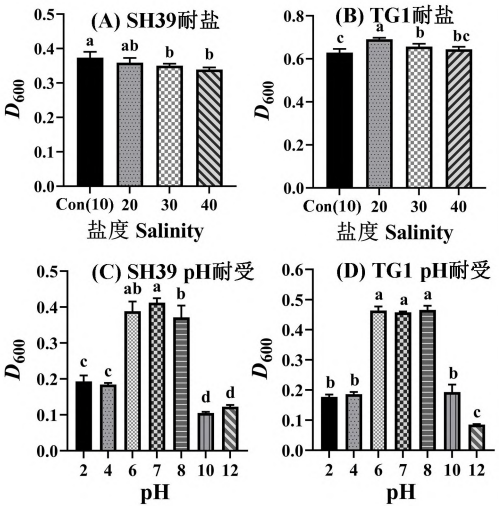


*表示数据间差异显著($P < 0.05$)。

*Indicates a significant difference between the data ($P < 0.05$).

图5　SH39与TG1成膜能力评估

Fig. 5　Evaluation of film-forming ability of SH39 and TG1

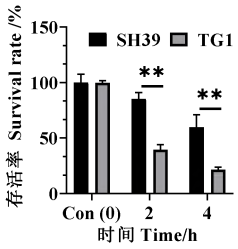


不同处理组凡含一个相同字母则表示差异不显著($P > 0.05$)。

Different treatment groups sharing the same letter indicate no significant difference between them ($P > 0.05$).

图6　SH39与TG1盐度与pH耐受评估

Fig. 6　Salinity and pH tolerance assessment of SH39 and TG1



** 表示数据间差异极显著($P < 0.01$)。** indicates extremely significant differences between data ($P < 0.01$).

图7　SH39与TG1胆盐耐受评估

Fig. 7　Bile salt tolerance assessment for SH39 and TG1

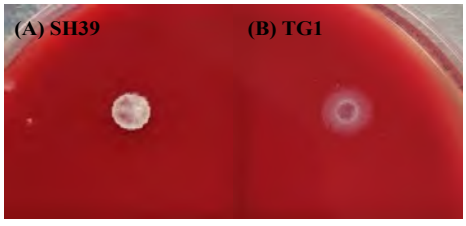


图8　SH39与TG1溶血性验证

Fig. 8　Hemolytic test of SH39 and TG1

表5　SH39与TG1抗生素敏感性评估

Table 5　Evaluation on antibiotic sensitivity of SH39 and TG1

抗生素 Antibiotics	浓度 Concentration/(μg/片)	抑菌圈直径判断标准 Standard of judgment/mm			敏感性 Sensitivities	
		R	I	S	SH39	TG1
恩诺沙星 Enrofloxacin	10	≤10	11 ~ 14	≥15	S	S
氟苯尼考 Florfenicol	30	≤10	11 ~ 14	≥15	S	S
磺胺甲恶唑 Sulfamethoxazole	30	≤10	11 ~ 14	≥15	S	S
新霉素 Neomycin	30	≤10	11 ~ 14	≥15	S	S
多西环素 Doxycycline	30	≤14	15 ~ 17	≥18	S	S
环丙沙星 Ciprofloxacin	5	≤15	16 ~ 20	≥21	S	S
磺胺间甲氧嘧啶 Sulfamethoxypyridimine	30	≤12	13 ~ 16	≥17	S	S
甲砜霉素 Thiamphenicol	30	≤15	16 ~ 20	≥21	S	S
氟甲喹 Flumequine	30	≤15	16 ~ 20	≥21	S	S

注:R,耐药;I,中介;S,敏感。

Note: R, resistant; I, intermediate; S, sensitive.

3　讨论

本研究采用高温预处理筛选策略,成功分离获得2株海洋源贝莱斯芽孢杆菌(*B. velezensis*)SH39与TG1。生理生化鉴定结果表明,2株菌均具有广泛的碳源代谢活性,这与先前研究报道的贝莱斯芽孢杆菌特性相符[11]。贝莱斯芽孢杆菌最先发现于西

中国知网　https://www.cnki.net

班牙南部的贝莱斯河[15]，已有研究表明，不同来源的贝莱斯芽孢杆菌在饲料添加剂、水质调控、病原拮抗及免疫调节等方面表现出显著益生潜力[16−18]。

3.1 贝莱斯芽孢杆菌的环境适应性

益生菌须具备良好生长特性，才能在动物体内发挥益生作用，而外源益生菌在海洋动物肠道内定植，则需要承受动物消化道酸性环境、胆盐以及高盐度胁迫[19−20]。贝莱斯芽孢杆菌属于厚壁菌门，在极端环境中能够产生内生芽孢以应对环境胁迫，具有一定抗逆性能。Gao等[11]报道一株从凡纳滨对虾（*Litopenaeus vannamei*）养殖环境中筛选到的贝莱斯芽孢杆菌，既能抵抗0.3%质量分数的胆盐胁迫，也能在pH值为2的TSB培养基中存活。广东海洋大学研究团队报道2株从珍珠龙胆石斑鱼消化道内筛选得到的贝莱斯芽孢杆菌，其能在低至1.0pH值下保持一定存活率，且耐受质量分数0.5%胆盐浓度[4]。Li等[21]对比从牦牛（*Bos grunniens*）肠道内容物分离得到枯草芽孢杆菌（*Bacillus subtilis*）与贝莱斯芽孢杆菌的耐酸和耐胆盐情况发现，贝莱斯芽孢杆菌表现更好耐受性能。本研究得到类似结果，SH39与TG1在pH为2 ~ 4培养环境中光密度显著高于pH为12菌液（$P < 0.05$），表明2株菌均具有良好耐酸性；在胆盐耐受实验中，2株菌在含质量分数0.4%牛胆盐LB培养基中表现良好耐受能力。酸碱与胆盐耐受实验表明SH39与TG1在肠道环境中拥有一定定植潜力。全基因组测序研究显示，贝莱斯芽孢杆菌能够利用8个ATP合成酶*atp*基因组成一个操作子，通过水解ATP从细胞质中挤出质子来维持酸性条件下质子平衡，同时，Na^+/H^+逆转运蛋白及其编码基因的存在，使贝莱斯芽孢杆菌拥有良好低pH耐受性[22]，基因组中*btlA*和*bshA*基因则是参与到胆盐耐受和分解过程，使贝莱斯芽孢杆菌在高胆盐浓度环境中保持活力[23]。良好耐盐性能是益生菌在海洋环境中发挥作用的先决条件。有研究从盐碱地分离出1株具有广谱真菌抗性的贝莱斯芽孢杆菌能够在盐度为0 ~ 120环境中生长[24]，油水富集液中筛选得到贝莱斯芽孢杆菌也被证明能够在质量浓度10 ~ 150 g/L NaCl培养基中存活[19]。本研究综合海水养殖实际盐度需求，发现分离株SH39与TG1均能在高盐度培养基中保证生长，支持其作为海水养殖益生菌的应用潜力。

3.2 贝莱斯芽孢杆菌胞外酶系提高水产饲料利用率

水产动物通常依靠自身各种消化酶对饲料进行消化与吸收，然而饲料中替代鱼粉的植物组分降低了水产动物饲料转化率，肠道内消化酶种类与活性不足直接或间接影响水产行业的进一步发展[25−26]。芽孢杆菌生长繁殖快，抗逆性好，其分泌的多种消化酶（如蛋白酶、脂肪酶和淀粉酶）能显著提高饲料利用率，常被用于饲料添加领域[2, 27]。研究表明，饲料中添加枯草芽孢杆菌可使石斑鱼饲料效率比提升25% ~ 60%[28]。贝莱斯芽孢杆菌有丰富的胞外酶系，Xia等[29]发现贝莱斯芽孢杆菌不仅能够产生蛋白酶、淀粉酶、脂肪酶、纤维素酶等多种胞外酶，而且能够刺激大口黑鲈（*Micropterus salmoides*）肠道内胰蛋白酶、淀粉酶以及血清脂肪酶活性增加，进而显著改善大口黑鲈生长性能；林淑华等[12]亦确定野猪（*Sus scrofa*）肠道来源的贝莱斯芽孢杆菌能够分解淀粉与纤维素。本研究中，SH39与TG1同样有蛋白、纤维素以及淀粉的胞外降解活性，表明其作为饲料添加剂具备促进水产动物生长的潜力。

3.3 芽孢杆菌的广谱抗菌作用与定植潜力

水产病害频发对水产养殖业造成重大经济损失[30−33]，益生菌因其显著病原拮抗作用和宿主免疫增强功能，在“无抗时代”背景下成为绿色病害防控策略的研究热点[34−35]。蜡样芽孢杆菌（*Bacillus cereus*）能够通过上调杂交石斑鱼脾脏和头肾中多种免疫和抗氧化基因（*CTL*、*CAT*、*SOD*、*HSP70*、*TLR3*、*TGF-β*和*IgM*）的表达，增强宿主免疫与抗氧化能力[36]，贝莱斯芽孢杆菌能够合成脂肽、多酮类、肽类等多类型强抗菌次生代谢物[37]。本研究通过体外抑菌实验确定SH39与TG1对细菌性水产病原有广谱性抑制效果。尽管SH39与TG1在分子生物学鉴定上被归为同一种，但2株菌不仅形态上存在明显差异，其对金黄色葡萄球菌、溶藻弧菌、哈维氏弧菌以及霍乱弧菌等6种病原抑制效果同样差异显著（$P < 0.05$），这可能是2株菌在生态位竞争以及次级代谢物的产生能力上存在差异。生物膜是由细菌及其分泌形成的胞外聚合物共同形成的复杂结构，该结构能够促进菌体与宿主黏膜之间定植，与游离状态相比，生物膜结构有更加稳定形式，能增强益生菌抗逆性以及与致病菌竞争肠道位点能力[38−39]。例如，枯草芽孢杆菌DG101能够通过形成生物膜保护本地肠道菌群不受肠道环境压力的影响[20]，相较于游离状态菌体，处于生物膜状态植物乳杆菌（*Lactiplantibacillus plantarum*）也被证明有更好黏附特性以及模拟肠胃液中更高存活率[40]。本研究通过结晶紫染色法体外分别评定SH39与TG1成膜能力，发现TG1成膜能力显著强于SH39（$P < 0.05$），这可能是

中国知网 https://www.cnki.net

TG1能够定植于珍珠龙胆石斑鱼体表重要原因。

3.4　贝莱斯芽孢杆菌安全性验证

益生菌安全性是其商业化应用前提。本研究使用9种常见抗生素进行耐药实验,结果表明,SH39和TG1对所有抗生素敏感,这排除了益生菌携带耐药基因在肠道微生物群落中水平转移的潜在风险[41]。此外,大多细菌致病性与其溶血特性相关,溶血活性评估也是评价益生菌安全性重要标准之一。研究表明,贝莱斯芽孢杆菌在哥伦比亚血平板上不具有β溶血性[42],本研究结果与之一致,分离菌在血平板上未表现出草绿色或透明溶血环,确定SH39与TG1为γ溶血。本研究活体实验也显示,腹腔注射SH39和TG1后,石斑鱼未出现异常状况,表明2株菌具有潜在生物安全性。

4　结论

本研究从珊瑚与石斑鱼体表黏液中分离获得2株耐高温芽孢杆菌SH39和TG1,经形态学观察、生理生化鉴定以及分子生物学鉴定,综合确定其为贝莱斯芽孢杆菌(*Bacillus velezensis*)。2株菌不仅对胆盐、盐度以及酸性环境有良好耐受性,而且对常见水产病原菌有着广谱抑菌活性,并且能够产生多种胞外消化酶,这提示SH39和TG1在海水养殖中有较大应用潜力,可作为水产养殖候选益生菌。未来将基于本研究获得的贝莱斯芽孢杆菌结合全基因组测序技术以及复合微生物菌剂等手段,在活体层面研究其对我国大中型名贵海产鱼类如珍珠龙胆石斑鱼的益生作用,为推动名贵海水鱼类的集约化高效健康养殖提供助力。

参考文献

[1] YILMAZ S, YILMAZ E, DAWOOD M A O, et al. Probiotics, prebiotics, and synbiotics used to control vibriosis in fish: a review[J]. Aquaculture, 2022, 547: 737514.

[2] GHOSH T. Recent advances in the probiotic application of the *Bacillus* as a potential candidate in the sustainable development of aquaculture[J]. Aquaculture, 2025, 594: 741432.

[3] 苏宏飞, 刘缘, 曾璐佳, 等. 珊瑚益生菌筛选及其益生特性分析[J]. 南方农业学报, 2024, 55(7): 1873-1886.

[4] AMOAH K, CAI J, HUANG Y, et al. Identification and characterization of four *Bacillus* species from the intestine of hybrid grouper (*Epinephelus fuscoguttatus*♀ × *E. lanceolatus* ♂), their antagonistic role on common pathogenic bacteria, and effects on intestinal health[J]. Fish & Shellfish Immunology, 2024, 152: 109795.

[5] WANG X H, LU C X, WAN F X, et al. Enhance the biocontrol efficiency of *Bacillus velezensis* Bs916 for white spot syndrome virus in crayfish by overproduction of cyclic lipopeptide locillomycin[J]. Aquaculture, 2023, 573: 739596.

[6] SUN H C, SHANG M, TANG Z L, et al. Oral delivery of *Bacillus subtilis* spores expressing *Clonorchis sinensis* paramyosin protects grass carp from *Cercaria* infection[J]. Applied Microbiology and Biotechnology, 2020, 104(4): 1633-1646.

[7] WANKA K M, DAMERAU T, COSTAS B, et al. Isolation and characterization of native probiotics for fish farming[J]. BMC Microbiology, 2018, 18(1): 119.

[8] ZHANG Y P, LIANG X F, HE S, et al. Dietary supplementation of exogenous probiotics affects growth performance and gut health by regulating gut microbiota in Chinese Perch (*Siniperca chuatsi*)[J]. Aquaculture, 2022, 547: 737405.

[9] SHEPHERD E S, DELOACHE W C, PRUSS K M, et al. An exclusive metabolic niche enables strain engraftment in the gut microbiota[J]. Nature, 2018, 557(7705): 434-438.

[10] LEÑINI C, RODRIGUEZ AYALA F, GOÑI A J, et al. Probiotic properties of *Bacillus subtilis* DG101 isolated from the traditional Japanese fermented food nattō[J]. Frontiers in Microbiology, 2023, 14: 1253480.

[11] GAO Y L, QIANG L, WU N, et al. Study on the potential probiotics isolated from marine aquaculture system and evaluation for aquaculture application[J]. Aquaculture Research, 2024, 2024(1): 9555271.

[12] 林淑华, 谭娟娟, 杨贝莹, 等. 野猪肠道菌群多样性分析及其益生菌的分离筛选[J]. 微生物学通报, 2025, 52(2): 757-770.

[13] 黄沁愉, 蒋学建, 苏宏飞, 等. 珊瑚来源群体淬灭活性产生菌的筛选与抑菌活性研究[J]. 广西科学, 2020, 27(5): 509-519.

[14] 任廷亿, 刘永相, 张永英, 等. 太行鸡源贝莱斯芽孢杆菌的益生特性及全基因组分析[J]. 微生物学通报, 2025, 52(4): 1697-1709.

[15] RUIZ-GARCÍA C, BÉJAR V, MARTÍNEZ-CHECA F, et al. *Bacillus velezensis* sp. nov., a surfactant-producing bacterium isolated from the river Vélez in Málaga, southern Spain[J]. International Journal of Systematic and Evolutionary Microbiology, 2005, 55(1): 191-195.

[16] THURLOW C M, WILLIAMS M A, CARRIAS A, et al. *Bacillus velezensis* AP193 exerts probiotic effects in channel catfish (*Ictalurus punctatus*) and reduces aquaculture pond eutrophication[J]. Aquaculture, 2019, 503: 347-356.

[17] GAO X Y, LIU Y, MIAO L L, et al. Characterization and mechanism of anti-*Aeromonas salmonicida* activity of a marine probiotic strain, *Bacillus velezensis* V4[J]. Applied Microbiology and Biotechnology, 2017, 101(9): 3759-3768.

中国知网 https://www.cnki.net

[18] LI J, WU Z B, ZHANG Z, et al. Effects of potential probiotic *Bacillus velezensis* K2 on growth, immunity and resistance to *Vibrio harveyi* infection of hybrid grouper (*Epinephelus lanceolatus* ♂ × *E. fuscoguttatus* ♀) [J]. Fish & Shellfish Immunology, 2019, 93: 1047-1055.

[19] YIN J, WEI X X, HU F T, et al. Halotolerant *Bacillus velezensis* sustainably enhanced oil recovery of low permeability oil reservoirs by producing biosurfactant and modulating the oil microbiome[J]. Chemical Engineering Journal, 2023, 453: 139912.

[20] YAO M F, LU Y M, ZHANG T, et al. Improved functionality of *Ligilactobacillus salivarius* Li01 in alleviating colonic inflammation by layer-by-layer microencapsulation[J]. NPJ Biofilms and Microbiomes, 2021, 7: 58.

[21] LI A Y. Isolation and identification of potential *Bacillus* probiotics from free ranging yaks of Tibetan Plateau, China [J]. Pakistan Veterinary Journal, 2019, 39(3): 377-382.

[22] TANG Y Y, LI T, HUANG Y H, et al. Comprehensive phenotypic characterization and genomic analysis unveil the probiotic potential of *Bacillus velezensis* K12[J]. Animals, 2025, 15(6): 798.

[23] KUEBUTORNYE F K A, LU Y S, WANG Z W, et al. Functional annotation and complete genome analysis confirm the probiotic characteristics of *Bacillus* species isolated from the gut of Nile tilapia[J]. LWT, 2022, 163: 113541.

[24] TORRES M, LLAMAS I, TORRES B, et al. Growth promotion on horticultural crops and antifungal activity of *Bacillus velezensis* XT1[J]. Applied Soil Ecology, 2020, 150: 103453.

[25] DA C T, LUNDH T, LINDBERG J E. Digestibility of dietary components and amino acids in animal and plant protein feed ingredients in striped catfish (*Pangasianodon hypophthalmus*) fingerlings[J]. Aquaculture Nutrition, 2013, 19(5): 741-750.

[26] NAYLOR R L, HARDY R W, BUREAU D P, et al. Feeding aquaculture in an era of finite resources[J]. Proceedings of the National Academy of Sciences of the United States of America, 2009, 106(36): 15103-15110.

[27] RAY A K, GHOSH K, RINGØ E. Enzyme-producing bacteria isolated from fish gut: a review[J]. Aquaculture Nutrition, 2012, 18(5): 465-492.

[28] HAN C J, SONG S Z, CUI C C, et al. Strain-specific benefits of *Bacillus* probiotics in hybrid grouper: growth enhancement, metabolic health, immune modulation, and *Vibrio harveyi* resistance[J]. Animals, 2024, 14(7): 1062.

[29] XIA L, CHENG G F, WANG P, et al. Screening and identification of probiotics from the intestinal tract of largemouth bass (*Micropterus salmoides*) for use as a feed additive and bacterial infection control[J]. Aquaculture, 2024, 584: 740661.

[30] 饶颖竹, 梁静真, 陈蓉, 等. 海水养殖斜带石斑鱼致病性鳗弧菌的分离鉴定及药敏试验[J]. 南方农业学报, 2016, 47(8): 1416-1422.

[31] 李辉, 冯伟, 唐永凯, 等. 中华绒螯蟹过氧化物还原酶基因克隆及其在鳗弧菌感染下的表达分析[J]. 南方农业学报, 2021, 52(8): 2267-2275.

[32] 刘明珠, 谢瑾琨, 余庆, 等. 激活式核酸适配体LYGV1c对石斑鱼虹彩病毒的特异性识别与检测[J]. 南方农业学报, 2025, 56(6): 1704-1714.

[33] 李梦梦, 韦红玲, 刘明珠, 等. 八角茴香水提物调控宿主免疫反应抗石斑鱼虹彩病毒的机制研究[J]. 南方农业学报, 2022, 53(10): 2756-2765.

[34] QI X Z, LUO F, ZHANG Y L, et al. Exploring the protective role of *Bacillus velezensis* BV1704–Y in zebrafish health and disease resistance against *Aeromonas hydrophila* infection [J]. Fish & Shellfish Immunology, 2024, 152: 109789.

[35] WEI D D, GUO Z B, CHEN F, et al. Gut microbiota of largemouth bass in response to temperature stress[J]. Aquaculture Reports, 2025, 43: 102912.

[36] XIE G T, CHEN X Y, FENG Y W, et al. Effects of dietary multi-strain probiotics on growth performance, antioxidant status, immune response, and intestinal microbiota of hybrid groupers (*Epinephelus fuscoguttatus* ♀ × *E. lanceolatus* ♂)[J]. Microorganisms, 2024, 12(7): 1358.

[37] KHALID F, KHALID A, FU Y C, et al. Potential of *Bacillus velezensis* as a probiotic in animal feed: a review[J]. Journal of Microbiology, 2021, 59(7): 627-633.

[38] LOU Z X, ZHENG X D, BEDE D, et al. New perspectives for mechanisms, ingredients, and their preparation for promoting the formation of beneficial bacterial biofilm[J]. Journal of Food Measurement and Characterization, 2023, 17 (3): 2386-2403.

[39] YAO B Q, YANG Z Q, ZHAO X R, et al. Biofilm-state probiotics: Advanced alternatives to traditional probiotics[J]. Trends in Food Science & Technology, 2025, 156: 104854.

[40] ZHANG L J, MENG Y, LI J Y, et al. *Lactiplantibacillus plantarum* Y42 in biofilm and planktonic states improves intestinal barrier integrity and modulates gut microbiota of balb/c mice[J]. Foods, 2022, 11(10): 1451.

[41] HE J T, HONG L, SONG M J, et al. Diverse *Acinetobacter* species and Plasmid-Driven spread of carbapenem resistance in pharmaceutical settings in China[J]. Environment International, 2025, 198: 109373.

[42] 檀茜倩, 王丹, 程笑笑, 等. 虾酱源芽孢杆菌的筛选及其益生特性[J]. 中国食品学报, 2023, 23(12): 51-60.

（**责任编辑：**刘岭）

中国知网 https://www.cnki.net

邹杰，王琳，陈祺琦，何旭聪，黄金梅，孙天奕，苏宏飞 . 珊瑚源噻虫嗪降解菌的分离、鉴定及其降解特性研究［J］. 广东农业科学，2025，52（5）：130-143.

ZOU Jie, WANG Lin, CHEN Qiqi, HE Xucong, HUANG Jinmei, SUN Tianyi, SU Hongfei. Isolation, purification, structure characterization and biological activity of polysaccharide from *Rubi fructus*［J］. Guangdong Agricultural Sciences, 2025，52（5）：130-143.

珊瑚源噻虫嗪降解菌的分离、鉴定及其降解特性研究

邹　杰[1,2,3]，王　琳[2]，陈祺琦[1,2,3]，何旭聪[3]，黄金梅[3]，孙天奕[3]，苏宏飞[1,3]

（1. 广西大学资源环境与材料学院，广西 南宁　530004；2. 中国科学院南海海洋研究所 / 中国科学院热带海洋生物资源与生态重点实验室，广东 广州　510301；
3. 广西大学海洋学院，广西 南宁 530004）

摘　要：【目的】分离珊瑚共附生微生物中的潜在噻虫嗪降解菌，并解析其相关降解特性。【方法】以珊瑚为试验材料，将珊瑚源微生物在以噻虫嗪为唯一碳源的培养基进行 3 轮富集培养，利用高通量测序技术分析富集培养物的多样性、丰富度及群落组成；对富集培养物中的潜在噻虫嗪降解菌株进行分离、鉴定及其噻虫嗪降解能力测试，确定噻虫嗪降解目的菌株；通过目的菌株对噻虫嗪的降解产物鉴定及毒性预测解析其对噻虫嗪的降解特征。【结果】经 3 轮富集培养，得到能以噻虫嗪为唯一碳源利用的珊瑚源富集培养物。富集培养物的高通量测序结果表明随着富集时间的增加，珊瑚源的噻虫嗪降解微生物群落结构趋于复杂，群落结构分析结果表明 3 轮富集中变形菌门、厚壁菌门、拟杆菌门为优势菌门，γ- 变形菌纲、α- 变形菌纲为优势菌纲，弧菌属（*Vibrio*）、交替单胞菌属（*Alteromonas*）和 *Epibacterium* 为优势菌属。从第 3 轮富集培养物中分离得到 27 株潜在噻虫嗪降解菌株，根据菌株形态筛选出 GXU 22002、GXU 22003、GXU 22031、GXU 22040 4 株菌株，通过 16S rRNA 比对确定 4 株菌株分别为 *Serratia marcescens*、*Vibrio sagamiensis*、*V. neocaledonicus*、*V. alginolyticus*。4 株菌株对噻虫嗪的降解能力试验结果表明，*S. marcescens* GXU 22002、*V. sagamiensis* GXU 22003、*V. neocaledonicus* GXU 22031、*V. alginolyticus* GXU 22040 对噻虫嗪具有不同程度的降解活性，在培养 7 d 后对噻虫嗪降解率分别为 14.7%、16.3%、20.7%、9.9%。通过菌株 *V. sagamiensis* GXU 22003 对噻虫嗪的降解产物鉴定得出其降解噻虫嗪的主要产物为 TMX-urea、TMX-NH、H-CLO-tri、CLO-tri 4 种化合物。ECOSAR 软件分析显示降解产物对鱼、水蚤、藻类 3 种水生生物的急性毒性相比噻虫嗪减弱。【结论】成功从珊瑚中分离出 4 株潜在的噻虫嗪降解菌，并解析其降解特征，为噻虫嗪农药污染治理提供菌种资源和理论依据。

关键词：珊瑚；农药污染；噻虫嗪；群落结构；菌株分离；弧菌属；微生物降解

中图分类号：S482.3+7；X592　　**文献标志码**：A　　**文章编号**：1004-874X（2025）05-0130-14

Isolation, Identification and Degradation Characteristics Study of Thiamethoxam Degrading Bacteria from Coral

ZOU Jie[1,2,3], WANG Lin[2], CHEN Qiqi[1,2,3], HE Xucong[3], HUANG Jinmei[3], SUN Tianyi[3], SU Hongfei[1,3]

（1. *School of Resources, Environment and Materials, Guangxi University, Nanning* 530004, *China*;
2. *South China Sea Institute of Oceanology, Chinese Academy of Sciences / Key Laboratory of Tropical Marine Bio-resources and Ecology, Chinese Academy of Sciences, Guangzhou* 510301, *China*;
3. *School of Marine Sciences, Guangxi University, Nanning*, 530004, *China*）

Abstract: 【Objective】This study aimed to isolate the potential thiamethoxam-degrading bacteria from coral and

收稿日期：2025-02-09
基金项目：广西自然科学基金（2023GXNSFAA026388）
作者简介：邹杰（1999—），男，在读硕士生，研究方向为农药的微生物降解，E-mail：yzsjc0827@163.com
通信作者：苏宏飞（1984—），男，博士，副教授，研究方向为海洋生物资源开发与利用，E-mail：shf2016@gxu.edu.cn

中国知网 https://www.cnki.net

to analyze their degradation-related characteristics.【Method】Coral samples were used as the experimental material, the symbiotic microorganisms from corals were enriched and cultured for three rounds in a medium with thiamethoxam served as the sole carbon source. The diversity, richness, and community composition of the enriched microbial cultures were analyzed using high-throughput sequencing. The potential thiamethoxam-degrading strains were isolated, identified, and their thiamethoxam-degrading ability was evaluated to determine the target thiamethoxam-degrading strains. The degradation-related characteristics of thiamethoxam of the target strain by identifying degradation products of thiamethoxam and predicting their toxicity.【Result】Following three rounds of enrichment culture with thiamethoxam, coral symbionts that could utilize thiamethoxam as the sole carbon source were obtained high-throughput sequencing analysis of the enriched cultures revealed that their community structure of coral symbiotic thiamethoxam-degrading microorganisms .gained complexity with time. Further analysis revealed that within three rounds of enrichment, Proteobacteria, Firmicutes, Bacteroidota and Actinobacteriota were the dominant phyla; γ- and α-Proteobacteria were the predominant classes; *Vibrio, Alteromonas* and *Epibacterium* emerged as the preeminent genera. In total, 27 potential thiamethoxam-degrading strains were isolated from the third enrichment culture . Of these, four strains including GXU 22002, GXU 22003, GXU 22031, and GXU 22040 were screened morphologically . By comparing the 16S rRNA sequences, they were identified as *Serratia marcescens*, *Vibrio sagamiensis*, *V. neocaledonicus* and *V. alginolyticus*, respectively. The thiamethoxam-degradation ability tests indicated that these strains exhibited varying levels of degradation activity. *S. marcescens* GXU 22002, *V. sagamiensis* GXU 22003, *V. neocaledonicus* GXU 22031, and *V. alginolyticus* GXU 22040 had degradation rates of 14.7%, 16.3%, 20.7%, and 9.9%, respectively, after 7 days. An analysis of the thiamethoxam-degradation products by GXU 22003 confirmed the presence of four main degradation products: TMX-urea, TMX-NH, H-CLO-tri, and CLO-tri. An assessment by the ECOSAR software showed that the acute toxicity of the products against three aquatic organisms (fish, daphnia, and green algae) was weaker than that of the parent compound, thiamethoxam.【Conclusion】This study isolated potential thiamethoxam-degrading bacteria from coral samples, and determined their degradatio--associated characteristics, thereby providing valuable resource strains and a theoretical foundation for the control of pesticide pollution.

Key words: coral; pesticide pollution; thiamethoxam; community structure; strain isolation; *Vibrio*; microbial degradation

【研究意义】噻虫嗪（Thiamethoxam，THM）又名阿克泰，是一种具有全新结构的第 2 代新烟碱类杀虫剂[1]，具有剂量低、高效、内吸性好等优点，被广泛运用于农业害虫防治[2-4]。特有的 2- 氯 -1,3- 噻唑 -5- 基结构提高了噻虫嗪对咀嚼式和刺吸式口器害虫的触杀及胃毒活性[5]，可有效防治蚜虫、粉虱、潜叶蛾等害虫，使噻虫嗪成为水稻、小麦、蔬菜等农作物不可或缺的农药[6-7]。已有研究表明，噻虫嗪主要通过引起氧化应激、抑制酶活性、阻碍基因表达等方式起作用，可引起生物产生代谢紊乱、细胞衰亡、蛋白表达异常等中毒现象[8-9]。环境中噻虫嗪可能成为一种有机污染物，危害人类及其他非靶向生物的健康与安全，因此，如何安全有效地去除噻虫嗪污染成为当前亟需解决的问题。

【前人研究进展】目前降解水体中噻虫嗪的方法有物理法、化学法和生物降解法。物理法主要运用吸附技术，利用良好的吸附剂去除水体中的噻虫嗪[10-11]。化学法主要利用高级氧化技术，使用 Fenton（芬顿）、电化学、光催化等技术氧化噻虫嗪[12-14]。物理法和化学法去除噻虫嗪的成本相对较高，还可能产生二次污染。生物降解法主要利用微生物对污染物的催化和代谢作用，该方法具有成本低、代谢产物毒性低、无二次污染等优点。目前已有来自陆地土壤的微生物降解噻虫嗪的研究报道，如 Pandey 等[15]从土壤中分离的 1 株假单胞菌（*Pseudomonas* sp. 1G）可在 14 d 内降解 70% 噻虫嗪，可将噻虫嗪杂环部分含有的硝基还原为亚硝基、氨基、羰基，使噻虫嗪转化为毒性更弱的尿素类噻虫嗪代谢物；Zhou 等[16]从海南大豆种植区的根系菌中分离得到黏着剑菌（*Ensifer adhaerens*）TMX-23，该菌对噻虫嗪具有良好的降解能力，还可释放多种植物促生物质；Rana 等[17]从土壤分离得到恶臭假单胞菌（*P. putida*）IMBL 5.2 和嗜气芽孢杆菌（*Bacillus aeromonas*）IMBL 4.1，在降解试验开始的 15 d 后噻虫嗪降解率分别达 38% 和 45%。此外，海洋微生物种类丰富、数量繁多、分布广泛，已有

中国知网　https://www.cnki.net

研究发现海洋微生物在降解污染物方面展现出广阔的应用潜力[18-19]。其中，珊瑚礁生态系统具有丰富的生物多样性和生产力[20]，已证实其共附生微生物可在海洋特有的高盐、高压、低营养、低光照等极端条件下生存，在海水中或陆地上温度、pH、盐度等条件较为极端的地区的噻虫嗪污染治理方面更具应用潜力[21]。目前已有研究表明珊瑚源微生物可降解有机污染物。Saranya 等[22]从珊瑚中分离出 1 株能有效吸附 Cu、Cr、Zn 等重金属元素的菌株 *Cronobacter muytjensii* KSCAS2，其在陆地农田土壤重金属污染的防治展示出良好性能。Ansari 等[23]从珊瑚组织液富集获得的微生物能有效降解石油原油。Jayasree 等[24]从大堡礁的美丽鹿角珊瑚粘液中分离出 1 株菌株 *Photobacterium ganghwense* T14，其对氟氯氰菊酯的降解率可达 92.13%。黄沁愉等[25]从三亚鹿回头的近海海域珊瑚中分离出潜在的 EHMC（对甲氧基肉桂酸辛酯）降解菌。这些研究表明珊瑚蕴藏丰富的污染物降解微生物，极可能筛选出噻虫嗪降解菌。目前珊瑚礁区已出现严重的有机污染，对珊瑚生态造成巨大危害，如多环芳烃和多氯联苯的污染会导致珊瑚藻的光合色素含量下降、细胞膜透性和丙二醛含量增加，最终导致珊瑚藻停止生长[26]；除草剂 PSII 通过与特定蛋白结合抑制珊瑚光合电子传递，导致活性氧产生，进而干扰共生菌的光合作用，加剧氧化损伤，最终损害珊瑚的健康[27]；有机磷类除草剂草胺膦和草甘膦会抑制珊瑚氮相关代谢、共生细胞周期和营养相关基因的表达，干扰珊瑚的代谢、钙化和减数分裂等基本生理过程[28]。然而，在污染物存在的情况下，珊瑚并未出现大量死亡，可能是数量巨大、种类繁多的共附生微生物降解作用使珊瑚获得新的生存希望。

【本研究切入点】噻虫嗪随着大气、河流最终注入海洋，危害日益增加，因此寻找来源于海洋的降解菌，或许更能适应海水理化性质，对海洋农药污染治理更具前景。然而，目前报道的噻虫嗪降解菌均来源于陆地，尚未见从海洋环境中分离得到噻虫嗪降解菌的研究报道。因此本研究尝试从珊瑚源微生物中分离得到噻虫嗪降解菌，丰富噻虫嗪降解功能菌株资源。【拟解决的关键问题】本研究从珊瑚中富集培养噻虫嗪降解菌，分析富集培养物的群落组成与结构，然后分离培养获得潜在噻虫嗪降解菌，最后进行菌株鉴定、降解活性测定、降解产物鉴定及毒性预测等分析噻虫嗪降解特征，为挖掘噻虫嗪降解菌以治理海洋农药污染提供物质资源和理论依据。

1 材料与方法

1.1 试验材料

1.1.1 *珊瑚样品* 珊瑚样品于 2023 年 4 月采集自海南省三亚鹿回头近岸海域的珊瑚礁（18°13'N、109°29'E）。按照唐小玉等[29]方法用锤子敲取健康的鹿角杯形珊瑚（*Pocillopora damicornis*）样本，并保存于装有海水的无菌样品袋，送往广西南海珊瑚礁研究实验室用于后续研究。

1.1.2 *主要培养基及试剂* （1）人工海水培养基（MMC）：氯化钠 24.0 g/L，硫酸铵 1.0 g/L，氯化钾 0.7 g/L，磷酸二氢钾 2.0 g/L，磷酸氢二钠 3.0 g/L，七水合硫酸镁 3.5 g/L，ddH_2O 1 L，pH 7.4，121℃灭菌 25 min。灭菌后添加 1% 微量元素原液；微量元素原液配制方法参考文献［30］，配制好后用 0.22 μm 滤膜过滤。（2）Marine Agar 培养基（MA）：胰蛋白胨 5 g，酵母提取粉 1 g，葡萄糖 0.5 g，柠檬酸铁 0.05 g，陈海水 0.5 L，ddH_2O 0.5 L，pH 7.4；105℃灭菌 40 min。

噻虫嗪标准品（95%）购自上海麦克林生化科技股份有限公司；70% 噻虫嗪水分散粒剂购自山东贵合生物科技有限公司；扩增细菌 16S rRNA 基因的通用引物 27F（5'-AGRGTTTGATYNTGGCTCAG-3'）和 1492R（5'-TASGGHTACCTTGTTASGACTT-3'）由生工生物工程（上海）股份有限公司合成；OMEGA 细菌 DNA 提取试剂盒购自广州飞扬生物工程有限公司。

1.2 潜在噻虫嗪降解菌群的富集培养

以噻虫嗪为唯一碳源，按终浓度 100 mg/L 配制人工海水－噻虫嗪（MMC-THM）液体培养基。取 1 g 鹿角杯形珊瑚枝条装入 50 mL 离心管，往离心管加入 10 mL 无菌海水，振荡 20 s，静置 5 min 去除骨骼碎片。用三层棉纱过滤，收集液体于另一支 50 mL 离心管，8 000 r/min 离心 2 min。弃上清液，取沉淀物至 15 mL 离心管，

中国知网 https://www.cnki.net

加入 10 mL 无菌海水振荡涡旋，使沉淀物在无菌海水中重悬，然后 8 000 r/min 离心 2 min，重复以上步骤 2~3 次，获得珊瑚共附生微生物菌悬液。取 200 μL 菌悬液接种于 100 mL MMC–THM 液体培养基中，150 r/min 28 ℃ 避光条件下进行第 1 轮富集培养，培养至培养基中富集培养物 OD_{600} 无明显变化时，按 1% 接种量接种至新培养基继续第 2 轮富集。第 3 轮富集操作同第 2 轮。试验设置 3 个处理：试验组 TC 在含有噻虫嗪的培养基中添加珊瑚菌悬液，第 1~3 轮富集培养物分别标记为 TC–1、TC–2、TC–3；对照组 C 单一添加珊瑚菌悬液，不添加噻虫嗪；对照组 T 单一添加噻虫嗪样品，不添加珊瑚菌悬液。每个处理 3 次重复，所有处理按相同条件培养。

1.3　潜在噻虫嗪降解菌群的高通量测序

每轮富集结束时，收集 2 mL 培养液，使用 OMEGA 细菌 DNA 提取试剂盒提取细菌总 DNA，使用 1% 琼脂糖凝胶电泳和 NanoDrop 2000 验证 DNA 的纯度和浓度，检验条带单一且浓度合格的总 DNA 样品送至上海凌恩生物科技有限公司进行微生物组高通量测序。数据分析步骤如下：首先利用 DADA2 方法从 QIIME2（V2020.6）中处理的 Reads 中提取扩增子序列变异（Amplicon sequence variant，ASVs，P<0.05）[31]；然后使用 Bayes 注释方法进行物种注释，利用 QIIME 软件估算微生物群落的 α 多样性指数，生成不同分类水平上的物种丰度表。

1.4　潜在噻虫嗪降解菌的分离培养

取 200 μL 第 3 轮富集培养液，涂布于含有 100 mg/L 噻虫嗪的 MMC–THM 固体培养基上，25 ℃避光培养 3 d。根据平板上单菌落的形态，挑取不同单菌落至含有 100 mg/L 噻虫嗪的 MMC–THM 固体培养基上进行划线分离纯化，于 25 ℃避光培养 3 d。对生长在 MMC–THM 固体培养基上的单菌落接种至 MA 固体培养基划线分离，对单菌落经过 2~3 次分离纯化后得到细菌纯培养物，获得潜在噻虫嗪降解菌株，并用 20% 甘油于 –80 ℃保藏。

1.5　潜在噻虫嗪降解菌的鉴定和系统进化分析

使用细菌基因组 DNA 提取试剂盒提取潜在降解菌的基因组 DNA，使用细菌通用引物 27F（5'–AGAGTTTGATCCTGGCTCAG–3'）和 1492R（5'–ACGGCTACCTTGTTACGACT–3'）进行 PCR 扩增。反应体系：模板 1.0 μL、27F 引物 1.0 μL、1492R 引物 1.0 μL、*Taq* 酶 12.5 μL、ddH_2O 9.5 μL，总共 25.0 μL。反应条件：95 ℃ 5 min，94 ℃ 30 s、55 ℃ 40 s、72 ℃ 90 s、30 个循环，72 ℃ 10 min。将 PCR 扩增产物送至生工生物工程（上海）股份有限公司完成测序。在 NCBI（https://www.ncbi.nlm.nih.gov）和 Ezbiocloud（https://eztaxon–e.ezbiocloud.net/）进行基因序列比对，根据序列比对结果选取具有较高同源性菌株的 16S rRNA 基因作为参照序列，使用 MEGA11 软件，以自展值为 1 000 次采用邻接法（Neighbor–Joining，N–J）进行聚类分析并构建系统发育树[32]。

1.6　噻虫嗪降解率测定

用 0.85% 生理盐水制备潜在噻虫嗪降解菌株的菌悬液，按 1% 接种量接种至 10 mL 含 100 mg/L 噻虫嗪的 MMC–THM 培养基中，25 ℃、160 r/min 振荡培养 7 d，以添加等量无菌生理盐水为对照组，测定菌株对噻虫嗪的降解率。培养结束后取各试验组的培养液 2 mL，置于分液漏斗中，加入 4 mL 二氯甲烷，剧烈振荡 5~6 次后静置分层。弃去上层水相，有机相加入适量无水硫酸钠脱水。取 1 mL 脱水后的有机相转移至 2 mL 离心管，使用氮吹仪将有机相吹干。加入 1 mL 乙腈（色谱纯）溶解，经 0.22 μm 有机尼龙微孔滤膜过滤后置于 2 mL 色谱进样瓶。用封口膜封好口后置于 4 ℃保存，供高效液相色谱（HPLC）检测[33]。HPLC 检测条件：流动相为 0.1% 甲酸（V/V）的乙腈：水（25 ∶ 75），色谱柱为 C18（250 mm × 4.6 mm，5 μm），进样量 20 μL，检测波长 251 nm，柱温 25 ℃，流速 1.0 mL/min。降解率计算公式如下：

$$降解率（\%）=〔（C_0 - C）/ C_0〕\times 100$$ [15]

式中，C_0 为对照组噻虫嗪浓度（mg/L），C 为试验组噻虫嗪残留浓度（mg/L）。

称取 10 mg 噻虫嗪标准品，用甲醇作为溶剂配制成浓度为 1 000 mg/L 噻虫嗪母液，用甲醇稀释配制浓度为 1、5、10、20、50、100 mg/L 的噻虫嗪标准溶液，参照上述方法测定其在 HPLC 的峰面积，制作标准曲线。

中国知网　https://www.cnki.net

1.7 噻虫嗪降解菌降解产物鉴定和毒性预测

噻虫嗪降解菌株培养液经二氯甲烷萃取后用乙腈定容至 1 mL，培养液中噻虫嗪降解产物的液相色谱－质谱联用（LC-MS）分析委托安徽春丰里检测科技有限公司完成。LC 参数：色谱柱为 Agilent EP-C18（2.1 mm × 100 mm，1.8 μm），进样体积为 20 μL，柱温为 40℃，波长为 251 nm。流动相：A 为 0.1% 甲酸水，B 为乙腈。流速：0.2 mL/min。梯度洗脱程序：0~1 min，5% B；1~7 min，5% → 95% B；7~12 min，95% B；12~17 min，95% → 5% B；17~22 min，5% B。MS 参数：离子源为 ESI（电喷雾电离源），模式为 MS2 Scan，极性为 Positive，m/z 范围为 50~600。使用 ECOSAR 软件对噻虫嗪降解产物进行毒性预测，预测噻虫嗪降解产物对鱼类、水蚤、藻类 3 种水生生物的急性毒性。

1.8 数据分析方法

使用 SPSS 27.0 软件对试验数据进行统计分析，以 P=0.05 为临界值，使用单因素方差分析方法（*ANOVA*）进行差异显著性分析。

2 结果与分析

2.1 噻虫嗪降解菌的富集生长情况

在 3 轮以噻虫嗪为唯一碳源的富集培养过程中，试验组 TC 样品的 3 轮富集培养细菌密度呈现增长趋势，其中前 2 轮富集培养物的 OD_{600} 增长尤为突出，从初始的 0.03 增长至 0.26。第 1 轮富集中，富集培养物的 OD_{600} 在培养第 6 天达到最高值；第 2 轮富集中，培养物的 OD_{600} 在培养第 4 天达到最高值，在第 6 天以后 OD_{600} 在 0.22 左右平稳。微生物生长速度在前 2 轮富集培养中相对较快、OD_{600} 最高达 0.2 以上，第 3 轮富集有所减缓、但均高于 0.1。相同条件下，单一添加噻虫嗪对照组 T 与单一添加珊瑚微生物对照组 C 的 OD_{600} 则几乎无变化（图 1）。可见，珊瑚噻虫嗪富集培养物中的微生物并非自养细菌，培养基的吸光度变化是由细菌自身变化引起，表明珊瑚源微生物可利用噻虫嗪为唯一碳源生长，具有潜在的噻虫嗪降解作用。

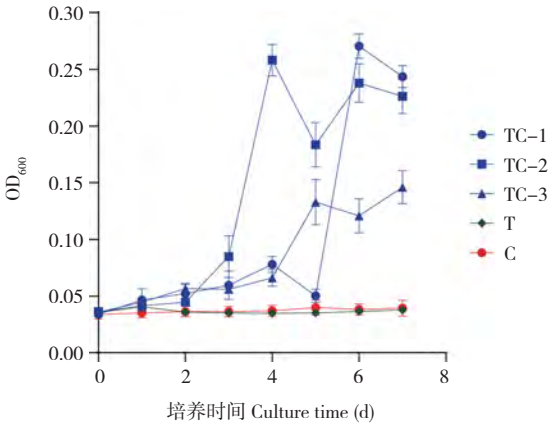


图 1 噻虫嗪富集培养物的细菌生长曲线

Fig. 1 Bacterial growth curve of thiamethoxam-enrichment samples

2.2 噻虫嗪富集培养物高通量测序分析

2.2.1 噻虫嗪富集培养物 α 多样性分析 通过 Chao1、ACE、Shannon、Simpson 等指标反映富集培养物样本内部的物种丰富度和多样性。测序结果分析发现，3 轮富集培养物的 Chao1 指数和 ACE 指数范围介于 163~177，第 2 轮富集培养物的 Chao1 指数和 ACE 指数的数值在 3 轮富集培养物中最高（表 1），表明在富集过程中细菌群落物种丰富度先增加后减少，但丰富度总体较低且差异较小。3 轮富集培养物的 Shannon 指数范围在 2.09~2.22，Simpson 指数也在 0.75~0.82 波动，其中第 3 轮富集培养物的 Shannon 指数和 Simpson 指数比前 2 轮富集大。可见，3 轮富集培养物的 Simpson 和 Shannon 指数值不高且差异较小，表明 3 轮富集培养物的物种多样性较低且差异不显著。

表 1 噻虫嗪富集样品的微生物群落多样性指数

Table 1 Diversity indexes of microbial communities isolated from thiamethoxam-enrichment samples

样品 Samples	Chao1 指数 Chao1 index	ACE 指数 ACE index	Shannon 指数 Shannon index	Simpson 指数 Simpson index
TC-1	168.34	166.11	2.09	0.76
TC-2	169.50	176.68	2.12	0.75
TC-3	163.68	169.86	2.22	0.82

2.2.2 噻虫嗪富集培养物微生物群落结构分析 珊瑚共附生微生物以噻虫嗪为唯一碳源富集培养所得样品经高通量测序，按照 97% 相似度进行 OTU 聚类并划分物种分类，共归属为 11 门 16 纲 37 目 62 科 90 属（表 2）。3 轮富集培养后，试验组 TC 在门、纲、目、科、属等各分类水平上

中国知网 https://www.cnki.net

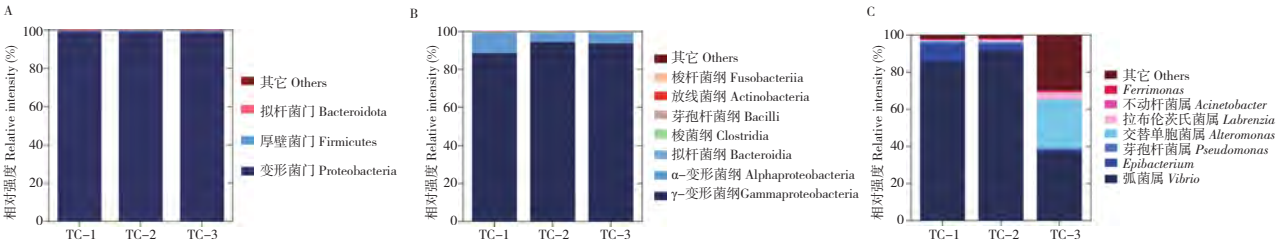
表 2　噻虫嗪富集样品中不同水平上的细菌种类数目

Table 2　Number of bacteria species at different levels in thiamethoxam–enrichment samples

样品 Samples	门 Phylum	纲 Class	目 Order	科 Family	属 Genus
TC–1	8	11	28	47	59
TC–2	8	11	29	51	67
TC–3	9	13	27	44	63

的细菌种类数目趋于平稳。在群落结构方面，在高浓度噻虫嗪驯化条件下，富集培养物在门水平和纲水平的组成无较大变化，但属水平的结构随着富集时间的推移而趋于复杂（图 2）。

在门水平上（图 2A），3 轮富集培养物菌群中变形菌门（Proteobacteria）、厚壁菌门（Firmicutes）、拟杆菌门（Bacteroidota）和放线



A：门水平；B：纲水平；C：属水平

A: Phylum level; B: Class level; C: Genus level

图 2　噻虫嗪富集样品细菌群落分布

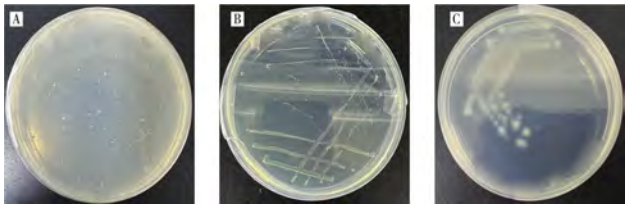
Fig. 2　Distribution of bacterial community in thiamethoxam–enrichment samples

菌门（Actinobacteriota）为优势菌门（相对丰度 > 0.1%），其中变形菌门占据绝大优势。在纲水平上（图 2B），3 轮富集培养物菌群中主要包括 γ–变形菌纲（Gammaproteobacteria）、α–变形菌纲（Alphaproteobacteria）、拟杆菌纲（Bacteroidia）、梭菌纲（Clostridia）、芽孢杆菌纲（Bacilli）等，其中 γ–变形菌纲与 α–变形菌纲为 3 轮富集培养物中的优势菌纲；α–变形菌纲的相对丰度为 TC–1>TC–3>TC–2，随着富集时间的推移呈先减后增的趋势。在属水平上（图 2C），以相对丰度 ≥ 5% 的属为优势属，3 轮富集培养物中的优势菌群为弧菌属（*Vibrio*）、*Epibacterium*、交替单胞菌属（*Alteromonas*），其中 *Epibacterium* 仅在第 1 轮富集过程中为优势菌属。*Epibacterium* 在第 1 轮富集中的相对丰度为 10.12%，随着富集次数的增加占比趋于减小，至第 3 轮富集时相对丰度仅 0.98%；交替单胞菌属在第 1、2 轮富集中的相对丰度仅为 0.49% 和 0.22%，至第 3 轮富集中相对丰度提高至 26.16%；弧菌属随着富集次数的增加占比先缓慢上升然后大幅下降，但在 3 轮富集中仍为优势菌属。

2.3　噻虫嗪降解菌株的分离培养与鉴定

对第 3 轮富集培养物进行涂布和划线培养以获得单株噻虫嗪潜在降解菌株。取第 3 轮富集培养液在 MMC–THM 固体培养基涂布 3 d，培养后在平板上生成大小不一致的白色圆形菌落（图 3A）。挑取 MMC–THM 平板上较大的单菌落至 MMC–THM 固体培养基继续划线培养 3 d，平板上的单菌落呈圆形，直径 1.5 mm 左右，乳白色（图 3B）。挑取 MMC–THM 固体培养基上的单菌落至 MA 固体培养基划线培养 3 d，平板上的单菌落呈圆形、乳白色、直径 0.5 cm 左右，周围有半透明光圈，边缘不整齐边，中间无隆起（图 3C）。

经筛选共分离出 27 株菌株，根据菌株生长形态选取 4 株菌株分别提取 16S rRNA，在 NCBI



A：MMC–THM 固体培养基（涂布）；B：MMC–THM 固体培养基（第 1 轮划线）；C：MA 固体培养基（第 2 轮划线）

A: MMC–THM solid medium (coating); B: MMC–THM solid medium (the first round of streaking); C: MA solid medium (the second round of streaking)

图 3　噻虫嗪潜在降解菌株在固体培养基上的分离情况

Fig. 3　Isolation of potential thiamethoxam degrading strains on solid medium

中国知网　https://www.cnki.net

和 Ezbiocloud 上在线比对，选取同源性较高的序列采用邻接法构建系统发育树。由表 3 和图 4 可知，菌株 GXU 22002 与 *Serratia marcescens* ATCC 13880 为同一簇，序列相似度为 98.75%；菌株 GXU 22003 与 *V. sagamiensis* LC2–047 的序列相似度为 98.77%；菌株 GXU 22031 与 *V. neocaledonicus* NC470 为同一簇，序列相似度为 99.65%；菌株 GXU 22040 与 *V. alginolyticus* CX–31 为同一簇，序列相似度为 99.21%。因此，将菌株 GXU 22002 鉴定为 *S. marcescens*，菌株 GXU 22003 鉴定为 *V. sagamiensis*，菌株 GXU 22031 鉴定为 *V. neocaledonicus*，菌株 GXU 22040 鉴定为 *V. alginolyticus*。

表 3 潜在噻虫嗪降解菌株信息

Table 3 Information of potential thiamethoxam–degradating strains

菌株 Strains	相似性高的菌株（序列号）Closest organism in GenBank (Accession No.)	相似度 Similarity (%)
GXU 22002	*Serratia marcescens* ATCC 13880 (JMPQ01000005)	98.75
GXU 22003	*Vibrio sagamiensis* LC2–047 (AB428909)	98.77
GXU 22031	*Vibrio neocaledonicus* NC470 (JQ934828)	99.65
GXU 22040	*Vibrio alginolyticus* CX–31 (MH368375)	99.21

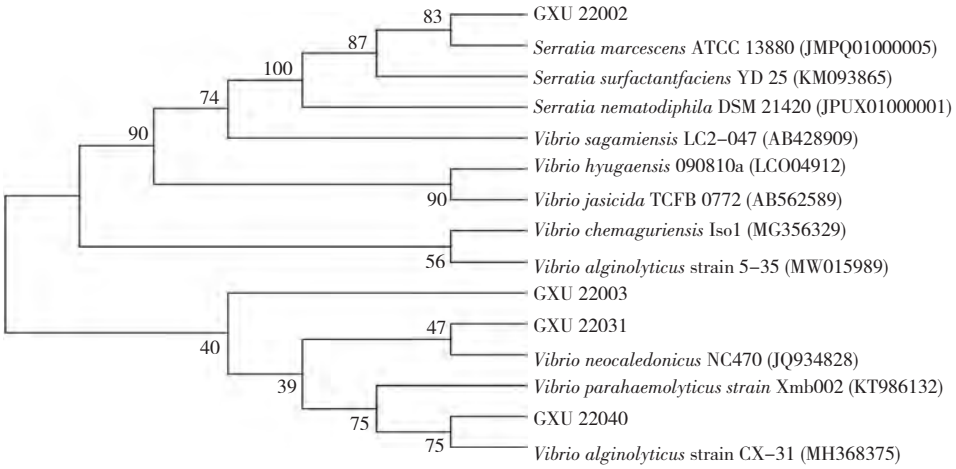


图 4 潜在噻虫嗪降解菌株系统发育树

Fig. 4 Phylogenetic tree of potential thiamethoxam degrading strains

2.4 噻虫嗪降解菌株的降解活性测试

以噻虫嗪浓度为横坐标、峰面积为纵坐标制作噻虫嗪的标准曲线（图 5）。标准曲线回归方程为 y=65.90x–0.01370，R^2=0.9995，线性关系良好。

使用 HPLC 测定潜在噻虫嗪降解菌株对噻虫嗪的降解率，结果（图 6）显示 4 株潜在噻虫嗪降解菌对噻虫嗪均有一定降解能力，其中菌株 *V. neocaledonicus* GXU 22031 对噻虫嗪的降解能力最好，降解率为 20.7%；其次是菌株 *V. sagamiensis* GXU 22003，降解率为 16.3%；菌株 *S. marcescens* GXU 22002 和菌株 *V. alginolyticus* GXU 22040 对噻虫嗪的降解率分别为 14.7% 和 9.9%。其中，菌株 *S. marcescens* GXU 22002 与菌株 *V. sagamiensis* GXU 22003 对噻虫嗪的降解率无显著差异（P>0.05），其余菌株对噻虫嗪的降解能力均存在显著差异（P<0.05）。

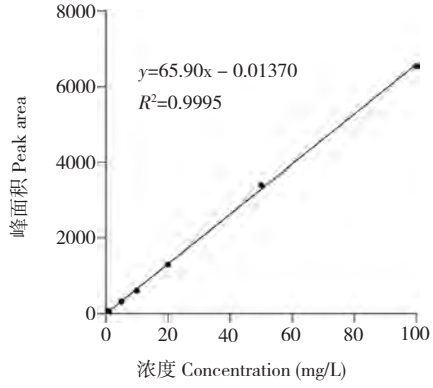


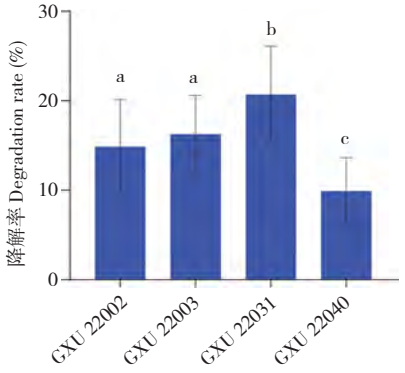
图 5 噻虫嗪标准曲线

Fig. 5 Standard curve of thiamethoxam

2.5 噻虫嗪降解产物鉴定及毒性预测

虽然 *V. neocaledonicus* GXU 22031 对噻虫嗪的降解率在 4 株菌株中最高，但 *V. neocaledonicus*

中国知网 https://www.cnki.net



小写英文字母不同者表示差异显著（$P<0.05$）

Different lowercase letter indicate significant differences ($P<0.05$)

图 6　4 株潜在噻虫嗪降解菌对噻虫嗪的降解率

Fig. 6　Degradation rate of thiamethoxam by four potential thiamethoxam degrading strains

会危害环境，对水生生物具有一定的致病性[34]，因此选择对噻虫嗪降解率仅次于 *V. neocaledonicus* GXU 22031 的菌株 *V. sagamiensis* GXU 22003 作进一步试验。通过 LC–MS 检测并分析菌株 *V. sagamiensis* GXU22003 降解噻虫嗪的产物，检测到 4 种降解产物并分析出其具体的分子结构（图 7）。降解产物 A 的分子式为 $C_8H_{10}ClN_3O_2S$，m/z 为 247.9【M+H】$^+$，为脲类噻虫嗪代谢物（Urea thiamethoxam，TMX–urea）；降解产物 B 的分子式为 $C_8H_{11}ClN_4OS$，m/z 为 246.2【M+H】$^+$，为亚胺类噻虫嗪代谢物（Imine thiamethoxam，THX–NH）；降解产物 C 和 D 的分子式分别为 $C_9H_{12}ClN_5OS$ 和 $C_9H_{10}ClN_5OS$，m/z 为 274.2【M+H】$^+$ 和 272.2【M+H】$^+$，分别为羟基三嗪类噻虫胺衍生物（Hydroxyl clothianidin triazinones，H–CLO–tri）和三嗪类噻虫胺衍生物（Clothianidin triazinones，CLO–tri）。

采用 ECOSAR 软件对噻虫嗪的 4 种降解产物进行其对鱼类、水蚤和藻类 3 种水生生物的急性毒性预测（表 4）。全球化学品统一分类与标签制度（Globally Harmonized System of Classification and Labelling of Chemicals，GHS）是全球使用范围最为广泛的化学品毒性分类制度，其在表示化

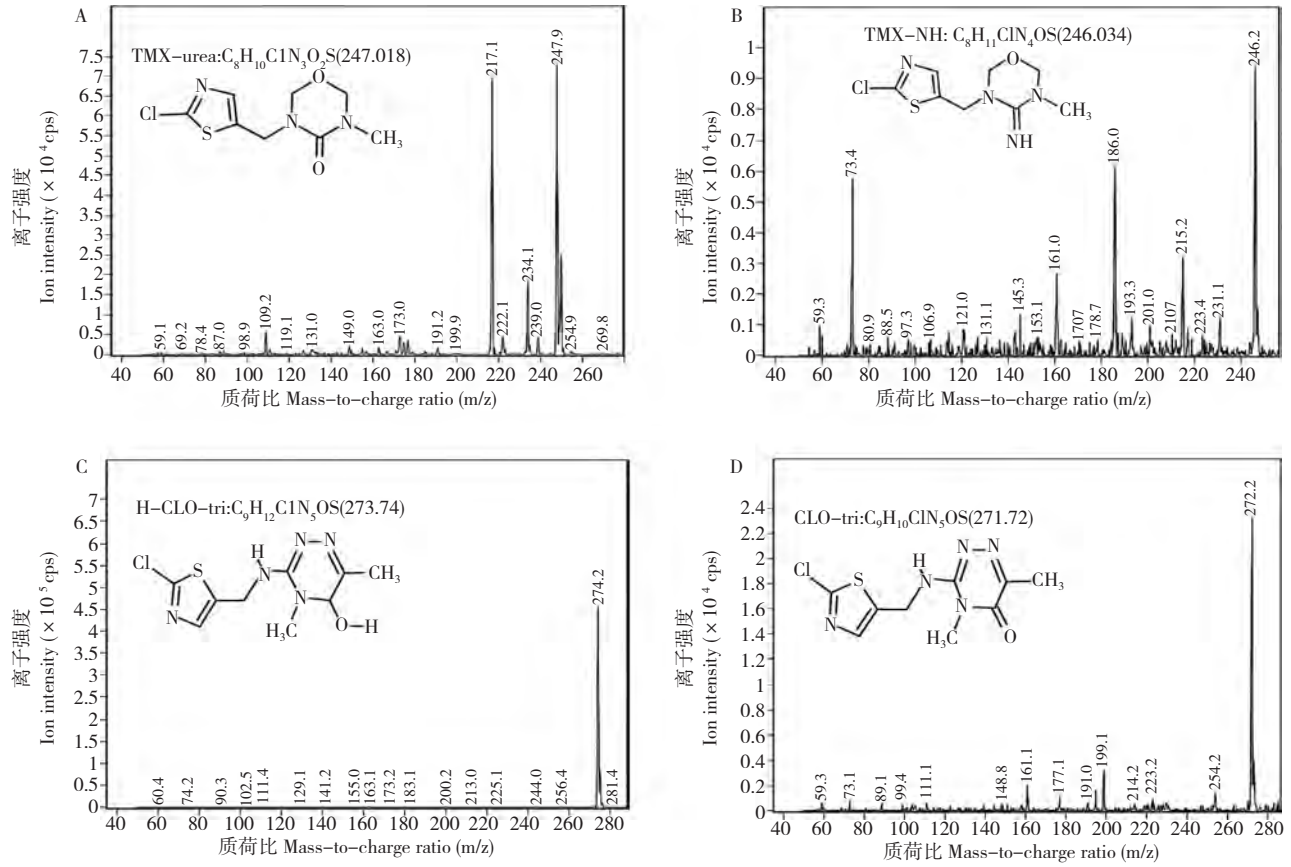


图 7　4 种噻虫嗪降解产物的 LC–MS 图谱

Fig. 7　LC–MS spectrum of four thiamethoxam degradation products

中国知网　https://www.cnki.net

表 4 噻虫嗪代谢产物的毒性预测

Table 4 Toxicty prediction of thiamethoxam metabolites

生物 Organisms	LC_{50} (EC_{50}) (mg/L)				
	THM	TMX-urea	TMX-NH	H-CLO-tri	CLO-tri
鱼类 Fish	345.80	582.86	288.07	1422.02	35.56
水蚤 Daphnia	35.84	329.67	29.89	131.56	4.37
藻类 Green algae	39.00	0.99	32.45	179.22	3.40

注：鱼类急性毒性指标为 96-h LC_{50}；水蚤急性毒性指标为 48-h LC_{50}；藻类急性毒性指标为 96-h EC_{50}。

Note: Acute toxicity of fish: 96-h LC_{50}; Acute toxicity of daphnia: 48-h LC_{50}; Acute toxicity of green algae: 96-h EC_{50}.

学品对水生生物的毒性方面具有一定的权威[35]。根据 GHS 的急性毒性分类，LC_{50}（EC_{50}）> 100 mg/L 为未分类（微毒），10 mg/L<LC_{50}（EC_{50}）≤ 100 mg/L 为急性 3 类（低毒），1 mg/L<LC_{50}（EC_{50}）≤ 10 mg/L 为急性 2 类（中毒），LC_{50}（EC_{50}）≤ 1 mg/L 为急性 1 类（高毒）。通过菌株 *V. sagamiensis* GXU 22003 对噻虫嗪的生物降解作用，噻虫嗪降解产物的毒性相较于噻虫嗪本身有所下降，尤其是产物 H-CLO-tri，对鱼类、水蚤、藻类的 LC_{50}（EC_{50}）分别为 1 422、132、179 mg/L。藻类暴露在 TMX-urea 溶液中 96 h 后的 EC_{50} 为 0.99 mg/L，尽管 TMX-urea 对鱼类和水蚤的毒性不高，TMX-urea 仍不可归类为无害物质。代谢物 CLO-tri 对 3 种水生生物的毒性相比其他 3 种代谢物高，但能进一步降解生成毒性较低的 H-CLO-tri，即使 CLO-tri 毒性高于噻虫嗪本身，但其进一步降解后的产物毒性明显低于噻虫嗪。

3 讨论

噻虫嗪是目前使用最广泛的新烟碱农药之一，其在农业施用过程中大部分未被农作物吸收，而是直接进入土壤和大气，经雨水冲刷进入地表径流，从而污染河流、湖泊、海洋等水体环境[36-37]。目前淡水及海水水体均已检测出噻虫嗪，最高浓度可达 281 ng/L[38-41]。已有研究发现斑马鱼[5]、中华蟾蜍蝌蚪[42]、鲫鱼[43]等水生生物均受到噻虫嗪毒害，出现氧化代谢功能异常和抗氧化系统混乱等功能障碍。噻虫嗪可通过食物链积累进入人体，对人体健康产生危害。人体摄入噻虫嗪后会出现发烧、定向障碍、头晕和呕吐、心动过速、呼吸急促等中毒症状[44-46]。长期暴露在噻虫嗪环境对人类的免疫功能、血液循环和生殖系统等均造成不利影响[9, 47]。

黄沁愉等[25]研究发现，原始珊瑚共附生微生物样品的 α 多样性指数较大，但经过 3 轮以有机紫外吸收剂 EHMC 为唯一碳源的培养基富集培养后，样品的 α 多样性指数显著下降，表明在高浓度 EHMC 驯化条件下物种的多样性和丰富度下降。此研究中 EHMC 富集培养物的 4 种 α 多样性指数与本研究中的数值相近，本研究中富集培养物 α 多样性指数较低，原因可能为高浓度的噻虫嗪抑制了珊瑚共附生微生物的丰富度与多样性。但与本研究略有不同的是，经 EHMC 多次驯化后，珊瑚共附生微生物的群落结构趋于简单，本研究与其产生差异的原因可能为本研究中富集培养物的部分菌群在污染物达到一定浓度或接触污染物达到一定时间时激发了其对污染物的降解利用能力[48]。在污染物长期胁迫条件下，环境中微生物群落结构会显著改变[49]。高浓度噻虫嗪导致抗逆性较弱的细菌逐渐消亡，对噻虫嗪具有较高耐受性的细菌则产生应对噻虫嗪的策略，逐渐在菌群中占据主导地位，这些菌群可能为潜在的噻虫嗪降解菌。

前人研究发现，健康珊瑚共附生微生物群落的主要菌属为弧菌属、交替单胞菌属、芽孢杆菌属、假单胞菌属、假交替单胞菌属等[25, 50]，而本研究中在经过噻虫嗪第 3 轮富集后的珊瑚共附生微生物优势菌属仅有弧菌属和交替单胞菌属，表明弧菌属和交替单胞菌属的细菌对噻虫嗪的耐受性较强，具有较大的噻虫嗪降解潜力。来自海洋的交替单胞菌属细菌能降解广泛存在于海洋中的甲基汞和芘等有机污染物[51-52]；弧菌属细菌被发现具有降解褐藻胶、几丁质等有机物的能力[53-54]，并被发现能降解在海洋中难降解的有机污染物聚丁二酸丁二醇酯（PBS）[55]。研究发现，沙雷氏菌（*Serratia*）能降解毒死蜱和溴氰菊酯等农药[56-57]，本次研究也首次发现其具有降解噻虫嗪的潜力。弧菌属细菌被成功分离出来，印证了富集培养试验中其具有噻虫嗪降解潜力的结果。弧菌具有一定生物致病性[58]，未来可通过基因改造降低菌株潜在的致病性[59]，

中国知网 https://www.cnki.net

或通过宏基因组分析菌株降解噻虫嗪的功能基因从而提取出具有噻虫嗪降解活性的酶[55]。在第3轮富集培养物中占有优势的交替单胞菌属细菌未被分离出来，这可能与本研究选用的筛选培养基有关。在以往的研究中分离出交替单胞菌属细菌的培养基有 LB 培养基[60]、2216E 培养基[61]以及 MSM 培养基[51]等，培养基的营养成分对可培养细菌的数量及种类具有重要影响[62]。而本研究使用以噻虫嗪为唯一碳源的 MMC 培养基和 MA 固体培养基作为分离培养基，可能不利于交替单胞菌的分离。在其他研究中已经针对芳香烃、氟氯氰菊酯等有机污染物进行珊瑚共附生微生物的驯化富集并获得对于对应底物耐受性大的菌群，成功分离出具有降解对应底物能力的功能菌株[24, 63]。因此，从珊瑚中分离可降解噻虫嗪的微生物具有可行性。

在以往的研究中，报道的噻虫嗪降解菌对噻虫嗪的降解率在 38%~87%[15-17]，与本研究的降解结果有较大的差异，这可能是由微生物来源、培养方法及条件、样品采集地等试验参数不同导致的。因此虽然本研究分离出的噻虫嗪降解菌对噻虫嗪的降解率较低，但仍有优化其降解率的空间。有研究对培养条件进行优化或对菌株进行改造，从而使菌株降解有机物的能力得到大幅优化。例如，Boufercha 等[64]从工业园区的沉积物分离出的菌株 *Labrys portucalensis* F11 在以噻虫嗪为唯一碳源的条件下培养 30 d 后对噻虫嗪的降解率为 43%，在培养基添加醋酸钠后对噻虫嗪的降解率达到 100%；Xiang 等[65]使用新型的聚乙烯醇 – 海藻酸钠 – 生物炭固定技术使噻虫嗪降解菌 *Chryseobacterium* sp. H5 固定化，固定后的菌株在 7 d 内对噻虫嗪的降解率为 90.47%，远高于固定前菌株对噻虫嗪的降解率（61.72%）。因此为提高珊瑚共附生噻虫嗪降解菌对噻虫嗪的利用能力，还需要进一步了解菌株最佳的生长条件及其对噻虫嗪的最佳降解条件，通过设计单因素试验与正交试验等菌株生长条件优化试验提升菌株对噻虫嗪的降解率。

Pandey 等[15]通过 LC–MS 鉴定出噻虫嗪通过脱氮生成 TMX–urea、TMX–NH、TMX–NNO（Nitrosoguanidine thiamethoxam）和 TMX–NH_2（Aminoguandine thiamethoxam）4 种代谢物，Zhou 等[14]通过 LC–MS 鉴定出噻虫嗪通过裂解恶二嗪环生成噻虫胺（Clothianidin，CLO）、CLO–tri 和 H–CLO–tri 3 种代谢物。这两项研究结果分别代表噻虫嗪的两个主要的降解途径，本研究中鉴定出的降解产物与这些研究一致，表明本研究中菌株 *V. sagamiensis* GXU 22003 对噻虫嗪的降解途径有可能为脱氮和裂解恶二嗪环。Boufercha 等[64]在使用菌株 *L. portucalensis* F11 处理后，从含噻虫嗪的无机盐培养基中检测出 12 种噻虫嗪代谢产物，这些产物包括本研究中检测出的 4 种噻虫嗪降解产物；同时测试该菌株处理前后的培养基对费氏另类弧菌（*Aliivibrio fischeri*）的毒性作用，结果显示处理前的培养基显著抑制费氏另类弧菌发光，而处理后的培养基则无抑制作用，由此推测本研究检测出的 4 种噻虫嗪降解产物对生物的毒性较小。由于本研究尚未鉴定出更多噻虫嗪的代谢产物，因此无法完全确定菌株 *V. sagamiensis* GXU 22003 对噻虫嗪的降解途径。但已明确菌株 *V. sagamiensis* GXU 22003 对噻虫嗪的降解产物对环境的危害与毒性相对较小，其可被视为有潜力运用于实际环境中噻虫嗪污染治理的功能菌株。

4　结论

对珊瑚共附生微生物进行 3 轮噻虫嗪胁迫下的富集，得到能以噻虫嗪为唯一碳源利用的富集培养物。高通量测序发现噻虫嗪富集培养物主要菌群有弧菌属、交替单胞菌属、*Epibacterium*，其中弧菌属和交替单胞菌属在 3 轮富集后对噻虫嗪具有较大的耐受能力。此外，在富集培养物菌群中筛选出 4 株噻虫嗪降解细菌，分别为 *S. marcescens* GXU 22002、*V. sagamiensis* GXU 22003、*V. neocaledonicus* GXU 22031、*V. alginolyticus* GXU 22040，接种 7 d 后对噻虫嗪的降解率分别为 14.7%、16.3%、20.7%、9.9%。通过 LC–MS 分析菌株 *V. sagamiensis* GXU 22003 降解噻虫嗪的降解产物，结果表明该菌株可将噻虫嗪降解为 TMX–urea、TMX–NH、H–CLO–tri、CLO–tri，这 4 种降解产物的毒性相比噻虫嗪有所减弱。综上，本研究首次从南海海域珊瑚中成功分离获得潜在

中国知网　https://www.cnki.net

的噻虫嗪降解菌资源，为噻虫嗪的生物降解技术提供新的方向。

参考文献（References）：

[1] 巩文雯, 刘庆菊, 胡彬, 王纪华, 韩平 . 农产品中新烟碱类杀虫剂噻虫嗪残留分析研究进展[J]. 广东农业科学, 2017, 44(12): 103–109. DOI: 10.16768/j.issn.1004–874X.2017.12.016.
GONG W W, LIU Q J, HU B, WANG J H, HAN P. Research progress of determination of neonicotinoid insecticide thiamethoxam residues in agricultural products[J]. *Guangdong Agricultural Sciences*, 2017, 44(12): 103–109. DOI: 10.16768/j.issn.1004–874X.2017.12.016.

[2] 张国生, 侯广新 . 烟碱类杀虫剂的应用、开发现状及展望 .[J]. 农药科学与管理, 2004(3): 22–26.DOI: 10.3969/j.issn.1002–5480.2004.03.009.
ZHANG G S, HOU G X. Present status of development and prospect of nicotinoid insecticides[J]. *Pesticide Science and Administration*, 2004(3): 22–26. DOI: 10.3969/j.issn.1002–5480.2004.03.009.

[3] 须志平 . 新烟碱类杀虫剂在作物保护方面的应用[J]. 世界农药, 2009, 31(1): 18–21. DOI: 10.3969/j.issn.1009–6485.2009.01.006.
XU Z P. The application of neonicotinoid insecticides in crop protection[J]. *World Pestcides*, 2009, 31(1): 18–21. DOI: 10.3969/j.issn.1009–6485.2009.01.006.

[4] 孙东磊, 赵欢欢, 安玉兴, 付建涛, 卢颖林, 陈立君, 戴思行, 龚恒亮 . 3 种新烟碱类杀虫剂对甘蔗螟虫的活性及防治效果[J]. 广东农业科学, 2017, 44(6): 109–113. DOI: 10.16768/j.issn.1004–874X.2017.06.016.
SUN D L, ZHAO H H, AN Y X, FU J T, LU Y L, CHEN L J, DAI S X, GONG H L. Toxicity and field efficacy of three kinds of neonicotinoid insecticides to sugarcane borer[J]. *Guangdong Agricultural Sciences*, 2017, 44(6): 109–113. DOI: 10.16768/j.issn.1004–874X.2017.06.016.

[5] 陈爱梅 . 吡虫啉和噻虫嗪对斑马鱼氧化胁迫及 DNA 损伤[D]. 泰安 : 山东农业大学, 2013.
CHEN A M. Oxidative stress and DNA damage induced by imidacloprid and thiamethoxam exposure in zebra–fish (*Danio rerio*)[D]. Tai'an: Shandong Agricultural University, 2013.

[6] 李萍, 方向群, 毕璋友, 陈春秋 , 章守富 . 南方水稻黑条矮缩病药剂防治效果试验[J]. 广东农业科学, 2015, 42(21): 97–101. DOI: 10.16768/j.issn.1004–874X.2015.21.015.
LI P, FANG X Q, BI Z Y, CHEN C Q, ZHANG S F. Control effect of pesticides against southern rice black–streaked dwarf disease[J]. *Guangdong Agricultural Sciences*, 2015, 42(21): 97–101. DOI: 10.16768/j.issn.1004–874X.2015.21.015.

[7] MENANDRO N A. Toxicity of thiamethoxam against Philippine subterranean termites[J]. *Journal of Insect Science,* 2007, 7(1): 1–6 DOI: 10.1673/031.007.2601.

[8] 刘佳涵, 张秀霞, 张泽龙, 郑佩华, 李军涛, 冼健安, 鲁耀鹏 . 新烟碱类杀虫剂对非靶标水生动物的毒性作用研究进展J]生态毒理学报, 2025, 20(1): 238–252. DOI: 10.7524/AJE.1673–5897.20240807002.
LIU J H, ZHANG X X, ZHANG Z L, ZHENG P H, LI J T, XIAN J A, LU Y P. Research progress on the toxicological effects of neonicotinoid pesticides on non–target aquatic animals[J]. *Asian Journal of Ecotoxicology,* 2025, 20(1): 238–252. DOI: 10.7524/AJE.1673–5897.20240807002.

[9] QAMAR W, SHAHID M U, IRFAN M, ABBAS R Z, FARAZ A, HUSSAIN R, ALVI M A. Thiamethoxam toxicity: a review in one–health perspective[J]. *Kafkas Universitesi Veteriner Fakultesi Dergisi*, 2023, 29(5): 557–570. DOI: 10.9775/kvfd.2023.30161.

[10] 贺艳, 邓月华 . 水环境中新烟碱类农药去除技术研究进展[J]. 环境化学, 2020, 39(7): 1963–1976. DOI: 10.7524/j.issn.0254–6108.2019082102.
HE Y, DENG Y H. A review on the removal technologies of neonicotinoid pesticides from aquatic environment[J]. *Environmental Chemistry*, 2020, 39(7): 1963–1976. DOI: 10.7524/j.issn.0254–6108.2019082102.

[11] PANIC S, RAKIC D, GUZSVÁNY V, KISS E, BOSKOVIC G, KóNYA Z, KUKOVECZ A. Optimization of thiamethoxam adsorption parameters using multi–walled carbon nanotubes by means of fractional factorial design[J]. *Chemosphere*, 2015, 141: 87–93. DOI: 10.1016/j.chemosphere.2015.06.042.

[12] MEIJIDE J, GÓMEZ J, PAZOS M, SANROMÁN M A. Degradation of thiamethoxam by the synergetic effect between anodic oxidation and fenton reactions[J]. *Journal of Hazardous Materials*, 2016, 319: 43–50. DOI: 10.1016/j.jhazmat.2016.02.064.

[13] YANG H, LIU H J, HU Z B, LIANG J W, PANG H L, YI B. Consideration on degradation kinetics and mechanism of thiamethoxam by reactive oxidative species (ROSs) during photocatalytic process[J]. *Chemical Engineering Journal*, 2014, 245: 24–33. DOI: 10.1016/j.cej.2014.02.016.

[14] YAO Y W, HUANG C J, YANG Y, LI M Y, REN B L. Electrochemical removal of thiamethoxam using three–dimensional porous PbO_2–CeO_2 composite electrode: electrode characterization, operational parameters optimization and degradation pathways[J]. *Chemical Engineering Journal*, 2018, 350: 960–970. DOI: 10.1016/j.cej.2018.06.036.

[15] PANDEY G, DORRIAN S J, RUSSELL R J, OAKESHOTT J G. Biotransformation of the neonicotinoid insecticides imidacloprid and thiamethoxam by *Pseudomonas* sp. 1G[J]. *Biochemical and Biophysical Research Communications*, 2009, 380(3): 710–714. DOI: 10.1016/j.bbrc.2009.01.156.

[16] ZHOU G C, WANG Y, ZHAI S, GE F, LIU Z H, DAI Y J, YUAN S, HOU J Y. Biodegradation of the neonicotinoid insecticide thiamethoxam by the nitrogen–fixing and plant–growth–promoting rhizobacterium *Ensifer adhaerens* strain TMX–23[J]. *Applied Microbiology and Biotechnology*, 2013, 97(9): 4065–4074. DOI: 10.1007/s00253–012–4638–3.

[17] RANA S, JINDAL V, MANDAL K, KAUR G, GUPTA V K. Thiamethoxam degradation by *Pseudomonas* and *Bacillus* strains isolated from agricultural soils[J]. *Environmental Monitoring and Assessment*, 2015, 187(5): 4532–4540. DOI: 10.1007/s10661–015–4532–4.

[18] KARL D M. Hidden in a sea of microbes[J]. *Nature*, 2002, 415(6872): 590–591. DOI: 10.1038/415590b.

[19] LAURO F M, MCDOUGALD D, THOMAS T, WILLIAMS T J, EGAN

中国知网 https://www.cnki.net

S, RICE S, DEMAERE M Z, TING L, ERTAN H, JOHNSON J, FERRIERA S, LAPIDUS A, ANDERSON I, KYRPIDES N, MUNK A C, DETTER C, HAN C S, BROWN M V, ROBB F T, KJELLEBERG S, CAVICCHIOLI R. The genomic basis of trophic strategy in marine bacteria[J]. *Proceedings of the National Academy of Sciences of the United States of America*, 2009, 106(37): 15527–15533. DOI: 10.1073/pnas.0903507106.

[20] XU L J, YU K F, LI S, LIU G H, TAO S C, SHI Q, CHEN T R, ZHANG H L. Interseasonal and interspecies diversities of *Symbiodinium* density and effective photochemical efficiency in five dominant reef coral species from Luhuitou fringing reef, northern South China Sea [J]. *Coral Reefs*, 2017, 36(2): 477–487. DOI: 10.1007/s00338–016–1532–y.

[21] VAN OPPEN M J H, BLACKALL L L. Coral microbiome dynamics, functions and design in a changing world[J]. *Nature Reviews Microbiology*, 2019, 17(9): 557–567. DOI: 10.1038/s41579–019–0223–4.

[22] SARANYA K, SUNDARAMANICKAM A, SHEKHAR S, MEENA M, SATHISHKUMAR R S, BALASUBRAMANIAN T. Biosorption of multi–heavy metals by coral associated phosphate solubilising bacteria *Cronobacter muytjensii* KSCAS2[J]. *Journal of Environmental Management*, 2018, 222: 396–401. DOI: 10.1016/j.jenvman.2018.05.083.

[23] ANSARI N, ROKHBAKHSH–ZAMIN F, HASSANSHAHIAN M, HESNI M A. Biodegradation of crude oil using symbiont crude–oil degrading bacteria isolated from corals collected at the Persian Gulf [J]. *Journal of Chemical Technology and Biotechnology*, 2021, 96(7): 1882–1892. DOI: 10.1002/jctb.6707.

[24] JAYASREE V S, SOBHANA K S, POULOSE P, BABU K R, JASMINE S, RANJITH L, SARAVANAN R, KINGSLY H J, SREENATH K R, JOSHI K K, GEORGE R M, GOPALAKRISHNAN A. Biodegradation of the pyrethroid pesticide cyfluthrin by the halophilic bacterium *Photobacterium ganghwense* isolated from coral reef ecosystem[J]. *Indian Journal of Fisheries*, 2020, 67(4): 116–131. DOI: 10.21077/ijf.2020.67.4.100553–14.

[25] 黄沁愉, 吕丽娜, 李洁, 琚慧敏, 苏宏飞. 珊瑚来源潜在降解对甲氧基肉桂酸辛酯的细菌物种多样性[J]. 热带海洋学报, 2025, 44: 133–145. DOI: 10.11978/2024059.
HUANG Q Y, LYU L N, LI J, JU H M, SU H F. Microbial diversity of potential EHMC–degrading bacteria from coral[J]. *Journal of Tropical Oceanography*, 2025, 44: 133–145. DOI: 10.11978/2024059.

[26] 聂磊, 王炳, 廖宝林, 彭丹. 持久性有机污染物对珊瑚藻生长和生理生态特性的影响[J]. 海洋湖沼通报, 2018(6): 75–84. DOI: 10.13984/j.cnki.cn37–1141.2018.06.011..
NIE L, WANG B, LIAO B L, PENG D. Impact of persistent organic pollutants on growth and physiological ecological characteristics of coral algae[J]. *Transactions of Oceanology and Limnology*, 2018(6): 75–84. DOI: 10.13984/j.cnki.cn37–1141.2018.06.011.

[27] ZHOU Y Y, LI Q L, ZHANG Q, YUAN M L, ZHU X S, LI Y C, LI Q P, DOWNS C A, HUANG D W, CHOU L M, ZHAO H W. Environmental concentrations of herbicide prometryn render stress–tolerant corals susceptible to ocean warming[J]. *Environmental Science & Technology*, 2024, 58(10): 4545–4557. DOI: 10.1021/acs.est.3c10417.

[28] ZHOU Z, NI X Z, WU Z J, TANG J. Physiological and transcriptomic analyses reveal the threat of herbicides glufosinate and glyphosate to the scleractinian coral *Pocillopora damicornis*[J]. *Ecotoxicology and Environmental Safety*, 2022, 229: 113074. DOI: 10.1016/j.ecoenv.2021.113074.

[29] 唐小玉, 张颖, 张文谦, 张燕英, 杨清松, 董俊德. 珊瑚共附生DMSP降解菌的分离及其多样性分析[J]. 海洋学报, 2021, 43(6): 108–117. DOI: 10.12284/hyxb2021110.
TANG X Y, ZHANG Y, ZHANG W Q, ZHANG Y Y, YANG Q S, DONG J D. Isolation and diversity analysis of coral–associated DMSP degrading bacteria[J]. *Haiyang Xuebao*, 2021, 43(6): 108–117. DOI: 10.12284/hyxb2021110.

[30] LYU L N, HE Y F, DONG C M, LI G Z, WEI G S, SHAO Z Z, ZHANG S. Characterization of chlorinated paraffin–degrading bacteria from marine estuarine sediments[J]. *Journal of Hazardous Materials*, 2022, 440: 129699. DOI: 10.1016/j.jhazmat.2022.129699.

[31] BOLYEN E, RIDEOUT J R, DILLON M R, BOKULICH N A, ABNET C C, AL–GHALITH G A, ALEXANDER H, ALM E J, ARUMUGAM M, ASNICAR F, BAI Y, BISANZ J E, BITTINGER K, BREJNROD A, BRISLAWN C J, BROWN C T, CALLAHAN B J, CARABALLO–RODRíGUEZ A M, CHASE J, COPE E K, DA SILVA R, DIENER C, DORRESTEIN P C, DOUGLAS G M, DURALL D M, DUVALLET C, EDWARDSON C F, ERNST M, ESTAKI M, FOUQUIER J, GAUGLITZ J M, GIBBONS S M, GIBSON D L, GONZALEZ A, GORLICK K, GUO J, HILLMANN B, HOLMES S, HOLSTE H, HUTTENHOWER C, HUTTLEY G A, JANSSEN S, JARMUSCH A K, JIANG L J, KAEHLER B D, BIN KANG K, KEEFE C R, KEIM P, KELLEY S T, KNIGHTS D, KOESTER I, KOSCIOLEK T, KREPS J, LANGILLE M G I, LEE J, LEY R, LIU Y X, LOFTFIELD E, LOZUPONE C, MAHER M, MAROTZ C, MARTIN B D, MCDONALD D, MCIVER L J, MELNIK A V, METCALF J L, MORGAN S C, MORTON J T, NAIMEY A T, NAVAS–MOLINA J A, NOTHIAS L F, ORCHANIAN S B, PEARSON T, PEOPLES S L, PETRAS D, PREUSS M L, PRUESSE E, RASMUSSEN L B, RIVERS A, ROBESON M S, ROSENTHAL P, SEGATA N, SHAFFER M, SHIFFER A, SINHA R, SONG S J, SPEAR J R, SWAFFORD A D, THOMPSON L R, TORRES P J, TRINH P, TRIPATHI A, TURNBAUGH P J, UL–HASAN S, VAN DER HOOFT J J J, VARGAS F, VáZQUEZ–BAEZA Y, VOGTMANN E, VON HIPPEL M, WALTERS W, WALTERS W, WAN Y, WANG M, WARREN J, WEBER K C, WILLIAMSON C H D, WILLIS A D, XU Z Z, ZANEVELD J R, ZHANG Y L, ZHU Q Y, KNIGHT R, CAPORASO J G. Reproducible, interactive, scalable and extensible microbiome data science using QIIME 2[J]. *Nature Biotechnology*, 2019, 37(9): 1091–1091. DOI: 10.1038/s41587–019–0252–6.

[32] KUMAR S, STECHER G, LI M, KNYAZ C, TAMURA K. MEGA X: Molecular evolutionary genetics analysis across computing platforms [J]. *Molecular Biology and Evolution*, 2018, 35(6): 1547–1549. DOI: 10.1093/molbev/msy096.

[33] 郭新强, 李荣, 林栋青, 朱彬, 李顺鹏, 蒋建东. 三唑磷降解菌株

中国知网 https://www.cnki.net

GS-1的分离鉴定及其降解特性的研究[J]. 微生物学通报, 2009, 36(8): 1143-1149. DOI: 10.13344/j.microbiol.china.2009.08.018.
GUO X Q, LI R, LIN D Q, ZHU B, LI S P, JIANG J D. Isolation and characterization of a triazophos-degrading strain GS-1 and its degrading characteristics[J]. *Microbiology China*, 2009, 36(8): 1143-1149. DOI: 10.13344/j.microbiol.china.2009.08.018.

[34] 耿真. 新喀里多尼亚弧菌分离鉴定及其对虾夷扇贝的致病性研究[D]. 大连: 大连海洋大学, 2022.
GENG Z. Isolation and identification of *Vibrio neocaledonicus* and its pathogenicity to Yesso scallop (*Patinopecten yessoensis*)[D]. Dalian: Dalian Ocean University, 2022.

[35] MACMILLAN D S, AMBURE P, ARANDA V, BAYONA Y, BONDEROVIC V, DAWICK J, FABRE N, FISCHER S, HODGES G, LLOBET-MUT A, LOISEL-JOUBERT S, RIVETTI C, ROBERTS J, SCHIRMER K, SERRANO-CANDELAS E, RAMON B S, STACKHOUSE R A. Addressing the challenges of acute fish toxicity hazard classification using a non-animal defined approach [J/OL]. *Environmental Toxicology and Chemistry*, 2025[2025-02-12]. https://doi.org/10.1093/etojnl/vgaf046

[36] 胡传鹤, 李永涛, 尚梦如, 陈欣敏, 田卓迅, 林学明. 5种新烟碱类农药在农田土壤中的吸附和淋溶行为[J]. 农业环境科学学报, 2023, 42(3): 539-546. DOI: 10.11654/jaes.2023-0023
HU C H, LI Y T, SHANG M R, CHEN X M, TIAN Z X, LIN X M. Adsorption and leaching behavior of five neonicotinoid pesticides in farmland soil[J]. *Journal of Agro-Environment Science*, 2023, 42(3): 539-546. DOI: 10.11654/jaes.2023-0023

[37] SHAO X S, LIU Z W, XU X Y, LI Z, QIAN X H. Overall status of neonicotinoid insecticides in China: Production, application and innovation[J]. *Journal of Pesticide Science*, 2013, 38(1-2): 1-9. DOI: 10.1584/jpestics.D12-037.

[38] CHEN Y C, ZHANG L, HU H M, WU R X, LING J, YUE S Q, YANG D, YU W F, DU W, SHEN G F, ZHAO M R. Neonicotinoid pollution in marine sediments of the East China Sea[J]. *Science of the Total Environment*, 2022, 842: 156658.DOI: 10.1016/j.scitotenv.2022.156658.

[39] LI X T, CHEN J H, HE X P, WANG Z W, WU D N, ZHENG X L, ZHENG L, WANG B D. Simultaneous determination of neonicotinoids and fipronil and its metabolites in environmental water from coastal bay using disk-based solid-phase extraction and high-performance liquid chromatography-tandem mass spectrometry[J]. *Chemosphere*, 2019, 234: 224-231. DOI: 10.1016/j.chemosphere.2019.05.243.

[40] MONTIEL-LEóN J M, MUNOZ G, DUY S V, DO D T, VAUDREUIL M A, GOEURY K, GUILLEMETTE F, AMYOT M, SAUVÉ S. Widespread occurrence and spatial distribution of glyphosate, atrazine, and neonicotinoids pesticides in the St. Lawrence and tributary rivers[J]. *Environmental Pollution*, 2019, 250: 29-39. DOI: 10.1016/j.envpol.2019.03.125.

[41] XIONG J J, WANG Z, MA X, LI H Z, YOU J. Occurrence and risk of neonicotinoid insecticides in surface water in a rapidly developing region: Application of polar organic chemical integrative samplers[J]. *Science of the Total Environment*, 2019, 648: 1305-1312. DOI: 10.1016/j.scitotenv.2018.08.256.

[42] 陈姣姣, 陈晓芳, 郑书梅, 张秋金, 耿宝荣. 噻虫嗪对中华蟾蜍蝌蚪抗氧化系统及丙二醛含量的影响[J]. 福建师范大学学报(自然科学版), 2019, 35(5): 61-66. DOI: 10. 12046/j. issn. 1000-5277. 2019. 05. 010.
CHEN J J, CHEN X F, JIN S M, ZHANG Q J, GENG B R. Effects of thiamethoxam on antioxidant system activity and malondialdehyd content in *Bufo gargarizans* tadpoles[J]. *Journal of Fujian Normal University* (*Natural Science Edition*), 2019, 35(5): 61-66. DOI: 10.12046/j. issn.1000-5277.2019.05.010.

[43] 王召, 彭舒, 孟立霞. 噻虫嗪对鲫鱼的急性毒性和抗氧化酶及乙酰胆碱酯酶活性的影响[J]. 水产科学, 2020, 39(6): 922-927. DOI: 10.16378/j.cnki.1003-1111.2020.06.018.
WANG Z, PENG S, MENG L X. Acute toxicity of thiamethoxam and activities of antioxidant enzymes and acetylcholinesterase in juvenile crucian carp *Carassius auratus*[J]. *Fisheries Science*, 2020, 39(6): 922-927. DOI: 10.16378/j.cnki.1003-1111.2020.06.018.

[44] AGARWAL R, SRINIVAS R. Severe neuropsychiatric manifestations and rhabdomyolysis in a patient with imidacloprid poisoning[J]. *American Journal of Emergency Medicine*, 2007, 25(7): 844-845. DOI: 10.1016/j.ajem.2006.11.044.

[45] HUANG N C, LIN S L, CHOU C H, HUNG Y M, CHUNG H M, HUANG S T. Fatal ventricular fibrillation in a patient with acute imidacloprid poisoning[J]. *American Journal of Emergency Medicine*, 2006, 24(7): 883-885. DOI: 10.1016/j.ajem.2006.03.008.

[46] WU I W, LIN J L, CHENG E T. Acute poisoning with the neonicotinoid insecticide imidacloprid in *N*-methyl pyrrolidone[J]. *Journal of Toxicology-Clinical Toxicology*, 2001, 39(6): 617-621. DOI: 10.1081/clt-100108494.

[47] RECIO-VEGA R, CARNPO-GóMEZ G, BORJA-ABURTO V H, MORAN-MARTíNEZ J, CEBRIAN-GARCIA M E. Organophosphorus pesticide exposure decreases sperm quality: Association between sperm parameters and urinary pesticide levels [J]. *Journal of Applied Toxicology*, 2008, 28(5): 674-680. DOI: 10.1002/jat.1321.

[48] 田蕴, 郑天凌. 海洋环境中降解多环芳烃的微生物[J]. 海洋科学, 2004, 28(9): 50-55.DOI: 10.3969/j.issn.1000-3096.2004.09.011
TIAN Y, ZHENG T L. PAH-degrading microorganisms in marine evnironment[J]. *Marine Sciences*, 2004, 28(9): 50-55. DOI: 10.3969/j.issn.1000-3096.2004.09.011

[49] YAKIMOV M M, DENARO R, GENOVESE M, CAPPELLO S, D'AURIA G, CHERNIKOVA T N, TIMMIS K N, GOLYSHIN P N, GILULIANO L. Natural microbial diversity in superficial sediments of Milazzo Harbor (Sicily) and community successions during microcosm enrichment with various hydrocarbons[J]. *Environmental Microbiology*, 2005, 7(9): 1426-1441. DOI: 10.1111/j.1462-5822.2005.00829.x.

[50] 陈金妮, 梁甲元, 余克服, 俞小鹏, 葛瑞琪, 覃良云, 许勇前. 涠洲岛2种造礁珊瑚共附生可培养潜在耐热细菌多样性[J]. 微生物学通报, 2023, 50(3): 909-923. DOI: 10.13344/j.microbiol.china.220344.
CHEN J N, LIANG J Y, YU K F, YU X P, GE R Q, QIN L Y, XU Y Q. Diversity of potential heat-tolerant bacteria associated with two species

中国知网 https://www.cnki.net

of scleractinian corals in Weizhou Island[J]. *Microbiology China*, 2023, 50(3): 909–923. DOI: 10.13344/j.microbiol.china.220344.

[51] 陈海宁, 田伟君, 赵婧, 江俊峰, 杨淑洁, 高惠子. 海洋芘降解菌 *Alteromonas* sp.P7 的降解特性及基因组初步分析[J]. 环境工程学报, 2022, 16(11): 3739–3749. DOI: 10.12030/j.cjee.202204072.
CHEN H N, TIAN W J, ZHAO J, JIANG J F, YANG S J, GAO H Z. Degradation characteristics and genome analysis of marine pyrene degrading bacteria *Alteromonas* sp. P7[J]. *Chinese Journal of Environmental Engineering*, 2022, 16(11): 3739–3749. DOI: 10.12030/j.cjee.202204072.

[52] ZHANG D X, CHU B W, YANG Q Q, ZHANG X Y, FANG Y Y, LIU G L, LIANG L A, GUO Y Y, YIN Y G, CAI Y, JIANG G B. Degradation of organic mercury in high salt environments by a marine aerobic bacterium *Alteromonas macleodii* KD01[J]. *Bioresource Technology*, 2024, 402: 130831. DOI: 10.1016/j.biortech.2024.130831.

[53] 张真庆, 于广利, 赵峡, 王远红, 吕志华, 管华诗. 一种海洋弧菌(*Vibrio* sp. WYA)褐藻胶裂合酶降解特性研究[J]. 高等学校化学学报, 2006, 27(1): 71–74. DOI: 10.3321/j.issn:0251–0790.2006.01.014
ZHANG Z Q, YU G L, ZHAO X, WANG Y H, LYU Z H, GUAN H S. Degradation character of an alginate lyase from *Vibrio* sp. WYA[J]. *Chemical Journal of Chinese Universities*, 2006, 27(1): 71–74. DOI: 10.3321/j.issn:0251–0790.2006.01.014

[54] HIRANO T, OKUBO M, TSUDA H, YOKOYAMA M, HAKAMATA W, NISHIO T. Chitin heterodisaccharide, released from Chitin by chitinase and chitin oligosaccharide deacetylase, enhances the chitin–metabolizing ability of *Vibrio parahaemolyticus*[J]. *Journal of Bacteriology*, 2019, 201(20): e00270–19.. DOI: 10.1128/jb.00270–19.

[55] KIMURA Y, FUKUDA Y, OTSU R, YU J, MINO S, MISAWA S, MARUYAMA S, IKEDA Y, MIYAMACHI R, NOGUCHI H, KATO S, YAMAMOTO Y, SAWABE T. A lesson from polybutylene succinate plastisphere to the discovery of novel plastic degrading enzyme genes in marine *vibrios*[J]. *Environmental Microbiology*, 2023, 25(12): 2834–2850. DOI: 10.1111/1462–2920.16512.

[56] 孙孝文, 刘诚, 王慧敏. 毒死蜱降解菌的驯化筛选及高活性毒死蜱降解菌群的构建[J]. 安徽农业科学, 2021, 49(13): 64–68, 73. DOI: 10.3969/j.issn.0517–6611.2021.13.017.
SUN X W, LIU C, WANG H M. Domestication and screening of chlorpyrifos–degrading bacteria and construction of composited flora with high chlorpyrifos–degrading capacity[J], *Journal of Anhui Agricultural Sciences*. 2021, 49(13): 64–68, 73. DOI: 10.3969/j.issn.0517–6611.2021.13.017.

[57] CYCON M, ZMIJOWSKA A, PIOTROWSKA–SEGET Z. Enhancement of deltamethrin degradation by soil bioaugmentation with two different strains of *Serratia marcescens*[J]. *International Journal of Environmental Science and Technology*, 2014, 11(5): 1305–1316. DOI: 10.1007/s13762–013–0322–0.

[58] 吴后波, 潘金培. 病原弧菌的致病机理[J]. 水生生物学报, 2003, 49(4): 422–426. DOI: 10.3321/j.issn:1000–3207.2003.04.018
WU H B, PAN J P. Virulence mechanisms of pathogenic *vibrio*[J]. *Acta Hydrobiologica Sinica*, 2003, 49(4): 422–426. DOI: 10.3321/j.issn:1000–3207.2003.04.018

[59] ARYAL M. Phytoremediation strategies for mitigating environmental toxicants[J]. *Heliyon*, 2024, 10(19): e38683. DOI: 10.1016/j.heliyon.2024.e38683.

[60] 王磊, 宿红艳, 杨润亚, 王晓杰, 林文杰. 海洋交替单胞菌 YTW–10 的鉴定及抑菌活性分析[J]. 海洋科学, 2011, 35(7): 14–19.
WANG L, SU H Y, YANG R Y, WANG X J, LIN W J. Identification and antimicrobial activity analysis of a marine *Alteromonas* YTW–10[J], *Marine Sciences*. 2011, 35(7): 14–19.

[61] IVANOVA E P, NG H J, WEBB H K, KURILENKO V V, ZHUKOVA N V, MIKHAILOV V V, PONAMOREVA O N, CRAWFORD R J. *Alteromonas australica* sp. nov., isolated from the Tasman Sea[J]. *Antonie Van Leeuwenhoek International Journal of General and Molecular Microbiology*, 2013, 103(4): 877–884. DOI: 10.1007/s10482–012–9869–x.

[62] 周楠, 姜成英, 刘双江. 从环境中分离培养微生物 : 培养基营养水平至关重要[J]. 微生物学通报, 2016, 43(5): 1075–1081. DOI: 10.13344/j.microbiol.china.160010.
ZHOU N, JIANG C Y, LIU S J. Cultivation of microorganisms from environments: Nutrient level of the culture medium is of great importance[J]. *Microbiology China*, 2016, 43(5): 1075–1081. DOI: 10.13344/j.microbiol.china.160010.

[63] AL–DAHASH L M, MAHMOUD H M. Harboring oil–degrading bacteria: A potential mechanism of adaptation and survival in corals inhabiting oil–contaminated reefs[J]. *Marine Pollution Bulletin*, 2013, 72(2): 364–374. DOI: 10.1016/j.marpolbul.2012.08.029.

[64] BOUFERCHA O, MONFORTE A R, BOUDEMAGH A, FERREIRA A C, CASTRO P M L, MOREIRA I S. Biodegradation and metabolic pathway of the neonicotinoid insecticide thiamethoxam by *Labrys portucalensis* F11[J]. *International Journal of Molecular Sciences*, 2022, 23(22): 14326. DOI: 10.3390/ijms232214326.

[65] XIANG X Z, YI X H, ZHENG W B, LI Y Q, ZHANG C, WANG X Z, CHEN Z G, HUANG M Z, YING G G. Enhanced biodegradation of thiamethoxam with a novel polyvinyl alcohol (PVA)/sodium alginate (SA)/biochar immobilized *Chryseobacterium* sp. H5[J]. *Journal of Hazardous Materials*, 2023, 443:130247. DOI: 10.1016/j.jhazmat.2022.130247.

【责任编辑　曾诗敏】

中国知网　https://www.cnki.net

◆珊瑚礁生态保护与修复◆

室内养殖条件下两种造礁石珊瑚的性腺发育研究*

黄菲菲[1,2],崔梦瑶[1,2],韦　芬[1,2**],杨溪月[1,2],潘晓媛[1,2,3],玉颢瑜[1,2]
(1.广西大学广西南海珊瑚礁研究重点实验室,广西大学珊瑚礁研究中心,广西南宁　530004;2.广西大学海洋学院,广西南宁　530004;3.广西大学资源环境与材料学院,广西南宁　530004)

摘要:为探究人工环境下造礁石珊瑚的性腺发育规律,本研究选取排卵型的美丽鹿角珊瑚(*Acropora formosa*)和丛生盔形珊瑚(*Galaxea fascicularis*)作为研究对象,自 2021 年 9 月起开展为期 1 年的室内养殖实验,观察其性腺发育过程,并与自然海域珊瑚对比。结果表明,室内养殖条件下美丽鹿角珊瑚的卵母细胞发育起始时间与自然海域珊瑚相同,但其性腺发育进程明显滞后;在整个观察周期内其仅发育至第Ⅱ时相。丛生盔形珊瑚性腺发育与自然群体同步,于 2022 年 4 月下旬达到性成熟。美丽鹿角珊瑚性腺发育停滞,可能由于光照强度不足导致自养营养受限,能量仅足以维持个体正常生长;而丛生盔形珊瑚自养与异养能力更强,故能维持正常的性腺发育,更适合于室内人工繁育。本研究为室内养殖条件下造礁石珊瑚的性腺发育提供了基础数据,并为珊瑚礁生态修复提供了理论依据。

关键词:美丽鹿角珊瑚;丛生盔形珊瑚;性腺发育;异位养殖;有性繁殖

中图分类号:P735　　**文献标识码**:A　　**文章编号**:1005-9164(2025)04-0820-08
DOI:10.13656/j.cnki.gxkx.20251114.017

珊瑚礁生态系统是生物多样性及生产力较高的生态系统之一,被称为“海洋中的热带雨林”[1-3]。受全球气候变化和人类活动的双重影响,全球多个海域的珊瑚礁生态系统已出现严重的退化[1,4-5],因此,珊瑚礁生态系统的保护与修复问题受到广泛关注。近年来,基于有性繁殖的珊瑚礁生态修复技术研究显著增加[6-8],而性腺发育是造礁石珊瑚有性繁殖的关键环节,由于大多数排卵型珊瑚每年仅排卵 1－2 次[6,9],因此,深入研究珊瑚的性腺发育过程,对利用有性繁殖技术促进珊瑚礁的修复具有重要意义。

目前,在野外环境下开展珊瑚性腺发育及排卵行为等繁殖相关的研究,主要依赖于人工观察和组织学分析的方法,这通常需要投入大量的人力和物力资源。此外,珊瑚样本的采集可能对供体珊瑚礁生态系

收稿日期:2024-11-18　　修回日期:2025-02-14
*国家自然科学基金项目(42090041),广西科技基地和人才专项(桂科 AD25069075),广西南海珊瑚礁研究重点实验室自主基金项目(GXLSCRSCS2023103)和广西大学大学生创新创业训练计划项目(202210593098)资助。
【第一作者简介】
黄菲菲(2004－),女,在读本科生,主要从事海洋生物与生态研究,E-mail:2706146103@qq.com。
【**通信作者简介】
韦　芬(1986－),女,博士,讲师,主要从事造礁石珊瑚的有性繁殖研究,E-mail:weifensky@163.com。
【引用本文】
黄菲菲,崔梦瑶,韦芬,等.室内养殖条件下两种造礁石珊瑚的性腺发育研究[J].广西科学,2025,32(4):820-827.
HUANG F F,CUI M Y,WEI F,et al. Gonadal Development of Two Scleractinian Coral Species under Indoor Cultivation Conditions [J]. Guangxi Sciences,2025,32(4):820-827.

中国知网　https://www.cnki.net

统造成破坏[10-11]。相比之下,在人工控制环境下开展珊瑚繁殖研究不仅操作更为便捷,而且对珊瑚礁生态系统的影响相对较小。2017 年,Craggs 等[12]首次在完全封闭的水族馆系统中成功实现了珊瑚的异位诱导产卵,为观察珊瑚在人工环境下的性腺发育提供了重要依据。2021 年,O′Neil 等[13]在人工培育条件下连续 2 年记录了柱珊瑚(*Dendrogyra cylindrus*)与迷宫珊瑚(*Meandrina meandrites*)的性腺发育过程,结果表明其性腺成熟及排卵时间与自然种群保持一致。2023 年,Wei 等[14]在异位养殖条件下研究发现,丛生盔形珊瑚(*Galaxea fascicularis*)的排卵时间集中在 4 月和 5 月,与自然海域中珊瑚的排卵时间完全同步。2024 年,Laforest 等[15]通过组织学方法,在室内循环水养殖系统(Recirculating Aquaculture System,RAS)中观察到经过 3 年培育后 *Montastraea cavernosa* 的性别变化及排卵行为。这些研究均表明,珊瑚在人工环境下的性腺发育周期及排卵时间与野外自然环境高度一致,为珊瑚的人工繁育和生态修复提供了重要的科学依据。

国外已有不少研究者对自然海域造礁石珊瑚的性腺发育进行了观察和报道。Wallace[16]调查了大堡礁 9 种鹿角珊瑚(*Acropora* spp.)配子发育情况,发现这些物种均为雌雄同体排卵型珊瑚,每年仅有一次配子发育周期;现有研究通常根据 Glynn 等[17]的标准,将珊瑚的性腺发育周期划分为 4 个时相;Shlesinger 等[18]则基于组织切片研究了红海北部 24 种珊瑚的性腺发育过程,发现该区域大部分珊瑚的性腺发育周期持续 6－7 个月。此外,新加坡、日本、墨西哥等地的研究者也陆续报道了本区域内造礁石珊瑚的性腺发育过程[19-21]。我国关于造礁石珊瑚性腺发育过程的研究起步较晚,相关报道较少,且主要集中在野外调查,研究方法主要是采用组织学分析。李元超等[22]于 2009 年观测了鹿回头海域的佳丽鹿角珊瑚(*Acropora pulchra*)卵母细胞的发育过程,并推断其排卵时间为 4 月底至 5 月初。杨小东[23]研究了徐闻灯楼角附近海域的澄黄滨珊瑚(*Porites lutea*)、大管孔珊瑚(*Goniopora djiboutiensis*)和丛生盔形珊瑚的性腺发育周期。张诗泽等[24]研究了三亚鹿回头海域多孔鹿角珊瑚(*A. millepora*)与丛生盔形珊瑚的繁殖类型,明确了丛生盔形珊瑚是假雌全异株排卵型珊瑚。韦芬等[25]研究了广西北海涠洲岛美丽鹿角珊瑚(*A. formosa*)和秘密角蜂巢珊瑚(*Favites abdita*)在自然海域的性腺发育过程,并确定了这两种珊瑚属排卵型珊瑚,均于 5 月下旬排卵。

美丽鹿角珊瑚因其较高的成活率和较快的生长速度[26],成为涠洲岛珊瑚礁人工生态修复的首选物种之一;丛生盔形珊瑚具有较强的环境耐受性,其野外种群白化发生率较低,在人工环境下容易饲养,可驯化程度高,是研究造礁石珊瑚理想的模式生物[27-28]。因此,本研究选取美丽鹿角珊瑚与丛生盔形珊瑚为研究对象,探索其在室内养殖的性腺发育规律,并与自然海域的珊瑚作比较,以期为人工养殖条件下造礁石珊瑚的性腺发育研究提供基础数据。

1 材料与方法

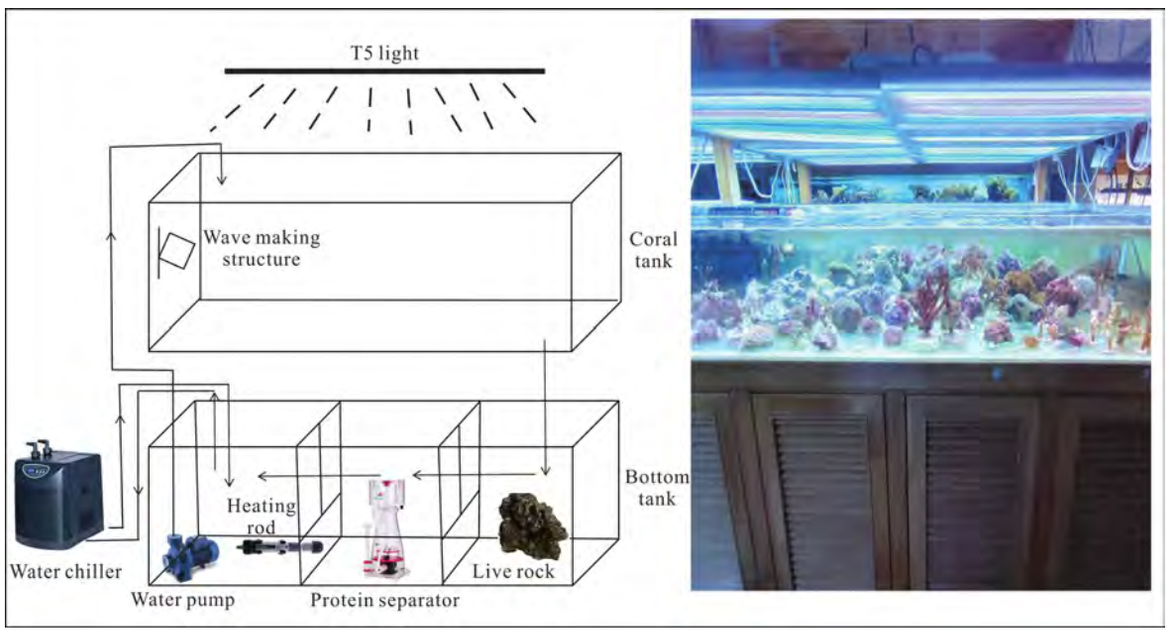
1.1 珊瑚养殖系统

本研究依据 RAS 人工繁育技术来设置光照、水流、水温等环境条件和珊瑚的异养饵料[12,29-31]。珊瑚养殖系统由主缸、底缸及灯光架构成(图 1),在底缸中放置蛋白分离器(品牌:Red Starfish,型号:RS-N230 Plus,工作电压:DC 24 V,功率:35 W,处理水量 2 600 L/h,购自深圳市鸿海水族设备有限公司)与活石(约 20 块,尺寸为 10－20 cm),用以降低水体营养盐水平。以 4 根 T5 灯(每根功率为 39 W,Giesemann GmbH,德国)为系统提供光源,利用定时器保持 12 h/d 的光照周期(上午 6:00 至下午 18:00),模拟日出、日落的自然现象,确保光照条件(强度约 3 500 lx)的稳定性和适宜性。利用水冷机(品牌:海利,型号:HC-1000BH,功率:746 W,购自广东海利集团有限公司)和加热棒(品牌:阿诺比,型号:FH-500,购自广东振华电器有限公司,)保持水温在(26±2) ℃。通过造浪结构模拟自然环境中的水流状态。养殖缸人工海水盐度为 32－35,pH 值控制在 8.1－8.3,每周更换 20%－30%的人工海水。每周投喂一次丰年虾卵(约 8 g)孵化的丰年虾(品牌:皇冠)作为珊瑚饵料。

1.2 样品采集与处理

美丽鹿角珊瑚(6 株)和丛生盔形珊瑚(6 株)于 2021 年 7 月采自广西北海涠洲岛海域(21°00′－21°10′N,109°00′－109°15′E)。将美丽鹿角珊瑚每株单独置于装有适量海水的聚乙烯塑料袋中,密封处理;从生盔形珊瑚每株单独采用海水完全浸湿的报纸进行包裹,最后分别放入不同的泡沫箱中,并于采集后 24 h 内转运至广西大学海洋学院岛礁生态修复实验室。造礁石珊瑚的性腺发育通常从秋季或冬季开始,在春季随着海水温度的逐渐升高,性腺发育进程

中国知网 https://www.cnki.net



The schematic diagram modified from reference [31].

图 1　珊瑚养殖系统

Fig. 1　Coral aquaculture system

显著加快[32]。因此,在性腺发育较慢的 9 月至翌年 2 月,每 2 个月取样一次;在性腺发育较快的 3—4 月,每个月取样一次。本研究分别于 2021 年 9 月 29 日、11 月 11 日和 2022 年 1 月 16 日对室内的美丽鹿角珊瑚进行取样,2022 年 3 月 17 日、4 月 22 日对室内美丽鹿角珊瑚和丛生盔形珊瑚都进行取样。同时,在 2021 年 9 月 28 日、11 月 18 日和 2022 年 3 月 8 日于涠洲岛海域 2—5 m 深处采集野外的美丽鹿角珊瑚。美丽鹿角珊瑚和丛生盔形珊瑚取样位置分别位于顶端下方和边缘约 5 cm 处,取样大小均为 1—3 cm。每次每种珊瑚各采集 3 株,采集后立即固定在用海水配制好的 5%(m ∶ V)多聚甲醛溶液中,4 ℃保存备用。

1.3　方法

固定的珊瑚样本参照文献[25]的方法进行处理:首先用 50%(V ∶ V)甲酸溶液对样本进行为期 5 d 的脱钙处理,随后进行梯度脱水处理,依次使用 75%乙醇、85%乙醇、90%乙醇、95%乙醇及无水乙醇进行脱水。脱水后的样本经二甲苯透明处理后,于 54 ℃石蜡中进行包埋,随后制备成厚度为 6—8 μm 的连续横向和纵向切片。切片经苏木精-伊红(Hematoxylin-Eosin,HE)双重染色后,采用凝胶树脂封片。使用光学显微镜[CX23,奥林巴斯(中国)有限公司,分辨率为 0.2 μm]进行组织学观察和拍照,并测量配子的最大直径,用 SPSS 26.0 软件计算平均直径及标准差。

2　结果与分析

本研究中造礁石珊瑚性腺发育过程的具体形态特征如表 1 和图 2 所示。

表 1　美丽鹿角珊瑚和丛生盔形珊瑚不同时相卵母细胞的平均直径

Table 1　Average diameters of oocytes in *A. formosa* and *G. fascicularis* at different stages

珊瑚种类 Coral species	时相 Stage	室内养殖 Indoor cultivation		自然海域 In the wild	
		取样日期 Sampling date	平均直径/μm Average diameter/μm	取样日期 Sampling date	平均直径/μm Average diameter/μm
A. formosa	Ⅰ	2021-09-29	60.31±15.62	2021-09-28	52.75±13.02
	Ⅰ	2021-11-11	58.12±18.22		
	Ⅰ	2021-01-16	61.89±15.53		
	Ⅱ	2022-03-17	109.09±40.08	2021-11-18	80.81±32.60
	Ⅲ			2022-03-08	176.66±24.57
G. fascicularis	Ⅲ	2022-03-17	305.45±28.57		
	Ⅳ	2022-04-22	365.57±37.25		

中国知网　https://www.cnki.net

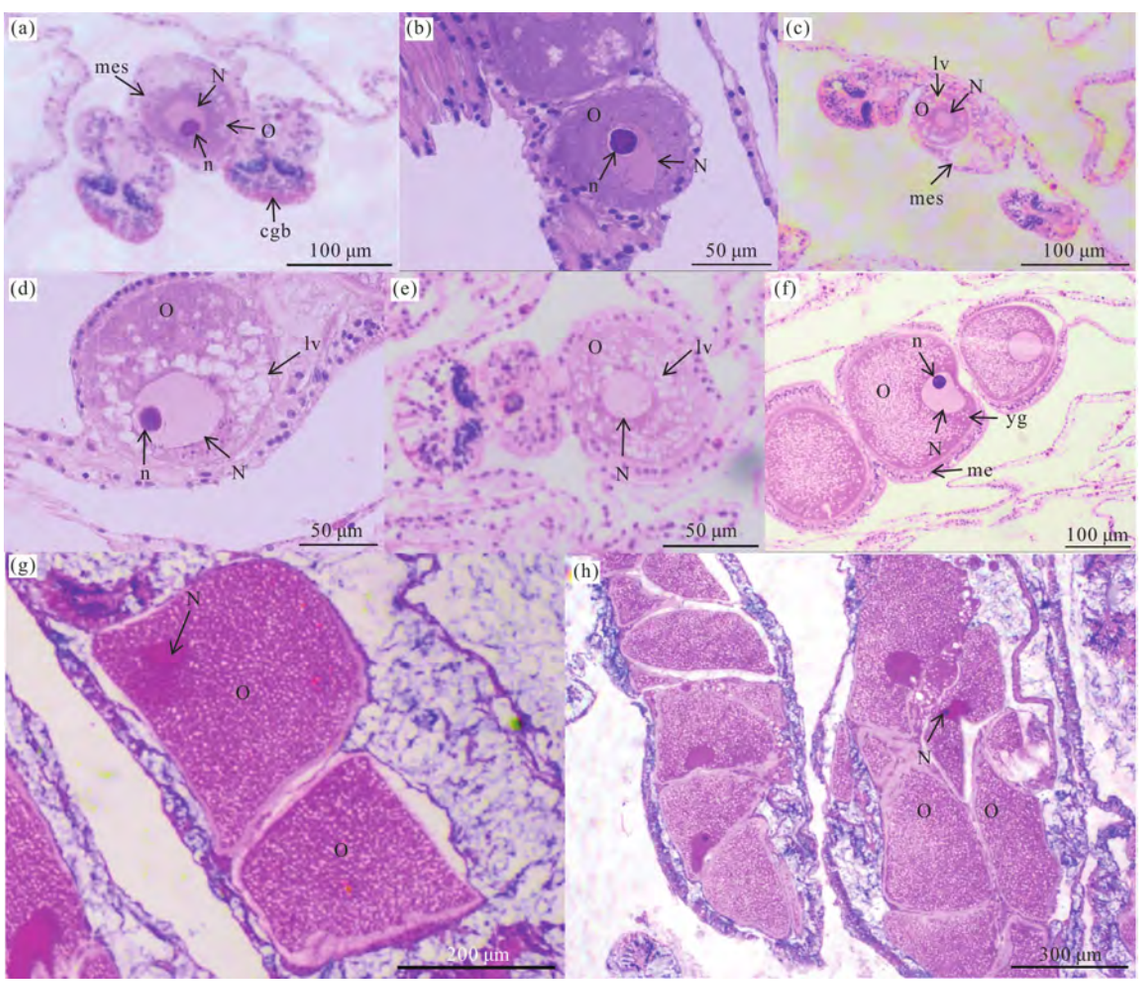
2021 年 9 月 29 日，在室内养殖条件下，美丽鹿角珊瑚的部分生殖腺中可观察到处于第Ⅰ时相的卵母细胞[图 2(a)]，卵母细胞数量较少且大小不一，形状不规则，细胞质致密，核质比高，细胞核位于细胞中间。2021 年 9 月 28 日，自然海域美丽鹿角珊瑚的卵母细胞同样处于第Ⅰ时相，其肠系膜中卵母细胞的细胞质更为致密，核质比依旧高[图 2(b)]。

2021 年 11 月 11 日，室内养殖美丽鹿角珊瑚的卵母细胞仍处于第Ⅰ时相，且数量稀少，零星分散在肠系膜上[图 2(c)]，卵母细胞中可见少量脂质泡。2021 年 11 月 18 日，自然海域美丽鹿角珊瑚的性腺已经发育至第Ⅱ时相，细胞质中可见大量的脂质泡，核仁染色清晰[图 2(d)]，相较于同时期在室内养殖的美丽鹿角珊瑚，其性腺发育的速度明显更快。

2022 年 1 月 16 日，室内养殖美丽鹿角珊瑚的卵母细胞依然为第Ⅰ时相。

2022 年 3 月 17 日，室内养殖美丽鹿角珊瑚的卵母细胞发育至第Ⅱ时相[图 2(e)]，数量稀少，仅部分生殖腺内可见，细胞呈圆形，细胞质中出现粗糙粒状的脂质泡，此时卵母细胞体积明显增大。2022 年 3 月 8 日，自然海域美丽鹿角珊瑚卵母细胞处于第Ⅲ时相[图 2(f)]，细胞多呈椭圆形，出现大量卵黄颗粒，细胞核向细胞膜迁移。

2022 年 4 月 22 日，室内养殖美丽鹿角珊瑚的卵母细胞仍处于第Ⅱ时相，卵母细胞未能发育成熟，卵子也无法正常排出。



O: oocyte; N: nucleus; n: nucleolus; mes: mesentery; cgb: cnidoglandular band; lv: lipid vesicle; yg: yolk granules; me: mesoglea. (a) Stage Ⅰ oocyte of *A. formosa* under indoor cultivation (2021-09-29); (b) Stage Ⅰ oocyte of *A. formosa* in the wild (2021-09-28); (c) Stage Ⅰ oocyte of *A. formosa* under indoor cultivation (2021-11-11); (d) Stage Ⅱ oocyte of *A. formosa* in the wild (2021-11-18); (e) Stage Ⅱ oocyte of *A. formosa* under indoor cultivation (2022-03-17); (f) Stage Ⅲ oocyte of *A. formosa* in the wild (2022-03-08); (g) Stage Ⅲ oocyte of *G. fascicularis* under indoor cultivation (2022-03-17); (h) Stage Ⅳ oocyte of *G. fascicularis* under indoor cultivation (2022-04-22).

图 2　美丽鹿角珊瑚与丛生盔形珊瑚的性腺发育过程

Fig. 2　Gonadal development of *A. formosa* and *G. fascicularis*

中国知网　https://www.cnki.net

2022 年 3 月 17 日,室内养殖的丛生盔形珊瑚发育至第Ⅲ时相[图 2(g)],卵母细胞形状为梯形,细胞质分布均匀,出现卵黄颗粒,细胞核移至细胞一侧。2022 年 4 月 22 日,室内养殖的丛生盔形珊瑚发育至第Ⅳ时相[图 2(h)],卵母细胞之间紧密连接,占据整个肠系膜,细胞形状变得不规则。细胞质分布均匀,富含卵黄颗粒。细胞核呈新月形或马鞍形,移至细胞边缘,紧紧黏附在细胞膜内侧。此时的卵母细胞已完全发育成熟,随时都可以排放到外界。

在室内养殖条件下,美丽鹿角珊瑚的性腺发育过程中始终未观察到精巢的发育。美丽鹿角珊瑚与丛生盔形珊瑚的性腺发育过程中,其卵母细胞内均未观察到虫黄藻,因此推测珊瑚共生的虫黄藻从周围环境中获取。

3 讨论

3.1 室内养殖的美丽鹿角珊瑚性腺发育落后于自然海域的原因分析

本研究发现,室内养殖条件下美丽鹿角珊瑚的卵母细胞发育起始时间与自然海域珊瑚一致(均从 9 月开始),然而,室内养殖珊瑚的卵母细胞在后续发育过程中明显滞后。造礁石珊瑚在室内养殖过程中的生长发育受多重因素影响,主要包括光照强度[33]、水温[34]、藻类竞争[35-36]以及营养供给[37]等。在本研究中,养殖缸的水温维持在(26±2) ℃,这是珊瑚生长的适宜温度[38]。此外,养殖系统稳定,定期清理大型藻类及其他有害生物,每周投喂 1 次丰年虾,因此排除了温度波动、营养限制及藻类竞争的影响。然而,本研究的光照强度维持在 3 500 lx,显著低于自然海域的平均光照强度(约 7 500 lx)[32]。本研究基于珊瑚-虫黄藻共生体的光合作用效率与光照强度呈正相关的观测结果,推测养殖系统的光照不足限制了珊瑚通过自养途径获取能量供应,这可能是导致室内养殖的美丽鹿角珊瑚性腺发育落后于自然海域群体的主要原因。

大量研究表明,光照强度是调控造礁石珊瑚生长和繁殖的关键环境因子。Wijgerde 等[39]研究发现辐照度对珊瑚特异性生长速率有显著的主效应,在较高辐照度条件下珊瑚表现出更高的生长速率;Villinski[40]发现在光照较弱的加勒比海海域,*Montastraea faveolata* 的繁殖力显著降低;Leuzinger 等[41]的研究显示指状蔷薇珊瑚(*Montipora digitata*)在光照最弱的环境下停止繁殖;Lin 等[42]的研究也表明,在辐照度较低的水族馆中,撕裂尖孔珊瑚(*Oxypora lacera*)和宝石刺孔珊瑚(*Echinopora gemmacea*)的卵母细胞较野生环境中的卵母细胞更小。尽管光照强度对美丽鹿角珊瑚繁殖的具体调控机制尚未完全阐明,但已有研究表明,鹿角珊瑚的生殖组织与体细胞组织的能量含量比较高[43],较弱的光照可能导致母体能量获取不足,从而减少繁殖投入,进而影响卵母细胞的发育。

3.2 室内养殖的美丽鹿角珊瑚与丛生盔形珊瑚性腺发育差异分析

本研究观察到,与美丽鹿角珊瑚相比,处于相同养殖环境下的丛生盔形珊瑚的卵母细胞能够发育成熟,且与自然海域丛生盔形珊瑚性腺发育成熟时间[14]同步。这可能与两种珊瑚的能量获取方式及其对饵料的偏好差异有关。

已有研究表明,造礁石珊瑚的能量获取方式存在种间差异。与枝状珊瑚相比,块状珊瑚表现出更强的异养摄食能力,其异养营养贡献率更高[41]。在自养能量不足的情况下,块状珊瑚能够通过调节异养与自养的能量比例来维持能量平衡,而枝状珊瑚则主要依赖脂质来维持能量供给的平衡[44]。张志楠[45]发现,在相同的环境条件下,块状珊瑚[如滨珊瑚属(*Porites*)、盘星珊瑚属(*Dipsastraea*)、角蜂巢珊瑚属(*Favites*)]的自养能力比枝状珊瑚[如鹿角珊瑚属(*Acropora*)]更强。此外,现有研究进一步证实,在人工培育条件下,中型浮游生物如丰年虾是丛生盔型珊瑚的理想饵料来源[46-47]。丛生盔型珊瑚能够通过摄食这些中型浮游生物,获得氮源、磷酸盐、维生素以及其他微量元素[48-51],从而维持其正常的生长发育。相比之下,鹿角珊瑚属对中型浮游生物的摄食能力较弱,而更适应摄食小型浮游生物如浮游植物等[52-53]。Conlan 等[53]的研究也表明,相较于投喂丰年虾,多孔鹿角珊瑚更容易从未经过滤的海水中获取营养物质。由此推测,本实验仅投喂丰年虾,可能不利于美丽鹿角珊瑚通过异养方式获取充足的能量。由于丛生盔型珊瑚的营养灵活性和可塑性比美丽鹿角珊瑚更高,因此该珊瑚更易于适应养殖缸内的生存环境,其性腺发育状况也更好。

4 结论

室内养殖条件下美丽鹿角珊瑚的卵母细胞发育起始时间与自然海域种群相同,然而,室内养殖群体的性腺发育进程明显滞后,最终仅能达到第Ⅱ时相,

中国知网 https://www.cnki.net

未能成熟,本研究推测是光照强度不足导致母体通过自养途径获取的能量受限,进而减少了对繁殖的能量投入,最终影响卵母细胞的正常发育。在同一养殖系统中,丛生盔形珊瑚性腺能够正常发育成熟,这可能由于其异养能力和自养能力比美丽鹿角珊瑚强,因此,性腺发育得更好。

参考文献

[1] MOBERG F,FOLKE C. Ecological goods and services of coral reef ecosystems [J]. Ecological Economics,1999,29(2):215-233.

[2] 余克服.珊瑚礁科学概论[M].北京:科学出版社,2018.

[3] 赵美霞,余克服,张乔民.珊瑚礁区的生物多样性及其生态功能[J].生态学报,2006,26(1):186-194.

[4] HUGHES T P,KERRY J T,ÁLVAREZ-NORIEGA M,et al. Global warming and recurrent mass bleaching of corals [J]. Nature,2017,543(7645):373-377.

[5] HUGHES T P,BAIRD A H,MORRISON T H,et al. Principles for coral reef restoration in the Anthropocene [J]. One Earth,2023,6(6):656-665.

[6] HARRISON P L. Sexual reproduction of scleractinian corals [M]//DUBINSKY Z, STAMBLER N. Coral reefs: an ecosystem in transition. Dordrecht: Springer Netherlands,2011:59-85.

[7] RANDALL C J,NEGRI A P,QUIGLEY K M,et al. Sexual production of corals for reef restoration in the Anthropocene [J]. Marine Ecology Progress Series,2020,635:203-232.

[8] MCLEOD I M,HEIN M Y,BABCOCK R,et al. Coral restoration and adaptation in Australia: the first five years [J]. PLoS One,2022,17(11):e0273325.

[9] 黄洁英.三亚鹿回头海域造礁石珊瑚的有性繁殖生物学研究[D].北京:中国科学院大学,2011.

[10] VARGAS-ÁNGEL B,COLLEY S B,HOKE S M,et al. The reproductive seasonality and gametogenic cycle of *Acropora cervicornis* off Broward County,Florida,USA [J]. Coral Reefs,2006,25(1):110-122.

[11] HARRISON P L. Sexual reproduction of reef corals and application to coral restoration [M]//WOLANSKI E,KINGSFORD M J. Oceanographic processes of coral reefs. 2nd ed. Boca Raton:CRC Press,2024:419-437.

[12] CRAGGS J,GUEST J R,DAVIS M,et al. Inducing broadcast coral spawning *ex situ*: closed system mesocosm design and husbandry protocol [J]. Ecology and Evolution,2017,7(24):11066-11078.

[13] O'NEIL K L,SERAFIN R M,PATTERSON J T,et al. Repeated *ex situ* spawning in two highly disease susceptible corals in the family Meandrinidae [J]. Frontiers in Marine Science,2021,8:669976.

[14] WEI F,CUI M Y,HUANG W,et al. *Ex situ* reproduction and recruitment of scleractinian coral *Galaxea fascicularis* [J]. Marine Biology,2023,170(3):30.

[15] LAFOREST K V,PETRIK C G,HYLTON A A,et al. Induced sexual reproduction *ex situ* reveals bidirectional sex change of the coral *Montastraea cavernosa* [J]. Coral Reefs,2024,43(5):1405-1416.

[16] WALLACE C C. Reproduction recruitment and fragmentation in nine sympatric species of the coral genus *Acropora* [J]. Marine Biology,1985,88:217-233.

[17] GLYNN P W,GASSMAN N J,EAKIN C M,et al. Reef coral reproduction in the eastern Pacific:Costa Rica,Panama,and Galapagos Islands (Ecuador) [J]. Marine Biology,1991,109(3):355-368.

[18] SHLESINGER Y,GOULET T L,LOYA Y. Reproductive patterns of scleractinian corals in the northern Red Sea [J]. Marine Biology,1998,132(4):691-701.

[19] GUEST J R. Reproductive patterns of scleractinian corals on Singapore's reefs [D]. Singapore: National University of Singapore,2004.

[20] NOZAWA Y,TOKESHI M,NOJIMA S. Reproduction and recruitment of scleractinian corals in a high-latitude coral community, Amakusa, southwestern Japan [J]. Marine Biology,2006,149(5):1047-1058.

[21] RODRÍGUEZ-TRONCOSO A P,CARPIZO-ITUARTE E,LEYTE-MORALES G E,et al. Sexual reproduction of three coral species from the Mexican South Pacific [J]. Marine Biology,2011,158:2673-2683.

[22] 李元超,黄晖,董志军,等.鹿回头佳丽鹿角珊瑚卵母细胞发育的组织学研究[J].热带海洋学报,2009,28(1):56-60.

[23] 杨小东.澄黄滨珊瑚、大管孔珊瑚和丛生盔形珊瑚性腺发育与生长规律的研究[D].湛江:广东海洋大学,2013.

[24] 张诗泽,黄晖,张浴阳,等.鹿回头多孔鹿角珊瑚与丛生盔形珊瑚性腺组织学研究[J].生态科学,2016,35(1):41-46.

[25] 韦芬,崔梦瑶,余克服,等.涠洲岛海域美丽鹿角珊瑚和秘密角蜂巢珊瑚的性腺发育研究[J].海洋学报,2023,45(12):92-100.

[26] 王欣,高霆炜,陈骁,等.涠洲岛园艺式珊瑚苗圃的架设与移植[J].广西科学,2017,24(5):462-467.

[27] PUNTIN G,CRAGGS J,HAYDEN R,et al. The reef-building coral *Galaxea fascicularis*: a new model system for coral symbiosis research [J]. Coral Reefs,

中国知网 https://www.cnki.net

2023,42:239-252.

[28] DIAS M,FERREIRA A,GOUVEIA R,et al. Synergistic effects of warming and lower salinity on the asexual reproduction of reef-forming corals [J]. Ecological Indicators,2019,98:334-348.

[29] OSINGA R,SCHUTTER M,GRIFFIOEN B,et al. The biology and economics of coral growth [J]. Marine Biotechnology,2011,13(4):658-671.

[30] 王淑红,洪文霆,陈纪新,等. 珊瑚人工繁育技术研究进展[J]. 应用生态学报,2015,26(9):2903-2912.

[31] 王永刚. 陆基养殖系统条件下的造礁石珊瑚人工繁育研究[D]. 南宁:广西大学,2021.

[32] LIN C H,NOZAWA Y. The influence of seawater temperature on the timing of coral spawning [J]. Coral Reefs,2023,42(2):417-426.

[33] 杨小东,肖宝华,廖宝林,等. 不同光照对稀杯盔形珊瑚生长及钙化的影响[J]. 海洋环境科学,2017,36(4):523-530.

[34] CRABBE M J C. Climate change,global warming and coral reefs:modelling the effects of temperature [J]. Computational Biology and Chemistry,2008,32(5):311-314.

[35] MCCOOK L,JOMPA J,DIAZ-PULIDO G. Competition between corals and algae on coral reefs:a review of evidence and mechanisms [J]. Coral Reefs,2001,19(4):400-417.

[36] HENRY J A,O'NEIL K L,PATTERSON J T. Native herbivores improve sexual propagation of threatened staghorn coral *Acropora cervicornis* [J]. Frontiers in Marine Science,2019,6:713.

[37] DING D S,SUN W T,PAN C H. Feeding of a scleractinian coral,*Goniopora columna*,on microalgae,yeast,and artificial feed in captivity [J]. Animals,2021,11(11):3009.

[38] JOKIEL P L,COLES S L. Effects of temperature on the mortality and growth of Hawaiian reef corals [J]. Marine Biology,1977,43:201-208.

[39] WIJGERDE T,HENKEMANS P,OSINGA R,et al. Effects of irradiance and light spectrum on growth of the scleractinian coral *Galaxea fascicularis*:applicability of LEP and LED lighting to coral aquaculture [J]. Aquaculture,2012,344/345/346/347/348/349:188-193.

[40] VILLINSKI J T. Depth-independent reproductive characteristics for the Caribbean reef-building coral *Montastraea faveolata* [J]. Marine Biology,2003,142:1043-1053.

[41] LEUZINGER S,WILLIS B L,ANTHONY K R N. Energy allocation in a reef coral under varying resource availability [J]. Marine Biology,2012,159:177-186.

[42] LIN C,ZHUO J M,CHONG G,et al. The effects of aquarium culture on coral oocyte ultrastructure [J]. Scientific Reports,2018,8:15159.

[43] LEUZINGER S,ANTHONY K R N,WILLIS B L. Reproductive energy investment in corals:scaling with module size [J]. Ecophysiology,2003,136:524-531.

[44] 莫洪燕. 西沙群岛珊瑚脂质的种间与季节性差异及其对能量供给的意义[D]. 南宁:广西大学,2024.

[45] 张志楠. 南海造礁石珊瑚营养方式的属种间、空间差异及其生态意义[D]. 南宁:广西大学,2021.

[46] HII Y S,SOO C L,LIEW H C. Feeding of scleractinian coral,*Galaxea fascicularis*,on *Artemia salina* nauplii in captivity [J]. Aquaculture International,2009,17:363-376.

[47] WIJGERDE T,DIANTARI R,LEWARU M W,et al. Extracoelenteric zooplankton feeding is a key mechanism of nutrient acquisition for the scleractinian coral *Galaxea fascicularis* [J]. The Journal of Experimental Biology,2011,214(Pt20):3351-3357.

[48] YU X L,LIU C Y,JIANG L,et al. Local adaptation of trophic strategy determined the tolerance of coral *Galaxea fascicularis* to environmental fluctuations [J]. Science of the Total Environment,2024,943:173694.

[49] MARTINEZ S,GROVER R,FERRIER-PAGÈS C. Unveiling the importance of heterotrophy for coral symbiosis under heat stress [J]. mBio,2024,15:e0196624.

[50] 俞晓磊,江雷,罗勇,等. 异养营养对丛生盔形珊瑚代谢及共生藻光合生理的影响[J]. 海洋科学,2019,43(12):81-88.

[51] YU X L,JIANG L,LUO Y,et al. Role of feeding and physiological trade-offs in sustaining resilience of the coral *Galaxea fascicularis* to light limitation [J]. Coral Reefs,2023,42:1297-1312.

[52] CONLAN J A,HUMPHREY C A,SEVERATI A,et al. Elucidating an optimal diet for captive *Acropora* corals [J]. Aquaculture,2019,513:734420.

[53] CONLAN J A,BAY L K,SEVERATI A,et al. Comparing the capacity of five different dietary treatments to optimise growth and nutritional composition in two scleractinian corals [J]. PLoS One,2018,13(11):e0207956.

中国知网 https://www.cnki.net

Gonadal Development of Two Scleractinian Coral Species under Indoor Cultivation Conditions

HUANG Feifei[1,2], CUI Mengyao[1,2], WEI Fen[1,2**], YANG Xiyue[1,2], PAN Xiaoyuan[1,2,3], YU Haoyu[1,2]

(1. Guangxi Laboratory on the Study of Coral Reefs in the South China Sea, Coral Reef Research Center of China, Guangxi University, Nanning, Guangxi, 530004, China; 2. School of Marine Sciences, Guangxi University, Nanning, Guangxi, 530004, China; 3. School of Resources, Environment and Materials, Guangxi University, Nanning, Guangxi, 530004, China)

Abstract: To investigate the gonadal development patterns of scleractinian corals under artificial conditions, this study focused on two broadcast-spawning species, *Acropora formosa* and *Galaxea fascicularis*. Beginning in September 2021, a one-year indoor cultivation experiment was conducted to observe their gonadal development, and the results were compared with corals in the wild. It was found that the initiation of oocyte development in *A. formosa* under indoor conditions was synchronous with that of wild corals. However, its gonadal development under indoor conditions was significantly delayed, reaching only stage Ⅱ by the end of the observation period. In contrast, the gonads of *G. fascicularis* cultivated indoors matured in late April, 2022, which was synchronous with that of wild populations. It is hypothesized the suspension of gonadal development in *A. formosa* cultivated indoors may be attributable to insufficient light, which limited autotrophic nutrition and was enough only to maintain normal growth. *G. fascicularis* exhibits strong autotrophic and heterotrophic abilities, thus being able to sustain normal gonadal development. This adaptability makes it more suitable for indoor artificial cultivation. This study provides baseline data on the gonadal development of indoor-cultivated scleractinian corals and offers theoretical support for the ecological restoration of coral reefs.

Key words: *Acropora formosa*; *Galaxea fascicularis*; gonadal development; *ex situ* cultivation; sexual reproduction

责任编辑:梁　晓


微信公众号投稿更便捷
联系电话:0771-2503923
邮箱:gxkx@gxas.cn
投稿系统网址:http://gxkx.ijournal.cn/gxkx/ch

中国知网　https://www.cnki.net



热带海洋学报
Journal of Tropical Oceanography
ISSN 1009-5470,CN 44-1500/P

《热带海洋学报》网络首发论文

题目：一株珊瑚来源二苯甲酮-3 降解菌 Sphingopyxis terrae SCSIO 90395 的分离鉴定及基因组特征

作者：刘名定，蔡永超，李洁，刘青，张健，吕丽娜，苏宏飞

网络首发日期：2025-12-10

引用格式：刘名定，蔡永超，李洁，刘青，张健，吕丽娜，苏宏飞．一株珊瑚来源二苯甲酮-3 降解菌 Sphingopyxis terrae SCSIO 90395 的分离鉴定及基因组特征[J/OL]．热带海洋学报. https://link.cnki.net/urlid/44.1500.P.20251209.1701.002



网络首发：在编辑部工作流程中，稿件从录用到出版要经历录用定稿、排版定稿、整期汇编定稿等阶段。录用定稿指内容已经确定，且通过同行评议、主编终审同意刊用的稿件。排版定稿指录用定稿按照期刊特定版式（包括网络呈现版式）排版后的稿件，可暂不确定出版年、卷、期和页码。整期汇编定稿指出版年、卷、期、页码均已确定的印刷或数字出版的整期汇编稿件。录用定稿网络首发稿件内容必须符合《出版管理条例》和《期刊出版管理规定》的有关规定；学术研究成果具有创新性、科学性和先进性，符合编辑部对刊文的录用要求，不存在学术不端行为及其他侵权行为；稿件内容应基本符合国家有关书刊编辑、出版的技术标准，正确使用和统一规范语言文字、符号、数字、外文字母、法定计量单位及地图标注等。为确保录用定稿网络首发的严肃性，录用定稿一经发布，不得修改论文题目、作者、机构名称和学术内容，只可基于编辑规范进行少量文字的修改。

出版确认：纸质期刊编辑部通过与《中国学术期刊（光盘版）》电子杂志社有限公司签约，在《中国学术期刊（网络版）》出版传播平台上创办与纸质期刊内容一致的网络版，以单篇或整期出版形式，在印刷出版之前刊发论文的录用定稿、排版定稿、整期汇编定稿。因为《中国学术期刊（网络版）》是国家新闻出版广电总局批准的网络连续型出版物（ISSN 2096-4188，CN 11-6037/Z），所以签约期刊的网络版上网络首发论文视为正式出版。

网络首发时间：2025-12-10 16:40:42　网络首发地址：https://link.cnki.net/urlid/44.1500.P.20251209.1701.002

一株珊瑚来源二苯甲酮-3 降解菌 *Sphingopyxis terrae* SCSIO 90395 的分离鉴定及基因组特征*

刘名定[1, 2, 3, 4],蔡永超[2, 3],李洁[2, 3],刘青[2, 3],张健[2, 3],吕丽娜[2, 3],苏宏飞[1, 4]
1. 广西大学资源环境与材料学院，广西 南宁 530004;
2. 热带海洋环境与岛礁生态全国重点实验室，中国科学院南海海洋研究所，广东 广州 510301;
3. 海南三亚海洋生态系统国家野外科学观测研究站，中国科学院海南热带海洋生物实验站，海南 三亚 572000;
4. 广西大学海洋学院，广西南海珊瑚礁研究重点实验室，广西 南宁 530004

摘要：二苯甲酮-3(2-Hydroxy-4-methoxybenzophenone, BP-3)是一种广泛添加于防晒霜和个人护理产品中的有机紫外线吸收剂，作为海洋新兴污染物，已被证实在珊瑚礁生态系统中存在富集风险并对生态安全构成潜在威胁。为探究 BP-3 在珊瑚礁生态系统中的生物去除途径，本研究从南海丛生盔型珊瑚(*Galaxea fascicularis*)组织样品中富集分离获得一株具备 BP-3(benzonphenone-3)降解功能的海洋细菌 *Sphingopyxis terrae* SCSIO 90395，并分析其降解活性和潜在代谢机制。结果表明：在以 BP-3 为唯一碳源的条件下，该菌株在 48h 内对 BP-3 的降解率达 30%。*S. terrae* SCSIO 90395 基因组大小为 3892925bp, GC(guanine-cytosine)含量为 64.81%，共预测到 3732 个编码基因，富含多个与芳香族化合物代谢和细胞色素 P450 相关的功能基因。分子对接分析结果进一步表明，由 gene0737 编码的细胞色素 P450 酶与 BP-3 之间具有较高的结合亲和力，具备启动 BP-3 生物降解的潜力。研究结果为发展基于珊瑚原位功能微生物的 BP-3 污染生物修复提供了新的菌种资源与理论支撑。

关键词：珊瑚共生菌；二苯甲酮-3；微生物降解；基因组分析

Isolation, identification and genomic characteristics of a coral-derived Benzophenone-3-degrading *Sphingopyxis terrae* SCSIO 90395*

LIU Mingding[1, 2, 3, 4], CAI Yongchao[2, 3], LI Jie[2, 3], LIU Qing[2, 3], ZHANG Jian[2, 3], LYU Lina[2, 3], SU Hongfei[1, 4]
1. School of Resources, Environment and Materials, Guangxi University, Nanning 530004, China;
2. State Key Laboratory of Tropical Oceanography, South China Sea Institute of Oceanology, Chinese Academy of Sciences, Guangzhou, 510301, China;
3. Sanya National Marine Ecosystem Research Station, Tropical Marine Biological Research Station in Hainan, Chinese Academy of Sciences, Sanya 572000, China;
4. School of Marine Sciences, Guangxi University, Guangxi Laboratory on the Study of Coral Reefs in the South China Sea, Nanning 530004, China

Abstract:. Benzophenone-3 (2-Hydroxy-4-methoxybenzophenone, BP-3) is an organic ultraviolet (UV) filter widely used in sunscreens and personal care products. As an emerging marine contaminant, BP-3 bioaccumulates in coral reef ecosystems, posing possible ecological risks. To explore its biodegradation pathways, a BP-3(benzonphenone-3) degrading bacteria, *Sphingopyxis terrae* SCSIO 90395, was isolated from the coral *Galaxea fascicularis* collected in the South China Sea. The strain degraded approximately 30% of BP-3 within 48 hours when provided as the sole carbon source. Genome analysis (3.89 Mb, 64.81%) revealed 3732 putative protein-coding sequences, including those associated with aromatic compound metabolism and cytochrome P450 enzymes. Molecular docking suggested that a cytochrome P450 enzyme encoded by gene0737 has high binding affinity to BP-3, implying a potential role in its biodegradation. These findings provided a novel microbial resource and establish a theoretical foundation for developing coral-associated microbial strategies for BP-3 bioremediation.
Key words: coral-associated bacteria; Benzophenone-3; microbial degradation; genomic analysis

二苯甲酮-3(2-Hydroxy-4-methoxybenzophenone, BP-3)是一种能够有效吸收 UVA(ultraviolet A)和 UVB (ultraviolet B)的有机紫外线吸收剂(Liu et al, 2011)。凭借良好的光稳定性和紫外线过滤性能，BP-3(benzonphenone-3)被广泛添加于防晒霜及多类个人护理产品中，在我国化妆品中的允许添加含量上限为 10%(Sánchez-Quiles et al, 2015)。据统计，全球热带地区每年使用防晒霜总量约为 16000~25000t，其中约有 4000~6000t 通过生活污水排放、工业活动和海滨旅游等途径进入水体，并最终汇入海洋环境(Tsui et al, 2019; Astel et al, 2020)。由于 BP-3 具有较高的辛醇—水分配系数，易在环境中富集，并表现出持久性、生物累积性与生态毒性(Apel et al, 2018)。

珊瑚礁生态系统作为最具生产力和生物多样性的生态系统之一，为大约 25%的海洋生物提供栖息地和食物来源(Moeller et al, 2021)，被誉为“海洋中的热带雨林”(赵美霞等, 2006)。然而，生态风险评估显示, BP-3 污染可能造成约

基金项目：国家自然科学基金项目(U23A2036)；广西科技基地和人才专项(桂科 AD25069075)；热带海洋环境与岛礁生态全国重点实验室自主项目(SKLTO2025PT002)
作者简介：刘名定(2001—)，男，湖南省衡阳市人，硕士研究生，从事海洋微生物相关研究。email: mingding_liu@163.com
通信作者：苏宏飞。email: shf2016@gxu.edu.cn
Foundation item: National Natural Science Foundation of China (U23A2036); Guangxi Science and Technology Program (GuiKe AD25069075); The program of State Key Laboratory of Tropical Oceanography, South China Sea Institute of Oceanology, Chinese Academy of Sciences (SKLTO2025PT002)
Corresponding author:. SU Hongfei. email: shf2016@gxu.edu.cn

73%的沿海珊瑚和 20%的近海珊瑚面临白化风险(Pei et al, 2023)。研究表明, BP-3 可在珊瑚体内积累(Tsui et al, 2017; Mitchelmore et al, 2019; Pei et al, 2023; Lyu et al, 2025), 导致珊瑚幼虫发育异常和基因变异(Danovaro et al, 2008; He et al, 2019; Wijgerde et al, 2020), 并诱发共生虫黄藻裂解, 加速珊瑚白化与死亡(Downs et al, 2016)。鉴于珊瑚礁在维持海洋生态平衡和沿海生态安全方面的重要作用, BP-3 的污染现状已对珊瑚礁生态系统构成严重威胁, 因此亟需开发高效、环境友好的去除途径, 以降低其对珊瑚礁的生态风险。

目前, 针对 BP-3 等有机污染物的环境治理技术主要包括物理吸附、化学氧化及生物降解等方式(Chen et al, 2015; Guo et al, 2016; Rajesha et al, 2019)。其中, 微生物降解法因其可持续、环境友好而更具应用潜力。已有研究学者从长期受到 BP-3 污染的沉积物或土壤中分离出多株降解菌, 如嗜甲基菌(*Methylophilus* sp.)、鞘氨醇单胞菌(*Sphingomonas wittichii*)、红球菌(*Rhodococcus* sp.)、华西克雷伯氏菌(*Klebsiella huaxiensis*)以及红色红球菌(*Rhodococcus ruber*)等(Jin et al, 2019; Fagervold et al, 2021; Baek et al, 2022; Omeroglu et al, 2025; Liu et al, 2025)。然而, 这些菌株大多来源于陆地环境, 若作为外来物种应用于海洋中 BP-3 污染修复时, 可能会对本地微生物群落造成干扰, 从而引发生态安全性问题。珊瑚作为典型的海洋生物, 其表面、黏液和组织中共生着丰富且高度适应的微生物群落(Reshef et al, 2006; Thompson et al, 2015; Bourne et al, 2016), 在长期的 BP-3 胁迫下, 可能演化出对 BP-3 具备降解潜力的土著微生物资源, 为针对性生物修复提供重要资源。

为此, 本研究选择南海优势造礁石珊瑚之一的丛生盔型珊瑚(*Galaxea fascicularis*)作为研究对象, 在以 BP-3 为唯一碳源的培养条件下进行多轮微生物富集, 并从中分离和鉴定得到一株具备 BP-3 降解能力的海洋细菌 *Sphingopyxis terrae* SCSIO 90395。通过系统分析该菌株的降解特性和基因组功能注释, 旨在揭示其在 BP-3 微生物修复中的潜在应用价值, 并为珊瑚礁生态系统防晒霜污染治理提供理论支撑和新的候选菌种资源。

1 材料和方法

1.1 材料

1.1.1 珊瑚样品驯养和 BP-3 胁迫处理

2023 年 11 月, 在海南省三亚市鹿回头海域(18°12′39.13″N, 109°28′50.09″E)采集丛生盔型珊瑚, 剪取适量珊瑚断枝置于自然海水循环缸内驯养 5~7d, 待生长状态恢复后转入室内珊瑚养殖系统, 并在 BP-3 胁迫条件下维持 20d。养殖条件设置如下: BP-3 初始浓度为 400ng·L^{-1}, 光照强度 120~140Lux(光照时间 12h:12h), 盐度 32‰~35‰, pH7.8~8.2, 实验期间, 每日更换 50%海水并补充 200ng·L^{-1} 的 BP-3。

1.1.2 培养基与试剂

BP-3 标准品(≥98%)购自 Sigma-Aldrich 公司; BP-1 标准品(≥99%)购自上海麦克林生化科技股份有限公司; 细菌 DNA 提取试剂盒购自天根生物科技有限公司; 用于扩增 16S rRNA 基因的通用引物 27F(5'-AGAGTTTGATCMTGGCTCAG-3')和 1492R(5'-GGTTACCTTGTTACGACTT-3')由生工生物工程(上海)股份有限公司合成; 2×SanTaq PCR Mix 购自广州欣凯莱生物技术有限公司。

富集培养和筛选使用人工海水培养基(marine microalgae culture medium, MMC): 23.7g·L^{-1} NaCl, 1.0g·L^{-1} KNO_3, 1.0g·L^{-1} NH_4Cl, 1.7g·L^{-1} KH_2PO_4, 3.0g·L^{-1} Na_2HPO_4, 0.3g·L^{-1} NaH_2PO_4, 3.5g·L^{-1} $MgSO_4·7H_2O$, 调节 pH 至 7.4 左右, 121℃灭菌 20min, 使用前添加 0.1%(*v*/*v*)的微量元素和维生素溶液(Liu et al, 2005)。分离培养使用 R2A 琼脂培养基(Dang et al, 2023): 0.25g·L^{-1} 胰蛋白胨, 0.5g·L^{-1} 酸水解酪蛋白, 0.5g·L^{-1} 酵母浸粉, 0.5g·L^{-1} 可溶性淀粉, 0.3g·L^{-1} K_2HPO_4, 0.1g·L^{-1} $MgSO_4$, 0.3g·L^{-1} 丙酮酸钠, 0.25g·L^{-1} 蛋白胨, 0.5g·L^{-1} 葡萄糖, 12.0g·L^{-1} 琼脂, 调节 pH 至 7.2, 121℃灭菌 20min。

1.2 方法

1.2.1 BP-3 降解菌的富集、分离和筛选

取在 BP-3 胁迫条件下培养 20d 的珊瑚断枝, 用无菌海水清洗表面后, 在无菌超净工作台内, 使用灭菌气枪分离丛生盔型珊瑚样品的组织与骨骼, 并用无菌海水收集组织均质液。取 1mL 均质液接种至含 29mL MMC 培养基和 400ng·L^{-1}BP-3 的无菌玻璃培养管内, 于 28℃、160r·min^{-1} 避光培养 20d。培养结束后, 按照 2%的接种量转移至新的 MMC-BP3 液体培养基中, 连续富集 3 轮。第 3 轮富集液梯度稀释后涂布于 R2A 琼脂平板, 在 25℃恒温培养箱培养 5~7d, 根据菌落形态特征挑取单菌落, 多次划线纯化后获得纯菌。将纯菌接种于 MMC-BP3 液体培养基中以验证其降解能力, 选择具有降解活性的菌株进行后续实验, 并进行编号和记录, 同时以 25%甘油作为保护剂于-80℃保藏。

1.2.2 菌株鉴定

从 R2A 琼脂平板上收集菌体, 采用细菌 DNA 提取试剂盒提取细菌基因组 DNA, 使用细菌通用引物 27F 和 1492R 对 16S rRNA 基因序列进行 PCR 扩增, 扩增反应体系为 50μL: DNA 模板 1μL, ddH_2O 20μL, 通用引物 27F 和 1492R 各 2μL, 以及 2×SanTaq PCR Mix 25μL。PCR 反应过程: 95℃预变性 5min30s, 54℃退火 30s, 72℃延伸 90s, 72℃终延伸 10min, 循环 30 次。PCR 扩增产物通过 1%(*w*/*v*)凝胶电泳检验扩增效果后, 回收扩增产物进行 16S rRNA 测序。获得的 16S rRNA 基因序列经 SeqMan 7.1 软件拼接后, 提交至 EzBioCloud 网站(https://www.ezbiocloud.net)进行比对鉴定(Yoon et al, 2017)。根据序列比对结果, 选取具有最高同源性的 16S rRNA 基因作为参照序列, 使用在线工具 genome-to-genome distance calculator(GGDC)

(https://ggdc.dsmz.de)构建系统发育树(Meier-Kolthoff et al, 2013; Meier-Kolthoff et al, 2021)。

将菌株 SCSIO 90395 的基因组数据上传至 TYGS(The Type Strain Genome Server, https://tygs.dsmz.de), 进行基于全基因组的系统发育分析(Meier-Kolthoff et al, 2019; Meier-Kolthoff et al, 2021)。

1.2.3 BP-3 降解率测定

从-80℃冰箱中取出保藏菌种, 在超净工作台中使用接种环蘸取菌液在 R2A 琼脂平板上进行划线, 置于 25℃恒温培养箱中培养 24h。刮取单菌落接种于 MMC-BP3 液体培养基中, 记录初始 OD_{600} 值后, 置于 25℃、160r·min^{-1}的恒温摇床振荡培养。空白对照组仅添加 BP-3, 每个处理设 3 个生物学重复。培养过程中每隔 24h 取样, 连续监测 6d。

参考 Omeroglu 等(2025)的方法, 使用乙酸乙酯萃取降解后的 BP-3 及其中间代谢产物(Omeroglu et al, 2025)。在实验不同时间点收集 2mL 培养物, 加入 2mL 乙酸乙酯, 于 25℃超声 10min, 收集有机相; 重复萃取一次后, 将两次萃取得到的有机相在氮气流下浓缩后并以甲醇复溶, 通过 0.22μm 滤膜过滤后利用高效液相色谱(HPLC)测定 BP-3 及其代谢物含量。

色谱分析采用 ZORBAX 300SB-C18 柱(4.6×250mm, 5μm)(Jin et al, 2019), 流动相为 0.01%甲酸水溶液与乙腈, 流速 1mL·min^{-1}, 柱温 25℃, 进样体积 20μL, 检测波长 290nm。BP-3 降解率计算公式: 降解率=[(C_0-C_t)/ C_0]×100%, 其中 C_0 为实验初始 BP-3 浓度(mg·L^{-1}), C_t 为各时间点测定的 BP-3 残留浓度(mg·L^{-1})。

采用外标法对 BP-3 及降解产物进行定量分析。将标准储备液用甲醇逐级稀释, 配制成不同浓度的标准液(1、5、10、20、50、100mg·L^{-1}), 按照上述方法依次进样, 记录峰面积, 以浓度为横坐标, 峰面积为纵坐标建立标准曲线。

1.2.4 BP-3 降解中间产物鉴定

参考 Baek 等(2022)的方法并进行适当修改(Baek et al, 2022)。采用高效液相色谱-串联质谱(HPLC-MS/MS)鉴定菌株 SCSIO 90395 降解 BP-3 过程中产生的中间产物。色谱条件如下: 使用Eclipse Plus C18色谱柱(4.6mm×250mm,5μm); 流动相 A 由 95%水、5%乙腈、0.01%甲酸和 2.5mmol 甲酸铵组成, 流动相 B 为 95%乙腈、5%水、0.01%甲酸和 2.5mmol 甲酸铵的混合液。梯度洗脱程序设置为: 0~23 min, 95%A; 23~25min, 5%A; 25~30min, 95%A。流速设定为 1mL·min^{-1}; 柱温为 30℃; 进样体积为 20μL。质谱条件为电喷雾(ESI)离子源, 正离子扫描, *m/z* 范围: 50-600。

1.2.5 全基因组测序

为解析该菌株对 BP-3 的降解机制和潜在功能基因, 对该菌株全基因组进行测序和注释分析。采用 illumina Nova Seq 6000 进行文库构建和测序, 原始数据经质控后进行基因组组装。基因组编码序列(CDS)使用 Prodigal v2.6.3(Hyatt et al, 2010)预测, 质粒基因采用 GeneMarkS(Besemer et al, 2005)预测, tRNA 和 rRNA 分别通过 tRNAscan-SE v2.0(Chan et al, 2019)和 Barrnapv0.9(https://github.com/tseemann/barrnap)进行预测。功能注释通过 BLASTP、Diamond、HMMER 等序列比对工具完成, 并结合蛋白质直系同源簇(cluster of orthologous groups of proteins,COG)、京都基因与基因组百科全书(KEGG, Kyoto encyclopedia of genes and genomes)数据库进行比对分析。

1.2.6 BP-3 与降解基因分子对接

分子对接参照 Adhish 等(2024)的方法(Adhish et al, 2024)。从 PubChem 数据库(https://pubchem.ncbi.nlm.nih.gov)下载 BP-3 的三维结构(Kim et al, 2024), 将潜在降解基因的蛋白质氨基酸序列上传至 SWISS-MODEL 服务器(https://swissmodel.expasy.org)预测三维结构(Kamguia et al, 2025)。利用 AutoDockTools-1.5.7 进行分子对接, 通过计算配体和蛋白质之间的相互作用力确定最佳结合模式, 并采用 PyMOL 对结果进行可视化分析。

1.2.7 数据统计与分析

数据处理和统计分析使用 SPSS 27, 采用方差分析(analysis of variance, ANOVA)和独立样本 T 检验进行统计学差异检验, P<0.05 表示差异显著。

2 结果与分析

2.1 BP-3 降解菌株的分离与鉴定

通过对丛生盔型珊瑚组织匀浆液进行以 BP-3 为唯一碳源的三轮富集培养, 共分离获得 10 株可在含 BP-3 培养基中生长的细菌。对纯培养菌株进行 BP-3 降解实验后, 筛选出一株能以 BP-3 为唯一碳源的降解菌 SCSIO 90395。为明确该菌株的系统分类地位, 首先基于 16S rRNA 基因序列构建系统发育树进行初步分析。结果显示(图 1a), 菌株 SCSIO 90395 与土地鞘氨醇盒菌(*Sphingopyxis terrae*) NBRC 15098 的 16S rRNA 基因序列具有最高相似性, 为 99.63%。进一步对其进行全基因组测序, 并在典型菌株基因组服务器(The Type Strain Genome Server, TYGS)上进行比对分析, 如图 1b 所示, SCSIO 90395 与 *S. terrae* NBRC 15098 的 dDDH 值(数字 DNA-DNA 杂交值)为 85.7%, 高于 70%的物种界定阈值(Deng et al, 2024), 且两者在系统发育树上聚为一支, 因此将菌株 SCSIO 90395 鉴定为土地鞘氨醇盒菌(*Sphingopyxis terrae*)。

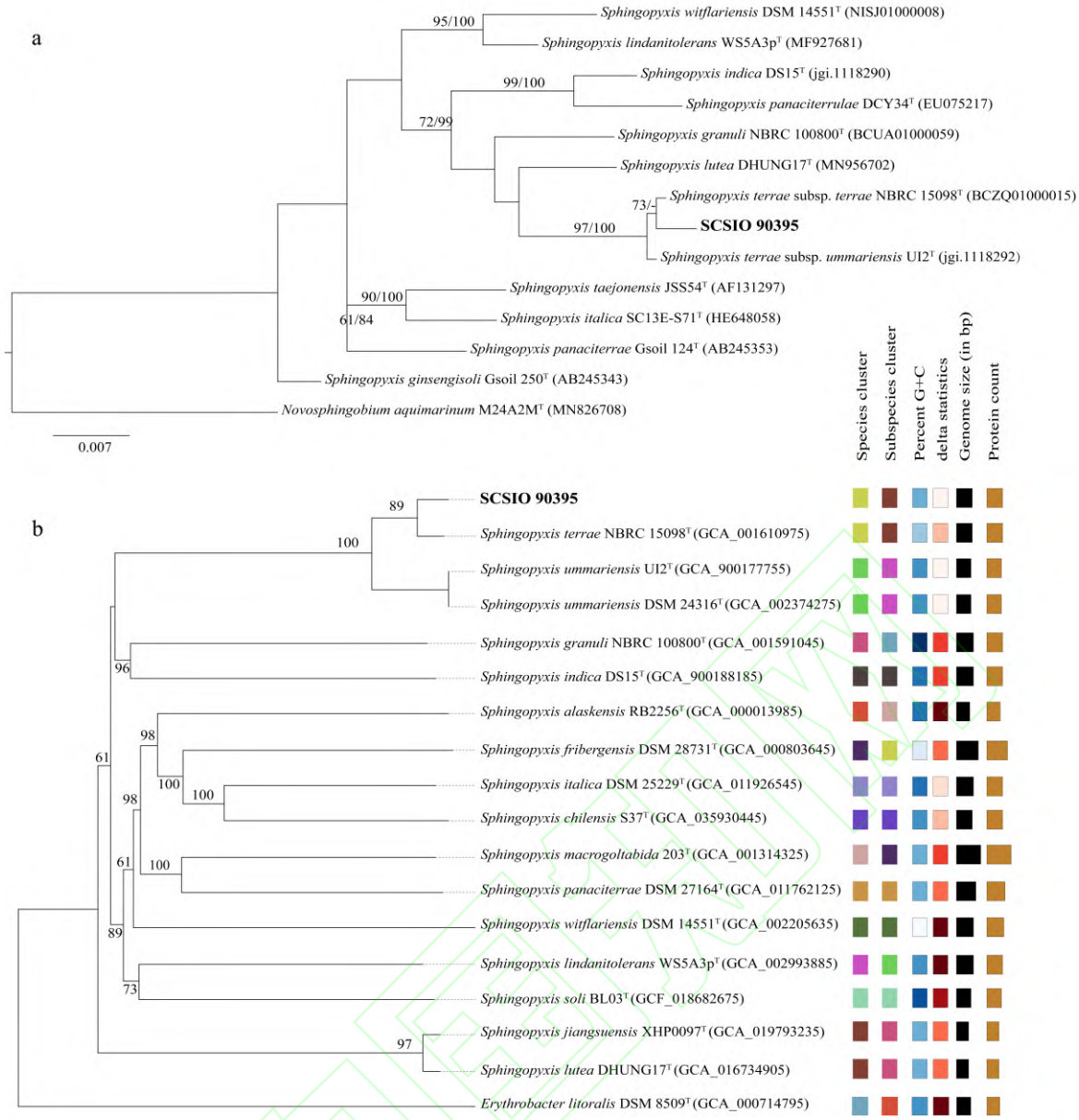


图 1　菌株 SCSIO 90395 的系统发育树。(a)基于 16S rRNA 基因序列的构建结果；(b)基于全基因组序列的构建结果

Fig. 1　Phylogenetic tree of strain SCSIO 90395. (a)Inferred from the 16S rRNA gene sequence; (b)Inferred from the whole-genome sequence

2.2　*S. terrae* SCSIO 90395 **对 BP-3 的降解**

由图 2 可知, BP-3 的标准曲线回归方程为 y=72.554x-3.5119, R^2=0.9999；BP-1 的标准曲线回归方程为 y=68.833x-71.575, R^2=0.9997。两者的相关系数均大于 0.999, 表明线性关系良好。

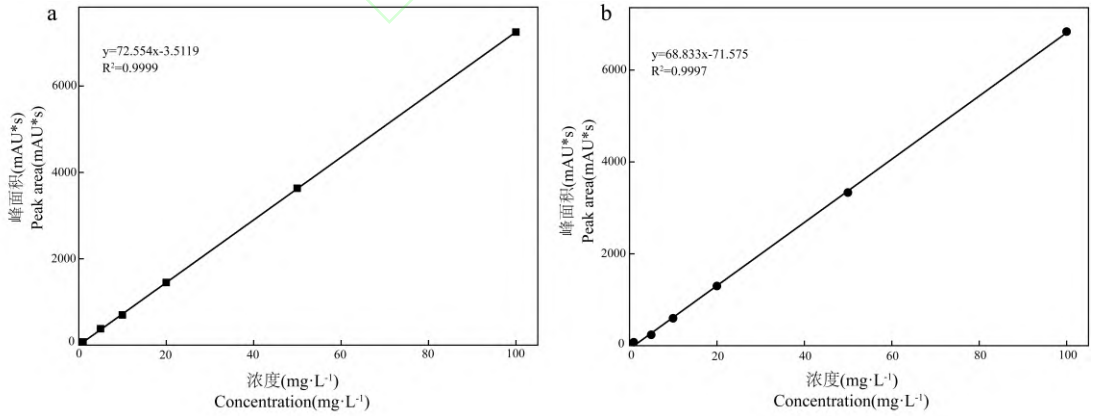


图 2　标准曲线 (a)BP-3；(b)BP-1

Fig. 2　Standard curve. (a)BP-3; (b)BP-1

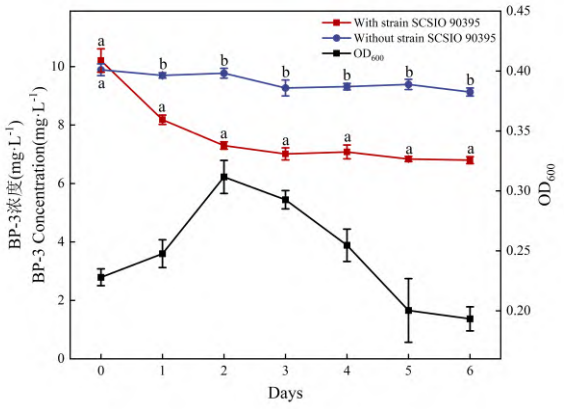


图 3　*S. terrae* SCSIO 90395 以 BP-3 为唯一碳源的降解和生长情况(具有不同标记的字母代表差异显著, p<0.05)

Fig. 3　Degradation and growth of *S. terrae* SCSIO 90395 using BP-3 as sole carbon source (different letters indicate significant differences, $p < 0.05$).

在以 BP-3 为唯一碳源的培养条件下, *S. terrae* SCSIO 90395 表现出一定的生长能力和显著的 BP-3 降解活性。如图 3 所示, 培养初期菌液的 OD_{600} 值为 0.22, 随后菌体浓度逐渐升高, 第 2 天达到约 0.32；与此同时, BP-3 浓度持续下降, 2 天内降解率约 30%, 显著高于空白对照组中的自然衰减水平。

2.3　BP-3 降解产物鉴定

为明确 *S. terrae* SCSIO 90395 在 BP-3 降解过程中产生的中间代谢产物, 采用 HPLC-MS/MS 进行检测。结果显示(图 4), 在菌株培养液中出现主要色谱峰, 其分子式为 $C_{13}H_{10}O_3$, 根据碎片离子峰 *m/z* 137.0236 和 *m/z* 105.0344, 将其鉴定为 BP-3 的主要去甲基化产物 BP-1(2,4-二羟基二苯甲酮)。进一步的量化分析显示, BP-3 浓度从初始的 0.045mmol·L^{-1} 逐渐下降至第 6 天的 0.03mmol·L^{-1}, 降解量为 0.015mmol·L^{-1}；同时, BP-1 在培养过程中逐渐累积, 在第 6 天达到 0.0029mmol·L^{-1}(图 5)。

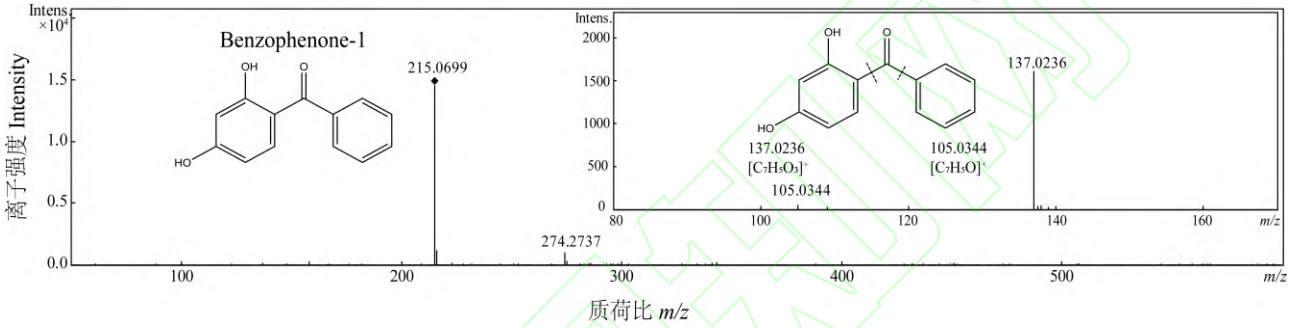


图 4　*S. terrae* SCSIO 90395 降解 BP-3 过程中间产物质谱图

Fig. 4　Mass spectra of intermediate substances during BP-3 degradation by *S. terrae* SCSIO 90395.

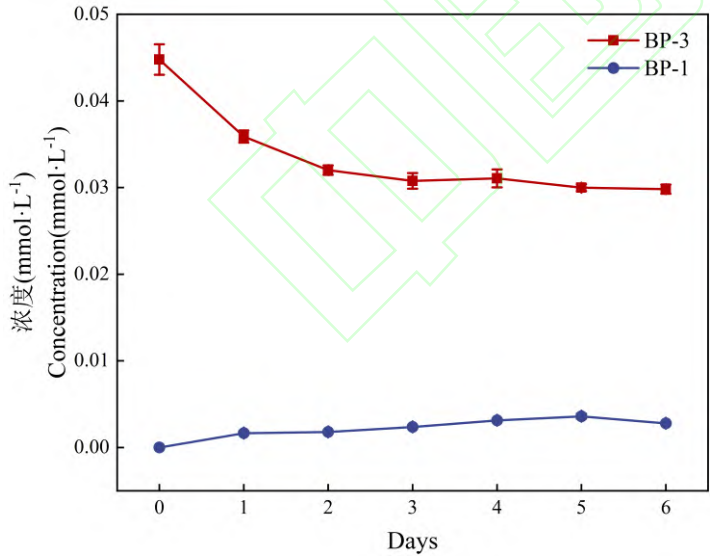


图 5　*S. terrae* SCSIO 90395 作用下 BP-3 降解及 BP-1 生成的浓度变化曲线

Fig. 5　Concentration profiles of BP-3 and the metabolite BP-1 during degradation by *S. terrae* SCSIO 90395.

2.4　*S. terrae* SCSIO 90395 基因组分析

2.4.1　基因组的基本特征

如图 6 所示, *S. terrae* SCSIO 90395 基因组全长 3,892,925bp, GC(guanine-cytosine)含量为 64.81%。预测编码基因(Coding sequence, CDSs)为 3732 个, 占整个基因组总长度的 91.14%。此外, 基因组中含有 46 个 tRNAs 基因、3 个 rRNA 基因(5S、16S、23S rRNA 各 1 个), 以及 16 个基因岛。

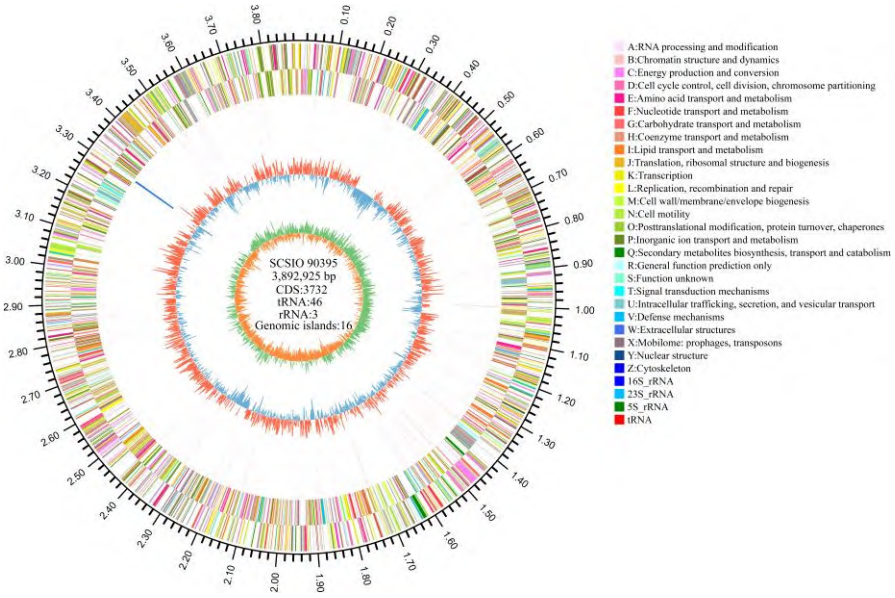


图 6　*S. terrae* SCSIO 90395 基因组图谱

(注：图谱的最外圈为基因组大小标识；第二圈和第三圈为正链和负链上的 CDS；第四圈为 rRNA 和 tRNA；第五圈为 GC 含量；最内圈为 GC-Skew 值)

Fig. 6　Whole genome map of *S. terrae* SCSIO 90395.

(Note: The outermost circle of the map indicates genome size; the second and third circles indicate CDS on the positive and negative strands; the fourth circle indicates rRNA and tRNA; the fifth circle indicates GC content; and the innermost circle indicates GC skew value).

2.4.2　基因功能注释

在预测的 3732 个编码基因中，共有 2973 个(79.66%)被注释到 COG 数据库(图 7a)。其中功能注释数量排名前五的类别依次为：一般功能预测(General function prediction only, R)、脂质转运与代谢(Lipid transport and metabolism, I)、转录(Transcription, K)、氨基酸转运与代谢(Amino acid transport and metabolism, E)以及细胞壁/膜/被膜生物合成(Cell wall/membrane/envelope biogenesis, M)。此外，基因组中共有 2639 个(70.71%)基因被注释到 KEGG 数据库中(图 7b)，其中 286 个基因与氨基酸代谢(Amino acid metabolism)相关，另有 193 个、189 个和 173 个基因分别归属于碳水化合物代谢(Carbohydrate metabolism)、辅因子与维生素代谢(Metabolism of cofactors and vitamins)以及能量代谢通路(Energy metabolism)。

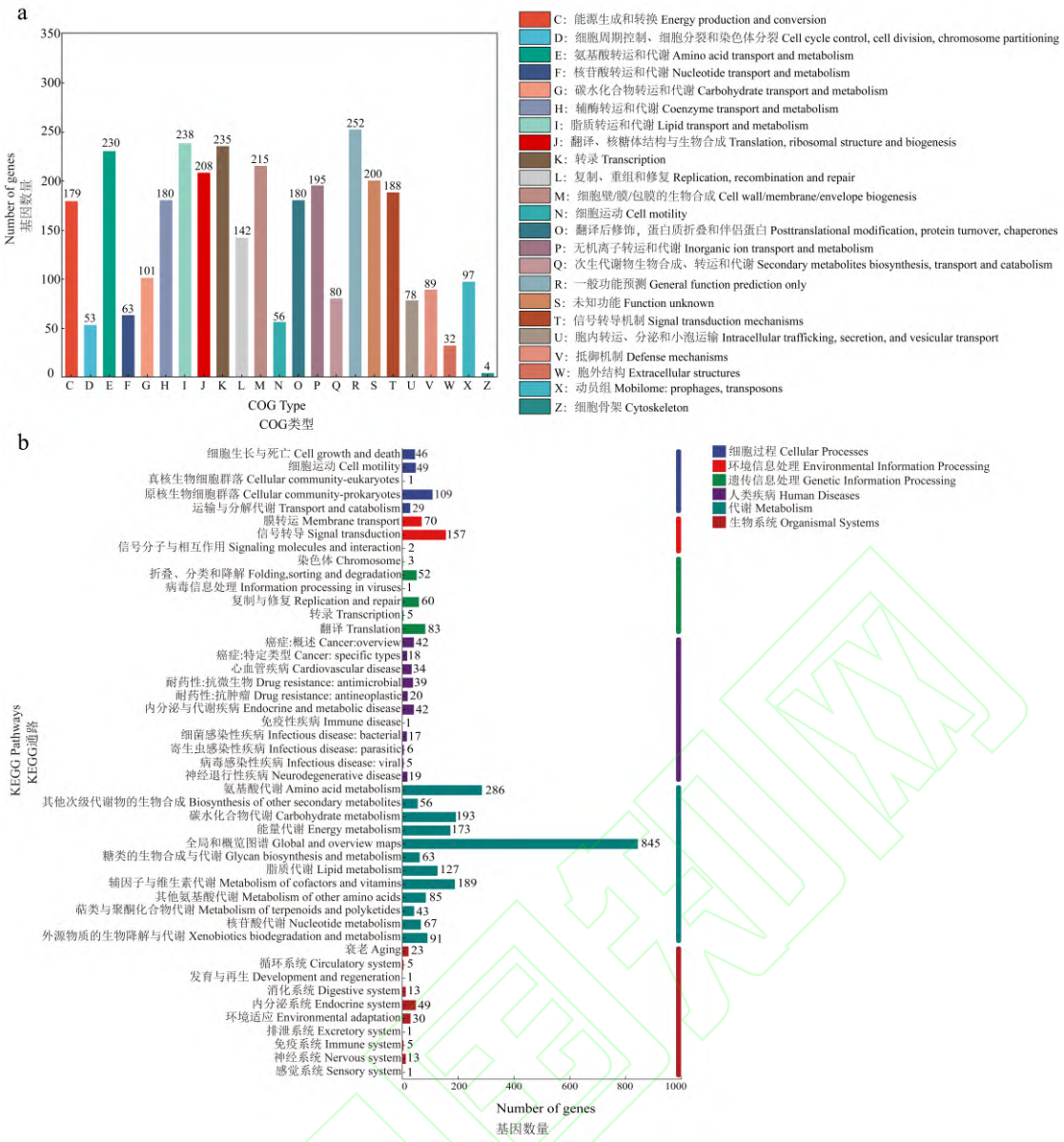


图 7　基因功能注释分类。(a)COG 功能注释；(b)KEGG 功能注释

Fig. 7　Functional classification of gene annotations. (a)COG functional annotation; (b)KEGG functional annotation

进一步分析 KEGG 功能注释结果发现, *S. terrae* SCSIO 90395 基因组中与物质代谢相关的基因占 72.9%, 涵盖了大多数微生物代谢通路及次级代谢产物的降解途径。并在此基础上, 筛查出多条与外源生物降解相关的代谢通路(表 1), 如苯甲酸盐降解通路、芳香族化合物降解通路、细胞色素 P450 代谢通路和多氯联苯代谢通路等, 表明该菌株具有较强的芳香族化合物降解潜力。

表 1　*S. terrae* SCSIO 90395 基因组中主要的生物降解和代谢调控通路及相关基因数量

Tab. 1　Major biodegradation and metabolic regulation pathways and related gene number in the genome of *S. terrae* SCSIO 90395

编号 r	通路	功能描述	注释数量/个
1	Ko00362	苯甲酸盐降解	37
2	Ko00980	细胞色素 P450 对异源化合物的代谢作用	20
3	Ko00626	萘降解	10
4	Ko00627	氨基苯甲酸盐降解	9
5	Ko00361	多氯联苯降解	8
6	Ko00622	二甲苯降解	7
7	Ko00643	苯乙烯降解	6
8	Ko00621	二噁英降解	5

2.4.3　BP-3 降解相关基因分析

在 *S. terrae* SCSIO 90395 基因组中, 注释到多种可能参与 BP-3 及其代谢产物降解和转化的关键功能基因(表 2)。其中, *acd* 基因编码的乙酰辅酶 A 脱氢酶在代谢过程中可催化脱氢反应(Qiu et al, 2024), *vanA* 基因编码的芳香环羟化双加氧酶 α 亚基能够介导芳香环的羟基化(Shan et al,

2024), *cypD_E* 属于细胞色素 P450 家族, 可催化去甲基化反应(Wang et al, 2023)。

表 2 *S. terrae* SCSIO 90395 基因组中与 BP-3 降解相关基因

Tab. 2 Genes of related to BP-3 degradation in the *S. terrae* SCSIO 90395 genome

KO 编号	同源基因	功能注释	注释数量/个
K00249	*acd*	乙酰辅酶 A 脱氢酶	26
K03862	*vanA*	芳香环羟化双加氧酶 α 亚基	2
-	*cypD_E*	细胞色素 P450	3
K00459	*npd*	硝酸盐单加氧酶	8
K00252	*gcdH*	戊二酰辅酶 A 脱氢酶	1
K01011	*sseA*	硫代硫酸盐/3-巯基丙酮酸硫转移酶	1

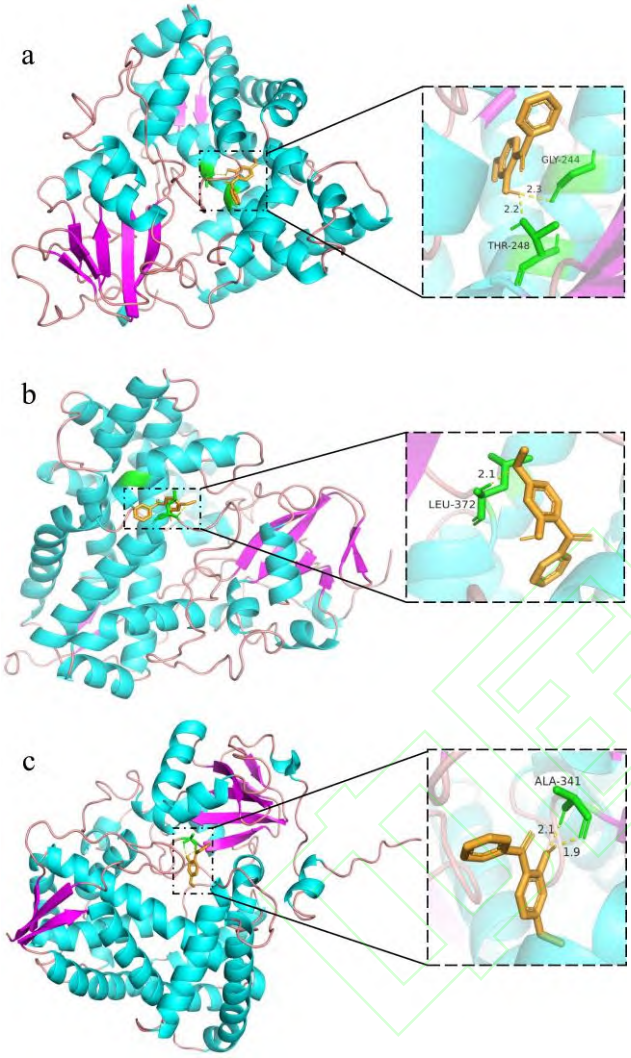


图 8 BP-3 和细胞色素 P450 的分子对接结果(a:gene0397; b:gene0433; c:gene0737)

Fig. 8 Molecular docking results of BP-3 and cytochrome P450(a:gene0397; b:gene0433; c:gene0737)

已有研究表明, 细胞色素 P450 酶可催化 BP-3 的去甲基化反应生成 BP-1(Baek et al, 2022)。因此, 为进一步分析 *S. terrae* SCSIO 90395 中细胞色素 P450 和 BP-3 的结合能力, 对编码 CYP450 的 gene0397(PDB ID:3LXH)、gene0433(PDB ID:6KBH)、gene0737(PDB ID: 2VE3)进行了分子对接。结合能是衡量复合物稳定性的核心指标, 负值越大, 表明结合能力越强, 形成的复合物越稳定(Yang et al, 2025)。结果显示, 三者与 BP-3 的结合能分别为-6.520、-6.520、-6.930kcal·mol^{-1}。进一步对对接结果进行可视化分析表明, 三者均与 BP-3 形成了氢键相互作用, 但结合模式存在差异。gene0397 与 BP-3 在对接位置通过 THR-248 和 GLY-244 两个氨基酸残基形成了 2 个氢键, 键长分别为 2.2Å 和 2.3Å(图 8a); gene0433 与 BP-3 在对接位置通过 LEU-372 形成 1 个氢键, 键长为 2.1Å, 并且 LEU-372 与 BP-3 的甲氧基形成结合位点(图 8b); gene0737 与 BP-3 在对接位置通过 ALA-341 形成 2 个氢键, 键长分别为 1.9Å、2.1Å(图 8c)。

3 讨论与结论

本研究通过以 BP-3 为唯一碳源的选择性富集, 从丛生盔型珊瑚样品中筛选获得一株具备 BP-3 降解功能的海洋细菌 SCSIO 90395, 经全基因组序列比对和系统发育分析, 将其鉴定为土地鞘氨醇盒菌(*Sphingopyxis terrae*)。已有研究表明, *Sphingopyxis* 属菌株能够降解多种难降解有机污染物, 具备较强的环境适应性和芳香族化合物降解潜力, 如三氯生、苯乙烯、四氢化萘等(Lee et al, 2012; Oelschlägel et al, 2015; Ledesma-García et al, 2016)。本研究的结果进一步表明 *Sphingopyxis terrae* 在珊瑚微生物群落中具备 BP-3 降解功能, 拓展了对该属菌株在海洋生态系统中的生态功能认知。与先前分离自污水处理厂活性污泥(Fagervold et al, 2021)、沉积物(Baek et al, 2022)等富营养且污染物稳定聚集环境的 BP-3 降解菌相比, *S. terrae* SCSIO 90395 来源于珊瑚内共生微生物群落, 更适应珊瑚礁生态系统的原位环境, 因此在用于珊瑚礁生物修复或污染治理中可能具备更好的生态适应性与应用潜力。

在 BP-3 的代谢过程中, 通过 HPLC-MS/MS 检测到其主要降解产物为 BP-1, 该产物已被多项研究报道为 BP-3 微生物降解的共同代谢中间体(Liu et al, 2011; Jin et al, 2019; Fagervold et al, 2021), 其生成机制主要依赖细胞色素 P450 催化的去甲基化反应(Baek et al, 2022), 该反应表现为苯环上的甲氧基被羟基取代。细胞色素 P450 酶(CYP450)是一类广泛存在于生物体内的血红素依赖型单加氧酶, 能够催化羟基化、去甲基化、环氧化等多种氧化反应, 在细菌降解外源有机污染物过程中发挥关键作用(Khmelevtsova et al, 2017; Yang et al, 2024; Wolf et al, 2024; Helvig et al, 2025)。全基因组分析结果显示, *S. terrae* SCSIO 90395 中注释到多种与芳香族化合物代谢相关的加氧酶编码基因, 这些基因

的存在表明该菌株在芳香环初步代谢方面具有较为丰富的酶学基础。利用分子对接技术发现 BP-3 与三个 CYP450 候选基因(gene0397、gene0433、gene0737)的结合能分别为-6.520、-6.520、-6.930kcal·mol^{-1}, 表明其与 BP-3 均具备较好的结合能力并形成稳定复合物(徐佳宁 等, 2025)。其中, gene0737 与 BP-3 具有更强的结合能和更短的氢键相互作用, 预示着它可能是 BP-3 降解的关键候选基因; 而 gene0433 与 BP-3 甲氧基的结合模式提示其可能参与初步去甲基化反应。这些结果为 *S. terrae* SCSIO 90395 降解 BP-3 提供了分子基础, 也为后续对关键 P450 酶的功能验证提供了明确靶点。

尽管 BP-1 是本研究中检测到的唯一中间代谢产物, 但其累积量未完全对应 BP-3 的消耗量。这一现象表明, 在本实验体系中, BP-3 的降解不只依赖于去甲基化生成 BP-1 的单一途径, 还可能涉及其他尚未检测到的并行或后续代谢反应。全基因组 KEGG 功能注释结果显示, *S. terrae* SCSIO 90395 在苯甲酸盐降解和芳香族化合物代谢等相关通路中富集了多种关键酶编码基因, 包括脱氢酶、羟化酶及苯环裂解酶等, 这表明该菌株具有进一步氧化 BP-1、裂解芳香环并将其转化成苯甲酸或小分子有机酸的潜能。已有研究指出, BP-1 可在氧化还原酶及双加氧酶等的协同作用下, 被转化为苯甲酸和 3-氧代己二酸(Baek et al, 2022)。因此, 虽然在本研究的单菌培养条件下未能直接检测到其他下游代谢产物, 但 *S. terrae* SCSIO 90395 的基因组功能注释结果表明其具备完成该降解过程所需的酶学基础。推测在单菌体系中, 相关关键酶的表达水平较低或部分代谢通路未被完全激活, 从而限制了降解过程的深入推进。

微生物群落在自然环境中通常具有高度复杂的代谢网络和功能互补性, 通过多种微生物间的协同作用实现有机污染物的高效降解(戴楚涵, 2022)。基于 *S. terrae* SCSIO 90395 的来源环境及其基因组潜力分析, 推测其在珊瑚共生体系中不仅能作为 BP-3 降解的启动者, 还可能通过与群落中其他微生物的协同互作, 形成完整代谢链, 加速 BP-3 的降解。因此, 未来研究可在珊瑚原位环境的条件下开展, 结合微生物群落间的相互作用分析, 深入探究 BP-3 在珊瑚生态系统中的完整降解途径。

综上所述, 本研究从丛生盔型珊瑚中分离获得一株具备 BP-3 降解能力的海洋细菌 *S. terrae* SCSIO 90395。该菌株能够在以 BP-3 为唯一碳源的条件下生长, 并将其转化为主要代谢产物 BP-1。基因组功能注释进一步揭示了其丰富的芳香族化合物代谢遗传背景, 为阐释 BP-3 生物降解机制提供了分子基础。本研究的菌株分离及功能研究为基于原位功能微生物的污染治理策略提供了理论支撑和新的菌种资源。

参考文献 References

戴楚涵, 2022. 1,4-二氧六环高效降解菌群富集、降解菌分离以及菌群互作机制初探[M]. 杭州: 浙江大学. DAI CHUHAN, 2022.Enrichment of an efficient 1,4-dioxane-degrading microbial culture, isolation of the degrading bacterium and the study of microbial interaction mechanisms[M]. Hangzhou: Zhejiang University (in Chinese with English abstract).

徐佳宁, 倪珞航, 刘舒予, 等, 2025. 基于网络药理学和细胞实验探究连翘苷对胆管癌的抑制作用[J]. 医学研究与战创伤救治, 38(7): 700–707. XU JIANING, NI LUOHANG, LIU SHUYU, et al, 2025. Mechanism of Phillyrin in inhibiting cholangiocarcinoma based on network pharmacology and cellular experiments[J]. Journal of Medical Research & Combat Trauma Care, 38(7): 700–707 (in Chinese with English abstract).

赵美霞, 余克服, 张乔民 等, 2006. 珊瑚礁区的生物多样性及其生态功能[J]. 生态学报, (1): 186–194. ZHAO MEIXIA, YU KEFU, ZHANG QIAOMIN, et al, 2006. Review on coral reefs biodiversity and ecological function[J]. Acta Ecologica Sinica, (1): 186–194 (in Chinese with English abstract).

ADHISH M, MANJUBALA I 2024. An in-silico approach to the potential modulatory effect of taurine on sclerostin (SOST) and its probable role during osteoporosis[J]. Journal of Biomolecular Structure and Dynamics, 42(17): 9002-9017.

APEL C, TANG J, EBINGHAUS R 2018. Environmental occurrence and distribution of organic UV stabilizers and UV filters in the sediment of Chinese Bohai and Yellow Seas[J]. Environmental Pollution, 235: 85-94.

ASTEL A, STEC M, RYKOWSKA I 2020. Occurrence and Distribution of UV Filters in Beach Sediments of the Southern Baltic Sea Coast[J]. Water, 12(11): 3024.

BAEK J H, KIM K H, LEE Y, et al, 2022. Elucidating the biodegradation pathway and catabolic genes of benzophenone-3 in Rhodococcus sp. S2-17[J]. Environmental Pollution, 299: 118890.

BESEMER J, BORODOVSKY M 2005. GeneMark: web software for gene finding in prokaryotes, eukaryotes and viruses[J]. Nucleic Acids Research, 33(suppl_2): W451-W454.

BOURNE D G, MORROW K M, WEBSTER N S 2016. Insights into the coral microbiome: underpinning the health and resilience of reef ecosystems[J]. Annual review of microbiology, 70(1): 317-340.

CHALITA M, KIM Y O, PARK S, et al, 2024. EzBioCloud: a genome-driven database and platform for microbiome identification and discovery[J]. International Journal of Systematic and Evolutionary Microbiology, 74(6): 006421.

CHAN P P, LOWE T M. tRNAscan-SE: Searching for tRNA Genes in Genomic Sequences[C]//M. KOLLMAR. Gene Prediction: Methods and Protocols. New York, NY:Springer New York,2019:1-14. 10.1007/978-1-4939-9173-0_1.

CHEN D-Y, GUO X-F, WANG H, et al, 2015. The natural degradation of benzophenone at low concentration in aquatic environments[J]. Water Science and Technology, 72(4): 503-509.

DANG B, JIA W, MA S, et al, 2023. Characterization of a novel nornicotine-degrading strain Mycolicibacterium sp. SMGY-1XX from a nornicotine-degrading consortium and preliminary elucidation of its biodegradation pathway by multi-omics analysis[J]. Journal of Hazardous Materials, 457: 131777.

DANOVARO R, BONGIORNI L, CORINALDESI C, et al, 2008. Sunscreens cause coral bleaching by promoting viral infections[J]. Environmental Health Perspectives, 116(4): 441-447.

DOWNS C A, KRAMARSKY-WINTER E, SEGAL R, et al, 2016. Toxicopathological Effects of the Sunscreen UV Filter, Oxybenzone (Benzophenone-3), on Coral Planulae and Cultured Primary Cells and Its Environmental Contamination in Hawaii and the U.S. Virgin Islands[J]. Archives of Environmental Contamination and Toxicology, 70(2): 265-288.

FAGERVOLD S K, ROHéE C, RODRIGUES A M S, et al, 2021. Efficient degradation of the organic UV filter benzophenone-3 by Sphingomonas wittichii strain BP14P isolated from WWTP sludge[J]. Science of The Total Environment, 758: 143674.

GUO Y, LIN Q, XU B, et al, 2016. Degradation of benzophenone-3 by the ozonation in aqueous solution: kinetics, intermediates and toxicity[J]. Environmental Science and Pollution Research, 23(8): 7962-7974.

HE T, TSUI M M P, TAN C J, et al, 2019. Comparative toxicities of four benzophenone ultraviolet filters to two life stages of two coral species[J]. Science of The Total Environment, 651: 2391-2399.

HELVIG C, KARIYAWASAM T, VRIENS B, et al, 2025. Genetically engineered bacteria and microalgae expressing a mutant of cytochrome P450 BM3 for efficient Diuron degradation in

wastewater treatment[J]. Microbiology Spectrum, 13(6): e02905-02924.
HYATT D, CHEN G-L, LOCASCIO P F, et al, 2010. Prodigal: prokaryotic gene recognition and translation initiation site identification[J]. BMC Bioinformatics, 11(1): 119.
JIN C, GENG Z, PANG X, et al, 2019. Isolation and characterization of a novel benzophenone-3-degrading bacterium Methylophilus sp. strain FP-6[J]. Ecotoxicology and Environmental Safety, 186: 109780.
KAMGUIA S D, NJABON E N, PATOUOSSA I, et al, 2025. A Comparative Analysis of Cockroach and Mosquito, Octopamine Receptor Homologues Produced Using Chimera, Swiss-Model, and AlphaFold Molecular Modeling Tools[J]. ACS Omega, 10(8): 7907-7919.
KHMELEVTSOVA L, SAZYKIN I, SAZYKINA M, et al, 2017. Prokaryotic cytochromes P450[J]. Applied Biochemistry and Microbiology, 53(4): 401-409.
KIM S, CHEN J, CHENG T, et al, 2024. PubChem 2025 update[J]. Nucleic Acids Research, 53(D1): D1516-D1525.
LEDESMA-GARCíA L, SáNCHEZ-AZQUETA A, MEDINA M, et al, 2016. Redox proteins of hydroxylating bacterial dioxygenases establish a regulatory cascade that prevents gratuitous induction of tetralin biodegradation genes[J]. Scientific Reports, 6(1): 23848.
LEE D G, ZHAO F M, REZENOM Y H, et al, 2012. Biodegradation of triclosan by a wastewater microorganism[J]. Water Research, 46(13): 4226-4234.
LIU C, SHAO Z 2005. Alcanivorax dieselolei sp. nov., a novel alkane-degrading bacterium isolated from sea water and deep-sea sediment[J]. International Journal of Systematic and Evolutionary Microbiology, 55(3): 1181-1186.
LIU F, MA Y, LI W, et al, 2025. How Rhodococcus ruber accelerated biodegradation of benzophenone-3[J]. Journal of Hazardous Materials, 482: 136566.
LIU Y S, YING G G, SHAREEF A, et al, 2011. Biodegradation of the ultraviolet filter benzophenone-3 under different redox conditions[J]. Environmental Toxicology and Chemistry, 31(2): 289-295.
LYU L, LI J, HUANG Q, et al, 2025. Exploring the Hidden Threat of Organic UV Filters to Corals and Macroalgae in Coral Reef Ecosystem from Luhuitou, Sanya, China[J]. Environmental Science & Technology, 59(16): 8130-8139.
MEIER-KOLTHOFF J P, CARBASSE J S, PEINADO-OLARTE R L, et al, 2021. TYGS and LPSN: a database tandem for fast and reliable genome-based classification and nomenclature of prokaryotes[J]. Nucleic Acids Research, 50(D1): D801-D807.
MEIER-KOLTHOFF J P, GöKER M, SPRöER C, et al, 2013. When should a DDH experiment be mandatory in microbial taxonomy?[J]. Archives of Microbiology, 195(6): 413-418.
MEIER-KOLTHOFF J P, GöKER M 2019. TYGS is an automated high-throughput platform for state-of-the-art genome-based taxonomy[J]. Nature Communications, 10(1): 2182.
MITCHELMORE C L, HE K, GONSIOR M, et al, 2019. Occurrence and distribution of UV-filters and other anthropogenic contaminants in coastal surface water, sediment, and coral tissue from Hawaii[J]. Science of The Total Environment, 670: 398-410.
MOELLER M, PAWLOWSKI S, PETERSEN-THIERY M, et al, 2021. Challenges in current coral reef protection–possible impacts of UV filters used in sunscreens, a critical review[J]. Frontiers in Marine Science, 8: 665548.
OELSCHLäGEL M, RüCKERT C, KALINOWSKI J, et al, 2015. Sphingopyxis fribergensis sp nov., a soil bacterium with the ability to degrade styrene and phenylacetic acid[J]. International Journal of Systematic and Evolutionary Microbiology, 65: 3008-3015.
OMEROGLU M A, BAKAN B, BALTACI M O, et al, 2025. Biodegradation of Benzophenone-3 in Non-Sterile Culture Process Using Klebsiella huaxiensis W2[J]. Water, Air, & Soil Pollution, 236(2): 106.
PEI J, HU J, ZHANG R, et al, 2023. Occurrence, bioaccumulation and ecological risk of organic ultraviolet absorbers in multiple coastal and offshore coral communities of the South China Sea[J]. Science of The Total Environment, 868: 161611.
QIU Z, LIU X, YU J, et al, 2024. Efficient conversion of aromatic and phenylpropanoid alcohols to acids by the cascade biocatalysis of alcohol and aldehyde dehydrogenases[J]. Synthetic and Systems Biotechnology, 9(2): 187-195.
RAJESHA B J, VISHAKA V H, BALAKRISHNA G R, et al, 2019. Effective composite membranes of cellulose acetate for removal of benzophenone-3[J]. Journal of Water Process Engineering, 30: 100419.
RESHEF L, KOREN O, LOYA Y, et al, 2006. The coral probiotic hypothesis[J]. Environmental microbiology, 8(12): 2068-2073.
SABAT A J, DURFEE T, BALDWIN S, et al, 2024. The complete genome sequence of unculturable Mycoplasma faucium obtained through clinical metagenomic next-generation sequencing[J]. Frontiers in cellular and infection microbiology, 14: 1368923.
SáNCHEZ-QUILES D, TOVAR-SáNCHEZ A 2015. Are sunscreens a new environmental risk associated with coastal tourism?[J]. Environment International, 83: 158-170.
SHAN B, MO J, YANG J, et al, 2024. Cloning and functional characterization of a cinnamate 4-hydroxylase gene from the hornwort Anthoceros angustus[J]. Plant Science, 341: 111989.
THOMPSON J R, RIVERA H E, CLOSEK C J, et al, 2015. Microbes in the coral holobiont: partners through evolution, development, and ecological interactions[J]. Frontiers in cellular and infection microbiology, 4: 176.
TSUI M M P, CHEN L, HE T, et al, 2019. Organic ultraviolet (UV) filters in the South China sea coastal region: Environmental occurrence, toxicological effects and risk assessment[J]. Ecotoxicology and Environmental Safety, 181: 26-33.
TSUI M M P, LAM J C W, NG T Y, et al, 2017. Occurrence, Distribution, and Fate of Organic UV Filters in Coral Communities[J]. Environmental Science & Technology, 51(8): 4182-4190.
WANG Z, WANG Z, WANG G, et al, 2023. New insight into biodegradation mechanism of phenylurea herbicides by cytochrome P450 enzymes: Successive N-demethylation mechanism[J]. Environment International, 182: 108332.
WIJGERDE T, VAN BALLEGOOIJEN M, NIJLAND R, et al, 2020. Adding insult to injury: Effects of chronic oxybenzone exposure and elevated temperature on two reef-building corals[J]. Science of The Total Environment, 733: 139030.
WOLF M E, HINCHEN D J, MCGEEHAN J E, et al, 2024. Characterization of a cytochrome P450 that catalyzes the O-demethylation of lignin-derived benzoates[J]. Journal of Biological Chemistry, 300: 11.
YANG C, DONG P-Z, JIANG Z-N, et al, 2025. Amino-functionalized Fe_3O_4-based covalent organic framework for efficient magnetic solid-phase extraction of three illegally added phosphodiesterase-5 inhibitors in functional food[J]. Food Bioscience, 65 : 106070.
YANG H, YU F, QIAN Z, et al, 2024. Cytochrome P450 for environmental remediation: catalytic mechanism, engineering strategies and future prospects[J]. World Journal of Microbiology and Biotechnology, 40(1): 33.
YOON S-H, HA S-M, LIM J, et al, 2017. A large-scale evaluation of algorithms to calculate average nucleotide identity[J]. Antonie van Leeuwenhoek, 110(10): 1281-1286.

崔梦瑶, 韦芬, 余克服. 造礁珊瑚有性繁殖的研究进展[J]. 海洋学报, 2025, 47(11): 13–26, doi:10.12284/hyxb2025134
Cui Mengyao, Wei Fen, Yu Kefu. Research progress on sexual reproduction of scleractinian corals[J]. Haiyang Xuebao, 2025, 47(11): 13–26, doi:10.12284/hyxb2025134

造礁珊瑚有性繁殖的研究进展

崔梦瑶[1], 韦芬[1*], 余克服[1,2*]

(1. 广西大学 广西南海珊瑚礁研究重点实验室/珊瑚礁研究中心/海洋学院, 广西 南宁 530004; 2. 南方海洋科学与工程广东省实验室(广州), 广东 广州 511458)

摘要: 造礁珊瑚的有性繁殖是维持珊瑚礁生态系统结构和功能的关键生物学过程, 直接决定珊瑚种群的动态更新与遗传多样性, 对于珊瑚礁生态系统的稳定与演化具有重要意义。本文综述造礁珊瑚有性繁殖的研究进展, 包括: (1) 珊瑚的繁殖类型; (2) 珊瑚的性腺发育; (3) 珊瑚的排卵与受精; (4) 珊瑚的胚胎发育; (5) 珊瑚幼虫的固着过程; (6) 珊瑚幼体的发育。现有进展表明, 珊瑚有性繁殖过程受内源生物机制与外源环境因子协同调控, 但其具体分子机制及过程仍不明了。未来需高度关注环境因子对造礁珊瑚排卵时间的影响、诱导珊瑚幼虫固着的机制、早期共生关系的建立与可塑性, 以及建立分子辅助育种方法筛选耐热型珊瑚等方面。

关键词: 造礁珊瑚; 有性繁殖; 性腺发育; 排卵与受精; 胚胎发育; 幼虫固着

中图分类号: Q954.4 **文献标志码:** A **文章编号:** 0253-4193(2025)11-0013-14

1 引言

珊瑚有性繁殖是指通过雌雄配子结合产生带有新基因型的新个体的生物学过程, 包括性腺发育、受精、胚胎发育、幼虫附着变态、幼体发育及子代再繁殖等 6 个阶段[1], 其中子代的成功繁殖标志着珊瑚已完成一个完整的有性繁殖周期, 实现了珊瑚幼体的有效补充[2]。有性繁殖产生大量具有遗传多样性的个体, 不仅有助于维持珊瑚种群数量的稳定, 还能增强其对环境变化的适应潜力, 对珊瑚礁生态系统的稳定、恢复和进化等具有重要的意义[3–4]。

现有研究表明, 尽管珊瑚可以在繁殖季产生大量配子, 但其有性繁殖过程中的各个阶段均表现出较高的死亡率[5–6]。如原肠期前的胚胎极易发生破裂、畸形和死亡[7–8]; 固着后的幼体受多种因素的影响, 导致第一年的死亡率可能高达 30%～99%[9–10], 特别是在全球气候变暖、人类活动加剧等破坏珊瑚生存环境的背景下, 这种现象严重制约了珊瑚群落的自然恢复能力[11]。因此, 本文基于文献总结了珊瑚有性繁殖过程中的生物学特性及调控机制, 梳理环境因素对珊瑚早期发育影响的认识, 希望有助于理解珊瑚早期生活史中的关键过程, 以及珊瑚幼体补充对种群结构的影响, 为珊瑚礁生态系统的管理与保护提供科学依据。

2 珊瑚的有性繁殖类型

在全球已知的 900 多种造礁珊瑚中, 有 400 多种的繁殖类型已经清楚[12], 这些珊瑚按照性别可分为雌雄同体型和雌雄异体型 2 类, 其中雌雄同体型珊瑚在同一株珊瑚体内同时产生卵子和精子 2 种配子, 而雌雄异体型则根据珊瑚的性别在不同的个体内分别产

收稿日期: 2025-07-29; **修订日期:** 2025-09-30。
基金项目: 国家自然科学基金(42090041); 广西科技基地和人才专项(桂科 AD25069075); 广西南海珊瑚礁研究重点实验室自主基金资助(GXLSCRSCS2023103)。
作者简介: 崔梦瑶(1997—), 女, 黑龙江省大庆市人, 博士研究生, 从事造礁珊瑚有性繁殖研究。E-mail: 2015392004@st.gxu.edu.cn
*** 通信作者:** 韦芬, 讲师, 主要从事造礁珊瑚有性繁殖研究。E-mail: weifensky@163.com; 余克服, 教授, 主要从事南海珊瑚礁地质、生态与环境研究。E-mail: kefuyu@scsio.ac.cn

生卵子或精子[10]。按照生殖方式，珊瑚可分为排卵型和排幼型，其中排卵型珊瑚通常会在1 a中的某个特定时间同步排出大量配子，在海水表面完成受精并发育为浮浪幼虫[13]；而排幼型珊瑚则在母体内完成受精，发育为浮浪幼虫后排出体外[5]。因此，珊瑚按繁殖类型可分为雌雄异体排卵型、雌雄同体排卵型、雌雄异体排幼型、雌雄同体排幼型等4种，其中雌雄同体排卵型珊瑚的比例最高，为63%[12]。

部分珊瑚物种表现出混合的性别或生殖方式[14]。例如，在不同海域，褶叶珊瑚科(Mussidae)、菌珊瑚科(Agariciidae)和滨珊瑚科(Porididae)的生殖方式有所不同，在印度−太平洋海域，这些珊瑚为排卵型，而在大西洋海域则为排幼型[15]。此外，在滨珊瑚科、菌珊瑚科和石芝珊瑚科(Fungiidae)等珊瑚中，已报道存在具有混合性别特征的物种(mixed or contrasting sexual patterns)，这些物种可以同时表现出雌性、雄性和雌雄同体3种性别类型[12, 14–17]。有研究认为混合性别可能是一种顺序雌雄同体(sequential hermaphrodites)，即珊瑚的性别可能受年龄、发育阶段、种群结构和温度等因素的影响而发生变化[15]。已有研究表明，某些雌雄异体珊瑚的雌雄株间存在生理差异，如澄黄滨珊瑚(*Porites lobata*)、巴拿马滨珊瑚(*Porites panamensis*)、椭圆星珊瑚(*Dichocoenia stokesi*)及柱状珊瑚(*Dendrogyra cylindrus*)等多种珊瑚雄株的钙化和生长速率显著高于雌株[18]；巴拿马滨珊瑚的雌雄株在珊瑚杯直径、单位面积珊瑚杯数量及相邻珊珊杯数量存在显著差异，体现出明显的二态性[19]。

3 珊瑚的性腺发育

造礁珊瑚没有真正的器官，其配子会周期性地在水螅体肠系膜特定部位产生，这一部位通常被称为性腺[20]。不同种间珊瑚性腺的发育时间不同，目前已知的排卵型珊瑚的性腺发育周期多为1 a，其中，大部分珊瑚的卵母细胞发育周期为4～12个月，精巢为1～8个月[21]，也有些卵母细胞需要14～15个月才能发育成熟，不同年份配子发育周期重叠，或1 a中有多个配子发育周期[22]。而排幼型珊瑚每年有多个配子形成周期，但具体周期、次数在不同种珊瑚间存在差异[23]。这可能与珊瑚的种类[24−25]及海水温度[26]有关。

珊瑚的配子发育分为4个时相[27](图1)。Ⅰ时相的卵原细胞发生于肠系膜内的中胶层附近；Ⅱ时相的初级卵母细胞被一层薄薄的中胶膜包裹，细胞形状变得不规则；Ⅲ时相的卵母细胞体积开始迅速增大，并逐渐积累卵黄蛋白等物质；Ⅳ时相的卵母细胞已经基本成熟，脂质泡内充满大量脂质，细胞核从中心位置移动到细胞膜附近，并在排卵前出现生发泡破裂(GVBD)[21, 27]。Ⅰ时相的精巢是由几十个精原细胞成簇地聚集而成的；Ⅱ时相的精巢被中胶层隔开，精母细胞数量增多，排列紧密；Ⅲ时相的精巢中间有腔隙，可见大部分精母细胞已完成减数分裂，形成精细胞；Ⅳ时相的精巢中含有大量精子，明显观察到精子尾部汇聚于一侧[27]。

相较于性腺组织学研究，珊瑚性腺发育过程中的关键基因及其表达的相关研究还较少，现有关研究主

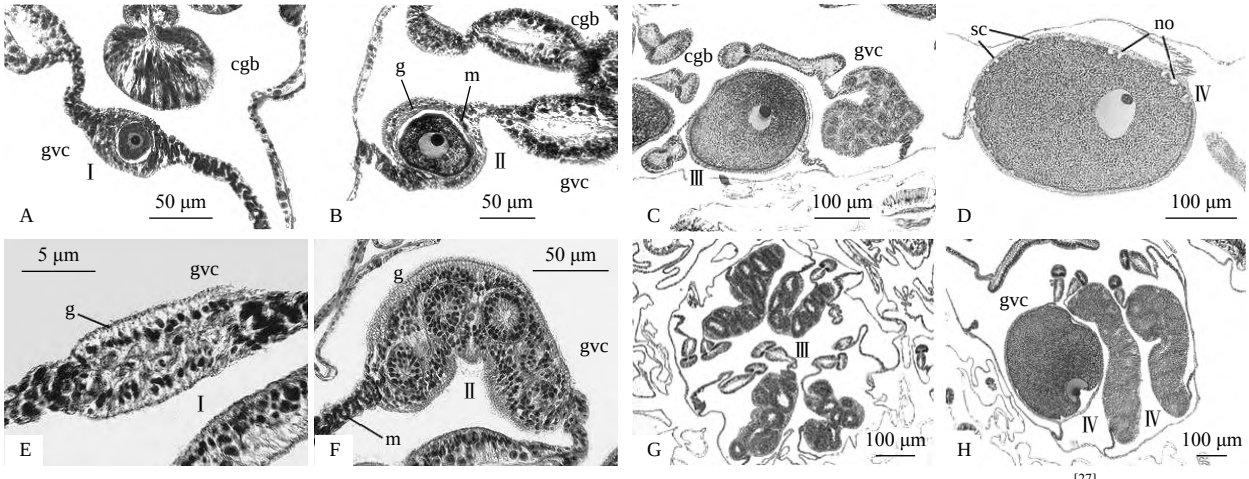


图1 摩羯鹿角珊瑚(*Acropora cervicornis*)不同时相配子的显微结构(图片改自Vargas-Ángel等[27])

Fig. 1 Micrographs of *A. cervicornis* during Gonadal Development (modified from Vargas-Ángel et al.[27])

A−D和E−H分别依次为第Ⅰ、Ⅱ、Ⅲ、Ⅳ时相的卵母细胞及精巢。cgb: 刺丝囊；g: 肠系膜；gvc: 消化循环腔；m: 中胶层；no: 凹痕；sc: 波浪形边缘

A−D and E−H represent oocytes and spermaries at stages Ⅰ, Ⅱ, Ⅲ, and Ⅳ, respectively. cgb: cnidoglandular band; g: gastrodermis; gvc: gastrovascular cavity; m: mesoglea; no: notches; sc: scalloping

要集中在肾形真叶珊瑚(*Euphyllia ancora*)中, 如 Shikina 发现 *piwi* 基因始终存在于肾形真叶珊瑚肠系膜组织的特定部位, 可以作为早期生殖细胞(精原细胞和卵原细胞)的标记基因[28]; 此外, 研究还发现了一些与配子成熟相关的基因, 如卵黄蛋白相关的基因(*Vg*、*Ep*)和促性腺释放激素(GnRH-like peptide)在雌株性腺发育的中期及末期大量表达; 乙酰化 α 微管蛋白(Acetylated alpha-Tubulin, Ac-α-Tu)及鸟苷酸环化酶受体(Receptor-type Guanylate Cyclases, rGCs)则在雄株中特异表达, 可以调控末期精子成熟[20, 29−30]。但这些特异表达的基因如何调节生殖细胞分化、发育及成熟的分子机制还尚未清楚。

4　珊瑚的排卵与受精

4.1　珊瑚的排卵及其影响因素

大多数造礁珊瑚具有同步排卵的行为, 即在配子成熟后, 同一海域的多种排卵型珊瑚会在满月前后若干个环境条件适宜的夜晚, 释放大量具有浮力的精卵束, 并在海面完成受精过程[22, 31]。珊瑚的同步排卵有助于增加海水中配子的浓度, 从而显著提高受精成功率。自 1982 年 Harrison 第一次在澳大利亚大堡礁观察到珊瑚大规模同步排卵现象后, 研究人员陆续在红海北部、日本琉球群岛、新加坡、菲律宾等地发现了珊瑚的同步排卵行为[32−35]。截至 2021 年, 研究人员已在印度−太平洋海域的 100 多个珊瑚礁区观察到 6 178 次造礁珊瑚(300 余种)的排卵行为[36], 然而, 具体的排卵日期受海区环境等多方面因素的影响仍难以精确预测。

现有研究表明, 珊瑚排卵时间主要受海水温度、月相、潮汐等环境因素影响[10, 37]。其中, 海温是决定排卵月份的关键因素, 造礁珊瑚通常在当地的春季至夏末期间进行排卵[38−39]。特定的季节性温度变化可能会诱发珊瑚排卵, Keith 等通过分析太平洋海区 34 个海域鹿角属珊瑚(*Acropora* spp.)的排卵时间, 发现海水温度的快速升高是促使鹿角珊瑚排卵的主要环境因素[40]; 同样, 台湾及三亚鹿回头等海域的造礁珊瑚排卵时间与当地海水温度上升的时段一致[41−42]。这可能是因为温度快速上升会增加海水中浮游生物和有机碎屑的数量, 从而加快珊瑚能量累积, 促进配子的成熟[27]。

月相是决定珊瑚具体排卵日期的关键因素[39, 43−44]。有研究表明, 珊瑚能够通过隐花色素(cryptochromes)来感知月光强度的变化[37, 45−46], 并利用满月时日落与月出之间的黑暗环境来调节排卵的具体日期[47−48]。同时, 大堡礁、日本高知岛及澳大利亚蜥蜴岛等地记录到珊瑚在满月后的小潮大规模排卵的行为, 推测月相引起的潮汐变化也是影响珊瑚排卵日期的环境因素之一[38, 49]。另外, 海况、珊瑚个体间的基因型差异以及邻近珊瑚排卵释放的激素等因素也会对珊瑚的排卵日期产生显著影响[50−51]。

综上所述, 珊瑚排卵时间受多种环境因素与内源生物节律所调节。然而, 现有研究尚不明确不同环境因素对珊瑚排卵时间的具体作用, 因此珊瑚的排卵日期仍难以准确预测[52]。此外, 人为活动引发的全球气候变暖、光污染等问题可能会显著影响珊瑚对环境的响应, 破坏其排卵的同步性, 甚至导致珊瑚在不适宜的环境条件下排卵[39, 53], 降低其繁殖的成功率。

4.2　珊瑚的受精及其影响因素

在已知繁殖类型的 400 多种造礁珊瑚中, 排卵型珊瑚占 85%, 其配子通常在排出后 1～2 h 内完成受精, 未受精的配子只能存活几个小时[5−6]。受精率作为衡量珊瑚繁殖成功的关键指标, 通常与珊瑚间距离、配子浓度、质量、接触时间及海水温度、酸碱度等因素密切相关[54−56]。其中, 个体间距离与精子密度是影响受精率的主要因素。研究表明, 风信子鹿角珊瑚(*Acropora hyacinthus*)的受精率随个体间距增大而显著下降: 当间距小于 0.5 m 时平均受精率为 30%, 间距达 10 m 时则低于 10%, 超过 15 m 时受精率趋近于 0[56]。在人工授精中, 精子密度约为 10^6 cells/mL 时受精率最高(＞75%), 降至 10^4 cells/mL 时则低于 50%[57]。然而, 海水酸化和暖化等环境现象导致的珊瑚白化会显著降低珊瑚种群密度, 减少配子的产量, 甚至可能在 1～2 年内不产生成熟配子, 或导致卵母细胞脂质过氧化, 从而降低特定海域珊瑚可用配子密度[58−60]。此外, 海洋环境的变化不仅影响珊瑚配子的生成, 还可能对释放到水体中的配子造成进一步损害, 例如, 海水的暖化和酸化均会导致鹿角珊瑚的精子活力降低, 从而影响受精率[61−62]。

全球气候变暖及人类活动引发的珊瑚白化和异步排卵现象, 导致自然繁殖过程中可用配子的数量减少、质量下降, 从而进一步加速了珊瑚礁生态系统的退化。因此, 研究人员尝试通过珊瑚精子的冷冻保存技术长期存储遗传物质, 以保护珊瑚的遗传和生物多样性[63−65]。该技术已成功储存了来自不同海域的 40 余种珊瑚精子, 并建立了珊瑚精子冷冻库(CryoDiversity Bank), 用于选择性育种实验[66−67], 然而, 目前仍缺乏通用的指标来评估冻融过程中精子质量的变化[68], 也尚未开发出合适的卵子低温保存方法, 限制

了珊瑚种质资源的长期保存[67]。

5 珊瑚的胚胎发育

造礁珊瑚的胚胎发育经历 5 个发育阶段：受精卵、卵裂期、囊胚期、原肠胚期、浮浪幼虫期（图 2）[69]。排幼型珊瑚的胚胎发育在体内完成，而排卵型珊瑚的胚胎发育则在体外完成，并且不同种类的发育时间存在差异[70−71]。大部分珊瑚排卵后 2 h 内受精卵开始分裂，2～7 h 完成卵裂，形成囊胚；胚胎在 15～24 h 内进入原肠阶段，并逐渐发展为原肠胚晚期，形成胚孔和双胚层结构；最终，在 24～36 h 内胚胎发育为初级浮浪幼虫，此时胚孔发育为幼体的口部，而内外胚层则分别分化为外表皮和肠腔，在显微镜下，早期浮浪幼虫明显观察到外面有一层透明的囊，并不停地转圈游动[72−74]。

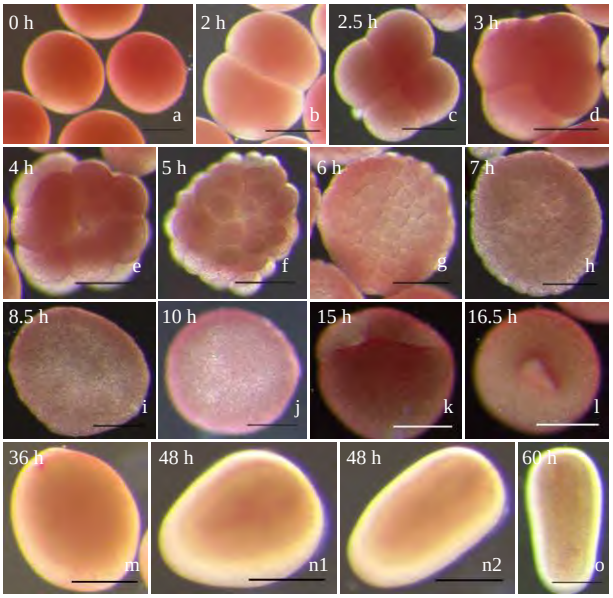


图 2 肉质扁脑珊瑚的胚胎及幼虫发育过程[69]

Fig. 2 The early development of *P.carnosus*[69]

a. 卵母细胞；b. 2 细胞期；c. 4 细胞期；d. 8 细胞期；e. 16 细胞期；f. 32 细胞期；g. 桑葚胚期（64 细胞期）；h. 桑葚胚期（128 细胞期）；i. 囊胚早期；j. 囊胚晚期；k. 原肠胚早期；l. 原肠胚中期；m. 浮浪幼虫早期；n1, n2. 浮浪幼虫中期；o. 浮浪幼虫晚期。所有标尺都为 200 μm

a. Oocytes; b. 2-cell stage; c. 4-cell stage; d. 8-cell stage; e. 16-cell stage; f. 32-cell stage; g. morula stage (64-cell stage); h. morula stage (128-cell stage); i. early blastula stage; j. later blastula stage; k. early gastrula stage; l. middle gastrula stage; m. early planula stage; n1, n2. middle planula stage; o. later planula stage. All rulers indicate 200 μm

珊瑚具有完整的原肠胚形成过程，是典型的刺胞动物发育模式。不同种类的珊瑚囊胚可分为“虾片状”和“坐垫状”2 种结构类型[75]，这两种类型分别通过内卷和内陷两种主要途径发育为原肠胚[76]。通常，复杂型珊瑚（complex corals）的囊胚呈虾片状，扁平且没有囊胚腔，在原肠形成的过程中，虾片状的囊胚内卷成碗状的结构，经过较长时间的变形才最终闭合成圆形的原肠胚，随后逐渐发育成带有口和咽的浮浪幼虫；坚实型珊瑚（robust corals）的囊胚多呈坐垫状，具有囊胚腔，这种囊胚先经历假内陷（出现假胚孔），然后恢复为空心球的形态，进入原肠胚期，随后再次内陷形成带有真胚孔及双胚层结构的原肠胚，最后发育为浮浪幼虫（图 3）[70, 77]。

此外，由于珊瑚胚胎较为脆弱，温度、pH、沉积物等多种环境因素都会对其发育产生影响，这些因素可能导致胚胎破裂、畸形和死亡。其中，温度是影响胚胎发育的最主要因素，适当地升高温度（＜30℃）能够加快胚胎的发育速度，但过高的温度则会显著增加胚胎的畸形率和死亡率[78−80]。例如，柔枝鹿角珊瑚（*Acropora tenuis*）在 32℃ 下，其胚胎畸形率比 27℃ 时增加了 15%，幼虫存活率降低了 1 倍[79]；佳丽鹿角珊瑚（*Acropora pulchra*）在正常温度（26℃）下胚胎畸形率为 3.6%，而在 30℃ 时增加至 7.6%，在 32℃ 时则显著上升至 39%[80]。

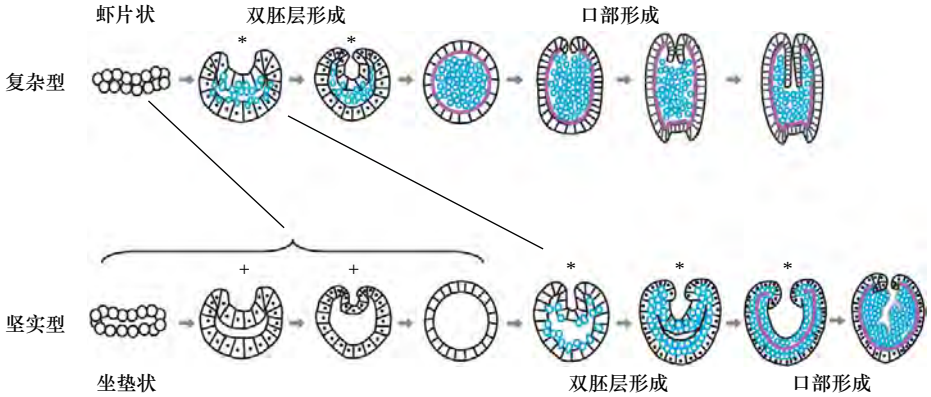


图 3 造礁珊瑚胚胎发育的两种模式（图片改自 Medina 等[70]）

Fig. 3 Diagrammatic representation of the two extreme forms of coral development (modified from Medina et al.[70])

6　珊瑚幼虫的固着过程

幼虫的附着与变态是浮浪幼虫从浮游生活过渡到固着底栖生活的过程[22]，包括寻找合适的线索(search)、附着(attach)和变态(metamorphosis)3 个阶段(图 4)[81]。排卵型珊瑚的幼虫一般在受精后 3 d 出现试探附着行为，并在 3～5 d 内完成附着[82]。排幼型珊瑚浮浪幼虫在排出后的几小时内即可开始附着，且更倾向于附着在亲本附近。幼虫附着时口端朝上，而反口端则紧贴基质，随着附着的进行，浮浪幼虫逐渐由椭圆形变为扁平的碟形结构，并通过钙化反应稳固地附着在基质上；附着 1～2 d 后，出现 6 个初级肠系膜，观察到球状触手(tentacle tips)标志着幼虫成功完成固着[83–84]。

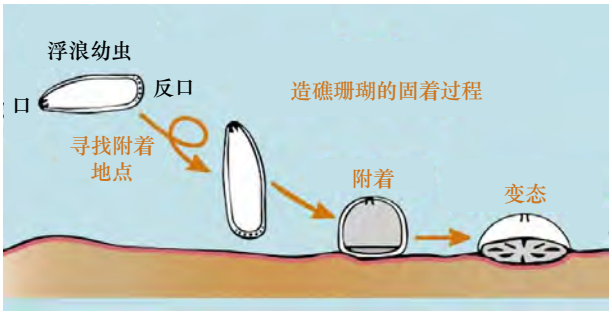


图 4　造礁珊瑚的固着过程(改自 Petersen 等[81])

Fig. 4　Settlement stages of scleractinian corals (from Petersen et al.[81])

浮浪幼虫在发现合适的线索后开始附着、变态

The steps of a coral larvae searching, attachment, and metamorphosis

研究表明，尽管一些珊瑚幼虫的存活时间可超过 200 d，但大多数幼虫在 4～13 d 内会迅速丧失附着能力[82, 85]。适宜的环境条件是浮浪幼虫完成固着的关键因素(表 1)[86–87]。现有研究普遍认为，壳状珊瑚藻(Crustose Coralline Algae, CCA)可以诱导大部分珊瑚幼虫固着[86–87]，其中一种石皮藻(*Titanoderma* cf. *tessellatum*)可使多种珊瑚幼虫的附着率(settlement rate)提升至 50% 以上[81, 88]。然而，不同种珊瑚的幼虫对壳状珊瑚藻的偏好存在差异。例如，鹿角珊瑚属(*Acropora*)的幼虫倾向于附着在孔石藻属(*Porolithon*)附近，而一种孢石藻(*Sporolithon* sp.)则能显著提高叶状珊瑚科(Lobophyllidae)幼虫的附着率[89]。另有研究表明，CCA 的提取物如糖甘油脂(glycoglycerolipids)和高分子多糖(high molecular weight polysaccharides)能诱导珊瑚幼虫固着[90]，而其他 CCA 提取物，如 11-脱氧笛鲷素 -3(11-deoxyfistularin-3)[91]及大环二内酯(macrodiolide luminaolide)[86]则仅能诱导幼虫变态。一些研究也发现，即使在没有 CCA 存在的情况下，海洋微生物膜同样能够诱导幼虫固着[92–94]。海洋微生物膜主要由多种细菌、单细胞藻类(包括硅藻)以及原生动物等组成。Kegler 等研究表明，伽马变形菌门(Gammaproteobacteria)及甲变形菌门(Alphaproteobacteria)中的多种细菌可能在幼虫固着过程中发挥诱导作用[95]。然而，目前仅从两株假交替单胞菌(*Pseudoalteromonas* sp. PS5、*Pseudoalteromonas* rubra #1783)中分离出四溴吡咯(tetrabromopyrrole)[96–98]和环丙菌红素(cycloprodigiosin)[99–100]，并证实其能有效诱导部分珊瑚物种的幼虫固着[96]。此外，GLW-酰胺神经肽(GLW-amide neuropeptides)、多巴胺(dopamine)、肾上腺素(epinephrine)、谷氨酸(glutamic acid)以及氯化钙($CaCl_2$)等化学物质也被证明能够有效诱导珊瑚幼虫的附着或变态行为[101–103]。

表 1　生物化学因素与物理因素对珊瑚幼虫固着过程的影响[86–87]

Table 1　Effects of biochemical and physical factors during larval settlement[86–87]

	影响因素	幼虫行为
生物化学因素	壳状珊瑚藻(Crustose Coralline Algae, CCA)及其代谢产物	诱导或排斥幼虫固着、不同种幼虫对CCA的选择存在差异
	微生物膜及其代谢产物	诱导或排斥幼虫固着
物理因素	环境光和附着基的颜色	影响固着深度、方向、位置
	附着基的材质和结构	影响附着率
	沉积物	影响附着率及对附着基的选择
	温度	影响附着率及寻找合适附着基的时间
	水流	影响幼虫的扩散能力和珊瑚连通性
	压强	影响固着深度

尽管生物化学因素被广泛认为是决定珊瑚固着的主要因素，但诸如环境光及附着基的颜色、附着基的材质和结构、沉积物等物理因素也会影响珊瑚幼虫的固着行为(表 1)[86–87]。其中，环境光和附着基的颜色被认为是影响幼虫固着的关键物理因素之一。Strader 等研究表明，珊瑚幼虫能够感知不同颜色的环境光，并表现出趋向红光的行为[104]；Mason 等则发现幼虫对红色或橙色的附着基表现出了显著的选择偏好[105]。此外，幼虫相比于平坦的表面，更倾向于在陶瓦、陶瓷等附着基的裂缝或凹陷处固着，从而减少其受到捕食者或草食动物干扰的风险[106–107]。

7 珊瑚的幼体发育

珊瑚幼体是指珊瑚通过有性繁殖产生的、尚不具备繁殖能力的小个体[2]，其早期发育过程包括口、肠系膜及触手的形成；骨骼发育与虫黄藻共生；新个体的形成等过程（图 5）[84]。新固着的幼体较为脆弱，易被捕食、藻类竞争等其他环境因素影响；多数珊瑚幼体早期的死亡率高达 30%～99%，符合Ⅲ型生存曲线[108–109]。因此，幼体获得合适的共生藻、提高幼体的生长速率、通过物理化学或生物的方法降低幼体被捕食和藻类竞争的风险等方法是提高幼体补充率的关键因素[110]。

7.1 幼体生长速率及存活率

珊瑚幼体死亡率与幼体的年龄和直径密切相关，现有研究表明，直径大于 5 mm 或年龄在 3～9 月以上的珊瑚幼体，其死亡率较低[111–112]。其中，食草鱼类捕食过程中的意外擦碰是导致 1～2 月龄幼体死亡的主要原因[113]，藻类及其他底栖生物与幼体竞争也是造成不同年龄珊瑚幼体死亡的重要因素[114–115]。研究人员已探索多种方法来减少意外擦碰或竞争导致的珊瑚幼体死亡现象[116–121]。例如，通过设计具有不同结构的附着基，可为幼体提供避难所，从而减少食草鱼类的干扰[116]；使用防污材料能够有效降低藻类等其他底栖生物与幼体之间的竞争压力[117]；将珊瑚幼虫与食草腹足类动物共同饲养，能够显著提高幼体的存活率[118–119]。这些方法在促进珊瑚幼体的存活和生长过程中展现出重要的应用潜力。

此外，海洋变暖和酸化会影响珊瑚幼体的生长发育及存活率。海洋变暖会干扰幼体的代谢过程，降低生长速率，并直接导致幼体死亡率的增加[120–121]。而海洋酸化会影响幼体的钙化能力，改变其骨骼形态及晶体微观结构，进而降低生长速率和骨骼密度，并显著提高幼体的死亡风险[122–123]。为应对海洋变暖和酸化对珊瑚幼体的负面影响，研究人员采取了辅助迁移策略，将相对耐热的亲本珊瑚迁移至需要修复的海域，与当地耐热性较低的个体进行杂交[124–127]。研究表明，亲本中至少一方具有较高的耐热性时，子一代（F1）的耐热性也会相应增强[128]。例如，Quiley 等研究发现，在热胁迫下，耐热性不同的亲本杂交产生的 F1 代个体在附着率、生长速率及基因表达模式等方面表现出显著差异，表明母体耐热性对 F1 代的耐热性具有多方面的调控作用[129]。尽管目前关于珊瑚 F1 耐受性的研究主要集中在鹿角珊瑚中，但 Kirk 等的研究表明，同一环境条件下的不同种珊瑚的 F1 普遍表现出相似的耐热特性[130]。因此，选择来自边缘地带的亲本进行杂交育种被认为是获得耐热性子代的有效策略。然而，这种基于表现型的传统选择方法存在选择周期长、成本高、准确性低等局限性，通过分子标记辅助选择技术则可以弥补这些缺点，已有许多研究通过重测序及转录组分析鉴定出多个与耐热性相关的候选基因，如：*Hsp70*、*Sacsin* 等[131]，但这些基因的具体遗传机制和功能尚不明确。目前仅有

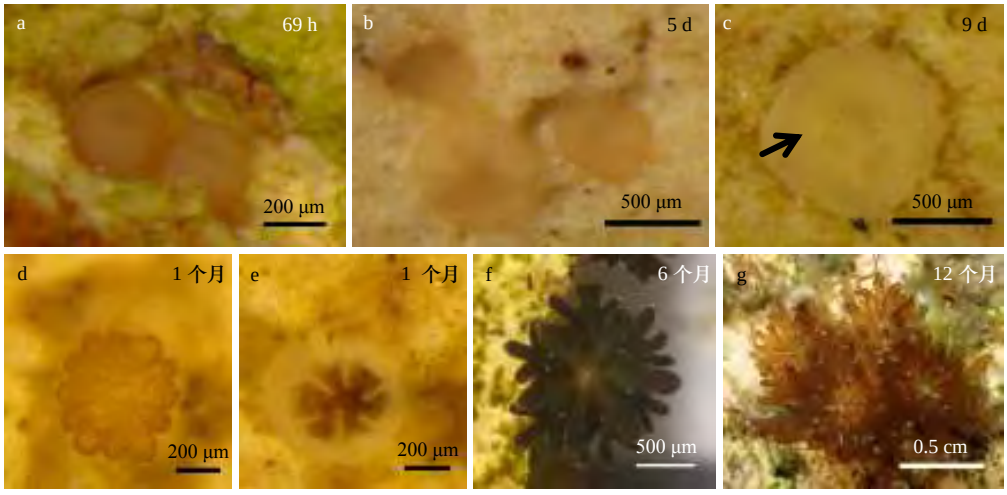


图 5 丛生盔形珊瑚的幼虫发育（改自 Wei 等[84]）

Fig. 5 *G. fascicularis* post-settlement development (modified from Wei et al.[84])

a. 幼虫在 69 h 时出现试探附着行为，b. 排卵后 5 d 观察到幼虫附着成功，有 6 个明显的肠系膜，c. 第 9 d 观察到共生虫黄藻和体壁，d、e. 1 个月后观察到 12 个触手和 6 个隔片，f、g. 后续幼体触手不断增长

a. Larvae started settling at 69 h; b. larvae settled successfully at 5 d, with 6 mesenteries; c. zooxanthellae and the body wall were observed at 9 d; d, e. after 1 month, 12 tentacles and 6 septa were evident; f, g. the juvenile tentacles continued to elongate

Cleves 等通过敲除多孔鹿角(*A.millepora*)的热休克转录因子 1(Heat Shock Transcription Factor 1, *HSF1*)基因, 证实了该基因在幼虫耐热性中的关键作用[132]。进一步阐明这些候选基因的功能将有助于提高珊瑚幼体在极端环境下的早期存活率。此外, 研究人员还发现, 珊瑚幼体在发育过程中可能与同种异体幼体发生融合, 形成嵌合体, 这些嵌合体表现出更快的生长速度、较早的性成熟时间以及更强的耐热和抗病能力[133–135]。

7.2　早期共生藻

在珊瑚早期的发育过程中, 主要通过 2 种方式获得共生藻: 一是通过来自母体的垂直传递, 二是通过环境中的水平传递[22]。现有研究表明, 排幼型珊瑚主要通过垂直传递获得共生藻, 在排卵前几日, 虫黄藻会进入卵母细胞或幼虫内, 子代的共生藻组成与母体相似[136]。而大部分排卵型珊瑚主要通过水平传递获得共生藻, 在幼虫附着后几日到 1 个月内, 幼体通过口从环境(水、底泥等)中获得虫黄藻, 这些虫黄藻先进入腔肠, 随后迁移到内胚层, 最后转移至外胚层细胞[137–139]。

虫黄藻作为珊瑚最重要的共生功能体之一, 为珊瑚宿主提供其生长发育所需的能量, 并在珊瑚骨骼形成过程中发挥关键作用[126, 140]。目前, 基于核糖体 DNA 序列分析, 虫黄藻已被划分为 9 个系群(Clade A—I), 每个系群又根据转录间隔区 ITS2 序列进一步划分为多个亚系群(如 C1、D1 等), 其中 Clade A、Clade B、Clade C 和 Clade D 是造礁珊瑚的主要共生系群[141]。珊瑚幼体可能与单一类型的虫黄藻形成严格的共生关系, 也可能与多种不同类型及亚型的虫黄藻共生, 幼体通过水平传递获得共生藻的种类及时间与珊瑚自身的种类、环境中虫黄藻的种类及密度, 以及环境条件密切相关[142–143]。有研究报道, 檐形石芝珊瑚(*Fungm scutaria*)在排卵后 4～5 d 便开始获取共生藻[144], 而黄癣盘星珊瑚(*Dipsastraea favus*)则在排卵后 26～30 d 才出现共生藻[145], 这表明不同种珊瑚在获取共生藻的时间差异较大。此外, 研究还表明, 宿主珊瑚能够主动调控其共生藻群落的组成, 而不是随机获取共生藻[146–148], 比如 Quigley 等发现, 鹿角珊瑚幼体在海水环境中获得的共生藻多样性远低于海洋沉积物中虫黄藻的多样性[148], 表明珊瑚幼体可以选择性地吸收合适的虫黄藻。

环境压力, 如光线不足或高温, 均会削弱珊瑚幼体获取共生藻的能力, 并改变其对虫黄藻的选择偏好[149–150], 而在 pCO_2≤1 200 μatm 下的海洋酸化对幼体共生藻的含量和组成几乎不产生影响[151]。研究表明, 在高温条件下, 珊瑚幼体会倾向于选择更耐热的 D 系群虫黄藻, 同时降低热敏感共生藻的相对丰度[150, 152–154]。珊瑚共生藻的群落组成被认为是影响幼体耐热性的关键因素之一[155], 接入耐热性更强的共生藻可显著提升珊瑚的耐热能力[156–157]。

8　展望

自 20 世纪 80 年代起, 国际上开始关注珊瑚有性繁殖并记录了不同海域多种珊瑚的有性繁殖过程, 探讨了环境因素对珊瑚有性繁殖过程的影响, 并提出了利用人工有性繁殖恢复受损珊瑚礁区的方法; 国内关于珊瑚有性繁殖的研究相对较晚, 迄今的研究主要是认识珊瑚的有性繁殖过程、探索环境因素对珊瑚早期共生关系的可塑性等[4, 18, 69, 105, 153]。目前, 国际上关于珊瑚的有性繁殖仍存在诸多未解之谜, 全面了解珊瑚的有性繁殖过程, 深入揭示影响珊瑚有性繁殖过程的关键因素及其调控机制, 对于理解珊瑚礁生态系统的内在属性、评估珊瑚礁生态系统的发育趋势、人工修复珊瑚礁生态系统及其保护和管理等均具有重要的意义。从已有的研究进展来看, 未来需要在以下方面尽快取得突破。

(1)环境因子对造礁珊瑚排卵时间的影响

近年来, 众多区域的研究人员已能够通过实地观测与历史数据分析相结合的方法, 对珊瑚的排卵时间进行初步预测。然而, 珊瑚的实际排卵时间受到多种环境因素的调控, 如海水温度、月相等。这些因素如何通过分子信号通路影响性腺发育成熟、排卵时间等机制尚不明确。未来需将多组学技术与长期原位监测结合, 解析温度波动、光周期等关键环境信号对生殖细胞发育的调控机制。同时, 通过室内实验模拟, 进一步揭示不同环境因子对珊瑚配子成熟及排卵时间的影响。该研究可为精确预测排卵时间及人工条件下诱导珊瑚全年排卵提供理论依据。

(2)诱导珊瑚幼虫固着的机制

珊瑚幼虫的固着是珊瑚早期发育的关键过程。尽管 CCA、海洋微生物膜及其提取物可以显著影响幼虫固着行为。但具体信号分子、受体蛋白及下游信号传导通路尚未完全阐明。未来研究应聚焦于 CCA、微生物膜的协同作用机制, 结合微生物组学、转录组学和代谢组学等多组学技术, 深入解析特定化学信号对幼虫附着行为及其调控机制的影响, 筛选有效的诱导物质。阐明固着机制可为提升珊瑚幼虫附着率提供必要的学术支撑。

(3)早期共生关系的建立与可塑性

虫黄藻作为珊瑚的关键共生功能体,其被获取过程受珊瑚种类、虫黄藻密度、环境压力等多种因素影响。然而,幼体识别并获取合适共生藻的分子机制尚未阐明,环境压力下幼虫如何调控共生藻组合以增强适应性仍待深入探究。未来将研究共生藻进入珊瑚幼体的过程,追踪其迁移路径,并筛选与共生藻获取相关的关键基因和蛋白,揭示幼体精准识别虫黄藻的分子机制。同时,在实验室条件下模拟不同环境压力,解析幼体各发育阶段共生体及基因表达动态。这些研究可以在全球气候变化和珊瑚白化加剧的背景下,为人工植入合适的共生藻提供理论和技术支持。

(4)建立分子辅助育种的方法,筛选耐热性珊瑚

全球气候变化导致海水温度持续升高,珊瑚白化现象频发,严重威胁海洋生态系统的稳定性。为应对这一危机,建立分子辅助育种方法筛选耐热性珊瑚具有重要意义。未来研究将通过基因组测序技术,挖掘珊瑚耐热相关功能基因(如热休克蛋白、抗氧化酶基因等),开发分子标记以精准筛选耐热表型个体。结合 CRISPR/Cas9 基因编辑技术开展功能验证,并通过人工诱导繁殖和共生藻适配实验,加速耐热性状的遗传改良。该方法突破传统育种的盲目性,显著提升育种效率,为珊瑚礁修复提供抗逆种质资源。

参考文献:

[1] Jones R, Ricardo G F, Negri A P. Effects of sediments on the reproductive cycle of corals[J]. Marine Pollution Bulletin, 2015, 100(1): 13−33.

[2] Randall C J, Negri A P, Quigley K M, et al. Sexual production of corals for reef restoration in the Anthropocene[J]. Marine Ecology Progress Series, 2020, 635: 203−232.

[3] Richmond, R. H. Reproduction and recruitment in corals[M]//Birkeland, C. Life and Death of Coral Reefs. New York: Springer, 1997: 175–197.

[4] Hughes T P, Tanner J E. Recruitment failure, life histories, and long-term decline of caribbean corals[J]. Ecology, 2000, 81(8): 2250−2263.

[5] Guest J, Heyward A, Omori M, et al. Rearing coral larvae for reef rehabilitation[J]. Reef Rehabilitation Manual, 2010: 73−92.

[6] Omori M, Fujiwara S. Manual for Restoration and Remediation of Coral Reefs[M]. Japan: Nature Conservation Bureau and Ministry of the Environment, 2004.

[7] Heyward A J, Negri A P. Turbulence, cleavage, and the naked embryo: a case for coral clones[J]. Science, 2012, 335(6072): 1064−1064.

[8] Humphrey C, Weber M, Lott C, et al. Effects of suspended sediments, dissolved inorganic nutrients and salinity on fertilisation and embryo development in the coral *Acropora millepora* (Ehrenberg, 1834)[J]. Coral Reefs, 2008, 27(4): 837−850.

[9] Riegl B, Purkis S J, Keck J, et al. Monitored and modeled coral population dynamics and the refuge concept[J]. Marine Pollution Bulletin, 2009, 58(1): 24−38.

[10] Harrison P L, Wallace C C. Reproduction, dispersal and recruitment of scleractinian corals[M]//Dubinsky Z. Coral Reefs. Netherlands: Elsevier Science Publishers, 1990, 25: 133−207.

[11] Byrne M. Global change ecotoxicology: identification of early life history bottlenecks in marine invertebrates, variable species responses and variable experimental approaches[J]. Marine environmental research, 2012, 76: 3−15.

[12] Baird A H, Guest J R, Willis B L. Systematic and biogeographical patterns in the reproductive biology of scleractinian corals[J]. Annual Review of Ecology, Evolution, and Systematics, 2009, 40: 551−571.

[13] 杨小东. 澄黄滨珊瑚、大管孔珊瑚和丛生盔形珊瑚性腺发育与生长规律的研究[D]. 湛江: 广东海洋大学, 2013.
Yang Xiaodong. Study of gonad development and growths of *Porites lutea*, *Goniopora djiboutiensis* and *Galaxea fascicularis*[D]. Zhanjiang: Guangdong Ocean University, 2013.

[14] Loya Y, Sakai K. Bidirectional sex change in mushroom stony corals[J]. Proceedings of the Royal Society B: Biological Sciences, 2008, 275(1649): 2335−2343.

[15] Eyal-Shaham L, Eyal G, Ben-Zvi O, et al. A unique reproductive strategy in the mushroom coral *Fungia fungites*[J]. Coral Reefs, 2020, 39(6): 1793−1804.

[16] Santiago-Valentín J D, Rodríguez-Troncoso A P, Carpizo-Ituarte E, et al. Reproductive pattern of the reef-building coral *Pavona gigantea* (Scleractinia: agariciidae) off southwestern Mexico[J]. Ciencias Marinas, 2015, 41(3): 233−246.

[17] Glynn P W, Gassman N J, Eakin C M, et al. Reef coral reproduction in the eastern Pacific: Costa Rica, Panama, and Galapagos Islands (Ecuador)[J]. Marine Biology, 1991, 109(3): 355−368.

[18] Cabral-Tena R A, Tortolero-Langarica J J A, Carricart-Ganivet J P, et al. Sex-associated differences in sclerochronology and sensitivity to thermal stress in Caribbean and eastern Pacific reef-building corals[J]. Marine Ecology Progress Series, 2024, 743: 167−183.

[19] Cruz-Ortega I, Cabral-Tena R A, Carpizo-Ituarte E, et al. Sensitivity of calcification to thermal history differs between sexes in the gonochoric reef-building corals *Dichocoenia stokesi* and *Dendrogyra cylindrus*[J]. Marine Biology, 2020, 167(7): 101.

[20] Shikina S, Chang C F. Sexual reproduction in stony corals and insight into the evolution of oogenesis in Cnidaria[M]//Goffredo S, Dubinsky Z. The Cnidaria, Past, Present and Future: The world of Medusa and Her Sisters. Cham: Springer, 2016: 249−268.

[21] Fadlallah Y H. Sexual reproduction, development and larval biology in scleractinian corals[J]. Coral Reefs, 1983, 2(3): 129−150.

[22] Harrison P L. Sexual reproduction of scleractinian corals[M]//Dubinsky Z, Stambler N. Coral Reefs: An Ecosystem in Transition. Dordrecht: Springer, 2011: 59-85.

[23] Tanner J E. Seasonality and lunar periodicity in the reproduction of Pocilloporid corals[J]. Coral Reefs, 1996, 15(1): 59−66.

[24] 韦芬, 崔梦瑶, 余克服, 等. 涠洲岛海域美丽鹿角珊瑚和秘密角蜂巢珊瑚的性腺发育研究[J]. 海洋学报, 2023, 45(12): 92−100.
Wei Fen, Cui Mengyao, Yu Kefu, et al. Gonadal development of *Acropora formosa* and *Favites abdita* in Weizhou Island[J]. Haiyang Xuebao, 2023, 45(12): 92−100.

[25] Gomez E J, Jamodiong E A, Maboloc E A, et al. Gametogenesis and reproductive pattern of the reef-building coral *Acropora millepora* in northwestern Philippines[J]. Invertebrate Reproduction & Development, 2018, 62(4): 202−208.

[26] Fan T Y, Dai C F. Reproductive plasticity in the reef coral *Echinopora lamellosa*[J]. Marine Ecology Progress Series, 1999, 190: 297−301.

[27] Vargas-Ángel B, Colley S B, Hoke S M, et al. The reproductive seasonality and gametogenic cycle of *Acropora cervicornis* off Broward County, Florida, USA[J]. Coral Reefs, 2006, 25(1): 110−122.

[28] Shikina S, Chung Y J, Wang H M, et al. Localization of early germ cells in a stony coral, *Euphyllia ancora*: potential implications for a germline stem cell system in coral gametogenesis[J]. Coral Reefs, 2015, 34(2): 639−653.

[29] Shikina S, Chiu Y L, Chen C J, et al. Immunodetection of acetylated alpha - tubulin in stony corals: evidence for the existence of flagella in coral male germ cells[J]. Molecular Reproduction and Development, 2017, 84(12): 1285−1295.

[30] Chiu Y L, Shikina S, Yoshioka Y, et al. De novo transcriptome assembly from the gonads of a scleractinian coral, *Euphyllia ancora*: molecular mechanisms underlying scleractinian gametogenesis[J]. BMC Genomics, 2020, 21(1): 732.

[31] Baird A H, Guest J R. Spawning synchrony in scleractinian corals: comment on Mangubhai & Harrison (2008)[J]. Marine Ecology Progress Series, 2009, 374: 301−304.

[32] Shlesinger Y, Goulet T L, Loya Y. Reproductive patterns of scleractinian corals in the northern Red Sea[J]. Marine Biology, 1998, 132(4): 691−701.

[33] Okubo N, Motokawa T. Embryogenesis in the reef-building coral *Acropora* spp[J]. Zoological Science, 2007, 24(12): 1169−1177.

[34] Chui A P Y, Wong M C, Liu S H, et al. Gametogenesis, embryogenesis, and fertilization ecology of *Platygyra acuta* in marginal non-reefal coral communities in Hong Kong[J]. Journal of Marine Biology, 2014, 2014: 953587.

[35] Guest J R, Baird A H, Goh B P L, et al. Seasonal reproduction in equatorial reef corals[J]. Invertebrate Reproduction & Development, 2005, 48(1/3): 207−218.

[36] Baird A H, Guest J R, Edwards A J, et al. An indo-pacific coral spawning database[J]. Scientific Data, 2021, 8(1): 35.

[37] Hoadley K D, Vize P D, Pyott S J. Current understanding of the circadian clock within Cnidaria[M]//Goffredo S, Dubinsky Z. The Cnidaria, Past, Present and Future: The World of Medusa and Her Sisters. Cham: Springer, 2016: 511−520.

[38] Babcock R C, Bull G D, Harrison P L, et al. Synchronous spawnings of 105 scleractinian coral species on the Great Barrier Reef[J]. Marine Biology, 1986, 90(3): 379−394.

[39] Shlesinger T, Loya Y. Breakdown in spawning synchrony: a silent threat to coral persistence[J]. Science, 2019, 365(6457): 1002−1007.

[40] Keith S A, Maynard J A, Edwards A J, et al. Coral mass spawning predicted by rapid seasonal rise in ocean temperature[J]. Proceedings of the Royal Society B: Biological Sciences, 2016, 283(1830): 20160011.

[41] 黄洁英. 三亚鹿回头海域造礁石珊瑚的有性繁殖生物学研究[D]. 北京: 中国科学院, 2011.
Huang Jieying. The sexual reproductive biology of hermatypic corals in Luhuitou, Sanya, China[D]. Beijing: University of Chinese Academy of Sciences, 2011.

[42] Lin C H, Nozawa Y. The influence of seawater temperature on the timing of coral spawning[J]. Coral Reefs, 2023, 42(2): 417−426.

[43] Fogarty N D, Marhaver K L. Coral spawning, unsynchronized[J]. Science, 2019, 365(6457): 987−988.

[44] Lin C H, Nozawa Y. Variability of spawning time (lunar day) in *Acropora versus* merulinid corals: a 7-yr record of in situ coral spawning in Taiwan[J]. Coral Reefs, 2017, 36(4): 1269−1278.

[45] Levy O, Appelbaum L, Leggat W, et al. Light-responsive cryptochromes from a simple multicellular animal, the coral *Acropora millepora*[J]. Science, 2007, 318(5849): 467−470.

[46] Shoguchi E, Tanaka M, Shinzato C, et al. A genome-wide survey of photoreceptor and circadian genes in the coral, *Acropora digitifera*[J]. Gene, 2013, 515(2): 426−431.

[47] Lin C H, Takahashi S, Mulla A J, et al. Moonrise timing is key for synchronized spawning in coral *Dipsastraea speciosa*[J]. Proceedings of the National Academy of Sciences, 2021, 118(34): e2101985118.

[48] Kaniewska P, Alon S, Karako-Lampert S, et al. Signaling cascades and the importance of moonlight in coral broadcast mass spawning[J]. eLife, 2015, 4: e09991.

[49] Wolstenholme J, Nozawa Y, Byrne M, et al. Timing of mass spawning in corals: potential influence of the coincidence of lunar factors and associated changes in atmospheric pressure from northern and southern hemisphere case studies[J]. Invertebrate Reproduction &

Development, 2018, 62(2): 98−108.
[50] Levitan D R, Fogarty N D, Jara J, et al. Genetic, spatial, and temporal components of precise spawning synchrony in reef building corals of the *Montastraea annularis* species complex[J]. Evolution, 2011, 65(5): 1254−1270.
[51] Sakai Y, Hatta M, Furukawa S, et al. Environmental factors explain spawning day deviation from full moon in the scleractinian coral *Acropora*[J]. Biology Letters, 2020, 16(1): 20190760.
[52] Harrison P L. Sexual reproduction of reef corals and application to coral restoration[M]//Wolanski E, Kingsford M J. Oceanographic Processes of Coral Reefs. 2nd ed. Boca Raton: CRC Press, 2024: 419−437.
[53] Gouezo M, Doropoulos C, Fabricius K, et al. Multispecific coral spawning events and extended breeding periods on an equatorial reef[J]. Coral Reefs, 2020, 39(4): 1107−1123.
[54] Lobov A A, Maltseva A L, Mikhailova N A, et al. The molecular mechanisms of gametic incompatibility in invertebrates[J]. Acta Naturae, 2019, 11(3): 4−15.
[55] Buccheri E, Ricardo G F, Babcock R C, et al. Fertilisation kinetics among common Indo-Pacific broadcast spawning corals with distinct and shared functional traits[J]. Coral Reefs, 2023, 42(6): 1351−1363.
[56] Mumby P J, Sartori G, Buccheri E, et al. Allee effects limit coral fertilization success[J]. Proceedings of the National Academy of Sciences of the United States of America, 2024, 121(52): e2418314121.
[57] Nozawa Y, Isomura N, Fukami H. Influence of sperm dilution and gamete contact time on the fertilization rate of scleractinian corals[J]. Coral Reefs, 2015, 34(4): 1199−1206.
[58] Martignago D C, Godoy L, Amaral A P, et al. Establishment of oxidative stress biomarkers in oocytes from healthy and bleached scleractinian corals[J]. Journal of Experimental Marine Biology and Ecology, 2024, 570: 151963.
[59] Paxton C W, Baria M V B, Weis V M, et al. Effect of elevated temperature on fecundity and reproductive timing in the coral *Acropora digitifera*[J]. Zygote, 2016, 24(4): 511−516.
[60] Briggs N D, Page C A, Giuliano C, et al. Dissecting coral recovery: bleaching reduces reproductive output in *Acropora millepora*[J]. Coral Reefs, 2024, 43(3): 557−569.
[61] Albright R, Mason B. Projected near-future levels of temperature and pCO_2 reduce coral fertilization success[J]. PLoS One, 2013, 8(2): e56468.
[62] Puisay A, Hédouin L, Pilon R, et al. How thermal priming of coral gametes shapes fertilization success[J]. Journal of Experimental Marine Biology and Ecology, 2023, 566: 151920.
[63] Hagedorn M, Page C A, O'Neil K L, et al. Assisted gene flow using cryopreserved sperm in critically endangered coral[J]. Proceedings of the National Academy of Sciences of the United States of America, 2021, 118(38): e2110559118.
[64] Hagedorn M, Carter V L, Henley E M, et al. Producing coral offspring with cryopreserved sperm: a tool for coral reef restoration[J]. Scientific Reports, 2017, 7(1): 14432.
[65] Daly J, Hobbs R J, Zuchowicz N, et al. Cryopreservation can assist gene flow on the great barrier reef[J]. Coral Reefs, 2022, 41(2): 455−462.
[66] Hobbs R J, O'brien J K, Bay L K, et al. A decade of coral biobanking science in Australia-transitioning into applied reef restoration[J]. Frontiers in Marine Science, 2022, 9: 960470.
[67] Bouwmeester J, Daly J, Zuchowicz N, et al. Cryopreservation to conserve genetic diversity of reef-building corals[M]//Van Oppen M J H, Lastra M A. Coral Reef Conservation and Restoration in the Omics Age. Cham: Springer, 2022: 225−240.
[68] Daly J, Hobbs R, Zuchowicz N, et al. A semi-automated workflow for the cryopreservation of coral sperm to support biobanking and aquaculture[J]. Journal of Visualized Experiments, 2024(208): e66233.
[69] 韦芬, 黄雯, 余克服, 等. 广西涠洲岛黄癣蜂巢珊瑚、肉质扁脑珊瑚的胚胎和幼虫的早期发育[J]. 海洋学报, 2020, 42(4): 87−95.
Wei Fen, Huang Wen, Yu Kefu, et al. Embryonic and larval early development of *Favia favus* and *Platygyra carnosus* in the Weizhou Island, Guangxi[J]. Haiyang Xuebao, 2020, 42(4): 87−95.
[70] Okubo N, Mezaki T, Nozawa Y, et al. Comparative embryology of eleven species of stony corals (Scleractinia)[J]. PLoS One, 2013, 8(12): e84115.
[71] Permata W D, Kinzie Iii R A, Hidaka M. Histological studies on the origin of planulae of the coral *Pocillopora damicornis*[J]. Marine Ecology Progress Series, 2000, 200: 191−200.
[72] Babcock R C, Heyward A J. Larval development of certain gamete-spawning scleractinian corals[J]. Coral reefs, 1986, 5(3): 111−116.
[73] Hirose M, Hidaka M. Early development of zooxanthella-containing eggs of the corals *Porites cylindrica* and *Montipora digitata*: the endodermal localization of zooxanthellae[J]. Zoological Science, 2006, 23(10): 873−881.
[74] 肖宝华, 廖宝林, 杨小东, 等. 肉质扁脑珊瑚的有性繁殖及早期发育[J]. 热带海洋学报, 2017, 36(1): 65−71.
Xiao Baohua, Liao Baolin, Yang Xiaodong, et al. Sexual reproduction and early development of *Platygyra carnosus*[J]. Journal of Tropical Oceanography, 2017, 36(1): 65−71.
[75] Technau U. Gastrulation and germ layer formation in the sea anemone *Nematostella vectensis* and other cnidarians[J]. Mechanisms of Development, 2020, 163: 103628.
[76] Okubo N, Hayward D C, Forêt S, et al. A comparative view of early development in the corals *Favia lizardensis*, *Ctenactis echinata*,

and *Acropora millepora*-morphology, transcriptome, and developmental gene expression[J]. BMC Evolutionary Biology, 2016, 16(1): 48.

[77] Marlow H Q, Martindale M Q. Embryonic development in two species of scleractinian coral embryos: Symbiodinium localization and mode of gastrulation[J]. Evolution & Development, 2007, 9(4): 355−367.

[78] Keshavmurthy S, Fontana S, Mezaki T, et al. Doors are closing on early development in corals facing climate change[J]. Scientific Reports, 2014, 4(1): 5633.

[79] Humanes A, Noonan S H C, Willis B L, et al. Cumulative effects of nutrient enrichment and elevated temperature compromise the early life history stages of the coral *Acropora tenuis*[J]. PLoS One, 2016, 11(8): e0161616.

[80] Puisay A, Pilon R, Goiran C, et al. Thermal resistances and acclimation potential during coral larval ontogeny in *Acropora pulchra*[J]. Marine Environmental Research, 2018, 135: 1−10.

[81] Petersen L E, Kellermann M Y, Schupp P J. Secondary metabolites of marine microbes: From natural products chemistry to chemical ecology[M]//Jungblut S, Liebich V, Bode-Dalby M. YOUMARES 9 - The Oceans: Our Research, Our Future. Cham: Springer, 2020: 159−180.

[82] Randall C J, Giuliano C, Stephenson B, et al. Larval precompetency and settlement behaviour in 25 Indo-Pacific coral species[J]. Communications Biology, 2024, 7(1): 142.

[83] Mass T, Putnam H M, Drake J L, et al. Temporal and spatial expression patterns of biomineralization proteins during early development in the stony coral *Pocillopora damicornis*[J]. Proceedings of the Royal Society B: Biological Sciences, 2016, 283(1829): 20160322.

[84] Wei Fen, Cui Mengyao, Huang Wen, et al. Ex situ reproduction and recruitment of scleractinian coral *Galaxea fascicularis*[J]. Marine Biology, 2023, 170(3): 30.

[85] Connolly S R, Baird A H. Estimating dispersal potential for marine larvae: dynamic models applied to scleractinian corals[J]. Ecology, 2010, 91(12): 3572−3583.

[86] Gleason D F, Hofmann D K. Coral larvae: from gametes to recruits[J]. Journal of Experimental Marine Biology and Ecology, 2011, 408(1/2): 42−57.

[87] Pysanczyn J W, Williams E A, Brodrick E, et al. The role of acoustics within the sensory landscape of coral larval settlement[J]. Frontiers in Marine Science, 2023, 10: 1111599.

[88] Whitman T N, Negri A P, Bourne D G, et al. Settlement of larvae from four families of corals in response to a crustose coralline alga and its biochemical morphogens[J]. Scientific Reports, 2020, 10(1): 16397.

[89] Abdul Wahab M A, Ferguson S, Snekkevik V K, et al. Hierarchical settlement behaviours of coral larvae to common coralline algae[J]. Scientific Reports, 2023, 13(1): 5795.

[90] Tebben J, Motti C A, Siboni N, et al. Chemical mediation of coral larval settlement by crustose coralline algae[J]. Scientific Reports, 2015, 5(1): 10803.

[91] Kitamura M, Schupp P J, Nakano Y, et al. Luminaolide, a novel metamorphosis-enhancing macrodiolide for scleractinian coral larvae from crustose coralline algae[J]. Tetrahedron Letters, 2009, 50(47): 6606−6609.

[92] Turnlund A C. Interactions between coral larval settlement, marine biofilms and crustose coralline algae microbiomes[D]. Brisbane: The University of Queensland, 2024.

[93] Bourne D G, Sato Y, Smith H A. Microbes guide corals looking to find a home[J]. Trends in Microbiology, 2024, 32(2): 120−121.

[94] Turnlund A C, Vanwonterghem I, Botté E S, et al. Linking differences in microbial network structure with changes in coral larval settlement[J]. ISME Communications, 2023, 3(1): 114.

[95] Kegler P, Kegler H F, Gärdes A, et al. Bacterial biofilm communities and coral larvae settlement at different levels of anthropogenic impact in the Spermonde Archipelago, Indonesia[J]. Frontiers in Marine Science, 2017, 4: 270.

[96] Tebben J, Tapiolas D M, Motti C A, et al. Induction of larval metamorphosis of the coral *Acropora millepora* by tetrabromopyrrole isolated from a *Pseudoalteromonas* bacterium[J]. PLoS One, 2011, 6(4): e19082.

[97] Alker A T, Farrell M V, Demko A M, et al. Linking bacterial tetrabromopyrrole biosynthesis to coral metamorphosis[J]. ISME Communications, 2023, 3(1): 98.

[98] Sneed J M, Sharp K H, Ritchie K B, et al. The chemical cue tetrabromopyrrole from a biofilm bacterium induces settlement of multiple Caribbean corals[J]. Proceedings of the Royal Society B: Biological Sciences, 2014, 281(1786): 20133086.

[99] Petersen L E, Kellermann M Y, Nietzer S, et al. Photosensitivity of the bacterial pigment cycloprodigiosin enables settlement in coral larvae—light as an understudied environmental factor[J]. Frontiers in Marine Science, 2021, 8: 749070.

[100] Petersen L E, Kellermann M Y, Fiegel L J, et al. Photodegradation of a bacterial pigment and resulting hydrogen peroxide release enable coral settlement[J]. Scientific Reports, 2023, 13(1): 3562.

[101] Erwin P M, Szmant A M. Settlement induction of *Acropora palmata* planulae by a GLW-amide neuropeptide[J]. Coral Reefs, 2010, 29(4): 929−939.

[102] Moeller M, Nietzer S, Schupp P J. Neuroactive compounds induce larval settlement in the scleractinian coral *Leptastrea purpurea*[J]. Scientific Reports, 2019, 9(1): 2291.

[103] Yang Qingsong, Zhang Wenqian, Zhang Ying, et al. Promoting larval settlement of coral *Pocillopora damicornis* by calcium[J]. Coral

Reefs, 2022, 41(1): 223−235.
[104] Strader M E, Davies S W, Matz M V. Differential responses of coral larvae to the colour of ambient light guide them to suitable settlement microhabitat[J]. Royal Society Open Science, 2015, 2(10): 150358.
[105] Mason B, Beard M, Miller M W. Coral larvae settle at a higher frequency on red surfaces[J]. Coral Reefs, 2011, 30(3): 667−676.
[106] Levenstein M A, Marhaver K L, Quinlan Z A, et al. Engineered substrates reveal species-specific inorganic cues for coral larval settlement[J]. ACS Sustainable Chem. Eng., 2022, 10: 3960−3971.
[107] Patterson J T, Flint M, Than J, et al. Evaluation of substrate properties for settlement of Caribbean staghorn coral *Acropora cervicornis* larvae in a land - based system[J]. North American Journal of Aquaculture, 2016, 78(4): 337−345.
[108] Wilson J, Harrison P. Post-settlement mortality and growth of newly settled reef corals in a subtropical environment[J]. Coral Reefs, 2005, 24(3): 418−421.
[109] Doropoulos C, Roff G, Bozec Y M, et al. Characterizing the ecological trade - offs throughout the early ontogeny of coral recruitment[J]. Ecological Monographs, 2016, 86(1): 20−44.
[110] Wolanski E, Kingsford M J. Oceanographic Processes of Coral Reefs: Physical and Biological Links in the Great Barrier Reef[M]. 2nd ed. Boca Raton: CRC Press, 2024.
[111] Babcock R, Mundy C. Coral recruitment: consequences of settlement choice for early growth and survivorship in two scleractinians[J]. Journal of Experimental Marine Biology and Ecology, 1996, 206(1/2): 179−201.
[112] Doropoulos C, Ward S, Marshell A, et al. Interactions among chronic and acute impacts on coral recruits: the importance of size - escape thresholds[J]. Ecology, 2012, 93(10): 2131−2138.
[113] Penin L, Michonneau F, Baird A H, et al. Early post-settlement mortality and the structure of coral assemblages[J]. Marine Ecology Progress Series, 2010, 408: 55−64.
[114] Nozawa Y. Micro-crevice structure enhances coral spat survivorship[J]. Journal of Experimental Marine Biology and Ecology, 2008, 367(2): 127−130.
[115] Chamberland V F, Petersen D, Guest J R, et al. New seeding approach reduces costs and time to outplant sexually propagated corals for reef restoration[J]. Scientific Reports, 2017, 7(1): 18076.
[116] Tebben J, Guest J R, Sin T M, et al. Corals like it waxed: paraffin-based antifouling technology enhances coral spat survival[J]. PLoS One, 2014, 9(1): e87545.
[117] Davies S W, Matz M V, Vize P D. Ecological complexity of coral recruitment processes: effects of invertebrate herbivores on coral recruitment and growth depends upon substratum properties and coral species[J]. PLoS One, 2013, 8(9): e72830.
[118] Toh T C, Ng C S L, Guest J, et al. Grazers improve health of coral juveniles in ex situ mariculture[J]. Aquaculture, 2013, 414−415: 288−293.
[119] Craggs J, Guest J, Bulling M, et al. Ex situ co culturing of the sea urchin, *Mespilia globulus* and the coral *Acropora millepora* enhances early post-settlement survivorship[J]. Scientific Reports, 2019, 9(1): 12984.
[120] Nozawa Y, Harrison P L. Effects of elevated temperature on larval settlement and post-settlement survival in scleractinian corals, *Acropora solitaryensis* and *Favites chinensis*[J]. Marine Biology, 2007, 152(5): 1181−1185.
[121] Ross C, Ritson-Williams R, Olsen K, et al. Short-term and latent post-settlement effects associated with elevated temperature and oxidative stress on larvae from the coral *Porites astreoides*[J]. Coral Reefs, 2013, 32(1): 71−79.
[122] Nakamura M, Ohki S, Suzuki A, et al. Coral larvae under ocean acidification: survival, metabolism, and metamorphosis[J]. PLoS One, 2011, 6(1): e14521.
[123] Cohen A L, McCorkle D C, de Putron S, et al. Morphological and compositional changes in the skeletons of new coral recruits reared in acidified seawater: insights into the biomineralization response to ocean acidification[J]. Geochemistry, Geophysics, Geosystems, 2009, 10(7): 2009GC002411.
[124] Chan Y L, Stock J H, Watson M W. A dynamic factor model framework for forecast combination[J]. Spanish Economic Review, 1999, 1(2): 91−121.
[125] Quigley K M, Marzonie M, Ramsby B, et al. Variability in fitness trade-offs amongst coral juveniles with mixed genetic backgrounds held in the wild[J]. Frontiers in Marine Science, 2021, 8: 636177.
[126] Torda G, Lundgren P, Willis B L, et al. Revisiting the connectivity puzzle of the common coral *Pocillopora damicornis*[J]. Molecular Ecology, 2013, 22(23): 5805−5820.
[127] Hoegh-Guldberg O, Hughes L, McIntyre S, et al. Assisted colonization and rapid climate change[J]. Science, 2008, 321(5887): 345−346.
[128] Chan W Y, Chung J, Peplow L M, et al. Maternal effects in gene expression of interspecific coral hybrids[J]. Molecular Ecology, 2021, 30(2): 517−527.
[129] Quigley K M, Randall C J, Van Oppen M J H, et al. Assessing the role of historical temperature regime and algal symbionts on the heat tolerance of coral juveniles[J]. Biology Open, 2020, 9(1): bio047316.
[130] Kirk N L, Howells E J, Abrego D, et al. Genomic and transcriptomic signals of thermal tolerance in heat - tolerant corals (*Platygyra daedalea*) of the Arabian/Persian Gulf[J]. Molecular Ecology, 2018, 27(24): 5180−5194.

［131］ Fuller Z L, Mocellin V J L, Morris L A, et al. Population genetics of the coral Acropora millepora: toward genomic prediction of bleaching[J]. Science, 2020, 369(6501): eaba4674.

［132］ Cleves P A, Tinoco A I, Bradford J, et al. Reduced thermal tolerance in a coral carrying CRISPR-induced mutations in the gene for a heat-shock transcription factor[J]. Proceedings of the National Academy of Sciences, 2020, 117(46): 28899−28905.

［133］ Rinkevich B, Shaish L, Douek J, et al. Venturing in coral larval chimerism: a compact functional domain with fostered genotypic diversity[J]. Scientific Reports, 2016, 6(1): 19493.

［134］ Huffmyer A S, Drury C, Majerová E, et al. Tissue fusion and enhanced genotypic diversity support the survival of *Pocillopora acuta* coral recruits under thermal stress[J]. Coral Reefs, 2021, 40(2): 447−458.

［135］ Jiang Lei, Zhang Yuyang, Liu Chengyue, et al. Gregarious larval settlement mediates the responses of new recruits of the reef coral *Acropora austera* to ocean warming and acidification[J]. Frontiers in Marine Science, 2022, 9: 964803.

［136］ Edmunds P J. Coral recruitment: patterns and processes determining the dynamics of coral populations[J]. Biological Reviews, 2023, 98(6): 1862−1886.

［137］ Bockel T, Rinkevich B. Rapid recruitment of symbiotic algae into developing scleractinian coral tissues[J]. Journal of Marine Science and Engineering, 2019, 7(9): 306.

［138］ Kenkel C D, Bay L K. Exploring mechanisms that affect coral cooperation: symbiont transmission mode, cell density and community composition[J]. PeerJ, 2018, 6: e6047.

［139］ McIlroy S E, Coffroth M A. Coral ontogeny affects early symbiont acquisition in laboratory-reared recruits[J]. Coral Reefs, 2017, 36(3): 927−932.

［140］ Quigley K M, Alvarez Roa C, Beltran V H, et al. Experimental evolution of the coral algal endosymbiont, *Cladocopium goreaui*: lessons learnt across a decade of stress experiments to enhance coral heat tolerance[J]. Restoration Ecology, 2021, 29(3): e13342.

［141］ Pochon X, Gates R D. A new *Symbiodinium* clade (Dinophyceae) from *Soritid foraminifera* in Hawai'i[J]. Molecular Phylogenetics and Evolution, 2010, 56(1): 492−497.

［142］ Adams L M, Cumbo V R, Takabayashi M. Exposure to sediment enhances primary acquisition of *Symbiodinium* by asymbiotic coral larvae[J]. Marine Ecology Progress Series, 2009, 377: 149−156.

［143］ Cumbo V R, Baird A H, Van Oppen M J H. The promiscuous larvae: flexibility in the establishment of symbiosis in corals[J]. Coral Reefs, 2013, 32(1): 111−120.

［144］ Schwarz J A, Krupp D A, Weis V M. Late larval development and onset of symbiosis in the scleractinian coral *Fungia scutaria*[J]. The Biological Bulletin, 1999, 196(1): 70−79.

［145］ Williams R B, Cornelius P F S, Hughes R G, et al. Coelenterate biology: recent research on cnidaria and ctenophora[C]//Proceedings of the Fifth International Conference on Coelenterate Biology. Dordrecht: Springer, 1991.

［146］ Yamashita H, Suzuki G, Kai S, et al. Establishment of coral–algal symbiosis requires attraction and selection[J]. PLoS One, 2014, 9(5): e97003.

［147］ Quigley K M, Willis B L, Bay L K. Heritability of the *Symbiodinium* community in vertically-and horizontally-transmitting broadcast spawning corals[J]. Scientific Reports, 2017, 7(1): 8219.

［148］ Quigley K M, Bay L K, Willis B L. Temperature and water quality-related patterns in sediment-associated Symbiodinium communities impact symbiont uptake and fitness of juveniles in the genus *Acropora*[J]. Frontiers in Marine Science, 2017, 4: 401.

［149］ Yorifuji M, Harii S, Nakamura R, et al. Shift of symbiont communities in *Acropora tenuis* juveniles under heat stress[J]. PeerJ, 2017, 5: e4055.

［150］ Turnham K E, Lewis A M, Kemp D W, et al. Limited persistence of the heat-tolerant zooxanthella, *Durusdinium trenchii*, in corals transplanted to a barrier reef where it is rare among natal colonies[J]. Coral Reefs, 2025, 44(2): 555−570.

［151］ Sun Youfang, Jiang Lei, Gong Sanqiang, et al. Impact of ocean warming and acidification on symbiosis establishment and gene expression profiles in recruits of reef coral *Acropora intermedia*[J]. Frontiers in Microbiology, 2020, 11: 532447.

［152］ Abrego D, Van Oppen M J H, Willis B L. Onset of algal endosymbiont specificity varies among closely related species of Acropora corals during early ontogeny[J]. Molecular Ecology, 2009, 18(16): 3532−3543.

［153］ Cumbo V R, Van Oppen M J H, Baird A H. Temperature and *Symbiodinium* physiology affect the establishment and development of symbiosis in corals[J]. Marine Ecology Progress Series, 2018, 587: 117−127.

［154］ Jiang Lei, Sun Youfang, Zhang Yuyang, et al. Impact of diurnal temperature fluctuations on larval settlement and growth of the reef coral *Pocillopora damicornis*[J]. Biogeosciences, 2017, 14(24): 5741−5752.

［155］ Quigley K M, Baker A C, Coffroth M A, et al. Bleaching resistance and the role of algal endosymbionts[M]//Van Oppen M J H, Lough J M. Coral Bleaching: Patterns, Processes, Causes and Consequences. Cham: Springer, 2018: 111−151.

［156］ Quigley K M, Alvarez-Roa C, Raina J B, et al. Heat-evolved microalgal symbionts increase thermal bleaching tolerance of coral juveniles without a trade-off against growth[J]. Coral Reefs, 2023, 42(6): 1227−1232.

［157］ Maire J, Van Oppen M J H. A role for bacterial experimental evolution in coral bleaching mitigation?[J]. Trends in Microbiology, 2022, 30(3): 217−228.

Research progress on sexual reproduction of scleractinian corals

Cui Mengyao[1], Wei Fen[1], Yu Kefu[1, 2]

(1. *Guangxi Laboratory on the Study of Coral Reefs in the South China Sea/Coral Reef Research Center of China/School of Marine Sciences*, *Guangxi University*, *Nanning* 530004, *China*; 2. *Southern Marine Science and Engineering Guangdong Laboratory* (*Guangzhou*), *Guangzhou* 519080, *China*)

Abstract: Sexual reproduction in scleractinian corals is a fundamental biological process that sustains the structure and function of coral reef ecosystems. It directly determines population dynamics and genetic diversity, thereby playing a crucial role in the stability and evolution of coral reefs. This review summarizes recent advances in the study of coral sexual reproduction, including: (1) reproductive strategies, (2) gonadal development, (3) spawning and fertilization, (4) embryogenesis, (5) larval settlement, and (6) juvenile development. Current research indicates that coral sexual reproduction is jointly regulated by endogenous biological mechanisms and exogenous environmental factors; however, the detailed molecular mechanisms underlying these processes remain largely unclear. Future studies should focus on elucidating the environmental regulation of spawning timing, mechanisms inducing larval settlement, establishment and plasticity of early symbiotic relationships, and the development of molecular-assisted breeding strategies for selecting thermotolerant coral strains.

Key words: scleractinian corals; sexual reproduction; gonadal development; spawning and fertilization; embryogenesis; larval settlement

◆珊瑚礁生态保护与修复◆

基于转录组学的造礁石珊瑚环境胁迫响应机制研究进展*

陈俊伶[1],马玉玲[1],郑　月[1],余克服[1,2**],俞小鹏[1**]

(1. 广西大学海洋学院,广西南海珊瑚礁研究重点实验室,广西大学珊瑚礁研究中心,广西南宁　530004;2. 南方海洋科学与工程广东省实验室(广州),广东广州　511458)

摘要:造礁石珊瑚的环境适应性取决于珊瑚共生功能体互作的分子调控机制,但这一机制尚未完全被阐明。近年来,随着高通量测序技术的发展,转录组学技术被广泛应用于珊瑚共生功能体的研究,成为解析珊瑚环境响应机制的关键工具,为揭示共生系统的分子互作网络提供了新视角。本文系统综述了转录组学在造礁石珊瑚环境适应性研究中的应用进展,重点阐述了不同环境胁迫下珊瑚共生功能体的转录响应,总结了珊瑚共生功能体各组分在应对不同环境胁迫时的差异响应机制。环境胁迫过程中珊瑚宿主和共生虫黄藻均表现出基因表达的可塑性,能够通过精确的转录调控网络来建立对环境胁迫的耐受性,并且能通过协同调控机制来维持共生关系的稳定。未来研究需进一步整合多组学数据,结合生理生态学验证,以全面揭示珊瑚共生功能体的调控网络。

关键词:转录组学;造礁石珊瑚;珊瑚共生功能体;虫黄藻;环境胁迫;适应性

中图分类号:Q178.53　　**文献标识码**:A　　**文章编号**:1005-9164(2025)04-0780-20

DOI:10.13656/j.cnki.gxkx.20251114.014

珊瑚礁生态系统是地球上生物多样性和生产力较高的生态系统之一,其生态功能的维持高度依赖于造礁石珊瑚这一关键框架生物[1]。然而,气候变暖、极端降水、海洋酸化和水体富营养化等环境胁迫会造成珊瑚宿主与共生虫黄藻的共生关系破裂,使得珊瑚将共生虫黄藻排出细胞外并致使共生虫黄藻的光合色素降解,最终导致珊瑚白化甚至死亡[2]。当响应环境胁迫时,珊瑚在其分子、细胞及生理生化水平都会产生一系列反应,是其应对环境胁迫的第一道防线。珊瑚及其共生虫黄藻都能通过基因表达的改变来重新配置代谢通路,以维持必需的新陈代谢并通过建立新的稳态来适应环境变化[3]。随着全球变暖不断加剧,珊瑚白化事件的频率和强度也在不断上升,但生态调查同时也发现部分珊瑚种群正在逐步建立环境

收稿日期:2025-06-19　　修回日期:2025-07-31

*国家自然科学基金重大项目(42030502),国家自然科学基金重点项目(42090041),国家自然科学基金项目(42406143),广西科技基地与人才专项(桂科 AD25069075),广西研究生教育创新计划项目(YCBZ2024045)资助。

【第一作者简介】

陈俊伶(1998—),女,硕士,主要从事生物与生态方向研究,E-mail:2227301003@st.gxu.edu.cn。

【**通信作者简介】

余克服(1969—),男,教授,主要从事南海珊瑚礁地质和生态环境研究,E-mail:kefuyu@scsio.ac.cn。

俞小鹏(1992—),男,助理教授,主要从事南海珊瑚生态与环境适应机制研究,E-mail:yuxiaopeng100@foxmail.com。

【引用本文】

陈俊伶,马玉玲,郑月,等. 基于转录组学的造礁石珊瑚环境胁迫响应机制研究进展[J]. 广西科学,2025,32(4):780-799.

CHEN J L,MA Y L,ZHENG Y,et al. Advances in Transcriptome-Based Mechanisms of Environmental Stress Responses in Scleractinian Corals [J]. Guangxi Sciences,2025,32(4):780-799.

中国知网　https://www.cnki.net

适应性,因此珊瑚环境响应的内在分子机制有待深入研究。

近年来,生物信息技术快速发展推动了以转录组为首的组学技术在珊瑚研究中的广泛应用,这从根本上改变了珊瑚环境适应性机制的研究范式[4-5]。转录组学技术能够识别珊瑚宿主和共生虫黄藻,为研究珊瑚与虫黄藻共生的内在分子机制提供了更为有效的方法[6]。作为在 RNA 水平上解析转录组图谱的研究技术,转录组学通过全面揭示生物体的基因表达情况,以阐述细胞、组织或器官在特定条件下的生命活动规律。目前,转录组学技术已被广泛应用于探究珊瑚共生功能体在高温、海水酸化、低盐胁迫、海水富营养化、污染物暴露等不同环境压力下的响应机制,为阐明珊瑚对环境胁迫的适应性机制提供了重要技术支撑[7]。本综述对国内外转录组学在造礁石珊瑚环境适应性中的应用进行了总结,深入分析了当前研究存在的局限性,并对未来相关的研究方向进行了展望。通过整合现有的研究成果,本文旨在为深入理解不同环境胁迫下珊瑚共生功能体环境适应性的分子机制及共生互作协同效应提供理论参考,同时也为珊瑚礁生态系统的保护与修复提供科学依据。

1 转录组学技术分类与发展

转录组是特定组织或细胞在某一发育阶段或功能状态下转录出来的全部 RNA 的集合[8]。作为一门从整体水平上研究细胞中基因转录情况及转录调控规律的学科,转录组学与静态稳定的基因组有所不同,其能够反映研究对象的动态变化。这种动态特性体现在同一基因在不同环境、不同时期和不同组分中的表达差异上。转录组学研究技术主要分为两大类:一类是杂交转录组学,以杂交图谱荧光信号的强弱来判断基因表达的丰度,包括微阵列(Microarray)技术、基因芯片(Gene chip)技术;另一类是测序转录组学,该技术通过组装、拼接得到相关序列,从而快速获取转录本相关信息,主要包括表达序列标签(Expressed Sequence Tags,EST)技术、基因表达序列分析(Serrial Analysis of Gene Expression,SAGE)、大规模平行测序(Massively parallel sequencing)技术、RNA Sequence (RNA-Seq)技术、单细胞转录组测序(Single cell transcriptome sequencing,scRNA-seq)技术等。

早期的转录组测序技术,如 Microarray、Gene chip、EST 等,虽然可以检测出基因的表达丰度,但是受限于物种基因组信息,难以应用到还未完成全基因组测序或者基因注释信息不完善的物种上。随着测序技术的革新,RNA-Seq 技术凭借其不依赖于预先设计的探针或已知序列信息的特点,逐渐成为目前主流的转录组测序技术。该技术具有通量高、准确性高、检测范围广、成本低等优势,可以应用于基因组图谱尚未完成组装的物种上[9]。在此基础上,scRNA-seq 技术作为新兴技术,能够解析组织细胞之间的基因表达异质性。该技术以单个细胞为检测单位,可以获得单个细胞的转录组信息,为揭示不同类型细胞在发育过程中的功能分化以及细胞间的调控网络提供了重要工具[10]。

目前,基于 Illumina 的下一代测序是主流的转录组测序技术。然而,由于读长较短,基于算法组装的全长转录本的质量相对较低。第三代全长转录本测序(TGS)的出现弥补了这一不足,其超长读长的特性显著提升了全长转录本组装的质量。转录组学技术的优缺点比较分析如表 1 所示。

表 1 转录组学技术比较分析

Table 1 The comparative analysis of transcriptomic technologies

技术 Technology	优点 Advantage	缺点 Disadvantage
Microarray	High throughput and reliability	Only detects sequences targeted by hybridization probes (fails to identify new species); exhibits cross-hybridization, non-specific hybridization, and limited detection efficiency of individual probes
Gene chip	Accurate detection of highly expressed genes; high throughput, miniaturization, automation, low cost, and anti-contamination	Unable to detect low-abundance genes (limited by gene copy number); limited database data potentially resulting in annotation errors
Expressed Sequence Tags	Relatively low cost and technical threshold; prior to 2003, the primary and most efficient method for rapid discovery and identification of unknown genes	Short length without complete expression sequences; low-abundance expressed genes difficult to acquire; high error rate; identical PCR product sizes in cDNA and genomic templates (due to intron absence); poor conservation of 3′UTR sequences, easily distinguishing single genes from closely related homologous gene families
RNA-Seq	High throughput, resolution, and sensitivity; not limited by prior knowledge; enables differentiation of symbiont components	Fails to reveal inter-individual cellular expression heterogeneity

中国知网 https://www.cnki.net

续表

Continued table

技术 Technology	优点 Advantage	缺点 Disadvantage
Single cell transcriptome sequencing	High sensitivity, accuracy, and specificity; high-quality high-throughput sequencing achievable with minimal sample input; avoids false-negative results from mixed cell populations; identifies rare cell subsets undetectable by bulk cell sequencing	Incompatible with high-throughput sample processing; challenging to capture full transcripts, entire transcriptomes, and full-length transcripts; only analyzes poly(A)-tailed mRNA [reliant on poly(T) primers for single-cell cDNA amplification]; stricter sample quality requirements; unable to detect most mRNA longer than 3 kb
Third-generation full-length transcriptome sequencing	Error correction via repeated sequencing; ultra-long read length; no requirement for template amplification; short runtime; direct detection of epigenetic modification sites and full-length transcripts	Relatively low sequencing accuracy; relies on polymerases and exonucleases with inadequate activity and stability; insufficient DNA extensibility prone to dimer formation

2 环境胁迫下的珊瑚共生功能体转录组学研究

珊瑚共生功能体由珊瑚宿主、共生虫黄藻及其他微生物共同组成,珊瑚宿主为共生虫黄藻提供生存场所和代谢产物,同时也依靠共生虫黄藻通过光合作用产生的光合产物(包括葡萄糖、甘油和氨基酸)易位来满足自身的能量需求。这种互利共生关系的稳定性对珊瑚共生功能体健康的维持至关重要。作为典型的共生功能体,造礁石珊瑚对环境胁迫的响应机制涉及多基因调控网络、多信号转导途径、多代谢通路以及复杂的共生互作机制[11]。因此,在利用转录组学研究珊瑚共生功能体环境适应性时,必须对珊瑚宿主和共生虫黄藻共同进行分析,以全面解析二者在环境压力下的基因表达变化情况及其相互作用机制。近年来,基于转录组学的珊瑚研究取得了一定的进展,揭示了一系列与环境适应性相关的重要基因和代谢通路。为深入了解珊瑚共生功能体转录组学研究,以“coral”“Microarray”“scRNA-seq”“Full-length transcriptome”“RNA-Seq”“Transcriptome”为检索关键词,并运用计算机检索语言将各个检索词进行联结,以美国科学信息研究所(Institute for Scientific Information,ISI)旗下的 Web of Science 核心合集[具体采用了其科学引文索引扩展版(SCIE)数据库]、中国知网(China National Knowledge Infrastructure,CNKI)数据库中 SCI 来源期刊、EI 来源期刊、中文核心期刊、硕博论文为来源数据,检索 2004—2024 年珊瑚转录组学研究相关文献。结果发现,随着转录组学技术的更新换代,RNA-Seq 技术已成为当前珊瑚研究的主流技术手段(图 1)。基于此,本文主要综述珊瑚共生功能体在不同环境胁迫下采用 RNA-Seq 技术的转录组学研究,以期为深入理解造礁石珊瑚环境适应性机制提供新的见解。

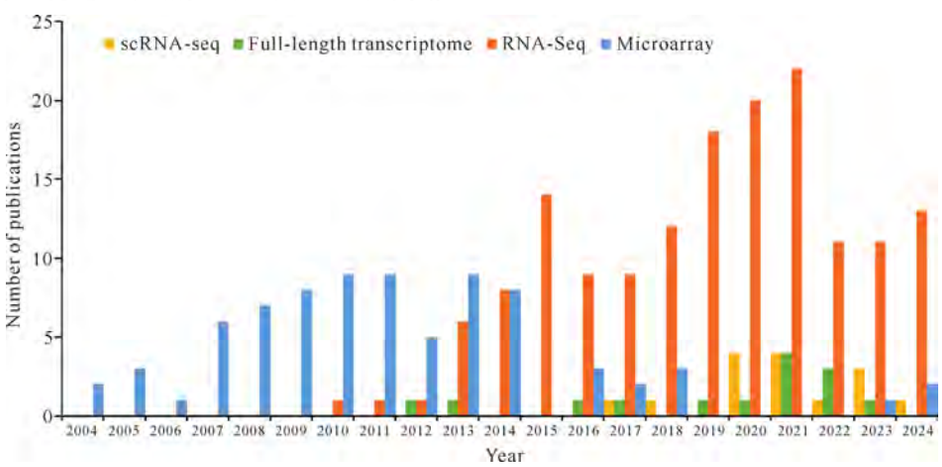


图 1 珊瑚转录组学研究的历年发文量统计

Fig. 1 Annual publication statistics in coral transcriptomic research

2.1 高温胁迫

随着全球变暖的加剧,海表温度的快速上升导致珊瑚热白化事件的频率和强度显著增加[12],高温已经成为引发珊瑚白化的最主要环境胁迫因素。为减

中国知网 https://www.cnki.net

轻热应激对细胞造成的损伤,珊瑚细胞内部发生了一系列反应,比如氧化还原调节、分子伴侣表达量上调、内质网应激和免疫反应等。在急性高温胁迫条件下,珊瑚对热应激产生巨大而快速的转录反应[13-15]。热应激首先广泛影响蛋白质加工、细胞生长周期和代谢,而后期的珊瑚白化反应则与 RNA 转运、细胞外基质、珊瑚钙化,以及 DNA 复制、修复活性相关。在珊瑚热白化的过程中,转录调控、蛋白质合成、细胞转运、细胞骨架重排和氧化还原稳态等这些与重要细胞功能和活动相关的通路显著表达。

在珊瑚共生功能体对高温胁迫的转录响应研究中,热休克蛋白(HSP)的编码基因是研究最为深入的基因。研究发现,热应激下珊瑚宿主细胞内大量热休克蛋白基因显著上调,表明其在热应激响应中发挥着关键作用[16-18]。Traylor-Knowles 等[19]研究表明,在急性高温胁迫期间,风信子鹿角珊瑚(*Acropora hyacinthus*)在 20 min 内上调与热应激相关的特定基因的表达,在 5 h 内约 20%的基因表达会显著上调。另外,珊瑚广义应激反应首先涉及转座子和转录因子的短期反应;然后启动下游过程[19](该过程得到了与热应激相关共表达基因网络的支持[20],并且该过程还伴随着 HSP 的短期上调和下调[19,21]);最后,转录组反应调控代谢过程的下调,限制珊瑚代谢、生长、细胞分裂、复制和蛋白质翻译相关的基因表达。热休克蛋白和转录因子在急性胁迫早期上调,表明热休克蛋白调控着热白化的整个过程。

经历热白化事件的珊瑚具有一定的自我恢复能力。Zhang 等[22]通过转录组分析发现,自然热白化的十字牡丹珊瑚(*Pavona decussata*)在自我恢复过程中,与有丝分裂、DNA 复制和重组相关的通路显著富集,这有助于珊瑚组织修复和能量代谢恢复。Li 等[23]在实验室条件下探究了鹿角杯形珊瑚(*Pocillopora damicornis*)共生功能体对逐渐升温的转录响应,结果发现随着温度的升高,鹿角杯形珊瑚对温度升高的反应比共生虫黄藻更快。另外,蛋白组学研究结果进一步验证了转录组学的研究结果。Petrou 等[24]发现,与对照组相比,高温胁迫下的多孔鹿角珊瑚(*Acropora millepora*)中参与氧化应激和蛋白质水解的相关蛋白酶显著增加,而共生虫黄藻中与光合作用、能量代谢相关的蛋白酶减少。上述结果均表明珊瑚正在通过相关变化来抵抗高温胁迫。

不同形状和种类珊瑚的热耐受性存在显著差异。块状珊瑚通常比片状、枝状珊瑚具有更高的热耐受性[19];而相对棕色丛生盔形珊瑚(*Galaxea fascicularis*)来说,绿色丛生盔形珊瑚具有更高的绿色荧光强度和 GFP 样蛋白编码基因转录水平,因而具有更高的耐热能力[25]。此外,共生虫黄藻的类型也会显著影响宿主的热耐受性。Cunning 等[26]通过控制实验发现,与 D 型虫黄藻共生的 *Montastraea cavernosa*,其与核糖体结构、翻译活性相关的基因显著上调,生长更快,并且在短期热应激下表现出更强的热耐受性。

为提高珊瑚共生功能体对高温的耐受性,研究人员开展了珊瑚热驯化研究。Yu 等[27]对霜鹿角珊瑚(*Acropora pruinosa*)进行热驯化后发现,珊瑚宿主中与代谢相关的基因,特别是氮代谢通路相关基因的表达显著下调,表明热驯化后的珊瑚可能通过降低新陈代谢水平来实现自我保护。因此,热驯化改变了珊瑚共生功能体的能量代谢途径,促进了营养物质从共生虫黄藻向珊瑚宿主转移,进而增强了其热适应性。

2.2 强光胁迫

大规模珊瑚白化事件不仅与持续高温有关,而且与太阳辐射强度、海面平静状态和海水透明度等其他自然环境因素共同作用有关。强光胁迫主要对珊瑚共生虫黄藻的光合系统和免疫系统造成损伤,而珊瑚宿主能够通过调节荧光蛋白和非荧光色蛋白基因的表达来减轻强光的不利影响。

朱乐等[28]在 26 ℃恒定温度下进行单因素光胁迫实验,发现强光胁迫导致短指软珊瑚(*Sinularia* sp.)共生虫黄藻密度骤降 98.69%,且多样性显著丧失、光合功能严重受损;与此同时,珊瑚宿主通过上调免疫通路(如 FcγR 吞噬作用、RIG-I 样受体通路)基因和异养营养(蛋白消化吸收)相关基因,并借助共生细菌(如 *Endozoicomonas* sp.)重组维持生存,证实宿主对强光的耐受性更强。而 Jia 等[29]研究同样发现,在排除高温干扰的条件下,强光胁迫不仅显著影响共生虫黄藻的光合系统功能,而且可对其免疫能力产生负面影响,但丛生盔形珊瑚宿主对强光的耐受性相对更强。然而,在自然海域环境中,持续的高温往往也伴随着强光的辐射[30],因此二者的协同作用可能加剧对珊瑚共生功能体的胁迫效应。

共生虫黄藻的类型显著影响珊瑚对强光和高温的耐受性。Yuyama 等[31]的研究发现,与 D 型虫黄藻共生的单独鹿角珊瑚(*Acropora solitaryensis*)表现出对强光和高温更强的耐受性。转录组分析显示,D 型虫黄藻中与光合作用相关的基因表达显著上调,

中国知网 https://www.cnki.net

而与离子转运、蛋白质折叠相关的基因表达显著下调,这种独特的基因表达模式可能是 D 型虫黄藻增强珊瑚功能共生体环境耐受性的重要机制[31]。为应对强光胁迫,珊瑚宿主也进化出有效的保护机制。在强光胁迫下,珊瑚体内荧光蛋白和非荧光色蛋白基因转录表达显著上调,这些蛋白能够吸收紫外线辐射,减少光损伤,从而增强珊瑚功能共生功能体对太阳辐射的抵抗能力[31]。这种光保护机制与珊瑚宿主的转录调控网络密切相关,是珊瑚适应强光环境的重要策略[31]。

2.3 海水酸化胁迫

大气中 CO_2 浓度的快速升高不仅加速了全球变暖,而且导致海水 pH 值下降,引起海水酸化现象,进而对珊瑚礁生态系统造成严重威胁。当有海水温度升高、重金属离子超标等其他环境因子协同作用时,海水酸化对生物体的影响将更加显著[32-33]。

海水酸化主要影响珊瑚钙化作用、代谢、细胞酸碱调节、应激响应等[34],而最直接的影响是与碳酸酐酶(CA)分泌相关基因的表达。Griffiths 等[35]发现来自不同低 pH 值环境下的 *Balanophyllia elegans* 转录响应存在差异。急性应激初期通常会引起基因的快速显著表达,从而恢复珊瑚体内平衡;而长期的慢性应激暴露意味着适应已经发生,相关基因的表达仅限于维持所必需的稳态。长期处于低 pH 值环境中的珊瑚具有更强的离子转运能力以适应环境并维持胞内 pH 稳态和钙化,而没有经历过低 pH 值环境驯化的珊瑚,在低 pH 胁迫下其细胞应激反应相关基因表达下调[35]。Kenkel 等[36]对长期适应低 pH 值自然环境的多孔鹿角珊瑚及共生虫黄藻进行转录组分析后发现,珊瑚宿主参与脂肪酸代谢相关的基因表达发生变化,共生虫黄藻细胞生长分裂增强,共生功能体转录反应复杂并对共生体之间相互作用产生影响。

不同种类的珊瑚对海水酸化的转录响应存在显著差异。Radice 等[37]通过将不同种类珊瑚移植到天然低 pH 值的野外环境中发现,耐受性低的 *Siderastrea siderea* 表现出更为固定的转录响应模式,而耐受性较高的两种滨珊瑚(*Porites astreoides* 和 *Porites porites*)则表现出更强的转录可塑性。这种物种特异性响应机制为理解珊瑚对海洋酸化的适应策略提供了重要的资料。

2.4 低盐胁迫

随着气候变暖,全球水循环加剧,导致极端降水事件的频率和强度不断增加。降水的变化对河口区域的珊瑚群落产生了极大影响——由于降水量增加和入海径流量增大,该区域的珊瑚更易受到低盐胁迫,进而出现白化现象。例如,香港的亚热带珊瑚群落在 2014 年和 2022 年都因夏季极端强降水导致珊瑚低盐白化事件的发生[38-40]。2022 年雨季,珠江三角洲地区强降雨事件增多,年降水量较 2021 年多 33.3%,较常年多 12.9%,而珠江年入海径流量较常年偏多 11.0%,这使得珠江冲淡水作用加剧,该海域底层海水盐度骤降至 26.975,导致该海域的珊瑚群落发生严重的低盐白化事件[41]。

Chen 等[41]研究表明,鹿角杯形珊瑚对低盐胁迫的响应模式因胁迫持续时间而异:在急性低盐胁迫下,与离子转运、细胞渗透压调节相关的基因显著上调;而在长期低盐驯化过程中,具有低盐耐受性的鹿角杯形珊瑚则表现出与代谢相关基因的显著下调。Aguilar 等[42]通过低盐胁迫实验揭示了多孔鹿角珊瑚在急性低盐胁迫下的转录组动态响应特征,发现与急性低盐胁迫 1 h 的珊瑚相比,经历 24 h 低盐胁迫的珊瑚中与蛋白质稳态、氨基酸和氮代谢相关的基因表达显著上调;同时,多孔鹿角珊瑚中许多与离子或有机分子转运相关的基因表达改变,特别是参与甘氨酸甜菜碱分解代谢的基因,其转录水平显著升高。珊瑚在低盐环境下的适应机制主要涉及细胞渗透压的调节,其对盐度波动的响应主要通过调节相容性有机渗透压物质(如甘油、游离氨基酸和多元醇)来实现[43-45]。除此之外,Chen 等[41]的研究揭示了不同低盐耐受性鹿角杯形珊瑚个体的转录组差异:低盐耐受性低的珊瑚个体受到了更严重的免疫损伤,其与免疫防御、细胞应激相关的基因显著上调;而耐受性更高的珊瑚个体中与糖酵解/糖异生相关的代谢基因显著下调。值得注意的是,在这些高耐受性珊瑚的共生虫黄藻中,与氧化磷酸化相关的基因显著上调,这可能是共生功能体补充能量需求以避免白化发生的重要机制之一[41]。

2.5 营养盐胁迫

海水营养富集(如溶解氮的增加)可能对造礁石珊瑚产生负面影响,导致珊瑚白化发生率上升。然而,营养盐胁迫下珊瑚共生功能体的响应机制复杂,营养盐胁迫对珊瑚的影响具有两面性。

Rosic 等[46]通过研究粗糙鹿角珊瑚(*Acropora aspera*)在铵态氮胁迫下的早期转录变化发现,与卵巢减数分裂相关的通路和参与分子摄取的内吞通路

中国知网 https://www.cnki.net

显著富集,这表明营养盐胁迫影响珊瑚的繁殖、降低酶活性、促进分解代谢并减少离子转运;另外,共生虫黄藻核酮糖二磷酸羧化酶和胡萝卜素、叶绿素(*a*、*b*、*c*)结合蛋白基因的表达上调,光合作用能力增强。氮含量的增加会对珊瑚的生长和共生体密度产生积极影响,但与此同时也会带来消极影响,如宿主释放藻类的百分比增加。高温应激会导致珊瑚氮含量增加,正如周榆鹏等[47]研究所示,高温胁迫下风信子鹿角珊瑚通过显著提升谷氨酰胺合成酶(GS)的活性来强化其氨氮同化能力,从而利于其共生藻密度及叶绿素含量的维持;相较之下,美丽鹿角珊瑚(*Acropora muricata*)在34 ℃时GS活性显著降低,导致其共生藻流失加速并呈现白化趋势。Yuan等[48]的研究结果表明,高浓度铵离子胁迫显著抑制了鹿角杯形珊瑚的核酸代谢和基因表达,调控了G蛋白偶联受体蛋白信号通路,使转录发生重构;同时,还诱导和调控了珊瑚细胞的凋亡和死亡。

铵态氮一方面对珊瑚造成了营养盐胁迫,另一方面又可能缓解珊瑚热应激反应。Zhou等[49]研究发现,铵态氮含量的升高对高温胁迫下的鹿角杯形珊瑚有积极的影响,不仅可以抑制热应激对珊瑚细胞凋亡和死亡的诱导,而且会抑制珊瑚细胞发育、分化等生理过程,减少能量消耗,将更多能量供给珊瑚必需的生命活动,从而提高珊瑚的恢复力。

2.6 缺氧胁迫

海洋变暖和海水富营养化使海水中的溶解氧含量不断降低,这种缺氧环境会导致珊瑚白化甚至死亡。据预测,到2100年全球海洋的脱氧率将达到7%[50]。随着缺氧事件和缺氧水域的不断增加,缺氧对珊瑚礁生态系统的潜在威胁日益凸显[51]。缺氧胁迫会激活珊瑚缺氧反应系统(HIF-HRS),导致其关键基因 *HIFα* 和 *HSP90* 的表达发生变化,进而影响珊瑚细胞内稳态、离子转运、细胞自噬以及脂质吸收等重要生理生化过程。

Alderdice等[52]通过RNA-Seq分析证实,细枝鹿角珊瑚(*Acropora tenuis*)具有与其他后生动物同源的、由完整活性缺氧诱导因子(HIF)介导的缺氧反应系统。这一系统是珊瑚应对缺氧胁迫的关键基因网络,其中关键基因 *HIFα* 的表达上调可能有助于改变珊瑚的白化敏感性[53]。此外,*HSP70* 和 *HSP90* 基因在提高珊瑚低氧胁迫耐受性中也发挥了重要作用,特别是 *HSP90* 的表达,它能够调控珊瑚HIF-HRS在缺氧胁迫下的代谢适应能力[53]。Alderdice等[52]研究还发现,具有更强低氧耐受性的细枝鹿角珊瑚往往表现出更高效的HIF-HRS,这些珊瑚通过维持更高的 *HIFα* 和HIF依赖性 *HSP90* 表达水平,能够快速协调 O_2 通过钾离子通道,抑制线粒体有氧活性并激活线粒体自噬以清除功能障碍的细胞器;同时,增强蛋白质稳态和脂质摄取能力;最终通过精细调控细胞周期与死亡,决定细胞的命运走向。另外,缺氧胁迫也会降低鹿角珊瑚(*Acropora* sp.)白化的温度阈值,高温和脱氧共同作用导致的过度氧化应激可能会干扰HIF-HRS信号传导、加剧光损伤,并使珊瑚免疫系统受损,进而使珊瑚更易发生白化[54]。

2.7 污染物胁迫

人类活动导致的化学污染物长期联合胁迫对珊瑚健康构成了严重威胁。污染物胁迫主要通过毒理效应影响珊瑚,在急性污染物胁迫下,珊瑚中与细胞应激相关的基因显著上调。

重金属、多环芳烃和农药残留是影响全球珊瑚礁生态系统健康的三大传统化学污染物。农业径流、城市及工业活动是重金属进入珊瑚礁生态系统的主要途径。Schwarz等[55]研究发现,在30 μg/L铜环境下暴露48 h的 *Montastraea franksi* 细胞出现了明显的DNA损伤和氧化应激反应。在急性镉胁迫下,鹿角杯形珊瑚中与蛋白质修饰、错误蛋白重折叠、内质网应激和细胞凋亡相关的基因表达显著上调,而与大分子代谢过程相关的基因表达显著下调,这种基因表达的正向调节有助于维持珊瑚共生体的平衡并提高其适应性[56]。多环芳烃主要通过石油烃类的燃烧和海上溢油进入海洋,并对珊瑚健康造成显著危害。在Liu等[57]的研究中,多环芳烃通过影响新陈代谢、抗氧化和解毒过程,对鹿角杯形珊瑚及其藻类共生体产生缓慢但持久的影响,但珊瑚可以通过神经内分泌调节来应对多环芳烃的胁迫。此外,除草剂、杀虫剂等残留农药通过地表径流和地下渗透进入河流,并最终汇入海洋,从而影响珊瑚健康。Zhou等[58]对暴露于草铵膦和草甘膦的鹿角杯形珊瑚进行转录组分析,发现草铵膦抑制了珊瑚的谷氨酰胺代谢,干扰了其应激反应、免疫调节和共生虫黄藻细胞生长周期;草甘膦则扰乱了珊瑚钙化、减数分裂和共生体营养物质输出。此外,除草剂扑草净严重影响虫黄藻的光合作用,破坏丛生盔形珊瑚共生虫黄藻的光系统修复机制,并且加剧高温对珊瑚关键能量和营养代谢通路的不利影响,最终导致珊瑚和虫黄藻共生关系破裂[59]。

中国知网 https://www.cnki.net

与传统污染物相比,新兴污染物对珊瑚礁生态系统的影响也日益受到关注。微塑料作为一种新兴污染物,通过溪流、表层土壤渗透、降水以及工业生活废水排放进入海洋,其在海洋生态系统中的移动与累积对珊瑚造成了新的胁迫,特别是微塑料可能携带大量病原体,可破坏珊瑚-虫黄藻的共生关系[60]。微塑料在珊瑚体内的积累会导致珊瑚组织缺陷、免疫系统受损、生长发育迟缓甚至白化。在急性微塑料胁迫下,鹿角杯形珊瑚发生应激反应,并通过 JNK 和 ERK 信号通路抑制其解毒和免疫系统[61]。另外,在微塑料胁迫下,虫黄藻中与解毒活性、营养吸收和光合作用相关的基因表达显著下调,而与氧化应激、离子转运和细胞凋亡相关的基因表达显著上调,这直接影响了珊瑚与虫黄藻共生关系的稳定性[62-63]。此外,随着滨海旅游业的快速发展,防晒霜污染问题日益凸显。Danovaro 等[64]研究表明,即使在极低的浓度水平下,防晒霜也可能引发鹿角珊瑚病毒感染,导致珊瑚白化。然而,Ishibashi 等[65]发现,防晒霜中常见的成分 benzophenone-3 (BP-3)对细枝鹿角珊瑚及其共生虫黄藻的毒性作用有限,这一发现为评估防晒霜对珊瑚的影响提供了新的视角。

2.8 疾病胁迫

气候变化带来的环境压力正在改变与珊瑚相关的微生物群落的组成,导致有益微生物向病原体转化,进而引起珊瑚白化和疾病暴发[66]。珊瑚疾病是珊瑚宿主、病原体和环境相互作用的结果[67]。在应对病原体入侵时,珊瑚的免疫反应表现出显著的转录变化。Silva-Lima 等[68]研究表明,受白色瘟疫病影响的 *Mussismilia braziliensis* 的免疫系统和细胞防御相关通路显著下调,而自噬和细胞黏附相关转录本的下调表明患病珊瑚宿主防御能力耗尽,无法有效抵御病原体的入侵而感染白化。Anderson 等[69]发现,受加勒比黄带病影响的 *Orbicella faveolata* 通过 Wnt 蛋白表达和 Notch 信号传导进行先天免疫调节,展现了珊瑚对疾病的不同防御策略。

珊瑚免疫系统的信号通路归纳为 4 个层次:模式识别受体的病原体感应、下游信号级联、炎症细胞因子表达的激活、一系列生存或死亡响应机制的启动[70]。珊瑚对疾病的免疫反应通常以炎症为特征,涉及多种复杂的分子机制。这些机制包括抗菌肽和活性氧的产生、抗氧化剂的生成、吞噬细胞向感染部位的迁移,以及黑色素的积累[71-72]。

不同种类珊瑚对病原体的耐受性存在显著差异。Wang 等[73]研究发现在溶珊瑚弧菌(*Vibrio coralliilyticus*)胁迫下,海孔角蜂巢珊瑚(*Favites halicora*)比鹿角杯形珊瑚呈现出更高的免疫相关基因转录可塑性。其中,海孔角蜂巢珊瑚中参与细胞凋亡途径的基因表达上调,而鹿角杯形珊瑚中核苷酸切除修复和碱基切除修复通路显著富集。He 等[74]研究发现,强壮鹿角珊瑚(*Acropora valida*)通过上调能量代谢途径和先天免疫反应来应对弧菌胁迫,同时抑制与细胞生长代谢相关基因的表达和细胞再生等过程。相比之下,盾形陀螺珊瑚(*Turbinaria peltata*)表现出更强的免疫系统调节能力,能够避免弧菌胁迫诱导的免疫失调,并通过上调特定的有机代谢途径来补充能量,但这种适应性响应可能以牺牲某些功能(如离子转运调节)为代价,该研究揭示了珊瑚对弧菌胁迫的特异性响应机制[74]。

2.9 复合胁迫

与单一环境胁迫相比,在自然环境中的珊瑚通常面临多种环境胁迫的共同作用。Wu 等[75]通过实验室模拟研究发现,温度和酸化对丛生盔形珊瑚和强壮鹿角珊瑚宿主基因表达的影响显著大于对其共生虫黄藻的影响;在高温和酸化的双重胁迫下,珊瑚宿主与共生虫黄藻之间参与光合作用、营养代谢与转移、共生体识别相关的基因表达普遍下调,表明营养物质从共生虫黄藻向珊瑚宿主的转移受到限制,最终导致共生关系的破裂。Kaniewska 等[76]研究报道,在高温和高 CO_2 分压的环境下,多孔鹿角珊瑚细胞内的三磷酸腺苷(ATP)被用于维持 pH 稳态、氧化应激反应、未折叠蛋白反应(UPR)及 DNA 修复,导致用于钙化和其他细胞功能的能量减少,从长远来看这可能导致珊瑚死亡率的增加。另外,热应激与有毒细菌溶珊瑚弧菌暴露的共同作用会加剧鹿角杯形珊瑚损伤,但高温仍是珊瑚主要的威胁[5]。

尽管热驯化已被证明能够提高珊瑚对海洋变暖的适应能力,但是当与其他环境胁迫因子叠加影响时,这种耐热性可能会受到损害。Zhou 等[59]研究表明,在高温和除草剂的双重胁迫下,耐受性较高的块状丛生盔形珊瑚及其共生虫黄藻中与光合作用、抗氧化能力和氮代谢相关的基因表达显著下调,这种转录组响应模式损害了珊瑚共生功能体的耐热机制。

环境变化不仅直接影响珊瑚的生理状态,而且可能通过影响珊瑚的免疫能力增加其感染特定或机会性病原体的风险。Takagi 等[77]发现在高温和溶珊瑚弧菌的共胁迫下,指形鹿角珊瑚(*Acropora digitif-*

中国知网 https://www.cnki.net

era)中与先天免疫反应相关的基因表达被抑制,但为了抵抗病原体的入侵,珊瑚上调了与蛋白质合成和分解相关的基因,显著增强了线粒体的氧化代谢、细胞外泌体的释放以及细胞外基质(ECM)成分转录物的生物合成。

珊瑚共生功能体在不同环境胁迫下的转录组学研究相关情况如表2所示。

表2 珊瑚共生功能体在不同环境胁迫下的转录组学研究

Table 2 Transcriptomic studies on coral holobionts under various environmental stresses

胁迫类型 Type of stress	胁迫环境 Stress environment	物种 Species	共生功能体组分 Holobiont composition	关键代谢通路/相关基因/蛋白 Key metabolic pathway/related gene/protein	假定功能 Putative function	胁迫下表达量变化 Differential expression under stress	参考文献 References
High temperature	Indoor	*Pocillopora damicornis*	Host	Tumor Necrosis Factor (TNF), p53 signaling pathway and caspase pathway	Apoptosis, immunity, translation, replication and repair	Upregulated	[23]
			Symbiodiniaceae	—	Translation, meiosis, signal transduction and circadian rhythm	Downregulated	
		Montastraea cavernosa	Host	Protein synthesis and processing, vesicle-mediated transport and secretion, ribosome structure and translational activity	Cell growth and development	Upregulated	[26]
				Carbohydrate metabolic process, DNA recombination and repair, extracellular matrix organization	Metabolism	Downregulated	
		Acropora aspera	Host	cytochrome c oxidase, NADH-ubiquinone oxidoreductase	Oxidative stress	Upregulated	[46]
				Green Fluorescent Protein (GFP)-like homologs	—	Downregulated	
			Symbiodiniaceae	Photosynthetic genes	—	Upregulated	
		Anomastraea irregularis	Host	Genes encoding senescence/apoptosis-related proteins	Apoptosis, maintenance of cell polarity and cytoskeletal changes	Upregulated	[78]
				Tubulin and deSUMOylating isopeptidases	Cellular stress, mitosis, nutrient transport	Downregulated	
		Pocillopora damicornis	Symbiodiniaceae	Bile acid-sodium symporter 2, acyl-CoA binding protein 3 and 6, sodium-coupled neutral amino acid transporter, sodium-dependent dicarboxylate transporter SDCS, sugar transporter SWEET1	Lipid biosynthesis, nutrient transport	Upregulated	[79]
		Galaxea fascicularis	Host	DNA integration pathway, DNA metabolic process, response to heat, unfolded protein response, protein folding	Regulation of genome integration and immunity	Upregulated	[80]
				Pantothenate metabolic process, positive regulation of epithelial cell migration, positive regulation of cell morphogenesis involved in differentiation	Metabolism, cell differentiation, development and migration	Downregulated	
		Acropora hyacinthus	Host (sensitive)	Tumor necrosis factor receptor-associated factor 3 homolog	Apoptosis, immune response	Upregulated	[81]
				Mannose-binding lectin	Immunomodulation, enzyme activity, enzyme biosynthesis	Downregulated	
			Host (tolerant)	*HSP70*, TNF, peroxidase and zinc metalloproteinase	—	Upregulated	
				Carbonic anhydrase, lectin and transcription factor	—	Downregulated	
	Natural seawater	*Millepora complanata*	Host	40S ribosomal protein S30, 60S ribosomal protein L15, 40S ribosomal protein S14, voltage-dependent L-type calcium channel subunit β-2, 10 kDa HSP	Protein biosynthesis, ion transport, oxidative stress	Upregulated	[82]
High temperature (heat acclimation)	Indoor	*Pocillopora damicornis*	Host	Transporters SLC16, SLC5A8	Nutrient transport	Upregulated	[79]
		Stylophora pistillata	Host (long-term heat stress)	Cellular stress response, protein folding, protein catabolism, regulation of cellular redox homeostasis, Reactive Oxygen Species (ROS) metabolism	Cellular stress, metabolism	Upregulated	[83]
				Regulation of biomineralization	—	Downregulated	

中国知网 https://www.cnki.net

续表

Continued table

胁迫类型 Type of stress	胁迫环境 Stress environment	物种 Species	共生功能体组分 Holobiont composition	关键代谢通路/相关基因/蛋白 Key metabolic pathway/related gene/protein	假定功能 Putative function	胁迫下表达量变化 Differential expression under stress	参考文献 References
			Host (short term heat stress)	Unfolded protein response signaling pathway	Cellular stress	Upregulated	
			Symbiodiniaceae	—	Photosynthesis	Downregulated	
High light	Indoor	*G. fascicularis*	Host	Pathways related to carbohydrate metabolism, energy metabolism, amino acid metabolism, glycan biosynthesis and metabolism, cofactor and vitamin metabolism, etc.	Cellular metabolism	Upregulated	[29]
Ocean acidification	Indoor	*Balanophyllia elegans*	Host	Calcium ion binding, voltage-gated Ca channel	Maintenance of membrane potential and ionic homeostasis	Upregulated	[35]
		Stylophora pistillata	Host	Bicarbonate transporter-like protein	—	—	[84]
			Symbiodiniaceae	Proton pump	—	—	
	Natural seawater	*Acropora millepora*	Host	FA synthesis gene (stearoyl-CoA desaturase)	Fatty acid metabolism	Downregulated	[36]
				FA catabolism gene (long-chain-fatty-acid-CoA ligase)	Fatty acid metabolism	Upregulated	
			Symbiodiniaceae	Ribosomal proteins	Cell growth/division	Upregulated	
		Porites astreoides	Host	*CA2* gene and Bcl-2-like apoptosis regulatory genes, HSPs and heat shock factors, calcium transporters	Apoptosis, ion transport	Upregulated	[37]
		Porites porites		Matrix metalloproteinases (MMPs), cytosolic phospholipase A2, rRNA processing proteins	Cell adhesion, phospholipid catalysis and calcium ion binding	Upregulated	
		Siderastrea siderea		Carbonic anhydrase 2-like gene, HSPs, TNF receptor-associated factor 3-like (TRAF3-like), MAP kinase cascade and serine/threonine protein kinases	Cellular stress, immune defense, transmembrane transport, calcium ion binding and activity	Upregulated	
				Solute carrier family genes (*SLC13*, *SLC39*, *SLC40*)	Ion transport	Downregulated	
Low salinity	Indoor	*Acropora millepora*	Host	Superoxide dismutase, Catalase (CAT), Glutathione S-Transferase (GST), transporter SLC24	—	Upregulated	[42]
				Transporter SLC6	—	Downregulated	
	Natural seawater	*Pocillopora damicornis*	Host (bleaching)	*TNF*, *CASP3*, *HSP90*	Immune defense, apoptosis	Upregulated	[41]
			Host (unbleaching)	Glycolysis/gluconeogenesis pathway, *CASP3*, *HSP90*	Substance and energy metabolism, immune response	Downregulated	
			Symbiodiniaceae	Oxidative phosphorylation	Amino acid metabolism	Upregulated	
		Orbicella faveolata, *O. franksi*	Host	Genes encoding proteins involved in antioxidant activity and mitochondrial structure composition	Oxidative stress	Upregulated	[85]
			Symbiodiniaceae (*Breviolum minutum*)	RNA decay proteins, Nonsense-Mediated mRNA Decay (NMD)	RNA modification	Downregulated	
Nutrient	Indoor	*Acropora aspera*	Host	Cellular meiosis, endocytosis, catabolism, ion transport, ROS scavenging pathway	Germ cells generating genetic diversity, mediating intracellular access and signal transduction of macromolecules, decomposing complex molecules to release energy and provide precursors, maintaining ion homeostasis and membrane potential inside and outside cells, maintaining cellular redox homeostasis	Upregulated	[46]

中国知网 https://www.cnki.net

续表

Continued table

胁迫类型 Type of stress	胁迫环境 Stress environment	物种 Species	共生功能体组分 Holobiont composition	关键代谢通路/相关基因/蛋白 Key metabolic pathway/related gene/protein	假定功能 Putative function	胁迫下表达量变化 Differential expression under stress	参考文献 References
			Symbiodiniaceae	Ribulose bisphosphate carboxylase, carotenoid-chlorophyll binding protein	Photosynthesis	Upregulated	
		Pocillopora damicornis	Host	Induction of apoptosis, caspase, Bcl-2-like protein, tumor necrosis factor receptor	Apoptosis	Upregulated	[49]
				Response to chemical	—	Upregulated	
				Metabolic process, nucleic acid metabolic process	—	Downregulated	
Hypoxia	Indoor	*Acropora tenuis*	Host	*HIFα*, *HSP90*, *HIF* target genes, pro-apoptotic gene *bnip3*, anti-apoptotic genes *bcl2* and *bclxl*	Hypoxic stress, mitophagy	Upregulated	[52]
		Acropora selago		*HIFα*, *HSP90*, *HIF* target genes, pro-apoptotic gene *bnip3*, anti-apoptotic genes *bcl2* and *bclxl*	Hypoxic stress, mitophagy, cell cycle regulation	Downregulated	
		Pocillopora damicornis	Host	JNK and ERK signaling pathways	—	Downregulated	[53]
Heavy metals	Indoor	*Montastraea franksi*	Host	Protein modification, unfolded protein response, endoplasmic reticulum stress, apoptosis	—	Upregulated	[55]
				Metabolic process, macromolecular localization	—	Downregulated	
Herbicides	Indoor	*Acropora tenuis*	Host	*GFP*, *cryl*, *Caspase*-8, *AmNR7* and chromogenic proteins	Oxidative stress, metabolism	Downregulated	[86]
			Symbiodiniaceae	Light-harvesting related genes, photosystem Ⅱ (PSⅡ)-related genes, *HSP* genes, ubiquitin system genes	Photosynthesis, oxidative stress, energy metabolism	Downregulated	
Microplastics	Indoor	*Pocillopora damicornis*	Symbiodiniaceae	Persulfide dioxygenase, haloacid dehalogenase-like hydrolase, domain-containing protein 3	Detoxification activity, nutrient absorption, photosynthesis	Downregulated	[61]
				Ubiquitin protein ligase HERC1, chloroplastic pentatricopeptide repeat-containing protein, 1,3-β-glucan synthase catalytic subunit Bgs3	Oxidative stress, ion transport, apoptosis	Upregulated	
Sunscreen	Indoor	*Acropora tenuis*	Host	Cytochrome P450 genes, *GXN*, G protein-coupled receptor (GPCR) genes, *CYP1A1* and *CYP17A*, poly-γ-glutamic homopolyglycan	Organic pollutant catabolism, oxidative stress, immune response, cell development	Upregulated	[87]
				HMCN1 and *MLP*	ECM homeostasis	Downregulated	
Triclosan	Indoor	*Porites lutea*	Host	Complement and coagulation cascade pathway, TNF signaling pathway, Notch signaling pathway	immune defense, reproduction	—	[88]
			Symbiodiniaceae	Ribosome biogenesis pathway, Integrin signaling pathway, flavonoid biosynthesis pathway, ribosomal proteins, RNA exonuclease complex	—	—	
Vibrio coralliilyticus	Indoor	*Favites halicora*	Host	Apoptosis	Immunomodulation	Upregulated	[73]
		Pocillopora damicornis		Nucleotide excision repair and base excision repair pathways	—	Downregulated	
		Acropora valida		GPCR signaling pathway, Toll-like receptor signaling pathway	Energy supply and immune response	Upregulated	[74]
				DNA integration, DNA recombination, nitrogen cycle metabolic process	Immunomodulation	Downregulated	
		Turbinaria peltata		JAK-STAT negative regulatory receptor signaling pathway, polysaccharide catabolic process, cellular response to potassium ions	Immunomodulation and energy metabolism	Upregulated	
				DNA integration, DNA recombination, nitrogen cycle metabolic process	Ion transport	Downregulated	
	Natural seawater	*Pocillopora damicornis*	Host	Arachidonic acid metabolism	—	—	[5]

中国知网 https://www.cnki.net

续表

Continued table

胁迫类型 Type of stress	胁迫环境 Stress environment	物种 Species	共生功能体组分 Holobiont composition	关键代谢通路/相关基因/蛋白 Key metabolic pathway/related gene/protein	假定功能 Putative function	胁迫下表达量变化 Differential expression under stress	参考文献 References
		Mussismilia braziliensis	Host	Immune response, cellular defense response, autophagy and DNA/RNA metabolic processes	Immune defense, autophagy	Downregulated	[68]
			Symbiodiniaceae	Photosynthetic dark reaction, carbohydrate and peptide biosynthesis processes	Photosynthesis, energy metabolism	Upregulated	
		O. faveolata	Host	Wnt signaling pathway, MAPK signaling pathway, Notch signaling pathway, phagocytosis pathway, RIG-I-like receptor signaling pathway, pathogenic bacterial invasion of epithelial cells pathway, NF-κB signaling pathway, complement activation pathway, leukocyte transendothelial migration pathway	Immune defense, cellular stress	Upregulated	[69]
High temperature+high light	Indoor	*G. fascicularis*	Host	Niemann-Pick C1 (NPC1) protein, lipoprotein, riboflavin protein and monocarboxylate transporter	Amino acid transport	Upregulated	[29]
				SLC transporters	Amino acid transport	Downregulated	
			Symbiodiniaceae	Photosystem Ⅰ (PSⅠ) and PSⅡ	Photosynthesis	Upregulated	
		Acropora solitaryensis	Symbiodiniaceae D	Photosynthesis, HSPs	Photosynthesis	Upregulated	[31]
				Ammonia transporters, zinc transporters and cationic amino acid transporters	Ion transport	Downregulated	
			Symbiodiniaceae C3	Photosynthesis, PSⅡ assembly, regulation of photosynthesis, light reaction	Photosynthesis	Downregulated	
High temperature+ocean acidification	Indoor	*G. fascicularis*	Host	NPC1, Lipid, riboflavin and monocarboxylates transporters	Amino acid transport	Upregulated	[75]
				Lipid transporter SLC family protein	Amino acid transport	Downregulated	
			Symbiodiniaceae	PSⅠ and PSⅡ	Photosynthesis	Upregulated	
		Acropora valida	Host	Lipoprotein, riboflavin protein and monocarboxylate transporter, NPC1 (Niemann-Pick disease, type C1), NPC2 (Niemann-Pick disease, type C2), solute carrier family protein SLC27A4, glucose transporter	Substance transport, nutrient metabolism/transfer, symbiont recognition	Downregulated	
				SLC23, mannose receptor and L-rhamnose-binding lectin	Vitamin C transport	Downregulated	
			Symbiodiniaceae	PSⅠ and PSⅡ, ammonium transporter	Photosynthesis, nitrogen metabolism	Downregulated	
High temperature+hypoxia	Indoor	*Acropora* sp.	Host	Prolyl hydroxylase EGLN1, photoprotective pigments, GFP	Promotion of cell survival and adaptation, photoprotection	Upregulated	[54]
				HIFα, Heat Shock Protein 90 Beta Family Member 1 (HSP90B1)	Hypoxic stress, immune response	Downregulated	
High temperature+herbicide	Indoor	*G. fascicularis*	Host	Cellular nitrogen compound biosynthetic process and cellular protein metabolic process, oxidative phosphorylation, fat digestion and absorption, protein digestion and absorption pathway, phagosome and lysosome pathway, carbon metabolism pathway, ribosomal proteins	Photosynthesis, energy metabolism	Downregulated	[59]
			Symbiodiniaceae	Photosynthesis, carbon fixation, nitrogen metabolism, glyoxylate metabolism	Conversion of light energy into chemical energy (ATP and NADPH), fixation of carbon dioxide to synthesize organic matter, metabolism	Downregulated	
High temperature+polycyclic aromatic hydrocarbons (PAHs)	Indoor	*Pocillopora damicornis*	Host	Neuroendocrine regulation, apoptosis process	—	Upregulated	[57]

中国知网 https://www.cnki.net

续表

Continued table

胁迫类型 Type of stress	胁迫环境 Stress environment	物种 Species	共生功能体组分 Holobiont composition	关键代谢通路/相关基因/蛋白 Key metabolic pathway/related gene/protein	假定功能 Putative function	胁迫下表达量变化 Differential expression under stress	参考文献 References
			Symbiodiniaceae	Cellular oxidative pressure	—	Upregulated	
				Photosynthesis efficiency	—	Downregulated	
High temperature+sediment	Indoor	*Pocillopora acuta*	Host	Small heat shock proteins (sHSPs), HSP16.1 and HSP16.2, Nuclear Factor Kappa B Subunit 1 (NFKB1)	Oxidative stress response, immune response, cell proliferation	Upregulated	[89]
				EF-Hand Domain Containing 1, growth arrest-specific protein 8, calcium/calmodulin-dependent protein kinase type Ⅳ	Cellular calcium homeostasis, cell division, apoptosis	Downregulated	

Note:"—" indicates that relevant research literature has not explored this part of the content.

3 环境胁迫下的珊瑚幼虫转录组学研究

珊瑚礁生态系统的持久性依赖于持续的珊瑚幼虫补充。在补充过程的各阶段,珊瑚幼虫对环境胁迫的耐受性可能成为珊瑚种群可持续发展的关键限制因素。与成体珊瑚相比,珊瑚幼虫对环境变化更为敏感,环境胁迫往往引发更显著的转录组变化[90]。

Jiang 等[79]的研究发现,热驯化后的鹿角杯形珊瑚幼虫中与细胞氧化应激反应、细胞生长周期和营养物质运输相关的基因表达显著上调,其共生虫黄藻中与代谢相关的基因表达显著下调且营养转运蛋白基因表达显著上调。在高温胁迫下,珊瑚幼虫通过抑制代谢过程来降低生存成本,从而维持高温条件下的能量平衡。然而,当高温与其他环境胁迫叠加时,其耐受机制可能被完全破坏。Chui 等[91]的研究表明,霜鹿角珊瑚幼虫对高温和低盐胁迫均表现出高度敏感性,其中,低盐对珊瑚幼虫定居的影响大于高温影响;而在高温和低盐的双重胁迫下,珊瑚幼虫完全丧失定居能力。另外,碳酸酐酶在无脊椎动物和脊椎动物的生物矿化中起重要作用,与碳酸酐酶分泌相关的基因表达的降低可直接影响珊瑚钙化。在珊瑚幼虫定居过程中,高 CO_2 浓度会干扰珊瑚幼虫的代谢、基因表达和蛋白质合成,破坏其精密有序的钙化过程,最终威胁珊瑚礁的补充和生存[92]。与此同时,Pinzón 等[93]发现高 CO_2 浓度增强了珊瑚幼虫细胞外有机基质的合成并抑制了其细胞代谢,与膜相关和碳酸酐酶分泌相关的基因表达量降低,而且骨骼有机基质中许多已知和假定成分的表达严重紊乱。这种生理层面的失调进一步体现在能量供应上,如 Yuan 等[94]的研究进一步表明,芽枝鹿角珊瑚(*Acropora gemmifera*)幼虫膜转运蛋白相关基因的下调会减少有机物质的运输,可能导致能量供应不足,进而影响幼虫的生长和发育。不仅如此,海水富营养化还会影响共生关系。Tong 等[95]发现,在高硝酸盐胁迫下,鹿角杯形珊瑚幼虫与共生虫黄藻之间的互惠关系可能向寄生关系转变——虫黄藻倾向于保留更多营养物质用于自身生长,导致分配给珊瑚幼虫的营养物质减少,从而阻碍珊瑚幼虫的正常发育。

面对全球海洋环境的变化,造礁石珊瑚早期生命阶段的幼虫依赖生理可塑性来适应新的环境条件。Meyer 等[96]研究发现,多孔鹿角珊瑚幼虫热休克蛋白在短期高温胁迫中倾向于上调,但在长期高温胁迫中则下调或保持不变。在热应激状态下,珊瑚幼虫通过激活细胞应激和免疫反应来维持蛋白质稳态,从而对抗热损伤[91]。而经过热适应的珊瑚幼虫则表现出内质网质量控制(ERQC)和免疫相关基因的下调或不变,其细胞生长发育未受到明显阻碍[83]。通过有性生殖产生的珊瑚幼虫通常携带共生虫黄藻,这不仅有助于满足处于扩散阶段的幼虫能量需求,而且使幼虫因携带不同虫黄藻亚群而表现出独特的转录组响应,从而增强其环境适应能力[83]。Jiang 等[79]研究表明,热驯化鹿角杯形珊瑚亲本所产下的幼虫在高温胁迫下表现出更强的抵抗力和光合自养能力。这些幼虫中与细胞周期、有丝分裂相关基因的上调,有助于缓解珊瑚宿主的细胞应激;同时,共生虫黄藻与光合作用相关的基因上调,维持了光收集、光保护和碳固定之间的平衡,从而优化了高温胁迫下共生功能体的光合活性。这种跨代适应现象表明,热驯化不仅增强了成体珊瑚的热适应性,而且也提高了其后代幼虫的热耐受性[79]。此外,不同表型的珊瑚幼虫在环境适应性方面同样存在差异。在环境胁迫下,多孔鹿角珊瑚红色荧光幼虫表现出细胞周期停滞和转录水平降

中国知网 https://www.cnki.net

低的特征,并且伴随核糖体的增加和抗氧化能力的增强,呈现出一种滞育状态。这种生理策略使珊瑚红色荧光幼虫在应对环境变化时具有更强的适应能力,有利于其进行长距离扩散,以逃离不利的生存环境[97]。珊瑚幼虫及其共生虫黄藻在不同环境胁迫下的转录组学研究如表 3 所示。

表 3　珊瑚幼虫及其共生虫黄藻在不同环境胁迫下的转录组学研究

Table 3　Transcriptomic study of coral larvae and its associated Symbiodiniaceae under different environmental stresses

胁迫类型 Type of stress	胁迫环境 Stress environment	珊瑚 Coral	共生功能体组分 Holobiont composition	关键代谢通路/相关基因/蛋白 Key metabolic pathway/related gene/protein	假定功能 Putative function	胁迫下表达量变化 Differential expression under stress	参考文献 References
High temperature	Indoor	*Pocillopora damicornis*	Coral larvae	Heat stress-related genes, transporter genes involved in transmembrane transport of nutrients	Cellular stress, nutrient transport	Upregulated	[79]
			Symbiodiniaceae	Photorespiration, nitrogen metabolism pathway	Photosynthesis, metabolism	Downregulated	
		Acropora pruinosa	Coral larvae	Carbohydrate metabolism, oxidative phosphorylation (ATP generation), MAPK signaling pathway, NF-κB signaling pathway	Apoptosis	Upregulated	[91]
		Acropora millepora	Coral larvae (long time heat stress)	*Cacna 1s*, Green Fluorescent Protein (GFP)	Ion transport	Upregulated	[96]
				Heat shock proteins, mitochondrial adenine transporter (Slc25a44), carbonic anhydrase genes *CA2* and *CA3*, ribosomal protein genes	Oxidative stress response, metabolism	Downregulated	
			Coral larvae (short time heat stress)	Coral cysteine-rich peptide genes, heat shock proteins (HSPA5, HSP90AA1 and HSP90B1), protein folding, ubiquitin-conjugating enzyme E2, non-fluorescent chromoproteins	Oxidative stress response, metabolism	Upregulated	
		Pocillopora damicornis	Coral larvae (sensitive)	Protein folding and endoplasmic reticulum quality control, Toll and Imd signaling pathways, NOD-like receptor signaling pathway, apoptosis	Maintenance of protein homeostasis and immune response	Upregulated	[98]
				DNA replication and repair, cell cycle checkpoint kinases, mitosis, respiration, metabolic processes	—	Downregulated	
			Coral larvae (tolerant)	Protein folding, metabolic processes, protein folding and endoplasmic reticulum quality control, immune and inflammatory responses	—	Downregulated	
			Coral larvae	ECM-receptor interaction, cell adhesion, glycosaminoglycan degradation and glycosphingolipid biosynthesis	—	Upregulated	[99]
				Lipid and carbohydrate metabolism, oxidative phosphorylation, cytochrome P450 metabolism of exogenous substances	—	Downregulated	
			Symbiodiniaceae	Genes encoding PSⅡ subunits	Photosynthesis	Downregulated	
			Coral larvae	Transferases (transferring phosphorus-containing groups)	Ion transport	Upregulated	[100]
				Structural proteins, oxidoreductases	—	Downregulated	
High light	Indoor	*Acropora millepora*	Coral larvae (green fluorescent)	ATP-dependent RNA helicases, sodium/potassium/chloride transporters (SLC12 transporters)	Regulation of cellular homeostasis	Upregulated	[97]
			Coral larvae (red fluorescent)	mTOR signaling pathway, ribosomal proteins, Cu/Zn superoxide dismutase, ferritin, catalase, glutathione peroxidase and thioredoxin	Antioxidant activity	Upregulated	
				Translation, ribosome structure and biogenesis	—	Downregulated	
Ocean acidification	Indoor	*Pocillopora damicornis*	Coral larvae	Spliceosome complex, RNA polymerase, protein secretion pathway and proteasome, amino acid biosynthesis and metabolism, steroid biosynthesis and glycosphingolipid biosynthesis, cell cycle	Genetic information processing	Upregulated	[99]

中国知网 https://www.cnki.net

续表

Continued table

胁迫类型 Type of stress	胁迫环境 Stress environment	珊瑚 Coral	共生功能体组分 Holobiont composition	关键代谢通路/相关基因/蛋白 Key metabolic pathway/related gene/protein	假定功能 Putative function	胁迫下表达量变化 Differential expression under stress	参考文献 References
			Symbiodiniaceae	Metabolism, ion transporters, cellular complexes	Ion transport	Upregulated	[100]
				Biosynthesis, RNA modification, isomerases, peptidases, hydrolases	Biosynthesis	Downregulated	
		Acropora millepora	Coral larvae	Glycoproteins, collagens, lipoproteins, lectins, cysteine-rich proteins, exopeptidases and matrix metalloproteinases	Extracellular Organic matrix synthesis	Upregulated	[92]
				Inner mitochondrial membrane complex proteins, ATP synthase subunits	Biomineralization, acid-base regulation, metabolism	Downregulated	
		Pocillopora damicornis	Coral larvae	Ca^{2+} transporters (SLC8, SLC24, SLC12 and SLC25), plasma membrane Ca^{2+} transporting ATPases, cadherins, thrombospondins	Ion transport, cell development and differentiation, coral calcification	Downregulated	[99]
Nutrient	Indoor	*Pocillopora damicornis*	Coral larvae	Unfolded protein response	Cellular stress	Upregulated	[95]
				Wnt signaling pathway, substance transport, substance metabolism	Cell development, ion transport	Downregulated	
			Symbiodiniaceae	ATP synthesis, carbohydrate metabolism, photosynthesis, respiration, substance transport and nitrogen compound metabolism	Cell division and growth, nutrient exchange, metabolism	Upregulated	
High temperature+ocean acidification	Indoor	*Pocillopora damicornis*	Coral larvae (transcriptional response of the high temperature + ocean acidification group vs. ocean acidification group)	ECM-receptor interaction pathway, cell adhesion	Genetic information process	Upregulated	[99]
				Carbohydrate, lipid and amino acid metabolism, as well as cytochrome P450 metabolism of exogenous substances	Metabolism	Downregulated	
			Coral larvae (transcriptional response of the high temperature+ocean acidification group vs. high temperature group)	Fatty acid biosynthesis and metabolism, phagosome maturation pathway and connexins	Provide lipid precursors for cell membrane repair and energy storage, clear damaged organelles or invading microorganisms, coordinate stress signal transmission among cell populations	Upregulated	
				ECM-receptor interaction pathway, cell adhesion, glycosaminoglycan degradation and glycosphingolipid biosynthesis	—	Downregulated	
			Symbiodiniaceae	Genes encoding PSⅡ subunits	Photosynthesis	Downregulated	
High temperature+low salinity	Indoor	*Acropora pruinosa*	Coral larvae	Caspase-independent apoptosis pathway, carbohydrate metabolism, oxidative phosphorylation (ATP generation), ribosomal proteins, neuropeptides and neurotransmitter receptors	Apoptosis	Upregulated	[91]
				Oxidative phosphorylation, fatty acid metabolism, lipid metabolism, nucleotide metabolism, carbohydrate metabolism	Metabolism	Downregulated	

Note:"—" indicates that relevant research literature has not explored this part of the content.

4 展望

转录组学技术为珊瑚环境适应性研究提供了新的技术手段,为解析环境胁迫下珊瑚环境适应性机制提供了新的视角,为环境压力风险预测、珊瑚白化程度和恢复能力评估等提供了科学依据。本文系统综述了转录组学技术在造礁石珊瑚环境适应性研究中的应用进展,重点阐明了珊瑚共生功能体在不同环境胁迫下的转录响应和适应机制。总的来说,在急性环境胁迫下,珊瑚宿主主要表现为氧化应激相关基因的上调表达和代谢相关基因的下调表达;而在长期的环境压力下,珊瑚逐渐建立起对环境胁迫的耐受性,表现为免疫应激相关基因表达的下调,以及共生虫黄藻中与代谢相关基因表达的上调,以满足珊瑚共生功能体的营养需求并维持共生关系的稳定。

尽管目前基于转录组学的珊瑚环境适应性研究已取得一定进展,但是未来仍需从以下 3 个方面开展

中国知网 https://www.cnki.net

进一步研究。

(1)完善造礁石珊瑚及其共生虫黄藻的基因组信息。造礁石珊瑚及其共生虫黄藻种类繁多,但现有基因组信息相对匮乏,而且珊瑚基因组质量普遍较低,这给基因注释和功能解析带来了挑战。因此,需要进一步扩展造礁石珊瑚基因组数据库,提高参考转录本的质量,为珊瑚环境适应性研究提供基础的组学数据。

(2)加强多重环境胁迫下珊瑚适应性的转录组学研究。随着气候变化日益复杂,珊瑚往往不再受单一环境胁迫的影响,而是面临多重环境胁迫的协同作用。因此,未来需要着重考虑多种环境胁迫因子对珊瑚的复合影响,多维度揭示珊瑚的环境适应机制。

(3)整合多组学技术深入解析珊瑚环境适应性机制。虽然转录组学技术已成功鉴定出环境胁迫下珊瑚共生功能体的关键基因和转录调控因子,但是仍需结合基因组学、蛋白质组学和代谢组学等多组学技术,系统开展环境耐受性基因和转录调控因子的功能研究。通过多组学数据的整合分析,从共生功能体水平上全面解析珊瑚白化机制及环境适应机制,为珊瑚礁生态系统的保护和管理提供理论支撑。

参考文献

[1] PLASS-JOHNSON J G,CARDINI U,VAN HOYTEMA N, et al. Coral bleaching [M]//ARMON R H, HÄNNINEN O. Environmental indicators. Dordrecht: Springer Netherlands,2015:117-146.

[2] HOEGH-GULDBERG O. Climate change,coral bleaching and the future of the world's coral reefs [J]. Marine and Freshwater Research,1999,50(8):839-866.

[3] SENECA F O,PALUMBI S R. The role of transcriptome resilience in resistance of corals to bleaching [J]. Molecular Ecology,2015,24(7):1467-1484.

[4] MILLER D J,BALL E E,FORÊT S,et al. Coral genomics and transcriptomics: ushering in a new era in coral biology [J]. Journal of Experimental Marine Biology and Ecology,2011,408(1/2):114-119.

[5] VIDAL-DUPIOL J,DHEILLY N M,RONDON R,et al. Thermal stress triggers broad *Pocillopora damicornis* transcriptomic remodeling, while *Vibrio coralliilyticus* infection induces a more targeted immuno-suppression response [J]. PLoS One,2014,9(9):e107672.

[6] SHINZATO C,INOUE M,KUSAKABE M. A snapshot of a coral "holobiont": a transcriptome assembly of the scleractinian coral, porites, captures a wide variety of genes from both the host and symbiotic zooxanthellae [J]. PLoS One,2014,9(1):e85182.

[7] WILLIAMS A. Multiomics data integration,limitations, and prospects to reveal the metabolic activity of the coral holobiont [J]. FEMS Microbiology Ecology, 2024, 100(5):fiae058.

[8] LICATALOSI D D,DARNELL R B. RNA processing and its regulation: global insights into biological networks [J]. Nature Reviews Genetics,2010,11(1):75-87.

[9] WANG Z,GERSTEIN M,SNYDER M. RNA-Seq: a revolutionary tool for transcriptomics [J]. Nature Reviews Genetics,2009,10(1):57-63.

[10] KHOZYAINOVA A A,VALYAEVA A A,ARBATSKY M S,et al. Complex analysis of single-cell RNA sequencing data [J]. Biochemistry (Moscow), 2023, 88(2):231-252.

[11] MIEOG J C,OLSEN J L,BERKELMANS R,et al. The roles and interactions of symbiont,host and environment in defining coral fitness [J]. PLoS One,2009, 4(7):e6364.

[12] SULLY S,BURKEPILE D E,DONOVAN M K,et al. A global analysis of coral bleaching over the past two decades [J]. Nature Communications, 2019, 10(1): 1264.

[13] GAO X,CHEN J L,MA Y L,et al. Differential physiological and microbial responses of the octocoral Junceella squamata to high-temperature and cadmium stress [J]. Marine Environmental Research, 2025: 106865. DOI:10.1016/j.marenvres.2024.106865.

[14] MCCARTHY O S,POMEROY M W,SMITH J E. Corals that survive repeated thermal stress show signs of selection and acclimatization [J]. PLoS One,2024, 19(7): e0303779. DOI: 10.1371/journal.pone.0303779.

[15] HAN T Y,LIAO X,GUO Z J,et al. Deciphering temporal gene expression dynamics in multiple coral species exposed to heat stress: implications for predicting resilience [J]. Science of the Total Environment,2024, 912:169021.

[16] MONTALBETTI E,BISCÉRÉ T,FERRIER-PAGÈS C,et al. Manganese benefits heat-stressed corals at the cellular level [J]. Frontiers in Marine Science,2021,8: 681119.

[17] THUMMASAN M,CASARETO B E,RAMPHUL C, et al. Physiological responses (Hsps 60 and 32,caspase 3,H_2O_2 scavenging,and photosynthetic activity) of the

中国知网 https://www.cnki.net

coral *Pocillopora damicornis* under thermal and high nitrate stresses [J]. Marine Pollution Bulletin, 2021, 171:112737. DOI:10.1016/j.marpolbul.2021.112737.

[18] CHOWDHURY S, KRUGER A, FETKENHOUR K, et al. Abstract 2207 investigating the molecular mechanisms of the heat shock response in corals: implications for thermal tolerance and resilience to climate change [J]. Journal of Biological Chemistry, 2025, 301(5S): 109972.

[19] TRAYLOR-KNOWLES N, ROSE N H, SHEETS E A, et al. Early transcriptional responses during heat stress in the coral *Acropora hyacinthus* [J]. The Biological Bulletin, 2017, 232(2): 91-100.

[20] ROSE N H, SENECA F O, PALUMBI S R. Gene networks in the wild: identifying transcriptional modules that mediate coral resistance to experimental heat stress [J]. Genome Biology and Evolution, 2015, 8(1): 243-252.

[21] KENKEL C D, SHERIDAN C, LEAL M C, et al. Diagnostic gene expression biomarkers of coral thermal stress [J]. Molecular Ecology Resources, 2014, 14(4): 667-678.

[22] ZHANG Y J, IP J C-H, XIE J Y, et al. Host-symbiont transcriptomic changes during natural bleaching and recovery in the leaf coral *Pavona decussata* [J]. Science of the Total Environment, 2022, 806(Pt 2): 150656.

[23] LI J, LONG L J, ZOU Y Y, et al. Microbial community and transcriptional responses to increased temperatures in coral *Pocillopora damicornis* holobiont [J]. Environmental Microbiology, 2021, 23(2): 826-843.

[24] PETROU K, NUNN B L, PADULA M P, et al. Broad scale proteomic analysis of heat-destabilised symbiosis in the hard coral *Acropora millepora* [J]. Scientific Reports, 2021, 11(1): 19061.

[25] GONG S Q, LIANG J Y, LI G, et al. Linking coral fluorescence phenotypes to thermal bleaching in the reef-building *Galaxea fascicularis* from the northern South China Sea [J]. Marine Life Science & Technology, 2023: 6(1): 155-167.

[26] CUNNING R, BAKER A C. Thermotolerant coral symbionts modulate heat stress-responsive genes in their hosts [J]. Molecular Ecology, 2020, 29(15): 2940-2950.

[27] YU X P, YU K F, HUANG W, et al. Thermal acclimation increases heat tolerance of the scleractinian coral *Acropora pruinosa* [J]. Science of the Total Environment, 2020, 733: 139319.

[28] 朱乐,沈贝祺,曹政,等.光胁迫下一种短指软珊瑚(*Sinularia* sp.)的白化响应研究[J].应用海洋学学报,2025,44(2):250-259.

[29] JIA S W, GENG X X, CAI Z F, et al. Comparison of physiological and transcriptome responses of corals to strong light and high temperature [J]. Ecotoxicology and Environmental Safety, 2024, 273: 116143.

[30] ZANDALINAS S I, FICHMAN Y, DEVIREDDY A R, et al. Systemic signaling during abiotic stress combination in plants [J]. Proceedings of the National Academy of Sciences of the United States of America, 2020, 117(24): 13810-13820.

[31] YUYAMA I, HIGUCHI T, MEZAKI T, et al. Metatranscriptomic analysis of corals inoculated with tolerant and non-tolerant symbiont exposed to high temperature and light stress [J]. Frontiers in Physiology, 2022, 13: 806171.

[32] 周洁,余克服,施祺.pCO_2 增加引起的海洋酸化对造礁珊瑚光合效率的影响[J].海洋与湖沼,2014,45(1):39-51.

[33] 刘昂,查广才,张振霞,等.环境胁迫下对虾免疫机制的研究进展[J].科学养鱼,2013,287(7):54-56.

[34] COLE C, FINCH A A, HINTZ C, et al. Effects of seawater pCO_2 and temperature on calcification and productivity in the coral genus *Porites* spp.: an exploration of potential interaction mechanisms [J]. Coral Reefs, 2018, 37: 471-481.

[35] GRIFFITHS J S, PAN T-C F, KELLY M W. Differential responses to ocean acidification between populations of *Balanophyllia elegans* corals from high and low upwelling environments [J]. Molecular Ecology, 2019, 28(11): 2715-2730.

[36] KENKEL C D, MOYA A, STRAHL J, et al. Functional genomic analysis of corals from natural CO_2-seeps reveals core molecular responses involved in acclimatization to ocean acidification [J]. Global Change Biology, 2018, 24(1): 158-171.

[37] RADICE V Z, MARTINEZ A, PAYTAN A, et al. Complex dynamics of coral gene expression responses to low pH across species [J]. Molecular Ecology, 2024, 33(1): e17186.

[38] LIU B Q, ZHU C W, XU K, et al. Record-breaking preflood rainfall over South China in 2022: role of historic warming over the Northeast Pacific and Maritime Continent [J]. Climate Dynamics, 2023, 61: 3147-3163.

[39] XIE J Y, LAU D C C, KEI K, et al. The 2014 summer coral bleaching event in subtropical Hong Kong [J].

中国知网 https://www.cnki.net

Marine Pollution Bulletin,2017,124(2):653-659.

[40] 陈学秋,杜勇,付宇鹏. 2022 年珠江流域暴雨洪水特点分析[J]. 中国水利,2022(22):28-32.

[41] CHEN J L,YU X P,YU K F,et al. Potential adaptation of scleractinian coral *Pocillopora damicornis* during hypo-salinity stress caused by extreme pre-flood rainfall over South China [J]. Environmental Research,2024,262:119848.

[42] AGUILAR C,RAINA J B,FÔRET S,et al. Transcriptomic analysis reveals protein homeostasis breakdown in the coral *Acropora millepora* during hypo-saline stress [J]. BMC Genomics,2019,20(1):148.

[43] MAYFIELD A B,GATES R D. Osmoregulation in anthozoan-dinoflagellate symbiosis [J]. Comparative Biochemistry and Physiology Part A:Molecular & Integrative Physiology,2007,147(1):1-10.

[44] HAGEDORN M,CARTER V L,LY S,et al. Analysis of internal osmolality in developing coral larvae,*Fungia scutaria* [J]. Physiological and Biochemical Zoology,2010,83(1):157-166.

[45] YANCEY P H,HEPPENSTALL M,LY S,et al. Betaines and dimethylsulfoniopropionate as major osmolytes in Cnidaria with endosymbiotic dinoflagellates [J]. Physiological and Biochemical Zoology,2010,83(1):167-173.

[46] ROSIC N,KANIEWSKA P,CHAN C K,et al. Early transcriptional changes in the reef-building coral *Acropora aspera* in response to thermal and nutrient stress [J]. BMC Genomics,2014,15(1):1052.

[47] 周榆鹏,肖遵勇,陈锦连,等. 美丽鹿角珊瑚(*Acropora muricata*)与风信子鹿角珊瑚(*Acropora hyacinthus*)的耐热性差异研究[J]. 海洋学报,2025,47(7):60-70.

[48] YUAN C,ZHOU Z,ZHANG Y D,et al. Effects of elevated ammonium on the transcriptome of the stony coral *Pocillopora damicornis* [J]. Marine Pollution Bulletin,2017,114(1):46-52.

[49] ZHOU Z,ZHANG G Q,CHEN G M,et al. Elevated ammonium reduces the negative effect of heat stress on the stony coral *Pocillopora damicornis* [J]. Marine Pollution Bulletin,2017,118(1/2):319-327.

[50] KEELING R F,KÖRTZINGER A,GRUBER N. Ocean deoxygenation in a warming world [J]. Annual Review of Marine Science,2010,2(1):199-229.

[51] ALTIERI A H,HARRISON S B,SEEMANN J,et al. Tropical dead zones and mass mortalities on coral reefs [J]. Proceedings of the National Academy of Sciences of the United States of America,2017,114(14):3660-3665.

[52] ALDERDICE R,SUGGETT D J,CÁRDENAS A,et al. Divergent expression of hypoxia response systems under deoxygenation in reef-forming corals aligns with bleaching susceptibility [J]. Global Change Biology,2021,27(2):312-326.

[53] DENGLER V L,GALBRAITH M,ESPINOSA J M. Transcriptional regulation by hypoxia inducible factors [J]. Critical Reviews in Biochemistry and Molecular Biology,2014,49(1):1-15.

[54] ALDERDICE R,PERNA G,CÁRDENAS A,et al. Deoxygenation lowers the thermal threshold of coral bleaching [J]. Scientific Reports,2022,12(1):18273.

[55] SCHWARZ J A,MITCHELMORE C L,JONES R,et al. Exposure to copper induces oxidative and stress responses and DNA damage in the coral *Montastraea franksi* [J]. Comparative Biochemistry and Physiology Part C:Toxicology & Pharmacology,2013,157(3):272-279.

[56] ZHOU Z,YU X P,TANG J,et al. Systemic response of the stony coral *Pocillopora damicornis* against acute cadmium stress [J]. Aquatic Toxicology,2018,194:132-139.

[57] LIU Z Q,AN M X,GENG X X,et al. The scleractinian coral *Pocillopora damicornis* relies on neuroendocrine regulation to cope with polycyclic aromatic hydrocarbons under heat stress [J]. Environmental Pollution,2023,316(Pt 1):120565.

[58] ZHOU Z,NI X Z,WU Z J,et al. Physiological and transcriptomic analyses reveal the threat of herbicides glufosinate and glyphosate to the scleractinian coral *Pocillopora damicornis* [J]. Ecotoxicology and Environmental Safety,2022,229:113074.

[59] ZHOU Y Y,LI Q L,ZHANG Q,et al. Environmental concentrations of herbicide prometryn render stress-tolerant corals susceptible to ocean warming [J]. Environmental Science & Technology,2024,58(10):4545-4557.

[60] RAHMAN M N,SHOZIB S H,AKTER M Y,et al. Microplastic as an invisible threat to the coral reefs:sources,toxicity mechanisms,policy intervention,and the way forward [J]. Journal of Hazardous Materials,2023,454:131522.

[61] TANG J,NI X Z,ZHOU Z,et al. Acute microplastic exposure raises stress response and suppresses detoxification and immune capacities in the scleractinian coral *Pocillopora damicornis* [J]. Environmental Pollution,

中国知网 https://www.cnki.net

2018,243(Pt A):66-74.

[62] RIPKEN C,KHALTURIN K,SHOGUCHI E. Response of coral reef dinoflagellates to nanoplastics under experimental conditions suggests downregulation of cellular metabolism [J]. Microorganisms,2020,8(11):1759.

[63] SU Y L,ZHANG K D,ZHOU Z,et al. Microplastic exposure represses the growth of endosymbiotic dinoflagellate *Cladocopium goreaui* in culture through affecting its apoptosis and metabolism [J]. Chemosphere,2020,244:125485.

[64] DANOVARO R,BONGIORNI L,CORINALDESI C,et al. Sunscreens cause coral bleaching by promoting viral infections [J]. Environmental Health Perspectives,2008,116(4):441-447.

[65] ISHIBASHI H,NISHIMURA S,TANAKA K,et al. Transcriptome analysis reveals limited toxic effects of the UV-filter benzophenone-3 (BP-3) on the hermatypic coral *Acropora tenuis* and its symbiotic dinoflagellates [J]. Marine Pollution Bulletin, 2024, 201:116260.

[66] PEIXOTO R S,SWEET M,VILLELA H D M,et al. Coral probiotics:premise,promise,prospects [J]. Annual Review of Animal Biosciences,2021,9(1):265-288.

[67] ROSENBERG E,KOREN O,RESHEF L,et al. The role of microorganisms in coral health,disease and evolution [J]. Nature Reviews Microbiology,2007,5(5):355-362.

[68] SILVA-LIMA A W,FROES A M,GARCIA G D,et al. *Mussismilia braziliensis* white plague disease is characterized by an affected coral immune system and dysbiosis [J]. Microbial Ecology, 2021, 81(3):795-806.

[69] ANDERSON D A,WALZ M E,WEIL E,et al. RNA-Seq of the Caribbean reef-building coral *Orbicella faveolata* (Scleractinia-Merulinidae) under bleaching and disease stress expands models of coral innate immunity [J]. PeerJ,2016,4:e1616.

[70] PALMER C V,TRAYLOR-KNOWLES N. Towards an integrated network of coral immune mechanisms [J]. Proceedings of the Royal Society B:Biological Sciences,2012,279(1745):4106-4114.

[71] TCHERNOV D,KVITT H,HARAMATY L,et al. Apoptosis and the selective survival of host animals following thermal bleaching in zooxanthellate corals [J]. Proceedings of the National Academy of Sciences of the United States of America,2011,108(24):9905-9909.

[72] VIDAL-DUPIOL J,LADRIÈRE O,DESTOUMIEUX-GARZÓN D,et al. Innate immune responses of a scleractinian coral to vibriosis [J]. The Journal of Biological Chemistry,2011,286(25):22688-22698.

[73] WANG S Y,LU C R,ZHANG Q,et al. Microbial community and transcriptional responses to *V. coralliilyticus* stress in coral *Favites halicora* and *Pocillopora damicornis* holobiont [J]. Marine Environmental Research,2024,196:106394.

[74] HE X C,ZOU J,CHEN Q Q,et al. Microbial and transcriptional response of *Acropora valida* and *Turbinaria peltata* to *Vibrio coralliilyticus* challenge:insights into corals disease resistance [J]. BMC Microbiology,2024,24(1):288. DOI:10.1186/s12866-024-03438-7.

[75] WU H,LI J L,SONG Q Q,et al. The synergistic negative effects of combined acidification and warming on the coral host and its symbiotic association with Symbiodiniaceae indicated by RNA-Seq differential expression analysis [J]. Coral Reefs,2023,42(5):1187-1201.

[76] KANIEWSKA P,CHAN C-K K,KLINE D,et al. Transcriptomic changes in coral holobionts provide insights into physiological challenges of future climate and ocean change [J]. PLoS One, 2015, 10(10):e0139223.

[77] TAKAGI T,YOSHIOKA Y,ZAYASU Y,et al. Transcriptome analyses of immune system behaviors in primary polyp of coral *Acropora digitifera* exposed to the bacterial pathogen *Vibrio coralliilyticus* under thermal loading [J]. Marine Biotechnology, 2020, 22(6):748-759.

[78] ONYANGO C A,GLASSOM D,MACDONALD A. De novo assembly of the transcriptome of scleractinian coral,*Anomastraea irregularis* and analyses of its response to thermal stress [J]. Molecular Biology Reports,2021,48(3):2083-2092.

[79] JIANG L,LIU C Y,CUI G X,et al. Rapid shifts in thermal reaction norms and tolerance of brooded coral larvae following parental heat acclimation [J]. Molecular Ecology,2023,32(5):1098-1116.

[80] HOU J,XU T,SU D J,et al. RNA-Seq reveals extensive transcriptional response to heat stress in the stony coral *Galaxea fascicularis* [J]. Frontiers in Genetics,2018,9:37.

[81] BARSHIS D J,LADNER J T,OLIVER T A,et al. Genomic basis for coral resilience to climate change [J].

中国知网 https://www.cnki.net

Proceedings of the National Academy of Sciences of the United States of America,2013,110(4):1387-1392.

[82] HERNÁNDEZ ELIZÁRRAGA V H,OLGUÍN-LÓPEZ N,HERNÁNDEZ-MATEHUALA R,et al. Transcriptomic differences between bleached and unbleached hydrozoan *Millepora complanata* following the 2015—2016 ENSO in the Mexican Caribbean [J]. PeerJ,2023,11:e14626.

[83] SAVARY R,BARSHIS D J,VOOLSTRA C R,et al. Fast and pervasive transcriptomic resilience and acclimation of extremely heat-tolerant coral holobionts from the northern Red Sea [J]. Proceedings of the National Academy of Sciences of the United States of America,2021,118(19):e2023298118.

[84] HERRERA M,LIEW Y J,VENN A,et al. New insights from transcriptomic data reveal differential effects of CO_2 acidification stress on photosynthesis of an endosymbiotic dinoflagellate in hospite [J]. Frontiers in Microbiology,2021,12:666510.

[85] WRIGHT R M,CORREA A M S,QUIGLEY L A,et al. Gene expression of endangered coral (*Orbicella* spp.) in flower garden banks national marine sanctuary after hurricane harvey [J]. Frontiers in Marine Science,2019,6:672.

[86] ISHIBASHI H,TAKAICHI D,TAKEUCHI I. Effects of the herbicide Irgarol 1051 on the transcriptome of hermatypic coral *Acropora tenuis* and its symbiotic dinoflagellates [J]. Science of the Total Environment,2021,780:146542.

[87] NISHIOKA S,MIYATA K,INOUE Y,et al. Deciphering mechanisms of UV filter (benzophenone-3)- and high temperature-induced adverse effects in the coral *Acropora tenuis*, using ecotoxicogenomics [J]. Science of the Total Environment,2024,954:176018.

[88] LIANG H,PAN C G,PENG F J,et al. Integrative transcriptomic analysis reveals a broad range of toxic effects of triclosan on coral *Porites lutea* [J]. Journal of Hazardous Materials,2024,480:136033.

[89] POQUITA-DU R C,HUANG D,CHOU L M,et al. Short term exposure to heat and sediment triggers changes in coral gene expression and photo-physiological performance [J]. Frontiers in Marine Science,2019,6:121.

[90] SAVARY R,BARSHIS D J,VOOLSTRA C R,et al. Fast and pervasive transcriptomic resilience and acclimation of extremely heat-tolerant coral holobionts from the northern Red Sea [J]. Proceedings of the National Academy of Sciences of the United States of America,2021,118(19):e2023298118.

[91] CHUI A P Y,WONG Y H,SUN J,et al. Effects of heat and hyposalinity on the gene expression in *Acropora pruinosa* larvae [J]. Frontiers in Marine Science,2023,10:1096407.

[92] MOYA A,HUISMAN L,BALL E E,et al. Whole transcriptome analysis of the coral *Acropora millepora* reveals complex responses to CO_2-driven acidification during the initiation of calcification [J]. Molecular Ecology,2012,21(10):2440-2454.

[93] PINZÓN J H,KAMEL B,BURGE C A,et al. Whole transcriptome analysis reveals changes in expression of immune-related genes during and after bleaching in a reef-building coral [J]. Royal Society Open Science,2015,2(4):140214.

[94] YUAN X C,YUAN T,HUANG H,et al. Elevated CO_2 delays the early development of scleractinian coral *Acropora gemmifera* [J]. Scientific Reports,2018,8(1):2787.

[95] TONG H Y,ZHANG F,SUN J,et al. Meta-organism gene expression reveals that the impact of nitrate enrichment on coral larvae is mediated by their associated Symbiodiniaceae and prokaryotic assemblages [J]. Microbiome,2023,11(1):89.

[96] MEYER E,AGLYAMOVA G V,MATZ M V. Profiling gene expression responses of coral larvae (*Acropora millepora*) to elevated temperature and settlement inducers using a novel RNA-Seq procedure [J]. Molecular Ecology,2011,20(17):3599-3616.

[97] STRADER M E,AGLYAMOVA G V,MATZ M V. Red fluorescence in coral larvae is associated with a diapause-like state [J]. Molecular Ecology,2016,25(2):559-569.

[98] JIANG L,ZHANG P,HUANG L T,et al. Life-stage specificity and temporal variations in transcriptomes and DNA methylomes of the reef coral *Pocillopora damicornis* in response to thermal acclimation [J]. Science of the Total Environment,2024,921:171098.

[99] JIANG L,SUN Y F,ZHOU G W,et al. Ocean acidification elicits differential bleaching and gene expression patterns in larval reef coral *Pocillopora damicornis* under heat stress [J]. Science of the Total Environment,2022,842:156851.

[100] RIVEST E B,KELLY M W,DEBIASSE M B,et al. Host and symbionts in *Pocillopora damicornis* larvae display different transcriptomic responses to ocean a-

中国知网 https://www.cnki.net

cidification and warming [J]. Frontiers in Marine Science, 2018, 5: 186.

Advances in Transcriptome-Based Mechanisms of Environmental Stress Responses in Scleractinian Corals

CHEN Junling[1], MA Yuling[1], ZHENG Yue[1], YU Kefu[1,2**], YU Xiaopeng[1**]

(1. Coral Reef Research Center of China, Guangxi Laboratory on the Study of Coral Reefs in the South China Sea, School of Marine Sciences, Guangxi University, Nanning, Guangxi, 530004, China; 2. Southern Marine Science and Engineering Guangdong Laboratory, Guangzhou, Guangdong, 511458, China)

Abstract: The environmental adaptability of scleractinian corals depends on the molecular regulatory mechanisms underlying the interactions within the coral holobiont, yet these mechanisms remain incompletely elucidated. In recent years, with the advancement of high-throughput sequencing technologies, transcriptomics has been widely applied to the study of coral holobionts, emerging as a key tool for deciphering the environmental response mechanisms of corals. It has provided new perspectives for unraveling the molecular interaction networks within symbiotic systems. This paper systematically reviews the application progress of transcriptomics in the research on coral environmental adaptability, focuses on elaborating the transcriptional responses of the coral holobiont under different environmental stresses, and summarizes the differential response mechanisms of each component of the coral holobiont in coping with various environmental stresses. Under environmental stress, both the coral host and its associated Symbiodiniaceae exhibit gene expression plasticity, which enables them to establish stress tolerance through precise transcriptional regulatory networks and maintain symbiotic stability via coordinated regulatory mechanisms. Future research should further integrate multi-omics data and combine physiological and ecological validation to comprehensively reveal the regulatory networks of coral holobionts.

Key words: transcriptomics; scleractinian corals; coral holobiont; Symbiodiniaceae; environmental stress; adaptation

责任编辑:米慧芝

微信公众号投稿更便捷
联系电话:0771-2503923
邮箱:gxkx@gxas.cn
投稿系统网址:http://gxkx.ijournal.cn/gxkx/ch

中国知网 https://www.cnki.net

◆珊瑚礁生态保护与修复◆

珊瑚共生蓝藻 *Synechococcus* sp. GXU01 对两种典型虫黄藻的代谢协调作用*

李志聪[1],胡思雨[1],梁祝清[1],杨雅婷[1],卢铭垚[1],余克服[1,2],梁甲元[1,2**],张　丽[3],冯宜合[3]
(1. 广西大学海洋学院,广西南宁　530004;2. 广西大学,广西南海珊瑚礁研究重点实验室,广西南宁　530004;3. 广西大学资源环境与材料学院,广西南宁　530004)

摘要:虫黄藻和蓝藻是珊瑚共生功能体中两种主要的光合共生微生物,在珊瑚共生系统的复杂交互作用中扮演重要角色。为探究二者之间的代谢协调机制,本研究通过离体共培养实验,将一株分离自十字牡丹珊瑚 *Pavona decussata* 的蓝藻 *Synechococcus* sp. GXU01(以下简称 GXU01)分别与两种典型的虫黄藻(环境敏感型的 *Cladocopium goreaui* 和环境耐受型的 *Durusdinium trenchii*)共培养,分析其在高温胁迫条件下生理代谢、光系统Ⅱ功能及固碳关键基因 *PsbA*、*rbcL* 表达等方面的协调响应。结果显示,GXU01 对两种虫黄藻的生长率均无显著影响,但在共培养初期,*D. trenchii* 的光合色素含量显著下降(24.5%－29.6%),而 *C. goreaui* 未受显著影响。无论在常温还是高温条件下,GXU01 均能显著提高两种虫黄藻的最大光化学效率(F_v/F_m)($P<0.05$)。在活性氧(ROS)方面,GXU01 使 *C. goreaui* 的 ROS 水平显著上升(9.83%－36.09%),而 *D. trenchii* 的 ROS 水平则显著降低(12.55%－23.12%)。在光系统Ⅱ修复关键基因表达方面,GXU01 对不同温度下 *C. goreaui* 的 *psbA* 表达无显著影响,但显著抑制高温胁迫下 *D. trenchii* 的 *psbA* 表达,其相对表达量下降 82.45%－85.01%。在固碳效率关键基因表达方面,GXU01 显著提高 *C. goreaui* 的 *rbcL* 表达(提高 25.37%－43.04%),同时也促进 *D. trenchii* 的 *rbcL* 表达(提高 51.62%－63.18%)。本研究从离体互作的角度揭示了 GXU01 与虫黄藻之间的协同作用,为共生态下虫黄藻的热适应机制与热白化响应提供了新见解。

关键词:珊瑚礁生态系统;共生功能体;蓝藻;虫黄藻;功能互作

中图分类号:Q178.53　　**文献标识码**:A　　**文章编号**:1005-9164(2025)04-0828-11
DOI:10.13656/j.cnki.gxkx.20251114.018

收稿日期:2025-07-15　　修回日期:2025-07-30
*科技基础资源调查专项(2023FY100804),广西科技基地与人才专项(桂科 AD25069075)资助。

【第一作者简介】
李志聪(1999－),男,硕士,主要从事海洋微生物生态学研究,E-mail:2227301021@st.gxu.edu.cn。
【**通信作者简介】
梁甲元(1986－),男,博士,副教授,主要从事珊瑚礁微生物生态学、海洋微生物资源开发与应用研究,E-mail:jyliang@gxu.edu.cn。

【引用本文】
李志聪,胡思雨,梁祝清,等. 珊瑚共生蓝藻 *Synechococcus* sp. GXU01 对两种典型虫黄藻的代谢协调作用[J]. 广西科学,2025,32(4):828-838.
LI Z C,HU S Y,LIANG Z Q,et al. Metabolic Interactions between the Coral-associated Cyanobacterium *Synechococcus* sp. GXU01 and Two Representative Symbiodiniaceae Species [J]. Guangxi Sciences,2025,32(4):828-838.

珊瑚及其共附生微生物,包括虫黄藻,以及与其长期互利共生的细菌、古菌、真菌、原生动物和病毒等,共同组成了珊瑚共生功能体(Coral holobiont)[1]。在该共生系统中,虫黄藻作为重要组成部分,通过光合作用为珊瑚提供超过95%的光合能量[2],使其得以在营养贫瘠的浅海环境中生存。研究表明,仅虫黄藻等共生藻对溶解无机氮、无机磷的吸收利用就可以满足珊瑚的快速生长所需[3]。此外,虫黄藻吸收的CO_2也参与珊瑚的钙化过程,促进其骨骼生长,为其他生物提供结构支持[4]。相应地,珊瑚则为虫黄藻提供受保护的栖息环境,并供应CO_2、氮、磷等无机营养物质[5]。蓝藻同样是珊瑚共生功能体中一类重要的光合微生物,也是优势共生藻之一[6]。已有研究显示,在某些珊瑚共生微生物组中,蓝藻的丰度仅次于虫黄藻,部分珊瑚共生功能体中蓝藻甚至占细菌总数的50%以上[7]。蓝藻能够通过固氮作用为珊瑚提供额外氮源,参与整个共生功能体的氮循环,提供细胞修复所需要的氮,促进光合作用[8-9],从而帮助珊瑚在逆境中维持稳态并增强其对热白化的抵抗能力[10-12]。需要指出的是,珊瑚的热白化并非单一物种作用的结果,而是"珊瑚-微生物"共生体失衡的综合体现。目前,关于虫黄藻在珊瑚热应激响应中的作用已有较为深入的研究,然而对共生微生物组中其他成员的功能机制,尤其是"虫黄藻-蓝藻"之间的代谢协调机理,仍了解不足。

关于珊瑚共生蓝藻的研究多聚焦于其在珊瑚宿主内发挥的能量供给、物质循环及环境适应等方面的多维功能。蓝藻可能通过代谢交互与虫黄藻形成互补网络,在珊瑚共生功能体中,二者的代谢协调对珊瑚的营养获取、环境适应力以及抗逆性具有关键作用。例如,有研究发现,加勒比海珊瑚 *Montastraea cavernosa* 中的虫黄藻会优先使用蓝藻固氮作用的产物[13],这些产物还可直接整合进珊瑚宿主的氨基酸合成途径[14]。在红海珊瑚 *Stylophora pistillata* 中,共生蓝藻甚至可满足宿主高达30%的氮源需求[15],其重要性不言而喻。此外,蓝藻还能通过抗氧化与耐高温机制直接增强珊瑚对环境胁迫的适应能力。高温胁迫下,蓝藻丰度显著上升,其合成的热休克蛋白(Hsp70)和超氧化物歧化酶(SOD)有助于清除宿主组织内的活性氧(ROS)[16]。蓝藻与虫黄藻之间也可能存在协同响应机制:夏季高温条件下,虫黄藻密度下降,蓝藻丰度显著上升,二者此消彼长的协同变化有助于提升珊瑚宿主应对环境变化的能力[17]。Liang 等[18]在研究杯形珊瑚(*Pocillopora* sp.)的高温胁迫与恢复过程时发现,尽管虫黄藻密度显著降低,蓝藻的相对丰度却明显上升,而珊瑚的最大光化学效率(F_v/F_m)未受显著影响,说明蓝藻可能在能量供给与恢复过程中发挥了补偿作用。在营养匮乏的情况下,虫黄藻还会通过主动摄食蓝藻以补充氮源。这一发现不仅更新了人们对虫黄藻营养模式(主要依赖光合作用)的传统认知,也揭示了虫黄藻在珊瑚共生功能体中更为复杂的营养互作关系[19]。因此,深入解析珊瑚共生功能体中虫黄藻与蓝藻之间的代谢协调机制,不仅有助于揭示珊瑚共生功能体的稳态维持机制,也为提升珊瑚应对气候变化与营养扰动的适应力提供新思路。

综上所述,目前关于内共生蓝藻和虫黄藻互作的研究多从珊瑚宿主角度展开。然而,由于共生体中复杂的生物互作网络,研究人员对蓝藻和虫黄藻之间代谢协调机制的整体认识仍较为有限。现有研究多关注高温[20]、高光[21]或酸化[22]等环境胁迫下虫黄藻的生理变化与基因表达,而对其与蓝藻共培养等生物互作情形的探讨相对不足。研究表明,虫黄藻在25 ℃条件下表现出较高的生长速率和光合活性[23];而当温度超过31 ℃时,F_v/F_m开始显著下降,32 ℃被认为已产生明显高温胁迫效应[24]。在珊瑚共生功能体中,32 ℃培养条件下虫黄藻会出现大量差异表达基因,说明该温度已超出其稳态耐受范围[25]。此外,珊瑚热白化会损伤虫黄藻的光合系统,导致其光合作用能力下降,研究也发现高温胁迫显著抑制虫黄藻光合作用相关基因的表达[26]。在光合作用相关基因中,*psbA* 基因编码光系统Ⅱ(PSⅡ)的D1蛋白,其表达水平反映光合系统的修复能力[27];*rbcL* 基因则编码核酮糖-1,5-二磷酸羧化酶/加氧酶(RuBisCO)大亚基,是评估碳固定效率的关键指标[28]。二者均为虫黄藻响应环境变化的核心功能基因,然而蓝藻是否调控其表达尚不明确。为深入探究蓝藻对虫黄藻生理生化特性的影响,特别是对其在 *psbA* 与 *rbcL* 基因表达、光合作用及碳同化能力方面的调控作用,本研究以环境敏感型虫黄藻 *Cladocopium goreaui*、环境耐受型虫黄藻 *Durusdinium trenchii* 以及蓝藻 *Synechococcus* sp.GXU01(以下简称GXU01)为研究对象,建立共培养体系,通过测定虫黄藻生长率、光合色素含量、F_v/F_m、ROS水平以及关键基因表达等指标,系统分析游离状态下珊瑚共生蓝藻对两种典型虫黄藻的代谢协调作用,以期为理解珊瑚共生功能体的

热适应机制与热白化响应提供新视角。

1 材料与方法

1.1 材料

GXU01 由本课题组从涠洲岛(21°10′－21°54′N,109°00′－109°15′E)十字牡丹珊瑚(*Pavona decussata*)中分离并保存[17]。实验时,将该菌株接种于含 3.5%海盐的蓝藻培养基(BG-11 培养基),置于温度 25 ℃、光照强度 4 000 Lux、光暗比 12∶12 的二氧化碳型人工气候箱(RDN-500D-CO_2,宁波扬辉仪器有限公司)中培养。虫黄藻 *C. goreaui* 和 *D. trenchii* 分别分离自涠洲岛的霜鹿角珊瑚(*Acropora pruinose*)和西沙群岛(15°46′－17°08′N,111°11′－112°54′E)的丛生盔形珊瑚(*Galaxea fascicularis*),其培养方法参照覃良云等[29]的研究。

1.2 实验设计

本研究采用双因素(温度、GXU01 共培养)实验设计,以探究虫黄藻 *C. goreaui*(C1)、*D. trenchii*(D1)分别与 GXU01 共培养的协调作用机理。实验分组设计如下:对照组(25C1,25D1),常温共培养组(25C1＋,25D1＋),高温胁迫组(32C1,32D1),高温共培养组(32C1＋,32D1＋),分别设 3 个生物学重复。其中,组名中的 25 和 32 分别指 25 ℃(对照)与 32 ℃(高温胁迫)两种温度条件。

将 GXU01 和 C1、D1 分别用 BG-11 培养基和 L1 培养基在 25 ℃条件下预培养至 4×10^5 cells/mL。随后,将 GXU01 以 10 000 r/min 离心 5 min,并用无菌海水洗涤沉淀 3 次。经预处理的 GXU01 以 0.5%(*V*/*V*)[17]接种至含等密度 C1、D1 的 L1 培养基。混合藻液分装至 250 mL 锥形瓶,置于二氧化碳型人工气候箱中培养。培养条件:温度 25 ℃/32 ℃,湿度 60% RH,CO_2 含量 1 964 mg/m^3,光照强度 4 000 Lux,光照周期 12 h。培养期间,每日早晚各摇匀一次培养基。

1.3 虫黄藻密度测定

分别取培养 1、4、7 d 的藻液 2 mL,使用浮游植物流式细胞仪(CytoSense,荷兰 CytoBuoy 公司)测定虫黄藻密度。测定前将藻液充分涡旋混匀,设置样品流速为 3 μL/s,测量时间 60 s,每组样品重复测量 9 次并取平均值。

1.4 细胞光合效率测定

在培养的第 1、3、5、7 天晚上,将藻液在黑暗环境中避光处理 30 min 后,使用连续监测荧光仪(Monitoring PAM,德国 WALZ 公司)测定 F_v/F_m。测量前摇匀藻液,并将探头垂直置于锥形瓶底部。电信号阻尼(Damping)和增益(Gain)分别设置为 1 和 2。每组样品重复测量 9 次,结果取平均值。

1.5 光合色素测定

在培养的第 1、4、7 天,取藻液各 1 mL 至离心管中,在 4 ℃条件下以 8 000 r/min 离心 5 min,去上清液,再加入 1 mL 100%甲醇后用锡纸覆盖,放入 4 ℃冰箱中黑暗保存 24 h,利用紫外分光光度计[UV-2700,岛津仪器(苏州)有限公司]分别测定其在 665、470、652 nm 处的吸光度(记为 A_{665}、A_{470}、A_{652}),并计算叶绿素 *a*(Chl *a*)、叶绿素 *b*(Chl *b*)和类胡萝卜素(Carotenoid)的含量。单细胞的色素含量用密度(cells/mL)换算。计算公式[30]如下:

Chl *a*(μg/mL)＝$16.72A_{665}-9.16A_{652}$,

Chl *b*(μg/mL)＝$34.09A_{652}-15.28A_{665}$,

Carotenoid(μg/mL)＝$(1000A_{470}-1.63\text{Chl }a-15.28\text{Chl }b)/221$。

1.6 ROS 含量测定

取培养至第 7 天的藻液各 1 mL,离心后取上清液加入 DCFH-DA 探针(终浓度为 10 μmol/L),取 200 μL 加入 96 孔板中,锡箔纸包裹于 37 ℃水浴孵育 30 min,立即放至酶标仪(Varioskan Lux 3020,美国 Thermo Fisher Scientific 公司)检测荧光强度,激发波长 488 nm,发射波长 525 nm。

1.7 RT-qPCR 功能验证

为验证蓝藻对虫黄藻光合作用的影响,挑选虫黄藻 *psbA* 和 *rbcL* 两个光合作用相关基因,分析藻液中基因表达的变化规律,虫黄藻内参基因选择 *GAPDH* 基因[31],相关基因引物序列见表 1。

表 1 RT-qPCR 所用基因引物

Table 1 Gene primers used for RT-qPCR

基因 Gene	引物序列 Primer sequence
psbA	F:5′-ATGCTTGGTGTGGCTTGTTG-3′ R:5′-AAGCTGCTACAACAGGTGCT-3′
rbcL	F:5′-TGAACGTGGAGGACATGTGG-3′ R:5′-TGATGAAGTCACCACCCTGC-3′
GAPDH[31]	F:5′-GTCGCATTGGTCGTATGGTCT-3′ R:5′-CGATTAGCTCGTCCTTCTCCC-3′

1.7.1 总 RNA 提取与反转录

取培养至第 7 天的藻液,使用 MolPure® Plant RNA Kit 植物 RNA 提取试剂盒[翌圣生物科技(上海)股份有限公司]提取总 RNA,并经紫外分光光度

计测定其浓度和质量。根据 PrimeScript™ RT reagent Kit 反转录试剂盒(日本 Takara Bio 公司)使用说明书,将 RNA 反转录为 cDNA。具体反应体系见表 2。反应程序如下:37 ℃孵育 15 min;84 ℃加热 5 s 使反转录酶失活;最后冷却至 4 ℃保存,用于后续实验。

表 2 反转录反应体系

Table 2 Reverse transcription reaction system **Unit:μL**

组分 Component	添加量 Addition amount
5×PrimeScript Buffer (real time)	2.0
PrimeScript RT Enzyme Mix Ⅰ	0.5
Oligo dT Primer (50 μmol/L)	0.5
Random 6 mers (100 μmol/L)	0.5
Total RNA	6.5

1.7.2 RT-qPCR 反应与分析

采用 ChamQ Universal SYBR qPCR Master Mix 试剂盒(Q711,南京诺唯赞生物科技股份有限公司),RT-qPCR 反应体系见表 3。RT-qPCR 反应程序设置如下:首先在 95 ℃下预变性 30 s;随后进行 40 个循环,每个循环包括 95 ℃ 10 s 与 60 ℃ 30 s 两个步骤;扩增结束后,进行熔解曲线分析,熔解条件采用仪器默认程序。所使用仪器为荧光定量 PCR 仪(7500Fast,美国 ABI 公司)。采用 $2^{-\triangle\triangle Ct}$ 法对基因相对表达量进行分析,虫黄藻基因相对表达量是以 *GAPDH* 作为内参基因,以 25 ℃无 GXU01 添加组为对照组计算获得。

表 3 RT-qPCR 反应体系

Table 3 RT-qPCR system **Unit:μL**

组分 Component	添加量 Addition amount
2×ChamQ Universal SYBR qPCR Master Mix	5.0
Primer 1 (10 μmol/L)	0.2
Primer 2 (10 μmol/L)	0.2
cDNA	2.0
ddH_2O	3.6

1.8 数据统计

使用 Excel 2021 对实验中获得的数据进行预处理,统计分析及绘图均在 GraphPad Prism 10.1.2 中进行,结果以平均值±标准差(Mean±SD)表示。若数据满足高斯正态分布,通过单因素方差分析(One-way ANOVA)对所有实验数据进行显著性检验,组间差异通过 Tukey 多重比较检验进行分析;若数据不满足高斯正态分布,则采用 Kruskal-Wallis 检验并使用 Dunn 多重比较检验进行组间比较,显著性水平设为 $P<0.05$。

2 结果与分析

2.1 共培养下虫黄藻生理生化指标

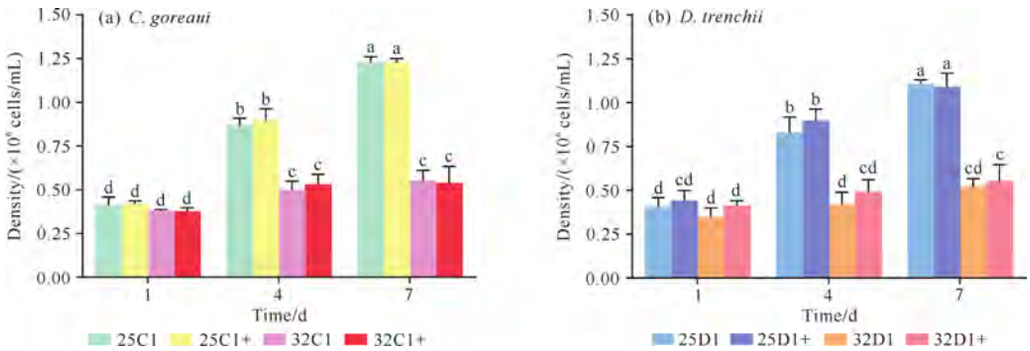
2.1.1 虫黄藻密度

(1)GXU01 对虫黄藻生长的影响。在 *C. goreaui* 中,第 4 天共培养组(25C1+与 32C1+)的细胞密度相较对照组(25C1 与 32C1)略有上升;但至第 7 天,两组间差异不明显[图 1(a)]。在 *D. trenchii* 中,第 1 天与第 4 天共培养组(25D1+与 32D1+)的细胞密度亦呈现上升趋势,但差异不显著[图 1(b)]。整体上,GXU01 对两种虫黄藻的生长均未产生显著影响。

(2)温度对虫黄藻生长的影响。高温处理显著抑制了两种虫黄藻的生长(第 7 天)。在 *C. goreaui* 中,32C1 组较 25C1 下降了 55.28%,32C1+较 25C1+下降了 56.23%;在 *D. trenchii* 中,32D1 较 25D1 下降了 52.95%,32D1+较 25D1+下降了 49.26%,两者均达到显著差异水平($P<0.05$)。综上,GXU01 对两种虫黄藻的生长均没有显著影响,而高温会显著抑制虫黄藻的生长。

2.1.2 虫黄藻光合色素

(1)*C. goreaui* 虫黄藻响应特征。实验前期(第 1 至第 4 天),共培养对 *C. goreaui* 的叶绿素 *b* 含量呈阶段性促进,共培养组(25C1+和 32C1+)叶绿素 *b* 含量显著高于对照组($P<0.05$),提升幅度分别为 20.44%-29.14%(25 ℃)和 10.21%-18.22%(32 ℃),到第 7 天差异不再显著。叶绿素 *a* 和类胡萝卜素则仅在第 4 天 25C1+显著高于对照组($P<0.05$),其他阶段无显著差异。25 ℃时 *C. goreaui* 色素含量随时间持续下降,32 ℃高温胁迫下则整体维持较高稳定水平。至第 7 天,32C1 相较于 25C1,叶绿素 *a*、叶绿素 *b* 和类胡萝卜素含量分别高出 53.23%、60.66%和 48.76%;共培养组(32C1+相较 25C1+)的提升幅度更高,分别为 61.00%、68.62%和 64.18%[图 2:(a)、(c)、(e)]。

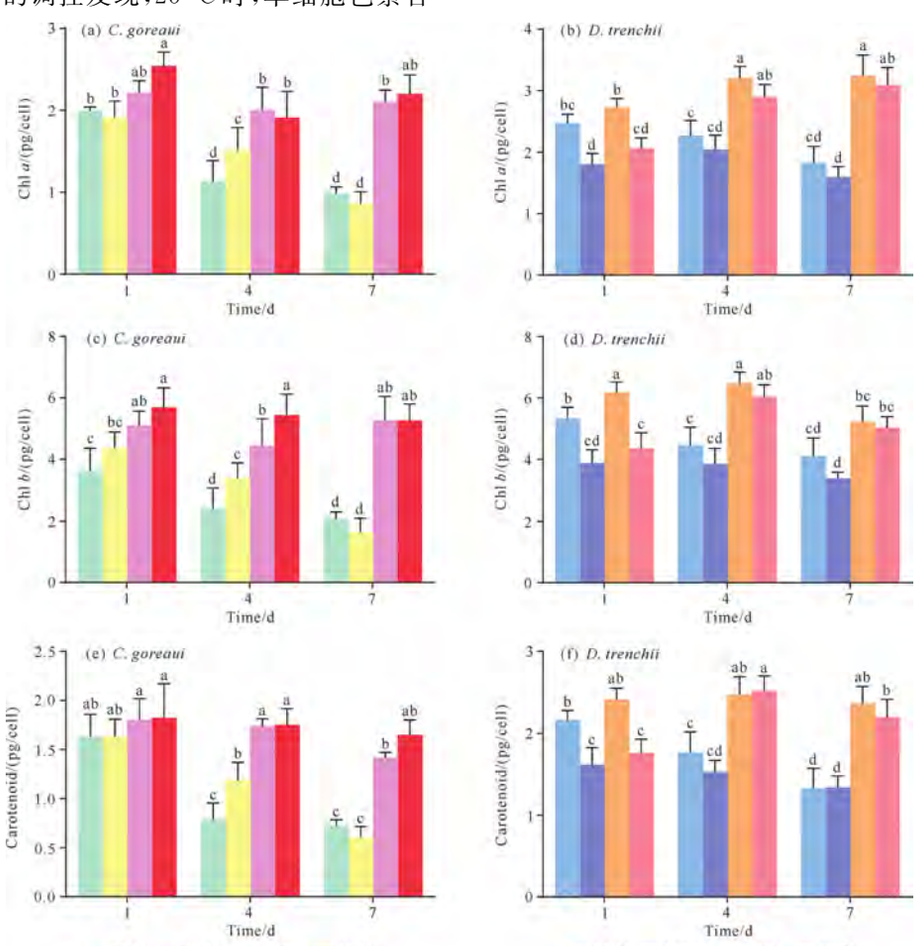


Different letters indicate significant differences among groups ($P<0.05$).

图 1　不同温度下虫黄藻密度变化

Fig. 1　Changes in density of Symbiodiniaceae at different temperatures

(2)*D. trenchii* 虫黄藻响应特征。共培养对 *D. trenchii* 光合色素有明显的抑制效应,在前期(第 1 天),共培养组光合色素含量显著降低,其中叶绿素 *a* 降低 24.50%－27.14%、叶绿素 *b* 降低 27.75%－29.60%、类胡萝卜素降低 25.10%－27.31%。随着时间推移,抑制效应减弱,第 4－7 天降幅收窄。分析温度对光合色素的调控发现,25 ℃时,单细胞色素含量随时间持续下降;32 ℃高温胁迫下,色素维持较高水平。第 7 天时,32D1 较 25D1 叶绿素 *a* 高出 43.58%、叶绿素 *b* 高出 21.63%、类胡萝卜素高出 43.81%;而共培养条件下,32D1＋较 25D1＋叶绿素 *a* 高出 48.51%、叶绿素 *b* 高出 32.91%、类胡萝卜素高出 39.16%[图 2:(b)、(d)、(f)]。



Different letters indicate significant differences among groups ($P<0.05$).

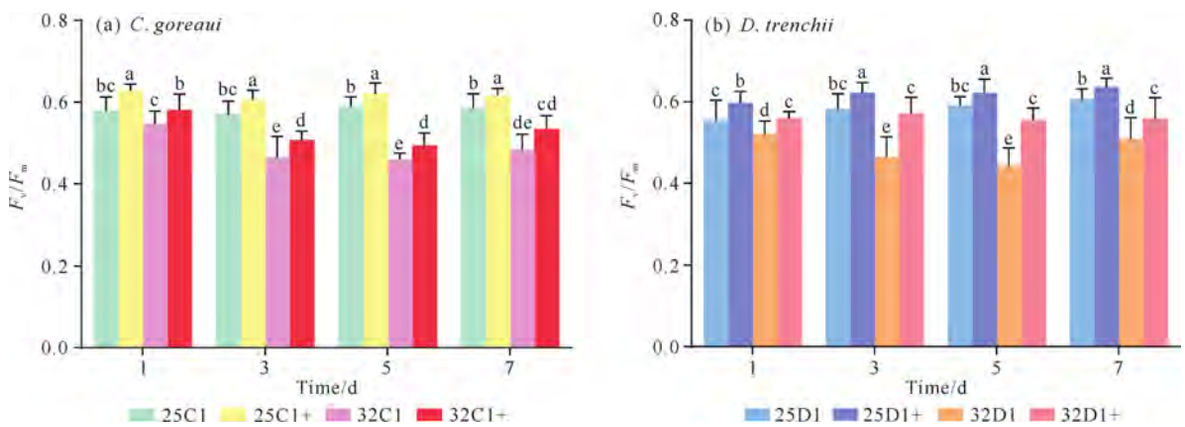
图 2　不同温度下虫黄藻光合色素含量变化

Fig. 2　Changes in photosynthetic pigment content of Symbiodiniaceae at different temperatures

C.goreaui 和 *D.trenchii* 在与 GXU01 共培养时物种特异性差异显著，*D.trenchii* 对共培养的敏感度高于 *C.goreaui*。

2.1.3 虫黄藻 F_v/F_m

如图 3 所示，*C.goreaui* 的 F_v/F_m 在 25 ℃时较为稳定，第 1 天 F_v/F_m 为 0.58±0.03，第 7 天保持在 0.59±0.03；而 *D.trenchii* 的 F_v/F_m 在第 1 天为 0.56±0.05，到第 7 天时，显著提升至 0.61±0.03（$P<0.05$）。32 ℃高温胁迫时，虫黄藻 F_v/F_m 出现显著下降，*C.goreaui* 的 F_v/F_m 从第 1 天的 0.55±0.03 显著降低至第 7 天的 0.48±0.04（$P<0.05$），降幅达 12.7%；*D.trenchii* 的 F_v/F_m 从 0.52±0.03 下降至 0.51±0.05，差异不显著（$P>0.05$）。



Different letters indicate significant differences among groups ($P<0.05$).

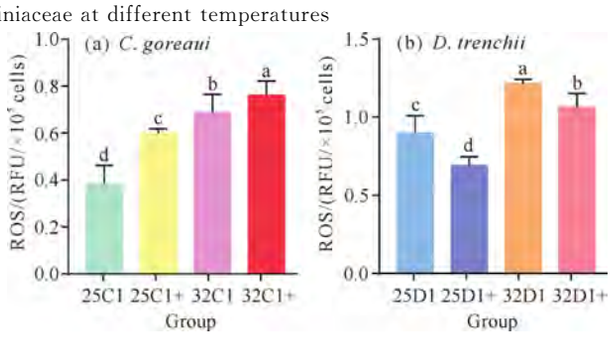
图 3 不同温度下虫黄藻 F_v/F_m 变化

Fig.3 Changes in F_v/F_m of Symbiodiniaceae at different temperatures

与 GXU01 共培养后，两种虫黄藻的 F_v/F_m 都有了显著提高（$P<0.05$）。*C.goreaui* 在 25 ℃时，第 1 天 F_v/F_m 提高 5.03%，第 7 天提高达 5.30%（25C1+对比 25C1）；而 32 ℃高温胁迫下，第 1 天提高 6.61%，第 7 天提高至 10.79%（32C1+对比 32C1）。*D.trenchii* 在 25 ℃时，第 1 天 F_v/F_m 提高 7.57%，第 7 天仅提高 4.95%（25D1+对比 25D1）；而 32 ℃高温胁迫下，第 1 天 F_v/F_m 提高 7.69%，第 7 天提高达 9.84%（32D1+对比 32D1）。

2.1.4 虫黄藻 ROS 水平

25 ℃时，与 GXU01 共培养的 *C.goreaui*（25C1+）ROS 水平相较于单独培养的对照组（25C1）显著提升 36.09%（$P<0.05$）；32 ℃高温胁迫时，共培养组依旧保持 9.83%的增幅[图 4(a)]，表明共生体会加剧 *C.goreaui* 的氧化应激。与之相反，*D.trenchii* 在共培养体系中的 ROS 水平呈现反向变化趋势，25 ℃共培养组（25D1+）较对照组（25D1）ROS 水平显著降低 23.12%，32 ℃共培养组则下降 12.55%[图 4(b)]，这提示共生关系对 *D.trenchii* 具备抗氧化保护效应。高温胁迫显著增强了两种共生藻的 ROS 积累，无论是单独培养还是共培养，32 ℃高温胁迫下的 ROS 水平均显著高于 25 ℃（$P<0.05$）。



Different letters indicate significant differences among groups ($P<0.05$).

图 4 不同温度下虫黄藻 ROS 含量变化

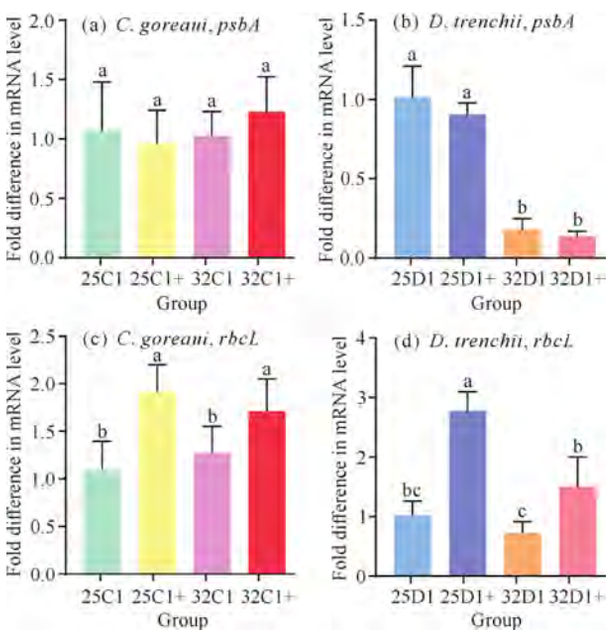
Fig.4 Changes in ROS content of Symbiodiniaceae at different temperatures

2.2 高温胁迫下 GXU01 对虫黄藻光照相关基因表达影响

与 GXU01 共培养对 *C.goreaui* 和 *D.trenchii* 的 *psbA* 基因相对表达量无显著影响。*C.goreaui* 的 *psbA* 基因受高温胁迫的影响不大，且共培养组（32C1+）表达量要高于对照组（32C1），这与常温的情况相反；而 *D.trenchii* 的 *psbA* 基因受高温胁迫影响后相对表达量显著降低（$P<0.05$），与常温组相比，下降了 82.45%－85.01%[图 5:(a)、(b)]。

C.goreaui 和 *D.trenchii* 的 *rbcL* 基因均表现出共培养组相对表达量显著高于对照组。25 ℃条件下，GXU01 添加使 *C.goreaui* 的 *rbcL* 基因表达量提

高 43.04%(25C1+相比 25C1),使 *D. trenchii* 提高 63.18%(25D1+相比 25D1)。32 ℃高温胁迫时提升的幅度减小,*C. goreaui* 共培养组 *rbcL* 表达量提高 25.37%(32C1 + 相比 32C1),*D. trenchii* 提高 51.62%(32D1+相比 32D1)[图 5:(c)、(d)]。以上结果表明,添加 GXU01 有助于提高虫黄藻的光合作用效率。



Different letters indicate significant differences among groups ($P<0.05$).

图 5 不同温度下虫黄藻 *psbA* 和 *rbcL* 基因相对表达量变化

Fig. 5 Changes in relative expression levels of *psbA* and *rbcL* in Symbiodiniaceae at different temperatures

3 讨论

3.1 虫黄藻生理生化响应规律

尽管有研究指出,含有蓝藻群体的珊瑚中虫黄藻的 DNA 含量较高,可能处于细胞分裂准备阶段[13],但这并不意味着蓝藻的固氮作用能显著提升虫黄藻密度。本实验中,两种虫黄藻(*C. goreaui* 与 *D. trenchii*)与蓝藻 GXU01 共培养时,仅在第 4 天虫黄藻密度略有增加,但差异均不显著($P>0.05$)。在 7 d 的实验周期中,高温胁迫抑制了虫黄藻的生长,但其密度仍缓慢上升;而在 25 ℃条件下,虫黄藻密度增长迅速,并在第 4 天后显著高于高温胁迫组。表明尽管高温会抑制 *C. goreaui* 和 *D. trenchii* 的生长,但两者对高温都有良好的适应能力。然而,前人研究将 D1 型虫黄藻归为耐热型虫黄藻,能适应极端高温环境,而 C1 型虫黄藻则属于热敏感型[32]。例如,以 *Durusdinium* 属为主比以 *Cladocopium* 属为主的鹿角杯形珊瑚表现出更强的热耐受性[33]。本研究推测,在离体培养条件下,培养基提供了充足营养,高温胁迫尚处于前期至中期阶段,虫黄藻抵御高温胁迫的能力较强。然而,若高温胁迫持续,两类虫黄藻的温度响应差异可能更为显著,值得进一步研究。

高温胁迫会直接破坏虫黄藻的 PSⅡ反应中心,而 F_v/F_m 是量化高温胁迫下虫黄藻 PSⅡ功能丧失的首选指标[34]。本研究中 *C. goreaui* 和 *D. trenchii* 的 F_v/F_m 在共培养条件下均高于单培养,高温则显著降低了这两种虫黄藻的 F_v/F_m。这与本课题组之前的研究结果[17]一致,进一步支持 GXU01 对虫黄藻代谢具有协调作用的结论,即蓝藻可在一定程度上缓解高温胁迫引起的 F_v/F_m 下降。值得注意的是,本实验共培养组仅添加 0.5%的蓝藻,在总藻密度中占比极低,因此蓝藻自身对光合色素、ROS 及光合参数测定的影响可忽略不计。尽管蓝藻添加量极少,但虫黄藻的 F_v/F_m 仍显著提升,提示 GXU01 可能通过固氮作用为虫黄藻提供氮源,进而提高其光合效率。已有研究也表明,添加无机氮可增强鳞砗磲(*Tridacna squamosa*)-虫黄藻共生体的光合作用[35],而氮限制条件下虫黄藻的 F_v/F_m 则较低[20],进一步说明氮供应对虫黄藻光合效率具有关键作用。

在高温胁迫和共培养条件下,*C. goreaui* 和 *D. trenchii* 表现出不同的光合色素响应模式。实验结果显示,*D. trenchii* 的叶绿素 *a*、叶绿素 *b* 和类胡萝卜素在共培养条件下,无论是常温还是高温,均有不同程度下降,且在第 1 天差异显著。而 *C. goreaui* 的色素变化较为复杂:常温下,其叶绿素 *a* 含量在第 1 天和第 7 天时共培养组低于对照组,高温下则相反,第 4 天表现相反;类胡萝卜素含量变化趋势与叶绿素 *a* 大致相同;叶绿素 *b* 含量在前 4 天共培养组显著高于对照组。值得注意的是,两种虫黄藻在高温胁迫下均表现出单细胞光合色素含量的上升,与已有研究结果[36-37]一致。类似地,杨晓红[20]也观察到虫黄藻 *Fugacium kawagutii* 叶绿素 *a* 含量在高温下上升的趋势,尽管差异不显著。

ROS 是一类化学性质活泼、氧化能力强的含氧物质,包括含氧自由基(如超氧自由基 $\cdot O_2^-$)和含氧非自由基(如单态氧 $^1O_2$ 和过氧化物 H_2O_2)[38]。虫黄藻在应激状态下会产生 ROS,导致 PSⅡ的光损伤[39]。研究表明,不同类型虫黄藻对高温胁迫的 ROS 响应差异显著:C1 型虫黄藻对高温高度敏感,

产生最多 ROS,而 D1 型虫黄藻是所研究的 7 种虫黄藻中唯一不受高温影响的类型[40]。本研究中,*C. goreaui* 和 *D. trenchii* 两种虫黄藻单细胞中的 ROS 含量均因高温胁迫而上升,与相关报道[41]一致。尽管一般认为热敏感型虫黄藻更易积累 ROS,本实验中 *D. trenchii* 的 ROS 水平相对更高。推测该差异可能与藻株生长状态有关:*C. goreaui* 在培养中表现出更好的细胞活性与稳定性,而 *D. trenchii* 的细胞状态较差,可能处于亚健康或代谢压力下,从而导致其 ROS 水平偏高。这提示 ROS 积累不仅与虫黄藻的固有耐热性有关,也可能受细胞培养状态及活力的影响。未来将结合细胞活性与抗氧化指标,进一步探讨这一机制。

GXU01 与这两种虫黄藻共培养也引发了不同的响应:与 *C. goreaui* 共培养导致 ROS 积累,推测该藻可能通过增加色素合成以竞争资源,从而引起氧化应激;而与 *D. trenchii* 共培养则减轻了其氧化损伤,推测 *D. trenchii* 通过降低色素合成以降低光捕获效率,避免 PSⅡ过度激发,从而减少 ROS 生成[37]。此外,蓝藻可能通过分泌类胡萝卜素协助 *D. trenchii* 淬灭多余光能,降低 ROS 水平,或通过其抗氧化系统(如超氧化物歧化酶和谷胱甘肽)协同增强 D1 型虫黄藻的 ROS 清除能力[38]。这表明 GXU01 对 *C. goreaui* 和 *D. trenchii* 两种虫黄藻具有不同的共生协调作用。已有研究指出,不同虫黄藻物种在资源竞争或受限时会表现出物种特异性的代谢调节策略[42],这为我们关于 *C. goreaui* 可能通过增强色素合成以竞争资源导致氧化应激,以及 *D. trenchii* 采取降低光捕获策略以避免过度激发的解释,提供了生态学层面的支持。

3.2 高温胁迫下 GXU01 对虫黄藻光照基因表达的影响

psbA 基因编码 PSⅡ反应中心的 D1 蛋白,是光合作用过程中的关键组分[43]。*rbcL* 基因编码 Rubisco 酶的大亚基,是卡尔文循环中催化 CO_2 固定的关键酶,其活性直接影响暗反应的碳同化效率,从而调控光反应与暗反应之间的能量平衡[44]。本研究结果显示,高温胁迫下,*C. goreaui* 中 *psbA* 基因的表达量虽有波动,但差异不显著;而 *D. trenchii* 的 *psbA* 基因表达量则显著下降($P<0.05$)。共培养处理并未对两种虫黄藻的 *psbA* 基因表达产生显著影响。高温胁迫导致 *D. trenchii* 的 *psbA* 基因表达下调,与沈城等[26]对稀杯盔形珊瑚(*Galaxea astreata*)共生虫黄藻的研究结果一致。然而,*C. goreaui* 并未表现出显著下降趋势,与通常的认识"敏感型虫黄藻对高温更为脆弱"存在一定差异。这种差异可能与实验初始状态有关。前期分析表明,在高温胁迫下,两种虫黄藻所承受的氧化应激水平不同:*D. trenchii* 的 ROS 积累量高于 *C. goreaui*。因此,基因表达模式的差异不仅取决于其耐热性,也可能受到氧化损伤程度的影响。此外,沈城等[26]的研究也发现,胁迫处理 5 d 时,28 ℃和 32 ℃条件下的 *psbA* 基因表达量相近,而 28 ℃仍处于虫黄藻的适宜温度范围[21]。

对 *rbcL* 基因表达的分析发现,高温胁迫未显著影响 *C. goreaui* 的基因表达量,而 *D. trenchii* 的基因表达量则出现不同程度的下降,其中高温胁迫共培养组的表达量显著低于对照组,其原因可能与上述分析一致。本研究还发现,共培养能够显著提高两种虫黄藻 *rbcL* 基因的相对表达量($P<0.05$),提示蓝藻可能通过提供额外碳源,缓解虫黄藻的碳限制,进而触发 Rubisco 合成的反馈调控机制。蓝藻进化出的无机 CO_2 浓缩机制(CCM)能够主动转运并积累高浓度 HCO_3^-,随后在羧酶体中经碳酸酐酶转化为 CO_2,供 Rubisco 固定[45-46]。当蓝藻细胞内 CO_2 浓度过高时,部分 CO_2 可能扩散至细胞外,形成局部高 CO_2 微环境,有利于虫黄藻吸收利用。此外,蓝藻在光合作用过程中可分泌蔗糖、葡萄糖等小分子糖类[47],虫黄藻可直接吸收这些有机物作为碳源和能量来源,从而调控激活 *rbcL* 的转录。另有研究显示,在亚高温和强光胁迫下,番茄幼苗的 *rbcL* 基因表达量下降 60%,同时 F_v/F_m 降低 40%[48],这一结果证实了 *rbcL* 基因对 PSⅡ的直接影响,从基因表达层面解释了本研究中共培养条件下虫黄藻 F_v/F_m 显著提升的现象。

4 结论

本研究从离体互作的角度,探讨了蓝藻 GXU01 与两种环境敏感性不同的虫黄藻(*C. goreaui* 和 *D. trenchii*)共培养过程中的代谢协调作用。结果表明,GXU01 对不同类型虫黄藻的生理响应具有差异性影响。在不显著影响虫黄藻生长的前提下,GXU01 能够调节其光合色素含量与 ROS 水平,并显著提高两种虫黄藻的 F_v/F_m;在分子水平上,GXU01 显著上调了虫黄藻 *rbcL* 基因的表达,表明其碳同化能力增强;而 *psbA* 基因的表达则未受到显著影响。以上结果表明,珊瑚共生蓝藻能够在不同虫黄藻类型中行使

差异化的调控机制,协同调节其光合作用与固碳能力。本研究为深入理解珊瑚共生功能体的热适应机制与热白化响应提供了新的研究视角。

参考文献

[1] BOURNE D G,MORROW K M,WEBSTER N S. Insights into the coral microbiome: underpinning the health and resilience of reef ecosystems [J]. Annual Review of Microbiology,2016,70:317-340.

[2] FALKOWSKI P G,DUBINSKY Z,MUSCATINE L,et al. Light and the bioenergetics of a symbiotic coral [J]. BioScience,1984,34(11):705-709.

[3] WIEDENMANN J,D′ANGELO C,MARDONES M L,et al. Reef-building corals farm and feed on their photosynthetic symbionts [J]. Nature,2023,620(7976):1018-1024.

[4] HILL M,HILL A. The magnesium inhibition and arrested phagosome hypotheses:new perspectives on the evolution and ecology of *Symbiodinium* symbioses [J]. Biological Reviews,2012,87(4):804-821.

[5] LIN S J,YU K F,ZHOU Z. Editorial:physiological regulation and homeostasis among coral holobiont partners [J]. Frontiers in Physiology,2022,13:921401.

[6] BAI C Z,WANG Q F,XU J Y,et al. Impact of nutrient enrichment on community structure and co-occurrence networks of coral symbiotic microbiota in *Duncanopsammia peltata*: zooxanthellae, bacteria, and archaea [J]. Microorganisms,2024,12(8):1540.

[7] WAINWRIGHT B J,ZAHN G L,AFIQ-ROSLI L,et al. Host age is not a consistent predictor of microbial diversity in the coral *Porites lutea* [J]. Scientific Reports,2020,10:14376.

[8] BEDNARZ V N,VAN DE WATER J A J M,RABOUILLE S,et al. Diazotrophic community and associated dinitrogen fixation within the temperate coral *Oculina patagonica* [J]. Environmental Microbiology, 2019, 21(1):480-495.

[9] KAYANNE H,HIROTA M,YAMAMURO M,et al. Nitrogen fixation of filamentous cyanobacteria in a coral reef measured using three different methods [J]. Coral Reefs,2005,24(2):197-200.

[10] CARDINI U,BEDNARZ V N,NAUMANN M S,et al. Functional significance of dinitrogen fixation in sustaining coral productivity under oligotrophic conditions [J]. Proceedings Biological Sciences,2015,282(1818):20152257.

[11] BENAVIDES M,BEDNARZ V N,FERRIER-PAGÈS C. Diazotrophs:overlooked key players within the coral symbiosis and tropical reef ecosystems [J]. Frontiers in Marine Science,2017,4:10.

[12] CEH J,KILBURN M R,CLIFF J B,et al. Nutrient cycling in early coral life stages:*Pocillopora damicornis* larvae provide their algal symbiont (*Symbiodinium*) with nitrogen acquired from bacterial associates [J]. Ecology and Evolution,2013,3(8):2393-2400.

[13] LESSER M P,FALCÓN L I,RODRÍGUEZ-ROMÁN A,et al. Nitrogen fixation by symbiotic cyanobacteria provides a source of nitrogen for the scleractinian coral *Montastraea cavernosa* [J]. Marine Ecology Progress Series,2007,346:143-152.

[14] KOPP C,PERNICE M,DOMART-COULON I,et al. Highly dynamic cellular-level response of symbiotic coral to a sudden increase in environmental nitrogen [J]. mBio,2013,4(3):e00052-13.

[15] BEDNARZ V N,NAUMANN M S,CARDINI U,et al. Contrasting seasonal responses in dinitrogen fixation between shallow and deep-water colonies of the model coral *Stylophora pistillata* in the northern Red Sea [J]. PLoS One,2018,13(6):e0199022.

[16] ROSIC N,KANIEWSKA P,CHAN C K,et al. Early transcriptional changes in the reef-building coral *Acropora aspera* in response to thermal and nutrient stress [J]. BMC Genomics,2014,15:1052.

[17] XU Y Q,LIANG J Y,QIN L Y,et al. The dynamics of Symbiodiniaceae and photosynthetic bacteria under high-temperature conditions [J]. Microbial Ecology, 2025,87(1):169.

[18] LIANG J Y,DENG C Q,YU K F,et al. Cross-linked regulation of coral-associated dinoflagellates and bacteria in *Pocillopora* sp. during high-temperature stress and recovery [J]. Microorganisms,2021,9(9):1972.

[19] JEONG H J,YOO Y D,KANG N S,et al. Heterotrophic feeding as a newly identified survival strategy of the dinoflagellate *Symbiodinium* [J]. Proceedings of the National Academy of Sciences, 2012, 109(31):12604-12609.

[20] 杨晓红. 高温及营养缺乏诱导虫黄藻氧化胁迫的初步研究[D]. 厦门:厦门大学,2020.

[21] 赵振鲁,刘甲星,张跃环,等. 离体培养的虫黄藻(*Symbiodinium voratum*)对温度和光照的生理响应[J]. 海洋与湖沼,2019,50(2):316-323.

[22] GE R Q,LIANG J Y,YU K F,et al. Regulation of the coral-associated bacteria and Symbiodiniaceae in *Acropora valida* under ocean acidification [J]. Frontiers in Microbiology,2021(12):767174.

[23] KARIM W,NAKAEMA S,HIDAKA M. Temperature effects on the growth rates and photosynthetic activities of *Symbiodinium* cells [J]. Journal of Marine Science and Engineering,2015,3(2):368-381.

[24] XIAO L H, JOHANSSON S, RUGHÖFT S, et al. Photophysiological response of Symbiodiniaceae single cells to temperature stress [J]. The ISME Journal, 2022, 16(8): 2060-2064.

[25] LI J, LONG L Y, ZOU Y Y, et al. Microbial community and transcriptional responses to increased temperatures in coral *Pocillopora damicornis* holobiont [J]. Environmental Microbiology, 2021, 23(2): 826-843.

[26] 沈城,刘楚吾,刘丽.温度胁迫及恢复初期稀杯盔形珊瑚共生虫黄藻 *Hsp*70、*Hsp*90、*psaA*、*psbA* 基因表达分析[J].热带海洋学报,2016,35(3):72-78.

[27] CHOTEWUTMONTRI P, BARKAN A. Light-induced *psbA* translation in plants is triggered by photosystem Ⅱ damage *via* an assembly-linked autoregulatory circuit [J]. Proceedings of the National Academy of Sciences of the United States of America, 2020, 117(35): 21775-21784.

[28] HU J L, LI T P, XU W, et al. Small antisense RNA RblR positively regulates RuBisCo in *Synechocystis* sp. PCC 6803 [J]. Frontiers in Microbiology, 2017, 8: 231.

[29] 覃良云,许勇前,陈金妮,等.造礁石珊瑚共生虫黄藻离体培养方法的优化[J].微生物学报,2023,63(4):1658-1671.

[30] 史何静.氧苯酮对虫黄藻和珊瑚-虫黄藻共生体系的毒理效应研究[D].海口:海南大学,2022.

[31] 刘春胜.三亚近海砗磲资源分布及番红砗磲光照适应机制[D].海口:海南大学,2021.

[32] LAJEUNESSE T C, SMITH R, WALTHER M, et al. Host-symbiont recombination versus natural selection in the response of coral-dinoflagellate symbioses to environmental disturbance [J]. Proceedings Biological Sciences, 2010, 277(1696): 2925-2934.

[33] WANG C W, ZHENG X Q, KVITT H, et al. Lineage-specific symbionts mediate differential coral responses to thermal stress [J]. Microbiome, 2023, 11(1): 211.

[34] GOMEZ-CAMPO K, BAUMS I B. Fitted *Fv*/*Fm* temperature response curves: applying lessons from plant ecophysiology to acute thermal stress experiments in coral holobionts [J]. Coral Reefs, 2025, 44(1): 77-84.

[35] FAM R R S, HIONG K C, CHOO C Y L, et al. Molecular characterization of a novel algal glutamine synthetase (GS) and an algal glutamate synthase (GOGAT) from the colorful outer mantle of the giant clam, *Tridacna squamosa*, and the putative GS-GOGAT cycle in its symbiotic zooxanthellae [J]. Gene, 2018, 656: 40-52.

[36] SHARP V A, BROWN B E, MILLER D. Heat shock protein (hsp 70) expression in the tropical reef coral *Goniopora djiboutiensis* [J]. Journal of Thermal Biology, 1997, 22(1): 11-19.

[37] FLORES-RAMÍREZ L A, LIÑÁN-CABELLO M A. Relationships among thermal stress, bleaching and oxidative damage in the hermatypic coral, *Pocillopora capitata* [J]. Comparative Biochemistry and Physiology Toxicology & Pharmacology, 2007, 146(1/2): 194-202.

[38] 李淑,余克服.珊瑚礁白化研究进展[J].生态学报,2007(5):2059-2069.

[39] REHMAN A U, SZABÓ M, DEÁK Z, et al. *Symbiodinium* sp. cells produce light-induced intra- and extracellular singlet oxygen, which mediates photodamage of the photosynthetic apparatus and has the potential to interact with the animal host in coral symbiosis [J]. The New Phytologist, 2016, 212(2): 472-484.

[40] MCGINTY E S, PIECZONKA J, MYDLARZ L D. Variations in reactive oxygen release and antioxidant activity in multiple *Symbiodinium* types in response to elevated temperature [J]. Microbial Ecology, 2012, 64(4): 1000-1007.

[41] 陈家琪.丛生盔形珊瑚两株内共生虫黄藻的体外驯化及应用[D].海口:海南大学,2021.

[42] MCILROY S E, WONG J C Y, BAKER D M. Competitive traits of coral symbionts may alter the structure and function of the microbiome [J]. The ISME Journal, 2020, 14(10): 2424-2432.

[43] 钟珍萍,吴乃虎.植物光合基因 *psbA* 的结构及表达调控综述[J].福建农业大学学报,1997(3):257-261.

[44] 任玲萱,方琰,孙双,等.基于 18S rDNA、*rbc*L 和 *atp*B 序列的轮藻科植物的系统发育研究[J].四川大学学报(自然科学版),2020,57(3):605-611.

[45] PRICE G D, BADGER M R, WOODGER F J, et al. Advances in understanding the cyanobacterial CO_2-concentrating-mechanism (CCM): functional components, Ci transporters, diversity, genetic regulation and prospects for engineering into plants [J]. Journal of Experimental Botany, 2008, 59(7): 1441-1461.

[46] BADGER M R, PRICE G D. CO_2 concentrating mechanisms in cyanobacteria: molecular components, their diversity and evolution [J]. Journal of Experimental Botany, 2003, 54(383): 609-622.

[47] SANTOS-MERINO M, YUN L, DUCAT D C. Cyanobacteria as cell factories for the photosynthetic production of sucrose [J]. Frontiers in Microbiology, 2023, 14: 1126032.

[48] 路涛.亚高温强光胁迫下番茄幼苗光抑制及光保护机制研究[D].沈阳:沈阳农业大学,2016.

Metabolic Interactions between the Coral-associated Cyanobacterium *Synechococcus* sp. GXU01 and Two Representative Symbiodiniaceae Species

LI Zhicong[1], HU Siyu[1], LIANG Zhuqing[1], YANG Yating[1], LU Mingyao[1], YU Kefu[1,2], LIANG Jiayuan[1,2**], ZHANG Li[3], FENG Yihe[3]

(1. School of Marine Sciences, Guangxi University, Nanning, Guangxi, 530004, China; 2. Guangxi Laboratory on the Study of Coral Reefs in the South China Sea, Guangxi University, Nanning, Guangxi, 530004, China; 3. School of Resources, Environment and Materials, Guangxi University, Nanning, Guangxi, 530004, China)

Abstract: Symbiodiniaceae and Cyanobacteria are the two major photosynthetic symbionts in the coral holobiont, playing critical roles in the complex metabolic interactions. This study aims to investigate the metabolic interactions between a cyanobacterial strain (*Synechococcus* sp. GXU01, hereinafter referred to as GXU01) isolated from *Pavona decussata* and two representative Symbiodiniaceae species: the thermally sensitive *Cladocopium goreaui* and the thermally tolerant *Durusdinium trenchii*. Co-culture experiments were conducted to explore the regulatory effects of GXU01 on the physiological metabolism and the expression of key genes related to photosystem Ⅱ and carbon fixation (*psbA* and *rbcL*) in response to heat stress. The results showed that GXU01 had no significant effect on the growth rate of *C. goreaui* or *D. trenchii*. However, during the initial stage of co-culture, the photosynthetic pigment content of *D. trenchii* decreased significantly (by 24.5%－29.6%), whereas that of *C. goreaui* was not significantly affected. Under both ambient and elevated temperature conditions, GXU01 enhanced the maximum photochemical efficiency (F_v/F_m) of both Symbiodiniaceae species ($P<0.05$). In terms of Reactive Oxygen Species (ROS) regulation, GXU01 markedly increased the ROS level in *C. goreaui* (by 9.83%－36.09%) but significantly reduced the ROS level in *D. trenchii* (by 12.55%－23.12%). Regarding photosystem Ⅱ repair, GXU01 showed no significant effect on the *psbA* expression in *C. goreaui* at different temperatures, but significantly downregulated the *psbA* expression in *D. trenchii* by 82.45%－85.01% under heat stress. In terms of carbon fixation, GXU01 significantly upregulated *rbcL* expression in both *C. goreaui* (by 25.37%－43.04%) and *D. trenchii* (by 51.62%－63.18%). This study provides new insights into the thermal adaptation and heat stress responses of Symbiodiniaceae in coral symbiotic systems from a perspective of in vitro interaction between GXU01 and Symbiodiniaceae.

Key words: coral reef ecosystem; symbiotic holobiont; Cyanobacteria; Symbiodiniaceae; functional interaction

责任编辑:陆媛峰

微信公众号投稿更便捷
联系电话:0771-2503923
邮箱:gxkx@gxas.cn
投稿系统网址:http://gxkx.ijournal.cn/gxkx/ch

◆珊瑚礁生态保护与修复◆

涠洲岛海域 7 种造礁石珊瑚的生长差异研究*

汪婷婷[1,2],周兴旺[2],谭何勇[2],肖遵勇[2],黄　雯[2],胡庭俊[1**]
(1. 广西大学动物科学技术学院,广西南宁　530004;2. 广西大学海洋学院,广西南海珊瑚礁研究重点实验室,广西大学珊瑚礁研究中心,广西南宁　530004)

摘要:在全球珊瑚礁持续退化的背景下,移植珊瑚物种的筛选是珊瑚礁生态修复过程中的关键环节。本研究选取涠洲岛自然海域的 7 种造礁石珊瑚,包括美丽鹿角珊瑚(*Acropora muricata*)、风信子鹿角珊瑚(*A. hyacinthus*)、霜鹿角珊瑚(*A. pruinosa*)等 3 种枝状珊瑚,十字牡丹珊瑚(*Pavona decussata*)、薄片刺孔珊瑚(*Echinopora lamellosa*)等 2 种片状珊瑚,以及澄黄滨珊瑚(*Porites lutea*)、五边角蜂巢珊瑚(*Favites pentagona*)等 2 种块状珊瑚,通过测定其相对体积增长倍数和相对质量增长倍数,比较不同珊瑚种类的生长差异。结果显示,7 种造礁石珊瑚的相对质量增长倍数依次为美丽鹿角珊瑚>风信子鹿角珊瑚>霜鹿角珊瑚>十字牡丹珊瑚>薄片刺孔珊瑚>澄黄滨珊瑚>五边角蜂巢珊瑚;但存活率呈相反趋势,五边角蜂巢珊瑚和十字牡丹珊瑚的存活率(95.00%)最高,风信子鹿角珊瑚的存活率(70.00%)最低。除澄黄滨珊瑚与 C15 亚群专性共生外,其余 6 种珊瑚均以 C1 为主导亚系群(占比超 75%)。枝状珊瑚的共生虫黄藻密度高于其他形态珊瑚,这可能是其生长优势大的原因之一。本研究结果可为相对高纬度海域珊瑚礁修复的物种选择提供科学依据。

关键词:珊瑚礁修复;珊瑚断枝;生长差异;虫黄藻;涠洲岛

中图分类号:P745　　**文献标识码**:A　　**文章编号**:1005-9164(2025)04-0812-08
DOI:10.13656/j.cnki.gxkx.20251114.016

珊瑚礁生态系统被誉为“海洋中的热带雨林”,具有极高的生产力和生物多样性。南海珊瑚礁不仅提供了渔业、旅游和海岸保护等关键的生态系统服务,还因其特殊的地理位置关乎着国家的海洋权益与战略地位[1]。然而,这一宝贵的生态系统正面临严峻的退化危机,过去 30 年,我国大陆和海南岛沿岸的珊瑚礁至少 80%已退化;过去 10－15 年,南海离岸较远的环礁和群岛的珊瑚礁覆盖度也从大于 60%退化至 20%左右[2-3]。

面对全球珊瑚礁急剧退化的严峻形势,各国珊瑚礁生态学家均在全力推进修复工作,并相继取得了一定效果[4]。国外主要的珊瑚礁修复技术包括针对破

收稿日期:2025-07-09　　修回日期:2025-07-31
*广西自然科学基金项目(2023GXNSFAA026510),广西科技基地与人才专项(桂科 AD25069075)资助。
【第一作者简介】
汪婷婷(1988－),女,硕士,主要从事动物生理学研究,E-mail:wttgood@qq.com。
【**通信作者简介】
胡庭俊(1965－),男,教授,主要从事动物用新药研发,E-mail:tingjunhu@126.com。
【引用本文】
汪婷婷,周兴旺,谭何勇,等. 涠洲岛海域 7 种造礁石珊瑚的生长差异研究[J]. 广西科学,2025,32(4):812-819.
WANG T T,ZHOU X W,TAN H Y,et al. Growth Differences of Seven Species of Scleractinian Corals in Weizhou Island [J]. Guangxi Sciences,2025,32(4):812-819.

中国知网　https://www.cnki.net

碎化生境的工程化修复技术、珊瑚礁基修复技术、简易修复技术、基于珊瑚苗圃的修复技术、有性繁殖技术等。我国珊瑚礁修复工作起步较晚,但近年发展迅速。李元超等[5]通过对佳丽鹿角珊瑚(*Acropora pulchra*)卵母细胞发育进行研究,推断出珊瑚的排卵时间,为幼虫捕获与修复提供了理论基础。段晓伟等[6]在深圳大澳湾构建断枝培育系统,发现霜鹿角珊瑚(*A. pruinosa*)生长速度最快,膨胀蔷薇珊瑚(*Montipora turgescens*)存活率最高。鲍鹰等[7]在人工养殖基地开展鹿角珊瑚(*Acropora* spp.)断枝培育,结果证实自然海域条件下的生长速率显著高于人工系统。王欣等[8]在涠洲岛架设铁架苗圃移植7种造礁石珊瑚,发现风信子鹿角珊瑚(*A. hyacinthus*)与粗野鹿角珊瑚(*A. humilis*)生长状况最佳,为涠洲岛修复选种提供了参考。但现有研究多聚焦于单一形态或少数物种,缺乏对不同形态珊瑚生长特性的系统对比,且共生藻对其生长的调控机制尚未明确。因此,珊瑚选种的科学性对修复成效具有决定性影响。合适的珊瑚种类不仅能显著提升移植成活率,还能通过快速生长加速礁区结构重建,进而增强生态系统韧性。不同珊瑚种类在生长速率、抗逆性及生态功能上存在显著差异[9]。枝状珊瑚通常比块状珊瑚生长更快,能迅速形成复杂的三维结构,为鱼类提供栖息地;而块状珊瑚虽然生长缓慢,但是抗风浪能力更强[10-11]。此外,珊瑚与共生藻的互作关系也影响选种:携带耐热共生藻系群的珊瑚在高温胁迫下表现出更强的适应性[12]。因此,基于区域环境特征与珊瑚生物学特性的精准选种,是珊瑚礁修复工程成功的前提。

涠洲岛是我国大陆沿岸最北缘的珊瑚礁分布区,在全球气候变暖的趋势下可能成为热带珊瑚的"避难所",兼具独特的生态价值与科研价值。近40年来,涠洲岛石珊瑚群落呈现明显的衰退趋势。活珊瑚覆盖率由1984年的50%下降至2015年的6%[12]。为保护和修复涠洲岛珊瑚礁,广西大学相关团队已经开展了一系列修复实践,包括投放梯形人工礁、1/4球形人工礁及铁架苗圃等,移植的珊瑚包括枝状的美丽鹿角珊瑚、风信子鹿角珊瑚等。本研究在涠洲岛自然海域设置的浮排上移植了7种造礁石珊瑚,从生态功能来看,选取的造礁石珊瑚涵盖涠洲岛珊瑚礁的关键类群:澄黄滨珊瑚(*Porites lutea*)与五边角蜂巢珊瑚(*Favites pentagona*)作为当前礁区的核心优势种,其稳定存续是维系礁体结构完整性的基础;美丽鹿角珊瑚与风信子鹿角珊瑚为历史优势种,通过浮排移植有望在修复区重建三维空间结构,恢复礁体的生态功能;十字牡丹珊瑚(*Pavona decussata*)与霜鹿角珊瑚代表了边缘珊瑚礁特有的适应性类群,其生理机制的研究可为全球变暖背景下珊瑚的适应性保护提供重要参考。本研究的珊瑚组合覆盖枝状、片状、块状等主要生长形态,以及礁坪、礁坡等关键生境的生态位,可为涠洲岛珊瑚礁修复提供定量生长与生理数据,旨在推动区域珊瑚礁修复的科学化与精准化。

1 材料与方法

1.1 材料

本研究选取的珊瑚断枝采集于涠洲岛自然海域,随后放置于该海域搭建的浮排上,浮排距水面高度约1 m。根据邹仁林[13]编著的《中国动物志 腔肠动物门 珊瑚虫纲 石珊瑚目 造礁石珊瑚》对实验珊瑚进行种、属鉴定。这些珊瑚断枝包括美丽鹿角珊瑚(Am)、风信子鹿角珊瑚(Ah)和霜鹿角珊瑚(Ap)等3种枝状珊瑚,十字牡丹珊瑚(Pd)和薄片刺孔珊瑚(El)等2种片状珊瑚,以及澄黄滨珊瑚(Pl)与五边角蜂巢珊瑚(Fp)等2种块状珊瑚。每种珊瑚断枝各选取20株,均使用等长的聚氯乙烯(PVC)塑料短管填充实心水泥制成珊瑚断枝苗托,并在PVC苗托上做好序号标记,放在自然海域浮排上进行7个月的生长实验。实验结束后,从每种珊瑚中随机选取5株具代表性的样本进行实验分析。

1.2 方法

1.2.1 珊瑚生长指标测定

珊瑚形态多样,仅测量其高度或面积难以精准表征其生长态势。为此,本研究通过拍照记录珊瑚断枝形态,采用排水法精确测定其相对体积增长倍数和相对质量增长倍数,客观反映珊瑚的生长情况。具体而言,通过测量珊瑚在烧杯中排开海水的质量来获取其体积,同时将珊瑚置于盛有海水的烧杯中直接称量,进而计算出珊瑚生长指标的相关数据,计算公式如下:

$$V_i = (m_{悬i} - m_{悬0})/\rho_{海水},$$

$$G_i = (V_i + V_0)/V_0,$$

$$M_i = m_{沉i}/m_{沉0},$$

式中,V_i 为初始到第 i 月内珊瑚体积增长量,$m_{悬i}$ 为珊瑚第 i 月的排水质量,$m_{悬0}$ 为珊瑚初始排水质量,$\rho_{海水}$ 为海水密度(1.002 g/cm^3),G_i 为初始到第 i 月珊瑚的相对体积增长倍数,V_0 为珊瑚初始体积,M_i

中国知网 https://www.cnki.net

为初始到第 i 月珊瑚的相对质量增长倍数,$m_{沉i}$ 为珊瑚第 i 月的质量,$m_{沉0}$ 为珊瑚初始质量。

1.2.2 7 种造礁石珊瑚共生虫黄藻分子系统分类

采用海洋动物基因组 DNA 提取试剂盒提取实验珊瑚共生虫黄藻 DNA。利用共生虫黄藻 ITS 特异性引物扩增 ITS 基因序列,正向引物为 ITS2-JIF(5′-GAATTGCAGAACTCCGTG-3′),反向引物为 ITS2-J2F(5′-GGGATCCATATGCTTAAGTTCAGCGGGT-3′)。扩增产物用 1%的琼脂糖凝胶电泳和凝胶成像仪(CLIN,上海勤翔科学仪器有限公司)进行检测,采用 Illumina MiSeq 测序仪(上海美吉生物医药科技有限公司)进行高通量测序。每种珊瑚送 5 个样品进行测序。由于薄片刺孔珊瑚和澄黄滨珊瑚分别有一个样品建库失败,因此这两种珊瑚只有 4 个重复样本。

1.2.3 7 种造礁石珊瑚内共生虫黄藻相关指标分析

(1)共生虫黄藻密度

采用洗牙器(WP-70EC,美国 Waterpik 公司)装入过滤海水(孔径为 0.45 μm 滤膜过滤)冲洗珊瑚样本,分离出珊瑚组织匀浆冲洗液和珊瑚骨骼,测量冲洗液总体积后,再取 2 mL 冲洗液在 4 ℃下以 5 000 r/min 离心 10 min,弃去上清液后用纯水定容至 4 mL,通过浮游植物流式细胞仪(CytoSense,荷兰 CytoBuoy 公司)检测单位体积的共生虫黄藻密度(C,单位为 cells/mL),同时采用铝箔技术法测量珊瑚的表面积[14],最终得出共生虫黄藻的密度(D,单位为 cells/cm^2),计算公式如下:

$$D=C\times 2\times V/(M/G),$$

式中,V 为冲洗液的总体积(mL),M 为贴合包裹珊瑚骨骼表面的铝箔纸质量(g),G 为铝箔纸单位面积质量(g/cm^2)。

(2)共生虫黄藻叶绿素 a 含量

共生虫黄藻叶绿素 a 含量的测定参考 Jeffrey 等[15]的吸光度测定法,并结合珊瑚表面积换算得到单位面积叶绿素 a 含量。具体步骤如下:从总冲洗液中取 15 mL,在 4 ℃条件下以 4 000 r/min 离心 5 min,去除上清液,向沉淀物中加入 10 mL 90%丙酮,于 4 ℃条件下萃取 24 h,萃取完成后,将溶液按相同参数再次离心,取上清液用酶标仪[Varioskan LUX,赛默飞世尔科技(中国)有限公司]分别测定 750、664、647、630 nm 波长处的吸光度(A),计算得出叶绿素 a 含量,具体公式如下:

$$\text{Chl } a=11.85\times(A_{664}-A_{750})-1.54\times(A_{647}-A_{750})-0.08\times(A_{630}-A_{750}),$$

式中,Chl a 为叶绿素 a 含量,单位为 μg/mL。结合总冲洗液体积(mL)和珊瑚骨骼样本表面积(cm^2),可计算得到单位面积叶绿素 a 含量(μg/cm^2)。

(3)最大光量子产量

叶绿素荧光是测量植物光合作用效率的方法之一[16-17],关闭系统光源后,经充分暗处理使珊瑚处于完全黑暗状态,再采用脉冲振幅调制荧光仪(DIVING-PAM-Ⅱ,德国 WALZ 公司)测定各珊瑚样本的最大光量子产量(F_v/F_m)。

1.2.4 数据分析

本研究数据描述性统计值采用平均值±标准差表示,使用 SPSS 27 统计软件对造礁石珊瑚各项数据进行单因素方差分析,使用 Games-Howell 进行事后检验,以 $P<0.05$ 为差异显著水平,使用 Origin 2024 软件进行绘图,并对共生虫黄藻 ITS2 序列的测序数据进行注释分析。

2 结果与分析

2.1 7 种造礁石珊瑚断枝的生长差异

7 种造礁石珊瑚断枝生长结果如图 1 所示。经浮排培育 7 个月后,不同种类珊瑚间表现出明显的生长差异。将第 0 个月与第 7 个月拍摄的照片进行对比,发现枝状的美丽鹿角珊瑚和霜鹿角珊瑚的生长表现为生长点数目增加及纵向生长,风信子鹿角珊瑚则以生长点数目增加和横向生长为主。片状的十字牡丹珊瑚同时兼顾纵向和横向生长,形成一个球状;薄片刺孔珊瑚仅呈横向生长。块状的澄黄滨珊瑚和五边角蜂巢珊瑚也同时兼顾纵向和横向生长,但生长速度缓慢。

7 种造礁石珊瑚断枝相对质量增长倍数的大小排序为美丽鹿角珊瑚>风信子鹿角珊瑚>霜鹿角珊瑚>十字牡丹珊瑚>薄片刺孔珊瑚>澄黄滨珊瑚>五边角蜂巢珊瑚(图 2)。其中,枝状的美丽鹿角珊瑚生长最快,其相对体积增长倍数与相对质量增长倍数分别为 11.7 倍和 11.4 倍;风信子鹿角珊瑚和霜鹿角珊瑚等枝状珊瑚的生长速度分别位列第 2 和第 3,其相对质量增长倍数分别为 5.9 倍和 5.1 倍;十字牡丹珊瑚和薄片刺孔珊瑚等片状珊瑚的生长速度分别位列第 4 和第 5;澄黄滨珊瑚和五边角蜂巢珊瑚等 2 种块状珊瑚的生长速度相对较慢,其相对质量增长倍数

中国知网 https://www.cnki.net

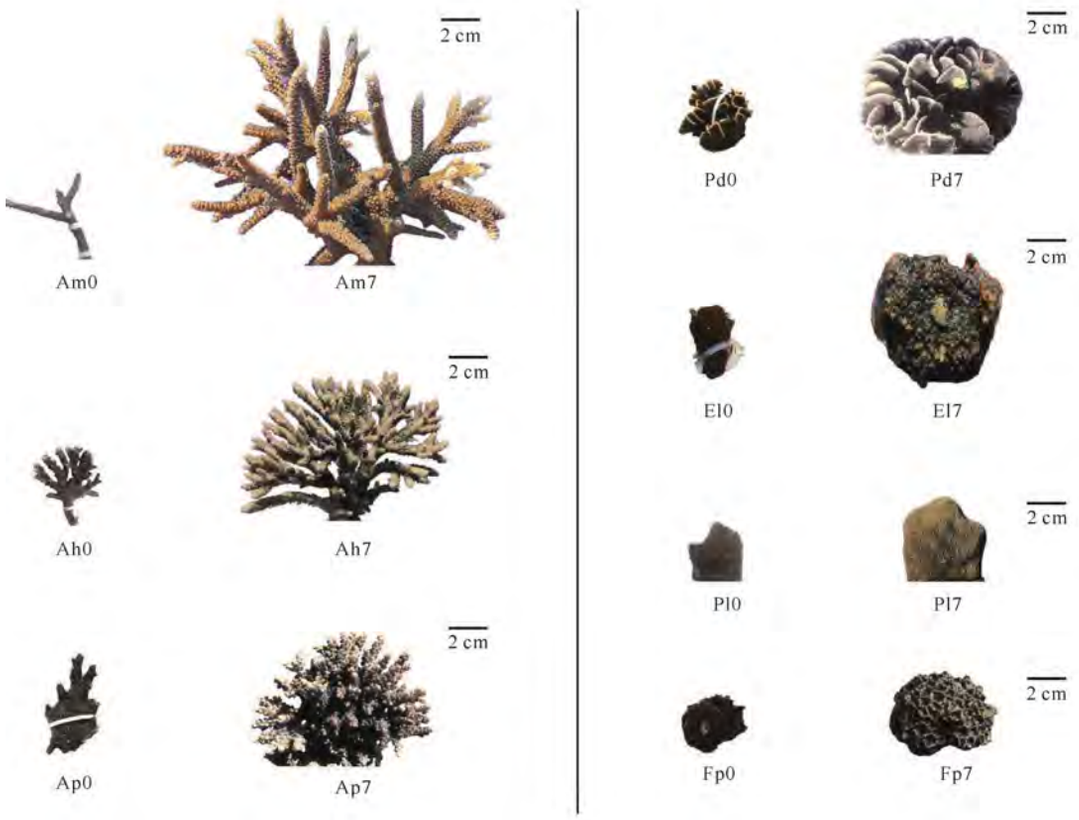
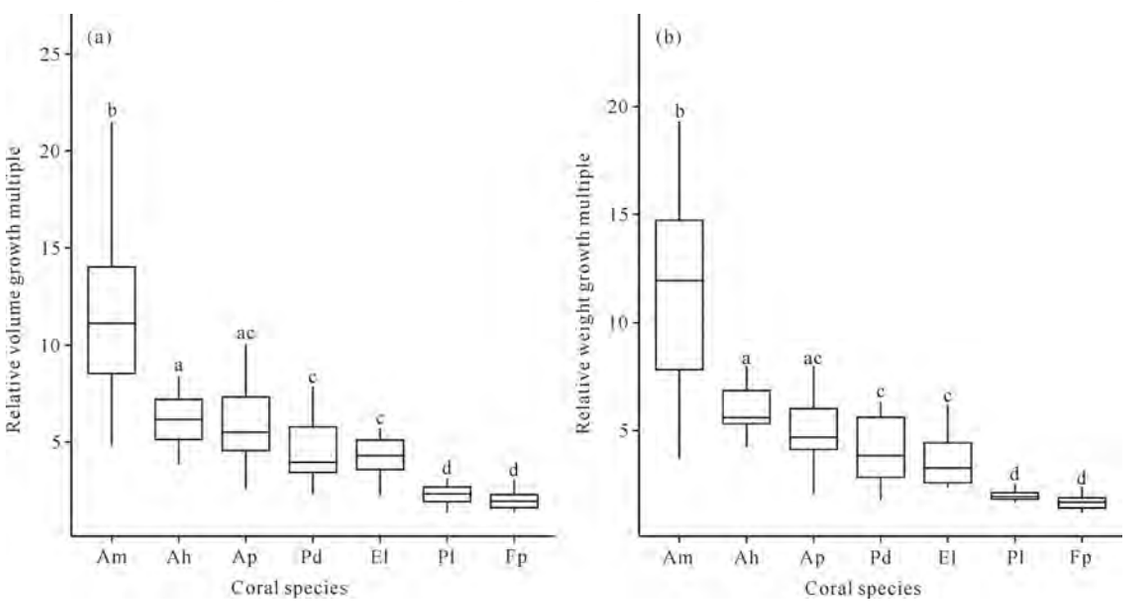


图1　7种造礁石珊瑚生长情况

Fig. 1　Growth comparison of 7 species of scleractinian corals



Different lowercase letters indicate significant differences ($P<0.05$).

图2　7种造礁石珊瑚的相对体积增长倍数和相对质量增长倍数

Fig. 2　Relative volume growth multiple and relative weight growth multiple of 7 species of scleractinian corals

仅分别为2.0倍和1.8倍。除风信子珊瑚与霜鹿角珊瑚、霜鹿角珊瑚与十字牡丹珊瑚、霜鹿角珊瑚与薄片刺孔珊瑚、五边角蜂巢珊瑚与澄黄滨珊瑚、十字牡丹珊瑚与薄片刺孔珊瑚间的相对质量增长倍数无显著差异外，其余各组间均存在显著差异($P<0.05$)。

7种造礁石珊瑚移植7个月后的存活率如表1

中国知网　https://www.cnki.net

所示。7 种造礁石珊瑚的平均存活率为 87.14%。五边角蜂巢珊瑚和十字牡丹珊瑚的存活率最高,为 95.00%;美丽鹿角珊瑚、霜鹿角珊瑚和澄黄滨珊瑚的存活率次之,为 90.00%;薄片刺孔珊瑚的存活率为 80.00%;风信子鹿角珊瑚的存活率最低,为 70.00%。

表 1　7 种造礁石珊瑚生长的存活率

Table 1　Survival rates of 7 species of scleractinian corals during their growth

珊瑚种类 Species of coral	移植个数 Number of transplants	存活个数 Number of survivors	移植存活率/% Transplant survival rate/%
Am	20	18	90.00
Ah	20	14	70.00
AP	20	18	90.00
Pd	20	19	95.00
El	20	16	80.00
Pl	20	18	90.00
Fp	20	19	95.00
Total	140	122	

2.2　7 种造礁石珊瑚共生虫黄藻系群及生理指标分析

除澄黄滨珊瑚外,其余 6 种珊瑚的共生虫黄藻主导系群均为 C1(占比 75%以上);澄黄滨珊瑚主要与 C15 虫黄藻共生,占比超过 90%(图 3)。C1ca 也广泛存在于 6 种珊瑚中,但占比较小,约为 3%。

7 种造礁石珊瑚的共生虫黄藻密度、单位面积叶绿素 *a* 含量和最大光量子产量 3 个指标的趋势各不相同(图 4)。3 种枝状珊瑚的共生虫黄藻密度($\geqslant 1.0\times10^6$ 个/cm^2)较高,澄黄滨珊瑚处于中间水平,十字牡丹珊瑚、薄片刺孔珊瑚和五边角蜂巢珊瑚的共生虫黄藻密度[$(0.3-0.4)\times10^6$ 个/cm^2]相对较低。五边角蜂巢珊瑚的单位面积叶绿素 *a* 含量显著高于美丽鹿角珊瑚和霜鹿角珊瑚($P<0.05$),其余均无显著差异($P>0.05$)。薄片刺孔珊瑚的最大光量子产量最高,霜鹿角珊瑚次之,十字牡丹珊瑚最低,余下 4 种珊瑚除美丽鹿角珊瑚与五边角蜂巢珊瑚具有显著差异外,其余均无显著差异($P>0.05$)。

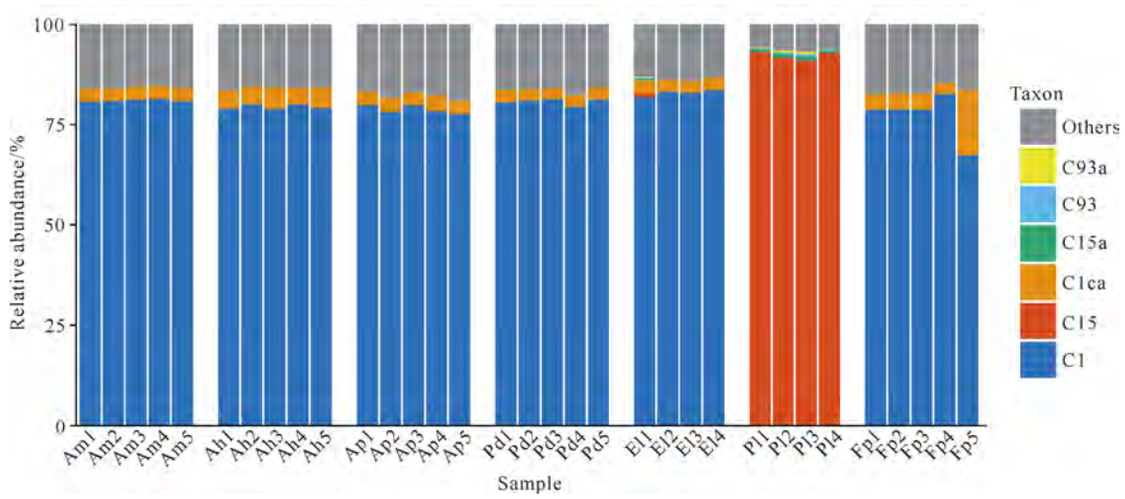
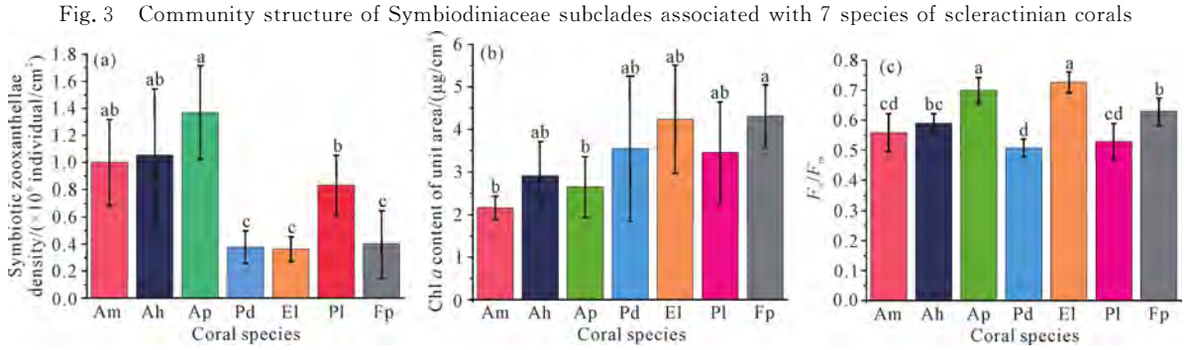


图 3　7 种造礁石珊瑚的共生虫黄藻系群群落结构

Fig. 3　Community structure of Symbiodiniaceae subclades associated with 7 species of scleractinian corals



Different lowercase letters indicate significant differences ($P<0.05$).

图 4　7 种造礁石珊瑚共生虫黄藻相关指标的变化

Fig. 4　Changes in indicators of Symbiodiniaceae associated with 7 species of scleractinian corals

中国知网　https://www.cnki.net

3 讨论

3.1 不同种珊瑚的生长差异

珊瑚礁的生态修复是遏制全球珊瑚礁退化的核心手段,而物种筛选直接决定着修复成效,不仅需要考虑物种的存活率、生长速率等基础生物学特性,还需要兼顾修复后群落的物种多样性与生态稳定性[18]。单一化的珊瑚种群抗干扰能力薄弱,在疾病暴发、极端气候等扰动下易引发生态系统崩溃[8],多形态、多物种的搭配移植已成为珊瑚礁修复的共识。因此,本研究聚焦涠洲岛海域7种优势造礁石珊瑚,系统评估其生长特性,旨在为高纬度珊瑚礁修复提供基础数据支撑,助力构建兼具功能性与稳定性的修复群落。不同形态珊瑚的生长量化需突破形态特异性限制。在珊瑚生长研究中,传统指标因形态适配性差异难以跨类群比较,如段晓伟等[6]和鲍鹰等[7]针对枝状珊瑚采用高度、分枝数及湿重等指标进行测定,王章义等[19]针对块状珊瑚以表面积为核心参数,这些研究均局限于单一形态。为解决这一问题,本研究创新性地采用排水法测定7种造礁石珊瑚的体积与质量,通过测定其相对体积增长倍数和相对质量增长倍数等标准化指标,消除了枝状、片状、块状珊瑚的形态差异对生长量化的干扰,建立了适用于不同形态珊瑚生长特性的统一且可靠的量化标准。

本研究结果显示,7种造礁石珊瑚的生长速率呈现显著差异,美丽鹿角珊瑚、风信子鹿角珊瑚和霜鹿角珊瑚等3种枝状珊瑚的相对体积增长倍数与相对质量增长倍数较大,十字牡丹珊瑚和薄片刺孔珊瑚等2种片状珊瑚处于中间水平,澄黄滨珊瑚和五边角蜂巢珊瑚等2种块状珊瑚较小。这一枝状>片状>块状的生长速率规律,与王永刚等[20]测定的3种造礁石珊瑚生长6个月的体积和质量结果类似,印证了珊瑚生长速率的形态依赖性。枝状珊瑚的生长速率大,可能由其内在机制的多维度作用共同驱动:(1)枝状珊瑚通常具有更高的钙化速率;(2)枝状珊瑚的疏松骨骼结构更有利于珊瑚虫与海水之间的物质交换;(3)本研究结果显示枝状珊瑚的共生虫黄藻密度更高(图4),虫黄藻通过光合作用将海水中的无机碳转换为有机化合物,为珊瑚生长提供了能量支撑,其光合产物的供给,可直接为珊瑚快速生长提供关键能量保障[21]。

从修复实践来看,高生长率的枝状珊瑚是构建珊瑚礁功能性结构的核心物种[22]。本研究结果显示,美丽鹿角珊瑚是生长速率最快的种类,经浮排培育7个月后其相对质量增长倍数为11.4倍,而风信子鹿角珊瑚与霜鹿角珊瑚等枝状珊瑚的相对质量增长倍数分别为5.9倍和5.1倍,表明即使同属枝状形态,生长速度仍存在明显分化。Zheng等[23]的研究表明,海南蜈支洲岛的两种枝状珊瑚[美丽鹿角珊瑚和花鹿角珊瑚(*A. florida*)]的生长速率可达11.0—12.1 cm/a,而同为枝状珊瑚的双叉鹿角珊瑚(*A. bifurcata*)的生长速率为5.6 cm/a。这种跨区域研究结果的一致性,进一步凸显了珊瑚不同种类之间的生长速度差异。本研究中,3种鹿角珊瑚的生长策略差异体现了枝状珊瑚的形态适应性:风信子鹿角珊瑚呈圆盘状,以平面横向生长为主;美丽鹿角珊瑚和霜鹿角珊瑚呈灌木状,以立体纵向生长为主[22,24]。这种差异化生长模式可快速提升珊瑚礁的三维结构复杂性,高生长率的鹿角珊瑚能在短期内形成多孔隙、多层次的栖息环境,有效提升礁栖生物(如鱼类)的丰富度与多样性[25-26]。从快速实现生态修复效果的角度考虑,建议在珊瑚礁修复过程中增加美丽鹿角珊瑚的苗种使用比例。同时,珊瑚的高存活率也是修复成功的关键因素[27]。Madin等[28]的研究表明,十字牡丹珊瑚在自然海域具有强的存活能力,本研究也发现块状的五边角蜂巢珊瑚表现出高存活率,二者共同为涠洲岛珊瑚礁修复中移植珊瑚种类的选择提供了科学依据。

3.2 珊瑚生长与共生虫黄藻的关系

虫黄藻作为珊瑚宿主的关键共生伙伴,通过光合作用为珊瑚提供生长所需的能量与有机化合物,是维持共生体系健康及响应环境变化的核心因素[29-30]。本研究发现,6种珊瑚的主导共生虫黄藻亚系群均为C1,仅澄黄滨珊瑚以C15为主要共生虫黄藻亚系群。这与涠洲岛区域虫黄藻的整体分布特征一致,即该区域多数珊瑚以C1为优势亚系群,而澄黄滨珊瑚与C15存在专性共生关系[31]。共生虫黄藻密度、叶绿素*a*含量和最大光量子产量等光合作用参数,既是反映珊瑚自养能力的关键指标,也是评估共生体系健康状态的重要依据[12,31]。本研究中,3种枝状珊瑚的共生虫黄藻密度($\geq 1.0\times10^6$个/cm^2)较高,澄黄滨珊瑚处于中间水平,十字牡丹珊瑚、薄片刺孔珊瑚及五边角蜂巢珊瑚的共生虫黄藻密度[$(0.3-0.4)\times10^6$个/cm^2]较低。这一结果与7种造礁石珊瑚的生长速率差异存在一定关联。具体而言,枝状珊瑚分枝发达,单位质量的表面积更大,且单位质量表面积上

中国知网 https://www.cnki.net

的共生虫黄藻密度更高,两者协同作用可使其获得更充足的光合产物供给,从而具有较片状和块状珊瑚更快的生长速率。

4 结论

本研究通过浮排培育实验,系统评估了涠洲岛自然海域 7 种优势造礁石珊瑚的生长特性、存活率及共生虫黄藻特征,为相对高纬度珊瑚礁修复提供了关键数据支撑。结果表明,7 种造礁石珊瑚生长速率呈现显著的形态差异,整体表现为枝状>片状>块状,美丽鹿角珊瑚生长最快。7 种造礁石珊瑚平均存活率达 87.14%,五边角蜂巢珊瑚与十字牡丹珊瑚存活率(95%)最高,风信子鹿角珊瑚(70%)最低。共生虫黄藻方面,除澄黄滨珊瑚以 C15 为优势系群外,其余 6 种珊瑚均以 C1 系群为主导(占比超 75%);枝状珊瑚共生虫黄藻密度高于片状与块状珊瑚,其高虫黄藻密度与形态优势的协同作用,通过提升光合产物供给,可能成为枝状珊瑚生长更快的重要机制。综合来看,美丽鹿角珊瑚可作为涠洲岛珊瑚礁修复的核心功能性物种,以快速构建礁体结构;五边角蜂巢珊瑚、十字牡丹珊瑚可作为补充物种,以提升群落稳定性,该"核心—补充"的物种搭配策略可为相对高纬度珊瑚礁生态修复实践提供科学参考。

参考文献

[1] 赵焕庭,王丽荣,袁家义. 南海诸岛珊瑚礁可持续发展[J]. 热带地理,2016,36(1):55-65.

[2] HUGHES T P,HUANG H,YOUNG M A L. The wicked problem of China′s disappearing coral reefs [J]. Conservation Biology,2013,27(2):261-269.

[3] 余克服. 南海珊瑚礁及其对全新世环境变化的记录与响应[J]. 中国科学:地球科学,2012,42(8):1160-1172.

[4] COMTE A,PENDLETON L H. Management strategies for coral reefs and people under global environmental change:25 years of scientific research [J]. Journal of Environmental Management,2018,209:462-474.

[5] 李元超,黄晖,董志军,等. 鹿回头佳丽鹿角珊瑚卵母细胞发育的组织学研究[J]. 热带海洋学报,2009,28(1):56-60.

[6] 段晓伟,肖宝华,廖宝林,等. 造礁石珊瑚自然海区断枝培育技术研究[J]. 广东海洋大学学报,2019,39(3):115-120.

[7] 鲍鹰,周学家,黄美霞,等. 鹿角珊瑚人工养殖的初步研究[J]. 海洋科学,2012,36(1):69-72.

[8] 王欣,高霆炜,陈骁,等. 涠洲岛园艺式珊瑚苗圃的架设与移植[J]. 广西科学,2017,24(5):462-467.

[9] 王文欢,余克服,王英辉. 北部湾涠洲岛珊瑚礁的研究历史、现状与特色[J]. 热带地理,2016,36(1):72-79.

[10] RAZAK T B,ROFF G,LOUGH J M,et al. Growth responses of branching versus massive corals to ocean warming on the Great Barrier Reef,Australia [J]. Science of the Total Environment,2020,705:135908.

[11] ACEVEDO-RAMIREZ C A,STEPHENSON W,WAKES S,et al. Wave transformation on a fringing reef system with spur and groove structures [J]. Journal of Geophysical Research:Oceans,2021,126(9):e2020JC-016910.

[12] 张海洋,赵美霞,钟瑜,等. 南海北部造礁石珊瑚共生体光合作用特征季节性监测[J]. 海洋地质前沿,2021,37(6):84-91.

[13] 邹仁林. 中国动物志:腔肠动物门 珊瑚虫纲 石珊瑚目 造礁石珊瑚[M]. 北京:科学出版社,2001.

[14] 刘旭. 造礁石珊瑚对温度胁迫的响应机制研究[D]. 南宁:广西大学,2020.

[15] JEFFREY S W,HUMPHREY G F. New spectrophotometric equations for determining chlorophylls a, b, c_1 and c_2 in higher plants,algae and natural phytoplankton [J]. Biochemie und Physiologie der Pflanzen,1975,167(2):191-194.

[16] BHAGOOLI R,HIDAKA M. Comparison of stress susceptibility of *in hospite* and isolated zooxanthellae among five coral species [J]. Journal of Experimental Marine Biology and Ecology,2003,291(2):181-197.

[17] ROWAN R. Coral bleaching:thermal adaptation in reef coral symbionts [J]. Nature,2004,430(7001):742.

[18] 覃祯俊,余克服,王英辉. 珊瑚礁生态修复的理论与实践[J]. 热带地理,2016,36(1):80-86.

[19] 王章义,师彦飞,宋莹莹,等. 水质与珊瑚增长速率关系研究[J]. 海洋湖沼通报,2018(4):82-90.

[20] 王永刚,黄雯,吴志强,等. 三种造礁石珊瑚断枝幼苗的生长及其与共生藻的关系研究[J]. 海洋湖沼通报,2022,44(1):91-98.

[21] RODOLFO-METALPA R,HOULBRÈQUE F,TAMBUTTÉ É,et al. Coral and mollusc resistance to ocean acidification adversely affected by warming [J]. Nature Climate Change,2011,1(6):308-312.

[22] LOHR K E,MCNAB A A C,MANFRINO C,et al. Assessment of wild and restored staghorn coral *Acropora cervicornis* across three reef zones in the Cayman Islands [J]. Regional Studies in Marine Science,2017,9:1-8.

[23] ZHENG X Q,LI Y C,LIANG J L,et al. Performance of ecological restoration in an impaired coral reef in the Wuzhizhou Island,Sanya,China [J]. Journal of Oceanology and Limnology,2021,39(1):135-147.

[24] OKUBO N,TANIGUCHI H,MOTOKAWA T. Succ-

中国知网 https://www.cnki.net

essful methods for transplanting fragments of *Acropora formosa* and *Acropora hyacinthus* [J]. Coral Reefs, 2005,24(2):333-342.
[25] DARLING E S,GRAHAM N A J,JANUCHOWSKI-HARTLEY F A,et al. Relationships between structural complexity, coral traits, and reef fish assemblages [J]. Coral Reefs,2017,36(2):561-575.
[26] ZHANG J L,KE J Z,LIU X B,et al. Survival and growth of "branches of opportunity" from ten coral species outplanted on framed reef modules [J]. Ecological Engineering,2025,212:107529.
[27] SOONG K,CHEN T A. Coral transplantation:regeneration and growth of *Acropora* fragments in a nursery [J]. Restoration Ecology,2003,11(1):62-71.
[28] MADIN J S,MCWILLIAM M,QUIGLEY K,et al. Selecting coral species for reef restoration [J]. Journal of Applied Ecology,2023,60(8):1537-1544.
[29] XU Y,ZHANG J,HUANG H,et al. Coral symbiosis carbon flow:a numerical model study spanning cellular to ecosystem levels [J]. Frontiers in Marine Science, 2022,9:749921.
[30] HINRICHS S,PATTEN N L,WAITE A M. Temporal variations in metabolic and autotrophic indices for *Acropora digitifera* and *Acropora spicifera*:implications for monitoring projects [J]. PLoS One, 2013, 8(5):e63693.
[31] HUANG W,HUANG Z H,YANG E G,et al. High- and low-temperature stress responses of *Porites lutea* from the relatively high-latitude region of the South China Sea [J]. Marine Environmental Research,2025, 204:106858.

Growth Differences of Seven Species of Scleractinian Corals in Weizhou Island

WANG Tingting[1,2],ZHOU Xingwang[2],TAN Heyong[2],XIAO Zunyong[2],HUANG Wen[2],HU Tingjun[1**]
(1. College of Animal Science and Technology,Guangxi University,Nanning,Guangxi,530004,China;2. Guangxi Laboratory on the Study of Coral Reefs in the South China Sea,Coral Reef Research Center of China,School of Marine Sciences,Guangxi University,Nanning,Guangxi,530004,China)

Abstract:In the context of persistent global coral reef degradation,the selection of coral species for transplantation is a critical step in the ecological restoration of coral reefs. This study evaluated the growth rates of seven scleractinian coral species,including three branching species(*Acropora muricata*,*A. hyacinthus*, and *A. pruinosa*),two foliose species(*Pavona decussata* and *Echinopora lamellosa*),and two massive species(*Porites lutea* and *Favites pentagona*). The relative volume growth multiple and relative weight growth multiple were measured to compare the growth differences among different coral species. The results showed that relative weight growth multiple of seven scleractinian coral species ranked as follows:*A. muricata*>*A. hyacinthus*>*A. pruinosa*>*Pavona decussata*>*E. lamellosa*>*Porites lutea*>*F. pentagona*. However,survival rates showed an opposite trend:*F. pentagona* and *Pavona decussata* had the highest survival rate (95.00%), while *A. hyacinthus* had the lowest survival rate (70.00%). The other six species were predominantly associated with clade C1(over 75% relative abundance) of Symbiodiniaceae,except *Porites lutea*,which maintained an obligate relationship with subclade C15. Notably,branching corals exhibited significantly higher density of Symbiodiniaceae,which may be one of the reasons for their significant growth advantage. These findings provide critical data to inform species selection for coral reef restoration in high-latitude marine ecosystems.
Key words:coral reef restoration;coral fragments;growth differences;Symbiodiniaceae;Weizhou Island

责任编辑:唐淑芬

中国知网 https://www.cnki.net

基于环境DNA技术的造礁石珊瑚物种多样性分析——以涠洲岛珊瑚礁区为例

曾心茹[1]，韦 芬[1,2]，崔梦瑶[1,3]，玉颢瑜[1]，潘晓媛[1]，余克服[1]

[1.广西大学 广西南海珊瑚礁研究重点实验室/珊瑚礁研究中心/海洋学院, 广西 南宁 530004; 2.广西大学 资源环境与材料学院, 广西 南宁 530004; 3.南方海洋科学与工程广东省实验室 (广州), 广东 广州 511458]

摘 要: 探究造礁石珊瑚物种多样性对于保护珊瑚礁生态系统具有重要意义，然而，传统调查造礁石珊瑚物种多样性的方法存在一定的局限性，因此，本研究采用高通量测序技术对涠洲岛珊瑚礁区海水环境 DNA（environmental DNA, eDNA）样品进行分析，并与前人传统调查数据相比较，以探讨 eDNA 技术在评估造礁石珊瑚多样性方面的应用潜力。结果显示：（1）eDNA 技术检测到涠洲岛海域共有 57 种石珊瑚，隶属于 13 科 33 属；近 6 年（2019—2024 年）的传统调查共记录了 11 科 29 属 68 种石珊瑚，其中 25 种珊瑚在 2 种方法中均检测到，且 2 种方法检测到的珊瑚优势物种相似。（2）α 多样性指数显示，涠洲岛珊瑚礁生态修复区（XFQ）的珊瑚物种多样性最高，而南湾湾内区域（SW2）的珊瑚物种多样性最低。（3）β 多样性分析及各站点聚类关系显示，涠洲岛南面的 SW1 站点与其他站点的物种组成差异最大，SW2 站点与北面的 W4 站点珊瑚物种组成较为相似。研究结果表明，eDNA 技术在涠洲岛造礁石珊瑚的物种多样性检测中具有可行性，可作为传统调查的有效补充手段，实现对涠洲岛海域造礁石珊瑚物种多样性的快速评估。

关键词: 石珊瑚；eDNA；物种多样性；涠洲岛

中图分类号: X176 **文献标识码:** A **文章编号:** 1007-6336(2025)05-0709-09

DOI:10.13634/j.cnki.mes.2025.05.016

Analysis of species diversity of scleractinian corals based on environmental DNA technology: A case study of Weizhou island coral reef area

ZENG Xinru[1], WEI Fen[1], CUI Mengyao[1,3], YU Haoyu[1], PAN Xiaoyuan[1], YU Kefu[1]

[1.Guangxi Laboratory on the Study of Coral Reefs in the South China Sea, Coral Reef Research Center of China, School of Marine Sciences, Guangxi University, Nanning 530004, China; 2.School of Resources, Environment and Materials, Guangxi University, Nanning 530004, China; 3.Southern Marine Science and Engineering Guangdong Laboratory (Guangzhou), Guangzhou 511458, China]

Abstract: Investigating the species diversity of scleractinian corals is essential for the protection of coral reef ecosystems. However, the traditional methods of investigating the species diversity of scleractinian corals are

收稿日期: 2024-08-26, **修订日期:** 2025-01-19

基金项目: 国家自然科学基金项目(42090041)；广西科技基地和人才专项(桂科 AD25069075)；广西南海珊瑚礁研究重点实验室自主基金资助项目(GXLSCRSCS2023103)

作者简介: 曾心茹(1999—)，女，广东阳江人，硕士，主要研究方向为海洋生物与生态，E-mail: xinruz@sina.cn

通信作者: 韦 芬(1986—)，女，广西融安人，壮族，讲师，博士，主要研究方向为珊瑚礁的生态与修复，E-mail: weifensky@163.com

中国知网 https://www.cnki.net

limited. In the study, we employed high-throughput sequencing technology to analyze environmental DNA(eDNA) samples collected from the coral reef area surrounding Weizhou island and compared them with historical survey data, to explore the potential application of eDNA technology in evaluating the diversity of reef-building corals. The results showed that (1) eDNA technology detected 57 species belonging to 13 families and 33 genera, while traditional survey data from the past six years (2019—2024) documented 68 species belonging to 11 families and 29 genera; Among them, 25 coral species were detected by both methods, and the dominant coral species identified by the two methods were similar. (2) The α-diversity index indicated that the coral species diversity was highest in the Weizhou island coral reef ecological restoration area (XFQ), whereas the inner South Bay area (SW2) exhibited the lowest coral species diversity. (3) β-diversity analysis and the clustering relationships among sites revealed that the SW1 site on the southern coast of Weizhou island exhibited the most distinct species composition compared to other sites, while the coral species composition of the SW2 site showed relatively higher similarity to that of the northern W4 site. These results underscore the feasibility of utilizing eDNA technology for assessing scleractinian coral species diversity at Weizhou island while serving as a valuable complement method for traditional transect surveys to achieve rapid assessment.

Key words: scleractinian corals; eDNA; species diversity; Weizhou island

珊瑚礁生态系统是全球初级生产力最高的生态系统之一, 具有极高的生物多样性, 因此被称为“海洋中的热带雨林”[1-3]。造礁石珊瑚是珊瑚礁生态系统的主要构建生物, 珊瑚物种多样性是珊瑚礁生物多样性的重要组成部分[4]。然而, 近年来由于全球变暖、人类活动、海洋污染、珊瑚病害及敌害生物的影响, 造礁石珊瑚发生大规模白化死亡, 珊瑚覆盖度和物种多样性急剧下降[5-7]。因此, 准确掌握造礁石珊瑚的群落特征和物种多样性对维持珊瑚礁生态系统的稳定与健康具有重要意义[8]。

目前珊瑚物种多样性调查主要依赖样本收集和野外生态调查(样带、样方及断面调查), 然后结合调查的样带录像和样本形态对珊瑚进行人工判读[9-11], 但这些方法容易受到地理、时间、人力和物力的限制, 同时调查结果的准确性还依赖站点的选择以及鉴定人员的珊瑚分类知识; 此外, 可能还存在样本获取不均衡的问题[12-15]。以上问题均可能导致对某些地区的珊瑚物种了解不足等情况发生。因此, 有必要结合一些新的技术和方法, 来辅助解决传统分类和物种多样性调查遇到的问题。

环境 DNA(environmental DNA, eDNA)技术具有操作简便、侵入性低、灵敏度高等优点, 被认为是一种非常有效、快速的方法[16]。该方法通过从环境介质(如水、土壤)中提取 DNA, 对特定基因片段进行 PCR 扩增和高通量测序, 从而实现对生物群落的监测[17]。早在 20 世纪末, eDNA 技术就开始应用于微生物学研究, 主要研究微生物的分类及其生理生化功能[18]。随着 eDNA 技术日益成熟, eDNA 技术逐渐被应用于单一物种检测、生物多样性以及生物量评估等, 例如, 研究人员将该技术应用于监测北部湾海域中华白海豚的分布[19]、长江口及邻近海域的鱼类群落特征[20]以及估算天然泻湖中鲤鱼的生物量和分布[21]等。

近年来 eDNA 技术也逐渐被应用于珊瑚监测。2018 年, Shinzato 等[22]从养殖海水的 eDNA 中检测到鹿角珊瑚; 2019 年, Nichols 和 Marko[23]的研究结果表明, 夏威夷珊瑚礁区海域 eDNA 检测珊瑚结果与样带调查结果高度相似; 2020 年, Alexander 等[24]利用 eDNA 技术在印度尼西亚和澳大利亚海岸交界处海域检测到 25 属 78 种石珊瑚, 与传统调查的 26 属 68 种石珊瑚存在显著差异, 同时还检测到该海域存在未被传统调查记录过的珊瑚; 2021 年, Shinzato 等[25]对日本冲绳海域的海水 eDNA 的检测结果表明, eDNA 可以揭示相隔 1 km 的珊瑚群落之间的差异; 2022 年, Dugal 等[26]利用 eDNA 技术在西澳大利亚罗利浅滩海水中检测出石珊瑚 37 个属 40 个种, 与传统珊瑚礁调查结果几乎一致。以上研究表明, eDNA 技术在珊瑚多样性调查中不仅具有较高的准确性, 还具有更高的灵敏性, 有望成为珊瑚监测的有力工具。

中国知网 https://www.cnki.net

涠洲岛珊瑚礁位于南海珊瑚礁分布的北缘[27]，是中国南海最重要的海洋生态系统之一。近几十年涠洲岛造礁石珊瑚物种多样性表现出明显的衰退趋势，据统计，活珊瑚平均覆盖率由1984 年的 42% 下降到 2015 年的 10%[28-29]。因此，开展珊瑚礁的保护工作刻不容缓，而实施有效的保护措施很大程度上依赖于对珊瑚物种多样性的了解。目前涠洲岛珊瑚礁生态调查是以样带和样方调查为主，导致涠洲岛珊瑚属种数量存在较大的差异[30-32]。因此，本研究利用 eDNA 技术对涠洲岛造礁石珊瑚进行分析，旨在探讨该技术用于检测珊瑚物种多样性的可行性，为造礁石珊瑚多样性监测及生物资源评估提供新的技术手段，同时为涠洲岛海域珊瑚礁保护工作提供基础数据支持。

1　材料与方法

1.1　样本采集

本研究样本分为室内珊瑚养殖缸（缸内放置 5 株美丽鹿角珊瑚【*Acropora muricata*】和 5 株丛生盔形珊瑚【*Galaxea fascicularis*】，阳性对照）、非珊瑚礁区自然海域（北海国际客运港码头，经纬度为 21°25′N, 109°07′E，阴性对照）以及涠洲岛珊瑚礁区海域（21°00′N—21°10′N, 109°00′E—109°15′E）水样。涠洲岛珊瑚礁区海域水样采于 2022 年 11 月，6 个采样站点位置列于表 1。SEb、SW1 和 SW2 站点位于涠洲岛南面，W3J、W4、XFQ 站点位于涠洲岛北面，其中 SW2 在南湾湾内，XFQ 是珊瑚礁生态修复区。每个站点使用采水器采集水深 2 ~ 3 m 的水样约 2 L，各 3 个平行，保存至已消毒的采样瓶中。为了能够最大程度地降低水样中 eDNA 的降解，所有水样在 12 h 内使用 0.45 μm 的混合纤维素滤膜进行抽滤。玻璃抽滤装置在使用前用 10% 次氯酸钠消毒液进行清洗消毒，为防止不同水样间的交叉污染，每抽滤完一个 2 L 水样，用纯净水对滤膜接触面进行清洗，然后再开始下一个水样抽滤。每个样品过滤后，将富集 eDNA 的滤膜保存在 5.0 mL 的无酶无菌离心管中，用干冰冷冻运输至实验室。

表 1　涠洲岛珊瑚礁区 eDNA 采样站点

Tab.1　eDNA sampling locations in coral reef area of Weizhou island

涠洲岛方位	站点名称	经度(°E)	纬度(°N)
南面	SEb	109.129	21.017
	SW1	109.077	21.019
	SW2	109.099	21.015
北面	W3J	109.126	21.082
	W4	109.142	21.067
	XFQ	109.113	21.080

1.2　eDNA 提取及扩增测序

使用海洋动物组织基因组 DNA 提取试剂盒（TianGen）进行 eDNA 提取（具体操作详见试剂盒说明书）。使用琼脂糖凝胶电泳对 eDNA 进行质量检测，将合格的 eDNA 保存于−80 ℃ 冰箱备用。根据文献 [24] 设计 ITS 基因高变区的通用引物为 SCLER5.8SFor（5′-GARTCTTTGAACGCAAATGGC-3′）和 SCLER28SRev（5′-GCTTATTAATATGCTTAAATTCAGCG-3′）。25 μL 的 PCR 扩增体系包含 DNA 模板 1 μL、正反引物各 1 μL、2×Taq PCR Mix 11 μL，最后用 ddH_2O 补足至 25 μL。PCR 扩增程序为：95 ℃ 预变性 5 min；95 ℃ 变性 30 s，55 ℃ 退火 30 s，72 ℃ 延伸 45 s，40 个循环；最后 72 ℃ 延伸 10 min。PCR 扩增完成后，经 1% 琼脂糖凝胶电泳检测后纯化回收样品。室内珊瑚缸养殖海水 eDNA 扩增产物采用一代测序，涠洲岛珊瑚礁区海水 eDNA 的 PCR 产物在 Illumina Miseq 平台（上海美吉生物医药科技有限公司）进行高通量双端测序。

1.3　数据分析

使用 dada2/deblur 降噪方法消除高通量测序数据中可能出现的测序错误，获得每个样本的 ASV（amplicon aequence variants）代表序列及丰度表，分析不同采样站点的共有 ASV 和独有 ASV，绘制差异物种的 Venn 图。采用 Blast best hit 注释算法[33]对获得的 ASVs 序列进行物种分类注释，将注释结果进行人工校对，手动去除非造礁石珊瑚的信息，如水母、软珊瑚等其他腔肠动物，剩余序列均是能注释为石珊瑚的高质量序列，用于珊瑚生物多样性分析[34]。

使用 QIIME2 软件计算 α 多样性指数，如 Sobs 指数、ACE 指数、Chao1 指数、Shannon

中国知网　https://www.cnki.net

指数和 Simpson 指数；基于各采样站点的珊瑚物种序列丰度，利用 Bray-Curtis 距离矩阵进行 PCoA 分析（β 多样性），绘制珊瑚物种组成热图，以此综合评价各站点珊瑚丰富度及多样性。

2 结果与讨论

2.1 造礁石珊瑚物种组成

室内珊瑚缸养殖海水 eDNA 测序所得的序列经 Blast 比对，结果显示物种均为鹿角珊瑚和丛生盔形珊瑚，与实际养殖环境中的珊瑚物种一致；涠洲岛非珊瑚礁区海水（阴性对照）未扩增出条带。珊瑚礁区的 18 个 eDNA 样本高通量测序共获得有效拼接序列 655661 条，平均序列长度为 270 bp。根据获得的分类单元丰度矩阵，绘制了 6 个采样站点共有分类单元的 Venn 图，各站点中共有和特有的分类单元数量如图 1 所示。6 个站点的共有分类单元数量为 21 个，北面 XFQ 站点（35 个）、W3J 站点（12 个）以及南面 SEb 站点（14 个）还具有较高数量的特有分类单元，南湾湾内 SW2 站点的特有分类单元数量最少（4 个）。经过数据库比对和人工校正，共注释到造礁石珊瑚 57 种，隶属于 13 科 33 属（详见附表 1 ①），有 3 个物种仅鉴定到属水平，分别为角孔珊瑚属（*Goniopora* sp.）、菊花珊瑚属（*Goniastrea* sp.）和石芝珊瑚属（*Fungiidae* sp.）。

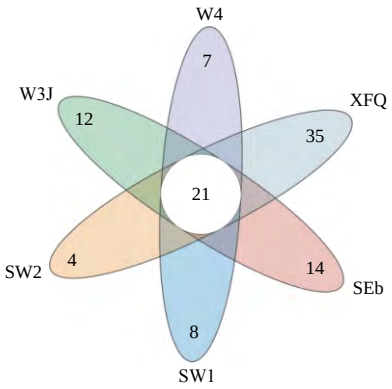


图 1 涠洲岛不同采样站点间共有 ASV 的 Venn 图

Fig. 1 Venn diagram of the common ASV of different station of Weizhou island

涠洲岛珊瑚礁区的珊瑚物种组成如图 2 所示，其中相对序列丰度前 10 位的珊瑚优势物种分别为梳状属珊瑚（*Pectinia teres*）、莫氏滨珊瑚（*Porites murrayensis*）、粗糙刺叶珊瑚（*Echinophyllia aspera*）、小刺叶珊瑚（*Lithophyllon scabra*）、斯氏伯孔珊瑚（*Bernardpora stutchburyi*）、黄癣盘星珊瑚（*Dipsastraea favus*）、锯齿刺星珊瑚（*Cyphastrea serailia*）、小斜花珊瑚（*Mycedium robokaki*）、加德纹珊瑚（*Gardineroseris planulata*）和帛琉腔星珊瑚（*Coelastrea palauensis*）。传统方法[28,31,35-36]检测到石珊瑚优势物种也有滨珊瑚（*Porites* sp.）、斯氏伯孔珊瑚、黄癣盘星珊瑚和粗糙刺叶珊瑚等，这在一定程度上说明了 eDNA 技术作为造礁石珊瑚物种多样性的调查方法具有较高的准确率和可靠性。

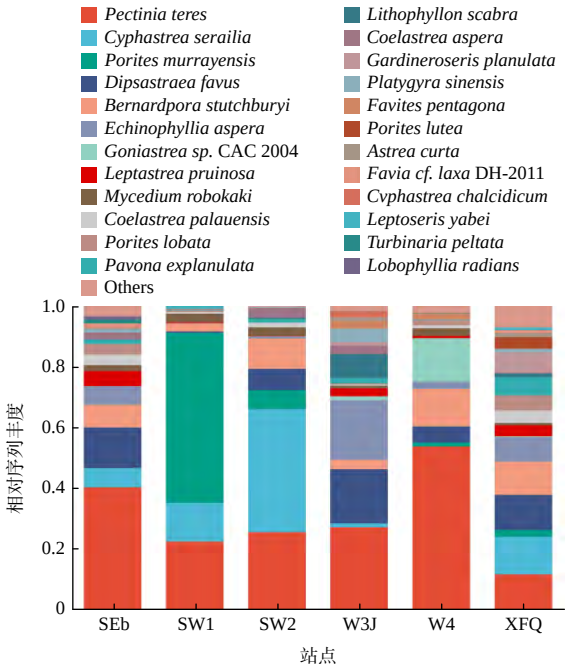


图 2 涠洲岛造礁石珊瑚物种组成

Fig. 2 Composition of scleractinian corals in Weizhou island

2019 年，Yu 等[28]在涠洲岛珊瑚礁区设置了 10 个调查站点 18 个生态断面和 24 个底质断面，共鉴定出 10 科 23 属 48 种珊瑚。2021 年，杨振雄等[35]在涠洲岛海域布设了 15 个站点 45 条断面，发现涠洲岛造礁石珊瑚有 9 科 22 属 42 种；同年，梁文等[31]也报道了涠洲岛西南部海域造

① 附表 1 请在本刊网站下载

中国知网 https://www.cnki.net

礁石珊瑚共有 9 科 38 种。2024 年，Zeng 等[36]在涠洲岛海域采集了 116 株珊瑚，鉴定为 49 种。综合以上 4 项研究结果，涠洲岛珊瑚礁区的造礁石珊瑚共计 11 科 29 属 68 种，以上数据作为本文的传统调查结果，具体的物种信息见表 2。

表 2　2019—2024 年涠洲岛造礁石珊瑚传统调查数据

Tab.2　Traditional survey data of scleractinian corals in Weizhou island from 2019-2024

科	属	种	拉丁名称	文献出处
滨珊瑚科	滨珊瑚属	*澄黄滨珊瑚	*Porites lutea*	[28,31,35-36]
		*团块滨珊瑚	*Porites lobata*	[31,35]
	伯孔珊瑚属	*斯氏伯孔珊瑚	*Bernardpora stutchburyi*	[28,31,35-36]
	角孔珊瑚属	大角孔珊瑚	*Goniopora djiboutiensis*	[28,35]
		二异角孔珊瑚	*Goniopora duofasciata*	[31]
		柱角孔珊瑚	*Goniopora columna*	[31]
菌珊瑚科	牡丹珊瑚属	小牡丹珊瑚	*Pavona minuta*	[28,36]
		易变牡丹珊瑚	*Pavona varians*	[28,35]
		叶形牡丹珊瑚	*Pavona frondifera*	[28,31,36]
		十字牡丹珊瑚	*Pavona decussata*	[28,31,35-36]
		*变形牡丹珊瑚	*Pavona explanulata*	[28,36]
鹿角珊瑚科	鹿角珊瑚属	霜鹿角珊瑚	*Acropora pruinosa*	[28,31]
		多孔鹿角珊瑚	*Acropora millepora*	[35-36]
		美丽鹿角珊瑚	*Acropora muricata*	[28,35-36]
	蔷薇珊瑚属	膨胀蔷薇珊瑚	*Montipora turgescens*	[31,35]
		单星蔷薇珊瑚	*Montipora monasteriata*	[28]
		鬃刺蔷薇珊瑚	*Montipora hispida*	[28]
		繁锦蔷薇珊瑚	*Montipora efflorescens*	[28,35-36]
裸肋珊瑚科	扁脑珊瑚属	精巧扁脑珊瑚	*Platygyra daedalea*	[28,31,35-36]
		交替扁脑珊瑚	*Platygyra crosslandi*	[28,31,35-36]
		肉质扁脑珊瑚	*Platygyra carnosa*	[28,35-36]
		*中华扁脑珊瑚	*Platygyra sinensis*	[28,35-36]
		小业扁脑珊瑚	*Platygyra verweyi*	[36]
		*小扁脑珊瑚	*Platygyra pini*	[36]
	刺柄珊瑚属	*腐蚀刺柄珊瑚	*Hydnophora exesa*	[28,31,35-36]
	刺孔珊瑚属	宝石刺孔珊瑚	*Echinopora gemmacea*	[28,36]
		*薄片刺孔珊瑚	*Echinopora lamellosa*	[28,35-36]
	刺星珊瑚属	*锯齿刺星珊瑚	*Cyphastrea serailia*	[28,35-36]
	角蜂巢珊瑚属	*秘密角蜂巢珊瑚	*Favites abdita*	[28,31,35-36]
		*五边角蜂巢珊瑚	*Favites pentagona*	[28,31,35-36]
		板叶角蜂巢珊瑚	*Favites complanata*	[31]
		海孔角蜂巢珊瑚	*Favites halicora*	[28,31,35-36]
		*多弯角蜂巢珊瑚	*Favites flexuosa*	[28,31,35-36]
		中华角蜂巢珊瑚	*Favites chinensis*	[31]
	菊花珊瑚属	*网状菊花珊瑚	*Goniastrea retiformis*	[28,35-36]
		似蜂巢菊花珊瑚	*Goniastrea favulus*	[36]
		*梳状菊花珊瑚	*Goniastrea pectinata*	[28,31,35-36]

中国知网　https://www.cnki.net

续表

科	属	种	拉丁名称	文献出处
裸肋珊瑚科	裸肋珊瑚属	阔裸肋珊瑚	*Merulina ampliata*	[28,31,35]
	盘星珊瑚属	*翘齿盘星珊瑚	*Dipsastraea matthaii*	[28,31,35-36]
		罗图马盘星珊瑚	*Dipsastraea rotumana*	[28,35-36]
		*黄癣盘星珊瑚	*Dipsastraea favus*	[28,31,35-36]
		*标准盘星珊瑚	*Dipsastraea speciosa*	[28,31,35-36]
		*海洋盘星珊瑚	*Dipsastraea maritima*	[28]
		圆突蜂巢珊瑚	*Favia veroni*	[31]
		带刺蜂巢珊瑚	*Favia stelligera*	[31]
		丹氏盘星珊瑚	*Dipsastraea danai*	[36]
		*疏盘星珊瑚	*Dipsastraea laxa*	[36]
	腔星珊瑚属	*粗糙腔星珊瑚	*Coelastrea aspera*	[28,35-36]
	斜花珊瑚属	鼻斜花珊瑚	*Mycedium elephantotus*	[28]
	圆星珊瑚属	*曲圆星珊瑚	*Astrea curta*	[28,35-36]
木珊瑚科	陀螺珊瑚属	复叶陀螺珊瑚	*Turbinaria frondens*	[28,35-36]
		*盾形陀螺珊瑚	*Turbinaria peltata*	[28,35-36]
		皱折陀螺珊瑚	*Turbinaria mesenterina*	[36]
		小星陀螺珊瑚	*Turbinaria.stellulata*	[28]
枇杷珊瑚科	盔形珊瑚属	丛生盔形珊瑚	*Galaxea fascicularis*	[28,35-36]
		稀杯盔形珊瑚	*Galaxea astreata*	[28,31,35]
石芝珊瑚科	足柄珊瑚属	壳形足柄珊瑚	*Podabacia crustacea*	[28,35-36]
	石叶珊瑚属	波形石叶珊瑚	*Lithophyllon.undulatum*	[28]
沙珊瑚科	沙珊瑚属	不等脊膛沙珊瑚	*Psammocora nierstraszi*	[36]
筛珊瑚科	筛珊瑚属	柱形筛珊瑚	*Coscinaraea columna*	[36]
同星珊瑚科	同星珊瑚属	*多孔同星珊瑚	*Plesiastrea versipora*	[28,35-36]
未定科	小星珊瑚属	紫小星珊瑚	*Leptastrea purpurea*	[28,31,35-36]
		横小星珊瑚	*Leptastrea transversa*	[28]
叶状珊瑚科	叶状珊瑚属	赫氏叶状珊瑚	*Lobophyllia hemprichii*	[28,35-36]
		*伞房叶状珊瑚	*Lobophyllia corymbosa*	[31,35-36]
	合叶珊瑚属	菌状合叶珊瑚	*Symphyllia agaricia*	[28,35]
	棘星珊瑚属	棘星珊瑚	*Acanthastrea echinata*	[31,36]
	刺叶珊瑚属	*粗糙刺叶珊瑚	*Echinophyllia aspera*	[28,31,35-36]

注: *表示该物种在eDNA检测到

本研究将 eDNA 检测到的珊瑚物种(57 种)与传统调查物种(68 种)进行比较(表 2),发现 eDNA 技术检测到的 25 种珊瑚与传统调查一致,占珊瑚总数(100 种)的 25%,与目前 eDNA 技术的预期检出范围相符[37-38]。其中,eDNA 检测到的梳状珊瑚(*Pectinia teres*、*Pectinia ayleni*)在中国造礁石珊瑚物种名录[39]中未被记录过,毗邻沙珊瑚(*Psammocora contigua*)、白斑小星珊瑚(*Leptastrea pruinosa*)、莫氏滨珊瑚(*P. murrayensis*)等 32 种珊瑚物种未在涠洲岛珊瑚礁区出现过;另外,涠洲岛传统调查确定存在的美丽鹿角珊瑚(*A. muricata*)、繁锦蔷薇珊瑚(*M. efflorescens*)和丛生盔形珊瑚(*G. fascicularis*)等 43 种珊瑚在 eDNA 检测中未被发现。这些发现揭示了 eDNA 检测可能存在假阳性和假阴性结果的问题。假阳性结果产生的原因可能是公共

中国知网 https://www.cnki.net

数据库中包含大量不同物种的序列信息，导致序列注释错误，从而使得比对结果中的物种并非来自本地调查水域；假阴性结果产生的原因可能是 eDNA 扩增的序列片段过短，导致信息位点不足以有效区分同属不同种的物种。由于涠洲岛尚未建立完善的本地造礁石珊瑚序列信息数据库，致使一些已知物种未能被 eDNA 技术检测到，特别是在鹿角珊瑚科物种的检测中，这一问题表现尤为突出，虽然有文献报道鹿角珊瑚有特异性引物[40]，但是无法满足本研究中整个涠洲岛珊瑚的扩增。此外，造礁石珊瑚的线粒体基因内部分化不足，导致系统发育分辨率仅在较高的分类水平上[41-43]，无法推断不同物种之间的遗传关系。已有研究发现[41-42]，珊瑚核基因的替代率远高于线粒体基因[44]。例如，Takabayashi 等发现了 ITS 的序列变异性在不同珊瑚种之间差异很大，因此，我们选择珊瑚的 ITS 序列作为 eDNA 扩增的目的基因。综上所述，eDNA 技术在造礁石珊瑚多样性调查中具有一定的可行性，可以对传统珊瑚调查数据进行补充，然而后续研究需进一步挖掘和完善珊瑚的分子数据库，开发新的引物，探索多引物联合使用的策略，以便更好地将该技术应用于造礁石珊瑚多样性调查。

2.2　造礁石珊瑚物种多样性分析

本研究利用 α 多样性指数分析涠洲岛海域造礁石珊瑚物种多样性（表 3），其中，Sobs 指数范围为 61 ~ 213，ACE 指数范围为 61.000 ~ 213.851，Chao1 指数范围为 61.0 ~ 213.3，Shannon 指数范围为 1.065 ~ 3.686，Simpson 指数范围为 0.010 ~ 0.569。在 6 个站点的样本中，涠洲岛北面 XFQ 站点的 Sobs 指数、ACE 指数、Chao1 指数和 Shannon 指数最高，Simpson 指数最低，表明该站点的珊瑚物种多样性最丰富；南湾湾内 SW2 站点的 Sobs 指数、ACE 指数和 Chao1 指数最低，说明该站点的珊瑚物种多样性最低。另外，南面的 SW1 站点 Sobs 指数（79）也较低，但南面 SEb 站点的 Sobs 指数（164）较高，与北面 W3J 站点（166）、W4 站点（134）的指数相差不大，物种多样性较高。Sobs 指数、ACE 指数和 Chao1 指数的分布趋势基本一致，Shannon 指数和 Simpson 指数分布趋势相反。

表 3　涠洲岛各站点造礁石珊瑚的 α 多样性指数

Tab.3　α diversity index of scleractinian coral at different sites in Weizhou island

样本编号	Sobs指数	ACE指数	Chao1指数	Shannon 指数	Simpson 指数
SEb	164	167.517	165.6	2.354	0.197
SW1	79	83.709	82.2	1.065	0.569
SW2	61	61.000	61.0	1.409	0.508
W3J	166	173.520	173.0	2.881	0.111
W4	134	139.515	139.2	1.891	0.365
XFQ	213	213.851	213.3	3.686	0.010

本研究利用 Bray-Curtis 距离矩阵对各采样站点的造礁石珊瑚物种序列丰度进行了 β 多样性分析，结果显示，涠洲岛南面的 SW1 和 SW2 站点物种组成与其他站点差异最大，其余站点物种组成相似（图 3）。基于种水平的造礁石珊瑚组成热图显示各站点的物种组成存在差异（图 4）。从聚类关系上看，南湾湾内 SW2 站点和北面的 W4 站点最先聚在一起，北面地理上相邻的站点 XFQ 和 W3J 也聚在一起，说明珊瑚物种组成相似，而与 XFQ 和 W3J 站点物种组成差异最大的是聚类关系最远的南面 SW1 站点；从物种相对丰度上看，涠洲岛北面的站点（XFQ、W3J 和 W4）相对于涠洲岛南面的站点（SW1、SW2、SEb）有着较高的相对丰度（图 4），这与 α 多样性和 β 多样性的分析结果基本一致。

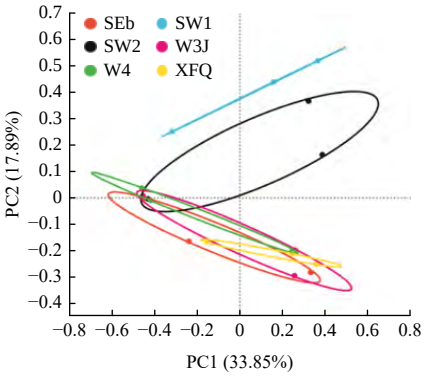


图 3　基于 Bray-Curtis 距离矩阵的涠洲岛造礁石珊瑚主坐标分析（PCoA）

Fig. 3　Principal coordinate analysis (PCoA) of Weizhou island scleractinian coral based on Bray-Curtis distance matrix

人类活动是造成涠洲岛各站点造礁石珊瑚

中国知网　https://www.cnki.net

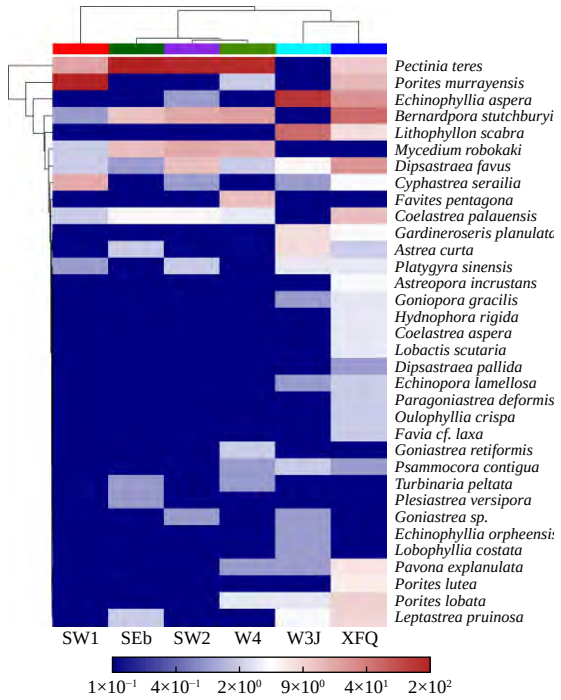


图 4 涠洲岛种水平造礁石珊瑚物种组成分布热图

Fig. 4 Heat map of species-level coral composition in Weizhou island

物种组成及多样性存在差异的重要因素。现场调研发现，XFQ 站点在涠洲岛珊瑚礁修复区内，目前该区域已投放 550 个珊瑚礁单体，200 个海上苗床，完成修复珊瑚礁面积 8.74875 公顷[45]，并且该站点的生态环境极少受到人类活动的干预，生物多样性得到很好的保护，因此其物种多样性和丰富度较其他几个站点高。而 SW2 站点位于涠洲岛南湾湾内，南湾主要为商业活动区域及渔船停靠地点，对生活在该区域的珊瑚影响较大[32]，因此，珊瑚物种多样性最低；SW1 站点位于石螺口附近，船舶往来与游客活动较为频繁，所以该站点的物种多样性也相对较低。SEb 站点周边开发了五彩滩景点，旅游活动也较多，但由于该站点位于坑仔珊瑚礁资源利用区[46]，该区域渔业资源与旅游资源的开发和利用较为合理，因此该站点比涠洲岛南面的另外两个站点 SW1 和 SW2 珊瑚物种多样性高，与北面的站点多样性相当。

此外，珊瑚礁区不同底质也会影响珊瑚群落的组成。于婉君[46]发现涠洲岛南面 SW2 站点的沙质基底占比高达 55.26%，远超过该断面的其他底质类型，而沙质基底不利于珊瑚的附着生长[46-47]，这也是该站点物种多样性最低的原因；此外，北面 W4 站点也是以泥沙为主的底质，因此，SW2 和 W4 站点的珊瑚物种组成相似。北面 XFQ 站点与 W3J 站点的物种组成相似可能是因为 2 个站点均在公山珊瑚礁生态保护区内，海域资源利用相同，底质地貌组成相似（均以沙质基底为主）[48]。涠洲岛西南部的 SW1 站点石珊瑚组成与其他站点间差异较大，物种多样性也相对较低，除了受人类活动的影响外，可能还因为该区域底质特殊，主要为礁坪沉积带，其底质组成以珊瑚遗体、贝壳以及陆源碎屑为主，活珊瑚覆盖率和多样性均较低[49]。

总之，由于人类活动的影响及珊瑚礁底质的差异，不同种类的珊瑚适应环境的能力和偏好方面存在差异，进而导致了涠洲岛各站点珊瑚物种多样性的差异。

3 结 论

（1）本研究利用 eDNA 技术检测到涠洲岛珊瑚礁区共有造礁石珊瑚 57 种，其中 25 种珊瑚与传统调查数据（68 种）一致，eDNA 检出率为 25%，2 种方法的珊瑚优势物种种类也大致相同。表明 eDNA 技术在造礁石珊瑚物种多样性调查中具有一定的可行性，但检测结果存在假阳性和假阴性，未来可考虑采用多引物联合并完善珊瑚序列数据库来进一步提高检出率。

（2）涠洲岛不同站点造礁石珊瑚的物种多样性和组成存在差异。珊瑚礁生态修复区（XFQ）的珊瑚物种多样性最高，南湾湾内区域（SW2）的珊瑚物种多样性最低；涠洲岛南面的 SW1 与其他站点的物种组成差异最大，SW2 站点和北面的 W4 站点珊瑚物种组成较为相似。人类活动的影响和珊瑚礁底质的差异是涠洲岛各站点珊瑚物种多样性存在差异的主要原因。

参考文献：

[1] KNOWLTON N, JACKSON J B C. The ecology of coral reefs[M]//BERTNESS M D, GAINES S, HAY M E. Marine Community Ecology. Sunderland: Sinauer Associates, 2001: 395-422.

[2] FISHER R, O'LEARY R A, LOW-CHOY S, et al. Species

中国知网 https://www.cnki.net

richness on coral reefs and the pursuit of convergent global estimates[J]. Current Biology, 2015, 25(4): 500-505.

[3] VOOLSTRA C R, PEIXOTO R S, FERRIER - PAGÈS C. Mitigating the ecological collapse of coral reef ecosystems: effective strategies to preserve coral reef ecosystems[J]. EMBO Reports, 2023, 24(4): e56826.

[4] 赵美霞, 余克服, 张乔民. 珊瑚礁区的生物多样性及其生态功能 [J]. 生态学报, 2006, 26(1): 186-194.

[5] PRATCHETT M S, CUMMING G S. Managing cross-scale dynamics in marine conservation: pest irruptions and lessons from culling of crown-of-thorns starfish (*Acanthaster* spp.)[J]. Biological Conservation, 2019, 238: 108211.

[6] DOVE S G, BROWN K T, VAN DEN HEUVEL A, et al. Ocean warming and acidification uncouple calcification from calcifier biomass which accelerates coral reef decline[J]. Communications Earth & Environment, 2020, 1(1): 55.

[7] PISAPIA C, BURN D, PRATCHETT M S. Changes in the population and community structure of corals during recent disturbances (February 2016-October 2017) on Maldivian coral reefs[J]. Scientific Reports, 2019, 9(1): 8402.

[8] MONTANO S. The extraordinary importance of coral-associated fauna[J]. Diversity, 2020, 12(9): 357.

[9] TEAGUE J, MEGSON-SMITH D A, ALLEN M J, et al. A review of current and new optical techniques for coral monitoring[J]. Oceans, 2022, 3(1): 30-45.

[10] SHOHAM E, BENAYAHU Y. Higher species richness of octocorals in the upper mesophotic zone in Eilat (Gulf of Aqaba) compared to shallower reef zones[J]. Coral Reefs, 2017, 36(1): 71-81.

[11] 黄　晖, 马斌儒, 练健生, 等. 广西涠洲岛海域珊瑚礁现状及其保护策略研究 [J]. 热带地理, 2009, 29(4): 307-312,318.

[12] HILL J, WILKINSON C. Methods for ecological monitoring of coral reefs[M]. Townsville: Australian Institute of Marine Science, 2004: 117.

[13] THRESHER R E, GUNN J S. Comparative analysis of visual census techniques for highly mobile, reef-associated piscivores (Carangidae)[J]. Environmental Biology of Fishes, 1986, 17(2): 93-116.

[14] PINHEIRO H T, GOODBODY-GRINGLEY G, JESSUP M E, et al. Upper and lower mesophotic coral reef fish communities evaluated by underwater visual censuses in two Caribbean locations[J]. Coral Reefs, 2016, 35(1): 139-151.

[15] 张涛锂, 练健生. 大亚湾造礁石珊瑚现状 [J]. 海洋与渔业, 2018(07): 104-105.

[16] 王　萌, 金小伟, 林晓龙, 等. 基于环境 DNA-宏条形码技术的底栖动物监测及水质评价研究进展 [J]. 生态学报, 2021, 41(18): 7440-7453.

[17] THOMSEN P F, WILLERSLEV E. Environmental DNA–An emerging tool in conservation for monitoring past and present biodiversity[J]. Biological Conservation, 2015, 183: 4-18.

[18] JUNIPER S K, CAMBON M A, LESONGEUR F, et al. Extraction and purification of DNA from organic rich subsurface sediments (ODP Leg 169S)[J]. Marine Geology, 2001, 174(1/2/3/4): 241-247.

[19] 杨嘉琪. 中华白海豚环境 DNA 检测技术的条件优化 [D]. 钦州: 北部湾大学, 2022.

[20] ZHANG H, YOSHIZAWA S, IWASAKI W, et al. Seasonal fish assemblage structure using environmental DNA in the Yangtze Estuary and its adjacent waters[J]. Frontiers in Marine Science, 2019, 6: 515.

[21] TAKAHARA T, MINAMOTO T, YAMANAKA H, et al. Estimation of fish biomass using environmental DNA[J]. PLoS One, 2012, 7(4): e35868.

[22] SHINZATO C, ZAYASU Y, KANDA M, et al. Using seawater to document coral-zoothanthella diversity: a new approach to coral reef monitoring using environmental DNA[J]. Frontiers in Marine Science, 2018, 5: 28.

[23] NICHOLS P K, MARKO P B. Rapid assessment of coral cover from environmental DNA in Hawai'i[J]. Environmental DNA, 2019, 1(1): 40-53.

[24] ALEXANDER J B, BUNCE M, WHITE N, et al. Development of a multi-assay approach for monitoring coral diversity using eDNA metabarcoding[J]. Coral Reefs, 2020, 39(1): 159-171.

[25] SHINZATO C, NARISOKO H, NISHITSUJI K, et al. Novel mitochondrial DNA markers for scleractinian corals and generic-level environmental DNA metabarcoding[J]. Frontiers in Marine Science, 2021, 8: 758207.

[26] DUGAL L, THOMAS L, WILKINSON S P, et al. Coral monitoring in northwest Australia with environmental DNA metabarcoding using a curated reference database for optimized detection[J]. Environmental DNA, 2022, 4(1): 63-76.

[27] 余克服, 蒋明星, 程志强, 等. 涠洲岛 42 年来海面温度变化及其对珊瑚礁的影响 [J]. 应用生态学报, 2004, 15(3): 506-510.

[28] YU W J, WANG W H, YU K F, et al. Rapid decline of a relatively high latitude coral assemblage at Weizhou Island, northern South China Sea[J]. Biodiversity and Conservation, 2019, 28(14): 3925-3949.

[29] ZOU R L, ZHANG Y L, XIE Y K. An ecological study of reef corals around Weizhou Island[C]//XU G Z, MORTON B. Proceedings on Marine Biology of South China Sea. Beijing: China Ocean Press, 1988.

[30] 梁　文, 黎广钊, 张春华, 等. 20 年来涠洲岛珊瑚礁物种多样性演变特征研究 [J]. 海洋科学, 2010, 34(12): 78-87.

（下转第 730 页）

中国知网　https://www.cnki.net

Environmental Science & Technology, 2020, 54(10): 6202-6212.

[54] KIM K, YOON H, CHOI J S, et al. Chronic effects of nano and microplastics on reproduction and development of marine copepod *Tigriopus japonicus*[J]. Ecotoxicology and Environmental Safety, 2022, 243: 113962.

[55] JEONG C B, WON E J, KANG H M, et al. Microplastic size-dependent toxicity, oxidative stress induction, and p-JNK and p-p38 activation in the monogonont rotifer (*Brachionus koreanus*)[J]. Environmental Science & Technology, 2016, 50(16): 8849-8857.

[56] KIM J, PARK Y, CHOI K. Phototoxicity and oxidative stress responses in *Daphnia magna* under exposure to sulfathiazole and environmental level ultraviolet B irradiation[J]. Aquatic Toxicology, 2009, 91(1): 87-94.

[57] 方海燕, 谢冰寒, 侯森淼, 等. PVC 微塑料对大型溞繁殖及应激与能量相关基因表达的影响 [J]. 环境科学学报, 2021, 41(5): 2056-2062.

[58] WANG Y, ZHANG M X, DING G H, et al. Polystyrene microplastics alleviate adverse effects of benzo[a]pyrene on tissues and cells of the marine mussel, *Mytilus galloprovincialis*[J]. Aquatic Toxicology, 2023, 256: 106430.

（本文编辑：胡莹莹）

（上接第 717 页）

[31] 梁　文, 周浩郎, 王　欣, 等. 涠洲岛西南部海域造礁石珊瑚的群落结构特征分析 [J]. 海洋学报, 2021, 43(11): 123-135.

[32] 王文欢. 近 30 年来北部湾涠洲岛造礁石珊瑚群落演变及影响因素 [D]. 南宁: 广西大学, 2017.

[33] NILSSON R H, RYBERG M, KRISTIANSSON E, et al. Taxonomic reliability of DNA sequences in public sequence databases: a fungal perspective[J]. PLoS One, 2006, 1(1): e59.

[34] BOLYEN E, RIDEOUT J R, DILLON M R, et al. Reproducible, interactive, scalable and extensible microbiome data science using QIIME 2[J]. Nature Biotechnology, 2019, 37(8): 852-857.

[35] 杨振雄, 张敬怀, 吕向立, 等. 涠洲岛造礁石珊瑚群落变化特征及其环境影响因子 [J]. 生态学报, 2021, 41(18): 7168-7179.

[36] ZENG X R, WEI F, CUI M Y, et al. Molecular phylogenetic classification of scleractinian corals from Weizhou Island, China[J]. Biological Journal of the Linnean Society, 2024, blae022.

[37] VALDIVIA-CARRILLO T, ROCHA-OLIVARES A, REYES-BONILLA H, et al. Integrating eDNA metabarcoding and simultaneous underwater visual surveys to describe complex fish communities in a marine biodiversity hotspot[J]. Molecular Ecology Resources, 2021, 21(5): 1558-1574.

[38] 陈文善, 陈泊霖, 卢　群, 等. 赤水河河源段鱼类资源现状调查 [J]. 渔业研究, 2024, 46(1): 60-68.

[39] 黄林韬, 黄　晖, 江　雷. 中国造礁石珊瑚分类厘定 [J]. 生物多样性, 2020, 28(4): 515-523.

[40] 耿涛年. 海南鹿角珊瑚属 DNA 条形码和系统进化研究 [D]. 海南: 海南大学, 2017.

[41] SHEARER T, VAN OPPEN M, ROMANO S, et al. Slow mitochondrial DNA sequence evolution in the Anthozoa (Cnidaria)[J]. Molecular ecology, 2002, 11(12): 2475-2487.

[42] HELLBERG M E. No variation and low synonymous substitution rates in coral mtDNA despite high nuclear variation[J]. BMC evolutionary biology, 2006, 6(1): 1-8.

[43] VAN OPPEN M J, WILLIS B L, MILLER D J. Atypically low rate of cytochrome b evolution in the scleractinian coral genus Acropora[J]. Proceedings of the Royal Society of London Series B: Biological Sciences, 1999, 266(1415): 179-183.

[44] TAKABAYASHI M, CARTER D, WARD S, et al. Inter- and intra-specific variability in ribosomal DNA sequence in the internal transcribed spacer region of corals[A]//Proceedings of the Australian Coral Reef Society 75th Anniversary Conference[C]. Brisbane: The University of Queensland, 1998: 241-248.

[45] 王　勤. 克服万难持续助推海岛生态修复项目 [EB/OL]. (2023-05-27)[2024-08-01].

[46] 于婉君. 涠洲岛珊瑚礁区的底质特征及其对珊瑚分布的影响 [D]. 南宁: 广西大学, 2022.

[47] YUEN Y S, YAMAZAKI S S, NAKAMURA T, et al. Effects of live rock on the reef-building coral *Acropora digitifera* cultured with high levels of nitrogenous compounds[J]. Aquacultural Engineering, 2009, 41(1): 35-43.

[48] 刘敬合, 黎广钊, 农华琼. 涠洲岛地貌与第四纪地质特征 [J]. 广西科学院学报, 1991, 7(1): 27-36.

[49] 莫永杰. 涠洲岛海岸地貌的发育 [J]. 热带地理, 1989, 9(3): 243-248.

（本文编辑：胡莹莹）

中国知网 https://www.cnki.net

Palaeogeography, Palaeoclimatology, Palaeoecology 663 (2025) 112805

Contents lists available at ScienceDirect

Palaeogeography, Palaeoclimatology, Palaeoecology

journal homepage: www.elsevier.com/locate/palaeo

Dominance of coralline algae in the South China Sea: Insights into their responses to paleoceanographic events over the last 20 million years

Yinqiang Li [a,b,c], Kefu Yu [c,*], Lizeng Bian [d], Baoqing Hu [a], Zhiheng Liao [a,c], Shengmin Huang [a], Zhiguang Song [a], Weihua Liao [e]

[a] Key Laboratory of Environment Change and Resources Use in Beibu Gulf, Ministry of Education & Guangxi Key Laboratory of Earth Surface Processes and Intelligent Simulation, Nanning Normal University, Nanning 530001, China
[b] Guangxi Beihai Wetland Ecosystem National Observation and Research Station, Beihai 536001, China
[c] Guangxi Laboratory on the Study of Coral Reefs in the South China Sea & School of Marine Sciences, Guangxi University, Nanning 530004, China
[d] School of Earth Sciences and Engineering, Nanjing University, Nanjing 210093, China
[e] Nanjing Institute of Geology and Palaeontology, Chinese Academy of Sciences, Nanjing 210008, China

ARTICLE INFO

Editor: Howard Falcon-Lang

Keywords:
Coralline red algae
Coral reefs
Paleoceanography
Xisha Islands

ABSTRACT

The evolution of Earth's climate is primarily reconstructed from deep-sea cores, while data from shallow-water carbonate successions play only a supplementary role. Furthermore, most available information originates from Western Europe, with limited data from the Middle East and almost none from the Americas and the Far East. While there has been significant discussion on the response of coralline algae to sea-level changes, their reactions to other paleoceanographic events and the long-term trends in their composition, abundance, and richness remain poorly understood. This study examines coralline algae in the carbonate rocks of Well CK2 in the northern South China Sea. A total of twelve genera, eight families, and three orders of coralline algae were identified in 666 petrologic thin sections. Coralline algal abundance was relatively high, between 10 and 4.28 Ma. In the early Miocene, coralline algal richness exhibited three distinct increases at 17.55 Ma, 17.45 Ma, and 17.44 Ma, corresponding to the Miocene Climate Optimum, likely as a response to global warming during this period. The distribution of *Mesophyllum* declined in response to a series of cooling events over the past 20 million years. Between 14.13 and 8.77 Ma, the concentration of *Aethesolithon* corresponded to a long-term sea-level fall, while its extinction indicated a rapid sea-level rise. At 6.71 Ma, the increasing abundance of *Lithothamnion* aligned with a rapid sea-level rise. A relative sea-level fall at 10 Ma was recorded by an increase in shallow-water coralline algae, which may be linked to regional uplift caused by the Dongsha movement. The algal distribution in the Xisha Islands reflects major geological and climatic events over the past 20 million years, underscoring the value of coralline algae as indicators of past climatic and environmental changes. These findings provide a new perspective on the late Cenozoic carbonate systems of the Far East.

1. Introduction

Calcareous red algae are important components of reefal carbonates, and their abundance and taxonomic composition result from a combination of climate, plate tectonics, oceanography, biogeography, and evolution (Halfar and Mutti, 2005; Pomar et al., 2017; Sarkar, 2017; Coletti et al., 2022). Recently, the potential of coralline algae as recorders of marine climate and their applications in paleoecology have been recognized (Braga and Aguirre, 2001, 2004; Coletti et al., 2019; Coletti and Basso, 2020; Li et al., 2021a, 2021b; Arnold et al., 2022). Additionally, Aguirre et al. (2000) used coralline algal groups with similar ecological requirements to analyze the diversification history of coralline algae. Therefore, understanding the evolution of coralline algae during different geological periods can enhance our knowledge of paleoceanographic events.

Coralline algae have a wide ecological distribution, ranging from polar to tropical settings within the euphotic zone (Nelson, 2009). They are major components of benthic assemblages and play important roles in coral reef development worldwide (Adey and Macintyre, 1973). Their contributions include binding coral frameworks (Rasser and Riegl, 2002; Littler and Littler, 1997), forming algal ridges (Steneck et al., 1997), trottoirs (Adey, 1986), and coralligène de plateau (Bosence, 1985),

* Corresponding author.
E-mail address: kefuyu@scsio.ac.cn (K. Yu).

https://doi.org/10.1016/j.palaeo.2025.112805
Received 21 October 2024; Received in revised form 4 February 2025; Accepted 5 February 2025
Available online 10 February 2025
0031-0182/© 2025 Elsevier B.V. All rights are reserved, including those for text and data mining, AI training, and similar technologies.

constructing algal build-ups (Bosence, 1983a), forming algal frameworks (Freiwald and Henrich, 1994), and developing free-living rhodoliths and branches (Bosence, 1983b). Due to their long and continuous growth over hundreds of years, coralline algae serve as valuable paleoenvironmental indicators (Halfar et al., 2011). The Mg content of coralline algae correlates with growth rates (Moberly Jr., 1968) and water temperature fluctuations (Chave and Wheeler Jr., 1965). Consequently, coralline algae have been used to reconstruct past temperature changes (Halfar et al., 2000) and historic marine cloud cover (Burdett et al., 2011). Coralline algae are also sensitive to changes in seawater carbonate chemistry associated with ocean acidification. Laboratory simulations indicate that the microscopic life history stage of *Arthrocardia corymbosa* is more vulnerable to environmental stress than the adult stage (Roleda et al., 2015). Correlation analyses of biotic and abiotic variables suggest that turbidity negatively affects coralline algal assemblages, whereas salinity has a positive effect (Lei et al., 2018). Additionally, well-preserved coralline algae in fossil reefs provide accurate records of past paleoenvironmental changes (Braga and Aguirre, 2001, 2004; Braithwaite, 2016).

Over the past 20 Ma, the Earth has experienced a series of tectonic and climatic events that have profoundly influenced global climate change (Wang, 1998). These include the early Miocene closure of the Tethyan Seaway, the middle Miocene expansion of the Antarctic ice sheet, the Miocene Climatic Optimum (MCO), the late Miocene negative carbon shift, the late Miocene–early Pliocene formation of the Isthmus of Panama, the late Pliocene intensification of Northern Hemisphere glaciation, and the middle Pleistocene climatic transition. Collectively, these events transformed the greenhouse-like conditions of the Paleogene into the Quaternary Ice Ages (Zachos et al., 2001; Mudelsee and Raymo, 2005; Lear et al., 2010; Guo et al., 2011; Knorr and Lohmann, 2014; Haywood et al., 2016; Hoorn et al., 2022). During these climatic shifts, global climate changed across different timescales. With increasing core depth (e.g., deep-sea sediments, ice cores), significant progress has been made in reconstructing climate change since the late Cenozoic (Wang et al., 2003; Tian et al., 2008; Jiang et al., 2019; Singh et al., 2023). However, data from shallow-water successions remain secondary. Additionally, most available information originates from Western Europe, with limited data from the Middle East and almost none from the Americas and the Far East. Moreover, the vast majority of studies provide only qualitative descriptions, which prevent accurate comparisons. Without such comparisons, large-scale reconstructions cannot be achieved. Therefore, the study of reefal carbonates in the SCS can provide valuable insights into the carbonate systems of the Far East. Coralline algae-rich intervals within shallow-water carbonates can be analyzed in relation to key environmental variables at regional and global scales, including temperature, nutrient and carbon cycles, water depth, tectonic activity, and global climatic events. Understanding climate change as recorded by coralline algae over the last 20 million years is crucial for interpreting long-term trends in the modern climate system.

The coral reefs of the South China Sea (SCS) are situated on the northern edge of the Coral Triangle (Yu and Zhao, 2009). They are classified into two main categories based on regional distribution: inshore coral reefs and offshore coral reefs (Yu, 2012). To investigate the development and evolution of coral reefs, at least six wells (Well XY-1, Well XY-2, Well XS-1, Well XC-1, Well XK-1, and Well CK2) have been drilled in the Xisha Islands and three in the Nansha Islands (Well NK-1, NY-1, NY-2) over the past half-century. Similar to Well CK2, Wells XK-1 and NK-1 also penetrated carbonate rock layers down to basaltic and volcaniclastic sequences. These wells have provided valuable materials for studying paleoecological and paleoenvironmental changes (Shao et al., 2017a, 2017b; Wang et al., 2018; Wu et al., 2019; Fan et al., 2020; Chen et al., 2021; Wu et al., 2021; Bi et al., 2024).

The Holocene carbonate sequences from Well NK-1 provide insights into reef growth (Zhao et al., 2022), while Pliocene paleoclimatic conditions and paleo-water depth variations have been inferred from coralline algae and foraminifera in Well XK-1 (Wu et al., 2023). Coralline algae from Well CK2 (Fig. 1A, B) accurately document sea-level changes and coral-reef evolution since the Miocene (Li et al., 2021a, 2021b). However, their role in recording and responding to paleoceanographic events remains unclear. In this study, we analyze the abundance, richness, and generic evolution of coralline algae from Well CK2 over a geological-historical period to investigate their responses to past paleoceanographic events.

2. Geological setting

As the largest marginal sea in the western Pacific Ocean, the SCS is connected to the East China Sea through the Taiwan Strait and to the Pacific Ocean through the Luzon Strait. Structurally, the SCS can be divided into three regions: the northern continental edge, the southern continental edge, and the ocean basin. Based on water depth and seafloor topography, the ocean basin is further subdivided into three subbasins: the northwest basin, the central basin, and the southwest basin (Li et al., 2015; Zhang et al., 2016).

The Xisha Islands (15°47′–17°08′ N, 110°10′–112°55′ E) are situated on a vast continental slope at the edge of the SCS and form one of the four largest archipelagos in the region. These islands consist of isolated carbonate platforms underlain by the Xisha-Zhongsha Block (Fig. 1B). Tectonically, they are part of the Xisha uplift, which formed due to the rifting of high-angle fault boundaries during the Paleocene (Tapponnier et al., 1990). The Xisha uplift was exposed at the surface before the Miocene (Wu et al., 2014). During the middle Miocene (15.5–10.5 Ma), the SCS region entered a phase of post-rift thermal subsidence (Wu et al., 2009). Strontium isotope dating indicates that the basement of the Xisha uplift consists of Precambrian gray granite gneiss and Mesozoic volcanic rocks (Wang et al., 1979). Tectonic subsidence curves and sedimentation rates from the three major depressions—the Huaguang Depression, Changchang Depression, and Zhongjiannan Basin (Fig. 1B)—near the Cenozoic Xisha uplift exhibit pronounced changes from 10.5 to 5.5 Ma (Wu et al., 2014).

The Xisha Islands extend approximately 250 km in length and 150 km in width (Yan, 2012) and comprise more than 40 sandbars, islands, and reefs. These formations include the Xuande Atoll on the eastern side and the Yongle Atoll on the southwestern side (Xu et al., 2010). The Xisha Islands have a tropical oceanic monsoon climate characterized by strong solar radiation and a physical marine environment influenced by the Asian monsoon and regional geomorphology. During summer, the East Asian monsoon is dominated by southwesterly winds, which blow from the ocean toward the mainland, whereas in winter, northeasterly winds prevail, blowing from the mainland toward the ocean (Wang et al., 2011). The region experiences relatively high temperatures, with an annual average of 26–27 °C, reaching a maximum of 28.9 °C in June and a minimum of 22.9 °C in January (Yan, 2012). The average annual humidity is approximately 81.6 %, and annual precipitation is around 1500 mm, with most rainfall occurring during the summer season (May–September) and the typhoon season (June–November; He and Zhang, 1986). These conditions indicate that the Xisha Islands provide a highly suitable environment for coral reef formation. The initiation of the Xisha carbonate platforms occurred during the early Miocene, facilitated by a stable tectonic setting and steep slopes formed in the Paleocene (Yu, 2012; Wu et al., 2014). Their development expanded significantly during the middle Miocene before declining in the late Miocene (Ma et al., 2011). This was followed by moderate to active carbonate platform growth during the Plio-Pleistocene (Shao et al., 2017a, 2017b).

3. Methods and material

3.1. Core logging

In 2013, a kilometer-scale drilling project, Well CK2, was conducted

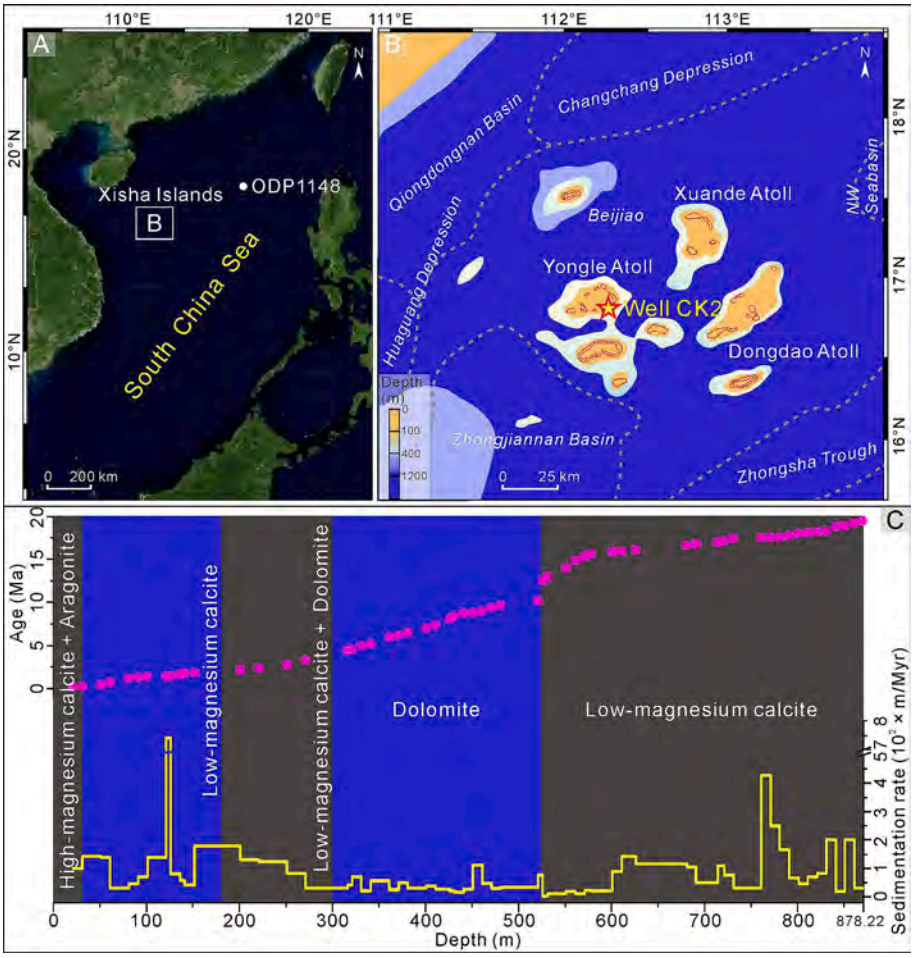


Fig. 1. Schematic diagram of the location, ages, and sedimentation rate of Well CK2. (A) Location of the Xisha Islands and Ocean Drilling Program (ODP) Site 1148 in the South China Sea (SCS). (B) Location of Well CK2, showing a tectonic sketch of the Xisha Islands and the depth of adjacent sea areas (modified from Wang et al., 2018). (C) Ages of Well CK2 based on changes in Sr isotope ratios with depth and variations in sedimentation rate, represented as core accumulation thickness per unit time (m/Myr) with depth. The primary mineral components, determined via X-ray diffraction (XRD), are indicated by black and blue filled boxes (modified from Fan et al., 2020). (For interpretation of the references to colour in this figure legend, the reader is referred to the web version of this article.)

on Chenhang Island, Xisha Islands, reaching a depth of 928.75 m with an average core recovery of approximately 70 %. Zircon U—Pb dating indicates that the Chenhang Island volcaniclastic rocks (878.22–928.75 m) were deposited as early as 35 Ma (Zhang et al., 2020). Based on Sr isotope stratigraphy and a magnetic stratigraphic chronology framework, the carbonate sequence (0–878.22 m) from Well CK2 spans nearly 20 Ma (Fan et al., 2020). The average growth rates of the Chenhang Island coral reef, as determined from Sr isotope dating, were 72.93 m/Myr during the early Miocene, 19.77 m/Myr during the middle Miocene, 28.57 m/Myr during the late Miocene, 39.63 m/Myr during the Pliocene, and 85.06 m/Myr during the Pleistocene (Fig. 1C).

Mineralogical analysis of the carbonate rocks revealed that the interval 0–21.4 m primarily consists of high-Mgcalcite and aragonite; the intervals 21.4–180 m and 522–878.22 m are mainly composed of low-Mgcalcite; the interval 180–300 m consists predominantly of low-Mgcalcite and dolomite; and the interval 300–522 m consists mainly of dolomite (Fig. 1C; Wang et al., 2018; Fan et al., 2020). High-precision U-series dating of Acropora coral demonstrated that Holocene coral reefs occupy the top 16.7 m of Well CK2 (Ma et al., 2021). Based on lithological characteristics, Well CK2 was divided into ten major lithological units, with volcaniclastic rocks considered separately (Li et al., 2021b). Petrologic features, such as rusty iron oxides and differential dissolution, allowed the identification of ten exposed surfaces (Yang et al., 2022). Coralline algal assemblages in Well CK2 record paleo-water depths ranging from < 5 m to > 25 m over the past 20 Ma, revealing three distinct sedimentary cycles from bottom to top (Li et al., 2021a, 2021b).

3.2. Sample description and methods

The 878.22 m carbonate sequence from Well CK2 was sampled systematically from top to bottom. In addition to the 414 samples studied by Li et al. (2021a, 2021b), an additional 252 samples were collected, resulting in a total of 666 standard petrologic thin sections (approximately 2 × 3 cm) analyzed in this study.

Coralline algae were examined under a polarizing microscope at the School of Marine Science, Guangxi University, following the methods of Li et al. (2021a, 2021b). The morphological classification of coralline algae followed the framework of Woelkerling et al. (1993). To ensure accurate comparisons with previously published datasets, a simplified higher-level taxonomic scheme was developed based on algal reproductive anatomy (Braga et al., 1993; Harvey et al., 2003; Le Gall and Saunders, 2007; Iryu et al., 2009; Rösler et al., 2016; Coletti and Basso, 2020; Li et al., 2021a). This scheme classifies coralline algae into three orders: Corallinales (characterized by uniporate conceptacles; Rösler et al., 2016), Hapalidiales (multiporate conceptacles; Nelson et al., 2015), and Sporolithales (sporangia grouped in sori; Le Gall et al., 2009). These orders can be distinguished based on reproductive characteristics: Corallinales are characterized by uniporate conceptacles, Hapalidiales by multiporate conceptacles, and Sporolithales by

sporangia grouped in sori. Coralline algal genera abundance and richness were determined and evaluated following the methods of Li et al. (2021a, 2021b). Rhodolith distribution was assessed using statistical analyses of their depth occurrence within the carbonate sequences. The size, morphology, and algal growth forms of rhodoliths were analyzed following Bosellini and Ginsburg (1971) and Woelkerling et al. (1993).

The carbonate sequence of Well CK2 was divided into 17 Subunits following Li et al. (2021a, 2021b). Coralline algal abundance was determined based on Li et al. (2021a, 2021b) and supplemented with data from additional samples collected from coralline algae-rich intervals. To infer the frequency of past sea-level fluctuations, long-term variations in the dominant distribution of Corallinales or Hapalidiales were analyzed. Student's *t*-test was used to assess the statistical significance of differences in coralline algal abundance across various Subunits, using IBM SPSS Statistics 22 software (IBM, Armonk, NY, USA). Statistical results are reported as means ± standard deviations ($n \geq 3$).

4. Results

4.1. Distribution of coralline algae over time in Well CK2

The carbonate sequence of Well CK2 is rich in coralline algae, which occur on corals, gravels, and other hard substrates. Twelve genera of coralline algae were identified from three orders.

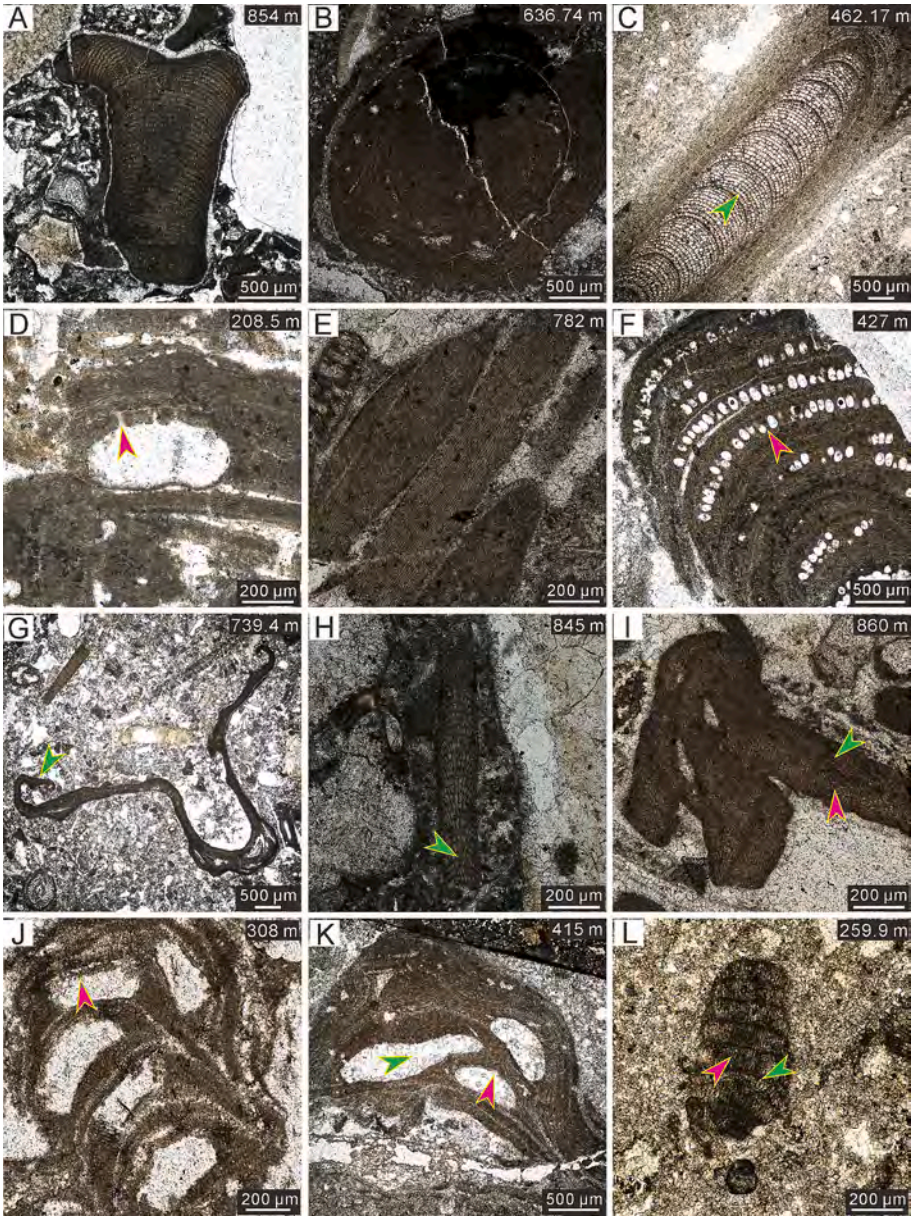


Fig. 2. Common coralline algae from Well CK2 and their typical features. (A) *Lithophyllum* (sample CK2-SS247). (B) *Hydrolithon* sp. (sample CK2-SS220). (C) *Aethesolithon nanhaiensis* (sample CK2-SS165), showing the arrangement of larger cells in arches (green arrowhead). (D) Hapalidiales (sample CK2-SS062), a well-preserved multi-porate conceptacle with conical pore canals (pink arrowhead). (E) *Corallina* sp. (sample CK2-SS234). (F) *Sporolithon* sp. (sample CK2-SS151), with well-preserved rows of sporangia (pink arrowhead). (G) Hooked coralline algae (Corallinales; sample CK2-SS225) with a distinct hook (green arrow). (H) Hypothallus of an encrusting coralline algae with a thin encrusting morphology (sample CK2-SS245), showing common cell fusions (green arrow). (I) *Mesophyllum* sp. (sample CK2-SS248), thallus showing distinct dorsal (green arrow) and ventral features (pink arrow). (J) *Lithothamnion magnum* (sample CK2-SS108), with a well-preserved multiporate conceptacle (pink arrow). (K) Corallinales (sample CK2-SS146), with well-preserved uniporate conceptacles (pink arrow) and borings (green arrow). (L) *Amphiroa* sp. (sample CK2-SS081) presenting a distinct arrangement of long (pink arrow) and short cells (green arrow). (For interpretation of the references to colour in this figure legend, the reader is referred to the web version of this article.)

Over the past 20 million years, coralline algal assemblages have been predominantly composed of Hapalidiales (Fig. 2D) and Corallinales (Fig. 2K), with relatively few representatives of Sporolithales. Corallinales dominate Subunits a-j and p-q, whereas Subunits k-o are primarily characterized by Hapalidiales (Fig. 3). Articulated forms include *Amphiroa* (Fig. 2L), *Corallina* (Fig. 2E), and *Jania*, while non-geniculate forms include *Aethesolithon* (Fig. 2C), *Lithothamnion* (Fig. 2J), *Mesophyllum* (Fig. 2I), Lithoporella, *Spongites*, *Lithophyllum* (Fig. 2A), *Neogoniolithon*, *Sporolithon* (Fig. 2F), and *Hydrolithon* (Fig. 2B). Additionally, some hooked coralline algae were observed (Fig. 2G). The stratigraphic distribution of *Corallina*, Lithoporella, *Lithophyllum*, and *Hydrolithon* has extended continuously throughout the past 20 million years. *Jania*, *Mesophyllum*, and *Lithothamnion* span the intervals 19.6–0.71 Ma, 19.48–1.19 Ma, and 17.45–2.18 Ma, respectively. The distributions of *Aethesolithon* and *Spongites* are relatively concentrated at 14.13–8.77 Ma and 6.35–4.28 Ma, respectively. *Neogoniolithon*, *Amphiroa*, and *Sporolithon* occur sporadically between 18.89 and 5.02 Ma, 6.94–2.17 Ma, and 16.5–6.74 Ma, respectively (Fig. 3). Coralline algal richness peaked at 789.85–689.07 m (17.73–16.78 Ma), with ten genera present, followed by a second peak at 9.77–7.35 Ma, with eight genera (Fig. 3). Core observations indicate that coralline algae in the Xisha Islands formed abundant ellipsoidal and spherical rhodoliths between 17.3 and 0.31

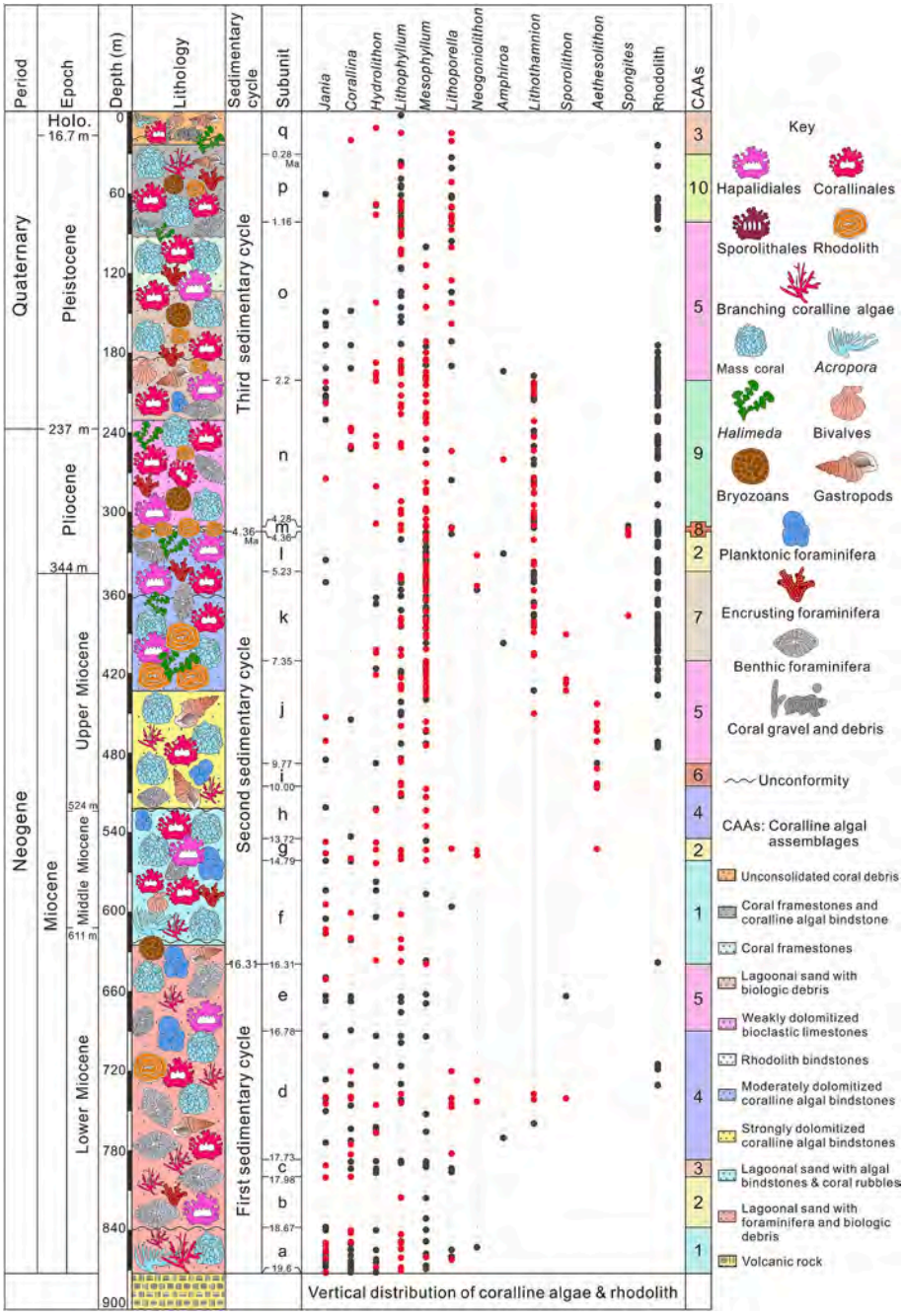


Fig. 3. Vertical distribution of coralline algae and rhodoliths. The rhodolith distribution was determined based on core descriptions and observations, while coralline algal genera distribution was identified from thin sections analyzed under a polarizing microscope. Samples (black dots) studied by Li et al. (2021a, 2021b) are compared with additional samples (red dots) collected for this study, including rhodoliths (black dots). Coralline algal assemblages (CAAs), sedimentary cycles (SCs), and Subunits follow Li et al. (2021a, 2021b). Intervals within the same assemblage are represented by colour-filled boxes. Some key symbols were modified from Coletti et al. (2021). (For interpretation of the references to colour in this figure legend, the reader is referred to the web version of this article.)

Ma, with diameters ranging from ~1 to 10 cm (Fig. 3).

4.2. Variations in coralline algal abundance

According to the main biological components and long-term changes in coralline algal abundance, we focused on the overall abundance of both coralline algae and coral. If the abundance of coralline algae and corals is relatively high during a certain period, it indicates that the climatic and environmental conditions at that time were favorable for the development of coral reefs. The intervals of high abundance occurred in the early Miocene (Interval I), upper Miocene to lower Pliocene (Interval III), and Pleistocene to Holocene (Interval V). In contrast, foraminifera were more dominant in the other intervals, particularly during the late early Miocene to early upper Miocene (Interval II) and late lowest Pliocene to lowest Pleistocene (Interval IV).

Interval I extends from the bottom of Well CK2 to 838.05 m (19.6–18.67 Ma; Subunit a). Interval II spans 838.05–506.1 m (18.67–10 Ma; Subunits b–h). Interval III covers 506.1–309 m (10–4.28 Ma; Subunits i–m). Interval IV extends from 309 to 200 m (4.28–2.2 Ma; Subunit n), and Interval V ranges from 200 m to the top (2.2–0 Ma; Subunits o–q). The primary biological frameworks in Intervals I, III, and V consist predominantly of coral and coralline algae, with minor or sporadic foraminifera (Figs. 4, 5). In contrast, Intervals II and IV exhibit a transition from coral and coralline algal dominance to a foraminifera-dominated assemblage (Fig. 4). Rhodoliths were particularly abundant between ~180–420 m (2.05–7.82 Ma), comprising 5–80 % of the carbonate deposits in this interval (Fig. 5). Overall, coralline algal abundance in Well CK2 was highest in the early Miocene and late Miocene–early Pliocene, with lower abundances recorded in other intervals (Fig. 5).

The analysis of thin sections from Well CK2 showed an average coralline algal abundance of 6.72 ± 0.45 %, with the highest abundance recorded in the 312–309 m interval (Subunit m; 4.36–4.28 Ma), where the average reached 34.06 ± 9.09 %. This value is significantly higher ($p < 0.05$) than those of other subunits (Fig. 6). During this period, numerous rhodoliths developed, contributing up to 80 % of the carbonate deposits (Fig. 5). The second highest algal abundance was recorded in Subunit c, approximately one-third of that in Subunit m. Significant differences in algal abundance were observed between Subunit c and Subunits b, f, h, and i. The abundance of coralline algae in Subunits b, h, and i was relatively low. Additionally, significant differences were found between Subunits b, h, and i and Subunits c, l, and m ($p < 0.05$). In summary, coralline algal abundance varied significantly across different subunits, with Subunit m displaying particularly intense coralline algal development (Fig. 6).

5. Discussion

5.1. Record and response of coralline algal taxa to changes in paleoceanographic events

In recent decades, more than 17 international research expeditions have drilled over 2000 wells in the SCS (Wang et al., 2014). The cores retrieved from these wells have provided extensive material and valuable insights into regional tectonics, paleoceanography, and the evolution of summer monsoon winds in East Asia (Wang et al., 2003). Paleoceanographic changes have been reconstructed from deep-sea sediments at ODP184 Site 1143 (Hess and Kuhnt, 2005; Wang et al., 2014). Our understanding of climatic and environmental changes in the SCS over the past 20 million years has largely been derived from studies of Ocean Drilling Program (ODP) and Integrated Ocean Drilling Program (IODP) cores (Wang et al., 2015; Miao et al., 2018).

More recently, drill-core research on coral reefs in the Xisha Islands has provided information on monsoon intensity (Jiang et al., 2019), carbon cycling (Xu et al., 2019), and sea-level fluctuations (Shao et al., 2017a; Wang et al., 2018; Li et al., 2021a, 2021b; Wu et al., 2023). The growth forms of coralline algae are primarily influenced by environmental factors (Iryu et al., 2009; Coletti et al., 2018). As key components of coral reefs, coralline algae serve as proxies for water depth and indicators of transgressive events (Adey and Macintyre, 1973; Varrone and D'Atri, 2007; Nalin et al., 2008; Abbey et al., 2011; Coletti et al., 2018). In geological contexts, the ratio of Corallinales to Hapalidiales is negatively correlated with increasing water depth (Cabioch et al., 1999; Aguirre et al., 2000; Coletti and Basso, 2020). Additionally, the development and extinction of coralline algal taxa are influenced by past climatic and environmental conditions (Aguirre et al., 2000). Therefore, changes in coralline algal composition, richness, abundance, and assemblages serve as valuable records of paleoenvironmental events throughout geological history (Braga and Aguirre, 2004).

These findings indicate that coralline algal abundance, richness, and

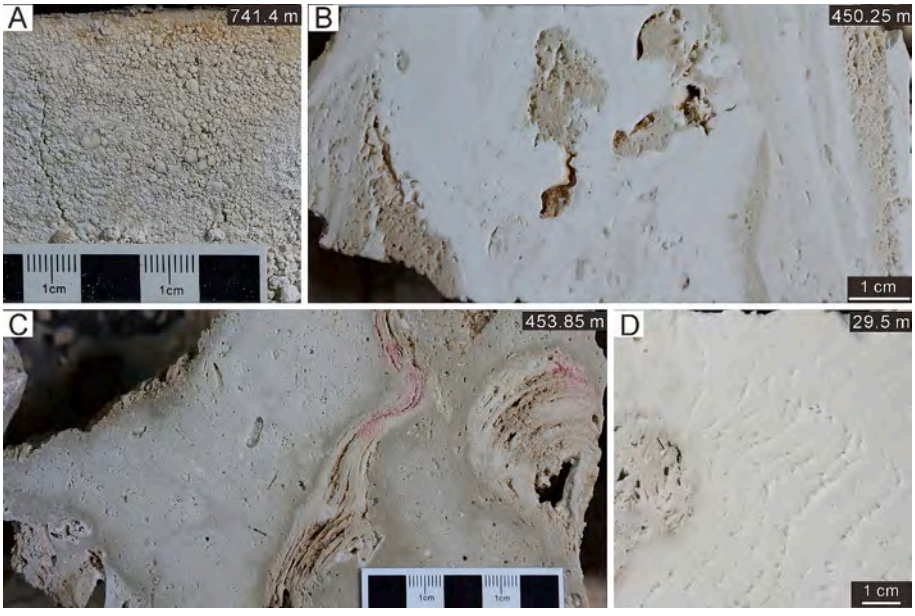


Fig. 4. Physical images of different intervals. (A) Numerous foraminiferal grains. (B) Bindstone formed by extensive coralline algae development. (C) Colonies of hermatypic Porites coral embedded in a bioclastic sediment containing fragments of coralline algae. (D) Growth band of well-preserved *Porites* coral.

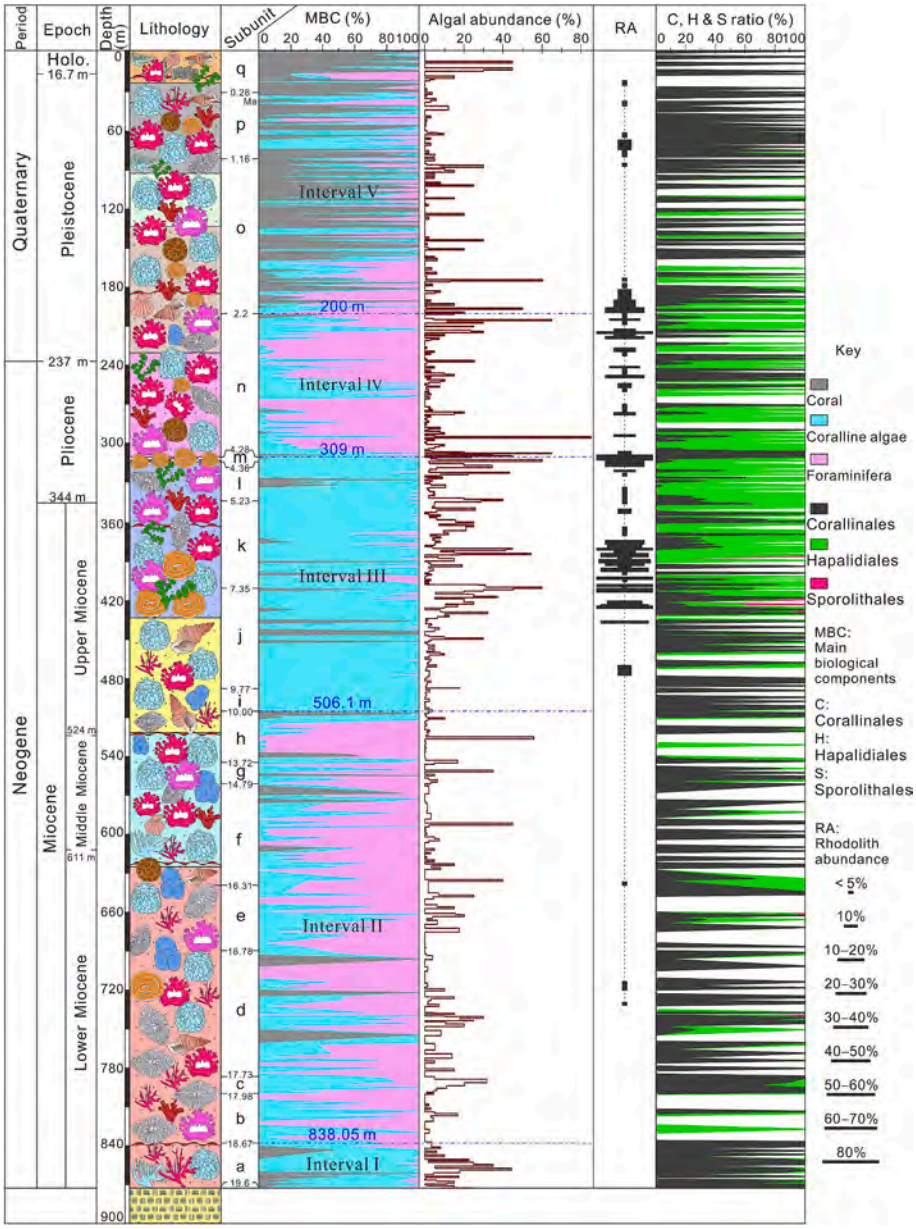


Fig. 5. Main biological components (MBC), abundance of coralline algae, rhodoliths, and coral, and the ratio of Corallinales, Hapalidiales, and Sporolithales. The MBC includes coral, coralline algae, and foraminifera, with foraminifera encompassing both benthic and planktonic species. Coralline algal abundance was recalculated using additional samples following Li et al. (2021a, 2021b). Coral abundance is based on Li et al. (2021a, 2021b). Rhodolith abundance represents the percentage of rhodoliths within the carbonate. For key symbols not included in this figure, refer to Fig. 3.

community composition are closely linked to paleoceanographic events, particularly sea-level fluctuations. In this study, coralline algal abundance and richness in Well CK2 exhibit pronounced temporal variations (Figs. 3–5), demonstrating their utility as paleoceanographic indicators. A total of 12 coralline algal genera were identified in Well CK2, with articulated and non-geniculate coralline algae distributed to varying degrees throughout the carbonate sequence (Fig. 3). The cumulative number of coralline algal genera increases in Subunits d (17.73–16.78 Ma), g (14.79–13.72 Ma), and k (7.35–5.23 Ma) (Fig. 7D). The most significant increase occurs in Subunit d, where three genera—*Amphiroa*, *Lithothamnion*, and *Sporolithon*—exhibit similar distributions within the core (Fig. 3). The coralline algal genera that show increased richness in Subunits g and k are *Aethesolithon* and *Spongites*, with notable increases at 552.74 m (14.13 Ma) and 376.5 m (6.35 Ma), respectively. Subunit d, which records the highest coralline algal richness and the first in-core occurrence of *Amphiroa*, *Lithothamnion*, and *Sporolithon*, corresponds to the mid-Miocene Climatic Optimum (Fig. 7). The occurrences of *Lithothamnion* and *Sporolithon* align closely with relative sea-level rises during the MCO (Fig. 7C; Haq et al., 1987; Miller et al., 2005; Miller et al., 2020). Sea surface temperature (SST) data also indicate that temperatures followed a similar pattern during this period (Fig. 7A; Hou et al., 2023, and references therein).

The MCO was a distinct period of climate change characterized by elevated biodiversity levels (Kohn and Fremd, 2008). Coralline algal species richness (Aguirre et al., 2000) and coral genus diversity (Budd, 2000) were relatively high during this interval. Consequently, the increase in coralline algal richness in the Xisha Islands (Fig. 7) during the MCO was likely driven by transient global warming or environmental conditions favorable for coral reef development.

As recorded by benthic foraminifera, the middle Miocene $\delta^{18}O$ values in the SCS suddenly increased between 14.2 and 13.6 Ma, coinciding with the largest expansion of the Antarctic ice sheet (Wang et al.,

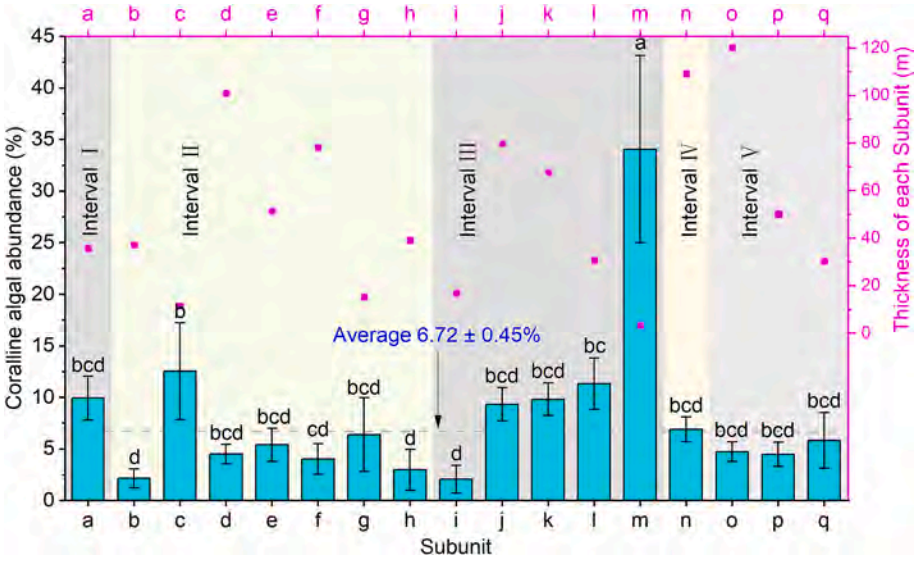


Fig. 6. Differences in coralline algal abundance across various Subunits of Well CK2. The gray dotted lines indicate the average coralline algal abundance throughout the entire drill core. Different colored bars are used to distinguish intervals. Values are presented as means ± SD. The completely inconsistent sets of letters (e.g., a, b, and bcd) on the bar graph indicate significant differences ($p < 0.05$) in coralline algal abundance among different Subunits.

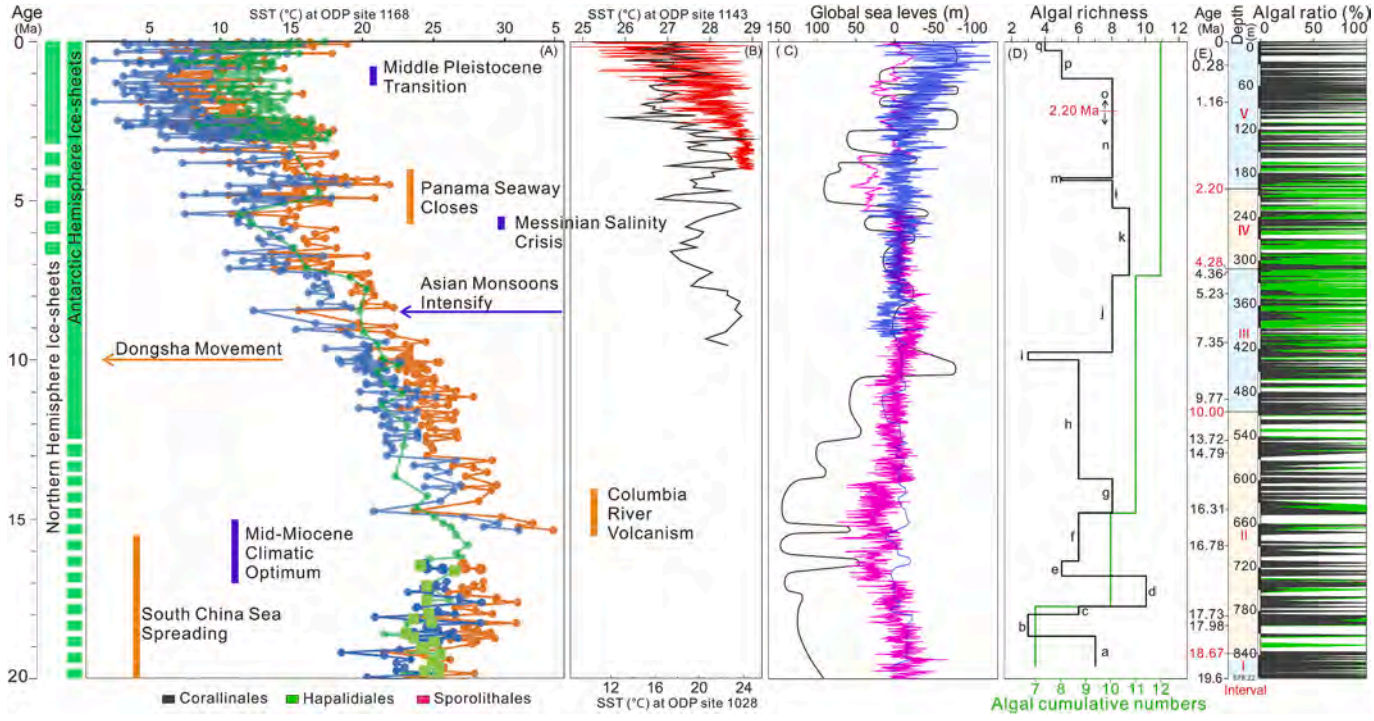


Fig. 7. Coralline algal richness and ratio vs. paleoceanographic events. (A) Sea surface temperature data from Hou et al. (2023) and references therein. (B) Sea surface temperature records are shown in red and black curves (Li et al., 2011; Matsuzaki, 2023, respectively). (C) Global sea-level records are shown in black, blue, and pink curves (Haq et al., 1987; Miller et al., 2005; Miller et al., 2020, respectively). (D) Coralline algal genus richness (black) and cumulative coralline algal genera (green) in Well CK2, determined from thin-section identifications. Letters a, b, c, …, q denote Subunit positions. (E) Ratio of Corallinales, Hapalidiales, and Sporolithales. Numbers highlighted in red indicate boundary ages of Intervals I—V. (For interpretation of the references to colour in this figure legend, the reader is referred to the web version of this article.)

2003). Meanwhile, the first occurrence of *Aethesolithon* in the core at 14.13 Ma (552.74 m) corresponds to the onset of climate cooling and declining SST (Hou et al., 2023). The occurrence of *Aethesolithon* is nearly synchronous with the permanent formation of the Antarctic ice sheet (Fig. 7). However, *Aethesolithon* disappeared from the record by 8.77 Ma (444.5 m) (Fig. 3). The paleo-water depth of the SCS increased during this period (Li et al., 2021b). Over the long-term growth period of *Aethesolithon*, global sea levels exhibited a downward trend (Fig. 7C), whereas *Aethesolithon* was primarily associated with the shallow, low-latitude-dominated mastophoroids (Braga and Aguirre, 2004). Thus, the development period of *Aethesolithon* coincided with a time of significant global climatic and environmental changes, suggesting that its disappearance may have resulted from multiple contributing factors. The increase in coralline algal richness in the SCS during the early and

middle Miocene was predominantly influenced by a combination of global and regional SST variations. Meanwhile, the disappearance of *Aethesolithon* and the subsequent occurrence of *Spongites* (Figs. 3, 6) after the late Miocene were associated with changes in regional sea levels.

Overall, coralline algal richness in Well CK2 exhibits a characteristic trend of initial increase followed by a decline from Interval I to Interval V (Fig. 7). Between 19.6 and 14.79 Ma, coralline algal richness fluctuated frequently, indicating shifts in ecological niches and the alternating evolution of multiple sedimentary microfacies. Subsequently, coralline algal richness began to decline and remained relatively stable over an extended period between 13.72 and 10 Ma. During this time, the paleo-water depth of the Xisha Islands was relatively shallow (Li et al., 2021b), global sea levels declined (Fig. 7C; Haq et al., 1987; Miller et al., 2005; Miller et al., 2020), and SSTs also showed a long-term decreasing trend (Fig. 7A; Hou et al., 2023, and references therein). These findings suggest that the environmental conditions supporting coral reef development during this period remained relatively stable.

5.2. Record and response of coralline algal abundance to changes in paleoceanographic events

During the early Miocene, when global temperatures were relatively high and ice volume was low, coralline algal abundance and richness in the SCS were also relatively high (Figs. 4, 7). This suggests that optimal temperature and sea-level conditions facilitated the growth and development of coralline algae. The highest coralline algal abundance and richness occurred during the late Miocene–early Pliocene (Figs. 3, 5). After 10 Ma, coralline algae became the dominant group among the three major reef-associated organisms (corals, coralline algae, and foraminifera) in the coral reef ecosystem (Fig. 5). A significant tectonic event, the Dongsha Movement, occurred following the cessation of SCS expansion (Du et al., 2021). This event led to uplift and erosion in certain regions, resulting in a hiatus in portions of the Miocene and Pliocene stratigraphic sequences. During this period, corals were nearly absent, and shallow-water coralline algae became the dominant group (Du et al., 2021). This shift is likely linked to the peripheral uplift caused by Dongsha tectonic activity, which also corresponded to a marked global sea-level decline (Fig. 7C; Haq et al., 1987). The late Miocene was a period of frequent geological events and intense global climate change (Zachos et al., 2008). A major global cooling event, the Late Miocene Cooling (LMC: ~7–5.4 Ma), was characterized by CO_2 concentrations falling below the glaciation threshold, leading to the expansion of the Northern Hemisphere ice sheets (Zachos et al., 2008). Regional tectonic activity during this time contributed to increased drought and seasonal variability, particularly around ~7 Ma (Herbert et al., 2016).

Global sea levels initially declined (7–6.72 Ma), then rose (6.72–5.9 Ma) before declining again (Fig. 7C; Miller et al., 2020). The sea surface temperature (SST) trends during this interval closely followed these sea-level fluctuations (Matsuzaki, 2023), while ice volume exhibited an inverse relationship (Rohling et al., 2021). This period corresponds to Subunit k in Well CK2, where *Mesophyllum*, *Lithothamnion*, and *Lithophyllum* are dominant. Coralline algal abundance in Subunit k was relatively high, averaging 9.81 ± 1.57 %. Among these taxa, *Lithothamnion* exhibited a notable increase in frequency after 6.71 Ma, with coralline algal assemblages indicating a relatively deeper paleo-water environment. Thus, the increase in *Lithothamnion* abundance corresponds to a global sea-level rise. *Mesophyllum* exhibited a long temporal range from 19.6 to 1.19 Ma but displayed a discontinuous distribution throughout the core. Notably, its abundance declined, and it disappeared at 13.72 Ma and 1.19 Ma, corresponding to the formation of the Antarctic ice sheet and the Mid-Pleistocene Transition (MPT), respectively. SST records show distinct downward and upward shifts following 13.72 Ma and 1.19 Ma, respectively (Fig. 7A, B; Li et al., 2011; Hou et al., 2023). These findings indicate that coralline algal evolution in Well CK2 is a key area for further research, as understanding these patterns may provide insights into the stratigraphic significance of coralline algae in deeper time.

The coralline algal ratio results reveal 22 instances of complete alternation among the orders Corallinales, Hapalidiales, and Sporolithales, where only one order was dominant in each instance (Fig. 7E). This suggests that at least 22 significant sea-level fluctuations occurred over the past 20 Ma. After 7.35 Ma, coralline algal assemblages were predominantly composed of Hapalidiales (Fig. 7E), with a corresponding increase in overall coralline algal abundance (Fig. 7D). These shifts suggest that the Xisha Islands entered a transgressive stage with frequent environmental changes. The observed patterns may be linked to a continuous decline in SST (Hou et al., 2023) and regional tectonic movements (Du et al., 2021).

5.3. Record and response of the main reefal organisms to changes in paleoceanographic events

The relationship between the abundance of corals, coralline algae, and foraminifera and ancient marine events was analyzed to understand how these reef-building organisms responded to paleoceanographic changes. Higher levels of coral and coralline algal abundance indicate periods of coral-reef development, which may have been influenced by climatic and environmental conditions favorable for reef growth. Based on the dominant reef-building organisms in different intervals, bioherms can be classified into coral-dominated reefs, coralgal reefs, and algal reefs (Abbey et al., 2011). The dominant corals, coralline algae, and foraminifera play key roles in high-productivity carbonate factories. In Well CK2, Intervals I and III are classified as coralgal reefs. Interval I, which exhibits relatively low coralline algal richness, is characterized by a higher sedimentation rate, whereas Interval III, with relatively high coralline algal richness, corresponds to a lower sedimentation rate. Interval V is a coral-dominated reef, and during this period, the sedimentation rate was relatively high, with lower coralline algal richness. In contrast, Intervals II and IV are more dominated by foraminifera, with coralline algae and a small proportion of coral (Fig. 9D). The carbonate deposition rates during Intervals II and IV were also relatively high (Fig. 1C), along with relatively high coralline algal richness (Fig. 3). From the perspective of coralline algal evolution, Corallinales was the dominant order in Intervals I, II, and V. In Interval III, coralline algal assemblages evolved from Corallinales to Hapalidiales, while Interval IV is characterized by the coexistence of Corallinales and Hapalidiales (Fig. 5). The evolution of coralline algae reflects changes in paleo-water depth, which in turn influenced reef growth and sedimentation rates. Specifically, the transition from Corallinales to Hapalidiales on a long-term scale suggests a decrease in sedimentation rate, which is reflected by the lowest sedimentation rate recorded in Interval III (Fig. 1C). This indicates a decline in carbonate factory productivity.

Foraminifera were nearly absent between the middle-late Miocene and early Pliocene (10–4.28 Ma; Fig. 5). A significant tectonic event, the Dongsha Movement, occurred along the northern edge of the SCS during this period, primarily impacting the Dongsha Uplift and its surrounding depressions (Du et al., 2021). The paleo-water depth recorded by coralline algal assemblages in Well CK2 shows a long-term deepening trend (Li et al., 2021a, 2021b), which corresponds with a parallel long-term rise in global sea levels (Haq et al., 1987; Miller et al., 2005; Miller et al., 2020). The two periods during which foraminifera became more abundant correspond to global sea-level declines (Haq et al., 1987; Miller et al., 2005; Miller et al., 2020) and SST variations (Hou et al., 2023).

6. Conclusions

The growth and development of coralline algae are predominantly influenced by environmental factors. Their distribution, abundance, and richness have responded significantly to major climatic and environmental events over the past 20 million years, demonstrating their potential as reliable paleoenvironmental indicators. Our findings highlight

the key responses of coralline algae and their proxy records to major climatic events in the Xisha Islands during this period, characterized by the following:

1) Variations in coralline algal richness. In the early Miocene (17.73–16.31 Ma), coralline algal richness was relatively high, with pronounced increases at 17.55 Ma (770.55 m), 17.45 Ma (744.74 m), and 17.44 Ma (741.74 m), reaching a peak of 10 genera in Subunit d. This period corresponds to the middle Miocene Climatic Optimum, reflecting a response to global warming. The genus *Aethesolithon* was extensively distributed in the 552.74–444.5 m interval (14.13–8.77 Ma), corresponding to a long-term regression, while its disappearance marks a rapid transgression.
2) Variations in coralline algal abundance. The coralline algal assemblages in Well CK2 are primarily composed of Hapalidiales and Corallinales, with Sporolithales occurring in minor quantities. Hapalidiales became predominant between 7.35 and 2.20 Ma, while Corallinales were present throughout the entire core, with a dominant phase from 19.6 to 10 Ma. Since 10 Ma, coralline algae have been mainly represented by Corallinales and Hapalidiales. Notably, *Mesophyllum* exhibited a long stratigraphic distribution (19.6–1.19 Ma) but showed a marked decline in abundance at 13.72 Ma and 1.19 Ma, eventually disappearing. In the late Miocene (6.71 Ma), the abundance of *Lithothamnion* increased significantly, corresponding to a period of rapid transgression. Additionally, the evolutionary patterns of coralline algae provide insights into the productivity of carbonate factories.
3) Significant changes in coralline algal abundance and genera composition. A major shift occurred at 10 Ma, driven by tectonic activity in the SCS (Dongsha Movement). During this period, coralline algal abundance increased, with the proliferation of shallow-water species, while corals were absent. Our results demonstrate that the abundance, richness, and evolutionary patterns of coralline algal genera in the Xisha Islands over the last 20 million years were shaped by a combination of climatic and environmental factors.

CRediT authorship contribution statement

Yinqiang Li: Writing – review & editing, Writing – original draft, Visualization, Validation, Methodology, Investigation, Formal analysis, Data curation, Conceptualization. **Kefu Yu:** Validation, Project administration, Funding acquisition, Conceptualization. **Lizeng Bian:** Data curation, Conceptualization. **Baoqing Hu:** Project administration, Funding acquisition, Conceptualization. **Zhiheng Liao:** Methodology, Data curation. **Shengmin Huang:** Project administration, Funding acquisition. **Zhiguang Song:** Validation, Project administration, Conceptualization. **Weihua Liao:** Methodology, Conceptualization.

Declaration of competing interest

This manuscript has not been published or presented elsewhere in part or in entirety and is not under consideration by another journal. We have read and understood your journal's policies, and we believe that neither the manuscript nor the study violates any of these. There are no conflicts of interest to declare.

Acknowledgements

This work was funded by the National Natural Science Foundation of China (Nos. 42030502 and 42090041), the Middle-aged and Young Teachers' Basic Ability Promotion Project of Guangxi (No. 2023KY0401), and the Opening Foundation of the Key Laboratory of Environment Change and Resources Use in Beibu Gulf, Ministry of Education, Nanning Normal University (No. NNNU-KLOP-X2204).

Data availability

All the data is presented in the article.

References

Abbey, E., Webster, J.M., Braga, J.C., Sugihara, K., Wallace, C., Iryu, Y., Potts, D., Done, T., Camoin, G., Seard, C., 2011. Variation in deglacial coralgal assemblages and their paleoenvironmental significance: IODP Expedition 310, "Tahiti Sea Level". Glob. Planet. Chang. 76, 1–15.
Adey, W.H., 1986. Coralline algae as indicators of sea-level. In: van de Plassche, O. (Ed.), Sea-Level Research: A Manual for the Collection and Evaluation of Data. Geo-Books, Norwich, pp. 229–280.
Adey, W.H., Macintyre, I.G., 1973. Crustose coralline algae: a re-evaluation in the geological sciences. Geol. Soc. Am. Bull. 84 (3), 883–904.
Aguirre, J., Riding, R., Braga, J.C., 2000. Diversity of coralline red algae: origination and extinction patterns from the Early Cretaceous to the Pleistocene. Paleobiology 26, 651–667.
Arnold, C.L., Bélanger, D., Gagnon, P., 2022. Growth Resilience of Subarctic Rhodoliths (*Lithothamnion* glaciale, Rhodophyta) to Chronic Low Sea Temperature and irradiance. J. Phycol. 58, 251–266. https://doi.org/10.1111/jpy.13231.
Bi, D., Zhai, S., Zhang, D., Liu, X., Dong, A., Shi, X., 2024. Magnesium isotopic compositions and origin of Neogene dolomites in Xisha Islands, South China Sea. J. Asian Earth Sci. 261, 105981.
Bosellini, A., Ginsburg, R.N., 1971. Form and internal structure of recent algal nodules (rhodolites) from Bermuda. J. Geol. 79, 669–682.
Bosence, D.W.J., 1983a. Coralline algal reef frameworks. J. Geol. Soc. Lond. 140, 365–376.
Bosence, D.W.J., 1983b. Description and classification of rhodoliths (Rhodoids, Rhodolites). In: Peryt, T.M. (Ed.), Coated Grains. Springer-Verlag, Berlin, pp. 217–224.
Bosence, D.W.J., 1985. The "Coralligène" of the Mediterranean-a recent analog for Tertiary coralline algal limestones. In: Toomey, D.F., Nitecki, M.H. (Eds.), Paleoalgology. Springer, Berlin-Heidelberg, pp. 216–225.
Braga, J.C., Aguirre, J., 2001. Coralline algal assemblages in upper Neogene reef and temperate carbonates in southern Spain. Palaeogeogr. Palaeoclimatol. Palaeoecol. 175, 27–41.
Braga, J.C., Aguirre, J., 2004. Coralline algae indicate Pleistocene evolution from deep, open platform to outer barrier reef environments in the northern Great Barrier Reef margin. Coral Reefs 23, 547–558.
Braga, J.C., Bosence, D.W.J., Steneck, R.S., 1993. New anatomical characters in fossil coralline algae and their taxonomy implications. Palaeontology 36, 535–547.
Braithwaite, C.J.R., 2016. Coral-reef records of Quaternary changes in climate and sea-level. Earth Sci. Rev. 156, 137–154.
Budd, A.F., 2000. Diversity and extinction in the Cenozoic history of Caribbean reefs. Coral Reefs 19 (1), 25–35.
Burdett, H., Kamenos, N.A., Law, A., 2011. Using coralline algae to understand historic marine cloud cover. Palaeogeogr. Palaeoclimatol. Palaeoecol. 302 (1–2), 65–70.
Cabioch, G., Montaggioni, L.F., Faure, G., Ribaud-Laurenti, A., 1999. Reef coralgal assemblages as recorders of paleobathymetry and sea level changes in the Indo-Pacific province. Quat. Sci. Rev. 18, 1681–1695.
Chave, K.E., Wheeler Jr., B.D., 1965. Mineralogic changes during growth in the red alga *Clathromorphum compactum*. Science 147, 621.
Chen, W., Huang, X., Wu, S., Liu, G., Wei, H., Wu, J., 2021. Facies character and geochemical signature in the late Quaternary meteoric diagenetic carbonate succession at the Xisha Islands, South China Sea. Acta Oceanol. Sin. 40 (3), 94–111.
Coletti, G., Basso, D., 2020. Coralline algae as depth indicators in the Miocene carbonates of the Eratosthenes Seamount (ODP Leg 160, Hole 966F). Geobios 60, 29–46.
Coletti, G., Basso, D., Corselli, C., 2018. Coralline algae as depth indicators in the Sommières Basin (early Miocene, Southern France). Geobios 51, 15–30.
Coletti, G., Basso, D., Betzler, C., Robertson, A.H.F., Spezzaferri, S., 2019. Environmental evolution and geological significance of the Miocene carbonates of the Eratosthenes Seamount (ODP Leg 160). Palaeogeogr. Palaeoclimatol. Palaeoecol. 530, 217–235.
Coletti, G., Balmer, E.M., Bialik, O.M., Cannings, T., Kroon, D., Robertson, A.H.F., Basso, D., 2021. Microfacies evidence for the evolution of Miocene coral-reef environments in Cyprus. Palaeogeogr. Palaeoclimatol. Palaeoecol. 584, 110670. https://doi.org/10.1016/j.palaeo.2021.110670.
Coletti, G., Commissario, L., Mariani, L., Bosio, G., Desbiolles, F., Soldi, M., Bialik, O.M., 2022. Palaeocene to Miocene southern Tethyan carbonate factories: a meta-analysis of the successions of South-western and Western Central Asia. Depositional Rec. 8 (3), 1031–1054.
Du, X., Liu, J., Xu, L., Zhang, Q., Zheng, J., Zhang, M., Wu, Q., Cai, G., Li, S., Suo, Y., 2021. The Dongsha Movement in the Jieyang Sag at the Northern South China Sea margin: Control on Hydrocarbon Traps (in Chinese). Geotecton. Metallog. 45, 201–210.
Fan, T., Yu, K., Zhao, J., Jiang, W., Xu, S., Zhang, Y., Wang, R., Wang, Y., Feng, Y., Bian, L., Qian, H., Liao, W., 2020. Strontium isotope stratigraphy and paleomagnetic age constraints on the evolution history of coral reef islands, northern South China Sea. Geol. Soci. Am. 131, 1–14. https://doi.org/10.1130/B35088.1.
Freiwald, A., Henrich, R., 1994. Reefal coralline algal build-ups within the Arctic Circle: morphology and sedimentary dynamics under extreme environmental seasonality. Sedimentology 41, 963–984.

Guo, J., Cheng, X., Chen, R., 2011. Response of palaeooceanography evolution of eastern and western Pacific Ocean and marginal sea to the Arctic Icecap formation. J. Palaeogeogr. 13, 334–346.
Halfar, J., Mutti, M., 2005. Global dominance of coralline red-algal facies; a response to Miocene oceanographic events. Geology 33, 481–484. https://doi.org/10.1130/G21462.1.
Halfar, J., Zack, T., Kronz, A., Zachos, J.C., 2000. Growth and high-resolution paleoenvironmental signals rhodoliths (coralline red algae): a new biogenic archive. J. Geophys. Res. 105, 22107–22116.
Halfar, J., Hetzinger, S., Adey, W., Zack, T., Gamboa, G., Kunz, B., Williams, B., Jacob, D. E., 2011. Coralline algal growth-increment widths archive North Atlantic climate variability. Palaeogeogr. Palaeoclimatol. Palaeoecol. 302, 71–80.
Haq, B.U., Hardenbol, J., Vail, P.R., 1987. Chronology of fluctuating sea levels since the triassic. Science 235, 1156–1167.
Harvey, A.S., Broadwater, S.T., Woelkerling, W.J., Mitrovski, P.J., 2003. Choreonema (Corallinales, Rhodophyta): 18S rDNA phylogeny and resurrection of the Hapalidiales for the subfamilies Choreonematoideae, Austrolithoideae, and Melobesioideae. J. Phycol. 39 (5), 988–998.
Haywood, A.M., Dowsett, H.J., Dolan, A.M., Rowley, D., Abe-Ouchi, A., Otto-Bliesner, B., Chandler, M.A., Hunter, S.J., Lunt, D.J., Pound, M., Salzmann, U., 2016. The Pliocene Model Intercomparison Project (PlioMIP) phase 2: scientific objectives and experimental design. Clim. Past 12, 663–675.
He, Q., Zhang, M., 1986. Reef Geology of the Xisha Islands. Science Press Beijing, China.
Herbert, T.D., Lawrence, K.T., Tzanova, A., Peterson, L.C., Caballerogill, R., Kelly, C.S., 2016. Late Miocene global cooling and the rise of modern ecosystems. Nat. Geosci. 9, 843–847.
Hess, S., Kuhnt, W., 2005. Neogene and Quaternary paleoceanographic changes in the southern South China Sea (Site 1143): the benthic foraminiferal record. Mar. Micropaleontol. 54 (1–2), 63–87.
Hoorn, C., Boschman, L., Kukla, T., Sciumbata, M., Val, P., 2022. The Miocene wetland of western Amazonia and its role in Neotropical biogeography. Bot. J. Linn. Soc. 199, 25–35.
Hou, S., Lamprou, F., Hoem, F.S., Hadju, M.R.N., Sangiorgi, F., Peterse, F., Bijl, P.K., 2023. Lipid-biomarker-based Sea surface temperature record offshore Tasmania over the last 23 million years. Clim. Past 19, 787–802.
Iryu, Y., Bassi, D., Woelkerling, W.J., 2009. Re-assessment of the type collections of fourteen Corallinalean species (Corallinales, Rhodophyta) described by W. Ishijima (1942–1960). Palaeontology 52, 401–427.
Jiang, W., Yu, K., Fan, T., Xu, S., Wang, R., Zhang, Y., Yue, Y., Zhao, J., Feng, Y., Wei, C., Wang, S., Wang, Y., 2019. Coral reef carbonate record of the Pliocene-Pleistocene climate transition from an atoll in the South China Sea. Mar. Geol. 411, 88–97.
Knorr, G., Lohmann, G., 2014. Climate warming during Antarctic ice sheet expansion at the Middle Miocene transition. Nat. Geosci. 7, 376–381.
Kohn, M.J., Fremd, T.J., 2008. Miocene tectonics and climate forcing of biodiversity, Western United States. Geology 36 (10), 783–786.
Le Gall, L., Saunders, G.W., 2007. A nuclear phylogeny of the Florideophyceae (Rhodophyta) inferred from combined EF2, small subunit and large subunit ribosomal DNA: establishing the new red algal subclass Corallinophycidae. Mol. Phylogenet. Evol. 43, 1118–1130.
Le Gall, L., Payyri, C., Bittner, L., Saunders, G.W., 2009. Multigene phylogenetic analyses support recognition of the Sporolithales ord. nov. Mol. Phylogenet. Evol. 54, 302–305.
Lear, C.H., Mawbey, E.M., Rosenthal, Y., 2010. Cenozoic benthic foraminiferal Mg/ca and Li/ca records: toward unlocking temperatures and saturation states. Paleoceanography 25, A4215.
Lei, X., Huang, Hui, Lian, J., Zhou, G., Jiang, L., 2018. Community structure of coralline algae and its relationship with environment in Sanya reefs, China. Aquat. Ecosyst. Health Manag. 21 (1), 19–29.
Li, L., Li, Q., Tian, J., Wang, P., Wang, H., Liu, Z., 2011. A 4-Ma record of thermal evolution in the tropical western Pacific and its implications on climate change. Earth Planet. Sci. Lett. 309, 10–20.
Li, X., Li, J., Yu, X., Wang, C., Jourdan, F., 2015. $^{40}Ar/^{39}Ar$ ages of seamount trachytes from the South China Sea and implications for the evolution of the northwestern sub-basin. Geosci. Front. 6, 571–577.
Li, Y., Yu, K., Bian, L., Fan, T., Wang, R., Jiang, W., Xu, S., Zhang, Y., Yang, Y., 2021a. Paleo-water depth variations since the Pliocene as recorded by coralline algae in the South China Sea. Palaeogeogr. Palaeoclimatol. Palaeoecol. 562, 110107.
Li, Y., Yu, K., Bian, L., Qin, Y., Liao, W., Yang, Y., Ma, Y., 2021b. Coralline algal assemblages record Miocene Sea-level changes in the South China Sea. Palaeogeogr. Palaeoclimatol. Palaeoecol. 584, 110673.
Littler, M.M., Littler, D.S., 1997. Disease-induced mass mortality of crustose coralline algae on coral reefs provides rationale for the conservation of herbivorous fish stocks. In: Proc. 8th Int. Coral Reef Symp., Panama. Smithonian Tropical Research Institute, Balboa, pp. 719–724.
Ma, Y., Wu, S., Lv, F., Dong, D., Gu, M., 2011. Seismic characteristics and development of the Xisha carbonate platforms, northern margin of the South China Sea. J. Asian Earth Sci. 40, 770–783.
Ma, Y., Qin, Y., Yu, K., Li, Y., Long, Y., Wang, R., Fan, T., Jiang, W., Xu, S., Zhao, J., 2021. Holocene coral reef development in Chenhang Island, Northern South China Sea, and its record of sea level changes. Mar. Geol. 440, 106593.
Matsuzaki, K.M., 2023. Evolution of Oceanography of the Central Northwest Pacific over the past 10 Million Years with Focus on late Miocene Global Cooling. Paleoceanogr. Paleoclimatol. 38 e2023PA004789.
Miao, Y., Warny, S., Clift, P.D., Gregory, M., Liu, C., 2018. Climatic or tectonic control on organic matter deposition in the South China Sea? A lesson learned from a comprehensive Neogene palynological study of IODP Site U1433. Int. J. Coal Geol. 190, 166–177.
Miller, K., Kominz, M., Browning, J., Wright, J., Mountain, G., Katz, M., Sugarman, P., Cramer, B., Christie-Blick, N., Pekar, S., 2005. The Phanerozoic Record of Global Sea-Level Change. Science 310, 1293–1298.
Miller, K.G., Browning, J.V., Schmelz, W.J., Kopp, R.E., Wright, J.D., 2020. Cenozoic Sea-level and cryospheric evolution from deep-sea geochemical and continental margin records. Sci. Adv. 6, z1346.
Moberly Jr., R., 1968. Composition of magnesian calcites of algae and pelecypods by electron microprobe analysis. Sedimentology 11, 61–82.
Mudelsee, M., Raymo, M.E., 2005. Slow dynamics of the Northern Hemisphere glaciation. Paleoceanogr. Paleoclimatol. 20, A4022. https://doi.org/10.1029/2005PA001153.
Nalin, R., Nelson, C.S., Basso, D., Massari, F., 2008. Rhodolith-bearing limestones as transgressive marker beds: fossil and modern examples from North Island, New Zealand. Sedimentology 55 (2), 249–274.
Nelson, W.A., 2009. Calcified macroalgae-critical to coastal ecosystems and vulnerable to change: a review. Mar. Freshw. Res. 60, 787–801.
Nelson, W.A., Sutherland, J.E., Farr, T.J., Hart, D.R., Neill, K.F., Kim, H.J., Yoon, H.S., 2015. Multi-gene phylogenetic analyses of New Zealand coralline algae: Corallinapetra Novaezelandiae gen. et sp. nov. and recognition of the Hapalidiales ord. nov. J. Phycol. 51, 454–468.
Pomar, L., Baceta, J.I., Hallock, P., Mateu-Vicens, G., Basso, D., 2017. Reef building and carbonate production modes in the west-central Tethys during the Cenozoic. Mar. Pet. Geol. 83, 261–304.
Rasser, M., Riegl, B., 2002. Holocene coral reef rubble and its binding agents. Coral Reefs 21, 57–72. https://doi.org/10.1007/s00338-001-0206-5.
Rohling, E.J., Yu, J., Heslop, D., Foster, G.L., Opdyke, B., Roberts, A.P., 2021. Sea level and deep-sea temperature reconstructions suggest quasi-stable states and critical transitions over the past 40 million years. Sci. Adv. 7, f5326.
Roleda, M.Y., Cornwall, C.E., Feng, Y., McGraw, C.M., Smith, A., M., Hurd, C.L., 2015. Effect of ocean acidification and ph fluctuations on the growth and development of coralline algal recruits, and an associated benthic algal assemblage. PLoS One 10 (10), e0140394.
Rösler, A., Perfectti, F., Pe, A., Braga, J.C., Gabrielson, P., 2016. Phylogenetic relationships of corallinaceae (Corallinales, Rhodophyta): taxonomic implications for reef-building corallines. J. Phycol. 52, 412–431.
Sarkar, S., 2017. Ecology of Coralline Red Algae and their Fossil Evidences from India. Thalassas Int. J. Mar. Sci. 33, 1–14.
Shao, L., Cui, Y., Qiao, P., Zhang, D., Liu, X., Zhang, C., 2017a. Sea-level changes and carbonate platform evolution of the Xisha Islands (South China Sea) since the early Miocene. Palaeogeogr. Palaeoclimatol. Palaeoecol. 485, 504–516.
Shao, L., Li, Q., Zhu, W., Qiao, P., Liu, X., You, L., Cui, Y., Dong, X., 2017b. Neogene carbonate platform development in the NW South China Sea: Litho-, bio- and chemo-stratigraphic evidence. Mar. Geol. 385, 233–243.
Singh, A.K., Sinha, D.K., Shrivastava, A., Singh, V.P., Mallick, K., Kaushik, T., 2023. Antarctic climate history and its Relationship with Global climate changes: Evidence from Ice Core Records. In: Khare, N. (Ed.), Climate Change and Geodynamics in Polar Regions. CRC Press, pp. 45–88.
Steneck, R.S., Macintyre, I.G., Reid, R.P., 1997. A unique algal ridge system in the Exuma Cays, Bahamas. Coral Reefs 16, 29–37.
Tapponnier, P., Lacassin, R., Leloup, P.H., Sch Rer, U., Dalai, Z., Haiwei, W., Xiaohan, L., Shaocheng, J., Lianshang, Z., Jiayou, Z., 1990. The Ailao Shan/Red River metamorphic belt: Tertiary left-lateral shear between Indochina and South China. Nature 343, 431–437.
Tian, J., Zhao, Q., Wang, P., Li, Q., Cheng, X., 2008. Astronomically modulated Neogene sediment records from the South China Sea. Paleoceanography 23, A3210.
Varrone, D., D'Atri, A., 2007. Acervulinid macroid and rhodolith facies in the Eocene Nummulitic Limestone of the Dauphinois Domain (Maritime Alps, Liguria, Italy). Swiss J. Geosci. 100, 503–515.
Wang, P., 1998. Deformation of Asia and global cooling: searching links between climate and tectonics (in Chinese). Q. Sci. 18, 213–221.
Wang, C., He, X., Qiu, S., 1979. Preliminary study about carbonate strata and micropaleontology of well Xiyong-1 in Xisha Islands. Pet. Geol. Exp. 23–32.
Wang, P., Zhao, Q., Jian, Z., Cheng, X., Huang, W., Tian, J., Wang, J., Li, Q., Li, B., Su, X., 2003. Deep-sea records in the South China Sea in the past 30 million years (in Chinese). Chin. Sci. Bull. 48, 2206–2215.
Wang, G., Xie, S.P., Qu, T., Huang, R.X., 2011. Deep South China Sea circulation. Geophys. Res. Lett. 38, L05601.
Wang, P., Li, Q., Tian, J., 2014. Pleistocene paleoceanography of the South China Sea: Progress over the past 20 years. Mar. Geol. 352, 381–396.
Wang, P., Li, Q., Dai, M., 2015. The South China Sea Deep: Introduction. Deep-Sea Res. II Top. Stud. Oceanogr. 122, 1–5.
Wang, R., Yu, K., Jones, B., Wang, Y., Zhao, J., Feng, Y., Bian, L., Xu, S., Fan, T., Jiang, W., Zhang, Y., 2018. Evolution and development of Miocene "island dolostones" on Xisha Islands, South China Sea. Mar. Geol. 406, 142–158.
Woelkerling, W.J., Irvine, L.M., Harvey, A.S., 1993. Growth-forms in Non-geniculate Coralline Red Algae (Coralliinales, Rhodophyta). Aust. Syst. Bot. 6, 277–293.
Wu, S., Yuan, S., Zhang, G., Ma, Y., Mi, L., Ning, X., 2009. Seismic characteristics of a reef carbonate reservoir and implications for hydrocarbon exploration in Deepwater of the Qiongdongnan Basin, northern South China Sea. Mar. Pet. Geol. 26, 817–823.
Wu, S., Yang, Z., Wang, D., Lü, F., Lüdmann, T., Fulthorpe, C., Wang, B., 2014. Architecture, development and geological control of the Xisha carbonate platforms, northwestern South China Sea. Mar. Geol. 350, 71–83.
Wu, F., Xie, X., Betzler, C., Zhu, W., Zhu, Y., Guo, L., Ma, Z., Bai, H., Ma, B., 2019. The impact of eustatic sea-level fluctuations, temperature variations and nutrient-level

changes since the Pliocene on tropical carbonate platform (Xisha Islands, South China Sea). Palaeogeogr. Palaeoclimatol. Palaeoecol. 514, 373–385.
Wu, F., Xie, X., Zhu, Y., Coletti, G., Betzler, C., Cui, Y., Bai, H., Chen, B., Shang, Z., 2021. Early development of carbonate platform (Xisha Islands) in the northern South China Sea. Mar. Geol. 441, 106629.
Wu, F., Xie, X., Coletti, G., Zhu, Y., Chen, B., Shang, Z., 2023. Coralline algal and foraminiferal records of the Pliocene paleoclimatic conditions and water-depth changes in the northern South China Sea. Mar. Pet. Geol. 153, 106276.
Xu, L., Liu, X.D., Sun, L., Yan, H., Liu, Y., Luo, Y.H., Huang, J., Wang, Y., 2010. Distribution of radionuclides in the guano sediments of Xisha Islands, South China Sea and its implication. J. Environ. Radioact. 101, 362–368.
Xu, S., Yu, K., Fan, T., Jiang, W., Wang, S., 2019. Coral reef carbonate δ13C records from the northern South China Sea: a useful proxy for seawater δ13C and the carbon cycle over the past 1.8 Ma. Glob. Planet. Chang. 182, 103003.
Yan, H., 2012. High Resolution Climatic and Environmental Changes in Xisha Islands of South China Sea during the Late Holocene. PhD Dissertation. University of Science and Technology of China.
Yang, Y., Yu, K., Wang, R., Fan, T., Jiang, W., Xu, S., Li, Y., Zhao, J., 2022. $^{87}Sr/^{86}Sr$ of coral reef carbonate strata as an indicator of global sea level fall: evidence from a 928.75-m-long core in the South China Sea. Mar. Geol. 445, 106758. https://doi.org/10.1016/j.margeo.2022.106758.
Yu, K., 2012. Coral reefs in the South China Sea: their response to and records on past environmental changes. Sci. China Earth Sci. 55, 1217–1229.
Yu, K., Zhao, J., 2009. Coral reefs. In: Wang, P., Li, Q. (Eds.), The South China Sea: Paleoceanography and Sedimentology. Springer, Netherlands, Dordrecht, pp. 229–254.
Zachos, J., Pagani, M., Sloan, L., Thomas, E., Billups, K., 2001. Trends, rhythms, and aberrations in global climate 65 Ma to present. Science 292, 686–693.
Zachos, J.C., Dickens, G.R., Zeebe, R.E., 2008. An early Cenozoic perspective on greenhouse warming and carbon-cycle dynamics. Nature 451, 279–283.
Zhang, J., Li, J., Ruan, A., Wu, Z., Ding, W., 2016. The velocity structure of a fossil spreading Centre in the Southwest Sub-basin, South China Sea. Geol. J. 51, 548–561.
Zhang, Y., Yu, K., Qian, H., Fan, T., Yue, Y., Wang, R., Jiang, W., Xu, S., Wang, Y., 2020. The basement and volcanic activities of the Xisha Islands: evidence from the kilometre-scale drilling in the northwestern South China Sea. Geol. J. 571–583.
Zhao, M., Zhong, Y., Zhang, S., Zhang, H., Yang, H., Shi, Q., Yan, H., Tong, H., Xu, W., Yan, W., 2022. Coral community of Holocene coral reef in the southern South China Sea and its significance for reef growth. Palaeogeogr. Palaeoclimatol. Palaeoecol. 602, 111152.

Palaeogeography, Palaeoclimatology, Palaeoecology 665 (2025) 112835



Contents lists available at ScienceDirect

Palaeogeography, Palaeoclimatology, Palaeoecology

journal homepage: www.elsevier.com/locate/palaeo



Holocene coral reef carbonate REY geochemistry during the neomorphism from aragonite to calcite: A case study in the South China Sea

Wei Jiang [a], Yuwen Xiao [a], Kefu Yu [a,b,*], Rui Wang [a], Shendong Xu [c], Ning Guo [a], Tingwu Gu [a]

[a] Guangxi Laboratory on the Study of Coral Reefs in the South China Sea, School of Marine Sciences, Guangxi University, Nanning, China
[b] Southern Marine Sciences and Engineering Guangdong Laboratory (Guangzhou), Guangzhou, China
[c] Key Laboratory of Coastal Zone Environmental Processes and Ecological Remediation, Yantai Institute of Coastal Zone Research, Chinese Academy of Sciences, Yantai, China

ARTICLE INFO

Editor: Howard Falcon-Lang

Keywords:
Rare earth element and yttrium
Coral reef
Microbialite
Neomorphism
Marine carbonate

ABSTRACT

The geochemistry of rare earth elements and yttrium (REY with Y, REE without Y) in reefal carbonates is increasingly used to investigate both palaeoceanography and modern oceans. Nevertheless, the application of these methods to elucidate climate dynamics of the geologic past is limited by their vulnerability to diagenetic alterations. Given the meteoric transformation of aragonite to calcite, which represents an extremely unfavorable scenario for preserving the original marine signature, we focused on the REY geochemistry of a Holocene coral reef, obtained from Well CK2 in the northern South China Sea, which initiated at ~7.8 ka BP, but ceased to grow vertically at ~3.9 ka BP. The Holocene reefal carbonates have undergone neomorphism, transforming aragonite into calcite in a meteoric environment and enabling a direct comparison of REY distributions between the original aragonite and neomorphic calcite. Despite the preserved REY patterns of stabilized calcite closely mirroring those initially present in surface seawater, the ΣREE contents and Ce anomalies vary significantly, reflecting mixing of REY from reefal microbialites. Despite these disturbances, the Nd_N/Yb_N and Y/Ho ratios of Holocene reefal carbonates still demonstrate a highly conservative behavior during diagenesis. Our study indicates that the initial REY parameters, such as Nd_N/Yb_N and Y/Ho ratios, are frequently preserved in Holocene reefal carbonates, thus offering significant support for employing ancient marine limestones as indicators of marine REY geochemistry. Nevertheless, prudence is advised when utilizing ΣREE contents and Ce anomaly.

1. Introduction

Modern and ancient marine carbonates incorporate rare earth elements and yttrium (REY with Y, REE without Y) in proportions akin to those observed in ambient seawater (Luo et al., 2021; Saha et al., 2019; Saha et al., 2021; Webb and Kamber, 2000; Webb et al., 2009; Wyndham et al., 2004; Zhao and Jones, 2013). In recent years, the REY proxy in marine carbonates, including scleractinian corals and microbialites, has been used successfully for tracing marine input origins (Falcone et al., 2022; Saha et al., 2018; Saha et al., 2019; Saha et al., 2021; Wei et al., 2023a; Zhao and Zheng, 2014), environmental pollution (Jiang et al., 2017; Nguyen et al., 2013; Xie et al., 2023), and palaeoceanography and paleoclimate (Bi et al., 2019; Della Porta et al., 2015; Jia et al., 2024; Jiang et al., 2019; Kamber et al., 2014; Li et al., 2019; Liu et al., 2022; Tostevin et al., 2016; Zhang and Shields, 2022; Zhao et al., 2021). Although the fidelity and robustness of modern/ancient marine carbonates REY proxies are empirically established, the efficacy still relies on the direct synsedimentary contamination degree of terrigenous detritus and preservation of original REY signals during subsequent diagenesis (Webb et al., 2009).

Direct terrigenous contamination can be identified through the concurrent presence of reduced mobile elements, such as thorium (Th) and zirconium (Zr) (Nothdurft et al., 2004; Webb and Kamber, 2000), and the effects of diagenesis on REY geochemistry of marine carbonates can be evaluated by the geochemical and mineralogical proxies for diagenesis alteration, such as manganese (Mn)/strontium (Sr) ratio and oxygen isotope ($\delta^{18}O$) (Derry et al., 1994; Higgins et al., 2018; Kaufman and Knoll, 1995). Over the last decades, the above methods have been extensively utilized to evaluate the preservation of original seawater REY signature, and most studies verifies the consistent conservative behavior of REY in reefal carbonates throughout a variety of diagenetic changes (Jia et al., 2024; Jiang et al., 2019; Li and Jones, 2014; Liu et al.,

* Corresponding author at: Guangxi Laboratory on the Study of Coral Reefs in the South China Sea, School of Marine Sciences, Guangxi University, Nanning, China.
E-mail address: kefuyu@scsio.ac.cn (K. Yu).

https://doi.org/10.1016/j.palaeo.2025.112835
Received 15 May 2024; Received in revised form 19 February 2025; Accepted 19 February 2025
Available online 20 February 2025
0031-0182/© 2025 Elsevier B.V. All rights are reserved, including those for text and data mining, AI training, and similar technologies.

2022; Luo et al., 2021; Shen et al., 2023; Webb et al., 2009; Zhao and Jones, 2013). However, the majority of prior studies have centered on the pre-Holocene limestones or dolomites, which have undergone compaction and lithification. Furthermore, despite the inclusion of Holocene data in some studies, the distinctive characteristics of Holocene carbonates might be obscured in the whole core study, due to their relatively scarce data compared to Pleistocene or other geological strata.

In general, except for the dissolution and recrystallization of metastable carbonate minerals, the characteristics of REY in carbonates are expected to maintain stability over geological timescales (Zhong and Mucci, 1995). Therefore, the REY signatures of marine carbonates are always susceptible to modification during the early diagenetic stage, e.g., neomorphism from aragonite to calcite (Tanaka et al., 2003; Webb and Kamber, 2000; Webb et al., 2009), which has been considered as one of the most unfavorable scenarios for preserving the original REY signature (Webb et al., 2009). Despite the transformation of aragonite to calcite can also be found in pre-Holocene stratum, e.g., the Pleistocene scleractinian coral skeletons of Florida (Webb et al., 2009), it is more readily observed in Holocene strata.

Coral reefs are extensively distributed throughout the South China Sea (SCS) (Yu, 2012), which initiated at the late Oligocene or early Miocene (Fan et al., 2020; Li et al., 2023). Well CK2, drilled on an isolated carbonate platform in the SCS (Fig. 1), yielded core recovery rates averaging ~70 %, with most sections exceeding 80 %, thus providing highly suitable research materials dating back to the early Miocene. According to high-precision uranium(U)-series dating, the initiation of Holocene reefal carbonates, measuring 16.7 m in thickness, occurred approximately 7.8 thousand years before present (ka BP), while vertical accretion ceased around 3.9 ka BP (Ma et al., 2021; Qin et al., 2019). Due to the minimal terrigenous influence, the Holocene reefal carbonates present an exceptional opportunity for investigating the response of REY behavior during neomorphism. This study investigates the REY signatures of the Holocene stratum in Well CK2 with an aim to assess the impact of neomorphism from aragonite to calcite on the REY signature of marine carbonates. The findings will contribute towards evaluating marine carbonates suitability as geochemical archives for environmental studies.

2. Geological settings

SCS is one of the largest low-latitude marginal sea on the globe with an area of ~3.5 × 10^6 km^2, originally formed due to rapid seafloor spreading during the Cenozoic era (Barckhausen and Roeser, 2013). The Xisha Islands (17°07′-15°43′N, 111°11′-112°54′E) constitute a cluster of atolls located on an elevated submarine plateau in the northwestern SCS, encompassed by seawater at depths exceeding 1 km. The Xisha Islands exhibit a tropical monsoon climate, characterized by an annual precipitation ranging from 1300 to 2000 mm, an average seawater surface temperature ranging from 22 to 30 °C, and near-surface salinity levels ranging from 33.14 to 34.24 ‰. The carbonate platforms surrounding the Xisha Islands exhibited extensive development, with reef and platform growth displaying relatively high activity levels during the middle Miocene, decreasing significantly during the late Miocene, and ranging from moderate to active during the Pliocene and Pleistocene periods (Fan et al., 2020; Shao et al., 2017; Wu et al., 2014). Well CK2, drilled in 2013 on Chenhang Island (16°27′ N, 111°43′ E) in the southeast of the Yongle Atoll, comprises a Cenozoic carbonate succession extending to a depth of 873.55 m, along with the volcaniclastic basement reaching a depth of 928.75 m. Considering the relative stability of neotectonic activities in the study area, as well as the fact that the reef flat of modern coral reefs in the SCS is predominantly situated at low tide height, and with Well CK2's borehole positioned approximately 2.9 m above this modern reef flat, it can be inferred that originally, the top of Well CK2 was located around 13.8 m below the low tide level of present-day sea (Qin et al., 2019).

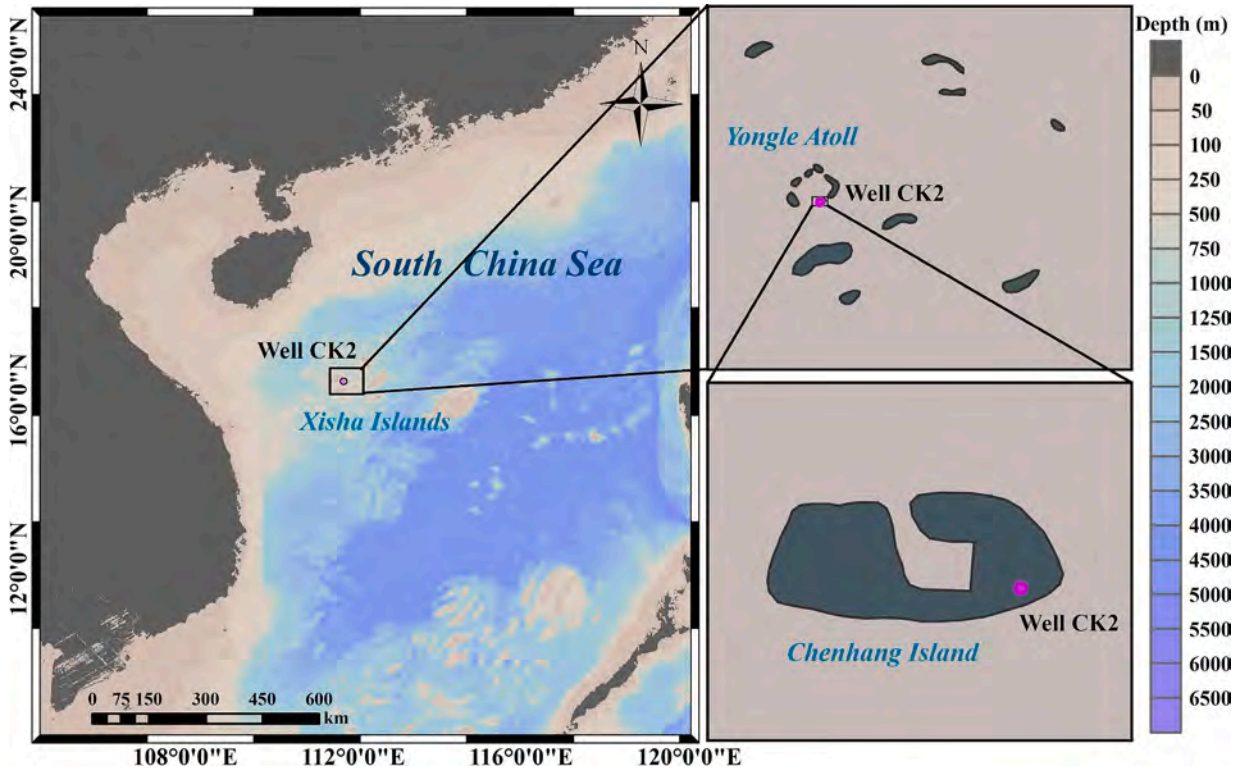


Fig. 1. Locality map of Well CK2 on the Chenhang Island of the Yongxing Atoll in the Xisha Islands, northern SCS.

3. Material and methods

3.1. Core chronology

Based on Qin et al. (2019) and Ma et al. (2021), the Pleistocene/Holocene boundary of Well CK2 was determined to be located 16.7 m below the drilling surface. The upper 16.7 m section of the core was sampled to obtain 18 well-preserved *Acropora* spp. Specimens (Fig. S1 in the Supplemental Materials) to establish a comprehensive chronostratigraphy of the Holocene coral reef. The samples were cleaned and sectioned to eliminate any surface impurities, e.g., drilling mud and loose sediments, subjected to ultrasonic oscillation in distilled water for debris particle removal, dried at 50 °C, and finally sealed in plastic bags. The U-series ages of the samples were determined by the Nu plasma multicollector inductively coupled plasma mass spectrometer at the University of Queensland, enabling precise determination of isotopic ratios and elemental concentrations with an accuracy within ±1–2 ‰ (2σ) (Clark et al., 2014). The U-thorium (Th) isotopic data and ^{230}Th dates can be seen in supporting information Table S1 and 11 samples were selected to establish the age framework based on the order from the youngest to the oldest in this study after removing age reversed samples (Fig. 2). The determination of age framework in details is provided in Ma et al. (2021).

3.2. Lithology and mineralogy

The mineral species and mass percentages were determined through the utilization of X'Pert PRO diffractometer according to 2θ angle and spectral peak intensity (Fig. S2). The lithological characteristics and mineralogy of Well CK2 were analyzed by conducting microscopic observations on about 300 thin sections using a polarizing microscope. The results indicate that the core from Well CK2, spanning from 16.7 to 0 m, predominantly consists of a coral debris mixture containing aragonite, high-Mg calcite and low-Mg calcite (Fig. 3). The entire core is comprised of identical constituent groups, predominantly coral (*Acropora* spp., accounting for 59.35 %) and fragments of coralline algae. The observation of coral, originally composed of aragonite, undergoing the aragonite-calcite transformation provided evidence for the existence of the aragonite-calcite transformation (Fig. S3).

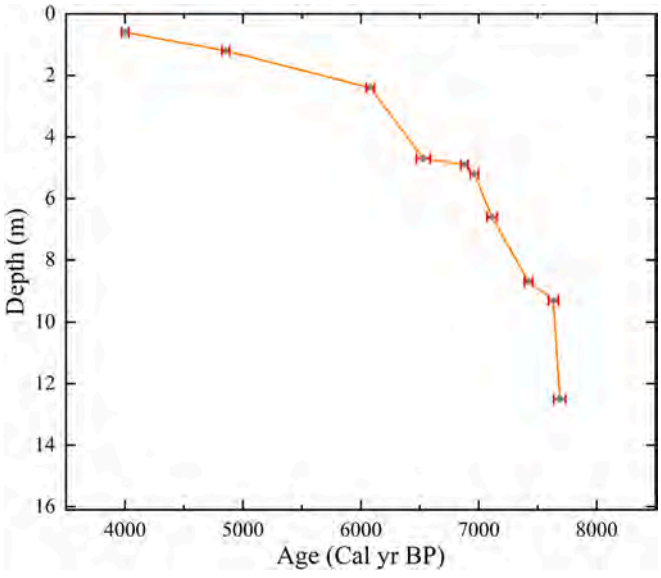


Fig. 2. Calibrated U-Th age framework of the Holocene section of Well CK2 core.

3.3. Geochemical analysis

Geochemical analyses of the samples were conducted at the Guangxi University, China. 14 carbonate powder samples from relatively well-preserved corals collected at an interval of ~1 m from the uppermost ~16.7 m section of Well CK2. The $\delta^{18}O$ analysis was conducted using a Finnigan MAT-253 stable isotope mass spectrometer coupled with a Fairbanks carbonate preparation device. The isotopic ratios were presented in the per mil (‰) convention and normalized to the V-PDB in accordance with the GBW04405 standard. Repeated measurements of this standard produced a standard deviation of 0.08 ‰ for $\delta^{18}O$. The carbonate samples were processed and analyzed for elemental compositions using standard techniques with an inductively coupled plasma emission mass spectrometer. The isotopes of REY (^{89}Y, ^{139}La, ^{140}Ce, ^{141}Pr, ^{146}Nd, ^{149}Sm, ^{153}Eu, ^{159}Tb, ^{160}Gd, ^{161}Dy, ^{165}Ho, ^{167}Er, ^{169}Tm, ^{172}Yb, and ^{175}Lu), along with other trace metals (^{31}P, ^{55}Mn, ^{57}Fe, ^{88}Sr, and ^{92}Zr), exhibit distinctive signals. The levels of barium oxid and rare earth oxide were determined by analyzing pure elemental solutions, with appropriate corrections made for any potential interferences. The concentrations of phosphorus pentoxide (P_2O_5) and ferric oxide (Fe_2O_3) applied in this study were determined based on the P and Fe concentrations. The analyzed data were assessed for accuracy and precision through a comprehensive quality assurance and quality control program, which encompassed the utilization of reagent blanks, duplicate tests, and certified geochemical reference materials (GBW07129, GBW07133, GBW07135) with deviations below 5 %. The detailed procedures were described in Xu et al. (2019) and Jiang et al. (2019).

3.4. Interpretations for proxies

The distribution patterns of REY in Holocene carbonate samples are demonstrated by normalizing the REY against the standard Post-Archean Average Shale (PAAS) (McLennan, 1989) and plotting them on a logarithmic scale as a function of the atomic numbers of the respective elements. The X_N represent the PAAS-normalized concentrations of X, and the Nd_N/Tb_N ratio is used to represent light REE (LREE)/heavy REE (HREE). The Y/Ho mass ratios are computed without undergoing any form of normalization. Ce anomaly ($Ce/Ce^* = Ce/(Pr^2/Nd)$) and Eu anomaly ($Eu/Eu^* = Eu \times 2/(Sm + Gd)$) are calculated by geometrically/linear extrapolating Pr and Nd, Sm and Gd, respectively.

4. Results

4.1. Lithofacies, depositional facies and mineralogy

The uppermost 16.7 m interval of Well CK2 consists predominantly of unconsolidated coarse sediments, comprising coral, large benthic foraminifera, mollusks, and coralline algae. The particle size distribution is dispersed and the frequency of the particle size is not well-defined or abrupt, indicating a shallow seawater environment characterized by moderate to high energy levels. The Holocene sedimentary environment of Well CK2 was characterized by unconsolidated bioclastic limestone and coral debris.

The upper 16.7 m section of Well CK2 can be classified into three units based on mineral compositions (Fig. 3). Unit I (0–~2 m) primarily consists of aragonite, with minor occurrences of high-Mg calcite. In Unit II (~2–~10 m), the majority of primary aragonite has undergone transformation to high-Mg calcite within this unit. Unit III (~10–16.7 m) is characterized by predominant low-Mg calcite, accompanied by minor amounts of aragonite or high-Mg calcite.

4.2. Elemental and isotopic geochemical characteristics

The REY proxies of the Well CK2 above 16.7 m are presented in Fig. 3. The Ce anomaly, Eu anomaly and Nd_N/Yb_N ratios do not exhibit any discernible trends except several extremes, with the respective

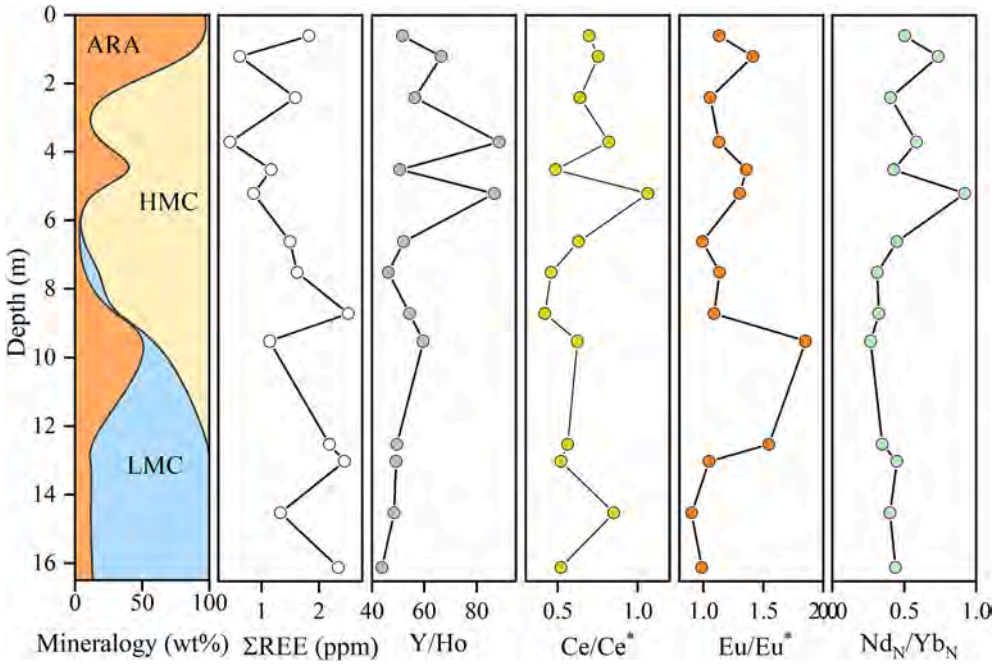


Fig. 3. Mineral compositions (ARA: aragonite; HMC: high-Mg calcite; LMC: low-Mg calcite) and REY profiles from the top ~16.7 m section of Well CK2 core.

ranges of 0.42–1.06 (average ± standard deviation (SD): 0.65 ± 0.17), 0.90–1.85 (average ± SD: 1.21 ± 0.25), and 0.27–0.92 (average ± SD: 0.47 ± 0.17). A visible secular variation trend can be observed in the sequence of ΣREE content and Y/Ho ratios, with the respective ranges of 0.45–2.50 ppm (average ± SD: 1.54 ± 0.64 ppm) and 43.70–88.58 (average ± SD: 57.37 ± 13.53). All the carbonate samples have typical seawater REY patterns, characterized by the depletion in LREE compared to the HREE, superchondritic Y/Ho ratios, a slight positive Eu anomaly, and a negative Ce anomaly, as observed in Fig. 4.

As a typical detrital element, Zr ranges from 0.26 to 1.99 ppm, with an average of 0.86 ± 0.42 ppm. The Mn and Sr have the ranges of 4.07–83.62 ppm (average ± SD: 30.98 ± 22.53 ppm) and 0.52–9.25 % (average ± SD: 1.41 ± 2.18 %), respectively. The P_2O_5 and Fe_2O_3 have the ranges of 0.04–0.15 % (average ± SD: 0.08 ± 0.03 %) and 0.06–0.33 % (average ± SD: 0.17 ± 0.08 %), respectively. The $\delta^{18}O$ values range from −5.06 to −2.10 ‰ (average ± SD: −3.43 ± 0.77 ‰) throughout the uppermost 16.7 m interval of Well CK2.

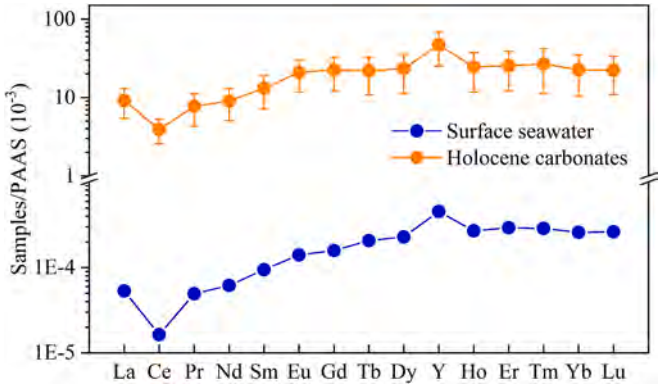


Fig. 4. The PAAS- normalized REY patterns of surface seawater samples from SCS and carbonates in the Well CK2 (0–16.7 m). The REY curve represented the average ± standard deviation. The data of SCS seawaters is from Alibo and Nozaki (2000).

5. Discussion

5.1. Impacts of contaminations and diagenesis

The exogenous sources, characterized by elevated REY contents and distinctive REY patterns, may overprint the carbonate REY signals (Nothdurft et al., 2004). This isolated carbonate system contained minimal fine siliciclastic particulates, which is consistent with the low ΣREE levels observed. In addition, the non-carbonate contaminations were always evaluated based on several criteria, including Zr for detritus, Fe for Fe-Mn(oxyhydr)oxides, and P for phosphates (Nothdurft et al., 2004; Zhao et al., 2022). The Zr, abundant in shale (~210 ppm), occurs in concentrations ~0.86 ppm in carbonate samples, indicating <1 % shale contamination. Despite the potential influences from the very small amounts of shale with high REY concentrations on REY patterns, this possibility has been dismissed due to the lack of significant correlation between ΣREE and Zr (Fig. 5). Likewise, the low Fe_2O_3 concentrations (<0.35 %) and absence of correlation observed in the plot depicting Fe_2O_3 concentrations against REY parameters (Fig. S4) suggests that Fe-Mn(oxyhydr)oxides do not exert a significant control over REY patterns. The P_2O_5 concentrations (<0.2 %) exhibit no significant correlation with the Y/Ho ratios and Nd_N/Yb_N, but they do display a strong correlation with ΣREE and Ce anomalies (Fig. 6). This suggests that phosphates, which can disproportionately incorporate REY and are susceptible to diagenesis alteration (German and Elderfield, 1990; Reynard et al., 1999), account for the observed effects. Therefore, while the ΣREE and Ce anomalies of carbonate samples may not accurately reflect the primary signal, it is expected that the signals of Y/Ho ratios and Nd_N/Yb_N ratios may be well-preserved in these samples.

The diagenetic processes involve the early marine diagenesis, chemical exchange between the solid phase and pore-fluid, transforming metastable aragonite and high-Mg calcite into low-Mg calcite rocks (Higgins et al., 2018). The sedimentary composition of the area is predominantly loose, with a notable lack of strong cementation. Only acicular aragonite cement can be observed within the interstices of certain coral fragments, which is commonly believed to have formed during the quasi-simultaneous period in a marine environment and likely shares similar REE chemical characteristics with seawater (Sholkovitz and Shen, 1995; Webb et al., 2009). Meanwhile, early

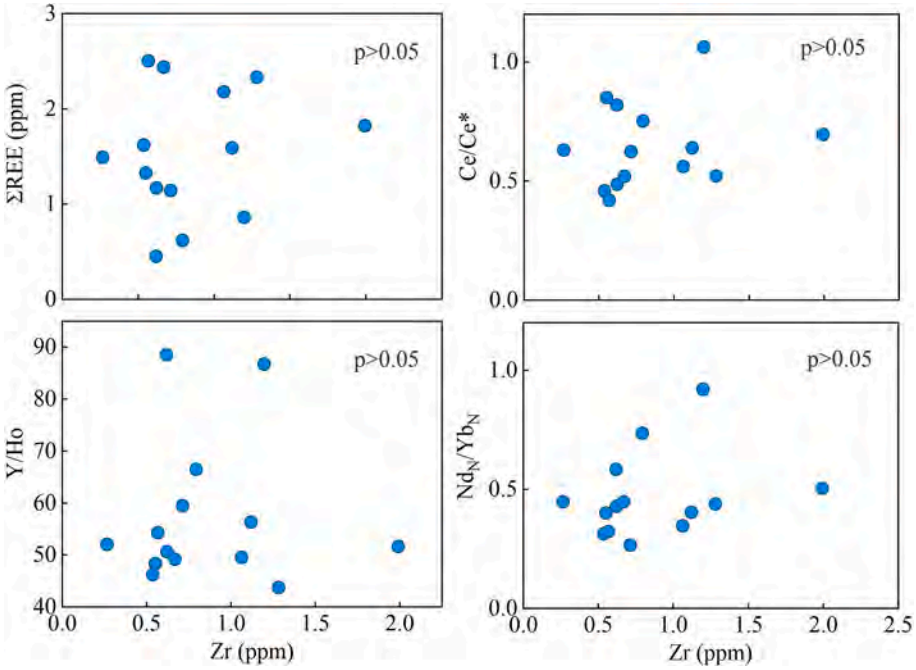


Fig. 5. Co-variation plots of REY parameters against Zr in the top ~16.7 m section of Well CK2 core.

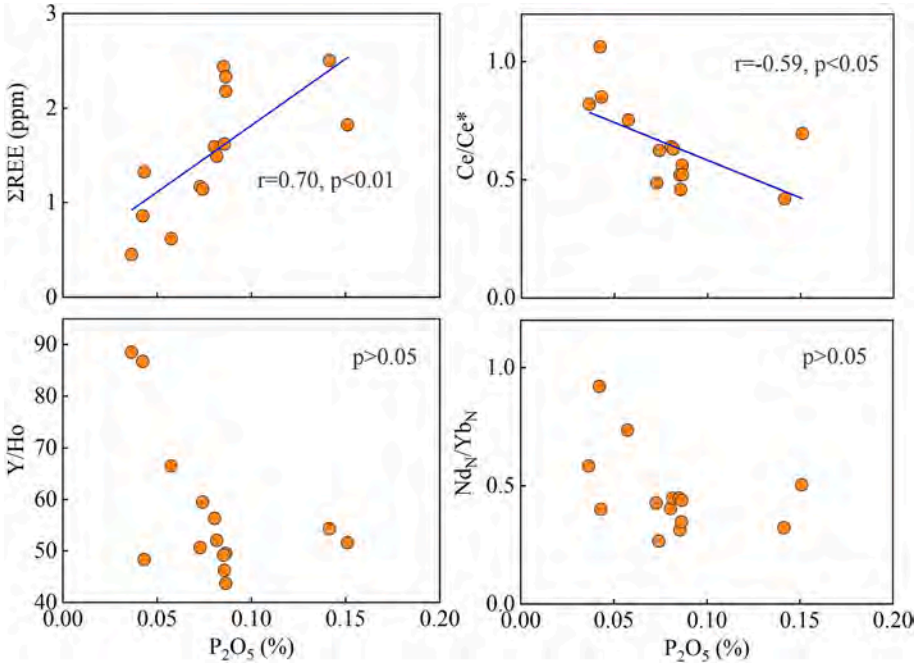


Fig. 6. Co-variation plots of REY parameters against P_2O_5 in the top ~16.7 m section of Well CK2 core.

marine diagenesis has been reported not to invalidate the utility of shallow-marine carbonates as proxies for the seawater chemistry (Wei and Zhang, 2024). Therefore early marine diagenesis can not affect the behavior of REY. The mineralogy (%) exhibits a poor correlation with the REY parameters (Fig. 7), indicating that the stabilization of the REY patterns of neomorphic calcites during the diagenetic processes (Frimmel, 2009; Webb and Kamber, 2000; Webb et al., 2009). From the view of geochemistry, the majority of diagenetic fluids typically exhibit low Sr concentrations and high Mn concentrations (Kaufman and Knoll, 1995). Additionally, meteoric fluids are characterized by isotopically depleted $\delta^{18}O$ values (Derry et al., 1994). The commonly employed thresholds for assessing the preservation of primary signals are about 1 for Mn/Sr ratios and − 10 ‰ for $\delta^{18}O$ values (Higgins et al., 2018). In the carbonate samples, the $\delta^{18}O$ results varied between −5.06 ‰ and − 2.10 ‰, with an average of −3.43 ‰, all surpassing the lower limit of −10 ‰. Meanwhile, the $\delta^{18}O$ values exhibit weak correlations with both the ΣREE and Y/Ho ratios across various sedimentary facies. Likewise, the Mn/Sr ratios ranged from 0.0005 to 0.0141, with an average value of 0.0036, significantly below the threshold of 1. The correlation between the Mn/Sr ratios and Y/Ho ratios is found to be poor, whereas a significant association between the Mn/Sr ratios and ΣREE can be observed (Fig. 8).

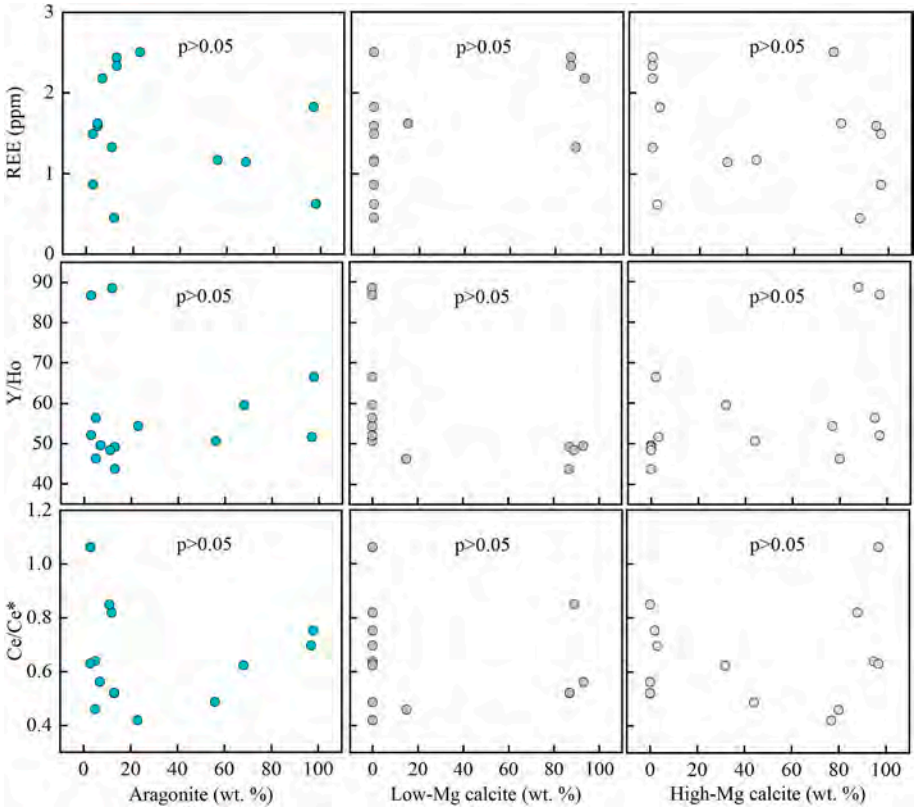


Fig. 7. Co-variation plots of REY parameters against mineral compositions in the top ~16.7 m section of Well CK2 core.

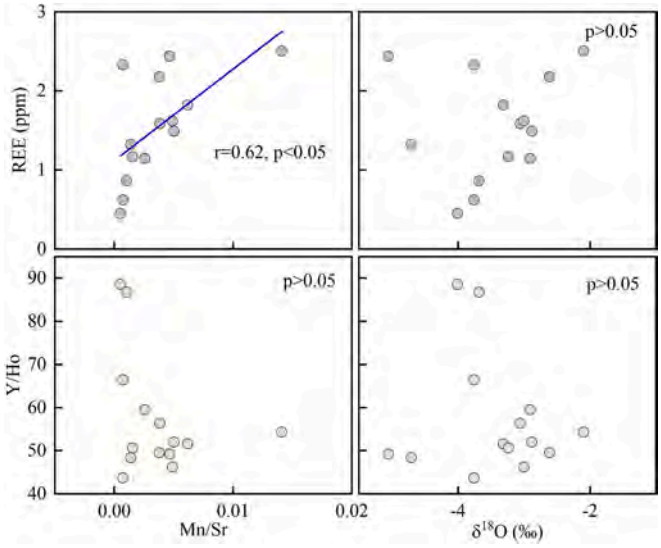


Fig. 8. Co-variation plots of REY parameters against Mn/Sr ratios and $\delta^{18}O$ values in the top ~16.7 m section of Well CK2 core.

Considering the significant correlations among Mn/Sr ratios, P_2O_5, and ΣREE (Figs. 6 and 8), we inferred that the phosphates were affected by diagenetic alteration, resulted in the variations in ΣREE (German and Elderfield, 1990; Reynard et al., 1999). In fact, there are a certain amount of phosphates, such as microbialites containing phosphate, fish teeth and bones, crustacea, lingulata etc., in the Holocene sediments, and P could also be bound to the carbonate grains (Dodd et al., 2021; Monbet et al., 2007; Ning et al., 2020). Furthermore, it is plausible that the recrystallization process of apatite contributes to the reenrichment of REY (Liu et al., 2023). The weak correlation between P_2O_5 and Ce/Ce* is likely transmitted from the strong negative correlation observed between ΣREE and Ce/Ce* ($r = 0.67$, $p < 0.01$).

5.2. REE behavior during neomorphism

In comparison to the overlying aragonite, the neomorphic calcite seems to exhibit distinctive characteristics (Fig. 3), including an increased ΣREE concentration, a heightened negative Ce anomaly, and an augmented depletion of light REE (lower Nd_N/Yb_N ratios), aligning with the REE parameters observed in Pleistocene scleractinian coral skeletons during meteoric diagenesis (Webb et al., 2009). Despite the weak correlation between ΣREE and mineralogy, a visible increase in REE concentration is observed from aragonite to calcite (Fig. 3). The majority of REY seem to be preserved through neomorphism, and the neomorphic calcite samples exhibit higher REY levels compared to aragonite (Fig. 3), albeit with predominantly similar PAAS-normalized patterns (Fig. 4). One hand, Webb et al. (2009) suggested that: (i) during the dissolution of calcite, the REY released are promptly sequestered by the adjacent deposited calcite; and (ii) upon the complete dissolution of marine limestone, the REY released will subsequently be sequestered by the newly formed calcite cement, leading to a slight enrichment of these elements within the new calcite. On the other hand, in comparison to the interactions between fluids and aragonite, the REY exhibit high distribution coefficients between calcite and diagenetic fluids, along with a strong tendency to bind to the surfaces of carbonate structures, which may result in the sequestration of REY during neomorphism (Lakshtanov and Stipp, 2004; Stipp et al., 2003). In general, the empirical distribution coefficients of REY between aragonite coral skeletons and fluids typically fall within the range of 1 to 5 (Akagi et al., 2004; Sholkovitz and Shen, 1995; Wyndham et al., 2004). Despite the empirical and experimental evidences are contradictory concerning calcite (Scherer and Seitz, 1980; Tanaka and Kawabe, 2006; Webb and Kamber, 2000; Zhong and Mucci, 1995), the REY partition coefficients between fluids and calcite exhibit significantly higher values (e.g., 2.5 to

10 (Terakado and Masuda, 1988), ~100 (Scherer and Seitz, 1980), ~300 (Toyama and Terakado (2019); Webb and Kamber, 2000)) compared to those observed between fluids and aragonite in equivalent experiments. Considering that the vast majority of samples, initially composed of aragonite, have now transformed into high-Mg calcite and low-Mg calcite, it is likely that the relatively higher ΣREY content in these carbonates can be attributed to their diagenetic processes. Despite the significant changes in ΣREE concentrations, the calcite REY patterns were retained largely intact due to proportionably scavenging of REY during the neomorphic calcite precipitation (Stipp et al., 2003) and the low levels of fluid REY concentrations.

Direct contamination by particulate matter and the dissolution of microbialites can also increase REY concentration (Cabioch et al., 2006; Webb et al., 2009; Webb and Kamber, 2000). Overall, the selective uptake of LREE by particulate matter could explain the nearly flat distribution and the minimal negative Ce anomaly (Webb et al., 2009). Obviously, the relatively low Nd_N/Yb_N ratios and well-developed negative Ce anomalies of neomorphic calcites (Fig. 3) ruled out the possibility of particulate matters. Reefal microbialites represent the advanced stage of encrustation on deceased coral colonies or, more commonly, on related encrusting organisms, thereby forming surface crusts (Camoin et al., 2006). Microbialites are commonly found within cavities of coral frameworks (Heindel et al., 2012) and have been demonstrated to contemporaneously develop alongside reef frameworks or slightly postdate associated corals by a few centuries (Webb and Jell, 2006; Westphal et al., 2010). As a feature of rapid sea-level rise and abrupt climatic changes, microbialites have been identified widespread development in the Holocene and modern reefs in the South China Sea (Gong et al., 2017; Heindel et al., 2012; Shen and Wang, 2008; Teng and Shen, 2008; Yang et al., 2023; Zhang et al., 2022). Reefal microbialites contain REY in higher concentration than corals (Webb and Kamber, 2000), thus enhancing testability to facilitate precise value assessment and providing robust seawater REY proxies for ancient reefs and carbonate platforms (Kamber and Webb, 2001; Kamber et al., 2014; Nothdurft et al., 2004; Olivier and Boyet, 2006). The dissolution of microbialite would not only result in an increased concentration of REY in pore fluids but also introduce an increasing negative Ce anomaly (Cabioch et al., 2006; Webb and Kamber, 2000). Therefore, we hypothesize that the microbialites, which exhibited sensitivity to diagenetic alteration, may account for the strong associations observed between ΣREE and Ce anomaly ($r = -0.67$, $p < 0.01$), as well as the correlation between ΣREE and Mn/Sr ratio (Fig. 8). It's worth noting that the growth of microbialites is typically succeeded by the formation of phosphatic-iron-manganese crusts, with phosphatic films frequently interlayering with microbial laminae on the external surfaces of the crusts and coating borings within both the microbialite and underlying red algal-foraminiferal encrustations (Camoin et al., 2006). Therefore, the microbialites containing phosphate might explain the significant correlations among P_2O_5, ΣREE and Ce anomaly (Fig. 6 and S2).

The reduction in LREE depletion in carbonates is thought to result from several factors, including the influences of terrigenous inputs (Nothdurft et al., 2004; Webb et al., 2009), variations in depositional settings (Kamber and Webb, 2001), and/or differences in diagenetic histories (Mazumdar et al., 2003). The Nd_N/Yb_N ratios, however, exhibit no discernible variations with respect to the diagenetic indices and mineral compositions (Fig. S5), implying that diagenesis exerted negligible influence on the depletion of LREEs. Salas-Saavedra et al. (2022) reported that reefal microbialit-hosted REY distributions (Nd_N/Yb_N and Y/Ho ratio) were consistent with shallow oxygenated seawater, and might provide high-quality proxies for ambient water quality. However, Mazumdar et al. (2003) proposed that the basicity of pore fluids in both the unsaturated and saturated zones, which increases due to organic matter degradation, facilitates the incorporation of HREE into the carbonate lattice. The transformation of aragonite and/or high-Mg calcite into low-Mg calcite potentially occurred within a mixed freshwater and seawater environment (MacNeil and Jones, 2003). Nevertheless, the limited depletion of LREE and the absence of any observed correlation between Nd_N/Yb_N ratios and diagenetic indices in carbonates may suggest negligible effects of meteoric processes throughout the transformation of aragonite and calcite. Actually, meteoric diagenesis does not invariably obscure the geochemical signature of primary carbonate minerals (Wei et al., 2023b). In this study, the Nd_N/Yb_N and Y/Ho ratios, which demonstrate limited correlations with both diagenetic alteration and non-carbonate contamination indexes, should be preserved as the primary REY signature during the neomorphism processes.

5.3. Interpretation of REY patterns

The Holocene carbonate REY patterns are characterized by (1) positive La anomalies, (2) negative Ce anomalies, (3) LREE depletion relative to HREE, and (4) superchondritic Y/Ho molar ratios (Fig. 4), similar to those found in other Quaternary marine carbonates (Jia et al., 2024; Luo et al., 2021; Webb and Kamber, 2000; Webb et al., 2009) and modern seawater in the South China Sea (Alibo and Nozaki, 1999, 2000). The Eu anomalies of most samples vary within the typical range of seawater (0.9–1.5) (Tostevin et al., 2016), and exhibit no clear trend. However, subtle distinctions exist among the REY patterns of the three units in terms of their Ce anomalies, Nd_N/Yb_N and Y/Ho ratios. All the Holocene carbonate samples exhibited negative Ce anomalies (Fig. 3). Tanaka et al. (2003) suggested that the Ce/Ce* of carbonates might indicate the depth of the seawater where the initial diagenetic processes occurred. The Ce/Ce* ratios of carbonates are consistent with those of modern surface seawater (Alibo and Nozaki, 2000), suggesting the presence of an oxygen-rich environment during their formation. The predominant process responsible for negative Ce anomalies in seawater is the oxidation of dissolved Ce(III) to particulate Ce(IV), associated with redox. Despite the possible influence of phosphates, the Holocene carbonate samples still exhibit the oxidation characteristics inherent to the original surface seawater.

Excluding the potential influences of mineralogy (Webb et al., 2009) and diagenesis (Azmy et al., 2011; Tanaka et al., 2003) on REY in carbonates, the variations in the Nd_N/Yb_N and Y/Ho ratios should primarily reflect the composition of the seawater during carbonate formation (Azmy et al., 2011). The observed variations in the Nd_N/Yb_N ratios of carbonates are likely attributed to fluctuations in the REY composition of seawater, as carbonates solely acquire REY from the surrounding seawater. The Nd_N/Yb_N ratios exhibit an increasing trend with depth in contemporary seawater (Alibo and Nozaki, 1999, 2000). Nonetheless, the gradual rise in Nd_N/Yb_N ratios with depth cannot be exclusively linked to differences in the initial depositional settings, since all the carbonates were formed in shallow marine environments. As a result, the recorded increase in Nd_N/Yb_N ratios with depth (Fig. 3) could indicate a long-term shift in the REY composition of seawater. The Nd_N/Yb_N ratio, indicative of LREE depletion, is consistently attributed to the preferential affinity of LREE towards scavenging processes prevalent in seawater (Wyndham et al., 2004). However, many factors including the continental weathering inputs (Akagi et al., 2004; Caetano-Filho et al., 2018; Saha et al., 2019; Wyndham et al., 2004) and mineralization and desorption processes occurring on the biogenic particles (Li et al., 2019) may influence the LREE depletion of seawater. Compared with modern seawaters in the SCS, the LREE depletion of carbonate samples are all within the range of surface seawater (Alibo and Nozaki, 2000). Considering the narrow range (0.27–0.92), the Nd_N/Yb_N ratios of Holocene carbonate might represent the secular change of LREE depletion of surface seawater in the open ocean, rather than being influenced by other impact factors.

Nozaki et al. (1997) proposed that Y and Ho exhibit relatively short residence times in the marine environment, with their fractionation primarily governed by scavenging processes associated with the complexation of Y and Ho on particles. The Y/Ho ratios are highest in open ocean settings, exceeding 44; they are intermediate in restricted marine environments, ranging from 25 to 44; and lowest in freshwater

systems and shale deposits, below 25 (Nozaki et al., 1997; Tostevin et al., 2016). The Y/Ho ratios of all samples, which are consistent with a seawater origin (Alibo and Nozaki, 2000), exhibit depth-dependent variations (Fig. 3). Overall, the Y/Ho ratios in surface seawater are primarily influenced by continental inputs and local oceanographic processes (Mazumdar et al., 2003). The Y/Ho ratios of Holocene carbonate samples fall between those of open ocean water and shale/freshwater (Nozaki et al., 1997; Tostevin et al., 2016), indicating a blend of terrigenous materials and oceanic seawater. In fact, the reef carbonate Y/Ho ratio has been utilized as reliable proxy for enhanced terrigenous inputs in the South China Sea (Jia et al., 2024). According to Fig. 3, our findings indicate an overall declining trend in terrigenous inputs over time.

6. Conclusions

We have conducted a REY analysis of a Holocene reef core in the Xisha Islands, northern SCS. Our findings suggest that Holocene reef carbonates preserve certain original REY signatures, such as Nd_N/Yb_N and Y/Ho ratios, derived from the surface seawater in which they formed, provided that they experience minimal terrigenous input and diagenetic alterations. Despite the REY parameters and patterns are consistent with those observed in other Holocene carbonate cores/corals in the SCS, the ΣREE contents should be impacted by both neomorphism and phosphates. In addition, the Ce anomaly variations were associated with the phosphates. We inferred that the reefal microbialites, which exhibited sensitivity to diagenetic alteration, might be responsible for the variations of ΣREE contents and Ce anomaly during the neomorphism. Hence, we postulate that the Nd_N/Yb_N and Y/Ho ratios of Holocene reef carbonates can serve as crucial indicators for understanding paleoceanography. However, caution is necessary when using ΣREE contents and Ce anomaly for analysis.

CRediT authorship contribution statement

Wei Jiang: Writing – review & editing, Writing – original draft, Visualization, Resources, Methodology, Investigation, Formal analysis, Data curation, Conceptualization. **Yuwen Xiao:** Writing – review & editing, Investigation, Formal analysis. **Kefu Yu:** Supervision, Resources, Investigation, Funding acquisition, Data curation, Conceptualization. **Rui Wang:** Investigation, Data curation. **Shendong Xu:** Investigation, Data curation. **Ning Guo:** Writing – review & editing. **Tingwu Gu:** Writing – review & editing.

Declaration of competing interest

The authors declare that they have no known competing financial interests or personal relationships that could have appeared to influence the work reported in this paper.

Acknowledgments

This work was financially supported by the National Natural Science Foundation of China (Grant Nos. 42030502, 41976059 and 42090041), National Key Research and Development Program of China (Grant No. 2023YFF0804801) and the major talent project of Guangxi Zhuang Autonomous Region (GXR-1BGQ2424020). The authors thank Dr. Tianlai Fan, Dr. Siqi Wu, Yeman Qin, Yifang Ma from Guangxi University for their work and helpful advices. Thanks are due to the responsible editor and anonymous reviewers for their critical reviews, which greatly improved our paper.

Appendix A. Supplementary data

Supplementary data to this article can be found online at https://doi.org/10.1016/j.palaeo.2025.112835.

Data availability

Data will be made available on request.

References

Akagi, T., Hashimoto, Y., Fu, F., Tsuno, H., Tao, H., Nakano, Y., 2004. Variation of the distribution coefficients of rare earth elements in modern coral-lattices: species and site dependencies. Geochim. Cosmochim. Acta 68, 2265–2273.
Alibo, D.S., Nozaki, Y., 1999. Rare earth elements in seawater: particle association, shale-normalization, and Ce oxidation. Geochim. Cosmochim. Acta 63, 363–372.
Alibo, D.S., Nozaki, Y., 2000. Dissolved rare earth elements in the South China Sea: Geochemical characterization of the water masses. J. Geophys. Res. Atmos. 105, 28771–28784.
Azmy, K., Brand, U., Sylvester, P., Gleeson, S.A., Logan, A., Bitner, M.A., 2011. Biogenic and abiogenic low-Mg calcite (bLMC and aLMC): Evaluation of seawater-REE composition, water masses and carbonate diagenesis. Chem. Geol. 280, 180–190.
Barckhausen, U., Roeser, H.A., 2013. Seafloor Spreading Anomalies in the South China Sea Revisited, Continent-Ocean Interactions within East Asian marginal Seas. Am. Geophys. Union 121–125.
Bi, D., Zhai, S., Zhang, D., Xiu, C., Liu, X., Liu, X., Jiang, L., Zhang, A., 2019. Geochemical Characteristics of the Trace and rare Earth elements in Reef Carbonates from the Xisha Islands (South China Sea): Implications for Sediment Provenance and Paleoenvironment. J. Ocean Univ. China 18, 1291–1301.
Cabioch, G., Camoin, G., Webb, G.E., Le Cornec, F., Garcia Molina, M., Pierre, C., Joachimski, M.M., 2006. Contribution of microbialites to the development of coral reefs during the last deglacial period: Case study from Vanuatu (South-West Pacific). Sediment. Geol. 185, 297–318.
Caetano-Filho, S., Paula-Santos, G.M., Dias-Brito, D., 2018. Carbonate REE + Y signatures from the restricted early marine phase of South Atlantic Ocean (late Aptian – Albian): the influence of early anoxic diagenesis on shale-normalized REE + Y patterns of ancient carbonate rocks. Palaeogeogr. Palaeoclimatol. Palaeoecol. 500, 69–83.
Camoin, G., Cabioch, G., Eisenhauer, A., Braga, J.C., Hamelin, B., Lericolais, G., 2006. Environmental significance of microbialites in reef environments during the last deglaciation. Sediment. Geol. 185, 277–295.
Clark, T.R., Zhao, J.-X., Roff, G., Feng, Y.-X., Done, T.J., Nothdurft, L.D., Pandolfi, J.M., 2014. Discerning the timing and cause of historical mortality events in modern Porites from the Great Barrier Reef. Geochim. Cosmochim. Acta 138, 57–80.
Della Porta, G., Webb, G.E., McDonald, I., 2015. REE patterns of microbial carbonate and cements from Sinemurian (lower Jurassic) siliceous sponge mounds (Djebel Bou Dahar, High Atlas, Morocco). Chem. Geol. 400, 65–86.
Derry, L.A., Brasier, M.D., Corfield, R.M., Rozanov, A.Y., Zhuravlev, A.Y., 1994. Sr and C isotopes in lower Cambrian carbonates from the Siberian craton: a paleoenvironmental record during the 'Cambrian explosion'. Earth Planet. Sci. Lett. 128, 671–681.
Dodd, M.S., Zhang, Z., Li, C., Algeo, T.J., Lyons, T.W., Hardisty, D.S., Loyd, S.J., Meyer, D.L., Gill, B.C., Shi, W., Wang, W., 2021. Development of carbonate-associated phosphate (CAP) as a proxy for reconstructing ancient ocean phosphate levels. Geochim. Cosmochim. Acta 301, 48–69.
Falcone, E.E., Federico, C., Boudoire, G., 2022. Geochemistry of trace metals and rare Earth elements in shallow marine water affected by hydrothermal fluids at Vulcano (Aeolian Islands, Italy). Chem. Geol. 593, 120756.
Fan, T., Yu, K., Zhao, J., Jiang, W., Xu, S., Zhang, Y., Wang, R., Wang, Y., Feng, Y., Bian, L., Qian, H., Liao, W., 2020. Strontium isotope stratigraphy and paleomagnetic age constraints on the evolution history of coral reef islands, northern South China Sea. GSA Bull. 132, 803–816.
Frimmel, H.E., 2009. Trace element distribution in Neoproterozoic carbonates as palaeoenvironmental indicator. Chem. Geol. 258, 338–353.
German, C.R., Elderfield, H., 1990. Application of the Ce anomaly as a paleoredox indicator: the ground rules. Paleoceanography 5, 823–833.
Gong, S.-Y., Li, H.-C., Siringan, F.P., Zhao, M., Kang, S.-C., Chou, C.-Y., 2017. AMS Carbon-14 dating of microbial carbonates in Holocene coral reefs, Western Luzon, Philippines. Quat. Int. 447, 27–34.
Heindel, K., Birgel, D., Brunner, B., Thiel, V., Westphal, H., Gischler, E., Ziegenbalg, S.B., Cabioch, G., Sjövall, P., Peckmann, J., 2012. Post-glacial microbialite formation in coral reefs of the Pacific, Atlantic, and Indian Oceans. Chem. Geol. 304-305, 117–130.
Higgins, J.A., Blättler, C.L., Lundstrom, E.A., Santiago-Ramos, D.P., Akhtar, A.A., Crüger Ahm, A.S., Bialik, O., Holmden, C., Bradbury, H., Murray, S.T., Swart, P.K., 2018. Mineralogy, early marine diagenesis, and the chemistry of shallow-water carbonate sediments. Geochim. Cosmochim. Acta 220, 512–534.
Jia, Y., Wu, H., Yan, W., Zhang, C., Hu, B., Zhang, J., Tian, L., Deng, C., 2024. Rare earth element geochemistry of reef carbonates in the South China Sea since the Miocene: Insights into paleoclimatic significance. J. Asian Earth Sci. 265, 106094.
Jiang, W., Yu, K.F., Song, Y.X., Zhao, J.X., Feng, Y.X., Wang, Y.H., Xu, S.D., 2017. Coral trace metal of natural and anthropogenic influences in the northern South China Sea. Sci. Total Environ. 607-608, 195–203.
Jiang, W., Yu, K., Fan, T., Xu, S., Wang, R., Zhang, Y., Yue, Y., Zhao, J.-X., Feng, Y.-X., Wei, C., Wang, S., Wang, Y., 2019. Coral reef carbonate record of the Pliocene-Pleistocene climate transition from an atoll in the South China Sea. Mar. Geol. 411, 88–97.

Kamber, B.S., Webb, G.E., 2001. The geochemistry of late Archaean microbial carbonate: implications for ocean chemistry and continental erosion history. Geochim. Cosmochim. Acta 65, 2509–2525.
Kamber, B.S., Webb, G.E., Gallagher, M., 2014. The rare earth element signal in Archaean microbial carbonate: information on ocean redox and biogenicity. J. Geol. Soc. Lond. 171, 745–763.
Kaufman, A.J., Knoll, A.H., 1995. Neoproterozoic variations in the C-isotopic composition of seawater: stratigraphic and biogeochemical implications. Precambrian Res. 73, 27–49.
Lakshtanov, L., Stipp, S., 2004. Experimental study of europium (III) coprecipitation with calcite. Geochim. Cosmochim. Acta 68, 819–827.
Li, G., Xu, W., Luo, Y., Liu, J., Zhao, J., Feng, Y., Cheng, J., Sun, Z., Xiang, R., Xu, M., Yan, W., 2023. Strontium isotope stratigraphy and LA-ICP-MS U-Pb carbonate age constraints on the Cenozoic tectonic evolution of the southern South China Sea. GSA Bull. 135, 271–285.
Li, R., Jones, B., 2014. Evaluation of carbonate diagenesis: a comparative study of minor elements, trace elements, and rare-earth elements (REE+Y) between Pleistocene corals and matrices from Grand Cayman, British West Indies. Sediment. Geol. 314, 31–46.
Li, X., Liu, Y., Wu, C.-C., Sun, R., Zheng, L., Lone, M.A., Shen, C.-C., 2019. Coral-inferred monsoon and biologically driven fractionation of offshore seawater rare earth elements in Beibu Gulf, northern South China Sea. Solid Earth Sci. 4, 131–141.
Liu, X., Fan, H., Zhang, H., Xiao, C., Yang, H., Zhou, T., Tang, Y., Shang, P., Zhu, C., Wen, H., 2023. The REY geochemistry of phosphorites during metamorphism of the Haizhou Group, NW Yangtze Block, China. Chem. Geol. 641, 121781.
Liu, X.-F., Zhai, S., Wang, X.-K., Liu, X., Liu, X.-M., 2022. Rare Earth Element Geochemistry of late Cenozoic Island Carbonates in the South China Sea. Minerals 12, 578.
Luo, Y., Li, G., Xu, W., Liu, J., Cheng, J., Zhao, J., Yan, W., 2021. The effect of diagenesis on rare earth element geochemistry of the Quaternary carbonates at an isolated coral atoll in the South China Sea. Sediment. Geol. 420, 105933.
Ma, Y., Qin, Y., Yu, K., Li, Y., Long, Y., Wang, R., Fan, T., Jiang, W., Xu, S., Zhao, J., 2021. Holocene coral reef development in Chenhang Island, Northern South China Sea, and its record of sea level changes. Mar. Geol. 440, 106593.
MacNeil, A., Jones, B., 2003. Dolomitization of the Pedro Castle Formation (Pliocene), Cayman Brac, British West Indies. Sediment. Geol. 162, 219–238.
Mazumdar, A., Tanaka, K., Takahashi, T., Kawabe, I., 2003. Characteristics of rare earth element abundances in shallow marine continental platform carbonates of late Neoproterozoic successions from India. Geochem. J. 37, 277–289.
McLennan, S., 1989. Rare earth elements in sedimentary rocks; influence of provenance and sedimentary processes. Rev. Mineral. Geochem. 21, 169–200.
Monbet, P., Brunskill, G.J., Zagorskis, I., Pfitzner, J., 2007. Phosphorus speciation in the sediment and mass balance for the central region of the Great Barrier Reef continental shelf (Australia). Geochim. Cosmochim. Acta 71, 2762–2779.
Nguyen, A.D., Zhao, J.X., Feng, Y.X., Hu, W.P., Yu, K.F., Gasparon, M., Pham, T.B., Clark, T.R., 2013. Impact of recent coastal development and human activities on Nha Trang Bay, Vietnam: evidence from a Porites lutea geochemical record. Coral Reefs 32, 181–193.
Ning, Z., Fang, C., Yu, K., Yang, B., Dan, S.F., Xia, R., Jiang, Y., Li, R., Wang, Y., 2020. Influences of phosphorus concentration and porewater advection on phosphorus dynamics in carbonate sands around the Weizhou Island, northern South China Sea. Mar. Pollut. Bull. 160, 111668.
Nothdurft, L.D., Webb, G.E., Kamber, B.S., 2004. Rare earth element geochemistry of late Devonian reefal carbonates, Canning Basin, Western Australia: confirmation of a seawater REE proxy in ancient limestones. Geochim. Cosmochim. Acta 68, 263–283.
Nozaki, Y., Zhang, J., Amakawa, H., 1997. The fractionation between Y and Ho in the marine environment. Earth Planet. Sci. Lett. 148, 329–340.
Olivier, N., Boyet, M., 2006. Rare earth and trace elements of microbialites in Upper Jurassic coral- and sponge-microbialite reefs. Chem. Geol. 230, 105–123.
Qin, Y., Yu, K., Wang, R., Jiang, W., Xu, S., 2019. The initiation time of the holocene coral reef at the Chenhang island (Xisha islands) and its significance as a sea level indicator. Trop. Geogr. 39, 319–328.
Reynard, B., Lécuyer, C., Grandjean, P., 1999. Crystal-chemical controls on rare-earth element concentrations in fossil biogenic apatites and implications for paleoenvironmental reconstructions. Chem. Geol. 155, 233–241.
Saha, N., Rodriguez-Ramirez, A., Nguyen, A.D., Clark, T.R., Zhao, J.-X., Webb, G.E., 2018. Seasonal to decadal scale influence of environmental drivers on Ba/Ca and Y/Ca in coral aragonite from the southern Great Barrier Reef. Sci. Total Environ. 639, 1099–1109.
Saha, N., Webb, G.E., Zhao, J.-X., Duc Nguyen, A., Lewis, S.E., Lough, J.M., 2019. Coral-based high-resolution rare earth element proxy for terrestrial sediment discharge affecting coastal seawater quality, Great Barrier Reef. Geochim. Cosmochim. Acta 254, 173–191.
Saha, N., Webb, G.E., Zhao, J.-X., Lewis, S.E., Duc Nguyen, A., Feng, Y., 2021. Spatiotemporal variation of rare earth elements from river to reef continuum aids monitoring of terrigenous sources in the Great Barrier Reef. Geochim. Cosmochim. Acta 299, 85–112.
Salas-Saavedra, M., Webb, G.E., Sanborn, K.L., Zhao, J.-X., Webster, J.M., Nothdurft, L. D., Nguyen, A., 2022. Holocene microbialite geochemistry records > 6000 years of secular influence of terrigenous flux on water quality for the southern Great Barrier Reef. Chem. Geol. 604, 120871.
Scherer, M., Seitz, H., 1980. Rare-earth element distribution in Holocene and Pleistocene corals and their redistribution during diagenesis. Chem. Geol. 28, 279–289.
Shao, L., Li, Q., Zhu, W., Zhang, D., Qiao, P., Liu, X., You, L., Cui, Y., Dong, X., 2017. Neogene carbonate platform development in the NW South China Sea: Litho-, bio- and chemo-stratigraphic evidence. Mar. Geol. 385, 233–243.
Shen, J., Wang, Y., 2008. Modern microbialites and their environmental significance, Meiji reef atoll, Nansha (Spratly) Islands, South China Sea. Sci. China Ser. D-Earth Sci. 51, 608–617.
Shen, R., Shen, A., Yu, K., McCormick, C.A., Jiang, W., Xiao, Y., Wu, L., Wang, R., 2023. Properties of dolomitizing fluids indicated by rare earth elements: a case study of the Upper Miocene to Pliocene dolostone on the Xisha Islands, South China Sea. Sediment. Geol. 455, 106475.
Sholkovitz, E., Shen, G.T., 1995. The incorporation of rare earth elements in modern coral. Geochim. Cosmochim. Acta 59, 2749–2756.
Stipp, S., Lakshtanov, L., Jensen, J., Baker, J., 2003. Eu 3+ uptake by calcite: preliminary results from coprecipitation experiments and observations with surface-sensitive techniques. J. Contam. Hydrol. 61, 33–43.
Tanaka, K., Kawabe, I., 2006. REE abundances in ancient seawater inferred from marine limestone and experimental REE partition coefficients between calcite and aqueous solution. Geochem. J. 40, 425–435.
Tanaka, K., Miura, N., Asahara, Y., Kawabe, I., 2003. Rare earth element and strontium isotopic study of seamount-type limestones in Mesozoic accretionary complex of Southern Chichibu Terrane, Central Japan: Implication for incorporation process of seawater REE into limestones. Geochem. J. 37, 163–180.
Teng, J., Shen, J., 2008. Microbial carbonates in Holocene beachrocks, Shuiweiling, Luhuitou Peninsula, Hainan Island. Sci. China Ser. D-Earth Sci. 51, 30–40.
Terakado, Y., Masuda, A., 1988. The coprecipitation of rare-earth elements with calcite and aragonite. Chem. Geol. 69, 103–110.
Tostevin, R., Shields, G.A., Tarbuck, G.M., He, T., Clarkson, M.O., Wood, R.A., 2016. Effective use of cerium anomalies as a redox proxy in carbonate-dominated marine settings. Chem. Geol. 438, 146–162.
Toyama, K., Terakado, Y., 2019. Estimation of the practical partition coefficients of rare earth elements between limestone and seawater: Discussion and application. Geochem. J. 53, 139–150.
Webb, G.E., Jell, J.S., 2006. Growth rate of Holocene reefal microbialites ? Implications for use as environmental proxies, Heron Reef southern Great Barrier Reef. ASEG Extend. Abstrac. 2006, 1–3.
Webb, G.E., Kamber, B.S., 2000. Rare earth elements in Holocene reefal microbialites: a new shallow seawater proxy. Geochim. Cosmochim. Acta 64, 1557–1565.
Webb, G.E., Nothdurft, L.D., Kamber, B.S., Kloprogge, J.T., Zhao, J.-X., 2009. Rare earth element geochemistry of scleractinian coral skeleton during meteoric diagenesis: a sequence through neomorphism of aragonite to calcite. Sedimentology 56, 1433–1463.
Wei, G.-Y., Zhang, F., 2024. Pristine or altered, what can early diagenesis tell us in shallow-water carbonates? Earth Planet. Sci. Lett. 641, 118806.
Wei, G.-Y., Zhang, F., Yin, Y.-S., Lin, Y.-B., Pogge von Strandmann, P.A.E., Cao, M., Li, N., Xiong, G., Chen, X., Fan, C., Xu, C., Tan, F., Zhang, X., Yang, H., Ling, H.-F., Shen, S.-Z., 2023b. A 13 million-year record of Li isotope compositions in island carbonates: Constraints on bulk inorganic carbonate as a global seawater Li isotope archive. Geochim. Cosmochim. Acta 344, 59–72.
Wei, H., Liu, G., Han, X., Zhao, Y., Wu, J., Yang, J., Li, S., Zhang, Y., Li, D., 2023a. Coral-based rare earth element proxy for hydrothermal fluid on the Yongxing Island, South China Sea. Ore Geol. Rev. 162, 105678.
Westphal, H., Heindel, K., Brandano, M., Peckmann, J., 2010. Genesis of microbialites as contemporaneous framework components of deglacial coral reefs, Tahiti (IODP 310). Facies 56, 337–352.
Wu, S., Yang, Z., Wang, D., Lü, F., Lüdmann, T., Fulthorpe, C., Wang, B., 2014. Architecture, development and geological control of the Xisha carbonate platforms, northwestern South China Sea. Mar. Geol. 350, 71–83.
Wyndham, T., McCulloch, M., Fallon, S., Alibert, C., 2004. High-resolution coral records of rare earth elements in coastal seawater: biogeochemical cycling and a new environmental proxy. Geochim. Cosmochim. Acta 68, 2067–2080.
Xie, S., Jiang, W., Sun, Y., Yu, K., Feng, C., Han, Y., Xiao, Y., Wei, C., 2023. Interannual variation and sources identification of heavy metals in seawater near shipping lanes: evidence from a coral record from the northern South China Sea. Sci. Total Environ. 854, 158755.
Xu, S., Yu, K., Fan, T., Jiang, W., Wang, R., Zhang, Y., Yue, Y., Wang, S., 2019. Coral reef carbonate δ13C records from the northern South China Sea: a useful proxy for seawater δ13C and the carbon cycle over the past 1.8 Ma. Glob. Planet. Chang. 182, 103003.
Yang, H.-Q., Zhang, X.-Y., Li, Y., Shi, Q., Tao, S.-C., Mu, X.-N., Wang, M.-Z., Liu, X.-J., Tan, F., Zhou, S.-N., Wang, G., 2023. Biogenetic peloidal micrites within coral skeletons cause geochemical anomalies in reef limestones, Zhongsha Atoll, South China Sea. Palaeogeogr. Palaeoclimatol. Palaeoecol. 610, 111337.
Yu, K., 2012. Coral reefs in the South China Sea: their response to and records on past environmental changes. Sci. China Earth Sci. 55, 1217–1229.
Zhang, K., Shields, G.A., 2022. Sedimentary Ce anomalies: Secular change and implications for paleoenvironmental evolution. Earth Sci. Rev. 229, 104015.
Zhang, X.-Y., Li, Y., Sun, F.-L., Tan, F., Shi, Q., Yan, H.-Q., Wang, G., Yang, H.-Q., 2022. Insights into microbially mediated cementation in modern beachrock in the Xisha Islands, South China Sea. Palaeogeogr. Palaeoclimatol. Palaeoecol. 592, 110904.
Zhao, H., Jones, B., 2013. Distribution and interpretation of rare earth elements and yttrium in Cenozoic dolostones and limestones on Cayman Brac, British West Indies. Sediment. Geol. 284-285, 26–38.
Zhao, M.-Y., Zheng, Y.-F., 2014. Marine carbonate records of terrigenous input into Paleotethyan seawater: Geochemical constraints from Carboniferous limestones. Geochim. Cosmochim. Acta 141, 508–531.
Zhao, Y., Wei, W., Li, S., Yang, T., Zhang, R., Somerville, I., Santosh, M., Wei, H., Wu, J., Yang, J., Chen, W., Tang, Z., 2021. Rare earth element geochemistry of carbonates as

a proxy for deep-time environmental reconstruction. Palaeogeogr. Palaeoclimatol. Palaeoecol. 574, 110443.
Zhao, Y., Wei, W., Santosh, M., Hu, J., Wei, H., Yang, J., Liu, S., Zhang, G., Yang, D., Li, S., 2022. A review of retrieving pristine rare earth element signatures from carbonates. Palaeogeogr. Palaeoclimatol. Palaeoecol. 586, 110765.
Zhong, S., Mucci, A., 1995. Partitioning of rare earth elements (REEs) between calcite and seawater solutions at 25 C and 1 atm, and high dissolved REE concentrations. Geochim. Cosmochim. Acta 59, 443–453.

Check for updates

JGR Earth Surface

RESEARCH ARTICLE
10.1029/2024JF008239

High-Resolution Coral Records of Rare Earth Elements and Yttrium in Seawater Driven by Submarine Groundwater Discharge in a Basalt Island: A Case Study in the Northern South China Sea

Tingwu Gu[1], Wei Jiang[1], Yansong Han[1], Chunmei Feng[1], Ning Guo[1], Caifeng Liu[1], Yu Zhang[1], and Kefu Yu[1,2]

[1]Guangxi Laboratory on the Study of Coral Reefs in the South China Sea, School of Marine Sciences, Guangxi University, Nanning, China, [2]Southern Marine Science and Engineering Guangdong Laboratory (Guangzhou), Guangzhou, China

Key Points:

- REY flux from basalt weathering driven by SGD is a major natural source of seawater
- Coral Nd_N/Yb_N ratios with seasonal cycles are driven by the SGD and the adsorption-desorption processes of marine biogenic particles
- Coral Y/Ho ratio serves as a potential proxy for basalt weathering

Supporting Information:

Supporting Information may be found in the online version of this article.

Correspondence to:

W. Jiang,
jianwe@gxu.edu.cn

Citation:

Gu, T., Jiang, W., Han, Y., Feng, C., Guo, N., Liu, C., et al. (2025). High-resolution coral records of rare earth elements and yttrium in seawater driven by submarine groundwater discharge in a basalt island: A case study in the northern South China Sea. *Journal of Geophysical Research: Earth Surface*, *130*, e2024JF008239. https://doi.org/10.1029/2024JF008239

Received 18 DEC 2024
Accepted 24 FEB 2025

Author Contributions:

Conceptualization: Wei Jiang
Data curation: Wei Jiang
Formal analysis: Tingwu Gu, Wei Jiang
Funding acquisition: Wei Jiang, Kefu Yu
Investigation: Tingwu Gu, Wei Jiang, Chunmei Feng, Ning Guo, Yu Zhang
Methodology: Tingwu Gu, Wei Jiang
Project administration: Kefu Yu
Resources: Wei Jiang
Supervision: Kefu Yu
Visualization: Wei Jiang
Writing – original draft: Tingwu Gu
Writing – review & editing: Wei Jiang, Yansong Han, Caifeng Liu

© 2025. American Geophysical Union. All Rights Reserved.

Abstract Rare earth elements and yttrium (REY) are widely employed as tracers for oceanic geochemical processes, which require a thorough understanding of their sources, sinks, and drivers of variability in the marine environment. However, significant uncertainties exist in the marine REY cycle, the so-called "missing Nd flux," particularly regarding the contribution of submarine groundwater discharge (SGD) and basalt weathering in volcanic islands. Here, we present a 10-year record of monthly *Porites* coral REY parameters from Weizhou Island, a volcanic island built up underwater from basalt eruptions during the Quaternary, to investigate the sources and seasonal characteristics of surface seawater REY. Results demonstrate a robust seasonal cycle in the coral Y/Ho ratios, exhibiting a strong correlation with the rainfall-controlled SGD on monthly timescales and East Asian Summer Monsoon on interannual timescales, both of which are associated with basalt weathering. Combined with multiple climatic and environmental data, we find that coral Nd_N/Yb_N ratios may be mainly controlled by precipitation associated with SGD and the adsorption-desorption processes of marine biogenic particles, whereas coral REY/Ca ratios are influenced by the remobilization of sediment driven by winter monsoon. Our research suggests that the high coral Y/Ho ratios may be primarily influenced by basalt weathering during the wet season, when SGD from the island is the chief source of REY to the coastal waters. This study provides new insights into the sources and characteristics of marine REY in volcanic islands, highlighting the potential for SGD-driven REY fluxes from basaltic islands.

Plain Language Summary Rare earth elements and yttrium (REY) are able to record marine geochemical processes. To better understand this process, it is necessary to comprehend the sources and track the changes of REY in the marine environment. However, the contribution of submarine groundwater discharge (SGD) and basalt weathering of volcanic islands to marine REY is still unclear. Here, a *Porites* coral, reflecting the historical changes in the REY composition of dissolved seawater, was collected from a volcanic island in the South China Sea. Comprehensive geochemical analyses have been conducted to explore the temporal variations and sources of REY in surface seawater. We discovered that basalt weathering driven by SGD is the main cause of REY changes in seawater. Furthermore, seasonal fluctuations in biogenic particles, combined with the dissolution of particulate REY within sediment driven by winter monsoon, played a substantial role. Another key point is that the REY parameters (e.g., Y/Ho ratio) may hold promise as an excellent indicator for assessing basalt weathering intensity. This study deepens our understanding of the origin and behavior of REY in marine systems, and improves the comprehension of how basalt weathering influences REY recorded in corals.

1. Introduction

Rare earth elements and yttrium (REY) are regarded as excellent tracers for water-mass transport, current transport, and particle settling, for example, in marine geochemical processes (Behrens et al., 2020; Deng et al., 2017; Elderfield & Greaves, 1982; Murphy & Dymond, 1984), due to their subtle but systematic differences in chemical properties related to their unique electronic structure (Elderfield et al., 1988). The main sources of dissolved REY in the modern oceans are riverine flux, submarine groundwater discharge (SGD), atmospheric/eolian flux, and hydrothermal inputs (Chen et al., 2015; Jiang et al., 2018b). In addition, there is important evidence that a deep, benthic flux and boundary exchange also likely contribute to the marine REY cycle (Abbott et al., 2015; Pearce et al., 2013). Analyzing the budget and pattern of oceanic dissolved REY provides valuable

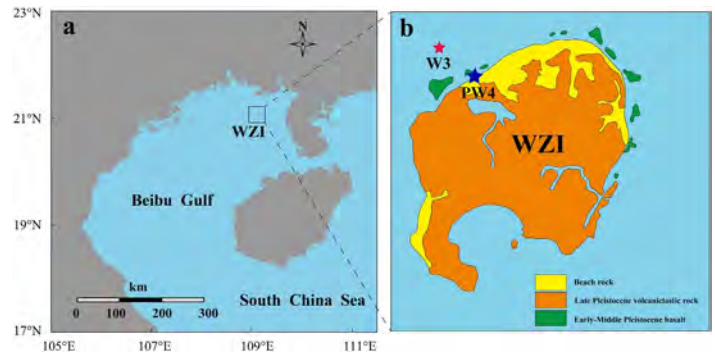


Figure 1. Location map of the study area. (a) Location map in WZI, and (b) Geological map in WZI (modified from Fan et al. (2006)) and sampling points of W3 coral and PW4 SGD (marked by stars).

insights into the geochemical signatures and climate evolution of the global or regional ocean (Adebayo et al., 2022; Garcia-Solsona & Jeandel, 2020; Garcia-Solsona et al., 2020; Pham et al., 2019). It is crucial to note that there is a difference between the combined river with atmospheric neodymium (Nd) fluxes and the flux required to balance the oceanic Nd budget, the so-called "missing Nd flux," which is a significant issue in marine REY research (Abbott et al., 2015; Arsouze et al., 2009; Lacan & Jeandel, 2005; Tachikawa et al., 2003). Recent research has shown that there are two promising candidates for "missing Nd flux," focusing on SGD (Chevis et al., 2015; Johannesson & Burdige, 2007; Johannesson et al., 2011) and the weathering of basaltic islands (Johannesson et al., 2017; Molina-Kescher et al., 2018). However, the geochemistry of REY in seawater remains relatively underexplored to date due to REY's low concentrations and complex chemical speciation (Schijf & Byrne, 2021). There is a lack of continuous high-resolution monitoring data to fully investigate the budget of REY in the oceans and their influencing factors.

Coral reefs, widespread in tropical and subtropical marine environments, provide an excellent high-resolution geochemical proxy due to their long growth histories, rapid annual growth rates, clear interannual boundaries, sensitivity to environmental changes, and suitable high-precision dating (Saha et al., 2016; Thompson, 2022; Yu et al., 2005). The concentrations of REY incorporated in coral skeletons are proportional to those in ambient seawater (Akagi et al., 2004; Sholkovitz & Shen, 1995), allowing for the historical changes in the dissolved REY composition of the surrounding seawater to be reliably represented by the changes in the REY composition along the growth bands in coral (Wyndham et al., 2004). Therefore, the records of REY provided by corals offer the potential to reveal past environmental and climatic parameters, including sea level change (Liu et al., 2006, 2011), human activities (Nguyen et al., 2013), continental weathering (Naqvi et al., 1996), SGD (Jiang et al., 2018b; Prouty et al., 2009), monsoon (Jiang et al., 2018a; Li et al., 2019), terrestrial runoff and associated coastal water quality (Saha et al., 2018). Despite numerous surveys of estuarine areas, much less is known about the coral REY variation in subterranean estuary areas as well as in basalt islands with SGD.

The Early-Middle Pleistocene flood basalts are the products of the largest volcanic eruption on Weizhou Island (WZI) (Zhang et al., 2020), which formed the volcanic terrain of the island (Fan et al., 2006). The natural conditions of WZI are conducive to the growth and reproduction of reef-building corals, which have developed since the mid-Holocene (Yu et al., 2019). Situated in a tropical zone with high precipitation and temperatures, the volcanic rocks in WZI primarily consist of basalt (Yu et al., 2021), which facilitates chemical weathering (Gislason et al., 2009). For this study, WZI was selected as the research area, where the high-resolution (monthly) coral records of REY were analyzed to investigate the impacts of climatic and environmental drivers (notably SGD and basalt weathering) on the seasonal variations of marine REY, aiming to enhance our understanding of marine REY budgets.

2. Materials and Methods

2.1. Study Area

WZI (20°00′–21°05′N, 109°04′–109°09′E), located in the northern South China Sea (SCS), is a volcanic island formed by subaqueous eruptions of Quaternary basaltic magma (Yue et al., 2024) (Figure 1). There are large areas

21699011, 2025, 3, Downloaded from https://agupubs.onlinelibrary.wiley.com/doi/10.1029/2024JF008239 by Wei Jiang - Guangxi University , Wiley Online Library on [11/03/2025]. See the Terms and Conditions (https://onlinelibrary.wiley.com/terms-and-conditions) on Wiley Online Library for rules of use; OA articles are governed by the applicable Creative Commons License

21699011, 2025, 3, Downloaded from https://agupubs.onlinelibrary.wiley.com/doi/10.1029/2024JF008239 by Wei Jiang - Guangxi University , Wiley Online Library on [11/03/2025]. See the Terms and Conditions (https://onlinelibrary.wiley.com/terms-and-conditions) on Wiley Online Library for rules of use; OA articles are governed by the applicable Creative Commons License

of spheroidal weathered basalt in the north of the island (Fan et al., 2006). WZI is an independent hydrogeological unit surrounded by the sea and characterized by a tropical oceanic monsoon climate. The average annual temperature is 23.5°C, and the average annual precipitation reaches ~1,423 mm, with nearly 85% occurring in the wet season (from May to October), which supports strong chemical weathering. Additionally, the island boasts abundant groundwater resources (Chen, 1999). The equal ^{224}Ra mass of the source and sink terms in the study area was used to estimate the SGD flux around the WZI to be 3.95×10^7 m^3 d^{-1} (26.57 cm d^{-1}) (Methods S1 and S2 in Supporting Information S1), which is comparable to those of Jeju Island (4.5×10^7 m^3 d^{-1}) (Kim & Kim, 2011).

2.2. Sample and Geochemical Analysis

A modern *Porites* coral labeled as W3 was collected at a water depth of 4 m in the northwest of WZI (21°4′7″N, 109°5′24″E) in October 2015 (Figure 1b). After washing with clean water, the coral was cut along the major growth axis using a rock saw to obtain a slab (approximately 24 cm long, 8 cm wide, and 1 cm thick). The annual growth bands of coral aragonite can be determined from the alternating light-dark density stripes of the X-ray image (Figure S1 in Supporting Information S1). Each high- and low-density band represents 1 year of growth (Knutson et al., 1972), while the outermost band represents the ongoing growth of coral skeletons in 2015. The slab was soaked in 10% H_2O_2 for 48 hr and washed 3 times in an ultrasonic bath with Milli-Q water to ensure the removal of any surface contamination that could potentially affect the accuracy of the trace elemental records. Subsequently, it was air-dried in an oven at 40°C for 48 hr.

Following pretreatment, preliminary grinding was conducted along the designated sample track of the slab, with the objective of removing approximately 1 mm of powder from the upper surface. Subsequently, based on the annual density stripes of the X-ray image, powdered calcium carbonate samples were taken at a fixed microsampling interval and continuously along the maximum growth axis to obtain 416 samples (32 years). The internal standard isotopes (^{103}Rh, ^{115}In, ^{187}Re) were used to prepare the 100 ml of 100 ppb internal standard stock solution. The national certified carbonate geochemical reference materials (GBW07129, GBW07133, GBW07135), as presented in Table S1 of the Supporting Information S1, were used as the external standards for the coral skeleton analysis (Jiang et al., 2022). Approximately 3 mg of the sample was weighed into an LDPE tube from the completely homogenized sample. Each tube was filled with 450 µl of 100 ppb internal standard stock solution, diluted approximately 3,000 times with 2% HNO_3, and then analyzed by inductively coupled plasma-mass spectrometry (ICP-MS) for geochemical analysis of REY. The signals of the REY isotopes (^{89}Y, ^{139}La, ^{140}Ce, ^{141}Pr, ^{143}Nd, ^{149}Sm, ^{153}Eu, ^{159}Tb, ^{160}Gd, ^{164}Dy, ^{165}Ho, ^{167}Er, ^{169}Tm, ^{174}Yb, and ^{175}Lu), other trace metals (^{43}Ca and ^{90}Zr), and the internal standard isotopes were simultaneously monitored and measured in the same aliquots. The signals were further corrected for any oxide, hydroxide, and isobaric interferences and calibrated against the certified elemental abundances in the standard to calculate the elemental concentrations in the coral samples (The levels of BaO and (REY)O were determined by analyzing pure elemental solutions, with appropriate corrections made for any potential interferences). All samples were measured 3 times with a relative standard deviation (RSD) of generally less than 5%. The details of the sample processing and analysis methods have been reported in our previous research (Jiang et al., 2022).

Previous studies have reported that the Ni/Ca and V/Ca ratios of the W3 coral were low and stable during the period 1994–2008, whereas these values fluctuated drastically and exhibited high levels during other periods of anthropogenic activity (Jiang et al., 2022; Wu et al., 2022). Thus, the coral REY time series was established for the decade of 1999–2008 in our study, which was the natural state relatively less affected by artificial disturbance in the WZI (Figure S2 in Supporting Information S1) and showed a more pronounced trend (Sun et al., 2022). The δ^{18}O values of W3 coral (selected from the same completely homogenized sample for the REY measurements) have been previously reported by Xu et al. (2018) and were applied in this study. The maximum δ^{18}O values corresponded to the lowest point of the sea surface temperature (SST) cycle and vice versa; then, each annual cycle variation of the same coral REY can be determined correspondingly (Tables S2 and S3 in Supporting Information S1). Subsequently, the REY data with the monthly resolution was obtained from linear interpolation. Because of the complex internal structure of the coral, the actual growth rate of the coral is not likely to be uniform. The interpolation method may result in slight deviations in the monthly resolution time series. Therefore, the data will be analyzed and discussed using a 5-month moving average, which effectively removes the disturbances in question.

21699011, 2025, 3, Downloaded from https://agupubs.onlinelibrary.wiley.com/doi/10.1029/2024JF008239 by Wei Jiang - Guangxi University , Wiley Online Library on [11/03/2025]. See the Terms and Conditions (https://onlinelibrary.wiley.com/terms-and-conditions) on Wiley Online Library for rules of use; OA articles are governed by the applicable Creative Commons License

2.3. SGD Sample Collection and Chemical Analysis

The groundwater sample (labeled as PW4, situated in close proximity to W3 coral) was collected in October 2022 in acid-cleaned high-density polyethylene (HDPE) bottles at the location shown in Figure 1b. In the field, salinity (~20‰) and pH (~6.66) were monitored using a portable multiparameter water quality analyzer until the parameters reached a stable state. Subsequently, the PW4 groundwater was filtered through a 0.45 μm filter membrane and collected in an acid-cleaned HDPE bottle. It was then acidified to a pH of less than 2 with ultra-pure HNO_3 and transported back to the laboratory under refrigeration. Since its return to the laboratory, the groundwater sample has been stored in the laboratory sample freezer at a temperature of approximately 0 degrees Celsius.

The PW4 groundwater sample was passed through Bio-Rad® Poly-Prep columns packed with ~2 mL of Bio-Rad AG® 50 W-X8 (100–200 mesh, hydrogen form) cation-exchange resin in order to separate the REY from the major salts. Two 3-mL acid rinses of 1.75 M ultra-pure HCl and 2 M ultra-pure HNO_3 were performed to elute Fe and Ba, respectively, from the columns. REY were then eluted from the column into a Teflon® beaker with 10 mL of 8 M ultra-pure HNO_3. Each sample was subsequently evaporated to dryness on a hot plate, and taken up in 10 mL of a 1% v/v ultra-pure HNO_3 solution for analysis (Johannesson et al., 2017). The sample was spiked with ^{115}In at 2 ppb for use as an internal standard and analyzed for the REY isotopes (^{89}Y, ^{139}La, ^{140}Ce, ^{141}Pr ^{146}Nd, ^{147}Sm, ^{153}Eu, ^{157}Gd, ^{159}Tb, ^{163}Dy, ^{165}Ho, ^{166}Er, ^{167}Er, ^{169}Tm, ^{172}Yb, and ^{175}Lu) by ICP-MS at Guangxi University. The analyzed data were assessed for accuracy and precision through quality assurance and quality control, which included reagent blanks, duplicate tests, and the National Research Council Canada Certified Reference Material (NASS-7). The analytical precision of REY analyses was consistently less than 10% RSD.

2.4. Climate and Environmental Data

Date on SST, rainfall, and wind speeds were collected from the WZI Weather Station. The East Asian Summer Monsoon (EASM) indices were obtained from the China Climate Bulletin (http://www.ncc-cma.net/channel/news/newsid/100060). Chlorophyll-*a* (Chl-*a*) concentration data were archived by the Environmental Research Division's Data Access Program (ERDDAP) of the National Oceanic and Atmospheric Administration (NOAA) (https://coastwatch.pfeg.noaa.gov/erddap/index.html). The sea surface salinity (SSS) data were obtained from the website http://www.ocean.iap.ac.cn/. The wet season of WZI is defined as the period between May and October, while the dry season is the interval between November and April.

2.5. REY Parameters

The REY parameters for W3 coral have been normalized using the Post Archean Australian Shales (PAAS) REY patterns (Pourmand et al., 2012). The ratio of $[Nd/Yb]_{PAAS}$ (Nd_N/Yb_N) is a common indicator to represent the fractionation of light rare earth elements (LREE, La-Eu) and heavy rare earth elements (HREE, Gd-Lu) (Henderson, 1984). Yttrium/holmium (Y/Ho) is commonly used in corals to indicate the degree of influence of continental sources, which are more enriched in Ho than in Y (Nguyen et al., 2013).

3. Results

3.1. Variation of the Coral REY

The total REE levels in W3 coral samples from 1999 to 2008 ranged from 136 to 775 ng/g, with an average of 202 ng/g (Figure 2). These values are substantially higher than those reported for sites in the SCS that have experienced minimal human disruption, such as Xiaodonghai Bay (average 106 ng/g) (Jiang et al., 2017, 2018b), Yongxing Island (average 42 ng/g) (Jiang et al., 2018a), and Longwan Bay (average 79 ng/g) (Liu et al., 2011), but lower than the areas that have been strongly impacted by human activities, such as Hong Kong (average 419 ng/g) (Liu et al., 2006, 2011) and Nha Trang Bay (average 340 ng/g) (Nguyen et al., 2013).

The monthly variation of REY parameters of W3 coral is shown in Figure 2. The coral had average REE/Ca and Y/Ca values of 149.03 ± 52.76 nmol/mol and 487.79 ± 41.57 nmol/mol, respectively. The coral REE/Ca showed a significant correlation ($r = 0.8$, $p < 0.001$, $n = 120$) to coral Y/Ca from 1999 to 2008. The average Y/Ho values for the coral are 152.53 ± 18.85. Notably, the Nd_N/Yb_N ratios (average 0.40, $n = 120$) exhibit a significant seasonal cyclicality, that is, high values in the wet season and low values in the dry season (Figure 2a). Additionally, a high value of REE/Ca (Y/Ca) occurs during the dry season (Figures 2c and 2d). The REY parameters in

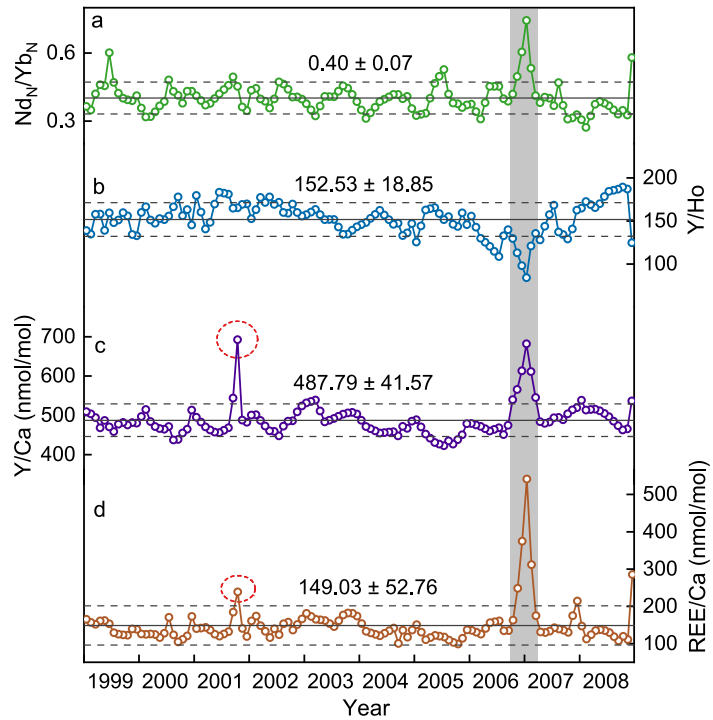


Figure 2. Monthly variation of REY parameters for W3 coral during 1999–2008. (a) Nd_N/Yb_N, (b) Y/Ho, (c) Y/Ca (nmol/mol), and (d) REE/Ca (nmol/mol). Solid lines represent the mean value, and dotted lines show the mean ± standard deviation. The red circles and gray background represent the anomalous peaks and valleys. The gray background corresponds to the middle and late construction period of the crude oil terminal project in the northwest of WZI (from October 2006 to March 2007).

the coral exhibit relative stability, except for anomalous peaks and valleys, which are primarily concentrated between September 2006 and March 2007. There was also an anomalous peak of REE/Ca (Y/Ca) in 2001, which may indicate an unconfirmed anthropogenic source (Jiang et al., 2022).

3.2. Normalized REY Patterns

The faithfulness and robustness of modern coral (e.g., W3 coral) marine REY proxies are empirical (Webb et al., 2009). The W3 coral samples have typical seawater REY patterns (Figure 3c), characterized by LREE depletions, HREE enrichments, negative Ce anomalies, and high Y/Ho ratios (~152, $n = 120$). Additionally, the lack of a correlation between the REY and Zirconium (Zr) (Figure S3 in Supporting Information S1) in the coral samples suggests that the coral REY can accurately record the surface seawater conditions (Jiang et al., 2018b). The REY concentration in the W3 coral was higher than that in the WZI coral (Li et al., 2019), despite both corals being from WZI (Figures 3c and 3d). Deviating from the surface seawater in the SCS (Alibo & Nozaki, 2000), the REY patterns for the WZI soil (Cai et al., 2021) and WZI basalt (Cai et al., 2021) are characterized by enrichment in LREE, positive Eu anomalies, and high REY concentrations (Figures 3a, 3b, and 3f).

4. Discussion

4.1. Factors Affecting REY Variations in Surface Seawater

The variations of REY in the SCS surface waters could be caused by several factors, including river runoff, dust and precipitation from the atmosphere, erosion of surrounding peninsulas and islands, and sediment remobilization from the shelf (Alibo & Nozaki, 2000). The impact of riverine inputs on REY, however, is deemed negligible due to the W3 coral site being far from large rivers on the Asian continent (Li et al., 2019; Wu et al., 2022). Furthermore, the offshore seawater REY in the WZI is not affected by eolian dust, as evidenced by the remarkably low eolian dust indexes reported by Nozaki et al. (1998), Amakawa et al. (2000), and Li et al. (2019).

21699011, 2025, 3, Downloaded from https://agupubs.onlinelibrary.wiley.com/doi/10.1029/2024JF008239 by Wei Jiang - Guangxi University , Wiley Online Library on [11/03/2025]. See the Terms and Conditions (https://onlinelibrary.wiley.com/terms-and-conditions) on Wiley Online Library for rules of use; OA articles are governed by the applicable Creative Commons License

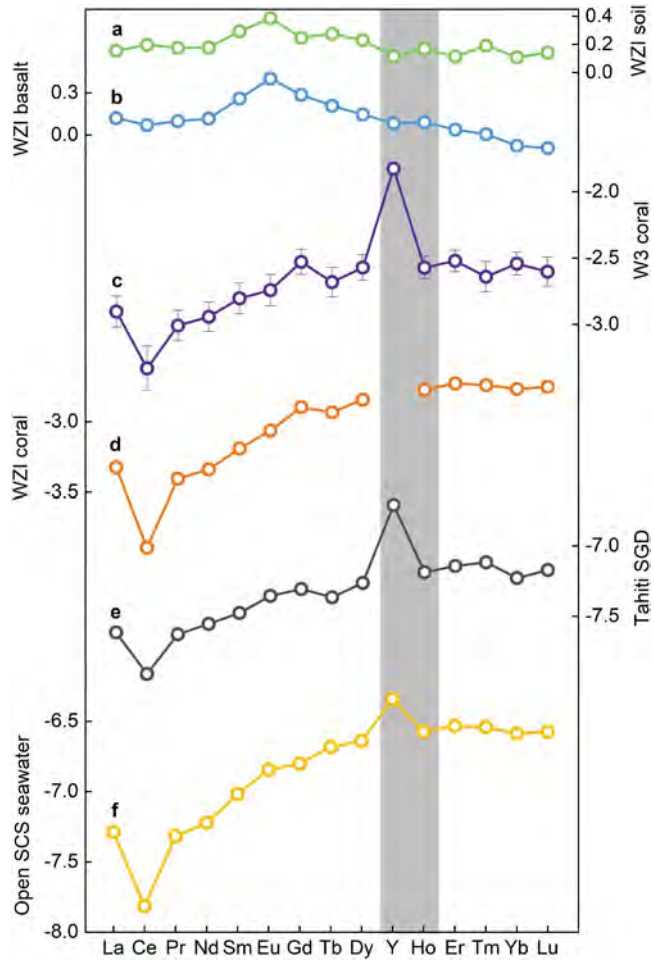


Figure 3. PAAS-normalized distribution patterns for REY. (a) WZI soil (Cai et al., 2021), (b) WZI basalt (Cai et al., 2021), (c) W3 coral (this study), (d) WZI coral (in the southwest of WZI) (Li et al., 2019), (e) Tahiti SGD (Molina-Kescher et al., 2018), and (f) open surface water of the SCS (Alibo & Nozaki, 2000). The ordinate is $\log_{10}$ (sample/PAAS) and the abscissa is REY. The gray background corresponds to the standardized Y and Ho.

Despite our previous research indicating that there were relatively small anthropogenic contributions of vanadium and nickel during the decade of 1999–2008 (Jiang et al., 2022; Wu et al., 2022), the REY parameters still demonstrate the impact of human activities due to their sensitivity. The REY parameters exhibited substantial anomalies between September 2006 and March 2007 (Figure 2). These anomalies are unlikely to be derived from natural sources and may be related to the construction of the crude oil terminal project in WZI during the middle and late stages. Coral V/Ca ratio is an effective indicator of oil pollution in coastal areas (Tanaka et al., 2013). It is worthy of note that an anomalous peak in the V/Ca ratio of W3 coral was also observed in late 2006 and early 2007, which may be correlated with the oil pollution events (Jiang et al., 2022). Furthermore, the observed depletion of Y/Ho ratios and the elevated Nd_N/Yb_N and REY/Ca in W3 coral during this period may be caused by the fact that when the dredged spoils were dumped into the seawater, the Ho-enriched and LREE-enriched terrigenous materials released an excess of Ho and LREE into the seawater (Nguyen et al., 2013). The REY/Ca ratios were significantly correlated with both the Nd_N/Yb_N ratios ($r = 0.99$, $p < 0.001$, $n = 6$) and the Y/Ho ratios ($r = -0.93$, $p < 0.01$, $n = 6$) (Figure S4 in Supporting Information S1) suggesting that total REY concentrations during this period exhibited a heightened sensitivity to increases in Ho and LREE, compared to HREE and Y. Consequently, the source of REY may be dominated by anthropogenic activity from September 2006 to March 2007. The study of natural drivers did not cover the changes in REY parameters during this period.

21699011, 2025, 3, Downloaded from https://agupubs.onlinelibrary.wiley.com/doi/10.1029/2024JF008239 by Wei Jiang - Guangxi University , Wiley Online Library on [11/03/2025]. See the Terms and Conditions (https://onlinelibrary.wiley.com/terms-and-conditions) on Wiley Online Library for rules of use; OA articles are governed by the applicable Creative Commons License

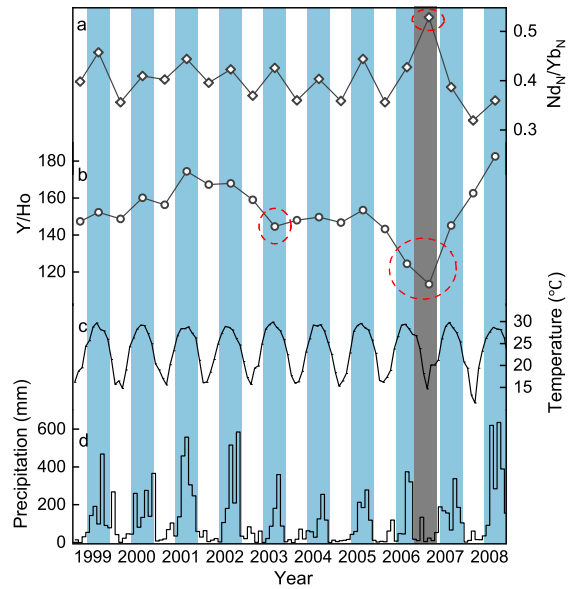


Figure 4. Seasonal variations of W3 coral REY parameters and environmental parameters during 1999–2008. (a) Nd_N/Yb_N, (b) Y/Ho, (c) temperature (°C), and (d) precipitation (mm). The white background represents the dry season of WZI (from November to April), and the blue background color represents the wet season of WZI (from May to October). The three red circles indicate a period characterized by inconsistent seasonal variation trends in REY parameters, and the gray background indicates a period with anthropogenic sources of REY.

In summary, to explore the natural drivers for the dissolved REY in WZI surface seawater, the following possibilities are studied: (a) Basalt chemical weathering driven by SGD, (b) remobilization of REY in the shelf sediments, and (c) biogeochemical cycle.

4.1.1. Basalt Chemical Weathering Driven by SGD

SGD is an important component of the global ocean hydrological cycle (Moore, 2010; Zhang et al., 2022) and is recognized as an essential flux of dissolved and particulate REY to coastal waters (Jiang et al., 2018b; Kim & Kim, 2011, 2014). The lithologic high permeability of marine islands is an important controlling factor for REY flux into the ocean (Kim & Kim, 2011). WZI exhibits high permeability due to its developed pore-fissure structure. This structure is composed of a series of basic volcanic rock types, including olivine basalt, basaltic tuff, and basaltic breccia (Chen, 1999). In contrast to the open surface seawater of the SCS (~0.023 μg/L), PW4 SGD (~0.087 μg/L) has been observed to exhibit elevated concentrations of REY. In general, terrestrial sources exhibit higher concentrations of REEs than seawater, especially LREEs. The coral Nd_N/Yb_N ratios exhibited a distinct seasonal variation pattern, characterized by elevated ratios during the wet season and reduced ratios during the dry season (Figure 4a). Thus, it is plausible to assert that SGD may contribute to REY fluxes of coastal areas in WZI.

Rock weathering converts primary minerals into secondary minerals and solutes, which are then transported to the ocean by SGD and surface runoff (Worthington et al., 2016). A similar effect occurs in volcanic rocks; thus, the weathering of volcanic islands is considered to be a significant source of REY in the seawater near volcanic islands (Johannesson et al., 2017; Molina-Kescher et al., 2018). Basalts are extremely susceptible to weathering (Louvat & Allègre, 1997), exhibiting a bulk weathering rate that is higher than that of many other silicate rocks (Dessert et al., 2001; Worthington et al., 2016). Previous studies have indicated that there are elevated REE contents in WZI basalt (ΣREE = 237 mg/kg) (Cai et al., 2021), with values approximately 160% of the upper continental crust (ΣREE = 146 mg/kg) (Taylor & McLennan, 1985). The chemical weathering of basalt may be an important source of REY in the surface seawater of WZI. In general, the rate of chemical weathering of groundwater on volcanic islands is always higher than that of surface water (Rad et al., 2007). Furthermore, young volcanic areas have generally higher hydraulic conductivity, facilitating the quick recharge of precipitation to

21699011, 2025, 3, Downloaded from https://agupubs.onlinelibrary.wiley.com/doi/10.1029/2024JF008239 by Wei Jiang - Guangxi University , Wiley Online Library on [11/03/2025]. See the Terms and Conditions (https://onlinelibrary.wiley.com/terms-and-conditions) on Wiley Online Library for rules of use; OA articles are governed by the applicable Creative Commons License

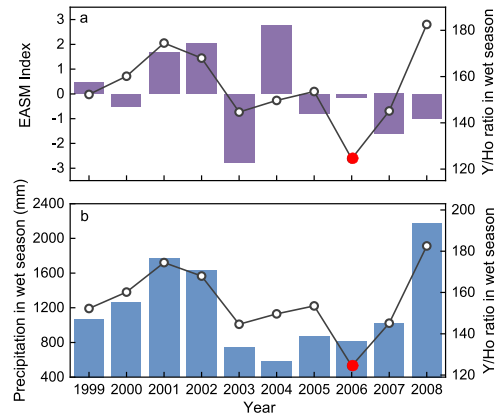


Figure 5. Comparison of the average W3 coral Y/Ho ratio of the wet season with the EASM index and precipitation of the wet season during 1999–2008. (a) Comparison of Y/Ho and the EASM index and (b) Comparison of Y/Ho and the precipitation. The red dot represents the coral Y/Ho value during the wet season of 2006, which was affected by the anthropogenic source of REY.

groundwater (Zang et al., 2023). In summary, the REY released by basalt weathering may be primarily discharged to the ocean via SGD rather than surface runoff due to the absence of rivers on WZI.

Weathering of basalt produces a solid mineral residue that is rich in Fe- and Mn- (hydro)oxides (Campodonico et al., 2019). The affinity of Y for Fe- and Mn- (hydro)oxides is substantially lower than that of holmium (Ho), despite their similar ionic radii (Bau, 1999; Bau et al., 1997). Thus, Y-Ho fractionation always occurs during basalt weathering (Thompson et al., 2013). The Y/Ho ratio of soil is lower than that of basalt on WZI (Figures 3a and 3b), confirming that Y is more mobile in weathering products from basalt compared to Ho. Notably, the majority of the erosion and migration of terrestrial materials in tropical islands predominantly occurs in the wet season (Nunes et al., 2023). The region's high precipitation during the wet season, combined with its high-permeability basalt aquifer, facilitates a rapid increase in groundwater fluxes, thereby promoting chemical weathering and water-rock interactions (Horta-Puga & Carriquiry, 2012; Kumar et al., 2019). Interestingly, the Y/Ho ratios of the W3 coral exhibit obvious seasonal cycles, with high values in the wet season and low values in the dry season, except for 2003 and 2006 (Figure 4b). The low Y/Ho ratios observed during the wet seasons of 2003 and 2006 may be related to the low EASM index (Figure 5a) and human activities, respectively. In particular, the PW4 SGD sample in WZI exhibited a high Y/Ho ratio (~123). Continuous rainwater leaching during the wet season provides a driving force for the downward migration of REY (especially Y), and groundwater with high Y/Ho ratios is transported to the surface seawater, where it is subsequently recorded by corals. Rainfall is the only natural source of replenishment for the abundant groundwater in WZI (Li & Qian, 2018). Therefore, precipitation data can be used to estimate SGD in WZI in the absence of groundwater data. The calculation of the coral residual $\delta^{18}O$ ($\Delta\delta^{18}O$) is achieved by subtracting the contribution of temperature from the coral $\delta^{18}O$ (Methods S3 in Supporting Information S1). Coral $\Delta\delta^{18}O$ can be used to indicate the seawater $\delta^{18}O$ isotope variations, which may correlate with SSS and precipitation (Corrège, 2006; Gagan et al., 1998). The 5-month moving average of $\Delta\delta^{18}O$ shows a significant positive correlation with SSS ($r = 0.39$, $p < 0.001$; Figure S5 in Supporting Information S1), whereas no significant correlation was observed with precipitation ($r = -0.22$, $p > 0.01$; Figure S5 in Supporting Information S1). It is interesting to note that the 5-month moving average variation of precipitation exhibited significant positive correlations with coral Nd_N/Yb_N ratios ($r = 0.34$, $p < 0.001$; Table S4 in Supporting Information S1) and Y/Ho ratios ($r = 0.45$, $p < 0.001$; Figure 6). Furthermore, there is also a notable correlation between coral Y/Ho ratios and precipitation during the wet season ($r = 0.37$, $p < 0.01$, $n = 60$; Figure S6 in Supporting Information S1), supporting that the Y/Ho may serve as an excellent proxy for basalt weathering in coastal seawater during the wet season, when SGD from the island represents the primary source of REY in the coastal waters.

Our findings suggest a substantial contribution of SGD from basaltic islands to the enrichment of REY in coastal seawater, which is supported by studies conducted in Kona, Hawaii (Johannesson et al., 2017), Jeju Island, Korea (Kim & Kim, 2011), and Tahiti Island (Molina-Kescher et al., 2018). It is noteworthy that our research, conducted in the WZI, may represent the inaugural report of this effect recorded by a coral.

21699011, 2025, 3, Downloaded from https://agupubs.onlinelibrary.wiley.com/doi/10.1029/2024JF008239 by Wei Jiang - Guangxi University , Wiley Online Library on [11/03/2025]. See the Terms and Conditions (https://onlinelibrary.wiley.com/terms-and-conditions) on Wiley Online Library for rules of use; OA articles are governed by the applicable Creative Commons License

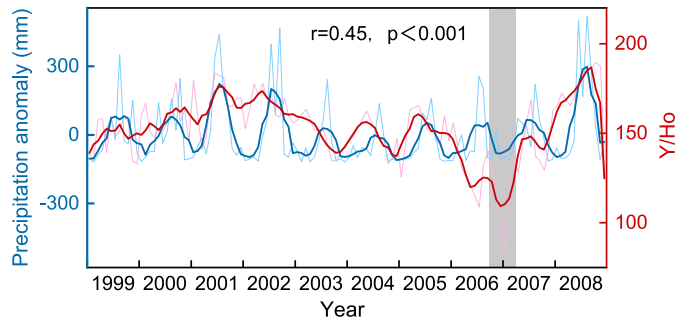


Figure 6. Comparison of W3 coral Y/Ho and precipitation anomaly during 1999–2008 (the average value of precipitation is 118.6 mm). The bold lines represent the 5-month moving average, and the fine lines represent the monthly variation. The gray background is the period with anthropogenic sources of REY.

4.1.2. Remobilization in the Bottom Sediments

Given that strong weathering and high SGD discharge would be expected to occur mostly during the summer seasons, however, this form seemed to contradict variations in the coral REE/Ca (Y/Ca) time series, which reach the peak value during the dry season (Figures 2c and 2d). In general, the majority of terrestrial dissolved and particulate REY in the near-coastal areas of WZI may be derived from SGD, due to the island's geographical positioning surrounded by the sea. Relevant to the high accumulation of REY in marine sediments, it is noteworthy that the resuspension of sediments and the upward diffusion of pore fluids may serve as important sources contributing to the presence of dissolved REY in surface seawater (Abbott et al., 2015; Crocket et al., 2018; Liao et al., 2022).

Strong winds have the potential to resuspend sediments, which may increase the concentration of dissolved elements in seawater. Approximately 50% of bottom sediments in shallow water areas can be resuspended when wind speeds exceed 4 m/s (Booth et al., 2000). The coastal seawater in WZI is very shallow, particularly at the W3 coral sampling site, with an average depth of approximately 5 m (Yu et al., 2019). The wind speed at WZI (average 4.2 m/s) exhibited a seasonal fluctuation under the impact of the strong East Asian Winter Monsoon (EAWM), displaying low wind speeds during the wet season and high wind speeds during the dry season (Figure 7 and Figure S7 in Supporting Information S1). During the dry season, wind speeds in excess of 4 m/s were a common occurrence in this region, creating favorable conditions for sediment resuspension. It is noteworthy that coral REY/Ca ratios also exhibited a similar trend, characterized by high values in the dry season (Figure 7). This pattern corresponds to the occurrence of winter monsoons and elevated average wind speeds observed during the same period. A 5-month moving average time series analysis showed a significant positive

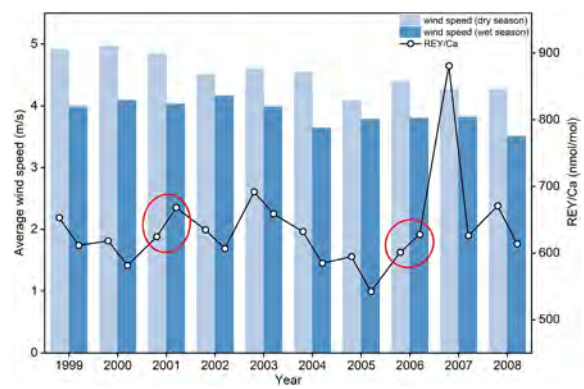


Figure 7. Seasonal variations of average wind speed and W3 coral REY/Ca ratios. The light blue and dark blue colors represent the dry season and the wet season of the average wind speed, respectively. The red circles indicate the year with inconsistent trends. The anomalous increase in REY/Ca values during the wet seasons of 2001 and 2006 interrupted the seasonal cycle of REY/Ca (an increase in the REY/Ca ratio was observed during the dry season), which should be related to artificial disturbances, as discussed above. This indicates that the increase in REY/Ca in surface seawater resulting from wind-induced sediment resuspension may be obscured by the effects of human-induced disturbances.

21699011, 2025, 3, Downloaded from https://agupubs.onlinelibrary.wiley.com/doi/10.1029/2024JF008239 by Wei Jiang - Guangxi University , Wiley Online Library on [11/03/2025]. See the Terms and Conditions (https://onlinelibrary.wiley.com/terms-and-conditions) on Wiley Online Library for rules of use; OA articles are governed by the applicable Creative Commons License

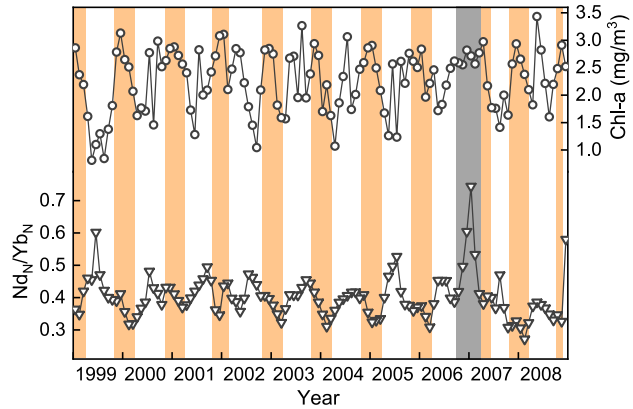


Figure 8. Comparison of W3 coral Nd_N/Yb_N and Chl-*a* during 1999–2008. The gray background is the period with anthropogenic sources of REY, and the orange background highlights that the high values of Chl-*a* correspond to low Nd_N/Yb_N ratios.

correlation between the average wind speed and coral REY/Ca in this area ($r = 0.34$, $p < 0.001$; Table S4 in Supporting Information S1). The occurrence of frequent hurricanes during the summer periods may also induce remobilization of bottom sediments. However, the absence of a correlation between coral REY/Ca ratios and the maximum wind speed ($p = 0.11$, $r > 0.05$; Table S4 in Supporting Information S1) precludes the possibility of an influence from the summer hurricane. In addition, we considered that the effects of summer hurricanes are not comparable to those of sustained winter winds in terms of their short-term impacts. Therefore, the concentrations of dissolved REY are substantially affected by the remobilization and resuspension of marine sediments in surface seawater caused by the strong winter monsoon. This conclusion is consistent with the findings reported by Li et al. (2019). Our study suggests that the signal of strong winter winds can be seen in the coral REY/Ca records on a longer timescale and with a monthly resolution.

4.1.3. Biogeochemical Cycle

Plankton plays an indispensable role in the biogeochemical cycle of trace elements in the ocean ecosystem (Martin & Knauer, 1973). For instance, rapid fluctuations in phytoplankton blooms and bio-particle variations can significantly impact the biogeochemical cycling of REY in shallow water environments (Hara et al., 2009). Seasonal variations in the WZI coral Nd_N/Yb_N ratios with peaks occurring during spring have been observed by Li et al. (2019), due to mineralization processes associated with biological particles.

Wind-induced sediment resuspension can also affect the light and nutrient limitation of phytoplankton, potentially increasing the nutrient supply for growth and enhancing phytoplankton production, as estimated by Chl-*a* (Schallenberg & Burns, 2004). A large number of biogenic particles are subsequently generated (Ma et al., 2014). The concentration of Chl-*a* in WZI generally exhibited a distinct seasonal pattern, with pronounced peaks during the dry season (Figure 8). Interestingly, the high Chl-*a* values observed in the dry season were inversely correlated with coral Nd_N/Yb_N ratios, and vice versa. The coral Nd_N/Yb_N ratios can still respond accurately to the changes in Chl-*a*, despite the potential presence of a time lag of 1–2 months in the time series due to the variable degree of annual growth rate of the coral (Gagan et al., 2012). The prevailing EAWM brings rich nutrients to the surface seawater in WZI during the dry season, promoting the proliferation of plankton. A substantial decrease in the Nd_N/Yb_N ratio was observed during the phytoplankton bloom (Figure 4a, shown with white background), due to biogenic particles preferentially absorbing LREE over HREE (Hara et al., 2009; Strady et al., 2015). Conversely, an increase in the Nd_N/Yb_N ratio was observed during the wet season, which may be caused by the release of LREE through the mineralization and desorption processes of biological particles during the waning winter monsoon. Interestingly, the 5-month moving average of coral Nd_N/Yb_N showed a negative correlation with Chl-*a* ($r = –0.29$, $p < 0.01$; Table S4 in Supporting Information S1). Therefore, the adsorption-desorption process of biological particles in the ocean may be an important factor influencing the REY pattern of seawater in WZI.

21699011, 2025, 3, Downloaded from https://agupubs.onlinelibrary.wiley.com/doi/10.1029/2024JF008239 by Wei Jiang - Guangxi University , Wiley Online Library on [11/03/2025]. See the Terms and Conditions (https://onlinelibrary.wiley.com/terms-and-conditions) on Wiley Online Library for rules of use; OA articles are governed by the applicable Creative Commons License

21699011, 2025, 3, Downloaded from https://agupubs.onlinelibrary.wiley.com/doi/10.1029/2024JF008239 by Wei Jiang - Guangxi University , Wiley Online Library on [11/03/2025]. See the Terms and Conditions (https://onlinelibrary.wiley.com/terms-and-conditions) on Wiley Online Library for rules of use; OA articles are governed by the applicable Creative Commons License

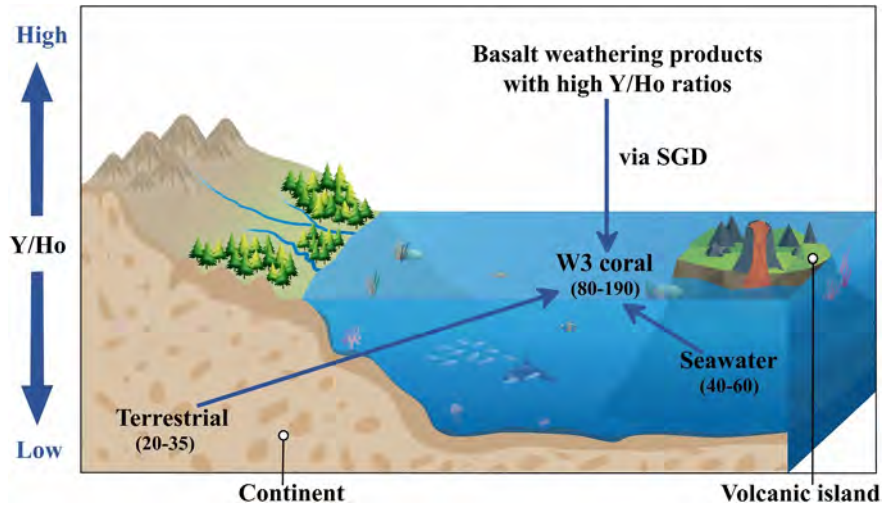


Figure 9. Schematic diagram of Y/Ho ratios in W3 coral and its end-members (terrestrial, seawater, and SGD), with ranges of Y/Ho values in parentheses.

4.2. Reliability of Coral Y/Ho Ratios as Basalt Weathering Proxies

Temperature, runoff, and precipitation are the most important parameters that control chemical weathering (Dessert et al., 2001; Shao et al., 2012). Indeed, the EASM controls the climatic regime of a region through changes in temperature and precipitation (Chen et al., 2017). The coral Y/Ho ratios are not only influenced by SGD associated with precipitation on monthly timescales but also affected by the EASM on interannual timescales (Figure 5). For instance, higher Y/Ho ratios were observed in 2001–2002 and 2008, which coincided with periods of elevated EASM index and heavy precipitation. Conversely, lower Y/Ho ratios were found in 2003 when the EASM index was weak and precipitation was low. In conclusion, the coral Y/Ho ratios exhibited a robust correlation with the EASM and rainfall-induced SGD, suggesting that the coral Y/Ho value is likely to be a potential novel and reliable proxy for chemical weathering intensity on basaltic islands.

The analysis showed noteworthy differences in the Y/Ho values of end-members between conventional continental sources and marine sources (Figure 9). However, the elevated Y/Ho values for W3 coral are too high to be explained by simple, binary mixing between seawater and terrestrial input. Instead, the high Y/Ho values for the coral indicate that there was an additional contribution derived from another flux. The W3 coral exhibits a REY pattern that is strikingly similar to that of Tahiti SGD, another Pacific volcanic island, particularly in terms of the elevated Y/Ho values (Figures 3c and 3e). In contrast to the open surface seawater of the SCS (Alibo & Nozaki, 2000), elevated Y/Ho ratios (~123) have also been observed in the PW4 SGD sample. The groundwater in the WZI was reported to be mainly basalt pore-fissure water (Ma et al., 2019). The coral average Y/Ho ratios during the wet season exhibit a significant positive correlation with precipitation, which controls SGD ($r = 0.95$, $p < 0.001$, $n = 9$; Figure 10). Accordingly, we suggest that the high Y/Ho ratio in W3 coral is most likely the result of the Y-Ho fractionation that occurred during basalt weathering. Ho is preferentially adsorbed onto secondary minerals during weathering, whereas Y is preferentially migrated away in solution, indicating that basalt weathering of the Y-Ho fractionation driven by the SGD contributes substantially to the coastal areas in WZI.

5. Conclusion

This study reconstructed the monthly variations of REY parameters in the surface seawater from 1999 to 2008, using the geochemical record of a coral from WZI. The Nd_N/Yb_N ratios exhibit a substantially seasonal cyclicity, which may be related to the precipitation associated with SGD and the adsorption-desorption processes of marine biogenic particles, with high values during the wet season and low values during the dry season. The combination of heavy rainfall and high temperature promotes basalt weathering and water-rock interaction during the wet season, which facilitates the release of REY and Y-Ho fractionation, resulting in high Y/Ho values in weathering solutions. Continued rainwater leaching provides a driving force for the downward migration of REY, and then SGD with high Y/Ho ratios is transported into the coastal seawater. Meanwhile, sediments resulting from the

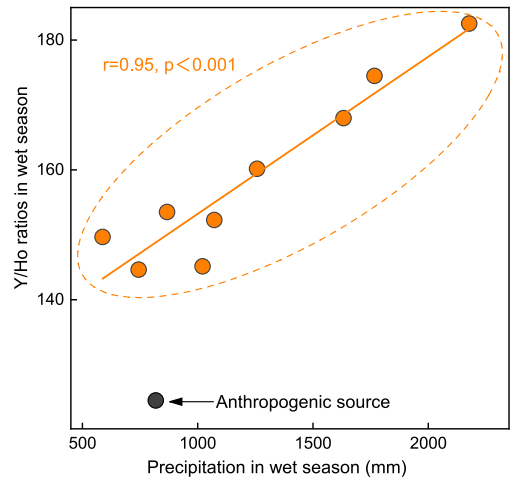


Figure 10. Comparison of the average Y/Ho ratios for W3 coral with the precipitation during the wet season during 1999–2008. The gray dot corresponds to the wet season of 2006, which was affected by the anthropogenic source of REY.

migration of basalt weathering products are deposited on the continental shelf around coastal areas of WZI. In the following dry season, the concentrations of REY in surface seawater are likely affected by the resuspension of marine sediments caused by winter winds, which is reflected in the coral REY/Ca ratios characterized by high ratios in the dry season.

The results suggest that REY fractionation in WZI is mainly controlled by basalt weathering associated with the EASM and SGD estimated by precipitation, as well as the biogeochemical cycle, whereas the total REY content is influenced by sediment resuspension driven by winter monsoon. REY flux from basalt weathering driven by SGD is the dominant natural source in the coastal areas of volcanic islands. This study presents for the first time that there is a substantial correlation between the coral Y/Ho ratio and basalt weathering, suggesting that coral Y/Ho could serve as a reliable proxy for basalt weathering intensity. Our study highlights the potential of this parameter in evaluating past and present basalt weathering. Furthermore, there is also the possibility that coral Nd_N/Yb_N could serve as a novel proxy for Chl-*a*. However, further high-precision data and longer time series are necessary for confirmation, and additional research is needed to strengthen the application of Y/Ho tracking for interannual EASM variability analysis.

Conflict of Interest

The authors declare no conflicts of interest relevant to this study.

Data Availability Statement

All data used in this study are accessible at Figshare (https://doi.org/10.6084/m9.figshare.28416318.v1) in Gu and Jiang (2025).

Acknowledgments
We thank the editor Mikael Attal, reviewers Karen H. Johannesson, Zhongbo Wang, Jaxon Dii Horne, and an anonymous reviewer for their careful work and constructive comments. This work was financially supported by the National Key R&D Program of China (Grant 2023YFF0804801), the major talent project of Guangxi Zhuang Autonomous Region (GXR-1BGQ2424020), and the National Natural Science Foundation of China (Grants 41976059 and 42030502).

References

Abbott, A. N., Haley, B. A., McManus, J., & Reimers, C. E. (2015). The sedimentary flux of dissolved rare earth elements to the ocean. *Geochimica et Cosmochimica Acta*, *154*, 186–200. https://doi.org/10.1016/j.gca.2015.01.010

Adebayo, S. B., Cui, M., Williams, T. J., Martin, E., & Johannesson, K. H. (2022). Evolution of rare earth element and εNd compositions of Gulf of Mexico seawater during interaction with Mississippi River sediment. *Geochimica et Cosmochimica Acta*, *335*, 231–242. https://doi.org/10.1016/j.gca.2022.08.024

Akagi, T., Hashimoto, Y., F-F, F., Tsuno, H., Tao, H., & Nakano, Y. (2004). Variation of the distribution coefficients of rare earth elements in modern coral-lattices: Species and site dependencies. *Geochimica et Cosmochimica Acta*, *68*(10), 2265–2273. https://doi.org/10.1016/j.gca.2003.12.014

Alibo, D. S., & Nozaki, Y. (2000). Dissolved rare earth elements in the South China Sea: Geochemical characterization of the water masses. *Journal of Geophysical Research*, *105*(C12), 28771–28783. https://doi.org/10.1029/1999JC000283

Amakawa, H., Alibo, D. S., & Nozaki, Y. (2000). Nd isotopic composition and REE pattern in the surface waters of the eastern Indian Ocean and its adjacent seas. *Geochimica et Cosmochimica Acta*, *64*(10), 1715–1727. https://doi.org/10.1016/S0016-7037(00)00333-1

21699011, 2025, 3, Downloaded from https://agupubs.onlinelibrary.wiley.com/doi/10.1029/2024JF008239 by Wei Jiang - Guangxi University , Wiley Online Library on [11/03/2025]. See the Terms and Conditions (https://onlinelibrary.wiley.com/terms-and-conditions) on Wiley Online Library for rules of use; OA articles are governed by the applicable Creative Commons License

Arsouze, T., Dutay, J. C., Lacan, F., & Jeandel, C. (2009). Reconstructing the Nd oceanic cycle using a coupled dynamical-biogeochemical model. *Biogeosciences*, *6*(12), 2829–2846. https://doi.org/10.5194/bg-6-2829-2009

Bau, M. (1999). Scavenging of dissolved yttrium and rare earths by precipitating iron oxyhydroxide: Experimental evidence for Ce oxidation, Y-Ho fractionation, and lanthanide tetrad effect. *Geochimica et Cosmochimica Acta*, *63*(1), 67–77. https://doi.org/10.1016/S0016-7037(99)00014-9

Bau, M., Möller, P., & Dulski, P. (1997). Yttrium and lanthanides in eastern Mediterranean seawater and their fractionation during redox-cycling. *Marine Chemistry*, *56*(1–2), 123–131. https://doi.org/10.1016/S0304-4203(96)00091-6

Behrens, M. K., Pahnke, K., Cravatte, S., Marin, F., & Jeandel, C. (2020). Rare earth element input and transport in the near-surface zonal current system of the Tropical Western Pacific. *Earth and Planetary Science Letters*, *549*, 116496. https://doi.org/10.1016/j.epsl.2020.116496

Booth, J. G., Miller, R. L., McKee, B. A., & Leathers, R. A. (2000). Wind-induced bottom sediment resuspension in a microtidal coastal environment. *Continental Shelf Research*, *20*(7), 785–806. https://doi.org/10.1016/S0278-4343(00)00002-9

Cai, Q., Fu, W., Wu, J., Zhao, Q., Yu, Y., Shao, Y., et al. (2021). Spatial distribution heterogeneity of rare earth element geochemistry in island soil under the joint constraints of volcanic rock and topography-A case study of Weizhou Island, Guangxi, China. *Quaternary Sciences*, *41*(5), 1294–1305. [in Chinese with English abstract]. https://doi.org/10.11928/j.issn.1001-7410.2021.05.06

Campodonico, V. A., Pasquini, A. I., Lecomte, K. L., García, M. G., & Depetris, P. J. (2019). Chemical weathering in subtropical basalt-derived laterites: A mass balance interpretation (Misiones, NE Argentina). *Catena*, *173*, 352–366. https://doi.org/10.1016/j.catena.2018.10.027

Chen, J., Algeo, T. J., Zhao, L., Chen, Z.-Q., Cao, L., Zhang, L., & Li, Y. (2015). Diagenetic uptake of rare earth elements by bioapatite, with an example from Lower Triassic conodonts of South China. *Earth-Science Reviews*, *149*, 181–202. https://doi.org/10.1016/j.earscirev.2015.01.013

Chen, Q., Liu, Z., & Kissel, C. (2017). Clay mineralogical and geochemical proxies of the East Asian summer monsoon evolution in the South China Sea during Late Quaternary. *Scientific Reports*, *7*(1), 42083. https://doi.org/10.1038/srep42083

Chen, X. (1999). State of groundwater resource and problem of geological environment in Weizhou Island, Baihai. *Guangxi Geology*, *12*(1), 64–68. [in Chinese with English abstract].

Chevis, D. A., Johannesson, K. H., Burdige, D. J., Tang, J., Bradley Moran, S., & Kelly, R. P. (2015). Submarine groundwater discharge of rare earth elements to a tidally-mixed estuary in Southern Rhode Island. *Chemical Geology*, *397*, 128–142. https://doi.org/10.1016/j.chemgeo.2015.01.013

Corrège, T. (2006). Sea surface temperature and salinity reconstruction from coral geochemical tracers. *Palaeogeography, Palaeoclimatology, Palaeoecology*, *232*(2–4), 408–428. https://doi.org/10.1016/j.palaeo.2005.10.014

Crocket, K. C., Hill, E., Abell, R. E., Johnson, C., Gary, S. F., Brand, T., & Hathorne, E. C. (2018). Rare Earth element distribution in the NE Atlantic: Evidence for benthic sources, longevity of the seawater signal, and biogeochemical cycling. *Frontiers in Marine Science*, *5*, 147. https://doi.org/10.3389/fmars.2018.00147

Deng, Y., Ren, J., Guo, Q., Cao, J., Wang, H., & Liu, C. (2017). Rare earth element geochemistry characteristics of seawater and porewater from deep sea in western Pacific. *Scientific Reports*, *7*(1), 16539. https://doi.org/10.1038/s41598-017-16379-1

Dessert, C., Dupré, B., François, L. M., Schott, J., Gaillardet, J., Chakrapani, G., & Bajpai, S. (2001). Erosion of Deccan Traps determined by river geochemistry: Impact on the global climate and the $^{87}Sr/^{86}Sr$ ratio of seawater. *Earth and Planetary Science Letters*, *188*(3–4), 459–474. https://doi.org/10.1016/S0012-821X(01)00317-X

Elderfield, H., & Greaves, M. J. (1982). The rare earth elements in seawater. *Nature*, *296*(5854), 214–219. https://doi.org/10.1038/296214a0

Elderfield, H., Whitfield, M., Burton, J. D., Bacon, M. P., Liss, P. S., Charnock, H., et al. (1988). The oceanic chemistry of the rare-earth elements. *Philosophical Transactions of the Royal Society of London, Series A*, *325*(1583), 105–126. https://doi.org/10.1098/rsta.1988.0046

Fan, Q., Sun, Q., Long, A., Yin, K., Su, I. J., Li, N., et al. (2006). Geology and eruption history of volcanoes in Weizhou Island and Xieyang Island, northern Bay. *Acta Petrologica Sinica*, *22*(6), 1529–1537. [in Chinese with English abstract].

Gagan, M. K., Ayliffe, L. K., Hopley, D., Cali, J. A., Mortimer, G. E., Chappell, J., et al. (1998). Temperature and surface-ocean water balance of the mid-Holocene tropical western Pacific. *Science*, *279*(5353), 1014–1018. https://doi.org/10.1126/science.279.5353.1014

Gagan, M. K., Dunbar, G. B., & Suzuki, A. (2012). The effect of skeletal mass accumulation in Porites on coral Sr/Ca and $\delta^{18}O$ paleothermometry. *Paleoceanography*, *27*(1), PA1203. https://doi.org/10.1029/2011PA002215

Garcia-Solsona, E., & Jeandel, C. (2020). Balancing rare earth element distributions in the northwestern Mediterranean Sea. *Chemical Geology*, *532*, 119372. https://doi.org/10.1016/j.chemgeo.2019.119372

Garcia-Solsona, E., Pena, L. D., Paredes, E., Pérez-Asensio, J. N., Quirós-Collazos, L., Lirer, F., & Cacho, I. (2020). Rare earth elements and Nd isotopes as tracers of modern ocean circulation in the central Mediterranean Sea. *Progress in Oceanography*, *185*, 102340. https://doi.org/10.1016/j.pocean.2020.102340

Gislason, S. R., Oelkers, E. H., Eiriksdottir, E. S., Kardjilov, M. I., Gisladottir, G., Sigfusson, B., et al. (2009). Direct evidence of the feedback between climate and weathering. *Earth and Planetary Science Letters*, *277*(1–2), 213–222. https://doi.org/10.1016/j.epsl.2008.10.018

Gu, T., & Jiang, W. (2025). High-resolution coral records of rare earth elements and yttrium in seawater driven by submarine groundwater discharge in a basalt island: A case study in the northern South China Sea [Dataset]. *Figshare*. https://doi.org/10.6084/m9.figshare.28416318.v1

Hara, Y., Obata, H., Doi, T., Hongo, Y., Gamo, T., Takeda, S., & Tsuda, A. (2009). Rare earth elements in seawater during an iron-induced phytoplankton bloom of the western subarctic Pacific (SEEDS-II). *Deep Sea Research Part II: Topical Studies in Oceanography*, *56*(26), 2839–2851. https://doi.org/10.1016/j.dsr2.2009.06.009

Henderson, P. (1984). *Rare earth element geochemistry*. Elsevier Science Publisher.

Horta-Puga, G., & Carriquiry, J. D. (2012). Coral Ba/Ca molar ratios as a proxy of precipitation in the northern Yucatan Peninsula, Mexico. *Applied Geochemistry*, *27*(8), 1579–1586. https://doi.org/10.1016/j.apgeochem.2012.05.008

Jiang, W., Wu, X., Yu, K., Yang, H., Xu, S., Wang, N., et al. (2022). Impacts of tropical cyclones and anthropogenic activities on marine vanadium: A unique perspective from high resolution Porites coral record. *Science China Earth Sciences*, *65*(12), 2285–2296. https://doi.org/10.1007/s11430-021-9993-9

Jiang, W., Yu, K., Song, Y., Zhao, J.-X., Feng, Y.-X., Wang, Y., et al. (2018a). Annual REE signal of East Asian winter monsoon in surface seawater in the northern South China Sea: Evidence from a century-long *Porites* coral record. *Paleoceanography and Paleoclimatology*, *33*(2), 168–178. https://doi.org/10.1002/2017PA003267

Jiang, W., Yu, K., Song, Y., Zhao, J.-X., Feng, Y.-X., Wang, Y., & Xu, S. (2018b). Coral geochemical record of submarine groundwater discharge back to 1870 in the northern South China Sea. *Palaeogeography, Palaeoclimatology, Palaeoecology*, *507*, 30–38. https://doi.org/10.1016/j.palaeo.2018.05.045

21699011, 2025, 3, Downloaded from https://agupubs.onlinelibrary.wiley.com/doi/10.1029/2024JF008239 by Wei Jiang - Guangxi University , Wiley Online Library on [11/03/2025]. See the Terms and Conditions (https://onlinelibrary.wiley.com/terms-and-conditions) on Wiley Online Library for rules of use; OA articles are governed by the applicable Creative Commons License

Jiang, W., Yu, K.-F., Song, Y.-X., Zhao, J.-X., Feng, Y.-X., Wang, Y.-H., & Xu, S. D. (2017). Coral trace metal of natural and anthropogenic influences in the northern South China Sea. *Science of the Total Environment*, *607–608*, 195–203. https://doi.org/10.1016/j.scitotenv.2017.06.105

Johannesson, K. H., & Burdige, D. J. (2007). Balancing the global oceanic neodymium budget: Evaluating the role of groundwater. *Earth and Planetary Science Letters*, *253*(1–2), 129–142. https://doi.org/10.1016/j.epsl.2006.10.021

Johannesson, K. H., Chevis, D. A., Burdige, D. J., Cable, J. E., Martin, J. B., & Roy, M. (2011). Submarine groundwater discharge is an important net source of light and middle REEs to coastal waters of the Indian River Lagoon, Florida, USA. *Geochimica et Cosmochimica Acta*, *75*(3), 825–843. https://doi.org/10.1016/j.gca.2010.11.005

Johannesson, K. H., Palmore, C. D., Fackrell, J., Prouty, N. G., Swarzenski, P. W., Chevis, D. A., et al. (2017). Rare earth element behavior during groundwater–seawater mixing along the Kona Coast of Hawaii. *Geochimica et Cosmochimica Acta*, *198*, 229–258. https://doi.org/10.1016/j.gca.2016.11.009

Kim, I., & Kim, G. (2011). Large fluxes of rare earth elements through submarine groundwater discharge (SGD) from a volcanic island, Jeju, Korea. *Marine Chemistry*, *127*(1), 12–19. https://doi.org/10.1016/j.marchem.2011.07.006

Kim, I., & Kim, G. (2014). Submarine groundwater discharge as a main source of rare earth elements in coastal waters. *Marine Chemistry*, *160*(2014), 11–17. https://doi.org/10.1016/j.marchem.2014.01.003

Knutson, D. W., Buddemeie, R. W., & Smith, S. V. (1972). Coral chronometers: Seasonal growth bands in reef corals. *Science*, *177*(4045), 270–272. https://doi.org/10.1126/science.177.4045.270

Kumar, M., Goswami, R., Awasthi, N., & Das, R. (2019). Provenance and fate of trace and rare earth elements in the sediment-aquifers systems of Majuli River Island, India. *Chemosphere*, *237*, 124477. https://doi.org/10.1016/j.chemosphere.2019.124477

Lacan, F., & Jeandel, C. (2005). Neodymium isotopes as a new tool for quantifying exchange fluxes at the continent–ocean interface. *Earth and Planetary Science Letters*, *232*(3–4), 245–257. https://doi.org/10.1016/j.epsl.2005.01.004

Li, P., & Qian, H. (2018). Water resources research to support a sustainable China. *International Journal of Water Resources Development*, *34*(3), 327–336. https://doi.org/10.1080/07900627.2018.1452723

Li, X., Liu, Y., Wu, C.-C., Sun, R., Zheng, L., Lone, M. A., & Shen, C. C. (2019). Coral-inferred monsoon and biologically driven fractionation of offshore seawater rare earth elements in Beibu Gulf, northern South China Sea. *Solid Earth Sciences*, *4*(4), 131–141. https://doi.org/10.1016/j.sesci.2019.09.003

Liao, J., Chen, J., Sun, X., Wu, Z., Deng, Y., Shi, X., et al. (2022). Quantifying the controlling mineral phases of rare-earth elements in deep-sea pelagic sediments. *Chemical Geology*, *595*, 120792. https://doi.org/10.1016/j.chemgeo.2022.120792

Liu, Y., Peng, Z., Wei, G., Ang, P. O., He, J., & Liu, G. (2006). Coral REE characters as an indictor of sea level rise in the Xigong waters, Hong Kong. *Geochimica et Cosmochimica Acta*, *70*(18), A367. https://doi.org/10.1016/j.gca.2006.06.743

Liu, Y., Peng, Z., Wei, G., Chen, T., Sun, W., He, J., et al. (2011). Interannual variation of rare earth element abundances in corals from northern coast of the South China Sea and its relation with sea-level change and human activities. *Marine Environmental Research*, *71*(1), 62–69. https://doi.org/10.1016/j.marenvres.2010.10.003

Louvat, P., & Allègre, C. J. (1997). Present denudation rates on the island of Réunion determined by river geochemistry: Basalt weathering and mass budget between chemical and mechanical erosions. *Geochimica et Cosmochimica Acta*, *61*(17), 3645–3669. https://doi.org/10.1016/S0016-7037(97)00180-4

Ma, C., Wu, X., Li, B., Gao, L., & Li, Q. (2019). The vulnerability evaluation of regional geo-environment: A case study in Beihai City, China. *Environmental Earth Sciences*, *78*(5), 129. https://doi.org/10.1007/s12665-019-8077-7

Ma, W., Chai, F., Xiu, P., Xue, H., & Tian, J. (2014). Simulation of export production and biological pump structure in the South China Sea. *Geo-Marine Letters*, *34*(6), 541–554. https://doi.org/10.1007/s00367-014-0384-0

Martin, J. H., & Knauer, G. A. (1973). The elemental composition of plankton. *Geochimica et Cosmochimica Acta*, *37*(7), 1639–1653. https://doi.org/10.1016/0016-7037(73)90154-3

Molina-Kescher, M., Hathorne, E. C., Osborne, A. H., Behrens, M. K., Kölling, M., Pahnke, K., & Frank, M. (2018). The influence of basaltic islands on the oceanic REE distribution: A case study from the tropical South Pacific. *Frontiers in Marine Science*, *5*, 50. https://doi.org/10.3389/fmars.2018.00050

Moore, W. S. (2010). The effect of submarine groundwater discharge on the ocean. *Annual Review of Marine Science*, *2*(1), 59–88. https://doi.org/10.1146/annurev-marine-120308-081019

Murphy, K., & Dymond, J. (1984). Rare earth element fluxes and geochemical budget in the eastern equatorial Pacific. *Nature*, *307*(5950), 444–447. https://doi.org/10.1038/307444a0

Naqvi, S. A. S., Nath, B. N., & Balaram, V. (1996). Signatures of rare-earth elements in banded corals of Kalpeni atoll-Lakshadweep archipelago in response to monsoonal variations. *Indian Journal of Marine Sciences*, *25*(1), 1–4. http://nopr.niscpr.res.in/handle/123456789/36379

Nguyen, A. D., Zhao, J. X., Feng, Y. X., Hu, W. P., Yu, K. F., Gasparon, M., et al. (2013). Impact of recent coastal development and human activities on Nha Trang Bay, Vietnam: Evidence from a Porites lutea geochemical record. *Coral Reefs*, *32*(1), 181–193. https://doi.org/10.1007/s00338-012-0962-4

Nozaki, Y., Dobashi, F., Kato, Y., & Yamamoto, Y. (1998). Distribution of Ra isotopes and the ^{210}Pb and ^{210}Po balance in surface seawaters of the mid Northern Hemisphere. *Deep Sea Research Part I: Oceanographic Research Papers*, *45*(8), 1263–1284. https://doi.org/10.1016/S0967-0637(98)00016-8

Nunes, M. C. M., Cardoso, D. P., Melo, T. V., Dorneles, V. R., Knapp, A. P., & Cecconello, S. T. (2023). Erosivity and seasonal rainfall for Pelotas-RS, Brazil with the RainfallErosivityFactor package and modified Fournier index. *Journal of South American Earth Sciences*, *132*, 104649. https://doi.org/10.1016/j.jsames.2023.104649

Pearce, C. R., Jones, M. T., Oelkers, E. H., Pradoux, C., & Jeandel, C. (2013). The effect of particulate dissolution on the neodymium (Nd) isotope and Rare Earth Element (REE) composition of seawater. *Earth and Planetary Science Letters*, *369–370*, 138–147. https://doi.org/10.1016/j.epsl.2013.03.023

Pham, V. Q., Grenier, M., Cravatte, S., Michael, S., Jacquet, S., Belhadj, M., et al. (2019). Dissolved rare earth elements distribution in the Solomon Sea. *Chemical Geology*, *524*, 11–36. https://doi.org/10.1016/j.chemgeo.2019.05.012

Pourmand, A., Dauphas, N., & Ireland, T. J. (2012). A novel extraction chromatography and MC-ICP-MS technique for rapid analysis of REE, Sc and Y: Revising CI-chondrite and Post-Archean Australian Shale (PAAS) abundances. *Chemical Geology*, *291*, 38–54. https://doi.org/10.1016/j.chemgeo.2011.08.011

Prouty, N. G., Jupiter, S. D., Field, M. E., & McCulloch, M. T. (2009). Coral proxy record of decadal-scale reduction in base flow from Moloka'i, Hawaii. *Geochemistry, Geophysics, Geosystems*, *10*(12), Q12018. https://doi.org/10.1029/2009GC002714

Rad, S. D., Allègre, C. J., & Louvat, P. (2007). Hidden erosion on volcanic islands. *Earth and Planetary Science Letters*, *262*(1), 109–124. https://doi.org/10.1016/j.epsl.2007.07.019

21699011, 2025, 3, Downloaded from https://agupubs.onlinelibrary.wiley.com/doi/10.1029/2024JF008239 by Wei Jiang - Guangxi University , Wiley Online Library on [11/03/2025]. See the Terms and Conditions (https://onlinelibrary.wiley.com/terms-and-conditions) on Wiley Online Library for rules of use; OA articles are governed by the applicable Creative Commons License

Saha, N., Rodriguez-Ramirez, A., Nguyen, A. D., Clark, T. R., Zhao, J.-X., & Webb, G. E. (2018). Seasonal to decadal scale influence of environmental drivers on Ba/Ca and Y/Ca in coral aragonite from the southern Great Barrier Reef. *Science of the Total Environment*, *639*, 1099–1109. https://doi.org/10.1016/j.scitotenv.2018.05.156

Saha, N., Webb, G. E., & Zhao, J.-X. (2016). Coral skeletal geochemistry as a monitor of inshore water quality. *Science of the Total Environment*, *566–567*, 652–684. https://doi.org/10.1016/j.scitotenv.2016.05.066

Schallenberg, M., & Burns, C. W. (2004). Effects of sediment resuspension on phytoplankton production: Teasing apart the influences of light, nutrients and algal entrainment. *Freshwater Biology*, *49*(2), 143–159. https://doi.org/10.1046/j.1365-2426.2003.01172.x

Schijf, J., & Byrne, R. H. (2021). Speciation of yttrium and the rare earth elements in seawater: Review of a 20-year analytical journey. *Chemical Geology*, *584*, 120479. https://doi.org/10.1016/j.chemgeo.2021.120479

Shao, J., Yang, S., & Li, C. (2012). Chemical indices (CIA and WIP) as proxies for integrated chemical weathering in China: Inferences from analysis of fluvial sediments. *Sedimentary Geology*, *265–266*, 110–120. https://doi.org/10.1016/j.sedgeo.2012.03.020

Sholkovitz, E., & Shen, G. T. (1995). The incorporation of rare earth elements in modern coral. *Geochimica et Cosmochimica Acta*, *59*(13), 2749–2756. https://doi.org/10.1016/0016-7037(95)00170-5

Strady, E., Kim, I., Radakovitch, O., & Kim, G. (2015). Rare earth element distributions and fractionation in plankton from the northwestern Mediterranean Sea. *Chemosphere*, *119*, 72–82. https://doi.org/10.1016/j.chemosphere.2014.05.049

Sun, Y., Jiang, W., Yu, K., Xu, S., Feng, C., Xie, S., & Wei, C. (2022). High-resolution coral records of cadmium in surface seawater: Biogeochemical cycling and a novel proxy for winter monsoon. *Geochemistry, Geophysics, Geosystems*, *23*(11), e2022GC010600. https://doi.org/10.1029/2022GC010600

Tachikawa, K., Athias, V., & Jeandel, C. (2003). Neodymium budget in the modern ocean and paleo-oceanographic implications. *Journal of Geophysical Research*, *108*(C8), 3254. https://doi.org/10.1029/1999JC000285

Tanaka, K., Ohde, S., Cohen, M. D., Snidvongs, A., Ganmanee, M., & McLeod, C. W. (2013). Metal contents of *Porites* corals from Khang Khao Island, Gulf of Thailand: Anthropogenic input of river runoff into a coral reef from urbanized areas, Bangkok. *Applied Geochemistry*, *37*, 79–86. https://doi.org/10.1016/j.apgeochem.2013.07.005

Taylor, S. R., & McLennan, S. M. (1985). *The continental crust: Its composition and evolution* (p. 312). Blackwell Scientific Publications.

Thompson, A., Amistadi, M. K., Chadwick, O. A., & Chorover, J. (2013). Fractionation of yttrium and holmium during basaltic soil weathering. *Geochimica et Cosmochimica Acta*, *119*, 18–30. https://doi.org/10.1016/j.gca.2013.06.003

Thompson, D. M. (2022). Environmental records from coral skeletons: A decade of novel insights and innovation. *Wiley Interdisciplinary Reviews: Climate Change*, *13*(1), e745. https://doi.org/10.1002/wcc.745

Webb, G. E., Nothdurft, L. D., Kamber, B. S., Kloprogge, J. T., & Zhao, J.-X. (2009). Rare earth element geochemistry of scleractinian coral skeleton during meteoric diagenesis: A sequence through neomorphism of aragonite to calcite. *Sedimentology*, *56*(5), 1433–1463. https://doi.org/10.1111/j.1365-3091.2008.01041.x

Worthington, S. R. H., Davies, G. J., & Alexander, E. C. (2016). Enhancement of bedrock permeability by weathering. *Earth-Science Reviews*, *160*, 188–202. https://doi.org/10.1016/j.earscirev.2016.07.002

Wu, X., Jiang, W., Yu, K., Xu, S., Yang, H., Wang, N., et al. (2022). Coral-inferred historical changes of nickel emissions related to industrial and transportation activities in the Beibu Gulf, northern South China Sea. *Journal of Hazardous Materials*, *424*, 127422. https://doi.org/10.1016/j.jhazmat.2021.127422

Wyndham, T., McCulloch, M., Fallon, S., & Alibert, C. (2004). High-resolution coral records of rare earth elements in coastal seawater: Biogeochemical cycling and a new environmental proxy. *Geochimica et Cosmochimica Acta*, *68*(9), 2067–2080. https://doi.org/10.1016/j.gca.2003.11.004

Xu, S., Yu, K., Wang, Y., Liu, T., Jiang, W., Wang, S., & Chu, M. (2018). Oil spill recorded by skeletal $\delta^{13}C$ of Porites corals in Weizhou Island, Beibu Gulf, northern South China Sea. *Estuarine, Coastal and Shelf Science*, *207*, 338–344. https://doi.org/10.1016/j.ecss.2018.04.031

Yu, H., Yang, W., Zhao, B., Chen, Z., Zhou, B., Nie, G., & Luo, H. (2021). Eruption sequences and characteristics of Weizhou Island Volcano, Guangxi Province, South of China. *Frontiers in Earth Science*, *9*, 713444. https://doi.org/10.3389/feart.2021.713444

Yu, K.-F., Zhao, J.-X., Wei, G.-J., Cheng, X.-R., & Wang, P.-X. (2005). Mid–late Holocene monsoon climate retrieved from seasonal Sr/Ca and $\delta^{18}O$ records of Porites lutea corals at Leizhou Peninsula, northern coast of South China Sea. *Global and Planetary Change*, *47*(2–4), 301–316. https://doi.org/10.1016/j.gloplacha.2004.10.018

Yu, W., Wang, W., Yu, K., Wang, Y., Huang, X., Huang, R., et al. (2019). Rapid decline of a relatively high latitude coral assemblage at Weizhou Island, northern South China Sea. *Biodiversity & Conservation*, *28*(14), 3925–3949. https://doi.org/10.1007/s10531-019-01858-w

Yue, Y., Xiang, X., Zhao, D., Yang, S., & Yao, Q. (2024). Late-Holocene ecosystem dynamics on Weizhou Island, China: A pollen and historical record of climate change and anthropogenic disturbances. *Quaternary Science Reviews*, *344*, 108977. https://doi.org/10.1016/j.quascirev.2024.108977

Zang, C., Sugita, M., Okita, A., & Bi, S. (2023). Runoff characteristics of headwater catchments in a young volcanic region. *Journal of Hydrology*, *620*, 129350. https://doi.org/10.1016/j.jhydrol.2023.129350

Zhang, Y., Wang, X., Xue, Y., Zou, C., Luo, M., Li, G., et al. (2022). Advances in the study of submarine groundwater discharge (SGD) in China. *Science China Earth Sciences*, *65*(10), 1948–1960. https://doi.org/10.1007/s11430-021-9946-x

Zhang, Y., Yu, K., Fan, T., Yue, Y., Wang, R., Jiang, W., et al. (2020). Geochemistry and petrogenesis of Quaternary basalts from Weizhou Island, northwestern South China Sea: Evidence for the Hainan plume. *Lithos*, *362–363*, 105493. https://doi.org/10.1016/j.lithos.2020.105493

21699011, 2025, 3, Downloaded from https://agupubs.onlinelibrary.wiley.com/doi/10.1029/2024JF008239 by Wei Jiang - Guangxi University , Wiley Online Library on [11/03/2025]. See the Terms and Conditions (https://onlinelibrary.wiley.com/terms-and-conditions) on Wiley Online Library for rules of use; OA articles are governed by the applicable Creative Commons License

Paleoceanography and Paleoclimatology

RESEARCH ARTICLE
10.1029/2024PA005080

The Potential of Benthic Foraminifera Carbon and Oxygen Isotopic Proxies as Environmental Indicators in Coral Reef Regions

Siqi Wu[1], Risheng Liang[1], and Kefu Yu[1,2]

[1]Guangxi Laboratory on the Study of Coral Reefs in the South China Sea, Coral Reef Research Center of China, School of Marine Sciences, Guangxi University, Nanning, China, [2]Southern Marine Science and Engineering Guangdong Laboratory (Guangzhou), Guangzhou, China

Key Points:

- Interspecific variations in $\delta^{13}C$ and $\delta^{18}O$ values of large benthic foraminifera are mainly influenced by symbionts and calcification pathway
- Different species display varying levels of intraspecific stability in $\delta^{13}C$ and $\delta^{18}O$ values, with only a few species showing high stability
- The isotopic values of certain species align with actual sea surface temperature and productivity levels

Correspondence to:
K. Yu,
kefuyu@scsio.ac.cn

Citation:
Wu, S., Liang, R., & Yu, K. (2025). The potential of benthic foraminifera carbon and oxygen isotopic proxies as environmental indicators in coral Reef regions. *Paleoceanography and Paleoclimatology*, *40*, e2024PA005080. https://doi.org/10.1029/2024PA005080

Received 2 DEC 2024
Accepted 22 APR 2025

Abstract Using reef-dwelling benthic foraminifera for paleoenvironmental reconstruction remains an unresolved challenge. Therefore, to evaluate the efficacy of using the $\delta^{18}O$ and $\delta^{13}C$ values obtained from benthic foraminifera species as environmental indicators in tropical reef regions, 233 specimens of 20 species collected from Huangyan Island and Lingyang Reef in the South China Sea were studied. The analyzed foraminifera species exhibited significant inter- and intraspecific variations for both $\delta^{18}O$ and $\delta^{13}C$ values, with $\delta^{13}C$ values displaying greater overall intraspecific variability. Clear distinctions were observed between the symbiont-bearing large benthic foraminifera (LBF) and symbiont-barren small benthic foraminifera, with the latter displaying slight oscillations around the isotopic values of the estimated equilibrium calcite and the $\delta^{18}O$ and $\delta^{13}C$ values of the LBF miliolids and rotaliids exhibiting markedly divergent trends. Miliolids generally showed higher isotopic values than equilibrium calcite, while rotaliids exhibited lower values, which may be attributed to variations in the calcification patterns and symbiotic algae associations. The $\delta^{18}O$ and $\delta^{13}C$ values of two LBF species at the two studied sites are generally consistent with the sea surface temperature and productivity levels, providing valuable insight into the utilization of reef-dwelling foraminifera as environmental indicators. The results of this study support the hypothesis that the $\delta^{18}O$ and $\delta^{13}C$ values of certain reef-dwelling foraminifera are reliable environmental indicators and offer valuable insights for paleoenvironmental reconstruction and marine ecosystem forecasting, although the limitations of this method should be considered in practical applications.

Plain Language Summary Coral reef sediments are invaluable archives for understanding environmental changes, yet the use of reef-dwelling foraminifera for paleoenvironmental reconstruction remains challenging. This study therefore assessed the potential of using isotopic values ($\delta^{18}O$ and $\delta^{13}C$) from foraminifera species as proxies for past environmental conditions in tropical reef regions. Specimens were collected from Huangyan Island and Lingyang Reef in the South China Sea. The results showed significant intraspecific and interspecific variability, influenced by a range of factors such as magnesium content, calcification pathways, growth rates, and symbiotic algae. Nevertheless, certain species exhibited relatively stable isotopic values that closely aligned with the actual environmental conditions, indicating their potential as reliable paleoenvironmental indicators. These findings underscore the potential of specific foraminifera species as effective tools for reconstructing the past environmental conditions in reef ecosystems, although further research is required to refine their application.

1. Introduction

Coral reef regions serve as critical marine habitats that are highly sensitive to environmental fluctuations. They have attracted considerable scientific interest due to their pivotal role in biodiversity conservation and their capacity to provide valuable insights into climate change (e.g., Bellwood et al., 2004; Graham et al., 2020). Large benthic foraminifera (LBF) are distinguished by their larger test sizes and their complex internal architecture that are frequently associated with symbiotic algae (e.g., Boudaugher-Fadel, 2018; Hallock, 2000; Walker et al., 2011). In contrast, small benthic foraminifera (SBF) have relatively smaller tests and generally lack symbiotic algae. Being among the most common inhabitants of reef environments, LBF play a pivotal role in shaping reef sediment composition (Doo et al., 2014; Langer, 2008; Pearson, 2012). The temporal and spatial distribution of LBF populations in reef regions provides a link between past and present, offering considerable potential for paleoenvironmental reconstruction (Maeda et al., 2017; Meng et al., 2022; F. Wu et al., 2023).

© 2025. American Geophysical Union. All Rights Reserved.

Furthermore, their strong responsiveness to external variations and remarkable resilience to events such as thermal stress enhance their utility as paleoenvironmental proxies (Benedetti et al., 2024; Coletti et al., 2022).

Geochemical analyses of deep-sea foraminiferal tests have become an effective tool for unraveling Earth's climatic history (Katz et al., 2010). The $\delta^{18}O$ signatures preserved within foraminifera tests have been extensively employed as proxy for paleotemperature and global ice volume, and for stratigraphic correlations (e.g., Lisiecki & Raymo, 2005; Prell et al., 1986; Waelbroeck et al., 2002), with the $\delta^{13}C$ values providing information about marine productivity levels and carbon cycling (e.g., Bickert & Mackensen, 2003; Mackensen, 2008; Zahn et al., 1986). However, despite the remarkable progress made in the geochemical analyses of deep-sea foraminifera, the application of these analytical tools faces considerable challenges when dealing with reef-dwelling species. Thus, the appropriateness of their geochemical signals for paleoenvironmental reconstruction is still debated (Billups et al., 2022; Saraswati, 2004).

Extensive research has consistently demonstrated that foraminiferal biomineralization is more susceptible to vital effects and abiotic factors in warm, shallow waters (Robbins et al., 2017; Wefer et al., 1999). Multiple studies on LBF have revealed their environmental implications in coral reef regions. Temperature-controlled culture experiments involving specific LBF species indicate a notable correlation between $\delta^{18}O$ and temperature, highlighting the promising nature of this methodology (Maeda et al., 2017). The application of in-situ microanalytical techniques has also shed light on the use of LBF carbon and oxygen isotopes in paleoenvironmental reconstructions (Rollion-Bard et al., 2008; Q. Zhang et al., 2020). However, comprehensive studies investigating the $\delta^{18}O$ and $\delta^{13}C$ values of naturally captured benthic foraminifera in reef areas have identified several limitations in their use as reliable environmental indicators. For instance, the isotopic analysis of various LBF species from Akajima in Japan indicated that shell size significantly impacts both $\delta^{18}O$ and $\delta^{13}C$ on the reef flat, while minimal impact is observed in deep water benthic foraminifera (Saraswati et al., 2004). Another study conducted at the Açu Reef, Brazil, found large intraspecific variability in the $\delta^{13}C$ and $\delta^{18}O$ values of all studied LBF (Billups et al., 2022).

The use of downcore foraminifera from coral reef regions in paleoenvironmental reconstruction is an emerging field (Fujita, 2020; Johnson et al., 2019; Meng et al., 2022). The interpretation and application of foraminifera in paleoenvironmental reconstructions require careful consideration and evaluation to mitigate potential biases and conflicting influences. The South China Sea (SCS) contains a substantial number of coral reefs; however, few studies focused on using reef-dwelling foraminifera as valuable environmental indicators in this area (A'ziz et al., 2021; Ma et al., 2018). This study therefore aimed to investigate the suitability of reef-dwelling benthic foraminifera as paleoenvironmental indicators and build a fundamental basis for future application in downcore samples without strong diagenesis. We conducted whole-test carbon and oxygen isotope analyses of different benthic foraminiferal species found in the surface reef sediments of the central SCS. The selected foraminifera encompassed four distinct orders, comprising a diverse array of species with varying test types, including both larger and smaller forms, and both symbiont-bearing and -barren species.

2. Geological Setting

The SCS is a maritime region that lies south of mainland China in the western Pacific Ocean (Figure 1). The area is characterized by a complex and dynamic tectonic setting that has been shaped over millions of years by a combination of plate tectonics, volcanism, and sedimentary processes (Shao et al., 2017; Sun, 2016; Y. Zhang et al., 2020). The Xisha Islands, also known as the Paracel Islands, are situated in the northwestern SCS and originated from the Xisha Uplift in the early Miocene (S. Wu et al., 2014). The Zhongsha Islands, also known as the Macclesfield Bank, are situated in the central SCS southeast of the Xisha Islands and feature atolls and an abundance of organic reefs that originated from the positive relief during the Middle Miocene (Huang et al., 2020).

The Lingyang Reef is located in the southwestern reef flat of the Yongle Atoll on the Xisha Islands. The reef is an atoll that comprises a roughly triangular contour spanning approximately 15 km^2, with a length of 5.6 km from north to south and a maximum width of approximately 4 km from east to west. A small lagoon within the reef has a diameter ranging from 2 to 3 km and a maximum depth exceeding 15 m. The western slope of the lagoon is characterized by a gentle incline, which stands in stark contrast to the steep slope of its eastern counterpart. Most of the reef platform is exposed above the water surface during low tides and only submerged during typhoons and extremely high tides. Numerous coral reefs are scattered throughout the lagoon. The sedimentary environment of

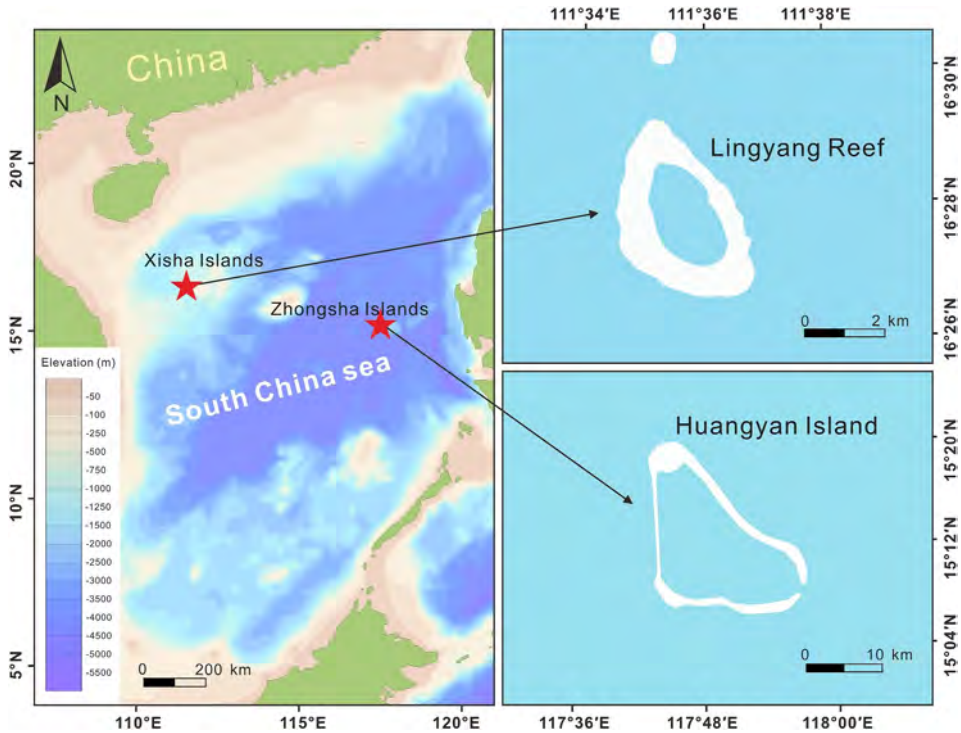


Figure 1. Map of South China Sea showing location and sampling sites in Lingyang Reef and Huangyan Island.

Lingyang Reef is relatively complex, including the a fore-reef slope, a reef flat, a lagoon slope, and a lagoon basin, which offers a diverse array of habitats suitable for foraminifera and other coral reef-associated organisms.

Huangyan Island, also known as Scarborough Shoal, is a triangular atoll located at the easternmost edge of the Zhongsha Islands. The total area of Huangyan Island is approximately 133 km^2, measuring ~15 km from east to west and north to south. The lagoon on Huangyan Island has a diameter ranging from 8 to 13 km and water depth varying between 9 and 11 m, with a maximum depth of 19.5 m. Huangyan Island is the only emergent area during low tides within the Zhongsha Islands. The sediment in the lagoon exhibits a distinct fining trend as the water depth increases, providing suitable habitats for foraminifera and other coral reef organisms.

3. Material and Methods

3.1. Surface Sediment Collection

Surface loose sediments were collected from the uppermost surfaces of the lagoon areas in the Lingyang Reef (16°28′N, 111°35′E, depth = 8 m) and Huangyan Island (15°07′N, 117°51′E, depth = 10 m) in the SCS (Figure 1). Sediments were stained immediately after collection using Rose Bengal to identify living and dead foraminifera. In subsequent procedures, a mixed foraminiferal assemblage was employed to represent a time period analogous to sampling from a specific layer in the sediment core. Samples were stored in the sample repository at the School of Marine Sciences, Guangxi University.

3.2. Foraminifera Specimen Preprocessing

Sediment samples were initially placed in beakers and agitated with distilled water before leaving to settle for one day. The upper suspension of the water was then decanted, and the washing process was repeated several times to reduce the clay content. Samples were then subjected to three cycles of 2-min ultrasonic cleaning in ultrapure water (70 W power, 40 kHz frequency) and immersed in a 5% buffered H_2O_2 solution for one day to degrade any organic matter. Subsequently, the samples were subjected to two additional cycles of 2-min ultrasonic cleaning and sieved to retain 0.063–2 mm particles. After drying in an oven at 60°C, foraminiferal specimens were then selected under a high-performance stereo microscope (ZEISS Stemi 508). Finally, careful observations were

conducted under a Scanning Electron Microscope (JXA-8230) to confirm that the samples have not undergone recrystallization.

3.3. Whole-Test Isotope Analysis

Larger individuals of uniform size and shape from each species were selected for isotopic analysis. Besides imperforate (porcelaneous) and perforate (hyaline) tests, foraminifera with agglutinated tests were also investigated, given that these species are primarily composed of calcareous cement and capable of self-secreting calcite (Loeblich & Tappan, 1989). To release their contents, the selected specimens were gently crushed and the fragments were collected using fine tweezers. Both individual and multiple specimens of the same species were analyzed using a stable isotope ratio mass spectrometer (ThermoScientific MAT253) in the laboratory at the School of Marine Sciences in Guangxi University. Standard deviations obtained for $\delta^{18}O$ and $\delta^{13}C$ were 0.08 and 0.04‰, respectively. Each species from the two study sites was analyzed, with a minimum of eight replicate samples, except for several species of lower abundance for which fewer than eight specimens were available. Calibration of the $\delta^{18}O$ and $\delta^{13}C$ results was performed using external standards from the Chinese national standard carbonate GBW04405 ($\delta^{18}O = -8.49 \pm 0.14$‰, $\delta^{13}C = 0.57 \pm 0.03$‰) and National Bureau of Standards 18 ($\delta^{18}O = -23.2 \pm 0.1$‰, $\delta^{13}C = -5.014 \pm 0.035$‰) and were reported per mille (‰) relative to the Vienna Pee Dee Belemnite (VPDB) isotope scale.

Analyzing individual specimens allowed us to capture unique isotopic signatures that may be masked when multiple specimens are combined, providing insights into the intraspecific variations critical for our research. Considering the potential bias from single-specimen analysis, future studies should incorporate multiple specimens. Mixed specimens can significantly reduce the testing time, which is especially beneficial in large-scale studies. Nevertheless, this approach may introduce additional errors, which we addressed by comparing the results of mixed specimens with the average isotopic values obtained for individual specimens. Specifically, *Sorites orbiculus* was chosen for analysis due to its relatively stable carbon and oxygen isotopic values and high abundance at both study sites.

3.4. Equilibrium Calcite Isotope Values Estimation

Oxygen and carbon isotope values of equilibrium calcite were calculated to assess the calcification of foraminifera relative to equilibrium conditions. The $\delta^{18}O_c$ ($\delta^{18}O$ of equilibrium calcite) can be derived using a modified equation (Kim & O'Neil, 1997):

$$\delta^{18}O_c = \frac{4.64 - \sqrt{21.53 - 0.36 \times (16.1 - T)}}{0.18} + \delta^{18}O_w - 0.27$$

where T is temperature in °C, $\delta^{18}O_c$ is in the VPDB scale, and $\delta^{18}O_w$ is in the Vienna Standard Mean Ocean Water (VSMOW) scale. The value 0.27 is derived from the VSMOW-VPDB conversion value, for which 0.27‰ is currently accepted (Hut, 1987). The $\delta^{18}O_w$ ($\delta^{18}O$ of ambient seawater) was obtained using the salinity-$\delta^{18}O_w$ isotope equation for surface to subsurface water in the SCS: $\delta^{18}O_w = 0.23S - 7.8$ (J. Wu et al., 2021). Salinity was derived from in-situ measurements using a YSI Pro30 conductivity meter, with both sites exhibiting a salinity of 34.5‰. According to an annually updated 1° × 1° grid global sea surface temperature (SST) data set (Rayner et al., 2003), the annual average SSTs for Lingyang Reef and Huangyan Island were set at 27.5°C and 28.5°C respectively. Using these parameters, the $\delta^{18}O_c$ of Lingyang Reef and Huangyan Island were calculated to be −2.49‰ and −2.68‰, respectively.

The $\delta^{13}C_c$ value ($\delta^{13}C$ of equilibrium calcite) was calculated using the carbon isotope fractionation relationship (Emrich et al., 1970):

$$\delta^{13}C_c = \delta^{13}C_b + 1.85 + 0.035\,(T - 20)$$

where T is temperature in °C, $\delta^{13}C$ is in the VPDB scale, and $\delta^{13}C_b$ is the $\delta^{13}C$ for dissolved HCO–3, which is approximated as the $\delta^{13}C$ of total dissolved organic carbon (DIC) since HCO–3 accounts for 91% in the DIC (Raven et al., 2005). The value of $\delta^{13}C_{DIC}$ was set to 0.35‰ in accordance with studies performed nearby (Ding et al., 2020). The $\delta^{13}C_c$ of Lingyang Reef and Huangyan Island were calculated as 2.46 and 2.50‰ respectively.

Table 1
Studied Foraminifera Species

Order	Family	Species	Test types	Symbiont	Number HY	Number LY
Miliolida	Hauerinidae	*Massilina intermedia*	Imperforate		0	10
		Quinqueloculina parkeri			8	11
		Schlumbergerina occidentalis			0	10
		Triloculina earlandi			8	4
	Peneroplidae	*Dendritina pacifica*		rhodophyte	0	10
		Peneroplis pertusus		rhodophyte	0	8
	Soritidae	*Sorites orbiculus*		dinoflagellate	9	10
Rotaliida	Amphisteginidae	*Amphistegina radiata*	Perforate	diatom	8	0
		A. lessonii		diatom	9	0
	Calcarinidae	*Calcarina hispida*		diatom	10	0
		Neorotalia calcar		diatom	11	11
	Nummulitidae	*Nummulites venosus*		diatom	0	7
		Heterostegina suborbicularis		diatom	0	8
	Elphidiidae	*Elphidium craticulatum*			0	11
		Elphidum crispum			0	10
		Elphidum sp.			9	10
	Almaenidae	*Anomalinella rostrata*			0	9
Textulariida	Valvulinidae	*Clavulina angularis*	Agglutinated		0	12
	Textulariidae	*Textularia agglutinans*			0	11
Lituolida	Verneuilinidae	*Gaudryina trullissata*			9	0
Total					81	152

Note. LBF species are marked in blue. Five species observed at both sites are marked in green. HY = Huangyan Island, LY = Lingyang Reef.

4. Results

The most abundant species from the LBF and SBF groups were selected for analysis. A total of 233 foraminiferal individuals from 20 species, with no signs of dissolution or recrystallization, were meticulously selected. Of these, 81 individuals representing 9 species were selected from Huangyan Island and 152 individuals representing 16 species from Lingyang Reef. The abundance and diversity of foraminifera are higher at Lingyang Reef than Huangyan Island. The genera and species identified in this study are listed in Table 1.

4.1. Isotopic Intraspecific and Interspecific Variability

The isotopic values showed significant intraspecific and interspecific variability in both study areas, with overall $\delta^{18}O$ values ranging from −4.26 to 1.20‰ (SD = 0.54) and overall $\delta^{13}C$ values from −1.44 to 4.78‰ (SD = 1.41), underscoring the complexity of isotopic signatures in reef-dwelling foraminifera. To better emphasize the variability in data stability among different foraminiferal species, we used variance instead of standard deviation (Figure 2). In general, the $\delta^{13}C$ data exhibited lower stability as compared to the $\delta^{18}O$ data, especially for Huangyan Island (Figure 2). The majority of $\delta^{18}O$ variance was below 0.15 with a maximum of 0.28, while four of the $\delta^{13}C$ variance were greater than 0.5, with one species, *Gaudryina trullissata*, surpassing 1.

4.2. Isotopic Variability of LBF and SBF

The 20 foraminifera species analyzed in this study include both LBF and SBF. Of the species observed, nine are LBF, including *Dendritina pacifica*, *Peneroplis pertusus*, *S. orbiculus*, *Amphistegina radiata*, *A. lessonii*, *Calcarina hispida*, *Neorotalia calcar*, *Nummulites venosus* and *Heterostegina suborbicularis*. Significant differences were observed in the $\delta^{18}O$ and $\delta^{13}C$ values obtained for the LBF and SBF groups. The highest degree of

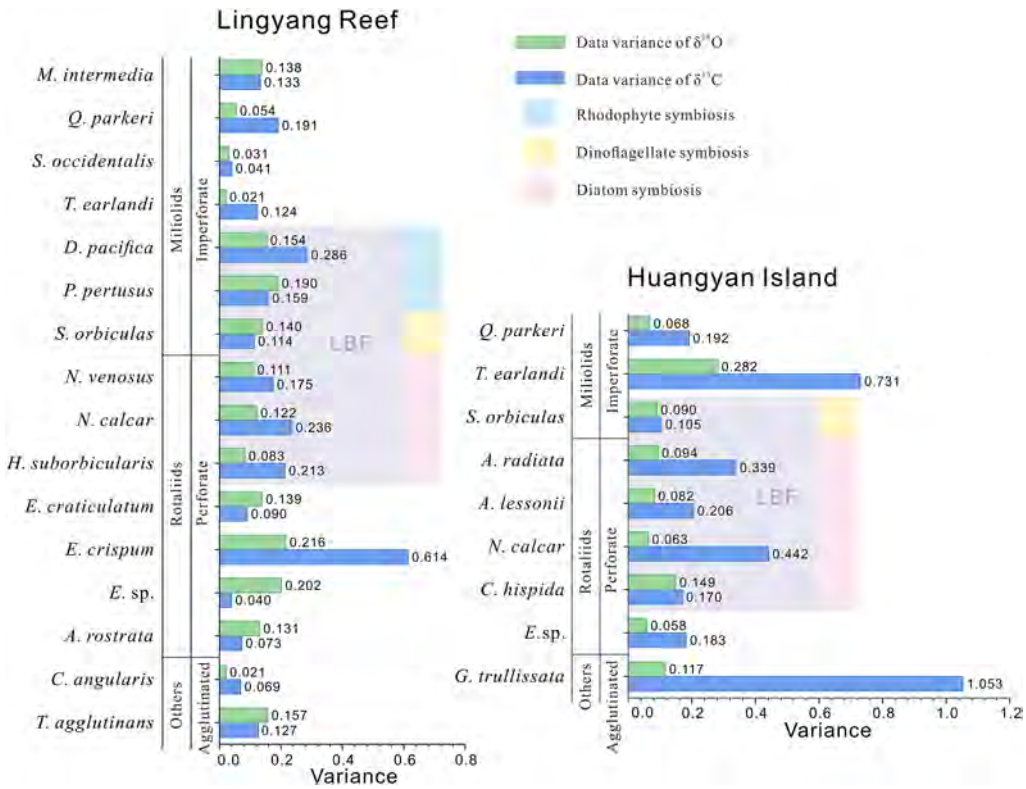


Figure 2. Variability in $\delta^{18}O$ and $\delta^{13}C$ values for analyzed foraminifera species at the two study sites.

intraspecific stability in the carbon and oxygen isotopic values was predominantly in the SBF group (Figure 2), especially *S. occidentalis* (0.031 and 0.041) and *Clavulina angularis* (0.020 and 0.069) from the Lingyang Reef. In the LBF group, the oxygen isotopic variances were generally lower (0.063∼0.190) than carbon isotopic variances (0.105∼0.442), with only *S. orbiculus* exhibiting relatively lower oxygen (0.090∼0.140) and carbon (0.105∼0.114) isotopic variances in both studied areas (Figure 2).

4.3. Spatial Variations in the Two Study Areas

4.3.1. Isotopic Results for Lingyang Reef

Sixteen foraminiferal species (152 individuals) were selected from the Lingyang Reef for carbon and oxygen isotope analyses, with six of them were LBF. The average $\delta^{18}O$ and $\delta^{13}C$ values for the 16 species were −2.60‰ (SD = 0.55) and 1.41‰ (SD = 1.39), respectively. The $\delta^{13}C$ data exhibited significant fluctuations ranging from −1.44 to 4.30‰, with the $\delta^{18}O$ data results fluctuating between −1.32‰ and −4.26‰ (Figure 3). The isotopic variances in Lingyang Reef were generally lower than 0.3, except for the $\delta^{18}O$ variance observed in *Elphidum crispum*, which reached 0.614 (Figure 2).

4.3.2. Isotopic Results for Huangyan Island

Nine benthic foraminiferal species (81 individuals) were selected from Huangyan Island, of which five were LBF. The average values of $\delta^{18}O$ and $\delta^{13}C$ were −2.73‰ (SD = 0.51) to 1.69‰ (SD = 1.51), respectively. The $\delta^{13}C$ values of all species fluctuated between −1.06 and 4.778‰, and the $\delta^{18}O$ values from −1.20‰ to −3.78‰ (Figure 4). In general, $\delta^{13}C$ data exhibited lower stability compared to $\delta^{18}O$ data in same site and the $\delta^{13}C$ data in Lingyang Reef (Figure 2). Only *S. orbiculus* displayed stability for both $\delta^{18}O$ and $\delta^{13}C$.

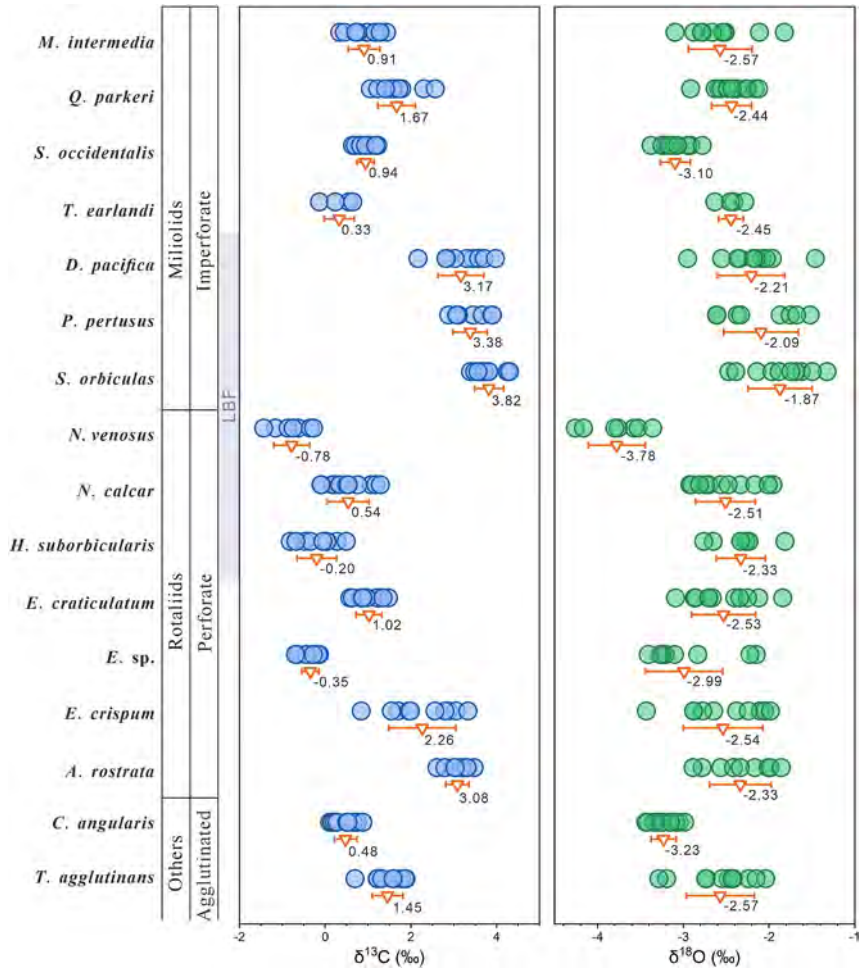


Figure 3. $\delta^{18}O$ (‰) and $\delta^{13}C$ (‰) values obtained for foraminiferal species in Lingyang Reef. Circles represent isotope values obtained for each specimen and triangles represent average values with standard deviation.

4.3.3. Isotopic Results for the Five Benthic Foraminifera Species Observed at Both Study Sites

Five of the 20 benthic foraminiferal species appeared in both the Huangyan Island and Lingyang Reef sediments (Figure 5), with average $\delta^{13}C$ values of 1.95 and 1.19‰ and average $\delta^{18}O$ values of −2.50‰ and −2.41‰ in Huangyan Island and Lingyang Reef, respectively.

The $\delta^{18}O$ and $\delta^{13}C$ values of different foraminifera species exhibit incongruent fluctuations across the two sites (Figure 5). The two LBF species *S. orbiculus* and *N. calcar* showed higher $\delta^{18}O$ values for Lingyang Reef (−1.87‰ and −2.51‰, respectively) as compared to Huangyan Island (−2.21 ‰ and −2.93‰, respectively), while for $\delta^{13}C$, *S. orbiculus* exhibited higher values in Huangyan Island (4.41‰) than Lingyang Reef (3.82‰), and *N. calcar* exhibited higher values in Lingyang Reef (0.54‰) than Huangyan Island (−0.17‰). All three SBF species exhibited higher $\delta^{18}O$ and $\delta^{13}C$ values in Huangyan Island (Figure 5).

4.4. Isotopic Variations Among Different Orders, Test Types, and Symbiont Types

The foraminiferal species studied belonged to four orders, with a corresponding relationship observed between the test types of the foraminifera and the orders to which they belonged (Table 1). *S. occidentalis* has an agglutinated structure and is placed in the imperforate group due to its evolutionary affinity with other Miliolida (Mikhalevich et al., 2008) and its retained typically imperforate arrangement (Wood, 1948).

Variation was observed in the $\delta^{18}O$ and $\delta^{13}C$ values among the different orders (test types). Both miliolid LBF and SBF exhibited higher $\delta^{18}O$ and $\delta^{13}C$ values in Huangyan Island (Figure 4), while only miliolid LBF exhibited

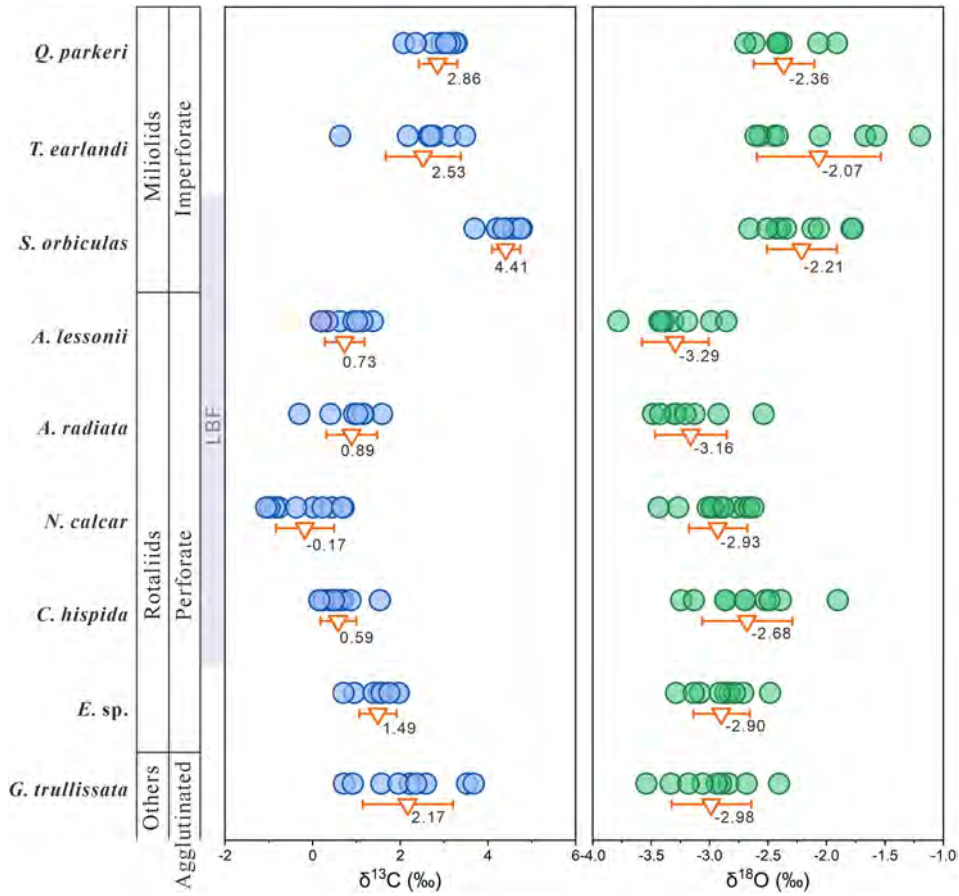


Figure 4. $\delta^{18}O$ (‰) and $\delta^{13}C$ (‰) values of analyzed foraminifera species in Huangyan Island. Circles represent isotope values obtained for each specimen; triangles represent average values with standard deviation.

higher $\delta^{18}O$ and $\delta^{13}C$ values in Lingyang Reef (Figure 3). The vast majority of the $\delta^{18}O$ and $\delta^{13}C$ values obtained for miliolid LBF were higher than the values estimated for equilibrium calcite, while rotaliid LBF exhibited the opposite pattern (Figure 6a). Thus, the LBF group is divided into two distinct parts on the $\delta^{13}C/\delta^{18}O$ scatter plot. In comparison, the isotopic values of the SBF group were closer to the estimated equilibrium calcite values and no clear distinction was assumed based on their test types (Figure 6b). Notably, while the results of agglutinated tests may theoretically be influenced by impurities, no distinct differentiation was observed in the SBF group as compared to the other two test types (Figure 6b).

The growth and development of LBF is typically accompanied by symbiotic algae, including rhodophytes, dinoflagellates, chlorophytes, and diatoms, which vary among different LBF species (e.g., Hallock, 2000; Prazeres & Renema, 2019). In this study, the nine LBF species were divided into three groups based on their symbiotic algae (Table 1). All studied rotaliids harbored diatoms, whereas the miliolids harbored only rhodophytes and dinoflagellates. In the miliolid group, the only species harboring dinoflagellate symbiont (*S. orbiculus*) exhibited the highest $\delta^{13}C$ values; however, little difference was observed in the $\delta^{18}O$ values for species with dinoflagellate symbionts and rhodophyte symbionts (Figure 6c).

4.5. The $\delta^{13}C$-$\delta^{18}O$ Relationship

Integrated data for all LBF species revealed moderate but positive $\delta^{13}C$-$\delta^{18}O$ correlations ($R^2 = 0.42$, Figure 6a), with the overall $\delta^{13}C$-$\delta^{18}O$ correlation weaker in the SBF group ($R^2 = 0.28$, Figure 6b). It is noteworthy that the higher correlation observed within the overall LBF group arises from the distinctly different isotopic distributions exhibited by miliolids and rotaliids. Specifically, miliolids (dark blue in Figure 6a) tend to demonstrate relatively higher $\delta^{13}C$ and $\delta^{18}O$ values, whereas rotaliids (red in Figure 6a) exhibit relatively lower $\delta^{13}C$ and $\delta^{18}O$ values.

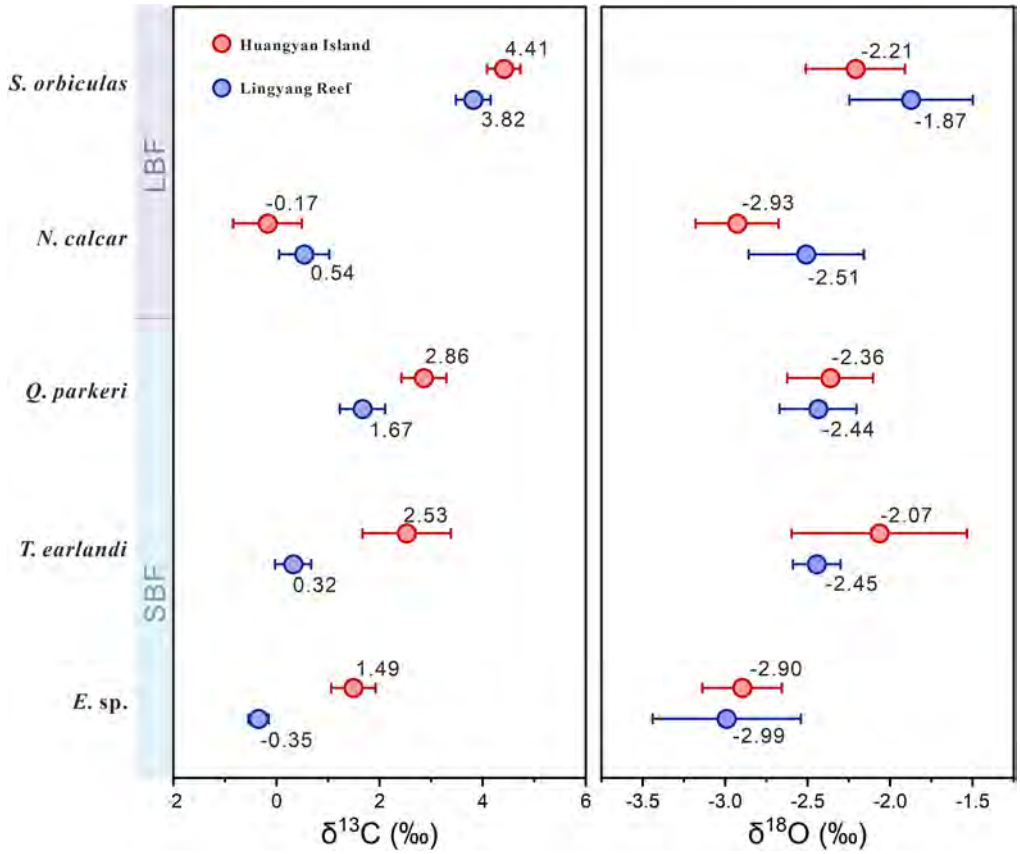


Figure 5. Average $\delta^{18}O$ (‰) and $\delta^{13}C$ (‰) values obtained for five foraminifera species observed at both studied sites.

However, when examining miliolids and rotaliids separately, the $\delta^{13}C$-$\delta^{18}O$ correlation within each group is weak ($R^2 = 0.00$ and 0.09, respectively).

The majority of species studied exhibit weak correlation, while several species (for which regression lines are plotted in Figures 7 and 8) show moderate positive $\delta^{13}C$-$\delta^{18}O$ correlation ($R^2 > 0.5$) with a slope greater than 1. Only one SBF species in the miliolid group from Huangyan Island, *Q. parkeri*, shows a notable correlation ($R^2 = 0.66$), while the others exhibit weak correlations (Figures 7 and 8). The rotaliid LBF *A. lessonii* and *N.*

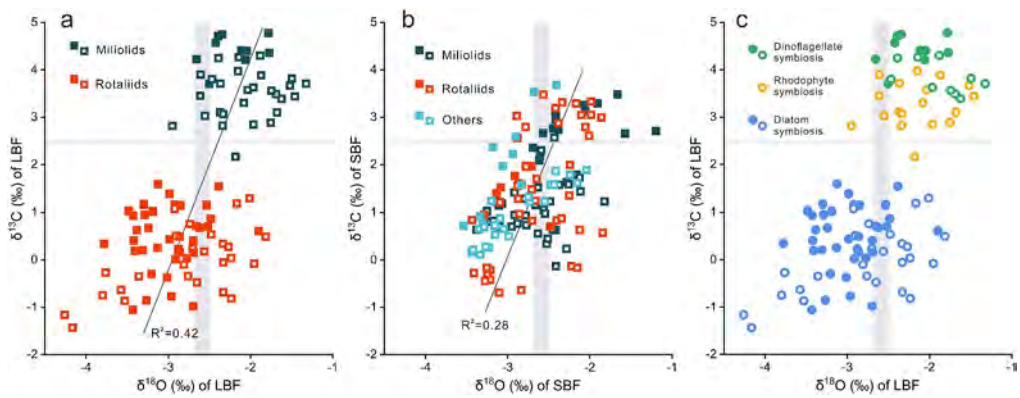


Figure 6. $\delta^{18}O$ versus $\delta^{13}C$ scatter plots. Vertical and horizontal gray bars represent $\delta^{18}O$ and $\delta^{13}C$ values estimated for equilibrium calcite, respectively. (a) large benthic foraminifera (LBF) group differentiated by test type; (b) small benthic foraminifera (SBF) group differentiated by test type; (c) LBF group differentiated by symbiont type. Solid and hollow symbols represent Huangyan Island and Lingyang reef, respectively.

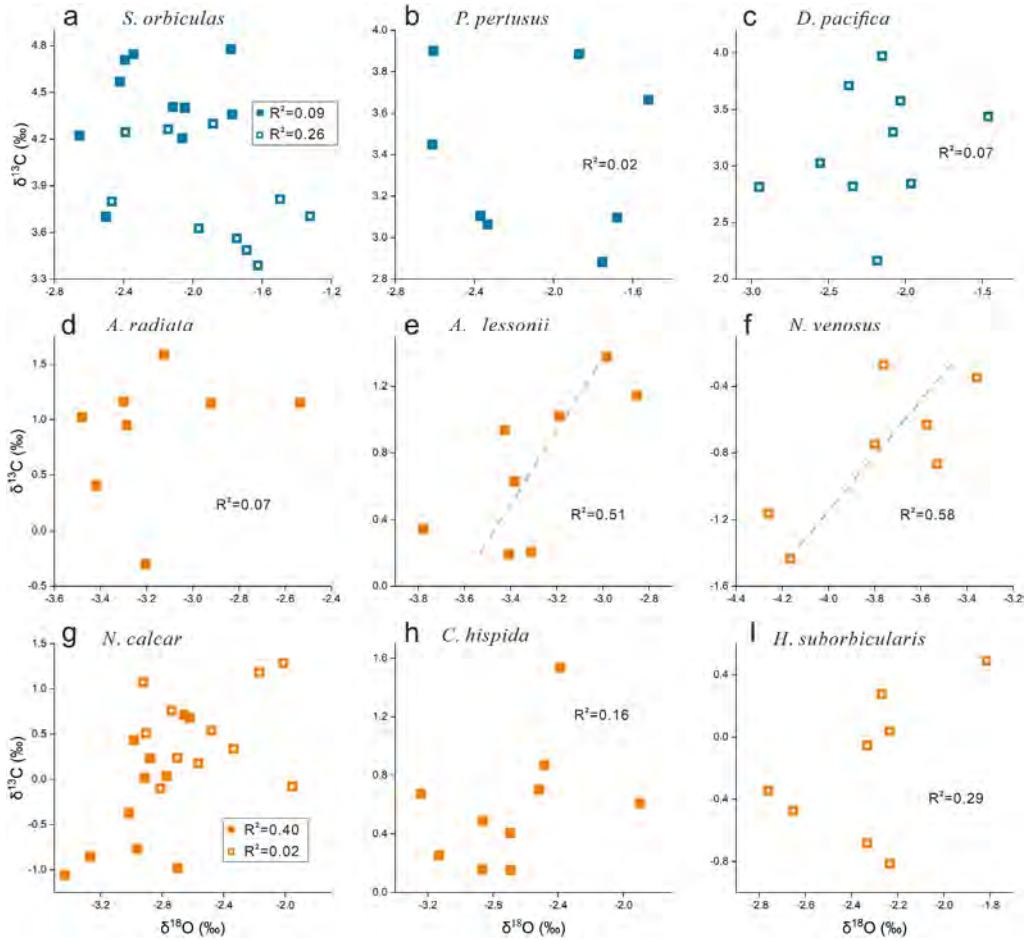


Figure 7. $\delta^{18}O$ versus $\delta^{13}C$ scatter plots of analyzed LBF. Blue and orange symbols represent miliolids and rotaliids, respectively. Solid and hollow symbols represent Huangyan Island and Lingyang reef, respectively.

venosus display moderate correlation ($R^2 = 0.51$ and 0.58), with weaker correlations observed in the remaining species (Figure 7). However, rotaliid SBF correlations are generally weak, except for *E. crispum* ($R^2 = 0.71$, Figure 8). Notably, two species, *Textularia agglutinans* and *G. trullissata*, which possessed agglutination tests, displayed the highest positive correlation ($R^2 = 0.76$ and $R^2 = 0.77$, Figures 8j and 8k).

4.6. Multiple Individual Analyses

Eight *S. orbiculus* individuals were mixed and subjected to carbon and oxygen isotope analyses, with results close to the mean values derived from single individuals (Table 2). Specifically, differences of 0.004 and 0.001‰ were obtained for $\delta^{13}C$ and $\delta^{18}O$ in the mixed results from Huangyan Island showed and differences of 0.049 and 0.090‰ were obtained for Lingyang Reef as compared to the mean. Considering the analytical precision, the results from both measurements can be regarded as consistent.

5. Discussion

5.1. Factors Affecting the Isotopic Variation in the 20 Foraminifera Species

The $\delta^{18}O$ and $\delta^{13}C$ values of the 20 studied species displayed significant overall interspecific, intraspecific, and spatial variations, with obvious variations between the LBF and SBF groups observed among species with different test types and LBF hosting different symbiont algae. The $\delta^{18}O$ and $\delta^{13}C$ values obtained for the foraminifera tests also differed from those presumed for equilibrium calcite. The differences in chemical composition of biogenic carbonate compared to inorganic carbonate within the same environmental conditions are known as

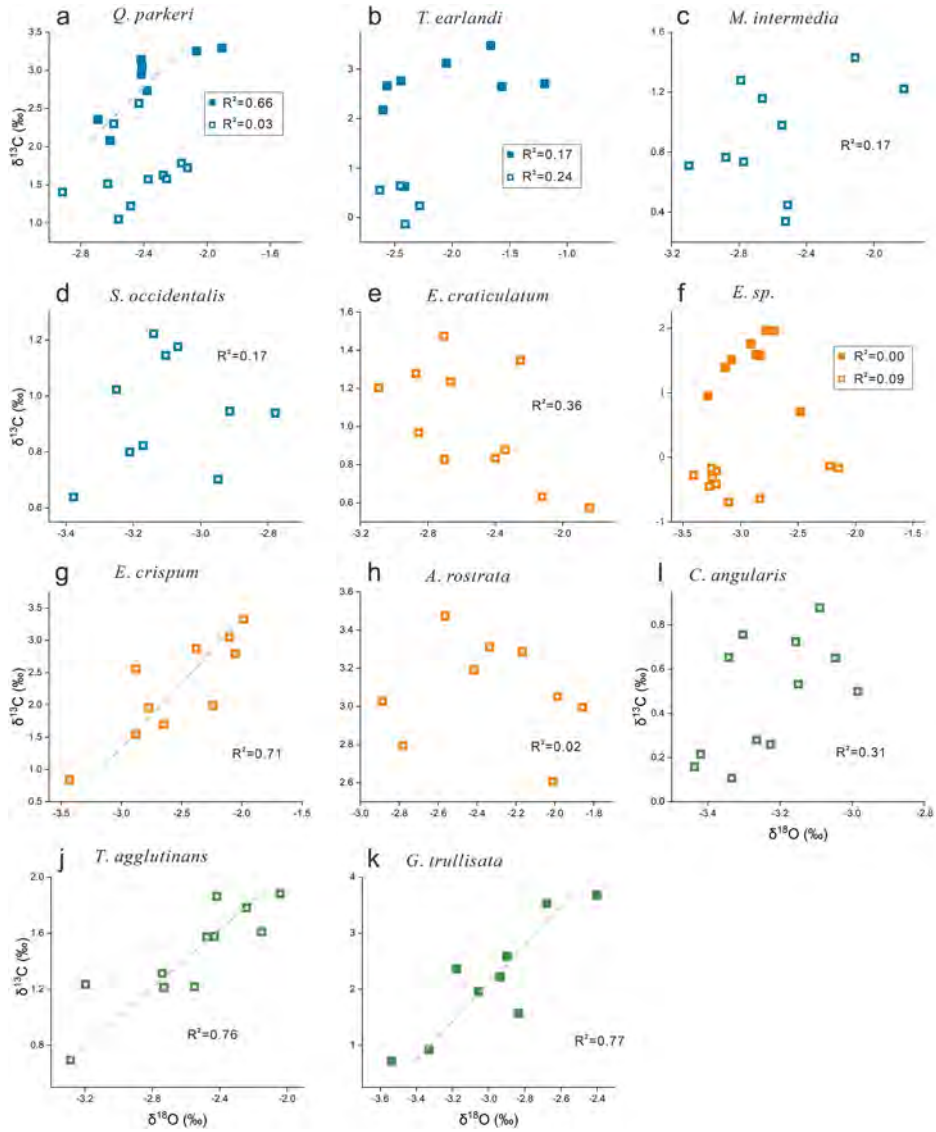


Figure 8. $\delta^{18}O$ versus $\delta^{13}C$ scatter plots of analyzed SBF. Blue, orange, and green symbols represent miliolids, rotaliids, and others, respectively. Solid and hollow symbols represent Huangyan Island and Lingyang reef, respectively.

"vital effects" (Dubicka et al., 2018; Erez, 1978; Grossman, 1987). Vital effects are associated with metabolic processes, including respiration, growth rate, and calcification pathways, as well as the photosynthetic activity of symbionts (Robbins et al., 2017; Rollion-Bard et al., 2008). A rapid growth rate leads to strong kinetic effects and linear associations between skeletal $\delta^{18}O$ and $\delta^{13}C$ in carbonates (McConnaughey, 1989). Previous studies consistently found the $\delta^{13}C$-$\delta^{18}O$ slopes to be greater than 1 (Billups et al., 2022), and this is also the case for the six species with observable correlation in our study (Figures 7 and 8), highlighting the distinct influence that these effects have on the $\delta^{18}O$ and $\delta^{13}C$ values. However, the majority of the species do not exhibit strong $\delta^{13}C$-$\delta^{18}O$ correlations, which suggests the influence of other factors.

Table 2
$\delta^{13}C$ and $\delta^{18}O$ Values Obtained From Mixed Multiple Specimens ($n = 8$) and the Average Obtained From Individual Sorites orbiculas Specimens ($n = 10$)

	Mixed		Individual average	
	$\delta^{13}C$ (‰)	$\delta^{18}O$ (‰)	$\delta^{13}C$ (‰)	$\delta^{18}O$ (‰)
Huangyan Island	4.406	−2.209	4.41	−2.21
Lingyang Reef	3.868	−1.963	3.819	−1.873

5.1.1. Influence of Magnesium Content

Magnesium substitution impacts the oxygen isotope fractionation for calcite and water, resulting in an ~0.14‰ $\delta^{18}O$ increase in magnesium calcite relative to pure calcite for each mole percent of $MgCO_3$ (Mavromatis

et al., 2012). This effect is significant enough that the presence of magnesium in LBF tests cannot be disregarded, as doing so would result in a deviation of several degrees when estimating paleotemperature. Symbiont-bearing benthic foraminifera exhibit significantly higher Mg/Ca ratios than planktonic or symbiont-barren benthic foraminifera (Raja et al., 2005). Considering this factor, LBF are expected to exhibit relatively higher $\delta^{18}O$ values. In our study, compared to the estimated equilibrium calcite, miliolid LBF exhibit higher $\delta^{18}O$ values overall, while rotaliid LBF generally display slightly lower values (Figure 6a), indicating a more intricate interplay of various controlling factors.

Previous studies have shown that the Mg content of LBF in the same genus typically falls within a fixed range despite temperature changes but varies among different genera and even species (Raja et al., 2005, 2007). For instance, the Mg/Ca ratio in *Amphistegina* ranges from 24 to 86 mmol/mol, whereas in *Neorotalia* it ranges from 214 to 290 mmol/mol (Raja et al., 2005, 2007). Such disparities may contribute to interspecies variation in terms of isotope value. In this study, *Amphistegina*, which exhibits substantially lower magnesium content as compared to other LBF genera, also shows lower $\delta^{18}O$ values relative to the other LBF genera in Huangyan Island (Figures 3 and 4), illustrating this point. Miliolids typically contain higher amounts of Mg compared to rotaliids (van Dijk et al., 2017), which aligns with the overall slightly higher oxygen isotope values observed in this study (Figure 6a). However, the isotopic differences between the miliolids and rotaliids cannot be solely attributed to the overall differences in their magnesium content. Specifically, the miliolids *P. pertusus* and *S. orbiculus* exhibit lower Mg/Ca ratios (Langer & Gehring, 1994; van Dijk et al., 2017) as compared to the rotaliids *C. hispida* and *N. calcar* (Raja et al., 2007), yet they demonstrate higher $\delta^{18}O$ values (Figures 3 and 4). Thus, while magnesium concentration is a significant factor influencing oxygen isotope fractionation, other species-specific traits are also crucial in driving isotopic variability.

5.1.2. Influence of Inherent Physiological Differences

The $\delta^{18}O$ and $\delta^{13}C$ values distinguished in the miliolids and rotaliids groups suggest that the vital effects associated with the foraminiferal order or test type play a crucial role in controlling the isotope values. Multiple studies have consistently demonstrated more negative $\delta^{13}C$ and $\delta^{18}O$ values for rotaliids as compared to miliolids in same environment (Billups et al., 2022; Langer, 1995; Robbins et al., 2017; Saraswati et al., 2004). Miliolids and rotaliids correspond to distinct test types and the divergent processes involved in their test formation may contribute to the observed variations in the isotope values. Different calcification pathways have been shown to influence their stable isotopic compositions (Robbins et al., 2017; Roepert et al., 2020; Ter Kuile et al., 1989). Rotaliids possess an internal carbon pool that accumulates elements from various sources to facilitate calcification, whereas miliolids, lacking such a pool, precipitate calcite within their vesicles by directly incorporating elements from seawater (Ter Kuile et al., 1989). Metabolic CO_2 enriches in the internal pool in rotaliids, leading to reduced $\delta^{13}C$ values as compared to species without pools (Ten Kuile & Erez, 1987; Ter Kuile, 1994). Furthermore, culture experiments have shown that miliolid $\delta^{13}C$ values are independent of pH and rotaliid $\delta^{13}C$ values are influenced by pH, which may be attributed to the lack of a relationship between pH and $\delta^{13}C$ for dissolved inorganic carbon in seawater (Robbins et al., 2017).

5.1.3. Influence of Symbiotic Algae

Symbionts serve as a crucial nutrient source for most coral reef LBF (Walker et al., 2011). The clear differentiation between miliolids and rotaliids in the Huangyan Island (Figure 4) indicates an inherent physiological control between these two types of foraminifera. However, it is worth noting that only the symbiont-bearing miliolids showed significantly higher isotope values in Lingyang Reef (Figure 3). Although concordance was observed between the symbiotic types and taxonomic classification in the symbiont-bearing group, the fact that symbiont-barren species did not exhibit order-associated differentiation (Figure 6b) suggests that order-associated factors, such as test type and calcification mode, do not control the isotopic values in this case. The study of benthic foraminifera from the continental shelf of tropical Brazil also reveals that LBF miliolids and rotaliids exhibit opposite $\delta^{13}C$ deviation trend compared to equilibrium calcite, while symbiont-barren species from both orders have $\delta^{13}C$ values close to that of equilibrium calcite (Billups et al., 2022), further confirming that the presence of symbionts appears to play a more critical role in influencing the $\delta^{13}C$. As for the oxygen isotope, study of larger foraminifera from a reef flat at Akajima, Okinawa, Japan, shows that symbiosis has little or no impact on the oxygen isotopic composition of the bulk carbonates in LBF (Saraswati et al., 2004). In our study, both $\delta^{13}C$ and $\delta^{18}O$ of LBF deviate from equilibrium calcite, but the $\delta^{13}C$ deviation is significantly more

pronounced compared to $\delta^{18}O$ (Figure 6), which may further corroborate the hypothesis that symbionts exert a primary influence on the carbon isotope values.

The variability produced by symbiotic algae is also linked to the presence of an internal carbon pool, and serves to enhance the influence of the pool on the isotopic results. Symbiont photosynthesis preferentially absorbs $^{12}CO_2$, leading to an increase in the proportion of $^{13}CO_2$ in ambient seawater and resulting in a positive shift in the $\delta^{13}C$ content of marine carbonates (Ravelo & Hillaire-Marcel, 2007). This phenomenon accounts for the elevated $\delta^{13}C$ values observed in the symbiont-bearing miliolids, as they calcify directly from ambient seawater rather than from an internal carbon pool. In contrast, the enhanced metabolic activity of the host-algae complex in rotaliids would result in an increased accumulation of metabolic CO_2 enriched with lighter oxygen and carbon in the internal carbon pool (Erez, 1978). Thus, photosynthetic activity tends to result in lower $\delta^{13}C$ and $\delta^{18}O$ values in symbiont-bearing rotaliids but higher $\delta^{13}C$ in symbiont-bearing miliolids.

Symbionts vary among different LBF, with rotaliids primarily hosting diatoms, while miliolids accommodate a diverse range of algae, including chlorophytes, rhodophytes, and dinoflagellates (Lee, 2006; Prazeres & Renema, 2019). Previous research on the photosynthetic plasticity of symbionts in LBF indicates that rhodophyte-bearing species exhibit a significantly lower maximum quantum efficiency compared to those associated with dinoflagellates, diatoms, or chlorophytes (Ziegler & Uthicke, 2011). This may clarify why miliolid species that host dinoflagellates show higher carbon isotope values than their rhodophyte-bearing counterparts (Figure 6b). The maximum quantum efficiencies of photosynthesis also differed among species that host the same symbiotic algae (Ziegler & Uthicke, 2011), potentially leading to the discrepancies observed among LBF with same algal symbionts. Species harboring diatoms are distributed over the largest depth range (Prazeres & Renema, 2019), and this extensive environmental distribution likely accounts for their broader $\delta^{13}C$ and $\delta^{18}O$ values when compared to species with other types of symbiotic algae (Figure 6c). Overall, the current evidence captures only the general influence of the presence of symbiotic algae, without fully elucidating the distinct impacts of different types of symbiotic algae, which requires further exploration.

Studies on planktic foraminifera have found that algal symbionts cause $\delta^{18}O$ depletion due to photosynthesis, which is possibly linked to kinetic fractionation (Spero, 1992; Spero & Lea, 1993). This, however, does not explain the overall high $\delta^{18}O$ values observed in symbiont-bearing miliolids, which are more likely influenced by the relatively higher Mg content, as mentioned previously. Hence, the isotopic offset in foraminifera cannot be attributed solely to the photosynthetic activity of symbiotic algae, and is instead the result of the combined effects of complex factors.

5.1.4. Factors Leading to Intraspecific Variation

Symbiotic photosynthetic intensity varies among individuals of the same species, potentially leading to intraspecific variation (Saraswati, 2004). In our study, greater intraspecific variations were observed for the $\delta^{13}C$ as compared to $\delta^{18}O$, indicating that the influence of vital effects more greatly affects $\delta^{13}C$. This may be attributable to the previously mentioned impact that symbiotic algae have on $\delta^{13}C$. However, the fact that LBF do not exhibit greater intraspecific variations than SBF suggests that symbiotic algae are not the primary drivers of variability, further supporting the conclusion that intraspecific variations are dominated by intrinsic vital effects.

The ontogenetic or ecotypic characteristics of foraminifera, potentially driven by lifespan, reproduction timing, and growth rates, lead to intraspecific variation (Saraswati, 2004; Staines-Urías & Douglas, 2009). In particular, lifespan and reproductive timing of foraminifera dictate the seasons they endure, ultimately shaping the seasonal variations observed in their tests (Saraswati, 2004). Higher growth rates correspond to elevated metabolic rates, likely resulting in greater metabolic CO_2 incorporation, affecting the $\delta^{13}C$ values (Staines-Urías & Douglas, 2009). Microanalysis indicates intra-test seasonal variation in LBF species (Rollion-Bard et al., 2008; Saraswati et al., 2004; Wefer & Berger, 1980), with a relatively rapid growth rate and extended lifespan observed across multiple seasons. Therefore, whole-test isotope data may have a stronger tendency to reflect the environmental conditions prevalent during the high growth rate season. Analysis of the similar growth stage is necessary to ensure comparability (Saraswati, 2004). To minimize this error, specimens with comparable sizes and morphologies were selected. Persistent intraspecific variations can be attributed only to uncontrollable factors. In LBF-based paleoenvironmental reconstruction, it is crucial to select multiple individuals of the same species and a similar size when averaging to reduce errors caused by intraspecific variation.

5.2. Environmental Information Revealed by Spatial Isotopic Variation

Five of the 20 benthic foraminiferal species appeared in both the Huangyan Island and Lingyang Reef sediments, with discernible variations in the $\delta^{18}O$ and $\delta^{13}C$ values (Figure 5). As discussed above, active photosynthetic symbionts would lead to a rise in the $\delta^{13}C$ content in miliolids and lower $\delta^{13}C$ values for rotaliids (due to the presence of the internal pool). Thus, the $\delta^{13}C$ values of the two common symbiont-bearing species (*S. orbiculus* and *N. calcar*) indicate a higher level of biological productivity in Huangyan Island, consistent with the established observation that the lagoon on Huangyan Island exhibits the highest phytoplankton biomass and primary productivity of the atolls in the Xisha area (Ke et al., 2016). The enhanced productivity levels of Huangyan Island may be attributed to nutrient input from fishing vessels and the aggregation of phytoplankton driven by southwestern winds (Ke et al., 2016). In addition, three of the SBF species in Huangyan Island exhibited higher $\delta^{13}C$ values compared to those in Lingyang Reef, which may be attributed to the overall higher primary productivity in the surrounding waters.

The $\delta^{18}O$ value of the foraminifera tests is mainly influenced by seawater temperature and $\delta^{18}O_w$ (Epstein et al., 1953; Pearson, 2012), with an inverse correlation between seawater temperature and the $\delta^{18}O$ value of carbonates when other conditions remain constant (Epstein et al., 1951). The modern annual SST in Huangyan Island is ∼1°C higher than it is in Lingyang Reef, according to a previously produced SST data set (Rayner et al., 2003), which is consistent with the $\delta^{18}O$ results of the two LBF species at the two studied sites (Figure 5). In contrast, inconsistencies were observed in the $\delta^{18}O$ values and SST of three SBF species at the two studied sites, suggesting that, in our case study, factors other than temperature exert a stronger influence on the $\delta^{18}O$ values in these species. LBF species, characterized by a larger size and longer lifespan, are expected to offer a more reliable representation of long-term average values and exhibit reduced susceptibility to temperature fluctuations during peak flux periods. The different environmental factors at Lingyang reef and Huangyan Island may have contributed to the observed differences in the coral reef health, which could also help explain the variations in foraminiferal abundance and diversity at the two sites. Nevertheless, the use of LBF species to quantify the relationship between the $\delta^{18}O$ values and environmental factors still poses a formidable challenge.

5.3. Application Potential of Benthic Foraminiferal Carbon and Oxygen Isotopes to Reconstruct Paleomarine Environments in Coral Reef Areas

Selecting benthic foraminiferal species with stable isotopic values that accurately reflect the prevailing environmental conditions is crucial for reliable paleoenvironmental reconstruction. Among the 20 benthic foraminiferal species analyzed, distinct intraspecific variations and different stability were observed in the $\delta^{13}C$ and $\delta^{18}O$ values, highlighting their varying potential as environmental proxies. Previous studies of LBF on a tropical continental shelf revealed the significant influence of vital and abiotic factors on stable isotopic variability, limiting their reliability as paleoenvironmental tracers (Billups et al., 2022; Saraswati et al., 2004). In this study, the $\delta^{13}C$ and $\delta^{18}O$ values of SBF fluctuated around equilibrium calcite. While some species displayed minor isotopic data variation (e.g., *S. occidentalis*, *C. angularis*), their utility in reflecting the reef paleoenvironmental conditions is limited due to their scarcity and discontinuity. LBF are more abundant, but more susceptible to vital effects: miliolid LBF generally exhibit higher $\delta^{18}O$ and $\delta^{13}C$ values and rotaliids display comparatively lower values. Despite the influence of vital effects, SST and productivity levels inferred from the $\delta^{18}O$ and $\delta^{13}C$ values of the shared LBF species *S. orbiculus* and *N. calcar* at the two study sites generally align well with the observed environmental conditions, indicating that these species possess the capacity to reflect the calcification environment.

Notably, *S. orbiculus*, the only species that hosts dinoflagellates, exhibited relatively stable $\delta^{18}O$ and $\delta^{13}C$ values in both studied sites and was not affected by the internal pool. However, *S. orbiculus* exhibited the highest $\delta^{18}O$ and $\delta^{13}C$ values of all the LBF species, and the greatest deviation from the equilibrium calcite. In other comprehensive studies involving multiple foraminifera species, *S. orbiculus* also exhibited higher $\delta^{18}O$ values and highest $\delta^{13}C$ values among the studied LBF species (Saraswati et al., 2004), indicating that the large isotopic migration of this species is consistent across different regions. The analysis of multiple individual mixed *S. orbiculus* samples indicates that they are closely aligned with the mean values obtained from single individuals, confirming their stability in reflecting the average environmental conditions over multiple years. Therefore, although the quantification of vital effects remains challenging, the isotopic results derived from certain LBF

species tests undeniably reveal the characteristics of the respective environments, such as the SST and productivity levels, providing invaluable insight for further paleoenvironmental research in coral reef regions.

When applied to downcore fossil samples, diagenetic alteration emerges as a critical factor. Current research has made progress in elucidating the effects that diagenesis has on stable isotopic compositions in SBF and planktonic species (e.g., Cisneros-Lazaro et al., 2022; Edgar et al., 2013; Poirier et al., 2021; Stainbank et al., 2020). Q. Zhang et al. (2020) employed a range of methods to effectively exclude diagenetic influences on LBF and successfully applied carbon isotopes from LBF to investigate the structure and magnitude of the carbon isotope excursion during the Paleocene-Eocene Thermal Maximum. However, the knowledge gap regarding LBF remains significant, and systematic investigations remain conspicuously absent. This deficiency could potentially be addressed through the following two approaches in future study: (a) controlled laboratory simulations replicating diagenetic processes under modern experimental conditions; (b) detailed observations and analysis of fossil samples. These complementary strategies could potentially establish diagnostic criteria for identifying and quantifying post-depositional modifications in LBF specimens, thereby enhancing the reliability of paleoenvironmental reconstructions derived from their geochemical signatures.

6. Conclusion

A total of 20 species were selected from surface sediments at Lingyang Reef and Huangyan Island in the SCS for $\delta^{13}C$ and $\delta^{18}O$ analysis. Several key observations were made:

1. The studied benthic foraminifera exhibited significant interspecific variations in stable isotopic values influenced by factors which included magnesium content, symbiotic algae and inherent vital effects among different species.
2. Intraspecific variation varied among species, with some species exhibiting stable data. These intraspecific variations were primarily attributed to ontogeny-related influences rather than symbiont influences.
3. Symbiont activity was found to have opposite influence on $\delta^{13}C$ values of miliolids and rotaliids. Additionally, SST and productivity levels derived from the $\delta^{18}O$ and $\delta^{13}C$ values of LBF species *S. orbiculus* and *N. calcar* generally align with the actual conditions at the two studied sites.

These findings provide valuable insights into the potential use of shallow-water benthic foraminiferal species as reliable environmental indicators, highlighting the necessity for further quantitative research to comprehensively understand the fundamental nature of vital effects and their broader implications, ultimately contributing to the refinement of paleoenvironmental reconstruction methodologies for reef areas using LBF stable isotope indicators.

Data Availability Statement

All isotope data related to this paper are available in the Zenodo data set (Wu, 2024).

Acknowledgments
This work was funded by the National Natural Science Foundation of China (Grant 42030502, 42090041 and 42402007) and Guangxi Natural Science Foundation (Grant 2024GXNSFBA010231). Gratitude is extended to Mei Li from School of Marine Sciences, Guangxi University, for her valuable assistance with proofreading.

References

A'ziz, N. A., Minhat, F. I., Pan, H. J., Shaari, H., Saelan, W. N. W., Azmi, N., et al. (2021). Reef foraminifera as bioindicators of coral reef health in southern South China Sea. *Scientific Reports*, *11*(1), 8890. https://doi.org/10.1038/s41598-021-88404-3

Bellwood, D. R., Hughes, T. P., Folke, C., & Nystrom, M. (2004). Confronting the coral reef crisis. *Nature*, *429*(6994), 827–833. https://doi.org/10.1038/nature02691

Benedetti, A., Papazzoni, C. A., & Bosellini, F. R. (2024). Unparallel resilience of shallow-water tropical calcifiers (foraminifera and scleractinian reef corals) during the early Paleogene global warming intervals. *Palaeogeography, Palaeoclimatology, Palaeoecology*, *651*, 112393. https://doi.org/10.1016/j.palaeo.2024.112393

Bickert, T., & Mackensen, A. (2003). Last glacial to holocene changes in south Atlantic deep water circulation. In *The South Atlantic in the Late Quaternary* (pp. 671–693). Springer. https://doi.org/10.1007/978-3-642-18917-3_29

Billups, K., Eichler, P. P. B., Ravelo, C., do Nascimento, L. L., Vital, H., & Gomes, M. P. (2022). Stable isotopic variability in individual benthic foraminifera from the continental shelf of tropical Brazil. *Journal of Foraminiferal Research*, *52*(4), 212–228. https://doi.org/10.2113/gsjfr.52.4.212

Boudaugher-Fadel, M. K. (2018). *Evolution and geological significance of larger benthic foraminifera*. UCL press.

Cisneros-Lazaro, D., Adams, A., Guo, J., Bernard, S., Baumgartner, L. P., Daval, D., et al. (2022). Fast and pervasive diagenetic isotope exchange in foraminifera tests is species-dependent. *Nature Communications*, *13*(1), 113. https://doi.org/10.1038/s41467-021-27782-8

Coletti, G., Commissario, L., Mariani, L., Bosio, G., Desbiolles, F., Soldi, M., & Bialik, O. M. (2022). Palaeocene to Miocene southern Tethyan carbonate factories: A meta-analysis of the successions of South-western and western central Asia. *The Depositional Record*, *8*(3), 1031–1054. https://doi.org/10.1002/dep2.204

Ding, L., Qi, Y., Shan, S., Ge, T., Luo, C., & Wang, X. (2020). Radiocarbon in dissolved organic and inorganic carbon of the South China Sea. *Journal of Geophysical Research: Oceans*, *125*(4), e2020JC016073. https://doi.org/10.1029/2020jc016073

Doo, S. S., Fujita, K., Byrne, M., & Uthicke, S. (2014). Fate of calcifying tropical symbiont-bearing large benthic foraminifera: Living sands in a changing ocean. *The Biological Bulletin*, *226*(3), 169–186. https://doi.org/10.1086/BBLv226n3p169

Dubicka, Z., Wierzbowski, H., & Wierny, W. (2018). Oxygen and carbon isotope records of upper cretaceous foraminifera from Poland: Vital and microhabitat effects. *Palaeogeography, Palaeoclimatology, Palaeoecology*, *500*, 33–51. https://doi.org/10.1016/j.palaeo.2018.03.029

Edgar, K. M., Pälike, H., & Wilson, P. A. (2013). Testing the impact of diagenesis on the δ18O and δ13C of benthic foraminiferal calcite from a sediment burial depth transect in the equatorial Pacific. *Paleoceanography*, *28*(3), 468–480. https://doi.org/10.1002/palo.20045

Emrich, K., Ehhalt, D., & Vogel, J. (1970). Carbon isotope fractionation during the precipitation of calcium carbonate. *Earth and Planetary Science Letters*, *8*(5), 363–371. https://doi.org/10.1016/0012-821x(70)90109-3

Epstein, S., Buchsbaum, R., Lowenstam, H., & Urey, H. C. (1951). Carbonate-water isotopic temperature scale. *Geological Society of America Bulletin*, *62*(4), 417–426. https://doi.org/10.1130/0016-7606(1951)62[417:cits]2.0.co;2

Epstein, S., Buchsbaum, R., Lowenstam, H. A., & Urey, H. C. (1953). Revised carbonate-water isotopic temperature scale. *Geological Society of America Bulletin*, *64*(11), 1315–1326. https://doi.org/10.1130/0016-7606(1953)64[1315:rcits]2.0.co;2

Erez, J. (1978). Vital effect on stable-isotope composition seen in foraminifera and coral skeletons. *Nature*, *273*(5659), 199–202. https://doi.org/10.1038/273199a0

Fujita, K., Yagioka, N., Nakada, C., Kan, H., Miyairi, Y., Yokoyama, Y., & Webster, J. M. (2020). Reef-flat and back-reef development in the Great barrier reef caused by rapid sea-level fall during the last glacial maximum. *Geology*, *48*(1), 39–43. https://doi.org/10.1130/G46792.1

Graham, N. A., Robinson, J. P., Smith, S. E., Govinden, R., Gendron, G., & Wilson, S. K. (2020). Changing role of coral reef marine reserves in a warming climate. *Nature Communications*, *11*(1), 2000. https://doi.org/10.1038/s41467-020-15863-z

Grossman, E. L. (1987). Stable isotopes in modern benthic foraminifera; a study of vital effect. *Journal of Foraminiferal Research*, *17*(1), 48–61. https://doi.org/10.2113/gsjfr.17.1.48

Hallock, P. (2000). Symbiont-bearing foraminifera: Harbingers of global change? Micropaleontology, 95–104.

Huang, X., Betzler, C., Wu, S., Bernhardt, A., Eagles, G., Han, X., & Hovland, M. (2020). First documentation of seismic stratigraphy and depositional signatures of Zhongsha atoll (Macclesfield Bank), South China Sea. *Marine and Petroleum Geology*, *117*, 104349. https://doi.org/10.1016/j.marpetgeo.2020.104349

Hut, G. (1987). Consultants' group meeting on stable isotope reference samples for geochemical and hydrological investigations.

Johnson, J., Perry, C., Smithers, S., Morgan, K. M., & Woodroffe, S. (2019). Reef shallowing is a critical control on benthic foraminiferal assemblage composition on nearshore turbid coral reefs. *Palaeogeography, Palaeoclimatology, Palaeoecology*, *533*, 109240. https://doi.org/10.1016/j.palaeo.2019.109240

Katz, M. E., Cramer, B. S., Franzese, A., Hönisch, B., Miller, K. G., Rosenthal, Y., & Wright, J. D. (2010). Traditional and emerging geochemical proxies in foraminifera. *Journal of Foraminiferal Research*, *40*(2), 165–192. https://doi.org/10.2113/gsjfr.40.2.165

Ke, Z., Liu, H., Wang, J., Liu, J., & Tan, Y. (2016). Abnormally high phytoplankton biomass near the lagoon mouth in the Huangyan Atoll, South China Sea. *Marine Pollution Bulletin*, *112*(1–2), 123–133. https://doi.org/10.1016/j.marpolbul.2016.08.028

Kim, S. T., & O'Neil, J. R. (1997). Equilibrium and nonequilibrium oxygen isotope effects in synthetic carbonates. *Geochimica et Cosmochimica Acta*, *61*(16), 3461–3475. https://doi.org/10.1016/S0016-7037(97)00169-5

Langer, M. R. (1995). Oxygen and carbon isotopic composition of Recent larger and smaller foraminifera from the Madang Lagoon (Papua New Guinea). *Marine Micropaleontology*, *26*(1–4), 215–221. https://doi.org/10.1016/0377-8398(95)00073-9

Langer, M. R. (2008). Assessing the contribution of foraminiferan protists to global ocean carbonate production 1. *The Journal of Eukaryotic Microbiology*, *55*(3), 163–169. https://doi.org/10.1111/j.1550-7408.2008.00321.x

Langer, M. R., & Gehring, A. U. (1994). Manganese (II) in tests of larger foraminifera from Madang (Papua New Guinea). *Journal of Foraminiferal Research*, *24*(3), 203–206. https://doi.org/10.2113/gsjfr.24.3.203

Lee, J. J. (2006). Algal symbiosis in larger foraminifera. *Symbiosis*, *42*(2), 63–75.

Lisiecki, L. E., & Raymo, M. E. (2005). A Pliocene-Pleistocene stack of 57 globally distributed benthic δ18O records. *Paleoceanography*, *20*(1), PA1003. https://doi.org/10.1029/2004pa001071

Loeblich, A. R., & Tappan, H. (1989). Implications of wall composition and structure in agglutinated foraminifers. *Journal of Paleontology*, *63*(6), 769–777. https://doi.org/10.1017/S0022336000036477

Ma, Z. L., Li, Q. Y., Liu, X. Y., Luo, W., Zhang, D. J., & Zhu, Y. H. (2018). Palaeoenvironmental significance of Miocene larger benthic foraminifera from the Xisha Islands, south China sea. *Palaeoworld*, *27*(1), 145–157. https://doi.org/10.1016/j.palwor.2017.05.007

Mackensen, A. (2008). On the use of benthic foraminiferal δ13C in palaeoceanography: Constraints from primary proxy relationships. *Geological Society, London, Special Publications*, *303*(1), 121–133. https://doi.org/10.1144/sp303.9

Maeda, A., Fujita, K., Horikawa, K., Suzuki, A., Yoshimura, T., Tamenori, Y., & Kawahata, H. (2017). Evaluation of oxygen isotope and Mg/Ca ratios in high-magnesium calcite from benthic foraminifera as a proxy for water temperature. *Journal of Geophysical Research: Biogeosciences*, *122*(1), 185–199. https://doi.org/10.1002/2016jg003587

Mavromatis, V., Schmidt, M., Botz, R., Comas-Bru, L., & Oelkers, E. H. (2012). Experimental quantification of the effect of Mg on calcite–aqueous fluid oxygen isotope fractionation. *Chemical Geology*, *310*, 97–105. https://doi.org/10.1016/j.chemgeo.2012.03.027

McConnaughey, T. (1989). ^{13}C and ^{18}O isotopic disequilibrium in biological carbonates: I. Patterns. *Geochimica et Cosmochimica Acta*, *53*(1), 151–162. https://doi.org/10.1016/0016-7037(89)90282-2

Meng, M., Yu, K., Hallock, P., Qin, G., Jiang, W., & Fan, T. (2022). Foraminifera indicate neogene evolution of yongle atoll from xisha islands in the south China Sea. *Palaeogeography, Palaeoclimatology, Palaeoecology*, *602*, 111163. https://doi.org/10.1016/j.palaeo.2022.111163

Mikhalevich, V., Kaminski, M. A., & Coccioni, R. (2008). Revised systematics of the Schlumbergerinida (phylum foraminifera). *7th International Workshop on Agglutinated Foraminifera, Urbino, ITALY*.

Pearson, P. N. (2012). Oxygen isotopes in foraminifera: Overview and historical review. *Paleontological Society Papers*, *18*, 1–38. https://doi.org/10.1017/s1089332600002539

Poirier, R. K., Gaetano, M. Q., Acevedo, K., Schaller, M. F., Raymo, M. E., & Kozdon, R. (2021). Quantifying diagenesis, contributing factors, and resulting isotopic bias in benthic foraminifera using the foraminiferal preservation index: Implications for geochemical proxy records. *Paleoceanography and Paleoclimatology*, *36*(5), e2020PA004110. https://doi.org/10.1029/2020PA004110

Prazeres, M., & Renema, W. (2019). Evolutionary significance of the microbial assemblages of large benthic Foraminifera. *Biological Reviews*, *94*(3), 828–848. https://doi.org/10.1111/brv.12482

Prell, W. L., Imbrie, J., Martinson, D. G., Morley, J. J., Pisias, N. G., Shackleton, N. J., & Streeter, H. F. (1986). Graphic correlation of oxygen isotope stratigraphy application to the late Quaternary. *Paleoceanography*, *1*(2), 137–162. https://doi.org/10.1029/pa001i002p00137

Raja, R., Saraswati, P. K., & Iwao, K. (2007). A field-based study on variation in Mg/Ca and Sr/Ca in larger benthic foraminifera. *Geochemistry, Geophysics, Geosystems*, *8*(10), Q10012. https://doi.org/10.1029/2006gc001478

Raja, R., Saraswati, P. K., Rogers, K., & Iwao, K. (2005). Magnesium and strontium compositions of recent symbiont-bearing benthic foraminifera. *Marine Micropaleontology*, *58*(1), 31–44. https://doi.org/10.1016/j.marmicro.2005.08.001

Ravelo, A. C., & Hillaire-Marcel, C. (2007). Chapter eighteen the use of oxygen and carbon isotopes of foraminifera in paleoceanography. *Developments in marine geology*, *1*, 735–764. https://doi.org/10.1016/s1572-5480(07)01023-8

Raven, J., Caldeira, K., Elderfield, H., Hoegh-Guldberg, O., Liss, P., Riebesell, U., et al. (2005). *Ocean acidification due to increasing atmospheric carbon dioxide*. The Royal Society.

Rayner, N., Parker, D. E., Horton, E., Folland, C. K., Alexander, L. V., Rowell, D., et al. (2003). Global analyses of sea surface temperature, sea ice, and night marine air temperature since the late nineteenth century. *Journal of Geophysical Research*, *108*(D14), 4407. https://doi.org/10.1029/2002jd002670

Robbins, L. L., Knorr, P., Wynn, J., Hallock, P., & Harries, P. (2017). Interpreting the role of pH on stable isotopes in large benthic foraminifera. *ICES Journal of Marine Science*, *74*(4), 955–964. https://doi.org/10.1093/icesjms/fsw056

Roepert, A., Polerecky, L., Geerken, E., Reichart, G. J., & Middelburg, J. J. (2020). Distribution of chlorine and fluorine in benthic foraminifera. *Biogeosciences*, *17*(18), 4727–4743. https://doi.org/10.5194/bg-17-4727-2020

Rollion-Bard, C., Erez, J., & Zilberman, T. (2008). Intra-shell oxygen isotope ratios in the benthic foraminifera genus Amphistegina and the influence of seawater carbonate chemistry and temperature on this ratio. *Geochimica et Cosmochimica Acta*, *72*(24), 6006–6014. https://doi.org/10.1016/j.gca.2008.09.013

Saraswati, P. K. (2004). Ontogenetic isotopic variation in foraminifera–Implications for palaeo proxy. *Current Science*, *86*(6), 858–860.

Saraswati, P. K., Seto, K., & Nomura, R. (2004). Oxygen and carbon isotopic variation in co-existing larger foraminifera from a reef flat at Akajima, Okinawa, Japan. *Marine Micropaleontology*, *50*(3–4), 339–349. https://doi.org/10.1016/S0377-8398(03)00099-9

Shao, L., Cui, Y., Qiao, P., Zhang, D., Liu, X., & Zhang, C. (2017). Sea-Level changes and carbonate platform evolution of the Xisha Islands (south China Sea) since the early Miocene. *Palaeogeography, Palaeoclimatology, Palaeoecology*, *485*, 504–516. https://doi.org/10.1016/j.palaeo.2017.07.006

Spero, H. J. (1992). Do planktic foraminifera accurately record shifts in the carbon isotopic composition of seawater ΣCO2? *Marine Micropaleontology*, *19*(4), 275–285. https://doi.org/10.1016/0377-8398(92)90033-g

Spero, H. J., & Lea, D. W. (1993). Intraspecific stable isotope variability in the planktic foraminifera Globigerinoides sacculifer: Results from laboratory experiments. *Marine Micropaleontology*, *22*(3), 221–234. https://doi.org/10.1016/0377-8398(93)90045-y

Stainbank, S., Spezzaferri, S., De Boever, E., Bouvier, A. S., Chilcott, C., De Leau, E. S., et al. (2020). Assessing the impact of diagenesis on foraminiferal geochemistry from a low latitude, shallow-water drift deposit. *Earth and Planetary Science Letters*, *545*, 116390. https://doi.org/10.1016/j.epsl.2020.116390

Staines-Urías, F., & Douglas, R. G. (2009). Environmental and intraspecific dimorphism effects on the stable isotope composition of deep-sea benthic foraminifera from the Southern Gulf of California, Mexico. *Marine Micropaleontology*, *71*(1–2), 80–95. https://doi.org/10.1016/j.marmicro.2009.01.007

Sun, W. (2016). Initiation and evolution of the South China sea: An overview. *Acta Geochimica*, *35*(3), 215–225. https://doi.org/10.1007/s11631-016-0110-x

Ten Kuile, B., & Erez, J. (1987). Uptake of inorganic carbon and internal carbon cycling in symbiont-bearing benthonic foraminifera. *Marine Biology*, *94*(4), 499–509. https://doi.org/10.1007/bf00431396

Ter Kuile, B. (1994). Mechanisms for calcification and carbon cycling in algal symbiont-bearing foraminifera. *Biology of Foraminifera*, 73–89.

Ter Kuile, B., Erez, J., & Padan, E. (1989). Mechanisms for the uptake of inorganic carbon by two species of symbiont-bearing foraminifera. *Marine Biology*, *103*(2), 241–251. https://doi.org/10.1007/bf00543354

Van Dijk, I., de Nooijer, L. J., & Reichart, G. J. (2017). Trends in element incorporation in hyaline and porcelaneous foraminifera as a function of pCO 2. *Biogeosciences*, *14*(3), 497–510. https://doi.org/10.5194/bg-14-497-2017

Waelbroeck, C., Labeyrie, L., Michel, E., Duplessy, J. C., Mcmanus, J. F., Lambeck, K., et al. (2002). Sea-level and deep water temperature changes derived from benthic foraminifera isotopic records. *Quaternary Science Reviews*, *21*(1–3), 295–305. https://doi.org/10.1016/S0277-3791(01)00101-9

Walker, R. A., Hallock, P., Torres, J. J., & Vargo, G. A. (2011). Photosynthesis and respiration in five species of benthic foraminifera that host algal endosymbionts. *Journal of Foraminiferal Research*, *41*(4), 314–325. https://doi.org/10.2113/gsjfr.41.4.314

Wefer, G., & Berger, W. (1980). Stable isotopes in benthic foraminifera: Seasonal variation in large tropical species. *Science*, *209*(4458), 803–805. https://doi.org/10.1126/science.209.4458.803

Wefer, G., Berger, W., Bijma, J., & Fischer, G. (1999). Clues to ocean history: A brief overview of proxies. *Use of proxies in paleoceanography: examples from the South Atlantic*, 1–68. https://doi.org/10.1007/978-3-642-58646-0_1

Wood, A. (1948). The structure of the wall of the test in the Foraminifera; its value in classification. *Quarterly Journal of the Geological Society*, *104*(1–4), 229–255. https://doi.org/10.1144/gsl.jgs.1948.104.01-04.11

Wu, F., Xie, X., Coletti, G., Zhu, Y., Chen, B., & Shang, Z. (2023). Coralline algal and foraminiferal records of the Pliocene paleoclimatic conditions and water-depth changes in the northern South China Sea. *Marine and Petroleum Geology*, *153*, 106276. https://doi.org/10.1016/j.marpetgeo.2023.106276

Wu, J., Lao, Q., Chen, F., Huang, C., Zhang, S., Wang, C., et al. (2021). Water mass processes between the South China sea and the western pacific through the Luzon strait: Insights from hydrogen and oxygen isotopes. *Journal of Geophysical Research: Oceans*, *126*(8), e2021JC017484. https://doi.org/10.1029/2021jc017484

Wu, S. (2024). Carbon and oxygen isotope data of foraminifera in coral reef regions [Dataset]. *Zenodo*. https://doi.org/10.5281/zenodo.14064938

Wu, S., Yang, Z., Wang, D., Lü, F., Lüdmann, T., Fulthorpe, C., & Wang, B. (2014). Architecture, development and geological control of the Xisha carbonate platforms, northwestern South China Sea. *Marine Geology*, *350*, 71–83. https://doi.org/10.1016/j.margeo.2013.12.016

Zahn, R., Winn, K., & Sarnthein, M. (1986). Benthic foraminiferal δ13C and accumulation rates of organic carbon: Uvigerina peregrina group and Cibicidoides wuellerstorfi. *Paleoceanography*, *1*(1), 27–42. https://doi.org/10.1029/pa001i001p00027

Zhang, Q., Ding, L., Kitajima, K., Valley, J. W., Zhang, B., Xu, X., et al. (2020). Constraining the magnitude of the carbon isotope excursion during the Paleocene-Eocene thermal maximum using larger benthic foraminifera. *Global and Planetary Change*, *184*, 103049. https://doi.org/10.1016/j.gloplacha.2019.103049

Zhang, Y., Yu, K., Qian, H., Fan, T., Yue, Y., Wang, R., et al. (2020). The basement and volcanic activities of the Xisha Islands: Evidence from the kilometre-scale drilling in the northwestern South China Sea. *Geological Journal*, *55*(1), 571–583. https://doi.org/10.1002/gj.3416

Ziegler, M., & Uthicke, S. (2011). Photosynthetic plasticity of endosymbionts in larger benthic coral reef Foraminifera. *Journal of Experimental Marine Biology and Ecology*, *407*(1), 70–80. https://doi.org/10.1016/j.jembe.2011.07.009

Acta Oceanol. Sin., 2025, Vol. 44, No. 9, P. 81–94
https://doi.org/10.1007/s13131-025-2511-3

Geochemical characteristics and petrogenesis of the basaltic pyroclastic rocks from the Xisha Islands, northwestern South China Sea

Yu Zhang[1], Yaqi Yuan[1], Kefu Yu[1, 2*]

[1] Guangxi Laboratory on the Study of Coral Reefs in the South China Sea and School of Marine Sciences, Guangxi University, Nanning 530004, China
[2] Southern Marine Science and Engineering Guangdong Laboratory (Guangzhou), Guangzhou 511458, China

Received 6 January 2025; accepted 25 April 2025
© Chinese Society for Oceanography and Springer-Verlag GmbH Germany, part of Springer Nature 2025

Abstract

As one of the micro-blocks dispersed in the South China Sea (SCS), the Xisha Islands are covered by thick Cenozoic sedimentary layers, making it challenging to obtain magmatic rocks. Well CK-2 is a kilometer-scale scientific drilling project on the Xisha Islands in the northwestern SCS. It penetrates the thick reef limestone and reaches basaltic pyroclastic rocks. This study presents the whole-rock and olivine compositions of the basaltic volcaniclastic rocks from Well CK-2. These rocks exhibited ocean island basalt signatures characterized by the enrichment of light rare earth elements and high-field-strength elements. Compared with partial melting products derived from mantle peridotite, whole-rock compositions showed elevated Fe/Mn and Zn/Fe mass ratios. Additionally, olivines were characterized by a lower Ca content, higher Ni content, elevated Fe/Mn mass ratios, and moderate Mn/Zn mass ratios compared to those crystallized from peridotitic melts. The compositions of both the whole-rock and olivine phenocrysts indicate the presence of pyroxenite in the mantle source, which likely formed through the reaction of recycled oceanic crust with the surrounding mantle peridotite. Using the olivine-liquid Mg-Fe exchange thermometer, this study derived mantle potential temperatures (T_p) ranging from 1 502℃ to 1 756℃, which is consistent with those of plume-related ocean island basalts. Furthermore, the basaltic volcaniclastic rocks exhibit low H_2O contents (0.01%–1.47%), which were significantly lower than those found in the primary magmas of Large Igneous Provinces. These results suggest that the basaltic volcaniclastic rocks on the Xisha Islands originated from a volatile-poor mantle plume source.

Key words South China Sea, Xisha Islands, basaltic pyroclastic rocks, olivine

Citation Zhang Yu, Yuan Yaqi, Yu Kefu. 2025. Geochemical characteristics and petrogenesis of the basaltic pyroclastic rocks from the Xisha Islands, northwestern South China Sea. Acta Oceanologica Sinica, 44(9): 81–94, doi: 10.1007/s13131-025-2511-3

1 Introduction

The South China Sea (SCS) is one of the largest marginal basins in the western Pacific that is located at the junction of the Pacific, Eurasian, and Indo-Australian Plates (Li et al., 2015; Yang and Fang, 2015; Yu et al., 2018; Zhang et al., 2018a, 2018b; Yu and Liu, 2020). Although the SCS basin is relatively small and its oceanic crust is very young, it has undergone a nearly complete Wilson cycle, from continental breakup to seafloor spreading to subduction (Li et al., 2014; Yang and Fang, 2015; Yang et al., 2019). Thus, the SCS serves as a natural laboratory for studying various lithospheric evolutionary processes, including continental margin breakup, ocean basin expansion, and subduction termination, and has attracted widespread attention from researchers worldwide (Li et al., 2014, 2015; Yu et al., 2018). The SCS can be divided into three main parts: northern, southern, and oceanic basins. The northern margin of the SCS lies between the South China Block and the ocean-continent transition zone of the SCS. In the past, the northern margin of the SCS was classified as a discrete, non-volcanic,

Foundation item: The National Natural Science Foundation of China under contract No. 42030502; the Guangxi Scientific Projects under contract Nos. AD17129063, AA17204074, and 2025GXNSFAA069324; the NSFC project under contract No. 42166003.
*Corresponding author, E-mail: kefuyu@scsio.ac.cn

passive continental margin (Clift et al., 2002). However, with the progression of research, it has been regarded as representing an intermediate mode of rifting, bearing characteristics that are closely aligned with a magma-poor margin (Gao et al., 2015). Unlike volcanic margins, which are characterized by extensive magmatic activity, Cenozoic volcanic rocks along the northern margin of the SCS are relatively limited in distribution. However, post-spreading magmatism is widespread throughout the SCS and surrounding areas (Xu et al., 2012).

The northern continental margin of the SCS has long been influenced by subduction of the Mesozoic Paleo-Pacific Plate and Cenozoic rifting processes (Suo et al., 2019; Li et al., 2020; Sun et al., 2021; Zhang et al., 2021a; Yang et al., 2023). Since the Late Cenozoic, the region has been influenced by a complex interplay of geological processes, including seafloor spreading, subduction along the Manila Trench, formation of the Taiwan Orogeny, uplift of the Tibetan Plateau, and extrusion of the Indosinian Block. These geological processes led to frequent and intense magmatic activity along passive continental margins during the Late Cenozoic (Zhang et al., 2014).

The Xisha Islands are overlain by thick Cenozoic sediments at the northern continental margin of the SCS, making it challenging to access magmatic rock samples through drilling. Consequently, studies on mantle-derived magmatism and tectonic evolution in the Xisha region remain scarce. Whether the Cenozoic magmatic activity in the Xisha region is related to the Hainan mantle plume remain unclear, which directly affects our understanding of critical scientific issues, such as the extensional processes of the northern SCS margin and the regional tectono-magmatic evolution. In this study, we present the mineral chemistry and whole-rock geochemistry of basaltic pyroclastic rocks from the basement of Well CK-2 to reveal the lithology of the mantle source and nature of the primary magma, which aids in our understanding of the genesis of Cenozoic basalts in the SCS and their geodynamic background.

2 Geological setting and sample description

The SCS is bounded by the East Vietnam fault to the west and the Manila Trench the east (Fig. 1). The deep-water basin of the SCS can be divided into three sub-basins: southwest, east, and northwest (Li et al., 2014, 2015; Liao et al., 2022; Zhang et al., 2024). Constrained by mapping magnetic anomalies and International Ocean Discovery Program Expedition (IODP) 349 drilling results, the onset of seafloor spreading near the northern continental margin of the SCS was dated to approximately 33 Ma. Subsequently, around 23.6 Ma, the ridge jumped southward and the seafloor extended into the southwest sub-basin. Seafloor spreading ceased at approximately 15 Ma in the eastern sub-basin and approximately 16 Ma in the southwestern sub-basin (Li et al., 2014). After the cessation of seafloor spreading, post-spreading magmatism occurred widely in the SCS and the surrounding areas (Wang et al., 2012; Xu et al., 2012; Yan et al., 2018, 2019; Yu et al., 2018; Qian et al., 2021, 2022).

There are several micro-blocks dispersed in the SCS, including Xisha, Nansha, Zhongsha, and Reed-northeastern Palawan blocks (Yan et al., 2008, 2014, 2015; Liu et al., 2011; Li et al., 2013; Zhang et al., 2020b, 2024). During the Paleo-Tethyes period, these micro-blocks were regarded as a single block, which was named the "Qiongdongnan block" (Liu et al., 2006; Yan et al., 2008). Since the Early Cenozoic, the regional stress field shifted from compression to extension, causing these micro-blocks to rift and drift away from the South China block (Clift et al., 2008; Yan et al., 2019 and references therein).

The Xisha micro-block is situated in the northwestern part of the northern continental slope of the SCS, bounded by the Xisha Trough in the north, the Qiongdongnan Basin in the northwest, and the Dongsha Trough in the east (Fig. 1). Composed of thinned continental crust, its basement is believed to have been affected by multiple phases of magmatism (Huang et al., 2011; Guo et al., 2016; Li et al., 2019; Zhang et al., 2024 and reference therein). With the subsidence of the Xisha micro-block and global sea-level fluctuations, coral reefs in the Xisha region began to develop since the Early Miocene (Shao et al., 2017; Fan et al., 2020). During the Middle Miocene, reefs flourished and expanded laterally, reaching their maximum extent (Wang et al., 2018). However, they began to contract during the Late Miocene and shrank further into isolated carbonate platforms during the Pliocene and Pleistocene (Wu et al., 2014).

Well CK2 was drilled in the Xisha micro-block of the northwestern SCS (Fig. 1). The well was drilled through thick reefal limestone (0–878.21 m) and reached the underlying basement (878.21–928.75 m) (Fig. 2). The basement of Well CK-2 consisted of basaltic pyroclastic rocks. The basaltic pyroclastic rocks contain minor amounts of marine bioclastic fossils, occasionally accompanied by reef limestone breccias (Fig. 3). They were predominantly gray-green, dark green, and yellow-brown in color. They underwent extensive alteration (chloritization, serpentinization and carbonation) and exhibited well-developed vesicular and amygdaloidal textures. The amygdalae were predominantly elliptical and circular, with a few irregularly shaped amygdales. The filling minerals mainly consisted of calcite, opal, chalcedony, and zeolite. The crystalline clastic minerals were primarily composed of clinopyroxene with minor amounts of plagioclase and olivine. The crystal clastics were mostly sub-angular to angular in shape, indicating that the basaltic pyroclastic rocks were formed in situ or near the site of volcanic activity. For a more detailed petrographic analysis, please refer to Zhang et al. (2018c, 2020b, 2024). The chemical characteristics of the clinopyroxene indicated that the parent magma belonged to a silica-undersaturated alkaline series, formed in an intraplate tectonic setting (Zhang et al., 2018c). The zircon U-Pb geochronology of the basaltic

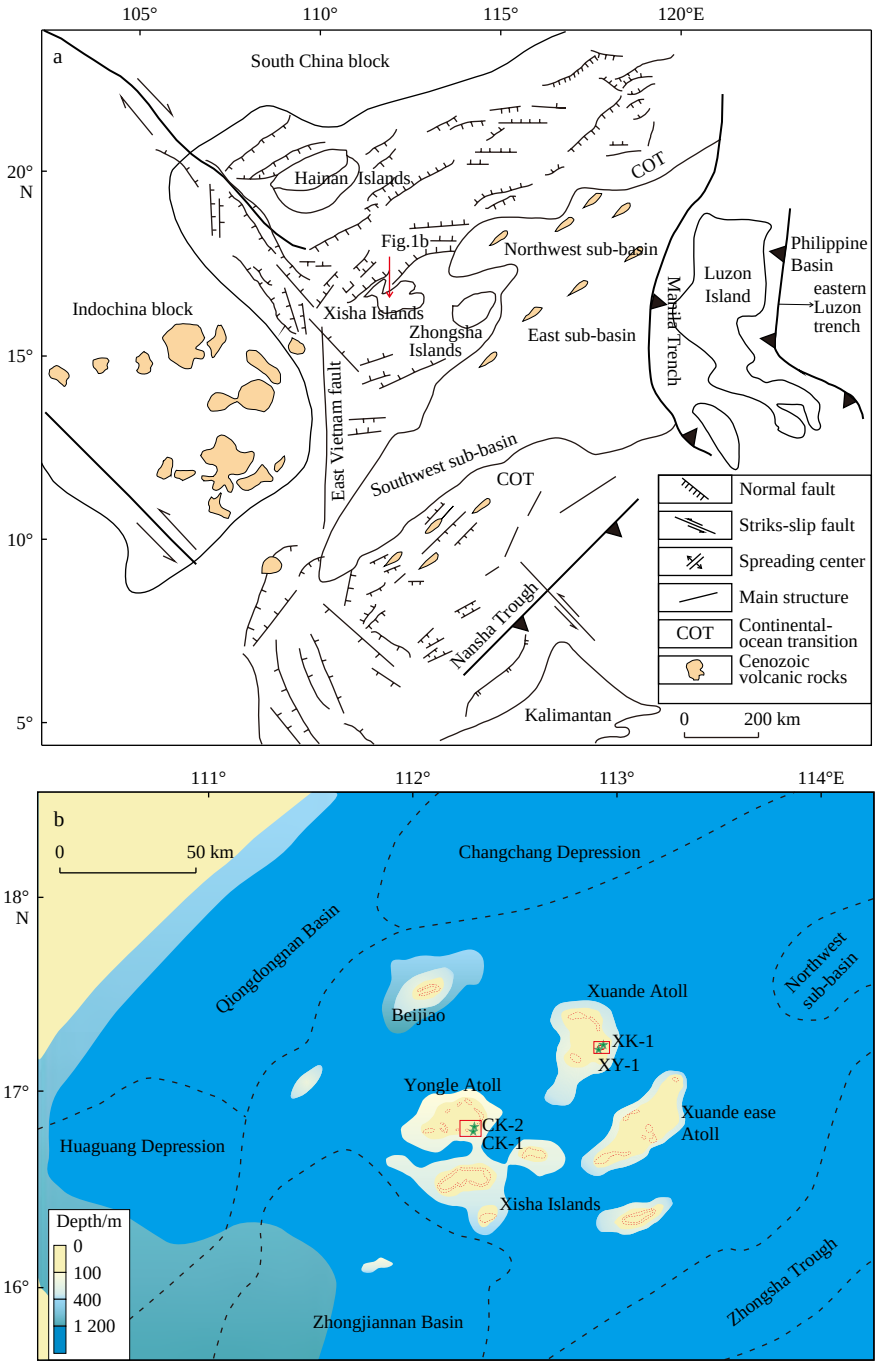


Fig. 1. Geological sketch of the SCS and its adjacent areas (a); location of Well CK-2 (b) (Wang et al., 2018; Zhang et al., 2024). The depth is below sea level and in meters.

pyroclastic rocks indicated that the Xisha micro-block likely developed on a uniform Late Jurassic metamorphic crystalline basement intruded by Cretaceous granitic magmatism (Zhang et al., 2024).

3 Analytical methods

In this study, whole-rock geochemical analyses of basaltic pyroclastic rocks were conducted using the LA-ICP-MS method. The sample selection adhered to the following two criteria: (1) microscopic observation ensured that the samples did not undergo significant alteration and (2) preference was given to fine-grained samples with evenly distributed mineral grains (Yang, 2015). Whole-rock LA-ICP-MS analyses were performed at the State Key Laboratory of Ore Deposit Geochemistry, Institute of Geochemistry, Chinese Academy of Sciences, using an Agilent 7 900 ICP-MS equipped with a GeoLasPro 193 nm ArF excimer laser. Helium was applied as a carrier gas which was mixed with Argon via a T-connector before entering the ICP-MS. The standard ablation cell was optimized with resin mold to get a small volume and to improve the washout efficiency. Analysis was run with 44 μm pit size, 10 Hz pulse frequency and 4−5 J/cm^2 fluence. El-

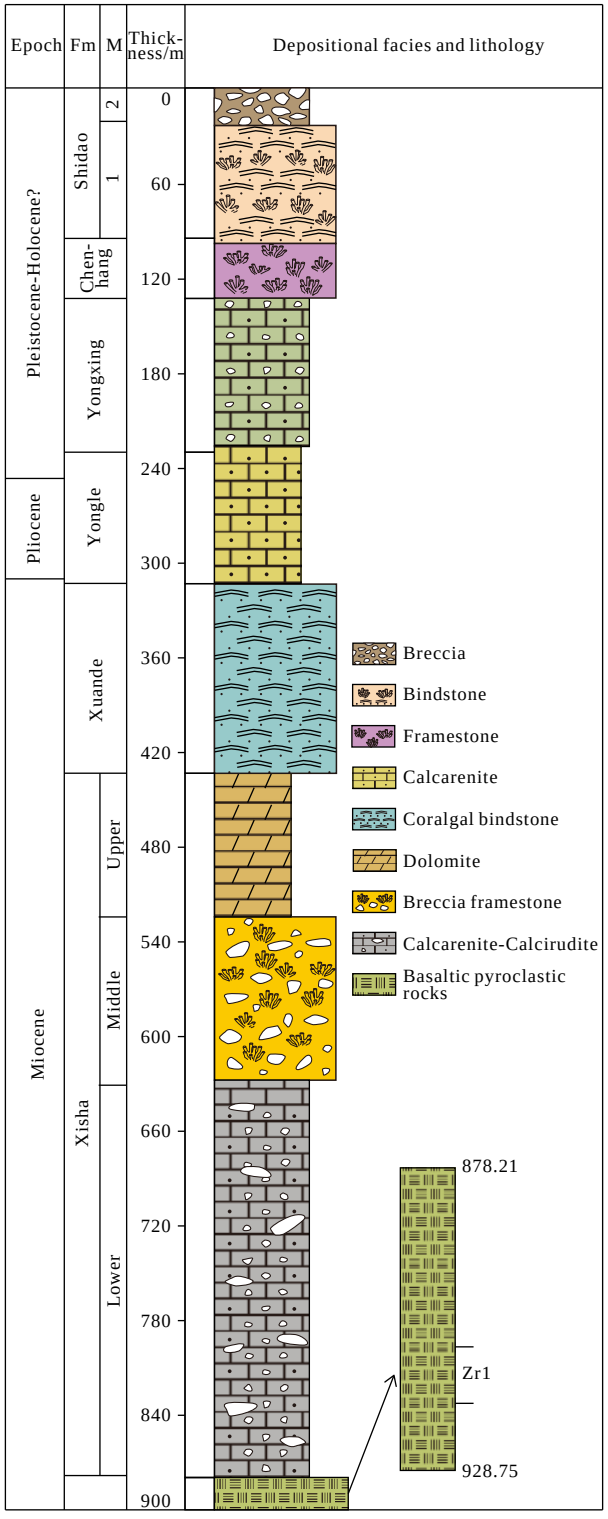


Fig. 2. Stratigraphy of Well CK-2, Xisha Islands (Zhang et al., 2020a). Fm: Formation; M: member.

ement contents were calibrated against multiple-reference materials (BHVO-2G, BCR-2G, and BIR-1G) without using an internal standard (Liu et al., 2008b). Off-line selection and integration of the background and analyte signals, time-drift correction, and quantitative calibration were performed using ICPMSDataCal (Liu et al., 2010).

In-situ trace element analyses of olivine were carried out using LA-ICP-MS at the Wuhan SampleSolution Analytical Technology Co., Ltd., Wuhan China. Detailed instrument parameters and analytical procedures are same as described by Zong et al. (2017).

4 Analytical results

4.1 *Whole-rock major and trace element compositions*

The whole-rock major and trace elements are listed in Table S1. The mass fraction of the pyroclastic rockschemical composition is as follows: 40.56%–48.89% for SiO_2; 12.79%–17.46% for Al_2O_3; 13.86%–20.63% for MgO; 11.45%–16.42% for ^{T}FeO; and 0.88%–4.77% for TiO_2. The Mg# values ranged from 66 to 75. The chondrite-normalized rare-earth element (REE) patterns showed that the pyroclastic rocks were enriched in light rare earth elements (LREEs) and had flat heavy rare earth element (HREE) patterns similar to those of the SCS and intraplate ocean island basalts (OIB) (Fig. 4) (Sun and McDonough, 1989; Yan et al., 2008). In the primitive mantle-normalized trace-element spider diagram (Fig. 5), the pyroclastic rocks were characterized by enrichment in high-field-strength elements (HFSEs), consistent with the features of OIB.

4.2 *Mineral chemistry*

Twenty olivine grains were analyzed for their chemical compositions. The results are summarized in Table S2. The analyzed olivines exhibited a narrow range of Fo contents (81–84). The major elemental compositions of the olivine from the basaltic pyroclastic rocks were as follows: SiO_2, 37.36%–39.23%; MgO, 43.28%–45.08%; NiO, 0.15%–0.24%; MnO, 0.21%–0.25%; CaO, 0.16%–0.25%. The high CaO content suggests that the analyzed olivines were phenocrysts formed during magma fractional crystallization (Thompson and Gibson, 2000; Foley et al., 2013).

5 Discussion

5.1 *Crustal contamination and fractional crystallization*

The composition of the basaltic magma is influenced by crustal contamination as it ascends through the crust to the surface. Therefore, it is necessary to evaluate the impact of crustal contamination on geochemical composition before interpreting the petrogenesis of basaltic pyroclastic rocks (Rudnick and Gao, 2003; Dai et al., 2018; Zhang et al., 2020a). Previous studies suggest that crustal contamination can be identified using whole-rock isotopes and trace-elements (Rudnick and Gao, 2003; Salters and Stracke, 2004). The basaltic pyroclastic rocks exhibited a relatively variable Nb/U mass ratio (23.29–89.22, with an average of 46.46) and Ce/Pb mass ratio (1.63–36.49, with an average of 13.04), which were substantially higher than those of the continental crust (Nb/U = 6.15 and Ce/Pb = 3.91; Rudnick and Gao, 2003; Salters and

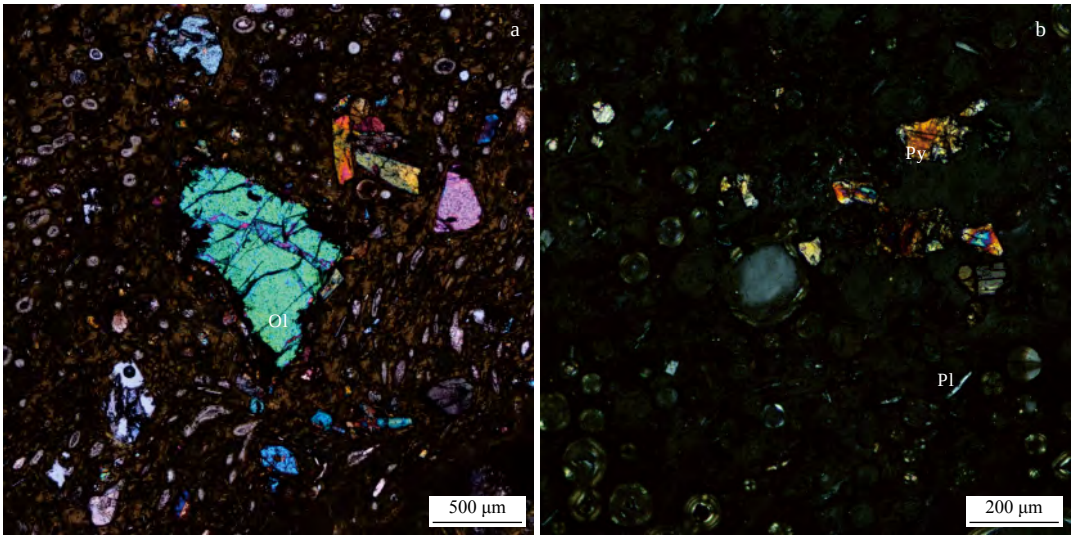


Fig. 3. Representative photomicrographs of the basaltic pyroclastic. Py: Pyroxene; Pl: Plagioclase; Ol: Olivine.

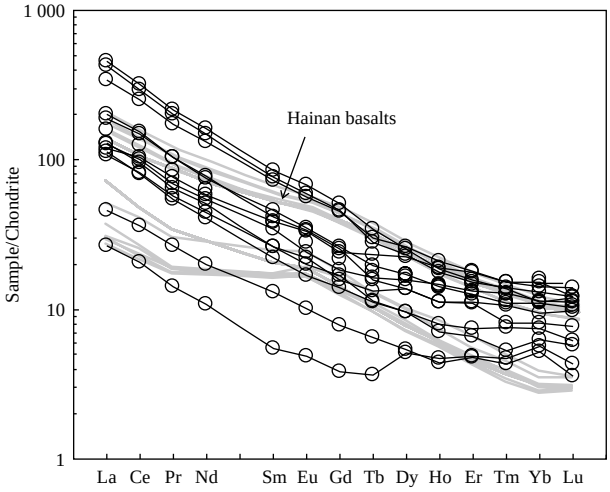


Fig. 4. Chondrite-normalized rare earth element patterns for the basaltic pyroclastic rocks from Well CK-2, Xisha Islands, SCS. The values for chondrite normalization are from Sun and McDonough (1989). Cenozoic basalt in Hainan Island is from literature (Liu et al., 2015; Gu et al., 2019).

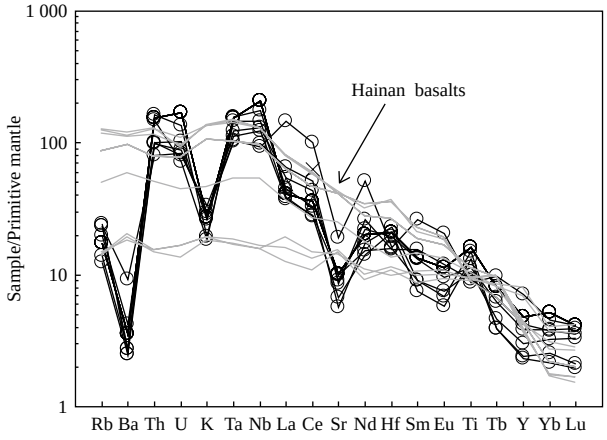


Fig. 5. Primitive mantle-normalized trace element diagrams for the basaltic pyroclastic rocks from Well CK-2, Xisha Islands, SCS. The values for primitive mantle normalization are from Sun and McDonough (1989). Cenozoic basalt in Hainan Island is from literature (Liu et al., 2015; Gu et al., 2019).

Stracke, 2004), suggesting limited crustal contamination. Furthermore, the primitive mantle-normalized trace element pattern lacked strong negative Nb or Ta anomalies (Fig. 5), implying that continental crustal contamination was negligible (Zou et al., 2003; Yang and Fang, 2015; An et al., 2017; Zhang et al., 2020a). In conclusion, the trace element characteristics suggest that crustal contamination of basaltic pyroclastic rocks was negligible, supporting the inference that these rocks were likely derived from a mantle source.

The basaltic pyroclastic rocks were characterized by low contents of Ni (131–247 μg/g), Co (16–77 μg/g), and Cr (23–73 μg/g) (Table S1). These results are inconsistent with the geochemical characteristics of primitive magma (Irving and Frey, 1978; Wilkinson and Le Maitre, 1987; An et al., 2017; Zhang et al., 2020a), implying that these basaltic pyroclastic rocks experienced a certain degree of fractional crystallization of olivine and clinopyroxene. In the primitive mantle-normalized trace-element spider diagram, the samples showed negative Eu and Sr anomalies (Fig. 5), indicating that the magmas that formed these basaltic pyroclastic rocks underwent plagioclase fractionation.

5.2 *Lithology of mantle source*

Identifying the lithology of mantle sources is essential for estimating the composition of the primary magma, assessing the mantle potential temperature, and understanding mantle heterogeneity. Traditionally, peridotite has been considered the primary mantle lithology in the source region of alkali basalts (Herzberg and O'Hara, 2002; Putirka, 2005; Rhodes et al., 2012). However, partial melting experiments have demonstrated that alkaline

basalts can also be generated through the partial melting of olivine-poor mantle lithologies, including carbonated peridotite, pyroxenite, and hornblendite (Hirschmann and Stolper, 1996; Hirschmann et al., 2003; Kogiso et al., 2003; Pertermann and Hirschmann, 2003a; Dasgupta et al., 2006, 2007; Kogiso and Hirschmann, 2006; Pilet et al., 2008; Sorbadere et al., 2013; Lambart et al., 2016).

Previous studies have suggested that carbonated peridotite and pyroxenite contribute to the mantle source of Late Cenozoic basalts in the SCS and its surrounding areas (Wang et al., 2012; Liu et al., 2015; An et al., 2017; Li et al., 2017; Zhang et al., 2017; Yan et al., 2018; Yang et al., 2020; Cao et al., 2022a, 2022b). Magmas generated through the partial melting of carbonated mantle peridotite exhibited significant negative Ti, Zr, and Hf anomalies (Zeng et al., 2010). However, the basaltic pyroclastic rocks exhibit positive Ti and Hf anomalies (Fig. 5), ruling out carbonatized mantle peridotite as the mantle source.

Experimental studies have demonstrated that the Fe/Mn mass ratio in basaltic melts serves as a reliable indicator of the mantle source lithology and can effectively distinguish between pyroxenite and peridotite mantle sources (Liu et al., 2008a; Wang et al., 2012). Pyroxenite-derived melts typically exhibit higher Fe/Mn mass ratios than those derived from peridotite (Liu et al., 2008a; Herzberg, 2011). Basaltic pyroclastic rocks are characterized by high Fe/Mn mass ratios, with an average of 86, which is significantly higher than the ratios observed in mid-ocean ridge basalt (MORB) and typical peridotite-derived melts (Wang et al., 2012). This elevated Fe/Mn mass ratio suggests the presence of a certain amount of pyroxenite in the mantle source of the basaltic pyroclastic rocks. Le Roux et al. (2010) demonstrated that high Zn/Fe mass ratios indicate a non-peridotite source. The basaltic pyroclastic rocks exhibited high Zn/Fe mass ratios (8.5–13.8, with an average of 10.7), which were substantially higher than the average values of the upper mantle (Le Roux et al., 2010). This further supported the presence of pyroxenite in the source rocks (Le Roux et al., 2010).

Olivine typically crystallizes first from mantle-derived melts, making it a key indicator for identifying the source lithology. In the basaltic pyroclastic rocks, the Fo of olivine exhibited no significant correlation with Ca content but shows a marked negative correlation with Mn content (Figs 6a and b). These systematic compositional relationships indicate that clinopyroxene fractionation has a limited influence on the olivine composition, suggesting that the observed olivine characteristics primarily reflect source-related processes. Previous studies suggest that the involvement of pyroxenite or eclogite in a mantle source can be identified by the presence of olivine phenocrysts with low content of Ca, high content of Ni, and high Fe/Mn mass ratios (Sobolev et al., 2005, 2007; Herzberg, 2011; Foley et al., 2013). The olivine phenocrysts from the basaltic pyroclastic rocks exhibited low Ca and high Ni contents, similar to the compositions of olivines in basalts from the SCS and its surrounding areas, which were derived from a pyroxenite source (Figs 6a and c) (Wang et al., 2012; Liu et al., 2015; An et al., 2017; Hoang et al., 2018; Zhang et al., 2018b; Yang et al., 2023)

Mn, Zn, and Fe have similar olivine–melt partition coefficients during the melting of mantle peridotite under specific whole-rock compositions, oxygen fugacity, pressure, and temperature conditions (Le Roux et al., 2010; Foley et al., 2013; Howarth and Harris, 2017). The proportions of these elements do not change significantly during partial melting or fractional crystallization but rather represent the characteristics of the source region (Sobolev et al., 2007; Foley et al., 2013; Herzberg et al., 2016). The Fe/Mn mass ratios of crystallized olivine from peridotite-derived melts generally ranged from 60 to 70 (Herzberg, 2011). The whole-rock high Fe/Mn ratios of the basaltic pyroclastic rocks were reflected in the Fe/Mn ratios of their olivine phenocrysts. As shown in the Fo vs. Fe/Mn diagram (Fig. 6d), most olivines from the basaltic pyroclastic rocks displayed high Fe/Mn mass ratios, indicating the presence of a pyroxenite mantle source. Howarth and Harris (2017) proposed that olivine crystallized from peridotite melts has high Mn/Zn values (>15), whereas olivine crystallized from pyroxenite melts has low Mn/Zn values (<13). The Mn/Zn values of olivine in the basaltic pyroclastic rocks range from 12 to 15, indicating a mixed pyroxenite-peridotite source. In summary, the compositions of both whole-rock (e.g., Fe/Mn and Zn/Fe mass ratios) and olivine phenocrysts (e.g., Ca and Ni contents and Fe/Mn and Zn/Fe mass ratios) suggest that the mantle source of basaltic pyroclastic rocks is a mixture of peridotite and pyroxenite.

Several hypotheses have been proposed to explain the genesis of pyroxenite, including (1) cumulative pyroxenite (Zhang and Xu, 2012), (2) metamorphosed oceanic crust (Herzberg, 2011; Lambart et al., 2013) and (3) reactions between recycled continental/oceanic crust and the surrounding mantle peridotite (Sobolev et al., 2005; Mallik and Dasgupta, 2012; Foley et al., 2013; Liu et al., 2015; Zhang et al., 2021b). Cumulative pyroxenite is characterized by low Ni content and cannot crystallize high-Ni olivine (Lee et al., 2006); therefore, the first hypothesis can be excluded. Additionally, most basaltic pyroclastic rocks have a higher MgO content than the melting products of silica-excess pyroxenite or bimineralic eclogite (MgO < 8.0%; Pertermann and Hirschmann, 2003b); the second hypothesis is not applicable for explaining the origin of the pyroxenite components in the mantle source of these rocks. Therefore, we argue that the third hypothesis is the most plausible mechanism for the genesis of pyroxenite in the source region of basaltic pyroclastic rocks.

The basaltic pyroclastic rocks exhibited positive Nb and Ta anomalies in the primitive mantle-normalized spidergrams (Fig. 5), suggesting that continental crust components were not present in the mantle source. Li is typically enriched in the crust and sediments (up to 70 μg/g) compared with the lithospheric mantle and mantle-de-

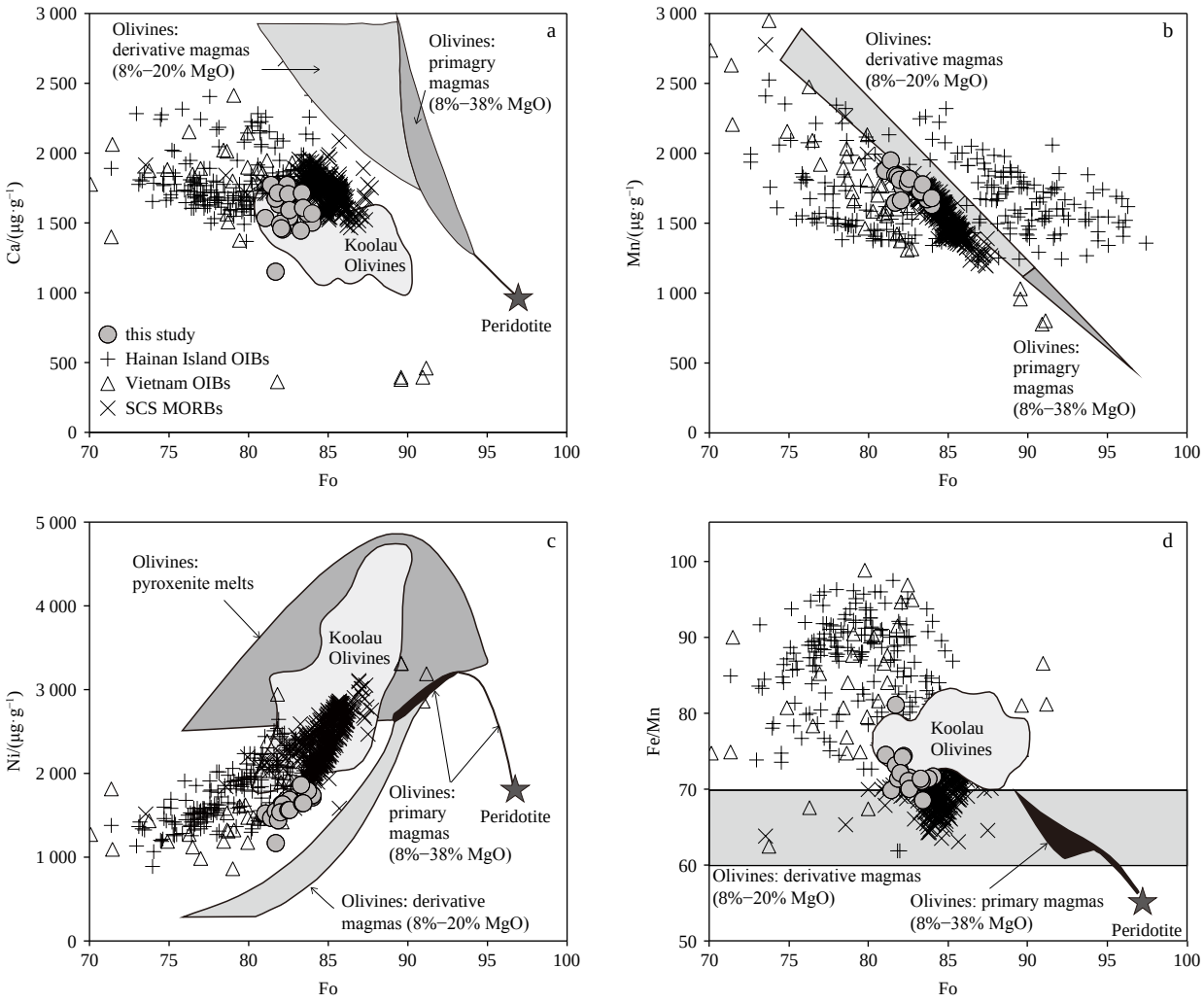


Fig. 6. Composition of olivine phenocrysts in basaltic pyroclastic rocks from Well CK-2 compared to calculated olivines from partial melts of a fertile peridotite and a stage 2 pyroxenite, after Herzberg (2011). Also shown are Koolau olivines (Sobolev et al., 2007). Data for the Hainan Island are from Gu et al. (2019); data for the Vietnam are from Hoang et al. (2018); data for SCS are from Zhang et al. (2018b).

rived melts (Foley et al., 2013). Based on the low Li content of olivine from Hawaii basalts, Ammannati et al. (2016) suggested that recycled subducted oceanic crust was involved in the production of the Hawaii basalts. The olivines from the basaltic pyroclastic rocks had low Li contents (mostly <5 μg/g), indicating that continental crust components were not present in the mantle source (Foley et al., 2013). Thus, we suggest that the recycled oceanic crust may have reacted with ambient mantle peridotite to form a relatively silica-rich mantle pyroxenite.

5.3 *Mantle potential temperature*

Potential temperature (T_p) refers to the hypothetical temperature of the mantle as it rises to Earth's surface without decompression or melting (Putirka, 2005). This serves as a critical parameter for characterizing the thermal state of the upper mantle (McKenzie and Bickle, 1988; Putirka, 2005, 2008; Campbell, 2007; Wang et al., 2012; Lee et al., 2009). It is widely recognized that magmas exhibiting OIB characteristics are not exclusively derived from mantle plumes (Xu et al., 2012). Mantle plumes are commonly linked to thermal anomalies characterized by elevated T_p values. Moreover, it is generally accepted that the generation of mafic magma associated with mantle plumes requires higher ambient T_p than that required for the formation of MORB (Herzberg and Asimow, 2008). To constrain mantle plumes, the concept of excess temperature (T_{ex}) has been proposed to identify thermal anomalies in the mantle ($T_{ex}=T_p^{hotspot}-T_p^{MORB}$). OIBs generated by mantle plumes typically exhibit elevated T_{ex}, which range between 100℃ and 300℃ (Kreutzmann et al., 2004; Putirka, 2005). Consequently, T_p can serve as a diagnostic parameter for identifying the presence of mantle plumes (Kreutzmann et al., 2004; Putirka, 2005).

The olivine-liquid Mg-Fe exchange thermometer was independent of the specific lithology of the mantle source (Putirka, 2005; Yu and Liu, 2020). In this study, we used an Fe-Mg exchange geothermometer to calculate the T_p of basaltic pyroclastic rocks. Using this method, the esti-

mated T_p for the basaltic pyroclastic rocks ranged from 1 502℃ to 1 756℃, with an average of 1 645℃. The T_p of Iceland basalt ranged from 1 480℃ to 1 520℃, and the T_p of Hawaii OIB was approximately 1 530℃ (Putirka, 2005). The estimated T_p of the basaltic pyroclastic rocks aligned closely with that of the plume-related OIBs (Iceland and Hawaii basalts), indicating an abnormally high mantle potential temperature in the study area. As discussed earlier, basaltic pyroclastic rocks exhibit OIB-like geochemical characteristics (Fig. 4). The combination of these OIB-type geochemical features and the evidence of high-temperature anomalies strongly supports the involvement of a mantle plume in their genesis.

Previous studies have proposed that the head of the Hainan mantle plume likely impinges on the base of the lithosphere at approximately 30 Ma (Wang et al., 2013). Yu et al. (2018) suggested that the SCS MORB which could have recorded plume-ridge interaction perhaps appeared since about 23.8 Ma. The initial-spreading MORB (Site U1500) of the SCS yielded a normal T_p (about 1 380℃) and was derived from a peridotite-dominated mantle source, suggesting that the opening of the SCS was not influenced by a mantle plume (Yu and Liu, 2020). In contrast, the late-spreading MORB (Site U1431E) yielded relatively high T_p (about 1 442℃) and originated from a pyroxenite-enriched mantle source (Zhang et al., 2018a, 2018b; Yang et al., 2019, 2023), indicating that the mantle plume impacted the final stages of SCS spreading. The uneven distribution of stagnant slab materials in the mantle transition zone is believed to have split and bifurcated the Cenozoic Hainan mantle plume into separate upwellings (Yang et al., 2023). Stronger portions of these stagnant slabs likely impeded the ascent of the mantle plume and hindere its upward migration. This bifurcation likely occurred as the mantle plume encountered stagnant slabs within the mantle transition zone, providing a plausible explanation for the uneven distribution of magmatic activity and discrepancies between the predicted magmatic distribution and topographic changes in classical mantle plume models (Yang et al., 2023).

5.4 *Water content of the magmas*

The formation of Large Igneous Provinces (LIP) involves various physical and chemical factors, including anomalously high mantle temperatures, the presence of fusible components in the mantle source, substantial decompression, and water enrichment (Sobolev et al., 2011; Liu et al., 2017). LIP are widely regarded as closely associated with mantle plume activity. Specifically, thermochemical mantle plumes originating from deep mantle are considered to account for the deep-sourced materials and the elevated thermal energy necessary for the extensive melting observed in LIP.

Water content of the mantle is important for studying magmatic processes in the deep mantle. Elevated water content increases the melting depth, leading to an increase in the volume of magma formed by melting. Recently, studies on the water content of major LIPs have been conducted worldwide (Xia et al., 2016; Liu et al., 2017, 2022; Ivanov et al., 2018; Gu et al., 2019; Lang et al., 2020). The primary magma water content of the picrites from the Emeishan LIP was 3.44%, corresponding to a mantle source water content of more than 6 000 μg/g. The formation of the Emeishan LIP was closely related to a high-temperature mantle plume enriched in water and fusible components (Liu et al., 2017).

The water content of the mantle plays a critical role in understanding magmatic processes occurring in the deep mantle. Elevated water content enhances the melting depth, which in turn increases the volume of magma produced during melting. Recent studies have investigated the water content of the mantle sources in major LIP (Xia et al., 2016a; Liu et al., 2017, 2022; Ivanov et al., 2018; Gu et al., 2019; Lang et al., 2020). For instance, the primary magma water content of the picrites from the Emeishan LIP exhibited a water content of 3.44%, corresponding to a mantle source water content exceeding 6 000 μg/g (Liu et al., 2017). The formation of the Emeishan LIP was closely related to a high-temperature mantle plume enriched in both water and fusible components (Liu et al., 2017).

In this study, the water content of the basaltic pyroclastic rocks was estimated using a Ca-in-olivine geohygrometer (Gavrilenko et al., 2016). This geohygrometer is based on experimental observations that demonstrate the influence of meltwater content on the partition coefficient of CaO between olivine and silicate melts ($D_{CaO}^{ol/liq}$). The geohygrometer calculated the meltwater content as a function of the MgO content and $D_{CaO}^{ol/liq}$ with an estimated uncertainty of 1.4%–1.8% H_2O (Gavrilenko et al., 2016). Using this method, we determined the H_2O contents of the primary magma in basaltic pyroclastic rocks to be 0.01%–1.47% (with an average of 0.66%), which is comparable to the water content of OIB (0.3%–2%, Métrich et al., 2014). However, these values were significantly lower than those of the mantle sources for many LIPs, such as the Emeishan LIP (3.44%, Liu et al., 2017) and the Tarim LIP (4.8%, Xia et al., 2016a) (Fig. 7).

5.5 *Implications*

Accumulating geophysical and geochemical evidence increasingly supports the existence of a Hainan mantle plume (Zou and Fan, 2010; Wang et al., 2013; Huang, 2014; Wei and Chen, 2016; Xia et al., 2016b; An et al., 2017; Fan et al., 2017; Yan et al., 2018, 2019; Yu et al., 2018; Zhang et al., 2018b, 2020a). A mushroom-shaped low-velocity seismic anomaly extending into the lower mantle was identified, suggesting the presence of a lower mantle root associated with the Hainan plume beneath southern China (Huang et al., 2015; Wei and Chen, 2016; Xia et al., 2016b; Fan et al., 2017). Several geophysical studies have further suggested that the Hainan mantle plume is one of the 12 plumes originating from the core-mantle boundary (Huang et al., 2015). The Cenozoic in-

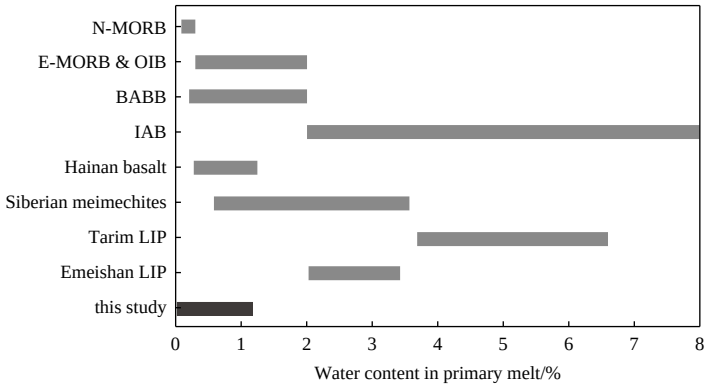


Fig. 7. Comparison of water contents in the primary melts of the basaltic pyroclastic rocks with those in other primary melts from different geological settings. The water contents of the Hainan basalts are from Gu et al. (2019) and those of other melts from Liu et al. (2017) and references therein. N-MORB: normal mid-ocean ridge basalt; E-MORB: enriched mid-ocean ridge basalt; OIB: oceanic island basalt; BABB: back-arc basin basalt; IAB: island arc basalt

traplate basalts of Southeast Asia are primarily distributed across the Leizhou Peninsula, Hainan Island, Indochina block, and SCS.

Gravity and magnetic anomaly data indicate that Cenozoic magmatism was widely distributed in the Xisha area (Zhang et al., 2016; Feng et al., 2017). Zhang et al. (2016) identified flat-topped and conical-topped seamounts in the Xisha area based on the geophysical data. Chenhang Island potentially represent one of the flat-topped seamounts (Zhang et al., 2024). The stratigraphic contact relationship and seismic reflection characteristics revealed three distinct phases of magmatism in the Xisha area: Paleocene and Eocene, early Oligocene to mid-Miocene, and mid-Miocene to recent (Zhang et al., 2016). In this study, the trace element patterns of the basaltic pyroclastic rocks exhibited typical OIB-like characteristics (Fig. 4). Additionally, the high T_p values further support the hypothesis that the mantle beneath the Xisha Islands was significantly influenced by the Hainan mantle plume. The northwestern SCS has experienced multiple phases of rifting since the Late Cretaceous, characterized by the extensive development of NE-NEE trending faults, which provide favorable pathways for magma upwelling. Furthermore, mantle plume material underwent lateral expansion at lithospheric depths, affecting the entire northern SCS from west to east (Xia et al., 2025). This process likely drives the widespread magmatic activity observed in the Xisha area. However, unlike classical mantle columns with large heads and thin tails that form large igneous provinces and age-progressive seamount chains, the Hainan mantle column did not exhibit these features.

6 Conclusions

This study presents the whole-rock and olivine chemical compositions of basaltic pyroclastic rocks from Well CK-2, SCS, and reaches to the following conclusions:

The compositions of both whole-rock and olivine phenocrysts indicate that the mantle source of the basaltic pyroclastic rocks was derived from a mixed source comprising peridotite and pyroxenite. The pyroxenite likely formed through the reaction of recycled oceanic crust with the surrounding mantle peridotite.

The calculated T_p values ranged from 1 502℃ to 1 756℃, which were comparable to those of plume-related OIB.

The basaltic pyroclastic rocks exhibited low H_2O contents (0.01%–1.47%), significantly lower than those observed in the primary magmas of LIPs.

References

Ammannati E, Jacob D E, Avanzinelli R, et al. 2016. Low Ni olivine in silica-undersaturated ultrapotassic igneous rocks as evidence for carbonate metasomatism in the mantle. Earth and Planetary Science Letters, 444: 64–74, doi: 10.1016/j.epsl.2016.03.039

An A R, Choi S H, Yu Y, et al. 2017. Petrogenesis of late Cenozoic basaltic rocks from southern Vietnam. Lithos, 272–273: 192–204, doi: 10.1016/j.lithos.2016.12.008

Campbell I H. 2007. Testing the plume theory. Chemical Geology, 241(3–4): 153–176, doi: 10.1016/j.chemgeo.2007.01.024

Cao Guangyue, Tong Ying, Li Xiang, et al. 2022a. Insights from olivine chemistry into crustal magmatic processes and the mantle source lithology of basalts from Hainan Island, China. Lithos, 430–431: 106852, doi: 10.1016/j.lithos.2022.106852

Cao Chuqi, Xiong Fahui, Yang Shengbiao, et al. 2022b. Geochemical characteristics and petrogenesis of Cenozoic basalt from the northern continental margin of the South China Sea. Acta Geologica Sinica (in Chinese), 96(8): 2683–2704

Cheng Zhiguo, Zhang Zhaochong, Wang Zhenchao, et al. 2020. Petrogenesis of transitional large igneous province: insights from bimodal volcanic suite in the Tarim large igneous province. Journal of Geophysical Research: Solid Earth, 125(5): e2019JB018382, doi: 10.1029/2019JB018382

Clift P, Lee G H, Anh Duc N, et al. 2008. Seismic reflection ev-

idence for a Dangerous Grounds miniplate: no extrusion origin for the South China Sea. Tectonics, 27(3): TC3008, doi: 10.1029/2007TC002216

Clift P, Lin Jian, Barckhausen U. 2002. Evidence of low flexural rigidity and low viscosity lower continental crust during continental break-up in the South China Sea. Marine and Petroleum Geology, 19(8): 951–970, doi: 10.1016/S0264-8172(02)00108-3

Dai Liqun, Zheng Fei, Zhao Zifu, et al. 2018. Geochemical insights into the lithology of mantle sources for Cenozoic alkali basalts in West Qinling, China. Lithos, 302–303: 86–98, doi: 10.1016/j.lithos.2017.12.013

Dasgupta R, Hirschmann M M, Smith N D. 2007. Partial melting experiments of peridotite + CO_2 at 3 GPa and genesis of alkalic ocean island basalts. Journal of Petrology, 48(11): 2093–2124, doi: 10.1093/petrology/egm053

Dasgupta R, Hirschmann M M, Stalker K. 2006. Immiscible transition from carbonate-rich to silicate-rich melts in the 3 GPa melting interval of eclogite + CO_2 and genesis of silica-undersaturated ocean island lavas. Journal of Petrology, 47(4): 647–671, doi: 10.1093/petrology/egi088

Fan Chaoyan, Xia Shaohong, Zhao Fang, et al. 2017. New insights into the magmatism in the northern margin of the South China Sea: spatial features and volume of intraplate seamounts. Geochemistry, Geophysics, Geosystems, 18(6): 2216–2239, doi: 10.1002/2016GC006792

Fan Tianlai, Yu Kefu, Zhao Jianxin, et al. 2020. Strontium isotope stratigraphy and paleomagnetic age constraints on the evolution history of coral reef islands, northern South China Sea. GSA Bulletin, 132(3–4): 803–816, doi: 10.1130/B35088.1

Feng Yingci, Zhan Wenhuan, Sun Jie, et al. 2017. The formation mechanism and characteristics of volcanoes in the Xisha waters since Pliocene. Journal of Tropical Oceanography (in Chinese), 36(3): 73–79

Foley S F, Prelevic D, Rehfeldt T, et al. 2013. Minor and trace elements in olivines as probes into early igneous and mantle melting processes. Earth and Planetary Science Letters, 363: 181–191, doi: 10.1016/j.epsl.2012.11.025

Gao Jinwei, Wu Shiguo, McIntosh K, et al. 2015. The continent–ocean transition at the mid-northern margin of the South China Sea. Tectonophysics, 654: 1–19, doi: 10.1016/j.tecto.2015.03.003

Gavrilenko M, Herzberg C, Vidito C, et al. 2016. A calcium-in-olivine geohygrometer and its application to subduction zone magmatism. Journal of Petrology, 57(9): 1811–1832, doi: 10.1093/petrology/egw062

Gu Xiaoyan, Wang Piaoyi, Kuritani T, et al. 2019. Low water content in the mantle source of the Hainan plume as a factor inhibiting the formation of a large igneous province. Earth and Planetary Science Letters, 515: 221–230, doi: 10.1016/j.epsl.2019.03.034

Guo Xiaoran, Zhao Minghui, Huang Haibo, et al. 2016. Crustal structure of Xisha block and its tectonic attributes. Chinese Journal of Geophysics (in Chinese), 59(4): 1414–1425

Herzberg C. 2011. Identification of source lithology in the Hawaiian and Canary Islands: implications for origins. Journal of Petrology, 52(1): 113–146, doi: 10.1093/petrology/egq075

Herzberg C, Asimow P D. 2008. Petrology of some oceanic island basalts: PRIMELT2. XLS software for primary magma calculation. Geochemistry, Geophysics, Geosystems, 9(9): Q09001, doi: 10.1029/2008GC002057

Herzberg C, O'Hara M J. 2002. Plume-associated ultramafic magmas of Phanerozoic age. Journal of Petrology, 43(10): 1857–1883, doi: 10.1093/petrology/43.10.1857

Herzberg C, Vidito C, Starkey N A. 2016. Nickel–cobalt contents of olivine record origins of mantle peridotite and related rocks. American Mineralogist, 101(9): 1952–1966, doi: 10.2138/am-2016-5538

Hirschmann M M, Kogiso T, Baker M B, et al. 2003. Alkalic magmas generated by partial melting of garnet pyroxenite. Geology, 31(6): 481–484, doi: 10.1130/0091-7613(2003)031<0481:AMGBPM>2.0.CO;2

Hirschmann M M, Stolper E M. 1996. A possible role for garnet pyroxenite in the origin of the "garnet signature" in MORB. Contributions to Mineralogy and Petrology, 124(2): 185–208, doi: 10.1007/s004100050184

Hoang T H A, Choi S H, Yu Y, et al. 2018. Geochemical constraints on the spatial distribution of recycled oceanic crust in the mantle source of late Cenozoic basalts, Vietnam. Lithos, 296: 382395, doi: 10.1016/j.lithos.2017.11.020

Holloway N H. 1982. North Palawan block, Philippine-its relation to Asian mainland and role in evolution of South China Sea. AAPG Bulletin, 66(9): 1355–1383, doi: 10.1306/03B5A7A5-16D1-11D7-8645000102C1865D

Howarth G H, Harris C. 2017. Discriminating between pyroxenite and peridotite sources for continental flood basalts (CFB) in southern Africa using olivine chemistry. Earth and Planetary Science Letters, 475: 143–151, doi: 10.1016/j.epsl.2017.07.043

Hu Zhaochu, Zhang Wen, Liu Yongsheng, et al. 2015. "Wave" signal-smoothing and mercury-removing device for laser ablation quadrupole and multiple collector ICPMS analysis: application to lead isotope analysis. Analytical Chemistry, 87(2): 1152–1157, doi: 10.1021/ac503749k

Huang Jinli. 2014. P- and S-wave tomography of the Hainan and surrounding regions: insight into the Hainan plume. Tectonophysics, 633: 176–192, doi: 10.1016/j.tecto.2014.07.007

Huang Haibo, Qiu Xuelin, Xu Yi, et al. 2011. Crustal structure beneath the Xisha Islands of the South China Sea simulated by the teleseismic receiver function method. Chinese Journal of Geophysics (in Chinese), 54(11): 2788–2798, doi: 10.3969/j.issn.0001-5733.2011.11.009

Huang Zhouchuan, Zhao Dapeng, Wang Liangshu. 2015. *P* wave tomography and anisotropy beneath Southeast Asia: insight into mantle dynamics. Journal of Geophysical Research: Solid Earth, 120(7): 5154–5174, doi: 10.1002/2015JB012098

Irving A J, Frey F A. 1978. Distribution of trace elements between garnet megacrysts and host volcanic liquids of kimberlitic to rhyolitic composition. Geochimica et Cosmochimica Acta, 42(6): 771–787, doi: 10.1016/0016-7037(78)90092-3

Ivanov A V, Mukasa S B, Kamenetsky V S, et al. 2018. Volatile

concentrations in olivine-hosted melt inclusions from meimechite and melanephelinite lavas of the Siberian Traps Large Igneous Province: evidence for flux-related high-Ti, high-Mg magmatism. Chemical Geology, 483: 442–462, doi: 10.1016/j.chemgeo.2018.03.011

Kogiso T, Hirschmann M M. 2006. Partial melting experiments of bimineralic eclogite and the role of recycled mafic oceanic crust in the genesis of ocean island basalts. Earth and Planetary Science Letters, 249(3–4): 188–199, doi: 10.1016/j.epsl.2006.07.016

Kogiso T, Hirschmann M M, Frost D J. 2003. High-pressure partial melting of garnet pyroxenite: possible mafic lithologies in the source of ocean island basalts. Earth and Planetary Science Letters, 216(4): 603–617, doi: 10.1016/S0012-821X(03)00538-7

Kreutzmann A, Schmeling H, Junge A, et al. 2004. Temperature and melting of a ridge-centred plume with application to Iceland. Part II: predictions for electromagnetic and seismic observables. Geophysical Journal International, 159(3): 1097–1111, doi: 10.1111/j.1365-246X.2004.02397.x

Kushiro I. 1996. Partial melting of a fertile mantle peridotite at high pressures: an experimental study using aggregates of diamond. In: Basu A, Hart S, eds. Earth Processes: Reading the Isotopic Code. Washington: American Geophysical Union, 109–122, doi: 10.1029/GM095p0109

Lambart S, Baker M B, Stolper E M. 2016. The role of pyroxenite in basalt genesis: melt-PX, a melting parameterization for mantle pyroxenites between 0.9 and 5 GPa. Journal of Geophysical Research: Solid Earth, 121(8): 5708–5735, doi: 10.1002/2015JB012762

Lambart S, Laporte D, Schiano P. 2013. Markers of the pyroxenite contribution in the major-element compositions of oceanic basalts: review of the experimental constraints. Lithos, 160–161: 14–36, doi: 10.1016/j.lithos.2012.11.018

Lang Mingde, Cheng Zhiguo, Zhang Zhaochong, et al. 2020. Hisingerite in trachydacite from Tarim: implications for voluminous felsic rocks in transitional large igneous province. Journal of Earth Science, 31(5): 875–883, doi: 10.1007/s12583-020-1330-x

Le Bas M J, Le Maitre R W, Streckeisen A, et al. 1986. A chemical classification of volcanic rocks based on the total alkali-silica diagram. Journal of Petrology, 27(3): 745–750, doi: 10.1093/PETROLOGY/27.3.745

Le Roux V, Lee C T A, Turner S J. 2010. Zn/Fe systematics in mafic and ultramafic systems: implications for detecting major element heterogeneities in the earth's mantle. Geochimica et Cosmochimica Acta, 74(9): 2779–2796, doi: 10.1016/j.gca.2010.02.004

Lee C T A, Cheng Xin, Horodyskyj U. 2006. The development and refinement of continental arcs by primary basaltic magmatism, garnet pyroxenite accumulation, basaltic recharge and delamination: insights from the Sierra Nevada, California. Contributions to Mineralogy and Petrology, 151(2): 222–242, doi: 10.1007/s00410-005-0056-1

Lee C T A, Luffi P, Plank T, et al. 2009. Constraints on the depths and temperatures of basaltic magma generation on Earth and other terrestrial planets using new thermobarometers for mafic magmas. Earth and Planetary Science Letters, 279(1–2): 20–33, doi: 10.1016/j.epsl.2008.12.020

Li Chunfeng, Li Jiabiao, Ding Weiwei, et al. 2015. Seismic stratigraphy of the central South China Sea basin and implications for neotectonics. Journal of Geophysical Research: Solid Earth, 120(3): 1377–1399, doi: 10.1002/2014JB011686

Li Chunfeng, Lin Jian, Kulhanek D K. 2014. South China Sea tectonics: opening of the South China Sea and its implications for Southeast Asian tectonics, climates, and deep mantle processes since the late Mesozoic. International Ocean Discovery Program Scientific Prospectus, 349: 1–111

Li Fucheng, Sun Zhen, Yang Hongfeng, et al. 2020. Continental interior and edge breakup at convergent margins induced by subduction direction reversal: a numerical modeling study applied to the South China sea margin. Tectonics, 39(11): e2020TC006409, doi: 10.1029/2020TC006409

Li Naisheng, Yan Quanshu, Chen Zhihua, et al. 2013. Geochemistry and petrogenesis of Quaternary volcanism from the islets in the eastern Beibu Gulf: evidence for Hainan plume. Acta Oceanologica Sinica, 32(12): 40–49, doi: 10.1007/s13131-013-0386-1

Li Shuguang, Yang Wei, Ke Shan, et al. 2017. Deep carbon cycles constrained by a large-scale mantle Mg isotope anomaly in eastern China. National Science Review, 4(1): 111–120, doi: 10.1093/nsr/nww070

Li Shiying, Yu Kefu, Zhang Yu, et al. 2019. Mineral chemistry of clinopyroxene in pyroclastic rocks of the Xisha Islands and their geological significance. Haiyang Xuebao (in Chinese), 41(7): 65–76

Liao Renqiang, Zhu Hongli, Li Congying, et al. 2022. Geochemistry of mantle source during the initial expansion and its implications for the opening of the South China Sea. Marine Geology, 447: 106798, doi: 10.1016/j.margeo.2022.106798

Liu Yongsheng, Gao Shan, Hu Zhaochu, et al. 2010. Continental and oceanic crust recycling-induced melt-peridotite interactions in the Trans-North China Orogen: U-Pb dating, Hf isotopes and trace elements in zircons from mantle xenoliths. Journal of Petrology, 51(1–2): 537–571, doi: 10.1093/petrology/egp082

Liu Yongsheng, Gao Shan, Kelemen P B, et al. 2008a. Recycled crust controls contrasting source compositions of Mesozoic and Cenozoic basalts in the North China Craton. Geochimica et Cosmochimica Acta, 72(9): 2349–2376, doi: 10.1016/j.gca.2008.02.018

Liu Yongsheng, Hu Zhaochu, Gao Shan, et al. 2008b. *In situ* analysis of major and trace elements of anhydrous minerals by LA-ICP-MS without applying an internal standard. Chemical Geology, 257(1–2): 34–43, doi: 10.1016/j.chemgeo.2008.08.004

Liu Jianqiang, Ren Zhongyuan, Nichols A R L, et al. 2015. Petrogenesis of Late Cenozoic basalts from North Hainan Island: constraints from melt inclusions and their host olivines. Geochimica et Cosmochimica Acta, 152: 89–

121, doi: 10.1016/j.gca.2014.12.023

Liu Jia, Xia Qunke, Kuritani T, et al. 2017. Mantle hydration and the role of water in the generation of large igneous provinces. Nature Communications, 8(1): 1824, doi: 10.1038/s41467-017-01940-3

Liu Jia, Xia Qunke, Sun Hao, et al. 2022. Compositional variation of picrites in the Emeishan large igneous province modulated by water in the mantle plume. Journal of Geophysical Research: Solid Earth, 127(1): e2021JB023584, doi: 10.1029/2021JB023584

Liu Hailing, Yan Pin, Liu Yingchun, et al. 2006. Existence of Qiongnan suture zone on the north margin of South China Sea. Chinese Science Bulletin, 51(S2): 107–120, doi: 10.1007/s11434-006-9107-x

Liu Hailing, Yan Pin, Zhang Boyou, et al. 2004. Pre-Cenozoic basements of the South China Sea and eastern Tethyan realm. Marine Geology & Quaternary Geology (in Chinese), 24(1): 15–28

Liu Hailing, Zheng Hongbo, Wang Yanlin, et al. 2011. Basement of the South China Sea area: tracing the Tethyan realm. Acta Geologica Sinica-English Edition, 85(3): 637–655, doi: 10.1111/j.1755-6724.2011.00457.x

Mallik A, Dasgupta R. 2012. Reaction between MORB-eclogite derived melts and fertile peridotite and generation of ocean island basalts. Earth and Planetary Science Letters, 329–330: 97–108, doi: 10.1016/j.epsl.2012.02.007

McKenzie D, Bickle M J. 1988. The volume and composition of melt generated by extension of the lithosphere. Journal of Petrology, 29(3): 625–679, doi: 10.1093/petrology/29.3.625

Métrich N, Zanon V, Créon L, et al. 2014. Is the 'Azores hotspot' a wetspot? Insights from the geochemistry of fluid and melt inclusions in olivine of Pico basalts. Journal of Petrology, 55: 377–393, doi: 10.1093/petrology/egt071

Pertermann M, Hirschmann M M. 2003a. Partial melting experiments on a MORB-like pyroxenite between 2 and 3 GPa: constraints on the presence of pyroxenite in basalt source regions from solidus location and melting rate. Journal of Geophysical Research: Solid Earth, 108(B2): 2125, doi: 10.1029/2000JB000118

Pertermann M, Hirschmann M M. 2003b. Anhydrous partial melting experiments on MORB-like eclogite: phase relations, phase compositions and mineral-melt partitioning of major elements at 2–3 GPa. Journal of Petrology, 44(12): 2173–2201, doi: 10.1093/petrology/egg074

Pilet S, Baker M B, Stolper E M. 2008. Metasomatized lithosphere and the origin of alkaline lavas. Science, 320(5878): 916–919, doi: 10.1126/science.1156563

Putirka K D. 2005. Mantle potential temperatures at Hawaii, Iceland, and the mid-ocean ridge system, as inferred from olivine phenocrysts: evidence for thermally driven mantle plumes. Geochemistry, Geophysics, Geosystem, 6(5): Q05L08, doi: 10.1029/2005GC000915

Putirka K D. 2008. Thermometers and barometers for volcanic systems. Reviews in Mineralogy and Geochemistry, 69(1): 61–120, doi: 10.2138/rmg.2008.69.3

Qian Shengping, Gazel E, Nichols A R L, et al. 2021. The origin of Late Cenozoic magmatism in the South China Sea and Southeast Asia. Geochemistry, Geophysics, Geosystems, 22(8): e2021GC009686, doi: 10.1029/2021GC009686

Qian Shengping, Salters V, McCoy-West A J, et al. 2022. Highly heterogeneous mantle caused by recycling of oceanic lithosphere from the mantle transition zone. Earth and Planetary Science Letters, 593: 117679, doi: 10.1016/j.epsl.2022.117679

Rhodes J M, Huang Shichun, Frey F A, et al. 2012. Compositional diversity of Mauna Kea shield lavas recovered by the Hawaii Scientific Drilling Project: inferences on source lithology, magma supply, and the role of multiple volcanoes. Geochemistry, Geophysics, Geosystems, 13(3): Q03014, doi: 10.1029/2011GC003812

Rudnick R L, Gao Shan. 2003. Composition of the continental crust. Treatise on Geochemistry, 3: 1–64, doi: 10.1016/B0-08-043751-6/03016-4

Salters V J M, Stracke A. 2004. Composition of the depleted mantle. Geochemistry, Geophysics, Geosystems, 5(5): Q05B07, doi: 10.1029/2003GC000597

Schlüter H U, Hinz K, Block M. 1996. Tectono-stratigraphic terranes and detachment faulting of the South China Sea and Sulu Sea. Marine Geology, 130(1–2): 39–78, doi: 10.1016/0025-3227(95)00137-9

Shao Lei, Li Qianyu, Zhu Weilin, et al. 2017. Neogene carbonate platform development in the NW South China Sea: litho-, bio- and chemo-stratigraphic evidence. Marine Geology, 385: 233–243, doi: 10.1016/j.margeo.2017.01.009

Sobolev A V, Hofmann A W, Kuzmin D V, et al. 2007. The amount of recycled crust in sources of mantle-derived melts. Science, 316(5823): 412–417, doi: 10.1126/science.1138113

Sobolev A V, Hofmann A W, Sobolev S V, et al. 2005. An olivine-free mantle source of Hawaiian shield basalts. Nature, 434(7033): 590–597, doi: 10.1038/nature03411

Sobolev S V, Sobolev A V, Kuzmin D V, et al. 2011. Linking mantle plumes, large igneous provinces and environmental catastrophes. Nature, 477(7364): 312–316, doi: 10.1038/nature10385

Sorbadere F, Médard E, Laporte D, et al. 2013. Experimental melting of hydrous peridotite-pyroxenite mixed sources: constraints on the genesis of silica-undersaturated magmas beneath volcanic arcs. Earth and Planetary Science Letters, 384: 42–56, doi: 10.1016/j.epsl.2013.09.026

Sun S S, McDonough W F. 1989. Chemical and isotopic systematics of oceanic basalts: implications for mantle composition and processes. Geological Society, London, Special Publications, 42(1): 313–345, doi: 10.1144/GSL.SP.1989.042.01.19

Sun Liheng, Sun Zhen, Zhang Yunying, et al. 2021. Multi-stage carbonate veins at IODP Site U1504 document Early Cretaceous to early Cenozoic extensional events on the South China Sea margin. Marine Geology, 442: 106656, doi: 10.1016/j.margeo.2021.106656

Suo Yanhui, Li Sanzhong, Jin Chong, et al. 2019. Eastward tectonic migration and transition of the Jurassic-Cretaceous Andean-type continental margin along southeast China. Earth-Science Reviews, 196: 102884, doi: 10.1016/j.earscirev.2019.102884

Thompson R N, Gibson S A. 2000. Transient high temperatures

in mantle plume heads inferred from magnesian olivines in Phanerozoic picrites. Nature, 407(6803): 502–506, doi: 10.1038/35035058

Walter M J. 1998. Melting of garnet peridotite and the origin of komatiite and depleted lithosphere. Journal of Petrology, 39(1): 29–60, doi: 10.1093/petroj/39.1.29

Wan Ling, Yao Bochu, Zeng Weijun, et al. 2006. Lithospheric structure and petroleum distribution in the South China Sea. Geology in China (in Chinese), 33(4): 874–884

Wang Xuance, Li Zhengxiang, Li Xianhua, et al. 2012. Temperature, pressure, and composition of the mantle source region of Late Cenozoic basalts in Hainan Island, SE Asia: a consequence of a young thermal mantle plume close to subduction zones? Journal of Petrology, 53(1): 177–233, doi: 10.1093/petrology/egr061

Wang Xuance, Li Zhengxiang, Li Xianhua, et al. 2013. Identification of an ancient mantle reservoir and young recycled materials in the source region of a young mantle plume: implications for potential linkages between plume and plate tectonics. Earth and Planetary Science Letters, 377–378: 248–259, doi: 10.1016/j.epsl.2013.07.003

Wang Rui, Yu Kefu, Jones B, et al. 2018. Evolution and development of Miocene "island dolostones" on Xisha Islands, South China Sea. Marine Geology, 406: 142–158, doi: 10.1016/j.margeo.2018.09.006

Wei S S, Chen Y J. 2016. Seismic evidence of the Hainan mantle plume by receiver function analysis in southern China. Geophysical Research Letters, 43(17): 8978–8985, doi: 10.1002/2016GL069513

Weller O M, Copley A, Miller W G R, et al. 2019. The relationship between mantle potential temperature and oceanic lithosphere buoyancy. Earth and Planetary Science Letters, 518: 86–99, doi: 10.1016/j.epsl.2019.05.005

Wilkinson J F G, Le Maitre R W. 1987. Upper mantle amphiboles and micas and TiO_2, K_2O, and P_2O_5 abundances and 100 Mg/(Mg+Fe^{2+}) ratios of common basalts and andesites: implications for modal mantle metasomatism and undepleted mantle compositions. Journal of Petrology, 28(1): 37–73, doi: 10.1093/petrology/28.1.37

Wu Shiguo, Yang Zhen, Wang Dawei, et al. 2014. Architecture, development and geological control of the Xisha carbonate platforms, northwestern South China Sea. Marine Geology, 350: 71–83, doi: 10.1016/j.margeo.2013.12.016

Xia Qunke, Bi Yao, Li Pei, et al. 2016a. High water content in primitive continental flood basalts. Scientific Reports, 6: 25416, doi: 10.1038/srep25416

Xia Shaohong, Gou Tao, Zhao Fang, et al. 2025. Late Cenozoic magmatism of the South China Sea driven by the Hainan mantle plume. Science Bulletin, 70(5): 604–608, doi: 10.1016/j.scib.2024.12.010

Xia Qunke, Liu Jia, Liu Shaochen, et al. 2013. High water content in Mesozoic primitive basalts of the North China Craton and implications on the destruction of cratonic mantle lithosphere. Earth and Planetary Science Letters, 361: 85–97, doi: 10.1016/j.epsl.2012.11.024

Xia Shaohong, Zhao Dapeng, Sun Jinlong, et al. 2016b. Teleseismic imaging of the mantle beneath southernmost China: new insights into the Hainan plume. Gondwana Research, 36: 46–56, doi: 10.1016/j.gr.2016.05.003

Xu Yigang, Wei Jingxian, Qiu Huaning, et al. 2012. Opening and evolution of the South China Sea constrained by studies on volcanic rocks: preliminary results and a research design. Chinese Science Bulletin, 57(24): 31503164, doi: 10.1007/s11434-011-4921-1

Yan Quanshu, Castillo P, Shi Xuefa, et al. 2015. Geochemistry and petrogenesis of volcanic rocks from Daimao Seamount (South China Sea) and their tectonic implications. Lithos, 218–219: 117–126, doi: 10.1016/j.lithos.2014.12.023

Yan Pin, Deng Hui, Liu Hailing, et al. 2006. The temporal and spatial distribution of volcanism in the South China Sea region. Journal of Asian Earth Sciences, 27(5): 647–659, doi: 10.1016/j.jseaes.2005.06.005

Yan Quanshu, Shi Xuefa, Castillo P R. 2014. The late Mesozoic-Cenozoic tectonic evolution of the South China Sea: a petrologic perspective. Journal of Asian Earth Sciences, 85: 178–201, doi: 10.1016/j.jseaes.2014.02.005

Yan Quanshu, Shi Xuefa, Metcalfe I, et al. 2018. Hainan mantle plume produced Late Cenozoic basaltic rocks in Thailand, Southeast Asia. Scientific Reports, 8(1): 2640, doi: 10.1038/s41598-018-20712-7

Yan Quanshu, Shi Xuefa, Wang Kunshan, et al. 2008. Major element, trace element, and Sr, Nd and Pb isotope studies of Cenozoic basalts from the South China Sea. Science in China Series D: Earth Sciences, 51(4): 550–566, doi: 10.1007/s11430-008-0026-3

Yan Quanshu, Straub S, Shi Xuefa. 2019. Hafnium isotopic constraints on the origin of late Miocene to Pliocene seamount basalts from the South China Sea and its tectonic implications. Journal of Asian Earth Sciences, 171: 162–168, doi: 10.1016/j.jseaes.2018.06.027

Yang Shuying. 2015. Geochemical characteristics of basalts from the Daimao seamount in the South China Sea (SCS) and from the SCS's neighboring lands: implications for the regional tectonic evolution (in Chinese)[dissertation]. Beijing: China University of Geosciences (Beijing)

Yang Shuying, Fang Nianqiao. 2015. Geochemical variation of volcanic rocks from the South China Sea and neighboring land: implication for magmatic process and mantle structure. Acta Oceanologica Sinica, 34(12): 112–124, doi: 10.1007/s13131-015-0759-8

Yang Fan, Huang Xiaolong, Xu Yigang, et al. 2019. Plume-ridge interaction in the South China Sea: thermometric evidence from Hole U1431E of IODP Expedition 349. Lithos, 324–325: 466–478, doi: 10.1016/j.lithos.2018.11.031

Yang Fan, Huang Xiaolong, Xu Yigang, et al. 2023. Bifurcation of mantle plumes by interaction with stagnant slabs in the mantle transition zone: evidence from late Cenozoic basalts within Southeast Asia. GSA Bulletin, 135(9–10): 2710–2720, doi: 10.1130/B36558.1

Yang Zongfeng, Li Jie, Liang Wenfei, et al. 2016. On the chemical markers of pyroxenite contributions in continental basalts in eastern China: implications for source lithology and the origin of basalts. Earth-Science Reviews, 157: 18–31, doi: 10.1016/j.earscirev.2016.04.001

Yang Wenjian, Yu Hongmei, Zhao Bo, et al. 2020. Mantle

sources and magma genesis of Late Cenozoic basalts in Weizhou Island, Guangxi, China. Acta Petrologica Sinica (in Chinese), 36(7): 2092–2110, doi: 10.18654/1000-0569/2020.07.11

Yao Bochu, Wan Ling, Wu Nengyou. 2004. Cenozoic plate tectonic activities in the Great South China Sea area. Geology in China (in Chinese), 31(2): 113–122

Yu Xun, Liu Zhifei. 2020. Non-mantle-plume process caused the initial spreading of the South China Sea. Scientific Reports, 10(1): 8500, doi: 10.1038/s41598-020-65174-y

Yu Mengming, Yan Yi, Huang Chiyue, et al. 2018. Opening of the South China Sea and upwelling of the Hainan Plume. Geophysical Research Letters, 45(6): 2600–2609, doi: 10.1002/2017GL076872

Zeng Gang, Chen Lihui, Xu Xisheng, et al. 2010. Carbonated mantle sources for Cenozoic intra-plate alkaline basalts in Shandong, North China. Chemical Geology, 273(1–2): 35–45, doi: 10.1016/j.chemgeo.2010.02.009

Zhang Guoliang, Chen Lihui, Jackson M G, et al. 2017. Evolution of carbonated melt to alkali basalt in the South China Sea. Nature Geoscience, 10(3): 229–235, doi: 10.1038/NGEO2877

Zhang Guoliang, Luo Qing, Zhao Jian, et al. 2018a. Geochemical nature of sub-ridge mantle and opening dynamics of the South China Sea. Earth and Planetary Science Letters, 489: 145–155, doi: 10.1016/j.epsl.2018.02.040

Zhang Cuimei, Sun Zhen, Manatschal G, et al. 2021a. Syn-rift magmatic characteristics and evolution at a sediment-rich margin: insights from high-resolution seismic data from the South China Sea. Gondwana Research, 91: 81–96, doi: 10.1016/j.gr.2020.11.012

Zhang Guoliang, Sun Weidong, Seward G. 2018b. Mantle source and magmatic evolution of the dying spreading ridge in the South China Sea. Geochemistry, Geophysics, Geosystems, 19(11): 4385–4399, doi: 10.1029/2018GC007570

Zhang Qiao, Wu Shiguo, Dong Dongdong. 2016. Cenozoic magmatism in the northern continental margin of the South China Sea: evidence from seismic profiles. Marine Geophysical Research, 37(2): 71–94, doi: 10.1007/s11001-016-9266-3

Zhang Qiao, Wu Shiguo, Lv Fuliang, et al. 2014. The seismic characteristics and the distribution of the igneous rocks in the Northernwest slope of the South China Sea. Geotectonica et Metallogenia (in Chinese), 38(4): 919–938

Zhang Yaling, Xu Yigang. 2012. Pyroxenites: high-pressure segregates or recycled oceanic crust? Geological Journal of China Universities (in Chinese), 18(1): 74–87

Zhang Yu, Yu Kefu, Fan Tianlai, et al. 2020a. Geochemistry and petrogenesis of Quaternary basalts from Weizhou Island, northwestern South China Sea: evidence for the Hainan plume. Lithos, 362–363: 105493, doi: 10.1016/j.lithos.2020.105493

Zhang Yu, Yu Kefu, Li Shiying. 2024. U-Pb zircon geochronology of basaltic pyroclastic rocks from the basement beneath the Xisha Islands in the northwestern South China Sea and its geological significance. Acta Oceanologica Sinica, 43(2): 83–93, doi: 10.1007/s13131-023-2198-2

Zhang Yu, Yu Kefu, Qian Handong. 2018c. LA-ICP-MS analysis of clinopyroxenes in basaltic pyroclastic rocks from the Xisha Islands, northwestern South China Sea. Minerals, 8(12): 575, doi: 10.3390/min8120575

Zhang Yu, Yu Kefu, Qian Handong, et al. 2020b. The basement and volcanic activities of the Xisha Islands: evidence from the kilometre-scale drilling in the northwestern South China Sea. Geological Journal, 55(1): 571–583, doi: 10.1002/gj.3416

Zhang Yunying, Yuan Chao, Sun Min, et al. 2021b. Contrasting compositions between phenocrystic and xenocrystic olivines in the Cenozoic basalts from central Mongolia: constraints on source lithology and regional uplift. American Mineralogist, 106(2): 251–264, doi: 10.2138/am-2020-7431

Zong Keqing, Klemd R, Yuan Yu, et al. 2017. The assembly of Rodinia: the correlation of early Neoproterozoic (ca. 900 Ma) high-grade metamorphism and continental arc formation in the southern Beishan Orogen, southern Central Asian Orogenic Belt (CAOB). Precambrian Research, 290: 32–48, doi: 10.1016/j.precamres.2016.12.010

Zou Haibo, Fan Qicheng. 2010. U-Th isotopes in Hainan basalts: implications for sub-asthenospheric origin of EM2 mantle endmember and the dynamics of melting beneath Hainan Island. Lithos, 116(1–2): 145–152, doi: 10.1016/j.lithos.2010.01.010

Zou Haibo, Reid M R, Liu Yongshun, et al. 2003. Constraints on the origin of historic potassic basalts from Northeast China by U-Th disequilibrium data. Chemical Geology, 200(1–2): 189–201, doi: 10.1016/S0009-2541(03)00188-8

Supplementary information:

Table S1. Major and trace element compositions of the basaltic pyroclastic rocks from Well CK-2, Xisha Islands, SCS.

Table S2. The chemical compositions of olivines of the basaltic pyroclastic rocks from Well CK-2, Xisha Islands, SCS.

The supplementary information is available online at https://doi.org/10.1007/s13131-025-2511-3 and http://www.aosocean.com/. The supplementary information is published as submitted, without typesetting or editing. The responsibility for scientific accuracy and content remains entirely with the authors.

Palaeogeography, Palaeoclimatology, Palaeoecology 675 (2025) 113082

Contents lists available at ScienceDirect

Palaeogeography, Palaeoclimatology, Palaeoecology

journal homepage: www.elsevier.com/locate/palaeo

Geochemical behavior of redox sensitive trace metals in marine environment and their applications as paleoredox proxies

Guo Ning [a], Jiang Wei [a,*], Li Yueer [a], Yu Kefu [a,b]

[a] Guangxi Laboratory on the Study of Coral Reefs in the South China Sea, School of Marine Sciences, Guangxi University, Nanning 530004, China
[b] Southern Marine Sciences and Engineering Guangdong Laboratory (Guangzhou), Guangzhou 528315, China

ARTICLE INFO

Editor: Bing Shen

Keywords:
Paleoredox
Rhenium
Uranium
Vanadium
Molybdenum
Marine deposits

ABSTRACT

The redox sensitive trace elements (RSTEs) are a group of trace metals that exhibit exceptional sensitivity to redox environments, with their transport and enrichment being constrained by prevailing redox conditions. Most of RSTEs are predominantly found in marine water as dissolved ions and tend to precipitate and accumulate in anoxic sediments under reducing conditions. The distinct behavior of RSTEs, such as rhenium (Re), uranium (U), vanadium (V), and molybdenum (Mo), has led to their widespread use as geochemical indicators to infer the redox state of marine sediments during deposition, and consequently, the oxygen levels in the overlying water and atmosphere. However, there are still gaps in our understanding of the redox transport and transformation processes of some RSTEs, and the application of certain indicators remains limited. In this review, we provide a detailed description of the geochemical behavior of typical RSTEs in the ocean. We also summarize a series of indicators that can be applied as proxies of seawater redox conditions. These indicators are based on the enrichment patterns of certain elements observed under varying redox conditions, including the elemental enrichment factor (TM_{EF}), excess trace metal concentration (TM_{XS}), elemental enrichment degree (TM/Al), bi-elemental ratios (Re/Mo, V/Cr, V/(V + Ni), V/Mn), Mo- and U-EF covariation patterns, and isotopic systems ($\delta^{98}Mo$, $\delta^{238}U$, $\delta^{51}V$, $\delta^{187}Re$). Considering local depositional environmental factors such as water chemistry, operation of Fe-Mn particle shuttle, sedimentation rate, and diagenesis are crucial for interpreting the enrichment patterns and the extent of isotope fractionation of RSTEs in marine sediments, providing valuable insights into the influence of hydrochemical conditions on the geochemical signatures of RSTEs across different geological periods. Therefore, the utilization of multiple independent geochemical proxies on the same sample and comparing data from temporally correlated profiles can yield a more robust and precise information about redox conditions and depositional environments of localized basins. Furthermore, we compiled data on the concentrations of Re, U, V, and Mo, as well as the isotope composition of Mo and U in ancient anoxic marine sediments from 3.5 billion years ago to the present. These data reveal the marine reservoirs of these elements, providing clues to the nature and timing of atmospheric oxidation on Earth. The results suggest that the Great Oxidation Event (GOE) was more like the climax of a long oxidation history starting from the Archean. In the millions of years after the end of the Lomagundi Event, the Earth may have remained well-oxygenated, until the oxygen level declined during the mid-Proterozoic. However, the records reveal at least two brief oxygenation events (ca. 1.4 Ga and 1.1 Ga) within this interval, contradicting the conventional view of persistently low oxygen concentrations throughout the mid-Proterozoic.

1. Introduction

In recent decades, the investigation of the geochemical behavior of redox sensitive trace elements (RSTEs) in seawater, such as vanadium (V), uranium (U), molybdenum (Mo), rhenium (Re), chromium (Cr), nickel (Ni), cadmium (Cd), and copper (Cu) and others, has garnered significant interest. These elements are highly sensitive to the redox conditions of the surrounding environment, and their distribution and migration in the ocean are regulated by many factors, mainly including dissolved oxygen, hydrogen sulfide concentration, and interactions with other substances. Among them, Mo, U, Re, and V in sediments are the four trace elements most commonly used to reconstruct redox conditions

* Corresponding author.
E-mail address: jianwe@gxu.edu.cn (J. Wei).

https://doi.org/10.1016/j.palaeo.2025.113082
Received 23 September 2024; Received in revised form 2 June 2025; Accepted 3 June 2025
Available online 6 June 2025
0031-0182/© 2025 Elsevier B.V. All rights are reserved, including those for text and data mining, AI training, and similar technologies.

and are important indicators for studying ocean oxygenation (Bennett and Canfield, 2020; Brumsack, 2006; Kunert and Kendall, 2023; Mänd et al., 2020; Ostrander et al., 2019; Sahoo et al., 2016; Tribovillard et al., 2012, 2006; Yang et al., 2023; Zhang et al., 2022b).

In this paper, we adopt the following the redox classification scheme for bottom waters based on dissolved oxygen and hydrogen sulfide concentrations: oxic (> 2.0 ml O_2 L^{-1}), dysoxic or suboxic (~0.2–2.0 ml O_2 L^{-1}), anoxic-nonsulfidic (< 0.2 ml O_2 L^{-1}, 0 ml H_2S L^{-1}), and anoxic-sulfidic or euxinic (0 ml O_2 L^{-1}, > 0 ml H_2S L^{-1}) (Fig. 1) (Algeo and Tribovillard, 2009). As two special minor elements, the redox cycles of iron (Fe) and manganese (Mn) profoundly influence the migration and enrichment processes of RSTEs (Tribovillard et al., 2006). Under oxic conditions, Fe and Mn accumulate in sediments as oxyhydroxides or oxides, which under suboxic and anoxic conditions can dissolve into the pore water and migrate to the sediment (Brumsack, 1989; Middelburg et al., 1987; Rajendran et al., 1992). Most RSTEs usually exist as soluble ions in oxic environment, with some being absorbed by plankton as nutrients/trace elements or co-cycled with redox-sensitive minerals such as Fe and Mn (oxy)hydroxides (Smrzka et al., 2019). Under low oxygen or reducing conditions, the behavior of RSTEs becomes more complicated, as they have the potential to precipitate from seawater as insoluble oxides, hydroxides, metal ligands, and organic complexes with lower valence (Crusius et al., 1996; Lv et al., 2021; McManus et al., 2006). This leads to varying distributions of RSTEs in different marine environments and their enrichment to varying extents (Fig. 1). Consequently, variations in the concentrations of RSTEs in siliciclastic rock (e.g., black shales or mudstones) have been commonly used for reconstructing environmental redox conditions. Furthermore, during the processes of redox, adsorption, and precipitation, RSTEs directly or indirectly experience measurable isotope fractionation (Ostrander et al., 2021). This property renders the isotope ratio of sedimentary rocks (e.g., siliciclastic rock and carbonates) yet another invaluable proxy in paleoredox investigations (Ostrander et al., 2021; Chen et al., 2021; Li et al., 2022).

Recent studies have found that RSTEs enrichment can be influenced by a range of factors beyond the redox conditions. Local depositional factors, such as the chemical composition of the water mass, variations in anoxic basins, fluctuations in sea level, and rates of sedimentation, all have significant impacts on the enrichment levels of RSTEs and the extent of their isotope fractionation (e.g., Liu and Algeo, 2020; Peng, 2022; Paul et al., 2023; Vind et al., 2023; Noordmann et al., 2015; Qin et al., 2022; Tan et al., 2023; Ostrander et al., 2019; Li et al., 2022; Lau et al., 2020). This is because these local depositional factors can regulate the distribution patterns of redox processes. For example, the presence of enclosed or semi-enclosed basins restricts water circulation, lowering the concentrations of RSTEs in seawater and subsequently influencing the extent of RSTEs enrichment and isotope compositions in sediments (e.g., Liu and Algeo, 2020; Noordmann et al., 2015; Tan et al., 2023; Ostrander et al., 2019; Kurzweil et al., 2015). Moreover, sedimentation rates exert a significant influence on the distribution/accumulation of RSTEs and their isotope compositions by modulating processes such as dilution of organic matter (via increased input of non-organic detrital components) and downward diffusion of trace metals (e.g., Crombez et al., 2020; Lau et al., 2020; Noordmann et al., 2015). Therefore, a comprehensive examination of the concentration, distribution, geochemical behavior, and isotopic composition of RSTEs in seawater and sediment is necessary for an advanced view of global environmental change, ecosystem functioning, and Earth's history.

In this paper, we aim to provide a thorough review of the geochemical behavior of RSTEs. Additionally, we will summarize the applications of RSTEs as widely accepted indicators for assessing the redox state of the marine environment, along with an examination of the local depositional and environmental parameters that exert influence on their distribution in sediments. Specifically, we provide a concise overview of the most important two minor elements, namely Fe and Mn, while placing emphasis on four RSTEs (Mo, U, Re, and V) and their isotopes. These RSTEs elements have been regarded as reliable indicators of paleoredox conditions due to their limited abundance in the Earth's crust, long residence times in seawater, diverse valence states, and deposition processes highly influenced by redox conditions.

2. Overview of RSTEs

Most RSTEs undergo biogeochemical cycling within the marine euphotic zone, either through primary producers or in conjunction with redox-sensitive minerals like Fe and Mn (oxy)hydroxides (Smrzka et al., 2019). The transport of RSTEs from the euphotic zone to the seafloor occurs at varying rates, including three primary carriers: (1) organic matter, (2) Fe(oxy)hydroxides, and (3) Mn(oxy)hydroxides, depending on their chemical speciation and association with solid-phase particles (e.g., Bertine and Turekian, 1973; Piper and Perkins, 2004; Smrzka et al., 2019; Goswami et al., 2012; Monien et al., 2014; Collier, 1984; Rudnicki and Elderfield, 1993; Auger et al., 1999), as visually depicted in Fig. 2. Typically, these particulate matters release RSTEs during the respiration and reductive dissolution processes near the sediment-water interface (Smrzka et al., 2019). Subsequently, these RSTEs may either diffuse into the oxic water column or become buried within the sediment (Smrzka et al., 2019).

2.1. Mn and Fe: key minor elements influencing RSTEs

The predominant species of Mn in seawater are Mn^{2+} and $MnCl^{+}$. However, under aerobic conditions, Mn(II) is inherently unstable and prone to oxidation, resulting in the formation of insoluble Mn(III) and particularly Mn(IV) (oxy)hydroxides (mainly MnO_2 and MnOOH) (Calvert and Pedersen, 1993; Rajendran et al., 1992). In oxic seawater, the most thermodynamically stable form of Fe is Fe(III), which undergoes rapid hydrolysis to generate various Fe(III) (oxy)hydroxides (mainly $Fe(OH)_3$) to its high insolubility (de Baar and de Jong, 2001). Under oxic conditions in marine water, both Mn(IV) and Fe(III) exist as (oxy)hydroxides, acting as oxidants during the oxidation of organic matter, following a predictable sequence (Froelich et al., 1979). After oxygen is consumed by organic matter, Mn(IV) generates Mn(II) in the pore water, and the subsequent production of Fe(II) in the pore water after nitrate is exhausted. Both of the aqueous ions can either diffuse upwards for re-oxidation or move downwards into sediment layers where sulfate reduction and methanogenesis dominate(Froelich et al., 1979). As the re-oxidation of Mn(II) generally occurs at a slower rate

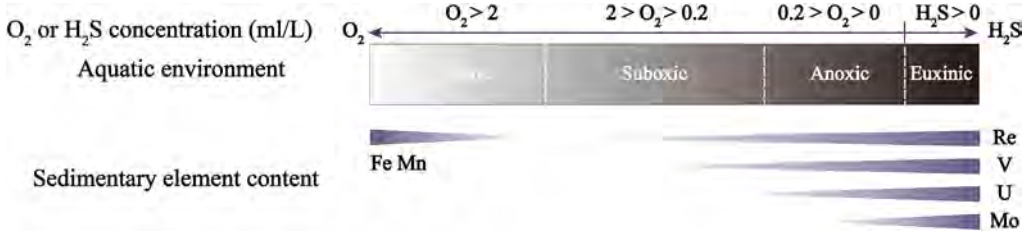


Fig. 1. Correlation between seawater ambient partitioning and variations in RSTEs concentration within sediments, modified from Tang et al. (2015).

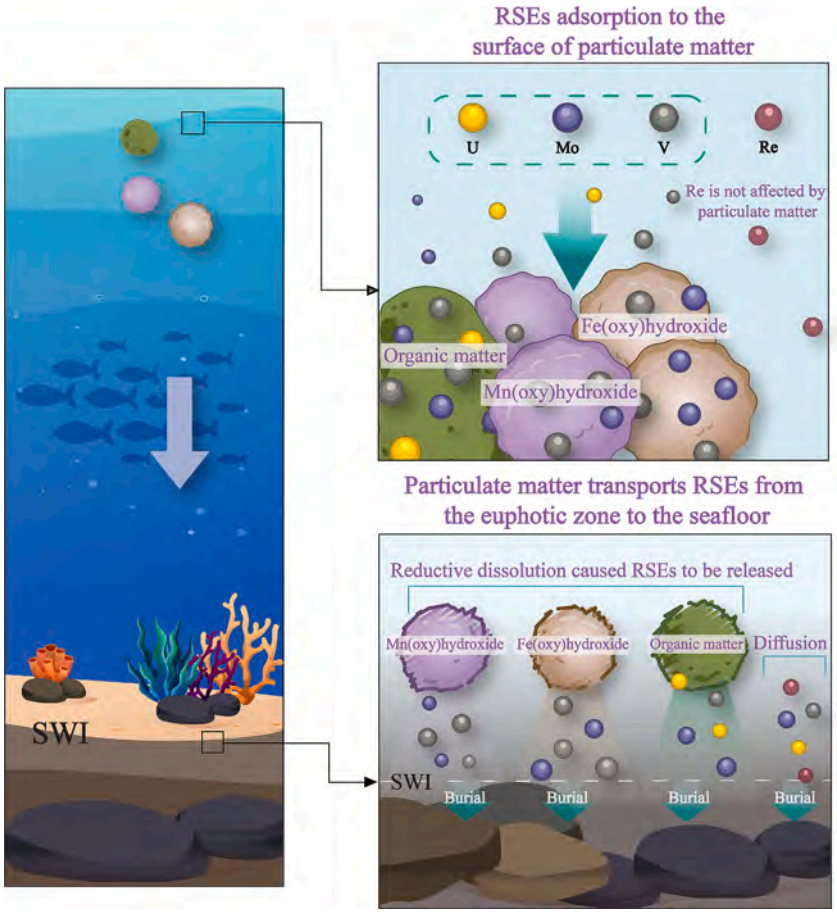


Fig. 2. Schematic representation of the circulation, adsorption, and transport of RSTEs in the water column to the seafloor, highlighting key solid-phase particles. SWI indicates sediment-water interface. The diagram incorporates three primary solid-phase particles: organic matter (depicted in green), Fe(oxy)hydroxide (depicted in brown), and Mn(oxy)hydroxide (depicted in purple). While it is possible for all four elements to adsorb onto all solid-phase particles, this depiction focuses on the most relevant elements associated with each phase, modified from Smrzka et al. (2019). (For interpretation of the references to colour in this figure legend, the reader is referred to the web version of this article.)

compared to that of Fe(II), Mn(II) released from the shallow layer preferentially diffuses into the overlying water column (Froelich et al., 1979; Olson et al., 2017). In contrast, Fe(II) released from deeper sulfate reduction zones is rapidly oxidized or sulfidized, which severely restricts its activity within the sediments (Froelich et al., 1979). When Fe(II) and Mn(II) diffuse downward into the sulfate reduction zone rich in H_2S, S (II) preferentially reacts with Fe(II) to form amorphous FeS (i.e., mackinawite). Subsequently, the FeS can be further transformed into pyrite (FeS_2) through the polysulfide pathway or the H_2S pathway (Rickard and Luther, 2007). Since the formation of FeS_2 in sediment is jointly controlled by the abundance of reactive Fe, H_2S, and partially oxidised sulphur in the water column, and is also highly reliant on the specific pathway of FeS_2 formation (e.g., Chang et al., 2020; Rickard, 1997; Rickard and Luther, 2007). Therefore, in pore waters rich in sulfides, Fe(II) may be depleted in the formation of FeS and FeS_2 (Rickard and Luther, 2007; Olson et al., 2017). Unlike the situation of Fe(II), Mn (II) typically precipitates as carbonate in the sulfate reduction zone (Jakobsen and Postma, 1989; Böttcher, 1998). This precipitation process significantly restricts the diffusion and migration of Mn(II) in pore water, ultimately resulting in almost no Mn available for the formation of authigenic pyrite (Böttcher, 1998). However, in sediments associated with pore waters enriched in sulfides and having a high Mn/Fe ratio, Mn (II) can serve as a secondary source of cations and partially substitute for Fe(II) in the pyrite lattice (Cui et al., 2023; Olson et al., 2017).

The distinctive geochemical behaviors of Fe and Mn are highly crucial in the transport of trace metals from the water column to the sediments, as well as their subsequent incorporation into the authigenic phase. In the oxic surface water column, the elevated concentration of dissolved oxygen facilitates the precipitation of Mn-(oxy)hydroxides and Fe-(oxy)hydroxides, thereby inducing substantial adsorption and precipitation of trace metals (Fig. 2). Upon approaching the sediment-water interface, trace metals adsorbed on Fe-Mn (oxy)hydroxides can be released and subsequently diffuse back into the water column or be captured by other solid phases (Fig. 2) (Olson et al., 2017; Tribovillard et al., 2006). The phenomenon, commonly referred to as the "particle shuttle," is essential for the enrichment of trace metals in suboxic-anoxic deposition systems by facilitating the transport and precipitation of trace metals from seawater into sediments (Algeo and Tribovillard, 2009).

In summary, the redox behavior of Fe and Mn controls the mobility and incorporation of trace metals. Mn and Fe (oxy)hydroxides efficiently scavenge specific reactive trace metals, such as Mo and V, either via surface adsorption or direct incorporation into their crystal lattice (Burdige, 1993). Consequently, these processes facilitate the cycling of associated RSTEs between the sediment and pore water, regulating their distribution and availability in the sedimentary environment.

2.2. Mo

Mo exhibits a significantly low abundance in the Earth's crust, with an average concentration of approximately 1.5 μg/g in the upper crust (McLennan, 2001). In contemporary seawater, Mo is found at an average concentration of approximately 0.010 μg/g (Collier, 1984). In oxic seawater, Mo predominantly exists as a stable molybdate oxyanion

(MoO_4^{2-}) (Bertine and Turekian, 1973). The residence time of Mo in seawater is estimated to be around 780 ka, which significantly exceeds the mixing time of seawater (1.5 ka) (Algeo and Tribovillard, 2009; Miller et al., 2011; Tribovillard et al., 2006).

Although MoO_4^{2-} has high solubility in oxic seawater, the adsorption of organic matter or Fe-Mn (oxy)hydroxides enables it to gradually accumulate even under oxic conditions (Bertine and Turekian, 1973; Piper and Perkins, 2004; Smrzka et al., 2019). This adsorption-mediated accumulation effectively facilitates the transportation of Mo from the water column to the sediment surface (Algeo and Lyons, 2006; Wagner et al., 2017). Under reducing conditions, the dissolution of Fe-Mn (oxy) hydroxides occurs, resulting in the release of MoO_4^{2-} into the ambient (pore) water. The fate of MoO_4^{2-} within the pore water depends on the concentration of ambient H_2S, as it may either re-diffuse back into the water column or be captured by more recalcitrant phases such as organic matter or Fe sulfides (Morford et al., 2005; Morford and Emerson, 1999). Under anoxic-euxinic conditions, MoO_4^{2-} undergoes sequential conversion to particle-reactive sulfur-containing Mo complexes such as thiomolybdates ($MoO_xS_{4-x}^{2-}$, x = 1–4) and molybdenum polysulphide (MoO$(S_4)S^{2-}$) (Helz et al., 1996). The thiomolybdate substances exhibit a pronounced affinity towards reactive surfaces and readily undergo adsorption or complexation onto metal-rich particles, organic matter, and iron sulfides for efficient removal (Fig. 3) (Emerson and Huested, 1991; Tribovillard et al., 2004; Zheng et al., 2002). As the ambient concentration of H_2S approaches the aquatic threshold, i.e., the "geochemical switch" of ~11 μM, MoO_4^{2-} is fully thiolated and converted into tetrathiomolybdate ion (MoS_4^{2-}) (Erickson and Helz, 2000). Therefore, Mo is typically highly enriched in euxinic sediments (Fig. 3C). It has also been demonstrated that sulfur-containing Mo complexes transform into an inert Fe-S-Mo nanomineral, and this transformation leads to a constant concentration of dissolved Mo in the water column or pore water, restricting further removal of Mo (Helz, 2022; Helz and Dolor, 2012). This process may explain why Mo enrichment in sediments is lower in strongly euxinic basins than in less euxinic basins (Helz et al., 2011; Helz and Dolor, 2012). However, significant fluctuations in the redox interface of the water column can potentially remobilize and release Mo from unstable euxinic sediments (e.g., Fe monosulfide (FeS)) back into the pore water (and subsequently bottom waters) (Dellwig et al., 2021; Hermans et al., 2019).

In summary, the enrichment of sedimentary Mo is largely influenced by the adsorption of Fe-Mn (oxy)hydroxides in oxic/suboxic water or by the sulphur effect of H_2S in euxinic ambient waters. In comparison to other RSTEs, Mo tends to exhibit greater vertical migration in sedimentary columns, and its immobilization is closely associated with the removal of iron sulphide phases or humic substances (Morford et al., 2009b; Morford and Emerson, 1999).

2.3. U

U is relatively scarce in the Earth's crust, with an average abundance of 2.8 μg/g in the upper crust (McLennan, 2001). In modern seawater, the average concentration of U is approximately 3.02×10^{-3} μg/g (Ku et al., 1977). Under oxic conditions and within the pH range of seawater, U mainly exists in the stable form of U(VI), where uranyl ions combine with carbonate ions to form soluble $UO_2(CO_3)_3^{4-}$ (Tribovillard et al., 2006). The residence time of U in seawater is shorter than that of Mo, averaging around 450 ka, yet still significantly higher than the mixing time of seawater (Ku et al., 1977).

In oxic seawater, U generally displays conservative behavior but can be adsorbed by organic matter (Goswami et al., 2012; Monien et al., 2014). The reduction and removal of U are primarily believed to occur in sediments instead of the water column due to the decoupling of U(VI)

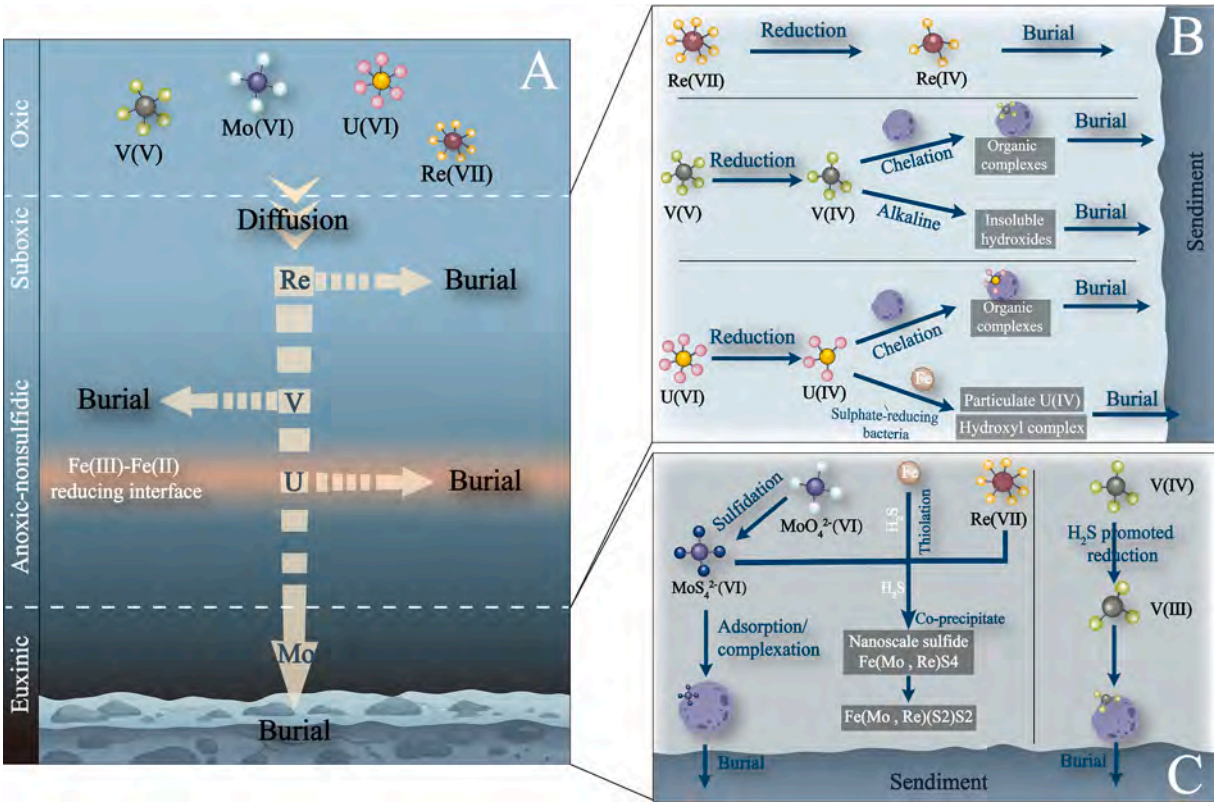


Fig. 3. Schematic illustration of the enrichment mechanism of RSTEs from water to sediment, no scale implied. A: Reduction sequence of RSTEs in waters with different degrees of oxidation, Referring to Algeo and Li (2020); B: Enrichment mechanism of RSTEs in suboxic-anoxic waters (no H_2S); C: Enrichment mechanism of RSTEs in euxinic waters. Enrichment of all RSTEs occurs under euxinic condition, the focus here, however, is on elements that are associated with H_2S in the water column.

reduction to U(IV) from the free H_2S concentration in the water column (Algeo, 2004; McManus et al., 2005; Zheng et al., 2002). Thus, the transport of U from the euphotic zone to the seafloor and sediments is primarily governed by dissolved oxygen concentrations and fluxes of organic matter (McManus et al., 2006, 2005). However, coupling between the cycling of Fe and U has been observed in sediments, indicating that Fe hydroxyoxides possess the capability to scavenge U or that microorganisms facilitate the transformation of these two substances (Beck et al., 2008; Lovley et al., 1993, 1991). Under the reduced state, U enrichment in sediments is promoted through two pathways: (1) the formation of organometallic ligands for U in humic acids (Klinkhammer and Palmer, 1991; McManus et al., 2005; Zheng et al., 2002), and (2) the conversion of soluble and unreactive U(VI) to insoluble and particulate-reactive U(IV) under the Fe(III)-Fe(II) reducing interface (Fig. 3) (Helz et al., 1996; Morford et al., 2007, 2005; Zheng et al., 2002). The result of this process is the formation of crystalline uraninite (UO_2) or its metastable precursor, along with highly surface-active hydroxyl complexes, ultimately leading to authigenic enrichment (Klinkhammer and Palmer, 1991; Zheng et al., 2002). The thermodynamic equilibrium governs the reduction kinetic process of U(VI) in sediments by synergistically modulating redox potential (Eh) and pH values (Zheng et al., 2002). Nevertheless, it is widely postulated that this reduction process is mediated by Fe and sulfate-reducing bacteria (Zheng et al., 2002). This is due to the fact that, in the absence of a catalyst, the abiotic reduction process of U(VI) is typically characterized by sluggish kinetics (Swarzenski et al., 1999). Within sediments, U is present in two forms: refractory crystalline uraninite and unstable monomeric "non-crystalline U(IV)", which is usually bound to organic matter and organic carbonaceous clays (Bernier-Latmani et al., 2010; Bone et al., 2017). The unstable mineral structure of monomeric U(IV) makes it susceptible to oxidation back to U(VI) through interactions with dissolved oxidants like oxygen (O_2) or solid oxides such as Fe-Mn (oxy)hydroxides can subsequently diffuse, either upward into the overlying water column or downward into the sediments (Cochran et al., 1986; Dellwig et al., 2021; McManus et al., 2005; Paul et al., 2023; Zheng et al., 2002).

In summary, the reduction of U occurs in close proximity to the Fe (III)-Fe(II) redox interface and is likely controlled by microbial-mediated Fe redox reactions, with little influence from the presence or absence of H_2S (Fig. 3). The deposition of U, unlike Mo, occurs under in sedimentary environment under less reducing conditions and at shallower depths (Fig. 3A). Its fixation primarily relies on the organic matter concentration present in the sediment.

2.4. V

Species of V in the environment is primarily governed by pH and redox conditions (Calvert and Pedersen, 1993). In marine environments, V exhibits a nutrient-like distribution and participates in biological cycling processes (Collier, 1984; Smrzka et al., 2019). The abundance of V is low in the Earth's crust, with an average of 2.7 μg/g in the upper crust and an average concentration of about 1.49×10^{-3} - 1.99×10^{-3} μg/g in modern seawater (Collier, 1984; Jeandel et al., 1987; Shen and Boyle, 1987). In oxic waters, V mainly exists as stabilized vanadate with the dominant species being HVO_4^{2-} and H_2VO^{4-}. V has a long residence time in the ocean ranging from approximately 50 ka to 130 ka (Morford and Emerson, 1999; Wanty et al., 1990).

In addition to being influenced by biological ingestion and release in oxic waters, the distribution of V is predominantly controlled by adsorption onto mineral surfaces, particularly Fe-Mn (oxy) hydroxides (Auger et al., 1999; Collier, 1984; Rudnicki and Elderfield, 1993). V readily adsorbs onto these sinking particles and subsequently diffuses from seawater, which is considered the most efficient transport mechanism of V from seawater to sediments (Piper and Calvert, 2009; Prange and Kremling, 1985). In weakly reducing environments, V(V) undergoes reduction to V(IV) and form vanadyl (VO^{2+}), which has a small ionic radius and is highly susceptible to chelation with organometallic ligands, leading to the formation of organic complexes or hydrides that are enriched in anoxic sediments (Fig. 3B) (Morford and Emerson, 1999). Under alkaline conditions in seawater, VO^{2+} species undergo hydrolysis to produce hydroxyl groups ($VO(OH)_3^-$) and the insoluble hydroxide $VO(OH)_2$ (Fig. 3B) (Emerson and Huested, 1991; Morford and Emerson, 1999). This process is more favorable in the presence of humic and fulvic acids (Emerson and Huested, 1991; Morford and Emerson, 1999). Although V(IV) does not form stable sulfides with H_2S, its adsorption onto particulate matter is significantly enhanced in the presence of sulfides in pore water (Fig. 3C) (Wehrli and Stumm, 1989). This is because V(IV) is more likely to form complexes with organic or inorganic ligands, and is more surface reactive compared to vanadates. Under euxinic conditions, free H_2S further reduces V(IV) to V(III), which can then be captured by surrounding porphyrin or precipitate as solid oxides such as V_2O_3 or the hydroxide $V(OH)_3$ (Breit and Wanty, 1991; Wanty and Goldhaber, 1992). Consequently, V typically tends to accumulate in the organic matter fraction of sediments rather than in pyrite or other euxinic minerals (Breit and Wanty, 1991). It has been suggested that the higher abundance of V in black shales under highly reducing conditions, which may be due to higher concentrations of H_2S, is a result of V reduction and sequestration in the sediments (Tribovillard et al., 2006). However, it has been noted that V enrichment in sediments from the oxygenated minimum zones is higher than in sediments deposited in the anoxic and euxinic water columns (Bennett and Canfield, 2020). Cui et al. (2023) and Kunert et al. (2020) have also concluded that highly euxinic conditions are not necessary for high V enrichment. They propose that elevated V concentrations in sediments could be attributed to (i) increased V concentrations in the water column resulting from the desorption and dissolution of Mn oxides following the influx of high Mn particulate flux into weakly anoxic environments, and (ii) moderately restricted environments with either strong or weak sulfidation, where robust water exchange at the seafloor continuously supplies V from the open ocean to the sediments.

To summarize, the removal of V from seawater is influenced by biological uptake, Fe-Mn (oxy)hydroxide, and redox processes. Both V and Mo are affected by the "particle shuttle," but there are significant differences between them. Surface seawater experiences a slight depletion in V due to the incorporation of biological or detrital particles (Collier, 1984). V enrichment occurs in suboxic-euxinic ambient and is shallower than Mo and deeper than Re in the sedimentary environment (Fig. 3A) (Tang et al., 2015). V tends to accumulate in the organic matter fraction of sediments due to stable complexation. During transient oxidation events, reduced V in sediments may undergo re-oxidation to V (V), which can destabilize the authigenic V phase (Wehrli and Stumm, 1989). Additionally, occasional bottom water oxidation can enhance carbon turnover and decrease the retention of recalcitrant organic compounds, potentially leading to the re-dissolution of solid-phase V (Wu et al., 2020).

2.5. Re

The crustal abundance of Re is extremely low, measuring approximately 0.4×10^{-3} μg/g, while its average concentration in modern seawater falls within the range of approximately 3.63×10^{-6} to 1.63×10^{-5} μg/g (Anbar et al., 1992; McLennan, 2001). Re is primarily delivered to the ocean via rivers and behaves conservatively in seawater, predominantly existing as dissolved oxidized perrhenate (ReO_4^-) (Anbar et al., 1992). Re demonstrates an extended residence time in seawater, averaging around 750 ka, surpassing significantly the mixing time of the oceanic water (Colodner et al., 1993).

In oxic seawaters, Re undergoes neither "particle shuttle" processes nor significant scavenging by organic or terrestrial particles, resulting in a sluggish accumulation rate (Colodner et al., 1993). In weakly oxic and anoxic seawater environments, the efficiency of Re enrichment is much higher (Colodner et al., 1993; Crusius et al., 1996; Morford et al., 2012). The migration of Re from the water column to sediments primarily

occurs through diffusion across the sediment-water interface, followed by the reduction of Re(VII) to Re(IV) solid-phase compounds in pore water (Fig. 3B) (Colodner et al., 1993). In suboxic water conditions prevalent in continental margin environments, authigenic Re enrichment occurs when shallow pore water becomes anoxic, with low H_2S concentrations but without simultaneous significant Mo accumulation, suggesting that Re enrichment is not strongly influenced by H_2S (Colodner et al., 1993; Morford et al., 2005; Morford and Emerson, 1999). However, it has also been suggested that dissolved sulfides in anoxic waters are key in controlling the speciation of Re by converting ReO_4^- to the dissolved sulphide species form, such as $Re(HS)_4^0$ (Helz, 2022; Helz and Dolor, 2012; Xiong, 2003; Živković et al., 2023). A positive correlation between Re concentration and total organic carbon (TOC) concentration was observed in some organic matter-rich sediments, indicating the scavenging of Re by organic matter (Rooney et al., 2010). Crusius and Thomson (2000) found in their study of marine sediments that Re concentration reached a minimum in the pyrite-enriched layer. This result suggests that the chemical properties of Re may prevent it from binding with pyrite. Therefore, its behavior is analogous to that of U, which is enriched in organic matter sediments and is not incorporated into pyrite under anoxic-euxinic conditions (Crusius and Thomson, 2000; Koide et al., 1987; Ravizza et al., 1991). Recent research proposes new perspectives on the removal mechanisms of Re and Mo in euxinic deposition environments, where both elements co-precipitate with Fe and S in euxinic waters (Helz, 2022; Helz and Dolor, 2012; Živković et al., 2023). The concentrations of Re and Mo in the euxinic water column are observed to start decreasing at the same location and reach asymptotes at similar depths, indicating their co-precipitation (Helz, 2022; Živković et al., 2023). The coprecipitate is a nanoscale sulphide, $Fe(Mo, Re)S_4$, which undergoes irreversible transformation by internal electron transfer to the product represented by $Fe(Mo, Re)(S_2)S_2$ (Helz, 2022; Živković et al., 2023).

When the bottom water column is weakly oxic or anoxic, Re can efficiently migrate into anoxic sediments at low levels of dissolved H_2S, making it a reliable proxy for tracking general marine anoxia (i.e., including euxinic and ferruginous anoxic) (Colodner et al., 1993; Crusius et al., 1996; Morford et al., 2012, 2005; Morford and Emerson, 1999). Although V and U exhibit similar behavior, the authigenic enrichment of Re in anoxic marine sediments is significantly higher than the crustal background concentration. This suggests that Re is more sensitive to O_2-deficient conditions than V and U, potentially providing more precise and quantitative information about the redox state of the deep ocean (Fig. 3A) (Sheen et al., 2018).

3. Influence of local depositional factors on RSTEs

Historically, it has been common to focus the causes of RSTEs enrichment in marine sediments on a narrow selection of factors, mainly the redox conditions (Algeo and Tribovillard, 2009; Helz et al., 1996; Paul et al., 2023; Peng, 2022). However, the enrichment of RSTEs in sediments is influenced by several "secondary" local depositional factors beyond the primary control of local redox conditions (Liu and Algeo, 2020; Peng, 2022). In recent years, geologists have started to address concerns regarding the impact of additional potential local depositional factors, such as the operation of Fe-Mn particle shuttle, the chemistry of the water column in the basin (seawater RSTEs concentrations), and the effects of sedimentation rates and diagenesis on the mechanisms of RSTEs enrichment in both modern and ancient marine sediments (e.g., Algeo and Rowe, 2012; Crombez et al., 2020; Liu and Algeo, 2020; Peng, 2022; Vind et al., 2023). The purpose of this section is not to reiterate the previous assessments of influences observed in RSTEs analyses (e.g., Xie et al., 2019; Zhang et al., 2022b). Instead, the emphasis is on discerning the impact of these "secondary" local depositional factors, which are crucial for reliably reconstructing paleo-redox depositional environments using geochemical indicators based on these elements.

3.1. Basin restriction

The concentration of dissolved RSTEs in the water column exerts a significant influence on RSTEs enrichment in sediments (Algeo and Lyons, 2006; Algeo and Rowe, 2012). Most RSTEs exhibit prolonged residence times in seawater (Tribovillard et al., 2006), resulting in minimal concentration changes in open ocean systems over short time scales. In open ocean basins, owing to well-circulated seawater, the concentration of RSTEs in sedimentary basins aligns with the global average seawater concentration (Tribovillard et al., 2012). Under these conditions, the enrichment of sedimentary RSTEs can reflect the reducing conditions of the underlying seawater (Fig. 4a). In semi-enclosed or closed ocean basins, the reduction in global ocean recharge of RSTEs into basin waters and their effective burial in sediments beneath anoxic conditions has resulted in a decrease in dissolved RSTEs reservoirs within local basins (Algeo and Lyons, 2006; Algeo and Rowe, 2012). Changes in the confinement degree of these basins, whether due to sea level fluctuations or tectonic processes, can subsequently impact the rate of RSTEs recharge or authigenic uptake (Liu and Algeo, 2020; Peng, 2022). These dynamics can lead to significant fluctuations in RSTEs abundance within sediments (Fig. 4bc). Therefore, when analyzing sedimentary redox environmental conditions, it is crucial to identify basin types that offer a plausible explanation for the depositional environment.

The Mo/TOC ratio is widely recognized as a valuable indicator for assessing the timing of water mass renewal under anoxic conditions. It reflects the availability of seawater elements and helps assess the degree to which hydrological conditions influence sedimentation in different basins (e.g., Algeo and Lyons, 2006; Liu and Algeo, 2020; Sahoo et al., 2012; Scott et al., 2008). Mo usually shows a strong positive correlation with TOC due to the significant uptake of organic matter (Algeo and Lyons, 2006). When the hydrological connection between the basin and the open ocean is weak, bottom water often has lower Mo availability, resulting in a lower Mo/TOC ratio in the sediments (Algeo and Lyons, 2006). Within several contemporary anoxic-euxinic marine systems with varying degrees of water body confinement, the sedimentary Mo/TOC ratios exhibit clear yet variable patterns (Tribovillard et al., 2012; Algeo and Lyons, 2006). Mo/TOC ratios in unconfined marginal sea basins hover around 45 ppm/%, aligning with seawater Mo concentrations close to global averages (e.g., Saanich Inlet, Canada; Algeo and Lyons, 2006). The Mo/TOC ratio in the weakly restricted, silled basins Cariaco Basin is about 25 ppm/% (Algeo and Lyons, 2006). Contrarily, Mo/TOC ranges from about 9 to 4.5 ppm/% in highly restricted Norwegian Framvaren Fjord and approximately 4.5 ppm/% in the strongly confined Black Sea, where seawater Mo concentrations exhibit a significant reduction compared to global averages (Algeo and Lyons, 2006). Therefore, when conducting analytical comparisons of marine sedimentary environments, it is feasible to juxtapose processed sample Mo/TOC ratio data against values from known modern ocean basin data points (Fig. 5). This approach allows for discriminating and assessing the extent of limitation in anoxic-sulfidic basins, furnishing crucial perspectives on the hydrological characteristics of marine sedimentary basins. However, it is important to consider a significant factor when using sediment Mo/TOC as a proxy for local water column limitation: during periods of widespread oceanic anoxia, the global marine reservoir of dissolved Mo was considerably lower than in the modern ocean (Fig. 13). Therefore, a low Mo/TOC ratio in sediments may not solely indicate strict basin-specific limitation but could also reflect global Mo depletion (e.g., Chen et al., 2022c; Tan et al., 2023; Zhu et al., 2022). Additionally, thermal maturation can lead to the loss of sedimentary TOC, impacting the use of metal/TOC ratios in inferring depositional conditions (Ardakani et al., 2016; Yang et al., 2023). To date, specific threshold qualifications akin to Mo have not been extensively established for other RSTEs in modern marine systems, although some RSTE/TOC analyses have been conducted (e.g., Gill et al., 2021; Liu and Algeo, 2020; Peng, 2022). Nonetheless, similar principles should theoretically

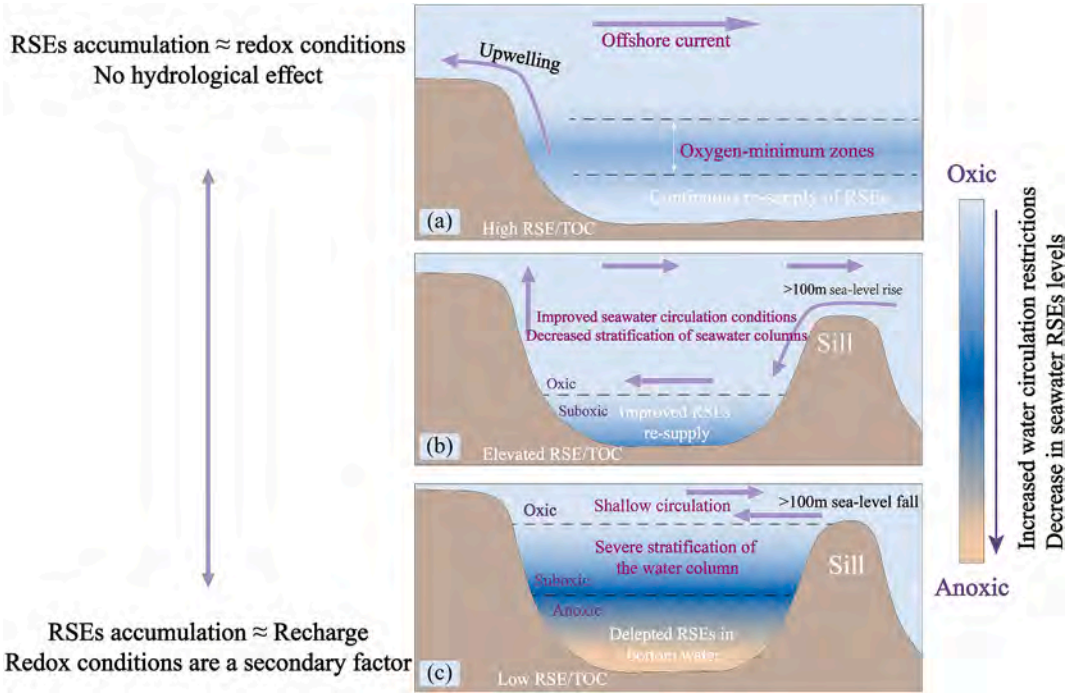


Fig. 4. Pattern diagram of the influence of water chemistry conditions on RSTEs enrichment patterns, modified from Tang et al. (2015) and Peng (2022).

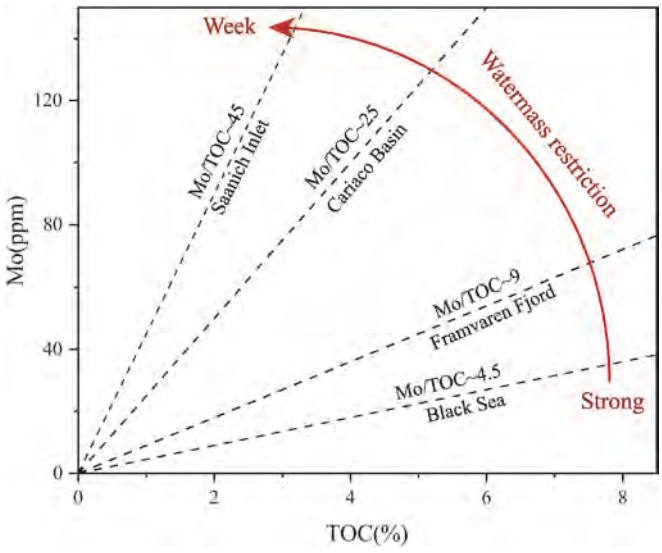


Fig. 5. TOC versus Mo concentration cross-plot, modified from Algeo and Lyons (2006). The dashed lines represent Mo/TOC in four modern basins with different degrees of limitation. The severity of limitation increases from Saanich Inlet to the Black Sea.

apply to other RSTEs as observed with Mo (Liu and Algeo, 2020).

3.2. Sedimentation rate

In recent years, sedimentation rate has been recognized as a potential factor influencing the extent of autochthonous RSTEs enrichment in marine sediments. It controls the extent of dilution of secondary sediment components (e.g., organic matter particles) and the downward diffusion of reactants (e.g., metallic elements, sulfates) (Andersen et al., 2014; Jobe et al., 2012; Sommerfield and Nittrouer, 1999). All else being equal, lower sedimentation rates increase the accumulation of RSTEs by prolonging the residence time of sediments in the RSTEs diffusion zone near the sediment-water interface (Liu and Algeo, 2020). However, it has been argued that low sedimentation rates increase the exposure time of surface sediments to oxygen, thereby enhancing the likelihood of their remobilization and consequent loss of RSTEs (Mangini et al., 2001; Crusius and Thomson, 2003). In contrast, high sedimentation rates facilitate rapid burial of sediments, reducing oxidation of organic matter (Crusius and Thomson, 2003; Mesa-Fernández et al., 2022) and thereby enhancing the preservation of RSTEs. Liu and Algeo (2020) demonstrated a linear negative correlation between authigenic Mo and U concentrations in sediments and sedimentation rates in basins with similar redox conditions, using a diffusion-reaction model. This indicates that sedimentation rate significantly impacts the authigenic enrichment levels of Mo and U in sediments (Liu and Algeo, 2020; Vind et al., 2023), crucially affecting the reliability of Mo- and U-based redox proxies. Failure to consider sedimentation rates when applying these elemental geochemical proxies across basin scales could potentially result in misinterpreting paleoenvironmental conditions. Crombez et al. (2020) suggested that differences in sedimentation rates exceeding an order of magnitude could significantly enrich (at low sedimentation rates) or dilute (at high sedimentation rates) the concentration of the authigenic component of RSTEs. When concentrations of the authigenic component of RSTEs surpass the detrital component by at least an order of magnitude, they become more robust indicators of paleoenvironmental change. Proxies based on the ratio of two authigenic compositions (e.g., Mo/TOC, Mo/U) may offer better correction for elemental enrichment in low detrital-origin samples rich in organic matter, as they respond proportionally to variations in sedimentation rates (Crombez et al., 2020).

3.3. Operation of the water column particle shuttle

Fe and Mn (oxy)hydroxides play a pivotal role in the distribution and enrichment of RSTEs by accelerating the uptake of certain elements from seawater into sediments and reactivating some of the elements in the vicinity of the aqueous chemocline (Morford et al., 2005; Algeo and Tribovillard, 2009; Tribovillard et al., 2012). This process is known as "particle shuttle". More specifically, insoluble Fe/Mn (oxy)hydroxides form in surface-oxygenated water and adsorb dissolved RSTEs as they

sink to the seafloor. When these particulate Fe/Mn (oxy)hydroxides enter the deep, anoxic bottom water environment, they dissolve under reducing conditions, releasing Fe, Mn, and adsorb RSTEs ions (Morford et al., 2005; Morford and Emerson, 1999). Once released, they engage in a new series of reactions, such as binding with sulfides and immobilization in solid phases, leading to a shift in the position of elemental enrichment (Algeo and Maynard, 2004; Helz et al., 1996; Helz and Vorlicek, 2019; Paul et al., 2023). Both Mo and V are impacted by Fe-Mn particle shuttle, whereas the adsorption of Re and U onto these phases is significantly weaker than Mo and V. Therefore, the operation of Fe-Mn shuttles does not substantially affect U and Re enrichment. As a result, active particle shuttle typically lead to notably higher authigenic Mo/U ratios compared to unrestricted oceanic systems (Morford et al., 2005; Algeo and Tribovillard, 2009; Tribovillard et al., 2012). This phenomenon is well documented in both modern (e.g., Cariaco Basin) and various paleoceanic systems (Algeo and Tribovillard, 2009; Tribovillard et al., 2012). Based on differences in geochemical behavior during Mo and U deposition, Algeo and Tribovillard (2009) proposed using Mo- and U-EF (EF is enrichment factor, see definition in Section 4.1) covariation patterns to identify trends in "particle shuttle", which have been widely applied to ancient and modern marine systems (e.g., Ostrander et al., 2019; Paul et al., 2023; Tan et al., 2023; Yang et al., 2023; Yuan et al., 2023; Zhu et al., 2022). The influence of "particle shuttle" effects in the water column can be discerned by examining the Mo_{EF}/U_{EF} ratio in sediments (Mo_{EF}/U_{EF} ratios typically ranging from 3 to 10 × seawater), as detailed in Section 4.3 below.

Additionally, Fe-Mn (oxy)hydroxides preferentially adsorb lighter Mo isotopes, resulting in lower δ^{98}Mo values in sediments (Barling and Anbar, 2004; Scholz et al., 2013; Cheng et al., 2016). Compared to other RSTEs, V exhibits a stronger affinity for oxide minerals, leading to its significant enrichment in Fe/Mn (oxy)hydroxides (Scott and Lyons, 2012; Tribovillard et al., 2012; Hein and Koschinsky, 2014; Ostrander et al., 2019). Therefore, the particle cycling effect of Fe/Mn (oxy)hydroxides not only decreases Mo isotopes in sediments but also results in notable enrichment of V relative to Mo, U, and Re. Consequently, the observation of a more pronounced negative correlation between the degree of V enrichment in sediments and δ^{98}Mo values has increasingly been used to identify the operation of Fe-Mn particle shuttle in the water column (Ostrander et al., 2019; Kunert et al., 2020; Chen et al., 2022c; Tan et al., 2023).

3.4. Diagenesis

Diagenesis is a pervasive process in sediments, and the element migration during diagenesis often modifies the degree of enrichment or depletion of RSTEs generated by the original depositional environment (Nameroff et al., 2002). This alteration leads to distributions of these elements that deviate from the original environmental conditions, introducing bias in the application of these elemental indicators for paleoenvironmental reconstruction (Tribovillard et al., 2006). For example, during early diagenesis, microbial-mediated organic matter degradation and mineralization, accompanied by the formation of authigenic minerals, induce simultaneous elemental redistribution and isotopic fractionation, modifying the primary geochemical records preserved in sediments (Berner, 1980; Deming and Baross, 1993; Aller, 2014; Scholz et al., 2011; Li et al., 2021; Lau et al., 2020; Kendall et al., 2009). This may be more pronounced in some sedimentary systems (Morford et al., 2009a), such as those experiencing seasonal or annual variations in sediment organic carbon fluxes, bottom water oxygen concentrations, oxygen penetration depths, and the intensity of bioturbation and irrigation due to water mass dynamics (e.g., in some lakes, Sholkovitz and Copland, 1982) or semi-enclosed basins with deep-water circulation (e.g., Saanich Inlet, Anderson and Devol, 1973). Diagenetic processes can superimpose sedimentary geochemical signatures on sedimentary rocks, which will further affect their record of the characteristics of the true historical environment. Therefore, diagenesis must be carefully considered when interpreting paleo-redox conditions.

Based on petrological and geochemical evidence, diagenesis and metamorphism of organic-rich mudstones and shales are characterised by the following features: high thermal maturity of organic matter; geochemical/mineralogical/structural indicators of thermochemical sulphate reduction and organic matter oxidation; the presence of coarse-grained pyrite nodules (indicative of diagenetic S and Fe elemental transport); the formation of diagenetic or metamorphic minerals (e.g., magnetopyrite is a metamorphic alteration product of pyrite); the formation of calcite veins, and the authigenic quartz fraction (e.g., Ardakani et al., 2016; Cai et al., 2015; Fantle et al., 2020; Zhao and Jin, 2021). Additionally, reasonable Re-Os isochron ages can demonstrate that post-depositional processes have not affected organic-rich mudstones and shales (Kendall et al., 2009; Rooney et al., 2010), providing a reliable basis for the use of redox proxies.

Currently, the assessment of the degree to which carbonate rocks have been altered during diagenesis and subsequent processes primarily relies on analyzing petrographic and mineralogical characteristics, supplemented by techniques based on elemental geochemistry for further interpretation. Techniques such as optical microscopy (diagenetic crystals and dolomite), scanning electron microscopy (detecting the presence of secondary mineral components in crystal structures), cathodoluminescence (spatial distribution of Fe^{2+} and Mn^{2+} contents), and X-ray diffraction (detecting mineral phase transitions and changes in lattice parameters) are applied to assess whether carbonates have undergone diagenesis and the extent of alteration (Swart, 2015; Li et al., 2023a; Fantle et al., 2020; Kaufman and Knoll, 1995; Warren, 2000; Kaczmarek and Thornton, 2017). Using multiple isotopic and trace element proxies (e.g., the loss of trace elements such as Sr and Mg; changes in isotopic ratios like δ^{13}C, δ^{18}O, $\delta^{44}/^{40}$Ca, and δ^{26}Mg; and characteristic trace element ratios such as Sr/Ca, Mg/Ca, and Mn/Sr) provides insights into carbonate diagenetic types, evolutionary history, and the degree to which redox indicators are affected across various spatial scales (e.g., Kaufman and Knoll, 1995; Peng et al., 2016; Brand and Veizer, 1981, 1980; Fantle and Higgins, 2014; Lau et al., 2017; Ahm et al., 2018, 2019; Higgins et al., 2018; Fantle et al., 2020; Murray et al., 2021; Lau and Hardisty, 2022). By integrating mass balance equations, isotope fractionation coefficients, and reactive transport models, researchers can invert diagenetic fluid compositions (e.g., freshwater/seawater mixing ratios), quantify diagenetic timescales of diagenetic events, and fluid fluxes (e.g., Ahm et al., 2018, 2019, 2021; Fantle et al., 2020; Lau and Hardisty, 2022; Akhtar et al., 2024). An example is the coupled Ca-Mg isotope system, whose synergistic fractionation pattern can serve as a precise geochemical fingerprint to distinguish between the "seawater-buffered" and "sediment-buffered" diagenetic conditions (Ahm et al., 2018, 2019, 2021; Lau and Hardisty, 2022; Akhtar et al., 2024). With the continuous improvement of these techniques and methods, we can integrate them to obtain more comprehensive and accurate diagenetic records. This allows for a more precise and detailed analysis of the geochemical characteristics of carbonate, thereby enhancing our understanding of diagenesis and sedimentary environments.

4. Methods for RSTEs to reconstruct the redox state

4.1. Extent of authigenic trace metal enrichment

Sediment RSTEs are crucial parameters for indicating the redox state of the depositional environment(e.g., Calvert and Pedersen, 1993; Crusius et al., 1996; Tribovillard et al., 2006; Scholz et al., 2011; Scott and Lyons, 2012). However, variations in the amount of RSTEs found in sediments, due to their diverse sources and characteristics, can significantly impact analysis results (Piper and Calvert, 2009). Therefore, it is necessary to process the concentration data of RSTEs obtained from rock samples through calibration or normalization. Only authigenic enrichment, which corrects for the detrital fraction, can be used to reconstruct

the redox state at the time of deposition. Various approaches exist for standardizing RSTEs in sediments, with the most widespread one being the use of Al levels (and also Th or Ti) as a standardizing element in sediments with low terrestrial detrital influx and high biogenic fraction (Van der Weijden, 2002). Although there are some limitations in adopting Al as a reference system, most studies have demonstrated that standardization of the obtained RSTEs elemental concentration by Al is still a practical and effective method (Tang et al. (2015) and their references therein). Currently, three proverbially recognized approaches are used for estimating authigenic trace metal enrichment: the enrichment factor (TM_{EF}, e.g., Calvert and Pedersen, 1993; Tribovillard et al., 2004), excess trace metal concentration (TM_{XS}, e.g., Jokinen et al., 2020; Scholz et al., 2013), and TM/Al ratio (e.g., Bennett and Canfield, 2020).

4.1.1. TM_{EF} and TM_{XS}

The TM_{EF} is a parameter used to evaluate the relative enrichment or depletion of a geochemical element in a sample compared to its abundance in the standard background (Tribovillard et al., 2012, 2006). It is typically expressed as:

$$TM_{EF} = \left(X/Al\right)_{Sample} \Big/ \left(X/Al\right)_{Pass} \quad (1)$$

Calculated TM_{EF} values can be categorized as follows: $TM_{EF} < 1$ indicates elemental depletion, $TM_{EF} > 1$ indicates elemental enrichment with respect to the crustal context, $TM_{EF} > 3$ indicates detectable autochthonous enrichment, and $TM_{EF} > 10$ indicates significant enrichment (Algeo and Lyons, 2006; Tribovillard et al., 2004). TM_{XS} is calculated by subtracting the amount of detrital input in sediments, to some extent reflecting the authigenic deposition of this element from seawater into sediment (Bennett and Canfield, 2020; Brumsack, 2006). TM_{XS} is calculated using the formula:

$$TM_{XS} = TM_{Sample} - \left(TM/Al\right)_{Reference} \times Al_{Sample} \quad (2)$$

The replacement values of the standard background values typically come from average shale (Turekian and Wedepohl, 1961), upper continental crust (UCC, McLennan, 2001), and Post-Archean Australian shale (PAAS, Taylor and McLennan, 1995). Both TM_{EF} and TM_{XS} are important parameters used to assess the redox conditions of depositional environments. TM_{XS} is mainly used to calculate the authigenic part of an element in sediments or sedimentary rocks to distinguish whether the element originates from seawater or terrigenous detritus. If the TM_{XS} value is large, the element is significantly affected by the processes within the sedimentary environment. Conversely, a small value indicates that the element mainly comes from terrigenous input. TM_{EF}, on the other hand, is used to determine whether an element in sediments or sedimentary rocks is enriched, and then infer the redox state of the sedimentary environment accordingly.

4.1.2. TM/Al ratio

To more accurately infer the redox state of ancient marine depositional environments, Bennett and Canfield (2020) recommended integrating enrichments of Mo, U, V, and Re for comprehensive analysis.

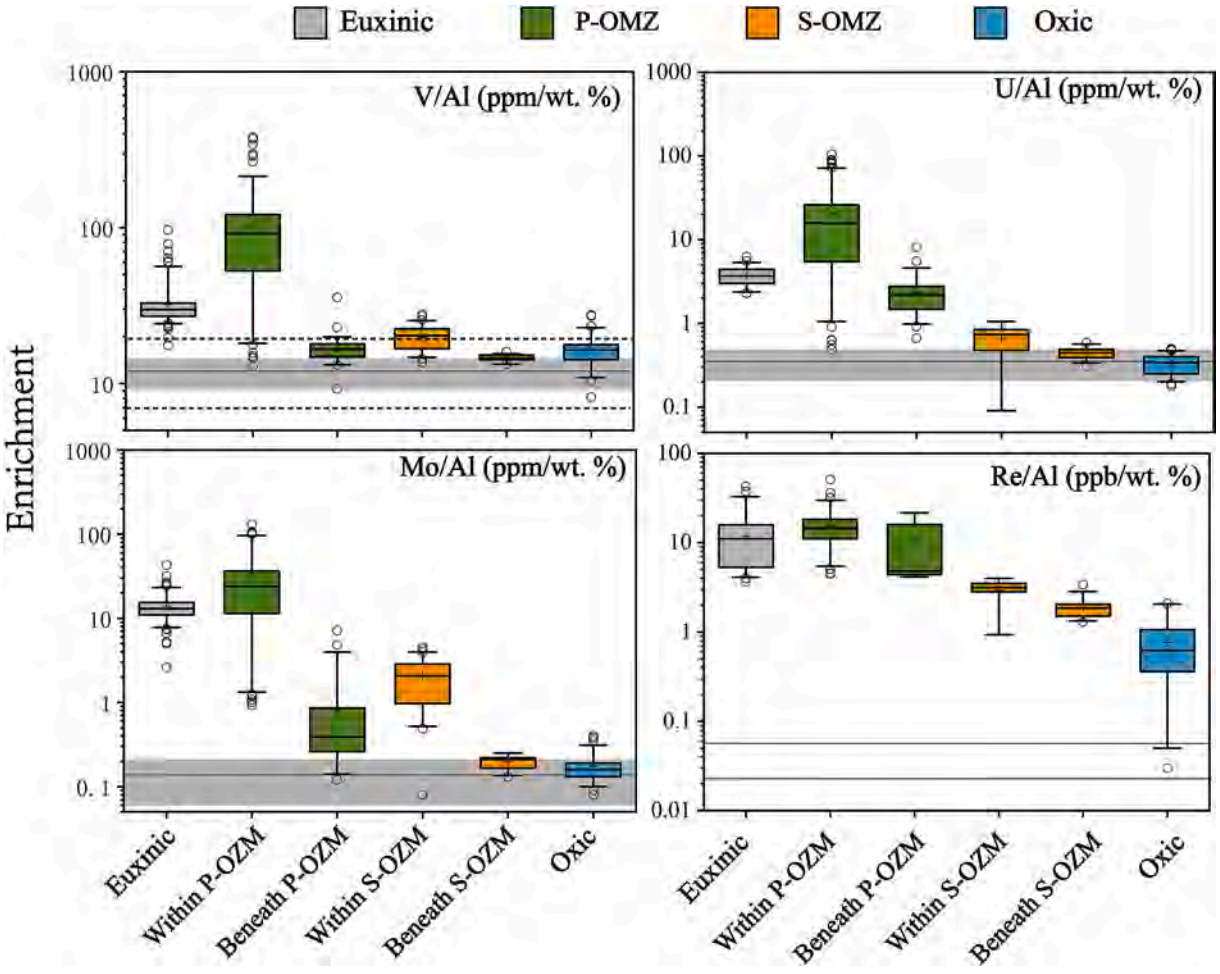


Fig. 6. RSTEs enrichment (lg scale) in different modern marine sedimentary environments. P-OMZ represents perennial oxygen-minimum zone, S-OMZ represents seasonal oxygen-minimum zone, modified from Bennett and Canfield (2020).

They compiled and analyzed data on Re, Mo, U, and V from modern marine sedimentary environments, including normal oxic depositional environments (such as the Washington margin), Seasonal Oxygen Minimum Zones (S-OMZs), or perennially low-oxygen areas at unrestricted continental margins (Perennial Oxygen Minimum Zones, P-OMZs, such as those off Chile and Namibia margins), as well as restrictive, permanently anoxic sulfide depositional basins (such as the Black Sea and Cariaço Basin) (Fig. 6). Based on the unique characteristics of RSTEs enrichment in different environments, they differentiated sedimentary environments using the enrichment ratios of TM (ppm)/Al (wt%) and established thresholds.

V showed the lowest enrichment in anoxic-euxinic depositional environments, with a median of 29.5 ppm/wt%, which is three times lower than the enrichment influenced by P-OMZ (median = 92.0 ppm/wt%) (Fig. 6). This enrichment pattern can be attributed to higher rates of input of reactive solids (such as organic matter particles and Fe-Mn (oxy) hydroxides) to the seafloor and faster turnover of the water column resulting in increased provision of soluble V in unrestricted marine setting (Algeo and Lyons, 2006; Sweere et al., 2016; Bennett and Canfield, 2020). Therefore, compared to the more restrictive conditions of euxinic basins, these factors provide a more favorable environment for the enrichment of V (Fig. 6). Compared to sediments in euxinic basins (median = 3.7 ppm/wt%), the highest U enrichment occurs in sediments beneath P-OMZ coverage (median = 15.8 ppm/wt%) (Fig. 6). This may be due to the higher rate of seawater renewal in the continental margin OMZ (Algeo and Lyons, 2006; Algeo and Tribovillard, 2009; Sweere et al., 2016). Furthermore, the upwelling zones with high primary productivity transport substantial organic carbon to the seafloor, enhancing the authigenic enrichment of U in sediments (Bennett and Canfield, 2020; McManus et al., 2006, 2005). U can also combine with biogenic particles in the water column to form particulate non-lithogenic uranium (PNU), which is an important source of authigenic U in sediments (Zheng et al., 2002). In sedimentary environments below P-OMZ compared to normal oxic conditions, the higher enrichment of U (median = 2.2 ppm/wt%, similar to euxinic basins) is likely due to these environments typically having shallower oxygen penetration depths and lower bottom water oxygen content, thereby preserving significant PNU signals (McManus et al., 2005; Morford and Emerson, 1999; Zheng et al., 2002). Similar to U and V, the highest enrichment of Mo is also observed in sediments beneath P-OMZ coverage (median = 23.9 ppm/wt%), which is approximately twice as high as that observed in sediments from euxinic basins (median = 12.9 ppm/wt%), and more than ten times higher than that observed in S-OMZ sediments (median = 2.07 ppm/wt %) (Fig. 6). This could be attributed to higher organic matter fluxes and active sulfate reduction beneath P-OMZ (Algeo and Lyons, 2006; Dahl et al., 2017; Helz and Vorlicek, 2019). Such conditions may lead to the formation of high concentrations of dissolved sulfides in shallow sediments, particularly in sediments with low reactive iron content. Consequently, effective removal of Mo can occur even in the absence of continuously high concentrations of free sulfides in the water column (as observed in euxinic basins) (Brüchert et al., 2003). Furthermore, due to hydrological restrictions, the rate of dissolved Mo supply from the open ocean to euxinic basins is much lower compared to OMZ environments (Algeo and Lyons, 2006; Bennett and Canfield, 2020; Sweere et al., 2016). The highest enrichment of Re in P-OMZ sediments (median = 14.6 ppb/wt%) slightly exceeds its enrichment in euxinic environments (median = 10.9 ppb/wt%) (Fig. 6). The enrichment of Re is primarily driven by reducing conditions generated by organic carbon respiration, thus the level of Re enrichment correlates with shallow oxygen penetration depths (Morford et al., 2012). Moreover, in OMZ and normal oxic sedimentary environments, Re enrichment also increases with productivity enhancements (Morford et al., 2012).

In general, normal oxic environments exhibit characteristic low ratios of RSTE/Al, notably Re/Al (<1.3 ppb/wt%), Mo/Al (<0.4 ppm/wt %) (Fig. 7). Evidence for euxinic basin sedimentary environments includes Mo/Al > 5 ppm/wt%, U/Al > 5 ppm/wt%, and V/Al between 23 and 46 ppm/wt% (Fig. 7). Mo/Al > 5 ppm/wt%, U/Al > 5 ppm/wt%, and V/Al > 46 ppm/wt% are strong indicators of perennial OMZ anoxic conditions, whereas U/Al > 1 ppm/wt%, V/Al < 23 ppm/wt%, and Mo/Al < 5 ppm/wt% suggest sediment deposition beneath oxic seawater in perennial OMZ regions (Fig. 7). It is noteworthy that applying modern sediment-defined thresholds to ancient oceans may lead to biases (Bennett and Canfield, 2020; Zhu et al., 2022; Absar et al., 2024), due to significant differences in RSTEs reservoirs between ancient and modern oceans (Fig. 13).

4.2. Re/Mo

Crusius et al. (1996) suggested that the Re/Mo ratio can be applied to differentiate between suboxic-anoxic deposition conditions. Re and Mo begin to enrich under suboxic and euxinic conditions respectively, therefore even minor expansions in anoxic seafloor areas can result in significant differences in their relative proportions in sediments (Crusius et al., 1996). Specifically, under oxic conditions, the Re/Mo ratio is

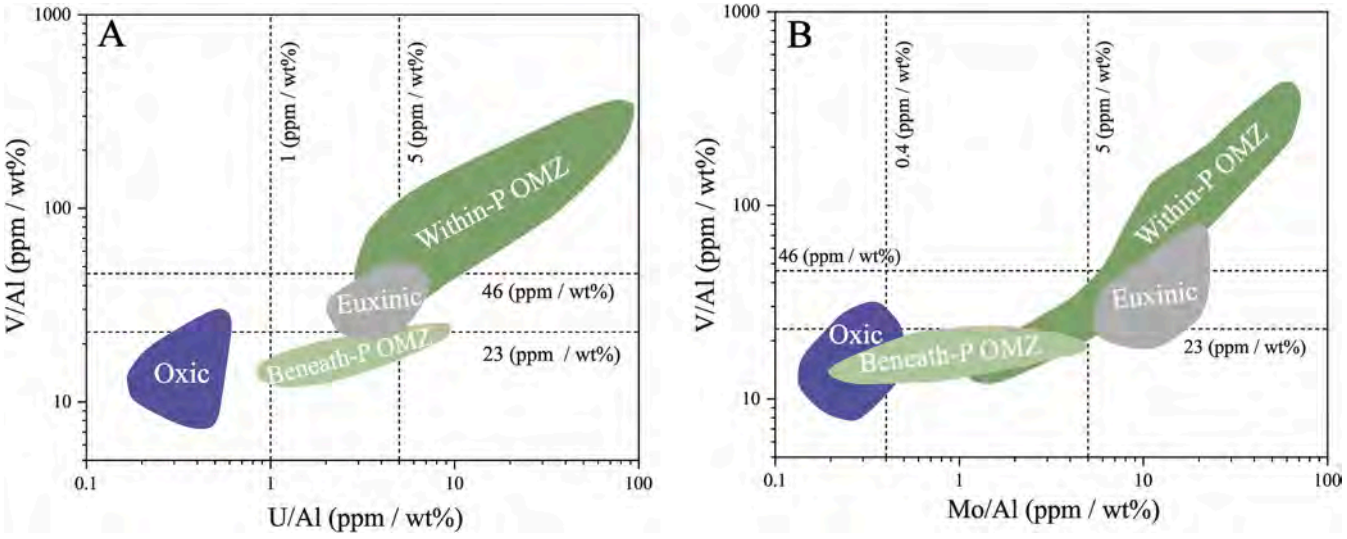


Fig. 7. V/Al-U/Al (A) and V/Al-Mo/Al (B) in modern marine. Dashed lines represent TM /Al thresholds suggested by Bennett and Canfield (2020) for various environmental settings. Purple, gray, and green regions correspond to oxic, euxinic basin, and P-OMZ interior and beneath, respectively. (For interpretation of the references to colour in this figure legend, the reader is referred to the web version of this article.)

usually similar to the crustal value (0.3×10^{-3}) (Nameroff et al., 2002). If the primary pathway for Mo removal from the oxic ocean involves the adsorption of Mo onto Fe and Mn (oxy)hydroxides, this process enriches Mo in these phases by more than 100-fold compared to the upper continental crust (Hein et al., 2013; McDaniel et al., 2004; Tagami and Uchida, 2007). Re is scavenged less efficiently, resulting in the Re/Mo ratios being lower than the crustal ratio (Nameroff et al., 2002). Under suboxic or mildly anoxic (absence of H_2S) conditions, the reduction of Fe-Mn (oxy)hydroxides releases adsorbed Mo and results in significant enrichment of Re in sediments (Crusius et al., 1996). Consequently, this results in a substantial increase in Re/Mo ratios, which can be much higher than the ratios in seawater, reaching 10×10^{-3} to 30×10^{-3} (Crusius et al., 1996; Nameroff et al., 2002). In anoxic-euxinic environments, both Re and Mo are highly enriched in sediments, bringing the Re/Mo ratio close to that found in seawater (0.8×10^{-3}) (Nameroff et al., 2002). Turgeon and Brumsack (2006) found that Re/Mo ratios between 4×10^{-3} to 15×10^{-3} and 0.8×10^{-3} to 4×10^{-3} could potentially characterize suboxic and anoxic-sulfidic sedimentary environments respectively. Recently, Kunert and Kendall (2023) have further refined the Re/Mo thresholds for distinguishing suboxic and anoxic-euxinic environments to Re/Mo = 10×10^{-3} and Re/Mo = 2×10^{-3} (Fig. 8). Furthermore, Crusius et al. (1996) proposed to determine the redox state of the water column or sediments—whether they are oxic, suboxic, or euxinic—by combining Re/Mo values with the depth of Re and Mo enrichment (Fig. 9A). In suboxic or euxinic environments, the original depth of enrichment of Re and Mo in sediments is around 1 cm, whereas in oxic environments, the depth of enrichment can reach 10 cm or more (Fig. 9A, Crusius et al., 1996).

Recent studies have provided researchers with new understandings of the mechanisms of Re and Mo removal from sediments, where Re and Mo co-precipitate with Fe and S in reducing water (Fig. 3) (Helz, 2022; Helz and Vorlicek, 2019; Vorlicek et al., 2018; Živković et al., 2023). The coprecipitate is a nanoscale sulfide, Fe(Mo, Re)S_4, which is irreversibly transformed to Fe(Mo, Re)(S_2)S_2 by internal electron transfer (Helz, 2022; Vorlicek et al., 2018). This irreversibility preserves information about the redox conditions at the time of deposition, unless the sedimentary rock subsequently undergoes oxidation or thermal maturation (Helz, 2022). Oxidation typically decreases the Re/Mo ratio as Re is more readily oxidized and leached from the sediment than Mo, while

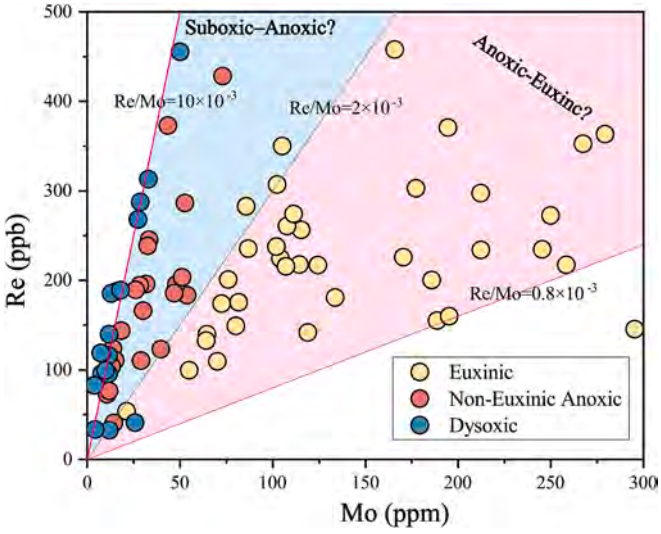


Fig. 8. Re versus Mo plots for Gordondale Member core. Trend lines are provided for suboxic and anoxic-sulfidic conditions, along with the modern seawater Re/Mo ratio (0.8×10^{-3}). Blue and pink shaded areas represent potential sedimentation under suboxic and anoxic-sulfidic conditions. Data from Kunert and Kendall (2023). (For interpretation of the references to colour in this figure legend, the reader is referred to the web version of this article.)

thermal maturation can either increase or decrease this ratio depending on temperature and mineral-phase changes (Helz, 2022). The Re/Mo ratio in the cumulative co-precipitate from the Rayleigh process is given by:

$$\left(Re_S/Mo_S\right)_{cum} = \left(Re^*_{aq,sat}/Mo^*_{aq,sat}\right) \times (1 - f^{\alpha})/(1 - f) \quad (3)$$

Where $\alpha = (Re/Mo)_{solid} / (Re/Mo)_{aqueous}$ is the distribution coefficient of Re and Mo during co-precipitation, typically assumed to be constant in the model to simplify calculations. Meanwhile, $f = Mo_{aqueous} / Mo^*_{aqueous}$ represents the remaining fraction of Mo in the aqueous phase, indicating the extent of Mo consumption during co-precipitation, where $Mo_{aqueous}$ and $Mo^*_{aqueous}$ are the current and initial concentrations of Mo in the aqueous phase, respectively (Helz, 2022). Helz (2022) calculated $(Re_s/Mo_s)_{sw}$ to be 0.94 by fitting Black Sea data, a result that closely aligns with the actual composition of the Black Sea sediment components (Fig. 9B). Other examples in Fig. 9 also confirm that $(Re_s/Mo_s)_{sw}$ can effectively represent local bottom water redox conditions, as originally proposed by Crusius et al. (1996). Živković et al. (2023) successfully used the $(Re_s/Mo_s)_{sw}$ model to predict sediment composition in Rogoznica Lake along the Adriatic coast of Croatia. However, the model may exhibit some complexity and requires appropriate parameterization. The accuracy and reliability of the model could be influenced by the choice of parameters, necessitating further research to validate and optimize it. For instance, the model assumes α to be constant, whereas in reality, it may vary under different environmental conditions.

4.3. Mo- and U-EF covariation patterns

Mo- and U-EF covariation patterns in sediments have been widely used to track redox and hydrological conditions in ancient and modern marine sediments (e.g., Algeo and Rowe, 2012; Algeo and Tribovillard, 2009; Gilleaudeau et al., 2020; Hu et al., 2023; Li et al., 2017; Tribovillard et al., 2012). The uptake of authigenic U in sediments begins at the redox boundary of Fe(II)-Fe(III) under low oxygen conditions, independent of the presence of seawater sulfides (Zheng et al., 2002). In contrast, authigenic Mo uptake requires the presence of at least trace H_2S (Helz et al., 1996). Based on the geochemical behaviors of Mo and U during sedimentation, Algeo and Tribovillard (2009) proposed that the Mo- and U-EF covariation patterns in sediments provide information on bottom water redox changes, operation of Fe-Mn particle shuttle in the water column, and hydrological conditions related to basin restriction levels. In their model, in an unrestricted marine system, U enrichment without Mo enrichment typically reflects suboxic conditions in the bottom water (Fig. 10 A1). When environmental conditions become more reducing, the degradation of organic matter and the increase in sulfides gradually lead to the accumulation of Mo surpassing that of U, resulting in a steeper Mo_{EF}-U_{EF} trend (Fig. 10 A2). Particle shuttle can effectively accelerate the enrichment of Mo in sediments, while U is largely unaffected by particle shuttle, causing Mo to accumulate more than U even in mildly reducing environments (Fig. 10 B). In a restricted environment with high concentrations of sulfides in the bottom water, Mo undergoes significant enrichment relative to U. However, due to hindered hydrological exchange with the open ocean and the equilibrium between $FeMoS_4$ and dissolved Mo in the presence of high sulfide concentrations (Paul et al., 2023), the supply of Mo to the bottom water is restricted (Fig. 10 C2). Consequently, the maximum achievable Mo enrichment factor is expected to be suppressed, leading to a gradual decrease in Mo_{EF}/U_{EF} ratio in the sediment, while U_{EF} continues to increase (Fig. 10 C2). Therefore, these authigenic Mo- and U-EF covariation patterns can not only be used to discern different redox conditions in sedimentary environments but also offer valuable clues about water mass properties and processes in various sedimentary basin marine systems.

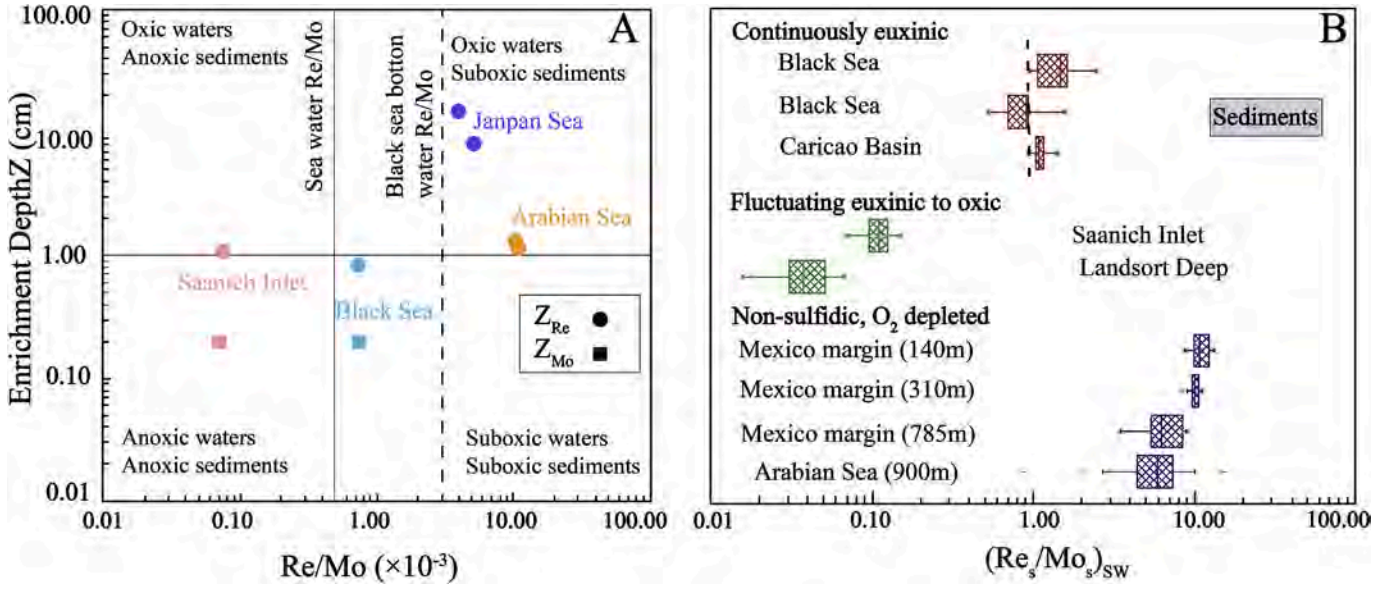


Fig. 9. Correlation between the original depth of enrichment Z and Re/Mo for sediment Re and Mo (A, modified from Crusius et al. (1996)); $(Re_s/Mo_s)_{sw}$ normalized to seawater in basin sediments classified according to the redox characteristics of the bottom water, with vertical dashed lines in the figure showing fitted Black Sea $(Re_s/Mo_s)_{sw}$ (B, modified from Helz (2022)).

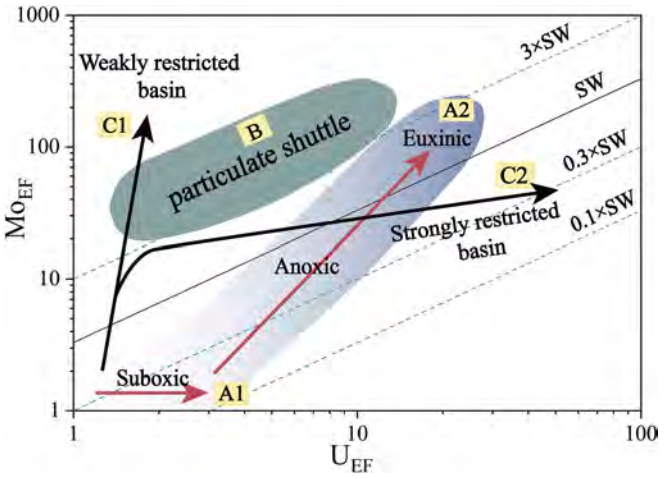


Fig. 10. Covariant patterns of Mo-EF and U-EF (modified after Tribovillard et al. (2012)). Solid diagonal lines represent Mo/U ratios equal to seawater values (1 × SW), while dashed lines indicate Mo/U ratios as fractions of seawater values (3 × SW, 0.3 × SW) (Algeo and Tribovillard, 2009; Tribovillard et al., 2012). The light blue area represents the "unrestricted ocean" trend. The green area represents the "particle shuttle" trend. Red arrows indicate bottom water redox trends, while black arrows denote basin water restriction trends. (For interpretation of the references to colour in this figure legend, the reader is referred to the web version of this article.)

4.4. V/Cr, V/(V + Ni), V/Mn

Over the years, ratios of V associated with other metals (e.g., V/Cr, V/(V + Ni)) have been widely utilized to infer oxygen levels in sedimentary environments. When V/Cr > 4.25, it indicates an anoxic environment; when V/Cr < 2.00, it suggests an oxic environment; and V/Cr in the range of 2.00 to 4.25 indicates suboxic conditions (Jones and Manning, 1994). Hatch and Leventhal (1992) compared the V/(V + Ni) ratio with other geochemical redox indicators and found that ratios less than 0.46, between 0.46 and 0.6, 0.6 to 0.84, and greater than 0.84 correspond to oxic, suboxic, anoxic, and euxinic conditions, respectively. However, Algeo and Liu (2020) pointed out that the fixed redox thresholds for these bimetallic ratios established in specific stratigraphic units may have limited applicability when analyzing other stratigraphic units. This is because under reducing conditions, the preferential enrichment of one metal element over another in a specific ratio cannot be guaranteed (Pan et al., 2022). Therefore, an accurate analysis of redox conditions in marine sedimentary systems must be based on specific stratigraphic contexts rather than relying on fixed redox thresholds (Algeo and Liu, 2020; Pan et al., 2022; Liu et al., 2023; Qian et al., 2024). Nevertheless, these redox proxies remain effective tools, although the redox thresholds for each ancient sediment layer need to be recalibrated.

Recently, Cui et al. (2023) investigated the impact of Mn oxides cycling in euxinic bottom waters and pore waters on V geochemistry in Chesapeake Bay, proposing the use of V/Mn molar ratios to track redox variations. The increase in dissolved V concentrations in waters primarily results from the transport of Mn particles to euxinic environments (Kunert et al., 2020; Cui et al., 2023). Desorption or dissolution of these Mn oxides leads to the substantial release of adsorbed V (Balistrieri and Murray, 1986; Beck et al., 2008). This exerts a more dominant control on V geochemistry compared to adsorption by pyrite and the formation of solid $V(OH)_3$ through reduction by H_2S (Wanty et al., 1990; Cui et al., 2023). Specifically, as environmental conditions become more euxinic, the dissolved V/Mn ratio increases while the solid-phase V/Mn ratio decreases. Due to the simultaneous negative correlation between solid-phase V/Mn molar ratio and H_2S concentration, and positive correlation between dissolved V/Mn molar ratio and H_2S concentration, the V/Mn molar ratio in sediments may serve as an effective tool for identifying marine redox conditions.

4.5. Isotope systems

Isotope geochemistry has experienced rapid development since the 21st century, with expanding applications in various fields due to theoretical breakthroughs, methodological innovations, and the development of high-precision analytical techniques (Kendall, 2021). In the field of earth sciences, isotopes have found extensive use in studies such as tracing the sources of substances, determining the ages of geological events, and revealing the redox conditions of depositional environments (e.g., Kendall et al., 2009; Kendall, 2021; Akhtar et al., 2024; Li et al., 2022). Changes in the depositional environment (e.g., variations in

organic matter burial rate, sedimentation rate, or basin hydrology and restriction) can result in the isotopic fractionation of elements during deposition, and the redox state of the environment can also impact the extent of isotopic fractionation (Kendall, 2021). Currently, two widely utilized isotope systems as redox tracers in the global oceans are Mo and U (e.g., Kendall et al., 2011; Andersen et al., 2014; Noordmann et al., 2015, 2016; Dickson, 2017; Rolison et al., 2017). Simultaneously, efforts are underway to develop Re and V isotopes for use as paleo-redox proxies (Kendall, 2021; Wei et al., 2023; Wu et al., 2022). Combined with isotope mass balance methods, researchers have found widespread application in global studies to estimate past oceanic hypoxic seafloor areas (e.g., Cheng et al., 2015; Cole et al., 2020b; Zhang et al., 2020; Wei et al., 2021a). By leveraging differences in the direction and/or magnitude of isotope fractionation in environments with distinct redox signatures, the degree of ocean oxygenation can be inferred through isotope mass balance models (Fig. 11, 12).

4.5.1. Mo isotopes

Mo isotopes have been the initial metal isotope system applied to quantify the redox state of the global ocean (Kendall, 2021). Recent studies have predominantly reported relative thousand-point deviations expressed relative to the NIST SRM 3134 standard (Nägler et al., 2014), denoted as:

$$\delta^{98}\mathrm{Mo}\ (‰) = \left[\left(\frac{^{98/95}\mathrm{Mo}_{Sample}}{^{98/95}\mathrm{Mo}_{Sample}}\right) - 1\right] \times 1000 \quad (4)$$

The modern open-ocean seawater (OSW) exhibits homogeneous δ^{98}Mo values ($\delta^{98}Mo_{OSW} = +2.34$ ‰) (Nakagawa et al., 2012; Siebert et al., 2003), significantly exceeding the Mo isotopic composition of riverine inputs (mean $\delta^{98}Mo_{river} = +0.7$ ‰). The transfer of Mo from water column to sediments induces distinct Mo isotopic fractionations controlled by the redox conditions of the depositional environment (Fig. 11). In oxic seawater, light Mo isotopes preferentially adsorb onto Fe and Mn (oxy)hydroxides, while heavy Mo isotopes remain in seawater (Barling and Anbar, 2004; Siebert et al., 2003; Wang et al., 2018). This process leads to a significant equilibrium isotopic fractionation between oxic sediment and open-ocean seawater with a fractionation factor of approximately $\Delta^{98}Mo_{OX\text{-}OSW} = -3$ ‰ (Barling and Anbar, 2004; Cheng et al., 2015). Under anoxic non-sulfide conditions ($O_2 = 0$ μM; $H_2S < 11$ μM), the reduction of Mo leads to highly variable δ^{98}Mo values between reduced sediments and open-ocean seawater, with $\Delta^{98}Mo_{RED\text{-}OSW}$ ranging from −0.5 ‰ to −2.9 ‰ (Azrieli-Tal et al., 2014;

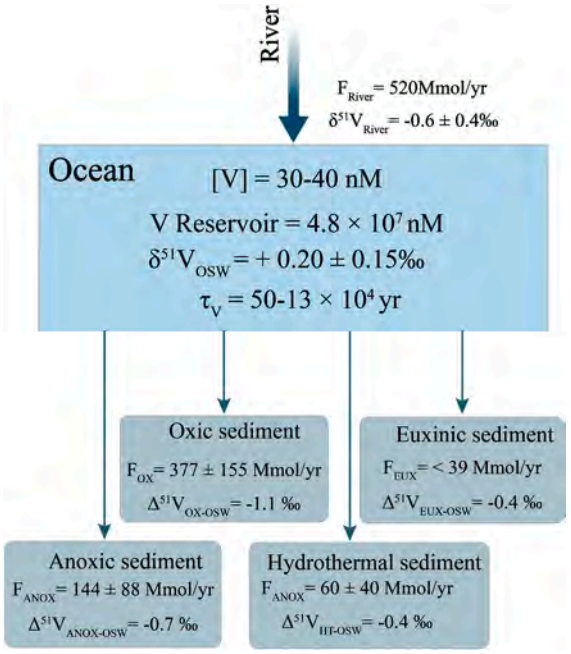


Fig. 12. Schematic diagram of a modern marine V isotope mass balance model, modified from Wei et al. (2023).

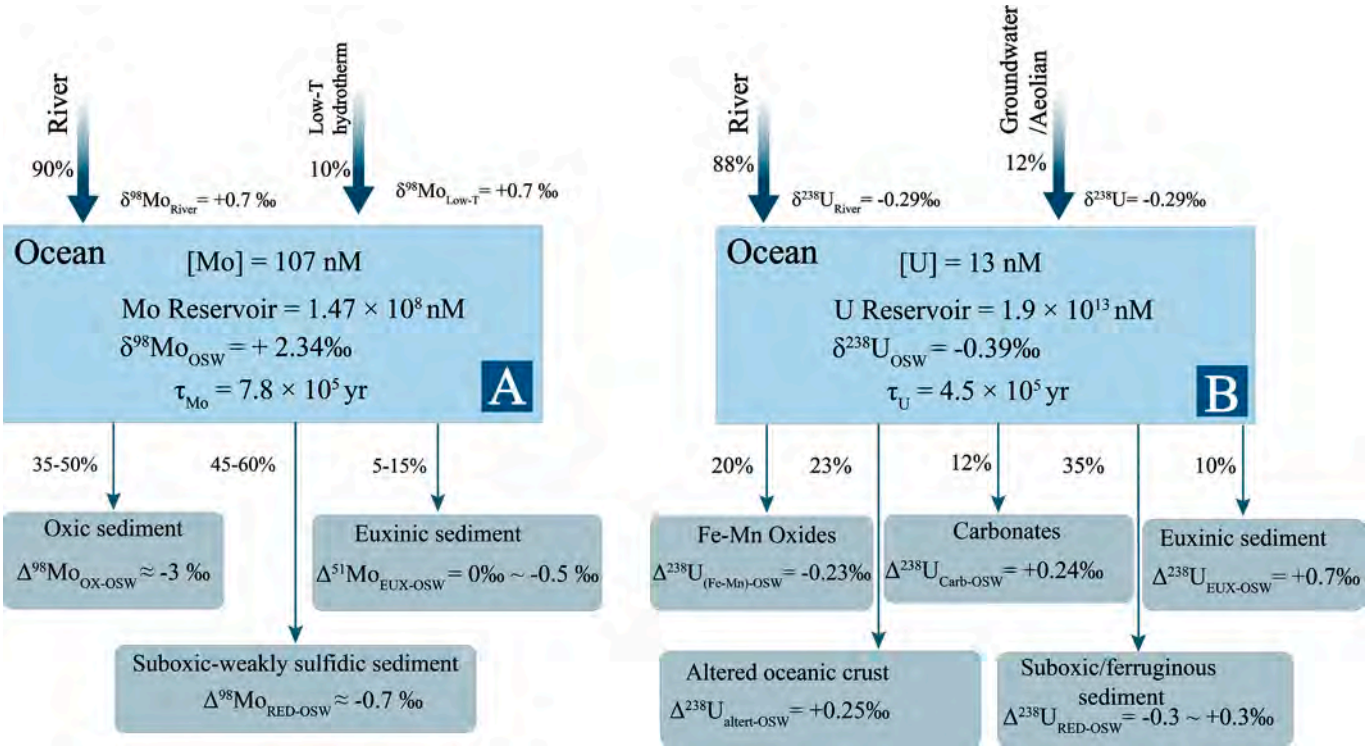


Fig. 11. Schematic of modern ocean (A) Mo, (B) U isotope mass balance models. (A) Modified from Wei et al. (2021a) and Wei et al. (2023), (B) Modified from Goto et al. (2014) and Wei et al. (2021a) U isotopes

Nägler et al., 2005; Noordmann et al., 2015). This variability likely arises from transport mechanisms (i.e., diffusion or Fe-Mn (oxy)hydroxide dissolution) mediating Mo transfer from bottom water to sediment porewater, coupled with incomplete conversion of molybdate to particle-reactive thiomolybdate (Eroglu et al., 2020; Wei et al., 2021a). Overall, the weighted mean $\Delta^{98}Mo_{RED\text{-}OSW} \approx -0.7$ ‰ represents the Mo isotope fractionation between non-sulfide sediments and seawater (Poulson et al., 2006). Under euxinic conditions ($H_2S \geq 11$ μM), the quantitative removal of Mo results in minimal Mo isotopic fractionation between sediments and the open ocean. MoO_4^{2-} is completely converted to MoS_4^{2-}, which either associates with Fe-S particles or adsorbs onto organic particles, leading to rapid removal from seawater (Helz et al., 1996; Erickson and Helz, 2000; Nägler et al., 2011; Dahl et al., 2017; Helz and Vorlicek, 2019). As a result, Mo is entirely incorporated into the sediments, where the δ^{98}Mo values of these sediments are similar to contemporaneous seawater values (Barling and Anbar, 2004; Noordmann et al., 2015; Helz et al., 2011; Lu et al., 2020). The non-quantitative removal of dissolved Mo allows for the preservation of variable δ^{98}Mo in sediments, and these values are significantly lower relative to seawater (Bura-Nakić et al., 2018; Nägler et al., 2011). This is due to isotopic fractionation of $\Delta^{98}Mo_{EUX\text{-}OSW}$ produced between MoS_4^{2-} and authigenic solid Mo phases in deep euxinic basins, ranging between 0 ‰ and − 0.5 ‰ (Nägler et al., 2011). As both strong and weak euxinic environments are much more Mo-enriched than non-euxinic environments, they are often considered to be oceanic Mo sinks. The average Mo isotope fractionation between overall euxinic sediments and open ocean seawater is $\Delta^{98}Mo_{EUX\text{-}OSW} = -0.5$ ‰ (Poulson et al., 2006).

Under euxinic conditions, Mo undergoes almost no fractionation as it transfers from seawater into sediments (Neubert et al., 2008; Nägler et al., 2011; Noordmann et al., 2015), thereby effectively preserving the δ^{98}Mo signature of seawater at the time. The Mo isotope composition of euxinic shale and carbonate serves as effective archives for reconstructing the global redox state of ancient oceans (e.g., Wille et al., 2007; Duan et al., 2010; Scheiderich et al., 2010; Voegelin et al., 2010; Kendall et al., 2011; Thoby et al., 2019). However, the isotope offset between sediments and seawater is influenced by complex local depositional factors, including Fe/Mn oxides, sea-level changes, and basin restrictions (Kendall et al., 2017; Ostrander et al., 2019; Qin et al., 2022). These factors pose challenges in accurately inferring the Mo isotope composition of ancient global seawater (Ostrander et al., 2019). The Fe-Mn particle shuttle significantly contributes to the decrease in the Mo isotope ratio in anoxic sediments (Hardisty et al., 2016; Ostrander et al., 2019; Qin et al., 2022; Tan et al., 2023). In this process, lighter Mo isotopes are preferentially adsorbed by Fe and Mn (oxy)hydroxides (Barling and Anbar, 2004; Siebert et al., 2003; Wang et al., 2018). When these particles sink into anoxic or weakly euxinic bottom waters and dissolve, the lighter Mo isotopes are released into the pore water, thus preserving the characteristics of lighter Mo isotopes in the sediment (Hardisty et al., 2016; Ostrander et al., 2019). The degree of basin restriction also influences the isotopic composition of Mo in sediments (Kurzweil et al., 2015; Noordmann et al., 2015; Ostrander et al., 2019; Tan et al., 2023). As restriction increases, the connectivity between the basin and the open ocean decreases, leading to a reduction in Mo supply, while the burial efficiency in sulfide-rich sediments increases, depleting the local dissolved Mo reservoir (Neubert et al., 2008; Scott and Lyons, 2012). At this time, Mo is almost quantitatively removed from the water and incorporated into the sediments, causing the euxinic sediments to retain a relatively high δ^{98}Mo value, which may mirror the coeval global seawater (Li et al., 2022; Tan et al., 2023). Additionally, hydrothermal activity may supply local seawater with abundant Mn, promoting the cycling of Mn oxides. Eventually, this leads to a decrease in the Mo isotopic value in sediments (Tan et al., 2023).

4.5.2. Uranium isotope

Analogous to Mo, the U isotope system can serve as a useful proxy for global oceanic redox oscillations, as U isotope fractionation exhibits distinct responses to varying levels of anoxic conditions (Kendall, 2021). Recent reports mostly express relative thousandths deviation ratios relative to the CRM145 standard (Andersen et al., 2014; He et al., 2021; Lu et al., 2020), denoted as:

$$\delta^{238}U\ (‰) = \left[\left({}^{238/235}U_{Sample} \Big/ {}^{238/235}U_{Standard} \right) - 1 \right] \times 1000 \quad (5)$$

The modern open-ocean seawater have a homogeneous value of $\delta^{2238}U_{OSW}$ of −0.39 ‰ (Andersen et al., 2015; Noordmann et al., 2016; Tissot and Dauphas, 2015). Despite inputs from groundwater and weathering sources (Dunk et al., 2002), U inputs to the modern ocean are predominantly riverine, with an average δ^{238}U value of −0.29 ‰ (Tissot and Dauphas, 2015; Wei et al., 2021a). The major modern marine U sinks consist of strongly anoxic (or euxinic) sediments, hypoxic (or non-euxinic) sediments, primary marine carbonates, Fe and Mn (oxy)hydroxides, and high-temperature hydrothermal alteration of oceanic crust (Fig. 11). Under anoxic-euxinic conditions, microbial-mediated U(VI) reduction produces significant U isotope fractionation between +0.8 ‰ and + 1.2 ‰, leading to a greater enrichment of heavy U isotopes in U(IV) solid-phase sediments (e.g., Basu et al., 2014; Stirling et al., 2015; Dang et al., 2016). Consistent with this, the average U isotope fractionation between sediments from modern anoxic basins and continental margins (e.g., Black Sea, Cariaco Basin, Gulf of Saanich, Baltic Sea, Namibian Margin (Abshire et al., 2020; Andersen et al., 2014; Brüske et al., 2020; Montoya-Pino et al., 2010; Stirling et al., 2007; Weyer et al., 2008)) and the overlying water column is $\Delta^{238}U_{EUX\text{-}OSW} = +0.7$ ‰ (Andersen et al., 2017). Authigenic U enrichment in suboxic sediments within sulphide-free suboxic or ferrous environments, such as in modern, highly productive continental margins (e.g., Peruvian continental margins, Namibian continental margins), is much lower than in euxinic depositional environments. The average δ^{238}U values range from −0.4 to −0.2 ‰ (Andersen et al., 2016; Weyer et al., 2008). During the precipitation of biogenic carbonate from seawater, the fractionation of U isotopes is relatively small (Chen et al., 2018b; Livermore et al., 2020; Romaniello et al., 2013). The offsets of $\Delta^{238}U_{Carb\text{-}OSW} = +0.24$ ‰ (Tissot et al., 2018) or $\Delta^{238}U_{Carb\text{-}OSW} = +0.27$ ‰ (Chen et al., 2018a) are considered to be indicative of the potential influence of early diagenetic alteration and authigenic U enrichment in carbonate sediments from anoxic water bodies or porewaters. However, these offsets may vary due to local depositional and burial environments of marine carbonate sediments (Hood et al., 2018). In contrast, U adsorbed onto Fe and Mn (oxy)hydroxides in the oceans will have a lighter isotopic composition, as observed in marine Fe-Mn crusts, with an isotopic fractionation of $\Delta^{238}U_{(Fe\text{-}Mn)\text{-}OSW} = -0.23$ ‰ (Brennecka et al., 2011; Goto et al., 2014). Furthermore, hydrothermal forcing and low-temperature alteration of oceanic crust are also considered significant sinks for marine U (Dunk et al., 2002). The δ^{238}U values derived from these processes are generally higher than seawater values (−0.17 ‰ to −0.25 ‰) (Andersen et al., 2015; Noordmann et al., 2016). Consequently, compared to other marine U sinks, the significant fractionation occurring in sediments formed in anoxic environments strengthens the utility of δ^{238}U as a paleo-redox indicator.

Recent studies have demonstrated that the extent of isotope fractionation during the removal of U to anoxic sediments is strongly influenced by various hydrological factors, including organic matter burial rate, sedimentation rate, primary productivity, and the degree of basin restriction (Lau et al., 2022; Rutledge et al., 2024). In high-productivity environments, such as upwelling zones, the input of organic carbon increases. Elevated organic carbon fluxes can prompt the transfer of a substantial quantity of heavy isotope U(IV) onto sinking organic particles (Lau et al., 2022; Rutledge et al., 2024). This process leads to a reduction in the δ^{238}U value of seawater, irrespective of whether the expansion of anoxic conditions is accompanied by ferruginous or euxinic states (Lau et al., 2022; Bruggmann et al., 2022; He et al.,

2021; Rutledge et al., 2024). Moreover, low sedimentation rates lead to the enrichment of U in sediments, as U has more time to undergo reduction and accumulation in the sediments (Lau et al., 2020, 2022). In contrast, high sedimentation rates dilute uranium concentrations and weaken the isotope fractionation effect (Lau et al., 2022). In basins with higher degrees of restriction, local U isotopes may be altered due to insufficient mixing with the open ocean. The reduction in uranium reserves results in a decrease in the $\delta^{238}U$ value of the sediments (Lau et al., 2020, 2022). Despite the complexity and diversity of these factors, the scale of anoxic uranium sinks in the ocean is a key factor controlling the $\delta^{238}U$ value of seawater (Lau et al., 2022; Remírez et al., 2024).

Typically, carbonate rocks are considered the most reliable archive for recording seawater $\delta^{238}U$ values, as they can directly and effectively capture the $\delta^{238}U$ composition of seawater. However, the use of $\delta^{238}U$ in carbonates for paleo-redox studies presents certain complexities, as they are subject to diagenetic processes, which can lead to deviations in $\delta^{238}U$ values of carbonates relative to seawater, ranging from approximately 0 ‰ to 0.6 ‰ (Chen et al., 2018a; Tissot et al., 2018). Nevertheless, after correcting for the $\delta^{238}U$ values in carbonates, they are still considered a reliable means for estimating the original seawater $\delta^{238}U$ composition (Zhang et al., 2020; Rutledge et al., 2024). Shale is also commonly used to calculate the U isotope composition of ancient seawater (Lau et al., 2022). However, when utilizing the $\delta^{238}U$ values of black shale to reconstruct ancient ocean redox states, special attention must be paid to accurately removing fractionation signals caused by local factors such as basin restriction, organic matter burial rates, and sedimentation rates (Lau et al., 2022).

4.5.3. V isotopes

The V isotope system is an emerging redox proxy with the ability to track short-term changes in the redox state of the global ocean (Wu et al., 2020). The isotopic composition of V is expressed as a relative thousandths deviation with respect to the Alfa Aesar (AA) standard solution first adopted by the University of Oxford (Nielsen et al., 2011), denoted as:

$$\delta^{51}V\ (‰) = \left[\left({}^{51/50}V_{Sample} \Big/ {}^{51/50}V_{Standard}\right) - 1\right] \times 1000 \qquad (6)$$

During continental chemical weathering, V in silicate rocks is dissolved into rivers, which is the main source of V in the modern oceans (Shiller and Mao, 2000), with a total (including both dissolved and particulate V) riverine input of $\delta^{51}V_{River} = -0.6$ ‰ (Wu et al., 2019). A V isotope study of seawater by Wu et al. (2019) showed that the V isotope composition of open-ocean seawater is homogeneous, with $\delta^{51}V_{OSW} = +0.20 \pm 0.15$ ‰ (Fig. 12). The incorporation of V into sediments varies according to different redox conditions, leading to significant differences in V isotopic compositions. In oxic seawater ($O_2 > 10$ μM), pentavalent vanadate (H_2VO^{4-}) tends to adsorb onto Fe-Mn (oxy)hydroxides and clay minerals (Morford et al., 2005; Prange and Kremling, 1985). This process results in a $\Delta^{51}V_{OX\text{-}OSW}$ value of −1.1 ‰ (Wu et al., 2020). In anoxic seawater ($O_2 < 10$ μM), the V isotopic composition of sediments depends on the isotopic fractionation of V(IV) enriched in organic matter particulate matter within the anoxic or strongly reducing fraction of the water column. Thus, the V isotope fractionation value between anoxic sediments and open ocean seawater is approximately $\Delta^{51}V_{ANOX\text{-}OSW} = -0.7$ ‰ (Wu et al., 2020). In analogy with anoxic sediments found on continental margins, the uptake of authigenic V in euxinic sediments of the Cariaco Basin primarily occurs through particle transport within the reduced water column rather than diffusive transport beneath the sediment-seawater interface (Calvert et al., 2015; Wu et al., 2020). Under euxinic conditions, characterized by high levels of sulphide, there is a $\Delta^{51}V_{EUX\text{-}OSW} = -0.42$ ‰ V isotope shift between the sulphide-rich sediments in the Cariaco Basin and oceanic seawater (Wu et al., 2020). Hydrothermal sediments represent another significant sink for marine V, primarily through the adsorption of Fe oxides, resulting in an associated V isotope shift of approximately $\Delta^{51}V_{HT\text{-}OSW} = -0.4$ ‰ (Wu et al., 2022).

V isotope paleoproxy is gradually emerging as an effective tool for quantifying the redox conditions of the global ocean in shale records (Wu et al., 2020; Heard et al., 2023; Li et al., 2023b; Wei et al., 2023). This proxy can also distinguish between different types of anoxic sediments (ferruginous vs. euxinic) and oxic sediments (Heard et al., 2023). Studies on different sedimentary environments in modern ocean basins have revealed that redox conditions are the main factor determining the characteristics of authigenic sedimentary V isotopes, while post-depositional diagenesis has a relatively minor impact on them (Wu et al., 2020; Chen et al., 2022b). However, the application of the V isotope system as a paleo-redox proxies is still in its infancy, and further studies on V isotopes are required to track the high-resolution evolution of redox conditions in the global ocean.

4.5.4. Re isotope

Re isotopes are generally expressed in terms of relative parts per thousand deviation, relative to the NIST SRM 989 standard, denoted as:

$$\delta^{187}Re\ (‰) = \left[\left({}^{187/185}Re_{Sample} \Big/ {}^{187/185}Re_{Standard}\right) - 1\right] \times 1000 \qquad (7)$$

Dickson et al. (2020) analyzed the Re isotopic composition of seawater in the Atlantic Ocean. They found a high degree of homogeneity in the open-ocean seawater, suggesting a $\delta^{187}Re_{OSW}$ value of approximately −0.17 ‰ for modern seawater. In the modern oceans, oxidative weathering of organic matter-rich mudstones with reducing minerals in the continental crust is the primary source of Re (Colodner et al., 1993), while low-temperature hydrothermal fluids may be a secondary source (Morford and Emerson, 1999). The sinks of Re in the modern ocean include sediment burial in three redox environments: oxic, suboxic, and anoxic (Sheen et al., 2018). Dellinger et al. (2021) made the first determination of the partitioning between Re and Atlantic seawater in the weathering products of the Mackenzie River, which was approximately −1.2 ‰. In recent years, the mechanisms driving redox fractionation of Re have been a subject of intense research (Zhang et al., 2022b). Miller et al. (2011) and Miller et al. (2015) suggested that reduction and sulfur substitution may be the primary mechanisms leading to isotopic fractionation of Re, with a predicted net isotopic fractionation of up to −1.5 ‰. However, stable Re isotope measurements are currently limited, primarily due to analytical method constraints and factors such as low concentrations of Re in geological samples (Miller et al., 2015). Given that Re isotopes share similar properties with Mo, U, and V isotopes, they hold significant potential for indicating redox conditions in sedimentary environments. Further investigation is needed to obtain detailed information on the extent of Re isotope fractionation in different oxidative environments.

5. Earth's oxygenation history: insights from the RSTEs

Tracking the oxidative history of Earth is challenging. Generally, the concentrations and isotopic compositions of RSTEs can be used to infer the redox conditions of the Earth (e.g., Kendall, 2021; Ostrander et al., 2021; Scott et al., 2008; Partin et al., 2013; Wei et al., 2023). The enrichment of RSTEs in organic-rich shales is widely regarded as providing a record of global marine redox conditions (Scott et al., 2008; Sahoo et al., 2012; Partin et al., 2013; Sheen et al., 2018; Mänd et al., 2020). In oxygen-rich seawater, RSTEs are primarily soluble, whereas in reducing marine environments, these metals are transported downward to the seafloor and accumulate in large quantities within the sediments (e.g., Morford and Emerson, 1999; Tribovillard et al., 2006). The burial flux of these metals is several orders of magnitude higher in the reducing environment than in the oxygenated environment (Sahoo et al., 2012). Globally, extensive weathering of RSTEs minerals under oxic conditions transports these metal elements from continental crusts to seawater via

rivers, thereby maintaining a large marine RSTEs reservoir. Conversely, during periods of global anoxia or low oxygen, the marine reservoir of these elements is minimized due to reduced continental weathering (Scott et al., 2008; Sahoo et al., 2012; Partin et al., 2013; Reinhard et al., 2013; Sheen et al., 2018). In relatively open local marine environments, where the degree of basin enclosure is slight or negligible, sediments deposited in anoxic and euxinic water bodies exhibit higher RSTEs concentrations when the marine RSTEs reservoir is large (indicating high marine oxidation states). Conversely, sediments show lower RSTEs concentrations when the marine RSTEs reservoir is small (indicating low marine oxidation states). Therefore, theoretically, insights into large-scale fluctuations in Earth's atmospheric-oceanic oxygen levels can be gained by examining RSTEs concentrations in anoxic shales (Scott et al., 2008; Sahoo et al., 2012; Partin et al., 2013; Reinhard et al., 2013; Lyons et al., 2014; Sheen et al., 2018). The U and Mo isotope systems, similar to the enrichment patterns of RSTEs, also respond to global oceanic redox environments. It is widely believed that well-oxidized oceans have higher Mo and U isotope values, whereas, in the new steady-state conditions following the expansion of oceanic sulfide environments, the Mo and U isotope compositions of global seawater are lower (Kendall et al., 2017; Zhang et al., 2020). We have updated the compilation of geological historical data on RSTEs concentrations in anoxic-euxinic marine sedimentary shales and the Mo and U isotope compositions in various types of anoxic-euxinic sediments across various epochs globally (Fig. 13). These RSTEs data predominantly originate from marine sedimentary rocks deposited in continental margins and basins, with some connection to open oceans. This allows us to correlate these data with global metal reservoirs in the oceans and further quantify the redox conditions of the global oceans.

Traditionally, it is believed that Earth experienced two critical oxygenation events during the Paleoproterozoic (Great Oxidation Event (GOE), starting around 2.43 Ga or 2.32–2.23 Ga, ending around 2.06 Ga) and the Neoproterozoic (the Neoproterozoic Oxidation Event (NOE), ~0.8–0.54 Ga), respectively, gradually establishing modern oxygen levels (Lyons et al., 2014) (Fig. 13). These two oxidation events serve as milestones to divide fluctuations in RSTEs contents in sedimentary deposits across the entire geological history into four main stages (e.g., Partin et al., 2013; Scott et al., 2008; Sheen et al., 2018). Before the GOE (>2.43 Ga), the concentration of RSTEs was generally low, indicating that the oxygen level in Earth's atmosphere may have been too low to significantly increase the input of terrestrial RSTEs through oxidative weathering. This restricts the storage of dissolved RSTEs in the upper ocean and the extent of RSTEs cycling (Anbar and Knoll, 2002; Scott et al., 2008; Scott and Lyons, 2012). Although early geological data points from the Archean are limited, the geological records prior to the Archean-Proterozoic boundary show some indications of trace oxygen in the Earth's atmosphere before the GOE, suggesting the presence of small amounts of oxygen. For example, in the McRae Shale, the concentrations of Mo and Re increased (Anbar et al., 2007), and the δ^{98}Mo of this unit is greater than the average value of the upper crust (0.7 ‰), with the δ^{98}Mo of some black shales reaching as high as 1.86 ‰ (Duan et al., 2010). In addition, the U- isotope composition of this horizon is also significantly heavier than the upper-crust value (Kendall et al., 2013). These phenomena are interpreted as evidence of oxygen production, leading to intensified oxidative weathering at ~2.5 Ga. Similar logic applies to the observed high Re enrichment in the organic-rich shales in the Klein Naute Formations at ~2.6–2.5 Ga (Kendall et al., 2010). Going further back in time, evidence of increased oxygen levels on Earth can still be found. Records from ~2.7 Ga show significant changes in elements such as Mo, U, and V, which may have resulted from an unusually rapid chemical weathering rate (Nesbitt et al., 2009). Moreover, shales and carbonates deposited during the period from 2.5 to 2.7 billion years ago exhibit much heavier δ^{98}Mo compared to the overall continental crust (Siebert et al., 2005; Wille et al., 2007; Voegelin et al., 2010; Eroglu et al., 2015; Thoby et al., 2019). While these localized enrichments themselves do not provide definitive evidence, combining various indicators such as MIF-S signals (Kurzweil et al., 2013; Ohmoto et al., 2006), δ^{53}Cr (Frei et al., 2009), and δ^{15}N (Thomazo et al., 2011) can further enhance the credibility of these short-term environmental oxidation events. Therefore, the GOE appears more like the culmination of Earth's long oxidative history beginning from the Archean (Ostrander et al., 2021). The increase in RSTEs concentrations and heavier Mo isotopic compositions at ~2.5 Ga reflects the rise in global atmospheric-oceanic oxygen levels associated with the GOE (Fig. 13). Currently, there is considerable controversy regarding the precise timing of the GOE. Geochemical evidence from multiple sulfur isotope systems constrain the GOE between 2.50 and 2.43 Ga (Warke et al., 2020). However, the permanent rise in atmospheric oxygen may not have occurred until ~2.32 Ga (Bekker et al., 2004; Luo et al., 2016). Asael et al. (2018) found that the increase in Mo isotopes in black shales during 2.32–2.06 Ga may have recorded the initial stage of the GOE: the rise in atmospheric oxygen levels led to large scale weathering of continental sulfides, which in turn enhanced the transport of sulfate to the ocean, providing a Mo sink for the euxinic environments at the ocean margins and ultimately affecting the composition of Mo isotopes. Other studies suggest that the culmination of permanent atmospheric oxygenation occurred at ~2.22–2.06 Ga, during the Lomagundi Event (LE) (Poulton et al., 2021). While geological records of RSTEs can capture indications of the GOE, data on elements like Re and V remain generally lacking. Further analysis of RSTEs concentrations during this period is needed to provide accurate evidence of the timing of the GOE. In addition, according to shale records from ~2 Ga Zaonega Formation in northwestern Russia, there is significant enrichment of Mo, U, and Re, as well as an increase in the isotope values of U and Cr (Mänd et al., 2020, 2022). Some researchers have proposed that even after the end of the LE, the oceans during the Paleoproterozoic maintained well-oxygenated for an extended period (Mänd et al., 2020, 2022). However, given the potential regional bias in the Zaonega Formation records (as indicated by conflicting conclusions of Bellefroid et al. (2018) and Ossa Ossa et al. (2018, 2022) regarding persistent global anoxia post LE), further research is necessary to elucidate the transient high oxidative levels that may have occurred after the LE.

The discussion on redox conditions in the mid-Paleozoic oceans and atmosphere has sparked considerable debate. Contrary to the widely accepted hypothesis of pervasive oceanic and atmospheric anoxia, an increasing body of research suggests that the mid-Paleozoic atmosphere-ocean system experienced several transient oxidation events. Specifically, records from RSTEs and other geochemical evidence indicate that at least two brief oxygenation events occurred at ~1.4Ga and ~ 1.1Ga (Diamond and Lyons, 2018; Diamond et al., 2018; Steadman et al., 2020; Wei et al., 2021b; He et al., 2022; Yu et al., 2022; Xu et al., 2024). Supporting this view, evidence such as increased Mo and V concentrations in Velkerri Group shales (Kendall et al., 2009; Cox et al., 2016; Zhang et al., 2016) is thought to correlate with weathering of phosphorus-rich flood basalts from large igneous provinces (Cox et al., 2016). Additionally, significant enrichment of Re and V in the Xiamaling Formation shales of North China is attributed to enhanced organic carbon burial due to strong upwelling events (Wang et al., 2020). Recent studies further support the point that the weathering of large igneous provinces may have increased initial ocean productivity and organic carbon burial, thereby increasing oxygen concentrations in the atmosphere-ocean system at ~1.4Ga (Diamond et al., 2021; Xu et al., 2024). Mo isotope data from black shales of the Xiamaling Formation in the North China Craton show that seawater δ^{98}Mo reached 1.8 ‰ at that time, higher than the average δ^{98}Mo of Mesoproterozoic seawater (about 1.1 ‰), consistent with extensive marine oxidation (Diamond et al., 2018; Zhang et al., 2019). Moreover, the Gaoyuzhuang Formation also records characteristic Mo isotope signals, with δ^{98}Mo values ranging from −4 ‰ to 2.51 ‰ (Luo et al., 2021; Ye et al., 2021). While Luo et al. (2021) attribute extremely heavy δ^{98}Mo to dolomitization, it could also represent a broad expansion of oxidized or weakly reduced environments (Ye et al., 2021). Related signals of a Mesoproterozoic

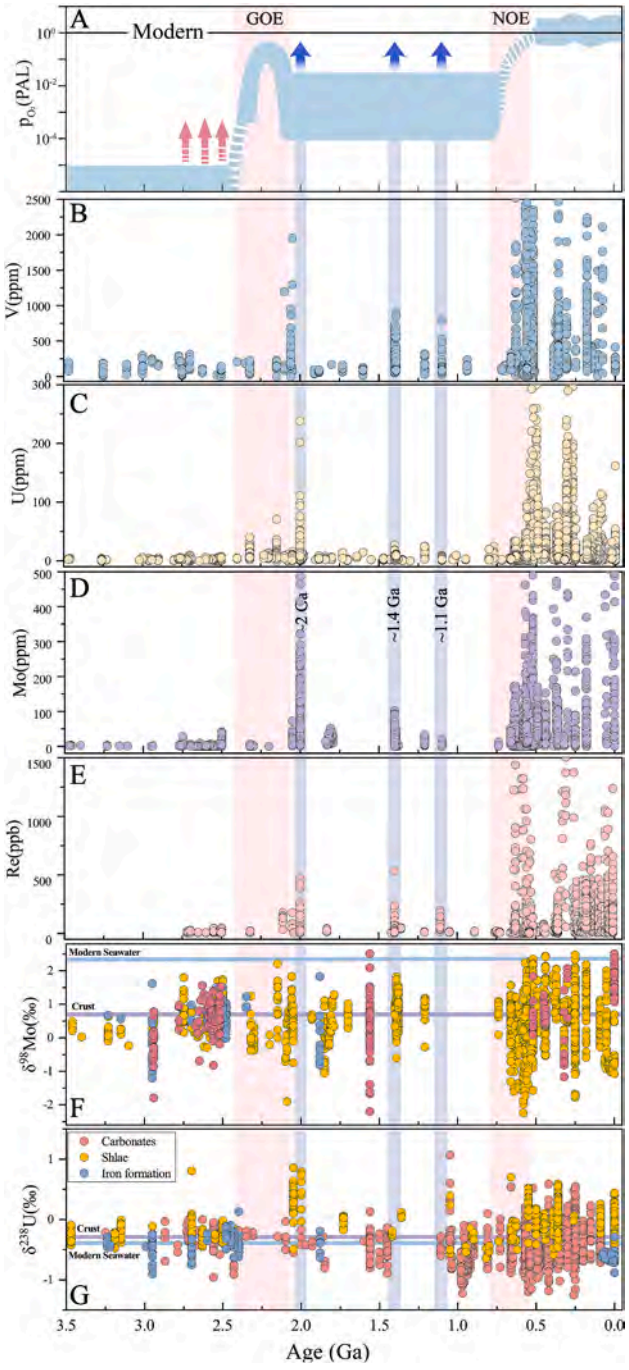


Fig. 13. Fig. Long-term record of RSTEs concentrations in anoxic shales. (A) Atmospheric O2 levels over time, adjusted from Lyons et al. (2014), with red arrows indicating O_2 'whiff' that may have been captured by the RSE geohistoric record, and blue arrows indicating Mesoproterozoic transient oxidative events that may have been identified by the RSTEs, and PAL = present atmospheric level. (B) V in anoxic shales through time, >2500 ppm data not shown. Modified after Sahoo et al. (2012, 2016). Other data from: Asael et al., 2018; Borchers et al., 2005; Cabral et al., 2013; Cox et al., 2016; Gilleaudeau et al., 2020; Gilleaudeau and Kah, 2013; He et al., 2022; Kunert and Kendall, 2023; Motomura et al., 2024; Piper and Dean, 2002; Roué et al., 2021; Tan et al., 2021, 2023; Wang et al., 2020; Wei et al., 2023; Yang et al., 2023; Yuan et al., 2023. (C) U in anoxic shales through time, >300 ppm data not shown. Modified after Partin et al. (2013) and Chen et al. (2015). Other data from: Cox et al., 2016; Gilleaudeau et al., 2020; He et al., 2022; Kendall et al., 2020; Lu et al., 2017; Mänd et al., 2020; Motomura et al., 2023; Ostrander et al., 2019; Roué et al., 2021; Sahoo et al., 2012, 2016; Stockey et al., 2020; Tan et al., 2021, 2023; Wang et al., 2020; Yang et al., 2023; Yuan et al., 2023; Dong et al., 2023; Zhao et al., 2023; Wei et al., 2023. (D) Mo in anoxic shales through time, >500 ppm data not shown. Modified after Chen et al. (2015) and Yuan et al., 2023. Other data from: Cox et al., 2016; Gilleaudeau et al., 2020; He et al., 2022; Kunert and Kendall, 2023; Mänd et al., 2020; Kendall et al., 2020; Roué et al., 2021; Sahoo et al., 2012, 2016; Stockey et al., 2020; Tan et al., 2021, 2023; Wang et al., 2020; Dong et al., 2023; Zhao et al., 2023; Wei et al., 2023; Yang et al., 2023. (E) Re in anoxic shales through time, >1500 ppb data not shown. Modified after Sheen et al. (2018). Other data from: Mänd et al., 2020; Ostrander et al., 2019; Sahoo et al., 2012, 2016; Wang et al., 2020; Yang et al., 2023; Kunert and Kendall, 2023. (F) δ^{98}Mo in anoxic sediments through time. Modified after Qin et al. (2022). Other data from: Stockey et al., 2020; Tan et al., 2021, 2023; He et al., 2022; Dong et al., 2023; Yuan et al., 2023; Zhao et al., 2023. (G) δ^{238}U in anoxic sediments through time. Modified after Chen et al. (2021). Other data from: Mänd et al., 2020; Abshire et al., 2022; Cherry et al., 2022; Dang et al., 2022; J. Chen et al., 2022a; Li et al., 2022; Zhang et al., 2022a; del Rey et al., 2023; Gong et al., 2023; Lu et al., 2023; Song et al., 2023; Wang et al., 2023; Zhao et al., 2023; Rutledge et al., 2024. (For interpretation of the references to colour in this figure legend, the reader is referred to the web version of this article.)

oxygenation event have also been observed in the 1.36 Ga strata of the McArthur Basin in northern Australia (Yang et al., 2017). Yang et al. (2017) reported that the average $\delta^{238}U$ of the upper black shales of the Velkerri Formation at 1.36 Ga was 0.13 ± 0.04 ‰, suggesting that the proportion of anoxic zones in the seafloor was less than 25 % during this period, indicating a relatively high degree of oceanic oxidation. Following this was the transient rise in atmospheric-oceanic O_2 at ~1.1Ga, evidenced primarily by multi-proxy shale data from the Taoudeni Basin, Mauritania (Rooney et al., 2010; Gilleaudeau and Kah, 2013, 2015; Gilleaudeau et al., 2016). Although the existing geochemical evidence is not as compelling as that for the ~1.4Ga, significant increases in Re and V concentrations in organic-rich shales and highly fractionated $\delta^{53}Cr$ in carbonates suggest the possibility of a transient oxidation event at ~1.1Ga (Diamond and Lyons, 2018; Gilleaudeau et al., 2016; Gilleaudeau and Kah, 2013, 2015; Rooney et al., 2010).

After ~1.1Ga, the concentration of RSTEs remained at low levels before the NOE. Multiple geochemical evidences indicate that continental oxidative weathering can be traced back to around 800 Ma (e.g., Cole et al., 2020a; Planavsky et al., 2014). However, the geological record of RSTEs seems unable to identify changes during this period, possibly due to relatively sparse data or low temporal resolution. Nevertheless, in black shales from Northwestern Canada, which are approximately 800 Ma old, the high $\delta^{238}U$ values indicate that there might have been transient oxygenation events in some parts of the ocean (Dang et al., 2022). The Doushantuo Formation in the South China Basin had close connections with the global oceans during the Ediacaran Period (635-560 Ma) (Yuan et al., 2023). The black shales of the Doushantuo Formation exhibit extremely high levels of RSTEs enrichment as well as high Mo and U isotope values (Sahoo et al., 2012, 2016; Ostrander et al., 2019; Yuan et al., 2023), indicating that these sediments captured the fundamental transition of Earth's oceans from predominantly anoxic conditions in the Precambrian to more broadly oxygenated conditions resembling today's oceans (Scott et al., 2008; Sahoo et al., 2012, 2016; Ostrander et al., 2019; Yuan et al., 2023). With the permanent establishment of widespread oceanic oxygenation, RSTEs in the oceans formed stable geochemical cycling processes similar to modern times. In today's predominantly oxygenated oceans, there are large reservoirs of RSTEs, leading to significant enrichment of RSTEs and varying degrees of fractionation of their isotopes in sediments at the anoxic-euxinic bottoms of a few oceanic areas (e.g., Scott et al., 2008; Sahoo et al., 2012, 2016; Partin et al., 2013; Sheen et al., 2018; Ostrander et al., 2019; Chen et al., 2021; Gangl et al., 2023; Yuan et al., 2023).

6. Conclusion and prospects

RSTEs exhibit unique geochemical behavior in the oceans, and differences in their behavior can be used to infer the redox state of the oceans. In suboxic-anoxic deposition environments, Re, U, and V are enriched, whereas Mo requires bottom-water sulphide for autogenous enrichment. As RSTEs respond differently to various redox potentials, the spatial extent of oxic, suboxic, and anoxic-euxinic ambient seawater can be estimated by measuring the concentrations of Re, U, V, and Mo in sediment or rocks. Commonly used assessment methods include the elemental enrichment factor (TM_{EF}), excess trace metal concentration (TM_{XS}), elemental enrichment (TM/Al), bi-elemental ratios (Re/Mo, V/Cr, V/(V + Ni), V/Mn), and Mo- and U-EF covariation patterns. Additionally, the extent of global ocean oxygenation can be inferred from RSTEs isotope mass balance models, utilizing differences in the direction and/or magnitude of isotope fractionation in different redox-characterized environments. Among these, $\delta^{98}Mo$ and $\delta^{238}U$ have been extensively used as oceanic redox tracers on a global scale, while $\delta^{51}V$ has been recognized for its potential to track short-term changes in the global oceanic redox state. Furthermore, the RSTEs concentrations from sediments of locally anoxic oceans can provide crucial evidence for revealing RSTEs oceanic reservoirs and the history of global redox structure. However, within the complex and lengthy sedimentary history of marine sediments, besides the primary control of local redox conditions, other factors such as water chemistry, particle shuttle, sedimentation rates, and post-depositional processes can lead to varying degrees of enrichment of RSTEs in sediments. Therefore, when inferring redox conditions across different spatial and temporal scales, these factors must be taken into consideration.

Currently, the geochemical mechanisms of RSTEs are not fully understood, including their processes of redox migration and transformation. Each geochemical proxy for ancient redox conditions has its own criteria and advantages and disadvantages in practical applications. By integrating multiple independent proxy indicators on the same sample and comparing data from temporally related profiles, more reliable and accurate information on redox and sedimentary environments in local basins can be obtained. Additionally, RSTEs data in ocean systems from different ages and locations are relatively limited, potentially exhibiting spatiotemporal variations in enrichment levels. The applicability of redox proxies developed from modern marine sediment systems or specific basins may be ambiguous when applied to ancient or different ocean basins. In the lengthy history of Earth's oxygenation, there are many controversies and unknowns regarding when and to what extent Earth began producing oxygen. Therefore, detailed stratigraphic and geochronological studies of key periods in Earth's oxygenation history are crucial for advancing our understanding of Earth's history. In the future, combining mass balance approaches of marine Mo, U, V, Re and leveraging the enrichment of RSTEs in sediment could potentially track long-term variations and extents of euxinic and non-euxinic seafloor distributions in the global ocean.

CRediT authorship contribution statement

Guo Ning: Writing – original draft, Methodology, Investigation, Formal analysis, Data curation. **Jiang Wei:** Writing – review & editing, Supervision, Resources, Investigation, Funding acquisition, Conceptualization. **Li Yueer:** Writing – review & editing. **Yu Kefu:** Supervision, Resources.

Declaration of competing interest

The authors declare that they have no known competing financial interests or personal relationships that could have appeared to influence the work reported in this paper.

Acknowledgments

This research was supported by the NSFC (42030502), Guangxi Science and Technology Program (No. AD25069075) and the major talent project of Guangxi (GXR-1BGQ2424020). Thanks are due to the responsible editor and anonymous reviewers for their critical reviews, which greatly improved our paper.

Appendix A. Supplementary data

Supplementary data to this article can be found online at https://doi.org/10.1016/j.palaeo.2025.113082.

Data availability

Data will be made available on request.

References

Absar, N., Kalam, T.D.A., Raza, M.Q., Ashok, M., Islam, R., 2024. Redox conditions of Early Cambrian Ocean as deciphered from multi-proxy geochemical and isotopic studies of Proto-Tethys carbonaceous sediments from Outer Lesser Himalaya, India. J. Earth Syst. Sci. 133, 26.

Abshire, M.L., Romaniello, S.J., Kuzminov, A.M., Cofrancesco, J., Severmann, S., Riedinger, N., 2020. Uranium isotopes as a proxy for primary depositional redox conditions in organic-rich marine systems. Earth Planet. Sci. Lett. 529, 115878.
Abshire, M.L., Riedinger, N., Clymer, J.M., Scott, C., Severmann, S., Romaniello, S.J., Puckette, J.O., 2022. Reconstructing the paleoceanographic and redox conditions responsible for variations in uranium content in North American Devonian black shales. Palaeogeogr. Palaeoclimatol. Palaeoecol. 587, 110763.
Ahm, A.-S.C., Bjerrum, C.J., Blättler, C.L., Swart, P.K., Higgins, J.A., 2018. Quantifying early marine diagenesis in shallow-water carbonate sediments. Geochim. Cosmochim. Acta 236, 140–159. Chemistry of Oceans Past and Present: A Special Issue in tribute to Harry Elderfield.
Ahm, A.-S.C., Maloof, A.C., Macdonald, F.A., Hoffman, P.F., Bjerrum, C.J., Bold, U., Rose, C.V., Strauss, J.V., Higgins, J.A., 2019. An early diagenetic deglacial origin for basal Ediacaran "cap dolostones.". Earth Planet. Sci. Lett. 506, 292–307.
Ahm, A.-S.C., Bjerrum, C.J., Hoffman, P.F., Macdonald, F.A., Maloof, A.C., Rose, C.V., Strauss, J.V., Higgins, J.A., 2021. The Ca and Mg isotope record of the Cryogenian Trezona carbon isotope excursion. Earth Planet. Sci. Lett. 568, 117002.
Akhtar, A.A., Cruger Ahm, A.-S., Higgins, J.A., 2024. Geochemical fingerprints of early diagenesis in shallow-water marine carbonates: insights from paired δ44/40Ca and δ26Mg values. Geochim. Cosmochim. Acta 383, 57–69.
Algeo, T.J., 2004. Can marine anoxic events draw down the trace element inventory of seawater? Geology 32, 1057–1060.
Algeo, T.J., Li, C., 2020. Redox classification and calibration of redox thresholds in sedimentary systems. Geochim. Cosmochim. Acta 287, 8–26. New Developments in Geochemical Proxies for Paleoceanographic Research.
Algeo, T.J., Liu, J., 2020. A re-assessment of elemental proxies for paleoredox analysis. Chem. Geol. 540, 119549.
Algeo, T.J., Lyons, T.W., 2006. Mo–total organic carbon covariation in modern anoxic marine environments: implications for analysis of paleoredox and paleohydrographic conditions. Paleoceanography 21, PA1016.
Algeo, T.J., Maynard, J.B., 2004. Trace-element behavior and redox facies in core shales of Upper Pennsylvanian Kansas-type cyclothems. Chem. Geol. 206, 289–318. Geochemistry of Organic-Rich Shales: New Perspectives.
Algeo, T.J., Rowe, H., 2012. Paleoceanographic applications of trace-metal concentration data. Chem. Geol. 324–325, 6–18. Special Issue Recent Advances in Trace Metal Applications to Paleoceanographic Studies.
Algeo, T.J., Tribovillard, N., 2009. Environmental analysis of paleoceanographic systems based on molybdenum–uranium covariation. Chem. Geol. 268, 211–225.
Aller, R.C., 2014. Sedimentary diagenesis, depositional environments, and benthic fluxes. In: Treatise on Geochemistry, Second ed. Elsevier, Oxford, pp. 293–334.
Anbar, A.D., Knoll, A.H., 2002. Proterozoic ocean chemistry and evolution: a bioinorganic bridge? Science 297, 1137–1142.
Anbar, A.D., Creaser, R.A., Papanastassiou, D.A., Wasserburg, G.J., 1992. Rhenium in seawater: confirmation of generally conservative behavior. Geochim. Cosmochim. Acta 56, 4099–4103.
Anbar, A.D., Duan, Y., Lyons, T.W., Arnold, G.L., Kendall, B., Creaser, R.A., Kaufman, A. J., Gordon, G.W., Scott, C., Garvin, J., Buick, R., 2007. A whiff of oxygen before the great oxidation event? Science 317, 1903–1906.
Andersen, M.B., Romaniello, S., Vance, D., Little, S.H., Herdman, R., Lyons, T.W., 2014. A modern framework for the interpretation of 238U/235U in studies of ancient ocean redox. Earth Planet. Sci. Lett. 400, 184–194.
Andersen, M.B., Elliott, T., Freymuth, H., Sims, K.W.W., Niu, Y., Kelley, K.A., 2015. The terrestrial uranium isotope cycle. Nature 517, 356–359.
Andersen, M.B., Vance, D., Morford, J.L., Bura-Nakić, E., Breitenbach, S.F.M., Och, L., 2016. Closing in on the marine $^{238}U/^{235}U$ budget. Chem. Geol. 420, 11–22.
Andersen, M.B., Stirling, C.H., Weyer, S., 2017. Uranium isotope fractionation. Rev. Mineral. Geochem. 82, 799–850.
Anderson, J.J., Devol, A.H., 1973. Deep water renewal in Saanich Inlet, an intermittently anoxic basin. Estuar. Coast. Mar. Sci. 1, 1–10.
Ardakani, O.H., Chappaz, A., Sanei, H., Mayer, B., 2016. Effect of thermal maturity on remobilization of molybdenum in black shales. Earth Planet. Sci. Lett. 449, 311–320.
Asael, Dan, Rouxel, Olivier, Poulton, S.W., Lyons, T.W., Bekker, Andrey, 2018. Molybdenum record from black shales indicates oscillating atmospheric oxygen levels in the early Paleoproterozoic, 318, 275–299.
Auger, Y., Bodineau, L., Leclercq, S., Wartel, M., 1999. Some aspects of vanadium and chromium chemistry in the English Channel. Cont. Shelf Res. 19, 2003–2018.
Azrieli-Tal, I., Matthews, A., Bar-Matthews, M., Almogi-Labin, A., Vance, D., Archer, C., Teutsch, N., 2014. Evidence from molybdenum and iron isotopes and molybdenum–uranium covariation for sulphidic bottom waters during Eastern Mediterranean sapropel S1 formation. Earth Planet. Sci. Lett. 393, 231–242.
de Baar, H., de Jong, J., 2001. Distributions. In: Wiley, J. (Ed.), Sources and Sinks of Iron in Seawater, in: Biogeochemistry of Fe in Seawater, SCOR - IUPAC. Baltimore, pp. 123–253.
Balistrieri, L.S., Murray, J.W., 1986. The surface chemistry of sediments from the Panama Basin: The influence of Mn oxides on metal adsorption. Geochim. Cosmochim. Acta 50, 2235–2243.
Barling, J., Anbar, A.D., 2004. Molybdenum isotope fractionation during adsorption by manganese oxides. Earth Planet. Sci. Lett. 217, 315–329.
Basu, A., Sanford, R.A., Johnson, T.M., Lundstrom, C.C., Löffler, F.E., 2014. Uranium isotopic fractionation factors during U(VI) reduction by bacterial isolates. Geochim. Cosmochim. Acta 136, 100–113.
Beck, M., Dellwig, O., Schnetger, B., Brumsack, H.-J., 2008. Cycling of trace metals (Mn, Fe, Mo, U, V, Cr) in deep pore waters of intertidal flat sediments. Geochim. Cosmochim. Acta 72, 2822–2840.
Bekker, A., Holland, H.D., Wang, P.-L., Rumble, D., Stein, H.J., Hannah, J.L., Coetzee, L. L., Beukes, N.J., 2004. Dating the rise of atmospheric oxygen. Nature 427, 117–120.
Bellefroid, E.J., Hood, A.V.S., Hoffman, P.F., Thomas, M.D., Reinhard, C.T., Planavsky, N.J., 2018. Constraints on Paleoproterozoic atmospheric oxygen levels. Proc. Natl. Acad. Sci. 115, 8104–8109.
Bennett, W.W., Canfield, D.E., 2020. Redox-sensitive trace metals as paleoredox proxies: A review and analysis of data from modern sediments. Earth Sci. Rev. 204, 103175.
Berner, R.A., 1980. Early diagenesis: a theoretical approach. Princeton University Press, New Jersey.
Bernier-Latmani, R., Veeramani, H., Vecchia, E.D., Junier, P., Lezama-Pacheco, J.S., Suvorova, E.I., Sharp, J.O., Wigginton, N.S., Bargar, J.R., 2010. Non-uraninite Products of Microbial U(VI) Reduction. Environ. Sci. Technol. 44, 9456–9462.
Bertine, K.K., Turekian, K.K., 1973. Molybdenum in marine deposits. Geochim. Cosmochim. Acta 37, 1415–1434.
Bone, S.E., Dynes, J.J., Cliff, J., Bargar, J.R., 2017. Uranium(IV) adsorption by natural organic matter in anoxic sediments. Proc. Natl. Acad. Sci. 114, 711–716.
Borchers, S.L., Schnetger, B., Böning, P., Brumsack, H.-J., 2005. Geochemical signatures of the Namibian diatom belt: Perennial upwelling and intermittent anoxia. Geochem. Geophys. Geosyst. 6, 2004GC000886.
Böttcher, M.E., 1998. Manganese(II) partitioning during experimental precipitation of rhodochrosite–calcite solid solutions from aqueous solutions. Mar. Chem. 62, 287–297.
Brand, U., Veizer, J., 1980. Chemical diagenesis of a multicomponent carbonate system–1: trace elements. J. Sediment. Res. 50, 1219–1236.
Brand, U., Veizer, J., 1981. Chemical diagenesis of a multicomponent carbonate system; 2, Stable isotopes. J. Sediment. Res. 51, 987–997.
Breit, G.N., Wanty, R.B., 1991. Vanadium accumulation in carbonaceous rocks: a review of geochemical controls during deposition and diagenesis. Chem. Geol. 91, 83–97. Trace Metals in Petroleum Geochemistry.
Brennecka, G.A., Wasylenki, L.E., Bargar, J.R., Weyer, S., Anbar, A.D., 2011. Uranium isotope fractionation during adsorption to Mn-oxyhydroxides. Environ. Sci. Technol. 45, 1370–1375.
Brüchert, V., Jørgensen, B.B., Neumann, K., Riechmann, D., Schlösser, M., Schulz, H., 2003. Regulation of bacterial sulfate reduction and hydrogen sulfide fluxes in the central namibian coastal upwelling zone. Geochim. Cosmochim. Acta 67, 4505–4518.
Bruggmann, S., Gilleaudeau, G.J., Romaniello, S.J., Severmann, S., Canfield, D.E., Anbar, A.D., Scholz, F., Frei, R., 2022. Uranium isotope cycling on the highly productive Peruvian margin. Chem. Geol. 590, 120705.
Brumsack, H.-J., 1989. Geochemistry of recent TOC-rich sediments from the Gulf of California and the Black Sea. Geol. Rundsch. 78, 851–882.
Brumsack, H.-J., 2006. The trace metal content of recent organic carbon-rich sediments: implications for Cretaceous black shale formation. Palaeogeogr. Palaeoclimatol. Palaeoecol. 232, 344–361.
Brüske, A., Weyer, S., Zhao, M.-Y., Planavsky, N.J., Wegwerth, A., Neubert, N., Dellwig, O., Lau, K.V., Lyons, T.W., 2020. Correlated molybdenum and uranium isotope signatures in modern anoxic sediments: implications for their use as paleo-redox proxy. Geochim. Cosmochim. Acta 270, 449–474.
Bura-Nakić, E., Andersen, M.B., Archer, C., de Souza, G.F., Marguš, M., Vance, D., 2018. Coupled Mo-U abundances and isotopes in a small marine euxinic basin: Constraints on processes in euxinic basins. Geochim. Cosmochim. Acta 222, 212–229.
Burdige, D.J., 1993. The biogeochemistry of manganese and iron reduction in marine sediments. Earth Sci. Rev. 35, 249–284.
Cabral, A.R., Creaser, R.A., Nägler, T., Lehmann, B., Voegelin, A.R., Belyatsky, B., Pašava, J., Seabra Gomes, A.A., Galbiatti, H., Böttcher, M.E., Escher, P., 2013. Trace-element and multi-isotope geochemistry of Late-Archean black shales in the Carajás iron-ore district, Brazil. Chem. Geol. 362, 91–104. Special Issue dedicated to H.D. Holland: Evolution of the atmosphere and ocean through time.
Cai, C., Xiang, L., Yuan, Y., He, X., Chu, X., Chen, Y., Xu, C., 2015. Marine C, S and N biogeochemical processes in the redox-stratified early Cambrian Yangtze ocean. J. Geol. Soc. Lond. 172, 390–406.
Calvert, S.E., Pedersen, T.F., 1993. Geochemistry of recent oxic and anoxic marine sediments: Implications for the geological record. Mar. Geol. 113, 67–88. Marine Sediments, Burial, Pore Water Chemistry, Microbiology and Diagenesis.
Calvert, S.E., Piper, D.Z., Thunell, R.C., Astor, Y., 2015. Elemental settling and burial fluxes in the Cariaco Basin. Mar. Chem. 177, 607–629.
Chang, X., Huang, Y., Chen, Z., Hou, M., 2020. The microscopic analysis of pyrite framboids and application in paleo-oceanography. Acta Sedimentol. Sin. 38, 150–165.
Chen, J., Montañez, I.P., Zhang, S., Isson, T.T., Macarewich, S.I., Planavsky, N.J., Zhang, F., Rauzi, S., Daviau, K., Yao, L., Qi, Y., Wang, Y., Fan, J., Poulsen, C.J., Anbar, A.D., Shen, S., Wang, X., 2022a. Marine anoxia linked to abrupt global warming during Earth's penultimate icehouse. Proc. Natl. Acad. Sci. 119, e2115231119.
Chen, X., Ling, H.-F., Vance, D., Shields-Zhou, G.A., Zhu, M., Poulton, S.W., Och, L.M., Jiang, S.-Y., Li, D., Cremonese, L., Archer, C., 2015. Rise to modern levels of ocean oxygenation coincided with the Cambrian radiation of animals. Nat. Commun. 6, 1–7.
Chen, X., Romaniello, S.J., Herrmann, A.D., Hardisty, D., Gill, B.C., Anbar, A.D., 2018a. Diagenetic effects on uranium isotope fractionation in carbonate sediments from the Bahamas. Geochim. Cosmochim. Acta 237, 294–311.
Chen, X., Romaniello, S.J., Herrmann, A.D., Samankassou, E., Anbar, A.D., 2018b. Biological effects on uranium isotope fractionation (238U/235U) in primary biogenic carbonates. Geochim. Cosmochim. Acta 240, 1–10.
Chen, X., Tissot, F.L.H., Jansen, M.F., Bekker, A., Liu, C.X., Nie, N.X., Halverson, G.P., Veizer, J., Dauphas, N., 2021. The uranium isotopic record of shales and carbonates through geologic time. Geochim. Cosmochim. Acta 300, 164–191.

Chen, X., Li, S., Newby, S.M., Lyons, T.W., Wu, F., Owens, J.D., 2022b. Iron and manganese shuttle has no effect on sedimentary thallium and vanadium isotope signatures in Black Sea sediments. Geochim. Cosmochim. Acta 317, 218–233.
Chen, Z., Wang, G., Jin, C., 2022c. Marine redox variation and hydrographic restriction in the early Cambrian Nanhua Basin, South China. Palaeogeogr. Palaeoclimatol. Palaeoecol. 607, 111263.
Cheng, M., Li, C., Zhou, L., Xie, S., 2015. Mo marine geochemistry and reconstruction of ancient ocean redox states. Sci. China Earth Sci. 58, 2123–2133.
Cheng, M., Li, C., Zhou, L., Algeo, T.J., Zhang, F., Romaniello, S., Jin, C.-S., Lei, L.-D., Feng, L.-J., Jiang, S.-Y., 2016. Marine Mo biogeochemistry in the context of dynamically euxinic mid-depth waters: a case study of the lower Cambrian Niutitang shales, South China. Geochim. Cosmochim. Acta 183, 79–93.
Cherry, L.B., Gilleaudeau, G.J., Grazhdankin, D.V., Romaniello, S.J., Martin, A.J., Kaufman, A.J., 2022. A diverse Ediacara assemblage survived under low-oxygen conditions. Nat. Commun. 13, 7306.
Cochran, J.K., Carey, A.E., Sholkovitz, E.R., Surprenant, L.D., 1986. The geochemistry of uranium and thorium in coastal marine sediments and sediment pore waters. Geochim. Cosmochim. Acta 50, 663–680.
Cole, D.B., Mills, D.B., Erwin, D.H., Sperling, E.A., Porter, S.M., Reinhard, C.T., Planavsky, N.J., 2020a. On the co-evolution of surface oxygen levels and animals. Geobiology 18, 260–281.
Cole, D.B., Planavsky, N.J., Longley, M., Böning, P., Wilkes, D., Wang, X., Swanner, E.D., Wittkop, C., Loydell, D.K., Busigny, V., Knudsen, A.C., Sperling, E.A., 2020b. Uranium isotope fractionation in non-sulfidic anoxic settings and the global uranium isotope mass balance. Glob. Biogeochem. Cycles 34, e2020GB006649.
Collier, R.W., 1984. Particulate and dissolved vanadium in the North Pacific Ocean. Nature 309, 441–444.
Colodner, D., Sachs, J., Ravizza, G., Turekian, K., Edmond, J., Boyle, E., 1993. The geochemical cycle of rhenium: a reconnaissance. Earth Planet. Sci. Lett. 117, 205–221.
Cox, G.M., Jarrett, A., Edwards, D., Crockford, P.W., Halverson, G.P., Collins, A.S., Poirier, A., Li, Z.-X., 2016. Basin redox and primary productivity within the Mesoproterozoic Roper Seaway. Chem. Geol. 440, 101–114.
Crombez, V., Rohais, S., Euzen, T., Riquier, L., Baudin, F., Hernandez-Bilbao, E., 2020. Trace metal elements as paleoenvironmental proxies: Why should we account for sedimentation rate variations? Geology 48, 839–843.
Crusius, J., Thomson, J., 2000. Comparative behavior of authigenic Re, U, and Mo during reoxidation and subsequent long-term burial in marine sediments. Geochim. Cosmochim. Acta 64, 2233–2242.
Crusius, J., Thomson, J., 2003. Mobility of authigenic rhenium, silver, and selenium during postdepositional oxidation in marine sediments. Geochim. Cosmochim. Acta 67, 265–273.
Crusius, J., Calvert, S., Pedersen, T., Sage, D., 1996. Rhenium and molybdenum enrichments in sediments as indicators of oxic, suboxic and sulfidic conditions of deposition. Earth Planet. Sci. Lett. 145, 65–78.
Cui, M., Luther, G.W., Gomes, M., 2023. Constraining the major pathways of vanadium incorporation into sediments underlying natural sulfidic waters. Geochim. Cosmochim. Acta 359, 148–164.
Dahl, T.W., Chappaz, A., Hoek, J., McKenzie, C.J., Svane, S., Canfield, D.E., 2017. Evidence of molybdenum association with particulate organic matter under sulfidic conditions. Geobiology 15, 311–323.
Dang, D.H., Novotnik, B., Wang, W., Georg, R.B., Evans, R.D., 2016. Uranium isotope fractionation during adsorption, (Co)precipitation, and biotic reduction. Environ. Sci. Technol. 50, 12695–12704.
Dang, D.H., Wang, W., Gibson, T.M., Kunzmann, M., Andersen, M.B., Halverson, G.P., Evans, R.D., 2022. Authigenic uranium isotopes of late Proterozoic black shale. Chem. Geol. 588, 120644.
Dellinger, M., Hilton, R.G., Nowell, G.M., 2021. Fractionation of rhenium isotopes in the Mackenzie River basin during oxidative weathering. Earth Planet. Sci. Lett. 573, 117131.
Dellwig, O., Wegwerth, A., Arz, H.W., 2021. Anatomy of the Major Baltic Inflow in 2014: impact of manganese and iron shuttling on phosphorus and trace metals in the Gotland Basin, Baltic Sea. Cont. Shelf Res. 223, 104449.
Diamond, C.W., Lyons, T.W., 2018. Mid-Proterozoic redox evolution and the possibility of transient oxygenation events. Emerg. Top. Life Sci. 2, 235–245.
Diamond, C.W., Planavsky, N.J., Wang, C., Lyons, T.W., 2018. What the 1.4 Ga Xiamaling Formation can and cannot tell us about the mid-Proterozoic ocean. Geobiology 16, 219–236.
Deming, J.W., Baross, J.A., 1993. The Early Diagenesis of Organic Matter: Bacterial Activity. In: Engel, M.H., Macko, S.A. (Eds.), Organic Geochemistry, Topics in Geobiology. Springer US, Boston, MA, pp. 119–144.
Diamond, C.W., Ernst, R.E., Zhang, S.-H., Lyons, T.W., 2021. Breaking the Boring Billion. In: Large Igneous Provinces. American Geophysical Union (AGU), pp. 487–501.
Dickson, A.J., 2017. A molybdenum-isotope perspective on Phanerozoic deoxygenation events. Nat. Geosci. 10, 721–726.
Dickson, A.J., Hsieh, Y.-T., Bryan, A., 2020. The rhenium isotope composition of Atlantic Ocean seawater. Geochim. Cosmochim. Acta 287, 221–228. New Developments in Geochemical Proxies for Paleoceanographic Research.
Dong, Z.-G., Peng, Z.-D., Robbins, L.J., Konhauser, K.O., Zhang, B.-L., Zhang, L.-C., Li, J., Li, W.-J., Zhang, L., Wang, C.-L., 2023. Episodic ventilation of euxinic bottom waters triggers the formation of black shale-hosted Mn carbonate depositsEuxinic. Geochim. Cosmochim. Acta 341, 132–149.
Duan, Y., Anbar, A.D., Arnold, G.L., Lyons, T.W., Gordon, G.W., Kendall, B., 2010. Molybdenum isotope evidence for mild environmental oxygenation before the Great Oxidation Event. Geochim. Cosmochim. Acta 74, 6655–6668.
Dunk, R.M., Mills, R.A., Jenkins, W.J., 2002. A reevaluation of the oceanic uranium budget for the Holocene. Chem. Geol. 190, 45–67. Geochemistry of Crustal Fluids-Fluids in the Crust and Chemical Fluxes at the Earth's Surface.
Emerson, S.R., Huested, S.S., 1991. Ocean anoxia and the concentrations of molybdenum and vanadium in seawater. Mar. Chem. 34, 177–196.
Erickson, B.E., Helz, G.R., 2000. Molybdenum(VI) speciation in sulfidic waters:: stability and lability of thiomolybdates. Geochim. Cosmochim. Acta 64, 1149–1158.
Eroglu, S., Schoenberg, R., Wille, M., Beukes, N., Taubald, H., 2015. Geochemical stratigraphy, sedimentology, and Mo isotope systematics of the ca. 2.58–2.50 Ga-old Transvaal Supergroup carbonate platform, South Africa. Precambrian Res. 266, 27–46.
Eroglu, S., Scholz, F., Frank, M., Siebert, C., 2020. Influence of particulate versus diffusive molybdenum supply mechanisms on the molybdenum isotope composition of continental margin sediments. Geochim. Cosmochim. Acta 273, 51–69.
Fantle, M.S., Higgins, J., 2014. The effects of diagenesis and dolomitization on Ca and Mg isotopes in marine platform carbonates: implications for the geochemical cycles of Ca and Mg. Geochim. Cosmochim. Acta 142, 458–481.
Fantle, M.S., Barnes, B.D., Lau, K.V., 2020. The role of diagenesis in shaping the geochemistry of the marine carbonate record. Annu. Rev. Earth Planet. Sci. 48, 549–583.
Frei, R., Gaucher, C., Poulton, S.W., Canfield, D.E., 2009. Fluctuations in Precambrian atmospheric oxygenation recorded by chromium isotopes. Nature 461, 250–253.
Froelich, P.N., Klinkhammer, G.P., Bender, M.L., Luedtke, N.A., Heath, G.R., Cullen, D., Dauphin, P., Hammond, D., Hartman, B., Maynard, V., 1979. Early oxidation of organic matter in pelagic sediments of the eastern equatorial Atlantic: suboxic diagenesis. Geochim. Cosmochim. Acta 43, 1075–1090.
Gangl, S.K., Stirling, C.H., Jenkyns, H.C., Preston, W.J., Clarkson, M.O., Moy, C.M., Dickson, A.J., Porcelli, D., 2023. Regional conditions cause contrasting behaviour in U-isotope fractionation in black shales: constraints for global ocean palaeo-redox reconstructions. Chem. Geol. 623, 121411.
Gill, B.C., Dahl, T.W., Hammarlund, E.U., LeRoy, M.A., Gordon, G.W., Canfield, D.E., Anbar, A.D., Lyons, T.W., 2021. Redox dynamics of later Cambrian oceans. Palaeogeogr. Palaeoclimatol. Palaeoecol. 581, 110623.
Gilleaudeau, G.J., Kah, L.C., 2013. Oceanic molybdenum drawdown by epeiric sea expansion in the Mesoproterozoic. Chem. Geol. 356, 21–37.
Gilleaudeau, G.J., Kah, L.C., 2015. Heterogeneous redox conditions and a shallow chemocline in the Mesoproterozoic ocean: evidence from carbon–sulfur–iron relationships. Precambrian Res. 257, 94–108.
Gilleaudeau, G.J., Frei, R., Kaufman, A.J., Kah, L.C., Azmy, K., Bartley, J.K., Chernyavskiy, P., Knoll, A.H., 2016. Oxygenation of the mid-Proterozoic atmosphere: clues from chromium isotopes in carbonates. Geochem. Perspect. Lett. 2, 178–187.
Gilleaudeau, G.J., Sahoo, S.K., Ostrander, C.M., Owens, J.D., Poulton, S.W., Lyons, T.W., Anbar, A.D., 2020. Molybdenum isotope and trace metal signals in an iron-rich Mesoproterozoic ocean: a snapshot from the Vindhyan Basin, India. Precambrian Res. 343, 105718.
Gong, Z., Wei, G.-Y., Fakhraee, M., Alcott, L.J., Jiang, L., Zhao, M., Planavsky, N.J., 2023. Revisiting marine redox conditions during the Ediacaran Shuram carbon isotope excursion. Geobiology 21, 407–420.
Goswami, V., Singh, S.K., Bhushan, R., 2012. Dissolved redox sensitive elements, Re, U and Mo in intense denitrification zone of the Arabian Sea. Chem. Geol. 291, 256–268.
Goto, K.T., Anbar, A.D., Gordon, G.W., Romaniello, S.J., Shimoda, G., Takaya, Y., Tokumaru, A., Nozaki, T., Suzuki, K., Machida, S., Hanyu, T., Usui, A., 2014. Uranium isotope systematics of ferromanganese crusts in the Pacific Ocean: Implications for the marine $^{238}U/^{235}U$ isotope system. Geochim. Cosmochim. Acta 146, 43–58.
Hardisty, D.S., Riedinger, N., Planavsky, N.J., Asael, D., Andrén, T., Jørgensen, B.B., Lyons, T.W., 2016. A Holocene history of dynamic water column redox conditions in the Landsort deep, Baltic Sea. Am. J. Sci. 316, 713–745.
Hatch, J.R., Leventhal, J.S., 1992. Relationship between inferred redox potential of the depositional environment and geochemistry of the Upper Pennsylvanian (Missourian) Stark Shale Member of the Dennis Limestone, Wabaunsee County, Kansas, U.S.A. Chem. Geol. 99, 65–82. Geochemistry of Metalliferous Black Shales.
He, Y., Zhu, X., Qiu, Y., Pang, L., Zhao, T., 2022. Extreme climate changes influenced early life evolution at ~ 1.4 Ga: Implications from shales of the Xiamaling Formation, northern North China Craton. Precambrian Res. 383, 106901.
He, Z., Clarkson, M.O., Andersen, M.B., Archer, C., Sweere, T.C., Kraal, P., Guthauser, A., Huang, F., Vance, D., 2021. Temporally and spatially dynamic redox conditions on an upwelling margin: The impact on coupled sedimentary Mo and U isotope systematics, and implications for the Mo-U paleoredox proxy. Geochim. Cosmochim. Acta 309, 251–271.
Heard, A.W., Wang, Y., Ostrander, C.M., Auro, M., Canfield, D.E., Zhang, S., Wang, H., Wang, X., Nielsen, S.G., 2023. Coupled vanadium and thallium isotope constraints on Mesoproterozoic ocean oxygenation around 1.38-1.39 Ga. Earth Planet. Sci. Lett. 610, 118127.
Hein, J.R., Koschinsky, A., 2014. 13.11 - Deep-Ocean ferromanganese crusts and nodules. In: Holland, H.D., Turekian, K.K. (Eds.), Treatise on Geochemistry, Second ed. Elsevier, Oxford, pp. 273–291.
Hein, J.R., Mizell, K., Koschinsky, A., Conrad, T.A., 2013. Deep-ocean mineral deposits as a source of critical metals for high- and green-technology applications: Comparison with land-based resources. Ore Geol. Rev. 51, 1–14.
Helz, G.R., 2022. The Re/Mo redox proxy reconsidered. Geochim. Cosmochim. Acta 317, 507–522.
Helz, G.R., Dolor, M.K., 2012. What regulates rhenium deposition in euxinic basins? Chem. Geol. 304–305, 131–141.

Helz, G.R., Vorlicek, T.P., 2019. Precipitation of molybdenum from euxinic waters and the role of organic matter. Chem. Geol. 509, 178–193.
Helz, G.R., Miller, C.V., Charnock, J.M., Mosselmans, J.F.W., Pattrick, R.A.D., Garner, C. D., Vaughan, D.J., 1996. Mechanism of molybdenum removal from the sea and its concentration in black shales: EXAFS evidence. Geochim. Cosmochim. Acta 60, 3631–3642.
Helz, G.R., Bura-Nakić, E., Mikac, N., Ciglenečki, I., 2011. New model for molybdenum behavior in euxinic waters. Chem. Geol. 284, 323–332.
Hermans, M., Lenstra, W.K., van Helmond, N.A.G.M., Behrends, T., Egger, M., Séguret, M.J.M., Gustafsson, E., Gustafsson, B.G., Slomp, C.P., 2019. Impact of natural re-oxygenation on the sediment dynamics of manganese, iron and phosphorus in a euxinic Baltic Sea basin. Geochim. Cosmochim. Acta 246, 174–196.
Higgins, J.A., Blättler, C.L., Lundstrom, E.A., Santiago-Ramos, D.P., Akhtar, A.A., Crüger Ahm, A.-S., Bialik, O., Holmden, C., Bradbury, H., Murray, S.T., Swart, P.K., 2018. Mineralogy, early marine diagenesis, and the chemistry of shallow-water carbonate sediments. Geochim. Cosmochim. Acta 220, 512–534.
Hood, A.V.S., Planavsky, N.J., Wallace, M.W., Wang, X., 2018. The effects of diagenesis on geochemical paleoredox proxies in sedimentary carbonates. Geochim. Cosmochim. Acta 232, 265–287.
Hu, R., Tan, J., Dick, J., Wang, Y., Li, G., Liu, C., 2023. Depositional conditions of siliceous microfossil-rich shale during the Ordovician–Silurian transition of south China: Implication for organic matter enrichment. Mar. Pet. Geol. 154, 106307.
Jakobsen, R., Postma, D., 1989. Formation and solid solution behavior of Ca-rhodochrosites in marine muds of the Baltic deeps. Geochim. Cosmochim. Acta 53, 2639–2648.
Jeandel, C., Caisso, M., Minster, J.F., 1987. Vanadium behaviour in the global ocean and in the Mediterranean sea. Mar. Chem. 21, 51–74.
Jobe, Z.R., Lowe, D.R., Morris, W.R., 2012. Climbing-ripple successions in turbidite systems: depositional environments, sedimentation rates and accumulation times. Sedimentology 59, 867–898.
Jokinen, S.A., Koho, K., Virtasalo, J.J., Jilbert, T., 2020. Depth and intensity of the sulfate-methane transition zone control sedimentary molybdenum and uranium sequestration in a eutrophic low-salinity setting. Appl. Geochem. 122, 104767.
Jones, B., Manning, D.A.C., 1994. Comparison of geochemical indices used for the interpretation of palaeoredox conditions in ancient mudstones. Chem. Geol. 111, 111–129.
Kaczmarek, S.E., Thornton, B., 2017. The effect of temperature on stoichiometry, cation ordering, and reaction rate in high-temperature dolomitization experiments. Chem. Geol. 468, 32–41.
Kaufman, A.J., Knoll, A.H., 1995. Neoproterozoic variations in the C-isotopic composition of seawater: stratigraphic and biogeochemical implications. Precambrian Res. 73, 27–49. Neoproterozoic Stratigraphy and Earth History.
Kendall, B., 2021. Recent Advances in Geochemical Paleo-Oxybarometers. Annu. Rev. Earth Planet. Sci. 49, 399–433.
Kendall, B., Creaser, R.A., Gordon, G.W., Anbar, A.D., 2009. Re–Os and Mo isotope systematics of black shales from the Middle Proterozoic Velkerri and Wollogorang Formations, McArthur Basin, northern Australia. Geochim. Cosmochim. Acta 73, 2534–2558.
Kendall, B., Reinhard, C.T., Lyons, T.W., Kaufman, A.J., Poulton, S.W., Anbar, A.D., 2010. Pervasive oxygenation along late Archaean ocean margins. Nat. Geosci. 3, 647–652.
Kendall, B., Gordon, G.W., Poulton, S.W., Anbar, A.D., 2011. Molybdenum isotope constraints on the extent of late Paleoproterozoic ocean euxinia. Earth Planet. Sci. Lett. 307, 450–460.
Kendall, B., Brennecka, G.A., Weyer, S., Anbar, A.D., 2013. Uranium isotope fractionation suggests oxidative uranium mobilization at 2.50 Ga. Chem. Geol. 362, 105–114. Special Issue dedicated to H.D. Holland: Evolution of the Atmosphere and Ocean Through Time.
Kendall, B., Dahl, T.W., Anbar, A.D., 2017. The stable isotope geochemistry of molybdenum. Rev. Mineral. Geochem. 82, 683–732.
Kendall, B., Wang, J., Zheng, W., Romaniello, S.J., Over, D.J., Bennett, Y., Xing, L., Kunert, A., Boyes, C., Liu, J., 2020. Inverse correlation between the molybdenum and uranium isotope compositions of Upper Devonian black shales caused by changes in local depositional conditions rather than global ocean redox variations. Geochim. Cosmochim. Acta 287, 141–164. New Developments in Geochemical Proxies for Paleoceanographic Research.
Klinkhammer, G.P., Palmer, M.R., 1991. Uranium in the oceans: where it goes and why. Geochim. Cosmochim. Acta 55, 1799–1806.
Koide, Minoru, Hodge, Vern, Yang, J.S., Goldberg, E.D., 1987. Determination of rhenium in marine waters and sediments by graphite furnace atomic absorption spectrometry. Anal. Chem. 59, 1802–1805.
Ku, T.-L., Mathieu, G.G., Knauss, K.G., 1977. Uranium in open ocean: concentration and isotopic composition. Deep-Sea Res. 24, 1005–1017.
Kunert, A., Kendall, B., 2023. Global ocean redox changes before and during the Toarcian Oceanic Anoxic Event. Nat. Commun. 14, 1–10.
Kunert, A., Clarke, J., Kendall, B., 2020. Molybdenum isotope constraints on the origin of vanadium hyper-enrichments in Ediacaran–Phanerozoic marine Mudrocks. Minerals 10, 1075.
Kurzweil, F., Claire, M., Thomazo, C., Peters, M., Hannington, M., Strauss, H., 2013. Atmospheric sulfur rearrangement 2.7 billion years ago: Evidence for oxygenic photosynthesis. Earth Planet. Sci. Lett. 366, 17–26.
Kurzweil, F., Drost, K., Pašava, J., Wille, M., Taubald, H., Schoeckle, D., Schoenberg, R., 2015. Coupled sulfur, iron and molybdenum isotope data from black shales of the Teplá-Barrandian unit argue against deep ocean oxygenation during the Ediacaran. Geochim. Cosmochim. Acta 171, 121–142.
Lau, K.V., Hardisty, D.S., 2022. Modeling the impacts of diagenesis on carbonate paleoredox proxie. Geochim. Cosmochim. Acta 337, 123–139.
Lau, K.V., Maher, K., Brown, S.T., Jost, A.B., Altıner, D., DePaolo, D.J., Eisenhauer, A., Kelley, B.M., Lehrmann, D.J., Paytan, A., Silva-Tamayo, J.C., Yu, M., Payne, J.L., 2017. The influence of seawater carbonate chemistry, mineralogy, and diagenesis on calcium isotope variations in Lower-Middle Triassic carbonate rocks. Chem. Geol. 471, 13–37.
Lau, K.V., Lyons, T.W., Maher, K., 2020. Uranium reduction and isotopic fractionation in reducing sediments: insights from reactive transport modeling. Geochim. Cosmochim. Acta 287, 65–92. New Developments in Geochemical Proxies for Paleoceanographic Research.
Lau, K.V., Hancock, L.G., Severmann, S., Kuzminov, A., Cole, D.B., Behl, R.J., Planavsky, N.J., Lyons, T.W., 2022. Variable local basin hydrography and productivity control the uranium isotope paleoredox proxy in anoxic black shales. Geochim. Cosmochim. Acta 317, 433–456.
Li, F., Ye, Y., Yu, Y., Guo, R., 2023a. Research progress of carbonate rock diagenesi. Bull. Geol. Sci. Technol. 42, 170–190.
Li, J., Azmy, K., Kendall, B., 2022. The Mo- and U-isotope signatures in alternating shales and carbonate beds of rhythmites: a comparison and implications for redox conditions across the Cambrian-Ordovician boundary. Chem. Geol. 602, 120882.
Li, L., Wang, X., Ren, Y., Su, H., Hu, L., Yang, G., Li, Z., Bosin, A.A., Astakhov, A.S., Chen, J., Liu, Y., Shi, X., 2021. Enrichment of Trace Metals (V, Cu, Co, Ni, and Mo) in Arctic Sediments—From Siberian Arctic Shelves to the Basin. J. Geophys. Res. Oceans 126, e2020JC016960.
Li, S., Friedrich, O., Nielsen, S.G., Wu, F., Owens, J.D., 2023b. Reconciling biogeochemical redox proxies: tracking variable bottom water oxygenation during OAE-2 using vanadium isotopes. Earth Planet. Sci. Lett. 617, 118237.
Li, Y., Zhang, T., Ellis, G.S., Shao, D., 2017. Depositional environment and organic matter accumulation of Upper Ordovician–Lower Silurian marine shale in the Upper Yangtze Platform, South China. Palaeogeogr. Palaeoclimatol. Palaeoecol. 466, 252–264.
Liu, J., Algeo, T.J., 2020. Beyond redox: control of trace-metal enrichment in anoxic marine facies by watermass chemistry and sedimentation rate. Geochim. Cosmochim. Acta 287, 296–317.
Liu, X., Chen, H., Mu, X., Zhang, H., Fan, J., Huang, Y., Zhao, K., Mansour, A., Gentzis, T., Ostadhassan, M., 2023. Organic matter preservation conditions in the third member of the Shahejie Formation (Dongpu Depression, China). Int. J. Coal Geol. 277, 104334.
Livermore, B.D., Dahl, T.W., Bizzarro, M., Connelly, J.N., 2020. Uranium isotope compositions of biogenic carbonates – Implications for U uptake in shells and the application of the paleo-ocean oxygenation proxy. Geochim. Cosmochim. Acta 287, 50–64.
Lovley, D.R., Phillips, E.J.P., Gorby, Y.A., Landa, E.R., 1991. Microbial reduction of uranium. Nature 350, 413–416.
Lovley, D.R., Roden, E.E., Phillips, E.J.P., Woodward, J.C., 1993. Enzymatic iron and uranium reduction by sulfate-reducing bacteria. Mar. Geol. 113, 41–53. Marine Sediments, Burial, Pore Water Chemistry, Microbiology and Diagenesis.
Lu, X., Kendall, B., Stein, H.J., Li, C., Hannah, J.L., Gordon, G.W., Ebbestad, J.O.R., 2017. Marine redox conditions during deposition of Late Ordovician and Early Silurian organic-rich mudrocks in the Siljan ring district, central Sweden. Chem. Geol. 457, 75–94.
Lu, X., Dahl, T.W., Zheng, W., Wang, S., Kendall, B., 2020. Estimating ancient seawater isotope compositions and global ocean redox conditions by coupling the molybdenum and uranium isotope systems of euxinic organic-rich mudrocks. Geochim. Cosmochim. Acta 290, 76–103.
Lu, X., Edwards, C.T., Kendall, B., 2023. No evidence for expansion of global ocean euxinia during the base Stairsian mass extinction event (Tremadocian, Early Ordovician). Geochim. Cosmochim. Acta 341, 116–131.
Luo, G., Ono, S., Beukes, N.J., Wang, D.T., Xie, S., Summons, R.E., 2016. Rapid oxygenation of Earth's atmosphere 2.33 billion years ago. Sci. Adv. 2, e1600134.
Luo, J., Long, X., Bowyer, F.T., Mills, B.J.W., Li, J., Xiong, Y., Zhu, X., Zhang, K., Poulton, S.W., 2021. Pulsed oxygenation events drove progressive oxygenation of the early Mesoproterozoic ocean. Earth Planet. Sci. Lett. 559, 116754.
Lv, J., Zhai, S., Yu, Z., Liu, X., Wang, K., 2021. Application and influence factors of redox-sensitive elements in a sedimentary environment. Mar. Sci. 45, 108–124.
Lyons, T.W., Reinhard, C.T., Planavsky, N.J., 2014. The rise of oxygen in Earth's early ocean and atmosphere. Nature 506, 307–315.
Mänd, K., Lalonde, S.V., Robbins, L.J., Thoby, M., Paiste, K., Kreitsmann, T., Paiste, P., Reinhard, C.T., Romashkin, A.E., Planavsky, N.J., Kirsimäe, K., Lepland, A., Konhauser, K.O., 2020. Palaeoproterozoic oxygenated oceans following the Lomagundi–Jatuli Event. Nat. Geosci. 13, 302–306.
Mänd, K., Planavsky, N.J., Porter, S.M., Robbins, L.J., Wang, C., Kreitsmann, T., Paiste, K., Paiste, P., Romashkin, A.E., Deines, Y.E., Kirsimäe, K., Lepland, A., Konhauser, K.O., 2022. Chromium evidence for protracted oxygenation during the Paleoproterozoic. Earth Planet. Sci. Lett. 584, 117501.
Mangini, A., Jung, M., Laukenmann, S., 2001. What do we learn from peaks of uranium and of manganese in deep sea sediments? Mar. Geol. 177, 63–78.
McDaniel, D.K., Walker, R.J., Hemming, S.R., Horan, M.F., Becker, H., Grauch, R.I., 2004. Sources of osmium to the modern oceans: new evidence from the 190Pt-186Os system11Associate editor: E. M. Ripley. Geochim. Cosmochim. Acta 68, 1243–1252.
McLennan, S.M., 2001. Relationships between the trace element composition of sedimentary rocks and upper continental crust. Geochem. Geophys. Geosyst. 2, 2000GC000109.
McManus, J., Berelson, W.M., Klinkhammer, G.P., Hammond, D.E., Holm, C., 2005. Authigenic uranium: relationship to oxygen penetration depth and organic carbon rain. Geochim. Cosmochim. Acta 69, 95–108.

McManus, J., Berelson, W.M., Severmann, S., Poulson, R.L., Hammond, D.E., Klinkhammer, G.P., Holm, C., 2006. Molybdenum and uranium geochemistry in continental margin sediments: paleoproxy potential. Geochim. Cosmochim. Acta 70, 4643–4662.
Mesa-Fernández, J.M., Martínez-Ruiz, F., Rodrigo-Gámiz, M., Jiménez-Espejo, F.J., García, M., Sierro, F.J., 2022. Paleocirculation and paleoclimate conditions in the western Mediterranean basins over the last deglaciation: new insights from sediment composition variations. Glob. Planet. Chang. 209, 103732.
Middelburg, J.J., De Lange, G.J., van Der Weijden, C.H., 1987. Manganese solubility control in marine pore waters. Geochim. Cosmochim. Acta 51, 759–763.
Miller, C.A., Peucker-Ehrenbrink, B., Walker, B.D., Marcantonio, F., 2011. Re-assessing the surface cycling of molybdenum and rhenium. Geochim. Cosmochim. Acta 75, 7146–7179.
Miller, C.A., Peucker-Ehrenbrink, B., Schauble, E.A., 2015. Theoretical modeling of rhenium isotope fractionation, natural variations across a black shale weathering profile, and potential as a paleoredox proxy. Earth Planet. Sci. Lett. 430, 339–348.
Monien, P., Lettmann, K.A., Monien, D., Asendorf, S., Wölfl, A.-C., Lim, C.H., Thal, J., Schnetger, B., Brumsack, H.-J., 2014. Redox conditions and trace metal cycling in coastal sediments from the maritime Antarctic. Geochim. Cosmochim. Acta 141, 26–44.
Montoya-Pino, C., Weyer, S., Anbar, A.D., Pross, J., Oschmann, W., Van De Schootbrugge, B., Arz, H.W., 2010. Global enhancement of ocean anoxia during Oceanic Anoxic Event 2: a quantitative approach using U isotopes. Geology 38, 315–318.
Morford, J.L., Emerson, S., 1999. The geochemistry of redox sensitive trace metals in sediments. Geochim. Cosmochim. Acta 63, 1735–1750.
Morford, J.L., Emerson, S.R., Breckel, E.J., Kim, S.H., 2005. Diagenesis of oxyanions (V, U, Re, and Mo) in pore waters and sediments from a continental margin. Geochim. Cosmochim. Acta 69, 5021–5032.
Morford, J.L., Martin, W.R., Kalnejais, L.H., François, R., Bothner, M., Karle, I.-M., 2007. Insights on geochemical cycling of U, Re and Mo from seasonal sampling in Boston Harbor, Massachusetts, USA. Geochim. Cosmochim. Acta 71, 895–917.
Morford, J.L., Martin, W.R., Carney, C.M., 2009a. Uranium diagenesis in sediments underlying bottom waters with high oxygen content. Geochim. Cosmochim. Acta 73, 2920–2937.
Morford, J.L., Martin, W.R., François, R., Carney, C.M., 2009b. A model for uranium, rhenium, and molybdenum diagenesis in marine sediments based on results from coastal locations. Geochim. Cosmochim. Acta 73, 2938–2960.
Morford, J.L., Martin, W.R., Carney, C.M., 2012. Rhenium geochemical cycling: insights from continental margins. Chem. Geol. 324–325, 73–86. Special Issue Recent Advances in Trace Metal Applications to Paleoceanographic Studies.
Motomura, K., Horie, K., Ikehara, M., Sano, T., Takehara, M., Kiyokawa, S., 2023. The nitrate-limited freshwater environment of the late Paleoproterozoic Embury Lake Formation, Flin Flon belt, Canada. Chem. Geol. 616, 121234.
Motomura, K., Bekker, A., Bleeker, W., Ikehara, M., Sano, T., Guilmette, C., Lin, Y., Kiyokawa, S., 2024. Nitrogen isotope gradient on continental margins during the late Paleoproterozoic. Geochim. Cosmochim. Acta 371, 144–161.
Murray, S.T., Higgins, J.A., Holmden, C., Lu, C., Swart, P.K., 2021. Geochemical fingerprints of dolomitization in Bahamian carbonates: Evidence from sulphur, calcium, magnesium and clumped isotopes. Sedimentology 68, 1–29.
Nägler, T.F., Neubert, N., Böttcher, M.E., Dellwig, O., Schnetger, B., 2011. Molybdenum isotope fractionation in pelagic euxinia: evidence from the modern Black and Baltic Seas. Chem. Geol. 289, 1–11.
Nägler, T.F., Anbar, A.D., Archer, C., Goldberg, T., Gordon, G.W., Greber, N.D., Siebert, C., Sohrin, Y., Vance, D., 2014. Proposal for an international molybdenum isotope measurement standard and data representation. Geostand. Geoanal. Res. 38, 149–151.
Nägler, Th.F., Siebert, C., Lüschen, H., Böttcher, M.E., 2005. Sedimentary Mo isotope record across the Holocene fresh–brackish water transition of the Black Sea. Chem. Geol. 219, 283–295.
Nakagawa, Y., Takano, S., Firdaus, M.L., Norisuye, K., Hirata, T., Vance, D., Sohrin, Y., 2012. The molybdenum isotopic composition of the modern ocean. Geochem. J. 46, 131–141.
Nameroff, T.J., Balistrieri, L.S., Murray, J.W., 2002. Suboxic trace metal geochemistry in the Eastern Tropical North Pacific. Geochim. Cosmochim. Acta 66, 1139–1158.
Nesbitt, H.W., Young, G.M., Bosman, S.A., 2009. Major and trace element geochemistry and genesis of supracrustal rocks of the North Spirit Lake Greenstone belt, NW Ontario, Canada. Precambrian Res. 174, 16–34.
Neubert, N., Nägler, T.F., Böttcher, M.E., 2008. Sulfidity controls molybdenum isotope fractionation into euxinic sediments: evidence from the modern Black Sea. Geology 36, 775–778.
Nielsen, S.G., Prytulak, J., Halliday, A.N., 2011. Determination of precise and accurate 51V/50V isotope ratios by MC-ICP-MS, Part 1: chemical separation of vanadium and mass spectrometric protocols. Geostand. Geoanal. Res. 35, 293–306.
Noordmann, J., Weyer, S., Montoya-Pino, C., Dellwig, O., Neubert, N., Eckert, S., Paetzel, M., Böttcher, M.E., 2015. Uranium and molybdenum isotope systematics in modern euxinic basins: Case studies from the central Baltic Sea and the Kyllaren fjord (Norway). Chem. Geol. 396, 182–195.
Noordmann, J., Weyer, S., Georg, R.B., Jöns, S., Sharma, M., 2016. $^{238}U/^{235}U$ isotope ratios of crustal material, rivers and products of hydrothermal alteration: new insights on the oceanic U isotope mass balance. Isot. Environ. Health Stud. 52, 141–163.
Ohmoto, H., Watanabe, Y., Ikemi, H., Poulson, S.R., Taylor, B.E., 2006. Sulphur isotope evidence for an oxic Archaean atmosphere. Nature 442, 908–911.
Olson, L., Quinn, K.A., Siebecker, M.G., Luther, G.W., Hastings, D., Morford, J.L., 2017. Trace metal diagenesis in sulfidic sediments: insights from Chesapeake Bay. Chem. Geol. 452, 47–59.
Ossa Ossa, F., Eickmann, B., Hofmann, A., Planavsky, N.J., Asael, D., Pambo, F., Bekker, A., 2018. Two-step deoxygenation at the end of the Paleoproterozoic Lomagundi Event. Earth Planet. Sci. Lett. 486, 70–83.
Ossa Ossa, F., Spangenberg, J.E., Bekker, A., König, S., Stüeken, E.E., Hofmann, A., Poulton, S.W., Yierpan, A., Varas-Reus, M.I., Eickmann, B., Andersen, M.B., Schoenberg, R., 2022. Moderate levels of oxygenation during the late stage of Earth's Great Oxidation Event. Earth Planet. Sci. Lett. 594, 117716.
Ostrander, C.M., Sahoo, S.K., Kendall, B., Jiang, G., Planavsky, N.J., Lyons, T.W., Nielsen, S.G., Owens, J.D., Gordon, G.W., Romaniello, S.J., Anbar, A.D., 2019. Multiple negative molybdenum isotope excursions in the Doushantuo Formation (South China) fingerprint complex redox-related processes in the Ediacaran Nanhua Basin. Geochim. Cosmochim. Acta 261, 191–209.
Ostrander, C.M., Johnson, A.C., Anbar, A.D., 2021. Earth's first redox revolution. Annu. Rev. Earth Planet. Sci. 49, 337–366.
Pan, Y., Huang, Z., Guo, X., Wang, R., Lash, G.G., Fan, T., Liu, W., 2022. A re-assessment and calibration of redox thresholds in the Permian Lucaogou Formation of the Malang Sag, Santanghu Basin, Northwest China. Mar. Pet. Geol. 135, 105406.
Partin, C.A., Bekker, A., Planavsky, N.J., Scott, C.T., Gill, B.C., Li, C., Podkovyrov, V., Maslov, A., Konhauser, K.O., Lalonde, S.V., Love, G.D., Poulton, S.W., Lyons, T.W., 2013. Large-scale fluctuations in Precambrian atmospheric and oceanic oxygen levels from the record of U in shales. Earth Planet. Sci. Lett. 369–370, 284–293.
Paul, K.M., van Helmond, N.A.G.M., Slomp, C.P., Jokinen, S.A., Virtasalo, J.J., Filipsson, H.L., Jilbert, T., 2023. Sedimentary molybdenum and uranium: Improving proxies for deoxygenation in coastal depositional environments. Chem. Geol. 615, 121203.
Peng, J., 2022. What besides redox conditions? Impact of sea-level fluctuations on redox-sensitive trace-element enrichment patterns in marine sediments. Sci. China Earth Sci. 65, 1985–2004.
Peng, Y., Shen, B., Lang, X.-G., Huang, K.-J., Chen, J.-T., Yan, Z., Tang, W., Ke, S., Ma, H.-R., Li, F.-B., 2016. Constraining dolomitization by Mg isotopes: a case study from partially dolomitized limestones of the middle Cambrian Xuzhuang Formation, North China. Geochem. Geophys. Geosyst. 17, 1109–1129.
Piper, D.Z., Calvert, S.E., 2009. A marine biogeochemical perspective on black shale deposition. Earth Sci. Rev. 95, 63–96.
Piper, D.Z., Dean, W.E., 2002. Trace-Element Deposition in the Cariaco Basin, Venezuela Shelf, under Sulfate-Reducing Conditions—A History of the Local Hydrography and Global Climate, 20 ka to the Present. US Government Printing Office, America, pp. 1–45.
Piper, D.Z., Perkins, R.B., 2004. A modern vs. Permian black shale—the hydrography, primary productivity, and water-column chemistry of deposition. Chem. Geol. Geochem. Organ 206, 177–197. Rich Shales: New Perspect.
Planavsky, N.J., Reinhard, C.T., Wang, X., Thomson, D., McGoldrick, P., Rainbird, R.H., Johnson, T., Fischer, W.W., Lyons, T.W., 2014. Low mid-proterozoic atmospheric oxygen levels and the delayed rise of animals. Science 346, 635–638.
Poulson, R.L., McManus, J., Siebert, C., Berelson, W.M., 2006. Molybdenum isotopes in modern marine sediments: unique signatures of authigenic processes. Geochim. Cosmochim. Acta 70, A501.
Poulton, S.W., Bekker, A., Cumming, V.M., Zerkle, A.L., Canfield, D.E., Johnston, D.T., 2021. A 200-million-year delay in permanent atmospheric oxygenation. Nature 592, 232–236.
Prange, A., Kremling, K., 1985. Distribution of dissolved molybdenum, uranium and vanadium in baltic sea waters. Mar. Chem. 16, 259–274.
Qian, L., Ding, X., Liu, H., Jiang, W., Yiming, A., Jiang, Z., Zha, M., 2024. Reconstructing salinity and redox variation of permian Lucaogou Formation in the Jimsar Sag, the Junggar Basin, China: combining trace elements and biomarkers as proxies. Mar. Pet. Geol. 162, 106737.
Qin, Z., Xu, D., Kendall, B., Zhang, X., Ou, Q., Wang, X., Li, J., Liu, J., 2022. Molybdenum isotope-based redox deviation driven by continental margin euxinia during the early Cambrian. Geochim. Cosmochim. Acta 325, 152–169.
Rajendran, A., Kumar, M.D., Bakker, J.F., 1992. Control of manganese and iron in Skagerrak sediments (northeastern North Sea). Chem. Geol. 98, 111–129.
Ravizza, G., Turekian, K.K., Hay, B.J., 1991. The geochemistry of rhenium and osmium in recent sediments from the Black Sea. Geochim. Cosmochim. Acta 55, 3741–3752.
Reinhard, C.T., Planavsky, N.J., Robbins, L.J., Partin, C.A., Gill, B.C., Lalonde, S.V., Bekker, A., Konhauser, K.O., Lyons, T.W., 2013. Proterozoic ocean redox and biogeochemical stasis. Proc. Natl. Acad. Sci. 110, 5357–5362.
Remírez, M.N., Gilleaudeau, G.J., Gan, T., Kipp, M.A., Tissot, F.L.H., Kaufman, A.J., Parente, M., 2024. Carbonate uranium isotopes record global expansion of marine anoxia during the Toarcian Oceanic anoxic event. Proc. Natl. Acad. Sci. 121, e2406032121.
del Rey, Á., Frýda, J., Calner, M., Frýdová, B., Zhang, F., Wang, C., Planavsky, N., Dahl, T.W., 2023. Mid-Ludfordian uranium isotope records distinguish the role of expansive marine anoxia in global carbon cycle dynamics during the late Silurian Lau/Kozlowskii bioevent. Glob. Planet. Chang. 229, 104248.
Rickard, D., 1997. Kinetics of pyrite formation by the H2S oxidation of iron (II) monosulfide in aqueous solutions between 25 and 125°C: the rate equation. Geochim. Cosmochim. Acta 61, 115–134.
Rickard, D., Luther, G.W., 2007. Chemistry of iron sulfides. Chem. Rev. 107, 514–562.
Rolison, J.M., Stirling, C.H., Middag, R., Rijkenberg, M.J.A., 2017. Uranium stable isotope fractionation in the Black Sea: modern calibration of the 238U/235U paleo-redox proxy. Geochim. Cosmochim. Acta 203, 69–88.

Romaniello, S.J., Herrmann, A.D., Anbar, A.D., 2013. Uranium concentrations and 238U/235U isotope ratios in modern carbonates from the Bahamas: assessing a novel paleoredox proxy. Chem. Geol. 362, 305–316.
Rooney, A.D., Selby, D., Houzay, J.-P., Renne, P.R., 2010. Re–Os geochronology of a Mesoproterozoic sedimentary succession, Taoudeni basin, Mauritania: Implications for basin-wide correlations and Re–Os organic-rich sediments systematics. Earth Planet. Sci. Lett. 289, 486–496.
Roué, L., Kurzweil, F., Wille, M., Wegwerth, A., Dellwig, O., Münker, C., Schoenberg, R., 2021. Stable W and Mo isotopic evidence for increasing redox-potentials from the Paleoarchean towards the Paleoproterozoic deep ocean. Geochim. Cosmochim. Acta 309, 366–387.
Rudnicki, M.D., Elderfield, H., 1993. A chemical model of the buoyant and neutrally buoyant plume above the TAG vent field, 26 degrees N, Mid-Atlantic Ridge. Geochim. Cosmochim. Acta 57, 2939–2957.
Rutledge, R.L., Gilleaudeau, G.J., Remírez, M.N., Kaufman, A.J., Lyons, T.W., Bates, S., Algeo, T.J., 2024. Productivity and organic carbon loading control uranium isotope behavior in ancient reducing settings: implications for the paleoredox proxy. Geochim. Cosmochim. Acta 368, 197–213.
Sahoo, S.K., Planavsky, N.J., Kendall, B., Wang, X., Shi, X., Scott, C., Anbar, A.D., Lyons, T.W., Jiang, G., 2012. Ocean oxygenation in the wake of the Marinoan glaciation. Nature 489, 546–549.
Sahoo, S.K., Planavsky, N.J., Jiang, G., Kendall, B., Owens, J.D., Wang, X., Shi, X., Anbar, A.D., Lyons, T.W., 2016. Oceanic oxygenation events in the anoxic Ediacaran ocean. Geobiology 14, 457–468.
Scheiderich, K., Zerkle, A.L., Helz, G.R., Farquhar, J., Walker, R.J., 2010. Molybdenum isotope, multiple sulfur isotope, and redox-sensitive element behavior in early Pleistocene Mediterranean sapropels. Chem. Geol. 279, 134–144.
Scholz, F., Hensen, C., Noffke, A., Rohde, A., Liebetrau, V., Wallmann, K., 2011. Early diagenesis of redox-sensitive trace metals in the Peru upwelling area – response to ENSO-related oxygen fluctuations in the water column. Geochim. Cosmochim. Acta 75, 7257–7276.
Scholz, F., McManus, J., Sommer, S., 2013. The manganese and iron shuttle in a modern euxinic basin and implications for molybdenum cycling at euxinic ocean margins. Chem. Geol. 355, 56–68.
Scott, C., Lyons, T.W., 2012. Contrasting molybdenum cycling and isotopic properties in euxinic versus non-euxinic sediments and sedimentary rocks: Refining the paleoproxies. Chem. Geol. 324–325, 19–27. Special Issue Recent Advances in Trace Metal Applications to Paleoceanographic Studies.
Scott, C., Lyons, T.W., Bekker, A., Shen, Y., Poulton, S.W., Chu, X., Anbar, A.D., 2008. Tracing the stepwise oxygenation of the Proterozoic ocean. Nature 452, 456–459.
Sheen, A.I., Kendall, B., Reinhard, C.T., Creaser, R.A., Lyons, T.W., Bekker, A., Poulton, S. W., Anbar, A.D., 2018. A model for the oceanic mass balance of rhenium and implications for the extent of Proterozoic ocean anoxia. Geochim. Cosmochim. Acta 227, 75–95.
Shen, G.T., Boyle, E.A., 1987. Lead in corals: reconstruction of historical industrial fluxes to the surface ocean. Earth Planet. Sci. Lett. 82, 289–304.
Shiller, A.M., Mao, L., 2000. Dissolved vanadium in rivers: effects of silicate weathering. Chem. Geol. 165, 13–22.
Sholkovitz, E.R., Copland, D., 1982. The chemistry of suspended matter in Esthwaite Water, a biologically productive lake with seasonally anoxic hypolimnion. Geochim. Cosmochim. Acta 46, 393–410.
Siebert, C., Nägler, T.F., von Blanckenburg, F., Kramers, J.D., 2003. Molybdenum isotope records as a potential new proxy for paleoceanography. Earth Planet. Sci. Lett. 211, 159–171.
Siebert, C., Kramers, J.D., Meisel, Th., Morel, Ph., Nägler, Th.F., 2005. PGE, Re-Os, and Mo isotope systematics in Archean and early Proterozoic sedimentary systems as proxies for redox conditions of the early Earth. Geochim. Cosmochim. Acta 69, 1787–1801.
Smrzka, D., Zwicker, J., Bach, W., Feng, D., Himmler, T., Chen, D., Peckmann, J., 2019. The behavior of trace elements in seawater, sedimentary pore water, and their incorporation into carbonate minerals: a review. Facies 65, 41.
Sommerfield, C.K., Nittrouer, C.A., 1999. Modern accumulation rates and a sediment budget for the Eel shelf: a flood-dominated depositional environment. Mar. Geol. 154, 227–241.
Song, Huyue, Algeo, T.J., Song, Haijun, Tong, J., Wignall, P.B., Bond, D.P.G., Zheng, W., Chen, X., Romaniello, S.J., Wei, H., Anbar, A.D., 2023. Global oceanic anoxia linked with the Capitanian (Middle Permian) marine mass extinction. Earth Planet. Sci. Lett. 610, 118128.
Steadman, J.A., Large, R.R., Blamey, N.J., Mukherjee, I., Corkrey, R., Danyushevsky, L. V., Maslennikov, V., Hollings, P., Garven, G., Brand, U., Lécuyer, C., 2020. Evidence for elevated and variable atmospheric oxygen in the Precambrian. Precambrian Res. 343, 105722.
Stirling, C.H., Andersen, M.B., Potter, E.-K., Halliday, A.N., 2007. Low-temperature isotopic fractionation of uranium. Earth Planet. Sci. Lett. 264, 208–225.
Stirling, C.H., Andersen, M.B., Warthmann, R., Halliday, A.N., 2015. Isotope fractionation of ^{238}U and ^{235}U during biologically-mediated uranium reduction. Geochim. Cosmochim. Acta 163, 200–218.
Stockey, R.G., Cole, D.B., Planavsky, N.J., Loydell, D.K., Frýda, J., Sperling, E.A., 2020. Persistent global marine euxinia in the early Silurian. Nat. Commun. 11, 1804.
Swart, P.K., 2015. The geochemistry of carbonate diagenesis: the past, present and future. Sedimentology 62, 1233–1304.
Swarzenski, P.W., McKee, B.A., Skei, J.M., Todd, J.F., 1999. Uranium biogeochemistry across the redox transition zone of a permanently stratified fjord: Framvaren, Norway. Mar. Chem. 67, 181–198.
Sweere, T., van den Boorn, S., Dickson, A.J., Reichart, G.-J., 2016. Definition of new trace-metal proxies for the controls on organic matter enrichment in marine sediments based on Mn, Co, Mo and Cd concentrations. Chem. Geol. 441, 235–245.
Tagami, K., Uchida, S., 2007. Determination of rhenium in manganese nodules by inductively coupled plasma mass spectrometry. J. Radioanal. Nucl. Chem. 273, 147–150.
Tan, Z., Jia, W., Li, J., Yin, L., Wang, S., Wu, J., Song, J., Peng, P., 2021. Geochemistry and molybdenum isotopes of the basal Datangpo Formation: implications for ocean-redox conditions and organic matter accumulation during the Cryogenian interglaciation. Palaeogeogr. Palaeoclimatol. Palaeoecol. 563, 110169.
Tan, Z., Wu, J., Jia, W., Li, J., Kendall, B., Song, J., Peng, P., 2023. Molybdenum isotope evidence from restricted-basin mudstones for an intermediate extent of oxygenation in the late Ediacaran ocean. Chem. Geol. 623, 121410.
Tang, D., Shi, X., Zhao, X., Wang, X., Song, G., 2015. Mo-U covariation as an important proxy for sedimentary environment redox conditions - progress, problems and prospects. GeoSci 29, 1–13.
Taylor, S.R., McLennan, S.M., 1995. The geochemical evolution of the continental crust. Rev. Geophys. 33, 241–265.
Thoby, M., Konhauser, K.O., Fralick, P.W., Altermann, W., Visscher, P.T., Lalonde, S.V., 2019. Global importance of oxic molybdenum sinks prior to 2.6 Ga revealed by the Mo isotope composition of Precambrian carbonates. Geology 47, 559–562.
Thomazo, C., Ader, M., Philippot, P., 2011. Extreme 15N-enrichments in 2.72-Gyr-old sediments: evidence for a turning point in the nitrogen cycle. Geobiology 9, 107–120.
Tissot, F.L.H., Dauphas, N., 2015. Uranium isotopic compositions of the crust and ocean: age corrections, U budget and global extent of modern anoxia. Geochim. Cosmochim. Acta 167, 113–143.
Tissot, F.L.H., Chen, C., Go, B.M., Naziemiec, M., Healy, G., Bekker, A., Swart, P.K., Dauphas, N., 2018. Controls of eustasy and diagenesis on the 238U/235U of carbonates and evolution of the seawater (^{234}U/^{238}U) during the last 1.4 Myr. Geochim. Cosmochim. Acta 242, 233–265.
Tribovillard, N., Riboulleau, A., Lyons, T., Baudin, F., 2004. Enhanced trapping of molybdenum by sulfurized marine organic matter of marine origin in Mesozoic limestones and shales. Chem. Geol. 213, 385–401.
Tribovillard, N., Algeo, T.J., Lyons, T., Riboulleau, A., 2006. Trace metals as paleoredox and paleoproductivity proxies: an update. Chem. Geol. 232, 12–32.
Tribovillard, N., Algeo, T.J., Baudin, F., Riboulleau, A., 2012. Analysis of marine environmental conditions based onmolybdenum–uranium covariation—Applications to Mesozoic paleoceanography. Chem. Geol. 324, 46–58. Special Issue Recent Advances in Trace Metal Applications to Paleoceanographic Studies.
Turekian, K.K., Wedepohl, K.H., 1961. Distribution of the elements in some major units of the Earth's crust. Geol. Soc. Am. Bull. 72, 175–192.
Turgeon, S., Brumsack, H.-J., 2006. Anoxic vs dysoxic events reflected in sediment geochemistry during the Cenomanian–Turonian Boundary Event (Cretaceous) in the Umbria–Marche Basin of central Italy. Chem. Geol. 234, 321–339.
Van der Weijden, C.H., 2002. Pitfalls of normalization of marine geochemical data using a common divisor. Mar. Geol. 184, 167–187.
Vind, J., Ofili, S., Mänd, K., Soesoo, A., Kirsimäe, K., 2023. Redox-sensitive trace metal hyper-enrichment in Tremadocian Alum Shale (graptolite argillite) in northwestern Estonia, Baltic Palaeobasin. Chem. Geol. 640, 121746.
Voegelin, A.R., Nägler, T.F., Beukes, N.J., Lacassie, J.P., 2010. Molybdenum isotopes in late Archean carbonate rocks: implications for early Earth oxygenation. Precambrian Res. 182, 70–82.
Vorlicek, T.P., Helz, G.R., Chappaz, A., Vue, P., Vezina, A., Hunter, W., 2018. Molybdenum burial mechanism in sulfidic sediments: iron-sulfide pathway. ACS Earth Space Chem. 2, 565–576.
Wagner, M., Chappaz, A., Lyons, T.W., 2017. Molybdenum speciation and burial pathway in weakly sulfidic environments: insights from XAFS. Geochim. Cosmochim. Acta 206, 18–29.
Wang, H., Zhang, Z., Li, C., Algeo, T.J., Cheng, M., Wang, W., 2020. Spatiotemporal redox heterogeneity and transient marine shelf oxygenation in the Mesoproterozoic ocean. Geochim. Cosmochim. Acta 270, 201–217.
Wang, W., Zhang, F., Zhang, S., Cui, Y., Zheng, Q., Zhang, Y., Yuan, D., Zhang, H., Xu, Y., Shen, S., 2023. Ecosystem responses of two Permian biocrises modulated by CO2 emission rates. Earth Planet. Sci. Lett. 602, 117940.
Wang, Z., Ma, J., Li, J., Wei, G., Zeng, T., Li, L., Zhang, L., Deng, W., Xie, L., Liu, Z., 2018. Fe (hydro) oxide controls Mo isotope fractionation during the weathering of granite. Geochim. Cosmochim. Acta 226, 1–17.
Wanty, R.B., Goldhaber, M.B., 1992. Thermodynamics and kinetics of reactions involving vanadium in natural systems: accumulation of vanadium in sedimentary rocks. Geochim. Cosmochim. Acta 56, 1471–1483.
Wanty, R.B., Goldhaber, M.B., Northrop, H.R., 1990. Geochemistry of vanadium in an epigenetic, sandstone-hosted vanadium-uranium deposit, Henry Basin, Utah. Econ. Geol. 85, 270–284.
Warke, M.R., Rocco, Di, Tommaso, Zerkle, A.L., Lepland, Aivo, Prave, A.R., Martin, A.P., Ueno, Y., Condon, D.J., Claire, M.W., 2020. The Great oxidation event preceded a paleoproterozoic "snowball Earth.". Proc. Natl. Acad. Sci. 117, 13314–13320.
Warren, J., 2000. Dolomite: occurrence, evolution and economically important associations. Earth Sci. Rev. 52, 1–81.
Wehrli, B., Stumm, W., 1989. Vanadyl in natural waters: adsorption and hydrolysis promote oxygenation. Geochim. Cosmochim. Acta 53, 69–77.
Wei, W., Frei, R., Klaebe, R., Tang, D., Wei, G.-Y., Li, D., Tian, L.-L., Huang, F., Ling, H.-F., 2021b. A transient swing to higher oxygen levels in the atmosphere and oceans at ~1.4 Ga. Precambrian Res. 354, 106058.

Wei, G.-Y., Planavsky, N.J., He, T., Zhang, F., Stockey, R.G., Cole, D.B., Lin, Y.-B., Ling, H.-F., 2021a. Global marine redox evolution from the late Neoproterozoic to the early Paleozoic constrained by the integration of Mo and U isotope records. Earth Sci. Rev. 214, 103506.
Wei, W., Chen, X., Ling, H.-F., Wu, F., Dong, L.-H., Pan, S., Jing, Z., Huang, F., 2023. Vanadium isotope evidence for widespread marine oxygenation from the late Ediacaran to early Cambrian. Earth Planet. Sci. Lett. 602, 117942.
Weyer, S., Anbar, A.D., Gerdes, A., Gordon, G.W., Algeo, T.J., Boyle, E.A., 2008. Natural fractionation of 238U/235U. Geochim. Cosmochim. Acta 72, 345–359.
Wille, M., Kramers, J.D., Nägler, T.F., Beukes, N.J., Schröder, S., Meisel, Th., Lacassie, J. P., Voegelin, A.R., 2007. Evidence for a gradual rise of oxygen between 2.6 and 2.5 Ga from Mo isotopes and Re-PGE signatures in shales. Geochim. Cosmochim. Acta 71, 2417–2435.
Wu, F., Owens, J.D., Huang, T., Sarafian, A., Huang, K.-F., Sen, I.S., Horner, T.J., Blusztajn, J., Morton, P., Nielsen, S.G., 2019. Vanadium isotope composition of seawater. Geochim. Cosmochim. Acta 244, 403–415.
Wu, F., Owens, J.D., Scholz, F., Huang, L., Li, S., Riedinger, N., Peterson, L.C., German, C. R., Nielsen, S.G., 2020. Sedimentary vanadium isotope signatures in low oxygen marine conditions. Geochim. Cosmochim. Acta 284, 134–155.
Wu, F., Owens, J.D., German, C.R., Mills, R.A., Nielsen, S.G., 2022. Vanadium isotope fractionation during hydrothermal sedimentation: Implications for the vanadium cycle in the oceans. Geochim. Cosmochim. Acta 328, 168–184.
Xie, X., Yuan, H., Song, J., Li, N., Li, X., Duan, L., Wang, Y., Ren, C., 2019. Indication of redox sensitive elements in marine sediments on anoxic condition of water environment. Geol. Rev. 65, 671–688.
Xiong, Y., 2003. Solubility and speciation of rhenium in anoxic environments at ambient temperature and applications to the Black Sea. Deep Sea Res. Part Oceanogr. Res. Pap. 50, 681–690.
Xu, L., Lechte, M., Shi, X., Zheng, W., Zhou, L., Huang, K., Zhou, X., Tang, D., 2024. Large igneous province emplacement triggered an oxygenation event at ~1.4 Ga: evidence from mercury and paleo-productivity proxies. Geophys. Res. Lett. 51, e2023GL106654.
Yang, S., Kendall, B., Lu, X., Zhang, F., Zheng, W., 2017. Uranium isotope compositions of mid-Proterozoic black shales: Evidence for an episode of increased ocean oxygenation at 1.36 Ga and evaluation of the effect of post-depositional hydrothermal fluid flow. Precambrian Res 298, 187–201.
Yang, S., Lu, X., Chen, X., Zheng, W., Owens, J.D., Young, S.A., Kendall, B., 2023. Uranium and molybdenum isotope evidence for globally extensive marine euxinia on continental margins and in epicontinental seas during the Devonian-Carboniferous Hangenberg Crisis. Geochim. Cosmochim. Acta 352, 133–156.
Ye, Y., Zhang, S., Wang, H., Wang, X., Tan, C., Li, M., Wu, C., Canfield, D.E., 2021. Black shale Mo isotope record reveals dynamic ocean redox during the Mesoproterozoic Era. Geochem. Perspect. Lett. 18, 16–21.
Yu, Y., Chen, Y., Li, D., Su, J., 2022. A transient oxygen increase in the Mesoproterozoic ocean at ~1.44 Ga: Geochemical evidence from the Tieling Formation, North China Platform. Precambrian Res. 369, 106527.
Yuan, L., Zhou, Y., Chen, X., Zhu, M., Poulton, S.W., Tian, Z., Li, D., Thirlwall, M., Shields, G.A., 2023. Multiple ocean oxygenation events during the Ediacaran Period: Mo isotope evidence from the Nanhua Basin, South China. Precambrian Res. 388, 107004.
Zhang, F., Lenton, T.M., del Rey, Á., Romaniello, S.J., Chen, X., Planavsky, N.J., Clarkson, M.O., Dahl, T.W., Lau, K.V., Wang, W., Li, Z., Zhao, M., Isson, T., Algeo, T. J., Anbar, A.D., 2020. Uranium isotopes in marine carbonates as a global ocean paleoredox proxy: a critical review. Geochim. Cosmochim. Acta 287, 27–49. New Developments in Geochemical Proxies for Paleoceanographic Research.
Zhang, F., Stockey, R.G., Xiao, S., Shen, S., Dahl, T.W., Wei, G.-Y., Cao, M., Li, Z., Kang, J., Cui, Y., Anbar, A.D., Planavsky, N.J., 2022a. Uranium isotope evidence for extensive shallow water anoxia in the early Tonian oceans. Earth Planet. Sci. Lett. 583, 117437.
Zhang, S., Wang, X., Wang, H., Bjerrum, C.J., Hammarlund, E.U., Costa, M.M., Connelly, J.N., Zhang, B., Su, J., Canfield, D.E., 2016. Sufficient oxygen for animal respiration 1,400 million years ago. Proc. Natl. Acad. Sci. 113, 1731–1736.
Zhang, S., Wang, X., Wang, H., Bjerrum, C.J., Hammarlund, E.U., Haxen, E.R., Wen, H., Ye, Y., Canfield, D.E., 2019. Paleoenvironmental proxies and what the Xiamaling Formation tells us about the mid-Proterozoic ocean. Geobiology 17, 225–246.
Zhang, X., Yuan, H., Song, J., Duan, L., 2022b. Indication to redox conditions of Re, Mo and U in marine environment. Adv. Earth Sci. 37, 358–369.
Zhao, J., Jin, Z., 2021. Mudstone diagenesis: research advances and prospects. Acta Sedimentol. Sin. 39, 58–72.
Zhao, Z., Pang, X., Zou, C., Dickson, A.J., Basu, A., Guo, Z., Pan, S., Nielsen, A.T., Schovsbo, N.H., Jing, Z., Dahl, T.W., 2023. Dynamic oceanic redox conditions across the late Cambrian SPICE event constrained by molybdenum and uranium isotopes. Earth Planet. Sci. Lett. 604, 118013.
Zheng, Y., Anderson, R.F., van Geen, A., Fleisher, M.Q., 2002. Preservation of particulate non-lithogenic uranium in marine sediments. Geochim. Cosmochim. Acta 66, 3085–3092.
Zhu, B., Yang, T., Wang, J., Chen, X., Pan, W., Chen, Y., 2022. Multiple controls on the paleoenvironment of the early Cambrian black shale-chert in the northwest Tarim Basin, NW China: trace element, iron speciation and Mo isotopic evidence. Mar. Pet. Geol. 136, 105434.
Živković, I., Bura-Nakić, E., Knežević, L., Helz, G.R., 2023. Deposition of Mo, Re and U under contrasting redox conditions; assessment of the [Re/Mo]sw redox proxy. Geochim. Cosmochim. Acta 359, 176–190.

Chemical Geology 681 (2025) 122724

Contents lists available at ScienceDirect

Chemical Geology

journal homepage: www.elsevier.com/locate/chemgeo

Molecular indicators of microbial community change linked to salinity variation and terrestrial inputs during the Ordovician-Silurian transition (East-Central USA)

Yi Song [a,b,c], Thomas J. Algeo [b,c,d,e], Carlton Brett [b], Zhanhong Liu [f], Shucheng Xie [c,*]

[a] School of Marine Sciences, Guangxi University, Nanning 530004, China
[b] Department of Geosciences, University of Cincinnati, Cincinnati, OH 45221-0013, USA
[c] State Key Laboratory of Geomicrobiology and Environmental Changes, School of Earth Sciences, China University of Geosciences, Wuhan 430074, China
[d] State Key Laboratory of Geological Processes and Mineral Resources, China University of Geosciences, Wuhan 430074, China
[e] State Key Laboratory of Oil and Gas Reservoir Geology and Exploitation, Chengdu University of Technology, Chengdu 610059, China
[f] Hubei Key Laboratory of Marine Geological Resources, College of Marine Science and Technology, China University of Geosciences, Wuhan 430074, China

ARTICLE INFO

Editor: Karen Johannesson

Keywords:
n-alkane
Sterane/hopane ratio
B/Ga
Bryophytes
Hirnantian
Kentucky

ABSTRACT

The end-Ordovician mass extinction (LOME), one of the largest biocrises of the Phanerozoic, was linked to a major climatic cooling event, continental glaciation, and oceanic environmental changes. To date, the effect of this biocrisis on marine microbial communities has received scant attention. Here, we generate biomarker records for Upper Ordovician to lower Silurian strata in eastern North America, along with geochemical proxies for watermass salinity and terrestrial fluxes, to investigate contemporaneous microbial community changes and possible controls thereon. Hopane-to-sterane ratios (H/S) exhibit reduced values related to enhanced eukaryotic inputs during the Hirnantian Ice Age. A decrease in the proportion of long-chain *n*-alkanes and an increase in moretane-to-hopane ratios reflect increased contributions from land plants to the organic fraction of marine sediments during the Ordovician-Silurian transition (OST). The high relative abundances of C_{19}-C_{20} long-chain tricyclic terpenes in the lower Silurian imply increased inputs from marine algae, possibly in response to enhanced nutrient fluxes from terrestrial sources to the ocean. The salinity proxies B/Ga and S/TOC indicate a shift in watermass conditions from marine to slightly brackish in the pre-Hirnantian to marine to slightly hypersaline in the Hirnantian and early Silurian, probably linked to shallowing of the Lexington Platform and climate aridification resulting from Gondwanan continental glaciation. This increase in salinity is consistent with rapid variation in hopane/sterane ratios, showing the influence of watermass salinity on microbial community composition. Thus, marine environmental changes (i.e., in salinity, redox, and nutrient fluxes) were the immediate cause of microbial community evolution during the OST, although the ultimate driver may have been expansion and diversification of terrestrial floras.

1. Introduction

The Late Ordovician to early Silurian was a protracted (~40-Myr-long) interval of global climate change, marine environmental perturbations, and major bioevolutionary events (Algeo et al., 2016). In the oceans, a major taxonomic radiation among invertebrates and increase in ecosystem complexity during the Early to Middle Ordovician, i.e., the Great Ordovician Biodiversification Event (GOBE; Servais and Harper, 2018), was accompanied by strong cooling and expanded oceanic anoxia (Zhang et al., 2022; Liu et al., 2025). The marine biodiversification event was terminated by the Late Ordovician Mass Extinction (LOME; Sheehan, 2001), which occurred in two main stages with contrasting effects on marine invertebrate and microbial communities (Liang et al., 2024). On land, the first simple (non-vascular, bryophyte-grade) land plants appeared in the Middle Ordovician and spread rapidly during the Late Ordovician (Servais et al., 2019), with possible attendant effects on terrestrial weathering fluxes (Liu et al., 2023). A long-term climatic cooling trend that commenced around the Early/Middle Ordovician boundary was associated with carbon-cycle perturbations (Zhang et al., 2024) and oceanic oxygenation (Wang et al., 2023), culminating in the

* Corresponding author.
E-mail address: xiecug@163.com (S. Xie).

https://doi.org/10.1016/j.chemgeo.2025.122724
Received 26 December 2024; Received in revised form 3 March 2025; Accepted 5 March 2025
Available online 8 March 2025
0009-2541/© 2025 Elsevier B.V. All rights are reserved, including those for text and data mining, AI training, and similar technologies.

Hirnantian Ice Age (Finnegan et al., 2011). With regard to tectonics, rapid plate motions heightened arc-terrane orogenic activity at a global scale (van Staal and Hatcher Jr., 2010; Scotese, 2023), possibly linked to a mantle superplume evidenced by a geomagnetic superchron (Algeo, 1996). Causal relationships among these biotic, climatic and tectonic events have been proposed but remain largely unresolved (Algeo and Shen, 2024).

The Lexington Platform in east-central Laurentia (i.e., Paleozoic North America) accumulated a near-continuous succession of shallow-marine carbonates, marls and shales during the Late Ordovician to early Silurian (Brett et al., 2004, 2020; Aucoin and Brett, 2016; Koirala et al., 2016). This platform was located marginally to the Iapetus Ocean and the intracratonic Sebree Trough and, thus, was subject to marine influences, yet it was sufficiently shallow that it experienced secular environmental changes (including watermass salinity) linked to sea-level and climatic variation (Kolata et al., 2001; Liu et al., 2024a). Moreover, it was adjacent to the Taconic Highlands, resulting in influences from terrestrial weathering and land plant productivity (Adiatma et al., 2019; Herrmann et al., 2023).

Biomarkers have the potential to reveal the interplay of climatic, tectonic, and biotic influences on the microbial community composition of this succession, yet it has been the subject of no detailed biomarker investigation to date. In this study, we generated biomarker and salinity proxy data from Upper Ordovician to lower Silurian strata of the Lexington Platform. The distribution patterns and relative abundances of *n*-alkanes and their alkylated homologues were measured to investigate terrestrial ecological changes, and various ratios of hopanes, steranes and terpanes were determined to investigate marine microbial community changes. We also generated salinity proxy data (i.e., B/Ga and S/TOC) to assess salinity conditions and their relationship to marine environmental changes and microbial community evolution. Our primary objectives were to: (1) generate records of variation in microbial-algal community composition and environmental conditions during the OST, with a special focus on the Hirnantian Ice Age, and (2) evaluate relationships between microbial-algal and paleoenvironmental proxies in order to draw inferences concerning controls thereon in Early Paleozoic marine ecosystems. The results of this study provide novel insights into factors influencing Ordovician-Silurian marine microbial-algal communities, with implications for terrestrial-marine teleconnections and life-environment co-evolution during the Early Paleozoic.

2. Background

2.1. Global events of Ordovician-Silurian transition

The Late Ordovician to early Silurian was an interval of major climatic and biotic changes (Algeo et al., 2016) [note: the Silurian Period has not been formally subdivided into early, middle, and late series, necessitating use of the lower case]. A protracted climatic cooling trend began around the Early/Middle Ordovician boundary and continued through the end of the Ordovician (Trotter et al., 2008), culminating in the Hirnantian Ice Age (~445 Ma) [note: although its total duration is thought to have been <1.0 Myr, it was marked by at least five glacial-interglacial cycles, making the term "Hirnantian Ice Age" more appropriate than "Hirnantian Glaciation"; Holmden et al., 2013; Algeo et al., 2016]. The peak of continental glaciation extended from the base of the *N. extraordinarius-N. ojsuensis* graptolite Zone to the lower *N. persculptus* Zone, during which global sea level is estimated to have fallen by 70–100 m (Finnegan et al., 2011). Smaller sea-level fluctuations in pre-Hirnantian Upper Ordovician and post-Hirnantian lower Silurian strata and other evidence demonstrate that continental glaciation persisted over a multi-million-year interval, albeit at lesser intensity than during the Hirnantian Stage (Saltzman and Young, 2005; Elrick et al., 2013; Pohl et al., 2016a; Liu et al., 2017; Li et al., 2021), suggesting that "Early Paleozoic Ice Age" might be the most suitable designation of all for this glacial event.

The Late Ordovician mass extinction (LOME, ~445 Ma) was possibly the second largest biocrisis of the Phanerozoic (Stanley, 2016), with large losses among the graptolite, brachiopod, conodont and trilobite clades (Rong et al., 2002; Algeo et al., 2016). The LOME comprised two episodes, one at the onset of the Hirnantian Ice Age (LOME-1) and the second at its termination (LOME-2; Fig. 1). Between these bioevents, the cool-water-adapted, brachiopod-dominated *Hirnantia* Fauna thrived in many marine settings (Rong et al., 2002, 2020). Recently, a prelude biocrisis has been recognized in the late Katian (LOME-0, Fig. 1), a few million years prior to the Hirnantian Stage extinction (Deng et al., 2021; Chen et al., 2024). In the Cincinnatian Series of east-central North America, detailed biostratigraphic analysis has revealed this event to be associated with the pulsed Richmondian invasion (Forsythe and Stigall, 2023) as well as with major regional unconformities in that region and in Baltica (Calner et al., 2010; Aucoin and Brett, 2016). Following the LOME, the lower Silurian was also characterized by several turnovers in the marine biosphere, among which the most severe was the Sandvika Event of the late Aeronian (~439 Ma), an event that eliminated ~23 % of conodont and trilobite families and severely affected the *Stimulograptus sedgwickii* graptolite community (Jeppsson, 1998; Stockey et al., 2020).

The causes of the LOME have been extensively debated (see Algeo et al., 2016, for a review), yet there is agreement on neither the proximate causes nor the ultimate driver. Various proximate environmental factors have been invoked, including sea-level fall (restricting habitable shelf area), global cooling, oceanic anoxia, and seawater acidification (Zhou et al., 2015; Luo et al., 2016; Liu et al., 2020; Zhang et al., 2022), with a similar range of factors inferred for the early Silurian Sandvika biocrisis (Aldridge et al., 1993; Rasmussen et al., 2019; Stockey et al., 2020). With regard to ultimate drivers, the main hypotheses include LIP magmatism (Jones et al., 2017) [but note problems with Hg evidence, as reviewed by Shen et al., 2019, 2022], tectonism and its weathering effects (Kump et al., 1999), and the spread of early land plants (Lenton et al., 2012) (Fig. 1). In fact, the general patterns of environmental change during the LOME are inconsistent with an LIP mechanism, and the tectonic hypothesis begs the question of why other tectonic episodes in Earth history have not had similar effects. On the other hand, the land plant hypothesis is consistent with the environmental proxy evidence and provides a mechanism uniquely related in time to the LOME (Algeo and Shen, 2024).

Fossil records indicate that bryophyte-grade land plants (i.e., lacking a vascular system, similar to modern mosses and lichens) began to appear in the earliest Middle Ordovician. The oldest cryptospores are from the Dapingian (Volkheimer, 1980; Wellman and Gray, 2000; Rubinstein et al., 2010), with slightly younger cryptospores from the Darriwilian (Vavrdová, 1984; Strother et al., 1996; Steemans et al., 2009) and Katian (Badawy et al., 2014), and the first trilete spores are from the Katian or Hirnantian (Steemans et al., 2009; Romero-Sarmiento et al., 2011; Lenton et al., 2012). However, the extent of such early plant cover on continents remains highly uncertain (Pohl et al., 2016b), and the initial impact of early land plants on terrestrial environments and global geochemical cycling and climate was likely relatively muted. By the OST, the pace of biological diversification and ecological spread of early land plants is thought to have accelerated, with observable effects on global weathering rates (Lenton et al., 2012; Pohl et al., 2016b).

2.2. Lipid biomarker proxies for paleoenvironmental conditions

Lipid biomarkers have the potential to document relationships between paleoenvironmental variation and microbial community change. The biosphere, especially concerning microbial communities and their metabolic processes, is highly responsive to alterations in marine and terrestrial habitats as well as atmospheric changes. Microbial metabolic products are typically found in rock with special functional groups that serve to preserve the original carbon skeleton of the compounds.

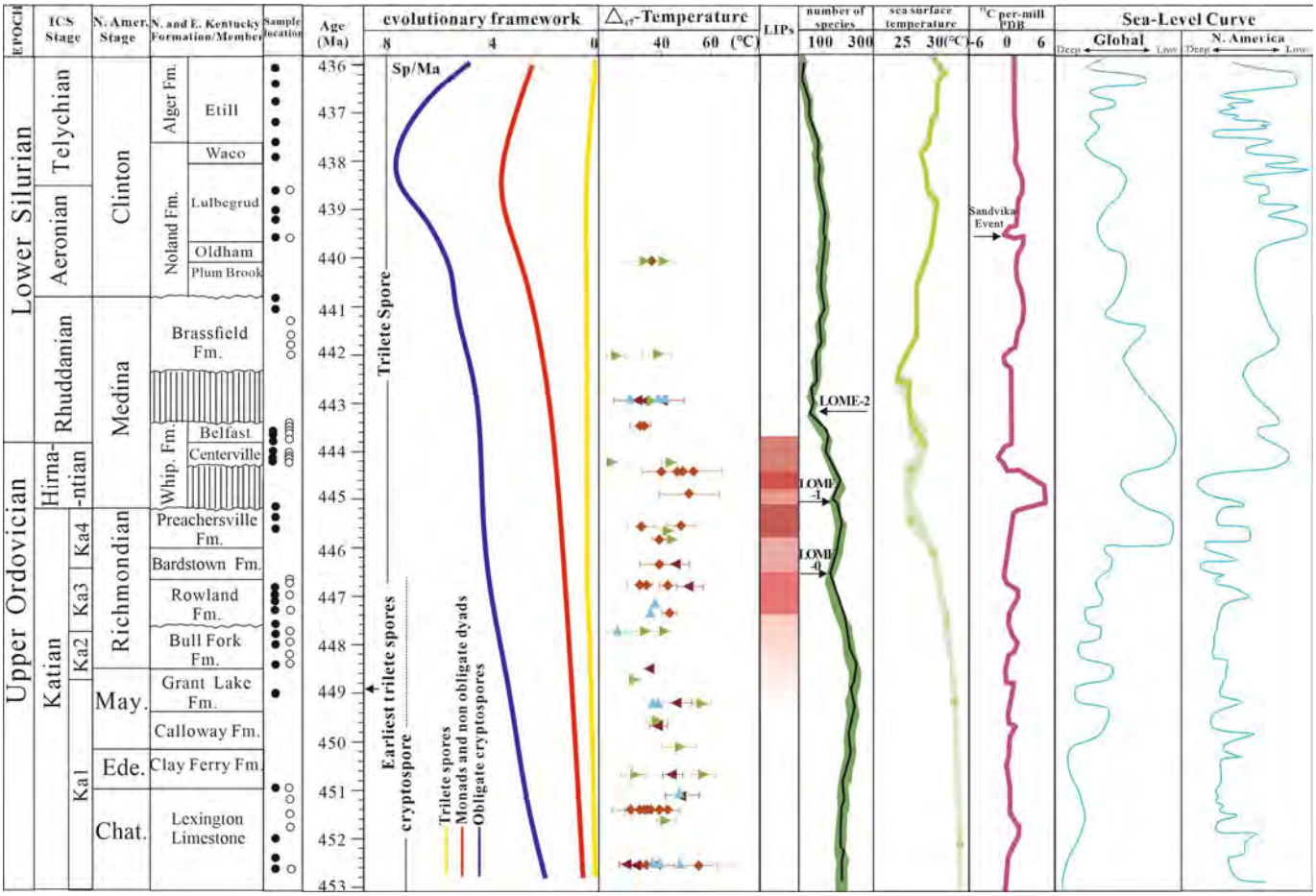


Fig. 1. Chronostratigraphy and stratigraphy of Upper Ordovician and lower Silurian units in eastern Laurentia. Source: Upper Ordovician stratigraphy (Brett et al., 2020; Stigall, 2023); lower Silurian stratigraphy (Ettensohn et al., 2013; Waid, 2018); timescale (Holland and Patzkowsky, 1996; Bergström et al., 2009a; Bergström et al., 2009b); early plant evolution (Wellman et al., 2013; Badawy et al., 2014; Algeo et al., 2016; Capel et al., 2022); Δ_{47}-temperature (Thiagarajan et al., 2024); LIPs with darker red bands corresponding to large volcanic eruptions (Rasmussen et al., 2019); number of species and LOME-0, LOME-1, LOME-2 (Deng et al., 2021; Chen et al., 2024); sea-surface temperature (Trotter et al., 2008); $\delta^{13}C_{carb}$ (Ogg et al., 2016); and global and North American sea-level curves (Ross and Ross, 1995; Brett et al., 2020). Abbreviations: Chat. = Chatfieldian Stage, Ede. = Edenian stage, May. = Maysvillian stage, Rhd. = Rhuddanian, Fm. = Formation, Mbr. = member, LOME = Late Ordovician Mass Extinction. (For interpretation of the references to colour in this figure legend, the reader is referred to the web version of this article.)

Consequently, lipid biomarkers can provide distinct insights into terrestrial and oceanic paleo-environmental conditions (Xie et al., 2017; Luo et al., 2019).

Alkanes—Alkanes, the most prevalent type of organic compound in sediments, originate mainly from bacteria and land plants, and the proportion of long-chain *n*-alkanes to total *n*-alkanes can be used as an indicator of land plant inputs to the marine environment. Immature source rocks with significant inputs of land-plant-sourced organic matter are dominated by the odd-numbered *n*-alkanes, particularly nC_{27}, nC_{29}, and nC_{31}, which either originate from epicuticular waxes synthesized by higher plants or are defunctionalized even-numbered acids, alcohols, or esters (Peters et al., 2005). Long-chain *n*-alkanes and terrestrial diterpane correlate significantly with the abundance of cryptospores and trilete spores in the Upper Ordovician to Lower Devonian of the North African Platform (Gondwana), demonstrating a clear signal of land plant inputs (Romero-Sarmiento et al., 2011), and increased long-chain *n*-alkanes and higher $\delta^{13}C$ values in Upper Devonian sediments of southern Euramerica may signal the expansion of early forests (Lu et al., 2019).

Steranes and hopanes—Steranes, which are derived mainly from eukaryotic algae, are the products of primary precursor sterols that serve to maintain the stability of the cell membrane. Hopanes, which are absent in eukaryotic algae and derived mainly from prokaryotic organisms, and bacteriohopanepolyols (BHP) are the primary precursor of C_{30} and higher hopane homologues. In marine sediments, the hopane/sterane ratio is indicative of the relative importance of bacteria and algae in the microbial community (Schwark and Empt, 2006). For example, high hopane/sterane ratios were reported for a warm interval during the end-Ordovician event, indicating climate-dependent changes in the balance of bacterial versus algal primary production (Rohrssen et al., 2013), and Upper Devonian shales in the Illinois Basin (North America) showed a correlation of hopane/sterane ratios with salinity variation, which controlled compositional changes in the microbial and algal plankton community (Song et al., 2021a).

Moretanes—'Moretane' is a designation for the 17β,21α(H)-hopane stereoisomers, thus distinguishing them from other hopane stereoisomers, which are referred to simply as 'hopanes'. In hopanoid stereoisomers, $\beta\beta$-hopanoids are the least thermodynamically stable compounds in the hopane stereoisomeric series, with rapid loss of $\beta\beta$-hopanoids due to thermal degradation or conversion to more thermodynamically stable forms such as $\beta\alpha$-moretane and $\alpha\beta$-hopane during burial (Seifert and Moldowan, 1980; Kolaczkowska et al., 1990; Peters et al., 2005). This transformation process typically occurs with clay minerals as catalysts, such as chlorite, illite, and mixed-layer illite/smectite (French et al., 2012). Moretane has no strictly delimited source, but high moretane abundance is commonly associated with large terrigenous inputs of immature organic matter, probably dominantly

from soil bacteria (Peters et al., 2005). The ratio of 17β,21α(H)-moretanes to 17α,21β(H)-hopanes (i.e., M/H) has been used to evaluate soil erosion events during end-Permian mass extinction event (Xie et al., 2007; Xie et al., 2017). Because moretanes are abundant in hypersaline, freshwater lakes and coal swamps (Quirk et al., 1984; Rullkötter and Marzi, 1988; Uemura and Ishiwatari, 1995; Rosa-Putra et al., 2001), detrital clays from terrestrial sources tend to have higher M/H than marine sediments (Wang, 2007; Xie et al., 2007; Song (Yi) et al., 2021).

Tricyclic terpenes—The homologues of the tricyclic terpanes, extending from C_{18} to C_{54} in crude oils and source rocks, can be used to evaluate the extent of thermal maturity and biodegradation of the organic fraction of the sediment. This series typically ranges from C_{19} to C_{30} with molecular structures of the regular 13β(H),14α(H), and C_{23} being the most common homologues. Additionally, the series of 13α(n-alkyl)-tricyclic terpanes features a substitution at the C-13 position of the main side chain (Azevedo et al., 2001). Owing to their structural similarities, regular tricyclic terpanes are thought to originate from cyclization of regular hexaprenols produced by *Tasmanites*, a prasinophycean alga (Simoneit et al., 1990; Aquino Neto et al., 1992). Because of their extreme resistance to biodegradation, tricyclic terpanes may also be produced by the thermal cleavage of the alkyl side chain in hopanes (Zumberge, 1987). Therefore, low-carbon-number (i.e., C_{19}-C_{20}) long-chain tricyclic terpanes primarily originate from eukaryotic algae and the cracking of hopanes from highly mature organic matter.

2.3. Elemental proxies for paleosalinity analysis

Elemental salinity proxies (i.e., B/Ga, Sr/Ba and S/TOC) can be used to infer the depositional salinity facies of deep-time shale and mudstone formations (Wei et al., 2018; Wei and Algeo, 2020). These proxies have now been widely applied to shale and marl formations ranging from Paleoproterozoic to Recent in age (e.g., Remírez and Algeo, 2020; Cheng et al., 2021, 2023; Gilleaudeau et al., 2021, 2023; Song (Yi) et al., 2021; Song (Yu) et al., 2021; Cao et al., 2023; Liu et al., 2024a, 2024b; Wang et al., 2024). The results of these studies demonstrated that many epicratonic formations previously regarded as uniformly marine in character were, in fact, brackish or fluctuating brackish-marine water bodies. In the present study, we will focus exclusively on B/Ga because (1) the Sr/Ba proxy cannot be applied owing to large amounts of carbonate-sourced Sr in the study units, and (2) all of the study samples have S/TOC values greater than 0.1, thus demonstrating an absence of freshwater indicators.

The boron/gallium (B/Ga) proxy is capable of discriminating between freshwater (<1 psu), low-brackish (1–15 psu), high-brackish (15–30 psu), marine (30–40 psu), and hypersaline conditions (>40 psu; n.b., psu = practical salinity unit), which correspond to B/Ga values of <3, 3–4.5, 4.5–6, 6–10, and > 10, respectively (Wei et al., 2018; Wei and Algeo, 2020; Wei et al., 2022; Remírez et al., 2025a, 2025b). It is based on the strong correlation of dissolved boron to salinity in modern aqueous systems (0.131 ppm/psu; Lee et al., 2010) and the fact that boron is readily taken up by clay minerals in the sediment (Keren and Mezuman, 1981). Gallium belongs to the same group of the periodic table (IIIA; boron group) and has the same valence (+3) as boron, but it is typically present only in the detrital fraction of sediments and is not adsorbed from the watermass by clay minerals. For normalization of B concentrations, Ga is used in preference to aluminum (Al) because its concentration in upper continental crust (17 ppm) is much closer to that of B (15 ppm) (McLennan, 2001; Algeo et al., 2025). Although developed for fine-grained siliciclastic sediments, the B/Ga proxy has been demonstrated to be robust in marls to an Al content as low as 2 % (Wei et al., 2025). B/Ga is unreliable in carbonate facies (i.e., Al < 2 %), but paleosalinity conditions can nonetheless be tentatively evaluated using "excess B" (B_{ex}, calculated as total B − 6 × Ga), with values of <0 ppm, ~10–20 ppm, and > 30 ppm indicative of brackish, marine, and hypersaline conditions, respectively (Wei et al., 2025).

3. Geological setting

3.1. Paleogeography

During the Late Ordovician to early Silurian, the paleogeographic location of the study area was in east-central Laurentia at 20–25°S paleolatitude (Cocks and Torsvik, 2021) (Fig. 2). Its location in a subtropical climate zone is consistent with the regional distribution of fossil and rock types (Brett et al., 2004, 2008, 2015, 2020; Aucoin and Brett, 2016; Koirala et al., 2016). The study site was located on the intracratonic Lexington Platform, an environmentally sensitive area of shallow to deep subtidal environments located between the Taconic foreland basin to the east and the Sebree Trough to the west. The Sebree Trough was an intracratonic sag within which cool nutrient-rich oceanic waters flowed, leading to accumulation of phosphatic carbonates on adjacent shelf margins (Kolata et al., 2001; Young et al., 2015). The Galena Shelf, located to the northwest of the Sebree Trough, was a broad, shallow carbonate-dominated region on the margin of the exposed Transcontinental Arch (Witzke, 1987).

3.2. Lithology and stratigraphy

The largely conformable Upper Ordovician-lower Silurian succession of the Lexington Platform consists of shallow-marine carbonates, marls and shales ranging up to 950 m in thickness (Weir et al., 1984; Brett et al., 2008, 2020; Koirala et al., 2016) (Fig. 1). The Upper Ordovician includes (1) the Lexington Limestone (Chatfieldian-lower Edenian), composed of thin-bedded, light- to medium-gray limestone (packstone to grainstone) interbedded with shale, both containing an abundance of shallow-marine biota (Borella and Osborne, 1978); (2) the Grant Lake

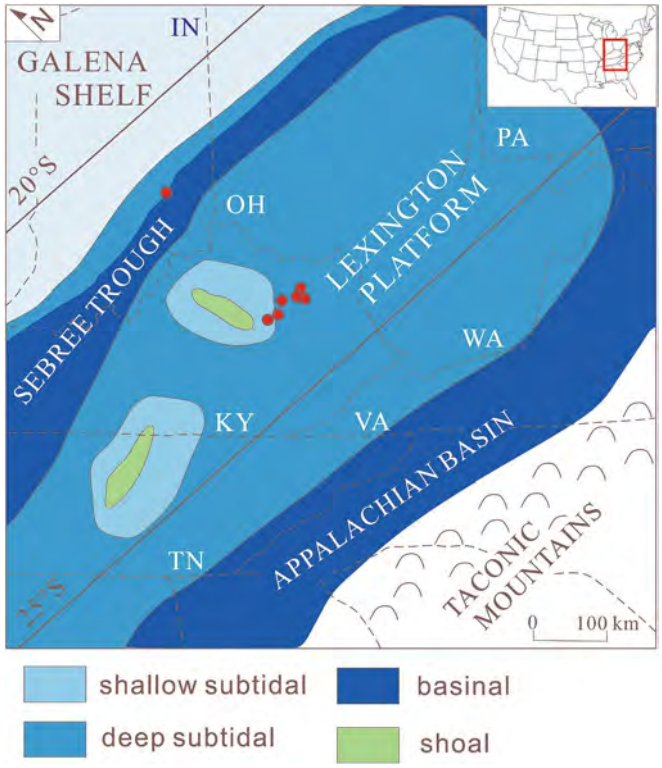


Fig. 2. Paleogeography and depositional environments of eastern Laurentia in late Cincinnatian time (Late Ordovician, ca. 450 Ma) (map modified from Brett et al., 2004). Red dots represent sample locations and dashed lines represent state boundaries. IN—Indiana; KY—Kentucky; OH—Ohio; PA—Pennsylvania; TN—Tennessee; VA—Virginia; WV—West Virginia. (For interpretation of the references to colour in this figure legend, the reader is referred to the web version of this article.)

Formation (Maysvillian), composed of fossiliferous wackestone, packstone, and grainstone (Brett et al., 2020); (3) the Bull Fork (or Arnheim) Formation (lower Richmondian), which grades upward from fossil-rich limestone to shale (Brett et al., 2015); (4) the Rowland Formation (mid-Richmondian), composed mainly of fossiliferous packstone and thin shale; (5) the Preachersville Member of the Drakes Formation (upper Richmondian), composed mainly of dolomitic to calcareous mudstone and dolomitic limestone that passes upward into green and red shale (Brett et al., 2015); and (6) the thin Centerville and Belfast members of the Whippoorwill Formation (lower Medinan), composed of calcareous and dolomitic siltstone, gray shale, and nodular argillaceous limestone (Waid, 2018).

The erosion surface at the O—S boundary is not well-developed in the study area, but clasts derived from underlying Ordovician strata are incorporated into the base of the Silurian Brassfield Formation (Weir et al., 1984). The Silurian succession in the study area is relatively thinner than the Ordovician due to tectonic uplift and erosion, and unconformities separate its stratigraphic sequences. The Silurian consists of (1) the Brassfield Formation (upper Medinan), composed of cherty dolostone; (2) the Plum Creek Shale (green) and overlying Oldham Limestone (dolomitic); (3) the Lulbegrud Shale Member of the Noland or Drowning Creek Formation (lower Clintonian), composed of green, mostly barren clay shale with a few discontinuous beds of dolomitic mudstone and wackestones with rare fossils (Sullivan et al., 2016); and (4) the Estill Shale Member of the Alger Formation (mid-Clintonian), composed of greenish gray to reddish clay shale and thin silty dolomite (Ettensohn et al., 2013; Sullivan et al., 2014; Brett et al., 2008, 2020; Stigall, 2023) (Fig. 1). The ages of the various study units have been established based on a combination of conodont biostratigraphy and regional stratigraphic correlation, with corresponding international stages (Late Ordovician Katian through early Silurian Telychian) shown in Fig. 1.

3.3. Sedimentary environments and sea-level variation

During the Late Ordovician, the Lexington Platform was covered by carbonate tidal and shelf facies, with carbonate and siliciclastic slope facies on its margins (Brett et al., 2004, 2008, 2015, 2020; Aucoin and Brett, 2016; Koirala et al., 2016). The Lexington Formation of central Kentucky documents the transition of a widespread carbonate platform into a ramp-to-basin system (Brett et al., 2004). The tectonic foreland basin (Appalachian Basin) to the southeast was the main source of siliciclastic debris to the study area (Fig. 2). The study succession records substantial sea-level fluctuations. A transgression from the Grant Lake Formation to Bull Fork Formation is marked by shallow-shelf grainstones overlain by thin shales and limestones deposited in a ramp setting, and by a decrease in carbonate content of the Bull Fork Formation from its base (~80 %) to its top (~20 %) (Brett et al., 2015, 2020). The Brassfield Formation, which forms the base of the Silurian System throughout the study area, consists mainly of dolostone in Kentucky but becomes progressively more limestone-rich northward into Ohio, where it records two early Silurian transgressive events. The Nowland Formation, which consists of alternating carbonate and shale with the latter increasing upsection, represents a transgressive unit (Ettensohn et al., 2013). Sea level rose from an early Silurian lowstand related to latest Ordovician (Hirnantian) glaciation to a peak in the late Llandovery-early Wenlock while displaying prominent short-term cyclicity (Brett et al., 2020).

4. Methods

4.1. Sampling

All samples were collected from Ordovician-Silurian outcrops in northeastern Kentucky and southeastern Indiana, USA. Upper Katian and younger rocks in the study area were removed by erosion from much of the axial region of the Cincinnati Arch, exposing strata down to the level of the Lexington Limestone. We collected 50 large (kg-sized) samples ranging in age from the upper Middle Ordovician (Shermanian) Lexington Limestone to the upper lower Silurian (Telychian) Alger Formation (see Table 1 for sample details). Apart from the Whippoorwill Formation samples, which came from the Sand Creek Section near Greensburg, Indiana, all other samples came from a relatively small area located about 50–60 km east of Lexington, Kentucky. Of the total of 50 samples, 34 were analyzed for biomarkers and 27 for elemental chemistry (n.b., 11 samples were tested for both types of proxies).

4.2. Organic geochemical analyses

The lipid extraction procedure used in this study followed that of Song (Yi) et al. (2021). Weathered surfaces were removed from each sample, and the freshest material was cut into small chips (~1 cm^3) that were ultrasonically cleaned three times in 18 MΩ ultrapure water. Then, the rock chips were ground to a fine powder (200 mesh) using a stainless-steel puck mill that was cleaned between samples by grinding three times with fired quartz sand and rinsing with ultrapure water and alcohol. About 5–10 g of powdered sample were dissolved in 9 % (by mass) hydrochloric acid and rinsed with ultrapure water for TOC pretreatment. About 40–50 g of powdered sample were extracted using a mixture of dichloromethane and methanol (9:1, v:v) in an accelerated solvent extractor (ASE 100 and ASE 150) at a pressure of 1500–1600 psi and a temperature of 100 °C, with static extractions proceeding through three cycles of 15 min per cycle. Total lipids were then separated using a clean activated silica gel column. Three lipid fractions (saturated hydrocarbons, aromatic hydrocarbons, and polar compounds) were successively eluted with solvent mixtures of increasing polarity (i.e., hexane, hexane/dichloromethane (1:1, v:v), and methanol, respectively).

Total organic carbon (TOC) and lipid detection analysis in this study also followed the procedures of Song (Yi) et al. (2021). The identification of lipids was performed by selected ion monitoring (SIM). The study samples were analyzed for a series of hydrocarbon biomarkers, including C_{13}–C_{33} *n*-alkanes, C_{27}–C_{35} 17α,21β-hopanes, C_{30}–C_{33} 17β,21α-hopanes (moretanes), C_{19}–C_{29} tricyclic terpanes and C_{27}–C_{29} steranes. Peak identification was based on comparison of retention times with standards and interpretation of mass spectrum fragmentation patterns from the literature. A solution of 5α(H),14β(H)-androstane with a concentration of 0.1032 mg/mL was used as an internal lab standard for quantification of saturated alkanes. Relative compound abundances were measured by comparing corresponding peak areas of mass chromatograms with those of the internal standard.

4.3. Inorganic geochemical analyses

Selected samples were analyzed for boron (B), gallium (Ga), and total sulfur (TS) contents at the Wuhan Center and the ALS Laboratory Group (see Table 2). For B analysis, a prepared sample (0.5 g) was fused with sodium hydroxide in a nickel crucible over a flame. The resulting melt was dissolved in deionized water and topped up to 100 mL. The solution was subsequently diluted by adding equal parts of HCl and analyzed by ICP-MS. For Ga analysis, the sample was digested with acid liquid and analyzed by ICP-MS. Data quality was monitored by analysis of a laboratory standard GSR-5 (B = 154 μg/g, Ga = 26 μg/g). For TS analysis, the sample was heated to approximately 1350 °C in an induction furnace while passing a stream of oxygen through the sample. Sulfur dioxide released from the sample was measured by an IR detection system and reported as total sulfur. Data quality was monitored using the U.S.G.S. SDO-1 standard (S = 5.35 %) and an internal laboratory standard (DBS-1, S = 1.97 %).

Table 1
Sample information.

Sample No.	Stage	Site	Formation	lithology	Age (Ma)
OST-MS	Telychian	Route 89, Kentucky	Alger Fm	shale	436.0
EST-2	Telychian	(37.9545°N, 84.1010°W)	Alger Fm	shale	436.4
EST-1	Telychian		Alger Fm	shale	436.8
89-s2	Telychian		Alger Fm	shale	437.2
89-s1	Telychian		Alger Fm	shale	437.6
OST-ES	Telychian		Alger Fm	shale	438.0
WAC-1	Telychian	Route 52, Kentucky	Noland Fm	dolostone	438.5
LUL-1	Telychian	(37.7251°N,84.3114°W)	Noland Fm	shale	438.6
OST-UL	Aeronian-Telychian		Noland Fm	dolostone	439.0
LUL-2	Aeronian		Noland Fm	shale	439.2
OW-11	Aeronian		Noland Fm	argillaceous dolostone	439.5
OST-LL	Aeronian		Noland Fm	argillaceous dolostone	439.6
OST-PC	Rhuddanian	Owingsville Manor, Kentucky (38.1269°N, 83.7545°W)	Brassfield Fm	argillaceous dolostone	440.8
OW-10	Rhuddanian		Brassfield Fm	argillaceous dolostone	441.2
OW-9	Rhuddanian		Brassfield Fm	argillaceous dolostone	441.4
OW-8	Rhuddanian		Brassfield Fm	argillaceous dolostone	441.6
OW-4	Rhuddanian		Brassfield Fm	shale	441.8
OW-2	Rhuddanian		Brassfield Fm	dolostone	442.0
S23	Hirnantian	Sand Creek Section, Greensburg, Indiana (39.2561°N, 85.5406°W)	Whippoorwill Fm	argillaceous limestone	443.4
S21	Hirnantian		Whippoorwill Fm	limestone	443.5
S17	Hirnantian		Whippoorwill Fm	argillaceous limestone	443.6
S16	Hirnantian		Whippoorwill Fm	argillaceous limestone	443.7
S14	Hirnantian		Whippoorwill Fm	marl	443.8
S8	Hirnantian		Whippoorwill Fm	argillaceous limestone	444.0
S4	Hirnantian		Whippoorwill Fm	calcareous shale	444.1
S1	Hirnantian		Whippoorwill Fm	limestone	444.2
S0	Hirnantian		Whippoorwill Fm	calcareous shale	444.3
OST-PRB	upper Richmondian	Owingsville Manor, Kentucky (38.1269°N, 83.7545°W)	Preachersville Fm	marl	445.3
OW-1	upper Richmondian		Preachersville Fm	marl	445.5
OST-DF	upper Richmondian		Preachersville Fm	marl	445.7
X123–8	middle Richmondian	I-64 (US Highway 60) near Owingsville, Bath County, Kentucky (38.1377°N, 83.7260°W)	Rowland Fm	calcareous shale	446.6
X123–5	middle Richmondian		Rowland Fm	marl	446.7
X123–3	middle Richmondian		Rowland Fm	marl	446.8
OST-MR	middle Richmondian		Rowland Fm	marl	447.0
X123–2	middle Richmondian		Rowland Fm	marl	447.1
X123–1	middle Richmondian		Rowland Fm	argillaceous limestone	447.3
SUN	lower Richmondian		Bull Fork Fm	marl	447.6
MM117-s2	lower Richmondian	I-64, Preston, Kentucky	Bull Fork Fm	marl	447.8
MM117-s3	lower Richmondian	(38.1112°N, 83.8089°W)	Bull Fork Fm	marl	448.0
MM1175–1	lower Richmondian		Bull Fork Fm	marl	448.2
MM1175–0	basal Richmondian		Bull Fork Fm	marl	448.4
GL-1	upper Maysvillian	Route 52, Kentucky (37.7251°N, 84.3114°W)	Grant Lake Fm	limestone	449.0
OST-BM	Maysvillian		Lexington Limestone	limestone	451.0
LX-SGM-8	upper Shermanian		Lexington Limestone	limestone	451.1
LX-SGM-7	upper Shermanian		Lexington Limestone	limestone	451.2
LX-SGM-5	upper Shermanian	Route 1958, east of Lexington, Kentucky (37.9984°N, 84.2340°W)	Lexington Limestone	limestone	451.4
LX-SGM-4	upper Shermanian		Lexington Limestone	limestone	451.8
LX-SGM-3	upper Shermanian		Lexington Limestone	limestone	452.0
LX-SGM-2	upper Shermanian		Lexington Limestone	limestone	452.4
LX-SGM-1	upper Shermanian		Lexington Limestone	argillaceous limestone	452.6

Table 2
Elemental salinity proxy data and salinity facies interpretations.

Sample No.	Ga (ppm)	B (ppm)	B/Ga	B_{xs} (ppm)	Salinity facies
WAC-1	1.2	24.9	21.7	18.0	marine to slightly hypersaline
OW-11	3.6	54.5	15.3	33.2	marine to slightly hypersaline
OW-9	2.4	38.1	15.7	23.6	marine to slightly hypersaline
OW-8	2.1	31.0	14.5	18.2	marine to slightly hypersaline
OW-4	21.8	151.6	6.9	20.6	marine
OW-2	1.0	29.0	28.1	22.8	marine to slightly hypersaline
S23	1.8	30.1	17.0	19.5	marine to slightly hypersaline
S21	0.28	11.9	42.8	10.2	marine to slightly hypersaline
S17	2.1	25.2	12.0	12.6	marine to slightly hypersaline
S14	4.2	50.4	11.9	25.0	marine to slightly hypersaline
S8	2.9	41.3	14.0	23.6	marine to slightly hypersaline
S4	8.7	95.9	11.0	43.6	marine to slightly hypersaline
S1	0.80	14.0	17.4	9.2	marine to slightly hypersaline
S0	9.7	105.0	10.8	46.7	marine to slightly hypersaline
X123–8	8.5	51.6	6.1	0.76	marine to slightly brackish
X123–5	7.3	55.6	7.6	11.7	marine
X123–3	7.8	45.4	5.8	−1.5	marine to slightly brackish
X123–1	1.2	4.5	3.7	−2.7	marine to slightly brackish
MM117–2	3.6	25.1	7.0	3.6	marine to slightly brackish
MM117–0	4.4	28.7	6.6	2.5	marine to slightly brackish
MM1175–3	4.1	28.6	7.0	4.1	marine to slightly brackish
MM1175–1	5.8	32.6	5.6	−2.1	marine to slightly brackish
LX-SGM-8	0.56	4.0	7.1	0.61	marine to slightly brackish
LX-SGM-7	0.36	2.3	6.5	0.18	marine to slightly brackish
LX-SGM-5	0.56	2.5	4.6	−0.80	marine to slightly brackish
LX-SGM-4	0.41	2.6	6.3	0.13	marine to slightly brackish
LX-SGM-1	2.4	9.5	4.0	−4.7	marine to slightly brackish

4.4. Data analysis

Changepoint analysis uses a numerical algorithm to objectively identify specific points in a time series at which the statistical properties of the data (i.e., their absolute values and/or patterns of variation) are abruptly altered, indicating a significant change in the underlying parameters, conditions, or processes controlling the data records (Reeves et al., 2007; Killick et al., 2021). In this study, we applied the envcpt() function from the EnvCpt package in R, which evaluates a variety of trend, changepoint, and autocorrelation models (i.e., time series analysis) for optimum performance (Killick and Eckley, 2014; Killick et al., 2021; Vollset et al., 2022). Since changepoint analysis requires data to be evenly spaced, this study used a combination of time window averaging and linear interpolation to convert non-equidistant data series (i.e., H/S data) into equidistant data series. We then chose "envcpt (data, model = 'mean')" in the 'EnvCpt' package to identify changepoints in our time series records (Zhang and Siegmund, 2007). This specific model identifies changepoints based on the mean and variance of data over a specific interval, and it has the lowest MBIC penalty value, making it advantageous for large and complex time series (Zhang and Siegmund, 2007). This statistical procedure allows for a relatively objective evaluation of the timing of changes in biomarker proxy records and their relationship to other proxy records.

5. Results

5.1. Distribution patterns of terrestrial geolipids

For the saturated fraction, the samples from Ordovician and Silurian strata show different distribution patterns in total ion chromatograms (TICs). The most abundant compounds in the saturated fraction are *n*-alkanes with a unimodal distribution in both Ordovician and Silurian samples, but the main peaks are different (Fig. 3). The main peak of *n*-alkanes in Upper Ordovician samples is C_{23} or C_{25} *n*-alkane, whereas the main peak in lower Silurian samples is C_{21} or C_{23} *n*-alkane, and odd-over-even predominance reveals substantial land plant inputs to marine facies of the study area (Fig. 3). Long-chain *n*-alkanes with odd-over-even dominance are mainly from the leaf wax of higher plants and, thus, are considered to be lipid biomarkers of higher plants, i.e., nC_{27}, nC_{29}, and nC_{31} alkanes (Peters et al., 2005), whereas medium-chain and short-chain *n*-alkanes are mainly derived from terrestrial aquatic plants and bacteria or algae, respectively.

In the study samples, the ratios of various *n*-alkane series (i.e., C_{14}-C_{20}, C_{21}-C_{26} and C_{27}-C_{33}) to total *n*-alkane content differ between the pre-Hirnantian and post-Hirnantian samples (Fig. 4). The proportion of C_{14}-C_{20} *n*-alkanes ranges from 0.25 to 0.42 with a median of 0.35 in the pre-Hirnantian Upper Ordovician and from 0.14 to 0.38 with a median of 0.26 in the Hirnantian and lower Silurian (note: all ranges are reported as the 16th-to-84th percentiles to avoid the influence of outliers). The proportion of C_{21}-C_{26} *n*-alkanes ranges from 0.30 to 0.43 with a median of 0.37 in the pre-Hirnantian Upper Ordovician, and from 0.33 to 0.49 with a median of 0.39 in the Hirnantian and lower Silurian. The proportion of C_{27}-C_{33} *n*-alkanes ranges from 0.21 to 0.30 with a median of 0.27 in the pre-Hirnantian, and from 0.18 to 0.46 with a median of 0.33 in the Hirnantian and lower Silurian. Compared with the values for the pre-Hirnantian Upper Ordovician, the proportion of short-chain *n*-alkanes decreased in the upper Hirnantian and lower Silurian, whereas the proportion of middle- and long-chain *n*-alkanes increased (Fig. 4).

The distributions of alkylated alkanes also show different patterns in the Ordovician versus the Silurian. The peak area of alkylated alkanes from Upper Ordovician samples is low, which is seen in the TIC of the saturated fraction, whereas the peak area of low-carbon-number alkylated alkanes (e.g., the alkylated homologues of short-chains alkanes) and high-carbon-number cycloalkanes (e.g., hopanes or tricyclic terpanes) from lower Silurian samples is high (Fig. 3).

High moretane concentrations have been observed in both terrestrial and marine facies with large terrestrial organic inputs (Xie et al., 2007). In this study, the main hopane compound is 17α(H),2β(H)-30-hopane (C_{30} hopane), followed by 17α(H),2β(H)-30-norhopane (C_{29} hopane). Similarly, the main moretane compound is C_{30} moretane, followed by C_{29} moretane. The moretane-to-hopane ratio (M/H), which is defined as the ratio of C_{30} moretane to C_{30} hopane, ranges from 0.41 to 0.50 with a median of 0.45 in the pre-Hirnantian Upper Ordovician, and from 0.40 to 0.54 with a median of 0.46 in the Hirnantian and lower Silurian (Fig. 4). These data indicate relatively uniform inputs of terrestrially derived material to the study area throughout the Late Ordovician-early Silurian interval.

5.2. Distribution patterns of marine geolipids

Hopanes in the saturated fraction are thought to be derived mainly from prokaryotes (Eglinton and Hamilton, 1967) and steranes mainly from eukaryotes (Rohmer et al., 1984). Therefore, the hopane-to-sterane

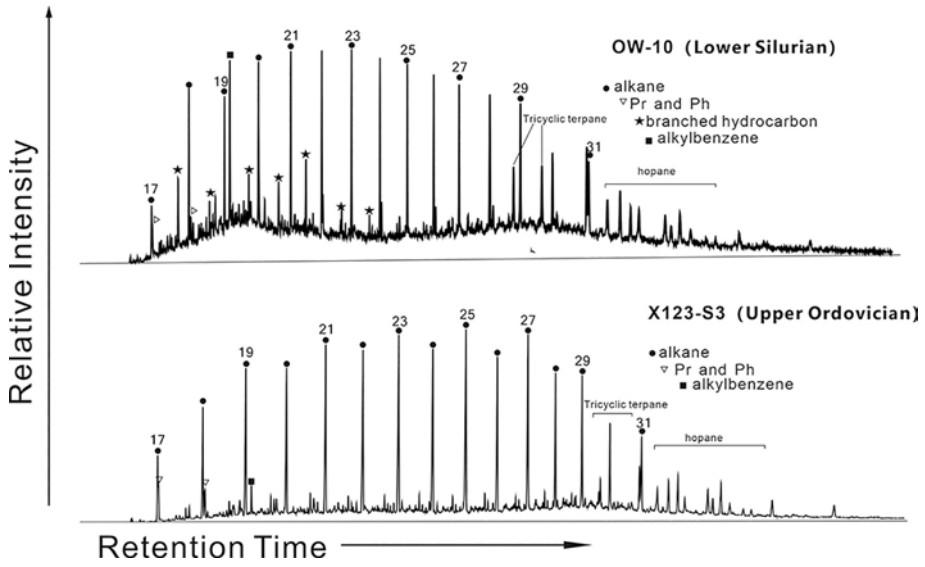


Fig. 3. Total ion chromatograms of the saturated fraction in a lower Silurian sample (above) and an Upper Ordovician sample (below), showing different distribution patterns of saturated alkanes.

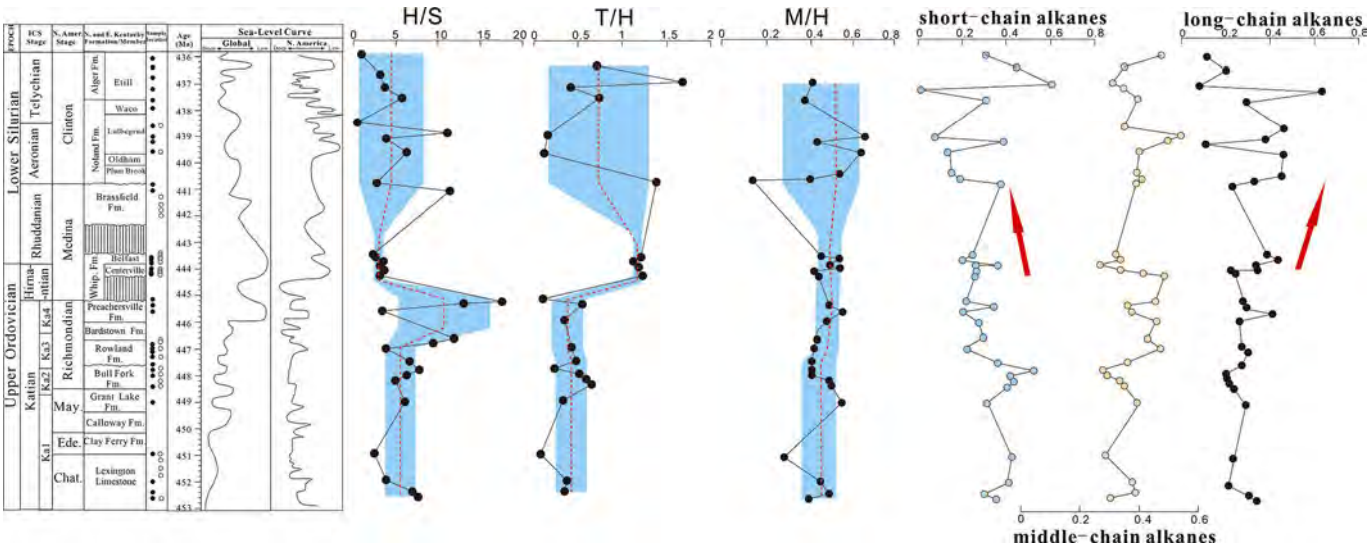


Fig. 4. Variation in biomarker proxies for the Upper Ordovician-lower Silurian succession in northeastern Kentucky and southeastern Indiana. M/H represents the ratio of C_{30} moretane to hopane; and short-chain, middle chain and long-chain n-alkanes represent the ratios of C_{14}-C_{20}, C_{23}-C_{26} and C_{27}-C_{33} *n*-alkanes to the total *n*-alkanes, respectively. Red dashed lines show variation in mean values. Blue fields show the mean ± 1SD (standard deviation). Abbreviations: T = C_{19}-C_{25} tricyclic terpanes, H = C_{30}-C_{34} $\alpha\beta$-hopanes, S = C_{27}-C_{29} regular steranes. (For interpretation of the references to colour in this figure legend, the reader is referred to the web version of this article.)

ratio (H/S) can indicate the relative contributions of prokaryotes and eukaryotes to the organic fraction. H/S ratios, which are defined as the ratio of $C_{30–34}$ $\alpha\beta$ hopanes and $C_{27\text{-}C29}$ regular steranes, range from 3.78 to 7.82 with a median of 6.52 in pre-Hirnantian samples, and from 1.49 to 5.48 with a median of 3.11 in Hirnantian and lower Silurian samples (Fig. 3). H/S ratios thus show a pronounced secular decrease from the Late Ordovician to early Silurian. These results indicate that prokaryotes (i.e., bacteria) were the dominant contributors of organic material to the study units throughout the Late Ordovician to early Silurian, although their relative dominance declined significantly at the time of the Hirnantian Ice Age.

Since hopanes are mainly derived from cell membrane lipids of prokaryotes such as bacteria, and tricyclic terpenes are derived from eukaryotic algae (see Section 2.2), the tricyclic terpene-to-hopane ratio (T/H) can be used to evaluate the relative inputs of marine eukaryotic algae and prokaryotes. T/H varied from 0.23 to 0.56 with a median of 0.39 in the pre-Hirnantian samples and increased significantly from 0.56 to 1.35 with a median of 1.18 in the Hirnantian to lower Silurian samples (Fig. 4). The results show that the prokaryotes largely contributed to the organic matter in the pre-Hirnantian while the relative input of eukaryotic algal sharply increased (by a factor of ~3×) at the time of the Hirnantian Ice Age, and then slightly declined in the early Silurian. Combined with T/H ratios, we can infer that decreased H/S ratios were linked to increased organic inputs from eukaryotic algae during the early Silurian.

5.3. Salinity variation

The present study samples all contain <4 % Al, ranging from limestones (Al <2 %) to marls (Al = 2–4 %) in composition. B/Ga is a robust

proxy for paleosalinity in the latter but not the former, so we also made use of the newly proposed "excess B" (B_{xs}) proxy to evaluate the salinity conditions of the limestone samples (Wei et al., 2025). For the Lexington Limestone and Bull Fork Formation samples (~90 % carbonate), B/Ga values are 4.5–7.0 with a median of 6.3 ($n = 13$), and B_{xs} ranges from about −5 to 5 ppm (see Table 2). Both proxies suggest marine to slightly brackish conditions with salinity fluctuations possibly in the range of ~25–35 psu. For the Hirnantian and lower Silurian samples (~70 % carbonate), B/Ga values are 11.1–21.4 with a median of 15.0 ($n = 14$), and B_{xs} ranges from ~10 to 30 ppm. Both proxies suggest marine to weakly hypersaline conditions with salinity fluctuations possibly in the range of ~35–45 psu. Thus, the study area appears to have experienced a modest but sustained increase in watermass salinity around the OST.

5.4. Changepoint analysis

The changepoint analysis in R shows that the main changepoints of all proxies are at ~445 Ma, i.e., the base of the Hirnantian Stage, although for some proxies secondary changepoints are present at ~447 Ma and ~441 Ma, i.e., within the late Katian and close to the Rhuddanian-Aeronian stage boundary, respectively (Fig. 4). These results confirm that the most far-reaching changes in marine microbial-algal community composition occurred at the onset of the Hirnantian Ice Age, although second-order changes also occurred in the prelude to this event (i.e., late Katian) and in its aftermath (i.e., mid-early Silurian).

6. Discussion

6.1. Thermal maturity and organic matter types

Thermal maturation during burial results in changes in the physical structure and chemical composition of organic matter (OM) as it passes from an immature state (prodiagenetic stage; sub-oil window) to at mature state (early to mid-diagenetic stages; oil window) and finally to an overmature state (late diagenetic stage; gas window) (Hunt, 1990; Peters et al., 2005). The degree of organic maturation of a sample can be evaluated using T_{max}, which represents the temperature of the peak rate of hydrocarbon generation from a sample during Rock-Eval analysis, with T_{max} values of < 435 °C, 435–455 °C, and > 455 °C corresponding to the stages above (Snowdon, 1995; Fig. 5a). Other metrics of thermal effects include vitrinite reflectance (R_o), which measures the brightness of figured organic macerals derived from land plants, with R_o values of 0.3 %, 0.5–1.0 % and 1.3 % corresponding to the stages above (Repetski et al., 2006), and the colour alteration index (CAI), which measures colour changes in conodonts as a function of thermal alteration of organic inclusions, with CAI values of 1, 2–4, and > 5 corresponding to the stages above (Epstein et al., 1977).

Organic matter can be derived from various sources including freshwater algae, marine algae, and terrestrial higher plants. Along with thermal maturation, OM source is the dominant influence on variation in crossplots of hydrogen index (HI) versus oxygen index (OI), i.e., the amounts of hydrogen and oxygen present per unit carbon in the kerogen fraction (Espitalité et al., 1977, Espitalié et al., 1988; Peters et al., 2005; Fig. 5b). Fresh OM has higher HI values and lower OI values than highly bacterially degraded or thermally altered OM. OM is assigned to several types: Type I, typical of freshwater algae, has initial HI of >800 mg/g TOC and OI of <100 mg/g TOC; Type II, typical of marine algae, has initial HI of ~600–700 mg/g TOC and OI of <100 mg/g TOC, including Type II-1 sapropel-sapropelic OM and Type II-2 sapropelic-humic OM; Type II-1, typical of marine algae with low terrestrial input, has HI of 350–700 mg/g TOC and OI of <100 mg/g TOC; Type II-2, typical of marine algae with high terrestrial input, has HI of 150–350 mg/g TOC and OI of <100 mg/g TOC; Type III, typical of terrestrial plants (but also of highly oxidized marine and mixed terrestrial-marine organic matter; Vitorović et al., 1984), has initial HI of <200 mg/g TOC and OI of <100 mg/g TOC. Each type of kerogen also has its own maturation pathway on an HI–OI plot (Fig. 5b), reflecting loss of H and O under conditions of anaerobic decay; however, aerobic decay leads to a gain of O by algal kerogen, generating low-HI, high-OI compositions that are similar to those of fresh terrestrial OM.

The study samples exhibit low HI values (< 25 mg/g) and low to intermediate T_{max} values of 420–438 °C (Fig. 5a), equivalent to R_o < 0.5–0.7 %, representing the immature stage to early oil-generation window and Type III kerogen with poor hydrocarbon-generating potential. The small range of T_{max} values indicates that the maturity of the study samples is nearly uniform. Regional studies of conodont CAI (Epstein et al., 1977) and clumped isotopes (Barney, 2020) demonstrated that the average burial temperature of the study formations is lower than 100 °C, verifying the relative immaturity of OM in the study units. Thus, most of the study samples contain Type III kerogen although

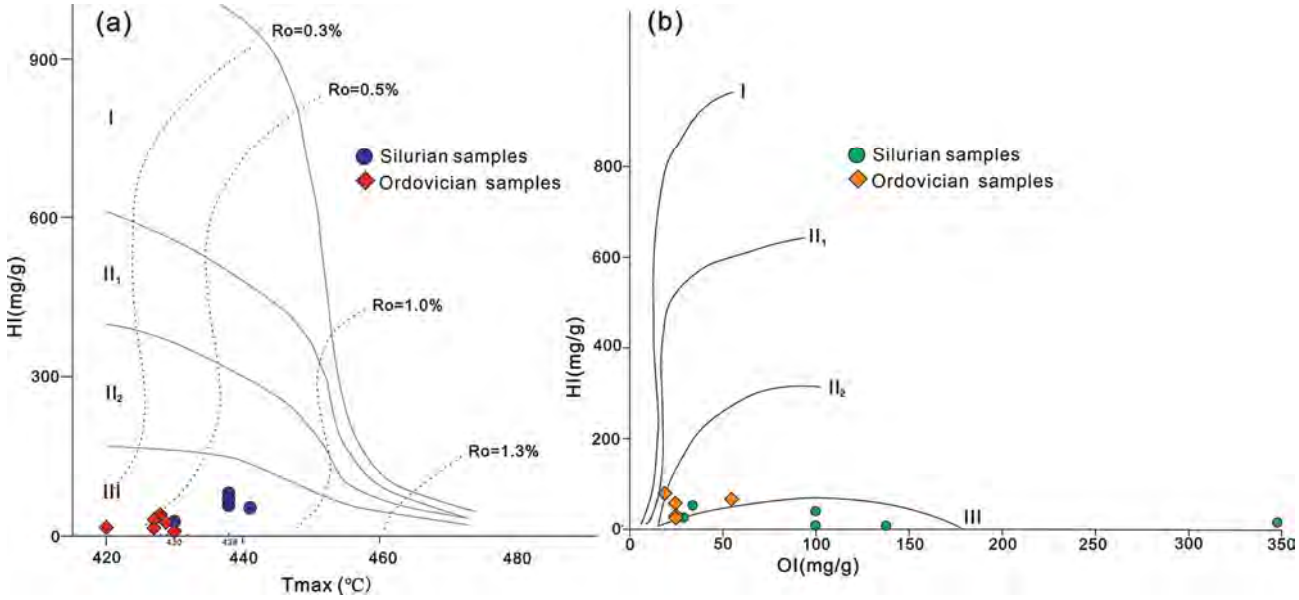


Fig. 5. (a) Hydrogen index (HI) versus T_{max}, indicating sample maturity; and (b) hydrogen index (HI) versus oxygen index (OI), indicating organic matter type (I, II or III).

some plot closer to the Type II pathway but close to its intersection with the Type III trend (Fig. 5b).

The TOC content differs between the stratigraphy units, showing relative lower TOC values ranging from 0.02 to 0.13 during Hirnantian, and much higher values than Hirnantian ranging from 0.32 to 2.53 during Rhuddanian while TOC is varied ranging from 0.03 to 0.59 during Katian (Supplementary Table 1). TOC maxima is observed in early Silurian and a major TOC depletion during the late Hirnantian have been found in study area. The decline in TOC during the Hirnantian stage may be related to increased dissolved oxygen caused by glacial cooling and the downward shift of the chemocline driven by sea-level drop (Yang and Fan, 2025). These changes created a relatively oxic marine environment on the continental shelf slope during the early Hirnantian.

The biomarker proxies in low maturity rocks and inorganic geochemical proxies, providing valuable insights into the effects of salinity and terrestrial inputs on microbial community composition and highlighting the dramatic environmental changes and their interconnections.

6.2. Secular variation in terrigenous inputs

Long-chain alkanes are mainly derived from terrestrial higher plants (i.e., vascular plants), middle-chain alkanes from mosses (e.g., sphagnum moss), non-marine algae or submerged/floating freshwater aquatic macrophytes (Ficken et al., 2000), and short-chain alkanes from marine algae and microbes (Eglinton and Hamilton, 1967; Song et al., 2020). Immature hydrocarbon source rocks with a large input of terrestrial organic matter are dominated by odd-carbon *n*-alkanes (i.e., nC_{27}, nC_{29} and nC_{31}), which are mainly degraded epidermal waxes. The long-chain n-alkanes are derived from land plants (Ficken et al., 2000; Pagani et al., 2006; Seki et al., 2012) or algae (Zegouagh et al., 1996), or in the case of some hypersaline carbonate and evaporate rocks (Peters et al., 2005). The kerogen type of the Silurian samples is Type III, which represents mainly terrestrial plant kerogen, whereas the Ordovician samples are closer to Type II and its intersection with the Type III trend, which is derived from marine algae via intense oxidative degradation (Vitorović et al., 1984) or via admixture of terrestrial organic matter. Thus, the long-chain *n*-alkanes are mainly thought to be terrestrially derived. An abundance of short-chain alkanes and hopanes indicates strong marine microbial activity. Long-chain alkanes are less stable than short-chain alkanes and tend to break into shorter chains with increasing maturity. Thus, short-chain alkanes can also be generated by bacterial degradation of long-chain alkanes (Zengler et al., 1999).

We compared the relative content of short- and long-chain alkanes to reflect the relative inputs of terrestrial plants and marine microbes. In the pre-Hirnantian Upper Ordovician, the contents of short- and long-chain *n*-alkanes are similar and nearly uniform, whereas in the Hirnantian and lower Silurian the proportion of short-chains *n*-alkanes decreases and that of long-chain *n*-alkanes increases. Based on change-point analysis, the trend of increasing long-chain *n*-alkanes started in the Hirnantian and persisted into the lower Silurian (Fig. 4). These results imply that organic matter inputs from land plants increased during the Hirnantian to early Silurian. Support for this inference is supplied by the spore record, which shows a shift in dominance from cryptospores to trilete spores during the Late Ordovician that reflects the evolution of new higher plant clades and the probable expansion of terrestrial floras (Romero-Sarmiento et al., 2011; Pšenička et al., 2021). Thus, the *n*-alkane evidence implies that land plant evolution had an impact on the marine environment of the study area during the OST. A gradual increase of terrestrial organic matter in marine successions during the Ordovician and Silurian periods is also seen in other global profiles (Pratt et al., 1978; Volkman, 1986; Libertín et al., 2018). For example, a section in southern Tunisia recorded the presence of various biomarkers indicative of land plant origin (e.g., retene, cadalene, simonellite, and isohexane-naphthalene) in the lower to mid-Silurian, although at fairly low concentrations (Volkman, 1986).

Although the flux of land plant-derived OM to marine sediments increased during the OST, total terrigenous inputs (as proxied by M/H in the study units) remained essentially unchanged, i.e., 0.41–0.55 (mean 0.45, $n = 15$) in the pre-Hirnantian versus 0.38–0.66 (mean 0.47, $n = 14$) in the Hirnantian and lower Silurian (Fig. 4). The increase in land plant-derived OM despite a nearly constant flux of soil-derived terrigenous material implies an expansion of higher plant floras on land during the OST rather than merely an increase in the total flux of land-derived detritus.

6.3. Microbial community changes during OST

The hopane/sterane (H/S) ratio shows marked variation during the Late Ordovician to early Silurian, which reflects significant microbial community changes during this interval. Hopanes and steranes are derived mainly from prokaryotes and eukaryotes, respectively, so the H/S ratio can reflect the relative inputs of organic matter from these sources (Song et al., 2021a). In this study, H/S ratios are similar in the Lexington Formation through Bull Fork Formation (range = 3.9–7.5) and then begin to increase at the top of the Rowland Formation (Fig. 4). A maximum H/S value of 17.8 is attained at the top of the Preachersville Formation, which far exceeds the range of 0.5–2.0 characteristic of the Phanerozoic (Peters et al., 2005). Increasing H/S at the onset of the Hirnantian Ice Age (and concurrent with LOME-1) reflects a sharp rise in prokaryotic inputs (e.g., marine bacteria). H/S then decreases to 2.9 with a range of 2.4–3.4 in the Centerville and Belfast members of the Whippoorwill Formation, reflecting enhanced and stable eukaryotic inputs (e.g., marine algae) during the main part of the Hirnantian Ice Age (Fig. 4).

The H/S ratio exhibits a second increase to 11.2 in the upper Brassfield Formation of the lower Silurian that is sustained into the Aeronian-lower Telychian Lulbegrud Shale, revealing a bacterial proliferation episode in the early Silurian. Although the graptolite extinctions of the Sandvika Event are not clearly delineated in our study profile, it appears that bacterial oceans persisted into the early Silurian (Jeppsson, 1998) (Figs. 1, 4). This is consistent with the phenomenon of bacterial oceans observed in most extinction events of the Phanerozoic (Xie et al., 2007, 2017; Cao et al., 2009; Liang et al., 2024). H/S then decreases slowly in the upper Telychian-lower Wenlock Estill Shale, indicating recovery of marine algae. These changes occurred in the context of strong $\delta^{13}C$ variation during the early Silurian indicative of contemporaneous climato-environmental instability (Saltzman, 2005; Cramer and Saltzman, 2007; Loydell, 2007; Cramer et al., 2011; Melchin et al., 2020). Various OST sections in North America and Europe have yielded ranges of H/S values for Katian and Rhuddanian strata that are both lower than (0.5–3.26, Smolarek et al., 2017) and similar to (2.62–12.8, Rohrssen et al., 2013) those of the present study. This variation may be attributed to differences between epeiric-sea and open-ocean depositional settings, because the composition of microbial communities is strongly influenced by local environmental conditions.

The tricyclic terpanes in the study samples may have been derived mainly from eukaryotic algae. Because tricyclic terpanes are common in strata enriched in *Tasmanites*, long-chain tricyclic terpanes are generally considered biomarkers for this algal taxon (Simoneit et al., 1990). However, the earliest macrofossils of *Tasmanites* appeared in the Middle Devonian, so tricyclic terpanes in Ordovician or Silurian strata were possibly derived from other algal taxa (Peters et al., 2005). Tricyclic terpanes can also originate from prokaryotic cell membrane lipids, which is a possible source of the high concentrations of these compounds in Neoproterozoic strata (Wang and Simoneit, 1995). Given that hopanes and steranes are characteristic of prokaryotes and eukaryotes, respectively, their relationship to tricyclic terpanes may be used to assess the origin of the latter. The study samples show a stronger correlation of C_{19-20} long-chain tricyclic terpanes with steranes ($r = +0.70$, $p = 0.003$, $n = 15$), than with hopanes ($r = +0.08$, $p = 0.8$, $n = 12$;

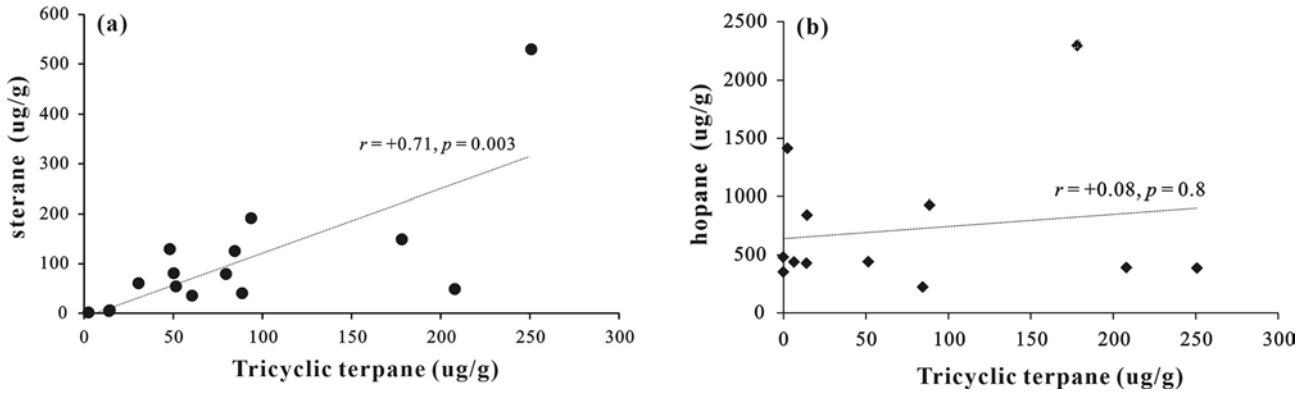


Fig. 6. Tricyclic terpanes versus (a) steranes and (b) hopanes in the study samples. The dotted lines are correlation trends, and *r* is Pearson's correlation coefficient.

Fig. 6), indicating derivation mainly from eukaryotes (e.g., microalgae).

This inference is consistent with the presence of a variety of algal fossils in the study units (Weir et al., 1984; Holland and Patzkowsky, 2004). Algal-coated grains are locally common in Upper Ordovician limestones of the Lexington Platform, suggesting that marine algae may have been the primary producers responsible for the formation of long-chain tricyclic terpanes in the study units during the Ordovician-Silurian Transition (OST) (Weir et al., 1984). Additionally, other reports of eukaryotic algae being the main primary producers in Canada and Africa highlight a significant turnover during the Late Ordovician, demonstrating the strong survival capabilities of oceanic plankton during periods of paleoenvironmental crisis (Vecoli, 2008; Delabroye et al., 2011; Khan et al., 2019).

The increasing, albeit fluctuating, trend toward higher ratios of tricyclic terpanes to hopanes in the lower Silurian suggests a flourishing of eukaryotic algae at that time. Conodont and brachiopod oxygen isotopes reveal comparatively cool temperatures in the early Silurian (~13–14 °C), and it was not until the Middle and Late Silurian that temperatures rose to 25 °C or higher within the paleotropics (Nardin et al., 2011; Cummins et al., 2014). Eukaryotic algal blooms and oxygen isotopic evidence from conodonts suggest that global temperatures continued to rise during the early Silurian, but more slowly than in the immediate aftermath of the Hirnantian Ice Age (Vecoli, 2008; Delabroye et al., 2011). The absolute concentration of tricyclic terpenes and hopanes decreased, but the ratio of tricyclic terpenes to hopanes increased, indicating that eukaryotic algal communities recovered more rapidly than prokaryotes during the early Silurian.*6.4. Effects of salinity and terrestrial inputs on microbial community composition.*

Microbial community compositions during the OST were impacted by environmental instability, i.e., variation in salinity, redox, and nutrient fluxes. Research on the modern Baltic Sea has shown that salinity changes are a primary trigger of rapid microbial community overturn, sometimes resulting in major changes in the core metabolisms of bacteria along salinity gradients from freshwater to marine (Gasiūnaitė et al., 2005; Dupont et al., 2014; Olofsson et al., 2020). In this study, the most significant change of microbial community occurred in conjunction with the Hirnantian Ice Age, coincident with a shift toward higher salinities during the OST. The shift is modest, from B/Ga values indicative of normal marine to slightly brackish conditions (4.0–7.6; ~25–35 psu) before glaciation to values indicative of moderate hypersalinity at its onset (6.9–42.8; ~35–45 psu), with marine to weakly hypersaline conditions persisting into the early Silurian. We infer that this salinity shift was due to climate aridification associated with the Hirnantian Ice Age, the effects of which were likely intensified by shallowing over the Lexington Platform (n.b., post-glacial eustatic levels were lower than pre-glacial levels, probably due to the continued existence of continental ice into the early Silurian; Grahn and Caputo, 1992; Finnegan et al., 2011; Fig. 1). The study area was located at paleolatitudes 15–20°S, i.e., in the dry subtropical belt, where the effects of climate aridification would have been most strongly felt (Liu et al., 2024b). The physiology and ecology of algae and microbes are highly sensitive to salinity variation, and the species of algae and microbes exhibit varying levels of adaptability to salinity, which directly have impact on microbial community composition (Dupont et al., 2014; Olofsson et al., 2020; Song et al., 2021a). Thus, the combined effects of sea-level fall and aridification contributed to secular variation in salinity, and increased salinity is consistent with the main changepoint of microbial community as evidenced by H/S ratios.

Climate aridification and sea-level fall can lead to enhanced terrestrial inputs through a less stable hydrological cycle (e.g., more frequent flash flooding) and increased physical erosion (Mather, 2007; Ravi et al., 2010). So we suggest that excepting lowering sea-level and aridification, the effect of terrestrial input on microbial community composition could also be more attention. The fossil records of terrestrial multicellular plants indicate the development/evolution of non-vascular plants had begun during the Middle Ordovician, and primitive land plants were structurally similar to modern mosses and lichens (Steemans et al., 2009; Lenton et al., 2012; Servais et al., 2019; Wellman et al., 2023). From the Middle Ordovician to the early Silurian, the spore assemblage changed from cryptospores to trilete spores as the dominant species, reflecting the evolution of vegetation on land. In this study, the ratio of long-chain *n*-alkanes to total *n*-alkanes content showed an increasing trend in the early Silurian, recording a rising contribution of terrestrial vegetation to the organic fraction of marine sediments. The spread of early land plants had a pronounced effect on marine sediments even though the terrestrialization process was still at an early stage, indicating a major role for vascular plants in accelerating weathering and chemical fluxes during the OST (Moulton and Berner, 1998; Ielpi and Lapôtre, 2020). This pronounced enhancement of terrestrial organic matter fluxes occurred despite total terrigenous inputs (i.e., including detrital siliciclastics) increasing only marginally from the Late Ordovician to early Silurian. Our data thus show that both salinity variation and the evolution of terrestrial ecosystems had observable effects on marine microbial community composition during the OST.

7. Conclusions

Analysis of an Upper Ordovician to lower Silurian succession that accumulated in eastern Laurentia reveals microbial community changes in the marine ecosystem and their relationship with salinity variation and early evolution of land plants. The hopane-to-sterane (H/S) and terpane-to-hopane (T/H) ratios show the change associated with B/Ga ratio, indicating algae blooms synchronized with the salinity variation at the onset of Hirnantian Ice Age. The evidence of terrestrial geolipids (long-chain alkanes and moretane-to-hopane ratio) shows that the input of organic matter derived from land plants increased during the Late Ordovician to early Silurian. Increased land plant inputs to marine sediments is consistent with a rapid expansion of land plants during the

OST. Although the relative proportion of eukaryote-derived organic matter increased again in the early Silurian, the secular trend of H/S shows the decreasing trend during the OST, suggesting influences related to both marine environmental perturbations (i.e., salinity variation) and early land plant evolution.

CRediT authorship contribution statement

Yi Song: Writing – original draft, Methodology, Funding acquisition, Formal analysis, Data curation, Conceptualization. **Thomas J. Algeo:** Writing – review & editing, Writing – original draft, Methodology, Investigation, Data curation, Conceptualization. **Carlton Brett:** Writing – review & editing, Resources, Methodology, Investigation. **Zhanhong Liu:** Writing – review & editing, Methodology, Data curation. **Shucheng Xie:** Methodology, Formal analysis, Conceptualization.

Declaration of competing interest

The authors declare that they have no known competing financial interests or personal relationships that could have appeared to influence the work reported in this paper.

Acknowledgments

This work was supported by the Guangxi Science and Technology Talent Base Special Program (grant no. GuikeAD21220131), the National Natural Science Foundation of China (NSFC) (grant no. 42302348, 42090041, 42166003). We thank Chao Gao for changepoint analysis in this study.

Appendix A. Supplementary data

Supplementary data to this article can be found online at https://doi.org/10.1016/j.chemgeo.2025.122724.

Data availability

I have shared my data at Supplementary File

References

Adiatma, Y.D., Saltzman, M.R., Young, S.A., Griffith, E.M., Kozik, N.P., Edwards, C.T., Leslie, S.A., Bancroft, A.M., 2019. Did early land plants produce a stepwise change in atmospheric oxygen during the late Ordovician (Sandbian ~458 Ma)? Palaeogeography, Palaeoclimatology. Palaeoecology 534, 109341.
Aldridge, R.J., Jeppsson, L., Dorning, K.J., 1993. Early Silurian oceanic episodes and events. J. Geol. Soc. Lond. 150 (3), 501–513.
Algeo, T.J., 1996. Geomagnetic polarity bias patterns through the phanerozoic. J. Geophys. Res. Solid Earth 101 (B2), 2785–2814.
Algeo, T.J., Shen, J., 2024. Theory and classification of mass extinction causation. Natl. Sci. Rev. 11 (1), nwad237.
Algeo, T.J., Marenco, P.J., Saltzman, M.R., 2016. Co-evolution of oceans, climate, and the biosphere during the 'Ordovician Revolution': a review. Palaeogeogr. Palaeoclimatol. Palaeoecol. 458, 1–11.
Algeo, T.J., Wei, W., Remírez, M.N., Wang, C.W., Liu, Z.H., Gilleaudeau, G., Brocks, J.J., 2025. Influence of clay-mineral assemblages on the B/Ga salinity proxy. Chem. Geol. (in review).
Aquino Neto, F.R., Trigüis, J., Azevedo, D.A., Rodriques, R., Simoneit, B.R.T., 1992. Organic geochemis¬try of geographically unrelated tasmanites. Org. Geochem. 18 (6), 791–803.
Aucoin, C.D., Brett, C.E., 2016. Refined stratigraphy of the late Ordovician (Katian; Richmondian) Waynesville formation across the northeastern and northwestern margin of the Cincinnati Arch. Stratigraphy 12, 307–317.
Azevedo, D., Zinu, C.A., Neto, F.A., Simoneit, B., 2001. Possible origin of acyclic (linear and isoprenoid) and tricyclic terpane methyl ketones in a Tasmanian Tasman¬ite bitumen. Org. Geochem. 32, 443–448.
Badawy, A.S., Mehlqvist, K., Vajda, V., Ahlberg, P., Calner, M., 2014. Late Ordovician (Katian) spores in Sweden: oldest land plant remains from Baltica. GFF 136 (1), 16–21.
Barney, B.B., 2020. Ocean Temperatures in the Late Ordovician: A Clumped Isotope Study of Brachiopods and Cements (Doctoral dissertation). Texas A&M University, p. 76.
Bergström, S.M., Chen, X., Gutierrez-Marco, J.C., Dronov, A., 2009a. The new chronostratigraphic classification of the Ordovician System and its relations to major regional series and stages and to $\delta^{13}C$ chemostratigraphy. Lethaia 42 (1), 97–107.
Bergström, S.M., Chen, X., Gutiérrez-Marco, J.C., Dronov, A., 2009b. The new chronostratigraphic classification of the Ordovician System and its relations to major regional series and stages and to $\delta^{13}C$ chemostratigraphy. Lethaia 42 (1), 97–107.
Borella, P.E., Osborne, R.H., 1978. Late middle and early late Ordovician history of the Cincinnati Arch province, Central Kentucky to Central Tennessee. GSA Bull. 89 (10), 1559–1573.
Brett, C.E., McLaughlin, P.I., Cornell, S.R., Baird, G.C., 2004. Comparative sequence stratigraphy of two classic Upper Ordovician successions, Trenton Shelf (New York–Ontario) and Lexington Platform (Kentucky–Ohio): implications for eustasy and local tectonism in eastern Laurentia. Palaeogeogr. Palaeoclimatol. Palaeoecol. 210 (2), 295–329.
Brett, C.E., Algeo, T.J., McLaughlin, P.I., 2008. Use of Event Beds and Sedimentary Cycles in High-Resolution Stratigraphic Correlation of Lithologically Repetitive Successions: The Upper Ordovician Kope Formation of Northern Kentucky and Southern Ohio. Springer, Netherlands, pp. 315–350.
Brett, C.E., Thomka, J.R., Schwalbach, C.E., Aucoin, C.D., Malgieri, T.J., 2015. Faunal epiboles in the Upper Ordovician of north-Central Kentucky: implications for high-resolution sequence and event stratigraphy and recognition of a major unconformity. Palaeoworld 24 (1–2), 149–159.
Brett, C.E., Aucoin, C.D., Dattilo, B.F., Freeman, R.L., Hartshorn, K.R., McLaughlin, P.I., Schwalbach, C.E., 2020. Revised sequence stratigraphy of the upper Katian Stage (Cincinnatian) strata in the Cincinnati Arch reference area: Geological and paleontological implications. Palaeogeogr. Palaeoclimatol. Palaeoecol. 540, 109483.
Calner, M., Lehnert, O., Nõlvak, J., 2010. Palaeokarst evidence for widespread regression and subaerial exposure in the Middle Katian (Upper Ordovician) of Baltoscandia: significance for global climate. Palaeogeogr. Palaeoclimatol. Palaeoecol. 296, 235–247.
Cao, C., Love, G.D., Hays, L.E., Wang, W., Shen, S., Summons, R.E., 2009. Biogeochemical evidence for euxinic oceans and ecological disturbance presaging the end-Permian mass extinction event. Earth Planet. Sci. Lett. 281 (3–4), 188–201.
Cao, G., Liu, Y., Li, C., Hou, M., Lash, G.G., Zhou, X., Li, Y., Song, Y., 2023. Salinity variations of the inner Yangtze Sea during the Ordovician-Silurian transition and its influences on marginal marine euxinia. Glob. Planet. Chang. 225, 104129.
Capel, E., Cleal, C.J., Xue, J., Monnet, C., Servais, T., Cascales-Miñana, B., 2022. The Silurian–Devonian terrestrial revolution: diversity patterns and sampling bias of the vascular plant macrofossil record. Earth Sci. Rev. 231, 104085.
Chen, C., Wang, J.S., Chen, X.H., Algeo, T.J., Wang, Z., Yang, W.W., Song, Q., 2024. Productivity and redox influences on the late ordovician 'katian extinction' and 'early silurian recovery'. Palaeogeogr. Palaeoclimatol. Palaeoecol. 642.
Cheng, M., Zhang, Z., Algeo, T.J., Liu, S., Liu, X., Wang, H., Chang, B., Jin, C., Pan, W., Cao, M., Li, C., 2021. Hydrological controls on marine chemistry in the Cryogenian Nanhua Basin (South China). Earth Sci. Rev. 218, 103678.
Cheng, M., Zhang, Z., Jin, C., Wei, W., Wang, H., Algeo, T.J., Li, C., 2023. Salinity variation and hydrographic dynamics in the early Cambrian Nanhua Basin (South China). Sci. China Earth Sci. 66 (6), 1268–1278.
Cocks, L.R.M., Torsvik, T.H., 2021. Ordovician palaeogeography and climate change. Gondwana Res. 100, 53–72.
Cramer, B.D., Saltzman, M.R., 2007. Fluctuations in epeiric sea carbonate production during Silurian positive carbon isotope excursions: a review of proposed paleoceanographic models. Palaeogeogr. Palaeoclimatol. Palaeoecol. 245 (1–2), 37–45.
Cramer, B.D., Munnecke, A., Schofield, D.I., Haase, K.M., Haase-Schramm, A., 2011. A revised $^{87}Sr/^{86}Sr$ curve for the Silurian: implications for global ocean chemistry and the Silurian timescale. J. Geol. 119 (4), 335–349.
Cummins, R.C., Finnegan, S., Fike, D.A., Eiler, J.M., Fischer, W.W., 2014. Carbonate clumped isotope constraints on Silurian Ocean temperature and seawater $\delta^{18}O$. Geochim. Cosmochim. Acta 140, 241–258.
Delabroye, A., Munnecke, A., Vecoli, M., Copper, P., Tribovillard, N., Joachimski, M.M., Desrochers, A., Servais, T., 2011. Phytoplankton dynamics across the Ordovician/Silurian boundary at low palaeolatitudes: correlations with carbon isotopic and glacial events. Palaeogeogr. Palaeoclimatol. Palaeoecol. 312 (1–2), 79–97.
Deng, Y., Fan, J., Zhang, S., Fang, X., Chen, Z., Shi, Y., Wang, H., Wang, X., Yang, J., Hou, X., Wang, Y., Zhang, Y., Chen, Q., Yang, A., Fan, R., Dong, S., Xu, H., Shen, S., 2021. Timing and patterns of the Great Ordovician biodiversification event and late ordovician mass extinction: perspectives from South China. Earth Sci. Rev. 220, 103743.
Dupont, C.L., Larsson, J., Yooseph, S., Ininbergs, K., Goll, J., Asplund-Samuelsson, J., McCrow, J.P., Celepli, N., Allen, L.Z., Ekman, M., Lucas, A.J., Hagström, Å., Thiagarajan, M., Brindefalk, B., Richter, A.R., Andersson, A.F., Tenney, A., Lundin, D., Tovchigrechko, A., Nylander, J.A.A., Brami, D., Badger, J.H., Allen, A.E., Rusch, D.B., Hoffman, J., Norrby, E., Friedman, R., Pinhassi, J., Venter, J.C., Bergman, B., 2014. Functional tradeoffs underpin salinity-driven divergence in microbial community composition. PLoS ONE 9 (2), e89549.
Eglinton, G., Hamilton, R.J., 1967. Leaf epicuticular waxes. Science 156 (3780), 1322–1335.
Elrick, M., Reardon, D., Labor, W., Martin, J., Desrochers, A., Pope, M., 2013. Orbital-scale climate change and glacioeustasy during the early late Ordovician (pre-Hirnantian) determined from $\Delta^{18}O$ values in marine apatite. Geology 41, 775–778.
Epstein, A.G., Epstein, J.B., Harris, L.D., 1977. Conodont Color Alteration; an Index to Organic Metamorphism, 995. U.S. Government Printing Office, Washington D.C.
Espitalié, J., Ungerer, P., Irwin, I., Marquis, F., 1988. Primary cracking of kerogens. Experimenting and modelling C1, C2–C5, C6–C15 and C15+ classes of hydrocarbons formed. Org. Geochem. 13 (4), 893–899.

Espitalité, J., Laporte, J.L., Madec, M., Marquis, F., Leplat, P., Paulet, J., 1977. A rapid method for source rocks characterisation and for determination of petroleum potential and degree of evolution. Rev. l'Instit. Franç. Pétrole 32, 23–42.
Ettensohn, F.R., Lierman, R.T., Mason, C.E., Andrews, W.M., Gordon, L.A., 2013. The silurian of Central Kentucky, U.S.a.: stratigraphy, palaeoenvironments and palaeoecology. Mem. Assoc. Austral. Palaeontol. 44 (44), 159–189.
Ficken, K.J., Li, B., Swain, D.L., Eglinton, G., 2000. An n-alkane proxy for the sedimentary input of submerged/floating freshwater aquatic macrophytes. Org. Geochem. 31, 745–749.
Finnegan, S., Bergmann, K., Eiler, J.M., Jones, D.S., Fike, D.A., Eisenman, I., Hughes, N. C., Tripati, A.K., Fischer, W.W., 2011. The magnitude and duration of late Ordovician–Early Silurian glaciation. Science 331 (6019), 903.
Forsythe, I.J., Stigall, A.L., 2023. Insights for modern invasion ecology from biotic changes of the Clarksville phase of the Richmondian Invasion (Ordovician, Katian). Paleobiology 49, 493–508.
French, K.L., Tosca, N.J., Cao, C., Summons, R.E., 2012. Diagenetic and detrital origin of moretane anomalies through the Permian–Triassic boundary. Geochim. Cosmochim. Acta 84, 104–125.
Gasiūnaitė, Z.R., Cardoso, A.C., Heiskanen, A.S., Henriksen, P., Kauppila, P., Olenina, I., Pilkaitytė, R., Purina, I., Razinkovas, A., Sagert, S., Schubert, H., 2005. Seasonality of coastal phytoplankton in the Baltic Sea: influence of salinity and eutrophication. Estuar. Coast. Shelf Sci. 65 (1–2), 239–252.
Gilleaudeau, G.J., Algeo, T.J., Lyons, T.W., Bates, S., Anbar, A.D., 2021. Novel watermass reconstruction in the early Mississippian Appalachian Seaway based on integrated proxy records of redox and salinity. Earth Planet. Sci. Lett. 558, 116746.
Gilleaudeau, G.J., Wei, W., Remírez, M.N., Song, Y., Lyons, T.W., Bates, S., Anbar, A.D., Algeo, T.J., 2023. Geochemical and hydrographic evolution of the late Devonian Appalachian Seaway: linking sedimentation, redox, and salinity across time and space. Geochem. Geophys. Geosyst. 24 (8), e2023GC010973.
Grahn, Y., Caputo, M.V., 1992. Early Silurian glaciations in Brazil. Palaeogeogr. Palaeoclimatol. Palaeoecol. 99 (1–2), 9–15.
Herrmann, A.D., Haynes, J.T., Robinet, R., Clift, P.D., Goggin, K.E., 2023. Testing tectonostratigraphic hypotheses of the Blountian phase of the Taconic Orogeny in the Southern Appalachians through an integrated geochronological and sedimentological study of Ordovician K-bentonites and quartz arenites. Minerals 13 (6), 807.
Holland, S.M., Patzkowsky, M.E., 1996. Sequence stratigraphy and long-term paleoceanographic change in the Middle and Upper Ordovician of the eastern United States. In: Witzke, B.J., Ludvigson, G.A., Day, J. (Eds.), Paleozoic Sequence Stratigraphy; Views from the North American Craton. Geological Society of America, Special Paper, vol. 306, pp. 117–130.
Holland, S.M., Patzkowsky, M.E., 2004. Ecosystem structure and stability: middle upper ordovician of central Kentucky, USA. Palaios 19 (4), 316–331.
Holmden, C., Mitchell, C.E., LaPorte, D.F., Patterson, W.P., Melchin, M.J., Finney, S.C., 2013. Nd isotope records of late Ordovician sea-level change-implications for glaciation frequency and global stratigraphic correlation. Palaeogeogr. Palaeoclimatol. Palaeoecol. 386, 131–144.
Hunt, J.M., 1990. Genaration and migration of petroleum from abnormal pressured fluid compartment. AAPG Bull. 74 (1), 1–2.
Ielpi, A., Lapôtre, M.G.A., 2020. A tenfold slowdown in river meander migration driven by plant life. Nat. Geosci. 13 (1), 82–86.
Jeppsson, L., 1998. Silurian oceanic events: Summary of general characteristics. In: Landing, E., Johnson, M.E. (Eds.), Silurian Cycles: Linkages of Dynamic Stratigraphy with Atmospheric, Oceanic and Tectonic Changes. New York State Museum Bulletin, New York, pp. 239–257.
Jones, D.S., Martini, A.M., Fike, D.A., Kaiho, K., 2017. A volcanic trigger for the late Ordovician mass extinction? Mercury data from South China and Laurentia. Geology 45 (7), 631–634.
Keren, R., Mezuman, U., 1981. Boron adsorption by clay minerals using a phenomenological equation. Clay Clay Miner. 29 (3), 198–204.
Khan, M.Z., Feng, Q., Zhang, K., Guo, W., 2019. Biogenic silica and organic carbon fluxes provide evidence of enhanced marine productivity in the Upper Ordovician-lower Silurian of South China. Palaeogeogr. Palaeoclimatol. Palaeoecol. 534, 109278.
Killick, R., Eckley, I.A., 2014. Changepoint: an R package for changepoint analysis. J. Stat. Softw. 58, 1–19.
Killick, R., Beaulieu, C., Taylor, S., Hullait, H., 2021. EnvCpt: Detection of Structural Changes in Climate and Environment Time Series. Retrieved From, Version 1.1.3.
Koirala, D.R., Ettensohn, F.R., Clepper, M.L., 2016. Eustatic and far-field tectonic control on the development of an intra-platform carbonate-shoal complex: upper tongue of the Tanglewood Member, Upper Ordovician Lexington Limestone, Central Kentucky, U.S.a. Sediment. Geol. 345, 1–18.
Kolaczkowska, E., Slougui, N.E., Watt, D.S., Maruca, R.E., Moldowan, J.M., 1990. Thermodynamic stability of various alkylated, dealkylated and rearranged 17α-and 17β-hopane isomers using molecular mechanics calculations. Org. Geochem. 16 (4–6), 1033–1038.
Kolata, D.R., Huff, W.D., Bergström, S.M., 2001. The Ordovician sebree trough: an oceanic passage to the Midcontinent United States. GSA Bull. 113 (8), 1067–1078.
Kump, L.R., Arthur, M.A., Patzkowsky, M.E., Gibbs, M.T., Pinkus, D.S., Sheehan, P.M., 1999. A weathering hypothesis for glaciation at high atmospheric during the late Ordovician. Palaeogeogr. Palaeoclimatol. Palaeoecol. 152 (1–2), 173–187.
Lee, K., Kim, T.W., Byrne, R.H., Millero, F.J., Feely, R.A., Liu, Y.M., 2010. The universal ratio of boron to chlorinity for the North Pacific and North Atlantic oceans. Geochim. Cosmochim. Acta 74 (6), 1801–1811.
Lenton, T.M., Crouch, M., Johnson, M., Pires, N., Dolan, L., 2012. First plants cooled the Ordovician. Nat. Geosci. 5 (2), 86–89.
Li, C., Zhang, J., Li, W., Botting, J., Chen, Q., Fan, J., Zhang, Y., 2021. Multiple glacio-eustatic cycles and associated environmental changes through the Hirnantian (late Ordovician) in South China. Glob. Planet. Chang. 207, 103668.
Liang, Y., Liu, Z.R., Algeo, T.J., Meng, L., Ming, C., Wang, J., Song, B., Liu, Z., Zhou, M.F., 2024. Contrasting dynamics of marine bacterial-algal communities between the two main pulses of the late Ordovician Mass Extinction. Earth Planet. Sci. Lett. 645, 118956.
Libertín, M., Kvaček, J., Bek, J., Žárský, V., Štorch, P., 2018. Sporophytes of polysporangiate land plants from the early Silurian period may have been photosynthetically autonomous. Nat. Plants 4 (5), 269–271.
Liu, Z., Algeo, T.J., Guo, X., Fan, J., Du, X., Lu, Y., 2017. Paleo-environmental cyclicity in the early Silurian Yangtze Sea (South China): tectonic or glacio-eustatic control? Palaeogeogr. Palaeoclimatol. Palaeoecol. 466, 59–76.
Liu, Y., Li, C., Fan, J., Peng, P.A., Algeo, T.J., 2020. Elevated marine productivity triggered nitrogen limitation on the Yangtze Platform (South China) during the Ordovician-Silurian transition. Palaeogeogr. Palaeoclimatol. Palaeoecol. 554, 109833.
Liu, Y., Li, Y., Hou, M., Shen, J., Algeo, T.J., Fan, J., Zhou, X., Chen, Q., Sun, Z., Li, C., 2023. Terrestrial rather than volcanic mercury inputs to the Yangtze Platform (South China) during the Ordovician-Silurian transition. Glob. Planet. Chang. 220, 104023.
Liu, Z., Algeo, T.J., Arefifard, S., Wei, W., Brett, C., Landing, E., Lev, S.M., 2024a. Testing the salinity of Cambrian to Silurian epicratonic seas. J. Geol. Soc. Lond. 181 (3), jgs2023-217.
Liu, Z., Algeo, T.J., Brocks, J.J., van Maldegem, L.M., Gilleaudeau, G.J., Kah, L.C., Cheng, M., Yu, W., 2024b. Salinity reconstruction in Proterozoic depositional systems. Geol. Soc. Am. Bull. 136 (in press).
Liu, M., Yuan, W., Fang, C., Wang, X., Tan, N., Zhao, M., Wang, X., Algeo, T.J., Sun, P., Feng, X., Chen, D., 2025. Mercury isotope evidence for Middle Ordovician photic-zone euxinia: implications for termination of the Great Ordovician biodiversification event. Gondwana Res. 137, 131–144.
Loydell, D.K., 2007. Early Silurian positive $\delta^{13}C$ excursions and their relationship to glaciations, sea-level changes and extinction events. Geol. J. 42 (5), 531–546.
Lu, M., Lu, Y., Ikejiri, T., Hogancamp, N., Sun, Y., Wu, Q., Carroll, R., Çemen, I., Pashin, J., 2019. Geochemical evidence of first forestation in the Southernmost Euramerica from Upper Devonian (Famennian) black shales. Sci. Rep. 9 (1), 7581.
Luo, G., Algeo, T.J., Zhan, R., Yan, D., Huang, J., Liu, J., Xie, S., 2016. Perturbation of the marine nitrogen cycle during the late Ordovician glaciation and mass extinction. Palaeogeogr. Palaeoclimatol. Palaeoecol. 448, 339–348.
Luo, G., Yang, H., Algeo, T.J., Hallmann, C., Xie, S., 2019. Lipid biomarkers for the reconstruction of deep-time environmental conditions. Earth Sci. Rev. 189, 99–124.
Mather, A., 2007. Arid environments. In: Perry, C., Taylor, K. (Eds.), Environmental Sedimentology. Blackwell, Oxford, pp. 144–189.
McLennan, S.M., 2001. Relationships between the trace element composition of sedimentary rocks and upper con¬tinental crust. Geochem. Geophys. Geosyst. 2 (4), 2000GC000109.
Melchin, M.J., Sadler, P.M., Cramer, B.D., 2020. The Silurian period. In: Gradstein, F.M., et al. (Eds.), Geologic Time Scale 2020. Elsevier, Amsterdam, pp. 695–732.
Moulton, K.L., Berner, R.A., 1998. Quantification of the effect of plants on weathering: Studies in Iceland. Geology 26 (10), 895–898.
Nardin, E., Godderis, Y., Donnadieu, Y., Hir, G.L., Blakey, R.C., Puceat, E., Aretz, M., 2011. Modeling the early Paleozoic long-term climatic trend. GSA Bull. 123 (5–6), 1181–1192.
Ogg, J.G., Ogg, G.M., Gradstein, F.M., 2016. Chapter 6 - Ordovician. In: Ogg, J.G., Ogg, G.M., Gradstein, F.M. (Eds.), A Concise Geologic Time Scale. Elsevier, Amsterdam, pp. 57–69.
Olofsson, M., Hagan, J.G., Karlson, B., Gamfeldt, L., 2020. Large seasonal and spatial variation in nano-and microphytoplankton diversity along a Baltic Sea—North Sea salinity gradient. Sci. Rep. 10 (1), 17666.
Pagani, M., Pedentchouk, N., Huber, M., Sluijs, A., Schouten, S., Brinkhuis, H., Sinninghe Damsté, J.S., Dickens, G.R., Backman, J., Clemens, S., Cronin, T., Eynaud, F., Gattacceca, J., Jakobsson, M., Jordan, R., Kaminski, M., King, J., Koc, N., Martinez, N.C., McInroy, D., Moore Jr., T.C., O'Regan, M., Onodera, J., Pälike, H., Rea, B., Rio, D., Sakamoto, T., Smith, D.C., St John, K.E.K., Suto, I., Suzuki, N., Takahashi, K., Watanabe, M., Yamamoto, M., Expedition, S., 2006. Arctic hydrology during global warming at the Palaeocene/Eocene thermal maximum. Nature 442 (7103), 671–675.
Peters, K.E., Walters, C.C., Moldowan, J.M., 2005. The Biomarker Guide: Biomarkers and Isotopes in Petroleum Systems and Earth History, 2. Cambridge University Press, Cambridge, UK, p. 490.
Pohl, A., Donnadieu, Y., Le Hir, G., Ladant, J.B., Dumas, C., Alvarez-Solas, J., Vandenbroucke, T.R.A., 2016a. Glacial onset predated late Ordovician climate cooling. Paleoceanography 31 (6), 800–821.
Pohl, A., Nardin, E., Vandenbroucke, T.R., Donnadieu, Y., 2016b. High dependence of Ordovician Ocean surface circulation on atmospheric CO_2 levels. Palaeogeogr. Palaeoclimatol. Palaeoecol. 458, 39–51.
Pratt, L.M., Phillips, T.L., Dennison, J.M., 1978. Evidence of non-vascular land plants from the early Silurian (Llandoverian) of Virginia, USA. Rev. Palaeobot. Palynol. 25 (2), 121–149.
Pšenička, J., Bek, J., Frýda, J., Žárský, V., Uhlířová, M., Štorch, P., 2021. Dynamics of Silurian plants as response to climate changes. Life 11 (9), 906.
Quirk, M.M., Wardroper, A.M.K., Wheatley, R.E., Maxwell, J.R., 1984. Extended hopanoids in peat environments. Chem. Geol. 42 (1–4), 25–43.
Rasmussen, C.M.Ø., Kröger, B., Nielsen, M.L., Colmenar, J., 2019. Cascading trend of early paleozoic marine radiations paused by late Ordovician extinctions. Proc. Natl. Acad. Sci. 116 (15), 7207–7213.

Ravi, S., Breshears, D.D., Huxman, T.E., D'Odorico, P., 2010. Land degradation in drylands: interactions among hydrologic–aeolian erosion and vegetation dynamics. Geomorphology 116 (3–4), 236–245.
Reeves, J., Chen, J., Wang, X.L., Lund, R., Lu, Q.Q., 2007. A review and comparison of changepoint detection techniques for climate data. J. Appl. Meteorol. Climatol. 46, 900–915.
Remírez, M.N., Algeo, T.J., 2020. Paleosalinity determination in ancient epicontinental seas: a case study of the T-OAE in the Cleveland Basin (UK). Earth Sci. Rev. 201, 103072.
Remírez, M.N., Schwarz, E., Gilleaudeau, G.J., Veiga, G.D., Algeo, T.J., 2025a. Seas to lakes and vice-versa: a test of facies versus elemental salinity proxies. Chem. Geol. 122663.
Remírez, M.N., Gilleaudeau, G.J., McBride, R., Pederson, C., Miller, C., Guerra, L., Piovano, E., Virtasalo, J., Wang, C.W., Algeo, T.J., 2025b. Calibrating elemental salinity proxies in Pleistocene-Holocene sedimentary environments. Chem. Geol. 122664.
Repetski, J.E., Ryder, R.T., Harper, J.A., Trippi, M.H., 2006. Thermal maturity patterns in the Ordovician and Devonian of Pennsylvania using conodont color alteration index (CAI) and vitrinite reflectance (%Ro). Northeast. Geol. Environ. Sci. 28 (3), 266–294.
Rohmer, M., Bouvier-Nave, P., Ourisson, G., 1984. Distribution of hopanoid triterpenes in prokaryotes. Microbiology 130 (5), 1137–1150.
Rohrssen, M., Love, G.D., Fischer, W., Finnegan, S., Fike, D.A., 2013. Lipid biomarkers record fundamental changes in the microbial community structure of tropical seas during the late Ordovician Hirnantian glaciation. Geology 41 (2), 127–130.
Romero-Sarmiento, M.-F., Riboulleau, A., Vecoli, M., Versteegh, G.J.M., 2011. Aliphatic and aromatic biomarkers from Gondwanan sediments of late Ordovician to early Devonian age: an early terrestrialization approach. Org. Geochem. 42 (6), 605–617.
Rong, J.Y., Xu, C., Harper, D.A.T., 2002. The latest Ordovician Hirnantia Fauna (Brachiopoda) in time and space. Lethaia 35 (3), 231–249.
Rong, J.Y., Harper, D.A.T., Huang, B., Li, R.Y., Zhang, X.L., Chen, D., 2020. The latest Ordovician Hirnantian brachiopod faunas: new global insights. Earth Sci. Rev. 208, 103280.
Rosa-Putra, S., Nalin, R., Domenach, A.M., Rohmer, M., 2001. Novel hopanoids from *Frankia* spp. and related soil bacteria. Eur. J. Biochem. 268 (15), 4300–4306.
Ross, C., Ross, J., 1995. North American depositional sequences and correlations, 309–313, Ordovician Odyssey: Short Papers. In: 7th International Symposium on the Ordovician System Book.
Rubinstein, C.V., Gerrienne, P., de la Puente, G.S., Astini, R.A., Steemans, P., 2010. Early Middle Ordovician evidence for land plants in Argentina (eastern Gondwana). New Phytol. 188 (2), 365–369.
Rullkötter, J., Marzi, R., 1988. Natural and artificial maturation of biological markers in a Toarcian shale from northern Germany. Org. Geochem. 13 (4–6), 639–645.
Saltzman, M.R., 2005. Phosphorus, nitrogen, and the redox evolution of the Paleozoic oceans. Geology 33 (7), 573–576.
Saltzman, M.R., Young, S.A., 2005. Long-lived glaciation in the late Ordovician? Isotopic and sequence-stratigraphic evidence from western Laurentia. Geology 33 (2), 109–112.
Schwark, L., Empt, P., 2006. Sterane biomarkers as indicators of palaeozoic algal evolution and extinction events. Palaeogeogr. Palaeoclimatol. Palaeoecol. 240 (1–2), 225–236.
Scotese, C.R., 2023. Ordovician plate tectonic and palaeogeographical maps. In: Harper, D.A.T., Lefebvre, B., Percival, I.G., Servais, T. (Eds.), A Global Synthesis of the Ordovician System: Part 1, 532. Geological Society of London, Special Publication, pp. 1–19.
Seifert, W.K., Moldowan, J.M., 1980. The effect of thermal stress on source-rock quality as measured by hopane stereochemistry. Phys. Chem. Earth 12, 229–237.
Seki, O., Harada, N., Sato, M., Kawamura, K., Ijiri, A., Nakatsuka, T., 2012. Assessment for paleoclimatic utility of terrestrial biomarker records in the Okhotsk Sea sediments. Deep-Sea Res. Part II Top. Stud. Oceanogr. 61-64, 85–92.
Servais, T., Harper, D.A., 2018. The great Ordovician biodiversification event (GOBE): definition, concept and duration. Lethaia 51 (2), 151–164.
Servais, T., Cascales-Miñana, B., Cleal, C.J., Gerrienne, P., Harper, D.A., Neumann, M., 2019. Revisiting the Great Ordovician diversification of land plants: recent data and perspectives. Palaeogeogr. Palaeoclimatol. Palaeoecol. 534, 109280.
Sheehan, P.M., 2001. The late Ordovician mass extinction. Annu. Rev. Earth Planet. Sci. 29 (1), 331–364.
Shen, J., Chen, J.B., Algeo, T.J., Yuan, S.L., Feng, Q.L., Yu, J.X., Zhou, L., O'Connell, B., Planavsky, N.J., 2019. Evidence for a prolonged Permian-Triassic extinction interval from global marine mercury records. Nat. Commun. 10, 1563.
Shen, J., Algeo, T.J., Feng, Q.L., 2022. Mercury isotope evidence for a non-volcanic origin of Hg spikes at the Ordovician-Silurian boundary, South China. Earth Planet. Sci. Lett. 594, 117705.
Simoneit, B.R.T., Leif, R.N., de Aquino, Radler, Neto, F., Almeida Azevedo, D., Pinto, A. C., Albrecht, P., 1990. On the presence of tricyclic terpane hydrocarbons in Permian tasmanite algae. Naturwissenschaften 77 (8), 380–383.
Smolarek, J., Marynowski, L., Trela, W., Kujawski, P., Simoneit, B.R.T., 2017. Redox conditions and marine microbial community changes during the end-Ordovician mass extinction event. Glob. Planet. Chang. 149, 105–122.
Snowdon, L.R., 1995. Rock-Eval T_{max} suppression: documentation and amelioration. AAPG Bull. 79 (9), 1337–1348.
Song, Y., Algeo, T.J., Wu, W., Luo, G., Li, L., Wang, Y., Xie, S., 2020. Distribution of pyrolytic PAHs across the Triassic-Jurassic boundary in the Sichuan Basin, southwestern China: evidence of wildfire outside the Central Atlantic Magmatic Province. Earth Sci. Rev. 201, 102970.
Song, Y., Gilleaudeau, G.J., Algeo, T.J., Over, D.J., Lyons, T.W., Anbar, A.D., Xie, S., 2021. Biomarker evidence of algal-microbial community changes linked to redox and salinity variation, Upper Devonian Chattanooga Shale (Tennessee, USA). GSA Bull. 133, 409–424.
Song, Y., Cao, Q., Li, S., Hu, S., Zhu, K., Ye, X., Wan, L., 2021. Salinized lacustrine organic-rich shale influenced by marine incursions: algal-microbial community, paleoenvironment and shale oil potential in the Paleogene Biyang Depression, East China. Palaeogeogr. Palaeoclimatol. Palaeoecol. 580, 110621.
Stanley, S.M., 2016. Estimates of the magnitudes of major marine mass extinctions in earth history. Proc. Natl. Acad. Sci. 113 (42), E6325–E6334.
Steemans, P., Hérissé, A.L., Melvin, J., Miller, M.A., Paris, F., Verniers, J., Wellman, C.H., 2009. Origin and radiation of the earliest vascular land plants. Science 324 (5925), 353-353.
Stigall, A.L., 2023. A review of the late Ordovician (Katian) Richmondian Invasion of eastern Laurentia. Palaeogeogr. Palaeoclimatol. Palaeoecol. 618, 111520.
Stockey, R.G., Cole, D.B., Planavsky, N.J., Loydell, D.K., Frýda, J., Sperling, E.A., 2020. Persistent global marine euxinia in the early Silurian. Nat. Commun. 11 (1), 1804.
Strother, P.K., Al-Hajri, S., Traverse, A., 1996. New evidence for land plants from the lower Middle Ordovician of Saudi Arabia. Geology 24 (1), 55–58.
Sullivan, N.B., Brett, C.E., McLaughlin, P.I., Kleffner, M.A., Cramer, B.D., 2014. Correlation of the waco member of the alger shale formation (Silurian; Llandovery; Telychian) in east-Central Kentucky and south-Central Ohio. GFF 136 (1), 254–258.
Sullivan, N.B., McLaughlin, P.I., Brett, C.E., Cramer, B.D., Kleffner, M.A., Thomka, J.R., Emsbo, P., 2016. Sequence boundaries and chronostratigraphic gaps in the Llandovery of Ohio and Kentucky: the record of early Silurian paleoceanographic events in east-Central North America. Geosphere 12 (6), 1813–1832.
Thiagarajan, N., Lepland, A., Ryb, U., Torsvik, T.H., Ainsaar, L., Hints, O., Eiler, J., 2024. Reconstruction of Phanerozoic climate using carbonate clumped isotopes and implications for the oxygen isotopic composition of seawater. Proc. Natl. Acad. Sci. USA 121 (36), e2400434121.
Trotter, J.A., Williams, I.S., Barnes, C.R., Lécuyer, C., Nicoll, R.S., 2008. Did cooling oceans trigger Ordovician biodiversification? Evidence from conodont thermometry. Science 321 (5888), 550–554.
Uemura, H., Ishiwatari, R., 1995. Identification of unusual 17β (H)-moret-22 (29)-ene in lake sediments. Org. Geochem. 23 (7), 675–680.
van Staal, C.R., Hatcher Jr., R.D., 2010. Global setting of Ordovician orogenesis. Glob. Ordovic. Earth Syst. Geol. Soc. Am. Spec. Pap. 466, 1–11.
Vavrdová, M., 1984. Some plant microfossils of possible terrestrial origin from the Ordovician of Central Bohemia. Věstník Ústředního ústavu geologického 59 (3), 165–170.
Vecoli, M., 2008. Fossil microphytoplankton dynamics across the Ordovician–Silurian boundary. Rev. Palaeobot. Palynol. 148 (2–4), 91–107.
Vitorović, D., Ambles, A., Djordjević, M., 1984. Relationship between kerogens of various structural types and the products of their multistep oxidative degradation. Org. Geochem. 6, 333–342.
Volkheimer, W., 1980. Liassic microfloras of the Neuquén Basin (Argentina): relations with other Gondwanic areas, Pap. 4th Int. Palynol. Conf. Lucknow t976.
Volkman, J.K., 1986. A review of sterol markers for marine and terrigenous organic matter. Org. Geochem. 9 (2), 83–99.
Vollset, K.W., et al., 2022. Ecological regime shift in the Northeast Atlantic Ocean revealed from the unprecedented reduction in marine growth of Atlantic salmon. Sci. Adv. 8 (9), eabk2542.
Waid, C.B.T., 2018. High-Resolution Subsurface Correlation of Late Ordovician–Wenlockian (Silurian) Strata in Southern and Southeastern Ohio: Columbus, Ohio, 14. Department of Natural Resources, Division of Geological Survey Geological Note, pp. 1–34.
Wang, C., 2007. Anomalous hopane distributions at the Permian–Triassic boundary, Meishan, China–evidence for the end-Permian marine ecosystem collapse. Org. Geochem. 38 (1), 52–66.
Wang, T.G., Simoneit, B.R.T., 1995. Tricyclic terpanes in Precambrian bituminous sandstone from the eastern Yanshan region, North China. Chem. Geol. 120 (1), 155–170.
Wang, X.L., Algeo, T.J., Li, C., Zhu, M., 2023. Spatial pattern of marine oxygenation set by tectonic and ecological drivers over the Phanerozoic. Nat. Geosci. 16 (11), 1020–1026.
Wang, X.Q., Zhan, C., Algeo, T.J., Shen, J., Liu, Z., 2024. Watermass architecture of the Ordovician–Silurian Yangtze Sea (South China) and its palaeogeographical implications. J. Geol. Soc. Lond. 181 (4), jgs2023-024.
Wei, W., Algeo, T.J., 2020. Elemental proxies for paleosalinity analysis of ancient shales and mudrocks. Geochim. Cosmochim. Acta 287, 341–366.
Wei, W., Algeo, T.J., Lu, Y., Lu, Y., Liu, H., Zhang, S., Peng, L., Zhang, J., Chen, L., 2018. Identifying marine incursions into the Paleogene Bohai Bay Basin lake system in northeastern China. Int. J. Coal Geol. 200, 1–17.
Wei, W., Yu, W., Algeo, T.J., Herrmann, A.D., Zhou, L., Liu, J., Wang, Q., Du, Y., 2022. Boron proxies record paleosalinity variation in the north American Midcontinent Sea in response to carboniferous glacio-eustasy. Geology 50 (5), 537–541.
Wei, W., Algeo, T.J., Meyer, D., Liu, J.S., Snihur, K.N., Lazowski, C., Yu, W.C., 2025. Utility of boron-based salinity proxies in carbonate and marly sediments. Chem. Geol. (in review).
Weir, G.W., Peterson, W.L., Swadley, W.C., Pojeta, J., 1984. Lithostratigraphy of upper Ordovician strata exposed in Kentucky. U. S. Geol. Surv. Prof. Pap. 1151-E, 1–121.
Wellman, C.H., Gray, J., 2000. The microfossil record of early land plants. Philos. Trans. R. Soc. Lond. Ser. B Biol. Sci. 355 (1398), 717–732.
Wellman C.H., Steemans, P. and Vecoli, M., 2013. Chapter 29 palaeophytogeography of Ordovician–Silurian land plants. From: Harper, D.A.T., Servais, T. (eds.) 2013. Early

Palaeozoic Biogeography and Palaeogeography. Geological Society of London, Memoir 38: 461–476.
Wellman, C.H., Cascales-Miñana, B. and Servais, T., 2023. Terrestrialization in the Ordovician. In: Harper, D.A.T., Lefebvre, B., Percival, I.G. and Servais, T. (eds.), 2023. A Global Synthesis of the Ordovician System: part 1. Geological Society of London, Special Publication 532, pp. 171–190.
Witzke, B.J., 1987. Models for circulation patterns in epicontinental seas applied to Paleozoic facies of North America craton. Paleoceanography 2 (2), 229–248.
Xie, S., Pancost, R.D., Huang, J., Wignall, P.B., Yu, J., Tang, X., Chen, L., Huang, X., Lai, X., 2007. Changes in the global carbon cycle occurred as two episodes during the Permian–Triassic crisis. Geology 35 (12), 1083–1086.
Xie, S., Algeo, T.J., Zhou, W., Ruan, X., Luo, G., Huang, J., Yan, J., 2017. Contrasting microbial community changes during mass extinctions at the Middle/late Permian and Permian/Triassic boundaries. Earth Planet. Sci. Lett. 460, 180–191.
Yang, S., Fan, J., 2025. Decreased marine organic carbon burial during the Hirnantian glaciation. Earth Planet. Sci. Lett. 654, 119240.
Young, A.L., Brett, C.E., McLaughlin, P.I., 2015. Upper Ordovician (Sandbian-Katian) sub-surface stratigraphy of the Cincinnati Region (Ohio, USA): transition into the Sebree Trough. Stratigraphy 12 (3–4), 297–305.
Zegouagh, Y., Derenne, S., Largeau, C., Saliot, A., 1996. Organic matter sources and early diagenetic alterations in Arctic surface sediments (Lena River delta and Laptev Sea, Eastern Siberia)—I. Analysis of the carboxylic acids released via sequential treatments. Org. Geochem. 24 (8), 841–857.
Zengler, K., Richnow, H.H., Rosselló-Mora, R., Michaelis, W., Widdel, F., 1999. Methane formation from long-chain alkanes by anaerobic microorganisms. Nature 401 (6750), 266–269.
Zhang, N.R., Siegmund, D.O., 2007. A modified Bayes information criterion with applications to the analysis of comparative genomic hybridization data. Biometrics 63 (1), 22–32.
Zhang, J., Li, C., Fang, X., Li, W., Deng, Y., Tu, C., Algeo, T.J., Lyons, T.W., Zhang, Y., 2022. Progressive expansion of seafloor anoxia in the Middle to late Ordovician Yangtze Sea: Implications for concurrent decline of invertebrate diversity. Earth Planet. Sci. Lett. 598, 117858.
Zhang, J., Li, C., Zhong, Y., Wu, X., Fang, X., Liu, M., Chen, D., Gill, B.C., Algeo, T.J., Lyons, T.W., Zhang, Y., 2024. Linking carbon cycle perturbations to the late Ordovician glaciation and mass extinction: a modeling approach. Earth Planet. Sci. Lett. 631, 118635.
Zhou, L., Algeo, T.J., Shen, J., Hu, Z., Gong, H., Xie, S., Huang, J., Gao, S., 2015. Changes in marine productivity and redox conditions during the late Ordovician Hirnantian glaciation. Palaeogeogr. Palaeoclimatol. Palaeoecol. 420, 223–234.
Zumberge, J.E., 1987. Terpenoid biomarker distributions in low maturity crude oils. Org. Geochem. 11 (6), 479–496.

Quaternary Science Reviews 369 (2025) 109636

Contents lists available at ScienceDirect

Quaternary Science Reviews

journal homepage: www.elsevier.com/locate/quascirev

The topographic features and sedimentary environment potentially influenced the vegetation reconstruction in southwestern China since the MIS3

Xiao Zhang [a], Yuanfu Yue [b,*], Ziyan Zhang [a], Liuying He [b], Xinmeng Yuan [b], Xintian Yu [b], Qiuchi Wan [c], Cong Chen [d], Yongjie Tang [d], Zhuo Zheng [d], Kangyou Huang [d]

[a] College of Life Sciences, Zhejiang Normal University, 321004, Jinhua, China
[b] Guangxi Laboratory on the Study of Coral Reef in the South China Sea, Coral Reef Research Centre, School of Marine Sciences, Guangxi University, Nanning, 530004, China
[c] School of Geography, South China Normal University, Guangzhou, 510635, China
[d] Guangdong Key Lab of Geodynamics and Geohazards, School of Earth Sciences and Engineering, Sun Yat–sen University, Zhuhai, 519082, China

ARTICLE INFO

Handling Editor: Dr Yan Zhao

Keywords:
Pollen record
Southwestern China
Peat bog
MIS3
Biome reconstruction
Climate change

ABSTRACT

A series of pollen records from southwestern (SW) China has provided substantial evidence for the reconstruction of paleovegetation and paleoclimate in the region since the Last Glacial Period (LGP). However, studies investigating the relationship between paleoclimate and ecosystem changes during MIS3 remain limited, thereby constraining our understanding of the response of vegetation to climatic fluctuations on the glacial–interglacial timescale. Moreover, in comparison to local–scale topographic pollen sources, traditional lake sedimentary environments introduce a higher degree of uncertainty into vertical vegetation reconstructions. Here, we present a pollen record derived from a peat core of the Niangniang (NN) Mountain Wetland, aiming to reconstruct biome and climate variations over the past 37 ka. Our findings indicate that during the LGP, the study area was predominantly covered by deciduous broadleaved forests (DBLF), with *Quercus* (D) and other Betulaceae taxa as the main components. Although a sedimentary hiatus occurred in the core sediments between 18.5 and 4.6 ka, it is still possible to infer that from the LGP to the late Holocene, the forests surrounding the NN wetland transitioned from DBLF to evergreen broadleaved forests (EBLF), which were predominantly composed of *Castanopsis* and *Cyclobalanopsis*. Over the past 2400 years, the rapid expansion of associated plants, including Poaceae and *Pinus*, along with secondary taxa such as *Alnus*, has driven a gradual transition to the Alpine Shrubland and Meadow (ALSM) biome. This shift is largely attributed to early human activities and fires. By comparing these results with other pollen and climate records, we conclude that DBLF expanded extensively at medium–to–high altitudes during the LGP, rather than evergreen sclerophyllous *Quercus* forest (ESQF). Consequently, previous estimates of mean annual temperature (MAT) based on pollen data may have been inflated from the Last Glacial Maximum (LGM) to the Holocene. In addition to the drivers operating at the glacial–interglacial scale, the Atlantic Meridional Overturning Circulation (AMOC) plays a pivotal role in modulating the variability of the Indian Monsoon precipitation, which in turn influences biome succession in SW China.

1. Introduction

The mountain ranges and valleys in southwestern (SW) China have provided important glacial refuges (Boufford and van Dijk, 2004), and are global hotspots of biodiversity due to their extreme topographical features, together with intense climatic fluctuations associated with the Indian summer monsoon (ISM) and recurrent glaciations (Tang et al., 2015). In recent years, a series of pollen records have furnished essential data for the quantitative reconstruction of paleovegetation and paleoclimate in SW China, particularly since the Last Glacial Maximum (LGM). For instance, at higher altitudes, such as Tengchongqinghai (TCQH) (Zhang et al., 2020), Heqing (HQ) (Jiang et al., 2001), Caohai (CH) (Zhang et al., 2024) and Dianchi (DC) (Xiao et al., 2020), the high proportion of *Quercus* (ES) during the LGM implies a significant

* Corresponding author.
E-mail address: yuanfu.yue@gxu.edu.cn (Y. Yue).

https://doi.org/10.1016/j.quascirev.2025.109636
Received 4 April 2025; Received in revised form 23 September 2025; Accepted 25 September 2025
Available online 29 September 2025
0277-3791/© 2025 Published by Elsevier Ltd.

southward expansion of evergreen sclerophyllous *Quercus* forests (ESQF) in this region. Simultaneously, other records indicate that deciduous broadleaved forests (DBLF), dominated by deciduous taxa like Betulaceae and *Quercus* (D), remained the dominant vegetation type in mid–to–high altitude mountains throughout the LGM (Deng et al., 2022; Li, K. et al., 2024). Moreover, studies on specialized taxa, such as *Pinus yunnanensis* (Pan et al., 2025), provide indirect evidence of small–scale vegetation evolution subsequent to the LGM. These studies on pollen records collected at different elevations in SW China have revealed distinct vegetation changes during the glacial–interglacial cycles (Shen and Xiao, 2018; Xiao et al., 2020) that have been closely linked to vertical biome shifts (Zhang et al., 2020). However, few investigated pollen records extend back through the Last Glacial Period (LGP, e.g., MIS3), and the low resolution of data acquired in previous works (Tang, 1992; Zhao et al., 2014; Zheng et al., 2016) has hindered precise spatial correlation and accurate dating of rapid climate changes during the LGP (Zhang et al., 2020).

Another critical issue that warrants attention is the limited focus in existing studies on the influence of topographic features and sedimentary environments on pollen–paleovegetation reconstruction. Pollen can be dispersed over distances ranging from dozens or even hundreds of km in flat terrain by wind and typically down to less than approximately 50 km in mountainous regions (Xu et al., 2016). Consequently, wind–dispersed pollen types with high productivity tend to be over-represented in pollen records. This over–representation leads to an overestimation of their proportion within vegetation types, such as *Pinus* (Wang et al., 2020). Most existing pollen records in SW China originate from lake sediments at various altitudes (Zhang et al., 2024). Larger lakes possess a robust ability to capture pollen transported by wind or water currents, thereby reflecting broader–scale mountain vegetation changes (Xu et al., 2016; Chevalier et al., 2020). In contrast, sedimentary environments with weaker pollen–trapping capabilities, such as wetlands, are more likely to accurately represent local vegetation succession characteristics (Deng et al., 2022). This divergence can result in significant differences in recorded vegetation types even among study sites in close proximity. For instance, during the LGP, the pollen record of TCQH lake in western SW China was predominantly characterized by ESQF. A significant portion of this pollen likely originates from the relatively high–altitude Gaoligong Mountain to the east (Xiao et al., 2015; Zhang et al., 2020). In contrast, merely 30 km to the north, Tengchongbeihai (TCBH) wetland was dominated by Coniferous and Mixed Forests (CLMX) during the same period (Zhang et al., 2019). Recent studies by Zeng et al. (2025) have utilized pollen analysis and ordination techniques to reconstruct the pollen dissemination characteristics of Gaoligong Mountain in SW China. Their findings indicate that the Asian summer monsoon, diurnally-varying orographic winds, and vegetation type characteristics all play roles in shaping pollen dispersal patterns in mountainous areas. Therefore, to achieve a more accurate reconstruction of the vegetation succession process in SW China since the LGP, it is essential to obtain additional pollen records from non–traditional lake sources.

Furthermore, the mechanisms driving biome changes in SW China since the LGP remain a subject of debate. Pollen records and simulation studies suggest that annual or monthly solar radiation may have been the primary factor influencing regional vegetation succession since the LGM (Xiao et al., 2015; Zhang et al., 2023). During the growing season, solar radiation plays a crucial role in influencing plant photosynthesis and growth, thereby determining the types and spatial distribution of vegetation over time. Other research has highlighted the significant impact of high–latitude ice volume on biome changes in the Yunnan–Guizhou Plateau (Zhang et al., 2024). High–latitude ice volume can significantly influence global sea level and atmospheric circulation patterns. These changes, in turn, have a profound impact on the climate of the Yunnan–Guizhou Plateau and contribute to local biome changes. Additionally, other factors such as surface temperature variations in the Indian Ocean–Western Pacific Warm Pool (a major driver of climate variability in the region; Xiao et al., 2014; Zhang et al., 2020), the north–south shifts of the Intertropical Convergence Zone (ITCZ) (Xiao et al., 2020), and fluctuations in the strength of the Atlantic Meridional Overturning Circulation (AMOC) (Zhang et al., 2024) have collectively exerted an influence on the characteristics of regional vegetation succession at various temporal scales. Thus, further research is necessary to elucidate the complex interactions of these influencing factors on biome change in SW China.

The Niangniang (NN) Mountain Wetland is situated in the western region of the Yunnan–Guizhou Plateau. The surrounding area features a karst peak cluster landform (Li, S.M. et al., 2024; Yue et al., 2024). Numerous cushion–shaped peat wetlands have developed and are distributed across the basaltic mountain plateau in this region. Our aim in this study is to reconstruct the biome succession in the eastern mountainous regions of the Tibetan Plateau and the Hengduan Mountains since MIS3. To achieve this, we present a pollen record retrieved from the NN subalpine wetland and quantitatively reconstruct local biome and climate variations since 37 ka. We systematically compare this pollen with numerous pollen and other paleoclimate records from SW China. Among these, especially noteworthy is the record of Caohai (CH) lake, which, despite its proximity, exhibits marked differences in sedimentary environments (Zhang et al., 2024). Through this comparison, we can reconstruct the biome succession in the target regions with greater precision and offer unique insights. This approach not only enhances the accuracy of quantitative climate reconstructions in the ISM region but also provides new perspectives on the mechanisms of related climate forcing.

2. Study area

2.1. Geographical setting

The NN Mountain is within the territory of the Yunnan–Guizhou Plateau, which is a transitional zone from the Tibetan Plateau to areas of lower altitude (Fig. 1). The wetland atop the NN Mountain (26°34′40″–26°36′38"N, 104°45′29″–104°48′45"E, 2050 m a.s.l.) represents one of the most well preserved plateau wetlands in SW China, renowned for its remarkable biodiversity (Zhou et al., 2022). The climate of the NN Mountain is mainly influenced by the ISM. The warm and moist air masses associated with the ISM lead to warm winters and hot summers. The study area has a subtropical humid monsoonal climate with around 78 % of its precipitation falling between May and October, when moist winds from the Arabian Sea and Bay of Bengal bring abundant rainfall. The mean annual temperature (MAT) of the study area is around 13.5 °C, while the mean annual precipitation (MAP) is approximately 1350 mm (Yue et al., 2024).

2.2. Modern vegetation

The current distribution of vegetation types in the NN Mountain and adjacent mountainous regions is closely correlated with the elevational gradients of the Tibetan Plateau. More specifically, the vegetation in the mountain ranges of SW China can be categorized into a series of distinct vegetation belts (Tang, 2015).

The lowest elevation belt, characterized by tropical rainforest (TRFO), occurs in Yunnan Province at the altitudes below 1000 m a.s.l. This ecosystem is predominantly composed of species from the families Fabaceae, Meliaceae, and Sapindaceae, with a minor presence of gymnosperms such as *Pinus*, Cycadaceae, and Podocarpaceae. Evergreen broadleaved forest (EBLF) typically develops between 1000 and 2400 m a.s.l, where it is primarily dominated by Fagaceae species including *Cyclobalanopsis delavayi*, *C. glaucoides*, and *Castanopsis delavayi*, alongside associated species like *Cinnamomum glanduliferum* and *Schima wallichii*. Coniferous forests, notably those dominated by *Pinus yunnanensis*, are prevalent in the upper elevations of this zone. Additionally, the lower boundary of this elevation belt exhibits some transitional

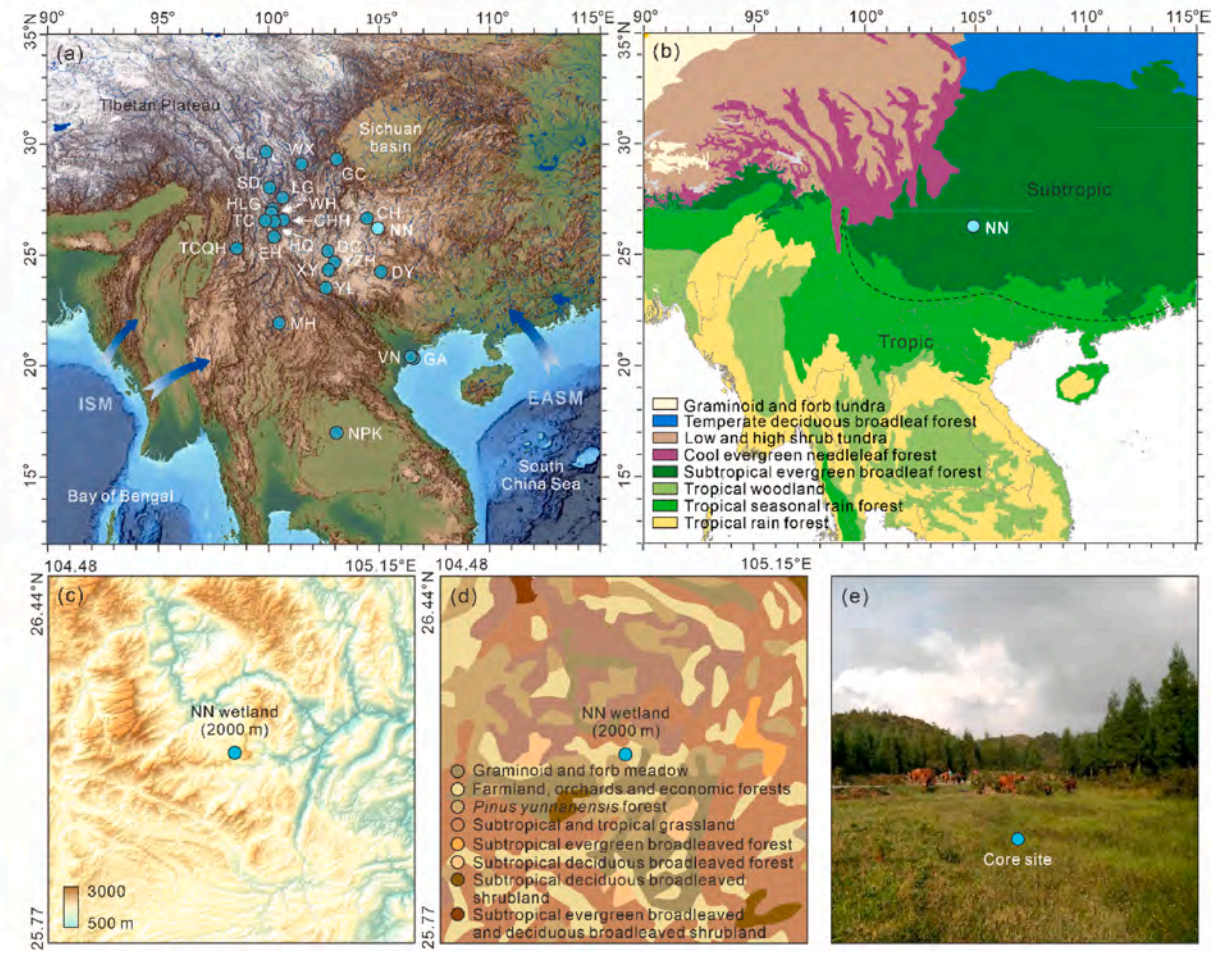


Fig. 1. (a) Topography and location of the NN wetland and the cores used for correlation. Dark green dots indicate the YSL profile (Shi et al., 2011), Wuxu (WX) (Zhang et al., 2016), Shudu (SD) (Cook et al., 2011, 2013; Yao et al., 2017), Haligu (HLG) (Song et al., 2012), Wenhai (WH) (Yao et al., 2015), Chenghai (CHH) (Xiao et al., 2017), Tiancai (TC) (Xiao et al., 2014), Lugu (LG) (Shen and Xiao, 2020), Tengchongqinghai (TCQH) (Xiao et al., 2015; Zhang et al., 2020), Dianchi (DC) (Xiao et al., 2020), Xingyun (XY) (Chen et al., 2014a, 2014b), Yangzhonghai (YZH) (Wang et al., 2020), Yilong (YL) (Li, K. et al., 2024) and Menghai (MH) lake (Tang, 1992); Ganchi (GC) wetland (Deng et al., 2022); Heqing (HQ) basin (Jiang et al., 2001; Xiao et al., 2007); Dayin (DY) cave (Zhang et al., 2024), VN/GA (Li et al., 2009), NPK (Penny, 2001); (b) Vegetation map of SW China (Zhang, 2007). (c) local topography and location of the NN wetland. (d) local vegetation around NN wetland (Zhang, 2007). (e) The surrounding environment of the core site. (For interpretation of the references to color in this figure legend, the reader is referred to the Web version of this article.)

forest types that incorporate elements of the tropical flora found at lower altitudes. From 2400 to 2700 m a.s.l., the vegetation types give way to conifers and deciduous broadleaved trees dominated by *Juniperus formosana*, *Pinus yunnanensis*, *Quercus fabri*, *Q. aliena*, *Corylus yunnanensis*, *Populus yunnanensis*, *Salix cavaleriei*, and *Alnus mengtze*. The dominant forest types here are deciduous broadleaved forest (DBLF) and mixed broadleaved forest (EBLF/DBLF). Between 2400 and 2700 m a.s.l, the vegetation transitions to DBLF, with dominant species including *Juniperus formosana*, *Pinus yunnanensis*, *Quercus fabri*, *Q. aliena*, *Corylus yunnanensis*, *Populus yunnanensis*, *Salix cavaleriei*, and *Alnus mengtze*. Additionally, evergreen sclerophyll *Quercus* forest (ESQF) dominated by sclerophyll *Quercus* species is common and/or dominant in a belt centered between 2500 and 3600 m in the southeastern parts of the Tibetan Plateau and SW China (Yang et al., 2009). Cold mixed forest (CLMX), primarily composed of cold–tolerant conifers such as *Abies*, *Picea*, and *Pinus*, is predominantly distributed between elevations of 3300 and 4200 m a.s.l. As elevation continues to increase, alpine shrubland, meadow, and tundra (ALSM) ecosystems are prevalent, characterized by dominant species from the Cyperaceae, Poaceae, and Ranunculaceae. The permanent ice belt generally forms at elevations above 4800–5000 m. The zonal vegetation of the NN Mountain primarily consists of EBLF, secondary forests, and certain cash crops, such as *Toxicodendron vernicifluum* and *Camellia oleifera* (Fig. 1d).

3. Materials and methods

3.1. Materials

The NN core was taken from the alpine wetland of the NN Mountain in the western Guizhou Province (Fig. 1e). The research site is not influenced by any rivers in its vicinity. The core is 150 cm long and covers all the sediment to the bedrock.

3.2. Methods

3.2.1. Laboratory analysis

The samples were collected at 1 cm intervals at the top 50 cm of the core and at 0.5 cm intervals towards the bottom (50–150 cm). In total, a collection of 245 samples was obtained. So, for each pollen sample, about 1 g of sediment was weighed and processed by heavy liquid separation (Moore et al., 1991; Yue et al., 2012). On average, 510 terrestrial pollen grains were counted per individual sample. Based on

the above counting method, all percentages quoted for pollen grains (from conifers, arboreal and non–arboreal taxa) in this work are based on the summed counts of pollen grains from terrestrial taxa. We used previously established morphological criteria to divide the complex *Quercus* pollen in SW China (Zhang et al., 2018). TILIA 3.0.1 (Grimm, 1991–1993) was used to calculate pollen percentages and plot the pollen diagram.

3.2.2. Biomization reconstruction

Vegetation reconstruction was conducted using the biomization technique based on previously reported plant functional types (PFTs) (Ni et al., 2014; Zheng et al., 2023), specifically employing the biome classifications derived from the pollen record of Caohai (CH) lake (~100 km southeast from NN site) (Zhang et al., 2024). Consistent with the CH lake records, all pollen taxa identified from the NN core were assigned to 17 PFTs and subsequently aggregated into 6 biomes relevant to the study area. When this biome reconstruction method was applied to modern pollen spectra for validation, the majority of samples were accurately classified according to previous studies (Zhang et al., 2024).

3.2.3. Statistical analysis

To simplify the analysis of the relationships between the ecological properties of the different pollen taxa and climatic variables, and to establish a quantitative framework for linking vegetation dynamics to paleoclimatic changes, we performed a principal component analysis (PCA) on the pollen dataset (Birks et al., 1998). Statistical analyses were based on the abundances (expressed as percentages) of pollen taxa detected in at least five samples with relative abundances exceeding 2 %; 30 pollen taxa satisfied these requirements. The gradient length was below 2 (1.32 in this study) standard deviation (SD) units, so the PCA method was considered appropriate for analyzing pollen assemblages with respect to interspecific correlations using square root transformation of pollen percentages. Statistical analyses were performed using Canoco 5.0 (Braak and Smilauer, 2002), with results visualized through biplot projections that simultaneously display taxon compositions and sample groupings. This integrative approach enabled us to identify dominant vegetation patterns and their climatic drivers across the studied stratigraphic interval.

4. Results

4.1. Sediment lithology and core chronology

Based on the color and lithological characteristics of the core sediments in the field, the 150 cm long NN sediment can be roughly divided into 5 layers from bottom to top (Fig. 2). The sediment from 150 to 126 cm consists of gray clay interbedded with wood fragments (140–136 cm) and plant remains. This is followed by a layer of dark peat with higher organic content (126–100 cm), which is identical to that observed between 80 and 50 cm. The deposits between 100 and 80 cm consist of silty dark gray clay and the uppermost 50 cm of the NN core mainly consists of silty gray clay.

The core's chronology was determined through accelerator mass spectrometry (AMS ^{14}C) dating of nine plant fragments and bulk sediment samples, which were analyzed at the Xi'an Accelerator Mass Spectrometry Center and Beta Analytic Inc. (Miami, USA) (Table 1). Given the study area's dominance of Carboniferous-Permian limestone, sandstone, and minor coal layers, the ^{14}C dating results from sediment samples collected at the NN wetland may be affected by the hard-water effect typical of karst sedimentary environment (Kong et al., 2010). This effect occurs when initial ^{14}C radioactivity in aquatic sediments is lower than contemporary atmospheric levels, causing apparent age overestimation of organic materials—an effect more pronounced in lake sediments. Notably, because the core was retrieved from an alpine wetland, the likelihood of hard-water effect influence is low. The age-depth model was established using the Bayesian Bacon method

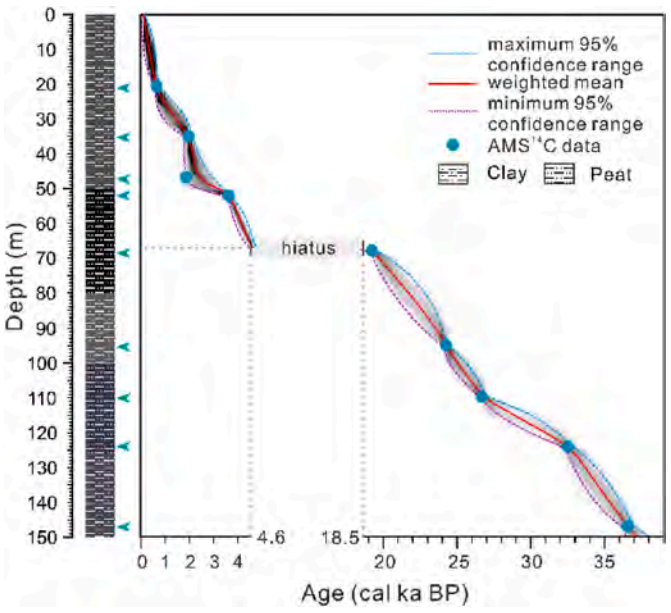


Fig. 2. Lithology and age/depth model of the NN core.

(Blaauw and Christen, 2011). It indicates that, due to the presence of a sedimentary hiatus, the core can be clearly divided into two distinct sections at a depth of 67 cm. The lower section spans from 150 to 67 cm, corresponding to an age range of 37.2 to 18.5 ka, while the upper section extends from 67 cm to the surface (0 cm) with an age range of 4.6 ka to the present (Fig. 2). The average temporal sampling resolutions of the two components are approximately 56 years and 114 years, respectively.

4.2. Fossil pollen and charcoal record

A total of 93 pollen and spore types were identified in 245 samples retrieved from the NN core. The most abundant and representative taxa are shown in the pollen diagram (Fig. 3). In samples from the glacial interval, the pollen assemblages are dominated by arboreal and herbaceous pollen. The most abundant taxa are *Quercus* (D), Betulaceae (*Corylus*, *Betula*, *Carpinus*) and Poaceae, which collectively account for 70–85 % of the total pollen content. These taxa are typical of a relatively cold and dry climate, which was characteristic of the glacial interval. Conversely, the dominant pollen taxa in assemblages from the Holocene are *Cyclobalanopsis* and *Castanopsis* followed by *Pinus*; other frequently detected taxa include arboreal taxa such as *Tsuga*, *Alnus*, *Eurya* and herbaceous taxa such as *Artemisia*, Asteraceae and Lamiaceae. To better understand the temporal variation of pollen assemblages, a Constrained Incremental Sum of Squares (CONISS) analysis was performed on the pollen data. Based on a CONISS analysis of the pollen data, the pollen sequence was divided into the following five main zones.

Zone 1 (37.2–27.4 cal ka BP, 150–112 cm)

In this zone, the mean percentage of arboreal pollen reaches a notably high value of 67.9 %, with *Quercus* (D) serving as the dominant taxon, accounting for an average of 24.9 %. Other common arboreal taxa include *Corylus* (6.9 %), *Carpinus* (5.1 %), *Betula* (3.2 %), and *Fagus* (3.3 %). Among non–arboreal pollen, Poaceae has the highest proportion at 18.7 %. This zone is further subdivided into two subzones, namely ***Zone 1a*** *(37.2–32.5* cal *ka BP, 150–*127 cm*)* and ***Zone 1b*** *(32.5–27.4* cal *ka BP, 127–*112 cm*)*. Compared to Zone 1a, the proportion of *Quercus* (D) in Zone 1b increased from 20.1 % to 29.1 %. Additionally, there were slight increases in other deciduous taxa such as *Betula* (from 2.5 % to 3.8 %), *Carpinus* (from 4.5 % to 5.5 %), and *Fagus* (from 2.9 % to 3.6 %), while the proportion of coniferous taxa decreased (from 9.1 % to 6.4 %). The composition of non–arboreal/herbaceous pollen remained largely

Table 1
AMS radiocarbon dates of samples from the NN core.

Depth (cm)	Lab code	Materials	^{14}C date (a BP)	Error (±a)	Calibrated age (cal a BP, 2σ)	Mid–point (cal a BP)
21	Beta 503983	Dark clay	480	30	496–542	518
35	Beta 503984	Dark clay	1880	30	1714–1840	1785
47	Xi'an 01	Dark clay	1617	28	1411–1538	1479
51.5	Beta 503985	Dark clay	3220	30	3375–3471	3426
68	Xi'an 02	Dark clay	15801	56	18909–19191	19054
95	Xi'an 03	Dark clay	20072	62	23879–24249	24071
110	Beta 506744	Dark clay	22240	80	26298–26936	26599
124	Xi'an 04	Dark clay	28250	120	31855–32934	32312
147	Beta 360342	Gray dark clay	32050	220	36000–36924	36391

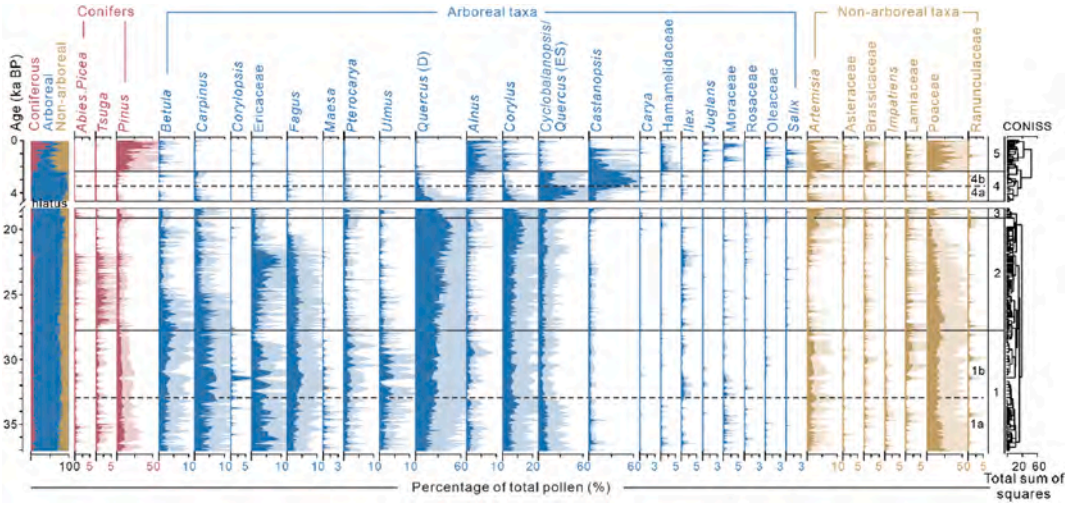


Fig. 3. Pollen percentage diagram of selected taxa in the NN core. There was a sedimentary hiatus between 4.6 and 18.5 ka. The solid and faded plots show the same percentage values on different scales.

unchanged.

Zone 2 (27.4–19.1 cal ka BP, 112–69 cm)

Compared to the preceding zone, Zone 2 exhibits an increased proportion of arboreal pollen (75.9 %), while the proportions of coniferous and non–arboreal pollen have both decreased to some extent. Notably, this zone is characterized by a significant rise in *Quercus* (D) to its highest percentage (36.9 %). Additionally, the proportion of *Corylus* has increased to 8.7 %. However, the proportions of other deciduous taxa that were relatively high in Zone 1 have slightly decreased, such as *Betula* (2.3 %), *Carpinus* (3.0 %) and *Fagus* (2.9 %). Among conifers, the most pronounced change is observed in *Tsuga*, which has increased from 0.7 % to 1.8 %. In terms of non–arboreal/herbaceous pollen, the proportion of Poaceae has decreased to 15.2 %, and *Artemisia* has also declined from 1.7 % to 1.0 %, with minimal changes in other herbaceous taxa.

Zone 3 (19.1–18.5 cal ka BP, 69–66 cm)

The variations in the proportions of conifer, arboreal, and non–arboreal pollen within Zone 3 were relatively minor. However, significant changes were observed among certain deciduous and evergreen taxa. Specifically, the proportions of *Quercus* (D) (27.7 %) and *Fagus* (0.3 %) exhibited a significant decline. Additionally, there was a slight decrease in *Betula* (1.1 %) and *Carpinus* (2.3 %). Conversely, the primary evergreen taxa, *Castanopsis* and *Cyclobalanopsis*, increased to 6.5 % and 18.4 %, respectively. Among non–arboreal pollen, *Artemisia* reached its highest proportion in the entire pollen diagram at 4.3 %, while Poaceae showed a slight reduction to 12.1 %.

Zone 4 (4.6–2.4 cal ka BP, 66–51 cm)

Zone 4 commenced at 4.6 ka due to the influence of the sedimentary hiatus. This zone is characterized by a markedly elevated arboreal pollen content (92.2 %), primarily dominated by *Cyclobalanopsis* (36.5 %) and *Castanopsis* (30.6 %). The proportions of coniferous and non–arboreal pollen both exhibit significant reductions. This zone can be further subdivided into two subzones:

Zone 4a (4.6–3.7 cal ka BP, 65–57 cm)

This zone exhibits the highest concentration of *Cyclobalanopsis* pollen (44.9 %) throughout the entire core. Additionally, several other evergreen taxa showed an increase, including *Ilex* (0.6 %). Conversely, the proportions of *Quercus* (D) and *Corylus* pollen declined significantly to 12.9 % and 5.6 %, respectively. The percentage of Poaceae within the non–arboreal pollen fraction also decreased from 12.1 % to 4.9 %.

Zone 4b (3.7–2.4 cal ka BP, 57–51 cm)

Compared to Zone 4a, the arboreal pollen content in Zone 4b is significantly higher at 94.5 %, while the proportions of coniferous and non–arboreal pollen are markedly lower at 1.8 % and 3.6 %, respectively. The most distinctive feature of this zone is the rapid increase in the proportion of *Castanopsis* pollen, which reaches its peak at 47.8 %, whereas the proportion of *Cyclobalanopsis* pollen declines to 28.1 %.

Zone 5 (since 2.4 cal ka BP, 51–0 cm)

In this zone, the proportion of arboreal pollen experienced a rapid decline to its lowest recorded level of 38.6 %, while both coniferous (27.1 %) and non–arboreal pollen (34.3 %) reached their highest levels. The increase in coniferous pollen was primarily attributed to a substantial rise in *Pinus* from 1.9 % to 26.9 %. The elevation in non–arboreal pollen was driven by significant increases in Poaceae, *Artemisia*, and Brassicaceae, with Poaceae notably rising to 25.8 %. Additionally, secondary taxa such as *Alnus* (5.6 %) and *Salix* (0.34 %) also exhibited marked upward trends.

4.3. Statistical analysis

PCA was conducted on the relative pollen frequencies to identify the key climatic factors influencing vegetation dynamics. The analysis of

245 NN core samples, encompassing 30 taxa, resulted in the first and second principal components (PCs), with their eigenvalues accounting for 51.3 % and 37.6 % of the total variance, respectively (Fig. 4). Taxa with positive loadings on PC1 primarily comprise common tropical and subtropical evergreen broadleaved forest species such as *Castanopsis* and *Cyclobalanopsis*. These evergreen species typically thrive in warmer climates. Conversely, taxa with negative loadings on PC1 predominantly include cold–tolerant deciduous trees like *Quercus* (D), *Fagus*, *Betula*, Ericaceae, and *Corylus*, as well as temperate conifers such as *Abies/Picea* and *Tsuga* (Fig. 4a). The presence of these cold–tolerant taxa in the negative loading group indicates that PC1 predominantly captures the influence of temperature on pollen taxa. Taxa with positive loadings for PC2 are primarily herbaceous taxa, including Poaceae, *Artemisia*, and certain deciduous taxa, whereas evergreen taxa such as *Castanopsis*, *Cyclobalanopsis*, and *Ilex* exhibit negative loadings. This suggests that PC2 may primarily reflect moisture conditions at the site, where positive values correspond to drier conditions and negative values indicate wetter conditions (Fig. 4a). Based on these interpretations of PC1 and PC2, Zone 2 is likely characterized by the driest or coldest conditions, while Zone 4a may represent the warmest or wettest environment (Fig. 4b).

To further explore the relationship between vegetation distribution and climate conditions over the past 21 ka in SW China, we compared the PC1 and PC2 curves with the TraCE–simulated MAT and MAP (Liu et al., 2009). By making this comparison, we aimed to validate whether the principal components obtained from the PCA could serve as reliable proxies for temperature and precipitation. Although a sedimentary hiatus exists between 18.5 and 4.6 ka, the trends identified in the PCA results align closely with those of the simulated reconstructions, indicating that the principal components may function as proxies for temperature (PC1) and precipitation (PC2), as suggested by earlier studies. (Fig. 4c). This finding implies that vertical biome shifts were predominantly influenced by temperature variations along elevation gradients and changes in monsoon precipitation intensity (Xiao et al., 2020; Zhang et al., 2024).

4.4. Biome reconstructions

Biome reconstructions play a crucial role in understanding the long–term ecological dynamics in SW China (Ni et al., 2014). In previous research, we effectively reconstructed the current biomes of SW China using modern pollen samples. The findings indicated that the shifts in pollen–based biomes were largely consistent with the vertical vegetation changes observed in the eastern mountains of the Tibetan Plateau (Zhang et al., 2024). As illustrated in Fig. 5, this study employed the same biome reconstruction method for the NN core. Biome scores indicated that during the LGP, the dominant biome was consistently

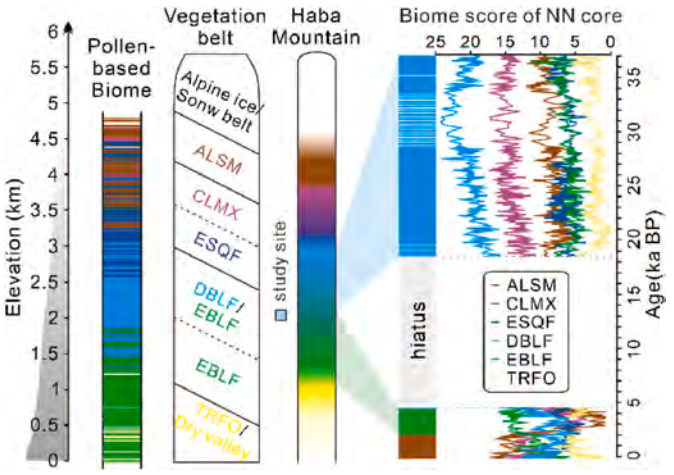


Fig. 5. Compare the pollen–based Biome in SW China (left) (Zhang et al., 2024), the modern mountainous vegetation types (middle) and the biome variations of the NN core (right). The elevated ALSM biome score observed between 2.4 and 0 ka are likely attributable to agricultural activities rather than natural factors.

DBLF (zones 1–3), especially prominent during MIS3, when the score peaked. During this time, CLMX and ALSM also showed relatively high biome scores, while the scores for EBLF and TRFO were the lowest. During the late Holocene (Zone 4), the biome score of EBLF reached its peak, indicating a significant shift in vegetation types during the transition from the LGP to the Holocene. Although the exact timing of the transition from DBLF to EBLF remains uncertain, a comparison with the biome reconstruction results from the adjacent CH core suggests that it likely occurred during the late deglaciation period or the early Holocene (Zhang et al., 2024). After 2.4 ka, ALSM emerged as the biome with the highest score, coinciding with a marked increase in *Pinus* and Poaceae pollen abundance (zone 5), which may be closely associated with human activities such as large–scale deforestation for agriculture and expansion of pastoral areas.

5. Discussion

5.1. Biome variations of NN and CH record

The most abundant pollen taxon in the NN fossil record from the LGP is *Quercus* (D), accompanied by other deciduous trees such as *Betula*, *Carpinus*, *Fagus*, Ericaceae (e.g., *Rhododendron*), and *Ulmus*. The biome result also indicates that the DBLF score has consistently been the highest, particularly during the MIS3 (Fig. 6). In modern East Asia, DBLF

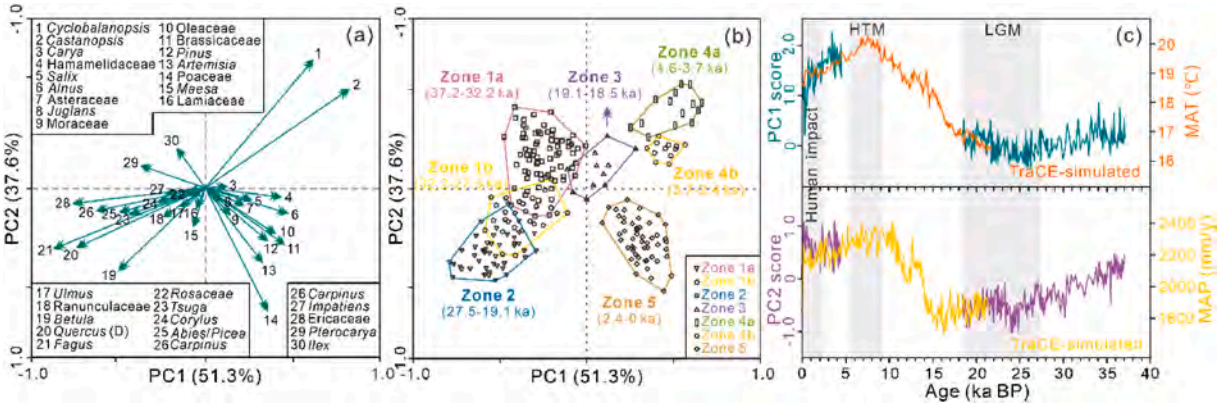


Fig. 4. PCA ordination of pollen percentage data. (a) PCA results based on selected pollen taxa. (b) Biplot of the PCA result for pollen data; (c) Comparison of PC1 (PC2) values and the local temperature (precipitation) simulated using TraCE21 (Liu et al., 2009).

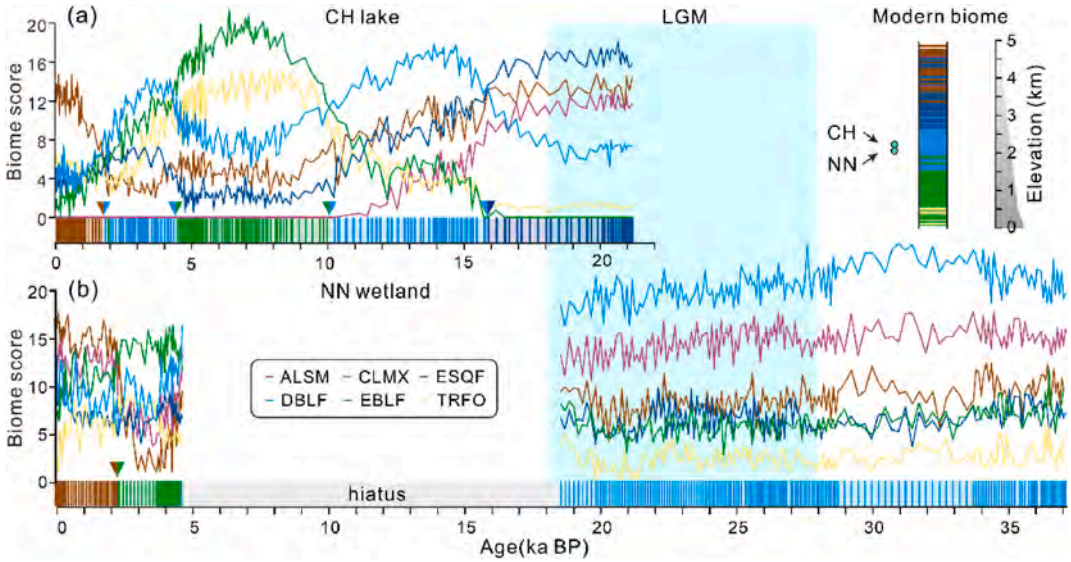


Fig. 6. Compare the biome scores recorded by (a) CH (Zhang et al., 2024) and (b) NN cores. The modern biomes found at different altitudes in SW China are also shown on the upper right side (Zhang et al., 2024). As illustrated in Fig. 5, the elevated biome scores of ALSM since 2.4 ka are closely associated with human activities.

is predominantly distributed north of 32° latitude, while in southwestern regions, only scattered patches of DBLF exist, likely due to the influence of the winter climate in this area (Tang, 2015). Although DBLF can be found within an elevation range of 300–3000 m a.s.l. (Flora of China Editorial Committee, 2013), they typically dominate at altitudes between 2000 and 2500 m a.s.l. (Zhou, 1981). This suggests that the vegetation types during the LGP exhibited a notable downward shift in altitude compared to contemporary vegetation (Tang, 2015).

To further understand the regional vegetation dynamics during the LGP, we compared the NN record with that of the CH core. The linear distance between the NN and CH cores is less than 100 km, and the sampling altitude difference is minimal (less than 200 m). Based on these geographical similarities, the vegetation types in the vicinity of these two records since the LGP were likely to have been relatively consistent. Wang et al. (2019) analyzed 14 pollen records from southern China and concluded that most of SW China was predominantly covered by temperate mixed coniferous and broadleaved forests or warm–temperate deciduous broadleaved forests during the LGP. While this general pattern provides a regional context, the records from the NN and CH show some unique characteristics. During this period, particularly at the LGM, the biome differences recorded by NN and CH were notably distinct (Fig. 6), highlighting the local–scale variability in vegetation responses to the glacial climate. Before 16 ka, the biome score of CH consistently indicated a dominance of *Quercus* (ES), while DBLF exhibited a significant prevalence around NN during this interval. *Quercus* (ES) species are commonly encountered and often dominate in an altitudinal belt centered between 2500 and 3600 m a.s.l. in the southeastern Tibetan Plateau and SW China (Yang et al., 2009). This elevation range is significantly higher, by approximately 500–800 m, than that of deciduous DBLF currently distributed in the southwestern region (Tang, 2015). *Quercus* (ES) exhibits notable adaptability to very cold and arid climates as well as nutrient–deficient soils. These conditions typically limit the growth of most deciduous broadleaved trees such as *Alnus*, *Betula*, and *Carpinus*, and other deciduous or evergreen Fagaceae members like *Quercus* (D) and *Cyclobalanopsis*, which are predominantly found at lower elevations (Zhou et al., 2007). Given the distinctive ecological characteristics of *Quercus* (ES) and its specific elevation range, it is plausible that these factors contributed to the notably lower vertical distribution of vegetation types recorded by the NN core compared to those documented in the CH record during the LGM.

We posit that the variation in pollen sources across different sites and the differing capacities of sedimentary environments to retain pollen are likely the primary factors contributing to this discrepancy. Firstly, CH is a typical karst lake formed under geological structural influences, with a catchment area of 380 km^2. It is surrounded by relatively high mountains, i.e. Xiliang (West, 2854 m), Yangjiao (East, 2519 m), Dalongcao (North, 2490 m) and Yingpan (South, 2360 m). Typically, pollen transport distances vary significantly depending on the terrain. For instance, in relatively flat terrains, pollen can be transported over distances ranging from dozens or even hundreds of kilometers, whereas in mountainous regions with dense vegetation, this distance is notably reduced to less than ~50 km (Xu et al., 2014). During summer, the ISM and associated precipitation transport pollen from the higher elevations of Xiliang Mountain on the western side to the CH water body, while during winter, the monsoon carries more pollen originating from Yangjiao Mountain on the eastern side. Unlike the CH core, the NN pollen sediments originated from the alpine wetland of NN Mountain. Within the pollen dissemination range, no other mountains with comparable or higher altitudes were present. Consequently, the pollen in the NN wetland primarily originated from a relatively localized area, which may lead to a more accurate representation of the local vegetation at that time but also limits the scope of regional vegetation information compared to the CH record. Thus, it is deduced that the high biome scores of ESQF and ALSM recorded by CH during the LGM do not straightforwardly imply that these high–altitude vegetation belts as a whole vertically descended by more than 1000 m (Zhang et al., 2024). This is because the composition of pollen records can be significantly affected by factors such as pollen sources and sedimentary environments. When calculated according to the altitude of the surrounding mountains of the CH core, the ESQF during this period is likely to have been concentrated within an altitude range of approximately 2300–2600 m. This indicates a downward shift of only about 500–800 m in comparison with the current situation (Fig. 7). Therefore, the area around CH may have been in the transition zone between DBLF and ESQF, while the area around NN was likely closer to the upper boundary of the DBLF belt during this period. Understanding these regional differences is crucial for comprehensively interpreting the vegetation evolution in this area, as it helps to identify the specific ecological niches and environmental gradients that influenced the distribution of different vegetation types. In previous studies, utilizing quantitative climate reconstruction results and the habitat characteristics of *Quercus* (ES), it

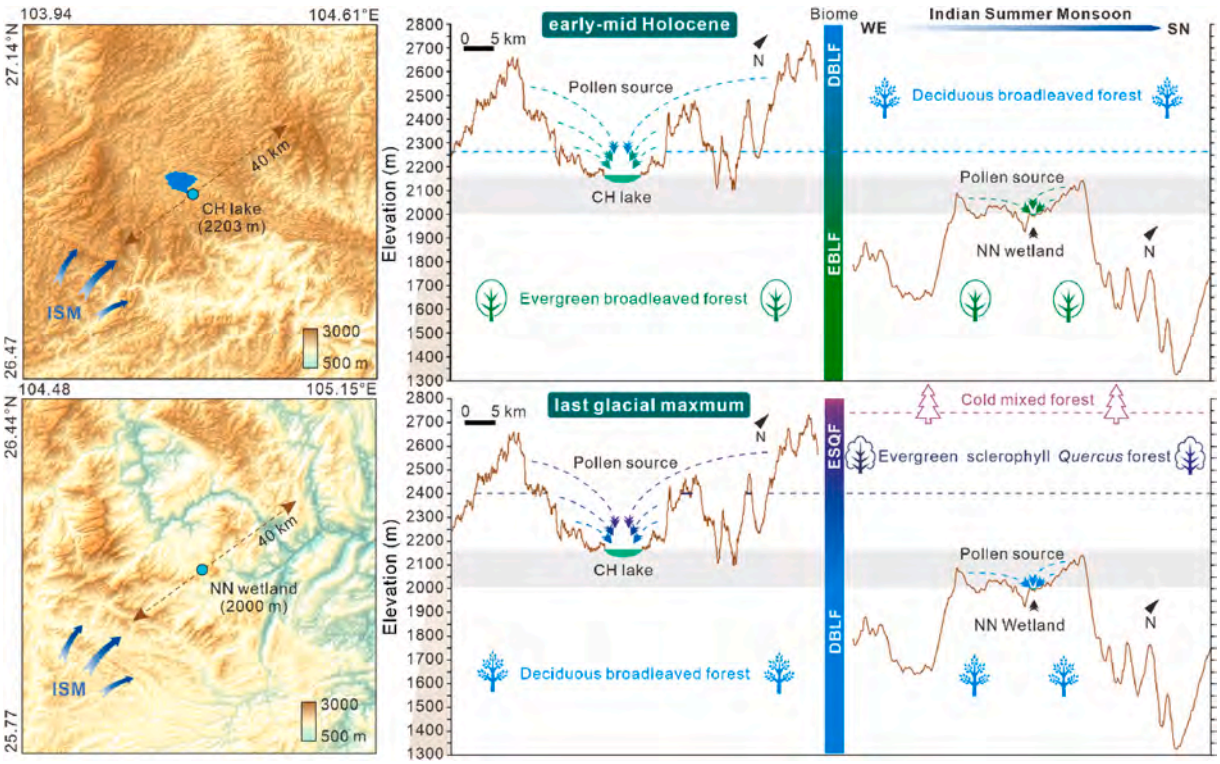


Fig. 7. The pollen sources of CH lake and NN wetland and the biome types of the mountain profiles during the early–mid Holocene and LGM.

was hypothesized that the biome transformation during the Heinrich event 1 (H1) period, as indicated by CH pollen records, could be closely associated with temperature fluctuations (Zhang et al., 2024). However, this conclusion may have underestimated the substantial influence of pollen sources. To gain a more accurate understanding of the biome transformation, it is essential to comprehensively consider factors such as pollen sources, sedimentary environments, and their interactions with climate change, in order to better reconstruct the historical vegetation dynamics in this area.

Since the deglaciation, with the gradual warming and increased humidity of the climate, the vertical vegetation zones in SW China have experienced an upward shift (Xiao et al., 2020). During this period, the CH sediment record clearly documented a transition in the surrounding mountain vegetation from DBLF to EBLF, which has been attributed to the intensification of the ISM (Zhang et al., 2024). Consistent with the CH records, the vegetation around NN also shifted from DBLF to EBLF between the LGP and the Holocene. Although sedimentary discontinuities prevent precise determination of the timing of this vegetation shift around NN site, evidence confirms that the EBLF boundary migrated upward by at least 300–500 m during the Holocene (Fig. 7). In the late Holocene (ca. 4–2 ka), the biome type in CH reverted from EBLF to DBLF, while regional vegetation type of NN wetland is EBLF, suggesting a slight downward migration of the alpine vegetation belt. The transition zone between EBLF and DBLF may be situated between 2000 and 2200 m during this period. Notably, since 2 ka, both CH and NN have recorded a clear shift to ALSM biome scores. We propose that the unusually high proportions of ALSM and DBLF during this period are attributable to elevated levels of Poaceae pollen (associated with ALSM) and *Alnus* pollen (linked to DBLF), likely resulting from human activities and fires. This also indirectly suggests that the anthropogenic disturbance in this area has been relatively consistent since around 2 ka.

5.2. Reassess the vegetation succession since the MIS3

To further elucidate the process in SW China since the MIS3, it is essential to understand the influence of topographic features and sedimentary environments on pollen records. Consequently, we systematically categorized previous pollen data, including those from NN, into four distinct types of study sites (Table 2).

1. The pollen source area is extensive, typically exceeding 30–50 km, with surrounding mountains of higher elevation. Most alpine lakes fall into this category. These pollen records typically offer a comprehensive overview of the regional high–altitude vegetation.
2. The pollen source area is also extensive, typically exceeding 30–50 km, but is devoid of surrounding mountains of higher elevation, such as the lower–altitude Menghai (MH) lake to the south (Tang, 1992). These records, similar to Type 1, encompass a diverse array of pollen sources and may also indicate vegetation changes across extensive regions. However, given the absence of high mountains in the surrounding area, the documented vegetation types are likely to resemble those in the vicinity of the sampling sites.
3. The pollen source area is limited, usually less than 10 km, yet surrounded by mountains of higher elevation, exemplified by the GC wetland (Deng et al., 2022). In this scenario, despite the presence of mountains surrounding the sedimentation site, the pollen assemblage is likely to be predominantly derived from local vegetation within the immediate area, owing to the limited capacity of the site to trap pollen grains.
4. The pollen source area is similarly limited (less than 10 km), without surrounding mountains of higher elevation, such as the NN wetland (this study). Pollen derived from this type of site predominantly reflects the composition of local vegetation, as there are no substantial topographic barriers that could interfere with pollen transport from distant sources. This characteristic renders it particularly valuable for investigating local–scale vegetation succession.

In summary, the first type of pollen records generally reflects regional high mountain vegetation, while the latter three types primarily represent local vegetation changes (Fig. 8).

Table 2
The basic information for pollen records in SW China.

Site	Long (°E)	Lan (°N)	Elevation (m a.s.l)	bottom Age (ka)	Sedimentary environment	Type	References
Tiancai (TC)	99.72	26.63	3898	21	Lake	1	Xiao et al., 2014a; Xiao et al., 2014b
Wuxu (WX)	101.40	29.15	3760	12.3	Lake	1	Zhang et al. (2016); Shen and Xiao (2018)
Shudu (SD)	99.94	27.91	3620	30	Lake	1	Cook et al. (2011); Cook et al. (2013); Yao et al., 2017
YSL profile	99.70	29.87	3310	32	Mountain	1	Shi et al. (2011)
Haligu (HLG)	100.18	27.00	3277	9.3	Lake	1	Song et al. (2012)
Wenhai (WH)	100.17	26.98	3080	23	Lake	1	Yao et al. (2015)
Lugu (LG)	100.78	27.72	2690	22	Lake	1	Shen and Xiao (2018)
Caohai (CH)	104.34	26.81	2203	22	Lake	1	Zhang et al. (2024)
Heqing (HQ)	100.17	26.56	2190	2780	Basin	1	Xiao et al. (2007); Jiang et al. (2001)
Niangniang (NN)	104.82	26.10	2000	37	Wetland	4	This study
Eryuanxihu (EYXH)	100.00	26.00	1980	17	Lake	1	Lin et al. (1986)
Erhai (EH)	100.18	25.73	1974	13	Lake	1	Shen et al. (2006)
Dianchi (DC)	102.68	25.02	1886	20	Lake	1	Xiao et al. (2020)
Tengchongqinghai (TCQH)	98.53	25.26	1885	68	Lake	1	Xiao et al. (2015); Yang et al. (2016); Zhang et al. (2020)
Ganchi (GC)	103.03	29.39	1805	25	Wetland	3	Deng et al. (2022)
Yangzonghai (YZH)	103.00	24.91	1800	13	Lake	1	Wang et al. (2020)
Xingyun (XY)	102.55	24.33	1717	37	Lake	1	Chen et al. (2014a); Chen et al. (2014b);
Chenghai (CHH)	100.67	26.53	1503	8.2	Lake	1	Xiao et al. (2017)
Yilong (YL)	102.58	23.68	1414	27	Lake	1	Li et al. (2024)
Dayin (DY)	105.04	24.23	991	47	Cave	4	Zhang et al. (2024)
Menghai (MH)	100.47	21.97	612	42	Lake	2	Tang, 1992

In numerous such records, from high–altitude regions in SW China and low–altitude areas on the southeastern margin of the Tibetan Plateau, it is evident that *Quercus* (ES) pollen was exceptionally abundant during the late MIS3 to the LGM. For instance, several lacustrine records, such as DC (Xiao et al., 2020), XY (Chen et al., 2014a), TCQH (Xiao et al., 2015; Zhang et al., 2020), and the HQ basin (Jiang et al., 2001), indicate the dominance of *Quercus* (ES) together with alpine *Abies/Picea* and cold–tolerant herbs in the vicinity of lakes in SW China. These pollen records, as described above, provide clear evidence that the ESQF expanded significantly southward and into lower-altitude regions during the period from MIS 3 to the LGM, in comparison to its modern distribution. Wang et al. (2023) utilized the MaxEnt model to simulate the potential distribution range of ESQF during the LGM, with results confirming this conclusion. However, it should be noted that all these pollen records belong to the Type 1 we previously classified (Table 2). Since these records may reflect surrounding mountain vegetation types rather than local vegetation changes, they might have overestimated the extent of ESQF expansion during the LGP. For instance, the pollen record from the relatively southern XY lake likely represents the mountain vegetation on its eastern side (1900–2500 m) (Chen et al., 2014a) (Fig. 8), while at an altitude of the core site (ca. 1700 m), it may be predominantly dominated by DBLF. This finding is also supported by records from the more southerly but lower–altitude YL lake (Li, K. et al., 2024). These examples demonstrate that failing to differentiate between regional (mountain–influenced) and local vegetation signals may result in misinterpretations regarding the actual extent of vegetation range shifts (Fig. 9a). In a recent study, three pollen records were utilized in the East Asian Monsoon Domain, comprising two from SW China (TCQH and CH) and one from central China (DJH), to quantitatively reconstruct the paleoclimate variations since the LGP (Zhang et al., 2023). The result shows that during the LGM, ESQF dominated around TCQH and CH lakes. Compared to modern vegetation, the altitudinal distribution of this vegetation zone shifted downward by ca. 900–1100 m (Zhang et al., 2020). Based on East Asian Pollen Database and quantitative models, it can be estimated that the MAT during the LGM was ca. 7–9 °C lower than during the Holocene (Zhang et al., 2023). However, given that the primary pollen sources of TCQH and CH predominantly originate from the surrounding alpine vegetation, it is plausible to infer that the ESQF did not extend to the same altitude around the two lakes during this period (Fig. 8). According to our NN records, the vegetation at ca. 2000 m likely represented either the lower boundary of the ESQF or the upper boundary of the DBLF. Consequently, the ESQF might have only undergone a vertical migration of 600–800 m during the LGM. Considering the slightly higher temperature gradient rate during the LGM compared to present–day conditions (Loomis et al., 2017), it is estimated that the MAT might have only decreased by an average of 5–7 °C relative to the Holocene. This finding is in good agreement with global model predictions (Osman et al., 2021), which not only validates the reliability of our estimations but also provides valuable insights into the regional climate changes during the LGM.

The deglaciation event since the LGM led to significant climatic changes, which in turn exerted profound impacts on the distribution and dynamics of vegetation types. As the climate gradually warmed and precipitation patterns altered, low–altitude vegetation types such as EBLF began to experience changes in their geographical ranges (Wang et al., 2019). Since the deglaciation, low–altitude vegetation types such as EBLF have restrictedly expanded northward (Zheng et al., 2023). However, the biome scores for DBLF recorded by NN, DC, and GC remained consistently high. Moreover, the proportion of deciduous components in southern sites, as documented by the studies of YZH (Wang et al., 2020), YL (Li, K. et al., 2024), and XY (Chen et al., 2014a), also remained relatively high. In contrast to the general northward expansion trend, the northward migration range of EBLF during this period was restricted, with its vertical distribution not exceeding 1400–1600 m a.s.l. This might be due to competition with other vegetation types, especially the persistent dominance of DBLF in some areas. Meanwhile, DBLF, ESQF and CLMX gradually migrated to higher–altitude areas in the eastern part of the Tibetan Plateau (Wang et al., 2019). For instance, the biome types in CH and TCQH underwent a clear transition from ESQF to DBLF, indicating that DBLF had vertically migrated to approximately 2000 m a.s.l. (Zhang et al., 2020, 2024). Nonetheless, records from HQ (Jiang et al., 2001), EYXH (Lin et al., 1986), and WH (Yao et al., 2015) still predominantly exhibit ESQF or CLMX, suggesting that DBLF in SW China was likely concentrated between 2000 and 2800 m a.s.l. during this period. Similarly, based on records from LG (Shen and Xiao., 2015), SD (Cook et al., 2011, 2013; Yao et al., 2017), WX (Zhang et al., 2016), TC (Xiao et al., 2014) and YSL (Shi et al., 2011), it can be inferred that ESQF in the area was distributed between 2400 and 3700 m a.s.l., while CLMX and ALSM were found at relatively higher altitudes (Fig. 9b).

With the gradual rise in temperature and precipitation, the EBLF, primarily consisting of *Castanopsis*, *Cyclobalanopsis*, and Euphorbiaceae,

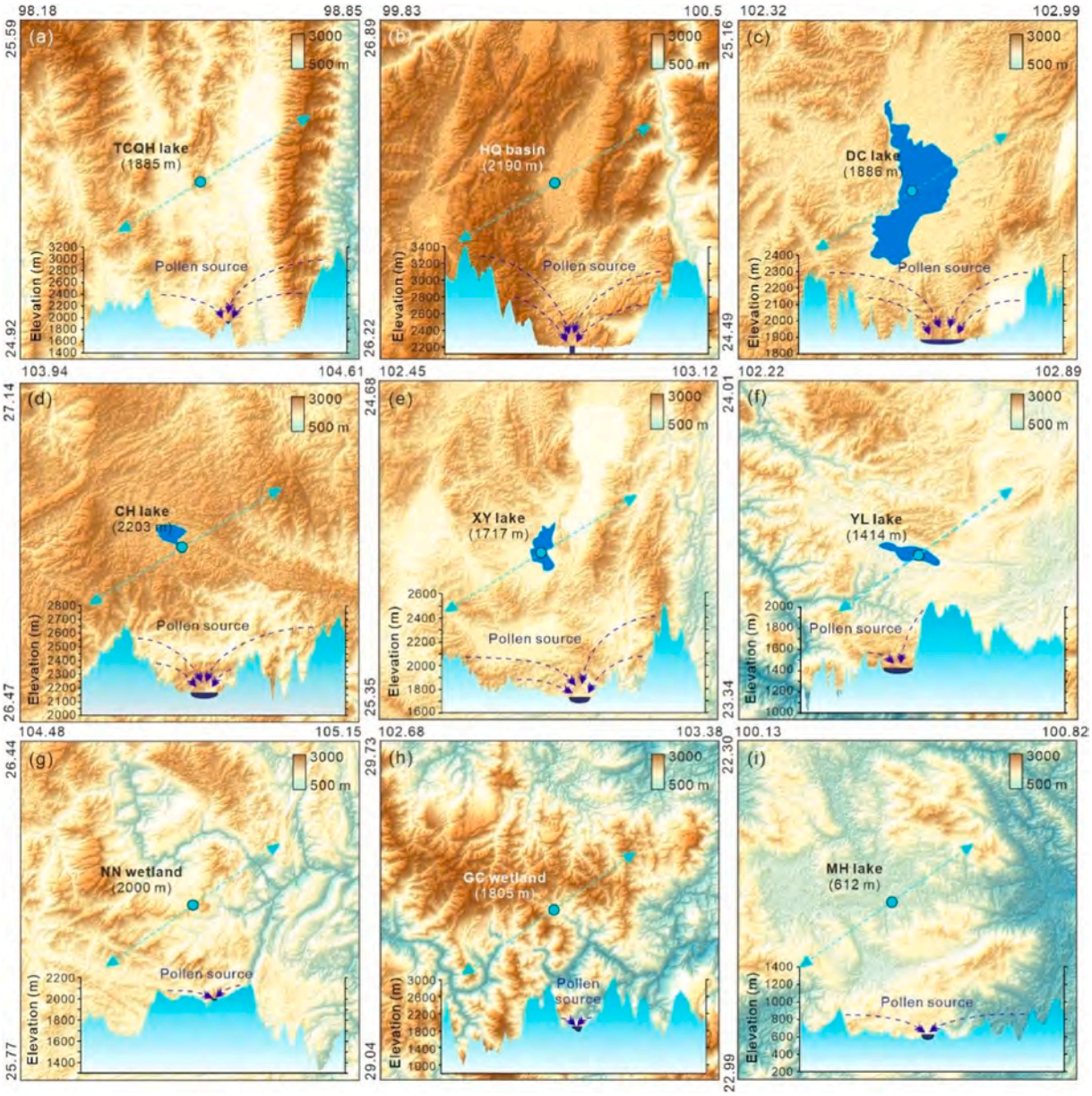


Fig. 8. The sedimentary environment and pollen sources documented by certain pollen records in SW China. (a) TCQH lake (Xiao et al., 2015; Zhang et al., 2020); (b) HQ basin (Jiang et al., 2001; Xiao et al., 2007); (c) DC lake (Xiao et al., 2020); (d) CH lake (Zhang et al., 2024); (e) XY lake (Chen et al., 2014a, 2014b); (f) YL lake (Li, K. et al., 2024); (g) NN wetland (this study); (h) GC wetland (Deng et al., 2022); (i) MH lake (Tang, 1992).

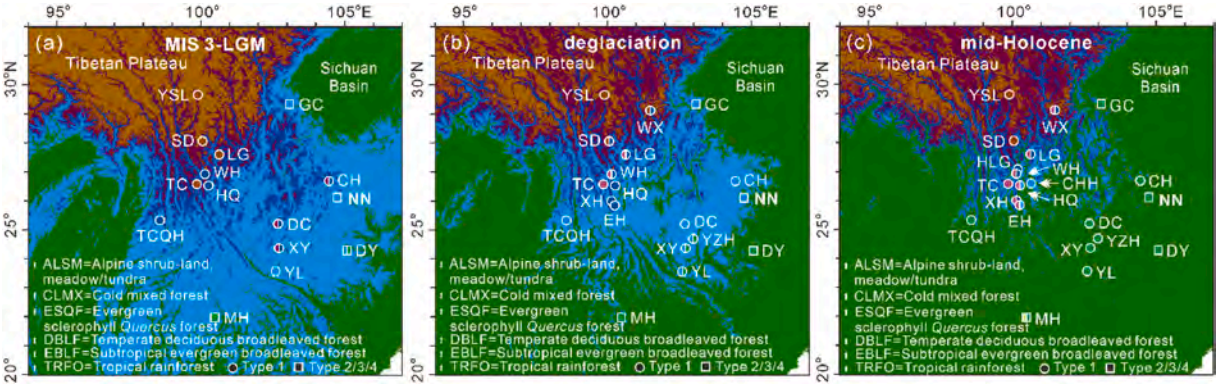


Fig. 9. Vegetation changes in Southwest China during (a) MIS3–LGM, (b) deglaciation and (c) early–mid Holocene inferred from pollen records and topographic feature.

experienced significant northward expansion during the early to mid-Holocene (Tang, 2015). This expansion and upward altitudinal shift not only demonstrated the vegetation's adaptability to climatic changes but also imposed ecological pressure on the distribution of DBLF, resulting in a marked contraction of its geographic range. Concurrently, paleovegetation records from high-altitude sites such as TCQH (Xiao et al., 2015; Zhang et al., 2020), CH (Zhang et al., 2024), GC (Deng et al., 2022), EH (Shen et al., 2006), and HQ (Jiang et al., 2001) reveal a transitional shift in vegetation composition, from DBLF dominance to an increased presence of evergreen elements. This suggests that the EBLF biome underwent a vertical shift to elevations of ca. 2200–2400 m a.s.l. (Fig. 9c). In contrast, the distribution range of DBLF was notably restricted. Based on records from WH (Yao et al., 2015), HLG (Song et al., 2012), LG (Xiao and Shen., 2018) and others, it can be inferred that the upper limit of DBLF distribution during this period was below approximately 3000 m a.s.l. A recent study by Zheng et al. (2023) examined the characteristics of EBLF and DBLF changes during the glacial to interglacial transition using pollen records from subtropical China. The findings revealed that most mountainous regions in the subtropical zone were predominantly covered by DBLF during the LGM, and the major biome replacement from deciduous to evergreen forest did not occur until around 8.1 ka. This suggests an earlier forest replacement in low–latitude regions compared to sites further north or at higher elevations. It not only provides additional evidence for the biome replacement process but also helps to establish a broader context for understanding the spatial and temporal patterns of vegetation changes in the region.

Following the LGP, the climate in the study region underwent significant changes, which had profound impacts on the distribution and migration of vegetation types. Among these, the ESQF, which exhibited a wide distribution during the LGP, gradually migrated to the southeastern edge of the Tibetan Plateau and the western margin of the Sichuan Basin. This migration resulted in its concentration primarily between 3000 and 3700 m a.s.l., similar to the modern distribution pattern (Yang et al., 2009). Meanwhile, pollen records from MH lake during the early–mid Holocene in southern regions highlighted specific components that are characteristic of TRFO (Tang, 1992). In contrast, NPK records from the Indochinese Peninsula at lower latitudes indicated that this region was predominantly covered by a typical TRFO biome during the same period (Penny, 2001). Consequently, it is reasonable to deduce that TRFO expanded from areas such as the Indochinese Peninsula into low–altitude regions south of ca. 22°N in SW China during this period. However, due to insufficient paleovegetation records, the precise extent of this expansion remains undetermined.

5.3. Possible climate forcing for the biome succession

Numerous studies have demonstrated that climate change since the LGP has significantly influenced biome succession across various regions in SW China (Xiao et al., 2020; Wang et al., 2019; Zhang et al., 2024). Understanding these impacts is essential for forecasting future ecosystem changes and for reconstructing the historical ecological dynamics of the region. For example, a continuous pollen record from 68 ka at TCQH lake indicates that vegetation during the MIS3 was highly productive (Zhang et al., 2020). By integrating this record with two additional sites (CH and DJH), the comprehensive dataset enabled the quantitative reconstruction of temperature and precipitation changes within the Asian monsoon domain since the MIS3 (Zhang et al., 2023). The pollen data from TCQH provided insights into the types and abundances of plants present, which were then correlated with known climate–vegetation relationships. The data from the other sites complemented this information, helping to fill in gaps and validate the reconstruction. These findings align with our PCA indicators for temperature (PC1) and precipitation (PC2), providing confirmation that the MIS3 period was characterized by significant climatic fluctuations, specifically cold and humid conditions (Fig. 10). On the

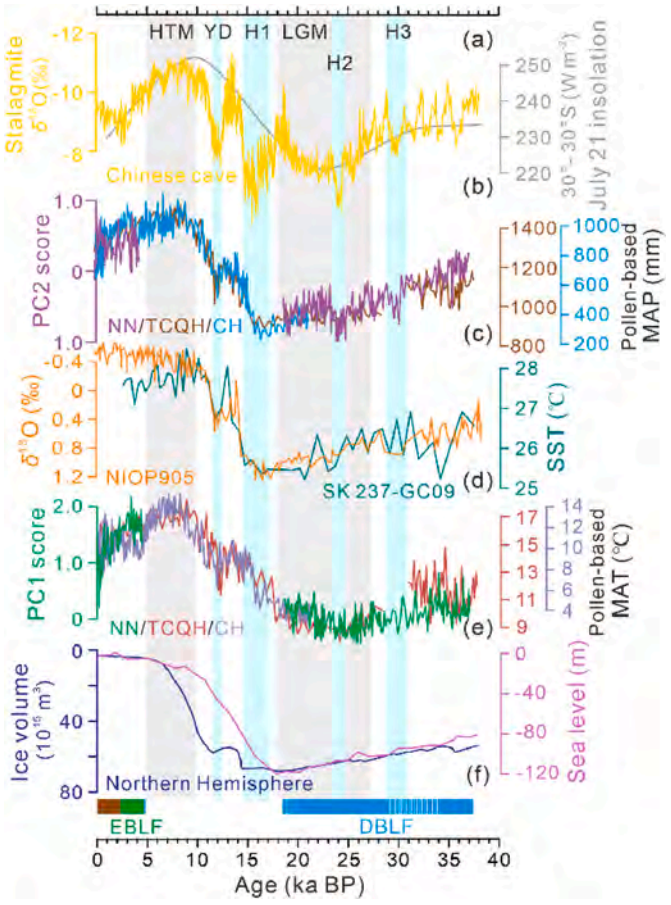


Fig. 10. Correlation of pollen proxies with other paleoclimatic records. (a) July 21 30°N–30°S insolation (Laskar et al., 2004) and Stalagmite $\delta^{18}O$ values from Chinese caves (Cheng et al., 2016); (b) PC2 for NN core and pollen–based MAP estimates for the TCQH and CH core (Zhang et al., 2023); (c) NIOP905 marine $\delta^{18}O$ *G. ruber* records (Jung et al., 2009) and SST from the SK237–GC09 core (Raza et al., 2017); (d) PC1 for NN core and pollen–based MAT estimates for the TCQH and CH core (Zhang et al., 2023); (e) ice volumes for the Northern Hemisphere simulated using ECHAM3 (Charbit et al., 2007) and sea level (Grant et al., 2014); (f) dominant biomes based on the NN core.

glacial–interglacial timescale, our PC1 and PC2 variations are closely correlated with Northern Hemisphere (NH) ice volume changes (Charbit et al., 2007) and the July insolation difference between 30°N and 30°S (Laskar et al., 2004), as shown in Fig. 10. This suggests that variations in ice sheets and the summer inter–tropical insolation gradient (SITIG) were critical factors influencing biome succession in SW China (Zhang et al., 2023, 2024). During the LGM, NH ice sheets significantly contributed to temperature reductions, intensifying the north–south temperature gradients. Consequently, this enhanced moisture transport from tropical oceans to the continent, increasing monsoonal precipitation over SW China and the eastern margin of the Tibetan Plateau (Lehmkuhl and Owen, 2005). The increased precipitation, in turn, influenced the growth and distribution of various plant taxa. Wet–adapted plants flourished, while drought–tolerant taxa encountered challenges, resulting in a shift in biome composition. Throughout this process, the Indo–Pacific Warm Pool played a crucial role in energy transmission, as evidenced by the high consistency between our pollen–based PC2 and other rainfall records in SW China (Xiao et al., 2020) with sea surface temperature (SST) and marine $\delta^{18}O$ data derived from planktonic foraminifera in the Bay of Bengal (Ahmad et al., 2012; Govil and Naidu, 2010; Jung et al., 2009).

Nonetheless, long–term climatic changes are insufficient to fully explain the intricate details of biome succession in SW China. For

instance, certain pollen records indicate that biomes underwent multiple distinct successions during deglaciation periods, frequently coinciding with rapid events such as the Younger Dryas (YD), Bolling–Allerød (BA), and H1 (Xiao et al., 2015; Zhang et al., 2024). Conversely, other pollen records suggest minimal or no significant changes in biome composition before and after these rapid events, with only a small fraction of species exhibiting minor alterations (Xiao et al., 2014; Shen and Xiao, 2018). This suggests that short–term fluctuations in regional climatic thresholds may have either facilitated or constrained the growth of certain taxa (Xu et al., 2023). Thus, the observed shifts in biomes in SW China are likely influenced by additional mechanisms rather than being solely a response to thermodynamic effects on a periodic scale. In this study, although YD and H1 are unrecorded, abrupt events H2 and H3 are distinctly evident in our precipitation indicators (PC2), indicating that the AMOC is an additional significant driver influencing changes in the Indian Monsoon, which profoundly affected the biome succession in SW China (Ng et al., 2018; Shen and Xiao, 2018). During the period of these abrupt events, the proportions of several taxa in our pollen records exhibited significant fluctuations. For example, Ericaceae, a taxon characterized by its representation as a typical deciduous shrub in subtropical regions (Tang, 2015), experienced a peak proportion of 11 % during the H2 event. In comparison with tree species such as *Quercus* (D), Ericaceae demonstrates a higher resilience to the strong winds and very dry conditions prevalent at mountain tops (Tang, 2015). Therefore, it is hypothesized that during the LGM, a period marked by an overall cold and dry climate, the exceptionally colder and drier conditions during the H2 event led to significant changes in certain taxa, such as Ericaceae. Similarly, biome transitions recorded by pollen analysis of CH lake since the LGM predominantly occurred during or immediately following global rapid events (i.e., H1, YD and the 4.2 ka event) (Zhang et al., 2024). Recently, the rainfall of the East Asian Summer Monsoon (EASM) was quantitatively reconstructed by using multi–proxy records from a maar lake in southern China, with the records dating back to the LGM (Lu et al., 2025). The analysis identified five critical tipping points in EASM rainfall variability since the LGM, which are also attributed to abrupt shifts in the AMOC and Saharan vegetation. Thus, the AMOC significantly impacts the degree of change in Asian monsoon precipitation through complex water vapor circulation processes, thereby influencing biome succession in SW China since the MIS3. These findings highlight the complex interplay between global climate systems, such as the AMOC, and regional ecological processes in the eastern margin of the Tibetan Plateau.

6. Conclusion

Studying the vegetation dynamics and biome variations in SW China is crucial for understanding the region's ecological history and its response to climate change. Our high–resolution pollen analysis yields a novel record of these aspects since 37 ka, enabling a detailed quantitative reconstruction of biome variations. The findings reveal that during the MIS3 period, the region surrounding the study site was dominated by DBLF, with *Quercus* (D) and other Betulaceae taxa serving as key components. The biome score for DBLF slightly decreased during the LGM, yet it remained the highest among all biomes. The discrepancies in biome composition during this period compared to records from the nearby CH lake may be attributed to variations in topographic characteristics and sedimentary environments. Through a comparative analysis of our findings with other pollen records from SW China, we infer that during the LGP, the DBLF likely expanded over extensive areas at medium to high altitudes in the region, whereas the ESQF may have experienced only a vertical migration of approximately 600–800 m during the LGM. Consequently, we hypothesize that the discrepancy in previous pollen-based MAT estimates may have been overestimated from the LGM to the Holocene.

In addition, during this period, the dominant vegetation type surrounding the NN wetland transitioned from DBLF to EBLF. This indicates that the EBLF biome in SW China underwent a vertical migration during the Holocene, establishing itself at elevations of approximately 2200–2400 m a.s.l. This shift not only indicates a response to changing climate conditions but also reflects the dynamic nature of the regional vegetation, adapting to gradual warming and other environmental factors. Over the past 2400 years, there has been a gradual shift towards the ALSM biome, with dominant taxa comprising pioneer plants and/or secondary shrubs associated with high fire frequencies. Consequently, we propose that this most recent biome transition is predominantly attributed to early human activities.

The PCA of the fossil pollen dataset revealed a strong correlation between the principal components and the simulated climate variables, indicating that PCA can serve as a robust proxy for assessing climate conditions. Given that abrupt events are clearly reflected in our precipitation indicators (PC2), we propose that, in addition to glacial–interglacial scale drivers such as solar radiation and variations in high–latitude ice volume, the AMOC plays an additional critical role in modulating changes in the Indian Monsoon. This, in turn, has significantly influenced biome transitions in SW China.

Author contributions

Xiao Zhang: Conceptualization, Data curation, Funding acquisition, Supervision, Writing–original draft, Writing–review & editing. Yuanfu Yue: Conceptualization, Data curation, Investigation, Formal analysis, Funding acquisition, Methodology, Supervision, Writing–review & editing. Ziyan Zhang: Software, Validation. Liuying He: Formal analysis, Writing–review & editing. Xinmeng Yuan: Formal analysis, Writing–review & editing. Xintian Yu: Formal analysis, Writing–review & editing. Qiuchi Wan: Investigation. Cong Chen: Investigation. Yongjie Tang: Investigation. Zhuo Zheng: Conceptualization, Methodology, Writing–review & editing. Kangyou Huang: Conceptualization, Writing–review & editing.

Declaration of competing interest

The authors declare that they have no known competing financial interests or personal relationships that could have appeared to influence the work reported in this paper.

Acknowledgments

This work was supported by the National Natural Science Foundation of China (41902184, 42366002 and 41702182) and National Key Research and Development Program of China (2022YFF0801501).

Data availability

A link to the data and/or code is provided as part of this submission.

References

Ahmad, S.M., Zheng, H.B., Raza, W., Zhou, B., Lone, M.A., Raza, T., Suseela, G., 2012. Glacial to Holocene changes in the surface and deep waters of the northeast Indian Ocean. Mar. Geol. 329, 6–23. https://doi.org/10.1016/j.margeo.2012.10.002.

Birks, H.J.B., Frey, D.G., Deevey, E.S., 1998. Review1: numerical tools in palaeolimnology progress, potentialities and problems. J. Paleolimnol. 20, 307–332. https://doi.org/10.1023/A:1008038808690.

Blaauw, M., Christen, J.A., 2011. Flexible paleoclimate age-depth models using an autoregressive gamma process. Bayesian Anal 6, 457–474. https://doi.org/10.1214/11-BA618.

Boufford, D.E., van Dijk, P.P., 2004. Mountains of Southwest China. In: Mittermeter, R. A., Gil, P.R., Hoffman, M., et al. (Eds.), Hotspot Revisited: Earth's Biologically Richest and Most Endangered Ecoregions. Cemex, Mexico, pp. 159–164, 2nd.

Braak, C.J.F.T., Smilauer, P., 2002. CANOCO Reference Manual and Cano-Draw for Windows User's Guide: Software for Canonical Community Ordination. Microcomputer Power, Ithaca, New York. Version 4. 5.

Charbit, S., Ritz, C., Philippon, G., Peyaud, V., Kageyama, M., 2007. Numerical reconstructions of the Northern Hemisphere ice sheets through the last glacial-interglacial cycle. Clim. Past. 3, 15–37. https://doi.org/10.5194/cp-3-15-2007.

Chen, F.H., Chen, X.M., Chen, J.H., Zhou, A.F., Wu, D., Tang, L.Y., Zhang, X.J., Huang, X. Z., Yu, J.Q., 2014b. Holocene vegetation history, precipitation changes and Indian Summer Monsoon evolution documented from sediments of Xingyun Lake, south-west China. J. Quat. Sci. 29, 661–674. https://doi.org/10.1002/jqs.2735.

Chen, X.M., Chen, F.H., Zhou, A.F., Huang, X.Z., Tang, L.Y., Wu, D., Zhang, X.J., Huang, X.Z., Yu, J.Q., 2014a. Vegetation history, climatic changes and Indian summer monsoon evolution during the Last Glaciation (36,400-13,400 cal yr BP) documented by sediments from Xingyun Lake, Yunnan, China. Paleogeogr. Paleoclimatol. Paleoecol. 410, 179–189. https://doi.org/10.1016/j.palaeo.2014.05.027.

Cheng, H., Edwards, R.L., Sinha, A., Spötl, C., Yi, L., Chen, S.T., Kelly, M., Kathayat, G., Wang, X.F., Li, X.L., Kong, X.G., Wang, Y.J., Ning, Y.F., Zhang, H.W., 2016. The Asian monsoon over the past 640,000 years and ice age terminations. Nature 534, 640–646. https://doi.org/10.1038/nature18591.

Chevalier, M., Davis, B.A.S., Heiri, O., Seppä, H., Chase, B.M., Gajewski, K., Lacourse, T., Telford, R.J., Finsinger, W., Guiot, J., Kühl, N., Maezumi, S.Y., Tipton, J.R., Carter, V.A., Brussel, T., Phelps, L.N., Dawson, A., Zanon, M., Vallé, F., Nolan, C., Mauri, A., Vernal, A., Izumi, K., Holmström, L., Marsicek, J., Goring, S., Sommer, P. S., Chaput, M., Kupriyanov, D., 2020. Pollen-based climate reconstruction techniques for late Quaternary studies. Earth Sci. Rev. 210, 103384. https://doi.org/10.1016/j.earscirev.2020.103384.

Cook, C.G., Jones, R.T., Langdon, P.G., Leng, M.J., Zhang, E.L., 2011. New insights on late Quaternary Asian palaeomonsoon variability and the timing of the Last Glacial Maximum in southwestern China. Quat. Sci. Rev. 30, 808–820. https://doi.org/10.1016/j.quascirev.2011.01.003.

Cook, C.G., Jones, R.T., Turney, C.S.M., 2013. Catchment instability and Asian summer monsoon variability during the early Holocene in southwestern China. Boreas 42 (1), 224–235. https://doi.org/10.1111/j.1502-3885.2012.00287.x.

Deng, Y.K., Ma, C.M., Huang, M., Zhao, L., Shang, G.C., Tang, L.Y., Lu, H.Y., 2022. Vegetation and climate changes since the Last Glacial Maximum inferred from high-resolution pollen records from the Sichuan Basin, southwest China. Palaeogeogr. Palaeoclimatol. Palaeoecol. 606, 111231. https://doi.org/10.1016/j.palaeo.2022.111231.

Flora of China Editorial Committee, 2013. Flora of China. Science Press, Beijing.

Govil, P., Naidu, P.D., 2010. Evaporation-precipitation changes in the eastern Arabian Sea for the last 68 ka: implications on monsoon variability. Paleoceanography 25, 1–19. https://doi.org/10.1029/2008PA001687.

Grant, K.M., Rohling, E.J., Ramsey, C.B., Cheng, H., Edwards, R.L., Florindo, F., Heslop, D., Marra, F., Roberts, A.P., Tamisiea, M.E., Williams, F., 2014. Sea-level variability over five glacial cycles. Nat. Commun. 5, 5076. https://doi.org/10.1038/ncomms6076.

Grimm, E.C., 1991. TILIA 2.0 (Computer Software) Illinois State. University Research and Collection Center.

Jiang, X.Z., Yang, X.D., Wang, S.M., Tong, G.B., 2001. The last glacial maximal pollen record in the lake sediments from ancient Heqing lake and its significance for paleomonsoon. Acta Micropalaeontol. Sin. 18, 263–267.

Jung, S.J.A., Kroon, D., Ganssen, G., Peeters, F., Ganeshram, R., 2009. Enhanced Arabian Sea intermediate water flow during glacial North Atlantic cold phases. Earth Planet Sci. Lett. 280, 220–228. https://doi.org/10.1016/j.epsl.2009.01.037.

Kong, F.C., Yang, R.D., Lin, S.J., 2010. Analysis of the evolution of Karst environment of Weining region, Guizhou Province west China: a proof from the sediment evolution of lake Caohai since about 73 million years. Earth Environ. 38, 138–145. https://doi.org/10.14050/i.cnki.1672-9250.2010.02.018.

Laskar, J., Robutel, P., Joutel, F., Gastineau, M., Correia, A.C.M., Levrard, B., 2004. A long term numerical solution for the insolation quantities of the Earth. Astron. Astro Phys. 428, 261–285. https://doi.org/10.1051/0004-6361:20041335.

Lehmkuhl, F., Owen, L.A., 2005. Late quaternary glaciation of tibet and the bordering mountains: a review. Boreas 34, 87–100. https://doi.org/10.1080/03009480510012908.

Li, K., Liao, M., Ni, J., 2024. Vegetation response to climate change and human activity in southwestern China since the last Glacial Maximum. Palaeogeogr. Palaeoclimatol. Palaeoecol. 636, 111990. https://doi.org/10.1016/j.palaeo.2023.111990.

Li, S.M., Wei, L.S., Zhao, W.W., Ren, W.H., Gu, Q.R., Che, Z.X., Cao, X.Y., Li, H., Zhang, X.J., Chen, C.Z., Zhao, Y., 2024. Environmental changes and human impacts over the past 1200 years: evidence from high-resolution pollen records from peat in the Yunnan-Guizhou Plateau, Southwest China. Palaeogeogr. Palaeoclimatol. Palaeoecol. 655, 112540. https://doi.org/10.1016/j.palaeo.2024.112540.

Li, Z., Saito, Y., Dang, P.X., Matsumoto, E., Vu, Q.L., 2009. Warfare Rather than Agriculture as a Critical Influence on Fires in the Late Holocene, Inferred from Northern Vietnam, vol 106. P.N.A.S, pp. 11490–11495. https://doi.org/10.1073/pnas.0813258106.

Lin, S.M., Qiao, Y.L., Walker, D., 1986. Late Pleistocene and Holocene vegetation history at Xi Hu, Er Yuan, Yunnan Province, southwest China. J. Biogeogr. 13, 419–440. https://doi.org/10.2307/2844966.

Liu, Z.Y., Otto-Bliesner, B.L., He, F., Brady, E.C., Tomas, R., Clark, P.U., Carlson, A.E., Lynch-Stieglitz, J., Curry, W., Brook, E., Erickson, D., Jacob, R., Kutzbach, J., Cheng, J., 2009. Transient simulation of last deglaciation with a new mechanism for Bølling-Allerød warming. Science 325, 310–314. https://doi.org/10.1126/science.1171041.

Loomis, S.E., Russell, J.M., Verschuren, D., Morrill, C., Cort, G.D., Damsté, J.S.S., Olago, D., Eggermont, H., Street-Perrott, F.A., Kelly, M.A., 2017. The tropical lapse rate steepened during the last glacial maximum. Sci. Adv. 3, e1600815. https://doi.org/10.1126/sciadv.1600815.

Lu, F.Z., Lu, H.Y., Gu, Y., Lin, P.Y., Lu, Z.Y., Zhang, Q., Zhang, H.Y., Yang, F., Dong, X.Y., Yi, S.W., Chen, D.L., Pausata, F.S.R., Ben-Yami, M., Mecking, J.V., 2025. Tipping point-induced abrupt shifts in east asian hydroclimate since the last glacial maximum. Nat. Commun. 16, 477. https://doi.org/10.1038/s41467-025-55888-w.

Moore, P.D., Webb, J.A., Collinson, M.E., 1991. Pollen analysis. J. Ecol. 80, 216.

Ng, H.C., Robinson, L.F., McManus, J.F., Mohamed, K.J., Jacobel, A.W., Ivanovic, R.F., Gregoire, L.J., Chen, T.Y., 2018. Coherent deglacial changes in western Atlantic Ocean circulation. Nat. Commun. 9, 1–10. https://doi.org/10.1038/s41467-018-05312-3.

Ni, J., Cao, X.Y., Jeltsch, F., Herzschuh, U., 2014. Biome distribution over the last 22,000 yr in China. Palaeogeogr. Palaeoclimatol. Palaeoecol. 409, 33–47. https://doi.org/10.1016/j.palaeo.2014.04.023.

Osman, M.B., Tierney, J.E., Zhu, J., Tardif, R., Hakim, G.J., King, J., Poulsen, C.J., 2021. Globally resolved surface temperatures since the last Glacial Maximum. Nature 599, 239–244. https://doi.org/10.1038/s41586-021-03984-4.

Pan, Z.K., Sun, Q.F., Wang, M., Meng, H.W., Huang, L.P., Shen, C.M., 2025. Dynamics of Yunnan pine (*Pinus yunnanensis*) forest since the Last Glacial Maximum in central Yunnan, SW China. Rev. Palaeobot. Palyno. 336, 105311. https://doi.org/10.1016/j.revpalbo.2025.105311.

Penny, D., 2001. A 40000 year palynological record from north-east Thailand; implications for biogeography and palaeo-environmental reconstruction. Paleogeogr. Paleoclimatol. Paleoecol. 171, 97–128. https://doi.org/10.1016/S0031-0182(01)00242-5.

Raza, T., Ahmad, S.M., Steinke, S., Raza, W., Lone, M.A., Beja, S.K., Suseela, G., 2017. Glacial to Holocene changes in sea surface temperature and seawater δ18O in the northern Indian Ocean. Paleogeogr. Paleoclimatol. Paleoecol. 485, 697–705. https://doi.org/10.1016/j.palaeo.2017.07.026.

Shen, J., Jones, R.T., Yang, X., Dearing, J.A., Wang, S., 2006. The holocene vegetation history of lake erhai, yunnan province southwestern China: the role of climate and human forcings. Holocene 16 (2), 265–276. https://doi.org/10.1191/0959683606hl923rp.

Shen, J., Xiao, X.Y., 2018. Evolution of the south Asian monsoon during the last 20 ka recorded in lacustrine sediments from southwestern China. Quat. Sci. 38, 799–820. https://doi.org/10.11928/j.issn.1001-7410.2018.04.01 (in Chinese).

Shi, S.Q., Yuan, D.X., Luo, L.D., Hao, X.D., Zhao, Z.Y., 2011. Comparative study on climatic change during later period of the late Pleistocene epoch with the sporopollen record from northwest Yunnan plateau and the stalagmite record from South China. Carsol. Sin./Zhong Guo Yan Rong 30 (2), 9. https://doi.org/10.3969/j.issn.1001-4810.2011.02.001 (in Chinese).

Song, X.Y., Yao, Y.F., Wortley, A.H., Paudayal, K.N., Blackmore, S., 2012. Holocene vegetation and climate history at haligu on the Jade Dragon Snow mountain, yunnan, sw China. Clim. Change 113 (3–4), 841–866. https://doi.org/10.1007/s10584-011-0364-6.

Tang, L.Y., 1992. Vegetation and climate history at Menghai, Yunnan during the past 42000 years. Acta Micropalaeontol. Sin. 9, 433–455 (in Chinese).

Tang, Q., 2015. The subtropical vegetation of Southwestern China. Plant Distribution, Diversity and Ecology. Springer, Netherlands. https://doi.org/10.1007/978-94-017-9741-2.

Wang, M., Meng, H.W., Huang, L.P., Sun, Q.F., Zhang, H.C., Shen, C.M., 2020. Vegetation succession and forest fires over the past 13000 years in the catchment of Yangzonghai Lake, Yunnan. Quaternary Science 40 (1), 175–189. https://doi.org/10.11928/j.issn.1001-7410.2020.01.17 (in Chinese).

Wang, W.M., Li, C.H., Shu, J.W., Chen, W., 2019. Changes of vegetation in southern China. Sci. China Earth Sci. 62, 1316–1328. https://doi.org/10.1007/s11430-018-9364-9.

Xiao, X.Y., Haberle, S.G., Shen, J., Yang, X.D., Han, Y., Zhang, E.L., Wang, S.M., 2014. Latest Pleistocene and Holocene vegetation and climate history inferred from an alpine lacustrine record, northwestern Yunnan Province, southwestern China. Quat. Sci. Rev. 86, 35–48. https://doi.org/10.1016/j.quascirev.2013.12.023.

Xiao, X.Y., Haberle, S.G., Li, Y.L., Liu, E.F., Shen, J., Zhang, E.L., Yin, J.J., Wang, S.M., 2017. Evidence of Holocene climatic change and human impact in northwestern Yunnan Province: High-resolution pollen and charcoal records from Chenghai Lake, southwestern China. Holocene 28, 127–139. https://doi.org/10.1177/0959683617715692.

Xiao, X.Y., Shen, J., Haberle, S.G., Han, Y., Xue, B., Zhang, E.L., Wang, S.M., Tong, G.B., 2015. Vegetation, fire, and climate history during the last 18500 cal a BP in south-western Yunnan Province, China. J. Quat. Sci. 30, 859–869.

Xiao, X.Y., Shen, J., Wang, S.M., Xiao, H.F., Tong, G.B., 2007. Palynological evidence for vegetational and climatic changes from the HQ deep drilling core in Yunnan Province, China. Sci. China Earth Sci. 50, 1189–1201.

Xiao, X.Y., Yao, A., Hillman, A., Shen, J., Haberle, S.G., 2020. Province based on high-resolution pollen and charcoal records from Dianchi, southwestern China. Quat. Sci. Rev. 236, 106297. https://doi.org/10.1016/j.quascirev.2020.106297.

Xu, D.K., Lu, H.Y., Chu, G.Q., Shen, C.M., Sun, Q., Wu, J., Li, F.J., Song, B., Cui, A.N., Li, H., Wu, N.Q., 2023. Fast response of vegetation in East Asia to abrupt climatic events during the last deglaciation. In: Proc. Natl. Acad. Sci. U.S.A. Nexus, 2, pp. 1–10. https://doi.org/10.1093/pnasnexus/pgad061.

Xu, Q.H., Zhang, S.R., Gaillard, M., Li, M.Y., Cao, X.Y., Tian, F., Li, F.R., 2016. Studies of modern pollen assemblages for pollen dispersal- deposition- preservation process understanding and for pollen-based reconstructions of past vegetation, climate, and human impact: a review based on case studies in China. Quaternary Sci. Rev. The International Multidisciplinary Review Journal 149.

Yang, Q.S., Chen, W.Y., Xia, K., Zhou, Z.K., 2009. Climatic envelope of evergreen sclerophyll oaks and their present distribution in the eastern Himalaya and Hengduan Mountains. J. Systemat. Evol. 47, 183–190. https://doi.org/10.1111/j.1759-6831.2009.00020.x.

Yang, Y.P., Zhang, H.C., Chang, F.Q., Meng, H.W., Pan, A.D., Zheng, Z., Xiang, R., 2016. Vegetation and climate history inferred from a Qinghai Crater Lake pollen record

from Tengchong, southwestern China. Paleogeogr. Paleoclimatol. Paleoecol. 461, 1–11. https://doi.org/10.1016/j.palaeo.2016.07.017.
Yao, Y.F., Song, X.Y., Wortley, A.H., Wang, Y.F., Blackmore, S., Li, C.S., 2017. Pollen-based reconstruction of vegetational and climatic change over the past ~30 ka at Shudu Lake in the Hengduan Mountains of Yunnan, southwestern China. PLoS One 12 (2), e0171967. https://doi.org/10.1371/journal.pone.0171967.
Yao, Y.F., Song, X.Y., Wortley, A.H., Blackmore, S., Li, C.S., 2015. A 22 570-year record of vegetational and climatic change from wenhai lake in the hengduan mountains biodiversity hotspot, yunnan, southwest China. Biogeosciences 12 (5), 1525–1535. https://doi.org/10.5194/bg-12-1525-2015.
Yue, Y., Zheng, Z., Huang, K., Chevalier, M., Chase, B.M., Carré, M., Ledru, M.P., Cheddadi, R., 2012. A continuous record of vegetation and climate change over the past 50,000 years in the Fujian Province of eastern subtropical China. Palaeogeogr. Palaeoclimatol. Palaeoecol. 365–366, 115–123. https://doi.org/10.1016/j.palaeo.2012.09.018.
Yue, Y.F., He, L.Y., Zheng, Z., Chen, C., Wan, Q.C., Tang, Y.J., Huang, K.Y., 2024. Late Holocene vegetation succession, climate change, and fire history in western Guizhou. Quaternary Science 44, 112–127. https://doi.org/10.11928/i.issn.1001-7410.2024.01.09 (in Chinese).
Zeng, H., Wang, Z.Y., Chen, G.X., Ferguson, D.K., Wang, Y.F., Yao, Y.F., 2025. Asian summer monsoon and orographic winds change the pollen flow in the Hengduan Mountains, southwestern China. Geophys. Res. Lett. 52, e2024GL113697. https://doi.org/10.1029/2024GL113697.
Zhang, E., Wang, Y., Sun, W., Shen, J., 2016. Holocene Asian monsoon evolution revealed by a pollen record from an alpine lake on the southeastern margin of the Qinghai–Tibetan Plateau. China, Clim. Past 12, 415–427. https://doi.org/10.5194/cp-12-415-2016.
Zhang, J.X., Xu, H., Gosling, W.D., Lan, J.H., Dodson, J., Lu, F.Y., Yu, K.K., Sheng, E.G., Liu, B., 2019. Vegetation and climate evolution during the Last Glaciation at Tengchong in Yunnan Province, Southwest China. Paleogeogr. Paleoclimatol. Paleoecol. 514, 441–452. https://doi.org/10.1016/j.palaeo.2018.11.008.
Zhang, X.S., 2007. Vegetation Map of the People's Republic of China (1:1 000 000). Geology Press, Beijing.
Zhang, X., Huang, K.Y., Zheng, Z., Zhang, Y.Z., Wan, Q.C., Tian, L.P., 2018. Pollen morphology of Quercus sect. Ilex and its relevance for fossil pollen identification in southwest China. Grana 57, 401–414. https://doi.org/10.1080/00173134.2018.1480653.
Zhang, X., Zheng, Z., Huang, K.Y., Cheng, J., Cheddadi, R., Zhao, Y., Chen Liang, C., Yang, X.Q., Wan, Q.C., Tang, Y.J., Chen, C., Li, J., 2023. Quantification of Asian monsoon variability from 68 ka BP through pollen-based climate reconstruction. Sci. Bull. 68, 713–722. https://doi.org/10.1016/j.scib.2023.03.013.
Zhang, X., Zheng, Z., Huang, K.Y., Yang, X.Q., Tian, L.P., 2020. Sensitivity of altitudinal vegetation in southwest China to changes in the Indian summer monsoon during the past 68000 years. Quat. Sci. Rev. 239, 106359. https://doi.org/10.1016/j.quascirev.2020.106359.
Zhang, Y., Yang, Q., Yang, F., Zeng, Y.M., Zhang, Z.T., Yang, W.S., Zou, Z.N., Shi, L., Zheng, H.B., 2024. Environment evolution and human activities since MIS3 at Dayindong site, Yunnan. Quaternary Sci. 44 (1), 29–47. https://doi/10.11928/j.issn.1001-7410.2024.01.03 (in Chinese).
Zhao, Y., Yu, Z.C., Herzschuh, U., Yang, B., Zhao, H., Fang, K.Y., Li, H., Li, Q., 2014. Vegetation and climate change during Marine Isotope Stage 3 in China. Chin. Sci. Bull. 59, 4444–4455. https://doi.org/10.1007/s11434-014-0611-0.
Zheng, Z., Chen, C., Huang, K.Y., Zhang, X., Kershaw, P., Cheng, J., Li, J., Yue, Y.F., Wan, Q.C., Zhang, Y.Z., Tang, Y.J., Wang, M.Y., Xiao, X.Y., Cheddadi, R., 2023. Holocene warming and evergreen/deciduous forest replacement across eastern China. Quat. Sci. Rev. 307, 108057. https://doi.org/10.1016/j.quascirev.2023.108057.
Zheng, Z., Zhang, X., Man, M.L., Wei, J.H., Huang, K.Y., 2016. Review and data integration of pollen-based quantitative Paleoclimate reconstruction studies in China and adjacent areas. Quat. Sci. 36, 503–519 (in Chinese).
Zhou, G.Y., 1981. Discussion on the boundary of warm temperature deciduous broad-leaf forest region in China. Acta Phytoecologia et Geo botanica Sinica 5. https://doi.org/10.1021/ol3026507 (in Chinese).
Zhou, X.P., Tang, L.Y., Xia, H.X., Peng, T., Deng, X.Y., Hou, M.D., Zhu, D., Xie, R.L., Wang, B., Guo, Y., 2022. Bryoflora characteristics in Niangniang Mountain national wetland Park. Liupanshui. Guizhou. J. Trop. Subtrop. Bot. 30, 111–124 (in Chinese).
Zhou, Z.K., Yang, Q.S., Xia, K., 2007. Fossils of *Quercus* sect. *Heterobalanus* can help explain the uplift of the Himalayas. Chin. Sci. Bull. 52, 238–247. https://doi.org/10.1007/s11434-007-0005-7.

Ore Geology Reviews 186 (2025) 106855

Contents lists available at ScienceDirect

Ore Geology Reviews

journal homepage: www.elsevier.com/locate/oregeorev

Microbially-mediated supergene dissolution and oxidization of solid manganese carbonate in the Malkantu manganese ore deposit in West Kunlun, Northwest China

Ling-Nan Zhao [a], Qin Huang [a,*], Dao-Hui Pi [b], Yi Zhang [c], Da-Qing Ding [d], Sasmaz Ahmet [e]

[a] Guangxi Laboratory on the Study of Coral Reefs in the South China Sea, Coral Reef Research Center of China, School of Marine Sciences, Guangxi University, Nanning 530004, China
[b] State Key Laboratory of Geological Processes and Mineral Resources, School of Earth Resources, China University of Geosciences, Wuhan 430074, China
[c] State Key Laboratory of Coal Mine Disaster Dynamics and Control, School of Resources and Safety Engineering, Chongqing University, Chongqing 400044, China
[d] China Metallurgical Geology Bureau of Geological Prospecting Institute of Guangxi, Nanning 530022, China
[e] Department of Geological Engineering, Fırat University, Elazığ 23119, Turkey

ARTICLE INFO

Keywords:
Supergene manganese oxide
Microbial dissolution
Malkantu Mn deposit
Weathering of manganese carbonate
West Kunlun

ABSTRACT

Supergenic manganese (Mn) oxide ores with high Mn concentrations, which are oxidized from sedimentary Mn carbonate ores, represent critical Mn resources and primary targets for industrial exploitation. Previous studies have suggested that most supergene Mn oxides are formed under warm and humid climatic conditions. However, the contribution of microbes to the formation of supergene Mn oxide deposits may have been significantly underestimated. In particular, under arid and cold conditions, where chemical weathering rates are extremely low, microbial processes may dominate, leading to Mn mineral alteration. In this study, we conducted a comprehensive morphological and mineralogical analysis of supergene Mn oxides in the Malkantu Mn deposit using advanced analytical methodologies, including X-ray diffraction, micro-Raman spectroscopy, scanning electron microscopy, and transmission electron microscopy. Our results revealed a range of microbially induced structures, including tubular borings, biofilm-like coatings, hyphae-like filaments, and nano-spherulite aggregations. These features provide compelling evidence for biologically mediated dissolution of Mn carbonates and the subsequent precipitation of secondary Mn oxides. The Mn carbonates, initially formed during the Late Carboniferous, were subsequently buried beneath the Permian volcanic-sedimentary sequences. The Cenozoic tectonic uplift exposed the Mn-rich layers to surface conditions characterized by arid climates, intense solar radiation, and minimal vegetation cover. Despite the seemingly inhospitable environment, microbial activity persisted, thus significantly influencing the alteration of Mn-bearing minerals. Our findings suggest a novel model for supergene Mn enrichment dominated by microbial processes rather than solely by climatic factors, offering new insights into supergene Mn ore genesis in arid, cold, and high-altitude settings.

1. Introduction

Manganese (Mn) is an essential metal with a wide-range of applications, particularly in battery and steel manufacturing (Zhang et al., 2022). Globally, sedimentary Mn ore deposits occur in a variety of sedimentary sequences, such as banded iron formations, carbonates, sandstone-mudstone, and black shale series, and have historically served as critical Mn sources (Force and Cannon, 1988; Fan et al., 1992; Calvert and Pedersen, 1996; Roy, 2006; Polgári et al., 2012; Beukes et al., 2016; Johnson et al., 2016; Yu et al., 2016, 2019, 2021a, 2021b; Sasmaz et al., 2020, 2021; Chen et al., 2023, 2022a,b; Dong et al., 2022, 2023). The prevailing understanding suggests that Mn initially precipitates as precursor oxides within oxic sediments, which subsequently undergo microbial reduction by heterotrophic microbes utilizing organic matter or methane (CH_4) as electron donors, resulting in the formation of Mn carbonates during early diagenesis (Calvert and Pedersen, 1996; Huang et al., 2023; Johnson et al., 2016; Zhang et al., 2020). In addition, several studies have proposed that Mn carbonates can form directly within anoxic water columns (Ai et al., 2023; Chen et al., 2023, 2022a,b; Gao et al., 2021). Thus, Mn carbonates, such as rhodochrosite,

* Corresponding author.
E-mail address: qinhuang@gxu.edu.cn (Q. Huang).

https://doi.org/10.1016/j.oregeorev.2025.106855
Received 30 April 2025; Received in revised form 22 August 2025; Accepted 23 August 2025
Available online 26 August 2025
0169-1368/© 2025 The Author(s). Published by Elsevier B.V. This is an open access article under the CC BY-NC license (http://creativecommons.org/licenses/by-nc/4.0/).

kutnohorite, and Mn-bearing calcite, typically dominate sedimentary Mn ore deposits (Johnson et al., 2016; Maynard, 2010; Yan et al., 2022). While primary Mn oxide deposits are rarely preserved, most sedimentary Mn deposits exhibit near-surface supergene Mn oxide zones where localized Mn enrichment can be economically significant (Beukes et al., 2016; Carmichael et al., 2017; Kuleshov, 2017a; Maynard, 2010; Tsikos et al., 2003; Vafeas et al., 2018). During weathering and soil formation, near-surface Mn carbonate ores commonly undergo extensive mineralogical alterations, leading to leaching of Mn carbonates and subsequent oxidation (Nimfopoulos et al., 1997). The presence of supergene zones in sedimentary Mn deposits profoundly influences their global economic viability because Mn oxides within these zones exhibit high Mn concentrations and are amenable to simplified mining processes (Beukes et al., 2016; Kuleshov, 2017b).

The supergene processes involving the leaching of Mn carbonates and subsequent oxidation of dissolved Mn^{2+} are typically considered products of warm and humid climatic conditions (Pack et al., 2000; Pharoe et al., 2020; Zhao et al., 2022). Therefore, supergene Mn oxides are often regarded as valuable proxies for dating tectonic and weathered events (Deng and Li, 2013; Deng et al., 2016; Gutzmer, 2012; Li et al., 2007; Poulton et al., 2015; Sethumadhav et al., 2010; Vafeas et al., 2018). However, many studies have ignored the microbial contribution during supergene or weathering processes. Indeed, the majority of natural Mn oxides are believed to form through direct or indirect microbial Mn^{2+} oxidation, as biotic pathways are significantly faster than abiotic ones (Learman et al., 2011; Romano et al., 2017; Tebo et al., 2005; Zhang et al., 2018). The ubiquity of Mn-oxidizing microorganisms, including bacteria and fungi, in terrestrial and marine ecosystems highlights their potential role in supergene processes (Tebo et al., 2005). The microbial oxidation of dissolved Mn^{2+} has been extensively reported in many studies (Geszvain and Tebo Bradley, 2010; Toyoda and Tebo, 2013), and experimental observations have demonstrated the ability of bacteria and fungi to facilitate the dissolution and surface modification of natural solid Mn carbonates (Tang et al., 2013; Wang et al., 2015). In arid and cold high-altitude environments, where chemical weathering rates are typically slow, the role of microbial processes in facilitating mineral transformation may be particularly pronounced (DiGregorio, 2005; Kuhlman et al., 2008; Lingappa et al., 2021; Wang et al., 2011). However, the evidence of microbially mediated supergene Mn mineralization under low chemical weathering conditions remains limited.

In recent years, the Malkansu Mn metallogenic zone, located within the West Kunlun orogenic belt in Northwest China, has emerged as a significant geological discovery (Zhang et al., 2020). This Mn metallogenic zone hosts a series of moderate to giant-sized sedimentary Mn ore deposits, including Ortokarnash, Muhu, and Malkantu. The Mn carbonate ores in this region exhibit extremely high grades, with an average Mn content exceeding 37 %, ranking among the richest Mn carbonate deposits documented in China to date (Gao et al., 2018). The Malkansu Mn metallogenic zone, located in an arid high-altitude environment, is an ideal natural laboratory for investigating these processes. Previous studies have identified Ca-bearing rhodochrosite as the dominant Mn mineral phase within the Malkansu Mn metallogenic zone (Zhang et al., 2020). Additionally, the near-surface environments within this zone contain abundant supergene Mn oxide ores, which are considered economically significant. In this study, we present mineralogical and microstructural evidence suggesting that microorganisms contribute significantly to the dissolution of solid Mn carbonate and the subsequent formation of Mn oxide phases during supergene weathering. Our findings highlight a novel biological pathway for Mn enrichment in both arid and cold environments.

2. Geological setting

Previous studies have provided a comprehensive description of the regional geological deposits of the Malkansu Mn carbonate metallogenic zone (Dong et al., 2020, 2023; Huang et al., 2022; Zhang et al., 2020; Dong et al., 2025). This section provides an overview of this study. The Malkansu Mn metallogenic belt is located at the junction of the Tarim Block and the West Kunlun orogenic belt at the northeastern edge of the Pamirs (Gao et al., 2018) (Fig. 1B). A giant Mn deposit (Ortokarnsh), two medium Mn deposits (Muhu and Malkantu), and several smaller zones of Mn mineralization have been found in the Malkansu Mn metallogenic belt (Dong et al., 2020, 2023; Zhang et al., 2020; Dong et al., 2025) (Fig. 1A). The Mn metallogenic belt preserves the Lower Carboniferous to Upper Permian strata and is controlled by the main west-to east-trending Malkansu compound anticline and a series of west-to east-trending regional faults (Zhang et al., 2020). During the late Paleozoic to early Mesozoic, the Paleo-Tethys Ocean began to subduct beneath the southern margin of the Tarim Plate and formed a back-arc basin in the Malkansu region (Zhang et al., 2018). A series of platform facies including conglomerate limestone, sandy limestone, and organic-rich marlstone were deposited in this basin. Subsequently, the residual basin closed and was covered by Permian volcanic and volcaniclastic rocks (Zhang et al., 2018). Since the Late Cenozoic, the western Kunlun region has experienced intense uplift, forming towering mountains that have been subjected to sustained weathering and erosion (Pan, 1990; Xiao and Wang, 1998). The progressive uplift of the Western Kunlun region led to the development of an arid, cold, sparsely vegetated plateau landscape.

The Early Carboniferous Wuluate Formation is composed of basic and acidic volcanic and volcaniclastic rocks with a small amount of carbonate rocks covering the eastern portion of the study area (Zhang et al., 2020). The Upper Carboniferous Kalaatehe Formation unconformably overlies the Wuluate Formation. The Kalaatehe Formation is an Mn-bearing stratum in which the first member consists of lenticular conglomerate and layered bioclastic limestones, the second member is composed of sandy limestone, and the third member includes organic-rich marlstone with two or three intervals of Mn ore bodies (Zhang et al., 2020). The rock assemblages of the Upper Carboniferous Kalaatehe Formation are indicative of transgression-regression. Lithological evidence, including dark grey to black coloration, well-developed horizontal bedding, and organic-rich marlstone of the third member, suggests a stable and low-energy depositional environment (Zhang et al., 2020). The Lower Permian Malkanquekusaishan Formation, which comprises a gray-purple conglomerate andesitic tuff with minor andesite, unconformably overlies the Kalaatehe Formation. The Malkantu Mn carbonate deposit is located in the eastern part of the Malkansu area, where the mining zone exhibits an approximately west-east orientation (Gao et al., 2018). Three layers of Mn ore are hosted in the organic-rich marlstone of the third member that consists of the Kalaatehe Formation in the Malkantu Mn deposit (Gao et al., 2018; Dong et al., 2025) (Fig. 2). The Malkantu Mn carbonate deposit is estimated to contain 30×10^6 tons of Mn ore and mainly consists of three laminated ore beds (Mn-1, Mn-2 and Mn-3) (Fig. 3), with Mn contents ranging from 17.5 to 41.3 wt%.

3. Samples and methods

Supergenic Mn ores were obtained by sampling two open profiles of Mn ore bodies (Fig. 3). Four samples were collected: two oxidized Mn carbonate ore samples from the Mn-1 open profile and two from the Mn-2 open profile. The Mn ore samples exhibited varying degrees of supergene weathering.

Thin sections of the re-oxidized Mn carbonate ores were systematically examined under a polarizing light microscope, and further analysis of the Mn ore thin-section samples was conducted using field-emission scanning electron microscopy (FE-SEM). Prior to FE-SEM observations, thin sections were coated with several nanometers of platinum (Pt) or gold (Au). These analyses were conducted at the State Key Laboratory of Geological Processes and Mineral Resources, China University of Geosciences, Wuhan, China, using a Zeiss Sigma 300 FE-SEM under specified

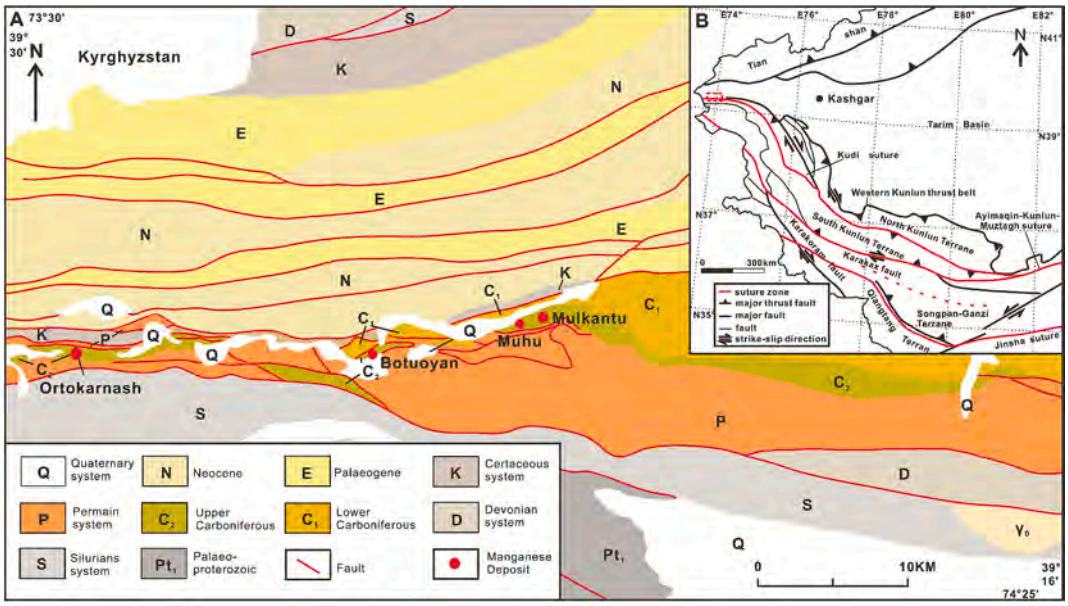


Fig. 1. A. Geological map of the Malkansu Mn metallogenic belt, showing the location of the Malkantu Mn carbonate deposit. B. Simplified tectonic units of the West Kunlun orogenic belt. Modified after Zhang et al. (2020).

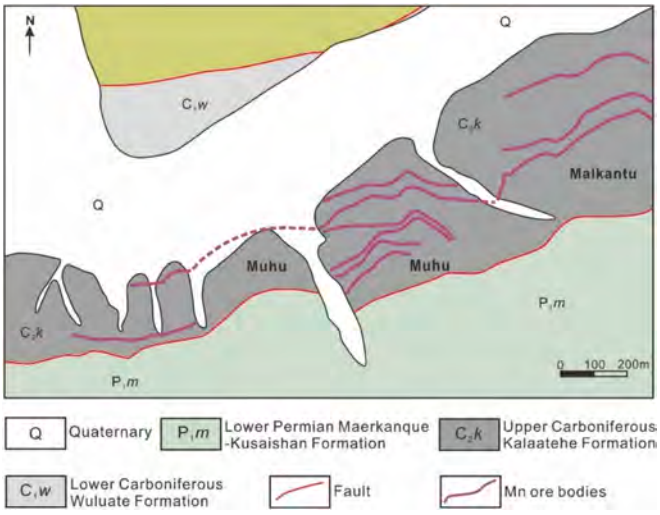


Fig. 2. Simplified geological map of the Malkantu manganese ore deposit. (modified from Dong et al., 2025).

operational conditions: a sample-to-detector distance of 8 mm, applied voltages of either 5 kV or 20 kV, and a beam current of 10nA.

For powder samples of Mn ores, X-ray diffraction (XRD) analysis was conducted using a Bruker D8 ADVANCE XRD instrument, covering a 2θ range of 5-75° with a count time of 1° min^{-1}. XRD analysis was carried out at the State Key Laboratory of Geological Processes and Mineral Resources, China University of Geosciences, Wuhan, China. Data processing and mineral identification were performed using Jade 6.0.

Raman spectroscopy was employed to identify the micro-minerals, and high-resolution micro-Raman analysis was conducted using a WITec300 Confocal Raman Imaging system at the State Key Laboratory of Biogeology and Environmental Geology, China University of Geosciences, Wuhan, China. All Raman spectra were processing used the WITec Project Five Plus software.

Transmission electron microscope (TEM) analyses were conducted using the Thermo Fisher Scientific FEI Talos F200× electron microscope, equipped with two windowless EDS detectors, at the Faculty of Materials Science and Chemistry, China University of Geosciences, Wuhan, China. EDS spectra and elemental mappings were obtained using a STEM system with an operating voltage of 200 kV.

4. Result

Polarizing light microscopy revealed a heterogeneous oxidation profile within the Mn carbonate ores, categorized into three distinct grades: mild, moderate, and severe alteration zones. In the mildly altered zone, the primary microstructures of Mn carbonate minerals remained notably intact. In the moderate alteration zone, the preservation of spherical and rod-shaped Mn carbonate grains was observed, while the interstitial spaces are filled with Mn oxides (Fig. 4A). In severe alteration zones, Mn carbonate minerals were completely replaced by Mn oxides and the formation of numerous dissolution holes ranged from 1 to 3 μm (Fig. 4B).

XRD analysis identified rhodochrosite, pyrolusite, todorokite, and quartz as the primary constituents of the supergene Mn ores (Fig. 4C). Micro-Raman spectroscopy analysis revealed the prevalence of todorokite in the severely oxidized regions (Fig. 4D). SEM revealed that spherical Mn carbonate and calcite cement were retained in the mildly oxidated area (Fig. 5A). Transitioning to regions of moderate oxidation, the calcite cement was replaced by Mn oxides, coinciding with the formation of a Mn oxide shell enveloping the spherical Mn carbonate (Fig. 5B-C). Residual Mn carbonate exhibited an array of eroded pits on its surfaces, predominantly irregular in shape and typically measuring less than 1 μm in diameter (Fig. 5D-F). Interstitially, micro-Mn oxide nodules, morphologically similar to modern oceanic ferromanganese nodules, were observed among the Mn carbonate grains, showing concentric layering (Fig. 5E-F). Within severely oxidized area, Mn carbonates were fully replaced by micro-Mn oxide spherulites and nodules (Fig. 6A-B). Numerous spherical Mn oxide coatings were observed, enveloping the micro-Mn oxide grains. Interstices between the Mn oxide grains and coatings were evident, along with the proliferation of micro-Mn oxide nodules (Fig. 6C-D).

Cross-sectional observations revealed concentric layering in micro-Mn oxide nodules, which were devoid of a central core and had irregular widths ranging down to several nanometers (Fig. 6E and F). The presence of network-like and fibrous structures interspersed between micro-Mn oxide nodules resembled fungal hyphae and biofilm

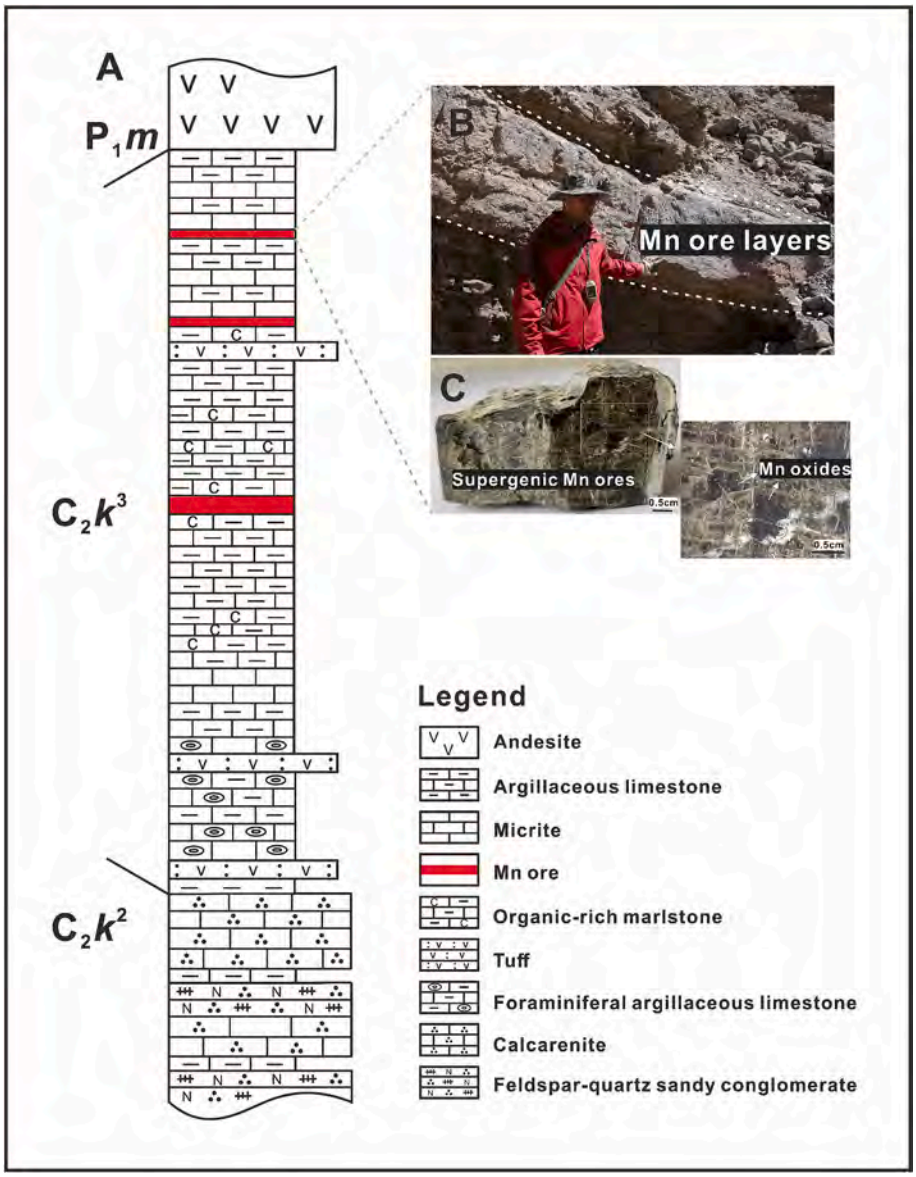


Fig. 3. A. Stratigraphic column of the sampling location: Carboniferous Kalaatehe Formation. B. Open Mn ore layers. C. Supergene Mn ores.

microstructures (Fig. 7A, D, and E). Moreover, the adhesion of numerous nano-spherulites with diameters ranging from 50 to 200 nm onto the surfaces of micro-Mn oxide and biofilm surfaces between nodules was observed (Fig. 7B). Some nano-spherulites exhibited elongated tail-like extensions akin to mucous substances adhering to their surfaces (Fig. 7F and G). The cumulative aggregation of these nano-spherulites resulted in the formation of thin concentric layers of Mn oxide (Fig. 7C). Furthermore, transmission electron microscopy analysis indicated that the nanospheres primarily comprised Mn, oxygen, and calcium (Fig. 7H–K). Thus, we speculated that these nano-spherulites predominantly consisted of todorokite.

5. Discussion

Since the Phanerozoic, the Western Kunlun Orogenic Belt has undergone three major tectonic events (Pan, 1990; Xiao and Wang, 1998). The first event occurred during the Middle to Late Early Paleozoic, when the subduction of the Proto-Tethys Ocean beneath the Kunlun Block led to the eventual closure of the ocean and the formation of the Kudi suture zone and the Western Kunlun Orogen. The second event occurred at the end of the Late Paleozoic and involved the northward subduction of the Paleo-Tethys Ocean beneath the Tarim Block. This process gave rise to a suite of intermediate-to-acidic island arc volcanic rocks in the foreland region of northern Western Kunlun, while a back-arc basin developed in the northern Malkansu region (Gao et al., 2018; Zhang et al., 2018). The Malkantu Mn carbonate deposit formed within this back-arc basin (Gao et al., 2018; Zhang et al., 2018). The third tectonic event began in the Late Cenozoic, during which the Western Kunlun region underwent rapid uplift, forming towering mountains that were subjected to intense weathering and erosion (Pan, 1990; Xiao and Wang, 1998). Previous studies have reported that large-scale tectonic uplift events are among the primary driving forces behind the development of extensive weathering crusts (Deng et al., 2016; Li et al., 2007). In the Malkantu Mn deposit, the Late Cenozoic uplift of the Western Kunlun region likely provided favorable conditions for the onset of supergene oxidation. This tectonic activity not only exhumed the Mn ore bodies from deep subsurface levels to near-surface or surface settings but also generated abundant fractures within the ore zone due to enhanced tectonic stress, thereby increasing the permeability and facilitating fluid access and oxidative alteration. Although the precise timing of the Mn oxide formation remains unconstrained, the supergene oxidation process likely occurred after the Cenozoic uplift event. Further geochronological

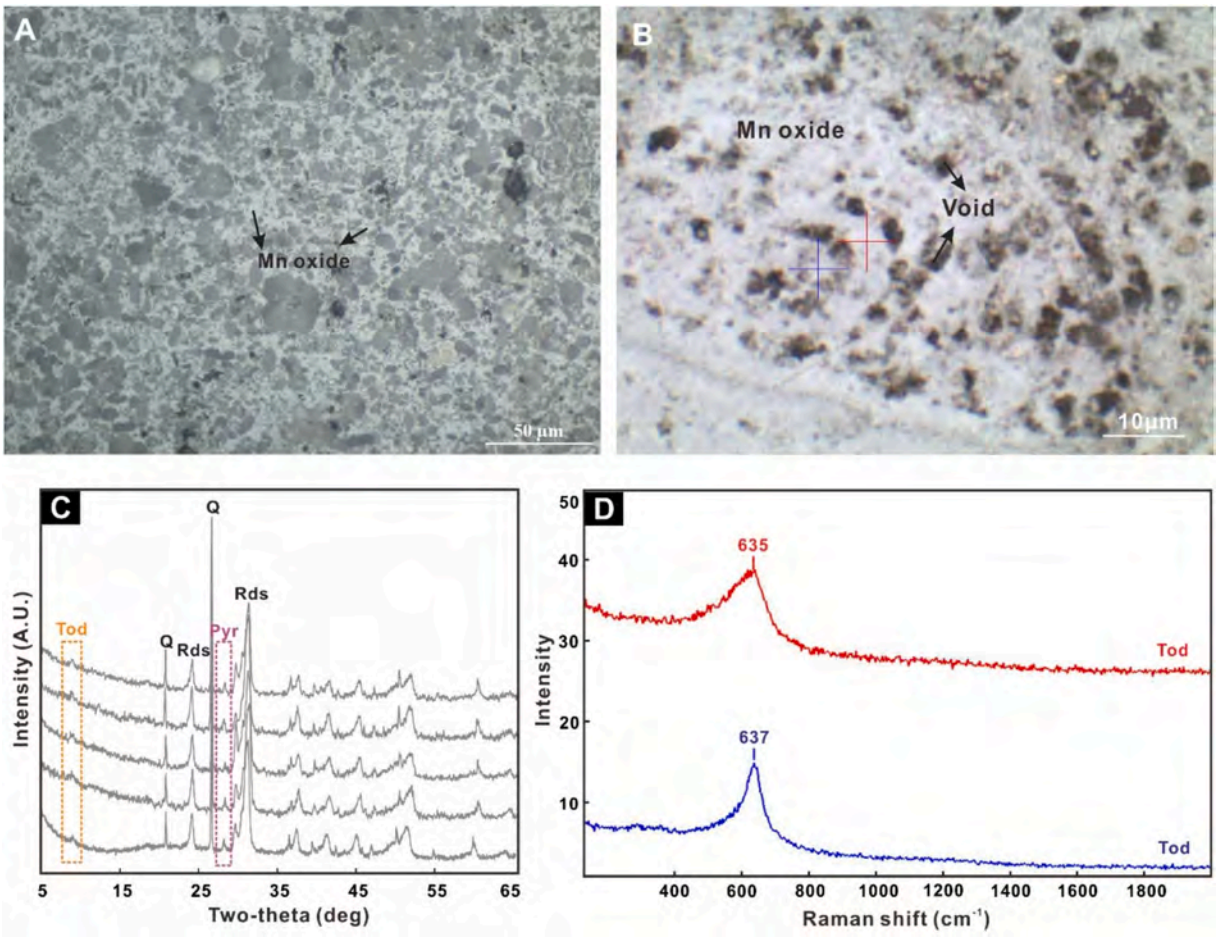


Fig. 4. . Polarizing microscope image (reflected light) of supergene Mn ore samples. A. Moderate oxidation area: Mn oxides is filling in pore of calcite cement. B. Severe oxidation area: Mn carbonate minerals fully replaced by Mn oxides, exhibiting numerous dissolution holes. C. XRD patterns of the supergene Mn ore. D. Micro-Raman patterns of the supergene Mn oxides in severe area. Q: Quartz; Rds: Rhodochrosite; Tod: Todorokite; Pyr: Pyrolusite.

constraints are required to validate this hypothesis.

The weathering of rocks encompasses a series of physical, chemical, and biological processes, with a notable emphasis on the vital contributions of organisms, particularly microorganisms, during the initial phases of rock weathering (Chen et al., 2022b). Microbial weathering of rock is a widely observed geological phenomenon on the Earth's surface, indicating the growth, proliferation, and metabolic byproducts of microorganisms that contribute to mineral dissolution, notably affecting mineral dissolution rates (Zhu and Li, 2004). The microorganisms capable of rock weathering primarily comprises bacteria, fungi, lichens, and algae. Carbonate minerals are abundantly distributed on Earth's surface and display significant susceptibility to microbial weathering (Lian et al., 2006). Biological weathering of carbonate minerals is evident in two distinct forms. First, microbial control involves microorganisms attaching to carbonate mineral surfaces, producing acidic substances that erode these minerals and forming dissolution holes with diameters ranging from 1 to 100 μm on these mineral surfaces (Fluegel, 2004; Lian et al., 2006; Neumann et al., 2002). Microorganisms with dissolution capabilities including bacteria, fungi, mosses, lichens, small animals, and plants (Gray and Engel, 2013; Hose et al., 2000; Lian et al., 2006). The nutrients in carbonate dissolution holes not only serve as energy sources for microbial metabolism but also significantly increase the available surface area for the chemical dissolution of carbonate (Gadd, 1999, 2007; Sterflinger, 2000; Viles, 1987). In addition, fungal hyphae can penetrate carbonate fissures, thereby accelerating dissolution (Breitenbach et al., 2022; van Breemen et al., 2000). Another aspect is microbially induced weathering, which is primarily characterized by the release of organic acids (e.g., formic acid, acetic acid, and vinegar) and CO_2 during microbial metabolism, effectively dissolving carbonate minerals (Smith and Ferry, 2000). Recent experimental studies have shown that Mn-oxidizers (bacteria and fungi) and their secretion of extracellular polymeric substances (EPS) facilitate the dissolution of solid rhodochrosite (Tang et al., 2013; Wang and Pan, 2014; Wang et al., 2015). In our samples, a substantial number of eroded pits were detected on the surfaces of Mn carbonate grains within the moderately oxidized zone, exhibiting irregular shapes with an approximate diameter of 1 μm, consistent with the morphology of microbial cells (Fig. 4D–F). Moreover, notable hole formations were observed in the Mn oxides within areas of severe oxidation, which are likely attributable to microbial dissolution processes (Fig. 4B). Given the weaker acid resistance of calcite than of Mn carbonate minerals, the initial calcite cement within the Mn carbonate preferentially undergoes dissolution. Microorganisms demonstrate a selective disruptive effect on minerals with varied crystal structures, showing an accelerated rate of mineral destruction in specimens with weaker weathering resistance to microorganisms (Lian, 1998; Lian et al., 2002, 2005). This phenomenon correlates with the presence of Mn oxides dispersed in a cement-like form among the Mn carbonate grains within the moderately oxidized zone. These findings indicate the active involvement of microorganisms in the weathering processes affecting Mn carbonate ores, thereby accelerating the weathering kinetics. Thus, we hypothesized that the weathering processes of Mn carbonate ores, especially when exposed near the surface, are significantly influenced by climatic conditions and microbial weathering processes.

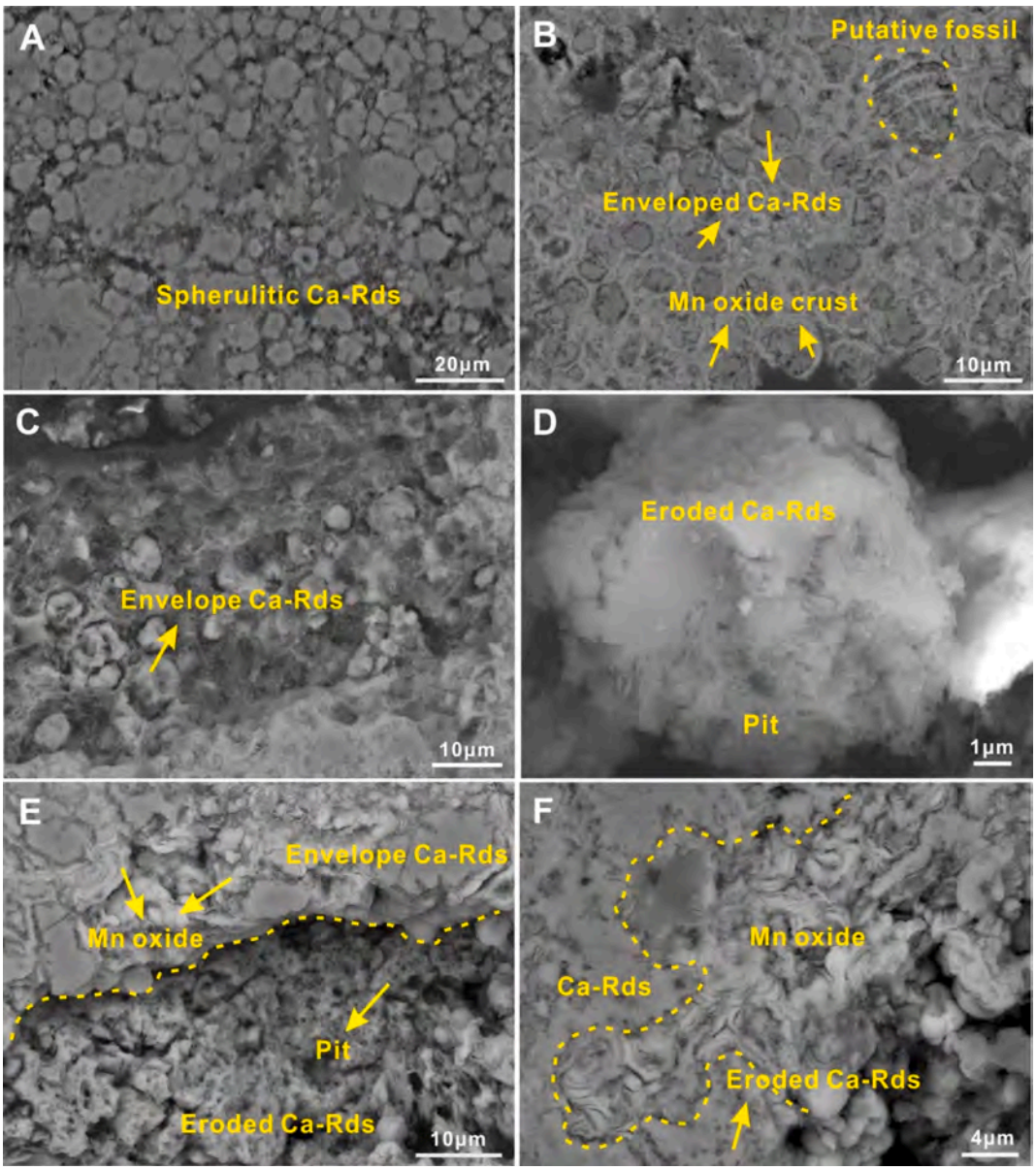


Fig. 5. Scanning electron microscope (SEM) images of moderate oxidation area in supergene Mn ores under BSE-SE2. A. Primary spherulitic Mn carbonate. B-C. Calcite cement is replaced by Mn oxides and Mn oxide shell enveloping spherical Mn carbonate. D-E. A large of eroded pit occurs in the surface Mn carbonate. F. Manganese oxide nodules are distributed among Mn carbonate grains. Rds: Rhodochrosite; Ca-Rds: Calcium-bearing rhodochrosite.

Microorganisms are ubiquitous in marine and terrestrial environments, including aphotic deep-sea environments (Bargar et al., 2009; Hansel, 2017; Lingappa et al., 2021; Tebo et al., 2005). Most of these microbes lack conducive conditions for fossilization, with only specific metabolic byproducts of certain bacteria preserved under particular environmental conditions, leading to the formation of microbial fossils (Nayak et al., 2013; Nealson and Tebo, 1980). Notably, iron-manganese oxidizers possess unique capability for preservation (Nealson and Tebo, 1980). Consequently, well-preserved bacterial microfossils found in Mn oxide sediments serve as crucial evidence of their biological origins (Jiang et al., 2017, 2019; Reykhard and Shulga, 2019; Rossi et al., 2010; Wang and Müller, 2009; Wang et al., 2009, 2011). However, the presence of microfossils does not necessarily imply direct microbial involvement in Mn oxidation processes (Bian et al., 1997; Huang et al., 2022; Rossi et al., 2010). Bian et al. (1997) classified the microfossil structures within Fe-Mn nodules into three microorganism categories: exogenous, parasitic, and constructive. Among these, only constructive microorganisms actively participate in Mn oxidation, whereas the former two play minimal roles (Jiang et al., 2019). Common examples of exogenous microorganisms in such environments include radiolarians and foraminifera (Nayak et al., 2013; Templeton et al., 2009). Previous studies have identified two types of constructive microorganisms, clumpy and filamentous, both belonging to primitive algal families in the East Pacific ferromanganese nodule area (Hu et al., 2000). Rossi et al. (2010) discovered abundant and well-preserved microbial fossils in ferromanganese crusts of cave environments. Our observations revealed the significant presence of enveloped spherical structures in the areas of severe oxidation in our samples (Fig. 6A and B), resembling the Fe-Mn-encrusted microfossils described by Levett et al. (2020) and Baele et al. (2008), whose mineralogical preservation offers strong support for a microbial origin. However, the lack of biogeochemical data for these structures presents a challenge for accurately assessing their reliability as microfossils. Despite these challenges, our findings on Mn oxide nodules highlighted a large number of biological structures, including fibrous materials that similar to fungal hyphae and mesh-like biofilms (Fig. 7D–G). These biological structures offer compelling evidence

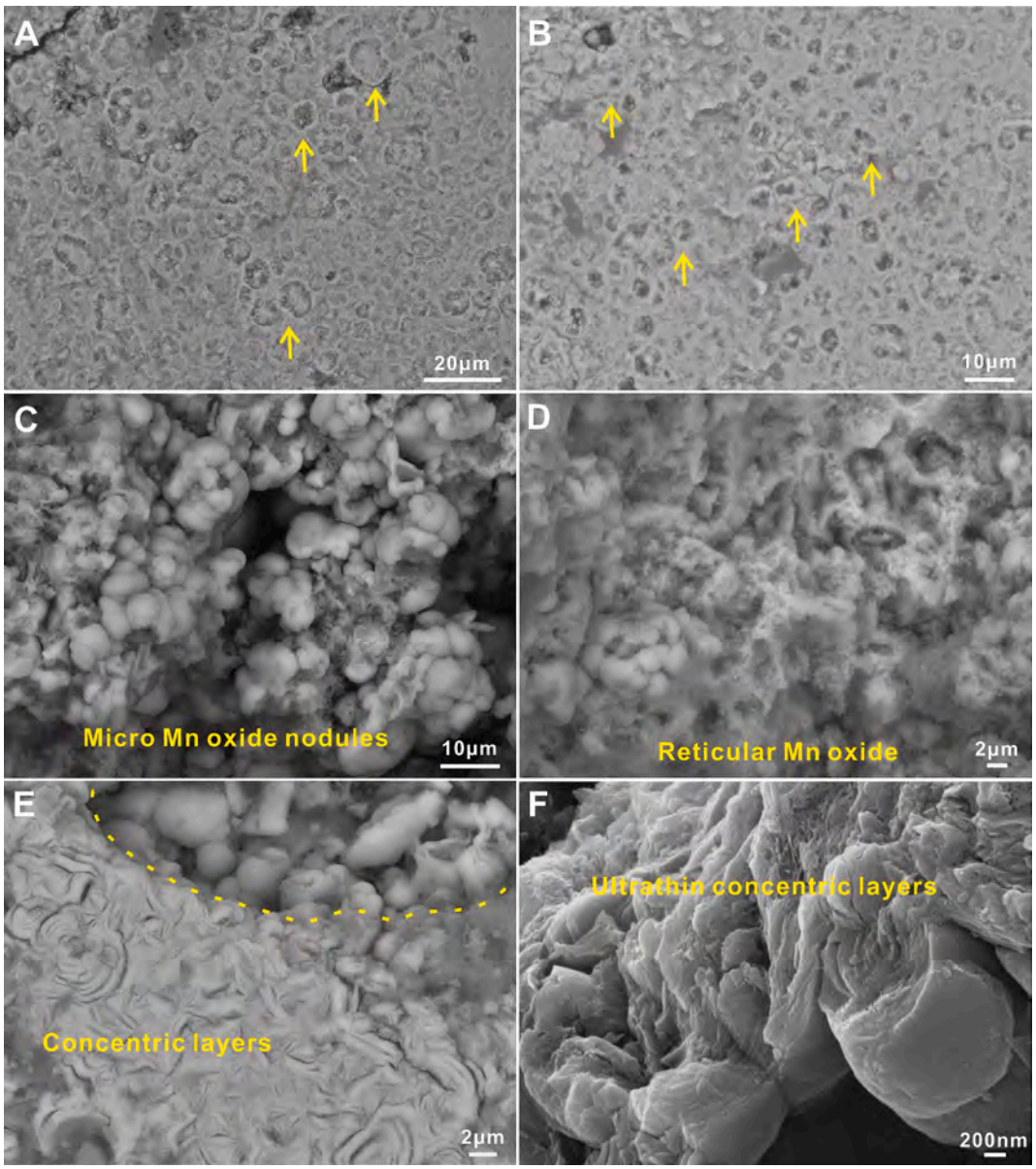


Fig. 6. Scanning electron microscope (SEM) images of severe oxidation area in supergene Mn ores under BSE-SE2. A-B. Spherical Mn oxide shells are enveloping micro-Mn oxide grains within. C. Micro-Mn oxide nodules. D. Reticular Mn oxides. E. Concentric layers of micro-Mn oxide nodules are similar with oceanic Fe-Mn nodules. F. Ultrathin concentric layers of micro-Mn oxide nodules.

supporting the microbial origin of Mn oxides.

The interpretation of nano-todorokite spherulites as ultra microfossils presents a plausible hypothesis (Nayak et al., 2013; Perri et al., 2018) (Fig. 7B). However, their heterogeneous sizes challenge this view, given the minor variations in the size of ultra microbial cell (Perri et al., 2018). Nano-todorokite spherulites typically adhere to the surfaces of biofilms, fibrous substrates, and Mn nodules, suggesting their potential role as initial byproducts of microbial Mn oxidation (Feng et al., 2010). Experimental evidence also supports the biological origin of nano-todorokite spherulites (Feng et al., 2010). Analysis of Mn nodule cross-sections revealed their coreless nature, contrasting sharply with modern oceanic ferromanganese nodules characterized by biogenic silica and calcite cores. Previous studies have postulated that biogenic silica and calcite debris act as nucleation sites, facilitating the precipitation of Mn oxide (Nayak et al., 2013; Wang et al., 2009, 2011). Our observations showed that the concentric layers of Mn oxide nodules were composed of nano-spherulites layers (Fig. 7C), indicating a possible primary nucleation role of these initially biogenic nano-todorokite spherulites. Microbial Mn oxidizers facilitate the oxidation of Mn^{2+} in the environment, resulting in the formation of nano-todorokite spherulites. These spherulites proliferate on biofilms or fibrous fungal hyphae, gradually aggregating to form larger spherulites that act as nucleation sites, attracting smaller spherulites and ultimately culminating in Mn oxide nodules with concentric layer arrangements. The presence of trailing mucilage around nano todorokite spherulites suggests inherent aggregation capabilities. In summary, our findings support the microbial oxidation origin of Mn oxide nodules.

Notably numerous spherulitic Mn carbonates were enveloped by Mn oxide coatings within the intermediate oxidation zone (Fig. 5B). The absence of eroded pits on the surfaces of Mn carbonate bearing Mn oxide coatings implied a potential passivation effect, impeding further dissolution and oxidation of Mn carbonate. The absence of corrosive eroded pits on the Mn carbonate grains encased in the Mn oxide coatings implied a potential passivation effect that impeded further oxidation. This phenomenon may be attributed to early-formed Mn oxide shells acting as physical barriers, microenvironmental variations in redox

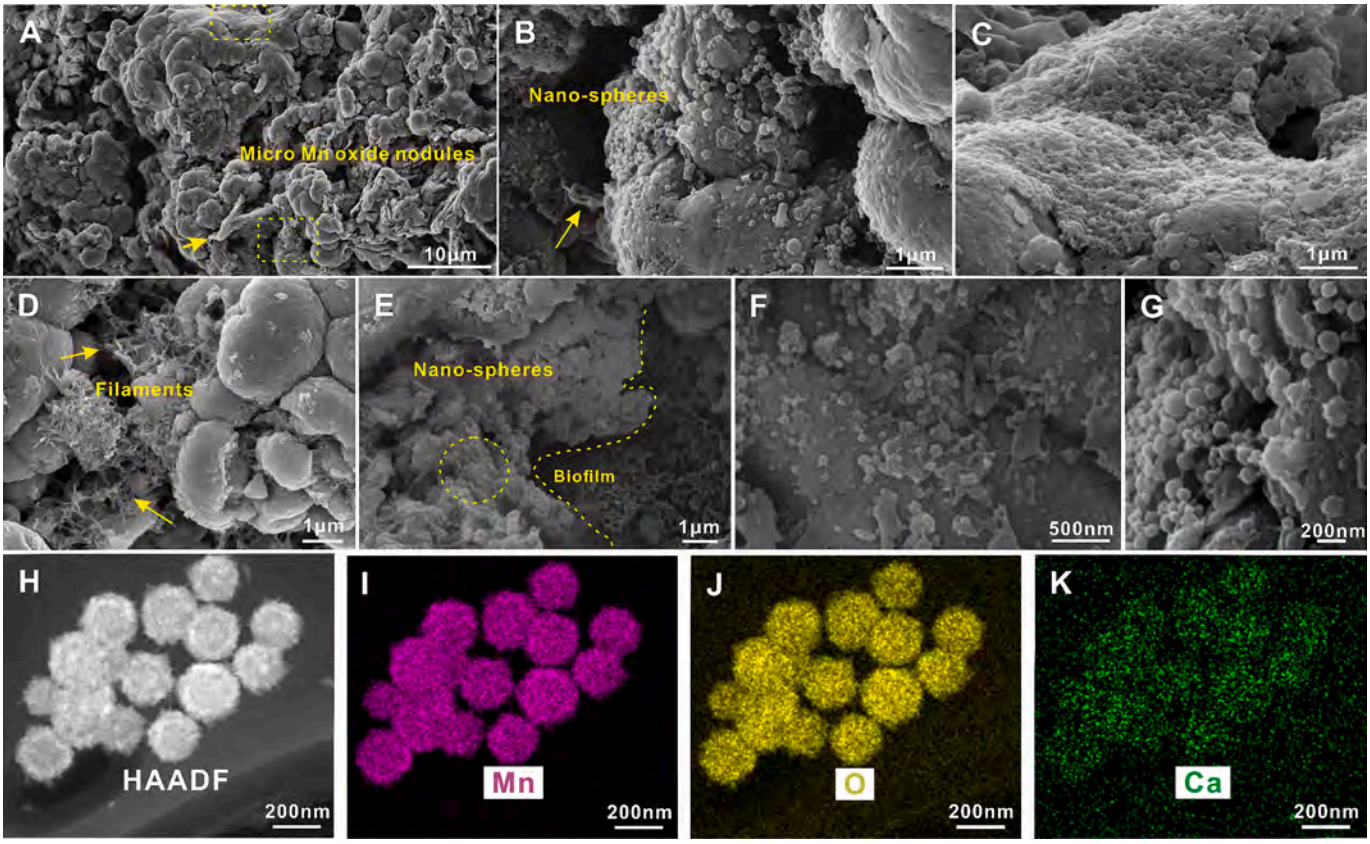


Fig. 7. Scanning electron microscope (SEM) and Transmission Electron Microscopy (TEM) images of severe oxidation area in supergene Mn ores under SE2 and HAADF. A. Micro-Mn oxide nodules. B. Numerous nanospheres with diameters ranging from 50 to 200 nm are attached to the surfaces of micro-Mn oxide nodules. C. Aggregation of abundant nanospheres generate thin concentric layers of micro-Mn oxide nodules. D-E. Network-like and fibrous materials interspersed between micro-Mn oxide nodules evokes resemblance to fungal hyphae and biofilm structures. F-G. Nanospheres exhibit elongated tail-like extensions. H-K. Elemental composition of nanospheres under the HAADF.

conditions that suppressed microbial oxidation, or restricted diffusion of oxidants through compact Mn oxide rims. However, the origin and effectiveness of such passivating rims remain speculative and require further experimental investigation. Broadly, microorganisms assume a pivotal role in driving the supergene weathering oxidation of near-surface Mn carbonate deposits. Our study revealed that microorganisms not only facilitate the dissolution of Mn carbonate but also catalyzed the in-situ oxidation of released Mn^{2+} in near-surface environments, thereby substantially enhancing the efficiency of supergene weathering oxidation processes. While previous studies have underscored the importance of warm and humid climates as prerequisites for supergene weathering and oxidation (Deng and Li, 2013; Deng et al., 2016; Li et al., 2007), recent findings have highlighted the persistence of abundant microorganisms capable of oxidizing Mn even in cold and arid settings (Dietzel et al., 2008; Whitley et al., 2017). Despite minimal rainfall, intense solar radiation, and absence of vegetation, microbial communities appear to mediate significant mineralogical alterations (Lingappa et al., 2021). In our study, although the observed features of microbial mediation were compelling, the relative contribution of biotic versus abiotic processes to overall oxidation remained difficult to determine. While the presence of tubular borings, biofilm-like structures, and nano-spherulite aggregates strongly suggests that microbial activity was a major mechanism, abiotic oxidation, such as O_2 diffusion, UV-induced redox reactions, or fluid-mediated weathering, may have also played a secondary role. Therefore, we tentatively propose that microbial oxidation holds significant potential in cold, arid, and high-altitude environments. However, the contribution of abiotic oxidation cannot be completely excluded. The Malkantu Mn deposit provides a compelling example of microbial resilience and mineralogical alterations in high-altitude, arid, and cold environments. These findings highlight the potential for biologically driven weathering and ore enrichment, even under seemingly inhospitable surface conditions.

6. Conclusion

This study revealed that microbial processes play a fundamental role in the supergene weathering and oxidation of Mn carbonate ores in the Malkantu Mn deposit in the West Kunlun region of Northwest China. Microscopic evidence, including the presence of micro-borings, biofilm-like structures, fungal hyphae analogs, and nanosphere aggregations, indicated active microbial involvement in both the dissolution of Mn carbonate and the precipitation of secondary Mn oxides. The observed paragenetic sequence, from partial carbonate dissolution to the formation of nanocrystalline todorokite and concentric Mn oxide nodules, supports a biologically mediated transformation pathway. These findings may challenge the conventional view that supergene Mn oxide formation is primarily climate-driven and emphasize the great potential of microorganisms in catalyzing and structuring oxidation processes near the surface. This study provides novel insights into the genesis of secondary Mn deposits and offers a biological perspective on arid and cold settings.

Declaration of competing interest

The authors declare that they have no known competing financial interests or personal relationships that could have appeared to influence the work reported in this paper.

Acknowledgments

This work was financially supported by the National Natural Science Foundation of China (Nos. 41972091) and Intensive Training Program under the Research Capacity Enhancement Project for Young and Middle-aged Faculty Members in Guangxi Universities (Nos. 2024KY0012).

Data availability

No data was used for the research described in the article.

References

Ai, J., Siljeström, S., Zhong, N., Chen, J., Wang, T., Qiu, N., George, S.C., 2023. Co-existing two distinct formation mechanisms of micro-scale ooid-like manganese carbonates hosted in Cryogenian organic-rich black shales in South China. Precambr. Res. 393, 107091.

Baele, J.-M., Bouvain, F., De Jong, J., Matielli, N., Papier, S., and Préat, A., 2008, Iron microbial mats in Modern and Phanerozoic environments, in Proceedings Instruments, Methods, and Missions for Astrobiology XI, v. 7097, SPIE, p. 171-182.

Bargar, J.R., Fuller, C.C., Marcus, M.A., Brearley, A.J., Perez De la Rosa, M., Webb, S.M., Caldwell, W.A., 2009. Structural characterization of terrestrial microbial Mn oxides from Pinal Creek, AZ. Geochim. Cosmochim. Acta 73 (4), 889–910.

Beukes, N., Swindell, E.P.W., Wabo, H., 2016. Manganese Deposits of Africa. Episodes 39, 285–317.

Bian, L., Chengyi, L., Fusheng, Z., De'an, D., Jianlin, C., 1997, Pelagic manganese nodules–A new type of oncolites: Acta Geologica Sinica, no. 01, p. 43-48, 115-116 (In Chinese with English abstract).

Breitenbach, R., Gerrits, R., Dementyeva, P., Knabe, N., Schumacher, J., Feldmann, I., Radnik, J., Ryo, M., Gorbushina, A.A., 2022. The role of extracellular polymeric substances of fungal biofilms in mineral attachment and weathering. npj Mater. Degrad. 6 (1), 42.

Calvert, S.E., Pedersen, T.F., 1996. Sedimentary geochemistry of manganese; implications for the environment of formation of manganiferous black shales. Econ. Geol. 91 (1), 36–47.

Carmichael, S. K., Doctor, D. H., Wilson, C. G., Feierstein, J., and McAleer, R. J., 2017, New insight into the origin of manganese oxide ore deposits in the Appalachian Valley and Ridge of northeastern Tennessee and northern Virginia, USA: Geological Society of America Bulletin, v. 129, no. 9-10, p. 1158-1180.

Chen, F., Pufahl, P.K., Wang, Q., Matheson, E.J., Shabaga, B.M., Zhang, Q., Zeng, Y., Le, X., Ruan, D., Zhao, Y., 2022a. A new model for the genesis of carboniferous Mn ores, Longtou Deposit, South China Block. Econ. Geol. 117 (1), 107–125.

Chen, F., Wang, Q., Pufahl, P.K., Matheson, E.J., Xian, H., Nan, J., Ma, H., Deng, J., 2023. Carbonate-hosted manganese deposits and ocean anoxia. Earth Planet. Sci. Lett. 622, 118385.

Chen, J., Li, F.B., Zhao, X.W., Wang, Y., Zhang, L.M., Yan, L.B., Yu, L.F., 2022b. Change in composition and potential functional genes of microbial communities on carbonatite rinds with different weathering times. Front. Microbiol. v. 13.

Deng, X.-D., Li, J.-W., 2013. $^{40}Ar/^{39}Ar$ dating of cryptomelane from the Baye manganese deposit SW Yunnan, China: implications for Growth Rate of Supergene Mn-Oxide Veins. Sci. China-Earth Sci. 56 (10), 1654–1663.

Deng, X.-D., Li, J.-W., Vasconcelos, P.M., 2016. $^{40}Ar/^{39}Ar$ dating of supergene Mn-oxides from the Zunyi Mn deposit, Guizhou Plateau, SW China: Implications for chemical weathering and paleoclimatic evolution since the late Miocene. Chem. Geol. 445, 185–198.

Dietzel, M., Kolmer, H., Pölt, P., Simic, S., 2008. Desert varnish and petroglyphs on sandstone - Geochemical composition and climate changes from Pleistocene to Holocene (Libya). Geochemistry 68 (1), 31–43.

DiGregorio, 2005. Rock Varnish and the Manganese Oxide connection. Anal. Chem. 77 (21), 433. A-438 A.

Dong, Z.-G., Zhang, L.-C., Dong, F.-Y., Zhang, B.-L., Xie, Y.-Q., Cha, B., Peng, Z.-D., Wang, C.-L., 2020. Geological Characteristics, Ore-controlling factors and metallogenic model of Muhu manganese deposit in west Kunlun, China. J. Jilin Univers. 50 (5), 1358–1372. In Chinese with English abstract.

Dong, Z., Peng, Z., Wang, C., Zhang, B., Zhang, L., Li, J., Zhang, X., Li, W., Zhang, L., 2022. Insight into the genesis of the Zhaosu Carboniferous Mn carbonate deposit (NW China): constraints from petrography, geochemistry, and C-Mo isotopes. Miner. Depos. 57 (7), 1269–1289.

Dong, Z.-G., Peng, Z.-D., Robbins, L.J., Konhauser, K.O., Zhang, B.-L., Zhang, L.-C., Li, J., Li, W.-J., Zhang, L., Wang, C.-L., 2023. Episodic ventilation of euxinic bottom waters triggers the formation of black shale-hosted Mn carbonate deposits. Geochim. Cosmochim. Acta 341, 132–149.

Dong, Z.-G., Zhang, B.-L., Zhang, L.-C., Dong, F.-Y., Li, J., Peng, Z.-D., Wan, B., and Wang, C.-L., 2025, Unravelling the mechanisms underlying marine redox shifts during sedimentary manganese metallogenesis: insights from the Carboniferous Muhu deposit, China: Mineralium Deposita. doi.org/10.1007/s00126-024-01343-7.

Fan, D., Liu, T., Ye, J., 1992. The process of formation of manganese carbonate deposits hosted in black shale series. Econ. Geol. 87 (5), 1419–1429.

Feng, X.H., Zhu, M., Ginder-Vogel, M., Ni, C., Parikh, S.J., Sparks, D.L., 2010. Formation of nano-crystalline todorokite from biogenic Mn oxides. Geochim. Cosmochim. Acta 74 (11), 3232–3245.

Fluegel, E., 2004. Microfacies of Carbonate Rocks. Speringer-Verlag, Berlin, pp. 366–367.

Force, E.R., Cannon, W.F., 1988. Depositional model for shallow-marine manganese deposits around black shale basins. Econ. Geol. 83 (1), 93–117.

Gadd, G.M., 1999. Fungal production of citric and oxalic acid: Importance in metal speciation, physiology and biogeochemical processes, *in* Poole, R. K., ed. Adv. Microb. Physiol. 41, 47–92.

Gadd, G.M., 2007. Geomycology: biogeochemical transformations of rocks, minerals, metals and radionuclides by fungi, bioweathering and bioremediation. Mycol. Res. 111, 3–49.

Gao, Y.-B., Teng, J.-X., Li, W.-Y., Chen, D.-H., Sui, Q.-L., Jing, D.-L., He, Y.-K., Bai, J.-K., 2018. Geology, geochemistry and ore genesis of the Aoertuokanashi manganese deposit, western Kunlun, Xinjiang, Northwest China. Acta Petrol. Sin. 34, 2341–2358. In Chinese with English abstract.

Gao, Z., Zhu, X., Wang, D., Pan, C., Yan, B., Li, J., 2021. Insights into hydrothermal controls and processes leading to the formation of the late Ediacaran Gaoyan stratiform manganese-carbonate deposit, Southwest China. Ore Geol. Rev. 139, 104524.

Geszvain, K., Tebo Bradley, M., 2010. Identification of a Two-component regulatory pathway essential for Mn(II) oxidation in Pseudomonas putida GB-1. Appl. Environ. Microbiol. 76 (4), 1224–1231.

Gray, C.J., Engel, A.S., 2013. Microbial diversity and impact on carbonate geochemistry across a changing geochemical gradient in a karst aquifer. ISME J. 7 (2), 325–337.

Gutzmer, J., 2012, Genesis and alteration of the Kalahari and Postmasburg manganese deposits, Griqualand West, South Africa. Ph.D. thesis, University of Johannesburg, Johannesburg.

Hansel, C.M., 2017. Chapter two – manganese in marine microbiology. In: Poole, R.K. (Ed.), Advances in Microbial Physiology, Volume 70. Academic Press, pp. 37–83.

Hose, L.D., Palmer, A.N., Palmer, M.V., Northup, D.E., Boston, P.J., DuChene, H.R., 2000. Microbiology and geochemistry in a hydrogen-sulphide-rich karst environment. Chem. Geol. 169 (3), 399–423.

Hu, W., Zhou, H., Gu, L., Zhang, W., Lu, X., Fu, Q., Pan, J., Zhang, H., 2000. New evidence of microbe origin for ferromanganese nodules from the East Pacific deep sea floor. Sci. China Ser. D Earth Sci. 43 (2), 187–192.

Huang, Q., Jiang, S.-Y., Pi, D.-H., Konhauser, K.O., Wen, X.-P., Lu, L.-Y., Yan, H., 2023. Thermochemical oxidation of methane by manganese oxides in hydrothermal sediments. Commun. Earth Environ. 4 (1), 224.

Huang, Q., Pi, D.-H., Jiang, S.-Y., Liu, D., Yan, H., Mänd, K., Kirsimäe, K., Bishop, B., Robbins, L.J., Yang, S.-S., 2022. The dual role of microbes in the formation of the Malkantu manganese carbonate deposit. NW China: Petrogr. Geochem. Exp. Evid. Chem. Geol. 606, 120992.

Jiang, X.-D., Sun, X.-M., Guan, Y., 2019. Biogenic mineralization in the ferromanganese nodules and crusts from the South China Sea. J. Asian Earth Sci. 171, 46–59.

Jiang, X.-D., Sun, X.-M., Guan, Y., Gong, J.-L., Lu, Y., Lu, R.-F., Wang, C., 2017. Biomineralisation of the ferromanganese crusts in the Western Pacific Ocean. J. Asian Earth Sci. 136, 58–67.

Johnson, J.E., Webb, S.M., Ma, C., Fischer, W.W., 2016. Manganese mineralogy and diagenesis in the sedimentary rock record. Geochim. Cosmochim. Acta 173, 210–231.

Kuhlman, K.R., Venkat, P., La Duc, M.T., Kuhlman, G.M., McKay, C.P., 2008. Evidence of a microbial community associated with rock varnish at Yungay, Atacama Desert, Chile. J. Geophys. Res. Biogeo. v. 113, no. G4.

Kuleshov, V., 2017a. Chapter 1 – Manganese Rocks and Ores. In: Maynard, J.B., Kuleshov, V. (Eds.), Isotope Geochemistry. Elsevier, pp. 1–4.

Kuleshov, V., 2017b. Chapter 3 - Genetic Types, Classifications, and Models of Manganese-Ore Formation. In: Maynard, J.B., Kuleshov, V. (Eds.), Isotope Geochemistry. Elsevier, pp. 63–352.

Learman, D.R., Voelker, B.M., Vazquez-Rodriguez, A.I., Hansel, C.M., 2011. Formation of manganese oxides by bacterially generated superoxide. Nat. Geosci. 4 (2), 95–98.

Levett, A., Gagen, E.J., Rintoul, L., Guagliardo, P., Diao, H., Vasconcelos, P.M., Southam, G., 2020. Characterisation of iron oxide encrusted microbial fossils. Sci. Rep. 10 (1), 9889.

Li, J.W., Vasconcelos, P., Duzgoren-Aydin, N., Yan, D.R., Zhang, W., Deng, X.D., Zhao, X. F., Zeng, Z.P., Hu, M.A., 2007. Neogene weathering and supergene manganese enrichment in subtropical South China: an $^{40}Ar/^{39}Ar$ approach and paleoclimatic significance. Earth Planet. Sci. Lett. 256 (3–4), 389–402.

Lian, B., 1998. A study on how silicate bacteria GY92 dissolves potassium from illite. Acta. Mineral. Sin. 18 (2), 234–238. In Chinese with English abstract.

Lian, B., Chen, J., Fu, Q.-P., Liu, C.-Q., Che, Y., 2005. Weathering of silicate minerals by microorganisms in culture experiments. Geol. J. China Univ. 11 (2), 181–186. In Chinese with English abstract.

Lian, B., Fu, Q.-P., Mo, D.-M., Liu, C.-Q., 2002. A comprehensive review of the mechanism of potassium releasing by silicate bacteria. Acta. Mineral. Sin. 22 (2), 179–183. In Chinese with English abstract.

Lian, B., Hu, Q., Chen, J., Ji, J., Teng, H.-H., 2006. Carbonate biomineralization induced by soil bacterium bacillus megaterium. Geochim. Cosmochim. Acta 70 (22), 5522–5535.

Lingappa, U.F., Yeager, C.M., Sharma, A., Lanza, N.L., Morales, D.P., Xie, G., Atencio, A. D., Chadwick, G.L., Monteverde, D.R., Magyar, J.S., Webb, S.M., Valentine, J.S., Hoffman, B.M., Fischer, W.W., 2021. An ecophysiological explanation for manganese enrichment in rock varnish. Proc. Natl. Acad. Sci. 118 (25), e2025188118.

Maynard, J.B., 2010. The chemistry of manganese ores throughtime: a signal of increasing diversity of Earth-surface environments. Econ. Geol. 105 (3), 535–552.

Nayak, B., Das, S.K., Munda, P., 2013. Biogenic signature and ultra microfossils in ferromanganese nodules of the Central Indian Ocean Basin. J. Asian Earth Sci. 73, 296–305.

Nealson, K.H., Tebo, B., 1980. Structural features of manganese precipitating bacteria. In: Proceedings Limits of Life, Dordrecht. Springer, Netherlands, pp. 173–182.
Neumann, T., Heiser, U., Leosson, M.A., Kersten, M., 2002. Early diagenetic processes during Mn-carbonate formation: evidence from the isotopic composition of authigenic Ca-rhodochrosites of the Baltic Sea. Geochim. Cosmochim. Acta 66 (5), 867–879.
Nimfopoulos, M.K., Pattrick, R.A.D., Michailidis, K.M., Polya, D.A., Esson, J., 1997. Geology, geochemistry, and origin of the continental karst-hosted supergene manganese deposits in the western Rhodope massif, Macedonia, Northern Greece. Explpor. Min. Geol. 6 (2), 171–184.
Pack, A., Gutzmer, J., Beukes, N.J., van Niekerk, H.S., 2000. Supergene ferromanganese wad deposits derived from Permian Karoo strata along the late Cretaceous-mid-Tertiary african land surface, Ryedale, South Africa. Econ. Geol. Bull. Soc. Econ. Geol. 95 (1), 203–220.
Pan, Y.-S. 1990, Tectonic features and evolution of the western kunlun mountain region: SCIENTIA GEOLOGICA SINICA, (03): 224-232 (In Chinese with English abstract).
Perri, E., Tucker, M.E., Słowakiewicz, M., Whitaker, F., Bowen, L., Perrotta, I.D., 2018. Carbonate and silicate biomineralization in a hypersaline microbial mat (Mesaieed sabkha, Qatar): Roles of bacteria, extracellular polymeric substances and viruses. Sedimentology 65 (4), 1213–1245.
Pharoe, B. K., Evdokimov, A. N., Gembitskaya, I. M., and Bushuyev, Y. Y., 2020, Mineralogy, geochemistry and genesis of the post-Gondwana supergene manganese deposit of the Carletonville-Ventersdorp area, North West Province, South Africa: Ore Geology Reviews, v. 120.
Polgári, M., Hein, J.R., Tóth, A.L., Pál-Molnár, E., Vigh, T., Bíró, L., Fintor, K., 2012. Microbial action formed Jurassic Mn-carbonate ore deposit in only a few hundred years (úrkút, Hungary). Geology 40 (10), 903–906.
Poulton, S.W., Henkel, S., März, C., Urquhart, H., Flögel, S., Kasten, S., Sinninghe Damsté, J.S., Wagner, T., 2015. A continental-weathering control on orbitally driven redox-nutrient cycling during cretaceous Oceanic Anoxic Event 2. Geology 43 (11), 963–966.
Reykhard, L.Y., Shulga, N.A., 2019. Fe-Mn nodule morphotypes from the NE clarion-clipperton fracture zone, pacific ocean: comparison of mineralogy, geochemistry and genesis. Ore Geol. Rev. 110, 102933.
Romano, C.A., Zhou, M., Song, Y., Wysocki, V.H., Dohnalkova, A.C., Kovarik, L., Paša-Tolić, L., Tebo, B.M., 2017. Biogenic manganese oxide nanoparticle formation by a multimeric multicopper oxidase Mnx. Nat. Commun. 8 (1), 746.
Rossi, C., Lozano, R.P., Isanta, N., Hellstrom, J., 2010. Manganese stromatolites in caves: El Soplao (Cantabria, Spain). Geology 38 (12), 1119–1122.
Roy, S., 2006. Sedimentary manganese metallogenesis in response to the evolution of the Earth system. Earth Sci. Rev. 77 (4), 273–305.
Sasmaz, A., Sasmaz, B., Hein, J.R., 2021. Geochemical approach to the genesis of the Oligocene-stratiform manganese-oxide deposit, Chiatura (Georgia). Ore. Geol. Rev. 128, 103910.
Sasmaz, A., Zagnitko, V.M., Sasmaz, B., 2020. Major, trace and rare earth element (REE) geochemistry of the Oligocene stratiform manganese oxide-hydroxide deposits in the Nikopol, Ukraine. Ore Geol. Rev. 126, 103772.
Sethumadhav, M.S., Gunnell, Y., Ahmed, M.M., Chinnaiah, 2010. Late Archean manganese mineralization and younger supergene manganese ores in the Anmod-Bisgod region, Western Dharwar Craton, southern India: Geological characterization, palaeoenvironmental history, and geomorphological setting. Ore Geol. Rev. 38 (1–2), 70–89.
Smith, K. S., and Ferry, J. G., 2000, Prokaryotic carbonic anhydrases: FEMS Microbiol Review, v. 24, no. 4, p. 335–366.
Sterflinger, K., 2000, Fungi as Geologic Agents: Geomicrobiology Journal, v. 17, no. 2, p. 97–124.
Tang, Y., Zeiner, C.A., Santelli, C.M., Hansel, C.M., 2013. Fungal oxidative dissolution of the Mn(II)-bearing mineral rhodochrosite and the role of metabolites in manganese oxide formation. Environ. Microbiol. 15 (4), 1063–1077.
Tebo, B.M., Johnson, H.A., McCarthy, J.K., Templeton, A.S., 2005. Geomicrobiology of manganese(II) oxidation. Trends Microbiol. 13 (9), 421–428.
Templeton, A.S., Knowles, E.J., Eldridge, D.L., Arey, B.W., Dohnalkova, A.C., Webb, S. M., Bailey, B.E., Tebo, B.M., Staudigel, H., 2009. A seafloor microbial biome hosted within incipient ferromanganese crusts. Nat. Geosci. 2 (12), 872–876.
Toyoda, K., Tebo, B.M., 2013. The effect of Ca^{2+} ions and ionic strength on Mn(II) oxidation by spores of the marine bacillus sp. SG-1. Geochim. Cosmochim. Acta 101, 1–11.
Tsikos, H., Beukes, N.J., Moore, J.M., Harris, C., 2003. Deposition, diagenesis, and secondary enrichment of metals in the paleoproterozoic hotazel iron formation, kalahari manganese Field, South Africa. Econ. Geol. 98 (7), 1449–1462.
Vafeas, N.A., Blignaut, L.C., Viljoen, K.S., Meffre, S., 2018. New evidence for the early onset of supergene alteration along the Kalahari unconformity. S. Afr. J. Geol. 121 (2), 157–170.
van Breemen, N., Lundström, U.S., Jongmans, A.G., 2000. Do plants drive podzolization via rock-eating mycorrhizal fungi? Geoderma 94 (2), 163–171.
Viles, H., 1987. A quantitative scanning electron microscope study of evidence for lichen weathering of limestone, Mendip Hills Somerset. Earth Surf. Process. Landforms 12 (5), 467–473.
Wang, H., and Pan, X., 2014, Role of extracellular polymeric substances (EPS) from Pseudomonas putida strain MnB1 in dissolution of natural rhodochrosite: Biogeosciences Discuss., v. 2014, p. 7273–7290.
Wang, H., Zhang, D., Song, W., Pan, X., Al-Misned, F.A., Golam Mortuza, M., 2015. Effect of exopolymers on oxidative dissolution of natural rhodochrosite by Pseudomonas putida strain MnB1: an electrochemical study. Appl. Geochem. 59, 95–103.
Wang, X., Müller, W.E.G., 2009. Marine biominerals: perspectives and challenges for polymetallic nodules and crusts. Trends Biotechnol. 27 (6), 375–383.
Wang, X., Peine, F., Schmidt, A., Schröder, H.C., Wiens, M., Schloßmacher, U., Müller, W. E.G., 2011. Concept of biogenic ferromanganese crust formation: coccoliths as bio-seeds in crusts from central atlantic ocean (senghor seamount/cape verde). Nat. Prod. Commun. 6 (5), 1934578X1100600522.
Wang, X., Schröder, H.C., Wiens, M., Schloßmacher, U., Müller, W.E.G., 2009. Manganese/polymetallic nodules: Micro-structural characterization of exolithobiontic- and endolithobiontic microbial biofilms by scanning electron microscopy. Micron 40 (3), 350–358.
Whitley, D.S., Santoro, C.M., Valenzuela, D., 2017. Climate change, rock coatings, and the archaeological record. Elements 13 (3), 183–186.
Xiao, X.-C. and Wang. J. 1998, A brief review of tectonic evolution and uplift of the Qinghai-Tibet plateau: Geological Review 1998, (04):372-381(In Chinese with English abstract).
Yan, H., Pi, D.-H., Jiang, S.-Y., Mao, J., Xu, L., Yang, X., Hao, W., Mänd, K., Li, L., Konhauser, K.O., Robbins, L.J., 2022. Mineral paragenesis in Paleozoic manganese ore deposits: depositional versus post-depositional formation processes. Geochim. Cosmochim. Acta 325, 65–86.
Yu, W.C., Polgári, M., Fintor, K., Gyollai, I., Szabó, M., Velledits, F., Liu, Z.C., Du, Y.S., 2021a. Contribution of microbial processes to the enrichment of Middle Permian manganese deposits in northern Guizhou. Ore Geology Reviews, v, South China, p. 136.
Yu, W., Algeo, T.J., Du, Y., Maynard, B., Guo, H., Zhou, Q., Peng, T., Wang, P., Yuan, L., 2016. Genesis of cryogenian datangpo manganese deposit: hydrothermal influence and episodic post-glacial ventilation of nanhua basin, South China. Palaeogeogr. Palaeoclimatol. Palaeoecol. 459, 321–337.
Yu, W., Polgári, M., Gyollai, I., Fintor, K., Huang, H., Szabó, M., Du, Y., 2021b. Microbial metallogenesis of early carboniferous manganese deposit in central Guangxi, South China. Ore Geol. Rev. 136, 104251.
Yu, W., Polgári, M., Gyollai, I., Fintor, K., Szabó, M., Kovács, I., Fekete, J., Du, Y., Zhou, Q., 2019. Microbial metallogenesis of Cryogenian manganese ore deposits in South China. Precambr. Res. 322, 122–135.
Zhang, B.-L., Wang, C.-L., Robbins, L.J., Zhang, L.-C., Konhauser, K.O., Dong, Z.-G., Li, W.-J., Peng, Z.-D., Zheng, M.-T., 2020. Petrography and geochemistry of the Carboniferous Ortokarnash manganese deposit in the western kunlun mountains, Xinjiang Province, China: implications for the depositional environment and the origin of mineralization. Econ. Geol. 115 (7), 1559–1588.
Zhang, B.-L., Zhang, L.-C., Feng, J., Xu, S.-Q., Feng, C.-R., Hao, Y.-H., Zheng, M.-T., Peng, Z.-D., and Dong, Z.-G., 2018, Genesis of the large-scale Ortokarnash manganese carbonate deposit in the Malkansu District, western Kunlun: Evidence from Geological Features: Geological Review, v. 64, p.361-377 (In Chinese with English abstract).
Zhang, Z., Li, W., Shen, Y., Wang, R., Li, H., Zhou, M., Wang, W., Wang, K., Jiang, K., 2022. Issues and opportunities of manganese-based materials for enhanced Zn-ion storage performances. J. Storage Mater. 45, 103729.
Zhao, L.Q., Niu, S.D., Niu, X.L., Chen, T., Wang, Y.C., Li, L., Huang, F., Wu, H.Y., Mo, L. C., Zhang, M., 2022. Manganese oxide minerals from the Xiangtan manganese deposit in south China and their application in formaldehyde removal. Minerals 12 (5).
Zhu, L.-J., Li, J.-Y., 2004. In: Carbonate Rock Weathering and Environmental Effects. Beijing: Geological Publishing Houes, pp. 80–100.

JGR Oceans

RESEARCH ARTICLE
10.1029/2024JC021890

Seasonal Variations in Coral Lipids and Their Significance for Energy Maintenance in the South China Sea

Shendong Xu[1,2,3], Hongyan Mo[3], Kefu Yu[1,3], Jie Gao[3], and Zheng Men[3]

[1]Southern Marine Science and Engineering Guangdong Laboratory (Guangzhou), Guangzhou, China, [2]Key Laboratory of Coastal Zone Environmental Processes and Ecological Remediation, Yantai Institute of Coastal Zone Research, Chinese Academy of Sciences, Yantai, China, [3]Guangxi Laboratory on the Study of Coral Reefs in the South China Sea, Coral Reef Research Centre of China, School of Marine Sciences, Guangxi University, Nanning, China

Key Points:

- The density and photosynthesis intensity of the symbiotic zooxanthellae decrease significantly accompanied by lipid content in summer
- The reduction of lipid $\delta^{13}C$ indicates that stored lipid was preferentially consumed in summer
- Stored lipid is an important type of alternative energy sources when autotrophic photosynthesis of zooxanthellae decreases

Correspondence to:

S. Xu and K. Yu,
sdxu@yic.ac.cn;
kefuyu@scsio.ac.cn

Citation:

Xu, S., Mo, H., Yu, K., Gao, J., & Men, Z. (2025). Seasonal variations in coral lipids and their significance for energy maintenance in the South China Sea. *Journal of Geophysical Research: Oceans*, *130*, e2024JC021890. https://doi.org/10.1029/2024JC021890

Received 25 SEP 2024
Accepted 5 MAY 2025

Author Contributions:

Conceptualization: Shendong Xu
Funding acquisition: Shendong Xu
Methodology: Shendong Xu
Project administration: Shendong Xu, Kefu Yu
Resources: Shendong Xu, Kefu Yu
Software: Hongyan Mo, Jie Gao
Supervision: Shendong Xu
Validation: Zheng Men
Writing – original draft: Shendong Xu, Hongyan Mo
Writing – review & editing: Shendong Xu

© 2025. American Geophysical Union. All Rights Reserved.

Abstract The degradation of coral reef ecosystems caused by coral bleaching has been increasing in recent years. Coral bleaching implies a decrease in the symbiodinianceae, such as endosymbiotic zooxanthellae, which in turn affects the energy supplied to coral hosts. However, as an alternative energy source, the energy supply mechanism of lipids during seasonal changes in zooxanthellae density (ZD) was not well explored and validated. In this study, 66 coral samples of *Acropora millepora* and *Pocillopora damicornis* were collected in March, June and October 2020 in Xisha Islands in the South China Sea. The response of lipids to the seasonal variations of ZD and photosynthetic rate was explored by combining physiological parameters (ZD) with geochemical indicators ($\delta^{13}C$ of zooxanthellae $\delta^{13}C_z$, host tissues $\delta^{13}C_h$ and total lipids $\delta^{13}C_{TL}$). The ZD and $\delta^{13}C_z$ of *Acropora millepora* and *Pocillopora damicornis* (ZD: 28.7% and 28.8%; $\delta^{13}C_z$: 0.47 and 0.57‰ respectively) decreased in summer compared to that in spring indicate a decrease in photosynthetic rate of zooxanthellae. Correspondingly, $\delta^{13}C_h$ decreased by 0.50 and 0.61‰, lipid content decreased by 60.82% and 53.56%, $\delta^{13}C_{TL}$ decreased by 2.1 and 2.07‰ respectively. This means that corals can maintain stable energy supply by increasing heterotrophic predation and consuming more lipid when autotrophic photosynthesis decreases in summer. We emphasize that the level of lipid reserves may be an important factor affecting the resistance to environmental stress. Coral species with higher lipid reserves could have a selective advantage and higher resistance to bleaching.

Plain Language Summary In recent years, global warming is causing coral bleaching to worsen. Coral bleaching means a decrease in the symbiodinianceae, such as endosymbiotic zooxanthellae. This is usually accompanied by a reduction in the photosynthetic intensity. Meanwhile, coral's energy obtained through photosynthesis will also decrease. Coral lipids contain components such as triglycerides and wax esters, and are potential alternative energy sources. However, the mechanism of lipid energy supplementation during symbiodinianceae reduction is not well understood. There were few studies on the seasonal changes of coral lipid contents and its mechanism for energy supply. Based on the $\delta^{13}C$ labeling technology, we explored the coupling between lipids consumption, autotrophic photosynthesis and heterotrophic predation. The results show that endosymbiotic zooxanthellae and the photosynthesis intensity decreased in summer. Correspondingly, the content and $\delta^{13}C$ of lipids decreased significantly. This means that storage lipids containing heavier carbon isotopes were consumed. Corals can maintain the stability of energy supply by consuming stored lipids when photosynthesis decreases. This energy maintenance mechanism has been rarely mentioned in previous research, which is important for improving coral's adaptability to the environmental stresses as well as resistance to bleaching.

1. Introduction

In recent years, the intensification of global warming and extreme climate have led to an increase in the frequency and severity of coral bleaching (Chen et al., 2019; Ferrier-Pagès et al., 2018; Jones et al., 2021; Sommer et al., 2024). For example, Fine et al. (2019) found that the increasingly warm and acidic marine environment caused some corals to bleach and die. And the number of coral species declined by 26% from 2015 to 2019 in the Great Barrier Reef of Australia. Xu et al. (2023) reported that coral bleaching and mortality rates in the northern South China Sea (SCS) have reached 84.78% and 10.68% respectively in recent years due to marine heat waves. Zooxanthellae is one kind of important endosymbiotic symbiodinaceae of coral. Coral bleaching means a decrease in endosymbiotic zooxanthellae density (ZD) and/or chlorophyll content (Chapron et al., 2022; Grottoli

et al., 2004; Suggett & Smith, 2020). From the perspective of energy supply, a decrease in ZD and/or chlorophyll content is usually accompanied by a decrease in the photosynthetic rate of the zooxanthellae which leads to a reduction in the amount of energy provided by photosynthesis to the coral host (Grottoli et al., 2006; Hughes et al., 2010; Lyndby et al., 2020). In this situation, corals need more energy to fill the energy gap. Almost all scleractinian corals are mixotrophic organisms, they can rely on both photosynthates translocated from their zooxanthellae and heterotrophic predation of the host (Houlbrèque & Ferrier-Pagès, 2009). It has been shown that corals can increase the intensity of host heterotrophic predation to maintain the balance of energy supply when autotrophic photosynthesis of the zooxanthellae decreases (Grottoli et al., 2006).

Coral lipids include structural lipids and storage lipids, therein sterols and phospholipids are important structural lipids which form the structural basis of coral cell membranes and zooxanthellae; triglycerides and wax esters are the main lipids for energy storage (Crandall et al., 2016; Imbs et al., 2010; Teece et al., 2011; Yamashiro et al., 1999). Each gram of lipid could produce 39.5 kj of energy and has a high energy value (Anthony et al., 2002; Palardy et al., 2008; Schoepf et al., 2015). Usually, a small portion of the substances synthesized by zooxanthellae through photosynthesis is used for their own growing and meeting their metabolic energy requirement; the remaining majority substances are transferred to the host in the form of organic compounds such as glucose and glycerol (Crossland et al., 1980; Patton & Burris, 1983; Yamashiro et al., 1999). Although the processes of lipid synthesis and storage are clear now, seasonal changes in lipid catabolism and their energy supply mechanism was still less studied. Yamashiro et al. (2005) found that there was a decrease in lipid content when coral reefs experienced bleaching in Okinawa, Japan. Schoepf et al. (2015) through a culture experiment found that *O. faveolate* corals had a 30% decrease in lipid content when they were exposed to high temperatures for 2.5 weeks. These studies investigated the changes in lipid content and other physiological parameters during bleaching and high-temperature stress. However, there are currently few studies conducted on the coupling analysis of the different energy supply patterns of coral in the context of seasonal variations in temperature and physiological parameters. This limits us to accurately understand the energy maintenance mechanism of corals under thermal stress. Especially considering the background of future climate scenarios characterized by more frequent thermal stress events, relatively higher surface seawater temperature (SST) in summer will be more likely to cause bleaching events.

Accurately obtaining information on changes in the rate of photosynthesis and intensity of heterotrophic predation is a prerequisite for further exploring the mechanism of lipid energy supply. Stable carbon isotope of different organic components of coral symbiotic tissues (i.e., $\delta^{13}C$ of zooxanthellae $\delta^{13}C_z$; $\delta^{13}C$ of hosts $\delta^{13}C_h$; $\delta^{13}C$ of total lipids $\delta^{13}C_{TL}$) have been proven to indicate changes in coral nutrition and the consumption process of lipids effectively (Alamaru et al., 2009; Ferrier-Pagès & Leal, 2019; Maier et al., 2010; Xu et al., 2021). During the process of photosynthesis, endosymbionts tend to absorb more CO_2 containing lighter ^{12}C which leads to carbon isotope fractionation and lower $\delta^{13}C_z$ values. When photosynthesis is enhanced, the demand for carbon increases and a heavier ^{13}C is absorbed. Generally, the stronger the photosynthesis of zooxanthellae, the weaker the fractionation effect and the more positive $\delta^{13}C_z$. On the contrary, when photosynthesis decreases, the fractionation effect increases, resulting in a decrease in $\delta^{13}C_z$ (Muscatine et al., 1989; Nahon et al., 2013; Rodrigues & Grottoli, 2006; Swart et al., 2005). With the increase in heterotrophic predation intensity of coral hosts, $\delta^{13}C_h$ will decrease due to the food source being usually poor in ^{13}C. This resulted in an increase in the difference between $\delta^{13}C_h$ and $\delta^{13}C_z$ (i.e., $\Delta^{h\text{-}z}\,^{13}C$). Based on this, we can further verify the changes in coral heterotrophic predation intensity through $\delta^{13}C_h$ and $\Delta^{h\text{-}z}\,^{13}C$ values variations. Generally, the lower heterotrophic predation intensity of corals is often accompanied by an increase in $\delta^{13}C_h$ and $\Delta^{h\text{-}z}\,^{13}C$; the stronger heterotrophy characterized by relatively lower $\delta^{13}C_h$ and $\Delta^{h\text{-}z}\,^{13}C$ values (Muscatine et al., 1989; Reynaud et al., 2002; Xu et al., 2021). The $\delta^{13}C_{TL}$ values are related to the consumption process. Because there are differences in $\delta^{13}C$ values between structural lipids and storage lipids, specifically storage lipids are relatively rich in ^{13}C. Generally, the $\delta^{13}C_{TL}$ value of the remaining total lipids decreases with the depletion of stored lipids during coral metabolism (Grottoli & Rodrigues, 2011; Rodrigues et al., 2008; Yamashiro et al., 2005). In this study we will explore seasonal variations in autotrophic photosynthesis, heterotrophic predation, and lipid consumption through measuring physiological parameters and stable carbon isotopes of different organic components of coral symbiotic tissues. And then, explore their significance for energy maintenance and environmental adaptability of corals.

The Xisha Islands are located in the central part of the SCS, about 330 km from the mainland (Figure 1). Being far away from the densely populated mainland, coral reefs in Xisha are less affected by human activities, but more affected by natural environmental stress. For example, ZD decreases significantly under the influence of higher

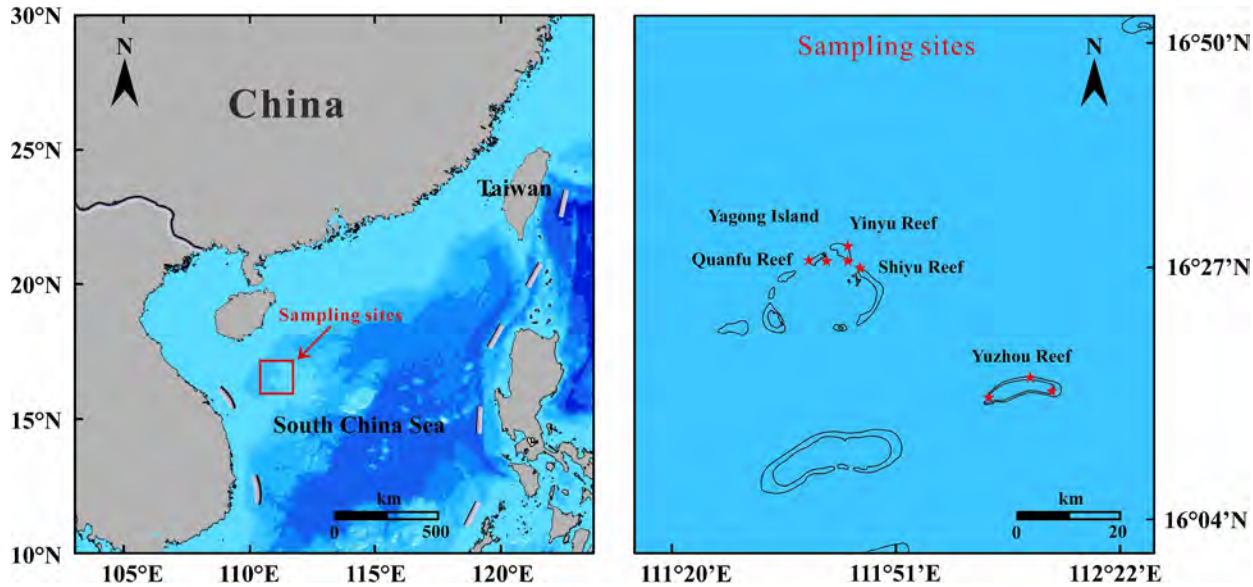


Figure 1. Study area (red box, on the left) and sampling location (red five-pointed star, on the right) of the Xisha Islands.

SST in summer (Qin, Yu, Chen, et al., 2019; Xu et al., 2021). Therefore, the Xisha Islands is an ideal site to explore the mechanism of energy replenishment of coral lipids under natural conditions when ZD decreases. Previous studies have shown that corals with different lipid contents have different survival advantages and coverage in this study area. Specifically, massive corals with higher lipid contents have more survival advantages compared to branching corals with lower lipid contents. The dominant position of massive corals was increasingly accompanied by a decrease in the coverage of branching corals in Xisha Islands in the SCS (Liao, 2021; Xu et al., 2022). However, it is unclear whether the level of lipid content can affect the environmental adaptability of corals through the stability of energy supply. We collected 66 samples of *Acropora millepora* (*A. millepora* $n = 33$) and *Pocillopora damicornis* (*P. damicornis* $n = 33$) corals in 2020 from the Xisha Islands. Physiological parameters, including ZD and lipid contents, were measured. Geochemical parameters, including $\delta^{13}C_z$, $\delta^{13}C_h$, and $\delta^{13}C_{TL}$ were measured and analyzed. As far as we know, this is the first study to examine $\delta^{13}C$ values of different organic components of coral symbiotic tissues in different seasons. This can enable us to further explore the energy supply mechanism of corals, especially during the summer when relatively higher SST lead to a decrease in ZD. We analyzed the seasonal changes in ZD and the photosynthetic rate of endosymbionts, and then we investigated the response of coral lipids to the changes in the ZD and the photosynthetic rate. This study has improved our understanding of the significance and energy maintenance mechanism of coral lipids, as well as providing insights about the effects of coral lipids on their environmental resilience.

The outline of the paper is as follows: Section 2 points out the sampling area, explains the experimental process and data analysis methods. Section 3 presents the data results and discussions. Section 4 gives conclusions, respectively.

2. Materials and Methods

2.1. Study Sites and Sample Collection

The study area Xisha Islands and the specific sampling area are shown in Figure 1. The prevailing tropical oceanic monsoon climate in the Xisha Islands leads to the obvious dry and wet seasons, as well as the ultra-high annual sunshine duration and abundant solar and thermal resources in this region (Zhang et al., 2014). In addition, the transparency of the seawater in the Xisha Islands is relatively high, about 15–30 m (Xu et al., 2021). These environmental conditions are very favorable for corals to photosynthesize, so coral reefs in this area have been well-developed and flourishing for hundreds of millions of years, with high ecological value (Zhang et al., 2014). The photosynthetically active radiation (PAR) and SST data are products of the MODIS (Moderate-Resolution Imaging Spectroradiometer) of the Terra satellite. These data were downloaded from the National Aeronautics

and Space Administration (NASA: https://oceandata.sci.gsfc.nasa.gov/directdataaccess/Level-3%20Mapped/Terra-MODIS/). The time range is from 1 January 2020 to 31 December 2020. The spatial range is from 111°E to 113°E and 15°N to 17°N, the spatial resolution is 4 km.

Coral samples were collected in March, June, and October 2020. In the Xisha Islands in the SCS, March corresponds to spring, June corresponds to summer, and October corresponds to autumn respectively. All these coral samples were randomly collected in sea areas where corals grow naturally in a healthy state. It was not a designated sampling area, nor was an artificially repaired sea area. However, it should be emphasized that all samples were collected at depths of approximately 2–4 m to prevent differences in coral physiological parameters caused by water depth. The surface area of each sample was approximately 50 cm^2. Then place in a ziplock bag and immediately freeze at −20°C to bring back to the laboratory.

2.2. Physiological Parameters Analysis

2.2.1. Surface Area of Coral Skeleton

Coral samples were rinsed in closed containers with a Waterpik washer (filtered through a 0.4 μm filter) to separate the coral skeleton and symbiotic tissues. A Waterpik scaler filled with seawater (filtered through a 0.4 μm membrane) was employed to rinse the corals to detach the coral skeleton from the symbiotic tissue, which formed a mixture with seawater (X). The mixture was poured into a measuring cylinder and the container was rinsed twice and combined and poured into the measuring cylinder, noting the total initial volume (V). The coral skeletons were placed in an oven at a temperature setting of 35°C, dried and then stored in PE plastic ziplock bags pending determination of their surface area. The surface of the coral skeleton was covered with aluminum foil and pressed, the foil was cut to cover the surface of the skeleton and weighed. A square of aluminum foil with 10 cm sides was cut and weighed, and the weight of the foil per square centimeter was calculated. Finally, the surface area of the skeleton (V_1) was determined by calculating the ratio of the weight of the foil covering the surface of the skeleton to the weight of the foil per square centimeter (Marsh, 1970; Xu et al., 2017).

2.2.2. ZD

The mixture of tissue and seawater (X) was centrifuged in 4 portions of 2 ml each in a table-top high-speed freezer centrifuge (Sigma-3K15) at 4,000 $r{\cdot}min^{-1}$ for 3 min. Then slowly removed the supernatant of the centrifuged solution. The remaining endosymbionts were added to 1 ml of 5% formaldehyde solution, fixed for 4 hr, and stored at 0°C. The preserved endosymbionts solution was mixed thoroughly, and the number of endosymbionts was counted under a microscope (Oakbass-BX53) using a hematocrit plate (covered with a thin slice), and the average value was taken 8 times, which was then converted to the number of endosymbionts in the total volume of the solution. Finally, the ZD was calculated based on the ratio of the number of endosymbionts contained in the initial total volume of solution to the surface area of the coral skeleton (V_1) (Fagoonee et al., 1999; Li et al., 2008).

2.2.3. Lipid Content

Samples were soaked in 10% aqueous formaldehyde solution for 24 hr. The samples were then rinsed with fresh water and dried at 35°C. Subsequently dried in a vial of chloroform-methanol mixture (chloroform: methanol = 2:1) to extract the lipids (Grottoli & Rodrigues, 2011). The extract was poured through a coarse paper filter into a pre-weighed aluminum tray after 24 hr. The coral sample and the filter were rinsed with 5 ml of freshly prepared chloroform-methanol solution, followed by evaporation of the solvent from the aluminum tray in a thermostatic blower oven at a regulated temperature (55°C), and the remaining material in the tray was the lipid (Stimson, 1987). The aluminum discs and residues were weighed and the mass of the discs was subtracted to obtain the mass of lipids from each coral (noted as M, accurate to 0.001 g). The weighed coral lipids were collected separately into 3 ml centrifuge tubes for subsequent determination of lipid carbon isotopes. Once lipid extraction, the remaining coral samples in the bottles were removed and dried. The coral surface was wrapped with aluminum foil and the coral skeletal surface area (V) was calculated based on the relationship between the weight and area of the foil. Finally, the ratio of lipid mass to coral skeletal surface area was calculated to obtain the lipid content of each coral sample. That is, lipid content (unit: mg/cm^2) = lipid mass (M)/coral skeletal surface area (V).

2.3. Stable Carbon Isotope Analysis

2.3.1. Separation of Endosymbionts and Host Tissue

The remaining mixture (X) after the determination of ZD was mixed thoroughly and poured into separate 50 ml centrifuge tubes and centrifuged at 4,000 $r{\cdot}min^{-1}$ for 5 min. The supernatant of the centrifuged samples (containing host tissues) was poured into clean centrifuge tubes slowly, and the separation was repeated until the endosymbionts were not visible in the solution with a microscope (Okbas-BX53). The solution was then poured into a filter fitted with a Whatman GF/F membrane (47 mm diameter, 0.7 μm pore size) and filter membranes enriched for coral hosts were placed in an oven at 35°C for 24 hr. After drying, the coral tissues were scraped off the membranes and collected in 3 ml centrifuge tubes for subsequent determination of the carbon isotopes of the coral hosts. The remaining lower layer of liquid in the 50 ml centrifuge tube (containing the endosymbionts) was supplemented with 0.5 ml of a hydrochloric acid solution at a concentration of 1 mol/L to remove carbonate material from the sample. Rinse the sample with distilled water, centrifuge and purify twice. And then placed in an oven at 35°C for 24 hr. After drying, the sample was collected and used for the determination of the carbon isotopes of endosymbionts (Papina et al., 2003; Seemann, 2013).

2.3.2. Determination of Stable Carbon Isotope

Samples of endosymbionts, host tissues, and lipids that had been processed for isotope measurements were sent to the Analytical Testing Center of the Third Institute of Oceanography, Ministry of Natural Resources. They were tested for $\delta^{13}C$ by Elemental Analysis-Stable Isotope Ratio Mass Spectrometry (EA-IRMS) using Sercon Integra 2, respectively. For the test, three blanks were set up in front of the samples, and two standards were inserted for every 12 samples (the standard sample was acetanilide, with $\delta^{13}C = -26.85‰$). Each sample was measured twice and the average value was taken. $\delta^{13}C_{TOC}$ values were determined relative to the PDB (Pee Dee Belemnite) with an analytical precision of ±0.2‰.

2.4. Statistical Analysis

The software used to analyze the data in this study was SPSS 25.0. One-way ANOVA tests were used to analyze whether the coral physiological parameters and carbon isotope ratios were significantly different in different seasons. Pearson's correlation analyses were used to analyze the correlation between the coral physiological parameters and the carbon isotope ratios. Independent-Sample *t*-tests were used to analyze whether there were significant differences between the two species of corals. Pearson's correlation analysis was used to analyze the correlation between coral physiological parameters and carbon isotope ratios. The statistical significance level was set at 0.05, that is, $p < 0.05$ is considered to be a significant correlation or significant difference. All results are expressed as mean ± 1 standard deviation (mean ± 1SD).

3. Results and Discussion

3.1. Seasonal Changes in ZD Lead to Changes in Photosynthetic Rate

3.1.1. Seasonal Changes in ZD

Corals have different thermal tolerances based on their genetics and the water depth, latitude, etc where they grow. Previous research work conducted in the study area have shown that the upper limit of SST suitable for branching corals is around 30°C (e.g., Qin, Yu, Wang, et al., 2019; Xu et al., 2022). When the SST exceeds this limit corals are induced to produce more destructive Reactive Oxygen Species, a substance that can lead to the destruction and loss of the coral endosymbionts (Bhagooli & Hidaka, 2004; Gustafsson et al., 2014; Venn et al., 2008; Yentsch et al., 2002). Many studies have shown that high SST can lead to the decrease in ZD. For example, Glynn and D'Croz (1990) found that ZD remained high when *P. damicornis* corals were at normal temperatures (26–28°C), but decreased to 68% of its original level when the corals were at temperatures of 30–32°C in an indoor experiment. Harithsa et al. (2005) conducted a field study of coral bleaching in the Laksha Islands in the Arabian Sea and found that the ZD of branching *A. formosa* corals decreased by 80% after experiencing abnormally high temperatures (30–32°C) for up to a month.

In this study SST showed significant seasonal variations in the Xisha Islands. Especially the average SST 30.27°C in June (Figure 2), which was close to or even exceeded the upper limit of the suitable growth temperature in the

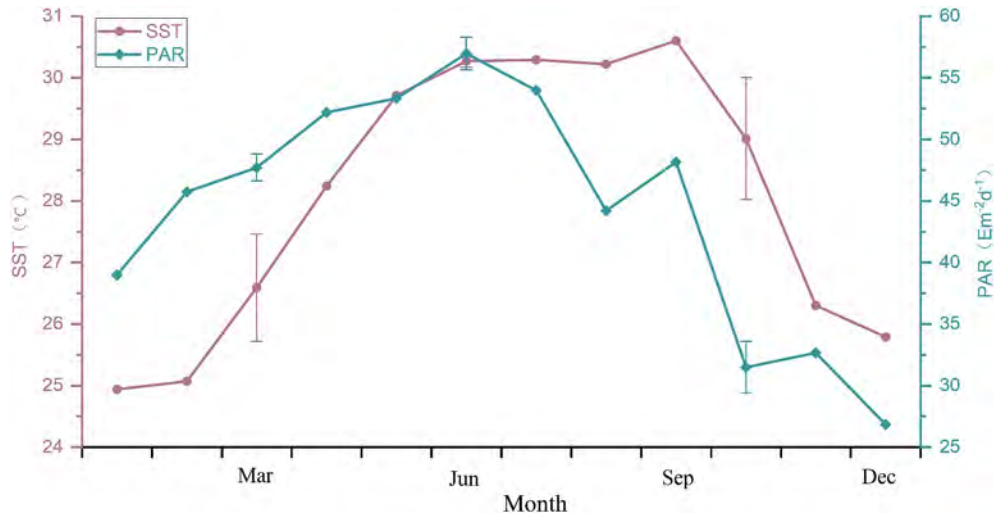


Figure 2. Monthly average surface seawater temperature and photosynthetically active radiation of Xisha islands in 2020.

study area (Qin, Yu, Chen, et al., 2019). Meanwhile, the ZD of the two coral species also showed significant seasonal differences. Specifically, the ZD of the *A. millepora* and *P. damicornis* corals decreased by 28.7% and 28.8% in June than that in March, and then increased by 59.1% and 36.2% in October than that in June, respectively (as shown in Table 1, Figure 3a). We conclude that ZD decreased due to high SST in summer and then recovered in autumn as SST decreased to the range suitable for coral survival.

3.1.2. Seasonal Changes in Photosynthetic Rate

The influencing factors of $\delta^{13}C_z$ mainly include two categories: $\delta^{13}C$ of seawater DIC and isotope fractionation effect related to photosynthesis. Therein, seawater DIC are related to the suess effect, river runoff and so on (Dassié et al., 2013; Deng et al., 2013); isotope fractionation effect during photosynthesis are related to the ZD, light intensity, water depth, water turbidity and so on (Alamaru et al., 2009; Browne et al., 2014). Among them, lighting is considered to be an important influencing factor of the photosynthetic intensity of zooxanthellae. It has been found that within a certain threshold range, the stronger the light, the higher the photosynthetic intensity of zooxanthellae and its $\delta^{13}C_z$ value. On the contrary, the lower the light, the lower the photosynthetic intensity of zooxanthellae and its $\delta^{13}C_z$ value (Ferrier-Pagès et al., 2018). In this study, the average PAR were 47.70 Em^{-2} d^{-1} in March (Spring), 56.97 Em^{-2} d^{-1} in June (Summer) and 31.48 Em^{-2} d^{-1} in October (Autumn) (Figure 2). The average PAR in June was about 19% higher than that in March (Spring) and 81% higher than that in October. Theoretically, $\delta^{13}C_z$ value in June should be higher than that in March and October if lighting conditions were the main factor influencing the seasonal variation of photosynthetic intensity of zooxanthellae. However, on the contrary, the $\delta^{13}C_z$ values in June were lower than those in March and October (Figure 4a). We consider that the effect of the reduced ZD on the photosynthetic intensity in June (summer) was greater than the

Table 1
The Results of Physiological Parameters

Species	Sampling month	ZD (10^6cells/cm^2)	Lipid content (mg/cm^2)
A. millepora	March	2.09 ± 0.56	3.42 ± 0.28
	June	1.49 ± 0.53	1.34 ± 0.20
	October	2.37 ± 0.75	1.77 ± 0.55
P. damicornis	March	1.98 ± 0.28	3.51 ± 0.39
	June	1.41 ± 0.42	1.63 ± 0.27
	October	1.92 ± 0.35	2.55 ± 0.34

Note. The mean values (mean ± 1SD) of physiological parameters (ZD and total lipid content) of *Acropora* and *P. damicornis* corals in March, June, and October.

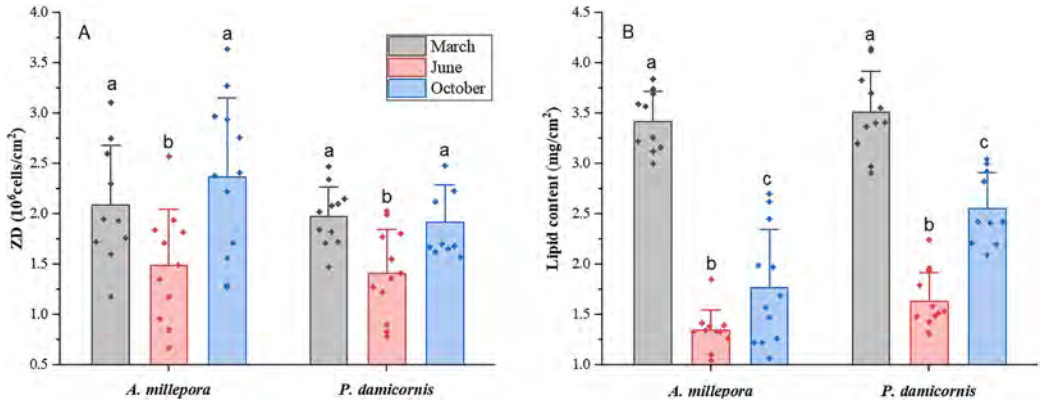


Figure 3. Seasonal differences in zooxanthellae density and lipid content of two coral species. (a) ZD; (b) Lipid content. The a, b and c indicate significant seasonal differences in physiological parameter of two genera of corals.

effect of elevated PAR. In other words, the magnitude of the increase in photosynthetic intensity and $\delta^{13}C_z$ due to the increase of PAR in June were offset by the impact of reduced ZD.

Nevertheless, we do not deny the potential influence of other factors on $\delta^{13}C_z$, what we want emphasize is that the changes in ZD was an important factor affecting $\delta^{13}C_z$ in this study. Coral derive their photosynthetic activity from the endosymbionts, whose chloroplasts contain chlorophyll and other accessory pigments indispensable for participation in photochemical reactions (Hoegh-Guldberg, 1999). The ZD can directly affect photosynthetic rate of endosymbionts. Generally, the higher the ZD, the higher the photosynthetic rate (Marubini & Davies, 1996;

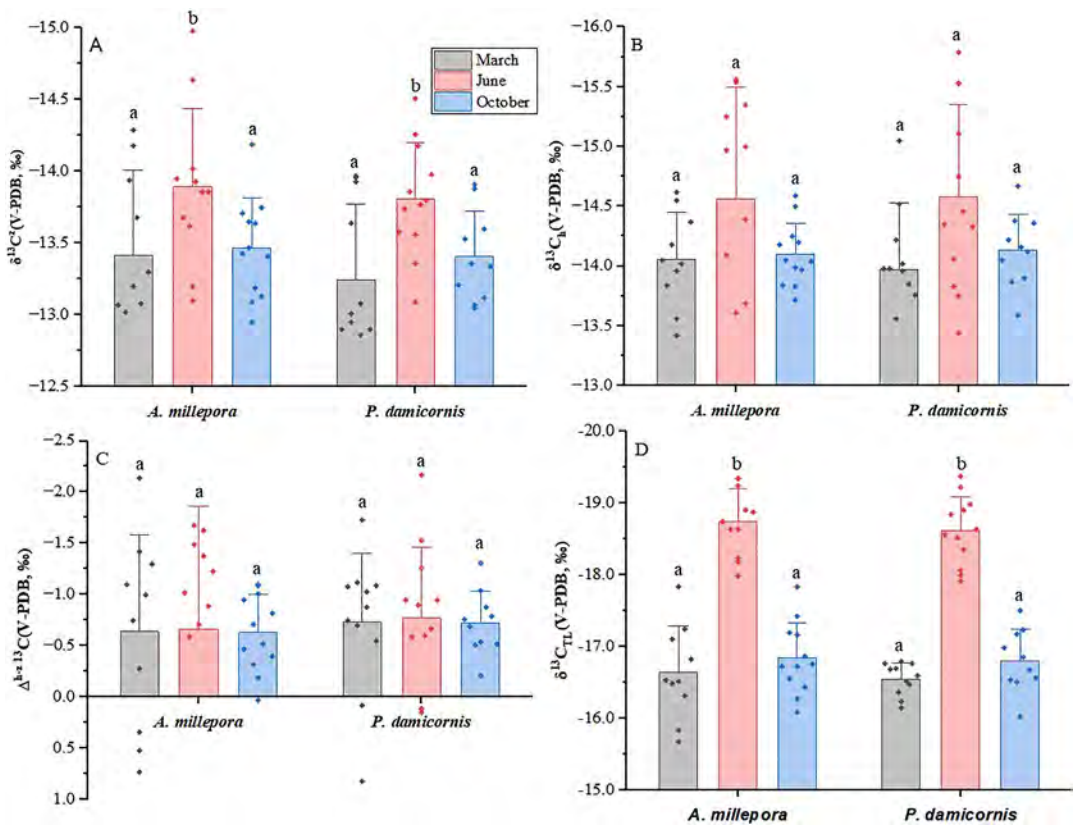


Figure 4. Carbon isotope ratios of two genera of corals in spring, summer and autumn. (a) $\delta^{13}C_z$; (b) $\delta^{13}C_h$; (c) $\Delta^{h\text{-}z}\,^{13}C$; (d) $\delta^{13}C_{TL}$. The error bars represent a standard error, and the letters a and b indicate statistical seasonal differences in coral carbon isotope ratios.

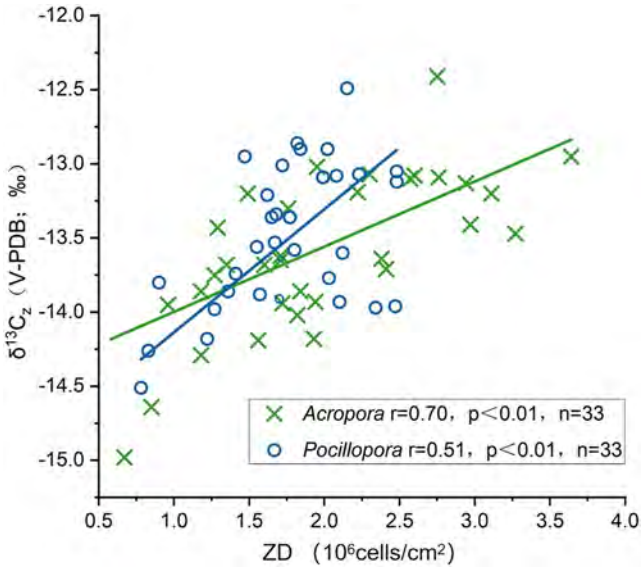


Figure 5. Relationship between zooxanthellae density and $\delta^{13}C_z$ of two coral species. In Pearson's correlation analysis, $p < 0.05$ was considered significant.

Porter et al., 1989; Wooldridge, 2014). As shown in Figure 5, the ZD and $^{13}C_z$ of both species of corals showed a significant positive correlation (*Acropora*: $r = 0.70$, $p < 0.01$; *P. damicornis*: $r = 0.51$, $p < 0.05$). This indicates that the $\delta^{13}C_z$ values of both species of corals were affected by ZD, that is, the higher the ZD, the stronger their autotrophic photosynthesis and the higher $\delta^{13}C_z$ values. In addition, average $\delta^{13}C_z$ was relatively higher in spring and autumn but lower in summer, which was consistent with the seasonal variation characteristics of ZD (Figures 3a and 4a). The consistent seasonal variations of characteristics ZD and $\delta^{13}C_z$ values imply that the variation of ZD leads to the variation of its photosynthetic rate as well as $\delta^{13}C_z$. The lower photosynthetic rate of corals in summer was mainly caused by the relatively lower ZD compared to that in spring and autumn.

3.2. Seasonal Changes in Heterotrophic Predation Intensity of Corals

Almost all scleractinian corals are mixotrophic organisms. They can obtain energy through both photosynthesis of endosymbionts and heterotrophic predation of the host (Alamaru et al., 2009; Conti-Jerpe et al., 2021; Grottoli et al., 2006; Oku et al., 2003). Normally photosynthetic nutrients from endosymbionts can provide most or even 100% of the daily metabolic energy requirements of corals (Davies, 1991; Muscatine & Cernichiari, 1969). When ZD decreases due to extreme environmental conditions, corals must rely on alternative sources of fixed carbon to meet their energy demand. Therefore, heterotrophic predation is an important alternative source. Some scholars have reported that corals can significantly increase their heterotrophic predation to maintain the stability of their energy supply during the decrease in ZD or even during bleaching (e.g., Grottoli et al., 2006; Hughes & Grottoli, 2013; Rodrigues & Grottoli, 2006). In addition, Alamaru et al. (2009) found that the heterotrophic predation intensity of corals significantly increased due to the decrease in autotrophic photosynthetic rate along a 60 m water depth gradient in the Red Sea. In this study, we speculate that corals rely more on heterotrophic predation to obtain energy in summer due to the decrease in ZD and autotrophic photosynthetic rate. This speculation can be proven by the decrease in $\delta^{13}C_h$ and $\Delta^{h\text{-}z\ 13}C$ values.

Due to the isotopic fractionation effect that accompanies carbon exchange between host and endosymbionts, the $\delta^{13}C_h$ values are slightly lower than $\delta^{13}C_z$ values (Muscatine et al., 1989; Maier et al., 2010). However, as heterotrophic predation enhanced, $\delta^{13}C_h$ became closer to the more ^{13}C-deficient food sources, resulting in lower $\delta^{13}C_h$ values and a more negative $\Delta^{h\text{-}z\ 13}C$ (Nahon et al., 2013). In our study, the two coral species exhibited decreases in $\delta^{13}C_h$ and $\Delta^{h\text{-}z\ 13}C$ in summer, although this was not statistically significant (Table 2, Figure 4). The $\delta^{13}C_h$ of *A. millepora* and *P. damicornis* corals decreased by 0.50 and 0.61‰, respectively compared to spring. Meanwhile, the $\Delta^{h\text{-}z\ 13}C$ values decreased by 0.03 and 0.04‰ compared to spring, respectively. This implied that the heterotrophic predation intensity of coral hosts of the two species increased during the summer when photosynthetic rate of the endosymbionts decreased, although there was no statistically significant difference.

Table 2
The Results of Geochemical Analysis

Species	Sampling month	$\delta^{13}C_z$ (V-PDB; ‰)	$\delta^{13}C_h$ (V-PDB; ‰)	$\Delta^{h\text{-}z\ 13}C$ (V-PDB; ‰)	$\delta^{13}C_{TL}$ (V-PDB; ‰)
A. millepora	March	−13.42 ± 0.56	−14.06 ± 0.37	−0.64 ± 0.89	−16.64 ± 0.61
	June	−13.89 ± 0.52	−14.56 ± 0.93	−0.67 ± 1.15	−18.74 ± 0.47
	October	−13.47 ± 0.33	−14.10 ± 0.25	−0.63 ± 0.35	−16.84 ± 0.48
P. damicornis	March	−13.24 ± 0.50	−13.97 ± 0.53	−0.73 ± 0.65	−16.55 ± 0.21
	June	−13.81 ± 0.38	−14.58 ± 0.74	−0.77 ± 0.67	−18.62 ± 0.45
	October	−13.41 ± 0.30	−14.13 ± 0.29	−0.73 ± 0.29	−16.81 ± 0.41

Note. The mean values (mean ± 1SD) of $\delta^{13}C_z$, $\delta^{13}C_h$, $\Delta^{h\text{-}z\ 13}C$, and $\delta^{13}C_{TL}$ of 2 different coral species in March, June, and October.

That is to say, coral hosts can increase their heterotrophic predation intensity when their energy supply is insufficient. The results are similar to relevant previous studies. For example, Palardy et al. (2005) conducted systematic experiments to test the autotrophic photosynthesis of endosymbionts and the intensity of host heterotrophic predation in three coral species from Panama at different water depths, and found that the photosynthetic rate of endosymbionts decreased, while the host predation intensity was enhanced significantly with depth.

3.3. Stored Lipid Is Another Important Type of Alternative Energy Sources

3.3.1. Seasonal Changes in Lipid Content

Coral's own stored nutrients are another potential source of energy, including proteins, carbohydrates and lipids (Leuzinger et al., 2012). Therein, proteins and carbohydrates account for only a small fraction of the coral's energy reserves, and the energy provided by these two substances is often used as a replenishment for coral in a short time (Hoogenboom et al., 2010; Porter et al., 1989). Scleractinian corals are lipid-rich organisms, with total lipids accounting for approximately 10%–46% of the tissue's dry weight (Al-Moghrabi et al., 1995; Harland et al., 1992, 1993). Lipids produce at least two-thirds more energy compared to the same unit mass of protein or carbohydrate, thus lipids have a relatively higher energy value (Conlan et al., 2020; Parrish, 2013). In this study, we compare and analyze the coupled changes in endosymbionts autotrophic photosynthesis, the host's heterotrophic predation, and coral's lipid content across different seasons, to better understand the mechanism of the role of lipids in maintaining a stable energy supply.

Our results showed that the total lipid content of two species of corals have decreased significantly in summer ($p < 0.05$, Figure 3b). Specifically, lipid content of *A. millepora* and *P. damicornis* corals decreased by about 2.08 and 1.88 mg cm^{-2} in summer than that in spring, representing 60.82% and 53.56% of lipid content in spring, respectively. And then increased by about 0.43 and 0.92 mg cm^{-2} in autumn than that in summer, representing 32.09% and 56.44% of summer, respectively (Table 1). The seasonal variation of lipid content was synchronized with ZD (Figure 3). So we suggest that corals consume more lipids to maintain the stability of energy supply in summer when the photosynthetic rate of endosymbionts decreases. In autumn, the density and photosynthesis of endosymbionts increased, the demand for lipid decreased, and the intensity of lipid catabolism decreased, leading to the recovery of lipid content. Previous studies have also found changes in coral lipid content under different conditions. For example, Al-Moghrabi et al. (1995) found that the autotrophic photosynthesis of coral endosymbionts decreased and corals' energy supply was insufficient under the shading state. The content of fatty acids, which are important components of lipid storage in the host tissue, is reduced significantly. Rodrigues et al. (2008) found that *P compressa* and *M capitata* corals consumed more stored lipids after bleaching by investigating the changes in lipid content before and after corals bleaching in Hawaiian. The synergistic changes of coral lipid, ZD and photosynthetic rate indicated that lipid could be used as an important supplement to maintain the balance of energy supply when corals were under environmental stress.

3.3.2. Isotopic Evidence of Lipid Consumption

The seasonal variation of $\delta^{13}C_{TL}$ can further verify that corals consume more lipids as an energy supplement in summer. Previous studies have shown that corals have different kinds of lipids, and not all of them were consumed equally. For example, Grottoli et al. (2004) found that the ratio of stored lipids to total lipids decreased and the ratio of structural lipids to total lipids increased in *P compressa* and *M verrucosa* corals after bleaching. This means that stored lipids were consumed as energy (Baumann et al., 2014; Grottoli et al., 2004). In addition, Grottoli and Rodrigues (2011) found that stored lipids have higher $\delta^{13}C$ values than structural lipids, and when corals consume stored lipids, the total lipids become more depleted in ^{13}C. Generally, the more lipids are consumed, the lower the $\delta^{13}C_{TL}$ value is. For example, a large amount of lipids were consumed after coral bleaching which result in decreases in $\delta^{13}C_{TL}$ of 1.9 and 3.4 ‰ in *Porites compressa* and *Montipora capitata* corals, respectively (Grottoli & Rodrigues, 2011). Besides, Alamaru et al. (2009) reported that $\delta^{13}C_{TL}$ values of *Stylophora pistillata* and *Favia favus* corals reduced by more than 4 ‰ along a 60 m water depth gradient in the Red Sea, due to the decrease in autotrophic photosynthetic rate and the consumption of more lipids. In our study, the $\delta^{13}C_{TL}$ values of both coral species showed significant seasonal differences ($p < 0.01$) with reduction amplitude 2.1 and 2.07 ‰ respectively (Table 2 and Figure 4d), which is roughly consistent with previous research results. This demonstrated that corals consumed more storage lipids enriched in ^{13}C to maintain adequate

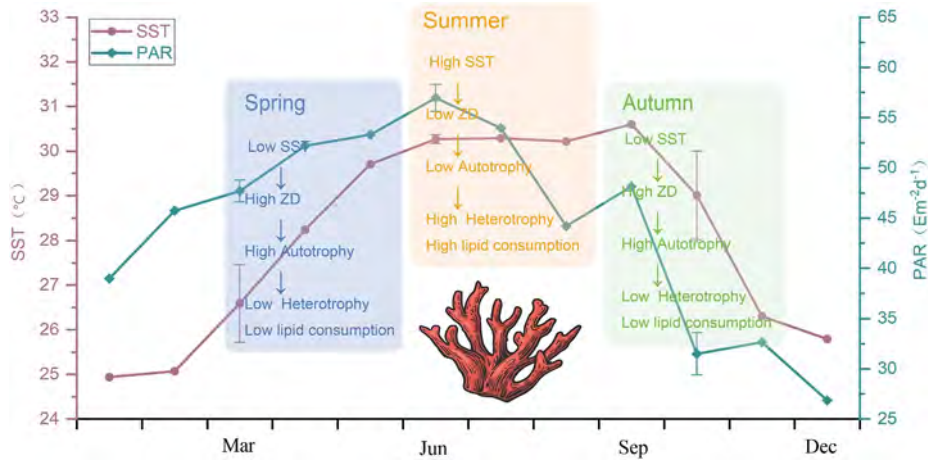


Figure 6. The graphical abstract about seasonal variations in coral zooxanthellae density, autotrophic rate of the symbiotic zooxanthellae, heterotrophic predation rate of the hosts, and the comsumption of lipids in the South China Sea.

energy supply when photosynthesis of endosymbionts was reduced in summer. In autumn, the lipid consumption became less due to the increase of ZD and photosynthesis. This study suggests that branching *A. millepora* and *P. damicornis* corals can maintain a stable energy supply by consuming more of their stored lipids when the energy supplied by the endosymbionts was insufficient. The seasonal changes in coral energy supply patterns in Xisha Islands reefs in the SCS are briefly summarized in Figure 6.

3.4. Implication of Coral Lipids for Their Environmental Stress Tolerance

The energy supply of organisms is the basis for maintaining their daily metabolic activities. Coral need to consume large amounts of lipids when they are exposed to high-frequency or prolonged environmental stress. Lipids as an important substance for corals to store energy, may affect their ability to survive under different environmental stresses. This study analyzed the seasonal changes in coral nutrition and lipids through $\delta^{13}C$ analysis. Results clearly demonstrate that storage lipid consumption is an important alternative energy source for corals when the energy obtained from autotrophic photosynthesis could not meet the daily metabolic demands due to ZD decreases in summer. It should be pointed out that the lipid reserves of corals are limited, and the lipid content of different species of corals also varies (Baumann et al., 2014; Grottoli & Rodrigues, 2011; Xu et al., 2022). Therefore, we consider that corals with different lipid contents may affect their environmental adaptability and bleaching sensitivity under the backdrop of global warming, and coral with higher lipid reserves may have greater environmental adaptability.

In our previous research, we have found significant differences in lipid contents between massive *Favia palauensis*, *Porites lutea* and the branching *Acropora millepora*, *Pocillopora damicornis* corals in Xisha Islands in the SCS (Xu et al., 2022). Specifically, massive *Favia palauensis* and *Porites lutea* have higher lipid contents than branching *Acropora millepora* and *Pocillopora damicornis* corals. Coincidentally, ecological surveys on coral community composition and live coral coverage data in the study area have shown that massive corals have more survival advantages compared to branching corals. For example, Liao (2021) found that the dominant position of massive corals was increasingly accompanied by a decrease in the coverage of branching corals when they conducted an investigation about the spatial distribution characteristics of coral communities in Xisha Islands in the SCS. Therefore, we consider that the level of coral lipid reserves is an important factor affecting their resistance to environmental stress, and may even further affect the species survival advantage of coral reefs. Coral species with higher lipid reserves could have a selective advantage and higher resistance to bleaching in the context of future climate scenarios characterized by more frequent thermal stress events.

What we want to emphasize is that the two coral species selected in this study *Acropora millepora* and *Pocillopora damicornis* were both branching corals, and there were no significant difference in their lipid content and lipid carbon isotopes (Table 3). In future research, studies can be conducted on corals of different species collected from reef areas at different latitudes and/or different water depths, and combining indoor conditioned

Table 3
Interspecific Differences in Zooxanthellae Density, Lipid Content and Stable Carbon Isotope Ratios of Two Coral Species (Independent-Sample t-Test)

Parameter	ZD	Lipid content	$\delta^{13}C_z$	$\delta^{13}C_h$	$\Delta^{h-z}\,^{13}C$	$\delta^{13}C_{TL}$
t	1.58	−1.82	−0.77	0.01	0.54	−0.12
p	0.12	0.07	0.44	0.99	0.59	0.90

Note. $p < 0.05$ was considered significant. The *t*-value represents the degree of difference between the means of two independent samples relative to the size of the sample's variability, The *p*-value represents the significance level of the difference, $p < 0.05$ was considered significant.

cultivation experiments. Further investigate and validate the impact mechanism of lipids on coral environmental adaptability and field community distribution.

4. Conclusions

In this study, we combined isotope geochemical indices and physiological parameters to investigate the response of lipids to the changes in density and photosynthetic rate of endosymbionts of *A. millepora* and *P. damicornis* corals in summer. And further analyzed the significance of lipids in maintaining the stability of energy supply. The results showed that the high SST in summer caused the corals to discard part of the endosymbionts. The photosynthetic rate of the endosymbionts were reduced, which in turn led to the decrease of the energy supplied by autotrophy. At this time, heterotrophic predation intensity of coral hosts increased and the lipid content decreased. This suggests that corals can maintain the stability of energy supply by increasing their heterotrophic predation and consuming their own stored lipids when the density of endosymbionts and photosynthesis decrease in summer. The $\delta^{13}C_{TL}$ value became significantly negative ($p < 0.001$) in summer which further confirmed that lipids were consumed. Lipid reserves is an effective supplement to the reduced autotrophic nutrient supply of the endosymbionts under environmental stress, which are important for improving coral's adaptability to environmental stresses as well as resistance to bleaching.

Data Availability Statement

The coral ZD, Lipid content, and $\delta^{13}C$ data can be retrieved from the Supplemental Information 1. In addition, the data used in this paper have been deposited in a general data repository [Dataset], they are available from the link https://doi.org/10.6084/m9.figshare.27085615 (Mo et al., 2024).

Acknowledgments
This work was funded by the National Natural Science Foundation of China (Grants 42090041, 42030502 & 41663001), the Opening Project of Guangxi Laboratory on the Study of Coral Reefs in the South China Sea (GXLSCRSCS2022001), Jiangsu Key Laboratory of Coast Ocean Resources Development and Environmental Security, Hohai University (JSCE202302).

References

Alamaru, A., Loya, Y., Brokovich, E., Yam, A., & Shemesh, A. (2009). Carbon and nitrogen utilization in two species of Red Sea corals along a depth gradient: Insights from stable isotope analysis of total organic material and lipids. *Geochimica et Cosmochimica Acta*, *73*(18), 5333–5342. https://doi.org/10.1016/j.gca.2009.06.018

Al-Moghrabi, S., Allemand, D., Couret, J., & Jaubert, J. (1995). Fatty acids of the scleractinian coral *Galaxea fascicularis*: Effect of light and feeding. *Journal of Comparative Physiology B*, *165*(3), 183–192. https://doi.org/10.1007/BF00260809

Anthony, K. R., Connolly, S. R., & Willis, B. L. (2002). Comparative analysis of energy allocation to tissue and skeletal growth in corals. *Limnology & Oceanography*, *47*(5), 1417–1429. https://doi.org/10.4319/lo.2002.47.5.1417

Baumann, J., Grottoli, A. G., Hughes, A. D., & Matsui, Y. (2014). Photoautotrophic and heterotrophic carbon in bleached and non-bleached coral lipid acquisition and storage. *Journal of Experimental Marine Biology and Ecology*, *461*(1), 469–478. https://doi.org/10.1016/j.jembe.2014.09.017

Bhagooli, R., & Hidaka, M. (2004). Photoinhibition, bleaching susceptibility and mortality in two scleractinian corals, *Platygyra ryukyuensis* and *Stylophora pistillata*, in response to thermal and light stresses. *Comparative Biochemistry and Physiology Part A: Molecular & Integrative Physiology*, *137*(3), 547–555. https://doi.org/10.1016/j.cbpb.2003.11.008

Browne, N. K., Precht, E., Last, K. S., & Todd, P. A. (2014). Photo-physiological costs associated with acute sediment stress events in three near-shore turbid water corals. *Marine Ecology Progress Series*, *502*, 129–143. https://doi.org/10.3354/meps10714

Chapron, L., Schoepf, V., Levas, S. J., Aschaffenburg, M. D., Warner, M. E., & Grottoli, A. D. (2022). Natural variability in Caribbean coral physiology and implications for coral bleaching resilience. *Frontiers in Marine Science*, *8*, 811005. https://doi.org/10.3389/fmars.2021.811055

Chen, B., Yu, K., Liang, J., Wen, H., Guanghua, W., Hongfei, S., et al. (2019). Latitudinal variation in the molecular diversity and community composition of Symbiodiniaceae in coral from the South China Sea. *Frontiers in Microbiology*, *10*, 1278. https://doi.org/10.3389/fmicb.2019.01278

Conlan, J., Bay, L., Jones, A., Thompson, A., & Francis, D. S. (2020). Seasonal variation in the lipid profile of *Acropora millepora* at Halfway Island. *Great Barrier Reef. Coral Reefs*, *39*(6), 1753–1765. https://doi.org/10.1007/s00338-020-02001-w

Conti-Jerpe, I., Thompson, P. D., Wong, C., Oliveira, N. L., Duprey, N., Moynihan, M., et al. (2021). Response to comment on trophic strategy and bleaching resistance in reef-building corals. *Science Advances*, *7*. https://doi.org/10.1126/sciadv.aaz5443

Crandall, J. B., Teece, M., Estes, B., Manfrino, C., & Ciesla, J. (2016). Nutrient acquisition strategies in mesophotic hard corals using compound specific stable isotope analysis of sterols. *Journal of Experimental Marine Biology and Ecology*, *474*, 133–141. https://doi.org/10.1016/j.jembe.2015.10.010

Crossland, C., Barnes, D., & Borowitzka, M. (1980). Diurnal lipid and mucus production in the staghorn coral *Acropora acuminata*. *Marine Biology*, *60*(2–3), 81–90. https://doi.org/10.1007/BF00389151

Dassié, E. P., Lemley, G. M., & Linsley, B. K. (2013). The Suess effect in Fiji coral $\delta^{13}C$ and its potential as a tracer of anthropogenic CO_2 uptake. *Palaeogeography, Palaeoclimatology, Palaeoecology*, *370*, 30–40. https://doi.org/10.1016/j.palaeo.2012.11.012

Davies, P. S. (1991). Effect of daylight variations on the energy budgets of shallow-water corals. *Marine Biology*, *108*(1), 137–144. https://doi.org/10.1007/BF01313481

Deng, W. F., Wei, G. J., Xie, L. H., & Yu, K. F. (2013). Environmental controls on coral skeletal $\delta^{13}C$ in the northern South China Sea. *Journal of Geophysical Research-Biogeosciences*, *118*(4), 1359–1368. https://doi.org/10.1002/jgrg.20116

Fagoonee, I., Wilson, H., Hassell, M., & Hassell, M. P. (1999). The dynamics of zooxanthellae populations: A long-term study in the field. *Science*, *283*(5403), 843–845. https://doi.org/10.1126/science.283.5403.843

Ferrier-Pagès, C., & Leal, M. C. (2019). Stable isotopes as tracers of trophic interactions in marine mutualistic symbioses. *Ecology and Evolution*, *9*(1), 723–740. https://doi.org/10.1002/ece3.4712

Ferrier-Pagès, C., Sauzéat, L., & Balter, V. (2018). Coral bleaching is linked to the capacity of the animal host to supply essential metals to the symbionts. *Global Change Biology*, *24*(7), 3145–3157. https://doi.org/10.1111/gcb.14141

Fine, M., Hoegh-Guldberg, O., Meroz-Fine, E., & Dove, S. (2019). Ecological changes over 90 years at Low Isles on the Great Barrier Reef. *Nature Communications*, *10*(1), 4409. https://doi.org/10.1038/s41467-019-12431-y

Glynn, P., & D'Croz, L. (1990). Experimental evidence for high temperature stress as the cause of El Nino-coincident coral mortality. *Coral Reefs*, *8*, 181–191. https://doi.org/10.1007/BF00265009

Grottoli, A., Rodrigues, L., & Juarez, C. (2004). Lipids and stable carbon isotopes in two species of Hawaiian corals, *Porites compressa* and *Montipora verrucosa*, following a bleaching event. *Marine Biology*, *145*(3), 621–631. https://doi.org/10.1007/s00227-004-1337-3

Grottoli, A. G., & Rodrigues, L. J. (2011). Bleached *Porites compressa* and *Montipora capitata* corals catabolize δ^{13} C-enriched lipids. *Coral Reefs*, *30*(3), 687–692. https://doi.org/10.1007/s00338-011-0756-0

Grottoli, A. G., Rodrigues, L. J., & Palardy, J. E. (2006). Heterotrophic plasticity and resilience in bleached corals. *Nature*, *440*(7088), 1186–1189. https://doi.org/10.1038/nature04565

Gustafsson, M. V., Aref, T., Kockum, A. F., Ekström, M. K., Johansson, G., & Delsing, P. (2014). Propagating phonons coupled to an artificial atom. *Science*, *346*(6206), 207–211. https://doi.org/10.1126/science.1257219

Harithsa, S., Raghukumar, C., & Dalal, S. (2005). Stress response of two coral species in the Kavaratti atoll of the Lakshadweep Archipelago, India. *Coral Reefs*, *24*(3), 463–474. https://doi.org/10.1007/s00338-005-0008-2

Harland, A., Fixter, L., Davies, P. S., & Anderson, R. A. (1992). Effect of light on the total lipid content and storage lipids of the symbiotic sea anemone *Anemonia viridis*. *Marine Biology*, *112*(2), 253–258. https://doi.org/10.1007/BF00702469

Harland, A., Navarro, J., Davies, P. S., & Fixter, L. M. (1993). Lipids of some Caribbean and Red Sea corals: Total lipid, wax esters, triglycerides and fatty acids. *Marine Biology*, *117*(1), 113–117. https://doi.org/10.1007/BF00346432

Hoegh-Guldberg, O. (1999). Climate change, coral bleaching and the future of the world's coral reefs. *Marine and Freshwater Research*, *50*, 839–866. https://doi.org/10.1071/MF99078

Hoogenboom, M., Rodolfo-Metalpa, R., & Ferrier-Pagès, C. (2010). Co-variation between autotrophy and heterotrophy in the Mediterranean coral *Cladocora caespitosa*. *Journal of Experimental Biology*, *213*(14), 2399–2409. https://doi.org/10.1242/jeb.040147

Houlbrèque, F., & Ferrier-Pagès, C. (2009). Heterotrophy in tropical scleractinian corals. *Biological Reviews*, *84*, 1–17. https://doi.org/10.1111/j.1469-185X.2008.00058.x

Hughes, A. D., & Grottoli, A. G. (2013). Heterotrophic compensation: A possible mechanism for resilience of coral reefs to global warming or a sign of prolonged stress? *PLoS One*, *8*(11), e81172. https://doi.org/10.1371/journal.pone.0081172

Hughes, A. D., Grottoli, A. G., Pease, T. K., & Matsui, Y. (2010). Acquisition and assimilation of carbon in non-bleached and bleached corals. *Marine Ecology Progress Series*, *420*, 91–101. https://doi.org/10.3354/meps08866

Imbs, A. B., Latyshev, N. A., Dautova, T. N., & Latypov, Y. Y. (2010). Distribution of lipids and fatty acids in corals by their taxonomic position and presence of zooxanthellae. *Marine Ecology Progress Series*, *409*, 65–75. https://doi.org/10.3354/meps08622

Jones, R. N., Brush, E. G., Dilley, E. R., & Hixon, M. A. (2021). Autumn coral bleaching in Hawai'i. *Marine Ecology Progress Series*, *675*, 199–205. https://doi.org/10.3354/meps13837

Leuzinger, S., Willis, B. L., & Anthony, K. (2012). Energy allocation in a reef coral under varying resource availability. *Marine Biology*, *159*(1), 177–186. https://doi.org/10.1007/s00227-011-1797-1

Li, S., Yu, K., Shi, Q., Chen, T., Zhao, M., & Zhao, J. (2008). Interspecies and spatial diversity in the symbiotic zooxanthellae density in corals from northern South China Sea and its relationship to coral reef bleaching. *Chinese Science Bulletin*, *53*(2), 295–303. https://doi.org/10.1007/s11434-007-0514-4

Liao, Z. H. (2021). Spatial distribution of coral community and benthic algae and their Ecological impacts across the South China Sea. *Guangxi University*. https://doi.org/10.27034/d.cnki.ggxiu.2021.000072

Lyndby, N. H., Holm, J. B., Wangpraseurt, D., Grover, R., Rottier, C., Kühl, M., & Ferrier-Pagès, C. (2020). Effect of temperature and feeding on carbon budgets and O2 dynamics in *Pocillopora damicornis*. *Marine Ecology Progress Series*, *652*, 49–62. https://doi.org/10.3354/meps13474

Maier, C., Weinbauer, M. G., & Pätzold, J. (2010). Stable isotopes reveal limitations in C and N assimilation in the Caribbean reef corals *Madracis auretenra, M. carmabi* and *M. formosa*. *Marine Ecology Progress Series*, *412*, 103–112. https://doi.org/10.3354/meps08674

Marsh, J. A. (1970). Primary productivity of reef-building calcareous red algae. *Ecology*, *51*(2), 255–263. https://doi.org/10.2307/1933661

Marubini, F., & Davies, P. (1996). Nitrate increases zooxanthellae population density and reduces skeletogenesis in corals. *Marine Biology*, *127*(2), 319–328. https://doi.org/10.1007/BF00942117

Mo, H., Xu, S., Yu, K., Gao, J., & Men, Z. (2024). Data for Seasonal variations in coral lipids and their significance for energy maintenance in the South China Sea [Dataset]. *Figshare*. https://doi.org/10.6084/m9.figshare.27085615

Muscatine, L., & Cernichiari, E. (1969). Assimilation of photosynthetic products of zooxanthellae by a reef coral. *The Biological Bulletin*, *137*(3), 506–523. https://doi.org/10.2307/1540172

Muscatine, L., Porter, J., & Kaplan, I. (1989). Resource partitioning by reef corals as determined from stable isotope composition. *Marine Biology*, *100*(2), 185–193. https://doi.org/10.1007/BF00391957

Nahon, S., Richoux, N. B., Kolasinski, J., Desmalades, M., Ferrier-Pages, C., Lecellier, G., et al. (2013). Spatial and temporal variations in stable carbon (δ^{13}C) and nitrogen (δ^{15}N) isotopic composition of symbiotic scleractinian corals. *PLoS One*, *8*(12), e81247. https://doi.org/10.1371/journal.pone.0081247

Oku, H., Yamashiro, H., Onaga, K., Sakai, K., & Iwasaki, H. (2003). Seasonal changes in the content and composition of lipids in the coral *Goniastrea aspera*. *Coral Reefs*, *22*(1), 83–85. https://doi.org/10.1007/s00338-003-0279-4

Palardy, J. E., Grottoli, A. G., & Matthews, K. A. (2005). Effects of upwelling, depth, morphology and polyp size on feeding in three species of Panamanian corals. *Marine Ecology Progress Series*, *300*, 79–89. https://doi.org/10.3354/meps300079

Palardy, J. E., Rodrigues, L. J., & Grottoli, A. G. (2008). The importance of zooplankton to the daily metabolic carbon requirements of healthy and bleached corals at two depths. *Journal of Experimental Marine Biology and Ecology*, *367*(2), 180–188. https://doi.org/10.1016/j.jembe.2008.09.015

Papina, M., Meziane, T., & Van Woesik, R. (2003). Symbiotic zooxanthellae provide the host-coral *Montipora digitata* with polyunsaturated fatty acids. *Comparative Biochemistry and Physiology Part B: Biochemistry and Molecular Biology*, *135*(3), 533–537. https://doi.org/10.1016/S1096-4959(03)00118-0

Parrish, C. C. (2013). Lipids in marine ecosystems. *International Scholarly Research Notices*, *2013*(1), 604045–604116. https://doi.org/10.5402/2013/604045

Patton, J. S., & Burris, J. E. (1983). Lipid synthesis and extrusion by freshly isolated zooxanthellae (symbiotic algae). *Marine Biology*, *75*(2–3), 131–136. https://doi.org/10.1007/BF00405995

Porter, J. W., Fitt, W. K., Spero, H. J., Rogers, C. S., & White, M. W. (1989). Bleaching in reef corals: Physiological and stable isotopic responses. *Proceedings of the National Academy of Sciences*, *86*(23), 9342–9346. https://doi.org/10.1073/pnas.86.23.9342

Qin, Z., Yu, K., Chen, B., Wang, Y., Liang, J., Luo, W., et al. (2019). Diversity of Symbiodiniaceae in 15 coral species from the southern South China Sea: Potential relationship with coral thermal adaptability. *Frontiers in Microbiology*, *10*, 2343. https://doi.org/10.3389/fmicb.2019.02343

Qin, Z., Yu, K., Wang, Y., Liang, J., Luo, W., Xu, L., et al. (2019). Spatial and intergeneric variation in physiological indicators of corals in the South China Sea: Insights into their current state and their adaptability to environmental stress. *Journal of Geophysical Research: Oceans*, *124*(5), 3317–3332. https://doi.org/10.1029/2018JC014648

Reynaud, S., Ferrier-Pages, C., Sambrotto, R., Juillet-Leclerc, A., Jaubert, J., & Gattuso, J. P. (2002). Effect of feeding on the carbon and oxygen isotopic composition in the tissues and skeleton of the zooxanthellate coral *Stylophora pistillata*. *Marine Ecology Progress Series*, *238*, 81–89.

Rodrigues, L. J., & Grottoli, A. G. (2006). Calcification rate and the stable carbon, oxygen, and nitrogen isotopes in the skeleton, host tissue, and zooxanthellae of bleached and recovering Hawaiian corals. *Geochimica et Cosmochimica Acta*, *70*(11), 2781–2789. https://doi.org/10.1016/j.gca.2006.02.014

Rodrigues, L. J., Grottoli, A. G., & Pease, T. K. (2008). Lipid class composition of bleached and recovering *Porites compressa* Dana, 1846 and *Montipora capitata* Dana, 1846 corals from Hawaii. *Journal of Experimental Marine Biology and Ecology*, *358*(2), 136–143. https://doi.org/10.1016/j.jembe.2008.02.004

Schoepf, V., Grottoli, A. G., Levas, S. J., Aschaffenburg, M. D., Baumann, J. H., Matsui, Y., & Warner, M. E. (2015). Annual coral bleaching and the long-term recovery capacity of coral. *Proceedings of the Royal Society B: Biological Sciences*, *282*(1889), 20151817. https://doi.org/10.1098/rspb.2015.1887

Seemann, J. (2013). The use of ^{13}C and ^{15}N isotope labeling techniques to assess heterotrophy of corals. *Journal of Experimental Marine Biology and Ecology*, *442*, 88–95. https://doi.org/10.1016/j.jembe.2013.01.004

Sommer, B., Hodge, J. M., Lachs, L., Cant, J., Pandolfi, J. M., & Beger, M. (2024). Decadal demographic shifts and size-dependent disturbance responses of corals in a subtropical warming hotspot. *Scientific Reports*, *14*(1), 6327. https://doi.org/10.1038/s41598-024-56890-w

Stimson, J. (1987). Location, quantity and rate of change in quantity of lipids in tissue of Hawaiian hermatypic corals. *Bulletin of Marine Science*, *41*(3), 889–904.

Suggett, D. J., & Smith, D. J. (2020). Coral bleaching patterns are the outcome of complex biological and environmental networking. *Global Change Biology*, *26*(1), 68–79. https://doi.org/10.1111/gcb.14871

Swart, P. K., Saied, A., & Lamb, K. (2005). Temporal and spatial variation in the $\delta^{15}N$ and $\delta^{13}C$ of coral tissue and zooxanthellae in *Montastraea faveolata* collected from the Florida reef tract. *Limnology & Oceanography*, *50*(4), 1049–1058. https://doi.org/10.4319/lo.2005.50.4.1049

Teece, M. A., Estes, B., Gelsleichter, E., & Lirman, D. (2011). Heterotrophic and autotrophic assimilation of fatty acids by two scleractinian corals, *Montastraea faveolata* and *Porites astreoides*. *Limnology & Oceanography*. https://doi.org/10.4319/lo.2011.56.4.128

Venn, A., Loram, J., & Douglas, A. (2008). Photosynthetic symbioses in animals. *Journal of Experimental Botany*, *59*(5), 1069–1080. https://doi.org/10.1093/jxb/erm328

Wooldridge, S. A. (2014). Differential thermal bleaching susceptibilities amongst coral taxa: Re-posing the role of the host. *Coral Reefs*, *33*(1), 15–27. https://doi.org/10.1007/s00338-013-1111-4

Xu, L., Liao, Z., Chen, H., Wang, Y., Huang, B., Lin, Q., et al. (2023). Community structure of scleractinian corals in the northern South China Sea and their responses to the marine heatwaves. *Journal of Tropical Oceanography*, *43*(3), 58–71. https://doi.org/10.11978/2023118

Xu, L. J., Yu, K. F., Li, S., Liu, G., Tao, S., Shi, Q., & Zhang, H. (2017). Interseasonal and interspecies diversities of Symbiodinium density and effective photochemical efficiency in five dominant reef coral species from Luhuitou fringing reef, northern South China Sea. *Coral Reefs*, *36*(2), 477–487. https://doi.org/10.1007/s00338-016-1532-y

Xu, S., Men, Z., Yu, K., Chen, H., Mo, H., Chen, B., & Qin, Z. (2022). Interspecific differences in the response of coral trophic status to the decrease in symbiotic zooxanthellae in summer. *Marine Ecology Progress Series*, *694*, 73–87. https://doi.org/10.3354/meps14108

Xu, S., Zhang, Z., Yu, K., Huang, X., Chen, H., Qin, Z., & Liang, R. (2021). Spatial variations in the trophic status of *Favia palauensis* corals in the South China Sea: Insights into their different adaptabilities under contrasting environmental conditions. *Science China Earth Sciences*, *64*(4), 839–852. https://doi.org/10.1007/s11430-020-9774-0

Yamashiro, H., Oku, H., Higa, H., Chinen, I., & Sakai, K. (1999). Composition of lipids, fatty acids and sterols in Okinawan corals. *Comparative Biochemistry and Physiology Part B: Biochemistry and Molecular Biology*, *122*(4), 397–407. https://doi.org/10.1016/S0305-0491(99)00014-0

Yamashiro, H., Oku, H., & Onaga, K. (2005). Effect of bleaching on lipid content and composition of Okinawan corals. *Fisheries Science*, *71*(2), 448–453. https://doi.org/10.1111/j.1444-2906.2005.00983.x

Yentsch, C. M., Yentsch, C. S., Cullen, J. J., Lapointe, B., Phinney, D. A., & Yentsch, S. W. (2002). Sunlight and water transparency: Cornerstones in coral research. *Journal of Experimental Marine Biology and Ecology*, *268*(2), 171–183. https://doi.org/10.1016/S0022-0981(01)00379-3

Zhang, H., Yu, K., Shi, Q., Yan, H., Liu, G., & Chen, T. (2014). Sea surface temperature variations during the Mid-Late Holocene reconstructed by *Porites* coral growth rates in the Xisha Islands. *Quaternary Sciences*, *34*(6), 1296–1305. https://doi.org/10.3969/j.issn.1001-7410.2014.06.19

Global and Planetary Change 257 (2026) 105259



Contents lists available at ScienceDirect

Global and Planetary Change

journal homepage: www.elsevier.com/locate/gloplacha



ENSO variations during the mid- to late Holocene: Evidence from coral growth rates spanning 2203 years in the northern South China Sea

Dahua Huang [a], Kefu Yu [a,b,*], Leilei Jiang [a], Wei Jiang [a]

[a] Guangxi Laboratory on the Study of Coral Reefs in the South China Sea, Coral Reef Research Center of China, School of Marine Sciences, Guangxi University, Nanning 530004, PR China
[b] Southern Marine Science and Engineering Guangdong Laboratory (Guangzhou), Guangzhou 511458, PR China

ARTICLE INFO

Editor: Dr. Fabienne Marret-Davies

Keywords:
Coral growth rate
Sea surface temperature
El Niño–Southern Oscillation
Mid- to late Holocene
Northern South China Sea

ABSTRACT

The El Niño–Southern Oscillation (ENSO) dominates global interannual climate variability and significantly impacts human societies. However, ENSO behavior during the Holocene remains poorly constrained and debated, limiting our ability to assess its long-term dynamics. Here, we present a 2203-year, discontinuous record of annual coral growth rates, derived from 113 U-series-dated fossil corals (*Porites lutea*) collected from eastern Hainan Island in the northern South China Sea (SCS), spanning 5829–2643 years before present (a BP, relative to 1950 Common Era [CE]). Using a robust calibration between coral growth rate and sea surface temperature (SST), we quantitatively reconstruct annual SST fluctuations in the northern SCS, ranging from 24.2 °C to 27.5 °C, with a mean of 25.6 ± 0.4 °C (1σ), approximately 0.7 °C lower than the baseline of 1982–2023 CE. The SST record reveals at least 18 cold periods occurring quasi-periodically at ~200-year intervals, with their durations shortening toward the Late Holocene. Since coral growth rates closely track local SST variability, interannual ENSO signals are reliably preserved in the coral archive. The inferred ENSO variability exhibits pronounced multidecadal modulation, transitioning from weaker-than-present, persistent La Niña-like conditions in the Mid-Holocene (~5800–4200 a BP) to stronger-than-present, prolonged El Niño-like conditions in the Late Holocene (~4200–2600 a BP). These ENSO shifts cannot be fully explained by external forcings such as orbital insolation or volcanic activity, highlighting the predominant role of internal ocean–atmosphere dynamics in modulating ENSO evolution during the Holocene.

1. Introduction

The El Niño–Southern Oscillation (ENSO) is the leading mode of interannual climate variability in the tropical Pacific and generates far-reaching hydroclimatic anomalies through coupled ocean–atmosphere teleconnections (Cai et al., 2020; Geng et al., 2023; McPhaden et al., 2006; Timmermann et al., 2018). During El Niño events, westerly wind anomalies generate downwelling Kelvin waves that deepen the eastern Pacific thermocline and warm the surface through the Bjerknes feedback, while the eastward shift of convection weakens the Walker circulation and induces drought across the western Pacific warm pool (Cai et al., 2021; Vialard et al., 2025). Conversely, La Niña events strengthen the trade winds and the zonal SST gradient, producing broadly opposite anomalies. ENSO is therefore a primary driver of global extremes, including droughts, floods, and heatwaves, and exerts substantial ecological and socioeconomic impacts (Cai et al., 2014; McPhaden, 2015). Although instrumental observations over the past ~150 years reveal pronounced decadal-scale ENSO fluctuations (Deser et al., 2010; Fedorov et al., 2020), major uncertainties remain regarding the influence of anthropogenic warming on ENSO variability (Lawman et al., 2022; Collins et al., 2010). Given that the instrumental record captures only a limited portion of ENSO's intrinsic variability, geological archives are essential for constraining its long-term behavior and improving climate model projections.

The Holocene (since 11,700 a BP, relative to 1950 Common Era [CE]) is particularly valuable as a climate analog for the present interglacial and provides an opportunity to investigate ENSO behavior under different background climate states. Coral-based reconstructions from the central and western tropical Pacific (Beck et al., 1997; Cobb et al., 2013; McGregor et al., 2013; Tudhope et al., 2001) suggest persistently weak ENSO variability during the Mid-Holocene, which is supported by marine sediment records from Peru (Rein et al., 2005). In contrast,

* Corresponding author at: School of Marine Sciences, Guangxi University, No. 100, Daxuedong Road, Xixiangtang District, Nanning 530004, Guangxi, China.
E-mail address: kefuyu@scsio.ac.cn (K. Yu).

https://doi.org/10.1016/j.gloplacha.2025.105259
Received 10 April 2025; Received in revised form 9 December 2025; Accepted 17 December 2025
Available online 18 December 2025
0921-8181/© 2025 Elsevier B.V. All rights are reserved, including those for text and data mining, AI training, and similar technologies.

sediment records from Laguna Pallcacocha (Moy et al., 2002) and evidence from archaeological sites in Peru (Keefer et al., 1998) indicate episodes of strong ENSO variability during the Mid-Holocene. In addition, whether ENSO variability is primarily driven by natural external forcings (Adams et al., 2003; Grothe et al., 2019; Jiménez-Moreno et al., 2021) or internal climate system variability (Cobb et al., 2003; Dee et al., 2020; Wittenberg, 2009) remains vigorously contested. These discrepancies are often attributed to the limited temporal resolution of many paleoclimate records, highlighting the need for more high-resolution ENSO reconstructions.

Porites corals are highly sensitive to environmental changes and provide climatic information at a monthly to annual resolution, making them reliable proxies for reconstructing ENSO variability during the Holocene (Cobb et al., 2003; Corrége et al., 2000; Dee et al., 2020). The northern South China Sea (SCS) hosts widespread *Porites* corals that effectively capture ENSO signals (Dang et al., 2024; Jiang et al., 2023; Yu, 2012). However, diagenetic alteration of coral aragonite can compromise the fidelity of geochemical proxy records (Brachert et al., 2016). In contrast, coral growth rates, measured along the skeletal primary growth axis, are largely insensitive to post-depositional diagenesis

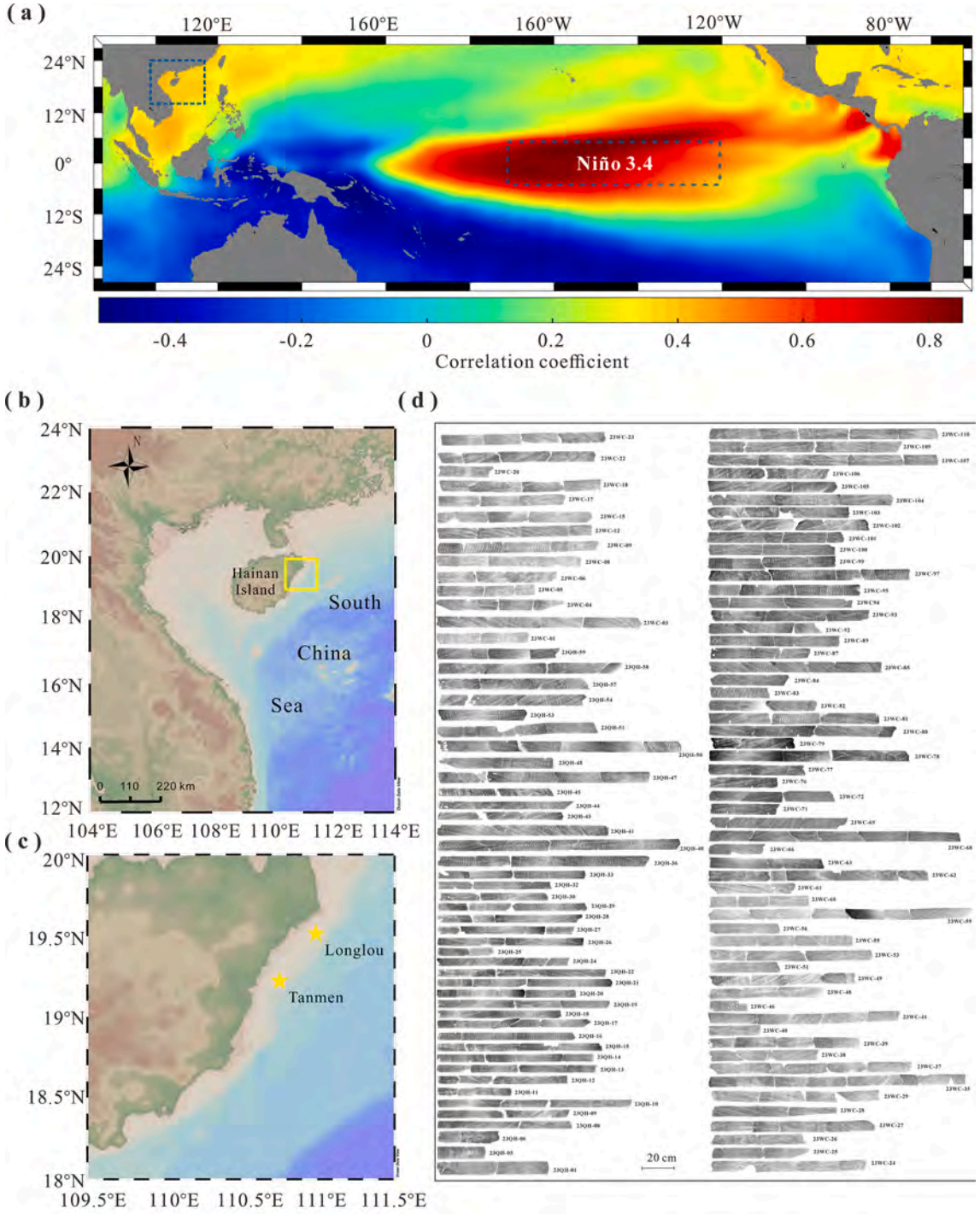


Fig. 1. Overview of the study area and fossil coral samples. (a) Spatial correlation between sea surface temperature (SST) in the Niño 3.4 region and SST in the study area (Jiang et al., 2021a). (b) Sampling locations. SST data are sourced from NOAA OISSTv2 (https://psl.noaa.gov/data/gridded/data.noaa.oisst.v2.html), and the map is generated using Ocean Data View program (https://odv.awi.de/). (c) X-ray images of the 113 fossil coral cores.

(Reuter et al., 2005), reducing this source of uncertainty. Consequently, analyzing *Porites* coral growth rates from the northern SCS offers a robust approach to improving the spatial and temporal resolution of ENSO reconstructions (Dang et al., 2020; Tao et al., 2024). Nonetheless, generating continuous multi-century coral records remains difficult due to the episodic preservation of corals and the discontinuous exposure of fossil colonies on uplifted reefs or reef flats (Cobb et al., 2013). As a result, most coral-based records are composite time series assembled from discrete samples, and truly long-term Holocene-scale continuous records remain scarce.

In this study, 113 fossil cores and one modern coral core (*Porites lutea*) collected from eastern Hainan Island in the northern SCS were analyzed. By integrating U-series dating of the fossils with annual growth-band counting from X-ray images, we constructed a discontinuous 2203-year record of annual coral growth rates, spanning approximately 5829 to 2643 a BP. Based on the relationship between modern coral growth rates and instrumental SST, a transfer function was developed to quantitatively reconstruct an annual SST record over this interval. Given that contemporary instrumental SST and coral growth rate–SST records effectively capture ENSO variability, this 2203-year-long record was used to assess long-term ENSO variability and its potential forcing mechanisms. The long-term, high-resolution SST series reconstructed from coral growth rates elucidates the dynamics of coral growth and ENSO variability over this interval, providing valuable insights into ENSO evolution and its driving mechanisms.

2. Study region

The SCS, located at the edge of the West Pacific Warm Pool, is influenced by the East Asian monsoon, with its interannual climate variability predominantly modulated by ENSO (Chen et al., 2023; Liu et al., 2016; Tan et al., 2016; Wang et al., 2023). Eastern Hainan Island (18°N–20°N, 110°E–111°E) is located in the northern SCS (Fig. 1a), where SST exhibits a distinct annual cycle, with higher SST from May to October (mean ~ 28.3 °C) and lower SST from January to March (~23.3 °C). The co-variability of SST between the northern SCS (including Hainan Island) and the Niño 3.4 region is attributed to the remote influence of ENSO activity through an "atmospheric bridge" (Klein et al., 1999). During El Niño events, weakening of the zonal SST gradient in the tropical Pacific enhances downward shortwave radiation and produces positive SST anomalies in the northern SCS (Jiang et al., 2021a, 2021b; Wang et al., 2000; Yan et al., 2011). Conversely, during La Niña events, negative SST anomalies are observed in the northern SCS as a result of a strengthened tropical Pacific gradient and reduced net solar radiation.

3. Materials and methods

3.1. Coral cores and dating

Coral samples (*Porites lutea*) were collected from eastern Hainan Island in 2023 CE (Fig. 1b–c). Coral cores were extracted from 113 dead colonies and one living colony using a hydraulic rig and a portable electric drill, with core diameters of 60 mm and 80 mm. The total lengths of the dead and living coral cores were approximately 111.9 m and 0.6 m, respectively. In the laboratory, each core was sliced into ~7 mm-thick sections. These sections were soaked in an 8 % H_2O_2 solution for 48 h to remove organic matter, then ultrasonically cleaned in deionized water for one hour to remove surface contaminants. Finally, after drying the sections in an oven at 37 °C, X-radiographs were obtained using a medical X-ray imaging system to identify annual growth-band patterns (Fig. 1d). Uranium-series dating of the dead coral cores was conducted using Multi-Collector Inductively Coupled Plasma Mass Spectrometer (MC-ICP-MS) at the University of Queensland, Australia, following the analytical methods detailed in Yu et al. (2006) and Zhao et al. (2009).

3.2. Growth rate measurement

Coral growth rate was quantified by measuring the distances between annual density bands visible in the X-ray images (Cooper et al., 2012; Helmle et al., 2011; Saenger et al., 2009; Tao et al., 2024). The RadiAnt DICOM Viewer software was used to convert the original X-ray negatives into positive grayscale images for analysis. Measurements were taken along the primary growth axis of each coral (DeLong et al., 2013), by measuring the distance between the midpoints of successive high-density bands, with each adjacent black–white band pair representing one year of skeletal extension. The mean of multiple measurements was calculated as the annual growth rate for that year. Annual growth-band counts derived from X-ray images were then integrated with Uranium-series dating results to establish the chronological framework, assigning each measured coral growth layer to a specific calendar year within dating uncertainties.

3.3. Data acquisition and processing

To evaluate the degree to which SST variability in the northern SCS reliably reflects ENSO variability, monthly SST data (1982–2023 CE) for eastern Hainan Island (18°N–20°N, 110°E–111°E) and for the Niño 3.4 region (5°S–5°N, 170°W–120°W) were compiled from the NOAA Optimum Interpolation SST Analysis dataset (OISSTv2, https://psl.noaa.gov/data/gridded/data.noaa.oisst.v2.html). Sea surface salinity (SSS) data were obtained from the UK Met Office EN4 dataset (https://www.metoffice.gov.uk/hadobs/en4/), and outgoing longwave radiation (OLR) data were extracted from the NOAA HIRS L1B product (Lee et al., 2007). These environmental parameters were used to assess their relative influence on coral growth and to quantify the extent to which SST is the dominant driver in the northern SCS.

Linear regression, spectral analysis, and wavelet transforms were conducted using PAST software. Linear interpolation was performed in SPSS software to facilitate comparison among datasets. In addition, SST anomalies (SSTA) were calculated as deviations from the climatology of the corresponding timescale for each SST record. The SST anomaly series was processed with a 3–7-year band-pass filter to isolate ENSO-frequency variability (Jiang et al., 2021a), and its total variance was taken as an indicator of ENSO intensity (Cobb et al., 2003; Comboul et al., 2015; Jiang et al., 2023). Furthermore, a 30-year sliding window was applied to calculate relative variance (Cobb et al., 2013; Dang et al., 2020), allowing ENSO intensity to be evaluated relative to 1994–2023 CE. In addition, probability density functions (PDFs) based on kernel density estimation were employed to characterize the temporal distribution of ENSO variance (Lawman et al., 2020).

The empirical calibration threshold method (Hereid et al., 2013) was applied to assess detection of ENSO events. Specifically, an initial threshold of 0.01 °C was incrementally adjusted by 0.01 °C to optimize detection of ENSO events (Jiang et al., 2021a; Tao et al., 2024). Based on the optimized thresholds, El Niño events were defined as SST anomalies exceeding 0.12 °C and La Niña events as those falling below −0.12 °C. Furthermore, the detection capability of the SST record from Hainan Island was quantified as the proportion of ENSO events correctly identified from the filtered SSTA series.

4. Results

4.1. Chronology construction

The modern coral core (24NH45) from Hainan Island spans 1982–2023 CE. The U and Th isotopic compositions and corresponding U-Th ages of the 113 fossil corals are listed in Table S1 (errors at 2σ). An age model for each coral was constructed by integrating U-Th ages with annual growth-band patterns identified in X-ray images. Across the 111.9 m of fossil cores and their associated X-ray images, a total of 7085 annual growth layers were identified. Individual fossil cores record

15–164 years of growth, with a mean length of ~63 years (Table S2).

Based on the established chronology, 1608 years of overlap were identified among the fossil corals (Fig. S1c), forming six continuous segments that together span 2203 years of the Mid- to Late Holocene. These segments (ages relative to 1950 CE) are 5829–5780 a BP (50 years), 5733–5149 a BP (585 years), 4667–4470 a BP (198 years), 4403–3212 a BP (1192 years), 3008–2939 a BP (70 years), and 2750–2643 a BP (108 years). The U-Th age uncertainties for each segment are reported at 2σ (Table S1). These discontinuous but temporally extensive segments constitute the high-resolution coral archive used in this study and substantially expand existing tropical coral records.

4.2. Characteristics of coral growth rate

The modern coral (1982–2023 CE) exhibits a mean annual growth rate of 1.246 ± 0.148 (1σ) cm/a, with a maximum of 1.700 cm/a, a minimum of 0.925 cm/a, and an overall amplitude of 0.775 cm/a. In comparison, the 113 fossil corals show a mean growth rate of 1.031 ± 0.138 (1σ) cm/a, with a maximum of 1.620 cm/a, a minimum of 0.584 cm/a, and an amplitude of 1.036 cm/a (Fig. S1a). On average, the fossil corals grew approximately 0.215 cm/a more slowly than the modern coral yet displayed substantially greater variability in annual growth rates.

Since the overlapping coral segments displayed broadly consistent trends, growth rates within the overlapping intervals were averaged to generate six composite continuous segments (Fig. S1b): (1) 5829–5780 a BP (50 years, mean 0.746 cm/a): growth rates declined from ~0.881 cm/a to 0.652 cm/a. (2) 5733–5149 a BP (585 years, 1.010 cm/a): growth rates exhibited an overall increasing trend, ranging from 0.653 cm/a to 1.385 cm/a, with minima occurring at ~5440 a BP (0.848 cm/a) and ~ 5250 a BP (0.821 cm/a). (3) 4667–4470 a BP (198 years, 1.058 cm/a): growth rates decreased sharply from 1.480 cm/a to 0.584 cm/a, yielding an amplitude of ~0.9 cm/a. (4) 4403–3212 a BP (1192 years, 1.034 cm/a): growth rates showed an overall decreasing trend with internal fluctuations. Notably low values occurred at ~4200 a BP (0.603 cm/a), ~4000 a BP (0.881 cm/a), ~3800 a BP (0.926 cm/a), ~3600 a BP (0.671 cm/a), ~3400 a BP (0.760 cm/a) and ~ 3200 a BP (0.754 cm/a), recurring at intervals of approximately 200 years. (5) 3008–2939 a BP (70 years, 0.940 cm/a): growth rates increased rapidly from 0.622 cm/a to 1.380 cm/a. (6) 2750–2643 a BP (108 years, 1.106 cm/a): growth rates rose from 0.818 cm/a to 1.450 cm/a (~2675 a BP) and subsequently declined to 0.707 cm/a.

Overall, the coral growth record can be divided into three broad phases: a period of increasing growth rates (~5800–4400 a BP), followed by a period of decreasing growth rates (~4400–4200 a BP), and a final period characterized by oscillatory growth-rate variability (~4200–2600 a BP). These patterns reflect the high sensitivity of coral growth to environmental variation and provide high-resolution insights into the climate dynamics during the Mid- to Late Holocene.

5. Discussion

5.1. Modern Calibration: coral growth rates as proxies for SST and ENSO

5.1.1. Coral growth rate thermometer

The primary environmental factors controlling coral skeletal growth include SST, SSS, and light availability (Cooper et al., 2012; Lough and Barnes, 1997). To assess their relative influence in the northern SCS, regression analyses were performed between coral growth rates and instrumental records of SST, SSS, and OLR (Fig. S2). The resulting coefficients of determination (R^2) are 0.836 for SST, but only 0.001 for SSS and 0.003 for OLR, indicating that SST is by far the dominant driver of coral growth-rate variability in this region. This interpretation is consistent with findings from Hainan Island (Nie et al., 1997) and the Xisha Islands (Tao et al., 2024), which similarly identified SST as the primary control on coral growth. A strong positive correlation ($r = 0.91$, $P < 0.0001$, $n = 42$) was observed between instrumental SST and coral growth rates from 1982 to 2023 CE in eastern Hainan Island (Fig. 2a). Based on this relationship, a coral growth rate–SST conversion equation (Fig. 2b) was developed using Reduced Major Axis (RMA) regression (Solow and Huppert, 2004):

$$\mathrm{SST}\ (^{\circ}\mathrm{C}) = 3.172\ (\pm 0.200) \times \mathrm{L}\ (\mathrm{cm}) + 22.356\ (\pm 0.251)\ (1\sigma) \quad (1)$$

$$R^2 = 0.84, n = 42, p < 0.0001.$$

where L denotes coral growth rate. From Eq. (1), an increase of 1 mm in coral growth rate corresponds to an increase of 0.3 ± 0.02 °C in SST. Using this calibration, the SST history for eastern Hainan Island from 1982 to 2023 CE was quantitatively reconstructed. The coral-derived SST values range from ~25.3 to 27.8 °C with a mean of 26.3 ± 0.4 °C (1σ), in excellent agreement with the instrumental SST range of 25.3–27.4 °C (26.3 ± 0.4 °C; Fig. S3a) over the same interval.

Over 1982–2023 CE, the coral-based SST closely tracks the instrumental SST in eastern Hainan Island (Fig. S3a), confirming that coral growth rates faithfully capture contemporary temperature variability. The two records exhibit consistent dominant periodicities in their spectral power (Fig. 2c-d), and the 2.5–97.5th percentile ranges of their probability density distributions almost entirely overlap (coral: −2.2 to 1.7, instrumental: −2.0 to 1.9; Fig. S3b), further demonstrating their strong similarity. Together, these results indicate that coral growth rates effectively capture contemporary SST variability in this region. These findings are consistent with observations from other regions, including the Great Barrier Reef (Cooper et al., 2008; Lough and Barnes, 1997), the southwestern Indian Ocean (Cooper et al., 2012), and the Caribbean Sea (Kwiatkowski et al., 2013; Saenger et al., 2009), where positive correlations between coral growth rates and SST have been documented. Notably, Lough and Barnes (2000) reconstructed twentieth-century SST in the Great Barrier Reef and reported that a 1 °C increase in SST corresponded to a 3 mm/year increase in coral growth rates. Such parallels provide further confidence that coral growth rate serves as a reliable "thermometer" proxy for past SST.

5.1.2. Modern ENSO variability

The modern instrumental and coral-derived SST records from Hainan Island both exhibit dominant interannual cycles of 2.3 years (Fig. 2c) and 2.2 years (Fig. 2d), respectively, consistent with the typical ENSO cycle. Furthermore, regression analyses between band-pass-filtered instrumental SST anomalies (detrended relative to the mean of 1982–2023 CE) in Hainan Island and those in the Niño 3.4 region, as well as between coral-derived SSTA from Hainan Island and instrumental SSTA in the Niño 3.4 region, yield statistically significant correlations ($r = 0.55$, $p < 0.001$, Fig. S4a; and $r = 0.31$, $p < 0.05$, Fig. 3c, respectively). In addition, the probability distribution of the coral-recorded SSTA closely matches that of the instrumental Niño 3.4 SSTA, exhibiting comparable 2.5–97.5 % ranges (coral-based: −2.2 to 1.7, Niño 3.4: −2.1 to 1.7; Fig. 3d). We further compared the coral growth rate record from Hainan Island to the coral $\delta^{18}O$ anomaly record from Fanning Island in the central tropical Pacific, which serves as a robust proxy for ENSO variability (Cobb et al., 2013). The two records exhibit a strong negative correlation ($r = -0.71$, $p < 0.001$, $n = 23$), and their probability density distributions show close agreement (Fig. 3a–b). In summary, these results demonstrate that SSTs in eastern Hainan Island are significantly modulated by ENSO variability. Because coral growth rates closely track local SST fluctuations, they enable robust reconstruction of ENSO-related climate variability.

To explicitly identify ENSO events, a 3–7-year band-pass filter and a standard event-threshold analysis were applied (Dang et al., 2024; Hereid et al., 2013; Jiang et al., 2021a), using a 30-year sliding window anchored to the period of 1994–2023 CE. Based on the threshold criterion, the annual SST records from the Niño 3.4 region correctly identify

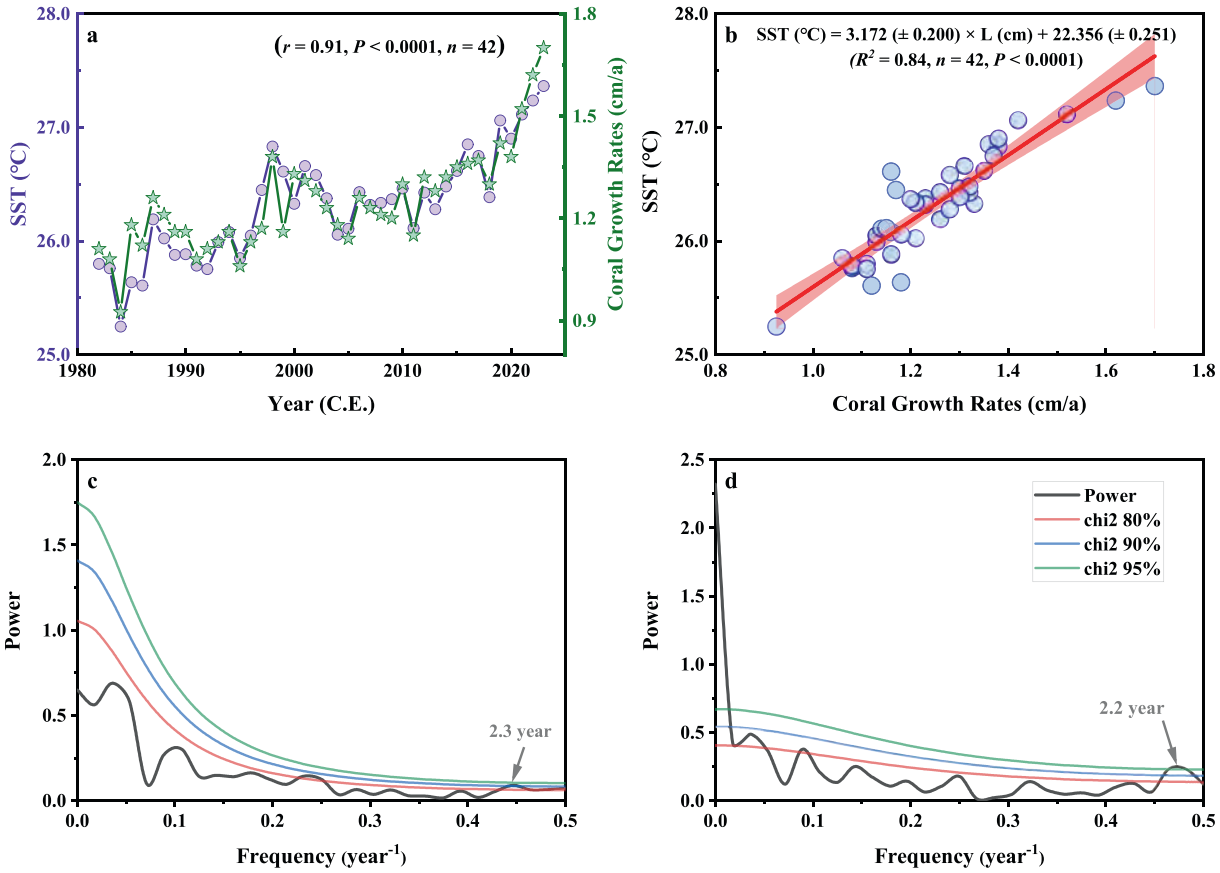


Fig. 2. Establishment of the coral growth rate–sea surface temperature (SST) conversion equation and spectral characteristics of SST variability in Hainan Island. (a) Comparison and (b) regression analysis of the relationship between coral growth rate and SST in the northern South China Sea. (c) Spectral analysis of instrumental SST (1982–2023 CE) and (d) coral growth rate–derived SST (1982–2023 CE). The green, blue, and red lines denote the 80 %, 90 %, and 95 % confidence levels, respectively. (For interpretation of the references to colour in this figure legend, the reader is referred to the web version of this article.)

7 El Niño events (missing 2) and 6 La Niña events (Fig. S4b). This corresponds to a detection rate of 78 % (7/9) for El Niño events and full detection (6/6) of La Niña events over 1994–2023 CE. The two missed El Niño events (1994 and 2004 CE) were likely weak in amplitude, and the conversion from monthly to annual resolution may have smoothed out these weaker ENSO signals. The instrumental SST record from Hainan Island correctly identified 7 El Niño events (missing 2) and 5 La Niña events (with 1 false alarm and 1 missed), achieving a detection rate of 78 % (7/9) for El Niño events and 83 % (5/6) for La Niña events (Fig. S4c). Similarly, our coral record from Hainan Island accurately captured 7 El Niño events (missing 2) and 4 La Niña events (with 1 false alarm and 2 missed), corresponding to a detection rate of 78 % (7/9) for El Niño events and 67 % (4/6) for La Niña events over 1994–2023 CE (Fig. 3e). Notably, both instrumental and coral records reveal an increasing trend in ENSO variance during 1982–2023 CE (Fig. S4d; Fig. 3f). Therefore, these results demonstrate that coral growth rates from Hainan Island reliably record ENSO variability at interannual timescales. Similar ENSO detectability based on growth rate has been documented for modern *Porites* coral from the Xisha Islands (Tao et al., 2024), further supporting the robustness of coral growth rate as an ENSO-sensitive proxy.

5.2. Fossil coral insights into SST fluctuation and ENSO variability

5.2.1. Reconstruction of SST changes during the mid- to late Holocene

Using the established calibration equation, SST variations in the northern SCS were quantitatively reconstructed during 5829–2643 a BP (Fig. 4a). The six continuous coral-derived segments (Table 1) indicate SST ranges of 24.4–25.2 °C (5829–5780 a BP), 24.4–26.8 °C (5733–5149 a BP), 24.2–27.1 °C (4667–4470 a BP), 24.3–27.2 °C (4403–3212 a BP), 24.3–26.7 °C (3008–2939 a BP), and 24.6–27.0 °C (2750–2643 a BP). The full 2203-year composite record yields a mean SST of 25.6 ± 0.4 °C, approximately 0.7 °C lower than the modern baseline (26.3 ± 0.4 °C, 1982–2023 CE). These results indicate that the Mid- to Late Holocene climate in the northern SCS was, on average, cooler than at present, consistent with previous coral-based reconstructions and marine sediment records from the northern SCS (Chen et al., 2024, Fig. 4h; Yang et al., 2019, Fig. 4d). Collectively, our coral record offers robust constraints on the timing and amplitude of oscillatory temperature variations during the Mid- to Late Holocene in this region.

Despite the overall cooling trend, at least 14 distinct warm episodes, with SSTs either comparable to or exceeding modern levels, can be identified within this 2203-year record (Fig. S5, Table S3). Several of these warming events coincide with well-documented periods of coral thermal stress and bleaching (Wang et al., 2021, Fig. 4f; Xu et al., 2017), including those occurring at ~5300 a BP, ~4568 a BP, ~3900 a BP, and ~ 3654 a BP. This pattern is further supported by coral records from Leizhou Peninsula (Yu et al., 2005, Fig. 4h), which report SSTs ~0.5 °C higher than in the 1990s around 4961 ± 54 a BP. These correlations suggest that modern-like or warmer SSTs have been reached repeatedly during the Mid- to Late Holocene, with deleterious impacts on reef ecosystems.

Using 25.2 °C (the annual minimum during 1982–2023 CE) as a threshold, at least 18 cold periods on an interannual scale are identified (Fig. S6–7; Table S4), with 5 pronounced multidecadal cold intervals using a 30-year sliding average (Fig. S6). The most severe cold interval occurred between 5829 and 5780 a BP (24.7 °C), representing a cooling of 1.6 °C relative to 1982–2023 CE. These prolonged cooling phases are

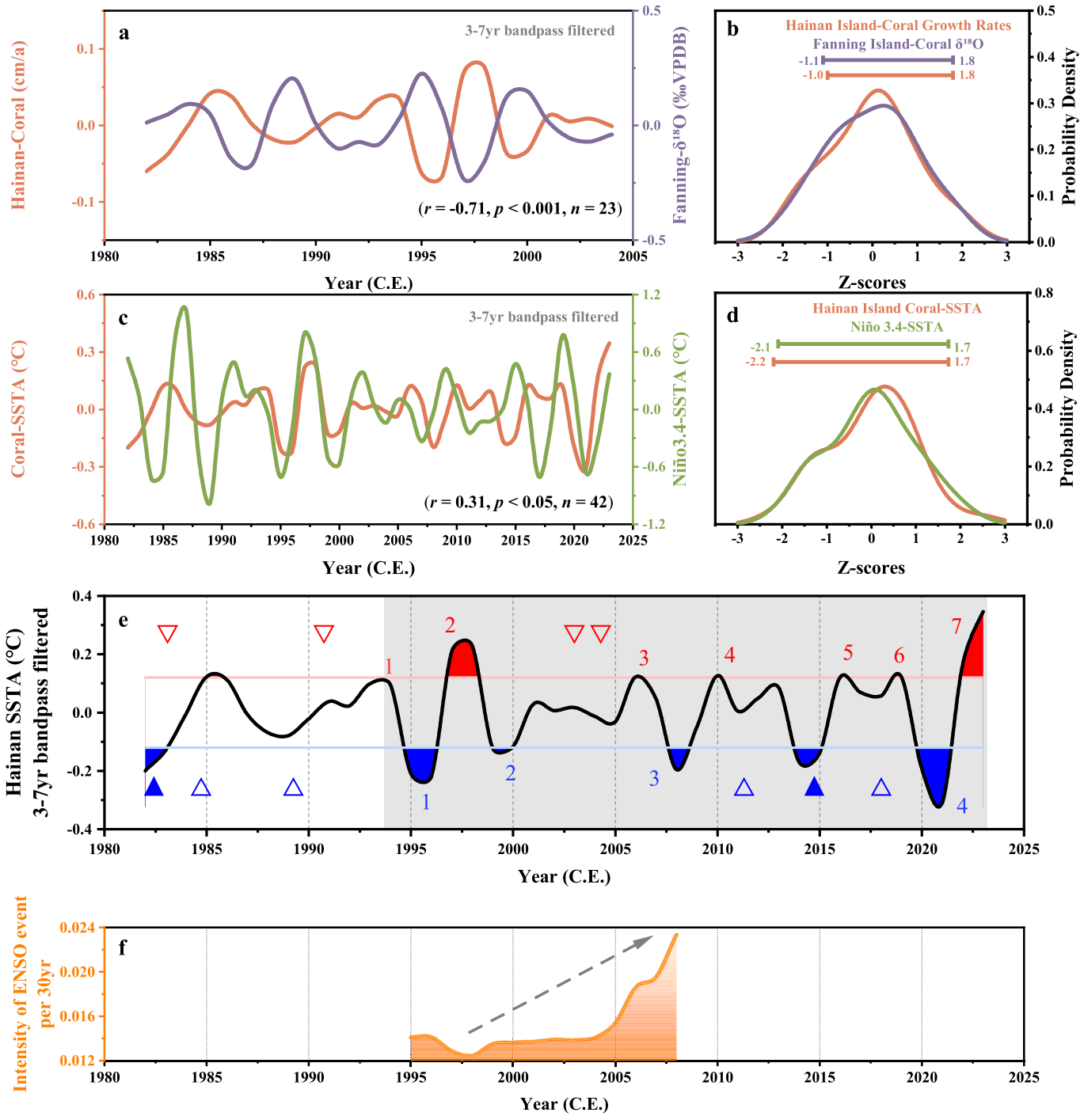
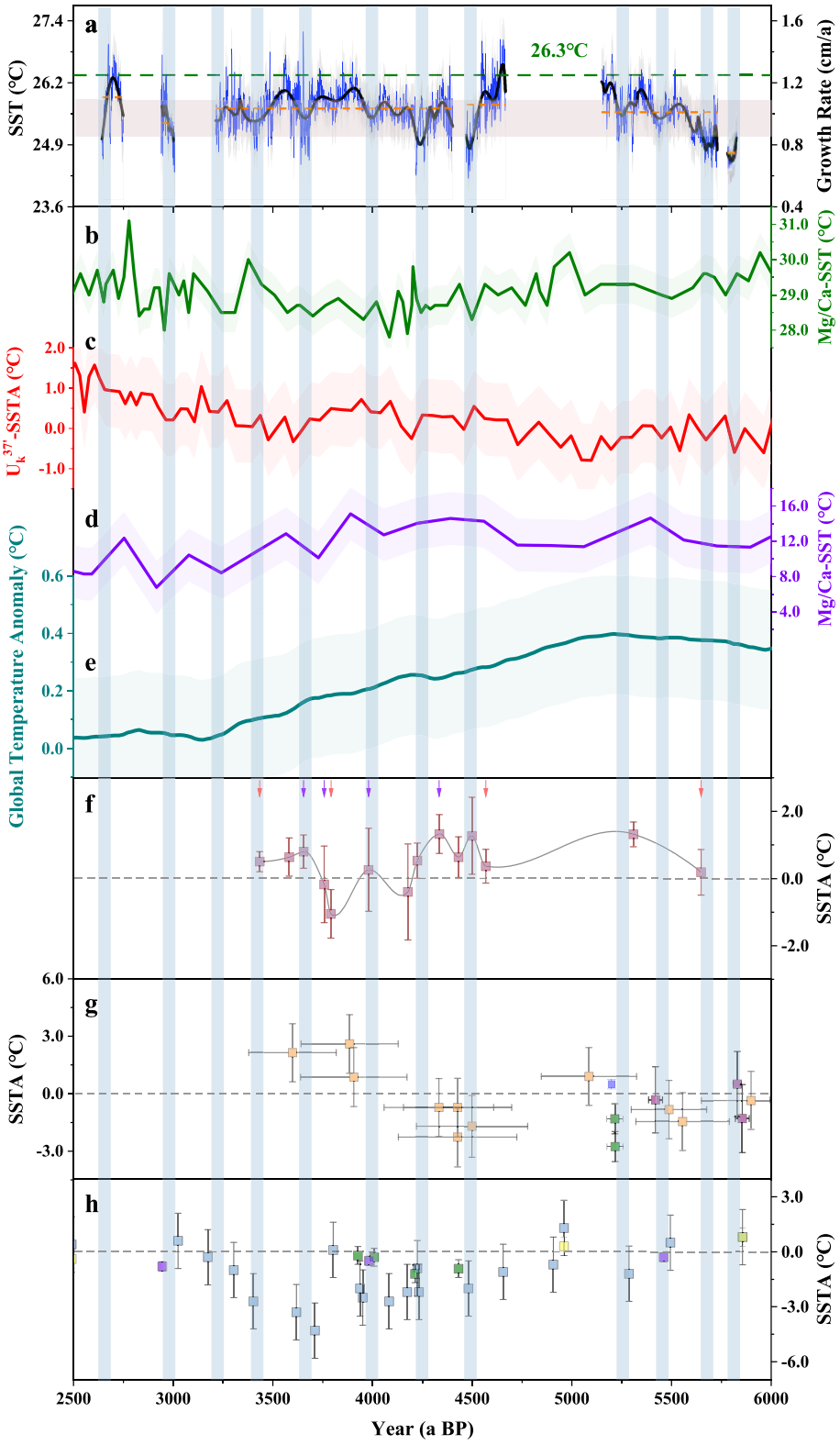


Fig. 3. El Niño–Southern Oscillation (ENSO) signals and variability inferred from modern coral records. (a) Filtered sea surface temperature anomalies (SSTA) and (b) probability density functions (PDFs) of coral records from Hainan Island (orange) and Fanning Island (purple; Cobb et al., 2013) during their overlapping interval (1982–2004 CE). (c) Relationship and (d) PDFs of 3–7-year band-pass-filtered SSTA from Hainan Island (orange) and the Niño 3.4 region (green) over their overlapping period (1982–2023 CE). (e) Extraction of ENSO events from coral-based SSTA using the defined threshold. Red and blue shading indicate identified El Niño and La Niña events, respectively; open triangles denote false negatives, and solid triangles denote false positives. The interval of 1994–2023 CE is highlighted by gray shading. (f) ENSO intensity derived from the variance of the extracted ENSO signal using a 30-year sliding window (1982–2023 CE). Horizontal bars in panels (b) and (d) indicate the 2.5–97.5 percentile ranges. All records in panels (b) and (d) are standardized using *Z*-scores for comparison. El Niño events are defined as SSTA exceeding 0.12 °C and La Niña events as SSTA below −0.12 °C. (For interpretation of the references to colour in this figure legend, the reader is referred to the web version of this article.)

not isolated features but are consistent with widespread paleoclimate evidence from the northern SCS and adjacent regions. Coral Sr/Ca records from Hainan Island indicate a rapid SST decline during the 4200 a BP event (Chen et al., 2023, 2024, Fig. 4h). Coral growth-rate archives from the Xisha Islands (Dang et al., 2020, Fig. 4h; Zhang et al., 2014, Fig. 4h) document SST reductions of 1.0 °C (4420–4312 a BP), 1.3 °C (4189–4112 a BP), and 0.9 °C (2985–2904 a BP) relative to 1887–2007 CE. Similarly, coral records from the Great Barrier Reef (Sadler et al., 2016, Fig. 4g), the central tropical Pacific and western Pacific (Bova et al., 2021, Fig. 4c; Rodriguez et al., 2019, Fig. 4g; Stott et al., 2004,

Fig. 4b), and Indonesia (Abram et al., 2009, Fig. 4g) indicate cooling events centered around 5800 a BP, ~5200 a BP, ~4400 a BP, ~4200 a BP, and ~ 3200 a BP, all of which correspond closely to cold intervals detected in our coral-derived SST record.

Significantly, these coral-based cold intervals exhibit a recurring periodicity of ~200 years. This cycle is consistent with independent Holocene climate reconstructions. For example, the global temperature stack compiled by (Marcott et al., 2013, Fig. 4e) documents cooling events at broadly similar ~200-year intervals. Additional support is provided by solar irradiance reconstructions, which highlight the de Vries (~208-year) solar cycle as a persistent feature of centennial-scale solar variability (Steinhilber et al., 2009, Fig. S8d). The recurrence of



(caption on next page)

Fig. 4. Growth rate–derived sea surface temperature (SST) reconstruction from fossil corals in Hainan Island compared with regional and global proxy records. (a) Reconstructed SST variability from this study. The gray shading represents the ±1σ uncertainty range; the orange dashed line denotes the mean SST of the six continuous segments (5829–5780 a BP, 5733–5149 a BP, 4667–4470 a BP, 4403–3212 a BP, 3008–2939 a BP, and 2750–2643 a BP); the red shaded band indicates the range of mean annual SST values across all fossil coral reconstructions; the green dashed line marks the instrumental mean SST for 1982–2023 CE; and the black curve shows the 30-year sliding mean. (b) SST reconstruction based on Mg/Ca of planktonic foraminifera from the western Pacific (Stott et al., 2004). (c) Alkenone-based, UK'_{37} SST reconstruction from the western Pacific (Bova et al., 2021). (d) SST reconstruction based on Mg/Ca of planktonic foraminifera from the northern South China Sea (Yang et al., 2019). (e) Holocene global temperature compilation sequence (Marcott et al., 2013). (f) Coral Sr/Ca-based SST anomaly reconstruction from the northern SCS (Wang et al., 2021). Arrows denote coral bleaching events: red arrows mark samples containing a single mortality surface, whereas purple arrows indicate samples exhibiting both mortality surfaces and growth discontinuities. (g) Coral-based SST anomaly reconstructions from the Mentawai Islands (Abram et al., 2009, orange squares), Muschu/Koil Island (Abram et al., 2009, purple squares), the Great Barrier Reef (Sadler et al., 2016, green squares), and the central tropical Pacific (Rodriguez et al., 2019, blue squares). (h) Coral Sr/Ca- and growth rate–based SST anomaly reconstructions from the northern SCS (Chen et al., 2024, blue squares; Dang et al., 2020, green squares; Yu et al., 2005, yellow squares; Zhang et al., 2014, purple squares). (For interpretation of the references to colour in this figure legend, the reader is referred to the web version of this article.)

Table 1
Distributional periods of fossil corals and the range of their growth rates and SST variations.

Distribution period ± 2σ (a BP)	Period duration (year)	Range of growth rates (cm/a)	Average growth rate (cm/a)	Range of SST (°C)	Average SST (°C)	SST Polarization (°C)
5829–5780	50	0.652–0.881	0.746	24.4–25.2	24.7 ± 0.4	0.8
5733–5149	585	0.653–1.385	1.010	24.4–26.8	25.6 ± 0.4	2.4
4667–4470	198	0.584–1.480	1.058	24.2–27.1	25.7 ± 0.4	2.9
4403–3212	1192	0.603–1.530	1.034	24.3–27.2	25.6 ± 0.4	2.9
3008–2939	70	0.622–1.380	0.940	24.3–26.7	25.3 ± 0.4	2.4
2750–2643	108	0.707–1.450	1.106	24.6–27.0	25.9 ± 0.4	2.4

~200-year cold intervals in our fossil coral record may therefore reflect sensitivity to these cyclic variations in solar output, superimposed on regional ocean–atmosphere feedbacks in the tropical Pacific.

However, solar forcing is unlikely to have acted as the sole driver of these cooling phases. The timing and magnitude of several SST anomalies do not align precisely with known solar minima, indicating that internal climate processes modulated their regional expression. ENSO-related ocean–atmosphere dynamics likely amplified or dampened the external solar signal, while the East Asian monsoon system, tightly coupled with tropical western Pacific SST, may have further reinforced these cooling intervals. The reconstructed SST minima coincide with reduced East Asian Summer Monsoon intensity inferred from cave speleothems and lacustrine records (Wang et al., 2005, Fig. S8c; Yancheva et al., 2007, Fig. S8b), suggesting that these cold phases formed part of broader shifts in the East Asian–western Pacific climate system.

In summary, the coral-derived cold events in the northern SCS are consistent with regional and global evidence for Holocene cooling. Their quasi-200-year recurrence pattern points to a potential solar pacing, yet the amplitude and timing of the cooling intervals also highlight the role of internal ocean–atmosphere variability and monsoon-ENSO interactions. These findings underscore the need to integrate coral archives with broader multi-proxy datasets to better constrain the mechanisms governing Holocene tropical climate variability.

5.2.2. Reconstruction of ENSO variability during the mid- to late Holocene

The coral-derived SST record during 5829–2643 a BP exhibits pronounced 2–7-year cycles (Fig. S9), consistent with canonical ENSO variability, but with dominant cycles that differ from those of the modern reference period (1982–2023 CE; Fig. 2c–d). High-frequency interannual ENSO signals (Fig. S10) are also identified during 5733–5149 a BP, 4667–4470 a BP, and 4403–3212 a BP. Together, these features indicate that ENSO variability during the Mid- to Late Holocene was neither stationary nor uniform, but instead characterized by notable changes in both frequency and amplitude. The distribution estimated from fossil-based SST anomalies (2.5–97.5 percentile range; Fig. S11) also departs from those of modern coral records (Fig. 3d), further reflecting the instability of ENSO behavior. Moreover, the probability distributions of three fossil coral segments (5829–5780 a BP, 3008–2939 a BP, and 2750–2643 a BP) are skewed toward positive anomalies, suggesting El Niño-like background states, whereas the interval of 5733–5149 a BP is skewed toward negative anomalies, indicating a potential association with La Niña-like conditions.

A 3–7-year band-pass filter was applied to isolate ENSO signals (Fig. 5a) in the coral-derived SST anomalies, and a 30-year moving window was used to reveal interdecadal fluctuations in SSTA from the northern SCS (Fig. 5c). The same 30-year window was employed to count El Niño events and La Niña events, thereby tracking interdecadal trends in ENSO event frequency (Fig. 5d). ENSO intensity was assessed by calculating the variance of the filtered SSTA within a 30-year sliding window (Fig. 5b), using the period of 1994–2023 CE (variance is 0.0233) as the modern reference. Based on these metrics, 15 periods of weak ENSO variability and 16 periods of strong ENSO variability were identified during the Mid- to Late Holocene (Fig. S12, Table 2). These results demonstrate that the Mid-Holocene was not a period of uniformly suppressed ENSO activity, but rather characterized by alternating phases of weak and strong ENSO expression. Notably, the marked increase in strong ENSO intervals after the 4.2 ka event suggests that ENSO variability intensified during the Late Holocene.

Multiple independent proxy records corroborate the evolutionary pattern of ENSO variability inferred from our coral data. For instance, marine radiocarbon reservoir age reconstructions from the northern SCS (Yu et al., 2010) indicate weakened ENSO variability around 5800–5600 a BP, consistent with the low ENSO variance identified for this interval. Coral records from New Caledonia (Lazareth et al., 2013) provide evidence for increased El Niño occurrence around 5500–5100 a BP, in agreement with speleothem $\delta^{18}O$ records that suggest wetter tropical conditions during this period (Tian et al., 2023, Fig. 6c), as well as the heightened El Niño activity reconstructed in our study. In contrast, coral fluorescence data from the Great Barrier Reef (Leonard et al., 2016) indicate reduced ENSO variability during 5200–4300 a BP, a trend reflected in eastern Hainan Island and central equatorial Pacific coral $\delta^{18}O$ records (McGregor et al., 2013; Sun et al., 2005), titanium concentrations in Cariaco Basin sediments (Haug et al., 2001, Fig. 6e), and our coral-derived variance.

Notably, during the 4.2 ka event, coral growth rates and Sr/Ca from the northern SCS (Dang et al., 2020, 2024) document a two-stage ENSO response in which variance decreased to 27 % of the modern level in the early phase and subsequently recovered to 63 % of the modern level in the late phase. This pattern matches the transient ENSO weakening followed by recovery observed in our reconstruction for this climate perturbation. After ~4200 a BP, ENSO variance exhibits a strengthening trajectory, supported by Tridacna records from the SCS that indicate

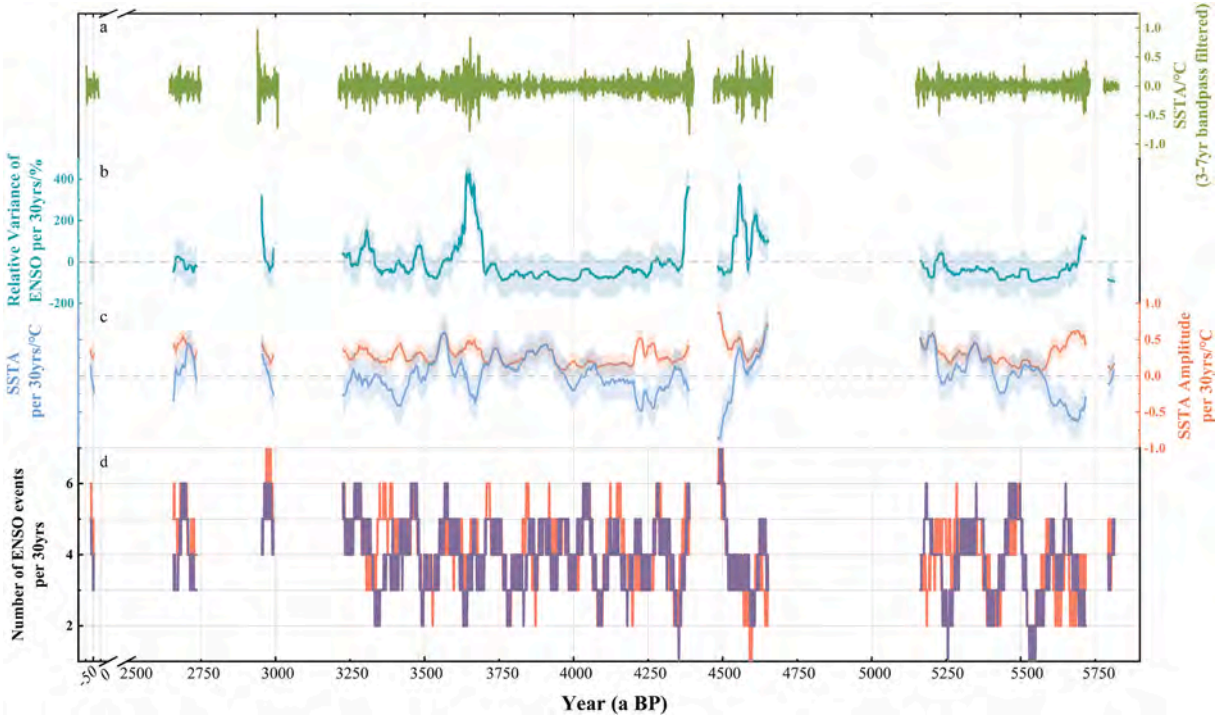


Fig. 5. El Niño–Southern Oscillation (ENSO) variability and sea surface temperature anomaly (SSTA) fluctuations inferred from fossil coral records in the northern South China Sea. (a) ENSO signals extracted from the coral-derived SSTA series using a 3–7-year band-pass filter. (b) ENSO intensity quantified as the variance of the filtered SSTA within a 30-year sliding window, expressed relative to the baseline of 1994–2023 CE. (c) Interdecadal variations in SSTA revealed by applying a 30-year sliding mean, where the blue curve represents the long-term trend and the orange curve denotes the corresponding amplitude changes. (d) Interdecadal ENSO frequency derived from a 30-year sliding window, with red and blue curves indicating the number of El Niño and La Niña events per 30-year window, respectively. (For interpretation of the references to colour in this figure legend, the reader is referred to the web version of this article.)

increasing ENSO variability during 4000–3000 a BP (Zhou et al., 2022). By ~3000 a BP, multiple proxies, including coral archives (Woodroffe et al., 2003), lake sediments (Konecky et al., 2016, Fig. 6f; Moy et al., 2002, Fig. 6b), and speleothem records (Hu et al., 2008, Fig. 6d; Zhu et al., 2017, Fig. 6g), document further ENSO intensification, which aligns with the high-variance phase identified in our reconstructions.

This cross-proxy and cross-regional agreement provides robust support for the validity of our findings and underscores the regional coherence of Holocene ENSO dynamics. A key insight from our reconstruction is the pronounced contrast in ENSO behavior between the Mid-Holocene (5829–4200 a BP) and the Late Holocene (4200–2643 a BP). The Mid-Holocene is characterized by generally weak ENSO variability, fewer extreme events, and a persistently La Niña-like background state. In contrast, ENSO variability intensified substantially after ~4200 a BP, with more frequent transitions between El Niño and La Niña, larger SST anomaly amplitudes, and a marked increase in overall ENSO variance, marking a shift toward a more dynamically unstable ENSO regime in the Late Holocene (Fig. 5, Figs. S13–14, Table S5).

5.3. SST–ENSO interactions and climate drivers

5.3.1. La Niña-like phases and SST cooling

Periods of markedly suppressed ENSO variability in our reconstruction are closely associated with prolonged SST cooling in the northern SCS and La Niña-like background states. The weakest ENSO variance occurred during 5814–5794 a BP, representing a 91 % reduction relative to the instrumental baseline of 1994–2023 CE (Table 2). During this interval, mean SST reached its minimum value of ~24.7 °C (Table S4), frequencies of ENSO events were reduced (4.24 El Niño and 3.90 La Niña events per 30 years, Fig. 5d), and interannual SSTA amplitudes were diminished (Fig. 5a,c). Similar, though less extreme, behavior is observed during the long weak-ENSO phase of 4265–3697 a BP, when variance remained on average 59 % below modern levels, frequencies revealed reduced ENSO events (4.06 El Niño events and 3.93 La Niña events per 30 years), and SST exhibited a relatively smooth warming trend with superimposed low-amplitude interannual variability.

Analogous to modern ENSO dynamics, these phases can be explained by a strengthened Walker circulation and enhanced equatorial upwelling, which favor a shallower thermocline in the western Pacific (Cai et al., 2021). In this configuration, relatively cool subsurface waters are more easily ventilated into the upper ocean of the western tropical Pacific and marginal seas such as the SCS, thereby promoting regional SST cooling and suppressing the growth of large ENSO anomalies. The low frequency and amplitude of ENSO events inferred for these intervals are therefore consistent with a dynamically stable, La Niña-biased background state. La Niña-dominated background conditions during comparable periods have been documented in marine sediment and coral records from the western Pacific (Cobb et al., 2013; McGregor et al., 2013).

These La Niña-like periods appear to have been accompanied by distinctive regional hydroclimatic responses. Increased precipitation over the maritime continent likely enhanced riverine discharge into the SCS, as indicated by coeval increases in terrigenous sediment input (Yang et al., 2019) and reductions in salinity. Concurrent weakening of the East Asian summer monsoon (Wang et al., 2005) may have further amplified continental runoff and upper-ocean stratification, thereby reinforcing surface cooling in the northern SCS. This interpretation is supported by synchronous cold anomalies recorded in coral, speleothem, and lacustrine archives across East and Southeast Asia (Asami et al., 2020; Hu et al., 2008; Zhang et al., 2023), suggesting a basin-scale hydroclimatic teleconnection under La Niña-dominated background states.

Table 2
Periods of stronger or weaker ENSO variability (referenced to a variance of 0.0233) on interdecadal scales during 5829–2643 a BP.

Distribution period ±2σ (a BP)	Period duration (year)	Mean ENSO Variance	Mean relative ENSO Variance (%)	Min Variance (%)	Max Variance (%)
5814–5794	21	0.0022	−91	−94	−85
5718–5691	28	0.0426	83	1	124
5690–5242	449	0.0108	−54	−93	2
5241–5214	28	0.0297	27	5	46
5213–5169	45	0.0128	−45	−79	−1
5168–5163	6	0.0242	4	1	6
4652–4588	65	0.0535	129	7	232
4587–4583	5	0.0206	−12	−40	−1
4582–4532	51	0.0686	194	5	372
4531–4484	48	0.0132	−43	−64	−20
4388–4365	24	0.0794	240	3	361
4364–4328	37	0.0181	−23	−43	−2
4327–4314	14	0.0251	8	0	14
4313–4290	24	0.0210	−10	−23	1
4289–4266	24	0.0252	8	0	24
4265–3697	569	0.0096	−59	−91	−1
3696–3563	134	0.0606	160	1	431
3562–3498	65	0.0109	−53	−80	−2
3497–3462	36	0.0346	48	0	84
3461–3416	46	0.0154	−34	−57	−1
3415–3412	4	0.0249	7	5	9
3411–3332	80	0.0147	−37	−62	−1
3331–3279	53	0.041	76	17	157
3278–3253	26	0.0203	−13	−22	0
3252–3226	27	0.0307	32	3	44
2993–2992	2	0.0371	59	57	61
2991–2969	23	0.0188	−19	−45	−1
2968–2953	16	0.0437	87	1	318
2730–2692	44	0.0172	−26	−50	−2
2691–2664	28	0.0272	17	2	26
2663–2657	7	0.0167	−28	−46	−2

5.3.2. *El Niño-like phases and SST warming*

Conversely, periods of intensified ENSO variability are associated with pronounced SST warming and more El Niño-like background conditions in the northern SCS. For example, during 4652–4588 a BP and 3696–3563 a BP (Table 2), anomalously warm SST conditions were identified in our coral records (Table S3), such as 4662–4640 a BP and 3583–3552 a BP. These periods are characterized by frequent El Niño events and greatly elevated ENSO variance. Both the ENSO event structure (Fig. S12b) and the dominant El Niño-like background state (Fig. S13) reflect this regime shift. Mechanistically, under persistently El Niño-like conditions, weakened trade winds and a reduced zonal SST gradient suppress equatorial upwelling and deepen the thermocline in the western tropical Pacific (Cai et al., 2021). Such a configuration reduces vertical mixing and tends to trap heat in the upper ocean of the western Pacific and marginal seas, leading to warmer SSTs and larger interannual anomalies. The large-amplitude ENSO cycles and elevated variance observed in the fossil record therefore reflect a dynamically unstable state of the ENSO system, in which frequent transitions between El Niño-like and La Niña-like conditions occur against a warm background.

These coupled patterns of intensified ENSO variability and regional SST warming are evident in other datasets from the northern SCS (Xu et al., 2017), indicating that prolonged El Niño-like conditions exert significant stress on regional climate and marine ecosystems. Strong interannual SST variability around 3600 a BP has been documented from Line Islands corals (Cobb et al., 2013), and disrupted reef accretion in Panama has been attributed to heightened ENSO variability during that interval (Toth and Aronson, 2019; Toth et al., 2015). Notably, coral bleaching events dated to ~4568 a BP and ~ 3900 a BP (Wang et al., 2021) coincide with intervals of sustained warming and strengthened ENSO variability identified in our reconstruction. This synchronicity suggests that ENSO-driven thermal stress played an important role in triggering bleaching during the Holocene, paralleling the mechanisms responsible for modern warming-induced coral degradation.

5.3.3. *Internally driven ENSO variability*

Our reconstruction suggests a strong correspondence between ENSO state and SST variability throughout the Mid- to Late Holocene. Cooler SSTs tended to occur during La Niña-like phases, whereas warmer conditions coincided with El Niño-like phases, implying a close linkage between ENSO dynamics and regional ocean temperatures in the northern SCS. However, only limited evidence supports external forcings as a major driver of long-term ENSO variability during the Mid- to Late Holocene. Neither reconstructed solar irradiance (Steinhilber et al., 2009, Fig. 6h) nor volcanic activity (Kobashi et al., 2017, Fig. 6i) shows a consistent correspondence with ENSO variance peaks or state transitions in our record. For instance, intervals of elevated ENSO variability (such as 4650–4580 a BP, 4580–4530 a BP, and 3700–3560 a BP) were not accompanied by marked declines in solar irradiance. Likewise, strengthened ENSO variance around 3700–3600 a BP did not coincide with enhanced volcanic forcing; rather, volcanic intensification around 3600–3500 a BP occurred during a period of reduced ENSO variability, suggesting a decoupling of these processes. Taken together, these patterns suggest that external forcings exerted only a limited influence on the long-term modulation of ENSO dynamics during the Mid- to Late Holocene.

Coral $\delta^{18}O$ records from Christmas and Fanning Islands indicate that orbital-scale insolation exerted only limited influence on ENSO dynamics, showing minimal sensitivity since ~7000 a BP (Cobb et al., 2013). Likewise, no statistically significant relationship has been identified between reconstructed ENSO variability and orbital forcing (Emile-Geay et al., 2016), and the impacts of even large volcanic eruptions appear weak and transient in coral $\delta^{18}O$ (Dee et al., 2020). Multiple studies also indicate that ENSO can undergo substantial fluctuations in the absence of clear external triggers (Cobb et al., 2003; Hereid et al., 2013; Zhu et al., 2022). Furthermore, the nonlinear and irregular nature of ENSO variability requires internal ocean–atmosphere processes to be considered in order to explain its Holocene evolution (McGregor and Gagan, 2004).

Taken together, coral-based records, supported by climate model results and other proxy reconstructions, suggest that internal climate dynamics were the primary driver of ENSO variability during the Mid- to Late Holocene. The irregular and oscillatory behavior of ENSO during this period was likely governed by ocean–atmosphere coupling and stochastic processes. Coral growth rate therefore represents a robust dual proxy, capable of recording both SST variations and ENSO-related interannual changes at annual resolution. The 2203-year fossil coral record from the northern SCS reveals complex climate behavior, including tightly linked SST–ENSO fluctuations, and highlights the predominant role of internal processes in modulating ENSO over the past ~6000 years.

6. Conclusion

This study establishes a 2203-year, high-resolution reconstruction of SST and ENSO variability derived from coral growth rates in the northern SCS during the Mid- to Late Holocene. Coral growth rate is demonstrated to be a reliable dual proxy for SST and ENSO variability, effectively capturing the amplitude and frequency of interannual climate fluctuations. The reconstructed annual SST record has a mean of 25.6 ± 0.4 °C (1σ), approximately 0.7 °C lower than the modern baseline (26.3 ± 0.4 °C, 1982–2023 CE). Over this interval, the coral-based SST series reveals at least 14 warm periods and 18 cold periods, with the latter recurring quasi-periodically at ~200-year intervals and shortening in duration toward the Late Holocene. Meanwhile, the reconstructed ENSO variability exhibits multiscale fluctuations, shifting from weaker-than-present, La Niña-like conditions (~5800–4200 a BP) to

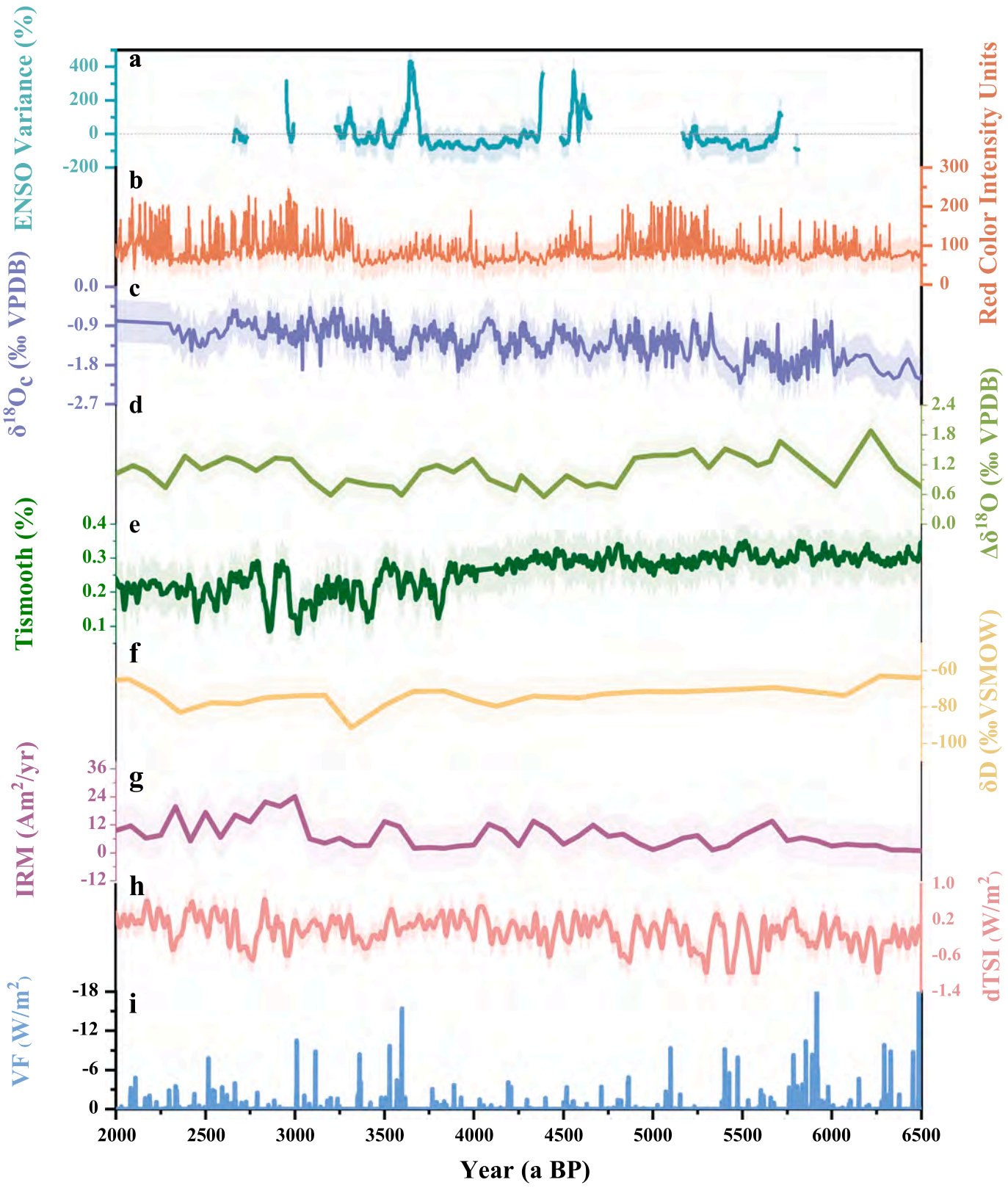


Fig. 6. Reconstructed El Niño–Southern Oscillation (ENSO) variability during the Mid- to Late Holocene compared with regional proxy records and external forcing datasets. (a) Relative ENSO variance derived from a 30-year sliding window (this study). (b) Red colour intensity from Laguna Pallcacocha sediments, southern Ecuador (Moy et al., 2002). (c) ENSO variability inferred from $\delta^{18}O$ records of Qunf Cave (Tian et al., 2023). (d) $\delta^{18}O$ differences between stalagmites from Heshang Cave and Dongge Cave (Hu et al., 2008). (e) Titanium concentrations in Cariaco Basin sediments off the Venezuelan coast (Haug et al., 2001). (f) Leaf-wax hydrogen isotope (δD) variations from Lake Towuti sediments in the Indo-Pacific Warm Pool (Konecky et al., 2016). (g) ENSO intensity reconstruction based on IRM magnetic minerals from a stalagmite in central China (Zhu et al., 2017). (h) Total solar irradiance reconstruction based on ice-core ^{10}Be records (Steinhilber et al., 2009). (i) Volcanic forcing reconstruction from the GISP2 ice core (Kobashi et al., 2017). (For interpretation of the references to colour in this figure legend, the reader is referred to the web version of this article.)

stronger-than-present, El Niño-like conditions (~4200–2600 a BP). Notably, La Niña-like intervals generally coincided with cooler SSTs, whereas El Niño-like phases corresponded to periods of SST warming, indicating strong SST–ENSO coupling. These patterns indicate that long-term ENSO variability cannot be attributed solely to external forcings, such as solar irradiance or volcanic eruptions. Instead, our findings highlight the dominant role of internal climate dynamics, particularly ocean–atmosphere interactions, in driving the nonlinear evolution of ENSO variability during the Mid- to Late Holocene.

CRediT authorship contribution statement

Dahua Huang: Writing – original draft, Software, Methodology, Investigation, Formal analysis. **Kefu Yu:** Writing – review & editing, Supervision, Resources, Project administration, Methodology, Funding acquisition, Conceptualization. **Leilei Jiang:** Writing – review & editing, Software, Formal analysis. **Wei Jiang:** Investigation.

Declaration of competing interest

The authors declare that they have no known competing financial interests or personal relationships that could have appeared to influence the work reported in this paper.

Acknowledgments

This work was funded by the National Natural Science Foundation of China (No. 42030502), Guangxi Scientific Project (No. AD25069075), and the National Key Research and Development Program of China (No. 2023YFF0804801).

Appendix A. Supplementary data

Supplementary data to this article can be found online at https://doi.org/10.1016/j.gloplacha.2025.105259.

Data availability

Supporting data for this study are available in the Zenodo data repository, doi: doi:https://doi.org/10.5281/zenodo.17853637.

References

Abram, N.J., McGregor, H.V., Gagan, M.K., et al., 2009. Oscillations in the Southern Extent of the Indo-Pacific warm Pool during the Mid-Holocene. Quat. Sci. Rev. 28 (25–26), 2794–2803. https://doi.org/10.1016/j.quascirev.2009.07.006.

Adams, J., Mann, M., Ammann, C., 2003. Proxy evidence for an El Niño-like response to volcanic forcing. Nature 426, 274–278. https://doi.org/10.1038/nature02101.

Asami, R., Yoshimura, N., Toriyabe, H., et al., 2020. High-resolution evidence for middle Holocene east Asian winter and summer monsoon variations: snapshots of fossil coral records. Geophys. Res. Lett. 47, e2020GL088509. https://doi.org/10.1029/2020GL088509.

Beck, J., Récy, J., Taylor, F., et al., 1997. Abrupt changes in early Holocene tropical sea surface temperature derived from coral records. Nature 385, 705–707. https://doi.org/10.1038/385705a0.

Bova, S., Rosenthal, Y., Liu, Z., et al., 2021. Seasonal origin of the thermal maxima at the Holocene and the last interglacial. Nature 589, 548–553. https://doi.org/10.1038/s41586-020-03155-x.

Brachert, T.C., Reuter, M., Krüger, S., et al., 2016. Low Florida coral calcification rates in the Plio-Pleistocene. Biogeosciences 13 (15), 4513–4532. https://doi.org/10.5194/bg-13-4513-2016.

Cai, W.J., Borlace, S., Lengaigne, M., et al., 2014. Increasing frequency of extreme El Niño events due to greenhouse warming. Nat. Clim. Chang. 4 (2), 111–116. https://doi.org/10.1038/nclimate2100.

Cai, W.J., McPhaden, M.J., Grimm, A.M., et al., 2020. Climate impacts of the El Niño-Southern Oscillation on South America. Nat. Rev. Earth Environ. 1, 215–231. https://doi.org/10.1038/s43017-020-0040-3.

Cai, W.J., Santoso, A., Collins, M., et al., 2021. Changing El Niño–Southern Oscillation in a warming climate. Nat. Rev. Earth Environ. 2, 628–644. https://doi.org/10.1038/s43017-021-00199-z.

Chen, X.F., Deng, W.F., Xiao, H.F., et al., 2023. Coral paleoclimate perspectives support the role of low-latitude forcing on the 4.2 ka BP event. Geophys. Res. Lett. 50, e2023GL104010. https://doi.org/10.1029/2023GL104010.

Chen, X.F., Deng, W.F., Zhao, J.X., et al., 2024. Interhemispheric synchrony of Mid–Late Holocene SST in the Indo-Pacific warm pool linked to upper water column dynamics. Quat. Sci. Rev. 346, 109064. https://doi.org/10.1016/j.quascirev.2024.109064.

Cobb, K.M., Charles, C., Cheng, H., et al., 2003. El Niño Southern Oscillation and tropical Pacific climate during the last millennium. Nature 424, 271–276. https://doi.org/10.1038/nature01779.

Cobb, K.M., Westphal, N., Sayani, H.R., et al., 2013. Highly variable El Niño-Southern Oscillation throughout the Holocene. Science 339 (6115), 67–70. https://doi.org/10.1126/science.1228246.

Collins, M., An, S.-I., Cai, W., et al., 2010. The impact of global warming on the tropical Pacific Ocean and El Niño. Nat. Geosci. 3 (6), 391–397. https://doi.org/10.1038/ngeo868.

Comboul, M., Emile-Geay, J., Hakim, G.J., et al., 2015. Paleoclimate sampling as a sensor placement problem. J. Clim. 28 (19), 7717–7740. https://doi.org/10.1175/JCLI-D-14-00802.1.

Cooper, T.F., De'Ath, G., Fabricius, K.E., et al., 2008. Declining coral calcification in massive *Porites* in two nearshore regions of the northern Great Barrier Reef. Glob. Chang. Biol. 14 (3), 529–538. https://doi.org/10.1111/j.1365-2486.2007.01520.x.

Cooper, T.F., O'Leary, R.A., Lough, J.M., 2012. Growth of western Australian corals in the Anthropocene. Science 335 (6068), 593–596. https://doi.org/10.1126/science.1214570.

Corrége, T., Delcroix, T., Recy, J., et al., 2000. Evidence for stronger El Niño-Southern Oscillation (ENSO) events in a Mid-Holocene massive coral. Paleoceanography 15, 465–470. https://doi.org/10.1029/1999PA000409.

Dang, S.H., Yu, K.F., Tao, S.C., et al., 2020. El Niño/Southern oscillation during the 4.2 ka event recorded by growth rates of corals from the North South China Sea. Acta Oceanol. Sin. 39 (1), 110–117. https://doi.org/10.1007/s13131-019-1520-5.

Dang, S.H., Liu, Z.F., Yu, K.F., et al., 2024. Reduced ENSO variability during the onset of the 4.2 ka event. Paleoceanogr. Paleoclimatol. 39, e2024PA004923. https://doi.org/10.1029/2024PA004923.

Dee, S.G., Cobb, K.M., Emile-Geay, J., et al., 2020. No consistent ENSO response to volcanic forcing over the last millennium. Science 367, 1477–1481. https://doi.org/10.1126/science.aax2000.

DeLong, K.L., Quinn, T.M., Taylor, F.W., et al., 2013. Improving coral-base paleoclimate reconstructions by replicating 350 years of coral Sr/Ca variations. Palaeogeogr. Palaeoclimatol. Palaeoecol. 373, 6–24. https://doi.org/10.1016/j.palaeo.2012.08.019.

Deser, C., Phillips, A.S., Bourdette, V., et al., 2010. Uncertainty in climate change projections: the role of internal variability. Clim. Dyn. 38 (3–4), 527–546. https://doi.org/10.1007/s00382-010-0977-x.

Emile-Geay, J., Cobb, K.M., Carré, M., et al., 2016. Links between tropical Pacific seasonal, interannual and orbital variability during the Holocene. Nat. Geosci. 9 (2), 168–173. https://doi.org/10.1038/ngeo2608.

Fedorov, A.V., Hu, S., Wittenberg, A.T., et al., 2020. ENSO low-frequency modulation and mean state interactions, El Niño Southern Oscillation in a changing climate. Geophys. Monogr. Ser. 173–198. https://doi.org/10.1002/9781119548164.ch8.

Geng, T., Jia, F., Cai, W.J., et al., 2023. Increased occurrences of consecutive La Niña events under global warming. Nature 619, 774–781. https://doi.org/10.1038/s41586-023-06236-9.

Grothe, P.R., Cobb, K.M., Liguori, G., et al., 2019. Enhanced El Niño-Southern Oscillation variability in recent decades. Geophys. Res. Lett. 47, 7. https://doi.org/10.1029/2019GL083906.

Haug, G.H., Hughen, K.A., Peterson, L.C., et al., 2001. Southward migration of the intertropical convergence zone through the Holocene. Science 293, 1304–1308. https://doi.org/10.1126/science.1059725.

Helmle, K.P., Dodge, R.E., Swart, P.K., et al., 2011. Growth rates of Florida corals from 1937 to 1996 and their response to climate change. Nat. Commun. 2, 215. https://doi.org/10.1038/ncomms1222.

Hereid, K.A., Quinn, T.M., Okumura, Y.M., 2013. Assessing spatial variability in El Niño-Southern Oscillation event detection skill using coral geochemistry. Paleoceanography 28 (1), 14–23. https://doi.org/10.1029/2012PA002352.

Hu, C.Y., Henderson, G.M., Huang, J.H., et al., 2008. Quantification of Holocene Asian monsoon rainfall from spatially separated cave records. Earth Planet. Sci. Lett. 266, 221–232. https://doi.org/10.1016/j.epsl.2007.10.015.

Jiang, L.L., Yu, K.F., Tao, S.C., et al., 2021a. ENSO variability during the medieval climate Anomaly as recorded by *Porites* corals from the northern South China Sea. Paleoceanography and Paleoclimatology 36, e2020PA004173. https://doi.org/10.1029/2020PA004173.

Jiang, L.L., Yu, K.F., Tao, S.C., et al., 2021b. Coral perspective on temperature seasonality and interannual variability in the northern South China Sea during the Roman warm period. Glob. Planet. Chang. 207, 103675. https://doi.org/10.1016/j.gloplacha.2021.103675.

Jiang, L.L., Yu, K.F., Tao, S.C., et al., 2023. Abrupt increase in ENSO variability at 700 CE triggered by solar activity. J. Geophys. Res. Oceans 128, e2022JC019278. https://doi.org/10.1029/2022JC019278.

Jiménez-Moreno, G., Anderson, R.S., Shinker, J.J., 2021. ENSO, sun and megadroughts in SW USA during the last 11,000 years. Earth Planet. Sci. Lett. 576, 117217. https://doi.org/10.1016/j.epsl.2021.117217.

Keefer, D.K., DeFrance, S.D., Moseley, M.E., et al., 1998. Early maritime economy and El Niño events at Quebrada Tacahuay, Peru. Science 281 (5384), 1833–1835. https://doi.org/10.1126/science.281.5384.1833.

Klein, S.A., Soden, B.J., Lau, N.C., 1999. Remote Sea surface temperature variations during ENSO: evidence for a tropical atmospheric bridge. J. Clim. 12 (4), 917–932. https://doi.org/10.1175/1520-0442(1999)012<0917:RSSTVD>2.0.CO;2.

Kobashi, T., Menviel, L., Jeltsch-Thömmes, A., et al., 2017. Volcanic influence on centennial to millennial Holocene Greenland temperature change. Sci. Rep. 7, 1441. https://doi.org/10.1038/s41598-017-01451-7.
Konecky, B., Russell, J., Bijaksana, S., 2016. Glacial aridity in Central Indonesia coeval with intensified monsoon circulation. Earth Planet. Sci. Lett. 437, 15–24. https://doi.org/10.1016/j.epsl.2015.12.037.
Kwiatkowski, L., Cox, P.M., Economou, T., et al., 2013. Caribbean coral growth influenced by anthropogenic aerosol emissions. Nat. Geosci. 6 (5), 362–366. https://doi.org/10.1038/ngeo1780.
Lawman, A.E., Partin, J.W., Dee, S.G., et al., 2020. Developing a coral proxy system model to compare coral and climate model estimates of changes in paleo-ENSO variability. Paleoceanography and Paleoclimatology 35 (7), e2019PA003836. https://doi.org/10.1029/2019PA003836.
Lawman, A.E., Di Nezio, P.N., Partin, J.W., et al., 2022. Unraveling forced responses of extreme El Niño variability over the Holocene. Sci. Adv. 8 (9), eabm4313. https://doi.org/10.1126/sciadv.abm4313.
Lazareth, C.E., Rosell, M.G.B., Turcq, B., et al., 2013. Mid-Holocene climate in New Caledonia (Southwest Pacific): Coral and PMIP models monthly resolved results. Quat. Sci. Rev. 69, 83–97. https://doi.org/10.1016/j.quascirev.2013.02.024.
Lee, H.T., Gruber, A., Ellingson, R.G., et al., 2007. Development of the HIRS outgoing longwave radiation climate dataset. J. Atmos. Ocean. Technol. 24 (12), 2029–2047. https://doi.org/10.1175/2007JTECHA989.1.
Leonard, N.D., Welsh, K.J., Lough, J.M., et al., 2016. Evidence of reduced Mid-Holocene ENSO variance on the Great Barrier Reef, Australia. Paleoceanography 31, 1248–1260. https://doi.org/10.1002/2016PA002967.
Liu, Z.F., Zhao, Y.L., Colin, C., et al., 2016. Source-to-sink transport processes of fluvial sediments in the South China Sea. Earth Sci. Rev. 153, 238–273. https://doi.org/10.1016/j.earscirev.2015.08.005.
Lough, J.M., Barnes, D.J., 1997. Several centuries of variation in skeletal extension, density and calcification in massive *Porites* colonies from the Great Barrier Reef: a proxy for seawater temperature and a background of variability against which to identify unnatural change. J. Exp. Mar. Biol. Ecol. 211 (1), 29–67. https://doi.org/10.1016/S0022-0981(96)02710-4.
Lough, J.M., Barnes, D.J., 2000. Environmental controls on growth of the massive coral *Porites*. J. Exp. Mar. Biol. Ecol. 245 (2), 225–243. https://doi.org/10.1016/S0022-0981(99)00168-9.
Marcott, S.A., Shakun, J.D., Clark, P.U., et al., 2013. A reconstruction of regional and global temperature for the past 11,300 years. Science 339 (6124), 1198–1201. https://doi.org/10.1126/science.1228026.
McGregor, H.V., Gagan, M.K., 2004. Western Pacific coral $\delta^{18}O$ records of anomalous Holocene variability in the El Niño-Southern Oscillation. Geophys. Res. Lett. 31, L11204. https://doi.org/10.1029/2004GL019972.
McGregor, H.V., Fischer, M.J., Gagan, M.K., et al., 2013. A weak El Niño/Southern Oscillation with delayed seasonal growth around 4,300 years ago. Nat. Geosci. 6 (11), 949–953. https://doi.org/10.1038/ngeo1936.
McPhaden, M.J., 2015. Playing hide and seek with El Niño. Nat. Clim. Chang. 5, 791–795. https://doi.org/10.1038/nclimate2775.
McPhaden, M.J., Zebiak, S.E., Glantz, M.H., 2006. ENSO as an integrating concept in earth science. Science 314 (5806), 1740–1745. https://doi.org/10.1126/science.1132588.
Moy, C.M., Seltzer, G.O., Rodbell, D.T., et al., 2002. Variability of El Niño/Southern Oscillation activity at millennial timescales during the Holocene epoch. Nature 460, 162–165. https://doi.org/10.1038/nature01194.
Nie, B.F., Chen, T.G., Liang, M.T., et al., 1997. Relationship between coral growth rate and sea surface temperature in the northern part of South China Sea during the past 100 a. Sci. China Ser. D Earth Sci. 40 (2), 173–182. https://doi.org/10.1007/BF02878376.
Rein, B., Lückge, A., Reinhardt, L., et al., 2005. El Niño variability off Peru during the last 20,000 years. Paleoceanography 20, PA4003. https://doi.org/10.1029/2004PA001099.
Reuter, M., Brachert, T.C., Kroeger, K.F., 2005. Diagenesis of growth bands in fossil Scleractinia corals: identification and modes of preservation. Facies 51 (1–4), 146–159. https://doi.org/10.1007/s10347-005-0064-7.
Rodriguez, L.G., Cohen, A.L., Ramirez, W., et al., 2019. Mid-Holocene, coral-based sea surface temperatures in the western tropical Atlantic. Paleoceanography and Paleoclimatology 34 (7), 1234–1245. https://doi.org/10.1029/2019PA003571.
Sadler, J., Webb, G.E., Leonard, N.D., et al., 2016. Reef core insights into Mid-Holocene water temperatures of the southern Great Barrier Reef. Paleoceanography 31 (10), 1395–1408. https://doi.org/10.1002/2016PA002943.
Saenger, C., Cohen, A.L., Oppo, D.W., et al., 2009. Surface-temperature trends and variability in the low-latitude North Atlantic since 1552. Nat. Geosci. 2 (7), 492–495. https://doi.org/10.1038/ngeo552.
Solow, A.R., Huppert, A., 2004. A potential bias in coral reconstruction of sea surface temperature. Geophys. Res. Lett. 31 (6), L06308. https://doi.org/10.1029/2003GL019349.
Steinhilber, F., Beer, J., Fröhlich, C., 2009. Total solar irradiance during the Holocene. Geophys. Res. Lett. 36 (19), L19704. https://doi.org/10.1029/2009GL040142.
Stott, L., Cannariato, K., Thunell, R., et al., 2004. Decline of surface temperature and salinity in the western tropical Pacific Ocean in the Holocene epoch. Nature 431, 56–59. https://doi.org/10.1038/nature02903.
Sun, D.H., Gagan, M.K., Cheng, H., et al., 2005. Seasonal and interannual variability of the Mid-Holocene East Asian monsoon in coral $\delta^{18}O$ records from the South China Sea. Earth Planet. Sci. Lett. 237 (43467), 69–84. https://doi.org/10.1016/j.epsl.2005.06.022.
Tan, W., Wang, X., Wang, W.Q., et al., 2016. Different responses of sea surface temperature in the South China Sea to various El Niño events during boreal autumn. J. Clim. 29, 1127–1142. https://doi.org/10.1175/JCLI-D-15-0338.1.
Tao, S.C., Liu, Kam-biu, Yan, H.Q., et al., 2024. SST and ENSO activity 282,000 years ago reconstructed from *Porites* coral in the South China Sea. Glob. Planet. Chang. 237, 104455. https://doi.org/10.1016/j.gloplacha.2024.104455.
Tian, Y., Fleitmann, D., Zhang, Q., et al., 2023. Holocene climate change in southern Oman deciphered by speleothem records and climate model simulations. Nat. Commun. 14, 4718. https://doi.org/10.1038/s41467-023-40454-z.
Timmermann, A., An, S.-I., Kug, J.-S., et al., 2018. El Niño–Southern Oscillation complexity. Nature 559 (7715), 535–545. https://doi.org/10.1038/s41586-018-0252-6.
Toth, L.T., Aronson, R.B., 2019. The 4.2ka event, ENSO, and coral reef development. Clim. Past 15, 105–119. https://doi.org/10.5194/cp-15-105-2019.
Toth, L.T., Aronson, R.B., Cobb, K.M., et al., 2015. Climatic and biotic thresholds of coral-reef shutdown. Nat. Clim. Chang. 5, 369–374. https://doi.org/10.1038/nclimate2541.
Tudhope, A.W., Chilcott, C.P., Mcculloch, M.T., et al., 2001. Variability in the El Niño–Southern Oscillation through a Glacial-Interglacial cycle. Science 291 (5508), 1511–1517. https://doi.org/10.1126/science.1057969.
Vialard, J., Jin, F.-F., McPhaden, M.J., et al., 2025. The El Niño Southern Oscillation (ENSO) recharge oscillator conceptual model: achievements and future prospects. Rev. Geophys. 63, e2024RG000843. https://doi.org/10.1029/2024RG000843.
Wang, B., Wu, R.G., Fu, X.H., 2000. Pacific-East Asian teleconnection: how does ENSO affect East Asian climate? J. Clim. 13 (9), 1517–1536. https://doi.org/10.1175/1520-0442(2000)013<1517:PEATHD>2.0.CO;2.
Wang, Y.J., Cheng, H., Edwards, R.L., et al., 2005. The Holocene Asian Monsoon: Links to solar changes and North Atlantic climate. Science 308 (5723), 587–854. https://doi.org/10.1126/science.1106296.
Wang, H., Yu, K.F., Tao, S.C., et al., 2021. New evidence for the periodic bleaching and recovery of *Porites* corals during the Mid–Late Holocene in the northern South China Sea. Glob. Planet. Chang. 197, 103397. https://doi.org/10.1016/j.gloplacha.2020.103397.
Wang, F., Li, X.G., Tang, X.H., et al., 2023. The seas around China in a warming climate. Nat. Rev. Earth Environ. 4, 535–551. https://doi.org/10.1038/s43017-023-00453-6.
Wittenberg, A.T., 2009. Are historical records sufficient to constrain ENSO simulations? Geophys. Res. Lett. 36 (12). https://doi.org/10.1029/2009GL038710.
Woodroffe, C.D., Beech, M.R., Gagan, M.K., 2003. Mid–Late Holocene El Niño variability in the equatorial Pacific from coral microatolls. Geophys. Res. Lett. 30 (7), 1358. https://doi.org/10.1029/2002GL015868.
Xu, S.D., Yu, K.F., Tao, S.C., et al., 2017. Evidence for the thermal bleaching of *Porites* corals from 4.0 ka B.P. In the Northern South China Sea. J. Geophys. Res. Biogeosci. 123, 79–94. https://doi.org/10.1002/2017JG004091.
Yan, H., Sun, L.G., Wang, Y.H., et al., 2011. A record of the Southern Oscillation Index for the past 2,000 years from precipitation proxies. Nat. Geosci. 4 (9), 611–614. https://doi.org/10.1038/ngeo1231.
Yancheva, G., Nowaczyk, N.R., Mingram, J., et al., 2007. Influence of the intertropical convergence zone on the East Asian monsoon. Nature 445 (7123), 74–77. https://doi.org/10.1038/nature05431.
Yang, Y.P., Xiang, R., Liu, J.G., et al., 2019. Inconsistent Sea surface temperature and salinity changing trend in the northern South China Sea since 7.0 ka BP. J. Asian Earth Sci. 171, 178–186. https://doi.org/10.1016/j.jseaes.2018.05.033.
Yu, K.F., 2012. Coral reefs in the South China Sea: their responses to and records on past environmental changes. Sci. China Earth Sci. 55 (8), 1217–1229. https://doi.org/10.1007/s11430-012-4449-5.
Yu, K.F., Zhao, J.X., Wei, G.J., et al., 2005. Mid–Late Holocene monsoon climate retrieved from seasonal Sr/Ca and $\delta^{18}O$ records of *Porites lutea* corals at Leizhou Peninsula, northern coast of South China Sea. Glob. Planet. Chang. 47 (2), 301–316. https://doi.org/10.1016/j.gloplacha.2004.10.018.
Yu, K.F., Zhao, J.X., Shi, Q., et al., 2006. U-series dating of dead *Porites* corals in the South China Sea: evidence for episodic coral mortality over the past two centuries. Quat. Geochronol. 1 (2), 129–141. https://doi.org/10.1016/j.quageo.2006.06.005.
Yu, K.F., Hua, Q., Zhao, J.X., et al., 2010. Holocene marine ^{14}C reservoir age variability: evidence from ^{230}Th-dated corals in the South China Sea. Paleoceanography 25, PA3205. https://doi.org/10.1029/2009PA001831.
Zhang, H.L., Yu, K.F., Shi, Q., et al., 2014. Sea surface temperature variations during the Mid–Late Holocene reconstructed by *Porites* coral growth rates in the Xisha Islands. Quat. Sci. 34 (6), 1296–1305. https://doi.org/10.3969/j.issn.1001-7410.2014.06.19.
Zhang, E.L., Meng, X.Q., Ning, D.L., et al., 2023. Holocene extreme hydroclimate events in the Asian monsoon region were more frequent during cooler intervals. Commun. Earth Environ. 4, 344. https://doi.org/10.1038/s43247-023-00997-x.
Zhao, J.X., Yu, K.F., Feng, Y.X., 2009. High-precision ^{238}U-^{234}U-^{230}Th disequilibrium dating of the recent past: a review. Quat. Geochronol. 4 (5), 423–433. https://doi.org/10.1016/j.quageo.2009.01.012.
Zhou, P.C., Yan, H., Han, T., et al., 2022. Mid to late Holocene ENSO variability reconstructed by high-resolution Tridacna Sr/Ca records from the northern part of the South China Sea. Palaeogeogr. Palaeoclimatol. Palaeoecol. 601, 111117. https://doi.org/10.1016/j.palaeo.2022.111117.
Zhu, Z.M., Feinberg, J.M., Xie, S.C., et al., 2017. Holocene ENSO-related cyclic storms recorded by magnetic minerals in speleothems of Central China. Proc. Natl. Acad. Sci. USA 114 (5), 852–857. https://doi.org/10.1073/pnas.1610930114.
Zhu, F., Emile-Geay, J., Anchukaitis, K.J., et al., 2022. A re-appraisal of the ENSO response to volcanism with paleoclimate data assimilation. Nat. Commun. 13, 747. https://doi.org/10.1038/s41467-022-28210-1.

Global and Planetary Change 257 (2026) 105238



Contents lists available at ScienceDirect

Global and Planetary Change

journal homepage: www.elsevier.com/locate/gloplacha



Research Article

Vegetation ecosystem responses to climate-human interactions since the Late Holocene from peat record of Niangniang Mountain, western Guizhou☆

Yuanfu Yue [a], Shixiong Yang [b,c,*], Liuying He [a], Zhuo Zheng [d], Xiao Zhang [e], Cong Chen [d], Qiuchi Wan [f], Yongjie Tang [d], Kangyou Huang [d], Fang Gu [g]

[a] Guangxi Laboratory on the Study of Coral Reef in the South China Sea, Coral Reef Research Center, School of Marine Sciences, Guangxi University, Nanning 530004, China
[b] Laboratory for Marine Geology, Marine Science and Technology Center, Qingdao 266237, China
[c] Qingdao Institute of Marine Geology, Qingdao 266237, China
[d] Guangdong Key Laboratory of Geodynamics and Geohazards, School of Earth Sciences and Engineering, Sun Yat-sen University, Zhuhai 519082, China
[e] College of Life Sciences, Zhejiang Normal University, 321004 Jinhua, China
[f] School of Geography, South China Normal University, Guangzhou 510635, China
[g] School of Ocean Sciences, China University of Geosciences, Beijing 100083, China

ARTICLE INFO

Editor: Dr. Jed O Kaplan

Keywords:
Vegetation ecosystem
Climate change
Human activities
Fire history
Late Holocene

ABSTRACT

This study presents a high-resolution multi-proxy analysis of a peat core from Niangniang Mountain in western Guizhou, China, to reconstruct vegetation dynamics, fire history, and human-environment interactions over the past 3400 years. By integrating pollen, charcoal, and sedimentological analyses, we identify four distinct phases of ecosystem change. Phase I (~3400–3200 cal yr BP) was characterized by stable, warm-humid conditions supporting dense subtropical evergreen broad-leaved forests (dominated by *Quercus*-E and *Castanopsis/Lithocarpus*) with minimal natural fire activity. Phase II (~3200–2100 cal yr BP) marked a transition to cooler-drier conditions, evidenced by declining evergreen taxa, expansion of *Pinus* and grasslands, and increased fire frequency, likely amplified by early human activities. Phase III (~2100–600 cal yr BP) saw sustained conifer dominance and grassland expansion under cool-dry climates, but fire activity paradoxically declined, possibly due to fuel limitation or land-use changes. Phase IV (~600 cal yr BP–present) recorded dramatic anthropogenic transformation, with *Pinus* peaking, evergreen taxa collapsing, and macroscopic charcoal (>125 μm) appearing, reflecting intensive agriculture during the Ming-Qing dynasties. Biodiversity trends revealed non-linear responses: low richness in stable climates (Phase I), intermediate peaks during transitional periods (Phase II), and maximum diversity in anthropogenic landscapes (Phase IV). The study highlights the interplay of monsoon variability and human activities in shaping subtropical ecosystems, with anthropogenic impacts have become dominant in recent centuries. These findings underscore the importance of local context in understanding long-term ecosystem resilience and biodiversity dynamics in monsoon-sensitive regions.

1. Introduction

The Late Holocene (~4200 cal yr BP to present) represents a critical transition in Earth system dynamics, marked by the intensifying influence of human activities on global landscapes through population growth and technological advancement (Stephens et al., 2019). Therefore, fire emerged as a primary catalyst and ecological engineer, fundamentally transforming ecosystems through deforestation, energy procurement, and swidden (slash-and-burn) agriculture (Yue et al., 2024a, 2024b; Bowman et al., 2011; Archibald et al., 2013). These anthropogenic practices substantially altered natural fire regimes, encompassing frequency, intensity, and spatial extent, across a variety of continental settings (Marlon et al., 2013; Power et al., 2008). Consequently, clarifying the interplay between climate variability,

☆ This article is part of a Special issue entitled: 'Fire' published in Global and Planetary Change.

* Corresponding author at: Qingdao Institute of Marine Geology, Qingdao 266237, China.
E-mail address: ysx_666@163.com (S. Yang).

https://doi.org/10.1016/j.gloplacha.2025.105238
Received 5 August 2025; Received in revised form 5 December 2025; Accepted 5 December 2025
Available online 9 December 2025
0921-8181/© 2025 Elsevier B.V. All rights are reserved, including those for text and data mining, AI training, and similar technologies.

anthropogenic ignition regimes, and vegetation feedbacks is fundamental to interpreting historical ecosystem dynamics and quantifying resilience trajectories under projected future climate scenarios (Yue et al., 2024a, 2024b; Marlon et al., 2013; Iglesias et al., 2021).

Wetland sediments, particularly peat bogs, are exceptional archives for investigating these complex interactions. Their continuous accumulation, high temporal resolution, and sensitivity to both climatic and anthropogenic signals make them particularly valuable (Yue et al., 2024a; Chambers and Charman, 2004; van der Knaap et al., 2011). Within these archives, microscopic charcoal particles act as "time capsules" of past fire events, resulting from the incomplete combustion of vegetation that were buried and preserved in the sediment (Whitlock and Larsen, 2001; Conedera et al., 2009). Charcoal analysis provides a vital quantitative tool for reconstructing regional fire history, including the frequency and intensity of fire events. These reconstructions help identify the drivers of fire activity—whether climatic (e.g., drought frequency), biotic (e.g., fuel load and type), or anthropogenic (e.g., land-use practices) (Yue et al., 2024a; Higuera et al., 2009; Colombaroli et al., 2013; Vachula et al., 2021). Although elevated charcoal concentrations are generally interpreted as indicators of more frequent or intense fires (Mooney et al., 2011), this relationship is inherently non-linear and mediated by complex interactions among climatic conditions (e.g., cold-dry phases conducive to burning; Marlon et al., 2009; Tan et al., 2015), vegetation flammability (Leys et al., 2018), and human activities (Bowman et al., 2011; Coughlan et al., 2018).

Complementing charcoal records, pollen analysis functions as a foundational palaeoecological proxy and remains central to reconstructing past vegetation composition, structure, and succession (Birks and Birks, 1980; Bennett and Willis, 2001). As direct and robust proxies of the past, pollen assemblages offer both qualitative and quantitative insights into historical plant communities and their associated climatic envelopes (Guiot et al., 1993; Xu et al., 2016; Herzschuh et al., 2019). Pollen data serve as indispensable proxy for reconstructing biomes, inferring palaeotemperature and palaeoprecipitation regimes, and elucidating the drivers of long-term vegetation dynamics (Prentice et al., 1996; Zheng et al., 2007; Herzschuh et al., 2019). Crucially, the integration of pollen and charcoal analyses provides a powerful, synergistic framework for exploring vegetation responses to concurrent changes in climate, fire disturbance regimes, and human land-use (Yue et al., 2024a, 2024b; Tinner et al., 2005; Colombaroli and Gavin, 2010; Blarquez et al., 2014). Reconstructing historical fire regimes and elucidating the driving mechanisms are thus essential for understanding the complex interplay among climate, vegetation, fire, human activity, and for developing robust models to predict future fire activity under global change (Marlon et al., 2013; Iglesias et al., 2021).

The Yunnan–Guizhou Plateau, located in Southwest China at the convergence of the Indian Summer Monsoon (ISM) and East Asian Summer Monsoon (EASM), represents a pivotal region for palaeoclimate and palaeoecological research due to its climatic complexity and ecological sensitivity (Yue et al., 2024a; Zhang et al., 2025). Its complex karst (limestone) topography, high biodiversity, and sensitivity to global changes make it uniquely valuable for studying past environmental dynamics (Yue et al., 2024a; Zhang et al., 2025; Xiao et al., 2014, 2015, 2017; Chen et al., 2014; Huang et al., 2018). The region experienced frequent and severe forest fires. Palaeoecological studies in this area reveal a significant increase in fire activity during the Late Holocene, driven by both climatic fluctuations, particularly cold-dry phases, and escalating human impacts (Yue et al., 2024a; Xiao et al., 2015, 2017; Huang et al., 2018; Yuan et al., 2022). While these studies have advanced our understanding of fire–vegetation–human relationships, for instance, anthropogenic activities such as deforestation introduced new ignition sources, they may have simultaneously suppressed fire occurrence by disrupting fuel continuity (Xiao et al., 2015; Xu et al., 2021; Huang et al., 2018). This underscores the non-linear and context-dependent nature of fire regime dynamics. Despite these insights, previous studies in Southwest China remain geographically uneven. In particular, western Guizhou is underrepresented relative to Yunnan and other subtropical regions, limiting our understanding of broader regional patterns (Yue et al., 2024a; Huang et al., 2018).

Niangniang Mountain Wetland (Fig. 1), located in western Guizhou on the eastern Yunnan-Guizhou Plateau, offers an ideal natural archive to address this gap (Yue et al., 2024a). Its continuous peat accumulation, high sensitivity to environmental changes, and unique geographic position make it particularly suitable for reconstructing Late Holocene palaeoclimate, fire history, and vegetation succession (Yue et al., 2024a). This study aims to: (1) reconstruct Late-Holocene climatic and environmental changes, (2) trace regional fire history, and (3) investigate how local and regional vegetation ecosystems responded to concurrent shifts in climate, fire activity, and human pressures.

2. Study area

Niangniang Mountain wetland (26°4′25″ – 26°8′24″N, 104°45′24″ – 104°51′41″E) is situated at the junction of Shuicheng District, Liupanshui City, and Panzhou City, Guizhou Province (Fig. 1). It lies in the transition zone between the mountainous plateau in western Guizhou and the hilly plains in central Guizhou. The wetland has an average altitude of 2100 m above sea level (m a.s.l.), stretches in a northwest-southeast direction, and covers a total area of approximately 2680 ha (including 1060 ha of wetland). As one of western Guizhou's largest and most ecologically significant peat swamp wetlands, its formation is primarily governed by the geological structure of the basalt bedrock and regional hydrological conditions. The combination of low bedrock permeability, abundant rainfall, and flat topography minimizes surface runoff, thereby promoting peat accumulation and supporting the development of the wetland ecosystem.

The study area lies within the subtropical plateau monsoon climate zone, characterized by warm, humid, and distinct seasons. The annual average temperature ranges from 13 to 16 °C. The annual precipitation ranges from 1100 to 1400 mm, with 60–70 % concentrated in summer (increasing from northwest to southeast). This precipitation pattern is tightly linked to the advance and retreat of the southwest monsoon. Additionally, the region has relatively short annual sunshine (1200–1500 h), and year-round relative humidity of 70–80 %, creating favorable hydrothermal conditions for subtropical evergreen broad-leaved forests.

Regional vegetation is dominated by subtropical evergreen broad-leaved forests, alongside coniferous forests, deciduous broad-leaved forests, and shrublands, showing clear vertical zonation (Liu, 1981). In the lower-elevation river valleys, evergreen broad-leaved tree species such as Lauraceae, Fagaceae and Theaceae are dominant, forming dense and complex evergreen broad-leaved forest communities. With rising elevation, vegetation shifts to coniferous forests (dominated by *Pinus yunnanensis* and *Pinus armandi*), and mixed coniferous and broad-leaved forests incorporating deciduous broad-leaved species. At high elevations, shrublands and meadows predominate, adapted to cold, windy conditions.

3. Materials and methods

3.1. Sampling

In September 2013, a 150-cm sediment core (NNS, 26.10°N, 104.82°E, 1999 m a.s.l., Fig. 1) was collected from the outer area of Niangniang Mountain wetland using a Russian peat corer. Immediately after retrieval, the core was sealed in plastic film and then stored at 4 °C to preserve sediment integrity and minimize external contamination. The upper 52 cm of core NNS was prioritized for detailed analysis, with sediment samples collected at 0.5-cm intervals throughout this interval, yielding 104 sediment samples for multi-proxy investigations.

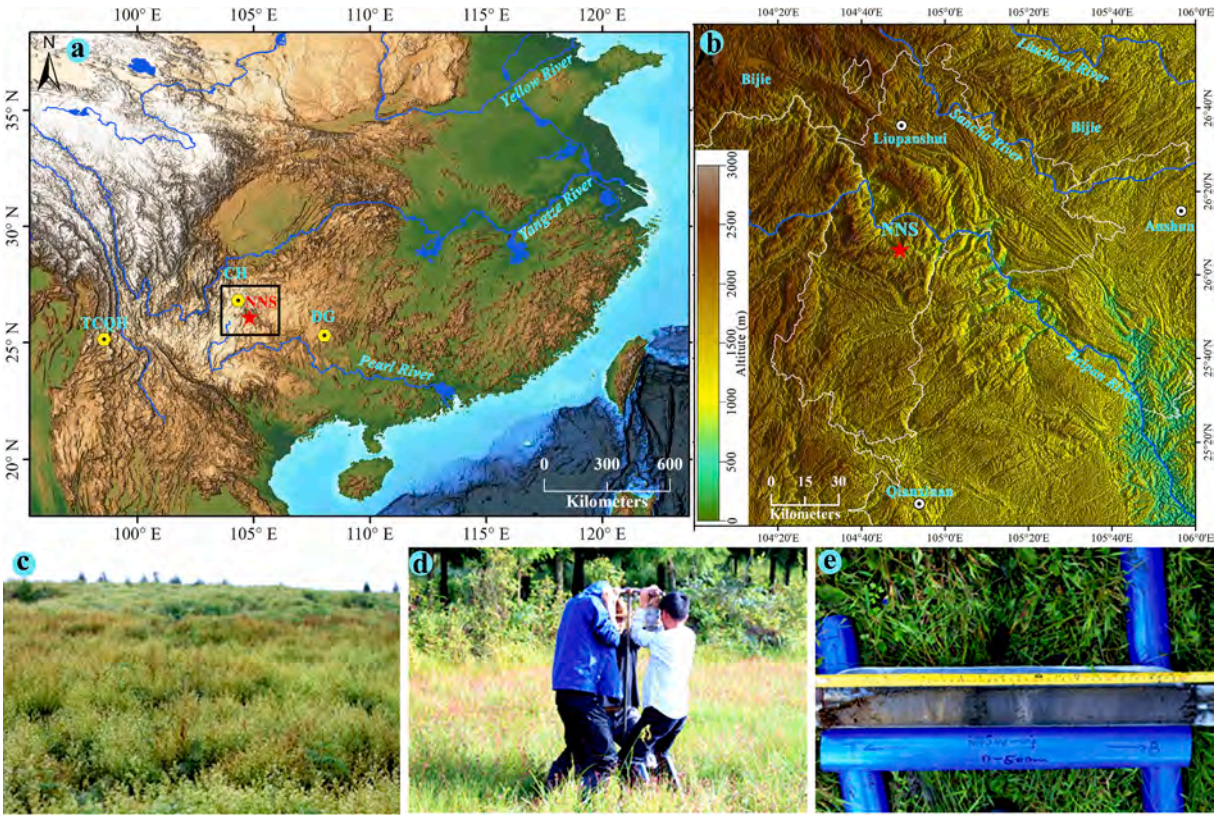


Fig. 1. (a) Geographic location and topography of the Niangniang Mountain (NNS) and comparison sites: Lake Tengcongqinghai (TCQH, Xiao et al., 2017), Chaohai Wetland (CH, Zhang et al., 2024), and Dongge Cave (Wang et al., 2005), (b) specific location of the peat drilling site in Niangniang Mountain wetland. (c-e). Field photos of the peat core extraction.

3.2. Particle size analysis

Grain-size analysis of the upper 52 cm sediments from the NNS borehole was conducted at 0.5-cm intervals using a Malvern Mastersizer 3000 laser diffraction system (School of Marine Sciences, Guangxi University), which measures particle sizes ranging from 0.02 to 3500 μm by analyzing light scattering patterns. Particle sizes were classified using the Krumbein phi (φ) scale (Krumbein, 1934), a logarithmic scale defined by the equation $\varphi = -\log_2(D/Do)$ (where D is the particle diameter in mm and Do = 1 mm as the reference diameter), establishing an inverse relationship between μm and φ: smaller μm values correspond to larger φ values (e.g., clay <4 μm equates to $\varphi > 8$, silt 4–63 μm to 4–8 φ, and sand >63 μm to $\varphi < 4$). This classification aligns with standard sedimentological categories—clay (<4 μm), silt (4–63 μm), and sand (>63 μm)—facilitating interpretation of depositional environments when integrated with other proxies (e.g., pollen and charcoal).

3.3. Chronology

To establish the age sequence of core NNS, well-preserved and uncontaminated plant remains from the core were selected for accelerator mass spectrometry (AMS) ^{14}C dating. In the laboratory, samples underwent pretreatment using the acid-base-acid method to remove humic acids, carbonates, and other impurities, ensuring the reliability of the dating data. Treated samples were then sent to the Xi'an Accelerator Mass Spectrometry Center and Beta Analytic Inc. (Miami, USA) for ^{14}C dating. Four samples were dated in total (Table 1). Radiocarbon dates were calibrated using Calib 8.2 software (Stuiver and Reimer, 1993) with the IntCal20 calibration curve (Reimer et al., 2020). The age-depth model was built using the recently developed Bayesian Bacon 2.5.4 algorithm (Blaauw and Christen, 2011) in RStudio (v4.3.1) with the rbacon package (v2.5.4) (Fig. 2). The chronology model indicates that the base of the upper 52 cm core segment dates to 3430 cal yr BP, with a sedimentation rate of just 0.015 cm/a.

3.4. Pollen and charcoal analysis

Fifty-two samples (1-cm interval) were selected for pollen and charcoal analysis. These samples were pretreated using the heavy liquid floatation method (Yue et al., 2012; Nakagawa et al., 1998). First, samples were sequentially treated with hydrochloric acid (HCl) and potassium hydroxide (KOH) to remove carbonates and organic matter. Samples were not bleached (to avoid destroying charcoal integrity). Residues were sieved through a 200 μm mesh. Next, pollen was enriched

Table 1
AMS ^{14}C dating results from the NNS wetland peat borehole.

Sample No.	Depth(cm)	Lab code	Material	Radiocarbon age (yr BP)	Error (±yr)	^{12}C/^{13}C ratio (‰)	Calibrated age range (cal yr BP)		
							min	max	median
NNS21	21.0	BETA 503983	Black clay	480	30	−26.5	499	541	519
NNS35	35.0	BETA 503984	Black clay	1880	30	−25.6	1730	1883	1821
NNS47	47.0	Xi'an-AMS	Black clay	1617	28		1411	1538	1479
NNS51.5	51.5	BETA 503985	Black peat	3220	30	−28.1	3375	3484	3439

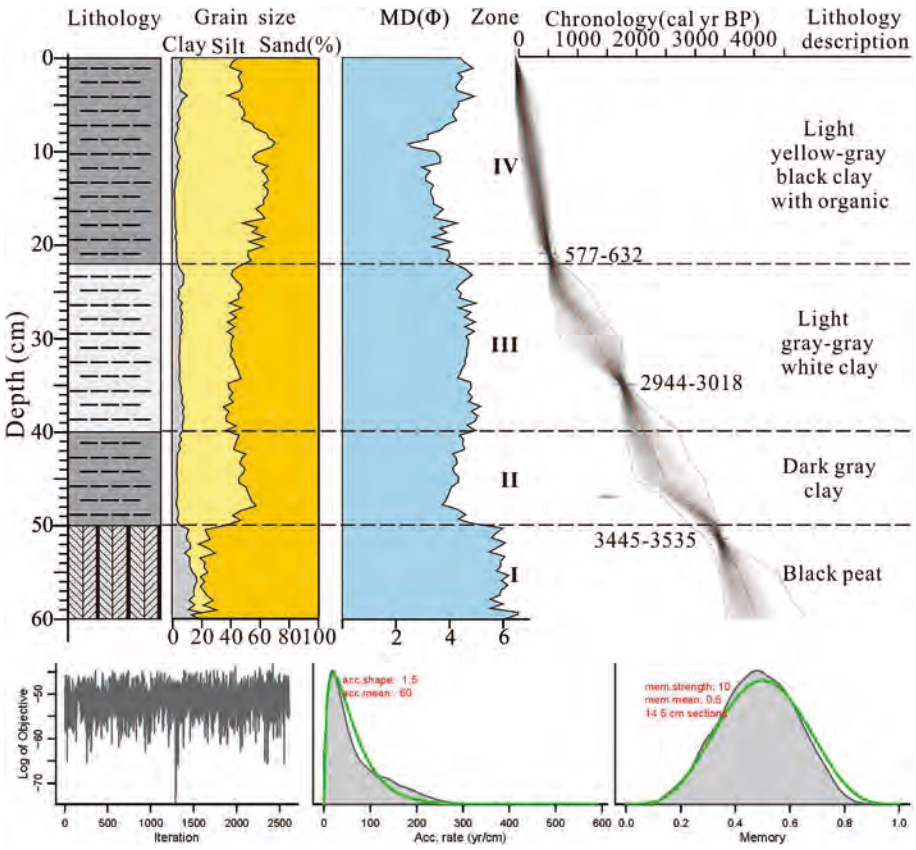


Fig. 2. The lithology, grain-size result, median particle size, Bayesian age-depth model, and lithology description from core NNS.

via heavy liquid flotation (density: 2.0 g/ml). To ensure the accuracy of pollen and charcoal concentration measurements, a known quantity of modern *Lycopodium clavatum* spores (27,560 grains per tablet) was added as an exotic pollen indicator during the processing of each sample.

Pollen identification was performed under a Nikon optical microscope at 400–1000× magnification, using authoritative references including *Angiosperm Pollen Flora of Tropic and Subtropical China* (Institute of Bontany and South China Institute of Bontany, Academia Sinica, 1982), *Pollen Flora of China* (Second Edition) (Wang et al., 1995) and *Chinese Quaternary Palynology* (Tang et al., 2016). For each sample, at least 400 pollen grains were counted to guarantee the representativeness and reliability. Relative percentages of pollen species were calculated based on the total terrestrial pollen count. Relative abundance of aquatic herbaceous pollen, fern spores, mosses, algae, and fungi were determined by their proportions within the total palynomorph assemblage (including terrestrial pollen), following the method outlined by Yue et al. (2012). Palynomorph diagrams were generated using Tilia 2.0.4 software with the CONISS cluster analysis method (Grimm, 1987), focused on taxa with a total content exceeding 5 %.

Charcoal analysis was conducted concurrently with pollen identification to ensure consistent sample processing. After undergoing pretreatment procedures including HCl-KOH digestion, 200 μm mesh sieving, and heavy liquid flotation), charcoal particles were hand-picked under a Nikon optical microscope at 400–1000× magnification. Distinguishing fire activity across different spatial scales is a key objective of palaeofire research (Whitlock and Larsen, 2001). To achieve this, we adopted a three-level size classification system validated through regional methodological studies (Li et al., 2006; Xu et al., 2021). The classification criteria and their ecological implications are as follows: (1) small microscopic charcoal (<50 μm), which is easily transported by wind over long distances and indicates regional fire events; (2) medium microscopic charcoal (50–125 μm), representing transitional fire signals between regional and local scales; and (3) macroscopic charcoal (>125 μm), which typically deposits within 3–7 km of the fire source and reflects near-source, localized burning (Ohlson and Tryterud, 2000; Vachula et al., 2021).

Charcoal particles were counted separately for each size class, and their concentrations (grains/g) were calculated using the *Lycopodium clavatum* spore (27,560 grains per tablet) as indicator. This approach standardizes for differences in sediment volume and preservation conditions. This workflow aligns with standardized palaeofire analysis protocols (Conedera et al., 2009) and has been validated in subtropical monsoon regions similar to our study area (Xu et al., 2021; Yue et al., 2024a, 2024b).

3.5. Principal Component Analysis (PCA)

To further clarify the role of the NNS borehole pollen assemblage in reflecting vegetation types and climate dynamics, Principal Component Analysis (PCA) was applied to pollen species with a total content greater than 5 % across all samples. This analysis focused on 29 dominant pollen types and was executed using Canoco 5 software to uncover ecological and climatic insights from the pollen data.

3.6. Rarefaction analysis

The palynological richness of core NNS was evaluated via rarefaction analysis in PAST software (Hammer et al., 2001). As a widely used statistical approach, rarefaction standardizes samples with varying pollen counts to estimate average richness at a constant reference level—typically the lowest pollen count in the dataset (Birks and Line, 1992). We utilized the uncorrected E (Sn) value derived from rarefaction analysis as an indicator of species richness, vegetation composition, and

landscape diversity. Specifically, the "Individual rarefaction" function in PAST's "Diversity" module was applied to pooled count data from each sampling site, generating rarefaction curves that illustrate how species richness changes with increasing sample size. This approach effectively revealed the differential responses of regional vegetation diversity to climate changes and human activities through reconstructed pollen richness, aligning with established palaeoecological methodologies.

4. Results

4.1. Sediment stratigraphy

This research investigated the sedimentary composition of the upper 52 cm of core NNS. Based on visual color, primary components, and sediment characteristics, the sequence was stratified into four lithological units (Fig. 2). Bulk sediment analysis revealed average contents of 4.97 % clay, 47.74 % silt, and 47.29 % sand with median particle size ranges from 2.37 to 5.96 φ. From bottom to top, the core is divided into four distinct zones (Fig. 2):

Zone I (52–50 cm): dark black peat. This zone shows a median particle size of 5.54 φ, with average clay, silt, and sand contents of 9.85 %, 65.23 %, and 24.93 %, respectively. It displays the highest clay and sand contents within the profile.

Zone II (50–40 cm): dark gray clay, showing a gradual boundary with underlying sediments. This zone has a median particle size of 4.18 φ, with average clay, silt, and sand contents of 4.14 %, 49.06 %, and 46.80 %, respectively. It exhibits the lowest clay content within the profile.

Zone III (40–22 cm): light grayish-white clay with sparse organic material. This unit has a median particle size of 4.57 φ, with average clay, silt, and sand contents of 6.13 %, 52.69 %, and 41.18 %, respectively. The clay content is higher than in Zone II.

Zone IV (22–0 cm): gray-yellow to gray-black organic-rich clay. This zone has a median particle size of 3.67 φ, with average clay, silt, and sand contents of 3.85 %, 41.06 %, and 55.09 %, respectively. It displays the highest silt content within the profile.

Grain-size distribution (sand: >63 μm; silt: 4–63 μm; clay: <4 μm) reflects significant shifts in hydrological regimes, erosion intensity, and depositional energy over the past 3400 years. For instance, Zone IV's high sand content (e.g., 55.09 %) indicates intensified runoff and high-energy depositional conditions, likely linked to enhanced precipitation events or anthropogenic-induced soil erosion (e.g., agricultural tillage; Zhang et al., 2024). In contrast, increased clay and silt proportions (e.g., 9.85 % clay and 65.23 % silt) in Zone I correspond to stable, low-energy environments under humid climatic conditions, as fine particles are transported and deposited only in calm water settings (Chambers and Charman, 2004). The transition from fine-grained sediments (Zone I) to coarser grains (Zone II–IV) parallels monsoon weakening and increasing human disturbance, highlighting the synergistic influence of climate and human activities on sedimentary processes. Integrating these grain-size insights with pollen and charcoal records strengthens multi-proxy interpretations: for example, the high sand content in Zone IV coincides with elevated macroscopic charcoal and Poaceae percentages, confirming intensive agricultural activities and associated erosion.

4.2. Facies description based on multi-proxy analysis

A total of 88 pollen and spore taxa were identified across 52 samples from core NNS. Pollen counts per sample ranged from 546 to 943 grains (729 grains). The pollen diagram (Fig. 3) illustrates the dominant and representative taxa (as seen in Fig. 4). Arboreal pollen (AP) was dominated by *Pinus*, deciduous *Quercus* (*Quercus*-D), *Corylus*, *Alnus*, *Betula*, *Carpinus*, *Morus*, *Hamamelis*, evergreen *Quercus* (Quercus-E), *Juglans*, *Tsuga*, and *Castanopsis/Lithocarpus*. Non-arboreal pollen (NAP) included Poaceae, *Artemisia*, Asteraceae, Chenopodiaceae and Brassicaceae. Aquatic/wetland herbs were primarily represented by Cyperaceae and *Myriophyllum*. Fern spores were dominated by monolete types (e.g., Polypodiaceae, Dryopteridaceae), with trilete spores identified in *Dicranopteris*. Based on variations in major pollen/spore percentages, and charcoal particles concentrations, CONISS cluster analysis divided core NNS into four distinct zones (Fig. 3):

4.2.1. Zone I (52–50 cm; ~3400–3200 cal yr BP)

This zone exhibits the highest pollen concentration in the profile (mean: 3.89 × 10^6 grains/g). AP dominates (92.05 %), with evergreen broad-leaved taxa (e.g., *Quercus*-E, *Castanopsis/Lithocarpus*) peaking at 76.72 %. Deciduous components (e.g., *Quercus*-D, *Alnus*) comprise 16.69 %, while coniferous *Pinus* is low (3.06 %). Terrestrial herbs (mainly Poaceae, *Artemisia*) account for 7.95 %. Fern spores (predominantly monolete) reach 20.81 %, with minimal aquatic herbs (0.76 %) and fungi (0.7 %). Charcoal concentrations are highest for particles <50

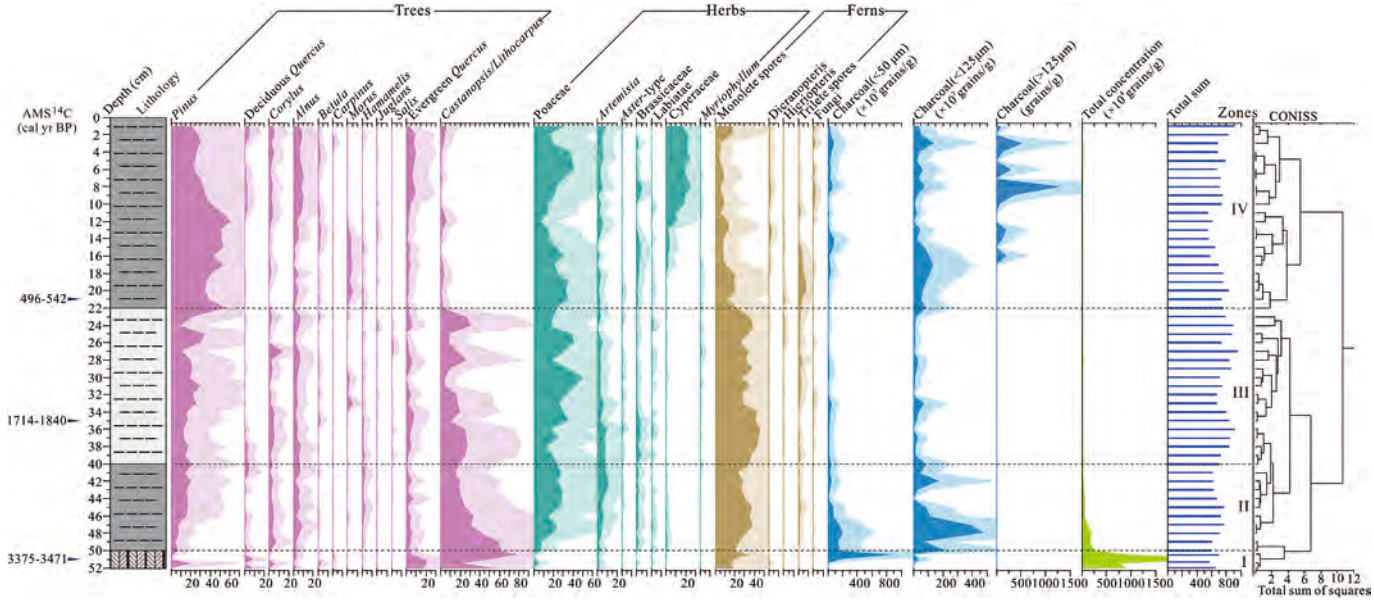


Fig. 3. Pollen percentage diagram of core NNS, including lithological column (color and texture, description see Fig. 2), radiocarbon ages (cal yr BP) with corresponding depths, relative frequency (%) of trees, herbs, ferns, concentrations of pollen and charcoal, and total sum (from left to right).

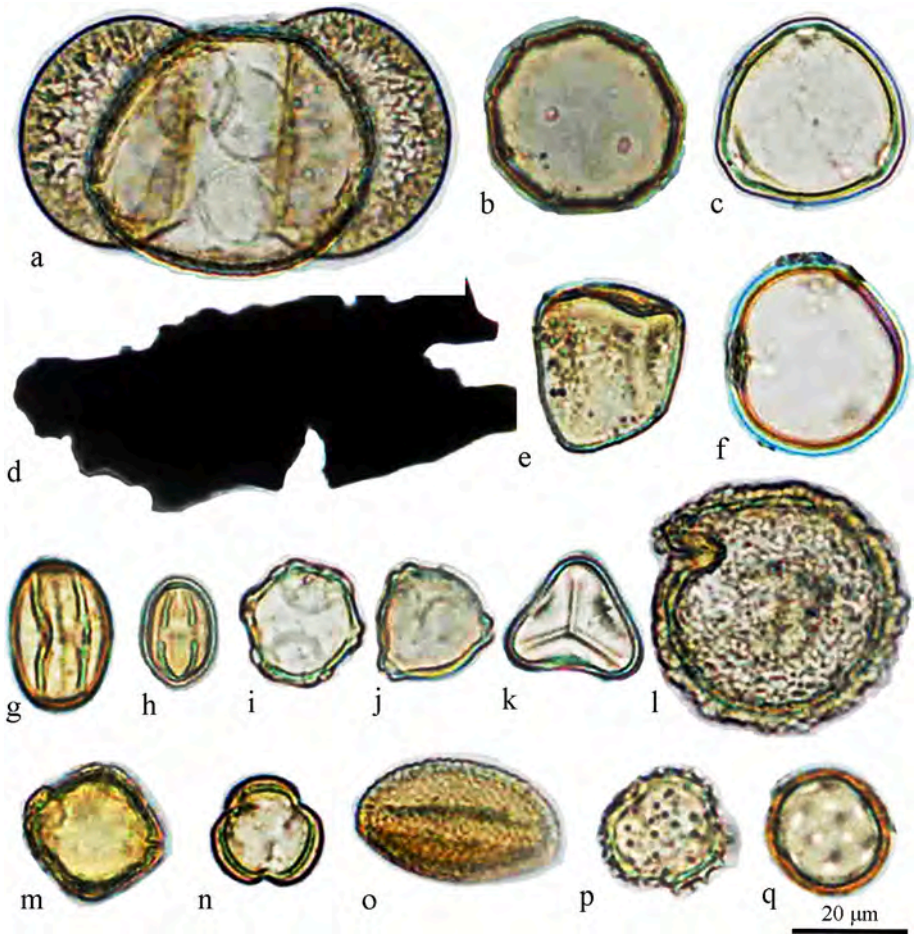


Fig. 4. Key palynomorph/charcoal micrographs from the Niangniang Mountain peat core. (a) *Pinus*; (b) *Juglans*; (c) *Carpinus*; (d) Charcoal particle; (e) Cyperaceae; (f) Poaceae; (g) Evergreen *Quercus* (*Quercus*-E); (h) *Castanopsis/Lithocarpus*; (i) *Alnus*; (j) *Betula*; (k) *Dicranopteris*; (l) *Tsuga*; (m) *Myriophyllum*; (n) *Artemisia*; (o) Brassicaceae; (p) Asteraceae; (q) Chenopodiaceae. All micrographs were taken under a Nikon optical microscope (400×)with bright-field illumination.

μm (mean: 439,121 grains/g), with a lower value for <125 μm particles (mean: 9212 grains/g); while particles >125 μm are absent. Total charcoal concentration ranges from 193,459 to 967,295 grains/g (mean: 448,333 grains/g).

4.2.2. Zone II (50–40 cm; ~3200–2100 cal yr BP)

Pollen concentration declines significantly (mean: 165,195 grains/g). AP decreases to 65.44 %, with evergreen broad-leaved taxa reduced to 33.40 %. Conifers (*Pinus*) increase to 14.87 %, and terrestrial herbs (Poaceae, *Artemisia*) peak at 34.56 %. Aquatic herbs (Cyperaceae, 1.13 %) and fern spores (33.54 %) show marked increases. Charcoal concentrations peak for 50–125 μm particles (mean: 15,236 grains/g). Particles <50 μm average 87,822 grains/g (range: 15,759–211,566 grains/g); while the particles >125 μm remain absent. Total charcoal averages 103,058 grains/g (range: 15,759–260,169 grains/g).

4.2.3. Zone III (40–22 cm; ~2100–600 cal yr BP)

AP declines slightly (60.26 %), dominated by coniferous Pinus (20.42 %). Evergreen broad-leaved taxa decrease to 24.01 % (*Castanopsis/Lithocarpus* dominant). Terrestrial herbs (dominated by Poaceae, 39.74 %) and monolete spores (39.05 %) show elevated percentages. Total pollen concentration averages 40,805 grains/g. Charcoal concentrations are the lowest in the profile: <50 μm (mean: 22,241 grains/g; range: 6816–53,539 grains/g), 50–125 μm (mean: 2232 grains/g). Particles >125 μm are absent. Total charcoal averages 24,437 grains/g (range: 8234–61,316 grains/g).

4.2.4. Zone IV (22–0 cm; ~600 cal yr BP–present)

AP comprises 66.59 % of the assemblage. Evergreen broad-leaved taxa decline to their minimum (9.64 %), while conifers (dominated by Pinus) peaks (40.37 %). Terrestrial herbs (Poaceae, Cyperaceae) reach their maximum (33.41 %). Fern spores decline to 16.27 %, with fungi at 1 %. Charcoal concentrations increase: <50 μm (mean: 40,786 grains/g; range: 8564–91,130), 50–125 μm (mean: 6357 grains/g). Notably, charcoal >125 μm first appears at 16 cm depth (~340 cal yr BP), averaging 158 grains/g (sporadic occurrence). Total charcoal concentration averages 47,300 grains/g (range: 10,581–106,755).

4.3. Principal component analysis (PCA)

Principal Components Analysis (PCA) of the pollen data reveals distinct environmental gradients (Fig. 5). The first two principal components (PC1 and PC2) together explain 62.51 % of the total variance, PC1 accounts for 50.65 % and PC2 for 11.86 %. It indicates that these axes capture the primary drivers of pollen assemblage variation.

PC1 exhibits strong positive loading for subtropical evergreen broad-leaved taxa (e.g., *Castanopsis/Lithocarpus*, evergreen *Quercus* (*Quercus*-E)), which favor warm-humid conditions (Fig. 5), and high negative loadings for cold/drought-tolerant taxa such as *Pinus* and Poaceae. This loading pattern indicates that PC1 captures a climatic gradient spanning warm-humid to cold-dry environments conditions.

PC2, by contrast, exhibits strong negative loadings for anthropogenic indicator taxa, particularly Poaceae, commonly associated with agricultural disturbance, and positive loadings for primary broad-leaved

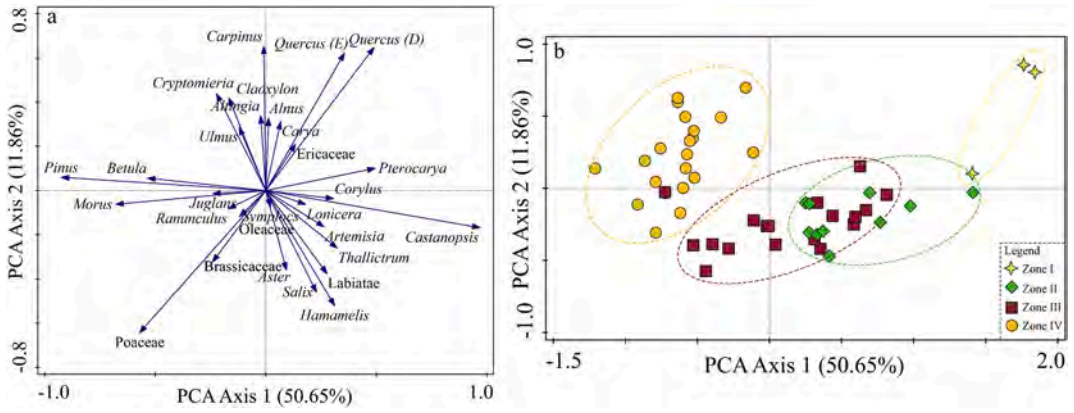


Fig. 5. PCA results from core NNS: (a) loading plots of dominant pollen taxa; (b) Sample distribution plot of pollen data for each zone.

forest taxa. Accordingly, PC2 likely represents a gradient of human-induced disturbance intensity.

Furthermore, the characteristics of pollen and spore assemblages across stratigraphic intervals provide compelling support for spatial distribution patterns of taxa (Fig. 5b). Although detailed species-level loadings require further analysis, the PCA results offer a robust foundational basis for interpreting vegetation responses to Late Holocene climatic variability and anthropogenic influence in this subalpine ecosystem.

PC2's ecological significance is phase-specific: in zone I (~3400–3200 cal yr BP), its positive loadings for evergreen broad-leaved taxa align with high clay content (stable humid conditions) and low charcoal concentrations (minimal disturbance), directly linking it to warm-humid climates. Particularly zone IV, PC2's negative loadings for anthropogenic indicators (e.g., Poaceae) correlate with elevated macroscopic charcoal (>125 μm) and sand content, confirming it reflects an anthropogenic disturbance gradient. This dual interpretation is validated by regional studies (Xiao et al., 2017; Xu et al., 2021), highlighting the shifting drivers of vegetation change over time.

4.4. Biodiversity

Palynology-based biodiversity models are used to evaluate the estimated number of pollen taxa for every sediment interval (1 cm

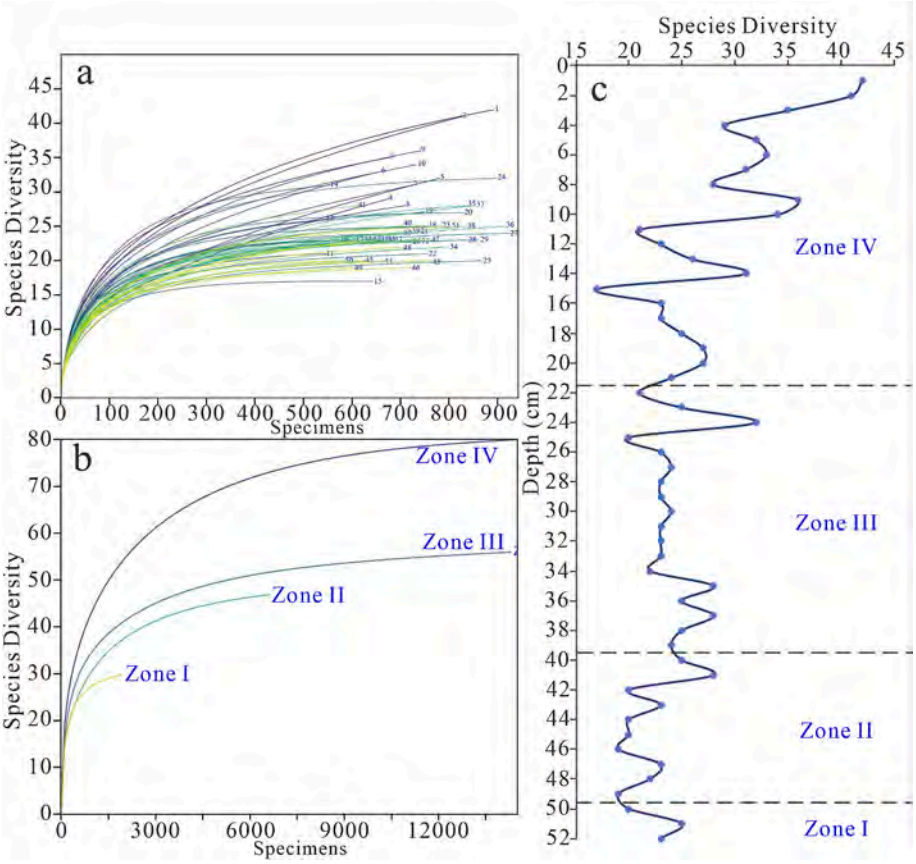


Fig. 6. Palynology-based rarefaction analysis: (a) Curves indicate estimated number of pollen taxa E (S_n) for every sediment interval (1 cm resolution) in core NNS, (b) estimated number of pollen taxa E (S_n) for each pollen zone in core NNS, (c) Palynological richness [E (S_n)] based on rarefaction analysis of pollen data from core NNS.

resolution) in core NNS. Rarefaction curves illustrate species diversity values for individual sample (Fig. 6a) and pollen zones (Fig. 6b). The estimated species richness fluctuated between 17 and 42 species per sample during the past 3400 years (Fig. 6c). Diversity metrics for the four zones (outlined in Section 4.2) are detailed below:

Zone I (~3400–3200 cal yr BP) contains 30 taxa and 2041 counts of pollen grains, with low species richness (E(Sn) = 20–25).

Zone II (~3200–2100 cal yr BP), taxa richness increased to 47 (6785 pollen grains), with moderate richness (E(Sn) = 19–28).

Zone III (~2100–600 cal yr BP), a total 56 taxa were recorded (14,410 pollen grains), the richness reached minimum levels (E(Sn) = 20–32).

Zone IV (~600 cal yr BP–present), a total 80 taxa were recorded (14,658 pollen grains), the richness rebounded to high levels (E(Sn) = 17–42).

These patterns of low richness in stable climates and peak richness in anthropogenic landscapes demonstrate that dynamic diversity may respond to climate and human impacts.

5. Discussions

5.1. Environmental fluctuation and ecosystem dynamics during the late Holocene

The Niangniang Mountain peat record provides a high-resolution archive of environmental and ecosystem dynamics spanning the last 3400 years. It reveals complex interactions among climate variability, vegetation succession, and anthropogenic influence in western Guizhou. This section synthesizes multi-proxy evidence to reconstruct palaeoenvironmental evolution and ecosystem responses across four distinct phases of the Late Holocene (Fig. 7).

5.1.1. Phase I (~3400–3200 cal yr BP)

The basal sediments of the Niangniang Mountain peat core record a period of exceptional ecosystem stability, driven by a strong summer monsoon influence. Pollen assemblages here are dominated by evergreen broad-leaved taxa (72.30 %), with evergreen *Quercus* and *Castanopsis/Lithocarpus* as the main components, indicating closed-canopy subtropical evergreen broad-leaved forests, a vegetation type characteristic of warm, humid conditions (Fig. 7). This interpretation is further corroborated by the high positive scores on both PC1 and PC2 (Fig. 7), though it is critical to clarify that PC2's linkage to warm-humid conditions is phase-specific to Phase I. Regional palaeoecological studies confirm both axes associated with warm-humid climatic conditions in this context (Xiao et al., 2015; Huang et al., 2018; Herzschuh et al., 2019).

Chronologically, this vegetation composition aligns with the late stage of the Holocene thermal maxima (HTM, Marcott et al., 2013), a global climatic optimum (Fig. 8a). Notably, this warm-humid optimum appears to have persisted longer at our site than in nearby records, including those from Lake Caohai (eastern Guizhou, Zhang et al., 2024), Lake Qinghai (Yunnan, Xiao et al., 2017), and other monsoon-influenced regions (Zhao et al., 2009). Exceptionally high pollen concentrations (3.89×10^6 grains/g) and minimal charcoal abundance further suggest limited ecological disturbance during this interval (Fig. 9), a pattern consistent with reduced fire activity during peak monsoon periods as documented in global fire-history syntheses (Marlon et al., 2013).

The 'peak monsoon period' in southwest China (including western Guizhou) is widely documented as 4000–3000 cal yr BP (Wang et al., 2005; Dykoski et al., 2005), corresponding to the late stage of the HTM. This period is characterized by maximum summer monsoon intensity, as recorded by speleothem $\delta^{18}O$ (Dongge Cave) and peat pollen records (Yue et al., 2012; Xiao et al., 2017). Our data align with this regional signal, but we emphasize that our 3400–3200 cal yr BP record captures only the tail end of this peak monsoon period—not its full duration—to avoid overinterpreting the scope of our core's basal interval.

Multiple proxies, including pollen assemblages, grain-size data, and charcoal concentrations converge to confirm Phase I's warm-humid regime. The high proportion of monolete fern spores (20.81 %) indicates moist understory conditions; when integrated with sedimentological and other proxy evidence, this collectively strengthens the case for Phase I's warm-humid climatic regime. The sedimentological evidence includes: (1) dark black peat with fine particle size (median 5.73 φ), which points to waterlogged conditions conducive to peat

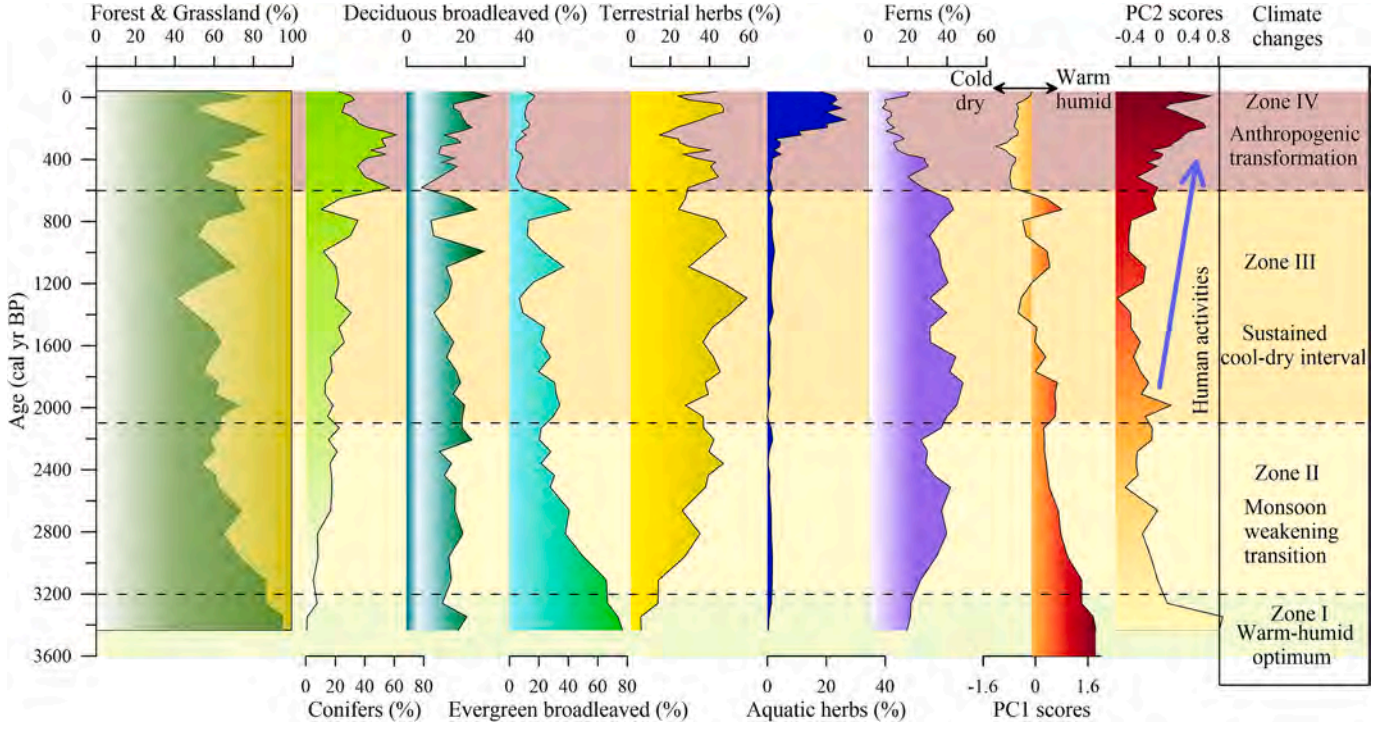


Fig. 7. The variations in primary pollen ecological types and the climate and environmental shifts signaled by PCA in the NNS wetland borehole.

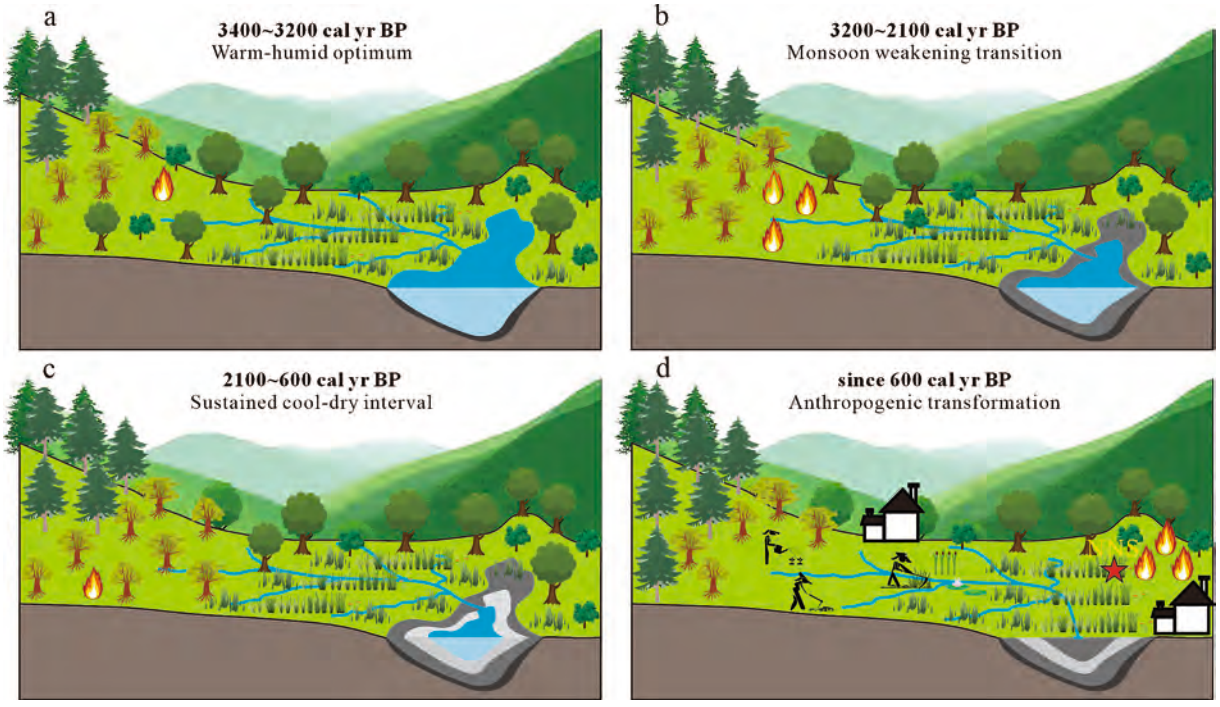


Fig. 8. Conceptual diagrams of environmental fluctuation and ecosystem dynamics on Niangniang Mountain since ~3400 cal yr BP: (a) 3400–3200 cal yr BP (warm-humid optimum); (b) 3200–2100 cal yr BP (monsoon weakening transition); (c) 2100–600 cal yr BP (sustained cool-dry interval); (d) since 600 cal yr BP (anthropogenic transformation).

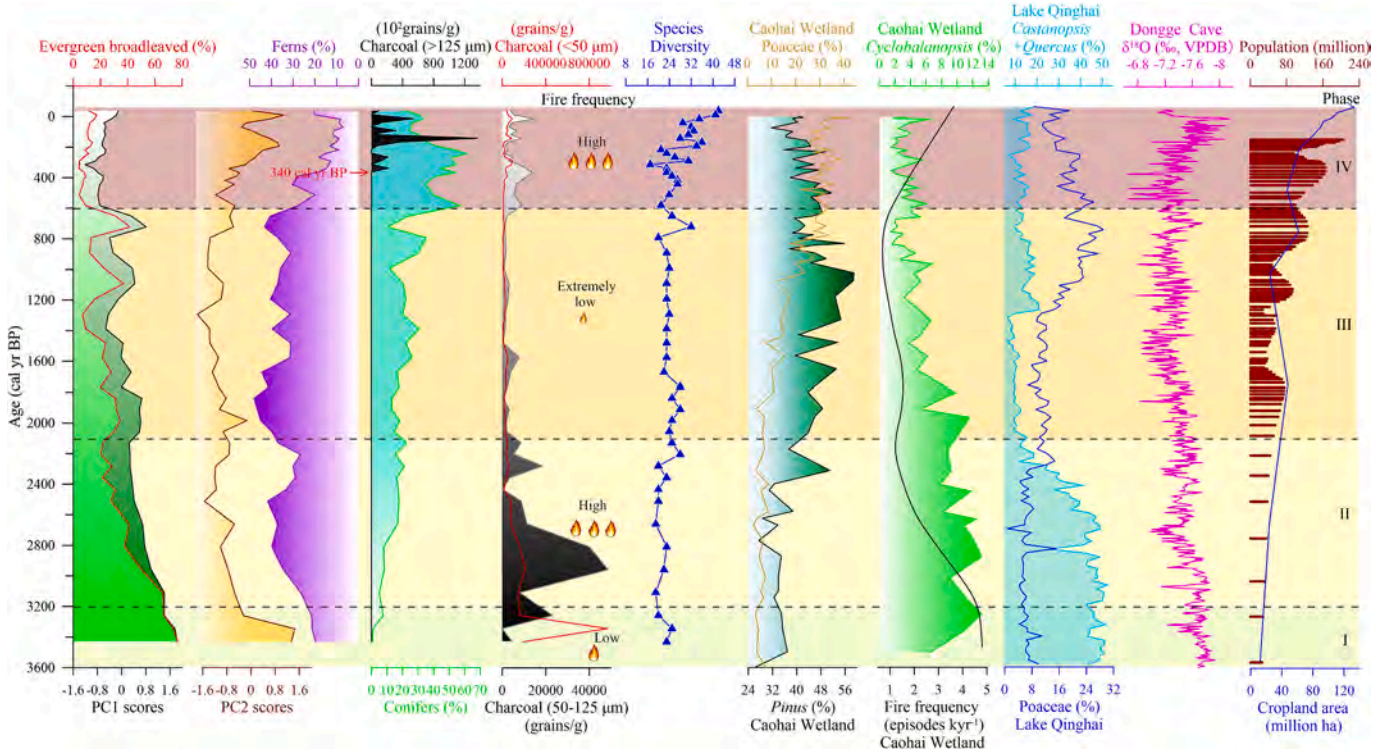


Fig. 9. Vegetation changes, climate dynamic, biodiversity, and fire activity records in the past 3400 years for this study, comparison to the record of Caohai Wetland (Zhang et al., 2024), Lake Qinghai (Xiao et al., 2017), δ^{18}Q of stalagmite of Dongge Cave (Wang et al., 2005), the estimated Holocene anthropogenic land use from China (Goldewijk et al., 2017), and the estimated human population of China (maroon) (Ge, 2002; Lu and Teng, 2000; Li et al., 2009). (For interpretation of the references to color in this figure legend, the reader is referred to the web version of this article.)

accumulation (Chambers and Charman, 2004). (2) higher clay content (Fig. 2), signaling stable, low-energy depositional environments, and (3) low charcoal concentrations (Fig. 4), further suggesting reduced fire activity under humid monsoon conditions.

As shown in Fig. 9, these findings align with regional speleothem $\delta^{18}O$ records that document the late stage of the maximum Holocene monsoon intensity (4000–3000 cal yr BP, Wang et al., 2005; Dykoski et al., 2005). Additionally, the delayed transition at Niangniang Mountain suggests (relative to other sites like Lake Caohai and Lake Qinghai) suggests local topographic buffering of monsoon weakening. This consistency across proxies and regional records confirms that local vegetation and environmental changes were embedded within broader southwest China monsoon dynamics.

5.1.2. Phase II (~3200–2100 cal yr BP)

This phase marks a significant ecological reorganization, driven by climatic deterioration, a shift toward cooler conditions and reduced monsoon-derived precipitation (consistent with regional speleothem records; Wen et al., 2017). Vegetation communities show clear responses to this climatic shift, for instance, evergreen broad-leaved taxa declined by 50 % (to 34.40 %), while drought-tolerant *Pinus* (14.87 %) and grassland species (Poaceae 34.56 %) increased notably (Fig. 7). This vegetation turnover indicates a shift toward cooler/drier conditions, aligns with both regional and global climate contexts. Regionally, it is consistent with records documenting weakened monsoon intensity during this period (Fig. 8b, Fig. 9, Wen et al., 2017; Zhou et al., 2023). While globally, we link this monsoon weakening—evident in our Phase II and corresponding to the late stage of the HTM—to hemispheric climate forcing (e.g., declining Northern Hemisphere insolation; Marcott et al., 2013), thereby clarifying how local ecological changes fit within broader global climatic processes.

Additionally, microscopic charcoal abundance (50–125 μm) increases tenfold (mean: 15,236 grains/g), suggesting heightened fire activity (Fig. 8b, Fig. 9). This increase likely stems from both climatic aridity (which dries fuel sources) and early human-induced disturbance. This pattern mirrors fire regime shifts observed in other monsoon transition zones during this period (Xu et al., 2021; Tan et al., 2015).

Interestingly, a key observation here is the apparent contradiction between sedimentological and pollen signals. Sediments shift to dark gray clay with reduced organic content, which indicates diminished peat accumulation under drier conditions consistent with regional lake level reconstructions (Chen et al., 2015). In contrast, pollen and spore data show expanded fern spores (33.54 %) and aquatic herbs, implying localized wetland expansion (Fig. 9). We attribute this discrepancy to episodic heavy rainfall events amid the overall drier trend. Increased slope runoff from these events may have created localized waterlogging in low-lying areas of the peatland, supporting wetland vegetation even as the broader regional climate became drier. This pattern has been observed in other subtropical peatlands during monsoon transition periods (Xiao et al., 2015).

5.1.3. Phase III (~2100–600 cal yr BP)

This phase records the most substantial vegetation reorganization (Fig. 7), with conifers expand to 20.42 %, while evergreen taxa decline to 24.01 %. This conifer-dominated landscape, accompanied by expanded grasslands (39.74 %), indicates prolonged cool/dry conditions, potentially linked to Northern Hemisphere cooling events like the Dark Ages Cold Period (DACP, ~500–900 CE), a well-documented cold-dry event that reinforced conifer dominance in Southwest China (Zhao et al., 2010; Wang et al., 2012). This prolonged cool-dry phase then overlaps with the Medieval Climate Anomaly (MCA, ~950–1250 CE), a period of regional climate instability rather than a uniform warm phase in this monsoon-sensitive area, which intensified summer monsoon fluctuations (Xiao et al., 2017). Episodic droughts and short wet spells during the MCA likely exacerbated conifer persistence and grassland expansion, as pine and Poaceae are more resilient to hydrological variability than evergreen broad-leaved taxa. Surprisingly, charcoal concentrations decline to a profile minimum (Fig. 8c, Fig. 9), despite the presumed flammability of pine forests. This contradiction may be attributed to three factors: (1) reduced fuel loads from prior deforestation (Huang et al., 2018), (2) active fire suppression as pastoralism expanded (Dietze et al., 2018), or climatic aridity insufficient to support frequent fires (Marlon et al., 2013). As shown in Fig. 9, similar fire-vegetation-climate decoupling has been documented in other subtropical regions during this period (Xiao et al., 2017; Xu et al., 2021; Zhang et al., 2024). The presence of light grayish-white clay with sparse organics further supports a prolonged moisture deficit, aligning with regional speleothem records showing weakened monsoon intensity (Wang et al., 2005).

5.1.4. Phase IV (~600 cal yr BP-present)

This phase documents dramatic ecosystem transformations fueled by intensive human activities (Fig. 8d). The dominance of *Pinus* (39.1 %), suppression of evergreen taxa (8.0 %), and continued grassland expansion (33.41 %) point to large-scale deforestation. Notably, this anthropogenic-driven vegetation transformation occurred amid enhanced El Niño-Southern Oscillation (ENSO) variability (Herzschuh et al., 2019). As a global climate mode, ENSO amplifies East Asian summer monsoon fluctuations in Southwest China, leading to more frequent extreme rainfall and drought events. However, such climatic variability did not reverse the vegetation trajectory: the first appearance of macroscopic charcoal (>125 μm) at ~340 cal yr BP (Fig. 9) marks localized slash-and-burn agriculture (Roos et al., 2023), and the concurrent surge in Poaceae (33.41 %) reflects widespread cropland expansion. These changes coincide with historical records of Han Chinese migration into Guizhou during the Ming-Qing dynasties (Yuan et al., 2022). This confirms that human impacts ultimately overwhelmed climatic controls, even as ENSO intensified monsoon variability. The resurgence of fire activity (charcoal mean: 47,300 grains/g), coupled with increased fungal spores and coarser sediments (55.09 % sand), points to landscape opening and soil erosion consistent with patterns observed across other Asian agricultural frontiers (Xiao et al., 2017; Zhang et al., 2024; Zhao et al., 2024). These shifts occurred despite the climatic backdrop of the Little Ice Age (LIA, ~1300–1850 CE), underscoring the dominant influence of human activity, in line with global Late Holocene human–environment interactions (Ellis et al., 2021).

The PCA ordination (PC1: 50.65 %, PC2: 11.86 %) provides quantitative support for these interpretations (Fig. 4). PC1 exhibits positive loadings for evergreen forest taxa and negative loadings for *Pinus* and Poaceae, reflecting a primary climate gradient from warm-humid to cool-dry conditions, explaining 50.65 % of total variance. This gradient aligns with regional reconstructions of Late Holocene monsoon weakening (Wang et al., 2012). Samples from Phase I cluster at the positive extreme, Phase III at the negative, with Phase II showing transitional positioning, a progression matching other monsoon-sensitive records (Zhao et al., 2010).

PC2 is characterized by negative loadings for *Pinus*, Brassicaceae and *Aster* (taxa linked to disturbed environments) and positive loadings for primary forest taxa, capturing an anthropogenic disturbance gradient that accounts for 11.86 % of variance. To strengthen this interpretation, we cross-validate PC2 with Phase IV's non-pollen proxies: the maximum PC2 scores in Zone IV samples correspond to the highest macroscopic charcoal concentrations (47,300 grains/g) and sand content (55.09 %) in the core, directly linking PC2's variation to intensified human activity (e.g., slash-and-burn agriculture, soil erosion). Notably, PC2's earlier association with warm-humid conditions is restricted to Zone I. In this interval, positive PC2 scores overlap with high clay content (stable humid conditions) and low charcoal (minimal disturbance), while Zone IV's PC2 signal is exclusively driven by anthropogenic factors. This phase-specific distinction avoids misinterpretation of PC2's ecological meaning across the core. This PCA pattern is consistent with analyses from other anthropogenically altered landscapes in subtropical China

(Xiao et al., 2017; Xu et al., 2021), confirming that human activity emerged as a secondary but increasingly significant ecological driver in the Late Holocene.

In addition, regional comparisons reveal both consistencies and unique aspects of Niangniang Mountain's environmental history. While the broad monsoon-weakening trend aligns with Yunnan records (Xiao et al., 2017), the persistence of evergreen taxa until ~3200 cal yr BP suggests western Guizhou remained favorable longer than eastern areas, likely due to topographic effects (Huang et al., 2018). Fire regime differences with other subtropical sites, where anthropogenic burning intensified steadily (Xu et al., 2021), highlight the role of local variables such as fuel availability and land-use practices in modulating fire–climate–human interactions (Archibald et al., 2013; Coughlan et al., 2018). These findings contribute to growing evidence that Late Holocene environmental change in monsoon Asia reflects complex interplay between global climate drivers, regional monsoon dynamics, and localized anthropogenic activities (Zhao et al., 2010; Zhou et al., 2023).

Notably, *Pinus* pollen is consistent over-representation throughout the record, a common phenomenon in subtropical peatland archives that requires explicit clarification to avoid misinterpreting vegetation dynamics.

Pinus pollen is consistently over-represented throughout the pollen record, a pattern common in subtropical peatland archives. Three key factors explain this phenomenon: (1) Ecologically, *Pinus yunnanensis* and *Pinus armandi*—dominant coniferous species in western Guizhou—exhibit strong adaptability to heterogeneous habitats (e.g., rocky slopes and degraded forests), maintaining large local populations (Xiao et al., 2017; Yuan et al., 2022). (2) Taphonomically, *Pinus* pollen grains have a thick, resistant exine layer that enhances preservation in anaerobic peat sediments, reducing decomposition rates compared to fragile broad-leaved pollen (Herzschuh et al., 2019; Xu et al., 2016). (3) Dispersally, as anemophilous species, *Pinus* releases massive amounts of lightweight pollen that can be transported over long distances by wind, increasing its relative abundance in the record even from non-local sources (Birks and Birks, 1980). This over-representation should be considered when interpreting vegetation dynamics, as *Pinus* pollen percentages may overestimate its actual coverage in the past landscape.

5.2. Climatic and anthropogenic drivers of biodiversity changes

The palynological richness index [E(Sn)] and PCA results from the Niangniang Mountain peat core provide detailed insights into the complex drivers of biodiversity change over the Late Holocene, revealing intricate interactions between climatic forcing and human disturbance (Fig. 8).

Phase I (~3400–3200 cal yr BP), characterized by low richness (E(Sn) = 20–24, Fig. 5c), reflects a period of climatic stability that favored the dominance of a few key taxa (Birks and Birks, 1980; Willis et al., 2010). The closed-canopy evergreen forest (72.30 %), dominated by evergreen *Quercus* and *Castanopsis/Lithocarpus*, created homogeneous environmental conditions that limited niche space for herbaceous species, resulting in low β-diversity (Huang et al., 2020). This pattern aligns with global observations that peak interglacial conditions often reduce plant diversity by favoring competitive exclusion of stress-tolerant species (Blarquez et al., 2014). The high pollen concentration (3.89×10^6 grains/g) further supports optimal growing conditions, as demonstrated in other subtropical peat archives (Huang et al., 2018).

Between Phase II (~3200–2100 cal yr BP), richness increased moderately (E(Sn) = 20–31, Fig. 5c) in response to greater climatic variability, which likely enhanced habitat heterogeneity. The coexistence of residual evergreen forests (34.40 %), expanding pine woodlands (*Pinus* 14.87 %), and grasslands (Poaceae 34.56 %) supported more species through niche partitioning (Colombaroli and Gavin, 2010; Steinbauer et al., 2018). This intermediate disturbance effect, where maximum diversity is achieved during ecotonal transitions, is also observed in European lake sediments (Giesecke et al., 2012). The expansion of fern spores (33.54 %) and aquatic herbs further suggests microhabitat diversification linked to fluctuating moisture conditions, a well-documented phenomenon in monsoon-sensitive environments (Ren et al., 2021).

In Phase III (~2100–600 cal yr BP), richness declined to its lowest levels (E(Sn) = 16–27, Fig. 5c), as habitat homogenization occurred through the dominance of stress-tolerant conifers (20.42 %, e.g., *Pinus*) and herbs (39.74 %, e.g., Poaceae) (Tinner et al., 2005; Zhao et al., 2009). This vegetation shift reflects a classic stress-filtering mechanism, where harsh environmental conditions eliminate all but the most adapted species (May et al., 2019). Despite *Pinus* dominance, charcoal concentrations declined, suggesting reduced fuel availability and lower structural complexity—conditions similar to those documented in other fire-suppressed coniferous ecosystems (Marlon et al., 2013).

In Phase IV (~600 cal yr BP-present), palynological richness reached its peak (E(Sn) = 26–36, Fig. 5c), despite intensive anthropogenic impact. This seemingly paradoxical increase aligns with the "intermediate disturbance hypothesis" (Xu et al., 2021; Ellis et al., 2021); agricultural activity, deforestation, and the expansion of secondary vegetation enhance habitat heterogeneity, which in turn supports greater biodiversity. Such a mosaic landscape supported both shade-intolerant ruderals (e.g., *Artemisia*, Brassicaceae) and forest-edge species, increasing γ-diversity despite reduced α-diversity in any single habitat type. Similar dynamics have been reported in European cultural landscapes, where moderate human disturbance maximizes biodiversity through intermediate disturbance effects (Dietze et al., 2018; Roberts et al., 2017). The appearance of macroscopic charcoal (>125 μm) at ~340 cal yr BP (Fig. 9) marks a critical threshold in land-use intensity, coinciding with Ming-Qing dynasty agricultural expansion (Yuan et al., 2022), the increase in Chinese population (Klein Goldewijk et al., 2017), and the expansion of cropland area (Ge, 2002; Lu and Teng, 2000; Li et al., 2009). This transformation led to novel ecosystems characterized by new disturbance regimes and the co-occurrence of fire-adapted taxa (e.g., *Pinus*) and disturbance indicators (e.g., Poaceae). Such patterns are increasingly recognized as characteristic of the early Anthropocene in East Asia (Stephens et al., 2019; Zhou et al., 2023).

The biodiversity patterns reveal non-linear responses to environmental change. The Phase II-III transition crossed an ecological threshold where cooling exceeded the tolerance of many evergreen taxa, causing irreversible forest reorganization (Wang et al., 2012). Sediment evidence, the presence of light grayish-white clay with low organics, corroborates this regime shift, reflecting prolonged moisture deficits that exceeded the buffering capacity of subtropical forest ecosystems (Huang et al., 2018). Likewise, the intensification of agricultural activity during Phase IV introduced fundamentally altered disturbance regimes, and along with elevated fungal spore abundances, this phenomenon signals accelerated decomposition and enhanced nutrient cycling—key hallmarks of anthropogenically modified landscapes (Leys et al., 2018; Roos et al., 2023). These findings support theoretical frameworks that emphasizing state shifts in coupled human-environment systems, particularly the "Anthropocene Biosphere" concept (Ellis et al., 2021).

The Niangniang Mountain diversity patterns show both similarities and differences with other Asian monsoon regions. While the general trend of increased diversity during intermediate disturbance phases matches Yunnan records (Xiao et al., 2015), the magnitude of anthropogenic enhancement in Phase IV exceeds that observed in less intensively cultivated areas (Ren et al., 2021). This contrast highlights the role of land-use intensity in mediating diversity responses, as proposed in global syntheses of palaeoecological data (Mottl et al., 2021). The study also contributes to ongoing debates about biodiversity conservation in cultural landscapes. The observed peak diversity during Phase IV supports the "intermediate disturbance hypothesis" in anthropogenic ecosystems (Fox, 2013), but raises questions about the long-term sustainability of such diversity given associated soil erosion (54.90 % sand content) and ecosystem simplification (8 % evergreen taxa). These trade-offs mirror contemporary concerns about biodiversity

conservation in rapidly developing Asian montane regions (Hua et al., 2022).

5.3. The history of human activities inferred from multi-proxy record

5.3.1. Proto-historical period (~3200–2100 cal yr BP)

While climatic deterioration drove broad vegetation shifts during Phase II, evidence of early human activity adds nuance to this transition. The charcoal peak during Phase II (mean: 15,236 grains/g for particles 50–125 μm, Fig. 9) suggests early human presence in western Guizhou, potentially linked to Bronze Age communities practicing limited forest deforestation. This period corresponds with archaeological evidence of Neolithic to Bronze Age transitions in surrounding regions (Ren et al., 2021; Zhao et al., 2009). However, the absence of macroscopic charcoal indicates that fire activity remained largely natural or involved low-intensity anthropogenic burning (Bowman et al., 2011; Marlon et al., 2013), consistent with patterns observed in other subtropical regions during initial human colonization (Yuan et al., 2022).

Notably, as shown in Fig. 7, >50 % decline in evergreen broad-leaved taxa (from 72.30 % to 34.40 %) and a concurrent increase in fire-prone *Pinus* (14.87 %) may represent unintentional landscape modification through selective burning, a pattern documented in other monsoon Asia regions (Colombaroli and Gavin, 2010). Such vegetation shifts likely triggered positive feedback, as pine-dominated ecosystems are generally more flammable than evergreen broad-leaved forests (Archibald et al., 2013). The concurrent expansion of grassland species (e.g., Poaceae, 34.56 %) further suggests initial forest opening, possibly for small-scale swidden agriculture or grazing, as evidenced by similar patterns in Yunnan (Xiao et al., 2015). This interval aligns with evidence of regional climate deterioration (Sun et al., 2015), complicating the disentanglement of climatic versus anthropogenic drivers. However, the timing of the charcoal peak (Fig. 9) indicates that human activity likely amplified climate-induced vegetation changes, as proposed in other Asian monsoon regions (Xu et al., 2021).

5.3.2. ~2100–600 cal yr BP (Phase III)

As shown in Fig. 9, charcoal concentration (mean: 2232 grains/g for 50–125 μm particles) dropped to a profile minimum during this phase, despite conditions generally conducive to fire (e.g., pine dominance up to 20.42 %, cool and dry climate). This apparent contradiction may be explained by multiple, non-mutually exclusive mechanisms.

Firstly, prior disturbances may have reduced fuel loads below thresholds necessary for frequent fire spread, as observed in other subtropical systems (Huang et al., 2018; Leys et al., 2018). Sedimentological evidence, as shown in Fig. 3, the light grayish-white clay with sparse organics, supports reduced biomass productivity under prolonged moisture deficits.

Secondly, a socio-economic shift away from fire-based land management may have occurred, with increasing reliance on pastoralism or more intensive agriculture reducing fire ignitions (Dietze et al., 2018). Historical records indicate increasing societal complexity in southwestern China during this period (Li et al., 2017), while political instability during the Han–Tang transition may have further limited anthropogenic fire use, as suggested by analogous patterns in central China (Zhao et al., 2010). The sustained conifers (*Pinus* dominance) likely reflect its value as a timber resource for construction (Fig. 7), consistent with archaeological evidence of building booms during Chinese imperial expansions (Xiao et al., 2017).

Additionally, climatic aridity may have been insufficient to sustain frequent fires. As shown in Fig. 7, the pollen record shows a continued decline in evergreen taxa (to 24.01 %) and expansion of grasslands (39.74 % e.g., Poaceae), indicating persistent landscape openness. This trajectory contrasts with some Yunnan records showing forest regeneration during this period (Fig. 9, Xiao et al., 2015), suggesting that ecosystems in western Guizhou may have crossed a critical ecological threshold (Wang et al., 2012). The sedimentological shift to finer particles (median 4.57 φ) with reduced organic content (Fig. 3) supports this interpretation, indicating altered hydrological regimes under changed vegetation cover.

5.3.3. ~600 cal yr BP to the present (Phase IV)

Dramatic ecological transformations occurred concurrent with historically recorded Han Chinese migration into Guizhou during the Ming–Qing dynasties (Yuan et al., 2022; Xu et al., 2021). The maximum PC2 scores in Phase IV samples and the first appearance of macroscopic charcoal particles (>125 μm) at approximately 340 cal yr BP (Fig. 9) provide unequivocal evidence of localized slash-and-burn agriculture. Palynological data reveal a pronounced decline in evergreen taxa and a sharp increase in Poaceae, consistent with widespread forest clearance for agriculture.

These changes reflect large-scale deforestation for agriculture (Fig. 8d), consistent with historical records of Ming-Qing agricultural expansion in southwest China (Stephens et al., 2019), the increase in Chinese population (Goldewijk et al., 2017), and cropland expansion (Ge, 2002; Lu and Teng, 2000; Li et al., 2009, Fig. 9). Sedimentological evidence shows a shift to organic-rich clay with a high sand fraction (55.09 %), indicative of accelerated hillslope erosion driven by cultivation patterns (Fig. 3), corroborated by both historical documentation and palaeoecological studies from the region (Xu et al., 2021; Zhou et al., 2023). Resurgent fire activity (mean charcoal concentration: 47,300 grains/g) and increased fungal spores further point to intensified decomposition and nutrient cycling, hallmarks of anthropogenically transformed landscapes (Roos et al., 2023). These transformations occurred despite the LIA climatic context, underscoring the overriding anthropogenic influence on ecosystem processes, a pattern observed across East Asia during this period (Ellis et al., 2021).

The Niangniang Mountain sequence exhibits both convergence and divergence with other East Asian palaeoecological records, underscoring the importance of local context in shaping human–environment interactions. As in the Loess Plateau (Zhao et al., 2009), human impacts in western Guizhou intensified after ~3000 cal yr BP, although ecological trajectories varied due to differences in topography, vegetation, and cultural development. In contrast to Yunnan records that show a later onset of human influence (Xiao et al., 2015), the early charcoal peak in the Niangniang profile suggests that this region may have been more vulnerable to anthropogenic burning, possibly due to its vegetation or topography. Additionally, the Ming-Qing transformation parallels agricultural intensification patterns across monsoon Asia (Stephens et al., 2019), but the magnitude of change at Niangniang surpasses many other sites, possibly reflecting its marginal position relative to Han Chinese settlement cores. These findings highlight how local biophysical and cultural factors modulate the intensity and character of human impacts across spatial and temporal scales (Archibald et al., 2013). The Niangniang Mountain record contributes to growing recognition of southwest China as a region where human activities have shaped ecosystems for millennia, challenging traditional narratives of pristine wilderness in montane subtropical Asia (Huang et al., 2018; Zhou et al., 2023).

6. Conclusions

The Niangniang Mountain peat record provides a detailed reconstruction of Late Holocene environmental changes in western Guizhou, revealing complex interactions between climate variability, vegetation succession, and human activities. Our key insights include:

(1) The mid-Holocene thermal maximum (HTM) persisted until ~3200 cal yr BP, supporting diverse evergreen forests under strong monsoon influence.
(2) Subsequent monsoon weakening and cooling shifted ecosystems to conifer-grassland dominance, with fire activity peaking initially but later declining due to climatic and anthropogenic factors.

(3) Human impacts, particularly during the Ming-Qing dynasties, overwhelmed climatic controls, leading to large-scale deforestation, intensified human-induced fire regimes, and biodiversity reorganization.
(4) Biodiversity exhibited threshold responses, with maximum richness occurring during intermediate disturbance phases and anthropogenic landscapes.

This study underscores the dual role of climate and humans in shaping subtropical ecosystems, with anthropogenic forces have become increasingly dominant in recent centuries. The findings align with regional patterns of monsoon-driven ecological change while highlighting unique local trajectories due to topographic and cultural factors. The persistence of evergreen forests longer than in eastern Guizhou suggests topographic buffering of monsoon shifts, whereas the intensity of Ming-Qing transformations reflects western Guizhou's marginal yet vulnerable position in China's agricultural expansion. These insights are critical for understanding long-term ecosystem resilience and informing conservation strategies in culturally modified landscapes under future climate change.

CRediT authorship contribution statement

Yuanfu Yue: Writing – review & editing, Writing – original draft, Visualization, Validation, Supervision, Software, Resources, Project administration, Methodology, Investigation, Funding acquisition, Formal analysis, Data curation, Conceptualization. **Shixiong Yang:** Writing – review & editing, Writing – original draft, Validation, Funding acquisition, Conceptualization. **Liuying He:** Formal analysis, Data curation. **Zhuo Zheng:** Writing – review & editing. **Xiao Zhang:** Writing – review & editing. **Cong Chen:** Investigation. **Qiuchi Wan:** Investigation. **Yongjie Tang:** Investigation. **Kangyou Huang:** Writing – review & editing, Methodology. **Fang Gu:** Writing – review & editing.

Declaration of competing interest

The authors declare that there are no known competing financial interests or personal relationships that could have appeared to influence the work reported in this manuscript.

All authors have approved the final version of the manuscript and agree to its submission.

Acknowledgments

This work was supported by the National Natural Science Foundation of China (41702182, 42366002 and 41902184), the Guangxi Scientific Projects (2025GXNSFAA069160), National Key Research and Development Program of China (2022YFF0801501), Shandong Provincial Natural Science Foundation, China (Grant No. ZR2024MD037), and the Ocean Negative Carbon Emissions (ONCE) Program (the action of No. 66.8).

Data availability

The data that support the findings of this study are available on request from the corresponding author, upon reasonable request.

References

Archibald, S., Lehmann, C.E.R., Gómez-Dans, J.L., Bradstock, R.A., 2013. Defining pyromes and global syndromes of fire regimes. Proc. Natl. Acad. Sci. 110, 6442–6447. https://doi.org/10.1073/pnas.1211466110.

Bennett, K.D., Willis, K.J., 2001. Pollen. In: Smol, J.P., Birks, H.J.B., Last, W.M., Bradley, R.S., Alverson, K. (Eds.), Tracking Environmental Change Using Lake Sediments: Terrestrial, Algal, and Siliceous Indicators. Springer Netherlands, Dordrecht, pp. 5–32. https://doi.org/10.1007/0-306-47668-1_2.

Birks, H.J.B., Birks, H.H., 1980. Quaternary Palaeoecology. University Park Press, Baltimore, pp. 1–289.

Birks, H.J.B., Line, J., 1992. The use of rarefaction analysis for estimating palynological richness from Quaternary pollen-analytical data. Holocene 2, 1–10.

Blaauw, M., Christen, J.A., 2011. Flexible paleoclimate age-depth models using an autoregressive gamma process. Bayesian Anal. 6, 457–474. https://doi.org/10.1214/11-BA618.

Blarquez, O., Vannière, B., Marlon, J.R., Daniau, A.L., Power, M.J., Brewer, S., Bartlein, P.J., 2014. Paleofire: an R package to analyze sedimentary charcoal records from the Global Charcoal Database to reconstruct past biomass burning. Comput. Geosci. 72, 255–261. https://doi.org/10.1016/j.cageo.2014.07.020.

Bowman, D.M.J.S., Balch, J., Artaxo, P., Bond, W.J., Cochrane, M.A., D'Antonio, C.M., DeFries, R., Johnston, F.H., Keeley, J.E., Krawchuk, M.A., Kull, C.A., Mack, M., Moritz, M.A., Pyne, S., Roos, C.I., Scott, A.C., Sodhi, N.S., Swetnam, T.W., 2011. The human dimension of fire regimes on Earth. J. Biogeogr. 38, 2223–2236. https://doi.org/10.1111/j.1365-2699.2011.02595.x.

Chambers, F.M., Charman, D.J., 2004. Holocene environmental change: contributions from the peatland archive. Holocene 14 (1), 1–6. https://doi.org/10.1191/0959683604hl684ed.

Chen, F., Chen, X., Chen, J., Zhou, A., Wu, D.U.O., Tang, L., Zhang, X., Huang, X., Yu, J., 2014. Holocene vegetation history, precipitation changes and Indian Summer Monsoon evolution documented from sediments of Xingyun Lake, south-west China. J. Quat. Sci. 29 (7), 661–674.

Chen, F., Xu, Q., Chen, J., Birks, H.J.B., Liu, J., Zhang, S., Jin, L., An, C., Telford, R.J., Cao, X., Wang, Z., Zhang, X., Selvaraj, K., Lu, H., Li, Y., Zheng, Z., Wang, H., Zhou, A., Dong, G., Zhang, J., Huang, X., Bloemendal, J., Rao, Z., 2015. East Asian summer monsoon precipitation variability since the last deglaciation. Sci. Rep. 5, 1–11. https://doi.org/10.1038/srep11186.

Colombaroli, D., Gavin, D.G., 2010. Highly episodic fire and erosion regime over the past 2,000 y in the Siskiyou Mountains, Oregon. Proc. Natl. Acad. Sci. 107 (45), 18909–18914. https://doi.org/10.1073/pnas.1007692107.

Colombaroli, D., Beckmann, M., van der Knaap, W.O., Curdy, P., Tinner, W., 2013. Changes in biodiversity and vegetation composition in the central Swiss Alps during the transition from pristine forest to first farming. Divers. Distrib. 19, 157–170. https://doi.org/10.1111/j.1472-4642.2012.00930.x.

Conedera, M., Tinner, W., Neff, C., Meurer, M., Dickens, A.F., Krebs, P., 2009. Reconstructing past fire regimes: methods, applications, and relevance to fire management and conservation. Quat. Sci. Rev. 28, 555–576. https://doi.org/10.1016/j.quascirev.2008.11.005.

Coughlan, M.R., Magi, B.I., Derr, K.M., 2018. A global analysis of hunter-gatherers, broadcast fire use, and lightning-fire-prone landscapes. Fire 1, 41. https://doi.org/10.3390/fire1030041.

Dietze, E., Theuerkauf, M., Bloom, K., Brauer, A., Dörfler, W., Feeser, I., Feurdean, A., Gedminienė, L., Giesecke, T., Jahns, S., Karpińska-Kołaczek, M., Kołaczek, P., Lamentowicz, M., Latałowa, M., Marcisz, K., Obremska, M., Pędziszewska, A., Poska, A., Rehfeld, K., Stančikaitė, M., Stivrins, N., Święta-Musznicka, J., Szal, M., Vassiljev, J., Veski, S., Wacnik, A., Weisbrodt, D., Wiethold, J., Vannière, B., Słowiński, M., 2018. Holocene fire activity during low-natural flammability periods reveals scale-dependent cultural human-fire relationships in Europe. Quat. Sci. Rev. 201, 44–56. https://doi.org/10.1016/j.quascirev.2018.10.005.

Dykoski, C., Edwards, R., Cheng, H., Yuan, D., Cai, Y., Zhang, M., Lin, Y., Qing, J., An, Z., Revenaugh, J., 2005. A high-resolution, absolute-dated Holocene and deglacial Asian monsoon record from Dongge Cave, China. Earth Planet. Sci. Lett. 233, 71–86. https://doi.org/10.1016/j.epsl.2005.01.036.

Ellis, E.C., Gauthier, N., Klein Goldewijk, K., Bliege Bird, R., Boivin, N., Díaz, S., Fuller, D. Q., Gill, J.L., Kaplan, J.O., Kingston, N., Locke, H., McMichael, C.N.H., Ranco, D., Rick, T.C., Shaw, M.R., Stephens, L., Svenning, J.-C., Watson, J.E.M., 2021. People have shaped most of terrestrial nature for at least 12,000 years. Proc. Natl. Acad. Sci. 118, 2023483118. https://doi.org/10.1073/pnas.2023483118.

Fox, J.W., 2013. The intermediate disturbance hypothesis should be abandoned. Trends Ecol. Evol. 28, 86–92. https://doi.org/10.1016/j.tree.2012.08.014.

Ge, J.X., 2002. The History of China Popolation. Fudan University Press, Shanghai (in Chinese).

Giesecke, T., Wolters, S., Jahns, S., Brande, A., 2012. Exploring Holocene changes in palynological richness in northern Europe – did postglacial immigration matter? PloS One 7, e51624. https://doi.org/10.1371/journal.pone.0051624.

Goldewijk, K.K., Beusen, A., Doelman, J., Stehfest, E., 2017. Anthropogenic land use estimates for the Holocene – HYDE 3.2. Earth Syst. Sci. Data 9, 927–953. https://doi.org/10.5194/essd-9-927-2017.

Grimm, E.C., 1987. CONISS: a FORTRAN 77 program for stratigraphically constrained cluster analysis by the method of incremental sum of squares. Comput. Geosci. 13, 13–35. https://doi.org/10.1016/0098-3004(87)90022-7.

Guiot, J., de Beaulieu, J.L., Cheddadi, R., David, F., Ponel, P., Reille, M., 1993. The climate in Western Europe during the last Glacial/Interglacial cycle derived from pollen and insect remains. Palaeogeogr. Palaeoclimatol. Palaeoecol. 103, 73–93. https://doi.org/10.1016/0031-0182(93)90053-L.

Hammer, Ø., Harper, D.A.T., Ryan, P.D., Voldgade, Ø., 2001. PAST: paleontological statistics software package for education and data analysis version 2.09. Palaeontol. Electron. 4, 1–9.

Herzschuh, U., Cao, X., Laepple, T., Dallmeyer, A., Telford, R.J., Ni, J., Chen, F., Kong, Z., Liu, G., Liu, K.-B., Liu, X., Stebich, M., Tang, L., Tian, F., Wang, Y., Wischnewski, J., Xu, Q., Yan, S., Yang, Z., Yu, G., Zhang, Y., Zhao, Y., Zheng, Z., 2019. Position and orientation of the westerly jet determined Holocene rainfall patterns in China. Nat. Commun. 10, 2376. https://doi.org/10.1038/s41467-019-09866-8.

Higuera, P.E., Brubaker, L.B., Anderson, P.M., Hu, F.S., Brown, T.A., 2009. Vegetation mediated the impacts of postglacial climate change on fire regimes in the south-central Brooks Range, Alaska. Ecol. Monogr. 79, 201–219. https://doi.org/10.1890/07-2019.1.

Hua, F., Bruijnzeel, L.A., Meli, P., Martin, P.A., Zhang, J., Nakagawa, S., Miao, X., Wang, W., McEvoy, C., Peña-Arancibia, J.L., Brancalion, P.H.S., Smith, P., Edwards, D.P., Balmford, A., 2022. The biodiversity and ecosystem service contributions and trade-offs of forest restoration approaches. Science 376, 839–844. https://doi.org/10.1126/science.abl4649.

Huang, X., Peng, W., Rudaya, N., Grimm, E.C., Chen, X., Cao, X., Zhang, J., Pao, X., Liu, S., Chen, C., Chen, F., 2018. Holocene vegetation and climate dynamics in the Altai Mountains and surrounding areas. Geophys. Res. Lett. 45, 6628–6636. https://doi.org/10.1029/2018GL078028.

Huang, X., Zhang, J., Storozum, M., Liu, S., Gill, J.L., Xiang, L., Ren, X., Wang, J., Qiang, M., Chen, F., Grimm, E.C., 2020. Long-term herbivore population dynamics in the northeastern Qinghai-Tibetan Plateau and its implications for early human impacts. Rev. Palaeobot. Palynol. 275, 104171. https://doi.org/10.1016/j.revpalbo.2020.104171.

Iglesias, A., Garrote, L., Bardají, I., Santillán, D., Esteve, P., 2021. Looking into individual choices and local realities to define adaptation options to drought and climate change. J. Environ. Manage. 293, 112861. https://doi.org/10.1016/j.jenvman.2021.112861.

Institute of Bontany and South China Institute of Bontany, Academia Sinica, 1982. AngiospermPollen Flora of Tropic and Subtropic China. Science Press, Beijing, pp. 1–453 (in Chinese).

Krumbein, W.C., 1934. Size frequency distributions of sediments. J. Sediment. Res. 4, 65–77. https://doi.org/10.1306/D4268EB9-2B26-11D7-8648000102C1865D.

Leys, B.A., Marlon, J.R., Umbanhowar, C., Vannière, B., 2018. Global fire history of grassland biomes. Ecol. Evol. 8, 8831–8852. https://doi.org/10.1002/ece3.4394.

Li, X., Zhou, X., Shang, X., Dodson, J., 2006. Different size method of charcoal analysis in loess and its significance in the study of fire variation. J. Lake Sci. 18, 540–544. https://doi.org/10.3321/j.issn:1003-5427.2006.05.017 (in Chinese).

Li, X.Q., Dodson, J., Zhou, J., Zhou, X.Y., 2009. Increases of population and expansion of rice agriculture in Asia, and anthropogenic methane emissions since 5000. Quat. Int. 202, 41–50. https://doi.org/10.1016/j.quaint.2008.02.009.

Li, J., Dodson, J., Yan, H., Zhang, D.D., Zhang, X., Xu, Q., Lee, H.F., Pei, Q., Cheng, B., Li, C., Ni, J., Sun, A., Lu, F., Zong, Y., 2017. Quantifying climatic variability in monsoonal northern China over the last 2200 years and its role in driving Chinese dynastic changes. Quat. Sci. Rev. 159, 35–46. https://doi.org/10.1016/j.quascirev.2017.01.009.

Liu, H., 1981. The vertical zonation of mountain vegetation in China. Acta Geograph. Sin. 36 (3), 267–279. https://doi.org/10.11821/xb198103003 (in Chinese with English abstract).

Lu, Y., Teng, Z.Z., 2000. General History of China Population. Shandong Peoples Press, Jinan (in Chinese).

Marcott, S.A., Shakun, J.D., Clark, P.U., Mix, A.C., 2013. A reconstruction of regional and global temperature for the past 11,300 years. Science 339, 1198–1201. https://doi.org/10.1126/science.1228026.

Marlon, J.R., Bartlein, P.J., Walsh, M.K., Harrison, S.P., Brown, K.J., Brown, K.J., Edwards, M.E., Edwards, M.E., Higuera, P.E., Power, M.J., Anderson, R.S., Briles, C. E., Brunelle, A., Carcaillet, C., Daniels, M.L., Hu, F.S., LaVoie, M.J., Long, C.J., Minckley, T.A., Richard, P.J.H., Scott, A.C., Shafer, D.S., Tinner, W., Umbanhowar, C.E., Whitlock, C., 2009. Wildfire responses to abrupt climate change in North America. Proc. Natl. Acad. Sci. 106, 2519–2524. https://doi.org/10.1073/pnas.0808212106.

Marlon, J.R., Bartlein, P.J., Daniau, A.-L., Harrison, S.P., Maezumi, S.Y., Power, M.J., Tinner, W., Vanniére, B., 2013. Global biomass burning: a synthesis and review of Holocene paleofire records and their controls. Quat. Sci. Rev. 65, 5–25. https://doi.org/10.1016/j.quascirev.2012.11.029.

May, F., Rosenbaum, B., Schurr, F.M., Chase, J.M., 2019. The geometry of habitat fragmentation: Effects of species distribution patterns on extinction risk due to habitat conversion. Ecol. Evol. 9, 2775–2790. https://doi.org/10.1002/ece3.4951.

Mooney, S.D., Harrison, S.P., Bartlein, P.J., Daniau, A.L., Stevenson, J., Brownlie, K.C., Buchman, S., Cupper, M., Luly, J., Black, M., Colhoun, E., D'Costa, D., Dodson, J., Haberle, S., Hope, G.S., Kershaw, P., Kenyon, C., Mckenzie, M., Williams, N., 2011. Late Quaternary fire regimes of Australasia. Quat. Sci. Rev. 30 (1–2), 28–46.

Mottl, O., Flantua, S.G.A., Bhatta, K.P., Felde, V.A., Giesecke, T., Goring, S., Grimm, E.C., Haberle, S., Hooghiemstra, H., Ivory, S., Kuneš, P., Wolters, S., Seddon, A.W.R., Williams, J.W., 2021. Global acceleration in rates of vegetation change over the past 18,000 years. Science 372, 860–864. https://doi.org/10.1126/science.abg1685.

Nakagawa, T., Brugiapaglia, E., Digerfeldt, G., Reille, M., Beaulieu, J.-L.D., Yasuda, Y., 1998. Dense-media separation as a more efficient pollen extraction method for use with organic sediment/deposit samples: comparison with the conventional method. Boreas 27, 15–24. https://doi.org/10.1111/j.1502-3885.1998.tb00864.x.

Ohlson, M., Tryterud, E., 2000. Interpretation of the charcoal record in forest soils: forest fires and their production and deposition of macroscopic charcoal. Holocene 10, 519–525. https://doi.org/10.1191/095968300667442551.

Power, M.J., Marlon, J., Ortiz, N., Bartlein, P.J., Harrison, S.P., Mayle, F.E., Ballouche, A., Bradshaw, R.H.W., Carcaillet, C., Cordova, C., Mooney, S., Moreno, P. I., Prentice, I.C., Thonicke, K., Tinner, W., Whitlock, C., Zhang, Y., Zhao, Y., Ali, A.A., Anderson, R.S., Beer, R., Behling, H., Briles, C., Brown, K.J., Brunelle, A., Bush, M., Camill, P., Chu, G.Q., Clark, J., Colombaroli, D., Connor, S., Daniau, A.L., Daniels, M., Dodson, J., Doughty, E., Edwards, M.E., Finsinger, W., Foster, D., Frechette, J., Gaillard, M.J., Gavin, D.G., Gobet, E., Haberle, S., Hallett, D.J., Higuera, P., Hope, G., Horn, S., Inoue, J., Kaltenrieder, P., Kennedy, L., Kong, Z.C., Larsen, C., Long, C.J., Lynch, J., Lynch, E.A., McGlone, M., Meeks, S., Mensing, S., Meyer, G., Minckley, T., Mohr, J., Nelson, D.M., New, J., Newnham, R., Noti, R., Oswald, W., Pierce, J., Richard, P.J.H., Rowe, C., Sanchez Goñi, M.F., Shuman, B.N., Takahara, H., Toney, J., Turney, C., Urrego-Sanchez, D.H., Umbanhowar, C., Vandergoes, M., Vanniere, B., Vescovi, E., Walsh, M., Wang, X., Williams, N., Wilmshurst, J., Zhang, J.H., 2008. Changes in fire regimes since the Last Glacial Maximum: an assessment based on a global synthesis and analysis of charcoal data. Climate Dynam. 30, 887–907. https://doi.org/10.1007/s00382-007-0334-x.

Prentice, C., Guiot, J., Huntley, B., Jolly, D., Cheddadi, R., 1996. Reconstructing biomes from palaeoecological data: a general method and its application to European pollen data at 0 and 6 ka. Climate Dynam. 12, 185–194. https://doi.org/10.1007/BF00211617.

Reimer, P.J., Austin, W.E.N., Bard, E., Bayliss, A., Blackwell, P.G., Bronk Ramsey, C., Butzin, M., Cheng, H., Edwards, R.L., Friedrich, M., Grootes, P.M., Guilderson, T.P., Hajdas, I., Heaton, T.J., Hogg, A.G., Hughen, K.A., Kromer, B., Manning, S.W., Muscheler, R., Palmer, J.G., Pearson, C., van der Plicht, J., Reimer, R.W., Richards, D.A., Scott, E.M., Southon, J.R., Turney, C.S.M., Wacker, L., Adolphi, F., Büntgen, U., Capano, M., Fahrni, S.M., Fogtmann-Schulz, A., Friedrich, R., Köhler, P., Kudsk, S., Miyake, F., Olsen, J., Reinig, F., Sakamoto, M., Sookdeo, A., Talamo, S., 2020. The IntCal20 northern hemisphere radiocarbon age calibration curve (0–55 cal kBP). Radiocarbon 62, 725–757. https://doi.org/10.1017/rdc.2020.41.

Ren, H., Wang, F., Ye, W., Zhang, Q., Han, T., Huang, Y., Chu, G., Hui, D., Guo, Q., 2021. Bryophyte diversity is related to vascular plant diversity and microhabitat under disturbance in karst caves. Ecol. Indic. 120, 106947. https://doi.org/10.1016/j.ecolind.2020.106947.

Roberts, P., Hunt, C., Arroyo-Kalin, M., Evans, D., Boivin, N., 2017. The deep human prehistory of global tropical forests and its relevance for modern conservation. Nat. Plants 3, 17093. https://doi.org/10.1038/nplants.2017.93.

Roos, C.I., Field, J.S., Dudgeon, J.V., 2023. Fire activity and deforestation in Remote Oceanian islands caused by anthropogenic and climate interactions. Nat. Ecol. Evol. 7, 2028–2036. https://doi.org/10.1038/s41559-023-02212-8.

Steinbauer, M.J., Grytnes, J.-A., Jurasinski, G., Kulonen, A., Lenoir, J., Pauli, H., Rixen, C., Winkler, M., Bardy-Durchhalter, M., Barni, E., Bjorkman, A.D., Breiner, F. T., Burg, S., Czortek, P., Dawes, M.A., Delimat, A., Dullinger, S., Erschbamer, B., Felde, V.A., Fernández-Arberas, O., Fossheim, K.F., Gómez-García, D., Georges, D., Grindrud, E.T., Haider, S., Haugum, S.V., Henriksen, H., Herreros, M.J., Jaroszewicz, B., Jaroszynska, F., Kanka, R., Kapfer, J., Klanderud, K., Kühn, I., Lamprecht, A., Matteodo, M., di Cella, U.M., Normand, S., Odland, A., Olsen, S.L., Palacio, S., Petey, M., Piscová, V., Sedlakova, B., Steinbauer, K., Stöckli, V., Svenning, J.-C., Teppa, G., Theurillat, J.-P., Vittoz, P., Woodin, S.J., Zimmermann, N.E., Wipf, S., 2018. Accelerated increase in plant species richness on mountain summits is linked to warming. Nature 556, 231–234. https://doi.org/10.1038/s41586-018-0005-6.

Stephens, L., Fuller, D., Boivin, N., Rick, T., Gauthier, N., Kay, A., Marwick, B., Armstrong, C.G., Barton, C.M., Denham, T., Douglass, K., Driver, J., Janz, L., Roberts, P., Rogers, J.D., Thakar, H., Altaweel, M., Johnson, A.L., Sampietro Vattuone, M.M., Aldenderfer, M., Archila, S., Artioli, G., Bale, M.T., Beach, T., Borrell, F., Braje, T., Buckland, P.I., Jiménez Cano, N.G., Capriles, J.M., Diez Castillo, A., Çilingiroğlu, Ç., Negus Cleary, M., Conolly, J., Coutros, P.R., Covey, R. A., Cremaschi, M., Crowther, A., Der, L., di Lernia, S., Doershuk, J.F., Doolittle, W.E., Edwards, K.J., Erlandson, J.M., Evans, D., Fairbairn, A., Faulkner, P., Feinman, G., Fernandes, R., Fitzpatrick, S.M., Fyfe, R., Garcea, E., Goldstein, S., Goodman, R.C., Dalpoim Guedes, J., Herrmann, J., Hiscock, P., Hommel, P., Horsburgh, K.A., Hritz, C., Ives, J.W., Junno, A., Kahn, J.G., Kaufman, B., Kearns, C., Kidder, T.R., Lanoë, F., Lawrence, D., Lee, G.-A., Levin, M.J., Lindskoug, H.B., López-Sáez, J.A., Macrae, S., Marchant, R., Marston, J.M., McClure, S., McCoy, M.D., Miller, A.V., Morrison, M., Motuzaite Matuzeviciute, G., Müller, J., Nayak, A., Noerwidi, S., Peres, T.M., Peterson, C.E., Proctor, L., Randall, A.R., Renette, S., Robbins Schug, G., Ryzewski, K., Saini, R., Scheinsohn, V., Schmidt, P., Sebillaud, P., Seitsonen, O., Simpson, I.A., Soltysiak, A., Speakman, R.J., Spengler, R.N., Steffen, M.L., Storozum, M.J., Strickland, K.M., Thompson, J., Thurston, T.L., Ulm, S., Ustunkaya, M.C., Welker, M.H., West, C., Williams, P.R., Wright, D.K., Wright, N., Zahir, M., Zerboni, A., Beaudoin, E., Munevar Garcia, S., Powell, J., Thornton, A., Kaplan, J.O., Gaillard, M.-J., Klein Goldewijk, K., Ellis, E., 2019. Archaeological assessment reveals Earth's early transformation through land use. Science 365, 897–902. https://doi.org/10.1126/science.aax1192.

Stuiver, M., Reimer, P.J., 1993. Extended ^{14}C data base and revised CALIB 3.0 14C age calibration program. Radiocarbon 35, 215–230. https://doi.org/10.1017/S0033822200013904.

Sun, W., Zhang, E., Jones, R.T., Liu, E., Shen, J., 2015. Asian summer monsoon variability during the late glacial and Holocene inferred from the stable carbon isotope record of black carbon in the sediments of Muge Co, southeastern Tibetan Plateau, China. Holocene 25, 1857–1868.

Tan, Z., Han, Y., Cao, J., Chang Huang, C., An, Z., 2015. Holocene wildfire history and human activity from high-resolution charcoal and elemental black carbon records in the Guanzhong Basin of the Loess Plateau, China. Quat. Sci. Rev. 109, 76–87. https://doi.org/10.1016/j.quascirev.2014.11.013.

Tang, L., Mao, L., Shu, J., Li, C., Shen, C., Zhou, Z., 2016. An Illustrated Handbook of Quaternary Pollen and Spores in China. Science Press, Beijing, pp. 1–601 (in Chinese).

Tinner, W., Conedera, M., Ammann, B., Lotter, A.F., 2005. Fire ecology north and south of the Alps since the last ice age. Holocene 15, 1214–1226. https://doi.org/10.1191/0959683605hl892rp.

Vachula, R.S., Sae-Lim, J., Li, R., 2021. A critical appraisal of charcoal morphometry as a paleofire fuel type proxy. Quat. Sci. Rev. 262, 106979. https://doi.org/10.1016/j.quascirev.2021.106979.

van der Knaap, W.O., Lamentowicz, M., van Leeuwen, J.F.N., Hangartner, S., Leuenberger, M., Mauquoy, D., Goslar, T., Mitchell, E.A.D., Lamentowicz, Ł., Kamenik, C., 2011. A multi-proxy, high-resolution record of peatland development

and its drivers during the last millennium from the subalpine Swiss Alps. Quat. Sci. Rev. 30, 3467–3480. https://doi.org/10.1016/j.quascirev.2011.06.017.
Wang, F.X., Qian, N.F., Zhang, Y.L., Yang, H.Q., 1995. Pollen Morphology of Chinese Plants. Science Press, Beijing, pp. 1–461 (in Chinese).
Wang, Y., Cheng, H., Edwards, R.L., He, Y., Kong, X., An, Z., Wu, J., Kelly, M.J., Dykoski, C.A., Li, X., 2005. The Holocene Asian monsoon: links to solar changes and North Atlantic climate. Science 308, 854–857. https://doi.org/10.1126/science.1106296.
Wang, L., Li, J., Lu, H., Gu, Z., Rioual, P., Hao, Q., Mackay, A.W., Jiang, W., Cai, B., Xu, B., Han, J., Chu, G., 2012. The East Asian winter monsoon over the last 15,000 years: its links to high-latitudes and tropical climate systems and complex correlation to the summer monsoon. Quat. Sci. Rev. 32, 131–142. https://doi.org/10.1016/j.quascirev.2011.11.003.
Wen, R., Xiao, J., Fan, J., Zhang, S., Yamagata, H., 2017. Pollen evidence for a mid-Holocene East Asian summer monsoon maximum in northern China. Quat. Sci. Rev. 176, 29–35. https://doi.org/10.1016/j.quascirev.2017.10.008.
Whitlock, C., Larsen, C., 2001. Charcoal as a fire proxy. In: Smol, J.P., Birks, H.J.B., Last, W.M., Bradley, R.S., Alverson, K. (Eds.), Tracking Environmental Change Using Lake Sediments: Terrestrial, Algal, and Siliceous Indicators. Springer Netherlands, Dordrecht, pp. 75–97. https://doi.org/10.1007/0-306-47668-1_5.
Willis, K.J., Bailey, R.M., Bhagwat, S.A., Birks, H.J.B., 2010. Biodiversity baselines, thresholds and resilience: testing predictions and assumptions using palaeoecological data. Trends Ecol. Evol. 25, 583–591. https://doi.org/10.1016/j.tree.2010.07.006.
Xiao, X., Haberle, S.G., Shen, J., Yang, X., Han, Y., Zhang, E., Wang, S., 2014. Latest Pleistocene and Holocene vegetation and climate history inferred from an alpine lacustrine record, northwestern Yunnan Province, southwestern China. Quat. Sci. Rev. 86, 35–48. https://doi.org/10.1016/j.quascirev.2013.12.023.
Xiao, X., Shen, J.I., Haberle, S.G., Han, Y., Xue, B., Zhang, E., Wang, S., Tong, G., 2015. Vegetation, fire, and climate history during the last 18 500 cal a BP in south-western Yunnan Province, China. J. Quat. Sci. 30, 859–869. https://doi.org/10.1002/jqs.2824.
Xiao, X., Haberle, S.G., Shen, J., Xue, B., Burrows, M., Wang, S., 2017. Postglacial fire history and interactions with vegetation and climate in southwestern Yunnan Province of China. Clim. Past 13, 613–627.
Xu, Q., Zhang, S., Gaillard, M.-j., Li, M., Cao, X., Tian, F., Li, F., 2016. Studies of modern pollen assemblages for pollen dispersal- deposition- preservation process understanding and for pollen-based reconstructions of past vegetation, climate, and human impact: a review based on case studies in China. Quat. Sci. Rev. 149, 151–166. https://doi.org/10.1016/j.quascirev.2016.07.017.
Xu, X., Li, F., Lin, Z., Song, X., 2021. Holocene fire history in China: responses to climate change and human activities. Sci. Total Environ. 753, 142019. https://doi.org/10.1016/j.scitotenv.2020.142019.
Yuan, Z., Wu, D., Wang, T., Ma, X., Li, Y., Shao, S., Zhang, Y., Zhou, A., 2022. Holocene fire history in southwestern China linked to climate change and human activities. Quat. Sci. Rev. 289, 107615. https://doi.org/10.1016/j.quascirev.2022.107615.
Yue, Y., Zheng, Z., Huang, K., Chevalier, M., Chase, B.M., Carré, M., Ledru, M.-P., Cheddadi, R., 2012. A continuous record of vegetation and climate change over the past 50,000 years in the Fujian Province of eastern subtropical China. Palaeogeogr. Palaeoclimatol. Palaeoecol. 365-366, 115–123. https://doi.org/10.1016/j.palaeo.2012.09.018.
Yue, Y., He, L., Zheng, Z., Chen, C., Wan, Q., Tang, Y., Huang, K., 2024a. Late Holocene vegetation succession, climate change, and fire history in western Guizhou. Quat. Sci. 44 (1), 112–127. https://doi.org/10.11928/j.issn.1001-7410.2024.01.09 (in Chinese with English abstract).
Yue, Y., Xiang, X., Zhao, D., Yang, S., Yao, Q., 2024b. Late-Holocene ecosystem dynamics on Weizhou Island, China: a pollen and historical record of climate change and anthropogenic disturbances. Quat. Sci. Rev. 344, 108977. https://doi.org/10.1016/j.quascirev.2024.108977.
Zhang, X., Huang, K., Cheng, J., Cheddadi, R., Wan, Q., Chen, C., Tang, Y., Yue, Y., Jia, X., Zheng, Z., 2024. Vertical biome shifts and climate changes since the last glacial maximum in the southeastern margin of the Tibetan plateau, Southwest China. Quat. Sci. Rev. 324, 108441. https://doi.org/10.1016/j.quascirev.2023.108441.
Zhang, X., Yue, Y., Zhang, Z., He, L., Yuan, X., Yu, X., Wan, Q., Chen, C., Tang, Y., Zheng, Z., Huang, K., 2025. The topographic features and sedimentary environment potentially influenced the vegetation reconstruction in southwestern China since the MIS3. Quat. Sci. Rev. 369, 109636. https://doi.org/10.1016/j.quascirev.2025.109636.
Zhao, Y., Yu, Z., Chen, F., Zhang, J., Yang, B., 2009. Vegetation response to Holocene climate change in monsoon-influenced region of China. Earth Sci. Rev. 97, 242–256. https://doi.org/10.1016/j.earscirev.2009.10.007.
Zhao, Y., Chen, F., Zhou, A., Yu, Z., Zhang, K., 2010. Vegetation history, climate change and human activities over the last 6200 years on the Liupan Mountains in the southwestern Loess Plateau in central China. Palaeogeogr. Palaeoclimatol. Palaeoecol. 293, 197–205. https://doi.org/10.1016/j.palaeo.2010.05.020.
Zhao, L., Zeng, Y., Rao, Z., Huang, C., Li, Y., Liu, L., Ma, C., 2024. Quantitative Holocene climate reconstruction and anthropogenic impact analysis based on the pollen records in peat sediment in Southern China. Global Planet. Change 234, 104390. https://doi.org/10.1016/j.gloplacha.2024.104390.
Zheng, Z., Cour, P., Huang, C., Duzer, D., Robert, G., Calleja, M., Beaudouin, C., Deng, Y., Huang, K., 2007. Dust pollen distribution on a continental scale and its relation to present-day vegetation along north-south transects in east China. Sci. China Ser. D Earth Sci. 50, 236–246. https://doi.org/10.1007/s11430-007-2059-4.
Zhou, S., Long, H., Xing, H., Zhang, K., Wang, R., Zhang, E., 2023. Human activities facilitated the decline of forest ecosystem in East Asia after 5000 a BP. Earth Sci. Rev. 245, 104552. https://doi.org/10.1016/j.earscirev.2023.104552.

地球环境学报
JEE
Journal of Earth Environment
Vol. 16 No. 4 | Aug. 2025
CSTR: 32259.14.JEE231017
DOI: 10.7515/JEE231017
综 述
REVIEW

珊瑚脂类生物标志物组成及对环境的响应：研究进展与问题

臧明思，王佳宝，宋 宜*，黄 雯，余克服
广西大学 海洋学院，广西南海珊瑚礁研究重点实验室，广西大学珊瑚礁研究中心，南宁 530004

摘 要：脂类是现代活珊瑚组织中细胞膜的结构成分以及重要的信号分子，在能量储存以及适应极端环境等方面发挥重要作用。珊瑚对海洋环境变化响应异常灵敏，能够通过改变自身脂类的组成和结构适应环境变化并产生特征性的脂类分子记录，对现代珊瑚以及化石珊瑚中脂类化合物进行研究，有助于深刻认识全球变化时期环境与生命协同演化过程。在国内外珊瑚脂类生物标志物的研究基础上，综述珊瑚及其文石骨骼中脂类化合物的分布特征，以及脂类对环境变化（如温度、光照、CO_2）响应的研究进展。珊瑚中的脂类化合物能够灵敏地响应环境变化，已有研究表明温度能明显地影响珊瑚组织中脂肪酸与甾醇的含量及分布。其中，珊瑚中的甾醇类受光照、温度以及营养方式等环境因素影响，并且种属间也表现出明显差异。研究表明珊瑚骨骼间微环境的物理化学特性是影响骨骼中脂类分布的重要因素。因此环境变化对珊瑚软组织以及骨骼中脂类的含量与分布具有显著影响，然而在现代过程中海洋环境对珊瑚组织中脂类分布的影响及定量关系还需进一步研究，其对环境响应的规律总结是研究珊瑚礁应对极端环境的基础。通过综述国内外珊瑚脂类的相关研究，为探究珊瑚脂类生物标志物记录生物地球协同演化过程提供更多见解。

关键词：珊瑚骨骼；环境胁迫；脂肪酸；甾醇；古环境

Response of coral lipid biomarkers to the environment: progress and problems

ZANG Mingsi, WANG Jiabao, SONG Yi*, HUANG Wen, YU Kefu
Coral Reef Research Center of China, Guangxi Laboratory on the Study of Coral Reefs in the South China Sea, School of Marine Sciences, Guangxi University, Nanning 530004, China

Abstract: ***Background, aim, and scope*** Lipids are the structural components of cell membranes and important signaling molecules in modern coral tissues that play an important role in energy storage and adaptation to extreme environments. Corals are highly responsive to changes in the marine environment; they can adapt to environmental changes and produce characteristic biogeochemical records by altering their lipid composition and structure. The study of lipid compounds in modern and fossil corals will help us understand the co-evolutionary

收稿日期：2022-12-30；**录用日期：**2023-04-12；**网络出版：**2023-04-30
Received Date: 2022-12-30; **Accepted Date:** 2023-04-12; **Online first:** 2023-04-30
基金项目：国家自然科学基金重大项目（42090041）
Foundation Item: Major Projects of the National Natural Science Foundation (42090041)
通信作者：宋 宜，E-mail：songyi_daisy@163.com
Corresponding Author: SONG Yi, E-mail: songyi_daisy@163.com
引用格式：臧明思，王佳宝，宋 宜，等. 2025. 珊瑚脂类生物标志物组成及对环境的响应：研究进展与问题 [J]. *地球环境学报*，16(4): 396−407. https://cstr.cn/32259.14.JEE231017.
Citation: Zang M S, Wang J B, Song Y, et al. 2025. Response of coral lipid biomarkers to the environment: progress and problems [J]. *Journal of Earth Environment*, 16(4): 396−407. https://cstr.cn/32259.14.JEE231017.

中国知网 https://www.cnki.net

process of the environment and life during the period of global change. ***Materials and methods*** Based on the research of coral lipid biomarkers at home and abroad, this paper reviews the distribution characteristics of coral and aragonite lipid compounds and the response of coral lipid compounds to environmental changes (temperature, light, and CO_2). ***Results*** Lipid compounds in corals respond sensitively to environmental changes. Temperature can significantly affect the content and distribution of fatty acids and sterols in coral tissues. Sterols in corals are influenced by environmental factors such as light, temperature, and nutritional modes, and show obvious differences among species. In addition, the physicochemical properties of the microenvironment between coral skeletons are important factors that affect the distribution of lipids in the skeletons. ***Discussion*** In the modern process, the influence of the marine environment on the distribution of lipids in coral tissues and their quantitative relationship needs to be further studied, and a rule summary of their response to the environment is the basis for studying the response of coral reefs to extreme environments. Previous studies have shown that temperature significantly affects the content and distribution of fatty acids and sterols in coral tissues. In addition, sterols in corals are affected by light, temperature, and nutritional mode, and their compositional characteristics differ among species. Moreover, the physical and chemical characteristics of the microenvironment between coral bones affect the distribution of lipids in the bones and play an important role in calcification. Therefore, environmental changes significantly affect the lipid content and distribution in coral tissues and bones. ***Conclusions*** Coral extracts are rich in lipid compounds and respond sensitively to environmental changes. In addition, coral lipids differ depending on the species and region. ***Recommendations and perspectives*** Currently, research on coral lipid compounds mainly focuses on analyzing the lipid content and composition of modern corals, as well as the response of coral lipids to environmental conditions. Therefore, it is necessary to conduct systematic research on the modern process of coral reef lipids in the future. For example, in addition to considering the impact of individual environmental factors on coral lipids, the synergistic response process between their lipid compounds and multiple environmental factors should also be explored. It is also necessary to further explore the influence of early diagenesis of reef-building corals on the distribution and content of lipid compounds in coral skeletons. This will help to better apply biomarker compounds in modern coral reefs to geological historical periods and provide relevant evidence for modern processes reflected in the paleoclimate and paleoenvironment of coral reef lipids in geological carriers.

Key words: coral skeleton; environmental stresses; fatty acid; sterol; paleoenvironment

现代珊瑚礁对环境变化非常敏感，尤其是全球变暖以及海洋酸化事件（Spalding and Brown，2015）。由于珊瑚具有生长周期较长、生长位置固定以及分布广等特点，也常被称作重建古气候的“载体”。其优势主要体现在以下几个方面：（1）造礁珊瑚的生长率较快，一般来说可以达到 1—2 $cm \cdot a^{-1}$，因此可用于进行年—月甚至更高分辨率的采样工作（Lought，2010）。（2）造礁珊瑚的持续生长时间可达几十年甚至上百年，因此它可以提供长时间尺度的气候变化记录（Falkowski et al.，1984）。（3）造礁珊瑚能够灵敏地响应气候变化并记录环境信号，因此珊瑚礁可以记录极端、突发、短期的事件。当温度、盐度、河流输入、海洋环流或其他海洋环境因子发生变化时，珊瑚骨骼中的一些同位素或微量元素都会产生相应的规律性变化（Roth，2014）。

脂类生物标志物具有化学稳定、结构多样以及具有特定来源等特征，因此常被用于古海洋环境和古海洋气候研究（Schubert et al.，1998；Werne et al.，2000；Zhang et al.，2006）。由于脂类化合物能对环境变化有很好的响应，因而可以为探究海洋地球化学过程提供丰富信息，包括母质来源（Weijers et al.，2009）以及沉积过程中的古环境条件。除此之外，某些脂类化合物如脂肪酸、甾醇等，可以用来指示特定的生物类群或者微生物功能群（Brocks，2005），因此这些脂类化合物也可以用作这些生物类群或代谢功能的标志物。

依照“将今论古”的原理，研究分析珊瑚中

中国知网 https://www.cnki.net

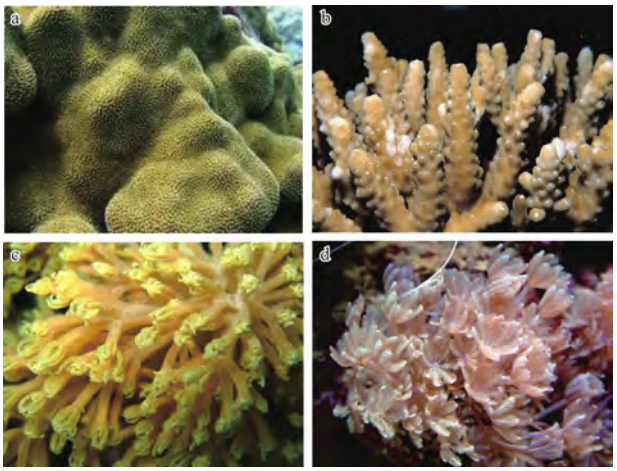
脂类化合物对现代环境条件（如温度、光照及 CO_2 等）变化的响应，有助于探究过去全球变化过程中珊瑚脂类化合物所反映的古环境信息。本文对近年来珊瑚脂类生物标志化合物的研究进展进行总结，尝试为珊瑚礁中脂类化合物古环境重建中“将今论古”这一方法提供理论支持。

1 脂类生物标志物在珊瑚组织及骨骼中的分布

1.1 珊瑚组织中脂类的组成与分布特征

珊瑚的脂质类型主要包括：蜡酯（wax ester，WE）、单烷基二酰甘油（monoalkyl-diacylglycerol，MADAG）、甘油三酯（triacylglycerol，TG）、极性脂质（polar lipid，PL）、以及甾醇（sterol，ST）（Imbs et al.，2015）。根据珊瑚的骨骼特性，可将其分为石珊瑚类与软珊瑚类。其中，石珊瑚具有分泌碳酸钙的能力，从而可以形成群体骨骼，它们是构成珊瑚礁体的主要部分，因此又被称为造礁珊瑚，如滨珊瑚（*Porites*）与鹿角珊瑚（*Acropora*）。软珊瑚没有坚硬的骨骼，只有细小的骨针分散在组织中，也被称为非造礁珊瑚（图 1）。不同类别珊瑚的脂质组成与含量也不相同。蜡酯与甘油三酯总含量在造礁珊瑚脂质含量中占主导地位（Imbs et al.，2010a），高达总脂质含量的 73%（Harland et al.，1993）。软珊瑚中脂质类型主要包括极性脂质与非极性脂质，其中非极性脂质主要为单烷基二酰甘油（Imbs et al.，2010b）。单烷基二酰甘油作为细胞膜调节过程中重要的脂类分子，在珊瑚脂类提取物中较为常见，前人研究表明软珊瑚中单烷基二酰基甘油的相对含量是造礁珊瑚中的 3 倍左右（Imbs et al.，2010b）（图 2）。

蜡酯是脂肪酸和一元醇所组成的酯，在海洋生物中广泛存在。珊瑚体内蜡酯是主要的能量贮存物质，也是珊瑚脂质中最主要的组成成分之一，其含量在不同种属和不同环境中均存在一定差别（Imbs et al.，2010b）。在热带珊瑚中，造礁珊瑚中蜡酯相对含量约是虫黄藻共生软珊瑚的 1.5 倍（图 2）（Harland et al.，1992）。受环境变化影响，珊瑚体内蜡酯含量也会发生较大改变。例如：随着气候季节性变化，夏季时珊瑚体内蜡酯含量会增加到冬季的 1.5 倍左右（Oku et al.，2003）。白化后的珊瑚体内蜡酯含量会急剧降低，绝对含量仅为健康珊瑚体内的 1/3—1/5（Grottoli et al.，2004），部分珊瑚白化后体内将不再含有蜡酯（Yamashiro et al.，2001），这可能是在白化事件中蜡脂作为储能物质，被当作主要能量来源被消耗。



a：滨珊瑚，b：鹿角珊瑚，c、d：软珊瑚。
a: *Porites*; b: *Acropora*; c, d: soft coral.

图 1 不同种类珊瑚
Fig. 1 Different coral species

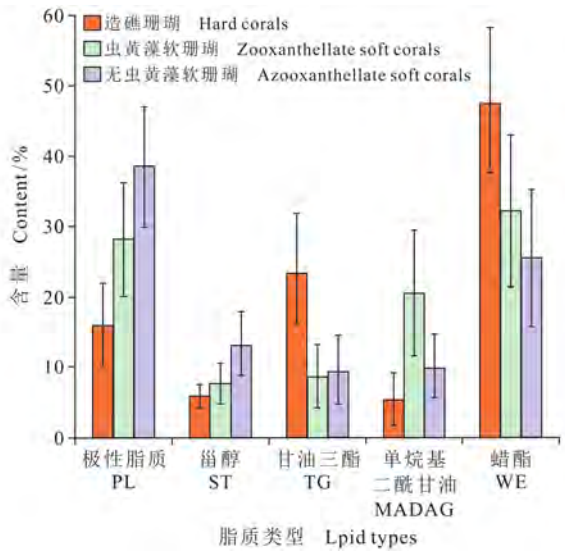


图 2 不同珊瑚群中各脂质类型的相对含量（占总脂质的百分比），改自 Imbs et al.（2010b）
Fig. 2 Relative contents of different lipid types in different coral groups (percentage of total lipids), modified from Imbs et al. (2010b)

脂肪酸在珊瑚中通常与脂肪醇结合形成蜡酯或直接以游离形式存在，是中性脂肪、磷脂和糖脂的主要成分。它广泛分布于生物体中，是构成生物体的主要成分之一。依据碳氢链的饱和程度，将脂肪酸进一步划分为饱和脂肪酸、单不饱和脂肪酸及

中国知网 https://www.cnki.net

多不饱和脂肪酸，其中，多不饱和脂肪酸依据双键位置的不同又可分为 ω-3 和 ω-6 系列多不饱和脂肪酸，ω-3 与 ω-6 由于其独特的结构在生物体内具有很强的生理功能。在造礁珊瑚中饱和脂肪酸以 $C_{16:0}$ 和 $C_{18:0}$ 为主，多不饱和脂肪酸以 $C_{20:4\omega6}$、$C_{20:5\omega3}$ 和 $C_{22:6\omega3}$ 为主，多不饱和脂肪酸含量在总脂肪酸中的占比可高达 50%（Imbs，2013）。Latyshev et al.（1991）对热带造礁珊瑚的多不饱和脂肪酸进行提取与分析后发现，ω-3 系列多不饱和脂肪酸主要由 $C_{20:5\omega3}$ 和 $C_{22:5\omega3}$ 组成，ω-6 系列多不饱和脂肪酸主要由 $C_{20:4\omega6}$ 和 $C_{22:4\omega6}$ 组成。与造礁石珊瑚相比，软珊瑚的脂肪酸种类有明显区别，软珊瑚中饱和脂肪酸以 $C_{16:0}$ 为主，多不饱和脂肪酸以 $C_{20:4\omega6}$ 为主（Kneeland et al.，2013）（图 3）。不仅如此，Vysotskii and Svetashev（1991）通过对比位于鄂霍次克海中不同水深下生长的软珊瑚体内的脂肪酸后发现：不同水深下的软珊瑚其脂肪酸主要组成也存在明显差别，表层暖水软珊瑚体内的脂肪酸主要是饱和脂肪酸 $C_{16:0}$ 和 $C_{18:0}$，而深层冷水软珊瑚体内的脂肪酸主要是多不饱和脂肪酸 $C_{20:4\omega6}$ 和 $C_{20:5\omega3}$。由此可见，珊瑚体内脂肪酸的组成与含量会受自身种属类型及生长环境等因素影响而产生差异，因此某些特定的脂肪酸类型也可用作珊瑚分类群的独特化学标记。例如：软珊瑚的脂质中含有 C_{24} 多不饱和脂肪酸 $C_{24:5\omega6}$ 和 $C_{24:6\omega3}$，但造礁珊瑚的脂质中却缺乏此类脂肪酸（Imbs et al.，2010b），因此上述多不饱和脂肪酸可作为软珊瑚的独特化学标记。虫黄藻共生珊瑚体内含有较多的多不饱和脂肪酸 $C_{18:3\omega6}$、$C_{18:4\omega3}$ 和 $C_{16:2\omega7}$（Imbs et al.，2009）（图 4），因而上述脂肪酸被认为是珊瑚有无虫黄藻的特征脂肪酸，也是研究珊瑚营养方式（即通过共生藻光合作用自养与异养营养）的关键。

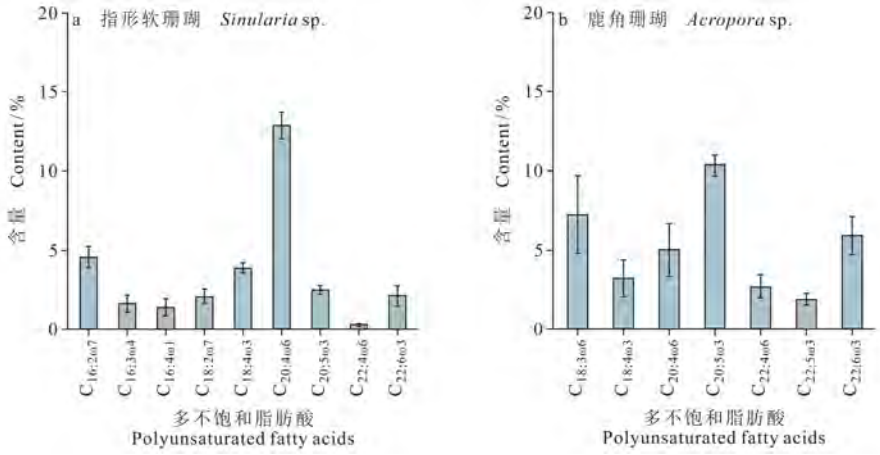


图 3　指形软珊瑚 *Sinularia* sp. 和鹿角珊瑚 *Acropora* sp. 中主要的多不饱和脂肪酸的相对含量（占总脂肪酸含量的百分比），改自 Imbs et al.（2010a）

Fig. 3　Relative content of major polyunsaturated fatty acids in soft coral *Sinularia* sp. and reef-building coral *Acropora* sp. (as a percentage of total fatty acid content), modified from Imbs et al. (2010a)

珊瑚体内同时含有较多的中性脂质，包括脂肪醇与甾醇等醇类化合物。脂肪醇是指羟基与脂肪烃基连接而形成的醇类，它能提供现代沉积物中有机质源（Zhang et al.，2014）、气候环境（Xie et al.，2003；Treignier et al.，2006）和有机质成岩变化（Sinninghe Damsté et al.，2002）等信息。在生物体中，脂肪醇一般会和脂肪酸结合在一起，以蜡酯的形式存在。珊瑚体内脂肪醇种类主要包括 $C_{14:0}$、$C_{16:0}$、$C_{16:1}$、$C_{18:0}$、$C_{18:1}$ 及 $C_{20:0}$，其中，以 $C_{16:0}$ 脂肪醇含量最高（Joseph，1979；Patton et al.，1983）。Oku et al.（2002）对蔷薇珊瑚（*Montipora* sp.）的顶部、中部以及底部的醇类含量分别进行研究，指出蔷薇珊瑚顶部的脂肪醇 $C_{16:0}$ 的相对含量高于底部含量。同时指出，$C_{16:0}$ 在珊瑚脂质中占据主导地位，占总脂肪醇含量的 80% 左右。除直链脂肪醇外，植醇也是珊瑚体内主要的醇类化合物。植醇主要来源于共生虫黄藻，占共生虫黄藻总脂肪醇含量的 13%—30%，与共生虫黄藻相比，宿主组织中的植醇相对含量非常低（Treignier et al.，2008）。除了脂肪醇，珊瑚

中国知网 https://www.cnki.net

脂类提取物中甾醇种类丰富并且含量较高，其分布特征在种属之间也存在明显差异。甾醇广泛分布于真核细胞中，是真核细胞膜重要的结构与调控成分（Bloch，1981）。它作为一种相对稳定的生物标志化合物，可以记录较长时间的地质信息（Volkman，1986）。由于甾醇的生物来源广泛且分子结构具有多样性，因此也被广泛用于有机质来源示踪及其变化过程的研究中（Frostegård and Bååth，1996）。珊瑚脂质中最主要的甾醇类型是胆固醇、菜油甾醇及 24-亚甲基胆固醇（Yamashiro et al.，1999）。与甾醇仅由胆固醇组成的哺乳动物细胞不同，珊瑚组织细胞会产生 C_{28}—C_{30} 植物甾醇（Yamashiro et al.，1999）。因为不同种属类型的珊瑚体内甾醇含量与分布存在差异性，所以甾醇也能被当作珊瑚分类群的独特标记（Yamashiro et al.，1999）。值得注意的是，甾醇含量与组成在珊瑚宿主与虫黄藻共生体之间也存在明显差异。Treignier et al.（2008）对比了石珊瑚的共生虫黄藻脂质与珊瑚虫宿主脂质中甾醇的组成成分与含量，发现两者脂质中最主要的甾醇类型均为菜油甾醇，不同的是，共生虫黄藻中 24-亚丙基胆固醇的相对含量比宿主组织中的高。由于甾醇具有良好的指向性，因此也可为研究珊瑚的营养方式提供独到见解。例如：甲藻甾醇主要是由甲藻共生体产生（Withers et al.，1982），因此甲藻甾醇可作为珊瑚光合自养来源的化学标志物。浮游动物是珊瑚重要的食物来源，通常含有大量胆固醇，因此胆固醇可作为珊瑚异养来源的化学标志物（Treignier et al.，2009）。

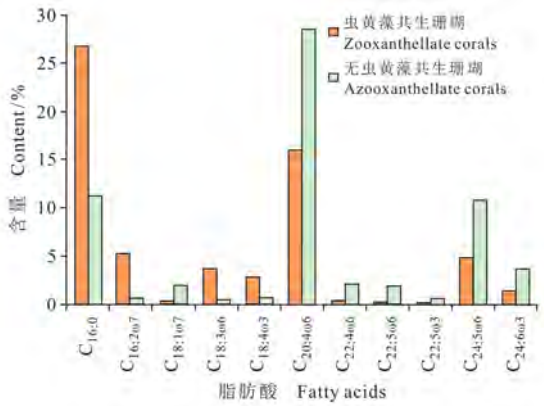


图 4 虫黄藻珊瑚与非虫黄藻珊瑚之间脂肪酸相对含量的差异，改自 Imbs et al.（2009）

Fig. 4 Differences in the relative content of fatty acids between zooxanthellate corals and azooxanthellate corals, modified from Imbs et al. (2009)

1.2 造礁石珊瑚文石骨骼中脂类的赋存形式及分布特征

造礁石珊瑚是热带海洋中常见的生物，主要生长在表层海水中。造礁石珊瑚在生长过程中会直接从海水中吸收 Ca^{2+} 和溶解的 CO_2 来分泌并沉淀碳酸钙，从而形成其特有的骨骼生长层。脂质是造礁石珊瑚骨骼中重要的组成成分，其含量占珊瑚骨骼干重的 1/10（Ingalls et al.，2003）。与珊瑚软组织中脂质组成成分不同，珊瑚骨骼中脂质的主要组成成分为极性脂质、甾醇以及甾醇酯（Farre et al.，2010）。脂质在造礁石珊瑚骨骼与组织中最明显的不同表现在蜡酯与甾醇酯的分布上：在珊瑚软组织中，蜡酯比甾醇酯的含量高；而在造礁石珊瑚骨骼中，蜡酯含量最低，而甾醇酯含量较高。

已有研究证明，有机质能够在造礁石珊瑚的文石骨骼中得到有效保存，这为重建珊瑚礁古环境提供了可能性（Ingalls et al.，2003）。珊瑚文石骨骼中的脂类总含量可占骨骼干重的 3%—10%，这包括骨骼微生物产生的脂类以及被包裹在碳酸钙晶体之间的脂类。珊瑚文石骨骼中分布着特定的生物群落并具有相应的功能作用，前人研究表明珊瑚骨骼中微生物群落产生的脂类化合物是骨骼中脂类的重要组成（Farre et al.，2010）。除此之外，在珊瑚骨骼纳米级微观结构中，造礁石珊瑚的文石骨骼中脂类化合物主要集中在富含有机质的钙化中心（von Euw et al.，2017）。造礁石珊瑚骨骼中存在两种微观结构：一种是由颗粒状晶体所构成的钙化中心，另一种是自钙化中心向外辐射的呈鱼鳞状的碳酸钙晶体纤维（Shirai et al.，2005）。

为进一步探究珊瑚骨骼中脂类化合物的组成与分布情况，Ingalls et al.（2003）对佛罗里达群岛附近的环圆菊珊瑚（*Montastraea annularis*）文石骨骼以及澄黄滨珊瑚（*Porites lutea*）文石骨骼的中性脂质含量及其组成进行研究，结果表明环圆菊珊瑚骨骼非晶格中的中性脂质含量是晶格中的 10 倍。不论是在环圆菊珊瑚骨骼的晶格内还是非晶格内，脂质中甾醇都以谷甾醇为主，脂肪醇都以 $C_{18:0}$ 为主，脂肪酸主要由 $C_{16:0}$ 与 $C_{18:0}$ 组成，且发现了少量的奇碳数脂肪酸。在澄黄滨珊瑚的文石骨骼中，中性脂质含量在晶格与非晶格中大致相同。澄黄滨珊瑚文石骨骼的脂质中饱和脂肪酸的主要组成是 $C_{16:0}$ 与 $C_{18:0}$，并且上述两种饱和脂肪酸在晶格内与非晶格中的含量相当，但是奇碳数脂

中国知网 https://www.cnki.net

肪酸主要富集在文石骨骼的非晶格中。综上，珊瑚骨骼晶格与非晶格中的化合物含量存在差异，但化合物种类基本相似。

脂类化合物不仅较好地保存在珊瑚骨骼当中，且它本身在珊瑚骨骼的钙化过程中也起着相当重要的作用。大多数生物的矿化过程需要通过有机基质进行调控，有机大分子指导矿物晶体的成核位点、生长方向，最终影响晶体生成的形状以及生成的物相（Putnis et al.，2021）。生物矿物中的有机基质是指参与生物矿物形成、调控或稳定过程的结构性物质（欧阳健明，2005），这其中也包括脂类化合物。研究表明造礁石珊瑚骨骼分泌的有机基质在调节或控制生物的矿化过程中发挥重要作用，其中脂类是造礁石珊瑚骨骼有机基质的主要组成成分（Gautret et al.，1997）。Reggi et al.（2016）对造礁石珊瑚骨骼有机基质中的脂质进行提取与分离后发现，脂质主要以游离脂肪酸的形式存在于骨骼的有机基质中，其中也包括少量甾醇、甾醇酯以及神经酰胺。骨骼有机基质中的脂肪酸以 $C_{16:0}$ 为主，其次是 $C_{18:0}$，这两种脂肪酸也是珊瑚软组织中最主要的饱和脂肪酸。与造礁珊瑚组织中脂肪酸组成成分不同的是，在骨骼脂类化合物中，不饱和脂肪酸以单不饱和脂肪酸 $C_{18:1}$ 为主，且其含量较低。该研究表明脂质与钙离子发生相互作用进而组装成颗粒，使得造礁石珊瑚骨骼内的脂质能够在方解石晶体中产生孔隙。这同时说明造礁石珊瑚骨骼内的脂质可促进方解石晶体内部孔隙的形成，从而影响珊瑚钙化过程及骨骼密度。

1.3　不同种属的珊瑚脂类分布差异

脂质是重要的能量储备，主要以蜡酯和甘油三酯的形式储存在动物组织中，或以甾醇和多不饱和脂肪酸的形式储存在细胞膜中（Samorì et al.，2017）。脂类由于生物来源不同通常具有不同的分布特征，因此不同种属之间其脂类分布存在一定差异。由于不同珊瑚种属之间可能存在营养方式、代谢水平以及区域分布的不同，本节综述种属间差异与脂类分布的关系。

珊瑚的营养方式包括两种，即通过共生藻的光合作用进行自养以及通过触手捕获和黏液吸附等方式进行异养。营养方式能够直接影响脂类来源，因此对脂类的分析可以提供有关珊瑚自养或异养起源的有用信息（Napolitano et al.，1997）。由于与珊瑚共生的虫黄藻是影响珊瑚脂质组成成分的重要因素之一，因此有虫黄藻共生与无虫黄藻共生的珊瑚之间其脂质分布存在明显差异。研究表明：热带虫黄藻共生珊瑚比热带非虫黄藻共生珊瑚含有更多的储存脂质（蜡酯与甘油三酯）以及更少的结构脂质（极性脂质和甾醇）（Yamashiro et al.，2005）（图 2）。每个珊瑚分类单元（从纲到属）都有各自特定的脂肪酸谱（Imbs et al.，2010b）。对于更高层次的分类水平而言，珊瑚群之间的这些差异则由脂肪酸生物合成途径的不同引起（Imbs，2013）。然而，珊瑚体内的脂肪酸并不都是由生物自身合成的，还有些脂肪酸是通过摄食转移而来（Mueller et al.，2014）。珊瑚属之间或同一属不同种之间脂肪酸组成的不同通常是由从食物中获得的脂肪酸的差异性造成（Imbs et al.，2007；Imbs et al.，2010b）。Imbs et al.（2010b）通过对比热带虫黄藻共生珊瑚与热带非虫黄藻共生珊瑚的脂肪酸组成后发现，前者脂肪酸以饱和脂肪酸 $C_{16:0}$ 为主，后者则以多不饱和脂肪酸 $C_{20:4\omega6}$ 和 $C_{24:5\omega6}$ 为主。从相对含量上看，与非虫黄藻共生珊瑚相比，虫黄藻共生珊瑚中多不饱和脂肪酸 $C_{18:4\omega3}$、$C_{18:3\omega6}$ 和 $C_{16:2\omega7}$ 的相对含量更高。珊瑚营养方式的差异也会影响珊瑚骨骼中脂肪酸组成，Samorì et al.（2017）对比虫黄藻共生珊瑚与非虫黄藻共生珊瑚骨骼中脂肪酸成分后发现，单不饱和脂肪酸 $C_{18:1}$ 仅在虫黄藻共生珊瑚的文石骨骼中检测到。

珊瑚群落中脂质的组成除与营养方式有关，也会受生存环境影响（Oku et al.，2003）。Imbs et al.（2016）对鄂霍次克海冷水水螅珊瑚（Stylasteridae）和我国南海热带水螅珊瑚（Milleporidae）的脂质组成成分进行比较后发现，两者中单烷基二酰甘油和甾醇的相对含量存在显著差异，冷水水螅珊瑚脂质中甾醇、极性脂质和甘油三酯的相对含量明显高于热带水螅珊瑚。该项研究同时表明：上述两种珊瑚中 C_{20} 和 C_{22} 多不饱和脂肪酸的绝对含量存在显著差异。首先，热带水螅珊瑚含有特有的多不饱和脂肪酸 $C_{22:5\omega6}$，冷水水螅珊瑚则缺乏此类脂肪酸；其次，冷水水螅珊瑚中最主要的多不饱和脂肪酸为 $C_{20:4\omega6}$ 和 $C_{20:5\omega3}$，但热带水螅珊瑚中最主要的多不饱和脂肪酸为 $C_{22:6\omega3}$；此外，冷水水螅珊瑚单不饱和脂肪酸 $C_{20:1\omega9}$ 相对含量明显高于热带水螅珊瑚（Imbs et al.，2016）。该项研究同时对比了鄂霍次克海冷水珊瑚群与我国南海热带软珊瑚群中主要的多不饱和酸的相对含量，结果表明同

中国知网 https://www.cnki.net

一类型的珊瑚群落在冷水与热带海洋中多不饱和脂肪酸 $C_{20:5\omega3}$ 的含量存在显著差异（Imbs et al.，2016）（图 5）。

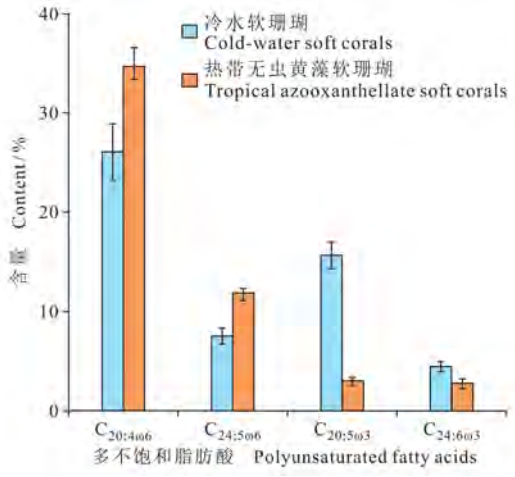


图 5 冷水软珊瑚与热带无虫黄藻珊瑚中主要的多不饱和脂肪酸的相对含量，改自 Imbs et al.（2016）

Fig. 5 Relative contents of major polyunsaturated fatty acids in cold-water soft corals and tropical azooxanthellate soft corals, modified from Imbs et al. (2016)

珊瑚群落中脂质的组成还会因珊瑚自身代谢水平的高低而产生差异。Samorì et al.（2017）对四种地中海珊瑚中的骨骼脂肪酸浓度和组成进行研究，选取的珊瑚具有不同层次的组织（独居或群居）和营养策略（共生或非共生）。结果表明：年轻珊瑚骨骼的脂肪酸浓度高于年老珊瑚，虫黄藻共生珊瑚骨骼的脂肪酸浓度高于非虫黄藻共生珊瑚，群居珊瑚的脂肪酸浓度也高于独居珊瑚。

2 珊瑚脂类对环境条件的响应

2.1 温度

温度是影响珊瑚异养营养以及共生虫黄藻光合效率的重要环境因素之一。珊瑚在遭受高温胁迫时，虫黄藻的光系统Ⅱ（PSII）反应中心将会受到破坏，从而导致光抑制，并最终导致珊瑚白化（李秀保等，2006）。在白化过程中，珊瑚依靠储备的能量，尤其是脂质得以生存。通过研究珊瑚脂质的组成成分，可以揭示脂质的来源，进而提供珊瑚白化和恢复期间代谢水平（即自养或异养）的证据（Rodrigues et al.，2008）。

研究表明珊瑚及其共生藻体内的脂质含量和脂肪酸分布会在高温胁迫下发生变化。对经受高温胁迫几周后的白化珊瑚进行脂质分析后发现，其总脂质浓度（Rodrigues and Grottoli，2007）、甘油三酯（Rodrigues et al.，2008）及蜡酯（Grottoli et al.，2004）含量均减少。Kneeland et al.（2013）研究了在不同温度（26、28、30 以及 32 ℃）和持续时间（4 周）下生长的虫黄藻 C1 型和虫黄藻 D1 型中脂质含量变化，结果表明虫黄藻中 C_{18} 多不饱和脂肪酸与 C_{18} 饱和脂肪酸在升温条件下呈明显下降趋势，并且脂肪酸与甾醇的比值在升温条件下也呈现下降趋势。该项研究表明虫黄藻体内游离脂肪酸和甾醇的比例可作为珊瑚受升温影响的敏感指标。Tolosa et al.（2011）通过对照实验，研究了短期热应力对肾形陀螺珊瑚（*Turbinaria reniformis*）体内脂肪酸、甾醇和脂肪醇含量的影响（图 6），发现珊瑚在经历高温胁迫后，其体内脂肪酸与甾醇的含量降低，但是脂肪醇的含量会增加（图 6）。此外，在对珊瑚体内脂肪酸的组成和含量进行对比后发现，$C_{16:0}$、$C_{18:0}$ 以及多不饱和脂肪酸的含量均减少（图 7）。值得注意的是，ω-3 多不饱和脂肪酸作为磷脂的主要成分，控制了许多细胞过程，如珊瑚生殖细胞的成熟（Pernet et al.，2002）。ω-3 系列多不饱和脂肪酸大量损失证实了在升温条件下珊瑚共生藻光合作用遭到部分损坏（Treignier et al.，2008），这是因为珊瑚体内必须的脂肪酸（如 ω-3 和 ω-6 系列多不饱和脂肪酸）主要来源于虫黄藻的生物合成（Papina et al.，2003）。

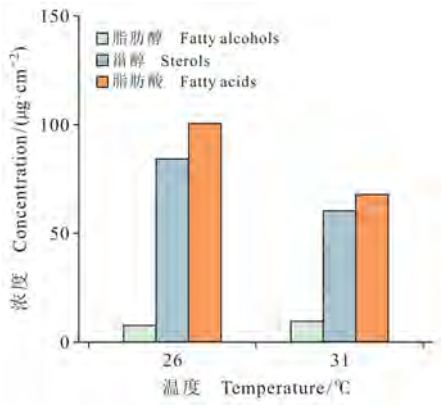


图 6 温度胁迫下（26 ℃和 31 ℃）珊瑚各脂类化合物含量，改自 Tolosa et al.（2011）

Fig. 6 Contents of lipid compounds in coral under temperature stress (26 ℃ and 31 ℃), modified from Tolosa et al. (2011)

珊瑚中脂质的含量与组成除了会受到极端温

中国知网 https://www.cnki.net

度影响，也会因温度的季节性不同产生差异。Oku et al.（2003）通过研究粗糙菊花珊瑚（*Goniastrea aspera*）脂质含量和组成的季节性变化后发现，随着气温增加，珊瑚中脂质含量呈线性上升，且在夏季保持较高水平。夏季较高的脂质水平被认为是夏季光照水平下，珊瑚共生虫黄藻在增强的光合作用下储存了更多的脂质。然而，虫黄藻密度和叶绿素含量的峰值则出现在冬季（Fitt et al.，2000），结合藻类数量与光合有效辐射水平之间存在显著负相关（Brown et al.，1999）的证据，推测这可能是珊瑚共生藻受光与温度季节性变化的影响。因此，珊瑚脂质水平的季节性变化主要受海水表面温度季节性变化的影响，而光照季节性变化的影响也不可忽视。

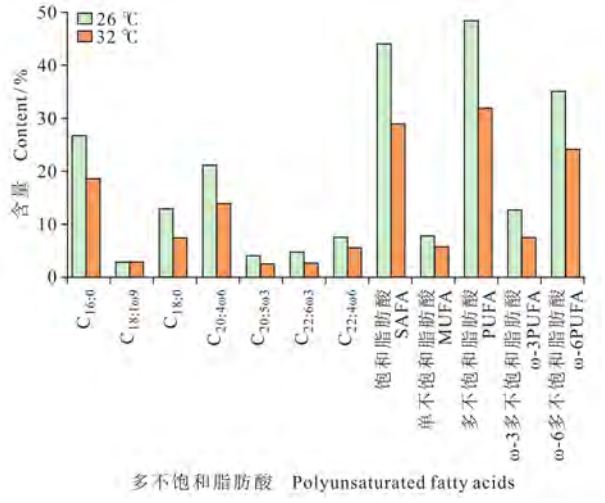
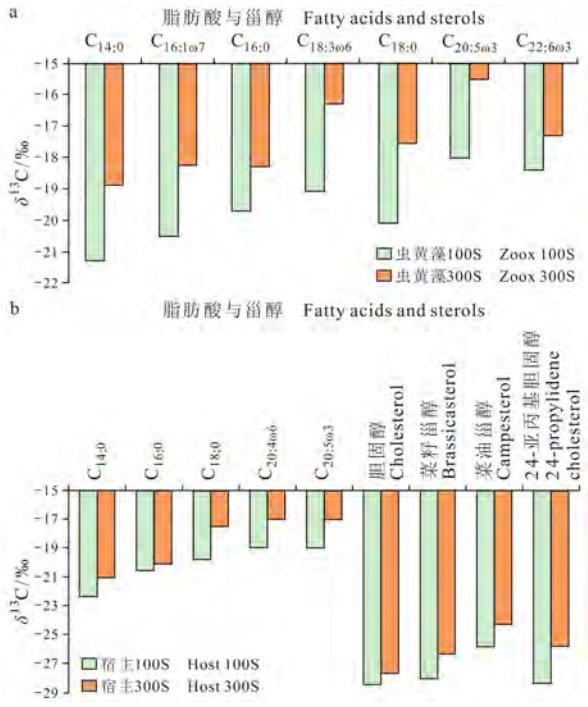


图 7　温度胁迫下（26 ℃和 31 ℃）珊瑚脂质中主要的多不饱和脂肪酸的相对含量，数据来源 Tolosa et al.（2011）

Fig. 7　Relative contents of major polyunsaturated fatty acids in coral lipids under temperature stress (26 ℃ and 31 ℃), data from Tolosa et al. (2011)

2.2　光照

光照是影响珊瑚共生虫黄藻光合速率的关键因素（周洁等，2014）。在珊瑚中，大部分光合作用固定的碳从共生体转移到珊瑚宿主体中，其主要成分是富含碳的有机物，用来维持珊瑚正常的能量消耗（Muscatine，1990）。多余的碳以脂质形式储存在宿主组织中，作为能量储备（Grottoli et al.，2004）。因此，光照条件会显著影响珊瑚体内脂质的含量与组成。对珊瑚进行人工遮蔽的实验表明在较低光照水平下的珊瑚通常含有较少的脂质（Stimson，1987）。与加勒比地区的浅层群落相比，生长在中光层深度附近的造礁石珊瑚的脂质水平下显著降低（Harland et al.，1992）。然而光照与脂质水平之间并非线性关系，Treignier et al.（2008）定量研究了在不同的光照以及摄食条件下，肾形陀螺珊瑚虫黄藻和宿主组织中脂肪酸和甾醇的组成，研究显示：光照影响所有珊瑚实验样品的叶绿素含量，光合作用速率以及脂质的生成；高光照（300 μmol 光子·m^{-2}·s^{-1}）使得饥饿珊瑚（即主要依赖共生光合产物提供营养的珊瑚）中除了植物醇以外的所有类脂物浓度增加了 1 倍。低光照（100 μmol 光子·m^{-2}·s^{-1}）则使珊瑚组织中脂质的含量降低，这是由于光合固定碳无法满足珊瑚日常代谢需求以及组织中脂质积累（图 8）。



Zoox 代表珊瑚虫黄藻，Host 代表宿主组织，100S 代表弱光条件 100 μmol 光子·m^{-2}·s^{-1}，300S 代表强光条件 300 μmol 光子·m^{-2}·s^{-1}，数据来源于 Treignier et al.（2009）。

Zoox represents coral zooxanthellate, Host represents host tissue, 100S represents 100 μmol photons·m^{-2}·s^{-1} for weak light conditions, and 300S represents 300 μmol photons·m^{-2}·s^{-1} for strong light conditions, data from Treignier et al. (2009).

图 8　在不同光照条件下宿主组织与珊瑚虫黄藻中脂肪酸与甾醇的碳稳定同位素值

Fig. 8　Carbon stable isotopes of fatty acids and sterols in host tissues and zooxanthellate under different light conditions

虫黄藻依靠日光进行光合作用以维持生命，因此光照条件同样会影响到虫黄藻中脂肪酸与脂肪醇的含量与组成。上述研究表明在强光条件下，

中国知网 https://www.cnki.net

虫黄藻中 ω-3 多不饱和脂肪酸、$C_{16:0}$ 脂肪醇以及植醇的含量都有所减少（Treignier et al.，2008）。24-亚丙基胆固醇作为虫黄藻脂质最主要的甾醇之一，也会受到光照条件影响，强光条件下虫黄藻中 24-亚丙基胆固醇的消耗会增加。

光照不仅会影响虫黄藻的光合速率，同时也会对珊瑚的碳利用产生影响。Treignier et al.（2009）通过控制变量的实验表明光照和喂食对肾形陀螺珊瑚虫黄藻以及宿主中脂类的碳稳定同位素（$\delta^{13}C$）组成有显著影响。虫黄藻和宿主中脂类生物标志物的 $\delta^{13}C$ 值随光照强度的增加而偏正，这是由于虫黄藻的光合速率随光照强度的增大而增加，^{13}C 固定也会随之增强（图 8）。

2.3 CO_2

自工业革命以来，人类活动产生的大量 CO_2 被排放到大气层中，不仅导致了严重的温室效应，也使得全球海洋出现酸化现象。由于造礁珊瑚在形成礁体的过程中需要利用 $CaCO_3$ 进行相关的生理生化过程，所以造礁珊瑚被认为是受海洋酸化影响最大的群体。

在 CO_2 分压（pCO_2）升高的情况下，珊瑚为了维持自身的钙化率，将会从以下一个或多个来源获取额外能量：（1）珊瑚自身能量储备（即脂质、蛋白质以及碳水化合物），（2）共生虫黄藻进行光合作用后提供的能量（Brading et al.，2011），（3）珊瑚异养所获取的能量（即浮游动物、颗粒物和溶解有机碳）（Drenkard et al.，2013）。Schoepf et al.（2013）分析了珊瑚在 pCO_2 为 39、62、75 Pa 的海水环境下脂质含量的变化。在研究的四种珊瑚中，有两种珊瑚的脂质含量受 pCO_2 影响。与现代海洋环境中 pCO_2（39 Pa）相比，多孔鹿角珊瑚（*A. millepora*）与鹿角杯形珊瑚（*Pocillopra damicornis*）的脂质含量均在高 pCO_2 的条件下有所增加。因此认为在海洋酸化条件下，珊瑚通常不会通过代谢能量储备（如脂质、碳水化合物及蛋白质）来维持其钙化过程。值得注意的是，虽然有些造礁珊瑚可以通过上调钙化点而抵消海洋酸化对自身钙化的消极影响（Schoepf et al.，2013），但也有研究表明造礁珊瑚的钙化率会随海洋酸化加剧而降低（Movilla et al.，2012）。Wall et al.（2017）通过分析对比在不同 pCO_2 条件下（pCO_2 为 44、97 Pa）锐枝杯形珊瑚（*P. acutas*）中脂质含量，得出珊瑚的脂质含量在高 pCO_2 下会减少的结论。该实验中珊瑚组织脂质含量的减少表明海洋酸化会诱导组织生物量的能量缺失，但是这与 Schoepf 的实验结果相悖。由此可见，在探究珊瑚脂类化合物对海水 pCO_2 的响应时，除了需要考虑造礁石珊瑚的种属差异性导致其钙化率对海洋酸化具有不同响应之外，也需要考虑 pCO_2 与珊瑚脂质之间是否存在非线性响应。然而探明造礁珊瑚脂质与海水 pCO_2 之间的关系仍需大量实验数据支持，后续还需进一步开展更多的有关海水 CO_2 对于珊瑚脂类影响的室内定量实验。

造礁珊瑚对海洋酸化的响应除因自身种属差异之外，还存在地区特异性（Comeau et al.，2014），因此探究海洋酸化对造礁珊瑚脂质的影响还应考虑多方面因素。然而现有文献中关于海洋酸化对珊瑚脂质影响方面的研究较少，且方法主要是定量对比实验。因此，还需要开展更多的有关海洋酸化对珊瑚脂类化合物影响方面的研究。

3 研究展望

研究珊瑚礁适应温度波动过程以了解其适应气候变化的能力具有十分重要的意义，也是珊瑚礁生态系统应对未来全球变化的根本挑战。我国南海珊瑚礁广泛发育，其碳酸盐岩全面记录了中新世以来珊瑚礁生态系统对古环境变化的响应过程。对珊瑚中的脂类化合物进行研究，不仅能更好地了解珊瑚自身生理生化过程，同时也能更好地对古环境进行重建。

目前，对珊瑚脂类化合物方面的研究主要集中在分析现代珊瑚的脂类含量与组成以及珊瑚脂质对环境条件的响应，后续还需要对珊瑚礁脂类的现代过程进行系统性研究，例如：除考虑单个环境因素对珊瑚脂类的影响之外，还应当探究其脂类化合物与多重环境因子的协同响应过程。对于现代过程的研究，能够更清晰地理解地质历史时期，尤其是气候环境突变期珊瑚礁对环境的响应策略。除此之外，也需深入探究造礁珊瑚早期成岩作用对珊瑚骨骼中脂类化合物分布特征及含量的影响。这将有助于将现代珊瑚礁中的生物标志化合物更好地应用于地质历史时期，并且为地质载体中的珊瑚礁脂类反映的古气候与古环境提供现代过程的相关依据。全球气候变化是当今世界的热点研究之一，准确预测未来全球气候变化的有效途径是以古鉴今。在未来工作中，可基

中国知网 https://www.cnki.net

于我国南海珊瑚礁碳酸盐岩样品，利用其中的脂类生物标志物研究珊瑚礁区脂类的分布特征，揭示珊瑚礁区生物对环境变化的生态响应和演变规律，从而为探讨全球气候变暖下珊瑚礁区微生物对环境变化的响应提供一定见解。

参考文献

李秀保，黄　晖，符　曲，等 . 2006. 鼻形鹿角珊瑚对不同温度的响应及白化研究 [J]. *热带海洋学报*，25(6): 58–62. [Li X B, Huang H, Fu Q, et al. 2006. Effects of temperature on bleaching of *Acropora nasuta* [J]. *Journal of Tropical Oceanography*, 25(6): 58–62.]

欧阳健明 . 2005. 生物矿物及其矿化过程 [J]. *化学进展*，17(4): 749–756. [Ouyang J M. 2005. Biominerals and their mineralization process [J]. *Progress in Chemistry*, 17(4): 749–756.]

周　洁，施　祺，余克服 . 2014. 三亚造礁石珊瑚虫黄藻光合作用效率的日周期及其调控因素 [J]. *热带海洋学报*，33(1): 81–89. [Zhou J, Shi Q, Yu K F. 2014. Exploration of factors that influence photosynthetic efficiency of symbiotic zooxanthellae of scleractinian corals in a Sanya fringing reef [J]. *Journal of Tropical Oceanography*, 33(1): 81–89.]

Bloch K. 1981. Sterol structure and membrane function [J]. *Current Topics in Cellular Regulation*, 18: 289–299.

Brading P, Warner M E, Davey P, et al. 2011. Differential effects of ocean acidification on growth and photosynthesis among phylotypes of *Symbiodinium* (Dinophyceae) [J]. *Limnology and Oceanography*, 56(3): 927–938.

Brocks J J. 2005. Building the biomarker tree of life [J]. *Reviews in Mineralogy and Geochemistry*, 59(1): 233–258.

Brown B E, Dunne R P, Ambarsari I, et al. 1999. Seasonal fluctuations in environmental factors and variations in symbiotic algae and chlorophyll pigments in four Indo-Pacific coral species [J]. *Marine Ecology Progress Series*, 191: 53–69.

Comeau S, Carpenter R C, Nojiri Y, et al. 2014. Pacific-wide contrast highlights resistance of reef calcifiers to ocean acidification [J]. *Proceedings Biological Sciences*, 281(1790): 20141339. DOI: 10.1098/rspb.2014.1339.

Drenkard E J, Cohen A L, McCorkle D C, et al. 2013. Calcification by juvenile corals under heterotrophy and elevated CO_2 [J]. *Coral Reefs*, 32(3): 727–735.

Falkowski P G, Dubinsky Z, Muscatine L, et al. 1984. Light and the bioenergetics of a symbiotic coral [J]. *BioScience*, 34(11): 705–709.

Farre B, Cuif J P, Dauphin Y. 2010. Occurrence and diversity of lipids in modern coral skeletons [J]. *Zoology*, 113(4): 250–257.

Fitt W K, McFarland F K, Warner M E, et al. 2000. Seasonal patterns of tissue biomass and densities of symbiotic dinoflagellates in reef corals and relation to coral bleaching [J]. *Limnology and Oceanography*, 45(3): 677–685.

Frostegård A, Bååth E. 1996. The use of phospholipid fatty acid analysis to estimate bacterial and fungal biomass in soil [J]. *Biology and Fertility of Soils*, 22(1): 59–65.

Gautret P, Cruit J P, Freiwald A. 1997. Composition of soluble mineralizing matrices in zooxanthellate and non-zooxanthellate scleractinian corals: biochemical assessment of photosynthetic metabolism through the study of a skeletal feature [J]. *Facies*, 36(1): 189–194.

Grottoli A G, Rodrigues L J, Juarez C. 2004. Lipids and stable carbon isotopes in two species of Hawaiian corals, *Porites compressa* and *Montipora verrucosa*, following a bleaching event [J]. *Marine Biology*, 145(3): 621–631.

Harland A D, Davies P S, Fixter L M. 1992. Lipid content of some Caribbean corals in relation to depth and light [J]. *Marine Biology*, 113(3): 357–361.

Harland A D, Navarro J C, Spencer Davies P, et al. 1993. Lipids of some Caribbean and Red Sea corals: total lipid, wax esters, triglycerides and fatty acids [J]. *Marine Biology*, 117(1): 113–117.

Imbs A B, Dang L P T, Rybin V G, et al. 2015. Fatty acid, lipid class, and phospholipid molecular species composition of the soft coral *Xenia* sp. (Nha Trang Bay, the South China Sea, Vietnam) [J]. *Lipids*, 50(6): 575–589.

Imbs A B, Demidkova D A, Dautova T N, et al. 2009. Fatty acid biomarkers of symbionts and unusual inhibition of tetracosapolyenoic acid biosynthesis in corals (Octocorallia) [J]. *Lipids*, 44(4): 325–335.

Imbs A B, Demidkova D A, Dautova T N. 2016. Lipids and fatty acids of cold-water soft corals and hydrocorals: a comparison with tropical species and implications for coral nutrition [J]. *Marine Biology*, 163(10): 202. DOI: 10.1007/s00227-016-2974-z.

中国知网　https://www.cnki.net

Imbs A B, Latyshev N A, Dautova T N, et al. 2010b. Distribution of lipids and fatty acids in corals by their taxonomic position and presence of zooxanthellae [J]. *Marine Ecology Progress Series*, 409: 65–75.

Imbs A B, Luu H V, Pham L Q. 2007. Intra-and interspecific variability of fatty acid composition of soft corals [J]. *Russian Journal of Marine Biology*, 33(1): 67–70.

Imbs A B, Yakovleva I M, Latyshev N A, et al. 2010a. Biosynthesis of polyunsaturated fatty acids in zooxanthellae and polyps of corals [J]. *Russian Journal of Marine Biology*, 36(6): 452–457.

Imbs A B. 2013. Fatty acids and other lipids of corals: composition, distribution, and biosynthesis [J]. *Russian Journal of Marine Biology*, 39(3): 153–168.

Ingalls A E, Lee C, Druffel E R M. 2003. Preservation of organic matter in mound-forming coral skeletons [J]. *Geochimica et Cosmochimica Acta*, 67(15): 2827–2841.

Joseph J D. 1979. Lipid composition of marine and estuarine invertebrates: porifera and cnidaria [J]. *Progress in Lipid Research*, 18(1): 1–30.

Kneeland J, Hughen K, Cervino J, et al. 2013. Lipid biomarkers in *Symbiodinium* dinoflagellates: new indicators of thermal stress [J]. *Coral Reefs*, 32(4): 923–934.

Latyshev N A, Naumenko N V, Svetashev V I, et al. 1991. Fatty acids of reef-building corals [J]. *Marine Ecology Progress Series*, 76: 295–301.

Lough J M. 2010. Climate records from corals [J]. *WIREs Climate Change*, 1(3): 318–331.

Movilla J, Calvo E, Pelejero C, et al. 2012. Calcification reduction and recovery in native and non-native Mediterranean corals in response to ocean acidification [J]. *Journal of Experimental Marine Biology and Ecology*, 438: 144–153.

Mueller C E, Larsson A I, Veuger B, et al. 2014. Opportunistic feeding on various organic food sources by the cold-water coral *Lophelia pertusa* [J]. *Biogeosciences*, 11(1): 123–133.

Muscatine L. 1990. The role of symbiotic algae in carbon and energy flux in reef corals [J]. *Coral Reefs, Ecosystems of the World*, 25(3): 75–87.

Napolitano G E, Pollero R J, Gayoso A M, et al. 1997. Fatty acids as trophic markers of phytoplankton blooms in the Bahía Blanca estuary (Buenos Aires, Argentina) and in Trinity Bay (Newfoundland, Canada) [J]. *Biochemical Systematics and Ecology*, 25(8): 739–755.

Oku H, Yamashiro H, Onaga K, et al. 2002. Lipid distribution in branching coral *Montipora digitata* [J]. *Fisheries Science*, 68(3): 517–522.

Oku H, Yamashiro H, Onaga K, et al. 2003. Seasonal changes in the content and composition of lipids in the coral *Goniastrea aspera* [J]. *Coral Reefs*, 22(1): 83–85.

Papina M, Meziane T, van Woesik R. 2003. Symbiotic zooxanthellae provide the host-coral *Montipora digitata* with polyunsaturated fatty acids [J]. *Comparative Biochemistry and Physiology Part B: Biochemistry and Molecular Biology*, 135(3): 533–537.

Patton J S, Battey J F, Rigler M W, et al. 1983. A comparison of the metabolism of bicarbonate ^{14}C and acetate 1-^{14}C and the variability of species lipid compositions in reef corals [J]. *Marine Biology*, 75(2): 121–130.

Pernet V, Gavino V, Gavino G, et al. 2002. Variations of lipid and fatty acid contents during the reproductive cycle of the anthozoan *Renilla koellikeri* [J]. *Journal of Comparative Physiology B*: *Biochemical, Systemic, and Environmental Physiology*, 172(6): 455–465.

Putnis C V, Wang L J, Ruiz-Agudo E, et al. 2021. Crystallization via nonclassical pathways: nanoscale imaging of mineral surfaces [M]// Zhang X. Crystallization via nonclassical pathways volume 2: aggregation, biomineralization, imaging & application. Washington DC: American Chemical Society: 1–35.

Reggi M, Fermani S, Samorì C, et al. 2016. Influence of intra-skeletal coral lipids on calcium carbonate precipitation [J]. *CrystEngComm*, 18(46): 8829–8833.

Rodrigues L J, Grottoli A G, Pease T K. 2008. Lipid class composition of bleached and recovering *Porites compressa* Dana, 1846 and *Montipora capitata* Dana, 1846 corals from Hawaii [J]. *Journal of Experimental Marine Biology and Ecology*, 358(2): 136–143.

Rodrigues L J, Grottoli A G. 2007. Energy reserves and metabolism as indicators of coral recovery from bleaching [J]. *Limnology and Oceanography*, 52(5): 1874–1882.

Roth M S. 2014. The engine of the reef: photobiology of the coral-algal symbiosis [J]. *Frontiers in Microbiology*, 5: 422. DOI: 10.3389/fmicb.2014.00422.

Samorì C, Caroselli E, Prada F, et al. 2017. Ecological relevance of skeletal fatty acid concentration and composition in Mediterranean scleractinian corals [J]. *Scientific Reports*,

中国知网 https://www.cnki.net

7: 1929. DOI: 10.1038/s41598-017-02034-2.

Schoepf V, Grottoli A G, Warner M E, et al. 2013. Coral energy reserves and calcification in a high-CO_2 world at two temperatures [J]. *PLoS One*, 8(10): e75049. DOI: 10.1371/journal.pone.0075049.

Schubert C J, Villanueva J, Calvert S E, et al. 1998. Stable phytoplankton community structure in the Arabian Sea over the past 200, 000 years [J]. *Nature*, 394(6693): 563–566.

Shirai K, Kusakabe M, Nakai S, et al. 2005. Deep-sea coral geochemistry: implication for the vital effect [J]. *Chemical Geology*, 224(4): 212–222.

Sinninghe Damsté J S, Rijpstra W I C, Reichart G J. 2002. The influence of oxic degradation on the sedimentary biomarker record Ⅱ. Evidence from Arabian Sea sediments [J]. *Geochimica et Cosmochimica Acta*, 66(15): 2737–2754.

Spalding M D, Brown B E. 2015. Warm-water coral reefs and climate change [J]. *Science*, 350(6262): 769–771.

Stimson J S. 1987. Location, quantity and rate of change in quantity of lipids in tissue of Hawaiian hermatypic corals [J]. *Bulletin of Marine Science*, 41(3): 889–904.

Tolosa I, Treignier C, Grover R, et al. 2011. Impact of feeding and short-term temperature stress on the content and isotopic signature of fatty acids, sterols, and alcohols in the scleractinian coral *Turbinaria reniformis* [J]. *Coral Reefs*, 30(3): 763–774.

Treignier C, Derenne S, Saliot A. 2006. Terrestrial and marine *n*-alcohol inputs and degradation processes relating to a sudden turbidity current in the Zaire canyon [J]. *Organic Geochemistry*, 37(9): 1170–1184.

Treignier C, Grover R, Ferrier-Pagés C, et al. 2008. Effect of light and feeding on the fatty acid and sterol composition of zooxanthellae and host tissue isolated from the scleractinian coral *Turbinaria reniformis* [J]. *Limnology and Oceanography*, 53(6): 2702–2710.

Treignier C, Tolosa I, Grover R, et al. 2009. Carbon isotope composition of fatty acids and sterols in the scleractinian coral *Turbinaria reniformis*: effect of light and feeding [J]. *Limnology and Oceanography*, 54(6): 1933–1940.

Volkman J K. 1986. A review of sterol markers for marine and terrigenous organic matter [J]. *Organic Geochemistry*, 9(2): 83–99.

von Euw S, Zhang Q H, Manichev V, et al. 2017. Biological control of aragonite formation in stony corals [J]. *Science*, 356(6341): 933–938.

Vysotskii M V, Svetashev V I. 1991. Identification, isolation and characterization of tetracosapolyenoic acids in lipids of marine coelenterates [J]. *Biochimica et Biophysica Acta (BBA): Lipids and Lipid Metabolism*, 1083(2): 161–165.

Wall C B, Mason R A B, Ellis W R, et al. 2017. Elevated pCO_2 affects tissue biomass composition, but not calcification, in a reef coral under two light regimes [J]. *Royal Society Open Science*, 4(11): 170683. DOI: 10.1098/rsos.170683.

Weijers J W H, Panoto E, van Bleijswijk J, et al. 2009. Constraints on the biological source(s) of the orphan branched tetraether membrane lipids [J]. *Geomicrobiology Journal*, 26(6): 402–414.

Werne J P, Hollander D J, Lyons T W, et al. 2000. Climate-induced variations in productivity and planktonic ecosystem structure from the Younger Dryas to Holocene in the Cariaco Basin, Venezuela [J]. *Paleoceanography*, 15(1): 19–29.

Withers N W, Kokke W C, Fenical W, et al. 1982. Sterol patterns of cultured zooxanthellae isolated from marine invertebrates: synthesis of gorgosterol and 23-desmethylgorgosterol by aposymbiotic algae [J]. *Proceedings of the National Academy of Sciences of the United States of America*, 79(12): 3764–3768.

Xie S C, Chen F H, Wang Z Y, et al. 2003. Lipid distributions in loess-paleosol sequences from northwest China [J]. *Organic Geochemistry*, 34(8): 1071–1079.

Yamashiro H, Oku H, Higa H, et al. 1999. Composition of lipids, fatty acids and sterols in Okinawan corals [J]. *Comparative Biochemistry and Physiology Part B: Biochemistry and Molecular Biology*, 122(4): 397–407.

Yamashiro H, Oku H, Onaga K, et al. 2001. Coral tumors store reduced level of lipids [J]. *Journal of Experimental Marine Biology and Ecology*, 265(2): 171–179.

Yamashiro H, Oku H, Onaga K. 2005. Effect of bleaching on lipid content and composition of Okinawan corals [J]. *Fisheries Science*, 71(2): 448–453.

Zhang S Y, Li S L, Dong H P, et al. 2014. An analysis of organic matter sources for surface sediments in the central South Yellow Sea, China: evidence based on macroelements and *n*-alkanes [J]. *Marine Pollution Bulletin*, 88(1/2): 389–397.

Zhang Z H, Zhao M X, Eglinton G, et al. 2006. Leaf wax lipids as paleovegetational and paleoenvironmental proxies for the Chinese Loess Plateau over the last 170 kyr [J]. *Quaternary Science Reviews*, 25(5/6): 575–594.

中国知网 https://www.cnki.net

https://doi.org/10.3799/dqkx.2024.000

南海北部滨珊瑚微环礁的海平面指示意义及其反映的中全新世海平面历史

乐远福[1*]，赵毅恒[1]，唐立超[2]，张 博[1]，熊海仙[3*]，张雅泽[4]

1. 广西南海珊瑚礁研究重点实验室，珊瑚礁研究中心，广西大学海洋学院，广西南宁 530004
2. 南京大学海岸与海岛开发教育部重点实验室，南京大学地理与海洋科学学院，江苏南京 210093
3. 中山大学海洋学院，广东珠海 519082
4. 广东省科学院广州地理研究所，广东广州 510070

摘 要：南海北部雷琼海岸的珊瑚礁是研究古海平面变化的重要标志物．但因重建标准不统一，海平面重建结果存在显著时空差异性．本研究通过对海南岛东部珊瑚礁区27块现代滨珊瑚微环礁的顶面高程进行实地测量，精确量化其海平面指示意义；同时对该区域65个已发表的海平面标志点数据进行重新校正，重建了更可靠的海平面变化历史．研究表明，这些顶部死亡但整体存活的现代滨珊瑚已达到生长上限，其顶面高程位于清澜港平均潮位以下146.09 cm，最低低潮位（lowest low tide，LLT）以下15.09 cm，且生长上限高差仅±8.35 cm，呈现典型的滨珊瑚微环礁发育形态，证实其生长主要受最低低潮位控制，是理想的海平面标志物．海平面重建结果显示，在（6 143±34）cal a BP至（3 013±9）cal a BP期间，南海北部相对海平面呈波动下降趋势，变化范围为（25.0±9.8）cm至（136.09±9.80）cm．与周边地区海平面记录对比发现，中全新世高海平面的出现时间和高度存在差异，这可能与标志物的高程估算方法及测年技术差异有关．此外，将研究结果和GIA模型（ICE-6G_HetML14）预测结果对比显示，南海北部雷琼海岸3个地点的中晚全新世海平面数据均低于模型预测曲线，表明该区域过去几千年可能经历构造沉降过程．本研究结果为预测南海北部未来海平面变化趋势提供重要科学依据，也为区域构造演化研究提供新视角．

关键词：南海北部；中全新世；相对海平面；滨珊瑚（微环礁）；海平面变化；构造沉降；海洋学．

中图分类号：P73 **文章编号：**1000－2383(2025)09－001－14 **收稿日期：**2024－00－00

The Sea-Level Indicative Meaning of *Porites* Microatolls and Its Application to Middle Holocene Sea-Level Reconstructions in the Northern South China Sea

Yue Yuanfu[1*], Zhao Yiheng[1], Tang Lichao[2], Zhang Bo[1], Xiong Haixian[3*], Zhang Yaze[4]

1. *Guangxi Laboratory on the Study of Coral Reefs in the South China Sea, School of Marine Sciences, Coral Reef Research Center of China, Guangxi University, Nanning* 530004, *China*
2. *Ministry of Education Key Laboratory for Coast and Island Development, School of Geographic and Oceanographic Sciences, Nanjing University, Nanjing* 210093, *China*

基金项目：国家自然科学基金项目（No. 42366002）；广西自然科学基金项目（No. 2025GXNSFAA069160）；国家重点研发计划项目（No. 2017YFA0603300）；自治区级大学生创新创业训练计划项目（No. S202410593449）．

作者简介：乐远福（1982—），男，博士，硕士生导师，主要从事全球变化与环境演变研究工作．ORCID：0000-0002-5248-0056．Email：yuanfu.yue@gxu.edu.cn

* **通讯作者：**乐远福，Email: yuanfu.yue@gxu.edu.cn

引用格式：乐远福，赵毅恒，唐立超，张博，熊海仙，张雅泽，2025．南海北部滨珊瑚微环礁的海平面指示意义及其反映的中全新世海平面历史．地球科学，50(9)：1－14．

Citation：Yue Yuanfu, Zhao Yiheng, Tang Lichao, Zhang Bo, Xiong Haixian, Zhang Yaze, 2025. The Sea-Level Indicative Meaning of *Porites* Microatolls and Its Application to Middle Holocene Sea-Level Reconstructions in the Northern South China Sea. *Earth Science*, 50(9): 1－14.

3. *School of Marine Sciences*, *Sun Yat-sen University*, *Zhuhai* 519082, *China*
4. *Guangzhou Institute of Geography*, *Guangdong Academy of Sciences*, *Guangzhou* 510070, *China*

Abstract: The coral reefs along the Leiqiong Coast in the northern part of the South China Sea are key indicators for studying paleo-sea level changes. However, due to the lack of unified standards, significant spatiotemporal discrepancies exist in coral-derived sea-level data. In this study, through field measurements of the top surface elevation of 27 modern *Porites* microatolls in the coral reef area of eastern Hainan Island, the sea level indicative meaning of *Porites* microatolls was first precisely quantified. Meanwhile, 65 published sea-level index proxies based on U-Th dated fossil *Porites* (microatoll) corals from the region were systematically recalibrated and integrated to reconstruct a more accurate and reliable sea-level change history during the Middle Holocene in the northern South China Sea. The research reveals that those modern *Porites* colonies with dead upper surfaces but intact overall viability have reached their growth limits. Their top elevation lies 146.09 cm below the mean tide level of Qinglan Port and 15.09 cm below the lowest low tide, and the height difference of the growth limit is only ±8.35 cm, representing a typical developmental pattern of *Porites* microatolls. It is confirmed that their growth limits are primarily controlled by the lowest low tide level, and they are ideal indicators for reconstructing past sea levels. Sea level reconstruction results indicate that the relative sea level in the northern South China Sea exhibited a fluctuating downward trend from (6 143±34) cal a BP to (3 013±9) cal a BP, ranging from (25.0±9.8) cm to (136.09±9.80) cm. Comparison with sea level records from surrounding South China Sea regions reveals spatiotemporal variations in the timing and magnitude of Middle Holocene high sea-level, which may be attributable to differences in indicator elevation estimation methods and dating techniques. In addition, a comparison of the research results with the sea level predicted by the GIA model (ICE-6G_HetML14), reveals that the Middle and Late Holocene sea-level data at three locations along the Leqiong coast are all below the model curve. This indicates that these regions may have undergone tectonic subsidence over the past several thousand years. The results of this study offer an important scientific basis for predicting the future sea-level change trend in the northern South China Sea, and provide a new perspective on regional tectonic evolution studies.

Key words: northern South China Sea; Middle Holocene; relative sea level, *Porites* coral/ microatoll; sea level changes; tectonic subsidence; oceanography.

0 引言

研究过去海平面变化的关键在于识别具有明确指示意义的海平面标志物(王绍鸿, 1989; 聂宝符, 1996; Yue *et al.*, 2024),并对其高程和年代进行精确测定(Yue *et al.*, 2024).海平面标志物的指示意义体现为其与特征潮汐水位/海平面之间可量化的高程关系(Yue *et al.*, 2024).高质量的标志物需具备几个关键特征:形成或分布于相对狭窄的垂直区间内,具备可重复测量的精确高程和年代数据,且在地质记录中保存状态良好.基于上述标准,海平面标志物可划分为两大类:生物标志物(如硅藻、有孔虫、珊瑚/珊瑚礁等)和沉积与地貌标志物(如海滩岩、盐沼泥类、泥炭等)(王绍鸿, 1989).

近年来,众多学者基于珊瑚(礁)、海滩岩、有孔虫、硅藻、盐沼、泥炭等典型海平面标志物,对南海北部全新世海平面历史开展了广泛研究,积累了丰富的海平面记录(聂宝符, 1996; Zhao and Yu, 2002; Zong, 2004; 时小军等, 2008; Yu *et al.*, 2009; Yao *et al.*, 2013; 唐立超和乐远福, 2023; 乐远福和唐立超, 2023).然而,对现有成果的深入分析表明,利用不同海平面标志物重建的南海北部全新世同期海平面高程存在显著差异.例如,U-Th定年的珊瑚礁记录显示中晚全新世海平面高于现代(时小军等, 2008; Yu *et al.*, 2009),而基于^{14}C定年的其他海平面标志物(如盐沼、泥炭等)重建的中全新世海平面却未显示高海平面(Zong, 2004).这一矛盾引发了关于南海北部是否存在中全新世高海平面的学术争议,表明该区域海平面历史研究的共识缺失.此外,研究表明,不同海平面标志物或方法反演的海平面曲线存在显著差异和不确定性,甚至在部分场景下缺乏可比性(乐远福和唐立超,2023).显然,若无法实现海平面标志物的精确识别、指示意义的明确界定以及多源数据的有效同化,将难以获得准确可靠的海平面曲线(乐远福等, 2022; Yue *et al.*, 2024).因此,在典型海区(如南海北部,图 1),选择指示意义明确的海平面标志物并结合高精度测年技术,是重建连续、高分辨率海平面变化序列的必要途径.

南海北部作为全球变化的敏感区域,也是全球

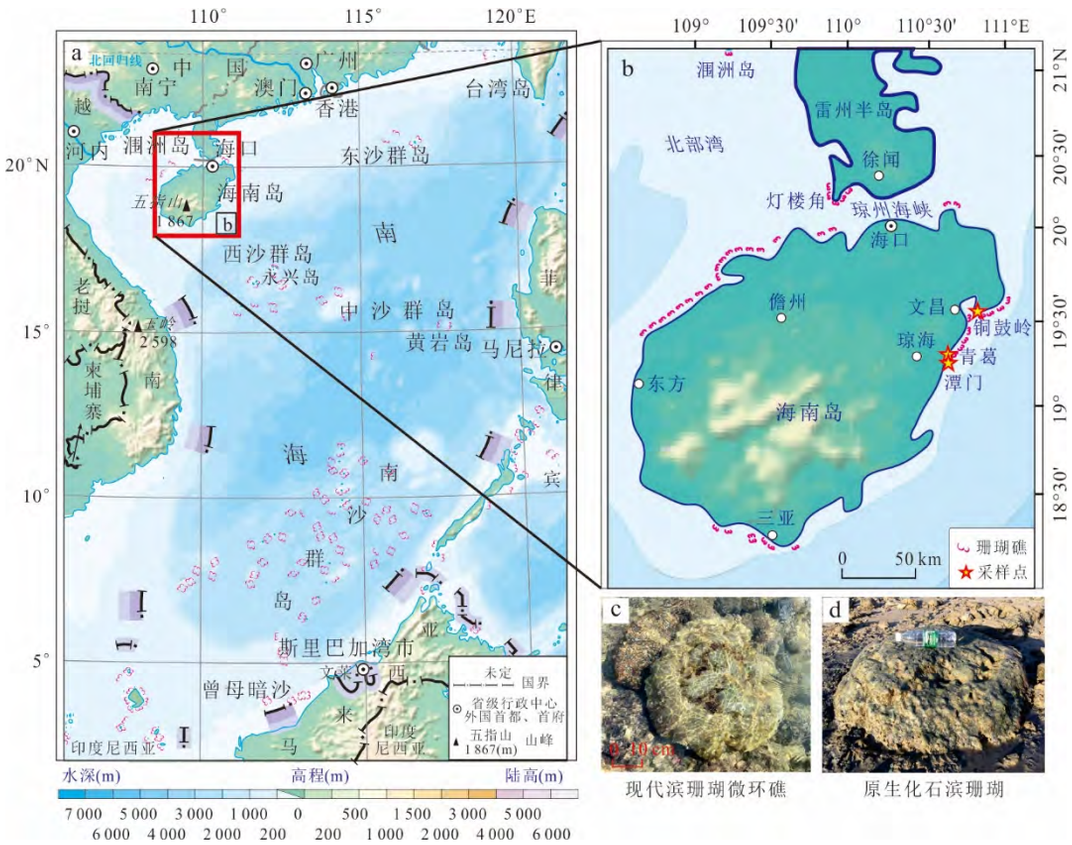


图 1　南海地理位置图(a)以及南海北部雷琼地区现代珊瑚礁空间分布(b),前期在海南岛东部沿海多个地点开展野外踏勘和滨珊瑚采样的地点(b),野外发现的现代滨珊瑚微环礁(c)及化石滨珊瑚(d)

Fig.1　Geographical location map of the South China Sea (a), spatial distribution of modern coral reefs in Leiqiong area in the north of the South China Sea (b), and field survey and coral sampling sites along the east coast of Hainan Island (b), modern *Porites* microatoll (c) and fossil *Porites* corals (d) found in the field

海平面研究的关键地带,全新世以来发育了丰富的海平面标志物,尤其在雷州半岛和海南岛沿海珊瑚礁区(图 1).珊瑚礁的发育严格受海平面制约,被认为是反映过去古海平面的重要标志(聂宝符, 1996).造礁珊瑚中的滨珊瑚,尤其是滨珊瑚微环礁,因具有清晰可辨的年生长纹层和持续的生长时间,且对铀-钍(uranium-thorium,U-Th)测年方法具有良好的适用性(Bard *et al.*, 1993; Zhao and Yu, 2002),被认为是理想的海平面标志物(Yue *et al.*, 2024).

当前,基于珊瑚礁的海平面变化研究主要依赖礁坪上出露海面的大型块状原生滨珊瑚(微环礁)的年代学与高程测量数据(聂宝符, 1996; Zhao and Yu, 2002; 时小军等, 2008; Yu *et al.*, 2009; Yao *et al.*, 2013; Hallmann *et al.*, 2018; 乐远福和唐立超, 2023; Yue *et al.*, 2024; Yan *et al.*, 2024).由滨珊瑚(微环礁)等大型块状珊瑚构成的礁顶面会随着海平面的变化而调整生长状态,呈现向上生长与侧向生长的双重趋势(Yu *et al.*, 2009; 乐远福和唐立超, 2023).关于滨珊瑚(微环礁)生长上限的界定,传统研究表明其最高生长上限通常不超过大潮低潮面,多数情况下位于大潮低潮面以下约 1 m 的位置(聂宝符, 1996; 余克服等, 2002;颜廷礼,2022).但部分学者以平均低低潮面作为滨珊瑚的生长上限开展海平面重建(例如,Yao *et al.*, 2013).此外,还有研究通过现代活滨珊瑚(微环礁)的顶面高程来进行相对海平面的重建(例如,时小军等, 2008; Yu *et al.*, 2009),或依据化石滨珊瑚(微环礁)的高程变化来重建特定时段的海平面波动历史(Yan *et al.*, 2024).

可见,目前南海北部广泛分布的滨珊瑚(微环礁)与现代海平面之间的定量关系仍存在较大的不确定性.一方面,不同研究采用的计算方法存在差异;另一方面,测年技术的多样性,部分年代区间的数据缺失,以及多数海平面重建缺乏区域构造校正.这些因素导致基于滨珊瑚(微环礁)重建的中全新世同期海平面结果差异显著,加剧了判断中全新世

是否存在高海平面的学术争议.例如,有学者质疑出露的化石滨珊瑚究竟是高海平面的产物,还是构造抬升的结果(Yao *et al.*, 2013).这表明,当前对滨珊瑚(微环礁)与海平面之间关系的探究仍处于半定量阶段,对作为海平面标志物的滨珊瑚(微环礁)的顶面高程与现代海平面的对应关系及潮位指示范围尚未明确界定.因此,亟需针对南海北部滨珊瑚(微环礁)开展高精度测量,精确量化其顶面高程与现代海平面之间的关系以及潮位指示范围,并基于"将今论古"原则,高质量重建过去海平面历史.

在此背景下,本研究对海南岛东部沿海已经达到生长上限的27块现代活滨珊瑚微环礁顶面高程开展测量,通过精确量化其与海平面的关系,建立海平面计算公式,验证滨珊瑚微环礁作为海平面标志物的可靠性.然后,以研究区礁坪上出露海面的大型块状原生化石滨珊瑚和滨珊瑚微环礁为研究对象,通过高程测量和U-Th定年,为南海北部提供新的可靠的海平面数据.同时,收集该区域已有的滨珊瑚(微环礁)海平面数据并进行系统性校正,集成新老数据以重建研究区中全新世的海平面变化历史,进一步讨论海平面变化与构造运动的关系.

1 研究区域

南海是我国近海中面积最大的海域(图1a).通过巴士海峡、苏禄海以及马六甲海峡等关键水道连接太平洋与印度洋.这一地理位置不仅赋予了南海独特的战略意义,也使其拥有丰富的海洋资源和生物多样性.作为远场区域,南海北部沿海低纬度地区(如北部湾中部海域涠洲岛、雷州半岛和海南岛等),自全新世以来气候与环境与构造相对稳定,为珊瑚礁和海滩岩等海平面标志物的发育提供了理想的环境.尤其是雷州半岛和海南岛沿海地区(图1b),珊瑚礁以岸边基岩为附着基底大面积发育,构成南海北缘和世界珊瑚礁重要的分布带.这些广泛分布的海平面标志物为研究过去海平面变化提供了宝贵的物质基础.

在海洋地质与珊瑚礁研究领域,大型块状滨珊瑚的礁顶面与海平面升降的动态关系一直是研究重点.理论上,大型块状滨珊瑚构成的礁顶面会随着海平面的升降而变化.当海平面稳定时,大型块状滨珊瑚生长至接近其生长上限后转为横向扩展,形成相对平坦的礁顶面.若海平面下降,珊瑚的生长上限亦随之降低,顶部因暴露于空气中而死亡,滨珊瑚在较低位置继续横向生长,围绕死亡顶面形成环带状新礁顶面.当海平面上升时,滨珊瑚持续向上及侧向生长,沿礁体边缘向上延伸,在原礁顶形成突起环带,直至达到新的生长上限并形成新的礁顶面.这种生长机制使得多数微环礁(microatoll)由顶部死亡但保持侧向生长的环带状大型块状原位珊瑚演化而来.其中,由滨珊瑚发育成的滨珊瑚微环礁尤为典型.类似的现象在印度洋Cocos群岛珊瑚礁区(Smithers and Woodroffe, 2000)、南纬3珊瑚礁区(Natawidjaja *et al.*, 2004)、海南岛青葛(时小军等,2008)以及雷州半岛徐闻灯楼角(Yu *et al.*, 2009)均有报道.这些区域的滨珊瑚微环礁,就是顶面已死亡但仍保持侧向生长呈环带状的滨珊瑚,个体顶面高程变化范围为2.0~8.5 cm(2σ),最低误差<3 cm.上述研究表明,同一珊瑚礁区由滨珊瑚(微环礁)等造礁珊瑚构成的礁顶面严格受海平面控制,因而被视为是热带区域高精度海平面标志物(Smithers and Woodroffe, 2000; Yu *et al.*, 2009),由这类珊瑚礁顶面构成的礁坪面亦成为推断古海平面的关键证据,为研究地质历史时期海平面变化提供了重要线索.

此外,南海作为西太平洋面积最大的边缘海,是太平洋与印度洋交汇的关键地带,该地区频繁遭受热带气旋/台风的侵袭(Yue *et al.*, 2019).由于紧邻印度-西太平洋暖池,且处于东亚季风区的核心区域,南海表层海洋环流深受东亚季风的显著调控(An, 2000),并呈现鲜明季节性特征:夏季,环流以东北向为主导,海水主要经卡里马塔海峡和卡斯帕海峡从爪哇海涌入南海,抵达南海北部后,大部分水体通过巴士海峡及巴林塘海峡流出并汇入黑潮主流,部分水流继续北上进入台湾海峡;冬季,环流则呈现逆时针方向流动,浙闽沿岸流与广东沿岸流自台湾海峡沿南海西部近岸向西南流动.

综上所述,南海北部作为南海向陆地过渡的关键地带,不仅是经济发达区域和大中城市集中区,更是全球气候变化的敏感、热点区域之一.研究南海北部过去海平面变化历史,不仅有助于人们深入理解南海海洋环境和生态系统,还能为应对全球气候变化和推动可持续发展提供重要科学依据.

2 材料和方法

2.1 数据来源及可靠性分析

本文数据主要来源于Yue *et al.*(2024)、颜廷礼

(2022)、Yan *et al.*(2024)及时小军等(2008).其中珊瑚顶面高程数据来源于海南岛东部文昌沿海开放海域珊瑚礁区的27块顶部已经死亡的现代活滨珊瑚微环礁(Yue *et al.*, 2024).65个海平面标志点数据则来源于海南岛东部文昌至琼海珊瑚礁区51块出露海面的大型块状原位化石滨珊瑚(微环礁),采样点分布见图1.其中包括Yue *et al.*(2024)的6个数据以及颜廷礼(2022)、Yan *et al.*(2024)的40个新近发表的数据.这些数据源自2020—2022年最低潮位期间在海南岛东部文昌铜鼓岭至琼海谭门沿海珊瑚礁区进行踏勘时采集的化石滨珊瑚(微环礁)样品.野外采样时利用徕卡(Leica)GS18 T GNSS接收机通过实时动态载波相位差分技术(Real Time Kinematic,RTK)对开放海域现代活以及化石原位滨珊瑚(微环礁)(图1c~1d)顶面进行了高精度高程测量.每个采样点至少进行2次独立测量,单次测量持续时间不少于5 min,取平均值作为最终高程数据;重复测量的误差范围控制在±2 cm以内,确保数据可靠性.另有19个滨珊瑚海平面数据来源于时小军等(2008)早年发表的研究.

本研究中当地平均潮位(mean tide level,MTL)数据基于海南清澜港长期潮位监测站(1985—2020年)实测记录计算,其高程基准与1985国家高程基准(即现代平均海平面,mean sea level,MSL)一致,两者差值可忽略不计.文中涉及的滨珊瑚微环礁顶面高程均以该基准为参照.

上述65个海平面标志点数据的年代均通过U-Th测年获得.为了便于与其他基于^{14}C测年的区域代用指标对比,所有U-Th测年结果均转换为距今年龄(cal a BP,起点为公元1950年).65个海平面标志点数据的原始数据、校正过程及最终结果详见附表,采样点分布见图1,其中高程基准统一转换为现代平均海平面(MSL).

为了验证数据,对65个海平面标志点数据进行了系统性、可靠性评估.(1)生长纹与测年精度验证:将化石珊瑚样品打磨至7 mm厚的珊瑚板,通过数字化X射线成像判断珊瑚样品生长纹清晰度.对生长纹清晰的新增珊瑚样品进行重复U-Th测试,以验证U-Th测年方法的精确性与结果的可靠性.举例来说,当数字化X射线成像清晰地展示出珊瑚的生长纹,则表明该珊瑚样品适合U-Th测年并可获得准确数据(Yue *et al.*, 2024).(2)$\delta^{234}U$值封闭系统检验:将所有化石滨珊瑚样品的$\delta^{234}U$与现代海水(144‰±2‰)(Chen *et al.*, 1986)及现代珊瑚(156‰±6‰)(Stirling *et al.*, 1995)的$\delta^{234}U$对比,若这些化石滨珊瑚样品在地质历史中保持封闭系统,其$\delta^{234}U$值应落于上述现代参照值范围内,相应测年数据视为可信;反之,若偏离此范围,则质疑数据的可信度.(3)铀浓度成岩作用评估:以南海北部276块珊瑚样品铀浓度平均值(3.0721×10^{-6})(Yue *et al.*, 2024)为基准,若珊瑚样品U浓度异常偏低,可能指示文石向方解石转化的成岩作用导致铀流失,相关数据判定为不可靠.

2.2　全新世海平面重建及验证

定量研究滨珊瑚微环礁顶面高程与现代海平面之间的关系及潮位指示范围,明确现代活滨珊瑚微环礁的指示意义(indicative meaning, *IM*)是开展过去海平面重建的基础.对于仅发现化石滨珊瑚(微环礁)但缺少现代活体滨珊瑚微环礁作为参照的区域,可采用以下公式估算当地古海平面高度:

$$RSL=H_{fossil}-IM, \tag{1}$$

其中,*RSL*为古海平面高度,H_{fossil}是原生化石滨珊瑚(微环礁)的顶面测量高程.对于同时存在化石滨珊瑚微环礁和活体滨珊瑚微环礁的海岸,古海平面高度为原生化石滨珊瑚微环礁与现代活体滨珊瑚微环礁顶面高程(H_{modern})的垂直高度差.公式如下:

$$RSL=H_{fossil}-H_{modern}, \tag{2}$$

注意,计算中*IM*、H_{fossil}和H_{modern}应转换为同一高程基准.若*RSL*为正值,表明古海平面高度高于现今海平面.由于大型块状原生滨珊瑚(微环礁)的侵蚀高度难以精确测定,本文所计算的海平面数值代表当时可能存在的最低海平面高度.

古海平面垂直高度的误差主要来源于海平面标志物的指示意义及其范围,以及样品采集和处理过程中的固有因素(如测量误差、样品厚度变化以及分样误差等).量化误差可采用以下公式(Shennan and Horton, 2002)进行计算:

$$E=(e_1^2+e_2^2+\cdots+e_n^2)^{1/2}, \tag{3}$$

其中,*E*代表海平面标志物所代表的*RSL*的总误差,$e_1\cdots e_n$代表各种误差来源.

最后,将南海北部中全新世海平面重建结果与冰川均衡调整(glacial isostatic adjustment, GIA)模型(ICE-6G_HetML140,数据来自南洋理工大学李堂华博士)进行对比,以分析海平面变化的驱动机制.该模型采用三维横向非均匀黏弹性地球模型

HetML140(Li and Wu, 2018; Li *et al.*, 2019)和ICE-6G_C冰盖模型(Peltier *et al.*, 2015),GIA响应通过耦合位扰动拉普拉斯方程的三维有限元算法(CLFE)计算(Wu, 2004).

3 结果

3.1 现代活滨珊瑚(微环礁)上顶面高程

根据野外勘探,海南岛文昌铜鼓岭珊瑚礁区开放海域随机选取的27块现代活滨珊瑚微环礁,除顶部已经死亡以外的其他部位均处于存活状态(Yue *et al.*, 2024).根据这27块样品的礁顶面高程测量数据(Yue *et al.*, 2024),这些滨珊瑚微环礁的顶面高程平均值为−43.09 cm(相对于MSL,后同)(图2a),个体变化高程范围为−51.6 cm至−34.94 cm,表明顶面高差最大为16.66 cm,相对高度变化幅度为±8.33 cm.以海南清澜港平均潮位(103 cm,1985国家高程基准),这些滨珊瑚微环礁顶面高度为−146.09 cm(图2b~2c),揭示其顶面高程与当地相对海平面存在可量化关系.

3.2 海平面数据对应的同位素数据和U-Th测年结果

65个海平面标志点数据对应的珊瑚同位素$\delta^{234}U(T)$变化、U浓度和U-Th年龄分布如图3所示.首先,65个海平面标志点数据所对应的化石滨珊瑚样品的$\delta^{234}U(T)$变化范围为(145.2±1.3)‰~(151.2±1.6)‰,平均值为148.50‰,处于现代珊瑚(Stirling *et al.*, 1995)和海水(Chen *et al.*, 1986)的$\delta^{234}U(T)$之间.其次,U浓度平均值为2.912×10^{-6},变化范围介于2.5753×10^{-6}~3.4326×10^{-6},与南海北部新近报道的的276个全新世珊瑚样品校正后U浓度(3.0721×10^{-6})(Yue *et al.*, 2024)高度吻合.最后,测年结果显示,这些滨珊瑚(微环礁)顶部年龄处于(3 013±9) cal a BP至(6 143±34) cal a BP之间,属于中全新世范围,年代跨度约3 100 a,年代误差(2σ)为8~34 a.

3.3 南海北部中全新世海平面重建结果

通过对海南岛东部沿海珊瑚礁区27块现代活滨珊瑚微环礁顶面高程的高精度测量,可以确定该区现代活滨珊瑚微环礁的海平面指示意义为当地平均潮位以下143.09 cm(图2b).采用误差计算公式,可以对新增珊瑚样品的海平面总误差进行量化.例如,27块现代活滨珊瑚微环礁顶面高程自身存在8.33 cm的误差,而RTK测量仪器总误差为5 cm,采样厚度1 cm,计算得海平面高程数据总误差为±9.8 cm.为了便于计算,对校正后的65个海平面标志点数据都赋予这个误差值.

基于3.2部分所述的海平面重建公式,获得了海南岛东部珊瑚礁区65个新的海平面标志点数据(附表和图4),为重建南海北部海南岛东岸中全新世的海平面变化历史奠定可靠基础.如图4所示,在(6 143±34) cal a BP到(3 013±9) cal a BP的3 100 a期间,南海北部的相对海平面波动范围为25~136.09 cm,整体呈现持续波动下降趋势.

4 讨论

4.1 滨珊瑚微环礁的海平面指示意义

滨珊瑚微环礁是高精度海平面重建的理想标志物.海南岛东部沿海珊瑚礁区27块现代活滨珊瑚微环礁野外测量结果显示,其分布于开放海域,顶面高程与海平面/参考潮位有可量化的垂直关系(Yue *et al.*, 2024).

首先,27块现代活滨珊瑚微环礁所在的海南岛东部沿海文昌铜鼓岭珊瑚礁区相对平坦,无显著局部凹陷,且与开放海域直接相通,即使是处于2020年7月的最低潮期间,海水也可以与外海自由交换.这就排除了局部地形对这27块现代活滨珊瑚微环礁生长的影响.更为重要的是,该区域属于海南铜鼓岭国家级自然保护区.据笔者2020年野外初步估算,该珊瑚礁区生态系统健康,珊瑚种类丰富(常见种包括*Porites*、*Platygyra*、*Montipora solanderi*、*Acropora austera*、*Facia speciose*、*Pocillopora*、*Fungia fungites*等),且活珊瑚覆盖度较高.这说明该区27块现代活滨珊瑚顶部死亡是因为达到本身的生长上限而导致的.

其次,从形态特征看,27块现代活滨珊瑚的顶面高程波动于−51.6 cm至−34.94 cm之间,变化范围为±8.33 cm,呈现出相对平坦却又在平顶中间凹凸不平的礁顶面,符合滨珊瑚微环礁的典型发育形态.此外,从生长状态分析,其顶部均已死亡,平均高程(−43.09 cm)较海南岛清澜港最低低潮位(−28 cm)低15.09 cm,较平均潮位(103 cm)低146.09 cm(图c),表明最低低潮是这些滨珊瑚微环礁理论生长上限.同时,这些现代活滨珊瑚顶面高度近乎一致、生长范围狭窄,指示其海平面变化响应区间狭窄且指示意义统一,符合滨珊瑚微环礁的典型特征,说明它们作为理想海平面标志物的可靠

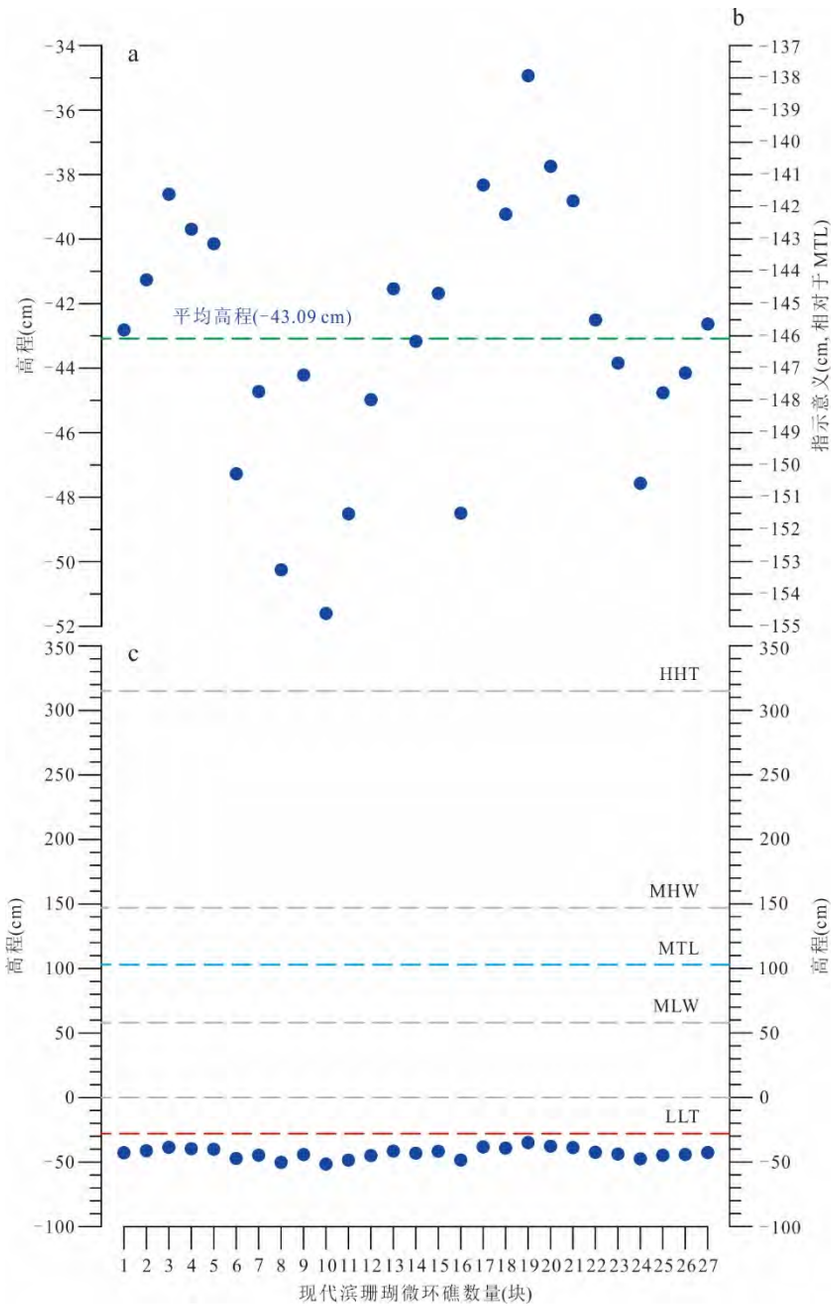


图 2　海南岛文昌铜鼓岭珊瑚礁区 27 块现代活滨珊瑚微环礁顶面高程与清澜港潮汐的关系

Fig.2　Relationship between the top elevation of 27 modern live *Porites* (microatolls) in Tongguling coral reef area and tides at Qinglan Harbor in Wenchang, Hainan Island

高程数据由 Leica GS18 T RTK 设备测量获取,为相对于 MSL 数值;清澜港属不正规日潮,基于 1985 年国家高程基准,其平均潮位为 103 cm,平均低潮位为 58 cm,平均高潮位为 147 cm,最高高潮位(Highest High Tide,HHT)为 315 cm,最低低潮位为−28 cm,平均潮差为 89 cm,最大潮差为 255 cm(中国人民解放军海军司令部航海保证部编制,2022)

性.基于上述特性,可通过这 27 块达到生长上限的现代活滨珊瑚微环礁,推算出目前出露海面的化石滨珊瑚(微环礁)礁顶面代表的最低海平面高度,为海平面研究提供关键数据支持.

4.2　中全新世海平面高程差异的原因分析

尽管以往基于滨珊瑚(微环礁)的海平面重建研究未深入探讨滨珊瑚(微环礁)的海平面指示意义,但需强调的是,现今沿海珊瑚礁区域礁坪上高出潮面的死亡大型块状原生滨珊瑚(微环礁),直接指示其发育时期海平面高于当前海平面.理论上,精确测定这些滨珊瑚(微环礁)顶面的年代及高程,即可有效推测其发育时期的海平面高度.基于此,

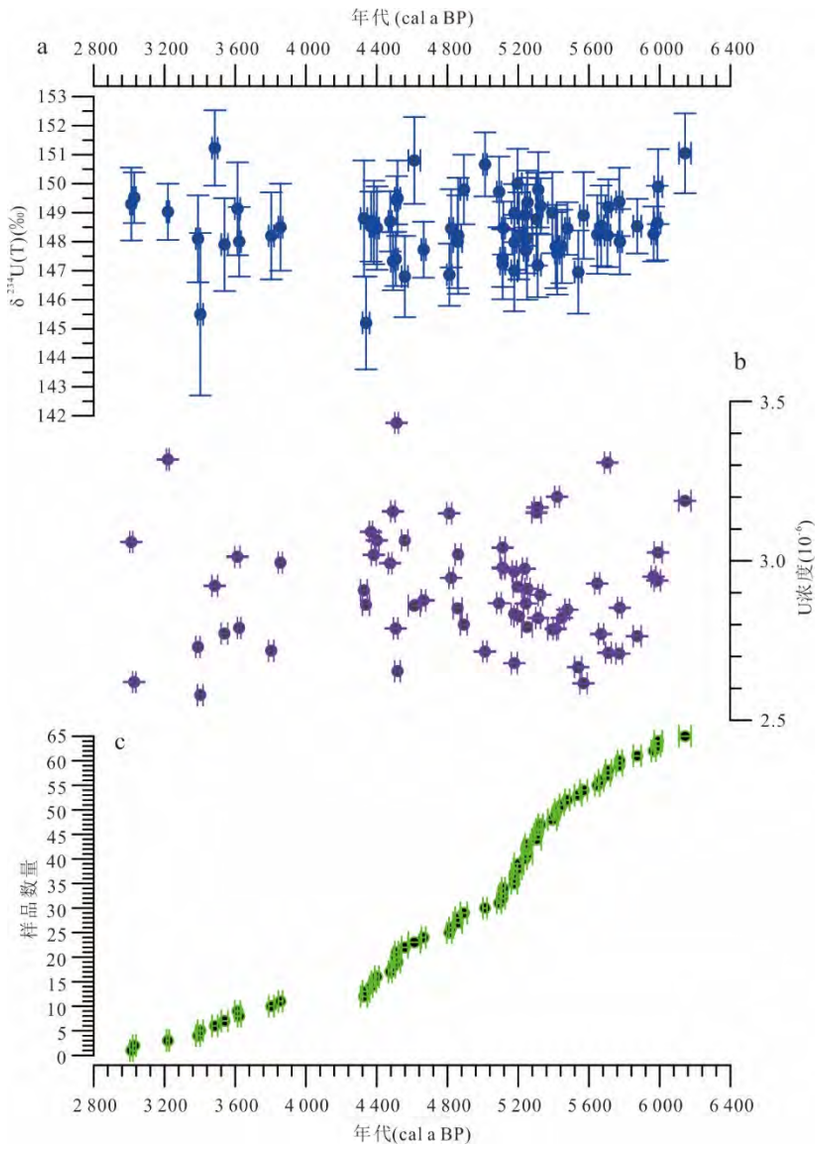


图 3 样品的 $\delta^{234}U(T)$ 变化 (a)、U 浓度(b) 和 U-Th 年龄分布(c)

Fig.3 $\delta^{234}U(T)$ change (a), U concentration (b) and U-Th age distribution (c)

有学者依据雷琼地区 4 个珊瑚礁的 ^{14}C 测年数据及其高程信息,推断该地区中全新世((7 120±165)至(4 010±110) a BP,未校正)海平面波动范围为 200～250 cm(余克服等,2002).同时,另有学者通过测量雷州半岛南部沿海的古珊瑚礁礁顶面高程,并结合 ^{14}C 测年技术,估算出中全新世期间(如(6 550±130)至(5 300±80) a BP,未校正)海平面比现今高出 300～400 cm(Ma *et al.*, 2003).在不考虑中全新世以来地壳升降影响的情况下,通过对该地区 7 块滨珊瑚进行的 16 个 U-Th 年龄年龄测定结果,进一步推测南海北部(7 240±319)至(5 009±54) a BP(相对于公元 2001 年)期间海平面高度至少比现代高出 290～380 cm(Zhao and Yu, 2002).然而,与上述 300～400 cm 高海平面结论不同,Yu *et al.*(2009)通过对比不同时期大型滨珊瑚微环礁与现代微环礁顶面高程,结合 5 个微环礁的 18 个 U-Th 年龄数据及微地貌结构特征,指出在(7 050±32)至(6 603±41) cal a BP(校正后,以公元 1950 年为基准)期间,雷州半岛海平面高度为现今水平之上(171.0±8.5)至(219.0±8.5) cm,并经历至少 4 次百年尺度的周期性波动.这些研究为南海北部中全新世高海平面提供了珊瑚礁证据.

从海平面高度时空变化视角分析,南海北部全新世海平面重建结果呈现出显著的差异性,根源可能在于所采用的海平面重建方法,其中海平面标志物的高程估算精度以及测年

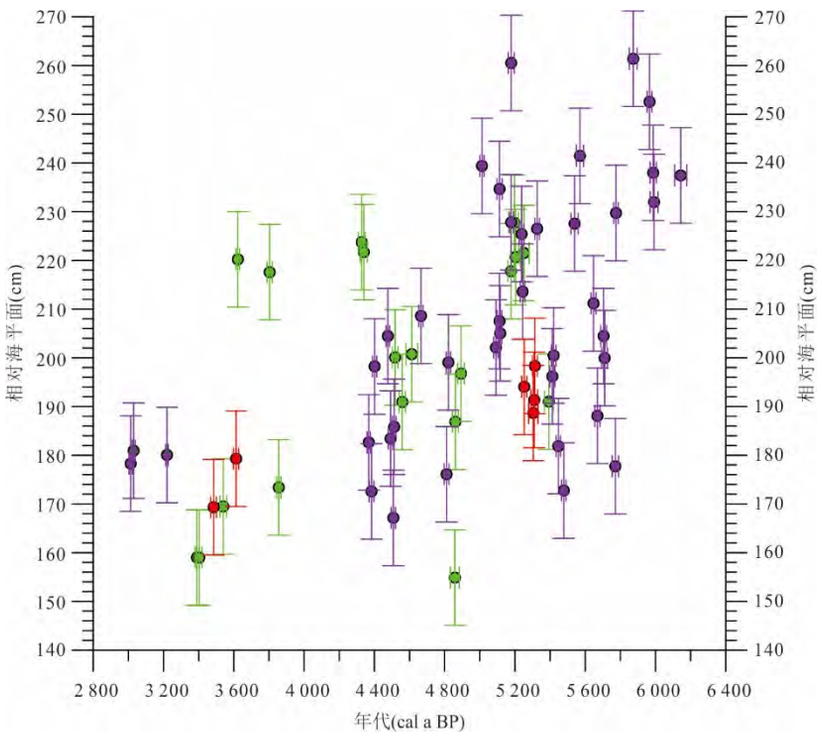


图 4　基于滨珊瑚及滨珊瑚微环礁重建的南海北部中全新世海平面

Fig.4　Middle Holocene sea level reconstruction of the northern South China Sea based on *Porites* corals and *Porites* microatolls

红色数据来源于 Yue *et al.*(2024);绿色数据来源于时小军等(2008);紫色数据来源于颜廷礼(2022)和 Yan *et al.*(2024)

技术是影响重建结果准确性的关键因素.

首先,在海平面高程估算方面,不同研究对滨珊瑚的海平面指示意义存在显著认知分歧.现有研究采用了多元参考标准,例如,有研究是以大潮低潮面/潮高基准面以下 1 m 作为滨珊瑚的实际生长上限(聂宝符,1996),也有研究以平均低潮面作为滨珊瑚的生长上限(Yao *et al.*, 2013),还有研究基于现代活滨珊瑚微环境顶面高程进行海平面重建(Yu *et al.*, 2009).尽管雷琼地区前人海平面重建结果均采用 1985 国家高程基准或与之可转换的潮高基准面,但在具体指标选取上存在明显分化——部分以平均低潮面为参考,部分以大潮低潮面为参考.这一差异成为导致区域海平面高程重建结果矛盾、限制横向可比性的主要原因.本研究通过将所有数据统一转换至现代平均海平面,有效消除基准差异对区域对比的影响,为区域对比提供了统一、可靠的分析基础.

本研究通过对海南岛东部沿海珊瑚礁区达到生长上限的现代滨珊瑚微环礁顶部进行高程测量,明确其顶面高程与现代海平面的关系以及潮位指示范围,量化滨珊瑚微环礁的海平面指示意义,为其他珊瑚礁区的滨珊瑚(微环礁)海平面重建提供了新范式和依据.

其次,在测年方法方面,研究表明珊瑚样品的 ^{14}C 测年结果相较于其对应的 U-Th 测年结果,系统性呈现约 200～1 000 a,甚至 3 000～3 500 a 的年轻化趋势,即使经过校正,仍可能存在 80～600 a 差距(Bard *et al.*, 1993).这种差异可能源于海洋碳库效应的时空变异性、环境的改变,或晚期成岩作用(Bard *et al.*, 1993).此外,不同软件或不同版本的同一软件对全新世 ^{14}C 年龄的校正结果,可能存在十年甚至上千年的差异(乐远福和唐立超,2023;唐立超和乐远福,2023).以本研究 65 个滨珊瑚(微环礁)海平面标志点数据为例,U-Th 测年的 2σ 误差范围为 14～34 a,且同一块滨珊瑚(微环礁)测年结果基本一致,凸显 U-Th 测年方法的高精度.同时,有学者通过对全新世珊瑚样品年代学数据,发现 U-Th 年龄与树木年代学校准结果高度吻合(Bard *et al.*, 1993),进一步验证了 U-Th 测年技术的准确性及其作为地质年代计的高精度特征.综上,选择指示意义明确的海平面标志物并采用精确测年方法,是高质量重建过去海平面的关键.对于滨珊瑚(微环礁)而言,U-Th 测年技术较 ^{14}C 测年方法具更高的海平面重建可信度.

在海平面重建研究中,无论采用何种海平面标志物,均需遵循以下关键流程:首先明确所选海平面标志物的指示意义.其次,提升定年技术精度并严格控制误差,同时开展必要的构造校正以消除地质构造运动的影响.在此基础上,通过多源数据交叉验证提升结果的可靠性,最后整合多元海平面记录以解决争议性问题.

与全球中全新世海平面记录对比表明,南海北部海平面变化既呈现全球共性,也存在区域分异.全球尺度上,中全新世早期海平面上升、中期维持相对高位是普遍特征,但不同区域的上升速率和高位持续时间差异显著.例如,泰国和越南现代海岸在8 000～7 000 cal a BP已出现明确海侵的证据,并在约6 000 cal a BP达到接近1.5 m的峰值(Tanabe, 2003; Stattegger *et al.*, 2013).与此同时,马来西亚半岛东海岸海平面在约7 000 cal a BP期间波动于1.4～3.0 m(Parham *et al.*, 2014),6 500 cal a BP时为1.5 m,至4 500 cal a BP进一步上升至2 m(Zhang *et al.*, 2021).此外,印度尼西亚勿里洞岛在6 800～6 600 cal a BP期间记录到1.8 m的海平面高度.此外,巽他陆架(Meltzner *et al.*, 2017)、澳大利亚大堡礁(Chappell, 1983)、太平洋波利尼西亚(Pirazzoli *et al.*, 1988)、和东印度洋科科斯环礁(Woodroffe *et al.*, 1999)的化石珊瑚礁记录均显示中全新世处于高海平面期.这表明南海北部中全新世高海平面的出现与南海周边区域基本同步,可能具有全球驱动背景.然而,热带太平洋地区中全新世早期海平面上升速率略高于南海北部,中期高位持续时间更长.这种差异可能与海洋地理环境、地壳均衡调整以及构造运动有关.南海北部受东亚季风和西太平洋暖池的影响,对区域气候系统变化更为敏感;而板块边界等构造活跃区,海平面变化则可能叠加了地壳升降运动的影响.

值得注意的是,中全新世是一个高温时期,南海北部海表温度较现在高0～2 ℃(Wei *et al.*, 2007).最新研究显示,基于滨珊瑚重建的南海北部中全新世高海平面和陆地孢粉重建的高温期高度重叠,表明高海平面可能与气候变暖密切相关(Yue *et al.*, 2024).在当前全球变暖背景下,1980－2020年全球海平面上升已经进入加速状态,且未来持续快速上升(乐远福和唐立超,2023),极有可能重现中全新世高海平面情景,这将对南海北部低洼地区的人类生存环境和沿海生态环境带来严重威胁,包括加剧海水入侵、土壤盐碱化等问题.因而,亟需采取有效措施应对海平面上升的潜在风险,以保障区域生态安全和居民生命财产安全.

4.3 区域构造升降运动因素分析

相对海平面变化是全球融冰过程、地壳均衡调整、局地构造运动和沉积压实等效应的综合响应.通过对比海平面变化地质数据与GIA模型的差异,有望从中分离出区域和当地的构造信号.为探讨南海北部雷琼海岸过去几千年的构造升降过程,本研究将海南岛东岸(本文研究区,图5a)、西岸(Yao *et al.*, 2013;图5b)和雷州半岛南端(Yu *et al.*, 2009;图5c)中晚全新世滨珊瑚(微环礁)海平面数据与GIA模型(ICE-6G_HetML140)进行对比.

假设GIA模型预测准确,其与海平面数据的差异理论上反映当地构造升降量.如图5所示,雷琼海岸中晚全新世海平面数据均位于GIA预测曲线下方,表明这些区域过去几千年处于构造沉降状态.其中,海南岛东岸中全新世数据与模型的差值小于1 m,至3 000 a BP缩小至约0.5 m,反映沉降速率较低((0.12±0.06) mm/a).尽管海南岛西岸和雷州半岛的海平面数据较少,不足以进行定量对比,但均表现出明显构造沉降迹象.

上述结果与前人提出的雷琼地区全新世构造抬升结论(詹文欢等,2006; Yao *et al.*, 2013)存在显著差异.例如,粤西与海南地区的中全新世高海平面(Zong *et al.*, 2004)及海南岛西部河流的全新世阶地(陈康林等,2024)常被解释为构造抬升证据.然而,本研究的最新数据-模型对比表明,雷琼海岸的中全新世高海平面现象可能是水动型GIA效应的结果,而非构造抬升——远场GIA高海平面效应掩盖了局地较弱的构造沉降信号,导致对全新世地质资料的误读.国家一等水准网垂直形变观测数据显示,近50 a来海南岛及雷州半岛海岸表现出明显沉降趋势(郭鑫伟等,2022),为本研究提出的中长期构造沉降提供了佐证.从新生代板块运动和南海的演变背景看,南海洋盆沉陷驱动南海北部大陆架向南扩张并伴随沉降(张健与石耀霖, 2003; Wang *et al.*, 2024),这可能是雷琼海岸中晚全新世构造沉降的区域动力学机制.

需要注意的是,以上推论依赖于GIA模型的准确性,而ICE-6G冰模型主要基于北极地区的融冰历史构建,对远场区域的预测存在不确定性.雷琼地区处于新构造活跃带,第四纪晚期经历复杂的间

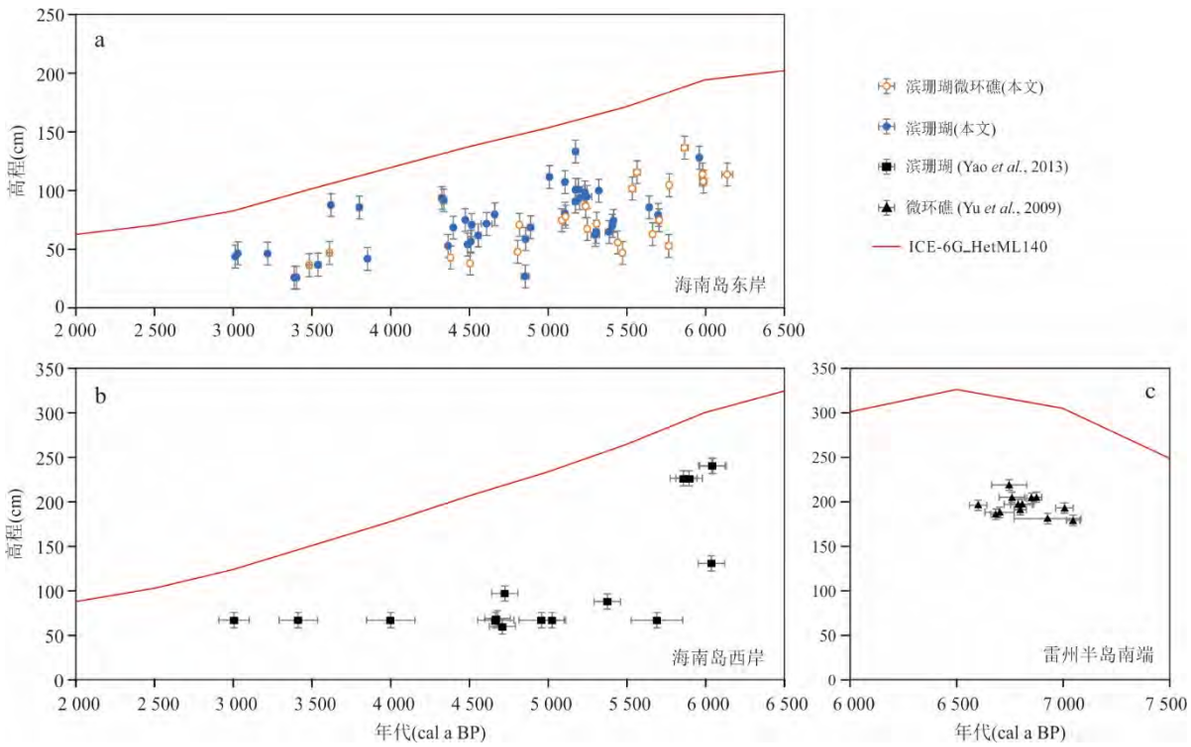


图 5　基于滨珊瑚及滨珊瑚微环礁重建的南海北部中全新世海平面与 GIA 模型预测海平面曲线对比图

Fig.5　Comparison of the Middle Holocene sea level reconstructed from *Porites* and *Porites* microatolls in the northern South China Sea with the sea level curves predicted by the GIA model

a,b 和 c 分别为海南岛东岸、西岸以及雷州半岛南端地区

歇性差异性升降(詹文欢等,2006;陈康林等,2024),内陆与海岸可能表现不同升降模式.因此,证实雷琼海岸长期构造升降模式并精确量化速率,仍需更多可靠的地质证据及模型交叉验证.

本研究受限于现有数据量与模型精度,暂未对海平面代用指标进行构造校正.研究中雷琼海岸 GIA 模型与实测数据的差异(图 5),已初步暗示构造因素对海平面变化的潜在影响,但量化分析仍需进一步探索.

5　结论和展望

本研究针对南海北部中全新世海平面变化争议及构造信号分离问题,通过分析海南岛东部珊瑚礁区 27 块顶面死亡的现代滨珊瑚微环礁顶面高程,明确其海平面指示意义,并对该区 65 个海平面标志点数据进行系统性评估与校正,进而重建南海北部中全新世海平面变化历史.主要结论如下:

(1)滨珊瑚微环礁海平面指示意义的精确量化.现代滨珊瑚微环礁平均高度(−43.09 cm)位于当地最低低潮位(−28 cm)以下 15.09 cm,证实最低低潮位是滨珊瑚微环礁的理论生长上限,表明海平面是该地区滨珊瑚微环礁发育的关键因素.这些滨珊瑚微环礁平均高程(−43.09 cm)相对于海南岛清澜港平均潮位(103 cm)为−146.09 cm,为滨珊瑚微环礁的海平面指示意义提供了量化基准,解决了前人因指示意义不明确导致的重建结果矛盾问题.

(2)中全新世海平面变化特征.本研究重建的是南海北部中全新世相对海平面变化,数据均以 MSL 为基准,确保与全球其他地区记录具有可比性.海平面重建结果显示,在(6 143±34) cal a BP 至(3 013±9) cal a BP 期间,南海北部的相对海平面波动范围为(25.0±9.8) cm 至(136.09±9.80) cm,整体呈波动下降趋势.与全球中全新世海平面记录相比,南海北部的海平面变化既呈现与全球一致的趋势,也存在区域差异特征,这可能与南海北部受东亚季风和西太平洋暖池的气候调控效应有关,以及叠加了地壳升降运动的影响.

(3)构造沉降的新证据.通过海平面变化地质数据与 GIA 模型的对比分析,发现南海北部雷琼海岸过去几千年整体处于构造沉降状态(海南岛东岸沉降速率为(0.12±0.06) mm/

a),修正了前人将中全新世高海平面归因于构造抬升的认识.远场GIA效应掩盖了局部沉降信号,导致对地质资料的误读.国家水准网观测数据与区域板块运动背景(南海洋盆沉陷驱动大陆架扩张)进一步支持了长期沉降机制.

(4)研究局限性与展望.本研究依赖北极融冰历史构建的GIA模型,对远场区域的预测存在不确定性.若要精确量化雷琼海岸长期构造升降速率,未来需结合更多钻孔资料、高精度测年数据及区域构造模型,验证长期沉降模式并量化速率,为准确分离气候与构造信号提供更坚实的基础.

References

An, Z. S., 2000. The History and Variability of the East Asian Paleomonsoon Climate. *Quaternary Science Reviews*, 19(1—5): 171—187. https://doi. org/10.1016/S0277-3791(99)00060-8

Bard, E., Arnold, M., Fairbanks, R. G., et al., 1993. ^{230}Th-^{234}U and ^{14}C Ages Obtained by Mass Spectrometry on Corals. *Radiocarbon*, 35(1): 191—199. https://doi.org/10.1017/s0033822200013886

Chappell, J., 1983. Evidence for Smoothly Falling Sea Level Relative to North Queensland, Australia, during the Past 6, 000 Yr. *Nature*, 302: 406—408. https://doi.org/10.1038/302406a0

Chen, J. H., Lawrence Edwards, R., Wasserburg, G. J., 1986. ^{238}U, ^{234}U and ^{232}Th in Seawater. *Earth and Planetary Science Letters*, 80(3—4): 241—251. https://doi.org/10.1016/0012-821X(86)90108-1

Chen, K. L., Jiang, T., Hu, Y. P., et al., 2024. The Origin and Evolution of Late Pleistocene River Terracesin Western Hainan Island. *Earth Science*, 49(8): 3043—3055 (in Chinese with English abstract).

Guo, X. W., Guo, C. X., Nie, J. L., et al., 2022. Vertical Movement Model in Chinese Mainland Based on First Order Leveling Results. *Geomatics and Information Science of Wuhan University*, 47(3): 361—368 (in Chinese with English abstract).

Hallmann, N., Camoin, G., Eisenhauer, A., et al., 2018. Ice Volume and Climate Changes from a 6000 Year Sea-Level Record in French Polynesia. *Nature Communications*, 9: 285. https://doi. org/10.1038/s41467‐017‐02695-7

Li, T. H., Wu, P., 2019. Laterally Heterogeneous Lithosphere, Asthenosphere and Sub-Lithospheric Properties under Laurentia and Fennoscandia from Glacial Isostatic Adjustment. *Geophysical Journal International*, 216(3): 1633—1647. https://doi.org/10.1093/gji/ggy475

Ma, Z. B., Xiao, J., Zhao, X., et al., 2003. Precise U-Series Dating of Coral Reefs from the South China Sea and the High Sea Level during the Holocene. *Journal of Coastal Research*, 19(2): 296—303.

Meltzner, A. J., Switzer, A. D., Horton, B. P., et al., 2017. Half-Metre Sea-Level Fluctuations on Centennial Timescales from Mid‐Holocene Corals of Southeast Asia. *Nature Communications*, 8: 14387. https://doi.org/10.1038/ncomms14387

Natawidjaja, D. H., Sieh, K., Ward, S. N., et al., 2004. Paleogeodetic Records of Seismic and Aseismic Subduction from Central Sumatran Microatolls, Indonesia. *Journal of Geophysical Research: Solid Earth*, 109(B4): B04306. https://doi.org/10.1029/2003JB002398

Navigation Guarantee Department, Commander Department of the People's Liberation Army Navy. 2022. Guide to China Ports C105 (South China Sea). China Navigation Publications Press, Tianjin (in Chinese).

Nie, B. F., 1996. Sea-Level Changes of the South China Sea in the Past 5000 Years. *Quaternary Sciences*, (1): 80—87 (in Chinese with English abstract).

Parham, P. R., Saito, Y., Sapon, N., et al., 2014. Evidence for Ca. 7‐ka Maximum Holocene Transgression on the Peninsular Malaysia East Coast. *Journal of Quaternary Science*, 29(5): 414—422. https://doi. org/10.1002/jqs.2714

Peltier, W. R., Argus, D. F., Drummond, R., 2015. Space Geodesy Constrains Ice Age Terminal Deglaciation: The Global ICE-6G_C (VM5a) Model. *Journal of Geophysical Research: Solid Earth*, 120(1): 450—487. https://doi.org/10.1002/2014JB011176

Pirazzoli, P. A., Montaggioni, L. F., Salvat, B., et al., 1988. Late Holocene Sea Level Indicators from Twelve Atolls in the Central and Eastern Tuamotus (Pacific Ocean). *Coral Reefs*, 7(2): 57—68. https://doi. org/10.1007/BF00301642

Shennan, I., Horton, B., 2002. Holocene Land‐ and Sea-Level Changes in Great Britain. *Journal of Quaternary Science*, 17(5—6): 511—526. https://doi.org/10.1002/jqs.710

Shi, X.J., Yu, K.F., Chen, T.G., et al., 2008. mid-to late-Holocene Sea Level Highstands: Evidence from Fringing Coral Reefs at Qionghai, Hainan Island. *Marine Geology & Quaternary Geology*, 28(5): 1—9 (in Chinese with English abstract).

Smithers, S. G., Woodroffe, C. D., 2000. Microatolls as Sea-Level Indicators on a Mid-Ocean Atoll. *Marine Ge-*

ology, 168(1－4): 61－78. https://doi. org/10.1016/S0025-3227(00)00043-8

Stattegger, K., Tjallingii, R., Saito, Y., et al., 2013. Mid to Late Holocene Sea-Level Reconstruction of Southeast Vietnam Using Beachrock and Beach‐Ridge Deposits. *Global and Planetary Change*, 110: 214－222. https://doi.org/10.1016/j.gloplacha.2013.08.014

Stirling, C. H., Esat, T. M., McCulloch, M. T., et al., 1995. High‐Precision U‐Series Dating of Corals from Western Australia and Implications for the Timing and Duration of the last Interglacial. *Earth and Planetary Science Letters*, 135(1－4): 115－130. https://doi.org/10.1016/0012-821X(95)00152-3

Tanabe, S., Hori, K., Saito, Y., et al., 2003. Song Hong (Red River) Delta Evolution Related to Millennium‐Scale Holocene Sea-Level Changes. *Quaternary Science Reviews*, 22(21－22): 2345－2361. https://doi. org/10.1016/S0277-3791(03)00138-0

Tang, L. C., Yue, Y. F., 2023. Application and Uncertainty Analysis of Beachrock to Mid-Late Holocene Sea-Level Reconstruction in the Northern South China Sea. *Marine Geological Frontiers*, 39(3): 1－19 (in Chinese with English abstract).

Wang, C. Q., Jia, L. Y., Hu, D. G., et al., 2024. Seismogenic Structure of the 1605 Qiongshan *M*7½ Earthquake and Its Holocene Activity History in Northern Hainan Island, China: Evidence from Cross‐Section Drilling and Shallow Seismic Profile. *Journal of Earth Science*, 35(3): 905－917. https://doi. org/10.1007/s12583-021-1585-x

Wang, S. H., 1989. Some Problem on Recognition of Sea Level Indicators. *Journal of Oceanography in Taiwan Strait*, 8(4): 329－337 (in Chinese with English abstract).

Wei, G. J., Deng, W. F., Yu, K. F., et al., 2007. Sea Surface Temperature Records in the Northern South China Sea from Mid-Holocene Coral Sr/Ca Ratios. *Paleoceanography*, 22(3): PA3206. https://doi. org/10.1029/2006PA001270

Woodroffe, C. D., McLean, R. F., Smithers, S. G., et al., 1999. Atoll Reef-Island Formation and Response to Sea-Level Change: West Island, Cocos (Keeling) Islands. *Marine Geology*, 160(1－2): 85－104. https://doi.org/10.1016/S0025-3227(99)00009-2

Wu, P., 2004. Using Commercial Finite Element Packages for the Study of Earth Deformations, Sea Levels and the State of Stress. *Geophysical Journal International*, 158 (2): 401－408. https://doi. org/10.1111/j. 1365‐246X.2004.02338.x

Yan, T. L., 2022. Records of Sea Level Changes over The Mid‐Holocene from U‐Series Ages of Shore Reefs in Tanmen, Hainan Island (Dissertation). Guangxi University, Nanning (in Chinese with English abstract).

Yan, T. L., Yu, K. F., Jiang, L. L., et al., 2024. Significant Sea-Level Fluctuations in the Western Tropical Pacific during the Mid‐Holocene. *Paleoceanography and Paleoclimatology*, 39(5): e2023PA004783. https://doi.org/10.1029/2023PA004783

Yao, Y. T., Zhan, W. H., Sun, J. L., et al., 2013. Emerged Fossil Corals on the Coast of Northwestern Hainan Island, China: Implications for Mid‐Holocene Sea Level Change and Tectonic Uplift. *Chinese Science Bulletin*, 58(23): 2869－2876. https://doi.org/10.1007/s11434-013-5692-7

Yu, K. F., Zhao, J. X., Done, T., et al., 2009. Microatoll Record for Large Century-Scale Sea-Level Fluctuations in the Mid‐Holocene. *Quaternary Research*, 71(3): 354－360. https://doi.org/10.1016/j.yqres.2009.02.003

Yu, K. F., Zhong, J. L., Zhao, J. X., et al., 2002. biological-Geomorphological Zones in a Coral Reef Area at Southwest Leizhou Peninsula Unveil Multiple Sea Level high-Stands in the Holocene. *Marine Geology & Quaternary Geology*, 22(2): 27－33 (in Chinese with English abstract).

Yue, Y. F., Tang, L. C., 2023. Characteristics of Sea Level Changes in the Northern South China Sea since the Holocene and Prediction of the Future Trends. *Marine Geology Frontiers*, 39(2): 1－16 (in Chinese with English abstract).

Yue, Y. F., Tang, L. C., Yu, K. F., 2022. General Characteristics of Sea-Level Changes along the North Atlantic Coast in the Past 2000 Years. *Marine Geology Frontiers*, 38(6): 1－15 (in Chinese with English abstract).

Yue, Y. F., Tang, L. C., Yu, K. F., et al., 2024. Coral Records of Mid‐Holocene Sea-Level Highstands and Climate Responses in the Northern South China Sea. *Acta Oceanologica Sinica*, 43(2): 43－57. https://doi. org/10.1007/s13131-023-2264-9

Yue, Y. F., Yu, K. F., Tao, S. C., et al., 2019.3500-Year Western Pacific Storm Record Warns of Additional Storm Activity in a Warming Warm Pool. *Palaeogeography, Palaeoclimatology, Palaeoecology*, 521: 57－71. https://doi.org/10.1016/j.palaeo.2019.02.009

Zhan, W. H., Zhu, Z. Y., Yao, Y. T., et al., 2006. Neotectonic Movement Recorded in Coral Reefs in the Northwestern South China Sea. *Quaternary Sciences*, 26(1):

77－84 (in Chinese with English abstract).

Zhang, J., Shi, Y. L., 2003. Thermodynamics Mechanism of the Marginal Extensional Belt of East Asia. *Geotectonica et Metallogenia*, 27(3): 222－227 (in Chinese with English abstract).

Zhang, Y. Z., Zong, Y. Q., Xiong, H. X., et al., 2021. The Middle-to-Late Holocene Relative Sea-Level History, Highstand and Levering Effect on the East Coast of Malay Peninsula. *Global and Planetary Change*, 196: 103369. https://doi.org/10.1016/j.gloplacha.2020.103369

Zhao, J. X., Yu, K. F., 2002. Timing of Holocene Sea-Level Highstands by Mass Spectrometric U-Series Ages of a Coral Reef from Leizhou Peninsula, South China Sea. *Chinese Science Bulletin*, 47(4): 348－352. https://doi.org/10.1007/BF02901194

Zong, Y. Q., 2004. Mid‐Holocene Sea‐Level Highstand along the Southeast Coast of China. *Quaternary International*, 117(1): 55－67. https://doi.org/10.1016/S1040-6182(03)00116-2

中文参考文献

陈康林, 姜涛, 胡亦潘, 等, 2024. 晚更新世以来海南岛西部河流阶地演化及其成因机制. 地球科学, 49(8): 3043－3055.

郭鑫伟, 郭春喜, 聂建亮, 等, 2022. 一等水准成果构建的中国大陆垂直运动模型研究. 武汉大学学报(信息科学版), 47(3): 361－368.

中国人民解放军海军司令部航海保证部, 2022. 中国港口指南C105(南海海区). 天津: 中国航海图书出版社.

聂宝符, 1996. 五千年来南海海平面变化的研究. 第四纪研究, (1): 80－87.

时小军, 余克服, 陈特固, 等, 2008. 中-晚全新世高海平面的琼海珊瑚礁记录. 海洋地质与第四纪地质, 28(5): 1－9.

唐立超, 乐远福, 2023. 海滩岩在南海北部中晚全新世海平面重建中的应用和不确定性分析. 海洋地质前沿, 39(3): 1－19.

王绍鸿, 1989. 海平面标志物识别的一些问题. 台湾海峡, 8(4): 329－337.

颜廷礼, 2022. 海南潭门镇珊瑚岸礁的铀系年代及其对中全新世海平面变化的记录(硕士学位论文). 南宁: 广西大学.

余克服, 钟晋梁, 赵建新, 等, 2002. 雷州半岛珊瑚礁生物地貌带与全新世多期相对高海平面. 海洋地质与第四纪地质, 22(2): 27－33.

乐远福, 唐立超, 2023. 南海北部全新世以来海平面变化特征及未来趋势预测. 海洋地质前沿, 39(2): 1－16.

乐远福, 唐立超, 余克服, 2022. 北大西洋沿岸过去2000年海平面变化的若干重要特征. 海洋地质前沿, 38(6): 1－15.

詹文欢, 朱照宇, 姚衍桃, 等, 2006. 南海西北部珊瑚礁记录所反映的新构造运动. 第四纪研究, 26(1): 77－84.

张健, 石耀霖, 2003. 东亚陆缘带构造扩张的深部热力学机制. 大地构造与成矿学, 27(3): 222－227.

海洋环境科学 doi: 10.11978/2024132 http://www.jto.ac.cn

近 30 年来涠洲岛海域海水磷含量变化及其影响因素—来自高分辨率珊瑚记录的证据

陈裕月[1], 姜伟[2], 杨浩丹[2], 余克服[2]

1. 中国地质大学(武汉)海洋学院, 湖北 武汉 430070;
2. 广西大学海洋学院, 广西南海珊瑚礁研究重点实验室, 广西 南宁 530004

摘要: 表层海水磷(P)含量变化是评价海洋生态系统营养含量的重要参数, 对地球环境演变过程起到重要调节作用。涠洲岛是我国最大最年轻的火山岛, 海水表层 P 含量变化缺乏长时间尺度记录, 影响因子尚未明确。珊瑚骨骼 P/Ca 是反演海水 P 含量的可靠指标, 被广泛用于重建高分辨率海水 P 含量变化历史。本研究以涠洲岛西北部连续生长珊瑚为研究对象, 基于珊瑚氧同位素建立 1985—2015 年的年龄框架, 重建 1985—2014 年月分辨率的珊瑚 P/Ca 变化历史。不同年份的珊瑚 P/Ca 值及其季节变化较大, 在 1998—2003 年之间珊瑚 P/Ca 值较低, 普遍低于年平均值。珊瑚 P/Ca 比值变化与季风强度变化存在极大相关性(P<0.05), 季风、台风盛行期珊瑚 P/Ca 值明显增加, 说明海表风速是该区域海水 P 含量变化的主控因素。此外, 火山爆发、石油泄露以及旅游业的发展也会造成 P 含量短暂性升高, 但影响时长有限。降雨量年际变化及干湿季变化与 P/Ca 值相关性不显著, 说明陆源物质对海水 P 含量变化的影响有限。

关键词: 涠洲岛; 磷; 珊瑚礁; 地球化学

中图分类号: X145 **文献标识码:** A **文章编号:** 1009-5470(2025)03-0206-11

Changes and controlling factors of seawater phosphorus in Weizhou Island over the past 30 years: Insights from high-resolution coral records

CHEN Yuyue[1], JIANG Wei[2], YANG Haodan[2], YU Kefu[2]

1. College of Marine Science and Technology, China University of Geosciences, Wuhan 430070, China;
2. Guangxi Laboratory on the Study of Coral Reefs in the South China Sea, School of Marine Sciences, Guangxi University, Nanning 530004, China

Abstract: The change in phosphorus (P) content in surface seawater is an important parameter to evaluate the nutrient content of marine ecosystem, and plays a significant role in regulating the evolution of the Earth's environment. Weizhou Island is the largest and youngest volcanic island in China. The change in surface phosphorus content in seawater over a long time scale is not well documented, and the influencing factors remain unclear. Coral skeleton P/Ca is a reliable index for retrieving seawater phosphorus content and is widely used to reconstruct the high-resolution history of seawater P content. In this study, continuously growing corals from northwest Weizhou Island were taken as the research object, and an age framework was established from 1985 to 2015 based on coral oxygen isotopes to reconstruct the P/Ca change history of surface seawater in monthly resolution from 1985 to 2014. The results showed that the coral P/Ca value varied greatly in different years and seasons, with low P/Ca values observed from 1998 to 2003, generally lower than the annual average. The change in coral P/Ca ratio was highly correlated with the change in monsoon intensity (P<0.05), and the coral P/Ca value increased significantly during the monsoon and typhoon periods, indicating that the sea

收稿日期: 2024-06-27; **修订日期:** 2024-07-29。林强编辑

基金项目: 国家重点研发计划项目(2023YFF0804801); 国家自然科学基金项目(41976059)

作者简介: 陈裕月(2000—), 女, 硕士研究生, 海洋科学专业, 主要从事海洋地质方面研究。email: chenyuyue@cug.edu.cn

通信作者: 姜伟。email: jianwe@gxu.edu.cn

Received date: 2024-06-27; **Revised date:** 2024-07-29. Editor: LIN Qiang

Foundation item: National Key Research and Development Program of China (2023YFF0804801); National Natural Science Foundation of China (41976059)

Corresponding author: JIANG Wei. email: jianwe@gxu.edu.cn

中国知网 https://www.cnki.net

~surface wind was the main factor controlling the change in seawater P content in this region. Additionally, volcanic eruptions, oil spills, and tourism can also cause a temporary increase in P content, but the effects are limited. However, there was no significant correlation between the inter-annual variations of rainfall and changes between wet and dry seasons and the P/Ca values, indicating that terrigenous materials had limited influence on the change in P content in seawater.

Key words: Weizhou Island; phosphorus; coral reefs; geochemistry

磷(P)是影响海洋浮游植物生物量和群落结构的关键营养元素, 对海洋初级生产力发挥着一定的抑制和促进作用(Delaney, 1998; Benitez-Nelson et al, 1999)。在地质时间尺度上, P 被认为是维持海洋初级生产力的最终限制营养元素(Kolowith et al, 2001; Paytan et al, 2007)。然而, 长期营养记录的缺乏限制了对营养污染程度和生态影响的理解。

热带造礁珊瑚对环境变化十分敏感, 连续生长时间长且珊瑚文石骨骼年际界限清楚, 结合高分辨率氧同位素可以建立精确的年龄框架, 因此热带造礁珊瑚是高分辨率记录海洋环境长时间尺度演化的重要载体(Hoppe, 2003; Lough, 2004; Yu et al, 2005; Yu, 2012)。Dodge 等人首先注意到珊瑚骨骼 P/Ca 值作为营养指标的潜力, 巴拿马湾的多个珊瑚群落说明了骨骼 P/Ca 值与海水溶解无机磷(dissolved inorganic phosphorus, DIP)之间存在相同的关系(Dodge et al, 1984b; LaVigne et al, 2010)。Chen 等(2011)通过南海大亚湾富营养环境下生长的滨珊瑚岩心发现, 在富营养化环境下, 珊瑚的 P/Ca 值与海水中总磷(total phosphorus, TP; 包括溶解和颗粒态)的线性关系更强。Mallela 等(2013)发现珊瑚 P/Ca 值与海水磷酸盐的强相关关系, 并建立了珊瑚 P/Ca 值与海水磷酸盐的线性关系, 随后通过大堡礁的多个珊瑚岩芯研究表明, 珊瑚 P/Ca 值的时间变异性与附近河流向珊瑚礁排放的总颗粒 P 呈强烈共变。Chen 等(2019)在此基础上进一步证实了珊瑚 P/Ca 值跟踪反演海水 DIP 变化的可靠性。以上研究都表明, 珊瑚骨骼 P/Ca 值与海水中各种形式的 P 有很强的相关性, 可以作为海水中 P 营养物质的代用指标。

涠洲岛是我国最大最年轻的火山岛, 也是广西面积最大的海岛, 表层海水温度平均 24.6℃, 光照充足, 造礁石珊瑚分布广泛(况雪源 等, 2007), 其珊瑚礁生态区是浮游植物生长受到 P 限制较明显的海区(何本茂等, 2013)。海水混合层 P 含量变化缺乏长时间尺度记录, P 含量演化的影响因子尚未明确。虽然前人对涠洲岛的海水化学性质和造礁珊瑚开展过一些研究, 但主要集中于古气候研究(Yu et al, 2001; Chen et al, 2009; Yu, 2012)。本研究利用涠洲岛 1985—2014 年高分辨率的珊瑚骨架地球化学数据(P/Ca、$\delta^{18}O$ 等)研究 1985—2014 年浅海珊瑚礁区海水 P 的变化规律, 通过分析 P/Ca 值与降雨量、海表风速、人类活动、火山爆发等的相关关系, 探讨了海水 P 的影响因素及其影响程度。本文的研究结果有助于了解涠洲岛营养污染程度和海水 P 对生态系统的影响, 从而为涠洲岛珊瑚礁区保护和发展提供科学依据。

1 研究区域、材料与方法

1.1 研究区域

涠洲岛(20°50′—21°10′N, 109°00′—109°15′E)隶属于广西北海市, 与雷州半岛、海南岛、越南相邻, 长约 7.5km, 宽约 5.5km, 全岛陆地面积约 24.98km^2(刘敬合等, 1991)(图 1)。涠洲岛是我国形成时间最晚, 由火山岩堆积成的岛屿, 环境承载能力和恢复能力十分有限(刘敬合 等, 1991; 况雪源 等, 2007)。受亚热带海洋性季风气候的影响, 涠洲岛夏季盛行偏南风, 冬季盛行偏北风, 春秋两季处于季风转换期, 风速较低(Gai et al, 2020)。根据涠洲岛月平均降水量, 5—10 月为雨季, 11 月至次年 4 月为干季(李嘉琪 等, 2018)。近年来, 涠洲岛人为活动的增加导致附近海水的营养通量显著增加, 过量的营养物质会影响珊瑚礁的健康程度, 出现珊瑚礁退化现象(McCook, 1999; Cloern, 2001; Glibert et al, 2006; Wang et al, 2018)。

1.2 材料与方法

分析的活体橙黄滨珊瑚 W3 于 2015 年 10 月采自涠洲岛西北部(21°04′07″N, 109°05′24″E) (图 1), 没有出现白化或疾病的迹象。样品运输至实验室后, 首先用清水冲刷去除珊瑚礁表面藻类、软体动物外壳等杂质, 使用高速切割机沿主要生长轴把 W3 珊瑚切割成 10mm 厚, 80~100mm 宽的薄板, 然后使用医用 X 光透视机获取 X 射线成像。为了去除表面污染物, 将珊瑚薄板放置在 10%H_2O_2 中浸泡 48h, 再加入超纯水(Milli-Q)超声清洗珊瑚薄板 3 次, 之后放置于 40℃鼓风干燥箱烘干。根据 X 射线成像和珊瑚骨骼一年内形成一个高密度段和一个低密度段的特征确定时间序列(Knutson et al, 1972; 龙雅婷 等, 2022)。为了测定珊瑚中的 P/Ca 值, 沿珊瑚最大生长轴连续取样, 每个样品约 10mg, 样品数量为 416 个。称取 0.5~1mg

中国知网 https://www.cnki.net

粉状样品与 100%H_3PO_4在 75℃的自动碳酸盐装置中反应, 并将提取出来的 CO_2 导入 Finnigan MAT-253 稳定同位素质谱仪, 采用 GBW04405 标准($\delta^{18}O$=–8.49‰)标准化为 V-PDB, 该标准的多次测量(n=15)得到 $\delta^{18}O$ 的标准偏差为 0.08%, 并用月分辨率 $\delta^{18}O$ 对年龄框架进行交叉验证。然后称取 3mg 的珊瑚骨骼粉末到离心管中, 加入 900μL 内标(^{115}In、^{187}Re 配置为 100ppb)消除 Ca 的基体效应, 然后用 2%HNO_3溶解稀释约 3000 倍至 6ppb。最后使用电感耦合等离子体质谱仪(ICP-MS)对获得的溶液进行 P、Ca 元素的测试。在 ICP-MS 测试前首先使用 ICP 分析专用标准溶液制作标准曲线, 测量中对所有样品进行三次测量, 每次测量结果的标准偏差普遍小于 5%, 有效减小了测试结果的误差。

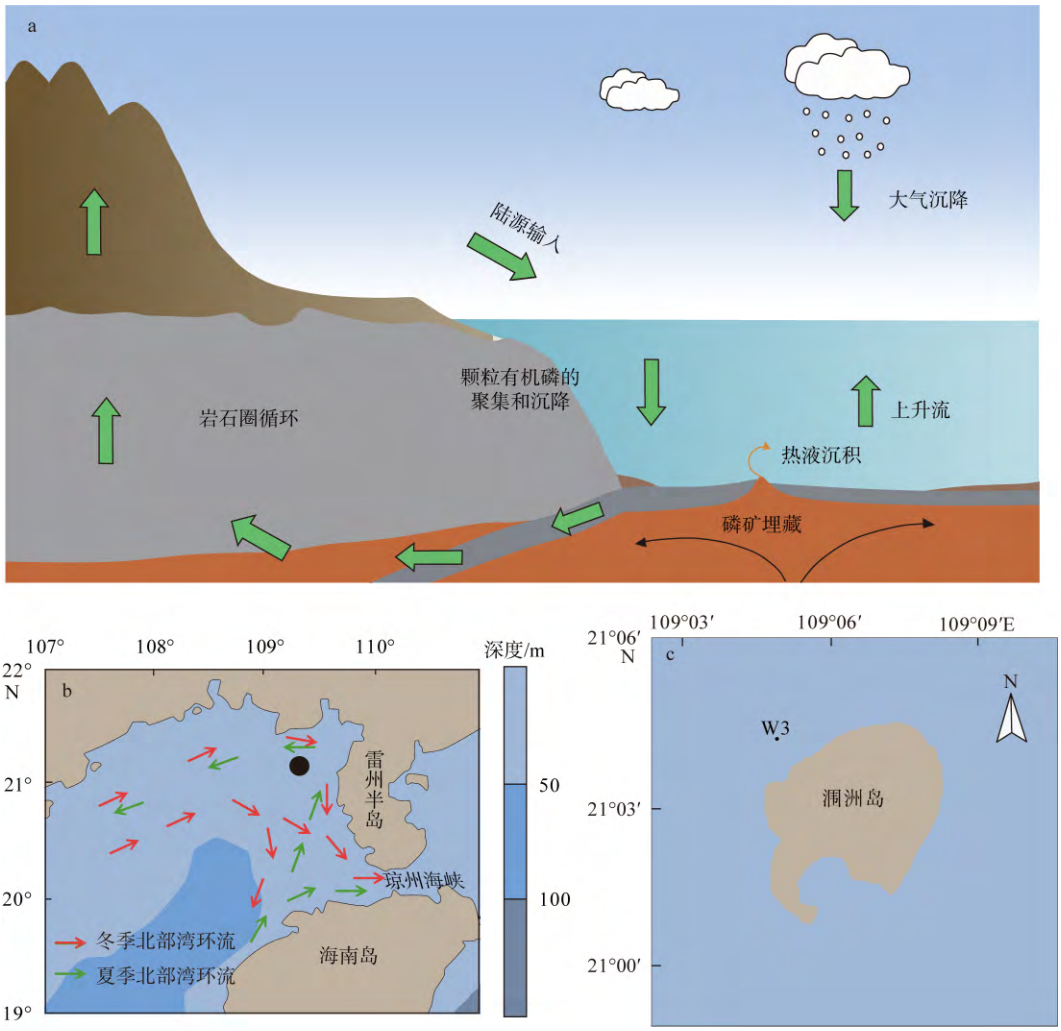


图 1 研究区位置示意图

a. 海洋磷循环示意图, 修改自 Benitez-Nelson (2000)和周强 等(2021); b. 北部湾环流图, 黑色圆点为采样站位, 基于自然资源部标准地图服务网站下载的审图号为 GS(2022)4309 号的标准地图制作; c. 采样站位图

Fig. 1 Schematic diagram of the marine phosphorus cycle (a) and diagram of circulation of the Beibu Gulf (b) and the sampling site (c)

本文所用到的涠洲岛降雨量、风速数据来自美国国家海洋和大气管理局自然科学部(www.esrl.noaa.gov/psd/data/), 涠洲岛溢油事件来自广西海洋局环境公报, 海水 TP 含量来自韦蔓新 等(2013)和吴敏兰(2014)。

2 结果

2.1 年代学框架

密度带成像结果显示 W3 珊瑚生长时间跨度为 1985—2015 年, 拥有 30 年珊瑚骨骼同位素记录(Xu et al, 2018)(图 2)。由于取样过程中, 沿着珊瑚最大生长轴均匀取 12~15 个样品, 所得数据不利于分析 P 干湿季的变化及季节特征, 因此利用 $\delta^{18}O$ 最大值与温度周期最低值相对应的特点, 即涠洲岛一年中 SST 最低的 1 月份对应于 $\delta^{18}O$ 最大值的月份, 对仪器测试数据进行 12 个月的插值处理, 处理后的数据以 12 个月均匀分布的形式呈现(图 2)。

中国知网 https://www.cnki.net

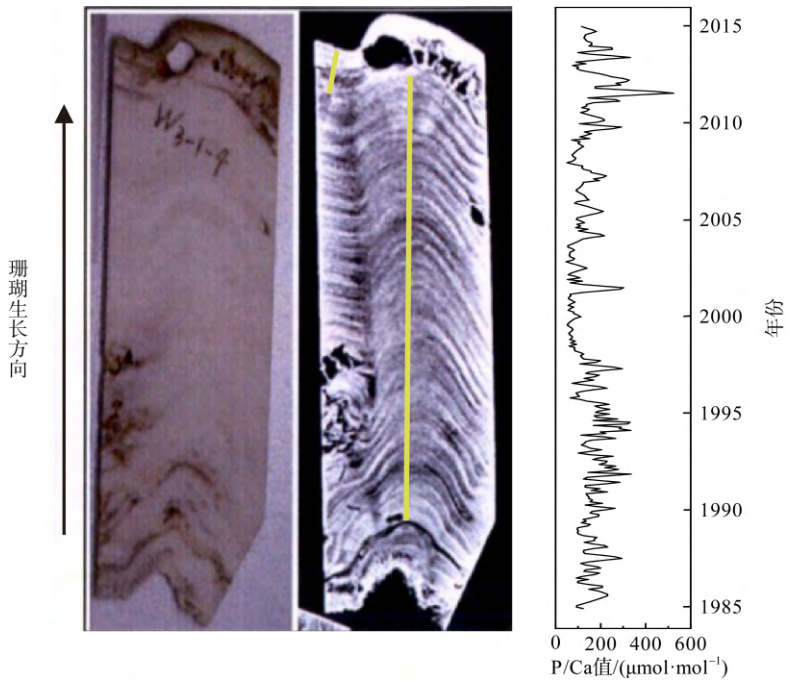


图 2 W3 珊瑚薄板和 X 射线照片及 P/Ca 值

骨架内的年带状由高(暗)密度和低(亮)密度的周期表示, 黄线表示珊瑚的最大生长轴。

Fig. 2 Slab photograph, X-ray image, and P/Ca ratios of Porites coral from the W3 site, Weizhou Island

2.2 P/Ca 值测试结果

ICP-MS 会检测骨骼内所有形式(有机、无机、可溶、不可溶)的 P, 因此, 本研究中 P/Ca 值信号反映了有机相和无机相的结合。全球平均 P/Ca 值和溶解无机磷 DIP 的线性关系表明, 珊瑚 P/Ca 值对低于 (4.9±1.4)μmol·mol^{-1} 的海水 DIP 不敏感, 且珊瑚骨骼 P/Ca 值的分析不确定度和异质性产生 1.4μmol·mol^{-1} 的额外误差。因此, 珊瑚 P/Ca 值接近或小于 6.3μmol·mol^{-1} 时, 不能精确反演海水 DIP(Chen et al, 2019)。本研究中 W3 珊瑚 P/Ca 值在 1985—2014 年期间的范围为 67.6~283.7μmol·mol^{-1}, 平均值为 152.3μmol·mol^{-1}, 大大超过 6.3μmol·mol^{-1}, 可以作为海水 P 的可靠代表。残余珊瑚组织内有大量 P 有机物的存在, 导致 2015 年珊瑚 P/Ca 值偏离正常轨迹(Dodge et al, 1984a; Alibert et al, 2003; LaVigne et al, 2008), 位于较高的状态, 因此忽略对该数据的分析。

1985—2014 年 W3 珊瑚的 P/Ca 值波动较大, 可以划分为三个时期, 分别是 1985—1997、1998—2003 和 2004—2014 年, 平均值分别为 174.48、88.76 和 160.87μmol·mol^{-1}, 分别称为前期、中期和后期。将一年内所有样品获取的 P/Ca 结果求平均可得到年平均 P/Ca 值, 三个时期的年平均 P/Ca 值的最大值分别位于 1992、2001 和 2011 年, 分别为 213.29、138.11 和 283.69μmol·mol^{-1}。前期年平均 P/Ca 值普遍较高, 从 1992 年开始出现一个下降的趋势, 在 1997 年有一个急剧的下降, 由 179.51μmol·mol^{-1}下降到 87.05μmol·mol^{-1}。中期为珊瑚 P/Ca 值低值期, P/Ca 年平均值低至 88.7μmol·mol^{-1}, 除个别月份外, 大多数月份珊瑚 P/Ca 值都低于总体平均值。2003 年后珊瑚 P/Ca 值开始升高, 由 73.74μmol·mol^{-1}上升到 135.18μmol·mol^{-1}。后期珊瑚 P/Ca 值缓慢增大, 2011 年急剧上升, 出现最大值, 随后 P/Ca 值不断下降(图 3)。

3 讨论

3.1 珊瑚 P/Ca 值代表海水 P 的变化

与其他珊瑚礁区相比, 涠洲岛 W3 珊瑚 P/Ca 值较高, 在其他已发表的研究范围之内(Montagna et al, 2006; Chen et al, 2011), 但显著高于公海和人类活动较少的海域中的珊瑚 P/Ca 值(Alibert et al, 2003; Chen et al, 2019)(表 1)。Chen 研究大亚湾珊瑚表明 P/Ca 值与海水 TP 具有较强的线性关系(P<0.001, r=0.9, n=16), 本文通过对该数据进行线性回归, 得到 P/Ca-TP 回归方程(Chen et al, 2011)。通过该方程推测海水 TP 含量, 绝大部分与涠洲岛实地采样所记录的海水 TP 含量相近, 随后将 W3 珊瑚 P/Ca 与海水实测数据与大亚湾数据进行相关性分析, 表明骨骼 P/Ca 值与 TP 之间存在较强的线性关系(P<0.001, r=0.969, n=22) (图 4)。进一步证实了该线性关系的可靠性以及在涠洲岛等高营养盐通量的地区珊瑚 P/Ca 值可以作为海水 P 的直接代理。

中国知网 https://www.cnki.net

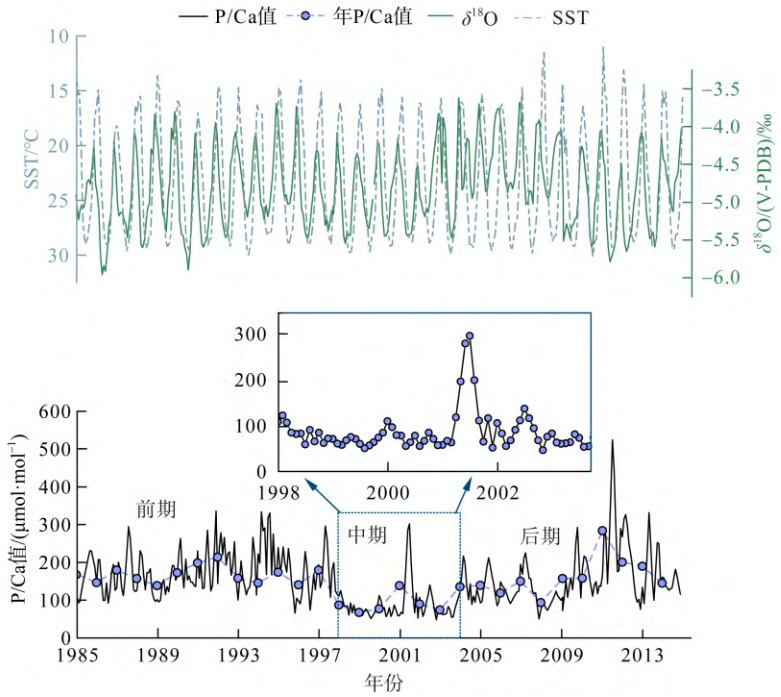


图 3 W3 珊瑚骨骼中基于珊瑚 δ^{18}O(V-PDB, ‰)构建的 P/Ca 值时间序列(1985—2014 年)

Fig. 3 P/Ca time series based on coral δ^{18}O (V-PDB, ‰) values in W3 coral skeletons over the period (1985–2014)

表 1 不同海域珊瑚 P/Ca 值对比

Tab. 1 P/Ca comparison from worldwide studies of scleractinian corals

海域	物种	P/Ca 值/(μmol·mol^{-1})	数据来源
涠洲岛	*Porites*	93.37~283.58	本研究
地中海 COBAS97a	*Desmophyllum dianthus*	125.8~139.4	Montagna et al, 2006
西太平洋 G16505		714.1~731.2	
大亚湾	*Porites* sp.	38.6~190.8	Chen et al, 2011
巴拿马湾	*Pavona gigantea*	4.1~10.3	Chen et al, 2019
列斯库拉索岛	*Montastrea*	11.4~52.7	
澳大利亚大堡礁	*Porites*	65.4	Alibert et al, 2003

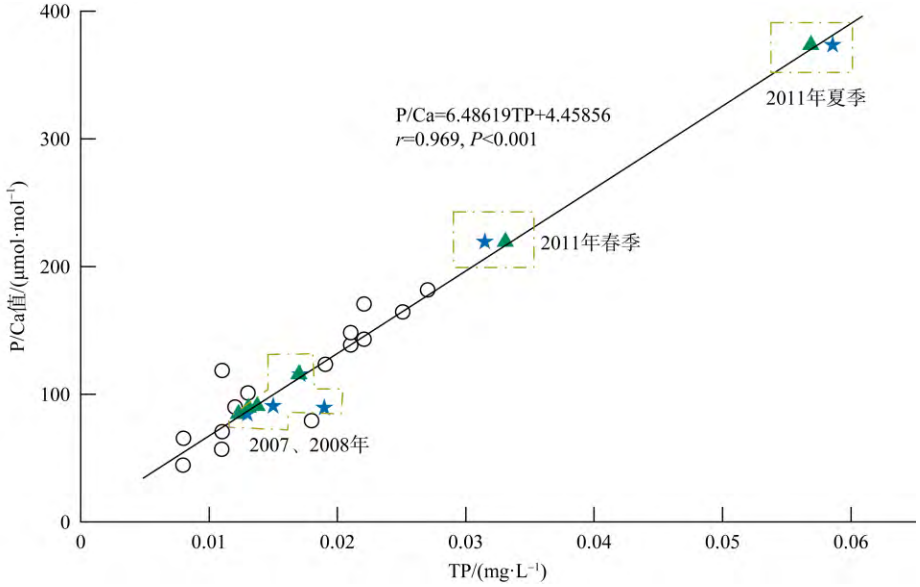


图 4 涠洲岛 W3 珊瑚与大亚湾珊瑚与海水 TP 的关系

黑色圆圈表示大亚湾珊瑚 P/Ca 值与海水 TP, 蓝色星形表示涠洲岛 W3 珊瑚 P/Ca 值与海水实测 TP, 绿色三角形表示涠洲岛 W3 珊瑚 P/Ca 值与由经验公式反演得到的海水 TP

Fig. 4 Relationship between seawater TP and corals from Weizhou Island (W3) and Daya Bay

中国知网 https://www.cnki.net

3.2 珊瑚骨骼 P/Ca 值与自然变量的关系

3.2.1 陆源输入

海洋中 P 来源主要有陆源输入、大气沉降、热液输送和火山喷发(图 1), 以下将从这几方面探讨影响珊瑚骨骼 P/Ca 值变化的自然因素(Moore et al, 2000; Slomp et al, 2004; Paytan et al, 2006)。河流和地下水是将物质从陆地运输到海洋的主要渠道, 降雨增加的季节径流承载入海的物质通量也相应增加(Shiller et al, 1987; Deng et al, 2009)。W3 珊瑚采样位置距离河流入海口较远, 最近的陆地为距离 51.66 km 的北海市(刘敬合 等, 1991), 且涠洲岛向海洋输送的河流少、流量小, 由涠洲岛河流输送入海的 P 含量小, 因此该海域海水 P 的径流输入较小。地下水是沿海海洋营养物质的重要和持续来源(Moore, 2010), 对珊瑚的丰度和多样性有潜在影响(Fabricius, 2005; Prouty et al, 2010)。一些沿海地区地下水陆源化合物含量高于河水(Slomp et al, 2004; Boehm et al, 2006; Santos et al, 2008)或者与河流流量相当(Burnett et al, 2003)。涠洲岛有丰富的地下水资源, 降雨是涠洲岛地下水资源的唯一天然来源(刘江宜 等, 2020)。W3 珊瑚骨骼 $\delta^{18}O$ 值和涠洲岛年降雨量与珊瑚 P/Ca 值相关性不显著(P=0.075, r=–0.330; P=0.988, r=0.003)(图 3、图 5), 表明来自地下水输入的营养盐对海水 P 变化的影响较小。涠洲岛受海洋气团和极地大陆气团的交替影响, 根据月平均降雨量, 可以将 5—10 月划分为湿季, 11 月至次年 4 月划分为干季(李嘉琪 等, 2018)。珊瑚骨骼 P/Ca 值干季的均值为 146.4μmol·mol^{-1}, 湿季 P/Ca 均值为 158.1μmol·mol^{-1}。珊瑚 P/Ca 值变化受到干湿季降雨的影响十分有限, 仅在 1987—1991 年, 湿季 P/Ca 值与降雨量呈正相关(P=0.001, r=0.989); 在 1985—2015 年, 干、湿季珊瑚 P/Ca 值与涠洲岛降雨量不相关(P=0.966, r=0.008; P=0.695, r=0.075)(图 5)。进一步说明了 W3 珊瑚骨骼 P/Ca 值和海水 P 含量受到陆地径流以及地下水的影响较小。

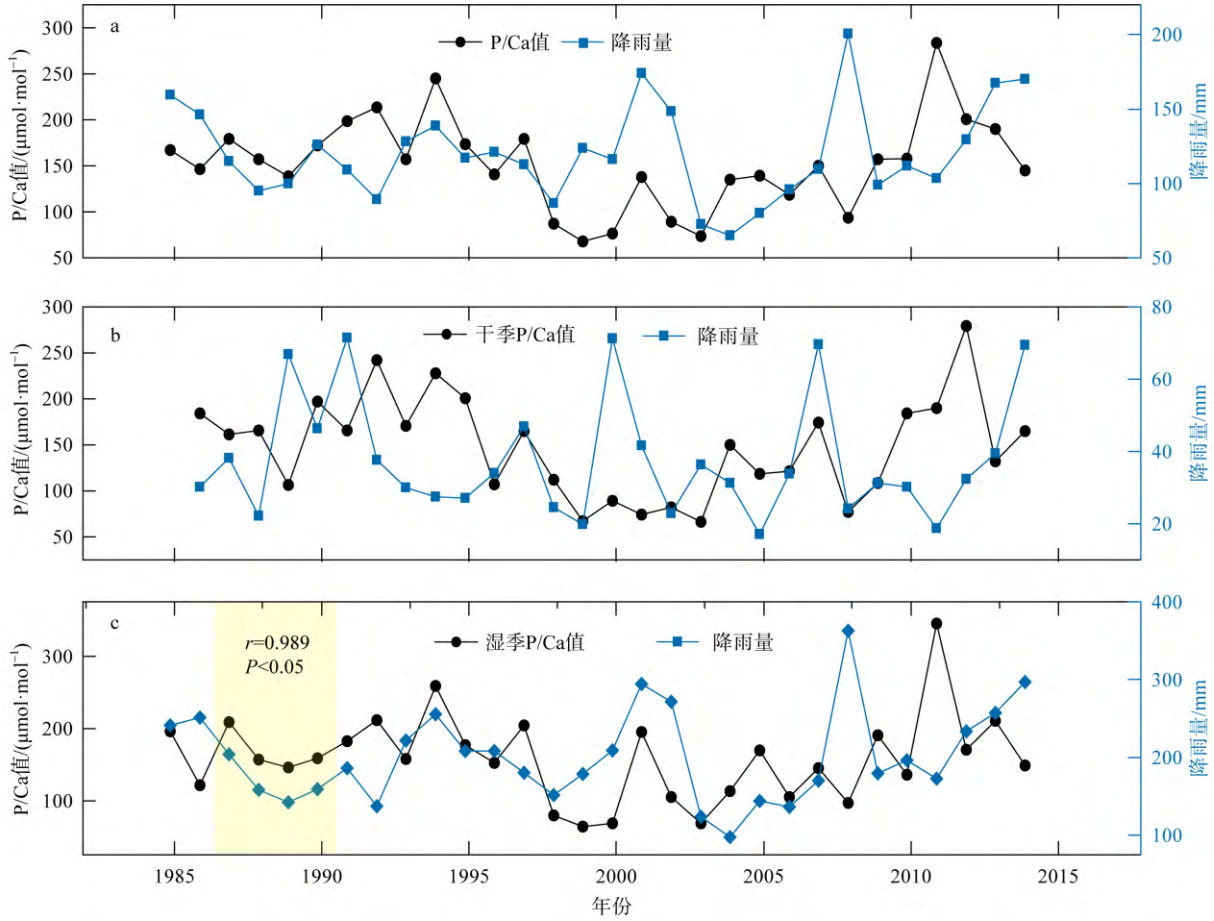


图 5 涠洲岛珊瑚骨骼 P/Ca 值和降雨量对比(1985—2014)

a. 珊瑚骨骼 P/Ca 值和年降雨量对比; b. 干季 W3 珊瑚骨骼 P/Ca 值和干季降雨量对比; c. 湿季 W3 珊瑚骨骼 P/Ca 值与湿季降雨量的变化

Fig. 5 Comparison of P/Ca of coral skeletons and annual rainfall in Weizhou Island (1985–2014)

3.2.2 大气沉降、热液输入和火山喷发

大气沉降是近海生态系统重要的营养来源, 且湿沉降是近海水体 P 的重要来源, 但大气湿沉降相对于其他因素(人为和自然)对 P 投入比例较低, 并且涠洲

中国知网 https://www.cnki.net

岛海域降雨量与珊瑚 P/Ca 值不相关, 因此大气沉降过程对该海域海水 P 的贡献较低(Lu et al, 2018)。在一个世纪以内, 涠洲岛附近没有火山喷发的记录(Li et al, 2018), 排除热液输入对海水 P 变化的影响。菲律宾吕宋岛的皮纳图博火山(120.35°E, 15.13°N)在 1991 年 6 月 12 日至 15 日爆发, 大量火山气溶胶被带入平流层(Hayashida et al, 1993), 同年底, 珊瑚骨骼 P/Ca 值逐渐升高, 在 1992 年达到前期(1985—1997 年)的最高值(图 3), 火山喷发通过大气远距离输送的影响时长较短, 经过一定时间的调整后逐渐恢复到正常海洋环境(魏浩天 等, 2020)。

3.2.3 海表风速

在东亚季风的控制下, 南海受到冬季干燥寒冷季风和夏季温暖潮湿季风的交替影响, 使得冬季风环流和夏季风降水均表现出较强的时空变异性(Deng et al, 2017; Gai et al, 2020)。南海夏季(6—8 月)盛行西南风, 表层海水易在该海域形成反气旋环流, 同时在沿岸地区形成离岸上升流, 冬季盛行东北风, 最大风速较夏季小。春秋两季处于季风转换期, 风速较低(Yu et al, 2005)。季风会驱动海水的垂直混合和水平混合, 且垂直混合强于水平混合, 因此在季风盛行期间, 海洋底部的 P 会被带到海表, 表层海水中 P 含量大大增加(李敏, 2009; Lao et al, 2023)。本研究中, 春秋两季 P/Ca 值在 1985—2000 年以及 2009—2013 年与平均风速呈现出明显的正相关关系(P=0.05, r=0.498; P=0.037, r=0.900), 且这种现象在风速较高的夏冬季节更加明显, 其 P/Ca 值在 1985—2010 年与平均风速具有正相关的关系(P=0.037, r=0.410)(图 6)。证实了该时段内季风是影响海水 P 含量变化的主导因素, 影响时间长且效果显著。尽管涠洲岛海域受到季风的主要影响, 但珊瑚 P/Ca 值季节性变化特征不明显, 因此还需考虑其他因素对海水 P 季节变化影响。热带气旋主要发生在湿季, 通过引起海水垂直混合将海水底部 P 带到海表(Walker et al, 2005; Gao et al, 2021), 从而影响海水表层 P 含量。本研究中, 1985—2007 年, 珊瑚年平均 P/Ca 值与年平均最大风速以及湿季平均 P/Ca 值与湿季平均最大风速存在显著相关性(P=0.007, r=0.542; P=0.043, r=0.426), 说明热带气旋也是影响海水 P 含量的主要原因。

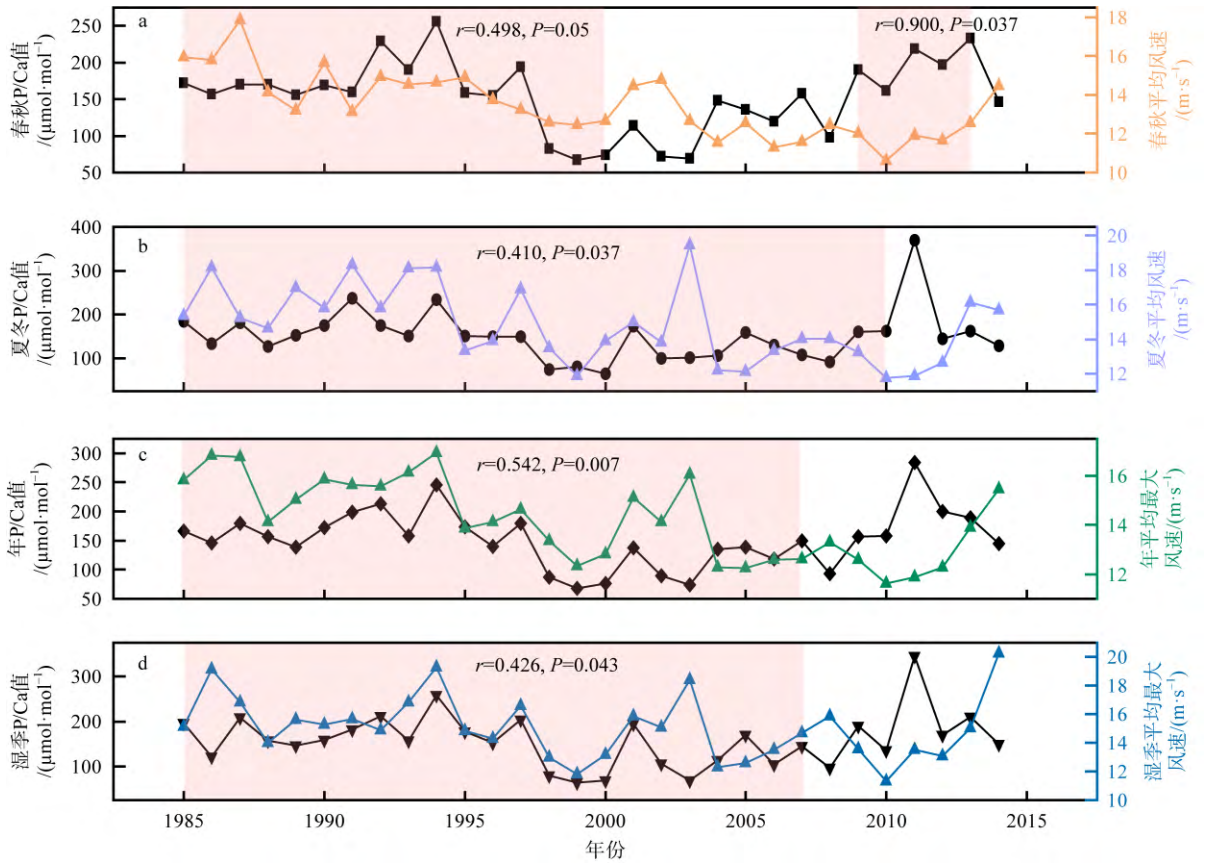


图 6 W3 珊瑚 P/Ca 值与风速的变化

a. 春秋季珊瑚 P/Ca 值与平均风速; b. 夏冬季珊瑚 P/Ca 值与平均风速; c.珊瑚年平均 P/Ca 值与年平均最大风速; d. 珊瑚湿季平均 P/Ca 值与湿季平均最大风速。阴影部分表示二者相关性显著

Fig. 6 Changes in P/Ca of W3 corals and wind speed. The shaded part is the range for which the P/Ca of W3 corals is significantly correlated with the wind speed

中国知网 https://www.cnki.net

为了进一步判断海表风速对海水 P 的影响, 我们将研究自然状态(1998—2003 年)海表风速对珊瑚骨骼 P/Ca 值变化的影响, 该时段涠洲岛人为活动少, 可以忽略人为因素对海水 P 的影响。该时间段内珊瑚骨骼 P/Ca 值较低, 平均值为 88.87μmol·mol^{-1}, 低于总体平均值。且除个别月份外, 大多数月份珊瑚 P/Ca 值都低于总体平均值。值得注意的是, 2001 年 6—9 月珊瑚 P/Ca 值异常高, 变化幅度非常大。4 月该比值较低, 仅为 64.7μmol·mol^{-1}, 但从 4 月份开始, 该比值开始大幅度上升, 幅值约为 80.0μmol·mol^{-1}, 同年 7 月份, 已经达到 285.48μmol·mol^{-1}(图 3)。根据中央气象台台风网, 2001 年 7 月 2 日, 0103 号台风“榴莲”经过涠洲岛海域; 同年, 7 月 7 日, 0104 号台风“尤特”经过涠洲岛海域; 7 月 26 日, 0107 号台风“玉兔”吹过北部湾涠洲岛海域; 8 月 11 日, 0110 号热带风暴“天兔”经过研究区域; 8 月 31 日, 0114 号热带风暴“菲特”经过研究海域; 9 月 21 日, 0116 号热带低压“百合”经过研究区域。台风会推动海水的水平运动, 以及加强水体的垂直混合, 因此在台风盛行期间, 台风影响区域的海水会产生强烈的混合。综上所述, 在自然状态下, 影响研究海域珊瑚骨骼 P/Ca 值变化的主导因素是海表风。

3.3 珊瑚骨骼 P/Ca 值与人类活动的关系

旅游业发展会极大地影响海水 P 含量变化。人类活动影响较强烈的海洋面积约占全球海洋面积的 41%(Halpern et al, 2008), 为了减轻环境污染和避免生态破坏, 1989 年 12 月 26 日, 会议通过了《中华人民共和国环境保护法》。根据 P/Ca 值时间序列, 1994 年后珊瑚 P/Ca 值呈现出明显下降趋势, 并在 1998—2003 年期间处于低值状态, 年平均值为 88.7μmol·mol^{-1}。这六年的珊瑚 P/Ca 年平均值都处于总体年平均 P/Ca 值水平以下, 这与环境保护方法的实施是密不可分的(图 3)。

随着经济发展和旅游资源不断开发, 涠洲岛吸引了越来越多游客的参观。2004 年, 涠洲岛游客为 9 万人/年, 到 2014 年, 上岛游客已经增加到 59.3 万人/年(王文欢 等, 2016)。2004 年到 2014 年涠洲岛上游客人数增长率为 5.03 万人/年, 污染物对附近海域也造成了明显的影响(郭芳, 2015)。值得注意的是, 2004—2012 年, W3 珊瑚 P/Ca 值与涠洲岛每年的游客人数具有显著的正相关性(P=0.03, r=0.855)(图 7)。与此同时, 根据海水实测数据, 从 2007 年到 2011 年涠洲岛海域海水 TP 含量不断增加, 从 0.013mg·L^{-1} 增加到 0.058mg·L^{-1}(韦蔓新 等, 2013; 吴敏兰, 2014)。以上研究都表明人类活动是引起周围海域海水 P 变化的重要原因之一。

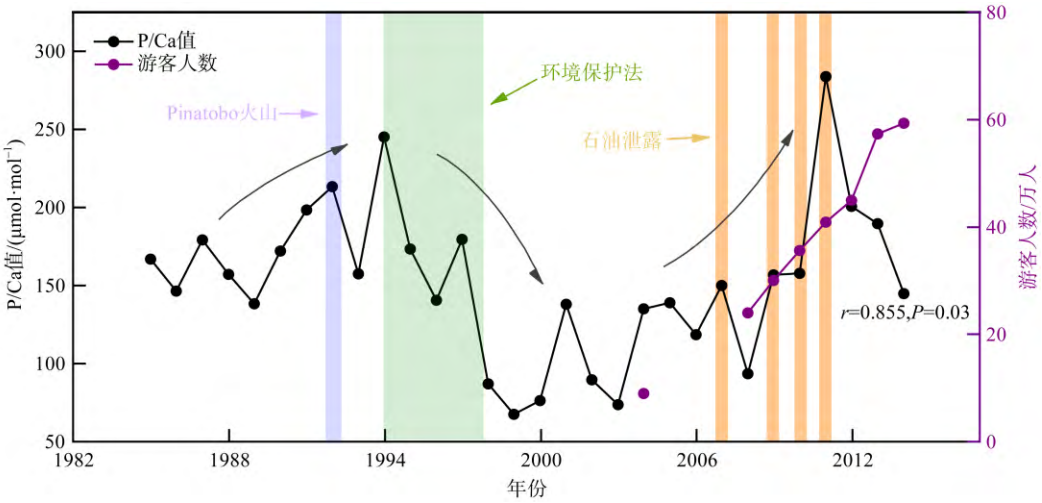


图 7 珊瑚骨骼 P/Ca 值(1985—2014)与游客人数(2004—2014)变化(Moore et al, 2000)

Fig. 7 Changes in P/Ca of coral skeletons (1985–2014) and number of tourists (2004–2014) (Moore et al, 2000)

石油是一种生物来源的天然产物, 富含碳、氢、磷等元素, 石油泄漏的海域海水磷含量较正常海水磷含量高(Medina-Bellver et al, 2005; 刘慧杰 等, 2012)。W3 珊瑚 P/Ca 值在 2007、2009、2010 和 2011 年(分别为 116.3、131.4、197.5 和 219.8μmol·mol^{-1})都比相邻年份的 P/Ca 值高, 与涠洲岛海域发生石油污染的时间相对应(图 7)。2006 年 7 月, 北海发生了严重的溢油事故, 污染物主要为黑色块状油污(陈圆 等, 2013), 受到石油泄漏事故的影响, 珊瑚岩芯 P/Ca 值大约增加了 24.6μmol·mol^{-1}。2008 年, 涠洲岛西南部海域发生了 4 次溢油事故, 污染物主要为黑色油块, 黏性较强, 其中污染最严重的溢油事故发生于 8 月份, 总溢油量高达 750 吨, 将近 129.96km^2 的海域面积都遭受了污染(李君光, 2009), 与此对应的是, 2008 年珊瑚骨骼 P/Ca

中国知网 https://www.cnki.net

值增加了 49.23μmol·mol^{-1}。2009 年, 一艘拖网渔船在北海码头沉没并出现溢油现象。2011 年 8 月 5 日, 涠洲镇也发生了一次石油溢油事故, 在西北方向距岸边约 5km 处出现大量漂浮油污(陈圆 等, 2013), 受到油污中有机物的影响, 2011 年 W3 珊瑚岩芯 P/Ca 值增加了 97.51μmol·mol^{-1}, 增加幅度较大。由于珊瑚钙化过程由多种机制参与进行, 最初钙化集中在表面, 随后经过缓慢的沉积逐渐增厚, 可能相对环境有一定的滞后性(Barnes et al, 1993; Taylor et al, 1995), 因此珊瑚 P/Ca 值出现峰值的时间滞后于溢油事故的时间。综上所述, 旅游业的发展和石油泄漏对海水 P 变化的相对影响较大。

4 结论

本次研究利用涠洲岛 1985—2014 年高分辨率珊瑚骨架的地球化学数据(P/Ca 值、δ^{18}O 等), 描述了珊瑚骨骼 P/Ca 值的变化和 1985—2014 年浅海珊瑚礁区海水 P 变化的影响因素, 主要研究结果如下。

1) W3 珊瑚骨骼 P/Ca 值作为海水表层 P 含量变化的有效代用指标, 能够可靠反演 1985—2014 年涠洲岛海域 P 含量变化, 涠洲岛海域海水 P 含量变化受陆源输入和大气沉降的影响较小, 可忽略不计。

2) 环境保护法的落实有利于缓解涠洲岛海域海水的污染程度。随着经济的发展, 游客人数增加和海上工程造成的溢油事故都是造成涠洲岛海域海水 P 含量增加的重要原因, 如果不加强对该海域的管理, 未来海水中的 P 可能会成为威胁珊瑚礁生存的重要因子。

3) 春秋季和秋冬季珊瑚 P/Ca 值与平均风速具有显著的相关性, 该海域海水 P 含量的变化受季风的强烈影响。台风盛行期间, 珊瑚 P/Ca 值也相应升高。因此海表风是影响海水 P 含量变化的主控因素, 而火山爆发、石油泄露以及旅游业的发展都是造成 P 含量短暂性升高的主要因素。

参考文献 References

陈圆, 青尚敏, 2013. 广西北部湾海洋油污染影响与应急管理浅析[J]. 海洋开发与管理, 30(3): 104–108 (in Chinese).

郭芳, 2015. 广西涠洲岛是如何成为“违建岛”的[J]. 中国经济周刊, (43): 34–37 (in Chinese).

何本茂, 黎广钊, 韦蔓新, 等, 2013. 涠洲岛珊瑚礁海域氮磷比值季节变化与浮游生物结构的关系[J]. 热带海洋学报, 32(4): 64–72. HE BENMAO, LI GUANGZHAO, WEI MANXIN, et al, 2013. Relationship between the seasonality of seawater N: P ratio and the structure of plankton on the reefs of Weizhou Island, northern South China Sea[J]. Journal of Tropical Oceanography, 32(4): 64–72 (in Chinese with English abstract).

况雪源, 苏志, 涂方旭, 2007. 广西气候区划[J]. 广西科学, 14(3): 278–283. KUANG XUEYUAN, SU ZHI, TU FANGXU, 2007. Climate regionalization of Guangxi[J]. Guangxi Sciences, 14(3): 278–283 (in Chinese with English abstract).

李嘉琪, 白爱娟, 蔡亲波, 2018. 西沙群岛和涠洲岛气候变化特征及其与近岸陆地的对比[J]. 热带地理, 38(1): 72–81. LI JIAQI, BAI AIJUAN, CAI QINBO, 2018. Climate change characteristics of the Xisha Islands and Weizhou Island in China and the comparison with the coastal land[J]. Tropical Geography, 38(1): 72–81 (in Chinese with English abstract).

李君光, 2009-06-08(001). 环境状况有喜有忧[N]. 北海日报 (in Chinese).

李敏, 2009. 南海海洋叶绿素 α 时空分布及对季风变动响应的研究[D]. 北京: 中国气象科学研究院. LI MIN, 2009. A study on the spatial and temporal Chl-α distribution in the South China Sea and a response to the South China Sea monsoon[D]. Beijing: Chinese Academy of Meteorological Sciences (in Chinese with English abstract).

刘慧杰, 张虎山, 2012. 海洋石油污染及治理措施[J]. 广州环境科学, 27(4): 35–38. LIU HUIJIE, ZHANG HUSHAN, 2012. Marine petroleum pollution and treatment measures[J]. Guangzhou Environmental Science, 27(4): 35–38 (in Chinese with English abstract).

刘江宜, 窦世权, 牟德刚, 2020. 海岛资源环境承载能力评价研究——以广西涠洲岛为例[J]. 中国渔业经济, 38(6): 109–120. LIU JIANGYI, DOU SHIQUAN, MOU DEGANG, 2020. Study on evaluation of resources and environment carrying capacity of islands: a case of Weizhou Island in Guangxi[J]. Chinese Fisheries Economics, 38(6): 109–120 (in Chinese with English abstract).

刘敬合, 黎广钊, 农华琼, 1991. 涠洲岛地貌与第四纪地质特征[J]. 广西科学院学报, 7(1): 27–36. LIU JINGHE, LI GUANGZHAO, NONG HUAQIONG, 1991. Features of geomorphy and quaternary geology of the Weizhou Island[J]. Journal of Guangxi Academy of Sciences, 7(1): 27–36 (in Chinese with English abstract).

龙雅婷, 余克服, 王瑞, 等, 2022. 涠洲岛珊瑚礁的发育过程及其与气候的对应关系[J]. 海洋地质与第四纪地质, 42(1): 184–193. LONG YATING, YU KEFU, WANG RUI, et al, 2022. Development of coral reefs around Weizhou Island and its bearing on climate[J]. Marine Geology & Quaternary Geology, 42(1): 184–193 (in Chinese with English abstract).

王文欢, 余克服, 王英辉, 2016. 北部湾涠洲岛珊瑚礁的研究历史、现状与特色[J]. 热带地理, 36(1): 72–79. WANG WENHUAN, YU KEFU, WANG YINGHUI, 2016. A review on the research of coral reefs in the Weizhou Island, beibu gulf[J]. Tropical Geography, 36(1): 72–79 (in Chinese with English abstract).

魏浩天, 刘刚, 韩孝辉, 等, 2020. 珊瑚礁对热液流体的地球化学记录——来自南海西沙永兴岛珊瑚礁稀土元素的证据[J]. 海洋地质与第四纪地质, 40(4): 78–95. WEI HAOTIAN, LIU GANG, HAN XIAOHUI, et al, 2020. Geochemical records of

中国知网 https://www.cnki.net

hydrothermal fluids in corals: Evidence of rare earth elements from coral reefs in the Yongxing Island, Xisha, South China Sea[J]. Marine Geology & Quaternary Geology, 40(4): 78–95 (in Chinese with English abstract).

韦蔓新, 黎广钊, 何本茂, 等, 2013. 涠洲岛珊瑚礁生态区各种形态磷含量的季节变化及其影响因素[J]. 应用海洋学学报, 32(2): 258–265. WEI MANXIN, LI GUANGZHAO, HE BENMAO, et al, 2013. Seasonal variation of different forms of phosphorus and the influential factors in coral reef ecoregion of Weizhou Island[J]. Journal of Applied Oceanography, 32(2): 258–265 (in Chinese with English abstract).

吴敏兰, 2014. 北部湾北部海域营养盐的分布特征及其对生态系统的影响研究[D]. 厦门: 厦门大学. WU MINLAN, 2014. The distribution feature of nutrients and the study of their influence on ecosystem in the northern Beibu Gulf[D]. Xiamen: Xiamen University (in Chinese with English abstract).

周强, 姜允斌, 郝记华, 等, 2021. 磷的生物地球化学循环研究进展[J]. 高校地质学报, 27(2): 183–199. ZHOU QIANG, JIANG YUNBIN, HAO JIHUA, et al, 2021. Advances in the study of biogeochemical cycles of phosphorus[J]. Geological Journal of China Universities, 27(2): 183–199 (in Chinese with English abstract).

ALIBERT C, KINSLEY L, FALLON S J, et al, 2003. Source of trace element variability in great barrier reef corals affected by the Burdekin flood plumes[J]. Geochimica et Cosmochimica Acta, 67(2): 231–246.

BARNES D J, LOUGH J M, 1993. On the nature and causes of density banding in massive coral skeletons[J]. Journal of Experimental Marine Biology and Ecology, 167(1): 91–108.

BENITEZ-NELSON C R, BUESSELER K O, 1999. Variability of inorganic and organic phosphorus turnover rates in the coastal ocean[J]. Nature, 398(6727): 502–505.

BENITEZ-NELSON C R, 2000. The biogeochemical cycling of phosphorus in marine systems[J]. Earth-Science Reviews, 51(1-4): 109–135.

BOEHM A B, PAYTAN A, SHELLENBARGER G G, et al, 2006. Composition and flux of groundwater from a California beach aquifer: Implications for nutrient supply to the surf zone[J]. Continental Shelf Research, 26(2): 269–282.

BURNETT W C, BOKUNIEWICZ H, HUETTEL M, et al, 2003. Groundwater and pore water inputs to the coastal zone[J]. Biogeochemistry, 66(1-2): 3–33.

CHEN MENGLI, MARTIN P, GOODKIN N F, et al, 2019. An assessment of P speciation and P:Ca proxy calibration in coral cores from Singapore and Bali[J]. Geochimica et Cosmochimica Acta, 267: 113–123.

CHEN TIANRAN, YU KEFU, SHI QI, et al, 2009. Twenty-five years of change in scleractinian coral communities of Daya Bay (northern South China Sea) and its response to the 2008 AD extreme cold climate event[J]. Chinese Science Bulletin, 54(12): 2107–2117.

CHEN TIANRAN, YU KEFU, 2011. P/Ca in coral skeleton as a geochemical proxy for seawater phosphorus variation in Daya Bay, northern South China Sea[J]. Marine Pollution Bulletin, 62(10): 2114–2121.

CLOERN J E, 2001. Our evolving conceptual model of the coastal eutrophication problem[J]. Marine Ecology Progress Series, 210: 223–253.

DELANEY M L, 1998. Phosphorus accumulation in marine sediments and the oceanic phosphorus cycle[J]. Global Biogeochemical Cycles, 12(4): 563–572.

DENG SHULIN, LI MANCHUN, SUN HAN, et al, 2017. Exploring temporal and spatial variability of precipitation of Weizhou Island, South China Sea[J]. Journal of Hydrology: Regional Studies, 9: 183–198.

DENG WENFENG, WEI GANGJIAN, LI XIANHUA, et al, 2009. Paleoprecipitation record from coral Sr/Ca and δ18O during the mid Holocene in the northern South China Sea[J]. The Holocene, 19(6): 811–821.

DODGE R E, GILBERT T R, 1984a. Chronology of lead pollution contained in banded coral skeletons[J]. Marine Biology, 82(1): 9–13.

DODGE R E, JICKELLS T D, KNAP A H, et al, 1984b. Reef-building coral skeletons as chemical pollution (phosphorus) indicators[J]. Marine Pollution Bulletin, 15(5): 178–187.

FABRICIUS K E, 2005. Effects of terrestrial runoff on the ecology of corals and coral reefs: review and synthesis[J]. Marine Pollution Bulletin, 50(2): 125–146.

GAI CONGCONG, LIU QINGSONG, ROBERTS A P, et al, 2020. East Asian monsoon evolution since the late Miocene from the South China Sea[J]. Earth and Planetary Science Letters, 530: 115960.

GAO XIAOFEI, CHEN HUIHUANG, GU BINHE, et al, 2021. Particulate organic matter as causative factor to eutrophication of subtropical deep freshwater: role of typhoon (tropical cyclone) in the nutrient cycling[J]. Water Research, 188: 116470.

GLIBERT P M, HARRISON J, HEIL C, et al, 2006. Escalating worldwide use of urea: a global change contributing to coastal eutrophication[J]. Biogeochemistry, 77(3): 441–463.

HALPERN B S, WALBRIDGE S, SELKOE K A, et al, 2008. A global map of human impact on marine ecosystems[J]. Science, 319(5865): 948–952.

HAYASHIDA S, SASANO Y, 1993. Stratospheric aerosol change in the early stage of volcanic disturbance by the Pinatubo eruption observed over Tsukuba, Japan[J]. Geophysical Research Letters, 20(7): 575–578.

HOPPE H G, 2003. Phosphatase activity in the sea[J]. Hydrobiologia, 493(1-3): 187–200.

KNUTSON D W, BUDDEMEIER R W, SMITH S V, 1972. Coral chronometers: seasonal growth bands in reef corals[J]. Science, 177(4045): 270–272.

KOLOWITH L C, INGALL E D, BENNER R, 2001. Composition and cycling of marine organic phosphorus[J]. Limnology and Oceanography, 46(2): 309–320.

LAO QIBIN, LU XUAN, CHEN FAJIN, et al, 2023. A comparative study on source of water masses and nutrient

中国知网 https://www.cnki.net

supply in Zhanjiang Bay during the normal summer, rainstorm, and typhoon periods: insights from dual water isotopes[J]. Science of the Total Environment, 903: 166853.

LAVIGNE M, FIELD M P, ANAGNOSTOU E, et al, 2008. Skeletal P/Ca tracks upwelling in Gulf of Panama coral: evidence for a new seawater phosphate proxy[J]. Geophysical Research Letters, 35(5): L05604.

LAVIGNE M, MATTHEWS K A, GROTTOLI A G, et al, 2010. Coral skeleton P/Ca proxy for seawater phosphate: multi-colony calibration with a contemporaneous seawater phosphate record[J]. Geochimica et Cosmochimica Acta, 74(4): 1282–1293.

LI FUCHENG, SUN ZHEN, YANG HONGFENG, 2018. Possible spatial distribution of the Mesozoic volcanic arc in the present-day South China Sea continental margin and its tectonic implications[J]. Journal of Geophysical Research: Solid Earth, 123(8): 6215–6235.

LOUGH J M, 2004. A strategy to improve the contribution of coral data to high-resolution paleoclimatology[J]. Palaeogeography, Palaeoclimatology, Palaeoecology, 204(1-2): 115–143.

LU HELI, ZHANG CHUANRONG, LIU GUIFANG, et al, 2018. Mapping China's ghost cities through the combination of nighttime satellite data and daytime satellite data[J]. Remote Sensing, 10(7): 1037.

MALLELA J, LEWIS S E, CROKE B, 2013. Coral skeletons provide historical evidence of phosphorus runoff on the Great Barrier Reef[J]. PLoS One, 8(9): e75663.

MCCOOK L J, 1999. Macroalgae, nutrients and phase shifts on coral reefs: scientific issues and management consequences for the Great Barrier Reef[J]. Coral Reefs, 18(4): 357–367.

MEDINA-BELLVER J I, MARÍN P, DELGADO A, et al, 2005. Evidence for *in situ* crude oil biodegradation after the Prestige oil spill[J]. Environmental Microbiology, 7(6): 773–779.

MONTAGNA P, MCCULLOCH M, TAVIANI M, et al, 2006. Phosphorus in cold-water corals as a proxy for seawater nutrient chemistry[J]. Science, 312(5781): 1788–1791.

MOORE J K, ABBOTT M R, RICHMAN J G, et al, 2000. The Southern Ocean at the last glacial maximum: a strong sink for atmospheric carbon dioxide[J]. Global Biogeochemical Cycles, 14(1): 455–475.

MOORE W S, 2010. The effect of submarine groundwater discharge on the ocean[J]. Annual Review of Marine Science, 2: 59–88.

PAYTAN A, SHELLENBARGER G G, STREET J H, et al, 2006. Submarine groundwater discharge: an important source of new inorganic nitrogen to coral reef ecosystems[J]. Limnology and Oceanography, 51(1): 343–348.

PAYTAN A, MCLAUGHLIN K, 2007. The oceanic phosphorus cycle[J]. Chemical Reviews, 107(2): 563–576.

PROUTY N G, FIELD M E, STOCK J D, et al, 2010. Coral Ba/Ca records of sediment input to the fringing reef of the southshore of Moloka'i, Hawai'i over the last several decades[J]. Marine Pollution Bulletin, 60(10): 1822–1835.

SANTOS I R, NIENCHESKI F, BURNETT W, et al, 2008. Tracing anthropogenically driven groundwater discharge into a coastal lagoon from southern Brazil[J]. Journal of Hydrology, 353(3-4): 275–293.

SHILLER A M, BOYLE E A, 1987. Dissolved vanadium in rivers and estuaries[J]. Earth and Planetary Science Letters, 86(2-4): 214–224.

SLOMP C P, VAN CAPPELLEN P, 2004. Nutrient inputs to the coastal ocean through submarine groundwater discharge: controls and potential impact[J]. Journal of Hydrology, 295(1-4): 64–86.

TAYLOR R B, BARNES D J, LOUGH J M, 1995. On the inclusion of trace materials into massive coral skeletons. 1. Materials occurring in the environment in short pulses[J]. Journal of Experimental Marine Biology and Ecology, 185(2): 255–278.

WALKER N D, LEBEN R R, BALASUBRAMANIAN S, 2005. Hurricane-forced upwelling and chlorophyll *a* enhancement within cold-core cyclones in the Gulf of Mexico[J]. Geophysical Research Letters, 32(18): L18610.

WANG BAODONG, XIN MING, WEI QINSHENG, et al, 2018. A historical overview of coastal eutrophication in the China Seas[J]. Marine Pollution Bulletin, 136: 394–400.

XU SHENDONG, YU KEFU, WANG YINGHUI, et al, 2018. Oil spill recorded by skeletal δ^{13}C of *Porites* corals in Weizhou Island, Beibu Gulf, northern South China Sea[J]. Estuarine, Coastal and Shelf Science, 207: 338–344.

YU KEFU, CHEN TEGU, HUANG DINGCHENG, et al, 2001. The high-resolution climate recorded in the δ^{18}O of *Porites lutea* from the Nansha Islands of China[J]. Chinese Science Bulletin, 46(24): 2097–2102.

YU KEFU, ZHAO JIANXIN, WEI GANGJIAN, et al, 2005. Mid-late Holocene monsoon climate retrieved from seasonal Sr/Ca and δ^{18}O records of *Porites lutea* corals at Leizhou Peninsula, northern coast of South China Sea[J]. Global and Planetary Change, 47(2-4): 301–316.

YU KEFU, 2012. Coral reefs in the South China Sea: their response to and records on past environmental changes[J]. Science China Earth Sciences, 55(8): 1217–1229.

中国知网 https://www.cnki.net

互联网在海洋科学研究生教育中的应用：现状、挑战与应对

姜伟，梁甲元，黄荣永，余克服
（广西大学 海洋学院，广西 南宁 530004）

【摘要】随着信息技术的迅猛发展，互联网已成为推动各学科教学改革的关键力量。作为一门涵盖自然、环境、技术及人文等多领域的综合性学科，海洋科学的研究生教育应紧跟时代步伐，充分利用现代信息技术，促进教学内容和方式的创新。本文探讨了互联网技术在海洋科学研究生教育中应用的现状，如线上课程、虚拟实验和大数据分析等，并分析了互联网技术应用存在问题和挑战。认为涉海高校通过实时更新课程内容、构建混合式教学模式、增强互动性和强化师资培训等措施，可有效提升教学质量与学生能力。
【关键词】海洋科学；研究生；互联网；教学改革；虚拟仿真
中图分类号：G642 文献标识码：A

The Application of Internet in Postgraduate Education of Marine Science: Current Situation, Challenges and Solutions

Jiang Wei, Liang Jiayuan, Huang Rongyong, Yu Kefu
(School of Marine Sciences, Guangxi University, Guangxi Nanning 530004, China)

【Abstract】With the rapid advancement of information technology, the Internet has emerged as a pivotal force driving educational reform across various disciplines. Given that marine science is an interdisciplinary field encompassing natural sciences, environmental studies, technology, and humanities, its postgraduate education must adapt to contemporary trends by leveraging modern information technology to foster innovation in teaching content and methodologies. This paper examines the current application of Internet technology in marine science postgraduate education, including online courses, virtual experiments, and big data analysis, while identifying the associated challenges and issues. It argues that marine universities can significantly enhance teaching quality and student competencies through measures such as timely updates to course content, development of hybrid teaching models, increased interactivity, and enhanced teacher training.
【Keywords】marine science; postgraduate; internet; teaching reform; virtual simulation

引言

党的二十大报告把“发展海洋经济，保护海洋生态环境，加快建设海洋强国”作为加快构建新发展格局和着力推动高质量发展的重要举措。高层次海洋人才和海洋科技创新是发展海洋新质生产力和建设海洋强国的基础保障。海洋科学类研究生教育作为海洋高等教育序列的顶端，是涉海高层次人才的集中培养高地。因此，扩大海洋专业研究生招收规模、培养海洋创新人才成为涉海高等院校支撑海洋强国战略的重要使命。

近年来，我国海洋科学类研究生招生规模持续增长，2024 年海洋科学类研究生招生人数达到了约 4700 人，较去年增加了约 10%。随着海洋科学类人才招生规模的不断扩大，海洋科学类研究生传统培养模式的存在受到时间和地点限制、资源利用率低、教学成本较高等不足，已不能满足对高素质海洋研究型人才的需求。互联网和信息技术的快速发展为海洋科学的教学改革提供了新的契机。借助互联网平台，教学内容得以更加灵活多样，学习方式也变得更加互动和个性化。近年来，线上教学在全球高等教育领域中得到了广泛应用，线上教学充分展现了其卓越的适应性和灵活性。本研究探讨了海洋科

中国知网 https://www.cnki.net

学研究生课程与培养中互联网应用的现状与挑战，提出将信息技术与海洋科学研究生培养有机结合的改革策略，为保障海洋人才高质量发展和海洋研究生教育现代化提供了建议和参考。

一、互联网在海洋科学研究生教育中的应用意义

近年来，互联网技术迅猛发展，其应用已渗透社会生活的各个领域，教育领域也不例外。互联网技术的快速发展为海洋科学研究生教育提供了新的思路和手段，使得教学资源的整合与共享、教学模式的创新与变革成为可能。通过互联网，学生可以随时随地获取全球范围内的优质教学资源，与国内外专家学者进行实时交流和合作，极大地开阔了学习视野和拓展了科研思路。首先，它打破了传统教育模式的时空限制，实现了教学资源的全球共享，使得学生能够接触到更多元化、更前沿的知识体系。其次，互联网技术支持下的新型教学模式，如混合式学习、翻转课堂等，能够激发学生的学习兴趣和主动性，提高他们的自主学习和创新思维能力。此外，互联网还为海洋科学研究生间的科研合作与学术交流提供了便捷平台，促进了科研成果共享和转化。

二、海洋科学研究生课程中互联网应用的现状

目前，海洋科学研究生课程教学与培养依旧存在传统的面对面课堂讲授、实验教学和论文写作等形式。然而，随着信息技术的普及，许多院校已开始尝试将互联网应用融入海洋科学教育中。

（一）线上资源建设初具规模

目前，许多涉海高校已逐步建立了涵盖海洋科学不同领域的在线课程资源。例如，部分涉海高校已经将传统的课堂教学内容进行数字化转型，提供了视频课程、电子教材、研究论文等在线学习材料，学生可以通过网络平台随时访问和学习。学术资源和教学资料的数字化极大地方便了学生的自主学习。此外，许多院校采用在线讨论论坛、学术交流群组等形式，增强学生与教师之间的互动，提升学生的学术交流能力。同时，一些高校利用MOOC（大规模开放在线课程）平台和网络视频会议等工具开展远程教育，使不同地区的研究生可共享优质教学资源。从传统的线下教学到线上教学的转型，不仅方便了学生的学习，也推动了海洋科学教育现代化。

（二）虚拟实验与仿真初步应用

由于海洋科学涉及大量的实验和实地调查，一些涉海高校尝试使用虚拟仿真技术和远程实验平台，可以让学生在计算机上模拟海洋现象和实验，降低了物理实验的局限性。例如，虚拟实验与仿真技术可用于海洋环境模拟，即模拟海洋中的各种物理、化学和生物过程，包括潮汐、海流、波浪、气候变化等，帮助研究生深入理解复杂的海洋现象，并预测不同情景下的海洋变化。目前，越来越多的虚拟实验平台和软件工具被开发出来，支持对海洋环境的高效仿真，如使用计算流体力学（CFD）、有限元分析（FEA）等技术模拟海洋动力学、生态系统、气候变化、灾害预测、海洋资源开发等。

（三）海洋大数据分析与模型构建

海洋科学中的数据分析与模型构建是当前研究的重要方向之一。随着卫星遥感、海洋传感器网络和无人潜水器等技术的迅猛发展，海洋科学研究获取的数据量呈指数级增长，涵盖了海洋表面温度、盐度、流速、潮汐以及气候变化等多个方面。如何高效处理和分析这些海量数据已成为海洋科学领域的一个核心挑战。通过互联网应用，学生能够更加便捷地进行数据分析和模型模拟等实践操作，从而加强了理论与实践的紧密结合。此外，海洋科学中的模型种类繁多，包括物理模型（如海洋流动模型、气候模型）、生物模型（如海洋生态系统模型）和化学模型（如污染扩散模型）。这些模型通常依赖数值模拟技术和方程求解方法，以实现对海洋环境的动态仿真与预测。近年来，海洋科学研究对多尺度建模的需求日益增加，即同时考虑从局部区域到全球尺度的海洋过程。这不仅要求模型具备更高的分辨率与精度，还必须能够适应不同空间尺度和时间尺度的数据输入。越来越多的海洋科学研究机构和政府部门建立了开放数据平台，提供免费的海洋数据集、模型和分析工具，促进了数据共享、合作研究，并推动了跨学科的合作与创新。

（四）科研合作与交流的促进

互联网技术的发展不仅为海洋科学研究生提供了丰富的学习资源和创新的教学模式，还极大地促进了他们之间的科研合作与学术交流。通过互联网平台，海洋科学研究生可以轻松跨越地域和学科界限，与国内外专家学者进行实时交流和合作。在科研合作方面，互联网平台为海洋科学研究生提供了便捷的沟通工具和协作平台。例如，通过视频会议、在线文档共享等工具，学生可以与导师、同学以及合作机构的科研人员进行实时沟通和协作，共同推进科研项目的进展。此外，一些专门的科研合作平台还提供了项目匹配、资金申请、成果展示等一站

中国知网 https://www.cnki.net

式服务，为海洋科学研究生的科研合作提供了有力支持。在学术交流方面，互联网平台也为海洋科学研究生提供了广阔的舞台。通过参加在线学术会议、研讨会等活动，学生可以了解最新的科研成果和学术动态，与国内外专家学者进行深入交流和探讨。同时，一些学术社区和论坛还为海洋科学研究生提供了发表文章、分享经验、交流心得的平台，促进了他们之间的学术交流和合作。

三、海洋科学研究生课程与培养中互联网应用的挑战

在海洋科学研究生课程中，互联网应用的普及和发展为教学和研究带来了诸多新的机遇与工具。然而，随着这一趋势的推进，也出现了一系列挑战。

（一）在线内容的更新滞后和匹配度低

海洋科学领域发展迅速，新技术和新发现层出不穷。然而，在线课程的内容更新和优化往往需要较长时间，特别是在涉及海洋科学前沿技术和研究时，可能会出现信息滞后现象，导致学生所学内容与当前的研究和技术应用间存在差距。此外，海洋科学课程内容复杂，涵盖理论知识和实验操作的结合，而现有的互联网应用多侧重于资源共享和线上学习，缺乏针对该学科特点的教学创新和技术支持。

（二）海洋科学特有的实践性与虚拟化限制

海洋科学课程具有显著的实践性特征，大量实验和观察活动必须在真实的海洋环境中进行，或依赖专门的海洋设备和技术。尽管虚拟实验和仿真工具能为学生提供一定程度的模拟体验，但它们无法完全替代实地的海洋观测和数据采集。此外，当前许多涉海学校及科研机构的互联网平台建设尚不完善，缺乏高效稳定的教学系统与虚拟仿真技术支持，导致在线学习体验不佳，从而影响了整体教学效果。

（三）在线数据安全性和实时性

在海洋科学研究中，数据收集与处理占据着核心地位，涵盖来自卫星遥感、传感器网络及实验室分析等多渠道的数据源。鉴于部分数据涉及敏感的地理信息、气候预测或国家安全等领域，因此对这些信息的安全保障和合规性提出了严格要求。此外，海洋科学研究还需要处理大量实时数据，例如海洋气候变化和海洋灾害等，此类数据具有快速变化和高度动态性的特点。为了确保全球海洋研究和应急响应的有效性，实时数据流的处理和分析不仅需要强大的计算资源和高效的数据传输能力，还必须保证数据的高度实时性和准确性。

（四）学习互动性与教师指导的缺失

在传统的面授课程中，学生享有明确的时间安排和教师的直接监督，而在互联网平台学习时，学生的自律性成为成功学习的关键因素。特别是在对学术要求较高的学科中，学生可能面临较大的学习压力，需要具备高度的自我管理能力。此外，尽管互联网课程提供了便捷的学习平台，但其缺乏面对面的互动和教师的即时指导，可能导致学生感到孤立，并在处理复杂理论和应用时因缺少及时答疑和讨论而影响学习效果。另外，海洋科学的教学团队主要由具有丰富传统教学经验的专家学者组成，他们在信息技术应用方面的知识和能力相对不足，难以高效地将互联网工具整合到课堂教学中。

四、海洋科学研究生课程与培养中互联网应用的改革策略

为了有效推动海洋科学教育的现代化，提升教育质量和效率，在海洋科学研究生课程中应采取一系列措施，以加强海洋科学研究生教育与互联网应用的有机结合。

（一）提高课程内容的实时更新与开放共享

海洋科学作为一门快速发展的学科，必须与时俱进，及时更新课程内容，并积极推动开放教育资源的共享。为此，应建立课程内容动态更新机制，确保最新的科研成果、技术进展和相关政策能够迅速融入教学体系。同时，加快开放教育资源平台的建设，提供免费或低成本的学习资料、实验工具及科研数据，促进全球范围内的海洋科学教育资源共享。此外，课程内容应采用模块化设计，使学生可以根据个人兴趣和需求灵活选择学习模块，深入探索海洋科学的前沿领域。涉海高校应加大投入，建设具有专业特色的在线教育平台，整合多学科知识，提供多样化的学习资源。该平台需要具备高效的互动功能，支持实时在线答疑、课后讨论及学术交流。

（二）构建混合式海洋教学模式

应将线上教学与传统线下教学有机结合，形成互补的混合式教学体系。对于海洋科学研究生课程而言，可以采用线上理论学习与线下实验、实地调查相结合的方式，充分利用线上平台提供的丰富学习资源，同时保留并强化传统教学中的实践环节。具体来说，可将课程内容划分为若干模块，每个模块包含在线学习部分和实验实习部分。研究生可以通过在线资源提前预习理论知识，在课堂上参与互动讨论、案例分析或实际操作，并通过实地实验和

中国知网 https://www.cnki.net

实习进一步巩固理论知识，掌握实验技能。

（三）增强互动性学习和加强师资培训

互联网应用应强化学生与课程内容、教师及同学之间的互动，通过灵活的学习路径设计满足学生的个性化需求，从而提升学习效果。引入智能学习系统，利用大数据分析和人工智能技术为每位学生提供定制化学习建议和规划。建立线上讨论平台、虚拟实验室和协作空间，促进学生与教师、同行间的实时互动和知识共享。开设在线辅导和答疑服务，借助视频会议和即时通信工具解决学生在学习过程中遇到的问题。设立专门的师资培训课程，帮助教师掌握互联网教育的核心技能和工具，学习如何设计互动性强且效果显著的在线课程。鼓励教师参与线上教育研究与实践，支持其开发创新性的海洋科学在线教学资源和课程。建立教学反馈机制，依据学生学习进度和满意度持续优化教学方法和内容。

（四）强化研究生自学能力和注重学科特性

提供丰富的自主学习资源，包括在线文献、案例分析和研究工具等，以支持学生在海洋科学各个领域的自主探索与深入理解。鼓励学生积极参与在线学术社区、科研项目及开源平台，以培养其创新精神和团队协作能力。建立在线导师制度，通过个性化指导帮助学生规划学术路径并提升自我管理能力。课程设计应充分考虑海洋科学的学科特点，结合互联网技术开发虚拟实验、在线模拟和数据分析工具，使学生能够在真实或模拟的海洋环境中进行实验操作、数据采集与分析。

（五）完善教学质量评估体系

在互联网教学模式下，如何确保教学质量和效果的有效评估是一个重要问题。为了解决这个问题，应建立完善的教学质量评估体系。首先，应制定科学的评估指标和方法，涵盖教学内容、教学方法、教学效果等多个方面。评估指标应具体、可量化，能够客观反映教学质量和效果。其次，应采用多种评估方式相结合的方法，如学生评价、同行评价、专家评价等。学生评价可以通过问卷调查、在线反馈等方式进行，了解学生对教学内容和方法的满意度和意见。同行评价和专家评价则可以通过教学观摩、教学研讨等方式进行，对教师的教学水平和能力进行全面评估。此外，还应加强对评估结果的反馈和应用。评估结果应及时反馈给教师和学生，帮助他们了解教学中存在的问题和不足，并及时改进。同时，评估结果也应作为教师晋升、奖励和评优的重要依据，激励教师不断提高教学质量和效果。

结语

在海洋强国战略的大背景下，国家对海洋科技人才的需求会越来越大，海洋科技人才则是国家实现建设海洋强国战略的重要支撑力量，对人才要求也会越来越高。互联网应用在海洋科学研究生课程和培养中的应用，能够突破传统教育模式的局限，推动教学内容和方法的改革。通过构建完善的互联网教学平台，加强师生互动，提高教师在线教学能力以及实施个性化评估，结合学科特点与信息技术，不仅能提高教学效率，优化学习体验，还能培养学生的创新思维和实践能力。未来，随着技术的不断发展，海洋科学研究生课程和教育将迎来更多创新和变革，推动海洋科学的可持续发展。

【参考文献】

[1] 高雪梅，于旭蓉，殷旭旺 . 需求 - 问题 - 路径：涉海类研究生协同培养模式优化探索与实践 [J]. 学位与研究生教育，2024(9):15-22.

[2] 刘航 . 涉海类研究生就业育人体系构建探究 [J]. 创新创业理论研究与实践，2022,5(20):92-94.

[3] 相雯，殷旭旺，王宏诗 . 提高海洋人才培养质量助力海洋强国建设 [J]. 中国多媒体与网络教学学报 (上旬刊)，2024,(2):118-121.

[4] 许红林，卢宇，向世林，等 . 海洋油气工程专业“虚实结合”生产实习教学改革与实践 [J]. 教育教学论坛，2024(50):118-121.

[5] 刘恩涛，成军，吕晓霞，等 . 校所协同的海洋科学硕士研究生联合培养模式探索与思考 [J]. 中国地质教育，2022,31(3):27-31.

[6] 易湘茜，邓家刚，高程海，等 . 海洋中药学线上线下混合式教学模式实践 [J]. 广西中医药大学学报，2023,26(4):93-95.

【基金项目】广西 2022 年度自治区级新工科研究与实践项目（项目编号：XGK2022002）。

【作者简介】姜伟（1989—），男，汉族，河北昌黎人，博士研究生，教授，研究方向：海洋地质学；梁甲元（1986—），男，汉族，广西桂平人，博士研究生，副教授，研究方向：海洋生物学；黄荣永（1985—），男，壮族，广西南宁人，博士研究生，副教授，研究方向：海洋遥感

【通讯作者】余克服（1969—），男，汉族，湖北公安人，博士研究生，教授，研究方向：南海珊瑚礁地质、生态与环境

中国知网 https://www.cnki.net

文章编号:0253-9985(2025)03-1006-13 doi:10.11743/ogg20250321

海相碳酸盐硼同位素反演古海水pH值模型及其应用

王 瑞[1,2,3],刘春彤[1,2,3],吴松烨[1,2,3],花 绘[1,2,3]
(1.广西大学 海洋学院,广西 南宁 530004;2.广西大学 珊瑚礁研究中心 广西 南宁 530004;3.广西南海珊瑚礁研究重点实验室,广西 南宁 530004)

摘要:硼元素(B)在自然界中广泛分布,其稳定同位素(^{10}B和^{11}B)的分馏特性使其成为古海洋和古气候重建的重要参数。依据硼同位素值($\delta^{11}B$)与海水pH值之间的敏感关系,科学家们建立了$\delta^{11}B$-古海水pH值模型,利用海相碳酸盐矿物中的硼同位素值来反演古海水的pH值,进而分析大气中CO_2浓度的变化,但模型的准确性仍面临挑战。基于海洋中硼循环和硼同位素测定方法分析,研究了$\delta^{11}B$-古海水pH值模型的构建机理及应用潜力。研究结果表明:影响该模型准确性的主要因素是生命效应产生硼偏差,硼同位素间分馏系数不准确,海水中硼同位素在$B(OH)_3$和$B(OH)_4^-$两种存在形式之间的交换过程不清楚,不能完全模拟自然环境中碳酸盐沉淀过程中硼同位素的分馏系数。为提高模型的准确性,应与B/Ca元素含量比值等其他指标结合使用,寻找受生命效应影响较小的碳酸盐样品;同时,要努力提高硼同位素分馏系数的计算精度,建立更科学的生命效应校正经验方法,使硼同位素在古海洋气候重建中的应用更加科学、发挥更大的作用。

关键词:古环境;古气候;古海水;pH值;硼同位素;海相碳酸盐
中图分类号:TE135 **文献标识码**:A

Proxy of paleo-seawater pH reconstruction based on boron isotopes of marine carbonates and its applications

WANG Rui, LIU Chuntong, WU Songye, HUA Hui

(1. *School of Marine Sciences, Guangxi University, Nanning, Guangxi* 530004, *China*; 2. *Coral Reef Research Center of China, Guangxi University, Nanning, Guangxi* 530004, *China*; 3. *Guangxi Laboratory on the Study of Coral Reefs in the South China Sea, Nanning, Guangxi* 530004, *China*)

Abstract: Boron (B) is widely distributed in nature. The fractionation of its stable isotopes ^{10}B and ^{11}B establishes boron as a significant tool for reconstructing paleoceanographic and paleoclimate conditions. The sensitivity of the $\delta^{11}B$ values to seawater pH makes it possible to establish a $\delta^{11}B$-paleo-seawater pH proxy. This proxy enables the inversion of paleo-seawater pH using the boron isotope values of marine carbonate minerals, which in turn facilitates the analysis of the atmospheric CO_2 concentration changes. Although the $\delta^{11}B$-paleo-seawater pH proxy has great theoretical potential, its accuracy remains a challenge. By analyzing the boron cycling in the ocean and methods for boron isotope determination, we investigate the underlying mechanisms and application potential of the $\delta^{11}B$-paleo-seawater pH proxy. The results indicate that major factors affecting the proxy accuracy include boron deviation caused by biological effects and inaccuracies in the fractionation coefficient between boron isotopes, insufficient understanding of the exchange processes between $B(OH)_3$ and $B(OH)_4^-$ in the seawater, and the inability of lab simulations to fully replicate the fractionation of boron isotopes during carbonate precipitation in the natural environment. To enhance the accuracy of the proxy, it is recommended to incorporate additional proxies such as the B/Ca ratio and to select carbonate samples less affected by biological effects. Furthermore, it is necessary to enhance the precision of boron isotope fractionation coefficient calculations, establishing a more scientific empirical method for correcting the biological effects. These advancements will contribute to more scientific and broader applications of boron isotopes in reconstructing paleoceanographic and

收稿日期:2024-09-29;**修回日期**:2024-12-26。
第一作者简介:王瑞(1983—),男,博士、副教授,碳酸盐岩沉积学。**E-mail**: wrzfl@gxu.edu.cn。
基金项目:国家自然科学基金项目(41962010,42030502,42090041);广西省自然科学基金项目(2021GXNSFAA220126)。

中国知网 https://www.cnki.net

paleoclimate conditions.

Key words: paleo-environment, paleoclimate, paleo-seawater, pH, boron isotope, marine carbonate

引用格式：王瑞，刘春彤，吴松烨，等. 海相碳酸盐硼同位素反演古海水 pH 值模型及其应用[J]. 石油与天然气地质，2025，46(3)：1006-1018. DOI：10. 11743/ogg20250321.

WANG Rui, LIU Chuntong, WU Songye, et al. Proxy of paleo-seawater pH reconstruction based on boron isotopes of marine carbonates and its applications[J]. Oil & Gas Geology, 2025, 46(3): 1006-1018. DOI: 10. 11743/ogg20250321.

古海洋特别是地球早期海水的 pH 值演化是科学家长期关注的一个重大科学问题。海水 pH 值在地质历史研究中扮演着至关重要的角色，其数值变化（特别是海洋酸化）直接影响着海洋生物碳酸盐的生长发育，进而影响海洋生态系统的平衡[1]。目前已知的反演古水体 pH 值信息的方法主要包括硼同位素[2-5]、锂同位素[6-7]、硅藻组合法[8-9]、brGDGTs（分支甘油二烷基甘油四醚）[10]和 3-羧基脂肪酸法[11]等。锂同位素值（δ^7Li）与海水 pH 值间存在负相关性[6-7]，但 δ^7Li-pH 值关系的研究仍处于起步阶段。硅藻组合法是根据沉积物中保存的硅藻的种类和丰度来重建古水体的 pH 值，在湖泊研究中有较多成功的应用[12]。brGDGTs 法是基于沉积物中 brGDGTs 的环化指数或异构化程度重建古水体 pH 值，而 3-羟基脂肪酸法是基于沉积物中 3-羟基脂肪酸的支链比反演古水体 pH 值[12]，但利用这两种方法反演的古海水 pH 值均存在较大的不确定性。在过去 20 年中，基于硼同位素与海水 pH 值之间的敏感关系而建立的硼同位素-海水 pH 值模型，使得硼同位素成为重建古海水 pH 值的有力工具，特别是利用钙质生物如珊瑚和有孔虫来推断古海水的 pH 值[2-5, 13]。

硼（B）的原子序数为 5，在化学元素周期表中属于轻量元素。硼的稳定同位素包括 ^{10}B 和 ^{11}B，其同位素组分丰度分别为 80. 1 %和 19. 9 %[14]。硼元素具有出色的溶解性，常见富集各类岩石及水相环境中，在海水中拥有长达约 16 Ma 的滞留期[15]，这一特性赋予了硼元素较好记录地质时间尺度原始沉积环境信息的能力。硼在水-岩反应过程中往往会发生显著的同位素分馏，从而导致水或岩石中的 ^{11}B/^{10}B 同位素含量比值变化幅度极大[16-17]。目前记载的数据显示自然界中不同物质的硼同位素值（δ^{11}B）在-70 ‰ ~ 75 ‰均有分布[18-19]，常见的环境流体及物质赋存的硼同位素值范围见图 1。因此，硼同位素的分馏特性可应用于判别沉积环境、反演洋壳构造运动过程、示踪流体来源和还原地球化学过程等，在过去的 10 余年大量应用于地幔地质学[20-24]、矿床地质学[25-28]和古海洋学[29-33]等领域，引起了学者们的广泛关注。

近年来全球气候变暖，温室效应愈演愈烈，其中关键的大气 CO_2 浓度与海水 pH 值联系密切。因此，硼同位素反演古海水 pH 值及大气 CO_2 浓度方面备受关注[31, 33-38]。对于硼同位素-古海水 pH 值模型而言，海水中的硼分馏过程、硼同位素分馏系数和硼同位素测定方法等因素均可能影响重建古海水 pH 值的结果和精确度。此外，鉴于硼同位素代用指标在碳酸盐尤其是生物碳酸盐样品的实际测定中存在生命效应（vital effect）的影响，基于硼同位素重建古海洋古气候的方法仍需进一步探索。因此，本文基于海洋中硼循环和硼同位素测定方法的背景分析，旨在梳理硼同位素-古海水 pH 值模型的构建机理及应用潜力，为利用硼同位素开展古海学和古气候学研究提供借鉴。

1　硼循环途径与模式

1. 1　输入方式

硼的输入与输出对于海洋中硼浓度和同位素比例有重要影响。目前认为海洋中硼的来源主要有 3 种：河流输入[40-43]、海底热液活动的释放和俯冲带增生楔的排出液[44-46]（图 2）。

地球表面岩石和土壤中的硼元素在自然风化过程中逐渐释放。物理风化如温差引起的岩石破碎，化学风化如溶解作用，共同促使硼溶解进入地表和地下水系统[47]。地下水与地表水的交互作用进一步促进了硼的迁移，使其以溶解态形式——包括自由离子和与有机物结合的复合物——被河流携带，最终汇入海洋，成为海洋硼循环的关键环节。据统计，陆地每年通过河流输送到海洋中的硼通量为 38.0×10^{10} g/a，δ^{11}B 为 10. 0 ‰[40]。然而，人类活动，特别是含硼洗涤剂的使用，对这一自然循环产生了影响。据估算，含硼洗涤产品的使用导致约 2.5×10^{10} g/a 的硼排放，占全球自然硼循环通量的近 7. 0 %[40, 43]。

在大洋中脊和其他洋壳活动区域，洋壳中的断裂为富含矿物质的热液流体提供了上升通道。这些流体携带着地幔中的硼，当它们与冷海水接触并混合时，硼

中国知网　https://www.cnki.net

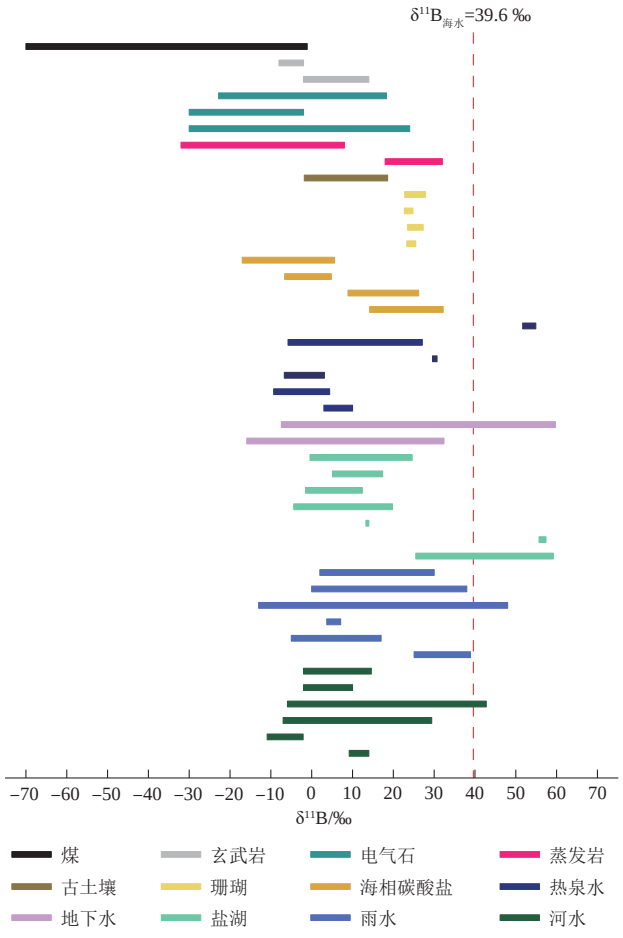


图1 自然界中的硼同位素组成与分布(修改自文献[39])

Fig. 1 Distribution of boron isotopic composition in nature (modified after reference [39])

元素便被释放到海洋环境中。这一过程对海洋硼循环贡献显著,输入硼通量平均为4.0×10^{10} g/a,而δ^{11}B则在−1.5‰~14.5‰之间波动[48-50],这一通量和同位素值受到3个关键因素的制约:硼从地幔转移到新的洋壳中的速率、洋壳生成速度和洋壳中的硼浓度值[48-51]。

与海底热液活动不同,增生楔排出液主要发生在板块汇聚带,尤其是俯冲带。在这一地质过程中,海洋板块向大陆板块或另一个海洋板块下方俯冲,进入地幔。随着板块的俯冲,板块表面的沉积物和部分地壳物质在压力和摩擦力共同作用下被加热并部分熔融,形成富含硼和其他化学物质的流体。这些流体通过地壳裂隙上升,最终排入海洋,为海洋硼循环贡献了新的硼源。这个过程输入海洋的平均硼通量和δ^{11}B分别为2.0×10^{10} g/a和20.0‰~30.0‰[48, 51-52]。这表明,虽然与河流输入相比,增生楔排出液对海洋硼的贡献较小,但它在海洋硼循环中扮演着独特而重要的角色。

总体而言,河流是硼元素进入海洋的主要输送者,其贡献显著高于海底热液活动和增生楔排出液。尽管后两者的贡献相对较小,但它们与河流输入共同构成了海洋硼循环的输送机制。

1.2 输出方式

海洋中的硼元素通过多种途径汇聚,包括洋壳低温蚀变[48, 53]、碎屑沉积物吸附[44, 54]和碳酸盐共沉淀[2](图2)。

洋壳低温蚀变是一种在低温条件(< 150 ℃)下发生的海水与洋壳相互作用的化学反应。在洋中脊和洋壳的形成过程中,海水通过裂缝和孔隙渗透到新形成的洋壳中,并与洋壳基岩接触,海水中的溶解硼与洋壳矿物(洋中脊玄武岩、蛇纹石和变质岩等)发生反应,随后被吸收并进入洋壳中[23, 48, 55]。在此过程中,进入洋壳的平均硼通量和δ^{11}B分别为27.0×10^{10} g/a和4.0‰[48],其主要受控于洋壳的矿物组成、海水的化学性质、温度和pH值,以及生物活动的影响[48, 53]。

碎屑沉积物吸附主要是沉积物颗粒通过物理或化学作用吸附硼元素,从而将硼从海水中移除。这些沉积物可能来源于陆地风化产物、海洋生物残骸或洋壳蚀变产物,因此沉积物的类型和粒径、海水中硼的浓度以及水动力学条件等因素均有可能影响沉积物对硼的吸附效率。沉积物吸附的平均硼通量和δ^{11}B值分别为13.0×10^{10} g/a和14.0‰~16.0‰[44, 54]。

碳酸盐共沉淀是在碳酸盐矿物(如方解石和文石)的形成过程中,硼同位素(^{10}B和^{11}B)与碳酸盐矿物共同沉淀。这一过程沉淀的平均硼通量约为6.0×10^{10} g/a,δ^{11}B平均值范围为15.0‰~25.0‰,主要受海水的碳酸盐饱和度、生物活动、pH值和温度等因素的控制[2]。

以上3种输出方式存在一定的物理化学条件(温度和pH值等)差异,并主导各自过程中硼的分馏,表现出不同的δ^{11}B值特征。整体而言,洋壳低温蚀变是硼元素的主要输出方式,但碎屑沉积物吸附和碳酸盐共沉淀对硼同位素分馏的影响更明显。

海洋中硼的输入和输出过程相互交织,共同塑造了海洋硼循环模式和全球硼同位素分布特征。现代海水中的硼浓度约为4.5×10^{-6},δ^{11}B平均约为39.6‰,不同海域间的硼浓度和同位素比值差异较小,δ^{11}B分布范围为37.7‰~40.4‰[56]。此外,大洋蚀变玄武岩、海底沉积物以及陆壳岩石的δ^{11}B也与它们对应的流体表现出高度的一致性[57],并且呈现出一定的规律性差异:大洋蚀变玄武岩的δ^{11}B最高,其次是海底沉积岩,而陆壳岩石的δ^{11}B相对较低[23, 58-59]。这种差异性反映了不同地质环境和物质来源对硼同位素分馏的影响。

中国知网 https://www.cnki.net

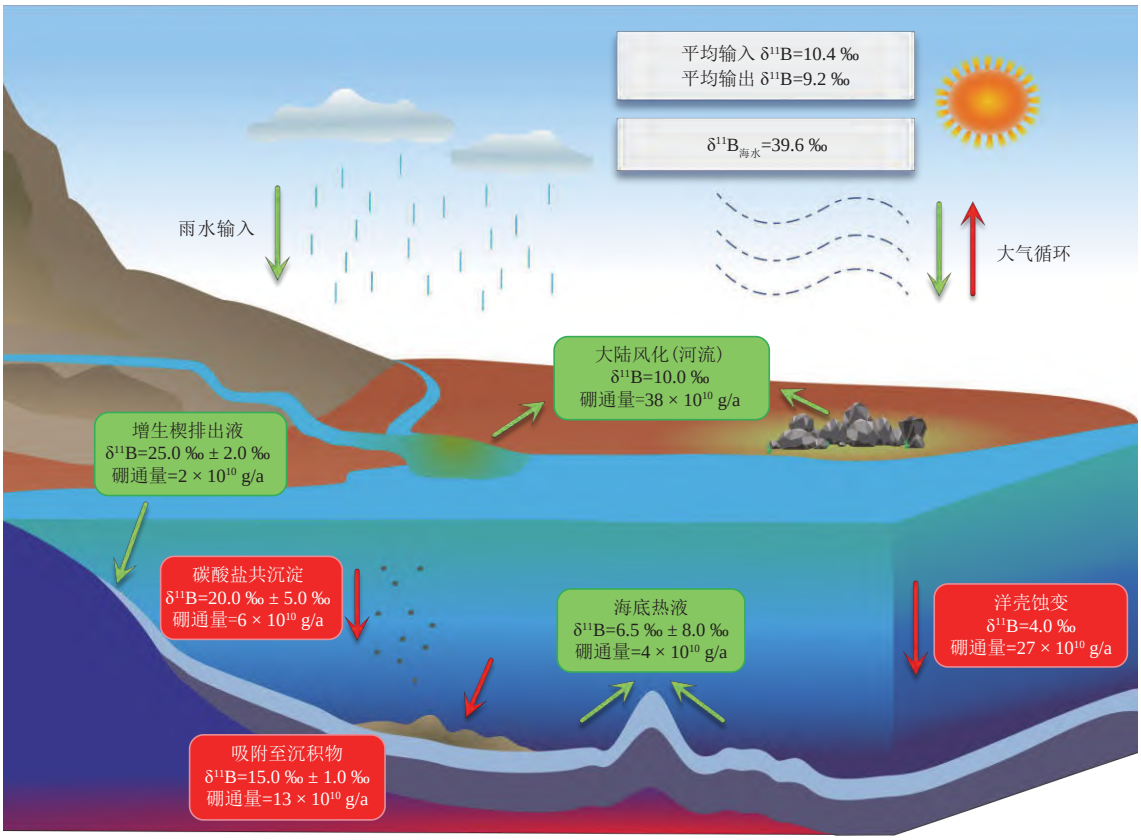


图 2　海洋中的硼循环（输入与输出）模式（修改自文献[37, 40]）

Fig. 2　Boron cycling patterns (inputs and outputs) in oceans (modified after references [37, 40])

2　硼同位素测定方法

硼同位素的测定可以追溯到20世纪60年代初期。然而，由于硼在自然中的浓度极低，早期的测定技术精度不足，难以满足高精度测定的需求，这成为了硼同位素研究发展的主要瓶颈。当时，硼含量的技术仅适用于盐湖等硼自然丰度高的环境[60-62]。随着20余年的技术发展和学者们的不懈努力，硼同位素高精度测量方法逐渐建立并完善，包括样品的消解、分离提纯和质谱分析等环节的改进[63-71]。这些技术的进步使得硼同位素分析得以广泛应用于地质研究，并催生了不同的科研群体和研究方向（如星云形成过程、壳-幔演化和核工业用富集硼等），为硼元素的广泛应用打下了坚实的基础[58, 72-73]。目前在国际上硼同位素测定普遍使用美国国家标准技术研究所生产的 NIST951（$^{11}B/^{10}B$ 的标准值为 4.046 9 ± 0.000 2）。在实际应用中，较为常见的硼同位素测定方法主要分为两大类：①溶液整体分析法，包括热电离质谱法（TIMS），电感耦合等离子体质谱法（ICP-MS）和多接收电感耦合等离子体质谱法（MC-ICP-MS）；②微区原位分析法，包括二次离子质谱法（SIMS）和激光剥蚀多接收电感耦合等离子体质谱法（LA-MC-ICP-MS）[71, 74]。这些方法的应用，为地质学研究提供了强有力的工具，推动了硼同位素应用的深入发展。

热电离质谱测定（TIMS）分为正热电离质谱（P-TIMS）和负热电离质谱（N-TIMS）。其中，P-TIMS是最早对高精度地质样品进行硼同位素分析的方法[75]，当时检测离子为 $Na_2BO_2^+$，相对质量差大，测定精度不高，误差约为±2 ‰[76]。然而现在P-TIMS通常利用 $Cs_2BO_2^+$ 作为发射离子，其相对质量足够大，可避免因硼同位素在测定过程中产生分馏而影响测定精度，最低可检测10 ng级硼含量的样品[77]，误差为±（0.1 ‰ ~ 0.4 ‰），被认为是目前硼同位素分析准确度最高的方法[74]。与之相比，N-TIMS的测定精度稍低，为0.4 ‰ ~ 0.7 ‰，但此方法的灵敏度极高，可分析硼含量为1 ng甚至到150 pg的样品[78-81]，并且对于海水、高盐卤水、地下水和碳酸盐等物质的前处理要求不高，无需对样品中的硼进行化学分离或浓缩即可进行分析[3]。但是N-TIMS检测的目标离子是 BO_2^-，由于不同的硼同位素对于测定离子的质量差较大，在测定过程中会发生分馏效应，由此影响精度[82]，因此其主要适用于量少且

中国知网　https://www.cnki.net

硼同位素分离比例大的样品。

电感耦合等离子体质谱法(ICP-MS)的优点主要为成本低、用时短,但测定得到的数据精度低,难以应用到精确分析研究中。ICP-MS的优点使其具有良好的竞争优势,因此许多学者尝试改进以提高其测定精度,多接收电感耦合等离子体质谱法(MC-ICP-MS)的出现提供了更好的解决办法[69],该技术已经逐渐成为硼同位素测试的主流方法。然而,硼的记忆效应一直是困扰MC-ICP-MS高精度测定$\delta^{11}B$的难题[83-84]。硼的记忆效应是指在仪器测试阶段样品在进样系统存在硼残留的现象,此效应将影响下一个样品的硼数据采集。目前消除硼的记忆效应的较优方法[85]是采用浓度0.6 mg/g的NaF溶液(浓度1 % HNO_3)作为洗液消除上一个样品硼同位素的残留,其优点在于清洗时间短、效率高、对测试结果影响小,同时操作简便、耗材少等,且能够显著提高MC-ICP-MS测定硼同位素的效率、稳定性和准确度。

二次离子质谱法(SIMS)适合直接分析固体样品,具有低前处理需求、高空间分辨率和稳定性,能分析不同位置和深度的同位素分布,目前广泛应用于珊瑚、双壳类、有孔虫和硼酸盐玻璃等硼同位素分析[86-89]。

激光剥蚀多接收电感耦合等离子体质谱法(LA-MC-ICP-MS)是一种微区原位高精度同位素比值分析测试技术,其不仅具有高空间分辨率、快速、实时、低样品消耗量和较少的水相关质谱干扰等特点,并且受到的记忆效应影响相对较低,被广泛应用于地质、环境科学、生物学、材料科学和考古学等领域[71]。需要注意的是,由于^{10}B和^{11}B之间存在10 %的质量差异,在激光剥蚀、传输和离子化过程中会产生同位素分馏,产生较大的质量歧视效应(mass discrimination)[90],影响测试结果的准确性,因此需采用样品标样交叉校正法(standard-sample bracketing,SSB)方法校正质量歧视和信号漂移,即在样品前后均插入标准样品进行测试,通过标准样品的质量歧视平均值对结果进行校正,并且需要精确控制仪器参数和校正方法等多种因素以确保数据的精确度和准确度。

3 硼同位素-古海水pH值模型

在古海洋古气候研究领域,通过精确测量海洋生物碳酸盐中的硼同位素比例,利用$\delta^{11}B$-古海水pH模型,能够重建古海水的pH值,进而可以推测大气CO_2含量和古气候变化。尽管一些研究发现海水硼同位素组成、硼酸电离常数和硼同位素分馏系数等不确定性因素会对$\delta^{11}B$-古海水pH值模型产生影响[3, 34, 91-94],但是近年来相关研究显示了该模型在解析古海洋古气候变化中的潜力。

生物碳酸盐类,如有孔虫、珊瑚、腕足类和腹足纲等,构成了海相环境中硼的主要储存库。硼进入这些碳酸盐结构时,海水的pH值对硼的同位素分馏具有显著影响。在自然水体中,硼通常以$B(OH)_3$和$B(OH)_4^-$两种溶解态形式存在。从微观角度看,$B(OH)_3$呈平面三角形结构,而$B(OH)_4^-$呈四面体结构。由于硼的轻质量和强溶解性,自然中的硼通常与氧结合,形成B—O键。四面体[$B(OH)_4^-$]中的B—O键键长为0.137 nm,C—O键的键长0.128 nm。这种相似性使得$B(OH)_4^-$能够以取代CO_3^{2-}的形式进入到碳酸盐晶格中[63, 95]。流体中的$B(OH)_3$和$B(OH)_4^-$通常存在一个动态交换平衡:

$$B(OH)_3 + H_2O \rightleftharpoons B(OH)_4^- + H^+ \quad (1)$$

硼的两种溶解态之间的转换并未发生价态变化,而发生这个交换反应的动力来源于轻、重同位素之间的分馏:

$$^{10}B(OH)_3 + {}^{11}B(OH)_4^- \rightleftharpoons {}^{11}B(OH)_3 + {}^{10}B(OH)_4^- \quad (2)$$

从反应式(2)中可以看出两种同位素在$B(OH)_4^-$和$B(OH)_3$中均有赋存,但两者主要富集的B同位素不同,其主要受^{10}B与^{11}B之间的分馏系数α_{4-3}和环境体系中的$^{11}B/^{10}B$同位素含量比值及反应平衡常数$^{11}_{10}K$的影响:

$$\alpha_{4-3} = \frac{1}{^{11}_{10}K} = \frac{^{11}B/{}^{10}B_{B(OH)_4^-}}{^{11}B/{}^{10}B_{B(OH)_3}} = \frac{R_{B(OH)_4^-}}{R_{B(OH)_3}} \quad (3)$$

式中:$^{11}B/{}^{10}B_{B(OH)_4^-}$及$^{11}B/{}^{10}B_{B(OH)_3}$分别表示$B(OH)_4^-$与$B(OH)_3$中两种同位素的含量比值,无量纲;$R$表示硼在某种相态中的$^{11}B/^{10}B$同位素含量比值,无量纲。

Oi等[96]通过研究多硼酸盐之间同位素效应,采用分子轨道理论并结合振动分析计算了单硼酸和多硼酸盐之间的同位素交换反应的平衡常数,得到多硼酸盐中硼同位素交换反应[公式(3)]的分馏系数α_{4-3}为1.019 4。如果流体体系中两种硼同位素交换反应的平衡常数大于1,说明^{11}B相对富集于$B(OH)_3$中,而^{10}B则相对富集于四面体$B(OH)_4^-$中。

在海水流体体系中,海水的pH值主要由碳酸盐系统进行宏观调控,大气中的CO_2通过海气交换被吸收到海水中,并且溶解后与水形成碳酸(H_2CO_3)。碳酸极易分解电离成H^+,HCO_3^-和CO_3^{2-},分离出的HCO_3^-仍可继续电离为CO_3^{2-}和H^+,也可与海水中的Ca^{2+}通过沉淀作用在海水体系沉积形成碳酸盐矿物(图3)。另外,海洋中生物的光合作用和呼吸作用会利用溶解态的CO_2,形成有机物CH_2O,并且通过代谢作用可再次回到海水中。

中国知网 https://www.cnki.net

碳酸盐系统帮助海水 pH 值维持在一定的范围内（通常在 7.9 ~ 8.4）[97]，以保持海水酸碱度的平衡（图 3）。

在海水-大气向海作用过程中，如果海水中溶解的 CO_2 增加，电离产生的 H^+ 随之增加，海水偏酸性，此时反应式（1）的平衡向左移动，海水中硼多以 $B(OH)_3$ 的形式存在；当溶解 CO_2 减少，海水 pH 值较高时，反应式（1）的平衡向右移动，此时硼主要以 $B(OH)_4^-$ 的形式赋存于流体体系中（图 4）。因此，对于 pH 值较高的海水（偏碱性），$\delta^{11}B$ 较低，而对于 pH 值较低的海水（偏酸性）则存在较高的 $\delta^{11}B$。

海水 pH 值对于两种溶解态硼相对含量的控制，主要是基于反应式（1）中的电离平衡，其中转换反应的反应平衡常数 pK_B^* 随海水 pH 值变化而变化[公式（4）]。根据 Hershy 等[98]的计算，当温度为 25 ℃时，$pK_B^* = 8.830$，随着温度升高，pK_B^* 增加，同时 $B(OH)_4^-$ 相对于 $B(OH)_3$ 的比例下降，此时流体中溶解的 $B(OH)_3$ 逐渐成为体系中硼的主导赋存形式。

$$pH = pK_B^* - \lg\frac{B(OH)_3}{B(OH)_4^-} \tag{4}$$

在已有研究中，关于利用硼同位素还原古海水 pH 值的理论关系式[3]如下：

$$pH = pK_B^* - \lg\left[\frac{\delta^{11}B_{海水} - \delta^{11}B_{样品}}{\alpha^{-1}\delta^{11}B_{样品} - \delta^{11}B_{海水} + 10^3(\alpha^{-1} - 1)}\right] \tag{5}$$

式中：$\delta^{11}B_{海水}$ 为海水中的 $B(OH)_3$ 和 $B(OH)_4^-$ 相对于国际标准 NIST951 的硼同位素值，$\delta^{11}B_{样品}$ 为两相溶解态

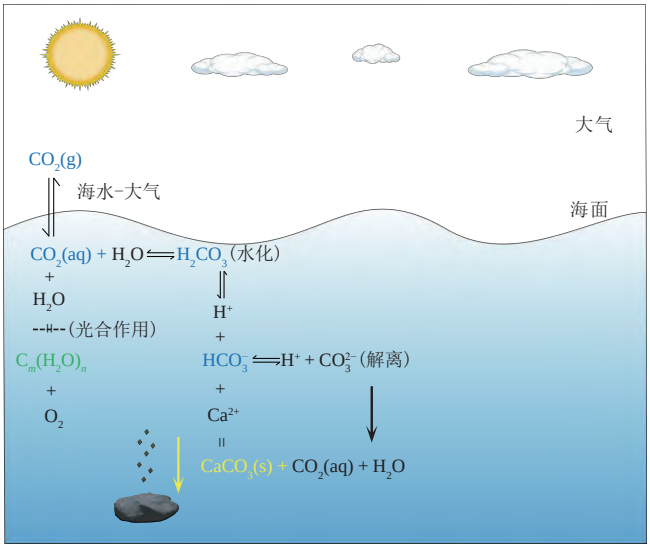


图 3　碳酸盐系统调控海水 pH 值示意图

Fig. 3　Schematic diagram showing the regulation of seawater pH by the carbonate system

g. 气态；aq. 水溶液；s. 固态

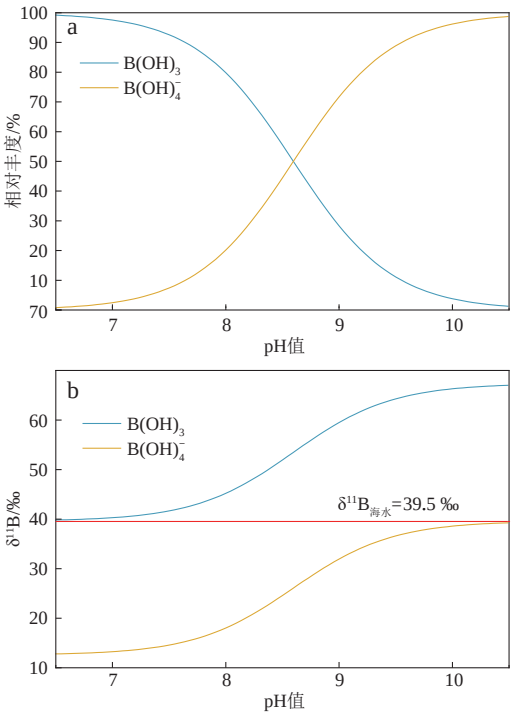


图 4　硼在海水中的存在形式和同位素组成与海水 pH 值的关系

Fig. 4　Relationships of boron occurrence forms and isotopic composition with seawater pH

a. 海水中硼的 2 种存在形式的相对丰度与 pH 值的关系；b. 硼的 2 种主导形式在不同 pH 值溶液中对应的 $\delta^{11}B$[3]

[计算使用反应平衡常数 $pK_B^* = 8.597$；分馏系数 $\alpha_{4-3} = 0.974$。]

硼共存的海水中 $B(OH)_4^-$ 相对于 NIST951 的值。但此模型关系式成立的前提是基于如下假设：硼主要以 $B(OH)_4^-$ 形式进入生物碳酸盐矿物，且几乎不发生同位素分馏[2, 3, 99]。此时，海相生物碳酸盐中的硼同位素值 $\delta^{11}B_c$ 即为共存海水中 $B(OH)_4^-$ 相对于国际标准 NIST951 的硼同位素值。在 $\delta^{11}B$-古海水 pH 值模型研究的起步阶段，有实验通过调制 pH = 8（与现代海水 pH 值相近）的溶液合成碳酸盐矿物（文石和方解石），对其进行硼同位素测定发现，合成得到的碳酸盐矿物的 $\delta^{11}B_c$ 几乎相同，并且与 $\delta^{11}B_{B(OH)_4^-}$ 的计算曲线吻合，据此将原理论式[公式（5）]中的 $\delta^{11}B_{样品}$ 替换成了 $\delta^{11}B_{B(OH)_4^-}$：

$$pH = pK_B^* - \lg\left[\frac{\delta^{11}B_{海水} - \delta^{11}B_{B(OH)_4^-}}{\alpha^{-1}\delta^{11}B_{B(OH)_4^-} - \delta^{11}B_{海水} + 10^3(\alpha^{-1} - 1)}\right] \tag{6}$$

从公式（5）中不难看出，分馏系数 α_{4-3}，$\delta^{11}B_{海水}$ 和 pK_B^* 这 3 个数值的可靠性对于 pH 理论计算值的精确程度有较大影响。其中，精确确定分馏系数 α_{4-3} 对于利用硼同位素值反演古海水 pH 值至关重要。

Kakihana 等[100]在 1977 年首次利用配分函数和光

中国知网　https://www.cnki.net

谱数据进行计算，得到α_{4-3}为0.981，这一结果在随后的一段时间内被广泛接受并应用。随着研究的深入，Kakihana的计算被再次验算，虽然得到的数值不变，但该方法被指出其计算结果对于实验所设定的$B(OH)_3$及$B(OH)_4^-$的分子振动频率和分子间作用力的理论计算值存在极高的敏感性，无法模拟自然环境中的分子行为，结果缺乏可靠性[101]。许多学者使用其他的计算测定方法（如分子轨道理论、同位素交换平衡理论等）得到α_{4-3}范围主要为0.972～0.975[102-104]，均低于此前广泛使用的0.981（表1）。刘羿等[103]对前人的方法（气相分子法和自洽反应场法）进行了全面对比与评价。其中，气相分子法假设$B(OH)_3$或$B(OH)_4^-$孤立于气相环境，忽略了实际环境（如溶剂或其他环境因素）对于分子振动的影响，难以准确反映实际溶液中的分子行为。自洽反应场法（self-consistent reaction field，简称SCRF）是指假设一个极性溶质分子位于极性溶剂中，极性溶剂会产生电场，这个电场则被称之为反应场；这个方法虽然考虑了溶液环境，但是该方法假设的极性溶剂拥有均匀的介电常数，可能无法充分考虑到溶剂分子与溶质分子之间的复杂相互作用，尤其是水溶液中重要的氢键效应。刘羿等最终选择了可能更贴近实际环境的“水滴法”（water-droplet method），即假设大量水分子环绕着$B(OH)_4^-$或$B(OH)_3$的排列模型，水分子之间形成氢键，这与真实水滴环状结构及氢键网络结构十分相似，可更为准确地模拟分子在自然环境流体中的行为。在计算过程中，他们发现之前关于$B(OH)_4^-$与硼酸盐中的BO_4键相同的假设有误。实际上，硼酸盐中的四面配位体比$B(OH)_4^-$轻，导致硼酸盐中的B同位素值显著较小；在这个模型中，α_{4-3}和pK_B^*对于曲线的预测有显著影响。基于这一发现，他们计算出新的分馏系数为0.974，并建立了基于$B(OH)_4^-$的pH值与$\delta^{11}B$的新理论曲线。肖军等[39]通过对北海涠洲岛、海南三亚和灯楼3个区域的活体珊瑚进行研究，计算得到α_{4-3}平均值为0.978 8。该值刚好落在$B(OH)_4^-$和$B(OH)_3$两者的计算曲线之间，表明在$B(OH)_4^-$为优先掺入形式的情况下，硼以$B(OH)_4^-$和$B(OH)_3$两种形式同时进入了珊瑚碳酸盐骨骼。由于活体样品的引入，使得该数值更适用于生物碳酸盐样品pH值的重建应用。

pK_B^*作为硼同位素重建古海水pH值理论式中的关键因子之一，已有大量相关研究对其进行实验并计算数值[105]。Hershey等[98]研究25 ℃时不同溶液介质中的$B(OH)_3$，得到$B(OH)_3$的平衡常数pK_B^*为8.830，这一数值得到了Hemming和Hanson的引用[3]。随后，Dickson在不同的温度和盐度条件下开展了计算实验[106]，得到了pK_B^*为8.597，并指出pK_B^*的大小随温度、盐度增高而减少。Roy等[107]在35‰盐度条件下对0～55 ℃的海水进行$B(OH)_3$的平衡常数研究，其结果与Dickson的结果具有高度的一致性。因此，截止目前，领域内普遍认可并广泛使用的pK_B^*为8.597[3]。

综上，目前大量研究通过各种方法对模型的相关参数（pK_B^*和α_{4-3}等）展开了广泛的讨论，但不同参数数值在实例应用上仍存在一定的争议，主要原因在于不同参数数值在部分研究对象的具体应用过程中仍存在一定的偏差，例如生物碳酸盐的生命效应使其体内硼同位素值与环境值间存在差异，对模型重建结果的准确度和可靠性带来了挑战。因此，未来关于$\delta^{11}B$重建古海水pH值的模型系数仍需要根据特定的物种建立经验公式对结果进行校正。

4 利用硼同位素反演古海水pH值

目前，利用硼同位素值反演古海水pH值的研究对象主要集中于生物碳酸盐，尤其是珊瑚和有孔虫。珊瑚（文石质）作为硼同位素分析样品，其重建结果具有高时间分辨率的特点，可提供短时间内的海水pH变化信息；而有孔虫（方解石质）载体则适用于构建较长时间序列的海水pH信息。

利用珊瑚反演古海水pH值主要集中于全新世时期（图5）。Wei等[29]和Pelejero等[108]利用澳大利亚大堡礁附近的珊瑚骨骼$\delta^{11}B$，重建了近300年的海水pH值演变过程，揭示了18世纪以来海洋酸化的趋势，特别是$\delta^{11}B$与碳同位素值（$\delta^{13}C$）之间的正相关性以及二者的共同下降趋势，表明燃烧化石燃料等人类活动可能导致

表1 计算硼同位素分馏系数的几种方法

Table 1 Summary of methods for calculating the boron isotope fractionation coefficient

方法	分馏系数（α_{4-3}）	特点	参考文献
分子轨道理论法	0.965 0～0.980 0	从微观角度深入理解，精确度高，但计算量大，成本高，对于参数的选择依赖性强	[96]
水滴法	0.974 0	可准确模拟分子的不同溶液环境下的实际情况，但计算成本高，且可能不适用于复杂环境体系	[103]
分光光度法	0.972 0	可直接测量，适合实际水样的分析计算，但对实验条件精确度要求高	[104]
活体珊瑚测定法	0.978 8	对自然样品的硼同位素理解深入，但成本高，样品需求量大，且易受样品的选择和处理过程影响	[39]

中国知网 https://www.cnki.net

大气 CO_2 浓度急剧上升，氧同位素值（$\delta^{18}O$）略微下降以及 Mg/Ca 元素含量比值（作为温度敏感性指标）稳步上升，进一步展示了与全球变暖趋势的一致性。他们的计算过程均选用了 pK_B^*= 8. 60；对于分馏系数，Pelejero 选用 α_{4-3} = 0. 981，而 Wei 则对比使用了 3 个不同系数值（α_{4-3} = 0. 974，0. 981 和 0. 980），前两者的反演结果与现代海水的平均 pH 值范围不符，因此 Wei 选用了 α_{4-3} = 0. 980，该结果更符合现代海水的酸碱情况，但 Wei 也指出，尽管选用了该系数，计算结果中仍存在异常低值。

柯婷等[31]采集了 47 个来自南海北部三亚湾的活体滨珊瑚骨骼，并开展约为月分辨率的硼同位素研究，重建了 2016—2019 年的海水 pH 值变化范围在 7. 77 ~ 8. 37，且呈季节性波动特征，与采样地点长期实测的海水 pH 值记录相符，为 $\delta^{11}B$-古海水 pH 值模型的可靠性提供了有力证据。柯婷等的计算过程选用了 pK_B^* = 8. 597，α_{4-3} = 0. 974，并且考虑到生命效应的影响使用滨珊瑚种的经验公式 $pH_{海水} = (pH_{ECF} - 5.95)/0.32$，对 pH 值重建结果进行了校正（ECF：extracytoplasmic calcifying fluid，细胞质外钙化液）。她们分析后发现虽然滨珊瑚的 $\delta^{11}B$ 受温度影响不明显（与 $\delta^{18}O$ 变化不同步），然而 $\delta^{11}B$ 重建的 pH 值与 $\delta^{18}O$ 却存在弱相关性，并从季节时间尺度上总结了海水 pH 的变化规律，即低温季节时海水倾向于偏碱性。这表明三亚湾珊瑚礁附近海水 pH 值的短时间变化可能受控于生物活动，而非海水 CO_2 的溶解度。另外，有研究测定南海多个岛礁珊瑚硼同位素特征并重建海水 pH 值（选用 α_{4-3} = 0. 981）发现，低 $\delta^{11}B$ 恰与 6 000 年前的极地冰雪消融-海平面升高事件对应，推测当时低碱度（pH = 5. 7 ~ 6. 2）[109]的雪融水汇入导致海水 pH 值降低，响应了中国南海的海平面变化的关键时期[110]。

以珊瑚作为研究对象并应用 $\delta^{11}B$-古海水 pH 值模型开展的研究通常会选用大型的块状珊瑚，以重建长时间（数百年）且连续的海水 pH 值序列。但珊瑚是复杂的多细胞生物，拥有调控自身钙化流体 pH 值的生命效应，且珊瑚生长过程中生物因素（光照、温度和营养盐浓度等）影响，可能存在个体差异[111]，因此珊瑚骨骼记录的 pH 信息可能与真实海水的存在偏差[3, 112]，为硼同位素代用指标的准确性和可靠性带来一定影响。未来解决珊瑚代用指标的局限性可能需要研究者针对选用的珊瑚属种建立更多物种经验公式，校正生命效应产生的 pH 值升高，尽可能消除生命效应的影响。

利用有孔虫反演古海水 pH 值可以追溯到新生代（60 Ma）（图 6）。Pearson 和 Palmer[93]分析了来自热带太平洋的 35 个有孔虫样本的硼同位素值，剔除了 3 个可能因为生命效应影响而发生强烈硼分馏的异常 $\delta^{11}B$ 低值后，重建了自新生代（60 Ma）以来海洋表面 pH 值（选取 pK_B^* = 8. 60，$\delta^{11}B_{海水}$ = 39. 5 ‰，α_{4-3} = 0. 981），发现早始新世—晚古新世（60 ~ 52 Ma）大气 CO_2 浓度基本平稳于 500×10^{-6} 左右，最大值甚至超过 $2\,000 \times 10^{-6}$，而在 55 ~ 40 Ma 期间出现了大气 CO_2 的不稳定下降，推测是由于洋中脊、火山和变质带排放的 CO_2 减少和碳埋藏的增加所导致。Spivack 等[113]利用有孔虫硼同位素对 21 Ma 的太平洋海水 pH 值重建的结果显示 pH 值为 7. 4，远低于现代海水（pH = 8. 2 ± 0. 2），并以此推测当时的大气 CO_2 浓度相比现代处于较高水平。此外，Sosdian 等[114]分析来自不同地理位置的 68 个有孔虫样本的碳酸钙壳中的 $\delta^{11}B$，考虑到有孔虫样品可能存在体内物种特异性硼偏移，对其使用校正公式：$\delta^{11}B_{borate} = (\delta^{11}B_{T.\ trilobus} - 2.69)/0.833$（$\delta^{11}B_{borate}$ 为进入该种有孔虫骨骼中的 $B(OH)_4^-$ 的 $\delta^{11}B$，$\delta^{11}B_{T.\ trilobus}$ 为有孔虫种 *Trilobatus trilobus* 的 $\delta^{11}B$），并选用 α_{4-3} = 0. 974 计算，重建了过去 22 Ma 的表层海水 pH 值及大气 CO_2 浓度，发现在中中

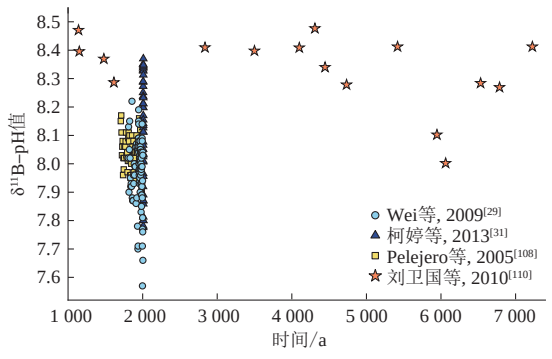


图 5　利用珊瑚重建的古海水 pH 值时间轴[29, 31, 108, 110]

Fig. 5　Timeline of paleo-seawater pH reconstructed from corals[29, 31, 108, 110]

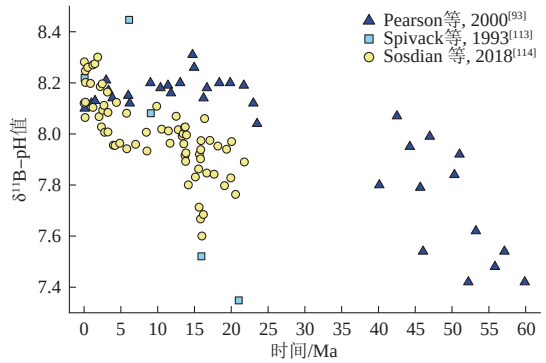


图 6　利用有孔虫重建的古海水 pH 值时间轴[93, 113, 114]

Fig. 6　Timeline of paleo-seawater pH reconstructed from foraminifer[93, 113, 114]

中国知网　https://www.cnki.net

新世气候适宜期(middle miocene climate optimum, MMCO),地球表面曾出现过大约7.6±0.1的pH值最低值,这一时期的CO_2浓度达到(470~630)×10^{-6}。在全新世时期,位于东大西洋塞拉利昂高迪的ODP-668B钻井中的有孔虫的硼同位素测定,建立了更新世中期(140~0 ka和420~300 ka)以来的表层海水pH值的演变规律,结果表明冰期的海水表面pH值高于间冰期,其差值达到0.18±0.03;也以此重建了该时间尺度内的大气CO_2变化,其结果与冰芯研究结果吻合,为有孔虫硼同位素在全新世古气候的应用提供有效支持[115];随后,Zeebe等[116]利用该研究重建的海水表面pH值序列,展开冰期—间冰期的气候震荡时期的追踪分析,发现硼同位素重建的数个冰期旋回pH值序列与$\delta^{18}O$呈现一致的波动趋势,且与Vostok冰芯[117]记录中推断的pCO_2变化一致。

利用有孔虫还原古海水pH值时,也可能会受到生命效应的影响。由于生物生长需求可能会调节体内的pH值,导致其与真实海水pH值存在偏差,且如果发生调控下偏碱性的体内环境,可能会促进$B(OH)_4^-$的形成,不利于保持原始硼记录[3, 112]。因此,需要通过实验建立经验模型,以校正生命效应带来的偏差[34, 118]。此外,有研究[119]指出浮游有孔虫的钙化过程可能会受到海水温度的影响,在这个阶段有孔虫的壳体内及周围会形成一个“微环境”,海水温度升高时,“微环境”的pH值和CO_3^{2-}浓度可能会被提高,促进钙化生长进程。

因此,$\delta^{11}B$-古海水pH值技术仍面临挑战和不确定性;目前对于海水中的硼同位素分馏及两种存在形式之间的交换过程的了解尚不充分,且受生命效应等因素的影响,模型中的关键参数α_{4-3}并不能完全消除生物碳酸盐中的硼同位素值偏差,未来仍需进一步探索。

5 结论与展望

基于硼同位素在海洋中的循环机制及其测定方法的分析,本文探讨了$\delta^{11}B$-古海水pH值模型在反演古海水pH值中的机制及应用。为了提高该模型的准确性,需要设计接近自然海水环境的模拟实验优化模型参数(α_{4-3}),采用多尺度模拟方法,整合微观模型与宏观模型,全面理解海水中硼同位素的分馏行为;针对不同碳酸盐生物物种(如珊瑚和有孔虫),建立全面的pH值校正公式库,减少生命效应对硼同位素值偏差的影响,并探索使用单一物种作为更可靠的碳酸盐样品,以降低种间差异和光合作用等生命活动对体内pH值的影响。目前,$\delta^{11}B$反演古海水pH值的研究主要集中于珊瑚和有孔虫,分别主要提供了全新世和新生代的海水pH值信息。尽管存在生命效应和硼同位素分馏等挑战,但该模型仍在揭示古海洋酸化和大气CO_2浓度变化方面显示出潜力。未来的研究应进一步优化模型系数,完善pH值校正公式,并扩展研究实例,以提高模型的准确性和可靠性。

同时,生物碳酸盐的硼/钙元素含量比值(B/Ca)和锂同位素值(δ^7Li)等指标也是反演古海水pH值的潜在有效指标。B/Ca用于计算海水pH值的原理是基于海水中硼与碳酸钙的相对含量,通过分析碳酸盐中的B/Ca比值,计算和重建海水的pH值[33, 63, 111]。另一方面,δ^7Li重建指标的依据是锂水合离子在进入碳酸盐晶格之前,其脱水过程的去溶能与pH值密切相关,且δ^7Li与海水pH值之间存在显著的负相关性[6-7]。通过结合这些指标,可以验证硼$\delta^{11}B$-古海水pH值模型反演古海水pH值的数据,进而增强对古海洋环境变化的理解。

参 考 文 献

[1] HALEVY I, BACHAN A. The geologic history of seawater pH [J]. Science, 2017, 355(6329): 1069-1071.

[2] VENGOSH A, KOLODNY Y, STARINSKY A, et al. Coprecipitation and isotopic fractionation of boron in modern biogenic carbonates [J]. Geochimica et Cosmochimica Acta, 1991, 55(10): 2901-2910.

[3] HEMMING N G, HANSON G N. Boron isotopic composition and concentration in modern marine carbonates [J]. Geochimica et Cosmochimica Acta, 1992, 56(1): 537-543.

[4] ISHIKAWA T, NAKAMURA E. Boron isotope systematics of marine sediments[J]. Earth and Planetary Science Letters, 1993, 117(3/4): 567-580.

[5] SANYAL A, HEMMING N G, HANSON G N, et al. Evidence for a higher pH in the glacial ocean from boron isotopes in foraminifera [J]. Nature, 1995, 373(6511): 234-236.

[6] ROBERTS J, KACZMAREK K, LANGER G, et al. Lithium isotopic composition of benthic foraminifera: A new proxy for paleo-pH reconstruction[J]. Geochimica et Cosmochimica Acta, 2018, 236: 336-350.

[7] VIGIER N, ROLLION-BARD C, LEVENSON Y, et al. Lithium isotopes in foraminifera shells as a novel proxy for the ocean dissolved inorganic carbon (DIC) [J]. Comptes Rendus Geoscience, 2015, 347(1): 43-51.

[8] BIRKS H J B, BRAAK C J F T, LINE J M, et al. Diatoms and pH reconstruction [J]. Philosophical Transactions of the Royal Society of London. B, Biological Sciences, 1990, 327(1240): 263-278.

[9] GINN B K, STEWART L J, CUMMING B F, et al. Surface-water acidification and reproducibility of sediment cores from Kejimkujik Lake, Nova Scotia, Canada[J]. Water, Air, and soil Pollution, 2007, 183(1): 15-24.

[10] XIAO Wenjie, WANG Yinghui, ZHOU Shangzhe, et al. Ubiquitous production of branched glycerol dialkyl glycerol

中国知网 https://www.cnki.net

tetraethers (brGDGTs) in global marine environments: A new source indicator for brGDGTs [J]. Biogeosciences, 2016, 13 (20): 5883-5894.

[11] WANG Canfa, BENDLE J, YANG Yi, et al. Impacts of pH and temperature on soil bacterial 3-hydroxy fatty acids: Development of novel terrestrial proxies [J]. Organic Geochemistry, 2016, 94: 21-31.

[12] 石鑫, 宋金明, 李学刚, 等. 海洋古 pH 重建的技术方法[J]. 海洋环境科学, 2019, 38(6): 954-962.
SHI Xin, SONG Jinming, LI Xuegang, et al. Methods for reconstruction of oceanic paleo-pH [J]. Marine Environmental Science, 2019, 38(6): 954-962.

[13] WANG Yijing, WEI Haizhen, JIANG Shaoyong, et al. Mechanism of boron incorporation into calcites and associated isotope fractionation in a steady-state carbonate-seawater system [J]. Applied Geochemistry, 2018, 98: 221-236.

[14] ZHANG Shuang, HENEHAN M J, HULL P M, et al. Investigating controls on boron isotope ratios in shallow marine carbonates [J]. Earth and Planetary Science Letters, 2017, 458: 380-393.

[15] TAYLOR S R, MCLENNAN S M. The continental crust: Its composition and evolution [M]. Oxford: Blackwell Scientific Publications, 1985.

[16] GAILLARDET J, LEMARCHAND D. Boron in the weathering environment [M]//MARSCHALL H, FOSTER G. Boron Isotopes. Cham: Springer International Publishing, 2018: 163-188.

[17] DEYHLE A, KOPF A. Deep fluids and ancient pore waters at the backstop: Stable isotope systematics (B, C, O) of mud-volcano deposits on the Mediterranean Ridge accretionary wedge [J]. Geology, 2001, 29(11): 1031-1034.

[18] WILLIAMS L B, HERVIG R L. Boron isotope composition of coals: A potential tracer of organic contaminated fluids [J]. Applied Geochemistry, 2004, 19(10): 1625-1636.

[19] HOGAN J F, BLUM J D. Boron and lithium isotopes as groundwater tracers: A study at the Fresh Kills Landfill, Staten Island, New York, USA [J]. Applied Geochemistry, 2003, 18 (4): 615-627.

[20] RYAN J G, LEEMAN W P, MORRIS J D, et al. The boron systematics of intraplate lavas: Implications for crust and mantle evolution [J]. Geochimica et Cosmochimica Acta, 1996, 60(3): 415-422.

[21] 蒋少涌, 于际民, 凌洪飞, 等. 壳-幔演化和板块俯冲作用过程中的硼同位素示踪[J]. 地学前缘, 2000, 7(2): 391-399.
JIANG Shaoyong, YU Jimin, LING Hongfei, et al. Boron isotope as a tracer in the study of crust-mantle evolution and subduction processes [J]. Earth Science Frontiers, 2000, 7(2): 391-399.

[22] PALMER M R. Boron cycling in subduction zones [J]. Elements, 2017, 13(4): 237-242.

[23] GUO Shun, ZHAO Kuidong, JOHN T, et al. Metasomatic flow of metacarbonate-derived fluids carrying isotopically heavy boron in continental subduction zones: Insights from tourmaline-bearing ultra-high pressure eclogites and veins (Dabie terrane, eastern China) [J]. Geochimica et Cosmochimica Acta, 2019, 253: 159-200.

[24] LI Yinchuan, WEI Haizhen, PALMER M R, et al. Equilibrium boron isotope fractionation during serpentinization and applications in understanding subduction zone processes [J]. Chemical Geology, 2022, 609: 121047.

[25] PALMER M R, SLACK J F. Boron isotopic composition of tourmaline from massive sulfide deposits and tourmalinites [J]. Contributions to Mineralogy and Petrology, 1989, 103 (4): 434-451.

[26] SU Zhikun, ZHAO Xinfu, LI Xiaochun, et al. Using elemental and boron isotopic compositions of tourmaline to trace fluid evolutions of IOCG systems: The worldclass Dahongshan FeCu deposit in SW China [J]. Chemical Geology, 2016, 441: 265-279.

[27] CODEÇO M S, WEIS P, TRUMBULL R B, et al. Chemical and boron isotopic composition of hydrothermal tourmaline from the Panasqueira W-Sn-Cu deposit, Portugal [J]. Chemical Geology, 2017, 468: 1-16.

[28] YANG Shuiyuan, JIANG Shaoyong, PALMER M R. Chemical and boron isotopic compositions of tourmaline from the Nyalam leucogranites, South Tibetan Himalaya: Implication for their formation from B-rich melt to hydrothermal fluids [J]. Chemical Geology, 2015, 419: 102-113.

[29] WEI Gangjian, MCCULLOCH M T, MORTIMER G, et al. Evidence for ocean acidification in the Great Barrier Reef of Australia [J]. Geochimica et Cosmochimica Acta, 2009, 73(8): 2332-2346.

[30] XIAO Jun, XIAO Yingkai, JIN Zhangdong, et al. Boron isotopic compositions in growing corals from the South China Sea [J]. Journal of Asian Earth Sciences, 2013, 62: 561-567.

[31] 柯婷, 韦刚健, 刘颖, 等. 南海北部珊瑚高分辨率硼同位素组成及其对珊瑚礁海水 pH 变化的指示意义[J]. 地球化学, 2015, 44(1): 1-8.
KE Ting, WEI Gangjian, LIU Ying, et al. High resolution boron isotopic compositions of a coral from the northern South China Sea and their implications for reconstruction of seawater pH [J]. Geochimica, 2015, 44(1): 1-8.

[32] 裴健翔, 郭潇潇, 薛海涛, 等. 莺歌海盆地中新统海相烃源岩形成环境及控制因素[J]. 石油与天然气地质, 2023, 44(4): 937-945.
PEI Jianxiang, GUO Xiaoxiao, XUE Haitao, et al. Environment and controlling factors of the Miocene marine source rocks in the Yinggehai Basin [J]. Oil & Gas Geology, 2023, 44 (4): 937-945.

[33] WEI Haizhen, ZHAO Yao, LIU Xi, et al. Evolution of paleo-climate and seawater pH from the Late Permian to postindustrial periods recorded by boron isotopes and B/Ca in biogenic carbonates [J]. Earth-Science Reviews, 2021, 215: 103546.

[34] XIAO J, JIN Z D, XIAO Y K, et al. Controlling factors of the $\delta^{11}B$-pH proxy and its research direction [J]. Environmental Earth Sciences, 2014, 71(4): 1641-1650.

[35] FARMER J R, HÖNISCH B, ROBINSON L F, et al. Effects of seawater-pH and biomineralization on the boron isotopic composition of deep-sea bamboo corals [J]. Geochimica et Cosmochimica Acta, 2015, 155: 86-106.

[36] NIR O, VENGOSH A, HARKNESS J S, et al. Direct measurement of the boron isotope fractionation factor: Reducing the uncertainty in reconstructing ocean paleo-pH [J]. Earth and Planetary Science Letters, 2015, 414: 1-5.

中国知网　https://www.cnki.net

[37] GREENOP R, HAIN M P, SOSDIAN S M, et al. A record of Neogene seawater $\delta^{11}B$ reconstructed from paired $\delta^{11}B$ analyses on benthic and planktic foraminifera[J]. Climate of the Past, 2017, 13(2): 149-170.

[38] 刘羿, 张春雷. 南海北部滨珊瑚礁同位素气候环境指示意义再研究[J]. 第四纪研究, 2017, 37(5): 1055-1063.
LIU Yi, ZHANG Chunlei. Revisiting paleoceanographic application of $\delta^{11}B$ in coral Porites from the northern South China Sea[J]. Quaternary Sciences, 2017, 37(5): 1055-1063.

[39] 肖军, 肖应凯, 金章东, 等. 活体珊瑚微量元素对硼同位素组成影响及硼掺入珊瑚的形式[J]. 地球化学, 2012, 41(5): 401-410.
XIAO Jun, XIAO Yingkai, JIN Zhangdong, et al. The influence of trace elements on boron isotopic composition of living corals and the incorporation species of boron into corals[J]. Geochimica, 2012, 41(5): 401-410.

[40] LEMARCHAND D, GAILLARDET J, LEWIN E, et al. The influence of rivers on marine boron isotopes and implications for reconstructing past ocean pH[J]. Nature, 2000, 408(6815): 951-954.

[41] LEMARCHAND D, GAILLARDET J, LEWIN É, et al. Boron isotope systematics in large rivers: Implications for the marine boron budget and paleo-pH reconstruction over the Cenozoic[J]. Chemical Geology, 2002, 190(1/4): 123-140.

[42] ROSE E F, CHAUSSIDON M, FRANCE-LANORD C. Fractionation of boron isotopes during erosion processes: the example of Himalayan rivers[J]. Geochimica et Cosmochimica Acta, 2000, 64(3): 397-408.

[43] CHETELAT B, GAILLARDET J. Boron isotopes in the Seine River, France: A probe of anthropogenic contamination[J]. Environmental Science & Technology, 2005, 39(8): 2486-2493.

[44] SPIVACK A J, PALMER M R, EDMOND J M. The sedimentary cycle of the boron isotopes[J]. Geochimica et Cosmochimica Acta, 1987, 51(7): 1939-1949.

[45] KOPF A, DEYHLE A. Back to the roots: Boron geochemistry of mud volcanoes and its implications for mobilization depth and global B cycling[J]. Chemical Geology, 2002, 192(3/4): 195-210.

[46] PALMER M R, SPIVACK A J, EDMOND J M. Temperature and pH controls over isotopic fractionation during adsorption of boron on marine clay[J]. Geochimica et Cosmochimica Acta, 1987, 51(9): 2319-2323.

[47] MEYBECK M. Global chemical weathering of surficial rocks estimated from river dissolved loads[J]. American Journal of Science, 1987, 287(5): 401-428.

[48] SMITH H J, SPIVACK A J, STAUDIGEL H, et al. The boron isotopic composition of altered oceanic crust[J]. Chemical Geology, 1995, 126(2): 119-135.

[49] HART S R, STAUDIGEL H. The control of alkalies and uranium in seawater by ocean crust alteration[J]. Earth and Planetary Science Letters, 1982, 58(2): 202-212.

[50] YOU Chenfeng, SPIVACK A J, SMITH J H, et al. Mobilization of boron in convergent margins: Implications for the boron geochemical cycle[J]. Geology, 1993, 21(3): 207-210.

[51] MARSCHALL H R. Boron isotopes in the ocean floor realm and the mantle[M]//MARSCHALL H, FOSTER G. Boron Isotopes. Cham: Springer International Publishing, 2018: 189-215.

[52] YOU Cf, SPIVACK A J, GIESKES J M, et al. Experimental study of boron geochemistry: Implications for fluid processes in subduction zones[J]. Geochimica et Cosmochimica Acta, 1995, 59(12): 2435-2442.

[53] SPIVACK A J, EDMOND J M. Boron isotope exchange between seawater and the oceanic crust[J]. Geochimica et Cosmochimica Acta, 1987, 51(5): 1033-1043.

[54] SCHWARCZ H P, AGYEI E K, MCMULLEN C C. Boron isotopic fractionation during clay adsorption from sea-water[J]. Earth and Planetary Science Letters, 1969, 6(1): 1-5.

[55] MARSCHALL H R, WANLESS V D, SHIMIZU N, et al. The boron and lithium isotopic composition of mid-ocean ridge basalts and the mantle[J]. Geochimica et Cosmochimica Acta, 2017, 207: 102-138.

[56] FOSTER G L, POGGE VON STRANDMANN P A E, RAE J W B. Boron and magnesium isotopic composition of seawater[J]. Geochemistry, Geophysics, Geosystems, 2010, 11(8): Q08015.

[57] JIANG Wanjun, SHENG Yizhi, WANG Guangcai, et al. Cl, Br, B, Li, and noble gases isotopes to study the origin and evolution of deep groundwater in sedimentary basins: A review[J]. Environmental Chemistry Letters, 2022, 20(2): 1497-1528.

[58] DE HOOG J C M, SAVOV I P. Boron isotopes as a tracer of subduction zone processes[M]//MARSCHALL H, FOSTER G. Boron Isotopes. Cham: Springer International Publishing, 2018: 217-247.

[59] COOPER G F, MACPHERSON C G, BLUNDY J D, et al. Variable water input controls evolution of the Lesser Antilles volcanic arc[J]. Nature, 2020, 582(7813): 525-529.

[60] FURST M J. Boron in siliceous materials as a paleosalinity indicator[J]. Geochimica et Cosmochimica Acta, 1981, 45(1): 1-13.

[61] HARDER H. Boron content of sediments as a tool in facies analysis[J]. Sedimentary Geology, 1970, 4(1/2): 153-175.

[62] LERMAN A. Boron in clays and estimation of paleosalinities[J]. Sedimentology, 1966, 6(4): 267-286.

[63] RAE J W B, FOSTER G L, SCHMIDT D N, et al. Boron isotopes and B/Ca in benthic foraminifera: Proxies for the deep ocean carbonate system[J]. Earth and Planetary Science Letters, 2011, 302(3/4): 403-413.

[64] HEMMING N G, HANSON G N. A procedure for the isotopic analysis of boron by negative thermal ionization mass spectrometry[J]. Chemical Geology, 1994, 114(1/2): 147-156.

[65] AL-AMMAR A, REITZNEROVÁ E, BARNES R M. Improving boron isotope ratio measurement precision with quadrupole inductively coupled plasma-mass spectrometry[J]. Spectrochimica Acta Part B: Atomic Spectroscopy, 2000, 55(12): 1861-1867.

[66] LEMARCHAND D, GAILLARDET J, GÖPEL C, et al. An optimized procedure for boron separation and mass spectrometry analysis for river samples[J]. Chemical Geology, 2002, 182(2/4): 323-334.

[67] AGGARWAL J K, MEZGER K, PERNICKA E, et al. The effect of instrumental mass bias on $\delta^{11}B$ measurements: A comparison between thermal ionisation mass spectrometry and multiple-collector ICP-MS[J]. International Journal of Mass Spectrometry, 2004, 232(3): 259-263.

中国知网 https://www.cnki.net

[68] FOSTER G L. Seawater pH, pCO_2 and $[CO^{2-}_3]$ variations in the Caribbean Sea over the last 130 kyr: A boron isotope and B/Ca study of planktic foraminifera[J]. Earth and Planetary Science Letters, 2008, 271(1/4): 254-266.

[69] GUERROT C, MILLOT R, ROBERT M, et al. Accurate and high-precision determination of boron isotopic ratios at low concentration by MC-ICP-MS (Neptune)[J]. Geostandards and Geoanalytical Research, 2011, 35(2): 275-284.

[70] MCCULLOCH M T, HOLCOMB M, RANKENBURG K, et al. Rapid, high-precision measurements of boron isotopic compositions in marine carbonates [J]. Rapid Communications in Mass Spectrometry, 2014, 28(24): 2704-2712.

[71] AGGARWAL S K, YOU Chenfeng. A review on the determination of isotope ratios of boron with mass spectrometry [J]. Mass Spectrometry Reviews, 2017, 36(4): 499-519.

[72] CHAUSSIDON M, ROBERT F. Nucleosynthesis of ^{11}B-rich boron in the pre-solar cloud recorded in meteoritic chondrules [J]. Nature, 1995, 374(6520): 337-339.

[73] 苏喜平, 杜爱兵, 韩晓辉, 等. 快堆控制棒组件用高富集度碳化硼芯块的热物理性能研究[J]. 山东陶瓷, 2015, 38(4): 3-5.
SU Xiping, DU Aibing, HAN Xiaohui, et al. Study on thermophysical properties of B_4C pellets used as control material in fast reactor[J]. Shandong Ceramics, 2015, 38(4): 3-5.

[74] 冯林秀, 李正辉, 曹秋香, 等. 硼同位素分析测试技术研究进展[J]. 岩矿测试, 2023, 42(1): 16-38.
FENG Linxiu, LI Zhenghui, CAO Qiuxiang, et al. A review on the development of boron isotope analytical techniques[J]. Rock and Mineral Analysis, 2023, 42(1): 16-38.

[75] RAMAKUMAR K L, PARAB A R, KHODADE P S, et al. Determination of isotopic composition of boron [J]. Journal of Radioanalytical and Nuclear Chemistry, 1985, 94(1): 53-61.

[76] SWIHART G H. Instrumental techniques for boron isotope analysis[J]. Reviews in Mineralogy and Geochemistry, 1996, 33(1): 845-862.

[77] ISHIKAWA T, NAGAISHI K. High-precision isotopic analysis of boron by positive thermal ionization mass spectrometry with sample preheating[J]. Journal of Analytical Atomic Spectrometry, 2011, 26(2): 359-365.

[78] KASEMANN S, MEIXNER A, ROCHOLL A, et al. Boron and oxygen isotope composition of certified reference materials NIST SRM 610/612 and reference materials JB-2 and JR-2 [J]. Geostandards Newsletter, 2001, 25(2/3): 405-416.

[79] YOU Chenfeng. Chapter 7-Thermal ionization mass spectrometry techniques for boron isotopic analysis: A review[M]//DE GROOT P A. Handbook of Stable Isotope Analytical Techniques. Amsterdam: Elsevier, 2004: 142-152.

[80] CLARKSON M O, KASEMANN S A, WOOD R A, et al. Ocean acidification and the Permo-Triassic mass extinction[J]. Science, 2015, 348(6231): 229-232.

[81] FARMER J R, HÖNISCH B, UCHIKAWA J. Single laboratory comparison of MC-ICP-MS and N-TIMS Boron isotope analyses in marine carbonates[J]. Chemical Geology, 2016, 447: 173-182.

[82] AGGARWAL S K, WANG B S, YOU Chenfeng, et al. Fractionation correction methodology for precise and accurate isotopic analysis of boron by negative thermal ionization mass spectrometry based on BO_2^- ions and using the $^{18}O/^{16}O$ ratio from ReO_4^- for internal normalization[J]. Analytical Chemistry, 2009, 81(17): 7420-7427.

[83] AGGARWAL J K, SHEPPARD D, MEZGER K, et al. Precise and accurate determination of boron isotope ratios by multiple collector ICP-MS: Origin of boron in the Ngawha geothermal system, New Zealand[J]. Chemical Geology, 2003, 199(3/4): 331-342.

[84] VANDERPOOL R A, HOFF D, JOHNSON P E. Use of inductively coupled plasma-mass spectrometry in boron-10 stable isotope experiments with plants, rats, and humans [J]. Environmental Health Perspectives, 1994, 102(S7): 13-20.

[85] 贺茂勇, 邓丽, 逯海, 等. NaF消除硼记忆效应的快速、高精度MC-ICP-MS硼同位素测定方法[C]//中国矿物岩石地球化学学会第17届学术年会论文摘要集. 贵阳: 中国矿物岩石地球化学学会, 2019: 1018.
HE Maoyong, DENG Li, LU Hai, et al. Rapid and high-precision MC-ICP-MS boron isotope determination method for eliminating boron memory effect using NaF[C]//Abstract Collection of Papers from the 17th Annual Conference of the Chinese Society of Mineral, Rock and Geochemistry. Guiyang: Chinese Society for Mineralogy Petrology and Geochemistry, 2019: 1018.

[86] ROLLION-BARD C, CHAUSSIDON M, FRANCE-LANORD C. pH control on oxygen isotopic composition of symbiotic corals[J]. Earth and Planetary Science Letters, 2003, 215(1/2): 275-288.

[87] BLAMART D, ROLLION-BARD C, MEIBOM A, et al. Correlation of boron isotopic composition with ultrastructure in the deep-sea coral *Lophelia pertusa*: Implications for biomineralization and paleo-pH [J]. Geochemistry, Geophysics, Geosystems, 2007, 8(12): Q12001.

[88] KASEMANN S A, SCHMIDT D N, BIJMA J, et al. *In situ* boron isotope analysis in marine carbonates and its application for foraminifera and palaeo-pH[J]. Chemical Geology, 2009, 260(1/2): 138-147.

[89] MARSCHALL H R, MONTELEONE B D. Boron isotope analysis of silicate glass with very low boron concentrations by secondary ion mass spectrometry [J]. Geostandards and Geoanalytical Research, 2015, 39(1): 31-46.

[90] JACKSON S E, GÜNTHER D. The nature and sources of laser induced isotopic fractionation in laser ablation-multicollector-inductively coupled plasma-mass spectrometry [J]. Journal of Analytical Atomic Spectrometry, 2003, 18(3): 205-212.

[91] 刘羿, 彭子成, 刘卫国, 等. 古海水pH值代用指标——海洋碳酸盐硼同位素研究进展[J]. 地球科学进展, 2007, 22(12): 1240-1250.
LIU Yi, PENG Zicheng, LIU Weiguo, et al. Advances in paleo-seawater pH proxy: Boron isotope in marine carbonates [J]. Advances in Earth Science, 2007, 22(12): 1240-1250.

[92] 肖军, 肖应凯, 刘丛强, 等. 海洋生物碳酸盐δ11B-pH技术影响因素[J]. 海洋地质与第四纪地质, 2010, 30(4): 215-222.
XIAO Jun, XIAO Yingkai, LIU Congqiang, et al. Study of influence factors on δ^{11}B-PH technique for marine bio-carbonate deposits [J]. Marine Geology & Quaternary Geology, 2010, 30(4): 215-222.

[93] PEARSON P N, PALMER M R. Atmospheric carbon dioxide concentrations over the past 60 million years[J]. Nature, 2000, 406(6797): 695-699.

中国知网　https://www.cnki.net

[94] PAGANI M, LEMARCHAND D, SPIVACK A, et al. A critical evaluation of the boron isotope-pH proxy: The accuracy of ancient ocean pH estimates [J]. Geochimica et Cosmochimica Acta, 2005, 69(4): 953-961.

[95] BRANSON O, KACZMAREK K, REDFERN S A T, et al. The coordination and distribution of B in foraminiferal calcite [J]. Earth and Planetary Science Letters, 2015, 416: 67-72.

[96] OI T. Ab initio molecular orbital calculations of reduced partition function ratios of polyboric acids and polyborate anions [J]. Zeitschrift für Naturforschung A, 2000, 55(6/7): 623-628.

[97] 陈敏. 化学海洋学[M]. 北京: 海洋出版社, 2009.
CHEN Min. Chemical oceanography[M]. Beijing: China Ocean Press, 2009.

[98] HERSHEY J P, FERNANDEZ M, MILNE P J, et al. The ionization of boric acid in NaCl, Na-Ca-Cl and Na-Mg-Cl solutions at 25°C[J]. Geochimica et Cosmochimica Acta, 1986, 50(1): 143-148.

[99] SANYAL A, BIJMA J, SPERO H, et al. Empirical relationship between pH and the boron isotopic composition of *Globigerinoides sacculifer*: Implications for the boron isotope paleo-pH proxy[J]. Paleoceanography and Paleoclimatology, 2001, 16(5): 515-519.

[100] KAKIHANA H, KOTAKA M, SATOH S, et al. Fundamental studies on the ion-exchange separation of boron isotopes [J]. Bulletin of the Chemical Society of Japan, 1977, 50 (1): 158-163.

[101] ZEEBE R E. Stable boron isotope fractionation between dissolved $B(OH)_3$ and $B(OH)_4^-$[J]. Geochimica et Cosmochimica Acta, 2005, 69(11): 2753-2766.

[102] 周进高, 徐哲航, 黄世伟, 等. 碳酸盐岩沉积储层研究前沿与未来发展方向[J]. 石油与天然气地质, 2024, 45(4): 929-953.
ZHOU Jingao, XU Zhehang, HUAN Shiwei, et al. Frontiers and trends in the research on carbonate sedimentology and reservoir geology[J]. Oil & Gas Geology, 2024, 45(4): 929-953.

[103] LIU Yun, TOSSELL J A. Ab initio molecular orbital calculations for boron isotope fractionations on boric acids and borates [J]. Geochimica et Cosmochimica Acta, 2005, 69(16): 3995-4006.

[104] BYRNE R H, YAO Wensheng, KLOCHKO K, et al. Experimental evaluation of the isotopic exchange equilibrium $^{10}B(OH)_3+^{11}B(OH)_4^-=^{11}B(OH)_3+^{10}B(OH)_4^-$ in aqueous solution [J]. Deep Sea Research Part I: Oceanographic Research Papers, 2006, 53(4): 684-688.

[105] 吴双, 王峻, 张春光, 等. 普光地区下三叠统富锂钾卤水成因与分布规律[J]. 断块油气田, 2024, 31(1): 96-105.
WU Shuang, WANG Jun, ZHANG Chunguang, et al. Genesis and distribution law of rich lithium-potassium brine in the Lower Triassic of Puguang area[J]. Fault-Block Oil & Gas Field, 2024, 31(1): 96-105.

[106] DICKSON A G. Thermodynamics of the dissociation of boric acid in synthetic seawater from 273.15 to 318.15 K[J]. Deep Sea Research Part A. Oceanographic Research Papers, 1990, 37(5): 755-766.

[107] ROY R N, ROY L N, LAWSON M, et al. Thermodynamics of the dissociation of boric acid in seawater at S = 35 from 0 to 55°C[J]. Marine Chemistry, 1993, 44(2/4): 243-248.

[108] PELEJERO C, CALVO E, MCCULLOCH M T, et al. Preindustrial to modern interdecadal variability in coral reef pH [J]. Science, 2005, 309(5744): 2204-2207.

[109] 秦大河. 南极冰盖表层雪内的现代环境气候记录研究(英)[J]. 冰川冻土, 1998, 20(4): 413-424.
QIN Dahe. A study of present climatic and environmental records in the surface snow of the Antarctic ice sheet[J]. Journal of Glaciology and Geocryology, 1998, 20(4): 413-424.

[110] 刘卫国, 肖军, HEMMING N G, 等. 冰雪融化导致海水pH值和海平面变化的硼同位素证据[J]. 地球环境学报, 2010, 1(1): 43-47.
LIU Weiguo, XIAO Jun, HEMMING N G, et al. Boron isotopic evidence for contribution of melting ice to ocean pH value and sea level during global warming[J]. Journal of Earth Environment, 2010, 1(1): 43-47.

[111] CHEN Xuefei, DENG Wenfeng, KANG Huiling, et al. A replication study on coral $\delta^{11}B$ and B/Ca and their variation in modern and fossil *Porites*: Implications for coral calcifying fluid chemistry and seawater pH changes over the last millennium[J]. Paleoceanography and Paleoclimatology, 2021, 36 (10): e2021PA004319.

[112] TROTTER J, MONTAGNA P, MCCULLOCH M, et al. Quantifying the pH 'vital effect' in the temperate zooxanthellate coral *Cladocora caespitosa*: Validation of the boron seawater pH proxy[J]. Earth and Planetary Science Letters, 2011, 303(3/4): 163-173.

[113] SPIVACK A J, YOU Chenfeng, SMITH H J. Foraminiferal boron isotope ratios as a proxy for surface ocean pH over the past 21 Myr [J]. Nature, 1993, 363(6425): 149-151.

[114] SOSDIAN S M, GREENOP R, HAIN M P, et al. Constraining the evolution of Neogene ocean carbonate chemistry using the boron isotope pH proxy[J]. Earth and Planetary Science Letters, 2018, 498: 362-376.

[115] HÖNISCH B, HEMMING N G. Surface ocean pH response to variations in pCO_2 through two full glacial cycles[J]. Earth and Planetary Science Letters, 2005, 236(1/2): 305-314.

[116] ZEEBE R E, BIJMA J, HÖNISCH B, et al. Vital effects and beyond: A modelling perspective on developing palaeoceanographical proxy relationships in foraminifera [J]. Geological Society, London, Special Publications, 2008, 303(1): 45-58.

[117] PETIT J R, JOUZEL J, RAYNAUD D, et al. Climate and atmospheric history of the past 420,000 years from the Vostok ice core, Antarctica[J]. Nature, 1999, 399(6735): 429-436.

[118] KRIEF S, HENDY E J, FINE M, et al. Physiological and isotopic responses of scleractinian corals to ocean acidification [J]. Geochimica et Cosmochimica Acta, 2010, 74(17): 4988-5001.

[119] 宋茜薇, 秦秉斌, 唐正, 等. 南大洋南极带现代浮游有孔虫*Neogloboquadrina pachyderma* (sinistral)钙化作用受控于海水温度而非海洋酸化[J]. 中国科学: 地球科学, 2022, 52(11): 2152-2165.
SONG Qianwei, QIN Bingbin, TANG Zheng, et al. Calcification of planktonic foraminifer *Neogloboquadrina pachyderma* (sinistral) controlled by seawater temperature rather than ocean acidification in the Antarctic Zone of modern Sothern Ocean[J]. Science China Earth Sciences, 2022, 52(11): 2152-2165.

(编辑 董奕含)

中国知网 https://www.cnki.net

微体古生物学报(中英文) 2025年3月; **42**(1): 58–70
Acta Micropalaeontologica Sinica **42**(1): 58–70; March, 2025

南海礁区大型底栖有孔虫Mg/Ca值微区分布及其应用潜力*

黄晓婷　李　玫　吴司琪**

广西南海珊瑚礁研究重点实验室, 南宁 530004

提要　生物碳酸盐Mg/Ca值是古水温的重要指标。然而作为珊瑚礁区沉积物重要组成部分的大型底栖有孔虫(LBF), 其Mg/Ca指标的应用受到诸多限制。为探究礁区LBF Mg/Ca值在海水古温度重建方面的应用潜力, 本研究使用微区分析方法, 深入探讨了西沙群岛永乐环礁表层沉积物中两种有孔虫*Amphistegina lobifera*和*Amphistegina lessonii*壳内Mg/Ca值的分布规律, 同时, 比较了两种微区方法——电子探针(EPMA)和激光剥蚀电感耦合等离子质谱(LA-ICP-MS)的差异。另外, 为了探究成岩作用对有孔虫Mg/Ca值的影响, 选取永乐环礁羚羊礁及琛航岛岩心中的*A. lobifera*进行了测试。结果表明, 两种LBF的Mg/Ca值展现出了极为相似的分布特征, 沿着生长方向均呈现出清晰的周期性分布模式, 这与初级和次级方解石层的交替生长有关, 但二者的Mg/Ca值在次级方解石层边缘的变化模式略有不同。结合壳内分布规律及两种微区方法的差异, 发现尽管有孔虫的Mg/Ca值受到初级方解石层影响, 但通过选择合适的微区原位分析方法和打点位置, 仍然具有反映海水温度变化的潜力。成岩作用对岩心深处有孔虫Mg/Ca值的影响不容忽视, 实际应用时需加以考虑。通过与现代表层沉积物同种有孔虫的Mg/Ca值范围对比, 同时结合扫描电镜观察结果, 可以判断成岩作用影响程度。

关键词　大型底栖有孔虫　Mg/Ca 指标　原位微区分析　古温度　永乐环礁
DOI:10.16087/j.cnki.1000-0674.20250106.001

前　言

珊瑚礁区以占全球海洋不足0.2%的面积, 养育超过了25%种类的海洋生物(Cox *et al.*, 2021)。在当前全球变暖、海平面上升的背景下, 珊瑚礁区在地质历史时期的环境演变是理解地球气候变迁的关键一环。珊瑚礁中的底栖有孔虫数量充足、种类繁多, 其死亡后残留的壳体是珊瑚礁区沉积物的重要组成部分(Hallock, 1981b; Fujita *et al.*, 2016; Doo *et al.*, 2017; Mcneil *et al.*, 2022; Förderer *et al.*, 2023)。有孔虫不断吸收周围海水中的元素构建其壳体, 从而记录了环境信息(Lea *et al.*, 1999)。Mg置换碳酸盐中的Ca是吸热过程, 温度升高会导致有孔虫壳体中Mg含量增加。基于这一特性, 有孔虫壳体Mg/Ca值可以反演海水温度的变化(Lea *et al.*, 1999)。

底栖有孔虫按常用的非系统分类类群可分为大型底栖有孔虫(LBF)与小底栖有孔虫(SBF)两类: LBF的壳体较大, 具有复杂的内部结构, 多与微体藻类共生。SBF的壳体则相对较小, 不含有共生藻类(Raja *et al.*, 2007)。在珊瑚礁区沉积物中, LBF在种类及数量上都占据优势地位(王丽荣和赵焕庭, 2008; Förderer *et al.*, 2018)。因此, 重建礁区古海洋环境, 对LBF的研究必不可少。然而, LBF的Mg/Ca指标在实际运用中存在各种问题。首先, 有孔虫壳体中的地球化学信号除了与生长时期的海洋环境有关, 其自身复杂的生长过程也会造成不同类群、不同个体、同一个体的不同圈层之间存有差异, 被称为生命效应(Bentov & Erez, 2006; Morse *et al.*, 2007)。由于个体较大及共生藻类的存在, LBF的生

*国家自然科学青年科学基金项目(42402007)及广西自然科学基金项目(2024GXNSFBA010231)。
**通讯作者(Corresponding author) E-mail: wusiqi@gxu.edu.cn
收稿日期 2024-09-30, **修改稿收到日期** 2024-12-25

中国知网 https://www.cnki.net

命效应尤为显著(Saraswati *et al*., 2004; Raja *et al*., 2005, 2007; Khanolkar *et al*., 2021; Charrieau *et al*., 2023)。另外, 与SBF相比, LBF的Mg/Ca值通常高出1−2个数量级(陈龙等, 2019), 因此, LBF的Mg/Ca值随海水温度变化的敏感程度较低。

目前, 对珊瑚礁区有孔虫的研究方法多为属种组合及分布, 研究领域多为对沉积相的指示和对珊瑚礁健康状况的评估(秦国权, 1987; Uthicke *et al*., 2010; Velásquez *et al*., 2011; Oliveira-Silva *et al*., 2012; Parker *et al*., 2012; Perrin & Bosellini, 2012; Stephenson *et al*., 2015; Chen & Lin, 2017; Renema, 2018; A'ziz *et al*., 2021), 缺乏利用有孔虫的地化指标对古环境进行定量分析重建, 亦缺乏对有孔虫壳体微量元素分布的深入解读。为了进一步提升礁区底栖有孔虫在古环境重建中的应用潜力, 本研究使用EPMA和LA-ICP-MS两种原位微区方法对*Amphistegina lobifera*和*Amphistegina lessonii*进行测试, 探讨其Mg/Ca值在壳体内部的分布规律, 并对比两种微区方法的差异, 为后续古环境重建的研究提供支撑。同时, 利用一个浅层岩心(底部年代约为2 665 aBP)及一个深层岩心(取样处年代约为3.6 Ma)中获取的*A. lobifera*来分析成岩改造对Mg/Ca值的影响, 综合探讨LBF的Mg/Ca指标作为海水古温度计的可行性。

1　材料与方法

1.1　样品及来源

本研究有孔虫来源于表层沉积物及岩心样品。所有样品均采集自中国南海西沙群岛永乐环礁(图1)。永乐环礁是西沙群岛西部岛群核心区域, 由羚羊礁、甘泉岛、珊瑚岛、全富岛、银屿等13个珊瑚岛礁及8个口门通道, 围绕中央潟湖组成, 属于典型的珊瑚环礁, 也是西沙群岛面积最大的环礁。永乐环礁的年际海水温度变化为23℃到32℃, 年均28℃(数据来自哥白尼海洋环境监测服务中心http://marine.copernicus.eu)。

表层沉积物样品(图2)均采集于2021年9月, *Amphistegina lobifera*采自银屿岛外礁坡(111°42′26″E, 16°35′51″N), *Amphistegina lessonii*采自甘泉岛外礁坡(111°34′51″E, 16°30′9″N)。LYJ2岩心(16°27'59.32"N, 111°36'09.62"E)于2013年采自羚羊礁封闭潟湖的内礁坪区域(相对海平面以下150 cm), 总长287 cm, 采集过程中没有任何损失。通过对岩心中有孔虫*Calcarina* sp.进行^{14}C测年得到LYJ2年代框架, 其底部年龄约为2 665 aBP (Yue *et al*., 2019)。CK2岩心(16°26'56.368"N, 111°0'53.557"E)于2013年钻自琛航岛东南部近礁突起处的碳酸盐岩。钻孔位置在地形上高出现代礁坪2.88 m, 钻井深度为928.75 m, 上部碳酸盐岩沉积物厚873.55 m, 下部火山碎屑岩基岩厚52.20 m, 整个钻孔平均取芯率为69.6%。锶同位素测定碳酸盐岩底部地层年龄为~19.6 Ma(Fan *et al*., 2020)。

1.2　测试属种及其测试区域的选取

LBF的Mg/Ca值变化范围较广(表1), 为15−375.85 mmol/mol, 绝大部分集中在50−350 mmol/mol。Mg/Ca值越低, 细微的Mg含量变化更加明显, 因此, 选取Mg/Ca值低的LBF更利于反映海水温度。LBF中*Amphistegina*属Mg/Ca值通常较低, 仅为15−90 mmol/mol。同时, 在珊瑚礁LBF中, *Amphistegina*属在全世界分布最广、数量最多(Hallock *et al*., 2024), 且具有时代连续性, 在CK2底部仍有出现, 可以一直追溯到晚中新世(孟敏, 2022)。该属含有硅藻共生体, 生活的深度范围很广(<1 m至~100 m), 但通常在水深20 m以内的岩石或海藻上出现(Hallock, 1999)。

*Amphistegina*属具有特征的钙化成壳方式, 其壳体在背腹两侧均呈现出渐开线状, 当形成新的房室时, 方解石由中心向两边不断沉淀, 从有孔虫的纵剖面(穿过背部与腹部顶点的剖面)看, 中部有一扇形无孔区域, 含有多层同心状纹层。其中, 较窄的深色层为初级方解石层, 较宽的浅色层为次级方解石层(Toler *et al*., 2001)。knob区域包含有孔虫整个生长阶段连续沉积的壳体, 面积大且无孔, 便于进行微区测试。

对表层沉积物样品中有孔虫进行挑选和鉴定后, 发现银屿岛外礁坡的优势种为*Amphistegina lobifera*, 甘泉岛外礁坡的优势种为*Amphistegina lessonii*, 故选择这两种有孔虫进行测试。LYJ2优势种为*A. lobifera*, 从岩心顶部到底部每间隔25~30 cm取一个样, 共取10个样。由于LYJ2长度较短, 为了更好地观测成岩作用的影响, 另取一较长岩心CK2约3.6 Ma处的*A. lobifera*进行测试。观察多个有孔虫均发现其高镁层溶解, 取两个样进行测试。

1.3　研究方法

1.3.1　样品前处理

考虑到礁区LBF直径的范围, 使用孔径0.063 mm及2 mm标准样筛将表层沉积物及岩心样品水洗过筛, 保留两筛之间的部分。为了去除有孔虫壳体中残留的有机质, 使用3%过氧化氢和0.4%

中国知网　https://www.cnki.net

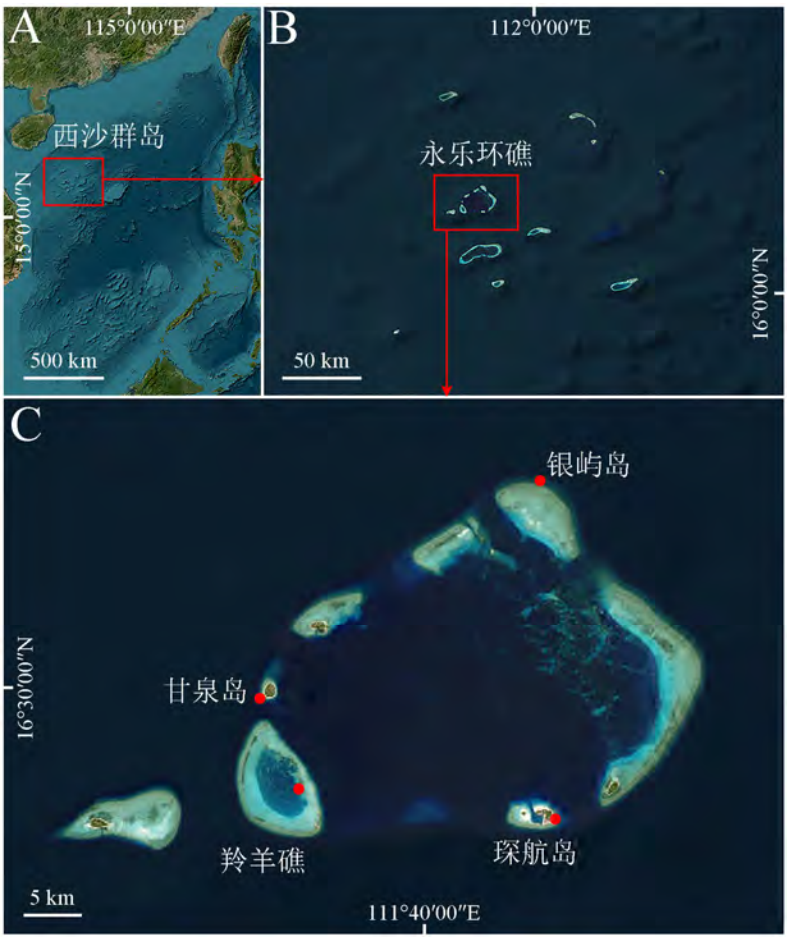


图1 研究区地图及采样位置

红点为采样位置，表层沉积物样品采自银屿岛和甘泉岛，岩心样品采自羚羊礁和琛航岛

Fig. 1 Map showing the sample locations

Red dots represent sampling sites. Surface sediment samples were collected from the Yinyu Island and the Ganquan Island, while core samples were obtained from the Lingyang Reef and the Chenhang Island

表 1 已知的LBF Mg/Ca值分布范围(包括全壳分析和微区分析)

Table 1 Reported distribution range of Mg/Ca values of LBF (whole-test and in-situ)

目	科	属	Mg/Ca值(mmol/mol)	来源
Rotaliida	Amphisteginidae	*Amphistegina*	15−90	(Raja *et al.*, 2007; Mewes *et al.*, 2014; Geerken *et al.*, 2018; Khanolkar *et al.*, 2021)
	Nummulitidae	*Heterostegina*	48.8−150	(宫巨嵩和史宇坤, 2017)
		Operculina	102.9−155.4	(Evans *et al.*, 2013; Evans *et al.*, 2015; 童铄云等, 2023)
	Calcarinidae	*Baculogypsina*	106.7−281.8	(Raja *et al.*, 2007; Gacutan *et al.*, 2017; 童铄云等, 2023)
		Calcarina	116.6−317.4	(Raja *et al.*, 2007; Gacutan *et al.*, 2017)
		Neorotalia	214−301.1	(Raja *et al.*, 2005; Raja *et al.*, 2007)
Miliolida	Soritidae	*Amphisorus*	224−256	(Raja *et al.*, 2005)
		Marginopora	213−375.85	(Raja *et al.*, 2005; Raja *et al.*, 2007)
		Archaias	55.5−150	(Toler *et al.*, 2001; Gacutan *et al.*, 2017; 宫巨嵩和史宇坤, 2017)
	Peneroplidae	*Laevipeneroplis*	130−150	(宫巨嵩和史宇坤, 2017)

中国知网 https://www.cnki.net

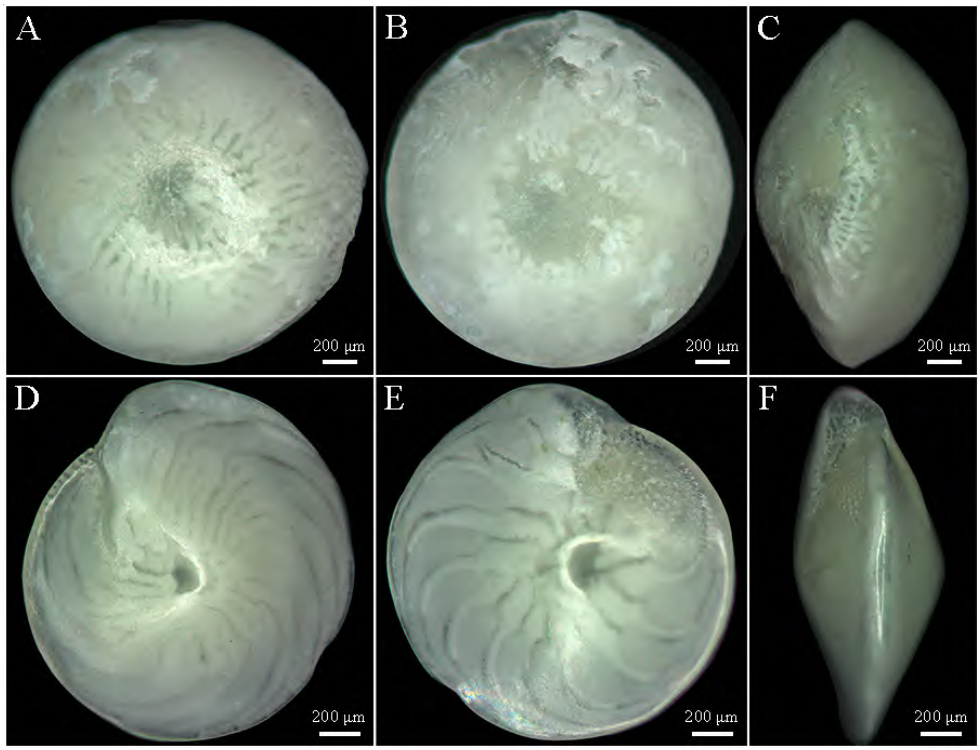


图 2　*A. lobifera*和*A. lessonii*的体视镜下照片

A−C. *A. lobifera*, 采自银屿岛: A. 背视; B.腹视; C.口视; D−F. *A. lessonii*, 采自甘泉岛: D. 背视; E. 腹视; F. 口视

Fig. 2　Light photos of *A. lobifera* and *A. lessonii*.

A−C. *A. lobifera* from the Yinyu Island: A. dorsal view; B. umbilical view; C. apertural view; D−F. *A. lessonii* from the Ganquan Island: D. dorsal view; E. umbilical view; F. apertural view

氢氧化钠混合溶液将其浸泡24h (Barker *et al.*, 2003), 然后使用超纯水清洗两遍。烘干后, 在体式镜(Zeiss Stemi 508)下挑取有孔虫样品, 然后用无水甲醇溶液超声清洗(＞5s), 移除沉积粘土, 烘干后将有孔虫封进环氧树脂, 待其凝固后, 脱模后打磨并抛光, 使其纵剖面knob区域生长纹层清晰。抛光完成后, 使用超纯水清洗, 再将其放在无水甲醇溶液中超声清洗(＞5s), 去除打磨抛光过程粘在样品上的杂质, 烘干后在偏光显微镜(Nikon LV100NPOL)反射光模式下拍摄并标记出所需测试区域(图3)。另外, 在EPMA测试前将样品镀碳。

1.3.2　微区Mg/Ca值测试

为了探讨两种有孔虫壳体中Mg/Ca值的分布规律, 使用EPMA对表层沉积物中*Amphistegina lobifera*和*Amphistegina lessonii*进行了面扫、线扫和点分析(分析位置见图3-A, 3-B, 3-D, 3-E)。面扫描及线扫描属于半定量分析, 点分析属于定量分析。面扫描能够获得直观的元素整体分布状况; 线扫时选择横纵两个方向, 纵向线扫从中心穿过全部生长纹层, 以获得整个生长过程元素的变化信息, 横向线扫尽量可能多地穿过同一次级方解石层, 便于追踪元素在层内的变化特征; 点分析能够获得准确的元素含量, 打点位置尽量选择在较宽的次级方解石层, 以最大限度排除Mg含量较高的初级方解石层的影响。为了比较EPMA和LA-ICP-MS两种微区分析方法的差异, 使用LA-ICP-MS对表层沉积物中的*A. lobifera*进行了Mg、Ca点分析, 打点位置紧靠EPMA(图3-B)。

为了分析成岩作用的影响, 使用EPMA对两个岩心LYJ2及CK2的*A. lobifera*进行了Mg、Ca面扫描(图7), 对LYJ2的*A. lobifera*还进行了Mg、Ca线性扫描(图3-C), 并使用LA-ICP-MS 对两个岩心的*A. lobifera*进行了点分析(图3-C, 3-F), 以便和表层沉积物样品作定量对比。

EPMA测试使用的仪器为日本电子JXA-8230, 测试条件为电流5×10^{-9}A, 电压15kV, 束斑大小10 μm。数据校正采用日本电子的ZAF校正方法。LA-ICP-MS测试使用的仪器为相干193 nm准分子激光剥蚀系统和安捷伦电感耦合等离子体质谱仪

中国知网　https://www.cnki.net

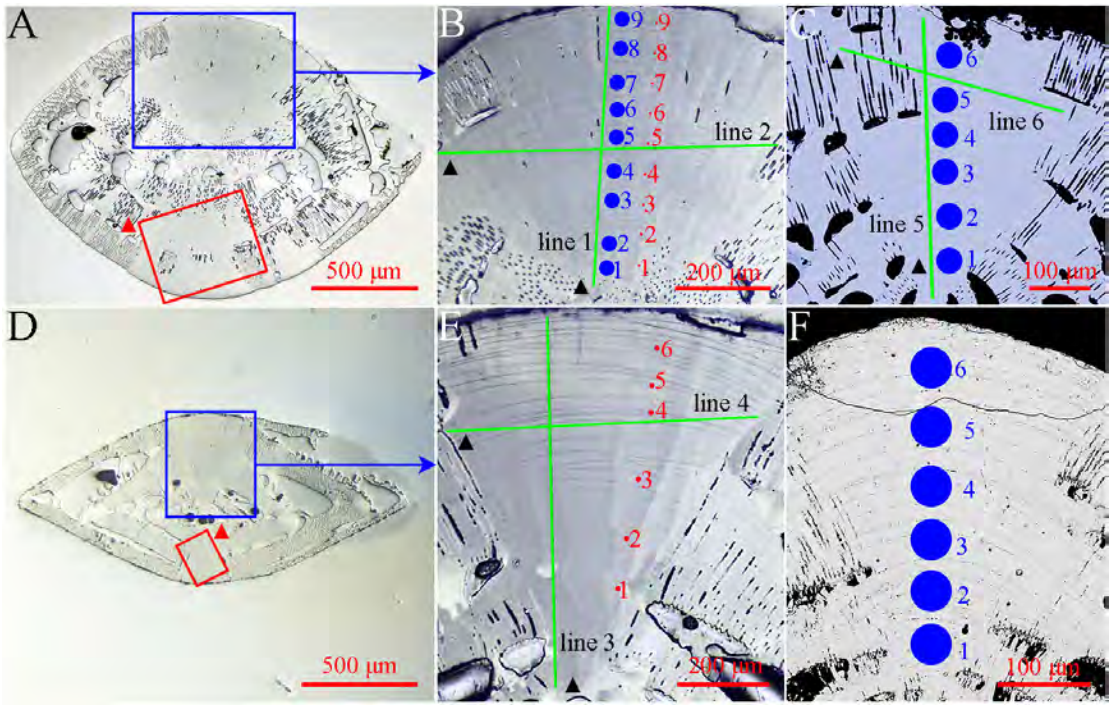


图 3 有孔虫测试区域示意图

A. 银屿岛表层*A. lobifera*.完整纵切面; B. 为图A中的蓝框放大, 显示测样位置; C. LYJ2 *A. lobifera*测样位置; D. 甘泉岛表层*A. lessonii*完整纵切面; E. 图D的蓝框区域放大; F. CK2 *A. lobifera*测样位置; 红框为面扫描区域, 红色三角标为面扫图左上角; 绿线为EPMA线扫位置, 实际宽度为1 μm, 黑色三角标为线扫起始位置; 红点和蓝点分别为EPMA和LA-ICP-MS打点位置, 其大小代表两种方法的束斑大小

Fig. 3 Analysis regions in the foraminiferal cross sections

A. Vertical section of *A. lobifera* from the Yinyu Island surface; B. close-up of the blue box in A showing analysis regions; C. analysis regions of *A. lobifera* from Core LYJ2; D. Vertical section of *A. lessonii* from surface sediments in the Ganquan Island; E. close-up of the blue box in D showing analysis regions; F. analysis regions of *A. lobifera* from Core CK2; red boxes represent EPMA mapping areas; red triangles represent the upper-left corner; green lines represent line-analysis position, with an actual width of 1 μm; black triangles marks the starting point; red and blue dots represent the point-analysis positions of EPMA and LA-ICP-MS, respectively, with their sizes corresponding to the spot sizes of the two methods

(Agilent 7900)联机, 测试条件为激光能量80 mJ, 激光束斑直径44 μm, 剥蚀频率5Hz。两种微区方法所得的元素结果全部转化为元素/钙形式。

2 结 果

2.1 表层沉积物两种有孔虫壳体的元素/钙分布规律及其Mg/Ca定量分析结果

表层沉积物中两种有孔虫的EPMA元素/钙面扫描结果(图4)显示, 二者的各元素/钙分布特征非常相似。Mg/Ca值远高于Na/Ca、Fe/Ca和P/Ca且变化范围较广, 在knob区域呈现出清晰的周期性分布, 在较窄的初级方解石层高, 在较宽的次级方解石层低。Na/Ca具有与Mg/Ca值相似的周期性分布特征, 但与Mg/Ca值相比变化不显著。Fe/Ca、P/Ca低, 分布均匀。共测试两组, 同种有孔虫面扫描结果具有相似性, 选择其中一组呈现(图4)。

表层沉积物两种有孔虫的EPMA Mg/Ca线性扫描结果(图5-A−D)与面扫描结果一致, 都显示出周期性规律变化。线扫结果还显示了两种有孔虫Mg/Ca分布的细微差别。两种有孔虫的Mg/Ca值均在次级方解石层内低而稳定, 在初级方解石层出现峰值。但初级方解石层的Mg/Ca峰值分别往内、外两侧过渡到次级方解石层边缘的Mg/Ca低值时, 两种有孔虫Mg/Ca值的变化幅度不一致, *Amphistegina lobifera*内侧平缓、外侧陡峭(图5-A红框中蓝色箭头指示内侧, 绿色箭头指示外侧), 而*Amphistegina lessonii*两侧都较为陡峭。

表层沉积物中*A. lessonii*的EPMA法Mg/Ca值范围为13.85−44.10 mmol/mol, *A. lobifera*的EPMA法和LA-ICP-MS法Mg/Ca值范围分别为18.11−42.86 mmol/mol和23.54−38.28 mmol/mol。整体上, 两种有孔虫的Mg/Ca值范围相近, *A. lessonii* EPMA的Mg/Ca值上下限均略大于*A. lobifera*的。与

中国知网 https://www.cnki.net

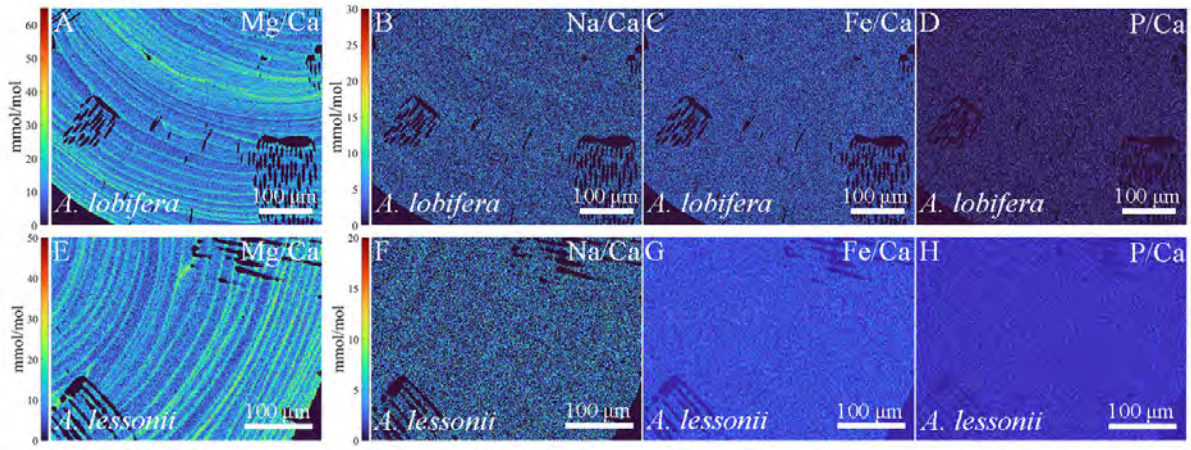


图 4　表层沉积物中*A. lobifera*和*A. lessonii*的元素/钙分布(具体面扫位置见图 3)

Fig. 4　Elements/Ca distribution maps of *A. lobifera* and *A. lessonii* from surface sediments (Detailed mapping positions provided in Fig. 3)

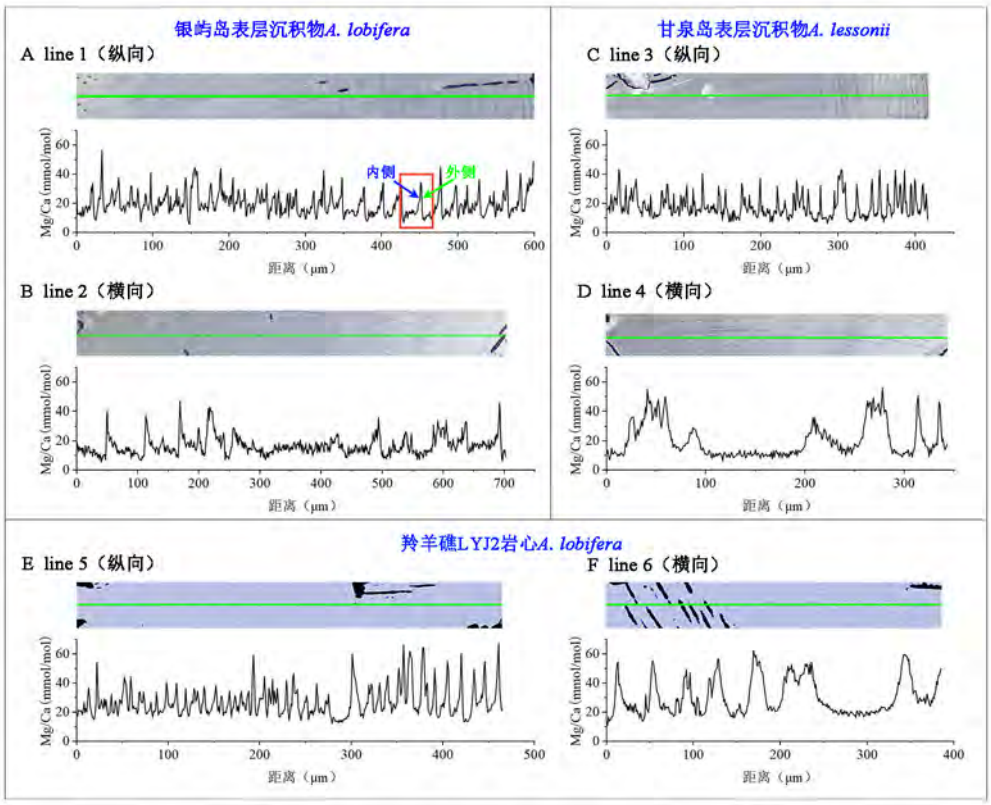


图 5　有孔虫Mg/Ca值EPMA线扫结果(具位分析置见图 3)

Fig. 5　EPMA Mg/Ca line-scan results of the foraminifers (Detailed scan positions provided in Fig. 3)

前人研究相比，本研究两种有孔虫微区Mg/Ca值均略微偏低(表2)。

A. lobifera 的两种微区方法对比显示，EPMA方法的Mg/Ca值上下限均略大于LA-ICP-MS方法的(图6-A)。

2.2　岩心*Amphistegina lobifera*壳体的Mg/Ca分布规律及其定量分析结果

LYJ2 *Amphistegina lobifera*的扫描电镜下照片(图7-B)显示，其knob区域保存完好，无明显的溶解现象，而CK2 *A. lobifera*高镁初级方解石层则

中国知网　https://www.cnki.net

表 2 *A. lobifera*和*A. lessonii*微区Mg/Ca值

Table 2 In-situ Mg/Ca values of *A. lobifera* & *A. lessonii*

属种	Mg/Ca值范围(mmol/mol)	方法	来源
A. lobifera	35.8−50.8	LA-ICP-MS	(宫巨嵩和史宇坤, 2017)
	23.54−38.28	LA-ICP-MS	本研究
	18.11−42.86	EPMA	本研究
A. lessonii	15−80	LA-ICP-MS	(Khanolkar *et al*., 2021)
	18−75	LA-ICP-MS	(Geerken *et al*., 2018)
	13.85−44.10	EPMA	本研究

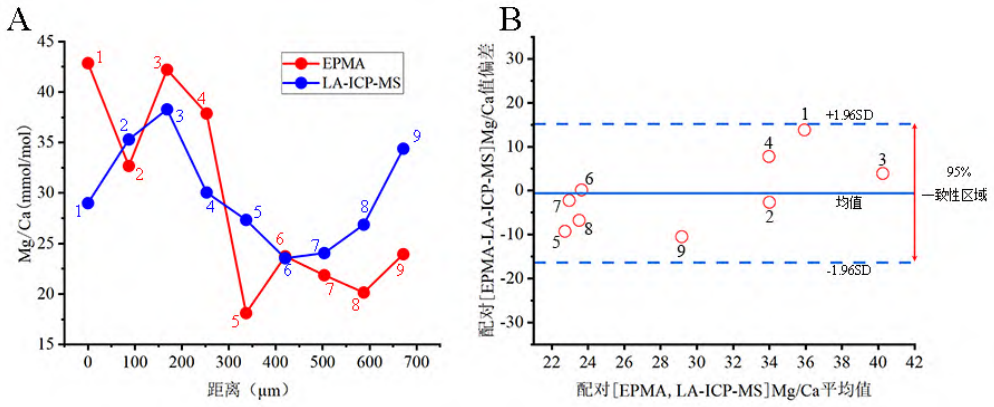


图 6 EPMA和LA-ICP-MS两种分析方法的比较

A. 同一个体相邻位置两种微区方法Mg/Ca点分析结果, 具体分析位置见图3-B; B. 两种微区方法Mg/Ca值的Bland-Altman图, 展示配对偏差与均值的关系

Fig. 6 Comparison of Mg/Ca between the EPMA and LA-ICP-MS methods

A. Mg/Ca ratios at adjacent positions of the same individual using two analysis methods, with detailed position shown in Fig. 3-B; B. Bland-Altman plot for the EPMA and LA-ICP-MS results, demonstrating the paired bias against the mean

发生了明显的溶解(图7-E)。Mg/Ca值面扫结果显示, LYJ2中*A. lobifera*的Mg/Ca值较高, 且具有与现代表层沉积物有孔虫相同的周期性分布特征, 而CK2中该种的Mg/Ca值明显降低, 周期性分布特征微弱。同时, LYJ2中*A. lobifera*的Mg/Ca的横纵线性扫描结果(图5-E, 5-F)都显示了与表层沉积物(图4-A)相似的变化特征。

LA-ICP-MS点分析结果显示(图8), LYJ2 *A. lobifera*的Mg/Ca分布范围略大于表层沉积物, 均值略小于表层沉积物, 二者整体接近。而CK2 *A. lobifera*的Mg/Ca最高值低于表层沉积物及LYJ2的最低值, 其整体Mg/Ca分布范围及Mg/Ca均值远低于表层沉积物及LYJ2的结果。

3 讨 论

3.1 微区分析的优势及不同微区分析方法的差异

3.1.1 全壳分析与微区分析的对比

全壳分析是有孔虫壳体微量元素测试最常使用的方法, 通常需要挑选大于25毫克的有孔虫样品(高剑峰等, 2003), 进行清洗、溶解后送进光谱仪或质谱仪进行测试(孟宪伟等, 2001)。全壳分析要求有孔虫壳体完整, 遇到残缺样品难以发挥作用, 其前处理步骤繁琐、冗长, 通常需要将有孔虫的元素含量稀释至一定倍数进行测试, 可能引入人为误差, 同时, 有孔虫壳体可能受到的次生作用或铝硅酸盐沾染, 都可能影响分析结果的准确性(宫巨嵩和史宇坤, 2017)。作为整体分析方法, 全壳分析无法提供足够高的空间分辨率, 通常只能对有孔虫属种间及个体间的地球化学元素进行研究, 不能深入解析有孔虫个体内部的地球化学元素变化。

原位微区分析通常能够在微米级的尺度上对固体样品进行元素定量分析, 微区原位分析技术省去了繁琐的样品消解、分离和富集等前处理流程, 具有简单、快速、实时在线等优点(Liu *et al*., 2013)。相较于全壳分析, 微区分析具有更高的分辨率、准确性及灵活度, 它可以针对有孔虫特定区域的化学成分、晶体结构等进行定量或定性的原

中国知网 https://www.cnki.net

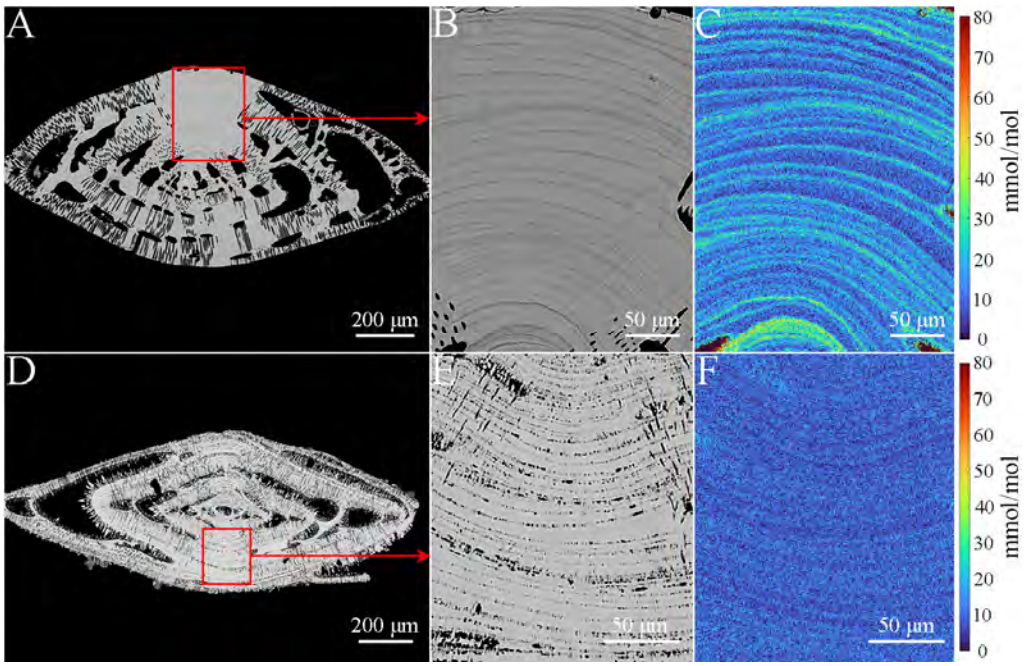


图 7　LYJ2 和CK2 中*A. lobifera*的EPMA面扫描区域细节特征及其Mg/Ca值分布

A−C. *A. lobifera*，来源于LYJ2: A. 完整纵切面; B. 为图A中面扫描红框区域放大，展示knob区域细节特征; C. 为图B中面扫描区域Mg/Ca值结果; D−F. *A. lobifera*，来源于CK2: D. 完整纵切面; E. 为图D中面扫描红框区域放大，展示knob区域细节特征; F. 为图E中面扫描区域Mg/Ca值结果

Fig. 7　The intra-test details and Mg/Ca distributions of *A. lobifera* from the cores of LYJ2 and CK2

A−C. *A. lobifera* from Core LYJ2: A. the cross section; B. close-up of the red box in A showing details of the knob area; C. Mg/Ca distribution of the knob area; D−F. *A. lobifera* from Core CK2: D. the cross section; E. close-up of the red box in D showing details of the knob area; F. Mg/Ca distribution of the knob area

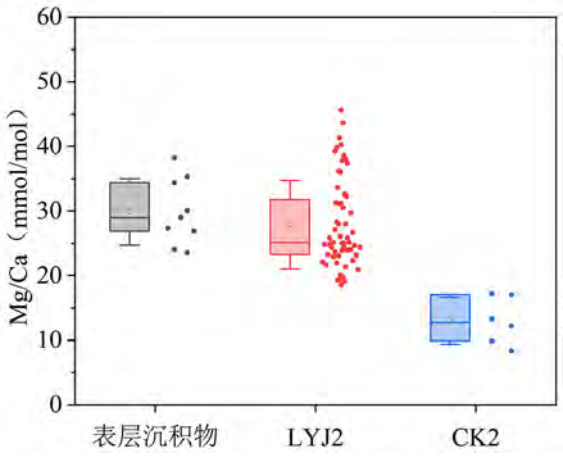


图 8　表层沉积物及岩心中*A. lobifera*的Mg/Ca值结果对比

LYJ2数据为从顶到底共取10个样的综合结果

Fig. 8　Comparison of the Mg/Ca values of *A. lobifera* from the surface sediments and cores

Data of Core LYJ2 represents the combined results from 10 samples

位研究，并且能够生成元素分布图像，直观地展示出壳体不同区域的元素分布情况，以及有孔虫的形貌和元素组成之间的关系(陈意等, 2021)。

LBF壳体的地球化学信号容易受到生命效应的影响，而微区分析有助于分析解读这一影响，提升其在古环境重建中的潜力(Raja *et al.*, 2005; Geerken *et al.*, 2019; Dijk *et al.*, 2020)。Raja(2005)等人对LBF *Marginopora kudakajimaensis*的外房室和其余部分进行了Mg/Ca值测试，发现其Mg/Ca值具有较高壳内异质性，可能是受共生藻类和个体寿命等因素的影响，虽然整个有孔虫壳体的Mg/Ca值与温度的相关性很差，但其外房室的Mg/Ca值与温度具有相关性，体现了选择合适位置进行微区分析的实际应用价值。

3.1.2　EPMA及LA-ICP-MS两种微区分析的差异

Balestra(2021)等人比较了EPMA和LA-ICP-MS两种方法在有孔虫Mg/Ca测试中的差异，使用的束斑分别为10 μm和12 μm。结果表明，当Mg/Ca值低于13 mmol/mol，两种微区方法具有一致性，当Mg/Ca值高于13 mmol/mol，EPMA的测量值偏高。由于预计两种仪器都不会出现尺度依赖性偏差，因此，这种差异可能是仪器灵敏度、光束饱和度影响导致。另外，LA-ICP-MS方法使用的束斑过小，可能对数据的准确性造成一定程度的影响。

中国知网　https://www.cnki.net

本研究使用EPMA和LA-ICP-MS对*Amphistegina lobifera*进行Mg、Ca点分析，并作Bland-Altman图展示两种微区方法Mg/Ca值的一致性情况(图6-B)。配对点全部落在95%一致限内，表明两种微区方法的一致性良好。然而它们的偏差并不是全正或全负，偏差可能来源于束斑大小及打点位置的差异。EPMA与LA-ICP-MS使用的束斑分别为10 μm和44 μm，而从图3-B可以看到，每一层的次级方解石的宽度不固定，宽度最小小于5 μm，最大约为40 μm。结合图3和图6-A可以看到，在配对点中，涵盖初级方解石层和靠近初级方解石层前侧的点Mg/Ca值偏高，这与*A. lobifera* EPMA线性扫描的Mg/Ca值分布规律细节(图5-A)吻合。这种Mg/Ca壳内分布特征导致了微区方法使用的束斑越小，受打点位置的影响更大，而较大的束斑反而能体现束斑范围内的平均情况。在*A. lobifera*两种微区分析方法的Mg/Ca值点分析结果中，EPMA的波动程度比LA-ICP-MS大，也印证了这一观点(图6-A)。为了数据的准确性，选择合适的微区方法及打点位置尤为重要。

3.2 大型底栖有孔虫Mg/Ca值微区分析的应用潜力

3.2.1 LBF Mg/Ca值的影响因素

LBF的Mg/Ca值，除了受到主要因素温度的影响外，还受海水盐度变化(Dissard *et al*., 2010; Geerken *et al*., 2018; Hauzer *et al*., 2021)、长时间内海水Mg/Ca值的波动(Segev & Erez, 2006)和生命效应(Raja *et al*., 2005, 2007; Khanolkar *et al*., 2021)等因素的影响，通过微区分析能够解读并帮助排除这些因素的影响。

环境相似的情况下，种间差异也会导致Mg/Ca值的不同。线扫结果表明，*Amphistegina lobifera*和*A. lessonii*的Mg/Ca值的细节分布规律略有不同(图5-A)，这可能与二者的钙化过程的差异有关。相较于*A. lessonii*, *A. lobifera*个体尺寸更大，寿命更长，碳酸钙沉积速率更快(Hallock *et al*., 1986)。在古环境重建的研究中，同属不同种的有孔虫往往被视作潜在的替代指标。然而，本研究表明，同属不同种的有孔虫Mg/Ca值壳内分布规律存在细节差异，这种差异可能会影响其Mg/Ca值的整体结果，也为实际应用中微区分析位置的选择提供了参考。因此，利用微区分析技术精确捕捉不同有孔虫壳内Mg/Ca比值差异，对于解析其原因及提升古环境重建的精度至关重要。

而利用岩心LBF的Mg/Ca值进行古温度重建时，还需考虑成岩作用的影响。本研究发现，通过扫描电镜观察并结合其Mg/Ca值分布范围，可以识别出其是否受明显的成岩作用影响。表层沉积物(图3-B, E)及LYJ2 (图7-B)中*A. lobifera*的knob区域完整，未观察到明显的溶解现象，并且其Mg/Ca值范围与表层沉积物的接近，表明在约2 600年尺度上，LYJ2有孔虫未受到明显的成岩作用影响，其Mg/Ca仍具有反映海水温度的潜力。相较于表层沉积物中的*A. lobifera*，LYJ2中*A. lobifera*的Mg/Ca上下限值略大，均值略低。其原因可能有：(1) 表层沉积物中*A. lobifera*的样品数量较少，受生命效应影响，其Mg/Ca可能不具有绝对的代表性；(2) *A. lobifera*的Mg/Ca值具有异质性，受打点位置的影响较大；(3) 岩心中的*A. lobifera*的Mg/Ca值反映了~2 665 aBP时期的海水温度变化；(4) 表层沉积物*A. lobifera*采集自外礁坡，LYJ2 *A. lobifera*采集自内礁坪，其受水动力等条件影响不同，例如，水动力影响与共生藻类光合作用相关的CO_2和O_2的交换(Hallock *et al*., 1986)；(5) LYJ2 *A. lobifera*可能已经发生轻微溶解。

而CK2 *A. lobifera*的knob区域的高镁层明显发生溶解，且其Mg/Ca最高值低于表层沉积物及LYJ2的最低值，表明在该岩心3.6Ma左右处，有孔虫明显受到了成岩作用的影响。因此，重建准确的古海水温度需要排除和量化这种影响。通过将测试位置尽量选择在低镁层，可以最大限度地排除高镁层溶解的影响；前人对浮游有孔虫的研究表明，水深、底部海水[CO_3^{2-}]、有孔虫壳体重量及有孔虫结晶度等指标具有校正有孔虫高镁层的溶解对Mg/Ca的影响的潜力(Lea *et al*., 2000; Broecker *et al*., 2001; Dekens *et al*., 2002; Tachikawa *et al*., 2003; Bassinot *et al*., 2004; Procter *et al*., 2024)。因此，通过选择合适的位置、寻找量化溶解程度的方法，即使受到成岩作用的影响，LBF仍然具有一定的反映古海水温度的潜力。

3.2.2 LBF Mg/Ca值微区分析应用潜力分析

Khanolkar (2021)等人在四个不同季节(2003年9月、11月、2004年1月和3月)从日本冲绳县赤岛海域的珊瑚礁中采集了多个*Amphistegina lessonii*活体成年样品(样品直径为900~1 200 μm)，使用LA-ICP-MS分析了样品从外房室到初房隔壁的元素/钙。并结合Hallock(1981a)通过培养实验得出的生长曲线，推断出了*A. lessonii*每个房室的生长时间。从而根据资料记录的海水温度，建立了该种的Mg/Ca值-温度经验公式。在2−3个月的生长期内，

中国知网 https://www.cnki.net

每个*A. lessonii*样品壳体的平均Mg/Ca值与其生长期的平均温度显著相关, 由以下指数方程和线性方程描述: ① Mg/Ca 值 (mmol/mol)=$26.8e^{0.0155T}$±0.94(R^2=0.45, p<0.05) 和 ② Mg/Ca 值 (mmol/mol)=0.607T+24.5±0.94(R^2=0.46, p<0.05)。同一采样月份*A. lessonii*样品壳体的平均Mg/Ca值与其生长期间的平均温度相关性更高, 由以下指数方程和线性方程描述: ③Mg/Ca值(mmol/mol)=$25.904e^{0.0172T}$±1.31(R^2=0.78, p<0.05) 和 ④ Mg/Ca 值 (mmol/mol)=0.67T+23.08±1.31(R^2=0.80, p<0.05)。

Khanolkar (2021)等人的研究中, 所有*A. lessonii*样品壳体Mg/Ca值范围约为15−80 mmol/mol, 明显超过了当地海水季节性变化的尺度, 但将壳体Mg/Ca值取平均值后, 仍与温度相关, 表明虽然初级方解石对结果有影响, 但由于其含量少, 不影响其整体趋势。因此, 选择合适的微区测试方法及测试位置, LBF的Mg/Ca值仍然具有重建地质历史时期海水温度的潜力。与Khanolkar(2021)等人的研究相比, 本研究的*A. lessonii*壳体Mg/Ca值偏低, 且变化幅度较小。只有将本研究*A. lessonii*的EPMA分析的Mg/Ca最大值44.10 mmol/mol代入④公式, 得到的温度结果29.42℃才在永乐环礁年际表层海水温度变化的范围内。本研究与Khanolkar(2021)等人研究的*A. lessonii*壳体Mg/Ca值的差异可能由以下原因导致:

(1) 初级方解石层的影响。Khanolkar (2021)等人的研究在有孔虫隔壁进行打点时, 未考虑初级方解石和次级方解石的差异, 部分Mg/Ca值高值可能受初级方解石层的影响。

(2) 微区分析方法的差异。本研究使用10 μm束斑EPMA方法, 而Khanolkar (2021)等人的研究使用30 μm束斑LA-ICP-MS方法对*A. lessonii*壳体的Mg/Ca值进行测试。而本研究使用*Amphistegina lobifera*对比两种微区方法的Mg/Ca值, 发现其受束斑大小及打点位置的影响。

(3) 高镁方解石的溶解。高镁方解石溶解度相对较高, 通常导致有孔虫壳体发生选择性溶解。Khanolkar (2021)等人的研究样品为活体有孔虫, 而本研究有孔虫样品采自表层沉积物, 可能已经沉积了一段时间, 其壳体高镁部分可能已经开始发生溶解。

(4) 地理环境差异间接影响有孔虫共生藻类的活性及生产力。LBF沉淀初级方解石受环境pH影响, 而共生藻类日间的光合作用和夜间的呼吸作用可改变有孔虫周围微环境的pH (Rink *et al.*, 1998; Köhler-Rink & Kühl, 2005)。Khanolkar (2021)等人研究的采样地点受潮汐及风暴影响, 海水浑浊和光强度降低, 间接影响了有孔虫共生藻类的光合作用和呼吸作用。

其他研究者利用微区分析方法, 还建立了以下几种LBF的Mg/Ca值-温度经验公式。Maeda (2017)等人通过实验室培养发现钙质有孔壳有孔虫*Calcarina gaudichaudi*和钙质无孔壳有孔虫*Amphisorus kudakajimaensis*的Mg/Ca值-温度变化相似。因此, 建立了两个种都适用的Mg/Ca值-温度经验公式: Mg/Ca=2.85T+81.20。Evans (2013)等人对*Operculina ammonoides*进行室内培养并建立了Mg/Ca值-温度经验公式。该种是已灭绝的始新世*Nummulites*属最亲近的现存亲近种, 因此, 根据该经验公式, 利用*Nummulites djokdjokartae*可重建始新世中期热带海面温度的季节性变化。结果表明, 始新世中期年温度变化范围为5−6℃, 其季节性变化大于现代的季节性变化, 这与始新世季节性表层海洋冷却一致。

*Amphistegina*属分布广泛、knob区域连续面积大且生长纹层明显、壳体Mg/Ca值在LBF中较低, 在重建海水温度方面有其独特的优势。本研究发现, 在*Amphistegina*两种有孔虫壳体中, Mg/Ca值均具有周期性的分布特征, 且在次级方解石中均较为稳定。另外, 两种有孔虫Mg/Ca值数值略具差异, 分布模式也稍有不同, 考虑到微区方法的高分辨率和精确性, 实际运用时同属不同种最好不要混用。同时, 结合有孔虫扫描电镜特征及其Mg/Ca值范围可以识别出其是否受明显的成岩作用影响。综上, *Amphistegina*属Mg/Ca值微区分析具有一定的应用潜力, 在实际应用中还需进一步评估。

4　结　论

为探究礁区LBF Mg/Ca值微区分析在重建海水温度中的应用潜力, 本研究使用EPMA及LA-ICP-MS对采自中国南海西沙岛礁表层沉积物及岩心中的*Amphistegina*属有孔虫进行了Mg/Ca值及其他元素/钙原位微区分析测试, 得到以下结论:

(1) *Amphistegina*属的Mg/Ca值相对其他LBF较低, 对温度的变化更敏感; 壳内含有硅藻共生体, 水深分布范围广泛, 在珊瑚礁中占据优势地位, 易于获取; 其含有的knob区域连续面积大, 能够记录连续的信息, 便于进行微区测试。

(2) 两种有孔虫壳体的Mg/Ca值均具有周期性分布特征。此外, 在两种有孔虫的同层次级方解石,

中国知网　https://www.cnki.net

Mg/Ca值均较为稳定，但存在细微差别。*Amphistegina lobifera*初级方解石层Mg/Ca峰值过渡到两侧次级方解石层Mg/Ca低值的变化幅度不一致，而*Amphistegina lessonii*则大致相同。因此，在探究LBF的微区分析重建海水温度的研究潜力时，需要考虑同属不同种有孔虫间Mg/Ca值分布差异的影响。

(3) 对比两种微区分析方法，发现有孔虫的Mg/Ca值，受初级方解石层的影响较大，当微区方法使用的束斑越小，受打点位置的影响越大。为了提升数据的可靠性，选择合适的微区方法及打点位置尤为重要。

(4) 岩心样品中的有孔虫可能会受到成岩作用影响，应进行检测及排除，提高分析测试结果的准确性。

综合本研究及前人研究结果，LBF的Mg/Ca值微区分析在古环境重建方面具有一定的应用潜力，但需注意样本选择、技术优化及影响因素评估等实际应用中的关键问题。

参考文献

王丽荣, 赵焕庭, 2008. 我国南海珊瑚礁区现代沉积底栖有孔虫的生态特征研究综述. 热带地理, **28**(4): 346–350

陈 龙, 黄明立, 史宇坤, 2019. 底栖有孔虫壳体微量元素地球化学指标及其“生命效应”. 微体古生物学报, **36**(2): 103–114

陈 意, 胡兆初, 贾丽辉等, 2021. 微束分析测试技术十年(2011~2020)进展与展望. 矿物岩石地球化学通报, **40**(1): 1–35, 253

孟宪伟, 杜德文, 程振波, 2001. 冲绳海槽有孔虫壳体的微量元素Sr, Nd同位素地球化学. 海洋学报, **23**(2): 62–68

孟 敏, 2022. 西沙群岛有孔虫分布特征及其对2000万年以来古环境演变的启示. 广西大学博士学位论文, 1–215

宫巨嵩, 史宇坤, 2017. 现代大型底栖有孔虫壳体地球化学元素的原位微区分析. 微体古生物学报, **34**(3): 291–301

秦国权, 1987. 西沙群岛“西永一井”有孔虫组合及该群岛珊瑚礁成因初探. 热带海洋, **6**(3): 10–20

高剑峰, 陆建军, 赖鸣远等, 2003. 岩石样品中微量元素的高分辨率等离子质谱分析. 南京大学学报: 自然科学版, **39**(6): 844–850

童铄云, 潘诗洋, 胡伟康等, 2023. 激光剥蚀-电感耦合等离子体质谱(LA-ICP-MS)法测定底栖有孔虫中的元素/钙比值. 中国无机分析化学, **13**(9): 967–974

A’ZIZ A N A, MINHAT F I, PAN H-J *et al*., 2021. Reef foraminifera as bioindicators of coral reef health in southern South China Sea. Scientific Reports, **11**(1): 8890

BALESTRA B, ROSE T, FEHRENBACHER J *et al*., 2021. In situ Mg/Ca measurements on foraminifera: comparison between Laser Ablation Inductively Coupled Plasma Mass Spectrometry and wavelength-dispersive X-ray spectroscopy by Electron Probe Microanalyzer. Geochemistry, Geophysics, Geosystems, **22**(2): e2020GC009449

BARKER S, GREAVES M, ELDERFIELD H, 2003. A study of cleaning procedures used for foraminiferal Mg/Ca paleothermometry: Mg/Ca paleothermometry. Geochemistry, Geophysics, Geosystems, **4**(9): 2003GC000559

BASSINOT F C, MÉLIÈRES F, GEHLEN M *et al*., 2004. Crystallinity of foraminifera shells: a proxy to reconstruct past bottom water CO_3^{2-} changes? Geochemistry, Geophysics, Geosystems, **5**(8): 2003GC000668

BENTOV S, EREZ J, 2006. Impact of biomineralization processes on the Mg content of foraminiferal shells: a biological perspective. Geochemistry, Geophysics, Geosystems, **7**(1): 2005GC001015

BROECKER W S, ANDERSON R, CLARK E *et al*., 2001. Record of seafloor $CaCO_3$ dissolution in the central equatorial Pacific. Geochemistry, Geophysics, Geosystems, **2**(6): 2000GC000151

CHARRIEAU L M, ROLLION-BARD C, TERBRUEGGEN A *et al*., 2023. Controls on lithium incorporation and isotopic fractionation in large benthic foraminifera. Minerals, **13**(1): 127

CHEN C, LIN H-L, 2017. Applying benthic foraminiferal assemblage to evaluate the coral reef condition in Dongsha Atoll lagoon. Zoological Studies, **56**: 20

CHEN L, HUANG M L, SHI Y K, 2019. Geochemical trace element proxies of benthic foraminiferal shells and their vital effects. Acta Micropalaeontologica Sinica, **36**(2): 103–114

CHEN Y, HU Z C, JIA L H *et al*., 2021. Progress of microbeam analytical technologies in the past decade (2011−2020) and prospect. Bulletin of Mineralogy, Petrology and Geochemistry, **40**(1): 1–35, 253

COX K D, WOODS M B, REIMCHEN T E, 2021. Regional heterogeneity in coral species richness and hue reveals novel global predictors of reef fish intra-family diversity. Scientific Reports, **11**(1): 18275

DEKENS P S, LEA D W, PAK D K *et al*., 2002. Core top calibration of Mg/Ca in tropical foraminifera: refining paleotemperature estimation. Geochemistry, Geophysics, Geosystems, **3**(4): 1–29

DIJK I V, NOOIJER L D, BARRAS C *et al*., 2020. Mn incorporation in large benthic foraminifera: differences between species and the impact of pCO_2. Frontiers in Earth Science, **8**: 567701

DISSARD D, NEHRKE G, REICHART G J *et al*., 2010. The impact of salinity on the Mg/Ca and Sr/Ca ratio in the benthic foraminifera *Ammonia tepida*: results from culture experiments. Geochimica et Cosmochimica Acta, **74**(3): 928–940

DOO S S, HAMYLTON S, FINFER J *et al*., 2017. Spatial and temporal variation in reef-scale carbonate storage of large benthic foraminifera: a case study on One Tree Reef. Coral Reefs, **36**: 293–303

EVANS D, EREZ J, ORON S *et al*., 2015. Mg/Ca-temperature and seawater-test chemistry relationships in the shallow-dwelling large benthic foraminifera *Operculina ammonoides*. Geochimica et Cosmochimica Acta, **148**: 325–342

EVANS D, MÜLLER W, ORON S *et al*., 2013. Eocene seasonality and seawater alkaline earth reconstruction using shallow-dwelling large benthic foraminifera. Earth and Planetary Science Letters, **381**: 104–115

FAN T, YU K, ZHAO J *et al*., 2020. Strontium isotope stratigraphy and paleomagnetic age constraints on the evolution history of coral reef islands, northern South China Sea. GSA Bulletin, **132**(3-4): 803–816

FUJITA K, OTOMARU M, LOPATI P *et al*., 2016. Shell productivity of the large benthic foraminifer *Baculogypsina sphaerulata*, based on the population dynamics in a tropical reef environment. Coral Reefs, **35**: 317–326

FÖRDERER E M, RÖDDER D, LANGER M R, 2023. Global diversity patterns of larger benthic foraminifera under future climate change. Global Change Biology, **29**(4): 969–981

中国知网 https://www.cnki.net

FÖRDERER M, RÖDDER D, LANGER M R, 2018. Patterns of species richness and the center of diversity in modern Indo-Pacific larger foraminifera. Scientific Reports, **8**(1): 8189

GACUTAN J, VILA-CONCEJO A, NOTHDURFT L D *et al.*, 2017. Mg/Ca and Sr/Ca as novel geochemical proxies for understanding sediment transport processes within coral reefs. Estuarine, Coastal and Shelf Science, **197**: 54–68

GAO J F, LU J J, LAI M Y *et al.*, 2003. Analysis of trace elements in rock samples using HR-ICPMS. Journal of Nanjing University, **39**(6): 844–850

GEERKEN E, DE NOOIJER L J, ROEPERT A *et al.*, 2019. Element banding and organic linings within chamber walls of two benthic foraminifera. Scientific Reports, **9**(1): 3598

GEERKEN E, DE NOOIJER L J, VAN DIJK I *et al.*, 2018. Impact of salinity on element incorporation in two benthic foraminiferal species with contrasting magnesium contents. Biogeosciences, **15**(7): 2205–2218

GONG J S, SHl Y K, 2017. In-situ LA-ICP-MS trace elemental analysis of modern larger benthic foraminifera. Acta Micropalaeontologica Sinica, **34**(3): 291–301

HALLOCK P, 1981a. Light dependence in *Amphistegina*. Journal of Foraminiferal Research, **11**(1): 40

HALLOCK P, 1981b. Production of carbonate sediments by selected large benthic foraminifera on two Pacific coral reefs. Journal of Sedimentary Research, **51**(2): 467–474

HALLOCK P, 1999. Symbiont-bearing foraminifera. Modern Foraminifera. Kluwer Academic Publishers. 123–139

HALLOCK P, FORWARD L B, HANSEN H J, 1986. Influence of environment on the test shape of *Amphistegina*. Journal of Foraminiferal Research, **16**(3): 224

HALLOCK P, KOUKOUSIOURA O, BADRELDIN A M, 2024. Why *Amphistegina lobifera*, a tropical benthic foraminiferal species, is thriving at temperate latitudes in the Mediterranean Sea. Journal of Foraminiferal Research, **54**(3): 237–248

HAUZER H, EVANS D, MÜLLER W *et al.*, 2021. Salinity effect on trace element incorporation in cultured shells of the large benthic foraminifer *Operculina ammonoides*. Paleoceanography and Paleoclimatology, **36**(6): e2021PA004218

KHANOLKAR S, SCHIEBEL R, SINGH A *et al.*, 2021. Intratest variations in trace element composition of *Amphistegina lessonii* using Femtosecond-Laser Ablation-ICP-Mass Spectrometry: a field study from Akajima, Okinawa prefecture, Japan. Geochemistry, Geophysics, Geosystems, **22**(3): e2020GC009443

KÖHLER-RINK S, KÜHL M, 2005. The chemical microenvironment of the symbiotic planktonic foraminifer *Orbulina universa*. Marine Biology Research, **1**(1): 68–78

LEA D W, MASHIOTTA T A, SPERO H J, 1999. Controls on magnesium and strontium uptake in planktonic foraminifera determined by live culturing. Geochimica et Cosmochimica Acta, **63**(16): 2369–2379

LEA D W, PAK D K, SPERO H J, 2000. Climate impact of Late Quaternary equatorial Pacific sea surface temperature variations. Science, **289**(5485): 1719–1724

LIU Y, HU Z, LI M *et al.*, 2013. Applications of LA-ICP-MS in the elemental analyses of geological samples. Chinese Science Bulletin, **58**: 3863–3878

MAEDA A, FUJITA K, HORIKAWA K *et al.*, 2017. Evaluation of oxygen isotope and Mg/Ca ratios in high-magnesium calcite from benthic foraminifera as a proxy for water temperature. Journal of Geophysical Research: Biogeosciences, **122**(1): 185–199

MCNEIL M, NOTHDURFT L D, HUA Q *et al.*, 2022. Evolution of the inter-reef Halimeda carbonate factory in response to Holocene sea-level and environmental change in the Great Barrier Reef. Quaternary Science Reviews, **277**: 107347

MENG M, 2022. Study of the foraminiferal distribution in the Xisha islands: implications for paleoenvironment evolution since the 20 Ma. Doctor Degree Dissertation of Guangxi University, 1–215

MENG X W, DU D W, CHENG Z B, 2001. Trace elemental and Sr-Nd isotopic geochemistry of foraminirera shell of the Okinawa Trough. Acta Oceanologica Sinica, **23**(2): 62–68

MEWES A, LANGER G, DE NOOIJER L J *et al.*, 2014. Effect of different seawater Mg^{2+} concentrations on calcification in two benthic foraminifers. Marine Micropaleontology, **113**: 56–64

MORSE J W, ARVIDSON R S, LÜTTGE A, 2007. Calcium carbonate formation and dissolution. Chemical Reviews, **107**(2): 342–381

OLIVEIRA-SILVA P, BARBOSA C F, DE ALMEIDA C M *et al.*, 2012. Sedimentary geochemistry and foraminiferal assemblages in coral reef assessment of Abrolhos, Southwest Atlantic. Marine Micropaleontology, **94**: 14–24

PARKER J H, GISCHLER E, EISENHAUER A, 2012. Biodiversity of foraminifera from late Pleistocene to Holocene coral reefs, South Sinai, Egypt. Marine Micropaleontology, **86**: 59–75

PERRIN C, BOSELLINI F R, 2012. Paleobiogeography of scleractinian reef corals: changing patterns during the Oligocene–Miocene climatic transition in the Mediterranean. Earth-Science Reviews, **111**(1-2): 1–24

PROCTER F A, PIAZOLO S, JOHN E H *et al.*, 2024. Electron backscatter diffraction analysis unveils foraminiferal calcite microstructure and processes of diagenetic alteration. Biogeosciences, **21**(5): 1213–1233

QIN G Q, 1987. A preliminary study on foraminiferal assemblages of Well 1 Xiyong, Xisha islands and their coral reef formation. Tropic Oceanology, **6**(3): 10–20

RAJA R, SARASWATI P K, IWAO K, 2007. A field-based study on variation in Mg/Ca and Sr/Ca in larger benthic foraminifera. Geochemistry, Geophysics, Geosystems, **8**(10): 2006GC001478

RAJA R, SARASWATI P K, ROGERS K *et al.*, 2005. Magnesium and strontium compositions of recent symbiont-bearing benthic foraminifera. Marine Micropaleontology, **58**(1): 31–44

RENEMA W, 2018. Terrestrial influence as a key driver of spatial variability in large benthic foraminiferal assemblage composition in the Central Indo-Pacific. Earth-Science Reviews, **177**: 514–544

RINK S, KÜHL M, BIJMA J *et al.*, 1998. Microsensor studies of photosynthesis and respiration in the symbiotic foraminifer *Orbulina universa*. Marine Biology, **131**: 583–595

SARASWATI P K, SETO K, NOMURA R, 2004. Oxygen and carbon isotopic variation in co-existing larger foraminifera from a reef flat at Akajima, Okinawa, Japan. Marine Micropaleontology, **50**(3-4): 339–349

SEGEV E, EREZ J, 2006. Effect of Mg/Ca ratio in seawater on shell composition in shallow benthic foraminifera. Geochemistry, Geophysics, Geosystems, **7**(2): 2005GC000969

STEPHENSON C M, HALLOCK P, KELMO F, 2015. Foraminiferal assemblage indices: a comparison of sediment and reef rubble samples from Conch Reef, Florida, USA. Ecological Indicators, **48**: 1–7

TACHIKAWA K, VIDAL L, SEPULCRE S *et al.*, 2003. Size-normalised test weights, Mg/Ca and Sr/Ca of planktonic foraminifera from the Arabian Sea. Geochimica et Cosmochimica Acta supplement, **67**(18): 464

中国知网　https://www.cnki.net

TOLER S K, HALLOCK P, SCHIJF J, 2001. Mg/Ca ratios in stressed foraminifera, *Amphistegina gibbosa*, from the Florida Keys. Marine Micropaleontology, **43**(3-4): 199–206

TONG S Y, PAN S Y, HU W K *et al*., 2023. Determination of Element/Calcium ratio in benthic foraminifera by Laser Ablation-Inductively Coupled Plasma Mass Spectrometry (LA-ICP-MS). Chinese Journal of Inorganic Analytical Chemistry, **13**(9): 967–974

UTHICKE S, THOMPSON A, SCHAFFELKE B, 2010. Effectiveness of benthic foraminiferal and coral assemblages as water quality indicators on inshore reefs of the Great Barrier Reef, Australia. Coral Reefs, **29**: 209–225

VELÁSQUEZ J, LÓPEZ-ANGARITA J, SÁNCHEZ J A, 2011. Evaluation of the FORAM index in a case of conservation: benthic foraminifera as indicators of ecosystem resilience in protected and non-protected coral reefs of the southern Caribbean. Biodiversity and Conservation, **20**: 3591–3603

WANG L R, ZHAO H T, 2008. A review of the studies in China on the ecological characteristics of modern sedimental benthic foraminifera of coral reef in South China Sea. Tropical Geography, **28**(4): 346–350

YUE Y, YU K, TAO S *et al*., 2019. 3500-year western Pacific storm record warns of additional storm activity in a warming warm pool. Palaeogeography, Palaeoclimatology, Palaeoecology, **521**: 57–71

IN-SITU MG/CA MICROANALYSIS IN LARGER BENTHIC FORAMINIFERA FROM THE SOUTH CHINA SEA REEF REGION AND THEIR APPLICATION POTENTIAL *

HUANG Xiaoting, LI Mei and WU Siqi**

Guangxi Laboratory on the Study of Coral Reefs in the South China Sea, *Guangxi University*, *Nanning 530004*, *China*

Abstract The Mg/Ca ratio in biogenic carbonates serves as a key indicator for paleotemperature reconstruction. However, the application of Mg/Ca ratio of larger benthic foraminifera (LBF), an important component of sediments in coral reef regions, is limited by various factors. To explore the application potential of Mg/Ca ratio in reef-dwelling LBF as a paleotemperature proxy, the intratest variation of Mg/Ca ratios of *Amphistegina lobifera* and *Amphistegina lessonii* obtained from the surface sediments of the Yongle Atoll in Xisha Islands was thoroughly investigated. Additionally, the differences between two methods [Electron Probe Microanalysis (EPMA) and Laser Ablation Inductively Coupled Plasma Mass Spectrometry (LA-ICP-MS)] were discussed. Furthermore, to examine the influence of diagenesis, the Mg/Ca ratios of *A. lobifera* from downcore samples of the Lingyang reef and the Chenhang Island in the Yongle Atoll were also analyzed. The results show that the Mg/Ca distributions of the two species exhibit notable similarities, both displaying a distinct periodic pattern along the growth direction, which is related to the alternate growth of primary and secondary calcite layers. However, the shifting trends in two species are slightly different near the edge of the secondary calcite layer. Combining the intratest distribution pattern and the differences between the two methods, it can be inferred that despite the influence of the primary calcite, the potential to reflect paleotemperature remains valid by selecting appropriate analytical methods and positions. The influence of diagenesis on the Mg/Ca ratio of downcore samples cannot be ignored and should be taken into account in applications. By comparing the Mg/Ca range with modern samples, and a thorough observation using scanning electron microscope, the extent of diagenetic influence can be assessed.

Key words larger benthic foraminifera, Mg/Ca ratio, in-situ microanalysis, paleotemperature, Yongle Atoll

* This research was supported by the National Natural Science Foundation of China (No. 42402007), Guangxi Natural Science Foundation Project (No. 2024GXNSFBA010231).

** **Corresponding author** E-mail: wusiqi@gxu.edu.cn

中国知网 https://www.cnki.net

余骄洋，俞小鹏，余克服，马玉玲．2025．西沙群岛太阳长棘海星（*Acanthaster solaris*）幽门盲囊细菌多样性及群落组成研究．热带地理，45（6）：1020-1033.

Yu Jiaoyang, Yu Xiaopeng, Yu Kefu, and Ma Yuling. 2025. Bacterial Diversity and Community Composition in the Pyloric Ceca of *Acanthaster solaris* in the Xisha Islands. *Tropical Geography*, 45 (6): 1020-1033.

西沙群岛太阳长棘海星（*Acanthaster solaris*）幽门盲囊细菌多样性及群落组成研究

余骄洋[1]，俞小鹏[1]，余克服[1,2]，马玉玲[1]

[1. 广西大学 广西南海珊瑚礁研究重点实验室//珊瑚礁研究中心//海洋学院，南宁 530004；
2. 南方海洋科学与工程广东省实验室（广州），广州 511458]

摘 要：长棘海星（Crown-of-Thorns Starfish, CoTS, *Acanthaster* spp.）是珊瑚的天敌，其周期性暴发并大量摄食珊瑚是导致珊瑚礁退化的重要原因。共生细菌对长棘海星的发育、繁殖和消化等具有重要意义，但迄今关于长棘海星体内细菌的组成与功能了解甚少。文章以采自西沙群岛珊瑚礁区的15个成年太阳长棘海星为研究对象，通过高通量测序技术检测其主要消化器官幽门盲囊内的细菌组成及其功能。结果显示：太阳长棘海星幽门盲囊中共检出833个细菌OTU，分别属于26个门、55个纲、115个目、171个科和278个属；优势门为变形菌门（Proteobacteria, 94.50%）；优势属为弧菌属（*Vibrio*, 60.61%）、罗尔斯通氏菌属（*Ralstonia*, 17.86%）和发光杆菌属（*Photobacterium*, 6.64%）。通过对比西沙群岛其他礁栖生物共生细菌的组成，发现不同食性的生物具有不同的细菌组成，表明摄食珊瑚可能是太阳长棘海星幽门盲囊细菌组成的重要影响因素。对比澳大利亚大堡礁和日本海域长棘海星消化道中的细菌组成，发现具有较大的区域差异，西沙群岛样品的弧菌含量远高于大堡礁和日本，这可能与2020—2021年西沙群岛珊瑚大面积白化有关，因为白化珊瑚共附生细菌中弧菌相对丰度会显著增加。此外，长棘海星作为潜在的弧菌传播载体，可能对南海珊瑚礁生态系统带来疾病风险。结合细菌功能预测的结果，推测长棘海星幽门盲囊细菌可能通过分泌水解酶来帮助其消化珊瑚。

关键词：长棘海星；共生细菌；幽门盲囊；珊瑚白化；西沙群岛

中图分类号：Q958.8；Q178.2 **文献标志码：**A **文章编号：**1001-5221(2025)06-1020-14

DOI：10.13284/j.cnki.rddl.20240365

长棘海星（Crown-of-Thorns Starfish, CoTS, *Acanthaster* spp.）是珊瑚的天敌，其周期性暴发是导致珊瑚礁生态系统退化的重要原因（姚秋翠 等，2022）。例如，2006—2010年长棘海星暴发导致西沙群岛的珊瑚覆盖率从60%多降低到不足5%（李元超 等，2019）；1985—2012年，澳大利亚大堡礁约42%的珊瑚礁退化是长棘海星造成的（De'ath et al.，2012）。有研究推测，随着气候变化的不断加剧，长棘海星暴发事件可能越来越频繁，对珊瑚礁生态系统的破坏也将更加严重（Kamya et al., 2017）。因此，长棘海星受到越来越多的关注。虽然国际上对长棘海星的研究已有60多年的历史，但对长棘海星的暴发机制及其应对策略等方面仍没有取得令人满意的进展（姚秋翠 等，2022）。中国对长棘海星的关注相对较晚，相关研究主要涉及其分类阶元厘定（李渊 等，2024）、生长繁殖（Tian et al., 2017；刘界宏 等，2024）、群体遗传（Chen et al., 2021a）、化学物质提取（蔡健 等，2021）、生物累积与分布特征（夏荣林 等，2022；赵思佳 等，2022；史敬文 等，2023；王辰燕 等，2023）、暴发原因（Yang et al., 2022; Peng et al., 2023）、危害与防治（郑金辉 等，2023；Li et al., 2024）、eDNA快

收稿日期：2024-06-05；**修回日期：**2024-08-23

基金项目：国家自然科学基金：印太交汇区代表性物种的生物多样性演变及其生态功能（42090041）；全新世南海珊瑚礁发育的时–空差异及其对全球变暖的适应机制（42030502）

作者简介：余骄洋（1998—），男，浙江杭州人，硕士研究生，主要从事珊瑚礁生物研究，（E-mail）yujiaoyang1998@outlook.com；

通信作者：余克服（1969—），男，湖北公安人，教授，博士生导师，主要从事珊瑚礁科学研究，（E-mail）kefuyu@scsio.ac.cn。

速检测（张颖 等，2022；闫智聪 等，2023；Wang et al., 2023）等方面。根据李渊等（2024）的研究，中国南海分布的长棘海星种类为太阳长棘海星（*Acanthaster solaris*）。

已有研究表明，长棘海星各组织中存在多种共附生细菌，且这些细菌在其发育、繁殖、和消化等重要生命活动过程中发挥作用（Carrier et al., 2018; Høj et al., 2018; Wada et al., 2020）。Wada等（2020）发现在长棘海星表皮下方普遍存在隶属于螺旋体门（Spirochaetes）并与其具有潜在共生关系的细菌COTS27，可能对适应海洋环境有一定作用。Carrier等（2018）对长棘海星幼虫的共附生细菌研究发现，一方面，营养条件能改变长棘海星幼虫的细菌组成，另一方面，光营养细菌（例如Rhodobacteraceae和Rhodospirillaceae）可能有助于增加长棘海星幼虫的存活机率。Høj等（2018）发现，长棘海星雄性生殖腺中的优势菌Mollicutes可能参与了长棘海星的配子成熟过程，而弓形菌属（*Arcobacter*）则与疾病显著相关。但迄今关于长棘海星细菌的研究仍较少（Wada et al., 2020）。因此，研究长棘海星的共附生细菌对于了解其暴发原因和防治具有重要作用。成年长棘海星摄食过程中翻出贲门胃包裹食物（如珊瑚等），并进行初步体外消化，然后将初步消化后的食物传递到幽门胃和幽门盲囊进一步消化（Jangoux, 1982）。幽门盲囊是最主要的消化场所之一，而消化道细菌不仅与宿主的栖息环境、食性等密切相关，还能通过宿主的排泄或死亡影响当地生态系统（Smriga et al., 2010; Ezzat et al., 2019; Velásquez-Rodríguez et al., 2021）。但关于南海太阳长棘海星幽门盲囊中的细菌组成及其功能尚不明确。

为进一步探究长棘海星幽门盲囊中菌群的结构及其功能，本研究在南海西沙群岛共采集了15只成年太阳长棘海星，通过16S rRNA高通量测序技术检测其幽门盲囊细菌的组成，并基于测序数据进一步对其多样性、群落组成以及潜在功能进行分析，以期有助于了解长棘海星的共生菌群与其宿主之间的关系。

1　材料与方法

1.1　样品采集

2021年春季在南海西沙群岛永乐环礁海域通过水肺潜水的方式在同一站位采集15个太阳长棘海星成体样本，迅速解剖采集幽门盲囊内部组织并用无菌海水清洗后放入液氮中冷冻。将冷冻样本带回广西南海珊瑚礁研究重点实验室进行幽门盲囊细菌DNA的提取（图1）。



图1　长棘海星摄食珊瑚（a）、反口面（b）、口面（c）和管足解剖（d）图

Fig.1　Photos of *Acanthaster solaris* which feeding on coral (a), aboral surface (b), oral surface (c), and tube foot anatomy (d)

注：照片由广西南海珊瑚礁研究重点实验室实验人员拍摄。

1.2　实验方法

使用无菌剪刀剪下约50 mg冰冻的太阳长棘海星幽门盲囊样品，然后使用粪便DNA提取试剂盒（广州美基生物科技有限公司，产地中国）提取其基因组总DNA。使用NanoDrop 2000（赛默飞世尔科技公司，产地美国）对获得的DNA进行质量和纯度检查后，使用条形码正向引物341F（5′-CCTACGGGNGGCWGCAG-3′）和反向引物806R（5′- GGACTACHVGGGTWTCTAAT-3′）按照先前报道的反应条件，对细菌16S rRNA基因的V3-V4区进行PCR扩增（Yu et al., 2021）。PCR扩增体系为50 μL混合物，包含10 μL 5×Q5@反应缓冲液、10 μL 5×Q5@ High GC Enhancer、1.5 μL 2.5 mM dNTPs、1.5 μL上下游引物（10 μM）、0.2 μL Q5@高保真DNA聚合酶和50 ng模板DNA。PCR相关试剂厂家为New England Biolabs，产地美国。使用AMPure XP Beads对扩增产物进行纯化，并使用ABI StepOnePlus实时PCR系统（Life Technologies，产地美国）进行定量。纯化后的产物根据Novaseg 6000的PE250模式pooling上机测序。

1.3 数据分析

使用FASTP（版本0.18.0）对Illumina平台的原始数据进行过滤，将过滤后获得的clean reads用于组装分析。使用FLSAH（版本1.2.11）将clean reads按最小重叠为10 bp，错配率最高2%的阈值合并为tag。使用Qiime2对低质量tags进行过滤，得到高质量的clean tags。使用UPARSE（版本9.2.64）流程将clean tags按97%的相似度聚类为OTUs（Operational Taxonomic Units，可操作分类单元）。使用UCHIME算法进行嵌合体检查，过滤嵌合体后得到的Effective tags进行OTU丰度统计和其他后续分析。选取丰度最高的tag序列作为每个OTU的代表序列。选择细菌16S：Silva（Release132）数据库，使用RDP Classifier（version 2.2，置信度阈值为0.8）对OTU代表序列进行物种注释。通过对OTU聚类分析和物种分类学分析，获得每个样本在不同分类层次的细菌群落组成和相对丰度（Yu et al., 2021）。使用Qiime2将在80%以上的样本中存在的OTUs判定为核心细菌微生物组成员（Bolyen et al., 2019）。

通过计算Good's物种覆盖度（Coverage）、群落丰富度（Ace richness estimator）、香农—威纳多样性指数（Shannon-wiener diversity index）、辛普森多样性指数（Simpson diversity index）、Sobs指数、Chao指数、PD-whole tree指数反映细菌群落的覆盖率、丰度和多样性（Schloss et al., 2011）。基于KEGG（Kyoto Encyclopedia of Genes and Genomes，京都基因与基因组百科全书）数据库的信息，利用PICRUSt， V2.1.4从16S rRNA标记基因序列预测细菌基因的功能。

通过Web of Science和中国知网检索西沙群岛生物的共附生细菌相关研究，并与本研究进行对比，包括以下物种：金带齿颌鲷（*Gnathodentex aurolineatus*）（王晶晶 等，2022）、圆舵鲣（*Auxis rochei*）、黄鳍金枪鱼（*Thunnus albacares*）、鸢乌贼（*Sthenoteuthis oualaniensis*）（Tang et al., 2023）、大马蹄螺（*Trochus niloticus*）（Zhang et al., 2023）、海鞘（*Atriolum robustum*）（Liu et al., 2021）、白化和健康的单独鹿角珊瑚（*Acropora solitaryensis*）（Liu et al., 2016）、健康和被长棘海星摄食的杯形珊瑚（*Pocillopora* sp.）（Qin et al., 2022）。同时，与澳大利亚大堡礁和日本地区的长棘海星共附生细菌进行比较（Høj et al., 2018; Wada et al., 2020）。

使用广州基迪奥生物技术有限公司在线平台[①]进行上述分析。利用Origin 2024绘制与其他文献来源数据的对比图，并使用Adobe Illustrator 2021进行整理和汇总。

2 结果分析

2.1 太阳长棘海星幽门盲囊共生细菌的群落组成和多样性

经过筛选和过滤后得到了1 845 047条细菌序列，并按照97%的相似度共分配了833个OTUs，分别属于26个门、55个纲、115个目、171个科和278个属。每个样本中的序列数为117 795~130 830，细菌序列长度均在204~476 bp，细菌序列的平均长度为466 bp。本研究每个样品的Good's coverage均＞99.9%，稀释曲线接近饱和，表明测序结果代表了样品中细菌分布的真实情况。太阳长棘海星幽门盲囊细菌群落的α-多样性指数平均值和标准差如表1所示，表明部分太阳长棘海星个体之间幽门盲囊细菌的丰度和多样性存在一定差异。如图2所示，在门水平上，太阳长棘海星幽门盲囊细菌中丰度最高的细菌都为变形菌门（Proteobacteria, 94.50%）；在属水平上，太阳长棘海星幽门盲囊细菌中的优势属为弧菌属（*Vibrio*, 60.61%），其他相对丰度＞5%的细菌属还包括罗尔斯通氏菌属（*Ralstonia*, 17.86%）和发光杆菌属（*Photobacterium*, 6.64%）。弧菌属（*Vibrio*）、罗尔斯通氏菌属（*Ralstonia*）和发光杆菌属（*Photobacterium*），分别是10、4和1个样本中的主导细菌，表明部分太阳长棘海星个体幽门盲囊细菌之间存在一定差异。

表1 15个太阳长棘海星幽门盲囊细菌多样性指数

Table 1 Bacterial diversity index of pyloric ceca of *Acanthaster solaris*

指数	平均值±标准差
Sobs	148.2±55.77
Ace	199.19±73.61
Chao	188.1±76.87
Shannon	1.52±0.99
Simpson	0.39±0.27
PD	25.47±8.43
Coverage	0.999 6±0.000 14

2.2 太阳长棘海星幽门盲囊中的核心细菌

按照在80%及以上的样品中出现的阈值筛选出42个核心细菌OTU。如图3所示，这42个核心细菌

① https://www.omicsmart.com/

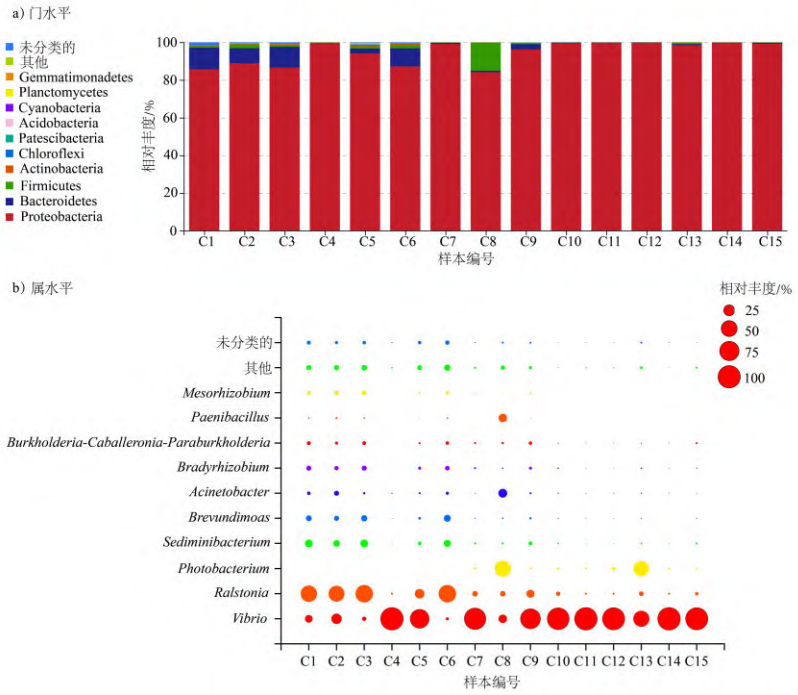


图2　门（a）和属（b）水平的太阳长棘海星幽门盲囊细菌群落组成

Fig.2　Bacterial community composition of the pyloric ceca in *Acanthaster solaris*, phylum (a) and genus (b) level

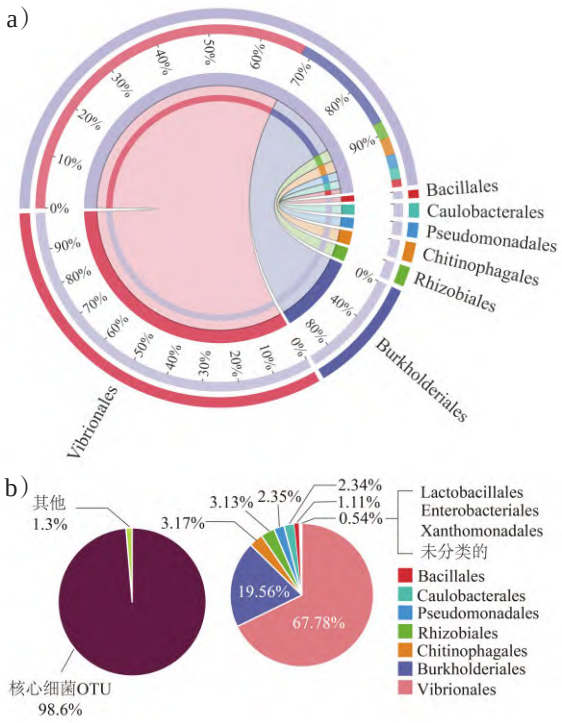


图3　太阳长棘海星幽门盲囊细菌（a）及其核心细菌（b）在目水平上的组成

Fig.3　Bacterial community composition (a) and core bacterial OTU (b) of the pyloric ceca in *Acanthaster solaris* (order level)

OTU 相对丰度总计 98.6%，分别属于以下 3 个门、10 个目和 23 个属：变形菌门（Proteobacteria）、厚壁菌门（Firmicutes）、拟杆菌门（Bacteroidetes）；弧菌目（Vibrionales）、伯克霍尔德氏菌目（Burkholderiales）、噬几丁质菌目（Chitinophagales）、柄杆菌目（Caulobacterales）、根瘤菌目（Rhizobiales）、假单胞菌目（Pseudomonadales）、乳杆菌目（Lactobacillales）、芽孢杆菌目（Bacillales）、肠杆菌目（Enterobacteriales）、黄单胞菌目（Xanthomonadales）；弧菌属（*Vibrio*）、罗尔斯通氏菌属（*Ralstonia*）、发光杆菌属（*Photobacterium*）、沉积杆菌属（*Sediminibacterium*）、短波单胞菌属（*Brevundimonas*）、慢生根瘤菌属（*Bradyrhizobium*）、不动杆菌属（*Acinetobacter*）、*Burkholderia-Caballeronia-Paraburkholderia*、中间根瘤菌属（*Mesorhizobium*）、类芽孢杆菌属（*Paenibacillus*）、*Bosea*、假单胞菌属（*Pseudomonas*）、*Pelomonas*、明串珠菌属（*Leuconostoc*）、嗜冷杆菌属（*Psychrobacter*）、赖氨酸芽孢杆菌属（*Lysinibacillus*）、芽孢杆菌属（*Bacillus*）、埃希氏–志贺氏菌属（*Escherichia-Shigella*）、*Delftia*、普罗威登斯菌属（*Providencia*）、寡养单胞菌菌属（*Stenotrophomonas*）、气球菌属（*Aerococcus*）、丛毛单胞菌属（*Comamonas*）。

2.3　太阳长棘海星幽门盲囊细菌与西沙群岛其他生物的差异

为进一步探究影响太阳长棘海星幽门盲囊细菌群落组成的因素，将其幽门盲囊细菌群落组成与西沙群岛其他礁栖生物的共附生细菌进行对比。礁栖生物的定义参照文献（高永利 等，2014）。如图 4 所示，在属水平上，圆舵鲣、黄鳍金枪鱼和鸢乌贼的肠道细菌以发光杆菌属（*Photobacterium*）为主（Tang et al., 2023）；金带齿颌鲷肠道细菌的优势菌属包括产丙酸菌属（*Propionigeniu*）、弧菌属（*Vibrio*）、*Intestinibacter* 等（王晶晶 等，2022）。大马蹄螺的肠道细菌以支原体属（*Mycoplasma*）为主（Zhang et al., 2023）；海鞘的共附生细菌中相对丰度

最高的是假单胞菌属（*Pseudomonas*）（Liu et al., 2021）。其中，圆舵鲣、黄鳍金枪鱼、鸢乌贼和金带齿颌鲷为肉食性生物（Mostarda et al., 2007；陶雅晋等，2017；王晶晶等，2022；Tang et al., 2023），大马蹄螺为植食性生物（Zhang et al., 2023），海鞘为滤食性生物（Liu et al., 2021）。健康的单独鹿角珊瑚共生细菌中的第一优势属为*Methylobacterium*，而白化的单独鹿角珊瑚中的优势属则为弧菌属（*Vibrio*）（Liu et al., 2016）；健康的杯形珊瑚的共生细菌以假单胞菌属（*Pseudomonas*）为主，而被长棘海星摄食的杯形珊瑚则以未分类的蓝藻门（n. Cyanobacteria）为主（Qin et al., 2022）。

相对而言，太阳长棘海星幽门盲囊细菌的组成与珊瑚共生细菌更为相似。本研究对比发现，太阳长棘海星幽门盲囊细菌与杯形珊瑚共生细菌共有13个细菌属（Qin et al., 2022），与健康单独鹿角珊瑚共生细菌共有13个细菌属，与白化单独鹿角珊瑚共生细菌共有8个细菌属（Liu et al., 2016）。此外，太阳长棘海星幽门盲囊细菌与白化单独鹿角珊瑚共生细菌中的主导细菌都为弧菌属，表明太阳长棘海星幽门盲囊细菌与白化珊瑚的共生细菌相似性更高。

2.4 西沙群岛太阳长棘海星幽门盲囊细菌组成与其他海域的差异

为了解不同地区之间长棘海星细菌群落组成的差异，将本研究结果与澳大利亚大堡礁和日本地区的长棘海星共附生细菌进行OTU水平比较。如图5所示，大堡礁地区长棘海星健康个体幽门盲囊中的优势菌主要包括隶属于Marine spirochetes、Flavobacteriales、Oceanospirillales、Anaeroplasmatales等目的OTU（Høj et al., 2018）；而日本地区长棘海星幽门胃的共附生细菌主要包括隶属于Marine spirochetes、Mycoplasmatales、Burkholderiales、Bacillales、Beggiatoales、Rhizobiales等目的OTU（Wada et al., 2020）。而本研究长棘海星幽门盲囊细菌中的主要OTU隶属于弧菌目（Vibrionales）、Burkholderiales、Chitinophagales、Caulobacterales、Rhizobiales、Pseudomonadales、Bacillales；这7个细菌目中有6个在澳大利亚大堡礁长棘海星幽门盲囊中被检出，有4个在日本地区的长棘海星幽门胃中被检出。并且，Vibrionales、Burkholderiales、Rhizobiales和Bacillales在所有地区的样品中都存在（Høj et al., 2018; Wada et al., 2020）。这表明西沙群岛太阳长棘海星幽门盲囊细菌群落组成与大堡礁和日本地区存在一定相似性。但是，西沙群岛太阳长棘海星幽门盲囊细菌群落组成与其他地区也存在较大差异，表现为西沙群岛太阳长棘海星幽门盲囊弧菌目（Vibrionales）细菌的相对丰度（67.3%）远高于大堡礁和日本地区长棘海星共生细菌中的弧菌目含量（均＜2%）。

2.5 太阳长棘海星幽门盲囊细菌基因功能预测

为了表征共生细菌的功能，利用PICRUSt V2.1.4基于16S rDNA测序数据预测共生细菌基因组功能。如图6所示，代谢类相关功能基因占比最高，在2级KEGG上包括碳水化合物代谢（Carbohydrate metabolism）、氨基酸代谢（Amino acid metabolism）、辅助因子和维生素的代谢（Metabolism of cofactors and vitamins）、脂类代谢（Lipid metabolism）、萜类和聚酮类物质的代谢（Metabolism of terpenoids and polyketides）、其他氨基酸的代谢（Metabolism of other amino acids）、异生素生物降解和代谢（Xenobiotics biodegradation and metabolism）、能量代谢（Energy metabolism）、聚糖生物合成和代谢（Glycan biosynthesis and metabolism）、其他次生代谢物的生物合成（Biosynthesis of other secondary metabolites）、核苷酸代谢（Nucleotide metabolism）。

2级KEGG上其他占比较高的功能包括复制和修复（Replication and repair）、折叠，分类和降解（Folding, sorting and degradation）、翻译（Translation）、转录（Transcription）、细胞运动（Cell motility）、膜转运（Membrane transport）、信号传导（Signal transduction）、细胞生长和死亡（Cell growth and death）、细胞群落—原核生物（Cellular community-prokaryotes）、运输和分解代谢（Transport and catabolism）等。在3级KEEG通路中还发现存在较高丰度的糖酵解/糖异生（Glycolysis/Gluconeogenesis）水平。

3 讨论

3.1 摄食珊瑚可能会影响太阳长棘海星幽门盲囊细菌

通过物种组成分析，发现弧菌属、罗尔斯通氏菌属和发光杆菌属是太阳长棘海星幽门盲囊细菌中的优势属。为进一步探究食性对细菌群落组成的影响，将太阳长棘海星幽门盲囊细菌与西沙群岛其他已经发现的常见生物的共附生细菌进行对比（图

4），发现均与本研究太阳长棘海星的幽门盲囊细菌有较大差异。相对而言，太阳长棘海星幽门盲囊细菌的群落组成与珊瑚更为相似，尤其是与白化珊瑚相似性更高。

饮食习性是驱动动物消化系统内细菌群落组成和多样性的重要因素（Miyake et al., 2015；向佳丽等，2022）。圆舵鲣和黄鳍金枪鱼通常以小型鱼类、头足类和甲壳类为食（Mostarda et al., 2007；陶雅晋等，2017）；大马蹄螺主要摄食大型藻类（Zhang et al., 2023），成体海鞘则以过滤海水为生（Liu et al., 2021），上述生物的饮食习性均与长棘海星不同。不同的摄食习惯将不同的食物引入肠道环境，导致特定微生物群体的生态位差异分化（Gao et al., 2020; Viver et al., 2023）。因此，本研究推测独特的珊瑚食性可能是导致太阳长棘海星幽门盲囊细菌群落组成与西沙群岛其他生物共附生细菌存在较大差异的主要原因。与本研究发现类似，Michl等（2017）对虹鳟（*Oncorhynchus mykiss*）的肠道细菌研究发现，植物性饲料能显著增加虹鳟肠道细菌中乳杆菌目（Lactobacillales）、芽孢杆菌目（Bacillales）和假单胞菌目（Pseudomonadales）等细菌的相对丰度，而动物性饲料则能增加拟杆菌目（Bacteroidales）、梭菌目（Clostridiales）和弧菌目（Vibrionales）等细菌的相对丰度。Cai等（2024）的研究也表明，西沙群岛植食性鱼类的肠道细菌群落组成及多样性与杂食性或肉食性鱼类显著不同，表明食物来源确实对肠道细菌有一定影响。

此外，太阳长棘海星幽门盲囊细菌的群落组成与珊瑚更为接近，并且主导细菌罗尔斯通氏菌属是南海珊瑚中常见的益生菌（Chen et al., 2021b），因此，本研究推测长棘海星摄食珊瑚之后，来自珊瑚的细菌也可能通过在消化道中定植，而改变共生细菌的群落组成（Ringø et al., 2016; Karlsen et al., 2022）。在其他地区也发现了类似现象，例如，加勒比海珊瑚礁区的蝴蝶鱼（*Chaetodon capistratus*）以珊瑚作为部分食物来源，其肠道中含有大量的珊瑚益生菌*Endozoicomonas*，而当珊瑚礁退化导致珊瑚食物来源大幅度减少之后，蝴蝶鱼肠道中*Endozoicomonas*的含量显著下降（Clever et al., 2022）。Velásquez-Rodríguez等（2021）在鹦嘴鱼（*Sparisoma viride*）粪便中检出大量与当地珊瑚相同的共生细菌，Ezzat等（2020）也发现鹦嘴鱼（*Chlorurus spilurus*）的口腔中存在与其所摄食珊瑚相同的细菌OTU。这些结果均表明珊瑚共生细菌可能通过摄食过程进入珊瑚摄食者的消化道，最终影响共生细菌的群落组成。

综上所述，本研究推测太阳长棘海星幽门盲囊细菌与其他生物的显著差异主要是由其摄食珊瑚的习性导致。

3.2　珊瑚健康状况可能会影响长棘海星幽门盲囊细菌组成

如图5所示，西沙群岛太阳长棘海星幽门盲囊细菌组成与大堡礁和日本地区存在一定相似性。但是，西沙群岛太阳长棘海星幽门盲囊弧菌目细菌的相对丰度远高于大堡礁和日本地区长棘海星共生细菌中的弧菌目含量，表明长棘海星幽门盲囊弧菌具有较大的区域差异。

共生细菌群落可塑性高，容易受到环境条件、食物供给和宿主发育阶段等因素的影响（Carrier et al., 2018; Egerton et al., 2018；向佳丽等，2022）。珊瑚礁是长棘海星等礁栖生物赖以生存的环境，珊瑚礁的健康状况会对礁栖生物的共生细菌产生显著影响（Clever et al., 2022; Zhang et al., 2023）。例如，Turon等

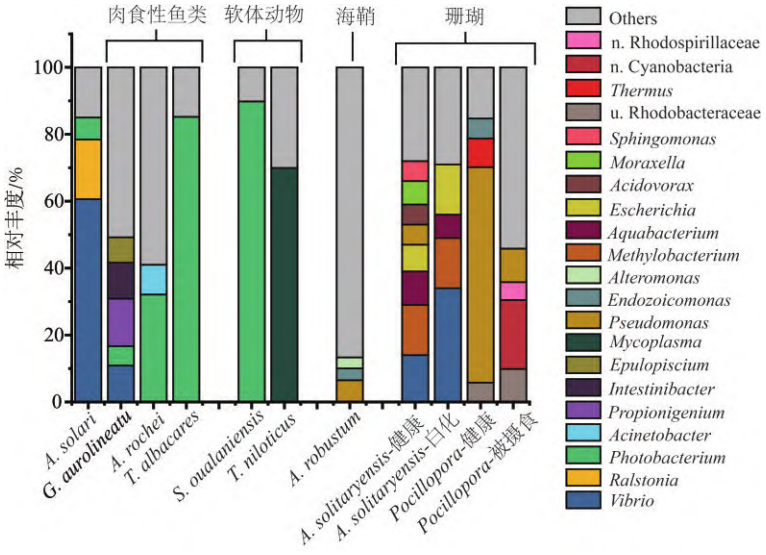


图4　太阳长棘海星幽门盲囊细菌与西沙群岛其他礁栖生物共附生细菌对比（属水平）

Fig.4　Comparison of pyloric cecal bacteria of *Acanthaster solaris* and symbiotic bacteria of other reef-associated organisms in the Xisha Islands on genus level

注：太阳长棘海星外的数据来自文献（Liu et al., 2016; Liu et al., 2021; Qin et al., 2022；王晶晶等，2022；Tang et al., 2023; Zhang et al., 2023）。

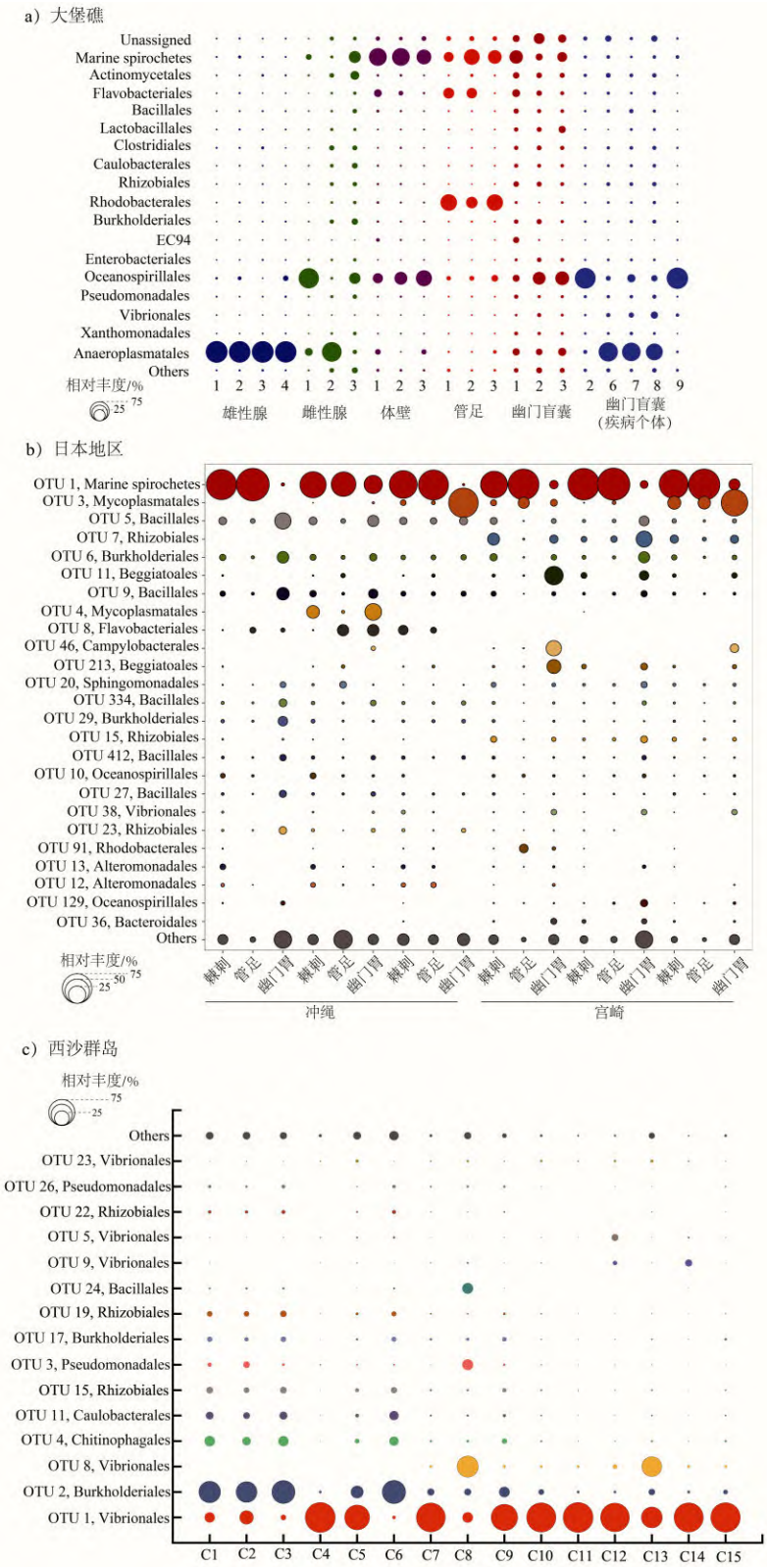


图5 不同地区长棘海星的主要细菌OTU的相对丰度和目水平的注释

Fig.5 The relative abundance and annotated results of the major symbiotic bacteria OTUs of the *Acanthaster solaris* in different regions

注：大堡礁和日本地区的数据结果来自文献（Høj et al., 2018; Wada et al., 2020）。

（2019）对芽庄湾的海绵群落研究发现，相比生长在健康珊瑚礁区的海绵群落，受人为干扰而衰退的珊瑚礁区的海绵具有更低的共附生细菌多样性。Zhang 等（2023）发现，大马蹄螺（*Trochus niloticus*）的肠道细菌的多样性和群落组成均在人为调控的海洋酸化和抗生素污染环境下发生改变。Cheutin 等（2021）发现，由珊瑚主导变为大型藻主导的生态相变显著地改变了珊瑚礁鱼类的肠道细菌群落组成。Clever 等（2022）在对兼性珊瑚食性的蝴蝶鱼（*Chaetodon capistratus*）肠道细菌研究中也发现，相比生活在健康珊瑚礁区的蝴蝶鱼，生活在衰退珊瑚礁区的蝴蝶鱼肠道细菌中益生菌 *Endozoicomonas* 含量减少，而弧菌科（Vibrionaceae）和红细菌科（Rhodobacteraceae）细菌的含量上升。西沙群岛珊瑚礁近年来退化严重，2019 年后高温导致的珊瑚白化事件和长棘海星暴发使西沙群岛的活珊瑚覆盖率急剧下降，2020 年西沙群岛珊瑚平均白化率为 23.9%，并且除永兴岛之外的区域都受到长棘海星暴发的威胁（Xiao et al., 2022；雷明凤 等，2024）。2021 年西沙永乐群岛的活珊瑚覆盖率已下降到 11%（郎尚昆，2022）。而 Høj 等（2018）采样时期（2014 年）的大堡礁区北部和 Wada 等（2020）采样时期（2017 年）的日本地区均具有较高的活珊瑚覆盖率（Emslie et al., 2024; Kimura et al., 2022）。因此，西沙群岛太阳长棘海星幽门盲囊细菌可能受到西沙珊瑚礁退化的影响。

本研究发现的主要差异是弧菌（*Vibrio*）相对丰度较高。众所周知，弧菌作为海洋中广泛分布的机会主义致病菌，其在健康珊瑚中的含量通常较低（Kvennefors et al., 2010; Liu et al., 2016）。然而，当珊瑚受到高温等环境胁迫时，其共生细菌中的弧菌含量急剧增长。例如在 2015/2016 年的全球性珊瑚白化事件中，南海南沙群岛

的石芝珊瑚（*Fungia fungites*）中弧菌的相对丰度急剧增长到52.9%，显著高于白化前1.61%的弧菌含量（Qin et al., 2020）。Liu等（2016）也发现西沙群岛中白化的鹿角珊瑚（*Acropora solitaryensis*）中的弧菌相对丰度为34%，远高于健康珊瑚中14%的弧菌含量。Zhao等（2023a）在2020年8—9月对西沙群岛海水和沉积物研究发现，西沙群岛海水中弧菌含量显著高于大亚湾，同时沉积物中的弧菌含量高达32.12%，显著高于周围海域，推测与2020年西沙珊瑚白化事件（Zhao et al., 2023b）有关。

因此，大规模白化事件可能导致珊瑚共附生细菌中的弧菌含量大量增加，并影响周围的环境和生物。成年长棘海星主要以珊瑚为食，并且长棘海星摄食珊瑚之后来自珊瑚的细菌也可能在其消化道中定植，从而改变共生细菌的群落组成（Ringø et al., 2016; Karlsen et al., 2022）。因此，摄食富含弧菌的珊瑚也可能导致本研究太阳长棘海星幽门盲囊中存在大量弧菌。并且本研究也发现不同太阳长棘海星个体的幽门盲囊细菌存在一定的差异（见图2），这可能是由于西沙群岛活珊瑚覆盖度持续降低，已经不能满足高密度长棘海星的食物需求，导致部分个体被迫摄食其他底栖生物（例如*Dendronephthya*、*Antipathes*、*Litophyton*等软珊瑚）（Jangoux, 1982; Kuo et al., 2021），而这可能导致不同个体之间细菌差异性增加（Michl et al., 2017; Viver et al., 2023）。

此外，弧菌作为机会致病菌是珊瑚礁生态系统中潜在的威胁，而海洋无脊椎动物可能是弧菌的储藏库（Dilmore & Hood, 1986）。弧菌可以在棘皮动物的消化道内增殖（Beleneva & Kukhlevskii, 2010），并可能通过宿主的摄食、排泄和移动传播到其他区域（Ezzat et al., 2019; Renzi et al., 2022）。因此，长棘海星可能是弧菌传播的潜在载体（Rivera-Posada et al., 2011; Caballes et al., 2012）。由于长棘海星的种群数量在暴发后期迅速下降（Pratchett, 2005），体内的弧菌将随着海星的死亡分解大量释放到周围环境中，从而给珊瑚礁生态系统带来疾病风险（Li et al., 2024）。因此，在长棘海星暴发后期，宜加强对珊瑚礁海域弧菌含量的检测，以更好地保护珊瑚礁生态系统。

综上所述，本研究推测太阳长棘海星幽门盲囊细菌可能受到西沙珊瑚礁退化的影响。南海西沙群岛太阳长棘海星幽门盲囊细菌与大堡礁、日本等地区的长棘海星共生细菌存在较大差异主要与珊瑚的健康状况相关。大面积白化事件导致白化珊瑚共生细菌和礁区环境中的弧菌暴发，太阳长棘海星可能由于摄食富含弧菌的珊瑚而导致体内含有大量弧菌。

3.3　幽门盲囊细菌可能参与太阳长棘海星消化过程

为分析共生细菌对长棘海星的作用，对幽门盲囊细菌进行功能预测，结果显示，太阳长棘海星幽门盲囊细菌的基因组功能最主要集中在代谢方面（图6）。在2级KEEG水平中相对丰度较高的通路包

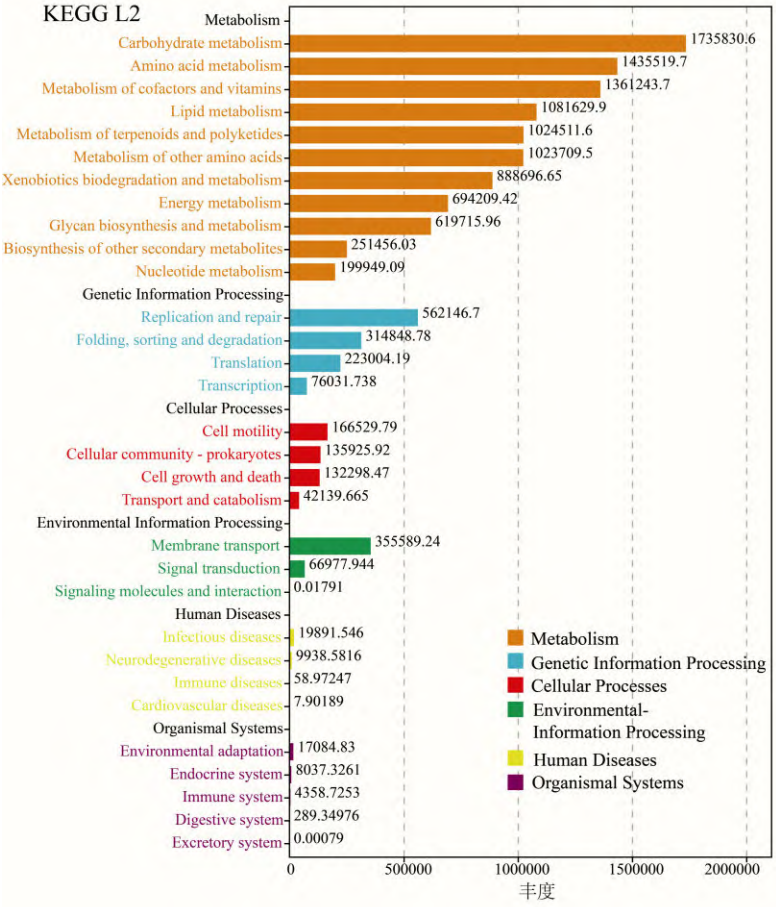


图6　基于KEGG的太阳长棘海星幽门盲囊细菌的基因功能预测

Fig.6　Gene function prediction of pyloric cecal bacteria of *Acanthaster solaris* based on KEGG

括碳水化合物代谢、氨基酸代谢、辅酶和维生素的代谢和脂类代谢等；在3级KEEG通路中还存在较高丰度的糖酵解/糖异生。这些结果表明，幽门盲囊细菌可能参与了太阳长棘海星的日常生理代谢过程。

碳水化合物、蛋白质、脂类是珊瑚中的主要储能物质（Schoepf et al., 2013）。例如，珊瑚黏液中包含阿拉伯糖、岩藻糖、半乳糖等多种糖类（Hadaidi et al., 2019）。动物消化道细菌的功能之一是通过向细胞外分泌水解酶，将碳水化合物（多糖）、蛋白质、脂肪等生物大分子水解成游离的单糖、氨基酸或脂肪酸，从而促进宿主对营养物质的转化和吸收（Ray et al., 2012）。因此，幽门盲囊细菌可能通过分泌水解酶，将多糖等碳水化合物分解为单糖，促进长棘海星对这类物质的吸收。与本研究发现类似，Beleneva & Kukhlevskii（2010）也发现海胆和海参肠道中存在具有能分泌半乳糖苷酶和岩藻多糖酶等多种水解酶的弧菌，可能具备帮助宿主消化食物的功能。此外，由于珊瑚组织中的蛋白质和脂类含量远高于糖类（Schoepf et al., 2013），因此，幽门盲囊细菌可能需要通过糖异生途径将氨基酸或脂肪酸等物质转化为糖类，以满足其生理需要（Thompson & Redak, 2000; Hecker et al., 2019）。

幽门盲囊细菌功能预测结果中的主要通路还包括脂类代谢。蜡酯（Wax ester）是珊瑚中重要的脂类贮能物质（Imbs et al., 2010）。尽管长棘海星被认为具有特异性消化珊瑚中蜡酯的酶系统（Benson et al., 1975; Brahimi-Horn et al., 1989），但是在其基因组中并没有发现编码相关酶的基因（Hall et al., 2017）。并且，长棘海星幼虫共生细菌与成体存在巨大差异（Carrier et al., 2018），而处在食性转换期的亚成体长棘海星也不具有完全消化珊瑚的能力（Deaker et al., 2021）。幽门盲囊是长棘海星主要的消化器官（Jangoux, 1982），因此，本研究推测珊瑚中的蜡酯可能被幽门盲囊中的产酶菌分泌的酯酶水解为游离的脂肪酸，从而促进长棘海星对珊瑚的消化吸收。赵书梅等（2017）也从溶藻弧菌（*Vibrio alginolyticus*）中克隆了酯酶基因，并将其在大肠杆菌（*Escherichia coli*）中表达后发现其具有较好的活性。

综上所述，本研究太阳长棘海星幽门盲囊细菌的主要功能集中在代谢方面，推测幽门盲囊细菌可能具有通过分泌水解酶来促进其消化吸收珊瑚的功能。

4 结论

本研究以南海西沙群岛的太阳长棘海星为对象，通过高通量测序研究其幽门盲囊细菌的群落组成及多样性，并对其潜在功能进行分析。得出以下主要结论：

1）西沙群岛太阳长棘海星幽门盲囊细菌群落中的优势门为变形菌门（94.50%）；优势属为弧菌属（*Vibrio*，60.61%），罗尔斯通氏菌属（*Ralstonia*，17.86%）和发光杆菌属（*Photobacterium*，6.64%）。太阳长棘海星幽门盲囊细菌的群落组成可能主要与其摄食珊瑚的习性相关；

2）太阳长棘海星幽门盲囊细菌可能受到西沙珊瑚礁退化的影响。白化事件导致珊瑚共生细菌和礁区环境中的弧菌暴发，太阳长棘海星可能由于摄食富含弧菌的珊瑚导致体内含有大量弧菌。同时，长棘海星作为潜在的弧菌传播载体，可能对南海珊瑚礁生态系统造成严重威胁；

3）太阳长棘海星幽门盲囊细菌的功能主要集中在代谢方面，幽门盲囊细菌可能通过分泌水解酶促进其消化吸收珊瑚。

参考文献（References）：

Beleneva I A and Kukhlevskii A D. 2010. Characterization of *Vibrio gigantis* and *Vibrio pomeroyi* Isolated from Invertebrates of Peter the Great Bay, Sea of Japan. *Microbiology*, 79: 402-407.

Benson A A, Patton J S, and Field C E. 1975. Wax Digestion in a Crown-of-Thorns Starfish. *Comparative Biochemistry and Physiology Part B*: *Comparative Biochemistry*, 52(2): 339-340.

Bolyen E, Rideout J R, Dillon M R, Bokulich N A, Abnet C C, Al-Ghalith G A, Alexander H, Alm E J, Arumugam M, Asnicar F, Bai Y, Bisanz J E, Bittinger K, Brejnrod A, Brislawn C J, Brown C T, Callahan B J, Caraballo-Rodríguez A M, Chase J, Cope E K, Silva R D, Diener C, Dorrestein P C, Douglas G M, Durall D M, Duvallet C, Edwardson C F, Ernst M, Estaki M, Fouquier J, Gauglitz J M, Gibbons S M, Gibson D L, Gonzalez A, Gorlick K, Guo J R, Hillmann B, Holmes S, Holste H, Huttenhower C, Huttley G A, Janssen S, Jarmusch A K, Jiang L J, Kaehler B D, Kang K B, Keefe C R, Keim P, Kelley S T, Knights D, Koester I, Kosciolek T, Kreps J, Langille M G I, Lee J, Ley R, Liu Y, Loftfield E, Lozupone C, Maher M, Marotz C, Martin B D, McDonald D, McIver L J, Melnik A V, Metcalf J L, Morgan S C, Morton J T, Naimey A T, Navas-Molina J A, Nothias L F, Orchanian S B, Pearson T, Peoples S L, Petras D, Preuss M L, Pruesse E, Rasmussen L B, Rivers A, Robeson II M S, Rosenthal P, Segata N, Shaffer M, Shiffer A, Sinha R, Song S J, Spear J R, Swafford A D, Thompson L R, Torres P J, Trinh P, Tripathi A, Turnbaugh P J, Ul-Hasan S, van der Hooft J J J, Vargas F,

Vázquez-Baeza Y, Vogtmann E, von Hippel M, Walters W, Wan Y H, Wang M X, Warren J, Weber K C, Williamson C H D, Willis A D, Xu Z Z, Zaneveld J R, Zhang Y L, Zhu Q Y, Knight R, and Caporaso J G. 2019. Reproducible, Interactive, Scalable and Extensible Microbiome Data Science Using QIIME 2. *Nature Biotechnology*, 37(8): 852-857.

Brahimi-Horn M C, Guglielmino M L, Sparrow L G, Logan R I, and Moran P J. 1989. Lipolytic Enzymes of the Digestive Organs of the Crown-of-Thorns Starfish (*Acanthaster planci*): Comparison of the Stomach and Pyloric Caeca. *Comparative Biochemistry and Physiology Part B*: *Comparative Biochemistry*, 92(4): 637-643.

Caballes C F, Schupp P J, Pratchett M S, and Rivera-Posada J A. 2012. Interspecific Transmission and Recovery of TCBS-Induced Disease between *Acanthaster planci* and *Linckia guildingi*. *Diseases of Aquatic Organisms*, 100(3): 263-267.

蔡健，梁曼颖，王健娇，周雪峰. 2021. 长棘海星中含氮类化学成分研究. 中国海洋药物，40（4）：45-49. [Cai Jian, Liang Manying, Wang Jianjiao, and Zhou Xuefeng. 2021. Nitrogenous Chemical Constituents from *Acanthaster planci*. *Chinese Journal of Marine Drugs*, 40(4): 45-49.]

Cai J Y, Yin B X, Wang Y H, Pan K, Xiao Y Y, and Wang X. 2024. Gut Microbiome Play a Crucial Role in Geographical and Interspecies Variations in Mercury Accumulation by Fish. *Science of The Total Environment*, 912: 169381.

Carrier T J, Wolfe K, Lopez K, Gall M, Janies D A, Byrne M, and Reitzel A M. 2018. Diet-Induced Shifts in the Crown-of-Thorns (*Acanthaster* sp.) Larval Microbiome. *Marine Biology*, 165(10): 1-8.

Chen B, Yu K F, Yao Q C, Liao Z H, Qin Z J, Yu X P, Wu Q, and He B. 2021a. Insights into the Environmental Impact on Genetic Structure and Larval Dispersal of Crown-of-Thorns Starfish in the South China Sea. *Frontiers in Marine Science*, 8: 728349.

Chen B, Yu K F, Liao Z H, Yu X P, Qin Z J, Liang J Y, Wang G H, Wu Q, and Jiang L L. 2021b. Microbiome Community and Complexity Indicate Environmental Gradient Acclimatisation and Potential Microbial Interaction of Endemic Coral Holobionts in the South China Sea. *Science of The Total Environmen*t, 765: 142690.

Cheutin M, Villéger S, Hicks C, Robinson J, Graham N, Marconnet C, Restrepo C, Bettarel Y, Bouvier T, and Auguet J. 2021. Microbial Shift in the Enteric Bacteriome of Coral Reef Fish Following Climate-Driven Regime Shifts. *Microorganisms*, 9(8): 1711.

Clever F, Sourisse J M, Preziosi R F, Eisen J A, Guerra E C R, Scott J J, Wilkins L G E, Altieri A H, McMillan W O, and Leray M. 2022. The Gut Microbiome Variability of a Butterflyfish Increases on Severely Degraded Caribbean Reefs. *Communications Biology*, 5 (1): 770.

De’ath G, Fabricius K E, Sweatman H, and Puotinen M. 2012. The 27-Year Decline of Coral Cover on the Great Barrier Reef and Its Causes. *Proceedings of the National Academy of Sciences of the United States of America*, 109(44): 17995-17999.

Deaker D J, Mos B, Lawson C, Dworjanyn S A, Budden C, and Byrne M. 2021. Coral Defences: the Perilous Transition of Juvenile Crown-of-Thorns Starfish to Corallivory. *Marine Ecology Progress Series*, 665: 115-125.

Dilmore L A and Hood M A. 1986. *Vibrios* of Some Deep-Water Invertebrates. *FEMS Microbiology Letters*, 35(2/3): 221-224.

Egerton S, Culloty S, Whooley J, Stanton C, and Ross R P. 2018. The Gut Microbiota of Marine Fish. *Frontiers in Microbiology*, 9: 873.

Emslie M J, Ceccarelli D M, Logan M, Blandford M I, Bray P, Campili A, Jonker M J, Parker J G, Prenzlau T, and Sinclair-Taylor T H. 2024. Changing Dynamics of Great Barrier Reef Hard Coral Cover in the Anthropocene. *Coral Reefs*, 43(3): 747-762.

Ezzat L, Lamy T, Maher R L, Munsterman K S, Landfield K, Schmeltzer E R, Gaulke C A, Burkepile D E, and Thurber R V. 2019. Surgeonfish Feces Increase Microbial Opportunism in Reef-Building Corals. *Marine Ecology Progress Series*, 631: 81-97.

Ezzat L, Lamy T, Maher R L, Munsterman K S, Landfield K M, Schmeltzer E R, Clements C S, Vega Thurber R L, and Burkepile D E. 2020. Parrotfish Predation Drives Distinct Microbial Communities in Reef-Building Corals. *Animal Microbiome*, 2: 1-5.

Gao Y M, Zou K S, Zhou L, Huang X D, Li Y Y, Gao X Y, Chen X, and Zhang X Y. 2020. Deep Insights into Gut Microbiota in Four Carnivorous Coral Reef Fishes from the South China Sea. *Microorganisms*, 8(3): 426.

高永利，黄晖，练健生，杨剑辉. 2014. 西沙群岛礁栖鱼类物种多样性及其食性特征. 生物多样性，22（5）：618-623. [Gao Yongli, Huang Hui, Lian Jiansheng, and Yang Jianhui. 2014. The Species Diversity and Trophic Structure of Reef Fishes in the Waters of the Xisha Archipelago. *Biodiversity Science*, 22(5): 618-623.]

Hall M R, Kocot K M, Baughman K W, Fernandez-Valverde S L, Gauthier M E A, Hatleberg W L, Krishnan A, McDougall C, Motti C A, Shoguchi E, Wang T F, Xiang X Y, Zhao M, Bose U, Shinzato C, Hisata K, Fujie M, Kanda M, Cummins S F, Satoh N, Degnan S M, and Degnan B M. 2017. The Crown-of-Thorns Starfish Genome as a Guide for Biocontrol of This Coral Reef Pest. *Nature*, 544(7649): 231-234.

Hadaidi G, Gegner H M, Ziegler M, and Voolstra C R. 2019. Carbohydrate Composition of Mucus from Scleractinian Corals from the Central Red Sea. *Coral Reefs*, 38(1): 21-27.

Hecker N, Sharma V, and Hiller M. 2019. Convergent Gene Losses Illuminate Metabolic and Physiological Changes in Herbivores and Carnivores. *Proceedings of the National Academy of Sciences of the United States of America*, 116(8): 3036-3041.

Høj L, Levy N, Baillie B K, Clode P L, Strohmaier R C, Siboni N, Webster N S, Uthicke S, and Bourne D G. 2018. Crown-of-Thorns Sea Star *Acanthaster* cf. *solaris* Has Tissue-Characteristic Microbiomes with Potential Roles in Health and Reproduction. *Applied and Environmental Microbiology*, 84(13): e00181.

Imbs A B, Latyshev N A, Dautova T N, and Latypov Y Y. 2010. Distribution of Lipids and Fatty Acids in Corals by Their

Taxonomic Position and Presence of Zooxanthellae. *Marine Ecology Progress Series*, 409: 65-75.

Jangoux M. 1982. Food and Feeding Mechanisms: Asteroidea. In: Jangoux M and Lawrence J M. *Echinoderm Nutrition*. London: CRC Press, 117-159.

Kamya P Z, Byrne M, Mos B, Hall L, and Dworjanyn S A. 2017. Indirect Effects of Ocean Acidification Drive Feeding and Growth of Juvenile Crown-of-Thorns Starfish, *Acanthaster planci*. *Proceedings of the Royal Society B-Biological Sciences*, 284 (1856): 20170778.

Karlsen C, Tzimorotas D, Robertsen E M, Kirste K H, Bogevik A S, and Rud I. 2022. Feed Microbiome: Confounding Factor Affecting Fish Gut Microbiome Studies. *ISME Communications*, 2 (1): 14.

Kuo C Y, Ho M J, Heng W K, Huang Y Y, Ko C Y, Jiang G C, Jeng M S, and Chen C A. 2021. What is for Dessert? Crown-of-Thorns Starfish Feeds on Non-Scleractinian Anthozoans at Taiping Island (Itu Aba), Spratlys, South China Sea. *Marine Biodiversity*, 52 (1): 2.

Kimura T, Chou L M, Huang D, Tun K, and Goh E. 2022. Status and Trends of East Asian Coral Reefs: 1983–2019. (2022-03-22) [2024-06-01]. https://icriforum. org/documents/status-and-trends-of-east-asian-coral-reefs-1983-2019/.

Kvennefors E C E, Sampayo E, Ridgway T, Barnes A C, and Hoegh-Guldberg O. 2010. Bacterial Communities of Two Ubiquitous Great Barrier Reef Corals Reveals Both Site and Species-Specificity of Common Bacterial Associates. *PLoS One*, 5(4): e10401.

Li Y X, Hao R X, Yu K F, and Chen X Y. 2024. Short-Term Impact of Decomposing Crown-of-Thorn Starfish Blooms on Reef-Building Corals and Benthic Algae: A Laboratory Study. *Water*, 16(2): 190.

郎尚昆 . 2022. 海南岛和西沙群岛珊瑚白化状况及原因分析 . 三亚 : 海南热带海洋学院 . [Lang Shangkun. 2022. The Status and Cause Analysis of Coral Bleaching in Hainan Island and Xisha Islands. Sanya: Hainan Tropical Ocean University.]

李元超，吴钟解，梁计林，陈石泉，赵建民 . 2019. 近 15 年西沙群岛长棘海星暴发周期及暴发原因分析 . 科学通报，64（33）: 3478-3484. [Li Yuanchao, Wu Zhongjie, Liang Jilin, Chen Shiquan, and Zhao Jianmin. 2019. Analysis on the Outbreak Period and Cause of *Acanthaster planci* in Xisha Islands in Recent 15 Years. *China Science Bulletin*, 64(33): 3478-3484.]

李渊，胡战彪，谢世君，刘世刚，妙星，王伟，肖家光，王芮，林龙山 . 2024. 南海长棘海星物种有效性探讨 . 应用海洋学学报，43（2）: 201-207. [Li Yuan, Hu Zhanbiao, Xie Shijun, Liu Shigang, Miao Xing, Wang Wei, Xiao Jiaguang, Wang Rui, and Lin Longshan. 2024. Discussion on Species Validity of Crown-of-Thorns Starfish in South China Sea. *Journal of Applied Oceanography*, 43(2): 201-207.]

Liu Z H, Chen C, Gao L, Zhang Y Y, Pei J J, Ren C H, and Hu C Q. 2016. Differences in Microbial Communities between Healthy and Bleached Coral *Acropora solitaryensis* from Xisha Islands, South China Sea. *Marine Biology Research*, 12(10): 1101-1108.

Liu Y, Wu P, Li C H, Xiao Y Y, Wang T, and Lin L. 2021. The Bacterial Composition Associated with *Atriolum robustum*, a Common Ascidian from Xisha Coral Reef, China. *Symbiosis*, 83(2): 153-161.

刘界宏，王鹏程，王智豪，夏文彤，谢松光，宋一清 . 2024. 西沙群岛长棘海星（*Acanthaster solaris*）繁殖生物学的初步研究 . 热带海洋学报，43（6）: 160-169. [Liu Jiehong, Wang Pengcheng, Wang Zhihao, Xia Wentong, Xie Songguang, and Song Yiqing. 2024. Preliminary Study on the Reproductive Biology of Crown-of-Thorns Starfish (*Acanthaster solaris*) in the Xisha Islands. *Journal of Tropical Oceanography*, 43(6): 160-169.]

雷明凤，余克服，廖芝衡，陈飚，黄学勇，陈小燕 . 2024. 西沙群岛银屿珊瑚礁的生态快速退化及其对鱼类的影响 . 热带海洋学报，43（3）: 87-99. [Lei Mingfeng, Yu Kefu, Liao Zhiheng, Chen Biao, Huang Xueyong, and Chen Xiaoyan. 2024. The Rapid Ecological Degradation and Its Impact on Fish of the Yinyu Island in the Xisha Archipelago. *Journal of Tropical Oceanography*, 43 (3): 87-99.]

Michl S C, Ratten J M, Beyer M, Hasler M, LaRoche J, and Schulz C. 2017. The Malleable Gut Microbiome of Juvenile Rainbow Trout (*Oncorhynchus mykiss*): Diet-Dependent Shifts of Bacterial Community Structures. *PLoS One*, 12(5): e177735.

Miyake S, Ngugi D K, and Stingl U. 2015. Diet Strongly Influences the Gut Microbiota of Surgeonfishes. *Molecular Ecology*, 24(3): 656-672.

Mostarda E, Campo D, Castriota L, Esposito V, Scarabello M P, and Andaloro F. 2007. Feeding Habits of the Bullet Tuna *Auxis rochei* in the Southern Tyrrhenian Sea. *Journal of the Marine Biological Association of the United Kingdom*, 87(4): 1007-1012.

Peng C H, Wang K, Wang W, Kuang F F, Gao Y H, Jiang R G, Sun X W, Dong X, Chen B H, and Lin H. 2023. Phytoplankton Community Structure and Environmental Factors During the Outbreak of Crown-of-Thorns Starfish in Xisha Islands, South China Sea. *Environmental Research*, 235: 116568.

Pratchett M S. 2005. Dynamics of an Outbreak Population of *Acanthaster planci* at Lizard Island, Northern Great Barrier Reef (1995–1999). *Coral Reefs*, 24(3): 453-462.

Qin Z J, Yu K F, Liang J Y, Yao Q C, and Chen B. 2020. Significant Changes in Microbial Communities Associated with Reef Corals in the Southern South China Sea During the 2015/2016 Global-Scale Coral Bleaching Event. *Journal of Geophysical Research-Oceans*, 125(7): e2019JC015579.

Qin Z J, Yu K F, Chen S C, Chen B, Yao Q C, Yu X P, Pan N B, and Wei X L. 2022. Significant Changes in Bacterial Communities Associated with *Pocillopora* Corals Ingestion by Crown-of-Thorns Starfish: An Important Factor Affecting the Coral's Health. *Microorganisms*, 10(2): 207.

Ray A K, Ghosh K, and Ringø E J. 2012. Enzyme-Producing Bacteria Isolated from Fish Gut: A Review. *Aquaculture Nutrition*, 18(5):

465-492.

Renzi J J, Shaver E C, Burkepile D E, and Silliman B R. 2022. The Role of Predators in Coral Disease Dynamics. *Coral Reefs*, 41(2): 405-422.

Rivera-Posada J A, Pratchett M, Cano-Gomez A, Arango-Gomez J D, and Owens L. 2011. Refined Identification of *Vibrio* Bacterial Flora from *Acanthasther planci* Based on Biochemical Profiling and Analysis of Housekeeping Genes. *Diseases of Aquatic Organisms*, 96(2): 113-123.

Ringø E Z, Zhou Z, Vecino J L G, Wadsworth S, Romero J, Krogdahl Å, Olsen R E, Dimitroglou A, Foey A, Davies S, Owen M, Lauzon H L, Martinsen L L, Schryver P D, Bossier P, Sperstad S, and Merrifield D L. 2016. Effect of Dietary Components on the Gut Microbiota of Aquatic Animals. A Never-Ending Story? *Aquaculture Nutrition*, 22(2): 219-282.

史敬文，王辰燕，王煜轩，覃素丽，康亚茹，颜安南，韩民伟，张瑞杰，余克服 . 2023. 南海长棘海星中多环芳烃的生物富集特征及来源解析 . 海洋环境科学，42（2）：209-216. [Shi Jingwen, Wang Chenyan, Wang Yuxuan, Qin Suli, Kang Yaru, Yan Annan, Han Minwei, Zhang Ruijie, and Yu Kefu. 2023. Bioaccumulation Characteristic and Source Analysis of Polycyclic Aromatic Hydrocarbons in *Acanthaster planci* from the South China Sea. *Marine Environmental Science*, 42(2): 209-216.]

Schloss P D, Gevers D, and Westcott S L. 2011. Reducing the Effects of PCR Amplification and Sequencing Artifacts on 16S rRNA-Based Studies. *PLoS One*, 6(12): e27310.

Schoepf V, Grottoli A G, Warner M E, Cai W J, Melman T F, Hoadley K D, Pettay D T, Hu X P, Li Q, Xu H, Wang Y C, Matsui Y, and Baumann J H. 2013. Coral Energy Reserves and Calcification in a High-CO_2 World at Two Temperatures. *PLoS One*, 8(10): e75049.

Smriga S, Sandin S A, and Azam F. 2010. Abundance, Diversity, and Activity of Microbial Assemblages Associated with Coral Reef Fish Guts and Feces. *FEMS Microbiology Ecology*, 73(1): 31-42.

陶雅晋，莫檬，何雄波，冯波，卢伙胜，颜云榕 . 2017. 南海黄鳍金枪鱼（*Thunnus albacores*）摄食习性及其随生长发育的变化 . 渔业科学进展，38（4）：1-10. [Tao Yajin, Mo Meng, He Xiongbo, Feng Bo, Lu Huosheng, and Yan Yunrong. 2017. Feeding Habits and Ontogenetic Diet Shifts of Yellowfin Tuna (*Thunnus albacores*) in the South China Sea. *Progress in Fishery Sciences*, 38(4): 1-10.]

Tang Y Z, Zhang L Y, Liu S G, Zhou J L, Ren Z J, Qu X Y, Li Y, and Lou F R. 2023. Intestinal Microbiota Analyses of Five Economic Fishery Resources in the South China Sea. *Comparative Biochemistry and Physiology Part D Genomics Proteomics*, 46: 101085.

Thompson S N and Redak R A. 2000. Interactions of Dietary Protein and Carbohydrate Determine Blood Sugar Level and Regulate Nutrient Selection in the Insect *Manduca sexta* L. *Biochimica et Biophysica Acta* (*BBA*)-*General Subjects*, 1523(1): 91-102.

Tian Y S, Yu Z H, Luo P, Yun L, Huang W, Hu C Q, Huo D, and Li H. 2017. Artificial Breeding and Culture of the Crown-of-Thorns Starfish *Acanthaster planci* (Linnaeus, 1758) Larvae in China. *Invertebrate Reproduction & Development*, 61(3): 157-163.

Turon M, Cáliz J, Triadó-Margarit X, Casamayor E, and Uriz M. 2019. Sponges and Their Microbiomes Show Similar Community Metrics Across Impacted and Well-Preserved Reefs. *Frontiers in Microbiology*, 10: 1961.

Velásquez-Rodríguez T M, Zuluaga-Arias C, Montaño-Salazar S M, González J M, and Sánchez J A. 2021. The Potential of Parrotfish Faeces in Replenishing Reefs with Coral-Associated Microbiome. (2021-01-15) [2024-06-03]. https://www. biorxiv. org/content/10. 1101/2020.09.15.298737v2.

Viver T, Ruiz A, Bertomeu E, Martorell-Barceló M, Urdiain M, Grau A, Signaroli M, Barcelo-Serra M, Aspillaga E, Pons A, Rodgers C, Gisbert E, Furones D, Alós J, Catalán I A, and Rossello-Mora R. 2023. Food Determines Ephemerous and Non-Stable Gut Microbiome Communities in Juvenile Wild and Farmed Mediterranean Fish. *Science of the Total Environment*, 889: 164080.

Wada N, Yuasa H, Kajitani R, Gotoh Y, Ogura Y, Yoshimura D, Toyoda A, Tang S L, Higashimura Y, Sweatman H and Forsman Z, Bronstein O, Eyal G, Thongtham N, Itoh T, Hayashi T, and Yasuda N. 2020. A Ubiquitous Subcuticular Bacterial Symbiont of a Coral Predator, the Crown-of-Thorns Starfish, in the Indo-Pacific. *Microbiome*, 8: 123.

Wang L W, Xu J R, Liu H J, Wang S P, Ou W C, Zhang M, Wei F, Luo S L, Chen B, Zhang S L, and Yu K F. 2023. Ultrasensitive and On-Site eDNA Detection for the Monitoring of Crown-of-Thorns Starfish Densities at the pre-Outbreak Stage Using an Electrochemical Biosensor. *Biosensors & Bioelectronics*, 230: 115265.

王辰燕，史敬文，颜安南，康亚茹，王煜轩，覃素丽，韩民伟，张瑞杰，余克服 . 2023. 有机磷酸酯在南海长棘海星中的生物富集特征及来源解析 . 热带海洋学报，42（5）：30-37. [Wang Chenyan, Shi Jingwen, Yan An'nan, Kang Yaru, Wang Yuxuan, Qin Suli, Han Minwei, Zhang Ruijie, and Yu Kefu. 2023. Bioaccumulation Characteristics and Source Apportionment of Organophosphate Esters in *Acanthaster planci* from the South China Sea. *Journal of Tropical Oceanography*, 42(5): 30-37.]

王晶晶，胡晓娟，曹煜成，苏浩昌，文国樑，张月星 . 2022. 南海岛礁海域金带齿颌鲷鳃组织和肠道菌群结构及其肠道菌群对碳源的利用特征 . 中国水产科学，29（12）：1788-1799. [Wang Jingjing, Hu Xiaojuan, Cao Yucheng, Su Haochang, Wen Guoliang, and Zhang Yuexing. 2022. Gill Tissue and Intestinal Flora Bacterial Community Structure and Carbon Source Utilization Characteristics of the Intestinal Flora of *Gnathodentex aurolineatus* in Reef Waters of the South China Sea. *Journal of Fishery Sciences of China*, 29(12): 1788-1799.]

夏荣林，宁志铭，余克服，方草，黄学勇，韦芬 . 2022. 长棘海星暴发对珊瑚礁区沉积物营养盐动力学的影响研究 . 海洋学报，44（8）：23-30. [Xia Ronglin, Ning Zhiming, Yu Kefu, Fang Cao, Huang Xueyong, and Wei Fen. 2022. Study on the Impacts

of Crown-of-Thorns Starfish on Nutrient Dynamics in the Coral Reef Sediments. *Acta Oceanologica Sinica*, 44(8): 23-30.]

Xiao J G, Wang W, Wang X L, Tian P, and Niu W T. 2022. Recent Deterioration of Coral Reefs in the South China Sea due to Multiple Disturbances. *PeerJ*, 10: e13634.

向佳丽，李渊，宋普庆，刘世刚，王芮，李海，妙星，张然，林龙山. 2022. 鱼类肠道微生物多样性及其与环境因子关系的研究进展. 渔业研究，44（2）：187-195. [Xiang Jiali, Li Yuan, Song Puqing, Liu Shigang, Wang Rui, Li Hai, Miao Xing, Zhang Ran, and Lin Longshan. 2022. Research Progress on Gut Microbial Diversity of Fish and Its Relationship with Environmental Factors. *Journal of Fisheries Research*, 44(2): 187-195.]

姚秋翠，余克服，廖芝衡，陈飚，俞小鹏，韦芬，胡宝清. 2022. 棘冠海星暴发及其对珊瑚礁的生态影响研究进展. 生态学报，42（18）：7517-7528. [Yao Qiuchui, Yu Kefu, Liao Zhiheng, Chen Biao, Yu Xiaopeng, Wei Fen, and Hu Baoqing. 2022. A Review of Research on Crown-of-Thorns Starfish and Their Ecological Effects on Coral Reefs. *Acta Ecologica Sinica*, 42(18): 7517-7528.]

Yang L T, Zhang Y, Chen H Z, Gao Q, Luo P, Hu J X, Zheng F Y, Yuan Y Y, Fu L, and Chen C. 2022. Physiological and Transcriptomic Responses to Starvation in the Corallivorous Crown-of-Thorn Starfish. *Frontiers in Marine Science*, 9: 1021377.

闫智聪，邢家杰，蔡文启，张开典，吴钟解，李元超，唐佳，周智. 2023. 基于环境DNA技术的西沙礁区长棘海星种群丰度研究. 海洋学报，45（3）：76-83. [Yan Zhicong, Xing Jiajie, Cai Wenqi, Zhang Kaidian, Wu Zhongjie, Li Yuanchao, Tang Jia, and Zhou Zhi. 2023. Study on the Population Distribution of *Acanthaster planci* in the Reef Area of the Xisha Islands Based on Environmental DNA Technology. *Acta Oceanologica Sinica*, 45 (3): 76-83.]

Yu X P, Yu K F, Liao Z H, Chen B, Deng C Q, Yu J Y, Yao Q C, Qin Z J, and Liang J Y. 2021. Seasonal Fluctuations in Symbiotic Bacteria and Their Role in Environmental Adaptation of the Scleractinian Coral *Acropora pruinosa* in High-Latitude Coral Reef Area of the South China Sea. *Science of The Total Environment*, 792: 148438.

赵思佳，张媛媛，余克服，俞小鹏，陈飚，许勇前，葛瑞琪. 2022. 南海珊瑚礁区棘冠海星重金属含量及其生物积累特征分析. 海洋环境科学，41（4）：579-585. [Zhao Sijia, Zhang Yuanyuan, Yu Kefu, Yu Xiaopeng, Chen Biao, Xu Yongqian, and Ge Ruiqi. 2022. Analysis of Heavy Metal Contents and Bioaccumulation Characteristics of *Acanthaster planci* in Coral Reef of South China Sea. *Marine Environmental Science*, 41(4): 579-585.]

赵书梅，王霖慧，唐嘉琦，赵静宜. 2017. 溶藻弧菌中酯酶基因的克隆表达及其酶学性质研究. 生物技术通报，33（6）：190-196. [Zhao Shumei, Wang Linhui, Tang Jiaqi, and Zhao Jingyi. 2017. Cloning, Expression and Characterization of the Esterase Gene *estZ* from *Vibrio alginolyticus*. *Biotechnology Bulletin*, 33 (6): 190-196.]

Zhao W B, Chen X, Liu R H, Tian P, Niu W T, Zhang X H, Liu J W, and Wang X L. 2023a. Distinct Coral Environments Shape the Dynamic of Planktonic *Vibrio* spp. *Environmental Microbiome*, 18 (1): 77.

Zhao W B, Chen L R, Liu M, Huang K Y, Ding Y Q, Xiao J G, Tian P, Liu J W, Zhang X H, Niu W T, and Wang X L. 2023b. Sedimentary *Vibrio* Blooms in the Xisha Islands May Associate with the 2020 Coral Bleaching Event. *Applied and Environmental Microbiology*, 89(7): e00543-23. DOI: 10.1128/aem.00543-23.

张颖，杨栎潼，刘冰，郑凡昱，罗鹏，陈偿. 2022. 长棘海星（*Acanthaster planci*）幼体特异性PCR检测技术与应用. 热带海洋学报，41（6）：125-131. [Zhang Ying, Yang Litong, Liu Bing, Zheng Fanyu, Luo Peng, and Chen Chang. 2022. Specific PCR Detection for *Acanthaster planci* Larvae and Its Application. *Journal of Tropical Oceanography*, 41(6): 125-131.]

Zhang T Y, Wang X, Qu Y, Zhang X L, Zhang Q Q, Yang D L, Wang Q, Dong Z J, and Zhao J M. 2023. Intestinal Microbiota Perturbations in the Gastropod *Trochus niloticus* Concurrently Exposed to Ocean Acidification and Environmentally Relevant Concentrations of Sulfamethoxazole. *Chemosphere*, 311: 137115.

郑金辉，任广波，胡亚斌，张飞飞，马毅，李明杰，王瑞富. 2023. 生物天敌暴发导致珊瑚礁退化的高分遥感监测与分析——以南海太平岛为例. 热带地理，43（10）：1856-1873. [Zheng Jinhui, Ren Guangbo, Hu Yabin, Zhang Feifei, Ma Yi, Li Mingjie, and Wang Ruifu. 2023. High Resolution Remote Sensing Monitoring and Analysis of Coral Reef Degradation Caused by Outbreaks of Biological Natural Enemies: A Case Study of the Taiping Island in the South China Sea. *Tropical Geography*, 43 (10): 1856-1873.]

作者贡献声明：

余骄洋：负责数据分析、论文撰写与修改；

俞小鹏：样品采集与论文修改；

余克服：论文思路和结构设计、论文修改；

马玉玲：校对与修改文字表述。

Bacterial Diversity and Community Composition in the Pyloric Ceca of *Acanthaster solaris* in the Xisha Islands

Yu Jiaoyang[1], Yu Xiaopeng[1], Yu Kefu[1,2], and Ma Yuling[1]

[1. Guangxi Laboratory on the Study of Coral Reefs in the South China Sea, Coral Reef Research Center of China, School of Marine Sciences, Guangxi University, Nanning 530004, China; 2. Southern Marine Sciences and Engineering Guangdong Laboratory (Guangzhou), Guangzhou 511458, China]

Abstract: Crown-of-Thorns Starfish (CoTS) are natural enemies of corals. Periodic outbreaks of CoTS and substantial feeding on corals lead to the degradation of coral reefs among the Indo-Pacific Ocean. Symbiotic bacteria play an important role in the development, reproduction, and digestion of CoTS. However, little is known about their composition and function. The pyloric ceca are the main digestive organ of CoTS. In this study, the composition and function of bacteria in the pyloric ceca of 15 adult *A. solaris* collected from the coral reef area of Xisha Islands were tested by high-throughput sequencing. A total of 833 bacterial OTUs were detected in the pyloric ceca, belonging to 26 phyla, 55 classes, 115 orders, 171 families, and 278 genera. The dominant phyla were Proteobacteria (94.50%), and the dominant genera were *Vibrio* (60.61%), *Ralstonia* (17.86%), and *Photobacterium* (6.64%). The symbiotic bacterial composition of other reef-associated organisms with different feeding habits, distributed in the Xisha Islands, were different. Composition of the pyloric cecal bacteria of CoTS were relatively similar to that of the coral symbiotic bacteria owing to the presence of some same bacteria genera in microbiome. Moreover, *Vibrio* was the dominant bacteria in both the pyloric cecal bacteria of CoTS and symbiotic bacteria of bleached *Acropora solitaryensis*, indicating high similarity. Therefore, the feeding habit of corals might be the important factor that affects the bacterial composition of the pyloric ceca of CoTS. The bacterial composition of the digestive tract of CoTS from the Great Barrier Reef of Australia and Japan showed the presence of Vibrionales, Burkholderiales, Rhizobiales, and Bacillales. However, significant regional differences were observed between the bacterial composition of the Xisha Island and Great Barrier Reef of Australia or Japan. *Vibrio* was more abundant in samples from the Xisha Islands than those from the Great Barrier Reef and Japan. This might be related to the massive coral bleaching events in the Xisha Islands from 2020 to 2021, which increased the relative abundance of *Vibrio* among the symbiotic bacteria of bleached corals. Additionally, as a potential *Vibrio* transmission vector, CoTS can pose a threat to the coral reef ecosystem in South China Sea. The results of bacterial function predict that their genome function was mainly focused on metabolism. The pathways with high relative abundance included carbohydrate, amino acid, cofactors and vitamins, and lipid metabolism. These results suggest that pyloric cecal bacteria may be involved in the daily physiological metabolic processes of CoTS. Thus, they might help digest corals by secreting hydrolytic enzymes. This study revealed the community composition, diversity, and affecting factors (feeding on coral) of pyloric cecal bacteria in CoTS from Xisha Islands, South China Sea.

Keywords: *Acanthaster solaris*; symbiotic bacteria; pyloric ceca; coral bleaching; Xisha Islands

Environmental Science & Technology

pubs.acs.org/est

Article

Organophosphate Ester Migration Mechanisms and Environmental Impacts in the Western South China Sea

Published as part of Environmental Science & Technology special issue "Ocean Health".

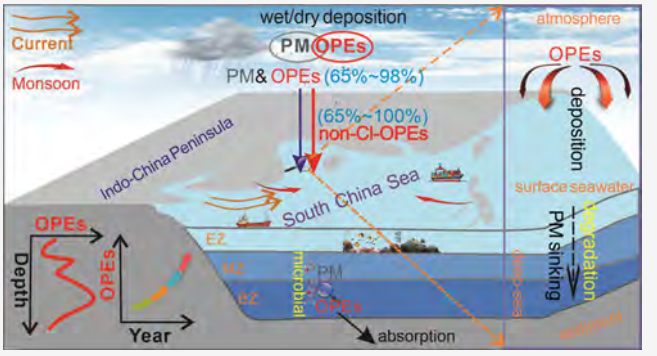
Minwei Han, Kefu Yu,* Ruijie Zhang, Biao Chen, Mei Xiong, Yaru Kang, Xiaopeng Yu, Zhenjun Qin, and Xiangrong Xu

Cite This: https://doi.org/10.1021/acs.est.5c09148

Read Online

ACCESS | Metrics & More | Article Recommendations | Supporting Information

ABSTRACT: Organophosphate esters (OPEs) are ubiquitous in various environmental media and are of concern because of their toxicity and potential ecological impacts. However, their transport mechanisms and ecological effects in marine environments remain poorly understood. Herein, we comprehensively investigated the occurrence and distribution of OPEs in multiple environmental media (atmosphere, rainwater, seawater, and sediments) in the western South China Sea (WSCS). Results show that OPEs are widespread in the WSCS. OPE concentrations in the atmosphere were higher than those reported in most other marine regions globally, whereas concentrations in seawater were either lower than or comparable to those in other oceanic regions. The biogeochemical cycling of OPEs is driven primarily by particulate matter (PM) and microbial activity. PM facilitates the transport of 65.3−98.4% of total OPEs and 60.5−100% of chlorinated OPEs from the atmosphere to the ocean. PM sinking strongly influences the vertical distribution of OPEs, while microorganisms contribute to OPE biodegradation through community succession, differentiation of ecological niches among key functional groups, and hydrolytic enzyme activity. Given the increasing concentrations of OPEs in the South China Sea, it is imperative to conduct comprehensive and continuous investigations of their migration mechanisms and impacts on marine ecosystems, particularly coral reefs.



KEYWORDS: *organophosphate esters, environmental behavior, migration mechanisms, particulate matter, microbial activity*

Downloaded via GUANGXI UNIV on October 25, 2025 at 02:10:18 (UTC).
See https://pubs.acs.org/sharingguidelines for options on how to legitimately share published articles.

1. INTRODUCTION

Organophosphate esters (OPEs) are widely used as flame retardants in polymers,[1,2] plasticizers,[3] defoamers[4] in various commercial and industrial products. Their production and use inevitably result in the release of residual OPEs into environmental media. Trace levels of OPEs have been detected in remote oceans, including the Southern Ocean and the polar regions.[1,5] The high lipophilicity of OPEs is of particular concern because it facilitates their accumulation in marine organisms such as corals, fish, and shellfish, and their subsequent transfer along the food chain, potentially posing threats to ecosystems and human health.[6−8]

The atmosphere influences the transport and distribution of OPEs in the environment, and the ocean is considered an important reservoir for these compounds.[1] The widespread distribution of OPEs in various environmental media underscores their considerable environmental transport properties.[7,9] Concurrently, their potential biotoxicity, including endocrine disruption abilities, neurotoxicity, reproductive toxicity, and carcinogenicity, is of high concern.[3,9] Remote marine environments are geographically distant from the direct impact of large-scale human activities and industrialized urban production. However, pollutants frequently enter the marine environment through multiple pathways, including atmospheric transport, riverine input, rainfall, and particulate matter (PM) deposition.[10,11] Under conditions of global warming and ocean acidification, these inputs may further exacerbate ecological threats to sensitive marine ecosystems such as coral reefs.[12,13] The biogeochemical cycling of OPEs in the marine environment is influenced by multiple factors, including their physical and chemical properties, ocean currents, atmospheric circulation, solar radiation, marine biological pumps (MBLPs), microbial activity, and particle deposition, leading to variations in their

Received: July 7, 2025
Revised: October 15, 2025
Accepted: October 15, 2025
Published: October 20, 2025

© 2025 American Chemical Society

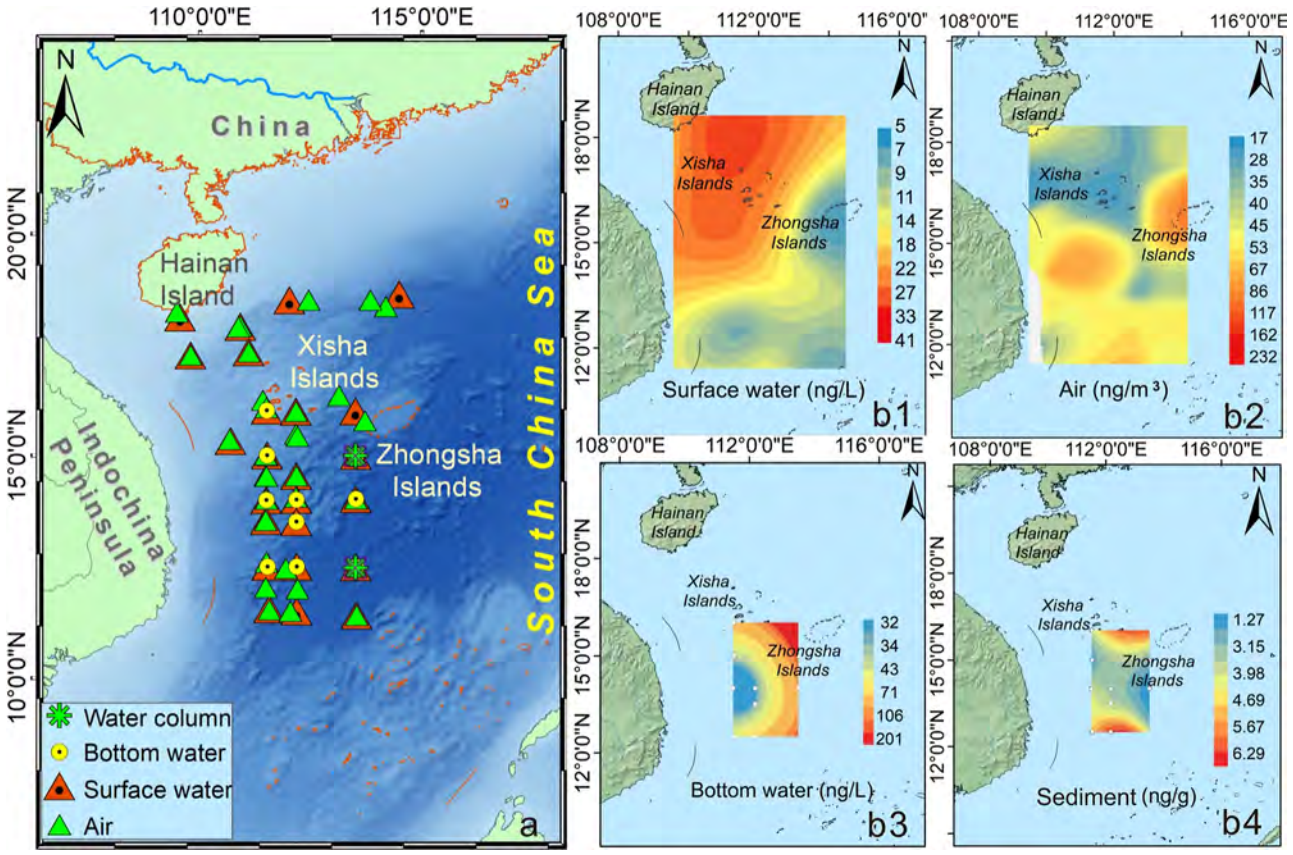


Figure 1. Sampling points (a) and distribution characteristics of OPEs (b) during the voyage in the WSCS.

behavior across different environmental media.[1,14−16] The diffusion patterns of ocean currents and sinking behavior of PM facilitate the diffusive transportation of semivolatile organic compounds (SVOCs) in surface systems and also impact their distribution and environmental behaviors within deep-sea systems.[17,18] The western South China Sea (WSCS) is influenced by intensive shipping activities and land-based runoff and is also impacted by the summer monsoon of the South China Sea (SCS). Pollution from shipping activities and rivers (e.g., Pearl and Mekong rivers) is transported into the SCS via diffusion with ocean currents,[19] and the terrigenous sources of SVOCs originating from excess human activities eventually end up in the SCS via the long-range transportation (LRT) of the atmosphere from land sources such as the Indochina Peninsula and Luzon Island.[20,21] The SCS is characterized by the presence of numerous coral reefs, which have been recognized for their remarkable biodiversity. However, currently, they are experiencing incessant bleaching and deterioration.[22] In the context of climate change, the damage to coral reefs due to intensified human activities appears to be more prominent, and the adverse effects of SVOCs on coral reefs are especially concerning. The deleterious effects of these pollutants on coral reefs predominantly include the destruction of coral symbiotic organisms, impacts on photosynthesis, changes in reef nutritional patterns, induction of oxidative stress, and inhibition of growth.[23−27] The WSCS serves as a transition zone for the migration of land-based pollution to coral reef regions of the SCS and is perennially exposed to various human activities, including terrestrial pollution, riverine input, and shipping.[17,19,28] However, the current status of OPE pollution and their environmental behavior in the region remain poorly understood, and the driving mechanisms of their biogeochemical cycling processes and ecological impacts are still unclear.

Therefore, this study aims to (1) quantify the occurrence and spatiotemporal trends of OPEs across multiple environmental compartments in the WSCS; (2) elucidate the vertical transport mechanisms of OPEs from the atmosphere to the ocean interior, including deep-sea systems; and (3) identify the key drivers governing the distribution and fate of OPEs in ocean vertical profiles. Collectively, these findings will advance understanding of the biogeochemical cycling, underlying mechanisms, and potential ecological impacts of OPEs as emerging contaminants in the marine environment.

2. MATERIALS AND METHODS

2.1. Chemicals and Reagents. Eleven widely used OPEs, including three chlorinated OPEs (Cl-OPEs) and eight nonchlorinated OPEs (non-Cl-OPEs), were selected as target compounds in this study. Their detailed physicochemical properties are provided in Text S1 and Table S1.

2.2. Sampling and Sample Pretreatment. All samples were collected during a cruise aboard the research vessel Xiangyanghong 3 in August 2021 (Figure 1). For the investigation of OPE concentrations, air, surface seawater, water column, bottom water, rainwater, and sediment samples (Tables S3−S6) were collected as described in our previous study.[17] In brief, atmospheric samples were collected using an active atmospheric sampler. Surface seawater was collected and passed through glass fiber filters (GFFs) and two tandem polyurethane foam (PUF) columns to enrich particle- and dissolved-phase OPEs. All the water column, bottom water, and rainwater samples were collected in brown glass bottles, stored

https://doi.org/10.1021/acs.est.5c09148
Environ. Sci. Technol. XXXX, XXX, XXX−XXX

at −4 °C, and, upon return to the laboratory, OPE extraction was performed using solid-phase extraction (SPE). All the solid-phase samples, including PUFs, GFFs, quartz fiber filters, and sediment samples, were wrapped in tinfoil zip-lock bags and stored at −20 °C. Detailed sampling and extraction procedures are provided in Text S2. For microbial community analysis, 20 L of seawater was collected using sterile Niskin bottles mounted on a CTD rosette. Water samples were filtered through a sterile stainless-steel disc filter (Sartorius, Göttingen, Germany) fitted with a sterile 0.22 μm pore-size polycarbonate membrane (Φ142 mm; Millipore, Billerica, USA). The filtration apparatus was cleaned with 75% ethanol prior to use. After filtration, the membrane was folded, placed into a 50 mL enzyme-free cryovial (Corning, Beijing, China), flash-frozen in liquid nitrogen, and stored at −80 °C. The total storage time from sampling to DNA extraction was less than 50 days.

2.3. Extraction and Instrumental Analysis. Two deuterium-labeled OPEs, i.e., tributyl phosphate-d_{27} (TNBP-d_{27}) and triphenyl phosphate-d_{15} (TPHP-d_{15}), were used as analytical surrogates. The target OPEs in all aqueous samples were extracted via SPE, and Soxhlet extraction was used for extracting other solid-phase samples (Text S2).[6,29,30] OPEs were qualitatively and quantitatively analyzed using an Agilent gas chromatography−tandem mass spectrometry (GC−MS/MS) instrument, and details of the instrumental parameters and temperature program are presented in Table S2 and Text S2.

2.4. Quality Assurance and Quality Control. Air samples were collected on the windward side of the ship's foredeck to minimize background contamination. Possible contamination was monitored using field blanks, experimental blanks, program blanks, and repeated samples. Instrumental detection limits (IDLs) were established based on a signal-to-noise ratio obtained from three times the analyte in the minimum standard. OPE concentrations in all blank samples were below or comparable to the IDLs, and all samples were corrected using field blanks. Method detection limits (MDLs) were calculated by dividing the 3-fold IDLs by the volume or mass of the sample. The MDLs for surface seawater, bottom seawater, atmospheric, and sediment samples were 0.0005−0.0300 ng/L, 0.0038−0.2415 ng/L, 0.0002−0.0112 ng/m^3, and 0.0075−0.4831 ng/g, respectively. TNBP-d_{27} and TPHP-d_{15} were used to monitor sample recovery, which ranged from 88.4% to 117%. The relative standard deviations of measured OPE concentrations in the spike matrix ranged from 0.52% to 18.9%. The reported concentrations were not corrected for surrogate recovery on an individual basis but were adjusted for procedural contamination by subtracting the mean concentration measured in the procedural blanks from each sample.

2.5. Bioinformatic Processing of 16S rRNA Sequencing Data. The methods for DNA extraction and 16S rRNA sequencing are described in Text S4. Raw sequencing reads (~50,000 reads per sample) were initially processed using fastp v0.19.[31] Quality control included the removal of low-quality bases (Q-score < 20) and adapter sequences. All samples demonstrated exceptionally high sequencing quality, with Phred quality scores ($Q30$) ranging from 97.9% to 98.9%, well above the widely adopted threshold for high-quality data ($Q30$ > 90%). These metrics indicate a very low error rate, confirm high sequence reliability, and support the robustness of the data for downstream bioinformatic analyses. Next, filtered high-quality reads were imported into QIIME2 v2022.2[32] for comprehensive microbiome analysis. Sequence processing was performed using the DADA2 algorithm,[33] which implemented a three-step denoising pipeline involving (i) the modeling of errors originating during amplification and sequencing and the use of this model to correct random sequencing errors, (ii) the precise merging of paired-end reads, and (iii) the generation of a high-resolution amplicon sequence variant (ASV) table containing exact biological sequences with their corresponding abundance profiles for all samples. For taxonomic classification, the representative sequences from each ASV were aligned with the SILVA ribosomal RNA database (SILVA; release 138; https://www.arb-silva.de/) using a naive Bayes classifier. The classification process used a bootstrap confidence threshold of 0.7 to ensure taxonomic assignment reliability.[34] To maintain data integrity, chimeric sequences and nonmicrobial sequences (i.e., mitochondrial, chloroplast, and eukaryotic-derived reads) were systematically filtered from the data set. Using these stringent quality control measures, only high-confidence bacterial ASVs were retained for the subsequent ecological analyses.

2.6. Data Analysis. *2.6.1. Microbial Community Characterization and Statistical Analyses.* Phylogenetic reconstruction was conducted by performing the multiple sequence alignment of representative ASV sequences using MAFFT v7.2[35] with default parameters, followed by maximum-likelihood tree construction using IQ-TREE.[36] The microbial α-diversity was estimated using the inverse Simpson index, and the β-diversity was calculated using Bray−Curtis dissimilarities between samples based on the high-confidence ASV data set. All diversity metrics were computed using the vegan package (v2.7-1) in R. Significant differences in the α-diversity among groups were assessed using Kruskal−Wallis tests. To evaluate variations in community structures, permutational multivariate analysis of variance (PERMANOVA) was performed on Bray−Curtis dissimilarity matrices with 9999 permutations, and results were visualized using nonmetric multidimensional scaling (NMDS) ordination plots.

The genus-level community composition was analyzed using relative abundance data normalized by the total sum scaling. Correlations between environmental variables and community structures were determined using partial Mantel tests, and microbial compositional variation among samples and environmental dissimilarity matrices were calculated using Canberra distance matrices while controlling for the dissolved oxygen concentration as a covariate. Community assembly processes were quantitatively assessed using a null model approach[37] with 999 randomizations, incorporating phylogenetic (β-nearest taxon index, βNTI) and taxonomic (Raup−Crick index, RCbray) metrics. Ecological processes were categorized as follows: (1) homogeneous selection (βNTI < −2), (2) heterogeneous selection (βNTI > +2), (3) dispersal limitation (|βNTI| < 2 and RC_{bray} > 0.95), (4) homogeneous dispersal (|βNTI| < 2 and RC_{bray} < −0.95), and (5) drift (|βNTI| < 2 and |RC_{bray}| < 0.95).

Depth-stratified microbial biomarkers were identified using the linear discriminant analysis effect size (LEfSe),[38] with significant differences in relative abundances (p < 0.05) confirmed using Kruskal−Wallis H tests. The functional potential was predicted from 16S rRNA gene sequences using the Phylogenetic Investigation of Communities by Reconstruction of Unobserved States (PICRUSt2)[39] with KEGG and MetaCyc pathway databases.[40,41] The abundance of OPE-degrading enzymes was visualized via heatmap analysis using the R heatmap package.

https://doi.org/10.1021/acs.est.5c09148
Environ. Sci. Technol. XXXX, XXX, XXX−XXX

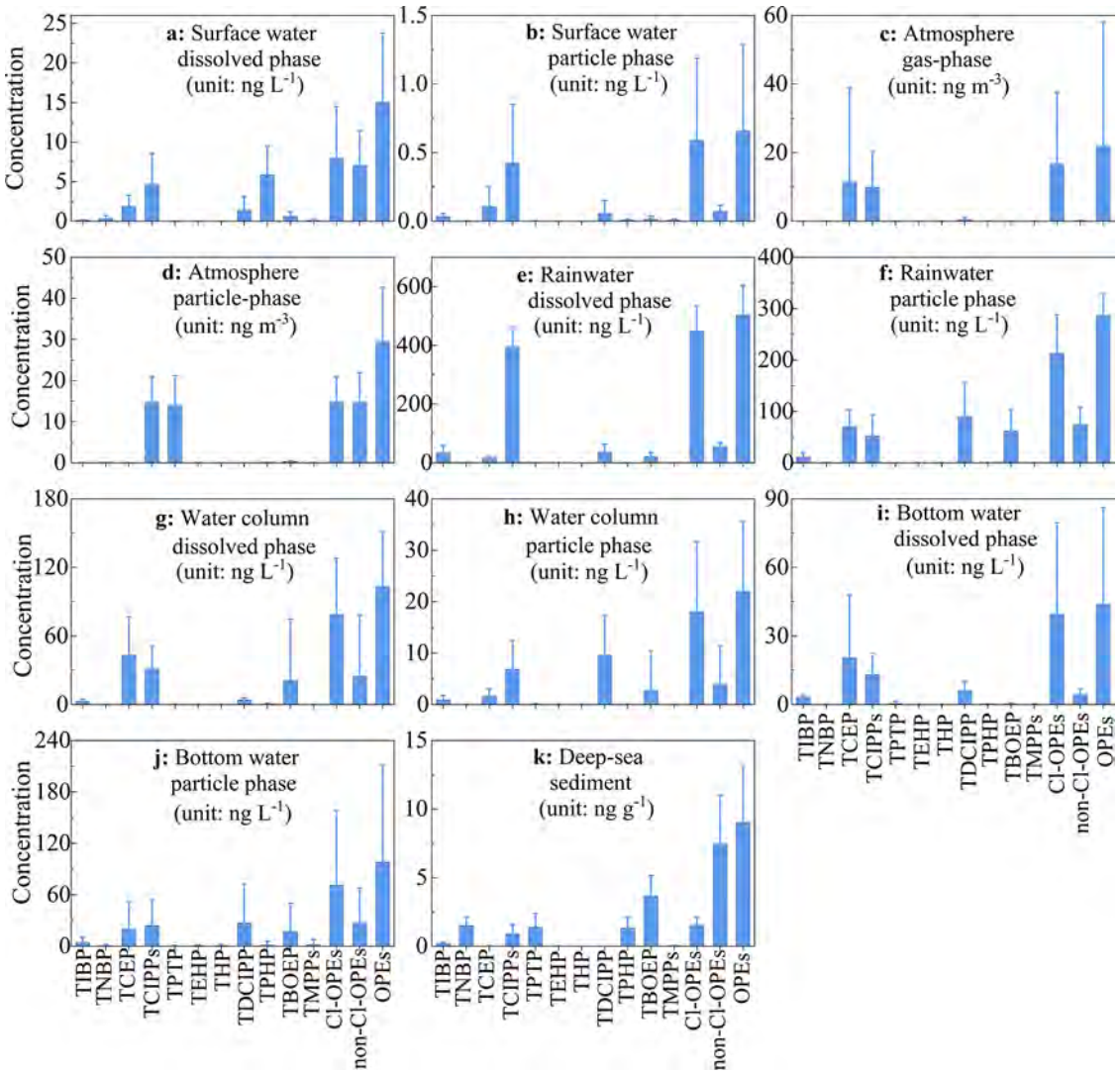


Figure 2. Organophosphate ester concentrations in different environmental media of the surface system (a–f) and deep-sea system (g–k) in the WSCS.

2.6.2. OPE Concentration Analysis. SPSS 26.0 was used for the statistical analysis of OPE concentrations. A student's *t*-test or a nonparametric test was used to ascertain the existence of differences in OPE concentrations between different groups. A *p*-value of <0.05 indicated a statistically significant result, and a *p*-value of <0.01 indicated a highly statistically significant result.

3. RESULTS AND DISCUSSION

3.1. Widespread Occurrence and Spatial Trends of OPEs in the WSCS. *3.1.1. Surface System.* Eleven target OPEs were simultaneously monitored in the gas and particle phases of the atmosphere, as well as in the dissolved and particle phases of surface seawater and rainwater in the WSCS. The majority of OPEs were detected across these environmental media. All 11 OPEs were detected in the atmospheric environment, with 11 in the gas phase and 9 in the particle phase. In surface seawater, nine OPEs were detected, with only tri(2-ethylhexyl) phosphate (TEHP) and trihexyl phosphate (THP) not detected. These results indicate that OPE contamination was pervasive within the WSCS surface system.

3.1.2. Atmosphere. The total concentrations of the 11 target OPEs ($\sum_{11}$OPEs) in the gas phase (21.9 ± 36.2 ng/m^3) were slightly lower than those in the particle phase (29.5 ± 13.2 ng/m^3) (Figures S2d and S3c). The total concentration of the eight non-Cl-OPEs ($\sum_{8}$non-Cl-OPEs) was approximately 40 times higher in the particle phase (48.6% ± 4.41%) than in the gas phase (1.39% ± 1.27%). For the 11 OPEs in the gas phase, the total concentration of the three chlorinated OPEs ($\sum_{3}$Cl-OPEs, 16.7 ± 21.0 ng/m^3) was significantly higher than that of the $\sum_{8}$non-Cl-OPEs (0.12 ± 0.13 ng/m^3) (nonparametric test, p < 0.01). In the particle phase, $\sum_{3}$Cl-OPEs (14.8 ± 6.12 ng/m^3) and $\sum_{8}$non-Cl-OPEs (14.7 ± 7.19 ng/m^3) were comparable. The atmospheric concentrations of OPEs observed in this study were higher than those reported in the Southern Ocean,[42] the Northern Pacific and Indian Oceans,[43] and the Atlantic, Pacific Oceans.[44]

3.1.3. Rainwater. $\sum_{11}$OPEs in the dissolved phase (505 ± 98.7 ng/L) was significantly higher than that in particle phase (287 ± 41.7 ng/L; *t*-test, p < 0.01; Figure 2e,f). $\sum_{3}$Cl-OPEs (dissolved phase: 448 ± 86.0 ng/L, particle phase: 213 ± 75.4 ng/L) was significantly higher than $\sum_{8}$non-Cl-OPEs (dissolved phase: 56.7 ± 12.8 ng/L, particle phase: 74.2 ± 33.6 ng/L). These concentrations were slightly higher than those in the intertropical convergence zone (ITCZ).[14]

https://doi.org/10.1021/acs.est.5c09148
Environ. Sci. Technol. XXXX, XXX, XXX−XXX

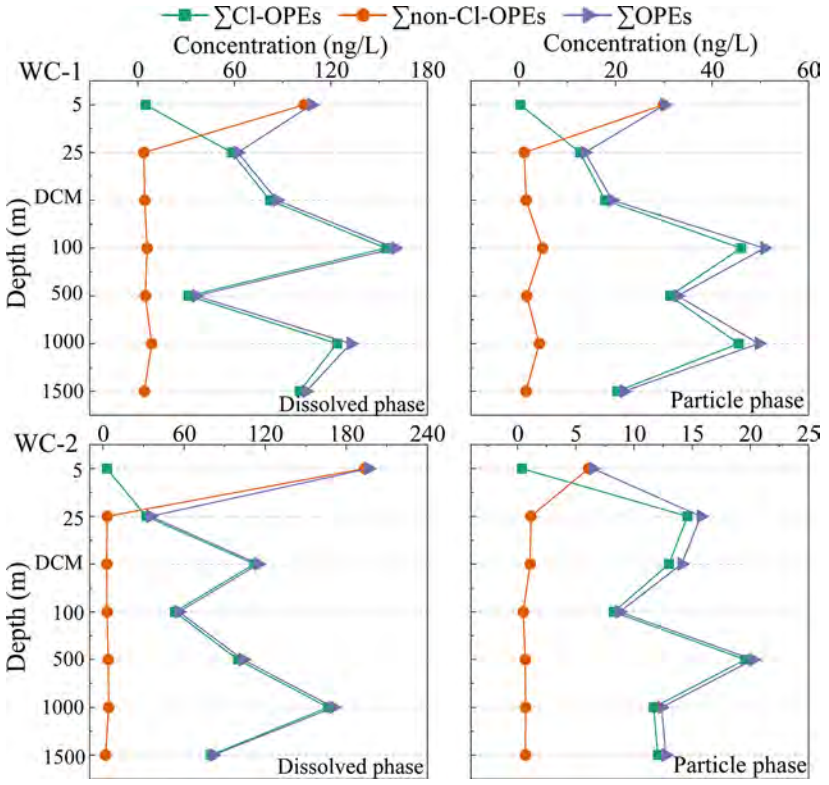


Figure 3. Variations in OPE concentrations in the two water columns (WC-1 is in the open water, deep chlorophyll maximum (DCM) = 75 m; WC-2 is close to the Zhongsha Atoll, DCM = 95 m) in the WSCS.

3.1.4. Surface Seawater. $\sum_{11}$OPEs in surface seawater were notably lower than those in rainwater. In the dissolved phase, $\sum_{11}$OPEs (15.0 ± 8.70 ng/L) were much higher than in the particle phase (0.66 ± 0.63 ng/L; *t*-test, $p < 0.01$; Figure 2a,b). Among these, $\sum_{3}$Cl-OPEs (7.95 ± 6.55 ng/L) and $\sum_{8}$non-Cl-OPEs (7.10 ± 4.37 ng/L) were comparable in the dissolved phase, whereas in the particle phase, $\sum_{3}$Cl-OPEs (0.59 ± 0.60 ng/L) were significantly higher than $\sum_{8}$non-Cl-OPEs (0.07 ± 0.05 ng/L). The OPE concentrations obtained were lower than those reported in the South Pacific,[45] the Atlantic Ocean,[14] Northwest Pacific and Arctic Oceans,[46] but close to those in the Southern Ocean.[5,14]

3.1.5. Deep-Sea System. All target OPEs were detected to varying extents in the dissolved and particle phases of seawater, with detection rates of 45.5−100% and 63.6−100%, respectively. Eight OPEs were detected in all deep-sea sediment samples, with a detection rate of 100%, while TEHP, THP, and tri(dichloroisopropyl) phosphate (TDCIPPs) were not detected.

3.1.6. Water Column Depth Profiles in Different Sea Areas. $\sum_{11}$OPEs in the dissolved phase (95.3 ± 42.6 ng/L) were significantly higher than in the particle phase (22.7 ± 13.7 ng/L; *t*-test, $p < 0.01$), and $\sum_{3}$Cl-OPEs were significantly higher than $\sum_{8}$non-Cl-OPEs in both the dissolved and particle phases (Figure 3). These concentrations were comparable to those reported in the Mariana Trench,[10] the Atlantic Ocean, and the Southern Ocean.[14]

In the open sea area (WC-1), $\sum_{11}$OPEs exhibited a consistent trend of change in particle and dissolved phases, i.e., $\sum_{11}$OPEs continuously increased from the surface to a depth of 100 m, suddenly decreased at a depth of 500 m, increased at a depth of 1000 m, and finally decreased at a depth of 1500 m. The highest $\sum_{11}$OPEs in the particle (50.8 ng/L) and dissolved (160 ng/L) phases were observed at a depth of 100 m (Figure 3).

In the sea area near the coral reef (WC-2), the observed trends in $\sum_{11}$OPEs exhibited notable differences between the dissolved and particle phases. The highest $\sum_{11}$OPEs in the dissolved phase was observed at the surface layer, while the highest $\sum_{11}$OPEs in the particle phase was observed at a depth of 500 m. From the surface to the subsurface layer (25 m), $\sum_{11}$OPEs in the dissolved phase decreased sharply and then significantly increased in the deep chlorophyll maximum (DCM) layer (Figure 3). This surface enrichment, accompanied by subsurface depletion, was attributed to the sinking and adsorption of PM, a process that is exacerbated by the nearby cold eddies. Conversely, the increased OPE concentration in the DCM layer was attributed to the increase in the phytoplankton biomass, which in turn affects the sinking of PM. Potential microbial activities may also be involved in OPE degradation. In the particle phase, $\sum_{11}$OPEs were highest at 25 m and gradually decreased with increasing depth, with the lowest concentrations observed at 100 m. Across all depth profiles from 100 to 1500 m, $\sum_{11}$OPEs first increased and then decreased; the difference was that the highest $\sum_{11}$OPEs in the dissolved phase (171 ng/L) occurred at 1000 m, whereas the highest $\sum_{11}$OPEs in the particle phase (20.2 ng/L) occurred at 500 m (Figure 3).

As mentioned above, the photochemical degradation process significantly reduced the concentration of Cl-OPEs in surface seawater compared to other layers in the vertical profile, and microbial activity in the subsurface layer of the ocean may dominate the degradation of non-Cl-OPEs in the vertical profile. Still, the distribution of OPEs in WC-1 and WC-2 water columns differed. Coral reef regions have a higher biodiversity and primary productivity, increasing PM concentration in the surrounding seawater. In WC-2, a high concentration of

https://doi.org/10.1021/acs.est.5c09148
Environ. Sci. Technol. XXXX, XXX, XXX−XXX

$\sum_{11}$OPEs in the dissolved phase may adsorb onto PM or coral mucus during the uninterrupted sinking process of PM. After obtaining the highest $\sum_{11}$OPEs in the particle phase at a 500 m depth, the sinking and dissolution of mucus and PM led to the re-entry of particle-phase OPEs into the dissolved phase of the water column. This process may have substantially increased $\sum_{11}$OPEs in the dissolved phase at a 1000 m depth. Additionally, the process of resuspension, induced by deep-sea currents, may have further increased the concentration of dissolved OPEs. Furthermore, except for surface seawaters, $\sum_{3}$Cl-OPEs was higher than $\sum_{8}$non-Cl-OPEs in all depth profiles. The exceptionally high value of $\sum_{8}$non-Cl-OPEs in surface seawater contributed to the high values of $\sum_{11}$OPEs (Figure 3).

3.1.7. Bottom Seawater. $\sum_{11}$OPEs in the particle phase (38.0 ± 49.1 ng/L) were comparable to those in the dissolved phase (44.0 ± 42.2 ng/L; *t*-test, $p < 0.01$), and $\sum_{3}$Cl-OPEs were significantly higher than $\sum_{8}$non-Cl-OPEs in both the dissolved and particle phases (Figure 2i,j). These concentrations were higher than those reported in the Atlantic and Southern Oceans,[14] but were comparable to those in the Mariana Trench.[10]

3.1.8. Deep-Sea Sediment. $\sum_{11}$OPEs ranged from 2.70 to 15.6 ng/g (8.13 ± 3.13 ng/g), and $\sum_{8}$non-Cl-OPEs (8.13 ± 3.63 ng/g) were significantly higher than $\sum_{3}$Cl-OPEs (0.92 ± 0.71 ng/g; Figure 2k). These OPE concentrations were higher than those reported in the Arctic Ocean,[47,48] but lower than those in the Eastern Indian Ocean,[49] the Mariana Trench,[10] and the Bohai Sea and East China Sea.[50]

3.1.9. Spatial Distribution of OPEs. 3.1.9.1. Spatial Differences and Influencing Factors in the Atmosphere. $\sum_{11}$OPEs in the atmospheric environment exhibited regional differences in the entire survey area, with higher values in the South and lower values in the North. High-$\sum_{11}$OPE regions were detected near the Indochina Peninsula and Zhongsha Islands (Figure 1b2). The southwest monsoon drives the transport of terrigenous pollution sources in the Indochina Peninsula, negatively affecting the SCS ecosystem.[51−53] The 72 h backward air mass trajectory showed the significant impact of the southwest monsoon on the SCS ecosystem during the sampling period (Figure S1). Terrestrial sources of pollution, such as electronics dismantling and waste incineration,[21,54] could continue releasing OPEs, which are transported to the SCS via the LRT of the air mass driven by the summer monsoon (Figure S2b). Additionally, the high-concentration zone of OPEs near the Zhongsha Islands was precisely located along the main shipping route in the SCS,[55] indicating that ship navigation could have been responsible for releasing OPE-related pollutants into the atmospheric environment.

The occurrence of OPEs in the atmosphere was influenced by monsoon and diurnal variations in the WSCS. Atmospheric OPE concentrations were markedly higher during the southwest monsoon than during the southeast monsoon, particularly in the gas phase (Figure S3d). The southwest monsoon likely contributed predominantly to the input of non-Cl-OPEs, whereas the southeast monsoon predominantly contributed to Cl-OPEs. Maritime human activities, including fishing, offshore oil drilling, and shipping, may have contributed to OPE inputs into the atmosphere (Figures S3a and 2d). The global electronic component manufacturing plant and supply base on Luzon Island was also responsible for transporting pollutants into the WSCS atmosphere via air masses (Figure 1b2). Diurnal variations influenced atmospheric OPE concentrations, with particle-phase OPE concentrations higher during daylight and gas-phase OPE concentrations higher at night (Figures S3e and 2h). This discrepancy was attributed to the higher photodegradation capacity of Cl-OPEs in the gas phase compared to the particle phase.

3.1.9.2. Gas/Particle Partitioning. Gas/particle partitioning determines the environmental fate of SVOCs, especially their LRT and migration in the atmosphere, and affects the bioavailability of SVOCs.[56,57] A comparison between the estimated K_P values of different models and the field values is shown in Figure S4. The comparison shows that the K_P values of the target OPEs predicted using the Harner−Bidleman adsorption model were close to the actual values (Figure S4e,f). The Junge−Pankow model fitted the correlation between the temperature-corrected subcooled liquid vapor pressure (P_L^0) and calculated values of K_P, but the slope was significantly different from the theoretical value at equilibrium (Figure S4a,b). By contrast, the K_P values for all 11 OPEs predicted using the $K_{soot\text{-}air}$ double-adsorption model were much lower than the actual values (Figure S4c,d). Furthermore, although the steady-state model predicted K_P values for some OPEs that were close to the actual values, there was a significant deviation between the predicted values and actual values for five OPEs (Figure S4g,h). New pollution sources, LRT, physical and chemical properties of OPEs, field sampling, air temperature, and activity coefficients affect the K_P of SVOCs, leading to the deviation between the actual and simulated values.[16,57,58]

3.1.9.3. Spatial Differences and Influencing Factors in the Surface Seawater. The high-value area of $\sum_{11}$OPEs covered the Hainan Island and Xisha Island (Figure 1b1), which experience frequent human activities. High concentrations of OPEs (28.0−40.5 ng/L) were detected in the northeastern region of the Hainan Island (W2 and W3). Of these, Cl-OPEs constituted 68.5−72.7% of the total, and the concentration of tris(2-carboxyethyl) phosphine (TCEPs) and tris(2-chloroisopropyl) phosphates (TCIPPs) reached their zenith, indicating that industrial discharges in the northeastern region of the Hainan Island (i.e., wastewater discharge and shipbuilding and maintenance) significantly impacted the spatial distribution of OPEs. Moreover, OPEs unintentionally generated during industrial activities in southern China entered the SCS via Pearl River runoff. There were well-established electronics dismantling and recycling industry chains in Qingyuan and Shantou, Guangdong Province, which may aggravate the pollution of OPEs in the Pearl River and SCS.[11,59] However, the current-driven transport and dispersion of OPEs in the northern SCS had a minimal impact on the distribution characteristics of OPEs in the surface water of the study area, as evidenced by the currents in the SCS during the sampling period (Figure S2a). Furthermore, the western boundary current (WBC), a primary driver of the northward migration and dispersion of water masses from the Mekong River and terrigenous pollution sources in the Central South Peninsula, could exacerbate OPE contamination (Figure S2a). Continuous runoff inputs from the Mekong River have exacerbated the pollution from dissolved black carbon, polycyclic aromatic hydrocarbons, and other organic matter in the WSCS.[17,52] Unfortunately, OPE pollution may pose a significant ecological threat to the numerous coral reefs in Hainan and Xisha Islands and increase the risk to human health through transfer along the food chain.[6,60] The target OPEs were significantly correlated in each environmental medium of the deep-sea and surface systems

https://doi.org/10.1021/acs.est.5c09148
Environ. Sci. Technol. XXXX, XXX, XXX−XXX

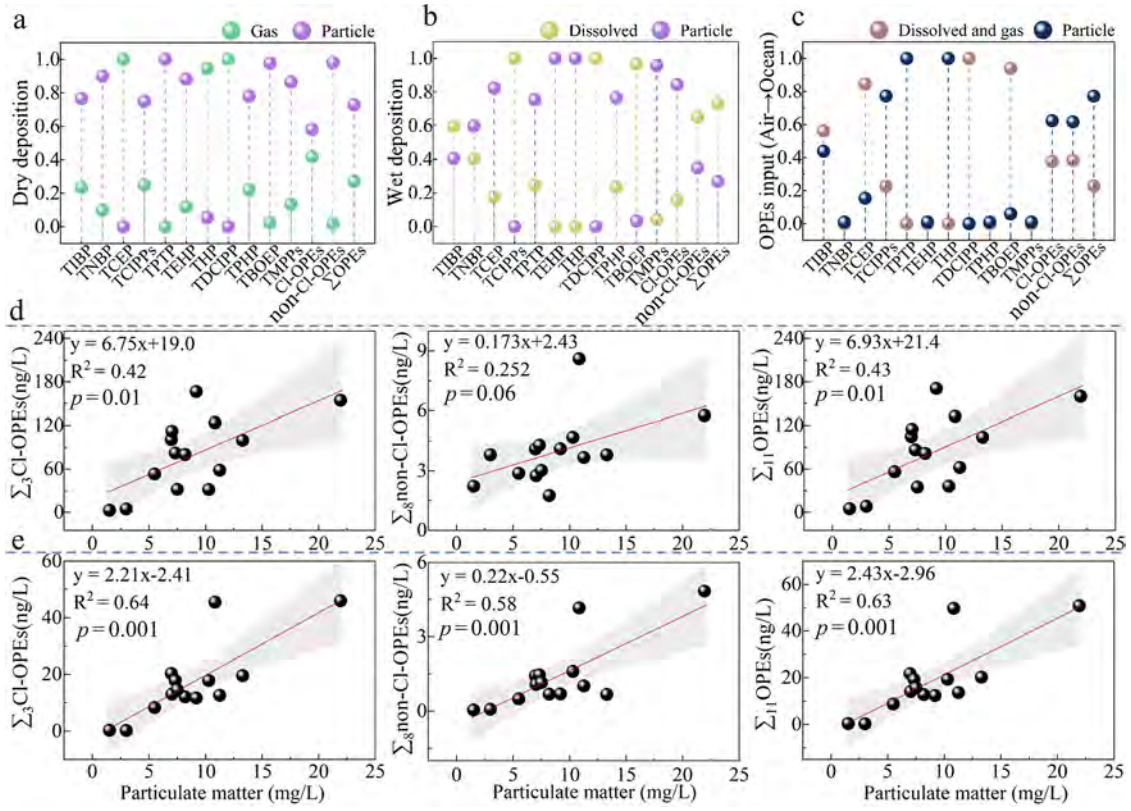


Figure 4. Contribution rates of different phases during OPE migration from the atmosphere to the ocean: (a) dry deposition, (b) wet deposition, and (c) total input flux. Correlation between particulate matter and OPE concentrations in the (d) dissolved and (e) particle phases of the water column.

(Figure S5), indicating that the OPEs in each environmental medium of the WSCS had similar potential sources.

3.2. Atmospheric Deposition as a Dominant Input Pathway. *3.2.1. Air–Water Exchange.* A modified two-layer model was used to calculate the air–water exchange flux of OPEs (Text S6).[61−63] The net flux range of the studied $\sum_{11}$OPEs was from 22.8 to 3012 ng/m^2/d, with an average value of 783 ± 810 ng/m^2/d, indicating that OPEs were evaporated from the ocean to the atmosphere during sampling period. Among them, the net flux of $\sum_3$Cl-OPEs (435 ± 564 ng/m^2/d) was higher than that of $\sum_8$non-Cl-OPEs (334 ± 314 ng/m^2/d), and TCIPPs and TPHPs were the dominant contributors to these two types of fluxes, respectively (Figure 4a).

3.2.2. Atmosphere Deposition. Atmospheric deposition has been successfully used to investigate the vertical migration of SVOCs (Text S6).[21,64] The calculated dry deposition fluxes ranged from 6161 to 58,165 ng/m^2/d (17,463 ± 9734 ng/m^2/d); the dry deposition fluxes of $\sum_3$Cl-OPEs (11,085 ± 8238 ng/m^2/d) were considerably higher than those of $\sum_8$non-Cl-OPEs (6379 ± 3105 ng/m^2/d; *t*-test, $p < 0.01$). The dry deposition fluxes of $\sum_{11}$OPEs in the particle phase (12,734 ± 5704 ng/m^2/d) were significantly higher than those in the gas phase (4729 ± 2592 ng/m^2/d; *t*-test, $p < 0.01$; Figure S7b,c). Some studies have demonstrated that wind speed, humidity, particle size, and physicochemical properties of compounds can affect dry deposition rates.[65,66] The wet deposition fluxes of OPEs ranged from 3521 to 9307 ng/m^2/d (6602 ± 2893 ng/m^2/d), and $\sum_8$non-Cl-OPEs were predominant (92.1% ± 1.74%; Figure S7d,e). Unlike dry deposition, wet deposition fluxes of $\sum_{11}$OPEs in the dissolved phase (4834 ± 2256 ng/m^2/d) were significantly higher than those in the particle phase (1768 ± 825 ng/m^2/d; *t*-test, $p < 0.01$; Figure S7b,c).

These results imply that PM plays an important role in the input of marine OPEs via atmospheric deposition and exerts a substantial influence on their vertical transport. For dry deposition, more than 27.1% of OPEs and 41.6% of Cl-OPEs deposited from the atmosphere into the ocean were attributable to PM (Figure 4a). Similarly, PM accounted for more than 27.0% of OPEs and 84.4% of Cl-OPEs transported vertically during wet deposition (Figure 4b).

3.2.3. Deep-Sea Sediment-Water Diffusion. The absorption/desorption characteristics of deep-sea sediments for OPEs were explored according to the procedures reported in our previous studies (Text S8).[17,20,67] As shown in Figure S8b, deep-sea sediments showed potential adsorption tendencies for the majority of OPEs in bottom seawater ($\log f < -0.12$), indicating that deep-sea sediments are potential sinks for OPEs in the water column of the WSCS. Moreover, the difference between the experimental K_{OC} and average field K_{OC} increased with increasing experimental K_{OC}, indicating that the adsorption capacity of sediments for OPEs increased with increasing KOC of the OPEs. The calculated log K_{OC} of OPEs was significantly correlated with their log K_{OW} ($R^2 = 0.65$, $p < 0.01$), demonstrating that the partitioning of OPEs between deep-sea sediment-water systems was significantly influenced by hydrophobic interactions (Figure S8a). The chemical structure of OPEs was closely related to the calculated log K_{OC}, which increased with increasing number of carbon atoms for non-Cl-OPEs and with increasing number of chlorine atoms for Cl-OPEs.[68]

In summary, the net atmospheric transport (20,460−27,085 ng/m^2/d) to the marine environment was the dominant process transporting OPEs to the WSCS, primarily via atmospheric deposition (Figure S7f). OPEs, especially chlorinated com-

https://doi.org/10.1021/acs.est.5c09148
Environ. Sci. Technol. XXXX, XXX, XXX−XXX

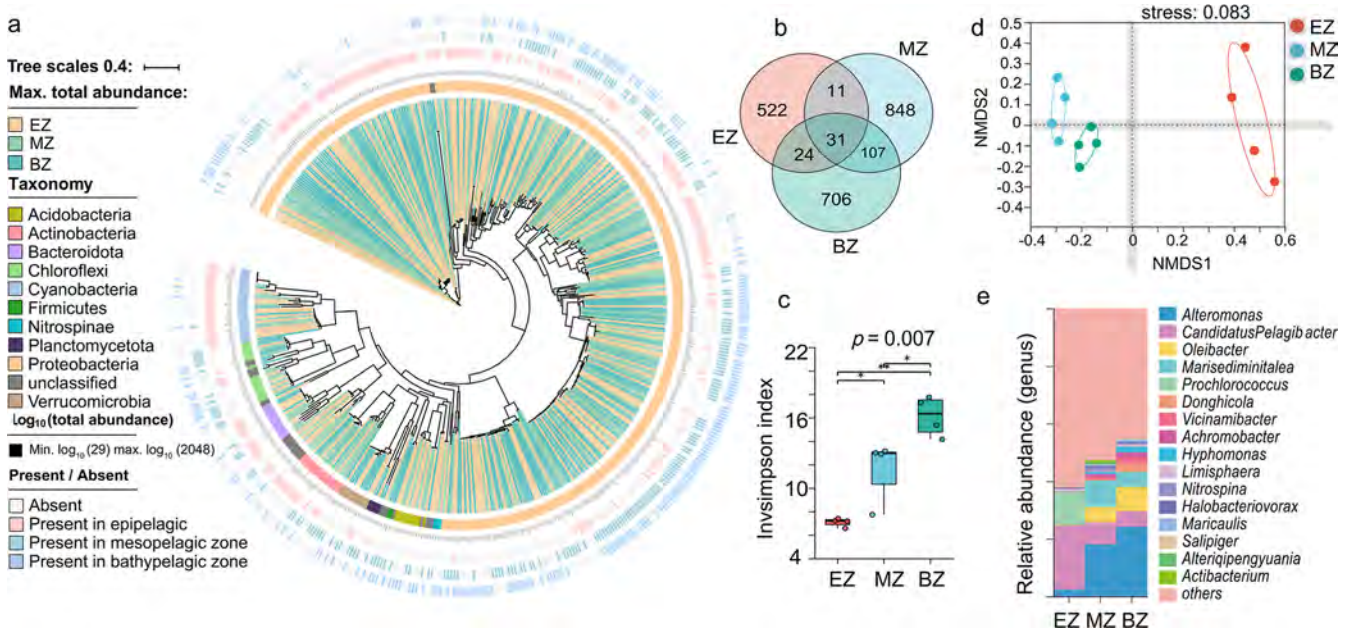


Figure 5. Vertical stratification characteristics of the bacterial diversity and community structure in seawater of the WSCS. (a) Phylum-level phylogenetic tree of the top 500 abundant ASVs (highlighting 10 dominant bacterial phyla). (b) Shared and unique ASVs among three zones (i.e., EZ, MZ, and BZ). (c) Taxonomic diversity (InvSimpson index) in three zones ($n = 12$; Kruskal–Wallis H test, $^{*}p < 0.05$, $^{**}p < 0.01$). (d) NMDS based on Bray–Curtis dissimilarities (PERMANOVA by Adonis, $n = 12$). (e) Relative abundance (%) of the top 16 bacteria in three zones.

pounds such as TCIPPs and TCEP, have high KP values and readily adsorb onto atmospheric PM. This results in high concentrations of OPEs in the atmospheric particle phase, and particulate-bound OPEs are more likely to enter the ocean via dry or wet deposition. Air–water exchange, however, depends on diffusion processes at the sea–air interface, and most OPEs have low Henry's constants, leading to weak volatilization from the sea surface to the atmosphere. Consequently, net atmospheric deposition was identified as the predominant pathway for OPEs entering the WSCS, exceeding the volatilization flux by orders of magnitude. Atmospheric deposition dominated the vertical transport of atmospheric OPEs, influencing their biogeochemical cycling and exacerbating ecological pressure on marine ecosystems, particularly coral reefs. Importantly, PM contributed 65.3–98.4% (58.6% ± 16.5%) of the total input of atmospheric OPEs into the ocean (Figure 4c), while deep-sea sediments were identified as a potentially significant sink for OPEs in the deep-sea environment (Figure S8).

3.3. Vertical Transport of OPEs and Biogeochemical Cycles. As shown in Figure 3, $\sum_{11}$OPEs in the two water columns of the WSCS exhibited significant differences. However, when the water column was divided into an epipelagic zone (EZ; 0–100 m), a mesopelagic zone (MZ; 100–500 m), and a bathypelagic zone (BZ; 1000–1500 m), OPEs exhibited a pronounced depletion in the surface layer and an enrichment in the deep sea. This distribution pattern was consistent in the dissolved and particle phases of seawater. The following order of $\sum_{11}$OPEs was observed in the dissolved and particle phases: BZ (106 ± 26.4 and 72.7 ± 29.2) > MZ (80.2 ± 17.5; 52.1 ± 3.45) > EZ (49.9 ± 31.6 and 31.6 ± 25.4; Figures S3 and S6). This pronounced heterogeneity may reflect the general pattern of the OPE distribution in the vertical profile of seawater in the WSCS.

3.3.1. Vertical Transport Driven by Particulate Matter. Material and energy transport in the ocean's vertical profile is linked to MBLPs, which play a crucial role in nutrient cycling and carbon sequestration in the deep sea.[69] The vertical transport processes of OPEs in the ocean affect their biogeochemical cycling processes in the global ocean.[49] OPEs in seawater depth profiles originate from the surface environment of oceans and combine with PM, phytoplankton, and biological detritus via biogeochemical cycling to sink to the deep sea under the action of MBLPs. Numerous studies have confirmed that organic pollution in the deep-sea environment originates from the surface system.[10,14,17,70] A clear correlation exists between OPEs in various environmental media in the surface and deep sea in the WSCS (Figure S5). As shown in Figure 4d,e, a notable positive correlation exists between OPE concentrations and PM in the WSCS vertical profile. The sinking of PM plays a pivotal role in shaping the distribution of OPEs along the depth profile, thereby influencing their vertical transport. Ocean snow, formed by the sinking of phytoplanktonic organic matter, organic particles, dead organisms, and feces, transports nutrients to the deep sea and also adsorbs and transports OPEs from surface waters to deeper ocean layers, thereby altering the concentration and composition of OPEs at different depths (Figure 4d,e). The interaction between sinking particles and OPEs may also influence the bioavailability of OPEs and their potential impacts on marine ecosystems throughout the water column. Therefore, PM in seawater drives the distributional characteristics of OPEs in the WSCS depth profile and also influences the environmental behavior of OPEs in the water column. PM plays an important role in the vertical transport of marine surface OPEs to the deep-sea environment, which most likely also influences the biogeochemical cycling of OPEs in the deep-sea environment.

3.3.2. Microbial Community Response and the Biological Pump of OPEs. The high-throughput 16S rRNA gene sequencing analysis of seawater samples from the EZ, MZ, and BZ showed distinct microbial community structures in these zones. Phylogenetic analysis of the top 500 most abundant ASVs demonstrated clear phylum-level clustering, with extremely low

https://doi.org/10.1021/acs.est.5c09148
Environ. Sci. Technol. XXXX, XXX, XXX–XXX

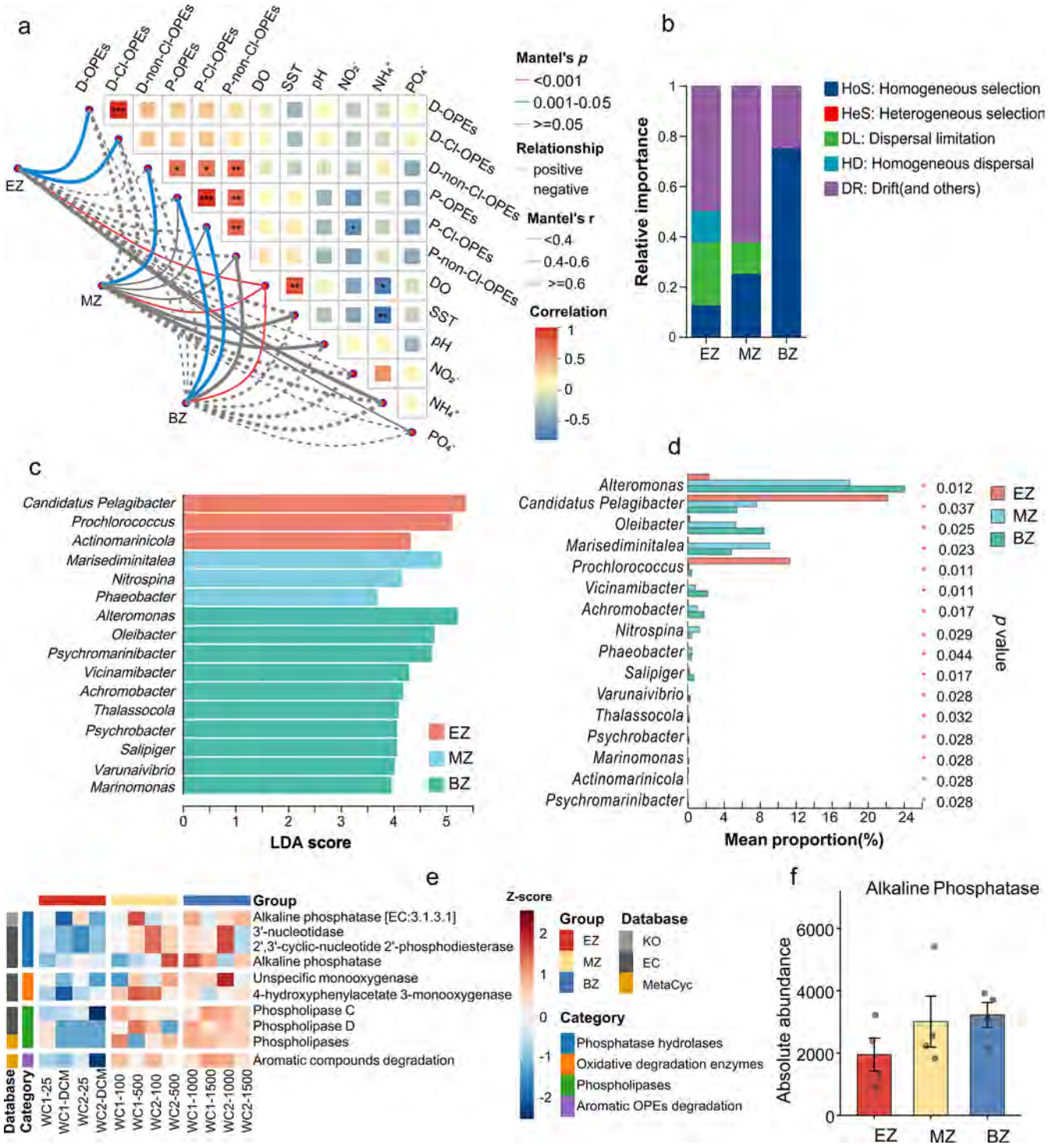


Figure 6. Microbial community assembly and degradation mechanisms driving the vertical partitioning of OPEs in the WSCS. (a) Associations between microbial community structure (based on Canberra distance) and environmental variables (based on Canberra distance) analyzed using partial Mantel tests. Partial Mantel's p values are indicated by edge color (solid and dashed lines represent positive and negative correlations, respectively), while partial Mantel's r values are represented by edge width. Statistical significance is denoted by edge color. Pairwise correlations between environmental variables are depicted using a color gradient reflecting Spearman's correlation coefficients, with statistical significance denoted as follows: $^{*}p < 0.05$, $^{**}p < 0.01$, and $^{***}p < 0.001$. (b) Relative contribution of each ecological process driving microbial community assembly within different water layers, based on null model analysis. (c) Identification of biomarkers in different zones by LEfSe. (d) Relative abundances of significantly differentiated biomarkers (Kruskal–Wallis H test, $p < 0.05$) in the EZ, MZ, and BZ. (e) Heatmap of the relative abundance of key OPE-degrading enzyme genes in different zones. (f) Alkaline phosphatase abundance increases with increasing water depth.

taxonomic overlap between the different zones (Figure 5a). These ASVs were predominantly distributed among the following phyla: Acidobacteria, Actinobacteria, Bacteroidota, Chloroflexi, Cyanobacteria, Firmicutes, Nitrospinae, Planctomycetota, Proteobacteria, unclassified taxa, and Verrucomicrobia (Figure 5a). Notably, only 31 ASVs (1.38%) were common

https://doi.org/10.1021/acs.est.5c09148
Environ. Sci. Technol. XXXX, XXX, XXX−XXX

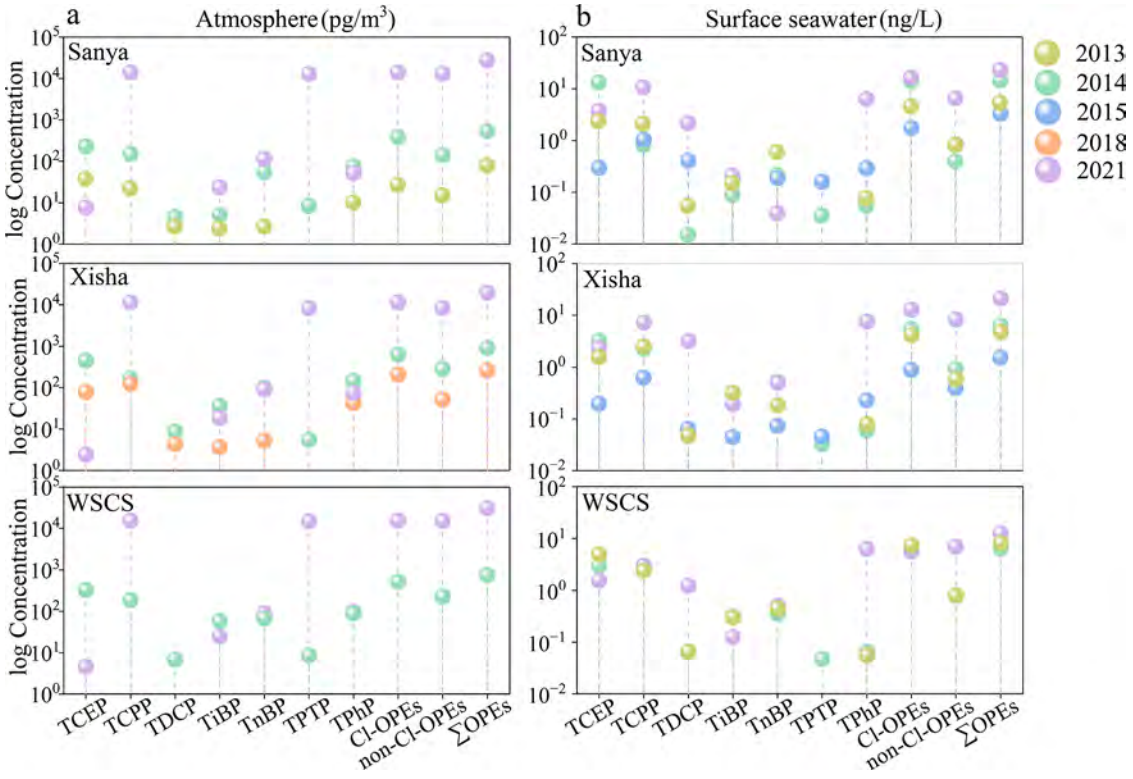


Figure 7. (a,b) Characteristics of interannual variability of OPE concentration levels in the SCS (atmosphere here represents only the atmospheric particle phase).

in all the three zones (Figure 5b). The MZ and BZ exhibited a higher community similarity (138 ASVs) but shared only 42−55 ASVs with the EZ. Furthermore, 522, 848, and 706 unique ASVs were detected in the EZ, MZ, and BZ, respectively, further corroborating the distinct community structures of these three zones (Figure 5b). The microbial α-diversity analysis (InvSimpson index) exhibited a significant increasing trend with depth (Kruskal−Wallis test, $p < 0.01$), following the order of BZ > MZ > EZ (Figure 5c). NMDS ordination based on Bray−Curtis dissimilarities (stress = 0.08) confirmed vertical stratification (PERMANOVA; $R^2 = 0.64$, $p = 0.001$), with distinct clustering of communities by zones (Figure 5d). At the genus level, the relative abundance of Alteromonas increased with increasing water depth (EZ = 2.36%, MZ = 18.0%, BZ = 24.1%), indicating the potential niche-specific adaptations to OPE-rich deep-sea environments. By contrast, the relative abundance of Pelagibacter decreased with increasing water depth (EZ = 22.3%, MZ = 7.68%, BZ = 5.46%), reflecting its reduced competitive fitness in deeper, more polluted seawater (Figure 5e).

Partial Mantel tests demonstrated a significant correlation between microbial community composition and OPE concentrations (Figure 6a). Dissolved OPEs (D-OPEs) and dissolved chlorinated OPEs (D-Cl-OPEs) exhibited significant correlations with the EZ microbial community structure, whereas dissolved non-Cl-OPEs (D-non-Cl-OPEs) showed stronger correlations with the MZ microbial community structure. Notably, particle-associated OPEs in the BZ were predominantly linked to the BZ community structure, indicating that microbial niche partitioning was the primary driver of the vertical stratification of OPEs (Figure 6a).

Distinct assembly mechanisms governed microbial communities in different zones (Figure 6b). In the EZ, drift (DR) and dispersal limitation were the dominant forces. In the MZ, the community assembly was jointly regulated by DR and homogeneous selection (HoS). In the BZ, the selective pressure of HoS significantly increased, collaborating with DR to mold the community structure (Figure 6b). These shifts in assembly mechanisms provided a foundation for the microbial degradation of OPEs.

LEfSe analysis further elucidated the microbial degradation mechanisms. The seawater in the EZ was dominated by typical oligotrophic microorganisms, while that in the MZ was enriched with bacterial genera such as *Phaeobacter* with potential for OPE degradation.[71,72] The seawater in the BZ was significantly enriched with highly efficient OPE-degrading bacteria, including *Alteromonas* and *Marinomonas*,[15,72] accompanied by the colonization of various piezophilic bacteria (Figure 6c). Kruskal−Wallis H tests confirmed significant differences ($p < 0.05$) in the relative abundances of these biomarkers in the three zones, indicating that the concentration gradient of OPEs and the vertical profile drive the niche differentiation of microbial functional communities (Figure 6d). These degrading bacteria regulated the concentration distribution of OPEs in the MZ and BZ via the MBLP effect. The microbial degradation of OPEs was mediated by phosphoester hydrolase (including alkaline phosphatase and phosphodiesterase),[73] oxidative degradation enzymes (e.g., oxygenases), phospholipase, and enzymes involved in the degradation of aromatic OPEs.[74] PICRUSt2-based functional inference elucidated the molecular mechanisms underlying OPE biodegradation. The abundance of key enzymes involved in OPE degradation, predicted using different databases, such as KEGG Orthology (KO), enzyme commission (EC) number, and MetaCyc, increased significantly in the MZ and BZ (Figure 6e). Notably, the alkaline phosphatase abundance increased with increasing water depth (EZ < MZ <

https://doi.org/10.1021/acs.est.5c09148
Environ. Sci. Technol. XXXX, XXX, XXX−XXX

BZ; Figure 6f), in agreement with the accumulation of OPEs in the MZ and BZ. This finding confirms that deep-sea microbial communities adapt to the high-OPEs environment by upregulating phosphoester hydrolase, enabling the efficient degradation of OPEs and regulating their vertical distribution.

In summary, we have systematically revealed the significant impact of deep-sea microbial activity on the distribution patterns of OPEs from the perspectives of microbial community assembly mechanisms and functional adaptive evolution. Concentration differences in OPEs and vertical profiles shape distinct marine microbial community structures, and these microbial communities drive the degradation of OPEs in the ocean via microbial activities such as ecological niche differentiation and significant upregulation of the relative abundance of key degrading taxa (e.g., *Phaeobacter*, *Alteromonas*, and *Marinomonas*) and enhanced activity of OPE-degrading enzymes (e.g., alkaline phosphatase). These phenomena are indicative of the significant ecological role of microbial communities in driving the biogeochemical cycling of OPEs in the marine environment via multidimensional adaptive strategies.

Consequently, in addition to the focus on the physical migration processes of PM in the ocean, the regulatory role of microbial activity on the biogeochemical cycling of OPEs in the ocean is equally important. The vertical distribution of OPEs in the ocean is influenced by a combination of physical−chemical processes (e.g., PM sinking) and biological processes (e.g., marine microbial activity). These processes collectively determine the concentration levels and distribution patterns of OPEs in the ocean, thereby impacting the biogeochemical cycling of OPEs in marine ecosystems.

3.4. OPE Pollution Trends and Potential Impacts. The analytical results and existing studies reveal that the pollution of OPEs in the SCS shows an increasing trend.[28,75−78] The pollution levels of OPEs in the atmosphere increased significantly (Figure 7a). Compared to earlier reports on the concentration of seven OPEs ($\sum_7$OPEs) in the atmosphere,[28,76,77] $\sum_7$OPEs in the Hainan Island increased from 77.9 ± 26.0 pg/m^3 in 2013 to 524 ± 330 pg/m^3 in 2014 and then to the current level of 13,040 ± 7191 pg/m^3. $\sum_7$OPEs in the Xisha Islands and WSCS increased from 912 ± 469 pg/m^3 and 730 ± 244 pg/m^3 in 2014 to 8501 ± 2576 pg/m^3 and 15,211 ± 8758 pg/m^3, respectively, during this survey.

The pollution levels of OPEs in the surface seawater of the SCS also showed a general increasing trend (Figure 7b). According to these results and existing reports on $\sum_7$OPEs in surface seawater in the SCS,[28,75,78] $\sum_7$OPEs in the Hainan and Xisha islands increased from 5.38 ± 2.83 ng/L and 4.73 ± 2.14 ng/L in 2013 to 14.5 ± 9.97 ng/L and 6.38 ± 2.12 ng/L in 2014, respectively, and even though there was a slight decrease in 2015, $\sum_7$OPEs have increased to 22.7 ± 10.4 ng/L and 21.1 ± 3.48 ng/L during the sampling period. In the WSCS, there was a slight decrease in 2014 (6.30 ± 2.55 ng/L) compared to 2013 (8.31 ± 5.74 ng/L), but the contamination level was significantly higher during the sampling period (12.7 ± 6.28 ng/L).

The non-Cl-OPE concentration increased at a higher rate than the Cl-OPEs, potentially owing to increased human activities such as paint and coating use as well as the growth of plastics and electronics industries.[79] The presence of long-term plastic waste in the SCS may also result in OPE release under the influence of ultraviolet rays or microorganisms. Furthermore, the rapid development of the electronics manufacturing industry in China (Guangdong, Fujian) and Vietnam have led to the continuous migration of OPEs in electronic components to long distances into the SCS via runoff and atmospheric transport. Concurrently, increase in maritime trade and use of SCS shipping lanes significantly raises the likelihood of antifouling paint wear and hydraulic oil leaks entering the ocean, thereby exacerbating OPE pollution. This could exert greater ecological pressure on marine ecosystems (e.g., coral reefs) in the SCS and influence deep-sea ecosystems through coupled physical, chemical, and biological processes. These processes may alter the composition of marine microbial communities, affect the natural succession of microbial community structures, and disrupt the ecological niche differentiation of key functional groups. Continued studies are needed to evaluate the potential impacts of increasing OPE pollution on ocean health. The methodologies and findings of this study will help advance research on the biogeochemical cycling of emerging contaminants in the marine environment and their ecological consequences. Collectively, these results highlight that the WSCS serves as a critical region for OPE deposition, transport, and microbial-mediated transformation, with important implications for both coral reef ecosystems and deep-sea environments.

4. ENVIRONMENTAL IMPLICATIONS

Escalating emissions of OPEs constitute a significant environmental threat to the SCS, highlighting the vulnerability of marine ecosystems to emerging contaminant inputs. This study demonstrates that atmospheric deposition—primarily mediated by PM—is the dominant pathway for OPE introduction, accounting for 65.3−98.4% of total inputs. This process efficiently transports OPEs to offshore and deep-sea environments, including ecologically sensitive zones such as coral reefs. The sinking of PM facilitates the vertical transfer of OPEs, resulting in unexpected contamination of deep-sea ecosystems and introducing these pollutants into fragile food webs. Critically, microbial communities respond through functional adaptation, including taxonomic niche partitioning and upregulation of hydrolytic enzymes, representing a natural yet potentially overwhelmed mechanism for OPE degradation. These findings underscore the urgent need to regulate PM-associated emissions from regional industrial and shipping activities. Furthermore, this study establishes a paradigm for understanding the fate of particle-reactive emerging pollutants, emphasizing the coupled roles of physical transport and biological transformation in determining their environmental impact. Mitigation strategies must consider the atmosphere−surface seawater−deep-sea continuum to effectively preserve ocean health.

■ ASSOCIATED CONTENT

Supporting Information

The Supporting Information is available free of charge at https://pubs.acs.org/doi/10.1021/acs.est.5c09148.

Calculation of gas−particle partitioning; calculation of air−water exchange and deposition; and additional figures and tables (PDF)

hmwASV_Taxon_Depth_asv.full.xlsx—ASV abundance table (count matrix for all sequenced samples). MetaCyc_pathway_pred.xlsx—Predicted MetaCyc metabolic pathways based on 16S data (functional prediction results). Prediction_enzyme.xlsx—Enzyme function pre-

https://doi.org/10.1021/acs.est.5c09148
Environ. Sci. Technol. XXXX, XXX, XXX−XXX

diction based on 16S data (EC number annotation). Prediction_KO.xlsx—KEGG Orthology (KO) functional prediction based on 16S data (ZIP)

AUTHOR INFORMATION

Corresponding Author

Kefu Yu − *Guangxi Laboratory on the Study of Coral Reefs in the South China Sea, Coral Reef Research Center of China, School of Marine Sciences, Guangxi University, Nanning 530004, China; Southern Marine Science and Engineering Guangdong Laboratory (Guangzhou), Guangzhou 511458, China;* orcid.org/0000-0003-3409-9945; Phone: +86-771-3231358; Email: kefuyu@scsio.ac.cn

Authors

Minwei Han − *Guangxi Laboratory on the Study of Coral Reefs in the South China Sea, Coral Reef Research Center of China, School of Marine Sciences, Guangxi University, Nanning 530004, China;* orcid.org/0000-0001-7231-8622

Ruijie Zhang − *Guangxi Laboratory on the Study of Coral Reefs in the South China Sea, Coral Reef Research Center of China, School of Marine Sciences, Guangxi University, Nanning 530004, China;* orcid.org/0000-0002-0246-2204

Biao Chen − *Guangxi Laboratory on the Study of Coral Reefs in the South China Sea, Coral Reef Research Center of China, School of Marine Sciences, Guangxi University, Nanning 530004, China*

Mei Xiong − *Institute of Genetics and Developmental Biology, Chinese Academy of Sciences, Beijing 100101, China*

Yaru Kang − *Guangxi Laboratory on the Study of Coral Reefs in the South China Sea, Coral Reef Research Center of China, School of Marine Sciences, Guangxi University, Nanning 530004, China*

Xiaopeng Yu − *Guangxi Laboratory on the Study of Coral Reefs in the South China Sea, Coral Reef Research Center of China, School of Marine Sciences, Guangxi University, Nanning 530004, China*

Zhenjun Qin − *Guangxi Laboratory on the Study of Coral Reefs in the South China Sea, Coral Reef Research Center of China, School of Marine Sciences, Guangxi University, Nanning 530004, China*

Xiangrong Xu − *Guangxi Laboratory on the Study of Coral Reefs in the South China Sea, Coral Reef Research Center of China, School of Marine Sciences, Guangxi University, Nanning 530004, China*

Complete contact information is available at: https://pubs.acs.org/10.1021/acs.est.5c09148

Author Contributions

Minwei Han: Writing original draft, Methodology, Investigation, Formal analysis, Data curation. Kefu Yu: Supervision, Resources, Funding acquisition. Ruijie Zhang: Data curation, Methodology. Biao Chen: Investigation, Supervision, Data curation. Mei Xiong: Visualization, Image retouching, Software. Yaru Kang: Methodology, Writing—review and editing. Xiaopeng Yu: Visualization, Writing—review and editing. Zhenjun Qin: Formal analysis, Writing—review and editing. Xiangrong Xu: Formal analysis, Writing—review and editing.

Notes

The authors declare no competing financial interest.

ACKNOWLEDGMENTS

This work was supported by the National Natural Science Foundation of China (No. 42030502), Guangxi Scientific Project (No. AD25069075), and Guangxi Natural Science Foundation (No. 2025GXNSFBA069537). The work was also supported by Southern Marine Science and Engineering Guangdong Laboratory (Zhuhai) (No. SML2021SI2005).

REFERENCES

(1) Xie, Z.; Wang, P.; Wang, X.; Castro-Jiménez, J.; Kallenborn, R.; Liao, C.; Mi, W.; Lohmann, R.; Vila-Costa, M.; Dachs, J. Organophosphate ester pollution in the oceans. *Nat. Rev. Earth Environ.* **2022**, *3* (5), 309−322.

(2) Ye, L.; Su, G. Elevated concentration and high Diversity of organophosphate esters (OPEs) were Discovered in Sediment from Industrial, and E-Waste Recycling Areas. *Water Res.* **2022**, *217*, 118362.

(3) Liu, Y.; Gong, S.; Ye, L.; Li, J.; Liu, C.; Chen, D.; Fang, M.; Letcher, R. J.; Su, G. Organophosphate (OP) diesters and a review of sources, chemical properties, environmental occurrence, adverse effects, and future directions. *Environ. Int.* **2021**, *155*, 106691.

(4) Dong, C.; Zhang, G.; Pei, Z.; Yang, R.; Li, Y.; Zhang, Q.; Jiang, G. Organophosphate esters in terrestrial environments of Fildes Peninsula, Antarctica: Occurrence, potential sources, and bioaccumulation. *J. Hazard. Mater.* **2024**, *478*, 135519.

(5) Trilla-Prieto, N.; Iriarte, J.; Berrojalbiz, N.; Casas, G.; Sobrino, C.; Vila-Costa, M.; Jiménez, B.; Dachs, J. Enrichment of Organophosphate Esters in the Sea Surface Microlayer from the Atlantic and Southern Oceans. *Environ. Sci. Technol. Lett.* **2024**, *11* (9), 1008−1015.

(6) Ding, Y.; Han, M.; Wu, Z.; Zhang, R.; Li, A.; Yu, K.; Wang, Y.; Huang, W.; Zheng, X.; Mai, B. Bioaccumulation and trophic transfer of organophosphate esters in tropical marine food web, South China Sea. *Environ. Int.* **2020**, *143*, 105919.

(7) Fu, J.; Fu, K.; Chen, Y.; Li, X.; Ye, T.; Gao, K.; Pan, W.; Zhang, A.; Fu, J. Long-Range Transport, Trophic Transfer, and Ecological Risks of Organophosphate Esters in Remote Areas. *Environ. Sci. Technol.* **2021**, *55* (15), 10192−10209.

(8) Huang, Q.; Hou, R.; Lin, L.; Li, H.; Liu, S.; Cheng, Y.; Xu, X. Bioaccumulation and Trophic Transfer of Organophosphate Flame Retardants and Their Metabolites in the Estuarine Food Web of the Pearl River, China. *Environ. Sci. Technol.* **2023**, *57* (9), 3549−3561.

(9) Gu, L.; Hu, B.; Fu, Y.; Zhou, W.; Li, X.; Huang, K.; Zhang, Q.; Fu, J.; Zhang, H.; Zhang, A.; Fu, J.; Jiang, G. Occurrence and risk assessment of organophosphate esters in global aquatic products. *Water Res.* **2023**, *240*, 120083.

(10) Xie, J.; Zhang, G.; Chen, C.; Luo, M.; Xu, H.; Chen, D.; Liu, R.; Li, Y.; Zhang, Q.; Zhang, Y.; Peng, X.; He, L.; Lin, T.; Jiang, G. Tracing Organophosphate Ester Pollutants in Hadal Trenches−Distribution, Possible Origins, and Transport Mechanisms. *Environ. Sci. Technol.* **2024**, *58* (9), 4392−4403.

(11) Lao, J.-Y.; Wu, R.; Cui, Y.; Zhou, S.; Ruan, Y.; Leung, K. M. Y.; Wu, J.; Zeng, E. Y.; Lam, P. K. S. Significant input of organophosphate esters through particle-mediated transport into the Pearl River Estuary, China. *J. Hazard. Mater.* **2022**, *438*, 129486.

(12) Jepson, P. D.; Law, R. J. Persistent pollutants, persistent threats. *Science* **2016**, *352* (6292), 1388−1389.

(13) Lamb, J. B.; Willis, B. L.; Fiorenza, E. A.; Couch, C. S.; Howard, R.; Rader, D. N.; True, J. D.; Kelly, L. A.; Ahmad, A.; Jompa, J.; Harvell, C. D. Plastic waste associated with disease on coral reefs. *Science* **2018**, *359* (6374), 460−462.

(14) Trilla-Prieto, N.; Berrojalbiz, N.; Iriarte, J.; Fuentes-Lema, A.; Sobrino, C.; Vila-Costa, M.; Jiménez, B.; Dachs, J. Biogeochemical Controls on Latitudinal (42°N to 70°S) and Depth Distribution of Organophosphate Esters in the Atlantic and Southern Oceans. *Environ. Sci. Technol.* **2025**, *59* (11), 5585−5595.

(15) Iriarte, J.; Trilla-Prieto, N.; Berrojalbiz, N.; Vila-Costa, M.; Dachs, J. Bacterial Production Modulates the Persistence of Organophosphate Ester Flame Retardants and Plasticizers in the Ocean. *Environ. Sci. Technol. Lett.* **2025**, *12* (2), 158−165.

https://doi.org/10.1021/acs.est.5c09148
Environ. Sci. Technol. XXXX, XXX, XXX−XXX

(16) Lv, S.; Tian, L.; Zhao, S.; Jones, K. C.; Chen, D.; Zhong, G.; Li, J.; Xu, B.; Peng, P. a.; Zhang, G. Aqueous secondary formation substantially contributes to hydrophilic organophosphate esters in aerosols. *Nat. Commun.* **2025**, *16* (1), 4463.
(17) Han, M.; Yu, K.; Zhang, R.; Chen, B.; Li, H.; Zhang, Z.-e.; Li, J.; Zhang, G. Sources of the Elevating Polycyclic Aromatic Hydrocarbon Pollution in the Western South China Sea and Its Environmental Implications. *Environ. Sci. Technol.* **2023**, *57* (49), 20750−20760.
(18) Liu, M.; Zheng, H.; Cai, M.; Leung, K. M. Y.; Li, Y.; Yan, M.; Zhang, Z.; Zhang, K.; Chen, M.; Ke, H. Ocean Stratification Impacts on Dissolved Polycyclic Aromatic Hydrocarbons (PAHs): From Global Observation to Deep Learning. *Environ. Sci. Technol.* **2023**, *57* (46), 18339−18349.
(19) Fang, Z.; Yang, W.; Chen, M.; Ma, H. Source and Fate of Dissolved Black Carbon in the Western South China Sea During the Southwest Monsoon Prevailing Season. *J. Geophys. Res.: Biogeosci.* **2017**, *122* (11), 2817−2830.
(20) Zhang, R.; Han, M.; Yu, K.; Kang, Y.; Wang, Y.; Huang, X.; Li, J.; Yang, Y. Distribution, fate and sources of polycyclic aromatic hydrocarbons (PAHs) in atmosphere and surface water of multiple coral reef regions from the South China Sea: A case study in spring-summer. *J. Hazard. Mater.* **2021**, *412*, 125214.
(21) Mi, L.; Xie, Z.; Zhang, L.; Waniek, J. J.; Pohlmann, T.; Mi, W.; Xu, W. Organophosphate Esters in Air and Seawater of the South China Sea: Spatial Distribution, Transport, and Air−Sea Exchange. *Environ. Health* **2023**, *1* (3), 191−202.
(22) Yu, K. Coral reefs in the South China Sea: Their response to and records on past environmental changes. *Sci. China: Earth Sci.* **2012**, *55* (8), 1217−1229.
(23) Lyu, L.; Li, J.; Huang, Q.; Liu, Q.; Yang, C.; Dong, J.; Su, H.; Zhang, S. Exploring the Hidden Threat of Organic UV Filters to Corals and Macroalgae in Coral Reef Ecosystem from Luhuitou, Sanya, China. *Environ. Sci. Technol.* **2025**, *59* (16), 8130−8139.
(24) Yuan, S.; Huang, J.; Qian, W.; Zhu, X.; Wang, S.; Jiang, X. Are Physical Sunscreens Safe for Marine Life? A Study on a Coral−Zooxanthellae Symbiotic System. *Environ. Sci. Technol.* **2023**, *57* (42), 15846−15857.
(25) Zhou, Z.; Tang, J.; Cao, X.; Wu, C.; Cai, W.; Lin, S. High Heterotrophic Plasticity of Massive Coral Porites pukoensis Contributes to Its Tolerance to Bioaccumulated Microplastics. *Environ. Sci. Technol.* **2023**, *57* (8), 3391−3401.
(26) Zhou, Y.; Li, Q.; Zhang, Q.; Yuan, M.; Zhu, X.; Li, Y.; Li, Q.; Downs, C. A.; Huang, D.; Chou, L.-M.; Zhao, H. Environmental Concentrations of Herbicide Prometryn Render Stress-Tolerant Corals Susceptible to Ocean Warming. *Environ. Sci. Technol.* **2024**, *58* (10), 4545−4557.
(27) Vuckovic, D.; Tinoco, A. I.; Ling, L.; Renicke, C.; Pringle, J. R.; Mitch, W. A. Conversion of oxybenzone sunscreen to phototoxic glucoside conjugates by sea anemones and corals. *Science* **2022**, *376* (6593), 644−648.
(28) Zhang, G.; Zhang, Y.; Mi, W.; Wang, Z.; Lai, S. Organophosphate esters in atmospheric particles and surface seawater in the western South China Sea. *Environ. Pollut.* **2022**, *292*, 118255.
(29) Casas, G.; Martinez-Varela, A.; Vila-Costa, M.; Jiménez, B.; Dachs, J. Rain Amplification of Persistent Organic Pollutants. *Environ. Sci. Technol.* **2021**, *55* (19), 12961−12972.
(30) Sun, Y.; De Silva, A. O.; St Pierre, K. A.; Muir, D. C. G.; Spencer, C.; Lehnherr, I.; MacInnis, J. J. Glacial Melt Inputs of Organophosphate Ester Flame Retardants to the Largest High Arctic Lake. *Environ. Sci. Technol.* **2020**, *54* (5), 2734−2743.
(31) Chen, S.; Zhou, Y.; Chen, Y.; Gu, J. fastp: an ultra-fast all-in-one FASTQ preprocessor. *Bioinformatics* **2018**, *34* (17), i884−i890.
(32) Bolyen, E.; Rideout, J. R.; Dillon, M. R.; Bokulich, N. A.; Abnet, C. C.; Al-Ghalith, G. A.; Alexander, H.; Alm, E. J.; Arumugam, M.; Asnicar, F.; Bai, Y.; Bisanz, J. E.; Bittinger, K.; Brejnrod, A.; Brislawn, C. J.; Brown, C. T.; Callahan, B. J.; Caraballo-Rodríguez, A. M.; Chase, J.; Cope, E. K.; Da Silva, R.; Diener, C.; Dorrestein, P. C.; Douglas, G. M.; Durall, D. M.; Duvallet, C.; Edwardson, C. F.; Ernst, M.; Estaki, M.; Fouquier, J.; Gauglitz, J. M.; Gibbons, S. M.; Gibson, D. L.; Gonzalez, A.; Gorlick, K.; Guo, J.; Hillmann, B.; Holmes, S.; Holste, H.; Huttenhower, C.; Huttley, G. A.; Janssen, S.; Jarmusch, A. K.; Jiang, L.; Kaehler, B. D.; Kang, K. B.; Keefe, C. R.; Keim, P.; Kelley, S. T.; Knights, D.; Koester, I.; Kosciolek, T.; Kreps, J.; Langille, M. G. I.; Lee, J.; Ley, R.; Liu, Y. X.; Loftfield, E.; Lozupone, C.; Maher, M.; Marotz, C.; Martin, B. D.; McDonald, D.; McIver, L. J.; Melnik, A. V.; Metcalf, J. L.; Morgan, S. C.; Morton, J. T.; Naimey, A. T.; Navas-Molina, J. A.; Nothias, L. F.; Orchanian, S. B.; Pearson, T.; Peoples, S. L.; Petras, D.; Preuss, M. L.; Pruesse, E.; Rasmussen, L. B.; Rivers, A.; Robeson, M. S., II; Rosenthal, P.; Segata, N.; Shaffer, M.; Shiffer, A.; Sinha, R.; Song, S. J.; Spear, J. R.; Swafford, A. D.; Thompson, L. R.; Torres, P. J.; Trinh, P.; Tripathi, A.; Turnbaugh, P. J.; Ul-Hasan, S.; van der Hooft, J. J. J.; Vargas, F.; Vázquez-Baeza, Y.; Vogtmann, E.; von Hippel, M.; Walters, W.; Wan, Y.; Wang, M.; Warren, J.; Weber, K. C.; Williamson, C. H. D.; Willis, A. D.; Xu, Z. Z.; Zaneveld, J. R.; Zhang, Y.; Zhu, Q.; Knight, R.; Caporaso, J. G. Reproducible, interactive, scalable and extensible microbiome data science using QIIME 2. *Nat. Biotechnol.* **2019**, *37* (8), 852−857.
(33) Callahan, B. J.; McMurdie, P. J.; Rosen, M. J.; Han, A. W.; Johnson, A. J.; Holmes, S. P. DADA2: High-resolution sample inference from Illumina amplicon data. *Nat. Methods* **2016**, *13* (7), 581−583.
(34) Bokulich, N. A.; Kaehler, B. D.; Rideout, J. R.; Dillon, M.; Bolyen, E.; Knight, R.; Huttley, G. A.; Gregory Caporaso, J. Optimizing taxonomic classification of marker-gene amplicon sequences with QIIME 2's q2-feature-classifier plugin. *Microbiome* **2018**, *6* (1), 90.
(35) Katoh, K.; Standley, D. M. MAFFT multiple sequence alignment software version 7: improvements in performance and usability. *Mol. Biol. Evol.* **2013**, *30* (4), 772−780.
(36) Nguyen, L. T.; Schmidt, H. A.; von Haeseler, A.; Minh, B. Q. IQ-TREE: a fast and effective stochastic algorithm for estimating maximum-likelihood phylogenies. *Mol. Biol. Evol.* **2015**, *32* (1), 268−274.
(37) Stegen, J. C.; Lin, X.; Fredrickson, J. K.; Konopka, A. E. Estimating and mapping ecological processes influencing microbial community assembly. *Front. Microbiol.* **2015**, *6*, 370.
(38) Segata, N.; Izard, J.; Waldron, L.; Gevers, D.; Miropolsky, L.; Garrett, W. S.; Huttenhower, C. Metagenomic biomarker discovery and explanation. *Genome Biol.* **2011**, *12* (6), R60.
(39) Douglas, G. M.; Maffei, V. J.; Zaneveld, J. R.; Yurgel, S. N.; Brown, J. R.; Taylor, C. M.; Huttenhower, C.; Langille, M. G. I. PICRUSt2 for prediction of metagenome functions. *Nat. Biotechnol.* **2020**, *38* (6), 685−688.
(40) Kanehisa, M.; Furumichi, M.; Sato, Y.; Kawashima, M.; Ishiguro-Watanabe, M. KEGG for taxonomy-based analysis of pathways and genomes. *Nucleic Acids Res.* **2023**, *51* (D1), D587−D592.
(41) Caspi, R.; Billington, R.; Keseler, I. M.; Kothari, A.; Krummenacker, M.; Midford, P. E.; Ong, W. K.; Paley, S.; Subhraveti, P.; Karp, P. D. The MetaCyc database of metabolic pathways and enzymes - a 2019 update. *Nucleic Acids Res.* **2020**, *48* (D1), D445−D453.
(42) Shi, T.; Li, R.; Fu, J.; Hou, C.; Gao, H.; Cheng, G.; Zhang, H.; Jin, S.; Kong, L.; Na, G. Fate of organophosphate esters from the Northwestern Pacific to the Southern Ocean: Occurrence, distribution, and fugacity model simulation. *J. Environ. Sci.* **2024**, *137*, 347−357.
(43) Möller, A.; Sturm, R.; Xie, Z.; Cai, M.; He, J.; Ebinghaus, R. Organophosphorus Flame Retardants and Plasticizers in Airborne Particles over the Northern Pacific and Indian Ocean toward the Polar Regions: Evidence for Global Occurrence. *Environ. Sci. Technol.* **2012**, *46* (6), 3127−3134.
(44) Castro-Jiménez, J.; González-Gaya, B.; Pizarro, M.; Casal, P.; Pizarro-Álvarez, C.; Dachs, J. Organophosphate Ester Flame Retardants and Plasticizers in the Global Oceanic Atmosphere. *Environ. Sci. Technol.* **2016**, *50* (23), 12831−12839.
(45) Li, R.; Gao, H.; Hou, C.; Fu, J.; Shi, T.; Wu, Z.; Jin, S.; Yao, Z.; Na, G.; Ma, X. Occurrence, source, and transfer fluxes of organophosphate esters in the South Pacific and Fildes Peninsula, Antarctic. *Sci. Total Environ.* **2023**, *894*, 164263.
(46) Na, G.; Hou, C.; Li, R.; Shi, Y.; Gao, H.; Jin, S.; Gao, Y.; Jiao, L.; Cai, Y. Occurrence, distribution, air-seawater exchange and atmos-

https://doi.org/10.1021/acs.est.5c09148
Environ. Sci. Technol. XXXX, XXX, XXX−XXX

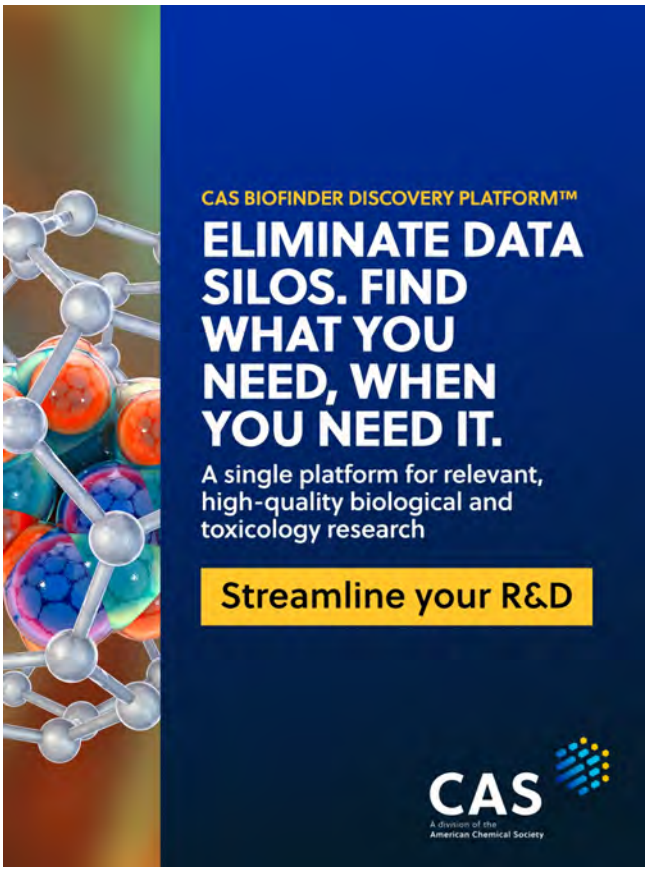
pheric deposition of organophosphate esters (OPEs) from the Northwestern Pacific to the Arctic Ocean. *Mar. Pollut. Bull.* **2020**, *157*, 111243.
(47) Fu, J.; Fu, K.; Hu, B.; Zhou, W.; Fu, Y.; Gu, L.; Zhang, Q.; Zhang, A.; Fu, J.; Jiang, G. Source Identification of Organophosphate Esters through the Profiles in Proglacial and Ocean Sediments from Ny-Ålesund, the Arctic. *Environ. Sci. Technol.* **2023**, *57* (5), 1919−1929.
(48) Ma, Y.; Xie, Z.; Lohmann, R.; Mi, W.; Gao, G. Organophosphate Ester Flame Retardants and Plasticizers in Ocean Sediments from the North Pacific to the Arctic Ocean. *Environ. Sci. Technol.* **2017**, *51* (7), 3809−3815.
(49) Cong, B.; Li, S.; Liu, S.; Mi, W.; Liu, S.; Zhang, Z.; Xie, Z. Source and Distribution of Emerging and Legacy Persistent Organic Pollutants in the Basins of the Eastern Indian Ocean. *Environ. Sci. Technol.* **2022**, *56* (7), 4199−4209.
(50) Liao, C.; Kim, U.-J.; Kannan, K. Occurrence and distribution of organophosphate esters in sediment from northern Chinese coastal waters. *Sci. Total Environ.* **2020**, *704*, 135328.
(51) Wang, X.; Zhang, H.; Lin, C.-J.; Fu, X.; Zhang, Y.; Feng, X. Transboundary transport and deposition of Hg emission from springtime biomass burning in the Indo-China Peninsula. *J. Geophys. Res.: Atmos.* **2015**, *120* (18), 9758−9771.
(52) Wu, G.; Ram, K.; Fu, P.; Wang, W.; Zhang, Y.; Liu, X.; Stone, E. A.; Pradhan, B. B.; Dangol, P. M.; Panday, A. K.; Wan, X.; Bai, Z.; Kang, S.; Zhang, Q.; Cong, Z. Water-Soluble Brown Carbon in Atmospheric Aerosols from Godavari (Nepal), a Regional Representative of South Asia. *Environ. Sci. Technol.* **2019**, *53* (7), 3471−3479.
(53) Jiang, H.; Li, J.; Zhang, R.; Pansak, W.; Zhong, G.; Li, K.; Zhao, S.; Bualert, S.; Phewnil, O.; Zhang, G. Mapping the Contribution of Biomass Burning to Persistent Organic Pollutants in the Air of the Indo-China Peninsula Based on a Passive Air Monitoring Network. *Environ. Sci. Technol.* **2023**, *57* (6), 2274−2285.
(54) Witstok, J.; Shivaei, I.; Smit, R.; Maiolino, R.; Carniani, S.; Curtis-Lake, E.; Ferruit, P.; Arribas, S.; Bunker, A. J.; Cameron, A. J.; Charlot, S.; Chevallard, J.; Curti, M.; de Graaff, A.; D'Eugenio, F.; Giardino, G.; Looser, T. J.; Rawle, T.; Rodríguez del Pino, B.; Willott, C.; Alberts, S.; Baker, W. M.; Boyett, K.; Egami, E.; Eisenstein, D. J.; Endsley, R.; Hainline, K. N.; Ji, Z.; Johnson, B. D.; Kumari, N.; Lyu, J.; Nelson, E.; Perna, M.; Rieke, M.; Robertson, B. E.; Sandles, L.; Saxena, A.; Scholtz, J.; Sun, F.; Tacchella, S.; Williams, C. C.; Willmer, C. N. A. Carbonaceous dust grains seen in the first billion years of cosmic time. *Nature* **2023**, *621* (7978), 267−270.
(55) Huang, C.; Qi, X.; Zheng, J.; Zhu, R.; Shen, J. A maritime traffic route extraction method based on density-based spatial clustering of applications with noise for multi-dimensional data. *Ocean Eng.* **2023**, *268*, 113036.
(56) Shi, S.; Zhao, B. Modeled Exposure Assessment via Inhalation and Dermal Pathways to Airborne Semivolatile Organic Compounds (SVOCs) in Residences. *Environ. Sci. Technol.* **2014**, *48* (10), 5691−5699.
(57) Yaman, B.; Dumanoglu, Y.; Odabasi, M. Measurement and Modeling the Phase Partitioning of Organophosphate Esters Using Their Temperature-Dependent Octanol−Air Partition Coefficients and Vapor Pressures. *Environ. Sci. Technol.* **2020**, *54* (13), 8133−8143.
(58) Okeme, J. O.; Rodgers, T. F. M.; Jantunen, L. M.; Diamond, M. L. Examining the Gas-Particle Partitioning of Organophosphate Esters: How Reliable Are Air Measurements? *Environ. Sci. Technol.* **2018**, *52* (23), 13834−13844.
(59) Zhang, K.; Zhang, B.-Z.; Li, S.-M.; Zeng, E. Y. Regional dynamics of persistent organic pollutants (POPs) in the Pearl River Delta, China: Implications and perspectives. *Environ. Pollut.* **2011**, *159* (10), 2301−2309.
(60) Kang, Y.; Zhang, R.; Yu, K.; Han, M.; Li, H.; Yan, A.; Liu, F.; Shi, J.; Wang, Y. Organophosphate esters (OPEs) in a coral reef food web of the Xisha Islands, South China Sea: Occurrence, trophodynamic, and exposure risk. *Chemosphere* **2023**, *313*, 137652.
(61) Whitman, W. G. The two film theory of gas absorption. *Int. J. Heat Mass Transfer* **1962**, *5* (5), 429−433.
(62) Han, M.; Zhang, R.; Yu, K.; Yan, A.; Li, H.; Zhang, R.; Zeng, W.; Zhang, Z.-e.; Liu, F. Environmental fate and effects of PAHs in tropical mariculture ponds near the northern South China Sea: Rainfall plays a key role. *Sci. Total Environ.* **2022**, *847*, 157442.
(63) Sanganyado, E.; Chingono, K. E.; Gwenzi, W.; Chaukura, N.; Liu, W. Organic pollutants in deep sea: Occurrence, fate, and ecological implications. *Water Res.* **2021**, *205*, 117658.
(64) Birgul, A.; Tasdemir, Y.; Cindoruk, S. S. Atmospheric wet and dry deposition of polycyclic aromatic hydrocarbons (PAHs) determined using a modified sampler. *Atmos. Res.* **2011**, *101* (1−2), 341−353.
(65) Xie, Z.; Möller, A.; Ahrens, L.; Sturm, R.; Ebinghaus, R. Brominated Flame Retardants in Seawater and Atmosphere of the Atlantic and the Southern Ocean. *Environ. Sci. Technol.* **2011**, *45* (5), 1820−1826.
(66) González-Gaya, B.; Zúñiga-Rival, J.; Ojeda, M.-J.; Jiménez, B.; Dachs, J. Field Measurements of the Atmospheric Dry Deposition Fluxes and Velocities of Polycyclic Aromatic Hydrocarbons to the Global Oceans. *Environ. Sci. Technol.* **2014**, *48* (10), 5583−5592.
(67) Lian, M.; Lin, C.; Li, Y.; Hao, X.; Wang, A.; He, M.; Liu, X.; Ouyang, W. Distribution, partitioning, and health risk assessment of organophosphate esters in a major tributary of middle Yangtze River using Monte Carlo simulation. *Water Res.* **2022**, *219*, 118559.
(68) Wang, X.; Zhu, L.; Zhong, W.; Yang, L. Partition and source identification of organophosphate esters in the water and sediment of Taihu Lake, China. *J. Hazard. Mater.* **2018**, *360*, 43−50.
(69) Arrieta, J. M.; Mayol, E.; Hansman, R. L.; Herndl, G. J.; Dittmar, T.; Duarte, C. M. Dilution limits dissolved organic carbon utilization in the deep ocean. *Science* **2015**, *348* (6232), 331−333.
(70) Liu, M.; Zheng, H.; Li, H.; Chen, F.; Cui, B.; Lou, L.; Wang, W.; Zhang, H.; Chen, C.; Lin, H.; Jiang, Y.; Ye, J.; Yan, M.; Leung, K. M. Y.; Cai, M. Pyrogenic PAHs Have Different Biogeochemical Fates in the Eastern Indian Ocean. *Environ. Sci. Technol.* **2024**, *58* (50), 22405−22416.
(71) Westermann, L. M.; Lidbury, I.; Li, C. Y.; Wang, N.; Murphy, A. R. .; Aguilo Ferretjans, M. D. M.; Quareshy, M.; Shanmugan, M.; Torcello-Requena, A.; Silvano, E.; Zhang, Y. Z.; Blindauer, C. A.; Chen, Y.; Scanlan, D. J. Bacterial catabolism of membrane phospholipids links marine biogeochemical cycles. *Sci. Adv.* **2023**, *9* (17), No. eadf5122.
(72) Despotović, D.; Aharon, E.; Trofimyuk, O.; Dubovetskyi, A.; Cherukuri, K. P.; Ashani, Y.; Eliason, O.; Sperfeld, M.; Leader, H.; Castelli, A.; Fumagalli, L.; Savidor, A.; Levin, Y.; Longo, L. M.; Segev, E.; Tawfik, D. S. Utilization of diverse organophosphorus pollutants by marine bacteria. *Proc. Natl. Acad. Sci. U.S.A.* **2022**, *119* (32), No. e2203604119.
(73) Liu, Q.; Wang, X.; Zhou, J.; Yu, X.; Liu, M.; Li, Y.; Sun, H.; Zhu, L. Phosphorus Deficiency Promoted Hydrolysis of Organophosphate Esters in Plants: Mechanisms and Transformation Pathways. *Environ. Sci. Technol.* **2021**, *55* (14), 9895−9904.
(74) Liang, Y.; Zhou, X.; Wu, Y.; Wu, Y.; Zeng, X.; Yu, Z.; Peng, P. Meta-omics elucidates key degraders in a bacterial tris(2-butoxyethyl) phosphate (TBOEP)-degrading enrichment culture. *Water Res.* **2023**, *233*, 119774.
(75) Yan, A.; Zhang, R.; Yu, K.; Kang, Y.; Huang, X.; Hu, J.; Xie, S.; Yang, X.; Wang, J. Organophosphate esters (OPEs) in corals of the South China Sea: Occurrence, distribution, and bioaccumulation. *Sci. Total Environ.* **2024**, *927*, 172212.
(76) Zhang, L.; Xu, W.; Mi, W.; Yan, W.; Guo, T.; Zhou, F.; Miao, L.; Xie, Z. Atmospheric deposition, seasonal variation, and long-range transport of organophosphate esters on Yongxing Island, South China Sea. *Sci. Total Environ.* **2022**, *806*, 150673.
(77) Lai, S.; Xie, Z.; Song, T.; Tang, J.; Zhang, Y.; Mi, W.; Peng, J.; Zhao, Y.; Zou, S.; Ebinghaus, R. Occurrence and dry deposition of organophosphate esters in atmospheric particles over the northern South China Sea. *Chemosphere* **2015**, *127*, 195−200.
(78) Sun, H.; Mi, W.; Li, X.; Wang, S.; Yan, J.; Zhang, G. Organophosphate ester in surface water of the Pearl River and South China Sea, China: Spatial variations and ecological risks. *Chemosphere* **2024**, *361*, 142559.

https://doi.org/10.1021/acs.est.5c09148
Environ. Sci. Technol. XXXX, XXX, XXX−XXX

(79) Lian, M.; Wang, J.; Wang, B.; Xin, M.; Lin, C.; Gu, X.; He, M.; Liu, X.; Ouyang, W. Spatiotemporal variations and the ecological risks of organophosphate esters in Laizhou Bay waters between 2019 and 2021: Implying the impacts of the COVID-19 pandemic. *Water Res.* **2023**, *233*, 119783.

NOTE ADDED AFTER ASAP PUBLICATION

After this article was published ASAP October 20, 2025, a correction was made to Figure 6a. The corrected version was posted October 22, 2025.



https://doi.org/10.1021/acs.est.5c09148
Environ. Sci. Technol. XXXX, XXX, XXX−XXX

Water Research X 27 (2025) 100294



Contents lists available at ScienceDirect

Water Research X

journal homepage: www.sciencedirect.com/journal/water-research-x





Emerging and legacy organophosphate flame retardants in the tropical estuarine food web: Do they exhibit similar bioaccumulation patterns, trophic partitioning and dietary exposure?

Qianyi Huang [a,g], Rui Hou [b,*], Yuchen Wang [d], Lang Lin [e], Hengxiang Li [a], Shan Liu [a], Xiangrong Xu [c,*], Kefu Yu [c,f], Xiaoping Huang [a]

[a] Key Laboratory of Tropical Marine Bio-resources and Ecology, Guangdong Provincial Key Laboratory of Applied Marine Biology, South China Sea Institute of Oceanology, Chinese Academy of Sciences, Guangzhou 510301, China
[b] Guangdong Provincial Key Laboratory of Water Quality Improvement and Ecological Restoration for Watersheds, School of Ecology, Environment and Resources, Guangdong University of Technology, Guangzhou 510006, China
[c] Guangxi Laboratory on the Study of Coral Reefs in the South China Sea, Coral Reef Research Center of China, School of Marine Sciences, Guangxi University, Nanning 530004, China
[d] College of Life Sciences and Engineering, Jinan University, Guangzhou 510632, China
[e] South China Sea Bureau of Ministry of Natural Resources, Guangzhou 510310, China
[f] Southern Marine Science and Engineering Guangdong Laboratory (Guangzhou), Guangzhou 511458, China
[g] University of Chinese Academy of Sciences, Beijing 100049, China

ARTICLE INFO

Keywords:
Legacy and emerging organophosphate flame retardants
Bioaccumulation
Trophic transfer
Organism partitioning
Biotransformation

ABSTRACT

Emerging organophosphate flame retardants (E-OPFRs) are a new class of pollutants that have attracted increasing attention, but their bioaccumulation patterns and trophodynamic behaviors in aquatic food webs still need to be validated by comparison with legacy OPFRs (L-OPFRs). In this study, we simultaneously investigated the bioaccumulation, trophic transfer, and dietary exposure of 8 E-OPFRs and 10 L-OPFRs in a tropical estuarine food web from Hainan Island, China. Notably, the Σ_{10}L-OPFRs concentration (16.1–1.18 × 10^5 lipid weight (lw)) was significantly greater than that of Σ_8E-OPFRs (nondetectable (nd) - 2.82 × 10^3 ng/g lw) among the investigated organisms, and they both exhibited similar trends: fish<mollusk<crustacean. Significant biomagnification was found only for triphenyl phosphate (TPHP, an L-OPFR) with a trophic magnification factor (TMF) of 1.55, whereas other E- and L-OPFRs showed limited trophic transfer potential. Storage lipid was the dominant adsorption phase for most E-OPFRs and L-OPFRs on the basis of the fugacity approach. The water content controls the main trophic partitioning for the L-OPFRs of triethyl phosphate (TEP) and tris(2-chloroethyl) phosphate (TCEP) in the food web. Storage lipid and structure protein are equally important for 2,2-bis(chloromethyl)-propane-1,3-diyltetrakis(2-chloroethyl) biphosphate (V6, an emerging OPFR). The investigation of metabolites and the biotransformation rate (K_M) confirmed the role of biotransformation in offsetting trophic transfer for both legacy and emerging OPFRs. Furthermore, the hazard quotients (HQs) were found to be <1 for South China residents for both the E- and L-OPFRs, but the health risks of these two kinds of OPFRs should be given sustained attention.

1. Introduction

Organophosphate flame retardants (OPFRs) have been commonly used as chemicals to increase the flame retardancy of various materials for decades, such as plastics, rubber, textiles, and electronic equipment (Du et al., 2019; Hou et al., 2016). The prohibition and restriction of the use of legacy OPFRs (L-OPFRs), such as TCEP, tris(1,3-dichloro-2-propyl) phosphate (TDCPP) and tri(chloro-2-propyl) phosphate (TCPP), in children's products, furniture, mattresses, and electronics have been pronounced by the US, Canada and the EU (Blum et al., 2019; Pantelaki and Voutsa, 2019; van der Veen and de Boer, 2012), and TCEP is also listed in the "Second batch of priority controlled

* Corresponding authors.
E-mail addresses: ruihou@gdut.edu.cn (R. Hou), xuxr@gxu.edu.cn (X. Xu).

https://doi.org/10.1016/j.wroa.2024.100294
Received 19 October 2024; Received in revised form 20 November 2024; Accepted 9 December 2024
Available online 10 December 2024
2589-9147/© 2024 The Authors. Published by Elsevier Ltd. This is an open access article under the CC BY-NC-ND license (http://creativecommons.org/licenses/by-nc-nd/4.0/).

chemicals list" in China (China MEE, 2020). In recent years, a growing number of nonhalogenated emerging OPFRs (E-OPFRs), such as diphenyl p-tolyl phosphate (CDP), 8-methylnonyl diphenyl phosphate (iDDPHP), and tris(4-tert-butylphenyl) phosphate (T4tBPP), have been introduced as substitutes for legacy OPFRs. The global OPFR market size was approximately ¥ 5.4 billion in 2022 and is expected to reach ¥ 7.9 billion in 2029 on the basis of QYResearch (2023).

Compared with legacy OPFRs, emerging OPFRs generally have higher molecular weights, longer half-lives and greater hydrophobicity (Luo et al., 2023; Ye et al., 2023). Notably, some emerging OPFRs exhibit comparable or even greater toxic effects than legacy OPFRs. For example, the effects of tris(4-isopropylphenyl) phosphate (iPPP) were greater than those of L-OPFRs (TPHP, tricresyl phosphate (TCP) and 2-ethylhexyl diphenyl phosphate (EHDPHP)) on mitochondrial activity, oxidative stress, and steroid secretion in mouse Leydig tumor cells (Schang et al., 2016), and energy metabolism was found to be more effectively inhibited by CDP than by L-OPFRs such as TPHP, TCEP, TDCPP, tris(2-ethylhexyl) phosphate (TEHP), tris(2-butoxyethyl) phosphate (TBOEP), and tris-n-butyl phosphate (TNBP) (Tsugoshi et al., 2020). In addition, emerging OPFRs have been detected in many aquatic environments, such as the Yangtze River Basin (Li et al., 2023), Taihu Lake (Ye et al., 2022; Zhao et al., 2019), and Laizhou Bay (Bekele et al., 2019). The effects on aquatic organisms and the potential risk of E-OPFRs have recently attracted widespread attention from scholars in the water environment field (Shi and Zhao, 2024; Xie et al., 2024b).

The extensive and widespread distribution of emerging OPFRs inevitably leads to increased exposure to aquatic animals (Shi and Zhao, 2024). Significantly increased E-OPFRs accumulation was detected in marine mammals (cetaceans and finless porpoises) from 2007 to 2020 (Xie et al., 2024a, 2024b). Previous studies have suggested that partitioning and biotransformation are the most important factors in the determination of bioaccumulation and trophic transfer of nonpersistent compounds in aquatic food webs (Huang et al., 2023; Kim et al., 2002). Compared with the commonly used Log K_{OW}, the organism-water partition coefficient ($K_{organism\text{-}water}$) is a more suitable descriptor for predicting bioaccumulation potential because of its partitioning in different tissue compartments (i.e., lipid, phospholipid, protein, and water) (Endo and Goss, 2014; Geisler et al., 2012; Huang et al., 2023). In addition, the estimated inherent K_M values and metabolite accumulation can provide insight into the biotransformation of OPFRs to characterize their compound-specific trophodynamics. Joint partitioning and biotransformation efforts can offer an opportunity to yield new insights into the bioaccumulation and trophic transfer mechanisms of E- and L-OPFRs in aquatic food webs.

To the best of our knowledge, whether the bioaccumulation potential and trophic transfer behavior of E-OPFRs are similar to those of legacy analogs in aquatic food webs remain unclear. For example, CDP showed trophic dilution in aquatic food webs for wild fish in Poyang Lake but exhibited significant trophic magnification potential in the marine food web of Laizhou Bay (Bekele et al., 2019; Yan et al., 2024). Bisphenol A bis (diphenyl phosphate) (BDP) was significantly biodiluted in Laizhou Bay, whereas no such trend was observed in Taihu Lake (Lian et al., 2024; Zhao et al., 2019). It is imperative to conduct pertinent studies without elucidation of the bioaccumulation and trophic transfer mechanisms involved. Hainan Island, China, is a region with distinctive characteristics, with relatively high levels of OPFRs pollution originating from both local and surrounding cities/countries (Mo et al., 2019). Therefore, the estuary (Nandu River Estuary) can be considered the ideal area to clarify the bioaccumulation pattern, the fugacity- and biotransformation-based mechanisms of trophic transfer, and the potential health risks of legacy and emerging OPFRs in the aquatic food web. The objectives of this study were to 1) compare the occurrence and accumulation of selected 8 emerging and 10 legacy OPFRs in marine environments and organisms; 2) characterize the different trophic partitioning of these OPFRs and introduce $K_{organism\text{-}water}$ and metabolite-quantified to clarify the primary influencing mechanisms; and 3) assess and compare the potential health risks of legacy and emerging OPFRs from seafood.

2. Results and discussion

2.1. Bioaccumulation of emerging and legacy OPFRs in the tropical estuarine food web

The concentrations of the 8 emerging and 10 legacy OPFRs in seawater and sediments from the Nandu River Estuary are provided in Fig. 1-A, B, Tables 1 and 2. Tris(2,4-di-tert-butylphenyl) phosphate (TDtBPP) (309±108 ng/L), iPPP (0.077±0.111 ng/L) and V6 (0.067 ±0.114 ng/L) are the most abundant E-OPFRs in seawater. TDtBPP was also the predominant E-OPFRs in the sediment samples (350±283 ng/g dw), which is not only produced industrially but also susceptible to the oxidation of tris(2,4-di-*tert*-butylphenyl) phosphite (AO168), leading to its high abundance in the environment (Gao et al., 2024; Liu and Mabury, 2018; Zhou et al., 2024). EHDPHP and TEHP are the most abundant legacy OPFRs in seawater, whereas TEP and TDCPP are dominant in sediment. Compared with those of the 10 legacy OPFRs, the total concentrations of the 8 emerging OPFRs were relatively greater in both seawater (309±109 ng/L) and sediments (350±283 ng/g dw).

In the food web samples, the mean total concentrations of Σ_{10}L-OPFRs and Σ_8E-OPFRs both showed an increasing trend among species: fish ($775 \pm 1.53 \times 10^3$ and 137 ± 209 ng/g lw) < mollusk ($1.60 \times 10^4 \pm 3.21 \times 10^4$ and 160 ± 246 ng/g lw) < crustacean ($4.63 \times 10^4 \pm 4.03 \times 10^4$ and 464 ± 881 ng/g lw), respectively (Fig. 1-A, Tables 1 and 2). (3-diphenoxyphosphoryloxyphenyl) diphenyl phosphate (RDP), iDDPHP and TDtBPP were the most accumulated emerging OPFRs, with average concentrations of 120 ng/g lw, 29.9 ng/g lw and 21.1 ng/g lw, respectively, whereas TDCPP (10,913 ng/g lw), TBOEP (259 ng/g lw), TCPP (89.9 ng/g lw), TCP (87.3 ng/g lw) and TPHP (70.7 ng/g lw) were important legacy OPFRs (Fig. 1-B). The average concentrations of the other emerging OPFRs were lower than 10.8 ng/g lw. A weak correlation of the total concentration was found between L- and E-OPFRs, which suggested that they may exhibit different environmental behaviors or sources (Figure S1). The concentrations of RDP and iDDPHP in the biota were higher than those in the water and sediment, which may be attributed to the moderate Log K_{OW} values of RDP (5.97) and iDDPHP (5.44) for bioaccumulation (Arnot and Gobas, 2006). Among legacy OPFRs, TDCPP and TCPP are well documented as important OPFR congeners in aquatic organisms because of their ubiquitous distribution and persistence in the environment (Choi et al., 2020; Fu et al., 2021; Xie et al., 2024b; Yan et al., 2024). Principal component analysis (PCA) revealed no distinct differences in the OPFRs distributions between the environmental matrices and biota or between the emerging and legacy OPFRs (Figure S2).

The log BAF value is usually employed as a metric to assess the bioaccumulation potential, where a value lower than 3.3 (wet weight-based, criterion B in Annex XIII of REACH) indicates a low bioaccumulation effect for the investigated chemicals. The log BAFs for the emerging OPFRs were in the range of −1.33–1.44, except for CDP, RDP and BDP (nd in seawater) (Fig. 1-C, Table S1). All legacy OPFRs had log BAF values ranging from −2.27–1.75 for all species (Fig. 1-C, Table S2). Overall, the studied emerging and legacy OPFRs have a limited bioaccumulation capacity in the investigated food web. The mean BSAF values of legacy and emerging OPFRs ranged from 0.004 to 27.4 and from 0.003 to 158, respectively (Tables S1 and S2). Among them, legacy OPFRs of TDCPP, TPHP, TBOEP, TCP and TEHP and emerging OPFRs of CDP, RDP, iDDPHP, iPPP and T4tBPP in some species were higher than 1, indicating that these compounds tend to accumulate in specific species rather than in sediment. In comparison, E-OPFRs have relatively high bioaccumulation potentials in the food web, and water uptake might be the main exposure route of most OPFRs in organisms.

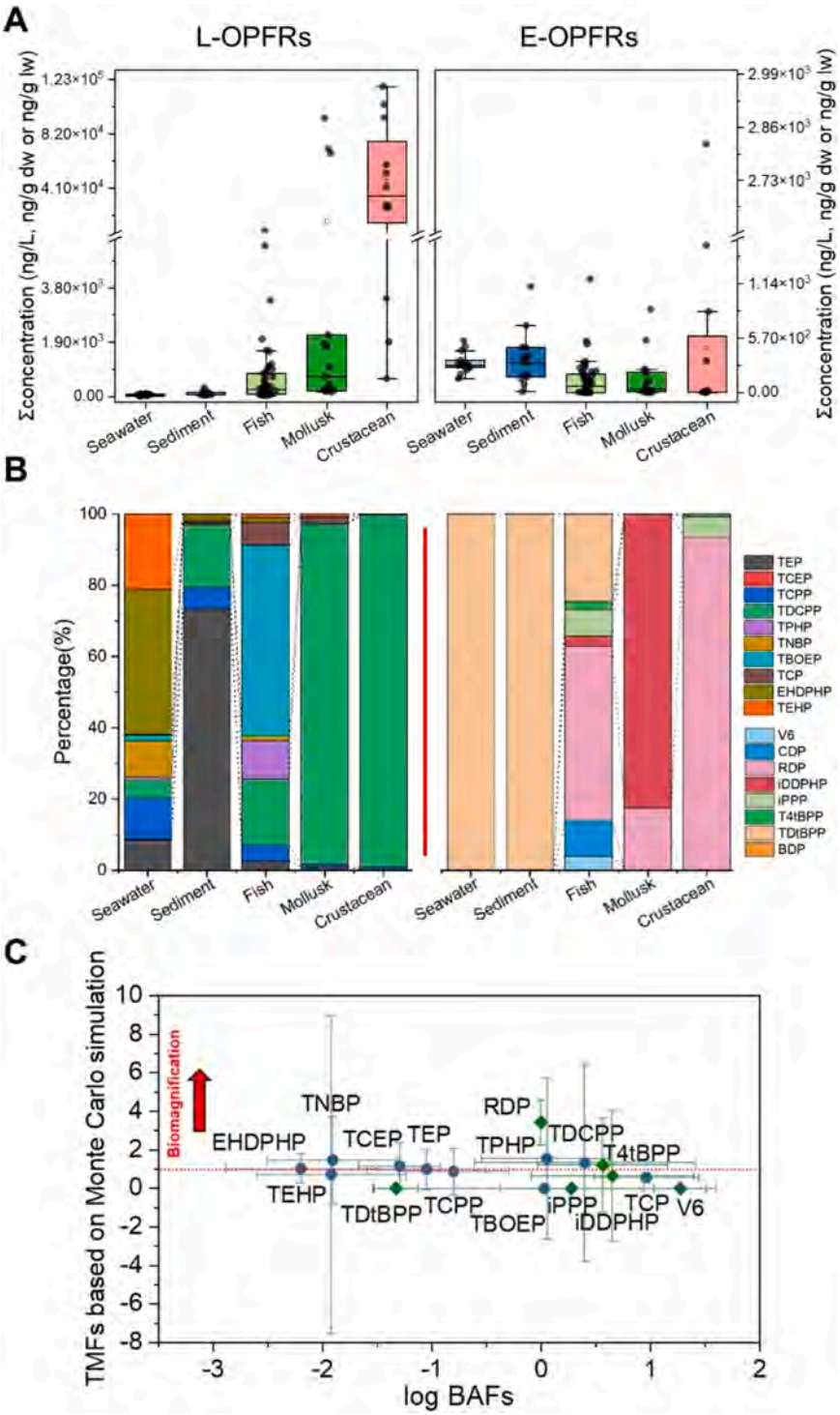


Fig. 1. Bioaccumulation of legacy and emerging OPFRs in the environment matrices and estuarine biotas from the Nandu River Estuary. (A) Total legacy and emerging OPFR concentrations, (B) legacy and emerging OPFR profiles, and (C) comparison of the log bioaccumulation factors (log BAFs) with the trophic magnification factor (TMF). The threshold values were set for bioaccumulation (log BAFs > 3.30) and biomagnification (TMF > 1). All the factor values are presented as the means ± standard deviations.

2.2. Trophodynamic differences between emerging and legacy OPFRs

The $\delta^{13}C$ and $\delta^{15}N$ values ranged from −23.8 ‰ to −14.7 ‰ and 3.44 ‰ to 15.8 ‰, respectively, in the food web (Figure S3-A and Table S3). A statistically significant correlation was observed between the $\delta^{13}C$ and $\delta^{15}N$ values ($r^2 = 0.4944$, $p < 0.001$), indicating analogous marine habitats for these species. The relative trophic levels (TLs) of the observed organisms ranged from 1.13 to 4.67 (Figure S3-B and Table S3). To reduce uncertainty, only OPFRs with detection frequency (DF) >30.0 % in the organisms were used to calculate the TMFs (Tables S1 and S2). The TMFs of TPHP, TCP and iDDPHP estimated by the slope of the concentration-TL relationship (TMF_{OLS}) were 1.55, 0.514 and 0.505, respectively ($p < 0.05$). In addition, TEHP showed a marginally significant relationship with TLs ($p = 0.05$, TMFs = 0.519; Fig. 2) in this study, indicating that TEHP tends to biodilute in this food web. The log-transformed concentrations of other legacy OPFRs (TCEP,

Table 1
Details on the concentrations of 8 emerging OPFRs in seawater (ng/L, $n = 14$), sediment (ng/g dw, $n = 14$), and biological samples (ng/g lipid weight).

Categories	Species name	V6	CDP	RDP	iDDPHP	BDP	iPPP	T4tBPP	TDtBPP	Σ_8E-OPFRs
Seawater	Dissolved phase	nd	nd	nd	nd	nd	nd	nd	178±95.7	178±95.7
	Detection frequency (%)	0.000	0.000	0.000	0.000	0.000	0.000	0.000	100	100
	Particulate phase	0.067 ±0.114	nd	nd	0.018 ±0.017	nd	0.077 ±0.111	0.010 ±0.019	131±64.2	131±64.1
	Detection frequency (%)	28.6	0.000	0.000	57.1	0.000	42.9	50.0	100	100
	Total	0.067 ±0.114	nd	nd	0.018 ±0.017	nd	0.077 ±0.111	0.010 ±0.019	309±108	309±109
	Detection frequency (%)	28.6	0.000	0.000	57.1	0.000	42.9	50.0	100	100
Sediment		0.077 ±0.198	0.004 ±0.012	0.020 ±0.075	0.022 ±0.026	nd	0.053 ±0.136	0.004 ±0.009	350±283	350±283
	Detection frequency (%)	14.3	14.3	7.14	50	0.000	14.3	14.3	100	100
Fish	*Epinephelus fasciatus*	nd	17.5 ± 30.3	108±57.4	2.26±3.91	nd	7.45±12.9	13.8 ± 12.7	344±596	493±598
	Chorinemus formosanus	nd	68.9 ± 119	nd	1.93±3.34	nd	nd	2.16±1.34	nd	73.0 ± 124
	Acanthopagrus latus	nd	nd	nd	0.503 ±0.524	nd	0.882 ±0.578	<MDL	108±188	110±187
	Terapon jarbua	nd	nd	nd	0.728 ±0.733	nd	0.556 ±0.963	1.08±1.23	nd	2.36±1.81
	Siganus canaliculatus	nd	42.2 ± 47.7	90.0 ± 85.2	2.84±2.70	nd	2.39±4.14	nd	nd	137±117
	Sillago sihama	38.1 ± 65.9	nd	nd	0.139 ±0.241	nd	nd	nd	nd	38.2 ± 65.8
	Leiognathus brevirostris	nd	nd	247±65.8	6.00±1.18	nd	77.5 ± 134	8.08±7.53	nd	338±183
	Pneumatophorus japonicus	43.2 ± 74.8	nd	35.2 ± 60.9	4.48±2.52	nd	26.6 ± 46.0	1.71±1.70	nd	111±108
	Gnathanodon speciosus	nd	59.2 ± 88.7	nd	2.56±1.25	nd	20.2 ± 27.6	0.494 ±0.856	nd	82.5 ± 117
	Plectorhinchus	nd	nd	nd	23.1 ± 38.6	nd	0.455 ±0.788	0.190 ±0.329	nd	23.8 ± 38.1
	Stolephorus chinensis	nd	18.7 ± 32.3	287±139	0.679 ±0.605	nd	2.38±4.13	0.946 ±0.839	nd	310±174
	Trachinotus ovatus	nd	nd	77.8 ± 87.4	0.874 ±0.757	nd	0.212 ±0.367	2.31±4.00	53.3 ± 92.4	135±62.6
	Pisodonophis boro	nd	nd	nd	2.00±1.77	nd	4.75±7.45	nd	nd	6.75±8.67
	Lutjanus johni	nd	nd	nd	<MDL	nd	<MDL	<MDL	nd	0.085 ±0.060
	Trachiocephalus myops	nd	nd	165±120	7.49±5.82	nd	9.44±8.20	18.4 ± 27.9	nd	201±98.6
Mollusk	*Turritella terebra bacillum*	nd	nd	nd	289±501	nd	nd	nd	nd	289±501
	Solen strictus	nd	nd	nd	14.3 ± 3.25	nd	nd	nd	nd	14.3 ± 3.25
	Meretrix meretrix	nd	nd	nd	326±190	nd	nd	nd	nd	326±190
	Loligo beka	nd	nd	19.8 ± 21.4	nd	nd	nd	nd	nd	19.8 ± 21.4
	Octopusocellatus	nd	nd	120±41.3	31.3 ± 42.2	nd	nd	nd	nd	152±83.2
Crustacean	*Penaeus penicillatus*	nd	nd	nd	nd	nd	nd	10.6 ± 10.0	nd	10.6 ± 10.0
	Parapenaeopsis hungerfordi	nd	nd	nd	nd	nd	nd	3.14±2.89	nd	3.14±2.89
	Metapenaeus affinis	nd	nd	110±191	nd	nd	nd	0.900 ±0.892	nd	111±190
	Oratosquilla oratoria	nd	nd	1625±904	nd	nd	107±126	nd	nd	1732±1002
Detection frequency in biota (%)		2.78	9.72	36.1	58.3	0.000	29.2	40.3	4.17	93.1

All the values are presented as the means ± standard deviations.
nd: all of the sample concentrations are lower than the MDL.
<MDL: the mean value is lower than the MDL.

TNBP, TEP, TCPP, TDCPP, and EHDPHP) and emerging OPFRs (T4tBPP and RDP) were not significantly related to TLs ($p > 0.05$, Figure S4).

Furthermore, we performed Monte Carlo simulations of the TMFs (TMF_{NPB}, $n = 10{,}000$) for all these OPFRs (Fig. 2 and S5). Bootstrap regression is frequently employed as a reliable supplementary method to OLS regression, as it is particularly suitable for the analysis of limited sample sizes and unequal samples. Among the E-OPFRs, the TMF_{NPB} of RDP was greater than 1, with probabilities of TMFs greater than 1 of 100 %. RDP has been found to have biomagnification potential in the food web of Poyang Lake, China, which is consistent with the results of this study (Yan et al., 2024). T4tBPP has a TMF_{NPB} of 1.21, with a 52.1 % probability of exceeding a value of 1, indicating moderate potential for biomagnification. In addition, iDDPHP has a TMF_{NPB} of 0.650 with a probability greater than 1 of 13.6 %, indicating its robust biodilution potential (Table S1). The TMF_{NPB} of the TPHP was 1.54, which is highly consistent with TMF_{OLS}. Significant biomagnification of TPHP has also been reported in the marine food webs of Laizhou Bay (Bekele et al., 2019), Pearl River Estury (Huang et al., 2023), and Liaodong Bay in China (He et al., 2023), suggesting its trophic transfer potential in the marine food web. The TMF_{NPB} values for legacy OPFRs (TEP, TCEP, TDCPP, TNBP and EHDPHP) were all >=1 in this food web, and the probabilities of observing TMFs > 1 were greater than 39.2 %. However, the TMF_{NPB} values for TCPP, TCP and TEHP were <1, and the probabilities of observing TMFs > 1 were <28.7 % (Table S2). A number of studies have reported the occurrence of trophic dilutions of TCP and TEHP in marine environments (Brandsma et al., 2015; He et al., 2023; Wang et al., 2023).

2.3. Partitioning and metabolic behavior of emerging and legacy OPFRs

In this study, we employed a fugacity-based approach to characterize the partition coefficients and mass distributions of legacy and emerging OPFRs in various biological phases accurately and assess their trophic transfer mechanisms in the estuarine food web. The pp-LFERs method allows for the normalization of contaminant concentrations in organisms to their mass fraction in each absorption phase. In general, the log $K_{lipid/water}$ values were greater than the log $K_{phospholipid/water}$ and log $K_{protein/water}$ values for OPFRs (Huang et al., 2023; Zhang et al., 2024).

Table 2
Details on the concentrations of 10 legacy OPFRs in seawater (ng/L, $n = 14$), sediment (ng/g dw, $n = 14$), and biological samples (ng/g lipid weight).

Categories	Species name	TEP	TCEP	TCPP	TDCPP	TPHP	TNBP	TBOEP	TCP	EHDPHP	TEHP	Σ_{10}L-OPFRs
Seawater	Dissolved phase	4.25 ±2.67	0.134 ±0.051	5.72 ±7.42	2.64±1.51	0.374 ±0.293	5.70 ±9.89	0.846 ±0.766	nd	9.33 ±6.21	0.570 ±0.403	29.6 ± 14.2
	Detection frequency (%)	100	100	71.4	92.9	100	100	100	0.000	100	100	100
	Particulate phase	0.530 ±0.324	0.001 ±0.002	0.625 ±0.391	0.217 ±0.286	0.054 ±0.030	0.021 ±0.030	0.032 ±0.034	0.148 ±0.307	13.4 ± 11.1	11.4 ± 8.67	26.4 ± 19.8
	Detection frequency (%)	100	7.14	100	71.4	100	78.6	92.9	57.1	100	100	100
	Total	4.78 ±2.76	0.135 ±0.051	6.34 ±7.63	2.86±1.61	0.428 ±0.312	5.72 ±9.91	0.878 ±0.776	0.148 ±0.307	22.7 ± 16.9	11.9 ± 8.82	55.9 ± 27.5
	Detection frequency (%)	100	100	100	100	100	100	100	57.1	100	100	100
Sediment		75.0 ± 60.8	0.014 ±0.006	5.91 ±3.99	17.9 ± 15.0	0.162 ±0.090	0.463 ±0.222	0.163 ±0.113	0.751 ±2.03	1.54 ±0.921	0.150 ±0.160	102±69.8
	Detection frequency (%)	100	100	100	100	100	100	100	57.1	100	78.6	100
Fish	*Epinephelus fasciatus*	44.1 ± 31.3	1.54 ±0.620	85.3 ± 86.5	210±203	126 ±60.4	74.0 ± 67.3	4721 ±2317	437 ±99.9	33.0 ± 11.6	22.5 ± 27.7	5755 ±2679
	Chorinemus formosanus	23.7 ± 10.4	0.267 ±0.287	nd	119±112	86.5 ± 119	5.51 ±3.31	1390 ±283	85.3 ± 89.0	1.26 ±2.18	12.5 ± 4.64	1724±238
	Acanthopagrus latus	6.01 ±3.75	0.113 ±0.035	6.54 ±6.09	26.1 ± 3.58	0.582 ±0.683	0.707 ±0.675	96.1 ± 166	nd	nd	0.652 ±0.072	137±168
	Terapon jarbua	59.1 ± 75.8	0.543 ±0.554	42.2 ± 50.9	167±257	29.0 ± 20.4	6.92 ±8.49	nd	nd	1.54 ±2.66	18.8 ± 27.8	325±441
	Siganus canaliculatus	0.962 ±1.67	0.474 ±0.527	nd	162±131	475 ±192	<MDL	nd	nd	nd	8.98 ±7.67	648±289
	Sillago sihama	19.4 ± 8.09	0.689 ±0.902	53.2 ± 51.0	96.9 ± 102	4.09 ±7.09	5.03 ±7.67	nd	5.01 ±8.68	nd	2.83 ±2.57	187±140
	Leiognathus brevirostris	49.7 ± 12.4	0.127 ±0.220	58.6 ± 49.8	nd	57.8 ± 24.0	nd	nd	nd	42.3 ± 21.8	7.98 ±13.8	217±59.9
	Pneumatophorus japonicus	13.3 ± 13.8	nd	0.748 ±1.30	95.1 ± 165	91.1 ± 51.1	13.1 ± 22.6	nd	nd	0.905 ±1.57	1.46 ±2.53	216±156
	Gnathanodon speciosus	3.29 ±3.60	0.414 ±0.380	59.4 ± 103	388±255	43.2 ± 37.3	11.9 ± 7.79	nd	50.5 ± 87.4	0.435 ±0.754	7.35 ±8.56	565±495
	Plectorhinchus	6.05 ±4.40	0.342 ±0.216	49.3 ± 85.3	21.0 ± 19.4	64.0 ± 39.6	2.57 ±1.08	nd	nd	<MDL	0.332 ±0.574	144±105
	Stolephorus chinensis	18.4 ± 0.910	1.15 ±0.568	nd	381±270	181 ±52.6	1.17 ±1.18	nd	46.6 ± 21.4	11.8 ± 9.30	6.46 ±4.62	648±345
	Trachinotus ovatus	44.9 ± 35.2	1.35 ±1.27	106 ±97.1	259±181	67.5 ± 48.1	27.3 ± 27.8	6.57 ±9.71	83.4 ± 123	36.0 ± 30.7	26.4 ± 23.7	658±488
	Pisodonophis boro	3.98 ±2.98	0.029 ±0.028	24.5 ± 39.2	184±200	7.71 ±6.72	0.966 ±1.67	0.035 ±0.060	19.3 ± 10.7	<MDL	2.39 ±2.25	243±262
	Lutjanus johni	0.738 ±1.28	0.091 ±0.091	7.93 ±7.31	37.2 ± 11.5	nd	1.35 ±2.17	nd	8.54 ±8.98	0.315 ±0.545	0.259 ±0.280	56.4 ± 15.6
	Trachiocephalus myops	nd	1.18 ±0.713	nd	26.4 ± 28.5	23.2 ± 6.67	8.88 ±11.3	nd	24.9 ± 21.9	12.1 ± 3.52	7.89 ±13.7	105±25.6
Mollusk	*Turritella terebra bacillum*	nd	1.96 ±1.29	414 ±217	76,328 ±13,968	25.6 ± 12.5	20.7 ± 6.84	nd	189 ±162	31.8 ± 35.4	81.2 ± 37.5	77,092 ±14,417
	Solen strictus	441 ±353	0.313 ±0.316	47.6 ± 82.4	50.9 ± 88.2	50.0 ± 17.6	nd	nd	466 ±373	28.6 ± 49.5	60.9 ± 53.0	1145±952
	Meretrix meretrix	216 ±193	0.212 ±0.106	33.2 ± 52.5	106±93.4	41.4 ± 2.59	nd	nd	313 ±271	297±259	414 ±209	1421±631
	Loligo beka	23.6 ± 20.7	0.296 ±0.165	2.97 ±5.15	141±38.4	21.4 ± 2.49	0.627 ±0.307	0.730 ±1.26	nd	0.251 ±0.316	9.85 ±17.1	201±42.9
	Octopusocellatus	61.0 ± 50.7	0.585 ±0.416	nd	nd	116 ±29.2	0.562 ±0.973	nd	82.8 ± 117	1.21 ±2.09	nd	262±136
Crustacean	*Penaeus penicillatus*	nd	1.77 ±0.564	373 ±48.0	26,850 ±883	2.77 ±0.728	14.2 ± 2.86	7.80 ±13.5	nd	0.662 ±1.15	7.33 ±12.7	27,258 ±920
	Parapenaeopsis hungerfordi	165 ±286	1.02 ±0.227	274 ±44.3	104,749 ±11,761	15.0 ± 10.9	0.163 ±0.283	nd	nd	nd	nd	105,205 ±11,780
	Metapenaeus affinis	192 ±225	2.10 ±0.250	211 ±74.3	37,264 ±30,019	45.8 ± 21.9	13.1 ± 9.34	1.17 ±2.03	285 ±359	25.1 ± 14.6	nd	38,039 ±30,159
	Oratosquilla oratoria	nd	1.43 ±0.878	307 ±218	14,242 ±23,084	122 ±118	11.1 ± 8.96	1.44 ±2.49	nd	40.4 ± 16.6	24.1 ± 41.7	14,750 ±23,370
Detection frequency in biota (%)		69.4	87.5	55.6	77.8	91.7	63.9	19.4	43.1	51.4	63.9	100

All the values are presented as the means ± standard deviations.
nd: all of the sample concentrations are lower than the MDL.
<MDL: the mean value is lower than the MDL.

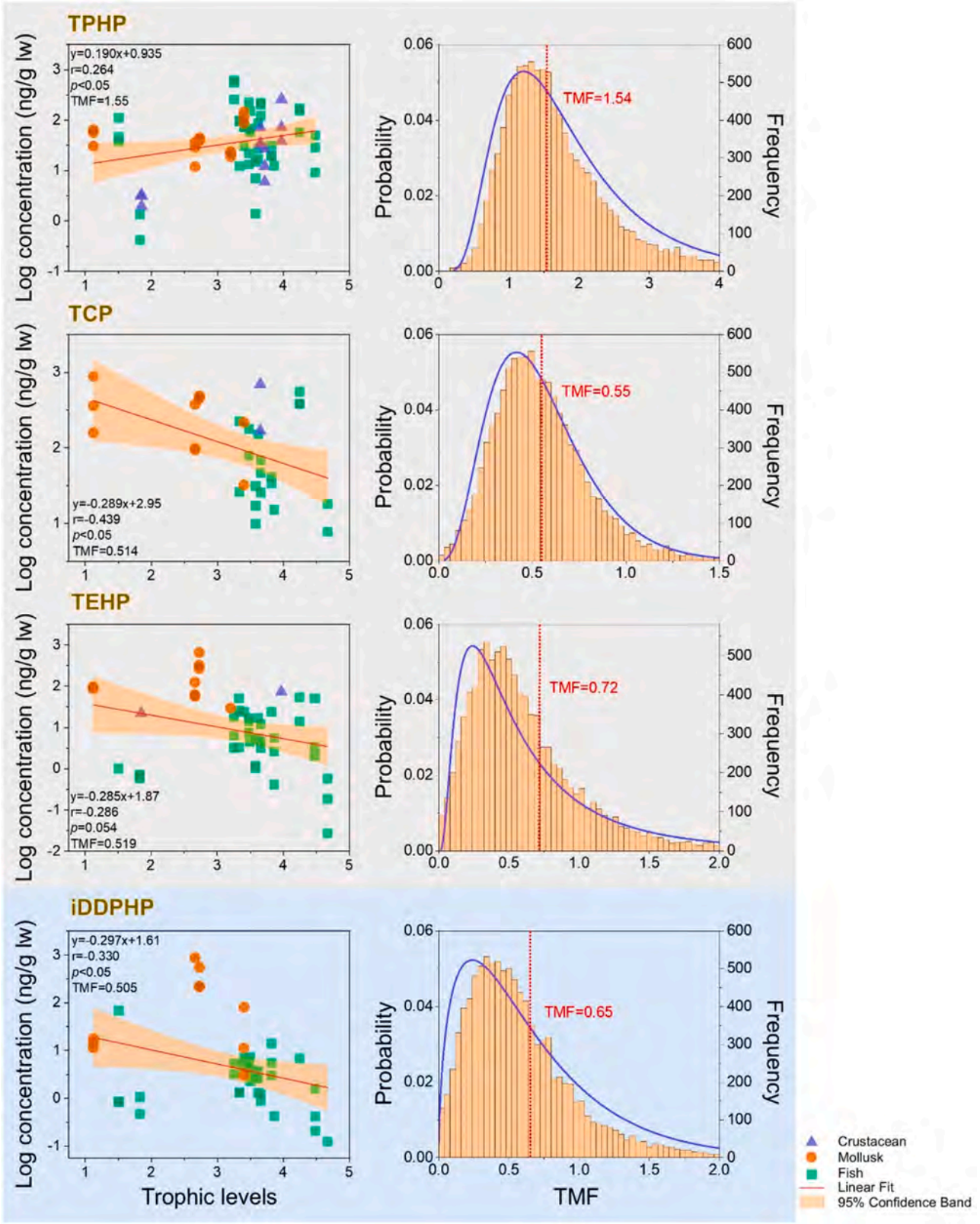


Fig. 2. Relationships between log-transformed concentrations of OPFRs (ng/g lw) and trophic levels (left side) and the frequency distributions of trophic magnification factors (TMFs) determined for lipid-normalized concentrations of OPFRs generated from bootstrapped Monte Carlo simulations (n = 10,000, right side) in estuarine food webs from Hainan Island, China.

Compared with legacy OPFRs, emerging OPFRs have relatively higher $K_{organism\text{-}water}$ values. The estimated $K_{organism\text{-}water}$ values were significantly correlated with Log K_{OW} for all the biota groups for OPFRs ($p < 0.01$, Fig. 3-A). These results confirmed the importance of hydrophobicity in the partitioning of OPFRs in marine organisms.

First, we found that the water content was the predominant absorption phase in all the biota samples (ranging from 66.6 % to 87.1 % of the mass), followed by structure protein (3.25–5.68 %), storage lipid (0.627–7.67 %) and phospholipids (0.120–0.200 %) (Figure S6). Considering that lipid, protein, phospholipid and water are important adsorption phases for the partitioning of organic pollutants, lipid-water/phospholipid-water/protein-water partition coefficients have been explored for their bioaccumulation/trophic magnification potential for emerging and legacy OPFRs (Droge, 2019; Fremlin et al., 2023). These results indicate that different trophic partitioning behaviors occurred for OPFR congeners in this food web. For TEP and TCEP, water content was the most important absorption phase for their mass distributions, and the mass distributions of storage lipid (29.1–85.4 %) and structural protein (13.2–65.9 %) were the two most important absorption phases for V6 (Fig. 3-B). The estimated mass fractions of the other 7 emerging OPFRs and 8 legacy OPFRs occurred mainly in storage lipid. Importantly, storage lipid did not significantly increase with increasing TLs ($r < 0$, $p = 0.591$; Figure S6), which may have resulted in an insignificant trophic transfer potential for most OPFRs in this study. Therefore, the variations in the absorption phase compositions may greatly control the partitioning of OPFRs in different food web members, which can also explain the different biomagnification conclusions for OPFRs across food webs (Borgå et al., 2012; Burkhard et al., 2013; Zhang et al., 2024).

A growing number of studies have indicated that the metabolism of OPFRs in organisms affects their bioavailability and limits their trophic transfer potential in food webs (Tang et al., 2019; Wang et al., 2019; Zhao et al., 2019). The total concentrations of the target OPFR metabolites increased in the following order: crustacean (30.7 ± 34.3 ng/g lw) < mollusk (49.5 ± 53.4 ng/g lw) < fish (50.6 ± 76.3 ng/g lw) ($p > 0.05$) (Table S4 and Figure S7-A). 4-hydroxyphenyl diphenyl phosphate (4-OH-TPHP) was the predominant OPFR metabolite, with a mean concentration of 27.5 ng/g lw, followed by di-n-butyl phosphate (DNBP), dibutyl-3-hydroxybutyl phosphate (3-OH-TNBP), and bis (2-butoxyethyl) phosphate (BBOEP) (Table S4 and Figure S7-B). The mass fraction of these OPFR metabolites in each absorption phase also did not show any positive correlations with the TLs (Figure S8). The significant relationships between TBOEP, TNBP and their corresponding metabolites suggest that there is a high probability that these two substances tend to be metabolized and accumulate in organisms (Figure S9). In the present study, we used the estimated K_M values via the EPA EPISuite BCFBAF™ for nonspecies-specific fish as a surrogate for the overall K_M of all OPFRs by various species in food webs (Table S5). The estimated K_M values of most legacy OPFRs were higher than those of emerging OPFRs (Fig. 3-A). It can be hypothesized that emerging OPFRs are inherently more difficult to metabolize in organisms and may accumulate more as parent compounds in the bodies of organisms.

2.4. Human dietary exposure and health risk assessment

In this study, we assessed the human health risks of target OPFRs and their metabolites via seafood consumption and used their concentrations in marine organisms to estimate daily intake (Fig. 4). HQ > 1 indicates a health risk for humans, whereas HQ < 1 indicates no risk. RfDs from references were adapted in this study and were calculated by applying the lowest NOAEL and reference maximum recommended composite uncertainty factors for the lowest reported NOAEL (Table S6). The HQs of all the OPFRs were in the range of 2.39×10^{-5}–7.93×10^{-2}. The relatively high HQs of TDCPP might be attributed to their relatively high exposure levels and low RfD. Generally, the total risk of human exposure to emerging OPFRs via seafood ingestion is relatively lower than that of legacy OPFRs. The bioavailability and permeability of compounds play key roles in the assessment of human exposure to OPFRs (Dahley et al., 2024; Pandey et al., 2024). Most legacy OPFRs have high gastrointestinal absorption according to an *in silico* tool (SwissADME; Table S7), indicating that emerging OPFRs may be relatively less bioavailable for humans. The probabilities of Caco-2 permeability were comparable between legacy and emerging OPFRs, but the aqueous solubilities of the emerging OPFRs, except for V6, were relatively lower (Log S < −4.0). This phenomenon may be attributed to the higher molecular mass of the emerging OPFRs. However, our study evaluated only OPFRs exposure via the dietary route, and the health risks of emerging OPFRs via multiple pathways should be assessed in the future. The high levels of some OPFR metabolites found in seafood cannot be ignored, which can provide valuable risk information for human exposure (Hou et al., 2023).

3. Conclusions

Understanding the partitioning and metabolism of OPFRs in marine organisms is far less understood but is key to assessing the trophic transfer potential of OPFRs in food webs. Although relatively high concentrations of the emerging OPFRs were detected in seawater and sediments from the investigated area, trophodynamic analysis revealed that the trophic transfer potential of the emerging OPFRs was lower than that of legacy OPFRs. Fugacity-based analysis indicated that different trophic partitioning behaviors occurred for the OPFR congeners in this food web. All the emerging OPFRs were found to be lipid-dominated in the organisms, but TEP and TCEP (the legacy OPFRs) showed significant water dominance in the food web members. Emerging OPFRs have relatively higher $K_{organism\text{-}water}$ values than legacy OPFRs do when accounting for the biological phase composition, but the relatively lower level of emerging OPFRs in the environment hinders their bioaccumulation and trophic transfer potential in the food web.

The consumption of seafood was found to present nonsignificant risks to local residents for both target legacy and emerging OPFRs. *In silico* bioavailability analysis also revealed a relatively lower gastrointestinal absorption potential of emerging OPFRs than legacy analogs. Nevertheless, it is advisable to maintain vigilance concerning the potential risks of emerging OPFRs from aquatic food webs, considering the gradual replacement of legacy OPFRs with emerging OPFRs in the future. Notably, we investigated only 8 metabolites of legacy OPFRs in this study. Comprehensive metabolite quantification of all OPFRs (especially E-OPFRs) can help characterize their bioaccumulation and trophodynamics in the food web.

4. Materials and methods

4.1. Chemicals and materials

The standards of 8 emerging OPFRs, including V6, CDP, RDP, iDDPHP, BDP, iPPP, T4tBPP and TDtBPP, and 10 legacy OPFRs, including TEP, TCEP, TCPP, TDCPP, TPHP, TNBP, TBOEP, TCP, EHDPHP and TEHP, were purchased with purities > 95 %. The 8 OPFR metabolites, including bis(2-butoxyethyl) hydroxyethyl phosphate (BBOEHEP), 3-OH-TNBP, 4-OH-TPHP, bis(2-butoxyethyl) 3-hydroxyl-2-butoxyethyl phosphate (3-OH-TBOEP), 2-ethyl-5-hydroxyhexyl diphenyl phosphate (5-OH-EHDPHP), diphenyl phosphate (DPHP), DNBP and BBOEP, were purchased with purities > 95 %. The detailed information of the abovementioned compounds is listed in Table S8. The isotope-labeled internal standard (IS) TNBP-d^{27} and surrogates for OPFRs (TPHP-d^{15}) and metabolites (BBOEP-d^{8}) were purchased from Toronto Research Chemicals (Toronto, ON, Canada). High-performance liquid chromatography-grade acetonitrile, dichloromethane, n-hexane, and methanol were purchased from OCEANPAK (Tianjin, China) or Merck (USA or Germany). The corresponding parent compounds for each of the metabolites are listed in Table S9.

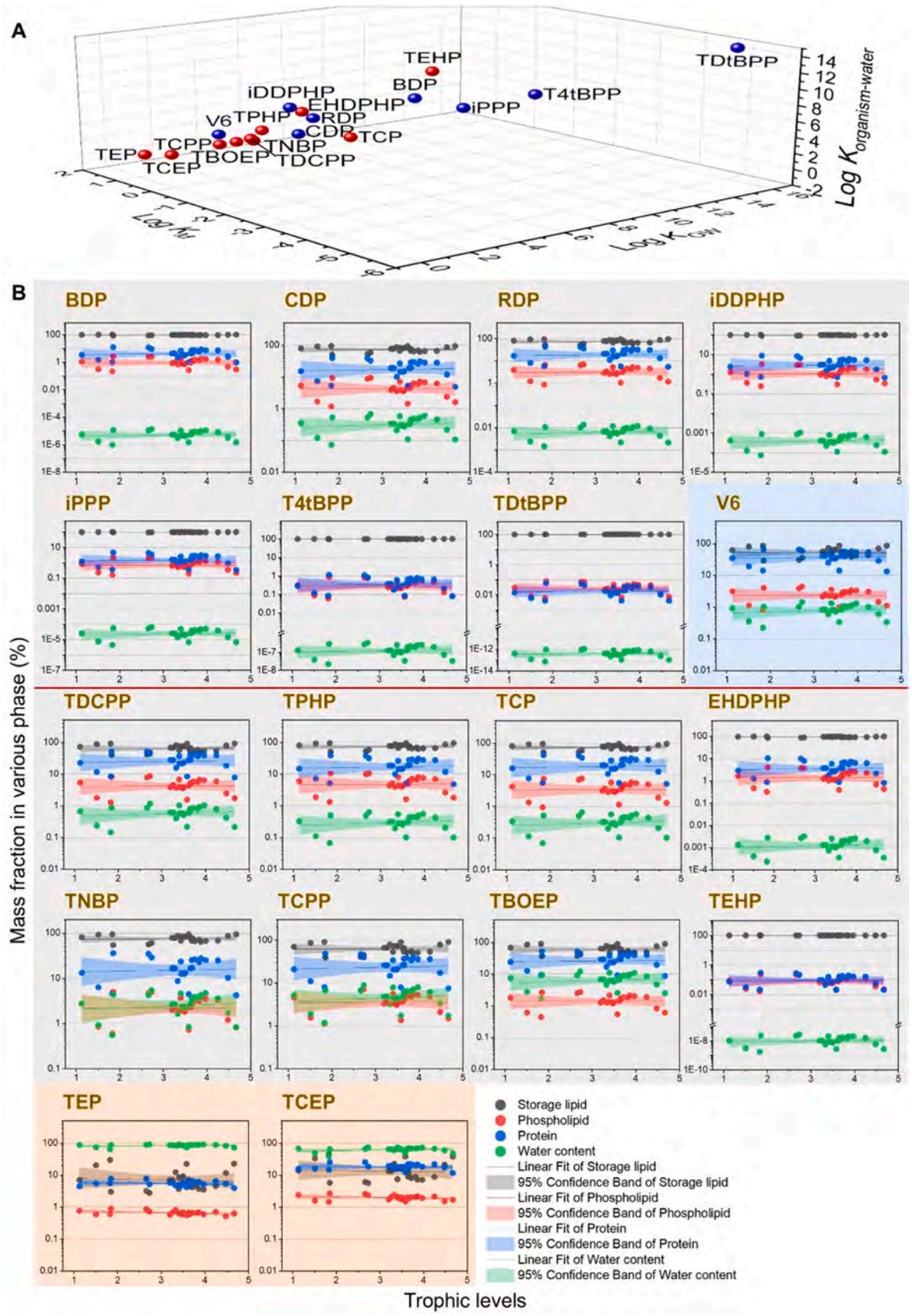


Fig. 3. (A) Estimated distributions of the Log $K_{organism\text{-}water}$ ratios of legacy OPFRs (red points) and emerging OPFRs (blue points) relative to Log K_{OW} and Log K_M. (B) Linear regressions between the mass fraction and TLs of 8 emerging and 10 legacy OPFRs.

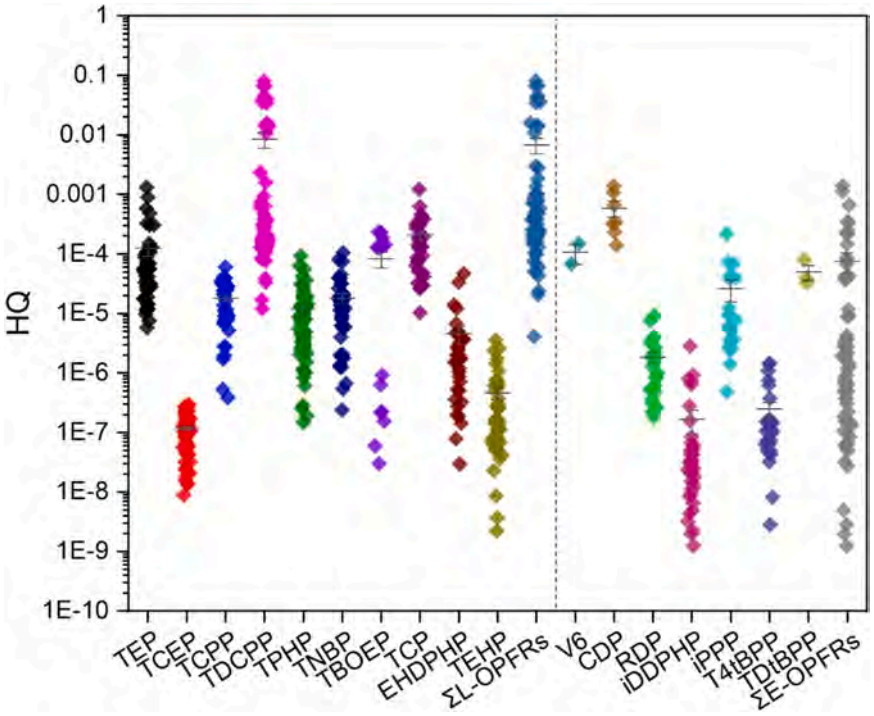


Fig. 4. Health risks of legacy and emerging OPFRs in seafood, measured in terms of hazard quotient (HQ).

4.2. Sampling sites and sample collection

All the environmental and faunal samples were collected from the Nandu River Estuary, China, in April 2023 (Figure S10). All the fauna samples were identified and classified on the basis of seafood databases (i.e., FishBase (https://www.fishbase.org), FishIDER (https://fishider.org/en), SeaLifeBase (https://www.sealifebase.org), and WoRMS (https://www.marinespecies.org)). The collected samples included fifteen fish species, including *Epinephelus fasciatus* (n = 3), *Chorinemus formosanus* (n = 3), *Acanthopagrus latus* (n = 3), *Terapon jarbua* (n = 3), *Siganus canaliculatus* (n = 3), *Sillago sihama* (n = 3), *Leiognathus brevirostris* (n = 3), *Pneumatophorus japonicus* (n = 3), *Gnathanodon speciosus* (n = 3), *Plectorhinchus* (n = 3), *Stolephorus chinensis* (n = 3), *Trachinotus ovatus* (n = 3), *Pisodonophis boro* (n = 3), *Lutjanus johni* (n = 1) and *Trachiocephalus myops* (n = 3). The five mollusk species included *Turritella terebra bacillum* (n = 3), *Solen strictus* (n = 3), *Meretrix meretrix* (n = 3), *Loligo beka* (n = 3) and *Octopusocellatus* (n = 3), and the four crustacean species included *Penaeus penicillatus* (n = 3), *Parapenaeopsis hungerfordi* (n = 3), *Metapenaeus affinis* (n = 3) and *Oratosquilla oratoria* (n = 3). Specifically, 54.1 % of these investigated species are carnivorous, 33.3 % are omnivorous, 4.17 % are deposit feeders, and 8.33 % are filter feeders. The majority of the species are benthic (62.5 %), with 33.3 % classified as coastal or pelagic and 4.17 % identified as coral reef fish. A detailed description of the collected organism samples is provided in Table S3. After collection, the samples were stored directly in a refrigerator at −20 °C and transported to the laboratory. Fourteen surface water samples and fourteen surface sediment samples were also collected in the sampling region.

4.3. Sample preparation and instrumental analysis

Detailed information on the preparation and treatment of the seawater, sediment and biota samples is provided in the Supporting Information (SI-1). Instrumental analysis of legacy and emerging OPFRs and metabolites was performed via Agilent 1290 Infinity ultra-high performance liquid chromatography coupled with Agilent 6470 triple quadrupole mass spectrometry (UPLC-MS/MS). The detailed UPLC and MS/MS parameters for the target analytes, surrogates, and IS are given in SI-2 and Table S10. The freeze-dried biota samples (0.5 mg) were used for analyzing stable isotopic ratios of carbon (δ^{13}C) and nitrogen (δ^{15}N) via a Flash EA 112 series elemental analyzer coupled with a Finnigan MAF ConFlo 111 isotope ratio mass spectrometer (Lu et al., 2023). The standard deviations for the δ^{13}C and δ^{15}N analyses were 0.02 % and 0.05 %, respectively. The water content of the biological samples was determined via the weighing method. The lipid content was determined gravimetrically using 0.1 g dw biological samples extracted with 1:1 v/v n-hexane and dichloromethane twice. Total protein and phospholipid levels in the biota samples were quantified via a Bicinchoninic Acid Assay Kit (Enzyme-linked Biotechnology Co., Shanghai, China) and a Phopholipid ELISA Kit (YJ218547, Yuanju Biotech, Shanghai, China), respectively.

4.4. Quality assurance and quality control (QA/QC)

All glassware was heated at 450 °C for 4 h before use, and all equipment (glassware, PTFE tube, etc.) was cleaned in sequence with methanol, dichloromethane, and n-hexane to decrease background interference. For each batch of samples (n = 12), a solvent blank, a method blank and a quality control (each target analyte at a concentration of 100 ng/mL) were run in sequence to check for carryover and system performance. Method blanks > 1 ng/mL were detected for TEP, TCPP, TDCPP, TPHP, and TDtBPP. The concentrations of the method blanks were subtracted from the corresponding samples. The surrogate recoveries for TPHP-d^{15} were 49.6–104 %, 65.4–85.0 %, and 53.4–138 % and those for BBOEP-d^{8} were 111–159 %, 85.4–123 % and 49.6–133 % for seawater, sediment and biological samples, respectively. The method detection limits (MDLs) and method quantitation limits (MQLs) were defined as the concentrations with signal-to-noise ratios of three and ten, respectively. The MDLs and MQLs of the target compounds ranged from 0.002 to 0.873 and 0.005–2.91 ng/g lw, respectively. The matrix effects for the target compounds ranged from 28.7 to 132 %. The utilization of matrix standards for the quantitative assessment of substances exhibiting high matrix effects. Spike recoveries were performed on the biological samples, with absolute recoveries ranging from 65.0 to

127 %. The intraday relative standard deviations (RSDs) were in the range of 0.957–22.0 %. Details of the QA/QC results for the seawater, sediment and biological samples are presented in Table S11.

4.5. Statistical analysis

The bioaccumulation factors (BAFs) are calculated to describe the transfer ratio of pollutants from water to biota via the following equations (Ma et al., 2014).

$$\mathrm{BAF}_{\mathrm{wet\ weight}} = C_{\mathrm{biota\ ww}} / C_{\mathrm{water}} \quad (1)$$

Where C_{water} is the sum of pollutant concentrations in the dissolved phase and particulate phase (ng/L) and C_{biota} is the concentration in biota (ng/g wet weight).

The biota-sediment accumulation factor (BSAF) is used to evaluate the bioavailability of pollutants from sediments and can be estimated via the following equation (Zhu et al., 2024):

$$\mathrm{BSAF} = C_{\mathrm{biota}} / C_{\mathrm{sediment}} \quad (2)$$

Where C_{biota} is the pollutant concentration in biota (ng/g wet weight) and C_{sediment} is the pollutant concentration in sediment (ng/g dry weight).

TLs of the analyzed organisms are estimated on the basis of the assumption that zooplankton occupy a TL of 2.0 and a $\Delta\sigma 15N$ of 3.4 via Eq. (3): (Yin et al., 2023)

$$TL_s = \left(\delta^{15}N_{\mathrm{samp}} - \delta^{15}N_{\mathrm{baseline}}\right) / \Delta\sigma^{15}N + \lambda \quad (3)$$

Where $\delta^{15}N_{\mathrm{samp}}$ and $\delta^{15}N_{\mathrm{baseline}}$ are the test $\delta^{15}N$ values of the biological sample and the baseline organism (zooplankton), respectively.

The calculation of TMFs is based on the correlations between lipid-normalized concentrations and the TLs of individual organisms via the following Eqs. (4)–(5):

$$\log\mathrm{OPFRs} = a + b{*}\mathrm{TLs} \quad (4)$$

$$\mathrm{TMFs} = 10^{b} \quad (5)$$

The partition coefficients for OPFRs and metabolites between the water and biological phases (i.e., lipid, protein and phospholipid) were estimated via the pp-LFERs method (SI-3 and Table S5). (Stenzel et al., 2013)

The relative fractions of the chemical mass of the target compounds (%) in each tissue phase can be estimated via Eq. (6): (Fremlin et al., 2023)

$$M_{tissue} = \frac{M_{tissue}}{M_{lipid} + M_{protein} + M_{phospholipid} + M_{water}} \times 100 \quad (6)$$

To evaluate the human health risk of OPFRs via seafood consumption, the estimated daily dietary intake (EDI) was calculated as follows: (Zhu et al., 2024)

$$EDI = C \times DC / BW \quad (7)$$

Where C is the concentration of the target compound in marine organisms (ng/g ww). DC represents the daily per capita seafood consumption of 82.4 g/person/day (Chen et al., 2023), and BW represents the average body weight of adults (70 kg) (Wang et al., 2020).

The health risk assessment via seafood consumption was evaluated (SI-4).

Univariate correlation analysis (Spearman correlation coefficients) was conducted to assess the concentrations between legacy and emerging OPFRs. All the statistical analyses were carried out via Origin 2022b software (Origin Lab Corporation, MA). A p value < 0.05, 0.01 or 0.001 was considered statistically significant. One-way analysis of variance (one-way ANOVA) was used to test the significance between groups, with a statistical significance level of 0.05. The chemical concentration below the MDLs was set to half of the MDLs for all the statistical analyses except linear regression.

CRediT authorship contribution statement

Qianyi Huang: Investigation, Data curation, Formal analysis, Visualization, Writing – original draft, Writing – review & editing. **Rui Hou:** Conceptualization, Investigation, Data curation, Writing – review & editing, Supervision, Funding acquisition. **Yuchen Wang:** Investigation, Data curation. **Lang Lin:** Investigation. **Hengxiang Li:** Investigation. **Shan Liu:** Investigation. **Xiangrong Xu:** Conceptualization, Investigation, Supervision, Project administration, Funding acquisition. **Kefu Yu:** Resources. **Xiaoping Huang:** Resources.

Declaration of competing interest

The authors declare that they have no known competing financial interests or personal relationships that could have appeared to influence the work reported in this paper.

Acknowledgments

This work was supported by the National Natural Science Foundation of China [No. 42277390], the Guangdong Basic and Applied Basic Research Foundation, China [No. 2024B1515020074], the Hainan Province Science and Technology Special Fund [No. ZDYF2022SHFZ317], and the Science and Technology Planning Project of Guangdong Province, China [No. 2023B1212060047].

Supplementary materials

Supplementary material associated with this article can be found, in the online version, at doi:10.1016/j.wroa.2024.100294.

Detailed information on the sampling, instrumental analysis, partition coefficient estimation and health risk assessment; tables showing the information on quality assurance and quality control results, biological parameters for individual samples, estimated partition coefficients, estimated bioaccumulation and biomagnification factors, acceptable daily intake values and human absorption parameters; figures showing sampling locations, bioaccumulation profiles of OPFR metabolites, relationships between legacy and emerging OPFR concentrations, relationships between log concentrations and trophic levels, relationships between metabolites and their parent OPFRs, frequency distributions of TMFs for some legacy and emerging OPFRs, and mass fractions of OPFR metabolites in the food web.

Data availability

The data that support the findings are available from the authors upon reasonable request.

References

China M.E.E., 2020. Priority chemicals list (second batch). https://www.mee.gov.cn/xxgk2018/xxgk/xxgk01/202011/t20201102_805937.html.

QYResearch, 2023. 2023–2029 Global and China Organophosphorus-based Flame Retardants Industry Research and 14th Five Year Plan Analysis Report.

Arnot, J.A., Gobas, F.A., 2006. A review of bioconcentration factor (BCF) and bioaccumulation factor (BAF) assessments for organic chemicals in aquatic organisms. Environ. Rev. 14 (4), 257–297.

Bekele, T.G., Zhao, H., Wang, Q., Chen, J., 2019. Bioaccumulation and trophic transfer of emerging organophosphate flame retardants in the marine food webs of Laizhou Bay, North China. Environ. Sci. Technol. 53 (22), 13417–13426.

Blum, A., Behl, M., Birnbaum, L.S., Diamond, M.L., Phillips, A., Singla, V., Sipes, N.S., Stapleton, H.M., Venier, M., 2019. Organophosphate ester flame retardants: are they a regrettable substitution for polybrominated diphenyl ethers? Environ. Sci. Technol. Lett. 6 (11), 638–649.

Borgå, K., Kidd, K.A., Muir, D.C., Berglund, O., Conder, J.M., Gobas, F.A., Kucklick, J., Malm, O., Powell, D.E., 2012. Trophic magnification factors: considerations of ecology, ecosystems, and study design. Integr. Environ. Assess. Manag. 8 (1), 64–84.

Brandsma, S.H., Leonards, P.E., Leslie, H.A., de Boer, J., 2015. Tracing organophosphorus and brominated flame retardants and plasticizers in an estuarine food web. Sci. Total Environ. 505, 22–31.
Burkhard, L.P., Borgå, K., Powell, D.E., Leonards, P., Muir, D.C.G., Parkerton, T.F., Woodburn, K.B., 2013. Improving the quality and scientific understanding of Trophic Magnification Factors (TMFs). Environ. Sci. Technol. 47 (3), 1186–1187.
Chen, X., Liang, X., Yang, J., Yuan, Y., Xiao, Q., Su, Z., Chen, Y., Lu, S., Wang, L., 2023. High-resolution mass spectrometry-based screening and dietary intake assessment of organophosphate esters in foodstuffs from South China. Sci. Total Environ. 905, 167169.
Choi, W., Lee, S., Lee, H.-K., Moon, H.-B., 2020. Organophosphate flame retardants and plasticizers in sediment and bivalves along the Korean coast: occurrence, geographical distribution, and a potential for bioaccumulation. Mar. Pollut. Bull. 156, 111275.
Dahley, C., Böckmann, T., Ebert, A., Goss, K.-U., 2024. Predicting the intrinsic membrane permeability of Caco-2/MDCK cells by the solubility-diffusion model. Eur. J. Pharm. Sci. 195, 106720.
Droge, S.T.J, 2019. Membrane–Water partition coefficients to aid risk assessment of perfluoroalkyl anions and alkyl sulfates. Environ. Sci. Technol. 53 (2), 760–770.
Du, J., Li, H., Xu, S., Zhou, Q., Jin, M., Tang, J., 2019. A review of organophosphorus flame retardants (OPFRs): occurrence, bioaccumulation, toxicity, and organism exposure. Environ. Sci. Pollut. Res. 26 (22), 22126–22136.
Endo, S., Goss, K.-U., 2014. Predicting partition coefficients of polyfluorinated and organosilicon compounds using Polyparameter Linear Free Energy Relationships (PP-LFERs). Environ. Sci. Technol. 48 (5), 2776–2784.
Fremlin, K.M., Elliott, J.E., Letcher, R.J., Harner, T., Gobas, F., 2023. Developing methods for assessing trophic magnification of perfluoroalkyl substances within an urban terrestrial avian food web. Environ. Sci. Technol. 57 (34), 12806–12818.
Fu, J., Fu, K., Chen, Y., Li, X., Ye, T., Gao, K., Pan, W., Zhang, A., Fu, J., 2021. Long-Range transport, trophic transfer, and ecological risks of organophosphate esters in remote areas. Environ. Sci. Technol. 55 (15), 10192–10209.
Gao, M., Zhang, Q., Wu, S., Wu, L., Cao, P., Zhang, Y., Rong, L., Fang, B., Yuan, C., Yao, Y., Wang, Y., Sun, H., 2024. Contamination status of novel organophosphate esters derived from organophosphite antioxidants in soil and the effects on soil bacterial communities. Environ. Sci. Technol. 58 (24), 10740–10751.
Geisler, A., Endo, S., Goss, K.-U., 2012. Partitioning of organic chemicals to storage lipids: elucidating the dependence on fatty acid composition and temperature. Environ. Sci. Technol. 46 (17), 9519–9524.
He, W., Ding, J., Liu, W., Zhong, W., Zhu, L., Zhu, L., Feng, J., 2023. Occurrence, bioaccumulation and trophic transfer of organophosphate esters in marine food webs: evidence from three bays in Bohai Sea, China. Sci. Total Environ. 861, 160658.
Hou, R., Sun, C., Zhang, S., Huang, Q., Liu, S., Lin, L., Li, H., Xu, X., 2023. The metabolism of novel flame retardants and the internal exposure and toxicity of their major metabolites in fauna - a review. J. Environ. Exposure Assess. 2 (2), 10.
Hou, R., Xu, Y., Wang, Z., 2016. Review of OPFRs in animals and humans: absorption, bioaccumulation, metabolism, and internal exposure research. Chemosphere 153, 78–90.
Huang, Q., Hou, R., Lin, L., Li, H., Liu, S., Cheng, Y., Xu, X., 2023. Bioaccumulation and trophic transfer of organophosphate flame retardants and their metabolites in the estuarine food web of the Pearl River, China. Environ. Sci. Technol. 57 (9), 3549–3561.
Kim, S.K., Lee, D.S., Oh, J.R., 2002. Characteristics of trophic transfer of polychlorinated biphenyls in marine organisms in Incheon North Harbor, Korea. Environ. Toxicol. Chem. 21 (4), 834–841.
Li, L., Chen, R., Wang, L., Jia, Y., Shen, X., Hu, J., 2023. Discovery of three organothiophosphate esters in river water using high-resolution mass spectrometry. Environ. Sci. Technol. 57 (18), 7254–7262.
Lian, M., Wang, J., Wang, Z., Lin, C., Gu, X., He, M., Liu, X., Wei, O., 2024. Occurrence, bioaccumulation and trophodynamics of organophosphate esters in the marine biota web of Laizhou Bay, Bohai Sea. J. Hazard. Mater. 469, 134035.
Liu, R., Mabury, S.A., 2018. Unexpectedly high concentrations of a newly identified organophosphate ester, tris(2,4-di-tert-butylphenyl) phosphate, in indoor dust from Canada. Environ. Sci. Technol. 52 (17), 9677–9683.
Lu, R., Cao, X., Zheng, X., Zeng, Y., Jiang, Y., Mai, B., 2023. Biomagnification and elimination effects of persistent organic pollutants in a typical wetland food web from South China. J. Hazard. Mater. 457, 131733.
Luo, W., Liu, Y., Yang, X., Aamir, M., Bai, X., Liu, W., 2023. Prenatal exposure to emerging and traditional organophosphate flame retardants: regional comparison, transplacental transfer, and birth outcomes. Environ. Pollut. 336, 122463.
Ma, X., Zhang, H., Wang, Z., Yao, Z., Chen, J., Chen, J., 2014. Bioaccumulation and trophic transfer of short chain chlorinated paraffins in a marine food web from Liaodong Bay, North China. Environ. Sci. Technol. 48 (10), 5964–5971.
Mo, L., Zheng, J., Wang, T., Shi, Y., Chen, B., Liu, B., Ma, Y., Li, M., Zhuo, L., Chen, S., 2019. Legacy and emerging contaminants in coastal surface sediments around Hainan Island in South China. Chemosphere 215, 133–141.
Pandey, N., Kumari, N., Roy, P., Mondal, S.K., Thakur, A., Sun, C.C., Ghosh, A., 2024. Tuning Caco-2 permeability by cocrystallization: insights from molecular dynamics simulation. Int. J. Pharm. 650, 123666.
Pantelaki, I., Voutsa, D., 2019. Organophosphate flame retardants (OPFRs): a review on analytical methods and occurrence in wastewater and aquatic environment. Sci. Total Environ. 649, 247–263.
Schang, G., Robaire, B., Hales, B.F., 2016. Organophosphate flame retardants act as endocrine-disrupting chemicals in MA-10 mouse tumor Leydig cells. Toxicol. Sci. 150 (2), 499–509.
Shi, H., Zhao, Y., 2024. Bringing the emerging organophosphate flame retardants (eOPFRs) into view: a hidden ecological and human health threat. Aquatic Toxicol. 267, 106833.
Stenzel, A., Goss, K.-U., Endo, S., 2013. Determination of Polyparameter Linear Free Energy Relationship (pp-LFER) substance descriptors for established and alternative flame retardants. Environ. Sci. Technol. 47 (3), 1399–1406.
Tang, B., Poma, G., Bastiaensen, M., Yin, S., Luo, X., Mai, B., Covaci, A., 2019. Bioconcentration and biotransformation of organophosphorus flame retardants (PFRs) in common carp (Cyprinus carpio). Environ. Int. 126, 512–522.
Tsugoshi, Y., Watanabe, Y., Tanikawa, Y., Inoue, C., Sugihara, K., Kojima, H., Kitamura, S., 2020. Inhibitory effects of organophosphate esters on carboxylesterase activity of rat liver microsomes. Chem. Biol. Interact. 327, 109148.
van der Veen, I., de Boer, J., 2012. Phosphorus flame retardants: properties, production, environmental occurrence, toxicity and analysis. Chemosphere 88 (10), 1119–1153.
Wang, H., Huang, W., Gong, Y., Chen, C., Zhang, T., Diao, X., 2020. Occurrence and potential health risks assessment of polycyclic aromatic hydrocarbons (PAHs) in different tissues of bivalves from Hainan Island, China. Food Chem. Toxicol. 136, 111108.
Wang, S., Zheng, N., Sun, S., Ji, Y., An, Q., Li, X., Li, Z., Zhang, W., 2023. Bioaccumulation of organophosphorus flame retardants in marine organisms in Liaodong Bay and their potential ecological risks based on species sensitivity distribution. Environ. Pollut. 317, 120812.
Wang, X., Zhong, W., Xiao, B., Liu, Q., Yang, L., Covaci, A., Zhu, L., 2019. Bioavailability and biomagnification of organophosphate esters in the food web of Taihu Lake, China: impacts of chemical properties and metabolism. Environ. Int. 125, 25–32.
Xie, Z., Zhang, X., Liu, F., Xie, Y., Sun, B., Wu, J., Wu, Y., 2024a. First determination of elevated levels of plastic additives in finless porpoises from the South China Sea. J. Hazard. Mater. 465, 133389.
Xie, Z., Zhang, X., Xie, Y., Liu, F., Sun, B., Liu, W., Wu, J., Wu, Y., 2024b. Bioaccumulation and potential endocrine disruption risk of legacy and emerging organophosphate esters in cetaceans from the Northern South China Sea. Environ. Sci. Technol. 58 (9), 4368–4380.
Yan, Z., Feng, C., Xu, Y., Wang, J., Huang, N., Jin, X., Wu, F., Bai, Y., 2024. Water temperature governs organophosphate ester dynamics in the aquatic food chain of Poyang Lake. Environ. Sci. Ecotechnol. 21, 100401.
Ye, L., Li, J., Gong, S., Herczegh, S.M., Zhang, Q., Letcher, R.J., Su, G., 2023. Established and emerging organophosphate esters (OPEs) and the expansion of an environmental contamination issue: a review and future directions. J. Hazard. Mater. 459, 132095.
Ye, L., Xing, L., Li, J., Kong, M., Su, G., 2022. Recognition of Organophosphate Esters (OPEs) in the sediment of 12 Lakes in the Taihu Lake Basin of China. ACS ES&T Water 2 (12), 2450–2459.
Yin, H., Chen, Y., Ma, W., Zhu, W., Wang, H., Zhou, Q., Li, J., Wang, A., Li, X., Xu, Q., 2023. δ13C and δ15N stable isotopes demonstrate seasonal changes in the food web of coral reefs at the Wuzhizhou Island of the South China sea. Ecol. Indic. 146, 109852.
Zhang, L., Yang, X., Low, W.V., Ma, J., Yan, C., Zhu, Z., Lu, L., Hou, R., 2024. Fugacity- and biotransformation-based mechanistic insights into the trophic transfer of organophosphate flame retardants in a subtropical coastal food web from the Northern Beibu Gulf of China. Water Res. 261, 122043.
Zhao, H., Liu, L., Li, Y., Zhao, F., Zhang, S., Mu, D., Liu, J., An, L., Wan, Y., Hu, J., 2019. Occurrence, bioaccumulation, and trophic transfer of oligomeric organophosphorus flame retardants in an aquatic environment. Environ. Sci. Technol. Lett. 6 (6), 323–328.
Zhou, R., Geng, J., Jiang, J., Shao, B., Lin, L., Mu, T., Wang, B., Liu, T., 2024. Contamination of dairy products with tris(2,4-di-tert-butylphenyl) phosphite and implications for human exposure. Food Chem. 448, 139144.
Zhu, R., Pan, C., Peng, F., Zhou, C., Hu, J., Yu, K., 2024. Parabens and their metabolite in a marine benthic-dominated food web from the Beibu gulf, South China Sea: occurrence, trophic transfer and health risk assessment. Water Res. 248, 120841.

Journal of Hazardous Materials 496 (2025) 139512

Contents lists available at ScienceDirect

Journal of Hazardous Materials

journal homepage: www.elsevier.com/locate/jhazmat

Cytochrome P450-mediated biotransformation of octocrylene in *Tetradesmus obliquus*: Integrative insights from transcriptomics, proteomics, molecular docking, and density functional theory calculation

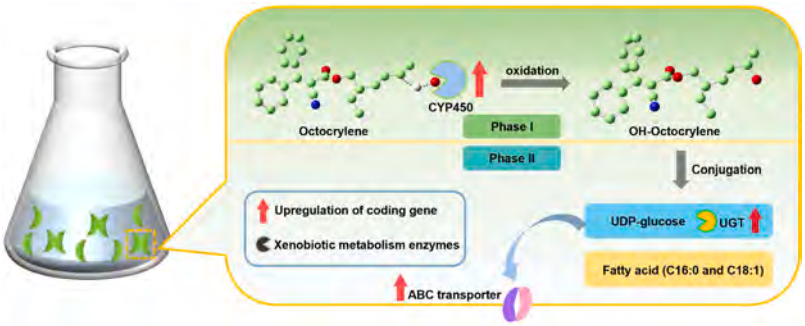
Jun-Jie Hu [a], Chang-Gui Pan [a,*], Xiang-Rong Xu [a,*], Feng-Jiao Peng [b,c], Shan Liu [a], Jiying Pei [a], Zhen-Zhu Liu [a], Hao Liang [a], Kefu Yu [a]

[a] *Guangxi Laboratory on the Study of Coral Reefs in the South China Sea, Coral Reef Research Center of China, School of Marine Sciences, Guangxi University, Nanning 530004, China*
[b] *Guangdong Provincial Key Laboratory of Chemical Pollution and Environmental Safety & MOE Key Laboratory of Theoretical Chemistry of Environment, SCNU Environmental Research Institute, South China Normal University, Guangzhou 510006, China*
[c] *School of Environment, South China Normal University, Guangzhou 510006, China*

HIGHLIGHTS

- *Tetradesmus obliquus* removed 95 % of OC in 10 days, mainly through biotransformation.
- Ten OC biotransformation products were identified, with 54.1 % being mono-hydroxylated.
- Seven CYP450s were significantly upregulated, confirming CYP450 involvement via ABT inhibition.
- Theoretical calculations indicate that CYP26-like mediates hydroxylation of the alkyl chain in OC.

GRAPHICAL ABSTRACT



ARTICLE INFO

Keywords:
Octocrylene
Tetradesmus obliquus
Cytochrome P450 enzymes
Biotransformation
Molecular docking

ABSTRACT

Octocrylene (OC), a sunscreen active ingredient, has received considerable attention due to its widespread occurrence and toxicity. However, little is known about its removal efficiency, elimination routes and the associated mechanisms by microalgae. Here, we investigated the removal efficiency, biotransformation products, pathways, and the cytochrome P450 (CYP450) catalytic reaction mechanism of OC by *Tetradesmus obliquus*. We found that *Tetradesmus obliquus* removed approximately 95 % of OC within 10 days, with biotransformation (82 %-99 %) being the primary removal route. Ten transformation products (TPs) were identified, of which mono-hydroxylated TPs accounted for 54.1 % of the total abundance. Transcriptomics and proteomics results both revealed that the expression of seven CYP450s was significantly upregulated, six of which were CYP26-like proteins. Furthermore, the non-specific CYP450 enzyme inhibitor 1-aminobenzotriazole (ABT) significantly inhibited the OC biotransformation rate, demonstrating the involvement of CYP450 in the biotransformation of OC in *Tetradesmus obliquus*. Molecular docking and DFT calculations jointly revealed that the specific binding conformation of OC with CYP26-like favored alkyl chain hydroxylation. Our findings demonstrate that

* Corresponding authors.
E-mail addresses: panchanggui@gxu.edu.cn (C.-G. Pan), xuxr@gxu.edu.cn (X.-R. Xu).

https://doi.org/10.1016/j.jhazmat.2025.139512
Received 9 June 2025; Received in revised form 30 July 2025; Accepted 8 August 2025
Available online 10 August 2025
0304-3894/© 2025 Elsevier B.V. All rights are reserved, including those for text and data mining, AI training, and similar technologies.

Tetradesmus obliquus can efficiently degrade OC, providing new insights for developing green and sustainable removal methods for emerging contaminants like OC.

1. Introduction

The global sunscreen market has experienced continuous growth due to increasing public awareness of UV-induced skin damage, including sunburn and skin cancer [39]. Among the most widely used UV filters, octocrylene (OC) holds a dominant position, accounting for 36.6 % of the market in Asia, 55.8 % in Europe, 52.0 % in North America, 74.0 % in South America, and 48 % in Australia as of 2021 [10]. However, OC's persistence in the environment poses significant concerns due to its resistance to photolysis and hydrolysis [16,30,42]. For example, OC has been shown to remain stable in surface water for over 144 h without degradation [48]. Additionally, conventional wastewater treatment plants (WWTPs) fail to effectively remove OC [63], allowing it to enter aquatic ecosystems through treated effluents and recreational water activities [41]. Environmental concentrations of OC have been reported to reach up to μg/L levels, with extremes exceeding 10^3 μg/L [15,58]. Due to its high lipophilicity (log K_{ow} = 6.88), OC can accumulate in aquatic organisms across various trophic levels [54], raising potential risks for non-target organisms. Adverse effects include endocrine disruption and growth inhibition as demonstrated in *Danio rerio*, where antiestrogenic, antiandrogenic, and estrogenic effects were observed [69]. Likewise, OC has been shown to inhibit the growth of marine species such as *Paracentrotus lividus* (sea urchin), *Mytilus galloprovincialis* (marine mussel) and *Artemia salina* (brine shrimp), with mortality occurring at concentrations between 100 μg/L to mg/L [22,55]. These findings underscore OC's toxicity to aquatic organisms and highlight the need for mitigation strategies.

Microalgae, as primary producers, constitute a significant biomass in various aquatic environments [50]. They play crucial ecological roles, such as providing oxygen and serving as the foundation of aquatic food webs [53]. Beyond their ecological importance, microalgae are utilized in industries for products like biofuels, nutritional supplements, cosmetics as well as wastewater treatment, highlighting their economic and environmental significance [4]. Among microalgal species, *Tetradesmus obliquus*, a green microalga commonly found in freshwater habitats, is noted for its rapid growth rate and robust adaptability to various environmental conditions [49,72]. This species has demonstrated efficacy in removing emerging contaminants (ECs), such as climbazole (CBZ), levofloxacin (LEV), and 17α-ethinyl estradiol (EE2) [50,51,66]. For example, *Tetradesmus obliquus* removed 23–29 % of benzophenone-3 (BP-3) mainly by biotransformation within 10 days [32]. Additionally, the heterotrophic microalga *Chromochloris zofingiensis* exhibited 76–97 % removal of LEV via biosorption and biotransformation processes [52]. The primary mechanism of EC removal by microalgae involved bioaccumulation, biotransformation and biosorption [29,51,68]. However, such studies have focused mostly on the removal rates and pathways, with the underlying molecular and biochemical mechanisms remaining largely unknown. This knowledge gap underscores the need for further research to elucidate the detailed processes governing microalgal remediation of ECs.

Cytochrome P450 (CYP450) enzymes, key members of the heme monooxygenase superfamily, play pivotal role in the metabolism of both endogenous and exogenous compounds in organisms [34]. These enzymes are recognized as key mediators of biotransformation for ECs, catalyzing reactions such as hydroxylation, oxidation, and decarboxylation [13]. For instance, CYP450 in zebrafish has been shown to mediate the formation of C5-OH and C6-OH hydroxylated metabolites from 2-ethylhexyl diphenyl phosphate (EHDPHP) [70]. Similarly, CYP450 participated in the metabolism of sulfamethoxazole (SMX) in *Chlorella sorokiniana* [13]. Despite their importance, our understanding of CYP450-mediated catalytic process remains limited, with only a few studies exploring their activity toward organic contaminants [17,61,74]. CYP450 was shown to drive microalgal biotransformation of bisphenol A (BPA), SMX and ciprofloxacin (CIP) through inhibitor assays, metabolomics, and molecular docking [12]. Here, we hypothesize that *Tetradesmus obliquus* can effectively remove OC through CYP450-mediated biotransformation, considering that the long carbon chains in OC that are amenable to such enzymatic modification [54,6]. However, it is crucial to note that biotransformation products may exhibit greater persistence, toxicity, or bioaccumulation potential than the parent compound (OC) itself [29]. Therefore, elucidating the structures and environmental behaviors of OC's transformation products is essential to understanding its fate, transport, and potential ecological risks in aquatic systems.

Thus, the present study aimed to achieve three primary objectives: i) to evaluate the efficiency and pathways of OC removal by *Tetradesmus obliquus*; ii) to identify the biotransformation products of OC, elucidate their formation pathways, and assess the associated toxicological risks; and iii) to investigate the catalytic mechanism of CYP450-mediated OC biotransformation in *Tetradesmus obliquus*. Collectively, the present study provides novel insights into the role of CYP450 in OC biotransformation within algal systems. The results not only advance out understanding of microalgal detoxification mechanism but also provide a scientific foundation for developing eco-friendly strategies for environmental remediation of OC and related contaminants.

2. Materials and methods

2.1. Chemicals and Tetradesmus obliquus culture

Octocrylene (OC, >98 %) was obtained from TCI (Tokyo, Japan). Dimethyl sulfoxide (DMSO) and LC-MS grade methanol were acquired from Macklin (Shanghai, China) and Sigma-Aldrich (St. Louis, Missouri, USA), respectively. Nitrogen-containing BG-11 culture medium stock solution (1000 ×) was purchased from Leding Tec (Shanghai, China).

Unicellular green alga *Tetradesmus obliquus* (FACHB-12) was purchased from the Freshwater Algae Culture Collection at Institute of Hydrobiology of Chinese Academy of Sciences (Wuhan, China). Microalgae were inoculated in sterile BG11 medium at pH of 7.0 ± 0.1. The algae were maintained in a climate chamber under controlled conditions of temperature (23.0 ± 0.2 °C), light intensity (3500 ± 100 *lux*), and a light-dark cycle of 12–12 h. Algae under exponential growth phase were collected for subsequent experiments.

2.2. Experimental setup

Tetradesmus obliquus in exponential growth phase was inoculated into 300 mL conical flasks, generating an initial algal cell density of approximately 4 × 10^5 cells/mL in 200 mL of BG11 medium. Four different treatments were performed: solvent control (0.01 % DMSO), 500 μg/L OC without algae (control), 500 μg/L OC with dead algae (control), and 500 μg/L OC with alive algae. Additionally, to investigate the role of CYP450 in the biotransformation of OC in algae, two more treatment groups were also conducted using 1-aminobenzotriazole (ABT; a non-specific inhibitor of CYP450 enzyme): ABT treatment group (5 μM) and ABT + OC treatment group (5 μM ABT + 500 μg/L OC) (Fig. S1). 5 μM ABT was validated in preliminary experiments and widely used in microalgae studies [13,60]. The flasks were shaken three times and repositioned daily to prevent uneven light exposure. The experimental conditions were the same as the culture conditions. All experiments were performed in triplicate, and lasted for 10 days. Measurements were conducted as follows: algal density and OC

concentration were measured every two days (days 0, 2, 4, 6, 8, and 10), OC biotransformation products were analyzed every five days (days 5 and 10), and transcriptome and proteomics analyses were performed after 10 days of exposure (day 10).

2.3. Determination of cell density

To investigate the effects of OC and ABT on algal growth, cell density was determined using a hemocytometer under an optical microscope. The optical density (OD) at 680 nm was measured using a microplate reader (Thermo Fisher, USA). A linear relationship between cell density (cells/mL) and OD_{680} was established, and the equation is provided below [25]:

$$\text{Cell density (cells/mL)} = 1.35\times 10^7 \times OD_{680} + 2.49 \times 10^4 \quad (1)$$

2.4. Removal of OC by algae

To determine OC concentrations in the culturing solution, 10 mL of algal solution was centrifuged at 3000 rpm for 10 min, and the supernatant was collected. The resultant algal cells were used to determine the amount of adsorbed (biosorption) and accumulated (bioaccumulation) OC. For biosorption, the algal cells were resuspended in 1 mL of 2:8 methanol/water, vortexed for 30 s, and centrifugated for 10 min at 3000 rpm. This procedure was repeated twice, and the resultant supernatants were combined for the determination of OC adsorbed onto the algal cells. Meanwhile, the resultant pellets were used to measure bioaccumulation by subjecting them to repeated freeze-thaw cycles and ultrasonic treatment, extraction with 1 mL of methanol each, vortex, and centrifugation (3000 rpm, 10 min). Details on calculating removal efficiency (R) and biotransformation rate (P_b), the pseudo-first-order kinetic model, and the Gompertz model are provided in Text S1.

2.5. OC and its transformation products (TPs) analysis

OC concentration was determined using an Agilent 1290 ultrahigh-performance liquid chromatography system coupled to a 6460 triple-quadrupole mass spectrometer (LC-MS/MS, Agilent, USA). Details on the LC-MS/MS parameters are shown in Table S1.

OC metabolites in algae were extracted following the method previously reported with minor modifications [67]. Briefly, at day 5 and day 10, 35 mL of algal solution from both the solvent control and the 500 μg/L OC treatment group were collected and centrifuged at 3000 rpm for 10 min. The pellet was subjected to ultrasonic disruption, followed by extraction with 1 mL of methanol. The mixture was vortexed for 30 s and then centrifuged. The supernatant was filtered through a 0.22 μm organic phase syringe filter. OC metabolites were then determined using an ultra-high-performance liquid chromatography system coupled to Q exactive™ plus hybrid quadrupole-orbitrap™ mass spectrometer (UHPLC-QE-Orbitrap-MS, Thermo Fisher Scientific, the United States). The spectra were analyzed using Compound Discoverer (CD) 3.3. The expected metabolite ID workflow was used to identify TPs, which were required to have a maximum mass error of less than 5 ppm accompanied by MS/MS spectra. Additionally, previous studies were used to assist in the TPs identification [54,6]. The instrument parameters and associated details are described in Text S2.

2.6. Transcriptomic and proteomic analysis

Transcriptomic and proteomic analysis were conducted in the solvent control group (DMSO) and the 500 μg/L OC treatment group on the 10th day to investigate changes in the expression of genes and proteins associated with biotransformation (such as CYP450 and ABC transporters) in *Tetradesmus obliquus* under OC exposure. Specifically, 200 mL of algal solution was centrifuged at 4000 rpm for 10 min, and the resultant pellet was washed twice with PBS (pH = 7), frozen in liquid nitrogen and stored at −80 °C. Detailed information on transcriptomics and proteomics analysis is provided in Text S3 and Text S4.

The reference genome version for transcriptomics and proteomics was GCA_030272155.1(https://www.ncbi.nlm.nih.gov/datasets/genome/GCA_030272155.1/). Differential expression genes (DEGs) were identified with p-value < 0.05 (Wald test) and an absolute log2-fold change > 0.585. Differential expression proteins (DEPs) were identified with p-value < 0.05 (student's t-test) and an absolute log2-fold change > 0.263. Gene ontology (GO), Kyoto Encyclopedia of Genes and Genomes (KEGG), and Swiss-Prot were used to note DEGs and DEPs functions.

2.7. In silico prediction and theoretical calculation

Quantum chemical calculations were conducted to investigate the structure-activity relationship of OC and the reactivity of active sites. Details of the density functional theory (DFT) calculations are provided in Text S5 [38]. The specific parameters for molecular docking are outlined in Text S6. The Cartesian coordinates of atoms, molecular docking parameters, and detailed docking results are provided in Tables S2-S4. Pairwise and multiple sequence alignments of protein sequences were performed using EMBOSS Needle and Clustal Omega [40], respectively, and visualized with Jalview [62]. Protein surface hydrophobicity was analyzed and visualized using ChimeraX 1.9 [44].

The ECOSAR Class Program (version 1.11) was used to assess toxic effects of OC and its TPs in aquatic environments. The toxicity of a chemical was classified according to the calculated $\log_{10}$ LC_{50}/EC_{50} values: very toxic ($\log_{10}$ $LC_{50}/EC_{50} < 0$), toxic ($0 < \log_{10}$ $LC_{50}/EC_{50} < 1$), harmful ($1 < \log_{10}$ $LC_{50}/EC_{50} < 2$), and not harmful ($2 < \log_{10}$ LC_{50}/EC_{50}) [21]. Subsequently, we used Swiss Target Prediction (http://www.swisstargetprediction.ch/) to predict the potential human protein targets of OC and its TPs by selecting targets with a probability greater than 0.1 ($P > 0.1$) for visualization using Cytoscape [71].

2.8. Statistical analyses

Statistical analyses were performed using SPSS (IBM, Statistics 26, USA). The normality of data was examined using Shapiro-Wilk test, and the homogeneity of variance between groups was checked by Levene's test. Normality (Shapiro-Wilk) and variance homogeneity (Levene's) were assessed at $\alpha = 0.05$. $p > 0.05$ indicated no significant deviations from assumptions. Significant differences in cell density between the treatment and control groups were estimated using one-way ANOVA, followed by least significant difference (LSD) test for multiple comparisons. For ANOVA, a statistically significant result ($p < 0.05$) indicates that at least two groups differ significantly. Subsequent post-hoc tests (LSD) with $p < 0.05$ identify which specific pairs of groups exhibit significant differences. The heatmaps of protein sequence identity and similarity were created using Chiplot (https://www.chiplot.online/), while other figures were generated with Origin 2024.

3. Results and discussion

3.1. OC removal by Tetradesmus obliquus

The cell density of *Tetradesmus obliquus* in 500 μg/L OC treatment group was slightly lower than the control group throughout the exposure, with the difference reaching approximately 10 % by the end of exposure (Fig. S2a). After 10 days, OC concentration decreased slightly in the abiotic group (without algae, < 5 %), suggesting negligible photolysis and hydrolysis of OC during the exposure period (Fig. S3). On the other hand, in the presence of *Tetradesmus obliquus*, OC concentration decreased by more than 90 % at the end of the exposure, demonstrating that biotic reactions were the main routes for OC removal.

Indeed, the OC removal observed here was primarily attributed to biotransformation (82 %-99 %) and bioaccumulation (1 %-17 %) (Fig. S2b), suggesting the important role of intracellular enzymes in the OC removal process. The Gompertz model fitted better than the pseudo-first-order kinetics model ($R^2 = 0.914$ and 0.868, respectively) (Fig. S2c-d). In this study, *Tetradesmus obliquus* required an adaptation period (lag phase) of approximately 0.8 days before transitioning into the exponential clearance phase of OC [9].

3.2. Identification of OC transformation products (TPs)

Ten TPs were identified with mass errors less than 5 ppm, seven of which are phase I TPs (TP249, TP359, TP375, TP377-Ph, TP377, TP391, and TP393; Where "xxx" in TPxxx denotes the relative molecular weight) while the remaining are phase II TPs (TP539, TP615 and TP641) (Fig. 1). The MS and MS/MS spectra of these TPs are shown in Fig. S4-S35. Among phase I TPs, both TP249 and TP359 were identified by fragments of *m/z* 250.08626 ($C_{16}H_{12}O_2N^+$), *m/z* 232.07569 ($C_{16}H_{10}O_2N^+$), and *m/z* 204.08078($C_{15}H_{12}N^+$) (Fig. S36). TP249 is known as 2-cyano-3,3-diphenylacrylic acid (CPAA) and a metabolite generated from the ester hydrolysis of OC [6], whereas TP359 was discovered for the first time for OC. Similarly, TP375, TP391 and TP393 were identified through the Na^+ adduct ions ($NaC_{16}H_{11}O_2N^+$, *m/z* 272.06820; Fig. S36). TP375 was identified as a carbonylated metabolite on the 2-ethylhexyl chain based on the fragment ions of *m/z* 272.06820 and *m/z* 127.11229 ($C_8H_{15}O^+$) (Fig. S36). Moreover, TP375 was likely a ketone metabolite as here we did not seek to identify carboxylated metabolites of OC. TP391 was identified by ions of *m/z* 272.06820 and *m/z* 288.06366, which suggests the occurrence of phenolic hydroxylation on the phenyl ring. In addition, other ions including *m/z* 165.08915 ($NaC_8H_{14}O_2^+$) and *m/z* 143.10720 ($C_8H_{15}O_2^+$) were also observed for TP391 (Fig. S36), which further confirms the occurrence of oxidation on the 2-ethylhexyl chain. TP391 was therefore a mono-carbonyl and mono-hydroxylated metabolite rather than a carboxylated metabolite. TP393 was identified as a dihydroxylation product by fragment ions of *m/z* 272.06820 and *m/z* 167.10480 ($NaC_8H_{16}O_2^+$) (Fig. S36). Unfortunately, phenyl ring hydroxylation was not observed for the di-hydroxylated metabolite, possibly due to low signal response and the lack of MS/MS spectra. Regarding TP377, it was a mono-hydroxylated metabolite identified through fragments of *m/z* 250.08626, *m/z* 232.07569 and *m/z* 204.08078, suggesting the occurrence of hydroxylation on the 2-ethylhexyl chain. Similarly, previous studies reported that 5-OH OC was a major product of alkyl chain hydroxylation of OC in *in vitro* studies, human urine, and coral symbionts [23,5,54,6]. Two additional fragments, *m/z* 272.06820 and *m/z* 288.06366 ($NaC_{16}H_{11}O_3N^+$), were also observed for TP377, indicating the simultaneous occurrence of hydroxylation on the phenyl ring, which was further confirmed by the detection of TP377-Ph.

Among phase II TPs, OC-glucoside conjugate (TP539) was identified through *m/z* 272.06820 and 2-ethylhexyl chain adduct with the glucoside ion ($NaC_{14}H_{26}O_6^+$, *m/z* 313.16174), which was reported for the first time for OC. In the MS/MS spectra of the sodium adduct ion, diagnostic fragment ions of *m/z* 382.17780 ($NaC_{24}H_{25}NO_2^+$) and *m/z* 272.06820 confirmed the presence of the two fatty acid conjugates, TP615 and TP641. It should be noted that fatty acid conjugates are extremely rare for natural biotransformation products of exogenous compounds. Nonetheless, because fatty acid conjugation would substantially increase compound's lipophilicity and thereby hinder its metabolism [54,8], we speculated this might be a strategy used by microalgae to reduce the bioavailability of OC, similar to acetylation and methylation in phase II metabolism reactions [18]. Likewise, fatty acid conjugates have been observed in coral symbionts and worms [14,54,56].

3.3. Proposed biotransformation pathway and toxicity assessment of TPs

Apart from the two newly reported TPs of 2-ethylhexyl chain desaturation (TP359) and OC-glucoside conjugate (TP539) (Fig. 1), the remaining eight TPs have been identified in human urine and coral symbionts as well [54,6]. As hydroxylation in the phase I metabolism serves as a prerequisite for the subsequent formation of oxidation/hydroxylation metabolites and phase II conjugation products, we provided a semi-quantitative assessment of the relative contributions of

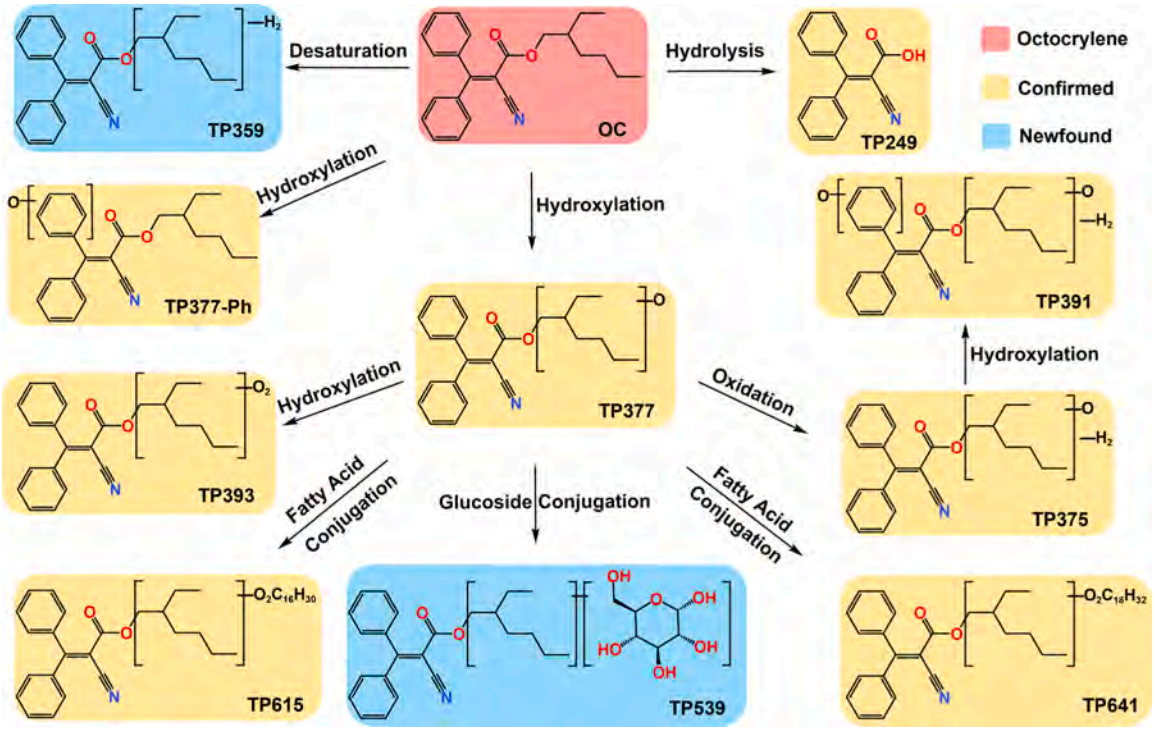


Fig. 1. Proposed transformation products and biotransformation pathways of OC by the green alga *Tetradesmus obliquus*. Where "xxx" in TPxxx denotes the relative molecular weight.

individual TPs based on their corresponding peak areas (Fig. 2a). On the 5th day, the proportions of phase I biotransformation products were 54.1 % for mono-hydroxylation (TP377 and TP377-Ph), 21.3 % for oxidation (TP375), 2.4 % for hydrolysis (TP249), 2.1 % for hydroxylation-oxidation (TP391), 1.8 % for di-hydroxylation (TP393) and 1.0 % for desaturation (TP359). Regarding the phase II biotransformation products, the proportions were 2.5 %, 7.2 %, and 7.6 % for glucoside conjugate (TP539), C16:0 fatty acid conjugate (TP615) and C18:1 fatty acid conjugate (TP641), respectively. Therefore, the mono-hydroxylation metabolites (TP377 and TP377-Ph) were the major identified TPs, with the 2-ethylhexyl chain hydroxylation metabolite (TP377) accounting for 97 % of the mono-hydroxylation products. In contrast to the OC metabolism in humans, hydroxylation rather than hydrolysis products dominated the TPs in microalgae [7]. However, on day 10, most of the TPs dissipated (e.g., TP249, TP391, etc., Table S5), with the abundance of all hydroxylated and hydrolyzed metabolites (TP249, TP377, TP377-Ph, TP391 and TP393) decreasing significantly by approximately 96.4–100 % as compared to day 5. Such reduction is likely due to their increased hydrophilicity, which facilitates their excretion from the algal cells. However, 7.8–10.2 % of the two fatty acid conjugates were retained (TP615 and TP641). None of the 10 metabolites were detected in the culture medium after 10 days, suggesting they may have undergone further degradation.

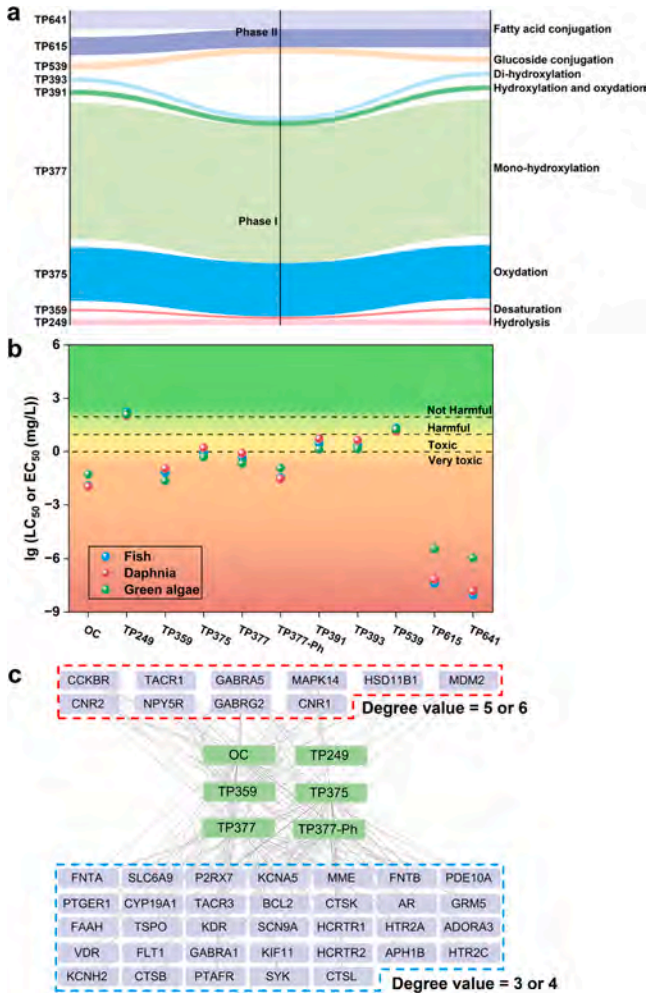


Fig. 2. The abundance (Peak area-based semi-quantification) (a), aquatic toxicity (b) and compounds-targets network (c) of OC biotransformation products. The abundance in (a) was measured on the day 5. The aquatic toxicity in (b) was predicted using ECOSAR. The compounds-targets network in (c) was created using Cytoscape and Swiss Target Prediction. The degree value indicates the number of compounds associated with a given target.

All observed TPs except TP359, TP615 and TP641 presented lower aquatic toxicity (fish, daphnia and green algae) than OC (according to ECOSAR, Fig. 2b and Table S6), which is probably related to the elevated hydrophilicity caused by the increased number of hydroxyl groups (e.g., TP377, TP393 and TP539), a common detoxification mechanism in organisms [11]. While TP359 showed relatively higher acute toxicity to green algae only, the two fatty acid conjugates (TP615 and TP641) exhibited relatively higher aquatic toxicity to fish, daphnia and green algae, possibly caused by elevated hydrophobicity. As a prior study of toxic effects of BP-3 (another sunscreen) on corals has demonstrated the phototoxicity of BP-3-glucoside [59], attention should be paid to the potential phototoxicity of OC-glucoside conjugates. Additionally, we identified 282 protein targets for six of the 11 examined compounds (OC, TP249, TP359, TP375, TP377 and TP377-Ph) using Swiss Target Prediction, which are related to growth and development, cardiovascular, neurological and immune system diseases (Fig. 2c).

3.4. Genes and proteins associated with biotransformation

Transcriptomic and proteomic analyses enable high-throughput screening of differentially expressed genes and proteins, revealing key factors in OC biotransformation [36,37]. The expression of a total of 13 genes along with their encoding proteins were simultaneously significantly upregulated, namely CYP450-monooxygenase (n = 7), Cu-monooxygenase (n = 1), UDP-glucuronosyltransferase (UGT) (n = 2) and ABC transporters (n = 3) (Fig. 3a and Table S7). Xenobiotic metabolism comprises both biotransformation and transport processes, which are involved in detoxification of exogenous compounds [57]. CYP450 are key enzymes participating in the metabolism of both endogenous and exogenous compounds, degrading substances primarily through oxidation and occasionally through dehydrogenation and hydrolysis [24]. They can biotransform lipophilic exogenous chemicals into more water-soluble compounds for excretion [65]. Here, we found significant upregulation (log_2FC of gene expression = 1.25–10.99, log_2FC of protein abundance = 1.12–5.00) of eight monooxygenase genes (OEZ86_000961, OEZ86_003108, OEZ86_003232, OEZ86_004050, OEZ86_004193, OEZ86_008212, OEZ86_011280 and OEZ86_013322) along with their encoding proteins (WIA30909.1, WIA32262.1, WIA32405.1, WIA35635.1, WIA35805.1, WIA36975.1, WIA28746.1 and WIA39880.1, respectively; coding gene names were used in the subsequent discussion to represent their corresponding proteins), which matches well our discovered biotransformation products. Therefore, we further performed BLASTP searches and domain analysis (https://www.ebi.ac.uk/interpro/; https://pantherdb.org) on these eight protein sequences to uncover their potential functions. BLASTP results showed that these proteins had the highest sequence identity (30.24 %-63.55 %) with CYP450s from *Monoraphidium sp.* (green algae) and were well-clustered within the CYP450 family of green algae (Figs. S37-S44). Domain analysis revealed that OEZ86_000961 and OEZ86_011280 were annotated as ABA-like proteins (abscisic acid hydroxylase) and DBH-like proteins (dopamine β-hydroxylase), respectively. Both ABA-like and DBH-like proteins mediate the hydroxylation of ABA and dopamine [2,35], respectively, with the hydroxylation sites located on their carbon chains. This suggests their potential activity in OC hydroxylation. The remaining proteins were classified as either CYP26-like proteins (retinoic acid hydroxylases in animals, uncharacterized) or CYP120A1-like proteins (retinoic acid hydroxylases in cyanobacteria, characterized) based on sequence similarity (Fig. 3b), indicating potential functional or substrate similarities. The representative proteins of the CYP26 family were CYP26A1, CYP26B1, and CYP26C1, which shared retinoic acid (RA) as their common substrate. This finding is intriguing, as some eukaryotic microalgae, such as *Chlamydomonas sp.*, have been reported to produce RA and its metabolites (e.g., at-4-oxo-retinoic acid) [64]. However, no such enzymes have been characterized or even mentioned in eukaryotic microalgae to date. The six CYP26-like proteins were compared pairwise, and they were

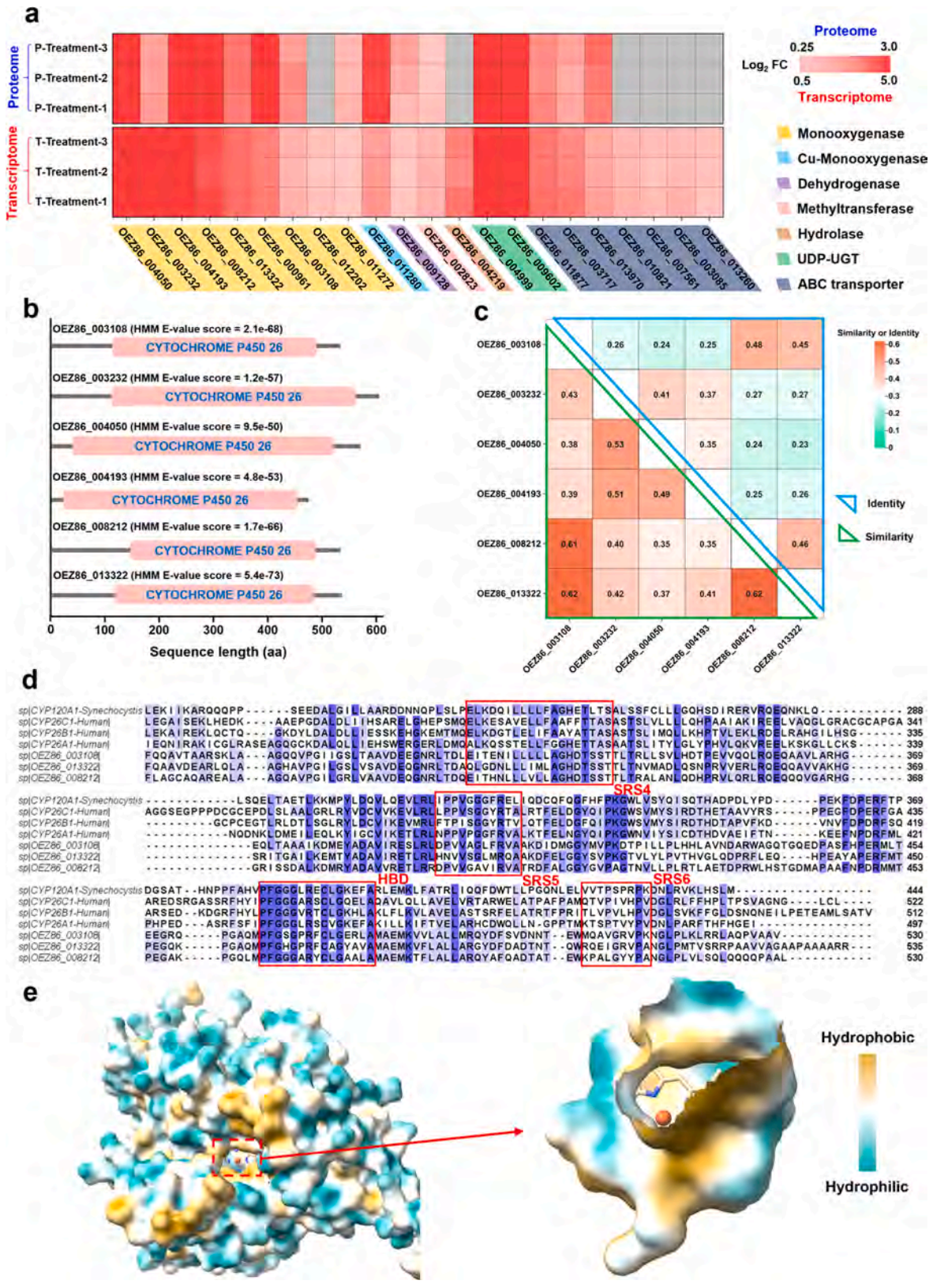


Fig. 3. Analysis of genes and proteins participating in xenobiotic metabolism. a) Expression fold changes of differentially expressed genes (DEGs) and differentially expressed proteins (DEPs) related to xenobiotic metabolism, b) Domain identification of the six CYP26-like proteins using the PANTHER classification system, c) Pairwise sequence alignment of the six CYP26-like proteins, d) Multiple sequence alignment of the three CYP26-like proteins, CYP120A1 and CYP26 family proteins (Complete sequence comparison is shown in Fig S45.), and e) Hydrophobicity analysis of the OEZ86_008212 protein surface. Treatment-1, Treatment-2 and Treatment-3 indicate biological replicates. T and P represent transcriptome and proteome, respectively. SRS and HBD indicate substrate recognition site and heme-binding domain, respectively.

grouped into two categories based on sequence similarity (Fig. 3c). High sequence similarity typically suggests functional similarity. If multiple proteins catalyze the same substrate, this could result in functional redundancy [26]. Therefore, we speculated that these proteins might catalyze multiple substrates or oxidation sites, which aligns with the presence of multiple TP377 isomers. Notably, the three members of the CYP26 family (CYP26A1, CYP26B1, and CYP26C1) exhibit distinct catalytic site preferences [26]. This suggests that the two groups identified in this study may preferentially catalyze different sites of the same substrate. To further investigate the differences in the substrate recognition sites (SRSs) and heme-binding domain (HBD) between the target proteins and CYP120A1 and CYP26, we performed a multiple sequence alignment of a set of proteins (OEZ86_003018, OEZ86_008212, OEZ86_013322) with CYP120A1 and CYP26 (Fig. 3d, Fig. S45). Consistent with a previous study, the sequence identity in the SRS5 region near the HBD was relatively high [28], indicating similarity in substrate catalysis. The three-dimensional structures of the proteins were modeled using AlphaFold (Fig. 3e). Taking OEZ86_008212 as an example, its substrate-binding channel and pocket exhibited high hydrophobicity, resembling those of CYP120A1 [31]. This was not unexpected as both RA and OC are highly hydrophobic compounds (log K_{ow} = 6.3 and 6.88, respectively). Based on their metabolites, the hydrophilic ends of both substrates likely oriented away from the heme group to optimize the catalytic site.

Consistent with TP539, we found that UDP-glucuronosyltransferase-like genes and proteins (UGT3A1-like and UGT3A2-like) were significantly upregulated. Notably, UGT3A1 and UGT3A2 utilized UDP N-acetylglucosamine, UDP-glucose, and UDP-xylose as sugar donors, instead of UDP-glucuronic acid, to metabolize a wide range of endogenous and exogenous compounds [20,43]. The upregulation of ABC transport proteins may also lead to enhanced detoxification capacity of algae [3,47]. Similarly, expression dysregulation of ABC transporters has been observed in algal cells exposed to tylosin and erythromycin [33,45].

3.5. The role of CYP450 in OC biotransformation

The preceding results of this study collectively supported the mediating role of CYP450 in OC biotransformation. To further strengthen this speculation, we used the non-specific CYP450 inhibitor ABT to explore the actual role of CYP450 in the metabolism (Fig. 4a-d) [46]. In comparison with the OC group, the addition of 5 μM ABT significantly decreased OC bioaccumulation rates by 0.1 %-13.0 % from day 2, 4, 6 and 8 (Fig. S46), and decreased biotransformation rates (1.4 %-7.3 %) (Fig. 4b). These effects are likely due to the inhibition of CYP450 enzyme activity. Additionally, ABT extended the lag phase and half-life of OC removal (Fig. 4c-d and S47), thereby slowing the early-stage biotransformation of OC in the algae. Similarly, a previous study reported that 5 μM of ABT significantly reduced the removal efficiency of SMX by *Chlorella sorokiniana* [13]. Therefore, it is highly likely that OC removal was primarily attributed to biotransformation mediated by CYP450.

Considering that hydroxylation was identified as the main metabolic reaction of OC in *Tetradesmus obliquus*, we used DFT to calculate the highest occupied molecular orbital-lowest unoccupied molecular orbital (HOMO-LUMO) gaps and condensed Fukui function of OC (Fig. S48). We found that the electron-rich and electron-poor regions were concentrated on the phenyl, nitrile and ester groups, which were confirmed by the condensed Fukui function results. Meanwhile, the atoms C5 ($f^- = 0.0643$), N26 ($f^- = 0.1004$) and C24 ($f^- = 0.0872$) were identified as the most susceptible sites for electrophilic attack. These results suggested that the phenyl group was more prone to electrophilic reagent attack than the alkyl chain [70]. However, this computational prediction did not fully align with our experimental observations of TPs abundance. This discrepancy may be explained by enzymatic reaction pathways, as hydroxylation, a major metabolic transformation, was predominantly catalyzed by CYP450 enzymes [34]. In such reactions, the alkyl chain was more susceptible to hydroxylation than the phenyl ring [19].

Transcriptomics and proteomics analysis demonstrated significant upregulation of CYP26-like proteins in *Tetradesmus obliquus* under the

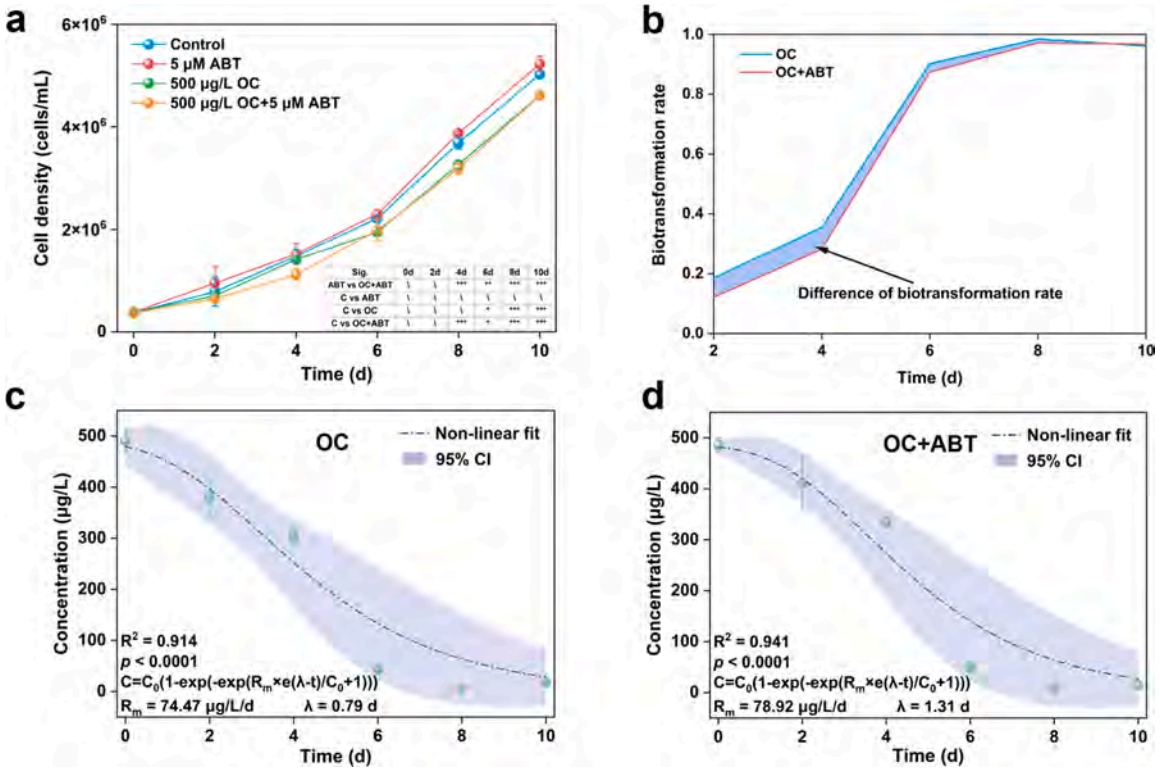


Fig. 4. Changes in algal cell density (a), OC biotransformation rates within 10 days with or without ABT addition (b), and Gompertz models for OC biotransformation in the OC (c) and OC+ABT (d) treatment groups. *, **, and *** represent $p < 0.05$, $p < 0.01$, and $p < 0.001$, respectively (post-hoc test: LSD).

OC exposure. CYP26 protein catalyzes RA mainly via hydroxylation [31], with the carbon chain of RA serving as the binding site [1]. Given the structural similarity between RA and OC, OC might be a substrate for CYP26-like proteins as well. Hence, we further conducted molecular docking of OC with CYP26-like proteins using AutoDock Vina. We employed the AlphaFold and Swiss-Model for protein modeling. With the exception of OEZ86_003108, which was modeled using CYP120A1 (PDB: 2VE4) as a homology template, all other proteins were predicted via AlphaFold. The results showed that all CYP26-like proteins met the criteria for molecular docking (Fig. S49, Table S8).

Six CYP26-like proteins exhibited strong binding affinity with OC, primarily mediated by van der Waals forces and hydrogen bonds, with binding energies ranging from −9.1 to −7.2 kcal/mol (Fig. 5a). For all CYP26-like proteins, RA and OC exhibited comparable binding energies, ranging from −9.4 to −7.3 kcal/mol. These results suggest that OC has the binding affinity required to serve as a substrate for CYP26-like enzymes (Fig. S50). However, the β-ionone ring of RA was positioned closer to the heme group rather than the long alkyl chain, consistent

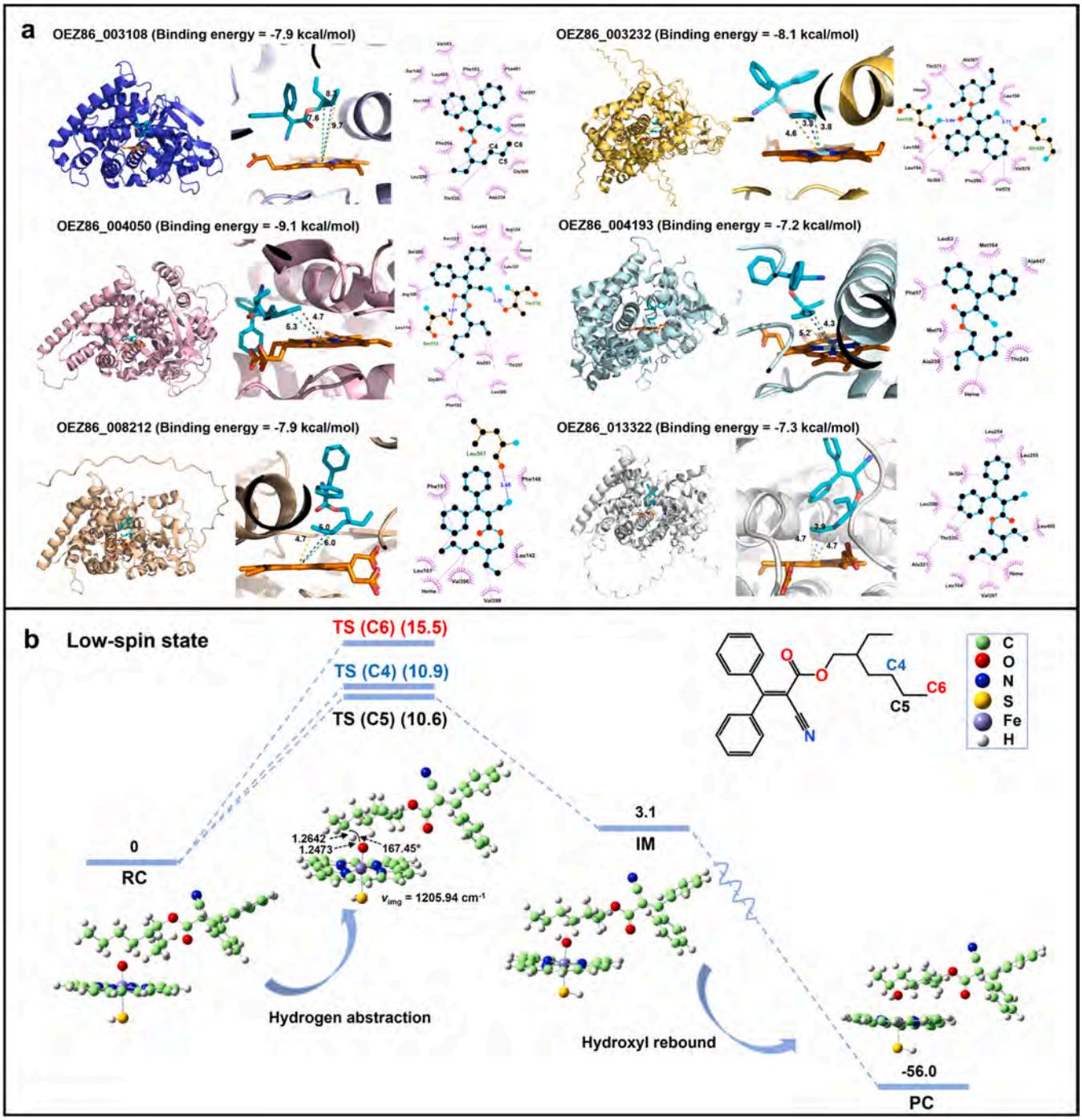


Fig. 5. Molecular docking of CYP26-like (OEZ86_003108, OEZ86_003232, OEZ86_004050, OEZ86_004193, OEZ86_008212 and OEZ86_013322) with OC (a) and energy profiles (in kcal/mol) for C-H abstraction and hydroxyl rebound of OC by Cpd I (b). The complete catalytic pathway was calculated exclusively for the hydroxylation occurring at C5. The distance between proteins and molecules was measured in angstroms (Å). In the 2D interaction diagram, purple and green dashed lines represent hydrophobic interaction and hydrogen bond, respectively. Abbreviation: Ala, alanine; Thr, threonine; Phe, phenylalanine; Pro, proline; Gly, glycine; Trp, tryptophan; Val, valine; Hem, heme; RC, reactant complex; TS, transition state; IM, intermediate; PC, product complex.

with the structure of its metabolic products [1]. Analysis of the binding conformations revealed that the alkyl chains of the six CYP26-like proteins were closer to the heme group than phenyl groups. Specifically, the distances between the iron atom at the heme center and the C4, C5, and C6 atoms were shorter than those of other atoms. This indicates that these three carbon atoms were more likely to be catalyzed by the active sites of CYP26-like proteins, owing to their strong binding affinity and specific conformational arrangement.

To further investigate the mechanism of OC hydroxylation, we calculated the reaction potential energy distribution and structure of the CYP450 active site with OC. In this study, only the low-spin (LS) state of Cpd I was considered. Previous reports indicate that reactions involving the high-spin (HS) state exhibit comparable or higher energy barriers [13,19,73]. The results showed that hydrogen abstraction (HAT) and hydroxyl rebound were the primary mechanisms for CYP450-mediated OC hydroxylation (Fig. 5b). HAT was identified as the rate-limiting step of the catalytic reaction. C5 (10.6 kcal/mol) exhibited a kinetic advantage over C4 (10.9 kcal/mol) and C6 (15.5 kcal/mol) during this step, as reflected in the condensed Fukui function (f^-), indicating that hydroxylation at C5 was more favorable. A previous study reported that C5 of EHDHPH had a lower hydrogen abstraction energy barrier than C6 of EHDHPH, facilitating the hydroxylation at C5 position [70]. Therefore, a complete catalytic pathway was calculated exclusively for the hydroxylation at the C5 position. Initially, the oxygen atom in Cpd I abstracts a hydrogen atom from the C5 position of OC, with a C-H-O bond angle reaching 167.45° and a distance of 1.25 Å between the abstracted hydrogen and the Fe^{IV}=O moiety in Cpd I. After hydrogen abstraction, an iron-hydroxy intermediate (IM) is formed [73]. Subsequently, the -OH radical rebounds from the iron-hydroxy group to the C5 position of the substrate, completing the reaction. The -OH rebound step proceeded without any barriers in the low-spin state [27], releasing approximately 59.1 kcal/mol of heat. Collectively, transcriptomics, proteomics, molecular docking and DFT calculation suggest that CYP26-like proteins are likely to be the primary proteins responsible for the hydroxylation of OC.

4. Conclusions

This study confirms the capability of *Tetradesmus obliquus* to effectively biotransform OC in aquatic environments, primarily via enzymatic processes. The biotransformation pathway was dominated by mono-hydroxylation, indicating a specific catalytic role of CYP450 enzymes. Transcriptomic and proteomic analyses highlighted significant activation of several CYP450s, particularly CYP26-like proteins, during the process. The use of the CYP450 inhibitor ABT further demonstrated the critical role of these enzymes. Molecular docking provided insights into the binding interactions, showing a preference for hydroxylation at specific sites on OC's alkyl chain. These findings underscore the potential of *Tetradesmus obliquus* in addressing ECs through bioremediation, presenting an environmentally friendly approach to pollution mitigation. However, the environmental behavior and toxicity of the resulting biotransformation products require further investigation to ensure the safety and sustainability of this method. This study provides a feasible strategy for establishing green and sustainable pollutant removal systems. Future research could optimize microalgal-based platforms or microalgal-bacterial consortia to enhance the elimination of ECs.

Environmental implication

The study highlights that the green alga *Tetradesmus obliquus* can effectively biotransform octocrylene (OC) in aquatic environments, offering a sustainable complement to existing water treatment methods. Enzymes such as cytochrome P450 play a key role in this process, suggesting potential for degrading other emerging contaminants. The use of algae-based systems could enhance the removal of persistent pollutants while minimizing ecological disruption. However, further research on transformation products will help optimize this approach and ensure its safe application in natural and engineered water systems.

CRediT authorship contribution statement

Jun-Jie Hu: Writing – original draft, Investigation, Data curation. **Chang-Gui Pan:** Writing – review & editing, Supervision, Funding acquisition, Conceptualization. **Jiying Pei:** Writing – review & editing. **Shan Liu:** Writing – review & editing, Visualization. **Feng-Jiao Peng:** Writing – review & editing, Data curation. **Xiang-Rong Xu:** Writing – review & editing, Supervision, Funding acquisition, Conceptualization. **Kefu Yu:** Writing – review & editing, Resources. **Hao Liang:** Writing – review & editing, Investigation. **Zhen-Zhu Liu:** Writing – review & editing, Methodology.

Declaration of Competing interest

The authors declare that they have no known competing financial interests or personal relationships that could have appeared to influence the work reported in this paper.

Acknowledgments

The authors would like to thank the financial support by the National Natural Science Foundation of China (42207322), Guangxi Science and Technology Program (No. AD25069075), Guangxi Natural Science Foundation (2023GXNSFAA026488), and the Innovation Project of Guangxi Graduate Education (YCBZ2025069).

Appendix A. Supporting information

Supplementary data associated with this article can be found in the online version at doi:10.1016/j.jhazmat.2025.139512.

Data availability

Data will be made available on request.

References

[1] Alder, A., Bigler, P., Werck-Reichhart, D., Al-Babili, S., 2009. In vitro characterization of synechocystis CYP120A1 revealed the first nonanimal retinoic acid hydroxylase. FEBS J 276, 5416–5431. https://doi.org/10.1111/j.1742-4658.2009.07224.x.

[2] Amin, N., Afkhami, A., Hosseinzadeh, L., Akbarzadeh, F., Madrakian, T., Nabiabad, H.S., 2020. Ratiometric bioassay and visualization of dopamine β-hydroxylase in brain cells utilizing a nanohybrid fluorescence probe. Anal Chim Acta 1105, 187–196. https://doi.org/10.1016/j.aca.2020.01.046.

[3] Bártíková, H., Skálová, L., Stuchlíková, L., Vokřál, I., Vaněk, T., Podlipná, R., 2015. Xenobiotic-metabolizing enzymes in plants and their role in uptake and biotransformation of veterinary drugs in the environment. Drug Metab Rev 47, 374–387. https://doi.org/10.3109/03602532.2015.1076437.

[4] Bhatt, P., Bhandari, G., Turco, R.F., Aminikhoei, Z., Bhatt, K., Simsek, H., 2022. Algae in wastewater treatment, mechanism, and application of biomass for production of value-added product. Environ Pollut 309, 119688. https://doi.org/10.1016/j.envpol.2022.119688.

[5] Bury, D., Belov, V.N., Qi, Y., Hayen, H., Volmer, D.A., Brüning, T., et al., 2017. Determination of urinary metabolites of the emerging UV filter octocrylene by online-SPE-LC-MS/MS. Anal Chem 90, 944–951. https://doi.org/10.1021/acs.analchem.7b03996.

[6] Bury, D., Modick-Biermann, H., Leibold, E., Bruning, T., Koch, H.M., 2019. Urinary metabolites of the UV filter octocrylene in humans as biomarkers of exposure. Arch Toxicol 93, 1227–1238. https://doi.org/10.1007/s00204-019-02408-7.

[7] Bury, D., Weber, T., Ebert, K.E., Zülz, S., Brüning, T., Koch, H.M., et al., 2023. Increasing exposure to the UV filters octocrylene and 2-ethylhexyl salicylate in Germany from 1996 to 2020: human biomonitoring in 24-h urine samples of the German environmental specimen bank (ESB). Environ Int 182. https://doi.org/10.1016/j.envint.2023.108334.

[8] Casey Laizure, S., Herring, V., Hu, Z., Witbrodt, K., Parker, R.B., 2013. The role of human carboxylesterases in drug metabolism: have we overlooked their importance? Pharm J Hum Pharmacol Drug Ther 33, 210–222. https://doi.org/10.1002/phar.1194.

[9] Çelekli, A., Yavuzatmaca, M., Bozkurt, H., 2010. An eco-friendly process: predictive modelling of copper adsorption from aqueous solution on spirulina platensis. J Hazard Mater 173, 123–129. https://doi.org/10.1016/j.jhazmat.2009.08.057.
[10] Chaiyabutr, C., Pruksaeakanan, C., Wongdama, S., Prasertsook, S., Kumpangsin, T., Boonchai, W., 2023. Characteristics and common ultraviolet filter usage of sunscreens purchased online: cross-cultural analysis across 5 continents. Photodermatol Photoimmunol Photomed 39, 27–38. https://doi.org/10.1111/phpp.12808.
[11] Chen, F., Huber, C., May, R., Schröder, P., 2016. Metabolism of oxybenzone in a hairy root culture: perspectives for phytoremediation of a widely used sunscreen agent. J Hazard Mater 306, 230–236. https://doi.org/10.1016/j.jhazmat.2015.12.022.
[12] Chu, Y., Zhang, C., Chen, X., Li, X., Ren, N., Ho, S.-H., 2023. Multistage defense response of microalgae exposed to pharmaceuticals in wastewater. Chin Chem Lett 34, 107727. https://doi.org/10.1016/j.cclet.2022.08.007.
[13] Chu, Y., Zhang, C., Wang, R., Chen, X., Ren, N., Ho, S.-H., 2022. Biotransformation of sulfamethoxazole by microalgae: removal efficiency, pathways, and mechanisms. Water Res 221. https://doi.org/10.1016/j.watres.2022.118834.
[14] Clergeaud, F., Fagervold, S.K., Rodrigues, A.M.S., Thorel, E., Stien, D., Lebaron, P., 2022. Transfer of 7 organic UV filters from sediment to the ragworm hediste diversicolor: bioaccumulation of Benzophenone-3 and further proof of octocrylene metabolism. Pollutants 2, 23–31. https://doi.org/10.3390/pollutants2010004.
[15] Downs, C.A., Akerlof, K.L., Stien, D., Rodrigues, A.M.S., Diaz-Cruz, M.S., Quintana, G., et al., 2024. Sunscreen pollution is abated during the COVID-19 "Anthropause" of 2020 in two U.S. National parks: cape lookout national seashore and Kaloko-Honokōhau national historical park. J Sea Res 200, 102510. https://doi.org/10.1016/j.seares.2024.102510.
[16] Duis, K., Junker, T., Coors, A., 2022. Review of the environmental fate and effects of two UV filter substances used in cosmetic products. Sci Total Environ 808, 151931. https://doi.org/10.1016/j.scitotenv.2021.151931.
[17] Fang, H., Oberoi, A.S., He, Z., Khanal, S.K., Lu, H., 2021. Ciprofloxacin-degrading paraclostridium sp. Isolated from sulfate-reducing bacteria-enriched sludge: optimization and mechanism. Water Res 191. https://doi.org/10.1016/j.watres.2021.116808.
[18] Farrukh, M., Shahzadi, S., Irfan, M., 2024. Drug Metabolism: Phase I and Phase Ii Metabolic Pathways. Drug Metabolism and Pharmacokinetics. IntechOpen.
[19] Fu, Z., Chen, J., Wang, Y., Hong, H., Xie, H., 2018. Quantum chemical simulations revealed the toxicokinetic mechanisms of organic phosphorus flame retardants catalyzed by P450 enzymes. J Environ Sci Health Part C 36, 272–291. https://doi.org/10.1080/10590501.2018.1537564.
[20] Fujiwara, R., Sumida, K., Kutsuno, Y., Sakamoto, M., Itoh, T., 2015. UDP-glucuronosyltransferase (UGT) 1A1 mainly contributes to the glucuronidation of trovafloxacin. Drug Metab Pharmacokinet 30, 82–88. https://doi.org/10.1016/j.dmpk.2014.09.003.
[21] Gao, Y., Ji, Y., Li, G., An, T., 2014. Mechanism, kinetics and toxicity assessment of OH-initiated transformation of triclosan in aquatic environments. Water Res 49, 360–370. https://doi.org/10.1016/j.watres.2013.10.027.
[22] Giraldo, A., Montes, R., Rodil, R., Quintana, J.B., Vidal-Liñán, L., Beiras, R., 2017. Ecotoxicological evaluation of the UV filters ethylhexyl dimethyl p-aminobenzoic acid and octocrylene using marine organisms isochrysis galbana, mytilus galloprovincialis and paracentrotus lividus. Arch Environ Contam Toxicol 72, 606–611. https://doi.org/10.1007/s00244-017-0399-4.
[23] Guesmi, A., Ohlund, L., Sleno, L., 2020. In vitro metabolism of sunscreen compounds by liquid chromatography/high-resolution tandem mass spectrometry. Rapid Commun Mass Spectrom 34, e8679. https://doi.org/10.1002/rcm.8679.
[24] Hrycay, E.G., Bandiera, S.M., 2015. In: Hrycay, E.G., Bandiera, S.M. (Eds.), Monooxygenase, Peroxidase and Peroxygenase Properties and Reaction Mechanisms of Cytochrome P450 Enzymes, Monooxygenase, Peroxidase and Peroxygenase Properties and Mechanisms of Cytochrome P450. Springer International Publishing, Cham, pp. 1–61.
[25] Hu, J.-J., Pan, C.-G., Peng, F.-J., Liang, H., Liu, Z.-Z., Yu, K., 2025. An integrated multi-omics approach reveals octocrylene disrupts tetradesmus obliquus growth by triggering a cascade of photosynthetic inhibition and metabolic dysregulation. J Hazard Mater 495, 139072. https://doi.org/10.1016/j.jhazmat.2025.139072.
[26] Isoherranen, N., Zhong, G., 2019. Biochemical and physiological importance of the CYP26 retinoic acid hydroxylases. Pharmacol Ther 204, 107400. https://doi.org/10.1016/j.pharmthera.2019.107400.
[27] Ji, L., Ji, S., Wang, C., Kepp, K.P., 2018. Molecular mechanism of alternative P450-catalyzed metabolism of environmental phenolic endocrine-disrupting chemicals. Environ Sci Technol 52, 4422–4431. https://doi.org/10.1021/acs.est.8b00601.
[28] Ke, N., Baudry, J., Makris, T.M., Schuler, M.A., Sligar, S.G., 2005. A retinoic acid binding cytochrome P450: CYP120A1 from synechocystis sp. Pcc 6803. Arch Biochem Biophys 436, 110–120. https://doi.org/10.1016/j.abb.2005.01.011.
[29] Kiki, C., Rashid, A., Wang, Y., Li, Y., Zeng, Q., Yu, C.-P., et al., 2020. Dissipation of antibiotics by microalgae: kinetics, identification of transformation products and pathways. J Hazard Mater 387, 121985. https://doi.org/10.1016/j.jhazmat.2019.121985.
[30] Kockler, J., Oelgemöller, M., Robertson, S., Glass, B., 2014. Influence of titanium dioxide particle size on the photostability of the chemical UV-filters butyl methoxy dibenzoylmethane and octocrylene in a microemulsion. Cosmetics 1, 128–139. https://doi.org/10.3390/cosmetics1020128.
[31] Kühnel, K., Ke, N., Cryle, M.J., Sligar, S.G., Schuler, M.A., Schlichting, I., 2008. Crystal structures of substrate-free and retinoic acid-bound cyanobacterial cytochrome P450 CYP120A1. Biochemistry 47, 6552–6559. https://doi.org/10.1021/bi800328s.
[32] Lee, S.H., Xiong, J.Q., Ru, S., Patil, S.M., Kurade, M.B., Govindwar, S.P., et al., 2020. Toxicity of benzophenone-3 and its biodegradation in a freshwater microalga scenedesmus obliquus. J Hazard Mater 389, 122149. https://doi.org/10.1016/j.jhazmat.2020.122149.
[33] Li, Q., Lu, D., Sun, H., Guo, J., Mo, J., 2021. Tylosin toxicity in the alga raphidocelis subcapitata revealed by integrated analyses of transcriptome and metabolome: photosynthesis and DNA replication-coupled repair. Aquat Toxicol 239, 105964. https://doi.org/10.1016/j.aquatox.2021.105964.
[34] Li, S., Chu, Y., Ren, N., Ho, S.-H., 2023. Cytochrome P450 enzyme-based biotransformation of pharmaceuticals and personal care products (PPCPs) by microalgae in the aquatic environment. Chem Eng J 476. https://doi.org/10.1016/j.cej.2023.146557.
[35] Li, S., Yuan, J., Zhou, F., Liu, Y., Xie, H., Jia, W., et al., 2025. Modulating ABA-dependent growth and development by overexpressing cytochrome P450 ABA 8′-hydroxylase in medicago truncatula. Environ Exp Bot 229, 106060. https://doi.org/10.1016/j.envexpbot.2024.106060.
[36] Liu, Z., Wang, G., Ye, X., Zhang, X., Jiang, Y., Han, Y., et al., 2025. Multigenerational toxic effects in daphnia pulex are induced by environmental concentrations of tire wear particle leachate. J Hazard Mater 486. https://doi.org/10.1016/j.jhazmat.2024.136977.
[37] Liu, Z., Zhang, Y., Jia, X., Hoskins, T.D., Lu, L., Han, Y., et al., 2024. Microcystin-LR induces estrogenic effects at environmentally relevant concentration in Black-Spotted pond frogs (Pelophylax nigromaculatus): in situ, in vivo, in vitro, and in silico investigations. Environ Sci Technol 58, 9559–9569. https://doi.org/10.1021/acs.est.4c01322.
[38] Lu, T., Chen, F., 2011. Multiwfn: a multifunctional wavefunction analyzer. J Comput Chem 33, 580–592. https://doi.org/10.1002/jcc.22885.
[39] Ma, Y., Yoo, J., 2021. History of sunscreen: an updated view. J Cosmet Dermatol 20, 1044–1049. https://doi.org/10.1111/jocd.14004.
[40] Madeira, F., Madhusoodanan, N., Lee, J., Eusebi, A., Niewielska, A., Tivey, A.R., et al., 2024. The EMBL-EBI job dispatcher sequence analysis tools framework in 2024. Nucleic Acids Res. https://doi.org/10.1093/nar/gkae241 gkae241.
[41] Manasfi, T., Coulomb, B., Ravier, S., Boudenne, J.-L., 2017. Degradation of organic UV filters in chlorinated seawater swimming pools: transformation pathways and bromoform formation. Environ Sci Technol 51, 13580–13591. https://doi.org/10.1021/acs.est.7b02624.
[42] Medici, A., Saviano, L., Siciliano, A., Libralato, G., Guida, M., Previtera, L., et al., 2022. Octocrylene: from sunscreens to the degradation pathway during chlorination processes: formation of byproducts and their ecotoxicity assessment. Molecules 27, 5286. https://doi.org/10.3390/molecules27165286.
[43] Meech, R., Rogers, A., Zhuang, L., Lewis, B.C., Miners, J.O., Mackenzie, P.I., 2012. Identification of residues that confer sugar selectivity to UDP-glycosyltransferase 3A (UGT3A) enzymes. J Biol Chem 287, 24122–24130. https://doi.org/10.1074/jbc.M112.343608.
[44] Meng, E.C., Goddard, T.D., Pettersen, E.F., Couch, G.S., Pearson, Z.J., Morris, J.H., et al., 2023. UCSF ChimeraX: tools for structure building and analysis. Protein Sci 32, e4792. https://doi.org/10.1002/pro.4792.
[45] Mo, J., Ma, Z., Yan, S., Cheung, N.K.M., Yang, F., Yao, X., et al., 2023. Metabolomic profiles in a Green alga (Raphidocelis subcapitata) following erythromycin treatment: ABC transporters and energy metabolism. J Environ Sci 124, 591–601. https://doi.org/10.1016/j.jes.2021.12.001.
[46] Montellano, P.R.Od, 2018. 1-aminobenzotriazole: a mechanism-based cytochrome P450 inhibitor and probe of cytochrome P450 biology. Med Chem 08. https://doi.org/10.4172/2161-0444.1000495.
[47] Nuruzzaman, M., Zhang, R., Cao, H.Z., Luo, Z.Y., 2014. Plant pleiotropic drug resistance transporters: transport mechanism, gene expression, and function. J Integr Plant Biol 56, 729–740. https://doi.org/10.1111/jipb.12196.
[48] O'Malley, E., McLachlan, M.S., O'Brien, J.W., Verhagen, R., Mueller, J.F., 2021. The presence of selected UV filters in a freshwater recreational reservoir and fate in controlled experiments. Sci Total Environ 754. https://doi.org/10.1016/j.scitotenv.2020.142373.
[49] Pal, M., Yesankar, P.J., Dwivedi, A., Qureshi, A., 2020. Biotic control of harmful algal blooms (HABs): a brief review. J Environ Manag 268, 110687. https://doi.org/10.1016/j.jenvman.2020.110687.
[50] Pan, C.-G., Peng, F.-J., Ying, G.-G., 2018. Removal, biotransformation and toxicity variations of climbazole by freshwater algae scenedesmus obliquus. Environ Pollut 240, 534–540. https://doi.org/10.1016/j.envpol.2018.05.020.
[51] Pazmino-Sosa, A.G., Blais, J.-F., Champagne, P., 2024. Effects of 17α-ethinyl estradiol (EE2) and removal potential by two microalgal species chlorella vulgaris and scenedesmus obliquus. Algal Res, 103634. https://doi.org/10.1016/j.algal.2024.103634.
[52] Peng, J., He, Y.-Y., Zhang, Z.-Y., Chen, X.-Z., Jiang, Y.-L., Guo, H., et al., 2022. Removal of levofloxacin by an oleaginous microalgae chromochloris zofingiensis in the heterotrophic mode of cultivation: removal performance and mechanism. J Hazard Mater 425. https://doi.org/10.1016/j.jhazmat.2021.128036.
[53] Ramanan, R., Kim, B.-H., Cho, D.-H., Oh, H.-M., Kim, H.-S., 2016. Algae–bacteria interactions: evolution, ecology and emerging applications. Biotechnol Adv 34, 14–29. https://doi.org/10.1016/j.biotechadv.2015.12.003.
[54] Stien, D., Clergeaud, F., Rodrigues, A.M.S., Lebaron, K., Pillot, R., Romans, P., et al., 2018. Metabolomics reveal that octocrylene accumulates in pocillopora damicornis tissues as fatty acid conjugates and triggers coral cell mitochondrial dysfunction. Anal Chem 91, 990–995. https://doi.org/10.1021/acs.analchem.8b04187.
[55] Thorel, E., Clergeaud, F., Jaugeon, L., Rodrigues, A.M.S., Lucas, J., Stien, D., et al., 2020. Effect of 10 UV filters on the brine shrimp artemia salina and the marine microalga tetraselmis sp. Toxics 8, 29. https://doi.org/10.3390/toxics8020029.

[56] Thorel, E., Clergeaud, F., Rodrigues, A.M.S., Lebaron, P., Stien, D., 2022. A comparative metabolomics approach demonstrates that octocrylene accumulates in stylophora pistillata tissues as derivatives and that octocrylene exposure induces mitochondrial dysfunction and cell senescence. Chem Res Toxicol 35, 2160–2167. https://doi.org/10.1021/acs.chemrestox.2c00248.

[57] Torres, M.A., Barros, M.P., Campos, S.C.G., Pinto, E., Rajamani, S., Sayre, R.T., et al., 2008. Biochemical biomarkers in algae and marine pollution: a review. Ecotoxicol Environ Saf 71, 1–15. https://doi.org/10.1016/j.ecoenv.2008.05.009.

[58] Tsui, M.M.P., Leung, H.W., Wai, T.-C., Yamashita, N., Taniyasu, S., Liu, W., et al., 2014. Occurrence, distribution and ecological risk assessment of multiple classes of UV filters in surface waters from different countries. Water Res 67, 55–65. https://doi.org/10.1016/j.watres.2014.09.013.

[59] Vuckovic, D., Tinoco, A.I., Ling, L., Renicke, C., Pringle, J.R., Mitch, W.A., 2022. Conversion of oxybenzone sunscreen to phototoxic glucoside conjugates by sea anemones and corals. Science 376, 644–648. https://doi.org/10.1126/science.abn2600.

[60] Wang, J., Chen, Z., Chen, H., Wen, Y., 2018. Effect of hydrogen peroxide on microcystic aeruginosa: role of cytochromes P450. Sci Total Environ 626, 211–218. https://doi.org/10.1016/j.scitotenv.2018.01.067.

[61] Wang, J., Ohno, H., Ide, Y., Ichinose, H., Mori, T., Kawagishi, H., et al., 2019. Identification of the cytochrome P450 involved in the degradation of neonicotinoid insecticide acetamiprid in phanerochaete chrysosporium. J Hazard Mater 371, 494–498. https://doi.org/10.1016/j.jhazmat.2019.03.042.

[62] Waterhouse, A.M., Procter, J.B., Martin, D.M., Clamp, M., Barton, G.J., 2009. Jalview version 2—a multiple sequence alignment editor and analysis workbench. Bioinformatics 25, 1189–1191. https://doi.org/10.1093/bioinformatics/btp033.

[63] Wu, D., Zhang, R., Lu, G., Lin, Q., Liu, F., Li, Y., 2017. Degradation of octocrylene using combined ozonation and electrolysis process: optimization by response surface methodology. Clean Soil Air Water 45. https://doi.org/10.1002/clen.201500664.

[64] Wu, X., Jiang, J., Wan, Y., Giesy, J.P., Hu, J., 2012. Cyanobacteria blooms produce teratogenic retinoic acids. Proc Natl Acad Sci 109, 9477–9482. https://doi.org/10.1073/pnas.1200062109.

[65] Xiong, J.-Q., Kurade, M.B., Abou-Shanab, R.A.I., Ji, M.-K., Choi, J., Kim, J.O., et al., 2016. Biodegradation of carbamazepine using freshwater microalgae chlamydomonas mexicana and scenedesmus obliquus and the determination of its metabolic fate. Bioresour Technol 205, 183–190. https://doi.org/10.1016/j.biortech.2016.01.038.

[66] Xiong, J.-Q., Kurade, M.B., Patil, D.V., Jang, M., Paeng, K.-J., Jeon, B.-H., 2017. Biodegradation and metabolic fate of levofloxacin via a freshwater Green alga, scenedesmus obliquus in synthetic saline wastewater. Algal Res 25, 54–61. https://doi.org/10.1016/j.algal.2017.04.012.

[67] Xiong, Q., Liu, Y.-S., Hu, L.-X., Shi, Z.-Q., Cai, W.-W., He, L.-Y., et al., 2020. Co-metabolism of sulfamethoxazole by a freshwater microalga chlorella pyrenoidosa. Water Res 175, 115656. https://doi.org/10.1016/j.watres.2020.115656.

[68] Yadav, N., Ahn, H.-J., Kurade, M.B., Ahn, Y., Park, Y.-K., Khan, M.A., et al., 2023. Fate of five bisphenol derivatives in chlamydomonas mexicana: toxicity, removal, biotransformation and microalgal metabolism. J Hazard Mater 454. https://doi.org/10.1016/j.jhazmat.2023.131504.

[69] Yan, S., Liang, M., Chen, R., Hong, X., Zha, J., 2020. Reproductive toxicity and estrogen activity in Japanese medaka (Oryzias latipes) exposed to environmentally relevant concentrations of octocrylene. Environ Pollut 261, 114104. https://doi.org/10.1016/j.envpol.2020.114104.

[70] Yang, R., Ye, Y., Chen, Y., Yang, Y., Yang, L., Yao, Y., et al., 2022. First insight into the formation of in vivo transformation products of 2-ethylhexyl diphenyl phosphate in zebrafish and prediction of their potential toxicities. Environ Sci Technol 57, 451–462. https://doi.org/10.1021/acs.est.2c05506.

[71] Zhang, F., Cui, S., Li, Z., Yuan, Y., Li, C., Li, R., 2020. A combination of metabolite profiling and network pharmacology to explore the potential pharmacological changes of secoisolariciresinol-diglycoside. RSC Adv 10, 34847–34858. https://doi.org/10.1039/d0ra06382g.

[72] Zhang, H., Zong, R., He, H., Huang, T., 2022. Effects of hydrogen peroxide on scenedesmus obliquus: cell growth, antioxidant enzyme activity and intracellular protein fingerprinting. Chemosphere 287. https://doi.org/10.1016/j.chemosphere.2021.132185.

[73] Zhang, R., Li, P., Zhang, R., Shi, X., Li, Y., Zhang, Q., et al., 2021. Computational study on the detoxifying mechanism of DDT metabolized by cytochrome P450 enzymes. J Hazard Mater 414, 125457. https://doi.org/10.1016/j.jhazmat.2021.125457.

[74] Zhao, C.-Y., Ru, S., Cui, P., Qi, X., Kurade, M.B., Patil, S.M., et al., 2021. Multiple metabolic pathways of enrofloxacin by lolium perenne L.: ecotoxicity, biodegradation, and key driven genes. Water Res 202, 117413. https://doi.org/10.1016/j.watres.2021.117413.

Environmental Science & Technology

pubs.acs.org/est

Article

Polymer Type, Oxidation, Size, and Abundance of Microplastics in Subsoils versus Topsoils with Varying Land Use in Beijing, China

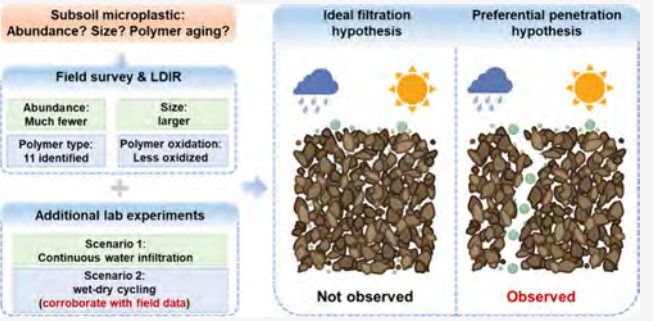
Liuwei Wang, Caide Huang, Junhao Cao, Pingfan Zhou, Siqi Han, Guangyu Qu, Michael S. Bank, and Deyi Hou*

Cite This: *Environ. Sci. Technol.* 2025, 59, 12933−12946

Read Online

ACCESS | Metrics & More | Article Recommendations | Supporting Information

ABSTRACT: The occurrence of microplastics (MPs) in topsoil is well documented; however, recent evidence has also shown that MPs can reach the subsoil, which may eventually enter groundwater aquifers posing a potential threat to drinking water. In this study, we examined polymer-type specific, small-sized MPs (20−500 μm) in both topsoil (5 cm) and subsoil (50 and 100 cm) in the megacity of Beijing, China, using Laser Direct Infrared (LDIR) Chemical Imaging Spectroscopy, focusing on variation in abundance, size, polymer type, and oxidation characteristics across 6 land use types. A total of 6085 MP particles with 11 polymer types were identified. MP abundance in subsoils was significantly lower, and they were surprisingly larger in size and less oxidized. MP distribution in subsoils was enhanced in fine-textured and iron (Fe)-depleted soils. Based on these findings, we conducted additional column migration experiments using different textured vadose zones, either with or without hematite, as a typical Fe oxide. Two scenarios were set, including continuous water infiltration and wet−dry cycling conditions. Field data strongly reflected our lab experiments under wet−dry cycling, suggesting that preferential penetration rather than filtration served as the likely primary mechanism of MP occurrence in subsoil.



KEYWORDS: *Soil contamination, Microplastic, LDIR, Aging, Migration*

Downloaded via GUANGXI UNIV on July 2, 2025 at 13:10:09 (UTC).
See https://pubs.acs.org/sharingguidelines for options on how to legitimately share published articles.

1. INTRODUCTION

Global production of plastic reached 413.8 million tons by 2023,[1] raising concerns about potential threats to ecosystems following the release of plastic debris into the environment.[2,3] It is estimated that ∼13−25 million tons of plastic debris is discarded into terrestrial ecosystems annually, leading to significant and irreversible accumulation in environmental compartments, including soil.[4,5] Moreover, plastics in soil become fragmented and oxidized over time, and this aging process produces tiny microplastics (MPs, <5 mm) and nanoplastics (NPs, <1 μm), which have much higher mobility and bioavailability.[4,6]

The abundance of MPs in topsoil, particularly in the surficial layer of ∼0−30 cm (plough layer), has been extensively reported and reviewed by previous studies.[7−9] The primary interest in MP explorations in topsoil is largely driven by concerns regarding agricultural soil pollution from plastic debris, such as mulching films.[7,10,11] Several pioneering studies have reported that small-sized MPs and NPs can be accumulated by crops via a crack-entry mode and ultimately transported to edible parts, thereby posing a potential threat to food security.[12−14] In addition, regional- and national-scale field surveys have been conducted to explore the spatial distributions of MPs in topsoils across various land use types, including agricultural soils.[6,7,10,15−22] These studies found that both local inputs from agricultural, domestic, and industrial activities and distal sources such as atmospheric deposition and runoff transport contributed to MP accumulation in topsoils.[6,16−22] For instance, a field survey in central Chile suggested that MP accumulation in soils was primarily due to the application of phosphate fertilizers rather than mining or traffic activities.[20] A field study in Coimbra, Portugal, found that urban greenspaces, in particular, parks, had the highest abundance of MPs compared to industrial and forest soils, which was possibly due to domestic emissions as well as the high retention of MPs by plants.[17] In contrast, another field survey in the metropolitan area of Seoul, Korea, found high MP abundance in agricultural and roadside soils compared to parks, suggesting the complexity of MP sources in urban settings.[22] In addition, a nationwide field study of Turkish soils suggested higher MP abundance in agricultural soils compared

Received: January 18, 2025
Revised: June 6, 2025
Accepted: June 10, 2025
Published: June 20, 2025



ACS Publications

© 2025 American Chemical Society

to urban soils, and MP accumulation was attributed to plastic mulching, domestic activities, and atmospheric deposition.[21] Furthermore, transport mechanisms of MPs in soil porous media have been explored through laboratory column migration tests.[23−29] Most of these studies utilized saturated porous media,[25−29] while several applied a more environmentally relevant scenario using unsaturated porous media.[23,24] These studies found that MPs were transported in porous media similarly to colloids and that one-site or two-site kinetic models for colloid/particle transport effectively described MP transport characteristics.[24−29]

Despite this, field evidence on the presence of MPs in subsoil (>30 cm) has only recently come to light, with a limited number of studies reporting that MPs have penetrated through the topsoil and accumulated in subsoils, typically ranging from 30 to 100 cm.[30−35] Similar to field studies focusing on topsoils, research on subsoil MPs has primarily examined agricultural soils compared to other land use types and has reported the abundance of MPs in subsoils.[30−32,35] However, several knowledge gaps still exist in subsoil MP research: (1) Despite the clear presence of MPs in subsoils, the mechanisms by which MPs accumulate in subsoils warrant further exploration. In particular, field evidence is needed to unravel transport mechanisms in real-world environments beyond laboratory column migration simulations. (2) Although MP abundance in subsoils has been reported by existing studies, field data on several other key factors of subsoil MPs affecting mobility and associated risks, such as size distribution patterns, polymer types, and polymer oxidation characteristics, remain very limited. (3) Field data on subsoil MPs in land use types other than agricultural soils are rare and have only been documented in a few studies,[33,34] thus our understanding of subsoil MP accumulation across land use types remains insufficient. Notably, a growing body of literature has documented the occurrence of MPs in groundwater aquifers[36−38] and non-negligible concentrations of MPs in tap water sourced from groundwater.[39,40] This provides direct evidence that MPs can be transported from topsoils through subsoils to groundwater, highlighting potential risks to drinking water safety. Unraveling the presence of MPs in subsoils is, therefore, crucial and a prerequisite for protecting drinking water sources.

In this study, we examined the presence and aging characteristics of MPs in subsoils to reveal the possible mechanisms of MP accumulation in the subsoil. First, we conducted a field survey in a metropolitan region to examine MP occurrence in topsoil (5 cm) and subsoil (50 and 100 cm). With the advancement of MP characterization techniques in recent years, we provided a polymer-type specific exploration of MPs using Laser Direct Infrared (LDIR) Chemical Imaging Spectroscopy, which can simultaneously capture a particle's spectral data and shape information, allowing for the determination of polymer type, oxidation characteristics, size, and shape of MPs.[41−43] Particles whose sizes range from 20 to 500 μm can be automatically detected by LDIR without the need for human intervention,[41,42,44] addressing a common challenge in MP characterization relying on manual scanning and measurement (in particular, individual point selection and analysis by conventional optical- or spectra-based approaches), which often introduces subjectivity and can compromise the accuracy and reliability of the results.[45−47] Previous studies have also shown that MPs within this size range are more prevalent in soil compared to larger MPs (>500 μm), with the mobility of these smaller MPs being significantly higher.[6,15,48] Various multivariate statistical analysis approaches were also employed to identify factors affecting the MP vertical distribution. Based on our field data, we formulated two hypotheses accounting for MP vertical distribution: (1) ideal filtration and (2) preferential penetration. Additional laboratory experiments were then conducted with different vadose zone types under two conditions: continuous water infiltration and wet−dry cycling. Finally, multiple lines of evidence from the field survey and additional laboratory experiments suggested possible mechanisms of MP vertical distribution in soil.

2. MATERIALS AND METHODS

2.1. Field Survey and Soil Sampling. A field survey was conducted in 2023 on August 30th and October 6th in the megacity of Beijing, China (39.4−41.1° N, 115.4−117.5° E). A total of 50 locations were selected, representing different land use types: arable land (n = 10), bare land (n = 5), forest (n = 10), grassland (n = 5), shrubland (n = 5), and urban greenspace (n = 15) (Figure S1). Paired topsoil (5 cm) and subsoil (50 cm) samples were simultaneously collected at all 50 locations using a stainless steel soil core sampler (0415SB, Eijkelkamp, The Netherlands). Representative photos for each land use type are provided in Figure S2. Furthermore, 8 additional samples with depths of 100 cm were also collected at 8 of the 50 sampling points (Figure S1). All 108 samples, each measuring 50 g, were transferred to aluminum boxes and brought to the lab for MP characterization. A detailed description of the field site is provided in Text S1. Soil moisture was measured *in situ* using a moisture meter (LY-601, Agatige, USA), while penetration resistance was also measured *in situ* using a soil compaction tester (PG-JSD-SC, Lankong, China). Bulk density of the soils was measured by using soil cores collected by a soil ring sampler.

Following these *in situ* measurements, an additional set of mixed soil samples (0−20 cm) measuring 1.5 kg was also collected at each sampling point using a stainless-steel shovel and transferred to the lab for the characterization of soil properties. The soils were first oven-dried at 40 °C and sieved below 2 mm. Soil pH was measured at a solid-to-liquid ratio of 1:2.5.[49] Soil electrical conductivity (EC) was measured at a solid-to-liquid ratio of 1:5.[50] Total organic carbon (TOC) content of the soil was determined with the potassium dichromate method.[51] Soil texture was determined with a laser particle size analyzer (LS13320, Beckman Coulter Inc., US) in wet mode[52] and classified as sand (>0.02 mm), silt (0.002−0.02 mm), and clay (<0.002 mm) according to the International Union of Soil Sciences (IUSS).[53] Soil CEC was determined using the ammonium acetate method.[51] Pseudo-total elemental compositions were determined by ICP-MS (7800, Agilent, USA) following aqua regia digestion.[54]

2.2. LDIR-Based Microplastic Characterization. Soil samples for LDIR characterization were subjected to MP separation following a well-established protocol with modifications.[55] Specifically, 10 g of sieved soil was placed in 60 mL glass serum bottles precleaned with nitric acid, and 20 mL of 30% hydrogen peroxide was added to the bottles; the slurry was heated at 60 °C for 12 h on a heating plate. The remaining liquid was evaporated, after which 50 mL of saturated $ZnCl_2$ solution (with a density of 1.7 g/cm^3) was added to the bottle, sonicated at 35 kHz for 10 min, and then allowed to settle for 24 h. The supernatant containing MPs was passed through a

https://doi.org/10.1021/acs.est.5c00871
Environ. Sci. Technol. 2025, 59, 12933−12946

10 μm stainless steel filter membrane, and the particles on the filter were transferred to another clean glass bottle. Next, 15 mL of 30% hydrogen peroxide and 5 mL of sulfuric acid were added to the bottle, which was then heated at 60 °C for another 12 h. Note that this protocol has been proven effective for efficient separation of MPs from solid matrices such as soil and sludge with relatively high natural organic matter content and will not alter the oxidation characteristics of MPs.[55] MPs were then collected on another 10 μm stainless steel filter membrane and washed with ultrapure water.

MPs on the filter membrane were resuspended in 1 mL of ethanol and loaded onto a high reflection window in the LDIR (8700, Agilent, USA) system for quantitative analysis. Small-sized MPs ranging from 20 to 500 μm could be characterized by LDIR and were automatically scanned by the system.[41,42,44] Clarity software was used to quantify the MPs after collecting infrared spectra within the wavenumber range of 1800 to 975 cm^{-1}. A matching degree of 70% was adopted in this study to identify specific polymer types.[42,44] A total of 11 plastic polymers were identified, including polyamide (PA), polycarbonate (PC), polyethylene (PE), polyethylene terephthalate (PET), poly(methyl methacrylate) (PMMA), polyoxymethylene (POM), polypropylene (PP), polystyrene (PS), polytetrafluoroethylene (PTFE), polyurethane (PU), and poly(vinyl chloride) (PVC). Characterization results such as average diameter, aspect ratio, polymer type, and original infrared spectra data of each particle were obtained for further analyses.

2.3. Field Survey Data Analysis. The size distribution of MPs was first described using a power law equation (eq 1):[56,57]

$$\lg y = \lg b - D\lg x \tag{1}$$

where x represents the size (μm) and y is the relative abundance of MPs. D is the fragmentation dimension, while parameter b is the intercept. It was observed that a higher absolute value of the power law slope indicates that MPs may have experienced more extensive aging.[56,58] It was reported by previous literature that the size distribution patterns of MPs in the environment usually followed this power law.[56,57,59] The power law was also used to normalize reported MP abundance across the literature to 1−5000 μm for comparison, whose details are provided in Text S2.

Following this, the cumulative size distribution of microplastics (MPs) was depicted using a conditional fragmentation model (eq 2):[6]

$$F(x) = 1 - e^{-\lambda x^{\alpha}} \tag{2}$$

where $F(x)$ represents the cumulative size distribution of MPs, λ stands for the range parameter, and α is the fragmentation parameter. Detailed assumptions and parameter definitions have been documented previously.[6]

In addition, the carbonyl index (CI) of the particles (as an indicator of polymer oxidation) was calculated following Zhang et al.[60] (eq 3):

$$\mathrm{CI} = \frac{I_{1750-1650}}{I_{1480-1440}} \tag{3}$$

where $I_{1750-1650}$ and $I_{1480-1440}$ refer to maximum infrared spectra absorbance within the wavenumber range of 1750−1650 cm^{-1} and 1480−1440 cm^{-1}, respectively.

An orthogonal partial least-squares-discriminant analysis (OPLS-DA) model was established to identify the key differentiating polymer types between topsoil and subsoil in field samples. This supervised method effectively determines the separating factor of 2 groups.[61−63] The OPLS-DA model is described with the following equations (eqs 4 and 5):[64]

$$X = t_p p_p^T + t_o p_o^T + E \tag{4}$$

$$Y = t_p q_p^T + F \tag{5}$$

where X is a matrix of predictors, Y is an matrix of responses, t_p and p_p are Y-predictive score matrix and loading matrix for X, t_o and p_o are Y-orthogonal score matrix and loading matrix for X, q_p is the Y-predictive loading matrix for Y, E is the residual matrix for X, and F is the residual matrix for Y, respectively. The OPLS-DA model splits the variability of the system into two components: predictive (correlated with the response Y) and orthogonal (not correlated with the response Y). Polymer types with a higher Variable Importance in Projection (VIP) value (VIP > 1) were identified as key separating types.[61−63]

We further explored potential relationships among variables through correlation analysis, principal component analysis (PCA), and hierarchical clustering. A debiased sparse partial correlation (DSPC) network was also used to reveal direct and indirect influences of soil properties and environmental factors on MP vertical distribution (eq 6):[65]

$$\hat{T} = vec(\hat{\Theta}) - \hat{\Theta} \otimes \hat{\Theta} vec(S - \hat{\Theta}^{-1}) \tag{6}$$

where $\hat{T}$ is the desparsified graphical lasso estimator, $\hat{\Theta}$ is the graphical lasso estimator of the inverse covariance matrix, and S is the sample covariance matrix. The DSPC network algorithm constructs partial correlation networks of variables, offering insights into their associations.[66,67] An edge was placed between the two nodes when p values were <0.05.

Furthermore, ridge regression (as a modification of multiple linear regression) was used to identify key factors affecting MP vertical distribution (eq 7):[68]

$$\hat{\beta}(k) = (X^T X + kI)^{-1} X^T Y \tag{7}$$

where $\hat{\beta}$ is the ridge estimator, I is the identity matrix, and k is the ridge parameter ($k \geq 0$). Ridge regression rather than multiple linear regression was adopted in this study because the independent variables were found to be highly correlated and to correct for potential overfitting.

Based on these exploratory statistical analyses, a structural equation model was constructed as a confirmatory analysis of potential pathways (eq 8):[69]

$$\eta = B\eta + \Gamma\xi + \zeta \tag{8}$$

where η is a vector of endogenous constructs, B is a matrix of coefficients representing the effects of the endogenous constructs on each other, Γ is a matrix of coefficients representing the effects of the exogenous constructs on the endogenous constructs, and ζ is a vector of residuals. Goodness of fit of the structural equation model was assessed via a χ^2 test, where a nonsignificant value ($p > 0.05$) indicated that the constructed pathways well describe the observed data.

One-way ANOVA with Fisher's LSD test was used to determine whether significant differences existed among groups with a significance level of $p < 0.05$. Different lowercase letters in the figures indicated significant differences among groups. Correlation analysis, PCA, and one-way ANOVA were conducted using Origin 2022, and ridge regression was

https://doi.org/10.1021/acs.est.5c00871
Environ. Sci. Technol. 2025, 59, 12933−12946

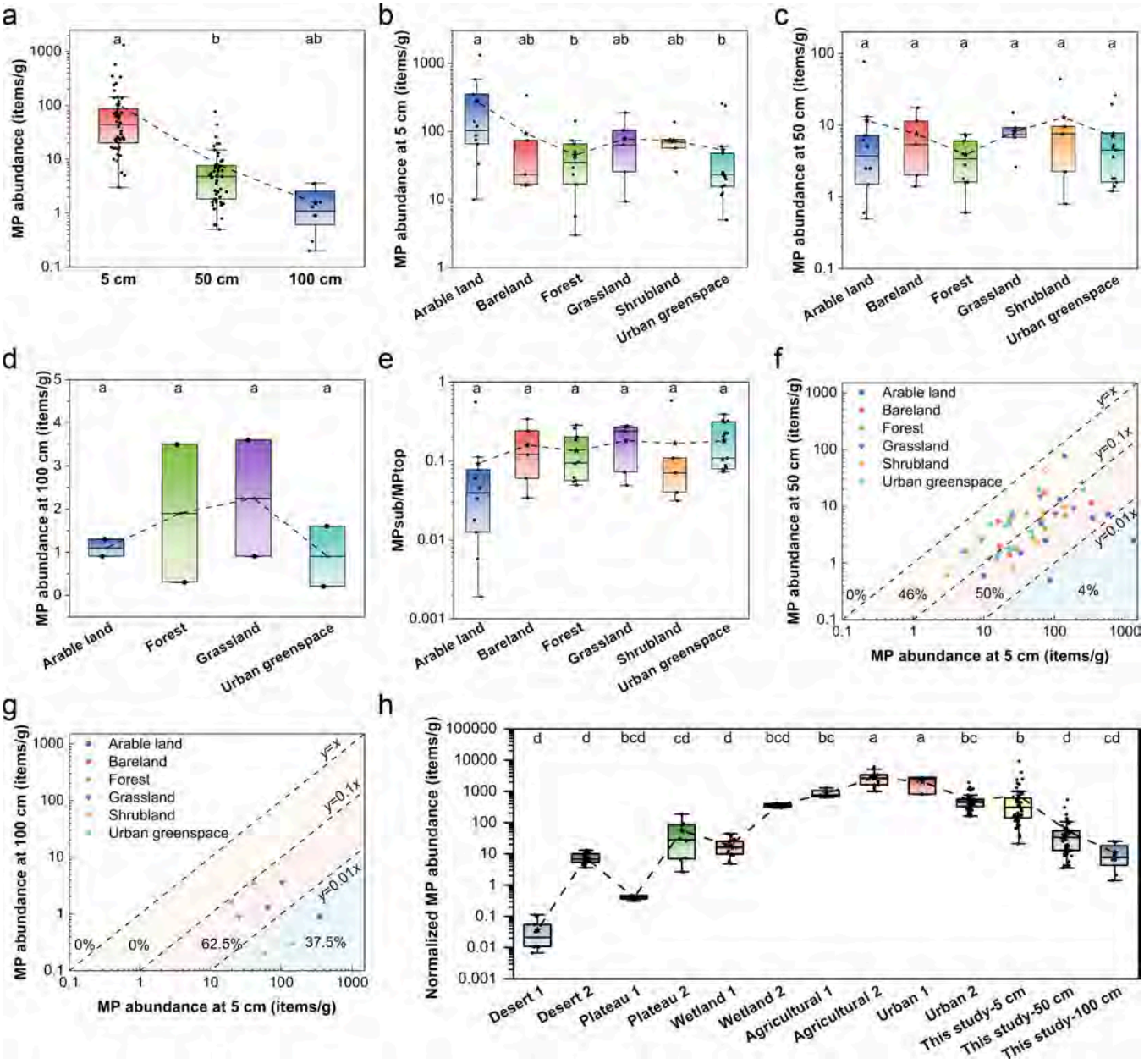


Figure 1. MP abundance in topsoil and subsoil, samples collected from a field survey in Beijing, China, 2023. (a) MP abundance in topsoil and subsoil (size range from 20 to 500 μm, same for panels b−g). (b) Soil MP abundance at 5 cm across different land use types. (c) Soil MP abundance at 50 cm across different land use types. (d) Soil MP abundance at 100 cm across different land use types. (e) Soil MP abundance at 50 cm divided by that at 5 cm (MPsub/MPtop) across different land use types. (f) Comparison of soil MP abundance at 5 and 50 cm. (g) Comparison of soil MP abundance at 5 and 100 cm. (h) Comparison of normalized soil MP abundance with literature data (size range normalized to 1 to 5000 μm according to Koelmans et al.[59] for comparison). Data sources: Desert 1 − Badain Jaran Desert;[81] Desert 2 − Mu Us Desert;[82] Plateau 1 − Southwest part of the Tibetan Plateau;[86] Plateau 2 − Southern Tibetan Plateau;[76] Wetland 1 − A tidal freshwater wetland in Kenilworth Park and Aquatic Gardens in Washington D. C., USA;[83] Wetland 2 − A karst wetland in Southwest China;[87] Agricultural 1 − Cotton field with long-term plastic mulching for 5 to over 30 years;[88] Agricultural 2 − Agricultural soil with long-term plastic mulching for 25 to 30 years;[84] Urban 1 − Soil collected from Wuhan City, China;[85] Urban 2 − Soil collected from Beijing City, China during our previous field survey.[6]

performed with XLSTAT, while other analyses were conducted using Program R scripts.

2.4. Additional Laboratory Column Migration Experiments. Following field survey and data analyses, additional column migration experiments were conducted in the laboratory to further test our hypotheses. Glass columns with an inner diameter of 5 cm and a length of 12 cm were used for this purpose. In this study, PE (LDPE, Dow, USA), PP (ExxonMobil, USA), PA (PA66, BASF, Germany), PET (DuPont de Nemours, USA), PVC (Tosoh, Japan), and PU (BASF, Germany) MPs with sizes ranging from 20 to 26 μm (controlled via wet sieving) were employed. The morphologies of the MPs were characterized by Field Emission Scanning Electron Microscopy (FESEM) (GEMINISEM500, ZEISS, Germany) (Figure S3). The surface functionalities of MPs were characterized by Fourier Transform Infrared Spectroscopy (FTIR) (Nicolet iS50, Thermo Fisher Scientific, USA) scanning within a wavenumber range of 4000 to 400 cm^{-1} with

https://doi.org/10.1021/acs.est.5c00871
Environ. Sci. Technol. 2025, 59, 12933−12946

a resolution of 4 cm^{-1} (Figure S4). Quartz sand and hematite (purity >99.9%), with particle diameters sieved between 90 and 100 μm, and kaolinite (purity 98.8% with 1.2% illite), with diameters ranging between 0.2 and 2.4 μm, were used. A 0.22 μm glass fiber filter membrane was placed at the bottom of each column. Four different vadose zones were created by combining different minerals, namely, 100% quartz sand (hereinafter referred to as 100Q), 90% quartz sand + 10% kaolinite (by mass) (90Q+10K), 40% quartz sand + 60% kaolinite (40Q+60K), 90% quartz sand + 10% hematite (90Q +10H), and 80% quartz sand + 10% hematite + 10% kaolinite (80Q+10H+10K). The side walls of each column were preroughened, and then, minerals were dry-packed into the columns with a packing height of 10 cm.[70] The porosity was held constant at 0.5 for each column. A leaching solution (1 mM NaCl at pH = 7)[24,71] was added to the columns from the top for 3 pore volumes (PVs) to achieve hydro-chemical equilibration. The leaching speed was maintained at 5 mm/h to prevent surface ponding, which is comparable to the water infiltration rate of natural fine-textured soils.[72] Subsequently, a 0.5 cm thick MP-spiked layer (13 g of quartz sand and 0.065 g of MPs, yielding an application rate of 0.5%[73]) was placed on top of the 10 cm vadose zone. Only one polymer type was used for each single column.

We conducted column experiments in two modes. In the first mode (continuous water infiltration), 10 pore volumes (PVs) of the leaching solution were continuously added to the column from the top. In the second mode (wet−dry cycling), we conducted 10 wet−dry cycles, each consisting of 1 PV of leaching solution injection followed by oven-drying at 50 °C for 48 h. After the experiments, soil samples were taken at 2.5 cm (calculated from the top, representing a 2 cm depth of penetration) and 8.5 cm from the top (representing an 8 cm depth of penetration) and dried at 50 °C. Triplicate samples were analyzed, where in each replicate, 1 g of dried solid sample was placed in a 40 mL glass serum bottle and 20 mL of saturated $ZnCl_2$ solution was added for separation. Particles trapped on the 10 μm stainless steel filter were characterized using confocal microscopy (FV 3000RS, Olympus, Japan) (with only one polymer type for each solid sample in a pure mineral vadose zone in lab experiments), whose applicability was thoroughly explored and cross-validated in our previous studies.[58,74,75]

2.5. Quality Control Measures. All chemicals used were of analytical grade. All liquids were passed through 10 μm stainless steel filters to prevent the introduction of MPs. For the analysis of field samples, three field blank samples were prepared by using aluminum boxes left open to test whether MPs were introduced during the sampling process. These samples were rinsed with 50 mL of ultrapure water, followed by flotation and MP quantification. Three soil blank samples were also prepared, where 50 g of ultrapure water-washed quartz sand, following flotation with $ZnCl_2$, was used to replace field-collected soils for MP separation. Additionally, considering that the soil core sampling process may induce vertical transport of MPs, we set up a 30 cm tall cleaned quartz sand layer in a bucket measuring 32 cm in height with a 34 cm inner diameter. The bulk density was 1.3 g/cm^3. We mixed an ultrahigh concentration of 600 g of MP mixture containing PE, PP, PET, PVC, PA, and PU MPs (100 g for each polymer type) with the top 5 cm quartz sand layer, resulting in an exceptionally high spiking rate of 10%. Afterward, we took three 20 cm long quartz sand core samples using the same core sampler and collected the bottom 50 g of quartz sand, which underwent the same quantification method.

In the aforementioned quality control samples, the number of particles detected was well below the MP concentration reported for soil samples (Table S1). The detection limit for LDIR using the protocol mentioned in this study was 0.056 items/g, while the quantification limit was 0.18 items/g. All reported data were above the quantification limit. Furthermore, we spiked 0.1 g of PE, PP, PET, PVC, PA, and PU MPs separately with 10 g of MP-free quartz sand and measured the spike recovery rates of MPs following sample pretreatment and LDIR characterization. The recovery rates of these polymers were 98.7%, 96.5%, 94.4%, 90.2%, 91.4%, and 92.7%, respectively, comparable with or higher than previously reported values using LDIR.[76,77]

For lab column migration experiments, a control column with a 100% quartz sand vadose zone was set, and triplicate solid samples at 2 and 8 cm penetration depths were collected following the same leaching experiments (a total of 6 samples were collected). The detection limit of MPs for confocal microscopy in lab column migration experiments was determined to be 2.9 items/g, while the quantification limit was 9.6 items/g. Observations above the quantification limit were reported with MP abundance values.

3. RESULTS AND DISCUSSION

3.1. Field Data Revealing MP Abundance in Topsoils and Subsoils. Average MP abundance decreased with increased sampling depth, with values of 104.8 ± 29.0 (mean and standard error), 8.1 ± 1.8, and 1.5 ± 0.5 items/g for 5, 50, and 100 cm, respectively (Figure 1a). MP abundance in arable land was highest at 5 cm (Figure 1b). This pattern aligns with previous findings showing higher MP abundance in agricultural soil compared to undisturbed natural soil.[7,20] A previous nationwide survey on topsoil MPs in Chinese arable lands also suggested that widespread use of plastic mulching and plastic packaging was the main cause of MP enrichment.[10] Several field surveys in other countries also suggested MP enrichment due to other agricultural activities such as phosphate fertilizer application (Chile's Región Metropolitana),[20] sludge application (Valencia, Spain),[78] and wastewater irrigation (Konya City, Türkiye).[79] However, at 50 and 100 cm, MP abundance in arable land was lower than that in shrubland (Figure 1c,d). Although arable land had the highest MP abundance, MP penetration into subsoils was not the highest in arable land (Figure 1e). These findings suggest that agricultural activities may strongly influence MP accumulation in topsoil yet may have less impact on MP enrichment in subsoil below the plough layer in this region. When comparing MP abundance at 5 and 50 cm, subsoil MP abundance was consistently lower than that in paired topsoil samples (with all observations falling below the $y = x$ line) (Figure 1f). Specifically, 46% of observations fell between the $y = x$ and $y = 0.1x$ lines, 50% fell between $y = 0.01x$ and $y = 0.1x$, and 4% fell below the $y = 0.01x$ line (Figure 1f). Similarly, when comparing abundances at 5 and 100 cm, all samples had MP abundance consistently <10% than that of topsoil, ranging from 0.2 to 3.6 items/g (Figure 1g). A recent *in situ* field trial in Zürich Reckenholz Switzerland suggested that MP penetration is relatively slow, with only 1% spiked PET MPs reaching below 8 cm soil depth in two years.[80]

Soil MP abundance in this region was further compared with that of other soils after normalization to 1−5000 μm following

https://doi.org/10.1021/acs.est.5c00871
Environ. Sci. Technol. 2025, 59, 12933−12946

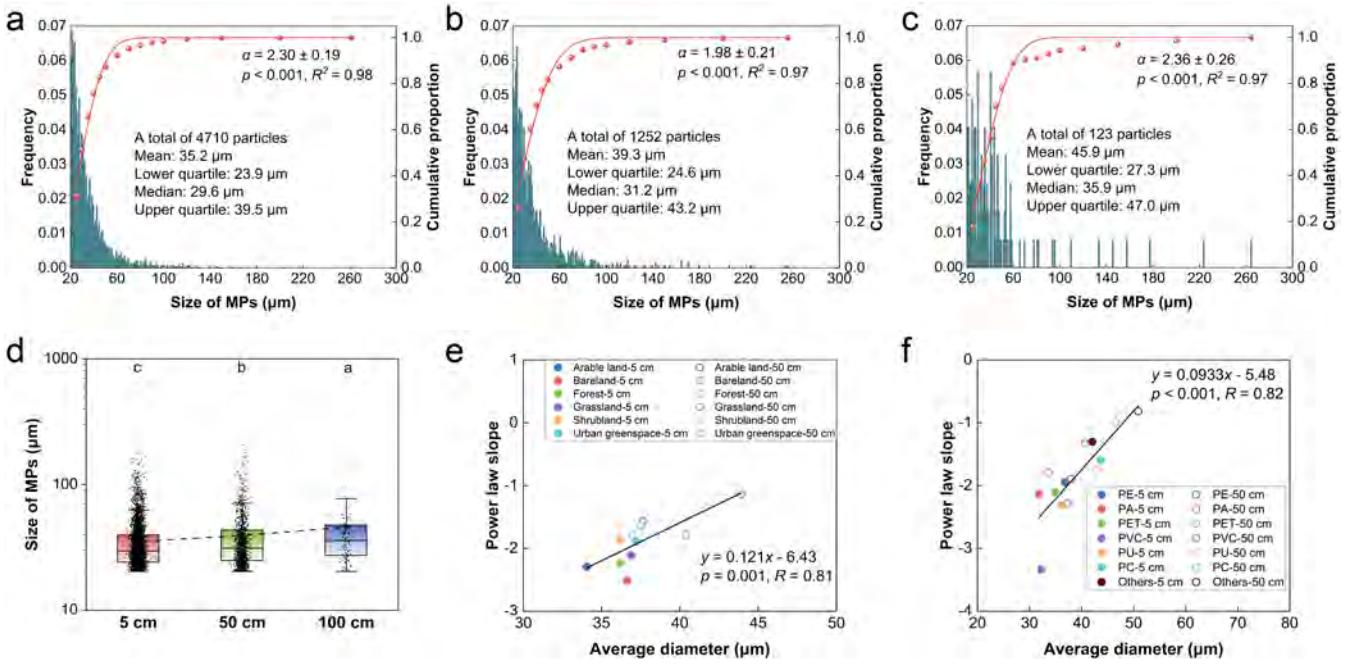


Figure 2. Size of MPs in topsoil and subsoil, samples collected from field survey in Beijing, China, 2023. (a) Size distribution of soil MPs at 5 cm. (b) Size distribution of soil MPs at 50 cm. (c) Size distribution of soil MPs at 100 cm. (d) Comparison of diameters of soil MPs across different sampling depths. (e) Correlation of power law slope with average diameters of MPs across various land use types. (f) Correlation of power law slope with average diameters of MPs with various polymer types.

methods described by Koelmans et al.[59] (Text S2). Normalized MP abundance in this study had ranges of 21.0−9212, 3.5−540, and 1.4−25.3 items/g at 5, 50, and 100 cm, respectively (Figure 1h). Topsoil MP abundance in this study was significantly higher ($p < 0.05$) than remote regions, such as the Badain Jaran Desert,[81] Mu Us Desert,[82] and the Southern Tibetan Plateau,[76] suggesting regional MP enrichment. Topsoil MP abundance was also significantly higher ($p < 0.05$) than protected areas such as a tidal freshwater wetland in Kenilworth Park and Aquatic Gardens in Washington D. C., USA.[83] Topsoil MP abundance observations were also significantly lower ($p < 0.05$) compared to agricultural soil with long-term (i.e., 25−30 years) plastic mulching[84] and urban soils collected from Wuhan City, China.[85] Notably, topsoil MP abundance reported in this study was not statistically different ($p > 0.05$) from our previous field survey in this region using a different MP characterization technique.[6] MP abundances at 50 and 100 cm were much lower than that of topsoil in this study and were comparable with MP abundance found in topsoil from remote regions.

3.2. Size Distribution of MPs in Topsoil and Subsoil. A total of 4710, 1252, and 123 MP particles were identified by LDIR at depths of 5, 50, and 100 cm, respectively (Figure 2). The size distribution characteristics of MPs were well described by the conditional fragmentation model, both for the entire data set at each sampling depth (Figure 2a−c) and for the land-type and polymer-type specific data sets (Table S2). The fragmentation parameter values were consistently >1 for all fittings (Figure 2a−c, Table S2), suggesting that the probability of MP fragmentation became higher for larger particles.[6] Previous studies also found that the conditional fragmentation model well described size distributions of MPs in different environmental samples such as soil, atmospheric deposition, freshwater, road dust, and sewage sludge.[6,89,90] Different fitting parameters were observed across samples, suggesting a possibility of using the size distribution parameters for source identification, which warrants further investigation.[6,89,90]

Surprisingly, a significant increase ($p < 0.05$) in MP size was found with increasing sampling depth (Figure 2a−d). This finding was somewhat counterintuitive regarding MP transport in porous media, where smaller particles were thought to have higher mobility.[91−93] The size distribution of MPs was also well described by power law, suggesting a pseudo-two-dimensional fragmentation pattern (Table S3). The absolute values of the power law slope or fragmentation dimension (D) were higher at 5 cm compared with those at 50 cm (Table S3). Furthermore, it was found that the higher the absolute value of the power law slope (i.e., the higher the fragmentation dimension), the lower is the average diameter of MPs (Figure 2e,f). Previous studies exploring the size distribution of MPs in natural aquatic environments[56] as well as those examining the size distribution of MPs generated under various accelerated aging conditions in the lab, including mechanical abrasion, freeze−thaw cycling, and ultraviolet (UV) irradiation,[58,75] also suggested a two-dimensional fragmentation pattern. For instance, by analyzing MP size distributions in various freshwater and marine aquatic environments on a global scale, Kooi and Koelmans[56] obtained an average fragmentation dimension of 1.6 ± 0.5 ($n = 19$).

3.3. Polymer Types of MPs in Topsoil and Subsoil. PA (12.4−26.3%), PE (8.0−12.3%), PET (16.8−17.1%), PU (16.5−23.6%), and PVC (12.7−24.3%) were the most abundant polymer types across different sampling depths, while other polymer types were less frequently detected (Figure 3a). These polymer types are widely fabricated and used,[1] and soil contamination by these diverse polymers suggests that soil MPs in this region may originate from several sources including domestic, construction, agricultural, atmospheric, and industrial. For example, PA is widely used in

https://doi.org/10.1021/acs.est.5c00871
Environ. Sci. Technol. 2025, 59, 12933−12946

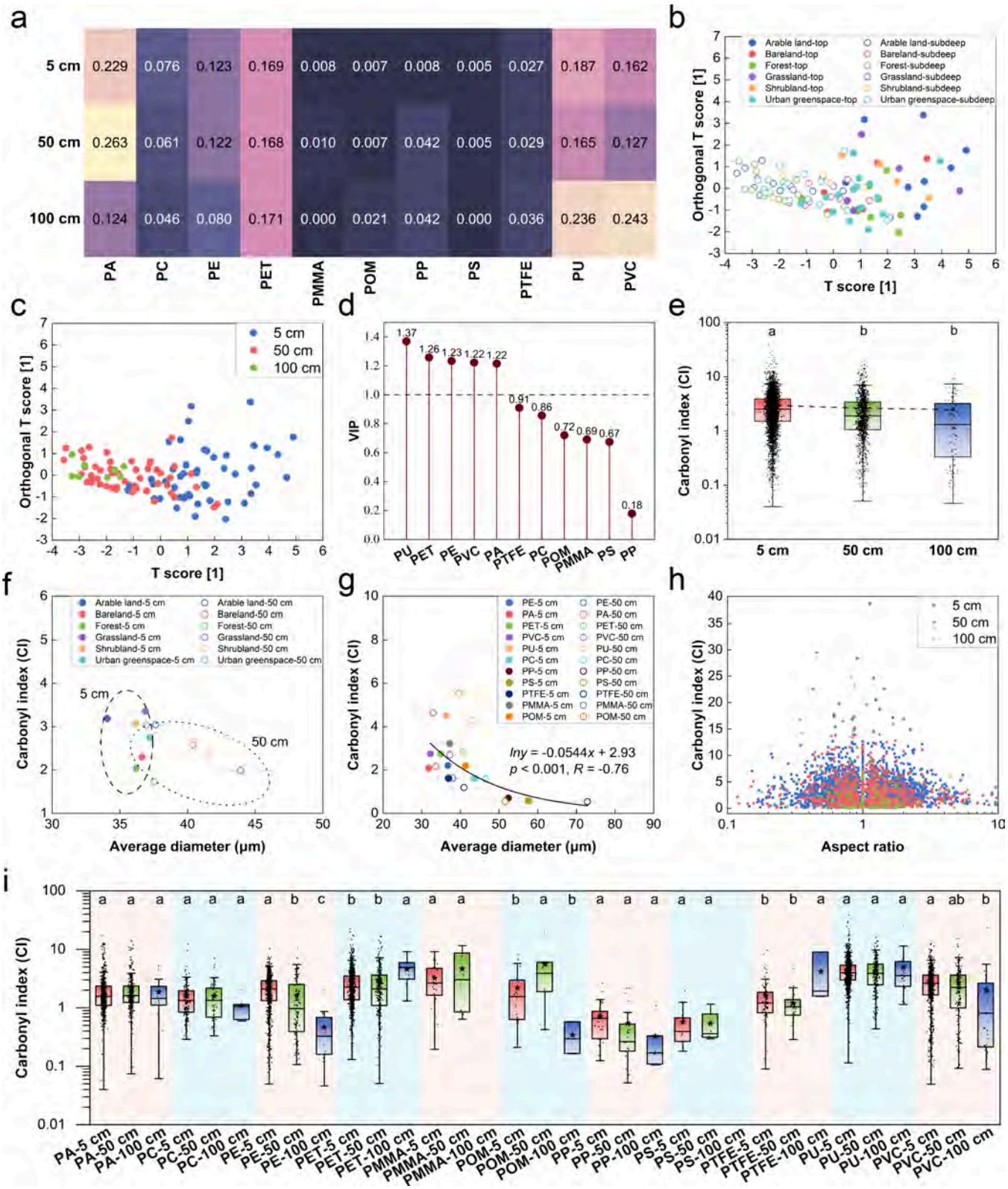


Figure 3. Polymer type and oxidation characteristics of MPs in topsoil and subsoil samples collected from the field survey in Beijing, China, 2023. (a) Heatmap revealing polymer type composition of soil MPs at different sampling depths. The numbers in the heatmap refer to proportions of each polymer types, and warmer colors suggest higher proportions. (b) OPLS-DA score plot of MP polymer composition across different land use types (top − 5 cm; subdeep − 50 and 100 cm). (c) OPLS-DA score plot of MP polymer composition at different sampling depths. (d) VIP values showing key separating polymer types. (e) CIs of all identified MPs at different sampling depths. (f) CI and average diameters of MPs across various land use types. (g) CI and average diameters of MPs across various polymer types. (h) CI and aspect ratios of MPs at 5, 50, and 100 cm. (i) Comparison of CIs for different polymer types at 5, 50, and 100 cm. Note that no PMMA or PS particles were detected at 100 cm.

https://doi.org/10.1021/acs.est.5c00871
Environ. Sci. Technol. 2025, 59, 12933−12946

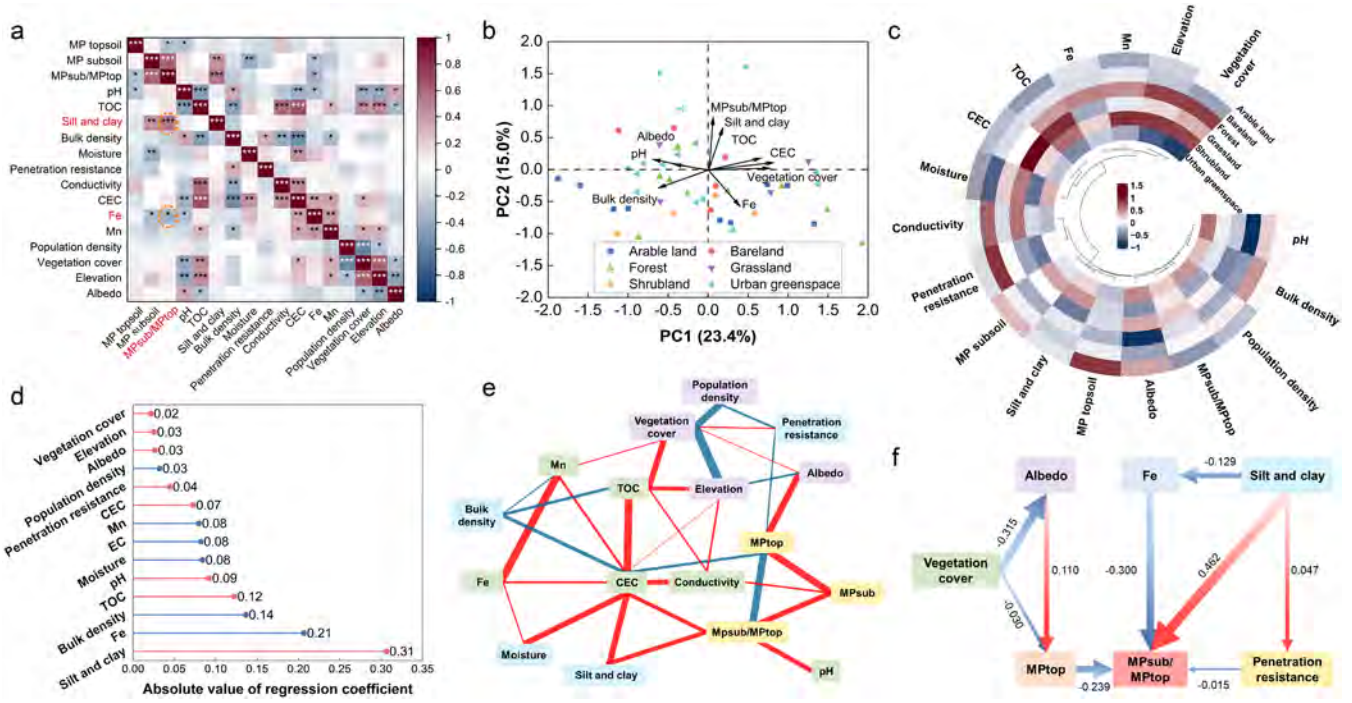


Figure 4. Statistical analyses unraveling factors affecting MP abundance and distribution in topsoil and subsoil samples collected from a field survey in Beijing, China, 2023. (a) Correlation analysis, (b) principle component analysis, (c) hierarchical clustering, (d) ridge regression, (e) DSPC network, and (f) structural equation model showing factors affecting microplastic distribution in subsoils versus topsoil.

various consumer goods such as textiles,[94,95] PE is commonly used in agricultural mulching films and plastic gauze at construction sites to prevent dusting;[10,58] PET is frequently used for food and beverage packaging as well as textiles.[95−97] PU is widely adopted in packaging as well as in many automotive applications,[98,99] and PVC is frequently used in building and construction, particularly for pipes.[100,101] A clear separation was observed using the OPLS-DA model, with $p < 0.001$, $R^2Y = 0.503$, and $Q^2 = 0.417$. Positive T score [1] values were reported for topsoil (5 cm), while negative T score [1] values were reported for most subsoils (50 and 100 cm) (Figure 3b,c). The key polymers contributing to the difference between topsoil and subsoil were identified as PU, PET, PE, PVC, and PA (VIP > 1) with VIP values of 1.37, 1.26, 1.23, 1.22, and 1.22, respectively (Figure 3d).

The relative abundances of PC and PE peaked at 5 cm; the abundances of PA, PMMA, PP, and PS peaked at 50 cm, while the abundances of other polymers peaked at 100 cm (Figure 3a). We originally assumed that polymers with a higher density would migrate to a greater extent; however, the findings from this study cannot be simply explained by this theory. For instance, PE and PP have low densities of <1, but their abundances showed different trends with increasing depth. PET and PVC are both polymers with high densities of >1.3, yet their relative abundances did not monotonically increase with depth. We further classified the 11 polymer types into low-density polymers (i.e., PE and PP, with densities lower than water) and high-density polymers (i.e., other polymers whose densities are usually higher than water). It was found that the proportion of high-density polymers first decreased and then increased with depth (Figure S5). Furthermore, we also classified the 11 polymer types into high-hydrophilicity polymers (i.e., polymers with oxygen-containing functional groups in their structure, including PA, PC, PET, PMMA, POM, and PU) and low-hydrophilicity polymers (i.e., other polymers, including PE, PP, PS, PTFE, and PVC). A gradual decrease in the proportion of high-hydrophilic polymers was observed (Figure S6). These findings suggest that density or hydrophilicity alone cannot explain the vertical distribution of MP polymers, further indicating the presence of other dominant transport mechanisms.

3.4. Polymer Oxidation Characteristics of MPs in Topsoil and Subsoil. The carbonyl indices (CIs) for MPs in subsoil were significantly lower ($p < 0.05$) than those in topsoil (Figure 3e), suggesting a lower degree of chemical oxidation for subsoil MPs. A lower degree of MP oxidation was also found to correlate with a higher average diameter for different land use types (Figure 3f). Furthermore, the degree of oxidation for different polymers showed an exponential decline with an increasing average diameter (Figure 3g). Similar patterns were also reported by previous field survey along the Japan coast[102] and accelerated aging experiments simulating coastal weathering of MPs,[103] which found that smaller MPs tended to have a higher extent of oxidation due to longer exposure to environmental aging processes.[102,103] It was also observed that particles with an aspect ratio closer to 1 (more spherical) tended to have a higher degree of oxidation (Figure 3h). Our previous field survey also suggested that MPs in the soil environment underwent shape changes from larger fragments to smaller granules.[6] Note that different polymers intrinsically possess different CIs due to their chemical structures; therefore, a polymer-type specific comparison of the degree of chemical oxidation was also conducted (Figure 3i), suggesting that PE and PVC were more oxidized in topsoil compared to the lesser oxidized PET, POM, and PTFE in the same media. Other polymer types showed no statistically significant difference across various sampling depths.

https://doi.org/10.1021/acs.est.5c00871
Environ. Sci. Technol. 2025, 59, 12933−12946

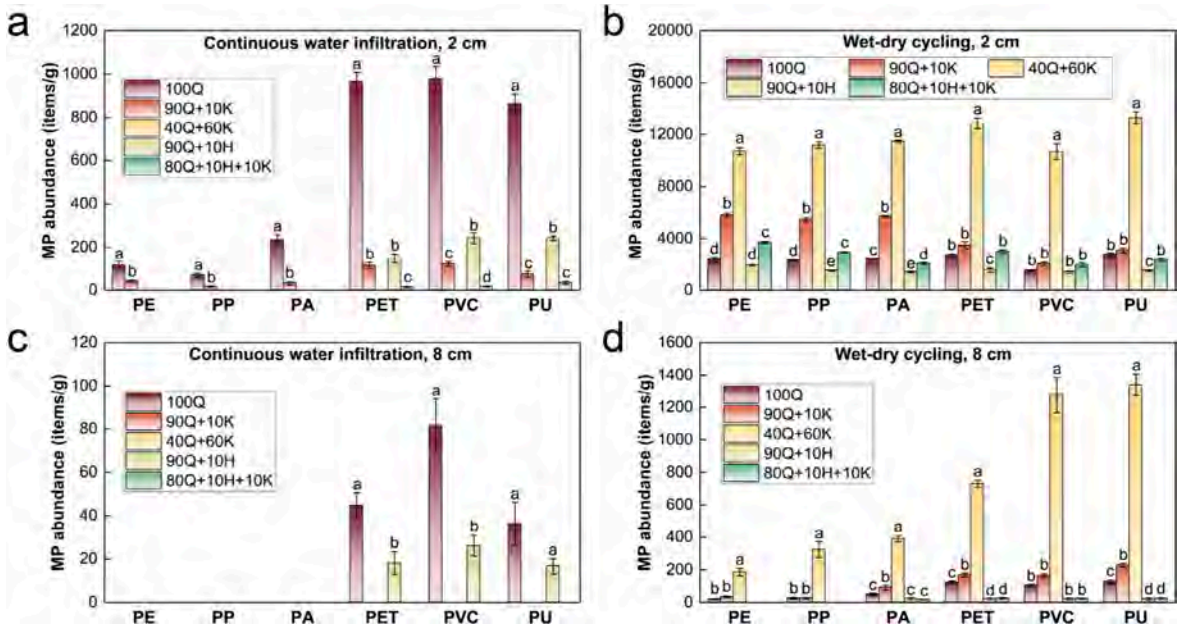


Figure 5. Additional evidence from laboratory simulation experiments. (a) Abundance of MPs under continuous water infiltration conditions at 2 cm. (b) Abundance of MPs under vadose zone wet−dry cycling conditions at 2 cm. (c) Abundance of MPs under continuous water infiltration conditions at 8 cm. (d) Abundance of MPs under vadose zone wet−dry cycling conditions at 8 cm.

3.5. Factors Affecting Vertical Distribution of MPs. We explored potential factors influencing MP vertical distribution, where a higher MPsub/MPtop ratio (soil MP abundance at 50 cm divided by that at 5 cm, based on paired data for 50 sample points) suggested a greater ability for MPs to migrate vertically. Correlation analysis showed that the proportion of fine particles (clay and silt) was significantly positively correlated with MPsub/MPtop, suggesting that soils with finer textures may have facilitated MP penetration (Figure 4a). This finding contradicted our original intuitive belief that coarse-textured soils should favor MP transport, while fine-textured soils would impede MP movement due to pore blockage. On the other hand, Fe content in soil exhibited a significant negative correlation with MPsub/MPtop ($p < 0.05$) (Figure 4a), indicating that higher Fe content in soils may hinder MP penetration. This impediment was expected, as previous studies from batch experiments have shown that positively charged or less negatively charged Fe oxides have a higher capacity for the attachment of negatively charged NPs/MPs due to electrostatic interactions, compared with silicates.[104,105] Previous studies with Fe-modified soil amendments also suggested a reduction in MP mobility following amendment.[106,107]

Results from PCA also suggested that soil texture and Fe content played key roles in affecting MP vertical distribution (Figure 4b), while hierarchical clustering results indicated that texture, albedo, penetration resistance, and population density are closely related to MP abundance in soils, in both topsoil and subsoil (Figure 4c). Ridge regression results corroborated the correlation analysis and PCA, further emphasizing the crucial impact of soil texture and Fe content on the MP distribution (Figure 4d).

Additionally, the DSPC network showed that albedo directly affected MP abundance in the topsoil (Figure 4e). It is well-established that UV irradiation promotes the fragmentation of large plastic debris into MPs. Our previous study using accelerated aging experiments also suggested that UV irradiation leads to the rapid generation of MPs with exponential kinetics.[75] Higher albedo indicates less protection from vegetation cover against UV irradiation,[108,109] which may contribute to higher MP abundance. In the DSPC network, texture had a direct impact on MP vertical distribution, while Fe content had an indirect impact by affecting soil CEC (Figure 4e).

Considering these findings collectively, we then established a structural equation model to characterize the potential pathways (Figure 4f). The p value was 0.78, indicating a close fit between the model and data (test statistic = 7.28 and df = 11). The standard root-mean-square residual (SRMR) was 0.074, suggesting a good fit of data to the proposed pathways. The pathways indicated that higher albedo led to higher MP abundance in topsoil, finer texture promoted MP migration to subsoils, and higher Fe content impeded MP migration. Although finer soil texture would result in higher penetration resistance, which is not favorable for MP migration, this impediment pathway played only a minor role compared to the enhancement (Figure 4f).

3.6. Additional Evidence from Laboratory Simulation Experiments. Findings from the field survey suggested that a finer texture and lower Fe content may have favored MP migration to subsoil. Here, we provided multiple lines of evidence using additional lab column migration experiments (Figure 5). In column experiments with continuous water infiltration, an increase in vadose zone kaolinite content (i.e., finer texture) significantly impeded MP transport ($p < 0.05$) (Figure 5a,c). Results from wet−dry cycling experiments were in stark contrast, showing a significant promotion of MP transport ($p < 0.05$) (Figure 5b,d). Furthermore, the introduction of hematite, a typical Fe oxide, significantly impeded MP transport in both scenarios ($p < 0.05$) (Figure 5). These phenomena were observed for different polymer types, including PE, PP, PA, PET, PVC, and PU, despite the intrinsic differences in the density, polymer structure, and surface hydrophobicity of these polymers.

https://doi.org/10.1021/acs.est.5c00871
Environ. Sci. Technol. 2025, 59, 12933−12946

3.7. Environmental Implications: Preferential Penetration as a Possible Cause. Here, we propose two scenarios for MP migration to subsoil based on the established knowledge of MP transport: the ideal filtration hypothesis and the preferential penetration hypothesis (Figure S7).

The ideal filtration hypothesis assumes that MPs migrate along soil pores in a manner similar to that of a filtration process. This hypothesis is inspired by the filtration process in environmental engineering, which traps and removes particles from aqueous media. In this case, larger MPs will be trapped to a greater extent, while smaller MPs will have a higher mobility. Additionally, fine-textured porous media will trap more particles, leading to lower mobility. Previous lab-based column migration tests using pure quartz sand as a representative porous medium supported this hypothesis, showing that coarser sand and smaller MPs result in greater MP penetration.[24,110−112]

Conversely, the preferential penetration hypothesis assumes that MPs mainly migrate through cracks generated by aging processes such as wet−dry cycling events. In this scenario, fine-textured soils will favor MP penetration due to a higher likelihood of desiccation cracking, and MPs that penetrate subsoils are not necessarily smaller when preferential penetration occurs. This hypothesis is inspired by knowledge from engineering geology, which suggests that silt and clay fractions in natural soils contain higher amounts of clay minerals, leading to desiccation cracking due to the swelling and shrinkage of these minerals.[113−115]

The findings from this study provide multiple lines of evidence, suggesting that MPs are likely transported from topsoil to subsoil via preferential penetration processes rather than ideal filtration. Field data showed that, while MP abundances in subsoil were lower compared to topsoil (Figure 1a), they were not smaller (Figure 2d) or more oxidized (Figure 3e), which contradicted the ideal filtration hypothesis. Additionally, results from column migration experiments suggested that vertical migration of MPs was significantly enhanced in fine-textured and Fe-depleted vadose zones under wet−dry cycling events (Figure 5). This finding strongly corroborates field data, which showed that the proportion of fine particles (clay and silt) was significantly positively correlated with MPsub/MPtop, while the Fe content was significantly negatively correlated with MPsub/MPtop (Figure 4a).

The findings from this field survey were also in stark contrast to the intuitive belief suggested by previous column migration studies of MP transport in porous media. Using quartz sand as a porous medium and adopting continuous flow conditions to examine MP transport mechanisms in soils, laboratory column migration experiments suggested that smaller MPs tended to have higher mobility in porous media compared to larger ones.[91−93] Furthermore, coarse-textured porous media were generally believed to favor MP transport due to larger pore spaces.[24,111] However, the results from this study provide robust evidence that MPs in subsoils are not necessarily smaller under real-world conditions and that fine-textured soils, in contrast, facilitate vertical MP transport. Therefore, we recommend revising current laboratory transport experiment simulations to better reflect natural conditions, including adopting natural soils or different textured minerals as vadose zone media and incorporating naturally occurring wet−dry cycling events, which were found to be important drivers of MP vertical distribution. Additionally, it is important to note that the groundwater level in this field region was >15 m;[116] therefore, fluctuations in groundwater level did not affect MP transport in this case. In other regions with a shallow groundwater table, however, it is highly likely that groundwater level fluctuations may also influence the MP vertical distribution.

The phenomenon of preferential penetration has implications for the risk assessment and mitigation of MPs in subsurface environments. Regions with lower soil Fe content, finer texture, more frequent precipitation events (i.e., leading to more wet−dry cycling in the vadose zone), and shallower groundwater are at a higher risk of MP penetration from topsoil to subsoil and then to the groundwater aquifer. The preferential penetration phenomenon may also apply to fractured rock vadose zones, including karst areas. In such regions, potential human and ecological risks induced by drinking MP-enriched groundwater should be explored by scientists, policymakers, and natural resource managers. On the other hand, a low-impact development (LID) infrastructure, such as bioretention ponds, has been proposed as a promising strategy to remove MPs from runoff water and prevent their migration across environmental compartments.[117,118] Such systems often apply a natural soil layer to trap aqueous contaminants including MPs, and high frequency wet−dry cycles occur in the vadose zone.[119,120] The risks of MP transport and leakage from these systems via preferential penetration should also be examined. The use of an Fe-rich surface layer for such systems for contaminant retention could be a potentially feasible mitigation measure.

3.8. Study Limitations. Although our investigation presents several novel findings, we feel it is important to highlight a few important study limitations. First, the LDIR system used in this study could only characterize MPs with sizes ranging between 20 and 500 μm, meaning larger MPs (>500 μm) and smaller MPs and NPs (<20 μm) were not modeled. Second, soil physicochemical properties were only measured for the surficial layer due to sampling mass restrictions. This limitation was partially overcome through additional support from lab column migration experiments, providing multiple lines of evidence to verify our hypotheses. Finally, other processes that may lead to soil cracking, such as freeze−thaw cycling,[121,122] were not considered in this region. Future studies may further verify whether the preferential penetration phenomenon and mechanisms also apply in high-latitude regions with both wet−dry cycling and freeze−thaw cycling.

■ ASSOCIATED CONTENT

Supporting Information

The Supporting Information is available free of charge at https://pubs.acs.org/doi/10.1021/acs.est.5c00871.

Detailed description of field site, MP abundance normalization method for comparison among literature, spatial distribution and land use types of sampling points, representative photos for each land use type and soil core sampling process, morphologies and FTIR spectra of MPs used for additional laboratory experiments, proportions of high-density and high-hydrophilicity polymers at different sampling depths, conceptual diagrams of the ideal filtration hypothesis and the preferential penetration hypothesis, particle quantification data of quality control experiments, regression

https://doi.org/10.1021/acs.est.5c00871
Environ. Sci. Technol. 2025, 59, 12933−12946

parameters of conditional fragmentation model, regression parameters of power law size distribution, and the original data set (PDF)

AUTHOR INFORMATION

Corresponding Author

Deyi Hou − *School of Environment, Tsinghua University, Beijing 100084, China; State Key Laboratory of Regional Environment and Sustainability, Tsinghua University, Beijing 100084, China;* orcid.org/0000-0002-0511-5806; Phone: +86-010-62781159; Email: houdeyi@tsinghua.edu.cn

Authors

Liuwei Wang − *School of Environment, Tsinghua University, Beijing 100084, China; Guangxi Laboratory on the Study of Coral Reefs in the South China Sea, Coral Reef Research Center of China, School of Marine Sciences, Guangxi University, Nanning 530004, China;* orcid.org/0000-0002-6176-6056

Caide Huang − *School of Environment, Tsinghua University, Beijing 100084, China*

Junhao Cao − *School of Environment, Tsinghua University, Beijing 100084, China;* orcid.org/0000-0001-7620-5633

Pingfan Zhou − *School of Environment, Tsinghua University, Beijing 100084, China*

Siqi Han − *School of Environment, Tsinghua University, Beijing 100084, China*

Guangyu Qu − *School of Environment, Tsinghua University, Beijing 100084, China*

Michael S. Bank − *Institute of Marine Research, Bergen NO-5817, Norway; University of Massachusetts Amherst, Amherst, Massachusetts 01003, United States;* orcid.org/0000-0001-5194-7171

Complete contact information is available at: https://pubs.acs.org/10.1021/acs.est.5c00871

Notes

The authors declare no competing financial interest.

ACKNOWLEDGMENTS

This work was supported by the National Natural Science Foundation of China (Grant No. 42225703) and Guangxi Science and Technology Program (Grant No. AD25069075).

REFERENCES

(1) PlasticsEurope. *Plastics - the fast Facts 2024*; PlasticsEurope: 2024.

(2) Stubbins, A.; Law, K. L.; Muñoz, S. E.; Bianchi, T. S.; Zhu, L. Plastics in the Earth system. *Science* **2021**, *373* (6550), 51−55.

(3) Thompson, R. C.; Courtene-Jones, W.; Boucher, J.; Pahl, S.; Raubenheimer, K.; Koelmans, A. A. Twenty years of microplastics pollution research - what have we learned? *Science* **2024**, *386* (6720), No. eadl2746.

(4) MacLeod, M.; Arp, H. P. H.; Tekman, M. B.; Jahnke, A. The global threat from plastic pollution. *Science* **2021**, *373* (6550), 61−65.

(5) Rillig, M. C.; Lehmann, A. Microplastic in terrestrial ecosystems. *Science* **2020**, *368* (6498), 1430−1431.

(6) Wang, L.; Li, P.; Zhang, Q.; Wu, W. M.; Luo, J.; Hou, D. Modeling the Conditional Fragmentation-Induced Microplastic Distribution. *Environ. Sci. Technol.* **2021**, *55* (9), 6012−6021.

(7) Büks, F.; Kaupenjohann, M. Global concentrations of microplastics in soils - A review. *Soil* **2020**, *6* (2), 649−662.

(8) Zhang, Z.; Zhao, S.; Chen, L.; Duan, C.; Zhang, X.; Fang, L. A review of microplastics in soil: Occurrence, analytical methods, combined contamination and risks. *Environ. Pollut.* **2022**, *306*, 119374.

(9) Shi, W.; Wu, N.; Zhang, Z.; Liu, Y.; Chen, J.; Li, J. A global review on the abundance and threats of microplastics in soils to terrestrial ecosystem and human health. *Sci. Total Environ.* **2024**, *912*, 169469.

(10) Chen, L.; Yu, L.; Li, Y.; Han, B.; Zhang, J.; Tao, S.; Liu, W. Spatial Distributions, Compositional Profiles, Potential Sources, and Intfluencing Factors of Microplastics in Soils from Different Agricultural Farmlands in China: A National Perspective. *Environ. Sci. Technol.* **2022**, *56* (23), 16964−16974.

(11) Qi, R.; Jones, D. L.; Li, Z.; Liu, Q.; Yan, C. Behavior of microplastics and plastic film residues in the soil environment: A critical review. *Sci. Total Environ.* **2020**, *703*, 134722.

(12) Li, L.; Luo, Y.; Li, R.; Zhou, Q.; Peijnenburg, W. J. G. M.; Yin, N.; Yang, J.; Tu, C.; Zhang, Y. Effective uptake of submicrometre plastics by crop plants via a crack-entry mode. *Nature Sustain.* **2020**, *3* (11), 929−937.

(13) Wang, J.; Zhang, X.; Li, X.; Wang, Z. Exposure pathways, environmental processes and risks of micro (nano) plastics to crops and feasible control strategies in agricultural regions. *J. Hazard. Mater.* **2023**, *459*, 132269.

(14) Wang, L.; Liu, B.; Zhang, W.; Li, Q.; Lin, B.; Wei, C. An unrecognized entry pathway of submicrometre plastics into crop root: The split of hole in protective layer. *J. Hazard. Mater.* **2023**, *457*, 131732.

(15) Scheurer, M.; Bigalke, M. Microplastics in Swiss Floodplain Soils. *Environ. Sci. Technol.* **2018**, *52* (6), 3591−3598.

(16) Zhang, S.; Liu, X.; Hao, X.; Wang, J.; Zhang, Y. Distribution of low-density microplastics in the mollisol farmlands of northeast China. *Sci. Total Environ.* **2020**, *708*, 135091.

(17) Leitão, I. A.; van Schaik, L.; Ferreira, A. J. D.; Alexandre, N.; Geissen, V. The spatial distribution of microplastics in topsoils of an urban environment - Coimbra city case-study. *Environ. Res.* **2023**, *218*, 114961.

(18) Li, Z.; Xu, B.; Zhang, R.; Wang, F.; Li, L.; Wang, K.; Zhang, R.; Jing, X.; Liu, Y.; Chen, P. Effects of land use on soil microplastic distribution adjacent to Danjiangkou reservoir, China. *Chemosphere* **2023**, *338*, 139389.

(19) Zhang, H.; Huang, Y.; An, S.; Li, H.; Deng, X.; Wang, P.; Fan, M. Land-use patterns determine the distribution of soil microplastics in typical agricultural areas on the eastern Qinghai-Tibetan Plateau. *J. Hazard. Mater.* **2022**, *426*, 127806.

(20) Corradini, F.; Casado, F.; Leiva, V.; Huerta-Lwanga, E.; Geissen, V. Microplastics occurrence and frequency in soils under different land uses on a regional scale. *Sci. Total Environ.* **2021**, *752*, 141917.

(21) Akca, M. O.; Gündoğdu, S.; Akca, H.; Delialioğlu, R. A.; Aksit, C.; Turgay, O. C.; Harada, N. An evaluation on microplastic accumulations in Turkish soils under different land uses. *Sci. Total Environ.* **2024**, *911*, 168609.

(22) Yoon, J. H.; Kim, B. H.; Kim, K. H. Distribution of microplastics in soil by types of land use in metropolitan area of Seoul. *Appl. Biol. Chem.* **2024**, *67* (1), 15.

(23) Keller, A. S.; Jimenez-Martinez, J.; Mitrano, D. M. Transport of Nano- And Microplastic through Unsaturated Porous Media from Sewage Sludge Application. *Environ. Sci. Technol.* **2020**, *54* (2), 911−920.

(24) Dong, S.; Zhou, M.; Su, X.; Xia, J.; Wang, L.; Wu, H.; Suakollie, E. B.; Wang, D. Transport and retention patterns of fragmental microplastics in saturated and unsaturated porous media: A real-time pore-scale visualization. *Water Res.* **2022**, *214*, 118195.

(25) Gui, X.; Ren, Z.; Xu, X.; Chen, X.; Chen, M.; Wei, Y.; Zhao, L.; Qiu, H.; Gao, B.; Cao, X. Dispersion and transport of microplastics in three water-saturated coastal soils. *J. Hazard. Mater.* **2022**, *424*, 127614.

(26) Ren, Z.; Gui, X.; Wei, Y.; Chen, X.; Xu, X.; Zhao, L.; Qiu, H.; Cao, X. Chemical and photo-initiated aging enhances transport risk of microplastics in saturated soils: Key factors, mechanisms, and modeling. *Water Res.* **2021**, *202*, 117407.
(27) Dong, S.; Xia, J.; Sheng, L.; Wang, W.; Liu, H.; Gao, B. Transport characteristics of fragmental polyethylene glycol terephthalate (PET) microplastics in porous media under various chemical conditions. *Chemosphere* **2021**, *276*, 130214.
(28) Li, W.; Brunetti, G.; Bolshakova, A.; Stumpp, C. Effect of particle density on microplastics transport in artificial and natural porous media. *Sci. Total Environ.* **2024**, *935*, 173429.
(29) Jiang, Y.; Zhou, S.; Fei, J.; Qin, Z.; Yin, X.; Sun, H.; Sun, Y. Transport of different microplastics in porous media: Effect of the adhesion of surfactants on microplastics. *Water Res.* **2022**, *215*, 118262.
(30) Cao, L.; Wu, D.; Liu, P.; Hu, W.; Xu, L.; Sun, Y.; Wu, Q.; Tian, K.; Huang, B.; Yoon, S. J.; Kwon, B.-O.; Khim, J. S. Occurrence, distribution and affecting factors of microplastics in agricultural soils along the lower reaches of Yangtze River, China. *Sci. Total Environ.* **2021**, *794*, 148694.
(31) Li, S.; Ding, F.; Flury, M.; Wang, Z.; Xu, L.; Li, S.; Jones, D. L.; Wang, J. Macro- and microplastic accumulation in soil after 32 years of plastic film mulching. *Environ. Pollut.* **2022**, *300*, 118945.
(32) Weber, C. J.; Santowski, A.; Chifflard, P. Investigating the dispersal of macro- and microplastics on agricultural fields 30 years after sewage sludge application. *Sci. Rep.* **2022**, *12* (1), 6401.
(33) Qiu, Y.; Zhou, S.; Zhang, C.; Chen, L.; Qin, W.; Zhang, Q. Vertical distribution and weathering characteristic of microplastics in soil profile of different land use types. *Sci. Total Environ.* **2023**, *905*, 166902.
(34) Li, J.; Zhu, B.; Huang, B.; Ma, J.; Lu, C.; Chi, G.; Guo, W.; Chen, X. Vertical distribution and characteristics of soil microplastics under different land use patterns: A case study of Shouguang City, China. *Sci. Total Environ.* **2023**, *903*, 166154.
(35) Zhang, S.; Bao, A.; Lin, X.; Jia, G.; Zhang, Q. Microplastic Accumulation in Agricultural Soils with Different Mulching Histories in Xinjiang, China. *Sustainability* **2023**, *15* (6), 5438.
(36) He, Y. Q.; McDonough, L. K.; Zainab, S. M.; Guo, Z. F.; Chen, C.; Xu, Y. Y. Microplastic accumulation in groundwater: Data-scaled insights and future research. *Water Res.* **2024**, *258*, 121808.
(37) Umeh, O. R.; Ophori, D. U.; Ibo, E. M.; Eke, C. I.; Oyen, T. P. Groundwater systems under siege: The silent invasion of microplastics and cock-tails worldwide. *Environ. Pollut.* **2024**, *356*, 124305.
(38) Viaroli, S.; Lancia, M.; Re, V. Microplastics contamination of groundwater: Current evidence and future perspectives. A review. *Sci. Total Environ.* **2022**, *824*, 153851.
(39) Pittroff, M.; Müller, Y. K.; Witzig, C. S.; Scheurer, M.; Storck, F. R.; Zumbülte, N. Microplastic analysis in drinking water based on fractionated filtration sampling and Raman microspectroscopy. *Environ. Sci. Pollut. Res.* **2021**, *28* (42), 59439−59451.
(40) Bäuerlein, P. S.; Hofman-Caris, R. C. H. M.; Pieke, E. N.; ter Laak, T. L. Fate of microplastics in the drinking water production. *Water Res.* **2022**, *221*, 118790.
(41) Liu, S.; Liu, X.; Guo, J.; Yang, R.; Wang, H.; Sun, Y.; Chen, B.; Dong, R. The Association Between Microplastics and Microbiota in Placentas and Meconium: The First Evidence in Humans. *Environ. Sci. Technol.* **2023**, *57* (46), 17774−17785.
(42) Lu, W.; Li, X.; Wang, S.; Tu, C.; Qiu, L.; Zhang, H.; Zhong, C.; Li, S.; Liu, Y.; Liu, J.; Zhou, Y. New Evidence of Microplastics in the Lower Respiratory Tract: Inhalation through Smoking. *Environ. Sci. Technol.* **2023**, *57* (23), 8496−8505.
(43) Ourgaud, M.; Phuong, N. N.; Papillon, L.; Panagiotopoulos, C.; Galgani, F.; Schmidt, N.; Fauvelle, V.; Brach-Papa, C.; Sempéré, R. Identification and Quantification of Microplastics in the Marine Environment Using the Laser Direct Infrared (LDIR) Technique. *Environ. Sci. Technol.* **2022**, *56* (14), 9999−10009.
(44) Fan, Y.; Zheng, J.; Deng, L.; Rao, W.; Zhang, Q.; Liu, T.; Qian, X. Spatiotemporal dynamics of microplastics in an urban river network area. *Water Res.* **2022**, *212*, 118116.
(45) Xie, J.; Gowen, A.; Xu, W.; Xu, J. Analysing micro- and nanoplastics with cutting-edge infrared spectroscopy techniques: a critical review. *Anal. Methods* **2024**, *16* (15), 2177−2197.
(46) Shi, H.; Sun, C. *Analysis of Microplastics and Nanoplastics*. Elsevier: Amsterdam, the Netherlands, 2024.
(47) Ivleva, N. P. Chemical Analysis of Microplastics and Nanoplastics: Challenges, Advanced Methods, and Perspectives. *Chem. Rev.* **2021**, *121* (19), 11886−11936.
(48) Lei, J.; Zhang, X.; Yan, W.; Chen, X.; Li, Z.; Dan, P.; Dan, Q.; Jiang, W.; Liu, Q.; Li, Y. Urban Microplastic Pollution Revealed by a Large-Scale Wetland Soil Survey. *Environ. Sci. Technol.* **2023**, *57* (21), 8035−8043.
(49) *Soil - Determination of pH - Potentiometry*; MEE, HJ 962-2018; Ministry of Ecology and Environment of the People's Republic of China: Beijing, China, 2018.
(50) *Soil quality-Determination of conductivity-Electrode method*; MEE, HJ 802-2016; Ministry of Ecology and Environment of the People's Republic of China: Beijing, China, 2016.
(51) Carter, M. R.; Gregorich, E. G. *Soil sampling and methods of analysis*; CRC Press: Boca Raton, FL, USA, 2007.
(52) Wang, L.; Guo, J.; Wang, H.; Luo, J.; Hou, D. Stimulated leaching of metalloids along 3D-printed fractured rock vadose zone. *Water Res.* **2022**, *226*, 119224.
(53) Brady, N. C.; Weil, R. R. *The Nature and Properties of Soils*, 15th ed.; Pearson Education Limited: Edinburgh Gate, 2017.
(54) *Soil and sediment-Determination of aqua regia extracts of 12 metal elements-Inductively coupled plasma mass spectrometry*; MEE, HJ 803-2016; Ministry of Ecology and Environment of the People's Republic of China: Beijing, China, 2016.
(55) Li, Q.; Wu, J.; Zhao, X.; Gu, X.; Ji, R. Separation and identification of microplastics from soil and sewage sludge. *Environ. Pollut.* **2019**, *254*, 113076.
(56) Kooi, M.; Koelmans, A. A. Simplifying Microplastic via Continuous Probability Distributions for Size, Shape, and Density. *Environ. Sci. Techno. Lett.* **2019**, *6* (9), 551−557.
(57) Cózar, A.; Echevarría, F.; González-Gordillo, J. I.; Irigoien, X.; Úbeda, B.; Hernández-León, S.; Palma, Á. T.; Navarro, S.; García-de-Lomas, J.; Ruiz, A.; Fernández-de-Puelles, M. L.; Duarte, C. M. Plastic debris in the open ocean. *Proc. Natl. Acad. Sci. U. S. A.* **2014**, *111* (28), 10239−10244.
(58) Gao, J.; Wang, L.; Wu, W. M.; Luo, J.; Hou, D. Microplastic generation from field-collected plastic gauze: Unveiling the aging processes. *J. Hazard. Mater.* **2024**, *467*, 133615.
(59) Koelmans, A. A.; Redondo-Hasselerharm, P. E.; Mohamed Nor, N. H.; Kooi, M. Solving the Nonalignment of Methods and Approaches Used in Microplastic Research to Consistently Characterize Risk. *Environ. Sci. Technol.* **2020**, *54* (19), 12307−12315.
(60) Zhang, Z. A.; Qin, X.; Zhang, Y. Using Data-Driven Methods and Aging Information to Quantitatively Identify Microplastic Environmental Sources and Establish a Comprehensive Discrimination Index. *Environ. Sci. Technol.* **2023**, *57* (30), 11279−11288.
(61) Hu, J.; Dai, J.; Sheng, N. Kynurenic Acid Plays a Protective Role in Hepatotoxicity Induced by HFPO-DA in Male Mice. *Environ. Sci. Technol.* **2024**, *58* (4), 1842−1853.
(62) Martella, G.; Gorokhova, E.; Sousa, P. F. M.; Tretyakova, N. Y.; Sundelin, B.; Motwani, H. V. DNA Adductomics for the Biological Effect Assessment of Contaminant Exposure in Marine Sediments. *Environ. Sci. Technol.* **2023**, *57* (29), 10591−10603.
(63) Zhou, Q.; Shen, Y.; Chou, L.; Guo, J.; Zhang, X.; Shi, W. Identification of Glucocorticoid Receptor Antagonistic Activities and Responsible Compounds in House Dust: Bioaccessibility Should Not Be Ignored. *Environ. Sci. Technol.* **2022**, *56* (23), 16768−16779.
(64) Boccard, J.; Rutledge, D. N. A consensus orthogonal partial least squares discriminant analysis (OPLS-DA) strategy for multiblock Omics data fusion. *Anal. Chim. Acta* **2013**, *769*, 30−39.
(65) Basu, S.; Duren, W.; Evans, C. R.; Burant, C. F.; Michailidis, G.; Karnovsky, A. Sparse network modeling and metscape-based visualization methods for the analysis of large-scale metabolomics data. *Bioinformatics* **2017**, *33* (10), 1545−1553.

(66) Janková, J.; van de Geer, S. Confidence intervals for high-dimensional inverse covariance estimation. *Electron. J. Stat.* **2015**, *9*, 1205−1229.
(67) Lu, X.; Lin, Y.; Qiu, X.; Liu, J.; Zhu, T.; Araujo, J. A.; Zhang, J.; Zhu, Y. Metabolomic Changes after Subacute Exposure to Polycyclic Aromatic Hydrocarbons: A Natural Experiment among Healthy Travelers from Los Angeles to Beijing. *Environ. Sci. Technol.* **2021**, *55* (8), 5097−5105.
(68) McDonald, G. C. Ridge regression. *Wiley Interdiscip. Rev. Comput. Stat.* **2009**, *1* (1), 93−100.
(69) Anderson, J. C.; Gerbing, D. W. Structural equation modeling in practice: A review and recommended two-step approach. *Psychol. Bull.* **1988**, *103* (3), 411.
(70) Lewis, J.; Sjöstrom, J. Optimizing the experimental design of soil columns in saturated and unsaturated transport experiments. *J. Contam. Hydrol.* **2010**, *115* (1−4), 1−13.
(71) Choudhary, A.; Khandelwal, N.; Ganie, Z. A.; Darbha, G. K. Influence of magnetite and its weathering originated maghemite and hematite minerals on sedimentation and transport of nanoplastics in the aqueous and subsurface environments. *Sci. Total Environ.* **2024**, *912*, 169132.
(72) FAO. *Irrigation Water Management: Training Manual No. 1 - Introduction to Irrigation*; Food and Agriculture Organization of the United Nations: Rome, Italy, 1985.
(73) De Souza MacHado, A. A.; Lau, C. W.; Till, J.; Kloas, W.; Lehmann, A.; Becker, R.; Rillig, M. C. Impacts of Microplastics on the Soil Biophysical Environment. *Environ. Sci. Technol.* **2018**, *52* (17), 9656−9665.
(74) Wang, L.; Bank, M. S.; Rinklebe, J.; Hou, D. Plastic-Rock Complexes as Hotspots for Microplastic Generation. *Environ. Sci. Technol.* **2023**, *57* (17), 7009−7017.
(75) Wang, L.; Gao, J.; Wu, W.-M.; Luo, J.; Bank, M. S.; Koelmans, A. A.; Boland, J. J.; Hou, D. Rapid Generation of Microplastics and Plastic-Derived Dissolved Organic Matter from Food Packaging Films under Simulated Aging Conditions. *Environ. Sci. Technol.* **2024**, *58* (45), 20147−20159.
(76) Liu, X.; Cheng, P.; Zhou, J.; Fan, Y.; Fu, Y.; Tan, L.; Lan, J.; Zhang, L.; Gu, H.; Bi, Y. Microplastic Characteristics in Equus kiang (Tibetan Wild Ass) Feces and Soil on the Southern Tibetan Plateau, China. *Environ. Sci. Technol.* **2023**, *57* (26), 9732−9743.
(77) Huang, S.; Huang, X.; Bi, R.; Guo, Q.; Yu, X.; Zeng, Q.; Huang, Z.; Liu, T.; Wu, H.; Chen, Y.; Xu, J.; Wu, Y.; Guo, P. Detection and Analysis of Microplastics in Human Sputum. *Environ. Sci. Technol.* **2022**, *56* (4), 2476−2486.
(78) van den Berg, P.; Huerta-Lwanga, E.; Corradini, F.; Geissen, V. Sewage sludge application as a vehicle for microplastics in eastern Spanish agricultural soils. *Environ. Pollut.* **2020**, *261*, 114198.
(79) Aydin, S.; Mucevher, O.; Ulvi, A.; Beduk, F.; Aydin, M. E.; Merken, O.; Uzun, C. Effects of long-term wastewater irrigation on microplastics pollution in agricultural soil. *Environ. Sci. Pollut. Res.* **2025**, *32* (20), 12340−12359.
(80) Schefer, R. B.; Koestel, J.; Mitrano, D. M. Minimal vertical transport of microplastics in soil over two years with little impact of plastics on soil macropore networks. *Commun. Earth Environ.* **2025**, *6* (1), 278.
(81) Wang, F.; Lai, Z.; Peng, G.; Luo, L.; Liu, K.; Huang, X.; Xu, Y.; Shen, Q.; Li, D. Microplastic abundance and distribution in a Central Asian desert. *Sci. Total Environ.* **2021**, *800*, 149529.
(82) Ding, L.; Wang, X.; Ouyang, Z.; Chen, Y.; Wang, X.; Liu, D.; Liu, S.; Yang, X.; Jia, H.; Guo, X. The occurrence of microplastic in Mu Us Sand Land soils in northwest China: Different soil types, vegetation cover and restoration years. *J. Hazard. Mater.* **2021**, *403*, 123982.
(83) Helcoski, R.; Yonkos, L. T.; Sanchez, A.; Baldwin, A. H. Wetland soil microplastics are negatively related to vegetation cover and stem density. *Environ. Pollut.* **2020**, *256*, 113391.
(84) Li, L.; Zhang, Y.; Kang, S.; Wang, S.; Gao, T.; Wang, Z.; Luo, X.; Kang, Q.; Sajjad, W. Characteristics of microplastics and their abundance impacts on microbial structure and function in agricultural soils of remote areas in west China. *Environ. Pollut.* **2024**, *360*, 124630.
(85) Zhou, Y.; Liu, X.; Wang, J. Characterization of microplastics and the association of heavy metals with microplastics in suburban soil of central China. *Sci. Total Environ.* **2019**, *694*, 133798.
(86) Feng, S.; Lu, H.; Yao, T.; Tang, M.; Yin, C. Analysis of microplastics in soils on the high-altitude area of the Tibetan Plateau: Multiple environmental factors. *Sci. Total Environ.* **2023**, *857*, 159399.
(87) Xia, F.; Liu, H.; Zhang, J.; Wang, D. Migration characteristics of microplastics based on source-sink investigation in a typical urban wetland. *Water Res.* **2022**, *213*, 118154.
(88) Jia, W.; Karapetrova, A.; Zhang, M.; Xu, L.; Li, K.; Huang, M.; Wang, J.; Huang, Y. Automated identification and quantification of invisible microplastics in agricultural soils. *Sci. Total Environ.* **2022**, *844*, 156853.
(89) Chen, Y.; Niu, J.; Xu, D.; Zhang, M.; Sun, K.; Gao, B. Wet Deposition of Globally Transportable Microplastics (<25 μm) Hovering over the Megacity of Beijing. *Environ. Sci. Technol.* **2023**, *57* (30), 11152−11162.
(90) Xu, D.; Gao, B.; Wan, X.; Peng, W.; Zhang, B. Influence of catastrophic flood on microplastics organization in surface water of the Three Gorges Reservoir, China. *Water Res.* **2022**, *211*, 118018.
(91) Li, M.; Zhang, M.; Rong, H.; Zhang, X.; He, L.; Han, P.; Tong, M. Transport and deposition of plastic particles in porous media during seawater intrusion and groundwater-seawater displacement processes. *Sci. Total Environ.* **2021**, *781*, 146752.
(92) Wang, Y.; Xie, Y.; Fan, W.; Yang, Z.; Tan, W.; Huo, M.; Huo, Y. Mechanism comparisons of transport-deposition-reentrainment between microplastics and natural mineral particles in porous media: A theoretical and experimental study. *Sci. Total Environ.* **2022**, *850*, 157998.
(93) Geng, C.; Gao, Y.; Zhang, H.; Xue, D.; Shan, H.; Wang, B.; Wang, X.; Zhao, J. Microplastic migration in porous media at various scales: a review. *Environ. Chem. Lett.* **2024**, *22* (2), 691−713.
(94) He, B.; Duan, H.; Yang, W.; Yabar, H.; Song, J. Decarbonizing polyamide textile production in China: Footprints and mitigation pathways from life cycle perspective. *Resour. Conserv. Recycl.* **2024**, *208*, 107705.
(95) Periyasamy, A. P.; Tehrani-Bagha, A. A review on microplastic emission from textile materials and its reduction techniques. *Polym. Degrad. Stab.* **2022**, *199*, 109901.
(96) Sousa, A. F.; Patrício, R.; Terzopoulou, Z.; Bikiaris, D. N.; Stern, T.; Wenger, J.; Loos, K.; Lotti, N.; Siracusa, V.; Szymczyk, A.; Paszkiewicz, S.; Triantafyllidis, K. S.; Zamboulis, A.; Nikolic, M. S.; Spasojevic, P.; Thiyagarajan, S.; Van Es, D. S.; Guigo, N. Recommendations for replacing PET on packaging, fiber, and film materials with biobased counterparts. *Green Chem.* **2021**, *23* (22), 8795−8820.
(97) Sheikhi, M.; Lupato, S.; Bianco, C.; Sethi, R.; Tiraferri, A. Plastic microfibers from household textile laundering: a critical review of their release and impact reduction. *Crit. Rev. Environ. Sci. Technol.* **2024**, *54* (20), 1501−1525.
(98) Akindoyo, J. O.; Beg, M. D. H.; Ghazali, S.; Islam, M. R.; Jeyaratnam, N.; Yuvaraj, A. R. Polyurethane types, synthesis and applications-a review. *RSC Adv.* **2016**, *6* (115), 114453−114482.
(99) Somarathna, H. M. C. C.; Raman, S. N.; Mohotti, D.; Mutalib, A. A.; Badri, K. H. The use of polyurethane for structural and infrastructural engineering applications: A state-of-the-art review. *Constr Build Mater.* **2018**, *190*, 995−1014.
(100) Edo, G. I.; Ndudi, W.; Ali, A. B. M.; Yousif, E.; Zainulabdeen, K.; Onyibe, P. N.; Ekokotu, H. A.; Isoje, E. F.; Igbuku, U. A.; Essaghah, A. E. A.; Ahmed, D. S.; Umar, H.; Ozsahin, D. U. Poly(vinyl chloride) (PVC): an updated review of its properties, polymerization, modification, recycling, and applications. *J. Mater. Sci.* **2024**, *59* (47), 21605−21648.
(101) Jiang, X.; Zhu, B.; Zhu, M. An overview on the recycling of waste poly(vinyl chloride). *Green Chem.* **2023**, *25* (18), 6971−7025.

(102) Celik, M.; Nakano, H.; Uchida, K.; Isobe, A.; Arakawa, H. Comparative evaluation of the carbonyl index of microplastics around the Japan coast. *Mar. Pollut. Bull.* **2023**, *190*, 114818.
(103) Syranidou, E.; Karkanorachaki, K.; Barouta, D.; Papadaki, E.; Moschovas, D.; Avgeropoulos, A.; Kalogerakis, N. Relationship between the Carbonyl Index (CI) and Fragmentation of Polyolefin Plastics during Aging. *Environ. Sci. Technol.* **2023**, *57* (21), 8130−8138.
(104) Nie, X.; Xing, X.; Xie, R.; Wang, J.; Yang, S.; Wan, Q.; Zeng, E. Y. Impact of iron/aluminum (hydr) oxide and clay minerals on heteroaggregation and transport of nanoplastics in aquatic environment. *J. Hazard. Mater.* **2023**, *446*, 130649.
(105) Zhang, Y.; Luo, Y.; Guo, X.; Xia, T.; Wang, T.; Jia, H.; Zhu, L. Charge mediated interaction of polystyrene nanoplastic (PSNP) with minerals in aqueous phase. *Water Res.* **2020**, *178*, 115861.
(106) Tong, M.; He, L.; Rong, H.; Li, M.; Kim, H. Transport behaviors of plastic particles in saturated quartz sand without and with biochar/Fe3O4-biochar amendment. *Water Res.* **2020**, *169*, 115284.
(107) Wang, X.; Dan, Y.; Diao, Y.; Liu, F.; Wang, H.; Sang, W.; Zhang, Y. Transport characteristics of polystyrene microplastics in saturated porous media with biochar/Fe3O4-biochar under various chemical conditions. *Sci. Total Environ.* **2022**, *847*, 157576.
(108) Hou, M.; Hu, Y.; He, Y. Modifications in vegetation cover and surface albedo during rapid urbanization: A case study from South China. *Environ. Earth Sci.* **2014**, *72* (5), 1659−1666.
(109) Myhre, G.; Kvalevåg, M. M.; Schaaf, C. B. Radiative forcing due to anthropogenic vegetation change based on MODIS surface albedo data. *Geophys. Res. Lett.* **2005**, *32* (21), 1−4.
(110) Hou, J.; Xu, X.; Lan, L.; Miao, L.; Xu, Y.; You, G.; Liu, Z. Transport behavior of micro polyethylene particles in saturated quartz sand: Impacts of input concentration and physicochemical factors. *Environ. Pollut.* **2020**, *263*, 114499.
(111) Li, F.; Huang, D.; Wang, G.; Cheng, M.; Chen, H.; Zhou, W.; Xiao, R.; Li, R.; Du, L.; Xu, W. Microplastics/nanoplastics in porous media: Key factors controlling their transport and retention behaviors. *Sci. Total Environ.* **2024**, *926*, 171658.
(112) Ranjan, V. P.; Joseph, A.; Sharma, H. B.; Goel, S. Preliminary investigation on effects of size, polymer type, and surface behaviour on the vertical mobility of microplastics in a porous media. *Sci. Total Environ.* **2023**, *864*, 161148.
(113) Tang, C. S.; Zhu, C.; Cheng, Q.; Zeng, H.; Xu, J. J.; Tian, B. G.; Shi, B. Desiccation cracking of soils: A review of investigation approaches, underlying mechanisms, and influencing factors. *Earth Sci. Rev.* **2021**, *216*, 103586.
(114) Bordoloi, S.; Ni, J.; Ng, C. W. W. Soil desiccation cracking and its characterization in vegetated soil: A perspective review. *Sci. Total Environ.* **2020**, *729*, 138760.
(115) Peron, H.; Hueckel, T.; Laloui, L.; Hu, L. B. Fundamentals of desiccation cracking of fine-grained soils: Experimental characterisation and mechanisms identification. *Can. Geotech. J.* **2009**, *46* (10), 1177−1201.
(116) Li, Y.; Wang, R.; Ma, H.; Zhang, J. M. Rising groundwater table due to restoration projects amplifies earthquake induced liquefaction risk in Beijing. *Nat. Commun.* **2025**, *16* (1), 1466.
(117) Smyth, K.; Drake, J.; Li, Y.; Rochman, C.; Van Seters, T.; Passeport, E. Bioretention cells remove microplastics from urban stormwater. *Water Res.* **2021**, *191*, 116785.
(118) Lange, K.; Magnusson, K.; Viklander, M.; Blecken, G. T. Removal of rubber, bitumen and other microplastic particles from stormwater by a gross pollutant trap - bioretention treatment train. *Water Res.* **2021**, *202*, 117457.
(119) García-Haba, E.; Hernández-Crespo, C.; Martín, M.; Andrés-Doménech, I. The role of different sustainable urban drainage systems in removing microplastics from urban runoff: A review. *J. Clean. Prod.* **2023**, *411*, 137197.
(120) Wang, C.; O'Connor, D.; Wang, L.; Wu, W. M.; Luo, J.; Hou, D. Microplastics in urban runoff: Global occurrence and fate. *Water Res.* **2022**, *225*, 119129.
(121) Wei, Y.; Tang, C. S.; Lu, Y.; Zhang, M.; Cheng, Q.; Li, L.; Shi, B. Evaporation and desiccation cracking of soils: Experiment evidence and insight on the freeze-thaw cycle dependence. *Eng. Geol.* **2024**, *329*, 107399.
(122) Liu, J.; Xu, H.; Tao, Y.; Lyu, Q. Effects of clay content and subfreezing temperature on the freeze−thaw deformation properties of clayey soils. *Catena* **2024**, *239*, 107916.

https://doi.org/10.1021/acs.est.5c00871
Environ. Sci. Technol. 2025, 59, 12933−12946

Journal of Hazardous Materials 495 (2025) 139072

Contents lists available at ScienceDirect

Journal of Hazardous Materials

journal homepage: www.elsevier.com/locate/jhazmat

An integrated multi-omics approach reveals octocrylene disrupts *Tetradesmus obliquus* growth by triggering a cascade of photosynthetic inhibition and metabolic dysregulation

Jun-Jie Hu [a], Chang-Gui Pan [a,*], Feng-Jiao Peng [b,c,**], Hao Liang [a], Zhen-Zhu Liu [a], Kefu Yu [a]

[a] *Guangxi Laboratory on the Study of Coral Reefs in the South China Sea, Coral Reef Research Centerof China, School of Marine Sciences, Guangxi University, Nanning 530004, China*

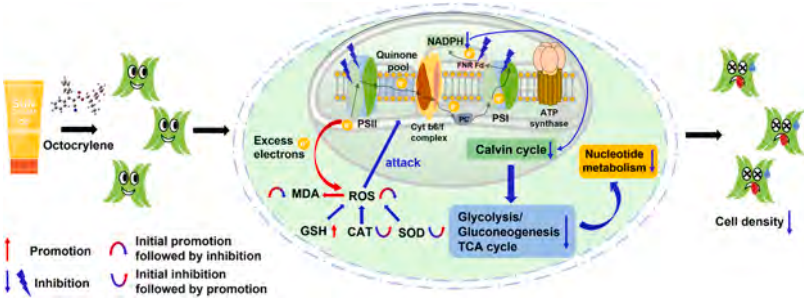
[b] *SCNU Environmental Research Institute, Guangdong Provincial Key Laboratory of Chemical Pollution and Environmental Safety, MOE Key Laboratory of Theoretical Chemistry of Environment, South China Normal University, Guangzhou, 510006, China*

[c] *School of Environment, South China Normal University, University Town, Guangzhou 510006, China*

HIGHLIGHTS

- The effects and mechanisms of *Tetradesmus obliquus* under OC exposure were explored.
- Environmental concentration of OC can inhibit the growth of *Tetradesmus obliquus*.
- OC disrupts *Tetradesmus obliquus*' photosynthetic and metabolism system.
- OC can activate the antioxidant system of *Tetradesmus obliquus*.

GRAPHICAL ABSTRACT



ARTICLE INFO

Keywords:
Octocrylene
Tetradesmus obliquus
Growth inhibition
Photosynthesis
Multi-omics analysis

ABSTRACT

Octocrylene (OC) is a widely used organic UV absorber and a common ingredient in coral-friendly sunscreen. Recent studies have highlighted its impact on microalgal growth, though the underlying mechanisms remain unclear. In this study, we investigated the growth inhibition and related mechanisms of green algae *Tetradesmus obliquus* exposed to OC at four concentrations (1, 10, 100, and 500 μg/L) over 7 days. Results demonstrated a concentration-dependent growth inhibition, with approximately 24 % growth reduction observed in the 500 μg/L group by the end of exposure. Chlorophyll fluorescence analysis showed that effective quantum yield (Y(II)) and photochemical quenching (qP) decreased by 8 %-29 %, while relative electron transport rate (rETR) declined by 10 %-36 %. These changes were supported by alterations in the expression of photosystem-related genes and proteins (*psbW*, *psaG*, *psaN*, *psbA*, *petF*, *Lhcb1*, *Lhcb2*, *psbS*, and *Lhcb4*). Additionally, suppression of the Calvin cycle and glycolysis pathways led to metabolic disruptions, with upregulated fatty acid degradation to compensate for tricarboxylic acid (TCA) cycle substrates. As energy reserves were diverted to counteract OC

* Corresponding author.
** Corresponding author at: SCNU Environmental Research Institute, Guangdong Provincial Key Laboratory of Chemical Pollution and Environmental Safety, MOE Key Laboratory of Theoretical Chemistry of Environment, South China Normal University, Guangzhou 510006, China.
E-mail addresses: panchanggui@gxu.edu.cn (C.-G. Pan), Fengjiaopeng@m.scnu.edu.cn (F.-J. Peng).

https://doi.org/10.1016/j.jhazmat.2025.139072
Received 9 January 2025; Received in revised form 4 June 2025; Accepted 25 June 2025
Available online 26 June 2025
0304-3894/© 2025 Elsevier B.V. All rights are reserved, including those for text and data mining, AI training, and similar technologies.

stress, the availability of precursors for DNA and RNA synthesis decreased, directly affecting cell growth and division. These findings contribute to a better understanding of the impact of OC in aquatic environments.

1. Introduction

Octocrylene (OC) is a widely utilized ultraviolet absorber known for its effective absorption of UVB and UVA-II radiation (320 ~ 340 nm). It is commonly used as a stabilizer for other UV absorbers, such as avobenzone (AVO), which offer broad-spectrum protection against UVA and UVB radiation [1]. In fact, OC has been found in 2999 sun protection factor (SPF) products in the United States [2], which accounted for approximately 49 % of the sunscreen products worldwide [3]. Moreover, it is expected that the levels of OC would be elevated due to the widespread banning of certain sunscreen ingredients, such as benzophenone-3 (BP-3) and ethylhexyl methoxycinnamate (EHMC) [4]. On the other hand, the high lipophilicity of OC ($\log K_{ow}$ = 6.88) [5], combined with its strong resistance to hydrolysis, photolysis, and aerobic biodegradation [6–8], contributes to its environmental persistence and bioaccumulation potential. It is generally recognized that short-term point source inputs, such as those from water-based recreational activities, are the primary contributors to elevated OC residues in aquatic environments [9], with concentrations reaching detectable levels of up to μg/L, and in some cases, exceeding 10^2 μg/L [10].

A previous toxicological study of OC revealed antiestrogenic, antiandrogenic, and estrogenic effects in *Danio rerio* [11]. Moreover, a prior study demonstrated that OC exposure affected both brain and liver development of zebrafish, accompanied by alterations of liver metabolic genes (*cebpa*, *rbp4* and *arntl1a*) [12]. More recent studies have revealed OC accumulation in coral tissues, forming complexes with fatty acids and inducing mitochondrial toxicity [13, 14]. In addition to endocrine disruption and metabolic disturbances, OC can also affect growth of aquatic organisms. For instance, the 48h-EC_{50} values for growth inhibition of OC in *Paracentrotus lividus* (sea urchin) and *Artemia salina* (brine shrimp) were 0.74 mg/L and 0.61 mg/L, respectively [15, 16]. Additionally, OC was shown to inhibit the growth of algae and marine bacteria, with EC_{50} values in the range of a few milligrams per liter [15–17].

Microalgae, as the primary producers, plays a fundamental role in the material cycling, energy flow, and enhancement of biodiversity throughout the ecosystem [18]. Furthermore, microalgae have the potential to accumulate pollutants and transfer them through the food chain [19]. *Tetradesmus obliquus*, a species of freshwater green algae, is widely distributed in aquatic environments [20, 21]. Additionally, it is a standard algal species widely used for toxic test, as recommended by the Organization for Economic Cooperation and Development (OECD) [22]. However, previous studies on OC have primarily focused on its effects on the growth inhibition of microalgae [15–17], the mechanisms underlying this inhibition remain poorly understood.

Therefore, the present study aimed to i) investigate the effects of OC on *Tetradesmus obliquus*, including parameters such as cell growth, the photosynthetic system and the antioxidant system, over a 7-day exposure period, and ii) illustrate the molecular mechanisms responsible for growth inhibition using metabolomic, transcriptomic and proteomic analyses.

2. Materials and methods

2.1. Chemicals and Tetradesmus obliquus culture

OC (> 98 %) was obtained from TCI (Tokyo, Japan), and its physicochemical properties are shown in Table S1. High performance liquid chromatography (HPLC) grade dimethyl sulfoxide (DMSO) and ethanol were both purchased from Macklin (Shanghai, China). Liquid chromatograph mass spectrometer (LC-MS) grade methanol and HPLC grade dichloromethane (DCM) were acquired from Sigma-Aldrich (St. Louis, Missouri, the United States). Nitrogen-containing BG-11 culture medium stock solution (1000 ×) was bought from Leding Tec (Shanghai, China), and the medium formulation can be referenced in [23]. Commercial kits for total protein (TP), reactive oxygen species (ROS), superoxide dismutase (SOD), catalase (CAT), malondialdehyde (MDA), and glutathione (GSH) were obtained from Nanjing Jiancheng Bioengineering Institute (Nanjing, China). The Elisa kit for Ribulose-1,5-bisphosphate carboxylase/oxygenase (rubisco) was purchased from Jingmei Biotechnology (Yancheng, China).

Unicellular green algae *Tetradesmus obliquus* (FACHB-12) was purchased from the freshwater algae culture collection of the Institute of Hydrobiology of Chinese Academy of Sciences (Wuhan, China). Microalgae were inoculated in sterile nitrogen-containing BG11 medium at a pH of 7.0 ± 0.1. The algae were maintained in a climate chamber under controlled conditions of temperature (23.0 ± 0.2°C), light intensity (3500 ± 100 *lux*), and a light-dark cycle of 12–12 h. The algae were cultured for at least 28 days before the experiment. Subsequently, algae were subcultured into fresh sterile medium every 7 days to ensure exponential growth until they were used for inoculating the test solutions.

2.2. Experimental setup

Tetradesmus obliquus in exponential growth phase was inoculated into 300 mL flasks, with the addition of 200 mL BG11 medium. The initial algal cell density was adjusted to about 4 × 10^5 cells/mL. Blank controls, solvent controls (0.01 % DMSO), and four OC treatment groups (1, 10, 100 and 500 μg/L) were set up with three replicates (n = 3). Here, the low concentrations of 1 and 10 μg/L were often found in natural water [10], while the high concentrations of 100 and 500 μg/L normally occurred in the recreational waterpark and river [24, 25]. These treatments were used to explore whether *Tetradesmus obliquus* were under stress after exposure to OC and how the responses differed among different treatments. The flasks were shaken three times and repositioned daily to prevent uneven light exposure, with the total duration of exposure lasting 7 days. Algal density was measured daily, while other physiological indicators, including photosynthetic pigments, enzyme activities, chlorophyll fluorescence and antioxidant system substances were assessed on days 0, 1, 3, 5, and 7. Omics, including metabonomic, transcriptomic and proteomic analyses were performed at the end of the exposure period (day 7).

2.3. Determination of physiological indicators

2.3.1. Determination of cell density

Cell density was determined using a hemocytometer under an optical microscope. The optical density (OD) at 680 nm was measured using a microplate reader (Thermo Fisher Scientific, the United States). A linear relationship between cell density (cells/mL) and OD_{680} was established, and the specific equation is provided below:

$$\text{Cell density (cells/mL)} = 1.35\times 10^7 \times OD_{680} + 2.49 \times 10^4 \quad (1)$$

2.3.2. Determination of photosynthetic pigment content

Briefly, 5 mL of algal solution were centrifuged at 4000 rpm for 10 min. After discarding the supernatant, 1 mL of 95 % ethanol was added into the centrifuge tube, and thoroughly mixed. Thereafter, the tube was stored in the dark at 4°C for 24 h and subsequently centrifuged at 10,000 rpm for 5 min. The absorbance at 470 nm, 649 nm, and

665 nm were measured for the supernatant using a microplate reader. The formulas for calculating the content of chlorophyll a (Chl a), chlorophyll *b* (Chl b), and carotenoids (CAR) are as follows [26]:

$$\text{Chl a (mg/L)} = 13.95\ OD_{665} - 6.88\ OD_{649} \quad (2)$$

$$\text{Chl b (mg/L)} = 24.96\ OD_{649} - 7.32\ OD_{665} \quad (3)$$

$$\text{CAR (mg/L)} = (1000\ OD_{470} - 2.05\ \text{Chl a} - 114.8\ \text{Chl b})/245 \quad (4)$$

2.3.3. Determination of chlorophyll fluorescence parameters

The microalgae were acclimated under darkness for 30 min to ensure accurate measurements. The maximum quantum yield (Fv/Fm), effective quantum yield (Y(II)), relative electron transport rate (rETR), photochemical quenching (qP), non-photochemical quenching (NPQ) and non-regulated excitation dissipation (Y(NO)) of *Tetradesmus obliquus* were determined by pulse amplitude modulation fluorometry (WALZ MONITORING-PAM, Germany) [27]. The interval between high-light pulses was set to 20 s. The maximum photosynthetic photon flux densities were 0, 90, 125, 190, 285, 420, 625, 820, and 1150 $\mu mol \cdot m^{-2}/s$.

2.3.4. Determination of total protein, antioxidant system, and rubisco

A 20 mL aliquot of the algal solution was centrifuged at 4000 rpm for 10 min, and the resulting pellet was washed twice with phosphate buffered saline (PBS, pH = 7) before being concentrated to 1 mL. Thereafter, the concentrated solution was grinded using an automated sample homogenizer (60 Hz, 5 min) with zirconium beads and subsequently centrifuged. After centrifugation, the supernatant was analyzed for total protein, antioxidant system, and rubisco using commercial kits [28].

2.4. Determination of OC

The method for OC determination was modified based on a previous study [29]. Briefly, 10 mL of algal solution was centrifuged at 4000 rpm for 10 min. The supernatant was extracted twice with 3 mL of DCM, concentrated with nitrogen, and re-dissolved in 0.5 mL of methanol. This solution was filtered through a 0.22 μm syringe filter, OC concentration was then determined using an Agilent 1290 ultrahigh-performance liquid chromatography system coupled to a 6460 triple-quadrupole mass spectrometer (LC-MS/MS, Agilent, the United States). Details on the LC-MS/MS parameters are shown in Table S2.

2.5. Metabolomics analysis

Briefly, 10 mL of algal solution (DMSO, 1 μg/L, and 500 μg/L) was centrifuged at 4000 rpm for 10 min, and the obtained pellet was washed twice with PBS (pH = 7). The cells were then frozen in liquid nitrogen and stored at −80 °C. Metabolites were extracted using a mixture of methanol and water (8:2, v:v), and analyzed using an ultrahigh-performance liquid chromatography system coupled to a Q-Exactive orbitrap mass spectrometer (UPLC-QE-Orbitrap-MS, Thermo Fisher Scientific, the United States). Details on metabolomics extraction and determination are provided in Text S1. Differentially expressed metabolites (DEMs) were identified based on a $p < 0.05$ and variable influence on projection (VIP) value > 1. DEMs were annotated using the Kyoto Encyclopedia of Genes and Genomes (KEGG) for metabolic pathway analysis and compound classification.

2.6. Transcriptomics analysis

A 200 mL aliquot of the algal solution (DMSO, 1 μg/L, and 500 μg/L) was centrifuged at 4000 rpm for 10 min and the obtained pellet was washed twice with PBS (pH = 7). The cells were then frozen in liquid nitrogen and stored at −80 °C. Detailed information on transcriptomics analysis is provided in Text S2. Transcriptome assembly, differential gene expression analysis, and functional enrichment were performed post-sequencing and sequence alignment. Differential expression genes (DEGs) were identified with adjust *p*-value < 0.05 (Benjamini-Hochberg method) and an absolute log2 fold change > 0.585. Functional enrichment analysis of DEGs involved KEGG pathway analyses.

Real-time quantitative polymerase chain reaction (RT-qPCR) was employed to validate key genes involved in pathways such as photosynthesis, ribosome, and metabolism, thereby confirming the accuracy of the transcriptomic analysis. Details of the RT-qPCR protocol are provided in Text S3, while the primer sequences for the selected genes are listed in Table S3.

2.7. Proteomics analysis

We performed proteomics analysis for solvent control (DMSO) and the high-concentration treatment group (500 μg/L). Sample preprocessing was consistent with the transcriptomics analysis until liquid nitrogen quenching. Subsequent protein extraction, digestion, and LC-MS/MS parameters are detailed in Text S4. The reference genome version for transcriptomics and proteomics was GCA_030272155.1 (https://www.ncbi.nlm.nih.gov/datasets/genome/GCA_030272155.1/). Differential expression proteins (DEPs) were identified with *p*-value < 0.05 (student's *t*-test method) and an absolute log2 fold change > 0.263 [30]. Functional enrichment analysis of DEPs involved KEGG pathway analyses.

2.8. Molecular docking and molecular dynamics (MD) simulation

To investigate the interaction between photosystem II subunit S (psbS) and OC, molecular docking and molecular dynamics simulations were performed. Using the psbS (4ri2.1.A) as a template, the three-dimensional configuration of the psbS was obtained through homology modeling with SWISS-MODEL (http://swissmodel.expasy.org/). The three-dimensional configuration of OC was obtained from PubChem (https://pubchem.ncbi.nlm.nih.gov/). Then, molecular docking was performed using AutoDock Vina 1.2.5 [31]. The conformation with the lowest binding energy was selected for molecular dynamics simulations, which were conducted using GROMACS 2024.3 package [32]. Detailed docking and simulation parameters are provided in Text S5.

2.9. Statistical analyses

All data were presented as mean ± standard deviation (SD). Statistical analyses were performed using SPSS Statistics 27 (IBM, the United States), with significance defined as $p < 0.05$. The normality of data was examined using Shapiro-Wilk test, and the homogeneity of variance between groups was checked by Levene's test. One-way analysis of variance (ANOVA) was employed to test the significance of differences in algal cell density, photosynthetic system, and antioxidant system indicators. Subsequently, post hoc least significant difference (LSD) tests were conducted to examine differences between treatment and control groups. Both Pearson and Spearman correlation analyses were employed to uncover potential relationships among the physiological indicators. The correlation heatmap was generated using ChiPlot (https://www.chiplot.online/), while all other figures were created with Origin 2024 (OriginLab, the United States).

3. Results

3.1. Effects on the growth

There was no significant difference between the DMSO control and the water control, suggesting that 0.01 % DMSO had no significant effect on the growth of *Tetradesmus obliquus* (Fig. 1a). After 7 days, algal cell

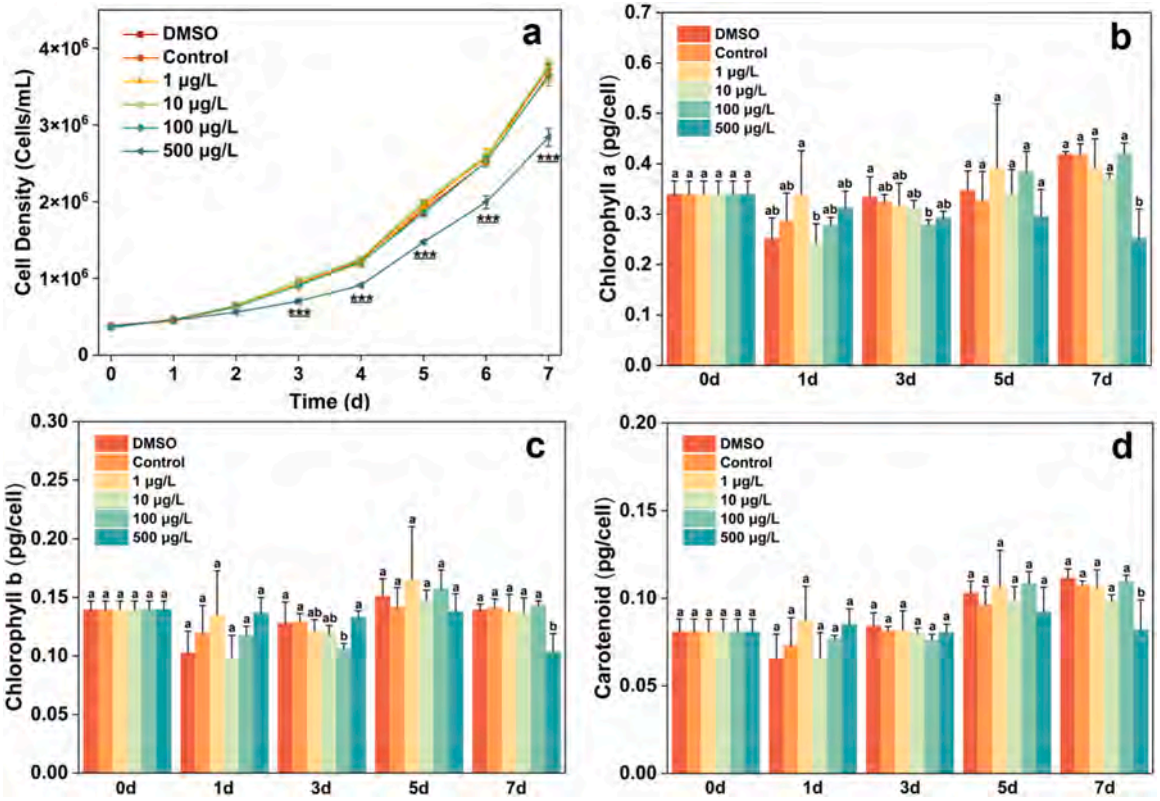


Fig. 1. The cell density (a), chlorophyll a (b), chlorophyll *b* (c) and carotenoids (CAR) content (d) of *Tetradesmus obliquus* exposed to OC. Note: ***: $p < 0.001$, different letters above error bars indicate significant differences ($p < 0.05$).

density increased approximately 7–9 fold in all groups. Moreover, there were significant reductions in algal cell density in the 500 μg/L group as compared to the DMSO group during the exposure period ($p < 0.05$), which increased with increasing exposure time, reaching approximately 24 % by the end of the experiment (day 7). On the other hand, there were no significant differences in the density of algal cells between the remaining OC treatment groups and the DMSO group.

3.2. Effects on the photosynthesis

On days 1, 3 and 5, there was no significant difference in the levels of the three photosynthetic pigments (Chl a, Chl b and CAR) between OC treatment groups and the DMSO group (Fig. 1b-d). However, on day 7, all three photosynthetic pigments decreased by approximately 20 %-40 % in the 500 μg/L group in comparison to the DMSO group ($p < 0.05$). On day 1, in comparison to the DMSO group, Fv/Fm significantly decreased by 0.025–0.065 in all OC groups, presenting a dose-response relationship ($p < 0.05$), except for the lowest OC treatment group (i.e., 1 μg/L), in which an increase of approximately 0.035 was observed (Fig. 2a). Noticeably, Fv/Fm decreased significantly from 0.64 on day 1–0.52 on day 3 in the 500 μg/L group ($p < 0.05$), and thereafter returned to 0.65 on days 5 and 7. In parallel, rubisco activity in the 500 μg/L group decreased significantly by 26 % as compared to the DMSO group on day 1, followed by a significant increase of 50 % on day 3 ($p < 0.05$), and thereafter remained at levels similar to the DMSO group (Fig. 2b).

In the 500 μg/L OC group, qP and Y(II) decreased by approximately 8 %-29 % across different light intensities compared to the DMSO control (Fig. 2c). rETR showed a greater reduction, ranging from 10 % to 36 %. NPQ exhibited a slight increase (4 %-7 %) under high light intensity on day 1 but continuously declined throughout the exposure period, with a maximum decrease of 19 %. Y(NO) increased steadily by approximately 1 %-10 % during the exposure. Photosynthetic parameters in the 1 μg/L OC treatment group were similar to the control, except on day 7. On day 7, Y(II), qP, rETR, and NPQ decreased by approximately 1 %-18 %, while Y(NO) increased by 1 %-4 %.

Molecular dynamics simulations showed a decrease in protein compactness upon ligand binding (Figs. 3a and 3b). The root mean square deviation (RMSD) of the ligand-free (apo) state reached equilibrium around 25 ns, while the bound state took up to 50 ns (Fig. 3c). The radius of gyration (Rg) remained stable overall in both states (Fig. 3d). However, the Rg value of the bound state was higher than that of the apo state, indicating that OC altered the compactness of both proteins. Root mean square fluctuation (RMSF) analysis revealed increased flexibility in amino acids around position 100 (Fig. 3e). Finally, the binding energy remained stable at approximately −43 kcal/mol (Fig. 3f).

3.3. Effects on the antioxidant system

There were no significant differences in ROS levels between the DMSO group and the two lower OC groups (1 and 10 μg/L) (Fig. 4a-e). ROS levels in the 100 μg/L and 500 μg/L group significantly increased by approximately 30–50 % as compared to the DMSO group on day 1 ($p < 0.05$), and afterwards decreased by approximately 10–65 %. The MDA content was similar between the DMSO group and the 1 μg/L group during the exposure period. On day1 and day 3, the MDA content in the 10 μg/L, 100 μg/L, and 500 μg/L groups increased by 30 %-59 %, compared to the DMSO group ($p < 0.05$). Except for the 500 μg/L group, the CAT activity showed no significant difference between other groups and DMSO group. CAT activity in the 500 μg/L group decreased by 33 % compared to the DMSO group on day 1 ($p < 0.05$), while on days 3, 5, and 7, it increased by 28 % ($p < 0.05$), 91 % ($p < 0.05$), and 18 %, respectively, compared to the DMSO group. SOD activity on the 10 μg/L, 100 μg/L, and 500 μg/L ($p < 0.05$) groups exhibited inhibition on day 1, with decreases ranging from 22 % to 56 %. After this, the SOD activity

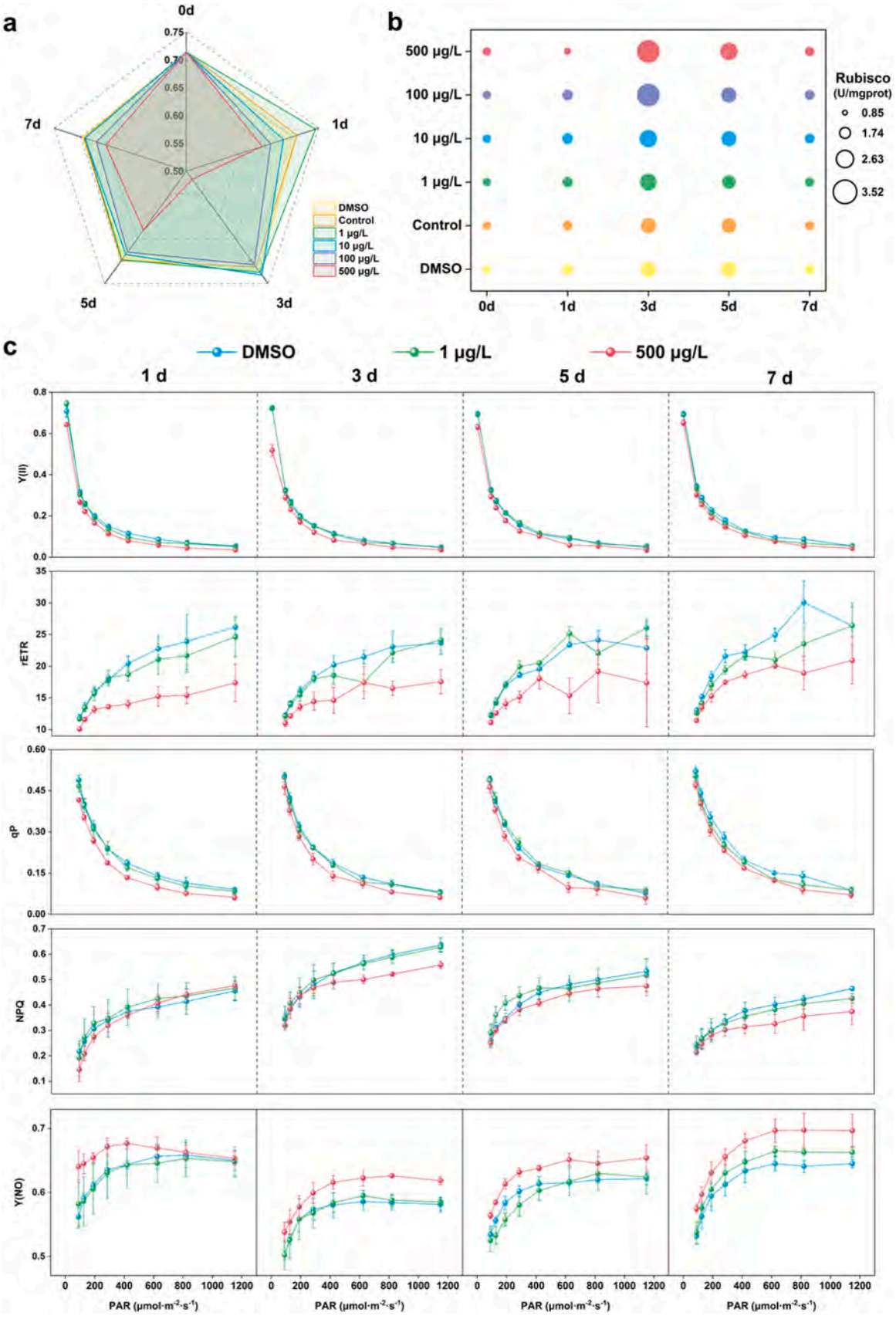


Fig. 2. The Fv/Fm value (a), rubisco activity (b), Y(II), rETR, qP, NPQ and Y(NO) values (c) of *Tetradesmus obliquus* exposed to OC.

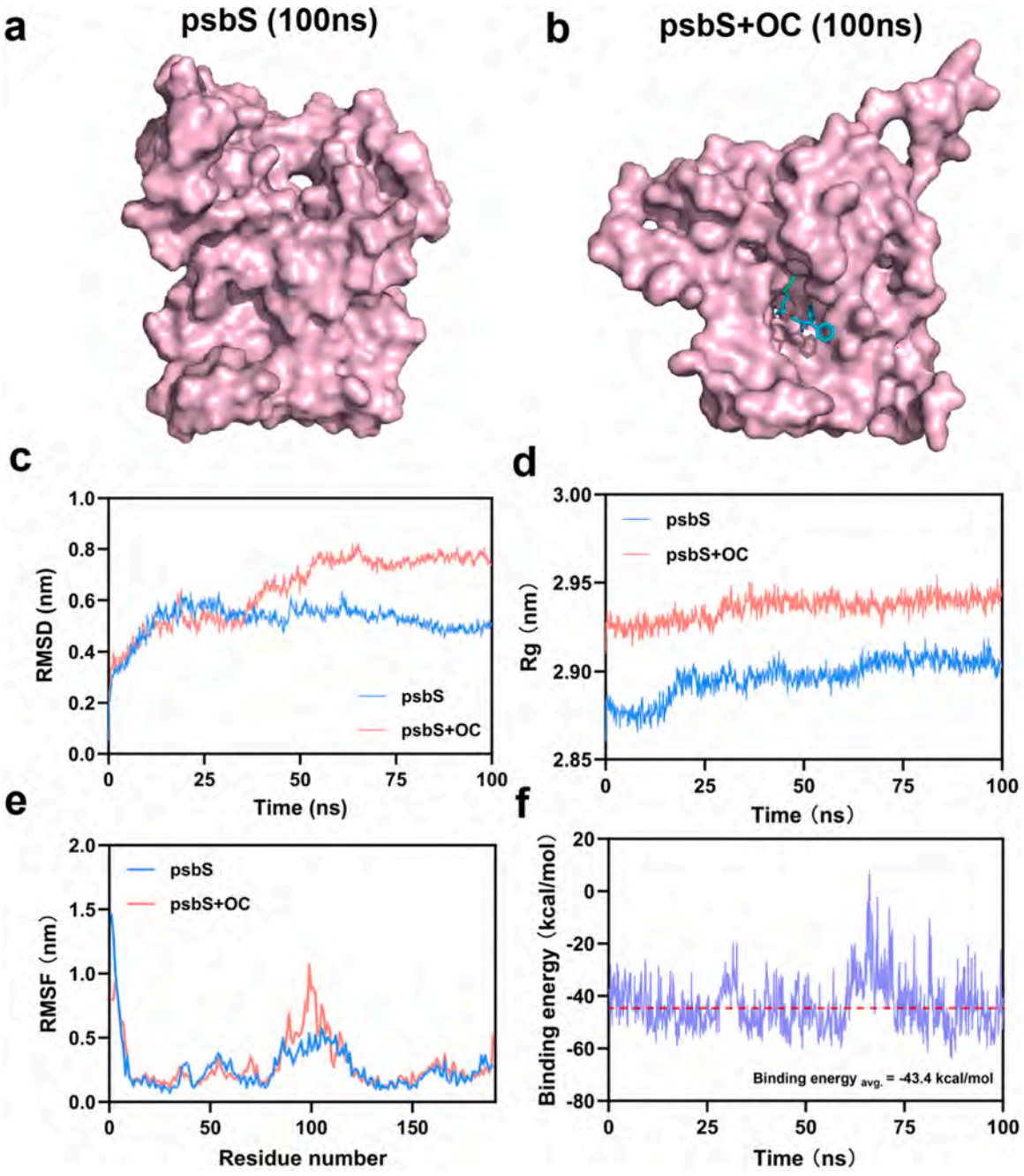


Fig. 3. Molecular docking and dynamics results. (a) psbS conformation, (b) psbS-OC binding conformation, (c) RMSD, (d) Rg, (e) RMSF, (f) Binding energy.

on the 100 μg/L and 500 μg/L ($p < 0.05$) groups continued to increase by 25–349 % compared to the DMSO group. Meanwhile, GSH content in the 500 μg/L group significantly increased by 59 %-97 % compared to the DMSO group on days 1, day 3 and day 5 ($p < 0.05$), with no significant difference observing on day 7.

3.4. *Effects on the metabolome, transcriptome and proteome*

The PCA score plot showed good clustering of replicates within the same group for metabolomics, transcriptomics, and proteomics (Figs. 5a and 5b , Fig. S1). The partial least squares discriminant analysis (PLS-DA) plot and permutation testing of PLS-DA confirmed the reliability of the metabolomics analysis model. (Fig. 5c, Fig. S2).

3.4.1. *Metabolomics analysis*

After 7 days of exposure, 69 DEMs were identified in 1 μg/L group (51 upregulated and 18 downregulated), while 208 DEMs were identified in 500 μg/L group (38 upregulated and 170 downregulated) (Fig. S3). Approximately 90 % of amino acids, lipids, carbohydrates, and nucleotides were downregulated in the 500 μg/L group, whereas approximately 67 % were upregulated in the 1 μg/L group (Fig. S4 and S5). The KEGG pathway enrichment analysis revealed that in the 1 μg/L group, the significantly enriched pathways included linoleic acid metabolism, carbon fixation in photosynthetic organisms, lysine biosynthesis, pentose phosphate pathway, and glyoxylate and dicarboxylate metabolism ($p < 0.05$, Fig. 5d, Fig. S6a), etc. In the 500 μg/L group, the significantly enriched KEGG pathways were associated with alpha-linolenic acid metabolism, nucleotide metabolism, purine metabolism, linoleic acid metabolism, and beta-alanine metabolism

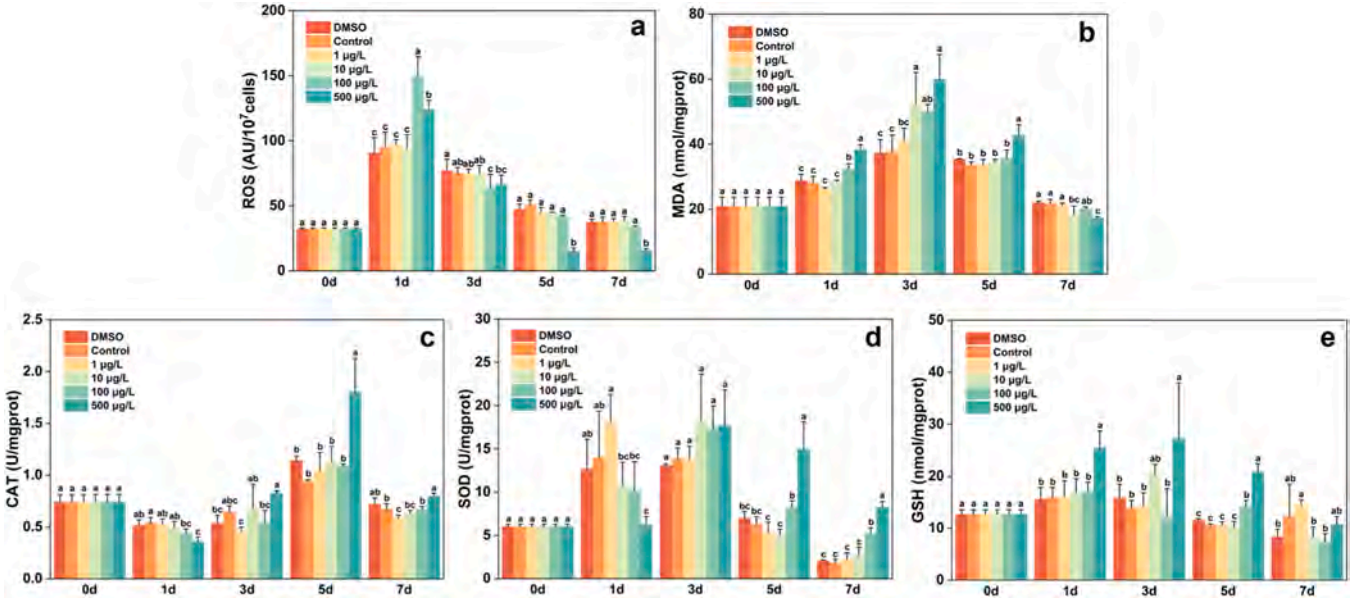


Fig. 4. The levels of ROS (a), MDA (b), CAT (c), SOD (d) and GSH (e) of *Tetradesmus obliquus* exposed to OC. Note: Different letters above error bars indicate significant differences ($p < 0.05$).

($p < 0.05$, Fig. 5e, Fig. S6b), etc.

3.4.2. Transcriptomics analysis

After 7 days of exposure, 401 (222 upregulated and 179 downregulated) and 612 (255 upregulated and 357 downregulated) DEGs were identified in the 1 and 500 μg/L groups, respectively (Fig. S7). The KEGG pathway enrichment analysis reveals that in the 1 μg/L group, the significantly enriched ($p < 0.05$) pathways were associated with cysteine and methionine metabolism, histidine metabolism, arginine biosynthesis, and arginine and proline metabolism (Fig. 5f, Fig S8a-b), etc. In the 500 μg/L group, the significantly enriched KEGG pathways included ABC transporters, nucleocytoplasmic transport, tryptophan metabolism, and spliceosome ($p < 0.05$, Fig. 5g, Fig S8c-d). The KEGG pathways related to genetic information processing are presented in Fig. S9-S13. Additionally, the RT-qPCR-validated genes showed high consistency with the transcriptomics data (Fig.S14).

3.4.3. Proteomics analysis

After 7 days of exposure, 573 (272 upregulated and 301 downregulated) DEPs were identified in the 500 μg/L group (Fig. S15). The heatmap of DEPs showed clear distinctions between the control and treatment groups (Fig. 5h). The KEGG pathway enrichment analysis reveals that in the 500 μg/L group, the significantly enriched ($p < 0.05$) pathways were associated with alpha-linolenic acid metabolism, valine, leucine and isoleucine degradation, fatty acid degradation, ABC transporters, glycerolipid metabolism (Fig. 5i).

4. Discussion

In the present study, *Tetradesmus obliquus* showed significant growth inhibition under the exposure of 500 μg/L OC group. It is considered that the attack on photosynthesis, energy metabolism, nucleotide and purine metabolism of *Tetradesmus obliquus* were responsible for this phenomenon.

4.1. OC disrupted electron transport and reduced photosynthetic activity

OC exposure impaired the photosynthetic system of *Tetradesmus obliquus*, as reflected in both functional parameters and molecular responses. A significant decrease in Fv/Fm on day 1 indicated inhibition of PSII [33], a primary target of OC stress. This inhibition was consistent with the downregulation of key PSII-related genes (Fig. 6, Fig. S16), such as *psbW* (encoding PSII reaction center subunit W protein) and *psbA* (encoding PSII D1 protein), which are essential for maintaining PSII stability and photochemical activity [34–36]. Although Fv/Fm significantly decreased, chlorophyll content remained stable from day 1 to day 5, demonstrating that the photosynthetic efficiency decline was independent of pigment loss [37]. Instead, the disruption of electron transport, evidenced by a decrease in rETR, likely contributed to reduced energy conversion efficiency (Fig. 4) [38]. This was further supported by the downregulation of *petF* (encoding ferredoxin I protein), which encodes an iron-sulfur protein critical for transferring electrons to downstream metabolic pathways like carbon fixation [39]. In addition , disruption of electron transport likely led to the accumulation of excess light energy, compounding photodamage. Under stress conditions, light-harvesting efficiency also declined, as indicated by reduced qP and the downregulation of *Lhcb1* (encoding chlorophyll a/b binding protein 1) and *Lhcb2* (encoding chlorophyll a/b binding protein 2), which are crucial for antenna pigment function [40, 41]. Concurrently, the photosynthetic system's capacity for thermal energy dissipation (NPQ) increased briefly on day 1, reflecting an initial photoprotective response [42]. However, prolonged exposure led to a decline in NPQ and a corresponding increase in Y(NO), signaling reduced heat dissipation capacity and photodamage [43]. psbS was significantly upregulated during exposure, a protein involved in photoprotection that is typically directly linked to NPQ values [44]. The upregulation of psbS was expected, as previous studies have demonstrated that psbS is consistently induced under abiotic stresses to protect chloroplasts from photodamage [45, 46]. However, this contrasting result may be attributed to the direct inhibition by OC. The longer equilibrium time, along with the higher RMSD and Rg values observed in the bound state, suggested that OC affected the stability of the psbS monomer [47]. This led to a reduction in the protein's compactness, which could further interfere with psbS function and hinder the formation of its dimer. At the PSI level, the downregulation of *psaG* (encoding PSI subunit G) and *psaN* (encoding PSI subunit N), subunits stabilizing the PSI complex and mediating electron transfer from plastocyanin, further disrupted electron transport [48, 49]. The combined downregulation of PSI and PSII-related genes ultimately impaired NADPH synthesis, hindering the Calvin cycle's conversion of 1,3-bisphosphoglycerate (1,3-BPG) to

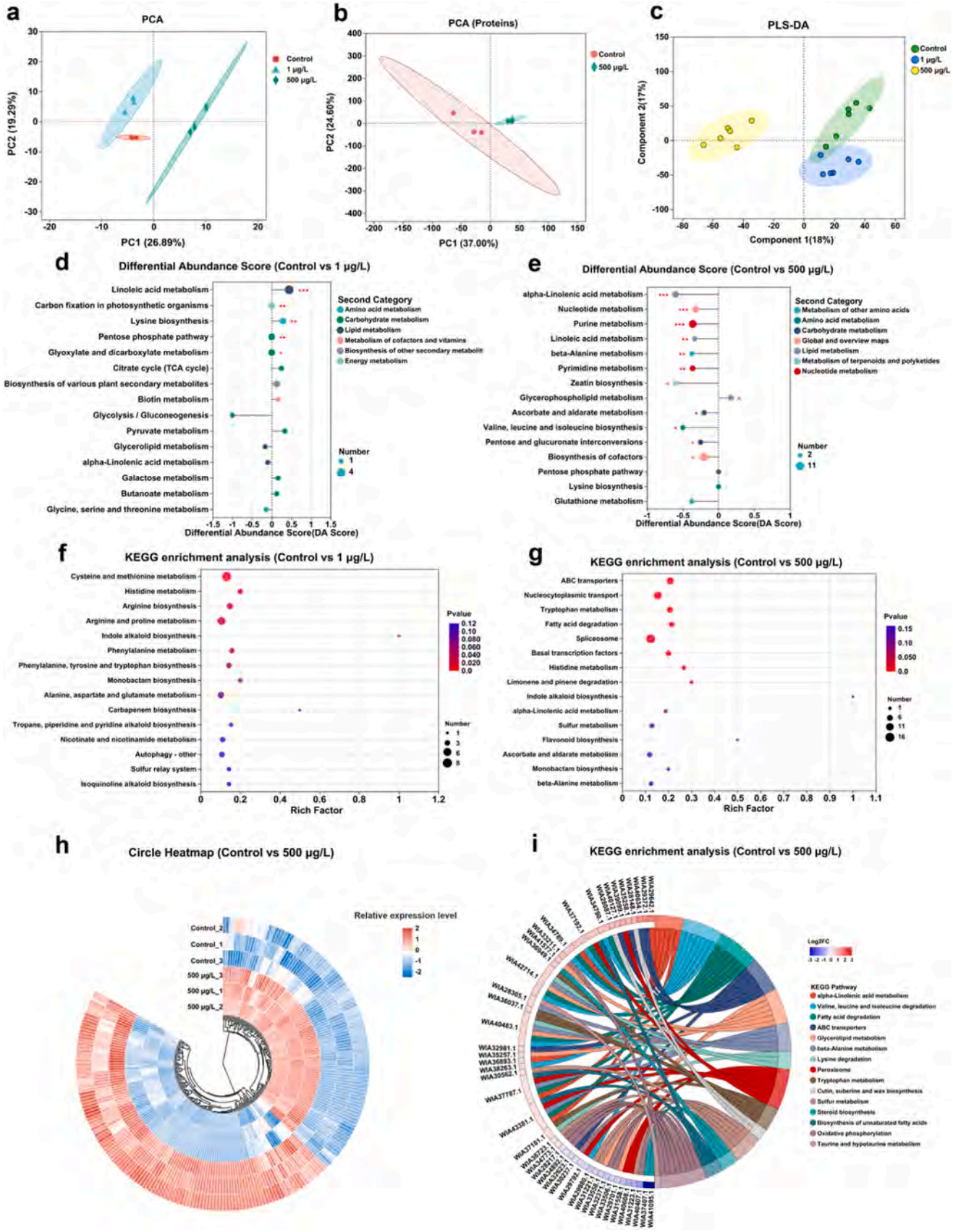


Fig. 5. Multi-omics analysis of *Tetradesmus obliquus* at the end of exposure (day 7). (a) Scores plot of PCA of transcriptome, (b) Scores plot of PCA of proteome, (c) Scores plot of PLS-DA of metabolome, KEGG enrichment analysis plot of DEMs in 1 μg/L OC (d) and 500 μg/L OC (e), KEGG enrichment analysis plot of DEGs 1 μg/L OC (f) and 500 μg/L OC (g), (h) Heatmap of protein abundance of DEPs and (i) KEGG enrichment analysis plot of DEPs. Note: *: $p < 0.05$, **: $p < 0.01$, ***: $p < 0.001$.

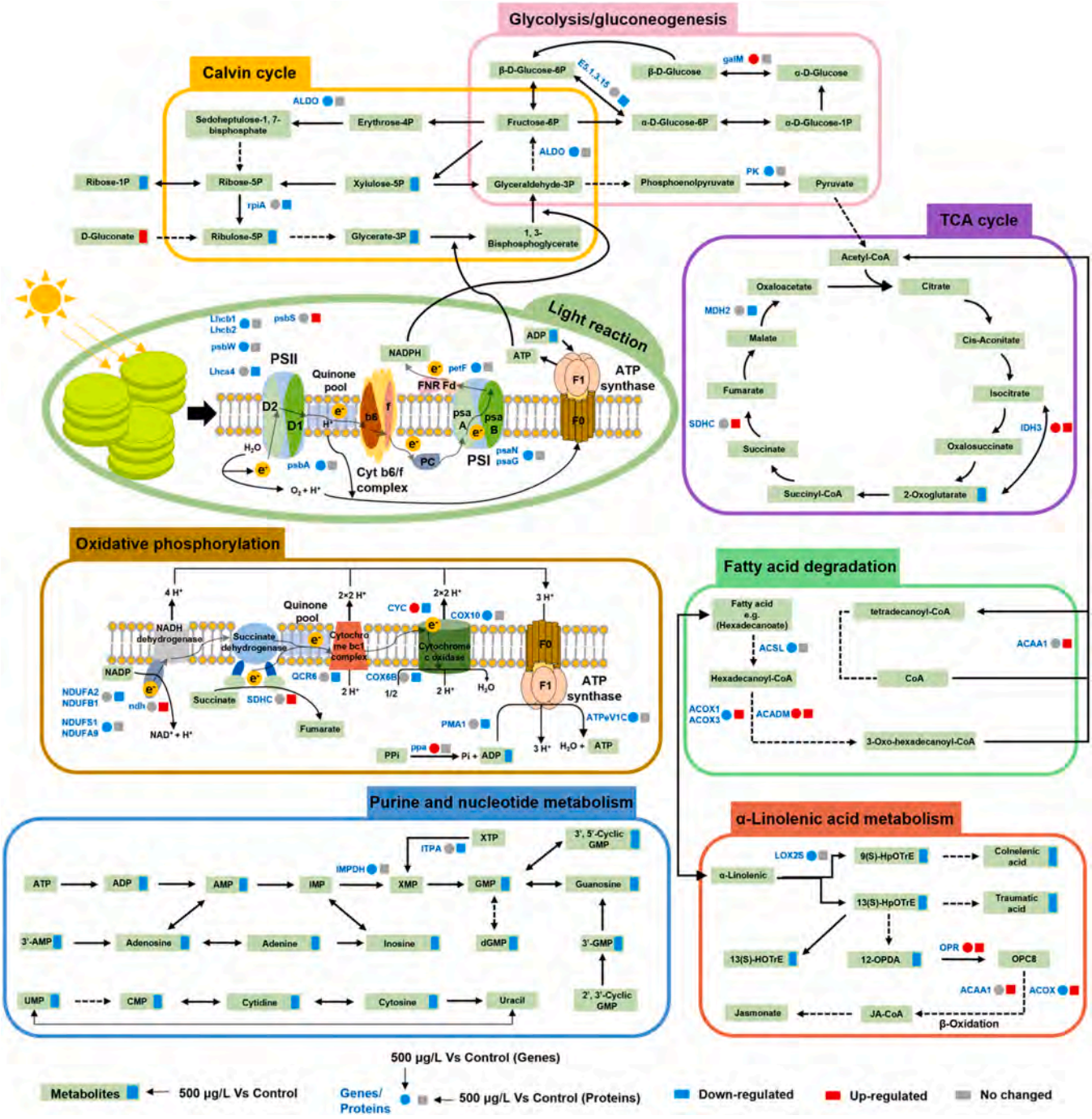


Fig. 6. Enrichment analysis of differentially expressed metabolites, genes and proteins in *Tetradesmus obliquus* after exposure to 500 μg/L OC. Note: The figure was modified based on KEGG.

glyceraldehyde-3-phosphate (G3P) [50]. Even at a concentration of 1 μg/L, OC caused photodamage by day 7. This indicated that the photosynthetic capacity of *Tetradesmus obliquus* was affected even under low environmental concentrations (1 μg/L). The downregulation of photosynthetic genes and proteins, combined with functional impairments in energy capture, electron transport, and photoprotection, underscores the severity of OC's impact on the *Tetradesmus obliquus* photosynthetic system.

Spearman's rank correlation analysis revealed strong negative correlations between ROS levels and both Fv/Fm ($r = -0.75$, $p < 0.001$) and $rETR_{max}$ ($r = -0.51$, $p < 0.05$) (Fig. S17), suggesting a potential mechanistic relationship between oxidative stress and photochemical efficiency impairment. In addition to gene-level changes, elevated ROS levels on day 1 suggested oxidative stress due to inhibited electron transport [51, 52]. The antioxidant system responded insufficiently, as enzymatic antioxidant activities were inhibited under high ROS conditions [53]. Previous studies also found that relatively lower concentrations of myclobutanil (50 μg/L) and p-chloroaniline (1.25 mg/L) induced higher antioxidant enzyme activity compared to higher concentrations (100 μg/L and 5 mg/L, respectively) [54, 55]. Non-enzymatic antioxidants, such as GSH, played a compensatory role in mitigating ROS but failed to fully prevent oxidative damage, as indicated by MDA accumulation (Fig. S18). Interestingly, as the OC concentrations declined both in the culture medium and intracellularly

(Table S4, Fig. S19), the 500 μg/L treatment group showed a slight recovery in antioxidant enzyme activities, concomitant with a reduction in ROS levels (Fig. S20, $p < 0.05$). This recovery, though partial, helped mitigate further oxidative stress and contributed to the elimination of excess MDA. However, the recovery did not fully reverse the damage to the photosynthetic system, particularly the impairment of photoprotective mechanisms and the decline in photosynthetic capacity. Together, these findings demonstrate that OC disrupted the coordinated function of photosynthetic proteins and genes, leading to impaired energy capture, electron transport, and photoprotection, ultimately reducing photosynthetic efficiency and causing photodamage.

4.2. Cascading effects: Photosynthetic inhibition disrupts energy metabolism

When the photosynthetic system was inhibited, the conversion of light energy into chemical energy decreased, leading to insufficient cellular energy supply and subsequent inhibition of metabolism [56]. As previously mentioned, the inhibition of the electron transport chain led to impaired NADPH synthesis, which subsequently affected carbon fixation in the Calvin cycle. The downregulation of the *ALDO* (encoding aldolase) gene and ribulose-5-phosphate isomerase (rpiA) likely impacted key enzymatic activities in both the Calvin cycle and glycolysis, resulting in reduced carbon metabolism efficiency [57, 58]. The downregulation of *ALDO* may have inhibited the production of three-carbon compounds in glycolysis, while the downregulation of rpiA protein may have obstructed the interconversion of five-carbon sugars in the Calvin cycle. These changes could directly lead to a decrease in the levels of metabolic intermediates such as ribulose-5-phosphate (Ribulose-5P), glycerate-3-phosphate (Glycerate-3P), and xylulose-5-phosphate (Xylulose-5P), thereby reducing carbon fixation efficiency[59]. Furthermore, the downregulation of *PK* (encoding pyruvate kinase) gene in the glycolysis pathway is noteworthy. In the final step of glycolysis, PK catalyzes the irreversible conversion of ADP and phosphoenolpyruvate to ATP and pyruvate [60, 61]. Pyruvate is then converted into acetyl coenzyme A (acetyl-CoA), a key substrate for the TCA cycle [62].

Due to the inhibition of photosynthesis and the resulting energy deficiency, fatty acid degradation was mobilized to supplement acetyl-CoA production [63]. This was also reflected in the lipid metabolic profile, where about 85 % of lipid molecules showed decreased abundance in the 500 μg/L OC group (Fig S5b). The upregulation of medium-chain acyl-CoA dehydrogenase (ACADM) and 3-ketoacyl-CoA thiolase (ACAA1) likely indicated enhanced activity of the fatty acid β-oxidation pathway [64], promoting fatty acid breakdown and energy supply [64, 65]. Additionally, in the α-linolenic acid metabolism pathway, the downregulation of oxylipins such as 12-oxophytodienoic acid (12-OPDA), hydroxy-octadecatrienoic acid (HOTrE), and traumatic acid (TA) suggested a suppression of certain lipid-derived defense metabolites under OC stress (Fig. 6). Despite this, the upregulation of key enzymes like ACADM, ACAA1, and 12-oxophytodienoate reductase (OPR) might contribute to jasmonic acid (JA) synthesis [66]. This dual response optimized energy production while selectively modulating defense-related metabolites to adapt to stress conditions.

Another key energy metabolism pathway, oxidative phosphorylation, was also altered. The downregulation of mitochondrial electron transport chain-related genes or proteins such as NADH: Ubiquinone oxidoreductase subunit A2 (NDUFA2) protein, NADH: Ubiquinone oxidoreductase subunit B1 (NDUFB1) protein, and *NDUFS1* (encoding NADH:Ubiquinone oxidoreductase core subunit S1 protein), along with oxidative phosphorylation-related proteins like cytochrome c (CYC) protein and cytochrome c oxidase subunit 6B (COX6B) protein (Fig. 6) [67], likely indicated reduced oxidative phosphorylation efficiency [68]. This suggests a decreased reliance on mitochondrial respiration, thereby reducing ROS production to cope with OC stress. This also implies that the increased activity of antioxidant enzymes was not the only mechanism for reducing ROS levels. Additionally, the upregulation of *ppa* (encoding pyrophosphatase) could have strengthened phosphate metabolism and ion transport functions [69], further helping the cell maintain metabolic homeostasis under low-energy-consuming conditions. A previous study found that OC leads to mitochondrial dysfunction in corals [13], which could be the underlying cause of the disruption in oxidative phosphorylation metabolism.

4.3. Reduction in substrates for cell growth and division inhibited cell growth

After photosynthesis and energy metabolism were affected, the cell required additional energy sources, such as fatty acids, to synthesize hormones to resist stress. This further reduced the availability of substrates needed for cell growth and division. In the 500 μg/L group, numerous genes involved in cell division and proliferation were enriched in pathways such as nucleocytoplasmic transport, spliceosome, basal transcription factors, RNA degradation. It should be noted that most of the DEGs in these pathways were downregulated, which is a common phenomenon in algae and plants under non-biological stress [70, 71]. However, no expression alterations in these genes were observed under the 1 μg/L group. The downregulation of genes related to genetic information processing indicated that cell growth and the synthesis of essential genetic materials may be inhibited (Fig. S10-S14), potentially contributing to the observed decrease in algal cell density. In 500 μg/L group, metabolites related to nucleobase metabolism were downregulated, corresponding to the previously mentioned downregulation of genes associated with genetic information processing. Notably, metabolites related to uridine (3′-UMP, 5′-UMP) exhibited downregulation, both being upstream products of uridine. The decreased levels of these two substances, which can be resynthesized from uridine in RNA degradation [72], may explain the observed inhibition of RNA synthesis identified in the transcriptomics, as UMP is a crucial component of RNA [73]. Other metabolites associated with RNA synthesis or precursor compounds for DNA synthesis, such as 3′-GMP, 5′-GMP, 3′-AMP, 5′-AMP, and 5′-CMP, also showed downregulation, which supported the hypothesis that DNA and RNA synthesis were inhibited.

Although no cell division-related pathways were enriched in the 1 μg/L group, alterations were still observed in certain energy metabolism pathways (e.g., linoleic acid metabolism and carbon fixation in photosynthetic organisms), particularly in amino acid metabolism pathways (including cysteine and methionine metabolism, histidine metabolism, arginine biosynthesis, arginine and proline metabolism, and lysine biosynthesis). These findings demonstrate that even at environmental relevant concentrations, metabolic disturbances were induced in the microalgae [74], although no significant reduction in algal density was detected.

In summary, the inhibition of the light reactions and electron transport in photosynthesis was a key event leading to the suppression of algal cell growth (Fig. 6). Insufficient and delayed NADPH supply disrupted carbon synthesis in the Calvin cycle. This chain reaction impaired the glycolytic pathway's ability to provide sufficient acetyl-CoA for the TCA cycle. As a result, fatty acid degradation was upregulated to supplement acetyl-CoA, while the oxidative phosphorylation pathway also became dysregulated, reducing electron transport chain activity to maintain cellular homeostasis. Under resource limitations, the synthesis of TA might have been suppressed to allocate resources to more immediate defense responses, such as the JA pathway. During energy shortages, more substrates were diverted to stress responses, and the downregulation of nucleotide metabolism pathways directly affected DNA and RNA synthesis [75], thereby impairing cell proliferation and division. This ultimately led to a reduction in cell density.

5. Conclusions

In conclusion, this study demonstrates that OC exposure leads to significant growth inhibition in the green alga *Tetradesmus obliquus* by disrupting photosynthesis and energy metabolism. The reduction in photosystem efficiency, along with suppressed Calvin cycle and glycolysis pathways, highlights how OC impairs energy production and metabolic balance. These disruptions resulted in increased fatty acid degradation to support energy demands and a decline in precursors for nucleic acid synthesis, directly affecting cell growth and division. As a widely used organic UV absorber, OC's impact on primary producers like *Tetradesmus obliquus* highlights the need for further research to understand its ecological effects and potential risks in aquatic environments.

CRediT authorship contribution statement

Zhen-Zhu Liu: Writing – review & editing, Investigation. **Kefu Yu:** Writing – review & editing, Resources. **Feng-Jiao Peng:** Writing – original draft, Supervision, Formal analysis, Conceptualization. **Hao Liang:** Writing – review & editing, Investigation. **Jun-Jie Hu:** Writing – original draft, Methodology, Investigation, Data curation. **Pan Chang-gui:** Writing – review & editing, Validation, Supervision, Conceptualization.

Environmental implications

The suppression of photosynthesis and energy metabolism pathways, along with shifts in metabolic processes, highlights how OC exposure disrupts energy balance and diminishes cellular function in primary producers. As OC continues to dominate the sunscreen market, its increasing environmental concentrations pose risks to aquatic ecosystems by altering species interactions and nutrient cycling, potentially reducing ecosystem resilience. These findings underscore the urgent need for further investigation into the broader environmental consequences of OC contamination.

Declaration of Competing Interest

The authors declare that they have no known competing financial interests or personal relationships that could have appeared to influence the work reported in this paper.

Acknowledgements

The authors would like to thank the financial support by the National Natural Science Foundation of China (42207322, and 42067054), the Guangzhou Municipal Science and Technology Project (2025A04J0904), and the Innovation Project of Guangxi Graduate Education (YCBZ2025069).

Appendix A. Supporting information

Supplementary data associated with this article can be found in the online version at doi:10.1016/j.jhazmat.2025.139072.

Data availability

Data will be made available on request.

References

[1] Cowden, A.M., Whittock, A.L., Holt, E.L., Stavros, V.G., Wills, M., 2023. Synthesis and characterisation of novel composite sunscreens containing both avobenzone and octocrylene motifs. RSC Adv 13, 17017–17027. https://doi.org/10.1039/d3ra02252h.

[2] Downs, C., DiNardo, J.C., Stien, D., Rodrigues, A.M., Lebaron, P., 2021. Benzophenone accumulates over time from the degradation of octocrylene in commercial sunscreen products. Chem Res Toxicol 34, 1046–1054. https://doi.org/10.1021/acs.chemrestox.0c00461.

[3] Chaiyabutr, C., Pruksaeakanan, C., Wongdama, S., Prasertsook, S., Kumpangsin, T., Boonchai, W., 2023. Characteristics and common ultraviolet filter usage of sunscreens purchased online: cross-cultural analysis across 5 continents. Photodermatol Photoimmunol Photomed 39, 27–38. https://doi.org/10.1111/phpp.12808.

[4] Miller, I.B., Pawlowski, S., Kellermann, M.Y., Petersen-Thiery, M., Moeller, M., Nietzer, S., et al., 2021. Toxic effects of UV filters from sunscreens on coral reefs revisited: regulatory aspects for "reef safe" products. Environ Sci Eur 33, 74. https://doi.org/10.1186/s12302-021-00515-w.

[5] Kameda, Y., Kimura, K., Miyazaki, M., 2011. Occurrence and profiles of organic sun-blocking agents in surface waters and sediments in Japanese rivers and lakes. Environ Pollut 159, 1570–1576. https://doi.org/10.1016/j.envpol.2011.02.055.

[6] Kockler, J., Oelgemöller, M., Robertson, S., Glass, B., 2014. Influence of titanium dioxide particle size on the photostability of the chemical UV-filters butyl methoxy dibenzoylmethane and octocrylene in a microemulsion. Cosmetics 1, 128–139. https://doi.org/10.3390/cosmetics1020128.

[7] Duis, K., Junker, T., Coors, A., 2022. Review of the environmental fate and effects of two UV filter substances used in cosmetic products. Sci Total Environ 808, 151931. https://doi.org/10.1016/j.scitotenv.2021.151931.

[8] Medici, A., Saviano, L., Siciliano, A., Libralato, G., Guida, M., Previtera, L., et al., 2022. Octocrylene: From sunscreens to the degradation pathway during chlorination processes: Formation of byproducts and their ecotoxicity assessment. Molecules 27, 5286. https://doi.org/10.3390/molecules27165286.

[9] Manasfi, T., Coulomb, B., Ravier, S., Boudenne, J.-L., 2017. Degradation of organic UV filters in chlorinated seawater swimming pools: transformation pathways and bromoform formation. Environ Sci Technol 51, 13580–13591. https://doi.org/10.1021/acs.est.7b02624.

[10] Tsui, M.M.P., Leung, H.W., Wai, T.-C., Yamashita, N., Taniyasu, S., Liu, W., et al., 2014. Occurrence, distribution and ecological risk assessment of multiple classes of UV filters in surface waters from different countries. Water Res 67, 55–65. https://doi.org/10.1016/j.watres.2014.09.013.

[11] Zhang, Q.Y., Ma, X.Y., Wang, X.C., Ngo, H.H., 2016. Assessment of multiple hormone activities of a UV-filter (octocrylene) in zebrafish (Danio rerio). Chemosphere 159, 433–441. https://doi.org/10.1016/j.chemosphere.2016.06.037.

[12] Blüthgen, N., Meili, N., Chew, G., Odermatt, A., Fent, K., 2014. Accumulation and effects of the UV-filter octocrylene in adult and embryonic zebrafish (Danio rerio). Sci Total Environ 476-477, 207–217. https://doi.org/10.1016/j.scitotenv.2014.01.015.

[13] Stien, D., Clergeaud, F., Rodrigues, A.M.S., Lebaron, K., Pillot, R., Romans, P., et al., 2018. Metabolomics reveal that octocrylene accumulates in Pocillopora damicornis tissues as fatty acid conjugates and triggers coral cell mitochondrial dysfunction. Anal Chem 91, 990–995. https://doi.org/10.1021/acs.analchem.8b04187.

[14] Thorel, E., Clergeaud, F., Rodrigues, A.M.S., Lebaron, P., Stien, D., 2022. A comparative metabolomics approach demonstrates that octocrylene accumulates in Stylophora pistillata tissues as derivatives and that octocrylene exposure induces mitochondrial dysfunction and cell senescence. Chem Res Toxicol 35, 2160–2167. https://doi.org/10.1021/acs.chemrestox.2c00248.

[15] Giraldo, A., Montes, R., Rodil, R., Quintana, J.B., Vidal-Liñán, L., Beiras, R., 2017. Ecotoxicological evaluation of the UV filters ethylhexyl dimethyl p-aminobenzoic acid and octocrylene using marine organisms Isochrysis galbana, Mytilus galloprovincialis and Paracentrotus lividus. Arch Environ Contam Toxicol 72, 606–611. https://doi.org/10.1007/s00244-017-0399-4.

[16] Thorel, E., Clergeaud, F., Jaugeon, L., Rodrigues, A.M.S., Lucas, J., Stien, D., et al., 2020. Effect of 10 UV filters on the brine shrimp Artemia salina and the marine microalga Tetraselmis sp. Toxics 8, 29. https://doi.org/10.3390/toxics8020029.

[17] Vieira Sanches, M., Oliva, M., De Marchi, L., Cuccaro, A., Puppi, D., Chiellini, F., et al., 2021. Ecotoxicological screening of UV-filters using a battery of marine bioassays. Environ Pollut 290, 118011. https://doi.org/10.1016/j.envpol.2021.118011.

[18] Pan, C.G., Peng, F.J., Ying, G.G., 2018. Removal, biotransformation and toxicity variations of climbazole by freshwater algae Scenedesmus obliquus. Environ Pollut 240, 534–540. https://doi.org/10.1016/j.envpol.2018.05.020.

[19] Guo, R., Du, Y., Zheng, F., Wang, J., Wang, Z., Ji, R., et al., 2017. Bioaccumulation and elimination of bisphenol a (BPA) in the alga Chlorella pyrenoidosa and the potential for trophic transfer to the rotifer Brachionus calyciflorus. Environ Pollut 227, 460–467. https://doi.org/10.1016/j.envpol.2017.05.010.

[20] Pal, M., Yesankar, P.J., Dwivedi, A., Qureshi, A., 2020. Biotic control of harmful algal blooms (HABs): a brief review. J Environ Manag 268, 110687. https://doi.org/10.1016/j.jenvman.2020.110687.

[21] Zhang, H., Zong, R., He, H., Huang, T., 2022. Effects of hydrogen peroxide on Scenedesmus obliquus: cell growth, antioxidant enzyme activity and intracellular protein fingerprinting. Chemosphere 287. https://doi.org/10.1016/j.chemosphere.2021.132185.

[22] Wang, P., Zhang, B., Zhang, H., He, Y., Ong, C.N., Yang, J., 2019. Metabolites change of Scenedesmus obliquus exerted by AgNPs. J Environ Sci 76, 310–318. https://doi.org/10.1016/j.jes.2018.05.017.

[23] Rippka, R., Deruelles, J., Waterbury, J.B., Herdman, M., Stanier, R.Y., 1979. Generic assignments, strain histories and properties of pure cultures of cyanobacteria. Microbiology 111, 1–61. https://doi.org/10.1099/00221287-111-1-1.

[24] Vila, M., Lamas, J.P., Garcia-Jares, C., Dagnac, T., Llompart, M., 2016. Ultrasound-assisted emulsification microextraction followed by gas chromatography–mass spectrometry and gas chromatography–tandem mass spectrometry for the analysis of UV filters in water. Microchem J 124, 530–539. https://doi.org/10.1016/j.microc.2015.09.023.
[25] Vila, M., Celeiro, M., Lamas, J.P., Garcia-Jares, C., Dagnac, T., Llompart, M., 2017. Simultaneous in-vial acetylation solid-phase microextraction followed by gas chromatography tandem mass spectrometry for the analysis of multiclass organic UV filters in water. J Hazard Mater 323, 45–55. https://doi.org/10.1016/j.jhazmat.2016.06.056.
[26] Wu, Y., Wan, L., Zhang, W., Ding, H., Yang, W., 2020. Resistance of cyanobacteria Microcystis aeruginosa to erythromycin with multiple exposure. Chemosphere 249, 126147. https://doi.org/10.1016/j.chemosphere.2020.126147.
[27] Zhang, Y., Luo, L., Gan, P., Chen, X., Li, X., Pang, Y., et al., 2024. Exposure to pentachlorophenol destructs the symbiotic relationship between zooxanthellae and host and induces pathema in coral Porites lutea. Sci Total Environ 907, 167956. https://doi.org/10.1016/j.scitotenv.2023.167956.
[28] Wang, G., Zhang, Q., Li, J., Chen, X., Lang, Q., Kuang, S., 2019. Combined effects of erythromycin and enrofloxacin on antioxidant enzymes and photosynthesis-related gene transcription in Chlorella vulgaris. Aquat Toxicol 212, 138–145. https://doi.org/10.1016/j.aquatox.2019.05.004.
[29] Miralles, P., Yusa, V., Sanchis, Y., Coscolla, C., 2021. Determination of 60 migrant substances in plastic food contact materials by vortex-assisted liquid-liquid extraction and GC-Q-Orbitrap HRMS. Molecules 26, 7640. https://doi.org/10.3390/molecules26247640.
[30] Lin, Y.-F., Liao, L.-Z., Wang, S.-Y., Zhang, S.-Z., Zhong, X.-B., Zhou, H.-M., et al., 2024. Causal association of golgi protein 73 with coronary artery disease: evidence from proteomics and Mendelian randomization. Int J Med Sci 21, 2127. https://doi.org/10.7150/ijms.94179.
[31] Eberhardt, J., Santos-Martins, D., Tillack, A.F., Forli, S., 2021. AutoDock Vina 1.2.0: new docking methods, expanded force field, and python bindings. J Chem Inf Model 61, 3891–3898. https://doi.org/10.1021/acs.jcim.1c00203.
[32] Abraham, M.J., Murtola, T., Schulz, R., Páll, S., Smith, J.C., Hess, B., et al., 2015. GROMACS: High performance molecular simulations through multi-level parallelism from laptops to supercomputers. SoftwareX 1, 19–25. https://doi.org/10.1016/j.softx.2015.06.001.
[33] Zhou, R., Yu, X., Kjær, K.H., Rosenqvist, E., Ottosen, C.-O., Wu, Z., 2015. Screening and validation of tomato genotypes under heat stress using Fv/Fm to reveal the physiological mechanism of heat tolerance. Environ Exp Bot 118, 1–11. https://doi.org/10.1016/j.envexpbot.2015.05.006.
[34] Knoppová, J., Sobotka, R., Yu, J., Bečková, M., Pilný, J., Trinugroho, J.P., et al., 2022. Assembly of D1/D2 complexes of photosystem II: binding of pigments and a network of auxiliary proteins. Plant Physiol 189, 790–804. https://doi.org/10.1093/plphys/kiac045.
[35] Cao, P., Su, X., Pan, X., Liu, Z., Chang, W., Li, M., 2018. Structure, assembly and energy transfer of plant photosystem II supercomplex. Biochim Et Biophys Acta (BBA) Bioenerg 1859, 633–644. https://doi.org/10.1016/j.bbabio.2018.03.007.
[36] Shi, L.-X., Lorkovic, Z.J., Oelmüller, R., Schröder, W.P., 2000. The low molecular mass PsbW protein is involved in the stabilization of the dimeric photosystem II complex in Arabidopsis thaliana. J Biol Chem 275, 37945–37950. https://doi.org/10.1074/jbc.M006300200.
[37] Faseela, P., Puthur, J.T., 2016. Chlorophyll a fluorescence changes in response to short and long term high light stress in rice seedlings. Indian J Plant Physiol 22, 30–33. https://doi.org/10.1007/s40502-016-0244-1.
[38] Ahammed, G.J., Xu, W., Liu, A., Chen, S., 2018. COMT1 silencing aggravates heat stress-induced reduction in photosynthesis by decreasing chlorophyll content, photosystem II activity, and electron transport efficiency in tomato. Front Plant Sci 9, 998. https://doi.org/10.3389/fpls.2018.00998.
[39] Lin, Y.-H., Pan, K.-Y., Hung, C.-H., Huang, H.-E., Chen, C.-L., Feng, T.-Y., et al., 2013. Overexpression of ferredoxin, PETF, enhances tolerance to heat stress in Chlamydomonas reinhardtii. Int J Mol Sci 14, 20913–20929. https://doi.org/10.3390/ijms141020913.
[40] Xie, M., Wang, X., Zeng, Q., Shen, J., Huang, B., 2024. Growth physiology and chlorophyll fluorescence analysis of two moss species under different LED Light qualities. Plant Physiol Biochem, 108777. https://doi.org/10.1016/j.plaphy.2024.108777.
[41] Pietrzykowska, M., Suorsa, M., Semchonok, D.A., Tikkanen, M., Boekema, E.J., Aro, E.-M., et al., 2014. The light-harvesting chlorophyll a/b binding proteins Lhcb1 and Lhcb2 play complementary roles during state transitions in Arabidopsis. Plant Cell 26, 3646–3660. https://doi.org/10.1105/tpc.114.127373.
[42] Gebara, R.C., LdOG, Alho, Mansano, da Silva, Rocha, A., Melão MdGG, G.S., 2023. Single and combined effects of Zn and Al on photosystem II of the green microalgae Raphidocelis subcapitata assessed by pulse-amplitude modulated (PAM) fluorometry. Aquat Toxicol 254, 106369. https://doi.org/10.1016/j.aquatox.2022.106369.
[43] Fan, H., Jin, M., Wang, H., Xu, Q., Xu, L., Wang, C., et al., 2019. Effect of differently methyl-substituted ionic liquids on Scenedesmus obliquus growth, photosynthesis, respiration, and ultrastructure. Environ Pollut 250, 155–165. https://doi.org/10.1016/j.envpol.2019.04.021.
[44] Fan, M., Li, M., Liu, Z., Cao, P., Pan, X., Zhang, H., et al., 2015. Crystal structures of the PsbS protein essential for photoprotection in plants. Nat Struct Mol Biol 22, 729–735. https://doi.org/10.1038/nsmb.3068.
[45] Ptushenko, V.V., Bondarenko, G.N., Vinogradova, E.N., Glagoleva, E.S., Karpova, O.V., Ptushenko, O.S., et al., 2022. Chilling Upregulates Expression of the PsbS and LhcSR Genes in the Chloroplasts of the Green Microalga Lobosphaera incisa IPPAS C-2047. Biochemistry 87, 1699–1706. https://doi.org/10.1134/S0006297922120240.
[46] Zhang, H., Zhao, L., Chen, Y., Zhu, M., Xu, Q., Wu, M., et al., 2021. Trophic transition enhanced biomass and lipid production of the unicellular green alga Scenedesmus acuminatus. Front Bioeng Biotechnol 9, 638726. https://doi.org/10.3389/fbioe.2021.638726.
[47] Li, N., Zeng, Z., Zhang, Y., Zhang, H., Tang, N., Guo, Y., et al., 2023. Higher toxicity induced by co-exposure of polystyrene microplastics and chloramphenicol to Microcystis aeruginosa: experimental study and molecular dynamics simulation. Sci Total Environ 866, 161375. https://doi.org/10.1016/j.scitotenv.2022.161375.
[48] Varotto, C., Pesaresi, P., Jahns, P., Leßnick, A., Tizzano, M., Schiavon, F., et al., 2002. Single and double knockouts of the genes for photosystem I subunits G, K, and H of Arabidopsis. Effects on photosystem I composition, photosynthetic electron flow, and state transitions. Plant Physiol 129, 616–624. https://doi.org/10.1104/pp.002089.
[49] Haldrup, A., Naver, Helle, Scheller, H.V., 1999. The interaction between plastocyanin and photosystem I is inefficient in transgenic Arabidopsis plants lacking the PSI-N subunit of photosystem. Plant J 17, 689–698. https://doi.org/10.1046/j.1365-313X.1999.00419.x.
[50] Bathellier, C., Tcherkez, G., Lorimer, G.H., Farquhar, G.D., 2018. Rubisco is not really so bad. Plant Cell Environ 41, 705–716. https://doi.org/10.1111/pce.13149.
[51] Wang, F., Gao, J., Shi, S., He, X., Dai, T., 2019. Impaired electron transfer accounts for the photosynthesis inhibition in wheat seedlings (Triticum aestivum L.) subjected to ammonium stress. Physiol Plant 167, 159–172. https://doi.org/10.1111/ppl.12878.
[52] Gururani, Mayank A., Venkatesh, J., Tran, L.S.P., 2015. Regulation of photosynthesis during abiotic stress-induced photoinhibition. Mol Plant 8, 1304–1320. https://doi.org/10.1016/j.molp.2015.05.005.
[53] Chamseddine, M., Wided, B.A., Guy, H., Marie-Edith, C., Fatma, J., 2008. Cadmium and copper induction of oxidative stress and antioxidative response in tomato (Solanum lycopersicon) leaves. Plant Growth Regul 57, 89–99. https://doi.org/10.1007/s10725-008-9324-1.
[54] Deng, Y., Zhang, W., Qin, Y., Liu, R., Zhang, L., Wang, Z., et al., 2019. Stereoselective toxicity of metconazole to the antioxidant defenses and the photosynthesis system of Chlorella pyrenoidosa. Aquat Toxicol 210, 129–138. https://doi.org/10.1016/j.aquatox.2019.02.017.
[55] Wang, X., Miao, J., Pan, L., Li, Y., Lin, Y., Wu, J., 2019. Toxicity effects of p-choroaniline on the growth, photosynthesis, respiration capacity and antioxidant enzyme activities of a diatom, Phaeodactylum tricornutu. Ecotoxicol Environ Saf 169, 654–661. https://doi.org/10.1016/j.ecoenv.2018.11.015.
[56] Bassi, R., Dall'Osto, L., 2021. Dissipation of light energy absorbed in excess: the molecular mechanisms. Annu Rev Plant Biol 72, 47–76. https://doi.org/10.1146/annurev-arplant-071720-015522.
[57] Sun, D., Zhou, X., Sun, X., Xu, N., 2023. Transcriptomic analysis reveals the regulatory mechanism of tetraspore formation in Gracilariopsis lemaneiformis. Front Mar Sci 9, 1080474. https://doi.org/10.3389/fmars.2022.1080474.
[58] Mao, W., Li, P., Wang, D., Hu, Z., Wei, S., Song, C., 2023. Effect of DACH-K2CO3 Mixed Absorbent on the Performance of a CO2 Absorption and Microalgae Conversion (CAMC) System. ACS Sustain Chem Eng 12, 120–129. https://doi.org/10.1021/acssuschemeng.3c04955.
[59] Sharma, S., Joshi, J., Kataria, S., Verma, S.K., Chatterjee, S., Jain, M., et al., 2020. Regulation of the Calvin cycle under abiotic stresses: an overview. Plant life under changing environment. 681–717. https://doi.org/10.1016/B978-0-12-818204-8.00030-8.
[60] Laporte, D., González, A., Moenne, A., 2020. Copper-Induced activation of MAPKs, CDPKs and CaMKs triggers activation of Hexokinase and inhibition of pyruvate kinase leading to increased synthesis of ASC, GSH and NADPH in ulva compressa. Front Plant Sci 11, 990. https://doi.org/10.3389/fpls.2020.00990.
[61] Schormann, N., Hayden, K.L., Lee, P., Banerjee, S., Chattopadhyay, D., 2019. An overview of structure, function, and regulation of pyruvate kinases. Protein Sci 28, 1771–1784. https://doi.org/10.1002/pro.3691.
[62] Oliver, D.J., Nikolau, B.J., Wurtele, E.S., 2009. Acetyl-CoA—life at the metabolic nexus. Plant Sci 176, 597–601. https://doi.org/10.1016/j.plantsci.2009.02.005.
[63] Izzo, L.T., Trefely, S., Demetriadou, C., Drummond, J.M., Mizukami, T., Kuprasertkul, N., et al., 2023. Acetylcarnitine shuttling links mitochondrial metabolism to histone acetylation and lipogenesis. Sci Adv 9, eadf0115. https://doi.org/10.1126/sciadv.adf0115.
[64] Wang, G., Li, T., Wan, Y., Li, Q., 2024. MYC expression and fatty acid oxidation in EGFR-TKI acquired resistance. Drug Resist Updates 72, 101019. https://doi.org/10.1016/j.drup.2023.101019.
[65] Long, B., Muhamad, R., Yan, G., Yu, J., Fan, Q., Wang, Z., et al., 2016. Quantitative proteomics analysis reveals glutamine deprivation activates fatty acid β-oxidation pathway in HepG2 cells. Amino Acids 48, 1297–1307. https://doi.org/10.1007/s00726-016-2182-7.
[66] Xin, Z., Chen, S., Ge, L., Li, X., Sun, X., 2019. The involvement of a herbivore-induced acyl-CoA oxidase gene, CsACX1, in the synthesis of jasmonic acid and its expression in flower opening in tea plant (Camellia sinensis). Plant Physiol Biochem 135, 132–140. https://doi.org/10.1016/j.plaphy.2018.11.035.
[67] Li, B., Yu, Y., Jiang, Y., Zhao, L., Li, A., Li, M., et al., 2021. Cloperastine inhibits esophageal squamous cell carcinoma proliferation in vivo and in vitro by suppressing mitochondrial oxidative phosphorylation. Cell Death Discov 7, 166. https://doi.org/10.1038/s41420-021-00509-w.
[68] Liu, J., Barrientos, A., 2013. Transcriptional regulation of yeast oxidative phosphorylation hypoxic genes by oxidative stress. Antioxid Redox Signal 19, 1916–1927. https://doi.org/10.1089/ars.2012.4589.

[69] Segami, S., Tomoyama, T., Sakamoto, S., Gunji, S., Fukuda, M., Kinoshita, S., et al., 2018. Vacuolar H+-pyrophosphatase and cytosolic soluble pyrophosphatases cooperatively regulate pyrophosphate levels in Arabidopsis thaliana. Plant Cell 30, 1040–1061. https://doi.org/10.1105/tpc.17.00911.

[70] Yang, Y., Li, A., Qiu, J., Yan, W., Han, L., Li, D., et al., 2023. Effects of lipophilic phycotoxin okadaic acid on the early development and transcriptional expression of marine medaka Oryzias melastigma. Aquat Toxicol 260, 106576. https://doi.org/10.1016/j.aquatox.2023.106576.

[71] Zhou, Y., Li, X., Chen, J., Li, W., Wang, F., 2023. Carbon sequestration performance, enzyme and photosynthetic activity, and transcriptome analysis of algae-bacteria symbiotic system after antibiotic exposure. Sci Total Environ 902, 166486. https://doi.org/10.1016/j.scitotenv.2023.166486.

[72] Li, G., Xie, C., Wang, Q., Wan, D., Zhang, Y., Wu, X., et al., 2019. Uridine/UMP metabolism and their function on the gut in segregated early weaned piglets. Food Funct 10, 4081–4089. https://doi.org/10.1039/c9fo00360f.

[73] Santos, J.P., Li, W., Keller, A.A., Slaveykova, V.I., 2024. Mercury species induce metabolic reprogramming in freshwater diatom Cyclotella meneghiniana. J Hazard Mater 465, 133245. https://doi.org/10.1016/j.jhazmat.2023.133245.

[74] Mo, J., Ma, Z., Yan, S., Cheung, N.K.M., Yang, F., Yao, X., et al., 2023. Metabolomic profiles in a green alga (Raphidocelis subcapitata) following erythromycin treatment: ABC transporters and energy metabolism. J Environ Sci 124, 591–601. https://doi.org/10.1016/j.jes.2021.12.001.

[75] Fan, T.W.M., Lane, A.N., 2015. Regulation of mammalian nucleotide metabolism and biosynthesis. Nucleic Acids Res 43, 2466–2485. https://doi.org/10.1093/nar/gkv047.

Journal of Hazardous Materials 495 (2025) 138958

Contents lists available at ScienceDirect

Journal of Hazardous Materials

journal homepage: www.elsevier.com/locate/jhazmat

Targeted and non-targeted analyses reveal trophic biomagnification of rubber-derived chemicals in an estuarine food web near China's largest rubber production region

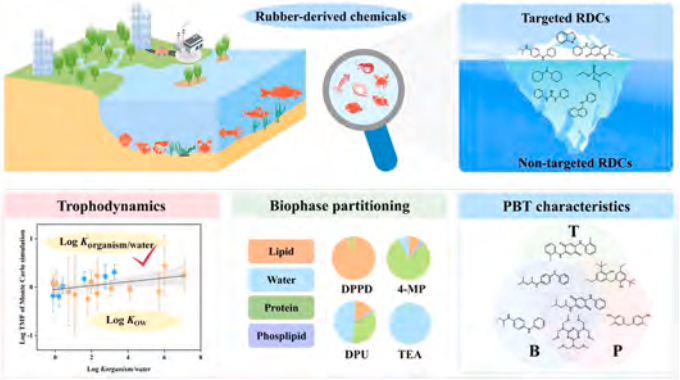
Yuan Liu [a,d], Jia-Ming Zhou [b], Nian-Nian Wu [c,f], Shan Liu [a,c,*], Xiao-Liang Liao [b], Haijiang Wu [e], Lin Zhu [e], Heng-Xiang Li [c], Lang Lin [c], Rui Hou [c], Zhi-Hua Li [d], Xiang-Rong Xu [a], Zhi-Feng Chen [b,**], Zongwei Cai [e]

[a] Guangxi Laboratory on the Study of Coral Reefs in the South China Sea, Coral Reef Research Center of China, School of Marine Sciences, Guangxi University, Nanning 530004, China
[b] Guangdong Key Laboratory of Environmental Catalysis and Health Risk Control, Guangdong-Hong Kong-Macao Joint Laboratory for Contaminants Exposure and Health, School of Environmental Science and Engineering, Guangdong University of Technology, Guangzhou 510006, China
[c] Key Laboratory of Tropical Marine Bio-Resources and Ecology, Guangdong Provincial Key Laboratory of Applied Marine Biology, South China Sea Institute of Oceanology, Chinese Academy of Sciences, Guangzhou 510301, China
[d] Marine College, Shandong University, Weihai, Shandong 264209, China
[e] State Key Laboratory of Environmental and Biological Analysis, Department of Chemistry, Hong Kong Baptist University, Hong Kong 999077, China
[f] University of Chinese Academy of Sciences, Beijing 100049, China

HIGHLIGHTS

- Targeted and non-targeted RDCs were first identified in estuarine species.
- Log $K_{organism/water}$ more accurately predicts RDC biomagnification than Log K_{ow}.
- Mass distribution analysis reveals phase-specific RDC partitioning in organisms.
- Most RDCs exhibit persistence, bioaccumulation, or toxicity (PBT) properties.

GRAPHICAL ABSTRACT



ARTICLE INFO

Keywords:
Rubber-derived chemicals
Bioaccumulation

ABSTRACT

The emergence of rubber-derived chemicals (RDCs) has garnered significant environmental attention, particularly *N*-(1,3-dimethylbutyl)-*N'*-phenyl-*p*-phenylenediamine quinone (6PPD-Q) linked to acute mortality in salmonids. However, the trophic transfer of RDCs within marine ecosystems is notably sparse. Here, we investigated

* Corresponding author at: Guangxi Laboratory on the Study of Coral Reefs in the South China Sea, Coral Reef Research Center of China, School of Marine Sciences, Guangxi University, Nanning 530004, China.
** Corresponding author.
E-mail addresses: liushan@scsio.ac.cn, liushan21137@163.com (S. Liu), chenzhf@gdut.edu.cn (Z.-F. Chen).

https://doi.org/10.1016/j.jhazmat.2025.138958
Received 12 February 2025; Received in revised form 23 May 2025; Accepted 14 June 2025
Available online 15 June 2025
0304-3894/© 2025 Elsevier B.V. All rights are reserved, including those for text and data mining, AI training, and similar technologies.

Biomagnification mechanisms
Non-targeted screening
Marine ecosystem

RDCs in the Nandu River estuary near China's largest rubber production region through an integrated targeted and non-targeted approach. Twelve targeted and 28 non-targeted RDCs were identified in biological samples. For targeted RDCs, total mean concentrations (ng/g, wet weight) showed a descending order of crab (702) > shellfish (531) > snail (491) > shrimp (392) > cuttlefish (342) > fish (190), while those for non-targeted RDCs followed the order of fish (3.91 $\times 10^3$) > shellfish (3.08 $\times 10^3$) > cuttlefish (2.96 $\times 10^3$) > shrimp (2.78 $\times 10^3$) > snail (1.61 $\times 10^3$) > crab (1.36 $\times 10^3$). Thirteen RDCs exhibited biomagnification potential with trophic magnification factors (TMFs) of 1.05–3.24, while nine compounds displayed biodilution trends (TMFs: 0.56–0.93). Organism-water partition coefficients, derived from multi-parameter linear free-energy relationships, more accurately elucidate biomagnification mechanisms of RDCs. Furthermore, 60 % of RDCs exhibited persistence, bioaccumulation and toxicity properties. This research underscores the importance of integrating targeted and non-targeted approaches of RDCs in biomonitoring, offering a more comprehensive view of cumulative chemical risks to humans and wildlife.

1. Introduction

Between 2004 and 2023, the global automotive industry, which had produced 1.6 billion vehicles with China contributing over 25 % to this output [41], necessitates the use of various additives in tire manufacturing to meet stringent performance standards. These additives, including antioxidants, vulcanization accelerators, crosslinking agents, and plasticizers, are predominantly high-production-volume compounds [40]. These additives can migrate to the tire surfaces and subsequently permeate diverse environmental matrices, exhibiting a spectrum of toxicities to aquatic organisms [28,38]. For example, antioxidant *N*-(1,3-dimethylbutyl)-*N'*-phenyl-*p*-phenylenediamine (6PPD) has been demonstrated to elicit developmental toxicity in *Danio rerio* embryos and larvae [42]. Notably, some tire additives undergo a suite of biotic and abiotic transformations, resulting in the generation of transformation products with potentially increased biotoxicity [30,35,48]. An illustrative case is the transformation of the pervasive rubber antioxidant 6PPD into 6PPD-quinone (6PPD-Q), which has been linked to acute mortality of wild salmon (*Oncorhynchus kisutch*) [47]. These tire additives and their transformation products, collectively known as rubber-derived chemicals (RDCs), can also enter the marine ecosystem, presenting hazards to aquatic life and potentially jeopardizing human health via the food webs [13,24,50,9].

Despite growing recognition of their ecological risks, the bioaccumulation and trophic transfer mechanisms of RDCs in aquatic food webs, particularly in estuarine ecosystems, remain poorly understood. Tropical estuaries, with their unique ecological sensitivity and environmental responsiveness, are ideal natural laboratories for studying contaminant behavior [1,18]. As biodiversity hotspots and essential nurseries for aquatic life, their susceptibility to organic pollutants makes them invaluable for pollution research. The accelerated biogeochemical cycling of contaminants in tropical regions, driven by elevated metabolic rates and warm temperatures, facilitates rapid transformations and biomagnification within food webs [12,22,4]. This positions tropical estuaries as critical indicators of global contaminant dynamics, offering unique insights into the environmental fate and ecological risks of emerging pollutants like RDCs.

The Nandu River Estuary (NRE), a tropical estuary in China, connects the Leizhou Peninsula to Haikou city, located on northern Hainan Province. Hainan Province, as China's largest rubber production base, hosts numerous rubber processing factories along the Nandu River basin, inevitably elevating the pollution levels of RDCs into the river [10]. Furthermore, NRE is situated in the most economically active region of Hainan Province, which experiences heavy traffic and abundant rainfall, making the NRE susceptible to pollution from RDCs. Therefore, this estuary is an ideal site for investigating the bioaccumulation and trophic transfer of RDCs. Recently, high-resolution mass spectrometry (HRMS) has become a critical tool for the detection and identification of unknown chemicals [11,14,45]. HRMS-based suspect and non-targeted screening strategies (commonly known as non-targeted analysis) have recently revealed a broad spectrum of RDCs across various environmental matrices, enhancing our understanding of these previously obscure compounds. However, existing research has largely focused on dust, surface runoff, and single-species exposures, with less attention given to the behavior and impacts of RDCs within food webs [27,31,8].

Thus, objectives of this research were to: (1) thoroughly profile the presence and composition of RDCs in tropical estuarine species utilizing both targeted and non-targeted approaches, (2) employ the organism-water partition coefficient ($K_{organism/water}$) and mass fraction to decipher their bioaccumulation and trophodynamic mechanisms, and (3) identify compounds with potential persistence, bioaccumulation, and toxicity (PBT) characteristics. This study, combining targeted and non-targeted analyses, can expand our understanding of the trophodynamics of RDCs in estuarine food webs and guide future biomonitoring strategies for compound prioritization and control.

2. Materials and methods

2.1. Reagents and materials

Seventeen RDCs, including five *p*-phenylenediamine antioxidants [PPDs: 6PPD, *N*-phenyl-*N'*-cyclohexyl-*p*-phenylenediamine (CPPD), *N,N'*-diphenyl-1,4-phenylenediamine (DPPD), *N,N'*-bis(methylphenyl)-1,4-benzenediamine (DTPD), and *N*-isopropyl-*N'*-phenyl-1,4-phenylenediamine (IPPD)], five corresponding PPD-derived quinones (PPD-Qs: 6PPD-Q, CPPD-Q, DPPD-Q, DTPD-Q, and IPPD-Q), five vulcanization accelerators [1H-benzotriazole (BT), benzothiazole (BTH), 2-methylthio-benzothiazole (2-Me-S-BTH), 2-hydroxybenzothiazole (2-OH-BTH), and *N,N'*-diphenylurea (DPU)], and two other additives [hexamethoxymethylmelamine (HMMM) and epsilon-caprolactam (CAP)] were selected (Table S1). Atrazine-d5, 6PPD-quinone-d5, and methylbenzotriazole-d6 were utilized as the internal standards. Details regarding solvents and reagents are delineated in the Supporting Information.

2.2. Sampling sites and sample collection

In April 2023, a total of 14 water samples, 12 sediment samples and 93 biological samples (encompassing 28 species) were procured from the NRE. The geographical coordinates of the sampling sites are delineated in Figure S1. The biological samples included three species of snail (BZL, *Turritella terebra bacillum*, n = 3; CWL, *Bufonaria rana*, n = 3; LFL, *Conomurex luhuanus*, n = 3), four species of shrimp (KXG, *Oratosquilla oratoria,* n = 3; HSFDX, *Parape naeopsis hungerfordi*, n = 3; JYXDX, *Metapenaeus affinis*, n = 3; CMDX, *Penaeus penicillatus*, n = 4), three species of shellfish (ZC, *Solen strictus*, n = 3; FLBCZ, *Ruditapes philippinarum*, n = 3; FCYB, *Perna canaliculus*, n = 3), two species of cuttlefish (DX, *Octopus ocellatus*, n = 3; HQWZ, *Loligo beka*, n = 3), and one species of crab (GZX, *Charybdis riversandersoni*, n = 3). We identified 15 species of fish (DLX, *Sillago sihama*, n = 3; CWCS, *Chorinemus formosanus*, n = 4; DCM, *Pisodonophis boro*, n = 3; HLWCS, *Gnathanodon speciosus*, n = 3; HBSBY, *Epinephelus fasciatus*, n = 4; DTGMY, *Trachiocephalus myops*, n = 3; TY, *Pneumatophorus japonicus*, n = 3; ST, *Cynoglossus semilaevis Gunther*, n = 3; XLL, *Terapon jarbua*, n = 4; LXCS, *Trachinotus ovatus*,

n = 3; HQJD, *Acanthopagrus latus*, n = 6; HBLZY, *Siganus canaliculatus*, n = 3; HJD, *Plectorhinchus*, n = 3; DWB, *Leiognathus brevirostris*; n = 4; ZHXGY, *Stolephorus chinensis*, n = 4). Upon collection, all samples were promptly stored in a freezer at −20°C and subsequently transported to the laboratory. For information on sampling locations, water quality, and biological samples, please refer to Figure S1 and Tables S2-S4 in the Supporting Information.

2.3. Sample extraction and targeted analysis

The extraction procedures for seawater, sediment, and biological samples followed our previous study with monitor modification [49]. Briefly, seawater samples (250 mL) were filtered and spiked with internal standards, and then enriched using solid-phase extraction (Waters, HLB, 500 mg) columns. Frozen-dried sediment samples (0.5 −1.5 g) were extracted using 2 mL of acetonitrile, 2 mL of methanol, and 2 mL of acetonitrile through ultrasonication. Muscle tissues (0.5 −2.0 g, wet weight) were collected as biological samples, extracted using acetonitrile and then purified using C18 adsorbent. Detailed information on the sample extraction can be found in the Supporting information.

RDCs were analyzed using an Agilent 1290 Infinity Ultra Performance Liquid Chromatography (UPLC) system coupled with an Agilent 6470 Triple Quadrupole Mass Spectrometer (MS/MS) in multiple reaction monitoring (MRM) mode. All targeted substances were analyzed in positive electrospray ionization mode (ESI+). The mobile phase consisted of Milli-Q water with 0.1 % formic acid (A) and methanol (B). Detailed operational conditions of the instrument, compound transitions, and retention times are listed in Table S5. The biological samples (0.1 g, dry weight) underwent extraction with a mixture of n-hexane and dichloromethane (1:1, v/v) in a two-step process. Subsequently, the lipid content was determined using gravimetric analysis (Table S4). Frozen-dried biological samples (0.5 mg) were analyzed for stable nitrogen ($\delta^{15}N$) isotope ratios using a Flash EA 112 series elemental analyzer coupled with a Finnigan MAF ConFlo 111 isotope ratio mass spectrometer [36] (Table S4). The accuracy of the nitrogen isotope analysis was maintained within ±0.05 %. The levels of total protein and phospholipid in the biota samples were quantified using a Bicinchoninic Acid Assay Kit (Enzyme-linked Biotechnology Co., Shanghai, China) and a Phopholipid ELISA Kit (YJ218547, Yuanju Biotech, Shanghai, China), respectively.

2.4. Non-targeted screening workflow for RDCs

Building on our previous studies with slight modifications [26,31], we identified potential RDCs beyond targeted substances in biological tissues using a Vanquish ultrahigh-performance liquid chromatography system coupled with an Orbitrap Exploris 120 quadrupole-orbitrap high-resolution mass spectrometer (UPLC-HRMS, Thermo Fisher Scientific, USA) in both positive and negative electrospray ionization modes. Non-targeted screening data were acquired by full-scan mass spectrometry (MS) of precursor ions, selecting those with signal values at least exceeding 5×10^3, followed by data-dependent acquisition in tandem MS ($ddMS^2$). Mass spectral features detected in quality control (QC) samples, prepared by combining 10 μL aliquots from each biological sample solution, but absent in blank controls or with QC responses exceeding five times that of the blank response, were classified as suspected features. These were analyzed using Compound Discoverer 3.3 (Thermo Fisher Scientific, USA) and structurally assigned based on the mzCloud mass spectral library (http://www.mzcloud.org). Features were prioritized if they met the following criteria: signal-to-noise ratio > 3, signal intensity $> 5 \times 10^4$, mass accuracy tolerance < 5 ppm, and a mzCloud match score or similarity match score > 60, with evidence of use in rubber or tire manufacturing verified via PubChem and Chemical Book databases. Features of interest were confirmed at confidence level 1 using commercially available reference standards via parallel reaction monitoring (PRM) fragmentation, or identified as probable structures at confidence level 2 [44]. Additionally, concentrations of confirmed and probable non-targeted RDCs in biological tissues were quantified using reference standard calibration and, when applicable, estimated via Quantem software (https://quantem.co/), respectively. Detailed calculations for non-targeted RDC concentrations (Text S6) and UPLC-HRMS operating parameters (Table S6) are provided in the Supplementary Information.

2.5. Quality assurance and quality control

All targeted substances have undergone strict quality control procedures. The recovery rates of 17 RDCs in water, sediment, and biological samples were 69.4–121 %, 54.0–125 %, and 60.9–118 % respectively (Tables S7-S8). The method detection limits (MDLs) and method quantification limits (MQLs) of RDCs across diverse environmental media were ascertained employing the signal-to-noise ratio approach. The MDLs for RDCs in water, sediments, and biological samples were delineated at 0.00493–2.25 ng/L, 0.00960–13.3 ng/g and 0.0127–3.95 ng/g, respectively. Their corresponding MQLs in water, sediments, and biological samples ranged from 0.0164 to 7.50 ng/L, 0.0321–44.2 ng/g and 0.0423–13.2 ng/g, respectively. To assess background contamination and instrument performance, each batch of samples underwent quality control measures such as field controls, field blanks, method blanks, solvent blanks, and standard solutions (each targeted substance at 100 μg/L). None of the targeted compounds were detected in method blank samples and solvent blanks. Only BTH, 2-OH-BTH, and HMMM were detected in field blank samples with levels greater than their MQLs. The final quantitative concentration was ascertained by subtracting the field blank concentration from the corresponding sample. For all quantification batches, the correlation coefficients (R^2) of the calibration curves (0.1–200 μg/L) exceeded 0.99. Moreover, calibration standards were assessed for each 12 samples to validate instrumental accuracy, ensuring analyte quantification variability remained within 20 %.

In non-targeted screening, an instrument blank, a standard solution, and a quality control (QC) sample, were analyzed before and after each batch during instrumental analysis. Additionally, a blank sample was measured every seven samples, and both a QC sample and a standard solution were analyzed every fourteen samples, with all procedures following the same method used for biological samples [6]. The relative standard deviation (RSD) of the peak areas of most RDCs in QC samples remained below 20 %. Outliers, such as *N*,*N*-dicyclohexylmethylamine (DCHMA), which had higher RSD values, were likely due to lower detection concentrations or reduced frequency in the samples rather than indicating absence. This interpretation is supported by DCHMA's identification at confidence level 1 using a reference standard.

2.6. Statistical analysis

The bioaccumulation factors (BAFs) for estuarine organisms were calculated as $1000 \times C_{biota}/C_w$, with C_{biota} representing the concentration of target chemical in each sample tissue (ng/g, wet weight, ww), and C_w denoting the mean concentration of RDCs in the estuarine water (ng/L). Levels of RDCs below the MQL are assigned a value equivalent to half of the MQL, while levels below the MDL are treated as zero.

Based on the premise that zooplankton occupy trophic level (TL) of 2.0 and $\delta^{15}N$ of 3.8 [54], the following equation was applied to deduce the TL of the surveyed organisms.

$$TL = 2 + \left[\left(\delta^{15}N_{sample} - \delta^{15}N_{plankton}\right)\right]/3.8 \quad (1)$$

The trophic magnification factors (TMFs) were calculated based on the correlation between lipid-normalized concentrations (ng/g, lipid weight, lw) and TLs of individual organisms, using Eqs. 2 and 3.

$$LogC_{biota} = a + b \times TL \quad (2)$$

$$TMF = 10^{b} \quad (3)$$

TMFs were calculated solely for RDCs found in biological samples at a detection frequency above 30 %. Linear regression was applied to forecast TMFs exhibiting clear concentration-TL relationships. Earlier research has proven that Monte Carlo simulations can reliably estimate TMF values of target compounds in food webs, even when no significant correlation exists between compound concentrations and TLs [22,23]. Therefore, besides linear regression, Monte Carlo simulations were also utilized for TMF value prediction. Log TMF values were derived through Monte Carlo simulations conducted using Crystal Ball software, which performed 10,000 predictions [22,23]. These simulations utilized lipid-normalized concentrations and TL values as input parameters, consistent with the approach employed in linear regression analyses.

The partition coefficients (log $K_{organism/water}$) for targeted and non-targeted RDCs between aqueous and biological phases (i.e., lipid, protein, and phospholipid) were determined utilizing the polyparameter linear free energy relationships (PP-LFERs) approach. Detailed information about the PP-LFERs method can be found in the Supporting information. PBT profiling was applied to assess the inherent hazards of targeted and non-targeted compounds. Refer to the Supplementary Information for detailed methodology. A single-factor correlation analysis (Spearman correlation coefficient) was performed to assess the impact of biological parameters on the bioaccumulation of RDCs, and one-way

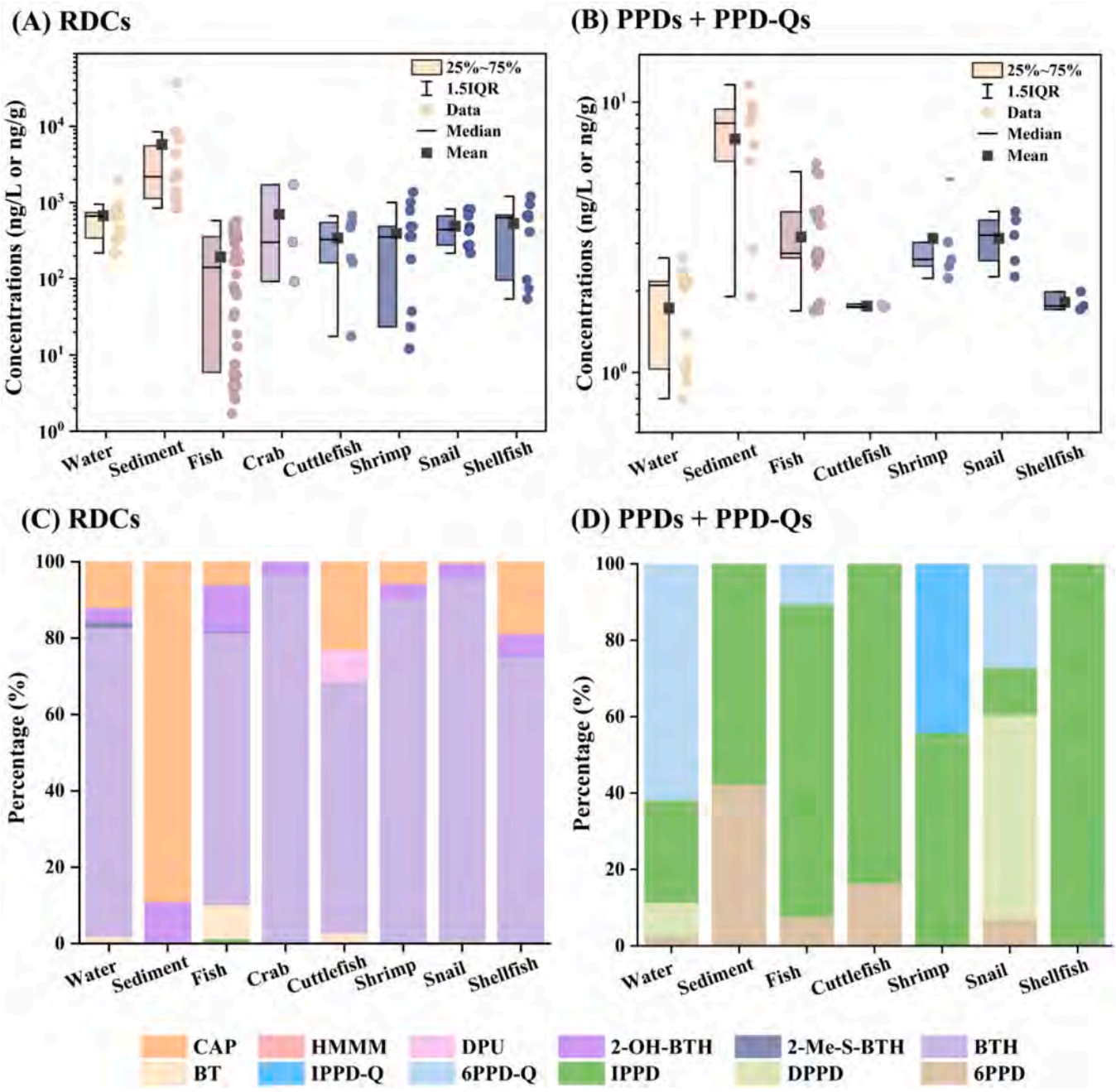


Fig. 1. Targeted determination of 17 RDCs in estuarine water, sediment, and biological samples. Box plots show (A) total concentrations of all targeted rubber-derived chemicals (RDCs) and (B) combined concentrations of *p*-phenylenediamines and their quinones (PPDs and PPD-Qs). Panels display proportions of (C) total targeted RDCs and (D) the combined proportions of PPDs and PPD-Qs. Concentrations, proportions (%), and BAFs of biological samples are expressed on a wet weight basis.

analysis of variance (ANOVA) was used to test the significance between groups. All statistical analyses were performed using SPSS v25.0 (SPSS Inc., Chicago) or Origin 2021b software (Origin Lab Corporation, Chicago). Statistical significance was set at $p < 0.05$.

3. Results and discussion

3.1. Contamination profiles and bioaccumulation of targeted RDCs in the biological tissues

Ten, six, nine, eight, seven and three targeted RDCs were identified in the tissues of fish, shellfish, snail, cuttlefish, shrimp and crab (Fig. 1C, Table S9). For the different groups, the total mean concentrations (ng/g, ww) decreased as follows: crab (702) > shellfish (531) > snail (491) > shrimp (392) > cuttlefish (342) > fish (190) (Fig. 1A), which were apparently higher than those documented in the biological species from Pearl River Estuary (45–67 ng/g) [49]. The observed differences might stem from the comparatively intense RDC contamination in the NRE (218–1.99 $\times 10^3$ ng/L, Fig. 1C, Tables S10-S11), exceeding those recorded in the Pearl River Estuary (119–942 ng/L) [49]. This elevated RDC pollution in the NRE could be linked to Hainan's status as China's predominant rubber producer and processing hub, consequently amplifying the environmental burden of RDCs in this region. Among the detected 12 targeted RDCs, BTH predominated with an average concentration proportion of 65.4–96.3 % in the tissues, followed by CAP (ND-23.0 %) and 2-OH-BTH (0.237–11.1 %), likely attributed to their high levels in water (Fig. 1C, Table S10). Interestingly, the mean levels of PPDs and PPD-Qs in tissues followed the order of snail (2.83 ng/g) > fish (2.68 ng/g) > shrimp (1.21 ng/g) > cuttlefish (1.05 ng/g) > shellfish (0.607 ng/g) > crabs (not detected) (Fig. 1B), indicating that snail and fish may have a greater enrichment capacity for PPDs and PPD-Qs. Significantly, PPDs and PPD-Qs displayed tissue-specific accumulation profiles; IPPD was predominantly enriched in fish, cuttlefish and shellfish, while 6PPD-Q and DPPD in snail, highlighting their differential bioaccumulation patterns (Fig. 1D).

BAFs were only ascertained for 11 targeted RDCs in biological samples, with IPPD-Q excluded due to its non-detection in water. Log BAF > 3.30 indicates bioaccumulation and log BAF > 3.70 indicates high bioaccumulation [3]. The mean log BAF values spanned 2.34–4.85 (Table 1), which were alignment with the calculated range for RDCs (1.1 −5.8) in the Pearl River Estuary [49]. Particularly, the mean log BAF values for 6PPD, DPPD, IPPD, BT, and DPU in at least one species surpassed 3.70, signifying a high bioaccumulative potential for these RDCs and underscoring the variability in their bioaccumulation among biological groups. Notably, the mean log BAF values for 6PPD-Q in fish (3.09) and snail (3.53) were lower than those of its parent compound 6PPD, with mean log BAF values of 4.76 in fish and 4.44 in snail. This variance could be ascribed to a combination of chemical hydrophobicity, environmental residual levels, and metabolic rates [19,31]. For the remaining RDCs, BTH, 2-OH-BTH and CAP demonstrated minimal bioaccumulation in most species (Log BAF < 3.30), while HMMM, and 2-Me-S-BTH exhibited bioaccumulation potential in a few species [3].

3.2. Non-targeted screening of RDCs in biological tissues beyond targeted substances

Non-targeted analysis of biological samples uncovered mass spectral features across a broad range of molecular weights, polarities, and peak intensities (Fig. 2A). Among these features, five RDCs were confirmed at level 1 using reference standards. These included two antioxidants, *N*-phenyl-1-naphthylamine (PNA) and diphenylamine (DPA), and three vulcanization accelerators, *N,N′*-dicyclohexylurea (DCU), *N,N′*-diphenylguanidine (DPG), and DCHMA (Fig. 2B and Table S12). Additionally, 23 features identified at level 2 as probable structures through mass spectral library matching included nine antioxidants [e.g., bisphenol A (BPA), 4-nonylphenol (4-NP), 2,2-methylenebis(4-ethyl-6-tert-

Table 1
Bioaccumulation factors (Log BAF) of targeted RDCs in the biota samples based on wet weight.

Compound	N[a]	Detection rate (%)[b]	Log BAF Range	Mean	Species for maximum Log BAF
Snail					
6PPD	9	22	4.40–4.48	4.44	*Bufonaria rana* (CWL)
DPPD	9	33	4.14–4.24	4.19	*Bufonaria rana* (CWL)
IPPD	9	22	3.69–3.75	3.72	*Turritella terebra bacillum* (BZL)
6PPD-Q	9	22	3.48–3.57	3.53	*Bufonaria rana* (CWL)
BTH	9	100	2.54–3.17	2.88	*Conomurex luhuanus* (LFL)
CAP	9	11	2.35–2.35	2.35	*Bufonaria rana* (CWL)
HMMM	9	67	2.73–4.36	3.52	*Conomurex luhuanus* (LFL)
2-Me-S-BTH	9	44	2.46–2.73	2.59	*Turritella terebra bacillum* (BZL)
2-OH-BTH	9	67	2.34–3.44	2.95	*Bufonaria rana* (CWL)
Shrimp					
IPPD	13	23	3.75–3.82	3.80	*Oratosquilla oratoria* (KXG)
BT	13	8	4.01–4.01	4.01	*Penaeus penicillatus* (CMDX)
BTH	13	54	2.73–3.38	3.00	*Metapenaeus affinis* (JYXDX)
CAP	13	62	1.63–3.08	2.47	*Metapenaeus affinis* (JYXDX)
HMMM	13	69	2.95–3.91	3.51	*Oratosquilla oratoria* (KXG)
2-Me-S-BTH	13	62	2.66–3.45	3.80	*Parapenaeopsis hungerfordi* (HSFDX)
Shellfish					
IPPD	9	33	3.57–3.63	3.59	*Perna canaliculus* (FCYB)
BTH	9	66	2.76–3.25	3.01	*Solen strictus* (ZC)
CAP	9	100	2.11–3.57	2.90	*Solen strictus* (ZC)
HMMM	9	100	3.20–3.81	3.48	*Perna canaliculus* (FCYB)
2-Me-S-BTH	9	33	2.39–2.50	2.43	*Perna canaliculus* (FCYB)
2-OH-BTH	9	56	2.84–3.59	3.31	*Solen strictus* (ZC)
Cuttlefish					
6PPD	6	17	4.30–4.30	4.30	*Loligo beka* (HQWZ)
IPPD	6	50	3.57–3.59	3.58	*Loligo beka* (HQWZ)
BT	6	17	3.67–3.67	3.67	*Loligo beka* (HQWZ)
BTH	6	50	2.51–3.09	2.85	*Loligo beka* (HQWZ)
CAP	6	33	2.40–3.74	3.07	*Octopusocellatus* (DX)
DPU	6	50	4.43–5.48	4.85	*Octopusocellatus* (DX)
2-Me-S-BTH	6	33	2.72–2.73	2.73	*Octopusocellatus* (DX)
2-OH-BTH	6	17	2.34–2.34	2.34	*Loligo beka* (HQWZ)
Crab					
BTH	3	100	2.23–3.49	2.80	*Charybdis riversandersoni* (GZX)
HMMM	3	100	3.19–3.66	3.37	*Charybdis riversandersoni* (GZX)
2-Me-S-BTH	3	67	3.20–3.25	3.23	*Charybdis riversandersoni* (GZX)
Fish					
6PPD	53	8	4.75–4.76	4.76	*Leiognathus brevirostris* (DWB)
IPPD	53	64	3.56–4.12	3.74	*Leiognathus brevirostris* (DWB)
6PPD-Q	53	19	3.08–3.44	3.09	*Leiognathus brevirostris* (DWB)
BT	53	28	2.75–4.44	3.63	*Chorinemus formosanus* (CWCS)
BTH	53	43	1.47–3.01	2.60	*Trachiocephalus myops* (DTGMY)
CAP	53	34	1.68–3.31	2.58	*Plectorhinchus* (HJD)
DPU	53	2	2.76–3.74	3.25	*Stolephorus chinensis* (ZHXGY)
HMMM	53	40	2.47–3.91	3.03	*Trachiocephalus myops* (DTGMY)
2-Me-S-BTH	53	34	2.20–2.85	2.56	*Trachinotus ovatus* (LXCS)
2-OH-BTH	53	36	2.34–4.27	2.89	*Plectorhinchus* (HJD)

[a] The total number of biota samples in each biota group.
[b] Detection frequencies in different biota groups.

butylphenol) (METBP), 4-nitroaniline (4-NA), 4-methylphenol (4-MP), butylhydroquinone (DTBHQ)], one ultraviolet absorber [bumetrizole (UV-326)], eight plasticizers [e.g., triethyl phosphate (TEP), diethyl phthalate (DEP), 2,4-di-tert-butylphenol (DTBP), diisodecyl phthalate (DIDP), monobutyl phthalate (MBP)], one polymerization catalyst [benzoic acid (BA)], and four vulcanization accelerators [e.g., triethanolamine (TEA), 4,4′-methylenebis(2-methylaniline) (MBA)] (Table S13). Concentrations of DPA, DCHMA, TEA, TEP, BPA, and 4-NP ranged from several dozen ng/L to several dozen mg/L in simulated water leachates from tire wear particles [16,26,43], while DCU, DPG, BA, and DEP were detected at μg/g levels in tire wear particles [2,53].

Twenty-three, 21, 20, 20, 17, and 9 non-targeted RDCs were identified in the tissues of fish, shellfish, snail, cuttlefish, shrimp, and crab, respectively (Fig. 2C). Total mean concentrations (ng/g, ww) were highest in fish (3.91×10^3), followed by shellfish (3.08×10^3), cuttlefish (2.96×10^3), shrimp (2.78×10^3), snail (1.61×10^3), and crab (1.36×10^3) (Table S14). These results suggest a higher enrichment capacity in fish, aligning with targeted determination results. Of the 28 identified non-targeted RDCs, four (PNA, DTBP, TEP, and TEA) were consistently detected across all biological tissues. Despite PNA's low concentrations ranging from 0.0477 to 69.7 ng/g ww (Table S14), it is noted for its high toxicity to *Chlorella vulgaris*, with a median effective concentration of 0.04 mg/L [25]. TEA was the predominant non-targeted compound in biological tissues, comprising 68–82 % of the total identified non-targeted compounds (Table S14). In a two-year dermal study, TEA induced liver tumors in female mice and may have contributed to a slight increase in live hemangiosarcomas in male mice [39]. Overall, non-targeted screening effectively complemented targeted analysis by prioritizing additional RDCs for identification with a confidence level of 2 or higher; however, reference standards are required to confirm probable structures at level 2. Given the ubiquitous detection of PNA and TEA across various species, additional analytical work is needed to integrate these two substances into routine surveillance programs.

3.3. Trophic transfer of targeted and non-targeted RDCs

RDCs with a detection rate of more than 30 % were used to estimate TMF [7]. For targeted RDCs, six compounds, namely BTH, 2-OH-BTH, 2-Me-S-BTH, IPPD, HMMM, and CAP, were selected for TMF estimations (Fig. 3). A significant correlation ($p < 0.05$) was observed between IPPD concentrations and TL (TMF = 1.95), indicative of biomagnification propensity (Fig. 3). Despite the absence of a statistically linear correlation between concentrations of BTH, 2-Me-S-BTH, and HMMM with their respective TLs, Monte Carlo simulation revealed a biomagnification potential for these compounds. Collectively, IPPD, BTH, 2-Me-S-BTH, and HMMM may accumulate at higher trophic levels, eventually implicating human exposure through the food chain. In contrast, there was a significant negative correlation ($p < 0.05$) between

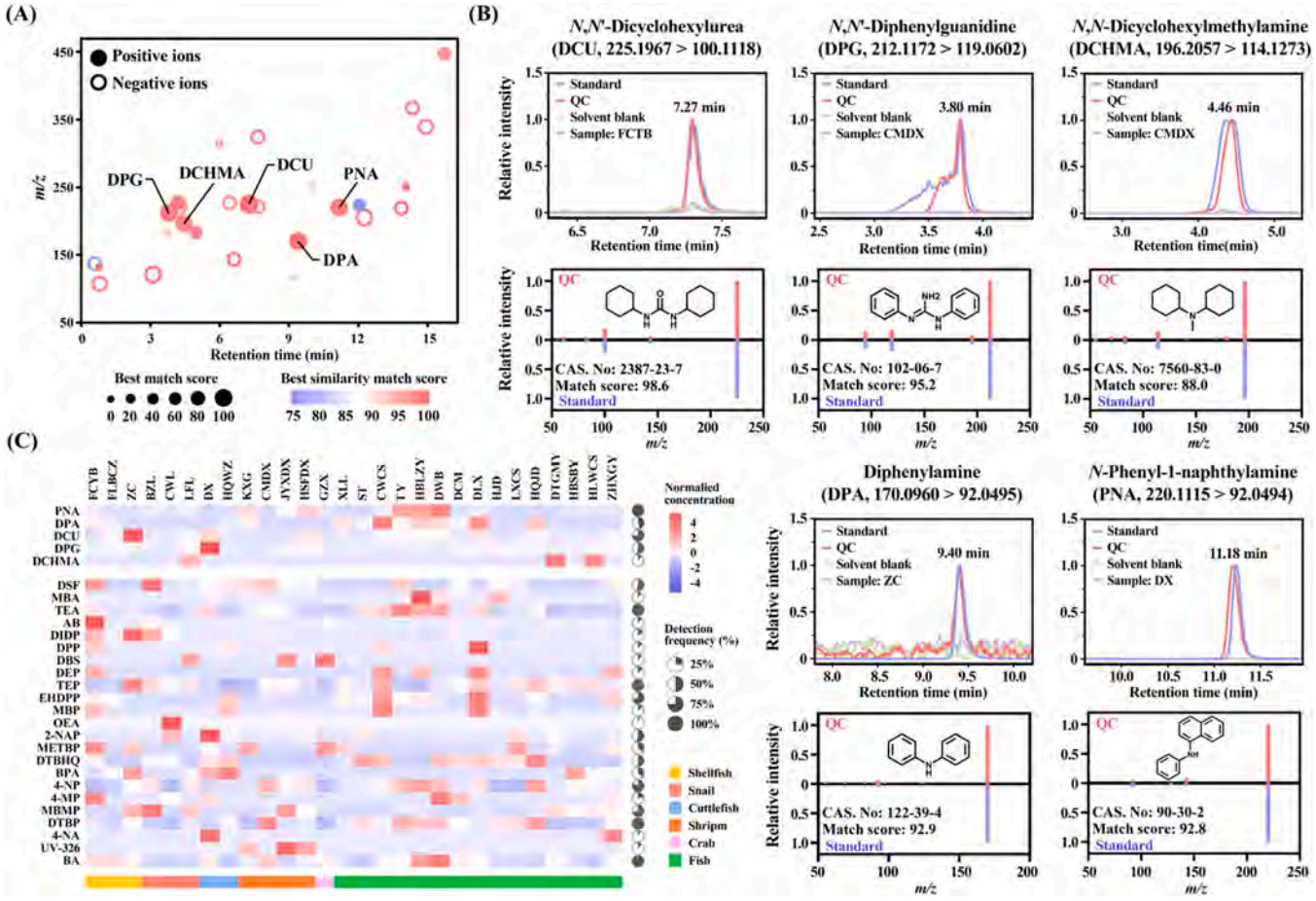


Fig. 2. Non-targeted screening of RDCs in biological samples. (A) Mass spectral features of RDCs identified with confidence levels 1 (compound name annotated) and 2. Circle size and color bar represent the mzCloud best match score and best similarity match score, respectively. (B) Extracted ion chromatograms and ddMS^2 spectra of five RDCs identified at confidence level 1. Chromatograms were obtained from the reference standard, quality control (QC), solvent blank samples, and a biological sample with minimal or no detection. ddMS^2 spectra are shown for the QC sample (top) and reference standard (bottom). (C) Normalized concentrations (color bar) and detection frequencies (circle black area size) of 5 RDCs at confidence level 1 and 23 at level 2 in tissues of 28 marine species in six biological groups.

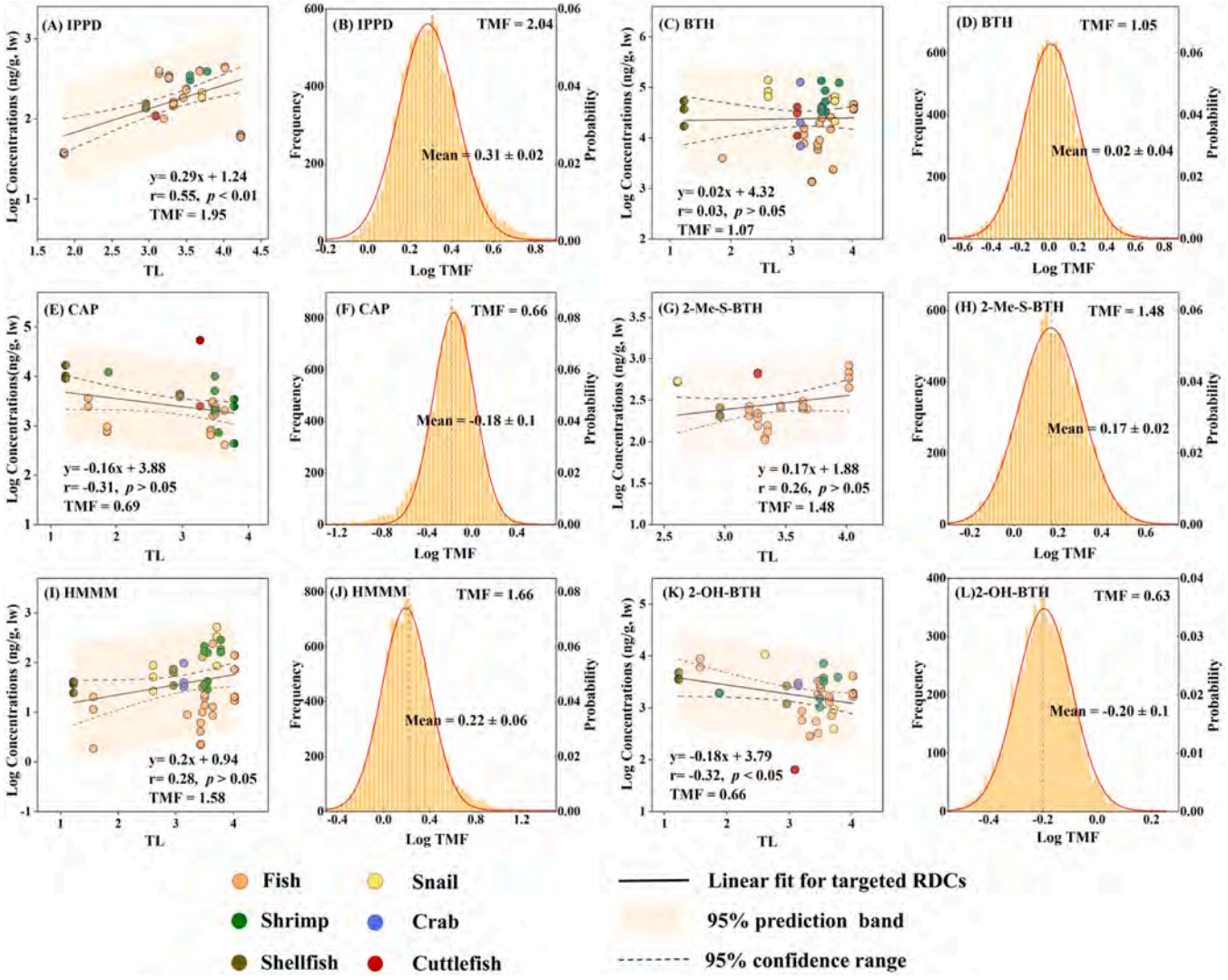


Fig. 3. Trophic transfer of targeted RDCs in estuarine species. Relationships between log-transformed levels (ng/g, lipid weight) of (A) IPPD, (C) BTH, (E) CAP, (G) 2-Me-S-BTH, (I) HMMM, and (K) 2-OH-BTH. Regression analysis was conducted based on the 95 % confidence interval for each compound. Frequency distribution of Trophic Magnification Factors (TMFs) estimated by bootstrap Monte Carlo simulations (n = 10,000) based on lipid normalized concentrations of (B) IPPD, (D) BTH, (F) CAP, (H) 2-Me-S-BTH, (J) HMMM, and (L) 2-OH-BTH in estuarine food webs.

the concentrations of 2-OH-BTH and TL (TMF = 0.66). Furthermore, Monte Carlo simulations hinted at the biodilution potential of CAP, despite the lack of a statistically linear correlation between log concentration of CAP and TL. This result suggests that species at higher trophic levels, such as fish, have livers that can metabolize contaminants more efficiently, which may reduce levels of 2-OH-BTH and CAP in higher trophic levels. Given the absence of a linear correlation between non-targeted RDC concentrations and their TLs, Monte Carlo simulations were used to identify their biomagnification trends (Table S15). Biodilution trends were observed for seven compounds, including 2-naphthol (2-NAP), BPA, 4-NP, 2,2′-methylenebis(4-methyl-6--tert-butylphenol) (MBMP), DTBP, DCU, and disulfiram (DSF), while the remaining nine compounds exhibited biomagnification trends. Notably, BTH and 2-Me-BTH showed a trend of biodilution in a subtropical estuary [49], as well as both BPA and 4-NP demonstrated biomagnification potential in a subtropical watershed [46], inconsistent with our findings. These disparities probably result from region-specific environmental pressures and ecological dynamics. Temperature's role in modulating the uptake and elimination kinetics of contaminants and the intricacy of aquatic food webs, particularly across latitudes, may intensify these differences [20,29]. Additional research is crucial for clarifying these dynamics and crafting environmental management strategies tailored to the specificities of diverse climatic and ecological settings.

3.4. Mass fraction in the biological phases

To further investigate the partitioning behavior of RDCs among different biological phases, the mass fractions and the partition coefficient of RDCs among water, lipid, phospholipid and protein were calculated. As depicted in Table S16 and Fig. 4, eight compounds, including TEA, CAP, TEP, BT, BA, 4-NA, 2-OH-BTH, and 4-MP exhibited a bioaccumulation propensity in aqueous phase of biological tissues (48.3–99.9 %), nine compounds (BPA, DPU, PNA, DPG, MBA, 2-NAP, MBP, DTBHQ, and DCU) preferred to be stored in proteins (51.7–84.2 %), and the remaining 28 substances showed a greater affinity for lipid storage (52.3–100 %). These findings indicate a pronounced variability in the distribution of RDCs across various biological phases. Interestingly, some transformation products, such as PPD-Qs, exhibited a diminished affinity for lipid storage relative to their parent compounds, such as PPDs. Concurrently, their aqueous and protein-bound fractions were augmented, potentially due to enhanced

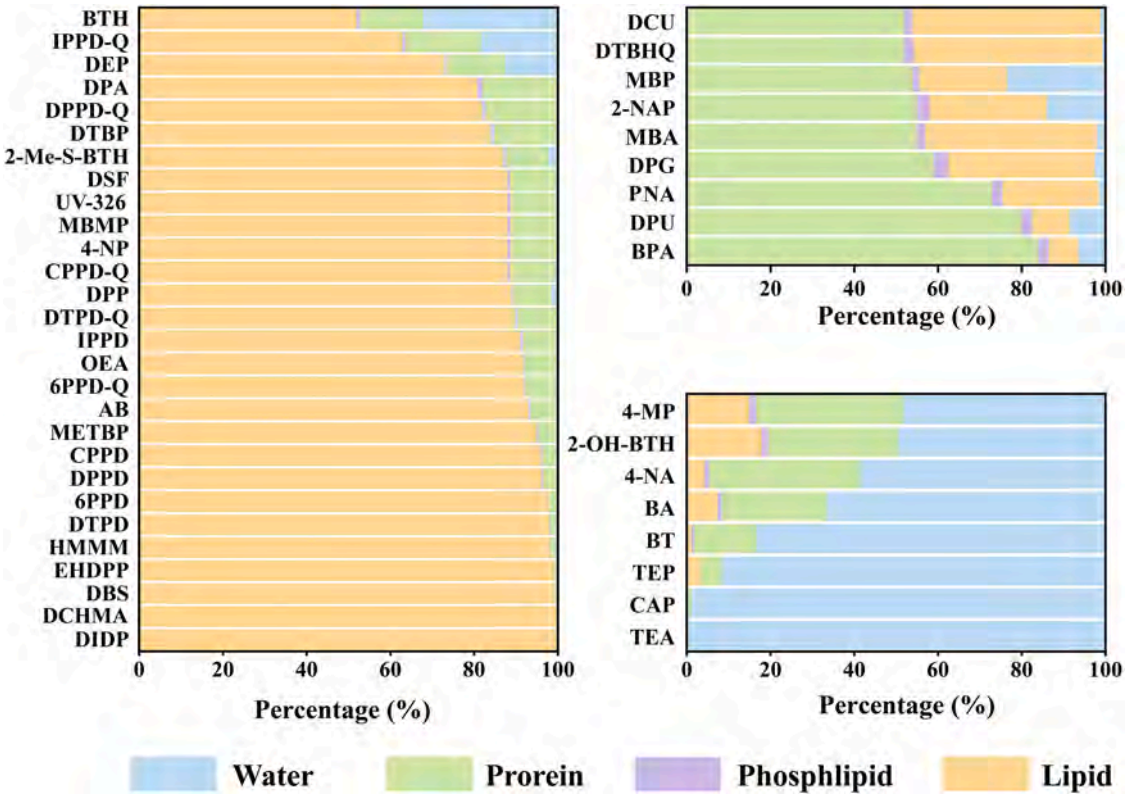


Fig. 4. Relative fractions of the mass of the target compounds in muscle tissue in different biological phases (lipid, phospholipid, protein and water).

hydrophilicity, a key facet of in vivo metabolic detoxification processes [34,37]. This result suggests that the metabolic conversion to more soluble forms may facilitate the compounds' clearance, thereby influencing their bioavailability, toxicity, and subsequent ecological impact. Despite some RDCs exhibiting higher log $K_{phosphlipid/water}$ than log $K_{lipid/water}$ and log $K_{protein/water}$, their mass fractions in the phospholipid phase were minimal (< 3.5 %), likely due to the low phospholipid content in tissues (0.01–0.02 %). Notably, the brain, a lipid-rich organ with high levels of phospholipids, has the second-highest lipid content among all human tissues, comprising 50 % of its dry weight [52]. These findings indicate a high accumulation potential of RDCs in the brain and suggest potential hazards, consistent with results from previous studies [31,32,5].

3.5. Partitioning and metabolic behavior impacting the bioaccumulation and trophodynamics

Hydrophobicity, defined as octanol-water partition coefficient (log K_{OW}), is a pivotal determinant in compound bioaccumulation and trophic transfer [21,22]. Nevertheless, log K_{OW} overlooks species-specific differences in lipid and non-lipid tissue composition [17]. Consequently, the organism-water partition coefficients (log $K_{organism/water}$) were employed as a refined alternative to K_{OW} for calculations [17]. For targeted RDCs, log $K_{organism/water}$ showed significant correlation with both log BAF and simulated TMF values, whereas log K_{OW} exhibited only a statistical positive correlation with log BAF ($p < 0.05$, Figs. 5A, 5C, and S4). Compared with log K_{OW} (r = 0.58) (Fig. 5A), log $K_{organism/water}$ demonstrated a stronger association with TMF (r = 0.94) (Fig. 5C), and similar consistency with log BAF (Figure S2). When non-targeted RDCs were included, log $K_{organism/water}$ maintained a significant correlation with simulated TMF values (Fig. 5D), unlike log K_{OW} (Fig. 5B). This implies that log $K_{organism/water}$ may serve as a more reliable predictor than log K_{OW} for the bioaccumulation and trophic transfer of RDCs within estuarine food webs.

Additionally, metabolic rates (k_m) of exogenous pollutants in organisms are reported to affect bioaccumulation and trophic transfer [3,46]. A negative linear correlation ($p = 0.05$) was observed between k_m and simulated TMF of targeted RDCs (Fig. 5E), and a comparable correlation ($p < 0.05$) between the log BAF values and k_m (Figure S3). When non-targeted RDCs were added, this trend became non-significant (Fig. 5F). The insignificance could stem from simulated metabolic rates in our fitting process, neglecting inter-species metabolic variances, thus weakening the effect of metabolic rates on the bioaccumulation and trophodynamics. Moreover, the accumulation of RDCs in organisms at higher trophic levels appears to be influenced by the metabolic transformation of their parent compounds, rather than being driven exclusively by bioaccumulation mechanisms. This metabolic alteration can lead to the phenomenon of "pseudo-biodilution or amplification" of the metabolites [22,51]. Future studies on the trophic transfer of RDCs should focus on accurately quantifying the biotransformation of parent compounds within organisms. Additionally, bioaccumulation and exposure time are pivotal for a comprehensive understanding of TMF. However, accurately determining the exposure duration of biological samples and whether bioaccumulation has reached a steady state poses a notable challenge under field conditions. More research is warranted to explore the combined effects of bioaccumulation and exposure time on trophic transfer of RDCs.

3.6. PBT properties

This research presents a first examination uncovering the pervasive presence of RDCs within tropical marine species through both targeted and non-targeted analyses. Despite the long-standing application of RDCs in rubber formulations, marine environmental assessments of these contaminants are conspicuously deficient. Specifically, there are notable gaps in knowledge regarding the PBT properties of RDCs, which are pivotal for accurate environmental management. To fill this gap, the present study evaluated the PBT characteristics of the targeted and non-

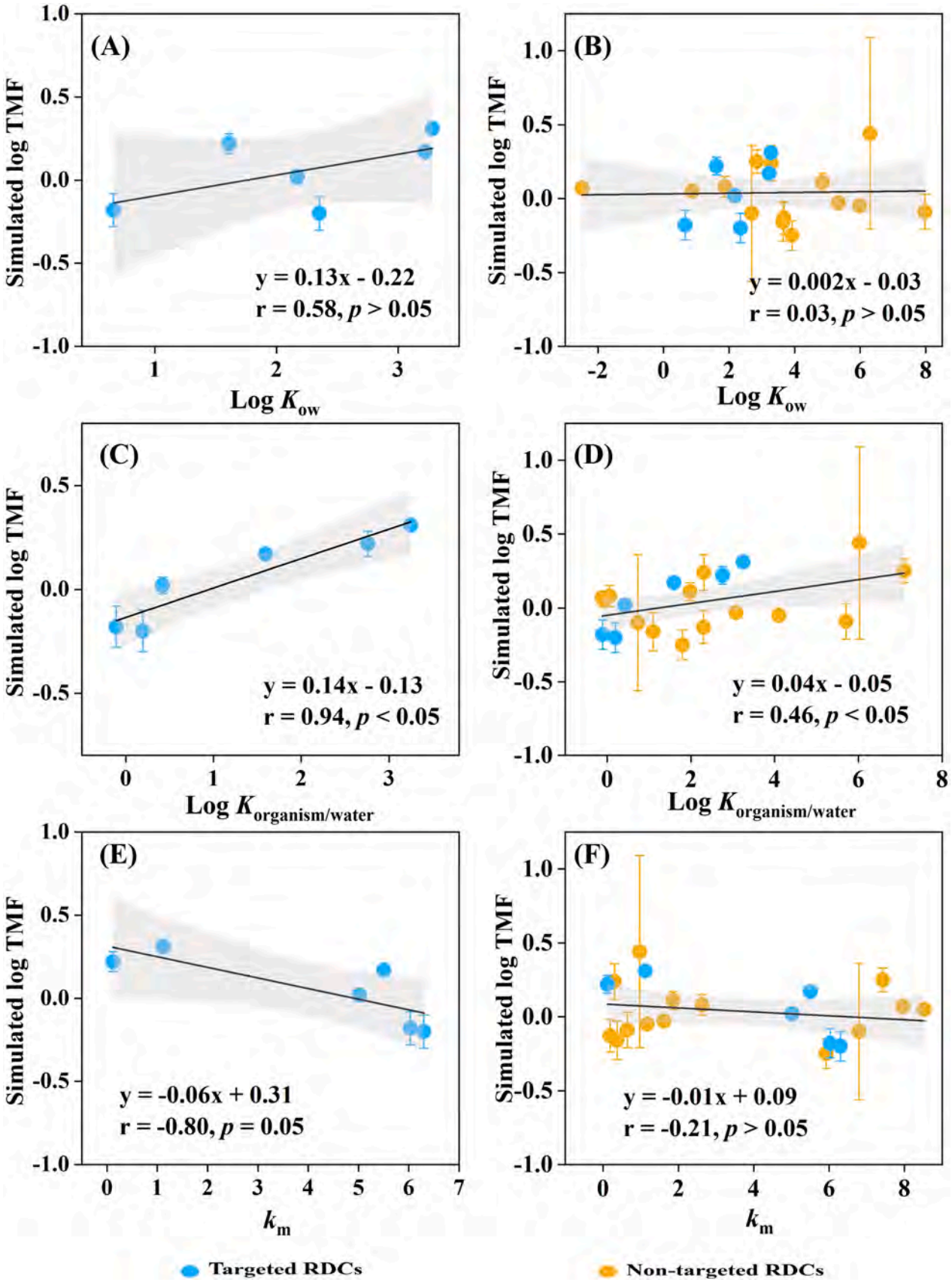


Fig. 5. Influence of partitioning and metabolic behavior on the trophodynamics of targeted and non-targeted RDCs. Correlations between the log TMF of RDCs from Monte Carlo simulations and their respective parameters: (A-B) log K_{OW}, (C-D) log $K_{organism/water}$, and (E-F) k_m. Regression analyses were conducted based on the 95 % confidence intervals for each compound.

targeted RDCs based on the field-measured and predicted data [15,33]. Specifically, 9 targeted and 15 non-targeted RDCs exhibited persistence with overall persistence (P_{OV}) exceeding 60 days (Fig. 6 and Table S17). Among them, HMMM (P_{OV}, 289 days) and DIDP (173 days) emerged as the most persistent compounds in the targeted and non-targeted categories, respectively. Eight targeted RDCs exhibited significant bioaccumulation (log BAF > 3.3), led by 6PPD with the largest BAF of 4.50. In contrast, non-targeted RDCs presented a low bioaccumulation propensity. Additionally, high toxicity was uniquely identified in the renowned 6PPD-Q and the non-targeted compound METBP, with median lethal concentrations below 0.01 mg/L. Notably, 60 % of RDCs exhibited PBT properties, with 15 out of 28 non-targeted compounds displaying one or more of these properties, underscoring their potential environmental risks.

4. Conclusions

This is the first study to integrate targeted and non-targeted approaches to assess the bioaccumulation and trophic transfer of RDCs in estuarine marine food webs. Twelve targeted RDCs and 28 non-targeted RDCs were identified in biological samples from the Nandu River estuary. Most PPDs were bioaccumulative or very bioaccumulative. Trophic transfer of RDCs was effectively predicted based on linear modeling and Monte Carlo simulation. Log $K_{organism/water}$ elucidated the biomagnification mechanism of RDCs more accurately than Log *K*ow. Mass distribution analysis showed that TEA, CAP, TEP, and BT tended to be distributed in the aqueous phase in organisms, while BPA, DPU, PNA, DPG, and MBA tended to be distributed in the protein phase. DIDP, DCHMA, DBS, and EHDPP exhibited greater affinity for lipid storage. PBT assessment showed that most RDCs exhibited at least one or more PBT characteristics, highlighting their potential environmental risk. This study emphasizes the importance of integrating targeted and untargeted approaches to RDCs in biomonitoring to provide a more comprehensive understanding of cumulative chemical risks to humans and wildlife. Future research is needed to elucidate the interspecies differences and detailed metabolic processes of RDC biotransformation, which is critical for refining ecological risk assessments and human health evaluations.

CRediT authorship contribution statement

Yuan Liu: Writing – original draft, Writing – review and editing, Visualization, Software, Methodology, Formal analysis, Data curation; **Jia-Ming Zhou:** Visualization, Software, Methodology, Data curation; **Nian-Nian Wu:** Investigation; **Shan Liu:** Conceptualization, Writing – review and editing, Funding acquisition; **Xiao-Liang Liao:** Data curation; **Haijiang Wu:** Methodology; **Lin Zhu:** Methodology; **Heng-Xiang Li:** Investigation; **Lang Lin:** Investigation; **Rui Hou:** Investigation; **Zhi-Hua Li:** Supervision; **Xiang-Rong Xu:** Funding acquisition, Resources, Writing – review and editing; **Zhi-Feng Chen:** Conceptualization, Writing – review and editing, Funding acquisition; **Zongwei Cai:** Methodology.

Environmental implication

This study integrates targeted and non-targeted approaches to elucidate the trophodynamics of rubber-derived chemicals (RDCs) in an estuarine food web. By identifying key RDCs with persistence, bioaccumulation, and toxicity, our findings underscore the necessity of incorporating non-targeted analysis into environmental biomonitoring. This comprehensive approach ensures a more accurate assessment of risks to aquatic organisms and public health, providing crucial guidance for prioritizing compounds in environmental management to safeguard both consumer health and aquatic ecosystems.

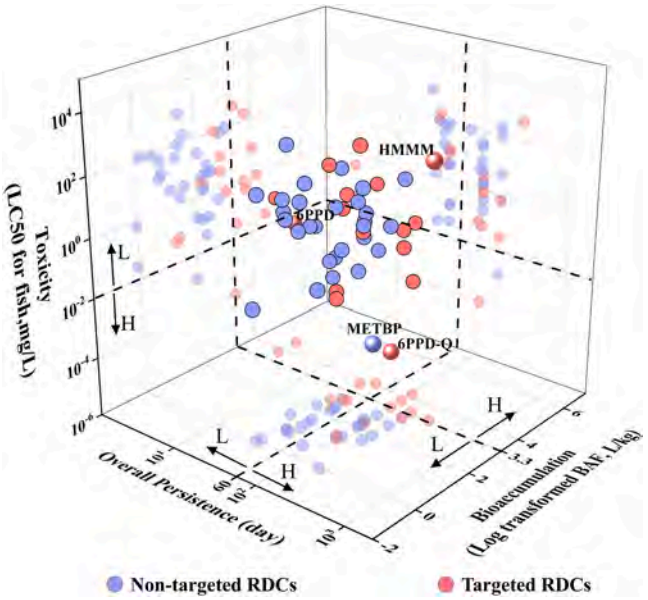


Fig. 6. Persistence, bioaccumulation, and toxicity based on field-measured and predicted data. The direction of the arrow indicates where the value of a specific attribute increases (H) or decreases (L). See Table S17 for detailed data.

Declaration of Competing Interest

The authors declare that they have no known competing financial interests or personal relationships that could have appeared to influence the work reported in this paper.

Acknowledgements

The authors would like to acknowledge the support by fund of the National Natural Science Foundation of China (Nos. 42177388, U21A2036, and 42177254), Hainan Province Science and Technology Special Fund (No. ZDYF2022SHFZ317), Science and Technology Innovation Special Project of Sanya City (No. 2022KJCX74), the Science and Technology Program of Guangzhou, China (2024A04J2991).

Appendix A. Supporting information

Supplementary data associated with this article can be found in the online version at doi:10.1016/j.jhazmat.2025.138958.

Data availability

Data will be made available on request.

References

[1] Adyasari, D., Oehler, T., Afiati, N., Moosdorf, N., 2018. Groundwater nutrient inputs into an urbanized tropical estuary system in Indonesia. Sci Total Environ 627, 1066–1079.
[2] Alves, C.A., Vicente, A.M.P., Calvo, A.I., Baumgardner, D., Amato, F., Querol, X., et al., 2020. Physical and chemical properties of non-exhaust particles generated from wear between pavements and tyres. Atmos Environ 224, 117252.
[3] Arnot, J.A., Gobas, F.A.P.C., 2004. A food web bioaccumulation model for organic chemicals in aquatic ecosystems. Environ Toxicol Chem 23 (10), 2343–2355.
[4] Bekele, T.G., Zhao, H., Wang, Q., Chen, J., 2019. Bioaccumulation and trophic transfer of emerging organophosphate flame retardants in the marine food webs of Laizhou Bay, North China. Environ Sci Technol 53 (22), 13417–13426.
[5] Blair, S.I., Barlow, C.H., McIntyre, J.K., 2020. Acute cerebrovascular effects in juvenile coho salmon exposed to roadway runoff. Can J Fish Aquat Sci 78 (2), 103–109.
[6] BP4NTA. Methods: study design. 2024. ⟨https://nontargetedanalysis.org/reference-content/methods/study-design/⟩. (accessed Nov 6, 2024).
[7] Castro-Jiménez, J., Bănaru, D., Chen, C.-T., Jiménez, B., Muñoz-Arnanz, J., Deviller, G., et al., 2021. Persistent organic pollutants burden, trophic

magnification and risk in a pelagic food web from coastal NW Mediterranean Sea. Environ Sci Technol 55 (14), 9557–9568.
[8] Chen, J., Tang, T., Li, Y., Wang, R., Chen, X., Song, D., et al., 2024. Non-targeted screening and photolysis transformation of tire-related compounds in roadway runoff. Sci Total Environ 924, 171622.
[9] Chibwe, L., Parrott, J.L., Shires, K., Khan, H., Clarence, S., Lavalle, C., et al., 2022. A deep dive into the complex chemical mixture and toxicity of tire wear particle leachate in Fathead Minnow. Environ Toxicol Chem 41 (5), 1144–1153.
[10] China Briefing, 2022. Investing in Hainan: industry, economics, and policy. Available from: ⟨https://www.china-briefing.com/news/investing-in-hainan-industry-economics-and-policy/⟩. [Accessed 4 November 2024].
[11] Diera, T., Thomsen, A.H., Tisler, S., Karlby, L.T., Christensen, P., Rosshaug, P.S., et al., 2023. A non-target screening study of high-density polyethylene pipes revealed rubber compounds as main contaminant in a drinking water distribution system. Water Res 229, 119480.
[12] Ding, Y., Han, M., Wu, Z., Zhang, R., Li, A., Yu, K., et al., 2020. Bioaccumulation and trophic transfer of organophosphate esters in tropical marine food web, South China Sea. Environ Int 143, 105919.
[13] Du, B., Liang, B., Li, Y., Shen, M., Liu, L.-Y., Zeng, L., 2022. First report on the occurrence of *N*-(1,3-dimethylbutyl)-*N*′-phenyl-*p*-phenylenediamine (6PPD) and 6PPD-quinone as pervasive pollutants in human urine from South China. Environ Sci Technol Lett 9 (12), 1056–1062.
[14] Du, B., Tian, Z., Peter, K.T., Kolodziej, E.P., Wong, C.S., 2020. Developing unique nontarget high-resolution mass spectrometry signatures to track contaminant sources in urban waters. Environ Sci Technol Lett 7 (12), 923–930.
[15] ECHA, 2023. Guidance on Information Requirements and Chemical Safety Assessment. Chapter R.11: PBT/vPvB assessment.
[16] Edeskär T, A.R., Håøya A.O., 2004. Leaching of phenol from tire shreds in a noise barrier. In: Sustainable waste management and recycling: challenges and opportunities; proceedings of the international conference organized by the concrete and masonry research group and held at Kingston University - London on 14-15 September 2004. London: Thomas Telford Ltd; 2004. p. 251–60.
[17] Endo, S., Brown, T.N., Goss, K.-U., 2013. General model for estimating partition coefficients to organisms and their tissues using the biological compositions and polyparameter linear free energy relationships. Environ Sci Technol 47 (12), 6630–6639.
[18] Feebarani, J., Joydas, T.V., Damodaran, R., Borja, A., 2016. Benthic quality assessment in a naturally- and human-stressed tropical estuary. Ecol Indic 67, 380–390.
[19] Grasse, N., Seiwert, B., Massei, R., Scholz, S., Fu, Q., Reemtsma, T., 2023. Uptake and biotransformation of the tire rubber-derived contaminants 6-PPD and 6-PPD quinone in the zebrafish embryo (*Danio rerio*). Environ Sci Technol 57 (41), 15598–15607.
[20] Hoondert, R.P.J., van den Brink, N.W., van den Heuvel-Greve, M.J., Ragas, A.J., Jan Hendriks, A., 2020. Implications of trophic variability for modeling biomagnification of pops in marine food webs in the svalbard archipelago. Environ Sci Technol 54 (7), 4026–4035.
[21] Hou, R., Huang, Q., Pan, Y., Lin, L., Liu, S., Li, H., et al., 2022. Novel brominated flame retardants (NBFRs) in a tropical marine food web from the South China Sea: the influence of hydrophobicity and biotransformation on structure-related trophodynamics. Environ Sci Technol 56 (5), 3147–3158.
[22] Huang, Q., Hou, R., Lin, L., Li, H., Liu, S., Cheng, Y., et al., 2023. Bioaccumulation and trophic transfer of organophosphate flame retardants and their metabolites in the estuarine food web of the Pearl River, China. Environ Sci Technol 57 (9), 3549–3561.
[23] Jia, H., Zhang, Z., Wang, C., Hong, W.-J., Sun, Y., Li, Y.-F., 2015. Trophic transfer of methyl siloxanes in the marine food web from coastal area of Northern China. Environ Sci Technol 49 (5), 2833–2840.
[24] Jia, J., Zhu, Q., Liu, N., Liao, C., Jiang, G., 2019. Occurrence of and human exposure to benzothiazoles and benzotriazoles in mollusks in the Bohai Sea, China. Environ Int 130, 104925.
[25] Jiang, J.-R., Cai, W.-X., Chen, Z.-F., Liao, X.-L., Cai, Z., 2024. Prediction of acute toxicity for *Chlorella vulgaris* caused by tire wear particle-derived compounds using quantitative structure-activity relationship models. Water Res 256, 121643.
[26] Jiang, J.-R., Chen, Z.-F., Liao, X.-L., Liu, Q.-Y., Zhou, J.-M., Ou, S.-P., et al., 2023. Identifying potential toxic organic substances in leachates from tire wear particles and their mechanisms of toxicity to *Scenedesmus obliquus*. J Hazard Mater 458, 132022.
[27] Jin, R., Wu, Y., He, Q., Sun, P., Chen, Q., Xia, C., et al., 2023. Ubiquity of amino accelerators and antioxidants in road dust from multiple land types: targeted and nontargeted analysis. Environ Sci Technol 57 (28), 10361–10372.
[28] Khan, F.R., Rødland, E.S., Kole, P.J., Van Belleghem, F.G.A.J., Jaén-Gil, A., Hansen, S.F., et al., 2024. An overview of the key topics related to the study of tire particles and their chemical leachates: from problems to solutions. TrAC Trends Anal Chem 172, 117563.
[29] Kortsch, S., Primicerio, R., Aschan, M., Lind, S., Dolgov, A.V., Planque, B., 2019. Food-web structure varies along environmental gradients in a high-latitude marine ecosystem. Ecography 42 (2), 295–308.
[30] Li, C., Zhang, Y., Yin, S., Wang, Q., Li, Y., Liu, Q., et al., 2023. First insights into 6PPD-quinone formation from 6PPD photodegradation in water environment. J Hazard Mater 459, 132127.
[31] Liao, X.-L., Chen, Z.-F., Liu, Q.-Y., Zhou, J.-M., Cai, W.-X., Wang, Y., et al., 2024. Tissue accumulation and biotransformation of 6PPD-quinone in adult zebrafish and its effects on the intestinal microbial community. Environ Sci Technol 58 (23), 10275–10286.
[32] Liao, X.-L., Chen, Z.-F., Ou, S.-P., Liu, Q.-Y., Lin, S.-H., Zhou, J.-M., et al., 2024. Neurological impairment is crucial for tire rubber-derived contaminant 6PPDQ-induced acute toxicity to rainbow trout. Sci Bull 69 (5), 621–635.
[33] Liu, Q., Li, L., Zhang, X., Saini, A., Li, W., Hung, H., et al., 2021. Uncovering global-scale risks from commercial chemicals in air. Nature 600 (7889), 456–461.
[34] Liu, X., Pan, G., 2019. Drug transporters in drug disposition, effects and toxicity. Springer Singapore, Singapore, pp. 293–340.
[35] Liu, Y.-H., Mei, Y.-X., Wang, J.-Y., Chen, S.-S., Chen, J.-L., Li, N., et al., 2024. Precipitation contributes to alleviating pollution of rubber-derived chemicals in receiving watersheds: combining confluent stormwater runoff from different functional areas. Water Res 264, 122240.
[36] Lu, R., Cao, X., Zheng, X., Zeng, Y., Jiang, Y., Mai, B., 2023. Biomagnification and elimination effects of persistent organic pollutants in a typical wetland food web from South China. J Hazard Mater 457, 131733.
[37] Matthee, C., Brown, A.R., Lange, A., Tyler, C.R., 2023. Factors determining the susceptibility of fish to effects of human pharmaceuticals. Environ Sci Technol 57 (24), 8845–8862.
[38] Müller, K., Hübner, D., Huppertsberg, S., Knepper, T.P., Zahn, D., 2022. Probing the chemical complexity of tires: identification of potential tire-borne water contaminants with high-resolution mass spectrometry. Sci Total Environ 802, 149799.
[39] National Toxicology Program, 2004. P.H.S., National Institutes of Health, US Department of Health and Human Services. NTP toxicology and carcinogenesis studies of triethanolamine (Cas No. 102-71-6) in B6C3F1 mice (dermal studies). National Toxicology Program technical report series, (518), 5–163. ⟨https://ntp.niehs.nih.gov/publications/reports/tr/500s/tr518⟩ [Accessed 4 November 2024].
[40] OECD HPV Database. ⟨https://hpvchemicals.oecd.org/ui/search.aspx⟩. [Accessed 4 September2024]. 2024.
[41] OICA, Organisation Internationale des Constructeurs d'Automobiles. ⟨https://www.oica.net/⟩. [Accessed 4 September 2024]. 2024.
[42] Peng, W., Liu, C., Chen, D., Duan, X., Zhong, L., 2022. Exposure to *N*-(1,3-dimethylbutyl)-*N*′-phenyl-*p*-phenylenediamine (6PPD) affects the growth and development of zebrafish embryos/larvae. Ecotoxicol Environ Saf 232, 113221.
[43] Rist, S., Le Du-Carrée, J., Ugwu, K., Intermite, C., Acosta-Dacal, A., Pérez-Luzardo, O., et al., 2023. Toxicity of tire particle leachates on early life stages of keystone sea urchin species. Environ Pollut 336, 122453.
[44] Schymanski, E.L., Jeon, J., Gulde, R., Fenner, K., Ruff, M., Singer, H.P., et al., 2014. Identifying small molecules via high resolution mass spectrometry: communicating confidence. Environ Sci Technol 48 (4), 2097–2098.
[45] Strynar, M., McCord, J., Newton, S., Washington, J., Barzen-Hanson, K., Trier, X., et al., 2023. Practical application guide for the discovery of novel PFAS in environmental samples using high resolution mass spectrometry. J Expo Sci Environ Epidemiol 33 (4), 575–588.
[46] Tang, J., Zhang, C., Zhang, J., Jia, Y., Fang, J., 2023. Trophodynamic of endocrine disrupting compounds in the aquatic food webs: association with hydrophobicity and biota metabolic rate. Sci Total Environ 868, 161731.
[47] Tian, Z., Zhao, H., Peter, K.T., Gonzalez, M., Wetzel, J., Wu, C., et al., 2021. A ubiquitous tire rubber–derived chemical induces acute mortality in coho salmon. Science 371 (6525), 185–189.
[48] Wang, W., Cao, G., Zhang, J., Qiao, H., Wang, F., Cai, Z., 2023. Recent applications of mass spectrometry in the analysis of transformation products of emerging contaminants in PM2.5. Anal Sci Adv 4 (3-4), 49–59.
[49] Wei, L.-N., Wu, N.-N., Xu, R., Liu, S., Li, H.-X., Lin, L., et al., 2024. First evidence of the bioaccumulation and trophic transfer of tire additives and their transformation products in an estuarine food web. Environ Sci Technol 58 (14), 6370–6380.
[50] Wu, J., Cao, G., Zhang, F., Cai, Z., 2023. A new toxicity mechanism of *N*-(1,3-Dimethylbutyl)-*N*′-phenyl-*p*-phenylenediamine quinone: formation of DNA adducts in mammalian cells and aqueous organisms. Sci Total Environ 866, 161373.
[51] Wu, N.-N., Liu, S., Xu, R., Huang, Q.-Y., Pan, Y.-F., Li, H.-X., et al., 2024. New insight into the bioaccumulation and trophic transfer of free and conjugated antibiotics in an estuarine food web based on multimedia fate and model simulation. J Hazard Mater 465, 133088.
[52] Yoon, J.H., Seo, Y., Jo, Y.S., Lee, S., Cho, E., Cazenave-Gassiot, A., et al., 2022. Brain lipidomics: from functional landscape to clinical significance. Sci Adv 8 (37), eadc9317.
[53] Zhao, H.N., Hu, X., Gonzalez, M., Rideout, C.A., Hobby, G.C., Fisher, M.F., et al., 2023. Screening *p*-phenylenediamine antioxidants, their transformation products, and industrial chemical additives in crumb rubber and elastomeric consumer products. Environ Sci Technol 57 (7), 2779–2791.
[54] Zheng, G., Wan, Y., Shi, S., Zhao, H., Gao, S., Zhang, S., et al., 2018. Trophodynamics of emerging brominated flame retardants in the aquatic food web of lake taihu: relationship with organism metabolism across trophic levels. Environ Sci Technol 52 (8), 4632–4640.

Water Research 287 (2025) 124366



Contents lists available at ScienceDirect

Water Research

journal homepage: www.elsevier.com/locate/watres



Rainfall, seasonal variation, and stream type governing the multi-media fate and ecological risks of tire additives and their transformation products in mega-urban streams

Li-Ni Wei [a,b], Nian-Nian Wu [c,e], Ru Xu [c,e], Yuan Liu [d], Shan Liu [a,*], Hai-Yan Zhang [b], Zi-Tong Li [b], Yue-Hong Liu [b], Xiang-Rong Xu [a], Jian-Liang Zhao [b,*], Guang-Guo Ying [b]

[a] Guangxi Laboratory on the Study of Coral Reefs in the South China Sea, Coral Reef Research Center of China, School of Marine Sciences, Guangxi University, Nanning, 530004, China
[b] Guangdong Provincial Key Laboratory of Chemical Pollution and Environmental Safety & MOE Key Laboratory of Theoretical Chemistry of Environment, School of Environment, South China Normal University, Guangzhou 510006, China
[c] Key Laboratory of Tropical Marine Bio-resources and Ecology, Guangdong Provincial Key Laboratory of Applied Marine Biology, South China Sea Institute of Oceanology, Chinese Academy of Sciences, Guangzhou 510301, China
[d] Marine College, Shandong University, Weihai, Shandong, 264209, China
[e] University of Chinese Academy of Sciences, Beijing, 100049, China

ARTICLE INFO

Keywords:
Tire additives and their transformation products
Stream multi-media
Seasonal dynamics
Road area
Partitioning pattern
Ecological risk

ABSTRACT

Tire additives and their transformation products (TATPs) are increasingly recognized for their toxicity and widespread environmental presence. However, the interplay of rainfall, seasonal variation, and stream type in governing their multi-media partitioning and risks remains largely unexplored. This study investigated the spatiotemporal distribution, environmental drivers, and ecological risks of 21 TATPs in three distinct urban streams (general road, expressway, and rural road-adjacent). Seventeen, 19, and 14 TATPs were quantified in water (514–6541 ng/L), suspended particulate matter (SPM, 12.8–244 ng/L), and sediment (1.71–248 ng/g), respectively. Rainfall significantly altered aqueous TATP levels, while stream type and seasonal variation influenced TATP pollution in SPM and sediment. Multiple linear regression identified pH, temperature, and road area as key aqueous-phase drivers, whereas precipitation and road area controlled the levels of TATPs in SPM and sediment, respectively. Hydrophobicity was a key determinant in TATP multi-media partitioning. High ecological risks were found across all water samples, primarily associated with 1,3-diphenylurea (DPU), 1,3-dicyclohexylurea (DCU), *N*-(1,3-dimethylbutyl)-*N'*-phenyl-*p*-phenylenediamine quinone (6PPD-Q), and hexa (methoxymethyl)melamine (HMMM). Eight TATPs exhibited persistence, bioaccumulation, or toxicity traits, warranting prioritized regulation. These insights are crucial for crafting effective environmental policies to mitigate =TATP impacts and protect urban aquatic ecosystems.

1. Introduction

Tire additives, such as antioxidants and vulcanizing agents, are integral to tire formulations because they enhance rubber durability and processing efficiency. *p*-Phenylenediamines (PPDs) are predominant antioxidants in tire and rubber products, with most of them including *N*-(1,3-dimethylbutyl)-*N'*-phenyl-*p*-phenylenediamine (6PPD), *N,N'*-diphenyl-1,4-phenylenediamine (DPPD), and *N*-isopropyl-*N'*-phenyl-*p*-phenylenediamine (IPPD) designated high-production volume (HPV) chemicals (OECD, 2024). Benzothiazoles (BTs), including benzothiazole (BTH), 2-hydroxybenzothiazole (2-OH-BTH), and 2-(methylthio)-benzothiazole (2-Me-S-BTH), act as vulcanizing agents (Capolupo et al., 2020; Fohet et al., 2023), and have been employed as tracers for tire pollution in surface runoff (Wu et al., 2022). Other additives are commonly used in tire manufacturing, such as 1,3-diphenylguanidine (DPG) is a vulcanization accelerator, whose transformation products are 1,3-diphenylurea (DPU) and 1,3-dicyclohexylurea (DCU) (Jin et al., 2021). Hexa(methoxymethyl)melamine (HMMM) is a crosslinking (Alhelou et al., 2019). These other additives have been frequently detected at high levels in tire leachates and surface waters (Rauert et al.,

* Corresponding authors.
E-mail addresses: liushan21137@163.com (S. Liu), jianliang.zhao@m.scnu.edu.cn (J.-L. Zhao).

https://doi.org/10.1016/j.watres.2025.124366
Received 25 March 2025; Received in revised form 6 July 2025; Accepted 6 August 2025
Available online 7 August 2025
0043-1354/© 2025 Elsevier Ltd. All rights are reserved, including those for text and data mining, AI training, and similar technologies.

2022; Müller et al., 2022; Liu et al., 2024a). These additives can produce a variety of transformation products through water immersion (Müller et al., 2022), gas-phase oxidation (Zhao et al., 2023), biodegradation (Xu et al., 2023), photodegradation, and thermal degradation (Fohet et al., 2023).

Tire additives and their transformation products (TATPs) can migrate to the tire surfaces and subsequently permeate diverse environmental matrices (Zoroufchi Benis et al., 2023; Zhang et al., 2024), exhibiting a spectrum of toxic effects on aquatic organisms. For example, 6PPD and *N*-(1,3-dimethylbutyl)-*N'*-phenyl-*p*-phenylenediamine quinone (6PPD-Q) have been demonstrated to significantly reduce spontaneous locomotion and heart rate in zebrafish (*Danio rerio*) embryos (Peng et al., 2022; Zhang et al., 2023c). IPPD is associated with developmental abnormalities and growth retardation in zebrafish (Zhong et al., 2022). Moreover, 2-OH-BTH and BTH can induce cytotoxicity and oxidative stress in the epithelial cells of rainbow trout (*Oncorhynchus mykiss*) (Zeng et al., 2016). Besides chronic toxicity, 6PPD-Q exhibited varying degrees of lethal effects on different fish species, with the median lethal concentrations (LC_{50}) ranging from 41 ng/L in juvenile coho salmon (*Oncorhynchus kisutch*) to 309 μg/L in zebrafish larvae (Lo et al., 2023; Hiki et al., 2021; Varshney et al., 2022).

Rainfall-induced surface runoff is a key source of TATPs in aquatic ecosystems (Liu et al., 2024a). Continuous inputs and inadequate management of surface runoff have driven TATPs to emerge as global environmental pollutants at high concentrations (μg/L or μg/g). Specifically, they have been identified in roadside dust in Japan (Hiki et al., 2022), wastewater treatment plants (WWTPs) in Germany (Seiwert et al., 2022), soil in Norway (Asheim et al., 2019), rivers in Australia (Rauert et al., 2022), seawater in China (Zhang et al., 2024), and atmospheric particulate matter in global megacities (Johannessen et al., 2022b). Significant spatial variations in TATP concentrations were observed globally. For instance, 6PPD-Q levels in Chinese rivers (0.26–11.3 ng/L) were much lower than those in American streams (<200–3500 ng/L) and some Canadian rivers (290–2350 ng/L) (Johannessen et al., 2022a; Tian et al., 2021; Zhang et al., 2023a). These concentration disparities underscore TATP pollution as a pressing global environmental concern. However, the comprehensive understanding of TATP partitioning mechanisms across multi-media (water, SPM, sediment), its spatial-temporal dynamics, and interplay of drivers (e.g., rainfall, seasonal variations, and stream type) in urban receiving environments remain largely elusive.

Urban streams are the linchpins of urban ecosystems, alleviating the urbanization impact on water cycles through rainwater infiltration and discharge. Yet, rapid urbanization has deteriorated rainwater quality, leading to substantial pollution in urban streams from direct surface runoff during rainfall (Anim and Banahene, 2021; Tian et al., 2021). A quintessential example of the detrimental effects of urbanization on water bodies is the "Urban Stream Syndrome" exacerbated by contaminants such as 6PPD-Q (Tian et al., 2021). Guangzhou is an exemplar of rapid urbanization in China, characterized by a subtropical monsoon climate, high population density, and intense economic activity. It has a well-developed river network, with major waterways like Dongjiang, Pearl River, and Liuxi River traversing the area. The region's frequent rainfall, extensive transportation infrastructure (225 km^2), and 3.18 million automobiles collectively create substantial environmental stress on urban streams and make it an exemplary case for studying urban stream pollution (GZSY, 2024). This extensive road network and substantial vehicle output inevitably exert significant environmental stress on urban water bodies, particularly in terms of pollution from TATPs. While there is a burgeoning interest in the pollution status of TATPs in urban water bodies (Peter et al., 2022; Zhang et al., 2023a), the impact of rainfall, seasonal fluctuation, and stream type on TATPs remains largely unexplored.

This study aims to (1) systematically characterize the multi-media distribution of 21 TATPs in urban streams adjacent to general road, expressway, and rural road; (2) quantify the impact of rainfall, seasonal variation, and stream type on TATP partitioning; (3) identify key drivers governing TATP fate across environmental compartments; and (4) evaluate the ecological risks, persistence, bioaccumulation, and toxicity (PBT) profiles of TATPs to prioritize compounds. By achieving these objectives, this study will deepen the understanding of TATP dynamics in urban water systems, guide the development of strategies to address their environmental and health impacts, and thereby enhance sustainable urban water management.

2. Materials and methods

2.1. Chemicals and materials

Four categories of TATPs, including five PPDs (6PPD, CPPD [*N*-cyclohexyl-*N'*-phenyl-1,4-benzenediamine], IPPD, DPPD, and DTPD [*N,N'*-ditolyl-*p*-phenylenediamine]), four PPDs-Q (6PPD-Q, CPPD-Q, DPPD-Q, and DTPD-Q), five BTs (BT [2Hbenzotriazole], BTH, 2-ABTH [2-aminobenzothiazol], 2-OH-BTH, and 2-Me-S-BTH), and seven other tire additives (DPG, DPU, DCU, HMMM, RD [poly(1,2-dihydro-2,2,4-trimethylquinoline)], TMTD [tetramethylthiuram disulfide]), and 4-OH-DPA [4-hydroxydiphenylamine] were selected. Atrazine-d5 and 6PPD-Q-d5 were used as internal standards, respectively. Stock standard solutions of each target compound were prepared in methanol and stored at −20 °C for later use. The purity of all standards exceeded 98 %, and all other reagents were of HPLC grade. Additional details can be found in Table S1 of the Supplementary materials.

2.2. Sampling stations and sample collection

Three representative urban streams in Guangzhou, China, were selected for sampling in the current study: streams near general roads (GRS), expressways (ES), and rural roads (RRS). GRS, adjacent to a major urban river, is subject to diverse pollution sources. RRS, situated at the residential area's edge, is vulnerable to domestic influences. ES, positioned beneath an expressway, is directly impacted by highway runoff but flows through an ecological park with minimal additional environmental perturbations. Three discrete sites were sampled for each stream type, yielding a total of nine sampling points, the geographic location and detailed information of the sampling sites are shown in Fig. S1 and Table S2. Water and sediment samples were collected at each sampling site both pre- and post-rainfall events, adhering to strict criteria: clear weather for at least one-week pre-rainfall and within three hours after the onset of rainfall (Liu et al., 2024a). Collections took place in September 2022, February 2023, and July 2023, representing the normal, dry, and wet seasons, respectively. The classification of these seasons was determined by referencing monthly rainfall patterns and published literature (GZSY, 2023; Huang et al., 2024). A total of 52 water, 54 SPM, and 46 sediment samples were amassed throughout the study period. Post-sampling, water quality parameters were measured *in situ* using a YSI Multiparameter Water Quality Monitor (YSI ProPlus, YSI Inc., USA). Water samples were collected and stored in 1-liter brown glass bottles, with 1 mL of 1 M glutathione solution and 20 mL of methanol added to attenuate microbial activity and chemical transformations. Sediment samples were collected using a grab sampler. All samples were stored at −20 °C and promptly transported to the laboratory. Then, the water samples were filtered through Whatman GF/F glass microfiber filters (0.7 μm) to separate the aqueous and particulate phases. Detailed information on water properties (including nitrate nitrogen [NO_3—N], ammonium nitrogen [NH_3—N], and total phosphorus [TP]), sediment properties (total organic carbon [TOC]) can be found in Tables S3-S4. Rainfall data were sourced from the daily records of meteorological stations in the districts where the sampling sites are located (China Meteorological Administration). The road area was determined by centering each sampling point, drawing a 500 m radius circle, and extracting the main road area (m^2) within this radius using Google Earth (version 7.3.4.8248, Google Inc). Population density

(people/km^2) is derived from the 2020 China Census data, representing the population density of the corresponding street at each sampling site (Table S2).

2.3. Sample extraction and instrumental analysis

Sample extraction for both water and sediment in this study adhered to established methodologies with minor modifications (Wei et al., 2024; Zhang et al., 2023a). Briefly, water samples (1 L) were processed via solid-phase extraction (SPE) using a Waters HLB cartridge (500 mg) for enrichment. For sediment samples (0.5 g), an ultrasonication method was employed with sequential extractions using 10 mL of methanol, 7 mL of acetonitrile, and 7 mL of dichloromethane. SPM samples were freeze-dried, crushed, and processed following the same ultrasonication protocol as for sediment. The targets were quantified using ultra-performance liquid chromatography coupled to a Xevo TQ-S triple quadrupole mass spectrometer (Waters Co., Milford, Massachusetts) with an electrospray ionization (ESI) source in multiple reaction monitoring mode. All the targets were analyzed in the ESI (+) mode, and the mobile phase consisted of Milli-Q water (with 0.1 % formic acid; A) and methanol (B). Detailed extraction methods, instrumental conditions, transitions and retention times of target compounds are provided in SI and Table S5.

2.4. Quality assurance and quality control (QA/QC)

Comprehensive quality assurance and quality control (QA/QC) measures were implemented throughout the analytical process, including field controls, blanks (field, procedural, solvent), and analytical standards (100 μg/L of each target), to monitor background contamination and ensure instrument performance. TATP concentrations in all samples were corrected by subtracting the mean field blank values. Recovery experiments ($n = 3$) for 21 TATPs in water, SPM, and sediment yielded ranges of 53.7–132 %, 53.0–124 %, and 53.0–121 %, respectively (Tables S6-S8). Method sensitivity was determined using signal-to-noise (S/N) ratios of 3 and 10 for the limits of detection (LOD) and quantification (LOQ), respectively. Target analytes were quantified using internal standardization, with calibration curves (0.1–200 μg/L) showing excellent linearity ($R^2 > 0.99$) across all batches.

2.5. Data analysis

All statistical analyses were performed using SPSS 26.0 (IBM Corp., Armonk, NY, USA) and OriginPro 2024 (OriginLab, Northampton, MA, USA). For TATP concentrations below the LOQs, statistical analysis incorporated values at 1/2 LOQs; whereas data below the LODs were assigned a zero value and denoted with ND (not detected). The Kolmogorov–Smirnov and Shapiro–Wilk tests were used to test for normality. The two-sample *t*-test and Mann-Whitney U test were utilized to evaluate alterations in TATP concentrations in water, SPM, and sediment under varying conditions (pre- and post-rainfall, season shifts, and stream types, as well as to examine seasonal variations in the water-SPM partition coefficients (K_p) and water-sediment partition coefficients (K_d). Spearman correlation analysis was employed to assess relationships between TATP concentrations. Multiple linear regression (MLR) was conducted to pinpoint the principal factors affecting TATP concentrations across various environmental matrices. β (unstandardized regression coefficient) represents the direction and magnitude of the independent effect of each predictor variable on TATP concentrations. To avoid multicollinearity, variance inflation factors (VIF < 5) were evaluated. Model significance was tested via ANOVA, and adjusted R^2 was reported.

The partition coefficients of K_p and K_d were calculated employing the subsequent equations (Xu et al., 2024a):

$$K_p = \frac{C_{SPM}}{C_{Water}} \quad (1)$$

$$K_d = \frac{C_{Sediment}}{C_{Water}} \times 1000 \quad (2)$$

where C_{Water} (ng/L), C_{SPM} (ng/L), and C_{Sediment} (ng/g), represent the concentrations of the target TATPs in the water, SPM, and sediment, respectively.

The fugacity fraction (*ff*) characterized TATP transfer directionality between water and sediment (Tan et al., 2024., Kong et al., 2023). The mass inventory calculation aimed to evaluate the sink potential of various environmental media for TATPs in streams. The hazard index (HI) and risk quotient (RQ) methods were adopted to evaluate the potential eco-environmental risk presented by TATPs (EPA, 2000; European, 2003), and HI depicted the total value of the ecological risk at the sampling site. To protect the environment and human health, the PBT characteristics (persistence, bioaccumulation potential, and toxicity) of TATPs in urban streams were evaluated based on PBT criteria (Muir and Howard, 2006). The specific calculation process of fugacity fraction, mass inventories, HI, RQ and PBT characteristics is included in the Texts S4-S5 and Tables S9-S10.

3. Results and discussion

3.1. Pervasive presence and compositional variability of TATPs in urban streams

3.1.1. Stream water

In the stream water samples ($n = 52$), 17 TATPs were identified, comprising 3 PPDs, 3 PPDs-Q, 5 BTs, and 6 others, with total levels varying from 514 to 6541 ng/L (median, 1504 ng/L) (Fig. 1A, Fig. S2). These levels consistently aligned with those documented in river waters (Zhang et al., 2023a; Rauert et al., 2022) and WWTP influent (Li and Kannan, 2024), but lower than those identified in road stormwater runoff (Liu et al., 2024a). Except for PPDs, CPPD-Q, DPPD-Q, DTPD-Q, 4-OH-DPA, RD, and TMTD, other TATPs showed high detection frequencies (92.3–100 %), suggesting their ubiquity in urban streams (Table S11). Compared with PPDs-Q (3.00 ng/L) and PPDs (1.15 ng/L), others (893 ng/L) and BTs (522 ng/L) had the highest median concentrations (Fig. 1B). Others (mean proportion, 51.85 %) and BTs (mean proportion, 47.73 %) predominantly contributed to the total TATP levels (Fig. 1E), likely due to their extensive application (Janna et al., 2011; Liu et al., 2017; Magami and Guthrie, 2012; Rink, 2008), high aqueous solubility (log K_{OW}: 1.40–3.30), and persistence (half-lives in water: 15.0–180 days, except 4-OH-DPA) (Table S10). 4-OH-DPA is a special case, in which the half-life of 4-OH-DPA in river water is only 0.14 days (Di et al., 2022). In contrast, PPDs (mean proportion, 0.07 %) and PPDs-Q (mean proportion, 0.35 %) constituted less of the total levels (Fig. 1E). Still, they can be highly toxic to aquatic life, even at low levels (Tian et al., 2021; Hiki et al., 2021; Brinkmann et al., 2022). Furthermore, the notably higher concentrations of PPD-Q (ND-41.5 ng/L) compared to its parent compound PPD (ND-6.17 ng/L) indicate that transformation products are more prevalent in water, highlighting the need to enhance the surveillance of PPDs-Q.

3.1.2. Stream SPM

In SPM samples ($n = 54$), 19 TATPs (encompassing 4 PPDs, 3 PPDs-Q, 5 BTs, and 7 others) were observed, with total levels ranging from 12.8 to 244 ng/L (median, 43.2 ng/L) (Fig. 1A, Fig. S3). The SPM levels of BTs exceeded those reported in the eastern shelf areas of China (Zhao et al., 2024), as did the levels of 6PPD and 6PPD-Q compared to Liuxi River Watershed (Zhang et al., 2023b). Except for CPPD, DPPD, CPPD-Q, DPPD-Q, BT, BTH, RD, TMTD, others were consistently detected in SPM (66.7–100 %, Table S11). The median total levels of TATPs in the four

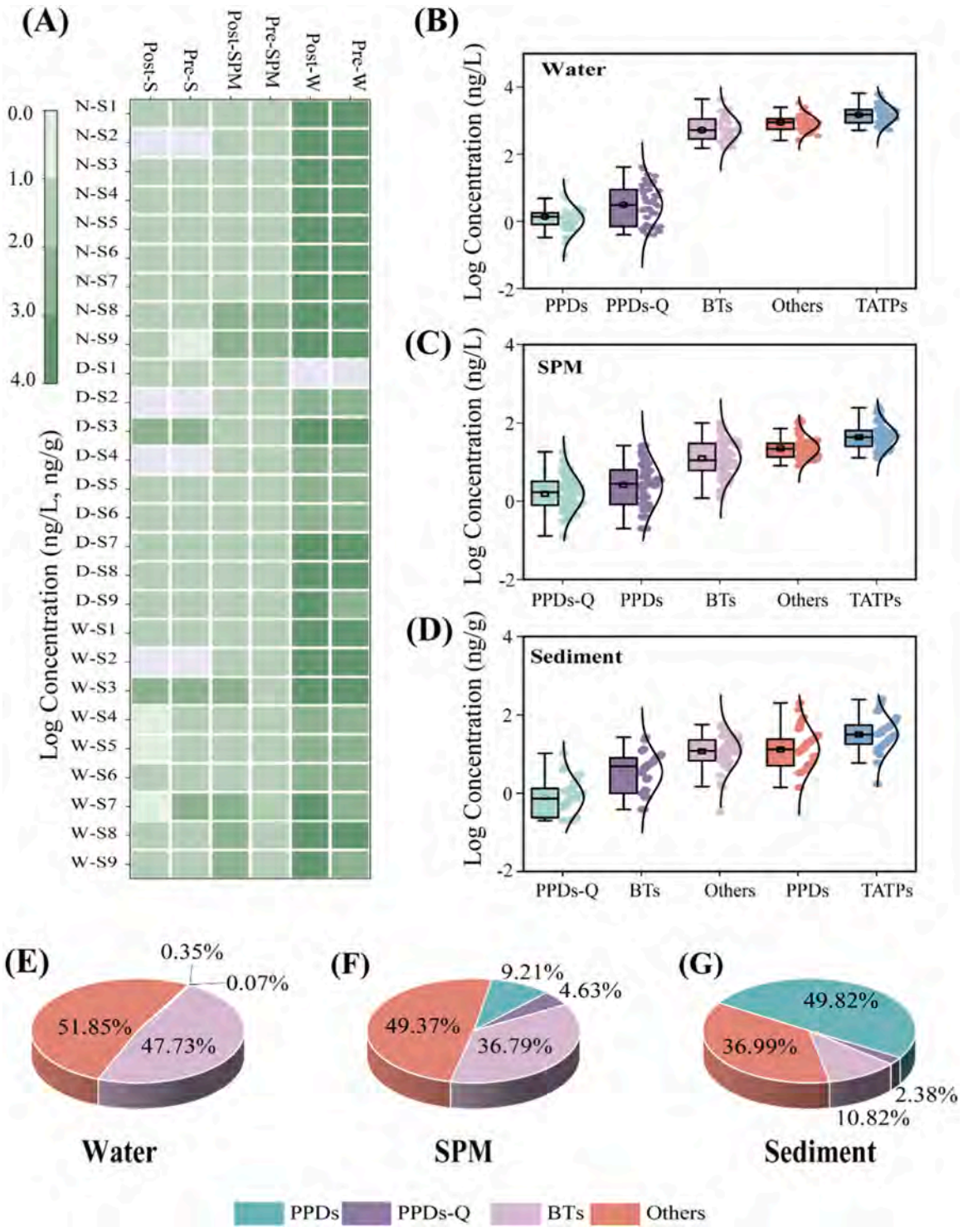


Fig. 1. Concentrations and compositions of tire additives and their transformation products in water, suspended particulate matter, and sediment. (A) The total concentrations of target compounds across various stations (S1-S9) and seasons (N, normal season; D, dry season; W, wet season); Pre- and Post- represent pre- and post-rainfall, respectively; W, SPM and S represent water, suspended particulate matter, and sediment, respectively. (B-D) Boxplots of log-transformed concentrations for PPDs-Q, PPDs, BTs, and others in water (B), SPM (C), and sediment (D); (E-G) Compositions of PPDs-Q, PPDs, BTs, and others in water (E), SPM (F), and sediment (G). Boxes represent the 25th and 75th percentiles; lines show medians; dots represent all data.

categories dropped in the following order: others (22.1 ng/L) > BTs (11.3 ng/L) > PPDs (2.65 ng/L) > PPDs-Q (1.69 ng/L) (Fig. 1C). Notably, the mean proportion of PPDs in SPM (9.21 %) was higher than in water (0.07 %). While PPDs are known for their limited long-distance transport in water due to rapid hydrolysis (Liu et al., 2024b), the role of SPM in facilitating the transport and the potential for broader environmental contamination by PPDs merits further scrutiny.

3.1.3. *Stream sediment*

In sediments ($n = 46$), 14 TATPs (including 4 PPDs, 2 PPDs-Q, 4 BTs, and 4 others) were detected with total levels spanning 1.71 to 248 ng/g (Fig. 1A, Fig. S4). These levels were lower than those found in roadside

soils (Jin et al., 2023), like river sediments (Zhang et al., 2024), but higher than estuarine and deep-sea sediments (Zeng et al., 2023; Wei et al., 2024). TATPs in sediments were dominated by PPDs (median, 12.5 ng/g), and others (median, 12.0 ng/g), followed by BTs (median, 4.25 ng/g), and PPDs-Q (median, 0.73 ng/g), a composition differing from that in water and SPM (Fig. 1). The dominance of PPDs likely reflects their high log K_{OC} values (2.70–3.70), promoting adsorption by the sediments (Table S1). The differential degradation rates of PPDs, with half-lives ranging from 0.17 to 1.89 days in water(Cao et al., 2023) and 338 to 542 days in sediments (EPI Suite), also significantly influence this distribution. More studies need to be carried out to reveal the multi-media partitioning mechanism of TATPs. Notably, 6PPD, a precursor to the highly toxic 6PPD-Q, peaked at 180 ng/g in sediment (Table S11). Given that 6PPD can transform into 6PPD-Q under anaerobic flooded soils (Xu et al., 2023), high concentrations of 6PPD in sediments may be converted to 6PPD-Q, thereby increasing the toxicity to aquatic life.

3.2. Rainfall, seasonal variation, and stream type influencing multi-media TATP concentrations

3.2.1. Rainfall

Post-rainfall (median, 1565 ng/L) water samples revealed the presence of 17 TATPs, significantly higher than the pre-rainfall (median, 1397 ng/L) (Independent samples *t*-test, $p < 0.05$, Fig. 2A, Table S12). This increase was mainly driven by elevated concentrations of others and PPDs-Q (Fig. S5). Additionally, the detection frequencies for TATPs (excluding 6PPD, CPPD, DPPD-Q, and BTH) were higher post-rainfall, with detection frequencies ranging from 73.1 % to 100 % (Table S12). This suggests rainfall-driven transport, potentially via road runoff or direct atmospheric deposition, may constitute significant TATP sources in urban streams. For the four TATP categories, the post-rainfall median concentrations followed the order: others (934 ng/L) > BTs (527 ng/L) > PPDs-Q (7.10 ng/L) > PPDs (0.87 ng/L). Interestingly, PPDs exhibited a lower maximum concentration post-rainfall (2.55 ng/L) than pre-rainfall (6.17 ng/L), likely due to rapid aqueous transformation, source variability, or rainfall dilution. The short half-lives of PPDs in river water (0.38–0.88 days for IPPD, CPPD, and 6PPD) likely contributed to their decrease (Xu et al., 2025). Dilution may also dominate if pollutant influx from rainfall is low. Conversely, concentrations and detection frequencies of 6PPD transformation products (6PPD-Q and 4-OH-DPA) increased post-rain. Our field-monitoring data limitations precluded definitive source identification for these products.

In SPM, 19 TATPs were identified post-rainfall, with slightly higher total levels (median, 47.4 ng/L) compared to pre-rainfall (median, 34.8 ng/L) (Independent samples *t*-test, $p > 0.05$, Fig. 2A, Table S13). This increase may stem from rainfall-driven particulate inputs like surface runoff and atmospheric deposition (Ge et al., 2024; Hiki and Yamamoto, 2022; Zhang et al., 2022), which enhance TATP concentrations in SPM. Among the four major categories, post-rainfall median concentrations were ranked as follows: others (23.1 ng/L) > BTs (16.6 ng/L) > PPDs (5.50 ng/L) > PPDs-Q (1.05 ng/L). Notably, BTs and PPDs levels were significantly elevated post-rainfall (Independent samples *t*-test, $p < 0.05$, Fig. S5). This further supports that post-rainfall SPM partly originates from road dusts and atmospheric deposition, as these sources are known to contain higher levels of BTs and PPDs (Wang et al., 2025; Liao et al., 2021).

In contrast to water and SPM samples, sediment TATP concentrations remained relatively stable, ranging from 5.93–192 ng/g pre-rainfall, compared to 1.71 to 248 ng/g post-rainfall, showing no significant increase ($p > 0.05$, Fig. 2A, Table S14). This consistency indicates that sediment TATP levels primarily represent long-term pollutant accumulation in urban streams, rather than being influenced by short-term weather variations.

3.2.2. Seasonal variations

Fig. 2B depicts pronounced seasonal fluctuations in TATP concentrations in water, with the median levels ranked as follows: normal season (2024 ng/L) > wet season (1153 ng/L) > dry season (901 ng/L) (Mann−Whitney U test, $p < 0.05$). BT, DPG, and DCU were identified as the primary contributors to elevated TATP concentrations during the normal season (Fig. S6). In contrast to water, SPM exhibited higher median levels of TATPs in the wet (55.9 ng/L) and normal seasons (52.8 ng/L) than in the dry season (21.8 ng/L) (Independent samples *t*-test, $p < 0.05$, Fig. 2B). These seasonal increases in SPM-associated TATPs are likely driven by enhanced surface runoff and the remobilization of sediment-bound TATPs during rainfall events (Xu et al., 2024b). Spearman correlation analysis revealed significant associations between total TATP concentrations and individual TATPs detected at frequencies above 30 %, except for DPPD-Q ($p < 0.05$; Fig. S7). This implies that these pollutants share similar sources or environmental behavior (Rauert et al., 2022; Xu et al., 2025, 2024b). In contrast, sediment TATP concentrations exhibited minimal seasonal variability, with only the dry season median (44.1 ng/g) being significantly higher than that of the normal season (20.1 ng/g) ($p < 0.05$, Fig. 2B), indicating sediment TATP levels are stable and less affected by seasonal changes. This consistency may arise from long-term sorption and sediment buffering, which could mitigate the impact of short-term climatic variations.

3.2.3. Stream type

In water, the median TATP levels of different stream types followed the order: GRS (2345 ng/L) > RRS (1565 ng/L) > ES (850 ng/L) (Mann−Whitney U test, $p < 0.05$; Fig. 2C). BT dominated in the water of GRS, representing 16.00–71.7 % of total TATPs and was found at μg/L levels in 63 % of sites (Fig. S2). Given BT's widespread use in industrial processes and consumer products, including corrosion inhibitors, antifogging and antifungal agents, washing powders, and brake fluids (Shi et al., 2019), its presence in GRS likely stems from urban runoff and other contaminated media such as industrial emissions, traffic-related sources, atmospheric deposition, construction activities, and improper waste disposal, highlighting the diverse pollution sources affecting GRS. In the water of ES and RRS, DPU was the dominant TATPs, constituting 16.00–61.13 %, and 1.32–56.34 % (Fig. S2), aligning closely with the composition found in urban road runoff (Liu et al., 2024a). This similarity suggests that road runoff is the primary source of TATPs in these receiving streams. Compared to ES, the higher total TATP concentrations in RRS are likely due to the larger road area in RRS, along with the influence of the surrounding environment (Table S2). Elevated levels of BTH, 2-OH-BTH, and 2-Me-S-BTH, which are associated with rubber products, were detected at higher concentrations in RRS (Liao et al., 2018), suggesting that the use of rubber products in nearby residential areas contributes to these higher levels.

For SPM, the median TATP concentrations exhibited a distinct pattern: RRS (50.5 ng/L) > GRS (44.9 ng/L) > ES (32.6 ng/L), with RRS being significantly higher than GRS and ES (Independent samples *t*-test, $p < 0.05$; Fig. 2C). Differently, median TATP concentrations in water and sediment followed the order: GRS > RRS > ES, reflecting the partitioning differences among various compartments. However, given the absence of SPM physicochemical data (e.g., particle size, TOC) and hydrodynamic conditions (e.g., flow velocity, retention time), the distinct TATP distribution in SPM remains unclear. Future research should prioritize SPM characterization and hydrodynamic modeling to clarify TATP behavior across environmental matrices.

The sediment distribution of TATPs mirrored that of the aqueous phase: GRS (median, 59.6 ng/g) > RRS (median, 30.2 ng/g) > ES (median, 23.2 ng/g) (Mann−Whitney U test, $p < 0.05$; Fig. 2C). Although there are significant differences between the total concentrations of TATP in different types of stream sediments, their compositions are relatively close, all dominated by 6PPD, followed by DPG, which also indicates that the distribution of TATP in river sediments from different cities is relatively stable.

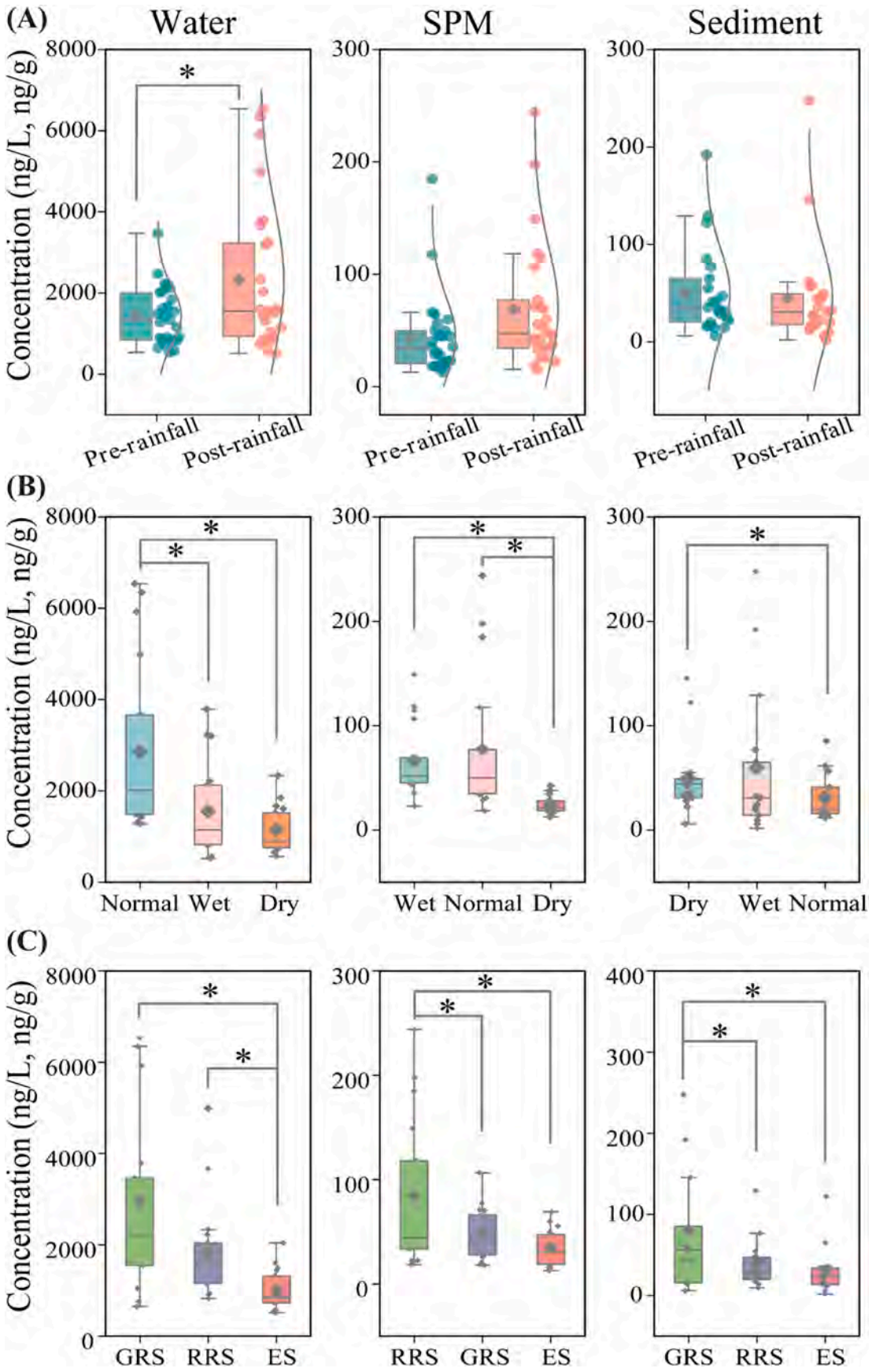


Fig. 2. Concentrations of tire additives and their transformation products in water, suspended particulate matter (SPM), and sediment under different conditions: (A) pre- and post-rainfall, (B) seasonal variation (normal, dry, and wet seasons), and (C) stream types (GRS, general road stream; ES, expressway stream; RRS, rural road stream). Asterisks indicate significant differences at $p < 0.05$.

3.3. Compartment-specific drivers of TATP distribution

Multiple linear regression analyses revealed compartment-specific determinants governing TATP distribution in urban streams (Table 1). For aqueous-phase TATPs, the robust model ($F = 5.83$, $p < 0.001$, $R^2 = 0.56$) identified three mechanistic drivers: pH ($\beta = 0.31$, $p = 0.016$), temperature ($\beta = 0.02$, $p = 0.049$), and log road area ($\beta = 2.00$, $p = 0.001$). The observed positive pH dependence implies that alkaline conditions may promote the leaching of tire-derived compounds, likely via desorption from particulate surfaces or dissolution of metal-TATP complexes. Temperature-driven increases likely stem from enhanced desorption kinetics and/or increased tire wear rates at higher temperatures. The robust correlation with road area ($\beta = 2.00$) quantitatively identifies vehicular traffic as a dominant emission source, with road expansion directly increasing TATP inputs. Importantly, the model's 56 % explanatory power suggests that other factors, such as hydrodynamic conditions or variations in tire formulation, may also influence aqueous-phase concentrations.

SPM demonstrated distinct control mechanisms ($F = 4.98$, $p < 0.001$; $R^2 = 0.52$), with precipitation as the sole significant predictor ($\beta = 0.004$, $p = 0.031$). This likely results from rainfall flushing accumulated tire wear particles and resuspending streambed sediments, thereby transporting TATP-containing particles into urban streams and elevating TATP concentrations in SPM. The lack of significance for road area in SPM, compared to its dominance in the dissolved phase, underscores differential fate processes. While dissolved TATP concentrations directly reflect source strength, particulate-bound TATPs appear to be governed by transport limitations rather than emission magnitude. Collectively, precipitation accounted for 52 % of the variability in TATP concentrations in SPM.

Sediment systems exhibited unique regulatory pattern ($F = 2.67$, $p = 0.036$; $R^2 = 0.26$), with only road area achieving significance ($\beta = 1.71$, $p = 0.05$). Although grain size distribution was not measured in this study, sediment TOC was quantified. However, TOC did not emerge as a statistically significant predictor ($p > 0.05$) of TATP sediment concentrations. This finding aligns with observations for PPDs in riverine and marine sediments, where TOC also showed no significant correlation (Zeng et al., 2023). Also, in estuarine sediments, TOC demonstrated significant associations only with 4 out of 20 TATPs (Zhang et al., 2024). These findings suggest that TOC levels do not predominantly control the partitioning for most TATPs in sediments. The relatively low explanatory power ($R^2 = 0.26$) of our sediment model strongly indicates that other sediment characteristics (e.g., grain size, mineral composition) or in-situ biogeochemical processes may significantly modulate TATP partitioning. Therefore, future work should incorporate comprehensive sediment characterization and investigate in-situ processes to fully elucidate the factors governing TATP sequestration in urban streambeds, particularly under varying hydrological conditions.

3.4. Hydrophobicity affecting the multi-media partitioning mechanisms

To elucidate the environmental behavior of TATPs within urban streams, examining the variations in their log K_p is imperative. Significant seasonal differences in log K_p values were observed pre-rainfall (Mann−Whitney U test, $p < 0.05$, Fig. S8, Tables S15–16), with the wet season exhibiting a wider range (−2.36 to 1.36) than the dry (−2.70 to 0.76) and normal seasons (−2.63 to 0.48). This suggests that the solubility or adsorptive potential of TATPs is sensitive to seasonal changes, likely driven by fluctuations in water physicochemical properties influenced by temperature and precipitation. Post-rainfall, the log K_p values were −2.70–1.34, −2.59–1.01, and −2.64–1.04 in the normal, dry and wet seasons, respectively. Notably, significant differences were observed only between the wet and normal seasons (Mann−Whitney U test, $p < 0.05$, Fig. S8, Tables S15–16). This suggests that precipitation might equalize TATP partitioning, mitigating seasonal water body effects.

Log K_d can delineate the partitioning behavior of TATPs between water and sediment. Before rainfall, log K_d values spanned 0.26–4.32 in normal, −0.44–5.18 in dry, and −0.39–6.00 in wet seasons. Post-

Table 1
Multiple linear regression analysis of concentrations (ng/L or ng/g) of tire additives and their transformation products in water, suspended particulate matter (SPM), and sediment against various variables.

	Analysis of variables [a]	Coefficient β (unitless unstandardized regression coefficients) [b]	*p* value	VIF	F	R^2	Adj R^2
Log C_{Water}	Regression	−6.17	<0.001		5.83	0.56	0.46
	Log Road area (m^2)	**2.00**	**0.001**	**2.15**			
	pH	**0.31**	**0.016**	**1.30**			
	T (°C)	**0.02**	**0.049**	**2.18**			
	DO (mg/L)	−0.03	0.164	1.24			
	NO_3-N (mg/L)	−0.007	0.465	1.74			
	NH_3-N (mg/L)	−0.037	0.601	1.18			
	TP (mg/L)	0.014	0.581	1.82			
	Precipitation (mm)	−0.003	0.120	1.93			
	Log Population density (person/km^2)	−0.70	0.438	1.83			
Log C_{SPM}	Regression	−6.67	<0.001		4.98	0.52	0.41
	Precipitation (mm)	**0.004**	**0.031**	**1.91**			
	pH	0.25	0.071	1.30			
	T (°C)	0.01	0.170	2.19			
	DO (mg/L)	−0.02	0.502	1.21			
	NO_3-N (mg/L)	−0.01	0.221	1.74			
	NH3-N (mg/L)	0.03	0.721	1.21			
	TP (mg/L)	0.04	0.175	1.54			
	Log Road area (m^2)	0.32	0.646	1.81			
	Log Population density (person/km^2)	1.17	0.239	1.67			
Log $C_{Sediment}$	Regression	5.52	0.036		2.67	0.26	0.16
	Log Road area (m^2)	**1.71**	**0.05**	**1.19**			
	TOC (%)	−0.12	0.367	1.45			
	T (°C)	−0.03	0.10	1.69			
	Precipitation (mm)	0.003	0.407	1.79			
	Log Population density (person/km^2)	−2.95	0.07	1.37			

[a] Analysis of variables includes pH, T (Temperature, °C), DO (Dissolved oxygen, mg/L) NO_3—N (nitrate nitrogen, mg/L), NH_3—N (ammonium nitrogen, mg/L), and TP (total phosphorus, mg/L) in water samples; TOC (total organic carbon content, %) in sediment samples. Precipitation (mm), log road area (m^2), and log Population density (person/km^2). [b] β coefficients are unitless unstandardized regression coefficients used to indicate the relative relationships between variables.

rainfall, these values modestly shifted to 0.18–3.29, −0.35–4.11, and −0.29–5.18, respectively (Fig. S8, Tables S17-S18. Notably, these log K_d values exceed log K_p by 2–5 orders of magnitude, owing to the particulate phase concentrations being used in ng/L versus ng/g. The log K_d values exhibited season-independent stability, with rainfall events failing to induce significant alterations. This unvarying pattern implies that sediments act as a reliable sink for TATPs, highlighting the importance of sediment management in curbing the ecological footprint of TATPs.

Recent investigation has highlighted that the partitioning behavior of TATPs within estuarine environments is primarily influenced by their octanol-water partition coefficient (log K_{OW}) and molecular weight (Zhang et al., 2024). As depicted in Fig. 3, positive correlations were observed between the partition coefficients (log K_p and log K_d) and log K_{OW} both pre-rainfall and post-rainfall. Conversely, molecular weight showed a negative correlation with log K_p exclusively post-rainfall ($p < 0.05$, $R^2 = 0.05$). This suggests that the partitioning of TATPs in urban streams is predominantly driven by log K_{OW} rather than molecular weight, contrasting with an earlier estuary-based study (Zhang et al., 2024). These correlations accentuate the pivotal influence of log K_{OW} on the environmental partitioning of TATPs. The marginal impact of molecular weight after rainfall suggests that variables, like dissolved organic carbon levels and sediment properties, exert a greater influence on partitioning.

The fugacity fraction (*ff*) characterized TATP transfer directionality between water and sediment (Fig. S9). Due to lack of data regarding particulate organic carbon, only water-sediment transfer was evaluated. The *ff* values of 0.25–0.75 indicates intercompartment equilibrium (Tan et al., 2024; Kong et al., 2023). Pre-rainfall, ff_{median} values >0.75 for BT, HMMM, and 6PPD-Q suggest predominant water phase origin with limited sediment transfer. Conversely, RD and 6PPD (*ff* < 0.25) preferentially partitioned from water to sediment. 2-ABTH, 2-OH-BTH, and IPPD exhibited few detections (*ff* consistently <0.25), indicating sediment partitioning tendency. Post-rainfall, 2-Me-S-BTH and DPG demonstrate aqueous-phase dominance with limited sediment transfer like BT, HMMM and 6PPD-Q with *ff* >0.75. RD, 6PPD, and IPPD maintained *ff* <0.25, implying minimal influence of rainfall inputs on their water-sediment distribution.

To clarify the distribution dynamics of TATPs across environmental compartments within urban streams, we conducted a meticulous assessment of their mass per unit area (Ikenoue et al., 2023; Xu et al., 2024) (Fig. S10). The mass per unit area of TATPs ranged from 1.26 −17.1 mg/m^2 in pre-rainfall and 1.00–26.9 mg/m^2 in post-rainfall. Sediments emerged as the primary repository for TATPs, accounting for an average proportion of 68.94 % (pre-rainfall) and 54.05 % (post-rainfall) of the total mass per unit area. This sedimentary sequestration is attributed to the hydrophobic nature of TATPs. Post-rainfall, a notable shift occurred, apart from PPDs, likely due to their accelerated degradation in aqueous environments. The subsequent increase in aqueous TATP concentrations suggests that rainfall-induced surface runoff significantly contributes to the urban stream's TATP load, highlighting the pivotal role of hydrological events in the mobilization and distribution of these compounds within urban ecosystems.

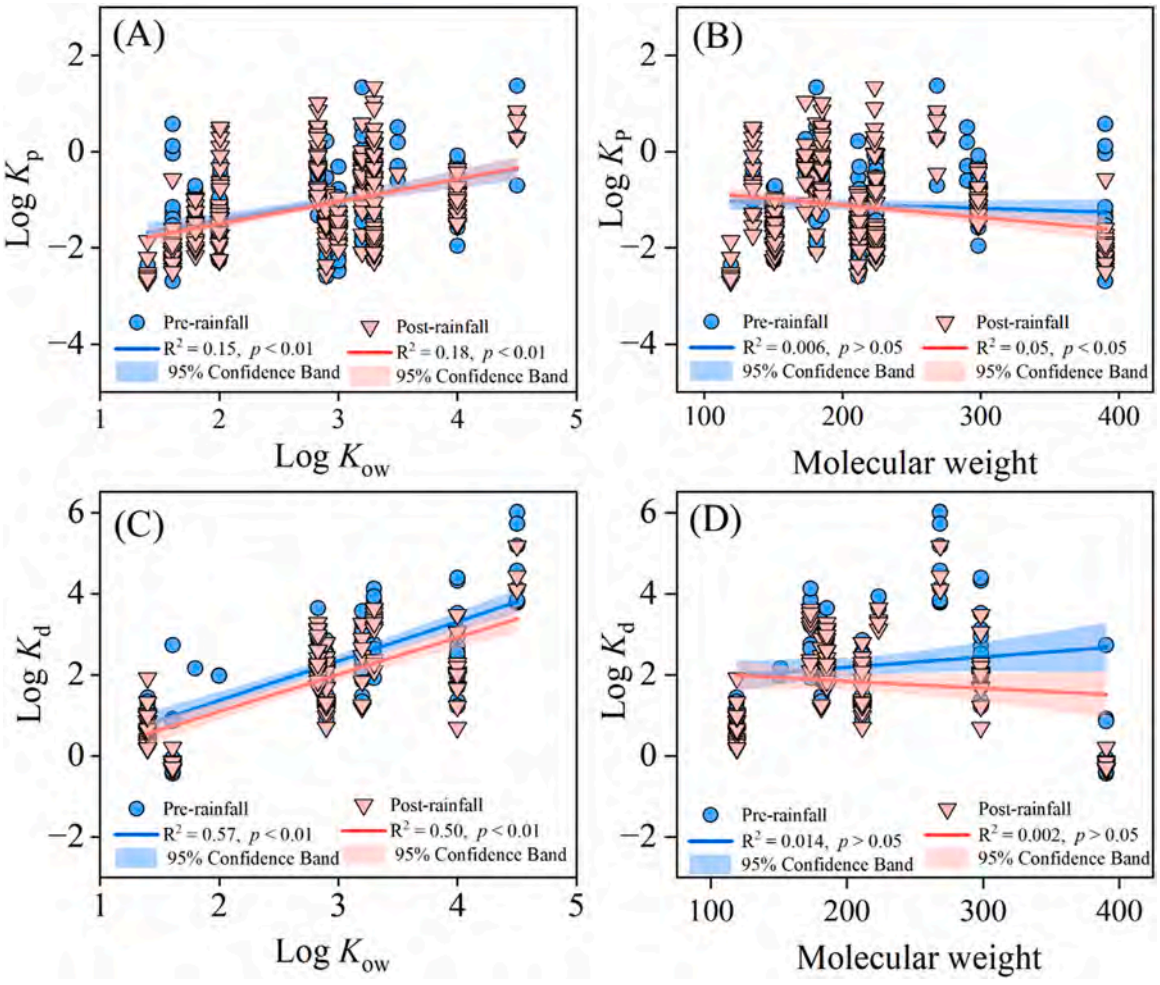


Fig. 3. Correlation between Log K_p of tire additives and their transformation products with Log K_{OW} (A) and molecular mass (B), and the correlation between Log K_d of tire additives and their transformation products with Log K_{OW} (C) and molecular mass (D).

3.5. High ecological risks and priority pollutants with PBT traits

As depicted in Fig. 4, the HI analysis of water samples from all sampling sites indicated high risks, with HI values escalating from 1.87 to 13.3 pre-rainfall to 2.09 to 24.9 post-rainfall, predominantly driven by DPU, DCU, 6PPD-Q, and HMMM. Post-rainfall, the impact on high-risk sites was further exacerbated by DPG, in addition to the four TATPs above. This suggests that rainfall may heighten the risk to urban water bodies. Notably, HMMM presented a high risk only at station D-S8 (dry season) pre-rainfall and at N-S8 (normal season) post-rainfall. This difference may be due to a combination of rainfall-induced TATP increase, dilution effect of rainfall, and compound degradation. Medium risks were observed for DPG, BT, IPPD, and 4-OH-DPA in 42.31 %, 7.76 %, 3.85 %, and 3.85 % of pre-rainfall samples, respectively; and for BT, 2-OH-BTH, and DPPD-Q in 23.08 %, 3.85 %, and 3.85 % of post-rainfall samples, respectively. Other TATPs, including BTH, 2-ABTH, 2-Me-S-BTH, RD, CPPD, and 6PPD, presented low risks due to their lower concentrations or toxicities.

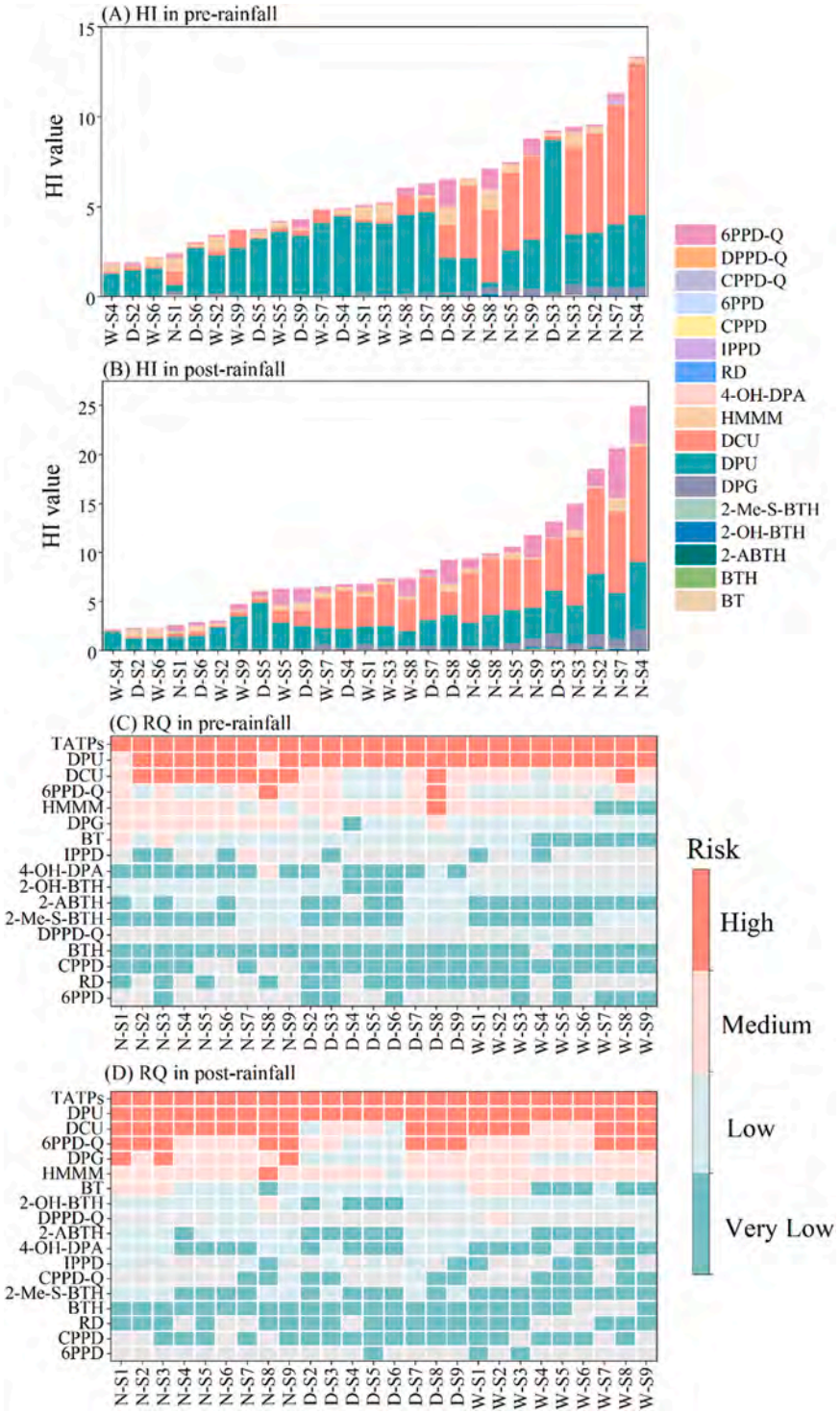


Fig. 4. Hazard index (HI) and risk quotient (RQ) values for tire additives and their transformation products pre-rainfall and post-rainfall across various stations (S1-S9) and seasons (N, normal season; D, dry season; W, wet season).

To understand the behavior and potential long-term effects of TATPs in the aquatic environment, the PBT characteristics of TATPs were identified based on measured and simulated data. HMMM and DPG showed half-lives in water exceeding 60 days, indicating considerable persistence (Fig. S11 and Table S10). Four compounds—CPPD, DPPD, DTPD and IPPD—exhibited bioaccumulation potential with log BAF values of 4.8, 4.8, 4.3, and 3.8, respectively (Wei et al., 2024), and consequent risk of biomagnification in the food chain. Furthermore, 6PPD-Q and TMTD, with extremely low LC_{50} (for fish) values of 41 ng/L and 340 ng/L (Lo et al., 2023; Padilla et al., 2012), respectively, demonstrated acute toxicity to fish, highlighting their harmful potential even at low concentrations. These findings highlight that eight TATPs possess one PBT characteristic, amplifying their risk profile in the environment. This knowledge is imperative for the development of stringent environmental regulations aimed at managing these substances effectively and safeguarding ecosystem health.

3.6. Limitations

Our study has some limitations. First, we collected 152 samples across multiple media over three seasons, with pre- and post-rainfall sampling at each of the nine sites. While this design captured the heterogeneity of major urban runoff sources and allowed statistical comparison of stream type impacts, it may not fully represent all stream environments. Future research with more sites and a broader range of stream types would enhance the generalizability of the results. Second, lack of SPM property data and hydrodynamics impeded full interpretation of TATP distribution patterns across streams. Future work should prioritize characterizing SPM properties and hydrodynamics to elucidate TATP partitioning. Third, toxicological information on TATPs remains limited, especially regarding their combined effects during multi-compound exposure. In this study, HI values were calculated using concentration-addition modelling. However, mixed TATPs in actual environments might exhibit synergistic effects, potentially resulting in higher risks than our assessment. Future research should focus on the combined toxicological effects of TATPs to improve the accuracy of risk assessments and inform more effective regulatory strategies.

4. Conclusions

This study offers new perspectives on the multi-media distribution and ecological risks of TATPs in urban streams, highlighting the significant roles of rainfall, seasonal variation, and stream type. Hydrophilic compounds (e.g., BTs) dominated aqueous phases and hydrophobic PPDs accumulated in sediments. Sediments acted as stable, long-term reservoirs, buffering short-term hydrological fluctuations. Precipitation events were a key driver in augmenting the concentrations of TATPs in the aqueous phase, whereas the extent of TATP contamination in SPM and sediment was primarily modulated by stream type and seasonal variation. Multivariate linear regression analysis elucidated compartment-specific factors governing TATP distribution: pH, temperature, and road area modulated aqueous-phase concentrations; precipitation exclusively dictated SPM levels; and road area was the sole determinant of sediment TATP concentrations. Hydrophobicity was a key determinant in their multi-media partitioning. Ecological risk assessments indicate high risks across all water samples. In a pioneering evaluation, eight TATPs exhibited persistence, bioaccumulation potential, or acute toxicity, warranting prioritization in regulatory frameworks. Urgent research is needed to uncover the partitioning dynamics of TATPs across environmental media and to assess their toxicological effects on aquatic life, prioritizing compounds with significant risk and notable PBT characteristics. To address TATP pollution in stormwater runoff, we propose installing stormwater filtration systems to enhance pollutant retention and implementing regular sediment dredging to remove contaminated stream sediments. These strategies should be integrated into comprehensive stormwater treatment plans optimizing stormwater collection, storage, and treatment. Future research should evaluate the effectiveness of these strategies in reducing TATP pollution under varying hydrological conditions.

CRediT authorship contribution statement

Li-Ni Wei: Writing – review & editing, Writing – original draft, Visualization, Software, Methodology, Investigation, Formal analysis, Data curation. **Nian-Nian Wu:** Investigation. **Ru Xu:** Investigation. **Yuan Liu:** Investigation. **Shan Liu:** Writing – review & editing, Funding acquisition, Conceptualization. **Hai-Yan Zhang:** Methodology. **Zi-Tong Li:** Data curation. **Yue-Hong Liu:** Methodology. **Xiang-Rong Xu:** Resources. **Jian-Liang Zhao:** Writing – review & editing, Supervision, Funding acquisition, Conceptualization. **Guang-Guo Ying:** Resources.

Declaration of competing interest

The authors declare that they have no known competing financial interests or personal relationships that could have appeared to influence the work reported in this paper.

Acknowledgments

The authors would like to acknowledge the support by the fund of the National Natural Science Foundation of China (Nos. U21A2036 and 42177388), the National Key Research and Development Program of China (2022YFC3105600), Special Fund of South China Sea Institute of Oceanology of the Chinese Academy of Sciences (SCSIO2023QY04).

Supplementary materials

Supplementary material associated with this article can be found, in the online version, at doi:10.1016/j.watres.2025.124366.

Data availability

Data will be made available on request.

References

Alhelou, R., Seiwert, B., Reemtsma, T., 2019. Hexamethoxymethylmelamine-A precursor of persistent and mobile contaminants in municipal wastewater and the water cycle. Water. Res. 165, 114973.

Anim, D.O., Banahene, P., 2021. Urbanization and stream ecosystems: the role of flow hydraulics towards an improved understanding in addressing urban stream degradation. Environ. Rev. 29 (3), 401–414.

Asheim, J., Vike-Jonas, K., Gonzalez, S.V., Lierhagen, S., Venkatraman, V., Veivåg, I.-L. S., Snilsberg, B., Flaten, T.P., Asimakopoulos, A.G., 2019. Benzotriazoles, benzothiazoles and trace elements in an urban road setting in Trondheim, Norway: re-visiting the chemical markers of traffic pollution. Sci. Total. Environ. 649, 703–711.

Brinkmann, M., Montgomery, D., Selinger, S., Miller, J.G.P., Stock, E., Alcaraz, A.J., Challis, J.K., Weber, L., Janz, D., Hecker, M., Wiseman, S., 2022. Acute toxicity of the tire rubber-derived chemical 6PPD-quinone to four fishes of commercial, cultural, and ecological importance. Environ. Sci. Technol. Lett. 9 (4), 333–338.

Cao, G., Wang, W., Zhang, J., Wu, P., Qiao, H., Li, H., Huang, G., Yang, Z., Cai, Z., 2023. Occurrence and fate of substituted *p*-phenylenediamine-derived quinones in Hong Kong wastewater treatment plants. Environ. Sci. Technol. 57 (41), 15635–15643.

Capolupo, M., Sørensen, L., Jayasena, K.D.R., Booth, A.M., Fabbri, E., 2020. Chemical composition and ecotoxicity of plastic and car tire rubber leachates to aquatic organisms. Water. Res. 169, 115270.

Di, S., Liu, Z., Zhao, H., Li, Y., Qi, P., Wang, Z., Xu, H., Jin, Y., Wang, X., 2022. Chiral perspective evaluations: enantioselective hydrolysis of 6PPD and 6PPD-quinone in water and enantioselective toxicity to *Gobiocypris rarus* and *Oncorhynchus mykiss*. Environ. Int. 166, 107374.

EPA, 2000. U.S. Environmental Protection Agency, Supplementary Guidance for Conducting Health Risk Assessment of Chemical Mixtures. Risk Assessment (accessed June 30, 2025).

European C., 2003. Technical Guidance Document on Risk Assessment in support of Commission Directive 93/67/EEC on risk assessment for new notified substances. Commission Regulation (EC) No. 1488/94 on risk assessment for existing substances, and Directive 98/8/EC of the European Parliament and of the Council concerning the placing of biocidal products on the market.

Fohet, L., Andanson, J.-M., Charbouillot, T., Malosse, L., Leremboure, M., Delor-Jestin, F., Verney, V., 2023. Time-concentration profiles of tire particle additives and transformation products under natural and artificial aging. Sci. Total. Environ. 859, 160150.

Ge, J., Hou, X., Liu, L., Deng, Q., Du, B., Zeng, L., 2024. Comprehensive identification and ubiquitous occurrence of eight classes of rubber-derived vulcanization accelerators in urban dusts. Environ. Sci. Technol. 58 (11), 5117–5128.

GZSY, 2023. Guangzhou Statistical Yearbook, Guangzhou Municipal Bureau of Statistics. https://tjj.gz.gov.cn/datav/admin/home/www_nj/2023/directory/01/html/01-03.htm (accessed July 1, 2025).

GZSY, 2024. Guangzhou Statistical Yearbook, Guangzhou Municipal Bureau of Statistics. http://tjj.gz.gov.cn/stats_newtjyw/zyxz/tjnjdzzz/content/post_10010720.html (accessed July 5, 2025).

Hiki, K., Yamamoto, H., 2022. Concentration and leachability of N-(1,3-dimethylbutyl)-N′-phenyl-*p*-phenylenediamine (6PPD) and its quinone transformation product (6PPD-Q) in road dust collected in Tokyo. Jap. Environ. Pollut. 302, 119082.

Hiki, K., Asahina, K., Kato, K., Yamagishi, T., Omagari, R., Iwasaki, Y., Watanabe, H., Yamamoto, H., 2021. Acute toxicity of a tire rubber-derived chemical, 6PPD quinone, to freshwater fish and crustacean species. Environ. Sci. Technol. Lett. 8 (9), 779–784.

Hou-R., Xu-R., Lin-L. Huang, Q.-Y., Li, H.-X., Liu, S., Pei, Y.-Q., Cheng, Y.-Y., Xu, X.-R., 2024. Organophosphate flame retardants and their metabolites in the Pearl River Estuary: occurrence, influencing factors, and ecological risk control strategies based on a mass balance model Environ. Int. 184, 108478.

Ikenoue, T., Nakajima, R., Fujiwara, A., Onodera, J., Itoh, M., Toyoshima, J., Watanabe, E., Murata, A., Nishino, S., Kikuchi, T., 2023. Horizontal distribution of surface microplastic concentrations and water-column microplastic inventories in the Chukchi Sea, western Arctic Ocean. Sci. Total. Environ. 855, 159564.

Janna, H., Scrimshaw, M.D., Williams, R.J., Churchley, J., Sumpter, J.P., 2011. From dishwasher to tap? Xenobiotic substances benzotriazole and tolyltriazole in the environment. Environ. Sci. Technol. 45 (9), 3858–3864.

Jin, J., van Swaaij, A.P.J., Noordermeer, J.W.M., Blume, A., Dierkes, W.K., 2021. On the various roles of 1,3-DIPHENYL guanidine in silica/silane reinforced sbr/br blends. Polym. Test. 93, 106858.

Jin, R., Wu, Y., He, Q., Sun, P., Chen, Q., Xia, C., Huang, Y., Yang, J., Liu, M., 2023. Ubiquity of amino accelerators and antioxidants in road dust from multiple land types: targeted and nontargeted analysis. Environ. Sci. Technol. 57 (28), 10361–10372.

Johannessen, C., Helm, P., Lashuk, B., Yargeau, V., Metcalfe, C.D., 2022a. The tire wear compounds 6PPD-quinone and 1,3-diphenylguanidine in an urban watershed. Arch. Environ. Contam. Toxicol. 82 (2), 171–179.

Johannessen, C., Saini, A., Zhang, X., Harner, T., 2022b. Air monitoring of tire-derived chemicals in global megacities using passive samplers. Environ. Pollut. 314, 120206.

H,H. Kong, J.J., Ma, T., Cao, X.Y., Li, W.D., Zhu, F.X., Sun, C., Yang, S.G., Li, S.Y., X, Q. M., 2023. Occurrence, partition behavior, source and ecological risk assessment of nitro-PAHs in the sediment and water of Taige Canal China. J. Environ. Sci. 124, 782–793.

Li, Z.-M., Kannan, K., 2024. Mass loading, removal, and emission of 1,3-diphenylguanidine, benzotriazole, benzothiazole, N-(1,3-Dimethylbutyl)-N′-phenyl-p-phenylenediamine, and their derivatives in a wastewater treatment plant in New York State, USA. ACS. ES. T. Water. 4 (6), 2721–2730.

Liao, C., Kim, U.-J., Kannan, K., 2018. A review of environmental occurrence, fate, exposure, and toxicity of benzothiazoles. Environ. Sci. Technol. 52 (9), 5007–5026.

Liao, X., Zou, T., Chen, M., Song, Y., Yang, C., Qiu, B., Chen, Z.-F., Tsang, S.Y., Qi, Z., Cai, Z., 2021. Contamination profiles and health impact of benzothiazole and its derivatives in PM2.5 in typical Chinese cities. Sci. Total. Environ. 755, 142617.

Liu, W., Xue, J., Kannan, K., 2017. Occurrence of and exposure to benzothiazoles and benzotriazoles from textiles and infant clothing. Sci. Total. Environ. 592, 91–96.

Liu, Y.-H., Mei, Y.-X., Liang, X.-N., Ge, Z.-Y., Huang, Z., Zhang, H.-Y., Zhao, J.-L., Liu, A., Shi, C., Ying, G.-G., 2024a. Small-intensity rainfall triggers greater contamination of rubber-derived chemicals in road stormwater runoff from various functional areas in Megalopolis cities. Environ. Sci. Technol. 58 (29), 13056–13064.

Liu, Y.-H., Mei, Y.-X., Wang, J.-Y., Chen, S.-S., Chen, J.-L., Li, N., Liu, W.-R., Zhao, J.-L., Zhang, Q.-Q., Ying, G.-G., 2024b. Precipitation contributes to alleviating pollution of rubber-derived chemicals in receiving watersheds: combining confluent stormwater runoff from different functional areas. Water. Res. 264, 122240.

Lo, B.P., Marlatt, V.L., Liao, X., Reger, S., Gallilee, C., Ross, A.R.S., Brown, T.M., 2023. Acute toxicity of 6PPDQuinone to early life stage juvenile chinook (*Oncorhynchus tshawytscha*) and coho (*Oncorhynchus kisutch*) salmon. Environ. Toxicol. Chem. 42 (4), 815–822.

Müller, K., Hübner, D., Huppertsberg, S., Knepper, T.P., Zahn, D., 2022. Probing the chemical complexity of tires: identification of potential tire-borne water contaminants with high-resolution mass spectrometry. Sci. Total. Environ. 802, 149799.

Magami, S., Guthrie, J., 2012. Amino resin cross-linked can coatings. Surf. Coat. Int. 95 (2), 64–73.

Muir, D.C.G., Howard, P.H., 2006. Are there other persistent organic pollutants? A challenge for environmental chemists. Environ. Sci. Technol. 40 (23), 7157–7166.

OECD. OECD HPV Database. https://hpvchemicals.oecd.org/ui/search.aspx (accessed October 18, 2024).

Padilla, S., Corum, D., Padnos, B., Hunter, D.L., Beam, A., Houck, K.A., Sipes, N., Kleinstreuer, N., Knudsen, T., Dix, D.J., Reif, D.M., 2012. Zebrafish developmental screening of the ToxCast™ Phase I chemical library. Reprod. Toxicol. 33 (2), 174–187.

Peng, W., Liu, C., Chen, D., Duan, X., Zhong, L., 2022. Exposure to N-(1,3-dimethylbutyl)-N′-phenyl-*p*-phenylenediamine (6PPD) affects the growth and development of zebrafish embryos/larvae. Ecotoxicol. Environ. Saf. 232, 113221.

Peter, K.T., Lundin, J.I., Wu, C., Feist, B.E., Tian, Z., Cameron, J.R., Scholz, N.L., Kolodziej, E.P., 2022. Characterizing the chemical profile of biological decline in stormwater-impacted urban watersheds. Environ. Sci. Technol. 56 (5), 3159–3169.

Rauert, C., Charlton, N., Okoffo, E.D., Stanton, R.S., Agua, A.R., Pirrung, M.C., Thomas, K.V., 2022. Concentrations of tire additive chemicals and tire road wear particles in an Australian urban tributary. Environ. Sci. Technol. 56 (4), 2421–2431.

Rink, H.-P., 2008. Automotive paints and coatings, second edition, chapter 7, poly-meric engineering for automotive coating applications (Eds.). In: Streitberger, H.-J., Dossel, K.-F. (Eds.), Automotive Paints and Coatings, 2nd ed. Wiley-VCH €Verlag, Weinheim, Germany.

Seiwert, B., Nihemaiti, M., Troussier, M., Weyrauch, S., Reemtsma, T., 2022. Abiotic oxidative transformation of 6-PPD and 6-PPD quinone from tires and occurrence of their products in snow from urban roads and in municipal wastewater. Water. Res. 212, 118122.

Shi, Z.-Q., Liu, Y.-S., Xiong, Q., Cai, W.-W., Ying, G.-G., 2019. Occurrence, toxicity and transformation of six typical benzotriazoles in the environment: a review. Sci. Total. Environ. 661, 407–421.

Tan, H.-D., Qiao, X., Ling, M., Wu, C.-Y., Zhang, X.-Y., He, X.-Y., Liang, Y.-F., Hao, R., 2024. Occurrence, multiphase partitioning, drivers, and ecological risks of current-use herbicides in a river basin dominated by rice–vegetable rotations in tropical China. Sci. Total. Environ. 908, 168270.

Tian, Z., Zhao, H., Peter, K.T., Gonzalez, M., Wetzel, J., Wu, C., Hu, X., Prat, J., Mudrock, E., Hettinger, R., Cortina, A.E., Biswas, R.G., Kock, F.V.C., Soong, R., Jenne, A., Du, B., Hou, F., He, H., Lundeen, R., Gilbreath, A., Sutton, R., Scholz, N.L., Davis, J.W., Dodd, M.C., Simpson, A., McIntyre, J.K., Kolodziej, E.P., 2021. A ubiquitous tire rubber–derived chemical induces acute mortality in coho salmon. Science (1979) 371 (6525), 185–189.

Varshney, S., Gora, A.H., Siriyappagouder, P., Kiron, V., Olsvik, P.A., 2022. Toxicological effects of 6PPD and 6PPD quinone in zebrafish larvae. J. Hazard. Mater. 424, 127623.

Wang, W., Zhang, J., Huang, G., Pryjomska-Ray, I., Volmer, D.A., Cai, Z., 2025. Tire-additive chemicals and their derivatives in urban road dust: spatial distributions, exposures, and associations with tire and road wear particles. J. Hazard. Mater. 490, 137749.

Wei, L.-N., Wu, N.-N., Xu, R., Liu, S., Li, H.-X., Lin, L., Hou, R., Xu, X.-R., Zhao, J.-L., Ying, G.-G., 2024. First evidence of the bioaccumulation and trophic transfer of tire additives and their transformation products in an estuarine food web. Environ. Sci. Technol. 58 (14), 6370–6380.

Wu, C.-C., Chen, L.-H., Wang, Z., Bao, L.-J., Song, L., Zeng, E.Y., 2022. Utility of benzothiazoles as markers of tire-derived inputs to estuarine waters assessed by polyethylene sheets. Environ. Pollut. 293, 118571.

Xu, Q., Li, G., Fang, L., Sun, Q., Han, R., Zhu, Z., Zhu, Y.-G., 2023. Enhanced formation of 6PPD-Q during the aging of tire wear particles in Anaerobic flooded soils: the role of iron reduction and environmentally persistent free radicals. Environ. Sci. Technol. 57 (14), 5978–5987.

Xu, R., Liu, S., Pan, Y.-F., Wu, N.-N., Huang, Q.-Y., Li, H.-X., Lin, L., Hou, R., Xu, X.-R., Cheng, Y.-Y., 2024. Steroid metabolites as overlooked emerging contaminants: insights from multimedia partitioning and source–sink simulation in an estuarine environment. J. Hazard. Mater. 461, 132673.

Xu, T.-T., Guo, J.-L., Yi, J.-F., Huang, S.-N., Liu, L.-Y., Guo, Y., 2024b. Occurrence and risk assessment of *p*-phenylenediamines and their quinones in aquatic environment: from city wastewater to deep sea. Sci. Total. Environ. 954, 176123.

Xu, S., Wang, Q., Lao, J.-Y., Cao, Y., Hong, P., Chen, C., Lam, E.Y., Fang, J.K.-H., Lee, S., Leung, K.M.Y., 2025. Typical tire additives in river water: leaching, transformation, and environmental risk assessment. Environ. Sci. Technol. 58, 18940–18949.

Zeng, F., Sherry, J.P., Bols, N.C., 2016. Evaluating the toxic potential of benzothiazoles with the rainbow trout cell lines, RTgill-W1 and RTL-W1. Chemosphere 155, 308–318.

Zeng, L., Li, Y., Sun, Y., Liu, L.-Y., Shen, M., Du, B., 2023. Widespread occurrence and transport of *p*-phenylenediamines and their quinones in sediments across urban rivers, estuaries, coasts, and deep-sea regions. Environ. Sci. Technol. 57 (6), 2393–2403.

Zhang, Y.-J., Xu, T.-T., Ye, D.-M., Lin, Z.-Z., Wang, F., Guo, Y., 2022. Widespread N-(1,3-Dimethylbutyl)-N′-phenyl-*p*-phenylenediamine quinone in size-fractioned atmospheric particles and dust of different indoor environments. Environ. Sci. Technol. Lett. 9 (5), 420–425.

Zhang, H.-Y., Huang, Z., Liu, Y.-H., Hu, L.-X., He, L.-Y., Liu, Y.-S., Zhao, J.-L., Ying, G.-G., 2023a. Occurrence and risks of 23 tire additives and their transformation products in an urban water system. Environ. Int. 171, 107715.

Zhang, R., Zhao, S., Liu, X., Tian, L., Mo, Y., Yi, X., Liu, S., Liu, J., Li, J., Zhang, G., 2023b. Aquatic environmental fates and risks of benzotriazoles, benzothiazoles, and *p*-phenylenediamines in a catchment providing water to a megacity of China. Environ. Res. 216, 114721.

Zhang, S.-Y., Gan, X., Shen, B., Jiang, J., Shen, H., Lei, Y., Liang, Q., Bai, C., Huang, C., Wu, W., Guo, Y., Song, Y., Chen, J., 2023c. 6PPD and its metabolite 6PPDQ induce different developmental toxicities and phenotypes in embryonic zebrafish. J. Hazard. Mater. 455, 131601.

Zhang, H.-Y., Liu, Y.-H., Wei, L.-N., Zhu, R.-Q., Zhao, J.-L., Liu, S., Xu, X.-R., Ying, G.-G., 2024. Unveiling spatiotemporal distribution, partitioning, and transport mechanisms of tire additives and their transformation products in a highly urbanized estuarine region. Sci. Total. Environ. 954, 176804.

Zhao, H.N., Hu, X., Tian, Z., Gonzalez, M., Rideout, C.A., Peter, K.T., Dodd, M.C., Kolodziej, E.P., 2023. Transformation products of tire rubber antioxidant 6PPD in

heterogeneous gas-phase ozonation: identification and environmental occurrence. Environ. Sci. Technol. 57 (14), 5621–5632.
Zhao, M.-L., Ji, X., He, Z., Yang, G.-P., 2024. Spatial distribution, partitioning, and ecological risk assessment of benzotriazoles, benzothiazoles, and benzotriazole UV absorbers in the eastern shelf seas of China. Water. Res. 248, 120885.
Zhong, L., Peng, W., Liu, C., Gao, L., Chen, D., Duan, X., 2022. IPPD-induced growth inhibition and its mechanism in zebrafish. Ecotoxicol. Environ. Saf. 239, 113614.
Zoroufchi Benis, K., Behnami, A., Minaei, S., Brinkmann, M., McPhedran, K.N., Soltan, J., 2023. Environmental occurrence and toxicity of 6PPD quinone, an emerging tire rubber-derived chemical: a review. Environ. Sci. Technol. Lett. 10 (10), 815–823.

Food Chemistry 495 (2025) 146185



Contents lists available at ScienceDirect

Food Chemistry

journal homepage: www.elsevier.com/locate/foodchem





Exploring the structural diversity and spatiotemporal dynamics of mogrosides in *Siraitia grosvenorii*

Jiying Pei [a], Qiong Su [a,b], Shuiyuan Jiang [c], Jianxiu Li [b,*], Nengzhong Xie [b,*]

[a] School of Resources, Environment and Materials, Guangxi University, Nanning 530004, China
[b] State Key Laboratory of Non-food Biomass Energy Technology, National Engineering Research Center for Non-Food Biorefinery, Guangxi Academy of Sciences, 98 Daling Road, Nanning 530007, China
[c] Guangxi Institute of Botany, Guangxi Zhuangzu Autonomous Region and the Chinese Academy of Sciences, Guilin 541006, China

ARTICLE INFO

Keywords:
Triterpenoid glycosides
Developmental stage
Cultivar
Environmental influence
Metabolomics
High-resolution mass spectrometry
Molecular networking

ABSTRACT

Mogrosides are the main non-caloric sweeteners in *Siraitia grosvenorii*, with sweetness determined by specific chemical structures. However, the diversity of triterpenoid skeletons and glucosylation patterns suggests that the variety of mogrosides remains insufficiently characterized. Here, high-resolution mass spectrometry (HRMS) coupled with Global Natural Products Social Molecular Networking (GNPS) was used to systematically profile mogrosides. A total of 88 distinct compounds were identified based on accurate molecular mass, MS/MS spectra, and retention time, and were classified into nine types of tetracyclic triterpene skeletons. Mogroside composition and abundance varied across developmental stages, cultivars, and environments. Fewer glucosyl units occurred during early development (15–30 days after pollination), while glucosylation increased in later stages (50–75 days after pollination). Greenhouse conditions accelerated growth, and the Xinning cultivar produced more mogroside V than Longji at maturity. This investigation facilitates novel mogroside discovery and reveals dynamic accumulation patterns, offering practical insights for cultivating high-sweetness *S. grosvenorii* fruits.

1. Introduction

Siraitia grosvenorii (Swingle) C. Jeffrey, commonly known as monk fruit or Luo Han Guo, is a fruit traditionally consumed in China for its natural sweetness and potential health benefits (Gong et al., 2019). It contains abundant bioactive compounds such as vitamin C, dietary fiber, and triterpene glycosides (Guo et al., 2024; Utami et al., 2024), which have attracted increasing interest in the functional food industry. The fruit's intense sweetness primarily arises from mogrosides, a group of triterpene glycosides (Xia, Rivero-Huguet, Hughes, & Marshall, 2008). Among these, mogroside V and siamenoside I are the predominant constituents, exhibiting sweetness approximately 425 and 563 times greater than sucrose, respectively (Cui et al., 2023). These non-caloric compounds are widely used as sugar substitutes in low-calorie and diabetic-friendly products (Gong et al., 2019), including beverages like Diet Coke sweetened with monk fruit extract. Beyond their sweetening properties, certain mogrosides—such as 11-oxo-mogroside V—also exhibit strong reactive oxygen species (ROS) scavenging activity (Chen, Wang, Qi, & Xie, 2007). This property indicates their potential as natural antioxidants, which may contribute to the reduction of oxidative stress when incorporated into a health-conscious diet (Huang et al., 2024; Lu et al., 2023). To fully harness these functional attributes, a comprehensive understanding of the structural diversity and distribution of mogrosides in *S. grosvenorii* is essential.

Mogrosides consist of a tetracyclic triterpenoid core decorated with varying glucosylation patterns, which significantly influence their sweetness and bioactivity (Li et al., 2014; Wu et al., 2022). Although numerous mogroside structures have been identified (Jia & Yang, 2009; Prakash & Chaturvedula, 2014), the complexity of their molecular frameworks suggests that many low-abundance or novel variants remain uncharacterized. Traditional analytical methods, such as isolation and structural elucidation, are labor-intensive and often miss these minor compounds. While liquid chromatography–mass spectrometry (LC–MS) has enhanced detection capabilities, the limited availability of comprehensive spectral databases continues to constrain the identification of new mogrosides.

We hypothesize that the diversity of triterpenoid skeletons and glucosylation patterns in *S. grosvenorii* leads to a far richer structural variety of mogrosides than currently recognized. To test this, we employed high-resolution mass spectrometry (HRMS) combined with Global Natural

* Corresponding authors.
E-mail addresses: jianxiuli@gxas.cn (J. Li), xienengzhong@gxas.cn (N. Xie).

https://doi.org/10.1016/j.foodchem.2025.146185
Received 20 May 2025; Received in revised form 13 August 2025; Accepted 30 August 2025
Available online 2 September 2025
0308-8146/© 2025 Elsevier Ltd. All rights are reserved, including those for text and data mining, AI training, and similar technologies.

Products Social Molecular Networking (GNPS). HRMS allows precise molecular formula determination, while GNPS facilitates visualization of molecular relationships and dereplication of unknown compounds based on MS/MS spectral similarity (Nothias et al., 2020; Wang et al., 2016; Xue et al., 2021). This integrated strategy enhances the efficiency of compound analysis by eliminating the need for isolation or purification. Furthermore, even low-abundance mogrosides, if subjected to MS/MS fragmentation, can be detected and annotated within molecular networks. This strategy has been successfully applied to other complex metabolite classes such as triterpenoid saponins and phenolics (Chen et al., 2023; Ge, Zhu, Yoshimatsu, & Komatsu, 2017). It offers a powerful platform for comprehensive mogroside profiling and novel compound discovery in *S. grosvenorii*.

In addition to analytical challenges, mogroside composition and content are known to vary significantly among cultivars and cultivation conditions (Dong et al., 2025; Wang et al., 2019). Genetic differences influence biosynthetic capacity, particularly through variation in the expression of key enzymes like UDP-glucosyltransferases involved in glycosylation (Qiao et al., 2019). Environmental factors—including temperature, light intensity, and humidity—also modulate enzyme activity and metabolic fluxes (Li, Kong, Fu, Sussman, & Wu, 2020; Yang et al., 2018). These modulations thereby affect mogroside accumulation patterns. Despite these known influences, the combined effects of cultivar genetics and environmental conditions on the temporal dynamics of mogroside biosynthesis remain poorly characterized. A deeper understanding of these interactions is essential to optimize cultivation strategies and improve the quality and yield of mogroside-rich products.

To address these knowledge gaps, we designed a systematic study to investigate the structural diversity and accumulation dynamics of mogrosides in *S. grosvenorii*. Using liquid chromatography–high-resolution mass spectrometry (LC–HRMS) integrated with GNPS, we aim to: 1) comprehensively characterize the chemical diversity of mogrosides, including low-abundance variants and a broad range of putative structures; 2) examine how cultivar type and cultivation conditions influence the spatiotemporal patterns of mogroside profiles during fruit development; and 3) quantify the impact of these factors on mogroside content across key developmental stages. This integrative strategy enables systematic, high-throughput investigation of mogroside diversity and accumulation dynamics, thereby facilitating their improved utilization in functional foods and food-derived ingredients.

2. Materials and methods

2.1. Materials of S. grosvenorii

S. grosvenorii plants were cultivated at the Guangxi Institute of Botany, Chinese Academy of Sciences (Guilin, China, GPS coordinates: E110.17 and N25.01). Two distinct cultivars were investigated: Longji and Xinning. The Longji cultivar was grown under two conditions: wild conditions (denoted as L) and greenhouse conditions (denoted as L'). The Xinning cultivar was exclusively grown in the wild (denoted as X). Pollination was standardized and conducted on July 22, 2020. Fruits were harvested at four critical stages: 15, 30, 50, and 75 days after pollination (DAP), representing the progression from early development to late maturity. For each experimental group (i.e., each combination of cultivar, growth condition, and developmental stage), six biological replicates were obtained. Each replicate consisted of an individual fruit of comparable size, harvested from a different plant to ensure biological independence. In total, 72 samples were collected for analysis. Immediately upon harvesting, fruits were flash-frozen in liquid nitrogen to preserve their biochemical integrity and natural properties. Following this, all samples were stored at −80 °C until subjected to further laboratory analysis. Due to post-processing laboratory errors, six contaminated samples were excluded, yielding a final total of 66 samples. The experimental design is schematically presented in Fig. 1.

2.2. Chemicals and reagents

Eighteen mogroside reference standards, including mogrol (MG), mogroside IA1 (IA1), mogroside IE1 (IE1), 11-oxo-mogroside IIA (11-O-IIA), mogroside IIE (IIE), mogroside IIA (IIA), mogroside IIA1 (IIA1), mogroside IIA2 (IIA2), 11-oxo-mogroside III (11-O-III), 11-oxo-mogroside IIIE (11-O-IIIE), mogroside III (III), mogroside IIIE (IIIE), mogroside IVA (IVA), mogroside IVE (IVE), siamenoside I (SI), 11-oxo-mogroside V (11-O-V), mogroside V (V), and mogroside VI (VI), were procured from Chengdu Biopurify Phytochemicals Ltd. (Chengdu, China). HPLC-grade methanol and acetonitrile were purchased from Thermo Fisher Scientific (Waltham, USA), and ultrapure water was obtained using a PURELAB Classic system (ELGA LabWater, High Wycombe, UK). Other chemicals and reagents utilized in this study were of analytical grade and above. Stock solutions of the 18 mogroside reference standards were prepared at a concentration of 1000 mg/L by dissolving 1 mg of each compound in 50:50 (v/v) methanol-water. These stock solutions were stored at −20 °C in amber vials for future analyses. Working solutions at various concentrations were subsequently prepared by diluting the stock solutions with methanol as needed.

2.3. Extraction of metabolites from S. grosvenorii

Frozen *S. grosvenorii* samples were initially dehydrated using a vacuum freeze dryer (Qingdao Yonghe Chuangxin Electronic Technology Co., Ltd., Qingdao, China) for 72 h. The dried fruit was then ground into

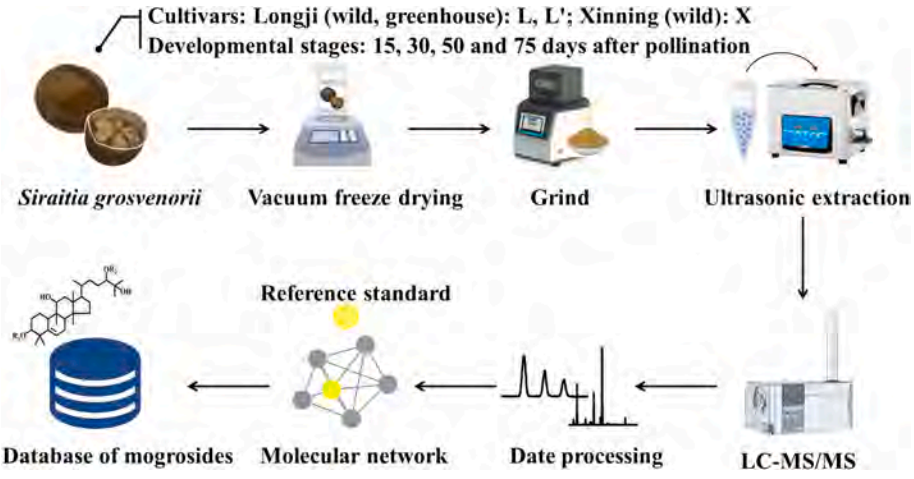


Fig. 1. A diagram of the experimental design.

fine powder using a high-throughput tissue grinder (SCIENTZ-48, Scientz Biotechnology Polytron Technologies Inc., Zhejiang, China) with stainless steel beads, operating at 60 Hz for 3 min. The ground powder was sieved through a 60-mesh screen to ensure uniform particle size. For metabolite extraction, 50 mg of the powdered sample, obtained from an individual fruit, was mixed with 0.5 mL of chilled methanol-water (80:20, v/v) solution. The mixture was sonicated for 15 min with a 40 kHz frequency at room temperature (Shenzhen Shenhuatai Ultrasonic Cleaning Equipment Co., Ltd., Shenzhen, China) and then centrifuged at 9660 ×*g* (rotor radius: 60 mm, 12,000 rpm) for 10 min at 4 °C (Micro 200 R Centrifuge, Andreas Hettich GmbH & Co. KG, Tuttlingen, Germany). The extraction was repeated twice, and supernatants from all three extractions were pooled. The pooled extracts were evaporated to dryness under a nitrogen stream. The dried residue was reconstituted in 1 mL of methanol-water solution (50:50, v/v). Prior to ultra-performance liquid chromatography–tandem mass spectrometry (UPLC–MS/MS) analysis, 0.1 mL of the reconstituted solution was filtered through a 0.22 μm Millipore filter and subsequently diluted 4.5-fold for sample injection.

2.4. Instrumental measurement and data pre-processing

Metabolic analysis was performed using UPLC coupled with Q-Exactive Orbitrap mass spectrometry (UPLC-Q-Exactive Orbitrap-MS) (Thermo Fisher Scientific, Waltham, USA). Chromatographic separation was achieved using an RRHD SB-C18 column (2.1 mm × 100 mm, 1.8 μm; Agilent Technologies, CA, USA). The mobile phases consisted of H_2O with 0.1 % formic acid (A) and acetonitrile with 0.1 % formic acid (B). The gradient elution program was as follows: 0–8 min, 25 % B; 8–11 min, 25 %–80 % B; 11–16.5 min, 80 % B; 16.6–20 min, 80 %–25 % B; and 20–23 min, 25 % B. The flow rate was maintained at 0.2 mL/min, with an injection volume of 2 μL and a column temperature set at 30 °C throughout the analysis.

Mass spectrometry data were acquired using a data-dependent acquisition (DDA) mode, controlled by Xcalibur software (Thermo Fisher Scientific, Waltham, USA). The electrospray ionization (ESI) source operated in negative ion mode with a spray voltage of 2.7 kV. The ionization source settings were configured as follows: capillary temperature, 320 °C; sheath gas flow rates, 30 arbitrary units (Arb); auxiliary gas flow rates, 10 Arb. Arb is a unit defined by the instrument software. For MS acquisition, full scan measurements were conducted at a resolution of 70,000 FWHM (at *m/z* 200), spanning a mass range from *m/z* 200 to 1800. Data-dependent MS/MS scans were carried out at a resolution of 35,000 FWHM (at *m/z* 200), with a normalized collision energy (NCE) of 15.

For data pre-processing, raw data files (.raw) were converted to mzXML format and analyzed using the open-source MZmine software (Version 2.51, Okinawa Institute of Science and Technology (OIST), Onna, Japan) for feature extraction. It is available at: https://github.com/mzmine/mzmine2/releases (accessed on September 15, 2021). During chromatogram construction, a minimum peak height threshold of 70,000 was applied, with an *m/z* tolerance of 5 ppm. Chromatograms were deconvoluted using the local minimum algorithm, with peak duration set from 0.07 to 1.20 min and a minimum absolute height of 70,000. Isotopic peaks were grouped with an *m/z* tolerance of 0.003 Da and a retention time tolerance of 0.05 min. Peak alignment was performed using the join aligner module, with *m/z* and retention time tolerances of 0.001 Da and 0.15 min, respectively. After alignment, gap filling was conducted with an intensity tolerance of 5 %, an *m/z* tolerance of 0.001 Da (or 5 ppm), and a retention time tolerance of 0.15 min. A detailed account of the MZmine parameters used in this study is presented in Table S1. Detailed settings are provided in Table S1.

2.5. Molecular network analysis

An MGF-formatted file and a feature quantification table, both exported from MZmine software, were uploaded to the GNPS website for feature-based molecular networking (FBMN) analysis. The FBMN was carried out with parameters set as follows: parent and fragment ion mass tolerance of 0.02 Da, a cosine score threshold of 0.7, a minimum of 2 matched peaks, a library search minimum matched peak count of 2, a library search score threshold of 0.7, and a minimum peak intensity of 100,000. The FBMN job can be accessed at: https://gnps.ucsd.edu/ProteoSAFe/status.jsp?task=a819779c1f5e477b9859018ca3051250. In total, 29 compounds were annotated using the GNPS database search. Additional unidentified compounds were manually characterized by comparing their MS/MS spectra with those of known compounds from the GNPS library and 18 mogroside reference standards. The results of the molecular networking were visualized using Cytoscape software (Version 3.8.0, Cytoscape Consortium, San Diego, USA).

2.6. Statistical analysis

A total of 66 samples were included in the statistical analysis, representing combinations of different developmental stages (DAP15, DAP30, DAP50, and DAP75), cultivars (Longji and Xinning), and growth environments (wild and greenhouse). Specifically, the Longji cultivar was grown under both wild (L) and greenhouse (L') conditions, while the Xinning cultivar was cultivated only under wild conditions (X), resulting in a total of 12 distinct sample groups, with 4–6 biological replicates per group.

To explore metabolic differences and clustering patterns among these conditions, multivariate statistical analyses including Principal Component Analysis (PCA), Orthogonal Partial Least Squares Discriminant Analysis (OPLS-DA), and Principal Coordinates Analysis (PCoA) were conducted. PCA and OPLS-DA were performed using SIMCA-P software (Version 14.1, Umetrics, Umea, Sweden), with data pre-processing involving unit variance scaling for PCA and Pareto scaling for OPLS-DA. The reliability of the OPLS-DA model was validated with 200 random permutation tests. Model performance was assessed using the R^2 (cum) for goodness-of-fit and Q^2 (cum) for prediction. Values approaching 1 indicate high accuracy, while Q^2 (cum) values greater than 0.5 suggest acceptable predictive reliability. PCoA was performed using R (Version 4.4.1, R Core Team, Vienna, Austria). To visualize the distribution of mogrosides in *S. grosvenorii* across different developmental stages and cultivars, Hierarchical Cluster Analysis (HCA) was performed using Chiplot (https://www.chiplot.online). For group comparisons (e.g., comparisons across different developmental stages, cultivars, or environments), statistical analyses were conducted using SPSS software (Version 17.0, SPSS Inc., Chicago, USA). Prior to hypothesis testing, data were checked for normality with the Shapiro–Wilk test and for homogeneity of variances using Levene's test. If both assumptions were met, two groups were compared using a two-tailed unpaired Student's *t*-test; otherwise, the Mann–Whitney *U* test was applied. For comparisons among multiple groups, one-way ANOVA followed by post-hoc tests was used when assumptions were satisfied; if not, the Kruskal–Wallis test was conducted. A *p*-value of <0.05 was considered statistically significant.

2.7. Data quality control

To assess system stability and technical reproducibility, a pooled quality control (QC) sample was prepared by mixing equal amounts (10 mg) of *S. grosvenorii* powder from all experimental samples. Ten 50 mg aliquots (QC1–QC10) were taken from the pooled material and processed using the same extraction and analysis procedures as the individual samples.

For instrument stability monitoring, one aliquot (QC1) was repeatedly injected—six times at the beginning of the UPLC–MS/MS run and then once after every six sample injections—resulting in ten total injections (labeled QC1–1 to QC1–10). The average relative standard deviation (RSD) of the extracted ion currents (EICs) for the ten most

intense peaks across QC1–1 to QC1–10 was 7.15 %, indicating good system stability (Fig. S1). To evaluate the technical reproducibility of the full workflow, all ten QC aliquots (QC1–QC10) were analyzed. PCA revealed that these QC samples clustered tightly near the center of the score plot (Fig. S2), confirming high technical consistency across both the extraction and instrumental analysis steps.

During feature extraction, variables with an RSD greater than 30 % across QC1–1 to QC1–10 were excluded to ensure data quality. Additionally, all experimental samples were analyzed in a randomized order to reduce systematic bias. For compound identification, mass accuracy was maintained within ±5 ppm for both precursor and product ions.

3. Results

3.1. Identification of unknown mogrosides with GNPS

Chromatographic separation coupled with HRMS enabled the identification of 2455 molecular features, which were subsequently organized into molecular networks. These molecular networks provided a comprehensive view of the relationships among the 2455 features. This facilitated the identification of unknown mogrosides through comparison with 18 mogroside reference standards. As shown in Fig. 2A, all 18 identified mogrosides share a common structural foundation of either a mogrol or 11-oxo-mogrol skeleton. Their key distinction lies in the number of attached glucosyl units, which varies from one to six across the different compounds. Under negative ESI mode, mogrosides are typically ionized as $[M + HCOO]^-$. Upon collision-induced dissociation (CID), these formate-adducted ions consistently lose formic acid (*m/z* 46.0055) (Fig. 2B). The loss of *m/z* 46.0055 represents a hallmark fragmentation behavior characteristic of mogrosides. This enables the grouping of mogroside-related compounds into clusters within the molecular network based on high cosine similarity scores.

Building on this characteristic fragmentation profile, we utilized 18 mogroside reference standards to guide the structural annotation of unknown mogrosides. The following example illustrates the approach used to identify the unknown mogrosides. Molecular network analysis revealed that several unknown compounds, with *m/z* values of 1167.5824 (ID 27977), 1169.5964 (ID 18370), 1313.6393 (ID 18378), 1329.6333 (ID 25544), and 1491.6883 (ID 18388), co-clustered with two known mogroside standards: mogroside III (*m/z* 1007.5449, $C_{48}H_{82}O_{19}$, ID 233) and mogroside V (*m/z* 1331.6509, $C_{60}H_{102}O_{29}$, ID 243) (Fig. 3A). Upon closer inspection of their MS/MS spectra, these unknown compounds displayed fragmentation patterns similar to the reference mogrosides, notably a consistent loss of *m/z* 46.0055 corresponding to formic acid loss (Fig. 3B). This consistent pattern suggested that these unknown compounds were likely mogrosides. To identify these compounds more precisely, we calculated their molecular formulas based on their exact masses. The molecular formulas for the unknown compounds were as follows: $C_{54}H_{90}O_{24}$ (2.23 ppm), $C_{54}H_{92}O_{24}$ (0.77 ppm), $C_{60}H_{100}O_{28}$ (1.22 ppm), $C_{60}H_{100}O_{29}$ (0.53 ppm), and $C_{66}H_{110}O_{34}$ (1.94 ppm). Mogrosides are characterized by a tetracyclic triterpenoid skeleton with attached glucosyl units, each having a molecular formula of $C_6H_{10}O_5$ (mass of 162 Da). By analyzing the molecular formulas of these unknown compounds, we were able to infer both the structure of the triterpenoid skeleton and the glucosyl units attached to each molecule. For instance, the compound with *m/z* 1167.5824 (ID 27977) corresponded to a mogrol skeleton ($C_{30}H_{50}O_4$) with four glucosyl units. Similarly, the compounds with *m/z* values of 1169.5964 (ID 18370), 1313.6393 (ID 18378), 1329.6333 (ID 25544), and 1491.6883 (ID 18388) corresponded to mogrol skeletons with variations. Specifically, they retained the original skeleton ($C_{30}H_{52}O_4$), lost one H_2O ($C_{30}H_{50}O_3$), lost two hydrogens ($C_{30}H_{50}O_4$), and lost two hydrogens ($C_{30}H_{50}O_4$), respectively. The glucosyl units attached to each compound were determined to be 4, 5, 5, and 6, respectively. Due to the limitations of mass spectrometry in differentiating structural isomers, the complete structures of these compounds could not be fully elucidated. Therefore, the unidentified mogrosides were tentatively designated as: 11-oxo-mogroside IV isomer (ID 27977), mogroside IV isomer (ID 18370), 25-dehydroxy-24-oxo-mogroside V isomer (ID 18378), 11-oxo-mogroside V isomer (ID 25544), and 11-oxo-mogroside VI isomer (ID 18388) (Fig. 3B).

Tetracyclic triterpenoids can have multiple structural isomers for a given molecular formula. These variations may arise from differences such as the positioning of double bonds, the location of hydroxyl groups, and the cis/trans configuration of carbon atoms. For instance, the molecular formula $C_{30}H_{50}O_5$ can correspond to two or more constitutional isomers, such as 7-oxo-mogrol (Li et al., 2014), 20-hydroxy-11-oxo-mogrol (Li et al., 2014), and 29-hydroxy-mogrol (Fig. 4A) (Wang et al., 2022). In the case of $C_{30}H_{52}O_4$, two epimers–mogrol and 11-epi-mogrol–can exist. This is due to the differing spatial orientation of the hydroxyl group at the C-11 position, which can either be in the α (downward) or *β* (upward) configuration (Fig. 4B) (Wu et al., 2022). However, distinguishing between these isomers using mass spectrometry remains challenging, as the tetracyclic triterpenoid skeletons exhibit minimal fragmentation in CID spectra. As a result, isomers with identical molecular masses but different structural configurations cannot always be distinguished. These isomers with the same molecular formula are grouped under a common core structure label designated as Mx, where "x" refers to the number of distinct molecular formulas identified. In this study, the core structures identified in the GNPS analysis correspond to the following molecular formulas: M1 (M, $C_{30}H_{52}O_4$), M2 (M – H_4O, $C_{30}H_{48}O_3$), M3 (M – H_2O, $C_{30}H_{50}O_3$), M4 (M – O, $C_{30}H_{52}O_3$), M5 (M – H_2, $C_{30}H_{50}O_4$), M6 (M – H_2 + O, $C_{30}H_{50}O_5$), and M7 (M + CH_2, $C_{31}H_{54}O_4$) (Fig. 4C) (Gong et al., 2019; Guo et al., 2024; Li et al., 2006; Li et al., 2014; Wu et al., 2022). To further expand the scope, our literature search revealed two additional core structures present within the molecular network: M8 (M + O, $C_{30}H_{52}O_5$) (Gong et al., 2019; Wu et al., 2022) and M9 (M + CH_2O, $C_{31}H_{54}O_5$) (Wu et al., 2022). However, these nodes did not cluster with the reference standards in the network, which may be attributed to FBMN parameter settings, such as MS/MS peak intensity thresholds or other spectral matching criteria.

In addition to structural isomerism of the tetracyclic triterpenoid skeleton, mogrosides with the same tetracyclic triterpenoid skeleton and the same glucosyl units can exist as multiple isomers. This is due to the structural flexibility in glucosyl unit attachment. Specifically, glucosyl units can attach to different hydroxyl positions on the tetracyclic triterpenoid skeleton, either as individual sugars or in chain-like structures. For example, when the M1 tetracyclic triterpenoid skeleton is conjugated with one to six glucosyl units, several distinct structural isomers can be formed (Fig. S3). Distinguishing mogroside isomers solely by MS/MS fragmentation is challenging due to their highly similar spectra. Therefore, chromatographic separation based on retention time differences, which arise from variations in polarity, is employed to differentiate them. For example, as shown in Fig. S4D, isomers IIE, IIA2, IIA, and IIA1 eluted at 11.22 min, 11.62 min, and 11.83 min (IIA and IIA1), respectively. Given the negligible difference in retention times between IIA and IIA1, they were considered indistinguishable. A threshold of 0.2 min—based on the typical peak width of reference standards (0.1–0.3 min)—was applied to define chromatographically resolvable isomers.

Additionally, analysis of the 18 mogroside reference standards revealed a trend of decreasing retention time with increasing glucosylation. This trend is consistent with increasing polarity (Fig. S4). For instance, mogrol exhibited an elution time of 13.52 min. In contrast, mogrosides with one to six glucosyl units eluted progressively earlier, with their elution times ranging from approximately 12.00 min down to 1.77 min. To avoid false positives, a retention time tolerance of ±4 min was applied around the expected elution window for each glucosylation level. This dual filtering strategy—based on MS/MS fragmentation and retention time—allowed for robust yet cautious annotation of mogroside features. In total, we identified 88 unique mogrosides (Table S2),

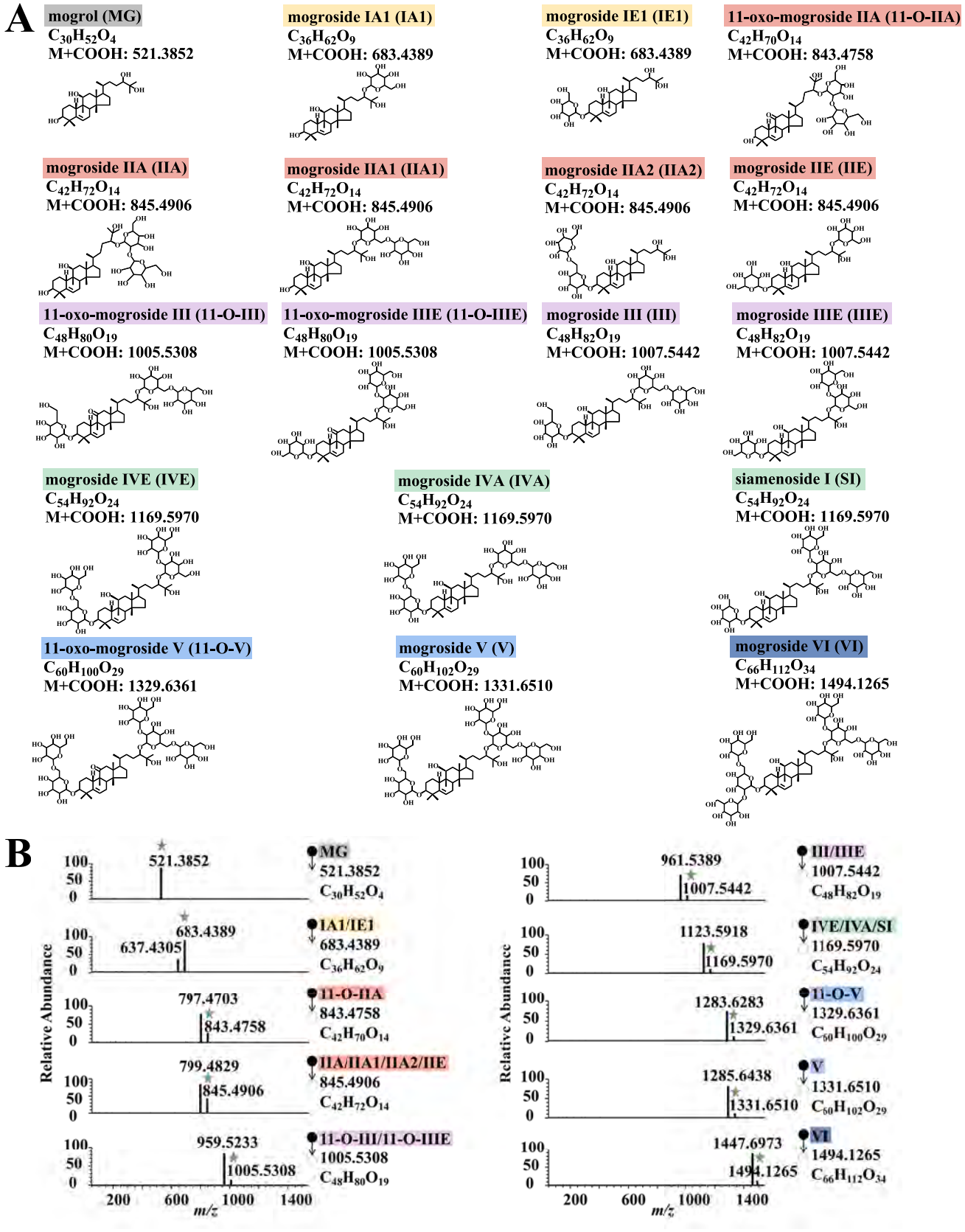


Fig. 2. (A) Structure and (B) MS/MS spectra of the 18 mogroside reference standards. The number of glucosyl units is highlighted by shading beneath the mogroside names.

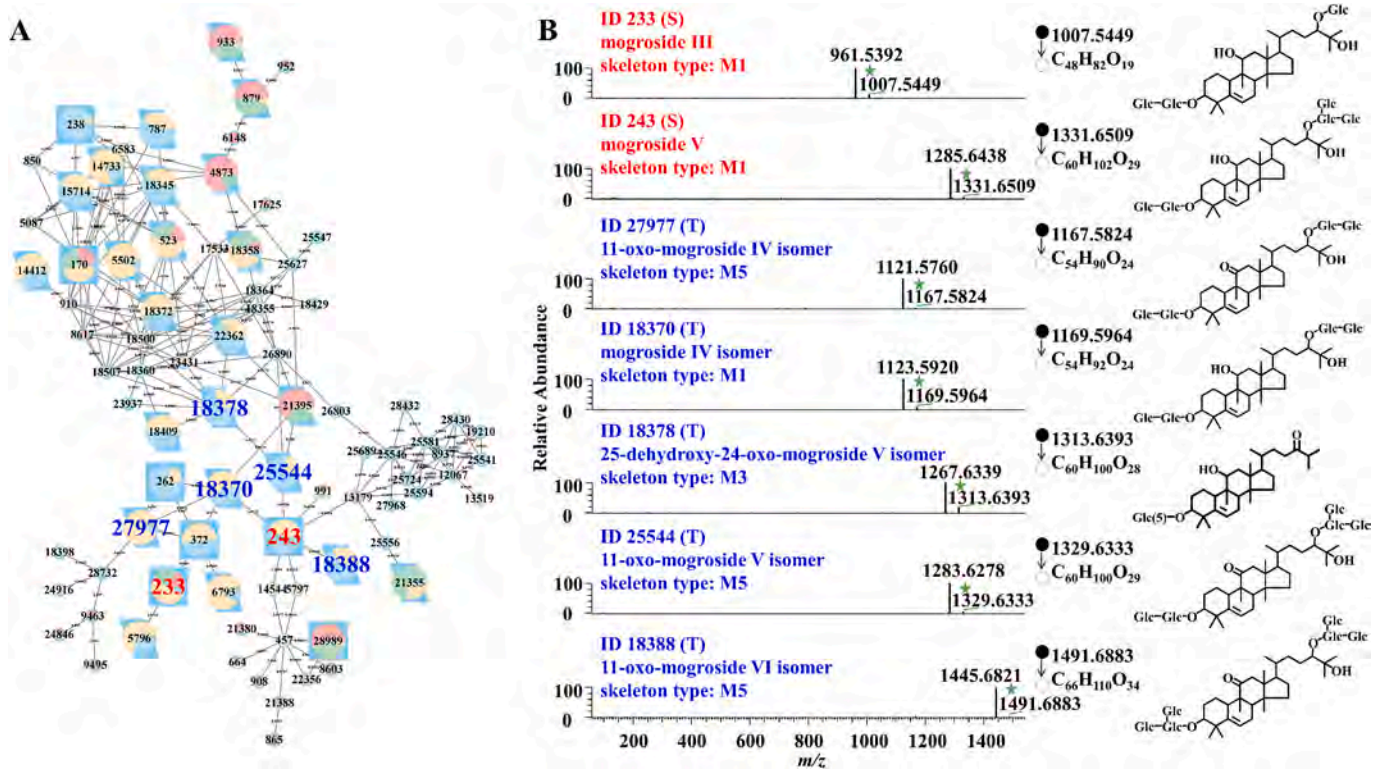


Fig. 3. (A) Submolecular network of *S. grosvenorii* metabolites. Rectangular nodes represent known mogroside reference standards, while parallelogram nodes correspond to mogrosides inferred from these standards. The unknown mogrosides (ID 27977, ID 18370, ID 18378, ID 25544, and ID 18388) were identified based on their structural similarity to reference standards (ID 233 and ID 243). Each pie chart illustrates the relative abundance of each compound at different developmental stages, with pink representing DAP15, green for DAP30, yellow for DAP50, and blue for DAP75. (B) MS/MS spectra of two known mogroside reference standards (mogroside III and mogroside V, labeled as "S") and five tentatively identified mogrosides (labeled as "T"). Peaks marked with an asterisk (*) indicate precursor ions. Representative structures are provided for the inferred mogrosides. (For interpretation of the references to colour in this figure legend, the reader is referred to the web version of this article.)

comprising 18 compounds confirmed by reference standards and 70 tentatively annotated based on HRMS and GNPS analysis. These correspond to 36 distinct molecular formulas derived from their *m/z* values. Based on their skeleton type, the 88 unique mogrosides are categorized as follows: 25 with M1 (mogrol), 3 with M2 (bryogenin), 10 with M3 (25-dehydroxy-24-oxo-mogrol), 13 with M4 (11-deoxy-mogrol), 20 with M5 (11-oxo-mogrol), 9 with M6 (7-oxo-mogrol), 1 with M7 (25-methoxy-mogrol), 6 with M8 (5α, 6α-epoxy-mogrol), and 1 with M9 (7*β*-methoxy-mogrol). In terms of glucosylation degree, the compounds were distributed as follows: 2 aglycones (no glucosyl units), 12 mono-glucosides, 20 di-glucosides, 16 tri-glucosides, 19 tetra-glucosides, 13 penta-glucosides, and 6 hexa-glucosides.

3.2. Spatiotemporal dynamics of metabolic profiles in S. grosvenorii

To investigate the metabolic dynamics of *S. grosvenorii* across different developmental stages, cultivation conditions, and cultivars, multivariate statistical analysis (PCA, OPLS-DA, and PCoA) was performed. The PCA and OPLS-DA analyses revealed significant differences in the metabolic profiles of wild-grown *S. grosvenorii* across different developmental stages (Fig. 5 and Fig. S5A, C). These differences were statistically supported by a PERMANOVA test based on the PCA distance matrix ($p < 0.05$, Fig. S5B). The OPLS-DA model exhibited strong explanatory and predictive power ($R^2 = 0.975$, $Q^2 = 0.965$), and the results of 200-time permutation testing confirmed the model's robustness and statistical reliability (Fig. S5D). The degree of separation observed in metabolic profiles closely correlates with the time intervals between developmental stages. Specifically, samples from adjacent developmental stages exhibited more similar profiles, while those from more widely separated stages displayed greater differences. Comparative analysis of cultivar L grown in wild and greenhouse conditions revealed significant differences in their metabolic profiles. Greenhouse-grown plants displayed more advanced metabolic characteristics, resembling those of older wild-grown plants, especially during early developmental stages. For instance, the metabolic profile of DAP15 greenhouse-grown plants was similar to that of DAP30 wild-grown plants. PCoA further confirmed consistent metabolic differences between wild-grown and greenhouse-grown cultivar L across all developmental stages ($p < 0.05$, Fig. S6A). Additionally, PCoA was used to compare the metabolic profiles of cultivars L and X. The results revealed significant differences during the early (DAP15) and late (DAP75) developmental stages ($p < 0.05$), but no significant differences were detected at mid-developmental stages (DAP30 and DAP50) ($p > 0.05$, Fig. S6B).

In the following, PCoA and HCA were performed to analyze the distribution of 88 identified mogrosides in *S. grosvenorii* across different developmental stages, cultivation conditions, and cultivars. The PCoA revealed significant differences in the metabolic profiles of mogrosides across developmental stages for all cultivars ($p < 0.05$, Fig. S7A). Notably, comparative analyses revealed significant metabolic divergence between wild-grown and greenhouse-grown cultivar L at all developmental stages ($p < 0.05$, Fig. S7B). Cultivars L and X exhibited distinct metabolic profiles at the late developmental stage ($p < 0.05$, DAP75), whereas no significant differences were observed between the two cultivars at the early (DAP15) and intermediate developmental stages ($p > 0.05$, DAP30 and DAP50) (Fig. S7C).

To further explore the distribution of mogrosides, we categorized the 88 identified mogrosides into two groups based on their glucosyl unit content: low-glucoside (0–3 glucosyl units) and high-glucoside (4–6 glucosyl units). HCA revealed that low-glucoside mogrosides were

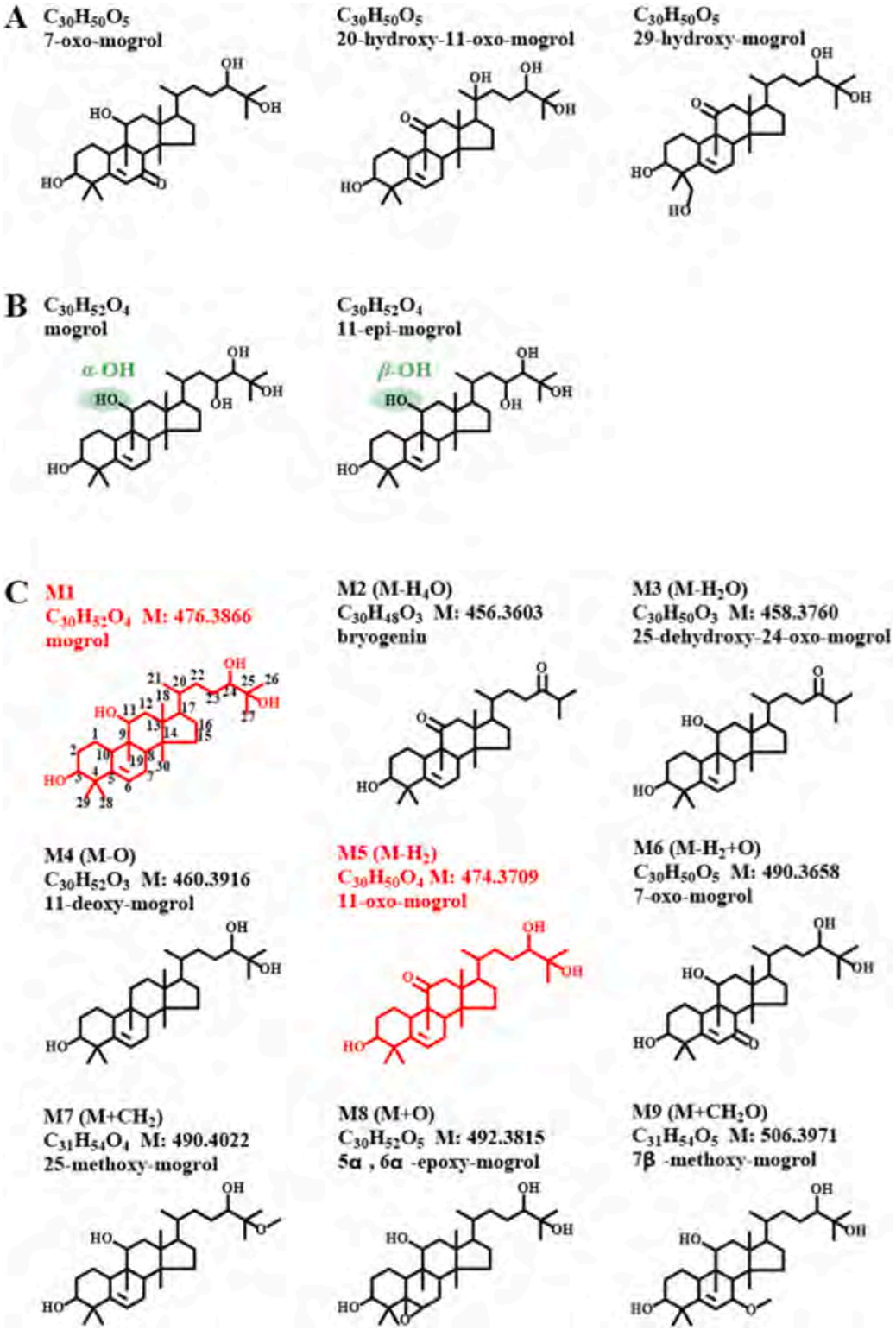


Fig. 4. (A) Three possible structures for the molecular formula $C_{30}H_{50}O_5$. (B) Two optical isomers for the molecular formula $C_{30}H_{52}O_4$. (C) Nine identified molecular formulas of tetracyclic triterpenoid skeletons (M1–M9) from *S. grosvenorii*, each paired with a representative structure. The two structures, M1 and M5, which match those in the 18 reference standards, are highlighted in red. The carbon sites in the tetracyclic triterpenoid skeleton are marked, with M1 (mogrol) used as an example. (For interpretation of the references to colour in this figure legend, the reader is referred to the web version of this article.)

predominantly found in early maturity fruits (DAP15 and DAP30), while high-glucoside mogrosides were mainly present in mid and late maturity fruits (DAP50 and DAP75) (Fig. 6). The HCA also revealed that mogroside distributions were more similar between samples from adjacent developmental stages. Specifically, the DAP15 and DAP30 samples formed one cluster, while the DAP50 and DAP75 samples formed another. This indicates a clear metabolic distinction between the early maturity and late maturity fruits.

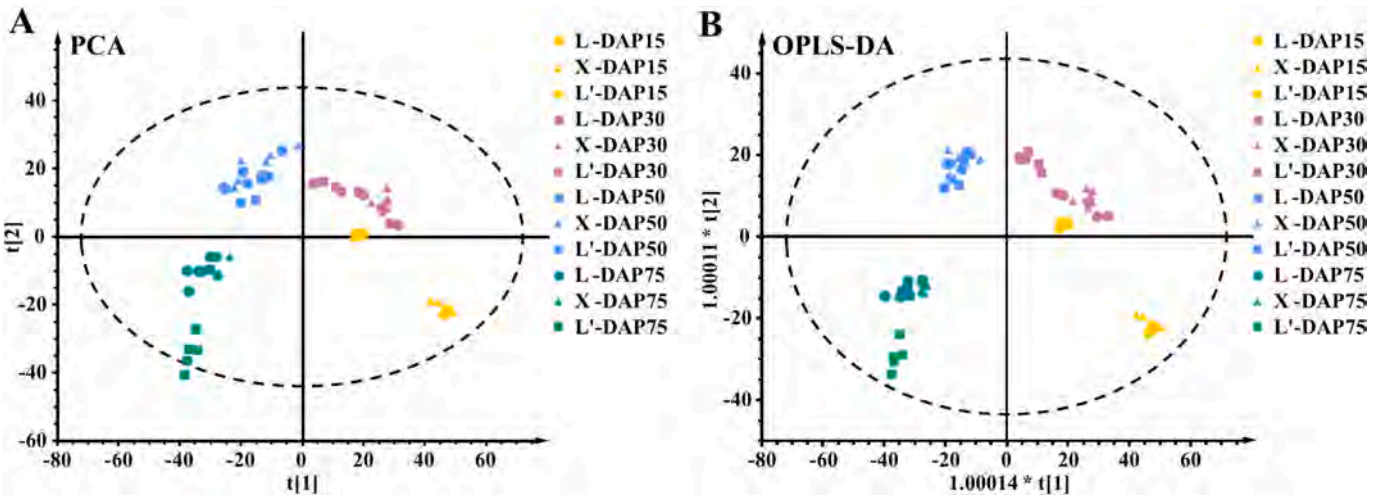


Fig. 5. (A) PCA and (B) OPLS-DA plots based on the metabolic profiling of *S. grosvenorii* at different developmental stages.

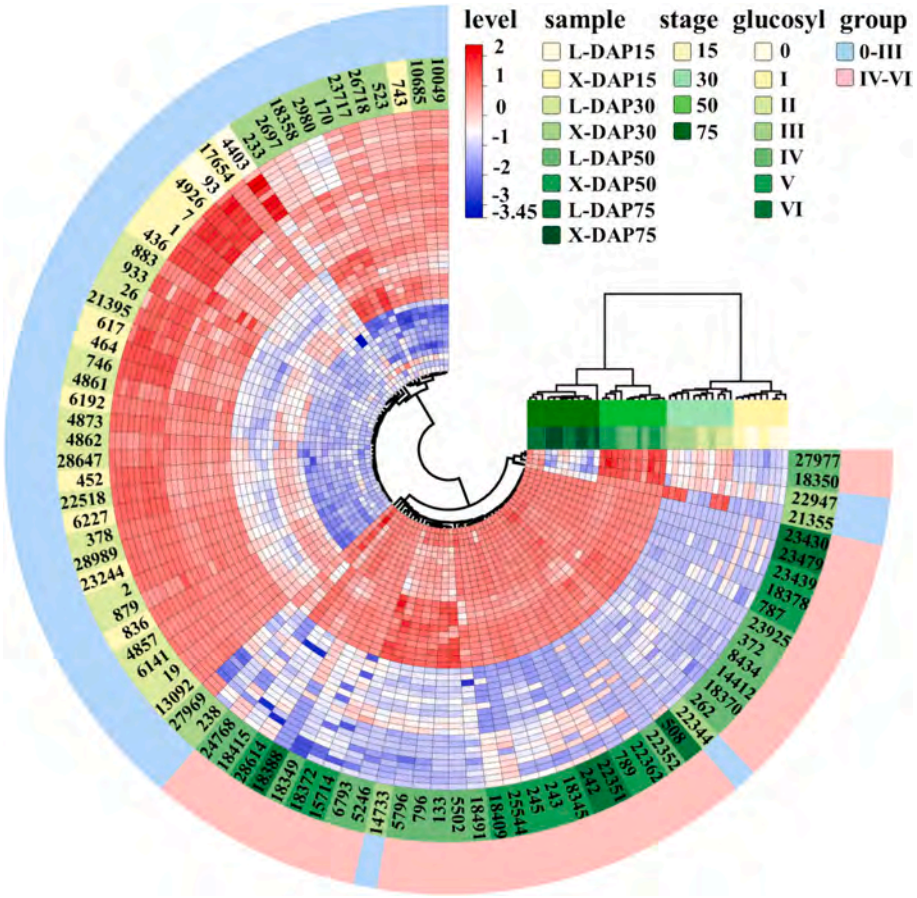


Fig. 6. HCA plot illustrating the distribution of identified mogrosides from *S. grosvenorii* across different developmental stages.

3.3. Spatiotemporal dynamics of mogroside content in S. grosvenorii

To quantitatively monitor changes in mogroside content during different developmental stages, cultivation conditions, and cultivars, calibration curves were constructed for 18 mogroside standards. These mogrosides were quantified directly using individual calibration curves prepared for each reference standard (Fig. S8A). For the remaining 70 inferred mogrosides lacking standards, an alternative calibration-by-proxy approach was employed. This method is based on the observed trend: except for MG, the ionization efficiency of mogrosides in ESI decreases as glucosyl units increase, while mogrosides containing the same glucosyl units exhibit relatively consistent ionization efficiencies (Fig. S9). This trend aligns with a previous report (Luo et al., 2016). Similar strategies have been documented in literature: Feng et al. (Feng et al., 2025) and Ling et al. (Ling et al., 2022), for example, used isotopically labeled internal standards with specific benzene ring counts to quantify quinones sharing the same ring count. Despite structural diversity, compounds with identical core structures often exhibit similar

ionization behavior (Wang, Wang, & Han, 2017), making calibration-by-proxy a practical alternative when individual standards or isotopic analogs are unavailable.

Accordingly, the 18 mogroside standards were grouped by glucosyl units, with the mean signal value for each group used to generate calibration curves. These curves estimated concentrations of inferred mogrosides with the same glucosyl unit count. For instance, a two-glucosyl-unit curve developed from five standards (11-O-IIA, IIA, IIA1, IIA2, and IIE) quantified 15 corresponding mogrosides across 70 samples. The resulting six calibration curves showed strong linearity (R^2: 0.9951–0.9999; *p*-values: 3.12×10^{-15}–2.41×10^{-9}) (Fig. S8B), indicating reliable fit and acceptable precision for quantifying mogrosides without available standards.

The total mogroside content peaked at DAP50, reaching 61.19 mg/g, which was significantly higher than at other developmental stages (Fig. 7A). However, highly glucosylated mogrosides such as mogroside V and mogroside VI peaked at DAP75, with levels of 11.26 mg/g and 1.04 mg/g, respectively (Fig. 7B). Throughout all developmental stages, the majority of the total mogroside content came from the 18 identified mogroside standards, while non-standard mogrosides contributed merely 23.13 %–29.59 % of the total content at each stage (Fig. 7B). For example, during the mature stage (DAP75), the predominant mogrosides were mogroside V, SI, and 11-O-V, which collectively accounted for 65.63 % of the total mogrosides. The variation in mogroside content based on glucosyl units followed a clear temporal pattern (Fig. 7C). At DAP15, early maturity fruits primarily contained mogrosides with two and three glucosyl units, at concentrations of 23.29 mg/g and 10.96 mg/g, respectively. By DAP30, the concentration of mogrosides with three glucosyl units increased to 16.82 mg/g, while those with two glucosyl units decreased to 19.06 mg/g. At DAP50, mogrosides with three, four, and five glucosyl units became the most abundant, with concentrations of 17.66 mg/g, 21.65 mg/g, and 16.85 mg/g, respectively. In the late maturity fruits at DAP75, mogrosides with five glucosyl units dominated, reaching a concentration of 21.65 mg/g. Meanwhile, those with four glucosyl units declined to 10.70 mg/g.

The progression of mogroside glucosylation revealed three distinct metabolic patterns during fruit development (Fig. S10). Low-glucosylation mogrosides (with one and two glucosyl units) showed a significant decrease ($p < 0.05$) in content prior to DAP50, indicating their early-stage predominance and subsequent metabolic conversion. Medium-glucosylation mogrosides (with three and four glucosyl units) exhibited a biphasic pattern. They showed a significant increase ($p < 0.05$) before DAP30, followed by a marked decrease ($p < 0.05$) from DAP50 to DAP75. This pattern suggests that they function as transitional metabolites during fruit development. The high-glucosylation mogrosides (with five and six glucosyl units) accumulated significantly ($p < 0.05$) between DAP30 and DAP50. Notably, mogrosides with six glucosyl units continued to increase significantly ($p < 0.05$) through DAP75, indicating sustained glucosylation activity for complex mogrosides during late maturation.

Comparative analysis of late-maturity fruits (DAP75) revealed significant variations in mogroside accumulation patterns across cultivation conditions and cultivars. Wild-grown cultivar L showed the highest total mogroside content (37.17 mg/g), significantly exceeding

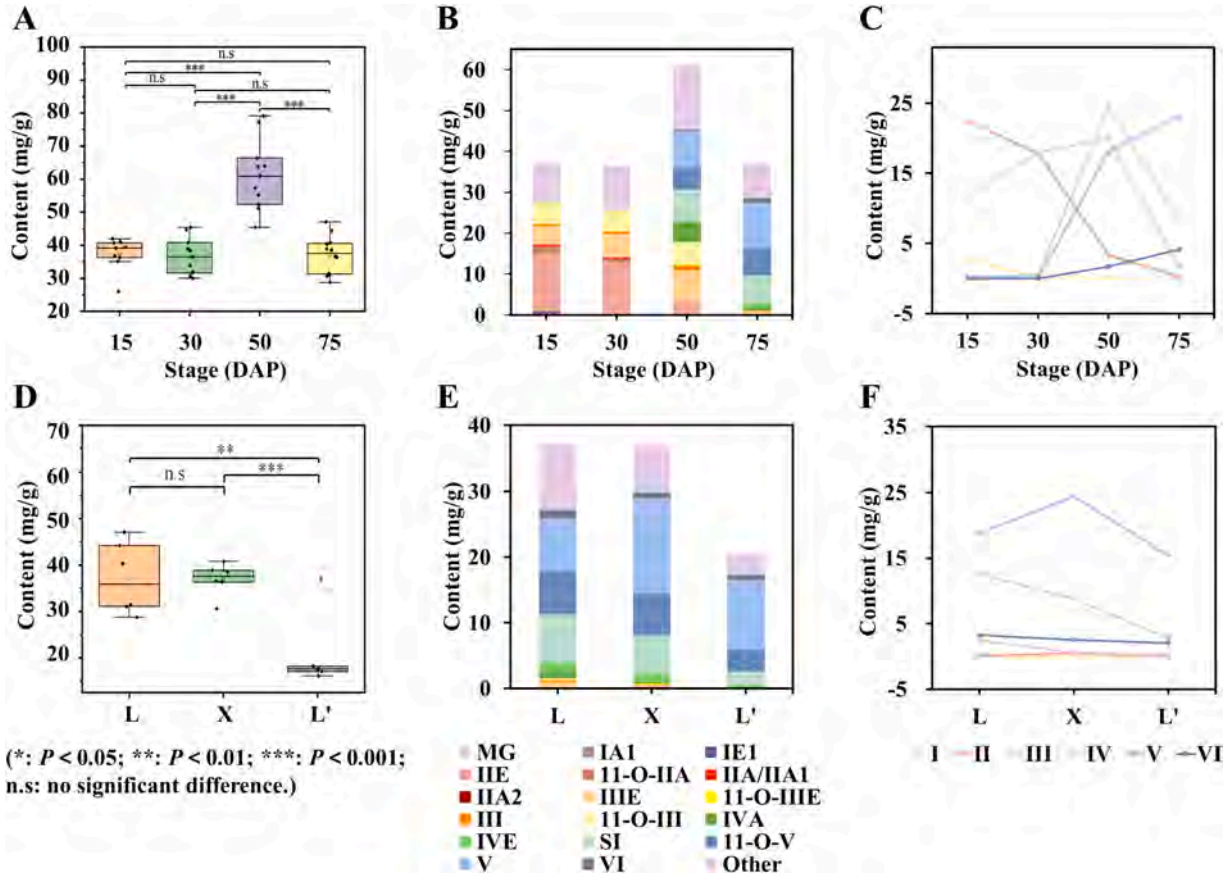


Fig. 7. Comparative analysis of mogroside distribution across developmental stages, cultivars, and growth environments. (A) Box plot showing the total mogroside content at four developmental stages (DAP15, DAP30, DAP50, and DAP75). (B) Stacked bar chart showing the composition of 18 mogroside reference standards and tentatively identified mogrosides across the developmental stages. (C) Line chart showing the distribution of mogrosides categorized by glucosyl units at each developmental stage. (D) Box plot showing the total mogroside content among different cultivars and growth environments (L, X, and L'). (E) Stacked bar chart showing the composition of 18 mogroside standards and tentatively identified mogrosides in L, X, and L'. (F) Line chart showing the distribution of mogrosides categorized by glucosyl units in L, X, and L'.

greenhouse-grown L' (20.59 mg/g, $p < 0.05$) while remaining comparable to wild-grown X (36.97 mg/g) (Fig. 7D). Interestingly, examination of individual mogrosides uncovered contrasting patterns. Despite its lower total content, cultivar L' accumulated 32.5 % more mogroside V (10.66 mg/g) than cultivar L (8.04 mg/g), with cultivar X demonstrating the highest mogroside V production (14.47 mg/g) (Fig. 7E). These differential patterns were also observed when analyzing mogrosides by the number of glucosyl units (Fig. S11). With five-glucosyl mogrosides as an example, cultivar X accumulated significantly higher levels than L' ($p < 0.05$), while showing comparable content to L (Fig. 7F and Fig. S11E).

4. Discussion

The combination of HRMS and molecular network analysis has significantly enhanced the high-throughput identification of unknown natural products. In our study, these advanced techniques identified 88 distinct mogrosides representing 9 unique tetracyclic triterpenoid skeletons. This finding substantially expands the known database of these compounds. This combined approach presents distinct advantages over conventional methods. Traditional approaches typically rely on targeted analyses using reference standards or a combination of isolation, purification, and spectroscopic techniques (Li et al., 2007; Shen et al., 2014). However, reference standards can only detect known compounds, which limits the discovery of novel mogrosides. Additionally, the isolation and purification steps are both labor-intensive and time-consuming processes. In contrast, HRMS coupled with molecular network analysis facilitates rapid, simultaneous identification of multiple unknown mogrosides, including low-abundance species that might otherwise remain undetected.

Like all analytical methods, this workflow has inherent limitations that warrant discussion. On the structural identification side, mass spectrometry inherently struggles to distinguish structural isomers (De Bruycker, Welle, Hirth, Blanksby, & Barner-Kowollik, 2020), making definitive structural assignment challenging. Although we could tentatively classify mogroside types based on accurate mass, characteristic MS/MS fragmentation, and retention time differences, their precise structures could not be confirmed. Further verification using nuclear magnetic resonance (NMR), chemical synthesis of standards, or other orthogonal techniques will be essential. Beyond identification, the quantification of mogrosides presents its own set of challenges and solutions. Our calibration-by-proxy approach offers practical utility for comprehensive metabolomic profiling but is not without constraints. Limitations arise from subtle structural variations beyond glucosyl unit count. Even among mogrosides sharing the same number of glucosyl units, ionization efficiencies may vary (Yang et al., 2023). It potentially compromises the accuracy of absolute quantification compared to analyses using individual authentic standards. Nonetheless, this method enabled both qualitative identification and quantification of numerous mogrosides that would otherwise be inaccessible due to the lack of commercial or synthesized standards. Importantly, this capability facilitated the identification of distinct accumulation patterns of mogrosides across developmental stages, cultivation environments, and cultivars of *S. grosvenorii*.

The accumulation of 88 distinct mogrosides during the developmental stages of *S grosvenorii* highlights the plant's dynamic biochemical changes throughout development. In early stages, the fruit predominantly contains simpler mogrosides with fewer glucosyl units. This aligns with the low glucosyl content observed at this stage. As the fruit matures, the glucosyl units gradually increase, supplying the necessary substrates for the synthesis of more complex mogrosides (Hong, Yang, Liu, Leong, & Chen, 2022). This biochemical transition shifts the dominant mogrosides: fewer glucosyl units dominate in early stages, whereas more glucosyl units accumulate at later stages (Lee, Salomon, Yu, & Jez, 2019). By full maturity, mogroside V–renowned for its intense sweetness–becomes the dominant component. The accumulation of intensely sweet mogrosides (e.g., mogroside V) in later stages reflects biochemical maturation. It may also represent an ecological adaptation. The increased accumulation of sweet mogrosides likely attracts animals, thereby promoting seed dispersal and reproduction in *S. grosvenorii* (Stevenson, Nicolson, & Wright, 2017).

The total mogroside content reported in this study at maturity (20.59–37.17 mg/g) aligns with the range of 30–40 mg/g reported in previous literature (Wang et al., 2019). The 18 mogroside reference standards comprised 70–90 % of total mogrosides across all developmental stages. The remaining 70 compounds occurred at significantly lower concentrations. From DAP50 to maturity (DAP75), the levels of highly glucosylated mogrosides (e.g., mogroside V and 11-oxo-mogroside V) increased. However, this period also saw a decrease in overall mogroside content, consistent with published literature reports (Qing et al., 2017). This indicates that incomplete conversion of the low glucosylated mogrosides to their highly glucosylated counterparts occurs during fruit maturation. Instead, some of these low glucosylated mogrosides likely undergo metabolic transformations. These processes, including hydroxylation (Zhang et al., 2008), oxidation (Miettinen et al., 2017), and sulfation (Kanwal, Adhikari, Hameed, Hafizur, & Musharraf, 2017), lead to the formation of other compounds.

The cultivation environments are pivotal factors in determining the metabolism of *S. grosvenorii*, particularly its mogroside V content. In greenhouse environments, key factors such as light intensity, temperature, water availability, and soil composition are carefully controlled. This optimization promotes plant growth and accelerates fruit maturation. The controlled setting shortens the cultivation period, reducing production costs while maintaining mogroside V levels. In contrast, wild environments face fluctuating temperatures, varying photoperiods, and limited soil nutrients. These conditions prolong the maturation period. However, these environmental stresses also drive metabolic shifts. Specifically, lower nutrient availability—particularly nitrogen deficiency—shifts plant metabolism toward the production of secondary metabolites (Zhang et al., 2023). This prioritizes compounds such as mogrosides over growth-related primary metabolic processes. Additionally, environmental stressors such as ultraviolet radiation, temperature fluctuations, and drought elevate ROS levels (Gill & Tuteja, 2010). These elevated ROS levels can accelerate the conversion of mogroside V to 11-oxo-mogroside V. As a result, wild-grown *S. grosvenorii* tends to accumulate a broader range of mogrosides, resulting in a higher total mogroside content compared to greenhouse-grown plants.

In addition to environmental factors, genetic variations among cultivars also significantly influence mogroside accumulation. For example, during maturation, cultivar X accumulates higher levels of mogrosides with five glucosyl units relative to cultivar L. This includes particularly high levels of mogroside V. This difference likely stems from genetic variations that regulate mogroside biosynthesis enzymes, particularly glycosyltransferases. These include UDP-glucosyltransferases, which are identified as key enzymes in mogroside biosynthesis (Itkin et al., 2016). These enzymes control the attachment of glucose molecules to the triterpene aglycone, a critical step in the formation of glucosylated mogrosides as characterized in the biosynthetic pathway analysis (Chen et al., 2024; Itkin et al., 2016). These genetic variations may lead to increased activity of glycosyltransferases in cultivar X, resulting in higher levels of highly glucosylated mogrosides like mogroside V. Therefore, genetic differences between cultivars X and L are likely a key contributing factor to the observed variation in mogroside accumulation.

5. Conclusions

In this study, non-targeted metabolomics combined with molecular networking enabled the systematic identification of 88 mogrosides in *S. grosvenorii*. These compounds span nine distinct tetracyclic triterpene skeletons, offering a comprehensive overview of mogroside diversity. This work lays a solid foundation for the future discovery of novel mogrosides, supported by complementary structural elucidation

techniques such as NMR and infrared spectroscopy to resolve structural ambiguities. Our results reveal that mogroside composition and content are significantly influenced by developmental stage, cultivar genotype, and cultivation conditions. As the fruit matures, low-glucosylated mogrosides undergo sequential glucosylation, culminating in a peak of five- and six-glucosylated forms around DAP75. Greenhouse cultivation was found to accelerate fruit development and promote mogroside V accumulation in cultivar L, whereas cultivar X exhibited higher mogroside V levels at physiological maturity. These findings offer valuable insights for optimizing cultivation strategies to enhance mogroside yield and sweetness in *S. grosvenorii*.

CRediT authorship contribution statement

Jiying Pei: Writing – review & editing, Writing – original draft, Project administration, Investigation, Funding acquisition, Formal analysis, Conceptualization. **Qiong Su:** Writing – original draft, Validation, Software, Methodology, Investigation, Formal analysis. **Shuiyuan Jiang:** Resources, Funding acquisition. **Jianxiu Li:** Supervision, Project administration, Funding acquisition, Conceptualization. **Nengzhong Xie:** Supervision, Project administration, Funding acquisition.

Declaration of competing interest

The authors declare the following financial interests/personal relationships which may be considered as potential competing interests: Reports a relationship with that includes: Has patent pending to. If there are other authors, they declare that they have no known competing financial interests or personal relationships that could have appeared to influence the work reported in this paper.

Acknowledgements

This work was supported by the Guangxi Science and Technology Major Program (GuikeAA24206051), Guangxi Natural Science Foundation (2023GXNSFAA026488), National Natural Science Foundation of China (32260245, 22264003), Guangxi Science and Technology Major Program (GuikeAA22117015-3), Central Guidance Fund for Local Scientific and Technological Development Program (ZY23055011), Guangxi Key Technologies R&D Program (AB21238011), Innovation and Science Foundation Program of Guangxi Academy of Sciences (2024YGFZ505-904).

Appendix A. Supplementary data

Supplementary data to this article can be found online at https://doi.org/10.1016/j.foodchem.2025.146185.

Data availability

Data will be made available on request.

References

Chen, H., Quynh, N. N., Akida, A., Ra, M. J., Jung, S. M., Yu, J. N., … Kim, K. H. (2023). Global natural products social (GNPS)-based molecular-networking-guided isolation of phenolic compounds from *Ginkgo biloba* fruits and the identification of estrogenic phenolic glycosides. *Plants, 12*(23), 3970. https://doi.org/10.3390/plants12233970

Chen, W. Q., Lin, X. D., Wang, Y., Mu, D. T., Mo, C. M., Huang, H. X., … Tang, Q. (2024). Selection of reference genes in *Siraitia siamensis* and expression patterns of genes involved in mogrosides biosynthesis. *Plants, 13*(17), 2449. https://doi.org/10.3390/plants13172449

Chen, W. J., Wang, J., Qi, X. Y., & Xie, B. J. (2007). The antioxidant activities of natural sweeteners, mogrosides, from fruits of *Siraitia grosvenori*. *International Journal of Food Sciences and Nutrition, 58*(7), 548–556. https://doi.org/10.1080/09637480701336360

Cui, S. R., Zang, Y. M., Xie, L., Mo, C. M., Su, J. X., Jia, X. L., … Ma, X. J. (2023). Post-ripening and key glycosyltransferase catalysis to promote sweet mogrosides accumulation of *Siraitia grosvenorii* fruits. *Molecules, 28*, 4697. https://doi.org/10.3390/molecules28124697

De Bruycker, K., Welle, A., Hirth, S., Blanksby, S. J., & Barner-Kowollik, C. (2020). Mass spectrometry as a tool to advance polymer science. *Nature Reviews Chemistry, 4*(5), 257–268. https://doi.org/10.1038/s41570-020-0168-1

Dong, F., Song, J. R., Fu, C. M., Huang, X. Y., Yang, X. R., Lu, F. L., & Li, D. P. (2025). Spatial variability and climate response characteristics of the chemical components in *Siraitia grosvenorii* (Luo Han Guo). *Industrial Crops and Products, 228*, Article 120897. https://doi.org/10.1016/j.indcrop.2025.120897

Feng, L. L., Tan, S. Y., Cheng, S. M., Feng, H. R., Xie, Z. H., Fang, X., … Dai, X. H. (2025). Rapid and sensitive detection of quinones by in-source microdroplet derivatization coupled with mass spectrometry. *Analytical Chemistry, 97*(18), 9771–9778. https://doi.org/10.1021/acs.analchem.4c06780

Ge, Y. W., Zhu, S., Yoshimatsu, K., & Komatsu, K. (2017). MS/MS similarity networking accelerated target profiling of triterpene saponins in *Eleutherococcus senticosus* leaves. *Food Chemistry, 227*, 444–452. https://doi.org/10.1016/j.foodchem.2017.01.119

Gill, S. S., & Tuteja, N. (2010). Reactive oxygen species and antioxidant machinery in abiotic stress tolerance in crop plants. *Plant Physiology and Biochemistry, 48*(12), 909–930. https://doi.org/10.1016/j.plaphy.2010.08.016

Gong, X., Chen, N. M. H., Ren, K., Jia, J. Y., Wei, K. H., Zhang, L., … Li, M. H. (2019). The fruits of *Siraitia grosvenorii*: A review of a Chinese food-medicine. *Frontiers in Pharmacology, 10*, 1400. https://doi.org/10.3389/fphar.2019.01400

Guo, Q. H., Shi, M. K., Sarengaowa, Xiao, Z. W., Xiao, Y., & Feng, K. (2024). Recent advances in the distribution, chemical composition, health benefits, and application of the fruit of *Siraitia grosvenorii*. *Foods, 13*(14), 2278. https://doi.org/10.3390/foods13142278

Hong, H. J., Yang, Q., Liu, Q., Leong, F., & Chen, X. J. (2022). Chemical comparison of monk fruit products processed by different drying methods using high-performance thin-layer chromatography combined with chemometric analysis. *Frontiers in Nutrition, 9*, Article 887992. https://doi.org/10.3389/fnut.2022.887992

Huang, H. X., Peng, Z., Zhan, S., Li, W., Liu, D., Huang, S., … Wang, W. (2024). A comprehensive review of *Siraitia grosvenorii* (Swingle) C. Jeffrey: Chemical composition, pharmacology, toxicology, status of resources development, and applications. *Frontiers in Pharmacology, 15*, Article 1388747. https://doi.org/10.3389/fphar.2024.1388747

Itkin, M., Davidovich-Rikanati, R., Cohen, S., Portnoy, V., Doron-Faigenboim, A., Oren, E., … Schaffer, A. (2016). The biosynthetic pathway of the nonsugar, high-intensity sweetener mogroside V from *Siraitia grosvenorii*. *Proceedings of the National Academy of Sciences of the United States of America, 113*(47), E7619–E7628. https://doi.org/10.1073/pnas.1604828113

Jia, Z. H., & Yang, X. G. (2009). A minor, sweet cucurbitane glycoside from *Siraitia grosvenorii*. *Natural Product Communications, 4*(6), 769–772. https://doi.org/10.1177/1934578x0900400606

Kanwal, N., Adhikari, A., Hameed, A., Hafizur, R. M., & Musharraf, S. G. (2017). Isolation and characterization of non-sulfated and sulfated triterpenoid saponins from *Fagonia indica*. *Phytochemistry, 143*, 151–159. https://doi.org/10.1016/j.phytochem.2017.08.005

Lee, S. G., Salomon, E., Yu, O., & Jez, J. M. (2019). Molecular basis for branched steviol glucoside biosynthesis. *Proceedings of the National Academy of Sciences of the United States of America, 116*(26), 13131–13136. https://doi.org/10.1073/pnas.1902104116

Li, C., Lin, L. M., Sui, F., Wang, Z. M., Huo, H. R., Dai, L., & Jiang, T. L. (2014). Chemistry and pharmacology of *Siraitia grosvenorii*: A review. *Chinese Journal of Natural Medicines, 12*(2), 89–102. https://doi.org/10.1016/S1875-5364(14)60015-7

Li, D. P., Ikeda, T., Huang, Y. L., Liu, J. L., Nohara, T., Sakamoto, T., & Nonaka, G. I. (2007). Seasonal variation of mogrosides in Lo Han Kuo (*Siraitia grosvenori*) fruits. *Journal of Natural Medicines, 61*(3), 307–312. https://doi.org/10.1007/s11418-006-0130-7

Li, D. P., Ikeda, T., Matsuoka, N., Nohara, T., Zhang, H., Sakamoto, T., & Nonaka, G. I. (2006). Cucurbitane glycosides from unripe fruits of Lo Han Kuo (*Siraitia grosvenori*). *Chemical and Pharmaceutical Bulletin, 54*(10), 1425–1428. https://doi.org/10.1248/cpb.54.1425

Li, Y. Q., Kong, D. X., Fu, Y., Sussman, M. R., & Wu, H. (2020). The effect of developmental and environmental factors on secondary metabolites in medicinal plants. *Plant Physiology and Biochemistry, 148*, 80–89. https://doi.org/10.1016/j.plaphy.2020.01.006

Ling, C., Shi, Q. F., Wei, Z. P., Zhang, J. J., Hu, J. J., & Pei, J. Y. (2022). Rapid analysis of quinones in complex matrices by derivatization-based wooden-tip electrospray ionization mass spectrometry. *Talanta, 237*, Article 122912. https://doi.org/10.1016/j.talanta.2021.122912

Lu, R. H., Hu, J. H., Liu, X. X., Yu, L. J., Hu, J. J., Jiang, H. M., … Liang, X. W. (2023). Mogroside-rich extract from *Siraitia grosvenorii* fruits protects against heat stress-induced intestinal damage by ameliorating oxidative stress and inflammation in mice. *Food & Function, 14*(2), 1238–1247. https://doi.org/10.1039/d2fo02179j

Luo, Z. L., Shi, H. W., Zhang, K. L., Qin, X. J., Guo, Y. H., & Ma, X. J. (2016). Liquid chromatography with tandem mass spectrometry method for the simultaneous determination of multiple sweet mogrosides in the fruits of *Siraitia grosvenorii* and its marketed sweeteners. *Journal of Separation Science, 39*(21), 4124–4135. https://doi.org/10.1002/jssc.201600563

Miettinen, K., Pollier, J., Buyst, D., Arendt, P., Csuk, R., Sommerwerk, S., … Goossens, A. (2017). The ancient CYP716 family is a major contributor to the diversification of eudicot triterpenoid biosynthesis. *Nature Communications, 8*, Article 14153. https://doi.org/10.1038/ncomms14153

Nothias, L. F., Petras, D., Schmid, R., Dührkop, K., Rainer, J., Sarvepalli, A., … Dorrestein, P. C. (2020). Feature-based molecular networking in the GNPS analysis

environment. *Nature Methods, 17*, 905–908. https://doi.org/10.1038/s41592-020-0933-6

Prakash, I., & Chaturvedula, V. S. P. (2014). Additional new minor cucurbitane glycosides from *Siraitia grosvenorii*. *Molecules, 19*(3), 3669–3680. https://doi.org/10.3390/molecules19033669

Qiao, J., Luo, Z. L., Gu, Z., Zhang, Y. L., Zhang, X. D., & Ma, X. J. (2019). Identification of a novel specific cucurbitadienol synthase allele in *Siraitia grosvenorii* correlates with high catalytic efficiency. *Molecules, 24*(3), 627. https://doi.org/10.3390/molecules24030627

Qing, Z. X., Zhao, H., Tang, Q., Mo, C. M., Huang, P., Cheng, P., … Zhang, J. G. (2017). Systematic identification of flavonols, flavonol glycosides, triterpene and siraitic acid glycosides from *Siraitia grosvenorii* using high-performance liquid chromatography/quadrupole-time-of-flight mass spectrometry combined with a screening strategy. *Journal of Pharmaceutical and Biomedical Analysis, 138*, 240–248. https://doi.org/10.1016/j.jpba.2017.01.059

Shen, Y., Lin, S. J., Han, C., Zhu, Z. O., Hou, X. D., Long, Z., & Xu, K. L. (2014). Rapid identification and quantification of five major mogrosides in *Siraitia grosvenorii* (Luo-Han-Guo) by high performance liquid chromatography–triple quadrupole linear ion trap tandem mass spectrometry combined with microwave-assisted extraction. *Microchemical Journal, 116*, 142–150. https://doi.org/10.1016/j.microc.2014.04.014

Stevenson, P. C., Nicolson, S. W., & Wright, G. A. (2017). Plant secondary metabolites in nectar: Impacts on pollinators and ecological functions. *Functional Ecology, 31*(1), 65–75. https://doi.org/10.1111/1365-2435.12761

Utami, M. M. D., Dewi, A. C., Hertamawati, R. T., Hariono, B., Zhuo, J., & Yong, T. (2024). Nutritional composition of monk fruit (*Siraitia grosvenorii*) as a candidate yogurt sweetener. *IOP Conference Series: Earth and Environmental Science, 1338*(1), 12021. https://doi.org/10.1088/1755-1315/1338/1/012021

Wang, B., Yang, Z., Xin, Z. Q., Ma, G., Qian, Y., Xie, T. P., & Prakash, I. (2019). Analysis of mogrosides in *Siraitia grosvenorii* fruits at different stages of maturity. *Natural Product Communications, 14*(9). https://doi.org/10.1177/1934578X19878621

Wang, M., Wang, C. Y., & Han, X. L. (2017). Selection of internal standards for accurate quantification of complex lipid species in biological extracts by electrospray ionization mass spectrometry-what, how and why? *Mass Spectrometry Reviews, 36*(6), 693–714. https://doi.org/10.1002/mas.21492

Wang, M. X., Carver, J. J., Phelan, V. V., Sanchez, L. M., Garg, N., Peng, Y., … Bandeira, N. (2016). Sharing and community curation of mass spectrometry data with global natural products social molecular networking. *Nature Biotechnology, 34*(8), 828–837. https://doi.org/10.1038/nbt.3597

Wang, Y. J., Yang, J., Li, X. N., Bai, H., Luo, J. F., He, Z. R., & Wang, Y. H. (2022). Cucurbitane-type triterpenoids from the branches and leaves of *Elaeocarpus sylvestris*. *Phytochemistry Letters, 51*, 39–45. https://doi.org/10.1016/j.phytol.2022.06.012

Wu, J. J., Jian, Y. Q., Wang, H. Z., Huang, H. X., Gong, L. M., Liu, G. G., … Wang, W. (2022). A review of the phytochemistry and pharmacology of the fruit of *Siraitia grosvenorii* (Swingle): A traditional Chinese medicinal food. *Molecules, 27*(19), 6618. https://doi.org/10.3390/molecules27196618

Xia, Y., Rivero-Huguet, M. E., Hughes, B. H., & Marshall, W. D. (2008). Isolation of the sweet components from *Siraitia grosvenorii*. *Food Chemistry, 107*(3), 1022–1028. https://doi.org/10.1016/j.foodchem.2007.09.014

Xue, X. X., Jiao, Q. S., Jin, R. N., Wang, X. Y., Li, P. Y., Shi, S. G., … Chen, S. L. (2021). The combination of UHPLC-HRMS and molecular networking improving discovery efficiency of chemical components in Chinese classical formula. *Chinese Medicine, 16*(1), 50. https://doi.org/10.1186/s13020-021-00459-6

Yang, L., Wen, K. S., Ruan, X., Zhao, Y. X., Wei, F., & Wang, Q. (2018). Response of plant secondary metabolites to environmental factors. *Molecules, 23*(4), 762. https://doi.org/10.3390/molecules23040762

Yang, X. R., Xu, F., Lu, F. L., He, W., Song, J. R., Yan, X. J., … Li, D. P. (2023). Metabolism of two mogroside isomers, mogroside III and mogroside IIIE, in normal and drug-metabolizing enzyme-induced rats. *Journal of Agricultural and Food Chemistry, 71*(51), 20735–20750. https://doi.org/10.1021/acs.jafc.3c07938

Zhang, W. J., Zhang, T., Zhang, J., Lei, W. W., Zhao, L., Wang, S., … Wei, M. (2023). Low nitrogen stress promotes root nitrogen uptake and assimilation in strawberry: Contribution of hormone networks. *Horticulturae, 9*(2), 249. https://doi.org/10.3390/horticulturae9020249

Zhang, Z. Z., Li, S. Y., Ownby, S., Wang, P., Yuan, W., Zhang, W. L., … Beasley, R. S. (2008). Phenolic compounds and rare polyhydroxylated triterpenoid saponins from *Eryngium yuccifolium*. *Phytochemistry, 69*(10), 2070–2080. https://doi.org/10.1016/j.phytochem.2008.03.020

Environmental Chemistry and Ecotoxicology 7 (2025) 2544–2555

Contents lists available at ScienceDirect

Environmental Chemistry and Ecotoxicology

journal homepage: www.keaipublishing.com/en/journals/environmental-chemistry-and-ecotoxicology/

Research Paper

Emerging microplastic and nanoplastic threats: Decoding winter survival mechanisms in hybrid groupers through hepatic metabolic disruption☆

Julong Wang [a,f], Yan Gao [b], Shanshan Yao [a,f], Lang Lin [c,*], Hengxiang Li [a], Shan Liu [d], Rui Hou [e], Zhijian Jiang [a], Xiangrong Xu [d,*]

[a] Guangdong Provincial Key Laboratory of Applied Marine Biology, South China Sea Institute of Oceanology, Chinese Academy of Sciences, Guangzhou 510301, China
[b] Institute of Environmental Research at Greater Bay Area, Key Laboratory for Water Quality and Conservation of the Pearl River Delta, Ministry of Education, Guangzhou University, Guangzhou 510006, China
[c] South China Sea Sea Area and Island Center (South China Sea Standard Measurement and Information Center), Ministry of Natural Resources, Guangzhou 510310, China
[d] Guangxi Laboratory on the Study of Coral Reefs in the South China Sea, Coral Reef Research Center of China, School of Marine Sciences, Guangxi University, Nanning 530004, China
[e] Guangdong Provincial Key Laboratory of Water Quality Improvement and Ecological Restoration for Watersheds, School of Ecology, Environment and Resources, Guangdong University of Technology, Guangzhou 510006, China
[f] University of Chinese Academy of Sciences, Beijing 100049, China

ARTICLE INFO

Keywords:
Nanoplastics
Lipids metabolism
Oxidative stress
Transcriptomics
Quantitative analysis

ABSTRACT

This study explores the impact of microplastics (MPs) and nanoplastics (NPs) on hepatic lipid metabolism in *pearl gentian grouper* (*Epinephelus fuscoguttatus*♀ × *Epinephelus lanceolatus*♂) during overwintering and elucidates the underlying mechanisms. Fish were exposed to polystyrene (PS) MPs and NPs of varying sizes (5 μm, 500 nm, and 50 nm) for a 15-day exposure period. Histopathological analysis, oxidative stress assessment, and gene expression profiling related to lipid metabolism revealed significant toxic effects on the liver. Results showed that NPs preferentially accumulated in the liver, causing hepatocyte swelling, inflammation, and lipid metabolism disorders. Smaller particle sizes intensified oxidative stress, reduced triglyceride (TG) content, and elevated low-density lipoprotein cholesterol (LDL-C) and total cholesterol (T-CHO) levels. Transcriptomic analysis indicated that MPs and NPs altered the expression of lipid metabolism genes, particularly those in glyceride metabolism and lipolysis pathways, with significant upregulation of *PNPLA2* and *LIPG* ($p < 0.05$) under cold stress. This led to excessive energy reserve depletion and hepatic lipid metabolism dysfunction. This study establishes a "environmental stress-gene-metabolism" response model and provides novel insights into the molecular mechanisms by which NPs disrupt lipid homeostasis in aquatic organisms, offering a theoretical basis for understanding the toxicological effects of emerging contaminants.

1. Introduction

Plastics are widely used due to their exceptional material properties [1]; however, they present significant environmental challenges. In 2023, global plastic production reached 400 million metric tons [2], with forecasts predicting an increase to 1.48 billion metric tons by 2050 [3]. Over 90 % of plastic waste is not adequately recycled, and approximately 10 % of terrestrial plastic debris enters marine ecosystems, constituting about 85 % of total marine litter [4]. Within marine environments, plastics undergo degradation through physical, chemical, and biological processes [5,6], resulting in the formation of microplastics (MPs, <5 mm) and nanoplastics (NPs, <100 nm) [7,8]. These particles have been identified in seawater, sediments, and marine organisms [9,10]. MPs and NPs can release harmful additives, such as phthalates and bisphenol A [3], and adsorb heavy metals and persistent organic pollutants [11,12]. Extensive research has demonstrated that MPs and NPs exhibit bioaccumulative potential and toxicological effects, presenting substantial risks to ecosystems and human health through food chain transfer [13].

MPs and NPs can accumulate in organisms, triggering toxic effects

☆ This article is part of a Special issue entitled: 'Persistent toxic substances' published in Environmental Chemistry and Ecotoxicology.

* Corresponding authors.
E-mail addresses: linlauncer@126.com (L. Lin), xuxr@gxu.edu.cn (X. Xu).

https://doi.org/10.1016/j.enceco.2025.07.021
Received 25 May 2025; Received in revised form 30 June 2025; Accepted 26 July 2025
Available online 6 August 2025
2590-1826/© 2024 The Authors. Publishing services by Elsevier B.V. on behalf of KeAi Communications Co. Ltd. CC BY 4.0 This is an open access article under the CC BY license (http://creativecommons.org/licenses/by/4.0/).

such as gastrointestinal obstruction, metabolic dysregulation, reproductive system abnormalities, and changes in biochemical parameters [14]. The liver, as the central metabolic and secretory organ of the digestive system, plays a critical role in protein synthesis, nutrient metabolism, xenobiotic detoxification, and immune regulation [15]. Upon internalization of MPs and NPs into organisms, these particles elicit a compensatory response, marked by the upregulation of genes such as the sodium/potassium-transporting ATPase subunit alpha-4 (*Atp1a4*) and the calcium-activated chloride channel regulator 3 A-1 (*Clca3a1*). This response enhances cellular energy metabolism and chloride homeostasis to mitigate the disruptions caused by MPs [16]. A substantial body of experimental evidence demonstrates that MPs and NPs exert significant toxic effects on the liver of marine organisms. Research has shown that exposure to MPs and NPs can induce pathological changes in liver tissue, including hepatocyte swelling, inflammatory cell infiltration, and structural damage [17]. At the molecular level, temporary exposure to MPs or NPs can activate the unfolded protein response, specifically through the PERK-Eif2a signaling pathway, leading to oxidative stress in the liver. This, in turn, results in lipid accumulation and hepatocyte degeneration [18]. Additionally, animal studies have confirmed that exposure to MPs and NPs significantly alters the expression of genes involved in lipid metabolism, including key regulatory factors such as PPAR, SREBP1, and AMPK [19].

Compared to MPs, NPs exhibit significantly higher bioaccumulation potential in hepatic tissue. Quantitative analyses in both fish and mammalian models consistently show a greater accumulation of NPs in the liver than MPs, likely due to their smaller size and increased cellular uptake efficiency [20]. This heightened accumulation and greater "availability" of NPs result in more severe hepatic injury, including inflammatory responses, oxidative stress, dysregulation of lipid metabolism (such as hepatic steatosis), and, in some cases, progression to cirrhosis and fibrosis [18,21]. These differences underscore the critical role of particle size in determining the toxicity of MPs and NPs [22,23]. Compared to MPs, NPs possess a smaller size and a larger specific surface area, which enable them to more readily penetrate biological barriers, such as the gaps between intestinal epithelial cells or gill mucosa, and reach the liver via the bloodstream [24]. The increased bioavailability of NPs enhances their interaction with cellular membranes, inducing endoplasmic reticulum stress and mitochondrial dysfunction. Consequently, this results in increased oxidative stress and inflammation [25]. These properties account for the typically greater toxicity of NPs compared to MPs at the same exposure levels [26].

Current toxicological research predominantly focuses on model organisms (such as *zebrafish* and *tilapia*), with a notable scarcity of studies on fish species of high economic importance. Taking the *pearl gentian grouper* as an example, this species accounts for over 70 % of China's total grouper aquaculture production [27]. In 2022, China's grouper farming output reached 205,800 tons, ranking it as the third largest marine aquaculture fish species and establishing it as a vital economic species in the southeastern coastal regions. Given the widespread presence and ingestion of MPs and NPs in marine environments [28], the *pearl gentian grouper* inevitably becomes a carrier of these contaminants [29,30]. The toxicity study of MPs and NPs for this species has not been reported in a systematic study, and its key scientific issues such as bioaccumulation patterns and molecular toxicological mechanisms need to be carried out urgently. Accordingly, the aim of this study is to investigate the transfer patterns of MPs and NPs in the *pearl gentian grouper*, and focus on the mechanism of NPs on hepatic lipid metabolism in *pearl gentian grouper*. Combined with histopathological analysis, oxidative stress indicators, biochemical parameters, and transcriptome analysis of lipid metabolism related genes, we systematically evaluate the interfering effects of NPs on hepatic lipid metabolism and its potential molecular mechanisms.

2. Methods

2.1. Materials and chemicals

In this study, spherical PS MPs and NPs with particle sizes of 5 μm, 500 nm, and 50 nm were utilized. These samples were procured from Jiangsu Zhichuan Technology Co., Ltd. (Jiangsu, China). The stock solutions of PS MPs and NPs were stored at 4 °C and subjected to ultrasonication for 30 min prior to use to ensure uniform dispersion of the particles. The morphological characteristics and dimensions of PS MPs and NPs were analyzed using a desktop scanning electron microscope (SEM, JSM-7800F, TESCAN, Czech) and a transmission electron microscope (TEM, TF30, JEOL Ltd., Japan). Particle size distribution is quantified by laser diffraction for MPs (Microtrac S3500, Malvern Instruments, England) and dynamic light scattering (DLS, Malvern Zetasizer Nano ZS90, Malvern Instruments, England) for NPs. Surface charge characteristics are determined via zeta potential measurements (DLS, Malvern Zetasizer Nano ZS90, Malvern Instruments, England).

2.2. Fishing rearing and sampling

The *pearl gentian grouper* used in this experiment were obtained from Daqiuzhuang Aquaculture Co., Ltd. (Guangdong, China). The initial body weight of the fish was 54.79 ± 8.11 g, and the body length was 15.38 ± 0.96 cm. The experimental conditions were natural winter conditions with a temperature range of 10–15 °C. After two weeks of acclimation, the fish were randomly assigned to four groups (n = 25 per group): a control group and three treatment groups exposed to PS microbeads with particle sizes of 5 μm, 500 nm, and 50 nm, respectively. Based on the sampling results, we chose 1 mg/L as the exposure concentration for all groups (Fig.S1), and there is a 15-day exposure period. Prior to exposure, the PS MPs and NPs were pre-treated to prepare suspensions following the method described by Zhang et al. [31] (Fig. S2). At the end of the experiment, the fish were euthanized using tricaine. Subsequently, samples of liver, gill, intestine, stomach, and muscle tissues were collected, and immediately frozen in liquid nitrogen, and then stored at −80 °C in an ultra-low temperature freezer for further analysis. Ethical approval was obtained from the Ethical Committees of the South China Sea Institute of Oceanology, Chinese Academy of Science.

2.3. Organ distribution analysis

The pyrolysis method in combination with gas chromatography–mass spectrometry (Py-GC/MS) established by Zhou et al. [32] was used for quantification of MPs and NPs in the main tissue organs (gills, intestine, liver, muscle and stomach) of the *pearl gentian grouper*. The detailed procedure was as follows: 1 mL of 25 % tetramethylammonium hydroxide (Shanghai Aladdin Biochemical Co., Ltd., Shanghai, China) solution was added to the tissue samples, followed by digestion on a constant temperature shaker (300 rpm, 25 °C) for 24 h. Subsequently, 10 mL of anhydrous ethanol was added, and the mixture was incubated in a water bath at 80 °C for 30 min. After centrifugation at 4000 rpm for 5 min, the supernatant was discarded. The pellet was then resuspended in 0.50 mL of ultrapure water, and 200 μL of the suspension was transferred to a pyrolysis target in three aliquots, dried at 70 °C, and prepared for analysis. For Py-GC/MS analysis, styrene trimer (m/z = 91) was used as the characteristic indicator for polystyrene quantification (pyrolyzer: Frontier EGA/PY-3030D, Frontier Laboratories Ltd., Fukushima, Japan; gas chromatograph: Agilent 5977B, Agilent Technologies, Inc., Santa Clara, USA; mass spectrometer: Agilent 8890, Agilent Technologies, Inc., Santa Clara, USA).

2.4. Pathological examination

Liver tissue samples were fixed in 4 % paraformaldehyde for 24 h,

followed by embedding in paraffin (for hematoxylin-eosin staining, H&E) and optimal cutting temperature compound (for Oil Red O staining). Serial sections with a thickness of 5–8 μm were prepared using a microtome. H&E sections were used to examine histopathological changes in the liver tissue, while Oil Red O sections were employed to assess lipid droplet accumulation within hepatocytes. All sections were observed under a light microscope, and quantitative analysis of histopathological alterations and lipid droplet accumulation was performed using ImageJ image analysis software (National Institutes of Health, USA).

2.5. Biochemical analysis

Precisely 100 mg of liver tissue from *pearl gentian grouper* was weighed and placed into a 2 mL sterile grinding tube. Pre-chilled phosphate-buffered saline (PBS, pH 7.40) was added at a 1:9 (w/v) ratio. The samples were then ground in a cryogenic grinder at −30 °C, followed by centrifugation at 4 °C and 15000 rpm for 10 min. The supernatant was collected, and commercial kits were used to measure the levels of superoxide dismutase (SOD), catalase (CAT), malondialdehyde (MDA), and glutathione (GSH) (Beijing MREDA Technology Co., Ltd., Beijing, China), as well as total cholesterol (T-CHO), triglycerides (TG), and low-density lipoprotein cholesterol (LDL-C) (Nanjing Jiancheng Bioengineering Institute, Nanjing, China).

2.6. RNA-sequencing analysis and quantitative real-time PCR (q-PCR)

After the exposure period, three *pearl gentian groupers* were randomly selected from each group, and their liver tissues were collected for transcriptomic analysis. Following established protocols, total RNA extraction, RNA integrity assessment, library construction, and high-throughput sequencing were performed [33]. Based on normalized gene expression levels, differentially expressed genes (DEGs) were identified between the control and treatment groups using a threshold of greater than 1.5-fold change ($|\log2foldchange| > 0.585$) and a significance level of $p < 0.05$. Functional annotation and enrichment analysis of DEGs were conducted using Gene Ontology (GO) and Kyoto Encyclopedia of Genes and Genomes (KEGG) pathway analyses. Additionally, KEGG enrichment analysis was employed to elucidate lipid metabolism pathways associated with the DEGs. Furthermore, the expression levels of 12 selected genes were validated using real-time quantitative polymerase chain reaction. Detailed information on gene names and primer sequences was provided in the supplementary materials (Table.S1).

2.7. Data analysis

Data visualization and graphical representation were performed using Origin 2023 (OriginLab Corporation, USA), SPSS (International Business Machines Corporation, USA), and GraphPad Prism 10 (GraphPad Software Corporation, USA). All data are presented as mean ± standard deviation. Statistical differences between the control and exposure groups were evaluated using one-way analysis of variance. p value less than 0.05 was considered indicative of a statistically significant difference between the exposure and control groups. Different numbers of asterisks represent different p values: * was for $p < 0.05$, ** was for $p < 0.01$, *** was for $p < 0.001$, **** was for $p < 0.0001$.

3. Results and discussion

3.1. Characterization of PS MPs and NPs

The purchased MPs and NPs of three different particle sizes were characterized using SEM, TEM, DLS, and Zeta potential measurements (Fig.S3). The SEM and TEM results revealed that the PS MPs and NPs of all three sizes used in this study were spherical in shape. The average particle sizes for $PS_{5\ \mu m}$, $PS_{500\ nm}$, and $PS_{50\ nm}$ were determined to be 4.66 ± 0.26 μm, 524.84 ± 22.26 nm, and 54.06 ± 2.38 nm, respectively. Zeta potential analysis indicated that the PS particles were predominantly negatively charged, with values of −14.90 ± 1.59 mV, −40.03 ± 11.77 mV, and − 1.75 ± 1.62 mV for the respective sizes. Notably, the 500 nm PS particles exhibited the highest Zeta potential value. We redispersed 50 nm NPs and measured their Zeta potential to be −28.75 ± 2.06 mV, indicating that under this method, NPs can be well dispersed (Fig.S2).

3.2. PS MPs and NPs have extensive absorption and distribution in various tissues of fish

In this study, the distribution characteristics of PS MPs and NPs in various tissues of *pearl gentian grouper* after a 15-day exposure at a concentration of 1 mg/L were determined using Py-GC/MS. The experimental results demonstrated that the polystyrene trimer, with a retention time of 24–26 min and a mass to charge ratio of 91, could serve as a characteristic marker for PS quantification without significant interference from the protein extraction process [32] (Fig. 1a, Fig. 1b, Fig. 1c, Fig.S4). Tissue distribution analysis revealed that $PS_{5\ \mu m}$ particles exhibited the highest accumulation in the digestive system, specifically in the stomach and intestine, with concentrations of 3.61 μg/g and 5.60 μg/g wet tissue, respectively, which were approximately 2–6 times higher than those of NPs. In respiratory organs, the accumulation of $PS_{50\ nm}$ particles in gill tissue was significantly greater than that of other sizes, reaching 5.60 μg/g wet tissue, compared to 0.56 μg/g and 0.94 μg/g wet tissue for the other particle sizes. In muscle tissue, PS content showed a particle size-dependent pattern, decreasing with smaller particle sizes (ranging from 2.67 ± 0.62 to 1.49 ± 0.71 μg/g wet tissue). The liver tissue displayed a distinct distribution profile, with the highest content of $PS_{50\ nm}$ (22.94 ± 6.46 μg/g wet tissue) and a notable increasing trend as particle size decreased (Fig. 1d, Fig. 1e, Fig. 1f, Fig. 1g, Fig. 1 h, Table.S2).

Particle size is a critical factor influencing the uptake and distribution of MPs. Due to their higher specific surface area and lipophilic properties, NPs tend to aggregate on the intestinal surface, whereas MPs are primarily excreted through feces [34]. Notably, regardless of size, both MPs and NPs can impair intestinal barrier function, thereby enabling their penetration through intestinal epithelial cells into the internal environment [35]. Once inside the body, MPs and NPs can bypass the protective barriers of the circulatory and lymphatic systems, resulting in widespread systemic distribution [36]. The liver, as a central organ for metabolism and detoxification, is the primary site for the accumulation of exogenous PS, with concentrations significantly higher than in other tissues, making it a primary target for the toxic effects of MPs and NPs. Furthermore, the presence of MPs and NPs has also been detected in other organs, such as the brain and kidneys [37,38]. In the respiratory system, NPs are easily absorbed through gill tissues and transported to various internal organs via the bloodstream, while MPs, although retained, are less prone to accumulation [39]. Despite extensive research on the impact of particle size on the tissue accumulation of MPs and NPs, variables such as exposure duration, exposure method, tissue type, and detection techniques can significantly influence experimental outcomes. Consequently, the widespread distribution and accumulation patterns of MPs and NPs in *pearl gentian grouper* underscore their potential risk to food safety, warranting further attention and investigation. In addition to this, the presence of MPs has been detected in other economically important species, such as *large yellow croaker* and *eel* [40]. Studies have shown that *eels*, due to their benthic habits, are more likely to come into contact with MPs in sediments. Consequently, the MPs detected in their intestines are often associated with higher concentrations of adsorbed pollutants [41,42]. With the continuous development of the aquaculture industry, food safety issues have increasingly garnered public attention. Therefore, reducing biological contamination and enhancing food safety at the table have become key areas of research.

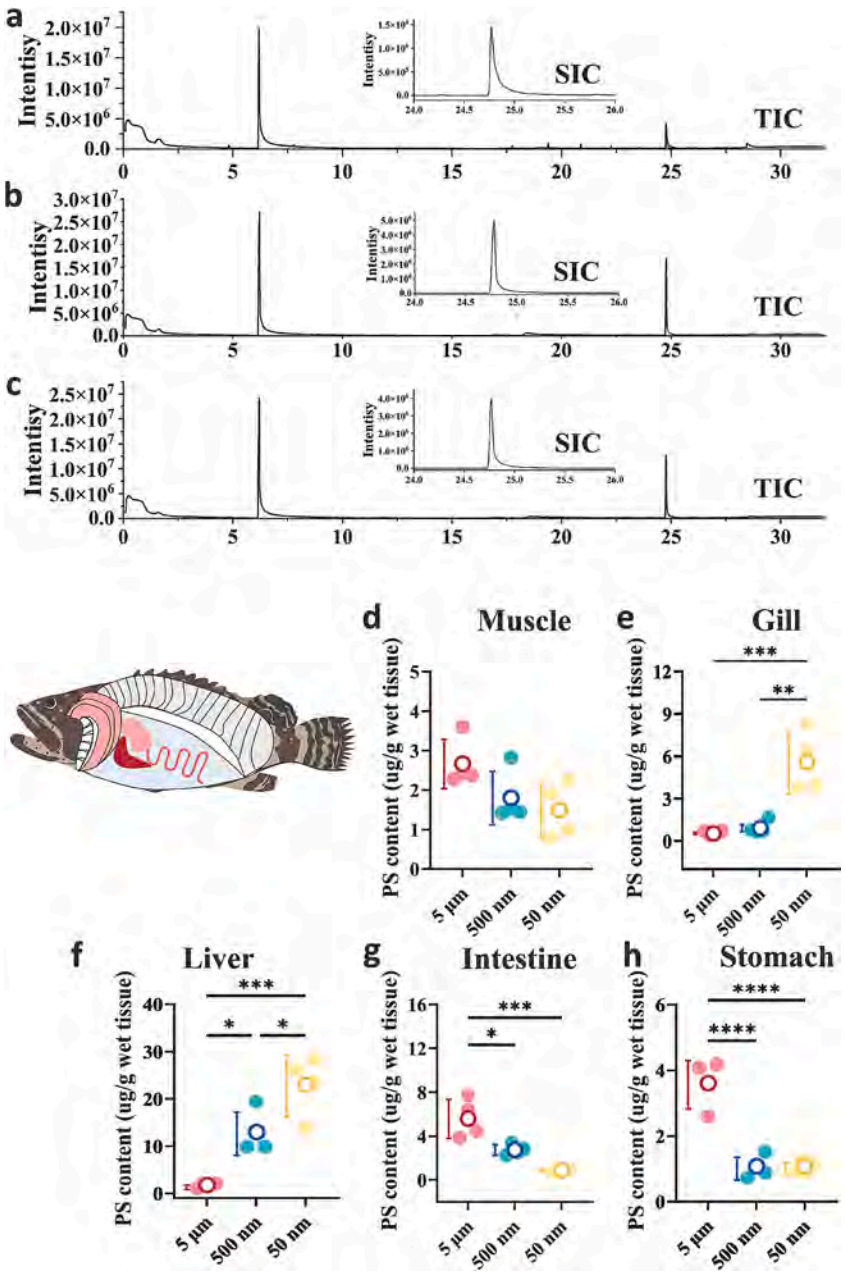


Fig. 1. (a-c) Py-GC/MS chromatogram of $PS_{5\ \mu m}$, $PS_{500\ nm}$ and $PS_{50\ nm}$. The total ion chromatogram (TIC), selected indicator ion chromatogram (SIC, m/z 91). (d-h) Determination of MPs and NPs content in major organs of *pearl gentian grouper* after exposure to MPs and NPs of different particle sizes, including (d) Muscle; (e) Gill; (f) Liver; (g) Intestine; (h) Stomach. Data are expressed as mean ± standard deviation. With four independent tests in every treatment.

3.3. Main pathological changes in liver following MPs and NPs exposure of different size

Following a 15-day exposure experiment, MPs and NPs caused significant pathological damage to liver tissue compared to the control group. Histopathological analysis revealed characteristic damage, including hepatocyte swelling, indistinct cell boundaries, vacuolar degeneration, inflammatory cell infiltration, fatty degeneration, and localized fibrous tissue proliferation (Fig. 2a, Fig.S5). Quantitative assessment using a liver injury scoring system indicated a clear particle size-dependent pattern in these pathological changes (Fig. 2c). Specifically, as the particle size of MPs and NPs decreased, their ability to penetrate the intestinal epithelial barrier and directly impact the liver via the circulatory system was significantly enhanced [43]. This finding aligns with previous studies [44], smaller NPs exhibited a broader tissue distribution within organisms and exerted stronger toxic effects when compared with MPs. It is noteworthy that the liver exhibits a degree of tissue damage closely associated with liver dysfunction [45]. This study revealed that MPs and NPs exposure not only caused typical hepatocyte damage but also triggered a distinctive disruption in lipid metabolism. Through Oil Red O staining analysis, we observed a significant reduction in lipid deposition area in the liver tissue of the exposure group (Fig. 2b, Fig. 2d, Fig.S6), a phenomenon that differs from previous reports. This finding suggests that MPs and NPs may exacerbate liver injury by interfering with lipid metabolism pathways in the liver [46]. Therefore, MPs and NPs exposure can lead to liver dysfunction through multiple mechanisms, including the induction of hepatic inflammation, promotion of fatty degeneration, and disruption of lipid metabolism.

The experimental results demonstrated that MPs and NPs exposure exerted a significant particle size-dependent effect on the levels of TG, T-

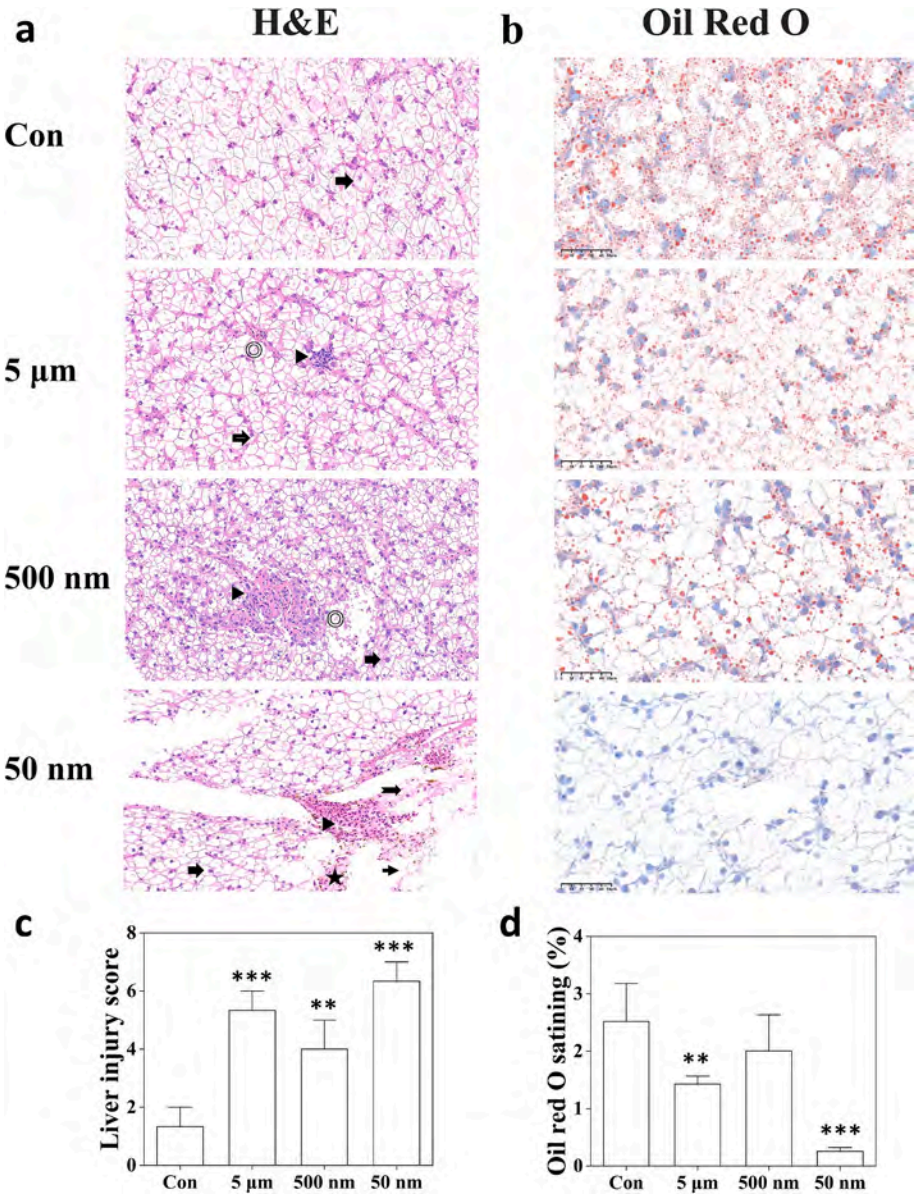


Fig. 2. Pathological changes in the liver after exposure to PS MPs and NPs of different particle sizes. (a) Hematoxylin-eosin staining images of liver. (Magnification:×20) (b) Quantitative analysis of liver damage. (c) Oil red o staining image of liver. (Magnification:×20) (d) Oil red o staining area percentage. Different symbols represent different types of damage. (▶: Inflammatory cell infiltration; ➧: Hepatocyte swelling; ➠: Fibrosis; →: Tissue damage; ◎: Liver lobule destruction; ★: Pigmentation). (For interpretation of the references to colour in this figure legend, the reader is referred to the web version of this article.)

CHO, and LDL-C in liver tissue. As particle size decreased, the TG content in the liver tissue exhibited a gradual declining trend (Fig. 3a), while the levels of T-CHO and LDL-C showed a marked increase (Fig. 3b, Fig. 3c), with the most pronounced changes observed in the 50 nm exposure group ($p < 0.05$). TG, as a critical regulator of energy homeostasis and lipid metabolism [47], is primarily stored in adipocytes in the form of lipid droplet, providing energy reserves for the organism [48]. The reduction in TG content suggests that MPs and NPs exposure may accelerate the breakdown of TG to meet energy demands. This observation is in accordance with the findings of Chen et al. [49], who reported that MPs exposure led to a decrease in TG levels in mouse liver, subsequently triggering liver dysfunction, hepatocyte damage, and lipid metabolism disorders.

LDL-C functions as a primary mediator of lipid transport and plays a pivotal role in shuttling lipids from the liver to peripheral tissues [19]. The elevated LDL-C levels observed in this study suggest a compensatory mechanism to alleviate metabolic stress induced by MPs and NPs exposure, though this adaptive response may concurrently disrupt lipid homeostasis and energy metabolism. As a critical regulator of fish metabolism, growth, and health, cholesterol is instrumental in governing lipid catabolism and energy allocation, while also modulating various physiological processes, including cellular signaling cascades [50]. Research by Lee et al. [51] has demonstrated that the accumulation of MPs and NPs in the body can induce liver damage accompanied by elevated cholesterol levels. This may represent an adaptive defense mechanism, whereby the organism provides additional energy to mitigate the toxic effects of MPs and NPs. Furthermore, exposure to MPs and NPs may also promote the development of atherosclerosis by triggering inflammatory responses. Specifically, the inflammatory environment can lead to the oxidation of LDL-C, which is subsequently engulfed by macrophages and transformed into cholesterol and lipid rich foam cells [52]. By comprehensively analyzing the changes in TG, LDL-C, and T-CHO levels, it can be inferred that MPs and NPs exposure significantly accelerates the organism's energy metabolism processes, mobilizing

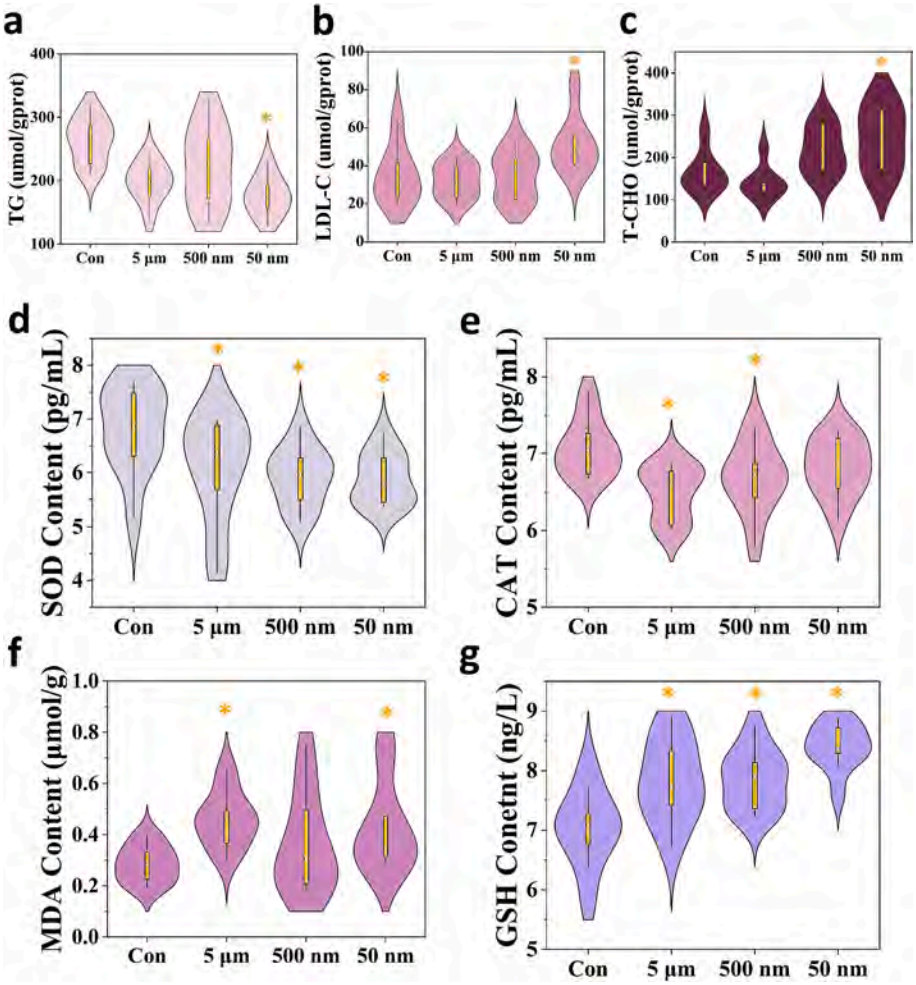


Fig. 3. Analysis of biochemical parameters and oxidative stress. (a) TG content; (b) LDL-C content; (c) T-CHO content; (d) SOD content; (e) CAT content; (f) MDA content; (g) GSH content.

lipid reserves to provide energy support in response to exogenous contaminants. This finding offers a crucial metabolic perspective for further elucidating the toxicity mechanisms of MPs and NPs.

3.4. *Effect of different particle size PS MPs and NPs on oxidative stress in liver tissues*

Exposure to MPs and NPs can trigger oxidative stress responses in organisms, with a pronounced particle size-dependent effect: as particle size decreases, the intensity of oxidative stress significantly increases [53]. This heightened oxidative stress prompts cells to release numerous inflammatory mediators, which activate the organism's immune system, leading to inflammatory responses and ultimately disrupting the homeostasis of hepatic lipid metabolism. Among these processes, the excessive production of reactive oxygen species (ROS) is regarded as a central mechanism contributing to hepatotoxicity and lipotoxicity.

In the *pearl gentian grouper*, we observed that MPs and NPs exposure significantly disrupted the balance of the antioxidant system. Specifically, the levels of SOD and CAT were markedly reduced (Fig. 3d, Fig. 3e), while the levels of MDA and GSH were significantly elevated (Fig. 3f, Fig. 3g). SOD and CAT, as the first line of defense in the antioxidant system, are responsible for converting superoxide radicals into hydrogen peroxide and further decomposing it into water and oxygen, respectively [54,55]. The decline in their activities indicates a significant impairment in the organism's ability to scavenge ROS. Under these conditions, GSH plays a vital role in mitigating MPs and NPs induced oxidative damage by converting peroxides into less toxic hydroxyl compounds [56].

It is noteworthy that MDA, a specific marker of lipid peroxidation in cell membranes [57], exhibited a significant increase in content, directly reflecting the extent of cell membrane damage caused by exposure to MPs and NPs. Previous studies have shown that MDA not only acts as a biomarker of oxidative stress but also induces apoptosis in various cell types, including hepatocytes [58]. Furthermore, due to their ability to directly penetrate cell membranes, NPs can more effectively disrupt the cellular microenvironment and metabolic processes, while the toxic additives they release further intensify oxidative stress levels. The findings of this study are highly consistent with those reported by Tao et al. [59], confirming that exposure to MPs and NPs significantly impairs the liver's antioxidant system function and leads to abnormal elevations in MDA and GSH levels.

3.5. *Overview of changes in hepatic transcriptome*

This study employed RNA-seq technology to systematically investigate the molecular regulatory mechanisms of lipid metabolism in the liver of the pearl gentian grouper under MPs and NPs exposure. Transcriptomic analysis revealed that 441, 397, and 499 DEGs were identified in the respective exposure groups, with 23 genes exhibiting a consistent differential expression pattern across all three groups (Fig. 4a, Fig. 4b, Fig. 4c). To gain deeper insights into the biological roles of these DEGs, we conducted comprehensive functional enrichment analyses

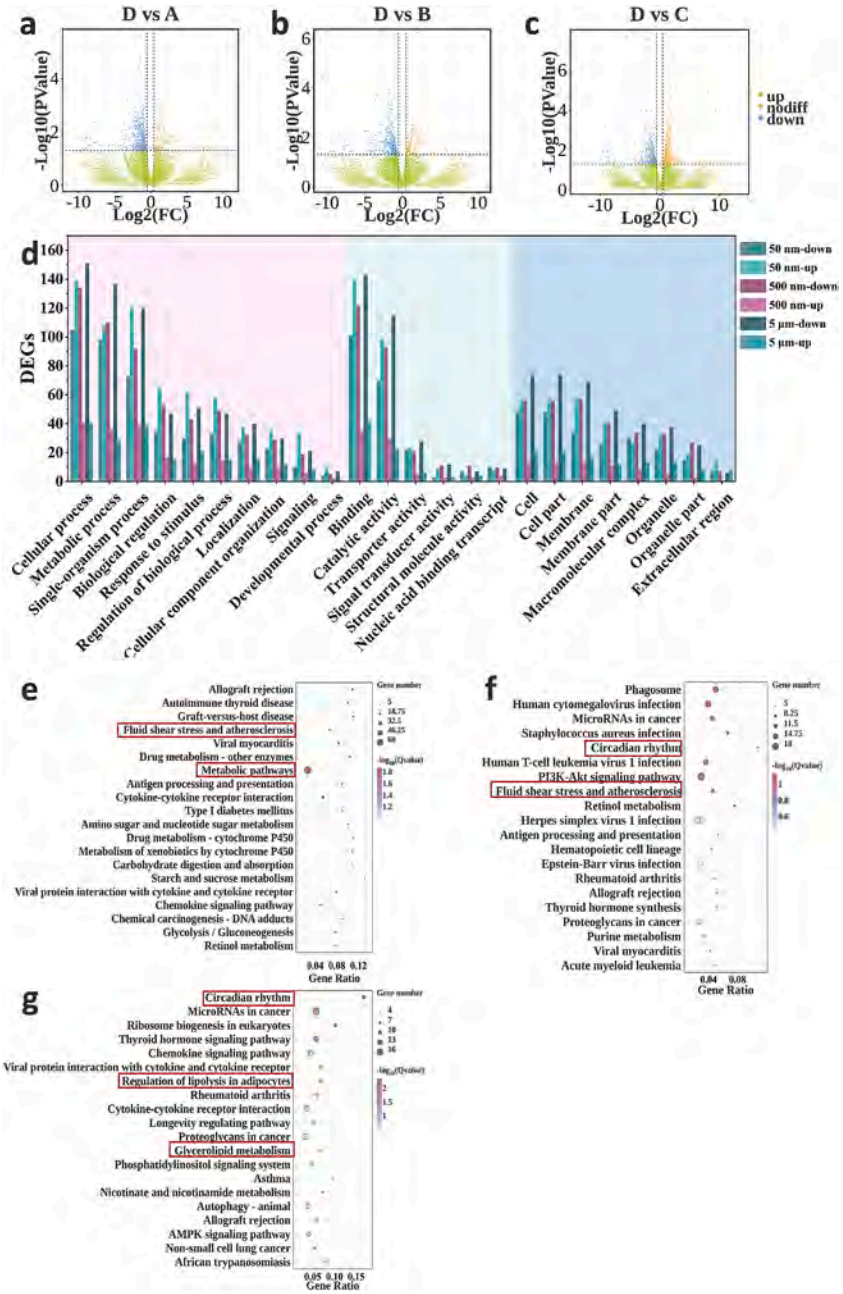


Fig. 4. Transcriptome analysis results of MPs of different particle sizes. (a-c) Volcano plot of expression differences between different particle size exposure groups and control groups. (a) 5 μm. (b) 500 nm. (c) 50 nm. (d) GO functional annotation analysis. (e-f) KEGG pathway enrichment analysis after exposure to MPs and NPs of different particle sizes. (e) 5 μm. (f) 500 nm. (g) 50 nm.

using GO and KEGG databases. GO annotation classified the DEGs into three primary categories: Biological Process, Cellular Component, and Molecular Function (Fig. 4d). The analysis revealed that significantly enriched DEGs were primarily associated with biological functions such as “cellular processes,” “metabolic processes,” “single-organism responses,” “binding,” and “catalytic activity.” Notably, the pronounced enrichment in “metabolic processes” suggests that MPs and NPs exposure may induce widespread disruptions in cellular metabolic homeostasis [60]. This finding aligns with the observed changes in TG, T-CHO, and LDL-C levels, as well as the results of Oil Red O staining, collectively confirming the substantial interference of MPs and NPs exposure on hepatic lipid metabolism. Furthermore, the significant enrichment in the “catalytic activity” category indicates that MPs and NPs exposure might influence the organism’s antioxidant defense system by affecting enzyme activity [61]. This hypothesis is supported by the observed variations in antioxidant enzyme activity in the present study. Additionally, research by Dar et al. [62] has demonstrated that the expression and activity of antioxidant enzymes exhibit a characteristic “biphasic response”: they are positively regulated under low stress conditions but significantly suppressed under high stress conditions. This phenomenon may account for the observed dysfunction in the antioxidant system in this study.

Based on transcriptomic data analysis, we categorized the 934 identified DEGs into 10 distinct gene clusters with varying expression patterns. Among these, the expression profiles of genes in Clusters 3, 4, 6, and 7 were significantly associated with disruptions in hepatic lipid metabolism (Fig.S7). KEGG pathway enrichment analysis revealed that these DEGs were predominantly involved in metabolic pathways such as triglyceride metabolism, adipocyte lipolysis regulation, glycerophospholipid metabolism, steroid biosynthesis, and pathological

processes like atherosclerosis. Notably, DEGs in other clusters were primarily linked to biological processes including apoptosis, immune response, and signal transduction. Further analysis indicated significant variations in the hepatic lipid metabolism pathways affected by MPs and NPs exposure. These particle size-dependent pathway differences are likely to reflect a close relationship between the toxicity mechanisms of MPs and NPs and their physicochemical properties. Specifically, MPs may primarily disrupt cellular functions through physical stimulation and surface adsorption, whereas NPs can penetrate cells directly, exerting toxic effects by interfering with organelle functions and molecular signaling pathways. This finding provides crucial molecular-level evidence for understanding the particle size-dependent toxicity mechanisms of MPs and NPs.

Transcriptomic analysis revealed that although PS MPs and NPs of varying particle sizes exhibited significant enrichment in lipid metabolism-related pathways, the specific metabolic pathways affected differed markedly (Fig. 4e, Fig. 4f, Fig. 4g). Specifically, $PS_{5\ \mu m}$ was predominantly enriched in pathways such as "atherosclerosis" and "regulation of lipolysis in adipocytes"; $PS_{500\ nm}$ showed significant enrichment in pathways related to "atherosclerosis" and "circadian rhythm"; while $PS_{50\ nm}$ primarily influenced pathways including "circadian rhythm," "regulation of lipolysis in adipocytes," and "triglyceride metabolism." These particle size-dependent pathway variations highlight fundamental differences in the toxicity mechanisms of MPs and NPs [63]. Notably, although MPs and NPs may induce similar toxic effects, the intensity and underlying mechanisms of their impact vary considerably. Due to their higher bioavailability, NPs are more readily absorbed and accumulated in tissues, leading to stronger oxidative stress and inflammatory responses [64]. In contrast, MPs primarily exert their effects by disrupting gut function and altering gut microbiota homeostasis [65]. This finding is consistent with the results reported by Choi et al. [66] and Jeong et al. [67]. However, existing studies are limited to indicate that both MPs and NPs can cause gut microbiota dysbiosis, the underlying mechanisms of these effects require further investigation.

To validate the reliability of the RNA-seq results, we performed q-PCR analysis on key genes involved in the regulation of adipocyte lipolysis and triglyceride metabolism (such as *PNPLA2*, *MGLL*, *LIPC*, and *LPIN1*) as well as other genes associated with lipid metabolism (*C1QL4* and *FABP3*) (Fig. 5a, Fig. 5b). Since the $PS_{500\ nm}$ exposure group showed limited enrichment in lipid metabolism pathways, q-PCR validation was conducted on the control group and other two treatment groups. The results demonstrated that the expression patterns of these genes were highly consistent with the Illumina sequencing data, exhibiting similar

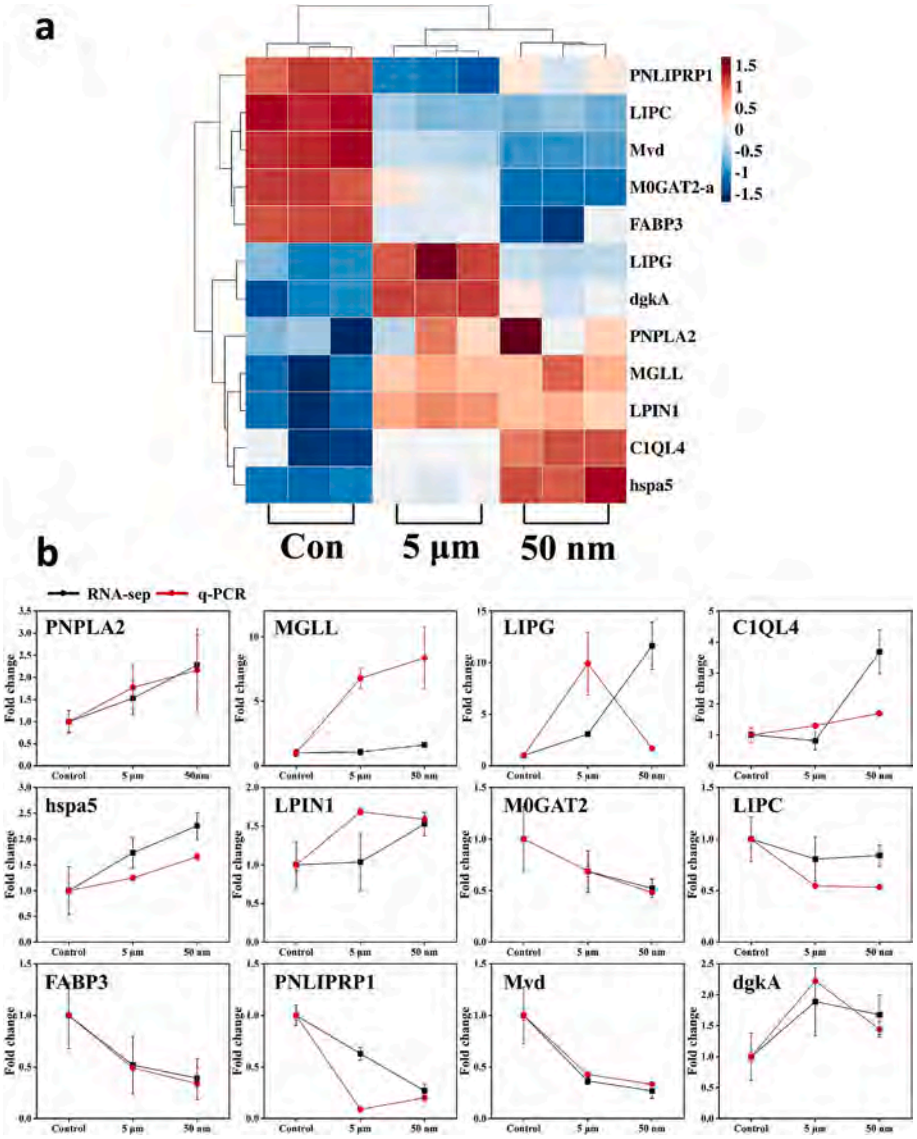


Fig. 5. (a) Heatmap of q-PCR gene expression; (b) q-PCR validation of RNA-sep. Up and down represent up-regulated genes and down-regulated genes, respectively.

upregulation and downregulation trends, thereby confirming the reliability of the DEGs analysis.

3.6. Potential mechanism of hepatic lipid metabolism disruption by small particle size PS MPs and NPs

Based on these findings, we propose the hypothesis of multiple mechanisms of action of MPs and NPs exposure leading to disorders of hepatic lipid metabolism (Fig. 6).

(1) MPs and NPs exposure during the overwintering period interferes with glyceride metabolism and adipocyte lipolytic regulatory processes. Research by Wang et al. [68] demonstrated that under cold stress, *perch* adapt to the demands of lipid metabolism by downregulating gene expression in the mTOR signaling pathway while upregulating *PPAR-a* expression. Notably, *pearl gentian grouper* exhibits a significant reduction in food intake when temperatures drop below 24 °C, and feeding ceases entirely at 13 °C [69]. Combining the Oil Red O staining and transcriptomic analysis results from this study, we found that MPs and NPs exposure accelerates lipid breakdown in adipose tissue, leading to premature depletion of energy reserves and thereby impairing the fish's ability to cope with cold stress. This observation aligns with findings by Biro et al. [70], who reported that small *oncorhynchus mykiss* experience significantly increased mortality rates due to early exhaustion of lipid reserves during winter. It is noteworthy that the smaller the particle size of MPs, the more pronounced the depletion of hepatic lipid reserves. Although this study did not directly measure fatty acid content, considering that fatty acids are central components of lipid metabolism, future research should prioritize examining changes in fatty acid profiles. This will contribute to a more comprehensive understanding of the molecular mechanisms underlying MPs and NPs induced lipid metabolism disorders, particularly by elucidating their toxic effects from the perspective of fatty acid metabolism.

(2) MPs and NPs exposure leads to energy metabolism imbalance. To cope with the physiological stress induced by MPs and NPs exposure, fish must increase their metabolic demands to maintain essential physiological functions, resulting in a significant reduction of energy allocated for growth and development, thereby causing an imbalance in energy distribution [71]. The reduction in lipid content is not only attributed to the lack of nutritional value in MPs and NPs but may also be linked to the increased energy demand caused by the inflammatory responses they trigger [72]. This finding is corroborated by the results of hematoxylin-eosin staining. Transcriptomic analysis further revealed significant enrichment in the IL-17 signaling pathway and autophagy-related pathways, which are energy-dependent biological processes that exacerbate energy consumption [73]. This phenomenon is consistent with the findings of Watts et al. [74], who reported that MPs exposure leads to a notable reduction in energy reserves and lipid depletion in crabs. Additionally, studies suggest that certain organisms may activate anaerobic metabolic pathways to cope with chemical stress induced by MPs and NPs exposure [75]. Collectively, these findings jointly explained that MPs and NPs exposure disrupts energy metabolism balance, resulting in reduced hepatic lipid storage and subsequently impairing the normal growth and development of organisms. Given that numerous studies have demonstrated a significant increase in the levels of inflammatory mediators (e.g., TNF-α, IL-1β) and their gene expression under exposure to MPs and NPs as well as cold stress conditions, we did not directly measure the concentrations of these inflammatory mediators or autophagy markers (e.g., LC3-II) to further validate the transcriptomic analysis results. Future studies could employ real-time sample collection and multi-omics approaches to further substantiate the related hypotheses [76–81].

(3) Disruption of TG metabolism and abnormal transport. TG plays a critical role in maintaining energy homeostasis and serves as the primary form of energy storage in adipose tissue. Under conditions of increased energy demand, such as fasting, TG can be

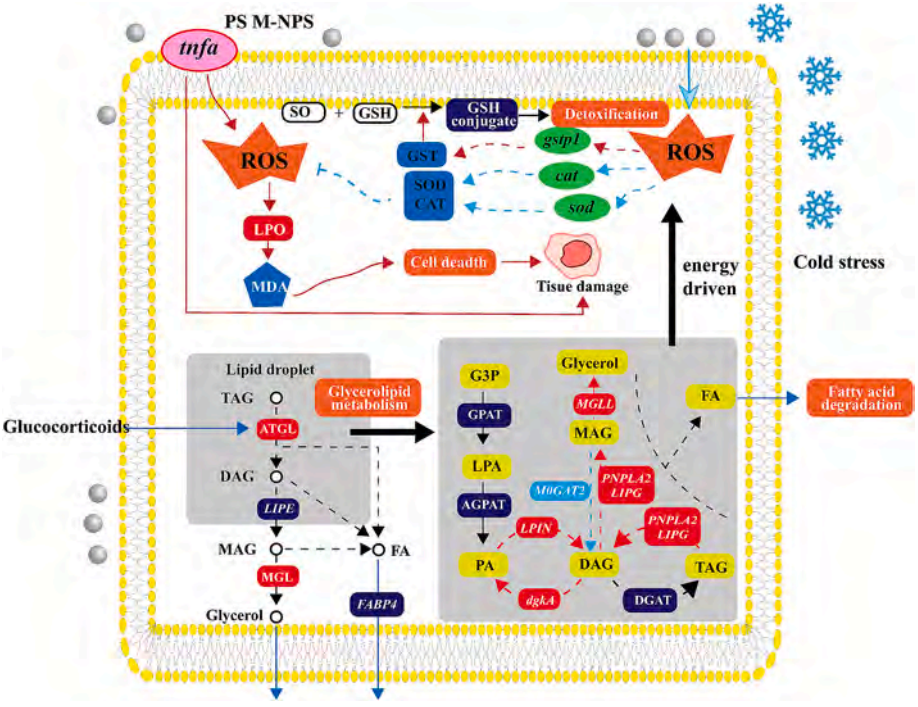


Fig. 6. Diagram of glycerol metabolism and lipid decomposition regulation in *pearl gentian grouper* exposed to 50 nm PS NPs. Red rectangles indicate up-regulated genes, and blue rectangles indicate down-regulated genes. (For interpretation of the references to colour in this figure legend, the reader is referred to the web version of this article.)

hydrolyzed to release fatty acids, providing energy for the organism [82]. Adipose triglyceride lipase (ATGL) acts as the rate-limiting enzyme in TG breakdown, primarily catalyzing the initial hydrolysis step of TG to produce diacylglycerol, which serves as a substrate for hormone-sensitive lipase (HSL), thereby supplying essential energy to the organism [83]. Following MPs and NPs exposure, the expression level of ATGL is significantly upregulated, which subsequently promotes the catabolism of TG in the liver. This process results in a reduction of hepatic TG content, while TG is transported from the liver to peripheral tissues in the form of LDL-C via apolipoprotein-mediated mechanisms to meet the energy demands of other tissues. This abnormal metabolism and transport of TG may represent a key mechanism underlying the disruption of hepatic lipid metabolism induced by MPs and NPs exposure.

3.7. Mitigation measure

To mitigate the adverse effects of MPs and low temperatures, we propose the following measures from the perspectives of the aquaculture environment and dietary interventions, taking into account both economic costs and practical benefits. Firstly, to address the issue of MPs pollution, we recommend implementing a dual-filtration system at the water inlets and outlets of aquaculture facilities. Specifically, a primary large-pore filter can be used to remove larger debris, followed by a secondary small-pore filter to effectively capture MPs. This approach can significantly reduce the entry and re-circulation of MPs within aquaculture systems. Additionally, we suggest the adoption of bacteria-microalgae combined bioremediation technology to improve water quality and yield in closed-loop aquaculture systems while specifically targeting the removal of MPs to prevent their re-entry into the environment [84,85].

Furthermore, as increased membrane lipid unsaturation and oxidative stress exacerbate cellular damage under low-temperature conditions [86], we recommend the use of functional feed additives to alleviate cold stress in fish. Specifically, diets enriched with antioxidants such as vitamin E and vitamin C, as well as other bioactive compounds including propolis, phycocyanin, highly unsaturated fatty acids, inositol, and phospholipids, can enhance fish resilience to cold stress [87]. Studies have shown that pre-winter feeding with high-oil diets improves the health status of *gilthead sea bream*, while winter diets supplemented with the aforementioned compounds significantly increase the survival rate of *gilthead sea bream* during cold periods [88]. These cost-effective and feasible dietary interventions can be readily adopted by aquaculture practitioners to improve the physiological adaptation of fish to temperature fluctuations.

4. Conclusion

This study shows that MPs and NPs enter systemic circulation via the respiratory and digestive systems, accumulating in the liver of *pearl gentian grouper*. This accumulation causes pathological damage, oxidative stress, and abnormal lipid metabolism, with effects intensifying as particle size decreases. During the overwintering phase, MPs and NPs exposure accelerates lipid degradation, likely as a compensatory mechanism to maintain energy homeostasis under thermal stress. Two potential mechanisms underlie this disruption: (1) immune-mediated energy demand, where the immune response to MPs and NPs increases energy needs, enhancing lipid reserve mobilization; and (2) direct modulation of lipid metabolism, with MPs and NPs upregulating hepatic TG catabolism through altered expression of genes like *PNPLA2*, *MGLL*, and *LIPG*, reducing hepatic TG levels while increasing circulating LDL-C. These findings offer novel insights into the mechanisms of hepatic lipid metabolism disruption by MPs and NPs during overwintering.

CRediT authorship contribution statement

Julong Wang: Writing – review & editing, Writing – original draft, Visualization, Formal analysis, Data curation. **Yan Gao:** Validation, Supervision. **Shanshan Yao:** Validation, Supervision. **Lang Lin:** Writing – review & editing, Supervision, Funding acquisition, Data curation, Conceptualization. **Hengxiang Li:** Validation, Supervision. **Shan Liu:** Validation, Supervision. **Rui Hou:** Validation, Supervision. **Zhijian Jiang:** Validation, Supervision. **Xiangrong Xu:** Validation, Supervision.

Declaration of competing interest

The authors declare that they have no known competing financial interests or personal relationships that could have appeared to influence the work reported in this paper.

Acknowledgments

This work was supported by the Basic and Applied Basic Research Project of Guangzhou Municipal Science and Technology Bureau (No. 2023A04J0194), the Natural Science Foundation of Hainan Province (No. 422QN443) and the National Natural Science Foundation of China (No. 42206149).

Appendix A. Supplementary data

Supplementary data to this article can be found online at https://doi.org/10.1016/j.enceco.2025.07.021.

Data availability

Data will be made available on request.

References

[1] K. Hu, Y. Yang, J. Zuo, W. Tian, Y. Wang, X. Duan, S. Wang, Emerging microplastics in the environment: properties, distributions, and impacts, CHEMOSPHERE 297 (2022) (Article 134118).
[2] Europe Plastic, Plastics - the Fast Facts 2023, Plastics Europe, 2024.
[3] N.R. Maddela, D. Kakarla, K. Venkateswarlu, M. Megharaj, Additives of plastics: entry into the environment and potential risks to human and ecological health, J. Environ. Manag. 348 (2023) (Article 119364).
[4] G. Bishop, D. Styles, P.N.L. Lens, Recycling of European plastic is a pathway for plastic debris in the ocean, Environ. Int. 142 (2020) (Article 105893).
[5] M. Zbyszewski, P.L. Corcoran, Distribution and degradation of fresh water Plastic particles along the beaches of Lake Huron, Canada, Water Air Soil Pollut. 220 (2011) 365–372.
[6] A.L. Andrady, Microplastics in the marine environment, Mar. Pollut. Bull. 62 (2011) 1596–1605.
[7] R.C. Thompson, Y. Olsen, R.P. Mitchell, A. Davis, S.J. Rowland, A.W.G. John, D. McGonigle, A.E. Russell, Lost at sea: where is all the Plastic? Science 304 (2004) 838.
[8] M. Cole, P. Lindeque, E. Fileman, C. Halsband, T.S. Galloway, The impact of polystyrene microplastics on feeding, function and fecundity in the marine copepod *Calanus helgolandicus*, Environ. Sci. Technol. 49 (2015) 1130–1137.
[9] M. Efendy, N. Amir, M.Z. Mahasin, F.M. Wahyu, M.K. Aroua, M. Gozan, Distribution and characteristics of microplastics in seawater, sediment, and crude salt from Madura Island, the largest solar salt production island in Indonesia, Reg. Stud. Mar. Sci. 78 (2024) (Article 103803).
[10] Y. Gong, Q. Wang, Y. Xiang, B. Liu, X. Chen, Y. Zhang, Invisible threat to mesopelagic fish: microplastics and artificial cellulose particles in bigfin lanternfish *Symbolophorus californiensis* from the Northwest Pacific Ocean, Reg. Stud. Mar. Sci. 78 (2024) (Article 103799).
[11] D. Brennecke, B. Duarte, F. Paiva, I. Cacador, J. Canning-Clode, Microplastics as vector for heavy metal contamination from the marine environment, Estuar. Coast. Shelf Sci. 178 (2016) 189–195.
[12] A.A. Koelmans, E. Besseling, A. Wegner, E.M. Foekema, Plastic as a carrier of POPs to aquatic organisms: a model analysis, Environ. Sci. Technol. 47 (2013) 7812–7820.
[13] B. Jadhav, A. Medynska-Juraszek, Microplastic and Nanoplastic in crops: possible adverse effects to crop production and contaminant transfer in the food chain, Plants-Basel 13 (2024) (Article 2526).
[14] A.I. Osman, M. Hosny, A.S. Eltaweil, S. Omar, A.M. Elgarahy, M. Farghali, P.S. Yap, Y. Wu, S. Nagandran, K. Batumalaie, S.C.B. Gopinath, O.D. John, M. Sekar, T. Saikia, P. Karunanithi, M.H.M. Hatta, K.A. Akinyede, Microplastic sources,

formation, toxicity and remediation: a review, Environ. Chem. Lett. 21 (2023) 2129–2169.
[15] H. Yang, F. Sun, H. Liao, Y. Guo, T. Pan, F. Wu, J.P. Giesy, Distribution, abundance, and risks posed by microplastics in surface waters of the Yangtze River basin, China, Environ. Pollut. 333 (2023) (Article 122086).
[16] H. Cui, X. Jiang, J. Cao, W. Yang, B. Yang, M. Li, Comparative analysis of metabolic dysfunctions associated with pristine and aged polyethylene microplastic exposure via the liver-gut Axis in mice, ACS Nano 19 (2025) 14272–14283.
[17] Y. Sun, Q. Deng, Q. Zhang, X. Zhou, R. Chen, S. Li, Q. Wu, H. Chen, Hazards of microplastics exposure to liver function in fishes: a systematic review and meta-analysis, Mar. Environ. Res. 196 (2024) (Article 106423).
[18] W. Wang, X. Mao, R. Zhang, X. Zhou, Y. Liu, H. Zhou, J. Jia, B. Yan, Nanoplastic exposure at environmental concentrations disrupts hepatic lipid metabolism through oxidative stress induction and endoplasmic reticulum homeostasis perturbation, Environ. Sci. Technol. 57 (2023) 14127–14137.
[19] S. He, J. Wang, L. Zhou, T. Jia, Z. Mao, X. Zhang, L. Zhang, J. Wang, M. Yang, P. Huang, Short term exposure to polystyrene nanoplastics in mice evokes self-regulation of glycolipid metabolism, Ecotox Environ. Safe 256 (2023) (Article 114906).
[20] W. Luo, M. Cao, C. Sun, J. Wang, M. Gao, X. He, L. Dang, Y. Geng, B. Li, J. Li, Z. Shi, X. Yan, Size-dependent internalization of polystyrene microplastics as a key factor in macrophages and systemic toxicity, J. Hazard. Mater. 490 (2025) (Article 137701).
[21] Y. Lu, Y. Zhang, Y. Deng, W. Jiang, Y. Zhao, J. Geng, L. Ding, H. Ren, Uptake and accumulation of polystyrene microplastics in zebrafish (*Danio rerio*) and toxic effects in liver, Environ. Sci. Technol. 50 (2016) 4054–4060.
[22] D.C. Bobori, A. Dimitriadi, K. Feidantsis, A. Samiotaki, D. Fafouti, I. Sampsonidis, S. Kalogiannis, G. Kastrinaki, D.A. Lambropoulou, G.Z. Kyzas, G. Koumoundouros, D.N. Bikiaris, M. Kaloyianni, Differentiation in the expression of toxic effects of polyethylene-microplastics on two freshwater fish species: size matters, Sci. Total Environ. 830 (2022) (Article 154603).
[23] H. Yang, H. Xiong, K. Mi, W. Xue, W. Wei, Y. Zhang, Toxicity comparison of nano-sized and micron-sized microplastics to goldfish *Carassius auratus* larvae, J. Hazard. Mater. 388 (2020) (Article 122058).
[24] L. Zhu, C. Xie, L. Chen, X. Dai, Y. Zhou, H. Pan, K. Tian, Transport of microplastics in the body and interaction with biological barriers, and controlling of microplastics pollution, Ecotox Environ. Safe 255 (2023) (Article 114818).
[25] J. Fan, L. Liu, Y. Lu, Q. Chen, S. Fan, Y. Yang, Y. Long, X. Liu, Acute exposure to polystyrene nanoparticles promotes liver injury by inducing mitochondrial ROS-dependent necroptosis and augmenting macrophage-hepatocyte crosstalk, Part. Fibre Toxicol. 21 (2024) (Article 20).
[26] G. Ye, X. Zhang, X. Liu, X. Liao, H. Zhang, C. Yan, Y. Lin, Q. Huang, Polystyrene microplastics induce metabolic disturbances in marine medaka (Oryzias melastigmas) liver, Sci. Total Environ. 782 (2021) (Article 146885).
[27] J. Lin, P. Liang, Q. Zhu, M. Qiu, Effect of Laminarin on growth and immunity of pearl gentian grouper, Fujian J. Agric. Sci. 32 (2017) 17–21.
[28] J.B. Koongolla, L. Lin, Y. Pan, C. Yang, D. Sun, S. Liu, X. Xu, D. Maharana, J. Huang, H. Li, Occurrence of microplastics in gastrointestinal tracts and gills of fish from Beibu gulf, South China Sea, Environ. Pollut. 258 (2020) (Article 113734).
[29] T.W.L. Lam, L. Fok, A.T.H. Ma, H. Li, X. Xu, L.T.O. Cheung, M.H. Wong, Microplastic contamination in marine-cultured fish from the Pearl River estuary, South China, Sci. Total Environ. 827 (2022) (Article 154281).
[30] Q. Wang, F. Huang, K. Liang, W. Niu, X. Duan, X. Jia, X. Wu, P. Xu, L. Zhou, Polystyrene nanoplastics affect digestive function and growth in juvenile groupers, Sci. Total Environ. 808 (2022) (Article 152098).
[31] H. Zhang, S. Zhang, Z. Duan, L. Wang, Pulmonary toxicology assessment of polyethylene terephthalate nanoplastic particles in vitro, Environ. Int. 162 (2022) (Article 107177).
[32] X. Zhou, S. He, Y. Gao, H. Chi, D. Wang, Z. Li, B. Yan, Quantitative analysis of polystyrene and poly(methyl methacrylate) Nanoplastics in tissues of aquatic animals, Environ. Sci. Technol. 55 (2021) 3032–3040.
[33] X. Lu, J. Tian, H. Wen, M. Jiang, W. Liu, F. Wu, L. Yu, S. Zhong, Microcystin-LR-regulated transcriptome dynamics in ZFL cells, Aquat. Toxicol. 212 (2019) 222–232.
[34] T. Atugoda, H. Piyumali, S. Liyanage, K. Mahatantila, M. Vithanage, Fate and behavior of microplastics in freshwater systems, in: Handbook of Microplastics in the Environment, Springer, 2022, pp. 781–811.
[35] X. Zhang, K. Wen, D. Ding, J. Liu, Z. Lei, X. Chen, G. Ye, J. Zhang, H. Shen, C. Yan, S. Dong, Q. Huang, Y. Lin, Size-dependent adverse effects of microplastics on intestinal microbiota and metabolic homeostasis in the marine medaka (Oryzias melastigma), Environ. Int. 151 (2021) (Article 106452).
[36] J.H. Kim, Y.B. Yu, J.H. Choi, Toxic effects on bioaccumulation, hematological parameters, oxidative stress, immune responses and neurotoxicity in fish exposed to microplastics: a review, J. Hazard. Mater. 413 (2021) (Article 125423).
[37] M. Atamanalp, M. Köktürk, A. Uçar, H.A. Duyar, S. Özdemir, V. Parlak, N. Esenbuğa, G. Alak, Microplastics in tissues (brain, gill, muscle and gastrointestinal) of *Mullus barbatus* and *Alosa immaculata*, Arch. Environ. Contam. Toxicol. 81 (2021) 460–469.
[38] S. Chisada, M. Yoshida, K. Karita, Polyethylene microbeads are more critically toxic to the eyes and reproduction than the kidneys or growth in medaka, *Oryzias latipes*, Environ. Pollut. 268 (2021) (Article 115957).
[39] M. van Pomeren, N.R. Brun, W.J.G.M. Peijnenburg, M.G. Vijver, Exploring uptake and biodistribution of polystyrene (nano)particles in zebrafish embryos at different developmental stages, Aquat. Toxicol. 190 (2017) 40–45.
[40] W. Lv, Q. Yuan, D. He, W. Lv, W. Zhou, Microplastic contamination caused by different rearing modes of Asian swamp eel (*Monopterus albus*), Aquac. Res. 52 (2020) 5084–5095.
[41] L. Rivas-Iglesias, Á. Gutiérrez, E. Dopico, S. Fernández, V. Soto-López, E. Garcia-Vazquez, Endangered, exploited glass eels (*Anguilla anguilla*) with critical levels of heavy metals and microplastics reveal both shipping and plastic spill threats, Environ. Pollut. 369 (2025) (Article 125824).
[42] D. Menéndez, A. Álvarez, S. Acle, P. Peón, A. Ardura, E. Garcia-Vazquez, Microplastics across biomes in diadromous species. Insights from the critically endangered *Anguilla anguilla*, Environ. Pollut. 305 (2022) (Article 119277).
[43] X. Meng, J. Zhang, W. Wang, G. Gonzalez-Gil, J.S. Vrouwenvelder, Z. Li, Effects of nano-and microplastics on kidney: physicochemical properties, bioaccumulation, oxidative stress and immunoreaction, Chemosphere 288 (2022) (Article 132631).
[44] K. Yin, Y. Wang, H. Zhao, D. Wang, M. Guo, M. Mu, Y. Liu, X. Nie, B. Li, J. Li, M. Xing, A comparative review of microplastics and nanoplastics: toxicity hazards on digestive, reproductive and nervous system, Sci. Total Environ. 774 (2021) (Article 145758).
[45] L.P. Bechmann, R.A. Hannivoort, G. Gerken, G.S. Hotamisligil, M. Trauner, A. Canbay, The interaction of hepatic lipid and glucose metabolism in liver diseases, J. Hepatol. 56 (2012) 952–964.
[46] X. Wang, K. Deng, P. Zhang, Q. Chen, J.T. Magnuson, W. Qiu, Y. Zhou, Microplastic-mediated new mechanism of liver damage: from the perspective of the gut-liver axis, Sci. Total Environ. 919 (2024) (Article 170962).
[47] K. Birsoy, W.T. Festuccia, M. Laplante, A comparative perspective on lipid storage in animals, J. Cell Sci. 126 (2013) 1541–1552.
[48] T. Fujimoto, R.G. Parton, Not just fat: the structure and function of the lipid droplet, Cold Spring Harb. Perspect. Biol. 3 (2011) 4831–4838.
[49] X. Chen, J. Zhuang, Q. Chen, L. Xu, X. Yue, D. Qiao, Chronic exposure to polyvinyl chloride microplastics induces liver injury and gut microbiota dysbiosis based on the integration of liver transcriptome profiles and full-length 16S rRNA sequencing data, Sci. Total Environ. 839 (2022) (Article 155984).
[50] T.M. Wu, J.J. Jiang, R.M. Lu, Y.H. Lin, Effects of dietary inclusion of soybean meal and cholesterol on the growth, cholesterol status and metabolism of the giant grouper (*Epinephelus lanceolatus*), Aquac. Nutr. 26 (2019) (Article 12997).
[51] J.H. Lee, J.C. Kang, J.H. Kim, Toxic effects of microplastic (polyethylene) on fish: accumulation, hematological parameters and antioxidant responses in Korean bullhead, Pseudobagrus fulvidraco, Sci. Total Environ. 877 (2023) (Article 162874).
[52] X. Lin, W. Zhang, C. Yang, P. Ma, K. He, G. Chen, Y. Tao, H. Yan, Z. Yang, L. Zhang, J. Fan, Q. Cui, W. Huang, G. Liu, X. Xian, Y. Wang, Depleting LCAT aggravates atherosclerosis in LDLR-deficient Hamster with reduced LDL-cholesterol level, J. Adv. Res. 63 (2024) 187–194.
[53] P. Zheng, R. Li, K. Lai, X. Zhang, Biological exposure to microplastics and nanoplastics and plastic additives: impairment of glycolipid metabolism and adverse effects on metabolic diseases, Environ. Sci. Pollut. Res. 31 (2024) 60778–60791.
[54] Z. Li, X. Chang, M. Hu, J.K.H. Fang, I.M. Sokolova, W. Huang, E.G. Xu, Y. Wang, Is microplastic an oxidative stressor? Evidence from a meta-analysis on bivalves, J. Hazard. Mater. 423 (2022) (Article 127211).
[55] S. Yedier, S.K. Yalçınkaya, D. Bostancı, Exposure to polypropylene microplastics via diet and water induces oxidative stress in *Cyprinus carpio*, Aquat. Toxicol. 259 (2023) (Article 106540).
[56] H.J. Forman, H. Zhang, A. Rinna, Glutathione: overview of its protective roles, measurement, and biosynthesis, Mol. Asp. Med. 30 (2009) 1–12.
[57] M. Uchiyama, M. Mihara, Determination of malonaldehyde precursor in tissues by thiobarbituric acid test, Anal. Biochem. 86 (1978) 271–278.
[58] M. Premanathan, K. Karthikeyan, K. Jeyasubramanian, G. Manivannan, Selective toxicity of ZnO nanoparticles toward gram-positive bacteria and cancer cells by apoptosis through lipid peroxidation, Nanomed-Nanotechnol 7 (2011) 184–192.
[59] J. Tao, P. Deng, M. Lin, C. Chen, Q. Ma, L. Yang, W. Zhang, Y. Luo, S. Chen, H. Pi, Z. Zhou, Z. Yu, Long-term exposure to polystyrene microplastics induces hepatotoxicity by altering lipid signatures in C57BL/6J mice, Chemosphere 347 (2024) (Article 140716).
[60] Y. Zhao, Z. Bao, Z. Wan, Z. Fu, Y. Jin, Polystyrene microplastic exposure disturbs hepatic glycolipid metabolism at the physiological, biochemical, and transcriptomic levels in adult zebrafish, Sci. Total Environ. 710 (2019) (Article 136279).
[61] T. Xu, Z. Li, H. Li, L. Lin, R. Hou, S. Liu, T. Li, E. Zeng, K. Yu, X. Xu, Unraveling the toxicity mechanisms of nanoplastics with various surface modifications on *Skeletonema costatum*: cellular and molecular perspectives, Sci. Total Environ. 953 (2024) (Article 176164).
[62] I. Dar, A. Barzilai, Cellular responses to oxidative stress, in: K.K. Khanna, Y. Shiloh (Eds.), The DNA Damage Response: Implications on Cancer Formation and Treatment, Springer, 2009, pp. 65–79.
[63] E. Besseling, P. Redondo-Hasselerharm, E.M. Foekema, A.A. Koelmans, Quantifying ecological risks of aquatic micro- and nanoplastic, Crit. Rev. Environ. Sci. Technol. 49 (2019) 32–80.
[64] X. Wang, H. Zheng, J. Zhao, X. Luo, Z. Wang, B. Xing, Photodegradation elevated the toxicity of polystyrene microplastics to grouper (Epinephelus moara) through disrupting hepatic lipid homeostasis, Environ. Sci. Technol. 54 (2020) 6202–6212.
[65] Z. Li, C. Feng, W. Pang, C. Tian, Y. Zhao, Anoplastic-induced genotoxicity and intestinal damage in freshwater benthic clams (*Corbicula fluminea*): comparison with microplastics, ACS Nano 15 (2021) 9469–9481.
[66] J.S. Choi, S.H. Hong, J.W. Park, Evaluation of microplastic toxicity in accordance with different sizes and exposure times in the marine copepod *Tigriopus japonicus*, Mar. Environ. Res. 153 (2020) (Article 104838).

[67] C.B. Jeong, E.J. Won, H.M. Kang, M.C. Lee, D.S. Hwang, U.K. Hwang, B. Zhou, S. Souissi, S.J. Lee, J.S. Lee, Microplastic size-dependent toxicity, oxidative stress induction, and p-JNK and p-p38 activation in the Monogonont rotifer (Brachionus koreanus), Environ. Sci. Technol. 50 (2016) 8849–8857.
[68] Z. Wang, Z. Dong, Y. Yang, J. Wang, T. Yang, X. Chen, L. Liang, W. Mu, Histology, physiology, and glucose and lipid metabolism of Lateolabrax maculatus under low temperature stress, J. Therm. Biol. 104 (2022) (Article 103161).
[69] S.K. Das, T.W. Xiang, N.M. Noor, M. De, S.K. Mazumder, M.P. Goutham-Bharathi, Temperature physiology in grouper (Epinephelinae: Serranidae) aquaculture: a brief review, Aquacult. Rep. 20 (2021) (Article 100682).
[70] P.A. Biro, A.E. Morton, J.R. Post, E.A. Parkinson, Over-winter lipid depletion and mortality of age-0 rainbow trout (*Oncorhynchus mykiss*), Can. J. Fish. Aquat. Sci. 61 (2004) 1513–1519.
[71] L. Yin, H. Liu, H. Cui, B. Chen, L. Li, F. Wu, Impacts of polystyrene microplastics on the behavior and metabolism in a marine demersal teleost, black rockfish (*Sebastes schlegelii*), J. Hazard. Mater. 380 (2019) (Article 120861).
[72] C.J.M. Silva, A.L. Patrício Silva, D. Campos, A.L. Machado, J.L.T. Pestana, C. Gravato, Oxidative damage and decreased aerobic energy production due to ingestion of polyethylene microplastics by *Chironomus riparius* (Diptera) larvae, J. Hazard. Mater. 402 (2021) (Article 123775).
[73] S.L. Wright, D. Rowe, R.C. Thompson, T.S. Galloway, Microplastic ingestion decreases energy reserves in marine worms, Curr. Biol. 23 (2013) 1031–1033.
[74] A.J.R. Watts, M.A. Urbina, S. Corr, C. Lewis, T.S. Galloway, Ingestion of Plastic microfibers by the crab *Carcinus maenas* and its effect on food consumption and energy balance, Environ. Sci. Technol. 49 (2015) 14597–14604.
[75] M. Oliveira, A. Ribeiro, K. Hylland, L. Guilhermino, Single and combined effects of microplastics and pyrene on juveniles (0+ group) of the common goby *Pomatoschistus microps* (Teleostei, Gobiidae), Ecol. Indic. 34 (2013) 641–647.
[76] W. Deng, T. Yang, R. Dong, Y. Yan, Q. Jiang, Astaxanthin protects tilapia head kidney cells against polystyrene microplastics-induced inflammation through MAPK and NF-κB signaling pathways, Aquaculture 574 (2023) (Article 739686).
[77] F. Del Piano, A. Lama, G. Piccolo, N.F. Addeo, D. Iaccarino, G. Fusco, L. Riccio, D. De Biase, G. Mattace Raso, R. Meli, M.C. Ferrante, Impact of polystyrene microplastic exposure on gilthead seabream (*Sparus aurata* Linnaeus, 1758): differential inflammatory and immune response between anterior and posterior intestine, Sci. Total Environ. 879 (2023) (Article 163201).
[78] J. Cui, Y. Zhang, L. Liu, Q. Zhang, S. Xu, M. Guo, Polystyrene microplastics induced inflammation with activating the TLR2 signal by excessive accumulation of ROS in hepatopancreas of carp (*Cyprinus carpio*), Ecotox Environ. Safe 251 (2023) (Article 114539).
[79] E. Ahmadifar, N. Kalhor, M.A.O. Dawood, M. Ahmadifar, M.S. Moghadam, S. Abarghouei, A. Hedayati, Effects of polystyrene microparticles on inflammation, antioxidant enzyme activities, and related gene expression in Nile tilapia (*Oreochromis niloticus*), Environ. Sci. Pollut. Res. 28 (2021) 14909–14916.
[80] Z. Sun, X. Tan, Q. Liu, H. Ye, C. Zou, M. Xu, Y. Zhang, C. Ye, Physiological, immune responses and liver lipid metabolism of orange-spotted grouper (*Epinephelus coioides*) under cold stress, AQUACULTURE 498 (2019) 545–555.
[81] J. Chen, H. Li, P. Xu, Y. Tang, S. Su, G. Liu, N. Wu, M. Xue, F. Yu, W. Feng, C. Song, H. Wen, Hypothermia-mediated apoptosis and inflammation contribute to antioxidant and immune adaption in freshwater drum, *Aplodinotus grunniens*, Antioxidants-Basel 11 (2022) (Article 1657).
[82] H. Wang, M.V. Airola, K. Reue, How lipid droplets "TAG" along: Glycerolipid synthetic enzymes and lipid storage, BBA-Mol. Cell Biol. L. 2017 (1862) 1131–1145.
[83] R. Zimmermann, J.G. Strauss, G. Haemmerle, G. Schoiswohl, R. Birner-Gruenberger, M. Riederer, A. Lass, G. Neuberger, F. Eisenhaber, A. Hermetter, R. Zechner, Fat mobilization in adipose tissue is promoted by adipose triglyceride lipase, Science 306 (2004) 1383–1386.
[84] C. Wang, C. Jiang, T. Gao, X. Peng, S. Ma, Q. Sun, B. Xia, Z. Bai, S. Xu, X. Zhuang, Improvement of fish production and water quality in a recirculating aquaculture pond enhanced with bacteria-microalgae association, Aquaculture 547 (2022) (Article 737420).
[85] A. Solomando, X. Capó, C. Alomar, M. Compa, J.M. Valencia, A. Sureda, S. Deudero, Assessment of the effect of long-term exposure to microplastics and depuration period in *Sparus aurata* Linnaeus, 1758: liver and blood biomarkers, Sci. Total Environ. 786 (2021) (Article 147479).
[86] A.F.M. El-Sayed, M. Izquierdo, The importance of vitamin E for farmed fish—a review, Rev. Aquac. 14 (2022) 688–703.
[87] M.J. Islam, A. Kunzmann, J. Henjes, M.J. Slater, Can dietary manipulation mitigate extreme warm stress in fish? The case of European seabass, *Dicentrarchus labrax*, Aquaculture 545 (2021) (Article 737153).
[88] A. Ibarz, F. Padrós, M.Á. Gallardo, J. Fernández-Borràs, J. Blasco, L. Tort, Low-temperature challenges to gilthead sea bream culture: review of cold-induced alterations and 'winter syndrome', Rev. Fish Biol. Fish. 20 (2010) 539–556.

The ISME Journal, 2025, **19(1)**, wraf215
https://doi.org/10.1093/ismejo/wraf215
Advance access publication: 30 September 2025
Review Article

Deciphering the universal role of gut microbiota in pollutant transformation

Rui Hou[1,‡], Xiaowei Jin[2,‡], Jingchun Feng[1,3,4,*], Jingchuan Xue[1,4], Chengzhi Chen[5], Yuanqiang Zou[6], Xiangrong Xu[7,*], Kefu Yu[3,7], Pei-Yuan Qian[3,8], Wei Zhang[9], Jizhong Zhou[10], Si Zhang[3], Zhifeng Yang[1,3,4]

[1]Guangdong Provincial Key Laboratory of Water Quality Improvement and Ecological Restoration for Watersheds, School of Ecology, Environment and Resources, Guangdong University of Technology, Guangzhou, Guangdong 510006, China
[2]China National Environmental Monitoring Centre, Beijing 100012, China
[3]Southern Marine Science and Engineering Guangdong Laboratory (Guangzhou), Guangzhou, Guangdong 511458, China
[4]Key Laboratory of City Cluster Environmental Safety and Green Development, Institute of Environmental and Ecological Engineering, Guangdong University of Technology, Guangzhou, Guangdong 510006, China
[5]Department of Occupational and Environmental Health, School of Public Health, Chongqing Medical University, Chongqing 400016, China
[6]State Key Laboratory of Genome and Multi-omics Technologies, BGI Research, Shenzhen, Guangdong 518083, China
[7]Guangxi Laboratory on the Study of Coral Reefs in the South China Sea, Coral Reef Research Centre of China, School of Marine Sciences, Guangxi University, Nanning, Guangxi 530004, China
[8]Department of Ocean Science, The Hong Kong University of Science and Technology, Hong Kong 999077, China
[9]Centre for Marine Bioproducts Development, College of Medicine and Public Health, Flinders University, Adelaide, South Australia 5001, Australia
[10]Institute for Environmental Genomics, University of Oklahoma, Norman, OK 74078, United States

*Corresponding authors. Jingchun Feng, School of Ecology, Environment and Resources, Guangdong University of Technology, 100 Waihuan Xi Road of Guangzhou University Town, Guangzhou, Guangdong 510006, China. E-mail: fengjc@gdut.edu.cn; Xiangrong Xu, School of Marine Sciences, Guangxi University, 100 Daxue Road, Nanning, Guangxi 530004, China. E-mail: xuxr@gxu.edu.cn
‡Rui Hou and Xiaowei Jin contributed equally to this work.

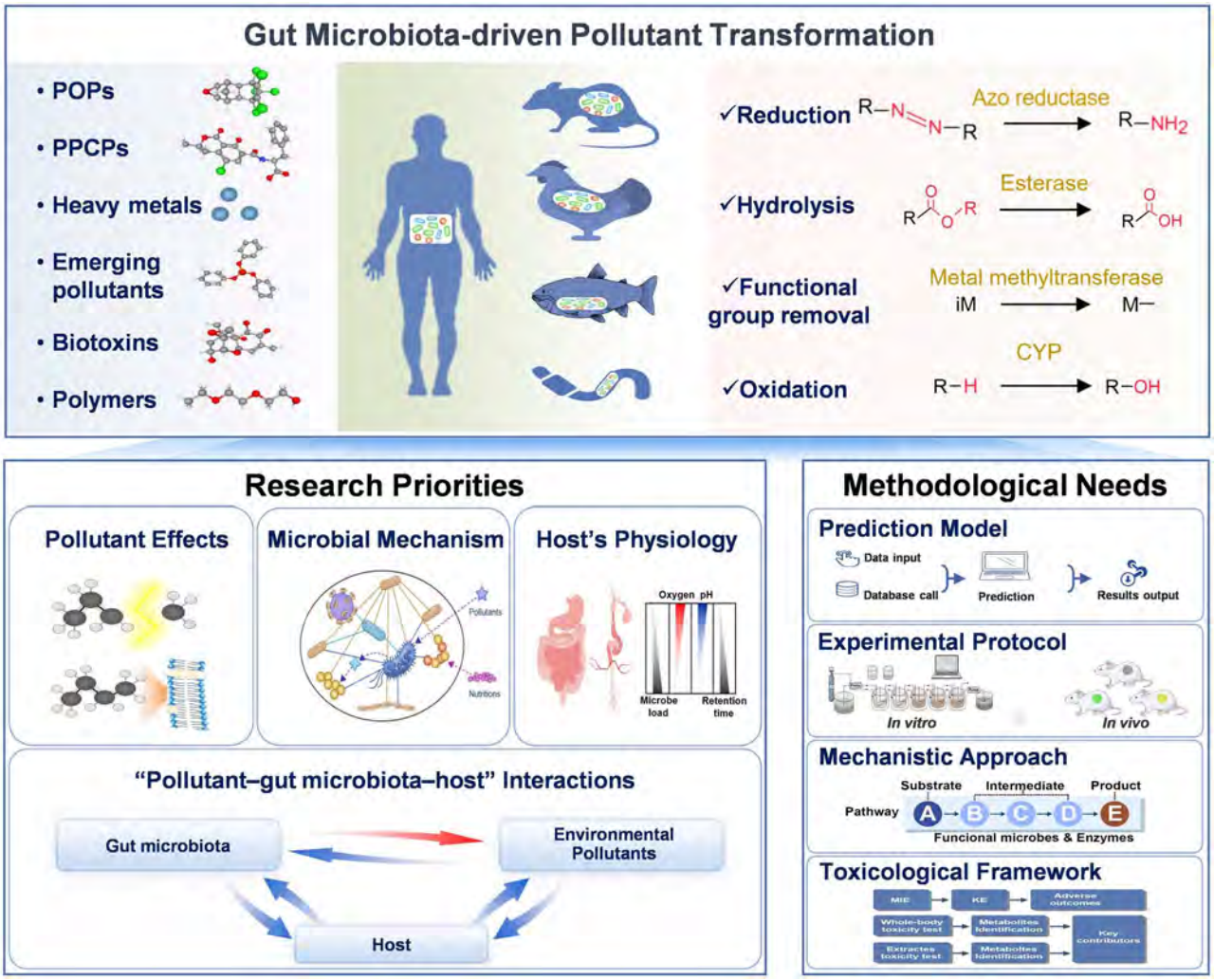
Abstract

The gut microbiota represents a critical yet underexplored "second genome" in the host that functions as a key driver of pollutant transformation across Earth's ecosystems. This review synthesizes the current understanding of over 490 pollutants across a wide range of species, highlighting the universal role of gut microbial communities in modifying pollutant exposure. We have demonstrated that gut microbial communities transform a broad spectrum of environmental pollutants through evolutionarily conserved pathways, fundamentally altering their bioavailability, fate, and toxicity potential within the host. Transformation reactions are elucidated with connections among the metabolic enzymes that are developed by specific gut microbes, emphasizing the markedly specific and complementary signatures of microbial biotransformation compared to the host process. By integrating multidisciplinary studies, the complex and dynamic interplay between the gut microbiota, host physiology, and environmental pollutants has been elucidated, and drivers involved in the biotransformation processes have been proposed. Furthermore, current methodologies are critically evaluated, and next-generation approaches to reveal the underlying mechanisms of gut microbiota-driven pollutant transformation are outlined. This review underscores the urgent need to systematize research on "pollutant–gut microbiota–host" interactions and advocates the integration of gut microbial perspectives into interdisciplinary research paradigms of toxicology, microbiology, and ecology.

Received: 11 May 2025. **Revised:** 25 July 2025. **Accepted:** 19 September 2025
© The Author(s) 2025. Published by Oxford University Press on behalf of the International Society for Microbial Ecology.
This is an Open Access article distributed under the terms of the Creative Commons Attribution License (https://creativecommons.org/licenses/by/4.0/), which permits unrestricted reuse, distribution, and reproduction in any medium, provided the original work is properly cited.

Downloaded from https://academic.oup.com/ismej/article/19/1/wraf215/8268573 by National Science & Technology Library user on 14 October 2025

Graphical abstract



Keywords: gut microbiota; pollutant transformation; toxicological outcomes; "pollutant–gut microbiota–host" interactions; interdisciplinary research framework

Introduction

Environmental pollutants pose unprecedented challenges to ecosystems and human health in the Anthropocene [1]. While traditional toxicology has focused primarily on direct host–pollutant interactions, emerging evidence reveals a critical yet underexplored driver in environmental toxicology: the gut microbiota. The gut microbiota, which can be found in virtually any metazoan, from invertebrates to vertebrates, serves as a crucial interface between environmental exposure and biological responses [2]. This complex microbial ecosystem, which comprises trillions of microbes with > 150-fold more genes than their host [3, 4], performs functions including resistance to pathogens, regulation of the immune system, fermentation of nondigestible dietary fibers, anaerobic metabolism of peptides and proteins, interaction with the circadian rhythm, and biotransformation of xenobiotics [5, 6]. There is now growing recognition that the gut microbiota functions as an "external" organ for the host [7, 8].

In recent years, the "game-changing potential" of the gut microbiota with respect to its effects on the mode of action (MOA) and the absorption, distribution, metabolism, and excretion (ADME) of pollutants have since shaped the ecological and environmental toxicology. The gut microbiota acts as the first physical and biological barrier against environmental pollutants from the diet as it resides at the site of exposure. Environmental pollutants, such as antibiotics [9], heavy metals [10, 11], persistent organic pollutants (POPs) [12, 13], pesticides [14–16], nanomaterials [17, 18], and other emerging pollutants [19], strongly influence the structure and activity of the gut microbiome. The gut-"X" axis of the gut is considered an important target of pollutant toxicity, such as intestinal injury [20], hepatic diseases [21], metabolic disorders [22], immune perturbations [23], and behavioral and neurochemical alterations [24, 25]. In addition, the gut microbiota harbors diverse enzyme families with xenobiotic-transformation potential, which function as modifiers of pollutant exposure in

Downloaded from https://academic.oup.com/ismej/article/19/1/wraf215/8268573 by National Science & Technology Library user on 14 October 2025

organisms. Many recent cutting-edge and innovative efforts in toxicology have made great strides toward gut microbiota-driven pollutant transformation in organisms ranging from invertebrates to humans [5, 26–28]. The gut microbiota has been revealed to play an important role in the biotransformation of pollutants, and different chemical transformation modes and toxicity modifications associated with the hepatic process have been described [29]. Overall, research on the gut microbiota has spurred a paradigm shift from focusing solely on host-level consequences to adopting a more integrative toxicological approach that emphasizes host–microbiota symbiosis as a key determinant of pollutant-induced adverse outcomes.

Over the past few years, the impact of environmental pollutants on the gut microbiota, together with induced host toxicology, has been described in various recent reviews [7, 19, 28, 30, 31]. Although some reviews have summarized the available information on pollutant biotransformation by the gut microbiota [5, 26–28, 32–35], most have focused primarily on the human gut microbiota as a major target. Globally, mechanistic and critical reviews of gut microbiota-driven pollutant transformation grounded in the "One Planet, One Health" concept (encompassing the multidisciplinary links among planet, human health, and animal health) are still lacking. Many recent cutting-edge and innovative efforts in toxicology have made great strides toward gut microbiota-driven pollutant transformation in organisms ranging from invertebrates to humans [5, 26–28], covering: (i) potential candidate microbes and their transformation activities; (ii) transformation kinetics, pathways, and mechanisms of target pollutants; and (iii) changes in pollutant bioavailability and toxicity during microbial transformation. Pollutant transformation by the gut microbiota may be far more diverse and complicated than previously believed because of the complex interplay of several factors. The gut microbiota encompasses diverse domains of life, including archaea, bacteria, fungi, and viruses, all of which could contribute to pollutant transformation. Differences in the amount and composition of the gut microbiota among species directly affect enzyme activities, resulting in significant variation in the effects on pollutant transformation; in contrast, pollutant structures and properties can also determine the intrinsic recalcitrance of pollutants to microbial transformation [36]. Moreover, various host-related factors, such as host genetics, lifestyle, diet, and environmental stress, can also dramatically modulate microbial capacity and efficiency in pollutant transformation [30, 37, 38]. To date, the "gut microbiota-driven transformation" is a research gap in which specialization has been neglected and research frequently overlooks, where the associated direct transformation modulations and the indirect modulations under "pollutant–microbiota–host" interactions are the key issues to be addressed.

By synthesizing insights from toxicological, microbiological, and ecological research, this review aims to provide a comprehensive framework for understanding how gut microbiota-driven biotransformation shapes the impact and fate of environmental pollutants. First, a panoramic overview of the role of the gut microbiota in the ADME processes of pollutants is provided, and scenarios where the gut microbiota participates in the pollutant transformation are proposed. Second, specific pathways (the enzymes involved), functional microbes, and their corresponding effects on toxicity in gut microbiota-driven transformation are summarized on the basis of the latest knowledge of pollutant transformation. Third, the drivers of this gut microbial transformation distribution are analyzed from the basic perspective of "pollutant–gut microbiota–host" interactions. Finally, methodological advances in the study of gut microbial transformation are presented, and key issues that should be addressed in the future are suggested. This timely and essential review of gut microbiota-driven transformation will not only advance scientific understanding but also facilitate the development of more accurate risk assessment models and innovative strategies to mitigate the ecological and human health impacts of environmental pollution.

A brief overview of gut microbiota-driven transformation and its influence on pollutant absorption, distribution, metabolism, and excretion (ADME) processes

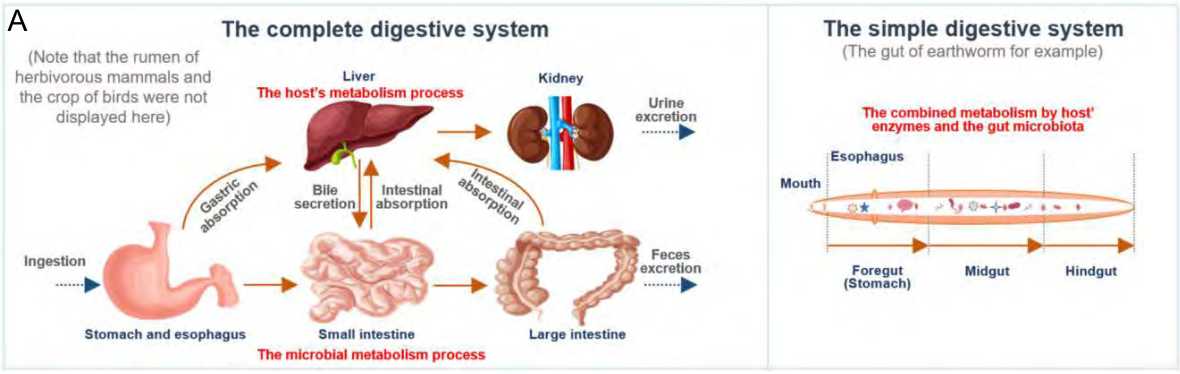
The ADME processes determine the internal exposure and toxic action of pollutants within the body. Among these factors, host-gut microbiota cooperative transformation is recognized as both the most influential and the least understood factor (Box 1A). Due to their distinct physiological and enzymatic properties, the host (particularly the liver, a primary site of chemical transformation) and the gut microbiota often exhibit divergent, or even opposing, capabilities in metabolizing pollutants. As a highly vascularized organ with a constant oxygen supply, the liver predominantly facilitates detoxifying transformation through the action of cytochrome P450 monooxygenases (CYPs), hydrolases, and conjugating enzymes [39, 40]. In contrast, much of the gut of large animals are located in reducing environments, where the gut microbiota cannot rely on oxygen as the terminal electron acceptor for respiration [41]. In general, hepatic transformation tends to exhibit broad substrate specificity, whereas the gut microbiota is capable of mediating a wide array of metabolic reactions, including reductive and hydrolytic processes [42].

In humans and other vertebrate animals with a complete digestive system, pollutants can encounter the gut microbiota through various pathways. Once absorbed by the gastrointestinal (GI) tract, the ingested pollutants often undergo "first-pass metabolism (presystemic metabolism)" by the host's enzymes and microbial enzymes before they reach the systemic circulatory system. Hepatic metabolites in the circulation may also be excreted via the bile back to the gut lumen and reprocessed by the gut microbiota [4, 26], where the subsequent deconjugation of the excreted phase II metabolites can result in "enterohepatic circulation" of chemicals in the body. Invertebrates possess a simple digestive system (a simple tube of enterocyte cells) harboring the gut microbiota [44], often resulting in a relatively simple host–gut microbiota transformation process. Overall, the host- and gut microbiota-driven transformations form a complex, complementary, and interactive metabolic network.

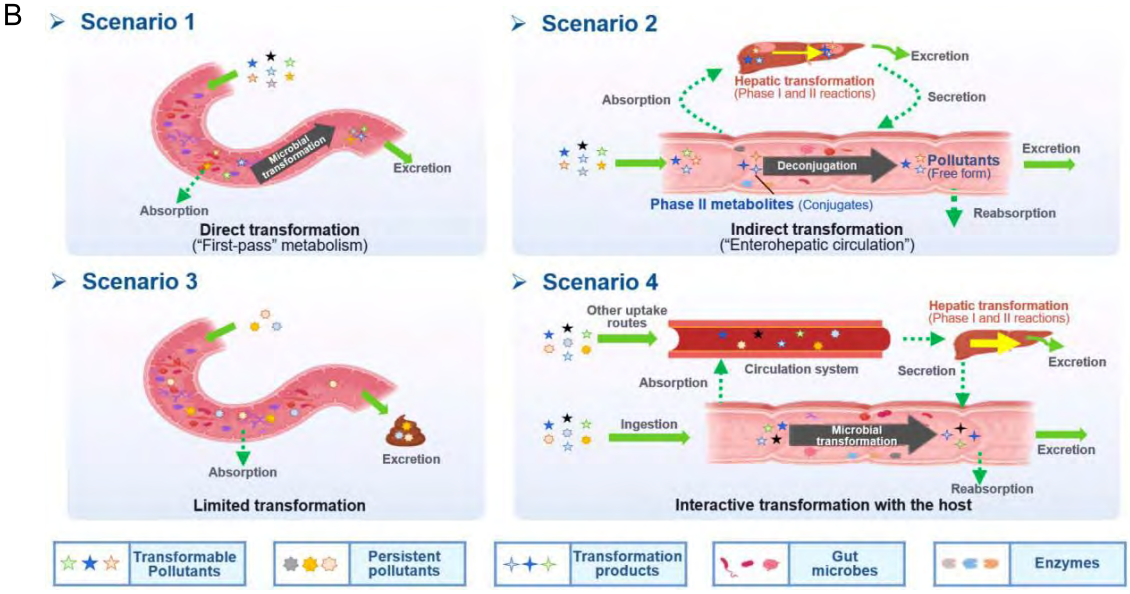
The role of the gut microbiota in pollutant transformation and the alteration of toxicokinetic and toxicodynamic properties are closely tied to the structure and exposure route of the pollutant. Briefly, gut microbiota-driven pollutant transformation in humans and other vertebrate animals can be categorized into four distinct scenarios (Box 1B). With respect to the susceptibility of pollutants to microbial transformation, "first-pass metabolism" by the gut microbiota can be considered the first barrier for the entry of pollutants into the blood circulation system (i.e. direct transformation). The easily absorbed and readily hepatically conjugated pollutants are more likely to be reproposed by the gut microbiota, thereby spending long periods in the systemic circulation through this process of "enterohepatic circulation" (i.e. indirect transformation) [4, 26]. In contrast to the previous two

Downloaded from https://academic.oup.com/ismej/article/19/1/wraf215/8268573 by National Science & Technology Library user on 14 October 2025

Box 1. Overview of the complex metabolic network of pollutants in the host-gut microbiota cooperative process (A) and the four proposed scenarios of pollutant transformation with respect to the gut microbiota (B).



There are different ADME processes for xenobiotics in the digestive system of invertebrates and high-trophic level organisms. In the complete digestive system, orally ingested chemicals first experience the extremely acidic environment of the stomach (pH 1.5) [43], where various pH-sensitive compounds can undergo abiotic hydrolysis and reduction reactions. Subsequently, these compounds can be jointly modified by digestive enzymes and the gut microbiota in the small intestine and colon. They are then absorbed by the intestinal tissues and enter into circulation. Compounds in the circulatory system can be processed by hepatic transformation and excreted via the kidneys. Bile excretion provides another opportunity for metabolism by the gut microbiota, in which the phase II metabolites can be transformed to the conjugated form then reabsorbed during the "enterohepatic cycle" [4, 26]. Eventually, chemicals and metabolites that are not absorbed by the large intestine can be excreted via feces. In the simple digestive system, host and microbial transformation processes are more likely to occur simultaneously and function together [44].



There are four scenarios in which the gut microbiota participates in pollutant transformation: (1) the "first-pass metabolism" of ingested pollutants by the gut microbiota; (2) the hepatic metabolites (mainly the phase II metabolites) of some pollutants in the circulatory system may also be excreted via the bile back to the gut lumen, after which they are reprocessed by the gut microbiota; (3) some persistent pollutants cannot be degraded due to their persistence and limited residence time in the GI tract; and (4) the gut microbiota participates in a complex and interactive process with the host.

scenarios, the gut microbiota can hardly modify rapidly absorbed or microbe-resistant chemicals (the third scenario). In addition, the gut microbiota mainly exerts direct effects on dietary compounds. Because the exposed pollutants bypass this "first-pass metabolism" to enter systemic circulation via another route (i.e. inhalation, dermal intake, or intravenous injection), only the bile-excreted proportion can be processed by the gut microbiota [26]. In real-world scenarios involving mixed pollutant exposure, host–gut microbiota cooperative biotransformation is the most common occurrence (the fourth scenario). Consequently, ADME studies must meticulously distinguish between these distinct transformation processes and account for exposure- and structure-specific mechanisms when evaluating the role of gut microbiota–pollutant interactions.

Universality of gut microbiota-driven pollutant transformation

The capacity of gut microbiota to transform environmental pollutants demonstrates remarkable universality, as shown by a comprehensive analysis of the biotransformation of over 490 structurally diverse pollutants by animal species across 13 taxonomic groups, spanning invertebrates, fish, birds, non-human mammals, and human. Supporting data on transformation

Downloaded from https://academic.oup.com/ismej/article/19/1/wraf215/8268573 by National Science & Technology Library user on 14 October 2025

pathways, functional microbes, and potential toxicity modulation are summarized from the environmental toxicology and ecotoxicology studies (Fig. 1; Table 1; Supplementary Tables S1–S6).

Substrate and reaction universality of the gut microbial transformation

Legacy organic pollutants

Even though legacy organic pollutants including POPs possess relatively stable chemical structures, substantial evidences have confirmed their biotransformation by gut microbiota of humans and rodents (Supplementary Fig. S1). For instance, dechlorination has been identified as a general reductive metabolic pathway for a wide range of chlorinated compounds [45, 46], including dichlorodiphenyl trichloroethane (DDT), organochlorine pesticides (OCPs) such as dieldrin, lindane, and methoxychlor, as well as polychlorinated biphenyls (PCBs). Similarly, the ester bonds in organophosphate pesticides (OPs) and other ester-containing raw chemicals render these compounds susceptible to hydrolysis by enzymes (e.g. phosphoesterases) derived from human gut microbiota [47, 48]. Furthermore, the nitro-containing pollutants, such as nitro-polycyclic aromatic hydrocarbons (nitro-PAHs), can be reduced by gut microorganisms to amino-polycyclic aromatic hydrocarbons (amino-PAHs), thereby enhancing their mutagenicity and carcinogenicity; for example, certain bacteria such as *Klebsiella* sp. C1, which are isolated from humans may be involved in this process [49, 50]. Similarly, azo dyes are susceptible to biotransformation by azo reductases produced by specific gut bacteria, including *Clostridium perfringens*, *Bacteroides ovatus*, *Enterococcus faecalis*, and *Ruminococcus obeum*, as well as the broader human gut microbiota [51–53], though which generates carcinogenic aniline derivatives. PAHs have also been reported to undergo hydroxylation by CYPs from the gut microbiota [54, 55], yielding products with elevated estrogenicity. Furthermore, the gut microbiota-mediated biotransformation of melamine has attracted much attention due to the significant increase in nephrotoxicity caused by the formation of cyanuric acid [56].

Metals

Microbial transformation of metals often involves complex networks of redox, methylation, and thiolation reactions, profoundly influencing their mobility and toxicity. Arsenic (As) metabolism provides a seminal example of this metabolic versatility, which display complex transformation networks: iAs^{V} can be reduced to iAs^{III} by sulfate-reducing bacteria (e.g. *Desulfovibrio*), subsequently methylated to monomethyl- (MMA^{V}) and dimethylarsinic acid (DMA^{V}), and thiolated to generate products such as monomethylmonothio- ($MMMTA^{V}$), dimethylmonothio- ($DMMTA^{V}$), dimethyldithioarsinic acid ($MMDTA^{V}$), and dimeth yldiothio-arsonic acid ($DMDTA^{V}$) [57–59]. Human gut microbiota can also oxidize iAs^{III} to iAs^{V} [60]. Meanwhile, organic arsenic compounds (e.g. MMA^{V}, DMA^{V}, AsB, and arsenic sugars) can also be transformed by the gut microbiota through hydrolysis to enhance their host absorption [61–63]. Critically, this capacity for biotransformation is not unique to As; similar bacterial methylation pathways have been confirmed for other metals including Hg, Bi, Sb, Se, and Te (Supplementary Fig. S2), highlighting a conserved functional role across metal substrates.

Pharmaceutical and personal care products (PPCPs)

The role of the gut microbiota in pharmaceutical transformation has long been recognized and considered in the field of pharmaceutical design (Supplementary Fig. S3). The reductive metabolism of pharmaceuticals represents a significant biotransformation process, particularly for structurally distinct groups such as azo (–N=N–), nitro ($–NO_2$), alkenes (–C=C–), ketones (–C=O), N-oxides (–N–O), and sulfoxides (–S=O). For example, the azo drugs (mainly the digestion-related drugs) of balsalazide, ipsalazide, neoprontosil, olsalazine, prontosil, and sulfasalazine are intentionally designed to avoid rapid adsorption to ensure their effective delivery to the colonic region [64]. These prodrugs rely on azo reductases secreted by the gut microbiota for azo bond cleavage to release active ingredients [4, 65]. Nitrazepam can be efficiently reduced to 7-aminonitrazepam by *Clostridium leptum* from human gut [66], whereas the cardiac drug digoxin can undergo alkene cleavage by the human gut microbiota to produce dihydrodigoxin [67]. Hydrolysis is another critical metabolic pathway for pharmaceuticals by the gut microbiota. For instance, *Helicobacter pylori*, a bacterium found in human gut, can initially inactivate L-DOPA by decarboxylating it to generate *m*-tyramine and *m*-hydroxyphenyl-acetic acid via hydrolase activity [68]. Similarly, antibiotics including benzylpenicillin and chloramphenicol can also be dealkylated by the gut microbiota to counteract their adverse effects [69]. In addition, deconjugation mediated by microbial β-glucuronidases and other hydrolases can transform the detoxified pharmaceuticals (the conjugates), such as itirican (SN38) [70], acetaminophen [71], diclofenac [72], indomethacin [73], and triclosan [74], extending their pharmacological or toxicological effects.

Mycotoxins

Although mycotoxins are natural fungal metabolites, they have attracted global attention as emerging pollutants that adversely affect human health [75]. The transformation of deoxynivalenol (DON) into deepoxy-deoxynivalenol by the gut microbiota is an efficient detoxifying transformation that occurs by the gut microbiota (Supplementary Fig. S4) [76]. In addition, hydrolysis can also be conducted by the gut microbiota to detoxify mycotoxins, such as ochratoxin A [77]. The sulfate and glucuronide conjugates of mycotoxins (e.g. DON [75, 76] and zearalenone [78]) can also be rapidly deconjugated by the gut microbiota, extending their half-lives in the body.

Polymers and nanomaterials

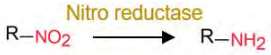
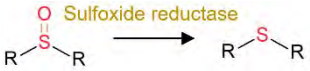
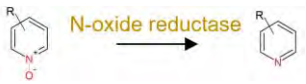
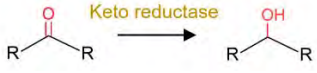
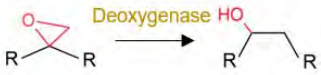
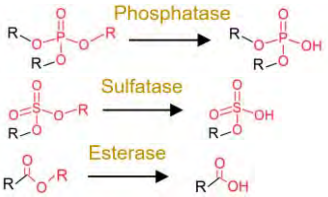
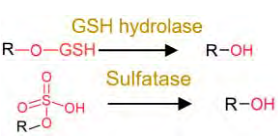
A key universal mechanism for polymer biotransformation by the gut microbiota involves enzymatic oxidative fragmentation initiated by microbial oxidases (e.g. cytochrome P450 and laccases), followed by depolymerization and assimilation. This pathway has been demonstrated for a range of synthetic polymers, such as polyethylene [79, 80], low-density polyethylene [81], polystyrene [82–84], polyvinyl chloride [85], and polylactic acid [86]. These processes ultimately metabolize polymers into monomers, low-molecular-weight organic compounds, and the subsequent CO_2 and H_2O. In addition, carbon nanomaterials have been confirmed to be transformed into endogenous organic metabolites via anaerobic fermentation in the gut, incorporating inorganic carbon into organic butyrate [87].

Other emerging pollutants

Bisphenol A and disinfection byproducts (e.g. chloroacetonitrile, dibromoacetic acid, and tetrabromopyrrole) are transformed in the simulator of human intestinal microbial ecosystem (SHIME), mitigating oxidative DNA damage [88, 89]. Furthermore, tetrabromobisphenol A and its analogs (e.g. tetrachlorobisphenol A and tetrabromobisphenol S) can suffer debromination and

Downloaded from https://academic.oup.com/ismej/article/19/1/wraf215/8268573 by National Science & Technology Library user on 14 October 2025

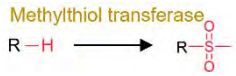
Table 1. General mechanisms and toxicological consequences of gut microbiota-driven transformation.

Category	Reaction types	General reaction mechanism	Representative chemical targets	Toxicology consequences
Reduction	Azo reduction		Azo-dyes and azo-antibacterial predrugs (i.e. balsalazide analogs and prontosil)	• Generate carcinogenic aromatic amines from azo-dyes; • Release products with efficacy (toxicity).
	Nitro reduction		Nitro-PAHs, benzodiazepines drugs (i.e. nitrazepam, clonazepam, and bromazepam), and metronidazole	• Decrease toxicity of nitro-PAHs; • Increase carcinogenicity of benzodiazepines.
	Alkene reduction		Deleobuvir and digoxin (the drugs)	• Decrease efficacy (toxicity).
	Sulfoxide reduction		Sulfur-containing drugs (i.e. omeprazole and sulfinpyrazone)	• Release products with efficacy (toxicity).
	N-oxide reduction		N-oxide prodrug (i.e. loperamide oxide) and H2 receptor antagonists (i.e. ranitidine and nitazidine)	• Release products with efficacy (toxicity) for the prodrug; • Decrease the efficacy of the antagonists.
	Keto reduction		Hydrocortisone (the endocrine drug) and zearalenone (the mycotoxin)	• Increase efficacy (toxicity) of zearalenone. • Increase toxicity of zearalenone.
	De-epoxidation		Mycotoxin (i.e. deoxynivalenol and nivalenol)	• Decrease toxicity.
	Dehalogenation		DDT, PCBs, and other organochlorine pesticides	• Decrease toxicity.
	Metal reduction		iAs^V	• Increase toxicity of iAs.
	Metal demethylation		CH_3Hg^I	• Decrease toxicity and bioavailability.
Hydrolysis	Dealkylation		Ester-containing drugs (i.e. carbetapentane citrate, ketorolac, and L-Dopa), organophosphate pesticides, organophosphate flame retardants and parabens	• Decrease toxicity and bioavailability in most cases.
	Deacetylation		N- or O-acetyl chemicals and drugs (i.e. acetaminophen, formanilide, and irinotecan) and acetyl mycotoxins (i.e. T-2 toxin)	• Increase bioavailability in most cases; • Sometimes increase toxicity (i.e. diltiazem, irinotecan, and spironolactone).
	Deglycosylation		Conjugates of drugs, personal care products, mycotoxins, pesticides, nirto-PAHs and plastic additive	• Increase bioavailability.
	Other deconjugation		Conjugates of drugs, personal care products, nirto-PAHs, and pesticides	• Increase bioavailability.

(continued)

Downloaded from https://academic.oup.com/ismej/article/19/1/wraf215/8268573 by National Science & Technology Library user on 14 October 2025

Table 1. Continued.

Category	Reaction types	General reaction mechanism	Representative chemical targets	Toxicology consequences
Functional group removal	Acetylation		Some drugs (i.e. 5-aminosalicylate, sulfapyridine and sulfasalazine)	• Decrease bioavailability in most cases.
	Methylthiolation		Organochlorine pesticides (i.e. PCB29 and chlorothalonil)	• Increase bioavailability in most cases.
	N-dealkylation		Some drugs and neonicotinoid pesticides	• Decrease toxicity
	Metal methylation		As, Bi, Hg, Sb, Se, and Te	• Decrease toxicity and increase bioavailability.
	Metal thiolation		As and Se	• Decrease toxicity and increase bioavailability.
Oxidation	Hydroxylation		PAHs and phenol	• Increase toxicity (estrogenicity) and bioavailability.
	Alkyl cleavage		Plastic additives	• Change toxicity (estrogenicity) and bioavailability.
	Oxidative depolymerization		Plastic and nanomaterials	• Decrease toxicity.

glycosylation by the human gut microbiota [90, 91], whereas microbial deglycosylation of the conjugates of these compounds is also observed [91]. Esters can increase the susceptibility of organophosphate flame retardants and phthalate esters to hydrolysis by the gut microbiota [92, 93]. In addition, our previous study on crucian carp has demonstrated that gut microbiota-mediated alkyl-cleavage significantly alters the estrogenic effects of bisphenol A and its analogs [94].

Overall, the gut microbiota-driven pollutant metabolic reactions generally include the following: (i) reduction (e.g. alkene reduction, azo reduction, de-epoxidation, dihydroxylation, dehalogenation, enoate reduction, hydrazine cleavage, keto reduction, nitro reduction, N-oxide reduction, and sulfoxide reduction); (ii) hydrolysis (e.g. deacylation, dealkylation, deamidation, decarboxylation, deconjugation, proteolysis, and thiazole ring-opening); (iii) functional group removal (e.g. acetylation, methylthiolation, N-dealkylation, and transamination); and (iv) oxidation. The extensive transformation of diverse environmental pollutants demonstrates the broad substrate diversity inherent to the gut microbiota metabolic capabilities.

Cross-species universality of the gut microbial transformation

Reduction reactions are widely prevalent microbial-mediated transformation processes for pollutants across 13 taxonomic groups (Fig. 1B). The metabolism mediated by the gut microbiota is widely regarded as a response-modifying process that reflects the energy demand of gut microbes [95]. Most of the gut parts of large animals are in reducing environments, and as a result the gut microbiota in the intestine cannot utilize oxygen as the terminal electron acceptor for respiration [41]. Consequently, in contrast to oxidation, which ranks first in host metabolic processes, the redox potential in the intestine is suitable for gut microbes because it transfers hydride equivalents or electrons (H^+ and $2e^-$) to substrates [5, 26, 27]. For example, dehalogenation reactions of halogenated organic compounds (primarily classified as POPs) have been widely observed in the guts of various species, including humans [46], rodents [45], earthworms [96], and apple maggots [97]. Parallel transformation conservation occurs for metal reduction. In studies of fish, rodents and humans, both the reduction and methylation could be mediated by the gut microbiota to inorganic and organic arsenic (iAs and oAs), encompassing the reduction, methylation, and thiolation pathways [61–63, 98, 99]. This metabolic versatility extends to the invertebrates' gut microbiota, where the *Escherichia coli*. From earthworm gut (*Eisenia foetida*) can reduce and methylate As [100]. Mycotoxin's detoxifying transformation further demonstrates cross-species conservation: reductive pathways efficiently transform DON, HT-2, nivalenol, verrucarol, and T-2 toxins in fish [101], chickens [102, 103], pigs [104], and humans [76].

Hydrolysis and functional group removal reactions are important mechanisms through which the gut microbiota participates in host energy metabolism; these two reactions can produce simple molecules that can be used for energetic purposes without relying on oxidants [26, 105]. For endosulfan, a special OCP with a sulfate group, endosulfan diol has been confirmed as a

Downloaded from https://academic.oup.com/ismej/article/19/1/wraf215/8268573 by National Science & Technology Library user on 14 October 2025

microbial triphenyl produced through hydrolysis by *Rhodococcus* found in earthworms [106]. The plasticizers with esters (e.g. di(2-ethylhexyl) phthalate and tri(2-butoxyethyl) phosphate) undergo hydrolysis by specific gut microbes from earthworms [92, 93] and fish [94], and the hydrolysis of OPs occurs exclusively in various mammals and invertebrates [107–109]. Deconjugation is also a widespread and highly efficient hydrolysis reaction that occurs across species (including humans [4, 70, 91, 110], other mammals [111, 112], fish [113], prawns [113], and mussels [113]) and across diverse xenobiotic classes, such as drugs, POPs, mycotoxins, and plasticizers. These reactions, which typically proceed rapidly, highlight the microbiota's inherent and host-independent capacity to transform conjugated compounds, regardless of specific host-microbiota interactions. In addition, N-dealkylation (the functional group removal reaction) can be rapidly conducted for pharmaceutical neonicotinoid pesticides or by the gut microbiota of worms and mammals [3, 114].

Evidence of pollutant oxidation reactions that are driven by the gut microbiota has also been reported from invertebrates to vertebrates, although oxidation reactions are typically oxygen-sensitive and require a significant amount of energy. In invertebrates, the relatively simple gut structure of invertebrates allows higher oxygen availability in their gut environment, thereby facilitating oxidative reactions [115, 116]; in contrast, vertebrate gut systems contain more anoxic gut environments, but CYP enzymes are highly abundant in several facultative anaerobic bacteria [117, 118]. For example, the ability of the gut microbiota to transform various plastics was discovered in studies based on earthworms [81], mealworms [83], superworms [84, 116], other invertebrates [119–121], and the mammals [122]. The facultatively anaerobic and strictly aerobic bacteria are ubiquitous in the gut may promote oxidation under both anoxic and oxic conditions [115, 116].

Although the gut microbiota across species shares a universality for the general pollutant transformations, species-specific differences in final outcomes often arise due to the simultaneous operation of diverse and intricate microbial transformation processes. For example, in earthworms, the gut microbiota primarily mediates the methylation of inorganic mercury (iHg) into methylmercury (MeHg), with sulfate-reducing bacteria (e.g. *Desulfovibrio*) serving as the key methylators [123]. In contrast, studies on fish have shown that while their gut microbiota can simultaneously drive both the methylation and demethylation of Hg [124, 125], where the demethylation process appears to be more efficient. Collectively, these cross-species examples illustrate conserved functional roles of the gut microbiota in pollutant transformation, serving as a critical modifier against environmental pollution.

General toxicological consequences of gut microbial transformation

Transformation processes driven by the gut microbiota have attracted much attention because they can significantly alter the bioavailability (pharmacokinetic parameters) of certain pollutants and induce changes in their toxicological effects (Table 1) [5, 7, 28]. The reduction reactions generally convert chemicals into more water-soluble metabolites and facilitate their excretion from microbial cells, but the toxicological outcomes are dependent on substrate specificity [26]. For example, nitro reduction generates amine metabolites with weak toxicity, and azo reduction generally induces compound carcinogenicity. The hydrolysis of the pollutant itself markedly reduces host exposure, whereas the deconjugation of the pollutant metabolites results in the reactivation of pollutants and increases their bioavailability in the gut (Table 1). In functional removal reactions, the installation or removal of specific groups can also affect the bioavailability and toxicity of pollutants. For example, the acetylation of pollutants (e.g. 5-aminosalicylate and sulfapyridine) has been shown to reduce toxicity (or efficacy) [126], whereas the methylation of heavy metals may increase their bioavailability and toxicity [127].

To date, few toxicokinetic studies have assessed the role of the gut microbiota in pollutant transformation and its combined impact on host metabolism. A bioavailability study of disinfection byproducts via SHIME revealed that ~ 60% of chloroacetonitrile, 45% of dibromoacetic acid, and 80% of tetrabromopyrrole underwent abiotic transformation in the stomach and small intestine. Subsequent transformation of the remaining compounds occurs in the colon, facilitated by the gut microbiota, underscoring the pivotal role of gastrointestinal transformation in the toxicology of these orally ingested pollutants [89]. Research has confirmed that the gut microbiota's efficiency in reducing nitrazepam to 7-aminonitrazepam is seven times greater than that of the liver [66]. A recent study utilizing a GF rat model for the global analysis of the physiological toxicokinetics of brivudine (a pharmaceutical) reported that 70% of the compound's transformation could be attributed to microbial processes [29]. In addition, a toxicokinetic model demonstrated that the gut microbiota contributed 44.0% and 18.4% to the metabolism of total and inorganic arsenic, respectively, in zebrafish [99]. However, current toxicokinetic studies remain insufficient in fully characterizing the contribution of the gut microbiota to pollutant ADME, thereby limiting the toxicological understanding of the microbiota's role in the context of pollutant exposure. Given the variable metabolic activity of the gut microbiota toward different pollutants and their inherent variability, this contribution is influenced by multiple factors, necessitating careful interpretation of existing data or context-specific application. Advanced models that integrate environmental complexity are imperative for evaluating the long-term toxicological impacts of gut microbiota-driven pollutant biotransformation in real-world exposure scenarios.

Major factors driving the gut microbial biotransformation

The intricate interplay among pollutants, the gut microbiota, and host physiology underscores the complexity of gut microbiota-driven pollutant transformation. To systematically deconstruct this complexity, our analysis progresses across three tiers: (i) pollutant structural and toxicological determinants of microbial susceptibility, (ii) the enzymatic machinery across bacterial phyla and their metabolic interplay with hosts, and (iii) host-specific modulators shaping microbial catalysis. This tripartite framework offers a unified perspective on how microbial pollutant transformation emerges from the confluence of chemical properties, microbial ecology, and host biology.

Pollutant effects on microbial transformation

The biotransformation potential of a chemical largely depends on its intrinsic structure and properties, which determine its resistance to transformation and ability to interact with specific enzymes [32, 36]. Multidimensional scaling clustering was employed to categorize the chemicals into groups of structurally similar compounds (SI-1; $n = 125$; Supplementary Table S7). This similarity-based clustering yielded 63 distinct clusters. To streamline the subsequent analysis, all clusters containing fewer than three molecules were consolidated into a single cluster,

Downloaded from https://academic.oup.com/ismej/article/19/1/wraf215/8268573 by National Science & Technology Library user on 14 October 2025

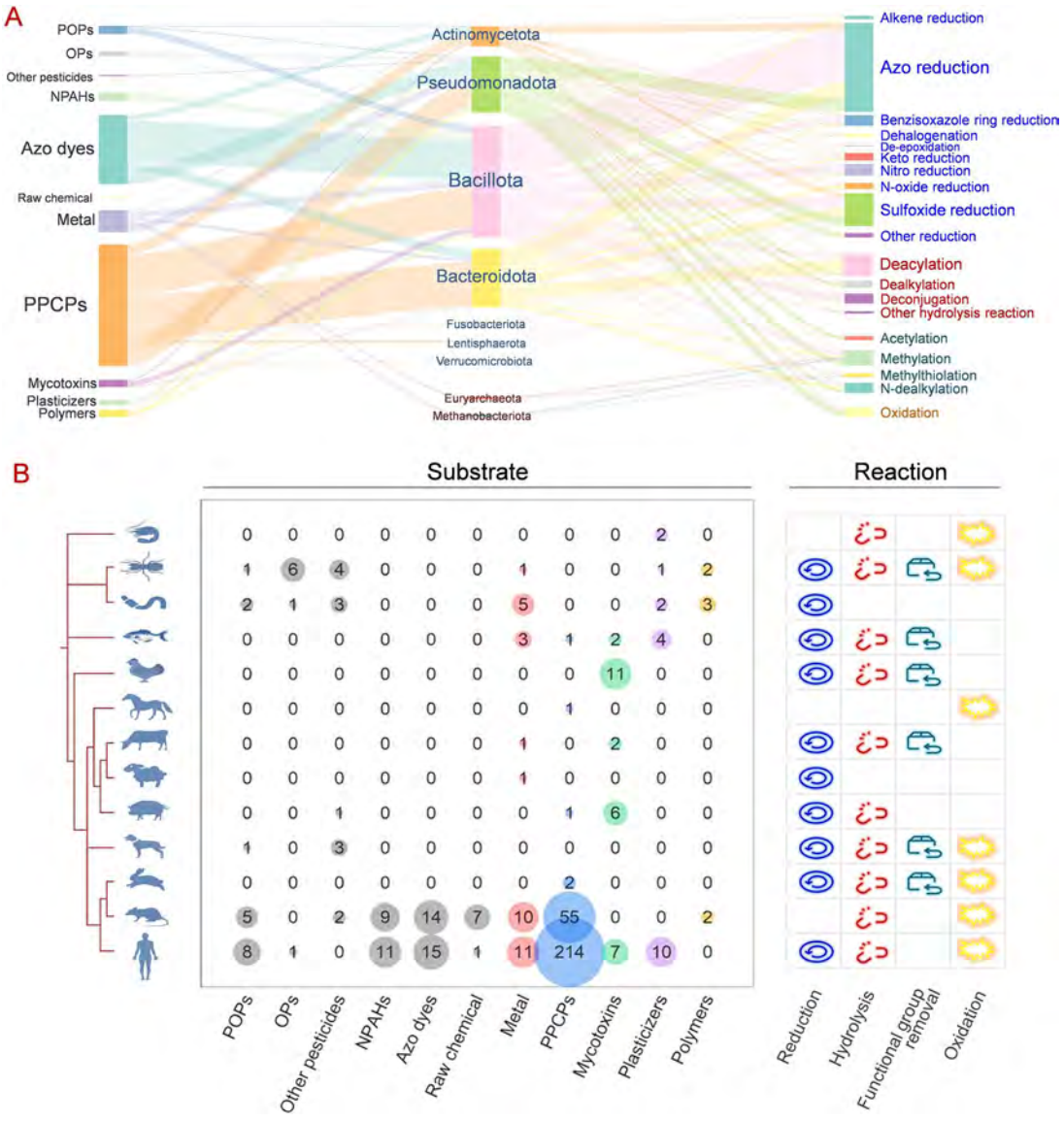


Figure 1. Distribution of pollutant biotransformation by gut microbes from mammals and non-mammal fauna. (A) Consensus evidence of pollutant–microbe–reaction triad can be found in Supplementary Tables S1–S6. (B) Diversity of transformable pollutants and reaction types across 13 taxonomic groups. The size of the circles represents in the left the number of transformable pollutants for a particular category on the left. The symbols on the right indicate whether a certain reaction was reported for the gut microbial transformation within a certain taxonomic group. Organisms categorized as follows (top to bottom): other invertebrates, diptera insects, worms, fish, chickens, horses, cattle, sheep, pigs, dogs, rabbits, rats, and humans. Abbreviations: OPs, organophosphate pesticides (OPs); NPAHs, nitrated polycyclic aromatic hydrocarbons; POPs, persistent organic pollutants; PPCPs, pharmaceuticals and personal care products.

designated Cluster 14 (Supplementary Fig. S5A). Consequently, certain clusters could be associated with specific transformation pathways (Supplementary Fig. S5B). Clusters 8, 10, and 12 are readily distinguishable by the presence of an azo group. The azo group is a key structural feature conducive to specific azo reduction reactions. For the compounds in Clusters 1 and 4, which encompass majority of nitro-PAHs, nitro reduction emerges as the most prevalent transformation reaction. In Cluster 1, chemicals lacking specialized functional groups are more likely to undergo oxidation or the removal of functional groups. Epoxy-containing compounds in Cluster 2 trigger de-epoxidation reaction, whereas halogenated compounds in Cluster 3 undergo dehalogenation. The Phase II conjugates in Clusters 9 and 13 primarily undergo glycosyl or glucuronosyl cleavage. Chemicals in Clusters 5, 6, and 11, which possess C-O, C-N, C-S, or ester bonds, are prone to hydrolysis reactions, including dealkylation and deacylation, as well as N-dealkylation. Overall, this analysis indicates that pollutant transformation by the gut microbiota is highly structure specific. Certain substructures, such as glycosidases-related groups, esters, nitro, azo, alkene, keto, N-oxide, sulfoxide, and epoxy substructures, increase the susceptibility of pollutants to microbial transformation.

Pollutants can exert dose-dependent constraints on biotransformation via direct toxicity to the gut microbiota. Antibiotics, as the most disruptive pollutants, can induce acute microbial suppression, compositional shifts, and metabolic capacity changes [128, 129]. Similarly, exposure to non-antibiotic, including pharmaceuticals and environmental chemicals, may disrupt enzymatic pathways (e.g. azoreductases and β-glucuronidases) critical for pollutant transformation, leading to the accumulation

Downloaded from https://academic.oup.com/ismej/article/19/1/wraf215/8268573 by National Science & Technology Library user on 14 October 2025

of toxic intermediates and compromised detoxification [130]. Polybrominated biphenyls (BDE-209) and perfluorooctane sulfonate reduce microbial diversity and short-chain fatty acid production in both carp and infants [131, 132], whereas digoxin enhances reductase activity and pollutant transporter expression [130]. Furthermore, exposure to dioxins and heavy metals has been linked to increased microbial transformation (and/or resistance) genes, as demonstrated by shotgun metagenomic analysis of 359 Italian subjects across contamination gradients [133]. This transformation capacity erosion illustrates a cascading effect within "One Health" frameworks, wherein antibiotics and other microbiologically toxic pollutants diminish the gut microbiota-driven transformation, thereby magnifying the adverse impacts of other pollutants. Within this framework, understanding how antibiotic and non-antibiotic pollutants alter the gut microbial function is vital not only for elucidating the gut microbiota-driven transformation to mixed pollutants but also for revealing the bidirectional interplay between pollutants and the gut microbiota.

Microbial mechanisms of transformation

One of the goals in gaining a mechanistic understanding of microbial transformation is identifying and classifying the functions of key microbes. We compiled information for 109 isolated gut microbes known to secrete core XME families: hydrolases, oxidoreductases, transferases, and lyases (Fig. 2; Supplementary Table S8). Overall, the xenobiotic-metabolizing microbes appeared to be dispersed across four major bacterial phyla (Bacillota, Pseudomonadota, Actinomycetota, and Bacteroidota). The phylum Bacillota was the most frequently observed phylum of XME microbes in these datasets, consisting of the genera *Clostridium* (25.4%), *Eubacterium* (14.5%), *Lactobacillus* (9.1%), and *Enterococcus* (9.1%). *Bifidobacterium* (69.2%) is the most common genus in the phylum Actinomycetota and is characterized by the activities of azo reductase, nitro reductase, β-glucuronidase, and arylsulfatase. The genera *Bifidobacterium* (in Actinomycetota), *Bacteroides* (in Bacteroidota), *Citrobacter* (in Pseudomonadota), *Klebsiella* (in Pseudomonadota), and *Escherichia* (in Pseudomonadota) are also possible sources of additional xenobiotic-metabolizing bacteria. *E. coli*, the gut species with the highest XME activity, is capable of catalyzing the hydrolysis, reduction, oxidation, and transfer reactions of xenobiotics [107, 134, 135]. However, the "bacteria-centric" perspective presented herein reflects the current state of the literature rather than disregarding the potential significance of other microbiota components, and the roles of archaea, fungi, and viruses in pollutant transformation should not be overlooked. For example, the archaeal genus *Methanobrevibacter* represents a primary source of cellulases in the gastrointestinal tract of ruminants [136, 137], whereas the human gut archaea such as *Methanosphaera stadtmanae* and *Methanobrevibacter smithii* have demonstrated methyltransferase activity toward arsenic (As) [58, 59].

Although the isolation method provides direct insights into the gut strains involved in pollutant transformation, it clearly overlooks those uncultured gut microbes and the microbial interactions. In a previous study of XMEs in human gut microbiota (397 gut metagenomes) using metagenomic approaches, 850 bacterial genera were found to encode at least one XME (including CYP, monoamine oxidase, epoxide hydrolase, alcohol and aldehyde dehydrogenase, thiopurine methyltransferase, *N*-acetyl transferase, and glutathione *S*-transferase) [136]. In many cases, the diversity of the gut microbiota leads to a greater variety of microbial enzymes, and the combination of synergistic, beneficial, and antagonistic interactions among members of the gut microbiota may have a significant effect on the microbial transformation of pollutants in the digestive system [137]. Horizontal gene transfer events among the gut microbiota can also expand their substrate utilization range, enhance fermentation capacity, and provide new electron transfer pathways, thereby improving adaptation to anaerobic environments and increasing pollutant transformation efficiency [138–140]. Metagenomics has enabled the discovery of previously unrecognized enzymes, reactions, and organism-specific pathways by systematically expanding the catalog of xenobiotic-metabolizing pathways beyond culturable species [133]. Therefore, this approach is preferable for clarifying the diverse genes and pathways expressed by poorly represented microbes, the interactions of transformation-associated microbes with other microbes, and their adaptive evolution to pollutants on the basis of microbial co-occurrence in future studies.

Host effects on the microbial transformation

The gut morphology, physiology, and function exert a combined influence on the colonization of the gut microbiota (Box 2), which reflects adaptations to ecological niches and environmental conditions (e.g. pH, lumen flux, and peristalsis). There is little microbial colonization in the stomach due to the extremely acidic environment (pH 1.5), whereas the density of the gut microbiota increases significantly in the distal small intestine (also known as the ileum) and colon [5, 141]. Another gradient of microbial distribution can be found along the tissue–lumen axis, wherein few bacteria adhere to the tissue or mucus but many bacteria are found in the lumen [142, 143]. Physiological characteristics of the host's digestive system are also important determinants of the pollutant retention time and their opportunities in contact with the gut microbiota. The slow dietary transport and abundant microbial colonization make the distal intestine an ideal site for pollutant transformation [5, 144, 145]. For example, the extended digesta retention time in ruminants also allows for more extensive microbial transformation of complex and persistent pollutants [146]. In addition, vertebrate microbial stability enables predictable pollutant transformation efficiency, whereas the structural simplicity and environmental sensitivity of invertebrate guts may lead to high variability in transformation pathways and outcomes across individuals [147].

The composition and activity of the gut microbiota are influenced by a combination of various internal factors (such as the host's sex, lifestyle, and genetic characteristics) and external factors (such as diet) [30, 37, 38]. Thus, the physiological functions and lifestyle habits of the host inevitably affect the gut microbial community and enzyme activity. In a recent large-scale metagenome analysis, community similarity across hosts was determined basis of the initial inoculum and niche-specific factors such as the oxygen level, temperature, pH, and organic carbon availability rather than the phylogenetic relatedness of the hosts [30]. Taking digestive enzymes as an example, there are visible differences in the composition of gut microbes with digestive enzyme activity across host species from humans, mammals, birds, amphibians, and fish to invertebrates (Supplementary Table S9). The activity levels of lipases, proteases, and trypsases in the gut microbiota of carnivorous animals are much higher than those in herbivorous species [161]. In omnivorous animals, the microbiome in the gut tract mainly consists of protein-hydrolyzing bacteria and starch-, lipid-, and cellulose-decomposing bacteria [161]. Feeding

Downloaded from https://academic.oup.com/ismej/article/19/1/wraf215/8268573 by National Science & Technology Library user on 14 October 2025

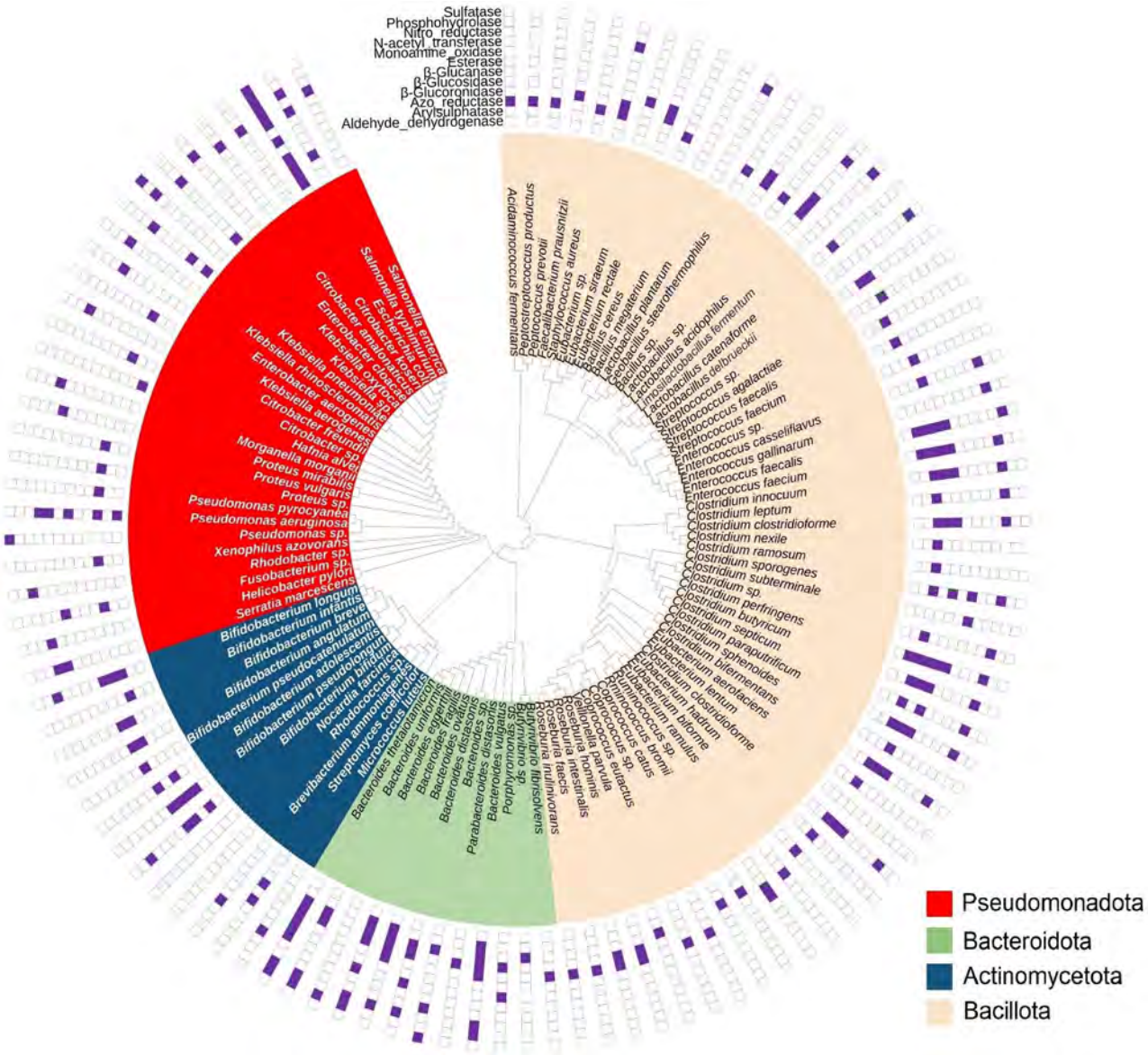


Figure 2. Phylogenetic tree showing the isolated gut bacterial strains with xenobiotic-metabolizing enzyme (XME) activities. The phylogenetic relationships among the reported bacterial strains were extracted from the National Center for Biotechnology Information (NCBI) taxonomic database classification system. The data points plotted outside the tree represent the xenobiotic metabolism ability of each species.

ruminants a starch-free diet allows the gut microbiota to require almost no intestinal amylase to function but results in the presence of a series of cellulose degraders in the rumen [162]. Moreover, amylase activity in the digestive tract of omnivorous fishes is generally greater than that in the digestive tract of carnivorous fishes [163]. Previous research revealed differences in the metabolism of both endogenous and xenobiotic substances in the enriched gut microbiota of six marine species caused by differences in their feeding habitats [113, 164]. Therefore, the understanding of the effects of the host's physiological signatures and feeding habits on the gut microbiota must be further improved to account for variations in the microbiota in response to pollutants, especially in comparisons across species. Such interspecific differences in gut anatomy and microbial function underscore the importance of considering host-specific gut models when predicting the biotransformation and toxicological consequences of pollutants.

Calling for novel methodologies for elucidating gut microbiota-driven transformation

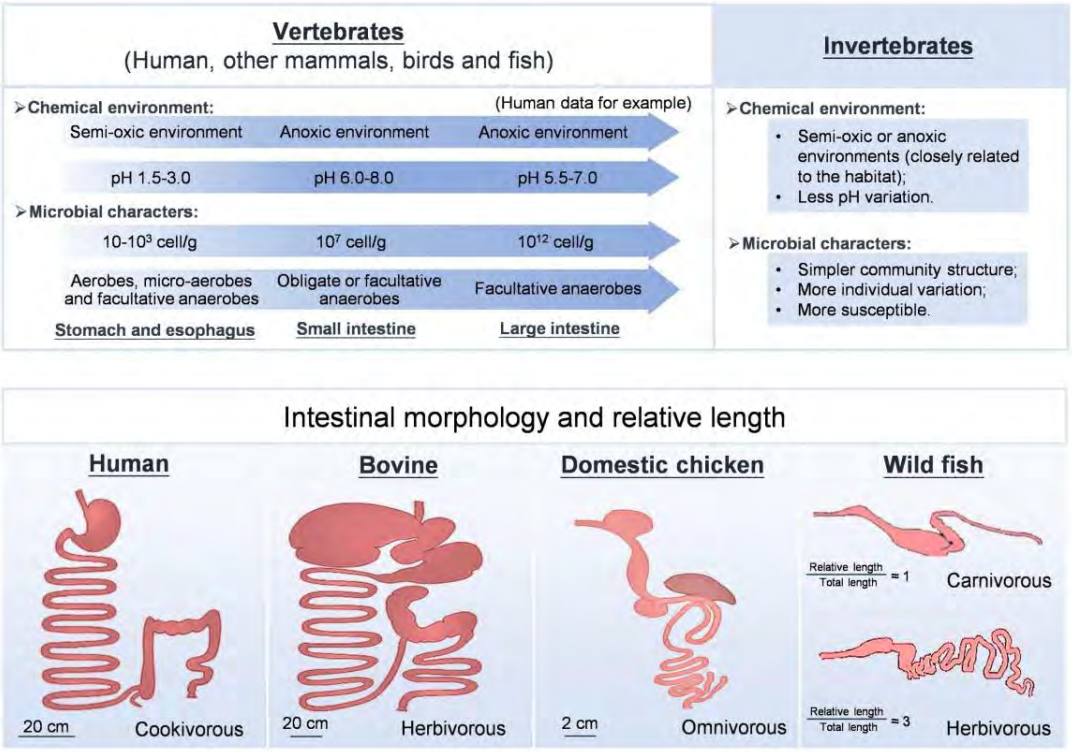
Although significant advances in recent years have paved the way for a more comprehensive toxicological perspective of gut microbiota-driven pollutant transformation, the major challenge is that the existing methodologies may no longer be adequate for gaining mechanistic insights into the transformation process under complex "pollutant–gut microbiota–host" interactions (Fig. 3).

Developing prediction tools for the gut microbiota-driven transformation of pollutants

Given the impracticality of experimentally investigating the gut microbial transformation of every environmental pollutant, computational prediction of transformation potential, scope, and

Downloaded from https://academic.oup.com/ismej/article/19/1/wraf215/8268573 by National Science & Technology Library user on 14 October 2025

Box 2. Distribution characteristics of the microbiota in the gut systems of humans and other animals.



Spatial heterogeneity of both chemical conditions and microbial signatures varies along the digestive tract [148]. In humans, the mucosal surface area of the gastrointestinal (GI) tract is ~ 200–300 m^2, harboring various microbes, including 10^{13}–10^{14} cells of 400 different microbial species and subspecies [149]. Anaerobic bacteria are the main components of the stable intestinal microbiota, and their numbers are 100 to 1000 times higher than those of aerobic bacteria and facultative anaerobes [150]. The general ranking for bacterial number in human tissues from high to low is as follows: large intestine > small intestine > duodenum and stomach [5, 141]. In addition, the core gut microbes across vertebrate species are relatively stable including bacterial phyla of Actinomycetota, Bacillota, Bacteroidota, Pseudomonadota, Fibrobacterota, Fusobacteriota, and Verrucomicrobiota, and other microbes of fungi, archaea, protozoa, and viruses [151, 152], while > 98% of isolated genetic sequences present in the gut come from bacteria in vertebrates [38, 153]. In invertebrates, the tube-like gut provides a semi-oxic or anoxic environment with stable moisture conditions and nutrient pools from the foregut to the hindgut, which facilitates colonization through facultatively anaerobic bacteria [44]. In contrast, the simple invertebrate digestive system induces environmentally susceptible gut microbiota with high interindividual variability and no consistent core microbiome [44]. All vertebrates, including fish, mammals, and humans, have relatively complex but different gut systems [154–156], which equipping them with distinct digestive capacities (the comparative gut structures illustrated were redrawn based on anatomical data from the cited literatures). The average total intestinal transit time for healthy adults is 70 h (in the range of 23–168 h), with a majority (~80%) of the time spent in the large intestine (colon) rather than other sections [5, 144, 145]. Ruminant mammals (e.g. bovine) have developed a downstream stomach or hindgut, thereby extending the digesta retention time in the hindgut by as long as 96 h [157]. In fish, the gut evacuation time measured *in situ* generally ranges from 6 to 86 h [158–160], with herbivorous species exhibiting extended digestion periods.

specificity is essential. Reaction mining and machine learning approaches have led to tools such as BioTransformer [165], DrugBug [166], and GutBug [167], which predict potential microbial biotransformation pathways and enzyme classes (EC numbers) based on chemical structure. However, reliable prediction remains challenging due to the complexity and dynamic nature of the gut microbiome and the scarcity of high-quality training data across diverse conditions. Advances in high-throughput technologies are aiding the development of better-curated databases. For example, integrated genetic and metabolomic analyses have been used to identify gut microbes and enzymes involved in drug metabolism [3], whereas microbiome-derived metabolic screening combines culturing, metagenomics, and transformation assays to link genes to functions [4]. Although not specifically designed for gut pollutant transformation studies, numerous databases containing biological and chemical information can be leveraged to develop accurate predictive models through integration or as foundational resources, such as the metabolism pathway databases (e.g. KEGG, MetaCyc, and Reactome), enzyme-specific databases (e.g. CAZy, Pfam, and UniProt), chemical–enzyme interaction databases (e.g. ChEMBL), and protein–protein interaction databases (e.g. STRING). Especially, genomic context prediction methods (i.e. gene co-occurrence, co-expression profiles, and genomic neighborhood) as implemented in tools such as STRING can provide a powerful "guilt-by-association" approach for hypothesizing novel pathway components in non-model organisms [168]. Artificial intelligence and the subdomains machine learning and natural language processing, which integrate pathways, enzymes, metabolites, and kinetics from many biotransformation studies, are recommended for chemoinformatic and bioinformatic analyses. This could enable more precise tools to quickly screen for pollutant candidates prone to microbial transformation, which will support more finely targeted mining and the mechanistic analysis of associations between enzymes and specific reactions.

Downloaded from https://academic.oup.com/ismej/article/19/1/wraf215/8268573 by National Science & Technology Library user on 14 October 2025

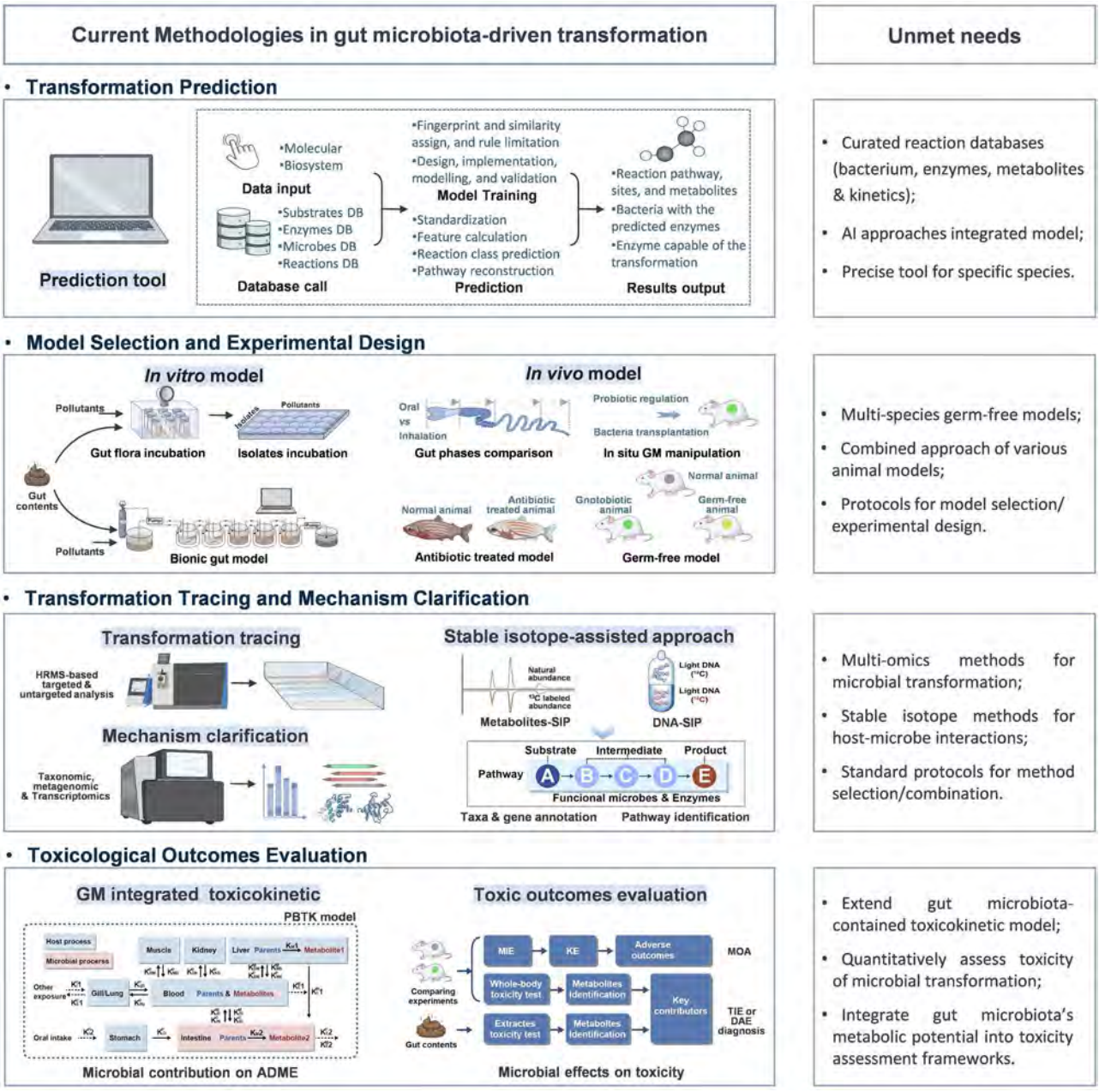


Figure 3. Existing methodologies and development directions for gut microbiota-driven pollutant transformation. Abbreviations: DB, database; AI, artificial intelligence; GM, gut microbiota; HRMS, high-resolution mass spectrometry; SIP, stable isotope probing; PBTK, physiologically based toxicokinetics; ADME, absorption, distribution, metabolism, and excretion; MIE, molecular initiating event; KE, key event; MOA, modes of action; TIE, toxicity identification evaluation; EDA, effect-directed analysis.

Constructing advanced experimental models and selection guidelines for gut microbiota-driven transformation of pollutants

Current experimental models for studying gut microbiota-driven pollutant transformation include both *in vitro* and *in vivo* systems, each with distinct advantages and limitations in replicating the gut physiology and microbial complexity. *In vitro* models, such as batch cultures with fecal samples [169], are accessible and ethically advantageous but are limited by the poor culturability of many gut species [170–172]. Continuous culture simulators (e.g. SHIME [59, 62, 89], the simulation of the mammal intestinal microbial ecosystem [173], and the fish digestion model [158]) can better mimic intestinal conditions and enable direct observation of microbial metabolism, but they still struggle to fully replicate critical gut features such as pH, redox potential, and microbial diversity. *In vivo* gut microbiota manipulation models, including germ-free (GF) animals, antibiotic-treated models, and fecal microbiota transplantation (FMT) models, can provide direct functional insights but face translational and practical challenges [5, 174, 175]. GF rodents are relatively ideal models but still exhibit anatomical and metabolic abnormalities and limited human extrapolation [5]. They also require stringent maintenance and exhibit morphological and functional abnormalities such as significant cecal enlargement and reduced absorption efficiency [5]. Among aquatic species, only GF zebrafish at the larval stage are available and widely used as a model for gut microbiome

Downloaded from https://academic.oup.com/ismej/article/19/1/wraf215/8268573 by National Science & Technology Library user on 14 October 2025

research [99, 158]. In addition, the FMT model is applicable only for studying specific bacteria upon successful colonization. To enhance reproducibility and biological relevance, future efforts should focus on developing multi-species gnotobiotic models, humanized microbiota mouse models, and integrated systems that combine *in vitro* realism with *in vivo* validity. Novel technologies such as intestinal organoids, 3D cell cultures, or gut-on-a-chip systems offer more accurate biological replication [176], enabling simulation of host responses and supporting reliable *in vitro–in vivo* extrapolation. There is also a growing need to develop standardized selection guidelines that consider research objectives, pollutant properties, and the microbial ecological context to facilitate model comparison and data integration.

Integrating technologies for the description and tracing of transformation mechanisms

Elucidating the complex interactions among microbial consortia and host cells during gut-driven pollutant transformation requires interdisciplinary strategies integrating microbiology, analytical chemistry, omics technologies, and computational biology. This requires interdisciplinary approaches that combine molecular biology, analytical chemistry, laboratory experiments, and data science [177]. Microbiological techniques, such as conventional culture, single-cell sequencing, metabarcoding, metagenomics, transcriptomics, proteomics, metabolomics, and their combinations, are essential for studying composition and function of the gut microbiota [19, 175]. The study of the enzymes and metabolic pathways of known gut microbes can also provide clues to support microbiome discoveries. Integrating multiomics data provides genetic insights into transformation enzymes, while combining omics with microbial metabolic network analysis helps clarify microbial relationships during metabolism.

Although advanced chemical analysis can detect trace levels of gut metabolites, host-microbe-metabolite interactions remain difficult to characterize. Stable isotopes (e.g. ^{13}C, ^{15}N, and ^{18}O) help trace low-level or cometabolic activities. The preferential breakage of bonds for light isotopes and heavy isotopes (^{13}C) results in a gradual increase in the enrichment of heavy isotopes in the parent compound compared with the metabolites [178]. Compound-specific isotope analysis examines isotope ratios to identify unique biotransformation pathways and fractionation-causing reactions [179], thereby distinguishing pollutant transformation from host–microbe interactions. Stable isotope-assisted metabolomics (SIAM) enables sensitive, untargeted detection of isotope-labelled pollutant metabolites, enhancing high-resolution mass spectrometry for unknown metabolite characterization [180, 181]. SIAM can be used to track isotopic labels globally without preconceptions about pollutant fate [182]. Stable isotopes can also link transformation activities with specific microbial populations and assimilation mechanisms. Stable isotope probing (SIP) methods, including DNA-SIP, metagenomic-SIP, transcriptome-SIP, protein-SIP, and single-cell SIP, provide sequence and functional data on potential transformation agents by monitoring labelled atom incorporation into nucleic acids [183, 184]. Time-dependent ^{13}C-metabolite flux analysis (^{13}C-MFA) traces isotopic ratios in key metabolic pathways, revealing gut transformation processes [185]. For example, ^{13}C-MFA successfully elucidated the microbial fermentation of ^{13}C-labelled carbon nanomaterials in mice [87], demonstrating its ability to uncover *in situ* gut symbiotic metabolism. These integrative, isotope-enabled approaches allow mechanistic exploration of pollutant transformation at the molecular, cellular, and ecosystem levels, offering a powerful framework for future gut microbiome research.

Advancing toxicological assessment approaches for gut microbiota-driven pollutant transformation

Despite early hints of its pollutant-transforming role, the gut microbiota's direct toxicity-related interactions with pollutants, drugs, and xenobiotics may represent just the tip of the iceberg [28, 186]. Beyond these direct impacts (e.g. "first-pass metabolism" and "enterohepatic circulation"), two key non-transformation mechanisms also influence pollutant bioavailability: (i) changes in bioavailability (e.g. gut mucosal barrier alterations or microbiota-mediated pollutant adsorption) [187] and (ii) interference with the host's detoxification mechanisms [5, 188]. For instance, gut microbes can alter pollutant absorption by affecting mucosal integrity or through direct adsorption. *Lactiplantibacillus plantarum* can reduce PAH uptake via surface binding [189], while some certain bacteria can deplete pharmaceuticals through bioaccumulation without structural modification [190]. Comparative studies in germ-free versus colonized animals have further revealed microbiota-induced changes in host gene expression related to xenobiotic metabolism in the gut and liver [191, 192], highlighting the microbiome's systemic influence on toxicological responses.

Toxicological assessments must be integrated into gut microbiota transformation studies. For example, product identification coupled with toxicity assessments (i.e. effect-directed analysis and toxicity identification evaluation) can reveal key mechanisms in *in vitro* gut microbiota models. *In silico* tools such as quantitative structure–activity relationships, quantitative cationic–activity relationships, quantitative structure–nanotoxicity relationships, and structural can be employed to predict the toxicity of gut metabolites. In addition, the application of a physiologically based toxicokinetic (PBTK) model incorporating gut microbial transformation can clarify associations between the microbiota and *in vivo* pollutant toxicokinetics. PBTK models can be developed for GF or antibiotic-treated animal comparisons to describe both microbiota- and host-driven transformation processes [29]. These approaches facilitate the elucidation of the microbially mediated toxicological effects of pollutants by providing a quantitative framework for understanding the role of the microbiota in pollutant toxicokinetics. Given the tremendous progress in biochemistry, microbiology, and toxicology, a comprehensive interdisciplinary methodological framework for the more in-depth exploration of the role of the gut microbiota in toxicology is urgently needed.

Conclusions and prospects for progress

The transformation of environmental pollutants by the gut microbiota greatly impacts the effects of exposure to and the toxicology of these pollutants in humans and animals. This review summarizes the emerging understanding of the contributions of the gut microbiota to pollutant transformation, covering a wide range of host species and chemical classes. The main transformation reactions that can be driven by the gut microbiota include reduction, hydrolysis, functional group removal, and oxidation. These reactions are connected to the metabolic enzymes that have developed in the gut microbiota, allowing them to directly transform specific pollutants and regulate their MOA and ADME properties in the host. In addition, this review provides an overview of existing methodologies and future

Downloaded from https://academic.oup.com/ismej/article/19/1/wraf215/8268573 by National Science & Technology Library user on 14 October 2025

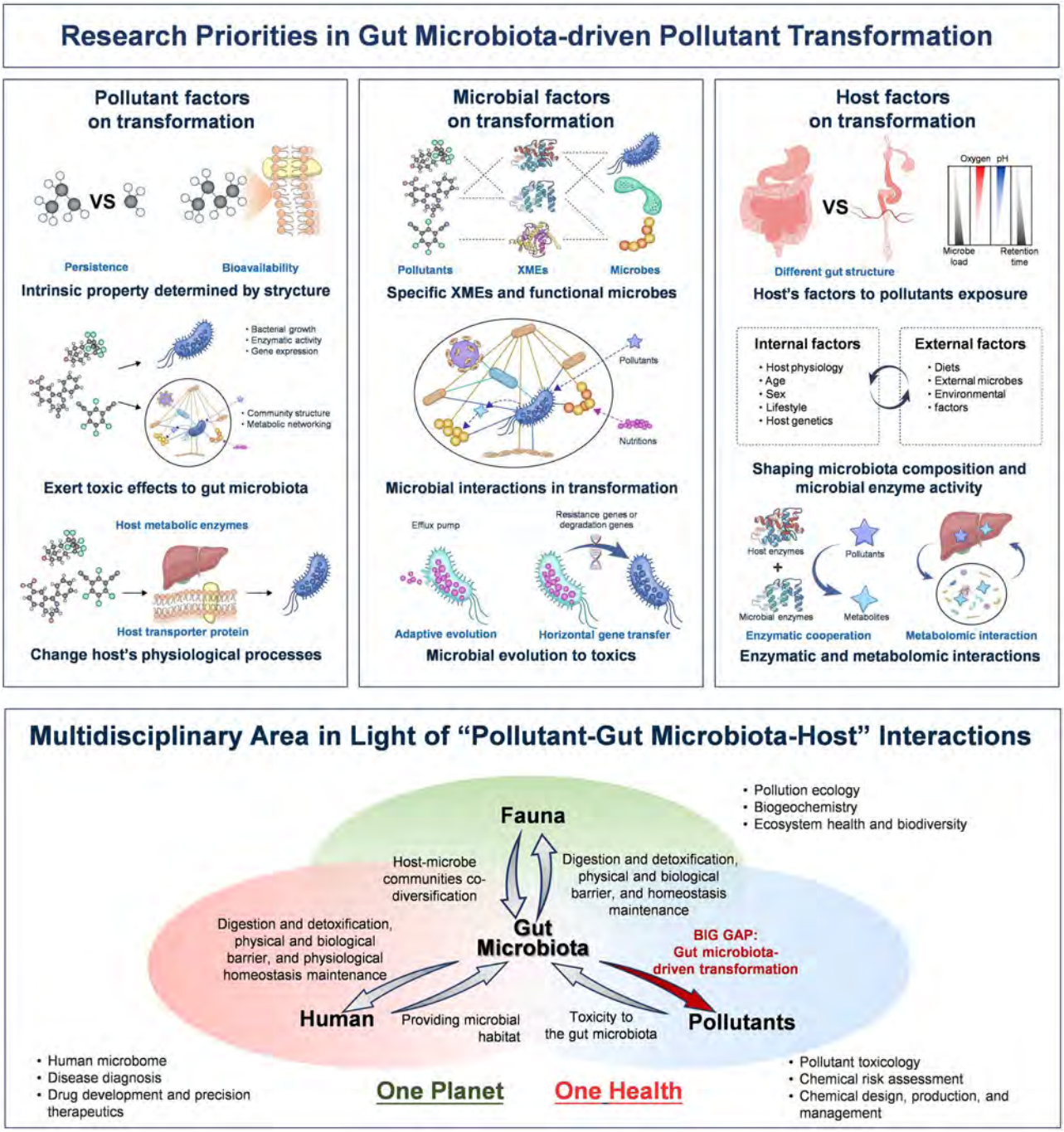


Figure 4. Key goals for investigating gut microbiota-driven transformation and multidisciplinary research in light of "pollutant–gut microbiota–host" interactions.

development directions to systematically elucidate gut microbiota-driven transformation and its toxicological consequences. The key to the successful investigation of gut microbiota-mediated transformation is to efficiently combine transformation consequences with microbial and compound-specific features, which requires highly multidisciplinary research dedicated to elucidating "pollutant–gut microbiota–host" interactions (Fig. 4). In the opinion of this research group, the following key issues should be addressed in the future:

- Pollutant transformation by gut microbial communities involves both dose effects and mixture effects. Future studies should clearly identify the long-term toxic effects and threshold concentrations for specific compounds and the co-metabolism of complex pollutant mixtures in the assessment of the effects of the host and gut microbiota on environmental pollutants in the real world.
- Owing to the complex structure of gut microbial communities, future studies should systematically explore the functional implications of bacteria and enzymes involved in transformation processes, the mechanistic characterization of interactions among bacteria, and the influence of ecosystem-wide changes in the microbiome on transformation outcomes.

Downloaded from https://academic.oup.com/ismej/article/19/1/wraf215/8268573 by National Science & Technology Library user on 14 October 2025

- Considering that pollutant transformation can be recognized as a combined host–microbiota process, a systems biology view of host–microbiota interactions should be established for pollutant transformation mechanisms, including microbial modulation, enzymatic cooperation, and metabolomic interactions.

Recognizing the gut microbiota's pivotal role as a universal modifier of pollutant exposure underscores the need to integrate "pollutant–gut microbiota–host" interactions into the"One Planet, One Health" concept. However, gut microbiota-driven transformation remains an underexplored research frontier and is often overlooked due to its inherent complexity and interdisciplinary nature. First, insights into gut microbiota-mediated pollutant transformations have led to advancements in chemical design, pollutant management, risk assessment, and toxicology. Beyond this, characterizing population-specific microbial metabolic functions could significantly enhance environmental health research, drug development, precision medicine, and other transdisciplinary fields aligned with the "One Planet, One Health" notion. Ultimately, given the potential relationships between healthy host microbiota relationships at the micro level and ecosystem health and homeostasis at the macro level, understanding gut microbial transformation holds promise as a path for ecological research on ecosystem changes and biodiversity loss across all ecosystems on Earth in the context of the Anthropocene.

Acknowledgements

This work was supported jointly by the National Natural Science Foundation of China (42277390, 42322710, 42325603, and 42494884), Guangdong Basic and Applied Basic Research Foundation, China (2024B1515020074), and Guangxi Science and Technology Program (AD25069075).

Author contributions

Rui Hou and Xiaowei Jin conceived the idea, compiled the metadata and undertook analysis, assembled the authorship team, and drafted the manuscript and figures. Jingchuan Xue, Chengzhi Chen, and Yuanqiang Zou contributed to the data analysis and methods. Kefu Yu, Peiyuan Qian, Wei Zhang, Jizhong Zhou, Si Zhang, and Zhifeng Yang provided valuable suggestions on different aspects of this review. Jingchun Feng and Xiangrong Xu reviewed and edited the manuscript. All the authors commented on the draft and gave final consent for the review.

Supplementary material

Supplementary material is available at *The ISME Journal* online.

Conflicts of interest

The authors declare no competing financial interest.

Funding

None declared.

Data availability

All data are available in the main text or the supplementary materials.

References

1. Alpizar F, Backhaus T, Decker N. *et al. Un Environment Global Chemicals Outlook ii-from Legacies to Innovative Solutions: Implementing the 2030 Agenda for Sustainable Development*. United Nations Environment Programme, 2019.
2. Lee W-J, Hase K. Gut microbiota–generated metabolites in animal health and disease. *Nat Chem Biol* 2014;**10**:416–24. https://doi.org/10.1038/nchembio.1535
3. Zimmermann M, Zimmermann-Kogadeeva M, Wegmann R. *et al.* Mapping human microbiome drug metabolism by gut bacteria and their genes. *Nature* 2019;**570**:462–7. https://doi.org/10.1038/s41586-019-1291-3
4. Javdan B, Lopez JG, Chankhamjon P. *et al.* Personalized mapping of drug metabolism by the human gut microbiome. *Cell* 2020;**181**:1661–79.e22. https://doi.org/10.1016/j.cell.2020.05.001
5. Sousa T, Paterson R, Moore V. *et al.* The gastrointestinal microbiota as a site for the biotransformation of drugs. *Int J Pharm* 2008;**363**:1–25. https://doi.org/10.1016/j.ijpharm.2008.07.009
6. Sommer F, Bäckhed F. The gut microbiota—masters of host development and physiology. *Nat Rev Microbiol* 2013;**11**:227–38. https://doi.org/10.1038/nrmicro2974
7. Wilson ID, Nicholson JK. Gut microbiome interactions with drug metabolism, efficacy, and toxicity. *Transl Res* 2017;**179**:204–22. https://doi.org/10.1016/j.trsl.2016.08.002
8. Clarke G, Stilling RM, Kennedy PJ. *et al.* Minireview: gut microbiota: the neglected endocrine organ. *Mol Endocrinol* 2014;**28**:1221–38. https://doi.org/10.1210/me.2014-1108
9. Zhu D, An X-L, Chen Q-L. *et al.* Antibiotics disturb the microbiome and increase the incidence of resistance genes in the gut of a common soil collembolan. *Environ Sci Technol* 2018;**52**:3081–90. https://doi.org/10.1021/acs.est.7b04292
10. Zhang S, Jin Y, Zeng Z. *et al.* Subchronic exposure of mice to cadmium perturbs their hepatic energy metabolism and gut microbiome. *Chem Res Toxicol* 2015;**28**:2000–9. https://doi.org/10.1021/acs.chemrestox.5b00237
11. Zhai Q, Yu L, Li T. *et al.* Effect of dietary probiotic supplementation on intestinal microbiota and physiological conditions of nile tilapia (*Oreochromis niloticus*) under waterborne cadmium exposure. *Antonie Van Leeuwenhoek* 2017;**110**:501–13. https://doi.org/10.1007/s10482-016-0819-x
12. Zhang L, Nichols Robert G, Correll J. *et al.* Persistent organic pollutants modify gut microbiota–host metabolic homeostasis in mice through aryl hydrocarbon receptor activation. *Environ Health Perspect* 2015;**123**:679–88. https://doi.org/10.1289/ehp.1409055
13. Choi Jeong J, Eum Sung Y, Rampersaud E. *et al.* Exercise attenuates pcb-induced changes in the mouse gut microbiome. *Environ Health Perspect* 2013;**121**:725–30. https://doi.org/10.1289/ehp.1306534
14. Xu C, Liu Q, Huan F. *et al.* Changes in gut microbiota may be early signs of liver toxicity induced by epoxiconazole in rats. *Chemotherapy* 2014;**60**:135–42. https://doi.org/10.1159/000371837
15. Luo Y, Wang X-R, Ji L-L. *et al.* Epr detection of hydroxyl radical generation and its interaction with antioxidant system in carassius auratus exposed to pentachlorophenol. *J Hazard Mater* 2009;**171**:1096–102. https://doi.org/10.1016/j.jhazmat.2009.06.132 1102.
16. Motta EVS, Raymann K, Moran NA. Glyphosate perturbs the gut microbiota of honey bees. *Proc Natl Acad Sci U S A* 2018;**115**:10305–10. https://doi.org/10.1073/pnas.1803880115

Downloaded from https://academic.oup.com/ismej/article/19/1/wraf215/8268573 by National Science & Technology Library user on 14 October 2025

17. Chen H, Wang B, Gao D. *et al.* Broad-spectrum antibacterial activity of carbon nanotubes to human gut bacteria. *Small* 2013;**9**:2735–46. https://doi.org/10.1002/smll.201202792
18. Wang H-T, Ding J, Xiong C. *et al.* Exposure to microplastics lowers arsenic accumulation and alters gut bacterial communities of earthworm *Metaphire californica*. *Environ Pollut* 2019;**251**:110–6. https://doi.org/10.1016/j.envpol.2019.04.054
19. Adamovsky O, Buerger AN, Wormington AM. *et al.* The gut microbiome and aquatic toxicology: an emerging concept for environmental health. *Environ Toxicol Chem* 2018;**37**:2758–75. https://doi.org/10.1002/etc.4249
20. Ohkusa T, Koido S. Intestinal microbiota and ulcerative colitis. *J Infect Chemother* 2015;**21**:761–8. https://doi.org/10.1016/j.jiac.2015.07.010
21. Le Roy T, Llopis M, Lepage P. *et al.* Intestinal microbiota determines development of non-alcoholic fatty liver disease in mice. *Gut* 2013;**62**:1787–94. https://doi.org/10.1136/gutjnl-2012-303816
22. Qin J, Li Y, Cai Z. *et al.* A metagenome-wide association study of gut microbiota in type 2 diabetes. *Nature* 2012;**490**:55–60. https://doi.org/10.1038/nature11450
23. Gensollen T, Iyer SS, Kasper DL. *et al.* How colonization by microbiota in early life shapes the immune system. *Science* 2016;**352**:539–44. https://doi.org/10.1126/science.aad9378
24. Heijtz RD, Wang S, Anuar F. *et al.* Normal gut microbiota modulates brain development and behavior. *Proc Natl Acad Sci U S A* 2011;**108**:3047–52. https://doi.org/10.1073/pnas.1010529108
25. Hsiao Elaine Y, McBride Sara W, Hsien S. *et al.* Microbiota modulate behavioral and physiological abnormalities associated with neurodevelopmental disorders. *Cell* 2013;**155**:1451–63. https://doi.org/10.1016/j.cell.2013.11.024
26. Koppel N, Maini Rekdal V, Balskus EP. Chemical transformation of xenobiotics by the human gut microbiota. *Science* 2017;**356**:eaag2770. https://doi.org/10.1126/science.aag2770
27. Collins SL, Patterson AD. The gut microbiome: An orchestrator of xenobiotic metabolism. *Acta Pharm Sin B* 2020;**10**:19–32. https://doi.org/10.1016/j.apsb.2019.12.001
28. Claus SP, Guillou H, Ellero-Simatos S. The gut microbiota: a major player in the toxicity of environmental pollutants? *NPJ Biofilms Microbi* 2016;**2**:16003. https://doi.org/10.1038/npjbiofilms.2016.3
29. Zimmermann M, Zimmermann-Kogadeeva M, Wegmann R. *et al.* Separating host and microbiome contributions to drug pharmacokinetics and toxicity. *Science* 2019;**363**:eaat9931. https://doi.org/10.1126/science.aat9931
30. Ley RE, Lozupone CA, Hamady M. *et al.* Worlds within worlds: evolution of the vertebrate gut microbiota. *Nat Rev Microbiol* 2008;**6**:776–88. https://doi.org/10.1038/nrmicro1978
31. Jin Y, Wu S, Zeng Z. *et al.* Effects of environmental pollutants on gut microbiota. *Environ Pollut* 2017;**222**:1–9. https://doi.org/10.1016/j.envpol.2016.11.045
32. Spanogiannopoulos P, Bess EN, Carmody RN. *et al.* The microbial pharmacists within us: a metagenomic view of xenobiotic metabolism. *Nat Rev Microbiol* 2016;**14**:273–87. https://doi.org/10.1038/nrmicro.2016.17
33. Seyed Hameed AS, Rawat PS, Meng X. *et al.* Biotransformation of dietary phytoestrogens by gut microbes: a review on bidirectional interaction between phytoestrogen metabolism and gut microbiota. *Biotechnol Adv* 2020;**43**:107576. https://doi.org/10.1016/j.biotechadv.2020.107576
34. Lindell AE, Zimmermann-Kogadeeva M, Patil KR. Multimodal interactions of drugs, natural compounds and pollutants with the gut microbiota. *Nat Rev Microbiol* 2022;**20**:431–43. https://doi.org/10.1038/s41579-022-00681-5
35. Alexander JL, Wilson ID, Teare J. *et al.* Gut microbiota modulation of chemotherapy efficacy and toxicity. *Nat Rev Gastro Hepat* 2017;**14**:356–65. https://doi.org/10.1038/nrgastro.2017.20
36. Fenner K, Elsner M, Lueders T. *et al.* Methodological advances to study contaminant biotransformation: new prospects for understanding and reducing environmental persistence? *ACS ES&T Water* 2021;**1**:1541–54. https://doi.org/10.1021/acsestwater.1c00025
37. Schmidt TSB, Raes J, Bork P. The human gut microbiome: from association to modulation. *Cell* 2018;**172**:1198–215. https://doi.org/10.1016/j.cell.2018.02.044
38. Turner PV. The role of the gut microbiota on animal model reproducibility. *Anim Model Exp Med* 2018;**1**:109–15. https://doi.org/10.1002/ame2.12022
39. Li Y, Meng Q, Yang M. *et al.* Current trends in drug metabolism and pharmacokinetics. *Acta Pharm Sin B* 2019;**9**:1113–44. https://doi.org/10.1016/j.apsb.2019.10.001
40. Chaira T, Subramani C, Barman TK. Adme, pharmacokinetic scaling, pharmacodynamic and prediction of human dose and regimen of novel antiviral drugs. *Pharmaceutics* 2023;**15**:15. https://doi.org/10.3390/pharmaceutics15041212
41. Arkhipova OV, Akimenko VK. Unsaturated organic acids as terminal electron acceptors for reductase chains of anaerobic bacteria. *Microbiology* 2005;**74**:629–39. https://doi.org/10.1007/s11021-005-0116-6
42. Pant A, Maiti TK, Mahajan D. *et al.* Human gut microbiota and drug metabolism. *Microb Ecol* 2023;**86**:97–111. https://doi.org/10.1007/s00248-022-02081-x
43. Walter J, Ley R. The human gut microbiome: ecology and recent evolutionary changes. *Ann Rev Microbiol* 2011;**65**:411–29. https://doi.org/10.1146/annurev-micro-090110-102830
44. Lobo-da-Cunha A. Structure and function of the digestive system in molluscs. *Cell Tissue Res* 2019;**377**:475–503. https://doi.org/10.1007/s00441-019-03085-9
45. Barker PS, Morrison FO, Whitaker RS. Conversion of ddt to ddd by proteus vulgaris, a bacterium isolated from the intestinal flora of a mouse. *Nature* 1965;**205**:621–2. https://doi.org/10.1038/205621b0
46. Yim Y-J, Seo J, Kang S-I. *et al.* Reductive dechlorination of methoxychlor and ddt by human intestinal bacterium *Eubacterium limosum* under anaerobic conditions. *Arch Environ Con Tox* 2008;**54**:406–11. https://doi.org/10.1007/s00244-007-9044-y
47. Velmurugan G, Ramprasath T, Swaminathan K. *et al.* Gut microbial degradation of organophosphate insecticides-induces glucose intolerance via gluconeogenesis. *Genome Biol* 2017;**18**:8. https://doi.org/10.1186/s13059-016-1134-6
48. Van Dexter S, Boopathy R. Biodegradation of phenol by *Acinetobacter tandoii* isolated from the gut of the termite. *Environ Sci Pollut Res* 2019;**26**:34067–72. https://doi.org/10.1007/s11356-018-3292-4
49. Kim H-Y, Song H-G. Purification and characterization of nad(p)h-dependent nitroreductase i from klebsiella sp. C1 and enzymatic transformation of 2,4,6-trinitrotoluene. *Appl Microbiol Biotechnol* 2005;**68**:766–73. https://doi.org/10.1007/s00253-005-1950-1
50. Hirayama K, Baranczewski P, Åkerlund J-E. *et al.* Effects of human intestinal flora on mutagenicity of and DNA adduct formation from food and environmental mutagens. *Carcinogenesis* 2000;**21**:2105–11. https://doi.org/10.1093/carcin/21.11.2105

Downloaded from https://academic.oup.com/ismej/article/19/1/wraf215/8268573 by National Science & Technology Library user on 14 October 2025

51. Morrison JM, Wright CM, John GH. Identification, isolation and characterization of a novel azoreductase from clostridium perfringens. *Anaerobe* 2012;**18**:229–34. https://doi.org/10.1016/j.anaerobe.2011.12.006
52. He Z, Chen L, Catalan-Dibene J. *et al.* Food colorants metabolized by commensal bacteria promote colitis in mice with dysregulated expression of interleukin-23. *Cell Metab* 2021;**33**:1358–1371.e5. https://doi.org/10.1016/j.cmet.2021.04.015
53. Xu H, Heinze TM, Paine DD. *et al.* Sudan azo dyes and Para red degradation by prevalent bacteria of the human gastrointestinal tract. *Anaerobe* 2010;**16**:114–9. https://doi.org/10.1016/j.anaerobe.2009.06.007
54. Van de Wiele T, Vanhaecke L, Boeckaert C. *et al.* Human colon microbiota transform polycyclic aromatic hydrocarbons to estrogenic metabolites. *Environ Health Perspect* 2005;**113**:6–10. https://doi.org/10.1289/ehp.7259
55. Humblot C, Combourieu B, Väisänen ML. *et al.* 1h nuclear magnetic resonance spectroscopy-based studies of the metabolism of food-borne carcinogen 2-amino-3-methylimidazo[4,5-f]quinoline by human intestinal microbiota. *Appl Environ Microbiol* 2005;**71**:5116–23. https://doi.org/10.1128/aem.71.9.5116-5123.2005
56. Zheng X, Zhao A, Xie G. *et al.* Melamine-induced renal toxicity is mediated by the gut microbiota. *Sci Transl Med* 2013;**5**:172ra22. https://doi.org/10.1126/scitranslmed.3005114
57. Chi L, Xue J, Tu P. *et al.* Gut microbiome disruption altered the biotransformation and liver toxicity of arsenic in mice. *Arch Toxicol* 2019;**93**:25–35. https://doi.org/10.1007/s00204-018-2332-7
58. Diaz-Bone RA, Van de Wiele TR. Biovolatilization of metal(loid)s by intestinal microorganisms in the simulator of the human intestinal microbial ecosystem. *Environ Sci Technol* 2009;**43**:5249–56. https://doi.org/10.1021/es900544c
59. Van de Wiele T, Gallawa Christina M, Kubachk Kevin M. *et al.* Arsenic metabolism by human gut microbiota upon in vitro digestion of contaminated soils. *Environ Health Perspect* 2010;**118**:1004–9. https://doi.org/10.1289/ehp.0901794
60. Yu H, Wu B, Zhang X-X. *et al.* Arsenic metabolism and toxicity influenced by ferric iron in simulated gastrointestinal tract and the roles of gut microbiota. *Environ Sci Technol* 2016;**50**:7189–97. https://doi.org/10.1021/acs.est.6b01533
61. Xue X-M, Wang H-Y, Yu X-W. *et al.* Gut microbiota control the bioavailability and metabolism of organoarsenicals of seaweeds in mice after oral ingestion. *Environ Sci Technol* 2023;**57**:8588–97. https://doi.org/10.1021/acs.est.2c09167
62. Rubin SSCDC, Alava P, Zekker I. *et al.* Arsenic thiolation and the role of sulfate-reducing bacteria from the human intestinal tract. *Environ Health Perspect* 2014;**122**:817–22. https://doi.org/10.1289/ehp.1307759
63. Potera C. Fire in the belly? Sulfur-reducing gut microbes fuel arsenic thiolation. *Environ Health Perspect* 2014;**122**:A222. https://doi.org/10.1289/ehp.122-A222
64. Jerca FA, Jerca VV, Hoogenboom R. Advances and opportunities in the exciting world of azobenzenes. *Nat Rev Chem* 2022;**6**:51–69. https://doi.org/10.1038/s41570-021-00334-w
65. Sousa T, Yadav V, Zann V. *et al.* On the colonic bacterial metabolism of azo-bonded prodrugsof 5-aminosalicylic acid. *J Pharm Sci* 2014;**103**:3171–5. https://doi.org/10.1002/jps.24103
66. Rafii F, Sutherland J, Hansen E Jr. *et al.* Reduction of nitrazepam by *Clostridium leptum*, a nitroreductase-producing bacterium isolated from the human intestinal tract. *Clin Infect Dis* 1997;**25**:S121–2. https://doi.org/10.1086/516204
67. Haiser HJ, Gootenberg DB, Chatman K. *et al.* Predicting and manipulating cardiac drug inactivation by the human gut bacterium *Eggerthella lenta*. *Science* 2013;**341**:295–8. https://doi.org/10.1126/science.1235872
68. Hashim H, Azmin S, Razlan H. *et al.* Eradication of helicobacter pylori infection improves levodopa action, clinical symptoms and quality of life in patients with Parkinson's disease. *PLoS One* 2014;**9**:e112330. https://doi.org/10.1371/journal.pone.0112330
69. Holt R. The bacterial degradation of chloramphenicol. *Lancet* 1967;**289**:1259–60. https://doi.org/10.1016/S0140-6736(67)92720-1
70. Parvez MM, Basit A, Jariwala PB. *et al.* Quantitative investigation of irinotecan metabolism, transport, and gut microbiome activation. *Drug Metab Disposition* 2021;**49**:683–93. https://doi.org/10.1124/dmd.121.000476
71. Lee SH, An JH, Lee HJ. *et al.* Evaluation of pharmacokinetic differences of acetaminophen in pseudo germ-free rats. *Biopharm Drug Disposition* 2012;**33**:292–303. https://doi.org/10.1002/bdd.1799
72. Amanda L, Bret DW, Lauren B. *et al.* Pharmacologic targeting of bacterial β-glucuronidase alleviates nonsteroidal anti-inflammatory drug-induced enteropathy in mice. *J Pharmacol Exp Ther* 2012;**341**:447–54. https://doi.org/10.1124/jpet.111.191122
73. Saitta KS, Zhang C, Lee KK. *et al.* Bacterial β-glucuronidase inhibition protects mice against enteropathy induced by indomethacin, ketoprofen or diclofenac: mode of action and pharmacokinetics. *Xenobiotica* 2014;**44**:28–35. https://doi.org/10.3109/00498254.2013.811314
74. Wang G, Zhang H, Zhang J. *et al.* Metabolic fate of environmental chemical triclocarban in colon tissues: roles of gut microbiota involved. *Sci Total Environ* 2021;**787**:147677. https://doi.org/10.1016/j.scitotenv.2021.147677
75. Omotayo OP, Omotayo AO, Mwanza M. *et al.* Prevalence of mycotoxins and their consequences on human health. *Toxicol Res* 2019;**35**:1–7. https://doi.org/10.5487/TR.2019.35.1.001
76. Gratz Silvia W, Duncan G, Richardson AJ. The human fecal microbiota metabolizes deoxynivalenol and deoxynivalenol-3-glucoside and may be responsible for urinary deepoxy-deoxynivalenol. *Appl Environ Microb* 2013;**79**:1821–5. https://doi.org/10.1128/AEM.02987-12
77. Ouethrani M, Van de Wiele T, Verbeke E. *et al.* Metabolic fate of ochratoxin a as a coffee contaminant in a dynamic simulator of the human colon. *Food Chem* 2013;**141**:3291–300. https://doi.org/10.1016/j.foodchem.2013.05.157
78. Gratz SW, Dinesh R, Yoshinari T. *et al.* Masked trichothecene and zearalenone mycotoxins withstand digestion and absorption in the upper GI tract but are efficiently hydrolyzed by human gut microbiota in vitro. *Mol Nutr Food Res* 2017;**61**:1600680. https://doi.org/10.1002/mnfr.201600680
79. Yang J, Yang Y, Wu W-M. *et al.* Evidence of polyethylene biodegradation by bacterial strains from the guts of plastic-eating waxworms. *Environ Sci Technol* 2014;**48**:13776–84. https://doi.org/10.1021/es504038a
80. Yang Y, Chen J, Wu W-M. *et al.* Complete genome sequence of bacillus sp. Yp1, a polyethylene-degrading bacterium from waxworm's gut. *J Biotechnol* 2015;**200**:77–8. https://doi.org/10.1016/j.jbiotec.2015.02.034
81. Huerta Lwanga E, Thapa B, Yang X. *et al.* Decay of low-density polyethylene by bacteria extracted from earthworm's guts: a potential for soil restoration. *Sci Total Environ* 2018;**624**:753–7. https://doi.org/10.1016/j.scitotenv.2017.12.144

Downloaded from https://academic.oup.com/ismej/article/19/1/wraf215/8268573 by National Science & Technology Library user on 14 October 2025

82. Yang Y, Yang J, Wu W-M. *et al.* Biodegradation and mineralization of polystyrene by plastic-eating mealworms: part 2. Role of gut microorganisms. *Environ Sci Technol* 2015;**49**:12087–93. https://doi.org/10.1021/acs.est.5b02663
83. Brandon AM, Gao S-H, Tian R. *et al.* Biodegradation of polyethylene and plastic mixtures in mealworms (larvae of *Tenebrio molitor*) and effects on the gut microbiome. *Environ Sci Technol* 2018;**52**:6526–33. https://doi.org/10.1021/acs.est.8b02301
84. Billen P, Khalifa L, Van Gerven F. *et al.* Technological application potential of polyethylene and polystyrene biodegradation by macro-organisms such as mealworms and wax moth larvae. *Sci Total Environ* 2020;**735**:139521. http://neimeng.zssgdsb-85176920tsgjnz.com:80/rwt/17/https/MSYXTLUQPJUB/10.1016/j.scitotenv.2020.139521
85. Zhang Z, Peng H, Yang D. *et al.* Polyvinyl chloride degradation by a bacterium isolated from the gut of insect larvae. *Nat Commun* 2022;**13**:5360. https://doi.org/10.1038/s41467-022-32903-y
86. Yuan J, Ma J, Sun Y. *et al.* Microbial degradation and other environmental aspects of microplastics/plastics. *Sci Total Environ* 2020;**715**:136968. https://doi.org/10.1016/j.scitotenv.2020.136968
87. Cui X, Wang X, Chang X. *et al.* A new capacity of gut microbiota: fermentation of engineered inorganic carbon nanomaterials into endogenous organic metabolites. *Proc Natl Acad Sci U S A* 2023;**120**:e2218739120. https://doi.org/10.1073/pnas.2218739120
88. Wang Y, Rui M, Nie Y. *et al.* Influence of gastrointestinal tract on metabolism of bisphenol a as determined by in vitro simulated system. *J Hazard Mater* 2018;**355**:111–8. https://doi.org/10.1016/j.jhazmat.2018.05.011
89. Yin J, Li D, Zheng T. *et al.* Gastrointestinal degradation and toxicity of disinfection byproducts in drinking water using in vitro models and the roles of gut microbiota. *Environ Sci Technol* 2023;**57**:16219–31. https://doi.org/10.1021/acs.est.3c04483
90. Lv M, Liu Y, Wang M. *et al.* Biotransformation of tetrabromobisphenol a and its analogs by selected gut bacteria strains: implications for human health. *Environ Sci Technol* 2024;**58**:20894–905. https://doi.org/10.1021/acs.est.4c10434
91. Zhang H, Zhang S, Hou X. *et al.* Deglycosylation of two typical plant-generated glycoconjugates of tetrabromobisphenol a through in vitro digestion processes. *Environ Sci Technol Lett* 2022;**9**:955–61. https://doi.org/10.1021/acs.estlett.2c00757
92. Luo S, Zhen Z, Teng T. *et al.* New mechanisms of biochar-assisted vermicomposting by recognizing different active di-(2-ethylhexyl) phthalate (dehp) degraders across pedosphere, charosphere and intestinal sphere. *J Hazard Mater* 2023;**458**:131990. https://doi.org/10.1016/j.jhazmat.2023.131990
93. Wu X, Zhu Y, Yang M. *et al.* Earthworms enhance the bioremediation of tris(2-butoxyethyl) phosphate-contaminated soil by releasing degrading microbes. *J Hazard Mater* 2023;**452**:131303. https://doi.org/10.1016/j.jhazmat.2023.131303
94. Hou R, Zhang S, Huang Q. *et al.* Role of gastrointestinal microbiota from crucian carp in microbial transformation and estrogenicity modification of novel plastic additives. *Environ Sci Technol* 2023;**57**:11476–88. https://doi.org/10.1021/acs.est.3c03595
95. Saad R, Rizkallah MR, Aziz RK. Gut pharmacomicrobiomics: the tip of an iceberg of complex interactions between drugs and gut-associated microbes. *Gut Pathogens* 2012;**4**:16. https://doi.org/10.1186/1757-4749-4-16
96. Mudziwapasi R, Mlambo SS, Chigu NL. *et al.* Isolation and molecular characterization of bacteria from the gut of *Eisenia fetida* for biodegradation of 4,4 ddt. *J Appl Biol Biotech* 2016;**4**:41–7. https://doi.org/10.7324/JABB.2016.40507
97. Boush MG, Matsumura F. Insecticidal degradation by pseudomonas melophthora, the bacterial symbiote of the apple maggot1. *J Econ Entomol* 1967;**60**:918–20. https://doi.org/10.1093/jee/60.4.918
98. Song D, Chen L, Zhu S. *et al.* Gut microbiota promote biotransformation and bioaccumulation of arsenic in tilapia. *Environ Pollut* 2022;**305**:119321. https://doi.org/10.1016/j.envpol.2022.119321
99. Zhong X, Zhang G, Huang J. *et al.* Effects of intestinal microbiota on the biological transformation of arsenic in zebrafish: contribution and mechanism. *Environ Sci Technol* 2024;**58**:2247–59. https://doi.org/10.1021/acs.est.3c08010
100. Zhou G-W, Yang X-R, Zheng F. *et al.* Arsenic transformation mediated by gut microbiota affects the fecundity of *Caenorhabditis elegans*. *Environ Pollut* 2020;**260**:113991. https://doi.org/10.1016/j.envpol.2020.113991
101. Guan S, He J, Young JC. *et al.* Transformation of trichothecene mycotoxins by microorganisms from fish digesta. *Aquaculture* 2009;**290**:290–5. https://doi.org/10.1016/j.aquaculture.2009.02.037
102. Young JC, Zhou T, Yu H. *et al.* Degradation of trichothecene mycotoxins by chicken intestinal microbes. *Food Chem Toxicol* 2007;**45**:136–43. https://doi.org/10.1016/j.fct.2006.07.028
103. Yu H, Zhou T, Gong J. *et al.* Isolation of deoxynivalenol-transforming bacteria from the chicken intestines using the approach of pcr-dgge guided microbial selection. *BMC Microbiol* 2010;**10**:182. https://doi.org/10.1186/1471-2180-10-182
104. Kollarczik B, Gareis M, Hanelt M. In vitro transformation of the fusarium mycotoxins deoxynivalenol and zearalenone by the normal gut microflora of pigs. *Nat Toxins* 1994;**2**:105–10. https://doi.org/10.1002/nt.2620020303
105. Lombard V, Bernard T, Rancurel C. *et al.* A hierarchical classification of polysaccharide lyases for glycogenomics. *Biochem J* 2010;**432**:437–44. https://doi.org/10.1042/BJ20101185
106. Verma A, Ali D, Farooq M. *et al.* Expression and inducibility of endosulfan metabolizing gene in rhodococcus strain isolated from earthworm gut microflora for its application in bioremediation. *Bioresour Technol* 2011;**102**:2979–84. https://doi.org/10.1016/j.biortech.2010.10.005
107. Harishankar MK, Sasikala C, Ramya M. Efficiency of the intestinal bacteria in the degradation of the toxic pesticide, chlorpyrifos. *3 Biotech* 2013;**3**:137–42. https://doi.org/10.1007/s13205-012-0078-0
108. Chen B, Zhang N, Xie S. *et al.* Gut bacteria of the silkworm bombyx mori facilitate host resistance against the toxic effects of organophosphate insecticides. *Environ Int* 2020;**143**:105886. https://doi.org/10.1016/j.envint.2020.105886
109. Cheng D, Guo Z, Riegler M. *et al.* Gut symbiont enhances insecticide resistance in a significant pest, the oriental fruit fly *Bactrocera dorsalis* (Hendel). *Microbiome* 2017;**5**:13. https://doi.org/10.1186/s40168-017-0236-z
110. Wallace BD, Wang H, Lane KT. *et al.* Alleviating cancer drug toxicity by inhibiting a bacterial enzyme. *Science* 2010;**330**:831–5. https://doi.org/10.1126/science.1191175
111. Jung M-A, Jang S-E, Hong S-W. *et al.* The role of intestinal microflora in anti-inflammatory effect of baicalin in mice. *Biomol Ther (Seoul)* 2012;**20**:36–42. https://doi.org/10.4062/biomolther.2012.20.1.036
112. Kasimir M, Behrens M, Schulz M. *et al.* Intestinal metabolism of α- and β-glucosylated modified mycotoxins t-2 and ht-2 toxin in the pig cecum model. *J Agric Food Chem* 2020;**68**:5455–61. https://doi.org/10.1021/acs.jafc.0c00576

Downloaded from https://academic.oup.com/ismej/article/19/1/wraf215/8268573 by National Science & Technology Library user on 14 October 2025

113. Zhang S, Hou R, Sun C. *et al.* Metabolic activity of gut microbial enrichment cultures from different marine species and their transformation abilities to plastic additives. *Environ Int* 2024;**190**:108882. https://doi.org/10.1016/j.envint.2024.108882
114. Elango D, Siddharthan N, Alaqeel SI. *et al.* Biodegradation of neonicotinoid insecticide acetamiprid by earthworm gut bacteria brucella intermedium pdb13 and its ecotoxicity. *Microbiol Res* 2023;**268**:127278. https://doi.org/10.1016/j.micres.2022.127278
115. Yang S-S, Wu W-M, Brandon AM. *et al.* Ubiquity of polystyrene digestion and biodegradation within yellow mealworms, larvae of *Tenebrio molitor* Linnaeus (Coleoptera: Tenebrionidae). *Chemosphere* 2018;**212**:262–71. https://doi.org/10.1016/j.chemosphere.2018.08.078
116. Chen Z, Zhang Y, Xing R. *et al.* Reactive oxygen species triggered oxidative degradation of polystyrene in the gut of superworms (*Zophobas atratus* larvae). *Environ Sci Technol* 2023;**57**:7867–74. https://doi.org/10.1021/acs.est.3c00591
117. Spiga L, Winter MG, Furtado de Carvalho T. *et al.* An oxidative central metabolism enables salmonella to utilize microbiota-derived succinate. *Cell Host Microbe* 2017;**22**:291–301.e6. https://doi.org/10.1016/j.chom.2017.07.018
118. Litvak Y, Byndloss MX, Bäumler AJ. Colonocyte metabolism shapes the gut microbiota. *Science* 2018;**362**:eaat9076. https://doi.org/10.1126/science.aat9076
119. LeMoine CMR, Grove HC, Smith CM. *et al.* A very hungry caterpillar: polyethylene metabolism and lipid homeostasis in larvae of the greater wax moth (*Galleria mellonella*). *Environ Sci Technol* 2020;**54**:14706–15. https://doi.org/10.1021/acs.est.0c04386
120. Cassone BJ, Grove HC, Elebute O. *et al.* Role of the intestinal microbiome in low-density polyethylene degradation by caterpillar larvae of the greater wax moth, galleria mellonella. *Proc Biol Sci* 2020;**287**:20200112. https://doi.org/10.1098/rspb.2020.0112
121. Lou Y, Ekaterina P, Yang S-S. *et al.* Biodegradation of polyethylene and polystyrene by greater wax moth larvae (*Galleria mellonella* l.) and the effect of co-diet supplementation on the core gut microbiome. *Environ Sci Technol* 2020;**54**:2821–31. https://doi.org/10.1021/acs.est.9b07044
122. Bao L, Cui X, Zeng T. *et al.* Incorporation of polylactic acid microplastics into the carbon cycle as a carbon source to remodel the endogenous metabolism of the gut. *Proc Natl Acad Sci U S A* 2025;**122**:e2417104122. https://doi.org/10.1073/pnas.2417104122
123. Kaschak E, Knopf B, Petersen JH. *et al.* Biotic methylation of mercury by intestinal and sulfate-reducing bacteria and their potential role in mercury accumulation in the tissue of the soil-living *Eisenia foetida*. *Soil Biol Biochem* 2014;**69**:202–11. https://doi.org/10.1016/j.soilbio.2013.11.004
124. Wang X, Wu F, Wang W-X. In vivo mercury demethylation in a marine fish (*Acanthopagrus schlegeli*). *Environ Sci Technol* 2017;**51**:6441–51. https://doi.org/10.1021/acs.est.7b00923
125. Yang T-T, Liu Y, Tan S. *et al.* The role of intestinal microbiota of the marine fish (*Acanthopagrus latus*) in mercury biotransformation. *Environ Pollut* 2021;**277**:116768. https://doi.org/10.1016/j.envpol.2021.116768
126. Deloménie C, Fouix S, Longuemaux S. *et al.* Identification and functional characterization of arylamine n-acetyltransferases in eubacteria: evidence for highly selective acetylation of 5-aminosalicylic acid. *J Bacteriol* 2001;**183**:3417–27. https://doi.org/10.1128/jb.183.11.3417-3427.2001
127. Li H, Lin X, Zhao J. *et al.* Intestinal methylation and demethylation of mercury. *Bull Environ Contam Toxicol* 2019;**102**:597–604. https://doi.org/10.1007/s00128-018-2512-4
128. Dethlefsen L, Relman DA. Incomplete recovery and individualized responses of the human distal gut microbiota to repeated antibiotic perturbation. *Proc Natl Acad Sci U S A* 2011;**108**:4554–61. https://doi.org/10.1073/pnas.1000087107
129. Jernberg C, Löfmark S, Edlund C. *et al.* Long-term impacts of antibiotic exposure on the human intestinal microbiota. *Microbiology* 2010;**156**:3216–23. https://doi.org/10.1099/mic.0.040618-0
130. Maurice Corinne F, Haiser Henry J, Turnbaugh PJ. Xenobiotics shape the physiology and gene expression of the active human gut microbiome. *Cell* 2013;**152**:39–50. https://doi.org/10.1016/j.cell.2012.10.052
131. Chang X, Kang M, Feng J. *et al.* Effects of bde-209 exposure on growth performance, intestinal digestive enzymes, and intestinal microbiome in common carp (*Cyprinus carpio* l.). *Aquacult Fish* 2023;**8**:33–41. https://doi.org/10.1016/j.aaf.2021.05.005
132. Iszatt N, Janssen S, Lenters V. *et al.* Environmental toxicants in breast milk of Norwegian mothers and gut bacteria composition and metabolites in their infants at 1 month. *Microbiome* 2019;**7**:34. https://doi.org/10.1186/s40168-019-0645-2
133. De Filippis F, Valentino V, Sequino G. *et al.* Exposure to environmental pollutants selects for xenobiotic-degrading functions in the human gut microbiome. *Nat Commun* 2024;**15**:4482. https://doi.org/10.1038/s41467-024-48739-7
134. Ervin SM, Simpson JB, Gibbs ME. *et al.* Structural insights into endobiotic reactivation by human gut microbiome-encoded sulfatases. *Biochemistry* 2020;**59**:3939–50. https://doi.org/10.1021/acs.biochem.0c00711
135. Zahran SA, Ali-Tammam M, Hashem AM. *et al.* Azoreductase activity of dye-decolorizing bacteria isolated from the human gut microbiota. *Sci Rep* 2019;**9**:5508. https://doi.org/10.1038/s41598-019-41894-8
136. Das A, Srinivasan M, Ghosh TS. *et al.* Xenobiotic metabolism and gut microbiomes. *PLoS One* 2016;**11**:e0163099. https://doi.org/10.1371/journal.pone.0163099
137. Faust K, Sathirapongsasuti JF, Izard J. *et al.* Microbial co-occurrence relationships in the human microbiome. *PLoS Comp Biol* 2012;**8**:e1002606. https://doi.org/10.1371/journal.pcbi.1002606
138. Brown BP, Wernegreen JJ. Genomic erosion and extensive horizontal gene transfer in gut-associated acetobacteraceae. *BMC Genomics* 2019;**20**:472. https://doi.org/10.1186/s12864-019-5844-5
139. Murphy Chelsea L, Youssef Noha H, Hanafy Radwa A. *et al.* Horizontal gene transfer as an indispensable driver for evolution of neocallimastigomycota into a distinct gut-dwelling fungal lineage. *Appl Environ Microbiol* 2019;**85**:e00988–19. https://doi.org/10.1128/AEM.00988-19
140. Moura de Sousa J, Lourenço M, Gordo I. Horizontal gene transfer among host-associated microbes. *Cell Host Microbe* 2023;**31**:513–27. https://doi.org/10.1016/j.chom.2023.03.017 527.
141. Aron-Wisnewsky J, Doré J, Clement K. The importance of the gut microbiota after bariatric surgery. *Nat Rev Gastro Hepat* 2012;**9**:590–8. https://doi.org/10.1038/nrgastro.2012.161
142. Sekirov I, Russell SL, Antunes LCM. *et al.* Gut microbiota in health and disease. *Physiol Rev* 2010;**90**:859–904. https://doi.org/10.1152/physrev.00045.2009
143. Nakashima K, Kimura S, Ogawa Y. *et al.* Chitin-based barrier immunity and its loss predated mucus-colonization by indigenous gut microbiota. *Nat Commun* 2018;**9**:3402. https://doi.org/10.1038/s41467-018-05884-0
144. Cummings JH, Bingham SA, Heaton KW. *et al.* Fecal weight, colon cancer risk, and dietary intake of nonstarch

Downloaded from https://academic.oup.com/ismej/article/19/1/wraf215/8268573 by National Science & Technology Library user on 14 October 2025

polysaccharides (dietary fiber). *Gastroenterology* 1992;**103**:1783–9. https://doi.org/10.1016/0016-5085(92)91435-7
145. Varum FJO, McConnell EL, Sousa JJS. *et al.* Mucoadhesion and the gastrointestinal tract. *Crit Rev Ther Drug Carrier Syst* 2008;**25**:207–58. https://doi.org/10.1615/CritRevTherDrugCarrierSyst.v25.i3.10
146. Roager HM, Hansen LBS, Bahl MI. *et al.* Colonic transit time is related to bacterial metabolism and mucosal turnover in the gut. *Nat Microbiol* 2016;**1**:16093. https://doi.org/10.1038/nmicrobiol.2016.93
147. Clark RI, Walker DW. Role of gut microbiota in aging-related health decline: insights from invertebrate models. *Cell Mol Life Sci* 2018;**75**:93–101. https://doi.org/10.1007/s00018-017-2671-1
148. Hacquard S, Garrido-Oter R, González A. *et al.* Microbiota and host nutrition across plant and animal kingdoms. *Cell Host Microbe* 2015;**17**:603–16. https://doi.org/10.1016/j.chom.2015.04.009
149. Hao W-L, Lee Y-K Microflora of the gastrointestinal tract. In: Spencer JFT, Ragout de Spencer AL (eds.). *Public Health Microbiology: Methods and Protocols*. Totowa, NJ: Humana Press, 2004, 491–502. https://doi.org/10.1385/1-59259-766-1:491
150. Clemente Jose C, Ursell Luke K, Parfrey Laura W. *et al.* The impact of the gut microbiota on human health: An integrative view. *Cell* 2012;**148**:1258–70. https://doi.org/10.1016/j.cell.2012.01.035
151. Ley RE, Bäckhed F, Turnbaugh P. *et al.* Obesity alters gut microbial ecology. *Proc Natl Acad Sci U S A* 2005;**102**:11070–5. doi:10.1073/pnas.0504978102
152. Eckburg PB, Bik EM, Bernstein CN. *et al.* Diversity of the human intestinal microbial flora. *Science* 2005;**308**:1635–8. https://doi.org/10.1126/science.1110591
153. Jandhyala SM, Talukdar R, Subramanyam C. *et al.* Role of the normal gut microbiota. *World J Gastroenterol* 2015;**21**:8787–803. https://doi.org/10.3748/wjg.v21.i29.8787
154. Furness JB. Comparative and evolutionary aspects of the digestive system and its enteric nervous system control. In: Spencer N.J., Costa M., Brierley S.M. (eds.), *The Enteric Nervous System II*. Cham: Springer International Publishing, 2023, 165–77.
155. Bindari YR, Gerber PF. Centennial review: factors affecting the chicken gastrointestinal microbial composition and their association with gut health and productive performance. *Poult Sci* 2022;**101**:101612. https://doi.org/10.1016/j.psj.2021.101612
156. Karachle PK, Stergiou KI. Gut length for several marine fish: relationships with body length and trophic implications. *Marine Biodiversity Records* 2010;**3**:e106. https://doi.org/10.1017/S1755267210000904
157. Stevens CE, Hume ID. *Comparative Physiology of the Vertebrate Digestive System*. Cambridge: Cambridge University Press, 2004.
158. Wang R, Mohammadi M, Mahboubi A. *et al.* In-vitro digestion models: a critical review for human and fish and a protocol for in-vitro digestion in fish. *Bioengineered* 2021;**12**:3040–64. https://doi.org/10.1080/21655979.2021.1940769
159. Specziàr A. In situ estimates of gut evacuation and its dependence on temperature in five cyprinids. *J Fish Biol* 2002;**60**:1222–36. https://doi.org/10.1111/j.1095-8649.2002.tb01716.x
160. Handeland SO, Imsland AK, Stefansson SO. The effect of temperature and fish size on growth, feed intake, food conversion efficiency and stomach evacuation rate of Atlantic salmon post-smolts. *Aquaculture* 2008;**283**:36–42. https://doi.org/10.1016/j.aquaculture.2008.06.042
161. Liu H, Guo X, Gooneratne R. *et al.* The gut microbiome and degradation enzyme activity of wild freshwater fishes influenced by their trophic levels. *Sci Rep* 2016;**6**:24340. https://doi.org/10.1038/srep24340
162. Yue Z-B, Li W-W, Yu H-Q. Application of rumen microorganisms for anaerobic bioconversion of lignocellulosic biomass. *Bioresour Technol* 2013;**128**:738–44. https://doi.org/10.1016/j.biortech.2012.11.073
163. Ray AK, Ghosh K, Ringø E. Enzyme-producing bacteria isolated from fish gut: a review. *Aquac Nutr* 2012;**18**:465–92. https://doi.org/10.1111/j.1365-2095.2012.00943.x
164. Zhang S, Hou R, Wang Y. *et al.* Xenobiotic metabolism activity of gut microbiota from six marine species: combined taxonomic, metagenomic, and in vitro transformation analysis. *J Hazard Mater* 2024;**480**:136152. https://doi.org/10.1016/j.jhazmat.2024.136152
165. Djoumbou-Feunang Y, Fiamoncini J, Gil-de-la-Fuente A. *et al.* Biotransformer: a comprehensive computational tool for small molecule metabolism prediction and metabolite identification. *J Cheminformatics* 2019;**11**:2. https://doi.org/10.1186/s13321-018-0324-5
166. Sharma AK, Jaiswal SK, Chaudhary N. *et al.* A novel approach for the prediction of species-specific biotransformation of xenobiotic/drug molecules by the human gut microbiota. *Sci Rep* 2017;**7**:9751. https://doi.org/10.1038/s41598-017-10203-6
167. Malwe AS, Srivastava GN, Sharma VK. Gutbug: a tool for prediction of human gut bacteria mediated biotransformation of biotic and xenobiotic molecules using machine learning. *J Mol Biol* 2023;**435**:168056. https://doi.org/10.1016/j.jmb.2023.168056
168. Park JM, Kim TY, Lee SY. Prediction of metabolic fluxes by incorporating genomic context and flux-converging pattern analyses. *Proc Natl Acad Sci U S A* 2010;**107**:14931–6. https://doi.org/10.1073/pnas.1003740107
169. Yin N, Cai X, Zheng L. *et al.* In vitro assessment of arsenic release and transformation from as(v)-sorbed goethite and jarosite: the influence of human gut microbiota. *Environ Sci Technol* 2020;**54**:4432–42. https://doi.org/10.1021/acs.est.9b07235
170. Feng Y, Wang Y, Zhu B. *et al.* Metagenome-assembled genomes and gene catalog from the chicken gut microbiome aid in deciphering antibiotic resistomes. *Commun Bio* 2021;**4**:1305. https://doi.org/10.1038/s42003-021-02827-2
171. Stewart RD, Auffret MD, Warr A. *et al.* Compendium of 4,941 rumen metagenome-assembled genomes for rumen microbiome biology and enzyme discovery. *Nat Biotechnol* 2019;**37**:953–61. https://doi.org/10.1038/s41587-019-0202-3
172. Chen C, Zhou Y, Fu H. *et al.* Expanded catalog of microbial genes and metagenome-assembled genomes from the pig gut microbiome. *Nat Commun* 2021;**12**:1106. https://doi.org/10.1038/s41467-021-21295-0
173. Dufourny S, Everaert N, Lebrun S. *et al.* Baby-spime: a dynamic in vitro piglet model mimicking gut microbiota during the weaning process. *J Microbiol Methods* 2019;**167**:105735. https://doi.org/10.1016/j.mimet.2019.105735
174. Shahid A, Hayat S, Munir S. *et al.* Chapter 16—modulation of human microbiome and drug metabolism. In: Hamid Akash M.S., Rehman K. (eds.), *Biochemistry of Drug Metabolizing Enzymes*. Amsterdam: Academic Press, 2022, 375–97. https://www.sciencedirect.com/science/article/pii/B9780323951203000129
175. Rowland I, Gibson G, Heinken A. *et al.* Gut microbiota functions: metabolism of nutrients and other food components. *Eur J Nutr* 2018;**57**:1–24. https://doi.org/10.1007/s00394-017-1445-8

Downloaded from https://academic.oup.com/ismej/article/19/1/wraf215/8268573 by National Science & Technology Library user on 14 October 2025

176. Puschhof J, Pleguezuelos-Manzano C, Clevers H. Organoids and organs-on-chips: insights into human gut-microbe interactions. *Cell Host Microbe* 2021;**29**:867–78. https://doi.org/10.1016/j.chom.2021.04.002
177. Meier MJ, Harrill J, Johnson K. *et al.* Progress in toxicogenomics to protect human health. *NAT Rev Genet* 2024;**26**:105–22. https://doi.org/10.1038/s41576-024-00767-1
178. Wanner P, Parker BL, Chapman SW. *et al.* Identification of degradation pathways of chlorohydrocarbons in saturated low-permeability sediments using compound-specific isotope analysis. *Environ Sci Technol* 2018;**52**:7296–306. https://doi.org/10.1021/acs.est.8b01173
179. Hofstetter TB, Bakkour R, Buchner D. *et al.* Perspectives of compound-specific isotope analysis of organic contaminants for assessing environmental fate and managing chemical pollution. *Nature Water* 2024;**2**:14–30. https://doi.org/10.1038/s44221-023-00176-4
180. Tian Z, Vila J, Yu M. *et al.* Tracing the biotransformation of polycyclic aromatic hydrocarbons in contaminated soil using stable isotope-assisted metabolomics. *Environ Sci Technol Lett* 2018;**5**:103–9. https://doi.org/10.1021/acs.estlett.7b00554
181. Chen K, Xiang Y, Yan X. *et al.* Global tracking of transformation products of environmental contaminants by 2h-labeled stable isotope-assisted metabolomics. *Anal Chem* 2022;**94**:7255–63. https://doi.org/10.1021/acs.analchem.2c00500
182. Creek DJ, Chokkathukalam A, Jankevics A. *et al.* Stable isotope-assisted metabolomics for network-wide metabolic pathway elucidation. *Anal Chem* 2012;**84**:8442–7. https://doi.org/10.1021/ac3018795
183. Li J, Luo C, Song M. *et al.* Biodegradation of phenanthrene in polycyclic aromatic hydrocarbon-contaminated wastewater revealed by coupling cultivation-dependent and -independent approaches. *Environ Sci Technol* 2017;**51**:3391–401. https://doi.org/10.1021/acs.est.6b04366
184. Zhan Y, Liu W, Bao Y. *et al.* Fertilization shapes a well-organized community of bacterial decomposers for accelerated paddy straw degradation. *Sci Rep* 2018;**8**:7981. https://doi.org/10.1038/s41598-018-26375-8
185. Bednarski TK, Rahim M, Young JD. In vivo 2h/13c flux analysis in metabolism research. *Curr Opin Biotechnol* 2021;**71**:1–8. https://doi.org/10.1016/j.copbio.2021.04.005
186. Lv M, Liu Y, Shi C. *et al.* A missing puzzle piece of pollutant metabolism in humans: the gut microbiota. *Environ Sci Technol Lett* 2024;**11**:48–50. https://doi.org/10.1021/acs.estlett.3c00833
187. Gulnaz A, Chang J-E, Maeng H-J. *et al.* A mechanism-based understanding of altered drug pharmacokinetics by gut microbiota. *J Pharm Invest* 2023;**53**:73–92. https://doi.org/10.1007/s40005-022-00600-z
188. Koontz JM, Dancy BCR, Horton CL. *et al.* The role of the human microbiome in chemical toxicity. *Int J Toxicol* 2019;**38**:251–64. https://doi.org/10.1177/1091581819849833
189. Zhao H, Zhou F, Qi Y. *et al.* Screening of lactobacillus strains for their ability to bind benzo(a)pyrene and the mechanism of the process. *Food Chem Toxicol* 2013;**59**:67–71. https://doi.org/10.1016/j.fct.2013.05.040
190. Klünemann M, Andrejev S, Blasche S. *et al.* Bioaccumulation of therapeutic drugs by human gut bacteria. *Nature* 2021;**597**:533–8. https://doi.org/10.1038/s41586-021-03891-8
191. Kuno T, Hirayama-Kurogi M, Ito S. *et al.* Effect of intestinal flora on protein expression of drug-metabolizing enzymes and transporters in the liver and kidney of germ-free and antibiotics-treated mice. *Mol Pharm* 2016;**13**:2691–701. https://doi.org/10.1021/acs.molpharmaceut.6b00259
192. Kim J-K, Choi MS, Kim J-Y. *et al.* Ginkgo biloba leaf extract suppresses intestinal human breast cancer resistance protein expression in mice: correlation with gut microbiota. *Biomed Pharmacother* 2021;**140**:111712. https://doi.org/10.1016/j.biopha.2021.111712

Downloaded from https://academic.oup.com/ismej/article/19/1/wraf215/8268573 by National Science & Technology Library user on 14 October 2025

© The Author(s) 2025. Published by Oxford University Press on behalf of the International Society for Microbial Ecology. This is an Open Access article distributed under the terms of the Creative Commons Attribution License (https://creativecommons.org/licenses/by/4.0/), which permits unrestricted reuse, distribution, and reproduction in any medium, provided the original work is properly cited.
The ISME Journal, 2025, **19(1)**, wraf215
https://doi.org/10.1093/ismejo/wraf215
Review Article

Environmental Chemistry and Ecotoxicology 7 (2025) 2619–2630

Contents lists available at ScienceDirect

Environmental Chemistry and Ecotoxicology

journal homepage: www.keaipublishing.com/en/journals/environmental-chemistry-and-ecotoxicology/

Research Paper

Nationwide occurrence, distribution drivers, and source apportionment of steroids in China's coastal wetlands: An urgent priority for 4-androstene-3,17-dione and progesterone

Shan Liu [a,1], Qin-Ge Zhou [d,e,1], Yuan Liu [f], Biao Li [b,g], Huabing Li [b,g], Ji-Xun Chen [a], Nian-Nian Wu [d,e], Man Wang [b,g], Xiang-Rong Xu [a], Li-Jun Zhou [b,g,*], Qinglong L. Wu [b,c,g,h,i,*]

[a] Guangxi Laboratory on the Study of Coral Reefs in the South China Sea, Coral Reef Research Center of China, School of Marine Sciences, Guangxi University, Nanning 530004, China
[b] State Key Laboratory of Lake and Watershed Science for Water Security, Nanjing Institute of Geography and Limnology, Chinese Academy of Sciences, Nanjing 211135, China
[c] Center for Evolution and Conservation Biology, Southern Marine Sciences and Engineering Guangdong Laboratory (Guangzhou), Guangzhou 511458, China
[d] State Key Laboratory of Tropical Oceanography; Laboratory of Tropical Marine Bio-resources and Ecology; Guangdong Provincial Key Laboratory of Applied Marine Biology, South China Sea Institute of Oceanology, Chinese Academy of Sciences, Guangzhou 510301, China
[e] University of Chinese Academy of Sciences, Beijing 100049, China
[f] Marine College, Shandong University, Weihai, Shandong 264209, China
[g] State Key Laboratory of Lake Science and Environment, Nanjing Institute of Geography and Limnology, Chinese Academy of Sciences, Nanjing 211135, China
[h] Sino-Danish Center for Science and Education, University of Chinese Academy of Sciences, Beijing 100039, China
[i] Lake Fuxian Ecological Research Station, Chinese Academy of Sciences, Chengjiang 652500, China

ARTICLE INFO

Keywords:
Steroids
Coastal wetlands
Mass inventory
Source apportionment
Priority list

ABSTRACT

Steroids are potent endocrine-disrupting compounds, yet their environmental behavior in coastal wetlands remains poorly understood. This first nationwide assessment of steroids along approximately 5000 km China's coastline analyzed 21 steroids across 136 water and 139 sediment samples from 10 regions. Eight and eleven steroids were identified in water and sediment, at total concentrations of not detected (ND) to 23 ng/L and ND to 32 ng/g, respectively, with spatial distributions showing significant heterogeneity. Sediments constitute the dominant reservoir, storing 97 % of the ~19-ton national steroid inventory, pinpointing them as a critical compartment for long-term monitoring. Steroid occurrence was primarily driven by socioeconomic inputs (livestock, aquaculture, and sewage), while their fate and partitioning were subsequently modulated by coastal environmental conditions (salinity, chlorophyll-*a*, temperature, total organic carbon). Source apportionment further demonstrated that water and sediment record pollution across different timescales: water reflects current wastewater inputs (64.3 % from wastewater treatment plants), whereas sediment preserves a legacy of historical domestic and livestock sources (96.6 %). Critically, risk-based prioritization showed that exposure potential outweighs intrinsic hazard, though steroid stanozolol exhibited the highest hazard, the most exposed steroids—4-androstene-3,17-dione and progesterone—were identified as high-priority contaminants. Our findings translated data into actionable management strategies, offering a scientific framework for targeted source control, optimized monitoring, and effective risk mitigation of steroid pollution in coastal ecosystems.

1. Introduction

Steroids, encompassing estrogens, androgens, glucocorticoids, and progestagens, are endocrine-disrupting chemicals (EDCs) that exhibit carcinogenicity in humans and exert deleterious effects on aquatic species [1,2]. Even at trace concentrations (ng/L), they can disrupt

* Corresponding authors at: Key Laboratory of Lake and Watershed Science for Water Security, Nanjing Institute of Geography and Limnology, Chinese Academy of Sciences, Nanjing 211135, China.
E-mail addresses: ljzhou@niglas.ac.cn (L.-J. Zhou), qlwu@niglas.ac.cn (Q.L. Wu).
[1] Shan Liu and Qin-Ge Zhou contributed equally to this paper.

https://doi.org/10.1016/j.enceco.2025.10.030
Received 11 September 2025; Received in revised form 8 October 2025; Accepted 27 October 2025
Available online 29 October 2025
2590-1826/© 2024 The Authors. Publishing services by Elsevier B.V. on behalf of KeAi Communications Co. Ltd. CC BY 4.0 This is an open access article under the CC BY license (http://creativecommons.org/licenses/by/4.0/).

sexual characteristic [3], inhibit reproduction [4], and dysregulate gene expression in aquatic species [5]. They originate from endogenous excretion by humans/animals through urine and feces and synthetic applications in healthcare, livestock and aquaculture [6,7]. Globally, annual emissions of six major natural steroids exceed 18,270 tons and grow by 10 % yearly [8]. Critically, conventional wastewater treatment plants (WWTPs) struggle to effectively remove steroids [9], and untreated or partially treated discharges also release steroids into the environment. Consequently, steroids exist as pervasive contaminants in diverse ecosystems [10].

Coastal wetlands are key transition zones between land and sea, offering key ecological functions like carbon storage, biodiversity protection, and shoreline stabilization [11]. Their biogeochemical processes naturally intercept land-derived pollutants, such as antibiotics [12], *per*- and polyfluoroalkyl substances [13], macro- and microplastics [14], mitigating fluxes to coastal oceans. However, escalating anthropogenic pressures (e.g., land reclamation, aquaculture intensification, climate change) degrade these habitats [15], potentially compromising their pollutant retention capacity and amplifying marine contamination risks.

Despite their ecological vulnerability, steroid occurrence and fate in coastal wetlands remain strikingly understudied. Existing research mostly targets freshwater systems (lakes, rivers, and WWTPs) [2,16,17], whereas coastal data are sparse, geographically fragmented, and restricted to isolated estuaries [18], bays [19], or deltas [20]. This gap is particularly acute for China, which hosts 13,373 km^2 of coastal wetlands (top 10 globally) [15], historically degraded by intensive human activities [21]. Although recent conservation efforts (since 2012) have expanded wetland area [22], the biogeochemical drivers governing steroid contamination status, partitioning, source apportionment, and risks in these ecosystems are virtually uncharacterized at a national scale, hindering evidence-based coastal management.

Here, we present the first comprehensive, coast-wide assessment of steroid distribution across China's coastal wetlands. We hypothesized that: (1) the distribution of steroids in coastal wetlands is governed by a combination of unique coastal environmental processes and distinct regional socioeconomic activities; (2) natural steroids would dominate the contamination profile in coastal wetlands, owing to their continuous and widespread input from human and animal excretion; (3) exposure potential, rather than intrinsic hazardous properties, would be the predominant factor in determining priority steroids for environmental management in coastal wetlands.

Hence, we quantified 21 steroids in water-sediment matrices from 10 major coastal cities, spanning 9 coastal provinces and representative wetland categories (natural wetlands, restored wetlands, and aquaculture ponds). Our aims were to (1) establish baseline contamination profiles of steroids in water-sediment system at a national scale; (2) identify key environmental and socioeconomic drivers modulating steroid partitioning and spatial trends; (3) quantify national steroid inventories via mass-load estimation; (4) apportion steroid sources via principal component analysis-multiple linear regression (PCA-MLR) modeling; (5) screen priority steroids. The findings from this study can offer comprehensive insights into steroids' environmental behavior in coastal wetlands and help with the control and management of steroids.

2. Materials and methods

2.1. Chemicals

In contrast to the predominant focus on estrogens in steroid research [23], this work prioritizes the investigation of other steroid classes (androgens, glucocorticoids, and progestagens). A total of 21 steroids were therefore targeted, encompassing 4 natural steroids [4-androstene-3,17-dione (AED), testosterone (T), cortisol (CRL) and progesterone (P)], 5 metabolites [11-deoxycorticosterone (DOC), 20α-dihydroprogesterone (20α-DHP), 17α,20α-dihydroxyprogesterone (17α,20α-DOHP), 17α,20β-dihydroxyprogesterone (17α,20β-DOHP), 17α-hydroxyprogesterone (17α-OHP)] and 12 synthetic steroids [17β-boldenone (17β-BOL), 19-nortestosterone (19-NT), stanozolol (S), 17α-methyltestosterone (17α-MT), prednisolone (PREL), 17α-hydroxyprogesterone acetate (17α-OHPA), 1-dehydroprogesterone (1-DHP), medroxyprogesterone acetate (MPA), norvinisterone (NVT), cyproterone acetate (CPTA), megestrol acetate (MGTA), norethindrone (NTD)]. Isotopically labeled internal standards, namely testosterone-d3 (T-d3), cortisol-d2 (CRL-d2) and progesterone-d9 (P-d9) were used to ensure analytical accuracy. More details on these compounds are provided in the Table S1 and Text S1 in the Supporting Information.

2.2. Study regions and sample collection

The study encompasses ten representative sampling regions (Fig. 1), strategically positioned across critical wetland areas along China's coastal provinces. These regions include the Liao River Estuary (LRE) in Panjin, Liaoning Province; Bohai Bay (BHB) in Qinhuangdao, Hebei Province; the Yellow River Estuary (YRE) in Dongying, Shandong Province; the Yangtze River Estuary (YZE) in Shanghai, which is a municipality directly under the central government; the Zhangjiang River Estuary (ZJR) in Zhangzhou, Fujian Province; the Pearl River Estuary (PRE) in Guangzhou, Guangdong Province; as well as coastal wetlands in Wenzhou (WZW), Zhejiang Province; Yancheng (YCW), Jiangsu Province; the Leizhou Peninsula (LZP), Guangdong Province; and Sanya (SYW), Hainan Province.

The samples were classified based on distinct wetland types into aquaculture ponds (AP), natural wetlands (NW), and restored wetlands (RW). A total of 136 water samples and 139 sediment samples were collected across various locations from July to August 2023 (Fig. 1). Comprehensive details regarding the sampling locations are delineated in Tables S2. Water samples were preserved in plastic containers, while sediment samples were collected using stainless-steel grab samplers. After sampling, all samples were stored at −20 °C for subsequent extraction.

2.3. Sample extraction and instrumental analysis

The extraction and analytical methods utilized in this study are described in the Text S2 and S3 in Supporting Information. Briefly, water samples were filtered through a 0.7 μm glass fiber filter (GF/F, Whatman, UK) to eliminate suspended particulate matter, followed by enrichment via solid phase extraction using HLB cartridges (Waters, 500 mg). The targeted steroids were eluted with 4.5 mL of methanol, 4 mL of ethyl acetate, and 4 mL of dichloromethane, then the eluted solution was dried by nitrogen and reconstituted in 1 mL of methanol. Sediment samples (0.5 g) underwent ultrasonic extraction using 2 mL of acetonitrile, 2 mL of methanol, and 2 mL of acetonitrile. The extracts were then concentrated and redissolved in 0.5 mL methanol for further analysis. Steroids were detected and quantified using LC-MS/MS (Agilent 1290 Infinity II liquid chromatography in conjunction with an Agilent 6470 triplequadrupole mass spectrometer) which was operated in multiple-reaction monitoring mode.

2.4. Quality assurance and quality control (QA/QC)

The recovery rates for the 21target steroids varied, with water samples showing a range of 68 % to 116 % and sediment samples ranging from 65 % to 107 % (Table S3). The method limits of detection (LOD) and method limits of quantification (LOQ) were determined using signal-to-noise ratios (SNR) of threefold and tenfold near the target peak, respectively. The LODs and LOQs for the target analytes in water samples ranging from 0.0076 to 2.3 ng/L and 0.025 to 7.8 ng/L, respectively. For sediment samples, LODs and LOQs were within the ranges of 0.00035–0.42 ng/g and 0.0012–1.4 ng/g, respectively (Table S3). Furthermore, each batch of samples was subjected to quality

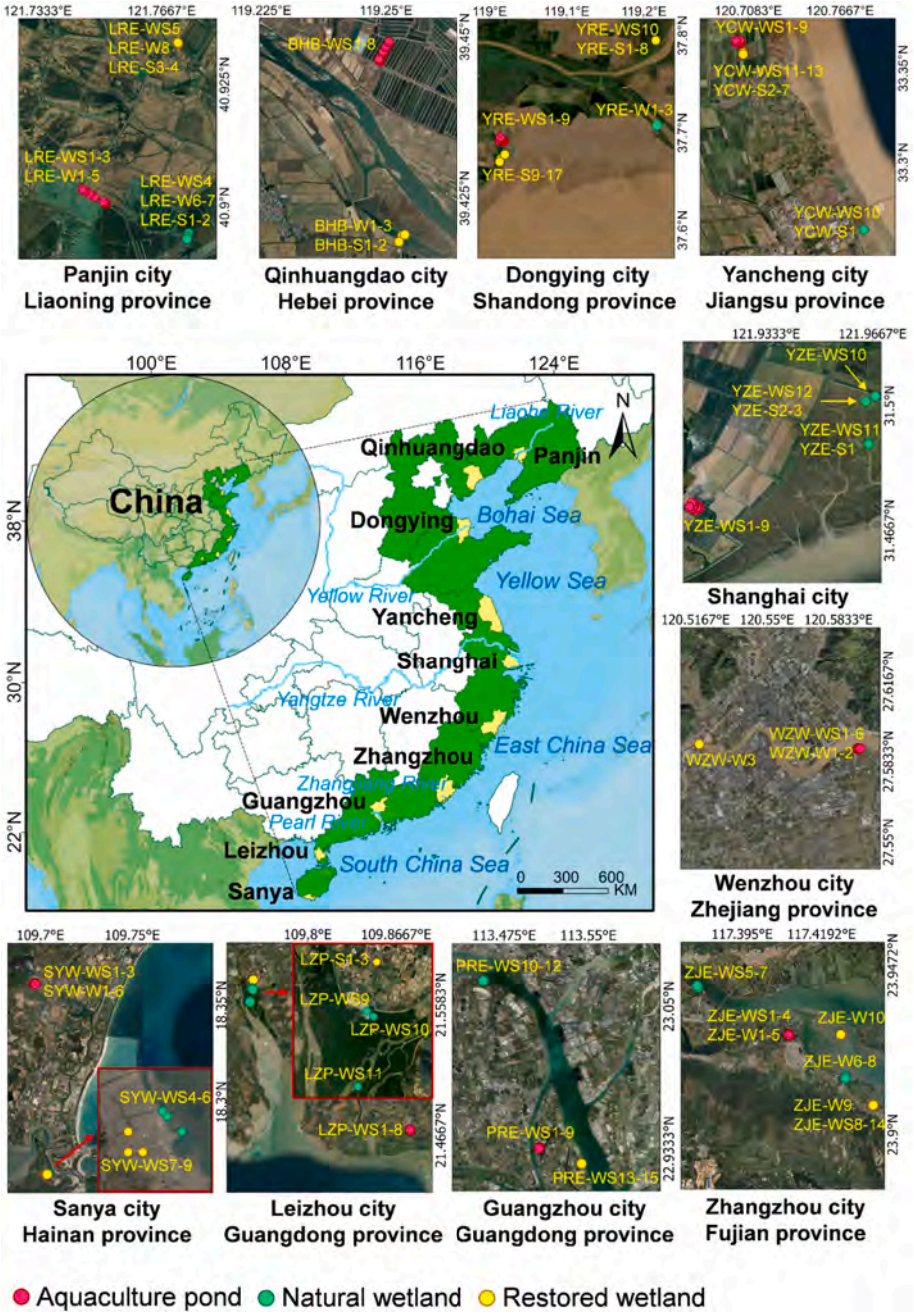


Fig. 1. Sampling sites of ten coastal wetland regions. In the map of China, yellow represent cities that contain sampling sites and green areas indicate provinces where the sampling sites are located. WS, W and S respectively indicate sample sites that both water and sediment, solely water, only sediment samples were gathered. (For interpretation of the references to colour in this figure legend, the reader is referred to the web version of this article.)

control checks including the use of field blanks, procedural blanks, solvent blanks, and standard solutions (100 μg/L of each steroid) to assess instrument performance and background contamination levels. All target steroids were not detected (ND) in the field, procedural, and solvent blanks, and thus no blank correction was applied to the sample data. The calibration curves (1.0–200 μg/L) of 21 object steroids displayed great linearity with strong correlation coefficient above 0.99. Further details can refer to the Supporting Information.

2.5. Data analysis

Steroid concentrations below the limit of detection (LOD) were designated as non-detectable (ND). Values between LOD and LOQ were estimated using half of the LOQ [24]. Additionally, data within LOD and LOQ range were factored into calculations of detected frequency (DF), whereas NDs were excluded. The Mann-Whitney *U* test was used to evaluate differences in total steroid levels across sampling areas and wetland types, due to non-normal distribution. To explore the associations between steroid concentrations and environmental and socioeconomic parameters, spearman's rank correlation analysis was employed. Socioeconomic data came from the local government's official statistical yearbook (Table S4). Statistical significance was determined using a single *p*-value threshold of $p < 0.05$ for all tests and analyses. Principal component analysis (PCA) and multiple linear regression (MLR) were employed to identify the different sources of steroids in water and sediment sample [20,25]. The mass inventory of steroids in water and sediment was estimated by integrating measured concentration, water depth, and sediment characteristics, and the final inventory represents

the median value derived from a Monte Carlo simulation, which incorporated the ranges of the input parameters to account for their variability. Moreover, a risk-based prioritization approach, which integrated the potential hazard effects and environmental exposure, was employed to identify priority steroids. This approach included three steps: (1) assigning a PBT (persistence, bioaccumulation, toxicity) score to each steroid; (2) quantifying exposure via detection frequency and measured concentration; (3) combining hazard and exposure to yield the final priority list. All calculation details and formulas regarding priority steroids, mass inventory, and PCA-MLR analysis are provided in the Text S5-S8 in Supporting Information. The visual map of sample sites was created using ArcGIS Pro and Microsoft PowerPoint 2021. Other figures and the Spearman rank correlation analysis were generated using Origin 2024. Furthermore, the PCA-MLR analysis was conducted using SPSS 27.

3. Results and discussion

3.1. Nationwide occurrence and spatial distribution of steroids in the coastal wetlands

Eight steroids were identified in water across ten major coastal wetlands, with the total concenrations ranging from ND to 23 ng/L (median: 0.30 to 4.8 ng/L; Fig. 2A, Table S5). Generally, our

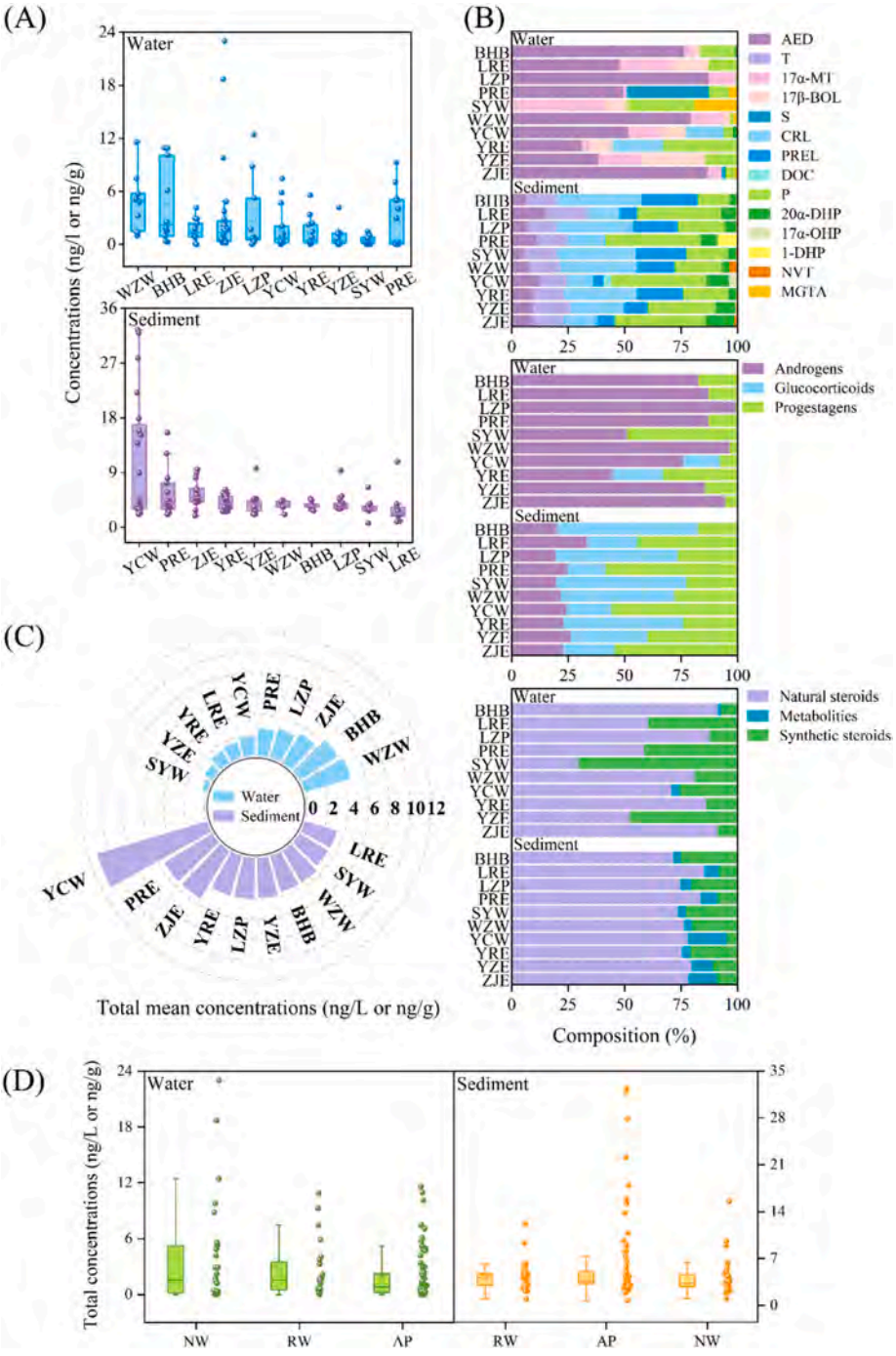


Fig. 2. The total concentrations of steroids (A), compositions of steroids categorized by their types, effects and sources (B), total mean concentration (C), and the total concentrations of steroids in water and sediment across different wetland types (D).

meseasurements are comparable to those in South China Sea bays [19], but lower than those in adjacent rivers [26] and inland lake [17], possibly driven by higher water mobility and dilution effects in coastal wetlands. The steroids in China's coastal wetlands within an intermediate range of global pollution levels. The comparability with Kenya's lake water [27], despite differing socioeconomic stages, indicate a similar level of anthropogenic pressure and highlight the ubiquitous nature of steroids as global pollutants. More importantly, the significantly lower concentrations compared to certain Canadian surface waters [28] and the Sundarbans wetland [29] underscore that regional socioeconomic factors and environmental fate processes are decisive. Efficient dilution, dynamic hydrography and—relative to the Sundarbans—more advanced wastewater infrastructure in China's coastal cities likely curtail steroid buildup. Thus, global comparison shows that steroid pollution reflects not only economic development but also the effectiveness of local environmental governance and natural attenuation capacity. Spatially, the total mean concentrations of steroids (ng/L) in water followed: WZW (4.6) > BHB (4.3) > ZJE (3.3) > LZP (2.9) > PRE (2.6) > YCW (1.8) > LRE (1.6) > YRE (1.3) > YZE (0.88) > SYW (0.47), though regional differences were marginal ($p > 0.05$). AED, 17α-MT and P showed high detection rates of 51 %, 76 % and 54 %, respectively, whereas the other compounds had detection rates below 50 %. Regarding individual compounds, natural androgen AED dominated in water samples from all study regions except in SYW, where 17α-MT was the primary compound (Fig. 2B). Androgens were the most prevalent class of steroids aross all the ten regions, followed by progestagens, while glucocorticoids (CRL, < 7.8 ng/L) were detected exclusively in YCW and YZE. These findings did not fully align with steroid distribution patterns documented in previous studies focusing on the Pearl River Estuary and coastal waters of the Guangdong-Hong Kong-Macao Greater Bay Area [30,31], likely due to a complex interplay of diverse pollution sources, seawater dilution, or bioaccumulation of wetland plants. The metabolite 20α-DHP (< 0.84 ng/L) was identified only in BHB and YCW. Notably, in SYW, synthetic steroids were presented comparatively high proportion (71.2 %) driven by 17α-MT (< 0.025–0.85 ng/L). This elevated level likely stems from the extensive use of 17α-MT in aquaculture. Therefore, tighter controls on synthetic steroids in aquaculture in SYW are essential.

Eleven steroids were detected in sediments, with total levels varing from ND to 32 ng/g (median: 2.3–4.6 ng/g; Fig. 2A, Table S6). Our measurements were lower than those in Chinese river [16], but comparable to Chinese fishing port [32]. Globally, these levels were lower than those reported in Canadian river [33], but higher than those in Italian coastal lagoon [34]. Globally, the sedimentary steroid burden in China's coastal wetlands is notable yet not extreme, reflecting a balance between large anthropogenic inputs from densely populated, economically active coastlines and the natural attenuation capacity of these dynamic systems. Spatially, the total mean concentrations of steroids (ng/g) in sediments followed: YCW (11) > PRE, ZJE (5.5) > YRE, LZP (4.0) > YZE (3.9) > BHB, WZW (3.6) > SYW (3.3) > LRE (3.2). Notably, except YCW, no significant differences of steroid levels in sediments were found, mainly attributed to high elevated concentrations in YCW aquaculture pond (Table S6). AED, T, CRL, PREL, P and 20α-DHP showed high detection rates at 97 %, 100 %, 90 %, 78 %, 99 % and 91 % respectively, whereas detection rates of other compounds below 50 %. Regarding individual compounds, 6 steroids were indentified across all regions, with mean concentrations (ng/g) in descending order: P (1.7), CRL (1.1), T (0.70), PREL (0.50), AED (0.53), and 20α-DHP (0.39) (Fig. 2B), indicating their long-term presence and coexistence in coastal wetland sediments. Unlike water, in sediments, androgens had the smallest proportion, while glucocorticoids and progestagens were the dominant classes. The natural steroid proportion was relatively consistent across all sampling regions (71.9 %–85.6 %), seemly due to their widespread sources like human and animal metabolism and excretion. Meanwhile, In YCW and ZJE, metabolites had higher percentages, while synthetic steroids were more prevalent in other regions.

We also analyzed the distribution and proportions of steroids by different wetland types. In water, the total steroid concentrations (ng/L) were ND–12 (median, 0.80), ND–23 (1.6), and ND–11 (1.5) for AP, NW and RW, respectively. In sediments, levels (ng/g) were 0.71–32 (3.7), 1.0–16 (3.3), and 0.95–12 (4.2) for AP, NW and RW, respectively (Fig. 2D and Tables S5, S6). Total concentrations showed no significant variation across wetland types in water or sediments (Mann-Whitney *U* test, $p > 0.05$). Additionally, steroid proportion in different wetland types, mirrored those in different study regions, regardless of whether steroids were categorized by individual compounds or different types (Fig. S2). These results indicate that wetland type exerts little influence on steroid distribution in coastal wetlands. Notably, aquaculture ponds at PRE had the highest average steroid concentration at 1.3 ng/L (Fig. S2), while their natural and restored wetland sediments showed significant contamination, possibly due to Guangdong's high population density and aquaculture industry. All wetland types contained the synthetic steroids 17α-MT and 17β-BOL in water, with aquaculture ponds exhibiting the highest percentages. These steroids, used as feed additives for sex manipulation [35], and growth promotion [36], suggest possible unauthorized use in some aquaculture operations.

3.2. Distribution drivers of steroids in wetland water and sediments

Steroid concentrations in coastal wetlands can be impacted by multiple environmental factors, and the wet-season conditions under which this study was conducted likely modulated these interactions. In water (Fig. 3A), salinity was positively correlated with 17α-MT and P, the opposite of the "salting-out effect" reported for most EDCs, whose aqueous solubility drops as salts accumulate, driving them into the non-aqueous phase [37]. This apparent contradiction may be a distinctive feature of the wet season, the large influx of freshwater likely created a low-salinity environment where steroids are likely influenced to a more strongly by other drivers. Consequently, in coastal wetlands experiencing intense hydrological cycles, traditional models governing steroid distribution may require seasonal adjustments. This is critical for accurately predicting their environmental behavior across both dry and wet seasons. Furthermore, the negative correlations between chlorophyll-*a* and steroid concentrations (17β-BOL and P) highlight a key natural purification process driven by phytoplankton. Algae can mitigate steroids through mutiple mechanisms, such as acting as a photosensitizer to enhance oxidative photodegradation [38], directly adsorbing the compounds, and facilitating biodegradation [39], making algal communities an efficient, multi-pathway removal system in the aquatic environment, a capability that can be harnessed in algae-based wastewater treatment to enhance steroid removal [40]. Given that aquaculture wastewater and livestock manure are rich in nutrients [41,42], the positive correlation of 17α-MT and 20α-DHP with nutrient indicators suggests a shared origin, directly implicating the aquaculture and livestock industries as major contributors to steroid contamination in these coastal wetlands. Conversely, the negative correlation between P and nutrients likely reflects enhanced surface-runoff transport of nutrients during the wet season, which stimulates algae proliferation and thereby accelerates the biodegradation and transformation of natural steroids [43,44]. The negative correlations of P with both dissolved organic carbon (DOC) and water temperature point to its enhanced degradation through two primary pathways: DOC-facilitated photodegradation [45] and temperature-dependent biodegradation [46] and photodegradation [47]. Hence, the synergistic action of sunlight, warm temperatures, and organic carbon leads to the most efficient natural attenuation of steroids in such conditions.

In sediment (Fig. 3B), AED, T, P, and 20α-DHP levels have strong positive correlations with nutrient indicators, implying that these steroids have a source rich in nutrients, such as domestic sewage, livestock and aquaculture wastewater [41,42]. Nevertheless, the negative correlations between PREL, 1-DHP and certain nutrients revealed the complexity of steroid adsorption and degradation in sediments,

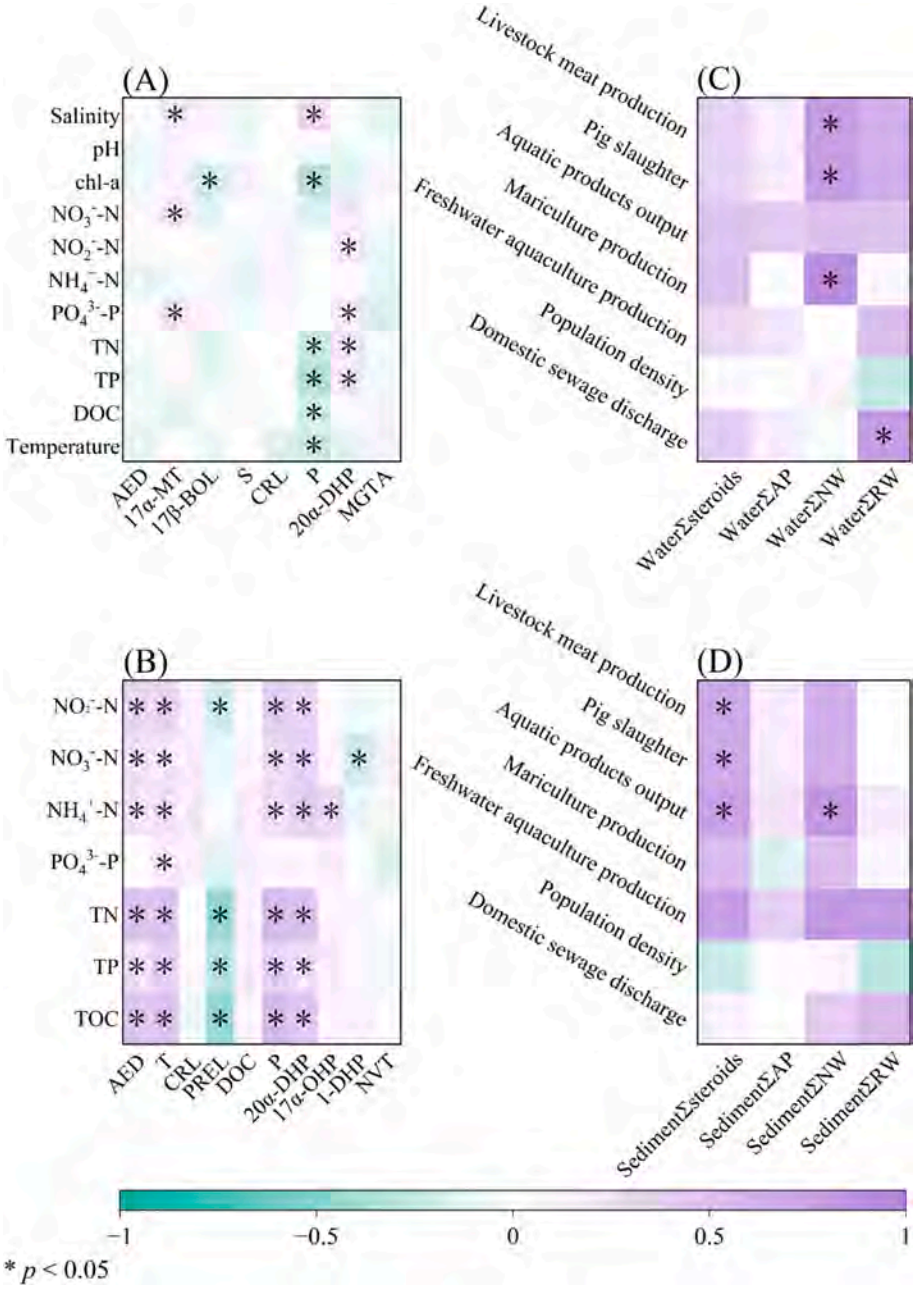


Fig. 3. Correlations between steroid concentrations and environmental parameters in water (A) and sediment (B), correlations between total steroid concentrations and socioeconomic parameters from ten districts in water (C) and sediment (D).

highlighting the need for future research on how multiple factors interact with steroid occurrence. Moreover, most steroids, including AED, T, P, and 20α-DHP, had significant positive relationships with total organic carbon (TOC) (r = 0.31–0.37, $p < 0.05$) (Fig. S3). This correlation, consistent with reports from estuarine [18] and fishing port sediments [32], can be attributed to the well-established role of TOC in facilitating the adsorption of hydrophobic organic compounds to sediments [48]. Consequently, TOC-rich sediments act as a significant sink, sequestering steroids and reducing their immediate bioavailability in the water column. Conversely, the concentrations of PREL were negatively correlated with TOC, possibly because factors beyond TOC also affect sediment steroid occurrence, such as sediment resuspension that enhances the bioavailability of DOC [49], promoting the biodegradation and transformation of steroids and thereby influencing their partitioning. Additionally, wet-season hydrology—dilution, resuspension, and high nutrient—sharply increases the complexity of interacting factors. Thus, while the detected correlations pinpoint core drivers of steroid fate, their magnitude and relative weight are specific to the monsoon phase and may differ under the stagnant, concentrated dry season.

Regarding socioeconomic parameters, steroid levels in natural wetland waters correlated positively with farming production (livestock meat, pig slaughter, mariculture) (Fig. 3C), implying possible discharge of untreated or inadequately treated livestock and aquaculture wastewater into natural wetlands. Manure composting can also introduce steroids into wetland water via surface runoff [50]. Similarly, the total steroid concentrations in sediments correlated strongly with farming production (livestock meat, pig slaughter and aquatic product) (Fig. 3D), indicating livestock and aquaculture are likely the main sources of steroids in coastal wetland sediments [51,52]. Furthermore, the strong link between steroid levels in restored wetland water and local sewage discharge shows domestic sewage is a key factor and potential steroid source. The strong correlation between aquatic yield and

natural wetland sediment steroids (Fig. 3D) underscores aquaculture's substantial impact on ecosystems and highlights the need for better environmental management and pollution control in aquaculture.

3.3. Mass inventory

We estimated steroid mass inventory in Chinese coastal wetlands by integrating our monitoring data from ten wetland regions spanning nine provinces (Fig. 4). Challenges in distinguishing natural and restored wetlands led us to separately quantify mass inventories in coastal wetlands (natural and restored) and aquaculture ponds. The total steroid mass inventory in Chinese coastal wetlands and aquaculture ponds was 19 tons, 1.3 % of China's national mass inventory [50]. Provincial-level inventories exhibited significant spatial heterogeneity, ranging from 558.6 (Hebei) to 5791 (Guangdong) kg (Fig. 4A). In water, the mass per unit area was 0.023–2.6 ng/cm^2 (Table S7), lower than the Jiulong River estuary [53]. In sediment, it was 0.17–0.50 mg/m^2 (Table S7), similar to Chinese estuaries [18] but significantly lower than fishing ports [32]. The sedimentary steroid mass inventory, which accounted for 97 % of the total mass inventory (Fig. 4B), highlights the critical role of sediments as a primary reservoir for steroids in wetland ecosystems. In coastal wetlands, water steroid mass inventory ranged from 0.56 kg in Hainan to 163 kg in Fujian, and sediment mass inventory from 312 kg in Hebei to 5108 kg in Guangdong (Fig. 4C). Liaoning, with the largest wetland area (10,338 km^2), had relatively low steroid mass inventory, which likely due to its sparse population (Table S4). Conversely, high mass inventories in Guangdong and Fujian emphasize the urgent need to address steroid pollution here.

For aquaculture ponds, steroid mass inventory in water ranged from 0.04 kg (Shanghai) to 5.9 kg (Guangdong), while in the sediment, it ranged from 18.4 kg (Shanghai) to 1055 kg (Jiangsu) (Fig. 4D). The low inventories in Shanghai likely stem from its minimal aquaculture pond areas (51.8 km^2). Although Shandong has the largest aquaculture area, its steroid mass inventory is relatively low, possibly due to effective aquaculture management and water quality control. Conversely, the high steroid inventories in both water and sediment in Guangdong may be related to its robust aquaculture economy [54]. High-density aquaculture can accelerate steroid accumulation in sediment. Jiangsu's aquaculture pond sediments have the highest steroid mass inventory (1055 kg), significantly exceeding the second place (Guangdong, 558 kg). Future monitoring of steroid pollution in aquaculture ponds should focus on Guangdong and Jiangsu, particularly aquaculture pond sediments in Jiangsu, as these may serve as a significant source of steroids entering the marine environment [32]. Overall, sediments emerged as a primary reservoir for steroids, thereby highlighting the critical importance of prioritizing sediments in future monitoring and restoration endeavors.

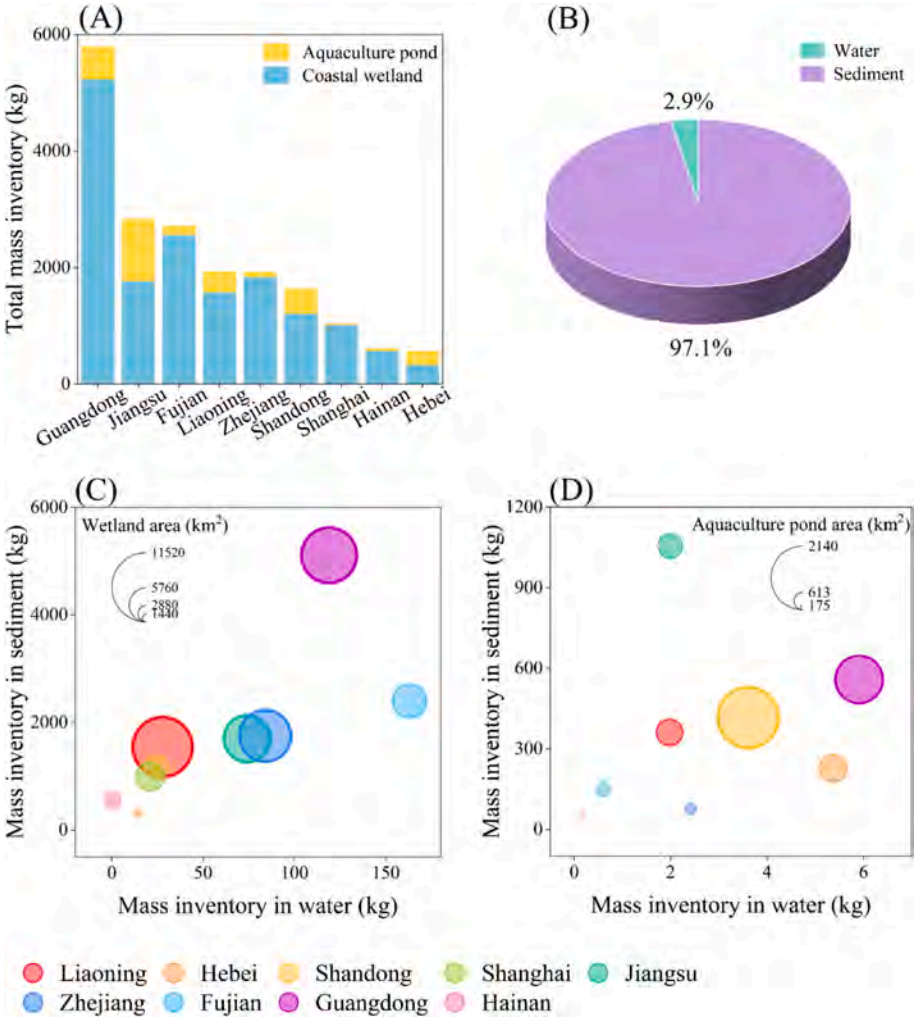


Fig. 4. Total steroid mass inventories of different provinces (A), the percentage of the total steroid mass inventories (B), each steroid mass inventories of different provinces within natural and restored wetlands (C) and aquaculture ponds (D).

3.4. Source apportionment

In water, four principal components (PC1-PC4) were identified, contributing 22.6 %, 16.2 %, 14.1 % and 14.0 % to the total variance, respectively (Table S8). PC1 was associated with S and MGTA. MGTA is extensively used in medical applications such as cachexia–anorexia syndrome [55], and S is commonly employed for treating cytopenia [56] and as a stimulant in athletes [57]. Hence, PC1 likely represents wastewater inputs from medical and pharmaceutical sources. PC2 was strongly associated with 17β-BOL and 20α-DHP. 17β-BOL was known as its employment in livestock growth promoting [58], and 20α-DHP was a natural metabolite of P and was commonly found in mammals [59]. Therefore, PC2 likely represents livestock wastewater. PC3 correlated highly with CRL, which was effectively removed in WWTPs (98 % removal rate) and detected at very low levels in effluents (0.55 ng/L) [10]. Thus, PC3 likely originated from untreated wastewater. PC4 was characterized by the endogenous androgen AED, which is mainly of human origin [50] excreted via urine [60]. Its high prevalence in WWTPs (up to 802 ng/L in influent, and 70 ng/L in effluent) indicates PC4 stands for WWTPs effluents [27,61]. The contributions of the four principal components were determined via MLR analysis using factor score (FS_k) and the standard normalized deviation ($\widehat{Z}_{sum}$) of target steroid concentrations, retaining only significance variables ($p < 0.05$), as following equation:

$$\widehat{Z}_{sum} = 0.244FS_1 + 0.145FS_2 + 0.088FS_3 + 0.8588FS_4 \ (R2 = 0.824)$$

Fig. 5A illustrated the mean percentage contributions of each source to the total steroid concentrations: 18.3 % from medical and pharmaceutical discharge (PC1), 10.9 % from livestock wastewater (PC2), 6.6 % from untreated wastewater (PC3), and 64.3 % from WWTPs effluents

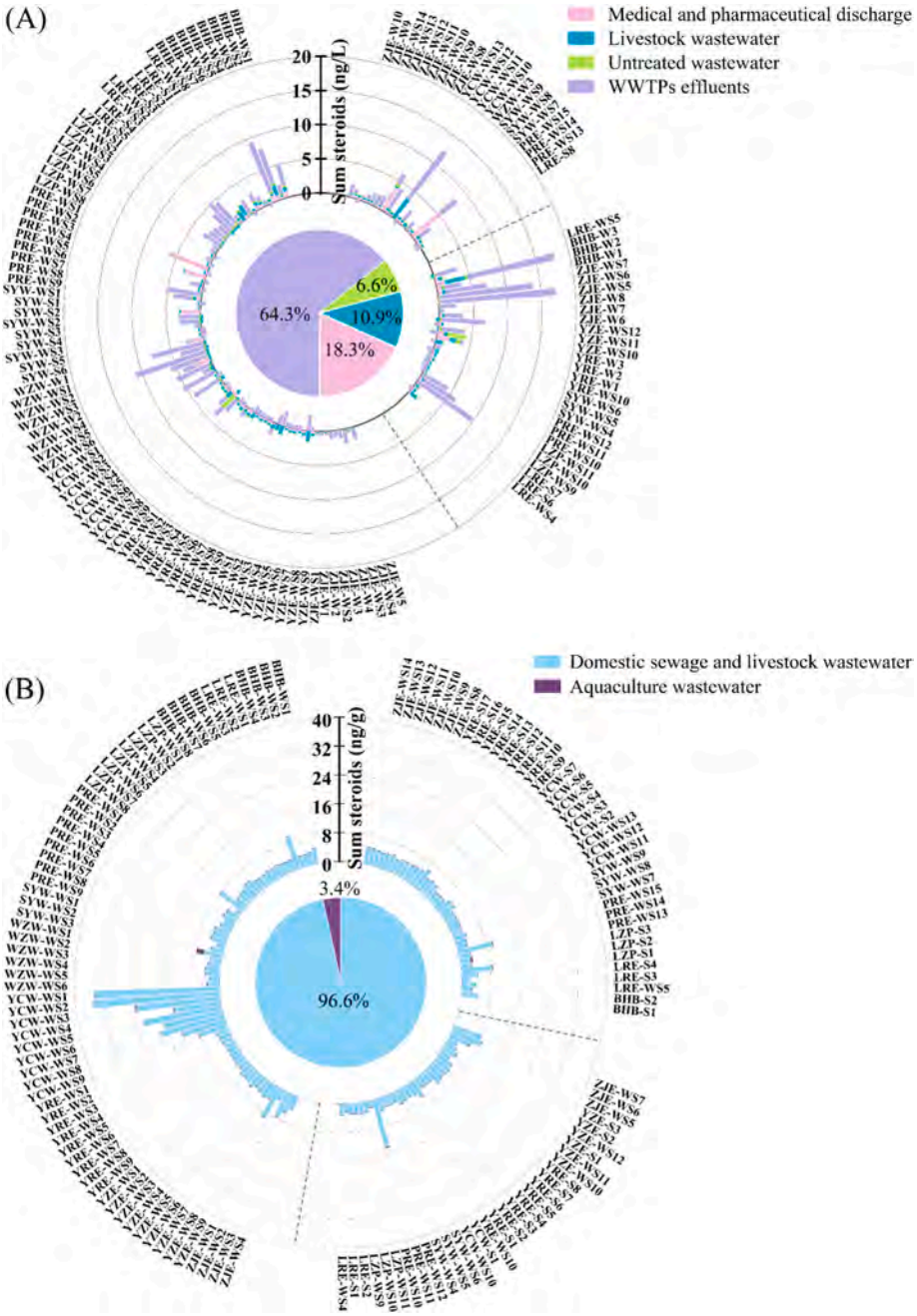


Fig. 5. Source contributions to steroids based on PCA-MLR analysis for water (A) and sediment (B).

(PC4). The dominance of WWTP effluents as the primary source of steroids in water is consistent with findings in rivers of Beijing [25]. However, this contrasts sharply with studies from surface water of the Yellow River Delta [20], where animal source was identified as the major contributor (42.3 %). This regional heterogeneity in sources underscores that steroid emissions are a direct reflection of local anthropogenic activities. Consequently, precise management of steroids are needed, such as upgrading WWTPs in urbanized zones and controlling waste in agricultural regions. The contributions of sources varied greatly among sampling points. WWTP effluents (PC4) were the main cause of high steroid levels at most sites, while other sources (PC1, PC2, PC3) dominated elsewhere. These differences likely stem from inadequate wastewater treatment and variable discharge conditions. Additionally, negative values from some sources at certain stations are typically attributed to improper variable scaling, a common issue in PCA [62].

In sediment, four principal components (PC1-PC4) were recognized, explaining 43.9 %, 14.3 %, 9.4 % and 9.3 % of the total variance, respectively (Table S9). PC1 was linked to four endogenous steroids (AED, T, P, and 20α-DHP) originating from human and animal sources, primarily via sewage and livestock farming [8]. Therefore, PC1 was identified as domestic sewage and livestock wastewater. PC2 strongly correlated with glucocorticoids CRL and PREL, both commonly found in WWTPs and efficiently removed (99 % for CRL and 96 % for PREL) [61]. Therefore, PC2 can be considered as untreated wastewater. PC3 was characterized by high loadings for 17α-MT, which was widely used in aquaculture for hormonal sex reversal [63]. Moreover, among the three types of wetlands, 17α-MT was found as the highest proportion in aquaculture pond water (Fig. S2). Therefore, PC3 can be inferred as originating from aquaculture wastewater. PC4 was strongly correlated with NVT, a well-known component of contraceptives. Therefore, PC4 was identified as pharmaceutical wastewater. Similarly, the equation for MLR as follows:

$$\widehat{Z}_{sum} = 0.982FS_1 + 0.035FS_3 \ (R2 = 0.967)$$

Results indicated that only PC1and PC3 were retained, with contributions of 96.6 % from domestic sewage and livestock wastewater (PC1), and 3.4 % from aquaculture wastewater (PC3) (Fig. 5B). Across all sediment sampling sites, the majority of steroid load originated from livestock wastewater and domestic sewage, with aquaculture wastewater contributing negligible proportions. The hydrophobic nature of steroids leads to their accumulation in sediments via sedimentation, making sediments a major storage [50]. Hence, steroid source analysis in sediment likely reflects the historical aquatic steroid pollution and accumulation. The findings highlight significant accumulation of natural steroids in coastal wetland sediments, which should not be overlooked, as these steroids can be resuspended and re-entered the water column. Our quantitative source apportionment provides a scientific basis for targeted mitigation strategies. The predominance of WWTP effluents necessitates prioritizing upgrades to treatment technologies in major coastal cities, with a focus on advanced oxidation processes such as photocatalysis, Fenton reactions, electrocatalytic oxidation, and catalytic ozonation [64]. To address the significant contributions from medical and livestock sources, policy measures should include the improved management of pharmaceutical waste and the enforcement of stricter regulations on waste discharge from livestock farms. The spatial heterogeneity of pollution sources calls for tailored, region-specific control strategies.

3.5. Screening of priority steroids in water

This study utilized a risk-based prioritization model, and integrated 12 PBT attributes (3 for persistence, 3 for bioaccumulation, and 6 for toxicity) with environmental exposure of steroids to identify priority steroids in coastal wetland water [65]. According to criteria for PBT substances (Table S11), 5 steroids (AED, S, 17α-MT, P and 20α-DHP) exhibited high persistence, indicating their extreme persistence (model-predicted total degradation times exceeding months), with S having the highest persistence. None of the detected steroids reached the bioaccumulation criteria, with S exhibiting the highest bioaccumulation potential (Log BAF = 3.1). Although the detected steroids do not meet the criteria for acute aquatic toxicity ($LC_{50}/EC_{50} < 0.1$ mg/L), their potential for inducing chronic and sublethal effects poses a significant threat to aquatic organisms. We found that all steroids have possible developmental toxicity, five steroids (AED, S, 17α-MT, P and 20α-DHP) have probable carcinogenicity, and four (S, CRL, P and MGTA) have potential hepatotoxicity. The combination of these toxicity endpoints, especially their endocrine-disrupting potential, means that these steroids, even at low environmental levels, exert a cascade of adverse effects on aquatic organisms, compromising reproduction, development, and overall health. The ToxPi scores based on PBT attributes indicate that steroid S poses the highest hazard among detected compounds, followed by 17α-MT (Fig. 6A). The predicted no-effect concentration (PNEC) of S is the lowest (47 ng/L), resulting in medium risks (RQs ≥ 0.1) at several sampling points in the PRE region, while 17α-MT exhibits minimal risk (RQs < 0.01) (Fig. S4). The high ToxPi score of S is attributed to its strong persistence and bioaccumulation characteristics. S is commonly used as veterinary medicine [66] and stimulant of sports [57], thus there was a potential for its misuse and underscoring the need for targeted monitoring of S in PRE.

Normalized exposure (Fig. 6B) showed AED, P, 17α-MT, 17β-BOL, and S as the most exposed compounds (normalized exposure ≥0.01). Integrating exposure levels and hazard data, AED and P were classified as high-priority steroids, and 17α-MT, S and 17β-BOL as medium-priority steroids in coastal wetland water (Fig. 6C). The high-risk indexes of AED and P stem predominantly from their high exposure levels in water, with PBT attributes contributing relatively little (Fig. 6C). Though AED and P are naturally secreted by humans and animals, their accumulation can cause ecological harm. Exposure to P can cause direct

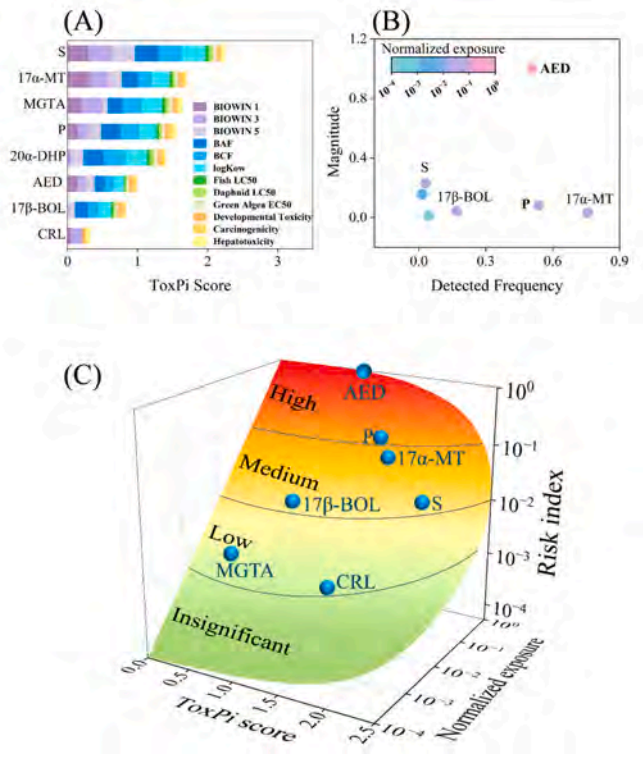


Fig. 6. ToxPi score (A), concentration magnitude versus detection frequency, and their respective contributions to normalized exposure (B), and ranking of priority steroids based on ToxPi score, normalized exposure and risk index in water samples (C).

pathological damage to vital organs, such as the liver and gills in fish [67]. More critically, at the physiological level, both steroids function as potent endocrine disruptors. P is proven to disrupt sex differentiation [68] and alter transcriptional profiles in the brain and ovary, adversely impacting reproduction [69]. Simultaneously, AED exhibits strong androgenic effects, leading to the masculinization of female fish across multiple species, including mosquitofish and fathead minnows [70–72]. Critically, the risk is magnified in real-world scenarios where mixtures prevail. Environmentally relevant mixtures of steroids exert additive adverse impacts on fish reproduction [73], and the co-regulation of several genes by multiple steroids suggests a convergent disruption of key developmental pathways [74]. Therefore, the co-occurrence of P and AED with other steroids likely leads to combined toxicities that pose a far greater threat to aquatic ecosystems than any single compound alone. In all coastal wetland water samples, AED and P exhibited low or minimal risks (RQs < 0.1) in coastal wetlands (Fig. S4). Specifically, AED showed low risk at BHB, ZJE, LZP, and WZW, while P exhibited low risk at BHB, ZJE, PRE, and YRE. Given these results, enhanced monitoring and management of AED and P are recommended for BHB and ZJE wetlands. To achieve this, wastewater treatment plants should establish specific monitoring indicators, and pre-treatment standards for aquaculture and livestock wastewater need to be strengthened. Overall, at 83 % of the sampling sites, steroids pose minimal ecological risk (RQs < 0.01, Fig. S4). Despite low concentrations, vigilance is needed, especially in PRE, where steroid mixtures have a higher hazard index (HI $>$ 0.1), potentially impacting organism endocrine systems.

3.6. Limitations

Several limitations should be acknowledged in this study. Firstly, the absence of comprehensive toxicity data restricted our risk assessments to only 8 steroids, which might lead to an underestimation of the cumulative risks in the environment. Secondly, the PCA-MLR model adopted herein simplifies the intricate interactions between pollution sources and fails short in precisely refining the identification of pollution sources. Thirdly, the snapshot sampling approach, conducted exclusively during wet season, fails to capture seasonal variations, which is critical for steroids influenced by hydrological and biological cycles. To address these gaps, future studies should incorporate longitudinal monitoring efforts, expand toxicity datasets, and employ multi-compartment modeling to enhance the precision of risk predictions.

4. Conclusions

This study established the first systematic, national-scale baseline for steroid occurrence in China's coastal wetlands, revealing key contamination characteristics. Steroid concentrations were found to be relatively low overall (ND to 23 ng/L in water and ND to 32 ng/g in sediment), with natural steroids predominating. Furthermore, no significant differences in steroid levels were observed across different wetland types (natural, restored, aquaculture). Environmental parameters (salinity, chlorophyll-*a*, temperature, and TOC) and socioeconomic drivers (livestock farming output, aquaculture production, domestic sewage discharge) significantly influenced steroid occurrence and partitioning. Crucially, sediments were identified as the dominant reservoir, holding an estimated 19-ton national inventory that constitutes 97 % of the total steroid mass. Based on this inventory assessment, Jiangsu and Guangdong provinces emerged as priority regions for future monitoring and management. WWTP effluents dominated steroid sources in wetland water; domestic sewage and livestock wastewater dominated in sediments. Moreover, the natural steroids 4-androstene-3,17-dione and progesterone were designated as priority steroids mainly due to their high environmental exposure levels. Consequently, these findings highlight the necessity to enhance steroid removal efficiency and treatment standards in wastewater, with particular focus on 4-androstene-3,17-dione and progesterone. This research provides critical scientific support for evidence-based policies aimed at protecting vulnerable coastal wetlands and mitigating steroid fluxes into the marine environment.

CRediT authorship contribution statement

Shan Liu: Writing – review & editing, Writing – original draft, Supervision, Methodology, Funding acquisition. **Qin-Ge Zhou:** Writing – review & editing, Writing – original draft, Data curation. **Yuan Liu:** Formal analysis, Data curation. **Biao Li:** Investigation. **Huabing Li:** Investigation. **Ji-Xun Chen:** Data curation. **Nian-Nian Wu:** Formal analysis. **Man Wang:** Investigation. **Xiang-Rong Xu:** Resources. **Li-Jun Zhou:** Writing – review & editing, Project administration, Funding acquisition, Conceptualization. **Qinglong L. Wu:** Funding acquisition, Conceptualization.

Declaration of competing interest

The authors declare that they have no known competing financial interests or personal relationships that could have appeared to influence the work reported in this paper.

Acknowledgments

We would like to thank National Key Research and Development Program of China (2023YFF1304501), National Natural Science Foundation of China (Grant No. 42293264, 32171629 and 42177388), the Youth Innovation Promotion Association of Chinese Academy of Sciences (No. 2022318), Science and Technology Planning Project of NIGLAS, China (No. NIGLAS2022TJ07), the Major Talent Project of Guangxi Zhuang Autonomous Region, and the Autonomous Deployment Project of Key Laboratory of Lake and Watershed Science for Water Security, China (NKL2023-KP01). We would also like to thank Hongwei Wang and Fangwei Fan for their assistance in the sample collection tasks.

Appendix A. Supplementary data

Supplementary data to this article can be found online at https://doi.org/10.1016/j.enceco.2025.10.030.

References

[1] IARC, The International Agency for Research on Cancer (IARC) Monographs on the Identification of Carcinogenic Hazards to Human. https://www.iarc.who.int/, 2020 (accessed 14 June 2025).
[2] R. Zhong, H. Zou, J. Gao, T. Wang, Q. Bu, Z.-L. Wang, M. Hu, Z. Wang, A critical review on the distribution and ecological risk assessment of steroid hormones in the environment in China, Sci. Total Environ. 786 (2021) 147452, https://doi.org/10.1016/j.scitotenv.2021.147452.
[3] A. Watanabe, T. Myosho, A. Ishibashi, J. Yamamoto, M. Toda, Y. Onishi, T. Kobayashi, Levonorgestrel causes feminization and dose-dependent masculinization in medaka fish (*Oryzias latipes*): endocrine-disruption activity and its correlation with sex reversal, Sci. Total Environ. 876 (2023) 162740, https://doi.org/10.1016/j.scitotenv.2023.162740.
[4] T.J. Runnalls, N. Beresford, S. Kugathas, L. Margiotta-Casaluci, M. Scholze, A. P. Scott, J.P. Sumpter, From single chemicals to mixtures—reproductive effects of levonorgestrel and ethinylestradiol on the fathead minnow, Aquat. Toxicol. 169 (2015) 152–167, https://doi.org/10.1016/j.aquatox.2015.10.009.
[5] Y.-Q. Liang, Z. Jing, C.-G. Pan, Z. Lin, Z. Zhen, L. Hou, Z. Dong, The progestin norethindrone alters growth, reproductive histology and gene expression in zebrafish (*Danio rerio*), Chemosphere 242 (2020) 125285, https://doi.org/10.1016/j.chemosphere.2019.125285.
[6] J.-P. Besse, J. Garric, Progestagens for human use, exposure and hazard assessment for the aquatic environment, Environ. Pollut. 157 (2009) 3485–3494, https://doi.org/10.1016/j.envpol.2009.06.012.
[7] S. Liu, H. Chen, X.-R. Xu, Q.-W. Hao, J.-L. Zhao, G.-G. Ying, Three classes of steroids in typical freshwater aquaculture farms: comparison to marine aquaculture farms, Sci. Total Environ. 609 (2017) 942–950, https://doi.org/10.1016/j.scitotenv.2017.07.207.
[8] Q.-Q. Zhang, C. Xing, Y.-Y. Cai, X.-T. Yan, G.-G. Ying, How much do human and livestock actually contribute to steroids emission and surface water pollution from

past to the future: a global research, Sci. Total Environ. 772 (2021) 145558, https://doi.org/10.1016/j.scitotenv.2021.145558.
[9] Q. Yu, J. Geng, X. Zong, Y. Zhang, K. Xu, H. Hu, Y. Deng, F. Zhao, H. Ren, Occurrence and removal of progestagens in municipal wastewater treatment plants from different regions in China, Sci. Total Environ. 668 (2019) 1191–1199, https://doi.org/10.1016/j.scitotenv.2019.02.327.
[10] H. Chang, J. Hu, B. Shao, Occurrence of natural and synthetic glucocorticoids in sewage treatment plants and receiving river waters, Environ. Sci. Technol. 41 (2007) 3462–3468, https://doi.org/10.1021/es062746o.
[11] X. Huang, Z. He, Y. Wang, F. Wang, Z. Zheng, Y. Zuo, Y. Cao, X. Yao, Z. She, Y. Ge, Y. Li, Assessment of soil microbial communities and diversity in typical coastal wetlands along a succession gradient: implications for reconstructing the long-term evolution of coastal wetlands, Environ. Technol. Innov. (2025) 104263, https://doi.org/10.1016/j.eti.2025.104263.
[12] J. Chen, K. Yuan, Z. Xue, G. Chen, S. Chen, D. Ou, P. Zheng, Y. Ye, Dredging wastewater discharge caused mangrove sediment antibiotic accumulation and affected functional microbes in carbon and nitrogen metabolism, Environ. Pollut. 375 (2025) 126326, https://doi.org/10.1016/j.envpol.2025.126326.
[13] S.E. Jones, N. Gutkowski, S. Demick, M. Curello, A. Pavia, A.R. Robuck, M.-L. Li, Assessing bivalves as biomonitors of per- and polyfluoroalkyl substances in coastal environments, Environ. Sci. Technol. 59 (2025) 5202–5213, https://doi.org/10.1021/acs.est.4c11215.
[14] X. Ouyang, C.M. Duarte, S.-G. Cheung, N.F.-Y. Tam, S. Cannicci, C. Martin, H.S. Lo, S.Y. Lee, Fate and effects of macro- and microplastics in coastal wetlands, Environ. Sci. Technol. 56 (2022) 2386–2397, https://doi.org/10.1021/acs.est.1c06732.
[15] Q. He, Z.A. Li, P. Daleo, J.S. Lefcheck, M.S. Thomsen, J.B. Adams, T.J. Bouma, Coastal wetland resilience through local, regional and global conservation, Nat. Rev. Biodivers. 1 (2025) 50–67, https://doi.org/10.1038/s44358-024-00004-x.
[16] R. Xu, S. Liu, H. Chen, Q.-W. Hao, Y.-X. Hu, H.-X. Li, L. Lin, R. Hou, B. Hong, S. Yu, X.-R. Xu, An effective tool for tracking steroids and their metabolites at the watershed level: combining fugacity modeling and a chemical indicator, Environ. Pollut. 326 (2023) 121499, https://doi.org/10.1016/j.envpol.2023.121499.
[17] L. Zhao, C. Wang, F. Sun, H. Liao, H. Chang, X. Jia, Assessment of occurrence, partitioning and ecological risk for 144 steroid hormones in Taihu Lake using UPLC-MS/MS with machine learning model, Chemosphere 354 (2024) 141598, https://doi.org/10.1016/j.chemosphere.2024.141598.
[18] R. Xu, S. Liu, Y.-F. Pan, N.-N. Wu, Q.-Y. Huang, H.-X. Li, L. Lin, R. Hou, X.-R. Xu, Y.-Y. Cheng, Steroid metabolites as overlooked emerging contaminants: insights from multimedia partitioning and source–sink simulation in an estuarine environment, J. Hazard. Mater. 461 (2024) 132673, https://doi.org/10.1016/j.jhazmat.2023.132673.
[19] C. Ren, Q. Fang, H. Long, F. Liu, W. Lan, G. Gao, Pollution characteristics, sources and ecological risks of steroid hormones in Fangchenggang Bay, South China Sea: significant impacts of rivers and domestic sewage entering the sea, J. Hazard. Mater. 489 (2025) 137556, https://doi.org/10.1016/j.jhazmat.2025.137556.
[20] X. Shen, Q. Zhang, Q. Xiang, J. Zhao, Y. Cao, K. Li, J. Song, Z. Wang, X. Zhao, Q. Chen, Occurrences, source apportionment, and potential risks of 55 progestins in surface water of the Yellow River Delta, China, J. Hazard. Mater. 480 (2024) 136098, https://doi.org/10.1016/j.jhazmat.2024.136098.
[21] M. Hu, J. Sardans, R. Yan, H. Wu, R. Ni, J. Peñuelas, C. Tong, Substantial increase in P release following conversion of coastal wetlands to aquaculture ponds from altered kinetic exchange and resupply capacity, Water Res. 230 (2023) 119586, https://doi.org/10.1016/j.watres.2023.119586.
[22] X. Wang, X. Xiao, X. Xu, Z. Zou, B. Chen, Y. Qin, X. Zhang, J. Dong, D. Liu, L. Pan, B. Li, Rebound in China's coastal wetlands following conservation and restoration, Nat. Sustain. 4 (2021) 1076–1083, https://doi.org/10.1038/s41893-021-00793-5.
[23] B. Du, G. Fan, W. Yu, S. Yang, J. Zhou, J. Luo, Occurrence and risk assessment of steroid estrogens in environmental water samples: a five-year worldwide perspective, Environ. Pollut. 267 (2020) 115405, https://doi.org/10.1016/j.envpol.2020.115405.
[24] USEPA, Guidance for Data Quality Assessment. https://www.epa.gov/quality/guidance-data-quality-assessment, 2003 (accessed 2 June 2024).
[25] H. Chang, Y. Wan, J. Hu, Determination and source apportionment of five classes of steroid hormones in Urban Rivers, Environ. Sci. Technol. 43 (2009) 7691–7698, https://doi.org/10.1021/es803653j.
[26] F. Zhang, L. Zhang, Y. Wang, H. Wang, Sexual hormones in a coastal river adjacent to the Bohai Sea: characteristic pollutants and dominantly influencing factors, Environ. Res. 212 (2022) 113133, https://doi.org/10.1016/j.envres.2022.113133.
[27] I.C. Tanui, F. Kandie, M. Krauss, A. Piotrowska, S. Finckh, A. Kiprop, H. Hollert, N. Shahid, M. Liess, W. Brack, Occurrence and potential risk of steroid hormones in selected surface water and wastewater treatment plants in western Kenya, Environ. Pollut. 367 (2025) 125623, https://doi.org/10.1016/j.envpol.2024.125623.
[28] K. Goeury, G. Munoz, S. Vo Duy, M. Prévost, S. Sauvé, Occurrence and seasonal distribution of steroid hormones and bisphenol a in surface waters and suspended sediments of Quebec, Canada, Environ. Adv. 8 (2022) 100199, https://doi.org/10.1016/j.envadv.2022.100199.
[29] P. Chakraborty, N.W. Shappell, M. Mukhopadhyay, S. Onanong, K.R. Rex, D. Snow, Surveillance of plasticizers, bisphenol a, steroids and caffeine in surface water of river ganga and Sundarban wetland along the bay of Bengal: occurrence, sources, estrogenicity screening and ecotoxicological risk assessment, Water Res. 190 (2021) 116668, https://doi.org/10.1016/j.watres.2020.116668.
[30] S. Liu, R. Xu, Y.-F. Pan, Q.-Y. Huang, N.-N. Wu, H.-X. Li, L. Lin, R. Hou, X.-R. Xu, Free and conjugated forms of metabolites are indispensable components of steroids: the first evidence from an estuarine food web, Water Res. 235 (2023) 119913, https://doi.org/10.1016/j.watres.2023.119913.
[31] Q.-G. Zhou, S. Liu, Y. Liu, N.-N. Wu, Q.-S. Yang, H.-X. Li, X.-R. Xu, J. Ling, Contamination, multimedia partitioning, and priority list of steroids and their metabolites in coastal regions of the Greater Bay Area, China, Process. Saf. Environ. Prot. 197 (2025) 106973, https://doi.org/10.1016/j.psep.2025.106973.
[32] S. Liu, F. Tian, Y.-F. Pan, H.-X. Li, L. Lin, R. Hou, L.-B. Zhang, Z. Zhang, S.-S. Liu, X.-R. Xu, Y.-Y. Cheng, H.-G. Chen, Contamination and ecological risks of steroid metabolites require more attention in the environment: evidence from the fishing ports, Sci. Total Environ. 807 (2022) 150814, https://doi.org/10.1016/j.scitotenv.2021.150814.
[33] H. Yarahmadi, S.V. Duy, M. Hachad, S. Dorner, S. Sauvé, M. Prévost, Seasonal variations of steroid hormones released by wastewater treatment plants to river water and sediments: distribution between particulate and dissolved phases, Sci. Total Environ. 635 (2018) 144–155, https://doi.org/10.1016/j.scitotenv.2018.03.370.
[34] E. Pignotti, E. Dinelli, Distribution and partition of endocrine disrupting compounds in water and sediment: case study of the Romagna area (North Italy), J. Geochem. Explor. 195 (2018) 66–77, https://doi.org/10.1016/j.gexplo.2018.02.008.
[35] S.K. Ong, P. Chotisukarn, T. Limpiyakorn, Sorption of 17α-methyltestosterone onto soils and sediment, Water Air Soil Pollut. 223 (2012) 3869–3875, https://doi.org/10.5740/jaoacint.14-281.
[36] L. Watson, R. Potter, C. Murphy, R. Gibbs, The development and single-laboratory validation of a method for the determination of steroid residues in fish and fish products, J. AOAC Int. 98 (2015) 580–587, https://doi.org/10.5740/jaoacint.14-281.
[37] L. Yang, Q. Cheng, L. Lin, X. Wang, B. Chen, T. Luan, N.F.Y. Tam, Partitions and vertical profiles of 9 endocrine disrupting chemicals in an estuarine environment: effect of tide, particle size and salinity, Environ. Pollut. 211 (2016) 58–66, https://doi.org/10.1016/j.envpol.2015.12.034.
[38] L. Ge, H. Deng, F. Wu, N. Deng, Microalgae-promoted photodegradation of two endocrine disrupters in aqueous solutions, J. Chem. Technol. Biotechnol. 84 (2009) 331–336, https://doi.org/10.1002/jctb.2043.
[39] W. Shi, L. Wang, D.P.L. Rousseau, P.N.L. Lens, Removal of estrone, 17α-ethinylestradiol, and 17ß-estradiol in algae and duckweed-based wastewater treatment systems, Environ. Sci. Pollut. Res. 17 (2010) 824–833, https://doi.org/10.1007/s11356-010-0301-7.
[40] Y. Zhang, M.Y. Habteselassie, E.P. Resurreccion, V. Mantripragada, S. Peng, S. Bauer, L.M. Colosi, Evaluating removal of steroid estrogens by a model alga as a possible sustainability benefit of hypothetical integrated algae cultivation and wastewater treatment systems, ACS Sustain. Chem. Eng. 2 (2014) 2544–2553, https://doi.org/10.1021/sc5004538.
[41] S.A. Moezzi, S. Rastgar, M. Faghani, Z. Ghiasvand, A. Javanshir Khoei, Optimization of carbon membrane performance in reverse osmosis systems for reducing salinity, nitrates, phosphates, and ammonia in aquaculture wastewater, Chemosphere 376 (2025) 144304, https://doi.org/10.1016/j.chemosphere.2025.144304.
[42] T. Tan, Z. Zhang, Z. Huang, C. Ma, G. Liu, T. Huhe, Y. Chen, J. Xie, Y. Chen, Evaluating the nutrient and pollutant flows of the Chinese livestock manure management system from 1949 to 2050, Resour. Conserv. Recycl. 215 (2025) 108092, https://doi.org/10.1016/j.resconrec.2024.108092.
[43] F. Zhang, Q. Yu, L. Yang, Watershed scale patterns in steroid hormones composition and content characters at a typical eutrophic lake in southeastern China, Environ. Sci. Pollut. Res. 26 (2019) 6107–6115, https://doi.org/10.1007/s11356-018-04120-y.
[44] L. Bai, Q. Ju, C. Wang, L. Tian, C. Wang, H. Zhang, H. Jiang, Responses of steroid estrogen biodegradation to cyanobacterial organic matter biodegradability in the water column of a eutrophic lake, Sci. Total Environ. 805 (2022) 150058, https://doi.org/10.1016/j.scitotenv.2021.150058.
[45] E. Caupos, P. Mazellier, J.-P. Croue, Photodegradation of estrone enhanced by dissolved organic matter under simulated sunlight, Water Res. 45 (2011) 3341–3350, https://doi.org/10.1016/j.watres.2011.03.047.
[46] Y.-Y. Yang, T. Borch, R.B. Young, L.D. Goodridge, J.G. Davis, Degradation kinetics of testosterone by manure-borne bacteria: influence of temperature, pH, glucose amendments, and dissolved oxygen, J. Environ. Qual. 39 (2010) 1153–1160, https://doi.org/10.2134/jeq2009.0112.
[47] T. Nejedly, J. Klimes, A model of natural degradation of 17-α-ethinylestradiol in surface water and identification of degradation products by GC-MS, Environ. Sci. Pollut. Res. 24 (2017) 23196–23206, https://doi.org/10.1007/s11356-017-9743-5.
[48] H. Feng, X. Xu, P. Peng, C. Yang, H. Zou, C. Chen, Y. Zhang, Sorption and desorption of epiandrosterone and cortisol on sewage sludge: comparison to aquatic sediment, Environ. Pollut. 329 (2023) 121663, https://doi.org/10.1016/j.envpol.2023.121663.
[49] X. Liu, C. Lan, L. Zhu, C. Yan, N. Wang, H. Chen, G. Zheng, Y. Che, Z. Yang, R. Bao, Sediment resuspension as a driving force for organic carbon transference and rebalance in marginal seas, Water Res. 257 (2024) 121672, https://doi.org/10.1016/j.watres.2024.121672.
[50] Q.Q. Zhang, J.-L. Zhao, G.-G. Ying, Y.-S. Liu, C.-G. Pan, Emission estimation and multimedia fate modeling of seven steroids at the river basin scale in China, Environ. Sci. Technol. 48 (2014) 7982–7992, https://doi.org/10.1021/es501226h.
[51] S. Liu, G.-G. Ying, L.-J. Zhou, R.-Q. Zhang, Z.-F. Chen, H.-J. Lai, Steroids in a typical swine farm and their release into the environment, Water Res. 46 (2012) 3754–3768, https://doi.org/10.1016/j.watres.2012.04.006.
[52] S.-S. Liu, G.-G. Ying, Y.-S. Liu, Y.-Y. Yang, L.-Y. He, J. Chen, W.-R. Liu, J.-L. Zhao, Occurrence and removal of progestagens in two representative swine farms:

effectiveness of lagoon and digester treatment, Water Res. 77 (2015) 146–154, https://doi.org/10.1016/j.watres.2015.03.022.
[53] R. Xu, N.-N. Wu, S. Liu, H. Chen, Q.-W. Hao, Y.-X. Hu, B. Hong, S. Yu, X.-R. Xu, Spatiotemporal distribution and priority assessment of steroids in the estuarine environment: implications for environmental risk management, Mar. Pollut. Bull. 216 (2025) 117980, https://doi.org/10.1016/j.marpolbul.2025.117980.
[54] P. Yuan, X. Wang, Y. Zhou, Z. Qi, K. Liu, Y. Fang, Y. Ning, Evolutionary pattern and influencing factors of the aquaculture development in the Guangdong-Hong Kong-Macao Greater Bay area during 1986–2020, Ecol. Indic. 161 (2024) 111952, https://doi.org/10.1016/j.ecolind.2024.111952.
[55] V. Ruiz-García, E. López-Briz, R. Carbonell-Sanchis, S. Bort-Martí, J.L. Gonzálvez-Perales, Megestrol acetate for cachexia–anorexia syndrome. A systematic review, J. Cachexia. Sarcopeni. 9 (2018) 444–452, https://doi.org/10.1002/jcsm.12292.
[56] Y. Liu, C. Yang, H. Xue, F. Ye, W. Sun, J. Wang, W. Qi, H. Niu, L. Hua, H. Wang, B. Han, Z. Shao, Stanozolol improves the progression-free survival of patients with high-risk myelodysplastic syndrome after decitabine treatment, Int. J. Hematol. 113 (2021) 807–814, https://doi.org/10.1007/s12185-021-03115-9.
[57] M. Derakhshandeh, F. Taghian, K. Jalali Dehkordi, S.A. Hosseini, Synchronized resistance training and bioactive herbal compounds of Tribulus Terrestris reverse the disruptive influence of Stanozolol, Steroids 182 (2022) 109000, https://doi.org/10.1016/j.steroids.2022.109000.
[58] M. Park, J. Sim, Y. Jeon, S. Yeon, J. Lee, S. In, Determination of boldenone in postmortem specimens including blood and urine samples using LC-MS/MS, J. Pharm. Biomed. Anal. 169 (2019) 111–115, https://doi.org/10.1016/j.jpba.2019.02.043.
[59] A.K. Hankele, K. Rehm, J. Berard, G. Schuler, L. Bigler, S.E. Ulbrich, Progestogen profiling in plasma during the estrous cycle in cattle using an LC-MS based approach, Theriogenology 142 (2020) 376–383, https://doi.org/10.1016/j.theriogenology.2019.10.005.
[60] Z.-H. Liu, Y. Kanjo, S. Mizutani, Urinary excretion rates of natural estrogens and androgens from humans, and their occurrence and fate in the environment: a review, Sci. Total Environ. 407 (2009) 4975–4985, https://doi.org/10.1016/j.scitotenv.2009.06.001.
[61] Z. Fan, S. Wu, H. Chang, J. Hu, Behaviors of glucocorticoids, androgens and progestogens in a municipal sewage treatment plant: comparison to estrogens, Environ. Sci. Technol. 45 (2011) 2725–2733, https://doi.org/10.1021/es103429c.
[62] C. Lin, J. Gong, Y. Zhou, D. Chen, Y. Chen, J. Yang, Q. Li, C. Wu, H. Tang, Spatiotemporal distribution, source apportionment, and ecological risk of corticosteroids in the urbanized river system of Guangzhou, China, Sci. Total Environ. 706 (2020) 135693, https://doi.org/10.1016/j.scitotenv.2019.135693.
[63] X. Zhang, C. Fang, X. Lou, G. Yang, C. Kong, Y. Shi, D. Huang, Determination of 17α-methyltestosterone in aquatic products using high-performance liquid chromatography-tandem mass spectrometry, Microchem. J. 183 (2022) 108119, https://doi.org/10.1016/j.microc.2022.108119.
[64] A.A. Bayode, S.S. Emmanuel, S.O. Sanni, O.A. Olalekan, O.T. Ore, D.T. Koko, M. O. Omorogie, Current status and performance evaluation of emerging advanced remediation techniques for the removal of steroidal hormones in water, Environ. Chem. Ecotoxicol. 6 (2024) 315–337, https://doi.org/10.1016/j.enceco.2024.07.006.
[65] J. Hu, Y. Lyu, H. Chen, L. Cai, J. Li, X. Cao, W. Sun, Integration of target, suspect, and nontarget screening with risk modeling for per- and polyfluoroalkyl substances prioritization in surface waters, Water Res. 233 (2023) 119735, https://doi.org/10.1016/j.watres.2023.119735.
[66] H. Li, X. Zhou, Solid-phase extraction of stanozolol abuse in athletes using a novel magnetic molecularly imprinted polymer sorbent, Alex. Eng. J. 116 (2025) 55–61, https://doi.org/10.1016/j.aej.2024.12.040.
[67] L. Hou, H. Xu, G. Ying, Y. Yang, H. Shu, J. Zhao, X. Cheng, Physiological responses and gene expression changes in the western mosquitofish (*Gambusia affinis*) exposed to progesterone at environmentally relevant concentrations, Aquat. Toxicol. 192 (2017) 69–77, https://doi.org/10.1016/j.aquatox.2017.09.011.
[68] Y.-Q. Liang, G.-Y. Huang, S.-S. Liu, J.-L. Zhao, Y.-Y. Yang, X.-W. Chen, F. Tian, Y.-X. Jiang, G.-G. Ying, Long-term exposure to environmentally relevant concentrations of progesterone and norgestrel affects sex differentiation in zebrafish (*Danio rerio*), Aquat. Toxicol. 160 (2015) 172–179, https://doi.org/10.1016/j.aquatox.2015.01.006.
[69] S. Zucchi, S. Castiglioni, K. Fent, Progesterone alters global transcription profiles at environmental concentrations in brain and ovary of female zebrafish (*Danio rerio*), Environ. Sci. Technol. 47 (2013) 12548–12556, https://doi.org/10.1021/es403800y.
[70] J.P. Stanko, R.A. Angus, In vivo assessment of the capacity of androstenedione to masculinize female mosquitofish (*Gambusia affinis*) exposed through dietary and static renewal methods, Environ. Toxicol. Chem. 26 (2007) 920–926, https://doi.org/10.1897/06-201R.1.
[71] Z.A. DeQuattro, J.D.C. Hemming, T.P. Barry, Effects of androstenedione exposure on fathead minnow (*Pimephales promelas*) reproduction and embryonic development, Environ. Toxicol. Chem. 34 (2015) 2549–2554, https://doi.org/10.1002/etc.3092.
[72] L.-P. Hou, Y. Yang, H. Shu, G.-G. Ying, J.-L. Zhao, G.-Z. Fang, L. Xin, W.-J. Shi, L. Yao, X.-M. Cheng, Masculinization and reproductive effects in western mosquitofish (*Gambusia affinis*) after long-term exposure to androstenedione, Ecotoxicol. Environ. Saf. 147 (2018) 509–515, https://doi.org/10.1016/j.ecoenv.2017.08.004.
[73] S. Zucchi, L. Mirbahai, S. Castiglioni, K. Fent, Transcriptional and physiological responses induced by binary mixtures of Drospirenone and progesterone in zebrafish (*Danio rerio*), Environ. Sci. Technol. 48 (2014) 3523–3531, https://doi.org/10.1021/es405584f.
[74] R.A. Willi, S. Castiglioni, N. Salgueiro-González, N. Furia, S. Mastroianni, S. Faltermann, K. Fent, Physiological and transcriptional effects of mixtures of environmental estrogens, androgens, progestins, and glucocorticoids in zebrafish, Environ. Sci. Technol. 54 (2020) 1092–1101, https://doi.org/10.1021/acs.est.9b05834.

Journal of Alloys and Compounds 1020 (2025) 179492

Contents lists available at ScienceDirect

Journal of Alloys and Compounds

journal homepage: www.elsevier.com/locate/jalcom

Construction of S-type CdS@$ZnIn_2S_4$ heterojunctions with core-shell hollow nanosphere and their application in visible light photocatalytic degradation of antibiotics

Qiqi Huang [a,1], Jiqiao Zhang [c,1], Ziwen Song [a], Xianwang Deng [a], Songlin Luo [a], Weizhi Yuan [a], Xiaofang He [a], Pengfei Zheng [d], Shaopeng Wang [a,d,*], Liwei Wang [a,b,*]

[a] Guangxi Laboratory on the Study of Coral Reefs in the South China Sea, Coral Reef Research Center of China, School of Marine Sciences, Guangxi University, Nanning 530004, PR China
[b] Southern Marine Science and Engineering Guangdong Laboratory, Guangzhou 511458, PR China
[c] China Institute of Atomic Energy, Beijing 102413, PR China
[d] Guangxi Key Laboratory of Beibu Gulf Marine Resources, Environment and Sustainable Development, Beihai 536015, PR China

ARTICLE INFO

Keywords:
CdS@$ZnIn_2S_4$
S-type heterojunction
Core-shell structure
Visible-light adsorption
Norfloxacin degradation

ABSTRACT

Semiconductor photocatalysis has been widely applied to address global environmental pollution. CdS has garnered significant attention due to its strong visible-light response and capability to form stable heterojunctions with other catalysts. However, the photocatalytic performance of CdS is still limited by fast recombination of photogenerated electron-hole pairs. In this study, various CdS@$ZnIn_2S_4$ heterojunctions with core-shell structure were successfully synthesized by a hydrothermal method, and the optimal component was determined as 5 %-CdS@$ZnIn_2S_4$ heterojunction due to the largest specific surface area and the smallest band gap (2.27 eV) through various characterizations. In addition, the results of norfloxacin degradation experiments demonstrated that the 5 %-CdS@$ZnIn_2S_4$ heterojunction showed the highest photocatalytic performance than CdS, $ZnIn_2S_4$ and other composites. Specifically, the degradation rate of norfloxacin reached 90.8 % within 2 h and decreased by only 8.3 % after five recycling experiments. Such S-type heterojunction photocatalyst obviously enhanced the light absorption and effectively promoted the spatial separation and transfer of photogenerated carriers, thus significantly improving the performance of photocatalytic reactions. Furthermore, the main active substances $\bullet O_2^-$ and •OH in the degradation process were identified through active species capture experiments, and the degradation mechanism was analyzed. This technology is anticipated to provide insights and theoretical guidance for developing novel photocatalysts, which is of great significance for promoting the construction of ecological civilization and realizing sustainable economic and social development.

1. Introduction

Norfloxacin, a typical broad-spectrum antibiotic, plays a significant role in numerous fields, including medicine and agriculture [1–3], but has the potential to exhibit ecotoxic effects at certain concentrations in the environment due to its limited absorption and utilization in living organisms [4–6]. Semiconductor photocatalytic technology, with the advantages of non-pollution, high efficiency, low energy consumption, etc. [7–9], has been widely used in the fields of photocatalytic water decomposition, antimicrobial applications, and pollutant degradation, showcasing a wide range of applications prospects since it can conduct environmental remediation and energy conversion through directly utilizing the solar energy [10–12]. However, despite various methods employed to enhance photocatalytic systems, such technology still faces challenges in practical applications, such as inefficient visible light utilization, rapid recombination of photogenerated charges, and low migration efficiency of electrons and holes [13–15]. Therefore, developing highly efficient photocatalysts is urgently needed to address antibiotic pollution, thus serving environmental protection and human health.

* Corresponding authors at: Guangxi Laboratory on the Study of Coral Reefs in the South China Sea, Coral Reef Research Center of China, School of Marine Sciences, Guangxi University, Nanning 530004, PR China.
E-mail addresses: wsp@gxu.edu.cn (S. Wang), wangliwei0427@163.com (L. Wang).
[1] These authors contributed equally to this work.

https://doi.org/10.1016/j.jallcom.2025.179492
Received 24 October 2024; Received in revised form 16 February 2025; Accepted 27 February 2025
Available online 27 February 2025
0925-8388/© 2025 Elsevier B.V. All rights are reserved, including those for text and data mining, AI training, and similar technologies.

It is worth noting that even the famous photocatalysts, CdS-based materials, are still limited by these inherent defects, including low charge separation efficiency or easy recombination of photogenerated carriers, poor light absorption, limited surface active sites, and noticeable photo-corrosion phenomena [16,17]. Many efforts have been made to overcome these shortcomings, including semiconductor-coupling methods such as morphological modifications and elemental doping. For example, Keerthana et al. prepared PVP-assisted Mn-CdS nanoparticles that enhanced cationic degradation [18], and Liu et al. developed carbon-coated Zn-doped CdS core-shell photocatalysts (Zn-CdS@C) that showed good performance in photocatalytic removal of antibiotics [19]. In photocatalysis, the method of coupling CdS to other semiconductors is of particular interest. This approach has been shown to significantly improve the separation of photogenerated electrons and holes, reduce carrier complexation, and modulate the band gap structure, expanding the light absorption range and improving the photocatalytic performance [20]. Notably, the functionalized core-shell and hollow structures provide advantages such as large specific surface area, improved light utilization efficiency, and reduced charge-carrier recombination, leading to significant performance optimization [21–23]. In particular, $ZnIn_2S_4$ has also been widely used with CdS and displayed excellent photocatalytic performances [24,25].

Based on this, x-CdS@$ZnIn_2S_4$ (x = 0, 5 %, 10 % and 15 %) heterojunctions with different ratios were synthesized by a simple hydrothermal method in this study, which possessed the advantages of mild and environment-friendly conditions, high crystallinity of the products, and controllable morphology, which significantly shortened the preparation time and lowering the cost, thus could be an ideal choice for the preparation of high-performance photocatalytic materials [26]. The core-shell hollow micro-nanostructures introduced in CdS@$ZnIn_2S_4$ heterojunctions [27] resulted in a large specific surface area, which enhanced the catalyst's light-absorbing ability and contact area with the reactants. The synergistic interaction between core and shell and the formation of heterojunction also enabled the CdS@$ZnIn_2S_4$ heterojunction to absorb more photons with lower energy, effectively promoting the separation and migration of photogenerated electrons and holes and reducing carrier complexation, which provided a strong support for the enhancement of photocatalytic performance [28,29]. This study demonstrated the aforementioned phenomenon using characterization methods such as XPS and EIS. The heterojunction formed between $ZnIn_2S_4$ and CdS extended the light absorption range of the material, resulting in better photocatalytic activity in visible light. The experimental findings demonstrated that the 5 %-CdS@$ZnIn_2S_4$ heterojunction exhibited the highest catalytic efficiency and the most optimal performance under UV-*vis* irradiation, surpassing the CdS@$ZnIn_2S_4$ heterojunction with a single component or other CdS content. This outcome was in agreement with the characterization results. The unique preparation method and the constructed core-shell structure resulted in high stability in aqueous solution. In addition, active species (•OH and $\bullet O_2^-$) for the photocatalytic degradation of norfloxacin in water were identified by active species capture experiments. Furthermore, the roles of the active species in the degradation process were investigated, which led to the establishment of the corresponding photocatalytic degradation mechanism and the elucidation of possible mechanistic pathways. Therefore, the successful combination of CdS and $ZnIn_2S_4$ enhances the photocatalytic degradation of norfloxacin under visible light irradiation, which will promote the development of water treatment technologies for the efficient degradation of pollutant antibiotics.

2. Experimental section

2.1. Hydrothermal synthesis CdS@$ZnIn_2S_4$

Specifically, various x-CdS@$ZnIn_2S_4$ (x = 0, 5 %, 10 % and 15 %) heterojunctions were synthesized using a hydrothermal method. The detailed processes were listed in **S1.1**, Supporting Information.

2.2. Characterization

All the characterizations of the photocatalysts were listed in **S1.2**, Supporting Information.

2.3. Photocatalytic degradation experiment

In this study, the photocatalytic degradation experiments of norfloxacin were carried out using a xenon lamp photocatalytic reactor (CEL-PF300-T8E, China) at room temperature (25 ℃), using 300 W xenon lamp photocatalytic reactor (CEL-PF300-T8E, China) to simulate the sunlight. Then 20 mg of each photocatalyst sample was weighed and dispersed in 100 mL of norfloxacin solution (20 mg/L), placed in the photocatalytic reactor and stirred under dark conditions for 1 h to reach the adsorption-desorption equilibrium. The xenon light source was switched on (the average light intensity was about 886 mW/cm^2). Meanwhile, the cold-water recirculation device of the photocatalytic reactor was opened throughout the experiment. Then, 4 mL of the solution was drawn from the vessel at a given time interval (15 min) and filtered with a 0.22 μm membrane to separate the catalyst from the supernatant. Finally, the supernatant was detected by using a UV-vis spectrophotometer (SHIMADZU UV-2700, Japan) to determine the absorbance at a specific wavelength of 272 nm, which was determined after full-wavelength scanning (Fig. S7a). Subsequently, the degradation rate of norfloxacin was calculated in conjunction with the plotted standard curve of norfloxacin to assess the photocatalytic performance of the photocatalysts (Fig. S7b), which was calculated according to the following formula:

$$\eta = \frac{C_0 - C_t}{C_0} \times 100\%$$

Where: η is the photocatalytic degradation rate; C_0 is the initial concentration of norfloxacin solution (mg/L); C_t is the concentration of norfloxacin solution after the reaction has been carried out for t min (mg/L).

The prepared CdS@$ZnIn_2S_4$ heterojunction's photocatalytic cycling performance was evaluated by carrying out five consecutive photocatalytic reactions. After the complete photocatalytic reaction, the samples were collected by centrifugation, and the catalysts were washed three times with deionized water and ethanol, respectively. They were dried in an oven at 60 °C, and subsequently used for the next photocatalytic experiment.

Reactive species capture experiments could identify the prominent reactive radicals affecting norfloxacin degradation in the reaction system, and the present study used TEOA, IPA, and BQ as h^+, •OH and $\bullet O_2^-$ trapping agents. After the adsorption-desorption equilibrium was reached at the end of the dark reaction of the photocatalytic experiment, the trapping agents were added to the solution for subsequent experiments.

3. Results and discussion

3.1. Characterization of photocatalysts

The XRD patterns of CdS hollow nanospheres and x-CdS@$ZnIn_2S_4$ (x = 0, 5 %, 10 % and 15 %) heterojunctions were shown in Fig. 1a. Among them, the line I and II corresponded to the hexagonal phase $ZnIn_2S_4$ standard card (JCPDS No. 72–0773) and hexagonal phase CdS standard card (JCPDS No. 01–077–2306), respectively [30–32]. The high-intensity peak of line II at 2θ = 26.62° (corresponding to the (002) crystal plane) indicated that CdS hollow nanospheres tended to grow along the c-axis [33]. The peaks found in lines III to V were all in the presence of CdS, $ZnIn_2S_4$ crystalline phases, including the characteristic peaks attributed to CdS (002), (100), (110) and (112) crystal faces and the characteristic peaks attributed to (006), (110), (202) and (213)

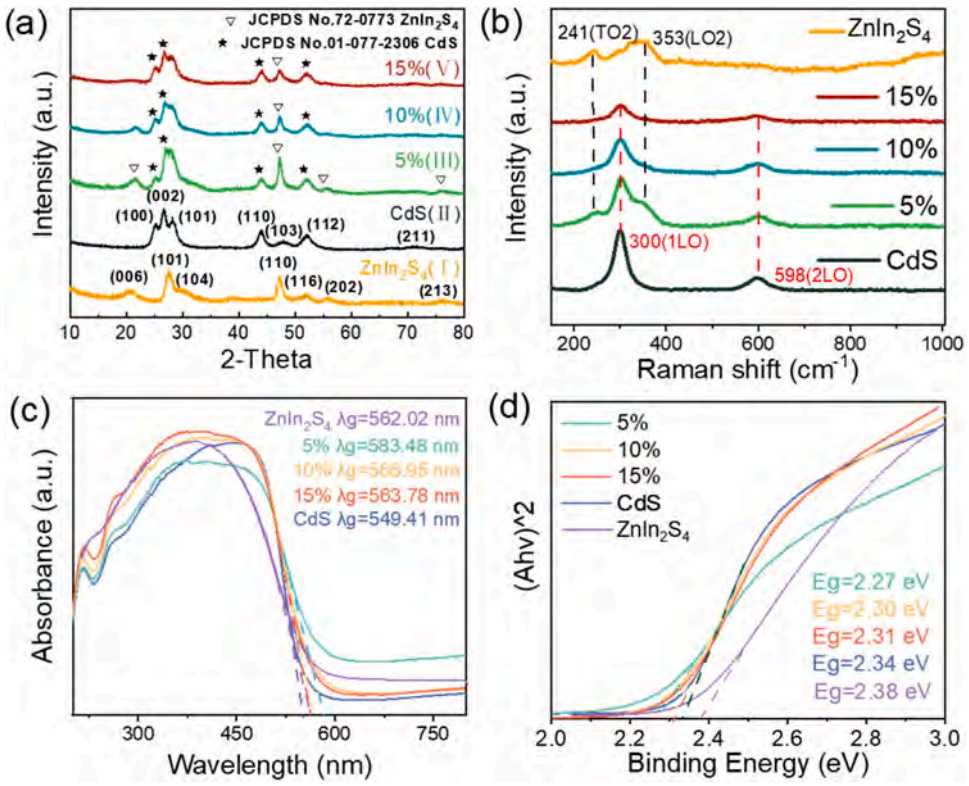


Fig. 1. CdS hollow nanospheres and x-CdS@$ZnIn_2S_4$ (x = 0, 5 %, 10 % and 15 %) heterojunctions: (a) XRD spectrum, (b) Raman spectrum, (c) UV-*vis* diffuse reflectance spectra, and (d) band gap calculated by Tauc plot method.

crystal faces, with the different compositional ratios leading to the differences in the peaks [34]. The above results indicated the successful preparation of CdS@$ZnIn_2S_4$ heterojunction with a well-maintained crystal structure.

The Raman spectra of CdS hollow nanospheres and x-CdS@$ZnIn_2S_4$ (x = 0, 5 %, 10 % and 15 %) heterojunctions were presented in lines I to V of Fig. 1b, respectively. As could be seen from line I, the characteristic peaks at 241 and 353 cm^{-1} were associated with the transverse optical mode (TO2) and longitudinal optical mode (LO2) vibrations of $ZnIn_2S_4$, respectively [35]. The characteristic peaks observed at approximately 300 and 598 cm^{-1} in line II were associated with the fundamental optical phonon mode (1LO) and the first overtone mode (2LO) vibrations of CdS [36]. The Raman spectra of the CdS@$ZnIn_2S_4$ heterojunctions showed four distinctive peaks at 241, 300, 353 and 598 cm^{-1}, which exhibited a high degree of correlation with the characteristic peaks of the Raman spectra of CdS and $ZnIn_2S_4$, respectively. Notably, the 1LO and 2LO vibrations of CdS increased with increasing CdS content in the composite, indicating the successful bonding of $ZnIn_2S_4$ sheets with CdS. Fourier transform infrared spectroscopy (FT-IR) could be employed to examine the chemical composition and functional groups of CdS hollow nanospheres and x-CdS@$ZnIn_2S_4$ (0 %, 5 %, 10 % and 15 %) heterojunctions (Fig. S1). The characteristic peaks at 1387 and 3440 cm^{-1} could be attributed to the -OH functional group (line I), while the peaks around 600–700 cm^{-1} represented the Cd-S stretching vibration (line II) [37]. This provided further evidence that the preparation of CdS@$ZnIn_2S_4$ heterojunction material was successful.

Fig. 1c illustrated the UV-*vis* diffuse reflectance spectra of CdS hollow nanospheres and x-CdS@$ZnIn_2S_4$ (x = 0, 5 %, 10 % and 15 %) heterojunctions, together with the corresponding band gap maps calculated by the Tauc plot method. The light absorption edges of CdS hollow nanospheres and x-CdS@$ZnIn_2S_4$ (x = 0, 5 %, 10 % and 15 %) heterojunctions were found to be 549.41, 562.02, 583.48, 566.95 and 563.78 nm, respectively. The UV-*vis* diffuse reflectance spectra of CdS clearly showed the absorption band edges due to the electronic transition from the valence band to the corresponding conduction band. The CdS@$ZnIn_2S_4$ heterojunctions exhibited a pronounced absorption at 583.48 nm with a red-shifted maximum wavelength, which could be attributed to the formation of a heterojunction between $ZnIn_2S_4$ and CdS, thereby increasing the absorption range and intensity [38]. Furthermore, the corresponding band gaps were calculated by the equation $(\alpha h\nu)^{1/n} = A(h\nu\text{-}Eg)$ [39], as illustrated in Fig. 1d. The band gaps of CdS nanospheres and x-CdS@$ZnIn_2S_4$ (x = 0, 5 %, 10 % and 15 %) heterojunctions were 2.34, 2.38, 2.27, 2.30, and 2.31 eV, respectively. It is noteworthy that the band gap of the CdS@$ZnIn_2S_4$ heterojunction diminished from 2.34 to 2.27 eV as the proportion of CdS in the composites was reduced, a development that is advantageous for enhancing the photocatalytic activity [40]. This phenomenon could be attributed to the following reasons: when the particle size decreases to a certain extent due to the increase in CdS content, the movement of electrons and holes is restricted, leading to the emergence of quantum confinement effects, which significantly changes the electronic structure of CdS [41]. Additionally, the rise in CdS content may affect the electric field and energy band bending at the heterojunction interface, altering the electronic density of states at the interface and changing the intrinsic band gap properties of CdS, which in turn leads to an increase in the band gap [42–44].

The successful synthesis of the heterojunction was verified by XRD, Raman and FT-IR characterization of CdS, x-CdS@$ZnIn_2S_4$ (x = 0, 5 %, 10 % and 15 %) heterojunctions. In particular, UV-*vis* diffuse reflectance spectroscopy and corresponding band calculations showed that the 5 %-CdS@$ZnIn_2S_4$ heterojunction has the lowest band gap value, so the optimized 5 %-CdS@$ZnIn_2S_4$ heterojunction is a promising candidate for further research and application.

Fig. 2a and Fig. S2 showed SEM images of CdS hollow nanospheres and pure $ZnIn_2S_4$. As can be seen, the CdS structure is hollow, and the spherical morphology remains intact throughout the etching process. Thus, the multistage CdS@$ZnIn_2S_4$ core-shell hollow spheres have been successfully prepared by *in-situ* chemical deposition. While the pure

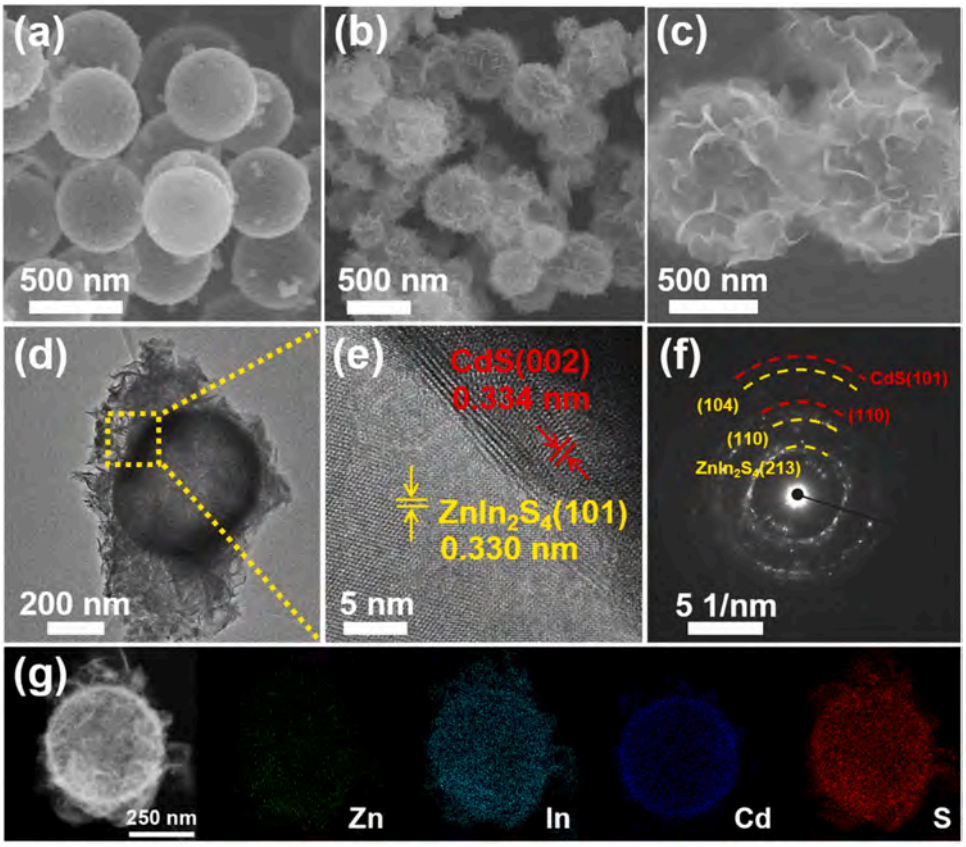


Fig. 2. SEM images of (a) CdS hollow nanosphere, (b) and (c) 5 %-CdS@$ZnIn_2S_4$ heterojunction. (d) TEM, (e) HRTEM, (f) SAED images, (g) TEM image and its corresponding EDS mapping images of Cd, S, Zn, In elements of 5 %-CdS@$ZnIn_2S_4$ heterojunction.

phase $ZnIn_2S_4$ presents a petal-like spherical structure composed of nanosheets. As illustrated in Fig. 2b and c, the disordered two-dimensional $ZnIn_2S_4$ flakes exhibited uniform growth on the surface of the thin shell layer of CdS. Not only did this effectively increase the specific surface area, but it also provided a much larger number of active sites for chemical reactions.

Fig. 2d displayed the TEM image of the 5 %-CdS@$ZnIn_2S_4$ heterojunction, which verified the core-shell hollow structure of multilevel CdS@$ZnIn_2S_4$. The thin-shell structure of CdS reduced the transport distance of electrons, reducing energy loss and improving stability. Furthermore, the core-shell structure protected the inner core from dissolution and exploited the synergistic effect between heterojunctions to accelerate electron transport [45]. Correspondingly, the lattice fringes of the $ZnIn_2S_4$ (101) facet at 330 nm and the CdS (002) facet at 0.334 nm could be observed in the HRTEM image of CdS in Fig. 2e. In addition, the SAED results in Fig. 2f showed the presence of a diffraction ring that spreads uniformly from the center to the surroundings, suggesting a polycrystalline structure for the CdS@$ZnIn_2S_4$ sample. Further measurements yielded diffraction rings attributed to the CdS (101), (110) crystal planes and the $ZnIn_2S_4$ (104), (110), and (213) crystal planes, which initially demonstrated the successful preparation of the heterojunction electrode material. Fig. 2g revealed the elemental distribution of Zn, In, Cd and S in 5 %-CdS@$ZnIn_2S_4$ heterojunction. The results exhibited that the 5 %-CdS@$ZnIn_2S_4$ heterojunction has four elements, Cd, S, Zn and In, which are uniformly distributed on the surface of the core-shell hollow spheres. The regular circular distribution of the Cd element on the surface was consistent with the regular hollow spheres of CdS used in the preparation process. In contrast, the elements S, Zn and In were partially dispersed outside the circle with the flake structure. It corresponded to the uniform growth of $ZnIn_2S_4$ flakes on the CdS hollow sphere substrate, further demonstrating the successful preparation of CdS@$ZnIn_2S_4$ heterojunction.

The samples were analyzed by XPS to determine the chemical state of the elements on the surface. The full spectrum of 5 %-CdS@$ZnIn_2S_4$ heterojunction, as illustrated in Fig. S3, demonstrated the presence of four elements, namely Cd, Zn, In and S, on the surface of the composite, which is in accordance with the EDS results. Fig. 3a showed the XPS spectra of Cd 3d attributed to two strong peaks of Cd $3d_{5/2}$ and $3d_{3/2}$ shifted to 405.7, 405.3 eV, and 412.7, 412.1 eV, respectively [46,47]. In Fig. 3b, the peaks at 451.4, 451.0 eV and 443.8, 443.4 eV were attributed to $3d_{3/2}$ and $3d_{5/2}$ of In, respectively, indicating the valence state + 3 [48]. It could be seen that the formation of the 5 %-CdS@$ZnIn_2S_4$ heterojunction leads to a change in the binding energy of the In 3d orbitals.

Fig. 3c reflected the high-resolution XPS spectra of Zn 2p, with the characteristic peaks of Zn $2p_{1/2}$ and $2p_{3/2}$ shifted to 1045.3, 1043.1 eV and 1021.8 and 1020.0 eV compared to $ZnIn_2S_4$. This proved the presence of Zn^{2+} in the 5 %-CdS@$ZnIn_2S_4$ heterojunction [49]. The XPS spectrum of S2p was shown in Fig. 3d, with two peaks at 162.1 and 160.2 eV, corresponding to $S2p_{1/2}$ and $S2p_{3/2}$, the characteristic peaks of S^{2-} [50]. The shifting phenomenon of the binding energies of the XPS characteristic peaks suggested that there is a tendency for the electrons in the composite CdS to spontaneously diffuse into $ZnIn_2S_4$, resulting in the formation of an electron-absorbing layer in CdS and an electron-accumulating layer in $ZnIn_2S_4$ [51]. In addition, the formation of heterojunction between CdS and $ZnIn_2S_4$ resulted in further splitting of Cd $3d_{3/2}$ and $3d_{5/2}$, and two packet peaks were observed next to the Cd $3d_{3/2}$ and $3d_{5/2}$ peaks. Similarly, this phenomenon was observed on the In $3d_{3/2}$ and $3d_{5/2}$ characteristic peaks of 5 %-CdS@$ZnIn_2S_4$ heterojunction.

In this study, the information regarding the specific surface area, pore volume, average pore diameter of all the samples were evaluated

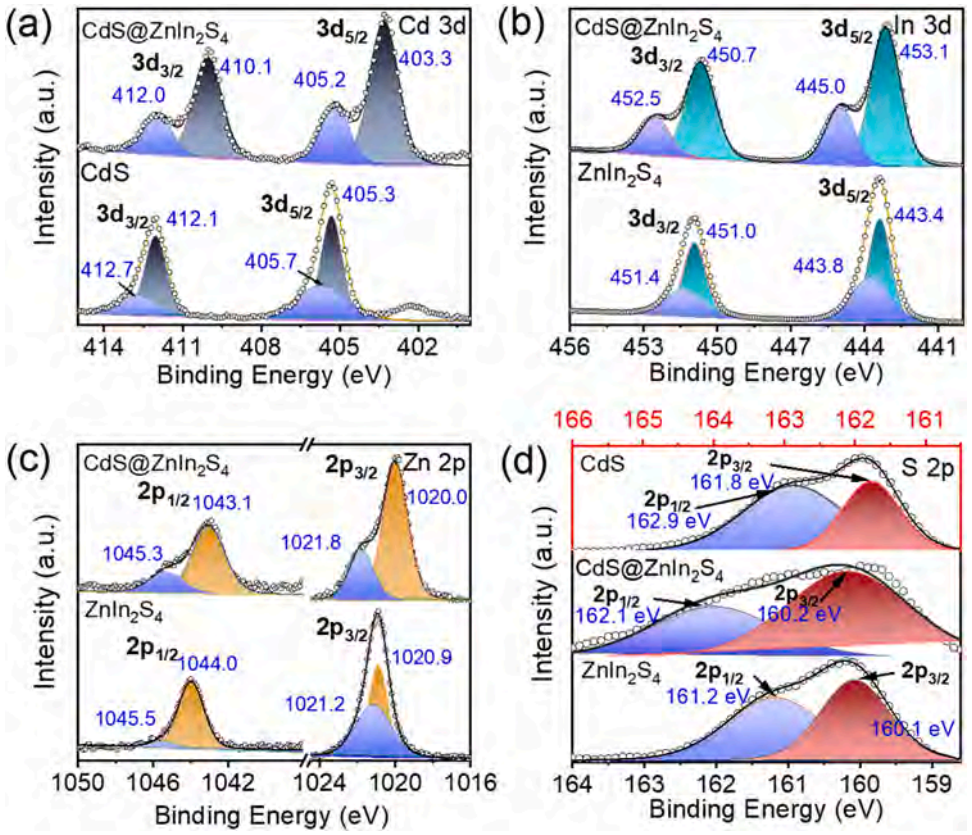


Fig. 3. (a)High-resolution XPS spectra of (a) Cd 3d, (b) In 2p, (c) Zn 3d, and (d) S 2p of 5 %-CdS@$ZnIn_2S_4$ heterojunction.

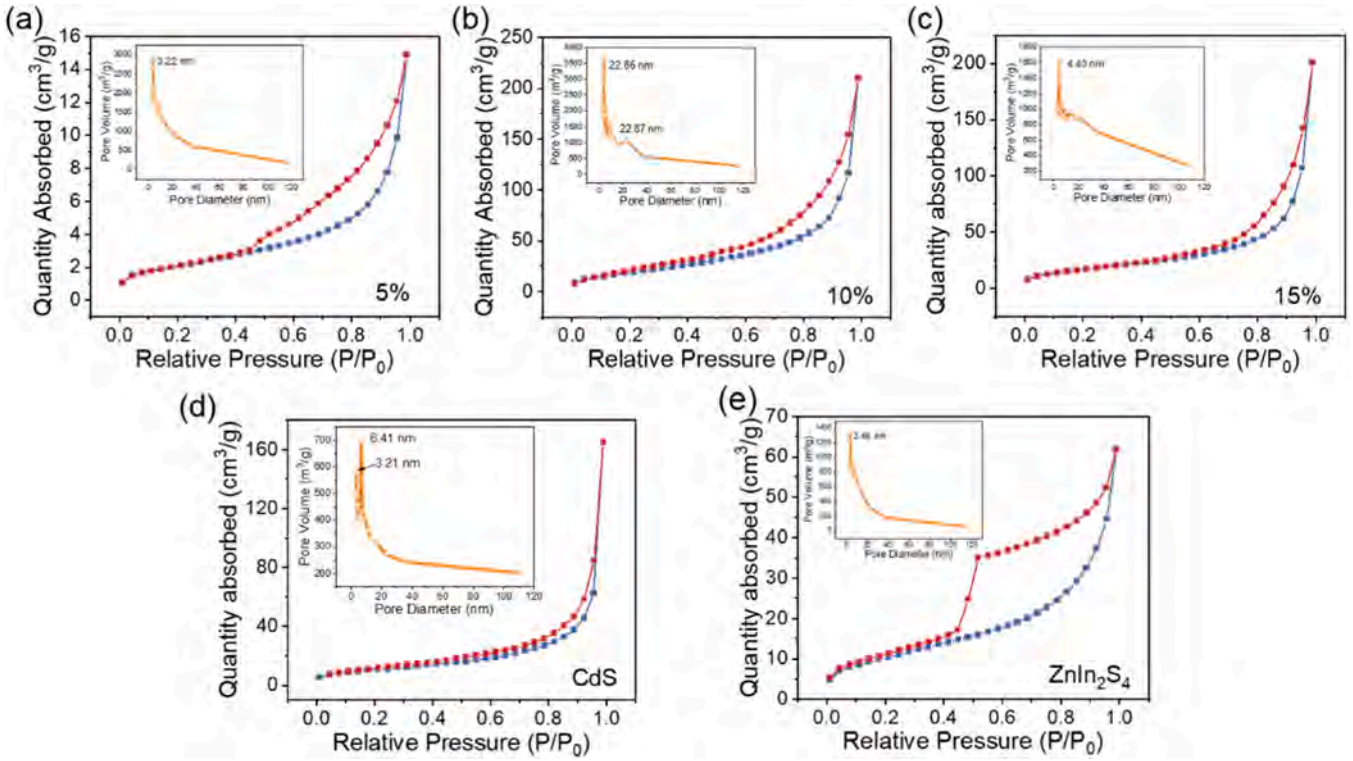


Fig. 4. Nitrogen adsorption/desorption isotherms and the corresponding pore size distribution graphs of CdS hollow nanospheres and x-CdS@$ZnIn_2S_4$ (x = 0, 5 %, 10 % and 15 %) heterojunctions from (a) to (e).

Table 1
Surface area, pore volume, average pore diameter, micro volume, micro area of CdS hollow nanospheres and x-CdS@$ZnIn_2S_4$ (x = 0, 5 %, 10 % and 15 %) heterojunctions.

Sample	Surface area (m^2/g)	Pore Volume (cm^3/g)	Pore Diameter (nm)	Micro Volume (cm^3/g)	Micro Area (m^2/g)
$ZnIn_2S_4$	38.365	0.087	3.462	0.002	3.885
5 %	75.256	0.218	3.222	0.003	3.926
10 %	71.838	0.317	4.053	-	-
15 %	63.223	0.302	4.399	-	-
CdS	39.114	0.250	6.412	-	-

"-" means no detection.

using nitrogen adsorption/desorption isotherms combined with BET, BJH and t-plot models, as illustrated in Fig. 4 and Table 1. The isotherms of the composites in Fig. 4a-e exhibited the characteristics of a type IV isotherm and H3 hysteresis loop, indicating that the material possessed a mesoporous structure. The specific surface areas of CdS hollow nanospheres and x-CdS@$ZnIn_2S_4$ (x = 0, 5 %, 10 % and 15 %) heterojunctions were found to be 39.114, 38.365, 75.256, 71.838 and 63.223 m^2/g, respectively. The composites revealed a considerable enhancement in the specific surface area compared to CdS and $ZnIn_2S_4$. Among the three doping components, 5 %-CdS@$ZnIn_2S_4$ heterojunction (specific surface area 75.256 m^2/g) revealed the largest specific surface area and the most active reactive sites. However, the specific surface area of the composites decreased as the CdS doping ratio increased. Besides, sharp peaks were observed at 6.41, 3.46, 3.22, 22.87, and 4.40 nm in CdS hollow nanospheres and x-CdS@$ZnIn_2S_4$ (x = 0, 5 %, 10 %, and 15 %) heterojunctions, respectively, indicating that a favorable distribution of pore sizes for 5 %-CdS@$ZnIn_2S_4$ heterojunction leads to an enhancement in the specific surface area, thus providing more active sites for the photocatalytic degradation of antibiotics. This suggested that the growth of the core-shell hollow sphere morphology was hindered by an increase in CdS content, leading to a decline in the specific surface area and the emergence of CdS-biased properties in the composites.

3.2. Photocatalytic activity and stability

The catalytic activity of the photocatalysts was evaluated using norfloxacin solution (20 mg/L) under UV-*vis* light irradiation. Firstly, norfloxacin was mixed with CdS hollow nanospheres and x-CdS@$ZnIn_2S_4$ (x = 0, 5 %, 10 % and 15 %) heterojunctions, respectively, and left to stand in the dark for 1 h to allow for the completion of the adsorption-desorption process. Thereafter, photocatalytic degradation experiments were conducted under UV-*vis* light. As illustrated in Fig. S4a and Table 2, the concentration of norfloxacin demonstrated slight fluctuations in the blank control group in the absence of a photocatalyst, indicating that norfloxacin possesses favorable photostability. After 2 h, the degradation rates of norfloxacin by CdS hollow nanospheres and x-CdS@$ZnIn_2S_4$ (x = 0, 5 %, 10 % and 15 %) heterojunctions were found to be 34.72 %, 43.74 %, 90.82 %, 84.3 % and 81.2 %, respectively.

Furthermore, combining the degradation efficiency (57.55 %) of norfloxacin by a physical mixture of CdS and $ZnIn_2S_4$ (1:1) under the same conditions (Fig. S4b) demonstrated that the synergistic effect between the two materials after successful compositing has a significant and positive role in improving the performance of the photocatalysts [52,53]. Among them, the 5 %-CdS@$ZnIn_2S_4$ heterojunction exhibited the most effective and pronounced photocatalytic degradation performance, confirming the optimal composition identified through characterization. As illustrated in Table 3, a comparative analysis of the photocatalysts reported in the literature revealed that the degradation efficiencies of g-C_3N_4/$CoFe_2O_4$, N-CQDs/Bi_2WO_6, and other similar photocatalysts are 86.8 % and 88.0 %, respectively. The photocatalysts in this study exhibited a marginal enhancement in the degradation efficiency, thereby signifying the superior degradation performance of the 5 %-CdS@$ZnIn_2S_4$ heterojunction for norfloxacin. Additionally, during the adsorption-desorption process, the composite photocatalyst possessed a greater adsorption capacity for norfloxacin than the pure component, attributing to the abundant adsorption sites formed by the high specific surface area of the CdS@$ZnIn_2S_4$ heterojunctions. In the EIS spectra of CdS hollow nanospheres and x-CdS@$ZnIn_2S_4$ (x = 5 %, 10 % and 15 %) heterojunctions (Fig. S5), the semicircle part is typically indicative of the charge transfer resistance, with a smaller radius indicating a higher electrochemical activity of the material and a more efficient charge transfer process. The straight line extending beyond the semicircle reflects the stability of the charge transfer and the ion diffusion rate at the interface. It is evident that the slope of 5 %-CdS@$ZnIn_2S_4$ heterojunction is greater than others, thus, the diffusion is faster, the charge transfer is more stable at the interface, and the electrochemical reaction is more favorable [54]. Compared with other composites, 5 %-CdS@$ZnIn_2S_4$ heterojunction had the most minor semicircle diameter, indicating the most efficient electron transfer rate and catalytic performance, consistent with the degradation experiments. Based on these results, 5 %-CdS@$ZnIn_2S_4$ heterojunction was selected as the photocatalyst for all subsequent degradation experiments.

Fig. 5a and b elucidated the kinetic processes of 5 %-CdS@$ZnIn_2S_4$ heterojunction for degrading norfloxacin under the irradiation of UV-visible and visible light, respectively. Firstly, the correlation between $Ln(C_0/C_t)$ and t was robust and linear, demonstrating that the photocatalytic reaction conformed to the first-order kinetic model; for the visible light, 5 %-CdS@$ZnIn_2S_4$ heterojunction was observed to degrade norfloxacin by 80 % within 2 h, with a rate constant (K) of 0.0071 min^{-1}. The degradation was reduced by 10 %, and the rate constant (K) was 0.002 lower than that under UV-visible conditions. Nevertheless, the photocatalyst proved effective in degrading norfloxacin. Furthermore, Fig. 5c displayed the variation curves of the UV-visible absorption spectra of norfloxacin solutions undergoing a photocatalytic degradation reaction. It was observed that the absorbance of norfloxacin gradually decreased with the prolongation of the exposure time, and no additional peaks appeared, implicating that 5 %-CdS@$ZnIn_2S_4$ heterojunction exerted a pronounced degradation effect on norfloxacin.

Table 2
The degradation efficiency of norfloxacin by CdS hollow nanospheres and x-CdS@$ZnIn_2S_4$ (x = 0, 5 %, 10 % and 15 %) heterojunctions under UV-visible light.

Sample	Degradation efficiency
CdS	34.72 %
$ZnIn_2S_4$	43.74 %
5 %	90.82 %
10 %	84.32 %
15 %	81.23 %

Table 3
Comparison of degradation efficiency of different photocatalysts in photocatalytic degradation of norfloxacin.

Photocatalysts	Degradation time (min)	Degradation rate (%)	Kinetic constants (k/min^{-1})	References
Fe_2O_3/g-C_3N_4	120	94.7	0.0111	[55]
Bi_2O_3/CdS	120	86.0	0.012	[56]
xC-TiO_2	150	74.0	0.0056	[57]
g-C_3N_4/$CoFe_2O_4$	120	86.8	0.012	[58]
g-C_3N_4@$CaCO_3$	180	76.0	0.0088	[59]
N-CQDs/Bi_2WO_6	180	88.0	0.0088	[60]
CdS@$ZnIn_2S_4$	120	90.82	0.0094	This work

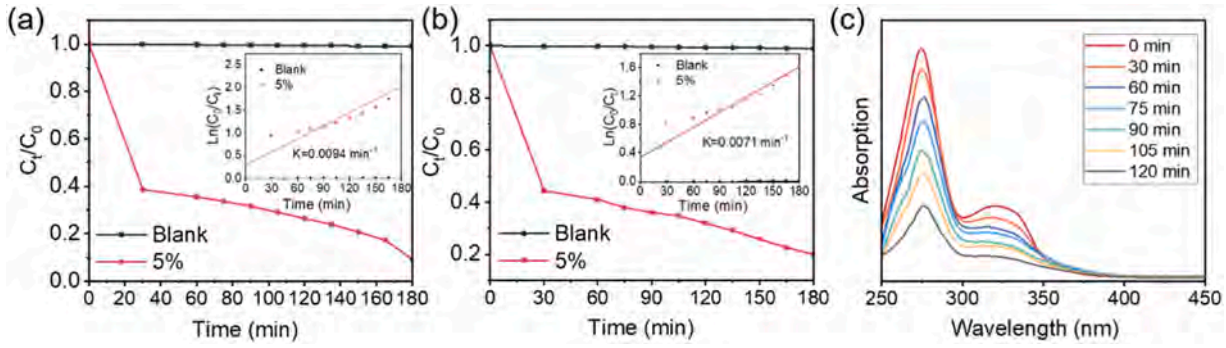


Fig. 5. Degradation and kinetic profiles (inset) of 5 %-CdS@$ZnIn_2S_4$ heterojunction: under UV-visible irradiation (a), under visible light (b), and (c) UV-visible absorption spectra of degraded norfloxacin.

In practical utilization, the stability and repeatability of photocatalysts represented the critical factors for the remediation of water contamination, and they constituted essential reference indicators for the assessment of photocatalyst performance. Therefore, to assess the reusability of 5 %-CdS@$ZnIn_2S_4$ heterojunction, this study performed SEM characterization of 5 %-CdS@$ZnIn_2S_4$ heterojunctions after a norfloxacin degradation experiment (Fig. S6). As can be seen from the figure, the nanostructure of the reacted 5 %-CdS@$ZnIn_2S_4$ heterojunction remains intact without any obvious agglomeration or structural disruption, indicating its good structural stability. In addition, recycling experiments under UV-visible light irradiation were carried out in this study. As illustrated in Fig. 6a and b, the degradation curve exhibited minimal variation after five degradation cycles, and the degradation rate decreased by only 8.3 %, signifying excellent photostability.

The identification of the active species generated during the photocatalytic process is of paramount importance for elucidating the degradation mechanism of norfloxacin. To this end, active species capture experiments were conducted in the present study. As shown in Fig. 6c, benzoquinone (BQ), isopropanol (IPA) and triethanolamine (TEOA) were introduced as scavengers of $\bullet O_2^-$, $\bullet OH$ and h^+, respectively. The addition of TEOA slightly altered the degradation efficiency, suggesting that h^+ was not the primary active substance. However, the degradation efficiency of norfloxacin decreased significantly from 90.8 % to 3.9 % and 16.9 % after the addition of BQ and IPA as the scavengers of $\bullet O_2^-$ and $\bullet OH$, respectively, suggesting that $\bullet O_2^-$ and $\bullet OH$ play an essential role in the photocatalytic process. The aforementioned results indicated that the photocatalytic degradation of norfloxacin resulted in the production of $\bullet O_2^-$, $\bullet OH$ and h^+, with the effects of these active substances on the degradation of norfloxacin occurring in the order of $\bullet O_2^- > \bullet OH > h^+$. As shown in Fig. 6d, the TOC was significantly reduced after 180 min of irradiation with 5 %-CdS@$ZnIn_2S_4$ heterojunction, indicating a high mineralization efficiency for TC photodegradation.

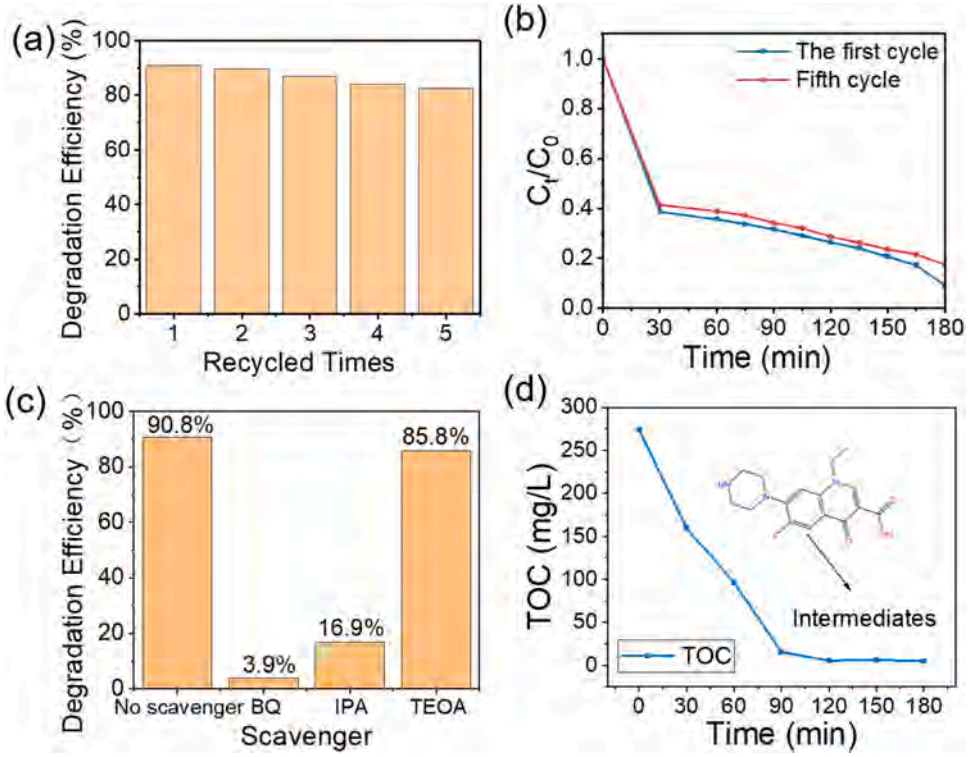


Fig. 6. (a) Cyclic recycling experiment for the photodegradation of norfloxacin, (b) comparison of the degradation profiles after the first and fifth cycle, (c) active species trapping experiment, and (d) TOC concentration of the degraded norfloxacin solution versus irradiation time. 5 %-CdS@$ZnIn_2S_4$ heterojunction was utilized throughout the above experiments.

3.3. Photocatalytic degradation mechanism

In this study, CdS hollow nanospheres were coupled with $ZnIn_2S_4$ nanosheets to form CdS@$ZnIn_2S_4$ heterojunctions with a core-shell structure. This approach has been shown to effectively improve the photocatalytic performance of the resulting materials for the following principal reasons. Firstly, the hollow structure of the CdS nanospheres enabled a larger specific surface area and higher porosity of the catalysts, which allowed for greater exposure of the active sites and good permeability characteristics. Furthermore, sufficient diffusion channels and multiple active surface areas enabled the effective adsorption of norfloxacin molecules, thereby enhancing the visible light absorption performance of the catalyst [61,62]. Secondly, the core-shell structure of the heterojunctions enhanced the light scattering from the hollow structure, provided a larger specific surface area and generated sufficient active sites, which significantly improved the light utilization rate, charge utilization efficiency, and photocatalytic performance of the photocatalysts [63,64]. Thirdly, in the S-type heterogeneity, photogenerated electrons were transferred from the conduction band of CdS to the conduction band of $ZnIn_2S_4$. In contrast, holes were transferred from the valence band of $ZnIn_2S_4$ to the valence band of CdS. This separated photogenerated electrons and holes at the interface and formed two built-in electric fields in opposite directions [65,66]. This facilitated the separation and migration of photogenerated carriers and improved the redox capacity, thereby further enhancing the photocatalytic efficiency.

Fig. 7 displayed the Mott-Schottky curves for 5 %-CdS@$ZnIn_2S_4$ heterojunction, $ZnIn_2S_4$, and CdS, with all three samples exhibiting n-type semiconductor characteristics. In n-type semiconductors, the flat-band potential is typically 0.2 eV higher than the CB potential [67]. Based on the intercepts of the MS curves on the X-axis, the flat-band potentials of the 5 %-CdS@$ZnIn_2S_4$ heterojunction, $ZnIn_2S_4$ and CdS were estimated to be −1.59, −0.92 and −0.69 eV (vs. NHE), respectively; the corresponding CB potentials were −1.39, −0.72 and −0.49 eV (vs. NHE). Combined with the band gap data in Fig. 1d, the corresponding VB potentials were 0.88, 1.66 and 1.85 eV (vs. NHE).

In light of the aforementioned findings, a potential photocatalytic mechanism for the degradation of norfloxacin by CdS@$ZnIn_2S_4$ heterojunction was put forth in this paper (Fig. 8). The CB potentials of $ZnIn_2S_4$ and CdS were −0.92 and −0.69 eV (vs. NHE). The corresponding VB potential values were 1.66 and 1.85 eV (vs. NHE), respectively. Among them, the CB values of $ZnIn_2S_4$ were more negative than those of CdS, whereas the VB values of CdS were more positive than those of $ZnIn_2S_4$, which agrees with the results of previous studies [67]. The successful preparation of the CdS@$ZnIn_2S_4$ heterojunction brought the two materials into proximity, thereby generating interfacial charge and energy band bending at the interface. During the photocatalytic degradation process, the CdS@$ZnIn_2S_4$ heterojunction generates e^- and h^+ ions under light, with the e^- of $ZnIn_2S_4$ and CdS entering the conduction band, while the h^+ remains in the valence band. This results in the creation of a built-in electric field, energy band bending and

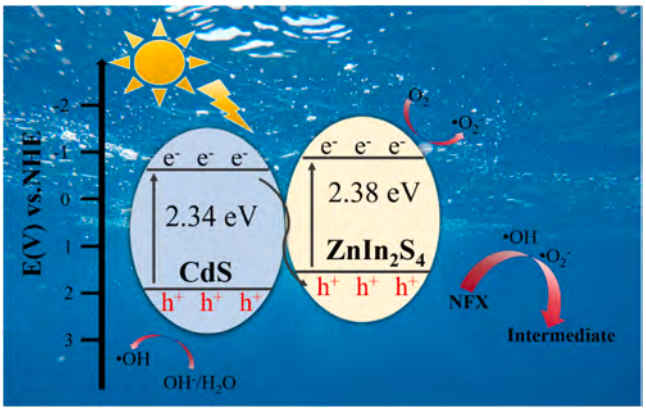


Fig. 8. Reaction mechanism diagram of CdS@$ZnIn_2S_4$ heterojunction.

Coulombic gravity between $ZnIn_2S_4$ and CdS, which in turn drives the transfer of charge-carrying electrons. Concurrently, the Coulomb force of electrons (e^-) and holes (h^+) propels the electrons in the conduction band (CB) of CdS to migrate to the valence band (VB) of $ZnIn_2S_4$ and re-combine to form an S-type heterojunction in the interfacial region. This facilitates the separation of the photo-generated electron-hole pairs and the elimination of the superfluous e^- and h^+ by recombination in the photocatalytic process. The light-generated electrons (e^-) and holes (h^+) react with water and dissolved oxygen to form hydroxyl (•OH) and oxygen ($•O_2^-$) groups. The •OH possesses a highly significant oxidizing capacity, which enables a direct attack on the norfloxacin molecule, resulting in the cleavage of carbon chains and the oxidation of its functional groups. Meanwhile, the $•O_2^-$ facilitates the oxidative degradation of the norfloxacin molecule through an electron transfer mechanism [68]. The initial attack on the norfloxacin molecule by •OH and $•O_2^-$ destroys its molecular structure, leading to the progressive decomposition of the molecule into smaller organic compounds, such as acetic acid, oxalic acid, and other intermediates. The final mineralization process produces CO_2 and H_2O [69].

4. Conclusion

In conclusion, this paper presented the successful construction of a CdS@$ZnIn_2S_4$ heterojunction photocatalyst with a core-shell structure for the efficient degradation of norfloxacin. The prepared CdS@$ZnIn_2S_4$ heterojunction exhibited superior photocatalytic performance relative to the individual catalysts CdS and $ZnIn_2S_4$. Wherein, the 5 %-CdS@$ZnIn_2S_4$ heterojunction demonstrated the most favorable characteristics, including the largest specific surface area, the narrowest band gap, and the most negligible impedance. Furthermore, the 5 %-CdS@$ZnIn_2S_4$ heterojunction photocatalyst achieved a high degree of norfloxacin degradation (80 %) and excellent stability (only an 8.3 % decrease after five cycles) within 2 h under the irradiation of visible

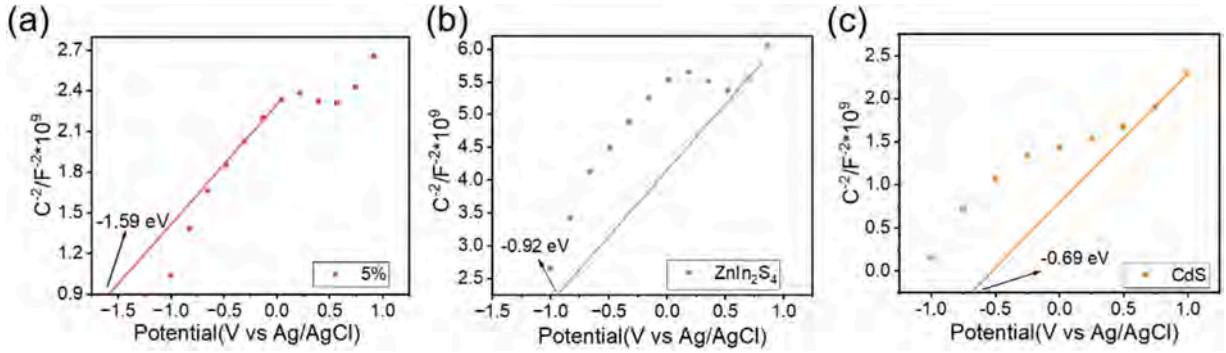


Fig. 7. Mott-Schottky curves of (a) 5 %-CdS@$ZnIn_2S_4$ heterojunction, (b) $ZnIn_2S_4$, (c) CdS.

light. Therefore, 5 %-CdS@$ZnIn_2S_4$ heterojunction was regarded as the optimal component photocatalyst in the present study. The excellent photocatalytic performances were attributed to the core-shell structure and highest light utilization rate of the photocatalysts, the formation of the S-type heterojunction to increase the charge transfer rate and reduce the recombination rate of the photogenerated carriers. Additionally, the study sought to elucidate the degradation mechanism of norfloxacin by CdS@$ZnIn_2S_4$ heterojunction by investigating the energy band structure of the composite catalysts and the generated active substances. Due to the multifaceted advantages of the photocatalysts prepared in this study, the core-shell CdS@$ZnIn_2S_4$ heterojunctions will provide new insights into the design and development of green photocatalytic technologies that are environmentally friendly, reusable, and effective in removing environmental contamination.

CRediT authorship contribution statement

Deng Xianwang: Software, Methodology, Investigation. **Luo Songlin:** Data curation, Conceptualization. **Yuan Weizhi:** Validation, Methodology. **He Xiaofang:** Validation, Methodology. **Song Ziwen:** Validation, Investigation, Data curation. **Huang Qiqi:** Writing – original draft, Methodology, Investigation, Data curation, Conceptualization. **Zhang Jiqiao:** Writing – original draft, Methodology, Data curation, Conceptualization. **Zheng Pengfei:** Validation, Software. **Wang Shaopeng:** Validation, Software. **Wang Liwei:** Writing – review & editing, Supervision, Resources, Project administration, Methodology, Conceptualization.

Declaration of Competing Interest

The authors declare that they have no known competing financial interests or personal relationships that could have appeared to influence the work reported in this paper.

Acknowledgments

This work was supported by the Self-Topic Project of Guangxi Laboratory on the Study of Coral Reefs in the South China Sea (No. GXLSCRSCS2023102); Guangxi Key Laboratory of Beibu Gulf Marine Resources, Environment and Sustainable Development, Fourth Institute of Oceanography (No. MRESD-2023C05); Natural Science and Technology Innovation and Development Doubling Plan Project, Guangxi University (Nos. 2022BZRC025, 2024BZRC009); National College Students' Innovation and Entrepreneurship Training Program (No. 202310593057) and College Students' Innovation and Entrepreneurship Training Program of Guangxi University (No. 202310593493).

Appendix A. Supporting information

Supplementary data associated with this article can be found in the online version at doi:10.1016/j.jallcom.2025.179492.

Data availability

Data will be made available on request.

References

[1] J. Wang, S. Xu, K. Zhao, G. Song, S. Zhao, R. Liu, Risk control of antibiotics, antibiotic resistance genes (ARGs) and antibiotic resistant bacteria (ARB) during sewage sludge treatment and disposal: a review, Sci. Total Environ. 877 (2023) 162772.
[2] S. Modi, G.K. Inwati, A. Gacem, S. Saquib Abullais, R. Prajapati, V.K. Yadav, R. Syed, M.S. Alqahtani, K.K. Yadav, S. Islam, Y. Ahn, B. Jeon, Nanostructured antibiotics and their emerging medicinal applications: an overview of nanoantibiotics, Antibiotics 11 (2022) 708.
[3] A. She, The potential of natural antibiotics as a novel antimicrobial strategy: a review of mechanisms and applications, Theor. Nat. Sci. 8 (2023) 21–27.
[4] S.M. Zainab, M. Junaid, N. Xu, R.N. Malik, Antibiotics and antibiotic resistant genes (ARGs) in groundwater: a global review on dissemination, sources, interactions, environmental and human health risks, Water Res. 187 (2020) 116455.
[5] S. Zeng, J. Sun, X. Lü, Z. Peng, B. Dong, X. Dai, B. Ni, Impacts of norfloxacin on sewage sludge anaerobic digestion: bioenergy generation and potential environmental risks, Results Eng. 20 (2023) 101392.
[6] T. Zhang, X. Wang, Q. Zhang, D. Yang, X. Zhang, H. Liu, Q. Wang, Z. Dong, J. Zhao, Interactive effects of multiple antibiotic residues and ocean acidification on physiology and metabolome of the bay scallops Argopecten irradians, Sci. Total Environ. 912 (2024) 168941.
[7] X. Bai, W. Chen, B. Wang, T. Sun, B. Wu, Y. Wang, Photocatalytic degradation of some typical antibiotics: recent advances and future outlooks, Int. J. Mol. Sci. 23 (2022) 8130.
[8] X. He, T. Kai, P. Ding, Heterojunction photocatalysts for degradation of the tetracycline antibiotic: a review, Environ. Chem. Lett. 19 (2021) 4563–4601.
[9] J. Xu, J. Shen, H. Jiang, X. Yu, W.Ahmad Qureshi, C. Maouche, J. Gao, J. Yang, Q. Liu, Progress and challenges in full spectrum photocatalysts: mechanism and photocatalytic applications, J. Ind. Eng. Chem. 119 (2023) 112–129.
[10] E. Pavitra, L. Antony, K.S. Ranjith, K. Alotaibi, J. Lee, S.K. Hwang, G.S.R. Raju, Y. Han, Y.S. Huh, Near-infrared light driven highly efficient and thermally stable $Gd_2Ti_2O_7$:Er^{3+}/Yb^{3+} sub-microspheres for photocatalytic and plant growth LED applications, J. Alloy. Compd. 979 (2024) 173574.
[11] D. Sun, M. Zhang, L. Huang, Y. Qu, Y. Yu, B. Lou, H. Du, B. Xu, K. Wang, Intermediate products driven one-pot in-situ synthesis of BiOCl/WO_3 heterojunction with enhanced photocatalytic hydrogen and oxygen evolution for potential industrial applications, J. Alloy. Compd. 969 (2023) 172433.
[12] S. Faisal, H. Jan, S.A. Shah, S. Shah, A. Khan, M.T. Akbar, M. Rizwan, F. Jan, Wajidullah, N. Akhtar, A. Khattak, S. Syed, Green synthesis of zinc oxide (ZnO) nanoparticles using aqueous fruit extracts of myristica fragrans: their characterizations and biological and environmental applications, ACS Omega 6 (2021) 9709–9722.
[13] X. Yang, Z. Chen, W. Zhao, C. Liu, X. Qian, M. Zhang, G. Wei, E. Khan, Y.H. Ng, Y. S. Ok, Recent advances in photodegradation of antibiotic residues in water, Chem. Eng. J. 405 (2021) 126806.
[14] X. Wu, G. Chen, J. Wang, J. Li, G. Wang, Review on S-scheme heterojunctions for photocatalytic hydrogen evolution, Acta Phys. -Chim. Sin. 39 (2023) 2212016.
[15] A. Haleem, A. Shafiq, S.Q. Chen, M. Nazar, A comprehensive review on adsorption, photocatalytic and chemical degradation of dyes and nitro-compounds over different kinds of porous and composite materials, Molecules 28 (2023) 1081.
[16] K. Sharma, V. Hasija, M. Malhotra, P.K. Verma, A.A. Parwaz Khan, S. Thakur, Q. Van Le, H.H. Phan Quang, V. Nguyen, P. Singh, P. Raizada, A review of CdS-based S-scheme for photocatalytic water splitting: synthetic strategy and identification techniques, Int. J. Hydrog. Energy 52 (2024) 804–818.
[17] I. Ahmad, S. Ben Ahmed, M. Shabir, M. Imran, A.M. Hassan, N.S. Alatawi, Review on CdS-derived photocatalysts for solar photocatalytic applications – advances and challenges, J. Ind. Eng. Chem. 130 (2024) 105–124.
[18] S. Keerthana, R. Yuvakkumar, G. Ravi, A.E.M.A. Mustafa, A.A. Al-Ghamdi, M. Soliman Elshikh, D. Velauthapillai, PVP influence on Mn–CdS for efficient photocatalytic activity, Chemosphere 277 (2021) 130346.
[19] T. Liu, B. Wang, T. Wang, C. Li, W. Wang, M. Wang, J. Zhang, One-pot synthesis of Zn–CdS@C nanoarchitecture with improved photocatalytic performance toward antibiotic degradation, Chemosphere 300 (2022) 134621.
[20] T. Huang, Z. Huang, X. Yang, S. Yang, Q. Gao, X. Cai, Y. Liu, Y. Fang, S. Zhang, S. Zhang, Green and regulable synthesis of CdNCN on CdS semiconductor: atomic-level heterostructures for enhanced photocatalytic hydrogen evolution, Adv. Powder Mater. 3 (2024) 100242.
[21] K. Dong, H. Li, C. Zhang, M. Zhou, Q. Liang, Y. Wang, Z. Li, S. Xu, Construction of in-situ core-shell Cu_2-xS@Mn0.3Cd0.7S S-scheme heterojunction with efficient photocatalytic H_2 evolution, Int. J. Hydrog. Energy 51 (2024) 1357–1365.
[22] N.J. Panicker, P.M. Ajayan, P.P. Sahu, Band-gap tuned hexagonal-boron nitride/reduced graphene oxide superlattice wrapped cadmium sulfide/Polypyrrole nanocomposite as an efficient supercapacitor electrode material, J. Energy Storage 56 (2022) 105901.
[23] M.H. Rashid, A. Koel, T. Rang, N. Nasir, N. Sabir, F. Ameen, A. Rasheed, Optical dynamics of copper-doped cadmium sulfide (CdS) and zinc sulfide (ZnS) quantum-dots core/shell nanocrystals, Nanomaterials 12 (2022) 2277.
[24] Y. Zhang, Y. Wu, L. Wan, H. Ding, H. Li, X. Wang, W. Zhang, Hollow core–shell Co_9S_8@$ZnIn_2S_4$/CdS nanoreactor for efficient photothermal effect and CO_2 photoreduction, Appl. Catal. B: Environ. 311 (2022) 121255.
[25] H. Feng, X. Zhang, Q. Yao, Y. Zhou, M. He, Y. Liu, A. Zhang, X. Bu, Cd(Eu)Se/CdS/CdZnS/ZnS quantum dots with hydrophilic alloy shell supported by flower-like $ZnIn_2S_4$: a S-scheme for efficient photocatalytic H_2 evolution, J. Alloy. Compd. 976 (2024) 173235.
[26] W. Zheng, G. Lu, X. Liu, S. Fan, Y. Hu, N. Pinna, J. Zhang, Mixed-dimensional heterojunction by 3D CdS nanowire arrays bridged with 2D WSe2 for ultrafast photoelectric gas sensor, Matter 8 (2025) 101914.
[27] H. Zou, Z. Luo, X. Yang, Q. Xie, Y. Zhou, Toward emerging applications using core–shell nanostructured materials: a review, J. Mater. Sci. 57 (2022) 10912–10942.
[28] Z. Du, J. Pan, C. Ma, Y. Guan, M. Sun, Z. Gao, H. Tang, X. Yan, CdS nanorods embedded in $ZnIn_2S_4$ nanosheets to construct n-n heterojunction for ultrahigh photocatalytic H_2 and H_2O_2 production, Colloids Surf. A: Physicochem. Eng. Asp. 706 (2025) 135774.

[29] Q. Yu, Y. Liu, Q. Zeng, Y. Yang, S. Ning, Y. Wei, X. Wang, D. Zeng, Efficient photocatalytic H_2 production and Cr(VI) reduction using a Cu_2-xSe/ZnSe heterojunction, J. Alloy. Compd. 1014 (2025) 178810.
[30] T. Jia, M. Liu, C. Zheng, F. Long, Z. Min, F. Fu, D. Yu, J. Li, J.H. Lee, N.H. Kim, One-pot hydrothermal synthesis of La-doped $ZnIn_2S_4$ microspheres with improved visible-light photocatalytic performance, Nanomaterials 10 (2020) 2026.
[31] X. Yang, Y. Yang, B. Wang, T. Wang, Y. Wang, D. Meng, Synthesis and photocatalytic property of cubic phase CdS, Solid State Sci. 92 (2019) 31–35.
[32] A. Rajwali Khan, Z. Rehman, A. Khan, H. Ambareen, H. Ullah, S.M. Abbas, Y. Khan, R. Khan, Solar-light driven photocatalytic conversion of p-nitrophenol to p-aminophenol on CdS nanosheets and nanorods, Inorg. Chem. Commun. 79 (2017) 99–103.
[33] A. Khan, Z. Rehman, A. Khan, H. Ambareen, H. Ullah, S.M. Abbas, Y. Khan, R. Khan, Solar-light driven photocatalytic conversion of p -nitrophenol to p-aminophenol on CdS nanosheets and nanorods, Inorg. Chem. Commun. 79 (2017) 99–103.
[34] L. Ye, Z. Wen, $ZnIn_2S_4$ nanosheets decorating WO_3 nanorods core-shell hybrids for boosting visible-light photocatalysis hydrogen generation, Int. J. Hydrog. Energy 44 (2019) 3751–3759.
[35] B. Ahmed, S. Kumar, S. Kumar, A.K. Ojha, Shape induced (spherical, sheets and rods) optical and magnetic properties of CdS nanostructures with enhanced photocatalytic activity for photodegradation of methylene blue dye under ultra-violet irradiation, J. Alloy. Compd. 679 (2016) 324–334.
[36] S. Shen, L. Zhao, X. Guan, L. Guo, Improving visible-light photocatalytic activity for hydrogen evolution over $ZnIn_2S_4$: a case study of alkaline-earth metal doping, J. Phys. Chem. Solids 73 (2012) 79–83.
[37] Q. Liang, W. Gao, C. Liu, S. Xu, Z. Li, A novel 2D/1D core-shell heterostructures coupling MOF-derived iron oxides with $ZnIn_2S_4$ for enhanced photocatalytic activity, J. Hazard. Mater. 392 (2020) 122500.
[38] J. Wang, S. Sun, R. Zhou, Y. Li, Z. He, H. Ding, D. Chen, W. Ao, A review: synthesis, modification and photocatalytic applications of $ZnIn_2S_4$, J. Mater. Sci. Technol. 78 (2021) 1–19.
[39] X. Luo, C. Liu, M. Chen, S. Zhang, Y. Xu, Electrochemical performance and enhanced photocatalytic activity of Ce-doped $BiVO_4$ under visible light irradiation, Mater. Res. Bull. 94 (2017) 428–434.
[40] J. Jiang, F. Gu, W. Shao, C. Li, Fabrication of spherical multi-hollow TiO_2 nanostructures for photoanode film with enhanced light-scattering performance, Ind. Eng. Chem. Res. 51 (2012) 2838–2845.
[41] Y. Ning, D. Lv, Q. Tang, H. Wang, X. Hu, Y. Cao, S. Yu, H. Tian, Novel 2D/2D/2D heterojunction of $ZnIn_2S_4$/g-C_3N_4/MoS_2 for enhanced photocatalytic hydrogen evolution reaction, Ceram. Int. 50 (2024) 48692–48699.
[42] Y. Liu, Y. Yang, B. Zhang, D. Deng, J. Ning, G. Liu, S. Xue, F. Zhang, X. Liu, W. Zhang, Electronic structure and optical properties of CdS/BiOI heterojunction improved by oxygen vacancies, J. Alloy. Compd. 955 (2023) 170235.
[43] N. Karamoschos, A. Katsamitros, L. Sygellou, K.S. Andrikopoulos, D. Tasis, Composition-regulated photocatalytic activity of $ZnIn_2S_4$@CdS hybrids for efficient dye degradation and H_2O_2 evolution, Molecules 29 (2024) 3857.
[44] S. Zhang, M. Du, Z. Xing, Z. Li, K. Pan, W. Zhou, Defect-rich and electron-rich mesoporous Ti-MOFs based NH_2-MIL-125(Ti)@$ZnIn_2S_4$/CdS hierarchical tandem heterojunctions with improved charge separation and enhanced solar-driven photocatalytic performance, Appl. Catal. B: Environ. 262 (2020) 118202.
[45] J. Zhang, J. Ma, J. Zhang, R. Cui, Z. Liu, X. Li, R. Sun, Core-shell structured cobalt sulfide/C. I. pigment yellow 53 photocatalysts with abundant sulfur vacancies for efficient photocatalytic co-production of xylonic acid and CO, Small 20 (2024) e2401977.
[46] X. He, T. Kai, P. Ding, Heterojunction photocatalysts for degradation of the tetracycline antibiotic: a review, Environ. Chem. Lett. 19 (2021) 4563–4601.
[47] B.R.C. Vale, R.S. Mourão, J. Bettini, J.C.L. Sousa, J.L. Ferrari, P. Reiss, D. Aldakov, M.A. Schiavon, Ligand induced switching of the band alignment in aqueous synthesized CdTe/CdS core/shell nanocrystals, Sci. Rep. 9 (2019) 8332.
[48] H. Pedersen, C. Hsu, N. Nepal, J.M. Woodward, C.R. Eddy, Atomic layer deposition as the enabler for the metastable semiconductor inn and its alloys, Cryst. Growth Des. 23 (2023) 7010–7025.
[49] W. Chen, R. Yan, J. Zhu, G. Huang, Z. Chen, Highly efficient visible-light-driven photocatalytic hydrogen evolution by all-solid-state Z-scheme CdS/QDs/$ZnIn_2S_4$ architectures with MoS_2 quantum dots as solid-state electron mediator, Appl. Surf. Sci. 504 (2020) 144406.
[50] M. Li, J. Qiu, L. Yang, Y. Feng, J. Yao, Fabrication of TiO_2 embedded $ZnIn_2S_4$ nanosheets for efficient Cr(VI) reduction, Mater. Res. Bull. 122 (2020) 110671.
[51] G. Han, F. Xu, B. Cheng, Y. Li, J. Yu, L. Zhang, Enhanced photocatalytic H_2O_2 production over inverse opal ZnO@ polydopamine S-scheme heterojunctions 0 (2022) 2112037.
[52] J. Luo, K. Wang, Y. Qiu, X. Zhou, X. Ning, L. Zhan, X. Zhou, Built-in electric field mediated S-scheme high-quality charge separation in $BiVO_4$/NiAl-LDH heterojunction for highly efficient photocatalytic degradation of antibiotics, J. Alloy. Compd. 1008 (2024) 176572.
[53] J. Luo, J. Chen, X. Chen, X. Ning, L. Zhan, X. Zhou, Construction of cerium oxide nanoparticles immobilized on the surface of zinc vanadate nanoflowers for accelerated photocatalytic degradation of tetracycline under visible light irradiation, J. Colloid Interface Sci. 587 (2021) 831–844.
[54] Q. Wang, J. Xie, H. Huang, W. Ni, Q. Xue, Enhanced ambient-stability and charge transport property of the $CsPbBr_3$@Polyaniline, J. Lumin. 275 (2024) 120770.
[55] G. Lu, W. Li, Z. Li, G. Gu, Q. Han, J. Liang, Z. Chen, Enhanced degradation of norfloxacin under visible light by s-scheme Fe_2O_3/g–C_3N_4 heterojunctions, Molecules 29 (2024) 5212.
[56] Z. Liu, M. Roosh, M. Lu, A. Arshad, W. Xian, Y. Shen, G. Liu, A. Bahadur, S. Iqbal, S. Mahmood, K.M. Alotaibi, Empowering wastewater treatment with step scheme heterojunction ternary nanocomposites for photocatalytic degradation of nitrophenol, Sci. Rep. 15 (2025) 3299.
[57] Kalsoom Adnan, F.M. Zada, Sarwat, H. Soonmin, B. Khan, M. Alamzeb, W. Sun, J. Ikram, N.U. Rehman, Visible light induced photocatalytic degradation of norfloxacin using xC-TiO_2, Heliyon 11 (2025) e41320.
[58] I. Abdelfattah, A.M. El-Shamy, A comparative study for optimizing photocatalytic activity of TiO2-based composites with ZrO_2, ZnO, Ta_2O_5, SnO, Fe_2O_3, and CuO additives, Sci. Rep. 14 (2024) 27175.
[59] G. Huang, D. Zeng, M. Wei, Y. Chen, A. Ma, S. Cheng, Efficient degradation of methylene blue by g-C_3N_4@$CaCO_3$ photocatalyst via synergistic adsorption and catalysis under visible light irradiation, Diam. Relat. Mater. 153 (2025) 112031.
[60] H. Ren, S. Wang, A. Labidi, B. Pan, J. Luo, C. Wang, Nanoengineering of ultrathin N-CQDs/Bi_2WO_6 S-scheme heterojunction for enhanced photodegradation of antibiotics as emerging contaminants: mechanism insight and toxicity assessment, Sep. Purif. Technol. 362 (2025) 131717.
[61] W. Wei, X. Sun, J. Sun, C. Hao, Shape-controlled growth and in situ characterization of CdS nanocrystals via liquid cell transmission electron microscopy, Molecules 29 (2024) 5342.
[62] Z. Yu, B. Yin, F. Qu, X. Wu, Synthesis of self-assembled CdS nanospheres and their photocatalytic activities by photodegradation of organic dye molecules, Chem. Eng. J. 258 (2014) 203–209.
[63] H. Zhu, H. Shi, J. Li, X. Qu, S. Zhao, H. Wang, A. Rong, Z. Chen, Construction of S-scheme $Cs_3PMo_{12}O_{40}$/$MnIn_2S_4$ heterojunction for efficient photocatalytic removal of antibiotics: degradation pathways, toxicity evaluation and mechanism insight, J. Alloy. Compd. 976 (2024) 173072.
[64] M. Chahkandi, M. Zargazi, K.B. Ghiasabadi, J.S. Chung, Core-shell structured Ag-HAp@Bi_2S_3 as effective S-scheme heterojunction photocatalyst: induced with internal polarization electric field effect and co-catalyst fashions, J. Mol. Liq. 399 (2024) 124423.
[65] X. Li, Q. Luo, L. Han, F. Deng, Y. Yang, F. Dong, Enhanced photocatalytic degradation and H_2 evolution performance of N CDs/S-C_3N_4 S-scheme heterojunction constructed by π-π conjugate self-assembly, J. Mater. Sci. Technol. 114 (2022) 222–232.
[66] J. Luo, R. Li, Y. Chen, X. Zhou, X. Ning, L. Zhan, L. Ma, X. Xu, L. Xu, L. Zhang, Rational design of Z-scheme $LaFeO_3$/SnS_2 hybrid with boosted visible light photocatalytic activity towards tetracycline degradation, Sep. Purif. Technol. 210 (2019) 417–430.
[67] W. Xu, W. Tian, L. Meng, F. Cao, L. Li, Interfacial chemical bond-modulated z-scheme charge transfer for efficient photoelectrochemical water splitting, Adv. Energy Mater. 31 (2021) 202003500.
[68] S. Sambyal, V. Chauhan, P. Shandilya, A. Priye, Photocatalytic norfloxacin degradation enabled by a dual S-scheme nanocellulose-based Ag_2WO_4/NiO/MoO_3 tertiary heterojunction, Catal. Sci. Technol. (2025).
[69] L. Yadav, M. Sharma, H. Laddha, M. Agarwal, R. Gupta, Insight into efficient photocatalytic degradation of norfloxacin over a simple, economical biochar-based magnetic photocatalyst under solar illumination: a statistical and experimental approach, Environ. Sci. Pollut. Res. 31 (2024) 60971–60987.

Journal of Alloys and Compounds 1017 (2025) 179019

Contents lists available at ScienceDirect

Journal of Alloys and Compounds

journal homepage: www.elsevier.com/locate/jalcom

Constructing of Bi_2O_3-In_2O_3 nanofibers for sensitive detection of freshness gas markers in aquatic products

Liwei Wang [a,b], Liping Gao [a,*], Hongjie Liu [c,*], Qian Zhang [b], Hao Fu [c], Zhelin Liu [a]

[a] Anhui Engineering Research Center of Intelligent Perception and Elderly Care, Chuzhou University, Chuzhou 239000, China
[b] School of Marine Sciences, Coral Reef Research Center of China, Guangxi Laboratory on the Study of Coral Reefs in the South China Sea, Guangxi University, Nanning 530004, China
[c] School of Chemistry and Chemical Engineering, Guangxi University, Nanning 530004, China

ARTICLE INFO

Keywords:
Bi_2O_3-In_2O_3 nanofibers
Oxygen vacancy
Gas sensor
Trimethylamine

ABSTRACT

In order to quickly and accurately detect and then evaluate the freshness of fish, trimethylamine is used as a landmark gas for detection. In this study, an alternative trimethylamine chemosensor based on Bi_2O_3-In_2O_3 nanofibers (NFs) was synthesized successfully through the electrospinning method. The structure, morphology and chemical states of Bi_2O_3-In_2O_3 NFs were characterized. The results of gas sensing tests indicated that after doping In_2O_3 with 3 % Bi_2O_3, the sensor displays better sensitivity to trimethylamine (48.6–100 ppm), which was 2.9 times higher than pure In_2O_3 (NTs) gas sensor (16.4) at the optimal operating temperature of 250 °C. Under low concentrations of trimethylamine (0.5 ppm), the 3 % Bi_2O_3-In_2O_3 NFs sensor still has a specific sensitivity (1.3). The increased sensitivity of 3 % Bi_2O_3-In_2O_3 NFs sensor is attributed to the increase of oxygen vacancy, which can be confirmed by XPS and UV-*vis* methods. The sensor sensitivity decreased as the relative humidity increased, but the response remained at approximately 10 even under a high humidity environment of 90 %. The excellent performances towards trimethylamine indicate that 3 % Bi_2O_3-In_2O_3 NFs are prospective candidates for trimethylamine gas sensor fabrication.

1. Introduction

Trimethylamine (TMA) is a typical kind of volatile organic compound that is mainly generated in the spoilage of fish [1]. TMA is one of the most effective indicators for assessing the freshness of fish and seafood because the concentration increases with the deterioration degree of the fishery products [2,3]. The fish is generally considered fresh if the concentration of TMA released from the fish is less than 10 ppm [4–6]. Therefore, it is essential to detect ppm levels of TMA in fish during storage and transport.

Metal oxide semiconductors (MOS) have been widely applied in gas detection due to their low cost, ease of manufacturing, convenient operation, rapid response, and portability and have achieved significant research results [7–10]. The performance and application effectiveness of gas sensors largely depend on the selected gas-sensitive materials [11,12]. Previous research reports have indicated that MOS-based nanomaterials have great potential for trimethylamine (TMA) detection [9,13,14].

Indium (III) oxide (In_2O_3) is a versatile material exhibiting n-type semiconducting properties. Due to its exceptional optical and electrical properties and its excellent chemical stability, it has garnered significant attention in gas sensing and photocatalysis [15–18]. By exploiting the morphology-dependent functional properties of nanomaterials, various nanostructures of In_2O_3 have been successfully synthesized, including nanoparticles, nanowires, nanosheets, nanocubes, and hollow spheres [19–25]. Fiber-structured materials are highly favored due to their high surface area and ultrafine nanocrystallites, which significantly increase the number of gas adsorption sites. More importantly, electrospinning technology can synthesize nanofibers simply and economically [26]. For example, The In_2O_3 nanofiber gas sensor prepared by electrospinning and hydrothermal methods demonstrated a response value of 5.44 at 160 °C to 50 ppm of trimethylamine [27]. In contrast, another sensor with a web-like structure of In_2O_3 nanofibers could detect trimethylamine down to 1 ppm at 80 °C, with a response value as high as 3.8 [28]. However, single-component materials often suffer from low sensitivity and poor selectivity. To solve this problem, constructing heterostructures is considered as an effective method to improve these properties. Due to their unique structural characteristics, heterostructure

* Corresponding authors.
E-mail addresses: gaozhangping@163.com (L. Gao), hongjieliu2008@163.com (H. Liu).

https://doi.org/10.1016/j.jallcom.2025.179019
Received 9 September 2024; Received in revised form 28 January 2025; Accepted 4 February 2025
Available online 6 February 2025
0925-8388/© 2025 Published by Elsevier B.V.

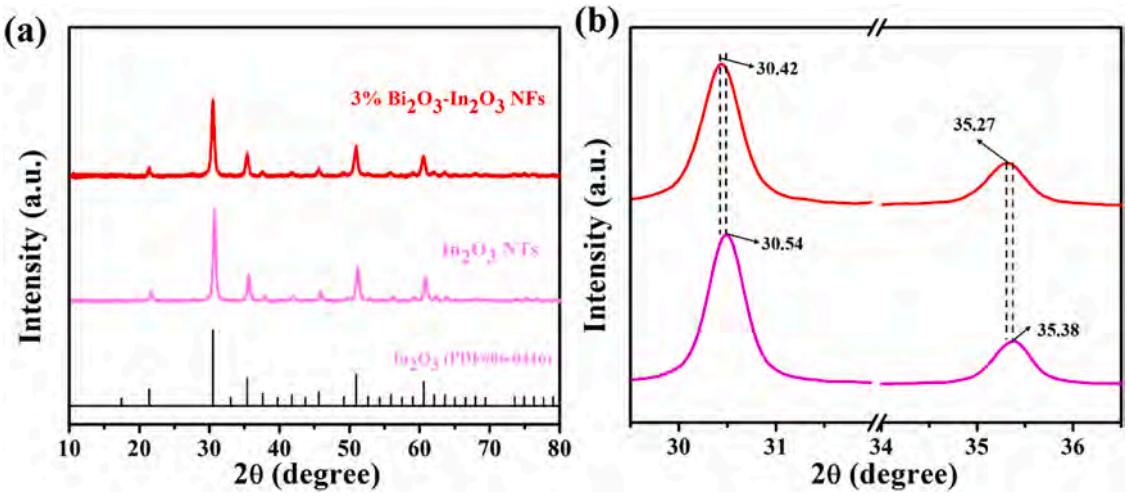


Fig. 1. XRD patterns of the prepared In_2O_3 NTs and 3 % Bi_2O_3-In_2O_3 NFs (a, b).

composites have garnered widespread attention and recognition from scholars. For instance, NiO-$BiVO_4$ p-n heterojunction microspheres exhibit excellent gas sensing properties, including fast response/recovery times, high humidity resistance, and low detection limit of 3.42 ppb toward TEA [29]. The TiO_2-$NiFe_2O_4$ heterojunction sensor synthesized by hydrothermal method exhibits better performance to trimethylamine under white light irradiation [30]. Li et al. used facile one-step electrospinning technology to synthesize hierarchical and porous SnO_2/In_2O_3 heterostructures, which showed that the optimal operating temperature is significantly reduced under UV light irradiation [31]. Nevertheless, there is still a need to further enhance TMA sensing performance for practical applications, particularly in selectivity and sensitivity.

In the present study, we successfully prepared Bi_2O_3-In_2O_3 nanofiber (NFs) heterojunction sensors. Compared to In_2O_3 nanotubes, the 3 % Bi_2O_3-In_2O_3 NFs heterojunction sensor exhibited higher sensitivity and selectivity to trimethylamine (TMA) gas. This enhanced gas sensing performance can be attributed to the increased number of active sites provided by the fiber structure, the spatial separation of charge carriers, rapid charge transfer characteristics, and the unique bandgap structure of the heterojunction.

2. Experimental

2.1. Chemicals

Analytical grade Polyvinylpyrrolidone (PVP, M_w = 1,300,000), Indium nitrate hydrate ($In(NO_3)_3{\cdot}5H_2O$), Bismuth nitrate pentahydrate ($Bi(NO_3)_3{\cdot}5H_2O$), N-N-Dimethylacetamide (DMF), absolute ethanol (EtOH) were all obtained from Aladdin (Shanghai, China). All materials were used without further purification. DI water was used throughout the experiments.

2.2. Fabrication of Bi_2O_3-In_2O_3 nanofibers and In_2O_3 nanotubes

In general, the Bi_2O_3-In_2O_3 NFs were prepared through the sol-gel electrospinning technique and the subsequent calcination treatment. First, DMF and absolute ethanol were mixed in a volume ratio of 8: 2. The Bismuth-Indium sol was then produced by adding $In(NO_3)_3{\cdot}5H_2O$ and $Bi(NO_3)_3{\cdot}5H_2O$ to the mixed solution. After vigorous stirring, PVP is further added and stirred to obtain a homogeneous spinning solution. Following this, electrospinning was performed on ET-2535H spinning equipment with a high electrostatic voltage of 18 kV and a stable propulsion velocity of 2 mL h^{-1}. The receiving distance is 20 cm and the receiving speed is 500 rpm. During the electrospinning process, the ambient temperature was maintained at 20 ± 3 °C and the relative humidity was kept at 45 ± 3 %. Finally, the as-spun hybrid nanofibers were annealed in air at 600 °C to obtain the Bi_2O_3-In_2O_3 NFs. Based on different Bi: In molar ratios, we define these mixtures as 1 % Bi_2O_3-In_2O_3, 3 % Bi_2O_3-In_2O_3, 5 % Bi_2O_3-In_2O_3, and 10 % Bi_2O_3-In_2O_3. For comparison, pure In_2O_3 NTs without the addition of $Bi(NO_3)_3{\cdot}5H_2O$ were prepared using the same procedure. The schematic illustration for the preparation of Bi_2O_3-In_2O_3 NFs is shown in Fig. S1.

2.3. Gas sensor assembly and sensing test

The detailed assembling process of the sensor was as follows: the powder was first ground with several drops of DI water to form a diluted paste, which was then spin-coated onto a special alumina ceramic tube that had been preinstalled with a pair of gold electrodes and two pairs of Pt wires. A Ni-Cr heating wire was inserted through the tube to serve as a heater. The alumina tube was subsequently welded onto a pedestal with six probes, resulting in the final sensor unit. Before the measurement, all sensors underwent aging at 150 °C for 48 h. Gas-sensing tests were performed on a CGS-8 intelligent static test system (Beijing Elite Tech Co. Ltd., China), which can precisely control the gas flow, the gas composition, and the measurement of electrical resistance. During the whole process, dry air was used as the reference and gas balance. The specific testing procedure is as follows: Firstly, a certain amount of water vapor, air, and target gas are pre-mixed uniformly through the humidity-controlled gas and liquid distribution system. Then, the mixed gas is introduced into the test chamber. Inside the test chamber is a ceramic tube that can be controlled to heat up to 400 °C to overcome adsorption energy or reaction barriers. Subsequently, the mixed gas diffuses onto the surface of the gas sensor, and the reacted gas is pumped out of the system, followed by re-filling with air to restore the sensor's resistance value. Besides, certain water vapor was pre-mixed with ethanol vapor and air at room temperature (20 °C) to reach tunable R.H. The sensor response is defined as $S = R_a/R_g$ for reductive gases, where R_a is the sensor resistance in air, and R_g is the sensor resistance in the target gas phase. The response time (Tres) is the time required to attain 90 % of the steady gas response value, whereas the recovery time (Trec) is when 10 % of the initial gas response value is attained.

2.4. Characterizations

The crystal structure of the material was characterized by powder X-ray diffraction (XRD) analysis (Rigaku Ultima IV, Japan, Cu Kα radiation, λ = 1.5418 Å). The morphology and microstructure were characterized by field-emission scanning electron microscopy (FESEM)

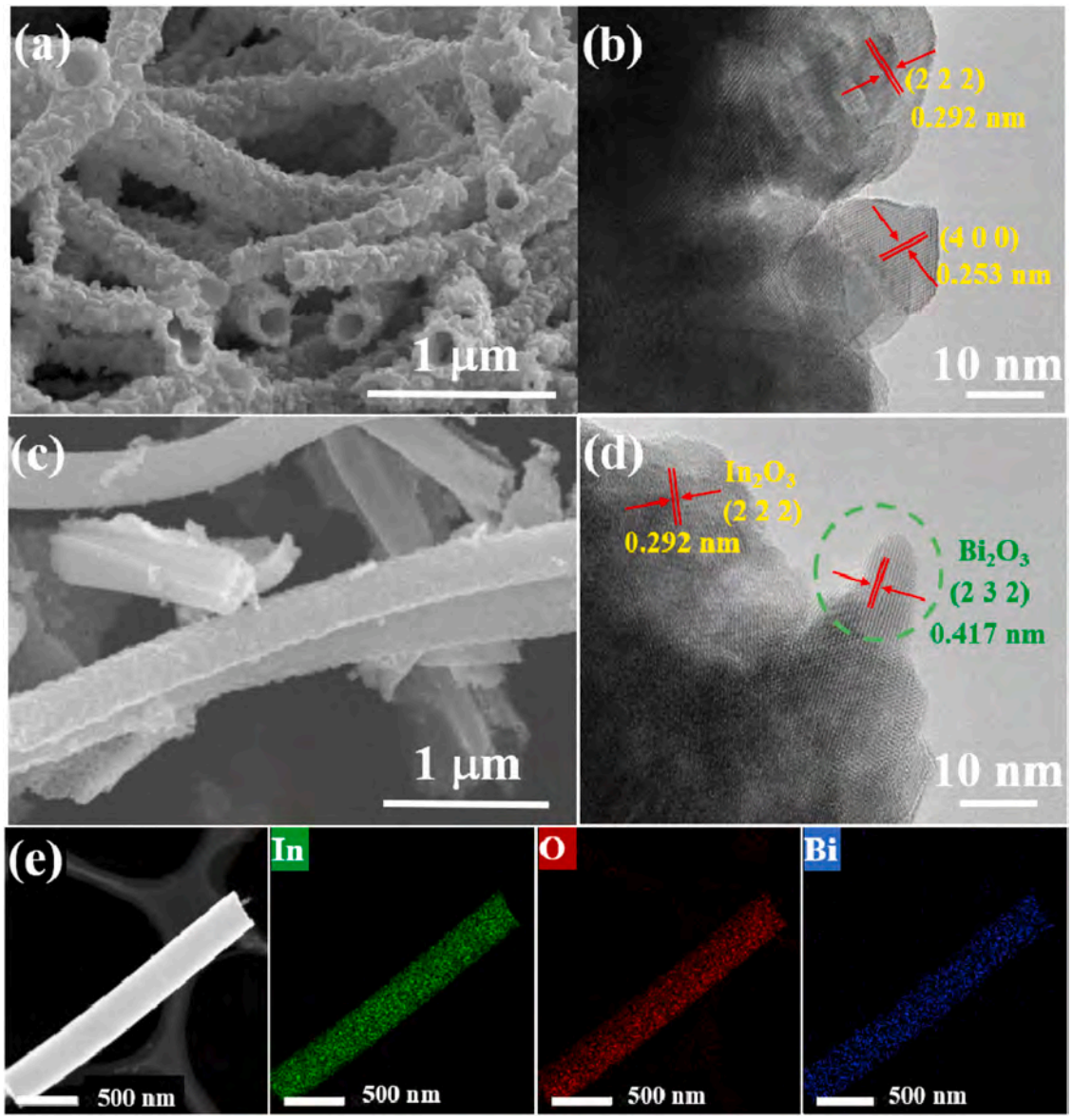


Fig. 2. (a, c) SEM of the prepared In_2O_3 NTs and 3 % Bi_2O_3-In_2O_3 NFs, (b, d) TEM images of In_2O_3 NTs and 3 % Bi_2O_3-In_2O_3 NFs, and (e) EDS elemental maps of 3 % Bi_2O_3-In_2O_3 NFs.

(Hitachi SU5000, Japan), transmission electron microscopy (TEM) and high-resolution TEM (HRTEM) (FEI Tecnai G2 f20 twin, 200 kV). X-ray photoelectron spectroscopy (XPS) (Thermo Scientific ESCALAB 250Xi, Al Kα X-ray monochromator) was used to analyze the elemental and solid surface of the materials. The photo adsorption performance of the sample is analyzed by ultraviolet-visible spectroscopy (UV-*vis*) (Lambda 1050+, America).

3. Results and discussion

3.1. Material characterizations

The effect of Bi_2O_3 doping on the crystal structure of In_2O_3 was analyzed by XRD. Fig. 1a shows the XRD patterns of the pure samples and Bi_2O_3-In_2O_3 samples. All the diffraction peaks of Bi_2O_3-In_2O_3 can be easily attributed to the cubic structure of standard In_2O_3 (PDF # 06-0416), which proves the successful preparation of pure In_2O_3. Compared with the diffraction peaks of pure In_2O_3 NTs, there are no other phases in the Bi_2O_3-In_2O_3 NFs sample, which may be because the content of Bi element is too low. However, the (222) and (400) peaks of the 3 % Bi_2O_3-In_2O_3 NFs sample have a significant left shift, as shown in Fig. 1b. This phenomenon can be explained by the difference in the ion radius of Bi^{3+} and In^{3+}. The radius of Bi^{3+} is 1.03 Å, which is larger than that of In^{3+} (0.81 Å) under the same coordination number [32]. Therefore, when In^{3+} ions are replaced by Bi^{3+} in the In_2O_3 lattice, the diffraction peak of In_2O_3 shifts to the low-angle region. With the increase of Bi^{3+}, the diffraction peaks shift will increase accordingly. The grain sizes calculated for the two materials are shown in Table S1. It can be observed from the table that the materials assembled from small particles have a size of approximately 20 nm.

SEM and TEM were used to observe the morphologies of 3 % Bi_2O_3-In_2O_3 NFs and In_2O_3 NTs. Fig. S2 shows that two precursor materials that have not been calcined at high temperatures have no noticeable difference in appearance, and they are all slender solid fibers. In_2O_3 becomes hollow tubes after high-temperature calcination. However, 3 % Bi_2O_3-In_2O_3 still maintains a solid structure after high-temperature calcination (Fig. 2a and c). Fig. S2c and f show that both 3 % Bi2O3-In2O3 NFs and In_2O_3 NTs have a diameter of 300 nm. Fig. S3 shows the SEM images of composites with different doping ratios. As the doping amount increases, the morphology of the composites gradually

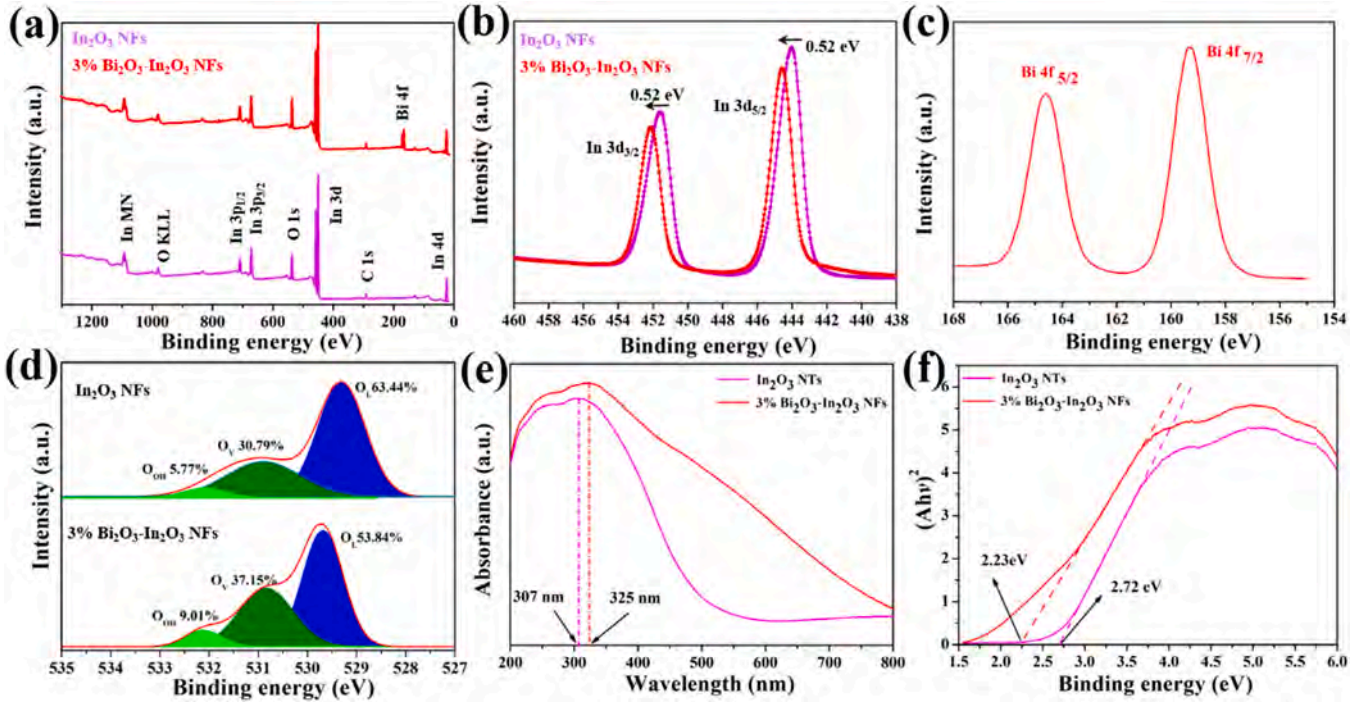


Fig. 3. XPS pattern of In_2O_3 NTs and 3 % Bi_2O_3-In_2O_3 NFs: (a) survey spectra, (b) In 3d spectra, (c) Bi 4f spectra, (d) O 1s spectra , (e) UV-*vis* absorption spectra, (f) Band gap energy diagram of In_2O_3 NTs and 3 % Bi_2O_3-In_2O_3 NFs.

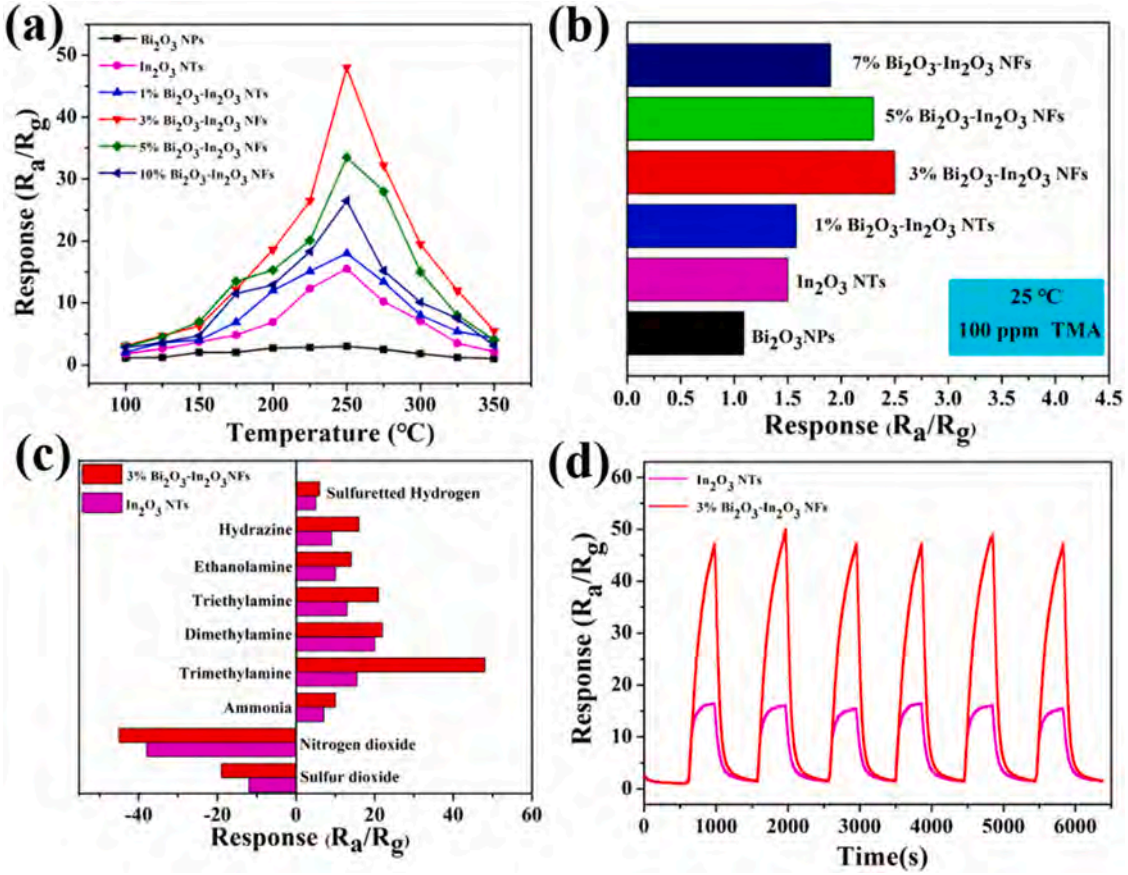


Fig. 4. (a) Response of the sensors to 100 ppm TMA at 100–300 °C, (b) Response of the sensors to 100 ppm TMA at 25 °C, (c) The selectivity of In_2O_3 NTs and 3 % Bi_2O_3-In_2O_3 NFs sensors toward various fish corruption gases (100 ppm), (d) The repeatability of In_2O_3 NTs and 3 % Bi_2O_3-In_2O_3 NFs sensors to 100 ppm of TMA.

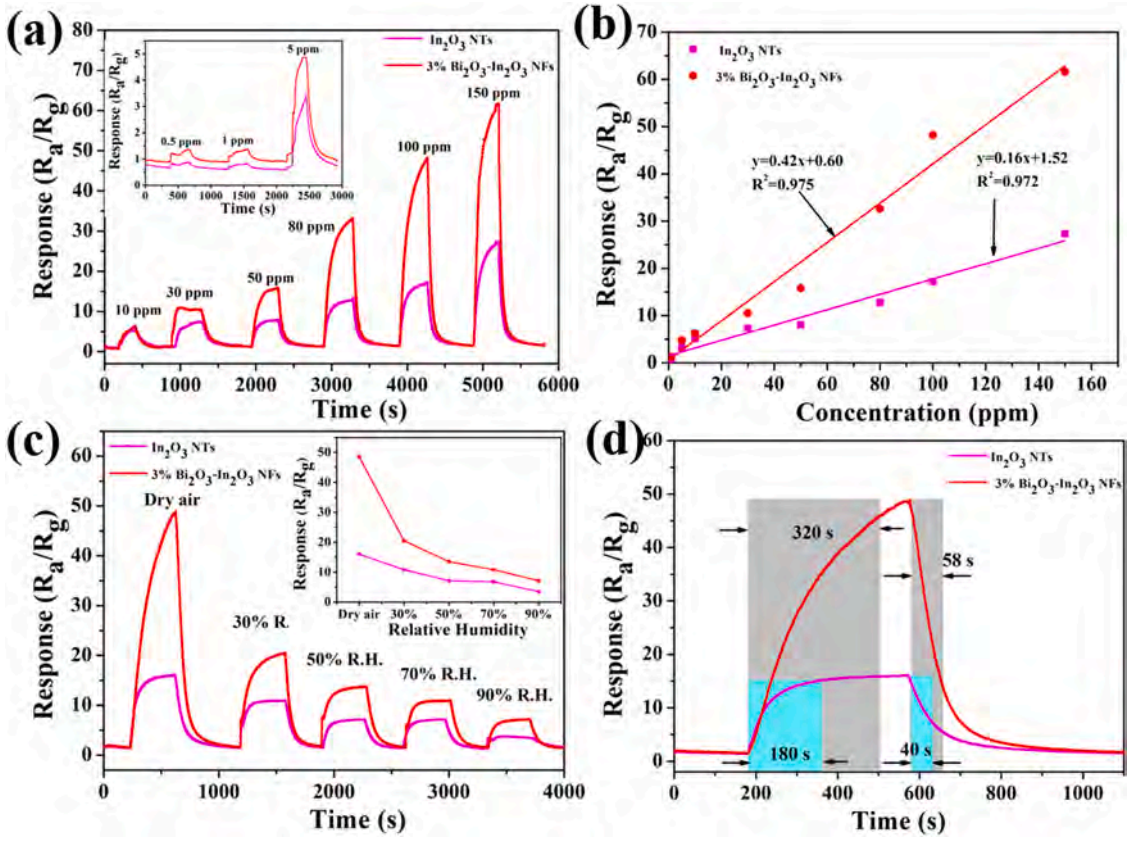


Fig. 5. Gas-sensing performance of In_2O_3 NTs and 3 % Bi_2O_3-In_2O_3 NFs sensors: (a) Response recovery curves of the sensors to 0.5–150 ppm TMA (Inset is the lower concentrations from 0.5 to 5 ppm), (b) The fitting curve between concentration and response, (c) TMA response recovery curves (Inset is the corresponding sensitivity curves) of the sensors with different R.H., (d) Response recovery curves of the sensors to 100 ppm TMA in dry air.

transitions from In_2O_3 tubes to nanofibers. As shown in Fig. 2b and d, the crystal plane spacing with a lattice stripe width of 0.417 nm, 0.292 nm and 0.253 nm corresponds to (232) crystal plane of Bi_2O_3 and (210) and (400) crystal plane of In_2O_3 respectively can be found. Fig. 2e is the EDS element diagram of 3 % Bi_2O_3-In_2O_3 NFs, which shows that the material is composed of In, O and Bi, and the elements are evenly distributed.

To further investigate the information on chemical states and chemical bonds in the materials, XPS spectra were measured. The XPS spectrum shown in Fig. 3a confirms the existence of O, In elements in In_2O_3 NTs, and the existence of O, In, and Bi elements in 3 % Bi_2O_3-In_2O_3 NFs. In the high-resolution XPS spectrum of In 3d (Fig. 3b), it is observed that the two binding energies of In 3d in pure In_2O_3 NTs are 444.12 eV and 451.61 eV, which belong to In $3d_{5/2}$ and $3d_{3/2}$, respectively. However, the two peaks in 3 % Bi_2O_3-In_2O_3 NFs shifted to higher energies compared to In_2O_3 NTs. This may be due to the substitution of In^{3+} by Bi^{3+}, resulting in the formation of higher binding energy for the In-O-Bi bond. Fig. 3c shows the high-resolution Bi 4f spectrum of 3 % Bi_2O_3-In_2O_3 NFs. The peaks of $4f_{7/2}$ (159.4 eV) and $4f_{5/2}$ (164.8 eV) are clearly visible. The measured distance between these two peaks is 5.4 eV, indicating that Bi is doped into In_2O_3 as Bi^{3+}. Fig. 3d is the high-resolution O 1s spectra of In_2O_3 NTs and 3 % Bi_2O_3-In_2O_3 NFs. These two curves can be fitted to three peaks, including lattice oxygen (O_L at 529.8 eV), oxygen vacancy (O_V at 531.1 eV) and chemisorption oxygen (O_C at 532.07 eV). The calculated O_V value of 3 % Bi_2O_3-In_2O_3 NFs is 37.15 %, which is higher than 30.79 % of In_2O_3 NTs. It is generally believed that in the process of gas sensing, surface oxygen vacancy defects can provide potentially more active sites for gas adsorption, and the dissociation chemisorption process provides high local charge density and strong electrostatic field to facilitate surface electron transport [33], thereby improving the gas sensitivity of the material.

UV-*vis* DRS was used to study the photo-adsorption properties of In_2O_3 NTs and 3 % Bi_2O_3-In_2O_3 NFs samples. As shown in Fig. 3e, both materials have obvious light absorption below 450 nm. Due to the presence of Bi_2O_3, the light absorption edge of 3 % Bi_2O_3-In_2O_3 NFs has a continuous red shift. The band gap energy is calculated according to the formula $(\alpha h\nu)1/n = A(h\nu\text{-}E_g)$, where h, ν, α, A, E_g are Planck's constant, optical frequency, absorption coefficient, constant and band gap energy, respectively. Since In_2O_3 is an indirect band gap semiconductor, n is defined as 2. Fig. 3f shows that the energy band energies (E_g) of In_2O_3 NTs and 3 % Bi_2O_3-In_2O_3 NFs are 2.72 and 2.23 eV, respectively. The band gap of 3 % Bi_2O_3-In_2O_3 NFs samples is significantly reduced, and it is used as an electron donor to regulate metal oxidation. Electron donors can modulate the electronic structure of metal oxides, thus narrowing the band gap [34], which is consistent with the XPS test results.

3.2. Gas sensing properties

To explore the optimal doping ratio, we synthesized Bi_2O_3-In_2O_3 materials with various doping ratios as well as Bi_2O_3 nanoparticles and characterized with SEM (Fig. S3, S4), and then investigated their gas-sensing performance towards trimethylamine at different testing temperatures. Among them, the XRD pattern of the Bi_2O_3 nanoparticles perfectly matched with PDF#71-2274, and its bandgap width was 2.79 eV (Fig. S4). Through comparative analysis, we found that all sensors show a similar response trend of "increasing-maximum-decreasing" for 100 ppm TMA as the temperature rose from 100 to 350 °C, wherein the highest sensitivity presents at 250 °C (Fig. 4a). Generally speaking, as the temperature increases, the thermal energy of gas gradually increases. It is easier to undergo oxidation-reduction reactions after overcoming the surface activation energy barrier of the material. However, when the temperature is too high, the penetration depth of gas

Table 1
Comparison of gas-sensitive performance of 3 % Bi_2O_3-In_2O_3 sensor with other sensors reported in the literature for TMA.

Materials & Morphology	Working Temperature (°C)	Concentration (ppm)	Response (R_a/R_g)	Limited of detection (ppm)	Ref.
In_2O_3 flower-like structures	200	100	~15	0.5	[35]
Pt/Bi_2O_3/In_2O_3 HS	140	100	347	1	[36]
In_2O_3-SnO_2	280	10	7.11	1	[37]
α-Fe_2O_3/ZnO	260	50	5.9	10	[38]
MIL−88B-6h@ Fe_2O_3	200	100	16.73	1	[39]
Flower-like Co_3O_4/In_2O_3	200	10	11.67	1	[40]
Mn_2O_3@In_2O_3 core shell	180	100	47	5	[41]
3 % Bi_2O_3-In_2O_3 NFs	250	100	48.6	0.5	This work

molecules decreases, resulting in the response value gradually reducing. In the entire test temperature range, the 3 % Bi_2O_3-In_2O_3 NFs showed a higher gas response than the pure In_2O_3 NTs sensor and other proportions of Bi_2O_3-In_2O_3 sensors, indicating that the doping of 3 % Bi_2O_3 effectively improved the sensitivity of the In_2O_3-based gas sensor to trimethylamine. For sensor applications, room temperature or near-room temperature operation is regarded as an important development direction. Therefore, we examined the sensing performance of the material towards trimethylamine at room temperature and found that the response value was relatively low (Fig. 4b), unable to meet the application requirements. Consequently, we adopted 250 °C as the testing temperature for subsequent experiments.

Selectivity is another important indicator for detecting the sensor's gas sensitivity. In general, gas sensitivity depends on the number of reactant molecules involved in the redox reaction between the chemisorbed oxygen and the target gas and the number of target gas molecules involved in the surface reaction. The higher the number of reactant molecules, the easier the gas to be adsorbed and react. To fully understand the selectivity of sensors for fish spoilage produced gas trimethylamine, In_2O_3 NTs and 3 % Bi_2O_3-In_2O_3 NFs gas sensors were prepared to detect different gases produced by fish spoilage under optimal operation. Selectivity testing of interfering gases is shown in Fig. 4c. Under the same conditions, the 3 % Bi_2O_3-In_2O_3 NFs sensor demonstrated the highest selectivity for trimethylamine among reducing gases, achieving a sensitivity of 48.6 at 100 ppm, followed by methylamine and triethylamine with responses of 22.3 and 20.8, respectively. Other reducing gases, such as ammonia, hydrogen sulfide, ethanolamine, etc., have a much lower response than trimethylamine. Besides, some typical oxidative gases, such as NO_2 and SO_2, were selected to comprehensively examine the selectivity of heterojunction sensors. As shown in Fig. 4c, the sensitivity of the 3 % Bi_2O_3-In_2O_3 NFs sensor to the oxidative gases NO_2 and SO_2 is slightly lower than that to trimethylamine (TMA). Considering that the volatile gases produced in the fish decay process are mainly reducing organic amine gases, this sensor exhibits the best selectivity for TMA, thus making it suitable for fish freshness detection.

In order to verify whether the gas sensors based on In_2O_3 NTs and 3 % Bi_2O_3-In_2O_3 NFs have good repeatability, we conducted a gas sensitivity test of six consecutive test cycles under the same environmental conditions. As shown in Fig. 4d, the gas response of the two sensors to 100 ppm trimethylamine does not have a significant drift at the test temperature of 250 °C, indicating that the two sensors have

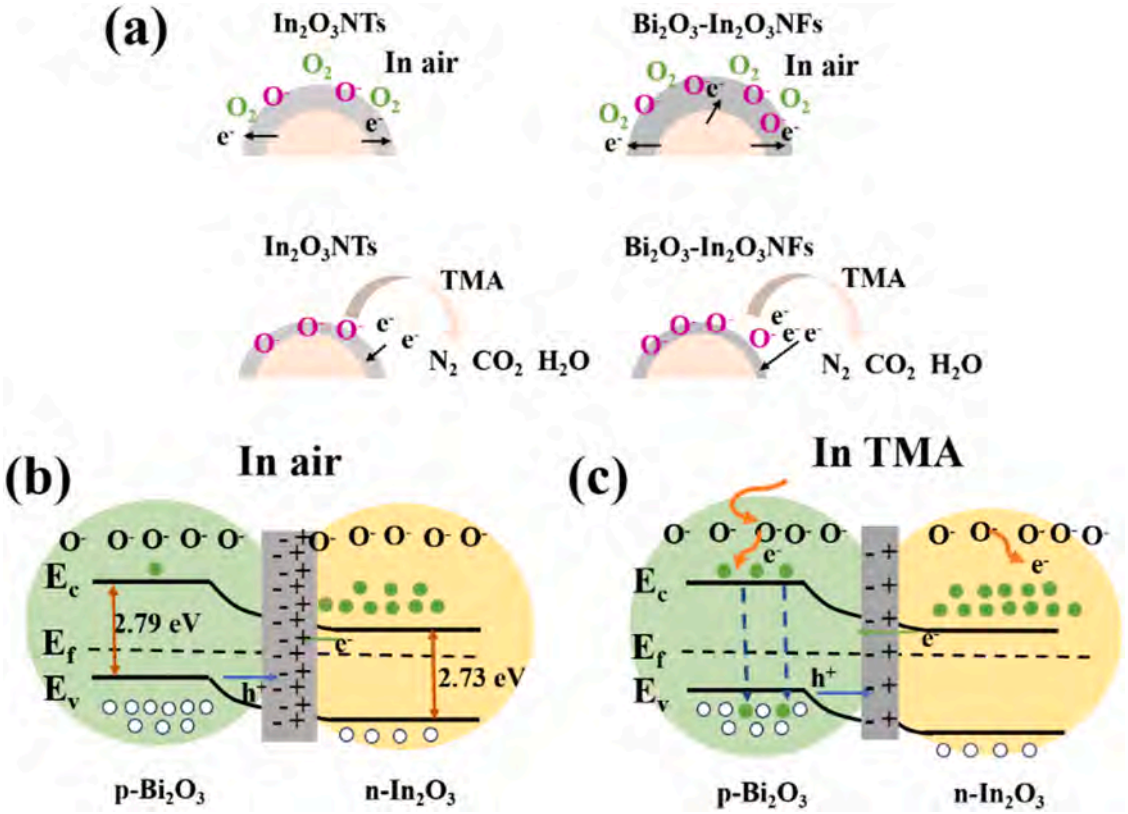


Fig. 6. (a) The TMA-sensing schematic diagram of sensing mechanism of pure In_2O_3 NTs and Bi_2O_3-In_2O_3 NFs, (b)Band diagram for Bi_2O_3-In_2O_3 interface in air, (c) Band diagram for Bi_2O_3-In_2O_3 after interface in TMA gas.

relatively good stability under continuous operation.

Based on the excellent sensing performance of In_2O_3 NTs and 3 % Bi_2O_3-In_2O_3 NFs gas sensors to trimethylamine gas, the response characteristics of sensors at different concentrations were further explored. As shown in Fig. 5a, the response of the two gas sensors in the range of 0.5–150 ppm increases with the trimethylamine concentration increased at the test temperature of 250 °C. Even under the low concentration of 0.5 ppm, the response value of 3 % Bi_2O_3-In_2O_3 NFs sensor is 1.3, indicating that the sensor can effectively detect low concentration of trimethylamine. It is expected to be applied to the detection of trimethylamine produced by spoilage of fish at low concentration. Fig. 5b shows the response-concentration linear relationship diagram of the sensors at 250 °C. The correlation coefficient of the In_2O_3 NTs gas sensor is R^2= 0.972, and the correlation coefficient of the 3 % Bi_2O_3-In_2O_3 NFs gas sensor is R^2= 0.975, indicating that both sensors have good linearity of the fitting curve and the sensitivity increasing sensitivity trend of the 3 % Bi_2O_3-In_2O_3 NFs gas sensor is more obvious.

Table 1 shows TMA sensing performances based on different structures. Obviously, compared to In_2O_3 flower-like structures [35], Pt/Bi_2O_3/In_2O_3 HS [36], In_2O_3-SnO_2 [37], α-Fe_2O_3/ZnO [38], MIL-88B-6h@Fe_2O_3 [39], Flower-like Co_3O_4/In_2O_3 [40] and Mn_2O_3@In_2O_3 core-shell [41], the 3 % Bi_2O_3-In_2O_3 NFs synthesized in this experiment exhibit significant sensitivity and detection limit advantages. The gas sensing enhancement may be attributed to more active centers obtained from the enhanced oxygen vacancy defects on Bi_2O_3-In_2O_3 NFs as shown in XPS and PL spectra.

It is important to point out that R.H. is an important factor affecting the gas sensing properties of a MOS-type sensor. Thus, the above sensor was investigated for detecting 100 ppm ethanol under different relative R.H. levels. As displayed in Fig. 5c, different R.H. exhibited a large influence on the sensing performance. Overall, the sensor response decreased with increasing R.H. from 0 % to 90 %. However, the response remained at approximately 10 even under a high humidity environment of 90 % and showed that the material had a certain humidity resistance. Furthermore, the response/recovery time is an important parameter to evaluate gas sensor performance. Fig. 5d shows that the response and recovery times of 3 % Bi_2O_3-In_2O_3 NFs and pure In_2O_3 NTs sensors in dry air toward 100 ppm trimethylamine were 320 s/58 s and 180 s/40 s, respectively. The response time of In_2O_3 NTs is about half of the response time after doping Bi_2O_3. The reason may be that In_2O_3 NTs is a hollow structure, so a larger specific surface area is more conducive to gas adsorption and passage. Due to the solid structure of the Bi_2O_3-In_2O_3 NFs gas sensor and the more active sites formed by its heterojunction structure (more gases can be adsorbed), so its adsorption time and recovery time are more prolonged than In_2O_3 NTs.

3.3. Sensing mechanism

In this work, the reason for the superior gas sensitivity of 3 % Bi_2O_3-In_2O_3 NFs can be attributed to the increase of oxygen vacancies and the formation of p-n heterojunctions. First, the XPS analysis spectrum in Fig. 3d shows that Bi_2O_3 doping adapts the lattice at the interface of the heterostructure and at the same time causes the content of surface oxygen vacancies to increase. The increase of oxygen vacancies increases the number of active sites related to gas adsorption on the surface of the gas-sensitive material, and a higher number of adsorption sites is conducive to enhancing sensing performance [42,43]. In this experiment, the presence of more oxygen vacancies in the material will promote the adsorption of oxygen molecules in the air on the surface of the material to form oxygen anions, which in turn cause more trimethylamine gas molecules undergoing redox reactions on the surface of gas-sensitive materials, finally improved the gas-sensitive performance of the material. Secondly, the electronic performance of the gas-sensitive material significantly impacts the performance of the gas sensor. Bi_2O_3 is a p-type semiconductor with a band gap of 2.79 eV, while the band gap of the synthesized In_2O_3 is 2.73 eV. As shown in Fig. 6c, when two different types of semiconductors are in contact, since the carriers of p-type semiconductors are holes and those of n-type semiconductors are electrons, holes in p-type Bi_2O_3 and electrons in n-type In_2O_3 will be attracted to each other [44]. The diffusion of these two types of carriers further forms a potential barrier at the interface between the two semiconductors. In this process, the energy difference will cause the energy band in the depletion layer to bend gradually until the Fermi level of the entire system reaches equilibrium [45,46]. Consequently, barriers for electrons and holes are formed at the p-n heterojunction and create an additional depletion layer [47], as is shown in Fig. 6a. When Bi_2O_3-In_2O_3 nanofibers (NFs) are exposed to air at 250 °C, oxygen molecules adsorb onto their surface and capture electrons from the material [48], transforming into O^- ions, as illustrated in the Fig. 6a and b. As a result of this transformation, the material's electron concentration decreases, leading to an increase in resistance. However, once these nanofibers are exposed to triethylamine (TEA) vapor, TEA molecules react with the O^- ions adsorbed on the Bi_2O_3-In_2O_3 nanofibers. The electrons released during this reaction return to the material's interior, subsequently narrowing the width of the electric double layer (EDL) and reducing the resistance, as shown in Fig. 6c. By utilizing this alteration in material resistivity, we can attain a sensitive reaction to the gas under measurement.

4. Conclusions

In summary, the hollow In_2O_3 NTs and solid 3 % Bi_2O_3-In_2O_3 NFs were prepared by combining electrospinning and high-temperature calcination. The surface morphology, structure and chemical components of the gas-sensitive materials were characterized. The characterization results show that 3 % Bi_2O_3-In_2O_3 nanofibers (NFs) exhibit more abundant oxygen vacancies. Due to the increased number of oxygen vacancies and the formation of p-n heterojunctions, the gas-sensing performance of the 3 % Bi_2O_3-In_2O_3 NFs sensor is significantly enhanced. The optimal operating temperature of the Bi_2O_3-In_2O_3 NFs gas sensor was determined to be 250 °C through a series of systematic trimethylamine gas tests. In addition, compared with the In_2O_3 NTs gas sensor, the 3 % Bi_2O_3-In_2O_3 NFs gas sensor has a highly sensitive response to trimethylamine (48.6/100 ppm and 1.3/0.5 ppm). This sensor is capable of effectively detecting low-concentration trimethylamine gas produced by fish meat. Humidity test research shows that by introducing an appropriate amount of Bi_2O_3, the sensor can maintain good sensitivity (10) in an environment with a relative humidity of 90 %.

CRediT authorship contribution statement

Liping Gao: Writing – review & editing, Data curation, Conceptualization. **Hongjie Liu:** Formal analysis, Data curation, Conceptualization. **Liwei Wang:** Writing – original draft, Funding acquisition, Conceptualization. **Zhelin Liu:** Data curation. **Qian Zhang:** Investigation, Data curation. **Hao Fu:** Data curation.

Declaration of Competing interest

The authors declare that they have no known competing financial interests or personal relationships that could have appeared to influence the work reported in this paper

Acknowledgments

This work was funded by the Open Foundation of Anhui Engineering Research Center of Intelligent Perception and Elderly Care, Chuzhou University, under Grant No. 20220PB04 and 20220PB05; Key Projects of Guangxi Natural Science Foundation (2020GXNSFDA297015); National Natural Science Foundation of China Department of Anhui Provincial (2023AH051602).

Appendix A. Supporting information

Supplementary data associated with this article can be found in the online version at doi:10.1016/j.jallcom.2025.179019.

Data availability

Data will be made available on request.

References

[1] S. Bourigua, S. El Ichi, H. Korri-Youssoufi, A. Maaref, S. Dzyadevych, N. Jaffrezic Renault, Electrochemical sensing of trimethylamine based on polypyrrole–flavin-containing monooxygenase (FMO3) and ferrocene as redox probe for evaluation of fish freshness, Biosens. Bioelectron. 28 (2011) 105–111.

[2] P. Wang, Z. Zheng, X. Cheng, L. Sui, S. Gao, X. Zhang, Y. Xu, H. Zhao, L. Huo, Ionic liquid-assisted synthesis of α-Fe_2O_3 mesoporous nanorod arrays and their excellent trimethylamine gas-sensing properties for monitoring fish freshness, J. Mater. Chem. A 5 (2017) 19846–19856.

[3] R. Yang, X. Huang, Z. Wang, Y. Zhou, L. Liu, A chemisorption-based microcantilever chemical sensor for the detection of trimethylamine, Sens. Actuators B: Chem. 145 (2010) 474–479.

[4] E. Chen, H. Fu, R. Lin, Y. Tan, J. Zhang, Highly selective and sensitive trimethylamine gas sensor based on cobalt imidazolate framework material, ACS Appl. Mater. Interfaces 6 (2014) 22871–22875.

[5] H.S. Woo, C.W. Na, I.D. Kim, J.H. Lee, Highly sensitive and selective trimethylamine sensor using one-dimensional ZnO-Cr_2O_3 hetero-nanostructures, Nanotechnology 23 (2012) 245501.

[6] K. Mitsubayashi, Y. Kubotera, K. Yano, Y. Hashimoto, T. Kon, S. Nakakura, Y. Nishi, H. Endo, Trimethylamine biosensor with flavin-containing monooxygenase type 3 (FMO3) for fish-freshness analysis, Sens. Actuators B: Chem. 103 (2004) 463–467.

[7] W. Zhang, W. Zhang, Fabrication of SnO_2-ZnO nanocomposite sensor for selective sensing of trimethylamine and the freshness of fishes, Sens. Actuators B: Chem. 134 (2008) 403–408.

[8] F. Zhang, X. Dong, X. Cheng, Y. Xu, X. Zhang, L. Huo, Enhanced gas-sensing properties for trimethylamine at low temperature based on $MoO_3/Bi_2Mo_3O_{12}$ hollow microspheres, ACS Appl. Mater. Interfaces 11 (2019) 11755–11762.

[9] Z. Sun, X. Yan, L. Huang, Y. Zhang, Z. Hu, C. Sun, X. Yang, G. Pan, Y. Cheng, AuPd bimetallic functionalized monodisperse In_2O_3 porous spheres for ultrasensitive trimethylamine detection, Sens. Actuators B: Chem. 381 (2023) 133355.

[10] Z. Qin, Z. Wu, Q. Sun, J. Sun, M. Zhang, T. Shaymurat, C. Lv, H. Duan, Biomimetic gas sensor derived from disposable bamboo chopsticks for highly sensitive and selective detection of NH_3, Chem. Eng. J. 462 (2023) 142203.

[11] W. Pi, X. Chen, M. Humayun, Y. Yuan, W. Dong, G. Zhang, B. Chen, Q. Fu, Z. Lu, H. Li, Z. Tang, W. Luo, Highly sensitive chemiresistive H_2S detection at subzero temperature over the Sb-doped SnO_2@g-C_3N_4 heterojunctions under UV illumination, ACS Appl. Mater. Interfaces 15 (2023) 14979–14989.

[12] T. Tang, Z. Li, Y. Cheng, K. Xu, H. Xie, X. Wang, X. Hu, H. Yu, B. Zhang, X. Tao, C. Hung, N. Hoa, G. Chen, Y. Li, J. Ou, Single-step growth of p-type 1D Se/2D $GeSe_xO_y$ heterostructures for optoelectronic NO_2 gas sensing at room temperature, J. Mater. Chem. A 11 (2023) 6361–6374.

[13] C. Zhao, J. Shen, S. Xu, J. Wei, H. Liu, S. Xie, Y. Pan, Y. Zhao, Y. Zhu, Ultra-efficient trimethylamine gas sensor based on Au nanoparticles sensitized WO_3 nanosheets for rapid assessment of seafood freshness, Food Chem. 392 (2022) 133318.

[14] F. Zhang, K. Liu, H. Li, S. Cui, D. Zhang, J. Zeng, Z. Yan, MoO_3 nanorods decorated by $PbMoO_4$ nanoparticles for enhanced trimethylamine sensing performances at low working temperature, ACS Appl. Mater. Interfaces 14 (2022) 24610–24619.

[15] L. He, T. Wood, B. Wu, Y. Dong, L. Hoch, L. Reyes, D. Wang, C. Kübel, C. Qian, J. Jia, K. Liao, P.O. Brien, A. Sandhel, J. Loh, P. Szymanski, N. Kherani, T. Sum, C. Mims, G. Ozin, Spatial separation of charge carriers in $In_2O_{3-x}(OH)_y$ nanocrystal superstructures for enhanced gas-phase photocatalytic activity, ACS Nano 10 (2016) 5578–5586.

[16] Q. Liu, Y. Liu, F. Wu, X. Cao, Z. Li, M. Alharbi, A.N. Abbas, M.R. Amer, C. Zhou, Highly sensitive and wearable In_2O_3 nanoribbon transistor biosensors with integrated on-chip gate for glucose monitoring in body fluids, ACS Nano 12 (2018) 1170–1178.

[17] Q. Liu, N. Aroonyadet, Y. Song, X. Wang, X. Cao, Y. Liu, S. Cong, F. Wu, M. E. Thompson, C. Zhou, Highly sensitive and quick detection of acute myocardial infarction biomarkers using In_2O_3 nanoribbon biosensors fabricated using shadow masks, ACS Nano 10 (2016) 10117–10125.

[18] K. Wan, D. Wang, F. Wang, H. Li, J. Xu, X. Wang, J. Yang, Hierarchical In_2O_3 @SnO_2 core–shell nanofiber for high efficiency formaldehyde detection, ACS Appl. Mater. Interfaces 11 (2019) 45214–45225.

[19] A. Shanmugasundaram, V. Gundimeda, T. Hou, D.W. Lee, Realizing synergy between In_2O_3 nanocubes and nitrogen-doped reduced graphene oxide: an excellent nanocomposite for the selective and sensitive detection of CO at ambient temperatures, ACS Appl. Mater. Interfaces 9 (2017) 31728–31740.

[20] Y. Sun, Z. Zhao, K. Suematsu, P. Li, Z. Yu, W. Zhang, J. Hu, K. Shimanoe, Rapid and stable detection of carbon monoxide in changing humidity atmospheres using clustered In_2O_3/CuO nanospheres, ACS Sens. 5 (2020) 1040–1049.

[21] Y. Meng, G. Liu, A. Liu, Z. Guo, W. Sun, F. Shan, Photochemical activation of electrospun In_2O_3 nanofibers for high-performance electronic devices, ACS Appl. Mater. Interfaces 9 (2017) 10805–10812.

[22] E.E. Miró, L. Gutiérrez, J.M. Ramallo López, F.G. Requejo, Perturbed angular correlation characterization of indium species on In/H-ZSM5 catalysts, J. Catal. 188 (1999) 375–384.

[23] Z. Cai, J. Dai, W. Li, K.B. Tan, Z. Huang, G. Zhan, J. Huang, Q. Li, Pd supported on MIL-68(In)-derived In_2O_3 nanotubes as superior catalysts to boost CO_2 hydrogenation to methanol, ACS Catal. 10 (2020) 13275–13289.

[24] K. Zhang, H. Dong, W. Dai, X. Meng, H. Lu, T. Wu, X. Zhang, Fabricating Pt/Sn-In_2O_3 nanoflower with advanced oxygen reduction reaction performance for high-sensitivity MicroRNA electrochemical detection, Anal. Chem. 89 (2017) 648–655.

[25] X. Wang, F. Liu, X. Chen, X. Song, G. Xu, Y. Han, J. Tian, H. Cui, In_2O_3 nanoparticles decorated ZnO hierarchical structures for n-butanol sensor, ACS Appl. Nano Mater. 3 (2020) 3295–3304.

[26] J.H. Lee, J.Y. Kim, A. Mirzaei, H.W. Kim, S.S. Kim, Significant enhancement of hydrogen-sensing properties of ZnO nanofibers through NiO loading, Nanomaterials 8 (2018) 902.

[27] Q. Xie, Y. Ding, Q. Wang, P. Song, Fabrication of 1D/2D In_2O_3 nanofibers/Ti_3C_2TX MXene composites for high performance detection of trimethylamine at low temperature, Sens. Actuators B: Chem. 405 (2024) 135338.

[28] X. Song, D. Tian, Y. Qiu, X. Sun, B. Jiang, C. Zhao, Y. Zhang, L. Fan, N. Zhang, Improving poisoning resistance of electrocatalysts via alloying strategy for high-performance lithium-sulfur batteries, Energy Storage Mater. 41 (2021) 248–254.

[29] Y. Shuai, R. Peng, Y. He, X. Liu, X. Wang, W. Guo, NiO/$BiVO_4$ p-n heterojunction microspheres for conductometric triethylamine gas sensors, Sens. Actuators B: Chem. 384 (2023) 133625.

[30] W. Wang, L. Zhang, Z. Liu, Y. Kang, Q. Chen, W. Wang, M. Liu, B. Ye, F. Yu, Y. Li, Visible-light-activated TiO_2-$NiFe_2O_4$ heterojunction for detecting sub-ppm trimethylamine, J. Alloy. Compd. 898 (2022) 162990.

[31] H. Li, Q. Zhang, J. Guo, X. Wang, Y. Wang, Q. Ma, In-situ growth of hierarchical SnO_2/In_2O_3 heterostructures with multiple effective n-n heterojunctions for superior triethylamine-sensing performances, Sens. Actuators B: Chem. 369 (2022) 132377.

[32] Y. Fang, Y. Zhang, Y. Zhang, Y. Zhang, X. Su, J. Hu, Bi^{3+}/Mn^{4+} co-activated phosphors for indoor plant growth and temperature sensing, J. Alloy. Compd. 934 (2023) 168049.

[33] P.G. Choi, N. Izu, N. Shirahata, Y. Masuda, SnO_2 nanosheets for selective alkene gas sensing, ACS Appl. Nano Mater. 2 (2019) 1820–1827.

[34] Y. Zhou, R. Cui, Y. Dang, Y. Li, Y. Zou, Doping controlled oxygen vacancies of $ZnWO_4$ as a novel and effective sensing platform for carbendazim and biomolecule, Sens. Actuators B: Chem. 296 (2019) 126680.

[35] D. Meng, T. Qiao, G. Wang, Y. Shen, X. San, Y. Pan, F. Meng, NiO-functionalized In_2O_3 flower-like structures with enhanced trimethylamine gas sensing performance, Appl. Surf. Sci. 577 (2022) 151877.

[36] X. Li, Y. Li, X. Xu, X. Wang, G. Sun, B. Zhang, Y. Wang, J. Cao, Persistently boosted TEA sensing performance of In_2O_3 hollow spheres by sequentially modified with Bi_2O_3 and Pt nanoparticles, Sens. Actuators B: Chem. 422 (2025) 136628.

[37] F. Li, X. Gao, R. Wang, T. Zhang, G. Lu, N. Barsan, Design of core-shell heterostructure nanofibers with different work function and their sensing properties to trimethylamine, ACS Appl. Mater. Interfaces 8 (2016) 19799–19806.

[38] R. Zhang, L. Wang, J. Deng, T. Zhou, Z. Lou, T. Zhang, Hierarchical structure with heterogeneous phase as high performance sensing materials for trimethylamine gas detecting, Sens. Actuators B: Chem. 220 (2015) 1224–1231.

[39] Y. Ji, Z. Pan, T. Ma, K. Wang, X. Zhao, Q. Jin, Hierarchical porous spindle-shaped MIL-88B@Fe_2O_3 with core-shelled structure for conductometric trimethylamine detection, Sens. Actuators B: Chem. 417 (2024) 136103.

[40] Y. Ji, N. Zhang, J. Xu, Q. Jin, X. San, X. Wang, Co_3O_4/In_2O_3 p-n heterostructures based gas sensor for efficient structure-driven trimethylamine detection, Ceram. Int. 49 (2023) 17354–17362.

[41] Z. Zhang, R. Wu, X. Chen, Y. Mu, Z. Yang, Z. Liu, C. Yue, D. Dastan, X. Yin, T. Liu, Enhancement of TEA gas-sensitive properties by Mn_2O_3@In_2O_3 core-shell structured p-n heterojunction, J. Alloy. Compd. 976 (2024) 173340.

[42] G. Li, X. Qi, G. Zhang, S. Wang, K. Li, J. Wu, X. Wan, Y. Liu, Q. Li, Low-cost voltammetric sensors for robust determination of toxic Cd(II) and Pb(II) in environment and food based on shuttle-like α-Fe_2O_3 nanoparticles decorated β-Bi_2O_3 microspheres, Microchem. J. 179 (2022) 107515.

[43] G. Li, X. Qi, J. Wu, X. Wan, T. Wang, Y. Liu, Y. Chen, Y. Xia, Highly stable electrochemical sensing platform for the selective determination of pefloxacin in food samples based on a molecularly imprinted-polymer-coated gold nanoparticle/black phosphorus nanocomposite, Food Chem. 436 (2024) 137753.

[44] X. Cheng, Q. Xu, S. Li, J. Li, Y. Zhou, Y. Zhang, S. Li, Oxygen vacancy enhanced Co_3O_4/ZnO nanocomposite with small sized and loose structure for sensitive electroanalysis of Hg(II) in subsidence area water, Sens. Actuators B: Chem. 326 (2021) 128967.

[45] D. Zhang, C. Su, S. Yao, H. Li, X. Pu, Y. Geng, Facile in situ chemical transformation synthesis, boosted charge separation, and increased photocatalytic activity of $BiPO_4$/BiOCl p-n heterojunction photocatalysts under simulated sunlight irradiation, J. Phys. Chem. Solids 147 (2020) 109630.

[46] P. Peljo, J.A. Manzanares, H.H. Girault, Contact potentials, fermi level equilibration, and surface charging, Langmuir 32 (2016) 5765–5775.
[47] Y.J. Kwon, S.Y. Kang, A. Mirzaei, M.S. Choi, J.H. Bang, S.S. Kim, H.W. Kim, Enhancement of gas sensing properties by the functionalization of ZnO-branched SnO_2 nanowires with Cr_2O_3 nanoparticles, Sens. Actuators B: Chem. 249 (2017) 656–666.
[48] J.H. Bang, A. Mirzaei, M.S. Choi, S. Han, H.Y. Lee, S.S. Kim, H.W. Kim, Decoration of multi-walled carbon nanotubes with CuO/Cu_2O nanoparticles for selective sensing of H_2S gas, Sens. Actuators B: Chem. 344 (2021) 130176.

Microchimica Acta (2025) 192:161
https://doi.org/10.1007/s00604-025-06966-9

RESEARCH

Electrochemical biosensor based on strand displacement reaction for on-site detection of *Skeletonema costatum*

Yaling Liu[1] · Yibo Zhang[2] · Changrui Ye[2] · Yayi He[1] · Shaopeng Wang[1] · Man Zhang[1] · Hao Fu[2] · Shan Lu[3] · Liwei Wang[1,2]

Received: 8 November 2024 / Accepted: 8 January 2025
© The Author(s), under exclusive licence to Springer-Verlag GmbH Austria, part of Springer Nature 2025

Abstract

An electrochemical biosensor was constructed for quantitatively detecting *Skeletonema costatum* (*S. costatum*) by combining the electrode modification material (NC-Au) with a strand displacement reaction (SDR). The SDR process addresses the issues of steric hindrance and electrostatic repulsion resulting from the large size of genomic DNA. It enhances the efficiency of the interfacial hybridization reaction and endows the biosensor with remarkable sensitivity. The limit of detection (LOD) and limit of quantification (LOQ) were 33.43 fg/μL (831 cells/L) and 87.21 fg/μL (2112 cells/L), respectively. Additionally, the biosensor has demonstrated excellent accuracy compared to methods such as microscopy and ddPCR ($P > 0.05$). Subsequent assessment of the adjacent waters of the Beibu Gulf using biosensors indicated a low risk of *S. costatum* red tide outbreaks in the region, which is consistent with the findings of the ecological survey. Therefore, we believe that this biosensor can provide a completely new idea for the dynamic monitoring and early warning of *S. costatum* red tide.

Keywords *Skeletonema costatum* · Strand displacement reaction · Electrochemical biosensor · On-site monitoring · Early red tide warning

Introduction

With the rapid development of modern industry, a large quantity of industrial wastewater is discharged into the ocean. Nutrients such as phosphorus, manganese, and iron in the wastewater are enriched in the ocean, which leads to the eutrophication of sea areas and the frequent occurrence of red tides [1–3]. *Skeletonema costatum* (*S. costatum*), as one of the critical species causing harmful red tides in coastal waters [4], usually occupies a dominant ecological niche during red tide outbreaks. Although *S. costatum* does not produce toxins, it usually causes seawater discoloration and alters its physical and chemical properties during epidemics. Severe *S. costatum* red tide can block the gills of fish, causing them to suffocate, and if it proliferates in economic seaweed aquaculture areas, it will also compete for nutrients with kelp, nori, etc., causing these seaweeds to discolor and rot, losing their edible and commercial value [5, 6]. However, as a natural phenomenon formed under specific marine environmental conditions, red tide cannot be eliminated artificially due to the complexity of its formation mechanism and the combined influence of multiple natural factors, given the current level of science and technology as well as the ability of humanity to intervene in the marine ecosystem. However, identifying and quantifying *S. costatum* through effective means is primary to achieve early warning of red tides and take preventive measures to avoid or mitigate the harm of red tides [7, 8]. At present, the detection of *S. costatum* mainly depends on microscopic examination methods

✉ Shan Lu
15007804705@163.com

✉ Liwei Wang
wangliwei0427@163.com

[1] Guangxi Laboratory on the Study of Coral Reefs in the South China Sea, Coral Reef Research Center of China, School of Marine Sciences, Guangxi University, Nanning 530004, China

[2] School of Resources, Environment and Materials; School of Chemistry and Chemical Engineering; State Key Laboratory for Conservation and Utilization of Subtropical Agro-Bioresources, College of Agriculture, Guangxi University, Nanning 530004, China

[3] Beibu Gulf Marine Ecological Environment Field Observation and Research Station of Guangxi, Marine Environmental Monitoring Centre of Guangxi, Beihai 536000, China

Published online: 13 February 2025

[9], high-performance liquid chromatography [10, 11], and some nucleic acid molecule–based detection technologies [12, 13] (such as qPCR and ddPCR, etc.). Although these technologies can all achieve sensitive detection of *S. costatum*, they often require professional operators, relatively long detection time, and large-scale instrument equipment. This does not apply to early warning of red tides that occur suddenly and proliferate. Therefore, developing a portable detection device with reliable results is necessary to meet the need for early warning of *S. costatum* red tides.

Electrochemical biosensors, extensively researched and developed over the past decades, have become a promising technology combining biorecognition mechanisms with physical transduction. They are characterized by miniaturization, ease of fabrication, rapid detection, low cost, and high efficiency, making them ideal for biological detection [14, 15]. Although electrochemical biosensors have demonstrated some advantages in bio-detection [16], their detection of *S. costatum* is still challenging. This is because the marine environment is affected by complex physical factors such as tides and ocean currents, and the density of *S. costatum* in the marine water column is often very low before the outbreak. In previous reports, most of the electrochemical biosensors used for algae detection have adopted a direct "sandwich" hybridization form of signal transmission, or the target RNA or DNA is fixed between the capture probe and the labeled reporter probe [17]. Nevertheless, this approach has obvious drawbacks owing to the existence of steric potential resistance and electrostatic repulsion of large-sized genomic DNA on the electrode surface, thus significantly reducing the collision efficiency of the hybridization reaction and leading to the inability of sensitive detection during the testing process. Nucleic acid strand detection techniques based on strand displacement reaction (SDR) show great potential in various fields [18, 19]. SDR primarily relies on the Watson–Crick base complementary pairing principle. For the response process, a nucleic acid strand (invading strand) can partially pair with one strand (template strand) of double-stranded nucleic acid by base complementation, thereby gradually replacing the other strand (displaced strand) from the double-stranded structure. On the one hand, since the replacement process strictly follows the principle of base complementary pairing, the designed recognition element can accurately recognize the target nucleic acid sequence, significantly reducing the probability of false positive results. On the other hand, the replaced DNA molecule is often tiny in volume and carries a less negative charge. Therefore, it can reach the electrode surface easily and generate a robust electrochemical signal [20].

Here, we present an electrochemical biosensor for quantitatively detecting *S. costatum* by combining NC-Au and SDR. This biosensor exhibits outstanding sensitivity, attributed to the sensitive response of NC-Au with excellent conductivity to the electrode surface and the enhanced hybridization efficiency on the electrode surface brought about by the SDR. In addition, the biosensor has been shown to have good reliability and accuracy compared to the microscopic examination method and ddPCR. The analysis of environmental samples proves that it can realize the rapid detection of *S. costatum* on-site. This work will provide new ideas for early warning of *S. costatum* red tide outbreaks.

Experimental section

Reagents and apparatus

Glucose ($C_6H_{12}O_6{\cdot}H_2O$), 1,2-diaminoethane ($NH_2CH_2CH_2NH_2$), $HAuCl_4$, tris (2-carboxyethyl) phosphine hydrochloride (TCEP), methylene blue (MB), and 6-mercaptoethanol (MCH), $K_3[Fe(CN)_6]$ and $K_4Fe(CN)_6{-}3H_2O$ were purchased from Aladdin Reagent Co. (Shanghai, China). Aluminum oxide powder (α-Al_2O_3) with particle sizes of 1.5, 0.5, and 0.05 μm was purchased from Tianjin Ada Hengsheng Technology Co. f/2 Medium was purchased from Cellbio (China). Tiangen Biochemical Technology Co. supplied the Plant Genomic DNA Extraction Kit (PGDK) for DNA extraction. MF-Millipore™ Mixed Cellulose Esters (MCE, 47-mm diameter, 0.22-μm pore size). All of the other reagents used in this study were of analytical grade. Furthermore, the resistance of the ultrapure water used throughout the experiment was 18.2 MΩ.

For the Chenhua electrochemical workstation (CHI660E), the working electrode was a glassy carbon electrode (GCE, 5 mm diameter), the counting electrode was a platinum sheet electrode (10 mm × 10 mm × 0.2 mm), and the reference electrode was an Ag/AgCl electrode (spec: R0305). A portable electrochemical workstation (MECART) with commercially available screen-printed carbon electrodes (SPCEs, 40 × 12.5 mm) was used as the test system. Other instruments include field emission scanning electron microscope (Thermo Fisher), high-resolution transmission electron microscope (HRTEM), transmission electron microscope (Tecnai G2 F20 S-Twin), powder X-ray diffractometer (XRD, Rigaku Ultima IV), X-ray photoelectron spectrometer (XPS, Thermo Science K-Alpha, USA), UV spectrophotometer (UV-2700), ultra-micro UV spectrophotometer (DeNovix DS-11, America), PCR (Eppendorf Mastercycler nexus, Germany), ddPCR (MicroDrop-100B, Guangzhou), BX53 biomicroscope (OLYMPUS, Japan), electrophoresis instrument (JUNYI, Beijing), electrophoretic gel imaging analysis system (Clinx Science Instruments), and air–liquid diaphragm vacuum pump (manufactured by Huankai Microbial Co., Ltd., Guangzhou, China).

Preparation of functional materials

Glucose and 1,2-diaminoethane are subjected to a hydrothermal reaction. Subsequently, after washing and drying, the material is activated in nitrogen to convert amorphous carbon into graphite carbon, denoted as NC.

The reduction of Au nanoparticles was achieved through the use of $NaBH_4$ and $C_{10}H_{17}N_3O_6S$, which served as reducing agents for this purpose. This process enabled the modification of the NC surface to form NC-Au. The detailed process of material preparation is described in **S1.1**, and the preparation flow is shown in Fig. S1.

S. costatum culture and DNA extraction

The culture method of *S. costatum* used in this work is detailed in S1.2. The DNA was extracted using a plant genomic DNA extraction kit.

Design of the specific primers

First, specific primers were designed using NCBI online (https://www.ncbi.nlm.nih.gov/). The designed primers were synthesized by Shanghai Sangon (Shanghai, China). Polymerase chain reaction (PCR) amplification was performed on the extracted DNA with specific primers. The PCR system was composed of 18 μL of sterilized water, 5 μL of premix, 0.5 μL of the upper and lower primers, and 1 μL of target DNA. The PCR thermal cycling program is as follows: pre-denaturation at 95 °C for 10 min, then 31 cycles are performed, each cycle including denaturation at 95 °C for 15 s, annealing at 57 °C for 30 s, extension at 72 °C for 35 s and finally extension at 72 °C for 10 min. Subsequently, agarose gel electrophoresis was performed on the PCR products to verify the specificity of the primers. As shown in Fig. S2, only the lane of *S. costatum* showed a distinct amplified band, while the other algae had no bands except for the dimer at the bottom. This indicates that the designed primers have excellent specificity. After electrophoresis, the gel strip containing *S. costatum* DNA was subjected to gel recovery treatment and sent to Shanghai Sangon Biotechnology Co. for sequencing. According to the sequencing results, target sequences were screened, and subsequent probe design was carried out. All oligonucleotide sequences used in the experiments were synthesized and purified by Shanghai Sangon Biotechnology Co. Afterwards, a calibrated amount of 1 × TE buffer was added to the lyophilized powder to prepare a 100 μM oligonucleotide stock solution, which was stored at 4 °C. The DNA sequences used in this work are shown in Table 1.

Table 1 Sequences of oligonucleotides are used in this work

Name	From 5' to 3'
Forward primer	GGTCCATCAGGGCAACACAA
Reverse primer	AGCCTCGGCTCGATCATTTC
Target DNA (T)	TCACTGACTCTGCTTGAGGGACGTGCT ATTC
Template strand (T1)	GAATAGCACGTCCCTCAAGCAGAGTCA GTGA
Capture probe (CP)	HS-$(CH_2)_6$-TCTTCCTGGGACGTCCCTCAA GCAGGCGGAAG
Reporter probe (RP)	TCCGCCTGCTTGAGGGACGTCCCA GGAA

Preparation of DNA probes

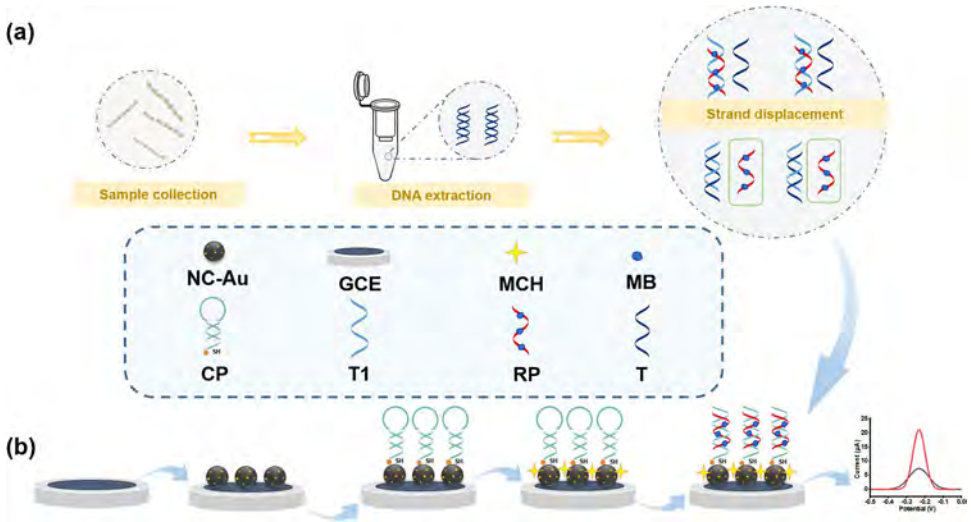
Process the original solution of the synthetic DNA probe as follows. Firstly, dilute the CP to 2 μM using 1 × TE buffer (pH = 7.4, 10 mM Tris–HCl, 1 mM EDTA, 1 M NaCl). Then, place it in a 95 °C water bath for 5 min and allow it to cool naturally to room temperature to form a hairpin structure. Subsequently, add 1 μL of TCEP with a concentration of 20 mM to 200 μL of the CP, mix them thoroughly, and conduct a pretreatment without light exposure at room temperature for 2 h. This aims to open the disulfide bond at the 5′ position of CP. Similarly, dilute the RP with TE buffer and then add an equal volume of MB solution (4 mM). React the mixture at 60 °C for 1 h. Next, mix the processed MB-RP and the diluted T1, keep them at 95 °C for 5 min, and then allow them to cool naturally to room temperature to form T1-RP. Specifically, mix 25 μL of RP (20 μM) with 25 μL of MB solution (4 mM) and react the mixture at 60 °C for 1 h. Subsequently, combine the reaction product with 50 μL of T1 (20 μM), maintain the mixture at 95 °C for 5 min, and let it cool naturally to room temperature to form T1-RP. When detecting DNA samples, mix 20 μL of the pre-prepared T1-RP (5 μM) with 20 μL of the T at different concentrations evenly by using 10 μL of 5 × PBS buffer (pH = 7.4, 10 mM Tris–HCl, 1 mM EDTA, 1 M NaCl) to form a 50-μL system. Incubate the mixture at room temperature for 30 min and then conduct the test using the biosensor.

DNA gel electrophoresis

The specificity of the selected primers was verified by agarose gel electrophoresis, and the construction process of the sensing interface was verified by polyacrylamide gel electrophoresis. Detailed information is provided in **S1.3**.

Preparation of biosensor

The glassy carbon electrodes (GCE) were ultrasonically washed with 95% ethanol and deionized water for 30 s,



Scheme 1 Schematic diagram of sensor interface construction process

respectively. Then, α-Al_2O_3 powder with particle sizes of 1.5, 0.5, and 0.05 μm was used to polish the surface of GCE sequentially. After thoroughly cleaning the electrode with deionized water, the surface of the GCE was wiped clean with dust-free paper. The preparation process of the biosensor is shown in Scheme 1. First, 10 μL of NC-Au (40 mg/mL) solution was dropped and coated on the surface of the treated GCE. After the dispersion had dried on the electrode surface, 10 μL of the CP was dropped onto the surface of NC-Au/GCE and incubated at room temperature for 100 min. Then, it was washed in PBS buffer to obtain CP/NC-Au/GCE. Subsequently, 10 μL of MCH was added dropwise onto the surface of CP/NC-Au/GCE and incubated at room temperature for 50 min. This step was taken to block the redundant active sites and prevent non-specific adsorption. Subsequently, the electrode was rinsed thoroughly with PBS to obtain MCH/CP/NC-Au/GCE. Finally, the treated T1-RP/T was added dropwise onto the electrode surface. The RP displaced by T underwent a hybridization reaction with CP on the electrode surface, generating an electrochemical signal and obtaining All/MCH/CP/NC-Au/GCE.

Electrochemical measurement

All the electrochemical tests conducted in this work were carried out on the three-electrode electrochemical workstation and the portable electrochemical workstation. Detailed information is provided in S1.4.

Information and processing of actual samples

The actual samples used in this study were collected from the coastal areas of the northern Beibu Gulf. The specific information on the samples and the detailed processing steps are provided in S1.5.

Data analysis and statistics

The experimental data processing methods in this paper are presented in S1.6.

Results and discussions

Working principle

As shown in Fig. 1, the designed reporter probe (denoted as RP; 28 bp) is first labeled by the electrochemical signal molecule MB through adsorption [21]. Subsequently, RP was annealed with the template strand (denoted as T1) to form a T1-RP double-stranded structure. In the presence of the target DNA (denoted as T), the overhanging region reserved in advance by RP in T1-RP guided T to hybridize with T1 to form a T-T1 duplex structure. At the same time, RP was forced to be released from T1-RP under thermodynamic driving. Subsequently, the released RP hybridizes with CP anchored on the NC-Au to form a DNA double strand. The above process mainly utilized the differences in thermodynamic stability of different DNA configurations (the ΔG of T1-RP was calculated as − 31.62 kcal/mol; the ΔG of T-T1 was calculated as − 61.99 kcal/mol). It was accomplished by initiating and driving the SDR through DNA fragments with specifically designed sequences. Since the amount of RP labeled by MB and finally enriched on the electrode surface was positively correlated with the concentration of the target substance, the quantification of the target substance could be achieved by measuring the redox current of MB. In addition, the effects of MB concentration and different addition stages on the electrochemical response were optimized (Fig. S3a and b). The best detection performance of the biosensor was achieved when a concentration of 2

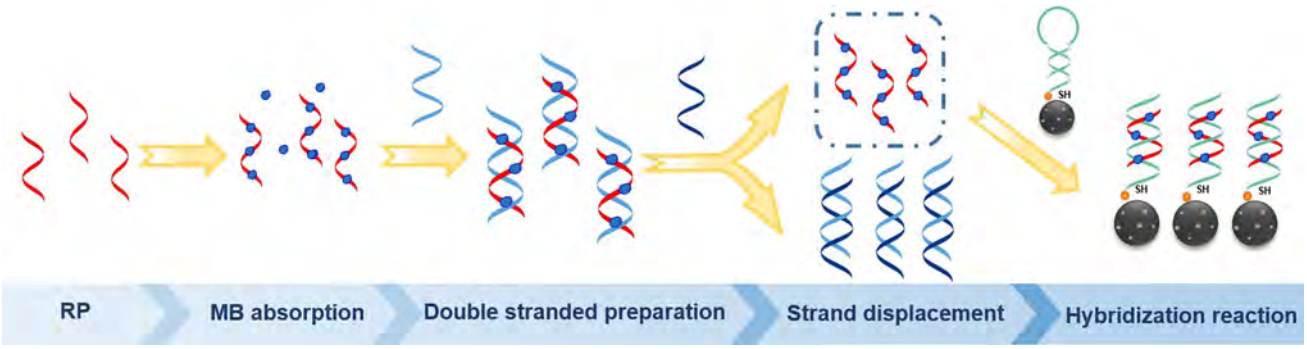


Fig. 1 Schematic diagram of sensing strategy

mM MB was added directly to the RP (Fig. S4). It is worth noting that the above strand substitution process can avoid the direct reaction between *S. costatum* DNA and CP, thus reducing the electrostatic repulsion and spatial site resistance for hybridization at the electrode interface to improve hybridization efficiency.

Characterization of NC-Au

The electrode's sensitive response to its surface perturbations was the basis for realizing signal transduction. NC-Au, with excellent electrochemical properties, was prepared by NC-doped Au as an electrode modification material. SEM was used to characterize the morphology of NC-Au and validate its successful synthesis. As shown in Fig. 2a and b, the synthesized NC-Au exhibited regular spherical structures with uniform sizes. Moreover, obvious Au nanoparticles can be observed on the NC surface. Through analysis, the average size of the Au nanoparticles was determined to be 0.126 μm (Fig. S5). The uniformly dispersed Au nanoparticles could serve as active sites for the subsequent connection of CP, enabling it to form a self-assembled monolayer on the surface of the modified electrode via Au–S bonds. To further verify the existence of Au nanoparticles, a high-resolution TEM image was taken, as shown in Fig. 2c; lattice fringes with a peak-to-peak spacing of 0.232 nm for Au nanoparticles could be observed, which corresponded to the (111) crystal plane of Au [22]. Energy dispersive X-ray

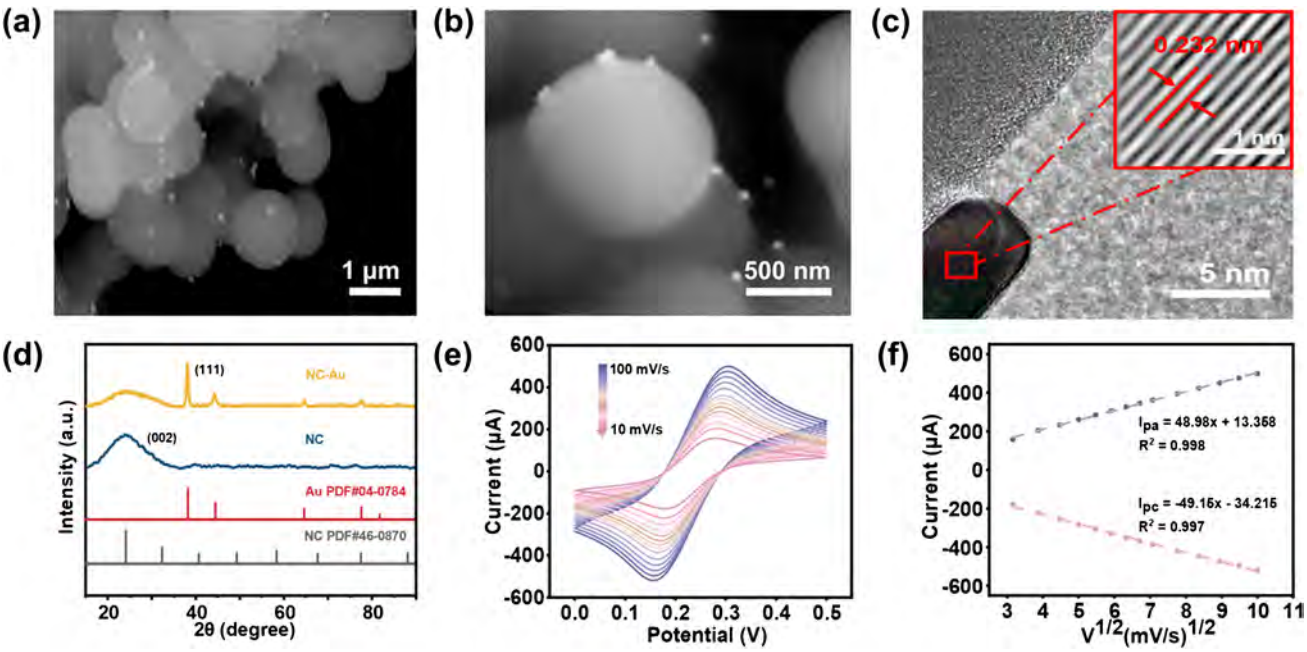


Fig. 2 **a** and **b** SEM of NC-Au, **c** TEM of NC-Au, **d** XRD patterns of NC and NC-Au, **e** CV curves of the NC-Au at different scan rates (mV/s) in 5 mM $[Fe(CN)_6]^{3-/4-}$ and 0.1M KCl, and **f** the corresponding linear correlation between redox peak current and the square root of scan rates for NC-Au

spectroscopy (EDS) demonstrated the sample's presence of Au, O, N, and C elements (Fig. S6).

In addition, it could be observed from the X-ray diffraction (XRD) spectrum in Fig. 2d that there were relatively intense characteristic peaks of the graphite phase at θ = 25° for both NC and NC-Au [23], suggesting that they exhibited the characteristics of the graphite phase. The π electrons present in the graphite phase can enhance the electrical conductivity of electrode materials. Moreover, excellent electrical conductivity significantly benefits the electrical signal conduction of sensors. In the spectrum of NC-Au, a distinct and narrow (111) diffraction peak of face-centered cubic Au crystal at θ = 38.1° could be observed [24], which further verified that NC had successfully been loaded with Au nanoparticles. In addition, the Raman spectrum in Fig. S7a shows that NC and NC-Au have characteristic peaks belonging to the D and G bands of carbon materials at around 1352 cm^{-1} and 1590 cm^{-1}, respectively. The ratio of the intensities of the two peaks (I_D/I_G) can be employed to measure the degree of graphitization of carbon materials [25, 26]. As can be seen from the figure, the I_D/I_G values of NC and NC-Au are comparable, indicating that with the loading of Au, the graphitized structure of NC is retained. In addition, the *N* in the sample was observed in the X-ray photoelectron spectroscopy (XPS) spectra of NC-Au to be predominantly in the form of pyrrole nitrogen [27] (Fig. S7b). Pyrrole nitrogen can change the material's electronic structure, increasing the electrode material's conductivity. In addition, the characteristic peaks of Au $4f_{5/2}$ (85.4 eV) and Au $4f_{7/2}$ (81.7 eV) in Au 4f indicate the presence of Au(0) in the sample [28] (Fig. S7c), proving that Au has been successfully modified on the surface of NC [29], which provides sites for subsequent anchoring of CP.

Subsequently, the kinetics of the modified electrode were studied by analyzing the influence of scan rate on redox current. Figure 2e shows that the peak current of the redox reaction increases linearly with the peak separation as the scan rate increases. The excellent linear correlation of the fitted curves of the square root of the oxidation and reduction peak currents versus scan rate ($V^{1/2}$) suggests that the electrochemical signals are generated by interfacial reactions controlled by diffusion processes [30] (Fig. 2f). In addition, the electrochemically active area (ENCA) of NC-Au was calculated to be 0.28 cm^2 (S2.4). A larger electrochemical active area means more reaction sites are available for the target substance to undergo electrochemical reactions, which in turn can improve the sensitivity of the biosensor. In conclusion, NC-Au has excellent electrical conductivity, a property that ensures efficient signal transduction and sensitive response to specific perturbations at the modified electrode.

Feasibility evaluation

Polyacrylamide gel electrophoresis was used to verify the feasibility of the SDR. As shown in Fig. 3a, the bright bands in lanes 1–3 represent the T, the T1, and the RP. Compared with lanes 2 and 3, the new band with slower migration in lane 4 indicated the successful preparation of double-stranded T1-RP. Since T has a higher molecular weight than RP, mixing the T with the double-stranded T1-RP resulted in a new, slower migrating band (T-T1, lane 5). In addition, a band similar to that in lane 3 (RP) was present in lane 5. The above results proved that T successfully displaced RP in double-stranded T1-RP and formed a T-T1 duplex structure. In addition, DPV further verified this process. As shown in Fig. S8, in the absence of T, T1-RP, which maintains the original conformation, prevents RP from hybridizing with CP, and only a weak MB redox peak appears in the DPV assay. However, a distinct redox peak could be observed after incubating the 1 nM T and T1-RP mixture on the electrode surface for a while. This indicates that the SDR successfully released the RP labeled by MB, while the

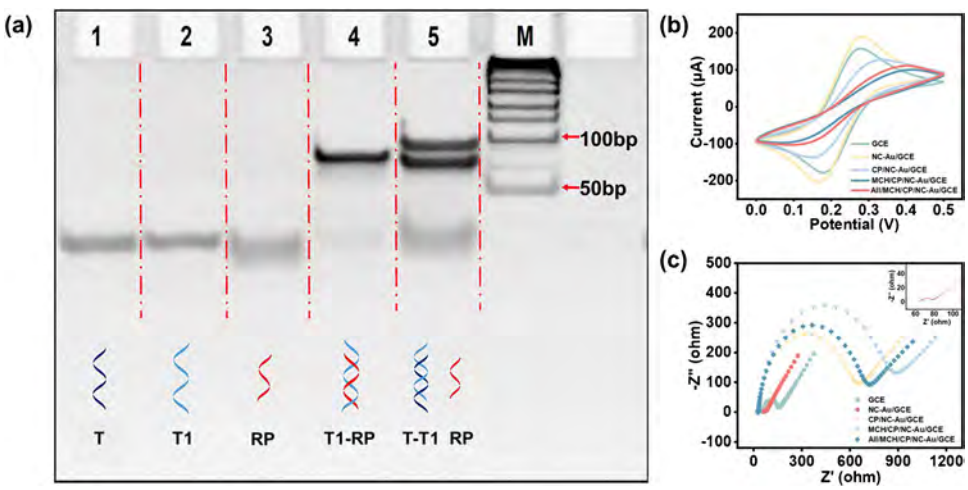


Fig. 3 **a** Polyacrylamide gel electrophoresis analysis of SDR process. Lane 1: T, lane 2: T1, lane 3: RP, lane 4: T1-RP, lane 5: T-T1/RP, M indicates the DNA markers for 50–500 bp. **b** CV curves, along with **c** Nyquist plots of the various stages of biosensor construction

hybridization of RP with CP allowed the enrichment of more signaling molecules on the electrode surface.

Construction of biosensor

Cyclic voltammetry (CV) and electrochemical impedance spectroscopy (EIS) were used to characterize the construction process of the sensing interface. As shown in Fig. 3b, NC-Au/GCE presented a pair of redox peaks with good reversibility, and its peak current was more significant than that of bare GCE. This indicates that NC-Au promotes electron transfer at the electrode interface and has good conductivity. When the sulfhydryl-modified CP was loaded onto the surface of the modified electrode, the transfer of the redox mediator to the electrode surface was inhibited due to the electrostatic repulsion between $[Fe(CN)_6]^{3-/4-}$ and the negatively charged phosphate backbone of DNA, so that the peak current of the CP/NC-Au/GCE was significantly reduced and the peak spacing significantly increased. Since MCH was electrochemically inert, when MCH was used to block the excess active sites on the electrode surface, the peak current of MCH/CP/NC-Au/GCE was further reduced. When the mixture of T1-RP/T was dropped on the electrode surface, the peak current of All/MCH/CP/NC-Au/GCE increased slightly. This may be due to the hybridization of MB-labelled RP with CP to form a double strand, resulting in decreased spatial site resistance of $[Fe(CN)_6]^{3-/4-}$. The above results all proved the successful construction of the sensing interface. In a typical impedance spectrum, the diameter of the semicircle at high frequency is related to the electron transfer resistance (Ret), which dominates the electron transfer of the redox probe on the sensing interface [31]. As shown in Fig. 3c, with the step-by-step modification of the electrode, Ret first increased and then decreased, which was consistent with the CV result and proved the successful construction of the biosensor.

Conditions optimization

CP's concentration, incubation time, hybridization time, and MCH blocking time were optimized to put the constructed biosensor in the optimal working state (Fig. S9a–d). After a series of experiments, CP with a concentration of 1 μM was selected for incubation for 100 min, the hybridization time was chosen as 120 min and the MCH blocking time was about 50 min. Detailed information can be obtained from S2.6.

Selectivity, short-term stability, and reproducibility of biosensor

In complex environmental samples, there are multiple interfering substances. Therefore, five common red tide algae (*Phaeocystis globosa*, *Prorocentrum donghaiense*, *Akashiwo sanguinea*, *Heterosigma akashiwo*, *Prorocentrum minimum*) were selected to evaluate the specificity of the biosensor. As shown in Fig. 4a, the current response of the interfering algal species was equivalent to the background value. In contrast, the current responses of the mixed and single *S. costatum* samples were significantly increased compared to the interfering samples ($P < 0.001$). This proves that the biosensor can accurately identify *S. costatum*. The excellent selectivity of the biosensor benefits from the particular gene fragments obtained through screening. In addition, the reproducibility of the biosensor was evaluated by comparing the measurement data between batches and within batches. As shown in Fig. 4b, the RSD within and between batches was calculated to be 4.48% and 1.80%, respectively. This indicates that the proposed biosensor has good reproducibility. Furthermore,

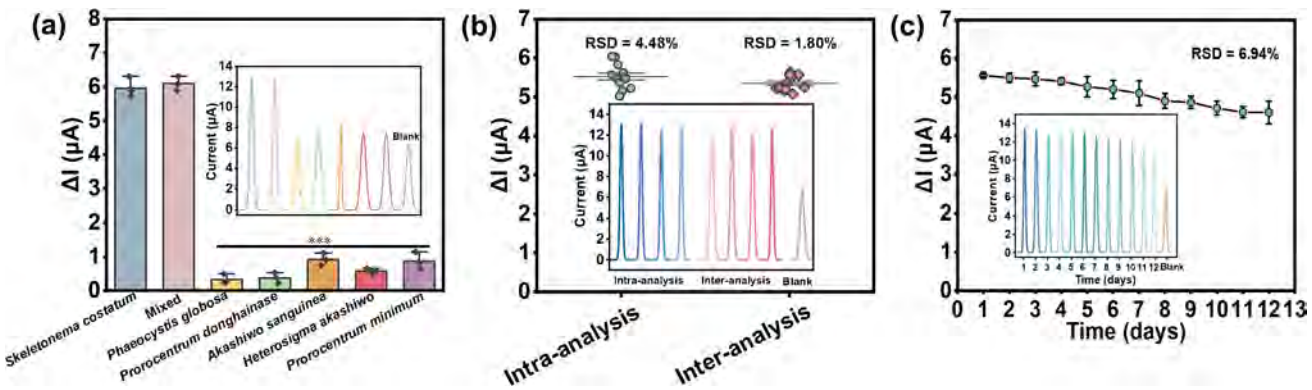


Fig. 4 **a** This sensing system can detect various interfering genomes. **b** The reproducibility of this sensing system (intra-analysis RSD = 4.48%, inter-analysis RSD = 1.80%), and **c** the short-term stability of this sensing system (RSD = 6.94%); ***: $P > 0.05$. The error bars represented the standard deviations ($n = 3$)

to enable the sensor to meet on-site testing requirements and provide valuable data for preliminary monitoring and assessment of red tides, we stored the fabricated biosensor at 4 °C and tested its stability. As shown in Fig. 4c, the relative standard deviation of the current signal was 6.94% within 12 days, demonstrating the short-term good stability of the biosensor.

Sensitivity of the biosensor

The sensitivity of the biosensor was evaluated by measuring the DPV response at different target DNA concentrations. As shown in Fig. 5a, the electrochemical signals gradually increased as the T concentration increased from 10 fM to 10 nM. This was because as the concentration of T increases, more RP is displaced to hybridize with CP, which in turn causes more MB to be enriched on the electrode surface. As shown in Fig. 5b, there is a linear relationship between the peak current of the electrochemical response and the logarithm of the concentration of T. The corresponding linear regression equation was $\triangle I = 20.301 + 2.287$ IgC, and the correlation coefficient R^2 was 0.987. Among them, ΔI was the peak current after deducting the background current of DPV, and lgC was the logarithm of the concentration of T. It was calculated that the LOD of this biosensor was 2.08 fM, and the LOQ was 5.97 fM (refer to S2.7 for the calculation formula), which indicated that the biosensor possessed good sensitivity. Moreover, the relatively high coefficient of determination R^2 ($R^2 = 0.987$) suggested that the signal response within the concentration range was closely related to the linear regression model, which was necessary for quantifying the response within this range. In addition, the spiked recovery method also proved the excellent accuracy of the biosensor (Table S1; recovery: 95.4–104.4%; RSD ≤ 1.4%).

Although the sensitivity of the biosensor has been verified, compared with the synthesized target DNA fragments, the detection performance of the biosensor for complex genomic samples is more important. Furthermore, the constructed biosensor must be portable to meet the requirements of on-site detection during red tide warnings. Therefore, a portable biosensor was constructed by stepwise modification of screen-printed electrodes, and *S. costatum* genomic DNA evaluated the performance of this portable biosensor. As shown in Fig. 6a, the peak current intensity of DPV gradually increases with the increase in genomic quality. In the range of genomic quality from 100 fg/μL to 10 ng/μL, there is an excellent linear relationship between the electrochemical response's peak current and the target genomic quality's logarithm.

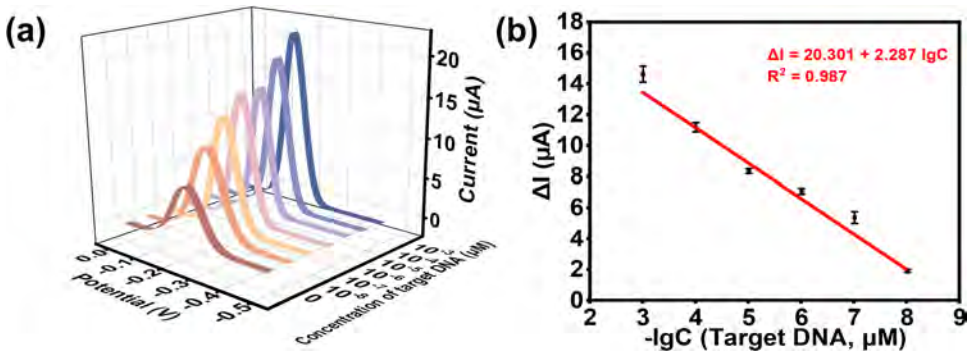


Fig. 5 **a** Representative DPV curves upon different concentrations of the target DNA. From bottom to top: blank (0 fM), 10 fM, 100 fM, 1 pM, 10 pM, 100 pM, and 1 nM. **b** A linear relationship between the electrochemical signal and concentration of the target DNA, accompanied by the corresponding regression equation (inset). The error bars represented the standard deviations ($n = 3$)

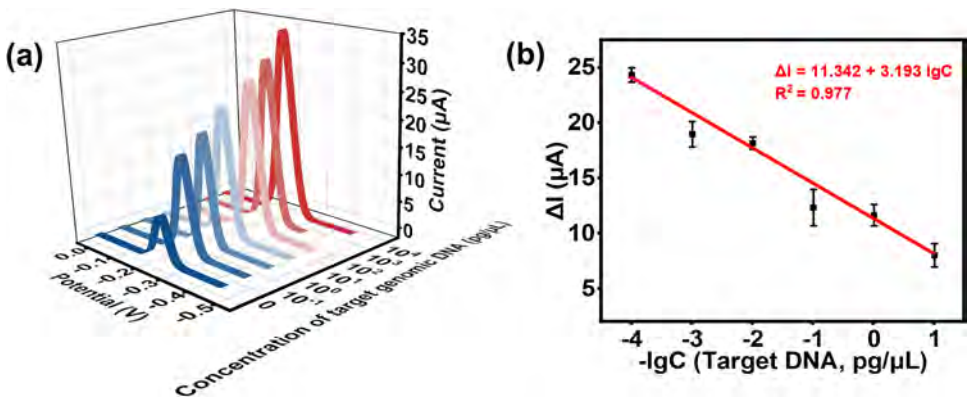


Fig. 6 **a** The biosensor measures the DPV response at different target genome masses. From bottom to top: blank (0 pg/μL), 100 fg/μL, 1 pg/μL, 10 pg/μL,100 pg/μL, 1 ng/μL, and 10 ng/μL. **b** A linear relationship between the electrochemical signal and concentration of the target DNA, accompanied by the corresponding regression equation (inset). The error bars represented the standard deviations ($n = 3$)

Table 2 Comparison of algae detection methods

Target sample	Detection method	Detection limit	Working range	References
Alexandrium minutum	I-t	2.478×10^{4} fM	0.12–1.0 nM	[32]
Aphanizomenon flos-aquae	CV and EIS	DIW: 81.2 fg /μL; Tap water: 9.99×10^{-3} fg/μL	10^{-1}–10^{3} ng/mL	[33]
Alexandrium minutum	EIS	3×10^{3} cells/L	5×10^{3}–10^{9} cells/L	[34]
Phaeocystis globosa	I-t	111.0 fM	150 fM–10 nM	[35]
Alexandrium minutum	DPV	69.1 fM	1×10^{-15}–1×10^{-5} M	[36]
Skeletonema costatum	DPV	33.43 fg/μL (831 cells/L; 2.08 fM)	100 fg/μL–10 ng/μL	This work

The linear equation was $\triangle I = 11.342 + 3.193$ IgC, and the correlation coefficient R^2 was 0.977 (Fig. 6b). The LOD and LOQ of this biosensor were calculated to be 33.43 fg/μL and 87.21 fg/μL (refer to S2.7 for the calculation formula), respectively. Compared with various methods for detecting algae, the proposed biosensor still has good sensitivity in the face of complex genomic samples while realizing miniaturization (Table 2).

The accuracy of the portable biosensor

The accuracy of the portable biosensor was evaluated by analyzing the culture samples from different life stages of *S. costatum*. As shown in Fig. 7a, we initially plotted the growth curve of *S. costatum* using the microscopic method and subsequently fitted it with OriginPro software (OriginLab Corporation). The growth stage was consistent with the BiHill function, and entered a stationary phase approximately the 8th day later and then a decline phase after the 11th day. Notably, the growth curve has no apparent slow growth period, which may be caused by the relatively high initial cell density of inoculation and sufficient nutrients in the culture medium. In addition, the growth curve obtained by measuring OD_{680} with an ultraviolet spectrophotometer was relatively consistent with this curve (Fig. S10). Subsequently, the samples mentioned above were analyzed using a portable biosensor. As illustrated in Fig. 7b, the curves plotted based on the current response of the portable biosensor exhibited a comparable trend to the growth curves. In addition, the quality of genomic DNA obtained by the portable biosensor was consistent with the results detected by the ultra-micro spectrophotometer (Fig. 7c). Since the individual counting method possesses a relatively high level of accuracy, it is frequently employed in the quantitative analysis of phytoplankton samples [13]. The cell density of *S. costatum* in 18-day samples was predicted by the current-algal density relationship curve (Fig. 7d) and compared with the results obtained by microscopic examination. As shown in Fig. 7e and f, the data obtained by the two methods are significantly correlated ($P = 0.979$). The results showed that the portable biosensor demonstrated consistent accuracy regardless of the stage of the *S. costatum* life cycle where the samples were taken.

Actual samples detection

The ability to detect *S. costatum* in a portable and accurate manner is crucial for the early warning of red tide outbreaks. This will enable those involved to take appropriate preventive measures more timely, thereby mitigating the damage. Since the growth and reproduction of *S. costatum* are affected by factors such as temperature and light, and historical data have shown that July and August in the Northern Hemisphere are the months with the highest incidence of red tides, these two months are thus the most important ones for monitoring. As shown in Fig. 8a, the samples were obtained by the research vessel in the adjacent waters of the Beibu Gulf, China, in July and August 2023. The information on the sampling points was reflected in Fig. 8b. To meet the on-site testing requirements, a portable electrochemical workstation was employed to measure the current signals of the sensor. Figure S11 showed the schematic diagram of the portable biosensing device test. The *S. costatum* DNA concentrations obtained using the portable biosensor were illustrated in Fig. 8c. The DNA concentrations of the two positive samples, S1 and S2, were not significantly different from the results of the ddPCR ($p > 0.05$). Furthermore, *S. costatum* was not detected in the remainder of the sea area. In addition, the calculated algal densities at site S1 and site S2 were 2.7×10^{5} cells/L and 0.38×10^{5} cells/L, respectively, indicating that the risk of *S. costatum* red tide was low in the current area (the benchmark concentration for red tide formation in Chinese inshore and the offshore regions is 1×10^{7} cells/L) (Fig. 8d). Although the number of samples subjected to analysis was relatively limited, the results demonstrate that the biosensor can quantitatively analyze *S. costatum* without needing a sophisticated instrument or the input of professional testing personnel.

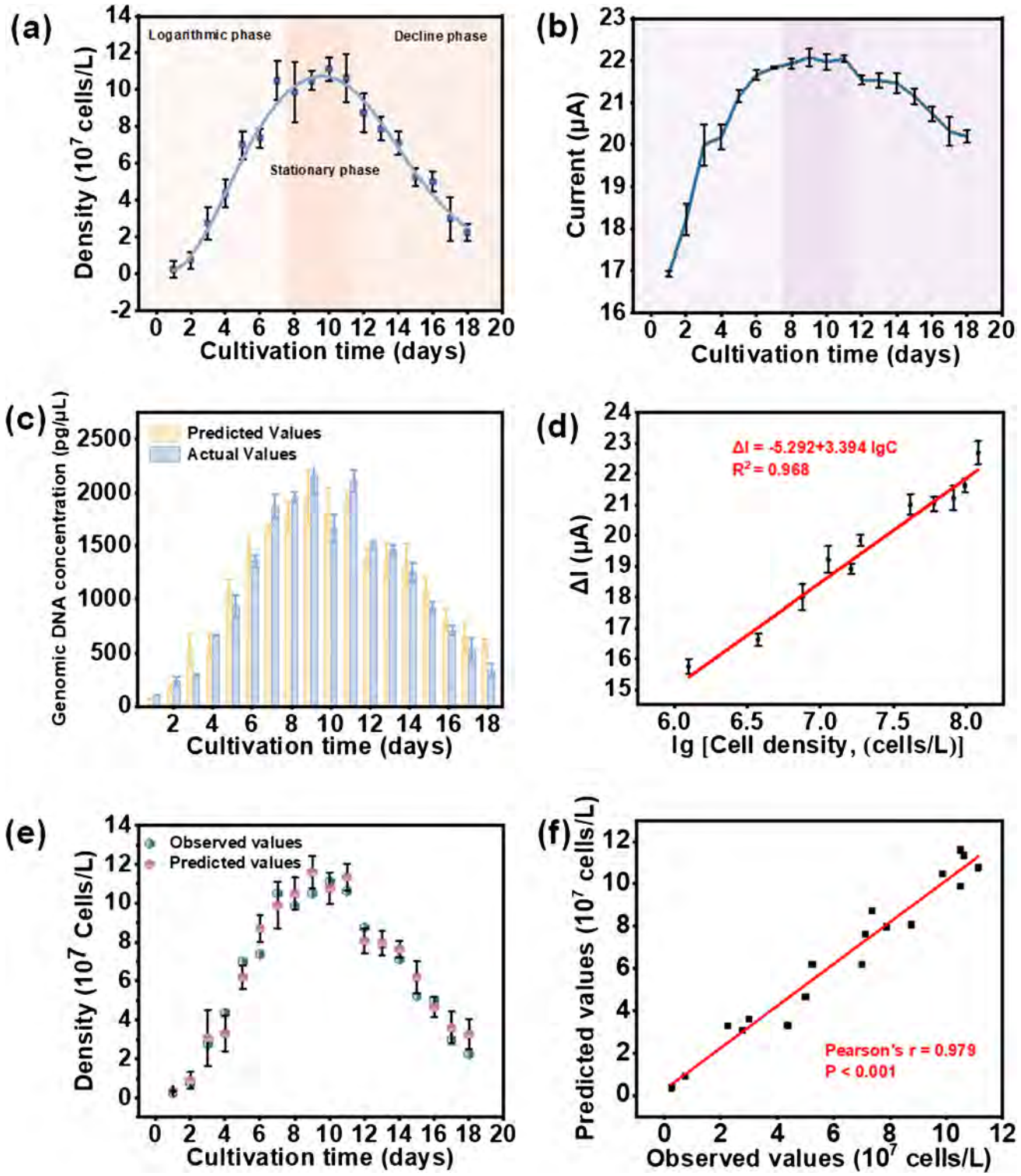


Fig. 7 **a** The density of algae was measured by microscopy, and the growth curve was drawn and fitted. **b** The sensor current response results draw the curve. **c** The quality of genomic DNA was measured by a portable biosensor and ultra-micro spectrophotometer, respectively. **d** Current-algal density relation curve. **e** The cell densities obtained by portable biosensors and microscopy, respectively, and **f** the correlation analysis of the results obtained by the two methods is performed ($P = 0.979$). The error bars represented the standard deviations ($n = 3$)

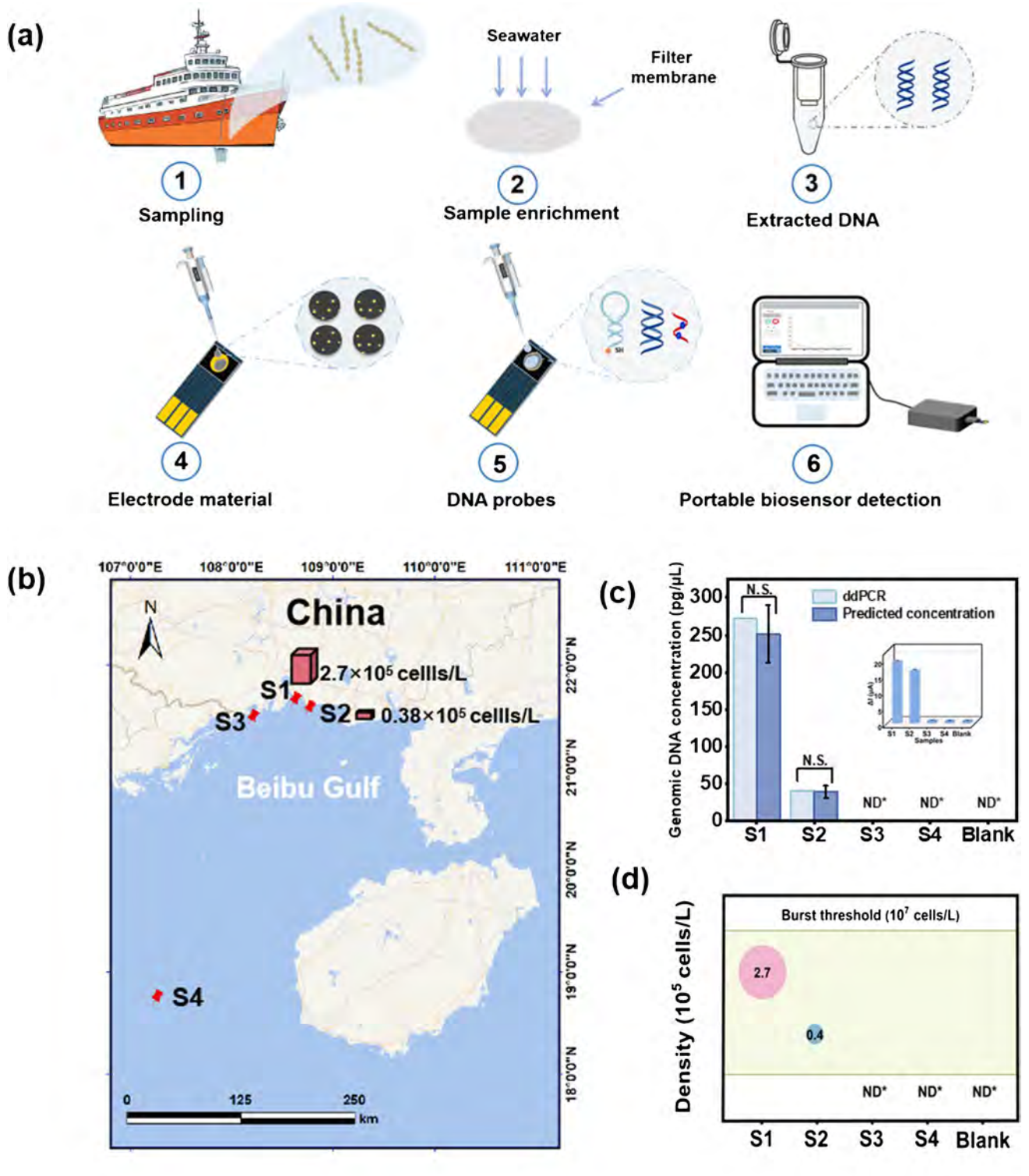


Fig. 8 **a** Schematic diagram of the process of on-site detection of *S. costatum* based on a portable device. **b** Information on the sampling sites. **c** The portable biosensor measured the current response of each site and the genomic DNA concentration of *S. costatum*, and the correlation analysis between the results and the ddPCR results showed no significant difference. **d** Cell density of *S. costatum* by portable biosensor. ND* means not detected. N.S. represents no significant difference. The error bars represented the standard deviations ($n = 3$)

Conclusion

In this study, an electrochemical biosensor for the detection of *S. costatum* was constructed to achieve an early warning of its red tide by combining NC-Au with excellent conductivity and the SDR. Benefiting from the sensitive response of NC-Au to the electrode response and the improvement of the hybridization efficiency on the electrode surface by the SDR, this biosensor showed good sensitivity. The LOD and LOQ of this biosensor were calculated as 33.43 fg/μL (or 831 cells/L) and 87.21 fg/μL (or 2112 cells/L), respectively. The LOQ was at least four thousand times lower than the baseline of the red tide outbreak threshold (10^7 cells/L). The high sensitivity of biosensors can shorten sample enrichment time and save the workforce. In addition, the excellent accuracy of the portable biosensor was proved by comparing the microscopic examination method and ddPCR ($p > 0.05$). More significantly, when analyzing water samples from the Beibu Gulf, China, the constructed portable biosensor successfully predicted a low risk of red tide outbreaks of *S. costatum*, and the results were in accordance with those obtained from ecological investigations. In conclusion, this biosensor can achieve sensitive and accurate detection of *S. costatum*. In the future, this biosensor is expected to provide a new idea for early warning of *S. costatum* red tide outbreaks.

Supplementary Information The online version contains supplementary material available at https://doi.org/10.1007/s00604-025-06966-9.

Acknowledgements This work was funded by the National Science Foundation of China (42090041, 42030502); Key Projects of Guangxi Natural Science Foundation (No. 2020GXNSFDA297015), China; Self-Topic Project of Guangxi Laboratory on the Study of Coral Reefs in the South China Sea, Nanning 530004, China (No. GXLSCRSCS2023102). In addition, we appreciate Prof. Kefu Yu for the assistance with the manuscript revision.

Author contributions Yaling Liu designed the experiments and initiated the experiments and writing of the manuscript. Yibo Zhang, Changrui Ye and Yayi He conducted literatures search, curated the graphs. Shaopeng Wang, Man Zhang and Hao Fu supplied constructive suggestions and the necessary funding. Shan Lu reviewed and investigation the study. Liwei Wang revised the manuscript. All authors contributed to reviewed the manuscript.

Funding This work was funded by the National Science Foundation of China (42090041, 42030502); Key Projects of Guangxi Natural Science Foundation (No. 2020GXNSFDA297015), China; Self-Topic Project of Guangxi Laboratory on the Study of Coral Reefs in the South China Sea, Nanning 530004, China (No. GXLSCRSCS2023102).

Data availability No datasets were generated or analysed during the current study.

Declarations

Ethical approval This study did not involve human or animal samples.

Competing interests The authors declare no competing interests.

References

1. Lee H-J, Shin M, Kim MS et al (2023) Removal of the red tide dinoflagellate Cochlodinium polykrikoides using chemical disinfectants. Water Res 242:120230. https://doi.org/10.1016/j.watres.2023.120230
2. Ji F, Sun Y, Yang Q (2023) Early warning of red tides using bacterial and eukaryotic communities in nearshore waters. Environ Res 216:114711. https://doi.org/10.1016/j.envres.2022.114711
3. Wei Y, Chen J, Wang M et al (2024) The double heterostructure photocatalyst MoS_2@ZIF-67/TiO_2: triumphant modification of TiO_2 and efficient removal of Karenia mikimotoi. Chem Eng J 479:147954. https://doi.org/10.1016/j.cej.2023.147954
4. Gao G, Fu Q, Beardall J et al (2019) Combination of ocean acidification and warming enhances the competitive advantage of Skeletonema costatum over a green tide alga Ulva linza. Harmful Algae 85:101698. https://doi.org/10.1016/j.hal.2019.101698
5. Wang H, Liu S, Xu Z et al (2023) Environmental light-activated nanozymes for efficient inactivation of harmful algae and associated hemolytic toxin. Chem Eng J 472:145029. https://doi.org/10.1016/j.cej.2023.145029
6. Yang J, Zhu Q, Chai J et al (2022) Development of environmentally friendly biological algicide and biochemical analysis of inhibitory effect of diatom Skeletonema costatum. Chin Chem Lett 33:1358–1364. https://doi.org/10.1016/j.cclet.2021.09.053
7. Qian J, Qian L, Pu N et al (2024) An intelligent early warning system for harmful algal blooms: harnessing the power of big data and deep learning. Environ Sci Technol 58:15607–15618. https://doi.org/10.1021/acs.est.3c03906
8. Xiao X, Peng Y, Zhang W et al (2024) Current status and prospects of algal bloom early warning technologies: a review. J Environ Manage 349:119510. https://doi.org/10.1016/j.jenvman.2023.119510
9. Liu F, Gaul L, Shu F et al (2022) Microscope-based light gradient generation for quantitative growth studies of photosynthetic micro-organisms. Lab Chip. https://doi.org/10.1039/d2lc00393g
10. Yu X, Yang JR, Chen J et al (2021) On the use of chemotaxonomy, a phytoplankton identification and quantification method based on pigment for quick surveys of subtropical reservoirs. Environ Sci Pollut Res 28:3544–3555. https://doi.org/10.1007/s11356-020-10704-4
11. Fasciotti M, Souza GHMF, Astarita G et al (2019) Investigating the potential of ion mobility-mass spectrometry for microalgae biomass characterization. Anal Chem 91:9266–9276. https://doi.org/10.1021/acs.analchem.9b02172
12. Wang J, Wang Y, Lai J et al (2023) Improvement and application of qPCR assay revealed new insight on early warning of Phaeocystis globosa bloom. Water Res 229:119439. https://doi.org/10.1016/j.watres.2022.119439
13. Zhang C, McIntosh KD, Sienkiewicz N et al (2023) Using cyanobacteria and other phytoplankton to assess trophic conditions: a qPCR-based, multi-year study in twelve large rivers across the United States. Water Res 235:119679. https://doi.org/10.1016/j.watres.2023.119679
14. Wu J, Liu H, Chen W et al (2023) Device integration of electrochemical biosensors. Nat Rev Bioeng 1:346–360. https://doi.org/10.1038/s44222-023-00032-w
15. Gong Q, Wang J, Guo Y et al (2024) A sandwich-type photoelectrochemical biosensor based on anthocyanin-sensitized ZnO/P5FIn heterojunction for the sensitive detection of CYFRA21-1. Microchim Acta 191:557. https://doi.org/10.1007/s00604-024-06636-2
16. Dong Z, Zhu X, Tang J et al (2024) An integrated smartphone-based electrochemical detection system for highly sensitive and

on-site detection of chemical oxygen demand by copper-cobalt bimetallic oxide-modified electrode. Microchim Acta 191:343. https://doi.org/10.1007/s00604-024-06399-w
17. Peng X-X, Guo T, Lu H et al (2020) Nanostructuring synergetic base-stacking effect: an enhanced versatile sandwich sensor enables ultrasensitive detection of microRNAs in blood. ACS Sens 5:2514–2522. https://doi.org/10.1021/acssensors.0c00772
18. Long J-B, Liu Y-X, Cao Q-F et al (2015) Sensitive and enzyme-free detection for single nucleotide polymorphism using microbead-assisted toehold-mediated strand displacement reaction. Chin Chem Lett 26:1031–1035. https://doi.org/10.1016/j.cclet.2015.05.036
19. Zhang Y, Xu G, Lian G et al (2020) Electrochemiluminescence biosensor for miRNA-21 based on toehold-mediated strand displacement amplification with $Ru(phen)_3^{2+}$ loaded DNA nanoclews as signal tags. Biosens Bioelectron 147:111789. https://doi.org/10.1016/j.bios.2019.111789
20. Liu F, Yang L, Yin X et al (2019) A facile homogeneous electrochemical biosensing strategy based on displacement reaction for intracellular and extracellular hydrogen peroxide detection. Biosens Bioelectron 141:111446. https://doi.org/10.1016/j.bios.2019.111446
21. Lu N, Pei H, Ge Z et al (2012) Charge transport within a three-dimensional DNA nanostructure framework. J Am Chem Soc 134:13148–13151. https://doi.org/10.1021/ja302447r
22. Xue H, Shi Y, Tian W et al (2024) Silver nanowires-based flexible gold electrode overcoming interior impedance of nanomaterial electrodes. Small 20:e2307328-n/a. https://doi.org/10.1002/smll.202307328
23. Xue X, Lou B, Wu C et al (2024) The impact of carbon material microstructure on li-ion storage behaviors of Si in Si/C anodes. Chem Eng J 488:150936. https://doi.org/10.1016/j.cej.2024.150936
24. Li Q, Zhao W, Zhai Z et al (2020) 2D/2D Bi_2MoO_6/g-C_3N_4 S-scheme heterojunction photocatalyst with enhanced visible-light activity by Au loading. J Mater Sci Technol 56:216–226. https://doi.org/10.1016/j.jmst.2020.03.038
25. Jalalah M, Han H, Nayak AK et al (2024) High-performance supercapacitor based on self-heteroatom-doped porous carbon electrodes fabricated from Mikania micrantha. Adv Compos Hybrid Mater 7:20. https://doi.org/10.1007/s42114-024-00833-6
26. Ayiania M, Weiss-Hortala E, Smith M et al (2020) Microstructural analysis of nitrogen-doped char by Raman spectroscopy: Raman shift analysis from first principles. Carbon 167:559–574. https://doi.org/10.1016/j.carbon.2020.05.055
27. Wang X, Xu Y, Liu X et al (2024) Delving into the dissimilarities in electrochemical performance and underlying mechanisms for sodium and potassium ion storage in N-doped carbon-encapsulated metallic Cu2Se nanocubes. J Energy Chem 95:336–347. https://doi.org/10.1016/j.jechem.2024.03.056
28. Medetalibeyoglu H, Kotan G, Atar N et al (2020) A novel and ultrasensitive sandwich-type electrochemical immunosensor based on delaminated MXene@AuNPs as signal amplification for prostate specific antigen (PSA) detection and immunosensor validation. Talanta 220:121403. https://doi.org/10.1016/j.talanta.2020.121403
29. Wang X, Wang W, Liu B et al (2023) Decrypting the electron-withdrawing effect of Au-decorated Bi_2O_3 for efficient CO_2-to-formate electroreduction. Small (Weinheim an der Bergstrasse, Germany) 19: n/a. https://doi.org/10.1002/smll.202304084
30. Du X, Zhang Z, Zheng X et al (2020) An electrochemical biosensor for the detection of epithelial-mesenchymal transition. Nat Commun 11:192–199. https://doi.org/10.1038/s41467-019-14037-w
31. Wang W, Gao Y, Wang W et al (2022) Ultrasensitive electrochemical detection of cancer-related point mutations based on surface-initiated three-dimensionally self-assembled DNA nanostructures from only two palindromic probes. Anal Chem 94:1029–1036. https://doi.org/10.1021/acs.analchem.1c03991
32. Morais SL, Barros P, Santos M et al (2021) Electrochemical genosensor for the detection of Alexandrium minutum dinoflagellates. Talanta 222:121416. https://doi.org/10.1016/j.talanta.2020.121416
33. Seo Y, Yoon Y, Lee M et al (2023) Rapid electrochemical biosensor composed of DNA probe/iridium nanoparticle bilayer for Aphanizomenon flos-aquae detection in fresh water. Colloids Surf B 225:113218. https://doi.org/10.1016/j.colsurfb.2023.113218
34. Oloketuyi S, Mazzega E, Zavašnik J et al (2020) Electrochemical immunosensor functionalized with nanobodies for the detection of the toxic microalgae Alexandrium minutum using glassy carbon electrode modified with gold nanoparticles. Biosens Bioelectron 154:112052. https://doi.org/10.1016/j.bios.2020.112052
35. Zhang T, Zhang C, Chen Y et al (2024) Rapid monitoring and early warning of Phaeocystis globosa bloom based on an effective electrochemical biosensor. Biochem Eng J 210:109444. https://doi.org/10.1016/j.bej.2024.109444
36 Zakariah EI, Ariffin EY, Nokarajoo D et al (2024) Highly sensitive of an electrochemical DNA biosensor detection towards toxic dinoflagellates Alexandrium minutum (A. minutum). Microchem J 199:109997. https://doi.org/10.1016/j.microc.2024.109997

Publisher's Note Springer Nature remains neutral with regard to jurisdictional claims in published maps and institutional affiliations.

Springer Nature or its licensor (e.g. a society or other partner) holds exclusive rights to this article under a publishing agreement with the author(s) or other rightsholder(s); author self-archiving of the accepted manuscript version of this article is solely governed by the terms of such publishing agreement and applicable law.

Journal of Water Process Engineering 69 (2025) 106756

Contents lists available at ScienceDirect

Journal of Water Process Engineering

journal homepage: www.elsevier.com/locate/jwpe

Comparison of UV based advanced oxidation processes (UV/H_2O_2, UV/NaClO, and UV/$Na_2S_2O_8$) for inactivating *Uronema marinum* in marine water

Xuan Chen, Pin Gan, Kunling Huang, Fangyu Liang, Tianhao Wu, Xudong Li, Yuanyuan Zhang *

Guangxi Laboratory on the Study of Coral Reefs in the South China Sea, Coral Reef Research Center of China, School of Marine Sciences, Guangxi University, Nanning 530004, China

ARTICLE INFO

Editor: Xiaying Xin

Keywords:
UV-AOPs
Uronema marinum
Marine water
Genetic information process
Cellular metabolism

ABSTRACT

The transmission of microorganisms via ballast water poses a potential threat of biological invasion, usually neglecting protozoa like *Uronema marinum* (*U. marinum*). This study inactivated *U. marinum* in seawater using UV based advanced oxidation processes (UV-AOPs) with 148.32 mJ·cm^{-2} UV dose and 10 μM oxidant. UV/Peroxydisulfate (1.29 log), UV/Hydrogen peroxide (1.08 log), and UV/Chlorine (1.05 log) significantly enhanced the UV (0.68 log) inactivation of *U. marinum*. Radical probe methods and radical quenching experiments indicate that the diverse radicals generated in UV-AOPs promote inactivation. Changes in extracellular DNA, K^+ concentration, and extracellular organic matter (EOM) fluorescence indicate that radicals act as global oxidants, exacerbating membrane damage and promoting DNA and intracellular substances release. Gene expression analysis reveals that RNA transcription is affected by UV/PDS and UV/H_2O_2, while UV/NaClO targets protein translation. In cellular metabolism, lipid metabolism is affected by UV/H_2O_2, whereas amino acid metabolism is affected by UV/NaClO and UV/PDS. Compared to UV/NaClO, metabolic pathways related to carbohydrates and energy are affected by UV/PDS. Equivalent THMs production of UV-AOPs, but more HAAs are generated in UV/NaClO process, likely linked to RCS concentration. UV/PDS is the most cost-efficient UV-AOPs based on electrical energy per order (EE/O).

1. Introduction

Global trade propels ocean transportation, as nearly 90 % of trade relying on maritime means [1]. Ballast water plays a crucial role in maintaining ship stability during loading and unloading, containing a diverse myriad of microorganisms like bacteria, zooplankton, and phytoplankton [2]. Tens of thousands of species are transferred through ballast water every hour, inadvertently introducing toxic and harmful aquatic organisms into new ecosystems, making ballast water as the main carrier of invasive species [3]. Addressing this, the International Ballast Water Management Convention, established by the International Maritime Organization (IMO) in 2004, mandates ballast water treatment following D-2 discharge limits (IMO, 2004). Thus, it is imperative to develop efficient, economical, and environmentally friendly disinfection technologies for ballast waters and harmful marine microorganisms.

Approximately 57 Ballast Water Treatment Systems (BWTS) have been approved and/or are commercially available, with methods related to UV constituting approximately 48 % of these systems [4]. Its efficacy lies in disrupting the genetic material (DNA/RNA) of microorganisms, allowing for effective Inactivation [5]. Compare to chemical disinfection processes, UV treatment has a lower propensity to generate toxic chemical disinfection by-products (DBPs) [6]. However, research has showed that specific microorganisms, such as dinoflagellates, diatoms and ballast water microbiological indicators *Enterococcus faecalis* (*E. faecalis*), demonstrate resistance to UV [7,8]. Furthermore, the effectiveness of UV disinfection is influenced by factors such as water quality turbidity, the presence of reflective or absorptive substances, salinity, and the concentration of dissolved organic matter (DOM) concentration [9].

Advanced oxidation processes (AOPs) are the process in which oxidants are activated to produce radicals with potent oxidation capabilities, and generate free radical chain reactions. Presently, research on

* Corresponding author.
E-mail address: yyzhang@gxu.edu.cn (Y. Zhang).

https://doi.org/10.1016/j.jwpe.2024.106756
Received 6 August 2024; Received in revised form 20 October 2024; Accepted 6 December 2024
Available online 13 December 2024
2214-7144/© 2024 Elsevier Ltd. All rights are reserved, including those for text and data mining, AI training, and similar technologies.

AOPs for ballast water treatment mainly includes electrochemical oxidation, photochemical oxidation, ozone oxidation, and ultrasonic oxidation [4]. UV-AOPs are easy to operate, and the low COD in seawater consumes less radicals. Therefore, UV-AOPs can effectively act on microorganisms in seawater [10,11]. This holds significant implications for integrating suitable ballast water technology. UV-AOPs (e.g., UV/PDS, UV/H_2O_2, UV/NaClO) surpass traditional disinfection methods in inactivating harmful microorganisms due to the generation of potent free radicals, such as sulfate radical ($\bullet SO_4^-$, $E^0 = 2.80$ V), hydroxyl radical ($\bullet$OH, $E^0 = 2.90$ V), chlorine radicals (RCS, e.g., $\bullet$Cl, $E^0 = 2.47$ V, $\bullet Cl_2^-$, $E^0 = 2.0$ V and $\bullet$ClO, $E^0 = 1.5$–1.8 V) [12]. Numerous studies have assessed UV-AOPs for disinfection. Moreno-Andres et al. reported that the D4 parameters of UV and UV/H_2O_2 (5 mg·L^{-1} H_2O_2) for inactivating *E. faecalis* in seawater were 24.64 mJ·cm^{-2} and 18.72 mJ·cm^{-2}, respectively, indicating that UV/H_2O_2 treatment significantly reduced UV dose [7]. Wen et al. used a combination of UVC-LED (265, 280 nm) and chlorine (0.6, 0.8 and 1 mg·L^{-1}) to inactivate *Tetraselmis* sp. in seawater. The results showed that the inactivation effect of the combined treatment was significantly greater than that of 400 mJ·cm^{-2} UV-LED alone or chlorine alone [13]. Our previous research demonstrated that activating PDS (0.1 mM) with UV-C (254 nm) increases *E. coli* inactivation by 2.28 s log and *Streptococcus agalactiae* (*S. agalactiae*) inactivation by 2.52 logs in seawater compared to UV treatment at 3.6 mJ·cm^{-2} [14]. Although many studies have evaluated the effectiveness and mechanisms of microbial inactivation, most of them focus on the inactivation in a single AOP. The comparative studies of UV/PDS, UV/H_2O_2, and UV/NaClO mainly focus on the degradation of pollutants such as benzopenone-8, dexamethasone, metronidazole [15–17]. To our best knowledge, the detailed comparative study of the inactivation effect and mechanism of microorganism in seawater in three commonly used UV-AOPs processes has not been investigated yet. Comparative research on microbial inactivation under various AOPs can help broaden our understanding of AOPs and microbial inactivation mechanism, and potentially provide more valuable insights.

In UV-AOPs processes, the process and impact of radical generation may be influenced by various factors, including the concentration, salinity, and pH of the starting substrates [7]. Several studies have indicated that the formation of potentially harmful disinfection by-products (DBPs) is influenced by factors such as halides, carbonates, NOM (non-biodegradable organic matter), and water pH [18]. For instance, chlorine would unexpectedly react with the organic matter in the water to produce various DBPs [19]. Notably, trihalomethanes (THMs) and haloacetic acids (HAAs) have been consistently detected in significant quantities across various ballast water treatment systems, as reported by Moreno-Andrés et al. [20]. Therefore, when inactivating harmful microorganisms in ballast water, it is important to compare diverse aspects, such as process performance and the generation of DBPs.

In comparison to harmful bacteria, fungi, algae and other microorganisms in seawater, marine protozoa have received limited attention. For instance, *Uronema marinum* (*U. marinum*), a prevalent marine single-celled organism measuring approximately 20–30 × 5–10 μm in size, primarily relies on asexual reproductive processes, and serves as a pathogenic parasite causing systemic scuticociliatosis in various marine fish species. The *U. marinum* are distributed worldwide and commonly found in a variety of habitats (e.g., seawater, sediment), especially in polluted waters. As a pathogenic parasite, *U. marinum* invade the surface, skin, fin, and muscle of fishes, as well as their abdominal cavity, kidney, pancreas, causing blackening of fish body color, bleeding of tissue and organs, ulcers, and other pathological changes, ultimately leading to the death of fish [21]. *U. marinum* causes systemic scuticociliatosis in various marine fish species, such as olive flounder (*Paralichthys olivaceus*), New Zealand groper (*Polyprion oxygeneios*), Atlantic salmon (*Salmo salar*), kelp grouper (*Epinephelus bruneus*), black rockfish (*Sebastes schlegelii*), and turbot (*Scophthalmus maximus*) [22]. Due to its highly infectivity, the outbreak of *U. marinum* can lead to significant mortalities and economic losses in farmed marine fish. Additionally, it has been detected in ballast water [22–24]. As stipulated by the D-2 ballast water discharge standard, the concentration of viable organisms with a size of 10–50 μm should be <10 per milliliter (IMO, 2004). And so far, the inactivation mechanism of microorganism has predominantly focus on the changes at the cellular level such as intracellular substances and cellular structures. Further research on the molecular level changes such as changes in microbial gene expression through molecular biology techniques has gradually received attention [25].

In this study, we investigate the inactivation of *U. marinum* vegetative cells by different UV-AOPs (UV/PDS, UV/H_2O_2, and UV/NaClO) in seawater, and the contributions of different reactive species to the inactivation of *U. marinum*. We monitor changes in morphology, the release of intracellular contents, and expression of differentially expressed genes (DEGs) to understand the inactivation process of *U. marinum* by different UV-AOPs. Furthermore, considering the potential environmental impact of active substances in ballast water treatment, it is essential to assess their potential toxic effects. Ultimately, we conducted a preliminary energy consumption analysis on three UV-AOPs inactivated *U. marinum* to compare their economic costs.

2. Materials and methods

2.1. Chemicals

All chemicals used in the experiments were of analytical grade, the details of chemical compounds and natural water are available in supplementary information (SI) Text S1.

2.2. Microbial surrogates

U. marinum was selected as representative surrogate of ciliate pathogenic protozoa, which was obtained from Institute of Hydrobiology, Chinese Academy of Sciences. A detailed description of *U. marinum* 's morphology is available in Text S2. Perform clone culture in a laboratory environment. Single individuals were isolated from the original population by capillary pipette and the clean single cell was reared in a Petrie dish with seawater.

U. marinum was cultured and maintained in seawater (temperature = 37 °C, salinity = 35 ‰; pH = 8.2) containing *Escherichia coli* (*E. coli*) and wheat grains, because bacteria served as the sustenance for *U. marinum*, and wheat grains provide nutrients for the growth of *E. coli* [26,27]. Synthetic seawater (SW) was prepared by dissolving sea salt, with the concentration of anions outlined in Table S1 [7].

2.3. Experimental procedures

A low-pressure mercury lamp (10 W) emitting light predominantly at 254 nm was designed for quasi-collimated beam in the photo-reactor, as shown in Fig. S1. The UV fluence rate (Ep^0) was determined as 1.24 mW·cm^{-2} by using the KI/KIO_3 actinometer, as detailed in Text S3 and Fig. S2 [28]. The UV dose (mJ·cm^{-2}) is calculated by Eq. (1).

$$\text{UV dose} = \text{UV Intensity} \times \text{Time} \quad (1)$$

where the intensity is the UV light intensity (mW·cm^{-2}), and time is the exposure time (s). The UV lamp was warmed up at least 20 min before the photolysis experiment to obtain stable irradiation. Centrifuge the *U. marinum* solution containing culture medium at 3000 rpm for 5 min, and discard the supernatant to remove the culture medium. Then suspended the cells that remain at the bottom in sterilized seawater with a salinity of 35 ‰ and pH of 8 that is representative of typical ballast water, aiming for a target concentration of 5000 cells·mL^{-1}. 20 mL *U. marinum* nutrient cells suspension was placed in a quartz reaction tube (diameter 2.5 cm, length 18 cm) for the Inactivation experiment. In accordance with previous investigations, the application of 10 μM of

PDS can significantly enhance the UV inactivation of *U. marinum* in seawater (Fig. S3) [12]. Oxidants (PDS, H_2O_2, NaClO) were added to achieve the same concentration (10 μM) in three systems, thereby facilitating uniformity for comparison. Collect the samples (0.1 mL) at the same time interval and add 0.1 mL of 0.4 % trypan blue solution to the sample, then dilute the sample with sterilized seawater to 1 mL. Live cells possess intact cell membranes that exclude the dye, while dead cells with compromised membranes take up the dye, appearing blue under a microscope. The density of living cell was determined based on the motility of live cells and their exclusion of TrypanBlue under a biological microscope (BX53F, Olympus) [29]. Inactivation rates of microorganisms were calculated by Eq. (2), The disinfection kinetic of *U. marinum* in UV-AOPs system was assessed by a Pseudo-first-order kinetic model.

$$S = log\left(\frac{N_0}{N_t}\right) = kt \tag{2}$$

where N_0 and N_t are the cell density (cells·mL^{-1}) before and after the inactivation processes, respectively; k is the Pseudo-first-order rate constant (s^{-1}); t is the experimental time (s). And the UV_{254} of the sample was measured with a UV spectrophotometer. To quantify the synergistic effect by coupling the oxidation process with the photolysis, the synergy factor was measured in Eq. (3) [30].

$$F_S = \frac{k_{uv/oxidant}}{k_{uv} + k_{oxidant}} \tag{3}$$

k_{uv} and $k_{oxidant}$ represent the Pseudo-first-order rate constants for UV and oxidant, respectively. The absorption spectrum of 1 mM oxidants solution(PDS, H_2O_2, NaClO) were measured by using a UV spectrophotometer (7500Fast, Thermo scientific, USA) at wavelengths of 254 nm.

Evaluate the contribution of free radicals by comparing microbial inactivation rates. The steady-state concentration of ROS in UV/PDS, UV/H_2O_2, or UV/NaClO conditions was determined through probe-based kinetic experiments. Nitrobenzene (NB), benzoic acid (BA), and 1, 4-dimethoxybenzene (DMOB) and anisole (AS) (5 μM) for quantifying •OH, $•SO_4^-$, •Cl, and •ClO, respectively, the details shown in Text S4 [16,18]. To evaluate the contribution of reactive species in the UV-AOPs system, scavenger methanol (MA: oxidant =10:1) was utilized to scavenge •OH and $•SO_4^-$, tert-butanol (TBA: oxidant =10:1) was employed as •OH and •Cl scavenger, NB (NB: oxidant =10:1) was employed as •OH scavenger [31].

2.4. Disinfection mechanisms experiments

Extracellular DNA (eDNA) of *U. marinum* was measured by spectrometry. In brief, *U. marinum* suspensions were centrifuged for 10 min at 8000 rpm, then the absorbance of supernatant was measured using a micro-spectrophotometer (VL0L00D0, Thermo Scientific, USA) [32]. 10 mL sample was centrifuged and the supernatant was filtered through 0.45 μm syringe filter, then the concentration of K^+ was measured by an Inductively Coupled Plasma Atomic Emitted Spectrometer (ICAP7400, Thermo Fisher, USA). Excitation emission matrix spectra (EEM) of *U. marinum* extracellular organic compounds (EOM) were determined by a three-dimensional fluorescence spectrometer (F-4700FL, Hitachi, Japan) [33].

In transcriptomics analysis, total RNA was extracted from samples [34]. Concentration and purity of the extracted RNA using Nanodrop2000. RNA quality was checked using RNase free agarose gel electrophoresis and assessed on an Agilent 2100 Bioanalyzer (Agilent Technologies, Palo Alto, CA, USA). After total RNA was extracted, eukaryotic mRNA was enriched by Oligo (dT) beads. Then the enriched mRNA was fragmented into short fragments using fragmentation buffer and reverse transcribed into cDNA with random hexamers. Second-strand cDNA was synthesized by DNA polymerase I, RNase H, dNTP and buffer. Then the cDNA fragments were purified with QiaQuick PCR extraction kit (Qiagen, Venlo, The Netherlands), end repaired, A base added, and ligated to Illumina sequencing adapters. The ligation products were size selected by agarose gel electrophoresis, PCR amplified, and sequenced using Illumina novaseq 6000. To get high quality clean reads, reads were further filtered by fastp [35]. Transcriptome denovo assembly was carried out with short reads assembling program–Trinity [36]. All transcripts obtained from this transcriptome sequencing were compared with six databases (NR, Swiss-Prot, Pfam, COG, GO and KEGG databases) to obtain annotation information in each database and to compile statistics on the annotation status of each database.

2.5. Disinfection by-products experiments

To evaluate the concentration of organic byproducts formed in three AOPs, THM and HAA were extracted by liquid/liquid extraction with methyl tert-butyl ether (MtBE), and then measured by using a gas chromatography–mass spectrometry (GC, 7890B—7000D, Agilent, USA) [18].

2.6. Electrical energy efficiency

The Electrical Energy per Order (EE/O) was provided a cost-effective evaluation for systems. EE/O (kW·h·m^{-3}) is defined as the electrical energy required to decompose pollutants in 1 m^3 of polluted water, which can be calculated by eqs. (4–7) [37].

$$EE/O_{total} = EE/O_{UV} + EE/O_{Oxidant} \tag{4}$$

$$EE \Big/ O_{UV} = \frac{P \times t \times 1000}{V \times 60 \times log\left(\frac{N_0}{N_t}\right)} \tag{5}$$

$$EE \Big/ O_{Oxidant} = Eq_{Oxidant} \times \frac{[Oxidant] \times 1000}{log\left(\frac{N_0}{N_t}\right)} \tag{6}$$

$$Eq_{Oxidant} = \frac{Price \times Mass}{10^6 \times Puritty \times EC} \tag{7}$$

where P represents lamp input power (i.e., 0.01 kW); V is the volume of the polluted water (i.e., 0.16 L); t is the irradiation time (i.e., 2 min); [oxidant] means the dosages of oxidant (i.e.,10^{-5} M); log (N_0/N_t) are the logarithm of the initial and final concentrations of *U. marinum*; $Eq_{oxidant}$ is the equivalent electrical energy consumption created per mole of oxidantis (Eq_{NaClO} = 0.479 kW·h·mol^{-1}, EqH_2O_2 = 0.074 kW·h·mol^{-1}, Eq_{PDS} = 0.208 kW·h·mol^{-1} [16].

2.7. Statistical analysis

To ensure reproducibility, all experiments were performed at least three times, and the standard deviation of the determinations was <5 %. Data statistical analysis was performed using SPSS 27.0 and Origin 2022 software. The inactivation kinetics were fitted by a linear fitting using the least-squares method in Origin. Statistically significant differences between independent groups were assessed through one-way analysis of variance (ANOVA). A significance level of 0.05 ($p < 0.05$) was considered as the threshold for determining statistical significance.

3. Result and discussion

3.1. Inactivation of U. Marinum with different UV-AOPs

The initial experiments focused on evaluating the effectiveness of *U. marinum* inactivation using various treatments, including UV at an intensity of 1.24 mW·cm^{-2} and three UV-AOPs (UV/H_2O_2, UV/PDS, and UV/NaClO) with same oxidant concentration (10 μM) in artificial

seawater. As shown in Fig. 1(a), the inactivation of *U. marinum* in the UV/PDS, UV/H_2O_2 and UV/NaClO (1.29 log, 1.08 log, and 1.05 log) was significantly higher than that in UV alone (0.68 log) with the 148.32 mJ·cm^{-2} UV dose. And *U. marinum* exhibited negligible inactivation when exposed to a single oxidant in seawater. UV-AOPs demonstrated robust inactivation capabilities attributable to the generation of radicals with strong oxidizing ability. •OH, •OH and •SO_4^-, •OH and •Cl were primarily produced in UV/H_2O_2, UV/PDS, and UV/NaClO processes, respectively, as indicated by eqs. (8–14).

$$S_2O_8^{2-} \xrightarrow{hv} 2 \bullet SO_4^- \quad (8)$$

$$\bullet SO_4^- + OH^- \rightarrow \bullet OH + SO_4^{2-} \quad (9)$$

$$H_2O_2 \xrightarrow{hv} 2 \bullet OH \quad (10)$$

$$OCl^- \xrightarrow{hv} \bullet OH + \bullet Cl \quad (11)$$

$$OCl^- + \bullet OH \rightarrow OH^- + \bullet ClO \quad (12)$$

$$\bullet Cl + OCl^- \rightarrow Cl^- + \bullet ClO \quad (13)$$

$$\bullet Cl + Cl^- \rightarrow \bullet Cl_2^- \quad (14)$$

The consumption of oxidants as shown in Fig. S4. Previous research has confirmed the effectiveness of UV/PDS for *U. marinum* inactivation due to the generation of •OH and •SO_4^- [12]. The inactivation kinetics of MS2 bacteriophage under UV/H_2O_2 treatment indicated an 11–15-fold increase in saltwater [38]. Moreover, Wen et al. demonstrated that UV-LED/chlorine treatments were more effective in inactivating *Tetraselmis* sp. than UV in seawater, underscoring the significant contributions of •OH or RCS [13]. The *k* for different processes follows the order: UV/PDS (8.47 × 10^{-3} s^{-1}) > UV/H_2O_2 (7.55 × 10^{-3} s^{-1}) > UV/NaClO (7.04 × 10^{-3} s^{-1}) > UV (4.68 × 10^{-4} s^{-1}). The variation in inactivation efficacy among these processes under the same conditions, such as UV wavelength and water composition, is attributed to the distinct types of radicals generated. It is widely accepted that •OH exhibits non-selective reactivity, while RCS (•Cl, •Cl_2^- and •ClO) are selective towards certain pollutants compared to •OH, and •SO_4^- also has strong oxidation selectivity, all of which have been proven to effectively inactivate microorganisms [33]. However, our results show that UV/H_2O_2 is more effective than UV/chlorine in inactivating *U. marinum*, which may be due to the lower selectivity of RCS towards *U. marinum*. Romero-Martínez et al. reported that the inactivation of *Tetraselmis suecica* under UV/peroxymonosulfate (UV/PMS) in ballast water was lower than under UV/H_2O_2 with 10 ppm oxidant [39]. However, compared to UV-LED/H_2O_2 (0.29 mM), UV-LED/PMS (0.008 mM) more effectively damages *Vibrio alginolyticus* under UV-C (λ_{max} = 275 nm, 0.39 ± 0.04 W·m^{-2}) conditions [40]. The inactivation efficacy of microbial in different processes may be attributed to species specific structural differences and the radicals generated by oxidation systems under different conditions. Therefore, it is important to choose the appropriate inactivation process based on the pathogen. Considering the complex composition of real marine water matrix, inactivation experiments of *U. marinum* in real marine water were studied. As shown in Fig. S5, the dynamic kinetics of *U. marinum* inactivation in the real marine water showed similar trend in the synthetic marine water. The inactivation of *U. marinum* in real marine water by UV, UV/H_2O_2, UV/NaClO, and UV/$Na_2S_2O_8$ treatments at 120 s were 0.32-log, 0.56-log, 0.50-log, and 1.10-log. The decrease in deactivation efficiency may be due to the competitive oxidation of organic matter in real seawater, as the TOC of real seawater (649 mg·L^{-1}) is higher than that of artificial seawater (240 mg·L^{-1}) (Table S2). The results indicate that different processes exhibit the same trend of inactivation in synthetic seawater and real seawater. Therefore, synthetic seawater prepared based on real seawater components can simulate real seawater, and the research conducted in the synthetic marine water matrix can represent the *U. marinum* inactivation in the real marine water matrix.

Fig. 1(b) shows the quantification of the relationship and synergistic effects between UV dose and inactivation. The value of *k* in UV, UV/H_2O_2, UV/NaClO, and UV/PDS were 4.74 × 10^{-4}, 7.55 × 10^{-3}, 7.23 × 10^{-3}, and 8.47 × 10^{-3} cm^2·mJ^{-1}, respectively. The *k* for the inactivation of *Tetraselmis suecica* by UV was found to be 0.010 ± 0.001 cm^2·mJ^{-1}, with an initial concentration of 7.27 × 10^4 cells·mL^{-1} [39]. The values of *k* for the inactivation of *E. coli* by UVC was 1.14 cm^2·mJ^{-1}, with an average initial concentration of 10^6 CFU·mL^{-1} [41]. These results suggest that *U. marinum* is less susceptible to UV inactivation compared to *Tetraselmis suecica* and *E. coli*. The overall inactivation of *U. marinum* can be attributed to the contributions of reactive radicals ($k_{radicals}$), UV irradiation (k_{UV}) and influence of oxidant ($k_{oxidant}$), respectively. The synergistic effect (Fs) of UV/H_2O_2, UV/NaClO, and UV/PDS are 1.42, 1.35 and 1.70, indicating a synergistic effect in UV-AOPs and the feasibility of the oxidant concentration. In addition, after treatment with UV, UV/PDS, UV/H_2O_2, and UV/NaClO for 120 s, the absorbance at 254 significantly decreased by 11.36 %, 21.46 %, 17.93 %, and 17.68 %, respectively (Fig. S6), indicating that the organic matter in the solution has been partially removed. The reduction of organic matter in the solution can increase the transmittance of UV, thereby further promoting

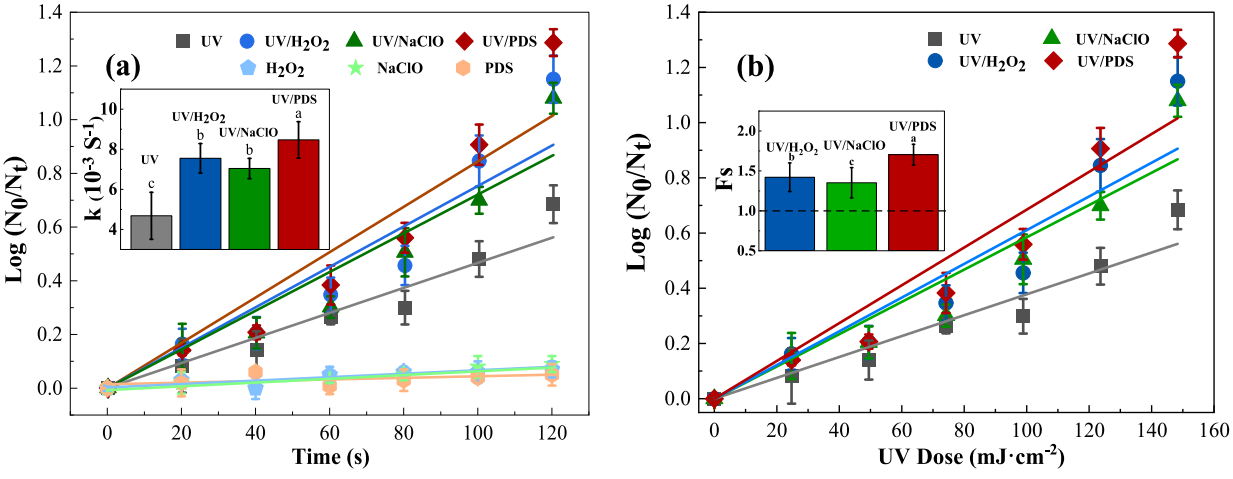


Fig. 1. **(a)** Comparison of UV alone and UV- AOPs for *U. marinum* inactivation in seawater, the insert shows the inactivation kinetics of different processes; **(b)** The relationship between the inactivation efficiency of *U. marinum* and UV dose, and the synergistic factor (inserted figure). (Experimental conditions: [*U. marinum*]$_0$ = 5000 cell·mL^{-1}, UV intensity = 1.24 mW·cm^{-2}, [H_2O_2]$_0$ = [PDS]$_0$ = [NaClO]$_0$ = 10 μM, pH = 8.2, *T* = 25 ± 2 °C).

the inactivation of microorganism. The synergistic inactivation of UV-AOPs on *U. marinum* may be linked to factors such as radical yield, steady-state free radical concentration, and the reactivity and selectivity of free radicals towards *U. marinum* [32]. As illustrated in Fig. S7, PDS exhibits a higher molar absorption coefficient under UV irradiation, making it easier to activate under UV_{254} compared to NaClO and H_2O_2. To elucidate which radicals are responsible for microbial inactivation, further studies were conducted.

3.2. Contribution of reactive species on the inactivation of U. Marinum

To gain insights into the *U. marinum* inactivation in the three UV-AOPs, we measured the concentrations of dominant reactive species, as depicted in Fig. 2. In the presence of anions in seawater, primary radicals have the potential to undergo transformations into secondary radicals through elementary reactions outlined as eqs. (15–31).

$$\bullet OH + Cl^- \rightarrow \bullet ClOH^- \quad (15)$$

$$\bullet ClOH^- + H^+ \rightarrow \bullet Cl + H_2O \quad (16)$$

$$\bullet Cl + OH^- \rightarrow \bullet ClOH^- \quad (17)$$

$$\bullet OH + OCl^- \rightarrow OH^- + \bullet ClO \quad (18)$$

$$\bullet Cl + OCl^- \rightarrow Cl^- + \bullet ClO \quad (19)$$

$$\bullet SO_4^- + Cl^- \rightarrow \bullet Cl + SO_4^{2-} \quad (20)$$

$$\bullet Cl + Cl^- \rightarrow \bullet Cl_2^- \quad (21)$$

$$\bullet SO_4^- + Br^- \rightarrow \bullet Br + SO_4^{2-} \quad (22)$$

$$\bullet Cl + Br^- \rightarrow \bullet Br + Cl^- \quad (23)$$

$$\bullet OH + Br^- \rightarrow \bullet BrOH^- \quad (24)$$

$$\bullet BrOH^- + Br^- \rightarrow \bullet Br_2^- + OH^- \quad (25)$$

$$\bullet Br + Br^- \rightarrow \bullet Br_2^- \quad (26)$$

$$\bullet Cl^- + Br^- \rightarrow \bullet ClBr^- \quad (27)$$

$$\bullet SO_4^- + HCO_3^- \rightarrow \bullet HCO_3 + SO_4^{2-} \quad (28)$$

$$\bullet SO_4^- + HCO_3^- \rightarrow \bullet HCO_3 + SO_4^{2-} \quad (29)$$

$$\bullet OH + HCO_3^- \rightarrow \bullet CO_3^- + H_2O \quad (30)$$

$$\bullet Cl + HCO_3^- \rightarrow \bullet CO_3^- + HCl \quad (31)$$

The abundant •ClO in UV/Chlorine has garnered attention due to its controversial performance in pollutant degradation [42,43]. In these UV-AOPs system, the production of secondary radicals is relatively lower, and their oxidative potential is weaker compared to •Cl and •ClO [44,45]. Therefore, the focus of the study was placed on the primary active species. Based on the probe degradation kinetics process and eqs. (S4-S7), the steady-state concentrations of $\bullet SO_4^-$ and •OH were calculated to be 1.86×10^{-14} M and 3.06×10^{-14} M in UV/PDS systems, as shown in Fig. 2(a). The High steady-state concentration and redox potential of $\bullet SO_4^-$ may explain why this process is more effective in inactivating microorganisms than others. In UV/H_2O_2 and UV/NaClO processes, the steady-state concentrations of •Cl are 6.25×10^{-14} M and 6.78×10^{-15} M, while the steady-state concentrations of •ClO are 3.26×10^{-15} M and 2.73×10^{-13} M, respectively. It is evident that the steady-state concentrations of •Cl are 1–2 orders of magnitude lower than those of •OH and •ClO in these processes. Consequently, the differences in *U. marinum* inactivation caused by •Cl are expected to be negligible. It is important to highlight that the steady-state concentrations of •OH among the three processes remain within one order of magnitude. The UV/NaClO process exhibits steady-state concentrations of •ClO two orders of magnitude higher than those in the UV/H_2O_2 process. However, the inactivation rate constant k of the UV/H_2O_2 process is higher by 0.51×10^{-3} s^{-1} than that of the UV/NaClO process. This observation suggests the importance of •OH in inactivation, and it implies that the selectivity and activity of •ClO towards *U. marinum* may not be particularly [12]. We acknowledge that differences in *U. marinum* inactivation in response to the concentration of primary radicals in the three types of AOPs may be subjective. To further elucidate the contributions of radicals, we conducted additional analyses by introducing radical scavengers.

Fig. 2(b) illustrate the contributions of reactive oxidizing specie of inactivation of *U. marinum* when treated with radical scavengers in UV and three UV-AOPs processes within 120 s. Detailed inactivation processes with different scavengers can be found in Fig. S8. The inactivation contribution rate of $\bullet SO_4^-$ and •OH accounted for 60 % of all reactive oxidizing species in UV/PDS, the inactivation contribution of •Cl and •OH were calculated as 52.87 % and 63.87 % in UV/H_2O_2 and UV/NaClO, respectively, which consistent with the primary radical concentration results.

3.3. Inactivation mechanisms

The concentration trends of eDNA during various treatment processes are presented in Fig. 3(a). Interestingly, the eDNA concentration exceeded 3 ng·μL^{-1} in response to UV/PDS, UV/H_2O_2, and UV/NaClO

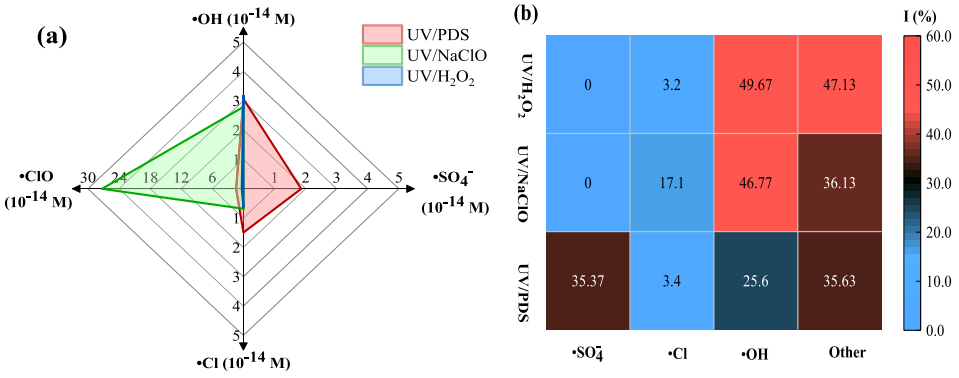


Fig. 2. (a) The steady state concentration of free radicals in the UV-AOPs processes; **(b)** Contribution of reactive radicals to the inactivation of *U. marinum*. (Experimental conditions: $[U. marinum]_0 = 5000$ cell·mL^{-1}, UV intensity = 1.24 mW·cm^{-2}, $[H_2O_2]_0 = [PDS]_0 = [NaClO]_0 = 10$ μM, $[NB]_0 = [TBA]_0 = [MeOH]_0 = 0.1$ mM, pH = 8.2, T = 25 ± 2 °C).

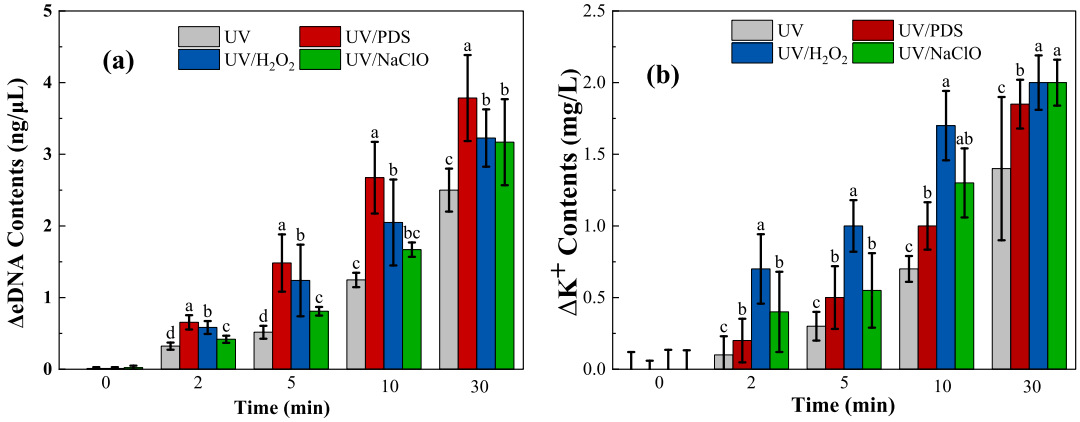


Fig. 3. (a) The extracellular DNA concentration of *U. marinum* in different processes; **(b)** The extracellular K^+ concentration of *U. marinum* in different processes. (Experimental conditions: $[U.\ marinum]_0$ = 5000 cells·mL^{-1}, UV intensity = 1.24 mW·cm^{-2}, $[H_2O_2]_0 = [PDS]_0 = [NaClO]_0$ = 10 μM, pH = 8.2, T = 25 ± 2 °C).

treatments, with values of 3.79, 3.23, and 3.17 ng·μL^{-1}, respectively, while UV treatment alone yielded a comparatively lower eDNA concentration of 2.73 ng·μL^{-1}. The results can be attributed to the action of ROS, which damage the cell wall or membrane, leading to the release of intracellular materials such as genetic material DNA into the surrounding environment [32]. On the other hand, the exposure of DNA to ROS and UV further induces structural and functional damage, impacting processes like DNA replication, repair, transcription, and translation. Consequently, aberrations in growth and metabolism occur, eventually resulting in inactivation. This phenomenon underscores one of the reasons why AOPs outperform UV treatment in terms of microbial inactivation. Wang et al. have indicated that the attack by $\bullet SO_4^-$ is associated with upregulation of intracellular ROS including H_2O_2, $\bullet O_2^-$ and •OH, initiating a chain oxidation reaction within the cell. These intracellular ROSs subsequently lead to cytoplasm oxidation and genomic DNA destruction, ultimately resulting in irreversible cell death [46]. And Wang et al. reported that reactive radicals such as $\bullet SO_4^-$ and •OH can damage the cell wall or membrane, promoting DNA exposure to UV, leading to DNA release into the solution and increased DNA strand breakages and fragments [31] It is worth noting that UV irradiation is renowned for its ability to inactivate microorganisms through DNA or RNA damage without destroying the cell wall. The increase in eDNA after UV treatment may be attributed to the elimination of harmful or superfluous DNA through cellular metabolism, maintaining cellular homeostasis [47]. In addition, we investigated the regrowth of *U. marinum* after different treatments, as illustrated in Fig. S9, the regrowth of *U. marinum* observed after UV inactivation, while there was no regrowth after UV-AOPs inactivation, demonstrating that the UV-AOPs systems could ensure the persistence and effectiveness of *U. marinum* inactivation. This may be due to the incomplete damage of UV to DNA, while UV-AOPs could destroy the structure of cell completely. Some studies have suggested that if DNA could not be destroyed in inactivation, the pathogen still have the potential to recover [48,49]. And it has reported that the ROS produced from AOPs can destroy the genetic components and cellular structure such as cell wall, cell membrane, resulting the inactivation of microorganisms [49].

The role of potassium ions (K^+) in maintaining cell osmotic pressure is pivotal, and variations in extracellular K^+ concentration can reflect changes in cell membrane permeability [50]. The degree of membrane damage is intricately linked to the selective permeability of cell membranes. As depicted in Fig. 3(b), the extracellular K^+ concentration exhibited an increasing trend during the *U. marinum* inactivation process, and UV-AOPs leads to a higher concentration of extracellular K^+ than UV, indicating that the active substance accelerates the damage to the cell membrane. The order of concentration increase is observed as UV/H_2O_2 > UV/NaClO > UV/PDS > UV, suggesting that UV/H_2O_2 induces the most substantial damage to membrane functionality. The changes in cell membrane permeability may be related to radical reactions with components on the cell membrane. Sun et al. reported that noncharged •OH may be more susceptible to attacking microbial surfaces than $\bullet SO_4^-$. In addition, the reaction rate between proteins and free radical species is higher than that of other biomolecules, such as polysaccharides and lipids [51]. Although extracellular secretions (proteins and polysaccharides) produced by cells are used to resist environmental stress, ultimately the cell membrane is damaged, impacting cellular metabolism [52]. Chen et al. found that an increase in cell membrane permeability could potentially disrupt the Proton Motive Force (PMF) that drives processes like ATP synthesis, nutrient transport, and other energy-dependent reactions in the cell. As a result, metabolic activity of *Staphylococcus aureus* (*S. aureus*) effectively reduced [53].

The fluorescence spectra of Extractable Organic Mater (EOM) were adopted to analyze releases cellular organic matter in *U. marinum* solutions, as depicted in Fig. 4. There are three main fluorescence peaks were discerned, which locate with $\lambda_{ex}/\lambda_{em}$ = 240/390 nm (peak A), 310/390 nm (peak C), 300/355 nm (peak D), corresponding to the fulvic acid-like, protein-like, and humic-like substance, respectively. To conduct a quantitative analysis, we divided the fluorescence spectra into five distinct regions and applied the Fluorescence Regional Integration (FRI) method, as described in Text S6. Table S3 provides a comprehensive list of typical representative substances within these regions. As illustrated in Fig. 4(a), the fluorescence spectrum of the solution containing normally growing cells exhibited Peak A and Peak C within regions III and V, indicating that natural organic matter through their metabolic activities in the solution primarily comprised fulvic acid-like and humic-like [54]. The treatment of UV, UV/H_2O_2, and UV/NaClO led to a weakening of Peaks A and C, indicating the degradation of fulvic acid-like and humic-like substances (Table S4). Notably, in UV/PDS processes, peaks in regions I, II, and IV, representing aromatic proteinoids I, aromatic proteinoids II, and dissolved microbial metabolites, respectively, displayed a significant enhancement. The Fluorescence Regional Integration values (Φi) in regions I, II, and IV increased by 1.48, 2.21, and 2.23 folds (Fig. 4(f)). This enhancement suggests that the inactivation of *U. marinum* by UV/PDS may result from the intracellular microbial organic matter (IMO) leaking into the extracellular space due to severe damage to the cell membrane. This observation aligns with a study by Peng et al., which explored the mechanism of cell disruption in harmful *Anabaena flosaquae* through ultrasound irradiation [25]. In addition, under UV/PDS treatment, the integral of the III and V also increased, signifying that protein-like substances can undergo degradation into humus-like substances. In comparison to UV treatment alone, the EEM spectra volumes of regions I and IV increased by 4.28 % and 61.39 % in the UV/NaClO treatment, while the region IV increased by 18.66 % in the UV/H_2O_2 treatment (Table S5). Regions I and IV are associated with aromatic proteinoids and dissolved microbial

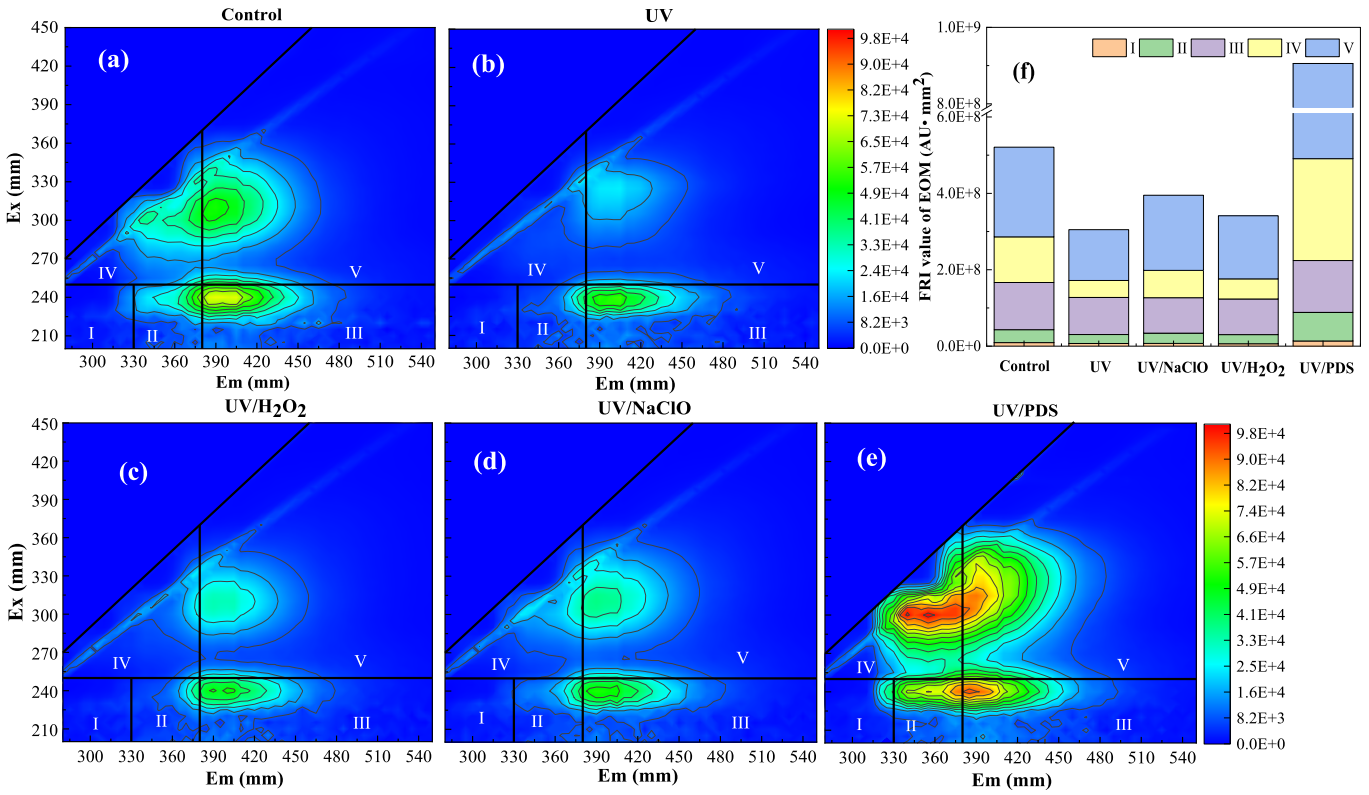


Fig. 4. The fluorescence EEM spectra of extracellular AOM after 2 min in different processes. **(a)** Control; **(b)** UV; **(c)** UV/NaClO; **(d)** UV/H_2O_2; **(e)** UV/PDS; **(f)** The fluorescence region integration of EEM spectra. (Experimental conditions: [*U. marinum*]$_0$ = 5000 cells·mL^{-1}, UV intensity = 1.24 mW·cm^{-2}, [H_2O_2]$_0$ = [PDS]$_0$ = [NaClO]$_0$ = 10 μM, pH = 8.2, T = 25 ± 2 °C).

metabolites, respectively. These findings indicate that the IMO leakage into the extracellular space due to damaged cell membranes was more pronounced under UV/NaClO and UV/H_2O_2 treatments than UV alone. UV/PDS induces the most substantial damage to the cell membrane with the primary component of the cell membrane being phospholipids, and subsequent inhibition of cellular activity [55,56]. Consequently, it can be hypothesized that UV/PDS may exert a more potent damaging effect on phospholipids compared to other treatments.

Compared with the control group, the DEGs of *U. marinum* were enriched in the pathways of DNA replication, nucleotide excisions repair, mismatch repair, and homologous recombination after UV and UV-AOPs treatments, all of which are related to replication and repair in genetic information processing **(**Fig. 5). This observation suggests that UV has a disruptive impact on the normal functioning of genetic material, specifically DNA, aligning with the well-established phenomenon of UV-induced DNA damage leading to the formation of pyrimidine dimers [5]. Moreover, the damaged to DNA exerts a detrimental influence on processes such as gene replication, transcription, and translation, consequently affecting the normal function and survival of cells [57].

The DEGs of *U. marinum* enriched pathways were not only genetic information processing but also metabolism and cellular processes following UV-AOPs treatment. Under UV/PDS and UV/H_2O_2 treatments, the DEGs were enriched in Spliceosome pathway, as illustrated in Fig. 5 **(b-c)**, the genes (Prp2 and Prp43) of Deah family ATPase/spinase, exhibited significant downregulation. Relevant studies have shown that Prp2 and Prp43 participate in the catalytic activation of splicosome play a pivotal role in mRNA splicing process [58,59]. Consequently, the transcription in genetic information processing of *U. marinum* is mainly affected under UV/PDS and UV/H_2O_2 systems. However, in contrast to the UV/PDS, the expression of PEX genes in Peroxisome pathway were significantly down-regulated by UV/H_2O_2 treatment. The PEX genes are known to play a central role in regulating peroxisome biogenesis [60]. Therefore, downregulation of PEX genes affects transport and catabolism in cellular processes may another factor contributing to cell inactivation in the UV/ H_2O_2 system. Fig. 5(d) reveals that under UV/NaClO treatment, DEGs were enriched in the Ribosome pathway, ribosome protein genes like EF-Tu (RP-L3, RP-L7, RP-L9, RP-L20, RP-S9, and RP-S16) displaying significantly down-regulated. Ribosomal protein genes are pivotal in constructing ribosomes and facilitating protein translation to uphold cell homeostasis and survival [61]. Therefore, the down-regulation of ribosomal protein gene expression affects translation in genetic information processing, may be the main cause of cellular structural and functional damage under the UV/NaClO system. In conclusion, the sensitivity of biological RNA transcription processes to radicals produced by UV/PDS and UV/H_2O_2 differs from the sensitivity of biological protein translation processes to UV/NaClO system. The life response mechanism of *U. marinum* during the inactivation process appears to be associated with changes in the types and levels of free radicals generated in the AOPs system.

We also attempt to delve deeper into the distinct responses of *U. marinum* when exposed to UV-AOPs relative to UV, the result show that UV-AOPs primarily exert their influence on cell metabolism (KEGG pathway enrichment analysis of *U. marinum* compare to UV is shown in Fig. 6 and Fig. S10). Specifically, the UV/H_2O_2 system appears to predominantly effect on pathways related to lipid metabolism, particularly glycerophospholipid metabolism and glycerolipid metabolism. The gene encoding important enzymes such as glyceronephate acyltransferase, and phosphatidylaerine synthase in glycerol phospholipid metabolism pathway significantly upregulated. Glycerophospholipids constitute a major component of cell membranes. The excessive ROS produced by UV/H_2O_2 attack all cell structures. The upregulation of gene expression in the phosphoglycerol metabolism pathway suggests that severely damaged cell membranes undergo self-repair [55]. In addition, genes associated with glycerolipid metabolism, such as DAK, TKFC, ALDH, MGLL, TGL2, LPT1, and DPPL, displayed significant upregulation, possibly reflecting the activation of cellular defense mechanisms.

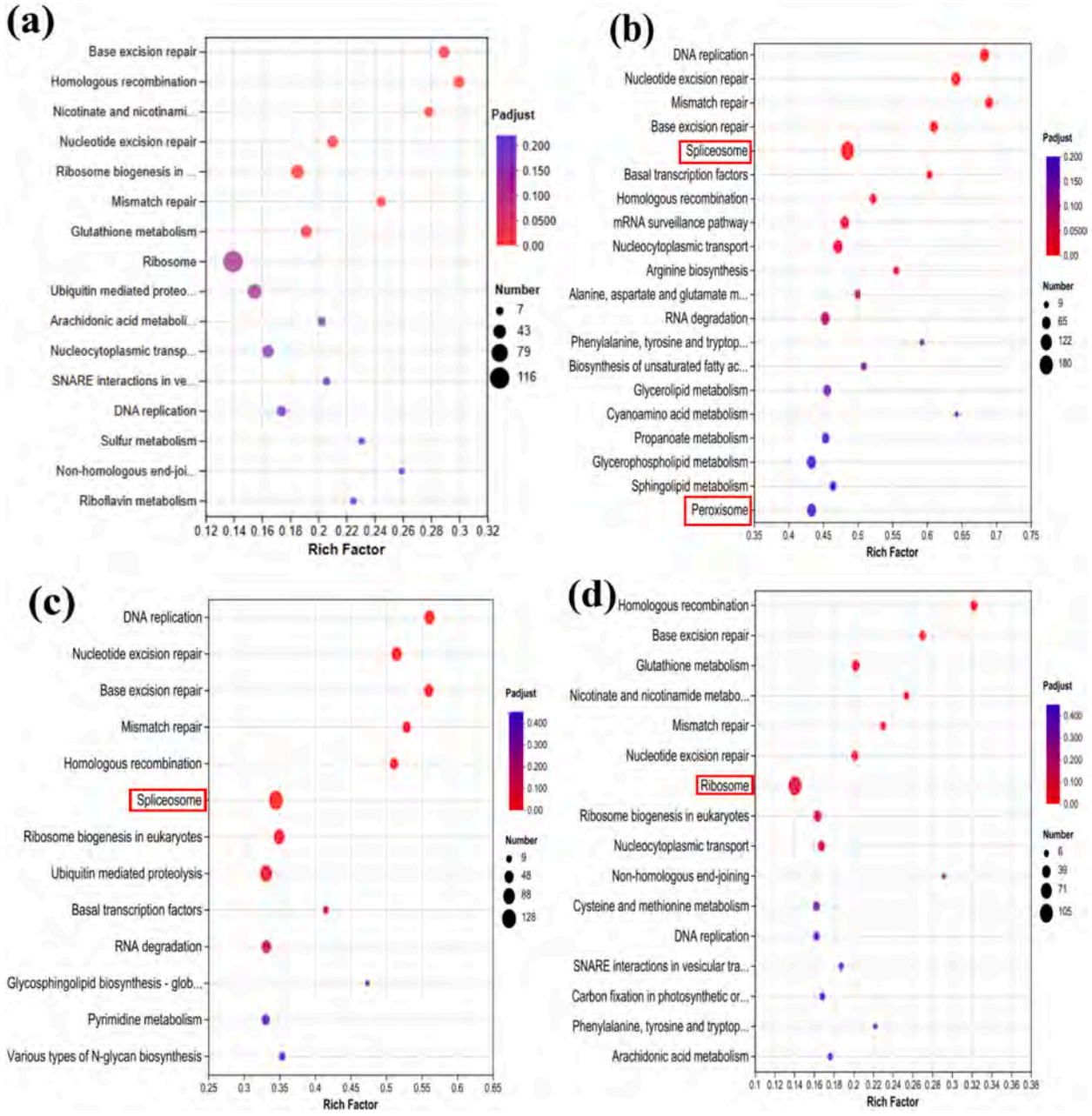


Fig. 5. KEGG pathway enrichment analysis of *U. marinum*. **(a)** UV; **(b)** UV/H_2O_2; **(c)** UV/PDS; **(d)** UV/NaClO.

Research by others has highlighted the role of glyceride metabolism in regulating defense gene expression in Arabidopsis through the modulation of oleic acid levels [62].

The primary pathways affected by UV/NaClO and UV/PDS treatments involve amino acid metabolism, encompassing glutathione metabolism and cysteine and methionine metabolism. In the case of glutathione metabolism, genes encoding glutathione synthase and glutathione S-transferase were upregulated, indicating their likely regulation in response to cellular redox changes, as glutathione is crucial for maintaining cellular and tissue redox homeostasis, protecting against oxidative stress, and participating in redox signaling pathways and detoxification reactions [63]. Similarly, in cysteine and methionine metabolism, the upregulation of genes such as serine *O*-acetyltransferase and cysteine synthase suggests an acceleration of cysteine and methionine metabolism. ROS primarily target proteins causing their oxidation to be essentially irreversible, particularly amino acids containing sulfur and thiol groups. Cysteine and methionine residues within peptide chains are particularly susceptible to ROS attacks [55]. Notably, glutathione is directly derived from the sulfur-containing amino acid cysteine and indirectly from methionine through the transformation pathway. As such, cells regulate the metabolism of glutathione, methionine, and cysteine to maintain redox homeostasis [64].

Compared with UV/NaClO, UV/PDS induces changes in gene expression within pathways related to carbohydrate metabolism and energy metabolism. The DEGs in Glycolysis pathway were downregulated, like key enzyme (hexokinase and phosphohexose isomerase) encoding genes, which suggests that ROS generated by UV/PDS may disrupt intracellular carbohydrate circulation. Glycolysis is the main metabolic pathway for energy production in highly proliferating cells, providing synthetic metabolic substrates to support cell proliferation and migration [65]. Consequently, UV/PDS may hinder glycolysis in *U. marinum*, potentially affecting its proliferation. Moreover, downregulation of glycolytic pathway expression may lead to abnormal gene expression on the TCA cycle pathway that downstream of Glycolysis.

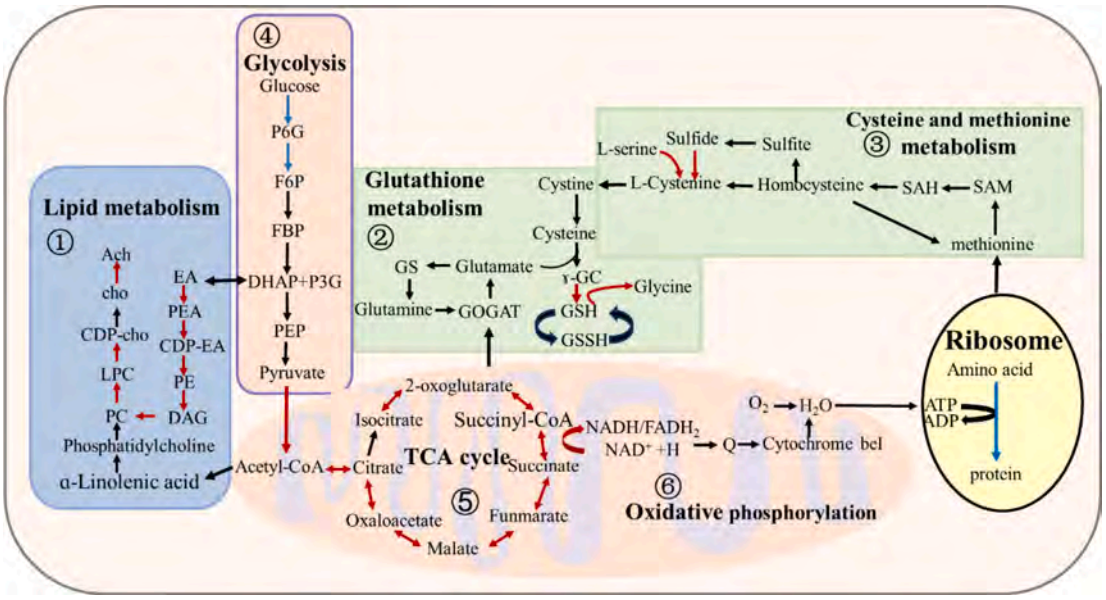


Fig. 6. Effect of UV-AOPs on the life response mechanism of *U. marinum*. (①: Lip metabolism; ②: Glutathione metabolism; ③: Cysteine and methionine metabolism; ④:Glycolysis; ⑤: Tricarboxylic acid cycle (TCA cycle); ⑥: Oxidative phosphorylation).

DEGs in TCA cycle pathway, such as citrate synthase, isocitrate dehydrogenase, and 2-oxoglutarate dehydrogenase genes are upregulated. The genes involved in oxidative phosphorylation, such as NADH dehydrogenase genes (Nduf), succinate dehydrogenase/fumarate reductase gene SDH, cytochrome reductase genes (Cyt1 and QCR7), cytochrome oxidase gene COX, and F-type ATPase gene alpha process gene expression were up-regulated. Oxidative phosphorylation provides most of the ATP, which is used by organisms to support life and is responsible for setting and maintaining metabolic homeostasis [66]. The results indicate that cells attempt to accelerate energy to maintain homeostasis. In summary, lipid metabolism is affected by UV/H_2O_2, whereas amino acid metabolism is more susceptible to the effects of UV/NaClO and UV/PDS. In comparison, carbohydrate metabolism and energy metabolism are affected by UV/PDS as opposed to UV/NaClO.

3.4. DBP formation after different treatments

The generation of disinfection by-products (DBPs) is an inadvertent outcome arising from the use of oxidants in the disinfection process. Existing studies have elucidated that radicals can induce DBP formation through two distinct mechanisms. Firstly, radicals can attack the precursors, exposing more reactive sites for chlorine to react and form DBPs. Secondly, halogen radicals themselves have the potential to form DBPs through radical addition to precursor molecules [67]. The investigations focused on the formation of classical DBPs within samples subjected to various UV-AOPs, and the results are presented in Fig. 7. For trihalomethanes (THMs) (Fig. 7(a)), there was no significant difference in concentration observed among the UV-AOPs systems after 2 min. The total concentration of haloacetic acids (HAAs) exhibited variations ranks as UV/NaClO> UV/H_2O_2 > UV/PDS, and the differing concentrations of Dichloroacetic Acid (DBAA) and Trichloroacetic Acid (TCAA) primarily contributed to the observed differences in HAAs concentration (Fig. 7 (b)). These discrepancies in DBAA and TCAA yields among the three UV-AOPs may stem from variations in radical speciation within these AOPs [68]. The selectivity of reactions between different types of free radicals and Natural Organic Matter (NOM) differs; for instance, •OH and RCS exhibit distinct reactivity patterns. RCS are known to selectively react with the electron-rich moieties of NOM [69]. Therefore, different AOPs generate distinct DBP precursors from NOM, resulting in varying HAAs formation [70]. Sun et al. also reported that under same UV fluence, the formation of HAAs using UV/chlorine and NOM was higher than that using UV/H_2O_2, attributing this difference to NOM's exposed to excessive free chlorine and RCS [68]. A noteworthy observation is the prevalence of Brominated-DBPs (Br-DBPs) as the predominant species,

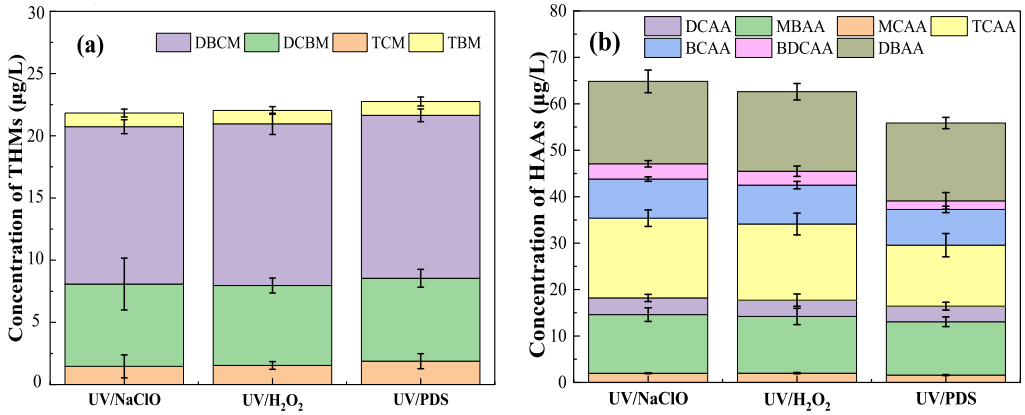


Fig. 7. The concentrations of classical DBPs during UV-AOPs treatment. **(a)** the concentrations of THMs; **(b)** the concentrations of HAAs. (Experimental conditions: [*U. marinum*]$_0$ = 5000 cell·mL^{-1}, UV intensity = 1.24 mW·cm^{-2}, [H_2O_2]$_0$ = [PDS]$_0$ = [NaClO]$_0$ = 10 μM, pH = 8.2, T = 25 ± 2 °C).

aligning with the influence of salinity as the primary factor favoring Br-DBPs over Chlorinated-DBPs (Cl-DBPs) in brackish and seawater conditions [7]. There are large number of halide ions in the seawater with a salinity of 35 ‰ that we use, the concentrations of chloride ions and bromide ions are approximately 19,000 and 65 mg·L^{-1}, respectively. Chen et al. have also suggested that in the presence of abundant bromide ions (Br^-), the predominant oxidant species shift towards bromine and reactive bromine species (RBSs) in LED-UV/Cl_2 [71]. Consequently, in the context of DBP control, it becomes evident that special attention should be directed towards systems characterized by lower concentrations of RCS.

3.5. Estimation of energy costs

The significant energy requirements associated with UV-AOPs and deemed it crucial to conduct an economic assessment of the various AOPs implemented [72]. The estimated cost for *U. marinum* inactivation in different UV-AOPs processes were list in Table 1, focusing on EE/O measurements. From the afore mentioned results, it becomes evident that employing any of the three UV-AOPs methods can significantly reduce the economic costs when compared to using UV alone. Notably, the most cost-effective process for *U. marinum* inactivation was observed in the UV/PDS system, boasting an EE/O_{total} of 1.655 kW·h·m^{-3}. Importantly, the required ultraviolet energy (EE/O_{UV}) diminishes as the synergistic effect of the combined UV and oxidant energies becomes more pronounced. This insight offers the potential for optimizing cost-effectiveness by strategically adjusting the ratio of UV energy to oxidant energy within the process.

4. Conclusion

This study conducted a comparative analysis of *U. marinum* inactivation in seawater using different UV-AOPs processes (UV/PDS, UV/H_2O_2 and UV/NaClO). This indicates the potential of UV-AOPs for seawater disinfection, with UV/PDS proving to be the most effective in *U. marinum* inactivation. The steady-state concentrations of •OH in the three processes are similar, and •OH played a significant role in the inactivation process. Despite a significantly higher steady-state concentration of •OCl in the UV/NaClO process compared to UV/H_2O_2, its inactivation of *U. marinum* was not substantial. Further investigation revealed that these UV-AOPs processes disrupt membrane structure and function, resulting in the leakage of DNA and EOM, and then disrupt genetic information expression and cellular metabolic processes. Transcriptome analysis highlighted the biological RNA transcription processes affected by radicals generated by UV/PDS and UV/H_2O_2, while protein translation processes responded more to radicals from UV/NaClO. Moreover, gene expression on lipid metabolism pathway was influenced by UV/H_2O_2, while amino acid metabolism pathway was affected by UV/NaClO and UV/PDS. Comparatively, gene expression related to enzymes involved in carbohydrate cycling and energy metabolism were affected by UV/PDS than UV/NaClO. From an economic standpoint, our cost analysis indicated that the UV/PDS system stood out, with 1.655 kW·h·m^{-3}. This research insights into the inactivation process of *U. marinum* and the differences among different UV-AOPs. Further research should be based on actual ballast water and its treatment devices to verify the stability and effectiveness of UV-AOPs in practical applications.

Table 1
EE/O of UV-AOPs for the inactivation of *U. marinum*.

System	EE/O_{UV}	$EE/O_{Oxidant}$	EE/O_{total} (kW·h·m^{-3})
UV	3.064	/	3.064
UV/ NaClO	1.984	0.005	1.989
UV/ H_2O_2	1.929	0.001	1.930
UV/PDS	1.653	0.002	1.655

CRediT authorship contribution statement

Xuan Chen: Writing – original draft, Methodology, Investigation, Formal analysis, Data curation, Conceptualization. **Pin Gan:** Methodology, Investigation, Conceptualization. **Kunling Huang:** Methodology, Investigation, Formal analysis, Conceptualization. **Fangyu Liang:** Methodology, Investigation, Conceptualization. **Tianhao Wu:** Methodology, Investigation, Conceptualization. **Xudong Li:** Methodology, Investigation, Conceptualization. **Yuanyuan Zhang:** Writing – review & editing, Supervision, Project administration, Funding acquisition, Data curation.

Declaration of competing interest

The whole or part of the work involved in this paper has not been published previously, and the publication of this manuscript is approved by all authors.

Acknowledgements

This study was supported by the National Science Foundation China (No. 42030502, No. 42090041), the College Students' Innovative Entrepreneurial Training Plan Program (No. 202310593494, No. 202310593257).

Appendix A. Supplementary data

Supplementary data to this article can be found online at https://doi.org/10.1016/j.jwpe.2024.106756.

Data availability

Data will be made available on request.

References

[1] A. Ardura, J.L. Martinez, A. Zaiko, E. Garcia-Vazquez, Poorer diversity but tougher species in old ballast water: biosecurity challenges explored from visual and molecular techniques, Mar. Pollut. Bull. 168 (2021) 112465.
[2] B. Lv, G. Zhu, W. Tian, C. Guo, X. Lu, Y. Han, T. An, Y. Cui, T. Jiang, The prevalence of potential pathogens in ballast water and sediments of oceangoing vessels and implications for management, Environ. Res. 218 (2022) 114990.
[3] S.A. Bailey, L. Brown, M.L. Campbell, J. Canning-Clode, J.T. Carlton, N. Castro, P. Chinho, F.T. Chan, J.C. Creed, A. Curd, J. Darling, P. Fofonoff, B.S. Galil, C. L. Hewitt, G.J. Inglis, I. Keith, N.E. Mandrak, A. Marchini, C.H. McKenzie, A. Occhipinti-Ambrogi, H. Ojaveer, L.M. Pires-Teixeira, T.B. Robinson, G.M. Ruiz, K. Seaward, E. Schwindt, M.O. Son, T.W. Therriault, A. Zhan, Trends in the detection of aquatic non-indigenous species across global marine, estuarine and freshwater ecosystems: a 50-year perspective, Divers, Distrib. 26 (2020) 1780–1797.
[4] O.-K. Hess-Erga, J. Moreno-Andrés, Ø. Enger, O. Vadstein, Microorganisms in ballast water: disinfection, community dynamics, and implications for management, Sci. Total Environ. 657 (2018) 704–716.
[5] E.A. Kouzminova, A. Kuzminov, Ultraviolet-induced RNA:DNA hybrids interfere with chromosomal DNA synthesis, Nucleic Acids Res. 49 (2021) 3888–3906.
[6] B. Werschkun, Y. Sommer, S. Banerji, Disinfection by-products in ballast water treatment: an evaluation of regulatory data, Water Res. 6 (2012) 4884–4901.
[7] J. Moreno-Andrés, L. Romero-Martínez, A. Acevedo-Merino, E. Nebot, UV-based technologies for marine water disinfection and the application to ballast water: does salinity interfere with disinfection processes? Sci. Total Environ. 581 (2016) 144–152.
[8] B. Sayinli, Y. Dong, Y. Park, A. Bhatnagar, S. Mika, Recent progress and challenges facing ballast water treatment-a review, Chemosphere 291 (2022) 132776.
[9] B. Werschkun, S. Banerji, O.C. Basurko, M. David, F. Fuhr, S. Gollasch, T. Grummt, M. Haarich, A.N. Jha, S. Kacan, A. Kehrer, J. Linders, E. Mesbahi, D. Pughiuc, S. D. Richardson, B. Schwarz-Schulz, A. Shah, N. Theobald, U. von Gunten, S. Wieck, T. Höfer, Emerging risks from ballast water treatment: the run-up to the international ballast water management convention, Chemosphere 112 (2014) 256–266.
[10] B. Zenati, A. Inal, F.-Z. Mesbaiah, S. Kourdali, S. Bachouche, J. Pinho, Pollutant load discharge from a southwestern Mediterranean river (Mazafran River, Algeria) and its impact on the coastal environment, Arab. J. Geosci. 3 (2023) 16.

[11] J. Varghese Manappallil, D. Susmita, F. Shaik, D. Geetha, Nanophotocatalytic treatment of seawater using TiO2 immobilized and suspension system under solar irradiation, journal of water, Process. Eng. 43 (2021) 102263.
[12] Y. Zhang, J. Xiang, J. Wang, H. Du, T. Wang, Z. Huo, W. Wang, M. Liu, Y. Du, Ultraviolet-based synergistic processes for wastewater disinfection: a review, J. Hazard. Mater. 14 (2023) 11393–11399.
[13] D. Wen, D. Chen, Y. Jiang, Synergistic algicidal effects of combined UV-LED/chlorine treatments on *Tetraselmis* sp.: optimization and mode-of-action, Chem. Eng. J. 422 (2021) 130043.
[14] Y. Zhang, M. Wei, K. Huang, K. Yu, J. Liang, F. Wei, J. Huang, X. Yin, Inactivation of *E. Coli* and *Streptococcus agalactiae* by UV/persulfate during marine aquaculture disinfection, Environ. Sci. Pollut. Res. 129 (2022) 45421–45434.
[15] K. Arman, M. Baghdadi, A. Pardakhti, Photochemical degradation of dexamethasone by UV/Persulphate, UV/hydrogen peroxide and UV/free chlorine processes in aqueous solution using response surface methodology (RSM), Int. J. Environ. Anal. Chem. 104 (2022) 2056–2074.
[16] J. Wang, J. Deng, E. Du, H. Guo, Reevaluation of radical-induced differentiation in UV-based advanced oxidation processes (UV/hydrogen peroxide, UV/peroxydisulfate, and UV/chlorine) for metronidazole removal: kinetics, mechanism, toxicity variation, and DFT studies, Sep. Purif. Technol. 301 (2022) 121905.
[17] Y.-M. Lee, G. Lee, T. Kim, K.-D. Zoh, Degradation of benzophenone-8 in UV/oxidation processes: comparison of UV/H2O2, UV/persulfate, UV/chlorine processes, J. Chem. Eng. 12 (2024) 111623.
[18] J. Zhao, J. Peng, R. Yin, M. Fan, X. Yang, C. Shang, Multi-angle comparison of UV/chlorine, UV/monochloramine, and UV/chlorine dioxide processes for water treatment and reuse, Water Res. 217 (2022) 118414.
[19] Y. Zhu, M. Wu, N. Gao, W. Chu, K. Li, S. Chen, Degradation of phenacetin by the UV/chlorine advanced oxidation process: kinetics, pathways, and toxicity evaluation, Chem. Eng. J. 335 (2017) 520–529.
[20] J. Moreno-Andrés, L. Peperzak, Operational and environmental factors affecting disinfection byproducts formation in ballast water treatment systems, Chemosphere 232 (2019) 496–505.
[21] Y. Huang, S. Wang, Y. Gao, J. Chen, X.-L. Wang, R.-J. Li, Comparison of mitochondrial genome and development of specific pcr primers for identifying two scuticociliates, *Pseudocohnilembus persalinus* and *Uronema marinum*, Parasit. Vectors 14 (2021) 318.
[22] G. Du, L. Qu, K. Shang, C. Sun, C. Wang, P. Gao, Ciliate *Uronema marinum* is the causative agent of scuticociliatosis in farm raised turbot Scophthalmus maximus, J. Oceanol. Limnol. 37 (2019) 1726–1735.
[23] G. Du, C. Sun, Y. Liu, Q. Dong, P. Gao, D. Li, L. Qu, In vitro anti-parasitic activity and mechanism of β-carboline derivatives isolated from the extracellular product of *Salinivibrio proteolyticus* strain YCSC6, Aquaculture 534 (2020) 736337.
[24] X. Pan, Z. Yi, J. Li, H. Ma, S.A. Al-Farraj, K.A.S. Al-Rasheid, Biodiversity of marine scuticociliates (Protozoa, Ciliophora) from China: description of seven morphotypes including a new species, Philaster sinensis spec. Nov, Eur. J. Protistol. 51 (2015) 142–157.
[25] Y. Peng, Z. Zhang, M. Wang, X. Shi, Y. Zhou, Y. Zhou, Y. Kong, Inactivation of harmful Anabaena flos-aquae by ultrasound irradiation: cell disruption mechanism and enhanced coagulation, Ultrason. Sonochem. 69 (2020) 105254.
[26] C. Wang, W.A. Bourland, W. Mu, X. Pan, Transcriptome analysis on chlorpyrifos detoxification in *Uronema marinum* (Ciliophora, Oligohymenophorea), Environ. Sci. Pollut. Res. 25 (2018) 33402–33414.
[27] H. Zeng, L. Shen, N. Lin, Z. Zhan, Effect of different culture conditions on the population growth of *Uronema marinum*, journal of Fujian Normal university, Natural Science Edition 31 (2015) 87–92.
[28] Z. Qiang, W. Li, M. Li, J.R. Bolton, J. Qu, Inspection of feasible calibration conditions for UV radiometer detectors with the KI/KIO3 actinometer, Photochem. Photobiol. 91 (2015) 68–73.
[29] B. Sayinli, Y. Dong, Y. Park, A. Bhatnagar, M. Sillanpää, Recent progress and challenges facing ballast water treatment – a review, Chemosphere 291 (2021) 132776.
[30] R. Pizzichetti, K. Reynolds, C. Pablos, C. Casado, E. Moore, S. Stanley, J. Marugán, Removal of diclofenac by UV-B and UV-C light-emitting diodes (LEDs) driven advanced oxidation processes (AOPs): wavelength dependence, kinetic modelling and energy consumption, Chem. Eng. J. 471 (2023) 144520.
[31] W. Wang, H. Wang, G. Li, T. An, H. Zhao, P.K. Wong, Catalyst-free activation of persulfate by visible light for water disinfection: efficiency and mechanisms, Water Res. 157 (2019) 106–118.
[32] G. Wen, X. Xu, H. Zhu, T. Huang, J. Ma, Inactivation of four genera of dominant fungal spores in groundwater using UV and UV/PMS: efficiency and mechanisms, Chem. Eng. J. 328 (2017) 619–628.
[33] Y.Q. Gao, J. Zhang, C. Li, F.X. Tian, N.Y. Gao, Comparative evaluation of metoprolol degradation by UV/chlorine and UV/H2O2 processes, Chemosphere 243 (2019) 125325.
[34] N. Ji, L. Lin, L. Li, L. Yu, Y. Zhang, H. Luo, M. Li, X. Shi, D.-Z. Wang, S. Lin, Metatranscriptome analysis reveals environmental and diel regulation of a *Heterosigma akashiwo* (raphidophyceae) bloom, Environ. Microbiol. 20 (2018) 1078–1094.
[35] S. Chen, Y. Zhou, Y. Chen, J. Gu, Fastp: an ultra-fast all-in-one FASTQ preprocessor, Bioinformatics 34 (2018) 884–890.
[36] M.G. Grabherr, B.J. Haas, M. Yassour, J.Z. Levin, D.A. Thompson, I. Amit, X. Adiconis, L. Fan, R. Raychowdhury, Q. Zeng, Z. Chen, E. Mauceli, N. Hacohen, A. Gnirke, N. Rhind, F. di Palma, B.W. Birren, C. Nusbaum, K. Lindblad-Toh, N. Friedman, A. Regev, Full-length transcriptome assembly from RNA-Seq data without a reference genome, Nat. Biotechnol. 29 (2011) 644–U130.
[37] F. Tian, W. Ye, B. Xu, X. Hu, S. Ma, F. Lai, Y. Gao, H. Xing, W. Xia, B. Wang, Comparison of UV-induced AOPs (UV/Cl2, UV/NH2Cl, UV/ClO2 and UV/H2O2) in the degradation of iopamidol: kinetics, energy requirements and DBPs-related toxicity in sequential disinfection processes, Chem. Eng. J. 398 (2020) 125570.
[38] Y. Yoon, H. Jee, S.H. Song, M.-H. Hwang, K.-J. Chae, B. Kim, E. Yang, Combination of H2O2-producing microbial desalination cells and UV/H2O2 advanced oxidation process: water salinity reduction and microbial inactivation, J. Chem. Eng. 11 (2023) 110110.
[39] L. Romero-Martínez, I. Rivas-Zaballos, J. Moreno-Andrés, I. Moreno-Garrido, A. Acevedo-Merino, E. Nebot, Improving the microalgae inactivating efficacy of ultraviolet ballast water treatment in combination with hydrogen peroxide or peroxymonosulfate salt, Mar. Pollut. Bull. 162 (2020) 111886.
[40] J. Moreno-Andrés, M. Tierno-Galán, L. Romero-Martínez, A. Acevedo-Merino, E. Nebot, Inactivation of the waterborne marine pathogen *vibrio alginolyticus* by photo-chemical processes driven by UV-A, UV-B, or UV-C LED combined with H2O2 or HSO5−, Water Res. 232 (2023) 119686.
[41] K. Song, M. Mohseni, F. Taghipour, Mechanisms investigation on bacterial inactivation through combinations of UV wavelengths, Water Res. 163 (2019) 114875.
[42] K. Guo, Z. Wu, S. Yan, B. Yao, W. Song, Z. Hua, X. Zhang, X. Kong, X. Li, J. Fang, Comparison of the UV/chlorine and UV/H2O2 processes in the degradation of PPCPs in simulated drinking water and wastewater: kinetics, radical mechanism and energy requirements, Water Res. 147 (2018) 184–194.
[43] Q. Kong, X. Lei, X. Zhang, S. Cheng, C. Xu, B. Yang, X. Yang, The role of chlorine oxide radical (ClO•) in the degradation of polychoro-1,3-butadienes in UV/chlorine treatment: kinetics and mechanisms, Water Res. 183 (2020) 116056.
[44] Z. Wu, K. Guo, J. Fang, X. Yang, H. Xiao, S. Hou, X. Kong, C. Shang, X. Yang, F. Meng, L. Chen, Factors affecting the roles of reactive species in the degradation of micropollutants by the UV/chlorine process, Water Res. 126 (2017) 351–360.
[45] L. Wang, C. Ye, L. Guo, C. Chen, X. Kong, Y. Chen, L. Shu, P. Wang, X. Yu, J. Fang, Assessment of the UV/chlorine process in the disinfection of Pseudomonas aeruginosa: efficiency and mechanism, Environ. Sci. Technol. 55 (2021) 9221–9230.
[46] W. Wang, H. Wang, G. Li, P.K. Wong, T. An, Visible light activation of persulfate by magnetic hydrochar for bacterial inactivation: efficiency, recyclability and mechanisms, Water Res. 176 (2020) 115746.
[47] A. Takahashi, R. Okada, K. Nagao, Y. Kawamata, A. Hanyu, S. Yoshimoto, M. Takasugi, S. Watanabe, M.T. Kanemaki, C. Obuse, E. Hara, Exosomes maintain cellular homeostasis by excreting harmful DNA from cells, Nature Comms. 8 (2017) 15287.
[48] Y. Chen, X. Duan, X. Zhou, R. Wang, S. Wang, N. Ren, S.-H. Ho, Advanced oxidation processes for water disinfection: features, mechanisms and prospects, Chem. Eng. J. 409 (2020) 128207.
[49] I. Assadi, A. Guesmi, O. Baaloudj, H. Zeghioud, W. Elfalleh, N. Benhammad, L. Khezami, A. Assadi, Review on inactivation of airborne viruses using non-thermal plasma technologies: from MS2 to coronavirus, Environ. Sci. Pollu. Res. 29 (2022) 4880–4892.
[50] X. Wang, H. Xu, H. Pei, Comparing the Effects and Mechanisms of Action of Permanganate, Chlorine, and Hydrogen Peroxide on the Membrane Integrity of Pseudanabaena Sp, Cells ,ACS ES&T Water 3 (2023) 588–597.
[51] P. Sun, C. Tyree, C.H. Huang, Inactivation of Escherichia coli, bacteriophage MS2, and *Bacillus* spores under UV/H2O2 and UV/Peroxydisulfate advanced disinfection conditions, Environ. Sci. Technol. 50 (2016) 4448–4458.
[52] Y. Chen, X. Duan, X. Zhou, R. Wang, S. Wang, N. Ren, S.H. Ho, Advanced oxidation processes for water disinfection: features, mechanisms and prospects, Chem. Eng. J. 409 (2020) 128207.
[53] X. Chen, Z. Chen, H. Liu, N. Huang, Y. Mao, K. Cao, Q. Shi, Y. Lu, H. Hu, Synergistic effects of UV and chlorine in bacterial inactivation for sustainable water reclamation and reuse, Sci. Total Environ. 845 (2022) 157320.
[54] Y. Kong, L. Ji, Y. Wang, J. Li, H. Lu, S. Mo, X. Wang, L. Zhu, X. Xu, X. Zheng, Combined Effect of NZVI and H2O2 on the Cyanobacterium *Microcystis aeruginosa*: Performance and Mechanism, Nano Materials 12 (2022) 3017.
[55] X. He, P. Wu, S. Wang, A. Wang, C. Wang, P. Ding, Inactivation of harmful algae using photocatalysts: mechanisms and performance, J. Clean. Prod. 289 (2020) 125755.
[56] J. Rodríguez-Chueca, S.I. Moreira, M.S. Lucas, J.R. Fernandes, P.B. Tavares, A. Sampaio, J.A. Peres, Disinfection of simulated and real winery wastewater using sulphate radicals: Peroxymonosulphate/transition metal/UV-A LED oxidation, J. Clean. Prod. 149 (2017) 805–817.
[57] A. Britt, Molecular genetics of DNA repair in higher plants, Trends Plant Sci. 4 (1999) 20–25.
[58] D.J. Combs, R.J. Nagel, M. Ares, S.W. Stevens, Prp43p is a DEAH-box spliceosome disassembly factor essential for ribosome biogenesis, Mol. Cell. Biol. 26 (2005) 234–523.
[59] S.H. Kim, R.J. Lin, Spliceosome activation by PRP2 ATPase prior to the first transesterification reaction of pre-mRNA splicing, Mol. Cell. Biol. 16 (1996) 6810–6819.
[60] Y. Fujiki, K. Okumoto, M. Honsho, Y. Abe, Molecular insights into peroxisome homeostasis and peroxisome biogenesis disorders, Biochimica et Biophysica Acta (BBA) - Molecular, Cell Res. 2022 (1869) 119330.
[61] C. Petibon, J. Parenteau, M. Catala, S.A. Elela, Introns regulate the production of ribosomal proteins by modulating splicing of duplicated ribosomal protein genes, Nucleic Acids Res. 44 (2016) 3878–3891.
[62] A. Kachroo, S.C. Venugopal, L. Lapchyk, D. Falcone, D. Hildebrand, P. Kachroo, Oleic acid levels regulated by glycerolipid metabolism modulate defense gene expression in Arabidopsis, Proc. Natl. Acad. Sci. USA 101 (2004) 5152–5157.

[63] H.J. Forman, H. Zhang, A. Rinna, Glutathione: overview of its protective roles, measurement, and biosynthesis, Mol. Asp. Med. 30 (2008) 1–12.
[64] F. Rezende, Renal Nox4 contributes to systemic redox homeostasis by controlling glutathione, methionine and cysteine metabolism, Free Radic. Biol. Med. 227 (2018) 719.
[65] J. Zlacká, M. Zeman, Glycolysis under circadian control, Int. J. Mol. Sci. 22 (2021) 13666.
[66] D.F. Wilson, Oxidative phosphorylation: regulation and role in cellular and tissue metabolism, J. Physiol. 595 (2017) 7023–7038.
[67] D.M. Bulman, C.K. Remucal, Role of reactive halogen species in disinfection byproduct formation during chlorine photolysis, Environ. Sci. Technol. 54 (2020) 9629–9639.
[68] J. Sun, D. Kong, E. Aghdam, J. Fang, Q. Wu, J. Liu, Y. Du, X. Yang, C. Shang, The influence of the UV/chlorine advanced oxidation of natural organic matter for micropollutant degradation on the formation of DBPs and toxicity during post-chlorination, Chem. Eng. J. 373 (2019) 870–879.
[69] Y. Xiang, J. Fang, C. Shang, Kinetics and pathways of ibuprofen degradation by the UV/chlorine advanced oxidation process, Water Res. 90 (2016) 301–308.
[70] X. Yang, J. Sun, W. Fu, C. Shang, Y. Li, Y. Chen, W. Gan, J. Fang, PPCP degradation by UV/chlorine treatment and its impact on DBP formation potential in real waters, Water Res. 98 (2016) 309–318.
[71] Y. Chen, I. Jafari, Y. Zhong, M. Chee, J. Hu, Degradation of organics and formation of DBPs in the combined LED-UV and chlorine processes: effects of water matrix and fluorescence analysis, Sci. Total Environ. 846 (2022) 157454.
[72] J.R. Bolton, K.G. Bircher, W. Tumas, C.A. Tolman, Figures-of-merit for the technical development and application of advanced oxidation technologies for both electric- and solar-driven systems (IUPAC technical report), Pure Appl. Chem. 73 (2001) 627–637.

Environmental Research 278 (2025) 121643

Contents lists available at ScienceDirect

Environmental Research

journal homepage: www.elsevier.com/locate/envres

Sorption and mechanisms of legacy and emerging per- and polyfluoroalkyl substances (PFASs) on different particle size fractions of marine sediments

Jun-Jie Hu [a,1], Shang-Ke Yu [a,1], Chao Yin [a], Feng-Jiao Peng [b,c], Shuang-Shuang Liu [d], Chang-Gui Pan [a,*], Kefu Yu [a]

[a] Guangxi Laboratory on the Study of Coral Reefs in the South China Sea, School of Marine Sciences, Guangxi University, Nanning, 530004, China
[b] SCNU Environmental Research Institute, Guangdong Provincial Key Laboratory of Chemical Pollution and Environmental Safety, MOE Key Laboratory of Theoretical Chemistry of Environment, South China Normal University, Guangzhou, 510006, China
[c] School of Environment, South China Normal University, University Town, Guangzhou, 510006, China
[d] Guangdong Provincial Key Laboratory of Fishery Ecology and Environment, South China Sea Fisheries Research Institute, Chinese Academy of Fishery Sciences, Guangzhou, 510300, China

ARTICLE INFO

Keywords:
Per- and polyfluoroalkyl substances
Marine sediment
Sorption
Particle sizes
Hydrophobic interactions

ABSTRACT

PFASs are ubiquitous in various environmental and biological media due to their extensive application and stability. However, the sorption of PFASs, especially emerging PFASs, on different particle size fractions of marine sediments remains unknown. Here, we investigated the sorption kinetics, isotherms, and mechanisms of six legacy and emerging PFASs on five different particle size fractions of marine sediments (F1 (69.4–190 μm), F2 (63.3–163 μm), F3 (5.25–72.6 μm), F4 (3.29–34.7 μm), and F5 (1.69–22.7 μm)). Our results indicated that the sorption kinetics and isotherms conformed well to the pseudo-second-order model and the Freundlich model, respectively, suggesting the nonlinear sorption of PFASs on marine sediments. The sorption capacities of PFASs decreased significantly with increasing sediment particle size from F5 to F1. Meanwhile, PFAS distribution coefficients (K_d) correlated positively with organic carbon content, specific surface area, and sediment pore volume. K_d values of PFOA and PFOS were 0.40–0.65 and 2.64–6.12 times higher than those of their substitutes, GenX and 6:2 FTSA. Hydrophobic interactions dominated PFAS sorption over electrostatic interactions. Overall, this study offers a comprehensive understanding of legacy and emerging PFAS distribution and mechanisms in marine sediments of varying particle sizes.

1. Introduction

Per- and polyfluoroalkyl substances (PFASs) are synthetic organic compounds in which hydrogen atoms in the carbon chain are partially or fully replaced by fluorine (Evich et al., 2022; Greene et al., 2024). Due to their carbon-fluorine chains (-CF_2) and hydrophilic functional groups (e.g., sulfonic and carboxylic acids), they exhibit surfactant properties and are widely used in firefighting foams, floor polishes, alkaline cleaners, paints, semiconductor production, photographic materials, pesticides, and carpets (Bogdan et al., 2024; Gaines, 2022; Pan et al., 2021). The high bond dissociation energy (536 kJ/mol) of the C-F bond makes PFAS extremely stable (Leung et al., 2022), leading to their occurrence in various environmental matrices, including air (Li et al., 2024), water (Shen et al., 2024), sediment (Zhu et al., 2024), biota (Marciano et al., 2024), and even humans (Zhang et al., 2024). Generally, the concentrations of PFASs ranged from ng/L to a few μg/L in water and ng/g to hundreds of ng/g dry weight (dw) in sediment (Yu et al., 2024; Zhang et al., 2025). Notably, long-chain PFASs are prone to bioaccumulation due to their chemical properties, which facilitates their transfer along food chains and results in biomagnification (Pan et al., 2021). Two representative PFASs, perfluorooctanoic acid (PFOA) and perfluorooctane sulfonate (PFOS), readily bind to serum proteins, affecting reproductive and developmental systems (Fischer et al., 2024; Yan et al., 2025). Moreover, PFOS has been characterized as an endocrine disruptor, and can also induce liver steatosis in zebrafish (Wang et al., 2022). Consequently, PFOA and PFOS, along with several other PFASs including perfluorohexanesulfonic acid (PFHxS), have been listed as persistent organic contaminants (POPs) under the Stockholm

* Corresponding author.
E-mail address: panchanggui@gxu.edu.cn (C.-G. Pan).
[1] These authors contributed equally to this work.

https://doi.org/10.1016/j.envres.2025.121643
Received 12 November 2024; Received in revised form 24 March 2025; Accepted 16 April 2025
Available online 16 April 2025
0013-9351/© 2025 Elsevier Inc. All rights are reserved, including those for text and data mining, AI training, and similar technologies.

Convention (UNEP, 2009; UNEP, 2023). In response, alternatives to PFASs including 6:2 fluorotelomer sulfonic acid (6:2 FTSA) and perfluoro-2-methyl-3-oxahexanoic acid (GenX), have been introduced into the market. Nevertheless, previous studies have revealed that some emerging PFASs not only demonstrate bioaccumulation potential but also exhibit significant toxicological effects (Gaballah et al., 2020; Wasel et al., 2023), thereby raising substantial concerns about their environmental persistence and potential human health implications.

In water-sediment system, pollutants' migration and bioavailability are directly impacted by their sorption behavior (Williams et al., 2017; Wu et al., 2015; Xiang et al., 2016). The sorption of PFASs on various adsorbents have been extensively explored, such as biochar (Liu et al., 2024), carbon materials (Dey et al., 2024), soils (Chen et al., 2020), and sediments (Fagbayigbo et al., 2022), etc. In fact, sediment has been demonstrated to be a crucial reservoir for PFASs, with their levels typically ranging from ng/g dw to μg/g dw (Ahmed et al., 2020). However, PFASs in sediment can be ingested by benthic organisms, potentially impacting aquatic ecosystems and, through consumption of these organisms, posing risks to human health.

Sediment consists of various particle size fractions with different physicochemical characteristics that collectively influence contaminant sorption (Chen et al., 2020; Qi and Zhang, 2016; Xiang et al., 2019). Therefore, sorption experiments with different sediment particle-size fractions offer a more refined insight into contaminants' sorption behavior than with whole sediment. Correspondingly, numerous studies have examined the sorption of emerging contaminants, such as polycyclic aromatic hydrocarbons (Tang et al., 2022), pesticides (El-Aswad et al., 2019) and antibiotics (Luo et al., 2019). The results demonstrate that the sorption of emerging contaminants is primarily governed by hydrophobic forces and electrostatic interactions, which are associated with the properties of emerging contaminants (e.g., organic carbon-water distribution coefficient (K_{oc})), solution (e.g., pH and ion concentrations) and sediment (e.g., organic matter (OM) and ferric oxides) (Li et al., 2023). For instance, the adsorbed concentrations of emerging contaminants (e.g., phthalic acid esters, PAEs) on different size fractions of soils and sediments have been found to usually follow the order: clay > fine silt > coarse silt > fine sand > coarse sand (Tan et al., 2016). Therefore, sorption of contaminants on various particle size fractions of sediments allows for comprehensively exploring contaminant sorption mechanisms and identifying the specific fractions responsible for the primary sorption on sediments (Chen et al., 2020; Qi and Zhang, 2016). To date, only two studies have examined the sorption behavior of legacy PFASs, particularly PFOS and PFOA, across various soil particle size fractions (Chen et al., 2020; Xiang et al., 2018). However, considering the widespread use of emerging PFASs and their different physicochemical properties compared to legacy PFASs, there is an urgent need for investigations into the sorption of emerging PFASs on different sediment fractions. Furthermore, due to distinct physicochemical properties (e.g., salinity) between marine sediment and freshwater sediments/soil (Sühring et al., 2016), contaminants often exhibit significantly different sorption behaviors in these two environments. Moreover, previous studies mainly relied on adsorption kinetics, isotherms, and Fourier transform infrared (FTIR) analysis, while paying insufficient attention to density functional theory (DFT) calculations for deeper insights. Specifically, DFT calculations can provide key parameters, such as electrostatic potentials, to reveal the fundamental driving forces behind sorption interactions (Parker et al., 2022).

In the present study, we aimed to: 1) investigate the sorption behavior of six legacy PFASs and emerging alternative PFASs on different particle size fractions of marine sediments; 2) clarify the main factors influencing PFASs sorption on different particle size fractions of marine sediments; and 3) elucidate the main mechanisms of PFASs sorption on marine sediments.

2. Materials and methods

2.1. Chemicals and standards

Six PFASs including three legacy PFASs (PFHxS, PFOA and PFOS) and three emerging alternative PFASs (perfluorobutanesulfonic acid (PFBS), 6:2 FTSA and GenX) were selected in the present study. PFOA and PFOS were purchased from AccuStandard (New Haven, Connecticut, the United States). PFBS, PFHxS, 6:2 FTSA and GenX were bought from Sigma-Aldrich (St. Louis, Missouri, the United States), Wellington laboratories (Ontario, Canada), International laboratory (San Francisco, California, the United States) and Apollo Scientific (Manchester, the United Kingdom), respectively. Besides, four mass labeled PFASs (MPFOA, MPFDA, MPFHxS and MPFOS) were utilized as internal standards, and all of them were provided by Wellington laboratories (Ontario, Canada).

2.2. Sediment collection and sieving

Sediment samples were collected from the Beibu Gulf, South China Sea, in April 2021. After freeze-drying, they were filtered through a 2 mm stainless steel screen to remove debris and then fractionated using the wet sieving method (Xiang et al., 2018). Briefly, 500 g of dry sediment was dispersed in water (5:1 mass ratio), stirred, and ultrasonically treated for 30 min. The suspension was sequentially passed through 180 μm, 60 μm, and 30 μm sieves to obtain coarse sand (F1, >180 μm), fine sand (F2, 60–180 μm), and coarse particles (F3, 30–60 μm). The remaining suspension was treated with 0.1 mol/L $Na_4P_2O_7$, settled for 4 h to collect fine particles (F4), and centrifuged at 5000 rpm for 10 min to obtain clay (F5). All fractions (F1-F5) were freeze-dried, weighed, and stored at −18 °C for further experiments.

2.3. Characterization of sediments

The physicochemical properties, including total organic carbon (TOC), pH, Brunauer-Emmett-Teller (BET) surface area, pore analysis and particle size analysis of different particle size fractions of sediments (F1-F5), were measured by elemental analyzer, pH meter, and automated gas sorption analyzer, respectively. Besides, the functional groups of these sediment fractions (F1-F5) were determined by FTIR spectroscopy. Detailed information on related analytical methods and physicochemical properties of F1-F5 are provided in Text S1 and Table S1, respectively.

2.4. Kinetics and isotherms of PFASs on different particle size fractions of sediments

The experiments were conducted following the OECD 106 standard (Lees et al., 2021). For the kinetics experiment, each 50-mL polypropylene (PP) centrifuge tube was prepared with 1.0 g of sediment. Subsequently, 40 mL of a 0.01 mol/L $CaCl_2$ solution and a PFAS solution targeting a nominal concentration of 10 μg/L per individual PFAS were added. After 1 min of vortex mixing, the tubes were placed in an oscillator and agitated at 25 °C. Sampling occurred at seven intervals: 0.5, 1, 2, 4, 8, 24, and 48 h. Following collection, samples were centrifuged at 5000 rpm for 10 min. Then, the separated water and sediment were extracted following our previous study with minor modification (Yin et al., 2022). The extraction methods are outlined in Text S2.

For isotherms, the sorption experiments were conducted under the same conditions as the kinetics experiment, but with a duration of 48 h and six concentrations of PFASs at 5, 10, 30, 50, 100 and 200 μg/L, respectively.

2.5. Determination of PFASs

PFASs concentrations were analyzed using an ultrahigh-performance

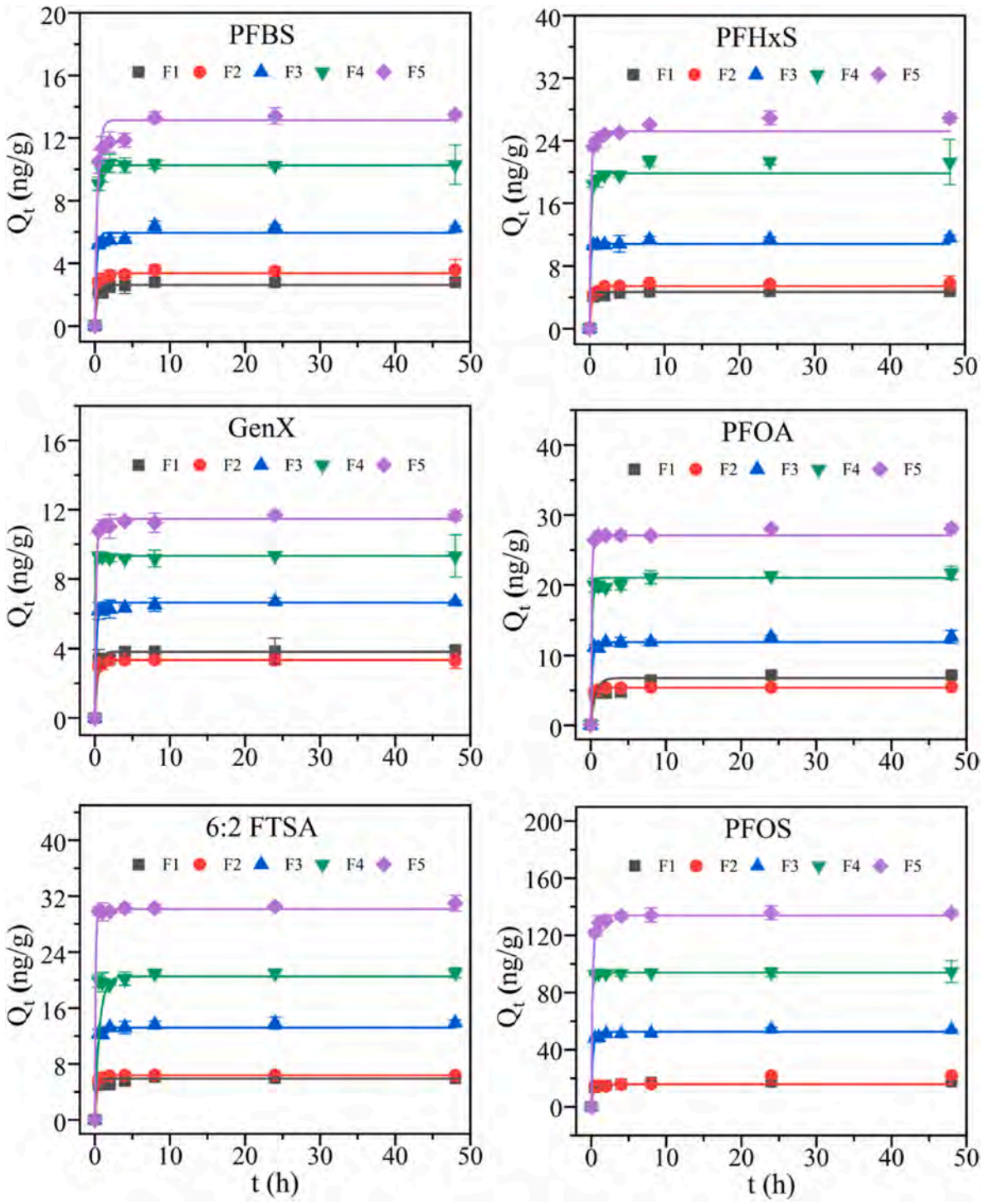


Fig. 1. The pseudo-first-order models for the sorption of PFASs on different particle size fractions of sediments.

liquid chromatography system coupled to a mass spectrometer (LC-MS/MS, Agilent Technologies, USA). Details on the LC-MS/MS parameters are shown in Text S3, Tables S2 and S3.

2.6. Theoretical calculation

The stereostructures of PFASs were obtained using GaussView 5.0. Conformational optimization of PFAS were performed in Gaussian 09w with the hybrid density functional B3LYP, all-electron basis set 6-31G+(d, p) and dispersion correction term (D3). Following this, surface electrostatic potentials were calculated. All wavefunction analyses were performed by Multiwfn 3.8 (Lu and Chen, 2011). Additionally, all isosurface maps were rendered using the Visual Molecule Dynamics (VMD) 1.9.3 program. The distribution coefficients (log D) for all target PFASs at pH 7 were estimated using the ChemAxon method in MarvinSketch (Xiao et al., 2018).

2.7. Quality assurance (QA) and quality control (QC)

Teflon materials were excluded from the experiments. The background concentrations of target PFASs in the whole sediment used for the sorption experiment ranged from 25 to 99 pg/g dw, which were

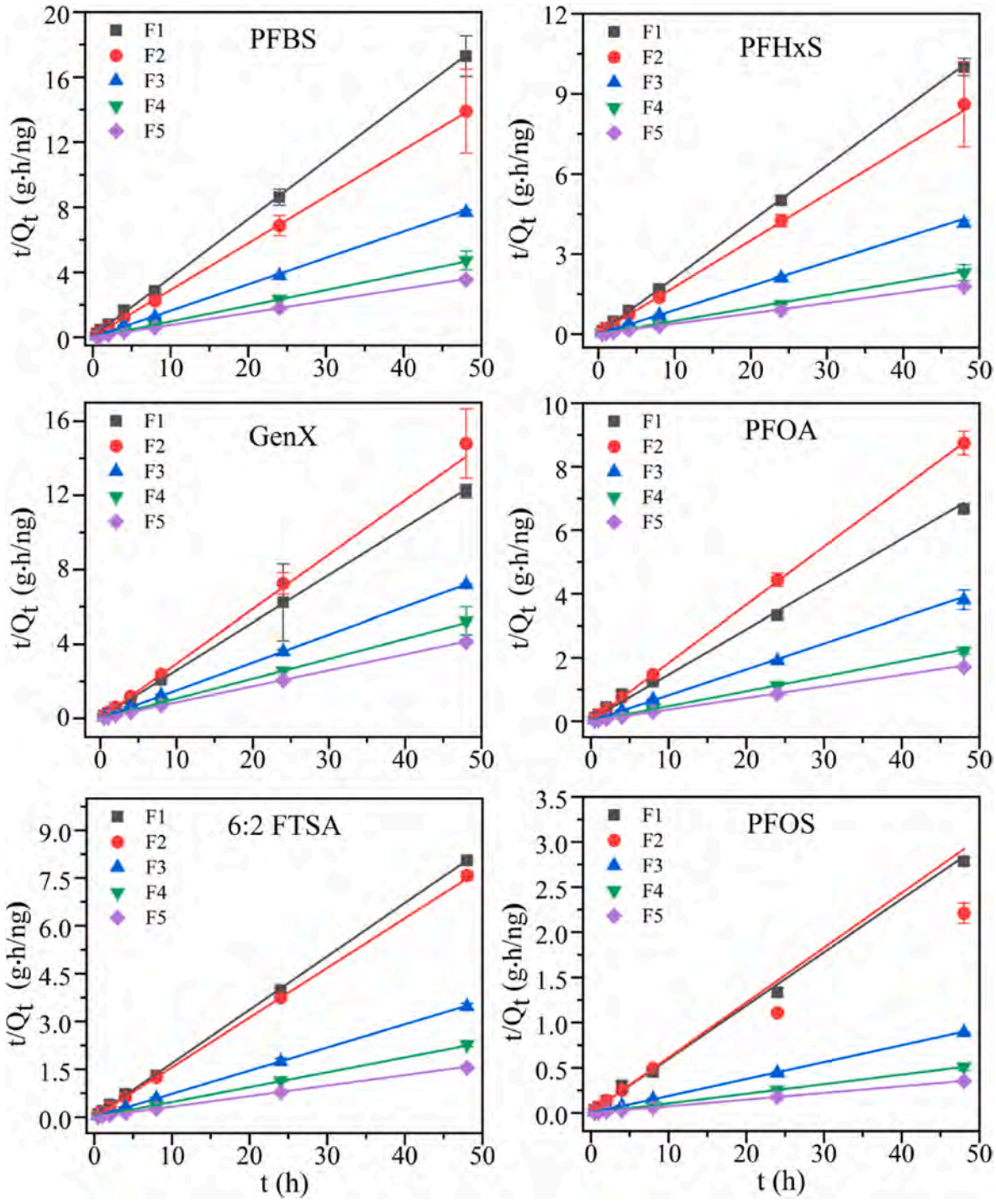


Fig. 2. The pseudo-second-order models for the sorption of PFASs on different particle size fractions of sediments.

considered negligible in our sorption experiment compared to the levels examined (ng/g dw-μg/g dw). Additionally, solvent blank, procedural blank, and recovery experiment were performed. The recovery of individual PFASs ranged from 69 % to 109 % and 93 %–119 % in water and sediment samples, respectively.

2.8. Data analysis

The intraparticle diffusion (Q_t) was calculated using the following formula:

$$Q_t = k_i t^{0.5} + C_i \quad (1)$$

where k_i represents the rate constant of stage i ($ng/g{\cdot}h^{-0.5}$); C_i is a constant indicating the intercept of stage i, which describes the resistance to mass transfer in the boundary layer effect (Kannan and Sundaram, 2001).

The isotherm data were fitted using the Freundlich model and Langmuir model listed below:

$$C_s = K_F C_e^n \quad (2)$$

$$C_s = C_m K_L C_e / (1 + K_L C_e) \quad (3)$$

where C_s represents the equilibrium concentration of PFAS in sediment

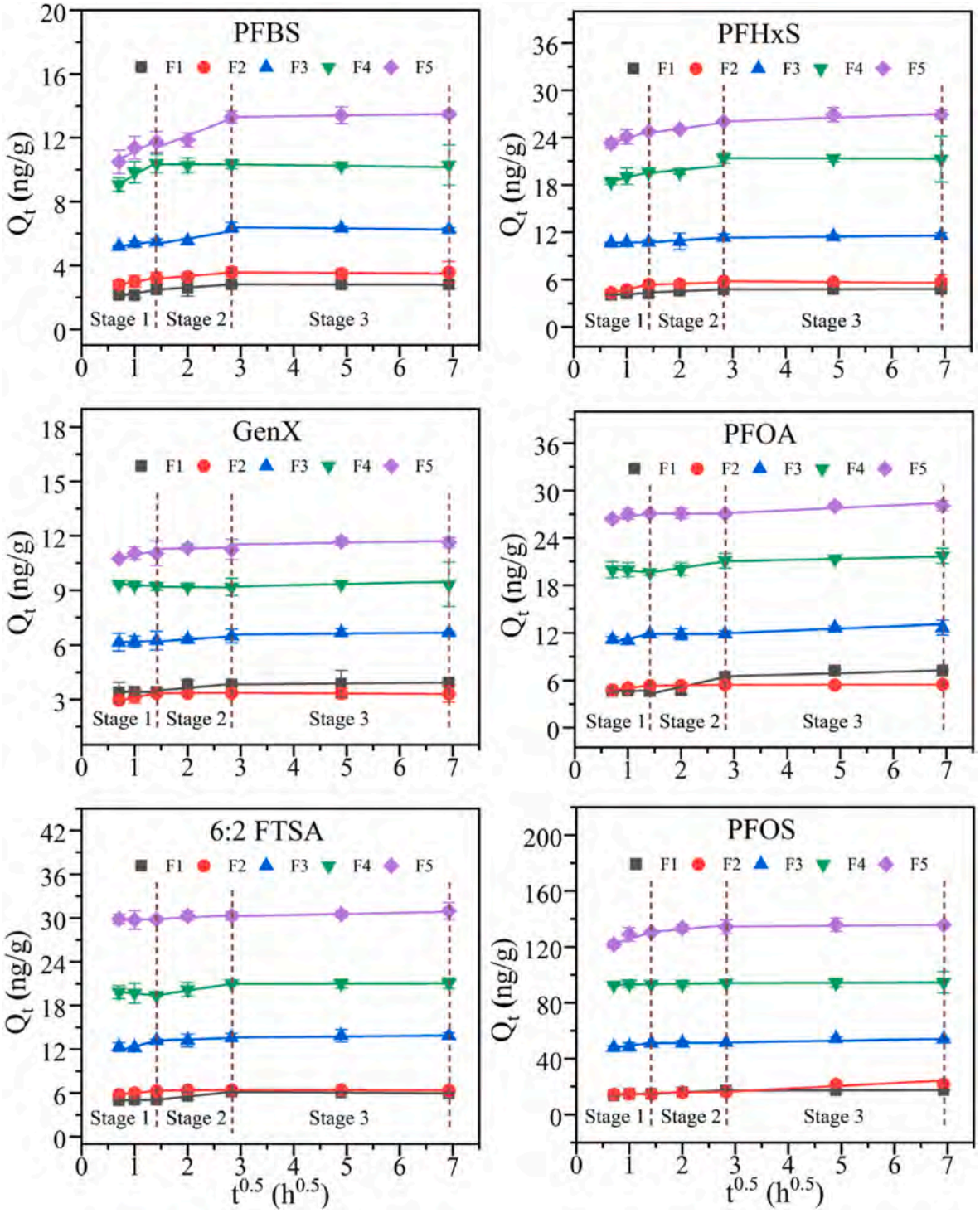


Fig. 3. The intraparticle diffusion models for the sorption of PFASs on different particle size fractions of sediments.

(ng/g dw), C_m is the maximum sorption capacity of PFASs in sediment (ng/g dw), C_e indicates the equilibrium concentration of PFASs in aqueous solution (ng/mL), K_F ((ng/g)/(ng/mL)^n) and K_L (mL/ng) are the sorption capacity constant, and n is an empirical dimensionless parameter describing the degree of isothermal non-linearity. The sorption isotherm is convex and non-linear when $n < 1$, but concave and linear when $n > 1$ (Milinovic et al., 2015).

Besides, pseudo-first-order and pseudo-second-order models, and the calculation method for the sediment-water distribution coefficient (K_d) are provided in Text S4.

2.9. Statistical analyses

Data are presented as mean ± standard deviation (SD). The Shapiro-Wilk test was used to assess data normality, and Levene's test evaluated variance homogeneity. Pearson correlation analysis was performed to investigate the relationships between the log K_{oc}, log D, and electrostatic potential (E_p). Statistical analyses were conducted using SPSS (IBM, Statistics 26, USA), with significance set at $p < 0.05$.

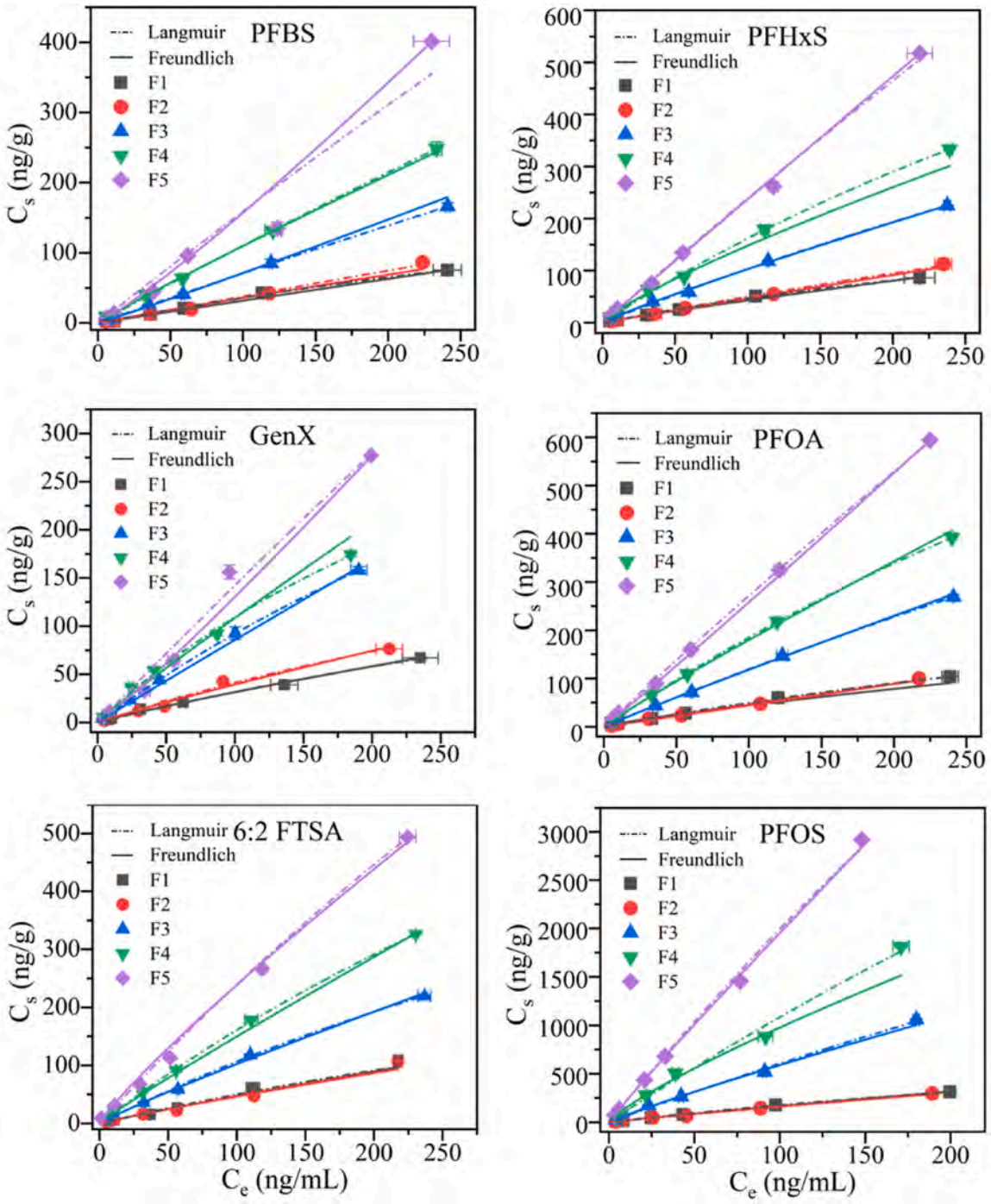


Fig. 4. The Freundlich models and Langmuir models for the sorption of PFASs on different particle size fractions of sediments.

3. Results and discussion

3.1. Characterization and contribution of particles with different sizes

The sediment was fractionated into five particle size categories: F1 (coarse sand, 69.4–190 μm), F2 (fine sand, 63.3–163 μm), F3 (coarse particles, 5.25–72.6 μm), F4 (fine particles, 3.29–34.7 μm), and F5 (clay particles, 1.69–22.7 μm) (Table S1). The mass fraction of each fraction varied, with F2 contributing the most (52.9 %), followed by F1 (22.3 %), and the smaller fractions F3 (6.0 %), F4 (9.1 %), and F5 (5.7 %). In terms of surface characteristics, F5 exhibited the highest TOC content (1.58 %) and BET surface area (37.98 m^2/g), while F1 and F2 had lower TOC content (0.14 % and 0.12 %, respectively). F5 also had the smallest pore size (3.05–3.83 nm), which is consistent with its higher organic content. The TOC content was higher in the finer fractions (F4 and F5) compared to the coarser ones (F1 and F2), which likely contributed to their higher sorption capacity for PFASs.

The sorption capacity of all PFASs on different fractions generally followed the order: F1 ≤ F2 < F3 < F4 < F5, with the maximum values ranging from 11.7 ng/g dw for GenX to 136 ng/g dw for PFOS. This can be ascribed to the relatively increased TOC content, BET surface area and pore volume in F5 than in the remaining fractions (Table S1). Likewise, previous studies reported a decrease in PFOS and PFOA sorption as soil particle size increased (Chen et al., 2020; Xiang et al., 2018). The sorption contribution of different fractions followed the order: F3 < F1 < F5 < F4 < F2. Although F2 had relatively low sorption

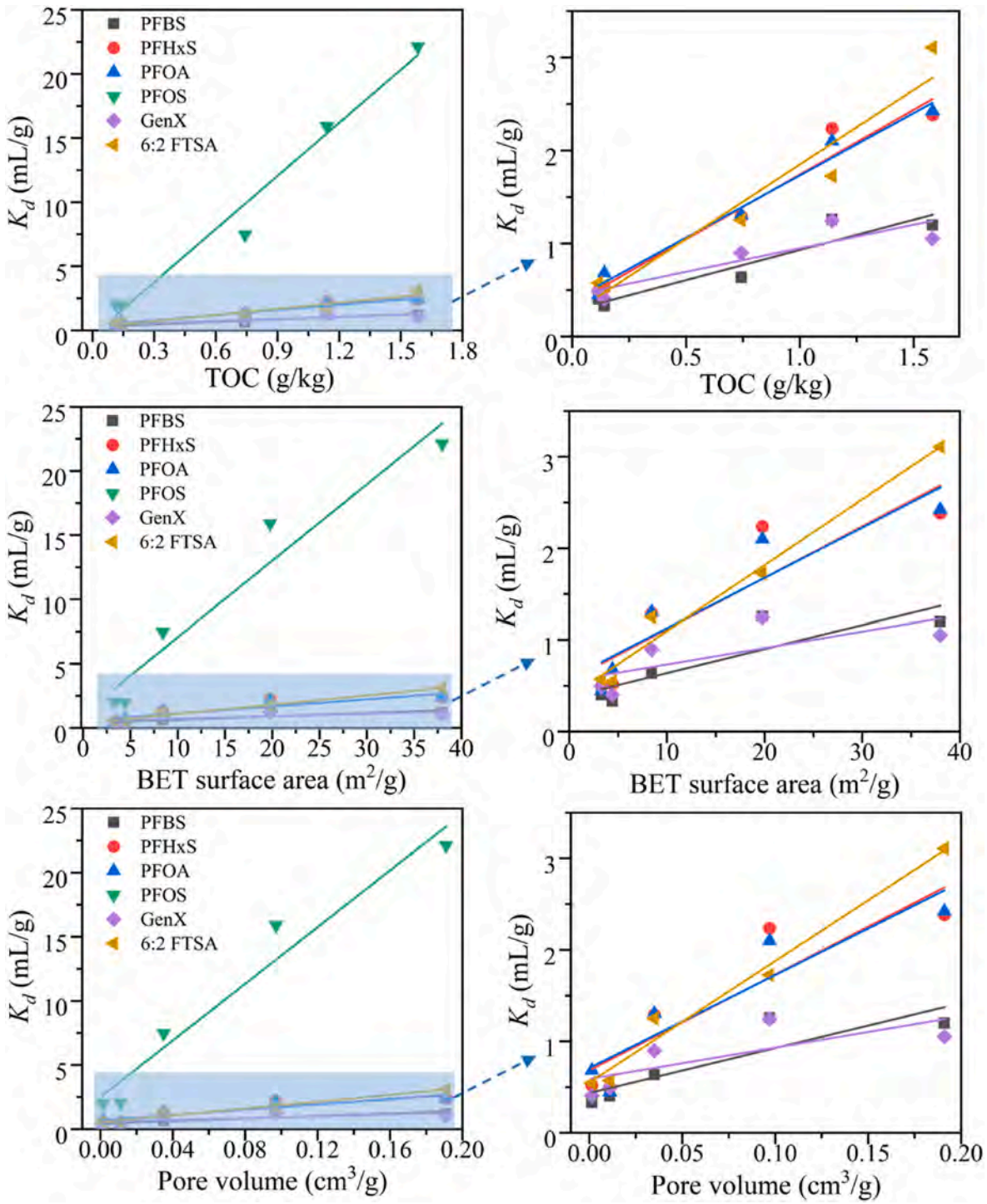


Fig. 5. Relationships between K_d values of PFASs and the physicochemical properties of the sediments.

capacity, its large mass fraction enabled it to dominate the sorption contribution of PFASs (32.9 %–41.2 %, Table S4). In contrast, F3 contributed the least due to its low organic matter content and small mass fraction (8.2 %–9.3 %).

3.2. Sorption kinetic of PFASs on different particle sizes of sediments

Fig. 1 shows the pseudo-first-order curves for the sorption of six PFASs on the five particle size fractions of sediments (F1, F2, F3, F4 and F5). Similar sorption trends were observed among different sediment fractions for all PFASs examined. Specifically, sorption occurred rapidly within 0–2 h while slowly during 2–8 h, and reached the dynamic equilibrium at approximately the 8th h. At equilibrium, the sorption concentrations of the six PFASs in different particle sizes of sediments (F1-F5) followed the order: PFOS (17.5–136 ng/g dw) > 6:2 FTSA (5.96–31.0 ng/g dw) > PFOA (5.50–28.1 ng/g dw) > PFHxS (4.80–26.9 ng/g dw) > PFBS (2.79–13.5 ng/g dw) > GenX (3.30–11.7 ng/g dw). These results suggest that the equilibrium concentrations of PFASs adsorbed onto the sediment increase with increasing length of -CF_2. Likewise, a higher equilibrium concentration has been found for PFOS as compared to PFOA (Chen et al., 2020; Xiang et al., 2018). Notably, the functional groups of PFASs also play a significant role in their sorption

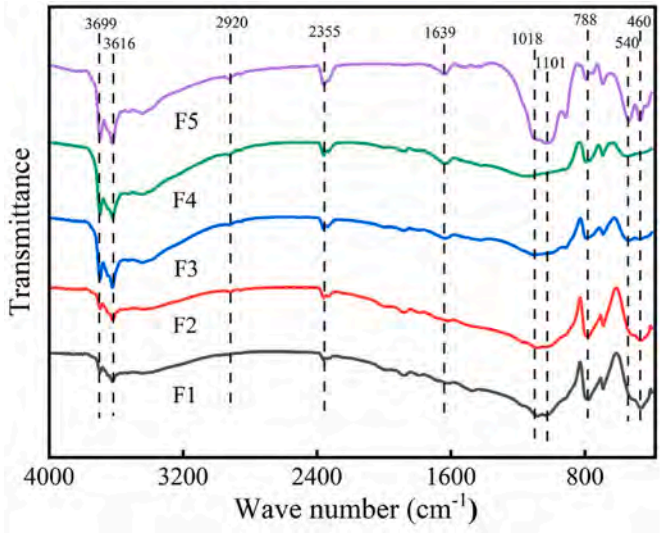


Fig. 6. The *Fourier transform infrared* (FTIR) spectra of different sediment particle size fractions (F1-F5).

behavior. Specifically, PFOS (pK_a = −3.3) exhibits stronger acidity, reactivity and metal affinity compared to PFOA (pK_a = −0.2) (Ali et al., 2024; Ordonez et al., 2022), which enhances its affinity for sediment particles. Similarly, the equilibrium level of 6:2 FTSA (5.50–28.1 ng/g dw) was much lower than that of PFOS (17.5–136 ng/g dw), even though these two PFASs have the same length of carbon chains. This difference can be attributed to the relatively lower hydrophobic contribution of -CH_2 in 6:2 FTSA (log D = 2.04) than -CF_2 in PFOS (log D = 3.71), given the smaller atomic size of H than F (Mejia-Avendaño et al., 2020).

The sorption of PFASs on sediment followed a pseudo-second-order kinetic model (R^2 > 0.99) (Fig. 2 and Table S4), with less than 5 % difference between the calculated (Q_e) and experimentally determined equilibrium sorption amount (Q_{exp}). This kinetic behavior suggests that sorption may be influenced by surface interactions rather than simple diffusion (Ho and McKay, 1999; Wei et al., 2017). Given the role of active sites such as organic matter in sediment sorption, further investigation is needed to clarify their contribution to PFASs binding mechanisms.

To enhance our understanding of the sorption mechanisms of PFASs on various particle size fractions of sediment, we further applied the particle diffusion model to interpret the sorption kinetics data (Fig. 3 and Table S5). We observed three stages involving in the sorption process, together with C_i values greater than 0 in all fitted models because a non-zero intercept (C_i) implies the involvement of multiple mechanisms in the sorption process according to diffusion theory (Wei et al., 2017; Xiang et al., 2018, 2019), this observed three-stage sorption process likely involves: i) film or boundary diffusion, with PFAS sorption primarily occurring on the surface of sediment particles of varying sizes; ii) particle diffusion, where sorption takes place within the pores of these particles; and iii) equilibrium sorption, as PFASs reach the inner surfaces of sediment fractions. Indeed, the pore size distribution predominantly ranged between 3.054 and 3.825 nm in all sediment fractions examined here (Table S1), and all examined PFASs had estimated molecular size radius ≤1.935 nm, with the largest molecular size being observed for PFOS based on the van der Waals radii for H (0.110 nm), C (0.170 nm), F (0.135 nm), O (0.140 nm) and S (0.180 nm). Hence, PFASs were able to diffuse freely in the pore of the sediment (Gavezzotti, 1983; Wei et al., 2017; Xiang et al., 2018).

3.3. Sorption isotherm of PFASs on different particle sizes of sediments

The PFAS sorption data fit well with both the Freundlich and Langmuir models (R^2 ≥ 0.954; Fig. 4 and Tables S6–S7); the former is commonly used to characterize PFAS sorption equilibrium when both models demonstrate a robust fit (Zhang et al., 2013). Here, none of n values were equal to 1 for F1-F5 fractions, suggesting nonlinear sorption of PFASs on these fractions. This nonlinear sorption is probably related to the heterogeneity of the sorption sites and the interaction between adsorbates (PFASs) and the adsorbent including the repulsive electrostatic interaction (Cheung et al., 2001; Higgins and Luthy, 2006). Moreover, the interaction among adsorbed PFASs may also have contributed to the observed non-linear isotherms, such as electrostatic repulsion generated by ionized functional groups (Li et al., 2019; Mejia-Avendaño et al., 2020). Among all tested fractions, F5 consistently exhibited the highest K_F values, particularly for long-chain PFASs, with values reaching 24.00 for PFOS and 2.27 for PFOA. These results indicate that the finer particle-size fraction possesses significantly enhanced sorption capacity compared to coarser fractions. This trend aligns with the observed log K_{oc} values, where PFOS showed the highest affinity (log K_{oc} = 4.15 in F5). The correlation between high K_F and log K_{oc} values in F5 suggests that sorption was strongly influenced by organic carbon content, reinforcing the role of hydrophobic interactions in PFAS retention. This can further be facilitated by the hydrophobic interactions between PFAS molecules, leading to the concave sorption isotherms for PFASs (Wang et al., 2015). Overall, these findings suggest that sorption of PFASs in sediments is primarily controlled by organic matter content, surface heterogeneity, and electrostatic interactions, rather than simple partitioning mechanisms.

3.4. Effect of physicochemical properties of sediment on PFASs sorption

To evaluate the sorption performance of various sediment fractions toward PFAS, the K_d values of PFASs sorption (10 μg/L) on these fractions (F1-F5) were obtained using the Freundlich model (Table S7). For the same sediment fraction, the K_d value increased with the increase in carbon-fluorine chain length, by approximately 0.414–5.22 mL/g per -CF_2 unit, depending on the particle size fractions. On all sediment fractions (F1-F5), PFOA and PFOS exhibited greater sorption than their respective substitutes, GenX and 6:2 FTSA. Specifically, the K_d values for these four PFASs were in the ranges of 0.68–2.42 mL/g for PFOA, 1.98–22.14 mL/g for PFOS, 0.41–1.25 mL/g for GenX and 0.55–3.11 mL/g for 6:2 FTSA, respectively. PFOA (log D = 2.27) demonstrated K_d values 0.40–0.65 times higher than its substitute GenX (log D = 0.74), while PFOS (log D = 3.71) exhibited 2.64–6.12 times greater K_d values compared to 6:2 FTSA (log D = 2.04). These results highlight the role of hydrophobic interactions in PFAS sorption onto sediment.

The relationships between the K_d values of PFASs and the physical properties (TOC, pore volume and BET surface area) of the different sediment fractions are shown in Fig. 5 and Table S8. Significant positive correlations were found between K_d and TOC for all PFASs examined (R^2 ≥ 0.795, p < 0.05), suggesting the impact of TOC on PFASs sorption. This is not unexpectedly since it has been demonstrated that sediment organic matter contained a large amount of sorption active functional groups that can facilitate PFASs sorption, such as -SO_3^-, -COO^-, -C=O and -OH (Adeola and Forbes, 2021; Xu et al., 2006; Zhang and He, 2010). Sulfonic acid group is a hard base while carboxylic acid group is a soft base according to the hard-soft acid-base theory (Wang et al., 2012). Correspondingly, here we found that perfluoroalkyl sulfonic acids (PFSAs: PFOS and 6:2 FTSA) with the same length of carbon chains (hard base) were more easily adsorbed onto oxide surfaces (hard acid) than their counterparts, perfluoroalkyl carboxylic acid (PFCA: PFOA) (Du et al., 2014). Similarly, certain surface functional groups (such as -C=O, -OH and metal-complexed groups) can be regarded as Lewis acid sites and thereby facilitate PFASs sorption, according to the Lewis acid and base concept (Punyapalakul et al., 2013; Yu et al., 2009). Similar to TOC, the pore volume of sediment fractions was also positively correlated with K_d values (R^2 ≥ 0.554, p ≤ 0.048). Therefore, higher pore volume is likely to result in greater sorption capacity of sediment for

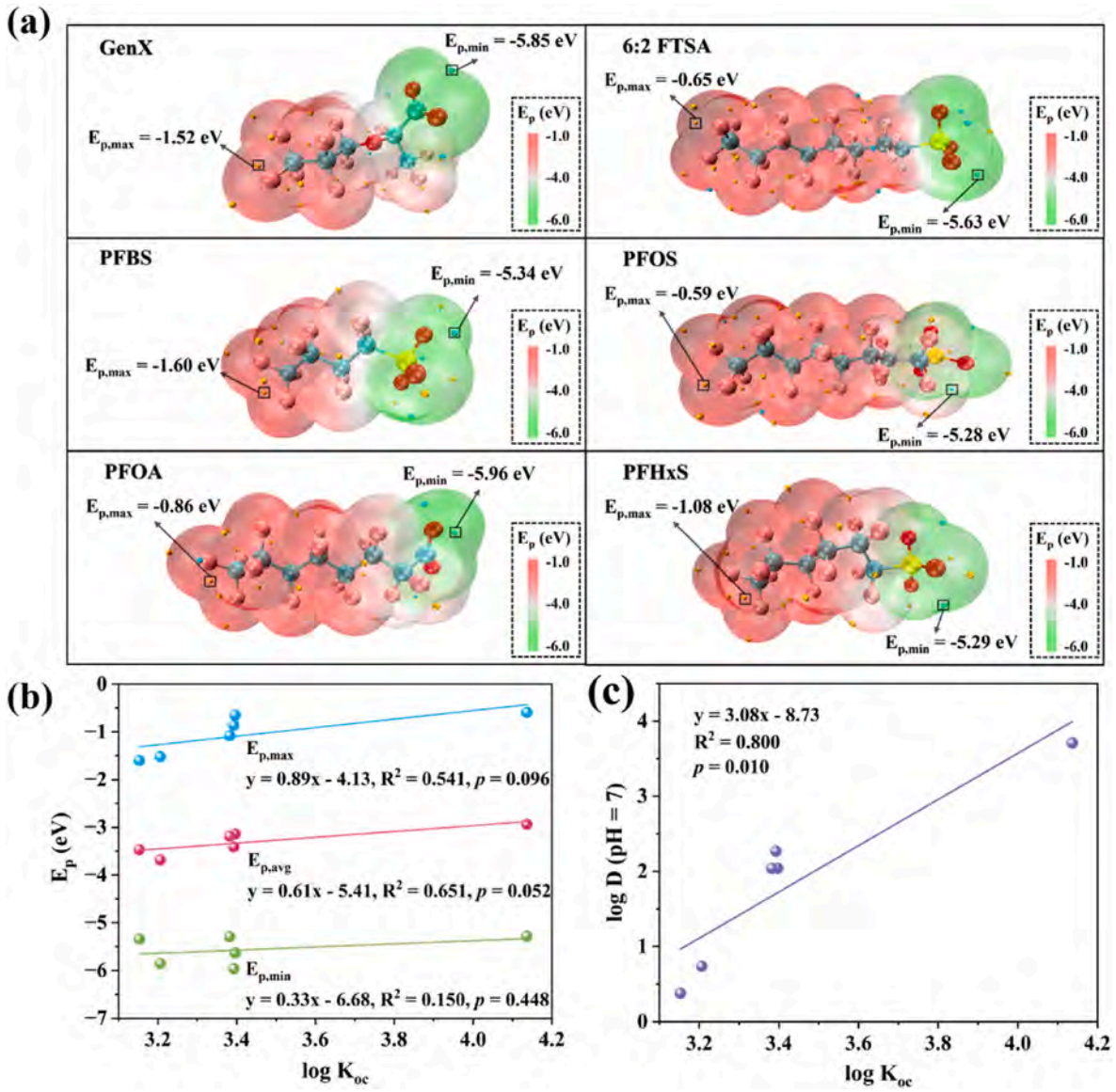


Fig. 7. The electrostatic potential of PFASs (a), Pearson correlation analysis between electrostatic potential and log K_{oc} (b), Pearson correlation analysis between log D and log K_{oc} (c).

Note: The yellow spheres on the electrostatic potential surface represent the $E_{p,max}$, while the blue spheres represent the $E_{p,min}$. (For interpretation of the references to colour in this figure legend, the reader is referred to the Web version of this article.)

PFASs. In agreement with our results, Du et al. (2014) found that the presence of pores enhanced PFASs sorption via providing sufficient space to accommodate large PFAS molecules and aggregates. Regarding BET surface area of sediment components, it was significantly positively correlated with the K_d values of all PFASs except GenX and PFBS ($R^2 \geq 0.808$, $p \leq 0.038$). Therefore, smaller sediment particles can present stronger sorption for PFASs, as they possess elevated specific surface areas and further more sorption sites than large sediment particles (Xiang et al., 2019). The lack of correlations between K_d values and specific surface area for GenX and PFBS might be related to their weak hydrophobicity caused by short chain.

Among the factors (e.g., TOC, BET surface area) that can influence the sorption of chemicals on sediment, TOC has been considered the main factor impacting the sorption of organic pollutants including PFASs (Adeola and Forbes, 2021; Huang et al., 2003; Wang et al., 2006; Zhang and He, 2010). Therefore, K_{oc} was calculated to compare the sorption potential of PFASs on F1-F5 (Table S7). Log K_{oc} values of PFASs ranged from 2.82 to 4.24, with ranges of 3.18–3.68 and 4.00–4.24 being found for PFOA and PFOS, respectively. Similar or relatively lower log K_{oc} values have been reported for these two PFASs in soil (Milinovic et al., 2015; Xiang et al., 2018). This variation may be linked to the differing physicochemical properties of sediment and soil. Among PFASs, log K_{oc} increased with increasing -CF_2 length, revealing the important role of hydrophobic interactions in the PFASs sorption process.

3.5. Influence of hydrophobic and electrostatic interactions

To further investigate the sorption mechanisms of PFASs on different sediment particle size fractions, we characterized these sediment fractions using Fourier transform infrared (FTIR) spectroscopy (Fig. 6). Multiple peaks were observed in all sediment fractions (F1-F5), including those well-known, namely 3699 cm^{-1} and 3616 cm^{-1} corresponding to the -OH stretching vibration, 2920 cm^{-1} representing the characteristic peak of fatty C-H bonds, and 2355 cm^{-1} corresponding to the -C=C=O stretching vibration. Peaks were also observed at

wavelengths of 788, 540, and 460 cm^{-1}, which correspond to the Fe-OH and Fe-O vibrations (Wang et al., 2016; Wei et al., 2017; Xiang et al., 2018). The -OH stretching vibrations, along with Fe-OH and Fe-O vibrations, suggested that PFAS sorption onto soil components likely involved hydrogen bonding and metal-mediated effects. A previous study found that the carboxyl group of PFOA could form inner-sphere Fe-carboxylate complexes in iron oxides through covalent metal-ligand bonding (Gao and Chorover, 2012). Similarly, the carboxyl groups on PFASs formed hydrogen bonds with hydroxyl groups in sediments (Jing et al., 2022). Notably, the C=C stretching vibration attributed to 1639 cm^{-1} appeared only in F4 and F5 while the C-O stretching vibration attributed to 1018 and 1101 cm^{-1} appeared only in F5, likely a result of the differences in organic matter content among different particle size fractions. These results suggest that F5 had the most abundant functional groups that can facilitate PFASs sorption, which can partially explain the greatest PFASs sorption capacity observed in this fraction (K_d = 1.05–22.14 mL/g). Furthermore, these rich functional groups suggest the presence of some cationic and anionic charges on sediments. Such positive charges can interact with PFASs through electrostatic interaction. Indeed, it has been demonstrated that electrostatic interaction was one of the primary mechanisms for PFASs sorption onto sediment (Li et al., 2018; Sima and Jaffe, 2021; Zhang et al., 2019).

The surface electrostatic potential of PFAS ions revealed that all of them were negatively charged (Fig. 7), indicating that they can be readily attracted to the positive charges on the sediment OM (Nguyen et al., 2020). with increasing -CF_2 length of the PFAS, suggesting a reduction in effective charge. In contrast, the -CF_2 did not significantly impact the absolute value of minimum E_p ($E_{p,min}$). However, this $E_{p,min}$ was influenced by the functional group (head) of PFASs, leading to PFSAs (PFOS, 6:2 FTSA, PFBS and PFHxS) having smaller absolute values of $E_{p,min}$ than PFCAs (PFOA and GenX). Noticeably, the -CH_2 group of 6:2 FTSA can reduce electron withdrawal by the head group through elevating the distance between the -CF_2 and the -SO_3^- (Parker et al., 2022); 6:2 FTSA had elevated net charge of the head group but lower net charge of the fluorinated tail than PFHxS. Since both tail and head groups affect the overall E_p of PFAS, the average E_p ($E_{p,avg}$) was utilized to represent the overall electrostatic potential. In fact, $E_{p,avg}$ has been shown to increase with an increase in -CF_2 length or when the head group changes from carboxylate to sulfonate (Parker et al., 2022). However, in the present study, $E_{p,max}$, $E_{p,min}$ and $E_{p,avg}$ were not significantly correlated with log K_{oc} (R^2 = 0.150–0.651, $p > 0.05$), which differ from the sorption behavior previously found for cationic and zwitterionic PFASs in natural soils (Xiao et al., 2019). Therefore, electrostatic interaction alone was not able to adequately explain the sorption of anionic PFASs on sediment.

Partition coefficient (log P) is commonly used as a parameter of the hydrophobicity of a chemical (Carotti et al., 2023). However, for ionizable compounds like PFASs, the distribution of both ionized and non-ionized forms in water need to be considered (Win et al., 2023). Hence, log D rather than log P is often used to represent the hydrophobicity of PFASs under different pH conditions. We observed a significant correlation between log K_{oc} and log D at pH = 7 (R^2 = 0.80, p = 0.01), which indicates that hydrophobic interaction played a significant role in the sorption of PFASs (Du et al., 2014; Higgins and Luthy, 2006). The difference in the sorption behavior observed between anionic PFASs and cationic or zwitterionic PFASs highlights that the sorption of anionic PFASs in soil and sediment is primarily driven by hydrophobic interaction (Xiao et al., 2019).

4. Conclusions

The present study found that the sorption kinetics of PFASs on different sediment particle size fractions fitted well the pseudo-second order model, with the sorption process involving membrane diffusion, intraparticle diffusion and boundary layer effects. Moreover, PFASs sorption isotherm data conformed well to the Freundlich equation, suggesting their nonlinear sorption behavior on the sediment. The K_d values of PFASs increased with sediment fractions' TOC, specific surface area and pore volume. In parallel, the sorption capacity of PFASs on sediment increased with the length of their -CF_2 chain while decreased with increasing sediment particle size. Our results further demonstrate that hydrophobic interactions can better explain the sorption of anionic PFASs on sediments than electrostatic interactions.

CRediT authorship contribution statement

Jun-Jie Hu: Writing – original draft, Investigation. **Shang-Ke Yu:** Writing – original draft, Investigation. **Chao Yin:** Methodology, Investigation. **Feng-Jiao Peng:** Writing – original draft. **Shuang-Shuang Liu:** Writing – review & editing. **Chang-Gui Pan:** Writing – review & editing, Supervision, Funding acquisition, Conceptualization. **Kefu Yu:** Writing – review & editing, Resources.

Declaration of competing interest

The authors declare that they have no known competing financial interests or personal relationships that could have appeared to influence the work reported in this paper.

Acknowledgments

The authors would like to thank the financial support by the National Natural Science Foundation of China (42067054; 42207322; 41673105) and the Innovation Project of Guangxi Graduate Education (YCBZ2023032).

Appendix A. Supplementary data

Supplementary data to this article can be found online at https://doi.org/10.1016/j.envres.2025.121643.

Data availability

Data will be made available on request.

References

Adeola, A.O., Forbes, P.B.C., 2021. Influence of natural organic matter fractions on PAH sorption by stream sediments and a synthetic graphene wool adsorbent. Environ. Technol. Innovat. 21. https://doi.org/10.1016/j.eti.2020.101202.

Ahmed, M., Johir, M., McLaughlan, R., Nguyen, L.N., Xu, B., Nghiem, L.D., 2020. Per-and polyfluoroalkyl substances in soil and sediments: occurrence, fate, remediation and future outlook. Sci. Total Environ. 748, 141251. https://doi.org/10.1016/j.scitotenv.2020.141251.

Ali, M.A., Thapa, U., Antle, J., Tanim, E.U.H., Aguilar, J.M., Bradley, I.M., et al., 2024. Influence of water chemistry and operating parameters on PFOS/PFOA removal using rGO-nZVI nanohybrid. J. Hazard Mater. 469, 133912. https://doi.org/10.1016/j.jhazmat.2024.133912.

Bogdan, A.R., Klos, K.S., Greene, C.W., Huset, C.A., Barry, K.M., Goeden, H.M., 2024. Per-and polyfluoroalkyl substances (PFAS) in powdered infant formula: potential exposures and health risks. Journal of Environmental Exposure Assessment 3, 14. https://doi.org/10.20517/jeea.2024.08.

Carotti, A., Varfaj, I., Pruscini, I., Abualzulof, G.W.A., Mercolini, L., Bianconi, E., et al., 2023. Estimating the hydrophobicity extent of molecular fragments using reversed-phase liquid chromatography. J. Separ. Sci. 46, 1–12. https://doi.org/10.1002/jssc.202300346.

Chen, X.T., Yu, P.F., Xiang, L., Zhao, H.M., Li, Y.W., Li, H., et al., 2020. Dynamics, thermodynamics, and mechanism of perfluorooctane sulfonate (PFOS) sorption to various soil particle-size fractions of paddy soil. Ecotoxicol. Environ. Saf. 206, 111105. https://doi.org/10.1016/j.ecoenv.2020.111105.

Cheung, C., Porter, J., Mckay, G., 2001. Sorption kinetic analysis for the removal of cadmium ions from effluents using bone char. Water Res. 35, 605–612. https://doi.org/10.1016/s0043-1354(00)00306-7.

Dey, D., Shafi, T., Chowdhury, S., Dubey, B.K., Sen, R., 2024. Progress and perspectives on carbon-based materials for adsorptive removal and photocatalytic degradation of perfluoroalkyl and polyfluoroalkyl substances (PFAS). Chemosphere, 141164. https://doi.org/10.1016/j.chemosphere.2024.141164.

Du, Z., Deng, S., Bei, Y., Huang, Q., Wang, B., Huang, J., et al., 2014. Adsorption behavior and mechanism of perfluorinated compounds on various adsorbents–a review. J. Hazard Mater. 274, 443–454. https://doi.org/10.1016/j.jhazmat.2014.04.038.

El-Aswad, A.F., Aly, M.I., Fouad, M.R., Badawy, M.E., 2019. Adsorption and thermodynamic parameters of chlorantraniliprole and dinotefuran on clay loam soil with difference in particle size and pH. Journal of Environmental Science and Health, Part B 54, 475–488. https://doi.org/10.1080/03601234.2019.1595893.

Evich, M.G., Davis, M.J.B., McCord, J.P., Acrey, B., Awkerman, J.A., Knappe, D.R.U., et al., 2022. Per- and polyfluoroalkyl substances in the environment. Science 375. https://doi.org/10.1126/science.abg9065.

Fagbayigbo, B., Opeolu, B., Fatoki, O., Olatunji, O., Akharame, M., Human, I., 2022. Sorption and partitioning of perfluorooctanoic acid (PFOA) and perfluorooctane sulfonate (PFOS) onto sediments of diep and plankenburg river systems Western Cape, South Africa. Environ. Technol. Innovat. 25, 102110. https://doi.org/10.1016/j.eti.2021.102110.

Fischer, F.C., Ludtke, S., Thackray, C., Pickard, H.M., Haque, F., Dassuncao, C., et al., 2024. Binding of per-and polyfluoroalkyl substances (PFAS) to serum proteins: implications for toxicokinetics in humans. Environmental Science & Technology 58, 1055–1063. https://doi.org/10.1021/acs.est.3c07415.

Gaballah, S., Swank, A., Sobus, J.R., Howey, X.M., Schmid, J., Catron, T., et al., 2020. Evaluation of developmental toxicity, developmental neurotoxicity, and tissue dose in zebrafish exposed to GenX and other PFAS. Environmental Health Perspectives 128, 047005. https://doi.org/10.1289/ehp5843.

Gaines, L.G.T., 2022. Historical and current usage of per- and polyfluoroalkyl substances (PFAS): a literature review. Am. J. Ind. Med. 66, 353–378. https://doi.org/10.1002/ajim.23362.

Gao, X., Chorover, J., 2012. Adsorption of perfluorooctanoic acid and perfluorooctanesulfonic acid to iron oxide surfaces as studied by flow-through ATR-FTIR spectroscopy. Environ. Chem. 9, 148–157. https://doi.org/10.1071/EN11119.

Gavezzotti, A., 1983. The calculation of molecular volumes and the use of volume analysis in the investigation of structured media and of solid-state organic reactivity. J. Am. Chem. Soc. 105, 5220–5225. https://doi.org/10.1021/ja00354a007.

Greene, C.W., Bogdan, A.R., Goeden, H.M., 2024. A revised and improved toxicokinetic model to simulate serum concentrations of bioaccumulative PFAS. Journal of Environmental Exposure Assessment 3, 12. https://doi.org/10.20517/jeea.2024.09.

Higgins, C.P., Luthy, R.G., 2006. Sorption of perfluorinated surfactants on sediments. Environmental Science & Technology 40, 7251–7256. https://doi.org/10.1021/es061000n.

Ho, Y.-S., McKay, G., 1999. The sorption of lead (II) ions on peat. Water Res. 33, 578–584. https://doi.org/10.1016/S0043-1354(98)00207-3.

Huang, W., Yu, Z., Fu, J., 2003. Effects of organic matter heterogeneity on sorption and desorption of organic contaminants by soils and sediments. Appl. Geochem. 18, 955–972. https://doi.org/10.1016/s0883-2927(02)00205-6.

Jing, H., Huang, X., Du, X., Mo, L., Ma, C., Wang, H., 2022. Facile synthesis of pH-responsive sodium alginate/carboxymethyl chitosan hydrogel beads promoted by hydrogen bond. Carbohydr. Polym. 278, 118993. https://doi.org/10.1016/j.carbpol.2021.118993.

Kannan, N., Sundaram, M.M., 2001. Kinetics and mechanism of removal of methylene blue by adsorption on various Carbons—A comparative study. Dyes Pigments 51, 25–40. https://doi.org/10.1016/s0143-7208(01)00056-0.

Lees, K.E., Fitzsimons, M.F., Snape, J., Tappin, A., Comber, S.D., 2021. Developing the OECD 106 fate testing protocol for active pharmaceuticals in soil. Environ. Technol. 42, 2551–2561. https://doi.org/10.1080/09593330.2019.1706643.

Leung, S.C.E., Shukla, P., Chen, D., Eftekhari, E., An, H., Zare, F., et al., 2022. Emerging technologies for PFOS/PFOA degradation and removal: a review. Sci. Total Environ. 827. https://doi.org/10.1016/j.scitotenv.2022.153669.

Li, F., Fang, X., Zhou, Z., Liao, X., Zou, J., Yuan, B., et al., 2019. Adsorption of perfluorinated acids onto soils: Kinetics, isotherms, and influences of soil properties. Sci. Total Environ. 649, 504–514. https://doi.org/10.1016/j.scitotenv.2018.08.209.

Li, X., Wang, Y., Cui, J., Shi, Y., Cai, Y., 2024. Occurrence and fate of per- and polyfluoroalkyl substances (PFAS) in atmosphere: size-dependent gas-particle partitioning, precipitation scavenging, and amplification. Environmental Science & Technology 58, 9283–9291. https://doi.org/10.1021/acs.est.4c00569.

Li, Y., Oliver, D.P., Kookana, R.S., 2018. A critical analysis of published data to discern the role of soil and sediment properties in determining sorption of per and polyfluoroalkyl substances (PFASs). Sci. Total Environ. 628–629, 110–120. https://doi.org/10.1016/j.scitotenv.2018.01.167.

Li, Z., Li, X., Wang, S., Che, F., Zhang, Y., Yang, P., et al., 2023. Adsorption and desorption of heavy metals at water sediment interface based on Bayesian model. J. Environ. Manag. 329. https://doi.org/10.1016/j.jenvman.2022.117035.

Liu, Z.-Z., Pan, C.-G., Peng, F.-J., Hu, J.-J., Tan, H.-M., Zhu, R.-G., et al., 2024. Rapid adsorptive removal of emerging and legacy per- and polyfluoroalkyl substances (PFASs) from water using zinc chloride-modified litchi seed-derived biochar. Bioresour. Technol. 408, 131157. https://doi.org/10.1016/j.biortech.2024.131157.

Lu, T., Chen, F., 2011. Multiwfn: a multifunctional wavefunction analyzer. J. Comput. Chem. 33, 580–592. https://doi.org/10.1002/jcc.22885.

Luo, Y., Chen, J., Wu, C., Zhang, J., Tang, J., Shang, J., et al., 2019. Effect of particle size on adsorption of norfloxacin and tetracycline onto suspended particulate matter in Lake. Environmental Pollution 244, 549–559. https://doi.org/10.1016/j.envpol.2018.10.066.

Marciano, J., Crawford, L., Mukhopadhyay, L., Scott, W., McElroy, A., McDonough, C., 2024. Per/Polyfluoroalkyl substances (PFASs) in a marine apex predator (White shark, carcharodon carcharias) in the northwest Atlantic Ocean. ACS Environmental Au 4, 152–161. https://doi.org/10.1021/acsenvironau.3c00055.

Mejia-Avendaño, S., Zhi, Y., Yan, B., Liu, J., 2020. Sorption of polyfluoroalkyl surfactants on surface soils: effect of molecular structures, soil properties, and solution chemistry. Environmental Science & Technology 54, 1513–1521. https://doi.org/10.1021/acs.est.9b04989.

Milinovic, J., Lacorte, S., Vidal, M., Rigol, A., 2015. Sorption behaviour of perfluoroalkyl substances in soils. Sci. Total Environ. 511, 63–71. https://doi.org/10.1016/j.scitotenv.2014.12.017.

Nguyen, T.M.H., Bräunig, J., Thompson, K., Thompson, J., Kabiri, S., Navarro, D.A., et al., 2020. Influences of chemical properties, soil properties, and solution pH on soil–water partitioning coefficients of per- and polyfluoroalkyl substances (PFASs). Environmental Science & Technology 54, 15883–15892. https://doi.org/10.1021/acs.est.0c05705.

Ordonez, D., Valencia, A., Sadmani, A.H.M.A., Chang, N.-B., 2022. Green sorption media for the removal of perfluorooctanesulfonic acid (PFOS) and perfluorooctanoic acid (PFOA) from water. Sci. Total Environ. 819, 152886. https://doi.org/10.1016/j.scitotenv.2021.152886.

Pan, C.G., Xiao, S.K., Yu, K.F., Wu, Q., Wang, Y.H., 2021. Legacy and alternative per- and polyfluoroalkyl substances in a subtropical marine food web from the beibu gulf, south China: fate, trophic transfer and health risk assessment. J. Hazard Mater. 403, 123618. https://doi.org/10.1016/j.jhazmat.2020.123618.

Parker, B.A., Knappe, D.R.U., Titaley, I.A., Wanzek, T.A., Field, J.A., 2022. Tools for understanding and predicting the affinity of per- and polyfluoroalkyl substances for anion-exchange sorbents. Environmental Science & Technology 56, 15470–15477. https://doi.org/10.1021/acs.est.1c08345.

Punyapalakul, P., Suksomboon, K., Prarat, P., Khaodhiar, S., 2013. Effects of surface functional groups and porous structures on adsorption and recovery of perfluorinated compounds by inorganic porous silicas. Separ. Sci. Technol. 48, 775–788. https://doi.org/10.1080/01496395.2012.710888.

Qi, Y., Zhang, T.C., 2016. Sorption and desorption of testosterone at environmentally relevant levels: effects of aquatic conditions and soil particle size fractions. J. Environ. Eng. 142, 04015045. https://doi.org/10.1061/(ASCE)EE.1943-7870.0001001.

Shen, N., Tang, J., Chen, J., Sheng, C., Han, T., He, X., et al., 2024. Occurrence and prevalence of per-and polyfluoroalkyl substances in the sediment pore water of mariculture sites: novel findings of PFASs from the bohai and yellow seas using a newly established analytical method. J. Hazard Mater. 471, 134256. https://doi.org/10.1016/j.jhazmat.2024.134256.

Sima, M.W., Jaffe, P.R., 2021. A critical review of modeling Poly- and perfluoroalkyl substances (PFAS) in the soil-water environment. Sci. Total Environ. 757, 143793. https://doi.org/10.1016/j.scitotenv.2020.143793.

Sühring, R., Busch, F., Fricke, N., Kötke, D., Wolschke, H., Ebinghaus, R., 2016. Distribution of brominated flame retardants and dechloranes between sediments and benthic fish — a comparison of a freshwater and marine habitat. Sci. Total Environ. 542, 578–585. https://doi.org/10.1016/j.scitotenv.2015.10.085.

Tan, W., Zhang, Y., He, X., Xi, B., Gao, R., Mao, X., et al., 2016. Distribution patterns of phthalic acid esters in soil particle-size fractions determine biouptake in soil-cereal crop systems. Sci. Rep. 6, 31987. https://doi.org/10.1038/srep31987.

Tang, L., Gudda, F.O., Wu, C., Ling, W., El-Ramady, H., Mosa, A., et al., 2022. Contributions of partition and adsorption to polycyclic aromatic hydrocarbons sorption by fractionated soil at different particle sizes. Chemosphere 301. https://doi.org/10.1016/j.chemosphere.2022.134715.

UNEP, 2009. Listing of perfluorooctane sulfonic acid, its salts and perfluorooctane sulfonyl fluoride. Stockholm Convention on Persistent Organic Pollutants. UNEP, Geneva, Switzerland.

Wang, F., Liu, C., Shih, K., 2012. Adsorption behavior of perfluorooctanesulfonate (PFOS) and perfluorooctanoate (PFOA) on boehmite. Chemosphere 89, 1009–1014. https://doi.org/10.1016/j.chemosphere.2012.06.071.

Wang, F., Shih, K., Leckie, J.O., 2015. Effect of humic acid on the sorption of perfluorooctane sulfonate (PFOS) and perfluorobutane sulfonate (PFBS) on boehmite. Chemosphere 118, 213–218. https://doi.org/10.1016/j.chemosphere.2014.08.080.

Wang, H., Zhu, J., Fu, Q., Hong, C., Hu, H., Violante, A., 2016. Phosphate adsorption on uncoated and humic acid-coated iron oxides. J. Soils Sediments 16, 1911–1920. https://doi.org/10.1007/s11368-016-1383-8.

UNEP, 2023. PFASs listed under the Stockholm Convention (overview). Stockholm Convention on Persistent Organic Pollutants. Secretariat of the Stockholm Convention.

Wang, Q., Huang, J., Liu, S., Wang, C., Jin, Y., Lai, H., et al., 2022. Aberrant hepatic lipid metabolism associated with gut microbiota dysbiosis triggers hepatotoxicity of novel PFOS alternatives in adult zebrafish. Environ. Int. 166, 107351. https://doi.org/10.1016/j.envint.2022.107351.

Wang, S., Jin, X., Bu, Q., Zhou, X., Wu, F., 2006. Effects of particle size, organic matter and ionic strength on the phosphate sorption in different trophic Lake sediments. J. Hazard Mater. 128, 95–105. https://doi.org/10.1016/j.jhazmat.2005.07.048.

Wasel, O., King, H., Choi, Y.J., Lee, L.S., Freeman, J.L., 2023. Differential developmental neurotoxicity and tissue uptake of the per-and polyfluoroalkyl substance alternatives, GenX and PFBS. Environmental science & technology 57, 19274–19284. https://doi.org/10.1021/acs.est.3c05023.

Wei, C., Song, X., Wang, Q., Hu, Z., 2017. Sorption kinetics, isotherms and mechanisms of PFOS on soils with different physicochemical properties. Ecotoxicol. Environ. Saf. 142, 40–50. https://doi.org/10.1016/j.ecoenv.2017.03.040.

Williams, K.L., Gladfelder, J.J., Quigley, L.L., Ball, D.B., Tjeerdema, R.S., 2017. Dissipation of the herbicide benzobicyclon hydrolysate in a model California rice field soil. J. Agric. Food Chem. 65, 9200–9207. https://doi.org/10.1021/acs.jafc.7b03679.

Win, Z.-M., Cheong, A.M.Y., Hopkins, W.S., 2023. Using machine learning to predict partition coefficient (log P) and distribution coefficient (log D) with molecular descriptors and liquid chromatography retention time. J. Chem. Inf. Model. 63, 1906–1913. https://doi.org/10.1021/acs.jcim.2c01373.

Wu, Y., Si, Y., Zhou, D., Gao, J., 2015. Adsorption of diethyl phthalate ester to clay minerals. Chemosphere 119, 690–696. https://doi.org/10.1016/j.chemosphere.2014.07.063.

Xiang, L., Sun, T.-F., Zheng, M.-J., Li, Y.-W., Li, H., Wong, M.-H., et al., 2016. Sorption of dodecyltrimethylammonium chloride (DTAC) to agricultural soils. Sci. Total Environ. 560, 197–203. https://doi.org/10.1016/j.scitotenv.2016.03.235.

Xiang, L., Wang, X.D., Chen, X.H., Mo, C.H., Li, Y.W., Li, H., et al., 2019. Sorption mechanism, kinetics, and isotherms of Di- n-butyl phthalate to different soil particle-size fractions. J. Agric. Food Chem. 67, 4734–4745. https://doi.org/10.1021/acs.jafc.8b06357.

Xiang, L., Xiao, T., Yu, P.F., Zhao, H.M., Mo, C.H., Li, Y.W., et al., 2018. Mechanism and implication of the sorption of perfluorooctanoic acid by varying soil size fractions. J. Agric. Food Chem. 66, 11569–11579. https://doi.org/10.1021/acs.jafc.8b03492.

Xiao, F., Hanson, R.A., Golovko, S.A., Golovko, M.Y., Arnold, W.A., 2018. PFOA and PFOS are generated from zwitterionic and cationic precursor compounds during water disinfection with chlorine or ozone. Environ. Sci. Technol. Lett. 5, 382–388. https://doi.org/10.1021/acs.estlett.8b00266.

Xiao, F., Jin, B., Golovko, S.A., Golovko, M.Y., Xing, B., 2019. Sorption and desorption mechanisms of cationic and zwitterionic per-and polyfluoroalkyl substances in natural soils: thermodynamics and hysteresis. Environmental Science & Technology 53, 11818–11827. https://doi.org/10.1021/acs.est.9b05379.

Xu, D., Zhu, S., Chen, H., Li, F., 2006. Structural characterization of humic acids isolated from typical soils in China and their adsorption characteristics to phenanthrene. Colloids Surf. A Physicochem. Eng. Asp. 276, 1–7. https://doi.org/10.1016/j.colsurfa.2005.09.038.

Yan, X.-Z., Peng, J., Liu, Y.-Q., Fan, R.-N., Ni, X.-Y., Gong, L., et al., 2025. Mixed exposure to PFOA and PFOS induces oocyte apoptosis and subfertility in mice by activating the hippo signaling pathway. Reprod. Toxicol. 132, 108829. https://doi.org/10.1016/j.reprotox.2024.108829.

Yin, C., Pan, C.G., Xiao, S.K., Wu, Q., Tan, H.M., Yu, K., 2022. Insights into the effects of salinity on the sorption and desorption of legacy and emerging per-and polyfluoroalkyl substances (PFASs) on marine sediments. Environmental Pollution 300, 118957. https://doi.org/10.1016/j.envpol.2022.118957.

Yu, L., Hua, Z., Liu, X., Xing, X., Zhang, C., Hu, T., et al., 2024. Multi-compartment levels and distributions of per- and polyfluoroalkyl substances surrounding fluorochemical manufacturing parks in China: a review of the current literature. J. Hazard Mater. 480, 136196. https://doi.org/10.1016/j.jhazmat.2024.136196.

Yu, Q., Zhang, R., Deng, S., Huang, J., Yu, G., 2009. Sorption of perfluorooctane sulfonate and perfluorooctanoate on activated carbons and resin: kinetic and isotherm study. Water Res. 43, 1150–1158. https://doi.org/10.1016/j.watres.2008.12.001.

Zhang, C., Yan, H., Li, F., Hu, X., Zhou, Q., 2013. Sorption of short- and long-chain perfluoroalkyl surfactants on sewage sludges. J. Hazard Mater. 260, 689–699. https://doi.org/10.1016/j.jhazmat.2013.06.022.

Zhang, D.Q., Zhang, W.L., Liang, Y.N., 2019. Adsorption of perfluoroalkyl and polyfluoroalkyl substances (PFASs) from aqueous solution - a review. Sci. Total Environ. 694, 133606. https://doi.org/10.1016/j.scitotenv.2019.133606.

Zhang, J., He, M., 2010. Effect of structural variations on sorption and desorption of phenanthrene by sediment organic matter. J. Hazard Mater. 184, 432–438. https://doi.org/10.1016/j.jhazmat.2010.08.123.

Zhang, J., Liu, J., Jin, R., Qiao, Y., Mao, J., Wang, Z., 2025. Prevalent per-and polyfluoroalkyl substances (PFASs) pollution in freshwater basins in China: a short review. Toxics 13, 135. https://doi.org/10.3390/toxics13020135.

Zhang, X., Zhou, X., Chen, H., Gao, X., Zhou, Y., Lee, H.K., et al., 2024. Changes in concentrations of polyfluoroalkyl substances in human milk over lactation time and effects of maternal exposure via analysis of matched samples. Environmental Science & Technology 58, 4115–4126. https://doi.org/10.1021/acs.est.3c09896.

Zhu, W., Liu, W., Jin, H., 2024. Sediment-seawater partitioning, bioaccumulation, and biomagnification of perfluorobutane sulfonamide in marine environment. Water Res. 255, 121466. https://doi.org/10.1016/j.watres.2024.121466.

Bioelectrochemistry 168 (2026) 109162



Contents lists available at ScienceDirect

Bioelectrochemistry

journal homepage: www.journals.elsevier.com/bioelectrochemistry





A ratiometric electrochemical DNA biosensor for the detection of crown-of-thorns starfish eDNA

Beihua Wen [a,1], Zhenyu Zhu [a,1], Junjie Zeng [a], Shiwei Wan [a], Chaoxin Zhang [a], Yingzhan Chen [a], Liwei Wang [a,b,*], Man Zhang [a,**], Kefu Yu [a]

[a] School of Resources, Environment and Materials; Guangxi Laboratory on the Study of Coral Reefs in the South China Sea, School of Marine Sciences, School of Chemistry and Chemical Engineering, Guangxi University, Nanning 530004, China
[b] Nansha Islands Coral Reef Ecosystem National Observation and Research Station, Guangzhou 510300, China

ARTICLE INFO

Keywords:
Ratiometric electrochemical DNA biosensor
Crown-of-thorns starfish
eDNA
Coral bleaching
Early warning

ABSTRACT

Recurring infestations of crown-of-thorns starfish (COTS) inflict severe harm on coral reef ecosystems. To prevent irreversible harm to coral ecosystems, early monitoring of COTS distribution before outbreaks is crucial for timely intervention and effective management. However, traditional monitoring methods are time-consuming, labor-intensive, and lack the sensitivity required for early warning and proactive control. In this study, a ratiometric electrochemical DNA biosensor was constructed for the detection of environmental DNA (eDNA) from COTS. This biosensor combines a dual-signal detection mechanism with internal calibration provided by a reference probe, along with a target recycling amplification strategy mediated by exonuclease III (Exo III). The biosensor exhibited outstanding analytical performance, with a low detection limit (LOD)of 93 fM and a linear response range spanning from 300 fM to 10 nM. Moreover, digital droplet PCR (ddPCR) verified the biosensor's accuracy and reliability ($P > 0.05$). The biosensor was successfully applied to detect COTS eDNA in environmental samples collected from the Paracel Islands. Therefore, the electrochemical biosensor is promising for detecting low-density COTS individuals or larvae before outbreaks, enabling early warning and facilitating timely ecological intervention.

1. Introduction

The coral reef ecosystem, with coral reefs at its core, possesses exceptionally high ecological and economic value [1]. The crown-of-thorns starfish (COTS), a type of echinoderm known for preying on live corals, particularly reef-building species, can trigger population surges that significantly disrupt coral reef ecosystems [2,3]. For instance, between 2017 and 2021, the rapid increase of COTS populations near Taiping Island within the Nansha Archipelago resulted in a dramatic reduction in coral coverage, dropping from 33 % to just 0.9 %, and causing over 97 % mortality of living corals [4]. Conventional approaches to detecting COTS mainly involve manta net tows as well as manual underwater surveys using scuba gear [5]. However, these methods require substantial human and material resources, and accurate quantification is challenging due to the cryptic nature of COTS. In light of the limitations of the methods mentioned above, it is crucial to develop more accurate and reliable detection strategies to enhance early monitoring capabilities. Recently, environmental DNA (eDNA)-based methods have gained widespread use in species monitoring, aquatic biodiversity assessment, and fish abundance analysis due to their simplicity, efficiency, non-invasiveness, and robust species identification capabilities. Studies have demonstrated a significant positive correlation between eDNA concentration and species biomass [6,7]. Uthicke et al. [8] showed that the population size and the spatial distribution of COTS across the Great Barrier Reef can be assessed by monitoring the dynamics of their eDNA using droplet digital PCR (ddPCR). However, ddPCR requires highly stringent reaction conditions, including precise thermal control and cycling parameters [9], which limits its excellent eDNA detection performance primarily to laboratory settings. Moreover, eDNA samples are susceptible to degradation during

* Corresponding author at: School of Resources, Environment and Materials; Guangxi Laboratory on the Study of Coral Reefs in the South China Sea, School of Marine Sciences, School of Chemistry and Chemical Engineering, Guangxi University, Nanning 530004, China.
** Corresponding author.
E-mail addresses: wangliwei@gxu.edu.cn (L. Wang), sdyczm@gxu.edu.cn (M. Zhang).
[1] These authors contributed equally to this work.

https://doi.org/10.1016/j.bioelechem.2025.109162
Received 22 August 2025; Received in revised form 30 October 2025; Accepted 2 November 2025
Available online 3 November 2025
1567-5394/© 2025 Elsevier B.V. All rights are reserved, including those for text and data mining, AI training, and similar technologies.

transport to the laboratory, and prolonged transit times can further increase costs [10]. Therefore, there is an urgent need to develop a simple and efficient detection method to enable on-site identification and application of eDNA.

Electrochemical biosensors offer an auspicious approach for on-site eDNA monitoring, thanks to their exceptional sensitivity, rapid responsiveness, low cost, portability, and user-friendly operation [11–19]. Wang et al. [20] were the first to develop an electrochemical DNA biosensor for identifying COTS eDNA, achieving a detection limit of 0.147 ng/μL. This pioneering work marked the initial application of such technology to enable early field alerts before the COTS outbreak. Building on this, Zhang et al. [21] proposed a cascade signal amplification strategy that combined catalytic hairpin assembly (CHA) and hybridization chain reaction (HCR), significantly enhancing detection sensitivity and reducing the detection limit to 18.4 fM, thereby offering a novel and ultrasensitive approach for detecting COTS eDNA. However, biosensors operating in a single-signal mode often struggle to distinguish signal variations caused by target binding from those resulting from electrode degradation. This uncertainty may compromise the accuracy, stability, and reproducibility of the biosensor, thereby limiting its practical application. To address this issue, it is necessary to develop ratiometric electrochemical biosensors with built-in calibration capabilities. By introducing internal reference elements, the concentration of the analyte can be determined by analyzing the peak current intensity ratio between two electroactive probes with distinct redox potentials, thereby enhancing measurement accuracy and reliability [22]. For example, Khodadoust et al. [23] constructed a dual-signal ratiometric sensing platform that demonstrated enhanced analytical capabilities compared to traditional single-signal detection strategies. However, in marine biological monitoring, the target DNA concentration in collected samples is often low due to dilution by ocean currents. To enhance the sensitivity of electrochemical DNA sensors, signal amplification strategies are commonly employed. For example, Hu et al. [24] realized ultrasensitive SARS-CoV-2 electrochemical sensing by utilizing exonuclease III (Exo III) for the degradation of double-stranded DNA. Exo III is an enzyme that sequentially removes nucleotides from the 3′ to 5′ end of double-stranded DNA, and it is commonly used in signal amplification systems to cyclically release target DNA, thereby generating a large number of detectable signals [25]. Because Exo III-mediated signal amplification operates independently of defined recognition sites, it represents an optimal and flexible approach for improving the performance of DNA biosensors.

This study developed a ratiometric electrochemical DNA biosensor for the quantitative detection of COTS eDNA. By integrating Exo III-assisted target recycling amplification with a dual-signal detection system based on internal reference calibration, the biosensor enhances detection sensitivity, signal stability, and reproducibility. Experimental results showed that Exo III-mediated cyclic amplification allowed for femtomolar-level detection, enabling highly sensitive eDNA detection. The ratiometric signal output corrected system errors, improving the accuracy of quantitative analysis. Compared to conventional methods, the biosensor offers advantages such as simplicity, low cost, and suitability for on-site applications. Additionally, a quantitative relationship between the electrochemical response and eDNA concentration was established, providing a reliable approach for early detection of low-density or cryptic COTS individuals, and laying the foundation for early warning and control of COTS outbreaks in coral reef ecosystems.

2. Materials and methods

2.1. Chemicals and apparatus

Detailed information on the chemicals and apparatus employed in this study is provided in Supplementary Information S1.1 and S1.2.

2.2. Primers and probes design

In this study, the mitochondrial COI gene of the COTS was selected as the target DNA sequence, with the reference sequence obtained from the NCBI database (accession number: AB116377.2). Primers were designed using the "Pick Primers" function of Primer-BLAST, with parameters set to a length of 15–30 bp and a GC content of 40 %–60 %. Among the 10 pairs of candidate primers generated, the pair with the lowest Self 3′ complementarity coefficient was selected as optimal. It targets the template strand from positions 136 to 437 bp, and its amplification specificity was verified via a BLAST search. To further confirm primer specificity, PCR amplification was performed using DNA templates from COTS and three common non-target species in coral reef ecosystems: *Choriaster granulatus*, *Pocillopora damicornis*, and *Chaetodon citrinellus*.

During probe design, both the secondary structural features of the sequences and the requirements for chemical modification were comprehensively considered. First, the DNA folding function of the UNA Fold web server was used to predict and optimize probe conformations. Its "Hybridization of Two Different Strands" function was then employed to analyze hybridization efficiency and thermodynamic parameters, thereby ensuring the structural stability and hybridization performance of the probes.

The DNA extraction method was described in Supplementary Information S1.3. The PCR reaction system and cycling conditions were detailed in Supplementary Information S1.4. The amplification products were analyzed by 1.25 % agarose gel electrophoresis, with specific electrophoresis conditions provided in Supplementary Information S1.5. The primer and probe sequences were listed in Table S1.

In the subsequent experiment, we used the same batch of DNA samples to systematically evaluate the biosensor's selectivity, setting the concentrations of the interfering DNA samples at 100 nM and the COTS at 10 nM.

2.3. eDNA enrichment

The eDNA enrichment process involved seawater collection, filtration, and DNA extraction. In September 2021, seawater samples were collected at multiple sites in the Paracel Islands using a plexiglass water sampler, with strict precautions to avoid contamination during sampling. eDNA extraction was conducted using the MagMAX™ Cell-Free DNA Isolation Kit (Applied Biosystems, Thermo Fisher Scientific, USA) with modifications to the standard protocol. Detailed experimental procedures were provided in Supplementary Information S1.6.

2.4. Fabrication and electrochemical testing of the biosensor

Following the method described in reference [26], the bare gold electrode (GE) was polished, ultrasonically cleaned, and electrochemically activated to obtain a uniform and active electrode surface. Subsequently, the capture probe (CP) treated with tris(2-carboxyethyl) phosphine (TCEP) was immobilized onto the electrode surface, and 6-mercaptohexanol (MCH) was then used to block unreacted sites, forming a stable DNA recognition interface. During the signal amplification process, the signal probe (SP), various concentrations of target DNA (TG), and Exo III were used to generate amplified products, which were then hybridized with the modified electrode for highly sensitive electrochemical detection. Detailed experimental procedures were provided in Supplementary Information S1.7.

All electrochemical tests were conducted on an electrochemical workstation equipped with a three-electrode system comprising a GE working electrode, an Ag/AgCl (3 M KCl) reference electrode, and a Pt counter electrode. Details of the electrochemical measurements were provided in Supplementary Information S1.8.

2.5. Blank control experiments

During the collection and processing of actual samples, negative controls were included at each step to monitor contamination. Blank control procedures were detailed in Supplementary Information S1.10.

2.6. Actual sample information

A field ecological survey was conducted in September 2021 in the coral reef habitats of the Paracel Islands, South China Sea. Based on previous outbreak records, six representative sampling sites (L1–L6) were selected for seawater collection. Detailed information on each site was summarized in Table S2.

2.7. Data processing and statistical analysis

All statistical analyses were performed using Excel 2016 and IBM SPSS Statistics 26. Experimental results are presented as mean values, with error bars representing the standard deviation from three parallel replicates. One-way analysis of variance (ANOVA) followed by Tukey's post hoc test was conducted to assess significant differences among groups. Statistical significance was determined at a 95 % confidence level, with the following notations: $*P > 0.05$; $**0.001 < P < 0.01$. Bar charts and line graphs were generated using Origin 2023.

3. Results and discussion

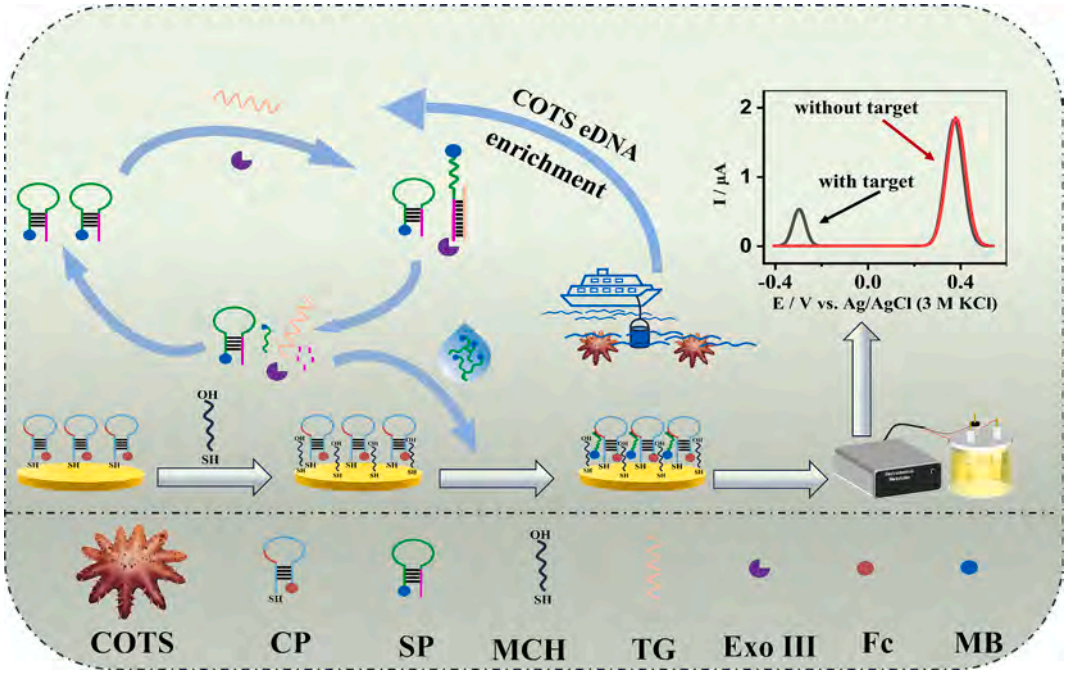
3.1. Principle of the ratiometric electrochemical DNA sensor

Scheme 1 illustrates the working principle of the biosensor developed in this study. The biosensor integrates an Exo III-assisted target recycling amplification method with a dual-signal strategy incorporating an internal reference probe for the detection of COTS eDNA. First, the CP was modified at the 3′ end with a thiol group (—SH) and immobilized on the gold electrode surface via the formation of Au—S bonds. The CP was further modified at the 5′ end with a ferrocene (Fc) group, which served as the internal reference signal. The stem structure of the CP was stabilized by multiple base pairs, ensuring that the Fc electrochemical signal remained stable during measurements. Importantly, the loop region of the CP was designed to be complementary to the MB-labeled DNA fragment generated after enzymatic cleavage.

In parallel, the SP was modified at the 5′ end with a methylene blue (MB) group. The SP also formed a stable stem–loop structure with multiple base pairs, leaving a protruding 3′ end that protected it from Exo III digestion in the absence of target DNA. Upon hybridization with COTS DNA, the SP underwent a conformational change from the closed to the open state, allowing Exo III to digest the SP from the 3′ to 5′ direction. After cleavage, the target DNA was released and participated in subsequent amplification cycles. Through multiple cycles of Exo III-assisted cleavage, a large number of MB-labeled DNA fragments were generated, which then specifically hybridized with the exposed loop region of the CP on the electrode surface via complementary base pairing. Notably, this hybridization event occurred without inducing any conformational change in the CP structure, as the CP loop remained statically accessible for binding.

The Exo III-mediated cleavage process and subsequent hybridization were further validated by polyacrylamide gel electrophoresis (PAGE). As shown in Fig. S2, after co-incubating the target DNA with SP, a distinct band with delayed migration appeared (lane 4), confirming the formation of a dimer complex. In the presence of Exo III (lane 5), the band formed by SP and target DNA completely disappeared, indicating that the complex was recognized by Exo III and cleaved specifically, with SP being degraded and releasing MB-labeled fragments along with the target DNA. At the same time, a clear delayed band formed by the MB-labeled fragments hybridizing with CP was observed, proving that the cleavage products were successfully captured by CP. In the control experiment, the co-incubation of SP and Exo III (lane 6) still showed the intact band, ruling out the possibility of nonspecific cleavage due to structural defects in SP, further validating the specificity and reliability of the biosensor design.

Within the appropriate potential window, the electrochemical signals of both Fc and MB were simultaneously recorded. The MB signal intensity was proportional to the target DNA concentration. At the same time, Fc served as an internal reference to correct for errors arising from electrode modification and to monitor potential contamination during electrode preparation. This dual-signal approach improved the detection accuracy, and the target DNA concentration was quantitatively



Scheme 1. Diagram of the working principle of the biosensor.

determined based on the I_{MB}/I_{Fc} ratio.

3.2. Characterization of the biosensor

Electrochemical impedance spectroscopy (EIS) is commonly applied as a reliable method for tracking the layer-by-layer assembly of biosensing interfaces [27,28]. In electrochemical impedance spectroscopy, the diameter of the semicircular portion displayed on the Nyquist plot is commonly interpreted as the charge transfer resistance (Rct) at the electrode-electrolyte interface, which quantifies the resistance encountered during electron exchange processes [29]. As illustrated in Fig. 1A, the bare gold electrode displayed a comparatively small semicircular arc on the Nyquist plot, which signified a low charge transfer resistance (Rct) and confirmed that the electrode surface is clean and possesses excellent electrical conductivity (curve a). Upon CP attachment on the electrode surface, the Rct showed a marked increase (curve b). This rise is mainly attributed to electrostatic repulsion occurring between the negatively charged phosphate groups of the CP and the ferricyanide/ferrocyanide redox pair $[Fe(CN)_6]^{3-/4-}$, which hinders efficient electron transfer at the interface. Further modification with MCH to block nonspecific binding sites resulted in a marked increase in Rct (curve c), as MCH was a poor electrical conductor that impeded electron transfer at the interface. Finally, after introducing the signal amplification solution, hybridization between CP and the residual DNA enhanced the local concentration of positively charged MB molecules. This process mitigated the repulsion from the phosphate groups and facilitated electron transport [30], thereby reducing the Rct value (curve d).

The variations in peak current and peak potential in cyclic voltammetry (CV) curves served as indicators to monitor the layered modification process of the electrode surface [31]. As illustrated in Fig. 1B, the unmodified gold electrode (GE, curve a) displayed distinct redox signals attributed to the $[Fe(CN)_6]^{3-/4-}$ couple, indicating that electron exchange at the electrode surface occurred efficiently. Following the self-assembly-mediated immobilization of the CP onto the GE surface, a significant reduction in the redox peak current was observed (curve b). This reduction is primarily ascribed to electrostatic interactions between $[Fe(CN)_6]^{3-/4-}$ ions and the negatively charged phosphate groups on the CP, which impede interfacial electron exchange at the electrode. To eliminate nonspecific adsorption, MCH was subsequently introduced to occupy the remaining reactive sites on the electrode, which further diminished the current response and led to an increased spacing between the oxidation and reduction peaks (curve c). Upon applying the signal amplification mixture to the MCH/CP/GE system, the redox peak current increased compared to the previous step. This enhancement was due to MB-tagged residual DNA molecules, whose positive charges reduced the electrostatic hindrance with the redox probe, thereby promoting electron movement. The results obtained from the CV were consistent with the trends revealed by electrochemical impedance spectroscopy EIS, further validating the successful construction of the biosensor.

3.3. Feasibility verification of the biosensor

The Mfold web server was used to analyze the feasibility of the conformations of the CP and SP (see Supplementary Information S1.9 and Fig. S3 for details).

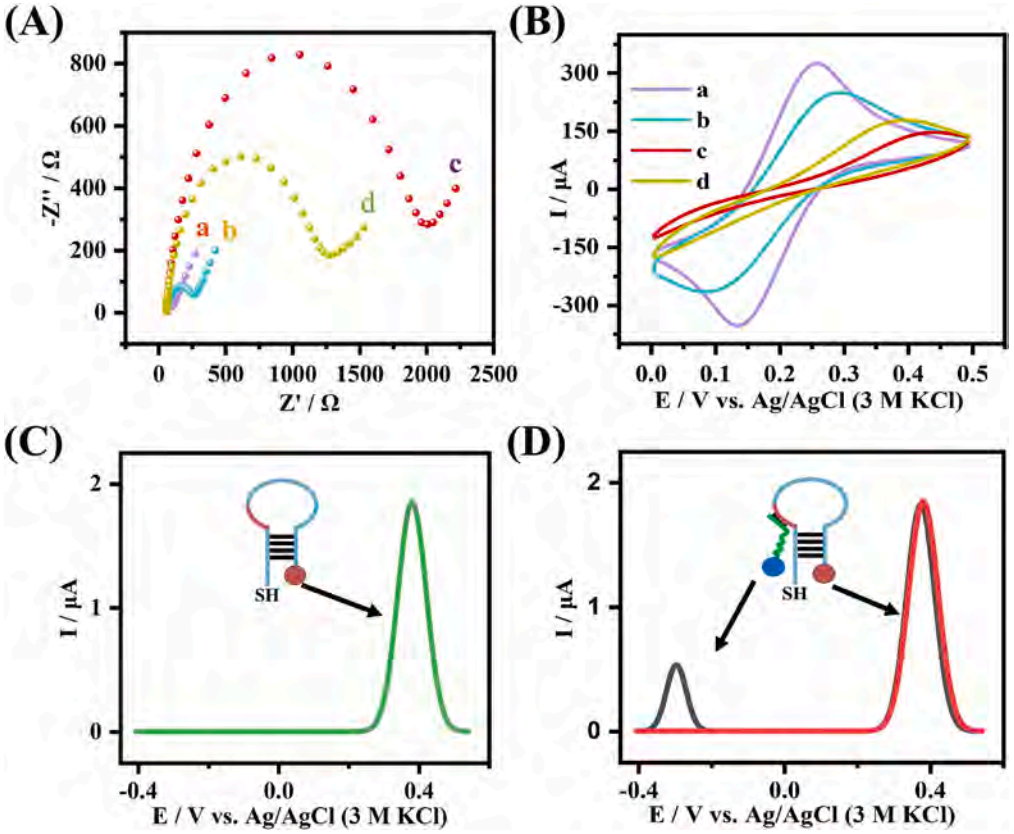


Fig. 1. (A) EIS and (B) CV of the stepwise modification process of the gold electrode, recorded in an aqueous solution containing 5 mM $[Fe(CN)_6]^{3-/4-}$ and 0.1 M KCl: (a) bare gold electrode (GE), (b) after capture probe immobilization (CP/GE), (c) after MCH blocking (MCH/CP/GE), and (d) after the addition of the reaction solution containing 10 nM target DNA (residual DNA/MCH/CP/GE). Feasibility verification: (C) The differential pulse voltammetric response of the MCH/CP-modified electrode (MCH/CP/GE) before adding the reaction solution, and (D) the differential pulse voltammetric responses of the MCH/CP-modified electrode (MCH/CP/GE) after adding the reaction solution containing 10 nM target DNA and the reaction solution without target DNA, respectively. (For interpretation of the references to colour in this figure legend, the reader is referred to the web version of this article.)

To evaluate the feasibility of the biosensor's signal response, differential pulse voltammetry (DPV) was employed to monitor the electrochemical signal changes during the CP and SP modification processes. As shown in Fig. 1C, a distinct Fc oxidation peak appeared near 0.39 V after the immobilization of CP and MCH, which was attributed to the efficient electron transfer facilitated by Fc on the electrode surface. Subsequently, the addition of residual DNA induced a pronounced MB current response around −0.3 V (Fig. 1D). The experimental results indicated that, under conditions where the probe remains uncleaved, the MB-labeled hairpin DNA cannot form complementary pairing with the CP on the electrode, thus failing to generate significant electrochemical signals. This phenomenon can be ascribed to the unique structural design of the hairpin CP and hairpin SP: the uncleaved SP probe maintains a closed hairpin structure, preventing the release of single-stranded DNA fragments that could be captured by the CP, and therefore, no signal is produced. In contrast, after enzymatic cleavage, the SP probe released specific MB-labeled single-stranded DNA fragments, which hybridized with the CP probe on the electrode surface, anchoring the MB molecules onto the electrode and producing detectable electrochemical signals, thereby validating the feasibility of this strategy.

3.4. Optimization of the biosensor

The experimental conditions of the biosensor were optimized to achieve optimal detection performance. As illustrated in Fig. 2A, the pretreated bare gold electrode showed a prominent broad peak (curve GE) with a peak current around 0.3 V. When the Fc-labeled CP was added, a more prominent broad peak (curve Fc/GE) appeared. The more prominent broad peak was likely the result of the combined oxidation peaks of the GE and Fc. The oxidation peak of Fc was not initially detected, possibly because numerous unmodified active sites on the gold electrode surface caused the oxidation signal of gold to overlap and obscure that of Fc. Upon treatment with MCH to block these active sites, no oxidation peak was observed (curve MCH/GE), thereby supporting this hypothesis. Following the incubation of Fc-labeled CP, the remaining exposed sites on the gold surface were again passivated using MCH. Under these conditions, an oxidation peak attributed to Fc appeared at approximately 0.39 V (curve MCH/Fc/GE), indicating the essential role of MCH in passivating the gold electrode to reveal the Fc signal. MCH blocking allowed the characteristic peak of Fc to become distinguishable from the broad peak of the gold electrode. Then, the effect of MCH blocking time on the experiment was investigated. As shown in Fig. 2B, with increasing MCH blocking time, the Fc (I_{Fc}) current initially increased and reached a maximum of 45 min. When the blocking duration was prolonged to 60 min, a decline in I_{Fc} was observed, due to the limited conductivity of MCH, as an overly passivated electrode surface suppressed electron transfer. Consequently, 45 min was selected as the optimal blocking time for MCH.

Since the surface density of the CP immobilized on the electrode significantly influences the efficiency of subsequent hybridization events, it was essential to carefully optimize the concentration of the CP. This optimization ensures sufficient probe coverage to facilitate effective target binding while minimizing nonspecific interactions, ultimately enhancing the overall sensitivity and reliability of the biosensor. As shown in Fig. 2C, I_{Fc} rose progressively as the CP concentration was elevated, peaking at 700 nM. However, under conditions where the SP concentration was 1000 nM and the target DNA concentration was 10 nM, I_{MB}/I_{Fc} decreased as the CP concentration increased (Fig. 2D).

At a CP concentration of 400 nM, the ratio remained relatively high (approximately 0.7), indicating that the system achieved an optimal balance: the electrode surface possessed sufficient CP coverage to provide ample target-binding sites while avoiding excessive electrostatic repulsion arising from densely packed negatively charged phosphate backbones, thereby maintaining efficient hybridization. Under these

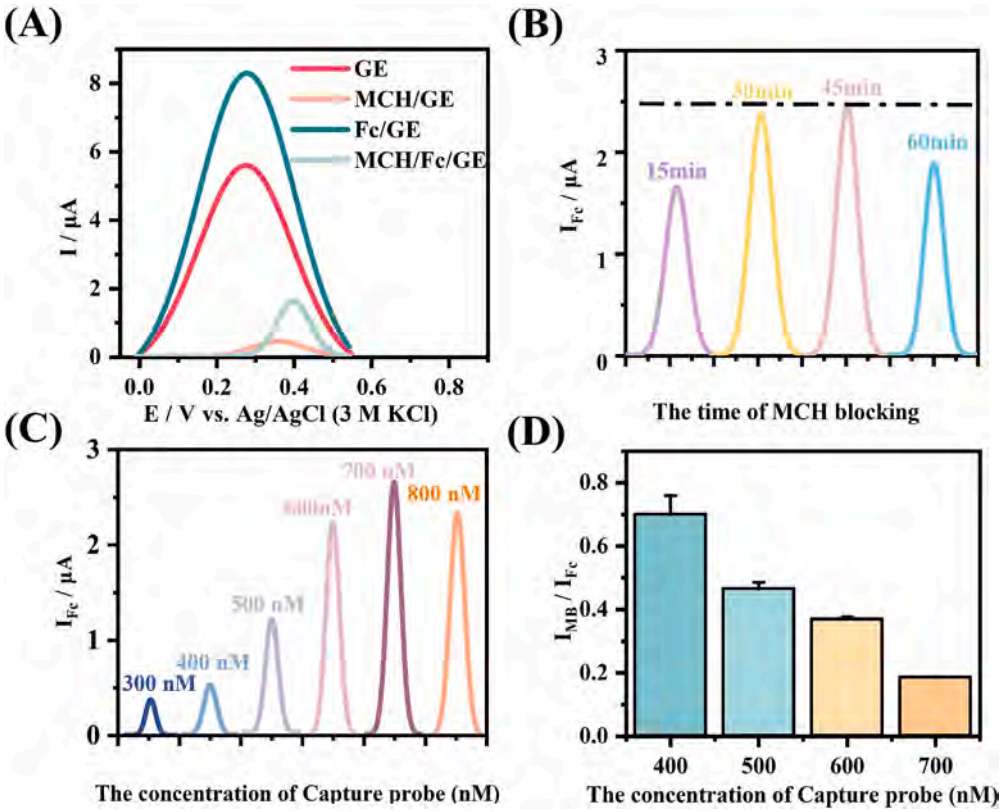


Fig. 2. Experimental condition optimization: (A) the role of MCH blocking, (B) duration of MCH blocking, (C) concentration of the capture probe, and (D) hybridization efficiency. The standard deviation of the mean is represented by the error bars, reflecting the variability observed among three independent replicates (n = 3).

conditions, the synergistic response between I_{MB} and I_{Fc} effectively amplified subtle signal variations induced by low-abundance targets, enabling their clear discrimination through ratiometric readouts. In contrast, when the CP concentration exceeded 400 nM, intensified electrostatic interference significantly suppressed hybridization efficiency. This resulted in a slower increase in I_{MB} relative to I_{Fc}, which in turn led to a decline in the I_{MB}/I_{Fc} ratio and reduced detection capability for low-concentration targets. Therefore, a CP concentration of 400 nM was selected as the optimal parameter for subsequent experiments.

3.5. Analytical performance of the biosensor

Excellent sensitivity was obtained under optimal conditions, as the target DNA could be recycled numerous times due to Exo III-assisted cleavage. This procedure generated a substantial amount of leftover DNA that was detectable in PBS.

As demonstrated in Fig. 3A, the I_{MB}/I_{Fc} signal progressively increased as the concentration of the target DNA rose, indicating a clear correlation between signal intensity and analyte amount. Conversely, the I_{Fc} signal stayed nearly unchanged, which contributed to stable performance and dependable results across various electrode fabrication batches. As demonstrated in Fig. 3B, a clear linear relationship was observed between the current ratio of I_{MB} to I_{Fc} and the logarithm of target DNA concentrations ranging from 300 fM to 10 nM. This result confirmed that the biosensor maintained reliable quantification performance over a broad dynamic concentration window and exhibited high sensitivity toward low-abundance DNA targets. The corresponding linear regression is expressed in Eq. (1):

$$I_{MB}/I_{Fc} = 0.12704x + 0.2577, R^2 = 0.997 \quad (1)$$

where I_{MB}/I_{Fc} was the ratio of dual signals, and x was the logarithm of the target DNA concentration.

The limit of detection (LOD) for the target DNA was determined to be as low as 93 fM. When I_{MB}/I_{Fc} equaled Eq. (2):

$$I_{MB}/I_{Fc} = S_0 + 3\sigma \quad (2)$$

where S_0 was the mean value of the I_{MB}/I_{Fc} of the blank sample, and σ was the standard deviation of S_0.

The limit of quantification (LOQ) for the target DNA was determined to be as low as 245 fM. When I_{MB}/I_{Fc} equaled Eq. (3):

$$I_{MB}/I_{Fc} = S_0 + 10\sigma \quad (3)$$

where S_0 was the mean value of the I_{MB}/I_{Fc} Of the blank sample, and σ was the standard deviation of S_0.

In the absence of Exo III-assisted cleavage, the target DNA could not be released into the cycling process, and the detected signal was reduced. As shown in Fig. 3C and D, a distinct linear correlation was successfully obtained between the I_{MB} to I_{Fc} signal ratio and the logarithmic transformation of the target DNA concentration across a wide range from 10 pM to 10 nM, which was quantitatively defined by the linear regression Eq. (4):

$$I_{MB}/I_{Fc} = 0.16489x + 0.08626, R^2 = 0.960 \quad (4)$$

Without Exo III-assisted cleavage, the LOD and LOQ were 1.76 pM and 3.70 pM, respectively, reducing the biosensor detection capability

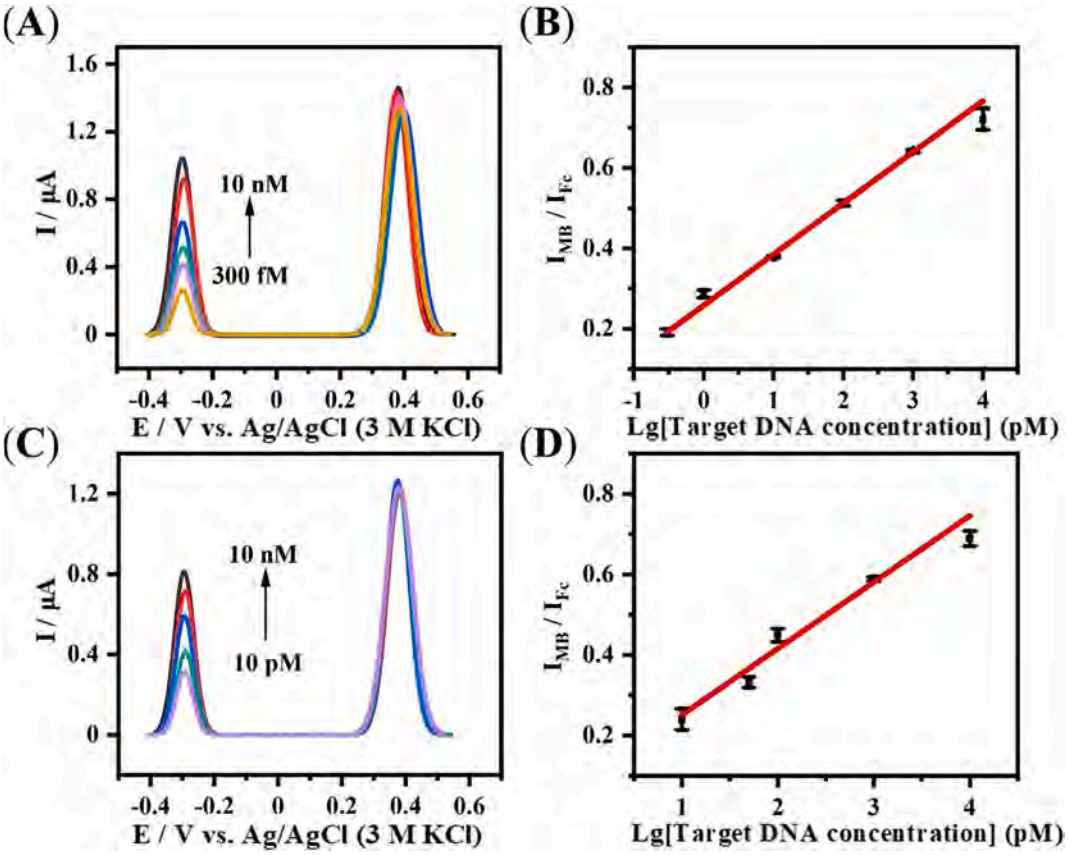


Fig. 3. (A) DPV signals of the biosensor recorded in response to varying concentrations of target DNA in the presence of Exo III. From bottom to top: 300 fM, 1 pM, 10 pM, 100 pM, 1 nM, and 10 nM. (B) Corresponding calibration plot of the I_{MB}/I_{Fc} ratio against the logarithmic values of target DNA concentrations ranging from 300 fM to 10 nM. (C) DPV profiles of the biosensor exposed to different target DNA concentrations in the absence of Exo III. From bottom to top: 10 pM, 50 pM, 100 pM, 1 nM, and 10 nM. (D) Calibration graph of I_{MB}/I_{Fc} versus the log-scale concentrations of target DNA (10 pM to 10 nM). The error bars indicate the standard deviation calculated from three separate and independent experimental measurements. ($n = 3$).

by more than 15-fold.

3.6. Assessment of selectivity, stability, and repeatability

Its repeatability was evaluated to guarantee that the Ratio Electrochemical DNA biosensor would be helpful in practice. Five parallel electrodes, each tested three times, were used to detect 10 pM target DNA under identical experimental conditions. Fig. 4A showed that the test results relative standard deviation (RSD) from the five parallel electrodes were 2.05 %, demonstrating that the designed biosensor had excellent repeatability.

To meet field monitoring requirements, biosensors needed to undergo preconditioning to shorten on-site detection time, making stability essential to ensure reliable performance during storage. In this study, the prepared biosensors were stored at 4 °C, with signal changes monitored every two days. As shown in Fig. 4B, the sensor retained 90.9 % of its initial signal after nine days, indicating good storage stability. The slight decrease in the I_{MB}/I_{Fc} ratio could mainly be attributed to slow conformational changes of the CP fixed on the electrode surface during storage, which reduced its hybridization efficiency with the signal probe enzyme cleavage products. Additionally, the SP in the solution might have undergone slow degradation, reducing the number of effective probes available for signal amplification. Although both the I_{MB} and I_{Fc} signal channels influenced the ratio, both signals maintained their primary electrochemical activity overall, with no significant imbalance or decline in detection accuracy. This level of stability was sufficient to cover typical field monitoring cycles (usually several days to a week), meeting practical application needs and providing important evidence for enhancing long-term stability through optimization of probe fixation strategies and storage conditions.

In addition, the actual marine environment contained not only COTS DNA but also a substantial amount of interfering DNA; therefore, evaluating the biosensor's selectivity was crucial. Herein, the cross-reactivity experiment was designed, and typical interfering species, such as *C. granulatus*, *P. damicornis*, and *C. citrinellus,* were selected as non-target samples (Fig. 4C). As shown in Fig. 4D, the I_{MB}/I_{Fc} signal ratios generated by these interfering DNA samples were similar to those of the blank control group. Notably, although the DNA concentration of each interferent was set at 10 times that of COTS, both the COTS samples with and without mixed interferents produced similarly enhanced response signals, with intensities exceeding three times that of any single interferent or the blank control. This result was consistent with the validation conclusion presented in Fig. S1, fully demonstrating that the primers and target gene regions designed in this study possessed high selectivity. This enabled the ratiometric electrochemical DNA biosensor to achieve efficient and accurate detection even in complex environmental samples.

3.7. Applicability analysis

In this work, six samples, including one negative control (with no recorded history of COTS outbreaks), were collected from five islands in the Paracel Islands, South China Sea (Fig. 5A–C). The sample information is listed in Table S2. Strict contamination control procedures were followed during sampling and processing (S1.10, Fig. S4). eDNA extraction was performed using the MagMAX™ Cell-Free DNA Isolation

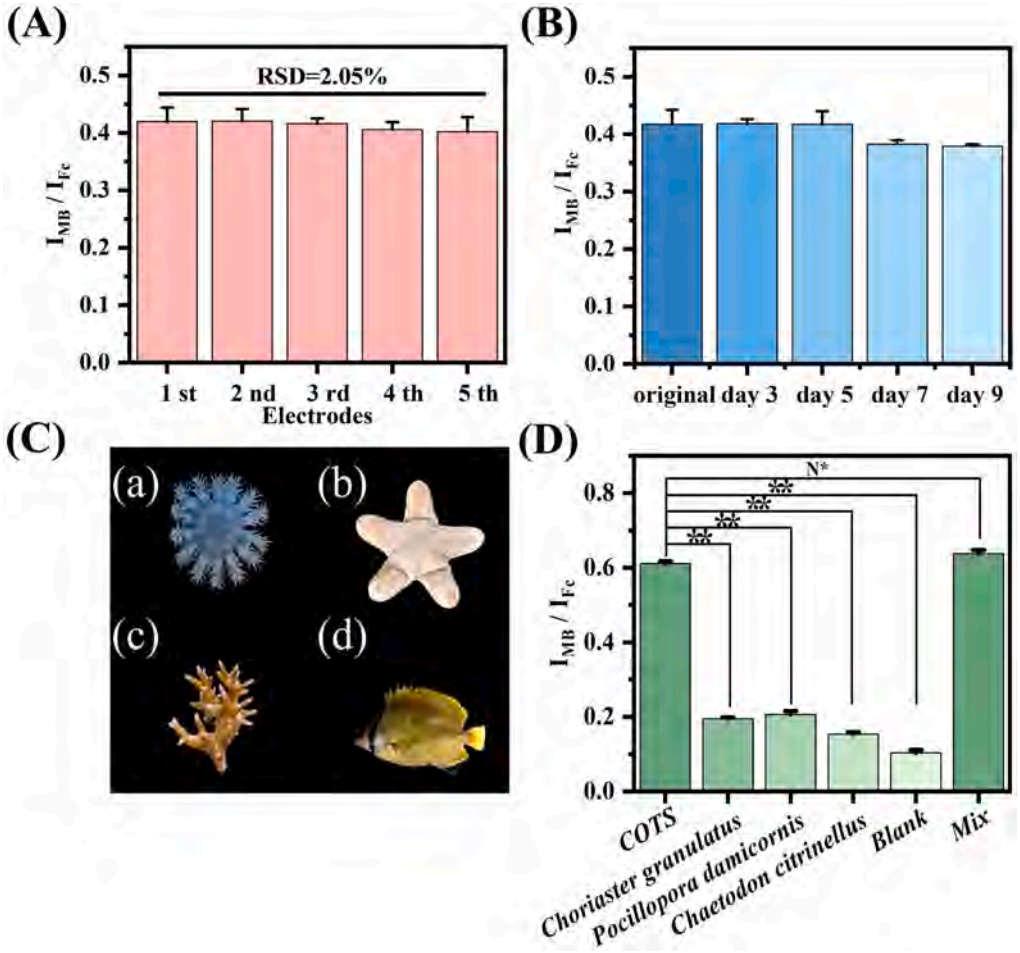


Fig. 4. (A) The repeatability, (B) stability, (C) photos of the interfering species and (D) selectivity of the biosensor: (a) COTS, (b) *C. granulatus*, (c) *P. damicornis*, and (d) *C. citrinellus*. The error bars represent the standard deviation of the mean, $n = 3$. N*: $P > 0.05$, **: $0.001 < P < 0.01$.

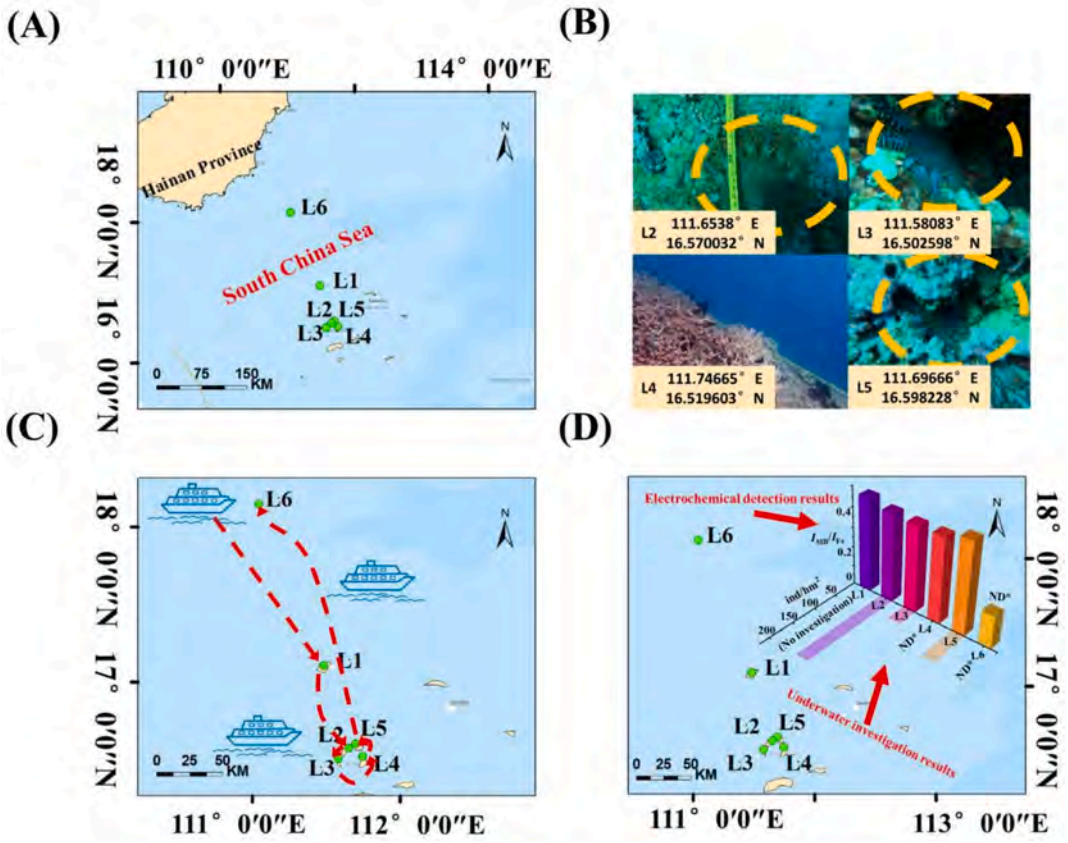


Fig. 5. (A) Paracel Islands. (B) Underwater investigation images. (C) Overview diagram of COTS dynamic distribution monitoring, showing the sampling points and the navigation path. (D) Underwater investigation results and Electrochemical detection results.

Kit, which effectively separated most of the common contaminants in marine samples, such as proteins, polysaccharides, and lipids, thereby minimizing their interference with subsequent biosensor detection. Additionally, the kit provided high DNA recovery efficiency, ensuring high-quality samples for biosensor detection.

As shown in Fig. 5D, samples L1, L2, L3, L4, and L5 exhibited strong electrochemical signals, indicating high concentrations of COTS eDNA. In contrast, sample L6 showed no detectable COTS in either electrochemical tests or ecological surveys. The ecological survey confirmed the presence of COTS populations in the areas corresponding to samples L2, L3, and L5. However, no COTS were observed in the L4 area, which was inconsistent with the biosensor results. Additionally, no underwater survey was conducted for the L1 site.

Underwater ecological surveys were limited in detecting hidden COTS, whereas biosensors functioned by detecting eDNA signals released by COTS. Sources of COTS eDNA included active individuals, hidden COTS within coral reefs, and microscopic larvae that were not visible in traditional surveys. Therefore, biosensors offer broader survey coverage and overcome the limitations of visual surveys, which often miss hidden and microscopic COTS. Based on the biosensor results, it was believed that COTS were present at North Reef and Longdong Island, where L1 and L4 were located. This finding was subsequently confirmed by an independent study conducted by Yan et al. [32], further demonstrating the reliability of the sensor.

Through one-way ANOVA combined with Tukey's post hoc test, no significant difference was found between the results of the biosensor and ddPCR ($P > 0.05$) (Table S3). To further validate the consistency between the two methods, we conducted a Pearson correlation analysis. As shown in Fig. S5, the results of the biosensor and ddPCR exhibited a strong positive correlation ($r = 0.998$, $p < 0.001$), further confirming the high consistency between the two methods. These results demonstrated that tracing COTS through biosensor detection of eDNA offered broader spatial coverage and higher sensitivity. The biosensor was expected to detect COTS larvae or low-density populations earlier than traditional underwater surveys, which typically relied on the visual detection of adult individuals. The early settlement of COTS larvae on coral reefs, considered a primary trigger of COTS outbreaks, undoubtedly provided critical information for understanding the mechanisms of COTS outbreaks.

The ratiometric electrochemical DNA biosensor demonstrated strong application potential in conventional coral reef ecological monitoring, which supported rapid on-site detection and avoided the degradation risk of eDNA during transport with ddPCR, based on a portable and lightweight electrochemical platform. It was suitable for shipboard surveys and real-time monitoring at island reefs, with the cost per sample controlled under $1.0. Compared to ddPCR, this biosensor simplified the workflow, with detection steps requiring no specialized personnel. In the future, combining the biosensor with microfluidic technology could enable automated sample enrichment and DNA extraction, further saving labor and time costs. Besides, ddPCR has advantages in high-throughput analysis, while this biosensor can enhance field survey efficiency by pre-modifying multiple electrodes. This enables rapid early warnings for key areas, making it a strong complementary tool to ddPCR. Integrating multi-channel microfluidic electrode arrays in the future could further improve detection throughput and automation levels.

4. Conclusion

In this research, a ratiometric electrochemical DNA biosensor was successfully constructed. Significantly, combining an exonuclease III-assisted target recycling amplification method with a dual-signal

strategy using an internal reference probe significantly improved the biosensor's sensitivity, reproducibility, and stability. After thorough optimization, the biosensor demonstrated outstanding analytical capabilities, featuring a wide linear detection range from 300 fM to 10 nM and a detection limit down to 93 fM. The primers and DNA targets were explicitly designed for COTS, enabling precise detection of COTS DNA even in complex sample environments. Moreover, ddPCR validation confirmed the biosensor's accuracy and reliability, showing no significant difference ($P > 0.05$). Ultimately, the biosensor developed here effectively detected COTS eDNA in multiple samples collected from the Paracel Islands in the South China Sea. It offered broader survey coverage and higher sensitivity than traditional ecological survey methods, overcoming the shortcomings of visual surveys that tend to overlook hidden and non-visible COTS. It is expected to be used to detect COTS larvae or low-density COTS, providing early field data and offering critical information for exploring the mechanisms of COTS outbreaks.

CRediT authorship contribution statement

Beihua Wen: Writing – original draft, Methodology, Investigation, Data curation, Conceptualization. **Zhenyu Zhu:** Writing – review & editing, Data curation, Conceptualization. **Junjie Zeng:** Writing – review & editing. **Shiwei Wan:** Investigation, Data curation. **Chaoxin Zhang:** Data curation. **Yingzhan Chen:** Validation, Software. **Liwei Wang:** Validation, Software. **Man Zhang:** Writing – review & editing. **Kefu Yu:** Writing – review & editing.

Declaration of competing interest

The authors declare that they have no known competing financial interests or personal relationships that could have appeared to influence the work reported in this paper.

Acknowledgments

This work received financial backing from the Guangxi Major Talent Project (Bagui Young Elite Talents Project), the Self-Topic Project of Guangxi Laboratory on the Study of Coral Reefs in the South China Sea, Nanning 530004, China (No. GXLSCRSCS2023102), and the Open Fund of Nansha Islands Coral Reef Ecosystem National Observation and Research Station, Guangzhou 510300, China (No. NSICR24204). We also gratefully acknowledge the valuable assistance provided by the Sansha Track Ocean Coral Reef Conservation Research Institute for their help in collecting specimens of COTS.

Appendix A. Supplementary data

Supplementary data to this article can be found online at https://doi.org/10.1016/j.bioelechem.2025.109162.

Data availability

Data will be made available on request.

References

[1] S. Hassan, B.S. Bali, A. Yaseen, M. Zaman, W. Muneer, S.A. Ganiee, A.J. Shah, B. A. Ganai, Bridging the gaps through environmental DNA: a review of critical considerations for interpreting the biodiversity data in coral reef ecosystems, Mar. Pollut. Bull. 209 (Pt B) (2024) 117242, https://doi.org/10.1016/j.marpolbul.2024.117242.

[2] R.J. Harris, D.A.L. Barnard, G. Paxton, S. Lockie, D.J. Craik, S.F. Cummins, C. K. Wang, C.A. Motti, The future of utilising semiochemical pest control methods to manage the destructive crown-of-thorns starfish outbreaks on coral reefs, Biol. Conserv. 302 (2025) 110984, https://doi.org/10.1016/j.biocon.2025.110984.

[3] K. Jensen, P.C. Doll, M.C.G. Cabrera, G. Diaz-Pulido, M. Logan, S. Uthicke, Feeding preferences and growth in herbivorous juvenile crown-of-thorns sea stars (*Acanthaster* cf. *solaris*), Mar. Biol. 172 (6) (2025) 86, https://doi.org/10.1007/s00227-025-04646-z.

[4] C.Y. Kuo, M.J. Ho, W.K. Heng, Y.Y. Huang, C.Y. Ko, G.C. Jiang, M.S. Jeng, C. A. Chen, What is for dessert? Crown-of-thorns starfish feeds on non-scleractinian anthozoans at Taiping Island (Itu aba), Spratlys, South China Sea, Mar. Biodivers. 52 (1) (2022) 2, https://doi.org/10.1007/s12526-021-01240-6.

[5] J. Doyle, S. Uthicke, Sensitive environmental DNA detection via lateral flow assay (dipstick)—a case study on corallivorous crown-of-thorns sea star (*Acanthaster* cf. *solaris*) detection, Environ. DNA 3 (2) (2020) 323–342, https://doi.org/10.1002/edn3.123.

[6] H.C. Rees, B.C. Maddison, D.J. Middleditch, J.R.M. Patmore, K.C. Gough, REVIEW: the detection of aquatic animal species using environmental DNA—a review of eDNA as a survey tool in ecology, J. Appl. Ecol. 51 (5) (2014) 1450–1459, https://doi.org/10.1111/1365-2664.12306.

[7] J. Zhang, X. Chen, Q. Zhou, C. Diao, H. Jia, W. Xian, H. Zhang, Species identification and biomass assessment of Gnathanodon speciosus based on environmental DNA technology, Ecol. Indic. 160 (2024) 111821, https://doi.org/10.1016/j.ecolind.2024.111821.

[8] S. Uthicke, B. Robson, J.R. Doyle, M. Logan, M.S. Pratchett, M. Lamare, Developing an effective marine eDNA monitoring: eDNA detection at pre-outbreak densities of corallivorous seastar (*Acanthaster* cf. *solaris*), Sci. Total Environ. 851 (Pt 1) (2022) 158143, https://doi.org/10.1016/j.scitotenv.2022.158143.

[9] Y. Hou, S. Chen, Y. Zheng, X. Zheng, J.M. Lin, Droplet-based digital PCR (ddPCR) and its applications, Trends Anal. Chem. 158 (2023) 116897, https://doi.org/10.1016/j.trac.2022.116897.

[10] T. Jo, M. Arimoto, H. Murakami, R. Masuda, T. Minamoto, Particle size distribution of environmental DNA from the nuclei of marine fish, Environ. Sci. Technol. 53 (16) (2019) 9947–9956, https://doi.org/10.1021/acs.est.9b02833.

[11] Y. Feng, D. Zhou, L. Gao, F. He, Electrochemical biosensor for rapid detection of bacteria based on facile synthesis of silver wire across electrodes, Biosens. Bioelectron. 168 (2020) 112527, https://doi.org/10.1016/j.bios.2020.112527.

[12] M. Mujeeb-U-Rahman, M.H. Nazari, M. Sencan, A novel semiconductor based wireless electrochemical sensing platform for chronic disease management, Biosens. Bioelectron. 124 (2019) 66–67, https://doi.org/10.1016/j.bios.2018.09.077.

[13] W.B.S. Machini, A.M. Oliveira-Brett, In situ electrochemical investigation of the interaction between bacteria *Xylella fastidiosa* DNA and copper(II) using DNA-electrochemical biosensors, Electrochem. Commun. 125 (2021) 106975, https://doi.org/10.1016/j.elecom.2021.106975.

[14] S. Jampasa, B. Jikul, C. Kreangkaiwal, W. Khamcharoen, W. Jesadabundit, W. Waiwinya, P. Saelim, T. Phanbunmee, K. Patarakul, O. Chailapakul, Multiple signaling probe-based ultrasensitive electrochemical DNA sensor integrated with NFC-enabled smartphone to diagnose leptospirosis, Sens. Actuat. B: Chem. 406 (2024) 135411, https://doi.org/10.1016/j.snb.2024.135411.

[15] P.S. Ganesh, S.E. Elugoke, S.H. Lee, S.Y. Kim, E.E. Ebenso, Smart and emerging point of care electrochemical sensors based on nanomaterials for SARS-CoV-2 virus detection: towards designing a future rapid diagnostic tool, Chemosphere 352 (2024) 141269, https://doi.org/10.1016/j.chemosphere.2024.141269.

[16] J. Liu, J. Chen, S. Jia, Y. Wang, D. Wu, Y. Wu, G. Li, CRISPR/Cas12a triggered SERS and naked eye dual-mode biosensor for ultrasensitive and on-site detection of nucleic acid via cascade signal amplification, Sens. Actuat. B: Chem. 404 (2024) 135249, https://doi.org/10.1016/j.snb.2023.135249.

[17] V. Chugh, S. Khurana, N. Kumar, P. Ish, S. Bose, R. Nayak, Development of an affordable microRNA electrochemical biosensor for identification and monitoring of obstructive sleep apnea and its associated comorbidities, Sens. Actuat. B: Chem. 394 (2023) 134349, https://doi.org/10.1016/j.snb.2023.134349.

[18] Y. Chen, Q. Bin, H. Liu, Y. Xie, S. Wang, J. Lu, W. Ou, M. Zhang, L. Wang, K. Yu, A novel biosensing strategy on the dynamic and on-site detection of *vibrio coralliilyticus* eDNA for coral health warnings, Bioelectrochemistry 158 (2024) 108697, https://doi.org/10.1016/j.bioelechem.2024.108697.

[19] J. Ye, W. Huang, X. Jia, H. Song, Y. Zhou, R. Yuan, W. Xu, Short-stranded DNA segment-modulated LAMP/H^+ as signal transducer to guide CHA-cooperated amplifiable electrochemical biosensing, Anal. Chim. Acta 1295 (2024) 342329, https://doi.org/10.1016/j.aca.2024.342329.

[20] L. Wang, J. Xu, H. Liu, S. Wang, W. Ou, M. Zhang, F. Wei, S. Luo, B. Chen, S. Zhang, K. Yu, Ultrasensitive and on-site eDNA detection for the monitoring of crown-of-thorns starfish densities at the pre-outbreak stage using an electrochemical biosensor, Biosens. Bioelectron. 230 (2023) 115265, https://doi.org/10.1016/j.bios.2023.115265.

[21] Z. Wei, X. Zhang, Y. Chen, H. Liu, S. Wang, M. Zhang, H. Ma, K. Yu, L. Wang, A new strategy based on a cascade amplification strategy biosensor for on-site eDNA detection and outbreak warning of crown-of-thorns starfish, Sci. Total Environ. 927 (2024) 172258, https://doi.org/10.1016/j.scitotenv.2024.172258.

[22] S. Cinti, G. Volpe, S. Piermarini, E. Delibato, G. Palleschi, Electrochemical biosensors for rapid detection of foodborne *Salmonella*: a critical overview, Sensors 17 (8) (2017) 1910, https://doi.org/10.3390/s17081910.

[23] C. Liu, T. Wu, W. Zeng, J. Liu, B. Hu, L. Wu, Dual-signal electrochemical aptasensor involving hybridization chain reaction amplification for aflatoxin B1 detection, Sens. Actuat. B: Chem. 371 (2022) 132494, https://doi.org/10.1016/j.snb.2022.132494.

[24] Y. Hu, F. Bao, S. Fu, S. Feng, J. Miao, P. Miao, Y. Xu, A facile electrochemical biosensor for coronavirus RNA assay with silver deposition, Talanta 266 (Pt 1) (2024) 125013, https://doi.org/10.1016/j.talanta.2023.125013.

[25] Y. Sun, X. Cheng, Y. Yi, K. Quan, Q. Chen, K. Zhang, J.J. Xu, The compact integration of multiple exonuclease III-assisted cyclic amplification units for high-

efficiency Ratiometric electrochemiluminescence detection of MRSA, Anal. Chem. 96 (2) (2024) 943–948, https://doi.org/10.1021/acs.analchem.3c05410.
[26] N. Khuda, S. Somasundaram, A.B. Urgunde, C.J. Easley, Ionic strength and hybridization position near gold electrodes can significantly improve kinetics in DNA-based electrochemical sensors, ACS Appl. Mater. Interfaces 15 (4) (2023) 5019–5027, https://doi.org/10.1021/acsami.2c22741.
[27] X. Zhang, G. Xie, D. Gou, P. Luo, Y. Yao, H. Chen, A novel enzyme-free electrochemical biosensor for rapid detection of *Pseudomonas aeruginosa* based on high catalytic cu-ZrMOF and conductive super, P, Biosens. Bioelectron. 142 (2019) 111486, https://doi.org/10.1016/j.bios.2019.111486.
[28] J. Qin, D.G. Jo, M. Cho, Y.K. Lee, Monitoring of early diagnosis of Alzheimer's disease using the cellular prion protein and poly(pyrrole-2-carboxylic acid) modified electrode, Biosens. Bioelectron. 113 (2018) 82–87, https://doi.org/10.1016/j.bios.2018.04.061.
[29] Y. Cao, J. Wang, Y. Xu, G. Li, Combination of enzyme catalysis and electrocatalysis for biosensor fabrication: application to assay the activity of indoleamine 2,3-dioxygensae, Biosens. Bioelectron. 26 (1) (2010) 87–91, https://doi.org/10.1016/j.bios.2010.05.019.
[30] R. Abedi, J.B. Raoof, M. Mohseni, A. Bagheri Hashkavayi, A signal-off aptasensor for the determination of *Acinetobacter baumannii* by using methylene blue as an electrochemical probe, Microchim. Acta 190 (8) (2023) 308, https://doi.org/10.1007/s00604-023-05901-0.
[31] S. Oloketuyi, E. Mazzega, J. Zavašnik, K. Pungjunun, K. Kalcher, A. de Marco, E. Mehmeti, Electrochemical immunosensor functionalized with nanobodies for the detection of the toxic microalgae *Alexandrium minutum* using glassy carbon electrode modified with gold nanoparticles, Biosens. Bioelectron. 154 (2020) 112052, https://doi.org/10.1016/j.bios.2020.112052.
[32] Z. Yan, J. Xing, W. Cai, K. Zhang, Z. Wu, Y. Li, J. Tang, Z. Zhou, Study on the population distribution of Acanthaster planci in the reef area of the Xisha Islands based on environmental DNA technology, Acta Oceanol. Sin. 45 (3) (2023) 76–83, https://doi.org/10.12284/hyxb2023038.

Journal of Hazardous Materials 496 (2025) 139272

Contents lists available at ScienceDirect

Journal of Hazardous Materials

journal homepage: www.elsevier.com/locate/jhazmat

Atmospheric transport of microplastics from land to sea is inefficient: Evidence from multimedia observations

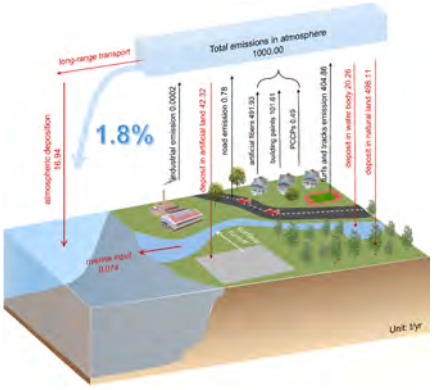
Xiangrong Xu [a,*], Zhen Yuan [b,h], Yanxu Zhang [c], Hengxiang Li [d], Lang Lin [e], Shan Liu [a], Rui Hou [f], Eddy Y. Zeng [g]

[a] Guangxi Laboratory on the Study of Coral Reefs in the South China Sea, Coral Reef Research Center of China, School of Marine Sciences, Guangxi University, Nanning 530004, China
[b] Key Laboratory of Marine Mineral Resources, Ministry of Natural Resources, Guangzhou Marine Geological Survey, China Geological Survey, Guangzhou 511458, China
[c] Department of Earth and Environmental Sciences, Tulane University, New Orleans, LA, USA
[d] Key Laboratory of Tropical Marine Bio-resources and Ecology, Guangdong Provincial Key Laboratory of Applied Marine Biology, South China Sea Institute of Oceanology, Chinese Academy of Sciences, Guangzhou 510301, China
[e] South China Sea Sea Area and Island Center, Ministry Of Natural Resources (South China Sea Standard Measurement and Information Center, Ministry Of Natural Resources), Guangzhou 510310, China
[f] Guangdong Provincial Key Laboratory of Water Quality Improvement and Ecological Restoration for Watersheds, School of Ecology, Environment and Resources, Guangdong University of Technology, Guangzhou 510006, China
[g] Institute of Environmental Health, School of Environment and Energy, South China University of Technology, Guangzhou 510006, China
[h] University of Chinese Academy of Sciences, Beijing 100049, China

HIGHLIGHTS

- A year-long synchronized observation of AMPs on both land and sea was carried out.
- Microplastics are mainly fibers in cities, and the pollution level is closely related to population density.
- Only 1.8 % of the atmospheric microplastic emissions could be transported from land to sea.
- Atmospheric transport is not an efficient way to transport AMPs from land to sea.
- The treatment of marine MP pollution should first reduce riverine input.

GRAPHICAL ABSTRACT



ARTICLE INFO

Keywords:
Microplastic pollution
Land-to-sea transport
Atmospheric transport

ABSTRACT

Microplastics have been recognized as a global marine environmental issue, but their sources, particularly the contribution of atmospheric transport, remain obscure. Here, we determine the transport efficiency of atmospheric microplastics (AMPs) from land to sea using multimedia observations from both sea and land in the South China Sea in conjunction with atmospheric trajectory modelling. Furthermore, we extrapolate AMP inputs to the

* Corresponding author.
E-mail address: xuxr@gxu.edu.cn (X. Xu).

https://doi.org/10.1016/j.jhazmat.2025.139272
Received 2 May 2025; Received in revised form 22 June 2025; Accepted 14 July 2025
Available online 23 July 2025
0304-3894/© 2025 Elsevier B.V. All rights are reserved, including those for text and data mining, AI training, and similar technologies.

Deposition
Fiber

ocean at a global scale. The results show that only 1.8 % of AMPs are transported and deposited into the sea, with most remaining on land. The global mass of AMPs entering the sea is 262.98 t, which is much less than the river exports. Therefore, we conclude that the atmospheric transport is not the main pathway for land-sourced microplastics to enter the sea, and suggest that the foremost step of curbing the worsening of marine MP pollution is to control the inflow of riverine MPs into the sea.

1. Introduction

Misuse and mismanagement of plastic products have caused masses of plastic waste to accumulate in the environment and eventually enter in the oceans [1]. The potential annual transfer of plastic waste from land to the oceans is estimated to be 4.8–12.7 Mt [2], resulting in a global concern of plastic pollution. Understanding the sources, transport and fate of plastics is a prerequisite for reducing plastic pollution. Studies have initially recognized rivers as the main pathway for plastic debris to enter the oceans, but a growing number of studies are emphasizing the role of atmospheric transport, especially for microplastics (MPs, < 5 mm) [3–5]. There have been many reports on the presence of atmospheric microplastics (AMPs) in various regions [6–9], but the transport and environmental fate of AMPs are unknown.

Observations of AMPs in remote areas, such as the French Pyrenees Mountain [10], the Alps [11], the Tibetan Plateau [12] and polar regions [13], have demonstrated the long-range transport of AMPs; however, their land-to-sea transport and transport efficiency are rarely discussed and have not been properly quantified. Several scientists have preliminarily estimated the global transport mass of AMPs into the sea, but the estimates vary greatly and are not comparable, ranging from 10.02 t/yr to 100 kt/yr [4,14–16]. The proposed AMP transport efficiencies in these studies are also ambiguous, ranging from 1.8 % to 34 % [14,16]. The key to these large gaps seems to be the original dataset used in estimations. Limitations in monitoring methods make it difficult for a single team to conduct large-scale monitoring of AMPs on a national or global scale, so existing studies usually utilize literature data to develop estimates. On the one hand, the lack of global field data contributes to the high level of uncertainty in these estimates. More importantly, it is a great challenge to integrate the noncomparable datasets across regions and periods, because the monitoring methods for these datasets vary widely [17,18]. The absence of standardized monitoring procedures would directly lead to a high level of uncertainty in global extrapolation. For example, the pore size of sampling filters is critical to AMP abundance. A filter with a large pore size used in AMP collection may result in an underestimation of AMP abundance. For example, in a previous study done in France [10], if only AMPs with a size larger than 100 μm were counted, the AMP abundance was 36 ± 18 items/m^2/d, but if a wider range of AMPs (> 5 μm) were considered, the abundance increased to 365 ± 69 items/m^2/d. However, the pore size of filters used varied widely among studies, with a range from 0.45 to 100 μm [19–22], making it a challenge to describe the distribution of AMP pollution by comparing different studies. Besides, the differences in reported AMP abundances caused by inconsistencies in sampling or analytical methods can easily be misinterpreted as real differences in the environment, thereby reducing the reliability and credibility of the estimates.

Here, almost all our estimates of AMP land-to-sea transport were made using simultaneous observations to ensure the reliability of the original data and transport efficiency (the framework for this study is shown in Fig. S1). We conducted simultaneous observations in the South China Sea (SCS) and four Chinese coastal cities, with sampling consisting of both deposited and suspended AMPs (see Methods). Notably, our sampling project spanned 2021, and the same sampling methods and processing procedures were employed among all sampling sites, thereby preventing errors across seasons and methods. According to the year-round observations from Guangzhou and Xiamen in 2021, we confirmed the proportion of MPs entering the atmosphere and estimated the AMP emission in four Chinese coastal provinces (Guangxi, Guangdong, Fujian and Hainan) further using primary MP emission inventory established by Wang, et al. after adjusting the emission sources [23]. There are two potential pathways for AMPs to enter the sea, both of which were accounted for. The first is long-distance atmospheric transport, which was estimated using air trajectories and AMP emissions estimation. The second is riverine transport, as they can enter the sea after being deposited in rivers. The sum of the two pathways was the total mass of land-sourced AMPs entering the SCS, and the transport efficiency of AMPs from land to sea was calculated accordingly. These findings serve as a foundation for comprehending the fate of MPs in terms of their sources and sinks, as well as their global cycling.

2. Materials and methods

2.1. Study sites and sampling methods

Sampling sites on land were set in five representative cities, including Beihai (Guangxi Zhuang Autonomous Region), Guangzhou (Guangdong Province), Xiamen (Fujian Province), Sanya (Hainan Province) and Yongxing Island (belonging to Sansha, Hainan Province), as shown in Fig. S2. The sampling methods were consistent with what we did in Guangzhou before [24]. In 2021, total atmospheric deposition (including dry deposition and wet deposition) was simultaneously collected at monthly intervals in all five cities ($n = 72$) using passive samplers. Atmospheric deposition was dropped into a glass collection bottle via a stainless-steel funnel and obtained by filtration (Fig. S3). The collection bottle was placed inside a stainless-steel box to prevent the escape of fallout and contamination from ground dust. In addition, to estimate the proportion of MPs entering the atmosphere, suspended AMPs were monitored throughout 2021 in Xiamen and Guangzhou. A total of 171 samples were collected using middle-flow suspended particulate samplers, which were installed on the roofs of laboratory buildings. The samplers were set approximately 1.5 m above the floor, effectively avoiding resuspended ground dust. Sampling was generally performed every other day, with an intake flow rate of 100 L/min for 24 h.

Marine AMP samples from the SCS were obtained during a cruise in April 2022, with a navigation route map depicted in Fig. S2. A suspended particulate sampler was secured on the upwind area of the back deck (approximately 2.8 m above sea level) to collect suspended AMPs. The suspended particulate sampler and sampling procedures agreed with sampling in cities to verify the validity of the samples. A total of 20 sampling transects were set along the cruise and one sample was collected at each section. The detailed geographic information of sampling transects was presented in Table S1.

All samples were collected on glass microfiber filters (Whatman GF/A, 1.6 μm), and detailed sampling procedures can be found in our previous study [24]. All filters were kept in aluminum foil for further examination.

2.2. MP identification

A total of 263 filters were collected, including deposited AMP samples ($n = 191$, 171 samples collected on land and 20 samples collected above the sea) and suspended AMP samples ($n = 72$). Each filter was evenly divided into two (deposited AMP samples) or four equal parts (suspended AMP samples), and one was chosen as a representative sample at random. In total, 263 representative samples were randomly

selected, all of which were tested for MP identification.

Three steps were necessary for MP identification, including MP extraction, observation and identification. Firstly, according to the typical features of plastic materials (such as no biological or cellular structures, uniform color and shiny) [12,24], all suspected MPs were visually screened out under a stereoscopic microscope (Olympus SZX10, Japan). The filter should be scanned back and forth under the microscope from top to bottom at least four times to ensure that every corner of the filter has been examined. But due to the limitation of human eyesight (< 20 μm), MPs of extremely small size may be unnoticed. The characteristics of all suspected MPs were observed and recorded, including shapes, colors and sizes (length and width). The micro-Fourier transform infrared spectroscopy (FT-IR) technique was used for qualitative identification of all collected AMPs. The screened suspected MPs were carefully flattened and straightened one by one, and transferred subsequently to a clean and dry copper sheet with steel tweezers, keeping the MPs to be tested as close as possible to the copper sheet. To obtain spectra, the FT-IR spectrometers (Thermo Scientific Nicolet iN10, USA) scanned the suspected MP placed on the copper with a resolution of 4 cm^{-1} for 16 scans each in reflection mode. All obtained spectra were compared with the standard spectra library individually, and the polymer composition could be confirmed when the match was > 60 %, which is a widely accepted and applied ratio [15,20,24]. All suspected MPs screened out were tested. Based on the random sampling proportion, the final total number of MPs for a sample was determined to be double or four times the identified numbers. However, due to the distribution randomness of environmental samples, the final MP data were subject to 2–4 times uncertainty.

2.3. Quality assurance and quality control

Quality assurance control measures were taken during sampling and identification to minimize contamination and subjective errors. During sampling, to minimize potential contamination, all filters and glass supplies were baked at 450 ℃ in a muffle for 4 h, and rinsed water was filtered by microfiber filters (Whatman GF/A, 47 mm, 1.6 μm) before use. In addition, cotton lab coats and nitrile gloves were worn throughout the sampling and pretreatment processes to prevent contamination. Procedural blanks were made by placing an open, wet and pretreated filter during the filtration of atmospheric deposition. A total of 72 procedure blanks were obtained and they were taken back to the laboratory and analyzed along with the samples. No MPs were detected in the procedural blanks, but a few cotton microfibers were detected (detected in 2 of 72 blanks). Ropes were used to secure the equipment on the board, and observable ropes near the sampler on the board were collected and tested, but no comparable materials were discovered in marine AMP samples. To avoid subjective errors in recognizing MPs, MP identification for all samples was performed by the same experimenter in this study, including scanning suspected MPs under microscope and FT-IR analysis.

2.4. Total MP emissions

In this study, we estimated the total MP emissions from four coastal provinces of the SCS based on the primary MP emission inventory established by Wang, et al.[23]. According to the actual observations, we adjusted the emission inventory, and the final inventory included seven emission sources: clothing, architectural coating, automotive paints, road markings, plastic raw materials, artificial turfs and running tracks, personal care and cosmetics products, with rubber tires and marine coating removed (Text S1). The MP emissions from each source can be calculated by the following equation.

$$Emission = A \times EF \quad (1)$$

The calculations of activity (A) and emissions factors (EF_s) of each source were detained in Text S1. The annual MP emission fluxes of each city were determined independently, and most of the socioeconomic statistics used in the calculation were obtained from official data published by the National Bureau of Statistics of China in 2021.

A Monte Carlo simulation was performed to characterize the uncertainty of MP emissions. Uncertainty in related activity data and emissions factors are two major causes of the uncertainty in MP emissions (Table S2) [24], where EF has been listed directly in the formulas mentioned in Text S1, and the remaining factors in the fomulas are grouped into A. Twenty-eight parameters (both A and EF) from seven MP emission sources were entered into Crystal Ball software (Oracle). All inputs were randomly selected and the MP emissions were repeatedly calculated 10,000 times according to the Eq. (1). The activity (A) data and emissions factors (EF_s) were listed in Table S2. The model gave a prediction range of 12.80–549.00 kt for MP emission, taking the 90 % confidence interval as the uncertainty range for MP emissions (Fig. S9).

2.5. The proportion of MPs entering the atmosphere

Although total MP emissions are initially quantified, the fraction of MPs that become airborne is highly uncertain, with reported proportions ranging from 1 % to 40 % [16]. The proportion of MPs entering the atmosphere calculated based on literature data may deviate from the actual value due to differences in sampling methods and sampling periods. In this case, we determined the proportion (α) using annual synchronic AMP data from Guangzhou and Xiamen, as shown in the following formula.

$$\alpha = \frac{M_{AMPs}}{E_{MPs}} \quad (2)$$

where E_{MPs} is the total mass of MP emissions calculated based on the emission inventory in Text S1 and M_{AMPs} is the mass of AMPs, which can be defined as:

$$M_{AMPs} = \frac{A \times H}{T} \quad (3)$$

where A is AMP abundance, H is the height of the atmosphere (assuming that AMPs were well mixed over a range of 1000 m), and T is the atmospheric residence time of AMPs. According to all measured AMPs (N = 703), the predominant aerodynamic diameter range of AMPs was 50–90 μm, and the main polymer type was PET (1.38 g/cm^3). Therefore, PET with an intermediate diameter of 70 μm was chosen as representative AMP and used to calculate the unit mass of AMPs. Based on the size of AMPs, T was estimated to be between 3 and 28 h (detailed calculations can be found in Materials and methods 2.7). Here, we denote T as 24 h to make calculations easier.

The average annual abundance from Guangzhou was used to determine α, while the dataset from Xiamen was used for verification (Table S3). The resulting α was proven to be valid and feasible when the estimated mass matched the mass of AMPs calculated from the field observations.

2.6. AMP deposition in terrestrial environments

Population density is highly correlated with MP pollution levels [6,7], and it has been widely considered in MP emission estimates [2,25]. Combining our field data from five cities with data from Dongguan [26], we developed a regression model on population density (p) and MP deposition flux (Dep), as shown in the following equation (Fig. 1c):

$$Dep = 0.004p + 12.63 \quad (4)$$

The R-squared (R^2) of the regression model was 0.86, which implied that this model could simulate the variation of MP deposition flux as well. As a result, the AMP deposition flux could be inferred from this model for each city (Fig. S4), and the total MP deposition could be calculated by multiplying it by the city area. However, different land use

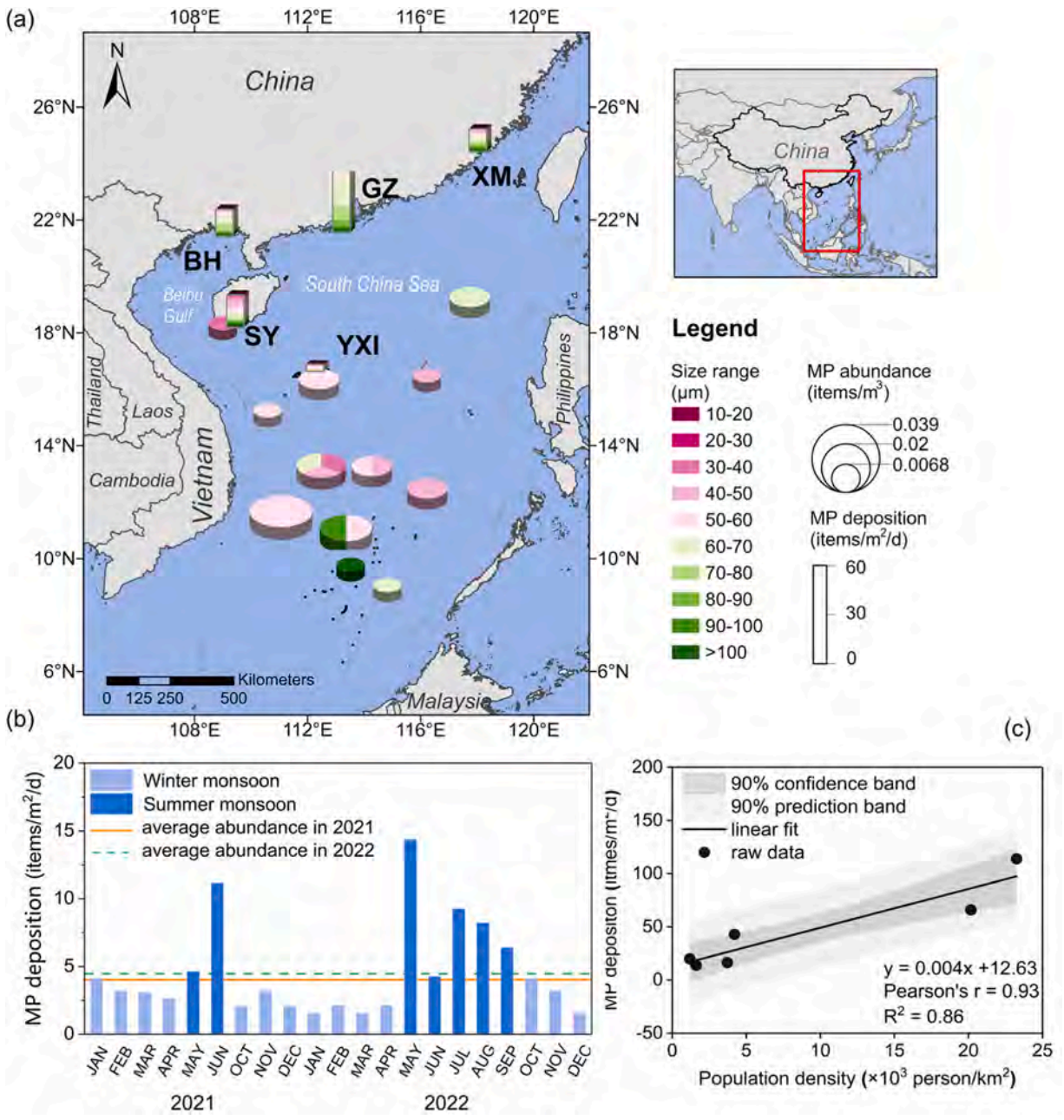


Fig. 1. AMP abundances in the South China Sea (SCS) region. The spatial distribution of AMP abundance (items/m^3), deposition fluxes (items/m^2/d) in the SCS region (including Beihai (BH) Guangzhou (GZ), Xiamen (XM) and Sanya (SY) and Yongxing Island (YXI)), aerodynamic size distribution (a) and AMP deposition at YXI from 2021 to 2022. The sampling on Yongxing Island in July, August and September of 2021 was interrupted due to a global pandemic of coronavirus disease 2019 and no data were obtained. Correlation between population density and AMP deposition (c), with one data from Huang, et al. and the rest were measured data from this work.

types where MPs are deposited may affect their fate. For example, AMPs deposited on artificial land could be washed into a water body via road runoff and then enter the ocean through river transport together with AMPs deposited directly into the water body [3,27,28]. Previous studies indicate that 6 % of AMPs can reach surface waters through road runoff [29,30]. The river transport probabilities of MPs from catchments to seas are suggested to be between 1.73–8.70 %, with an average value of 3.24 % for the top-ten catchments in Asia [31]. Therefore, the AMP deposition in each city was calculated separately for four land use types, including natural land (cultivated land, forest, grassland and semi-natural land), water bodies, artificial land and marine (Fig. S5). Land use data with a spatial resolution of 1 km were provided by the National Resources and Environment Database of the Chinese Academy of Sciences [32].

2.7. AMP transport trajectory model

The Hybrid Single-Particle Lagrangian Integrated Trajectory (HYSPLIT) model was applied to simulate the transport trajectory of air masses using Global Data Assimilation System (GDAS) meteorological data. Guangzhou was the most polluted site in study area (Fig. 2), so it was set as the starting point for the release of AMP pollution. The model was run in forward mode with a total run time of 28 h, starting at 100 m elevation above ground level (main altitude ranges of human activities). The model running time was determined by the maximum atmospheric residence time of AMPs, which was related to their aerodynamic

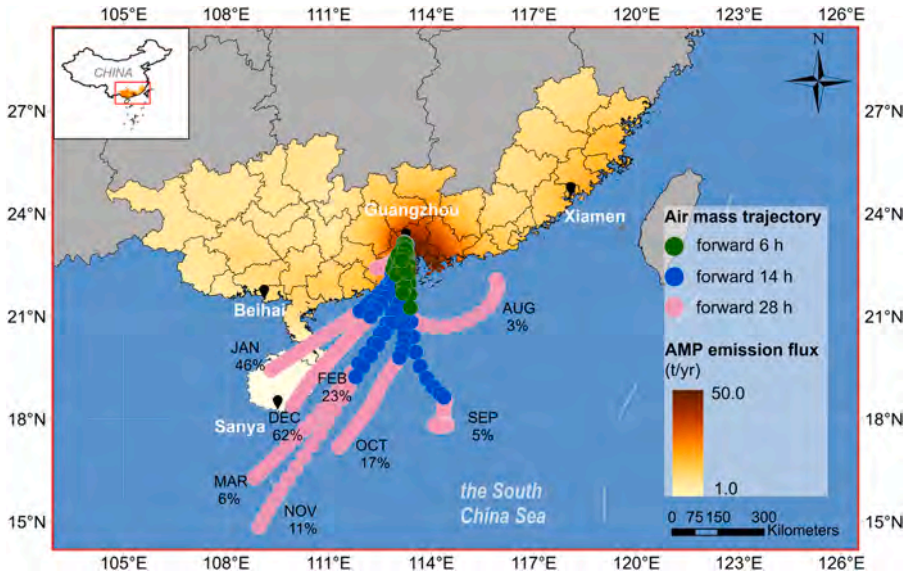


Fig. 2. Annual AMP emission for the four provinces adjacent to the South China Sea in 2021 and the distribution of seaward air masses according to forward trajectory modeling.

diameter. The atmospheric residence time and aerodynamic diameter could be calculated using the equations seen below [33,34].

$$D = \left(d_p \ln 2\theta\right)^{1/2} D_P \tag{5}$$

where D is the aerodynamic diameter, d_p is the density of plastics, θ is the aspect ratio of plastics and D_P is the cylindrical diameter of plastics.

$$V_t = \frac{gD^2\left(d_p - d_m\right)}{18\mu} \tag{6}$$

where V_t is the terminal velocity, g is the gravitational acceleration, D is the aerodynamic diameter, d_p is the density of plastics, d_m is the density of the air, and μ is the viscosity of air.

$$T = \frac{H}{V_t} \tag{7}$$

where T is the atmospheric residence time, and H is the height of air (assumed to be 1000 m).

The terminal velocity of AMPs followed a lognormal distribution (Fig. S6), and their 90 % confidence interval corresponded to an atmospheric residence time of 3–28 h. All trajectories were clustered at one-hour time intervals with a trajectory skip of 1 and analyzed for comparison by month.

Seaward trajectories were selected for further analyses (Fig. 2, approximately 15 % of a total of 7134 trajectories), and transport distances were calculated along the trajectory from the starting location to the deposition point. To ensure that most AMPs could reach the SCS, the transport distance should be at least 200 km, implying a 14 h atmospheric residence time. According to our measured size distribution of deposited AMPs (Fig. S6), only 11.3 % of AMPs met the conditions for a terminal velocity of less than 0.02 m/s and an atmospheric residence time over 14 h.

2.8. Data analysis

The Cystal Ball software (Oracle) was used to finish the Monte Carlo simulation, and Excel 2019 and SPSS 24.0 software (IBM, U.S.A.) were utilized for descriptive and statistical analysis. All analyses were carried out at a significance level of 0.05, and the data were reported as mean ± standard error (SE). A number of programs, including Origin 2022b, ArcGIS pro 2.8.6, and MATLAB R 2023a, were used to visualize the data.

3. Results and discussion

3.1. AMP abundance in the SCS region

Microplastics were widely present in all deposited samples, with deposition fluxes ranging from 4.11 to 109.34 items/m^2/d (Fig. S7a). For cities, the mean AMP deposition flux was significantly higher in Guangzhou (65.94 ± 7.53 items/m^2/d, Kruskal—Wallis test, $p < 0.05$), followed by Sanya (19.89 ± 3.19 items/m^2/d), Beihai (16.51 ± 2.88 items/m^2/d) and Xiamen (13.89 ± 1.83 items/m^2/d), as shown in Fig. 1a. However, there were no discernible differences in size distribution and shape between cities (see Supplementary Information for more AMP characteristics). The high AMP pollution level in Guangzhou may be because there were more AMP sources in densely populated cities with a high degree of anthropogenic activity [35,36]. The correlation analysis also confirmed a strong correlation between population density and AMP pollution (Pearson's correlation, $r = 0.93$, $p < 0.05$, Fig. 1c).

The two-year (from January 2021 to December 2022, Fig. 1b) AMP observations at Yongxing Island revealed that AMP deposition on islands far from land was markedly lower than that in cities, with an average deposition flux of 4.94 ± 0.83 items/m^2/d. Similarly, the analysis of marine air samples shown an average AMP abundance of 1.41 ± 0.23 items/100 m^3 in the SCS, which was obviously lower than our observations in cities, such as 0.17 ± 0.01 items/m^3 in Guangzhou and 0.07 ± 0.04 items/m^3 in Xiamen (detailed in Tables S1 and S3). As shown in Fig. 1a, AMP abundances were higher in the southwestern SCS, which may be attributed to emissions from neighboring Southeast Asian countries. The cruise occurred in April, and the SCS was in the summer wind period, so AMPs emitted from Southeast Asian land could be transported to the SCS by southwest winds (Fig. S8a), resulting in an increase in AMP abundance. These findings suggested a remarkable impact of land-based emissions on marine AMP distribution. The AMP abundance at Yongxing Island (1.40 items/100 m^3) was comparable to the mean (1.41 ± 0.23 items/100 m^3) and median values (1.39 items/100 m^3), according to our measured data during the cruise. Therefore, Yongxing Island was chosen as a representative site to calculate the total AMP deposition in the SCS. Based on the average AMP deposition flux at Yongxing Island, the total deposition of AMPs in the SCS was estimated to be 1.56 kt/yr (0.49–4.55 kt/yr) (Table S4).

3.2. Atmospheric MP emission

Our MP emission modelling revealed that a total of 166.61 kt MPs were discharged into the environment annually from four provinces adjacent to the SCS, with an uncertainty range of 12.80–549.00 kt (Fig. S9a). The estimation of primary MP emissions from seven sources was conducted by employing a range of socioeconomic data, such as population, residential area, and consumption of plastic products. Emission estimates were derived from the city level as the most basic unit, and 63 cities in Guangdong, Guangxi, Fujian and Hainan provinces were estimated. Synthetic fibers and artificial turfs accounted for approximately 90 % of MP emissions, which was compatible with our field observations that it was virtually all fibers (Text S2, Table S5). Synthetic fibers have long been recognized as a significant source of AMPs, and artificial turfs with a high nylon and polyethylene content have recently been proposed as an important source of AMPs [37,38].

Based on the MP emissions obtained previously and the field AMP data from Guangzhou and Xiamen, it has been defined that the fraction of MPs entering the atmosphere is 0.6 % (Table S3). Accordingly, a total of 1000.00 t AMPs were released annually into the atmosphere from the four provinces, with a distinct regional heterogeneity (Fig. 2). The Guangdong-Hongkong-Macao Greater Bay Area (GBA) is one of the most populous and rapidly developing areas in China, and MP contamination tends to be greater in densely urban agglomerations. The nine GBA cities in Guangdong Province were responsible for 67.5 % of Guangdong Province emissions and 33.2 % of total AMP emissions in the four provinces. These results indicated that the GBA is the most polluted area in the coastal regions of the SCS (Table S6). The high AMP abundances observed in GBA cities such as Guangzhou and Dongguan also demonstrate the high pollution level here [24,26,39]. Consequently, we reasonably considered Guangzhou as a center of AMP pollution and commenced the air mass projection from here.

3.3. The AMP budget

The direction of air mass flow and the residence time are the two most important determinants of whether AMPs can be transported to the sea. Due to the impact of monsoons, the seasonality of continental air pollution transport in Asia is pronounced [40,41]. Contaminated air masses can be only transported from mainland China to the SCS during the winter monsoon (northeastern winds) [42,43]. The air mass trajectories for each month in 2021 were acquired using the Hysplit forward trajectory model. Subsequent cluster analysis revealed that only 15 % of the air masses observed during this period exhibited a trajectory directed towards the sea (Fig. 2). On the other hand, a sufficiently long atmospheric residence time is necessary for AMPs to be effectively transported to the sea, which is constrained by their sizes. Only 11.3 % of AMPs could be transported over great distances and deposited in the SCS, according to the results of the size analysis. Therefore, it is estimated that 16.94 t AMPs could be transported through the atmosphere and deposited into the sea each year.

Some AMPs are deposited in response to precipitation or gravity [24,44]. A total of 560.69 t AMPs were deposited locally. Furthermore, the deposition was calculated for each of the four typical land use types, including natural land, artificial land, water bodies and marine (Fig. 3). The maximum deposition (498.11 t/yr) occurred on natural land due to the largest natural land area. The downward mobility of AMPs to groundwater is a complicated process, and the upper 25 cm of soil is regarded as a transient or persistent sink for MPs [45–47]. The potential contribution of groundwater to marine MP was therefore disregarded. Even in coastal areas, the area of the sea in the city is still very small and therefore the mass of AMPs directly deposited into the sea is negligible, weighing only 0.0004 t. Approximately 20.26 t AMPs settled annually into water bodies and entered the sea with rivers, which are the major pathway for MP transport into the seas [48,49]. On the other hand, approximately 42.32 t of AMPs were deposited on artificial land, a portion of which could be transported downstream by rivers after being washed into the water bodies [50]. As a result, the total mass of AMPs entering the sea through rivers was 0.74 t. We emphasize that this flux is for only the AMPs, not accounting for the MPs in the other environmental compartment. Therefore, this flux could not be directly comparable with the total riverine MP fluxes.

The remaining 422.05 t of AMPs were transported inland, with a low possibility of their eventual arrival in the ocean. Considering all pathways of AMPs to the sea, the ultimate input of AMPs from land to sea was 17.68 t. Our measurements in the SCS indicate that the sea received

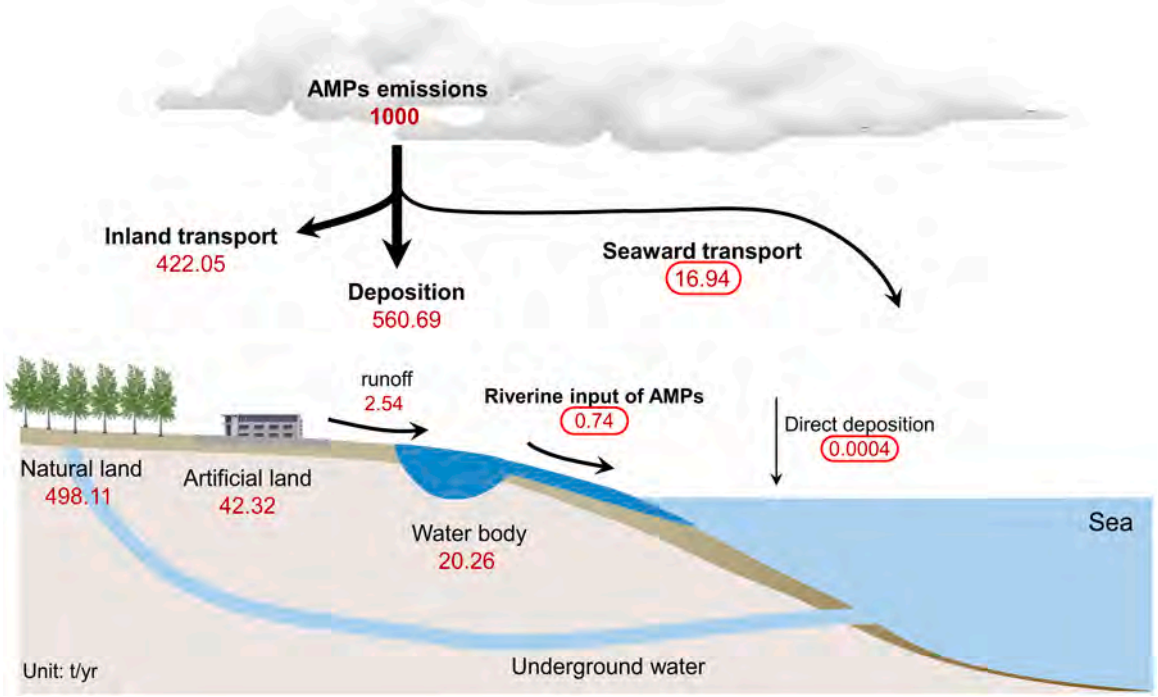


Fig. 3. Transfer fluxes for AMPs in four provinces adjacent to the SCS in China in 2021 (t/yr).

1.56 kt of AMPs deposition annually (Table S4), which come from all sources. It has demonstrated that our estimates of land-to-sea transport of AMPs are within an acceptable order of magnitude, since there is no question that any one source contributes less than the total deposition. This quantity represents a mere 1.8 % of the total AMP emissions, indicating that most AMPs tend to be retained on land. Moreover, for AMPs, the most of them enter the seas by atmospheric transport, with just a minor percentage sinking into the oceans with rivers following atmospheric deposition.

3.4. Land-to-sea transport of AMPs

The MP emissions from the four coastal provinces accounted for 23 % of the total MP emissions in China (737.29 Gg) [23], which could be considered the main contributor of MP emissions from mainland China to the SCS. However, China coasts may not be the primary source of AMPs in the SCS. This conclusion is reasonable and explainable. Our field observation in the SCS showed higher AMP abundance close to the coast of Southeast Asia, but almost none of the air masses along the coast of the SCS moved toward the sea in April (Fig. 2). Two years of AMP deposition monitoring in the SCS reveal that the summer months are a period of high AMP pollution, and at this time the winds are from the southwest. Slower summer winds extend the residence time of AMPs emitted from South Asian countries over the SCS and would favor AMP deposition. In contrast, winter winds are swift and short-lived, making it difficult to transport AMPs from mainland China into the sea (Fig. S8). On the other hand, countries bordering the SCS are also greatly affected by AMP pollution, especially Vietnam (172–292 items/m^2/d) [51], the Philippines (0.02 items/m^3) [52] and Malaysia (97–775 items/m^3) [53]. The estimation indicates that only approximately 1.1 % of the total deposition might originate from the four Chinese coastal provinces (Table S4), and more measured data from Southeast Asian countries are needed to completely clarify the source-sink of AMPs in the SCS.

We found a lower transport efficiency of AMPs from land to sea (17.68 t/yr, 1.8 % of the atmospheric emissions of MPs) compared to previous global studies, e.g., 21 % as proposed by Fu, et al. [4] and 34 % proposed by Evangeliou, et al. [16]. There are two possible reasons for these differences. First, these differences may be attributed to AMP emission estimates. Tire emissions were incorporated in previous emission estimates and are the greatest source, accounting for 84 % of the total [4,54]. However, the main component of tires is natural rubber, which is not listed in the ISO definition for plastics. Furthermore, tire wear particles are typically black fragments [55–57], but black did not make up a high percentage of observed particles in our observations, only roughly 11.7 %. Some black fragments were found only in the road dust and their polymer composition is not rubber or other tire additives [19,58], so the high 84 % share of tire emission need more supporting field data and further confirmation [5,54]. For the observed black particles, we matched their spectra to standard spectra library of rubber, resin and other common tire compounds, but the results were negative. Therefore, we excluded it from the MP emission inventory for the time being. The α of MPs entering the atmosphere is the most crucial factor in estimating AMP emissions. Long, et al. [54] suggested the α to be 12.5 % based on published AMP data; however, due to the fact that the data came from four research teams during 2016 and 2019, the results are greatly affected by the uncertainty of data integration across different teams and methodologies. On the basis of measured data from Guangzhou and Xiamen, we determined the α to be 0.6 % and ensured that the sampling method and processing procedures were completely consistent so that the resulting α is more reliable and conforms to reality. Notably, there is a possibility of overestimation, although our estimated α is much lower than the previous values. Our group conducted a vertical investigation of AMPs in 2021 and found that AMP abundance at 500 m was significantly lower than that at ground level [59]. Consequently, the assumption of uniform mixing of AMPs within the atmospheric boundary layer (set to 1000 m) in estimating the total mass of AMPs in Guangzhou and Xiamen may result in an exaggerated mass and an increased fraction of AMPs. The overestimated atmospheric transport efficiency of MPs is largely influenced by the high proportion of atmospheric emissions.

Another reason for the difference is the estimation of AMP deposition on land. Most studies estimated AMP deposition in their study areas based on published AMP deposition fluxes [14,21], but the comparability and availability of these data need to be validated. For instance, two research groups examined AMPs in Shanghai in 2018 and 2019, while the results differed by a factor of 200, with abundances of 1.42 $\pm$ 1.42 items/m^3 [60] and 267 $\pm$ 227 items/m^3 [7] respectively. Therefore, different choices of datasets could alter the estimated mass of AMPs deposited on land, potentially resulting in inflated atmospheric transport. To reduce data-related inaccuracies, we have standardized sampling and analytical procedures to ensure the availability of AMP data, and we have also used statistics from the same year as much as feasible. In addition to data errors, the mass calculation of MP is also a nonnegligible reason for differences. In previous studies, MPs were viewed as solid heterogeneous objects, and their mass was estimated by multiplying their polymer density by volumes [5,21,27,44]. MPs in actual environments may suffer density variations due to ageing and curling into hollow objects [61], leading to a large variance in overall mass. It is not yet known how much AMP mass is lost in the environment due to weathering or ageing; however, the conclusion that the atmospheric transport of MPs from land to sea is inefficient is unaffected.

The SCS has emerged as a hotspot for MP research [62,63], necessitating an urgent need to elucidate their origins. The Pasig River (Philippines), the Pearl River (China), and the Mekong River (Vietnam) are the major rivers that flow into the SCS and annually discharge 38.8 kt, 13.6 kt and 22.8 kt MPs into the sea, respectively [48]. The riverine input from any given river is considerably greater than the annual deposition of AMPs in the SCS (1.56 kt/yr), suggesting that atmospheric transport may be not the primary source of MPs in the SCS.

3.5. Uncertainty

The estimation of MP emissions is the basis of all further calculation, which is one source of uncertainty. Due to the uncertainties related to activity levels and emissions factors of MP sources, the estimated range of MP emissions is 12.80–549.00 kt (Fig. S9a). One aspect that is missing from our estimation is potential resuspension of deposited AMPs. Strong winds or turbulence may re-suspend previous deposited AMPs and allow them secondary transport [22,64]. However, there is currently no clear allocation factor between emission sources and resuspended sources of MPs, making it difficult to quantify the uncertainty in this part because of limitations imposed by research gaps. Another issue we need to mention and concern is the variability in the MP emission inventory. Synthetic fibers are the most prominent contributing source in our MP emission estimation, and while our field observations have confirmed this estimate, it is not set in stone. Urban planning and plastic emissions regulations will cause changes in MP emission inventory as well as AMP emissions, which need to be considered in further estimation in the future.

Another major source of uncertainty is the proportion of MPs entering the atmosphere. Values reported in the literature range from 1 % to 40 %, and some studies have even extended the upper limit to 83 % [16,54], which may not be conducive to further accurate estimation. Assuming that all MPs emitted into the air are deposited, and then estimate the corresponding α is 0.1 %–4.4 % using the AMP deposition calculated from measured data. Besides, based on the year-round AMP observations in Guangzhou, the α varies from 0.03 % to 1.5 % (Table S3). Combining these two results, the uncertainty range for α can be further narrowed to 0.1 %–1.5 %. It will be more scientific and accurate to confirm this ratio using a different dataset. However, we insisted on using synchronized measured data for estimation whenever possible, so the limitation of field data prevented us from further

validating.

We eventually estimate the uncertainty of our simulated AMP land-sea transport efficiency to be between 1.7 % and 7.5 %. Efficiency of land-sea transport of AMPs in different regions of the world ranged from 0.5 % to 40 %, with the South China Sea at about 2 % [16]. Our results are consistent with previous findings and give a finer range of AMP transport efficiency. It should be noted that the data used in our estimates are from coastal land, and therefore may be overestimated for inland areas far from the sea. More field studies are needed in the future, especially to complement the measured data from inland areas, to further understand the land-sea transport of AMPs.

3.6. Global Implications

We extrapolated our MP emission model and transport efficiency to the global level for a direct comparison between atmospheric transport and riverine input (Text S3). The annual global AMP emissions from land sources were estimated to be 14.61 kt, of which only 262.98 t (uncertainty range of 248.37–1095.76 t) could be deposited into the seas. This estimate is significantly lower in magnitude compared to earlier global estimates, such as the 13 kt/yr reported by Brahney, et al. [5] and 25 kt/yr reported by Fu, et al. [4]. The total annual global riverine emissions of plastics from land to sea are generally estimated to range from 0.1 to 1270 Mt [2,25,48,65], and the global export of MPs to the sea can also reach 47 kt per year [66]. We note that our worldwide estimation, which is based solely on field observations from the SCS region, is subject to considerable uncertainty. The 1.8 % land-to-sea transport efficiency should be used carefully, especially for inland areas with climates that differ significantly from the SCS, since AMP environmental fate will be directly impacted by variations in the weather. AMPs are supposed to have a poorer land-to-sea atmospheric transport efficiency than coastal areas due to the greater transport distances for inland locations from land to sea. Therefore, using the MP atmospheric transport efficiency from the SCS may lead to an overestimation of the land-sea transport in inland areas. But on the other hand, low precipitation in inland locations may result in less wet deposition of AMPs, which will increase the likelihood that the AMPs could be driven by the wind and travel long distance. However, there is still a lack of field observations to verify the final impact of the two effects mentioned above. On a global scale, population and plastic emissions tend to be concentrated in coastal regions [1]. From this perspective, the SCS region might be able to serve as a representative region, and the global extrapolated estimates based on these regional observations could be used as a reference value until more accurate observations are available. Despite the imperfection of our estimates, the huge order of magnitude difference between riverine input and atmospheric transport suggested that the riverine transport of MPs surpasses their atmospheric transport. The size of MPs may be the key to explaining the immense differences between atmospheric transport and riverine transport because larger plastic debris can float with rivers but cannot travel through the air. These results indicated that atmospheric transport is unlikely to be the primary channel for land-sourced MPs into the seas, and their land—sea transport efficiency is much lower than previously believed. We suggest that atmospheric transport may be not the main culprit for current serious marine MP pollution, and therefore the key to mitigating marine MP pollution depends on controlling and reducing riverine MP discharges to the seas.

Environmental Implication

Marine microplastic pollution is a serious and rapidly growing global problem that requires urgent action to reduce marine microplastics and their impacts. Clarifying the source of marine microplastics is a prerequisite for reducing microplastic pollution. For the first time, this study presents synchronized observations of atmospheric microplastics in five coastal cities throughout the year and determines the land-to-sea atmospheric transport efficiency of microplastics to be 1.8 % based on field data, which has been overstated in previous models. The findings provide valuable insights and scientific support for clarifying the source-sink of marine microplastics, with direct implications for future management strategies.

CRediT authorship contribution statement

Rui Hou: Software. **Eddy Y. Zeng:** Writing – review & editing. **Lang Lin:** Investigation. **Shan Liu:** Investigation. **Yanxu Zhang:** Writing – review & editing, Formal analysis. **Li Heng-Xiang:** Methodology, Investigation. **Xu Xiang-Rong:** Writing – review & editing, Project administration, Funding acquisition, Formal analysis, Conceptualization. **Zhen Yuan:** Writing – original draft, Visualization, Methodology, Investigation, Funding acquisition, Data curation.

Declaration of Competing Interest

The authors declare that they have no known competing financial interests or personal relationships that could have appeared to influence the work reported in this paper.

Acknowledgement

This work was supported by Guangxi Science and Technology Program (No. AD25069075), Hainan Province Science and Technology Special Fund (No. ZDYF2022SHFZ317), National Natural Science Foundation of China (No. U2005207), the Director General's Scientific Research Fund of Guangzhou Marine Geological Survey, China (No. 2024GMGS-QN-02). We thank Daning Li, Chang Chen, Zhenhua Long, and Fanyu Zheng of the Xisha Marine Science Comprehensive Experimental Station, South China Sea Institute of Oceanology, Chinese Academy of Sciences for their assistance. We acknowledge Prof. Minggang Cai from Xiamen University, Prof. Hongmei Jing from Institute of Deep-sea Science and Engineering, Chinese Academy of Sciences, Mr. Bin Li from Guangxi Mangrove Research Center and Mr. Liangming Wang from South China Sea Fisheries Research Institute, Chinese Academy of Fishery Sciences and other researchers involved in sample collection.

Appendix A. Supporting information

Supplementary data associated with this article can be found in the online version at doi:10.1016/j.jhazmat.2025.139272.

Data availability

Data will be made available on request.

References

[1] Lebreton, L., Andrady, A., 2019. Future scenarios of global plastic waste generation and disposal. Palgrave Commun 5 (1), 6.
[2] Jambeck, J.R., Geyer, R., Wilcox, C., Siegler, T.R., Perryman, M., Andrady, A., Narayan, R., Law, K.L., 2015. Plastic waste inputs from land into the ocean. Science 347 (6223), 768–771.
[3] Allen, D., Allen, S., Abbasi, S., Baker, A., Bergmann, M., Brahney, J., Butler, T., Duce, R.A., Eckhardt, S., Evangeliou, N., Jickells, T., Kanakidou, M., Kershaw, P., Laj, P., Levermore, J., Li, D., Liss, P., Liu, K., Mahowald, N., Masque, P., Materić, D., Mayes, A.G., McGinnity, P., Osvath, I., Prather, K.A., Prospero, J.M., Revell, L.E., Sander, S.G., Shim, W.J., Slade, J., Stein, A., Tarasova, O., Wright, S., 2022. Microplastics and nanoplastics in the marine-atmosphere environment. Nat Rev Earth Environ 3 (6), 393–405.
[4] Fu, Y., Pang, Q., Suo Lang Zhuo, G., Wu, P., Wang, Y., Mao, M., Yuan, Z., Xu, X., Liu, K., Wang, X., Li, D., Zhang, Y., 2023. Modeling atmospheric microplastic cycle by GEOS-Chem: An optimized estimation by a global dataset suggests likely 50 times lower ocean emissions. One Earth 6 (6), 705–714.
[5] Brahney, J., Mahowald, N., Prank, M., Cornwell, G., Klimont, Z., Matsui, H., Prather, K.A., 2021. Constraining the atmospheric limb of the plastic cycle. Proc Natl Acad Sci USA 118 (16), e2020719118.

[6] Perera, K., Ziajahromi, S., Bengtson Nash, S., Manage, P.M., Leusch, F.D.L., 2022. Airborne Microplastics in Indoor and Outdoor Environments of a Developing Country in South Asia: Abundance, Distribution, Morphology, and Possible Sources. Environ Sci Technol 56 (23), 16676–16685.
[7] Zhu, X., Huang, W., Fang, M., Liao, Z., Wang, Y., Xu, L., Mu, Q., Shi, C., Lu, C., Deng, H., Dahlgren, R., Shang, X., 2021. Airborne Microplastic Concentrations in Five Megacities of Northern and Southeast China. Environ Sci Technol 55 (19), 12871–12881.
[8] Roblin, B., Ryan, M., Vreugdenhil, A., Aherne, J., 2020. Ambient Atmospheric Deposition of Anthropogenic Microfibers and Microplastics on the Western Periphery of Europe (Ireland). Environ Sci Technol 54 (18), 11100–11108.
[9] Boucher, J.; Friot, D., Primary microplastics in the oceans: a global evaluation of sources. In IUCN Gland: Switzerland, 2017.
[10] Allen, S., Allen, D., Phoenix, V.R., Le Roux, G., Durántez Jiménez, P., Simonneau, A., Binet, S., Galop, D., 2019. Atmospheric transport and deposition of microplastics in a remote mountain catchment. Nat Geosci 12 (5), 339–344.
[11] Bergmann, M., Mutzel, S., Primpke, S., Tekman, M.B., Trachsel, J., Gerdts, G., 2019. White and wonderful? Microplastics prevail in snow from the Alps to the Arctic. Sci Adv 5 (8), eaax1157.
[12] Dong, H., Wang, L., Wang, X., Xu, L., Chen, M., Gong, P., Wang, C., 2021. Microplastics in a Remote Lake Basin of the Tibetan Plateau: Impacts of Atmospheric Transport and Glacial Melting. Environ Sci Technol 55 (19), 12951–12960.
[13] Mishra, A.K., Singh, J., Mishra, P.P., 2021. Microplastics in polar regions: An early warning to the world's pristine ecosystem. Sci Total Environ 784, 147149.
[14] Evangeliou, N., Tichý, O., Eckhardt, S., Zwaaftink, C.G., Brahney, J., 2022. Sources and fate of atmospheric microplastics revealed from inverse and dispersion modelling: From global emissions to deposition. J Hazard Mater 432, 128585.
[15] Liu, K., Wang, X., Song, Z., Wei, N., Ye, H., Cong, X., Zhao, L., Li, Y., Qu, L., Zhu, L., Zhang, F., Zong, C., Jiang, C., Li, D., 2020. Global inventory of atmospheric fibrous microplastics input into the ocean: An implication from the indoor origin. J Hazard Mater 400, 123223.
[16] Evangeliou, N., Grythe, H., Klimont, Z., Heyes, C., Eckhardt, S., Lopez-Aparicio, S., Stohl, A., 2020. Atmospheric transport is a major pathway of microplastics to remote regions. Nat Commun 11 (1), 3381.
[17] Zhang, Y., Kang, S., Allen, S., Allen, D., Gao, T., Sillanpää, M., 2020. Atmospheric microplastics: A review on current status and perspectives. EarthSci Rev 203, 103118.
[18] Yuan, Z., Li, H.-X., Lin, L., Pan, Y.-F., Liu, S., Hou, R., Xu, X.-R., 2022. Occurrence and human exposure risks of atmospheric microplastics: A review. Gondwana Res 108, 200–212.
[19] Yukioka, S., Tanaka, S., Nabetani, Y., Suzuki, Y., Ushijima, T., Fujii, S., Takada, H., Van Tran, Q., Singh, S., 2020. Occurrence and characteristics of microplastics in surface road dust in Kusatsu (Japan), Da Nang (Vietnam), and Kathmandu (Nepal). Environ Pollut 256, 113447.
[20] Liu, K., Wu, T., Wang, X., Song, Z., Zong, C., Wei, N., Li, D., 2019. Consistent Transport of Terrestrial Microplastics to the Ocean through Atmosphere. Environ Sci Technol 53 (18), 10612–10619.
[21] Brahney, J., Hallerud, M., Heim, E., Hahnenberger, M., Sukumaran, S., 2020. Plastic rain in protected areas of the United States. Science 368 (6496), 1257–1260.
[22] Zhang, Q., Zhao, Y., Du, F., Cai, H., Wang, G., Shi, H., 2020. Microplastic Fallout in Different Indoor Environments. Environ Sci Technol 54 (11), 6530–6539.
[23] Wang, T., Li, B., Zou, X., Wang, Y., Li, Y., Xu, Y., Mao, L., Zhang, C., Yu, W., 2019. Emission of primary microplastics in mainland China: Invisible but not negligible. Water Res 162, 214–224.
[24] Yuan, Z., Pei, C., Li, H., Lin, L., Liu, S., Hou, R., Liao, R., Xu, X., 2023. Atmospheric microplastics at a southern China metropolis: Occurrence, deposition flux, exposure risk and washout effect of rainfall. Sci Total Environ 869, 161839.
[25] Mai, L., Sun, X.-F., Xia, L.-L., Bao, L.-J., Liu, L.-Y., Zeng, E.Y., 2020. Global Riverine Plastic Outflows. Environ Sci Technol 54 (16), 10049–10056.
[26] Cai, L., Wang, J., Peng, J., Tan, Z., Zhan, Z., Tan, X., Chen, Q., 2017. Characteristic of microplastics in the atmospheric fallout from Dongguan city, China: preliminary research and first evidence. Environ Sci Pollut Res 24 (32), 24928–24935.
[27] Sonke, J.E., Koenig, A.M., Yakovenko, N., Hagelskjær, O., Margenat, H., Hansson, S.V., De Vleeschouwer, F., Magand, O., Le Roux, G., Thomas, J.L., 2022. A mass budget and box model of global plastics cycling, degradation and dispersal in the land-ocean-atmosphere system. Micro Nanoplastics 2 (1), 28.
[28] Werbowski, L.M., Gilbreath, A.N., Munno, K., Zhu, X., Grbic, J., Wu, T., Sutton, R., Sedlak, M.D., Deshpande, A.D., Rochman, C.M., 2021. Urban Stormwater Runoff: A Major Pathway for Anthropogenic Particles, Black Rubbery Fragments, and Other Types of Microplastics to Urban Receiving Waters. Environ Sci Technol Water 1 (6), 1420–1428.
[29] Clayer, F., Jartun, M., Buenaventura, N.T., Guerrero, J.-L., Lusher, A., 2021. Bypass of Booming Inputs of Urban and Sludge-Derived Microplastics in a Large Nordic Lake. Environ Sci Technol 55 (12), 7949–7958.
[30] Boucher, J., Faure, F., Pompini, O., Plummer, Z., Wieser, O., Felippe de Alencastro, L., 2019. Micro) plastic fluxes and stocks in Lake Geneva basin. TrAC TrAC Trends Anal Chem 112, 66–74.
[31] Schmidt, C., Krauth, T., Wagner, S., 2017. Export of Plastic Debris by Rivers into the Sea. Environ Sci Technol 51 (21), 12246–12253.
[32] Xu, X.; Liu, J.; Zhang, S.; Li, R.; Yan, C.; Wu, S., China's multi-period land use land cover remote sensing monitoring data set (CNLUCC). *Resource and Environment Data Cloud Platform: Beijing, China* 2018.
[33] Allen, S., Allen, D., Baladima, F., Phoenix, V.R., Thomas, J.L., Le Roux, G., Sonke, J.E., 2021. Evidence of free tropospheric and long-range transport of microplastic at Pic du Midi Observatory. Nat Commun 12 (1), 7242.
[34] Wright, S.L., Ulke, J., Font, A., Chan, K.L.A., Kelly, F.J., 2020. Atmospheric microplastic deposition in an urban environment and an evaluation of transport. Environ Int 136, 105411.
[35] Gonzalez-Pleiter, M., Edo, C., Aguilera, A., Viudez-Moreiras, D., Pulido-Reyes, G., Gonzalez-Toril, E., Osuna, S., de Diego-Castilla, G., Leganes, F., Fernandez-Pinas, F., Rosal, R., 2021. Occurrence and transport of microplastics sampled within and above the planetary boundary layer. Sci Total Environ 761, 143213.
[36] O'Brien, S., Okoffo, E.D., Rauert, C., O'Brien, J.W., Ribeiro, F., Burrows, S.D., Toapanta, T., Wang, X., Thomas, K.V., 2021. Quantification of selected microplastics in Australian urban road dust. J Hazard Mater 416, 125811.
[37] Cheng, H., Hu, Y., Reinhard, M., 2014. Environmental and Health Impacts of Artificial Turf: A Review. Environ Sci Technol 48 (4), 2114–2129.
[38] Mehmood, T., Peng, L., 2022. Polyethylene scaffold net and synthetic grass fragmentation: a source of microplastics in the atmosphere? J Hazard Mater 429, 128391.
[39] Huang, Y., He, T., Yan, M., Yang, L., Gong, H., Wang, W., Qing, X., Wang, J., 2021. Atmospheric transport and deposition of microplastics in a subtropical urban environment. J Hazard Mater 416, 126168.
[40] Lelieveld, J., Bourtsoukidis, E., Brühl, C., Fischer, H., Fuchs, H., Harder, H., Hofzumahaus, A., Holland, F., Marno, D., Neumaier, M., Pozzer, A., Schlager, H., Williams, J., Zahn, A., Ziereis, H., 2018. The South Asian monsoon—pollution pump and purifier. Science 361 (6399), 270–273.
[41] Tian, L., Li, J., Zhao, S., Tang, J., Li, J., Guo, H., Liu, X., Zhong, G., Xu, Y., Lin, T., Lyv, X., Chen, D., Li, K., Shen, J., Zhang, G., 2021. DDT, Chlordane, and Hexachlorobenzene in the Air of the Pearl River Delta Revisited: A Tale of Source, History, and Monsoon. Environ Sci Technol 55 (14), 9740–9749.
[42] Ou-Yang, C.-F., Hsieh, H.-C., Wang, S.-H., Lin, N.-H., Lee, C.-T., Sheu, G.-R., Wang, J.-L., 2013. Influence of Asian continental outflow on the regional background ozone level in northern South China Sea. Atmos Environ 78, 144–153.
[43] Jeong, J.I., Park, R.J., 2017. Winter monsoon variability and its impact on aerosol concentrations in East Asia. Environ Pollut 221, 285–292.
[44] Chen, Y., Niu, J., Xu, D., Zhang, M., Sun, K., Gao, B., 2023. Wet Deposition of Globally Transportable Microplastics (<25 μm) Hovering over the Megacity of Beijing. Environ Sci Technol 57 (30), 1152–11162.
[45] Gao, J., Pan, S., Li, P., Wang, L., Hou, R., Wu, W.-M., Luo, J., Hou, D., 2021. Vertical migration of microplastics in porous media: Multiple controlling factors under wet-dry cycling. J Hazard Mater 419, 126413.
[46] Koutnik, V.S., Leonard, J., Glasman, J.B., Brar, J., Koydemir, H.C., Novoselov, A., Bertel, R., Tseng, D., Ozcan, A., Ravi, S., Mohanty, S.K., 2022. Microplastics retained in stormwater control measures: Where do they come from and where do they go? Water Res 210, 118008.
[47] Waldschläger, K., Lechthaler, S., Stauch, G., Schüttrumpf, H., 2020. The way of microplastic through the environment – Application of the source-pathway-receptor model (review). Sci Total Environ 713, 136584.
[48] Lebreton, L.C.M., van der Zwet, J., Damsteeg, J.-W., Slat, B., Andrady, A., Reisser, J., 2017. River plastic emissions to the world's oceans. Nat Commun 8 (1), 15611.
[49] Meijer, L.J.J., van Emmerik, T., van der Ent, R., Schmidt, C., Lebreton, L., 2021. More than 1000 rivers account for 80% of global riverine plastic emissions into the ocean. Sci Adv 7 (18), eaaz5803.
[50] Wang, C., O'Connor, D., Wang, L., Wu, W.-M., Luo, J., Hou, D., 2022. Microplastics in urban runoff: Global occurrence and fate. Water Res 225, 119129.
[51] Truong, T.-N.-S., Strady, E., Kieu-Le, T.-C., Tran, Q.-V., Le, T.-M.-T., Thuong, Q.-T., 2021. Microplastic in atmospheric fallouts of a developing Southeast Asian megacity under tropical climate. Chemosphere 272, 129874.
[52] Romarate 2nd, R.A., Ancla, S.M.B., Patilan, D.M.M., Inocente, S.A.T., Pacilan, C.J. M., Sinco, A.L., Guihawan, J.Q., Capangpangan, R.Y., Lubguban, A.A., Bacosa, H. P., 2023. Breathing plastics in Metro Manila, Philippines: presence of suspended atmospheric microplastics in ambient air. Environ Sci Pollut Res 30 (18), 53662–53673.
[53] Afiq Daniel Azmi, M., Yasin, N.L.N.M., NorRuwaida, J., Hasnatul, A.H., Dewika, M., Sara, Y.Y., 2023. Analysis of suspended atmospheric microplastics size at different elevation in Universiti Teknologi Malaysia, Kuala Lumpur. IOP Conference Series Earth Environmental Science 1144 (1), 012009.
[54] Long, X., Fu, T.M., Yang, X., Tang, Y., Zheng, Y., Zhu, L., Shen, H., Ye, J., Wang, C., Wang, T., Li, B., 2022. Efficient Atmospheric Transport of Microplastics over Asia and Adjacent Oceans. Environ Sci Technol 56 (10), 6243–6252.
[55] Liu, C., Li, J., Zhang, Y., Wang, L., Deng, J., Gao, Y., Yu, L., Zhang, J., Sun, H., 2019. Widespread distribution of PET and PC microplastics in dust in urban China and their estimated human exposure. Environ Int 128, 116–124.
[56] Jia, Q., Duan, Y., Han, X., Sun, X., Munyaneza, J., Ma, J., Xiu, G., 2022. Atmospheric deposition of microplastics in the megalopolis (Shanghai) during rainy season: Characteristics, influence factors, and source. Sci Total Environ 847, 157609.
[57] Purwiyanto, A.I.S., Prartono, T., Riani, E., Naulita, Y., Cordova, M.R., Koropitan, A. F., 2022. The deposition of atmospheric microplastics in Jakarta-Indonesia: The coastal urban area. Mar Pollut Bull 174, 113195.
[58] Klein, M., Fischer, E.K., 2019. Microplastic abundance in atmospheric deposition within the Metropolitan area of Hamburg, Germany. Sci Total Environ 685, 96–103.
[59] Yuan, Z., Pei, C.-L., Li, H.-X., Lin, L., Hou, R., Liu, S., Zhang, K., Cai, M.-G., Xu, X.-R., 2023. Vertical distribution and transport of microplastics in the urban atmosphere: New insights from field observations. Sci Total Environ 895, 165190.

[60] Liu, K., Wang, X., Fang, T., Xu, P., Zhu, L., Li, D., 2019. Source and potential risk assessment of suspended atmospheric microplastics in Shanghai. Sci Total Environ 675, 462–471.
[61] Alimi, O.S., Claveau-Mallet, D., Lapointe, M., Biu, T., Liu, L., Hernandez, L.M., Bayen, S., Tufenkji, N., 2023. Effects of weathering on the properties and fate of secondary microplastics from a polystyrene single-use cup. J Hazard Mater 459, 131855.
[62] Cai, M., Liu, M., Qi, H., Cui, Y., Zhang, M., Huang, P., Wang, L., Xie, M., Li, Y., Wang, W., Ke, H., Liu, F., 2022. Transport of microplastics in the South China Sea: A review. Gondwana Res 108, 49–59.
[63] Matsushita, K., Uchiyama, Y., Takaura, N., Kosako, T., 2022. Fate of river-derived microplastics from the South China Sea: Sources to surrounding seas, shores, and abysses. Environ Pollut 308, 119631.
[64] Khodabakhshloo, N., Abbasi, S., Turner, A., 2023. Resuspension of microplastics and microrubbers in a semi-arid urban environment (Shiraz, Iran). Environ Pollut 316, 120575.
[65] Weiss, L., Ludwig, W., Heussner, S., Canals, M., Ghiglione, J.-F., Estournel, C., Constant, M., Kerhervé, P., 2021. The missing ocean plastic sink: Gone with the rivers. Science 373 (6550), 107–111.
[66] Van Wijnen, J., Ragas, A.M.J., Kroeze, C., 2019. Modelling global river export of microplastics to the marine environment: Sources and future trends. Sci Total Environ 673, 392–401.

Marine Pollution Bulletin 216 (2025) 117980

Contents lists available at ScienceDirect

Marine Pollution Bulletin

journal homepage: www.elsevier.com/locate/marpolbul

Spatiotemporal distribution and priority assessment of steroids in the estuarine environment: Implications for environmental risk management

Ru Xu [a], Nian-Nian Wu [b,e], Shan Liu [b], Hui Chen [b], Qin-Wei Hao [b], Yong-Xia Hu [b], Bing Hong [d], Shen Yu [d], Xiang-Rong Xu [c,*]

[a] Jiangxi Provincial Key Laboratory of Environmental Pollution Control, Jiangxi Academy of Eco-Environmental Sciences and Planning, Nanchang 330039, China
[b] Key Laboratory of Tropical Marine Bio-resources and Ecology, Guangdong Provincial Key Laboratory of Applied Marine Biology, South China Sea Institute of Oceanology, Chinese Academy of Sciences, Guangzhou 510301, China
[c] Guangxi Laboratory on the Study of Coral Reefs in the South China Sea, Coral Reef Research Center of China, School of Marine Sciences, Guangxi University, Nanning 530004, China
[d] CAS Key Laboratory of Urban Environment and Health, Institute of Urban Environment, Chinese Academy of Sciences, Xiamen 361021, China
[e] University of Chinese Academy of Sciences, Beijing 100049, China

ARTICLE INFO

Keywords:
Steroids and metabolites
Spatiotemporal patterns
Distribution behavior
Mass inventory
Priority pollutant screening
Estuarine environment

ABSTRACT

Steroids, known for their endocrine-disrupting capabilities, have become a subject of considerable concern in the scientific community. This research offers a thorough evaluation of steroid contaminants within the Jiulong River Estuary (JRE), examining their spatiotemporal distribution, multimedia distribution, and mass inventory. Seven steroids were detected in water samples, while ten steroids were identified in sediments, with concentrations ranging from 0.2 to 51 ng/L in water and no-detectable (ND) to 12 ng g^{-1} in sediments. In both water and sediments, natural steroids were the most prevalent throughout both the dry and wet seasons. The distribution of these compounds within the aquatic-sediment system was governed by their hydrophobicity and a suite of environmental factors, such as temperature, salinity, pH, chlorophyll-a, and total organic carbon content. Mass inventory analysis revealed that over 90 % of the total steroid mass inventory was stored in the sediments, underscoring their pivotal role as a repository for these substances within the JRE. Furthermore, this research represents the first comprehensive screening to identify priority contaminants in this region. Utilizing a multimetric evaluation approach, progesterone and testosterone were identified as high-priority pollutants during the dry season, with progesterone alone ranking as a high-priority pollutant in the wet season. This study provides crucial insights for the management of steroid-related pollution and the assessment of environmental risks in estuarine ecosystems.

1. Introduction

Steroids, ubiquitously detected in aquatic systems as emerging contaminants (Runnalls et al., 2010), have attracted considerable concern due to their potential carcinogenicity (IARC, 2020) and proven ecological risks. Even at low concentrations, as minimal as nanograms per liter (ng/L), steroids can induce intersex characteristics in fish and disrupt aquatic populations (Runnalls et al., 2015; Dang and Kienzler, 2019; Kidd et al., 2007; Azizi-Lalabadi and Pirsaheb, 2021). Endogenous steroids and their metabolites are naturally excreted by humans, livestock, and aquatic species through urine and feces. Additionally, synthetic steroids, which are commonly used in both human and veterinary medicine, as well as for promoting growth, further contribute to environmental pollution (Chang et al., 2009; Fent, 2015). Through sewage treatment plants and runoff from agricultural activities, these compounds make their way into the environment (Zhong et al., 2021; Adeel et al., 2017). Additionally, global steroid emissions have been rising at an approximate rate of 10 % annually (Zhang et al., 2021). As a result, a wide variety of different steroids are present at very low concentrations in surface waters across the world (Ojoghoro et al., 2021), highlighting a growing concern about their ecological impact.

Estuaries, as intricate and dynamic interfaces between terrestrial and marine ecosystems, serve crucial roles in facilitating interactions between land and sea and in channeling terrestrial compounds towards the

* Corresponding author.
E-mail address: xuxr@gxu.edu.cn (X.-R. Xu).

https://doi.org/10.1016/j.marpolbul.2025.117980
Received 30 December 2024; Received in revised form 9 April 2025; Accepted 10 April 2025
Available online 18 April 2025
0025-326X/© 2025 Elsevier Ltd. All rights are reserved, including those for text and data mining, AI training, and similar technologies.

ocean. However, they also face significant anthropogenic stressors (Zhen et al., 2021; Wang et al., 2022; Bianchi et al., 2018). Annually, an estimated 2.5 × 10^{10} tones of terrestrial-derived compounds are conveyed to the ocean, with approximately 90 % of this flux passing through estuaries (Wu et al., 2017a). Within the diverse mixture of contaminants found in estuarine environments, steroids have emerged as prevalent pollutants (Korkmaz et al., 2022; Omar et al., 2019; Meador et al., 2016), posing a significant threat to both fisheries and human health.

The Jiulong River (JR), Fujian Province's second-largest river, drains approximately 12 % of the region's land area (Guo et al., 2011). It traverses through the cities of Longyan, Zhangzhou, and Xiamen, providing essential water resources to these areas (Wu et al., 2019). The river eventually flows into the JRE, a shallow estuary in a subtropical region that connects Xiamen Bay to the Taiwan Strait. The merging of several tributaries, combined with the monsoon-driven coastal currents in the Taiwan Strait, makes the dynamics at the interface within the JRE highly complex (Guo et al., 2011). The Jiulong River Watershed (JRW) exerts a substantial impact on the water quality of the JRE and the Xiamen coastline, significantly contributing to the pollutant load within the estuary (Chen et al., 2014; Guo et al., 2011). Over recent decades, increasing human activities—such as population growth, urban and industrial wastewater discharge, expansion of agricultural fertilizer use, and livestock farming have intensified environmental pressures on the JRE (Zhang et al., 2011; Chen et al., 2015; Cao et al., 2014; Li et al., 2017). Especially noteworthy is the profound impact of the swift economic growth in the Xiamen Special Economic Zone, which has led to considerable anthropogenic perturbations in the estuarine ecosystems and adjacent regions (Yan et al., 2012; Wu et al., 2016). The synergistic impacts of these variables have markedly compromised the environmental integrity of the JRE. A wide range of research has emphasized the detection of different contaminants in the JRE, including perfluoroalkyl substances (PFAS) (Cai et al., 2018), pesticides (Lin et al., 2013), antibiotics (Zheng et al., 2011), and polybrominated diphenyl ethers (Wu et al., 2017b). Nevertheless, the prevalence of steroid pollution, particularly its metabolites, within this region remains largely underexplored. Given that agricultural runoff and household waste are primary sources of steroid contamination, it is essential to evaluate the

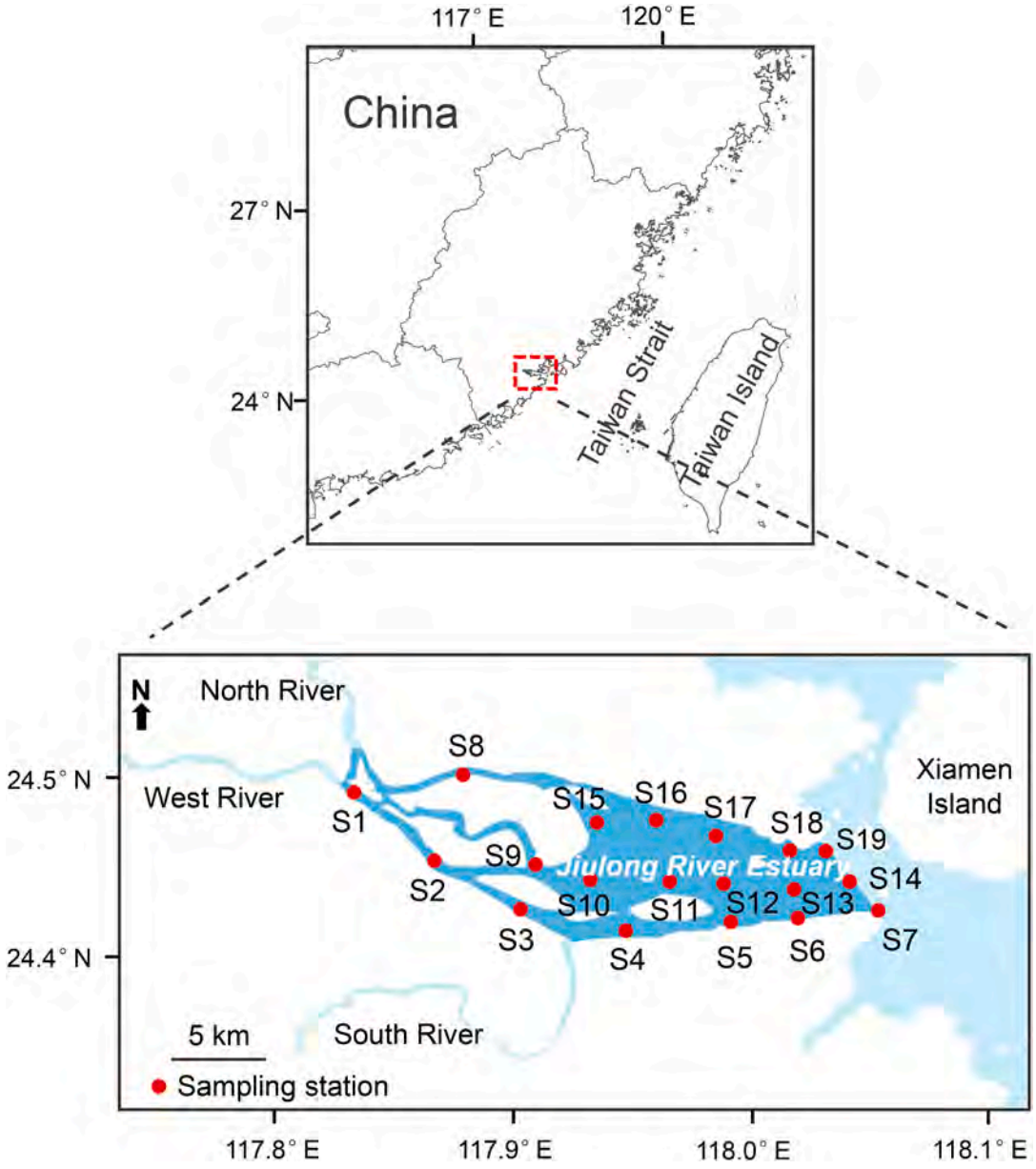


Fig. 1. Locations of the sampling sites in the JRE.

extent of steroid pollution in the JRE.

Therefore, the aim of this research was: (1) to clarify the spatial and temporal distribution of steroids within an estuarine water-sediment system, (2) to identify the factors shaping their distribution behaviors, (3) to quantify the pollution load via a mass inventory estimation, and (4) to prioritize pollutants employing a multi-criteria integrated assessment approach. The findings will contribute valuable scientific knowledge for the protection of estuarine ecosystems and pollutant management, providing a theoretical foundation for policy development and the optimization of pollution control strategies.

2. Materials and methods

2.1. Study area and sampling collection

The JRE, situated along the southeast coast of Fujian Province, China, is influenced by freshwater inputs from the JR, which has an average yearly runoff of 1.49×10^{10} m^3 (Chen et al., 2015). The JRE is primarily shaped by the confluence of three major streams, with two of the principal tributaries contributing significantly to its discharge. The North and West streams deliver average annual runoffs of 8.22×10^9 m^3 and 3.68×10^9 m^3, respectively (Fig. 1). Notably, the JRE is located in a region with high concentrations of sewage, livestock, and aquaculture activities, leading to substantial wastewater discharges, including steroids, directly into the estuary via river runoff (Zhang et al., 2011; Chen et al., 2015).

Samples of surface water and sediment were obtained from 19 locations (S1 − S19) within the JRE during both the dry season (November 2014) and the wet season (June 2015) (Fig. 1). A comprehensive overview of the sampling sites is provided in Table S1. At each site, 5 L of surface water was gathered using plastic containers, while sediment samples (from a 0–5 cm depth) were collected with a stainless-steel grab sampler. However, sediment samples could not be retrieved from several sites (S1, S3, S4, S7, S11, S15, S17) during the wet season. Following collection, the water samples were acidified to a pH of 3 with sulfuric acid (Yu et al., 2022) and preserved with a 5 % methanol solution (*v*/v) to prevent microbial activity. All samples were kept at −20 °C until they were analyzed further. Additional information about the sampling procedure is available in Text S1.

2.2. Sample extraction and instrumental analysis

Existing studies suggested that estrogens are likely to be very important steroids in aquatic environments (Ojoghoro et al., 2021), especially 17α-ethynylestradiol (EE2), which has been confirmed to have strong ecological toxicity (Runnalls et al., 2015; Caldwell et al., 2012). However, compared to estrogens, there was a significant knowledge gap in the environmental behavior and ecological risks of androgens, progestagens, and glucocorticoids, which severely limits the comprehensive ecological risk assessment of steroid pollution. Based on globally published data, this study selected three different types of steroids (androgens, progestagens, glucocorticoids) with high detection rates or concentrations in the environment as research targets, aiming to systematically analyze the spatiotemporal distribution patterns of characteristic pollutants in the JRE.

This research focused on analyzing a total of 22 steroids, including three androgens: 4-androstene-3,17-dione (AED), testosterone (T), and 17β-boldenone (17β-BOL); five glucocorticoids: cortisol (CRL), cortisone (CRN), 11-deoxycorticosterone (DOC), tetrahydrocortisol (3α,5β-THCRL), and prednisolone (PREL); and fourteen progestagens: progesterone (P), 17α,20α-dihydroxyprogesterone (17α,20α-DOHP), 17α,20β-dihydroxyprogesterone (17α,20β-DOHP), 17α-hydroxyprogesterone (17α-OHP), 17α-hydroxyprogesterone acetate (17α-OHPA), 11-ketoprogesterone (11-KP), 1-dehydroprogesterone (1-DHP), 16-dehydroprogesterone (16-DHP), medroxyprogesterone acetate (MPA), norvinisterone (NVT), dydrogesterone (DGT), norgestrel (NGT), cyproterone acetate (CPTA), and megestrol acetate (MGTA) (Table S2). A comprehensive list of the chemicals employed in this study is available in the Text S1.

The methods used for sample extraction were modified from previous research (Zhou et al., 2012; Liu et al., 2011). Initially, filtered water samples (5 L) were followed by processing with Oasis HLB solid-phase extraction (SPE) cartridges (6 mL, 500 mg). For sediment samples (2 g), ultrasonic-assisted extraction was performed using a mixture of acetonitrile and citric acid buffer, after which enrichment and cleanup were carried out with SAX-HLB cartridges. Steroid analysis was conducted using LC-MS/MS, employing an Agilent 1290 Infinity II liquid chromatograph in combination with an Agilent 6470 triple quadrupole mass spectrometer, operated in multiple-reaction monitoring (MRM) mode. Comprehensive details on the extraction and quantification methods are available in the Supplementary Information (SI).

2.3. Quality assurance and quality control (QA/QC)

The steroid recovery rates for water samples ranged from 63 % to 149 %, whereas for sediments, the recovery values fluctuated between 68 % and 155 % (Table S3). For each steroid analyzed, the detection limit (LOD) and quantitation limit (LOQ) for each steroid analyzed were calculated based on the signal-to-noise ratio and the corresponding value for the target compounds in the extraction process fell within the following ranges: for water samples, 0.029–1.4 $ng{\cdot}L^{-1}$ and 0.10–4.6 $ng{\cdot}L^{-1}$, and for sediments, 0.033–1.4 $ng{\cdot}g^{-1}$ and 0.11–4.8 $ng{\cdot}g^{-1}$ for sediments (Table S3). To evaluate background contamination and ensure the proper performance of the instrument, several blanks including field blanks, procedural blanks, solvent blanks and standard solutions were included in the analysis. The calibration curves for all the target analytes, spanning concentrations from 1.0 to 100 $\mu g{\cdot}L^{-1}$, demonstrated excellent linearity with correlation coefficients exceeding 0.995. The relative standard deviations for standard solutions, both intra-day and inter-day, varied between 1.4 % and 12 % and 6.4 % and 22 %, respectively.

2.4. Priority pollutant screening

In recent years, pinpointing priority pollutants has emerged as a critical environmental concern; however, a standardized protocol for their identification remains to be developed. Prior studies have focused on pinpointing priority contaminants in wastewater treatment plants (WWTPs) and surface waters, predominantly utilizing ecological risk assessments as a framework (Wang et al., 2023; Lu et al., 2023). However, such methodologies may fall short in capturing the intricacies inherent to actual environmental settings. Thus, it is imperative to encompass a holistic approach that accounts for the prevalence and ecological hazards of contaminants, alongside their propensity for persistence and bioaccumulation, especially within the context of estuarine ecosystems.

To address these concerns, a modified methodology was developed, which employs a multi-criteria scoring technique to prioritize contaminants (Gong et al., 2024; Wei et al., 2024; Zhang et al., 2024). This methodology integrates four pivotal criteria: occurrence (O), persistence (P), bioaccumulation (B), and ecotoxicity (E), with each criterion being accorded equal significance in the assessment. The criterion for occurrence encompasses the concentration levels and detection frequencies of the targeted pollutants within the JRE, with each factor being given equal consideration in the evaluation. Persistence is assessed based on the biodegradation half-life data available through the CompTox Chemicals Dashboard, whereas the bioaccumulation potential is evaluated using data from the EPI Suite 4.1 (Table S4). Ecotoxicity is determined by calculating the ecological risk of each compound (Table S4). The values assigned to each criterion are categorized into five classes using geometric progression, and a two-thirds cumulative rating method is applied to derive a conclusive score (Table S5). The total score for each compound is calculated by summing the scores across the four

criteria. Based on the total scores, the target contaminants are categorized into five priority classes (I – V), with Classes I and II representing high- and medium-priority pollutants, respectively. Further details on the identification process for priority contaminants can be found in Supporting Information (Text S2).

2.5. Data analysis

Details on how the distribution coefficients (K_d and K_{oc}) were calculated in Text S3. Further information on the mass inventories and deposition flux of steroids in the JR can be found in Text S4. The sampling map of the JRE was created using ArcGIS Pro v.2022. Mann-Whitney *U* test was carried out with IBM SPSS Statistics® 24, while Origin Pro v.2021 was used for generating figures and performing correlation analysis. A significance level of *p*-values <0.05 or < 0.01 was applied for all statistical tests.

3. Results and discussion

3.1. Occurrence of steroids in the JRE

3.1.1. Water

A total of seven steroids were identified in water samples collected over two seasons, with concentrations varying between 0.27 and 51 ng·L^{-1} (Fig. 2A and B, Table S6). The observed levels were found to exceed those previously reported in the Malaysia Estuary (Omar et al., 2019), the Sado River Estuary (Portugal) (Rocha et al., 2013), and Pearl River Estuary (Xu et al., 2024).

Among the identified steroids, natural steroids AED and P were found to have the highest prevalence, with detection rates reaching 89 %

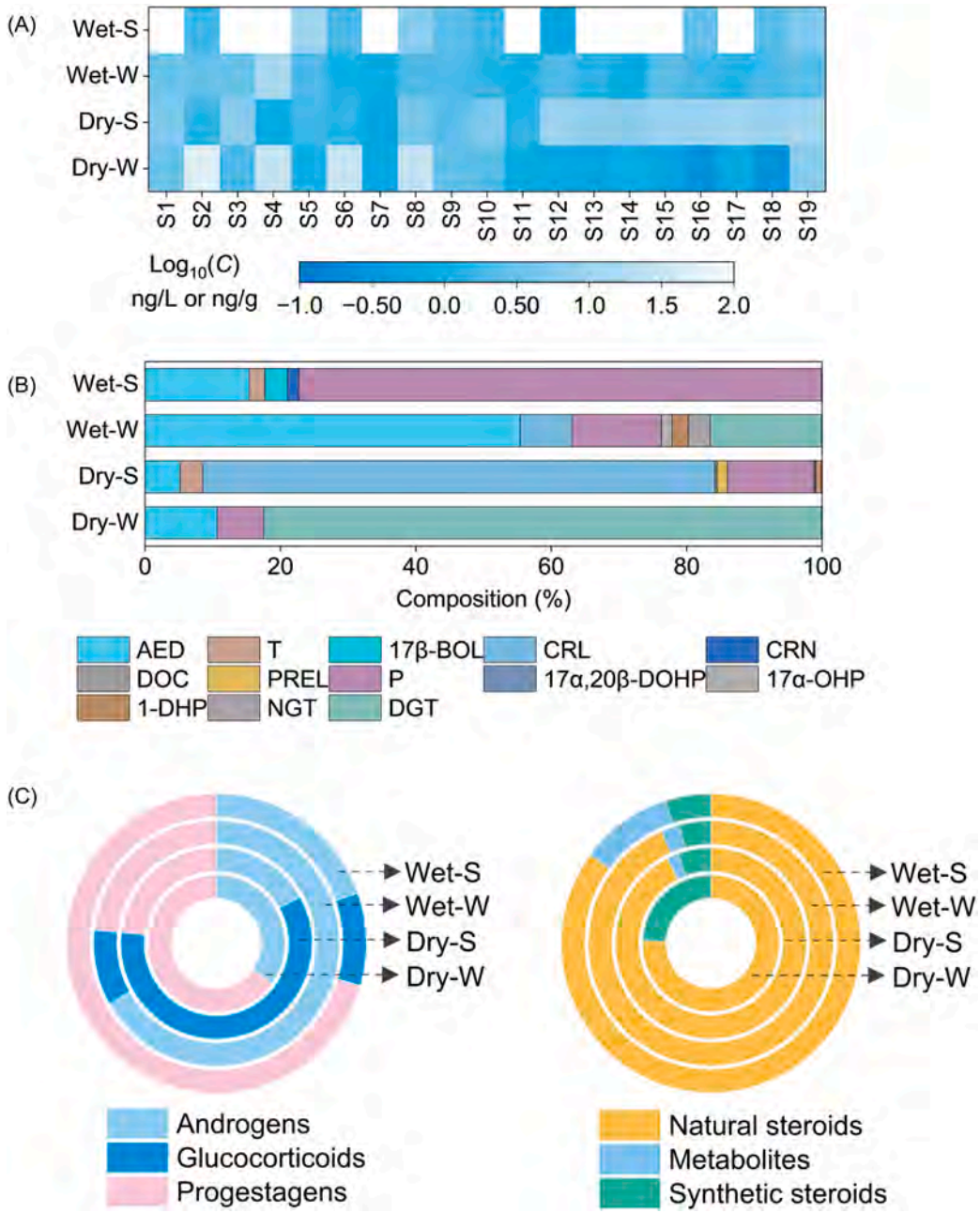


Fig. 2. Total concentrations (A), composition profiles (B), and percentages (C) of steroids in the surface water (Dry-W and Wet-W) and sediments (Dry-S and Wet-S) in dry and wet seasons.

and 100 % in the dry and wet seasons, respectively (Table S6). Concentrations of AED and P peaked at 3.2 ng·L^{-1} and 1.4 ng·L^{-1}, respectively (Table S6). The higher concentration of AED in water relative to P is likely due to its lower Log K_{oc} value (2.8), enhancing its mobility in water, in contrast to a higher Log K_{oc} (3.5) of P, which favors binding to sediments (Table S2). During the dry season, synthetic steroid DGT predominated in water, with concentrations peaking at 48 ng·L^{-1} (Fig. 2B). Its ubiquity in the dry season may be attributed to DGT's extensive application in contraception and for treating menstrual irregularities and endometriosis in the human and veterinary sectors within the JRW (Rižner et al., 2011). Other steroids such as CRL, 17α-OHP, 1-DHP, and NGT were only sporadically detected during the wet season. In terms of steroid classification, progestogens and androgens were predominant in both seasons, constituting 65 % and 67 % of the total steroid levels, respectively, surpassing glucocorticoids (Fig. 2C). Natural steroids constituted the majority of detected steroids, representing 76 % and 96 % of the total steroid levels in the dry and wet seasons, respectively (Fig. 2C). The higher occurrence of natural steroids in water may be attributed to the high human population density and extensive farming activities in the JRW.

3.1.2. Sediments

Overall, ten steroids were identified in sediments, with total concentrations varying from non-detectable (ND) to 12 ng·g^{-1} (Fig. 2A and B, Table S7). These values were similar to those observed in the Pearl River Estuary (Xu et al., 2024), but exceeded the levels found in estuarine sediments in Portuguese Estuaries (Amorim et al., 2024), Markman Canal and Swartkops River Estuary (Ohoro et al., 2021), and mariculture sediments in Malaysia (Ismail et al., 2020). However, they were lower than concentrations reported in the sediments of the Golden Horn Estuary (Korkmaz et al., 2022), the fishing ports in China (Liu et al., 2022) and river in Canada (Yarahmadi et al., 2018).

Paralleling the aqueous findings, natural steroids AED and P were widely identified in sediments. In the dry season, the detection rate for these compounds was 100 %, whereas in the wet season, detection rates varied from 58 % to 75 % (Table S7). The mean concentration of P (8.6 ng·g^{-1}) in sediments exceeded that of AED (1.6 ng·g^{-1}), contrasting with their aqueous concentrations where AED predominated. This disparity may stem from the higher Log *K*oc value of P, enhancing its affinity for sediment sorption relative to AED (Table S2). Interestingly, steroid metabolites like CRN were only detected in sediments during the wet season, whereas DOC and 17α,20β-DOHP were detected solely in the dry season (Table S7). This suggests that steroid metabolite profiles are highly influenced by seasonal variations. In terms of steroid classification, glucocorticoids and progestagens were dominant in the sediments, constituting 60 % and 70 % of the total steroids in the dry and wet seasons, respectively (Fig. 2C). In both seasons, natural steroids constituted the majority of detected compounds, accounting for 85 % to 92 % of the total steroid concentrations (Fig. 2C), consistent with their aquatic prevalence.

3.1.3. Potential threats posed by steroids to aquatic organisms

The concentrations of steroids and their metabolites detected in the JRE water samples were notably low (0.27–51 ng/L), yet these trace levels merit significant concern. Aquatic organisms, especially fish, demonstrate remarkable sensitivity to steroids in the water (Ojoghoro et al., 2021). While individual steroid concentrations might fall below thresholds for observable ecological impacts, the mixture of multiple steroids can induce adverse biological responses, a synergistic phenomenon termed the "a lot from a little" (Thrupp et al., 2018). Of particular note was the detection of 17α-OHP (ND − 0.28 ng/L), a hydroxylated progesterone metabolite. Unlike mammalian systems where parent compounds typically exhibit greater bioactivity, fish physiology shows heightened responsiveness to such hydroxylated metabolites, which function as biologically active progestagens (Scott et al., 1982). These combined findings suggest that multiple steroids and their metabolites, even at environmental concentrations of ng/L, require significant attention.

3.2. Spatiotemporal variations of steroids in the JRE

3.2.1. Water

No statistical variations in steroid concentrations were observed between two seasons (Mann-Whitney *U* test, $p > 0.05$) (Fig. 2, Table S6). This aligns with previous studies in the Pearl River estuary (Xu et al., 2024) and Jiaozhou Bay (Lu et al., 2021). In the dry season, three steroids (AED, P, and DGT) were detected in water, while seven steroids (AED, CRL, P, 17α-OHP, 1-DHP, NGT, and DGT) were detected in the wet season. The heightened riverine discharge during the wet season is hypothesized to facilitate the transport of a greater volume of steroids from the JRW, subsequently enriching steroid levels in the JRE. Furthermore, the increased anthropogenic activities, notably shipping and sewage discharge, is likely responsible for the elevated steroid concentrations observed in the wet season compared to the dry season (Wu et al., 2019). The maximum concentration of DGT in water was notably higher in the dry season (48 ng·L^{-1}) compared to the wet season (7.8 ng·L^{-1}), likely due to the dilution effects of precipitation and seawater influx during the wet season.

Spatial gradients in steroid concentrations within the estuary exhibited a decline from the riverine confluence towards the marine environment (Fig. S1). For instance, total steroid concentrations at sampling sites S1 and S7 in the dry season were 3.4 ng·L^{-1} and 0.68 ng·L^{-1}, respectively, while in the wet season, the concentrations were 3.3 ng·L^{-1} and 1.0 ng·L^{-1}. Similar trends were observed in previous studies (Sun et al., 2016; Yan et al., 2013). High steroid concentrations proximal to the river mouth likely indicate significant anthropogenic contributions to the area, encompassing discharges from sewage treatment plants in the downstream region of the western JR and the presence of untreated wastewater (Lv et al., 2014). The decline in steroid levels towards the open sea can be attributed to dilution by seawater. In the dry season, higher concentrations were observed at sampling sites S2 (57 ng·L^{-1}), S4 (26 ng·L^{-1}), and S8 (25 ng·L^{-1}), which located at the outlets where the North Stream, West Stream, and South Stream, respectively, enter the estuary. These regions experience substantial pollution from dense human populations, livestock farming, and aquaculture, which are likely significant contributors to the elevated steroid concentrations observed (Xu et al., 2023). Notably, site S4, which is near an aquaculture area and the outlet of the South Stream (Li et al., 2017), recorded the highest steroid concentration during the wet season (13 ng·L^{-1}). This is mainly attributed to substantial surface runoff, which carries a high volume of pollutants, including steroids, into the estuarine environment (Wang et al., 2010; Zhang et al., 2017). Site S14, located near the estuarine outlet, recorded the lowest concentration (0.91 ng·L^{-1}) in the wet season, influenced by the dilution effects of rainfall and river runoff (Liu et al., 2022).

3.2.2. Sediments

Based on steroid concentration levels, no notable seasonal variations were detected in the sediments when comparing the dry and wet seasons. (Mann-Whitney *U* test, $p > 0.05$) (Fig. 2a, Table S7), suggesting relatively stable steroid levels in the sediments. A similar seasonal trend has been reported in the Pearl River Estuary (Xu et al., 2024). The greater occurrence rates of natural steroids (such as AED, T, CRL, and P) were significantly reported in the dry season (74 %–100 %) (Fig. S2, Table S7). The diminished detection frequency of steroids in the wet season can be ascribed to heightened precipitation and the intensified hydrodynamic forces resulting from the interplay of riverine and marine waters in the estuary, potentially facilitating sediment resuspension (Wu et al., 2017b).

Spatially, steroid concentrations in the sediments of the lower estuary zone (sites S11-S19) were higher than those in the upper zone (sites S1-S4, S8-S10) during the dry season. Specifically, the northern bank of

the estuary (sites S15-S19) exhibited higher steroid concentrations compared to the southern bank (Fig. S1). The observed fluctuations in steroid concentrations could be attributed to a multitude of factors, such as localized pollution sources, hydrological regimes, and the influence of coastal effluents. Notably, the maximum concentration of steroids during the dry season was recorded at site S19 (12 ng·g^{-1}), located at the outlet of the JRE (Fig. S1, Table S7). This high concentration is presumably influenced by coastal effluents, enhanced sedimentation rates, and diminished sediment mobility, due to the proximity to adjacent islands (Lao et al., 2022). Conversely, the lowest concentration was observed at site S7, near the open ocean (0.59 ng·g^{-1}). During the wet season, steroid concentrations at individual stations exhibited variable patterns of increase and decrease (Fig. S1, Table S7). Specifically, the total steroid concentrations gradually declined from sites S8 and S16 to S18, suggesting that the upstream areas along the northern bank contribute significantly to the steroid load (Fig. S1). Relatively high total steroid concentration (11 ng·g^{-1}) was observed at Site S5, likely due to sewage discharge from the South Stream, a tributary that receives substantial wastewater inputs. Similarly, the total steroid concentration was 6.0 ng·g^{-1} at site S8, situated downstream of the North Stream outlet. High steroid concentration was also observed at the JRE outlet (S19, 5.5 ng·g^{-1}), reinforcing the idea that coastal discharges play a crucial role in the distribution of these contaminants. Interestingly, steroid concentrations were below detectable levels at sites S13 and S14, suggesting minimal contamination at these locations. This highlights the complex spatial distribution of steroids within the estuary and suggests that local hydrological and anthropogenic factors influence the sedimentary load of these compounds.

3.3. Partitioning behavior and influencing factors of steroids in the JRE

To better understand the distribution of steroids within the water-sediment system of the JRE, Log K_d values for the target steroids were determined over two seasons. The Log K_d values varied between 1.7 and 3.9 in the dry season and between 2.4 and 4.3 during the wet season (Fig. S2). A strong positive correlation was found between Log K_d and Log K_{ow} for the detected steroids (AED and P) during the wet season ($R = 0.88$, $p < 0.05$) (Fig. S2), indicating that hydrophobicity is a key factor in determining how steroids partition between water and sediments in this season. In contrast, the relationship between Log K_d and Log K_{ow} was weak ($R = 0.39$, $p > 0.05$) (Fig. S2), implying that steroid partitioning in the dry season is also influenced by factors other than hydrophobicity.

Besides hydrophobicity, various environmental variables influenced steroid distribution between water and sediments across both seasons (Fig. 3A). Temperature showed a significant positive relationship with AED, P, and overall steroid concentrations in water throughout the seasons (Fig. 3A). This could be attributed to its effect on enzyme activities such as arylsulfatase and β-glucuronidase, which aid in the deconjugation process of steroid conjugates present in water (Liu et al., 2015). Moreover, in the dry season, a negative correlation was observed between pH and both AED and total steroid concentrations in water (Fig. 3A), possibly because the fact that fluctuations in pH can affect steroid sorption by modifying the physical and chemical properties of organic matter (Neale et al., 2009). Salinity showed a negative correlation with AED and the total steroid concentration in water across both seasons (Fig. 3A), suggesting that steroid distribution may be influenced by salting-out and dilution, which are driven by factors such as rainfall, river inflows, and the discharge of domestic wastewater from land-based sources (Liu et al., 2022). Furthermore, chlorophyll-a (Chl-a) exhibited a

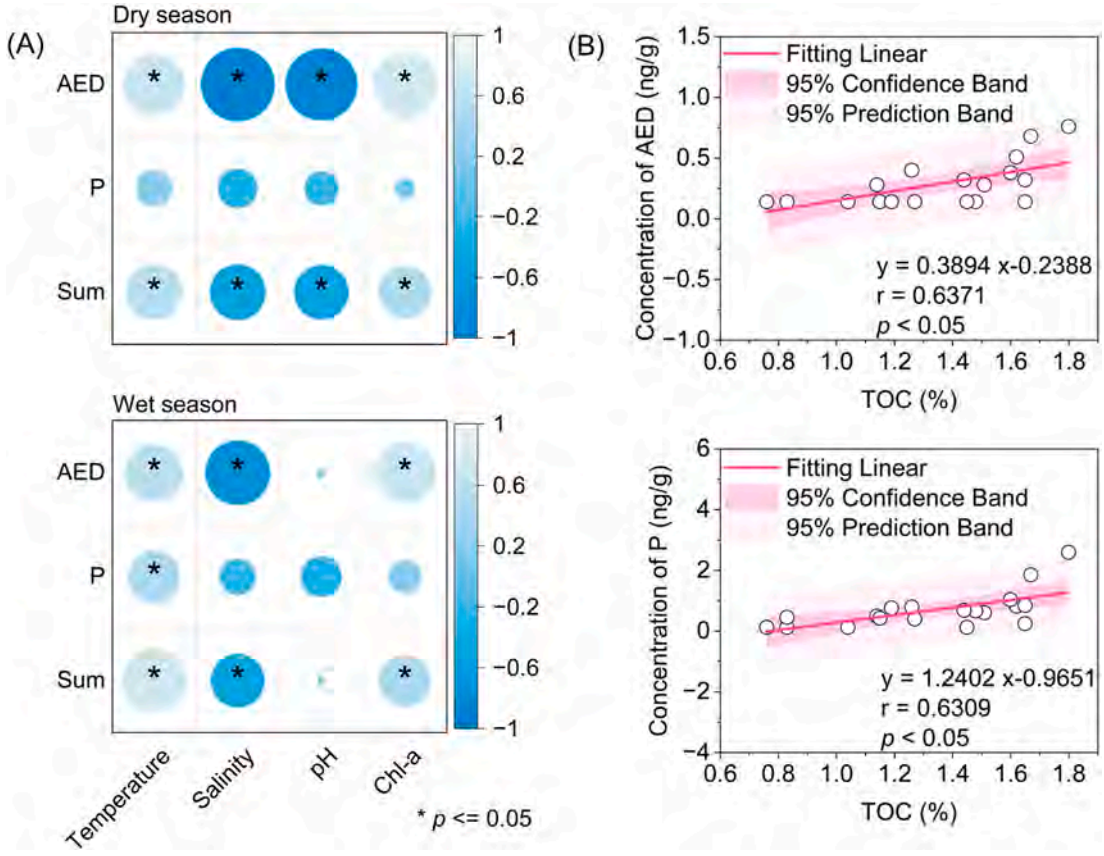


Fig. 3. (A) Correlations between detected steroids and environmental parameters for water in the JRE. Sum, total concentrations of steroids; (B) Correlations between detected steroids and TOC in sediments of the JRE during the dry season.

positive correlation with AED and the total steroid concentration in water during both seasons (Fig. 3A). This relationship can be attributed to the role of Chl-a as an indicator of phytoplankton biomass, which might be influence the bioavailability and distribution of pollutants including steroids in aquatic environments (Falkowski, 1994; Davies et al., 2018; Boyer et al., 2009). Higher Chl-a concentrations might reflect increased biological activity, which could affect the cycling and transformation of steroids in the water column.

In sediment samples, a significant positive relationship was observed between total organic carbon (TOC) and most of the steroids identified, such as AED and P, during the dry season ($p < 0.05$) (Fig. 3B). This suggests that higher TOC concentrations enhance the capacity of sediments to adsorb steroids (Huang et al., 2020; Li et al., 2019). Similar trends have been documented in other research on sediments collected from fishing ports and estuaries (Liu et al., 2022; Omar et al., 2018). However, in the wet season, no significant correlation was found between TOC and the detected steroids (AED, P, and the total steroid concentration) in the sediments (Fig. S3, $p > 0.05$), indicating that other factors could have a more prominent influence on the adsorption of steroids to sediments in this period.

3.4. Mass inventory and deposition flux

In the study, the mass inventories of steroids in the water of the JRE ranged from 0.36 to 0.76 ng cm^{-2} (androgens), 0 to 0.14 ng cm^{-2} (glucocorticoids), and 0.34 to 2.8 ng cm^{-2} (progestogens), respectively, over two seasons. Notably, the greater steroid mass inventory in the water was found during the dry season (Table S8). Glucocorticoids and progestagens collectively constituted over 75 % of the total mass inventories across both seasons (Table S8). Concordantly, the higher sedimentary steroid mass inventory was reported in the dry season, with natural steroids being the predominant contributors (Table S9). The estimated sedimentary steroid mass inventory was 0.11–0.32 mg m^{-2}, which is notably one to two orders of magnitude lower than the concentrations observed in fishing ports (2.1–16 mg m^{-2}) (Liu et al., 2022) and the Pearl River estuary (17–20 mg m^{-2}) (Xu et al., 2024). The sedimentary steroid mass inventory accounting for 91 % and 90 % of the overall mass inventory over two seasons, respectively (Fig. 4, Table S10). These results underscore the important role of sediments as a major reservoir for steroids in the JRE.

As a key reservoir for steroids, the deposition flux of steroids in the sediments warrants further attention. Deposition flux is a widely used indicator of contaminant accumulation in marine sediments, as it is not influenced by dilution from contaminant input sources or land-based runoff (Fang et al., 2015; Wang et al., 2020). The deposition flux of steroids in the JRE ranged from 0.28 to 5.4 ng cm^{-2} yr^{-1} (average: 2.5 ng cm^{-2} yr^{-1}) in the dry season and from 0 to 5.1 ng cm^{-2} yr^{-1} (average: 1.4 ng cm^{-2} yr^{-1}) in the wet season (Fig. 4). Notably, the burial capacity of steroids exhibited considerable spatial variability (Fig. 5). In the dry season, the highest deposition flux (5.4 ng cm^{-2} yr^{-1}) was observed at the outlet of the JRE (S19), likely due to the elevated sedimentation rates. In contrast, the highest flux during the wet season (5.1 ng cm^{-2} yr^{-1}) was recorded at site S5, possibly influenced by high-intensity human activities in the surrounding area.

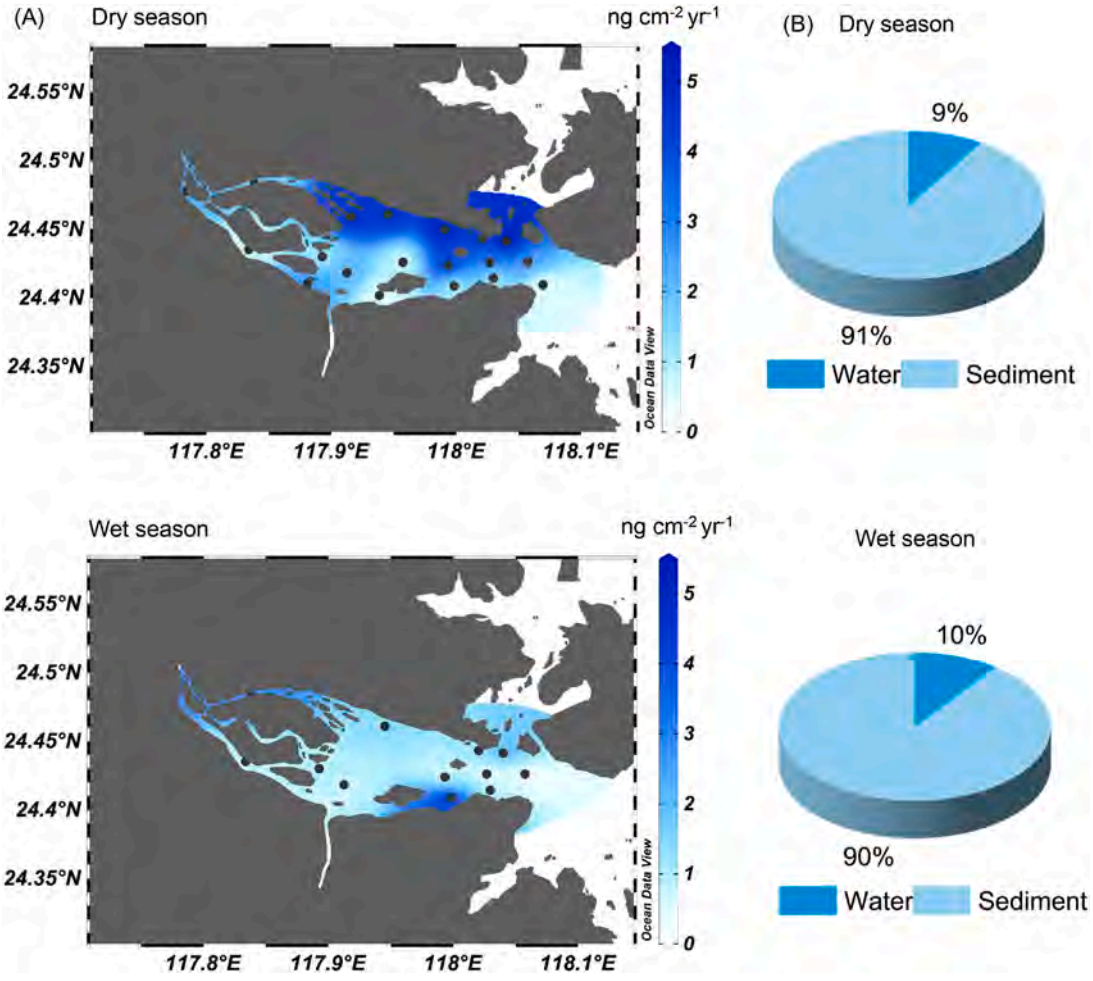


Fig. 4. Distribution pattern of steroids deposition fluxes (ng cm^{-2} yr^{-1}) in dry season and wet season (A) and the percentage of steroids in water and sediment during dry and wet season (B).

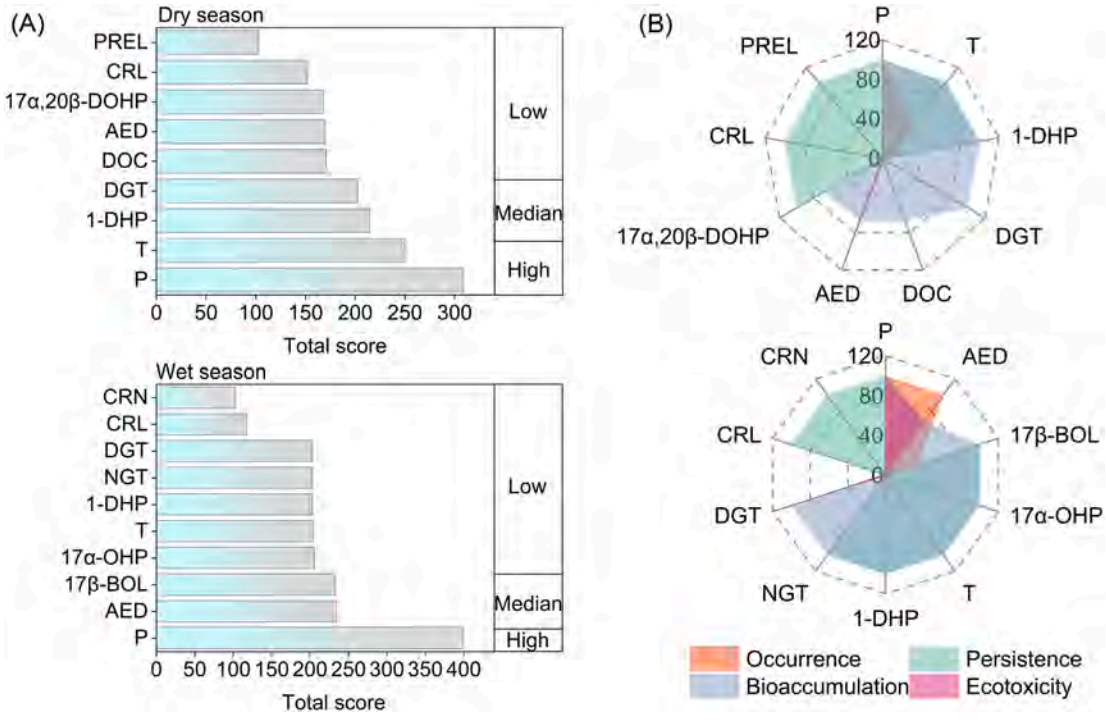


Fig. 5. The total scores for priority contaminants were determined using the multi-criteria scoring method (A). High, median, and low represent high-, medium-, and low-priority contaminants, respectively. The score for each criterion responsible for prioritization (B).

Based on our prior research, the riverine flux of steroids from the JR to the JRE was estimated at 94 kg per year (Xu et al., 2023). Steroids in the estuarine environment originate from both river discharge in the Jiulong River watershed and from aquaculture activities, undergoing various environmental processes, including degradation, water-sediments transformations, burial in deeper sediments, and transport to the open ocean (Xu et al., 2024). Despite the relatively low levels of steroid mass inventories and deposition fluxes in the JRE, the risk of steroid contamination remains significant and should not be overlooked.

3.5. Identification of priority pollutants

A multi-criteria assessment approach was employed to rank steroids within the JRE. The target compounds were scored and subsequently categorized into five categories (I − V) using a geometric progression scale (Table S11). Compounds with scores ranging from 248 to 309 in the dry season, and from 305 to 400 in the wet season were designated as high-priority pollutants (Class I). Similarly, compounds scoring between 199 and 248 in the dry season, and between 232 and 305 in the wet season, were classified as medium-priority pollutants (Class II). Any remaining contaminants with scores below 199 (dry season) or 232 (wet season) were designated as low-priority pollutants (Class III − V). Notably, P was identified as a high-priority pollutant in both seasons, while T was considered high-priority only during the dry season (Fig. 5). The elevated scores for P were attributed to its widespread presence (with a 100 % detection rate), strong bioaccumulation potential (log BAF values of 2.7), its persistence (half-life of 98 days), and its high toxicity, as shown by the predicted no-effect concentration (PNEC) of 0.1 ng/L. Despite relatively low detection rates and concentrations of T in the JRE, its high scores could be explained by its significant bioaccumulation potential (log BAF value of 2.2) and notable persistence (half-life of 98 days). This suggests that evaluating contaminants based solely on their environmental concentrations may not always be appropriate. Moreover, considering factors like bioaccumulation potential and biodegradability could offer more reliable indicators of contamination levels, particularly for steroids. Surprisingly, AED, a widely detected contaminant, was classified as a low-priority pollutant (Class III) during the dry season and a medium-priority pollutant (Class II) in the wet season. This classification was due to AED's rapid degradation and minimal ecotoxicity, respectively. In contrast, synthetic steroids (such as 1-DHP, DGT, and 17β-BOL) were identified as a medium priority (Class II), emphasizing their significance for monitoring and management efforts within the JRE. As for compounds like 17α,20β-DOHP, CRL, PREL, and CRN, despite their low degradability in the JRE, their overall scores were low due to their infrequent detection, limited bioaccumulation, and low toxicity, making them less likely to pose considerable ecological threats to estuarine ecosystems. Therefore, to optimize environmental monitoring and regulation efforts, it is recommended to focus on compounds classified as high- and medium-priority.

Although certain parameters within this comprehensive multi-criteria assessment rely on predictive modeling, the approach reveals that substances with lower scores could substantially affect the outcomes, thereby underscoring the limitations inherent in relying solely on a single indicator—such as toxicity—to assess and characterize contaminants. Incorporating temporal and spatial variability, distribution patterns, physicochemical properties, and ecological risks of target pollutants, a holistic system for identifying and prioritizing pollutants surpasses the efficacy of relying on static priority lists. This framework can provide critical technical support to governments in monitoring steroid pollutants, facilitating more scientifically grounded and efficient pollutant management and environmental safeguarding.

3.6. Environmental implication and limitations

Incorporating prioritized assessment into environmental risk management is crucial for effectively addressing complex environmental contaminants like steroids in estuarine environments. A prioritized assessment allows for the identification and ranking of risks based on their occurrence, persistence, and potential impacts on human health and ecosystems. This approach enables environmental managers and policymakers to allocate resources more efficiently, targeting the most harmful pollutants first and devising specific management strategies for

each identified risk. For instance, in the case of steroids in the JRE, a prioritized assessment can help distinguish between high-priority areas with severe contamination and low-priority zones where risk levels are manageable. Factors such as the concentration of steroids, their toxicity, bioaccumulation potential, and their effects on aquatic life can all be considered in the prioritization process.

Our research still has several limitations. Due to the lack of experimentally derived aquatic ecotoxicity data for the majority of steroids, we had to rely on ECOSAR model predictions for risk assessment. Although ECOSAR provides comparable toxicity benchmarks for substances with limited data through structure-activity relationships, its predictions mainly focus on acute lethal endpoints (e.g., LC50) and functional group generalization, which may not accurately reflect the unique low-concentration chronic effects of steroids (such as endocrine disruption and reproductive suppression). For instance, an experimental study demonstrated that the fish reproduction NOEC (100 ng/L) for synthetic progestin levonorgestrel was four orders of magnitude lower than ECOSAR-predicted chronic values (Runnalls et al., 2013), suggesting ECOSAR may significantly underestimate ecological risks of certain steroids. Furthermore, ECOSAR does not incorporate receptor-mediated toxicity pathways, which represent the core mechanisms through which steroids induce ecological effects at ng/L concentrations. This omission may result in predictions failing to reflect the most critical toxic effects. To address these limitations, we propose two key directions for future research: First, prioritizing standardized chronic testing of steroids could provide more robust experimental evidence for ecological risk assessment. Second, enhancing predictive models by incorporating additional environmental factors and biological response variables would help improve model predictive capability and accuracy.

4. Conclusions

This research provides an in-depth examination of the spatiotemporal patterns and behavior of 22 steroids and their metabolites in the JRE, marking the first attempt to establish a prioritized list of pollutants for management in this region. Among the steroids examined, seven steroids were detected in water samples, and ten steroids in sediments, with natural steroids being more prevalent. The distribution patterns of these compounds varied significantly across different temporal and spatial scales. Higher concentrations of steroids in water were predominantly observed near the outflows of the three primary tributaries of the JR. In the dry season, elevated steroid levels were mainly found in sediments on the northern side of the JRE, whereas during the wet season, the southern side exhibited higher concentrations. The variation in steroid distribution can be attributed to both their hydrophobic characteristics and environmental factors such as temperature, salinity, pH, chlorophyll *a*, and total organic carbon content. Mass inventory analyses revealed that over 90 % of the steroid mass was retained in sediments during both dry and wet seasons, highlighting a significant accumulation of steroids in sedimentary environments. The highest deposition flux was recorded at 5.4 ng cm^{-2} yr^{-1}, which, though low, suggests a gradual buildup of these compounds. A multi-criteria assessment approach identified two steroids (P and T) as the highest-priority pollutants in the dry season, while steroid P was singled out as the primary concern in the wet season. Notably, AED, a commonly detected natural steroid, was classified as a medium-to-low priority pollutant. These findings provide crucial insights into steroid pollution dynamics and offer valuable information for effective environmental management and risk mitigation in estuarine ecosystems.

CRediT authorship contribution statement

Ru Xu: Writing – original draft, Visualization, Methodology, Formal analysis, Data curation. **Nian-Nian Wu:** Methodology, Formal analysis. **Shan Liu:** Writing – review & editing, Methodology, Investigation. **Hui Chen:** Methodology, Investigation. **Qin-Wei Hao:** Methodology, Investigation. **Yong-Xia Hu:** Methodology, Investigation. **Bing Hong:** Investigation. **Shen Yu:** Resources, Conceptualization. **Xiang-Rong Xu:** Writing – review & editing, Supervision, Funding acquisition.

Declaration of competing interest

The authors declare that they have no known competing financial interests or personal relationships that could have appeared to influence the work reported in this paper.

Acknowledgments

The authors would like to acknowledge the support by fund of Hainan Province Science and Technology Special Fund (No. ZDYF2022SHFZ317), Science and Technology Innovation Special Project of Sanya City (No. 2022KJCX74), Jiangxi Provincial Key R & D Program (20232BBG70011).

Appendix A. Supplementary data

Supplementary data to this article can be found online at https://doi.org/10.1016/j.marpolbul.2025.117980.

Data availability

Data will be made available on request.

References

Adeel, M., Song, X.M., Wang, Y.Y., Francis, D., Yang, Y.S., 2017. Environmental impact of estrogens on human, animal and plant life: a critical review. Environ. Int. 99, 107–119.
Amorim, V.E., Morais, H., Ferreira, A.C.S., Pardal, M.A., Cruzeiro, C., Cardoso, P.G., 2024. Application of a robust analytical method for quantifying progestins in environmental samples from three Portuguese Estuaries. Mar. Pollut. Bull. 199, 115967.
Azizi-Lalabadi, M., Pirsaheb, M., 2021. Investigation of steroid hormone residues in fish: a systematic review. Process. Saf. Environ. Prot. 152, 14–24.
Bianchi, T.S., Cui, X., Blair, N.E., Burdige, D.J., Eglinton, T.I., Galy, V., 2018. Centers of organic carbon burial and oxidation at the land-ocean interface. Org. Geochem. 115, 138–155.
Boyer, J.N., Kelble, C.R., Ortner, P.B., Rudnick, D.T., 2009. Phytoplankton bloom status: chlorophyll a biomass as an indicator of water quality condition in the southern estuaries of Florida, USA. Ecol. Indic. 9, S56–S67.
Cai, Y.Z., Wang, X.H., Wu, Y.L., Zhao, S.H., Li, Y.Y., Ma, L.Y., Chen, C., Huang, J., Yu, G., 2018. Temporal trends and transport of perfluoroalkyl substances (PFASs) in a subtropical estuary: Jiulong River Estuary, Fujian, China. Sci. Total Environ. 639, 263–270.
Caldwell, D.J., Mastrocco, F., Anderson, P.D., Länge, R., Sumpter, J.P., 2012. Predicted-no-effect concentrations for the steroid estrogens estrone, 17β-estradiol, estriol, and 17α-ethinylestradiol. Environ. Toxicol. Chem. 31, 1396–1406.
Cao, D., Cao, W.Z., Fang, J., Cai, L.Y., 2014. Nitrogen and phosphorus losses from agricultural systems in China: a meta-analysis. Mar. Pollut. Bull. 85, 727–732.
Chang, H., Wan, Y., Hu, J.Y., 2009. Determination and source apportionment of five classes of steroid hormones in urban rivers. Environ. Sci. Technol. 43, 7691–7698.
Chen, N.W., Wu, Y.Q., Wu, J.Z., Yan, X.L., Hong, H.S., 2014. Natural and human influences on dissolved silica export from watershed to coast in Southeast China. J. Geophys. Res.:Biogeosci. 119, 95–109.
Chen, N.W., Wu, J.Z., Zhou, X.P., Chen, Z.H., Lu, T., 2015. Riverine N2O production, emissions and export from a region dominated by agriculture in Southeast Asia (Jiulong River). Agric. Ecosyst. Environ. 208, 37–47.
Dang, Z., Kienzler, A., 2019. Changes in fish sex ratio as a basis for regulating endocrine disruptors. Environ. Int. 130, 104928.
Davies, C.H., Ajani, P., Armbrecht, L., Atkins, N., Baird, M.E., Beard, J., Bonham, P., Burford, M., Clementson, L., Coad, P., Crawford, C., Dela-Cruz, J., Doblin, M.A., Edgar, S., Eriksen, R., Everett, J.D., Furnas, M., Harrison, D.P., Hassler, C., Henschke, N., Hoenner, X., Ingleton, T., Jameson, I., Keesing, J., Leterme, S.C., James McLaughlin, M., Miller, M., Moffatt, D., Moss, A., Nayar, S., Patten, N.L., Patten, R., Pausina, S.A., Proctor, R., Raes, E., Robb, M., Rothlisberg, P., Saeck, E.A., Scanes, P., Suthers, I.M., Swadling, K.M., Talbot, S., Thompson, P., Thomson, P.G., Uribe-Palomino, J., van Ruth, P., Waite, A.M., Wright, S., Richardson, A.J., 2018. A database of chlorophyll a in Australian waters. Sci. Data 5, 180018.
Falkowski, P.G., 1994. The role of phytoplankton photosynthesis in global biogeochemical cycles. Photosynth. Res. 39, 235–258.
Fang, Y., Chen, Y.J., Tian, C.G., Lin, T., Hu, L.M., Huang, G.P., Tang, J.H., Li, J., Zhang, G., 2015. Flux and budget of BC in the continental shelf seas adjacent to Chinese high BC emission source regions. Global Biogeochem. Cycles 29, 957–972.

Fent, K., 2015. Progestins as endocrine disrupters in aquatic ecosystems: concentrations, effects and risk assessment. Environ. Int. 84, 115–130.
Gong, X.H., Xiong, L.L., Xing, J.S., Deng, Y.Q., Su, Q.H., Sun, J., Qin, Y., Zhao, Z.H., Zhang, L., 2024. Implications on freshwater lake-river ecosystem protection suggested by organic micropollutant (OMP) priority list. J. Hazard. Mater. 461, 132580.
Guo, W.D., Yang, L.Y., Hong, H.S., Stedmon, C.A., Wang, F.L., Xu, J., Xie, Y.Y., 2011. Assessing the dynamics of chromophoric dissolved organic matter in a subtropical estuary using parallel factor analysis. Mar. Chem. 124, 125–133.
Huang, Y.Q., Wang, Y., Huang, Y.Z., Zhang, L.X., Ye, F., Wang, J.L., Shang, J.G., Liao, Q. J.H., 2020. Impact of sediment characteristics on adsorption behavior of typical antibiotics in Lake Taihu, China. Sci. Total Environ. 718, 137329.
IARC, 2020. The International Agency for Research on Cancer (IARC) Monographs on the Identification of Carcinogenic Hazards to Human.
Ismail, N.A.H., Wee, S.Y., Haron, D.E.M., Kamarulzaman, N.H., Aris, A.Z., 2020. Occurrence of endocrine disrupting compounds in mariculture sediment of Pulau Kukup, Johor, Malaysia. Mar. Pollut. Bull. 150, 110735.
Kidd, K.A., Blanchfield, P.J., Mills, K.H., Palace, V.P., Evans, R.E., Lazorchak, J.M., Flick, R.W., 2007. Collapse of a fish population after exposure to a synthetic estrogen. PNAS 104, 8897–8901.
Korkmaz, N.E., Caglar, N.B., Aksu, A., 2022. Presence and distribution of selected pharmaceutical compounds in water and surface sediment of the Golden Horn Estuary, Sea of Marmara, Turkey. Reg. Stud. Mar. Sci. 51, 102221.
Lao, J.Y., Wu, R.B., Cui, Y.S., Zhou, S.W., Ruan, Y.F., Leung, K.M.Y., Wu, J.X., Zeng, E.Y., Lam, P.K.S., 2022. Significant input of organophosphate esters through particle-mediated transport into the Pearl River Estuary, China. J. Hazard. Mater. 438, 129486.
Li, R.L., Liang, J., Gong, Z.B., Zhang, N.N., Duan, H.L., 2017. Occurrence, spatial distribution, historical trend and ecological risk of phthalate esters in the Jiulong River, Southeast China. Sci. Total Environ. 580, 388–397.
Li, Z.H., Zhang, W.Q., Shan, B.Q., 2019. The effects of urbanization and rainfall on the distribution of, and risks from, phenolic environmental estrogens in river sediment. Environ. Pollut. 250, 1010–1018.
Lin, P., Guo, L.D., Chen, M., Cai, Y.H., 2013. Distribution, partitioning and mixing behavior of phosphorus species in the Jiulong River estuary. Mar. Chem. 157, 93–105.
Liu, S., Ying, G.G., Zhao, J.L., Chen, F., Yang, B., Zhou, L.J., Lai, H.J., 2011. Trace analysis of 28 steroids in surface water, wastewater and sludge samples by rapid resolution liquid chromatography-electrospray ionization tandem mass spectrometry. J. Chromatogr. A 1218, 1367–1378.
Liu, Z.H., Lu, G.N., Yin, H., Dang, Z., Rittmann, B., 2015. Removal of natural estrogens and their conjugates in municipal wastewater treatment plants: a critical review. Environ. Sci. Technol. 49, 5288–5300.
Liu, S., Tian, F., Pan, Y.F., Li, H.Y., Lin, L., Hou, R., Zhang, L.B., Zhang, Z., Liu, S.S., Xu, X. R., Cheng, Y.Y., Chen, H.G., 2022. Contamination and ecological risks of steroid metabolites require more attention in the environment: evidence from the fishing ports. Sci. Total Environ. 807, 150814.
Lu, S., Lin, C.Y., Lei, K., Xin, M., Wang, B.D., Wei, O.Y., Liu, X.T., He, M.C., 2021. Endocrine-disrupting chemicals in a typical urbanized bay of Yellow Sea, China: distribution, risk assessment, and identification of priority pollutants. Environ. Pollut. 287, 117588.
Lu, S., Wang, J., Wang, B.D., Xin, M., Lin, C.Y., Gu, X., Lian, M.S., Li, Y., 2023. Comprehensive profiling of the distribution, risks and priority of pharmaceuticals and personal care products: a large-scale study from rivers to coastal seas. Water Res. 230, 119591.
Lv, M., Sun, Q., Hu, A.Y., Hou, L.Y., Li, J.W., Cai, X., Yu, C.P., 2014. Pharmaceuticals and personal care products in a mesoscale subtropical watershed and their application as sewage markers. J. Hazard. Mater. 280, 696–705.
Meador, J.P., Yeh, A., Young, G., Gallagher, E.P., 2016. Contaminants of emerging concern in a large temperate estuary. Environ. Pollut. 213, 254–267.
Neale, P., Escher, B., Schafer, A., 2009. pH dependence of steroid hormone—organic matter interactions at environmental concentrations. Sci. Total Environ. 407, 1164–1173.
Ohoro, C.R., Adeniji, A.O., Okoh, A.I., Okoh, O.O., 2021. Spatial and seasonal variations of endocrine disrupting compounds in water and sediment samples of Markman Canal and Swartkops River Estuary, South Africa and their ecological risk assessment. Mar. Pollut. Bull. 173, 113012.
Ojoghoro, J.O., Scrimshaw, M.D., Sumpter, J.P., 2021. Steroid hormones in the aquatic environment. Sci. Total Environ. 792, 148306.
Omar, T.F.T., Aris, A.Z., Yusoff, F.M., Mustafa, S., 2018. Occurrence, distribution, and sources of emerging organic contaminants in tropical coastal sediments of anthropogenically impacted Klang River estuary, Malaysia. Mar. Pollut. Bull. 131, 284–293.
Omar, T.F.T., Aris, A.Z., Yusoff, F.M., Mustafa, S., 2019. Risk assessment of pharmaceutically active compounds (PhACs) in the Klang River estuary, Malaysia. Environ. Geochem. Hlth. 41, 211–223.
Rižner, T.L., Brožič, P., Doucette, C., Turek-Etienne, T., Müller-Vieira, U., Sonneveld, E., van der Burg, B., Böcker, C., Husen, B., 2011. Selectivity and potency of the retroprogesterone dydrogesterone in vitro. Steroids 76, 607–615.
Rocha, M.J., Cruzeiro, C., Reis, M., Rocha, E., Pardal, M.A., 2013. Determination of 17 endocrine disruptor compounds and their spatial and seasonal distribution in the Sado River Estuary (Portugal). Toxicol. Environ. Chem. 95, 237–253.
Runnalls, T.J., Luigi, M.-C., Subramaniam, K., Sumpter, J.P., 2010. Pharmaceuticals in the aquatic environment: steroids and anti-steroids as high priorities for research. Hum. Ecol. Risk Assess. Int. J. 16, 1318–1338.
Runnalls, T.J., Beresford, N., Losty, E., Scott, A.P., Sumpter, J.P., 2013. Several synthetic progestins with different potencies adversely affect reproduction of fish. Environ. Sci. Technol. 47, 2077–2084.
Runnalls, T.J., Beresford, N., Kugathas, S., Margiotta-Casaluci, L., Scholze, M., Scott, A. P., Sumpter, J.P., 2015. From single chemicals to mixtures–reproductive effects of levonorgestrel and ethinylestradiol on the fathead minnow. Aquat. Toxicol. 169, 152–167.
Scott, A.P., Sheldrick, E.L., Flint, A.P.F., 1982. Measurement of 17alpha, 20beta -dihydroxy-4-pregnen-3-one in plasma of trout (Salmo gairdneri Richardson): seasonal changes and response to salmon pituitary extract. Gen. Comp. Endocr. 46, 444–451.
Sun, Q., Li, Y., Li, M.Y., Ashfaq, M., Lv, M., Wang, H.J., Hu, A.Y., Yu, C.P., 2016. PPCPs in Jiulong River estuary (China): spatiotemporal distributions, fate, and their use as chemical markers of wastewater. Chemosphere 150, 596–604.
Thrupp, T.J., Runnalls, T.J., Scholze, M., Kugathas, S., Kortenkamp, A., Sumpter, J.P., 2018. The consequences of exposure to mixtures of chemicals: something from 'nothing' and 'a lot from a little' when fish are exposed to steroid hormones. Sci. Total Environ. 619-620, 1482–1492.
Wang, J.Z., Guan, Y.F., Ni, H.G., Liu, G.J., Zeng, E.Y., 2010. Fecal steroids in riverine runoff of the Pearl River Delta, South China: levels, potential sources and inputs to the coastal ocean. J. Environ. Monit. 12, 280–286.
Wang, P., Mi, W.Y., Xie, Z.Y., Tang, J.H., Apel, C., Joerss, H., Ebinghaus, R., Zhang, Q.H., 2020. Overall comparison and source identification of PAHs in the sediments of European Baltic and North Seas, Chinese Bohai and Yellow Seas. Sci. Total Environ. 737, 139535.
Wang, C., Ding, Y., Guo, Z.H., Lin, H., Wu, J.W., 2022. Spatial–temporal distribution of total organic carbon and its transportation in the Jiulong River Estuary. Sci. Rep. 12, 9395.
Wang, S., Qian, J.S., Zhang, B.L., Chen, L., Wei, S., Pan, B.C., 2023. Unveiling the occurrence and potential ecological risks of organophosphate esters in municipal wastewater treatment plants across China. Environ. Sci. Technol. 57, 1907–1918.
Wei, L.N., Wu, N.N., Xu, R., Liu, S., Li, H.X., Lin, L., Hou, R., Xu, X.R., Zhao, J.L., Ying, G. G., 2024. First evidence of the bioaccumulation and trophic transfer of tire additives and their transformation products in an estuarine food web. Environ. Sci. Technol. 58, 6370–6380.
Wu, Y.L., Wang, X.H., Ya, M.L., Li, Y.Y., Hong, H.S., 2016. Distributions of organochlorine compounds in sediments from Jiulong River Estuary and adjacent Western Taiwan Strait: implications of transport, sources and inventories. Environ. Pollut. 219, 519–527.
Wu, G.J., Cao, W.Z., Huang, Z., Kao, C.M., Chang, C.T., Chiang, P.C., Wang, F.F., 2017a. Decadal changes in nutrient fluxes and environmental effects in the Jiulong River Estuary. Mar. Pollut. Bull. 124, 871–877.
Wu, Y.L., Wang, X.H., Li, Y.Y., Ya, M.L., Luo, H., Hong, H.S., 2017b. Polybrominated diphenyl ethers, organochlorine pesticides, and polycyclic aromatic hydrocarbons in water from the Jiulong River Estuary, China: levels, distributions, influencing factors, and risk assessment. Environ. Sci. Pollut. Res. 24, 8933–8945.
Wu, Y.L., Wang, X.H., Ya, M.L., Li, Y.Y., Hong, H.S., 2019. Seasonal variation and spatial transport of polycyclic aromatic hydrocarbons in water of the subtropical Jiulong River watershed and estuary, Southeast China. Chemosphere 234, 215–223.
Xu, R., Liu, S., Chen, H., Hao, Q.W., Hu, Y.X., Li, H.X., Lin, L., Hou, R., Hong, B., Yu, S., Xu, X.R., 2023. An effective tool for tracking steroids and their metabolites at the watershed level: combining fugacity modeling and a chemical indicator. Environ. Pollut. 326, 121499.
Xu, R., Liu, S., Pan, Y.F., Wu, N.N., Huang, Q.Y., Li, H.X., Lin, L., Hou, R., Xu, X.R., Cheng, Y.Y., 2024. Steroid metabolites as overlooked emerging contaminants: insights from multimedia partitioning and source–sink simulation in an estuarine environment. J. Hazard. Mater. 461, 132673.
Yan, X.L., Zhai, W.D., Hong, H.S., Li, Y., Guo, W.D., Huang, X., 2012. Distribution, fluxes and decadal changes of nutrients in the Jiulong River estuary, Southwest Taiwan Strait. Chinese Sci. Bull. 57, 2307–2318.
Yan, C.X., Yang, Y., Zhou, J.L., Liu, M., Nie, M.H., Shi, H., Gu, L.J., 2013. Antibiotics in the surface water of the Yangtze Estuary: occurrence, distribution and risk assessment. Environ. Pollut. 175, 22–29.
Yarahmadi, H., Duy, S.V., Hachad, M., Dorner, S., Sauve, S., Prevost, M., 2018. Seasonal variations of steroid hormones released by wastewater treatment plants to river water and sediments: distribution between particulate and dissolved phases. Sci. Total Environ. 635, 144–155.
Yu, Q.M., Yang, X.D., Zhao, F.Z., Hu, X.D., Fan, F., Ren, H.Q., Geng, J.J., 2022. Occurrence and removal of progestogens from wastewater treatment plants in China: spatiotemporal variation and process comparison. Water Res. 211, 118038.
Zhang, D.D., Lin, L.F., Luo, Z.X., Yan, C.Z., Zhang, X., 2011. Occurrence of selected antibiotics in Jiulongjiang River in various seasons, South China. J. Environ. Monit. 13, 1953–1960.
Zhang, M., Shi, Y.J., Lu, Y.L., Johnson, A.C., Sarvajayakesavalu, S., Liu, Z.Y., Su, C., Zhang, Y.Q., Juergens, M.D., Jin, X.W., 2017. The relative risk and its distribution of endocrine disrupting chemicals, pharmaceuticals and personal care products to freshwater organisms in the Bohai Rim, China. Sci. Total Environ. 590-591, 633–642.
Zhang, Q.Q., Xing, C., Cai, Y.Y., Yan, X.T., Ying, G.G., 2021. How much do human and livestock actually contribute to steroids emission and surface water pollution from past to the future: a global research. Sci. Total Environ. 772, 145558.
Zhang, H.Y., Liu, Y.H., Wei, L.N., Zhu, R.Q., Zhao, J.L., Liu, S., Xu, X.R., Ying, G.G., 2024. Unveiling spatiotemporal distribution, partitioning, and transport mechanisms of tire additives and their transformation products in a highly urbanized estuarine region. Sci. Total Environ. 954, 176804.

Zhen, X.M., Li, Y.F., Tang, J.H., Wang, X.M., Liu, L., Zhong, M.Y., Tian, C.G., 2021. Decabromodiphenyl ether versus decabromodiphenyl ethane: source, fate, and influencing factors in a coastal sea nearing source region. Environ. Sci. Technol. 55, 7376–7385.
Zheng, S.L., Qiu, X.Y., Chen, B., Yu, X.G., Liu, Z.H., Zhong, G.P., Li, H.Y., Chen, M., Sun, G.D., Huang, H., Yu, W.W., Freestone, D., 2011. Antibiotics pollution in Jiulong River estuary: source, distribution and bacterial resistance. Chemosphere 84, 1677–1685.
Zhong, R.Y., Zou, H.Y., Gao, J., Wang, T., Bu, Q.W., Wang, Z.L., Hu, M., Wang, Z.Y., 2021. A critical review on the distribution and ecological risk assessment of steroid hormones in the environment in China. Sci. Total Environ. 786, 147452.
Zhou, L.J., Ying, G.G., Liu, S., Zhao, J.L., Chen, F., Zhang, R.Q., Peng, F.Q., Zhang, Q.Q., 2012. Simultaneous determination of human and veterinary antibiotics in various environmental matrices by rapid resolution liquid chromatography-electrospray ionization tandem mass spectrometry. J. Chromatogr. A 1244, 123–138.

Journal of Environmental Chemical Engineering 13 (2025) 119889

Contents lists available at ScienceDirect

Journal of Environmental Chemical Engineering

journal homepage: www.elsevier.com/locate/jece

Hydrothermal carbonization of model compounds of municipal sludge: Effects of reaction conditions and aqueous phase recirculation

Yiming Feng [a], Xueling Hu [b], Yuyang Xue [c], Xingying Tang [d,*], Donghai Xu [e], Yingying Zhang [d], Yumeng Wu [a]

[a] School of Resources, Environment, and Materials, Guangxi University, Nanning 530004, China
[b] Schoool of Green Building and Low-carbon technology, Guangxi Technological College of Machinery and Electricity, Nanning 530007, China
[c] Institute of Industry Hygiene of Ordnance Industry, Xi'an 710065, China
[d] Guangxi Laboratory on the Study of Coral Reefs in the South China Sea, Coral Reef Research Center of China, School of Marine Sciences, Guangxi University, Nanning 530004, China
[e] School of Energy and Power Engineering, Xi'an Jiaotong University, Xi'an 710049, China

ARTICLE INFO

Keywords:
Model compounds
Hydrothermal carbonization
Aqueous phase recirculation
Nitrogen retention

ABSTRACT

In this study, lauric acid (fatty acid), glutamic acid (amino acid), and cellulose (carbohydrate) were employed as model compounds of municipal sludge (MSM) to investigate the effects of hydrothermal carbonization (HTC) conditions (temperature and time) and aqueous phase recirculation (APR) on the properties of hydrochar and process liquid. Increasing temperature and prolonging reaction time promoted the formation and transformation of organic acids and nitrogenous compounds, leading to a decrease in hydrochar yield. At 270 °C for 60 min, the hydrochar exhibited a higher N/C ratio (0.019), indicating enhanced nitrogen retention. This condition was selected for four cycles of APR. With increasing recirculation cycles, the hydrochar N/C ratio (0.019–0.050) further decreased, while the yield (24.3 %–22.5 %) slightly declined. APR enhanced reactions such as aromatization and Maillard reaction, increasing the content of O-containing functional groups in the hydrochar and accumulating more N-derived compounds, thereby accelerating the HTC process. Under APR, the N-doped hydrochar demonstrates improved potential as a functional carbon-based material, and the HTC liquid rich in organic matter shows broad prospects for use as aqueous carbon source.

1. Introduction

Municipal sludge, a solid waste from urban wastewater treatment, is rich in organic matter and nutrients such as N, P, and K [1]. It is considered a potential source of biomass energy. Conventional disposal techniques including landfilling, aerobic composting, anaerobic digestion, and incineration exhibit limitations in either treatment efficiency or cost [2,3]. Among these technologies, HTC has emerged as a widely adopted method for treating municipal sludge. HTC is typically carried out in a closed system under temperatures of 180–300 °C and pressures of 20–30 bar, using water as the reaction medium. The process involves a series of reactions including hydrolysis, dehydration, decarboxylation, polymerization, condensation, and aromatization [4]. A distinct advantage of HTC is its ability to directly process wet feedstocks with high moisture content without requiring pre-dewatering or drying [5]. Compared to incineration and landfilling, HTC consumes less energy and presents a lower risk of secondary pollution.

The primary products from municipal sludge treated via HTC are hydrochar, HTC liquid, and a small amount of gas. In-situ doping facilitates the preparation of functional materials from hydrochar, which are doped with O and N functional groups [6]. The HTC liquid is an organically enriched stream containing organic acids, phenols, aromatic hydrocarbons and nutrients [7]. Its high organic content allows it to be utilized as the feedstock for biofuels (e.g., biodiesel), an aqueous carbon source in wastewater treatment or a substrate for microbial fermentation. This facilitates sludge resource recovery. Strategies promoting the conversion of N-containing compounds into carbon sources within the aqueous phase may directly impede N retention within hydrochar. Conversely, processes designed to maximize N retention within hydrochar may alter the composition and biodegradability of the aqueous phase. Consequently, systematic and synchronised research is required to establish a green and efficient "solid-liquid dual-product recovery"

* Corresponding author.
E-mail address: tangxingying@gxu.edu.cn (X. Tang).

https://doi.org/10.1016/j.jece.2025.119889
Received 6 September 2025; Received in revised form 16 October 2025; Accepted 18 October 2025
Available online 27 October 2025
2213-3437/© 2025 Elsevier Ltd. All rights are reserved, including those for text and data mining, AI training, and similar technologies.

model, thereby promoting environmental management and energy recycling.

After HTC, 40–60 % of carbon and a substantial amount of organic compounds remain in the aqueous phase [8]. Direct treatment of the HTC liquid with high organic load would significantly increase operational costs and undermine the energy-saving advantages of the process [9]. Existing technologies struggle to effectively degrade the soluble organic compounds in aqueous phase, making its resource recovery a critical bottleneck for industrial application [10]. APR was applied to address this issue by reusing the HTC liquid as a solvent in subsequent batches [11], thereby reducing freshwater consumption and minimizing wastewater treatment demands. Through APR, active substances accumulated, leading to optimized reaction conditions and thus enhanced the carbonization and polymerization degree of the hydrochar [12]. Furthermore, chemical species and nutrients dissolved in HTC liquid can be effectively recovered [13]. APR is widely recognized as an optimized strategy for HTC, contributing to the sustainable utilization of biomass resources [14,15].

Municipal sludge has a complex composition, comprising organic matter, inorganic salts, heavy metals, and pathogenic microorganisms, with organic substances (such as cellulose, proteins, and lipids) being the most abundant components. This intricate composition and the interactions among its constituents result in multiple hydrothermal reaction pathways, making it difficult to investigate the behavior and reaction mechanisms of specific components [16]. Moreover, research combining MSM with APR remains relatively scarce. Most previous research has focused on optimizing the fuel properties and yield of hydrochar, while few studies have simultaneously delved into nitrogen retention in hydrochar and the potential utilization of aqueous products as a carbon source. To circumvent the complexity of actual sludge systems and precisely elucidate the transformation behaviour of key constituents (cellulose, proteins, lipids) during hydrothermal processes alongside their response mechanisms to APR, this study employs model compounds (cellulose, glutamic acid, lauric acid) to simulate sludge components [17].

The specific objectives of this study were to (i) investigate the effects of reaction temperature, reaction time, and APR on the HTC of MSM; (ii) explore the reaction pathways and mechanisms of MSM during HTC and APR. The findings are expected to provide guidance for optimizing the HTC process of municipal sludge and facilitating the resource utilization of its products.

2. Materials and methods

2.1. Materials

L-glutamic acid (99 %) was purchased by Shandong Keyuan Biochemical Co., Ltd. (Shandong, China). Lauric acid (98 %) and cellulose powder (d50,90–150 μm) were purchased from Shanghai Macklin Biochemical Co., Ltd. (Shanghai, China). All the chemicals used are of AR grades. Ultrapure water used throughout the experiments was obtained from a Milli-Q millipore system (18.2 MU).

2.2. Experimental procedure

2.2.1. HTC experiments

The mixing ratio of L-glutamic acid, lauric acid and cellulose powder was selected as 2:1:1 and the mixture was homogenized. The substances obtained after mixing were MSM, and their physicochemical properties are shown in Table 1.

MSM and ultrapure water were mixed at 1:9 (m/V) ratio, and hydrothermally carbonized in a high-pressure stainless steel reaction tube (316 L) using a tube furnace. Four temperatures (180 °C, 210 °C, 240 °C, 270 °C) and three residence times (30/60/120 min) were set for 12 cross-tests (labeled HC-01 to HC-12). The numbers and corresponding reaction conditions are shown in Table 1. Samples were heated at 9 °C/min to target temperatures in the tube furnace and held isothermally. Post-reaction, products were centrifuged (4000 rpm, 15 min): The supernatant was filtered as HTC liquid (HC-XX-L) and stored in brown glass vials, the solid phase was vacuum-dried (24 h), ground through a 100-mesh sieve to obtain hydrochar (HC-XX-S), and stored in darkness within a desiccator.

Table 1
Physicochemical properties of and the hydrochar.

Samples	Elemental analysis (wt%)				N/C	O/C	HHV (MJ/kg)
	C	H	O	N			
MSM	49.68	7.43	38.15	4.76	0.096	0.768	22.08
HC−01 (180 °C, 30 min)	64.02	6.19	28.92	0.87	0.014	0.452	26.64
HC−02 (210 °C, 30 min)	52.98	8.20	38.13	0.69	0.013	0.720	24.20
HC−03 (240 °C, 30 min)	52.09	7.80	39.69	0.42	0.008	0.762	23.27
HC−04 (270 °C, 30 min)	80.53	6.25	12.67	0.55	0.007	0.157	34.16
HC−05 (180 °C, 60 min)	50.10	8.22	40.96	0.72	0.014	0.818	22.93
HC−06 (210 °C, 60 min)	51.71	6.24	41.65	0.40	0.008	0.805	21.09
HC−07 (240 °C, 60 min)	67.33	2.62	29.51	0.54	0.008	0.438	23.53
HC−08 (270 °C, 60 min)	68.28	6.05	24.34	1.33	0.019	0.356	28.43
HC−09 (180 °C, 120 min)	71.95	10.39	16.53	1.13	0.016	0.230	35.63
HC−10 (210 °C, 120 min)	43.66	6.76	48.95	0.63	0.014	1.121	18.14
HC−11 (240 °C, 120 min)	67.59	1.82	30.08	0.51	0.008	0.445	22.62
HC−12 (270 °C, 120 min)	69.14	5.91	23.35	1.6	0.023	0.338	28.66

MSM—Model compounds of municipal sludge.

2.2.2. Aqueous phase recycling experiments

In APR experiments, the HTC liquid from the prior cycle fully replaced ultrapure water. HC-08 (270 °C, 60 min) was chosen as the initial cycle. The initial cycle (HC-R0) used 9 mL ultrapure water, yielding HC-R0-L (liquid) and HC-R0-S (hydrochar). Subsequent cycles (HC-R1–HC-R4) employed the preceding HTC liquid (e.g., HC-R0-L for HC-R1) as the solvent for HTC, generating corresponding products. Four cycles were labeled HC-R0 to HC-R4, with other procedures identical to baseline HTC tests.

2.3. Analytical methods

The yield of hydrochar (Y_{hc}) obtained in the HTC process was defined as the weight ratio of hydrochar (M_{hc}) to MSM (M_m) used as feedstock on a dry basis (Eq. (1)).

$$Y_{hc}\ (\mathrm{wt,\ \%}) = \frac{\mathrm{M_{hc}}}{\mathrm{M_m}} \times 100\% \quad (1)$$

An elemental analyzer (Vario EL cube, Elementar, Germany) was used to detect the elemental compositions (C, H, N, S) of the MSM and hydrochar. The O content was calculated by difference (O% = 100% − (C% + H% + N% + S% + Ash%)). The higher heating value (HHV) was calculated based on the elemental composition HHV = 0.3491C + 1.1783H + 0.1005S - 0.1034 O - 0.015N - 0.0211A.

Surface functional groups of hydrochar were characterized by Fourier transform infrared spectroscopy (FTIR, IRTrace-100, Japan) with a scanning range of 400–4000 cm^{-1} and 32 cumulative scans. X-ray photoelectron spectroscopy (XPS, Thermo Scientific Nexsa, USA) was used to analyse the surface elemental composition of hydrochars and their existence morphology. Al Kα-rays were selected as the excitation

source, with the accelerating voltage set at 10 kV and the current at 50 mA.

The pH of HTC liquid was measured by pH meter (E-201-L). TN was determined using Hach persulfate oxidation method reagents (Cat. 2714100-CN). Ammonia nitrogen (NH_3-N) concentration was measured with Hach salicylate method reagents (Cat. 2606945-CN). Total organic carbon (TOC) was quantified using a TOC analyzer (ET1020A). Chemical oxygen demand (COD) was measured using Hach TNTplus™ digestion vials (Cat. 2415915-CN). Untargeted screening of compounds in HTC liquid was performed using liquid chromatography-mass spectrometry (LC-MS; Q-EXACTIVE, Thermo Fisher Scientific) for comprehensive component characterization.

3. Results and discussions

3.1. Influence of reaction conditions on properties and yield of hydrochar

3.1.1. Hydrochar yields

The hydrochar yields under different reaction conditions are presented in Fig. 1. As the temperature increased, the hydrochar yield exhibited an decreasing trend. For instance, from HC-01 (30 min, 180 °C) to HC-04 (30 min, 270 °C), the hydrochar yield decreased by 4.7 %. A similar trend was observed in HC-05 to HC-08 and HC-09 to HC-12. This indicates that elevated temperatures promoted the depolymerization and decomposition of the feedstock, generating soluble low-molecular-weight substances such as organic acids, aldehydes, and alcohols. These substances then dissolved and accumulated in the aqueous phase [18,19]. Prolonging the reaction time also facilitated the degradation of MSM and led to a reduction in hydrochar yield. At 180 °C and 270 °C, extending the reaction time from 30 min to 120 min resulted in a decrease in hydrochar yield from 31.5 % and 26.8–22.2 % and 19.3 %, respectively. Notably, the yields at 60 min were close to those at 120 min (and even slightly lower at certain temperatures), and the decline from 60 min to 120 min was less pronounced than that from 30 min to 60 min. This suggests that the influence of reaction time on hydrochar yield is significantly less marked compared to that of temperature.

Compared to the hydrochar yields typically observed in real sludge (40 %–80 %) [20–22], the yields obtained from MSM in this study (19.3–31.5 %) were significantly lower. This observation is consistent with findings reported by Liu et al. [23]. The discrepancy can be attributed to the fact that the model compounds selected in this study were of analytical grade and were used to simulate the major organic components of sludge. In contrast, real sludge contains a high ash content, including substantial amounts of non-reactive substances such as sandy grit. These substances are insoluble in water and remain in the solid residue after HTC, thereby increasing the hydrochar yield. Furthermore, intermediate products formed during HTC can react with radicals generated from cellulose. This inhibited subsequent condensation and polymerization reactions involved in hydrochar formation [24], which also contributed to the lower hydrochar yield from MSM. When evaluating hydrochar of actual sludge, greater emphasis should be placed on carbon recovery rate, changes in content of organic matter and HHV. This provides a more accurate reflection of the HTC process's efficiency in converting organic matter.

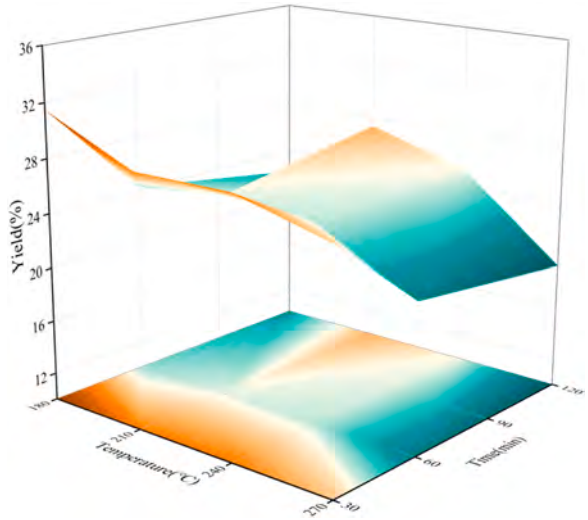


Fig. 1. Hydrochar yield of different reaction conditions.

Compared to other real biomass feedstocks such as food waste, faecal sludge, and eucalyptus bark (often >40 %), The hydrochar yield from MSM (19.3–31.5 %) was notably lower (Table 2). This discrepancy can be primarily attributed to two factors. First, real biomass contains a significant proportion of inorganic ash content, which is inert during HTC and remains in the solid product. Second, the complex structure of natural biomass, particularly the presence of recalcitrant components such as lignin, results in higher solid retention. In contrast, the MSM used in this study was ash-free and composed of highly reactive pure compounds, rendering them more readily susceptible to hydrolysis and dissolution. Their yields thus reflects the true conversion efficiency of the organic components.

3.1.2. Hydrochar properties

Elemental analysis was performed on the hydrochar derived from MSM under various reaction conditions (Table 1). Compared to the feedstock, a slight decrease in O and H content was observed. This can be attributed to dehydration and decarboxylation reactions occurring during the hydrothermal process, which release O-containing functional groups such as -OH and -COOH into the HTC liquid [18,30]. Due to the absence of ash, the hydrochar had higher C content , higher HHV and lower N/C ratio compared with that produced from real sludge. The C content generally increased with rising temperature. It is noteworthy that in the groups with reaction times of 30 min and 120 min, the C content initially decreased and then increased. This behaviour can be explained by the temperature at which cellulose hydrolyses, which is around 200 °C. At a temperature of 180 °C, hydrolysis did not proceed significantly, whereas substantial hydrolysis took place at 210 °C and above, generating small-molecule sugars that dissolved into the liquid phase, This reduced the C content in the solid product. At 270 °C, intermediates derived from the decomposition of feedstock condensed and recombined, forming insoluble polymers and polycyclic aromatic hydrocarbons [31]. These then re-accumulated in the hydrochar, leading to an increase in its C content.

As temperature increased and reaction time extended, the O/C ratio initially rised before decreasing. At lower temperatures and shorter reaction times, this increase in the resulted from the combined effects of hydrolysis reactions alongside dehydration and decarboxylation processes. However, as reaction intensity increased, dehydration and decarboxylation reactions became markedly enhanced [30]. Nitrogen was derived from glutamic acid. As the temperature increased, glutamic acid increasingly degraded. Following decarboxylation and deamination, it further decomposed into volatile fatty acids, hydrocarbons,

Table 2
Summary of HTC research with some key parameters and hydrochar yield from different biomass.

Samples	Temperature (°C)	Time	Yield (%)	Ref
Food waste	180–260	1 h	35.0–53.8	[25]
Defective coffee beans	150–250	40 min	34.2–64.2	[26]
Apple waste	180–230	2–4 h	53–73	[27]
Lemon peel waste	180–250	1 h	40.9–50.1	[28]
Faecal sludge	250	5 h	70–73	[29]
Petrochemical sludge	210–270	2 h	75.7–79.9	[19]
Eucalyptus bark	220–300	2–10 h	40.0–46.4	[24]

aldehydes, amines, and ammonia, which dissolved into the HTC liquid [32,33]. This led to a gradual decrease in N content in the solid phase. Meanwhile, the concurrent increase in C content resulted in a lower N/C ratio. In contrast to reaction temperature, varying the reaction time showed no significant differences among the groups, indicating that temperature is the key factor governing the elemental composition and yield of hydrochar.

3.1.3. FTIR analysis of hydrochar

The FTIR results of hydrochar under different conditions were presented in Fig. 2. Except for the 180 °C group, the stretching vibrations of -OH/N-H (3700–3300 cm^{-1}) weakened significantly with increasing temperature and prolonged reaction time, indicating enhanced dehydration of the MSM during HTC [10]. The C–H stretching vibrations of aliphatic methylene groups at 2922 cm^{-1} and 2855 cm^{-1} diminished as reaction severity increased, which can be attributed to the oxidation and decomposition of aliphatic chains in the MSM. The band near 1728 cm^{-1} is assigned to the C═O stretching vibration. In the 30-min and 60-min groups, its intensity initially increased and then decreased, whereas in the 120-min group, it declined gradually. This behavior can be explained by the degradation of cellulose and lauric acid generating intermediates such as carboxylic acids, aldehydes, and ketones, while higher temperatures promoted decarboxylation reactions. The band around 1660 cm^{-1} was attributed to the stretching vibration of C═N in amides. The band near 1514 cm^{-1} represented stretching vibrations of C═C and C–N in aromatic compounds. The C–O stretching vibration of alcohols and ethers at 1025 cm^{-1} weakened with increasing reaction severity, suggesting enhanced dehydration and decarboxylation.

3.2. Influence of reaction conditions on properties of HTC liquid

3.2.1. pH analysis

The influence of reaction conditions on the pH of the HTC liquid was shown in Fig. 3. The HTC liquid was strongly acidic, with pH values ranging from 2.4 to 3.6. According to previous studies [30,34,35], this mainly came from organic acids produced by hydrolysis of cellulose and lauric acid, and decarboxylation of glutamic acid. As the temperature increased, the pH value rose significantly. This is because elevated temperatures promoted further reactions of the organic acids, consuming functional groups such as carboxyl groups [30,34]. Meanwhile, the NH_3-N generated from the deamination of glutamic acid partially neutralized organic acids [36]. This phenomenon was more pronounced in groups with longer reaction times. Specifically, at a reaction time of 120 min, the pH value increased from 2.48 to 3.59 as the temperature increased from 180 °C to 270 °C. This suggests that extending the reaction time in conjunction with raising the temperature can enhance the aforementioned reactions. However, at a reaction time of 30 min, the pH value first decreased and then increased with rising temperature. A possible explanation is that the mild conditions at 180 °C and 30 min limited the hydrolysis of cellulose, resulting in less organic acid production. As the temperature increased, more extensive decomposition of cellulose generated additional organic acids, leading to a decrease in pH value. Under more severe conditions, however, the decomposition of organic acids became the dominant pathway, resulting in a rebound of the pH value.

3.2.2. COD and TOC analyses

To further investigate the effect of reaction conditions on the HTC liquid, COD and TOC were measured. As shown in Fig. 4a, the COD values were generally higher than 30 g/L, confirming its enrichment with organic substances. This phenomenon originated from the dissolution and accumulation of small-molecular-weight organic compounds derived from the decomposition of model compounds, namely glutamic acid, cellulose, and lauric acid [37]. When the reaction time was 30 min, the influence of temperature elevation on COD was negligible. However,

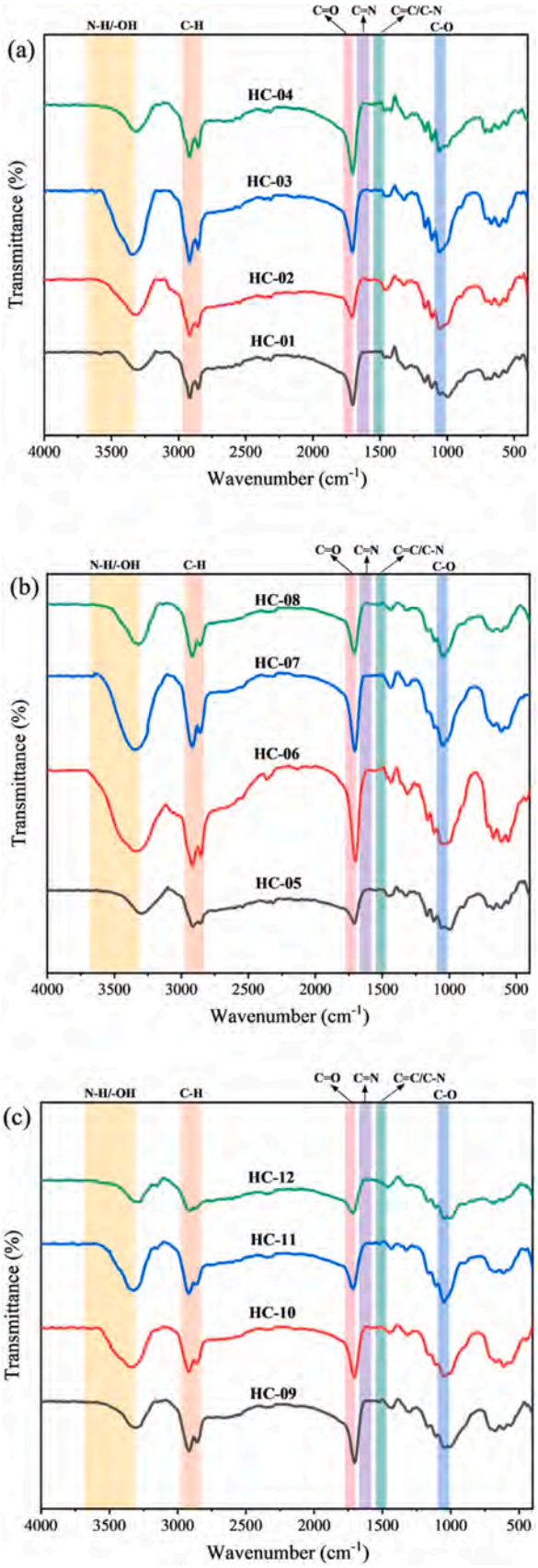


Fig. 2. FTIR of hydrochar under different reaction conditions. (a) HC-01–HC-04; (b) HC-05–HC-08; (c) HC-09–HC-12.

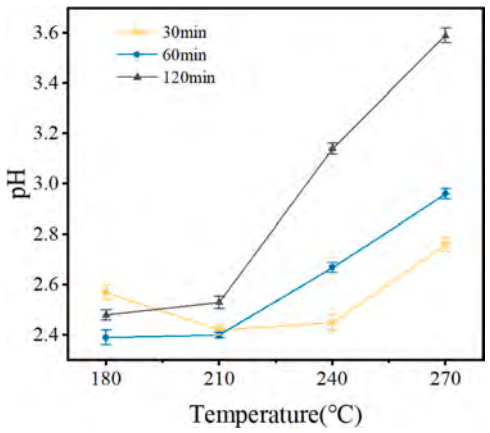


Fig. 3. pH of hydrothermal carbonization liquid under different reaction conditions.

under severe conditions (e.g., HC-08, HC-11, HC-12), COD decreased significantly, and this reduction became more pronounced with prolonged reaction time. According to previous studies [38], this behavior is likely attributed to the re-polymerization of small-molecular-weight organic compounds into insoluble polymers that transferred to the hydrochar, coupled with the mineralization of some organics into gases such as CO_2/CH_4.

The variation of TOC showed a high degree of synchronization with COD. As illustrated in Fig. 4b, a sharp decrease in TOC was observed under higher temperatures and longer reaction times, except for minor fluctuations at 30 min. This confirms that C primarily existed in the form of small organic molecules. The COD/TOC ratios for all groups remained below 3.0 (Fig. 4c), suggesting high biodegradability of the organic compounds. This ratio increased with rising temperature, indicating the conversion of small organic molecules into aromatic compounds and polymers that migrated to the solid phase [39]. However, extending the reaction time did not exhibit a similar effect.

3.2.3. NH_3-N and TN analyses

Fig. 5 shows the variations in NH_3-N and TN concentrations in the HTC liquid under different reaction conditions. As temperature increased, the value of NH_3-N increased significantly, with a particularly notable increase beyond 210 °C in the 30-min and 60-min groups, while the 120-min group exhibited a more gradual increase (Fig. 4a). This is attributed to enhanced reaction severity, which intensified the deamination of glutamic acid, promoting the generation of organic acids and NH_3-N. This finding aligns with the research conducted by Wang et al. [40]. It is worth noting that in the 30-min group, the value of NH_3-N initially decreased and then increased with rising temperature. This trend is consistent with the variation in pH value, indicating that under mild conditions (180 °C, 30 min), cellulose was not effectively degraded into organic acids, resulting in limited consumption of NH_3-N through neutralization with organic acids [41]. When the temperature reached 210 °C, accelerated decomposition of cellulose produced more organic

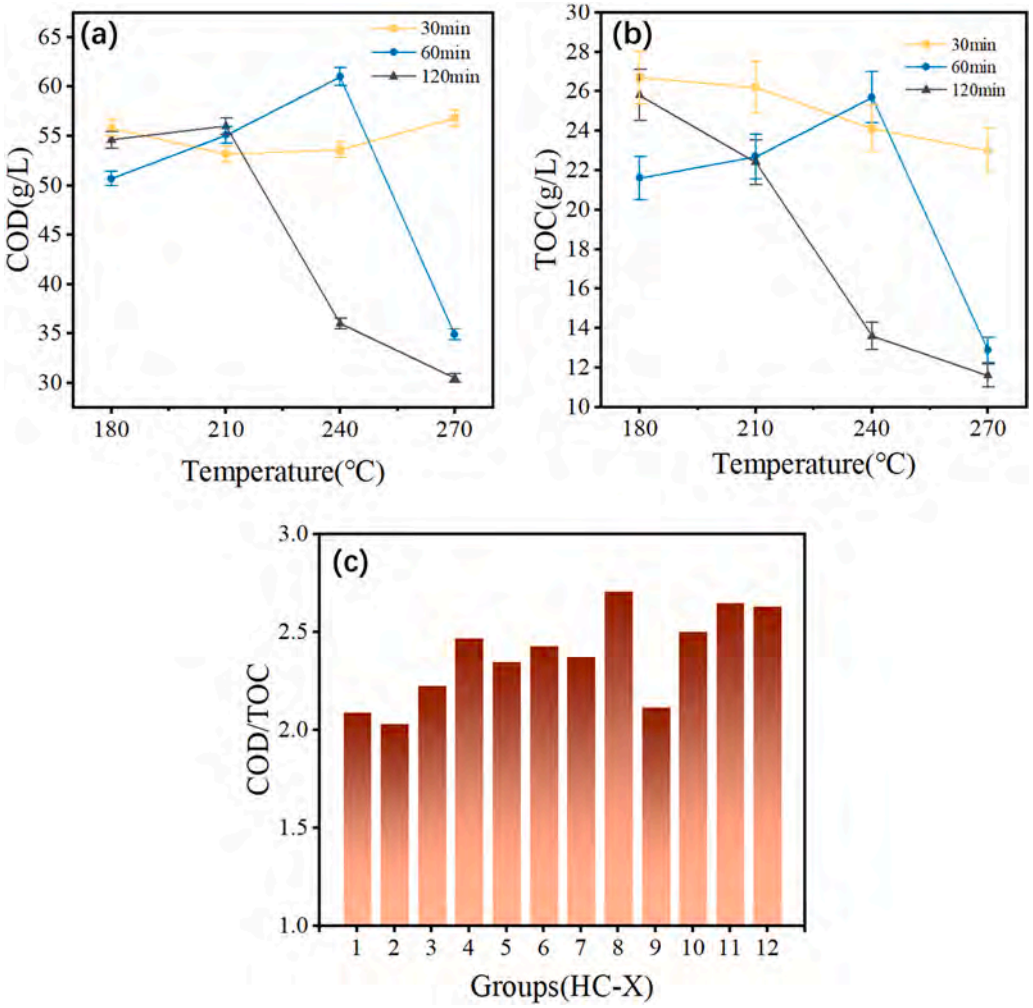


Fig. 4. COD and TOC of hydrothermal carbonization liquid under different reaction conditions. (a) COD; (b) TOC; (c) COD/TOC.

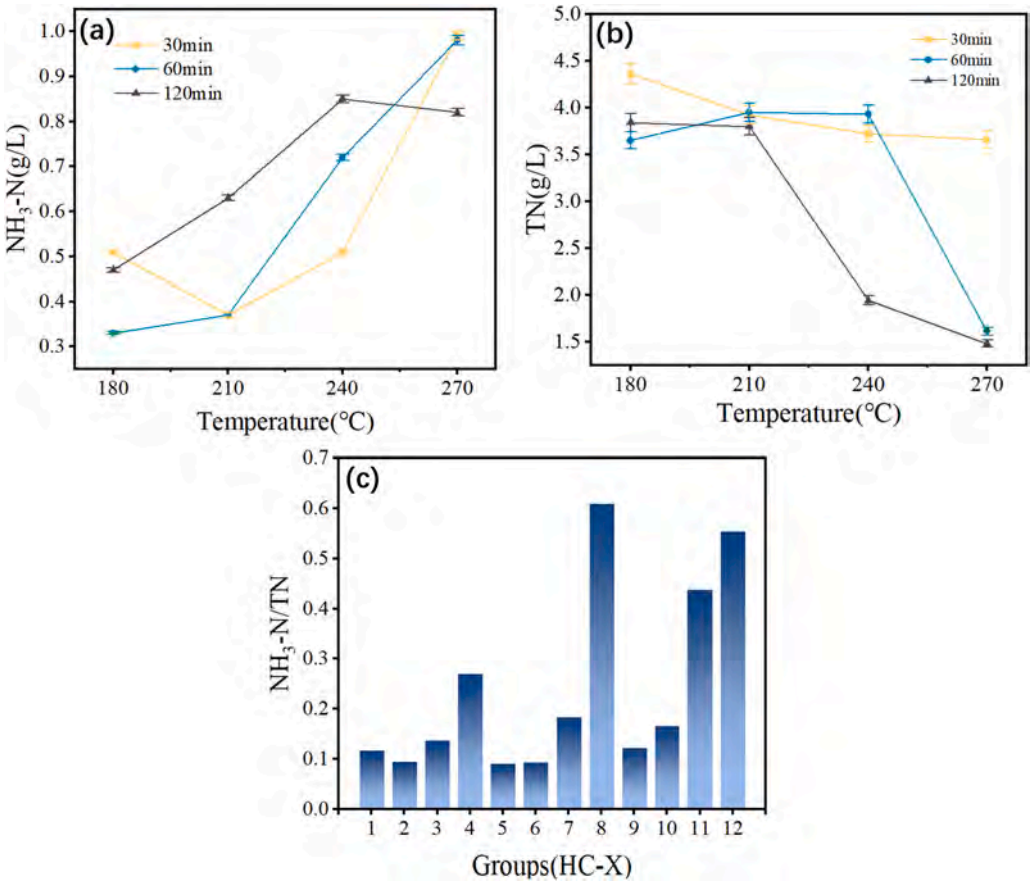


Fig. 5. The values of NH_3-N and TN of hydrothermal carbonization liquid under different reaction conditions. (a) NH_3-N; (b) TN; (c) NH_3-N/TN.

acids, which neutralized NH_3-N. Subsequently, under more severe reaction conditions, further degradation of organic acids occurred alongside accelerated deamination, leading to a renewed increase in NH_3-N.

As reported by Fakkaew et al. [29], proteins in sludge undergo accelerated hydrolysis with increasing temperature, decomposing into amino acids, dipeptides, polypeptides, and other nitrogenous substances. This phenomenon was also described by Xu et al. [42], who observed that the value of TN in the HTC liquid increased at higher temperatures. However, such a trend was not observed in the present study. This was due to the progressive hydrolysis of the actual sludge limiting the effective migration of N. The conversion of N can be influenced through pre-treatment or process optimization [8]. As shown in Fig. 5b, the value of TN remained relatively high (3.5–4.5 g/L) at 180 °C. This can be attributed to the model compounds employed in this study bypassing the protein hydrolysis step. Glutamic acid could directly participate in reactions, generating amines, amides, and other N-containing compounds that dissolved in the HTC liquid. As the temperature increased, the TN value decreased. This decline became more pronounced with longer reaction times, consistent with the variations in COD and TOC. Furthermore, in conjunction with the increasing NH_3-N/TN ratio shown in Fig. 5c, these results indicate that NH_3-N gradually became the dominant form of nitrogen in the HTC liquid, suggesting the conversion of organic-N into inorganic-N.

3.3. Influence of APR on properties and yield of hydrochar

To obtain hydrochar with a higher N/C ratio while considering energy consumption, HC-08 (270 °C, 60 min) was selected as the initial group for APR during hydrothermal process.

3.3.1. Yields and properties of hydrochar

Table 3 presents the physicochemical properties and yields of hydrochar before and after four cycles of APR. There was a slight decrease in the hydrochar yield, which declined from 24.3 % to 21.5 %, before rebounding to 22.5 %. This initial reduction can be attributed to the fact that the recirculated aqueous phase contained a substantial amount of intermediate products, such as organic acids, which acted as catalysts to promote the hydrolysis of the feedstock into small organic molecules that dissolved in aqueous phase [43]. As the HTC liquid approached saturation in later cycles, the reaction rate decreased, resulting in the subsequent recovery of the hydrochar yield. This is consistent with the trend observed by Xu et al. [10]. However, the primary constituents of their aqueous phase were soluble proteins and sugar hydrolysates, exhibiting alkalinity. Yield fluctuations are frequently attributed to the dissolution and repolymerization of organic matter.

With increasing times of APR, the C content of the hydrochar slightly increased, while the O content and O/C ratio decreased. This is probably because the APR promotes dehydration and decarboxylation reactions, resulting in O-containing functional groups being transferred from the hydrochar to aqueous phase [10]. This enhanced the degree of condensation and aromaticity [30,44]. The notable increase in the N/C ratio was primarily due to an increase in N content resulting from Maillard reactions between accumulated reducing sugars and glutamic acid in the aqueous phase. These reactions caused the substances to polymerise and be incorporated into the hydrochar. Previous studies have indicated that the Maillard reaction serves as a key mechanism for N retention in hydrochar [13,45]. Furthermore, the H content and HHV of the hydrochar showed only minor fluctuations.

Table 3
Physicochemical properties and yield of hydrochar under aqueous phase recycling.

Samples	Elemental analysis (wt%)				N/C	O/C	HHV (MJ/kg)	Yield (%)
	C	H	O	N				
HC-R0	68.28	6.05	24.34	1.33	0.019	0.356	28.43	24.3
HC-R1	67.40	6.35	24.20	2.05	0.030	0.359	28.48	25.1
HC-R2	67.05	6.17	24.99	1.79	0.027	0.373	28.07	24.8
HC-R3	70.70	6.06	18.82	4.42	0.063	0.266	29.81	21.5
HC-R4	69.22	5.88	21.46	3.44	0.050	0.310	28.83	22.5

3.3.2. Functional groups

The FTIR results for hydrochar were listed in Fig. 6. The broad overlapping band in the range of 3700–3300 cm^{-1} was attributed to O–H and N–H stretching vibrations [46]. According to Xu et al. [10], the recycling number had little influence on the O–H groups. The variation in N–H vibration may result from the decomposition of glutamic acid and the formation of amides through dehydration and condensation of N-containing intermediates. As the number of APR increased, the C–H stretching vibrations of aliphatic methylene groups at 2922 cm^{-1} and 2855 cm^{-1} weakened. This is due to the oxidative decomposition of lauric acid in the feedstock into volatile fatty acids, which transferred into the aqueous phase, indicating that APR effectively promotes the conversion and decomposition of materials [47,48]. The C═O stretching vibration near 1728 cm^{-1} weakened from HC-R0 to HC-R3 due to the degradation of feedstock, and then intensified in HC-R4 as compounds such as furfurals and ketones re-polymerized. This trend aligns with that of the N–H groups, confirming the presence of amides. The band around 1660 cm^{-1} was assigned to the stretching vibration of C═N in amides [10]. The band near 1514 cm^{-1} represented stretching vibrations of C═C and C–N in aromatic compounds. Its gradual enhancement with increasing recycling number indicates that APR promotes aromatization reactions of intermediates. The peak at 1025 cm^{-1} corresponded to C–O stretching vibrations in alcohols and ethers. Increased recycling numer facilitated the hydrolysis and further conversion of cellulose in the feedstock, leading to a reduction in the intensity of this peak.

To further investigate the effect of APR on the chemical states and speciation of surface functional groups, XPS was used to analyze the hydrochar under APR. The C1s spectra of hydrochar, as shown in Fig. 7, could be deconvoluted into four component peaks: the peak at a binding energy of 284.8 eV corresponded to aliphatic or aromatic carbon groups (CH_X, C–C/C═C); the peak at 285.6 ± 0.3 eV was assigned to hydroxyl or amino groups (-C-OR/-C-NR); the peak at 287.0 ± 0.4 eV represented carbonyl or imine groups (-C═O/-C═N); and the peak at 288.6 ± 0.2 eV was attributed to carboxyl, ester, or similar groups (-COOR) [23,39]. Visually, the main spectral envelope between 284 eV and 288 eV gradually evolved from a doublet into a singlet, primarily due to changes in the ratio of aromatic carbon groups to hydroxyl/amino groups. Concurrently, a new peak emerged between 288 eV and 290 eV. Compared to HC-R0 and HC-R1, the content of C–C/C═C groups decreased in HC-R2, HC-R3, and HC-R. This corresponds to the weakening of aliphatic C-H bonds observed in FTIR, indicating an increase in the proportion of O-containing functional groups. This suggests that organic acids accumulated in the aqueous phase may have catalyzed the hydrolysis and oxidation of the aromatic carbon framework [8]. The content of -C-OR and-C-NR groups increased significantly (21.14 %–37.00 %), indicating that APR promotes the Maillard reaction between glutamic acid and reducing sugars. APR also facilitated condensation and polymerization reactions, leading to the formation of N-heterocyclic compounds [23]. The content of C═O/C═N groups showed a slight increase in HC-R2 but a decreasing trend in subsequent cycles, indicating that the chemical structure of the hydrochar was transitioning from unstable intermediate states toward more stable terminal products. The -COOR content exhibited minor fluctuations, which may result from the oxidation of reducing sugars from lauric acid and cellulose, combined with intensified decarboxylation reactions during APR.

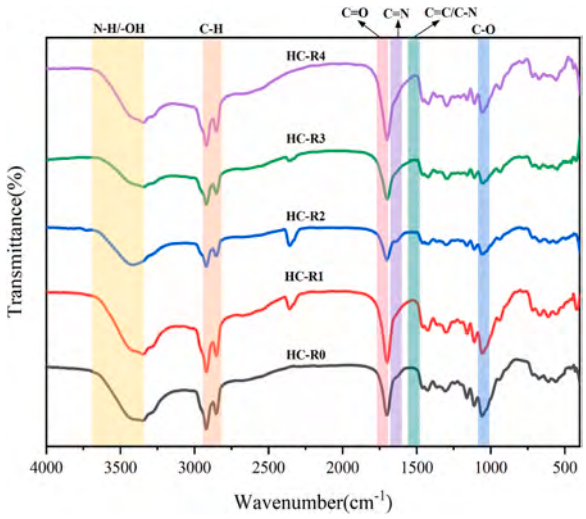


Fig. 6. FTIR of hydrochar under aqueous phase recycling.

Fig. 8 showed the O1s spectra, which were composed of four types of O-containing functional groups: C═O (furan or carbonyl groups) at a binding energy of 531.3 eV, -COOR (carboxyl or ester groups) at 532.4 eV, -C-O-R (ether groups) at 533.3 eV, and -C-OH (hydroxyl groups) at 534.3 eV [23]. The content of -COOR groups exhibited slight fluctuations, which was consistent with the observations in the C1s XPS spectra. The content of C═O groups increased slightly. In conjunction with the C1s analysis, the decrease in C═O/C═N ratio was attributed to a reduction in C═N content. The content of -C-O-R first increased and then decreased, which can be attributed to hydrolysis and aromatization of ether compounds formed by the condensation of alcohols, ultimately leading to a more stable structure.

The transformation of N species was further identified via N1s spectra (Fig. 9), which consist of four forms: pyridinic-N at a binding energy of 398.5 ± 0.3 eV, amide-N at 399.4 ± 0.3 eV, pyrrolic-N at 400.0 ± 0.3 eV, and quaternary-N at 401.0 ± 0.3 eV. After APR, pyrrolic-N and amide-N were converted into more stable forms, namely pyridinic-N and quaternary-N, consistent with FTIR findings. This indicates that recirculation enhanced polymerization and cyclization reactions, thereby effectively promoting nitrogen retention [49]. According to Wang et al. [45], the Maillard reaction between carbohydrate derivatives and amino acids serves as the primary mechanism for nitrogen fixation. In this study, cellulose and glutamic acid provided ideal precursors for the Maillard reaction, which played a key role in the efficient and stable incorporation of nitrogen into the carbon framework of hydrochar, ultimately enhancing its nitrogen doping level and structural stability.

3.4. Influence of APR on properties and components of HTC liquid

3.4.1. Properties of HTC liquid

As shown in Fig. 10, APR led to a progressive darkening of the HTC liquid and a reduction in its transparency. After four cycles, the liquid

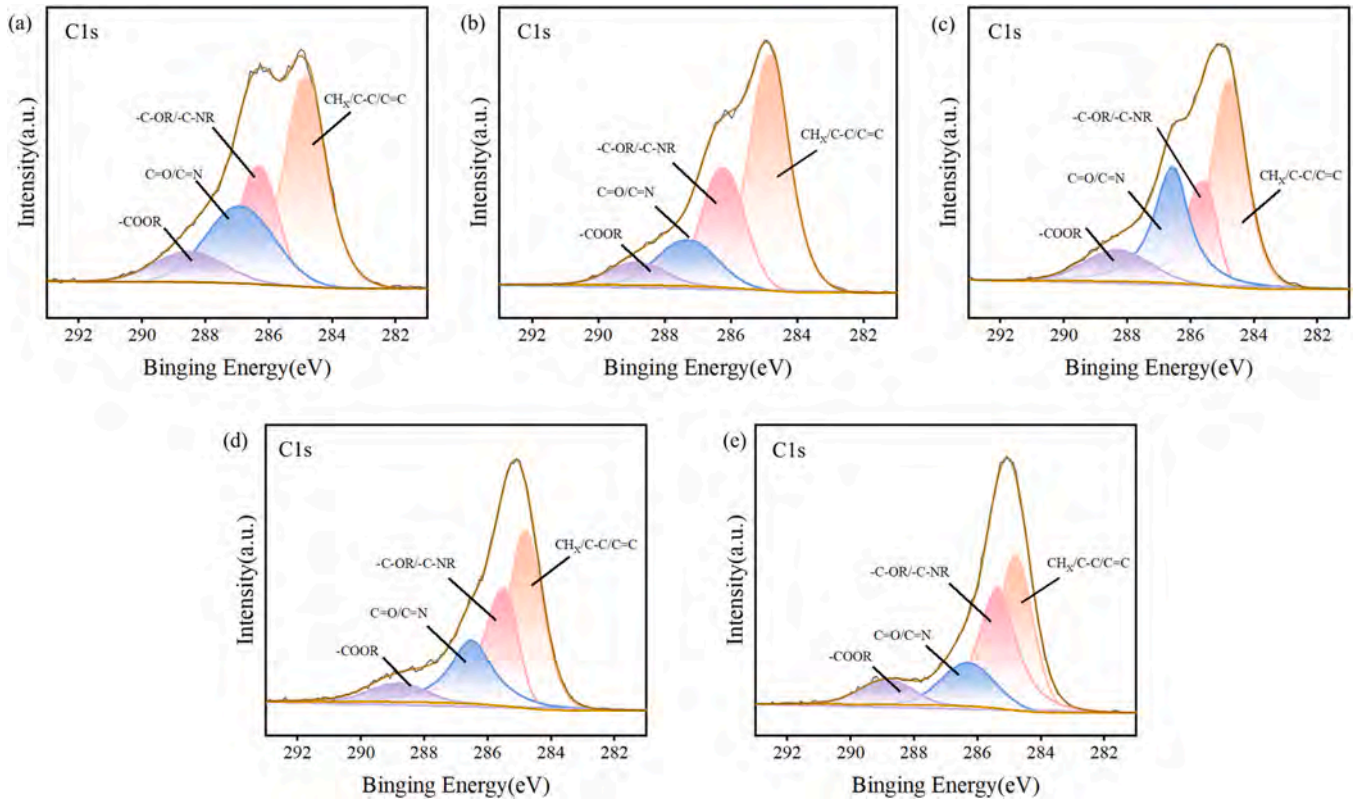


Fig. 7. XPS C1s spectra of hydrochar under aqueous phase recycling: (a) HC-R0; (b) HC-R1; (c) HC-R2; (d) HC-R3; (e) HC-R4.

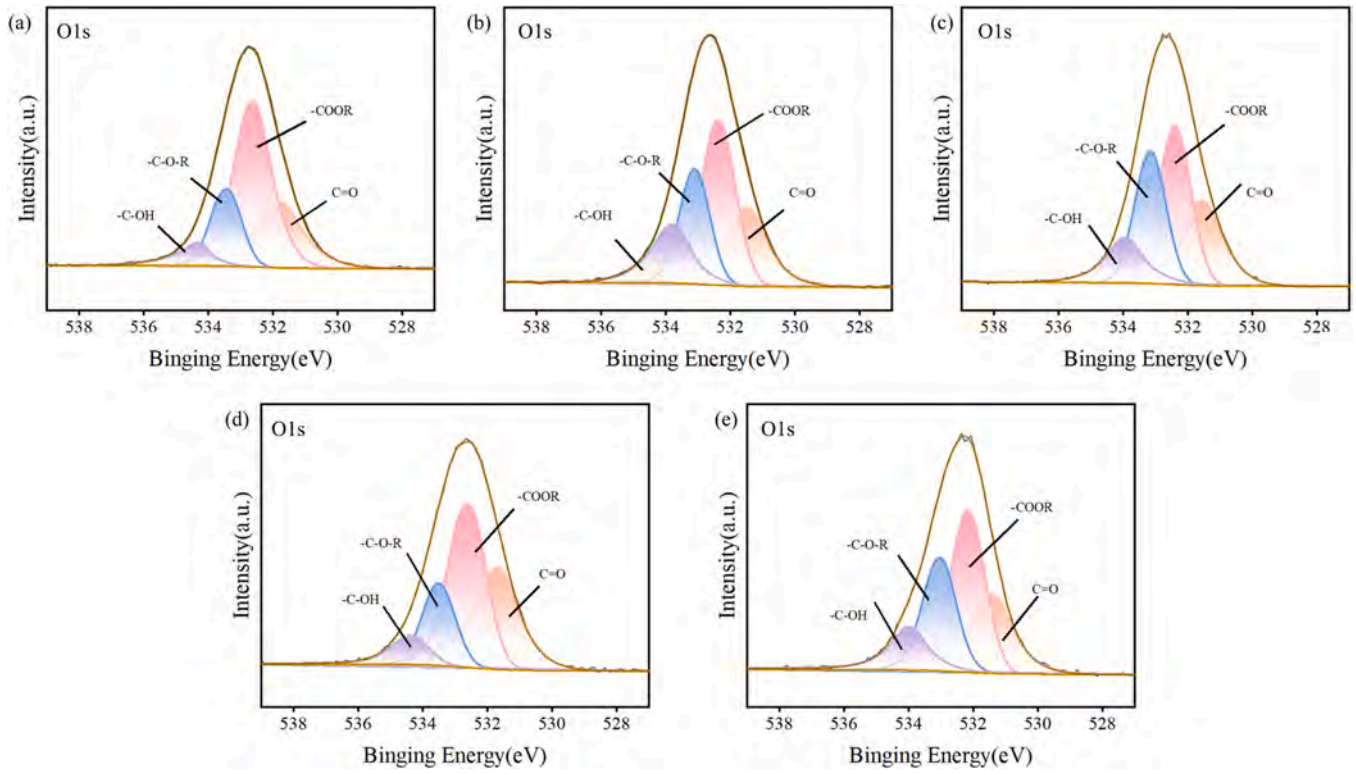


Fig. 8. XPS O1s spectra of hydrochar under aqueous phase recycling: (a) HC-R0; (b) HC-R1; (c) HC-R2; (d) HC-R3; (e) HC-R4.

appeared black. This darkening is attributed to the polymerization of organic matter into aromatic compounds and the formation of melanoidins via the Maillard reaction as the number of APR increased [50].

APR significantly increased the value of pH, TOC, COD, NH_3-N and TN of the HTC liquid, indicating the accumulation of intermediate products (Fig. 11). This conclusion is consistent with Fig. 10. The pH

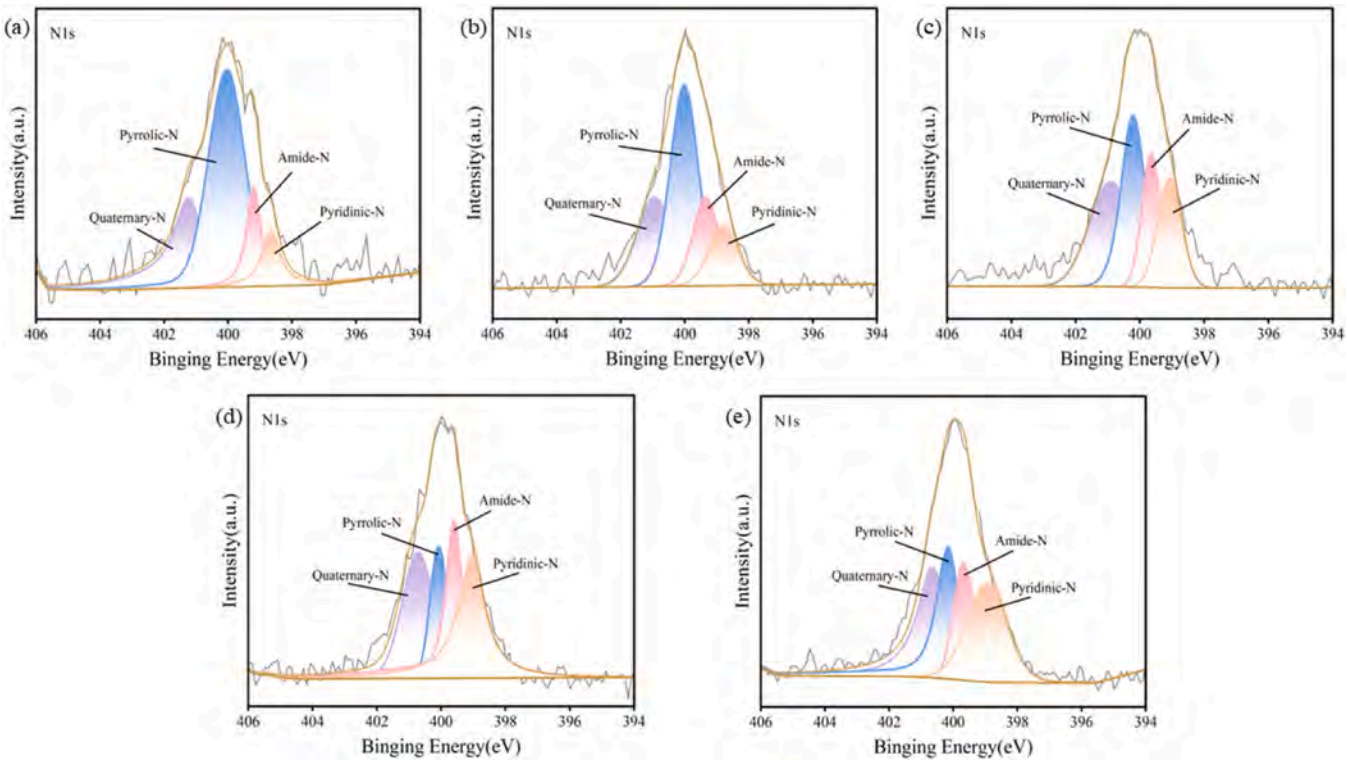


Fig. 9. XPS N1s spectra of hydrochar under aqueous phase recycling: (a) HC-R0; (b) HC-R1; (c) HC-R2; (d) HC-R3; (e) HC-R4.

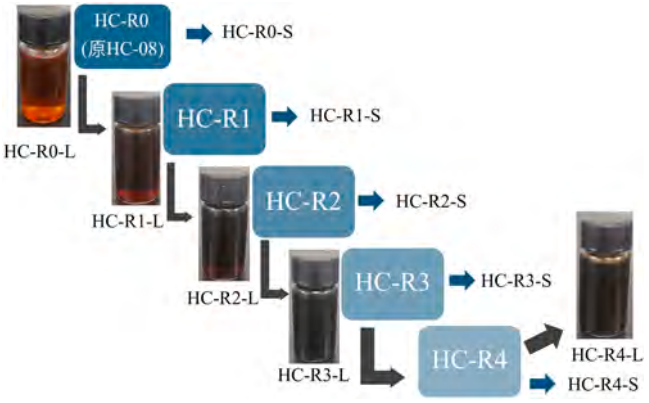


Fig. 10. Schematic diagram of aqueous phase recycling.

value increased from 2.96 in HC-R0–3.16 in HC-R4, which can be attributed to the accumulation of amides derived from glutamic acid and their subsequent conversion into amines [8], alongside the decomposition of organic acids in the aqueous phase. This is supported by the results of the XPS C1s. The sources of COD and TOC primarily included three aspects: volatile fatty acids from the decarboxylation and decomposition of lauric acid; organic acids and amines generated through the hydrolysis of glutamic acid; and alcohols, aldehydes, and ethers produced by the hydrolysis and further decomposition of cellulose. These intermediates also catalyzed and participated in the hydrothermal carbonation reactions. As the number of APR increased, the rate of increase in COD and TOC slowed, suggesting that the organic matter in the liquid phase approached saturation. An appropriate number of APR can markedly enhance the organic content of the HTC liquid, demonstrating considerable potential for producing high-quality aqueous carbon sources.

The TN primarily originated from amides and amines formed

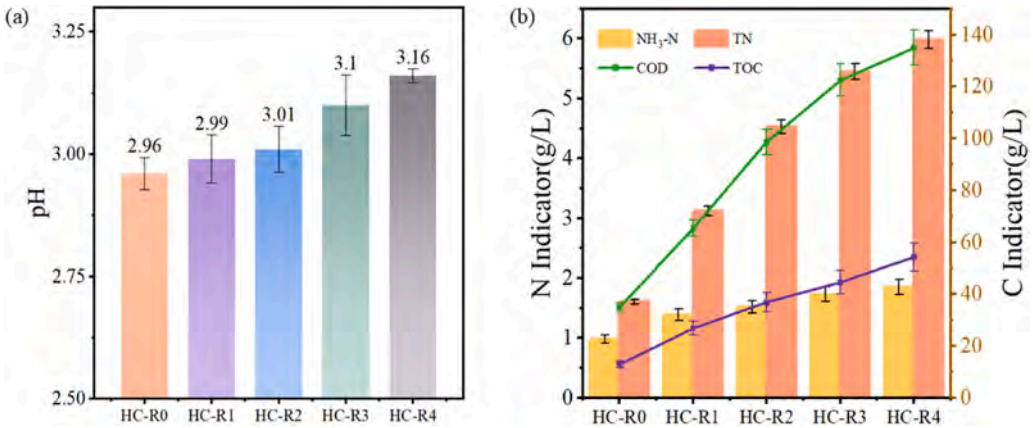


Fig. 11. pH, physical and chemical properties of hydrothermal carbonization liquid under aqueous phase recycling: (a) pH; (b) chemical properties.

through the hydrolysis of glutamic acid, which were further converted into NH_3-N and inorganic-N. Although both TN and NH_3-N increased during APR, their rates of increase slowed, consistent with the trends for COD and TOC. It is also noteworthy that the proportion of NH_3-N in TN decreased during recirculation, indicating a rise in the content of N-heterocyclic compounds in the aqueous phase, which became a major form of N in HTC liquid. Moreover, N-containing compounds in the aqueous phase directly contributed to N enrichment in the hydrochar. This was convincingly demonstrated by the significant increase in the N content of hydrochar and the transformation of N species towards more stable forms, namely pyridinic-N and quaternary-N.

3.4.2. *Components of HTC liquid*

To investigate the effect of APR on the composition of organic matter in HTC liquid, LC-MS characterization of the hydrochar under APR was performed, as shown in Fig. 12. The organic compounds detected were categorized into organic acids, hydrocarbons, amides, N-heterocyclic compounds, esters, ketones, and aromatic compounds. Organic acids accounted for a high proportion of the organic components, which explains the acidic nature of the HTC liquid [23]. These acids originated from three main sources: first, the hydrolysis of cellulose into small-molecular sugars followed by their decomposition and oxidation into organic acids; second, the decarboxylation and oxidation of lauric acid producing volatile fatty acids; and third, organic acids generated via decarboxylation of glutamic acid. With the increasing recirculation, organic acids participated in further reactions or were oxidized, leading to a rebound in pH [8]. This was consistent with the enhanced degree of aromatization observed in hydrochar. The increase in N-heterocyclic compounds was attributable to the further dehydration of Maillard reaction products [51]. Owing to the high content of glutamic acid in the feedstock, the amount of amides resulting from its hydrolysis also gradually increased with recirculation. The relative content of esters decreased, likely due to their participation in condensation reactions, which generated aromatic clusters and N-heterocyclic compounds, resulting in an increase in aromatic content. The decline in the relative content of hydrocarbons can be attributed to their participation in the Maillard reaction with glutamic acid, as well as their oxidation into organic acids and other compounds.

4. Conclusions

This study investigated the effects of reaction temperature, reaction time, and APR on properties of hydrochar and HTC liquid during the HTC of model compounds of municipal sludge (glutamic acid, lauric acid, and cellulose). The following conclusions can be drawn:

1) Increasing severity of reaction conditions significantly promoted the formation and transformation of organic acids and nitrogen, resulting in decreased COD, TOC and TN in aqueous phase, along with elevated pH and NH_3-N value. The hydrochar exhibited an overall decrease in the N/C ratio and yield. The O/C ratio first increased and then decreased.

2) APR increased the abundance of O-containing functional groups on the hydrochar surface, promoted the formation of N-heterocyclic and aromatic compounds, and facilitated the conversion of nitrogen into more stable forms, namely pyridinic-N and quaternary-N. The N/C ratio increased while the hydrochar yield and the O/C ratio decreased. The results indicate that recirculation enhanced the hydrolysis, decarboxylation, and deamination of the feedstock, as well as the repolymerization of intermediate products, thereby endowing the hydrochar with improved potential as a functional carbon-based material.

3) APR exerted an enrichment effect on substances in HTC liquid, leading to a gradual increase in pH and elevated levels of NH_3-N, TN, COD and TOC. The content of organic acids decreased, while the amounts of N-heterocyclic compounds and amides increased. These changes indicate that recirculation promoted aromatization and Maillard reactions among intermediate products, thereby enhancing the potential utilization value of the HTC liquid as a carbon source.

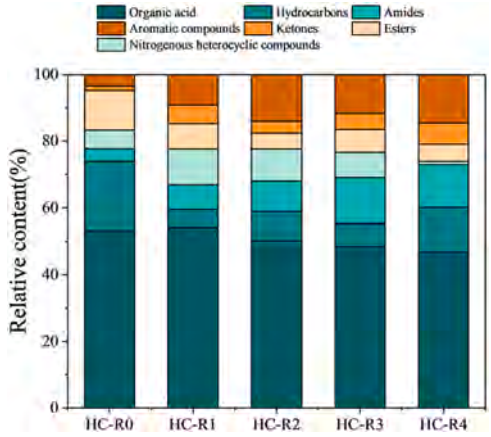


Fig. 12. Compounds identified in the hydrothermal carbonization liquid under aqueous phase recycling of model compounds of municipal sludge.

CRediT authorship contribution statement

Yiming Feng: Validation, Data curation, Conceptualization. **Xueling Hu:** Writing – review & editing, Validation. **Yuyang Xue:** Writing – original draft, Methodology, Investigation, Formal analysis. **Xingying Tang:** Writing – review & editing, Validation, Project administration, Investigation, Funding acquisition. **Donghai Xu:** Validation, Supervision. **Yingying Zhang:** Writing – review & editing, Validation. **Yumeng Wu:** Writing – review & editing, Visualization.

Declaration of Competing Interest

The authors declare that they have no known competing financial interests or personal relationships that could have appeared to influence the work reported in this paper.

Acknowledgment

The authors gratefully·acknowledge the financial support from the General Program of Guangxi Natural Science Foundation (No.2025GXNSFAA069823). Xing-ying Tang reports financial support was provided by the General Program of Guangxi Natural Science Foundation (No. 2025GXNSFAA069823) and the Guangxi Science and Technology Major Program (No. AA22117014).

Data availability

Data will be made available on request.

References

[1] N. Kossińska, A. Grosser, M. Kwapińska, W. Kwapiński, H. Ghazal, H. Jouhara, R. Krzyżyńska, Co-hydrothermal carbonization as a potential method of utilising digested sludge and screenings from wastewater treatment plants towards energy application, Energy 299 (2024) 131456.
[2] G. Zhen, X. Lu, H. Kato, Y. Zhao, Y.-Y. Li, Overview of pretreatment strategies for enhancing sewage sludge disintegration and subsequent anaerobic digestion: Current advances, full-scale application and future perspectives, Renew. Sustain. Energy Rev. 69 (2017) 559–577.
[3] P. Verlicchi, E. Zambello, Pharmaceuticals and personal care products in untreated and treated sewage sludge: occurrence and environmental risk in the case of application on soil—a critical review, Sci. Total Environ. 538 (2015) 750–767.
[4] A. Picone, M. Volpe, F. Codignole Lùz, W. Malik, R. Volpe, A. Messineo, Co-hydrothermal carbonization with process water recirculation as a valuable strategy to enhance hydrochar recovery with high energy efficiency, Waste Manag. 175 (2024) 101–109, https://doi.org/10.1016/j.wasman.2024.01.002.
[5] J. Watson, T. Wang, B. Si, W.-T. Chen, A. Aierzhati, Y. Zhang, Valorization of hydrothermal liquefaction aqueous phase: pathways towards commercial viability, Prog. Energy Combust. Sci. 77 (2020) 100819.

[6] Z.-X. Xu, X.-Q. Deng, S. Zhang, Y.-F. Shen, Y.-Q. Shan, Z.-M. Zhang, R. Luque, P.-G. Duan, X. Hu, Benign-by-design N-doped carbonaceous materials obtained from the hydrothermal carbonization of sewage sludge for supercapacitor applications, Green. Chem. 22 (2020) 3885–3895, https://doi.org/10.1039/D0GC01272F.
[7] K. Czerwińska, A. Marszałek, E. Kudlek, M. Śliz, M. Dudziak, M. Wilk, The treatment of post-processing liquid from the hydrothermal carbonization of sewage sludge, Sci. Total Environ. 885 (2023) 163858, https://doi.org/10.1016/j.scitotenv.2023.163858.
[8] S. Leng, L. Leng, L. Chen, J. Chen, J. Chen, W. Zhou, The effect of aqueous phase recirculation on hydrothermal liquefaction/carbonization of biomass: a review, Bioresour. Technol. 318 (2020) 124081.
[9] K. Mehrez, L. Fryda, H. Djelal, M. Mercier, H. Wray, A. Kane, N. Leblanc, R. Visser, Hydrothermal treatment of contaminated sorghum: hydrochar properties and characterization/phytotoxicity evaluation of the liquid phase, J. Environ. Chem. Eng. 13 (2025) 117710, https://doi.org/10.1016/j.jece.2025.117710.
[10] Z.-X. Xu, H. Song, P.-J. Li, Z.-X. He, Q. Wang, K. Wang, P.-G. Duan, Hydrothermal carbonization of sewage sludge: effect of aqueous phase recycling, Chem. Eng. J. 387 (2020) 123410, https://doi.org/10.1016/j.cej.2019.123410.
[11] H. Song, T. Yang, B. Li, Y. Tong, R. Li, Hydrothermal liquefaction of sewage sludge into biocrude: Effect of aqueous phase recycling on energy recovery and pollution mitigation, Water Res. 226 (2022) 119278, https://doi.org/10.1016/j.watres.2022.119278.
[12] Y.Z. Belete, S. Leu, S. Boussiba, B. Zorin, C. Posten, L. Thomsen, S. Wang, A. Gross, R. Bernstein, Characterization and utilization of hydrothermal carbonization aqueous phase as nutrient source for microalgal growth, Bioresour. Technol. 290 (2019) 121758, https://doi.org/10.1016/j.biortech.2019.121758.
[13] L. Leng, L. Yang, S. Leng, W. Zhang, Y. Zhou, H. Peng, H. Li, Y. Hu, S. Jiang, H. Li, A review on nitrogen transformation in hydrochar during hydrothermal carbonization of biomass containing nitrogen, Sci. Total Environ. 756 (2021) 143679.
[14] Y. Xiao, A. Leghari, L. Liu, F. Yu, M. Gao, L. Ding, Y. Yang, X. Chen, X. Yan, F. Wang, Effect of aqueous phase recycling on iron evolution and environmental assessment during hydrothermal carbonization of dyeing sludge, Fuel 356 (2024) 129477.
[15] J. Wang, Y. Wang, F. Yu, J. Wang, X. Wang, J. Luo, C. He, X. Cui, B. Yan, G. Chen, Efficient reclamation of phosphorus from wetland biomass waste via liquid-recirculated hydrothermal carbonization and precipitation, Water Res. 265 (2024) 122278.
[16] L. Ding, M. Yang, C. Areeprasert, X. Cheng, X. Chen, F. Wang, G. Yu, Analysis of micro-particle effect and methanogenic potential of food waste model compounds by hydrothermal pretreatment, Fuel 331 (2023) 125686.
[17] C. Peng, Y. Zhai, A. Hornung, B. Wang, S. Li, T. Wang, C. Li, Y. Zhu, In-depth comparison of morphology, microstructure, and pathway of char derived from sewage sludge and relevant model compounds, Waste Manag. 102 (2020) 432–440.
[18] C. Zhang, X. Ma, T. Huang, Y. Zhou, Y. Tian, Co-hydrothermal carbonization of water hyacinth and polyvinyl chloride: Optimization of process parameters and characterization of hydrochar, Bioresour. Technol. 314 (2020) 123676.
[19] X. Liu, Y. Zhai, S. Li, Q. Niu, X. Liu, Z. Wang, Y. Liu, Z. Qiu, C. Li, Y. Zhu, Hydrothermal carbonization of petrochemical sludge: The fate of hydrochar and oil components, J. Environ. Chem. Eng. 10 (2022) 108234.
[20] Q. Wang, S. Wu, D. Cui, H. Zhou, D. Wu, S. Pan, F. Xu, Z. Wang, Co-hydrothermal carbonization of organic solid wastes to hydrochar as potential fuel: a review, Sci. Total Environ. 850 (2022) 158034.
[21] R. Wang, K. Lin, D. Ren, P. Peng, Z. Zhao, Q. Yin, P. Gao, Energy conversion performance in co-hydrothermal carbonization of sewage sludge and pinewood sawdust coupling with anaerobic digestion of the produced wastewater, Sci. Total Environ. 803 (2022) 149964.
[22] Y. Wang, Y. Yu, H. Huang, C. Yu, H. Fang, C. Zhou, X. Yin, W. Chen, X. Guo, Efficient conversion of sewage sludge into hydrochar by microwave-assisted hydrothermal carbonization, Sci. Total Environ. 803 (2022) 149874.
[23] T. Liu, H. Jiao, L. Yang, W. Zhang, Y. Hu, Y. Guo, L. Yang, S. Leng, J. Chen, J. Chen, H. Peng, L. Leng, W. Zhou, Co-hydrothermal carbonization of cellulose, hemicellulose, and protein with aqueous phase recirculation: Insight into the reaction mechanisms on hydrochar formation, Energy 251 (2022) 123965, https://doi.org/10.1016/j.energy.2022.123965.
[24] P. Gao, Y. Zhou, F. Meng, Y. Zhang, Z. Liu, W. Zhang, G. Xue, Preparation and characterization of hydrochar from waste eucalyptus bark by hydrothermal carbonization, Energy 97 (2016) 238–245.
[25] S. Wu, Q. Wang, M. Fang, D. Wu, D. Cui, S. Pan, J. Bai, F. Xu, Z. Wang, Hydrothermal carbonization of food waste for sustainable biofuel production: Advancements, challenges, and future prospects, Sci. Total Environ. 897 (2023) 165327, https://doi.org/10.1016/j.scitotenv.2023.165327.
[26] M.S. Santana, R.P. Alves, W.M. da Silva Borges, E. Francisquini, M.C. Guerreiro, Hydrochar production from defective coffee beans by hydrothermal carbonization, Bioresour. Technol. 300 (2020) 122653.
[27] L. Suárez, I. Benavente-Ferraces, C. Plaza, S. de Pascual-Teresa, I. Suárez-Ruiz, T. A. Centeno, Hydrothermal carbonization as a sustainable strategy for integral valorisation of apple waste, Bioresour. Technol. 309 (2020) 123395.
[28] A. Picone, M. Volpe, M.G. Giustra, G. Di Bella, A. Messineo, Hydrothermal carbonization of lemon peel waste: Preliminary results on the effects of temperature during process water recirculation, Appl. Syst. Innov. 4 (2021) 19.
[29] K. Fakkaew, T. Koottatep, C. Polprasert, Faecal sludge treatment and utilization by hydrothermal carbonization, J. Environ. Manag. 216 (2018) 421–426.
[30] M. Cavali, H. Benbelkacem, B. Kim, R. Bayard, N.L. Junior, D.G. Domingos, A. L. Woiciechowski, A.B. de Castilhos Junior, Co-hydrothermal carbonization of pine residual sawdust and non-dewatered sewage sludge–effect of reaction conditions on hydrochar characteristics, J. Environ. Manag. 340 (2023) 117994.
[31] J. Zhang, L. Zhang, C. Lin, C. Wang, P. Zhao, Y. Li, Co-hydrothermal carbonization of polyvinyl chloride and lignocellulose biomasses: Influence of biomass feedstock on fuel properties and combustion behaviors, Sci. Total Environ. 868 (2023) 161532.
[32] H. Wang, Y. Xue, D. Hou, Y. Lu, F. Yang, C. Liu, X. Lin, C. Liu, Z. Zheng, Y. Zheng, Hydrothermal co-carbonization of medium-density fiberboard with N-rich compounds to produce N-containing compounds and N-doped biochar: product distribution, nitrogen transformation pathway and electrochemical performance, Fuel 381 (2025) 133584.
[33] R. Wang, Z. Lin, S. Meng, S. Liu, Z. Zhao, C. Wang, Q. Yin, Effect of lignocellulosic components on the hydrothermal carbonization reaction pathway and product properties of protein, Energy 259 (2022) 125063, https://doi.org/10.1016/j.energy.2022.125063.
[34] Y. Xu, B. Wang, S. Ding, M. Zhao, Y. Ji, W. Xie, Z. Feng, Y. Feng, Hydrothermal carbonization of kitchen waste: An analysis of solid and aqueous products and the application of hydrochar to paddy soil, Sci. Total Environ. 850 (2022) 157953.
[35] X. Zhang, R. Huang, Y. Cao, C. Wang, Rapid conversion of red mud into soil matrix by co-hydrothermal carbonization with biomass wastes, J. Environ. Chem. Eng. 9 (2021) 106039.
[36] W. Dominik, A. Pablo, H. Sonja, C. Fernando, F. Luca, K. Andrea, Process water recirculation during hydrothermal carbonization as a promising process step towards the production of nitrogen-doped carbonaceous materials, Waste Biomass. Valoriz. 13 (2022) 2349–2373.
[37] X. Yang, B. Wang, X. Song, F. Cheng, Evolution characteristics and mechanism of carbon structure during co-hydrothermal carbonization of sewage sludge and sub-bituminous coal, J. Clean. Prod. 434 (2024) 140382.
[38] H. Dang, R. Xu, J. Zhang, M. Wang, K. Xu, Hydrothermal carbonization of waste furniture for clean blast furnace fuel production: physicochemical, gasification characteristics and conversion mechanism investigation, Chem. Eng. J. 469 (2023) 143980.
[39] X. Yang, B. Wang, X. Song, F. Yang, F. Cheng, Co-hydrothermal carbonization of sewage sludge and coal slime with sulfuric acid for N, S doped hydrochar, J. Clean. Prod. 354 (2022) 131615, https://doi.org/10.1016/j.jclepro.2022.131615.
[40] J. Wang, B. Zhang, Q. Xu, W. Zuo, H. Zhou, S. Wu, Z. Xu, J. Fang, Y. Huang, H. Zhang, Enhancing nitrogen removal from sludge-derived hydrochar via hydrothermal carbonization fortified with advanced oxidation process pretreatment, J. Anal. Appl. Pyrolysis 174 (2023) 106132, https://doi.org/10.1016/j.jaap.2023.106132.
[41] Z.-X. Xu, R. Dou, F. Gao, Y.-X. Chen, L.-J. Leng, S.M. Osman, R. Luque, Bio-adhesives derived from sewage sludge via hydrothermal carbonization: Influence of aqueous phase recycling, Chem. Eng. J. 490 (2024) 151685.
[42] Z.-X. Xu, X.-Q. Ma, J. Zhou, P.-G. Duan, W.-Y. Zhou, A. Ahmad, R. Luque, The influence of key reactions during hydrothermal carbonization of sewage sludge on aqueous phase properties: A review, J. Anal. Appl. Pyrolysis 167 (2022) 105678.
[43] D. Ilanidis, S. Stagge, L.J. Jönsson, C. Martín, Hydrothermal pretreatment of wheat straw: Effects of temperature and acidity on byproduct formation and inhibition of enzymatic hydrolysis and ethanolic fermentation, Agronomy 11 (2021) 487.
[44] D. Cui, B. Zhang, S. Wu, X. Xu, B. Liu, Q. Wang, X. Zhang, J. Zhang, From sewage sludge and lignocellulose to hydrochar by co-hydrothermal carbonization: mechanism and combustion characteristics, Energy 305 (2024) 132414, https://doi.org/10.1016/j.energy.2024.132414.
[45] J. Wang, L. Zhang, J. Weng, J. Wei, D. Xu, B. Li, S. Zhang, M. Gholizadeh, E. Silva Lora, H. Zhang, Retention and transformation of nitrogen in hydrochars from co-hydrothermal carbonization of fiberboard and glucose, Fuel 352 (2023) 129023, https://doi.org/10.1016/j.fuel.2023.129023.
[46] J. Wang, X. Peng, X. Chen, X. Ma, Co-liquefaction of low-lipid microalgae and starch-rich biomass waste: The interaction effect on product distribution and composition, J. Anal. Appl. Pyrolysis 139 (2019) 250–257, https://doi.org/10.1016/j.jaap.2019.02.013.
[47] S. Leng, W. Li, C. Han, L. Chen, J. Chen, L. Fan, Q. Lu, J. Li, L. Leng, W. Zhou, Aqueous phase recirculation during hydrothermal carbonization of microalgae and soybean straw: a comparison study, Bioresour. Technol. 298 (2020) 122502.
[48] X. Ning, H. Teng, G. Wang, J. Zhang, N. Zhang, C. Huang, C. Wang, Physiochemical, structural and combustion properties of hydrochar obtained by hydrothermal carbonization of waste polyvinyl chloride, Fuel 270 (2020) 117526.
[49] T. Liu, Y. Guo, N. Peng, Q. Lang, Y. Xia, C. Gai, Z. Liu, Nitrogen transformation among char, tar and gas during pyrolysis of sewage sludge and corresponding hydrochar, J. Anal. Appl. Pyrolysis 126 (2017) 298–306, https://doi.org/10.1016/j.jaap.2017.05.017.
[50] T. Wang, Y. Zhai, Y. Zhu, C. Li, G. Zeng, A review of the hydrothermal carbonization of biomass waste for hydrochar formation: Process conditions, fundamentals, and physicochemical properties, Renew. Sustain. Energy Rev. 90 (2018) 223–247.
[51] C. Zhang, X. Ma, C. Zheng, T. Huang, X. Lu, Y. Tian, Co-hydrothermal carbonization of water hyacinth and sewage sludge: effects of aqueous phase recirculation on the characteristics of hydrochar, Energy Fuels 34 (2020) 14147–14158.

Corrosion Science 258 (2026) 113397

Contents lists available at ScienceDirect

Corrosion Science

journal homepage: www.elsevier.com/locate/corsci

A novel phosphorus segregation–driven chromium depletion mechanism for intergranular corrosion of inconel 625 in SCWO–HyMoS environments

Ke Li [a,b], Jiquan Chen [a,b], Guiyuan Xie [b], Xingying Tang [b,*], Donghai Xu [c], Jianqiao Yang [c]

[a] School of Resources, Environment, and Materials, Guangxi University, Nanning 530004, China
[b] Guangxi Laboratory on the Study of Coral Reefs in the South China Sea, Coral Reef Research Center of China, School of Marine Sciences, Guangxi University, Nanning 530004, China
[c] School of Energy and Power Engineering, Xi'an Jiaotong University, Xi'an 710049, China

ARTICLE INFO

Keywords:
Supercritical water oxidation
Inconel 625
Hydrothermal molten salt corrosion

ABSTRACT

This study investigated the intergranular corrosion (IGC) behavior of Inconel 625 sensitized at different temperatures (600–800°C) in supercritical water (SCW) environments containing phosphate-based hydrothermal molten salts (HyMoS). The results reveal that the IGC is driven by a dynamic chromium-depletion process induced by phosphorus segregation, which differs from the classical carbide-precipitation-induced chromium depletion theory. In addition, grain-boundary precipitates formed at 800 °C, such as MoNbP, further intensified the corrosion.

1. Introduction

Supercritical water oxidation (SCWO) is a treatment technology that exploits the unique thermophysical properties of supercritical water to efficiently and thoroughly remove organic pollutants [1–6]. However, its large-scale application still faces significant challenges. In high-concentration wastewater, the solubility of inorganic salts and their neutralization products in supercritical water is extremely low, leading to precipitation and scaling, which can result in channel blockages and local overheating [7–17]. Salt deposits, or the high local ion concentrations beneath them, can further exacerbate severe localized corrosion, posing a substantial threat to the long-term safe operation of SCWO systems [18–21]. To mitigate salt deposition and clogging, the HyMoS technique has been proposed [22–25]. This approach employs inorganic salts such as Na_2HPO_4, which has a melting point of 245°C below water's critical temperature [26,27], upon reaching saturation in supercritical water, these salts melt into fluid droplets with increasing temperature, enabling liquid-state transport and preventing blockages from solid deposition.

While the HyMoS strategy effectively alleviates salt deposition and clogging, it introduces new material challenges: the corrosion behavior of structural materials in contact with molten HyMoS remains unclear. Inconel 625 is widely used in SCWO reactors and other critical equipment due to its excellent high-temperature strength, oxidation resistance, corrosion resistance, and good machinability [28,29]. Our previous studies unexpectedly revealed that even in SCW environments rich in phosphate-based HyMoS, the corrosion-resistant Inconel 625 exhibits pronounced intergranular corrosion (IGC) susceptibility [30,31]. This selective attack along grain boundaries significantly weakens intergranular cohesion, markedly reducing the mechanical integrity and overall corrosion resistance of the alloy, thereby posing serious risks to SCWO system safety [32].

Current studies on SCWO systems containing phosphates indicate a dual role of phosphate ions [33]: at low concentrations, they may form protective films, whereas at high concentrations, corrosion is exacerbated. Existing studies have demonstrated that high phosphate concentrations can disrupt the Cr(III) protective layer, facilitating the formation of phosphate-containing products within the oxide film of the alloy [34,35]. In systems containing Cl^-, SO_4^{2-}, and PO_4^{3-}, eutectic salts may also form, further accelerating alloy corrosion [36]. However, these studies primarily focus on dissolved ionic phosphate species and do not explicitly clarify the specific contribution of the HyMoS phase to corrosion. In our preliminary experiments under HyMoS conditions, IGC was observed even in non-sensitized Inconel 625. Spectroscopic analysis revealed carbon segregation at the grain boundaries, accompanied by notable chromium enrichment. Under the present testing conditions (400°C), it remains uncertain whether these features meet the classical criteria for intergranular carbide precipitation. The underlying

* Corresponding author.
E-mail address: tangxingying@gxu.edu.cn (X. Tang).

https://doi.org/10.1016/j.corsci.2025.113397
Received 21 August 2025; Received in revised form 4 October 2025; Accepted 6 October 2025
Available online 8 October 2025
0010-938X/© 2025 Elsevier Ltd. All rights are reserved, including those for text and data mining, AI training, and similar technologies.

mechanisms by which this unique molten HyMoS phase induces IGC, particularly in relation to conventional IGC theories—such as Cr depletion caused by carbide precipitation [37,38], second-phase formation [39], or impurity segregation at grain boundaries [40]—remain largely unexplored.

This study aims to elucidate the distinctive IGC behavior and propagation mechanisms of Inconel 625 in phosphate-rich HyMoS SCW environments, thereby clarifying the critical influence of the HyMoS phase on grain boundary stability. The key innovation of this work lies in elucidating a novel corrosion pathway induced by the HyMoS environment, which is distinct from the classical carbide precipitation theory. The findings are expected to provide essential scientific guidance for assessing material reliability in SCWO systems utilizing HyMoS technology and will serve as a theoretical foundation for developing corrosion-resistant alloys and protective strategies for such extreme environments.

2. Experiment

2.1. Experimental materials

The Inconel 625 nickel-based alloy used in this study was supplied by Shenzhen Junhang Tezhong Alloy Materials Co., Ltd. Its chemical composition (wt%) is listed in Table 1. The original billets were machined into standard specimens measuring 5 mm × 5 mm × 3 mm using wire-cutting technology. The specimens were subjected to solution treatment at 1100°C for 1 h, followed by water quenching. Subsequently, the samples underwent sensitization treatment at three temperature gradients (600°C, 700°C, and 800°C) with a holding time of 4 h at each temperature. After sensitization, the specimens were removed and allowed to cool naturally to room temperature, constituting the sensitized state samples. The treated samples were flushed with nitrogen gas inside sample bags and stored in a drying oven prior to testing.

To simulate the corrosive environment encountered during the treatment of high-concentration wastewater through SCWO technology, and to ensure the stable formation of phosphate molten salts under the experimental conditions (400°C, 25 MPa), a phosphate-containing corrosive solution with a concentration of 5000 mg/L was employed in this study.

2.2. Experimental apparatus

This experiment utilized a 316 L stainless steel high-pressure reactor with a designed volume of 20 mL, operated under a rated pressure of 30 MPa, and a maximum operating temperature of 600°C to test molten phosphate corrosion [31]. To prevent galvanic corrosion interference between the specimen and the reactor body, the system was equipped with an Inconel 625 alloy liner tube, with the specimen placed inside an independent container within it.

2.3. Molten salt corrosion test

The pretreated Inconel 625 specimens were fixed onto the alloy liner tube sample holder. The system was purged three times with high-purity nitrogen gas (99.2 %) at 0.2 MPa for 2 min, ensuring an oxygen content of less than 10 ppm and eliminating oxygen interference. Subsequently, a quantified volume of corrosion solution was injected under nitrogen protection, and the liner tube assembly was placed into the main reactor. After sealing the reactor, a second nitrogen purge was performed. The specimens were then subjected to isothermal corrosion testing at 400 °C under a pressure of 25 MPa for 100 h in a programmable temperature-controlled box resistance furnace (KSL-1700X). At the end of the predetermined reaction time, the reaction system was immediately cooled by air to prevent subcritical state effects. After cooling to room temperature, the specimens were retrieved and sequentially cleaned with deionized water and acetone using ultrasonic cleaning (40 kHz, 20 min). They were then vacuum-dried for 30 min and stored in a desiccator for further use.

Table 1
Composition of the main elements of the tested Inconel 625 alloy in wt%.

Alloy	Ni	Cr	Mo	Fe	Nb	C
Inconel 625	62.88	20.69	8.81	3.69	3.21	0.10

2.4. Electrochemical testing

Double-loop electrochemical potentiokinetic reactivation (DL-EPR) testing [41] was employed to quantitatively evaluate the degree of sensitization (DOS) of Inconel 625 to IGC. The DL-EPR tests were conducted at room temperature using a Chenhua electrochemical workstation with a three-electrode system (working electrode: Inconel 625; reference electrode: Ag/AgCl; counter electrode: Pt). The electrolyte consisted of 0.5 mol/L H_2SO_4 and 0.01 mol/L KSCN. Before testing, the specimens were embedded in epoxy resin, sequentially polished to a mirror finish, and ultrasonically cleaned with acetone. The specimens were stabilized at open circuit potential (OCP) for 30 min. Anodic polarization was performed by scanning from −0.4 V to + 0.4 V at a scan rate of 1.67 mV/s, followed by a reverse scan back to the initial potential. The DOS value was calculated using the formula DOS = (ir/ia) × 100 %, where ia and ir represent the peak current densities during the forward and reverse scans, respectively.

2.5. Analytical testing methods

Surface morphology was observed using a field emission scanning electron microscope (FE-SEM, Zeiss Sigma 300) at an accelerating voltage of 5 kV. Elemental distribution was analyzed with an Oxford EDS spectrometer (acquisition time 60 s, count rate ≥10,000 cps). IGC morphology was measured by atomic force microscopy (AFM, Bruker Dimension Icon) over scan ranges of 1–5 μm, and surface potential was characterized using scanning Kelvin probe force microscopy (SKPFM) within 5–10 μm ranges. Surface elemental valence states were analyzed by X-ray photoelectron spectroscopy (XPS, Thermo ESCALAB 250XI, Al-Kα source) with a sampling depth of 0.5–3 nm. Microstructure was observed by field emission transmission electron microscopy (TEM, JEOL JEM-F200, 200 kV). Specimens for TEM were prepared by focused ion beam (FIB, Thermo Scios 2 Dual Beam) milling.

3. Results

3.1. Electrochemical analysis

The DL-EPR method was used to quantitatively assess the IGC susceptibility of Inconel 625 alloy after sensitization treatments at 600°C, 700°C, and 800°C. Before testing, the OCP of all samples reached a stable state. As shown in Fig. 1, the DL-EPR curves of the three sensitized states indicate that the activation peak shifts to lower potentials with increasing sensitization temperature. The activation peak current density (i_a) and reactivation peak current density (i_r) were statistically analyzed, and the DOS was calculated according to the formula in Fig. 1. The i_a value initially decreased and then increased, indicating a depassivation phenomenon at 700°C sensitization; however, the overall surface activity of the alloy continued to increase. The DOS value increased significantly with increasing sensitization temperature, reaching a maximum of 43.4 % at 800°C. This value far exceeds the IGC risk threshold (DOS > 5 %), confirming a moderate to high risk of IGC for sensitized Inconel 625.

3.2. Morphology and elemental analysis

The morphological evolution of Inconel 625 sensitized at 600°C,

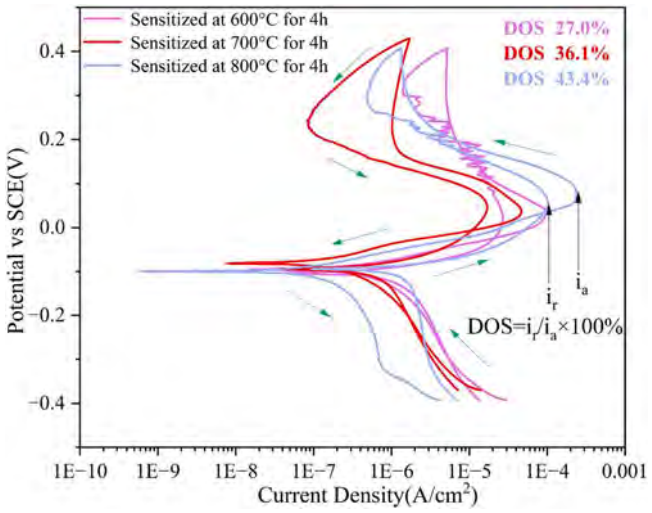


Fig. 1. DL-EPR of Inconel 625 alloy after 4 h sensitization at three sensitization temperatures.

700°C, and 800°C after 100 h of corrosion in SCW containing phosphate molten salt was analyzed by scanning electron microscopy (SEM). In the sample sensitized at 600°C (Fig. 3a), blocky oxides were observed growing along the grain boundaries, with continuous shallow grooves forming at the base of the grain boundaries, while deep penetration is absent. The matrix exhibited a lamellar stacked structure accompanied by small oxide patches. EDS surface mapping confirmed a significant chromium depletion at the grain boundaries; the blocky oxides surrounding the grain boundaries were identified as nickel oxides. Three raised oxide islands remained on the matrix surface, which, compared to the surrounding matrix height, were identified as intact inner oxides composed of Cr2O3. This protective layer effectively inhibited phosphate penetration, while phosphorus was uniformly distributed without localized accumulation. When the sensitization temperature increased to 700°C (Fig. 3b), the grain boundary width increased, and the edges exhibited a serrated morphology. EDS analysis revealed that the grain boundary aggregates consisted of Na3PO4, CrPO4, and Cr2O3, while the perforated regions were mainly composed of the Ni matrix, NiO, and Cr2O3. Under the 800°C sensitization condition (Fig. 3c), both the depth and width of the grain boundaries further increased, with more severe IGC. Adjacent to the intact oxide film, a characteristic step-like layered structure was detected, and the maximum height at the grain boundary was seen to gradually decrease towards the matrix. EDS surface mapping showed Cr-enriched zones adjacent to Cr-depleted zones at the grain boundariesas revealed by the blue dashed lines; however, no carbon enrichment was detected. This indicates that the Cr-depleted zones were not caused by conventional chromium carbide precipitation but rather resulted from continuous Cr consumption induced by phosphorus segregation [42]. This is fundamentally different from the traditional theory of intergranular corrosion [29,37,38,40]. At lower sensitization temperatures, less Cr precipitated and was directly spalled off by corrosion from phosphate molten salt. At higher sensitization temperatures, where chromium precipitation increases, the precipitates can react with phosphate molten salts deposited at grain boundaries to form CrPO4. With continuous segregation and attack by the phosphate molten salts, chromium is progressively consumed, leading to the development of chromium-depleted zones. In other words, phosphate molten salt induces a "formation-spallation cycle": Cr reacts with the molten salt to form CrPO4, which subsequently spalls, accelerating metal depletion. Residual analysis showed that the areas circled in yellow correspond to Cr2O3, while the remaining grain boundary regions mainly consisted of a Cr2O3/CrPO4 mixture, with Ni present primarily in the same regions.

3.3. AFM analysis

To quantify the effect of sensitization temperature on the depth of IGC, AFM was employed to characterize the three-dimensional morphology of Inconel 625 after 100 h of corrosion in SCW containing phosphate molten salt (Fig. 3). In the 600°C sensitized sample (Fig. 3a), AFM revealed protrusions approximately 650 nm in height, corresponding to the $NiO/NiCr_2O_4/FeCr_2O_4$ spinel oxides observed at the grain boundaries in the SEM image (Fig. 2a). Localized corrosion pits reached depths of up to 300 nm, with an overall surface height variation of 800 nm. When the sensitization temperature increased to 700°C (Fig. 3b), the grain boundary corrosion depth stabilized at approximately 210 nm, while the corrosion length extended to 600 nm, and spot-like phosphate deposits were scattered across the surface. Under the 800°C sensitization condition (Fig. 3c), the corrosion depth remained at 210 nm but spread across the entire grain boundary length. This morphological evolution is entirely consistent with SEM observations. These AFM results collectively confirm the strong corrosive capability of phosphate molten salt in SCW environments and demonstrate that IGC susceptibility significantly increases with sensitization temperature. This temperature dependence originates from dynamic changes in the corrosion mechanism. At 600°C, sensitization, accompanied by limited carbide precipitation, failed to form a continuous chromium-depleted zone. XPS and EDS detected residual Cr_2O_3 oxide islands, which effectively impeded the penetration of phosphate molten salt into the matrix [43]. However, with increasing sensitization temperature, Cr enrichment at the grain boundaries was eroded by molten salt, resulting in Cr loss. Under the drive of concentration gradients, chromium is continuously transported from the matrix interior to the grain boundaries. This leads to chromium depletion around the grain boundaries and impedes the formation of stable Cr_2O_3 films, thereby triggering an autocatalytic corrosive cycle: The protection offered by the oxide layer is weakened by Cr depletion, resulting in the accelerated dissolution of Ni and Cr elements. The penetration of phosphate molten salt is subsequently enhanced, ultimately resulting in the expansion of both the width and depth of grain boundary corrosion.

3.4. XPS analysis

Fig. 4 presents representative XPS spectra of Inconel 625 samples exposed for 100 h in SCW containing phosphate molten salts at different sensitization temperatures (600°C, 700°C, and 800°C).

In the Ni $2p_{3/2}$ spectra, three central components were identified with binding energies of 852.1 ± 0.4 eV, 855.8 ± 0.2 eV, and 861.8 ± 0.4 eV, which, according to the NIST database and previously published data, correspond to metallic Ni, $Ni(OH)_2$, and NiO, respectively [44]. The Cr $2p_{3/2}$ spectra exhibited four peaks with binding energies of 574.2 ± 0.3 eV, 576.2 ± 0.3 eV, 577.8 ± 0.5 eV, and 579.2 ± 0.4 eV, assigned to metallic Cr, Cr_2O_3, Cr^{3+}, and Cr^{6+}[48], respectively. At 800°C, grain boundary chromium depletion was exacerbated, metallic Cr gradually disappeared, and the oxidation states shifted from Cr_2O_3 and Cr^{6+} toward the more stable $Cr^{3+}/CrPO_4$.

3.5. TEM analysis

To characterize the nanoscale grain boundaries, TEM combined with EDS was used to examine the nanoscale grain boundary evolution of samples sensitized at 600°C, 700°C, and 800°C after 100 h of corrosion in SCW.

The sample sensitized at 600°C formed a single-layer oxide film approximately 810 nm thick (Fig. 5a), exhibiting a straightforward interface but lacking the typical bilayer structure observed in conventional SCWO [34,35], namely an outer NiO/Fe_2O_3 layer and an inner Cr_2O_3 layer. The film surface was covered by an approximately 200 nm thick phosphate corrosion layer, indicating selective dissolution of the outer oxide by the phosphate molten salt. The grain boundary region

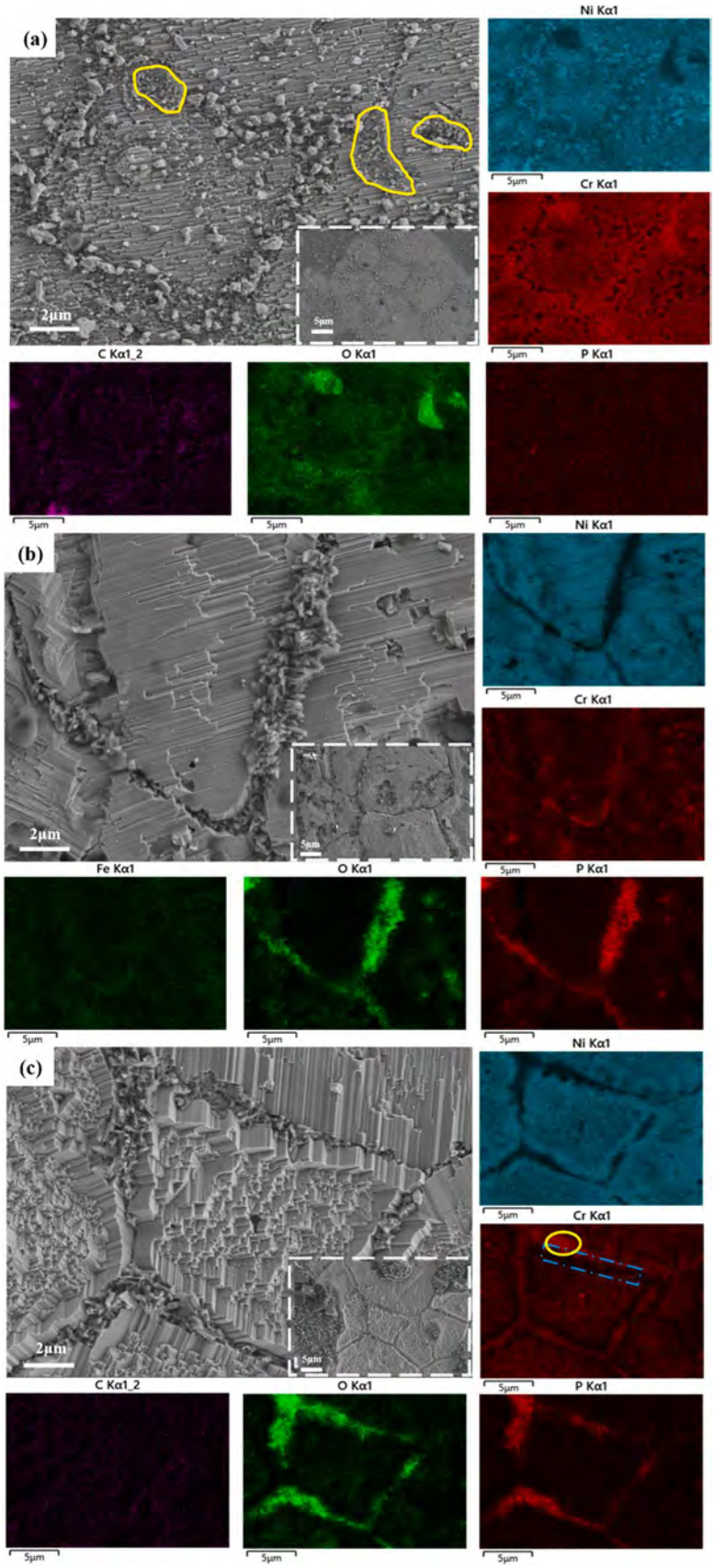


Fig. 2. SEM and EDS mapping of IGC of Inconel 625 at different sensitization states after 100 h exposure in SCW containing phosphate molten salts: (a) 600℃; (b) 700℃; (c) 800℃.

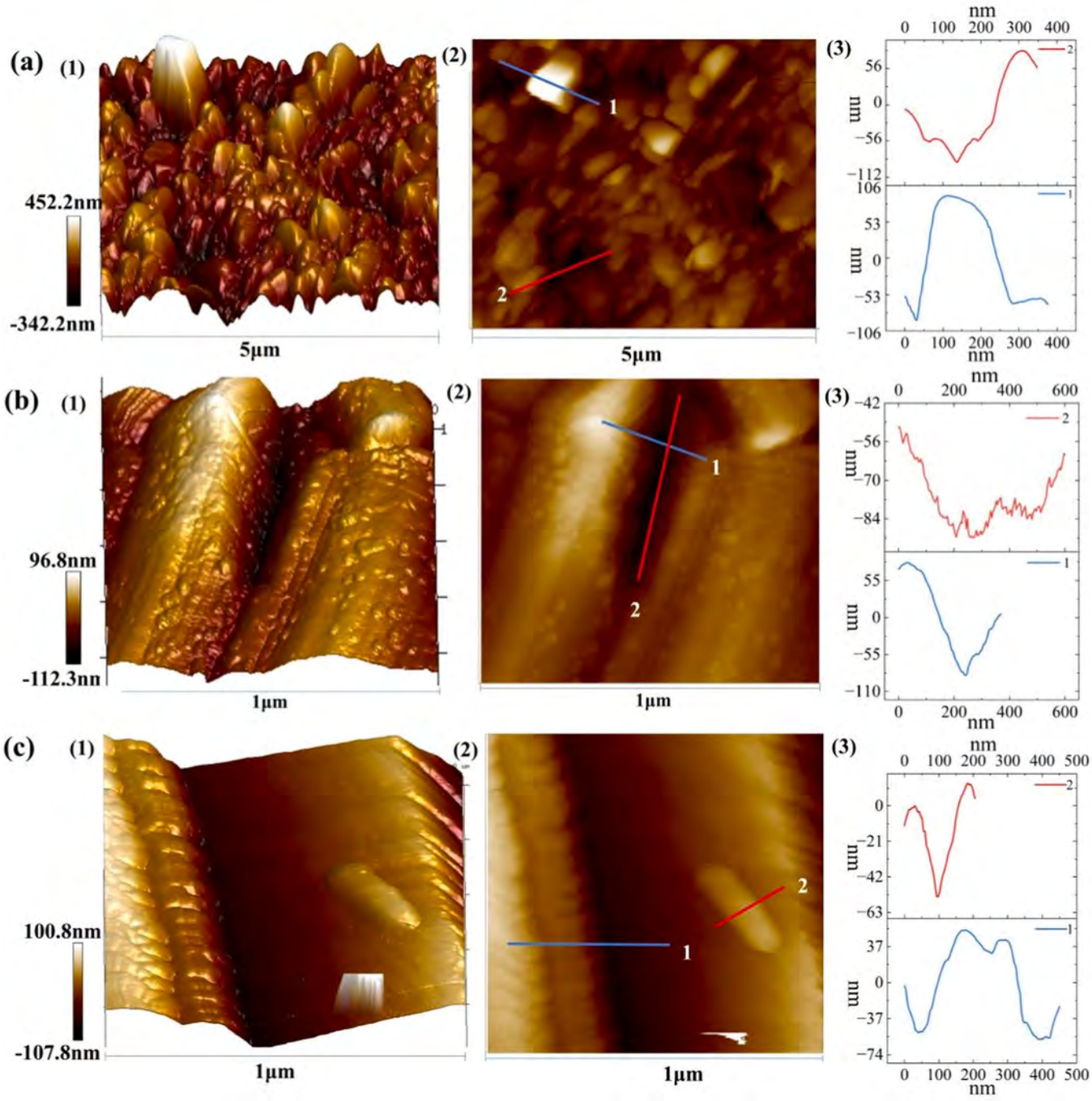


Fig. 3. AFM of three sensitized Inconel 625 samples after reaction in phosphate-containing molten salt SCW for 100 h: (A) Sensitized at 600℃ for 4 h; (B) Sensitization at 700℃ for 4 h; (C) Sensitization at 800℃ for 4 h; (1) Surface topography; (2) Height difference map; (3) (2) Height diagram corresponding to the two lines.

was clean, showing no signs of carbide precipitation or nucleation (Fig. 5b), which fundamentally contradicts the traditional chromium depletion mechanism caused by carbide precipitation [37,38]. Atomic-scale high-resolution TEM, combined with inverse FFT analysis, measured lattice fringe spacings of 0.16 nm and 0.09 nm longitudinally; these low spacing values are directly associated with low susceptibility to IGC [50]. Selected area electron diffraction (SAED) confirmed the presence of only the matrix phase (PDF#70–1849, (200) plane) (Fig. 5b). EDS mapping (Fig. 5e) further revealed that there was no grain boundary segregation of Cr or C, while phosphorus diffused along the grain boundaries, forming rapid corrosion channels. Additionally, Ni enrichment at dislocation sites suggested a risk of σ phase nucleation. These results indicate that IGC in this environment is dominated by phosphorus diffusion rather than carbide precipitation.

The oxide film on the sample sensitized at 700°C thickened to 3.0 μm and developed a differentiated inner and outer layer structure (Fig. 6a). Cross-sectional observation revealed a phosphate corrosion layer approximately 450 nm thick, with its deposition initiating several tens to hundreds of nanometers below the matrix interface. Multiple cracks appeared at the grain boundary base, indicating a risk of stress corrosion cracking. HRTEM analysis revealed an increase in the lattice spacing to 0.17 nm (Fig. 6c), which directly correlates with elevated IGC susceptibility [45]. However, no carbide or secondary phase precipitates were observed at the grain boundaries (Fig. 6b). SAED maintained the single matrix phase characteristic of the (200) plane (Fig. 6b). EDS elemental mapping (Fig. 6e) indicated a uniform distribution of Cr, C, and Ni at the

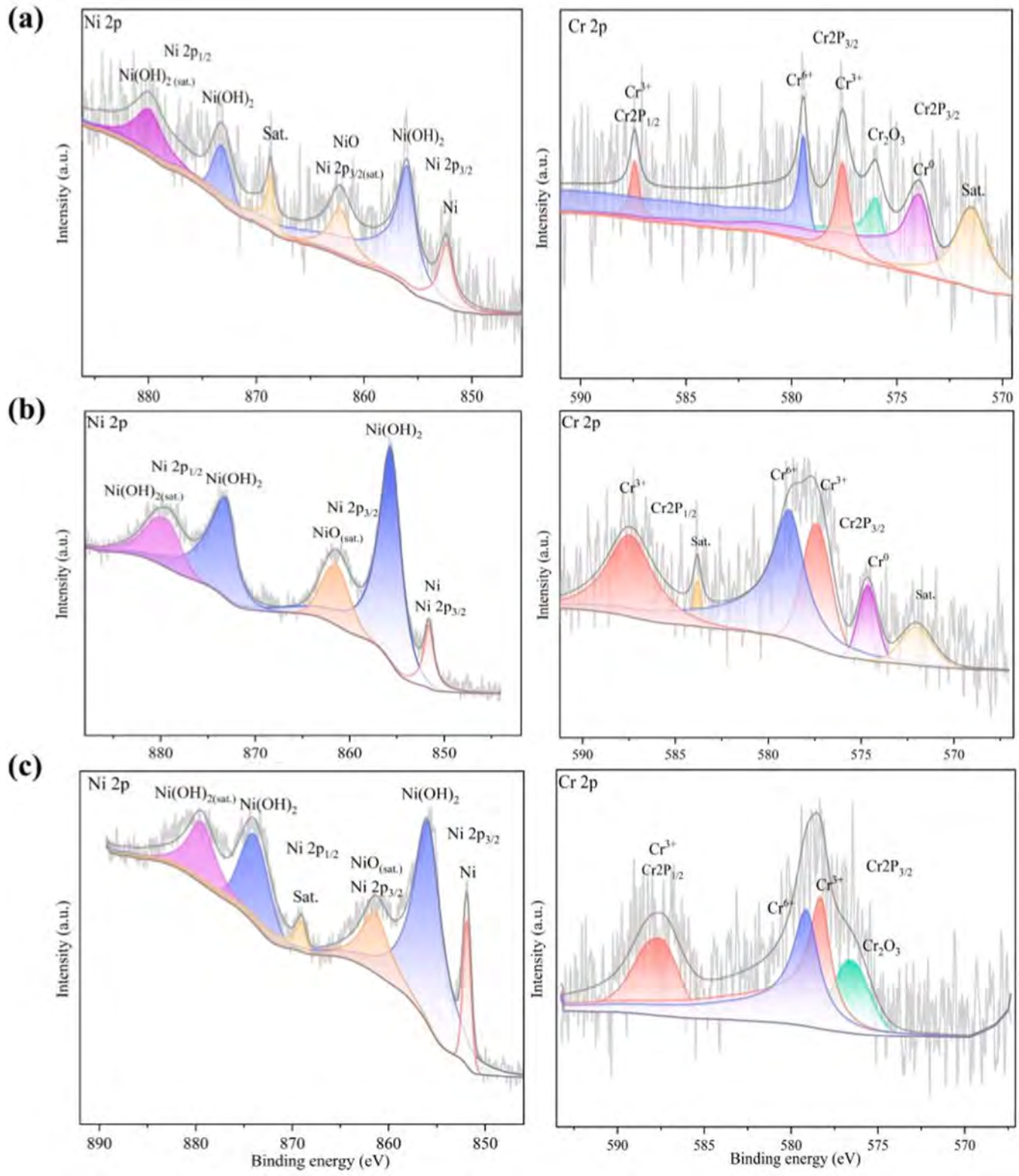


Fig. 4. Ni and Cr characteristic spectra of XPS after 100 h reaction of Inconel 625 with different sensitized states in phosphate-containing molten salt SCW: (a) sensitized at 600℃ for 4 h; (b) Sensitization at 700℃ for 4 h; (c) Sensitization at 800℃ for 4 h.

grain boundaries, contradicting the typical spectra of Cr-rich carbides [46]. However, SEM-EDS independently detected chromium-depleted zones, suggesting a Cr depletion mechanism unrelated to such a deviation from the conventional carbide theory is indicated by this observation [37,38]. Still, it is potentially consistent with reports attributing Cr depletion to Cr-C co-segregation preceding carbide nucleation [42,47].

The 800°C sensitized sample exhibited more pronounced changes: the inner oxide layer was thinned due to phosphate deep penetration along the grain boundaries (Fig. 8a), while the phosphate deposition layer thickened to 1.6 μm. Although no carbide precipitates were detected at the grain boundaries, EDS mapping (Fig. 7e) identified a second phase enriched with Mo, Nb, and P. SAED analysis confirmed this

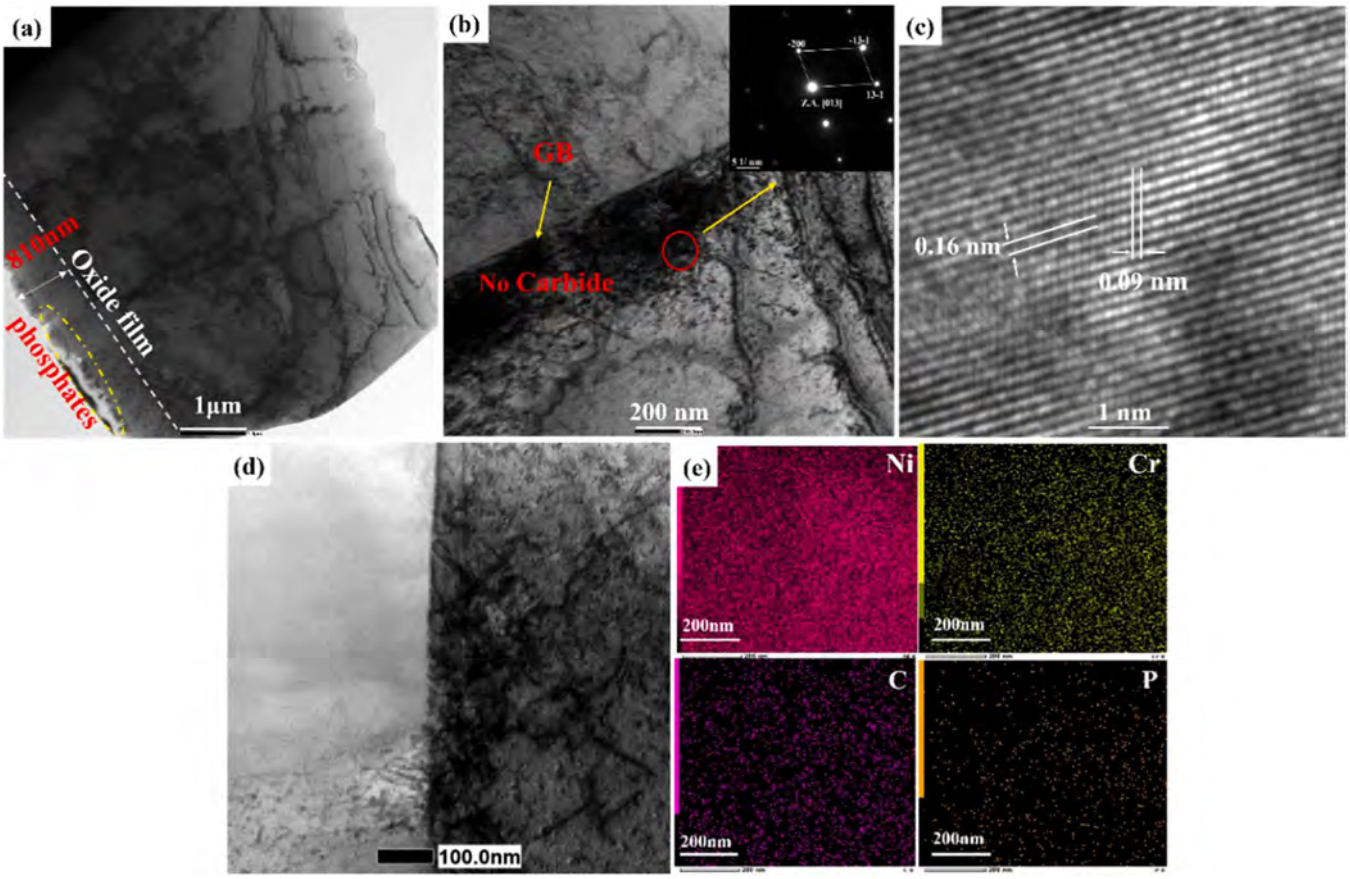


Fig. 5. TEM images of Inconel 625 sensitized at 600℃ for 4 h and corroded in phosphate-containing molten salt SCW for 100 h: (a) overall morphology; (b) bright field image of grain boundary and corresponding electron diffraction pattern; (c) inverse FFT transform image; (d) TEM image of grain boundary; (e) EDS elemental mapping of (d).

phase as a brittle intermetallic compound MoNbP, with an orthorhombic unit cell of approximately a = 5.86–6.0 Å, b = 3.18–3.3 Å, and c = 6.86–7.0 Å [48–51]. This phase was identified for the first time in a supercritical water corrosion environment. Grain boundary cohesion is reduced by this compound, thereby increasing the risk of intergranular fracture. The matrix lattice spacing further increased to 0.19 nm corresponding to the (111) plane, and the precipitate lattice spacing measured 0.23 nm corresponding to the (101) plane, confirming the presence of MoNbP [52].

Depth-resolved analysis of the phosphate deposition layer (Fig. 10) revealed a compositional gradient at the interface between the corrosion layer and the oxide layer. The yellow region was mainly composed of $CrPO_4$, $Mo_3(PO_4)_2$, and $FePO_4$, with no $Ni_3(PO_4)_2$ detected. The purple region exhibited stratification, with the upper part enriched in NiO and the lower part showing co-enrichment of P and Ni, indicating. This indicates that Ni had not been fully converted to phosphate due to its lower ionic transport rate compared to Cr, Mo, and Fe. The gray protrusions corresponded to residual oxides of Cr, Mo, and Fe. This spatial heterogeneity confirms that phosphate molten salt accelerates grain boundary degradation through three synergistic pathways: preferential dissolution of NiO and selective conversion of Cr, Mo, and Fe oxides into phosphates.

3.6. SKPFM analysis

To establish the relationship between microstructure and corrosion performance, SKPFM was employed to analyze the Volta potential distribution of the samples. Materials with higher Volta potential exhibit enhanced electrochemical inertness and superior corrosion resistance [53–55], whereas regions with lower potential are more prone to corrosion. Potential differences within the same material create micro-galvanic cells, where the lower potential zones act as anodes and preferentially dissolve [56,57] In this study, SKPFM characterization revealed that after 100 h of corrosion in SCW containing phosphate molten salt, the Volta potential difference between grain boundaries and matrix in the Inconel 625 sample sensitized at 800°C for 4 h reached approximately 50 mV (Fig. 9). Due to polishing during measurement, some surface phosphate layers were removed, so the actual potential difference is likely significantly higher, satisfying the conditions for intense galvanic corrosion. Combined with EDS detection of chromium-depleted zones and the absence of carbide precipitation observed by TEM, the results demonstrate that the galvanic corrosion between the grain boundary and the matrix aggravated the susceptibility to IGC in the phosphate-containing molten salt environment.

4. Discussion

4.1. Effect of sensitization

Sensitized Inconel 625 exhibited pronounced IGC susceptibility in DL-EPR testing. Temperature-dependent investigations further revealed that under sensitization at 600 °C, the DOS measured by DL-EPR was relatively low. The widening of grain boundary channels was limited, and chromium still retained the ability to form protective Cr2O3 oxide films locally. At 700 °C, however, the DOS value increased significantly, with corrosion evolving from isolated pits to continuous attack. The rapid diffusion of metallic elements led to the formation of an unstable and dense oxide film, while the efficient heat transfer in the SCW

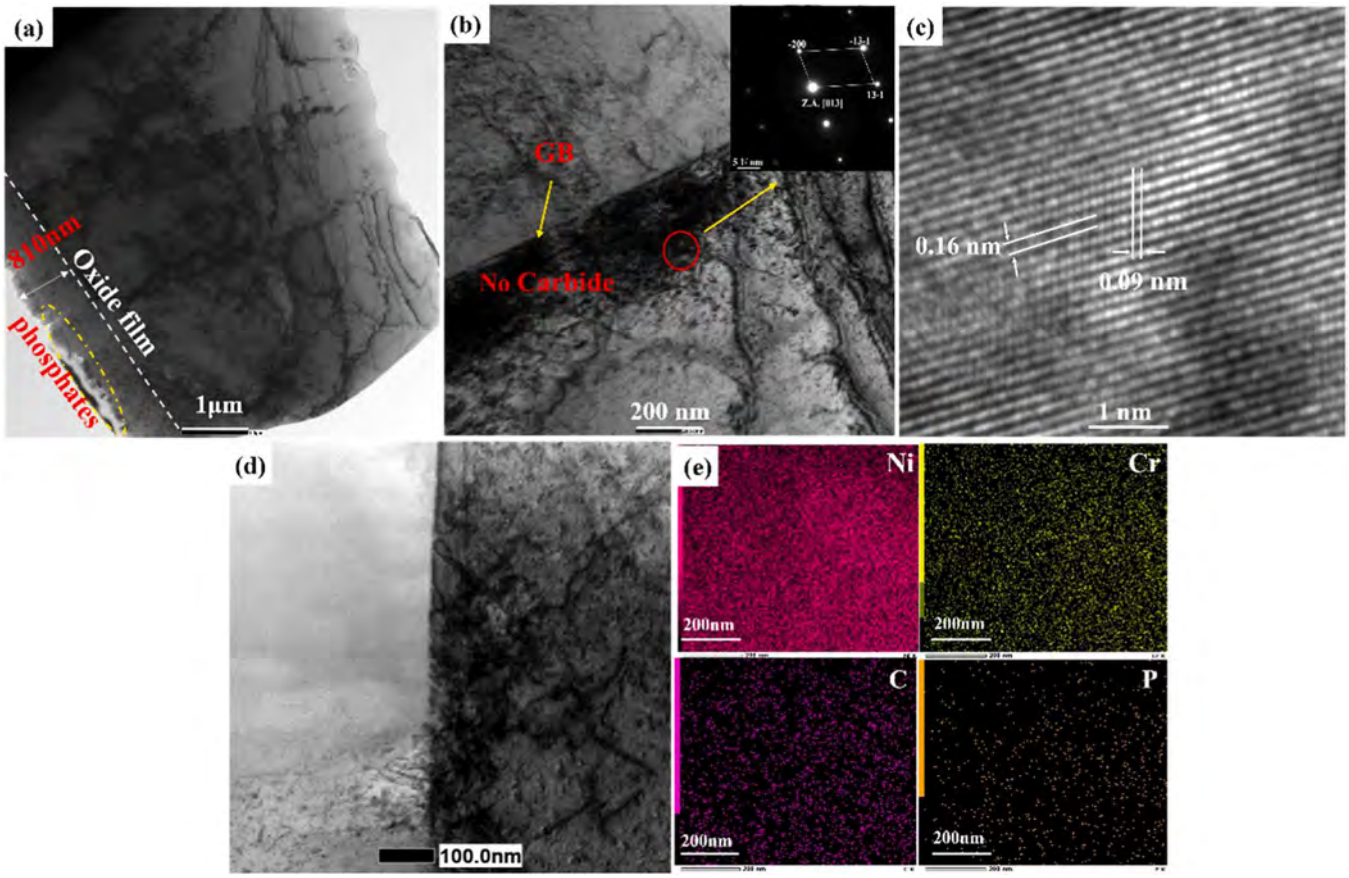


Fig. 6. TEM images of Inconel 625 sensitized at 700℃ for 4 h and corroded in phosphate-containing molten salt SCW for 100 h: (a) overall morphology; (b) bright field image of grain boundary and corresponding electron diffraction pattern; (c) inverse FFT transform image; (d) TEM image of grain boundary; (e) EDS elemental mapping of (d).

environment induced thermal stress cracking [58]. The synergistic effect of dissolution and spallation by phosphate molten salts further promoted crack propagation [59]. When the sensitization temperature increased to 800 °C, the DOS value reached as high as 43.4 %. The markedly widened grain boundary channels provided efficient pathways for elemental diffusion, accompanied by the precipitation of brittle phases, such as MoNbP, which led to severe degradation of material performance. The sensitization process, as a result, significantly activated and widened the grain boundaries, creating favorable conditions for the penetration of corrosive media and for the depletion of elements. With increasing sensitization temperature, atomic diffusivity was enhanced and intergranular mass transport accelerated, resulting in further broadening of grain boundaries. The inward penetration of corrosive PO_4^{3-}, the short-range migration of chromium toward grain boundaries, and the outward migration of nickel were consequently promoted.

4.2. *Effects of phosphorus segregation*

The results demonstrate that the IGC behavior of sensitized Inconel 625 in SCW containing phosphate molten salts is primarily driven by a dynamic dissolution-reprecipitation cycle dominated by phosphorus segregation, which deviates from the conventional chromium depletion theory caused by carbide precipitation [37,38] Although sensitization treatment initiates carbide precipitation along grain boundaries and broadens the boundary channels, these carbides are rapidly stripped away by the highly mobile phosphate molten salts, leaving behind initial erosion pathways. This process promotes substantial chromium migration and depletion along the grain boundaries, hindering the formation of a continuous protective Cr_2O_3 layer. Meanwhile, the widened boundary channels accelerate the mass transfer of Ni, Mo, and other metallic elements, resulting in the growth of an abnormally thick, yet porous and loose, oxide scale. It is noteworthy that the strong corrosivity of phosphate molten salts can directly dissolve Cr_2O_3 into Cr^{3+}, while Cr^{3+} is further converted into soluble Cr^{6+} species (CrO_4^{2-}) by the oxidative environment of SCW [60,61]. Under the combined effect of salt dissolution and mechanical flushing, Spallation occurs in the oxide scale, triggering a cyclic mechanism of "oxidation-spallation-erosion-reoxidation". This not only intensifies the progression of IGC but also accelerates general corrosion by continuously consuming key alloying elements such as Ni and Cr. Chromium from the alloy matrix migrates rapidly to the surface through the boundary channels and is transformed into soluble CrO_4^{2-}. However, the continuous flushing of molten salts establishes a dynamic "diffusion-oxidation-loss" cycle, in which the supply of chromium from the matrix cannot keep pace with the rate of oxidation and dissolution, ultimately leading to the development of pronounced chromium-depleted zones at the grain boundaries [62]. A critical finding is that no carbon enrichment was detected around the chromium-depleted zones, confirming that the underlying cause is not carbide precipitation, but rather phosphorus segregation [42]. In addition, the significant potential difference between the phosphate deposits and the alloy matrix gives rise to galvanic corrosion, which leads to a synergistic acceleration of IGC propagation.

4.3. *Effects of intergranular precipitates*

TEM analysis confirmed the absence of $Cr_{23}C_6$ or other carbide precipitates at grain boundaries in sensitized Inconel 625 exposed to SCW phosphate molten salt environment. This phenomenon is

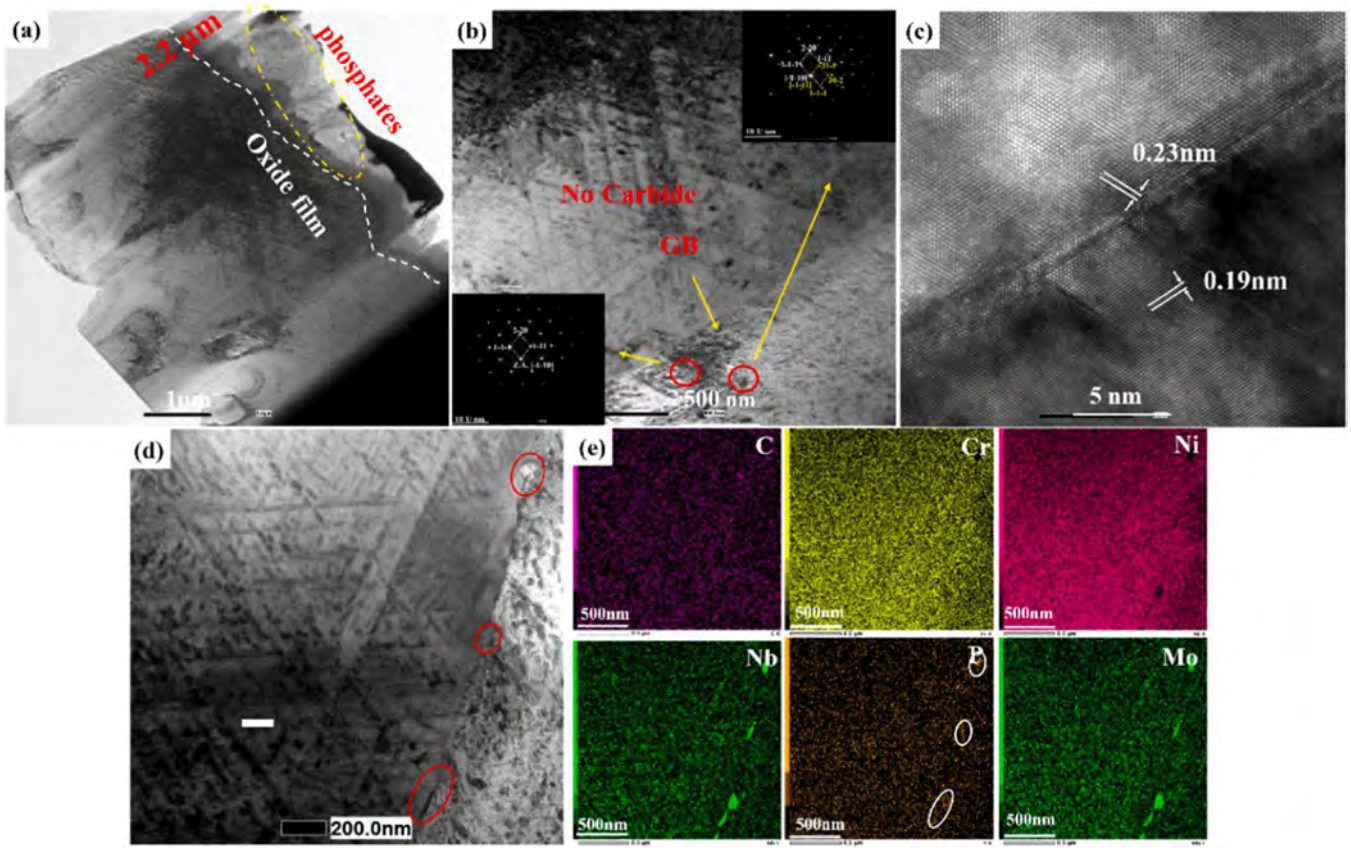


Fig. 7. TEM images of Inconel 625 sensitized at 800°C for 4 h and corroded in phosphate-containing molten salt SCW for 100 h: (a) overall morphology; (b) bright field image of grain boundary and corresponding electron diffraction pattern; (c) HRTEM images at the IGC interface of the sample (d) TEM image of grain boundary; (e) EDS elemental mapping of (d).

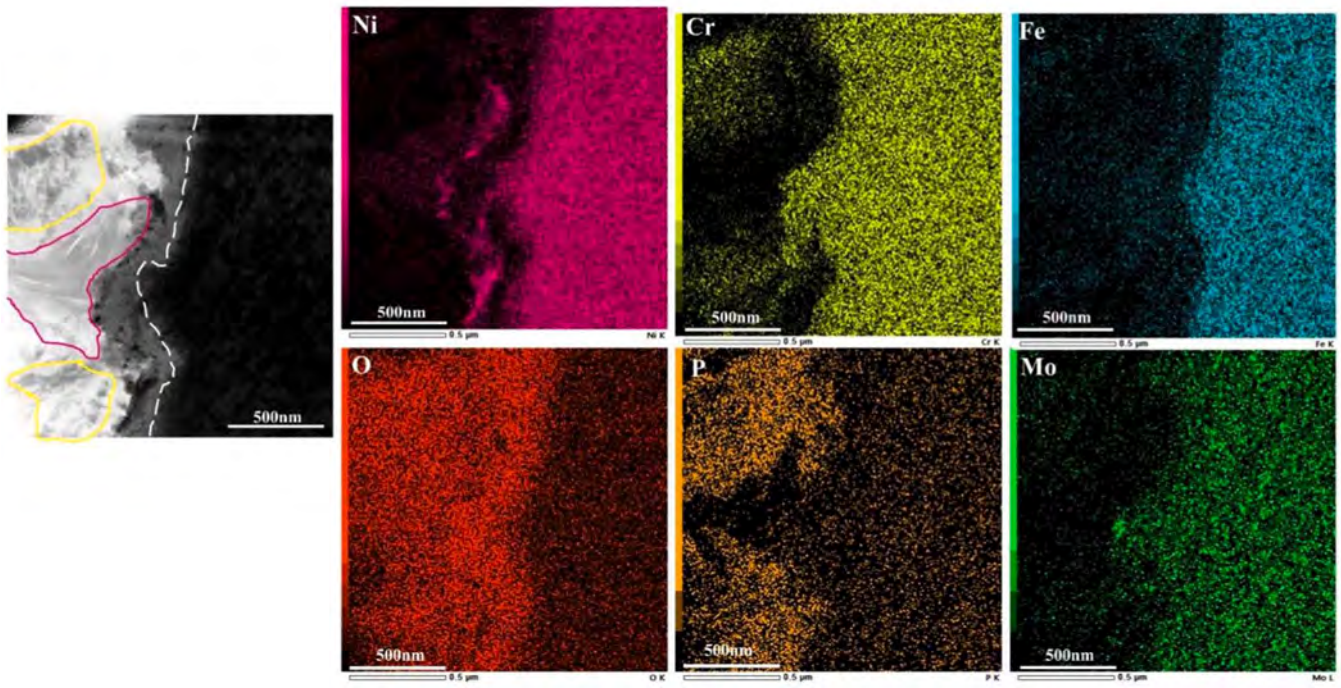


Fig. 8. EDS mapping of grain boundary oxide cross sections after sensitization at 800°C for 4 h and phosphate corrosion in SCW for 100 h.

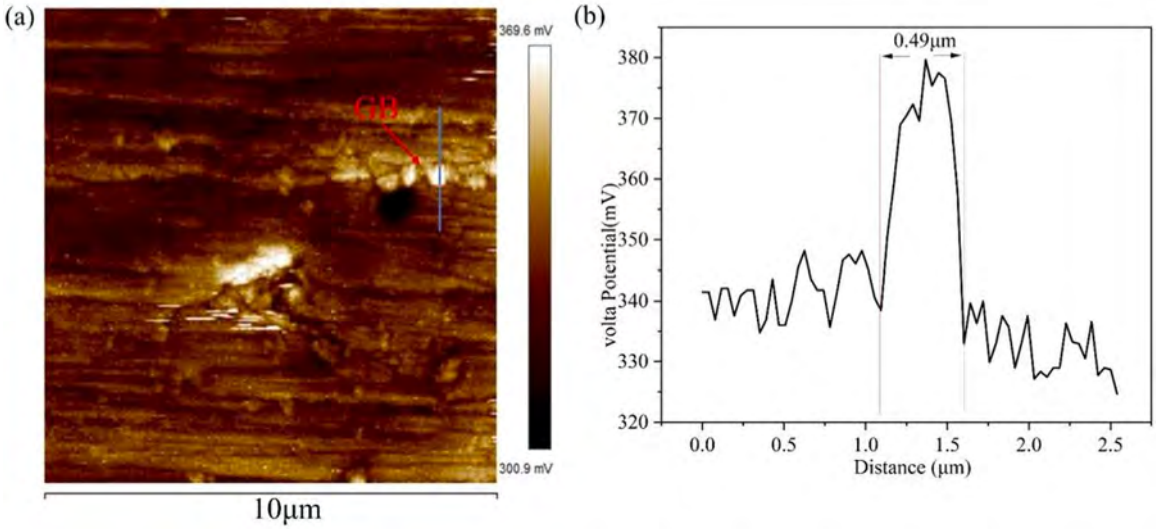


Fig. 9. SKPFM images of grain boundaries of 800°C sensitized specimens after 100 h of corrosion in SCW with phosphate molten salt: (a) Volta potential distribution around the grain boundaries; (b) Volta potential line scan distribution along the blue line crossing the grain boundaries.

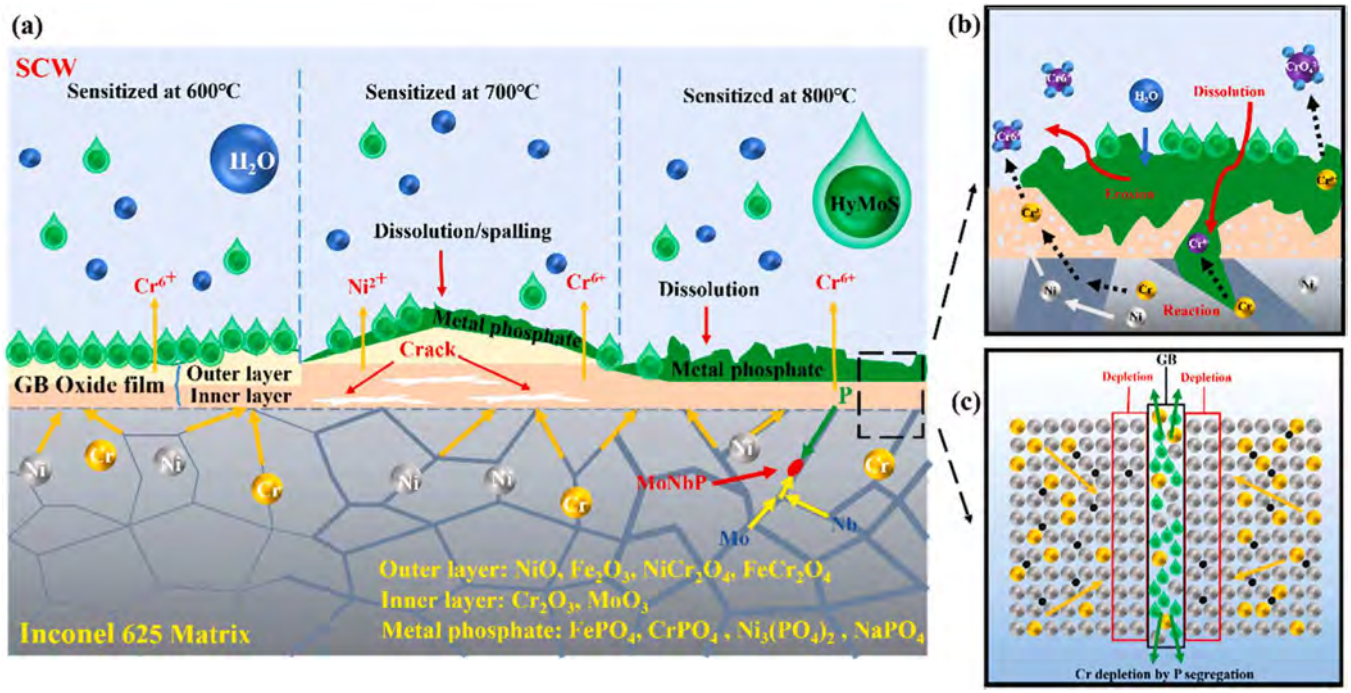


Fig. 10. Schematic of corrosion mechanism: (a) Propagation mechanism of IGC for the sensitized alloy in SCW containing phosphate molten salt; (b) Magnified view of grain boundary; (c) Mechanism of segregation-induced IGC.

attributed to the low carbon content of the alloy and the synergistic inhibition of carbide nucleation by phosphorus segregation. In the 800°C sensitized sample, the observed MoNbP intermetallic compound forms through a phosphate molten salt reaction: PO_4^{3-} deposits release active phosphorus at the grain boundaries, which diffuse and accumulate along the boundaries during corrosion, and subsequently coordinate with molybdenum and niobium that migrate due to sensitization. The role of this precipitate as a galvanic cathode, which accelerates the anodic dissolution of grain boundaries in the phosphate molten salt environment, was first revealed in this study. This precipitate induces dual grain boundary degradation mechanisms: high-resolution TEM revealed an increase in the matrix lattice spacing from 0.16 nm to 0.19 nm, confirming lattice distortion caused by chromium loss and molten salt corrosion; the potential difference between MoNbP and the matrix results in the initiation of galvanic corrosion; together, these effects significantly reduce grain boundary cohesion, collectively leading to "autocatalytic" failure characteristics [42] , and accelerating IGC propagation.

5. Conclusion

Through investigation of the IGC behavior of sensitized Inconel 625 alloy in SCW with phosphate molten salts, the main conclusions are as follows:

(1) Phosphate molten salts induce severe IGC in sensitized Inconel 625, with the evolution process proceeding through five stages: grain boundary activation and exposure, phosphate deposition, growth of phosphorus oxides, oxide scale spallation, and grain-boundary penetration by molten salts.
(2) The penetration depth of phosphate molten salt corrosion increases significantly with sensitization temperature. At 600 °C, protective circumferential grain-boundary oxides form without phosphate deposition. At 700 °C, grain boundary exposure, phosphate deposition, and cracks within the internal oxide film are observed. At 800 °C, grain boundaries are significantly widened, resulting in the development of a characteristic sawtooth corrosion morphology.
(3) IGC in the phosphate molten salt HyMoS system is essentially governed by a phosphorus-segregation-dominated, self-catalyzed dynamic chromium-depletion cycle. This mechanism differs from the conventional carbide-precipitation-induced chromium depletion theory.
(4) In specimens sensitized at 800 °C, the electrochemical potential difference between the precipitated MoNbP phase and the alloy matrix triggers galvanic corrosion, leading to reduced grain-boundary cohesion and an increased risk of brittle fracture, thereby serving as a critical factor exacerbating intergranular corrosion.

CRediT authorship contribution statement

Ke Li: Writing – original draft, Writing – review & editing, Data curation, Vallidation. **Jiquan Chen:** Writing – review & editing, Vallidation. **Guiyuan Xie:** Writing – review & editing, Vallidation. **Xingying Tang:** Writing – original draft, Writing – review & editing, Visualization, Methodology, Project admistaration, Funding acquisition. **Donghai Xu:** Writing – review & editing, Vallidation , Methodology. **Jianqiao Yang:** Writing – review & editing, Vallidation, Methodology.

Declaration of Competing interest

The authors declare the following financial interests/personal relationships which may be considered as potential competing interests: Xing-ying Tang reports financial support was provided by the General Program of Guangxi Natural Science Foundation. If there are other authors, they declare that they have no known competing financial interests or personal relationships that could have appeared to influence the work reported in this paper.

Appendix A. Supporting information

Supplementary data associated with this article can be found in the online version at doi:10.1016/j.corsci.2025.113397.

Data availability

Data will be made available on request.

References

[1] J. Li, S. Wang, Y. Li, L. Wang, T. Xu, Y. Zhang, Z. Jiang, Supercritical water oxidation of semi–coke wastewater: effects of operating parameters, reaction mechanism and process enhancement, Sci. Total Environ. 710 (2020) 134396, https://doi.org/10.1016/j.scitotenv.2019.134396.
[2] W. He, G. Li, L. Kong, X. Zhao, H. Wang, J. Huang, Progress in supercritical water oxidation based on corrosion and salt blockage problems (in Chinese), Environ. Eng. J. 1 (5) (2007) 1–6, https://doi.org/10.3969/j.issn.1673-9108.2007.05.001.
[3] X. Tang, Y. Zheng, Z. Liao, Y. Wang, J. Yang, J. Cai, A review of developments in process flow for supercritical water oxidation, Chem. Eng. Commun. 208 (2021) 1494–1510, https://doi.org/10.1080/00986445.2020.1783537.
[4] M.D. Bermejo, M.J. Cocero, Supercritical water oxidation: a technical review, AIChE J. 52 (2006) 3933–3951, https://doi.org/10.1002/aic.10993.
[5] Z. Yan, B. Örmeci, Y. Han, J. Zhang, Supercritical water oxidation for treatment of wastewater sludge and recalcitrant organic contaminants, Environ. Technol. Innov. 18 (2020) 100728, https://doi.org/10.1016/j.eti.2020.100728.
[6] G.B.M. De Souza, M.B. Pereira, L.C. Mourão, M.P. Dos Santos, J.A. De Oliveira, I.A. A. Garde, C.G. Alonso, V. Jegatheesan, L. Cardozo-Filho, Supercritical water technology: an emerging treatment process for contaminated wastewaters and sludge, Rev. Environ. Sci. Biotechnol. 21 (2022) 75–104, https://doi.org/10.1007/s11157-021-09601-0.
[7] P. Kritzer, N. Boukis, E. Dinjus, The corrosion of nickel-base alloy 625 in sub- and supercritical aqueous solutions of oxygen: A long time study, (n.d.).
[8] D. Xu, C. Huang, S. Wang, G. Lin, Y. Guo, Salt deposition problems in supercritical water oxidation, Chem. Eng. J. 279 (2015) 1010–1022, https://doi.org/10.1016/j.cej.2015.05.040.
[9] Y. Zhang, S. Wang, Y. Li, J. Zhang, D. Xu, C. Yang, J. Yang, J. Li, T. Xu, Inorganic salts in sub-/supercritical water—Part A: behavior characteristics and mechanisms, Desalination 496 (2020) 114674, https://doi.org/10.1016/j.desal.2020.114674.
[10] H. Shi, Z. Gao, Z. Fan, Y. Ding, Y. Qiao, Z. Zhu, Corrosion behavior of alloy C-276 in supercritical water, Adv. Mater. Sci. Eng. 2018 (2018) 1027640, https://doi.org/10.1155/2018/1027640.
[11] S. Bsat, B. Xiao, X. Huang, S. Penttilä, Oxidation behaviour of alloys 800H, 3033 and 304 in High-Temperature supercritical water, Oxid. Met 89 (2018) 151–163, https://doi.org/10.1007/s11085-017-9784-7.
[12] P. Kritzer, Corrosion in high-temperature and supercritical water and aqueous solutions: a review, J. Supercrit. Fluids 29 (2004) 1–29, https://doi.org/10.1016/S0896-8446(03)00031-7.
[13] J. Yang, S. Wang, X. Tang, Y. Wang, Y. Li, Effect of low oxygen concentration on the oxidation behavior of Ni-based alloys 625 and 825 in supercritical water, J. Supercrit. Fluids 131 (2018) 1–10, https://doi.org/10.1016/j.supflu.2017.07.008.
[14] S. Guo, D. Xu, Y. Li, Y. Guo, S. Wang, D.D. Macdonald, Corrosion characteristics and mechanisms of typical Ni-based corrosion-resistant alloys in sub- and supercritical water, J. Supercrit. Fluids 170 (2021) 105138, https://doi.org/10.1016/j.supflu.2020.105138.
[15] B.-H. Zhu, H.-C. Qiu, W. Jiang, Q.-H. Yu, Oxidation behavior of Al0.2CoCrFeNi high-entropy alloy film in supercritical water environment, Rare Met 41 (2022) 1217–1222, https://doi.org/10.1007/s12598-021-01859-1.
[16] M. Sun, X. Wu, Z. Zhang, E.-H. Han, Oxidation of 316 stainless steel in supercritical water, Corros. Sci. 51 (2009) 1069–1072, https://doi.org/10.1016/j.corsci.2009.03.008.
[17] W. Gao, C. Shen, L. Zhang, Corrosion behavior of T91 steel in supercritical water environment (in Chinese), Corros. Prot. 37 (6) (2016) 502, https://doi.org/10.11973/fsyfh-201606002.
[18] J. Yang, Y. Ding, F. Zhao, S. Wang, Y. Li, D. Xu, Under-deposit corrosion of Cr-coated Ni-based alloys in supercritical water oxidation environment at 500 °C, J. Supercrit. Fluids 208 (2024) 106213, https://doi.org/10.1016/j.supflu.2024.106213.
[19] J. Yang, S. Wang, Y. Li, D. Xu, Under-deposit corrosion of Ni-based alloy 825 and Fe-Ni based alloy 800 in supercritical water oxidation environment, Corros. Sci. 167 (2020) 108493, https://doi.org/10.1016/j.corsci.2020.108493.
[20] J. Yang, S. Wang, Y. Li, X. Tang, Y. Wang, D. Xu, Y. Guo, Effect of salt deposit on corrosion behavior of Ni-based alloys and stainless steels in supercritical water, J. Supercrit. Fluids 152 (2019) 104570, https://doi.org/10.1016/j.supflu.2019.104570.
[21] Z. Mi, S. Wang, L. Ding, X. Huang, Y. Zhang, Y. Li, Characterization of calcium and magnesium salt removal and inorganic salt crystallization deposition in supercritical water oxidation system, J. Environ. Chem. Eng. 13 (2025) 115554, https://doi.org/10.1016/j.jece.2025.115554.
[22] T. Voisin, A. Erriguible, C. Aymonier, Influence of multiphasic systems on salt(s) solubility in supercritical water: the case of NaCl and NaCl-Na2SO4, J. Supercrit. Fluids 152 (2019) 104567, https://doi.org/10.1016/j.supflu.2019.104567.
[23] T. Voisin, A. Erriguible, C. Aymonier, A new solvent system: hydrothermal molten salt, Sci. Adv. 6 (2020) eaaz7770, https://doi.org/10.1126/sciadv.aaz7770.
[24] N. Wei, D. Xu, B. Hao, S. Guo, Y. Guo, S. Wang, Chemical reactions of organic compounds in supercritical water gasification and oxidation, Water Res. 190 (2021) 116634, https://doi.org/10.1016/j.watres.2020.116634.
[25] P. Feng, D. Xu, Y. Zhi, B. He, S. Wang, Y. He, Y. Guo, Macro-characteristics and micro-mechanisms of Na2SO4 precipitation dissolved by KNO3 molten salt in a continuous supercritical water system, Water Res. 259 (2024) 121869, https://doi.org/10.1016/j.watres.2024.121869.
[26] Z. Lin, Y. Wang, X. Tang, R. Zhu, Corrosion behavior of inconel 625 in supercritical hydrothermal phosphoric acid molten salt environment (in Chinese), Public Sci. Technol. 24 (9) (2022) 50–53, https://doi.org/10.3969/j.issn.1008-1151.2022.09.014.
[27] E. Duverger-Nédellec, T. Voisin, A. Erriguible, C. Aymonier, Unveiling the complexity of salt(s) in water under transcritical conditions, J. Supercrit. Fluids 165 (2020) 104977, https://doi.org/10.1016/j.supflu.2020.104977.
[28] S. Guo, D. Xu, Y. Liang, Y. Li, J. Yang, G. Chen, D.D. Macdonald, Corrosion characteristics of typical Ni–Cr alloys and Ni–Cr–Mo alloys in supercritical water: a review, Ind. Eng. Chem. Res. 59 (2020) 18727–18739, https://doi.org/10.1021/acs.iecr.0c04292.
[29] D. Rodriguez, A. Merwin, Z. Karmiol, D. Chidambaram, Surface chemistry and corrosion behavior of inconel 625 and 718 in subcritical, supercritical, and ultrasupercritical water, Appl. Surf. Sci. 404 (2017) 443–451, https://doi.org/10.1016/j.apsusc.2017.01.119.

[30] Lin Z. Effect of Phosphate in Supercritical Water Environment on the Corrosion Behavior of Inconel 625 Alloy [D]. Guangxi University, Nanning, China, 2023. doi: 10.27034/d.cnki.ggxiu.2023.001338.
[31] J. Chen, Z. Lin, X. Tang, K. Li, R. Zhu, J. Yang, Comparative study of the corrosion behavior of inconel 625 in supercritical water containing dissolved and molten phosphates, J. Supercrit. Fluids 218 (2025) 106495, https://doi.org/10.1016/j.supflu.2024.106495.
[32] Z. Chen, L. Xiong, P. Zhang, Z. Zheng, G. Wang, H. Chen, D. Li, F. Xu, J. Xiao, Q. Chen, Tube explosion during continuous supercritical water oxidation of sludge: an incident investigation, Process Saf. Environ. Prot. 181 (2024) 131–142, https://doi.org/10.1016/j.psep.2023.11.017.
[33] S. Chen, X. Zhang, T. Li, J. Liu, K. Wu, Research progress on corrosion of device materials in supercritical water oxidation environment for hazardous waste treatment (in Chinese), Mater. Rev. 37 (8) (2023) 108–114, https://doi.org/10.11896/cldb.21100176.
[34] P. Kritzer, N. Boukis, E. Dinjus, The corrosion of alloy 625 (NiCr22Mo9Nb; 2.4856) in high-temperature, high-pressure aqueous solutions of phosphoric acid and oxygen. Corrosion at sub- and supercritical temperatures, materials and corrosion 49 (1998) 831–839, https://doi.org/10.1002/(SICI)1521-4176(199811)49:11<831::AID-MACO831>3.0.CO;2-V.
[35] Z. Ma, D. Xu, S. Guo, Y. Wang, S. Wang, Z. Jing, Y. Guo, Corrosion properties and mechanisms of austenitic stainless steels and Ni-Base alloys in supercritical water containing phosphate, sulfate, chloride and oxygen, Oxid. Met 90 (2018) 599–616, https://doi.org/10.1007/s11085-018-9855-4.
[36] T. Xu, S. Wang, X. Tang, Y. Li, J. Yang, J. Li, Y. Zhang, Corrosion mechanism of inconel 600 in oxidizing supercritical aqueous systems containing multiple salts, Ind. Eng. Chem. Res. 58 (2019) 23046–23056, https://doi.org/10.1021/acs.iecr.9b04527.
[37] Z. Wang, F. Gao, S. Tang, P. Zhou, W. Zhang, Z. Liu, Effect of twin-related boundaries distribution on carbide precipitation and intergranular corrosion behavior in nuclear-grade higher carbon austenitic stainless steel, Corros. Sci. 209 (2022) 110791, https://doi.org/10.1016/j.corsci.2022.110791.
[38] Mou L. Mechanism of Improving Intergranular Corrosion Resistance of 304 Stainless Steel by Regulating C/Cr Content and Precipitation Strengthening [D]. Taiyuan University of Science and Technology, Taiyuan, China, 2024. doi: 10.27721/d.cnki.gyzjc.2024.000762.
[39] W. Tian, D. Wu, Y. Li, S. Lu, Precipitation behavior and mechanical properties of a 16Cr-25Ni superaustenitic stainless steel weld metal during Post-weld heat treatment, Acta Metall. Sin. (Engl. Lett.) 35 (2022) 577–590, https://doi.org/10.1007/s40195-021-01274-6.
[40] O.V. Kasparova, Intergranular corrosion of nickel alloys (Review), Prot. Met. 36 (2000) 524–532, https://doi.org/10.1023/A:1026668925565.
[41] A. Keogh, E. Aradi, M. Taylor, A. Cook, E. Pickering, Z. Obadia, P. Prangnell, F. Scenini, Effect of ageing temperature on the microstructure and localised corrosion of 15–5PH stainless steel, Corros. Sci. 248 (2025) 112800, https://doi.org/10.1016/j.corsci.2025.112800.
[42] L. Mou, T. Bian, S. Zhang, B. Liu, P. Wu, J. Zhang, Y. Yu, Y. Zhang, X. Wang, New sights on intergranular corrosion resistance mechanism of type 304 austenitic stainless steel by adjusting carbon contents, J. Mater. Res. Technol. 26 (2023) 666–680, https://doi.org/10.1016/j.jmrt.2023.07.220.
[43] Y. Zhang, H. Wu, X. Yu, D. Tang, Role of cr in the high-temperature oxidation behavior of CrxMnFeNi high-entropy alloys at 800 °C in air, Corros. Sci. 200 (2022) 110211, https://doi.org/10.1016/j.corsci.2022.110211.
[44] Karishma, N. Tripathi, R.K. Pandey, A. Tripathi, K. Asokan, V. Bhushan, V. Sharma, Comparative analysis of structural, optical, and electronic properties of nickel oxide and Potassium-Doped nickel oxide nanocrystals, Energy Storage 6 (2024) e70065, https://doi.org/10.1002/est2.70065.
[45] J. Yang, L. Wei, H. Huang, P. Lu, Q. Ren, X. Xu, H. Xie, Effect of sc micro-alloying on microstructure and corrosion behavior of 7085 alloy friction stir welded joints, Vacuum 220 (2024) 112863, https://doi.org/10.1016/j.vacuum.2023.112863.
[46] R. Wang, Q. Zhou, Z. Zheng, Y. Gao, The negative effect of high-intensity shot-peening on the intergranular corrosion behavior of the Super304H austenitic stainless steel, Corros. Sci. 143 (2018) 390–402, https://doi.org/10.1016/j.corsci.2018.08.026.
[47] H. Li, S. Xia, B. Zhou, W. Liu, C–Cr segregation at grain boundary before the carbide nucleation in alloy 690, Mater. Charact. 66 (2012) 68–74, https://doi.org/10.1016/j.matchar.2012.02.008.
[48] R.G. Ding, Z.W. Huang, H.Y. Li, I. Mitchell, G. Baxter, P. Bowen, Electron microscopy study of direct laser deposited IN718, Mater. Charact. 106 (2015) 324–337, https://doi.org/10.1016/j.matchar.2015.06.017.
[49] S. Zhang, A. Zhang, L. Chang, W. Wang, X. Xin, W. Sun, Effect of phosphorus on the stress rupture properties of IN706 superalloy, Materials Science Engineering A 761 (2019) 137981, https://doi.org/10.1016/j.msea.2019.05.111.
[50] S. Zhang, L. Huang, A. Zhang, L. Yu, X. Xin, W. Sun, X. Sun, Segregation of phosphorus and precipitation of MNP-Type phosphide at the grain boundary of IN706 superalloy, J. Mater. Sci. Technol. 33 (2017) 187–191, https://doi.org/10.1016/j.jmst.2016.09.010.
[51] R. Nakkalil, N.L. Richards, M.C. Chaturvedi, A study of precipitates and insolubles in an ni Fe-based superalloy by analytical electron microscopy, Materials Science Engineering A 157 (1992) 89–100, https://doi.org/10.1016/0921-5093(92)90102-7.
[52] Y. Wu, C. Wang, X. Qin, J. Hou, L. Zhou, Segregation sequence of phosphorus and its effect on impact toughness of GH984G alloy during thermal exposure, J. Mater. Res. Technol. 18 (2022) 200–209, https://doi.org/10.1016/j.jmrt.2022.02.098.
[53] A. Davoodi, J. Pan, C. Leygraf, S. Norgren, The role of intermetallic particles in localized corrosion of an aluminum alloy studied by SKPFM and integrated AFM/SECM, J. Electrochem. Soc. 155 (2008) C211, https://doi.org/10.1149/1.2883737.
[54] C. Senöz, S. Borodin, M. Stratmann, M. Rohwerder, In situ detection of differences in the electrochemical activity of Al2Cu IMPs and investigation of their effect on FFC by scanning kelvin probe force microscopy, Corros. Sci. 58 (2012) 307–314, https://doi.org/10.1016/j.corsci.2012.02.006.
[55] E. Rahimi, A. Rafsanjani-Abbasi, A. Imani, S. Hosseinpour, A. Davoodi, Correlation of surface volta potential with galvanic corrosion initiation sites in solid-state welded Ti-Cu bimetal using AFM-SKPFM, Corros. Sci. 140 (2018) 30–39, https://doi.org/10.1016/j.corsci.2018.06.026.
[56] S. Zheng, C. Li, Y. Qi, L. Chen, C. Chen, Mechanism of (Mg,Al,Ca)-oxide inclusion-induced pitting corrosion in 316L stainless steel exposed to sulphur environments containing chloride ion, Corros. Sci. 67 (2013) 20–31, https://doi.org/10.1016/j.corsci.2012.09.044.
[57] C.F. Mallinson, A. Harvey, J.F. Watts, Characterization of carbide particles in S-65 beryllium by scanning kelvin probe force microscopy, J. Electrochem. Soc. 164 (2017) C342, https://doi.org/10.1149/2.0271707jes.
[58] Z. Zhang, Z.F. Hu, L.F. Zhang, K. Chen, P.M. Singh, Effect of temperature and dissolved oxygen on stress corrosion cracking behavior of P92 ferritic-martensitic steel in supercritical water environment, J. Nucl. Mater. 498 (2018) 89–102, https://doi.org/10.1016/j.jnucmat.2017.10.024.
[59] C. He, T. Guo, Q. Zhao, Z. Liang, Failure behavior analysis of oxide film formed on super-heater tubes of boiler during deep peak process, J. Supercrit. Fluids 218 (2025) 106474, https://doi.org/10.1016/j.supflu.2024.106474.
[60] E. Asselin, A. Alfantazi, S. Rogak, Corrosion of nickel–chromium alloys, stainless steel and niobium at supercritical water oxidation conditions, Corros. Sci. 52 (2010) 118–124, https://doi.org/10.1016/j.corsci.2009.08.053.
[61] L. Royer, X. Ledoux, S. Mathieu, P. Steinmetz, On the oxidation and nitridation of chromium at 1300 °C, Oxid. Met 74 (2010) 79–92, https://doi.org/10.1007/s11085-010-9198-2.
[62] Y. Hou, Z. Xu, S. Zhou, G. Li, Atomic-scale mechanism of effect of co-separation of elements at interface of ferrite and austenite on Cr-depleted zone of duplex stainless steel, J. Iron Steel Res. Int. 31 (2024) 710–718, https://doi.org/10.1007/s42243-023-01083-4.

Biomass and Bioenergy 193 (2025) 107557

Contents lists available at ScienceDirect

Biomass and Bioenergy

journal homepage: www.elsevier.com/locate/biombioe

Regulation of slow-release performance of high-sugar biomass waste filter mud and sugarcane bagasse by co-hydrothermal carbonization and potential evaluation of hydrochar-based slow-release fertilizers

Sisi Chen [a], Xingying Tang [b,*], Jiquan Chen [a], Yuyang Xue [a], Yinghui Wang [b,c], Donghai Xu [d]

[a] School of Resources, Environment and Materials, Guangxi University, Nanning, 530004, China
[b] School of Marine Sciences, Guangxi University, Nanning, 530004, China
[c] Guangxi Institute of Green and Low Carbon Technology Co., Ltd, Nanning, 530022, China
[d] Key Laboratory of Thermo-Fluid Science & Engineering, Ministry of Education, School of Energy and Power Engineering, Xi'an Jiaotong University, Xi'an, 710049, China

ARTICLE INFO

Keywords:
Hydrothermal carbonization
Filter mud
Slow-release fertilizer
Resource recycling
Optimal condition

ABSTRACT

In this study, we investigated the impact of process parameters, including reaction temperature (180–300 °C), residence time (30–120 min), and mixing ratios (1:0~5:1), on hydrochar properties of high-sugar biomass waste filter mud and sugarcane bagasse in the co-hydrothermal carbonization. The hydrochar is comprehensively characterized using Proximate analysis, industrial analysis, scanning electron microscopy, multi-point Brunauer-Emmett-Teller, Fourier-transform infrared spectroscopy, Raman spectroscopy, and thermogravimetric analysis. The urea release patterns from hydrochar-based slow-release fertilizers were assessed across different hydrochar-to-fertilizer ratios, and the reaction path during co-hydrothermal carbonization was analyzed. The findings reveal that hydrochar produced 240°C-60min-5:1 had a notably high specific surface area (45.921 m^2/g), abundant functional groups, and exceptional adsorption capabilities, which was suitable for preparing slow-release fertilizers. The hydrochar-based slow-release fertilizer formulated at a hydrochar-to-fertilizer ratio of 5:1 had the optimal slow-release performance, and the cumulative release rate of urea in 7d was 49.65 %, which was more than 40 % lower than that of pure urea. These results underscore the promising agricultural applications of products derived from the co-hydrothermal carbonization of filter mud and sugarcane bagasse.

1. Introduction

In recognition of environmental sustainability, conversion of biomass to bioenergy has increased in importance recently [1]. By 2030, biomass will account for 60 % of global energy production, making it the most important renewable resource, according to the International Renewable Energy Agency's (IRENA) Global Renewable Energy Roadmap [2]. As one of the most valuable commercial crops in the world, sugarcane also serves as the primary raw material in the worldwide sugar industry, supplying 80 % of the world's sugar needs [3,4]. One of the most challenging biomass by-products to dispose of in the sugar industry is filter mud (FM) [5], which is usually fertilized by fields or dumped carelessly. In addition to consuming a significant amount of land resources, it is also highly susceptible to rotting and stinking, breeding bacteria, polluting the air, and causing serious negative impacts on the environment due to its high-water content and richness in organic matter and sugar, among other things. Given this, there is an urgent need for a technology that is environmentally, economically, and socially trustworthy, improves biomass utilization, realizes product-added value, and incorporates sustainable development and climate change mitigation into the circular economy, helping to implement current policy requirements and achieve the goals of sustainable development [6].

Hydrothermal carbonization (HTC), as one of the thermochemical treatment methods, has attracted a lot of attention owing to the effectiveness of its process, economic viability, and high product yield of products [7]. As opposed to other thermochemical treatment methods like pyrolysis, gasification, and incineration, HTC reduces the hydrogen and oxygen content of biomass waste through dehydration and decarboxylation at low operating temperatures, pressures, and energy

* Corresponding author.
E-mail address: tangxingying@gxu.edu.cn (X. Tang).

https://doi.org/10.1016/j.biombioe.2024.107557
Received 27 May 2024; Received in revised form 6 December 2024; Accepted 15 December 2024
Available online 21 December 2024
0961-9534/© 2024 Elsevier Ltd. All rights are reserved, including those for text and data mining, AI training, and similar technologies.

Table 1
Elemental and ash content of raw materials and hydrochar.

Samples	Ultimate analysis (wt.%)					C/N value	ASH (wt.%)	HHV[a] (MJ/kg)	pH	EC (ms/cm)	Hydrochar Yield (%)
	C	H	O	N	S						
Filter Mud	19.59	3.94	16.52	1.10	3.58	17.8	56.13	8.93	6.82	1.38	–
Sugarcane Bagasse	44.16	5.78	47.96	0.55	0.23	80.8	1.32	17.26	–	–	–
HC 180°C-60min-2:1	25.66	4.22	26.88	0.85	1.78	30.3	40.62	10.46	6.79	1.70	74.02
HC 210°C-60min-2:1	25.90	4.61	18.50	0.72	1.15	36.1	49.12	11.63	5.98	0.67	54.37
HC 240°C-60min-2:1	25.37	4.24	17.88	0.72	1.41	35.4	50.39	11.07	6.14	1.05	56.98
HC 270°C-60min-2:1	25.81	3.96	15.06	0.75	1.84	34.4	52.58	11.18	6.21	0.80	53.33
HC 300°C-60min-2:1	26.91	3.67	7.01	0.90	2.50	29.9	59.01	11.99	6.75	0.49	45.89
HC 240°C-30min-2:1	25.68	4.28	21.39	0.73	1.03	35.3	46.89	10.90	6.11	0.65	57.08
HC 240°C-90min-2:1	27.39	4.25	16.94	0.74	1.33	37.2	49.37	11.89	5.96	0.50	54.57
HC 240°C-120min-2:1	27.43	3.38	14.26	0.74	1.49	37.2	52.70	11.11	5.97	0.60	54.24
HC 240°C-60min-1:0	15.01	2.62	10.61	0.66	2.25	22.8	68.86	5.99	7.05	1.63	71.23
HC 240°C-60min-1:1	31.66	5.10	21.11	0.76	1.04	41.8	40.35	14.11	5.83	1.22	58.43
HC 240°C-60min-3:1	23.11	3.60	14.79	0.72	1.50	32.0	56.28	9.73	6.11	0.98	58.94
HC 240°C-60min-4:1	23.63	3.68	11.42	0.75	1.73	31.5	58.79	10.32	6.58	1.03	59.56
HC 240°C-60min-5:1	19.64	3.20	9.89	0.73	1.93	26.9	64.61	8.42	6.35	1.43	62.38

[a] HHV (Higher heating value) = 0.3491C + 1.1783H + 0.1005S-0.1034O-0.015N-0.0211A, where C, H, O, N, S, and A represent the mass percentages on a dry basis of carbon, hydrogen, oxygen, nitrogen, sulfur, and ash contents of samples, respectively.

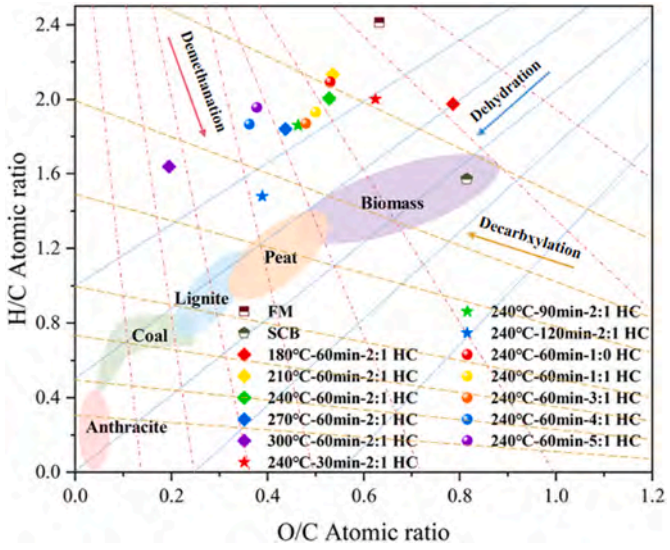


Fig. 1. Van Krevelen diagram of raw materials and hydrochar.

consumption without pre-drying, producing hydrochars with high carbon content. This method has been investigated for a variety of practical applications, including fuels, precursors for energy storage technologies, soil conditioners, and fertilizers [8,9]. For example, activated carbon prepared by HTC through sunflower stalk has a unique mesoporous layer-stacking structure, which demonstrates that the biomass-derived carbon materials have the potential of high electrochemical performance in the field of energy storage, using different natural waste biomass types as raw materials [10]. The sewage sludge is subjected to the Fenton reaction after HTC, and the hydrotchar obtained is used as a soil amendment, effectively enhancing the adsorption of nutrients, promoting plant growth, and reducing environmental impacts [11]. However, the degree of biomass dehydration and the gradual formation of carbonization products during the reaction process result in the production of hydrochars with low carbon content, specific surface area, porosity, and poor thermal stability, which restricts the use of hydrochar in practical applications [12].

Co-hydrothermal carbonization (co-HTC) technology of high-moisture organic waste and low-moisture biomass provides a potential avenue to reduce preprocessing energy costs while simultaneously enhancing the efficiency of thermal hydrolysis [13]. Low-moisture biomass with different compositions of lignocellulosic fibers has a crucial influence on the physicochemical properties of the generated carbon materials during HTC [14]. On the one hand, lignocellulosic biomass contains abundant organic components that assist in the coalification of proteinaceous organic waste, providing a framework and bridge for small molecules. On the other hand, the organic acids formed from lignocellulose after HTC act as catalysts, enhancing the yield of hydrochar [15]. Sugarcane bagasse (SCB) is a typical lignocellulosic biomass from the juice extraction process in the sugar industry, containing significant amounts of volatile matter, cellulose, hemicellulose, and lignin. With significant pollutant emissions and little additional value, it is mostly utilized for boiler fuel or pulp manufacture [16]. As a result, the sugar sector should combine FM and SCB for co-HTC, generate high-value products, realize resourceful and safe usage, and establish a whole-process utilization system. The latest research findings indicate that co-HTC of organic waste with a high moisture content and low-moisture biomass has notable favorable synergistic effects [15]. For instance, co-HTC of sludge and bagasse can adsorb Pb (II) in water [17], co-HTC of sludge and kitchen waste improved combustion performance [18], water hyacinth and sludge co-HTC promotes the enhancement of Maillard and Mannich reactions, improves the yield of hydrochar, and lowers energy consumption [19], hydrochars were fabricated by combination of rape straw and industrial sewage sludge to remove $NH4^+$ and PO_4^{3-} from hoggery effluent, which can provide extra N and P elements when made into fertilizer and also promote to release available K in soil [20]. Currently, there is a lack of research investigating the solid-phase properties of hydrochar produced from the co-HTC of FM and SCB.

The low nutrient utilization rate of traditional fertilizers and the irrational application of traditional fertilizers can cause soil quality degradation and environmental pollution, which not only leads to a decline in the quality of agricultural products but also poses a threat to ecological and environmental safety, so there is an urgent need to transform and improve fertilizer products that can meet the nutritional needs of crop growth while reducing environmental pollution. Currently, researchers and scientists have demonstrated that biochar-based slow-release fertilizers can reduce nutrient loss and nitrogen leaching, increase crop nutrition in the long term, improve soil properties, and increase crop yields compared to conventional fertilizers [21–23]. However, it is not yet clear whether co-HTC for the preparation of hydrochar-based slow-release fertilizer (HBSRF) represents a viable avenue for further research.

Therefore, this paper focuses on the influence of different process parameters (reaction temperature, residence time, and the mixing ratio of FM and SCB) on the characteristics of hydrochar. The physical and chemical structure features of hydrochar under different process parameters were studied utilizing different analytical techniques such as

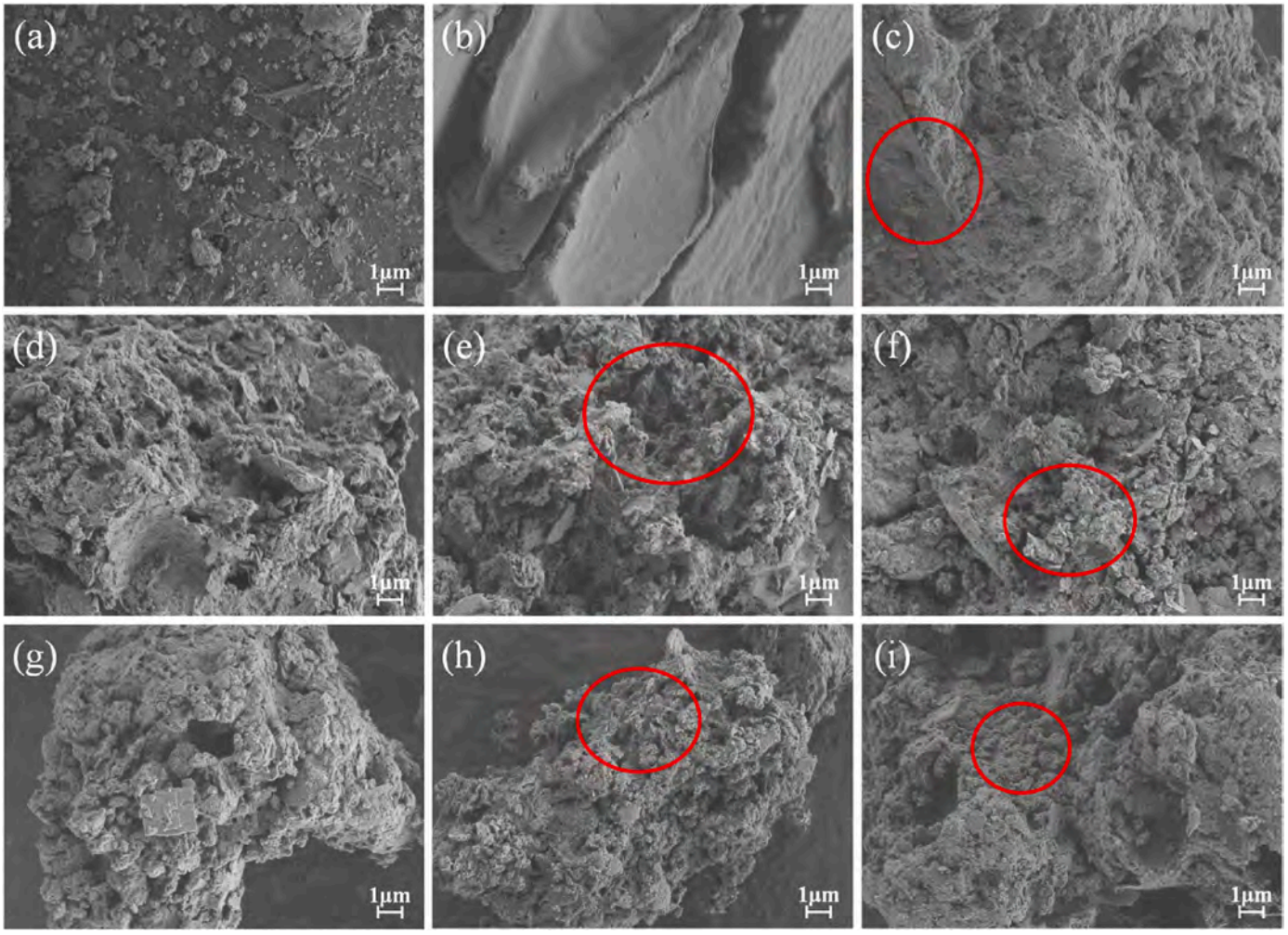


Fig. 2. Scanning electron microscope (SEM) images of raw materials and representative hydrochars: (a) filter mud (FM); (b) sugarcane bagasse (SCB); (c) HC 180°C-60min-2:1; (d) HC 240°C-60min-2:1; (e) HC 270°C-60min-2:1; (f) HC 240°C-120min-2:1; (g) HC 240°C- 60min-1:0; (h) HC 240°C-60min-1:1; (i). HC 240°C-60min-5:1.

elemental analysis, scanning electron microscopy, N_2 adsorption/desorption, Fourier-transform infrared spectroscopy, Raman spectroscopy, and thermogravimetric analysis. By preparing HBSRF using urea and hydrochar, column leaching experiments are conducted to study the urea release patterns of HBSRF, evaluate its potential for soil application, and explore possible reaction path during co-HTC, which provides a theoretical basis for the development of a new type of green fertilizers and the improvement of organic waste resource utilization industry chain in the sugar industry.

2. Materials and methods

2.1. Raw materials

The FM and SCB in the experiment were provided by the Guangxi Agricultural Reclamation Sugar Factory. The water content of the FM was about 70 %, the sucrose content was 1.5 %, the protein content was 13.43 %, the cellulose content was 36.02 %, the hemicellulose content was 20.09 % and the lignin content was 14.3 %. The SCB was composed of 49.02 % cellulose, 25.79 % hemicellulose, and 17.82 % lignin. Before the experiment, using a vacuum oven set at 105 °C for 24 h, the samples were dried., crushed, and 100 mesh sieved. Finally, all the samples were stored in a sealed bag for later use.

2.2. Co-HTC experiment

Experiments on HTC were conducted in a tube furnace (OTF-1200X-II, HF-Kejing, China). Considering the substantial volume and elevated water content of the FM and SCB in practical applications, the FM and SCB were mixed in 1:0, 1:1, 2:1, 3:1, 4:1, and 5:1 mass ratio before the experimental procedure. The feedstock and deionization were combined and supplied to the reactor in a proportion of 1:9 (w: v) for each experiment. Next, the reactor was heated to 180 °C, 210 °C, 240 °C, 270 °C, and 300 °C degrees Celsius at a rate of 5 °C per minute with residence times of 30 min, 60 min, 90 min, and 120 min, repeating the experiment several times and taking the average value to calculate After the experiment, the reactor was cooled to room temperature, and the reaction's solid and liquid phases were removed and later separated by vacuum filtration. The resultant solid phase product, hydrochar, was further dried under vacuum for 24 h at 105 °C, ground to 100 mesh, and stored in a self-sealing bag protected from light. This measurement is represented by the formula HC T-t-X, where T is the reaction's temperature, t is its residence time, and X is the mixing ratio. The liquid phase product, after filtering, was placed in a brown glass vial and kept chilled at 0–4 °C. The yield of hydrochar is calculated according to the formula:

$$\text{Hydrochar Yield}(\%) = \frac{m_{\text{hydrochar}}}{m_{\text{solid}}} \times 100\% \quad (1)$$

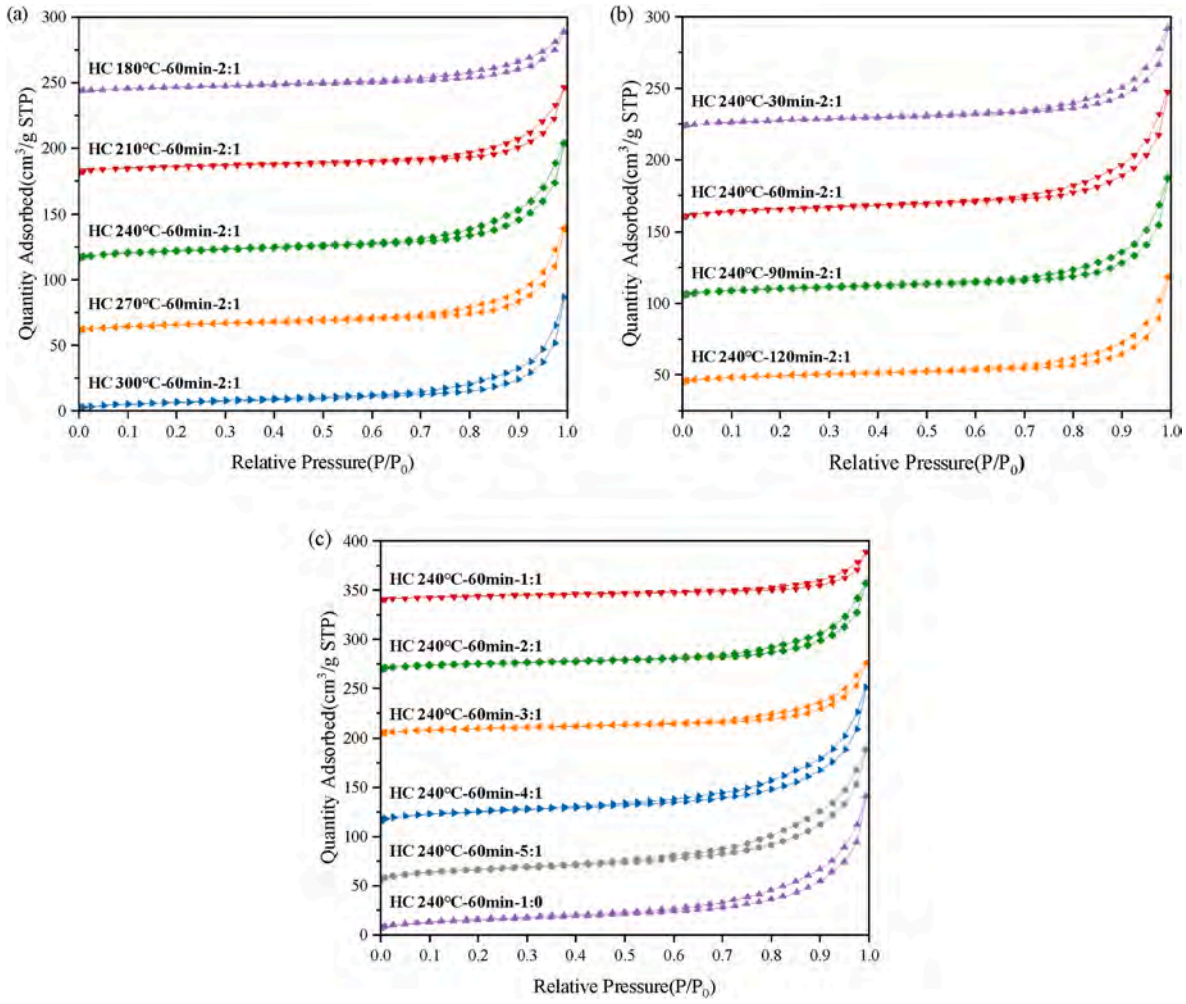


Fig. 3. N_2 adsorption/desorption curves for hydrochar: (a) reaction temperature of 180–300 °C; (b) residence time of 30–120 min; (c) mixing ratio of 1:0–5:1.

In the formula, $m_{hydrochar}$ is the hydrochar's quality, and m_{solid} is the raw material's quality.

2.3. Analytical methods

2.3.1. Ultimate and proximate analyses

The muffle furnace (YSD-12-12T, Yaoshi Instrument Co. Ltd., China) used the Chinese national standard GB/T 212–2008 to calculate the Proximate analysis of the raw materials and hydrochar. The elemental analyzer (Vario EL Cube, Germany) was used to characterize the content of carbon (C), hydrogen (H), nitrogen (N), and sulfur (S), while the proportion of oxygen (O) was then computed using differential subtraction.

2.3.2. pH and electrical conductivity (EC)

The pH and EC of hydrochar have an impact on the soil environment. These measurements were made using a pH meter (E−201-L, Leici, China) and an EC meter (DJS-1-L, Leici Co. Ltd, China), respectively, and were done right after mixing the sample and deionized water in a specific ratio (1:20, w/v) for 1 h [24].

2.3.3. Microscopic morphology and surface characteristics

The N_2 adsorption-desorption isothermal curves of the feedstock and hydrochar were calculated using a fully automated gas adsorption meter (Autosorb-IQ-MP, Quantachrome, USA), the specific surface area was calculated using the multi-point Brunauer-Emmett-Teller (BET) method, and the pore size distribution was calculated via the Barret-Joyner-Halenda (BJH) model [25]. Scanning electron microscopy (SEM) (Sigma500, Zeiss, Germany) was used to assess the surface morphology of raw materials and hydrochar. SEM images were produced by magnification to 5000 times.

2.3.4. Fourier-transform infrared spectroscopy analysis (FTIR)

Fourier-transform infrared spectroscopy (FTIR) (IRTrace-100, Shimadzu, Japan) was used to investigate the sample powder with 32 scans covering a scanning range of 400–4000 cm^{-1} to track the development of surface organic functional groups in the samples.

2.3.5. Micro-Raman spectroscopy analysis (Raman)

The carbonaceous structure of raw materials and hydrochar was assessed with a micro-Raman spectrometer (InVia, Renishaw, UK) set up with a laser wavelength of 532 nm, an exposure time of 10 s, and three scans in the range of 500–2500 cm^{-1}.

2.3.6. Thermogravimetric analysis (TGA)

The thermal stability of the hydrochar was examined by measuring the mass loss using a thermogravimetric analyzer (HCT-3, Henven Co. Ltd., China) in an inert atmosphere (N_2 = 99.999 %) between 50 °C and 800 °C with a heating rate of 20 °C/min and a gas flow rate of 80 mL/min.

Table 2
Specific surface area, pore volume, and pore size of hydrochar from raw materials and under different conditions.

Samples	Surface area (m^2/g)	Total Pore Volume (cm^3/g)	Average pore size (nm)
HC 180°C-60min-2:1	14.354	0.0696	2.968
HC 210°C-60min-2:1	16.912	0.0100	3.135
HC 240°C-60min-2:1	23.387	0.1356	10.028
HC 270°C-60min-2:1	19.649	0.1206	4.719
HC 300°C-60min-2:1	19.546	0.1316	4.435
HC 240°C-30min-2:1	18.514	0.1059	5.798
HC 240°C-90min-2:1	19.819	0.1271	3.310
HC 240°C-120min-2:1	18.081	0.1139	4.718
HC 240°C-60min-1:0	36.174	0.2075	3.932
HC 240°C-60min-1:1	16.432	0.0754	5.051
HC 240°C-60min-3:1	21.491	0.1111	3.704
HC 240°C-60min-4:1	41.608	0.2109	8.939
HC 240°C-60min-5:1	45.921	0.2061	2.972

2.4. Hydrochar-based slow-release fertilizer

2.4.1. Preparation of hydrochar-based slow-release fertilizer

Hydrochar and urea were mixed in the ratios of 0:1, 1:1, 3:1, and 5:1, respectively, with the addition of appropriate amounts of bentonite agent and deionized water, stirred homogeneously and then vacuum-dried at 50 °C, and HBSRFs were prepared by granulation in a granulator. The slow-release fertilizers with hydrochar and urea ratios of 1:1, 3:1, and 5:1 were named $HBSRF_1$, $HBSRF_3$, and $HBSRF_5$, respectively.

2.4.2. Column leaching experiment

Leaching columns were made from used 6 cm diameter by 20 cm high mineral water bottles. At the base of every column, place two layers of 100-mesh nylon mesh and secure them with ropes secured. The columns are coarse quartz sand and fine quartz sand. Place a conical bottle at the bottom of each column to collect the leachate. Add 50 mL of distilled water to each column every 24h for leaching for 7d, collect the leachate, and record its volume. The content of urea nitrogen in the leachate is determined using the dimethyl benzaldehyde method (GB/T 23348-2009).

2.4.3. Urea slow-release kinetics

This work examined the release mechanism of urea by fitting the cumulative release data of HBSRF using the zero-order, first-order, Higuchi, and Korsmeyer-Peppas models [26]. The model-fitting equations are as follows:

Zero-order model:

$$\frac{M_t}{M_\infty} = k_0 t \quad (2)$$

First-order model:

$$\frac{M_t}{M_\infty} = 1\text{-}e^{-k_1 t} \quad (3)$$

Higuchi model:

$$\frac{M_t}{M_\infty} = k_H t^{1/2} \quad (4)$$

Korsmeyer-Peppas model:

$$\frac{M_t}{M_\infty} = k_{kp} t^n \quad (5)$$

Where M_t and M_∞ stand for the mass of urea at various release periods t and release equilibrium, respectively; k0 denotes the diffusion kinetic constant of the zero-order model; k_1 and k_H denote the release constants of the first-order model and Higuchi model, respectively. The Korsmeyer-Peppas model's release index is denoted by n, and its rate constant is symbol k_{kp} [26].

3. Results and discussion

3.1. Physical and chemical characterization of hydrochar

3.1.1. Elemental composition and ash content

Table 1 displays the findings of the elemental composition (C, H, O, N, S) and ash of raw materials and hydrochar. Hydrochar mostly contains the elements C (15.01–31.66 wt%) and O (7.01–26.88 wt%), with lesser amounts of N, H, and S. With increasing reaction temperature and residence time, the content of C and ash gradually increased, while the H and O contents showed a decreasing trend. This was mainly due to the dehydration reaction, which involved the removal of hydroxyl (-OH), and the decarboxylation reaction, which involved the release of carboxyl (-COOH) and carbonyl (-C=O), while the HTC procedure was underway [27,28]. The H level exhibited a concomitant decline as the intensity of the aromatization reaction increased with rising temperature. Comparative analysis revealed that the C content of hydrochar with the addition of SCB exhibited an increase of over 30.85 % relative to that obtained from the single HTC of FM, reaching a maximum at a 1:1 ratio. This increase in C content soluble lignin in SCB is converted into highly condensed polycyclic aromatic hydrochar through dehydration, decarboxylation, and condensation [29]. It has been suggested that hydrochars with low N content are more environmentally friendly and cleaner than direct combustion of feedstocks. The main reason is that the N content of hydrochars is lower than that of feedstocks, which is due to the thermal hydrolysis of proteins of raw FM to ammoniated in the range of HTC temperature [30–32]. As evidenced in the literature [24,33,34], the N content of the feedstock has a significant impact on the C/N ratio of the hydrochar, which is higher than that of the other materials because of the lignocellulose content of the feedstock. The C/N ratio of the hydrochar is also one of the most important factors affecting its utilization and microbial activity in soil. The N-fixation and mineralization processes are in balance and within the range of ambient microbial activity when the ratio of C/N is 20∼30 [33]. Therefore, for soil applications, it may be more appropriate to use the hydrochar contains a ratio of C/N of 26.9 (HC 240°C-60min-5:1).

Van Krevelen plots based on the H/C and O/C atomic ratios of the feedstock and hydrochars were plotted as shown in Fig. 1 and contrasted with four typical coals and biomasses to further assess the degree of carbonization of hydrochar [29,35]. After the HTC reaction, the H/C and O/C atomic ratios shifted from higher to lower regions, which were tightly connected to the operating conditions. The two atomic ratios of hydrochar decreased significantly as reaction temperature and residence time increased, particularly at high temperatures and lengthy residence times. Nevertheless, the H/C ratio increased slightly at 210 °C and 240 °C, primarily because the high temperature accelerated the dehydration and decarboxylation reaction, which led to more oxygen loss. The occurrence further demonstrated that the demethylation reaction was negligible and that the decarboxylation and dehydration processes had a substantial impact on the hydrochar throughout the HTC procedure [36]. The majority of the hydrochar was identified close to the peat and biomass regions, which is consistent with the earlier studies in the literature [37,38]. These researches revealed that hydrochar in this range is more effective in enhancing soil fertility and improving soil

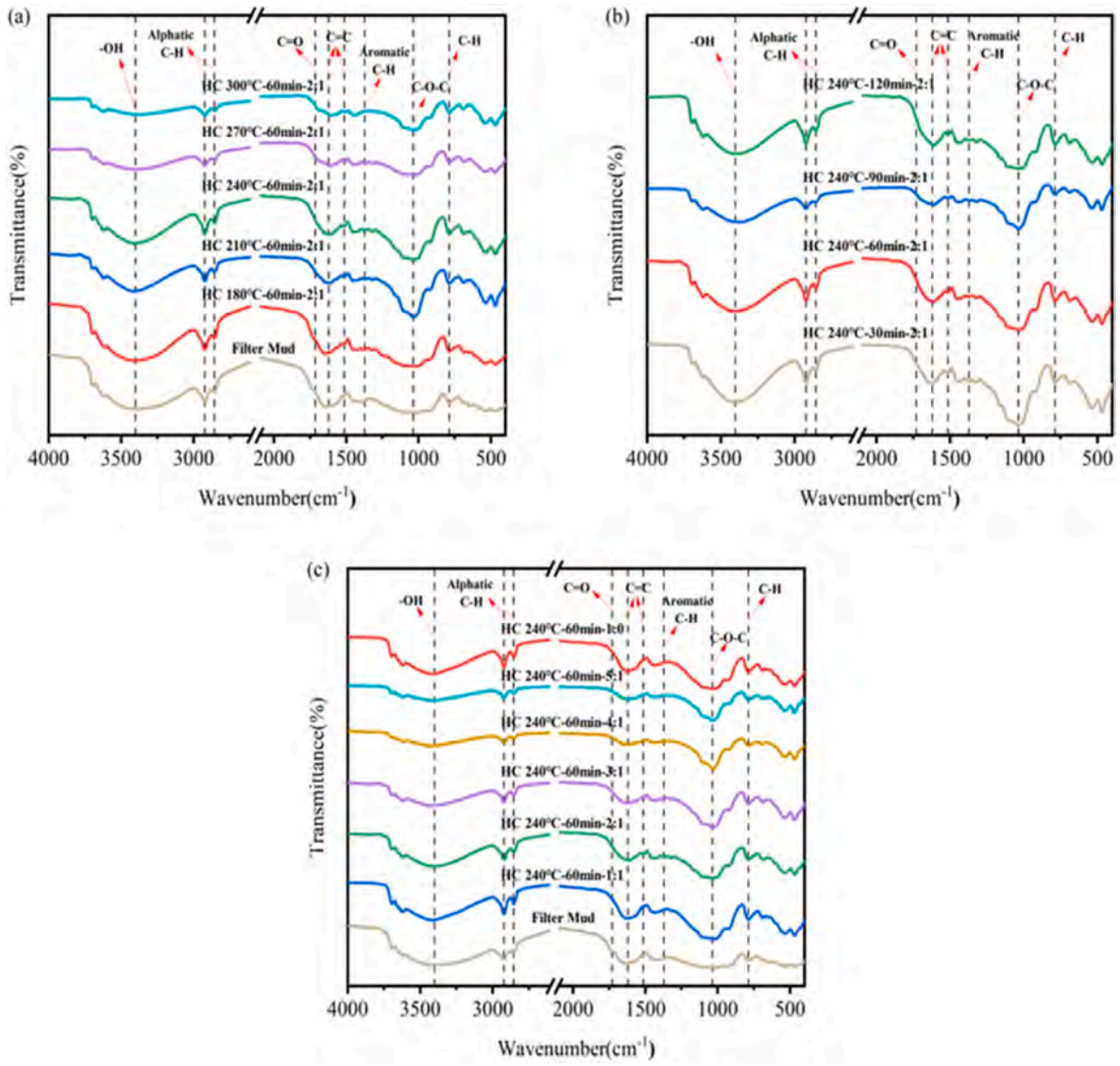


Fig. 4. FTIR of hydrochar generated under different conditions: (a) reaction temperature of 180–300 °C; (b) residence time of 30–120 min; (c) mixing ratio of 1:0–5:1.

properties and that hydrochars at 300°C-60min-2:1 are in the lignite range, which can be considered as prospective alternatives to coal [39]. This demonstrates yet again the pivotal role played by the reaction temperature in determining the composition of hydrochar [32]. In addition, the range of H/C atomic ratios in this study is slightly wider than that of the four common coals due to the large amount of oils and fats contained in FM and SCB [37].

3.1.2. pH, EC and HHV

Table 1 reports the pH, EC, and HHV of the hydrochar. The pH of the hydrochar remained relatively stable and ranged from neutral to slightly acidic. With the temperature increased, the pH of hydrochar started to decrease sharply, followed by a gradual increase. This phenomenon is likely attributed to the generation of organic acids resulting from the decomposition of carbohydrates in the raw material, leading to an initial reduction in pH. At elevated temperatures, the ongoing degradation of organic acids results in the depletion of acidic functional groups, such as carboxyl and hydroxyl, ultimately causing an elevation in the pH of hydrochar [27,34,40]. In contrast, the influence of residence time on the pH of hydrochar is relatively insignificant. Moreover, the pH of hydrochar produced exclusively through the HTC of FM tended to be neutral. This can be ascribed to the marginal presence of CaO and MgO in the raw material of FM, which neutralizes with organic acids after the HTC process. As the mixing ratio increased from 1:0 to 5:1, the concentrations of sucrose, cellulose, and other components in the raw material augmented. The hydrolysis process resulted in the generation of additional organic acids, leading to a gradual decrease in the pH of the hydrochar. This concurs with the observations of others [41], indicating that an increase in biomass content during co-HTC and the generation of bio-acids through thermal decomposition are contributing factors to the pH reduction.

Electrical conductivity (EC) serves to evaluate the soluble salt content in the sample. The HTC minimally affects soil salinity when used as a soil amendment [42,43]. The electrical conductivity of hydrochar produced at 180 °C is highest (1.70 mS/cm), and at 300 °C, it is lowest (0.49 mS/cm); both values are consistent with A-type soil salinity (<2.00 mS/cm) [44]. Interestingly, the electrical conductivity values for HTC produced at 180 °C and 300 °C were found to be exceptionally high similarly [42]. They proposed that the variation in conductivity after HTC is attributed to the disproportionate leaching of inorganic minerals from biomass. Examination of Table 1 indicates a substantial correlation between the HHV and the carbon content (C content) of hydrochar [45].

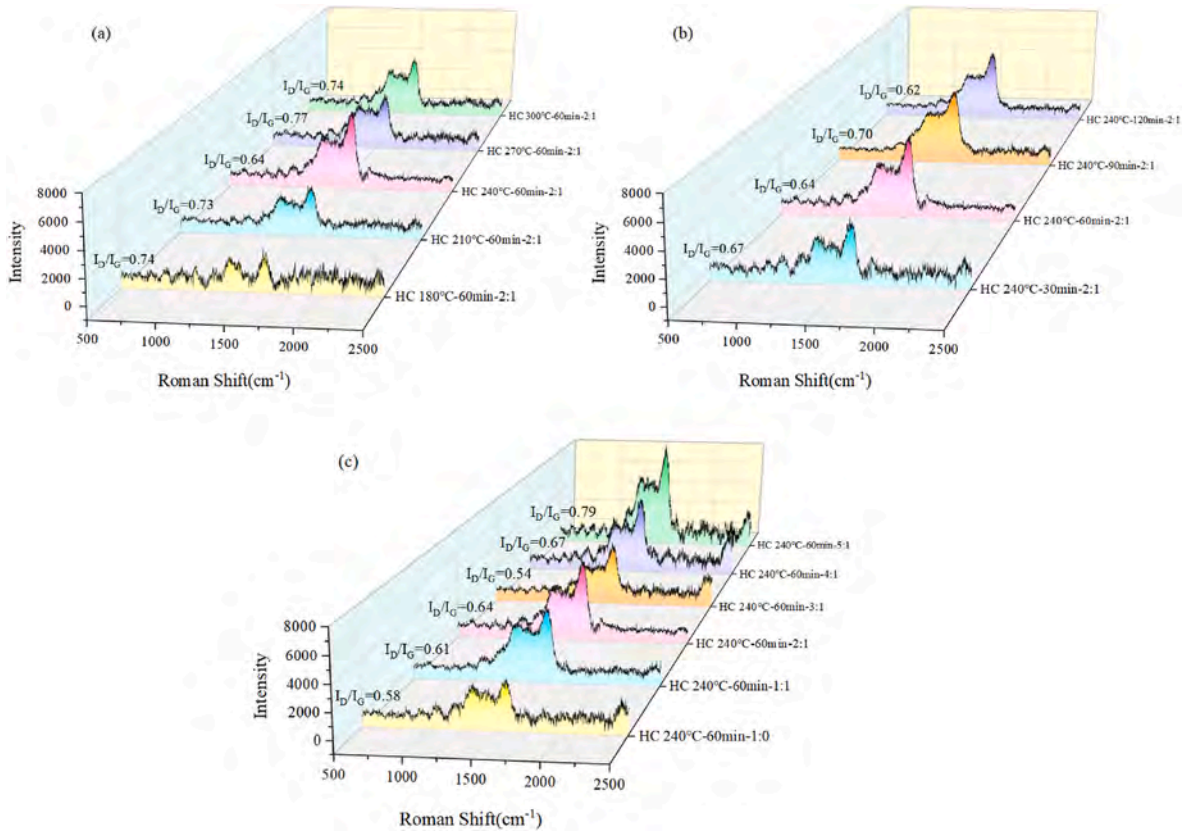


Fig. 5. Raman spectra of hydrochar produced under different conditions: (a) reaction temperature of 180–300 °C; (b) residence time of 30–120 min; (c) mixing ratio of 1:0–5:1.

The HHV of hydrochar increased accordingly to the increase in the content of C. Furthermore, the HHV of hydrochar can be enhanced by adjusting reaction temperature and residence time. Nevertheless, the HHV exhibits significant variation across different mixing ratios (5.99–14.11 MJ/kg), and the rise in HHV does not demonstrate a linear correlation with the increase in mixing ratio. These outcomes align with the conclusions of implying that the non-linear HHV increase during co-HTC is mainly a result of the swift aggregation and aromatization reactions of hydrochar [28]. These reactions result in agglomeration, slag formation, inadequate contact between the two feedstocks, and a subsequent reduction in the intensity of the thermal reaction.

3.1.3. Hydrochar yield from different HTC process conditions

Table 1 presents the hydrochar yield under various reaction conditions. The hydrochar yield dramatically dropped as the reaction temperature rose. On the one hand, elevated temperature supplies energy to break intermolecular bonds in biomass, causing the degradation of macromolecular organic matter in the feedstock. This leads to the generation of soluble substances such as 5-hydroxymethyl furfural, aldehydes, furfural, organic acids, alcohols, diols, and polyols, transferring to the liquid phase [24,28]. On the other hand, Lignin, cellulose, and hemicellulose are the primary constituents of the raw material, decompose at 180 °C, 200 °C, and 220 °C, respectively, contributing to the reduction in hydrochar yield [46]. The prolonged residence time results in a modest decrease in hydrochar yield, dropping from 57.08 % to 54.24 % as the residence time extends from 30 to 120 min, which is consistent with reported findings by Ref. [43], indicating that longer residence times lead to additional decomposition of liquid-phase products, generating gaseous byproducts. Additionally, co-HTC yields less compared to the exclusive HTC of FM. This can be attributed to the reaction of intermediates formed during FM degradation with free radicals produced by cellulose. This interaction stabilizes the co-HTC process, impeding subsequent condensation and re-polymerization [47].

It is noteworthy that as the mixing ratio increased, the hydrochar yield showed a gradual increase. This phenomenon is attributed to the increased carbohydrate content of the raw material, which intensifies the Maillard reaction, promoting hydrolysis and the production of a substantial amount of decreasing amino acids and sugars, which then come together to generate Amadori compounds, consequently facilitating the formation of hydrochar and leading to an increase in hydrochar yield [19,48].

3.2. Physical structure analysis of hydrochar

3.2.1. Surface morphology of hydrochar

The SEM images illustrated in Fig. 2 show significant changes in the physical structure and surface morphology of raw materials and hydrochars under various conditions. The untreated raw material features a smooth and intact surface. However, the surface of hydrochar became roughly textured, showcasing a loose and porous structure. This alteration was ascribed to the elimination of volatile substances from biomass during HTC, resulting in the formation of gaseous by-products such as CO_2 and H_2O. The emission of these gases creates the porous structure observed on the surface [49,50]. As the reaction temperature and residence time increased, there was an augmented generation of spherical carbon particles on the surface of hydrochar. Notably, when temperatures exceeded 240 °C or the residence time was extended to 90 min, the highly organized fibrous structure was disrupted to varying degrees, which hastened the appearance of additional microspheres on hydrochar's surface [48,51]. Furthermore, when FM was hydrothermally carbonized alone, its surface displayed a relatively loose structure, whereas when SCB was added to the mixture at a 1:1 ratio, the pores of hydrochar shrank, and the structure became tighter. This observation corresponds with the findings of an examination of the co-HTC of

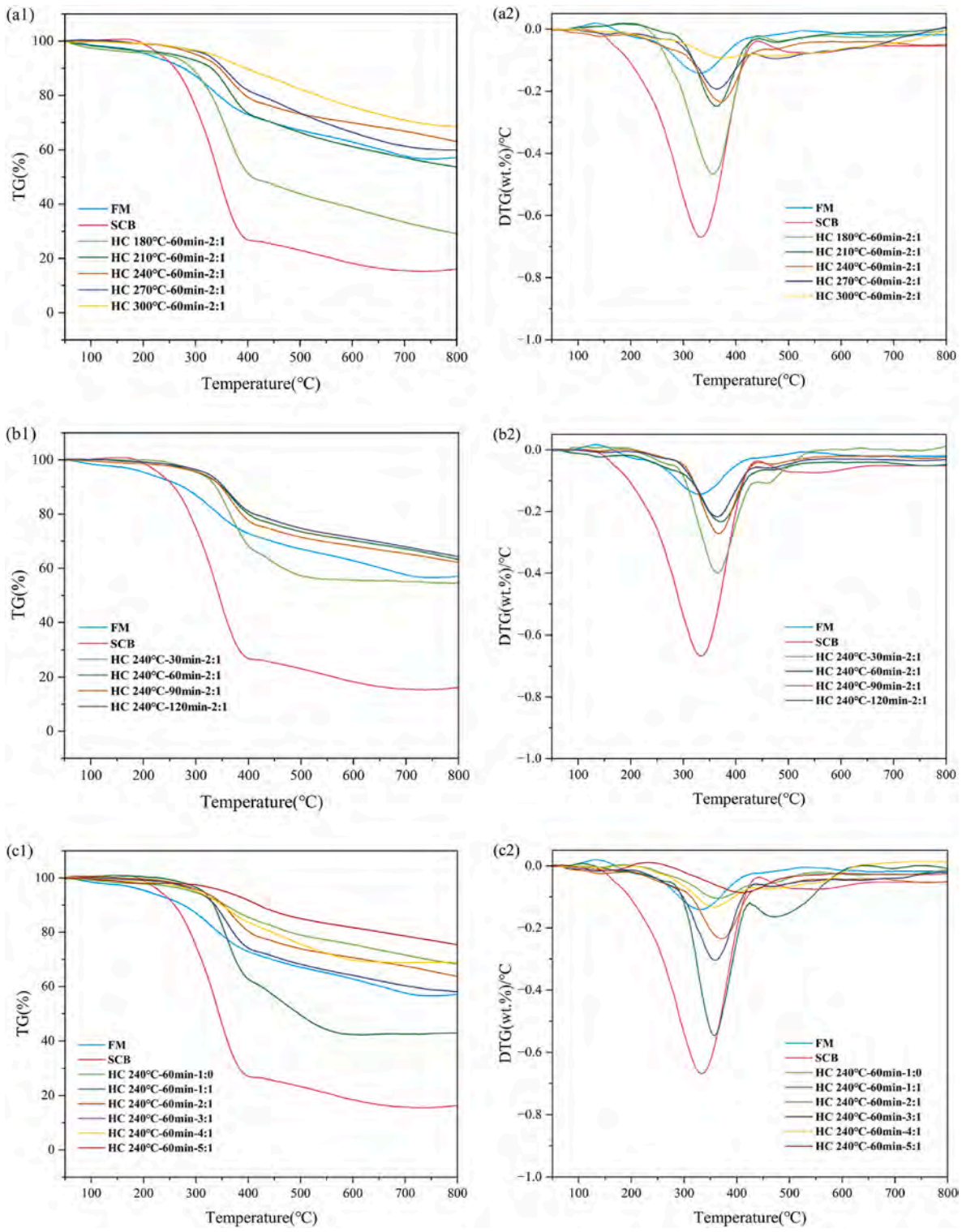


Fig. 6. TG and DTG curves for raw materials and hydrochar: (a) reaction temperatures from 180–300 °C; (b) residence times from 30–120 min; (c) mixing ratios from 1:0–5:1.

cellulose and pig manure [47]. They posit that co-HTC disrupts the structure of raw materials, resulting in microspheres derived from cellulose materials to the solid surface of the raw substance, subsequently obstructing or covering pores. Interestingly, the surface cracking of hydrochar was more severe, and the pores expanded as the FM ratio increased. This observation suggests that the increased FM content may facilitate the cleavage of cellulose and hemicellulose, the organic components of SCB, ultimately contributing to the formation of microspheres in hydrochar. Interestingly, as the proportion of FM increased, there was a corresponding escalation in the degree of surface cracking in hydrochar, resulting in larger pores. It is speculated that the higher content of FM intensifies the cleavage of organic components, including cellulose and hemicellulose, thereby playing a more significant role in the formation of hydrochar microspheres [52].

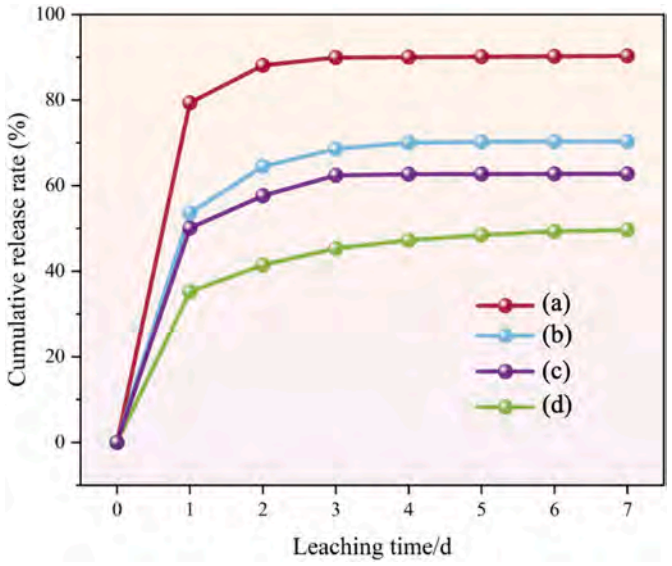


Fig. 7. Cumulative release rate of urea from different hydrochar fertilizer ratios: (a) Urea; (b) $HBSRF_1$; (c) $HBSRF_3$;(d) $HBSRF_5$.

Table 3
Urea release kinetic modeling parameters for different fertilizers.

Kinetic models	Parameter	Fertilizers			
		Urea	$HBSRF_1$	$HBSRF_3$	$HBSRF_5$
Zero-order	R^2	0.31477	0.42706	0.39758	0.52398
	K_0	0.53598	0.10065	0.09829	0.10574
	SSE	0.49825	0.41059	0.43321	0.32364
First-order	r^2	0.99991	0.99922	0.99807	0.99158
	K_1	0.99723	0.99585	0.99649	0.97205
	SSE	6.47E-05	5.59E-04	0.00139	0.00573
Higuchi	r^2	0.31477	0.42706	0.39758	0.52398
	K_H	0.18259	0.2013	0.19658	0.21147
	SSE	0.49825	0.41059	0.43321	0.32364
Korsmeyer-Peppas	r^2	0.99583	0.98896	0.99092	0.99626
	K_{kp}	0.91105	0.81335	0.83951	0.73499
	n	0.05747	0.12498	0.10687	0.17155
	SSE	0.00303	0.00791	0.00653	0.00254

3.2.2. Pore structure of hydrochar

Fig. 3 presents the N_2 isothermal adsorption/desorption curves of hydrochar under diverse conditions. The illustration reveals that all hydrochars display similar isotherm curves and exhibit a distinctive hysteresis loop in the adsorption-desorption process. The classification criteria outlined by the International Union of Pure and Applied Chemistry (IUPAC) correspond to the features of type IV curves, indicating that the hydrochar generated in this study qualifies as a mesoporous material with an average pore diameter ranging between 2.0 and 50.0 nm [53].

According to Table 2, hydrochar had the greatest pore volume and specific surface area at 240°C-60min-5:1 and 240°C-60min-4:1. When the temperature of HTC reached 240 °C, the specific surface area and total pore volume of hydrochar increased significantly, whereas the average pore size decreased slightly, indicating an increase for particles in the hydrochar. Nevertheless, with the further elevation of the carbonization temperature, the preceding pores commenced to collapse, thereby engendering an augmentation in the mean pore size and a diminution in the total pore volume and specific surface area of the water and coal [54]. According to Fig. 2(g), (h), and (i), the observed surface morphology of hydrochar in SEM analysis corresponds to its specific surface area, pore volume, and pore diameter results. As the mixing ratio increased, both the pore volume and specific surface area of hydrochar increased significantly. This larger specific surface area not only enhanced the active adsorption sites of hydrochar but also fostered soil microbial activity, contributing to the overall health of the soil ecosystem and nutrient cycling [55]. Furthermore, upon comparison, the hydrochar produced by FM and SCB co-HTC(14.35–45.92 m^2/g) exceeded the hydrochar produced by the hydrochar produced by food waste and corn stover co-HTC (0.98–2.81 m^2/g) and the biochar produced from the co-pyrolysis of sewage sludge and sawdust/rice straw (3.9–6.6 m^2/g) in terms of specific surface area on comparison [48,53]. This finding further underscores the robust adsorption capacity of hydrochar produced from the co-HTC of FM and SCB.

3.3. Analysis of functional groups and chemical structure of hydrochar surface

3.3.1. FTIR analysis

The transformation of functional groups in FM and hydrochar is clarified using FTIR analysis. Fig. 4(a), (b), and (c) depict the impact of reaction temperature, residence time, and mixing ratio on the surface functional groups of hydrochar. The broad peak at around 3402 cm^{-1} corresponded to the O-H stretching vibration, and its intensity diminished with the heightened severity of HTC, signifying dehydration reactions taking place throughout the process [51]. The peaks 2922 cm^{-1} and 2855 cm^{-1} were associated with C-H stretching vibrations in aliphatic compounds [56,57]. The peaks of the lignin aromatic ring, lignin aromatic skeleton C=C, and aliphatic molecule C-H were shown at 1620 cm^{-1}, 1514 cm^{-1}, and 1372 cm^{-1}, respectively. All three decreased as the reaction degree increased, further confirming the decomposition of lignin and the generation of aromatic compounds [57,58]. The peak at approximately 1035 cm^{-1} was attributed to the stretching vibration of C-O-C present in cellulose and hemicellulose. This peak exhibited a reduction in intensity with increasing reaction temperatures and prolonged residence times. This trend suggests that the carbohydrates and lipids are progressively degraded as the reaction occurs [59]. However, as observed in Fig. 4(c), an increase in the co-HTC ratio slightly enhances the peak intensity compared to the 1:0 condition. This enhancement may be ascribed to initial organic components remaining in the hydrochar after the condensation reaction in feedstocks [60]. Finally, the aromatic compound C-H, which is present at 788 cm^{-1}, demonstrates the high level of aromatization of the product [61]. In summary, hydrochar is rich in surface functional groups that make it more stable for microbial and chemical degradation, contributing to the sustainable retention of nutrients. This characteristic adds value to its potential applications in land use and adsorption [62].

3.3.2. Raman analysis

Raman spectroscopy is a potent tool for analyzing the chemical structure evolution of biochar, enabling the study of the degree of ordering in various hydrochars [49,63]. The Raman spectra shown in Fig. 5 pertain to hydrochars produced under different conditions. The Raman spectra of carbonaceous materials predominantly feature the D band (1350–1325 cm^{-1}), as well as the G band (1610–1580 cm^{-1}), representing the structural flaws in carbon atoms and the sp^2 hybridized carbon atoms' in-plane stretching vibration, respectively [64,65]. These two bands' relative intensity ratio (I_D/I_G) provides an effective indication of the graphitization degree of carbonaceous materials. A higher I_D/I_G value signifies a greater degree of disorder and a lower degree of graphitization [61,66]. These data indicate the existence of minor aromatic clusters in hydrochar, confirming the aromatization reactions as observed in the previously mentioned FTIR analysis [61].

Analysis indicates that, during the HTC process conducted at temperatures ranging from 180–240 °C, the degree of graphitization increases due to processes such as crystallization, gas elimination, and graphite formation. However, as the carbonization temperature steadily ascended, the I_D/I_G ratio also increased, signifying an increasing number of defective aromatic structures in hydrochar [67]. It has been proposed that this phenomenon is a result of the heightened intensity of the

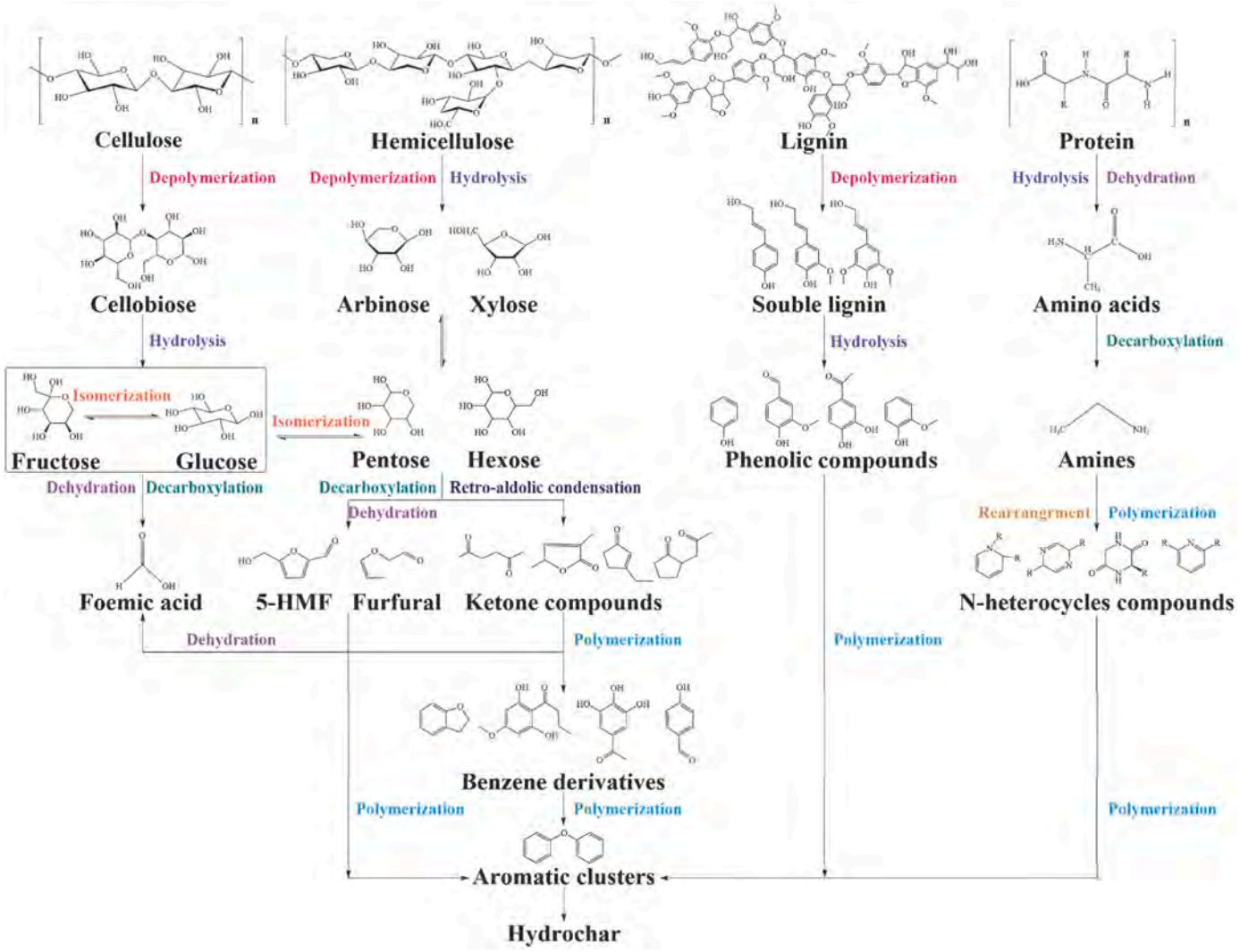


Fig. 8. Reaction path for the co-HTC process of FM and SCB.

aromatic ring condensation reaction within hydrochar at elevated temperatures [50]. Simultaneously, the reduction in substituents or aliphatic-branched chains occurred, contributing to the augmentation of medium and large aromatic ring systems in hydrochar. The extension of residence time showed no significant change in the I_D/I_G value. However, with an increase in the mixing ratio, the I_D/I_G value gradually increases, reaching its maximum at a mixing ratio of 5:1. This also confirms the maximum disorderliness of hydrochar under this condition, exhibiting more functional groups and active sites, which contribute to its strong adsorption capacity [65]. Overall, the I_D/I_G ratio of hydrochar fell within the range of 0.5–0.8, displaying observable amorphous carbon characteristics. Hydrochar can be applied in adsorption, soil improvement, and other related fields because of its faulty crystalline structure [66].

3.3.3. *Thermal stability analysis*

The thermal stability of hydrochar was assessed by thermogravimetric analysis shown in Fig. 6, which displays the TG and DTG curves of hydrochar derived from raw materials such as FM and SCB. There are three major phases in the combustion process: the dehydration stage, the devolatilization stage, and the combustion stage [48,68]. First of all, the evaporation of water caused a slight hydrochar's weight loss in the region of 100–200 °C, thus validating the vibration phenomenon of hydroxyl O-H stretching bands observed in FTIR analysis [48,56]. In the range of 200–400 °C, it is primarily associated with the decomposition of hemicellulose and cellulose [28]. Previous studies have demonstrated that the composition of biomass significantly influences its pyrolysis, with higher contents of cellulose and hemicellulose resulting in a faster rate of pyrolytic weight loss [69]. The third stage is a sluggish combustion phase (500–800 °C) of ash melting [70].

Comparing the plots in Fig. 6(a1), (a2), (b1), and (b2), it is evident that the increase in the operational parameters expedites the decomposition of volatile components, causing a significant decrease in the weight loss of the hydrochar and a gradual decrease in the temperature range [68]. It can be observed that FM and the hydrochar are both higher than SCB, indicating that the HTC process could remove unstable functional groups and small molecular substances in biomass [20]. When compared with the HTC with FM only, the hydrochar produced with a ratio of 1:1of co-HTC exhibits a new peak of around 450–500 °C, which can be related to the inclusion of SCB, leading to an elevated content of residual lignin in the hydrochar. Additionally, at the ratio of 5:1, the stability of the hydrochar is notably superior compared to the other conditions, which might be attributed to the hydrolysis intermediates of cellulose and hemicellulose (such as 5-HMF) promoting the aromatization reactions and forming more stable aromatic structures in hydrochars [20,28].

3.4. Evaluation of slow-release performance of HBSRF

3.4.1. Slow-release behavior

The comprehensive analysis of hydrochar properties mentioned above reveals that hydrochar, synthesized at 240°C-60min-5:1, has great potential as a slow-release fertilizer. This is attributed to its surface abundant functional groups, expansive specific surface area, and robust stability [71]. To explore its application prospects in agriculture, an evaluation of the slow-release performance of HBSRF was conducted through column leaching experiments involving urea at different hydrochar-to-fertilizer ratios.

Fig. 7 depicts the cumulative release rates of urea under different ratios of hydrochar to fertilizer. The results reveal that urea was released at the fastest rate on the first day, with a cumulative release rate of 79.37 %. In contrast, the cumulative release for $HBSRF_1$, $HBSRF_3$, and $HBSRF_5$ were 53.58 %, 50.07 %, and 35.19 %, respectively. This underscores the fact that pure urea dissolves readily after leaching. Thus, nutrient release is faster than in HBSRF. A comparative analysis showed that nearly all urea dissolved after four days, whereas the hydrochar-based fertilizer didn't reach equilibrium until the seventh day, indicating that the addition of hydrochar had an excellent slow-release effect. Additionally, on the seventh day, the cumulative release rates of urea for $HBSRF_1$, $HBSRF_3$, and $HBSRF_5$ were 70.31 %, 62.76 %, and 49.65 %, respectively. As the hydrochar-to-fertilizer ratio increased, the cumulative urea release performance of HBSRF gradually diminished, which was mainly ascribed to urea adsorption onto the hydrochar surface, penetration into the porous structure of hydrochar and chemical reactions with functional groups on the surface of hydrochar. These interactions effectively amplified the slow-release efficacy [72,73].

3.4.2. The kinetics of urea release

The cumulative release data of urea from slow-release fertilizers with varying hydrochar-to-fertilizer ratios were investigated using four distinct kinetic model types. The parameters of different kinetic models are presented in Table 3. It was found that, except for the $HBSRF_5$, the other three models conformed to the first-order kinetic equation for fertilizer release mechanisms ($R^2 > 0.99$). This indicates that the urea release rate is dependent on urea concentration [72]. For the $HBSRF_5$, the Korsmeyer-Peppas model had the highest R^2 and the lowest SSE, conforming to the Korsmeyer-Peppas model. This implies that urea was released slowly by pore diffusion, where n represents the diffusion index. The fitted n value was 0.172 (<0.45), suggesting that the fertilizer release behavior was determined by Fickian diffusion. This could be attributed to the increased content of hydrochar, allowing more nutrients to be stored in the pores of hydrochar, promoting the adsorption of urea by the pores [26,72,74]. During the entire release process, in addition to the predominant role played by the pores, the surface characteristics of hydrochar also dictated the urea release rate. The neutral to weakly acidic pH and the functional groups, such as aliphatic, phenolic hydroxyl, and carbonyl, on the surface of hydrochar effectively reduced the hydrolysis rate of urea [75].

3.5. Reaction path for co-HTC processes

Analyzing hydrochar characteristics, we deduce a reaction path for the co-HTC of FM and SCB. Fig. 8 illustrates that the primary constituents of both feedstocks, FM and SCB, include cellulose, hemicellulose, lignin, and protein. During the HTC process, hemicellulose in FM and SCB depolymerizes and breaks down into polysaccharides. Subsequently, the xylose formed in this process was hydrolyzed to produce pentose or hexose sugars by isomerization. Bond breaking in the lignocellulose matrix caused the creation of oligomers from cellulose, such as cellobiose, whereby glucose and fructose, respectively, were produced from polysaccharides (starch) and disaccharides (sucrose) and similarly isomerized to pentose and hexose [36,39]. The monosaccharides obtained were subjected to dehydration and decarboxylation reactions to yield furfural, 5-HMF, and other substances, and ketone compounds via reverse aldol condensation reactions [39,48,60]. Simultaneously, a sequence of dehydration and decarboxylation reactions was initiated by glucose and aldehyde-ketone compounds, resulting in the generation of organic acids and the production of H^+, which served as catalysts in the process [48,60]. Amino acids were produced by hydrolysis of proteins in FM. The organic amines obtained after decarboxylation can be converted into N-heterocyclic compounds [47].

In the Maillard reaction, glucose and amino acids reacted to produce Amadori compounds, which were further dehydrated to form N-heterocyclic compounds. Lignin was divided into soluble lignin and insoluble lignin. Soluble lignin was hydrolyzed into phenols, and unhydrolyzed lignin could directly carbonize into the hydrochar matrix [36,39,48]. During polymerization, furfural, 5-HMF, benzene derivatives, phenols, aldehydes, ketones, and N-heterocyclic compounds were converted to aromatic clusters, which further polymerized to form hydrochars [39,48,60,76]. This also verifies the previously mentioned situation that the hydrochar yield and specific surface area increased with an increase in mixing ratio during the co-HTC process. This was mainly because the higher the mixing ratio, the higher the concentration of proteins and carbohydrates, and the more sugars and amino acids were produced during hydrolysis. This accelerated the Maillard process, which in turn encouraged the creation of hydrochar microspheres [60].

3.6. Economic analysis

The processing of FM and SCB by hydrothermal carbonization technology results in the production of approximately 620 kg of hydrochar. Based on the yield obtained in the experiments, the addition of 60 % hydrochar allows to produce approximately one tone of hydrochar-based slow-release fertilizer. The market price of slow-release fertilizer is calculated at $415/t, while urea fertilizer is priced at $275/t. The financial implications of treating 1 tone of FM and SCB with natural gas are determined to be approximately $20. The cost of incorporating 30 % of the amount of urea into the production of 1 tone of hydrochar-based slow-release fertilizer is calculated to be $124, which equates to a total cost of $144. These figures illustrate that the economic viability of the process can be enhanced by reducing the initial investment costs.

In addition, the release of slow-release fertilizers is slower than that of traditional fertilizers, with a longer cycle. Hydrochar-based slow-release fertilizers can reduce the number of applications and waste of fertilizers, particularly in areas with high rainfall. They extend the release cycle, provide nutrients continuously, effectively improve the utilization rate of fertilizers, and save farmers time and labor costs.

4. Conclusion

The study proposes the co-HTC of high-sugar organic waste, FM, and low-moisture biomass, SCB. The research explores the impact of different conditions on the characteristics and structure of hydrochar. During co-HTC, the Maillard reaction, occurring among various components of feedstocks, accelerated dehydration and decarboxylation reactions and promoted the formation of hydrochar microspheres. Based on physical and chemical property characterization, the obtained hydrochar exhibited a maximum carbon content of 31.66 wt%, low ash content, conductivity within the range of Class A soils, and a surface rich in functional groups. It displayed a loose and porous structure, which enhanced soil water retention and aeration when used for land application. This significantly improved the nutrient uptake and retention capacity of the soil. Combined with the characteristics of hydrochar and the demands of energy consumption, it was found that hydrochar produced at 240°C-60min-5:1 provided optimal conditions for land application. It exhibited a C/N ratio of 26.9, a remarkably high specific surface area of 45.921 m^2/g, and a pore volume of 0.2061 cm^3/g, with a strong adsorption capacity. The optimal hydrochar conditions at 240°C-

60min-5:1 was selected as the carrier of HBSRF, and addition of different hydrochar-to-fertilizer ratios were added, which reveals that all HBSRF variants effectively slowed down urea release. Among them, $HBSRF_5$ exhibited superior slow-release performance, and its release kinetics aligned with the Korsmeyer-Peppas model. This implies that urea nitrogen was released through pore diffusion, thus validating the potential for agricultural application of slow-release fertilizers prepared from co-HTC of FM and SCB.

To authenticate its efficacy in agricultural settings, it is crucial to conduct soil fertility experiments on HBSRF. Furthermore, in large-scale industrial applications, the overall techno-economic assessment requires an in-depth analysis of the problems arising from the discharge or recovery of the liquid phase products of the HTC process to improve the sustainability of the process in large-scale facilities. It is imperative to carry out additional experiments focusing on the extracted liquid phase into the hydrothermal carbonation reaction as a solvent for the co-hydrothermal carbonation cycle experiment until the liquid is entirely depleted, which approach not only curtails the utilization of fresh water but also mitigates the financial burden associated with wastewater treatment in hydrothermal carbonation, enhancing the overall efficacy of the hydrothermal carbonation system.

CRediT authorship contribution statement

Sisi Chen: Conceptualization, Methodology, Investigation, Formal analysis, Visualization, Writing – original draft, Writing – review & editing. **Xingying Tang:** Supervision, Funding acquisition, Writing – review & editing. **Jiquan Chen:** Writing – review & editing. **Yuyang Xue:** Writing – review & editing. **Yinghui Wang:** Methodology, Writing – review & editing, Funding acquisition. **Donghai Xu:** Methodology, Writing – review & editing.

Declaration of competing interest

The authors declare that they have no known competing financial interests or personal relationships that could have appeared to influence the work reported in this paper.

Acknowledgments

This work was supported by the National Natural Science Foundation of China (No. 22068003) and the Guangxi Science and Technology Major Program (No. AA22117014).

Data availability

Data will be made available on request.

References

[1] X. Zhou, J. Zhao, M. Chen, G. Zhao, S. Wu, Influence of catalyst and solvent on the hydrothermal liquefaction of woody biomass, Bioresour. Technol. 346 (2022) 126354, https://doi.org/10.1016/j.biortech.2021.126354.
[2] Z. Hameed, M. Aslam, Z. Khan, K. Maqsood, A.E. Atabani, M. Ghauri, M. S. Khurram, M. Rehan, A. Nizami, Gasification of municipal solid waste blends with biomass for energy production and resources recovery: current status, hybrid technologies and innovative prospects, Renew. Sustain. Energy Rev. 136 (2021) 110375, https://doi.org/10.1016/j.rser.2020.110375.
[3] N. Aguilar-Rivera, M.T. Khan, I.A. Khan, R. Iqbal, M.M. Aslam, Sustainable conversion of wastes into green bioproducts to introduce diversification and green economy in the sugar industry. A review, Sugar Tech 24 (2022) 1198–1211, https://doi.org/10.1007/s12355-022-01167-7.
[4] S. Ou, J. Zhao, Y. Wang, Y. Tian, J. Wang, Preparation of octacosanol from filter mud produced after sugarcane juice clarification, Lwt - Food Science and Technology 45 (2012) 295–298, https://doi.org/10.1016/j.lwt.2011.08.011.
[5] M. Meghana, Y. Shastri, Sustainable valorization of sugar industry waste: status, opportunities, and challenges, Bioresour. Technol. 303 (2020) 122929, https://doi.org/10.1016/j.biortech.2020.122929.
[6] N. Ramanauske, T. Balezentis, D. Streimikiene, Biomass use and its implications for bioeconomy development: a resource efficiency perspective for the European countries, Technol. Forecast. Soc. Change 193 (2023) 122628, https://doi.org/10.1016/j.techfore.2023.122628.
[7] J. González-Arias, M.E. Sánchez, J. Cara-Jiménez, F.M. Baena-Moreno, Z. Zhang, Hydrothermal carbonization of biomass and waste: a review, Environ. Chem. Lett. 20 (2022) 211–221, https://doi.org/10.1007/s10311-021-01311-x.
[8] O.S. Djandja, R.K. Liew, C. Liu, J. Liang, H. Yuan, W. He, Y. Feng, B.G. Lougou, P. Duan, X. Lu, S. Kang, Catalytic hydrothermal carbonization of wet organic solid waste: a review, Sci. Total Environ. 873 (2023) 162119, https://doi.org/10.1016/j.scitotenv.2023.162119.
[9] Y.X. Seow, Y.H. Tan, N.M. Mubarak, J. Kansedo, M. Khalid, M.L. Ibrahim, M. Ghasemi, A review on biochar production from different biomass wastes by recent carbonization technologies and its sustainable applications, J. Environ. Chem. Eng. 10 (2022) 107017, https://doi.org/10.1016/j.jece.2021.107017.
[10] X. Wang, S. Yun, Wen Liang Fang, C. Zhang, X. Liang, Z. Lei, Z.-H. Liu, Layer-stacking activated carbon derived from sunflower stalk as electrode materials for high-performance supercapacitors, Sustainable Chemistry & Engineering 6 (2018) 11397–11407, https://doi.org/10.1021/acssuschemeng.8b01334.
[11] A.A. Gebretsadkan, Y.Z. Belete, L. Krounbi, I. Gelfand, R. Bernstein, A. Gross, Soil application of activated hydrochar derived from sewage sludge enhances plant growth and reduces nitrogen loss, Sci. Total Environ. 949 (2024) 174965, https://doi.org/10.1016/j.scitotenv.2024.174965.
[12] H. Zhao, X. Lu, Y. Wang, B. Sun, X. Wu, H. Lu, Effects of additives on sucrose-derived activated carbon microspheres synthesized by hydrothermal carbonization, J. Mater. Sci. 52 (2017) 10787–10799, https://doi.org/10.1007/s10853-017-1258-4.
[13] Q. Chen, H. Liu, J. Ko, H. Wu, Q. Xu, Structure characteristics of bio-char generated from co-pyrolysis of wooden waste and wet municipal sewage sludge, Fuel Process. Technol. 183 (2019) 48–54, https://doi.org/10.1016/j.fuproc.2018.11.005.
[14] M. Kim, J.F.S. Fernando, Z. Li, A. Alowasheeir, A. Ashok, R. Xin, D. Martin, A. Kumar Nanjundan, D.V. Golberg, Y. Yamauchi, N. Amiralian, J. Li, Ultra-stable sodium ion storage of biomass porous carbon derived from sugarcane, Chem. Eng. J. 445 (2022) 136344, https://doi.org/10.1016/j.cej.2022.136344.
[15] Q. Wang, S. Wu, D. Cui, H. Zhou, D. Wu, S. Pan, F. Xu, Z. Wang, Co-hydrothermal carbonization of organic solid wastes to hydrochar as potential fuel: a review, Sci. Total Environ. 850 (2022) 158034, https://doi.org/10.1016/j.scitotenv.2022.158034.
[16] S.P. Singh, M. Jawaid, M. Chandrasekar, K. Senthilkumar, B. Yadav, N. Saba, S. Siengchin, Sugarcane wastes into commercial products: processing methods, production optimization and challenges, J. Clean. Prod. 328 (2021) 129453, https://doi.org/10.1016/j.jclepro.2021.129453.
[17] M. Ebrahim Malool, M. Keshavarz Moraveji, J. Shayegan, Co-hydrothermal carbonization of digested sewage sludge and sugarcane bagasse: integrated approach for waste management, optimized production, characterization and Pb (II) adsorption, Alex. Eng. J. 74 (2023) 79–105, https://doi.org/10.1016/j.aej.2023.05.018.
[18] C. Zheng, X. Ma, Z. Yao, X. Chen, The properties and combustion behaviors of hydrochars derived from co-hydrothermal carbonization of sewage sludge and food waste, Bioresour. Technol. 285 (2019) 121347, https://doi.org/10.1016/j.biortech.2019.121347.
[19] C. Zhang, X. Ma, C. Zheng, T. Huang, X. Lu, Y. Tian, Co-Hydrothermal carbonization of water hyacinth and sewage sludge: effects of aqueous phase recirculation on the characteristics of hydrochar, Energy Fuels 34 (2020) 14147–14158, https://doi.org/10.1021/acs.energyfuels.0c01991.
[20] C.-L. Xu, A. Li, X. Xu, Z. Yang, G. Wang, Z. Cheng, S. Zhang, T. Li, Y. Pu, Guochun Lv, J. Cai, W. Zhou, Z. Pu, X. Qi, Co-hydrothermal carbonization of rape straw and industrial sewage sludge – applications of hydrochar for N and P adsorptions and for agricultural/horticultural purposes, J. Clean. Prod. 451 (2024) 142154, https://doi.org/10.1016/j.jclepro.2024.142154.
[21] D. Dong, J. Li, S. Ying, J. Wu, X. Han, Y. Teng, M. Zhou, Y. Ren, P. Jiang, Mitigation of methane emission in a rice paddy field amended with biochar-based slow-release fertilizer, Sci. Total Environ. 792 (2021) 148460, https://doi.org/10.1016/j.scitotenv.2021.148460.
[22] W. Shi, Y. Ju, R. Bian, L. Li, S. Joseph, D.R.G. Mitchell, P. Munroe, S. Taherymoosavi, G. Pan, Biochar bound urea boosts plant growth and reduces nitrogen leaching, Sci. Total Environ. 701 (2020) 134424, https://doi.org/10.1016/j.scitotenv.2019.134424.
[23] J. Santana, I. José, Bárbara Olinda Nardis, Cristiane Muniz Barbosa, José Fernandes Filho, C. Azevedo, Long-term Effect of Biochar-Based Fertilizers Application in Tropical Soil: Agronomic Efficiency and Phosphorus Availability, vol. 760, 2021, https://doi.org/10.1016/j.scitotenv.2020.143955, 143955–143955.
[24] C. Li, R. Cai, A. Hasan, X. Lu, X. Yang, Y. Zhang, Fertility assessment and nutrient conversion of hydrochars derived from co-hydrothermal carbonization between livestock manure and corn cob, J. Environ. Chem. Eng. 11 (2023) 109166, https://doi.org/10.1016/j.jece.2022.109166.
[25] Y. Li, K. Li, M. Su, Y. Ren, Y. Li, J. Chen, L. Li, Fabrication of carbon/SiO 2 composites from the hydrothermal carbonization process of polysaccharide and their adsorption performance, Carbohydr. Polym. 153 (2016) 320–328, https://doi.org/10.1016/j.carbpol.2016.07.072.
[26] H. Zhang, L. Xing, H. Liang, S. Liu, W. Ding, J. Zhang, C. Xu, Preparation and characterization of biochar-based slow-release nitrogen fertilizer and its effect on maize growth, Ind. Crop. Prod. 203 (2023) 117227, https://doi.org/10.1016/j.indcrop.2023.117227.
[27] M. Cavali, H. Benbelkacem, B. Kim, R. Bayard, N. Libardi Junior, D. Gonzaga Domingos, A.L. Woiciechowski, A.B.D. Castilhos Junior, Co-hydrothermal carbonization of pine residual sawdust and non-dewatered sewage sludge – effect

of reaction conditions on hydrochar characteristics, J. Environ. Manag. 340 (2023) 117994, https://doi.org/10.1016/j.jenvman.2023.117994.
[28] C. Zhang, X. Ma, T. Huang, Y. Zhou, Y. Tian, Co-hydrothermal carbonization of water hyacinth and polyvinyl chloride: optimization of process parameters and characterization of hydrochar, Bioresour. Technol. 314 (2020) 123676, https://doi.org/10.1016/j.biortech.2020.123676.
[29] J. Zhang, L. Zhang, C. Lin, C. Wang, P. Zhao, Y. Li, Co-hydrothermal carbonization of polyvinyl chloride and lignocellulose biomasses: influence of biomass feedstock on fuel properties and combustion behaviors, Sci. Total Environ. 868 (2023) 161532, https://doi.org/10.1016/j.scitotenv.2023.161532.
[30] X. Liu, Y. Zhai, S. Li, Q. Niu, X. Liu, Z. Wang, Y. Liu, Z. Qiu, C. Li, Y. Zhu, M. Xu, Hydrothermal carbonization of petrochemical sludge: the fate of hydrochar and oil components, J. Environ. Chem. Eng. 10 (2022) 108234, https://doi.org/10.1016/j.jece.2022.108234.
[31] M. Paneque, J.M. De la Rosa, J. Kern, M.T. Reza, H. Knicker, Hydrothermal carbonization and pyrolysis of sewage sludges: what happen to carbon and nitrogen? J. Anal. Appl. Pyrolysis 128 (2017) 314–323, https://doi.org/10.1016/j.jaap.2017.09.019.
[32] Z. Xu, H. Song, S. Zhang, S. Tong, Z. He, Q. Wang, B. Li, X. Hu, Co-hydrothermal carbonization of digested sewage sludge and cow dung biogas residue: investigation of the reaction characteristics, Energy 187 (2019) 115972, https://doi.org/10.1016/j.energy.2019.115972.
[33] G.A.G. Kavindi, Z. Lei, T. Yuan, K. Shimizu, Z. Zhang, Use of hydrochar from hydrothermal co-carbonization of rice straw and sewage sludge for Cr(VI) bioremediation in soil, Bioresour. Technol. Rep. 18 (2022) 101052, https://doi.org/10.1016/j.biteb.2022.101052.
[34] Y. Xu, B. Wang, S. Ding, M. Zhao, Y. Ji, W. Xie, Z. Feng, Y. Feng, Hydrothermal carbonization of kitchen waste: an analysis of solid and aqueous products and the application of hydrochar to paddy soil, Sci. Total Environ. 850 (2022) 157953, https://doi.org/10.1016/j.scitotenv.2022.157953.
[35] R. Wang, H. Lei, S. Liu, X. Ye, J. Jia, Z. Zhao, The redistribution and migration mechanism of nitrogen in the hydrothermal co-carbonization process of sewage sludge and lignocellulosic wastes, Sci. Total Environ. 776 (2021) 145922, https://doi.org/10.1016/j.scitotenv.2021.145922.
[36] D. Lachos-Perez, P. César Torres-Mayanga, E.R. Abaide, G.L. Zabot, F. De Castilhos, Hydrothermal carbonization and Liquefaction: differences, progress, challenges, and opportunities, Bioresour. Technol. 343 (2022) 126084, https://doi.org/10.1016/j.biortech.2021.126084.
[37] Y.Z. Belete, V. Mau, R. Yahav Spitzer, R. Posmanik, D. Jassby, A. Iddya, N. Kassem, J.W. Tester, A. Gross, Hydrothermal carbonization of anaerobic digestate and manure from a dairy farm on energy recovery and the fate of nutrients, Bioresour. Technol. 333 (2021) 125164, https://doi.org/10.1016/j.biortech.2021.125164.
[38] A. Giannouli, S. Kalaitzidis, G. Siavalas, A. Chatziapostolou, K. Christanis, S. Papazisimou, C. Papanicolaou, A. Foscolos, Evaluation of Greek low-rank coals as potential raw material for the production of soil amendments and organic fertilizers, Int. J. Coal Geol. 77 (2009) 383–393, https://doi.org/10.1016/j.coal.2008.07.008.
[39] R. Wang, Q. Jin, X. Ye, H. Lei, J. Jia, Z. Zhao, Effect of process wastewater recycling on the chemical evolution and formation mechanism of hydrochar from herbaceous biomass during hydrothermal carbonization, J. Clean. Prod. 277 (2020) 123281, https://doi.org/10.1016/j.jclepro.2020.123281.
[40] Y. Fei, D. Zhao, Y. Liu, W. Zhang, Y. Tang, X. Huang, Q. Wu, Y. Wang, T. Xiao, C. Liu, Feasibility of sewage sludge derived hydrochars for agricultural application: nutrients (N, P, K) and potentially toxic elements (Zn, Cu, Pb, Ni, Cd), Chemosphere 236 (2019) 124841, https://doi.org/10.1016/j.chemosphere.2019.124841.
[41] X. Zhang, R. Huang, Y. Cao, C. Wang, Rapid conversion of red mud into soil matrix by co-hydrothermal carbonization with biomass wastes, J. Environ. Chem. Eng. 9 (2021) 106039, https://doi.org/10.1016/j.jece.2021.106039.
[42] C. Nzediegwu, M.A. Naeth, S.X. Chang, Carbonization temperature and feedstock type interactively affect chemical, fuel, and surface properties of hydrochars, Bioresour. Technol. 330 (2021) 124976, https://doi.org/10.1016/j.biortech.2021.124976.
[43] J. Xiong, Z. Pan, X. Xiao, H. Huang, F. Lai, J. Wang, S. Chen, Study on the hydrothermal carbonization of swine manure: the effect of process parameters on the yield/properties of hydrochar and process water, J. Anal. Appl. Pyrolysis 144 (2019) 104692, https://doi.org/10.1016/j.jaap.2019.104692.
[44] L.C.D.A. Monica Puccini, Hydrothermal carbonization of municipal woody and herbaceous prunings: hydrochar valorisation as soil amendment and growth medium for horticulture, Sustainability (2018), https://doi.org/10.3390/su10030846.
[45] P. Gao, Y. Zhou, F. Meng, Y. Zhang, Z. Liu, W. Zhang, G. Xue, Preparation and characterization of hydrochar from waste eucalyptus bark by hydrothermal carbonization, Energy 97 (2016) 238–245, https://doi.org/10.1016/j.energy.2015.12.123.
[46] H.A. Murillo, J. Pagés-Díaz, L.A. Díaz-Robles, F. Vallejo, C. Huiliñir, Valorization of oat husk by hydrothermal carbonization: optimization of process parameters and anaerobic digestion of spent liquors, Bioresour. Technol. 343 (2022) 126112, https://doi.org/10.1016/j.biortech.2021.126112.
[47] Q. Li, H. Lin, S. Zhang, X. Yuan, M. Gholizadeh, Y. Wang, J. Xiang, S. Hu, X. Hu, Co-hydrothermal carbonization of swine manure and cellulose: influence of mutual interaction of intermediates on properties of the products, Sci. Total Environ. 791 (2021) 148134, https://doi.org/10.1016/j.scitotenv.2021.148134.
[48] Q. Wang, S. Wu, D. Cui, S. Pan, F. Xu, F. Xu, Z. Wang, G. Li, Co-hydrothermal carbonization of corn stover and food waste: characterization of hydrochar, synergistic effects, and combustion characteristic analysis, J. Environ. Chem. Eng. 10 (2022) 108716, https://doi.org/10.1016/j.jece.2022.108716.
[49] H. Dang, R. Xu, J. Zhang, M. Wang, K. Xu, Hydrothermal carbonization of waste furniture for clean blast furnace fuel production: physicochemical, gasification characteristics and conversion mechanism investigation, Chem. Eng. J. 469 (2023) 143980, https://doi.org/10.1016/j.cej.2023.143980.
[50] X. Yang, B. Wang, X. Song, F. Cheng, Evolution characteristics and mechanism of carbon structure during co-hydrothermal carbonization of sewage sludge and subbituminous coal, J. Clean. Prod. 434 (2024) 140382, https://doi.org/10.1016/j.jclepro.2023.140382.
[51] C. Li, R. Cai, Preparation of solid organic fertilizer by co-hydrothermal carbonization of peanut residue and corn cob: a study on nutrient conversion, Sci. Total Environ. 838 (2022) 155867, https://doi.org/10.1016/j.scitotenv.2022.155867.
[52] E.I.N.C. Assis, B. Gidudu, E.M.N. Chirwa, Hydrothermal carbonisation of paper sludge: effect of process conditions on hydrochar fuel characteristics and energy recycling efficiency, J. Clean. Prod. 373 (2022) 133775, https://doi.org/10.1016/j.jclepro.2022.133775.
[53] H. Huang, T. Yang, F. Lai, G. Wu, Co-pyrolysis of sewage sludge and sawdust/rice straw for the production of biochar, J. Anal. Appl. Pyrolysis 125 (2017) 61–68, https://doi.org/10.1016/j.jaap.2017.04.018.
[54] Q. He, C. Cheng, A. Raheem, L. Ding, S. Shiung Lam, G. Yu, Effect of hydrothermal carbonization on woody biomass: from structure to reactivity, Fuel 330 (2022) 125586, https://doi.org/10.1016/j.fuel.2022.125586.
[55] S. Yu, Y. Feng, L. Xue, H. Sun, L. Han, L. Yang, Q. Sun, Q. Chu, Biowaste to treasure: application of microbial-aged hydrochar in rice paddy could improve nitrogen use efficiency and rice grain free amino acids, J. Clean. Prod. 240 (2019) 118180, https://doi.org/10.1016/j.jclepro.2019.118180.
[56] T. Wang, B. Si, Z. Gong, Y. Zhai, M. Cao, C. Peng, Co-hydrothermal carbonization of food waste-woody sawdust blend: interaction effects on the hydrochar properties and nutrients characteristics, Bioresour. Technol. 316 (2020) 123900, https://doi.org/10.1016/j.biortech.2020.123900.
[57] M. Wang, M. Zhang, X. Chen, A. Chen, R. Xiao, X. Chen, Hydrothermal conversion of Chinese cabbage residue for sustainable agriculture: influence of process parameters on hydrochar and hydrolysate, Sci. Total Environ. 812 (2022) 152478, https://doi.org/10.1016/j.scitotenv.2021.152478.
[58] X. Chen, X. Fan, K. Gao, Y. Cheng, K. Zhang, L. Liu, L. Fang, J. Park, X. Chen, R. Xiao, Impacts of EDTA on the fate of nutrients and heavy metals during the hydrothermal carbonization of poultry manure, J. Environ. Chem. Eng. 11 (2023) 110061, https://doi.org/10.1016/j.jece.2023.110061.
[59] M.P. Olszewski, S.A. Nicolae, P.J. Arauzo, M. Titirici, A. Kruse, Wet and dry? Influence of hydrothermal carbonization on the pyrolysis of spent grains, J. Clean. Prod. 260 (2020) 121101, https://doi.org/10.1016/j.jclepro.2020.121101.
[60] T. Liu, H. Jiao, L. Yang, W. Zhang, Y. Hu, Y. Guo, L. Yang, S. Leng, J. Chen, J. Chen, H. Peng, L. Leng, W. Zhou, Co-hydrothermal carbonization of cellulose, hemicellulose, and protein with aqueous phase recirculation: insight into the reaction mechanisms on hydrochar formation, Energy 251 (2022) 123965, https://doi.org/10.1016/j.energy.2022.123965.
[61] S. Hao, Q. Zhang, Y. Shi, Q. Guo, P. Li, J. Huang, Preparation and characterization of the poplar micro-nano cellulose sustainable carbon spheres, Biomass Convers. Biorefinery (2022), https://doi.org/10.1007/s13399-022-03003-0.
[62] A. Khosravi, H. Zheng, Q. Liu, M. Hashemi, Y. Tang, B. Xing, Production and characterization of hydrochars and their application in soil improvement and environmental remediation, Chem. Eng. J. 430 (2022) 133142, https://doi.org/10.1016/j.cej.2021.133142.
[63] J. Xu, Q. He, Z. Xiong, Y. Yu, S. Zhang, X. Hu, L. Jiang, S. Su, S. Hu, Y. Wang, J. Xiang, Raman spectroscopy as a versatile tool for investigating thermochemical processing of coal, biomass, and wastes: recent advances and future perspectives, Energy Fuels 35 (2021) 2870–2913, https://doi.org/10.1021/acs.energyfuels.0c03298.
[64] W. Liang, G. Wang, R. Xu, X. Ning, J. Zhang, X. Guo, L. Ye, J. Li, C. Jiang, P. Wang, C. Wang, Hydrothermal carbonization of forest waste into solid fuel: mechanism and combustion behavior, Energy 246 (2022) 123343, https://doi.org/10.1016/j.energy.2022.123343.
[65] A.J. Ramiro De Castro, G.D. Saraiva, A.C. Oliveira, V.O. Sousa Neto, A.J. Paula, A. G. Souza Filho, O.P. Ferreira, Ordered porous carbons from hydrothermally treated biomass: effects of the thermal treatments on the structure and porosity, Vib. Spectrosc. 111 (2020) 103175, https://doi.org/10.1016/j.vibspec.2020.103175.
[66] Y. Zhao, W. Chen, F. Liu, P. Zhao, Hydrothermal pretreatment of cotton textile wastes: biofuel characteristics and biochar electrocatalytic performance, Fuel 316 (2022) 123327, https://doi.org/10.1016/j.fuel.2022.123327.
[67] X. Yang, B. Wang, X. Song, F. Yang, F. Cheng, Co-hydrothermal carbonization of sewage sludge and coal slime with sulfuric acid for N, S doped hydrochar, J. Clean. Prod. 354 (2022) 131615, https://doi.org/10.1016/j.jclepro.2022.131615.
[68] J. Cai, B. Li, C. Chen, J. Wang, M. Zhao, K. Zhang, Hydrothermal carbonization of tobacco stalk for fuel application, Bioresour. Technol. 220 (2016) 305–311, https://doi.org/10.1016/j.biortech.2016.08.098.
[69] T. Shen, F. Zhang, S. Yang, Y. Wang, H. Liu, H. Wang, J. Hu, Comprehensive study on the pyrolysis process of chestnut processing waste (chestnut shells): kinetic triplet, thermodynamic, in-situ monitoring of evolved gasses and analysis biochar, Fuel 331 (2023) 125944, https://doi.org/10.1016/j.fuel.2022.125944.
[70] M. He, X. Zhu, S. Dutta, S.K. Khanal, K.T. Lee, O. Masek, D.C.W. Tsang, Catalytic co-hydrothermal carbonization of food waste digestate and yard waste for energy application and nutrient recovery, Bioresour. Technol. 344 (2022) 126395, https://doi.org/10.1016/j.biortech.2021.126395.

[71] D.H.H. Sim, I.A.W. Tan, L.L.P. Lim, B.H. Hameed, Encapsulated biochar-based sustained release fertilizer for precision agriculture: a review, J. Clean. Prod. 303 (2021) 127018, https://doi.org/10.1016/j.jclepro.2021.127018.
[72] X. Liu, J. Liao, H. Song, Y. Yang, C. Guan, Z. Zhang, A biochar-based route for environmentally friendly controlled release of nitrogen: urea-loaded biochar and bentonite composite, Sci. Rep. 9 (2019), https://doi.org/10.1038/s41598-019-46065-3.
[73] M. Wang, A. Xiang, Z. Gao, K. Zhang, Y. Ren, Z. Hu, Study on the nitrogen-releasing characteristics and mechanism of biochar-based urea infiltration fertilizer, Biomass Convers. Biorefinery 13 (2023) 9795–9805, https://doi.org/10.1007/s13399-021-01848-5.
[74] H. Wei, H. Wang, H. Chu, J. Li, Preparation and characterization of slow-release and water-retention fertilizer based on starch and halloysite, Int. J. Biol. Macromol. 133 (2019) 1210–1218, https://doi.org/10.1016/j.ijbiomac.2019.04.183.
[75] S. Bakshi, C. Banik, D.A. Laird, R. Smith, R.C. Brown, Enhancing biochar as scaffolding for slow release of nitrogen fertilizer, Acs Sustain. Chem. Eng. 9 (2021) 8222–8231, https://doi.org/10.1021/acssuschemeng.1c02267.
[76] R. Wang, Z. Lin, S. Meng, S. Liu, Z. Zhao, C. Wang, Q. Yin, Effect of lignocellulosic components on the hydrothermal carbonization reaction pathway and product properties of protein, Energy 259 (2022) 125063, https://doi.org/10.1016/j.energy.2022.125063.

Journal of Environmental Chemical Engineering 13 (2025) 117574

Contents lists available at ScienceDirect

Journal of Environmental Chemical Engineering

journal homepage: www.elsevier.com/locate/jece

Efficient and selective recovery of lithium from spent lithium-ion batteries by biomass single-component regulated pyrolysis with synergistic water leaching approach

Yumeng Wu [a,e], Jianjun Cai [b,c,d,*], Xingying Tang [e,f,**], Shubin Wang [g], Mingkang Fang [b], Shengfeng Yao [b], Jiafeng Zhang [c,h]

[a] School of Resources, Environment, and Materials, Guangxi University, Nanning 530004, China
[b] Mizuda Group Co., Ltd., Huzhou 310000, China
[c] National Engineering Laboratory for High-Efficiency Recovery of Refractory Nonferrous Metals, School of Metallurgy and Environment, Central South University, Changsha 410083, China
[d] School of Architecture and Traffic, Guilin University of Electronic Technology, Guilin 541004, China
[e] Guangxi Laboratory on the Study of Coral Reefs in the South China Sea, Coral Reef Research Centre of China, School of Marine Sciences, Guangxi University, Nanning 530004, China
[f] School of Marine Sciences, Guangxi University, Nanning 530004, China
[g] State Environmental Protection Key Laboratory of Urban Ecological Environment Simulation and Protection, South China Institute of Environmental Sciences, Ministry of Ecology and Environment (MEE), Guangzhou 510655, China
[h] School of Metallurgy and Environment, Central South University, Changsha 410083, China

ARTICLE INFO

Keywords:
Spent lithium-ion battery
Cellulose
Hemicellulose
Lignin
Pyrolysis gas reduction

ABSTRACT

In this study, we developed a synergistic recycling technology based on biomass pyrolysis, roasting, and water leaching of biomass single components (cellulose, hemicellulose, and lignin), aiming to address the environmental risks posed by spent lithium-ion batteries due to the rapid growth of the new energy battery industry. By innovatively utilizing the reducing gases (H_2, CO) produced during the biomass pyrolysis process, we have not only achieved the structural cracking of ternary cathode materials but also reduced high-valent metal oxides (such as nickel, cobalt, and manganese oxides) to metallic states, thereby realizing selective lithium leaching. This study systematically explored how biomass type, dosage ratio, roasting temperature, and roasting time affect lithium reduction efficiency and leaching behaviour. Experimental results demonstrated that lignin exhibited the most potent synergistic effect under pyrolysis at 600 ℃. At a dosage ratio of 1:0.25, the lithium leaching rate exceeded 90 %, outperforming cellulose and hemicellulose under equivalent low-temperature and low-dosage conditions. A component-property database of biomass could be established to optimize dosing strategies for diverse cathode materials. Economic and environmental impact analyses using the Everbatt model indicate that biomass reduction leads to reduced energy consumption and greenhouse gas emissions, resulting in significant energy and environmental benefits. This study proposes a green and low-carbon lithium recycling method that integrates with metal recovery, providing technological innovation and practical significance for promoting sustainable development in the new energy sector.

1. Introduction

Under the dual goals of "carbon peaking" and "carbon neutrality", sustainable development has become a central focus of modern society [1]. The global energy landscape is shifting toward low-carbon technologies and renewable energy systems, with lithium-ion batteries playing a key role as enablers for electric vehicles (EVs) and grid-scale energy storage applications [2,3]. Lithium-ion batteries are valued as clean, safe, and efficient energy storage capabilities. Their technological advantages - including high energy density, extended lifespan, superior

* Corresponding author at: Mizuda Group Co., Ltd., Huzhou 310000, China.
** Corresponding author at: Guangxi Laboratory on the Study of Coral Reefs in the South China Sea, Coral Reef Research Centre of China, School of Marine Sciences, Guangxi University, Nanning 530004, China.
E-mail addresses: caijianjun@guet.edu.cn (J. Cai), tangxingying@gxu.edu.cn (X. Tang).

https://doi.org/10.1016/j.jece.2025.117574
Received 9 March 2025; Received in revised form 11 June 2025; Accepted 12 June 2025
Available online 13 June 2025
2213-3437/© 2025 Elsevier Ltd. All rights are reserved, including those for text and data mining, AI training, and similar technologies.

cycling performance, and environmental benefits - have established them as essential components in modern electronics and EVs [4,5]. This growing utilisation continues to drive sustained demand in the market. However, the relatively short lifespan of EVs (typically 3–10 years) has led to a significant rise in the disposal of lithium-ion batteries. Projections indicate that by 2030, the global lithium-ion battery decommissioning wave driven by treatment demand may exceed 11 million metric tons. In addition, the recycling industry market size is expected to grow to 23.72 billion U.S. dollars [6,7]. Recovering valuable metals from spent batteries is essential for conserving resources. Furthermore, this process plays an increasingly important role in ensuring the sustainable development of the lithium-ion battery industry.

To recycle nickel-cobalt-manganese (NCM) batteries, pre-treatment processes such as discharge, disassembly, and electrode stripping are applied to spent batteries [8]. Traditional recycling approaches include bio-metallurgy, hydrometallurgy, and pyrometallurgy [9,10]. In bio-metallurgical recovery, valuable metals are extracted from cathode materials using acids produced by microorganisms [11]. Although this method offers high leaching efficiency under mild operating conditions, it remains underdeveloped. Key challenges include strict microbial strain cultivation requirements and difficulties maintaining bacterial viability, limiting its industrial adoption [12,13]. Hydrometallurgical recovery employs reducing and leaching agents (e.g., inorganic acids such as H_2SO_4, HCl, and HNO_3 [14–16] or organic acids like citric acid and malic acid) to dissolve transition metals [17–19]. This method demonstrates high recovery rates, low energy consumption, and high product purity with multi-metal extraction capabilities [20,21]. Nevertheless, the large consumption of chemical reagents and the generation of toxic gases and high-salinity wastewater raises environmental concerns [22]. Regarding pyrometallurgical Recovery, current research focuses on reductant selection during the roasting [16,23].

Reduction roasting is an effective method to significantly improve the recovery of valuable metals from used batteries [24]. Notably, pyrolysis, a key pretreatment technology for spent cathode powder, is vital in biomass energy conversion [25]. Studies indicate that biomass offers advantages over traditional reductants in lithium battery recycling due to its abundant availability, renewable nature, and low environmental footprint [26]. During thermochemical decomposition under oxygen-limited conditions (e.g., anaerobic environments), biomass mainly produces three valuable products: reducing gases (H_2, CO, and CH_4), bio-oils, and bio-char. This process simultaneously inhibits toxic emissions such as fluorinated compounds or sulphur-containing species [27]. With near-zero emissions and high energy efficiency, this conversion pathway offers an environmentally sustainable approach to lithium-ion recovery. The reducing gases and biochar can react with spent cathode powder, a process enhanced by reducing gases from decomposed battery organic matter [28]. Additionally, the metals Ni and Co can catalyse the cracking of bio-oil into small-molecule gases, thereby enhancing the reaction efficiency. Recent studies demonstrate successful applications of green biomass materials—including macadamia nut shells [29], Bidens pilosa [30], Crofton's weed [31], and wood chips [32]—in lithium-ion battery reduction roasting. These materials provide a sustainable alternative to conventional reductants, such as graphite and coal.

Biomass primarily consists of cellulose, hemicellulose, and lignin. However, existing research has not reported the use of individual biomass components as reducing agents for the recovery of lithium battery materials. Building on previous work, we present a novel pyrolysis-driven reduction method using single-component biomass. Specifically, cellulose, hemicellulose, and lignin are selected as reducing agents. During pyrolysis, the generated gases and biochar minimize cathode oxides from spent lithium-ion batteries. This reduction process converts metal oxides into metallic Ni, Co, MnO, and Li_2CO_3. Through comprehensive characterization (XRD, TG-DSC, XPS, and SEM) of pyrolysis products, we propose potential chemical reaction pathways during the pyrolysis process. In addition, the synergistic effect of gas and biochar was experimentally investigated, and the effects of the three components on the lithium leaching rate were explored at the various roasting temperatures, dosage ratios, and roasting times. The method significantly expands the application options of the biomass reduction roasting method in lithium battery recycling by optimizing the mixing ratio of single biomass components in recycling spent lithium battery cathode materials, screening efficient primary biomass based on data, and systematically optimizing the recycling strategy.

2. Experimental section

2.1. Material preparation

The spent lithium ternary batteries used in the study were sourced from a battery recycling company in Guangxi Province, China. To ensure the safe handling of the batteries, they were first immersed in a 20 % sodium chloride solution for 24 h to ensure they were fully discharged. After discharge, it was manually disassembled and separated under a fume hood to obtain the cathode material. The cathode material was then cut into 2 × 2 cm pieces, placed in a crucible, and calcined in a muffle furnace at 550 ℃ for 2 h. This process effectively removed the binder between the cathode powder and the aluminum foil [33]. The calcined sample was manually ground and sieved with a 100-mesh standard sieve to finally obtain a refined sample of used lithium battery cathode material [34]. An inductively coupled plasma optical emission spectroscopy (ICP-OES) technique was used to analyze the elemental composition of the NCM materials. The main metal element content in the cathode powder is shown in Table S1, and the XRD pattern is shown in Figure S1. The three single-component biomass reductants (cellulose, hemicellulose, lignin) used in this study were purchased from Aladdin Reagents Ltd. Among them, cellulose was a white microcrystalline powder (CAS#9004–34–6). Basic lignin (CAS#8068–05–1) was in brown powder and was chosen as the lignin representative. Due to the commercial unavailability of purified hemicellulose, xylan (CAS#9014–63–5) is a representative substitute for hemicellulose in this study. The xylan sample used in the experiment was in the form of a white powder and was used as a source of hemicellulose.

2.2. Procedure

The schematic diagram of the experimental setup is shown in Fig. 1. Each of the three reducing agents was homogeneously mixed with cathode powder in a crucible and placed in a nitrogen-filled tube furnace for roasting. Before the experiment, the furnace chamber was purged with nitrogen for 10 min to remove the original air. The samples were heated to the desired temperature at a rate of 10 ℃/min and maintained at that temperature for a specified time. A valve controlled the gas flow rate, introducing the gas into a beaker filled with water. Nitrogen was continuously used until the reaction temperature dropped to approximately 60 ℃. After the roasting, the samples were ground for subsequent characterization and separation. The ICP-OES technique was used to determine the concentrations of Li, Ni, Co, and Mn. In this study, the effects of roasting temperature, cathode powder-to-reducing agent dosage ratio, and roasting time on the lithium leaching rate were investigated for each of the three reducing agents.

After calcination, the product was naturally cooled to room temperature and leached with deionized water (liquid-to-solid ratio = 30 mL/g, leaching time 40 min). The filter residue and filtrate were obtained through filtration and separation. The filter residue was dried at 80 ℃ for 6 h and then kept ready for use. The metal content in leachate was analyzed by inductively coupled plasma optical emission spectrometry to evaluate the leaching efficiency of lithium. The lithium leaching rate is calculated according to formula (1):

$$\eta = \frac{n \times C \times V}{m \times w} \times 100\% \quad (1)$$

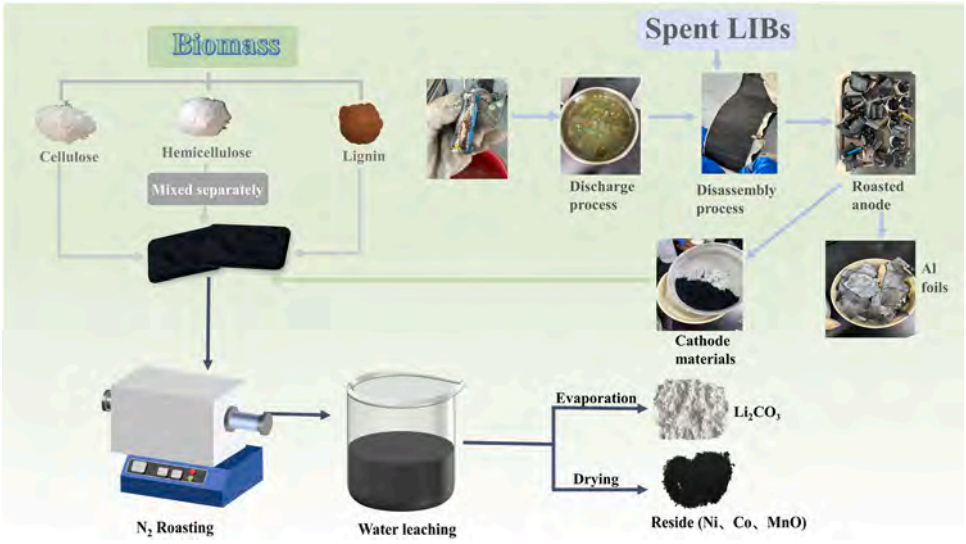


Fig. 1. Schematic diagram of the reduction process of waste lithium-ion batteries.

where η (%) denotes the leaching rate of lithium, *C* denotes the concentration of lithium ions in the leach solution, *V* denotes the volume of the leach solution, *m* denotes the mass of the reduced roasted product, and w denotes the mass fraction of lithium in the reduced roasted product.

2.3. Characterization

ICP-OES (Agilent, USA) was used to determine the content of metallic elements (Li, Ni, Co, Mn) and the concentration of Li. Scanning electron microscopy (SEM, Hitachi SU5000, Japan), X-ray diffraction (XRD, Bruker D8 Advance A25 ×, Germany), and X-ray photoelectron spectroscopy (XPS, Thermo Scientific K-Alpha, USA) were used to analyze the surface morphology, crystal structure, and chemical composition of the spent cathode materials, roasting samples, and leaching slag. The thermochemical behaviour during roasting was systematically investigated using a thermogravimetric analyzer (TG/DSC, Mettler Toledo, Switzerland). The mixed samples were heated from room temperature to 1000 ℃ at a heating rate of 10 ℃/min in a high-purity nitrogen atmosphere. Subsequently, the temperature-dependent Gibbs free energy values for relevant chemical reactions were computationally determined using HSC Chemistry 9.0 software.

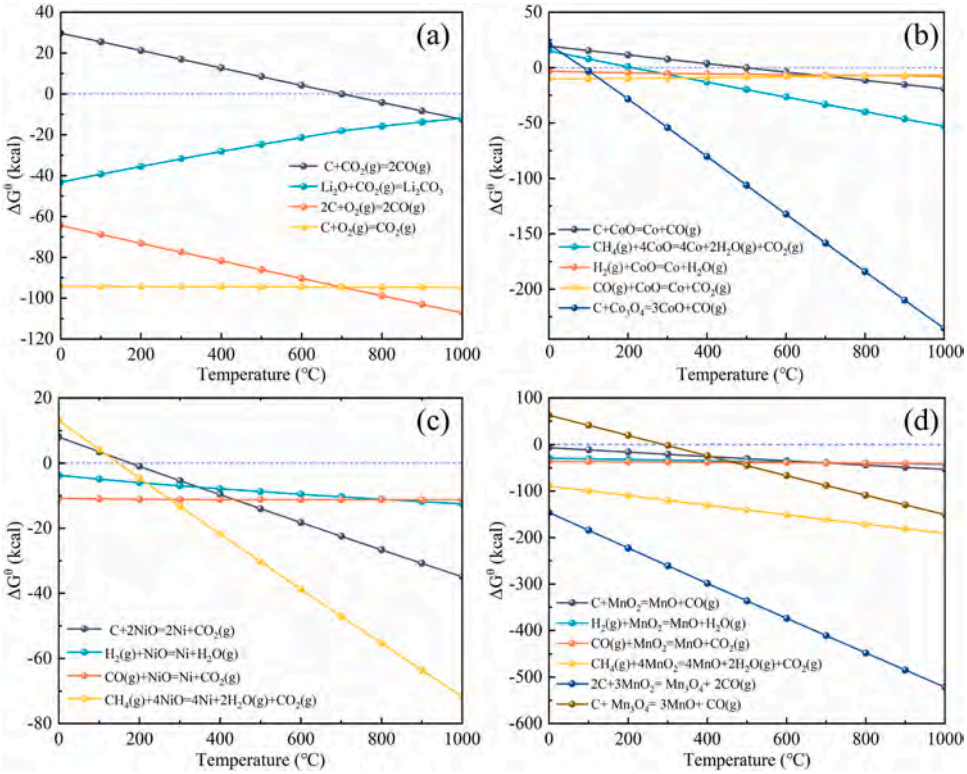


Fig. 2. Schematic representation of gibbs free energy as a function of temperature during the reduction roasting process.

3. Results and discussion

3.1. Thermodynamic analysis

During calcination, the primary pyrolysis products of cellulose, hemicellulose, and lignin include reducing gases (CH_4, CO, and H_2), as well as biochar [35]. Figure S2 shows the evolution processes of three biomass components at a specific heating rate. The HSC Chemistry 9.0 software was used to calculate the reaction of $LiNi_xCo_yMn_zO_2$ (NCM) with the three reducing agents over the temperature range from 0 to 1000 ℃ to evaluate potential reaction pathways. Fig. 2a shows that Li_2O obtained from NCM reduction reacts with CO_2 from the pyrolysis process to form Li_2CO_3 with consistently negative ΔG^θ values ($\Delta G^\theta < 0$), indicating a spontaneous reaction behaviour throughout the temperature range studied. Moreover, the lower the temperature, the more favourable the formation of Li_2CO_3. The thermal reduction mechanisms of transition metal oxides are illustrated in Fig. 2b-d, respectively: for Co (Fig. 2b), CoO and the reducing gas react at about 240 ℃, whereas the reaction between C and CoO starts at 500 ℃, and the response of C and Co_3O_4 at 100 ℃ leads to CoO. Because of the lower stability of Ni_2O_3, the thermodynamic data for NiO were calculated (Fig. 2c) [29]. A distinctive feature of nickel reduction is that nickel oxides can be reduced to nickel metal at relatively low temperatures (about 200 ℃). As the temperature increases, the ΔG^θ value becomes progressively more negative, similar to the reduction of cobalt, but exhibiting a more pronounced thermodynamic spontaneity. The oxides of Mn (Fig. 2d), which are estimated to pass through the following stages during the reaction, MnO_2, Mn_2O_3, Mn_3O_4, and MnO, are not reduced to monomeric Mn by the reducing gas. Therefore, Mn oxide remains the dominant form of manganese throughout the reaction. Thermodynamic analyses confirmed the feasibility of lowering the NCM cathode material with a single-component biomass reductant. The final reduction products determined from thermodynamic equilibrium calculations were Li_2CO_3, Ni, Co, and MnO.

3.2. The effect of synergistic reductive roasting of cellulose

Figs. 3a and 3b show the TG-DTG curves of cellulose alone and the mixed samples of NCM and cellulose. As shown in Fig. 3a, within the range of 50–150 ℃, the TG curve of cellulose decreases slowly due to the release of free water and some chemical water by cellulose. The thermogravimetric curve decreases within the 200–400 ℃ range, indicating cellulose molecules' β-1, 4-glycosidic bonds are broken [36]. In addition to releasing other volatile organic compounds (such as aldehydes, ketones, etc.), many volatile gases (such as CO, CO_2, and H_2) are also released. Above 400 ℃, the decomposition rate of cellulose gradually slows down, the weight loss rate tends to stabilize, and the remaining carbon structure reorganizes to form more stable coke [37]. In Fig. 3b, the TG curve of the mixed sample is similar to that of cellulose. In the initial stage, the weight loss of the mixture occurred earlier than the starting temperature, indicating that NCM might have accelerated the decomposition of cellulose. When the temperature is between 600 and 800 ℃, additional weight loss occurs, corresponding to the decomposition of ternary lithium materials. This might be due to the release of oxygen by NCM, which reacts with cellulose coke to form CO/CO_2, resulting in further mass loss. Compared with pure cellulose, the DTG peak also shifted to a certain extent, and a new peak appeared at > 600 ℃, corresponding to the decomposition or interaction of NCM. As the temperature increases, the octahedral structure collapses, and the metal oxides are further reduced by reducing gases (e.g., H_2, CO, CH_4, etc.) from the pyrolysis of cellulose as well as by biochar [28].

The effects of cellulose roasting temperature, dosage ratio, and roasting time on lithium leaching rate are systematically presented in Fig. 3c. Under fixed experimental conditions (NCM/cellulose = 1:1, 2 h roasting), insufficient thermal energy at lower temperatures results in suboptimal lithium recovery. This observation aligns with the reaction mechanism: Initial-stage cellulose pyrolysis produces reducing gases and biochar, whereas most metal oxides remain chemically inert below 500 ℃. The lithium leaching rate progressively increases when the reaching temperature exceeds 500 ℃, with a maximum value of 96.4 % at 700 ℃. During the heating process, the collapsed ternary lithium structure undergoes carbon-thermal reactions and gas reduction

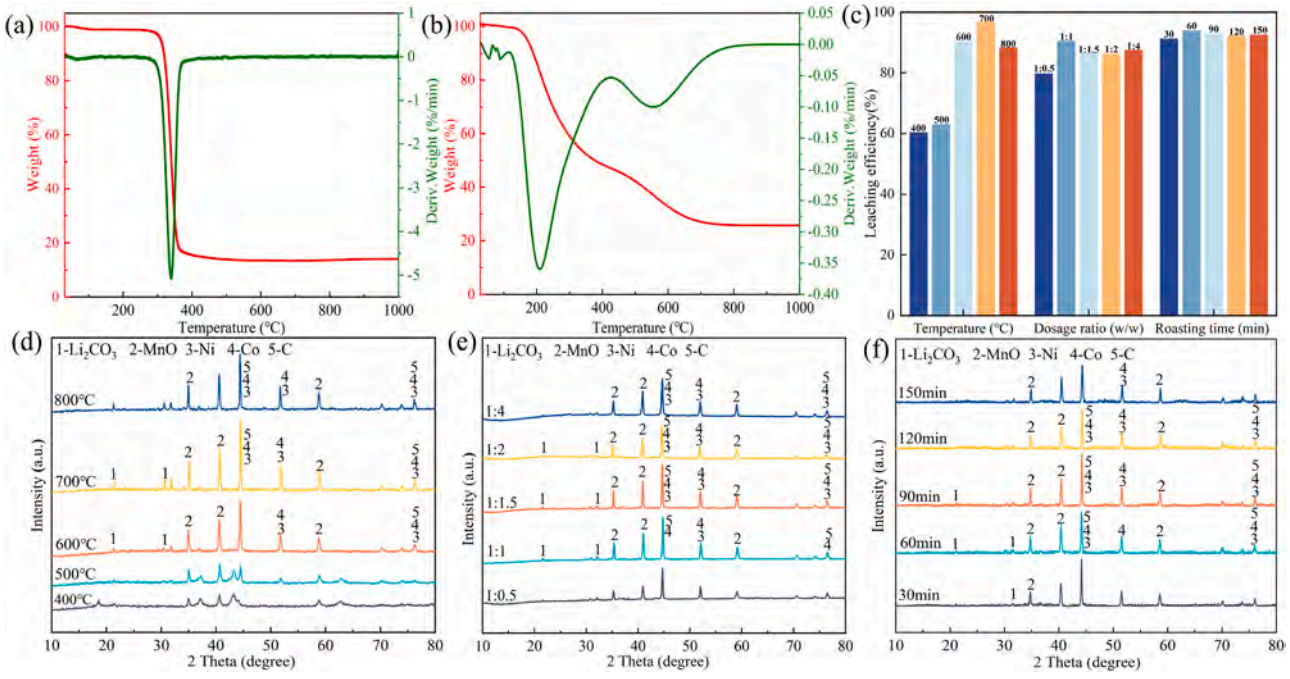


Fig. 3. TG/DTG (10 ℃/min) curves of (a) cellulose and (b) mixed NCM and cellulose (dosage ratio 1:1) in nitrogen atmosphere and (c) lithium leaching rate under different conditions (temperature, dosage ratio, roasting time) and (d-f) XRD patterns of the roasted products with different roasting temperatures, dosage ratios, and roasting times.

reactions, facilitated by the gas produced from cellulose pyrolysis, thereby intensifying the reaction. Moreover, the transition metal oxides decrease, and the generated CO_2 reacts with Li_2O to form Li_2CO_3. It can be seen from the XRD pattern Fig. 3d that peaks corresponding to Ni, Co, and MnO are present. However, exceeding 700 ℃ causes lithium loss, presumably due to high-temperature volatilization. The dosage ratio plays a critical role in determining the lithium leaching rate. As demonstrated in Fig. 3c, under standard conditions of 700 ℃ and 2 h roasting time, insufficient cellulose content fails to generate adequate reducing gases, leading to significantly low leaching efficiency. It can also be seen from the XRD pattern in Fig. 3e that when the mixing ratio of ternary lithium and cellulose is 1:1, the leaching rate of lithium reaches the maximum value of 90.34 %. This means that reducing gases and biochar are produced during the cellulose pyrolysis process, which can ensure that the reducing agent participates in the lithium reduction process. However, if the amount of cellulose used is excessive, although it can provide more reducing gas, it may lead to other side reactions and even cause the loss of some substances. As can be seen from Fig. 3c, with the roasting time extending from 30 min to 150 min, the leaching rate of lithium does not change significantly, indicating that the roasting time has no significant influence on the leaching rate of lithium. Furthermore, it can be seen from the XRD pattern in Fig. 3f that the generated product remains unchanged with increasing calcination time, indicating that the entire reduction process is instantaneous. The calcination time only affects the reaction rate. Therefore, 60-minute roasting achieves dual optimization: maximal metal oxide reduction and minimal lithium loss, yielding a 93.78 % leaching efficiency.

3.3. *The effect of synergistic reductive roasting of hemicellulose*

Figs. 4a and 4b show the pyrolysis behaviour studies of hemicellulose and hemicellulose mixed with Li-ion ternary battery materials, respectively. As shown in Fig. 4a, the pyrolysis process of hemicellulose mainly consists of the following stages: from room temperature to 150 ℃, the TG curve slightly decreases and becomes flat, during which the physically adsorbed and weakly bound water in hemicellulose escapes. 150–250 ℃, the acetyl group and some sugar units in the side chain of hemicellulose begin to decompose [38], which releases small molecule gases such as carbon dioxide. When the temperature exceeds 250 ℃, the glycosidic bond in hemicellulose is broken, and the furan ring is opened, releasing a large number of volatile substances. Volatile organic compounds such as CO, CO_2, H_2O, and acetic acid are mainly produced [39]. Due to the two different structural units of hemicellulose, there are double peaks in the DTG curve of hemicellulose. When the temperature is higher than 400 ℃, the TG curve tends to stabilize, the unstable components (e.g., oxygen-containing functional groups) in the remaining coke are further decomposed to form a more stable carbon structure, and some oxygen-containing groups ((e.g., hydroxyl and carboxyl) are further decomposed, releasing CO_2 and H_2O, and then finally tend to stabilize. The thermogravimetric curve of the mixture of NCM and hemicellulose is shown in Fig. 4b. In the low-temperature stage (< 200 ℃), the weight loss in this stage is relatively flat. The TG curve decreases slowly, which may be due to the evaporation of adsorbed water and the volatilization of a small amount of low-molecular-weight organic matter. When the temperature was 200–400 ℃, corresponding to the main decomposition stage of hemicellulose, the DTG peak was significant. Volatile products such as CO, CO_2, and aldehydes are generated in the process, accompanied by partial dehydration and carbonization of sugars, which is dominated by dehydration and bond breaking under anaerobic conditions, and the residual carbon skeleton may be partially retained until high temperatures. At temperatures greater than 400 ℃, mainly attributed to the decomposition of NCM materials, the ternary material $LiNi_xCo_yMn_zO_2$) may undergo lamellar collapse at high temperatures, releasing oxygen (residual metal oxides such as Li_2O, NiO, CoO, and so on), while the residual carbonaceous mass is further decomposed. Notably, the reducing gases such as CO released from hemicellulose may be adsorbed on the surface of the NCM or react with the residual carbon to promote the reduction of the high-valent metal oxides in the high-temperature section.

Roasting temperature significantly affects lithium's leaching rate, as shown in Fig. 4c, which investigates the leaching rate of lithium at 400–800 ℃ (NCM/ hemicellulose = 1:2, 2 h roasting). Similar to cellulose, the leaching rate of lithium is not more than 60 % at lower temperatures. However, with the increase in temperature, the high

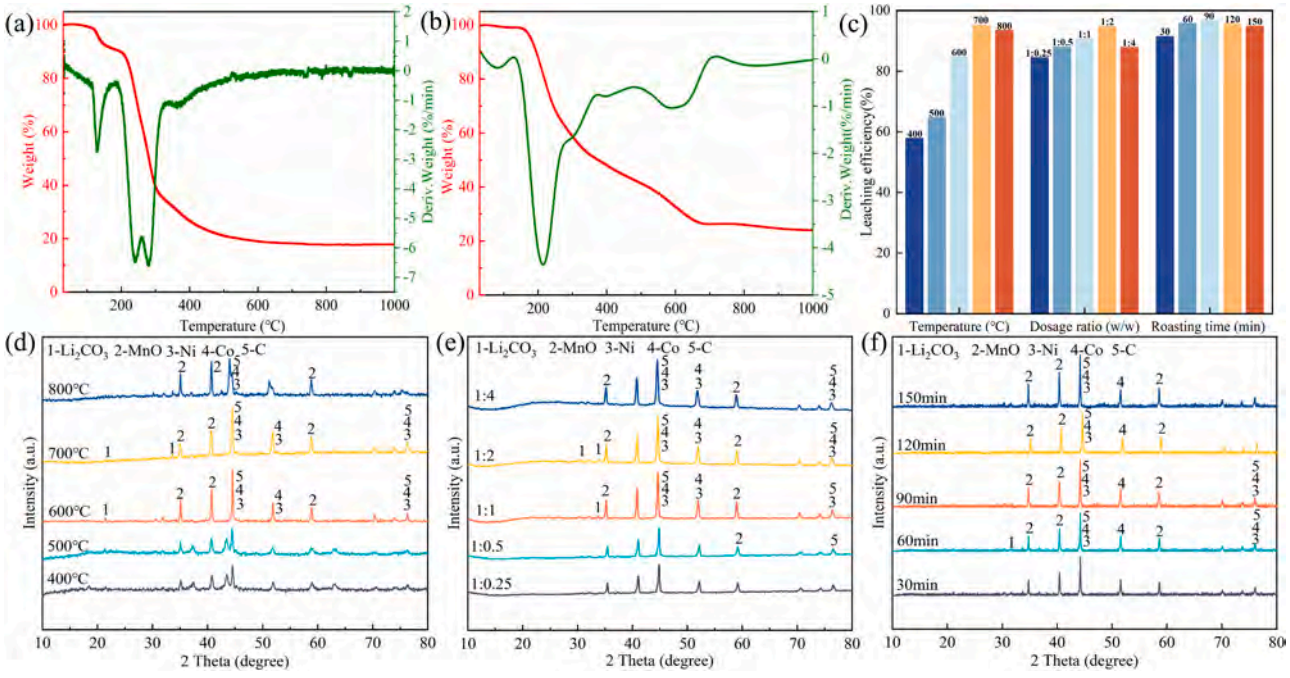


Fig. 4. TG/DTG (10 ℃/min) curves of (a) hemicellulose and (b) mixed NCM and hemicellulose (dosage ratio 1:2) in nitrogen atmosphere and (c) lithium leaching rate under different conditions (temperature, dosage ratio, roasting time) and (d-f) XRD patterns of the roasted products with different roasting temperatures, dosage ratios, and roasting times.

temperature (700 ℃) accelerates the kinetic process of the reduction reaction, shortens the reaction time, and promotes the formation of lithium salts (Li_2CO_3). When the temperature is more significant than 700 ℃, the lithium leaching rate decreases because high temperatures lead to the volatilization of lithium or densification of the material sintering, which impedes the aqueous leaching process in the lithium dissolution during water leaching. In Fig. 4d, Li_2CO_3, Ni, Co, and MnO peaks are observed at 700 ℃, indicating that the metal oxides are reduced to low valence metals. At a temperature of 700 ℃, the effect of the hemicellulose dosage ratio on the leaching rate of lithium was explored in Fig. 4c, where the dosage ratio was 1:2. From the XRD results in Fig. 4e, it can be seen that insufficient reducing gas under low dosage ratio conditions leads to incomplete reduction. The leaching rate of lithium would decrease, whereas the leaching rate of Li reached a maximum (94.64 %) when the feed ratio was 1:2, which was attributed to the fact that the hemicellulose provides sufficient reducing gas to efficiently reduce more metal oxides, especially at high temperatures (700 ℃), ensuring that the reaction proceeds adequately. To explore the effect of roasting time on the leaching rate of lithium, the roasting temperature and dosage ratio were controlled at 700 ℃ and 1:2. As can be seen in Fig. 4c, the extension of the roasting time from 30 min to 150 min, the leaching rate of lithium did not change significantly. Corresponding XRD patterns (Fig. 4f) exhibited no significant phase structure changes, indicating rapid reaction completion within the initial stages. This suggests that roasting time primarily influences reaction rate rather than final conversion. Therefore, 60 min was selected as the optimal balance to maximize lithium recovery.

3.4. The effect of synergistic reductive roasting of lignin

Lignin is a three-dimensional polymer consisting mainly of phenylpropane units interconnected by β-O-4 and C-C bonds, and its pyrolysis results from the cleavage of these bonds [40]. Fig. 5a shows the thermogravimetric curve of lignin when the temperature is below 200 ℃; a trace weight loss occurs, which is mainly attributed to the volatilization of adsorbed water or residual solvent. At temperatures in the range of 200–400 ℃, homocleavage of the β-O-4 bond occurs, giving rise to phenoxy (Ph-O-) and carbon-centred radicals. These reactive intermediates initiate chain cleavage reactions, releasing small molecular volatiles (e.g., CO_2, CO, methanol) [41], along with the formation of phenolic compounds and carbonaceous residues. When the temperature is higher than 500 ℃, it mainly involves the breaking of more stable bonds (e.g., C-C bonds, aromatic ring side-chain bonds) and rearrangement of aromatic structures, leading to secondary cleavage of the tars (mainly larger molecular weight phenolic compounds) and generation of gases (e.g., CH_4, H_2, etc.). Compared to the first two single-component reductants, lignin, due to its complex cross-linked structure, has a wider distribution temperature range and is more inclined to produce more coke, which is consistent with literature reports [42]. Fig. 5b shows the thermogravimetric curves of the ternary cell powder and lignin mixtures. The behaviour is similar to lignin alone pyrolysis at temperatures below about 200 ℃. When the temperature is in the range of 200–400 ℃, the weight loss in this phase is accelerated, which may involve the interaction between the initial products of lignin pyrolysis and the surface of the NCM material or the released reactive oxygen species. When the temperature is at 400–600 ℃, dramatic weight loss occurs. During this process, lattice oxygen (O^{2-}) is released from the lithium ternary cell material (NCM), and the reducing gases generated by lignin pyrolysis (CO/H_2, where CO can be generated by the combination of benzyl radicals generated by the cleavage of β-O-4 with oxygen, and H_2 can be generated by the complexation of hydroxyl radicals) utilize this oxygen to react. These reducing gases promote the reduction of high-valent metal ions (e.g., Ni^{3+}, Co^{3+}) in the NCM, leading to a decrease in the stability of its lattice structure, which enhances the release of lithium ions. When the temperature exceeds 600 ℃, a secondary weight loss peak occurs, and the process corresponds to the metal oxide (MO_X) catalyzed residual carbon gasification reaction. As the reaction proceeds, this redox process stabilizes when the residual carbon is consumed or the reaction reaches equilibrium.

Compared to cellulose and hemicellulose, lignin demonstrates superior performance as a reductant for Li-ion ternary battery materials, requiring lower reduction temperatures (Fig. 5c). The maximum lithium leaching rate (93.28 %) was achieved at 600 ℃ (NCM/lignin = 1:0.25, 2 h roasting), significantly higher than values observed for cellulose and

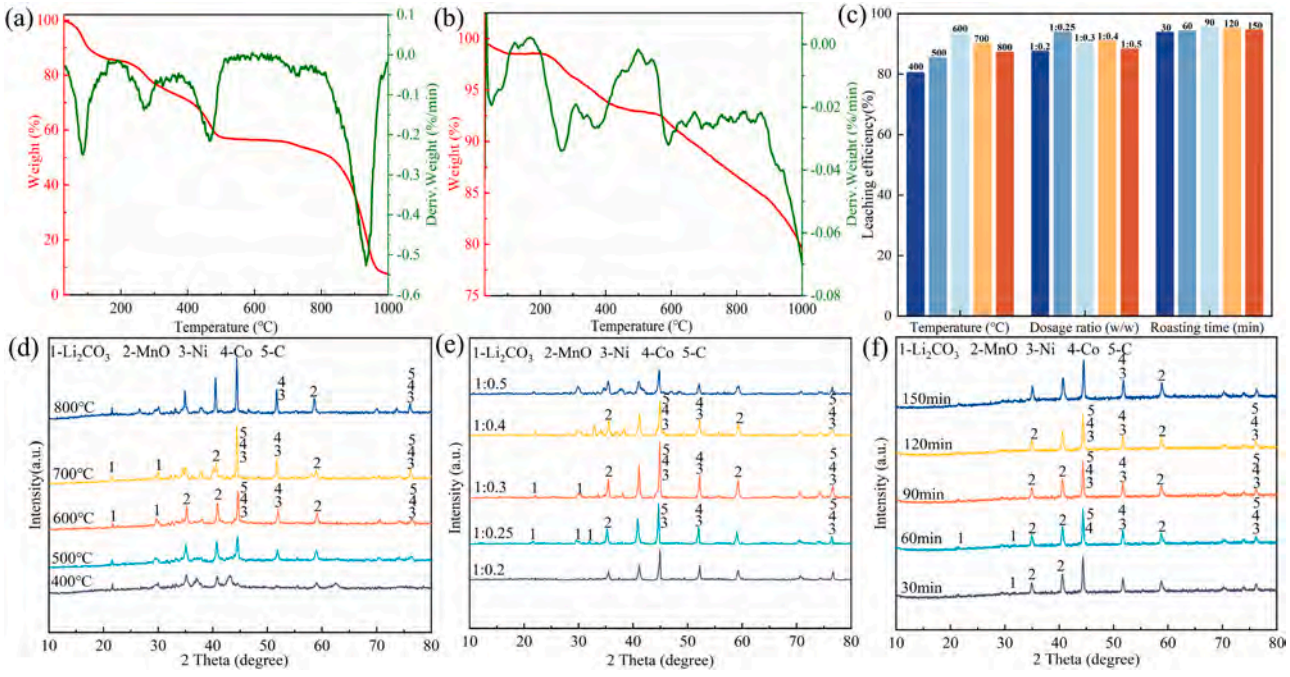


Fig. 5. TG/DTG (10 ℃/min) curves of (a) lignin and (b) mixed NCM and lignin (dosage ratio 1:0.25) in nitrogen atmosphere and (c) lithium leaching rate under different conditions (temperature, dosage ratio, roasting time) and (d-f) XRD patterns of the roasted products with different roasting temperatures, dosage ratios, and roasting times.

hemicellulose under equivalent conditions. At lower temperatures, reduced leaching efficiency may originate from insufficient generation of reactive gases. Lignin is a complex aromatic polymer. Its pyrolysis produces a more graphitized biochar that forms a stable conjugated system [36,43]. This enhances electronic conductivity and improves the carbon-based reduction process. In contrast, cellulose and hemicellulose—composed of linear/branched glucose units—yield disordered carbon structures upon pyrolysis. These amorphous carbons exhibit lower reactivity, necessitating higher temperatures (~700 ℃) to activate their reducing capacity. As shown from the XRD pattern in Fig. 5d, the phases at maximum leaching rates indicate that the high valent metal oxides are reduced to lower valent states. In exploring the effect of the lignin-to-lithium ratio on the lithium leaching rate, it was found that the leaching rate was very low at low feed ratios. As the feed ratio increased, the lithium leaching rate reached a maximum (93.56 %) when the NCM to lignin ratio was 1:0.25 (Fig. 5c). Further studies have shown that, compared with the other two reducing agents, less lignin mass is required to achieve the same reduction effect, which may be attributed to the higher carbon content of lignin. This resulted in more fixed carbon being produced during the pyrolysis process, as pyrolysis of lignin is more likely to make a carbon-rich residue, thus increasing carbon utilization efficiency. Fig. 5c and Fig. 5f discuss the effect of roasting time on the lithium leaching rate (roasting temperature of 600 ℃ and NCM/lignin mass ratio of 1:0.25). The effect of roasting time on lignin was similar to its impact on cellulose and hemicellulose, suggesting that the whole reduction process is rapid during roasting. The roasting time mainly affects the reaction rate and has little effect on the final.

4. Mechanistic analysis

Scanning electron microscopy (SEM) was employed to characterize the morphological evolution of cathode powder through comparative analysis of pre-calcination and post-calcination states. As reference benchmarks, cellulose, hemicellulose, and lignin microstructures are provided in Figure S3. The pristine cathode material (Fig. 6a–b) exhibits a well-defined spherical architecture with uniform particle distribution. Following cellulose-assisted calcination (Fig. 6c–d), complete structural reorganization occurs: Original spheroids are replaced by irregular polyhedral particulates showing angular surface features. In stark contrast, hemicellulose-NCM composites (Fig. 6e–f) demonstrate lamellar structure formation post-calcination, indicating more pronounced structural deformation than cellulose counterparts. Lignin-derived residues (Fig. 6g–h) present unique morphological differentiation, manifesting rod-like aggregates through the tight coalescence of submicron particles.

This study employed X-ray photoelectron spectroscopy (XPS) to analyze the reduction behaviours of Li, Ni, Co, and Mn in NCM ($LiNi_xCo_yMn_zO_2$) to investigate the valence state evolution of high-valent metal ions during the reaction of cellulose, hemicellulose, and lignin with waste cathode powder. Figure S4 presents the C 1 s spectra of the cathode powder and calcined samples. As shown in Fig. 7a, the Co 2p spectrum in NCM exhibits two primary peaks at 780.3 eV ($2p_{3/2}$) and 795.4 eV ($2p_{1/2}$), consistent with the Co^{3+} state. In addition, satellite peaks at 787.8 eV and 798.2 eV indicate the presence of Co^{4+}. After roasting, the Co $2p_{3/2}$ and $2p_{1/2}$ binding energies shifted to 781.1 eV and 796.5 eV in cellulose, 781.5 eV and 796.3 eV in hemicellulose, and 780.3 eV and 796.3 eV in lignin, respectively. These shifts indicate the reduction of Co^{3+} to Co^{2+} during the reaction. The Ni 2p spectrum of NCM (Fig. 7b) displays two prominent peaks at 854.9 eV ($2p_{3/2}$) and 872.7 eV ($2p_{1/2}$), with satellite peaks corresponding to Ni^{2+}. Post-roasting, the Ni $2p_{3/2}$ and $2p_{1/2}$ binding energies increased to 856.7 eV and 874.0 eV in cellulose, 856.8 eV and 874.8 eV in hemicellulose, and 855.3 eV and 873.2 eV in lignin. These results suggest that metallic Ni^0 and Ni^{2+} species are forming, likely due to oxidation [43]. In NCM (Fig. 7c), the Mn $2p_{3/2}$ and $2p_{1/2}$ peaks at 642.5 eV and 654.1 eV confirm the dominance of Mn^{4+}, while a minor peak at 645.4 eV corresponds to Mn^{3+}. After roasting, the Mn $2p_{3/2}$ and $2p_{1/2}$ peaks shifted to 642.1 eV and 653.6 eV in cellulose, 642.0 eV and 653.8 eV in hemicellulose, and 640.8 eV and 652.6 eV in lignin. Despite these shifts, XPS analysis revealed that high-valent Mn species (Mn^{3+}/Mn^{3+}) retained elevated binding energies during reduction and roasting [44]. The combined results demonstrate that the oxygen octahedra in S-NCM is disrupted during reduction and roasting. Furthermore, elevated temperatures promote the gradual decrease in high-valent metal ions to their lower-valent states.

Fig. 8a illustrates the reaction mechanisms of three single-component reductants (cellulose, hemicellulose, and lignin) in reducing ternary lithium-ion batteries. Cellulose, primarily composed of β-1,4-glucose units, undergoes pyrolysis to generate small-molecule volatile organic compounds, coke, and gases (CO, CO_2, H_2) [45]. During high-temperature roasting, the reducing gases (e.g., H_2 and CO) derived from cellulose pyrolysis effectively reduce metal oxides in the cathode material, enhancing lithium recovery. Concurrently, due to its high carbon content, cellulose-derived coke acts as a solid reductant and participates in carbothermal reduction with NCM, further facilitating lithium-ion release. The molecular structure of hemicellulose is more complex than cellulose, incorporating diverse sugar units (e.g., xylose, arabinose). It decomposes at lower temperatures, yielding more pyrolysis products such as small-molecule ketones, aldehydes, and organic acids. These compounds contribute to gas-phase reduction by generating H_2 and CO, synergistically enhancing the overall reducing capacity and

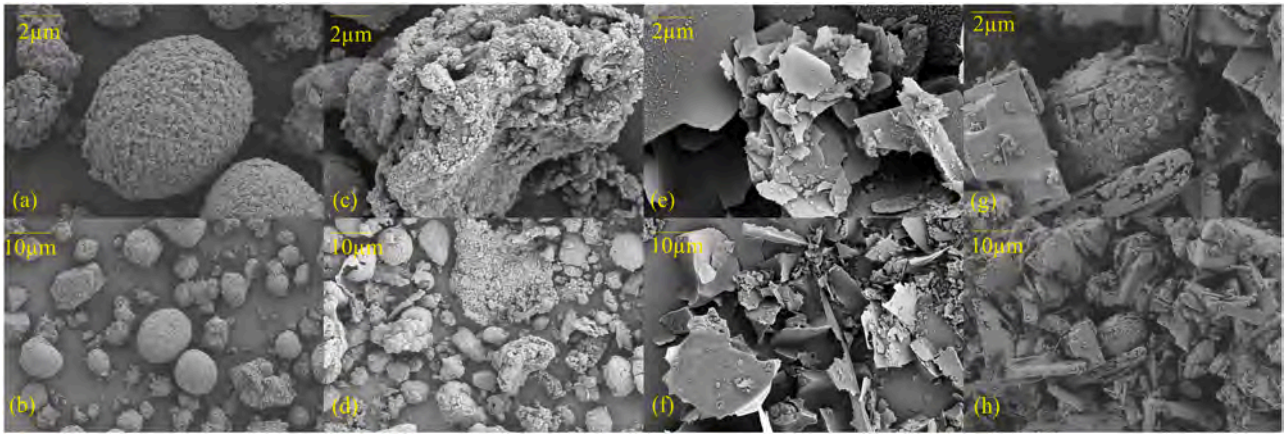


Fig. 6. SEM image: SEM image: (a-b) spent cathode powder (c-d) cellulose and NCM roasting samples (e-f) hemicellulose and NCM roasting samples (g-h) lignin and NCM roasting sample.

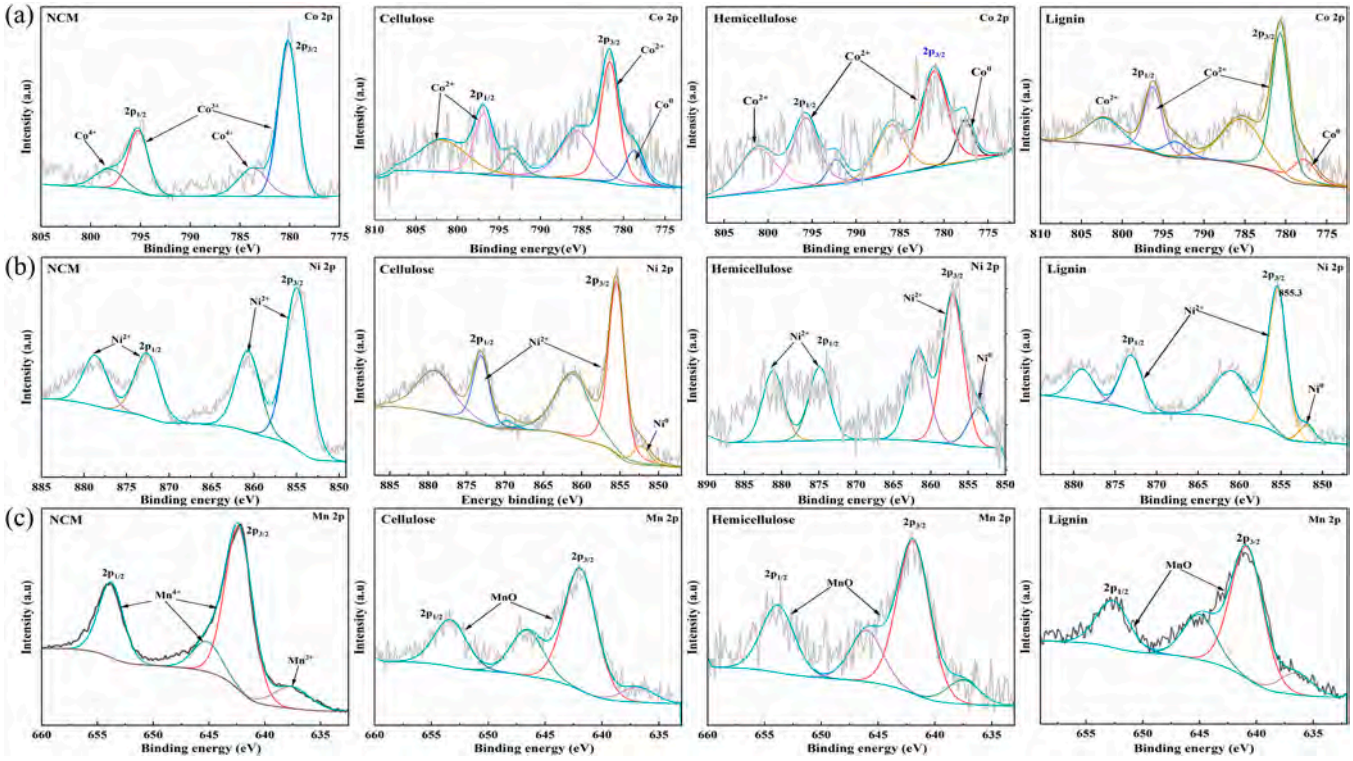


Fig. 7. XPS images of different metals: (a) Co; (b) Ni; (c) Mn.

supporting NCM reduction. As an aromatic polymer rich in benzene rings and methoxy groups, lignin decomposes into phenolic compounds, methoxy derivatives, and coke during pyrolysis [40]. Lignin-derived coke exhibits strong reducing properties, significantly promoting the carbothermal reduction of NCM. However, excessive coke residues may destabilize the NCM structure and reduce lithium recovery efficiency.

$LiNi_xCo_yMn_zO_2$, as a layered oxide, has a crystal structure containing a large number of oxygen octahedral units, as shown in Fig. 8b. The central element of the octahedron is usually a transition metal or Li^+, and Li^+ is intercalated between layers through ionic bonds and combined with oxygen through a mixture of covalent and ionic bonds. As the temperature rises, active lithium ions are released from the lattice. In addition, charge compensation of high-valent metals occurs, leading to the disorder of cations [46]. At the same time, unstable oxygen atoms are released from the lattice. The release of oxygen negatively charges the oxygen plane, enhancing the electrostatic repulsion between adjacent oxygen ion layers, thereby causing the lattice parameters to expand first and then contract[46,47]. In particular, Li^+ (0.76 Å) and Ni^{2+} (0.69 Å) with similar ionic radii are more likely to form the Li^+/Ni^{2+} barrier. Nickel ions migrate from the octahedral positions in the transition metal layer to the octahedral positions in the lithium layer [48,49]. During the pyrolysis of cellulose, hemicellulose, and lignin, these three single-component reducing agents generate small-molecule volatile substances. CO and CH_4 are mainly produced through deoxidation and side chain breakage, while H_2 is generated through aryl ring rearrangement and condensation reactions, generating biochar rich in active sites. Reducing gases diffuse to the surface of NCM and react with lattice oxygen to form CO_2/H_2O, promoting the transformation from lithium-oxygen octahedra to lithium-oxygen tetrahedra. Therefore, the lattice collapse theory can explain the thermochemical reaction mechanism of biomass pyrolysis on NCM. Research has found that compared with metals, the reducing gases (CO, H_2, CH_4) and biochar generated by biomass pyrolysis have a stronger affinity for oxygen in the lattice structure. This preferred adsorption effect makes the metal-oxygen bond more prone to breakage[28,50]. As the reaction proceeds, oxygen gradually escapes from the lattice, and the covalent bonds between the metal and oxygen keep breaking. Subsequently, transition metals and lithium will continue to be released from the octahedral lattice, eventually destroying the crystal structure of NCM and providing a possible way for further lithium recovery.

5. Economic and environmental analysis

Based on the Everbatt model [51] developed by Argonne National Laboratory, pyrometallurgical and hydrometallurgical processes were systematically evaluated, and the economics and environmental impacts of biomass pyrolysis reduction (GRR) were further analyzed. As hydrometallurgy is currently the mainstream method for lithium battery recycling, this paper analyses hydrometallurgy as a baseline, choosing NCM (nickel-cobalt-manganese) materials and pine wood chips as raw materials, and conducts an in-depth study of its economics. For more information on the Everbatt model, please refer to the main text, please refer to Text S1.

Assuming that a solid waste recycling company in China processes 10,000 tons of used lithium batteries per year, three different recycling processes are simulated and compared, as shown in the figure. Energy consumption and greenhouse gas (GHG) emissions are key indicators for evaluating recycling methods. As shown in Fig. 9a, the material consumption and energy use of the biomass reduction method is significantly lower than those of the pyrometallurgical and hydrometallurgical processes throughout the entire battery reduction process, primarily due to the method's lower smelting temperatures and reduced material inputs. Fig. 9b shows that when pine shavings are used as feedstock, the total GHG emissions from biomass reduction recovery are lower than the other two processes. This result is primarily attributed to its lower melting temperature and the avoidance of significant emissions from high-temperature roasting and fuel combustion in the conventional process. Since water leaching is required for the recovery and separation of Li, the biomass pyrolysis reduction method (GRR) adopted in our research process consumes more water than the other two methods, as shown in Fig. 9c.

The results of the economic modeling are shown in Fig. 9d, where the

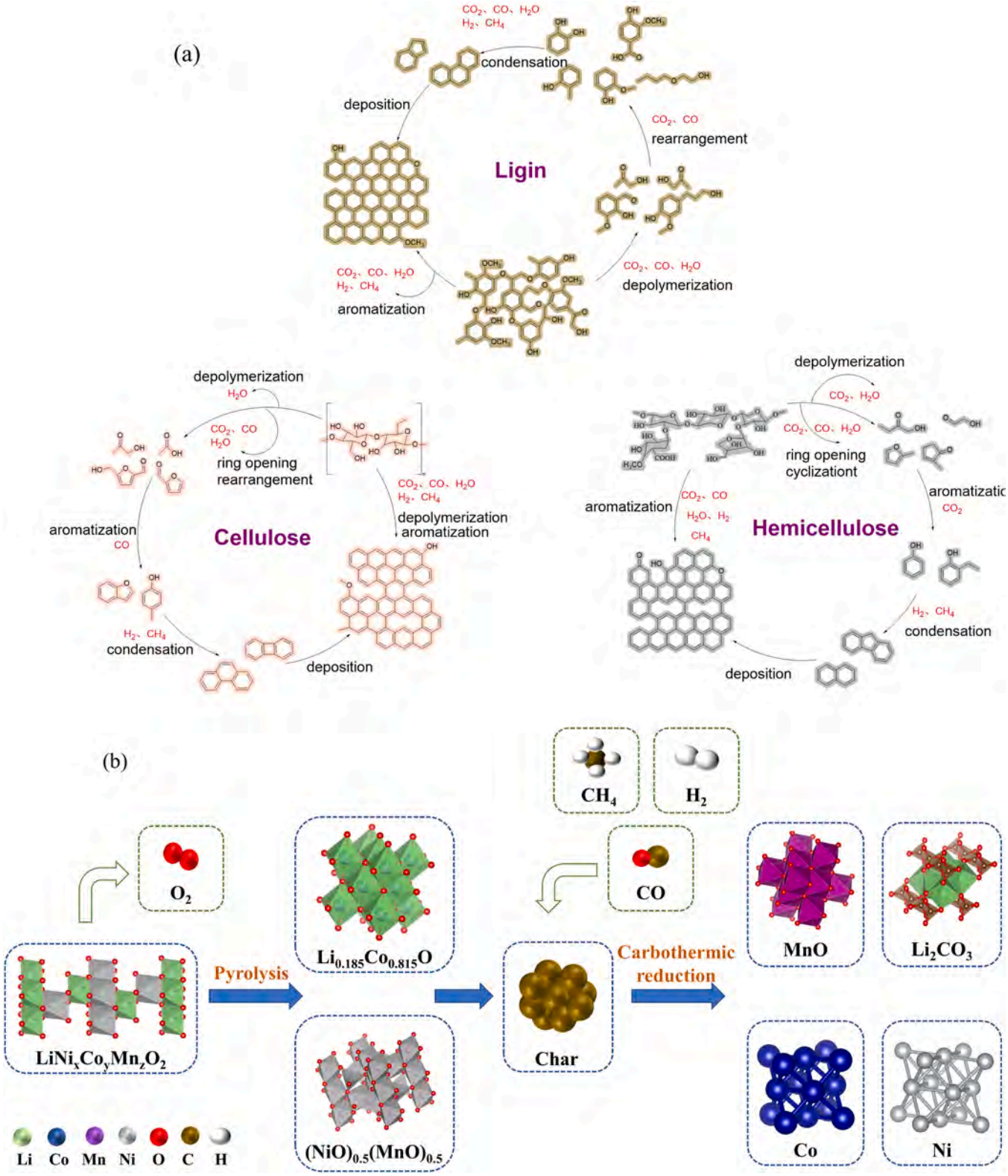


Fig. 8. Fig (a) pyrolysis mechanism process of cellulose, hemicellulose and lignin, (b) carbon-thermal reduction mechanism.

biomass reduction recovery is far superior to the pyrometallurgical and hydrometallurgical processes in terms of economics. This is not only because the recovery process can directly utilize oxides and lithium salts to produce new NCMs, but also because the method significantly reduces energy and chemical consumption, resulting in a high-value, high-purity product output at a low-cost input. The spider web diagram in Fig. 9e further conducts a comprehensive comparison of the three recovery methods. It can be seen that biomass reduction recovery is significantly superior to pyrometallurgical and wet methods in terms of energy efficiency, low emissions, throughput, and process simplicity. This is due to the safety of this process. It does not require the use of strong acids, strong alkalis, or organic solvents. The GRR method operates at a

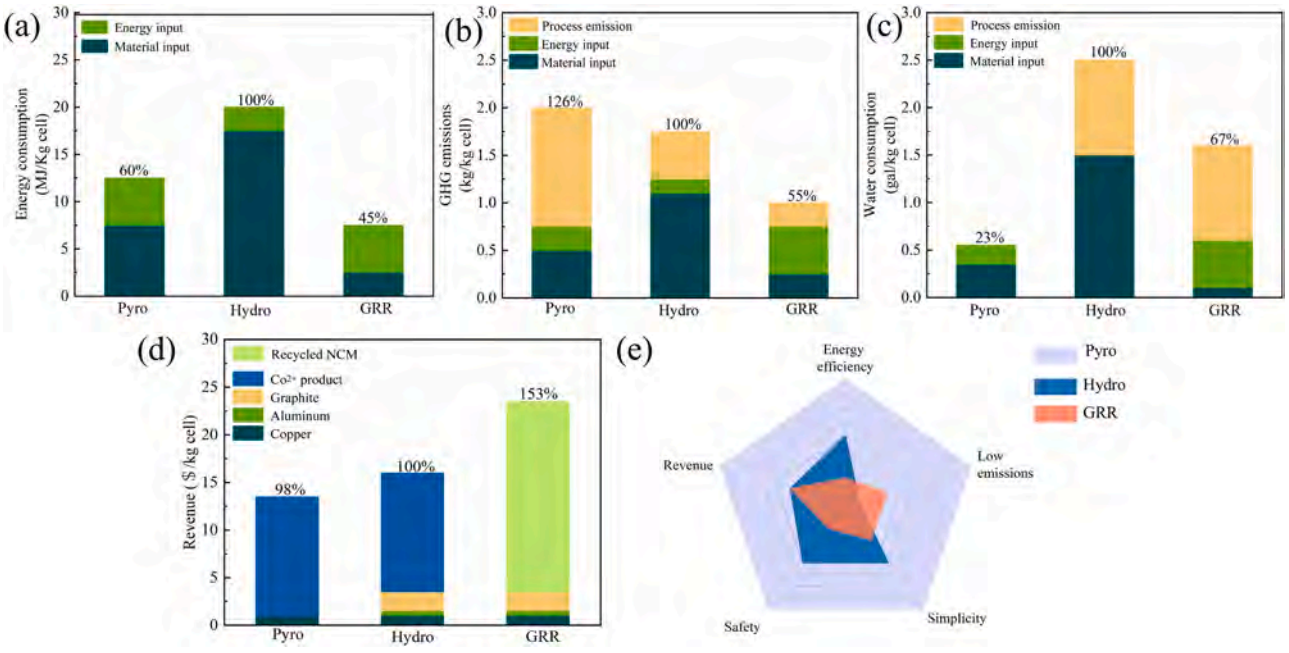


Fig. 9. Economic and environmental analyses of pyrometallurgical (Pyro), hydrometallurgical (Hydro) and biomass reduction (GRR) recovery processes: (a) energy consumption, (b) greenhouse gas emissions, (c) water consumption, (d) potential revenues, (e) comparative charts of pyro, hydro and direct recovery processes.

medium temperature, separating the electrode material from the current collector while ensuring the integrity of the current collector. Compared with hydrometallurgy and pyrometallurgy (Figures S5 and S6), GRR recovers cathode materials through direct calcination of pyrolysis gas, generating $LiCoO_2$ without the need for additional chemicals. This makes biomass pyrolysis (GRR) for lithium reduction more efficient and cost-effective, thereby guiding the possibility of commercial feasibility. However, it has not yet been verified in large-scale industrial applications, and further evaluation of more precise commercial economics is needed.

6. Conclusions

This study systematically investigates the thermal reduction of NCM cathodes using biomass-derived components (cellulose, hemicellulose, and lignin) as green reductants combined with a subsequent water-leaching process for efficient lithium recovery. The reduction mechanism was elucidated by comparative analyses of process parameters such as calcination temperature (500–800 ℃), stoichiometric ratio (0.25:1–2:1), and roasting time. Mechanistic studies showed that these three biopolymers produce reducing gases (CO, CH_4, H_2) during pyrolysis, resulting in an optimal gas-solid reaction environment. These reactive species effectively extract lattice oxygen from the NCM structure, leading to structural collapse and reducing high-valent transition metal oxides to low-valent states. It is worth noting that when the dosage ratio of NCM to biomass is 1:1 and 1:2, respectively, the lithium leaching efficiency of cellulose and hemicellulose at 700℃ reaches 90 %. In contrast, lignin exhibited superior reduction characteristics under milder conditions (600 ℃, 1:0.25 ratio), with comparable performance achieved with only 75 % less biomass input than polysaccharide-based reductants. This comparative study establishes criteria for biomass selection based on reduction efficiency and process economics. We can optimize the biomass single-component mixing ratios suitable for recycling cathode materials for used lithium-ion batteries, compare the biomass component gene pools to find suitable primary biomass, and finally, develop an innovative process for recycling used lithium-ion batteries by combined biomass pyrolysis reduction roasting-water leaching, which combines controlled thermal reduction with water leaching in an integrated approach to achieve a lithium recycling efficiency of 92–95 % while minimizing secondary pollution. Secondary pollution is minimized. In particular, the layered pore structure of lignin-derived carbon improves solid-gas contact efficiency, resulting in superior performance at low temperatures. The findings advance sustainable closed-loop lithium-ion battery recycling by synergizing resource recovery (lithium, transition metals) with biomass waste valorization. This dual benefit addresses both electronic waste management and circular economy objectives.

CRediT authorship contribution statement

Jianjun Cai: Supervision, Funding acquisition, Conceptualization. **Xingying Tang:** Supervision, Data curation. **Yumeng Wu:** Writing – review & editing, Writing – original draft, Software. **Shengfeng Yao:** Visualization, Conceptualization. **Jiafeng Zhang:** Visualization, Project administration. **Shubin Wang:** Data curation, Conceptualization. **Mingkang Fang:** Data curation, Conceptualization.

Declaration of Competing Interest

The authors declare that they have no known competing financial interests or personal relationships that could have appeared to influence the work reported in this paper.

Acknowledgements

This study was supported by the China Postdoctoral Science Foundation (2023M741516), the National Natural Science Foundation of China (52266011), and the Guangdong Basic and Applied Basic Research Foundation (2022A1515010970).

Appendix A. Supporting information

Supplementary data associated with this article can be found in the online version at doi:10.1016/j.jece.2025.117574.

Data availability

Data will be made available on request.

References

[1] Y. Wang, C.-h Guo, X.-j Chen, L.-q Jia, X.-n Guo, R.-s Chen, M.-s Zhang, Z.-y Chen, H.-d Wang, Carbon peak and carbon neutrality in China: goals, implementation path and prospects, China Geol. 4 (4) (2021) 720–746.

[2] Z. Chen, R. Feng, W. Wang, S. Tu, Y. Hu, X. Wang, R. Zhan, J. Wang, J. Zhao, S. Liu, Reaction-passivation mechanism driven materials separation for recycling of spent lithium-ion batteries, Nat. Commun. 14 (1) (2023) 4648.

[3] H. Ji, J. Wang, J. Ma, H.-M. Cheng, G. Zhou, Fundamentals, status and challenges of direct recycling technologies for lithium ion batteries, Chem. Soc. Rev. 52 (23) (2023) 8194–8244.

[4] A. Dehghani-Sanij, E. Tharumalingam, M. Dusseault, R. Fraser, Study of energy storage systems and environmental challenges of batteries, Renew. Sustain. Energy Rev. 104 (2019) 192–208.

[5] H. Hao, R. Tan, C. Ye, C.T.J. Low, Carbon-coated current collectors in lithium-ion batteries and supercapacitors: materials, manufacture and applications, Carbon Energy 6 (12) (2024) e604.

[6] Sahle-Demessie, E., 2023. End-of-Life Management of Lithium-Ion Batteries.

[7] S.-X. Yan, Y.-Z. Jiang, X.-P. Chen, L. Yuan, T.-T. Min, Y. Cao, W.-L. Peng, T. Zhou, Engineering classification recycling of spent lithium-ion batteries through pretreatment: a comprehensive review from laboratory to scale-up application, Rare Met. 43 (3) (2024) 915–941.

[8] L. Yu, X. Liu, S. Feng, S. Jia, Y. Zhang, J. Zhu, W. Tang, J. Gong, Recent progress on sustainable recycling of spent lithium-ion battery: efficient and closed-loop regeneration strategies for high-capacity layered NCM cathode materials, Chem. Eng. J. 476 (2023) 146733.

[9] V.S. Lakshmi, C.R. Satya, D.N. Aravind, Electronic waste: overview, recycling and metal extraction methods. IOP Conf. Ser. Mater. Sci. Eng, IOP Publishing, 2021 012069.

[10] C.-c Nie, X.-g Li, Q.-y Sun, Q. Gao, X.-n Zhu, X.-j Lyu, L. Li, X.-f You, Clean and efficient process for the recycling of all components from waste printed circuit boards: pre-treatment, bio-metallurgy, and deep utilization, J. Clean. Prod. (2024) 142810.

[11] M. Sethurajan, S. Gaydardzhiev, Bioprocessing of spent lithium ion batteries for critical metals recovery–a review, Resour. Conserv. Recycl. 165 (2021) 105225.

[12] B.K. Biswal, R. Balasubramanian, Recovery of valuable metals from spent lithium-ion batteries using microbial agents for bioleaching: a review, Front. Microbiol. 14 (2023) 1197081.

[13] J.J. Roy, B. Cao, S. Madhavi, A review on the recycling of spent lithium-ion batteries (LIBs) by the bioleaching approach, Chemosphere 282 (2021) 130944.

[14] H. Chen, S. Gu, Y. Guo, X. Dai, L. Zeng, K. Wang, C. He, G. Dodbiba, Y. Wei, T. Fujita, Leaching of cathode materials from spent lithium-ion batteries by using a mixture of ascorbic acid and HNO3, Hydrometallurgy 205 (2021) 105746.

[15] C. Peng, J. Hamuyuni, B.P. Wilson, M. Lundström, Selective reductive leaching of cobalt and lithium from industrially crushed waste Li-ion batteries in sulfuric acid system, Waste Manag. 76 (2018) 582–590.

[16] J. Wang, Y. Zhang, L. Yu, K. Cui, T. Fu, H. Mao, Effective separation and recovery of valuable metals from waste Ni-based batteries: a comprehensive review, Chem. Eng. J. 439 (2022) 135767.

[17] S. Li, W. Zhang, Y. Xia, Q. Li, Enhanced reducing capacity of citric acid for lithium-ion battery recycling under microwave-assisted leaching, Waste Manag. 189 (2024) 23–33.

[18] P. Ning, Q. Meng, P. Dong, J. Duan, M. Xu, Y. Lin, Y. Zhang, Recycling of cathode material from spent lithium ion batteries using an ultrasound-assisted DL-malic acid leaching system, Waste Manag. (Oxf.) 103 (2020) 52–60.

[19] K. Yang, C. Zhu, J. Li, B. Meng, K. Zhong, W. Huang, J. Yu, Z. Fang, Electric field-assisted leaching of valuable metals from spent lithium-ion batteries in a mixture of acetic acid and ascorbic acid, Hydrometallurgy 221 (2023) 106152.

[20] E. Asadi Dalini, G. Karimi, S. Zandevakili, M. Goodarzi, A review on environmental, economic and hydrometallurgical processes of recycling spent lithium-ion batteries, Miner. Process. Extr. Metall. Rev. 42 (7) (2021) 451–472.

[21] M. Sethurajan, E.D. van Hullebusch, D. Fontana, A. Akcil, H. Deveci, B. Batinic, J. P. Leal, T.A. Gasche, M. Ali Kucuker, K. Kuchta, Recent advances on hydrometallurgical recovery of critical and precious elements from end of life electronic wastes-a review, Crit. Rev. Environ. Sci. Technol. 49 (3) (2019) 212–275.

[22] K. Binnemans, P.T. Jones, The twelve principles of circular hydrometallurgy, J. Sustain. Met. 9 (1) (2023) 1–25.

[23] C. Pan, Y. Shen, Pyrometallurgical recycling of spent lithium-ion batteries from conventional roasting to synergistic pyrolysis with organic wastes, J. Energy Chem. 85 (2023) 547–561.

[24] Y. Zhang, W. Wang, Q. Fang, S. Xu, Improved recovery of valuable metals from spent lithium-ion batteries by efficient reduction roasting and facile acid leaching, Waste Manag. 102 (2020) 847–855.

[25] G. Lombardo, B. Ebin, M.R. St. J. Foreman, B.-M. Steenari, M. Petranikova, Chemical transformations in Li-ion battery electrode materials by carbothermic reduction, ACS Sustain. Chem. Eng. 7 (16) (2019) 13668–13679.

[26] E. Fan, L. Li, Z. Wang, J. Lin, Y. Huang, Y. Yao, R. Chen, F. Wu, Sustainable recycling technology for Li-ion batteries and beyond: challenges and future prospects, Chem. Rev. 120 (14) (2020) 7020–7063.

[27] Y. Shen, Recycling cathode materials of spent lithium-ion batteries for advanced catalysts production, J. Power Sources 528 (2022) 231220.

[28] Y. Zhao, B. Liu, L. Zhang, S. Guo, Microwave pyrolysis of macadamia shells for efficiently recycling lithium from spent lithium-ion batteries, J. Hazard. Mater. 396 (2020) 122740.

[29] J. Lu, C. Tian, C. Ren, M. Omran, F. Zhang, L. Gao, G. Chen, Priority recovering of lithium from spent lithium-ion battery cathode powder by pyrolysis reduction of bidens pilosa, J. Clean. Prod. 439 (2024) 140775.

[30] J. Lu, Y. Zhang, W. Huang, M. Omran, F. Zhang, L. Gao, G. Chen, Reductive roasting of cathode powder of spent ternary lithium-ion battery by pyrolysis of invasive plant crofton weed, Renew. Energy 206 (2023) 86–96.

[31] F. Zhou, X. Qu, Y. Wu, J. Zhao, S. Gao, D. Wang, H. Yin, Vacuum pyrolysis of pine sawdust to recover spent lithium ion batteries: the synergistic effect of carbothermic reduction and pyrolysis gas reduction, ACS Sustain. Chem. Eng. 10 (3) (2022) 1287–1297.

[32] F. Zhou, X. Li, S. Wang, X. Qu, J. Zhao, D. Wang, Z. Chen, H. Yin, Recovery of valuable metals from spent lithium-ion batteries through biomass pyrolysis gas-induced reduction, J. Hazard. Mater. 459 (2023) 132150.

[33] S. Yasa, O. Aydin, M. Al-Bujasim, B. Birol, M. Gencten, Recycling valuable materials from the cathodes of spent lithium-ion batteries: a comprehensive review, J. Energy Storage 73 (2023) 109073.

[34] A. Demirbaş, Sustainable cofiring of biomass with coal, Energy Convers. Manag. 44 (9) (2003) 1465–1479.

[35] S. Zhang, Y. Mei, G. Lin, Pyrolysis interaction of cellulose, hemicellulose and lignin studied by TG-DSC-MS, J. Energy Inst. 112 (2024) 101479.

[36] W.-J. Liu, H. Jiang, H.-Q. Yu, Development of biochar-based functional materials: toward a sustainable platform carbon material, Chem. Rev. 115 (22) (2015) 12251–12285.

[37] F. Lin, M. Xu, K.K. Ramasamy, Z. Li, J.L. Klinger, J.A. Schaidle, H. Wang, Catalyst deactivation and its mitigation during catalytic conversions of biomass, ACS Catal. 12 (21) (2022) 13555–13599.

[38] W.-H. Chen, C.-W. Wang, H.C. Ong, P.L. Show, T.-H. Hsieh, Torrefaction, pyrolysis and two-stage thermodegradation of hemicellulose, cellulose and lignin, Fuel 258 (2019) 116168.

[39] H. Yang, M. Gong, J. Hu, B. Liu, Y. Chen, J. Xiao, S. Li, Z. Dong, H. Chen, Cellulose pyrolysis mechanism based on functional group evolutions by two-dimensional perturbation correlation infrared spectroscopy, Energy Fuels 34 (3) (2020) 3412–3421.

[40] Y. Tong, T. Yang, J. Wang, B. Li, Y. Zhai, R. Li, A review on the overall process of lignin to phenolic compounds for chemicals and fuels: from separation and extraction of lignin to transformation, J. Anal. Appl. Pyrolysis (2024) 106663.

[41] S. Xie, X. Yang, Q. Sun, Z. Wang, Y. He, Research progress and prospects on thermal safety of lithium-ion batteries in aviation low-temperature and low-pressure environments, J. Energy Storage 83 (2024) 110734.

[42] L. Zhu, Z. Zhong, Effects of cellulose, hemicellulose and lignin on biomass pyrolysis kinetics, Korean J. Chem. Eng. 37 (2020) 1660–1668.

[43] A. Born, F.O. Johansson, T. Leitner, D. Kühn, A. Lindblad, N. Mårtensson, A. Föhlisch, Separation of surface oxide from bulk ni by selective ni 3 p photoelectron spectroscopy for chemical analysis in coincidence with ni M-edge auger electrons, Sci. Rep. 11 (1) (2021) 16596.

[44] J. Ju, Y. Feng, H. Li, R. Wu, Z. Xue, R. Ma, High-efficiency and environment-friendly separation and recovery of manganese from braunite via the ammonium sulfate roasting-water leaching process: behavior and mechanism, Chem. Eng. J. 466 (2023) 143218.

[45] S. Shen, C. Wang, B. Cai, H. Li, Y. Han, T. Wang, H. Qin, Heterogeneous hydrolysis of cellulose into glucose over phenolic residue-derived solid acid, Fuel 113 (2013) 644–649.

[46] C. Liang, L. Jiang, Z. Wei, W. Zhang, Q. Wang, J. Sun, Insight into the structural evolution and thermal behavior of LiNi0. 8Co0. 1Mn0. 1O2 cathode under deep charge, J. Energy Chem. 65 (2022) 424–432.

[47] J. Zheng, T. Liu, Z. Hu, Y. Wei, X. Song, Y. Ren, W. Wang, M. Rao, Y. Lin, Z. Chen, Tuning of thermal stability in layered li (Ni x Mn y Co z) O2, J. Am. Chem. Soc. 138 (40) (2016) 13326–13334.

[48] H. Konishi, M. Yoshikawa, T. Hirano, K. Hidaka, Evaluation of thermal stability in Li0. 2NixMn (1− x)/2Co (1− x)/2O2 (x= 1/3, 0.6, and 0.8) through X-ray absorption fine structure, J. Power Sources 254 (2014) 338–344.

[49] P. Liu, L. Xiao, Y. Tang, Y. Chen, L. Ye, Y. Zhu, Study on the reduction roasting of spent LiNi x co y mn z o 2 lithium-ion battery cathode materials, J. Therm. Anal. Calorim. 136 (2019) 1323–1332.

[50] J. Mao, J. Li, Z. Xu, Coupling reactions and collapsing model in the roasting process of recycling metals from LiCoO2 batteries, J. Clean. Prod. 205 (2018) 923–929.

[51] F. Arshad, J. Lin, N. Manurkar, E. Fan, A. Ahmad, M.-u-N. Tariq, F. Wu, R. Chen, L. Li, Life cycle assessment of lithium-ion batteries: a critical review, Resour. Conserv. Recycl. 180 (2022) 106164.

ACS ES&T Water

pubs.acs.org/estwater

Article

Parabens and Their Metabolites in Surface Sediment from Estuaries to the Sea: Occurrence, Spatial Distribution, and Potential Sources

Feng-Jiao Peng,[‖] Rong-Gui Zhu,[‖] Chang-Gui Pan,* Chao-Yang Zhou, Jun-Jie Hu, Sen Li, Xing-Jun Feng, and Kefu Yu

Cite This: *ACS EST Water* 2025, 5, 3739−3748

Read Online

ACCESS | Metrics & More | Article Recommendations | Supporting Information

ABSTRACT: Parabens have received significant attention due to their endocrine-disrupting properties. However, there is little information on paraben pollution in surface sediments across estuary, coastal, and marine environments within the same geographical areas. In this study, we investigated thoroughly the occurrence, spatial distribution, potential sources, and ecological risks of parabens and 4-hydroxybenzoic acid (4-HB) in estuarine, coastal, and marine sediments across the Beibu Gulf, South China Sea. Methylparaben (MeP) and 4-HB were the predominant target analytes in sediment samples, with concentrations ranging from 0.19 to 11.5 and from 5.80 to 130 ng/g dry weight, respectively. The estimated annual mass inventories deposited in the Beibu Gulf sediments were 3.00 tonnes for MeP and 45.4 tonnes for 4-HB. There was a distinct decrease in analyte concentrations from estuaries to the sea, suggesting that riverine input and point-source pollution from Weizhou Island were probably the primary sources of paraben pollution in the Beibu Gulf. All target analytes posed negligible ecological risks in the study region. This study presents the first comprehensive survey of parabens in sediments in the Beibu Gulf and contributes to our understanding of their environmental behavior and potential ecological risks.



KEYWORDS: *parabens, sediment, spatial distribution, pollution source, Beibu Gulf*

Downloaded via SOUTH CHINA NORMAL UNIV on August 21, 2025 at 00:00:58 (UTC).
See https://pubs.acs.org/sharingguidelines for options on how to legitimately share published articles.

1. INTRODUCTION

Parabens are a class of alkyl esters formed by the reaction of *p*-hydroxybenzoic acid with alcohols containing various alkyl groups.[1] Their broad-spectrum antimicrobial activity, coupled with high solubility and stability, has led to their extensive use as preservatives in food products, pharmaceuticals, and personal care items.[2,3] Among the commonly used parabens, methylparaben (MeP), ethylparaben (EtP), propylparaben (PrP), butylparaben (BuP), and benzylparaben (BzP) are the most prominent and representative paraben compounds.[4] Estimates from the European Chemical Substances Information System (ECSIS) indicate that the annual production of MeP ranges from 1,000 to 10,000 tonnes.[5] Moreover, the global cosmetics market value reached €500 billion in 2018.[6] Consequently, the occurrence of parabens has been documented in a wide range of environmental and biota media, including air, indoor dust, wastewater treatment plants, seawater, sediments, various marine organisms, and food products.[7−15] Meanwhile, parabens have been detected in almost all human matrices, including hair, urine, serum, milk, cord blood, placenta, and amniotic fluid tissue.[16−22] Despite being generally deemed safe, recent studies have demonstrated the potential adverse effects of parabens on human nervous, reproductive, and endocrine systems.[23−27] Furthermore, parabens have even been linked to the development of breast cancer.[28] Likewise, 4-hydroxybenzoic acid (4-HB), the primary metabolite and hydrolyzate of parabens, has also been demonstrated to possess endocrine-disrupting properties.[29] However, due to the increasing consumer demand for cosmetics, the use of parabens is expected to rise, leading to higher paraben production and consumption in the foreseeable future.[30] For example, a compound annual growth rate of 6.70% is projected for the parabens market from 2023 to 2030.[31] Consequently, there is growing concern about the presence of parabens in the environment.

It has been well demonstrated that wastewater treatment plants (WWTPs) cannot fully eliminate parabens.[32] Consequently, effluents from WWTPs along with direct sewage discharges from residential and industrial origins are significant sources of paraben release into the environment, with a part of parabens being subsequently partitioned into the sediment

Received: January 6, 2025
Revised: June 11, 2025
Accepted: June 11, 2025
Published: June 17, 2025



ACS Publications

© 2025 American Chemical Society

https://doi.org/10.1021/acsestwater.5c00018
ACS EST Water 2025, 5, 3739−3748

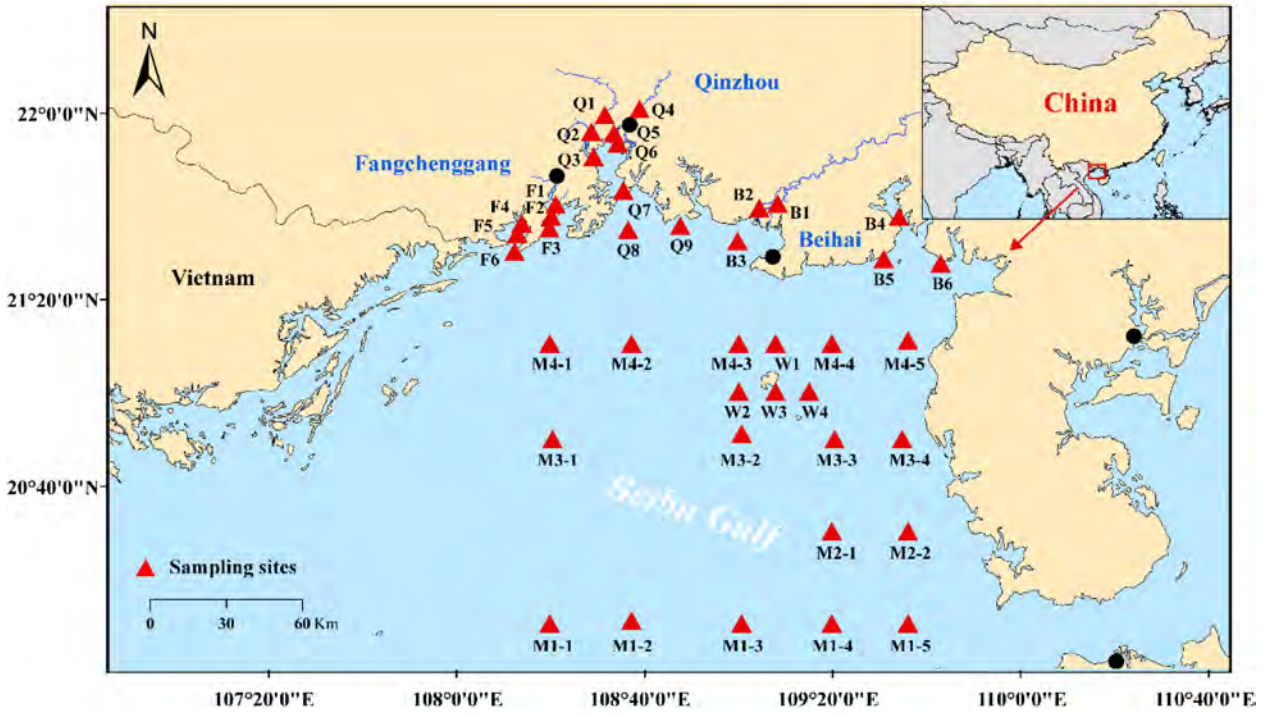


Figure 1. Map showing the sampling sites in estuaries, coastal areas, and the sea in the Beibu Gulf, South China Sea.

phase.[33] Further, as parabens trapped in sediment can be released under biological or physical disturbances, sediment is generally considered both a sink and a source of parabens in aquatic ecosystems. In fact, Ge et al. regarded marine surface sediments as the ultimate reservoir for organic contaminants including parabens and proposed that they may facilitate the transfer of these contaminants to benthic organisms.[34] Therefore, parabens in sediments may pose risks to benthic organisms, which underscores the importance of conducting comprehensive studies on the occurrence and ecological risks of parabens in sediments. Until now, several studies have investigated the occurrence of parabens in surface sediments and have demonstrated the ubiquitous presence of parabens in sediments worldwide. For instance, average concentrations of 2.40 and 120 ng/g dry weight (dw) have been reported for parabens and 4-HB in marine surface sediments in Korea, respectively.[35] Similar average levels of MeP and 4-HB (1.97 and 74.9 ng/g dw, respectively) were also found in coastal sediments in northern China.[36] In contrast, relatively higher mean MeP concentrations have been detected in sediments from the Turia River in Spain (152 ng/g dw) and urban rivers in Guangzhou in China (29.2 ng/g dw).[37,38] However, most previous studies have focused solely on either riverine or marine sediments, with none simultaneously investigating parabens in river, coastal, and marine surface sediments within the same geographical areas. This highlights the need for comprehensive studies to provide clearer and more direct insights into the sources, distribution, and migration patterns of parabens.

The Beibu Gulf, covering approximately 128,000 km^2, is a semienclosed bay located in the northwest of the South China Sea. It is surrounded by Vietnam and southern China such as Guangxi Province, the Leizhou Peninsula, and Hainan Island (17−22°N, 105−110°E). Along the coast of the Beibu Gulf, there are numerous harbors, such as Zhenzhu Port, Fangcheng Port, Qinzhou Bay, Beihai Port, and Tieshan Port.[39,40] The main rivers flowing into the Beibu Gulf include the Nanliu River, Qin River, Maoling River, and Fangcheng River. In recent decades, rapid industrialization and urbanization in the Beibu Gulf Economic Zone have caused the inevitable discharge of various pollutants into the surrounding waters, including emerging organic contaminants (ECs). Among these ECs, parabens have not received much attention in previous studies of this region. In fact, currently, it still remains largely unknown regarding the pollution characteristics and spatial distribution of parabens in the Beibu Gulf.

The present study aimed to investigate the occurrence, spatial distribution, potential sources, and ecological risks of parabens and 4-HB in estuarine, coastal, and marine sediments across the Beibu Gulf. In addition, we estimated the annual mass inventory of parabens and 4-HB deposited in sediments to better understand their environmental behavior and potential impacts. To achieve these objectives, sediment samples were collected from 41 locations across the Beibu Gulf and analyzed for six commonly used parabens (i.e., MeP, EtP, PrP, BuP, BzP, and heptylparaben (HeP)) and their metabolite 4-HB. To the best of our knowledge, this is the first study to comprehensively examine paraben pollution in surface sediments across estuarine, coastal, and marine environments within the same geographical area.

2. MATERIALS AND METHODS

2.1. Chemicals and Reagents. Six parabens (i.e., MeP, EtP, PrP, BuP, BzP, and HeP) and their metabolite, 4-HB, were selected as target analytes based on their prevalent use in cosmetic products, pharmaceuticals, and food products, their analytical feasibility,[41] and the results of previous studies.[12,35,42,43] Mass-labeled (^{13}C and ^{2}H) internal standards, including MeP, PrP, BuP, and 4-HB, were employed for quantification and qualification. These standards and internal standards were obtained from Sigma-Aldrich (St. Louis, MO) and Cambridge Isotope Laboratories (Andover, MA),

https://doi.org/10.1021/acsestwater.5c00018
ACS EST Water 2025, 5, 3739−3748

separately. Additional details about the standards, reagents, and chemicals can be found in the Supporting Information, specifically in Text S1 and Table S1.

2.2. Sample Collection. Forty-one sampling sites were investigated across the Beibu Gulf (Figure 1 and Table S2), namely, nine estuarine sites (F1, Q1−Q6 and B1−B2), 18 coastal sites (F2−F6, Q7−Q9, B3−B6, W1−W4, M3-4, and M4-5), and 14 marine sites (M1-1 to M1-5, M2-1 to M2-2, M3-1 to M3-3, and M4-1 to M4-4). Moreover, the sampling sites F1−F6, Q1−Q9, B1−B6, and W1−W4 are located around Fangchenggang City, Qinzhou City, Beihai City, and Weizhou Island, respectively, whereas M1-1 to M4-5 represent the remaining sites not part of the aforementioned regions (i.e., miscellaneous). Samples from F1−F6, Q1−Q9, and B1−B6 were collected in 2017, while those from the remaining sites (W1−W4 and M1-1 to M4-5) were collected in 2019. Surface sediment samples were collected at each site using a grab sampler, placed in sealable plastic bags, and stored at −18 °C. Subsequently, all samples were freeze-dried, homogenized using an agate mortar and pestle, sieved through an 80-mesh stainless steel sieve, and stored at −18 °C. The content of total organic carbon (TOC) in the sediment samples was determined using an elemental analyzer (Vario Macro Cube, Elementar Company, Germany).

2.3. Sample Extraction and Instrumental Analysis. The extraction of parabens and 4-HB was performed following methods established in previous studies with minor modification.[41,44] Briefly, each sediment sample (dry weight: 5 g) was spiked with internal standards (20 ng per compound), equilibrated for 30 min at room temperature, and extracted with 5 mL of a methanol/water mixture (5:3, v/v) by shaking in an orbital shaker for 60 min. The resulting extract was centrifuged at 4500 *g* for 5 min. This extraction process was repeated twice. The combined supernatant was first concentrated to 3 mL under a gentle stream of nitrogen and then diluted to 10 mL with ultrapure water containing 0.2% formic acid (pH = 2.5) for solid-phase extraction (SPE) using Oasis HLB cartridges (6 mL, 200 mg; Waters, Milford, MA, USA). Specifically, each SPE cartridge was preconditioned with 6 mL of methanol and 6 mL of ultrapure water under gravity (∼5 mL/min) in sequence. Following this, the sample was loaded and passed through the cartridge at a speed of approximately 5 mL/min. Thereafter, the cartridge was dried under vacuum and eluted with 9 mL of methanol. The eluent was concentrated to near dryness under a gentle stream of nitrogen, reconstituted in 1 mL of methanol, filtered through a 0.22 μm filter into a 2 mL amber glass vial, and stored at −18 °C until instrumental analysis.

The levels of the target analytes were measured using a 1290 ultraperformance liquid chromatography system coupled to a 6460 triple quadrupole mass spectrometer (UPLC−MS/MS, Agilent Technologies, USA). The system operated in negative ionization mode and utilized multiple reaction monitoring (MRM) for detection. Detailed information about the instrumental method is provided in Text S2, with the optimized instrumental parameters outlined in Tables S3 and S4.

2.4. Quality Assurance/Quality Control (QA/QC). A series of quality control measures were applied during both sampling and indoor laboratory analysis. Glass containers used for sampling and pretreatment procedures were thoroughly cleaned by rinsing with Milli-Q water and methanol, followed by baking at 450 °C for 4 h. Each sample batch included procedural blanks, blank spike, and matrix spike experiments. Quantification of target compounds was performed by using the internal standard curve method. The limit of detection (LOD) and limit of quantitation (LOQ) were determined as three and ten times the signal-to-noise (S/N) ratio, respectively. No target compounds were detected in any of the blanks. LOQs and recovery efficiencies for the target compounds in the sediment samples ranged from 0.03 to 0.20 ng/g dw and from 96.5% to 112.4%, respectively. Additional details on LODs, LOQs, and recoveries are available in Table S5.

2.5. Mass Inventory and Ecological Risk Assessment. The preliminary annual mass inventory (*I*, tonnes) of parabens and 4-HB deposited in the sediments in the Beibu Gulf was estimated using the following equation:[45]

$$\text{Mass inventory} = C \times \rho \times A \times D \quad (1)$$

where C is the mean concentration (ng/g dw) of individual parabens in the sediment; ρ represents the bulk density (g/cm^3) of the dry sediments, which was assumed to be 1.5 g/cm^3; A represents the area of the Beibu Gulf (128,000 km^2);[46] D is the sedimentation rate, which has been reported to vary from 0.5 to 0.9 cm/yr in the Beibu Gulf,[47] and accordingly, a median value of 0.7 cm/yr was used in the present study.

The potential ecological risks of parabens and 4-HB in the surface sediments of the Beibu Gulf were evaluated using the risk quotient (RQ) approach:[48]

$$\text{RQ} = \text{MEC}/\text{PNEC} \quad (2)$$

where MEC represents the measured environmental concentration, and PNEC is the predicted no-effect concentration. The PNEC values used here were all referenced from previous studies, where the values were derived from pelagic species due to the availability of toxicity data.[49,50] RQ ≥ 1 indicates high risk to sensitive aquatic organisms, 0.1 ≤ RQ < 1 means medium risk, and RQ < 0.1 indicates low risk.[51]

Due to the lack of toxicity information on parabens and 4-HB in sediments, the MECs of parabens and 4-HB in the sediment ($\text{MEC}_{\text{sediment}}$) were converted into their corresponding pore water concentrations ($C_{\text{pore water}}$) using the following equation:[52]

$$\text{MEC}_{\text{sediment}} = C_{\text{pore water}} = \frac{C_{\text{sediment}}}{K_{\text{oc}} \times \%\text{TOC}} \quad (3)$$

where C_{sediment} is the measured concentration of parabens and 4-HB in the sediment (ng/g dw), and K_{oc} represents the organic carbon-normalized sorption coefficient for parabens and 4-HB in the soil/sediment-water system. The K_{oc} values were obtained using the KOCWIN model of the EPI Suite program.[53]

2.6. Statistical Analysis. All statistical analyses were performed using the R program (version 4.3.2). Concentrations below the LOD were assigned a 1/2 LOD for each compound. Data normality and homogeneity were checked using the Shapiro−Wilk test and Levene's test, respectively. Accordingly, correlations between pollutant concentrations and TOC content were determined using the Spearman correlation coefficient (r). One-way analysis of variance (ANOVA) and Kruskal−Wallis tests were used, as appropriate, to examine differences in pollutant concentrations among geographical groups (estuarine, coastal, and marine groups; and Fangchenggang, Qinzhou, and Beihai cities). Moreover, a principal component analysis (PCA) was conducted on $\log_{10}$-

https://doi.org/10.1021/acsestwater.5c00018
ACS EST Water 2025, 5, 3739−3748

transformed pollutant concentrations to identify possible sources and spatial variation of parabens and 4-HB. The criterion for statistical significance was set at $p < 0.05$.

3. RESULTS AND DISCUSSION

3.1. Concentrations of Parabens and 4-HB in the Surface Sediments. Tables 1 and S6 summarize the detection frequencies and concentrations of parabens and 4-HB. All compounds except HeP were detected in the surface sediment samples. Specifically, MeP and 4-HB were detected in 100% of samples, followed by PrP (51.2%), EtP (41.5%), BzP (29.3%), BuP (17.1%), and HeP (0%). These results highlight the widespread occurrence and environmental persistence of MeP and 4-HB. The less frequent detection of PrP, EtP, BzP, BuP, and HeP may be attributed to their comparatively lower usage relative to MeP in consumer products, as documented in previous studies.[54,55] As parabens are known as endocrine disruptors, their presence in the environment raises concerns about potential impacts on aquatic organisms. The concentration of MeP ranged from 0.19 to 11.5 ng/g dw, with a mean of 2.32 ng/g dw. On average, the MeP concentration accounted for 87.0% of the total paraben concentration. Similarly, a high detection rate and percentage contribution of MeP have been observed in sewage sludge across the United States.[56] Regarding 4-HB, its concentration ranged from 5.80 to 130 ng/g dw, with a mean of 33.8 ng/g dw, which was approximately 10 times higher than that of MeP. This is not unexpected, given that 4-HB is a common metabolite of parabens.[42] The highest concentrations of both MeP and 4-HB were detected at site Q5 (Figure S1), likely due to its proximity to WWTPs and/or industrial discharge points, given its location within the urban area of Qinzhou City. To reduce paraben pollution in aquatic environments, several strategies can be considered: strengthening regulations on paraben use in consumer products to limit their environmental release, enhancing wastewater treatment processes to reduce their input into water bodies, and increasing public awareness about the environmental risks associated with parabens. For example, microalgae-based bioremediation has gained increasing attention as a sustainable and cost-effective approach for removing ECs, including parabens, from wastewater.[33]

Table 1. Concentrations (ng/g dw) of Parabens and 4-HB in the Sediment Samples Collected from Estuaries, Coastal Areas, and the Sea in the Beibu Gulf, South China Sea

Compound	DF (%)	Mean	Median	Range
MeP	100	2.32	1.18	0.19−11.5
EtP	41.5	0.06	nd	nd −0.38
PrP	51.2	0.08	0.03	nd −0.87
BuP	17.1	0.02	nd	nd −0.14
BzP	29.3	0.12	nd	nd −1.03
HeP	0	nd	nd	nd
$\sum_6$Parabens	-	2.59	1.59	0.19−11.7
4-HB	100	33.8	18.5	5.80−130

In comparison with the concentrations of parabens and 4-HB reported in the literature (Table S7), the mean MeP concentration detected in the Beibu Gulf (2.32 ng/g dw; the present study) was markedly lower than that found in the Turia River of Spain (152 ng/g dw)[37] and 2.79−11.6 times lower than those detected in other regions of China, including the Songhua Catchment (8.80 ng/g dw),[57] urban rivers in Guangzhou (29.2 ng/g dw),[38] Yellow River (13.0 ng/g dw),[58] and Huai River (11.6 ng/g dw).[58] These differences are not unexpected, given that estuarine sampling sites in the present study were observed to have higher levels of parabens and 4-HB than coastal and marine sampling sites. In parallel, this MeP concentration was comparable to those detected in Northern Chinese coastal areas (1.97 ng/g dw),[36] Korean coastal areas (2.30 ng/g dw)[35] and several watersheds in the United States, Japan, and Korea (4.31−4.69 ng/g dw).[59] In addition, the average concentration of 4-HB (33.8 ng/g dw; the present study) was one to seven times lower than those detected in other regions, including Korean coastal regions (115 ng/g dw),[35] Northern Chinese coastal areas (74.9 ng/g dw),[37] Huai River (100 ng/g dw), and Yellow River (273 ng/g dw).[58] These discrepancies can be attributed to several factors, including differences in regional urbanization and industrialization, sediment characteristics, hydrodynamic conditions, and environmental degradation.[60−63] For instance, the Beibu Gulf is less urbanized and industrialized and therefore presents relatively lower levels of paraben pollution. Overall, the Beibu

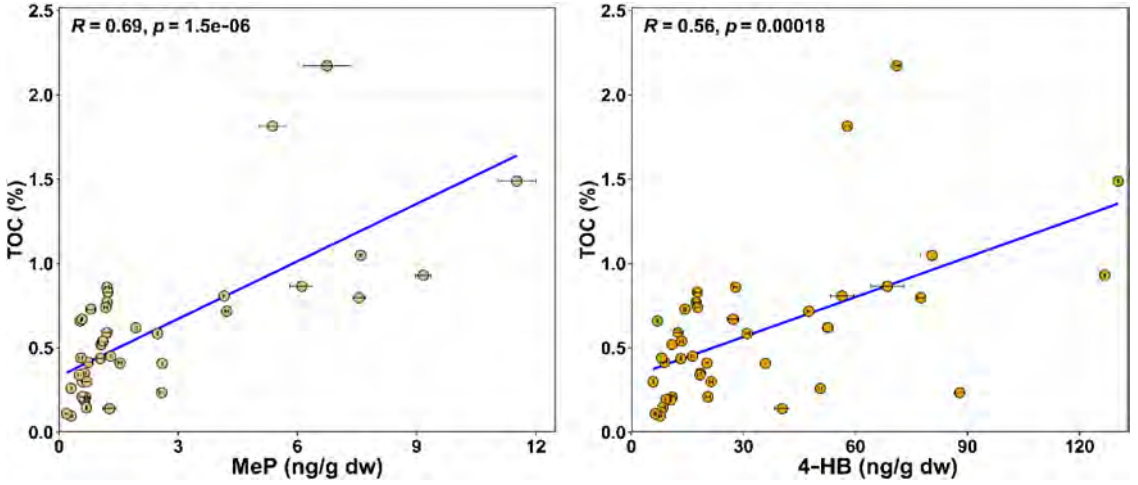


Figure 2. Spearman correlations between total organic carbon (TOC) content and methylparaben (MeP, left) or 4-hydroxybenzoic acid (4-HB, right) concentration in the sediment samples collected from estuaries, coastal areas, and the sea in the Beibu Gulf, South China Sea.

https://doi.org/10.1021/acsestwater.5c00018
ACS EST Water 2025, 5, 3739−3748

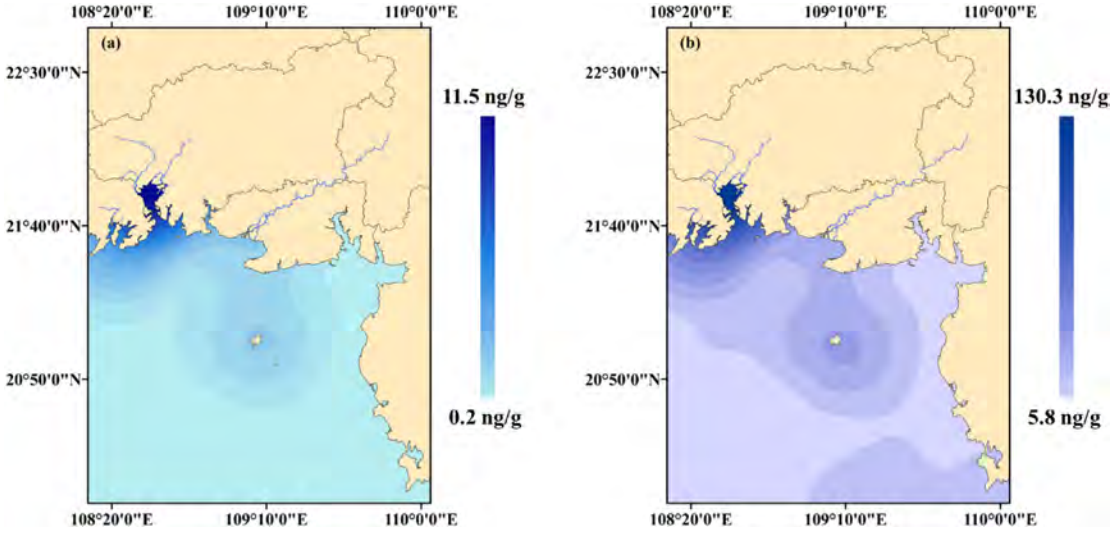


Figure 3. Spatial distribution of methylparaben (MeP, left) and 4-hydroxybenzoic acid (4-HB, right) in the sediment samples collected from estuaries, coastal areas, and the sea in the Beibu Gulf, South China Sea.

Gulf has relatively low levels of MeP and 4-HB pollution in its surface sediments on a global scale.

Previous studies have demonstrated that TOC content can influence the partitioning of organic contaminants in sediments.[64,65] Likewise, here the TOC content was significantly positively correlated with MeP (r = 0.69; p < 0.001) and 4-HB (r = 0.56; p < 0.001) concentrations in the sediment (Figure 2). These positive associations are not surprising, given the moderate hydrophobicity of parabens (e.g., Log K_{ow} of 1.96 and 1.39 for MeP and 4-HB, respectively; Table S1) and the fact that TOC provides binding sites that facilitate the sorption of organic contaminants, including parabens, through hydrophobic interactions and van der Waals forces.[62,66] Moreover, these results are in agreement with those obtained from studies on parabens in sediments collected from elsewhere, including the Huai River in China and watersheds in the United States, Japan, and Korea.[59,67] Besides TOC, various other factors may affect the partitioning of parabens and 4-HB in sediments, including their physicochemical properties, concentrations in the overlying water, degradation rates, sediment characteristics (e.g., grain size and mineral composition), and local hydrodynamic conditions.[61−63,66]

3.2. Spatial Distribution of Parabens and 4-HB. Based on the geographic difference, the sampling sites were categorized into three groups: estuarine, coastal, and marine sites. In each group, the average concentrations of MeP and 4-HB were 6.17 and 79.1 ng/g dw, 1.49 and 20.6 ng/g dw, and 0.90 and 21.7 ng/g dw, respectively (Figure S2). The concentrations of both compounds were significantly higher in the estuarine sediments than in the coastal and marine sediments (p < 0.01). Moreover, the overall spatial distribution pattern of MeP and 4-HB showed a trend of higher concentrations in estuaries > coast > sea (Figure 3). Such a distribution pattern has also been observed in previous studies on other organic pollutants, such as polycyclic aromatic hydrocarbons, polyhalogenated carbazoles, and p-phenylenediamines.[68−70] This pattern suggests that paraben pollution in the surface sediments of the Beibu Gulf is closely linked to anthropogenic activities. Corroborating this, W3, located near Weizhou Island, had relatively higher concentrations of both MeP and 4-HB (1.94 and 52.6 ng/g dw, respectively) than its neighboring sites in the sea, such as M3-2, M3-3, M4-3, and M4-4 (Figure S1). This is not surprising because Weizhou Island is a tourist hotspot with annual visitor counts over 2 million (https://www.gxnews.com.cn/staticpages/20231226/newgx658a1a7a-21391066.shtml). This heavy tourism would have contributed to the paraben pollution observed in the surrounding sea, as parabens can be released into the water when washed off the skin during showers or seaside activities.[71,72]

We further compared MeP and 4-HB concentrations among the sampling sites located in Fangchenggang (F1−F6), Qinzhou (Q1−Q9), and Beihai (B1−B6) cities (Figure S3). For both compounds, their concentrations followed the order: Qinzhou (mean: 5.83 and 67.5 ng/g dw, respectively) > Fangchenggang (mean: 2.30 and 36.5 ng/g dw, respectively) > Beihai (mean: 1.60 and 21.1 ng/g of dw, respectively), though these differences did not reach statistical significance. The relatively lower pollution observed in Beihai could be attributed to the lower inputs of WWTP effluents and road runoff into its primary river as compared to Qinzhou and Fangchenggang, as it has been shown that these sources can contain certain amounts of parabens and 4-HB.[73,74] Indeed, the primary rivers of both Qinzhou (Qin River) and Fangchenggang (Fangcheng River) run through their urban areas, but the one (Nanliu River) of Beihai does not. Consistent with our findings, in the sediments of the Xiaoqing River that runs through several megacities in Shandong Province and ultimately flows into Laizhou Bay (China), paraben concentrations were much higher than in other nearby rivers.[75]

3.3. Potential Sources of Parabens and 4-HB. Correlation analysis is a valuable tool for inferring potential sources of organic pollutants.[76] Here, we found a significant positive correlation between MeP and 4-HB concentrations (p < 0.001; Figure S4), indicating their similar sources and transport pathways. Results from PCA analysis revealed that the first and second principal components (PC1 and PC2, respectively) explained 37.4% and 34.5% of the total variation in the concentrations of parabens and 4-HB across sampling sites, respectively (Figure 4). PC1 was characterized by high loadings of EtP, PrP, BuP, and BzP, representing the variation

https://doi.org/10.1021/acsestwater.5c00018
ACS EST Water 2025, 5, 3739−3748

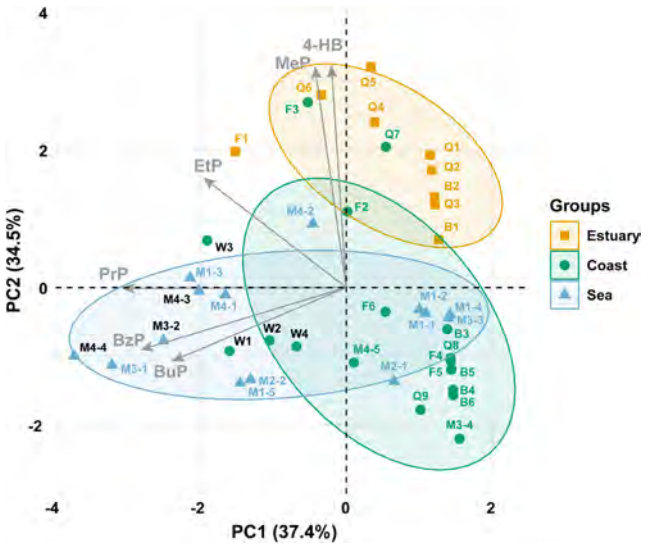


Figure 4. Principal component analysis (PCA) biplot showing sample scores (symbols) and chemical loadings (arrows). PC1 and PC2 represent the first and second principal components, which explain 37.4% and 34.5% of the total variance, respectively. The direction and length of each arrow indicate the contribution of each chemical variable (PrP, EtP, BuP, BzP, MeP, and 4-HB) to the principal components. Sampling sites located close together share similar chemical profiles. MeP, methylparaben; EtP, ethylparaben; PrP, propylparaben; BuP, butylparaben; BzP, benzylparaben; 4-HB, 4-hydroxybenzoic acid.

associated with these compounds across sampling sites, whereas PC2 was highly weighted for MeP and 4-HB, capturing another major source of variation in the dataset. The estuarine group (yellow square symbols) was clearly separated from the coastal and marine groups, with its sampling sites clustered in the upper-right quadrant of the PCA ordination diagram. Moreover, although sites F3 and Q7 belonged to the coastal group, they clustered with the estuary group, which aligns well with their geographic proximity.

Noticeably, some sampling sites (F4−F6, Q8, Q9, and B3−B6) in the coastal group clustered in the lower right quadrant of the diagram, exhibiting relatively lower levels of all examined pollutants. These sites shared a key characteristic that they are located in coastal bays without input from major rivers, suggesting that PC2 may represent riverine pollution sources. Indeed, parabens are commonly used in household personal care products (e.g., shampoo, body wash, and toothpaste) and some food packaging,[77] which are indirectly (through WWTP effluents) and/or directly discharged into rivers and can thus be partitioned into sediments. Meanwhile, the sampling sites located near Weizhou Island (W1−W4, M3-2, M4-3, and M4-4) were placed on the left side of the diagram, suggesting that PC1 may represent point source pollution from the island. At these sites, relatively higher concentrations of PrP, BuP, and BzP were detected, reflecting a different profile of paraben pollution compared to those located in Qinzhou, Fangchenggang, and Beihai cities. This difference is probably related to differences in the use and usage of products that contain different types of parabens. For example, the paraben pollution around Weizhou Island can be attributed mainly to tourists using sunscreen and skincare products.[78] Notably, BzP, a long-chain paraben, was not detected at the estuarine sampling sites but was detected at M3-1 with the highest concentration of 1.03 ng/g dw. This sampling site is located near Vietnam and may therefore be influenced by sources from there as well. Indeed, surveys in Vietnam have revealed that BzP was commonly detected at high concentrations in Vietnamese seawater and marine fish.[43,79] Furthermore, there are differences in the types and frequency of use of medicine and personal care products between countries or regions. Therefore, variations in the composition of parabens added to different products may have contributed to the bias observed in sampling sites near Weizhou Island toward PC1.[80]

3.4. Mass Inventory and Ecological Risk of Parabens and 4-HB. Pollutants trapped in the sediment can be released under biological disturbance and jet disturbance caused by the propeller,[81,82] thereby leading to sediment becoming a source of pollutants in addition to being a sink. In fact, sediment has been demonstrated to be a significant source of paraben pollution in the adjacent aquatic environment, posing potential risks to aquatic organisms and human beings.[83,84] Furthermore, our recent study found that MeP accumulated in benthic organisms and even biomagnified in benthic food webs.[41] Therefore, it is essential to assess the potential of sediment as a pollution source to the nearby environment. To do this, annual mass inventories were estimated for parabens and 4-HB deposited in the sediments in the Beibu Gulf (Table S8). The maximum annual mass inventory of individual chemicals reached 45.4 tonnes, which was found for 4-HB. For parabens, the annual mass inventories were ranked in the following order: MeP (3.00 tonnes) > BzP (0.16 tonnes) > PrP (0.11 tonnes) > EtP (0.08 tonnes) > BuP (0.03 tonnes). However, it should be noted that these estimates were subject to high uncertainty due to the use of mean concentration values and the median sedimentation rate, which may not have fully captured spatial and temporal variability. Despite this limitation, to our knowledge, this is the first study assessing the mass inventory of parabens and 4-HB in sediments, which provides baseline data to interpret results obtained from future studies. To improve accuracy in future assessments, incorporating high-resolution sedimentation rate data and flux modeling approaches would be beneficial.

Negligible risks to aquatic organisms were observed for parabens and 4-HB in the sediments (RQs ≤ 0.014; Table S9), which is consistent with findings reported for sediments from the Persian Gulf and the transboundary river Ganga.[85,86] However, the RQ calculation did not account for potential mixture toxicity, and the toxicity data used were not generated from benthic or marine organisms. To improve our understanding of paraben pollution and its ecological risks in marine environments, future monitoring studies should consider both halogenated and nonhalogenated parabens, given their distinct environmental persistence and toxicity, while toxicological studies should also focus on the sublethal effects of long-term paraben exposure on marine organisms, such as reproductive, developmental, and endocrine disruptions. Noticeably, the RQs of 4-HB were even relatively higher than those of MeP. Therefore, future studies should pay attention to paraben metabolites as well.

3.5. Environmental Implications. Although parabens are not classified as persistent organic pollutants (POPs), their continuous production, widespread application, and daily use have led to their constant release into the environment, thereby exhibiting pseudopersistence. Therefore, we predicted their characteristic travel distances (CTDs) and transport efficiencies (TEs) using the OECD Pov and LRTP Screening

https://doi.org/10.1021/acsestwater.5c00018
ACS EST Water 2025, 5, 3739−3748

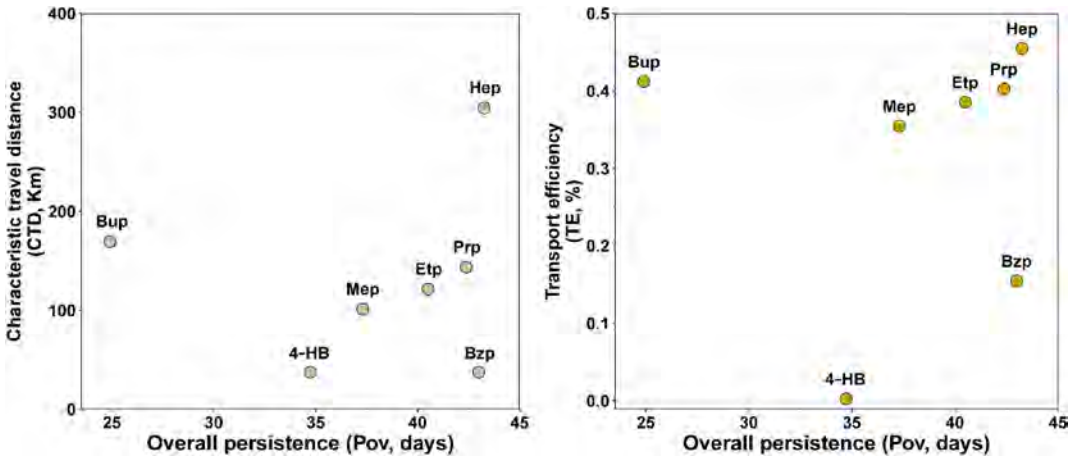


Figure 5. Calculated overall persistence (Pov), characteristic travel distance (CTD), and transport efficiency (TE) of the target compounds. MeP, methylparaben; EtP, ethylparaben; PrP, propylparaben; BuP, butylparaben; BzP, benzylparaben; HeP, heptylparaben; 4-HB, 4-hydroxybenzoic acid.

Tool based on the following physicochemical properties obtained from the EPI Suite 4.1 software: degradation half-lives in air, water, soil, and sediment, air/water partition coefficient (log K_{aw}), and octanol/water partition coefficient (log K_{ow}).[70] The results are shown in Figure 5 and Table S10. CTDs ranged from 37.37 km for BzP to 304.7 km for HeP. Regarding MeP, it had a CTD of 101.2 km, suggesting the potential for MeP originating from rivers and coastal areas to migrate across the entire Beibu Gulf and reach remote regions of the South China Sea (SCS). In contrast, the predicted CTD for 4-HB was only 37.4 km, which suggests that the occurrence of 4-HB in the Beibu Gulf is likely due to the degradation of parabens during the transport process rather than direct emission of 4-HB. This hypothesis is further confirmed by the strong correlation observed between MeP and 4-HB (Figure S4). The transport efficiencies (TE, %) through atmospheric deposition were very low for all target compounds (<0.5%). Therefore, both theoretical calculations and data from field samples indicate that river runoff is the primary pathway for transporting parabens and 4-HB to the ocean, whereas the contribution of atmospheric transport is minimal.

4. CONCLUSIONS

We present the first study of paraben pollution in surface sediments across estuarine, coastal, and marine environments within the same geographical area. In general, the paraben pollution in the Beibu Gulf was relatively low on a global scale. MeP and 4-HB were the predominant analytes detected in the sediment samples. The overall spatial distribution of MeP and 4-HB showed a trend of higher concentrations in estuaries > coast > sea. Riverine input and point source pollution from Weizhou Island are likely to be the primary sources of paraben pollution in the Beibu Gulf. Despite the widespread occurrence of MeP and 4-HB in the study region, none of the target compounds posed significant ecological risks. Future research should explore sediment cores, halogenated parabens, and metabolites other than 4-HB, as well as the long-term effects of paraben exposure on marine organisms to improve our understanding of paraben pollution and its ecological risks in marine environments.

■ ASSOCIATED CONTENT

Supporting Information

The Supporting Information is available free of charge at https://pubs.acs.org/doi/10.1021/acsestwater.5c00018.

Materials include details on chemical reagents and instrumental analysis, information on target analytes and sampling sites, and additional data and figures supporting the conclusions of the study (PDF)

■ AUTHOR INFORMATION

Corresponding Author

Chang-Gui Pan − *Guangxi Laboratory on the Study of Coral Reefs in the South China Sea, School of Marine Sciences, Guangxi University, Nanning 530004, China;* orcid.org/0000-0002-7090-0122; Email: panchanggui@gxu.edu.cn, panchanggui@hotmail.com

Authors

Feng-Jiao Peng − *SCNU Environmental Research Institute, Guangdong Provincial Key Laboratory of Chemical Pollution and Environmental Safety, MOE Key Laboratory of Theoretical Chemistry of Environment, South China Normal University, Guangzhou 510006, China; School of Environment, South China Normal University, Guangzhou 510006, China*

Rong-Gui Zhu − *Guangxi Laboratory on the Study of Coral Reefs in the South China Sea, School of Marine Sciences, Guangxi University, Nanning 530004, China*

Chao-Yang Zhou − *Guangxi Laboratory on the Study of Coral Reefs in the South China Sea, School of Marine Sciences, Guangxi University, Nanning 530004, China*

Jun-Jie Hu − *Guangxi Laboratory on the Study of Coral Reefs in the South China Sea, School of Marine Sciences, Guangxi University, Nanning 530004, China*

Sen Li − *SCNU Environmental Research Institute, Guangdong Provincial Key Laboratory of Chemical Pollution and Environmental Safety, MOE Key Laboratory of Theoretical Chemistry of Environment, South China Normal University, Guangzhou 510006, China; School of Environment, South China Normal University, Guangzhou 510006, China*

Xing-Jun Feng − *SCNU Environmental Research Institute, Guangdong Provincial Key Laboratory of Chemical Pollution*

and Environmental Safety, MOE Key Laboratory of Theoretical Chemistry of Environment, South China Normal University, Guangzhou 510006, China; School of Environment, South China Normal University, Guangzhou 510006, China

Kefu Yu − *Guangxi Laboratory on the Study of Coral Reefs in the South China Sea, School of Marine Sciences, Guangxi University, Nanning 530004, China*

Complete contact information is available at: https://pubs.acs.org/10.1021/acsestwater.5c00018

Author Contributions

‖F.-J.P. and R.-G.Z. contributed equally and are joint first authors.

Notes

The authors declare no competing financial interest.

■ ACKNOWLEDGMENTS

The authors would like to thank the financial support by the National Natural Science Foundation of China (42067054, 42207322, 41673105), the Guangzhou Municipal Science and Technology Project (2025A04J0904), and the Innovation Project of Guangxi Graduate Education (YCBZ2025069).

■ ABBREVIATIONS

DF, detection frequency; nd, no detected; MeP, methylparaben; EtP, ethylparaben; PrP, propylparaben; BuP, butylparaben; BzP, benzylparaben; HeP, heptylparaben; 4-HB, 4-hydroxybenzoic acid

■ REFERENCES

(1) Fransway, A. F.; Fransway, P. J.; Belsito, D. V.; Warshaw, E. M.; Sasseville, D.; Fowler, J. F.; DeKoven, J. G.; Pratt, M. D.; Maibach, H. I.; Taylor, J. S.; Marks, J. G.; Mathias, C. G. T.; DeLeo, V. A.; Zirwas, J. M.; Zug, K. A.; Atwater, A. R.; Silverberg, J.; Reeder, M. J. Parabens. *Dermatitis* **2019**, *30* (1), 3−31.

(2) Soni, M. G.; Carabin, I. G.; Burdock, G. Safety assessment of esters of *p*-hydroxybenzoic acid (parabens). *Food Chem. Toxicol.* **2005**, *43* (7), 985−1015.

(3) Petric, Z.; Ružić, J.; Žuntar, I. The controversies of parabens-an overview nowadays. *Acta Pharmaceut.* **2021**, *71* (1), 17−32.

(4) Nowak, K.; Ratajczak-Wrona, W.; Górska, M.; Jabłońska, E. Parabens and their effects on the endocrine system. *Mol. Cell. Endocrinol.* **2018**, *474*, 238−251.

(5) SUBSPORT (Substitution Support Portal) *SUBSPORT Specific Substances Alternatives Assessment-Parabens*; SUBSPORT, 2013.

(6) Wei, F.; Mortimer, M.; Cheng, H.; Sang, N.; Guo, L. Parabens as chemicals of emerging concern in the environment and humans: A review. *Sci. Total Environ.* **2021**, *778*, 146150.

(7) Liao, C.; Chen, L.; Kannan, K. Occurrence of parabens in foodstuffs from China and its implications for human dietary exposure. *Environ. Int.* **2013**, *57*−*58*, 68−74.

(8) Xue, J.; Sasaki, N.; Elangovan, M.; Diamond, G.; Kannan, K. Elevated accumulation of parabens and their metabolites in marine mammals from the United States coastal waters. *Environ. Sci. Technol.* **2015**, *49* (20), 12071−12079.

(9) Xue, X.; Xue, J.; Liu, W.; Adams, D. H.; Kannan, K. Trophic magnification of parabens and their metabolites in a subtropical marine food web. *Environ. Sci. Technol.* **2017**, *51* (2), 780−789.

(10) Emnet, P.; Gaw, S.; Northcott, G.; Storey, B.; Graham, L. Personal care products and steroid hormones in the Antarctic coastal environment associated with two Antarctic research stations, McMurdo Station and Scott Base. *Environ. Res.* **2015**, *136*, 331−342.

(11) Kung, T. A.; Lee, S. H.; Yang, T. C.; Wang, W. H. Survey of selected personal care products in surface water of coral reefs in Kenting National Park, Taiwan. *Sci. Total Environ.* **2018**, *635*, 1302−1307.

(12) Chen, J.; Meng, X.; Bergman, A.; Halden, R. U. Nationwide reconnaissance of five parabens, triclosan, triclocarban and its transformation products in sewage sludge from China. *J. Hazard. Mater.* **2019**, *365*, 502−510.

(13) Zhu, Q.; Wang, M.; Jia, J.; Hu, Y.; Wang, X.; Liao, C.; Jiang, G. Occurrence, distribution, and human exposure of several endocrine-disrupting chemicals in indoor dust: a nationwide study. *Environ. Sci. Technol.* **2020**, *54* (18), 11333−11343.

(14) Hajizadeh, Y.; Pourzamani, H.; Ebrahimpour, K.; Chavoshani, A.; Rahimi, B. Monitoring of paraben compounds in indoor and outdoor air of a populated city. *Atmos. Pollut. Res.* **2021**, *12*, 43−49.

(15) Fenni, F.; Sunyer-Caldú, A.; Ben Mansour, H.; Diaz-Cruz, M. S. Contaminants of emerging concern in marine areas: First evidence of UV filters and paraben preservatives in seawater and sediment on the eastern coast of Tunisia. *Environ. Pollut.* **2022**, *309*, 119749.

(16) Dualde, P.; Pardo, O.; Corpas-Burgos, F.; Kuligowski, J.; Gormaz, M.; Vento, M.; Pastor, A.; Yusà, V. Biomonitoring of parabens in human milk and estimated daily intake for breastfed infants. *Chemosphere* **2020**, *240*, 124829.

(17) Reimann, B.; Vrijens, K.; Roels, H. A.; Wang, C.; Cosemans, C.; Van Overmeire, I.; Nawrot, T. S.; Plusquin, M. *In utero* exposure to parabens and early childhood BMI z-scores - Associations between placental ethyl paraben, longitudinal BMI trajectories and cord blood metabolic biomarkers. *Environ. Int.* **2021**, *157*, 106845.

(18) Bräuner, E. V.; Uldbjerg, C. S.; Lim, Y.; Gregersen, L. S.; Krause, M.; Frederiksen, H.; Andersson, A. Presence of parabens, phenols and phthalates in paired maternal serum, urine and amniotic fluid. *Environ. Int.* **2022**, *158*, 106987.

(19) Chae, H.; Lee, I.; Jeong, Y.; Kim, S.; Choi, G.; Kim, S.; Park, J.; Moon, H.; Choi, K. Urinary paraben concentrations of adult women by fasting status: Comparison between Korea and the United States. *Sci. Total Environ.* **2022**, *849*, 157761.

(20) Li, Y.; Zheng, N.; Sun, S.; Wang, S.; Li, X.; Pan, J.; Li, M.; Lang, L.; Yue, Z.; Zhou, B. Exposure estimates of parabens from personal care products compared with biomonitoring data in human hair from Northeast China. *Ecotoxicol. Environ. Saf.* **2023**, *267*, 115635.

(21) Sunyer-Caldú, A.; Peiró, A.; Díaz, M.; Ibáñez, L.; Gil-Solsona, R.; Gago-Ferrero, P.; Silvia diaz-Cruz, M. Target analysis and suspect screening of UV filters, parabens and other chemicals used in personal care products in human cord blood: Prenatal exposure by mother-fetus transfer. *Environ. Int.* **2023**, *173*, 107834.

(22) Mao, W.; Jin, H.; Guo, R.; Chen, P.; Zhong, S.; Wu, X. Distribution of parabens and 4-HB in human blood. *Sci. Total Environ.* **2024**, *914*, 169874.

(23) Ren, X.; Deng, Y.; Liu, W.; Fu, J.; Huang, Z.; Zhang, D.; Xiao, Q.; Li, X.; Chen, X.; Huang, X.; Liu, J.; Lu, S. Co-exposure to parabens and triclosan and associations with cognitive impairment in an elderly population from Shenzhen, China. *Chemosphere* **2023**, *331*, 138699.

(24) Tung, C.-J.; Chen, M.-H.; Lin, C.-C.; Chen, P.-C. Association between parabens exposure and neurodevelopment in children. *Environ. Int.* **2024**, *188*, 108671.

(25) Kek, T.; Geršak, K.; Virant-Klun, I. Exposure to endocrine disrupting chemicals (bisphenols, parabens, and triclosan) and their associations with preterm birth in humans. *Reprod. Toxicol.* **2024**, *125*, 108580.

(26) Chatterjee, S.; Adhikary, S.; Bhattacharya, S.; Chakraborty, A.; Dutta, S.; Roy, D.; Ganguly, A.; Nanda, S.; Rajak, P. Parabens as the double-edged sword: Understanding the benefits and potential health risks. *Sci. Total Environ.* **2024**, *954*, 176547.

(27) Pan, J.; Liu, P.; Yu, X.; Zhang, Z.; Liu, J. The adverse role of endocrine disrupting chemicals in the reproductive system. *Front. Endocrinol.* **2023**, *14*, 1324993.

(28) Wan, M.; Co, V. A.; El-Nezami, H. Endocrine disrupting chemicals and breast cancer: a systematic review of epidemiological studies. *Crit. Rev. Food Sci. Nutr.* **2022**, *62* (24), 6549−6576.

(29) Boberg, J.; Taxvig, C.; Christiansen, S.; Hass, U. Possible endocrine disrupting effects of parabens and their metabolites. *Reprod. Toxicol.* **2010**, *30* (2), 301−312.
(30) Nowak, K.; Jablonska, E.; Ratajczak-Wrona, W. Controversy around parabens: Alternative strategies for preservative use in cosmetics and personal care products. *Environ. Res.* **2021**, *198*, 110488.
(31) *Global Parabens Market - Industry Trends and Forecast to 2030*. https://www.databridgemarketresearch.com/reports/global-parabens-market?srsltid=AfmBOop3pVNMUDhA25oDJ3wjG25rAvqNiKPKb6jUUNCg0M3z9Y65i8DU. accessed March 24, 2025.
(32) Wang, W.; Kannan, K. Fate of parabens and their metabolites in two Wastewater treatment plants in New York State, United States. *Environ. Sci. Technol.* **2016**, *50* (3), 1174−1181.
(33) Vale, F.; Sousa, C. A.; Sousa, H.; Santos, L.; Simões, M. Parabens as emerging contaminants: Environmental persistence, current practices and treatment processes. *J. Cleaner Prod.* **2022**, *347*, 131244.
(34) Ge, Y.; Zhang, H.; Fu, J.; Guo, Z.; Dong, Q.; Yu, J.; Mo, Z.; Lai, Y.; Yang, J.; Lu, S. Parabens, bisphenols, and triclosan in coral polyps, algae, and sediments from sanya, China: Occurrence, profiles, and environmental implications. *Environ. Pollut.* **2024**, *361*, 124839.
(35) Lee, J.; Lee, H.; Moon, H. Contamination and spatial distribution of parabens, their metabolites and antimicrobials in sediment from Korean coastal waters. *Ecotoxicol. Environ. Saf.* **2019**, *180*, 185−191.
(36) Liao, C.; Shi, J.; Wang, X.; Zhu, Q.; Kannan, K. Occurrence and distribution of parabens and bisphenols in sediment from northern Chinese coastal areas. *Environ. Pollut.* **2019**, *253*, 759−767.
(37) Carmona, E.; Andreu, V.; Picó, Y. Occurrence of acidic pharmaceuticals and personal care products in Turia River Basin: From waste to drinking water. *Sci. Total Environ.* **2014**, *484*, 53−63.
(38) Huang, C.; Wu, L.; Liu, G.; Shi, L.; Guo, Y. Occurrence and ecological risk assessment of eight endocrine-disrupting chemicals in urban river water and sediments of south China. *Arch. Environ. Contam. Toxicol.* **2018**, *75* (2), 224−235.
(39) Guan, Y.; He, H.; Fan, K.; Wang, S.; Guo, Z.; Wang, H.; Cui, L.; Chen, W.; Huang, C.; Liu, Z.; He, X.; Guo, K.; Zhang, J.; Xu, Z. Spatial distribution, source identification, and transportation paths of plutonium in the Beibu Gulf, South China Sea. *Mar. Pollut. Bull.* **2024**, *199*, 115972.
(40) Zhang, R.; Yu, K.; Li, A.; Zeng, W.; Lin, T.; Wang, Y. Occurrence, phase distribution, and bioaccumulation of organophosphate esters (OPEs) in mariculture farms of the Beibu Gulf, China: A health risk assessment through seafood consumption. *Environ. Pollut.* **2020**, *263*, 114426.
(41) Zhu, R.; Pan, C.; Peng, F.; Zhou, C.; Hu, J.; Yu, K. Parabens and their metabolite in a marine benthic-dominated food web from the Beibu gulf, South China Sea: Occurrence, trophic transfer, and health risk assessment. *Water Res.* **2024**, *248*, 120841.
(42) Liao, C.; Kannan, K. Temporal trends of parabens and their metabolites in mollusks from the Chinese Bohai Sea during 2006−2015: species-specific accumulation and implications for human exposure. *Environ. Sci. Technol.* **2018**, *52* (16), 9045−9055.
(43) Le, T. M.; Pham, P. T.; Nguyen, T. Q.; Nguyen, T. Q.; Bui, M. Q.; Nguyen, H. Q.; Vu, N. D.; Kannan, K.; Tran, T. M. A survey of parabens in aquatic environments in Hanoi, Vietnam and its implications for human exposure and ecological risk. *Environ. Sci. Pollut. Res.* **2022**, *29* (31), 46767−46777.
(44) Zhao, X.; Qiu, W.; Zheng, Y.; Xiong, J.; Gao, C.; Hu, S. Occurrence, distribution, bioaccumulation, and ecological risk of bisphenol analogues, parabens and their metabolites in the Pearl River Estuary, South China. *Ecotoxicol. Environ. Saf.* **2019**, *180*, 43−52.
(45) Mi, L.; Xie, Z.; Zhao, Z.; Zhong, M.; Mi, W.; Ebinghaus, R.; Tang, J. Occurrence and spatial distribution of phthalate esters in sediments of the Bohai and Yellow seas. *Sci. Total Environ.* **2019**, *653*, 792−800.
(46) Yang, C.; Wang, L.; Liu, Y.; Shan, B.; Sun, D. Spatial distribution, potential risks and source identification of heavy metals in the coastal sediments of the northern Beibu Gulf, south China sea. *Int. J. Environ. Res. Public Health* **2022**, *19* (16), 10205.
(47) Li, P.; Xue, R.; Wang, Y.; Zhang, R.; Zhang, G. Influence of anthropogenic activities on PAHs in sediments in a significant gulf of low-latitude developing regions, the Beibu Gulf, South China Sea: Distribution, sources, inventory and probability risk. *Mar. Pollut. Bull.* **2015**, *90* (1−2), 218−226.
(48) Xiao, S.; Wu, Q.; Pan, C.; Yin, C.; Wang, Y.; Yu, K. Distribution, partitioning behavior and potential source of legacy and alternative per- and polyfluoroalkyl substances (PFASs) in water and sediments from a subtropical Gulf, South China Sea. *Environ. Res.* **2021**, *201*, 111485.
(49) Kühn, R.; Pattard, M.; Pernak, K. D.; Winter, A. Results of the harmful effects of selected water pollutants (anilines, phenols, aliphatic compounds) to *Daphnia magna*. *Water Res.* **1989**, *23* (4), 495−499.
(50) Li, W.; Shi, Y.; Gao, L.; Liu, J.; Cai, Y. Occurrence fate and risk assessment of parabens and their chlorinated derivatives in an advanced wastewater treatment plant. *J. Hazard. Mater.* **2015**, *300*, 29−38.
(51) Wu, Q.; Xiao, S.; Pan, C.; Yin, C.; Wang, Y.; Yu, K. Occurrence source apportionment and risk assessment of antibiotics in water and sediment from the subtropical Beibu Gulf, South China. *Sci. Total Environ.* **2022**, *806*, 150439.
(52) Peng, F.-J.; Pan, C.-G.; Zhang, M.; Zhang, N.-S.; Windfeld, R.; Salvito, D.; Selck, H.; Van den Brink, P. J.; Ying, G.-G. Occurrence and ecological risk assessment of emerging organic chemicals in urban rivers: Guangzhou as a case study in China. *Sci. Total Environ.* **2017**, *589*, 46−55.
(53) Lin, H.; Zhou, L.; Lu, S.; Yang, H.; Li, Y.; Yang, X. Occurrence and spatiotemporal distribution of natural and synthetic steroid hormones in soil, water, and sediment systems in suburban agricultural area of Guangzhou City, China. *J. Hazard. Mater.* **2024**, *470*, 134288.
(54) Guo, Y.; Kannan, K. A survey of phthalates and parabens in personal care products from the United States and its implications for human exposure. *Environ. Sci. Technol.* **2013**, *47* (24), 14442−14449.
(55) Guo, Y.; Wang, L.; Kannan, K. Phthalates and parabens in personal care products from China: concentrations and human exposure. *Arch. Environ. Contam. Toxicol.* **2014**, *66* (1), 113−119.
(56) Chen, J.; Pycke, B. F. G.; Brownawell, B. J.; Kinney, C. A.; Furlong, E. T.; Kolpin, D. W.; Halden, R. U. Occurrence temporal variation, and estrogenic burden of five parabens in sewage sludge collected across the United States. *Sci. Total Environ.* **2017**, *593*−*594*, 368−374.
(57) Li, W.; Zhang, Z.; Li, Y.; Hung, H.; Yuan, Y. Assessing the distributions and fate of household and personal care chemicals (HPCCs) in the Songhua Catchment, Northeast China. *Sci. Total Environ.* **2021**, *786*, 147484.
(58) Feng, J.; Zhao, J.; Xi, N.; Guo, W.; Sun, J. Parabens and their metabolite in surface water and sediment from the Yellow River and the Huai River in Henan Province: Spatial distribution, seasonal variation and risk assessment. *Ecotoxicol. Environ. Saf.* **2019**, *172*, 480−487.
(59) Liao, C.; Lee, S.; Moon, H.; Yamashita, N.; Kannan, K. Parabens in sediment and sewage sludge from the United States, Japan, and Korea: spatial distribution and temporal trends. *Environ. Sci. Technol.* **2013**, *47* (19), 10895−10902.
(60) Zhao, X.; Wang, Y.; Li, Z.; Chen, T. The source of parabens in urban river water: The evidence from outdoor multimedia environment in six metropolitan cities, China. *Environ. Sci. Technol.* **2024**, *11* (5), 485−491.
(61) Iglesias, I.; Almeida, C. M. R.; Teixeira, C.; Mucha, A. P.; Magalhães, A.; Bio, A.; Bastos, L. Linking contaminant distribution to hydrodynamic patterns in an urban estuary: The Douro estuary test case. *Sci. Total Environ.* **2020**, *707*, 135792.

https://doi.org/10.1021/acsestwater.5c00018
ACS EST Water 2025, 5, 3739−3748

(62) Al-Khazrajy, O. S. A.; Boxall, A. B. A. Impacts of compound properties and sediment characteristics on the sorption behaviour of pharmaceuticals in aquatic systems. *J. Hazard. Mater.* **2016**, *317*, 198−209.
(63) Soriano, Y.; Gimeno-García, E.; Campo, J.; Hernández-Crespo, C.; Andreu, V.; Picó, Y. Exploring organic and inorganic contaminant histories in sediment cores across the anthropocene: Accounting for site/area dependent factors. *J. Hazard. Mater.* **2024**, *470*, 134168.
(64) Cheng, J.; Ko, F. Occurrence of PBDEs in surface sediments of metropolitan rivers: Sources, distribution pattern, and risk assessment. *Sci. Total Environ.* **2018**, *637*−*638*, 1578−1585.
(65) Zhong, M.; Wu, H.; Mi, W.; Li, F.; Ji, C.; Ebinghaus, R.; Tang, J.; Xie, Z. Occurrences and distribution characteristics of organophosphate ester flame retardants and plasticizers in the sediments of the Bohai and Yellow Seas, China. *Sci. Total Environ.* **2018**, *615*, 1305−1311.
(66) Peng, F. J.; Zhou, L. J.; Ying, G. G.; Liu, Y. S.; Zhao, J. L. Antibacterial activity of the soil-bound antimicrobials oxytetracycline and ofloxacin. *Environ. Toxicol. Chem.* **2014**, *33* (4), 776−783.
(67) Feng, J.; Zhao, J.; Guo, W.; Su, X.; Ru, X.; Dong, S.; Sun, J. Pollution characteristics, temporal records, and risks associated with parabens and mercury in sediments from the upper Huai River, Henan Province. *J. Geochem. Explor.* **2021**, *223*, 106726.
(68) Lu, Z.; Tian, W.; Zhang, S.; Chu, M.; Zhao, J.; Liu, B.; Yang, K.; Cao, H.; Chen, Z. Spatiotemporal variability of PAHs and their derivatives in sediments of the Laizhou Bay in the eastern China: Occurrence, source, and ecological risk assessment. *J. Hazard. Mater.* **2023**, *460*, 132351.
(69) Peng, L.; Liu, L.; Li, P.; Lin, K. Spatial and temporal distribution of polyhalogenated carbazoles in sediments from the Yangtze River estuary and adjacent East China Sea. *Environ. Pollut.* **2023**, *319*, 120957.
(70) Zeng, L.; Li, Y.; Sun, Y.; Liu, L.; Shen, M.; Du, B. Widespread occurrence and transport of *p*-phenylenediamines and their quinones in sediments across urban rivers, estuaries, coasts, and deep-sea regions. *Environ. Sci. Technol.* **2023**, *57* (6), 2393−2403.
(71) Lv, M.; Sun, Q.; Hu, A.; Hou, L.; Li, J.; Cai, X.; Yu, C. Pharmaceuticals and personal care products in a mesoscale subtropical watershed and their application as sewage markers. *J. Hazard. Mater.* **2014**, *280*, 696−705.
(72) Sun, Q.; Li, Y.; Li, M.; Ashfaq, M.; Lv, M.; Wang, H.; Hu, A.; Yu, C. PPCPs in Jiulong River estuary (China): Spatiotemporal distributions, fate, and their use as chemical markers of wastewater. *Chemosphere* **2016**, *150*, 596−604.
(73) Juksu, K.; Zhao, J.-L.; Liu, Y.-S.; Yao, L.; Sarin, C.; Sreesai, S.; Klomjek, P.; Jiang, Y.-X.; Ying, G.-G. Occurrence, fate and risk assessment of biocides in wastewater treatment plants and aquatic environments in Thailand. *Sci. Total Environ.* **2019**, *690*, 1110−1119.
(74) Zhao, X.; Zheng, Y.; Quan, F.; Hu, S.; Wu, Q.; Luo, M.; Gu, Y.; Tang, S.; Jiang, J. Road runoff as a significant nonpoint source of parabens and their metabolites in urban rivers. *Chemosphere* **2022**, *301*, 134632.
(75) Lu, S.; Wang, B.; Xin, M.; Wang, J.; Gu, X.; Lian, M.; Li, Y.; Lin, C.; Ouyang, W.; Liu, X.; He, M. Insights into the spatiotemporal occurrence and mixture risk assessment of household and personal care products in the waters from rivers to Laizhou Bay, southern Bohai Sea. *Sci. Total Environ.* **2022**, *810*, 152290.
(76) Pan, C.; Wang, Y.; Yu, K.; Zhang, W.; Zhang, J.; Guo, J. Occurrence and distribution of perfluoroalkyl substances in surface riverine and coastal sediments from the Beibu Gulf, south China. *Mar. Pollut. Bull.* **2020**, *150*, 110706.
(77) Li, W.; Yuan, Y.; Wang, S.; Liu, X. Occurrence spatiotemporal variation, and ecological risks of organophosphate esters in the water and sediment of the middle and lower streams of the Yellow River and its important tributaries. *J. Hazard. Mater.* **2023**, *443*, 130153.
(78) Pei, J.; Hu, J.; Zhang, R.; Liu, N.; Yu, W.; Yan, A.; Han, M.; Liu, H.; Huang, X.; Yu, K. Occurrence bioaccumulation and ecological risk of organic ultraviolet absorbers in multiple coastal and offshore coral communities of the South China Sea. *Sci. Total Environ.* **2023**, *868*, 161611.
(79) Tran-Lam, T. T.; Phung, A. T. T.; Pham, P. T.; Bui, M. Q.; Dao, Y. H.; Le, G. T. biomagnification, and risk assessment of parabens and their metabolites in marine fish: The case study of Vietnam. *Chemosphere* **2023**, *344*, 140221.
(80) Lei, K.; Zhu, Y.; Chen, W.; Pan, H.; Guo, B.; Zhang, X.; Cao, Y.; Sweetman, A. J.; Lin, C. The occurrence of home and personal care products in the Haihe River catchment and estimation of human exposure. *Sci. Total Environ.* **2018**, *643*, 63−72.
(81) Ma, Y.; Hua, Z.; Wang, P.; Yang, Y.; Dong, Y.; Yu, L. Mechanisms of propeller jet-induced migration, release, and distribution of perfluoroalkyl acids in sediment-water systems. *Water Res.* **2023**, *238*, 120048.
(82) Zhang, S.; Xu, D.; Tian, W.; Lu, Z.; Zhou, Y.; Chu, M.; Zhao, J.; Liu, B.; Cao, H.; Zhang, R.; Chen, Z. The effect of bioturbation on the release behavior of polycyclic aromatic hydrocarbons from sediments: A sediment-seawater microcosm experiment combined with a fugacity model. *Environ. Pollut.* **2024**, *349*, 123933.
(83) Lin, Y.; Deng, W.; Li, S.; Li, J.; Wang, G.; Zhang, D.; Li, X. Congener profiles, distribution, sources and ecological risk of parent and alkyl-PAHs in surface sediments of Southern Yellow Sea, China. *Sci. Total Environ.* **2017**, *580*, 1309−1317.
(84) Lu, M.; Jones, S.; McKinney, M.; Kandow, A.; Donahoe, R.; Cobb Faulk, B.; Chen, S.; Lu, Y. Assessment of phthalic acid esters plasticizers in sediments of coastal Alabama, USA: Occurrence, source, and ecological risk. *Sci. Total Environ.* **2023**, *897*, 165345.
(85) Arfaeinia, H.; Asadgol, Z.; Ramavandi, B.; Dobaradaran, S.; Kalantari, R. R.; Poureshgh, Y.; Behroozi, M.; Asgari, E.; Asl, F. B.; Sahebi, S. Monitoring and eco-toxicity effect of paraben-based pollutants in sediments/seawater, north of the Persian Gulf. *Environ. Geochem. Health* **2022**, *44* (12), 4499−4521.
(86) Chakraborty, P.; Mukhopadhyay, M.; Sampath, S.; Ramaswamy, B. R.; Katsoyiannis, A.; Cincinelli, A.; Snow, D. Organic micropollutants in the surface riverine sediment along the lower stretch of the transboundary river Ganga: Occurrences, sources and ecological risk assessment. *Environ. Pollut.* **2019**, *249*, 1071−1080.



Marine Pollution Bulletin 215 (2025) 117908



Contents lists available at ScienceDirect

Marine Pollution Bulletin

journal homepage: www.elsevier.com/locate/marpolbul



Occurrence, spatiotemporal distribution and environmental behavior of dissolved, particulate, and sedimentary black carbon in a subtropical coastal environment: Differences between semi-enclosed and open estuaries

Jingyu Wang [a,b], Ruijie Zhang [a,b,*], Jingzhen Wang [c,**], Liwei Mo [b], Zhehong Ji [a,b], Pan Wei [a,b], Chaoshuai Wei [b], Kefu Yu [b,d]

[a] School of Resources, Environment and Materials, Guangxi University, Nanning 530004, China
[b] Guangxi Laboratory on the Study of Coral Reefs in the South China Sea, Coral Reef Research Center of China, School of Marine Sciences, Guangxi University, Nanning 530004, China
[c] Guangxi Key Laboratory of Marine Environmental Change and Disaster in the Beibu Gulf, Bubei Gulf University, Qinzhou 535011, China
[d] Southern Marine Science and Engineering Guangdong Laboratory (Guangzhou), Guangzhou 511458, China

ARTICLE INFO

Keywords:
Black carbon
BPCA
Estuary
Beibu gulf
South China Sea

ABSTRACT

Black carbon (BC) plays a critical role in climate change and the carbon cycle as a long-term carbon sink. Estuaries, as key interfaces between land and ocean, are important not only for BC transport but also for its transformation and deposition. This study used the benzene polycarboxylic acid (BPCA) method to quantify BC concentrations in the surface waters and sediments of semi-enclosed and open estuaries in the North Beibu Gulf, South China Sea, across different seasons. Results showed that hydrological factors, such as urban riverine input, particle settling, and sediment resuspension, significantly influence BC dynamics. Dissolved BC (DBC) concentrations were highest in summer (125.5 ± 67.3 μg/L), driven by riverine input, while particulate BC (PBC) concentrations decreased rapidly along the river-estuary-coastal gradient (4.1–187.7 μg/L) due to particle settling. In winter, reduced riverine input increased the role of sediment resuspension, elevating PBC concentrations in the open estuary compared to the semi-enclosed estuary. Seasonal variations in BPCA composition showed differences in BC aromatic condensation, influenced by photodegradation, adsorption, and resuspension. Sedimentary BC (SBC) levels were stable (0.087 ± 0.048%dw), accounting for 14.0 ± 4.21 % of sedimentary organic carbon (SOC), which is a higher proportion compared to the contributions of DBC to dissolved organic carbon (DOC) (5.58 ± 2.74 %) and PBC to particulate organic carbon (POC) (6.81 ± 2.94 %). The aggregation of PBC and SBC was higher than that of DBC, emphasizing the sequestration potential of sedimentary environments. Semi-enclosed bays, less influenced by tides and waves, may provide better long-term BC storage, supporting coastal carbon sequestration.

1. Introduction

Black Carbon (BC), as a key participant in the global carbon cycle, is derived from the incomplete combustion of biomass and fossil fuels (Bird et al., 2015; Coppola et al., 2022). These processes convert relatively unstable biomass carbon into environmentally persistent forms of BC, creating a long-term carbon sink (Santín et al., 2015). In the context of global climate change, the increase in biomass burning events has led to a rise in BC production (Jones et al., 2024), further intensifying its role in the global carbon cycle (Santín et al., 2015). A substantial portion of BC is transported to marine environments via atmospheric deposition and river discharge (Bao et al., 2017; Fang et al., 2021). In aquatic systems, BC is present in both dissolved and particulate forms (Coppola et al., 2022, 2018; Wagner et al., 2018). Estuaries, acting as dynamic transition zones, regulate BC transport and transformation between terrestrial and marine systems (Raymond and Bauer, 2001). The fluxes of DBC (Dissolved BC) and PBC (Particulate BC) from rivers to oceans are estimated at 66.3 Tg yr^{-1} (Fang et al., 2021) and 17–37 Tg yr^{-1} (Coppola et al., 2018), respectively.

BC consists of a continuum ranging from the less condensed

* Corresponding author at: School of Resources, Environment and Materials, Guangxi University, Nanning 530004, China.
** Corresponding author.
E-mail addresses: rjzhang@gxu.edu.cn (R. Zhang), wangjingzhen-1@163.com (J. Wang).

https://doi.org/10.1016/j.marpolbul.2025.117908
Received 19 November 2024; Received in revised form 25 March 2025; Accepted 27 March 2025
0025-326X/© 2025 Published by Elsevier Ltd.

aromatic, partially charred biomass to highly condensed aromatic soot (Masiello, 2004). The classification of DBC and PBC is derived from the operational experimental methods traditionally used in oceanography to distinguish between dissolved and particulate organic carbon (Coppola et al., 2022). PBC undergoes dissolution and degradation processes within soils, subsequently entering aquatic systems as DBC (Ding et al., 2013). A portion of the PBC in the water may result from the photo-flocculation of existing DBC (Coppola et al., 2014). High concentrations of PBC can shift carbon from the dissolved phase to the particulate phase by adsorbing and aggregating organic carbon (Fang et al., 2021). Therefore, simultaneous analysis of both DBC and PBC is essential to comprehensively understand BC cycling, yet consistent analytical approaches are often lacking. Different methods target various components of BC along the BC continuum (Hammes et al., 2007; Roth et al., 2012), making it crucial to standardize approaches for better comparability. By doing so, we can achieve a clearer understanding of the relationship between the PBC and DBC pools, thereby gaining a more comprehensive insight into the regional and global BC cycles (Coppola et al., 2014; Wagner et al., 2018).

Estuaries, connecting terrestrial and marine systems, exhibit sharp gradients in biogeochemical variables such as salinity, turbidity, and organic carbon (Bauer et al., 2013). The interaction between riverine inputs, internal cycling, and ocean exchange is the primary driver of these spatial and temporal variations (Ward et al., 2017). Semi-enclosed bays (such as Jiaozhou Bay, Yellow Sea, North China) become key hotspots for BC burial through the effective settling and sequestration of BC and particulate pollutants (Feng et al., 2021). Resuspension, particularly in shallow systems, can return organic matter from sediments into the water column (Osterholz et al., 2021). In winter, strong wave action leads to intense resuspension, markedly increasing PBC levels near the Yellow River Delta and promoting its long-distance transport in the water column (Fang et al., 2021).

Accurately and reliably identifying and quantifying black carbon in various complex samples is essential but remains challenging (Coppola et al., 2022; Vaezzadeh et al., 2023b). The benzene polycarboxylic acid (BPCA) method is applicable to a wide range of environmental matrices, including soil (Glaser et al., 1998), water (Dittmar et al., 2008; Wagner et al., 2015; Ziolkowski et al., 2011), and sediment (Li et al., 2023; Sánchez-García et al., 2013; Vaezzadeh et al., 2021). The BPCA method chemically oxidizes the aromatic ring structure of BC, generating BPCAs with 3–6 carboxylic acid groups, which indicate BC content (Dittmar, 2008). The composition of BPCAs reflects the degree of aromatic condensation, providing information on the origin of BC (Brodowski et al., 2005; Dittmar, 2008; Glaser et al., 1998). However, challenges remain, such as the uncertainty of conversion factors between yields of BPCAs and BC (Brodowski et al., 2005; Ziolkowski et al., 2011), and interference from BPCAs in the environment (Barton et al., 2024).

Given the uncertainties in the behavior and fate of BC in nearshore systems, we have selected two estuaries in Qinzhou Bay, Beibu Gulf, South China, as our study area. The region's subtropical monsoon climate results in significant seasonal variation in river discharge, providing an ideal setting for studying the influence of riverine inputs on BC dynamics. The two estuaries offer contrasting hydrodynamic conditions. The environment of the semi-enclosed estuary is more stable, while the open estuary experiences higher resuspension and transport due to stronger tidal and wave action.

In this study, we aimed to (1) measure the concentrations of DBC and PBC in the waters using the BPCA method, as well as the content of SBC in surface sediments, and their respective proportions in the organic carbon pool; (2) investigate the seasonal variations and spatial differences in semi-enclosed and open estuaries, along with their underlying causes; (3) explore the implications of the molecular information provided by BPCA analysis; and (4) estimate the fluxes of BC entering the sea and the burial fluxes within this region.

2. Materials and methods

2.1. Study area and sample collection

Qinzhou Bay has a subtropical climate with characteristics of a marine monsoon climate, transitioning from subtropical to tropical conditions. There are significant differences in river runoff in dry and wet seasons (Table S1, "S" means Supplementary Materials). Our research area includes two parts: Maowei Sea (MWS) and Dafeng Estuary (DFE), MWS is a typical semi-enclosed bay, while DFE is an open estuary connected to the offshore ocean. In July 2023 (summer/rainy season) and December 2023 (winter/dry season), we collected water and sediment from 36 sites (Fig. S1). Physicochemical parameters (salinity, temperature, and pH) were measured in situ using a YSI sensor (Table S2). Surface water samples were collected using pre-cleaned buckets and filtered through nylon sieves to remove large particles, then immediately transferred to acid-washed polypropylene bottles. Sediment samples were collected from the surface 1–5 cm using a stainless steel grab sampler. Water and sediment samples were stored at 4 °C and − 20 °C, respectively, until laboratory analysis.

2.2. Preparation

Homogenized water samples were filtered through pre-combusted (450 °C, 6 h) GF/F filters (Whatman, nominal pore size 0.7 μm, diameter 47 mm). The mass concentration of total suspended solids (TSS) was determined by dividing the mass of particulates on the filter by the total volume of stream water passed through the filter. For the dissolved phase, DBC was extracted from the filtrate using solid phase extraction (SPE) cartridges (Agilent Bond Elut PPL, 500 mg, 6 mL) (Dittmar et al., 2008). Briefly, filtered water samples were acidified to pH = 2 with 32 % HCl. Samples were loaded onto the PPL cartridges at a flow rate of no >5 mL/min. After extraction, the cartridges were desalted with 12 mL ultrapure water (pH = 2), dried under an airstream, and stored frozen until further analysis.

2.3. Organic carbon and sediment grain size analysis

A portion of the filtrate was used to measure the DOC concentration using a total organic carbon (TOC) analyzer (TOC-VCPH Shimadzu). The analytical error based on duplicates was <10 % on average ($n = 3$). Deep seawater reference samples from the Sargasso Sea (D.A. Hansell, University of Miami, Florida) were used to verify data quality (Bao et al., 2023). A standard curve with a series of glucose solutions determined daily was used for calibration.

The dried filters were acidified with HCl vapor for 24 h to remove inorganic carbon before measuring the POC content (Yang et al., 2023a). Sediment samples were acidified with HCl to pH = 2, centrifuged, adjusted to neutral pH, and then freeze-dried(Li et al., 2023). The filters and sediment samples were wrapped in tin foil and analyzed for POC and SOC using an elemental analyzer (Elementar vario macro cube). Sulfanilamide was used as the standard, and the results were corrected for mass with an accuracy of ≤0.01 %.

The sediment grain size was analyzed using a Malvern Mastersizer 3000 laser particle size analyzer. Sediments were pre-treated with 2 mol/L HCl and 5 % H_2O_2 to remove inorganic carbon and organic matter, respectively. $(NaPO_3)_6$ was used as a dispersant (Fang et al., 2015). The relative standard deviation of the replicate samples was <3 % (n = 3). The particle sizes were <4 μm for clay, 4–63 μm for silt, and larger than 63 μm for sand.

2.4. BC analysis

Quantification of DBC, PBC, and SBC was performed using the BPCA method (Li et al., 2023; Wagner et al., 2015; Wiedemeier et al., 2016). The quantification procedures for DBC, PBC, and SBC differ only in the

pretreatment steps (see Text S1). Briefly, the pretreated samples were placed in 5 mL Teflon-lined stainless steel reaction vessels, to which 2 mL of 65 % nitric acid was added. The vessels were sealed and heated at 180 °C in an oven for 8 h. After digestion, the remaining HNO_3 and water were evaporated to dryness at 50 °C under a stream of high-purity nitrogen. The samples were redissolved in 1 mL of ultrapure water and then transferred into autosampler vials. Subsequently, they were separated and quantified using high-performance liquid chromatography (HPLC) (see Text S2).

2.5. Statistical analysis

The spatial distribution was analyzed using ordinary kriging interpolation in ArcGIS 10.8. Statistical analysis was performed using IBM SPSS Statistics 23, and data visualization was conducted using Origin 2021.

3. Results and discussion

3.1. General properties of water and sediment

During our sampling, water temperatures remained stable across different sites at the same sampling time, but exhibited significant seasonal variations ($p<0.01$). In the summer, temperatures ranged from 31.1 to 34.7 °C, while in the winter, from 21.3 to 25 °C (Table S2). Seasonal rainfall, river flow fluctuations, and tidal strength significantly influence estuarine salinity (Matsoukis et al., 2023). Fig. 1a clearly shows the salinity gradients and seasonal differences due to river-seawater mixing. In summer, riverine input predominates, with precipitation exceeding evaporation (Guo et al., 2024), salinity ranging from 0.24 ‰ to 24.6 ‰ (mean 9.24 ± 7.16 ‰). In winter, reduced river runoff and seawater return increase inner bay salinity, ranging from 2.37 ‰ to 28.9 ‰ (mean 21.1 ± 6.28 ‰). Spatially, the salinities in summer and winter are both significantly lower in the semi-close bay (MWS) than in the open estuary (DFE) (Fig. 1a), indirectly reflecting the varying degrees of influence from the river and ocean on the two regions with distinguishing hydrological characteristics.

In MWS, the summer TSS content (18.9 ± 13.6 mg/L) surpassed winter levels (12.2 ± 7.3 mg/L), likely due to enhanced riverine input during the rainy season. Conversely, in DFE, winter TSS (39.9 ± 21.2 mg/L) exceeded summer levels (22.7 ± 10.7 mg/L) (Fig. 1b), driven by sediment resuspension due to stronger winter tides and waves (Mouyen et al., 2018). MWS's semi-enclosed nature and the presence of numerous small islands mitigate tides effects in winter. Particle size, a key physical property of sediments, is mainly influenced by hydrodynamic conditions and sediment sources. Fig. 1c shows the spatial distribution of mean particle size (Mz), ranging from 1.58φ to 6.81φ. Fig. S2 displays the sediment type ternary diagram. Most sediments in the area are silty sand and sandy silt, with coarser sediments concentrated at the estuaries.

3.2. Abundance, seasonal differences and spatial distribution

3.2.1. DOC and DBC

During both summer and winter, DOC concentrations ranged from 0.55 to 3.16 mg/L (MWS: 1.88 ± 0.57 mg/L; DFE: 1.31 ± 0.45 mg/L) and 0.86 to 3.58 mg/L (MWS: 1.61 ± 0.49 mg/L; DFE: 2.18 ± 0.73 mg/L), respectively (Fig. 2a). In summer, DOC levels decreased with distance from urban areas, indicating rivers as the primary source of terrestrial organic matter to estuaries (Raymond and Bauer, 2001). Tidal mixing in estuaries further modulates DOC distribution through dilution, adsorption, aggregation, and flocculation, removing significant amounts of riverine DOC and Colored Dissolved Organic Matter (Zhou et al., 2021). In winter, elevated DOC concentrations in the DFE are likely due to sediment resuspension (Bauer et al., 2013) and/or higher primary production in winter than in summer in this region (Guo et al., 2017; Pan et al., 2015).

DBC was detected in all water samples, with concentrations varying by more than an order of magnitude (20.5–256 μg/L). In the summer, DBC concentrations were 158.2 ± 65.8 μg/L in MWS and 78.8 ± 33.3 μg/L in DFE, decreasing to 74.3 ± 27.8 μg/L in MWS and 55.5 ± 21.7 μg/L in DFE during winter, showing a clear decreasing trend from riverine to nearshore areas (Fig. 2b). Hydrology plays a crucial role in determining DBC concentrations and composition in global river outputs (Wagner et al., 2015). Due to significant differences in DBC concentrations between riverine and coastal waters, high riverine DBC readily diffuses into the sea upon entering estuaries (Fang et al., 2021). DBC

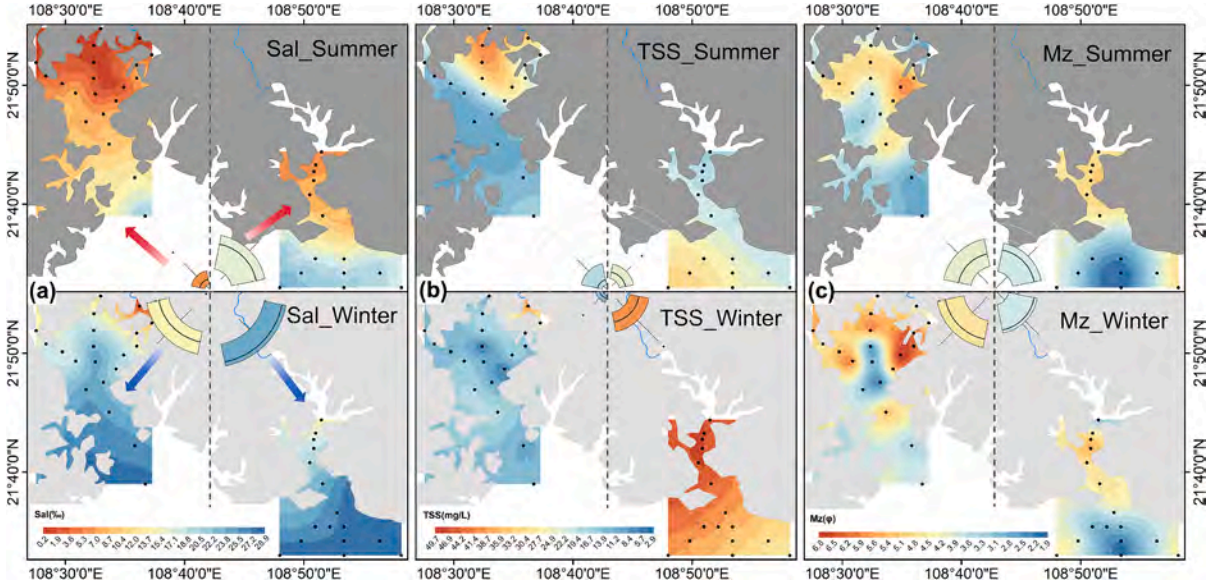


Fig. 1. Spatiotemporal distribution of salinity (a), total suspended solids (TSS) (b), and mean particle size (Mz) (c) plotted using ordinary Kriging spatial interpolation. The dark gray background indicates summer sampling, while the light gray background indicates winter sampling. The left region represents the Maowei Sea (MWS), and the right region represents the Dafeng River Estuary (DFE). In the center of the figure, box plots display five statistical data points: minimum, 25th percentile, median, 75th percentile, and maximum. The color of the boxes represents the mean value, corresponding to the color scale used in the spatial interpolation method (applies to Fig. 2 as well).

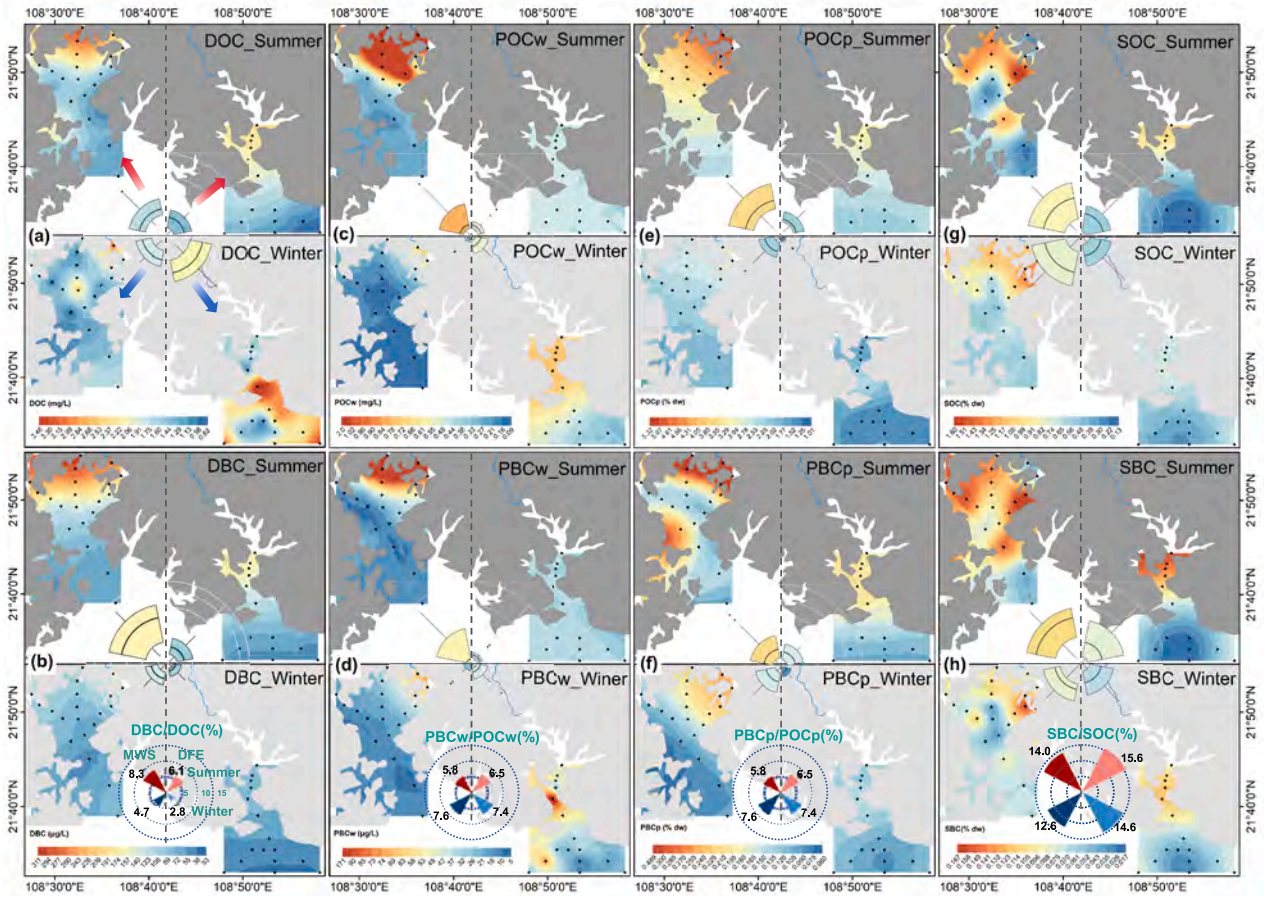


Fig. 2. Spatial distribution and concentrations of dissolved and particulate organic carbon (OC) and black carbon (BC) in Maowei Sea (MWS) and Dafeng River Estuary (DFE) during summer and winter. (a) Dissolved organic carbon (DOC), (b) dissolved black carbon (DBC), (c) particulate organic carbon per unit volume (POC_W), (d) particulate black carbon per unit volume (PBC_W), (e) particulate organic carbon per unit dry weight (POC_P), (f) particulate black carbon per unit dry weight (PBC_P), (g) sedimentary organic carbon (SOC), and (h) sedimentary black carbon (SBC).The central box plots show the concentrations of each parameter. At the very bottom of the figure, fan-shaped diagrams represent the proportions of DBC, PBC, and SBC within their respective OC pools. Colors indicate sampling locations and seasons: dark red for MWS in summer, light red for DFE in summer, dark blue for MWS in winter, and light blue for DFE in winter. (For interpretation of the references to color in this figure legend, the reader is referred to the web version of this article.)

concentrations in the two regions and two seasons all consistently showed a significant negative correlation with salinity ($r = -0.85$, $p < 0.01$) (Fig. 3a), indicating that urban runoff is the primary BC source in coastal areas. Compared to major rivers worldwide, such as the Amazon River (181–802 μg/L) and the Congo River (444–912 μg/L) (Wagner et al., 2019), the DBC concentrations in our study area are lower, yet significantly higher than those in certain nearshore and open ocean regions, like the western South China Sea (5.9–19.2 μg/L) (Fang et al., 2017), and the surface waters of the Atlantic, Pacific, and Arctic Oceans (16.8–31.2 μg/L) (Coppola and Druffel, 2016). Higher DBC concentrations in the estuarine area, particularly in MWS, are likely due to riverine input from the Qin River, which passes through the densely populated city of Qinzhou. Elevated summer levels likely result from increased precipitation, enhancing wet deposition of atmospheric BC particles and river runoff (Bao et al., 2019; Letourneau et al., 2021).

A linear relationship occurred between DBC and DOC concentrations, particularly in the summer with strong correlations ($r = 0.72$ and 0.78, $p < 0.01$) (Fig. 3b). This linear relationship is attributed to similar diagenetic processes driving the release of DOC and DBC from soils, or molecular associations between DOC and DBC via hydrophobic

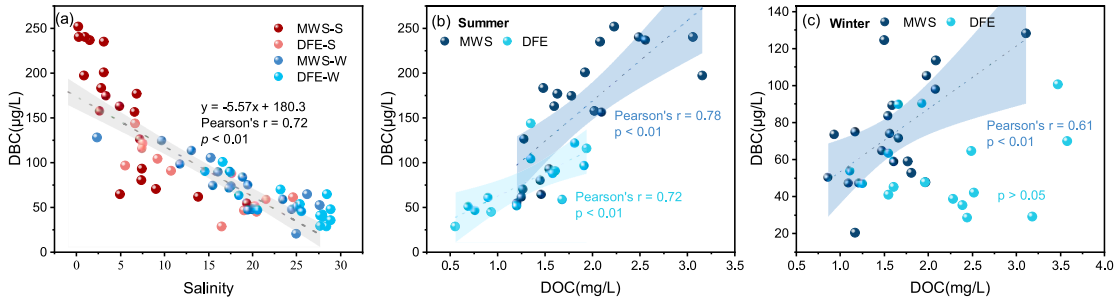


Fig. 3. Correlation analysis between dissolved black carbon (DBC) and other parameters. (a) Relationship between DBC and salinity, (b) Relationship between dissolved organic carbon (DOC) and DBC in summer, (c) Relationship between DOC and DBC in winter.

interactions (Jaffé et al., 2013). In winter, the correlation between DBC and DOC concentrations in MWS weakened ($r = 0.61$, $p < 0.01$), and the two were completely decoupled in DFE ($p > 0.05$) (Fig. 3c), suggesting different sources, transport, and transformation mechanisms. Some studies suggest that increased DOC may be linked to phytoplankton production and microbial transformation (Kragh and Søndergaard, 2009), with the decoupling of these parameters further supporting a terrestrial origin for DBC.

It is estimated that approximately 10 % of the riverine DOC exported to the global oceans originates from DBC (Jaffé et al., 2013). The average abundances of DBC determined for the samples accounted for 8.27 ± 2.47 % (MWS-Summer), 6.09 ± 1.69 % (DFE-Summer), 4.74 ± 1.59 % (MWS-Winter) and 2.82 ± 1.34 % (DFE-Winter) of the total DOC pool (Fig. 2b). The spatial decrease in DBC/DOC ratios along the river-to-nearshore gradient further supports the terrestrial origin of DBC (Fig. S3). The seasonal decrease in DBC/DOC ratios from summer to winter further indicates that surface runoff in summer is the main source of marine DBC.

3.2.2. POC and PBC

In this study, PBC_W and POC_W are used to express the concentrations of PBC and POC in water with unit mg/L, while PBC_P and POC_P are used to express the content of PBC and POC in particles with unit %dw. Both water-based (PBC_W, POC_W) and particle-based (PBC_P, POC_P) metrics are reported to distinguish between bulk water column dynamics and particle-specific contributions. POC_W and PBC_W were in the range of 0.05–2.39 mg/L and 4.08–188 μg/L, respectively, with the mean values of 34.6 ± 36.9 mg/L and 6.81 ± 2.94 μg/L(Table S3). They generally are lower than the corresponding DOC and DBC concentrations (Coppola et al., 2018; Fang et al., 2021; Osterholz et al., 2021). The average contribution of POC_W to OC_{IW} (OC in water, ie., POC_W + DOC) is 20.7 ± 12.4 % (3.3–56.3 %), and the average contribution of PBC_W to BC_{IW} (BC in water, ie., PBC_W + DBC) is 25.1 ± 14.7 % (4.8–72.1 %), reflecting the important contributions of particles to the OC and BC in the aquatic environment(Coppola et al., 2018; Wang et al., 2016).

In summer, the PBC_W concentration was 48.7 ± 56.7 μg/L, in the estuarine inlet region of MWS, where PBC_W concentrations peaked, followed by a rapid decrease downstream (Fig. 2d). This phenomenon is likely associated with the substantial input of particulate organic matter from rivers, especially during the rainy summer season, when surface runoff carries terrestrial particulates into the river system, eventually flowing into the estuarine region (Wagner et al., 2015). Simultaneously, the rapid attenuation of PBC_W at the estuary during summer suggests significant removal of PBC from the water column, leading to its deposition in nearshore sediments, which supports the formation of a more stable carbon sink (Yang et al., 2023a). In contrast, PBC_W (20.6 ± 20.68 μg/L) in MWS significantly decreased during winter ($p < 0.01$), indicating reduced BC and OC inputs in the winter season because of the declining river input.

DFE showed an increase in PBC_W ($p > 0.05$), from 30.9 ± 16.2 μg/L in summer to 37.8 ± 25.6 μg/L in winter (Fig. 2d). The shallower waters of DFE, influenced by winter wave action, caused sediment resuspension, leading to higher particulate levels in winter compared to summer. In contrast, the semi-enclosed MWS experiences less resuspension due to weaker hydrodynamic conditions, resulting in lower TSS, PBC_W, and POC_W concentrations in MWS than in DFE during winter (Figs.1b, 2c and 2d). The combined effect of strong winter monsoons and sediment resuspension significantly regulates the sources and dynamics of TSS and associated PBC_W and POC_W in coastal waters, with resuspension likely reintroducing BC from stable sedimentary environments back into the water column, potentially hindering BC preservation in sediments and prompting transport of BC from nearshore to offshore. Sediment resuspension, a key driver of organic carbon transport and rebalancing in marginal seas (Liu et al., 2024a), greatly impacts carbon dynamics of coastal ecosystems.

For POC_P and PBC_P, they are in the range of 0.88–6.30 % and 0.035–0.55 %, respectively, with mean values of 2.44 ± 1.34 % and 0.16 ± 0.11 %. For their spatiotemporal distribution, they are both higher in the MWS than in the DFE, and higher in the summer than in the winter (Fig. 2f), reflecting that particles from surface runoff in summer and urban areas own relatively high levels of POC_P and PBC_P than in winter and rural areas. These metrics are essential for understanding the intrinsic properties of suspended particles, providing insights into the sources and transformations of BC and OC that are not captured by water-column concentrations alone.

The correlation between PBC_W and POC_W ($r = 0.89$, $p < 0.01$) is stronger than that between PBC_P and POC_P ($r = 0.65$, $p < 0.01$), which is also reflected in the correlation between PBC_W and PBC_P with TSS ($r = 0.6$, $p < 0.01$ and $p > 0.05$, respectively) (Fig. 4).This disparity in correlations underscores that PBC_W and POC_W are directly influenced by the total suspended solids, reflecting bulk water column dynamics, whereas PBC_P and POC_P are more indicative of the specific composition of the particulate matter, which can vary independently of TSS concentrations. When quantifying PBC and POC in "per unit volume of water" resulting in a consistent fluctuation pattern of PBC_W and POC_W. Moreover, PBC_W and POC_W better reflect the effects of short-term external inputs or disturbances, such as a man-made flood events in the Yellow River (Wang et al., 2016; Xu et al., 2016). However, the actual relationship between PBC and POC may not be as strong, the use of a parameter related to the volume of water (PBC_W and POC_W) may have enhanced the correlation between PBC and POC.TSS and POC_W, PBC_W covary (Coppola et al., 2018), whereas the relationship between TSS and PBC_P, POC_P is less pronounced. For instance, high TSS from muddy or sandy sediments can lower PBC_P and POC_P as these materials have lower BC and OC content. Resuspension events further dilute PBC_P by introducing non-BC materials, even as TSS rises. This complexity is crucial in estuarine systems with mixed riverine and resuspended inputs.

The PBC/POC ratio (range 2.03–15.7 %, mean 6.81 ± 2.94 %) (Figs. 2f and S3) in the study area is comparable to the average global ocean value (6 %) (Coppola and Druffel, 2016), and lower than the global riverine range (15.8 ± 0.9 %) (Coppola et al., 2018), as riverine particulates typically have higher PBC/POC ratios than marine particulates (Flores-Cervantes et al., 2009). The higher PBC/POC ratios in winter compared to summer may result from increased combustion sources in winter (Wang et al., 2016) and/or sediment resuspension in winter. After all, sedimentary particles own higher BC/OC radio because a higher portion of OC is degraded than BC.

3.2.3. SOC and SBC

The SOC content in surface sediments ranged from 0.055%dw to 1.654%dw (mean 0.71 ± 0.44 %), while SBC varied between 0.012%dw and 0.191%dw (0.087 ± 0.048%dw) (Fig. 2g and h). They are both lower than the corresponding POC_P and PBC_P, i.e., average POC_P /SOC and PBC_P /SBC ratios are 6.4 ± 7.3 and 2.7 ± 2.9. This may be caused by the different composition and size between suspended particles and sedimentary particles. For example, suspended particles are generally finer and have lower density with more organic matter than sedimentary particles. Therefore, suspended particles themself not only have a higher content of OC and BC, but also have a strong ability to adsorb OC and BC.

Spatially, high concentrations of SOC and SBC were predominantly found in estuarine regions, particularly where urban rivers discharge into MWS and in the upper segment of DFE (Figs.2g and 2h). This spatial distribution correlates with sediment type and grain size, as river systems transport substantial particulate matter to estuarine areas, influencing the OC and BC content in coastal sediments (Fig. 5a and b). Most of this particulate matter is deposited in river deltas and adjacent coastal regions (Xue et al., 2017). Grain size is crucial for organic matter preservation in sediments, with finer grains generally hosting more organic matter due to their larger surface area and greater adsorption capacity (Dahl et al., 2016). SBC exhibits a significant correlation with SOC ($r = 0.9$, $p < 0.01$), showing no variation across seasons or watersheds (Fig. 5c). As a crucial component of sedimentary SOC, SBC is more

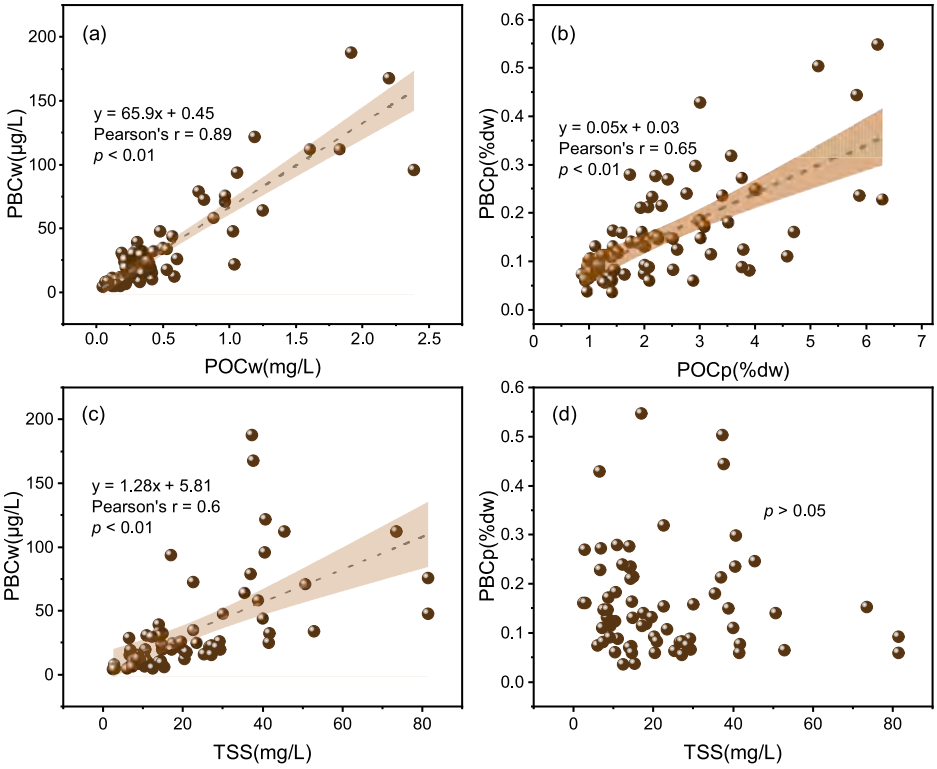


Fig. 4. Relationship between total suspended solids (TSS), particulate black carbon (PBC), and particulate organic carbon (POC) in water. (a) Correlation between PBC per unit volume (PBC_W) and POC per unit volume (POC_W), (b) Correlation between PBC per unit dry weight (PBC_P) and PBC per unit dry weight (POC_P), (c) Correlation between PBC_W and TSS, (d) Correlation between PBC_P and TSS. Note: PBC_W (mg/L) and POC_W (mg/L) are calculated from measured PBC_P (%dw) and POC_P (%dw) using $PBC_W = PBC_P \times TSS \times 0.01$ and $POC_W = POC_P \times TSS \times 0.01$, where TSS is in mg/L. POC_P and PBC_P are directly determined from filter-collected particles via elemental analysis and BPCA-HPLC, offering particle-specific insights, while PBC_W and POC_W quantify water column concentrations.

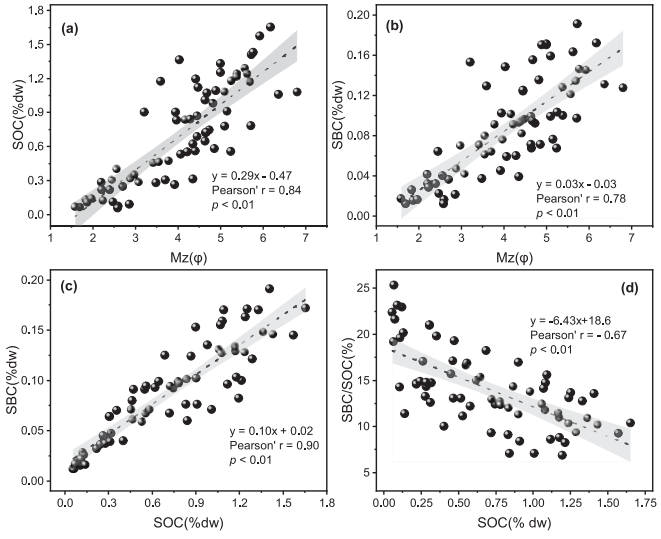


Fig. 5. Correlation analysis between mean particle size and sedimentary organic and black carbon. (a) Relationship between mean particle size (Mz) and sedimentary organic carbon (SOC), (b) Relationship between Mz and sedimentary black carbon (SBC), (c) Relationship between SBC and SOC, (d) Relationship between the ratio of SBC/SOC and SOC.

resistant to degradation than other forms of SOC due to its recalcitrant nature (Sánchez-García et al., 2012; Vaezzadeh et al., 2021) In a depositional environment characterized by fine-grained sediments and weak hydrodynamics, higher sedimentation rates favor organic matter burial. SBC concentrations are higher in fine-grained muddy areas and lower in sandy regions, indicating that hydrodynamic conditions largely dictate BC distribution in sediments. Semi-enclosed bays like MWS, where small islands naturally attenuate hydrodynamic forces, create favorable conditions for organic carbon burial (Feng et al., 2021). Additionally, the widespread aquaculture zones in MWS, with weak hydrodynamics, further promote fine-grained sediment dominance, enhancing organic carbon preservation. Low dissolved oxygen levels in bottom waters further reduce organic carbon degradation, increasing preservation potential (Raja and Rosell-Melé, 2020; Yang et al., 2023b).

SBC accounted for 6.86–25.33 % of SOC (mean 14.0 ± 4.2 %) (Table S3), comparable to levels in the Yellow River estuary (15.4 ± 6.1 %) and Yangtze River estuary (13.3 ± 4.9 %) (Fu et al., 2023), and within the global range for coastal sediments (3–20 %) (Fang et al., 2015; Ren et al., 2019). This consistency suggests that SBC is a significant carbon sink across the global sediment. Moreover, the average SBC/SOC ratio is more than twice the corresponding PBC/POC (6.81 ± 2.94 %) and DBC/DOC (5.58 ± 2.74 %), reflecting the much stronger stability of SBC than SOC during the preservation process of sediment. Sediments are well-recognized as the ultimate BC repository, with the potential for millennial-scale preservation, as observed in the Amazon River delta (Schmidt and Noack, 2000). This underscores SBC's key role in estuarine carbon storage and its broader impact on the global carbon cycle.

In this study, we observed that, areas with lower SOC content tend to have higher SBC/SOC ratios (Fig. 5d). Lower concentrations of SOC and SBC are found in coarser, sand-type sediments, likely because the chemical stability of BC makes it less susceptible to degradation, allowing it to be better preserved compared to other organic matter. In regions with low TOC content, other organic matter may have already decomposed or been lost, resulting in a relative increase in the proportion of BC and consequently a higher SBC/SOC ratio. Other studies have suggested that when using the BPCA method, higher clay content may

hinder the oxidation of BC by nitric acid (Sánchez-García et al., 2013), potentially leading to an underestimation of SBC in finer-grained areas and consequently lower SBC/SOC ratios.

3.3. Influence of estuarine resuspension on BC dynamics

The spatial and temporal distribution patterns of BC components highlight the impact of key sources: urban runoff, marine contributions, and sediment resuspension. Typically, without significant estuarine resuspension, BC levels peak in summer and decline in winter, as rainfall and runoff in the rainy season wash residual OC and BC from the land surface into coastal zones. Concentrations are higher in MWS (urban region, higher human activity) and lower in DFE (rural region, less human impact). However, in open estuaries during winter, strong winds and tidal action disrupt this pattern, increasing DOC, POC_W, and PBC_W concentrations. DOC rises as OC in sediments decomposes and is released into the water, supplemented by nutrient inputs and winter's suitable light and temperature conditions (Pan et al., 2015), which enhance primary productivity and decouple DOC from DBC.

RDA analysis (Fig. 6a) further elucidates the influence of environmental variables on BC components. RDA1 and RDA2 account for 76.91 % and 23.04 % of the variance, respectively, indicating that these axes effectively capture the relationship between environmental factors and BC dynamics. TSS shows a strong positive correlation with PBC_W, aligning along the positive RDA1 axis, which suggests that sediment resuspension plays a critical role in elevating PBC_W levels. Salinity, conversely, is negatively correlated with DBC and PBC_P, suggesting that freshwater input modulates their distribution in the estuarine environment.

In MWS, the output of DBC and PBC_W is coupled ($r = 0.60$ and 0.64, $p < 0.01$) (Fig. 6b and c), with the spatial pattern of PBC abundance indicating that most estuarine PBC_W settles within short distances, supporting a mechanism for the rapid removal of DBC in coastal areas, thereby weakening the riverine DBC signal in open seas (Wagner et al., 2019; Yang et al., 2023a). In contrast, in DFE, DBC and PBC_W are decoupled ($p > 0.05$), as sediment resuspension at the estuary increases PBC significantly. Although the photochemical oxidation of PBC may also be a source of DBC in aquatic systems (Alan Roebuck et al., 2017). Winter resuspension significantly increases TSS levels in DFE, elevating PBC_W and POC_W concentrations. However, PBC_P and POC_P do not increase proportionally; rather, higher TSS lowers their content per unit mass. Despite this, resuspension remains critical as it reintroduces stable sedimentary BC back into the water, potentially enabling further offshore transport under wave action. As previously noted, particulate BC and OC are major aquatic components and are more condensed than sedimentary BC, strengthening their role in aquatic BC dynamics.

Another noteworthy phenomenon is the relationship between TSS and DBC. As TSS increases, DBC also appears to rise; however, in areas with particularly high TSS levels, DBC concentrations are significantly lower (Fig. 6d). The relationship between TSS and DBC exhibits clear seasonal and watershed differences, influenced by the sources of DBC riverine input. In summer, MWS, which is closer to urban areas, shows elevated DBC and TSS concentrations, while in winter, the DFE region exhibits high TSS levels but lower DBC concentrations. Although DBC concentration is largely influenced by its source input, it may also be modulated by TSS. This result may be due to the fact that, although photochemical degradation is considered the primary pathway for DBC loss and alteration in aquatic environments, it is typically negligible in high-turbidity waters with limited light penetration (Medeiros et al., 2015). Conversely, at higher TSS levels, particle adsorption becomes the dominant process for DBC removal (Zhao et al., 2023). Calmer waters with minimal TSS and higher light exposure may serve as hotspots for DBC transformation and removal, as indicated by the majority of sample points located at low TSS and low DBC levels in the Fig. 6d. The reasons for the decoupling of PBC and DBC during sediment resuspension remain unclear and require further investigation through higher-resolution sampling and laboratory simulations.

The significant correlation between DBC, PBC_P, and salinity indicates that freshwater-seawater mixing plays a dominant role in modulating BC concentration in estuarine regions. A simple two-endmember mixing model was applied (see Text S4), revealing additional sources of DBC and PBC in MWS during summer (Fig. 6e). Atmospheric deposition of

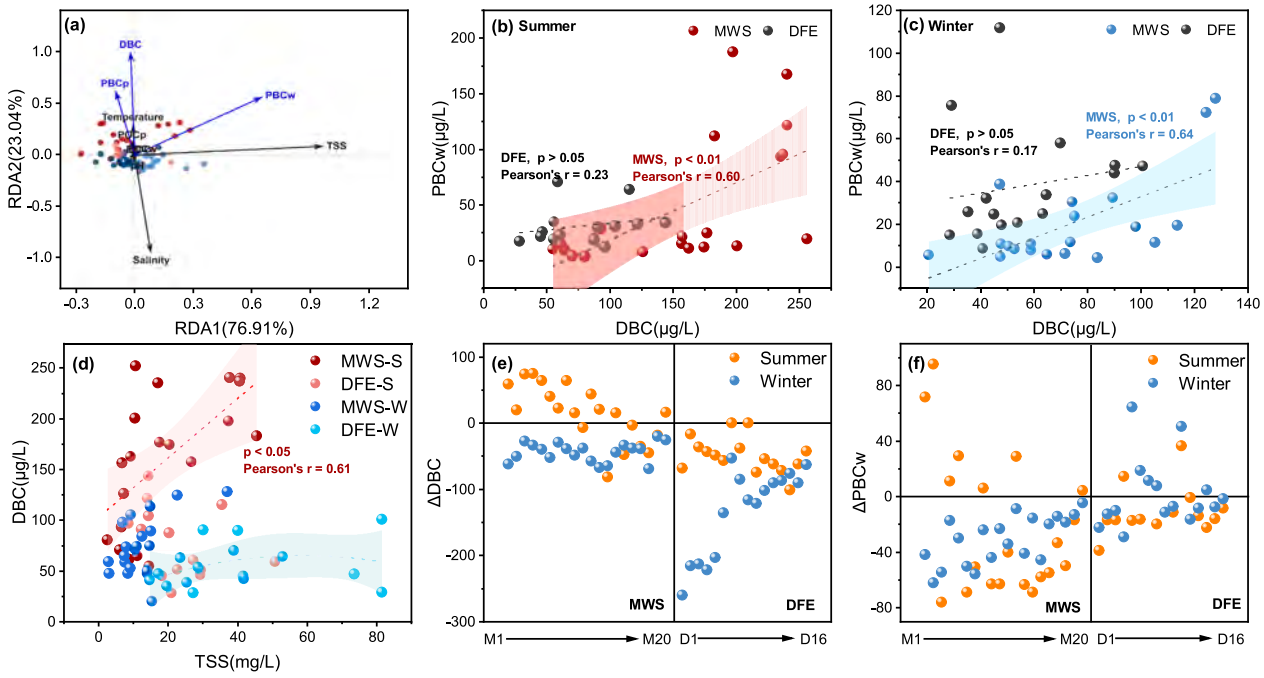


Fig. 6. Relationships between black carbon fractions and environmental factors in the water phase. (a) Redundancy analysis (RDA) of dissolved black carbon (DBC), particulate black carbon per unit volume (PBC_W), and particulate black carbon per unit dry weight (PBC_P) with environmental factors (TSS, salinity, temperature, pH, POC, DOC), (b-c) Correlation analysis between PBC_W and DBC in summer and winter, (d)Relationship between DBC and TSS, (e-f) Two-endmember mixing model, where ΔDBC and ΔPBC represent the difference between measured values and model estimates.

BC, recognized as significant on both global and regional scales (Bao et al., 2017), is unlikely to cause notable spatial differences in our study area due to its limited scope. However, it may contribute to seasonal variations. Additionally, emissions from frequent shipping and offshore activities may serve as potential BC sources in estuarine regions (Lack and Corbett, 2012). In winter, DBC shows a marked reduction, especially in the DFE area, likely due to particulate adsorption as previously discussed (Fig. 6f). The presence of additional PBC sources in winter in DFE further suggests contributions from sediment resuspension and emissions from combustion sources during the winter.

3.4. Molecular information and implications of BPCAs

The relative concentrations of BPCAs indicate the degree of aromatic condensation (Hammes et al., 2007; Roth et al., 2012). Overall, this study shows significant differences in BPCA composition between DBC and PBC or SBC. DBC is primarily composed of B5CA and B4CA (36 % and 32 %), consistent with previously reported BPCA profiles for coastal waters (Dittmar, 2008). In both PBC and SBC, B6CA is the most concentrated among the BPCAs, accounting for approximately 35 % of the total BPCAs. (Fig. 7a).

The B6/B5 ratio serves as an aromatic condensation indicator (Stubbins et al., 2012), with DBC in this study showing B6/B5 ratios from 0.28 to 0.60, aligning with major river DBC globally (Wagner et al., 2019). Seasonal variations in B6/B5 ratios range from 0.32 to 0.60 in summer and 0.28 to 0.39 in winter, decreasing toward offshore areas. This spatial and seasonal pattern of B6/B5 aligns with trends in DBC and the DBC/DOC ratio (Fig. 7b), reflecting a progressive decrease in aromatic condensation along the salinity gradient. The removal of DBC from the water column is mainly driven by photodegradation and particle adsorption, both of which preferentially eliminate condensed aromatic structures, resulting in lower B6/B5 ratios (Coppola et al., 2014; Stubbins et al., 2012). Furthermore, the influence of river flow on DBC density is significant. The low B6/B5 ratios (0.16–0.43) observed in Arctic rivers during periods of low runoff underscore the potential impact of hydrological factors on the aromatic condensation of DBC (Stubbins et al., 2012).

PBC exhibits regional and seasonal variations in BPCAs composition. In MWS, B6/B5 ratios are higher in summer, whereas in DFE, ratios peak in winter (Fig. 7c). Winter resuspension in DFE, driven by stronger winds and waves, remobilizes finer particles into the water column, increasing aromatic condensation. Additionally, higher PBC condensation in DFE during winter may be attributed to heating emissions from rural areas (Wang et al., 2016). Across urban areas in Asia, industrial coal combustion and vehicle emissions are major sources of carbon emissions, whereas rural biomass burning is the primary PBC source in suburban regions (Liu et al., 2024b). The seasonal variation in PBC sources across different global watersheds is significant and is strongly influenced by regional activities. For example, in the PBC transported by the Yellow and Yangtze Rivers in China, approximately 75 % of the PBC during winter months is derived from anthropogenic sources, compared to about 50 % in non-winter months. PBC samples collected in winter show significantly older ^{14}C ages than those collected in other seasons, indicating a higher contribution of aged PBC from coal combustion during winter (Wang et al., 2016).

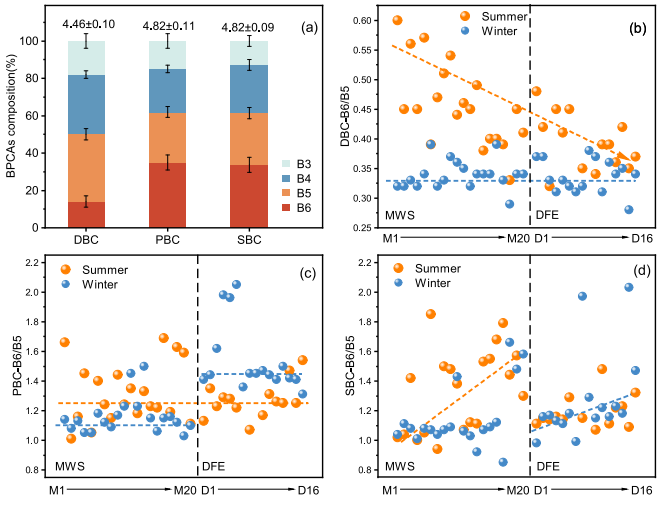


Fig. 7. BPCA composition and B6/B5 ratios of black carbon fractions. (a) BPCA composition of dissolved black carbon (DBC), particulate black carbon (PBC), and sedimentary black carbon (SBC), with mean acid numbers shown above the bars. (b-d) B6/B5 ratios for (b) DBC, (c) PBC, and (d) SBC.

Compared to DBC and PBC, SBC displays more stable condensation levels (B6/B5 ratio: 1.2 ± 0.25) along the salinity gradient, with higher values near the estuarine-sea interface (Fig. 7d). SBC shows minimal seasonal and spatial variation due to stable deposition environments, with most river-transported PBC preserved in coastal sediments. Coppola et al. (2014) propose that the photodegradation and/or hydrophobic properties of highly condensed DBC can lead to the formation of aggregated particles, which eventually settle, contributing to the high degree of aromatic condensation observed in PBC and SBC. The similarity in BPCA composition between SBC and PBC suggests that much of the river-transported PBC is deposited and preserved in coastal sediments, where its association with minerals likely plays a key role in its preservation. Stable sedimentary environments are particularly conducive to the long-term preservation of BC.

The BPCA method is an effective tool for tracing the origins of BC, as the relative abundance of different BPCAs provides a distinct signature of the combustion conditions, with higher B6/B5 ratios indicating high-temperature, fossil fuel-derived BC, while lower ratios point to biomass burning (Schneider et al., 2010). However, BC's transition from particulate to dissolved phases and photochemical degradation processes alter BPCA profiles, complicating source attribution. For example, BPCAs generated from the direct oxidation of urban dust particles are primarily composed of B6CA (Roth et al., 2012), whereas DBC leached from urban dust produces only trace amounts of B5CA and B6CA (Ding et al., 2014). Additionally, photochemical degradation tends to target B6CA over B5CA (Stubbins et al., 2012), adding complexity to the use of BPCA ratios for constraining BC sources (Wagner et al., 2018). This highlights the necessity for complementary tools, such as isotopic analysis and additional molecular markers like polycyclic aromatic hydrocarbons, to reliably elucidate BC sources (Vaezzadeh et al., 2023a, 2023b).

3.5. The flux of DBC and PBC and the buried flux of SBC

Watershed hydrology is considered one of the primary factors influencing the temporal variation of riverine DBC and PBC fluxes (Bao et al., 2019; Roebuck et al., 2018; Wagner et al., 2015). Based on the runoff data of the region's rivers (Text S5), we estimated the DBC and PBC flux in the study area. In this study, the fluxes of DBC and PBC are estimated to be 1.06 Gg/year and 0.25 Gg/year, respectively. The lower PBC flux is attributed to its source and the tendency to settle in estuarine regions. The DBC flux is lower than those observed in larger estuaries such as the Yangtze River (47.4 Gg/year; Wang et al., 2016) and the Pearl River (11.2–16.3 Gg/year; Zhang et al., 2023), but it is comparable to that of the Jiulong River (0.2–0.6 Gg/year; Zhao et al., 2023), which has a similar runoff volume. The flux is largely dependent on the river runoff.

Based on the SBC content in surface sediments and the sedimentation rate (Text S6), we calculated the burial flux of SBC. The burial flux of SBC in sediments ranges from 58 to 1848 μg/cm^2/yr, which is lower than that in the Pearl River Estuary (197–6480 μg/cm^2/yr; Liu et al., 2024b) and comparable to Daya Bay (212 ± 228 μg/cm^2/yr; Dan et al., 2022). However, it is higher than the values reported for other Chinese marginal seas, such as the Bohai Sea, Yellow Sea, and East China Sea

(67–425 μg/cm^2·yr; Fang et al., 2015) as well as the Gulf of Cádiz (120–245 μg/cm^2·yr; Sánchez-García et al., 2013). These results, although covering data from different time periods over the past decade, reflect that the burial flux is primarily influenced by sedimentation rate and sediment properties, with a concentration of BC burial in large estuarine areas and along continental shelf margins.

Given the lack of precise river runoff and sedimentation rate data, our estimates of DBC and PBC fluxes and BC burial fluxes in this region may have inherent uncertainties. Research on BC in the Beibu Gulf remains limited. However, the substantial contribution of terrestrial inputs from rivers, particularly those along the Vietnamese coast (Gao et al., 2015), underscores their significant role in this semi-enclosed shelf sea. Meanwhile, the construction of the Pinglu Canal is expected to further enhance the influx of terrestrial materials into the Beibu Gulf. This study provides an exploratory basis for future comprehensive research on BC in the Beibu Gulf. Future work could focus on monitoring BC in the rivers discharging into the gulf and estimating BC stocks across the entire Beibu Gulf.

4. Conclusions

This research provides comprehensive data on the spatial distribution and seasonal characteristics of BC in a semi-enclosed bay and an open estuarine located in subtropical areas, including detailed analyses of DBC and PBC concentrations within the surface water, as well as SBC content in sediments. By utilizing the BPCA method, this study represents a holistic attempt to assess BC content across different environmental matrices within the same region. The spatial distribution and seasonal variation of PBC and DBC suggest that riverine input is the primary source of BC in this region. Environmental factors lead to rapid deposition and transformation at river estuaries, where the decoupling of DBC and PBC seasonally is attributed to their different sources. The study highlights the distinct environmental roles of semi-enclosed bays and open river estuaries in BC dynamics, emphasizing the impact of sediment resuspension processes. It was observed that BC shows an increasing trend in aggregation from dissolved to particulate phases, a difference driven mainly by their sources, behaviors in the aquatic environment, and environmental degradation processes. The research further elaborates on the relationship between BC and its proportion within organic carbon, alongside other environmental factors, underscoring the stability of BC in sedimentary environments. Understanding these processes is crucial for predicting the impacts of future climate change on the global carbon cycle.

CRediT authorship contribution statement

Jingyu Wang: Writing – original draft, Visualization, Methodology, Formal analysis, Data curation. **Ruijie Zhang:** Writing – review & editing, Supervision, Project administration, Methodology, Funding acquisition, Conceptualization. **Jingzhen Wang:** Writing – review & editing, Methodology, Investigation, Funding acquisition. **Liwei Mo:** Investigation, Data curation. **Zhehong Ji:** Investigation, Data curation. **Pan Wei:** Investigation, Data curation. **Chaoshuai Wei:** Validation, Investigation. **Kefu Yu:** Funding acquisition.

Declaration of competing interest

The authors declare that they have no known competing financial interests or personal relationships that could have appeared to influence the work reported in this paper.

Acknowledgments

This work was supported by the Guangxi Natural Science Foundation (2025GXNSFAA069701), the Guangxi Young Elite scholar Program (Jingzhen Wang), and the National Natural Science Foundation of China (42030502 and 42090041).

Appendix A. Supplementary data

Supplementary data to this article can be found online at https://doi.org/10.1016/j.marpolbul.2025.117908.

Data availability

Data will be made available on request.

References

Alan Roebuck, J., Podgorski, D.C., Wagner, S., Jaffé, R., 2017. Photodissolution of charcoal and fire-impacted soil as a potential source of dissolved black carbon in aquatic environments. Org. Geochem. 112, 16–21. https://doi.org/10.1016/j.orggeochem.2017.06.018.

Bao, H., Niggemann, J., Luo, L., Dittmar, T., Kao, S.-J., 2017. Aerosols as a source of dissolved black carbon to the ocean. Nat. Commun. 8, 510. https://doi.org/10.1038/s41467-017-00437-3.

Bao, H., Niggemann, J., Huang, D., Dittmar, T., Kao, S., 2019. Different responses of dissolved black carbon and dissolved lignin to seasonal hydrological changes and an extreme rain event. JGR Biogeosciences 124, 479–493. https://doi.org/10.1029/2018JG004822.

Bao, H., Niggemann, J., Du, M., Zhao, W., Huang, D., Yi, Y., Yang, J.T., Dittmar, T., Kao, S., 2023. Deciphering sources and processing of dissolved black carbon in coastal seas. Limnology & Oceanography 68, 2562–2575. https://doi.org/10.1002/lno.12442.

Barton, R., Winston, I., Wagner, S., 2024. The presence of free benzenepolycarboxylic acids (BPCAs) may result in the overestimation of dissolved black carbon in aqueous samples. Org. Geochem. 190, 104765. https://doi.org/10.1016/j.orggeochem.2024.104765.

Bauer, J.E., Cai, W.-J., Raymond, P.A., Bianchi, T.S., Hopkinson, C.S., Regnier, P.A.G., 2013. The changing carbon cycle of the coastal ocean. Nature 504, 61–70. https://doi.org/10.1038/nature12857.

Bird, M.I., Wynn, J.G., Saiz, G., Wurster, C.M., McBeath, A., 2015. The pyrogenic carbon cycle. Annu. Rev. Earth Planet. Sci. 43, 273–298. https://doi.org/10.1146/annurev-earth-060614-105038.

Brodowski, S., Rodionov, A., Haumaier, L., Glaser, B., Amelung, W., 2005. Revised black carbon assessment using benzene polycarboxylic acids. Org. Geochem. 36, 1299–1310. https://doi.org/10.1016/j.orggeochem.2005.03.011.

Coppola, A.I., Druffel, E.R.M., 2016. Cycling of black carbon in the ocean. Geophys. Res. Lett. 43, 4477–4482. https://doi.org/10.1002/2016GL068574.

Coppola, A.I., Ziolkowski, L.A., Masiello, C.A., Druffel, E.R.M., 2014. Aged black carbon in marine sediments and sinking particles. Geophys. Res. Lett. 41, 2427–2433. https://doi.org/10.1002/2013GL059068.

Coppola, A.I., Wiedemeier, D.B., Galy, V., Haghipour, N., Hanke, U.M., Nascimento, G.S., Usman, M., Blattmann, T.M., Reisser, M., Freymond, C.V., Zhao, M., Voss, B., Wacker, L., Schefuß, E., Peucker-Ehrenbrink, B., Abiven, S., Schmidt, M.W.I., Eglinton, T.I., 2018. Global-scale evidence for the refractory nature of riverine black carbon. Nat. Geosci. 11, 584–588. https://doi.org/10.1038/s41561-018-0159-8.

Coppola, A.I., Wagner, S., Lennartz, S.T., Seidel, M., Ward, N.D., Dittmar, T., Santín, C., Jones, M.W., 2022. The black carbon cycle and its role in the earth system. Nat Rev Earth Environ 3, 516–532. https://doi.org/10.1038/s43017-022-00316-6.

Dahl, M., Deyanova, D., Gütschow, S., Asplund, M.E., Lyimo, L.D., Karamfilov, V., Santos, R., Björk, M., Gullström, M., 2016. Sediment properties as important predictors of carbon storage in Zostera marina meadows: a comparison of four European areas. PLoS One 11, e0167493. https://doi.org/10.1371/journal.pone.0167493.

Dan, S.F., Cui, Dongyang, Yang, B., Wang, X., Ning, Z., Lu, D., Kang, Z., Huang, H., Zhou, J., Cui, Dandan, Zhong, Q., 2022. Sources, burial flux and mass inventory of black carbon in surface sediments of the Daya bay, a typical mariculture bay of China. Mar. Pollut. Bull. 179, 113708. https://doi.org/10.1016/j.marpolbul.2022.113708.

Ding, Y., Yamashita, Y., Dodds, W.K., Jaffé, R., 2013. Dissolved black carbon in grassland streams: is there an effect of recent fire history? Chemosphere 90, 2557–2562. https://doi.org/10.1016/j.chemosphere.2012.10.098.

Ding, Y., Cawley, K.M., Da Cunha, C.N., Jaffé, R., 2014. Environmental dynamics of dissolved black carbon in wetlands. Biogeochemistry. https://doi.org/10.1007/s10533-014-9964-3.

Dittmar, T., 2008. The molecular level determination of black carbon in marine dissolved organic matter. Org. Geochem. 39, 396–407. https://doi.org/10.1016/j.orggeochem.2008.01.015.

Dittmar, T., Koch, B., Hertkorn, N., Kattner, G., 2008. A simple and efficient method for the solid-phase extraction of dissolved organic matter (SPE-DOM) from seawater: SPE-DOM from seawater. Limnol. Oceanogr. Methods 6, 230–235. https://doi.org/10.4319/lom.2008.6.230.

Fang, Y., Chen, Y., Tian, C., Lin, T., Hu, L., Huang, G., Tang, J., Li, J., Zhang, G., 2015. Flux and budget of BC in the continental shelf seas adjacent to Chinese high BC emission source regions. Glob. Biogeochem. Cycles 29, 957–972. https://doi.org/10.1002/2014GB004985.

Fang, Y., Chen, Y., Huang, G., Hu, L., Tian, C., Xie, J., Lin, J., Lin, T., 2021. Particulate and dissolved black carbon in coastal China seas: spatiotemporal variations, dynamics, and potential implications. Environ. Sci. Technol. 55, 788–796. https://doi.org/10.1021/acs.est.0c06386.

Fang, Z., Yang, W., Chen, M., Ma, H., 2017. Source and fate of dissolved black carbon in the Western South China Sea during the southwest monsoon prevailing season. J. Geophys. Res. Biogeo. 122, 2817–2830. https://doi.org/10.1002/2017JG004014.

Feng, N., Yang, W., Zhao, X., Chen, M., Qiu, Y., Zheng, M., 2021. Semi-enclosed bays serve as hotspots for black carbon burial: a case study in Jiaozhou Bay, western Yellow Sea. Sci. Total Environ. 797, 149100. https://doi.org/10.1016/j.scitotenv.2021.149100.

Flores-Cervantes, D.X., Plata, D.L., MacFarlane, J.K., Reddy, C.M., Gschwend, P.M., 2009. Black carbon in marine particulate organic carbon: inputs and cycling of highly recalcitrant organic carbon in the Gulf of Maine. Mar. Chem. 113, 172–181. https://doi.org/10.1016/j.marchem.2009.01.012.

Fu, W., Qi, Y., Luo, C., Zhang, H., Wang, X., 2023. Distinct radiocarbon ages reveal two black carbon pools preserved in large river estuarine sediments. Environ. Sci. Technol. 57, 6216–6227. https://doi.org/10.1021/acs.est.2c09079.

Gao, J., Chen, B., Shi, M., 2015. Summer circulation structure and formation mechanism in the Beibu gulf. Sci. China Earth Sci. 58, 286–299. https://doi.org/10.1007/s11430-014-4916-2.

Glaser, B., Haumaier, L., Guggenberger, G., Zech, W., 1998. Black carbon in soils: the use of benzenecarboxylic acids as specfic markers. Org. Geochem. 29, 811–819. https://doi.org/10.1016/S0146-6380(98)00194-6.

Guo, J., Yang, F., Costa, O.S., Yan, X., Wu, M., Qiu, H., Li, W., Xu, G., 2024. Nutrient budgets and biogeochemical dynamics in the coastal regions of northern Beibu gulf, South China Sea: implication for the severe impact of human disturbance. Mar. Environ. Res. 197, 106447. https://doi.org/10.1016/j.marenvres.2024.106447.

Guo, L., Xiu, P., Chai, F., Xue, H., Wang, D., Sun, J., 2017. Enhanced chlorophyll concentrations induced by Kuroshio intrusion fronts in the northern South China Sea. Geophys. Res. Lett. 44, 11,565-11,572. doi:https://doi.org/10.1002/2017GL075336.

Hammes, K., Schmidt, M.W.I., Smernik, R.J., Currie, L.A., Ball, W.P., Nguyen, T.H., Louchouarn, P., Houel, S., Gustafsson, Ö., Elmquist, M., Cornelissen, G., Skjemstad, J.O., Masiello, C.A., Song, J., Peng, P., Mitra, S., Dunn, J.C., Hatcher, P.G., Hockaday, W.C., Smith, D.M., Hartkopf-Fröder, C., Böhmer, A., Lüer, B., Huebert, B.J., Amelung, W., Brodowski, S., Huang, L., Zhang, W., Gschwend, P.M., Flores-Cervantes, D.X., Largeau, C., Rouzaud, J.-N., Rumpel, C., Guggenberger, G., Kaiser, K., Rodionov, A., Gonzalez-Vila, F.J., Gonzalez-Perez, J.A., De La Rosa, J.M., Manning, D.A.C., López-Capél, E., Ding, L., 2007. Comparison of quantification methods to measure fire-derived (black/elemental) carbon in soils and sediments using reference materials from soil, water, sediment and the atmosphere: BLACK CARBON QUANTIFICATION RING TRIAL. Glob. Biogeochem. Cycles 21. https://doi.org/10.1029/2006GB002914 n/a-n/a.

Jaffé, R., Ding, Y., Niggemann, J., Vähätalo, A.V., Stubbins, A., Spencer, R.G.M., Campbell, J., Dittmar, T., 2013. Global charcoal mobilization from soils via dissolution and riverine transport to the oceans. Science 340, 345–347. https://doi.org/10.1126/science.1231476.

Jones, M.W., Kelley, D.I., Burton, C.A., Di Giuseppe, F., Barbosa, M.L.F., Brambleby, E., Hartley, A.J., Lombardi, A., Mataveli, G., McNorton, J.R., Spuler, F.R., Wessel, J.B., Abatzoglou, J.T., Anderson, L.O., Andela, N., Archibald, S., Armenteras, D., Burke, E., Carmenta, R., Chuvieco, E., Clarke, H., Doerr, S.H., Fernandes, P.M., Giglio, L., Hamilton, D.S., Hantson, S., Harris, S., Jain, P., Kolden, C.A., Kurvits, T., Lampe, S., Meier, S., New, S., Parrington, M., Perron, M.M.G., Qu, Y., Ribeiro, N.S., Saharjo, B.H., San-Miguel-Ayanz, J., Shuman, J.K., Tanpipat, V., Van Der Werf, G.R., Veraverbeke, S., Xanthopoulos, G., 2024. State of wildfires 2023–2024. Earth Syst. Sci. Data 16, 3601–3685. https://doi.org/10.5194/essd-16-3601-2024.

Kragh, T., Søndergaard, M., 2009. Production and decomposition of new DOC by marine plankton communities: carbohydrates, refractory components and nutrient limitation. Biogeochemistry 96, 177–187. https://doi.org/10.1007/s10533-009-9357-1.

Lack, D.A., Corbett, J.J., 2012. Black carbon from ships: a review of the effects of ship speed, fuel quality and exhaust gas scrubbing. Atmos. Chem. Phys. 12, 3985–4000. https://doi.org/10.5194/acp-12-3985-2012.

Letourneau, M.L., Schaefer, S.C., Chen, H., McKenna, A.M., Alber, M., Medeiros, P.M., 2021. Spatio-temporal changes in dissolved organic matter composition along the salinity gradient of a marsh-influenced estuarine complex. Limnology & Oceanography 66, 3040–3054. https://doi.org/10.1002/lno.11857.

Li, H., Zhang, R., Yan, A., Xie, W., Wang, M., Yu, K., 2023. Black carbon in Deep-Sea seamount sediment cores: vertical variation and non-negligible char black carbon. Environ. Sci. Technol. 57, 14602–14610. https://doi.org/10.1021/acs.est.3c04208.

Liu, Xiaoqing, Lan, C., Zhu, L., Yan, C., Wang, N., Chen, H., Zheng, G., Che, Y., Yang, Z., Bao, R., 2024a. Sediment resuspension as a driving force for organic carbon transference and rebalance in marginal seas. Water Res. 257, 121672. https://doi.org/10.1016/j.watres.2024.121672.

Liu, Xinyi, Li, Y., Lin, T., Guo, N., Yuan, J., Yang, Y., Zhai, W., 2024b. Characterizing sedimentary black carbon in the Pearl River estuary. Southern China. Marine Chemistry 261, 104383. https://doi.org/10.1016/j.marchem.2024.104383.

Masiello, C.A., 2004. New directions in black carbon organic geochemistry. Marine chemistry, New approaches in marine organic biogeochemistry: a tribute to the life and science of John I. Hedges 92, 201–213. https://doi.org/10.1016/j.marchem.2004.06.043.

Matsoukis, C., Amoudry, L.O., Bricheno, L., Leonardi, N., 2023. Numerical investigation of river discharge and tidal variation impact on salinity intrusion in a Generic River Delta through idealized modelling. Estuar. Coasts 46, 57–83. https://doi.org/10.1007/s12237-022-01109-2.

Medeiros, P.M., Seidel, M., Ward, N.D., Carpenter, E.J., Gomes, H.R., Niggemann, J., Krusche, A.V., Richey, J.E., Yager, P.L., Dittmar, T., 2015. Fate of the Amazon River dissolved organic matter in the tropical Atlantic Ocean. Glob. Biogeochem. Cycles 29, 677–690. https://doi.org/10.1002/2015GB005115.

Mouyen, M., Longuevergne, L., Steer, P., Crave, A., Lemoine, J.-M., Save, H., Robin, C., 2018. Assessing modern river sediment discharge to the ocean using satellite gravimetry. Nat. Commun. 9, 3384. https://doi.org/10.1038/s41467-018-05921-y.

Osterholz, H., Burmeister, C., Busch, S., Dierken, M., Frazão, H.C., Hansen, R., Jeschek, J., Kremp, A., Kreuzer, L., Sadkowiak, B., Waniek, J.J., Schulz-Bull, D.E., 2021. Nearshore dissolved and particulate organic matter dynamics in the southwestern Baltic Sea: environmental drivers and time series analysis (2010−2020). Front. Mar. Sci. 8. https://doi.org/10.3389/fmars.2021.795028.

Pan, X., Wong, G.T.F., Tai, J.-H., Ho, T.-Y., 2015. Climatology of physical hydrographic and biological characteristics of the northern South China Sea shelf-sea (NoSoCS) and adjacent waters: observations from satellite remote sensing. Deep Sea research part II: topical studies in oceanography. The Oceanography of the Northern South China Sea Shelf-sea (NoSoCS) and Adjacent Waters 117, 10–22. https://doi.org/10.1016/j.dsr2.2015.02.022.

Raja, M., Rosell-Melé, A., 2020. Appraisal of sedimentary alkenones for the quantitative reconstruction of phytoplankton biomass. Proc. Natl. Acad. Sci. USA 118, e2014787118. https://doi.org/10.1073/pnas.2014787118.

Raymond, P.A., Bauer, J.E., 2001. Riverine export of aged terrestrial organic matter to the North Atlantic Ocean. Nature 409, 497–500. https://doi.org/10.1038/35054034.

Ren, P., Liu, Y., Shi, X., Sun, S., Fan, D., Wang, X., 2019. Sources and sink of black carbon in Arctic Ocean sediments. Sci. Total Environ. 689, 912–920. https://doi.org/10.1016/j.scitotenv.2019.06.437.

Roebuck, J.A., Seidel, M., Dittmar, T., Jaffé, R., 2018. Land use controls on the spatial variability of dissolved black carbon in a subtropical watershed. Environ. Sci. Technol. 52, 8104–8114. https://doi.org/10.1021/acs.est.8b00190.

Roth, P.J., Lehndorff, E., Brodowski, S., Bornemann, L., Sanchez-García, L., Gustafsson, Ö., Amelung, W., 2012. Differentiation of charcoal, soot and diagenetic carbon in soil: method comparison and perspectives. Org. Geochem. 46, 66–75. https://doi.org/10.1016/j.orggeochem.2012.01.012.

Sánchez-García, L., Cato, I., Gustafsson, Ö., 2012. The sequestration sink of soot black carbon in the northern European shelf sediments. Glob. Biogeochem. Cycles 26, 2010GB003956. https://doi.org/10.1029/2010GB003956.

Sánchez-García, L., De Andrés, J.R., Gélinas, Y., Schmidt, M.W.I., Louchouarn, P., 2013. Different pools of black carbon in sediments from the Gulf of Cádiz (SW Spain): method comparison and spatial distribution. Mar. Chem. 151, 13–22. https://doi.org/10.1016/j.marchem.2013.02.006.

Santín, C., Doerr, S.H., Preston, C.M., González-Rodríguez, G., 2015. Pyrogenic organic matter production from wildfires: a missing sink in the global carbon cycle. Glob. Chang. Biol. 21, 1621–1633. https://doi.org/10.1111/gcb.12800.

Schmidt, M.W.I., Noack, A.G., 2000. Black carbon in soils and sediments: analysis, distribution, implications, and current challenges. Glob. Biogeochem. Cycles 14, 777–793. https://doi.org/10.1029/1999GB001208.

Schneider, M.P.W., Hilf, M., Vogt, U.F., Schmidt, M.W.I., 2010. The benzene polycarboxylic acid (BPCA) pattern of wood pyrolyzed between 200 °C and 1000 °C. Org. Geochem. 41, 1082–1088. https://doi.org/10.1016/j.orggeochem.2010.07.001.

Stubbins, A., Niggemann, J., Dittmar, T., 2012. Photo-lability of deep ocean dissolved black carbon. Biogeosciences 9, 1661–1670. https://doi.org/10.5194/bg-9-1661-2012.

Vaezzadeh, V., Yi, X., Rais, F.R., Bong, C.W., Thomes, M.W., Lee, C.W., Zakaria, M.P., Wang, A.J., Zhong, G., Zhang, G., 2021. Distribution of black carbon and PAHs in sediments of peninsular Malaysia. Mar. Pollut. Bull. 172, 112871. https://doi.org/10.1016/j.marpolbul.2021.112871.

Vaezzadeh, V., Zhong, G., Gligorovski, S., Wang, Y., Zhang, G., 2023a. Characteristics of dissolved black carbon in riverine surface microlayer. Mar. Pollut. Bull. 194, 115301. https://doi.org/10.1016/j.marpolbul.2023.115301.

Vaezzadeh, V., Zhong, G., Zhang, G., 2023b. Benzene polycarboxylic acids as molecular markers of black carbon: progresses and challenges. Chemosphere 341, 140112. https://doi.org/10.1016/j.chemosphere.2023.140112.

Wagner, S., Cawley, K.M., Rosario-Ortiz, F.L., Jaffé, R., 2015. In-stream sources and links between particulate and dissolved black carbon following a wildfire. Biogeochemistry 124, 145–161. https://doi.org/10.1007/s10533-015-0088-1.

Wagner, S., Jaffé, R., Stubbins, A., 2018. Dissolved black carbon in aquatic ecosystems. Limnology and Oceanography Letters 3, 168–185. https://doi.org/10.1002/lol2.10076.

Wagner, S., Brandes, J., Spencer, R.G.M., Ma, K., Rosengard, S.Z., Moura, J.M.S., Stubbins, A., 2019. Isotopic composition of oceanic dissolved black carbon reveals non-riverine source. Nat. Commun. 10, 5064. https://doi.org/10.1038/s41467-019-13111-7.

Wang, X., Xu, C., Druffel, E.M., Xue, Y., Qi, Y., 2016. Two black carbon pools transported by the Changjiang and Huanghe Rivers in China. Glob. Biogeochem. Cycles 30, 1778–1790. https://doi.org/10.1002/2016GB005509.

Ward, N.D., Bianchi, T.S., Medeiros, P.M., Seidel, M., Richey, J.E., Keil, R.G., Sawakuchi, H.O., 2017. Where carbon Goes when water flows: carbon cycling across the aquatic continuum. Front. Mar. Sci. 4. https://doi.org/10.3389/fmars.2017.00007.

Wiedemeier, D.B., Lang, S.Q., Gierga, M., Abiven, S., Bernasconi, S.M., Früh-Green, G.L., Hajdas, I., Hanke, U.M., Hilf, M.D., McIntyre, C.P., Scheider, M.P.W., Smittenberg, R.H., Wacker, L., Wiesenberg, G.L.B., Schmidt, M.W.I., 2016. Characterization, quantification and compound-specific isotopic analysis of pyrogenic carbon using benzene Polycarboxylic acids (BPCA). JoVE 53922. https://doi.org/10.3791/53922.

Xu, C., Xue, Y., Qi, Y., Wang, X., 2016. Quantities and fluxes of dissolved and particulate black carbon in the Changjiang and Huanghe Rivers, China. Estuar. Coasts 39, 1617–1625. https://doi.org/10.1007/s12237-016-0122-0.

Xue, Y., Zou, L., Ge, T., Wang, X., 2017. Mobilization and export of millennial-aged organic carbon by the Yellow River. Limnology & Oceanography 62. https://doi.org/10.1002/lno.10579.

Yang, W., Fang, Z., Zhang, Q., Chen, M., Zheng, M., 2023a. Dynamics of particulate black carbon in the South China Sea: magnitude, resident timescale, sinking speed, and flux. Sci. Total Environ. 877, 162847. https://doi.org/10.1016/j.scitotenv.2023.162847.

Yang, Y., Li, Y., Huang, C., Chen, F., Chen, C., Zhang, H., Deng, W., Ye, F., 2023b. Anthropogenic influences on the sources and distribution of organic carbon, black carbon, and heavy metals in Daya Bay's surface sediments. Mar. Pollut. Bull. 196, 115571. https://doi.org/10.1016/j.marpolbul.2023.115571.

Zhang, Q., Zhou, J., Fang, Z., Yang, W., Chen, M., Zheng, M., 2023. Sources and Dynamics of Dissolved Black Carbon in the Pearl River Estuary and Shelf. J Oceanogr, Northern South China Sea. https://doi.org/10.1007/s10872-023-00708-2.

Zhao, W., Bao, H., Huang, D., Niggemann, J., Dittmar, T., Kao, S.-J., 2023. Evidence from molecular marker and FT-ICR-MS analyses for the source and transport of dissolved black carbon under variable water discharge of a subtropical estuary. Biogeochemistry 162, 43–55. https://doi.org/10.1007/s10533-022-00987-9.

Zhou, Y., He, D., He, C., Li, P., Fan, D., Wang, A., Zhang, K., Chen, B., Zhao, C., Wang, Y., Shi, Q., Sun, Y., 2021. Spatial changes in molecular composition of dissolved organic matter in the Yangtze River estuary: implications for the seaward transport of estuarine DOM. Sci. Total Environ. 759, 143531. https://doi.org/10.1016/j.scitotenv.2020.143531.

Ziolkowski, L.A., Chamberlin, A.R., Greaves, J., Druffel, E.R.M., 2011. Quantification of black carbon in marine systems using the benzene polycarboxylic acid method: a mechanistic and yield study: BC via the BPCA method: mechanism and yield. Limnol. Oceanogr. Methods 9, 140. https://doi.org/10.4319/lom.2011.9.140.

LIMNOLOGY and OCEANOGRAPHY

ASLO

Limnol. Oceanogr. 9999, 2025, 1–15
© 2025 Association for the Sciences of Limnology and Oceanography.
doi: 10.1002/lno.70139

RESEARCH ARTICLE

Further increasing nitrogen concentration does not enhance the denitrification and DNRA potentials in eutrophic reefs: Insights from the differences in benthic categories

Zhiming Ning,[1] **Zhijin Liu**,[1] **Kefu Yu**,[1,2] **Ronglin Xia**,[1] **Wei Jiang**,[1] **Bin Yang**,[3] **Guodong Song**[4*]

[1]Guangxi Laboratory on the Study of Coral Reefs in the South China Sea, School of Marine Sciences, Guangxi University, Nanning, China; [2]Southern Marine Science and Engineering Guangdong Laboratory (Guangzhou), Guangzhou, China; [3]Jiangsu Key Laboratory of Marine Biotechnology, Jiangsu Ocean University, Lianyungang, China; [4]Frontiers Science Center for Deep Ocean Multispheres and Earth System, and Key Laboratory of Marine Chemistry Theory and Technology, Ministry of Education, Ocean University of China, Qingdao, China

Abstract

Low nitrogen (N) availability is critical to coral health and resilience. Dissimilatory nitrate reduction processes, such as denitrification, anammox, and dissimilatory nitrate reduction to ammonium (DNRA), play a vital role in regulating seawater N content. Thus, quantifying the rates of these processes is essential for assessing the overall health and recovery potential of N-enriched coral reefs. However, the diversity and complexity of benthic categories in coral reefs severely limit our understanding of the overall nitrate reduction capacity of these ecosystems. To address this, we utilized the ^{15}N isotope tracing technique to assess denitrification, anammox, and DNRA for various benthic categories, including live corals, turf algae, sediments, biogenic rock, and coral rubble in the coral reefs of Weizhou Island. Our findings indicate that, except for sediments, the denitrification potential (0.1–5.6 mmol N m^{-2} d^{-1}) significantly exceeded that of DNRA (0.1–1.8 mmol N m^{-2} d^{-1}), while anammox (0.01–0.10 mmol N m^{-2} d^{-1}) was negligible. There was a significant difference in denitrification rate among benthic categories, with massive corals *Galaxea fascicularis* and biogenic rock exhibiting the highest rate. Extrapolated to the respective reef area, both live corals and biogenic rock contributed the most to the integrated rates of denitrification and DNRA (27–41%). However, no significant change in the rate was observed when the nitrate concentration increased from 10 to 20 μM. Consequently, it is crucial to strictly control N emissions in N-enriched reefs impacted by human activities, while also prioritizing the protection of benthic categories that significantly contribute to denitrification.

Coral reefs are among the most biodiverse and resource-rich ecosystems in the ocean, playing an extremely important role in resource and ecological functions (Normile 2009). However, under multiple stressors such as climate warming, water pollution, and outbreaks of crown-of-thorns starfish, coral reefs worldwide are experiencing severe degradation (Eakin et al. 2019; Morrison et al. 2019). Excess nitrogen (N) emissions from human activities have also become a significant driver of coral reef degradation. On one hand, excess N impairs the photosynthesis of symbiotic dinoflagellates, directly contributing to coral bleaching (Wiedenmann et al. 2013; Rosset et al. 2017; Morris et al. 2019). On the other hand, excess N promotes the growth of benthic macroalgae, further exacerbating coral reef degradation (McManus and Polsenberg 2004). Therefore, N cycling processes involving the removal of N from coral reefs are essential for regulating and balancing N concentrations and maintaining the health of coral reef ecosystems in the face of excess N.

The N cycle is the most complex of Earth's biogeochemical cycles, characterized by an unusually diverse set of transformations (Thamdrup 2012). First, biological dinitrogen (N_2) fixation, that is, the conversion of atmospheric N_2 into bioavailable ammonimu (NH_4^+) by prokaryotic microbes (diazotrophs), can alleviate N limitation for primary producers

*Correspondence: gsong@ouc.edu.cn

Associate editor: Bradley Eyre

Data Availability Statement: The data related to this article are available online (https://doi.org/10.6084/m9.figshare.26867287).

in coral reefs (Cardini et al. 2016). Then, NH_4^+ is oxidized into nitrite (NO_2^-) or nitrate (NO_3^-) by nitrifying bacteria and archaea in aerobic environments through nitrification (Rädecker et al. 2015). However, in anoxic environments, NO_3^- replaces dissolved oxygen (DO) as the primary electron acceptor and undergoes microbial dissimilatory reduction (Fossing et al. 1995; Kamp et al. 2011). The dissimilatory nitrate reduction primarily involves processes such as anaerobic ammonium oxidation (anammox), dissimilatory nitrate reduction to ammonium (DNRA), and denitrification (Devol 2015). Denitrification is a process in which organic matter provides energy for the dissimilatory reduction of NO_3^- or NO_2^- to N_2 or nitrous oxide (N_2O). Anammox, on the other hand, is a process carried out by chemolithoautotrophic bacteria, where NO_2^- serves as the electron acceptor and NH_4^+ acts as the electron donor, leading to the production of N_2 (Dalsgaard et al. 2005). However, the rates of anammox in coral reef ecosystems are consistently low (Eyre et al. 2008; Rädecker et al. 2015), though anammox bacteria are widely distributed in coral reefs (Zhang et al. 2015). Thus, denitrification is the most important pathway for N removal in coral reefs, which helps mitigate eutrophication in nearshore coral reef regions but may exacerbate N limitation in offshore coral reef areas (Eyre et al. 2008). Conversely, the DNRA process reduces NO_3^- to NH_4^+ and retains it within the ecosystem, contributing to the high productivity of oligotrophic reef areas (Erler et al. 2014).

In coral reef ecosystems, sediments are the most common anoxic environments where denitrification was first investigated (Miyajima et al. 2001). Additionally, denitrifying bacteria are present in the coral holobiont, within compartments that anoxic conditions required for denitrification through respiration (Siboni et al. 2008). However, it was not until Tilstra et al. (2019) that denitrification in corals was first confirmed using the acetylene inhibition method, which has certain limitations. Specifically, at low NO_3^- concentrations, acetylene may incompletely inhibit nitrous oxide reduction while also suppressing nitrification, thereby leading to an underestimation of the denitrification rate (El-Khaled et al. 2020; Table 1). Adding NO_3^- can avoid incomplete inhibition but may result in overestimation of the rate (Joye et al. 1996). The application of the ^{15}N isotope tracing technique avoids these drawbacks and quantifies the denitrification of various coral species, indicating species-specific differences in the denitrification capabilities of corals (Babbin et al. 2021; Glaze et al. 2022). Additionally, other benthic categories of coral reefs such as turf algae and coral rubble also exhibit denitrification capabilities, which increase with higher NO_3^- levels (El-Khaled et al. 2021a). However, since these studies used the acetylene inhibition method, the observed NO_3^--dependent denitrification might be influenced by methodological limitations, making it uncertain whether the trend reflects an inherent regulatory mechanism. Indeed, as primary producers, turf algae also assimilate NO_3^-, benefiting from increased NO_3^- availability (Hutchins and Capone 2022). With the rise in terrestrial N input, this could further degrade coral reef ecosystems, turning them into habitats for macroalgae and turf algae (McManus and Polsenberg 2004; Ren et al. 2017; Pan et al. 2021). Nonetheless, it remains unclear how denitrification in these benthic categories responds to the increase in NO_3^- in N-enriched coral reefs.

Dissimilatory nitrate reduction to ammonium is an active N cycling pathway in tropical corals, with a rate reaching 0.46–0.60 mmol N m^{-2} d^{-1} (Babbin et al. 2021; Glaze et al. 2022). Corals can alter the composition of dissolved inorganic N (DIN) through DNRA to regulate their response to thermal stress (Marangoni et al. 2020). Due to the same reactive substrates (i.e., NO_3^-), the DNRA process competes with the denitrification process. However, there are many conditions that stimulate DNRA and permit it to outcompete denitrification on living coral surfaces, such as hypoxic to anoxic boundary conditions, limited NO_3^- compared with organic carbon, higher salinity, and temperature (Dunn et al. 2013; Kraft et al. 2014; Glaze et al. 2022). In addition to the coral holobiont, significant DNRA activity has been demonstrated in reef sediments (Erler et al. 2014), but the DNRA processes in other benthic categories remain unquantified (Table 1). Quantifying both denitrification and DNRA processes is crucial for evaluating the overall health and recovery potential of N-enriched coral reef ecosystems.

As a typical coral reef severely degraded by high-intensity human activities (Yu et al. 2019), the NO_3^- concentration in the seawater around Weizhou Island in the northern South China Sea is significantly higher than that of the Great Barrier Reef (Glaze et al. 2022) and the Caribbean reef ecosystem (Babbin et al. 2021), and continues to rise, exacerbating coral reef degradation (Yu et al. 2019; Pan et al. 2021; Ning et al. 2022). However, there has been no research on the response of denitrification and DNRA processes to elevated N levels in eutrophic coral reefs. Based on documented significant differences in N_2 fixation rates and denitrification activities across benthic categories such as living corals, turf algae, sands, biogenic rock, and coral rubble (El-Khaled et al. 2021b), we hypothesized that DNRA and denitrification activities in eutrophic reefs would exhibit significant differences across various benthic categories. Hypothetically, denitrification and DNRA rates in different categories could be influenced by light conditions, as numerous studies have revealed light-mediated regulation of these processes in coral holobionts (Babbin et al. 2021; Glaze et al. 2022; Yang et al. 2024). Additionally, we hypothesized that, in response to increased NO_3^- concentrations, the N removal capacity through denitrification does not improve in eutrophic coral reefs.

To verify the differences in NO_3^- reduction across various benthic categories in eutrophic coral reefs, this study focuses on the coral reefs of Weizhou Island. Using the ^{15}N isotope tracer technique, we conducted controlled incubations of live corals, turf algae, sand sediments, biogenic rock, and coral rubble to

Table 1. Summary of previously reported rates ($\times 10^{-2}$ mmol N m^{-2} d^{-1}) of denitrification, DNRA, and anammox across benthic categories under light vs. dark conditions in coral reef ecosystems.*

		Denitrification		DNRA		Anammox			
Locations	Categories	Light	Dark	Light	Dark	Light	Dark	Methods	References
Caribbean reef	Hard corals	0–3.1	0–11	n.d.	n.d.	n.d.	n.d.	^{15}N tracing	(Babbin et al. 2021)
Great barrier reef	Hard corals	0.05–0.14	0.1–0.4	0–30	46–60	n.d.	n.d.	^{15}N tracing	(Glaze et al. 2022)
Luhuitou peninsula	Hard corals	n.d.	1.4–6.7	n.d.	n.d.	n.d.	0–0.1	^{15}N tracing	(Yang et al. 2024)
Red Sea	Hard corals	n.d.	0.04–0.5**	n.d.	n.d.	n.d.	n.d.	Acetylene inhibition	(Tilstra et al. 2019)
Red Sea	Turf algae	n.d.	0.12–0.17**	n.d.	n.d.	n.d.	n.d.	Acetylene inhibition	(El-Khaled et al. 2021b)
Red Sea	Coral rubble	n.d.	0.26–0.33**	n.d.	n.d.	n.d.	n.d.	Acetylene inhibition	(El-Khaled et al. 2021b)
Red Sea	Soft coral	n.d.	0.67–1.1**	n.d.	n.d.	n.d.	n.d.	Acetylene inhibition	(El-Khaled et al. 2021b)
Red Sea	Biogenic rock	n.d.	0.29–0.36**	n.d.	n.d.	n.d.	n.d.	Acetylene inhibition	(El-Khaled et al. 2021b)
Red Sea	Reef sands	n.d.	0.20–0.34**	n.d.	n.d.	n.d.	n.d.	Acetylene inhibition	(El-Khaled et al. 2021b)
Great barrier reef	Reef sands	n.d.	5.0	n.d.	n.d.	n.d.	11.7	^{15}N tracing	(Erler et al. 2013)

*n.d. = not determined.
**Rates measured under a 12 : 12 h dark/light cycle.

measure their potential rates of denitrification, DNRA, and anammox. The study aimed to assess the activity of these pathways under variable NO_3^- concentrations of 10 and 20 μM, as well as under light and dark conditions. The findings were subsequently extrapolated to estimate a preliminary N budget for distinct benthic categories within the coral reefs of Weizhou Island. These results will enhance our understanding of coral reef ecosystems resilience to eutrophication and provide a scientific basis for optimizing N pollution management strategies.

Materials and methods

Study sites and sampling

Weizhou Island (21°00′–21°10′N, 109°07′–109°15′E) is 7 km long, 5 km wide, 26 km^2 in area and is 48 km offshore of the southern Chinese mainland coast. It is a volcanic island located in the Beibu Gulf, and its comparatively high-latitude position provides an optimal habitat for coral growth. However, the mean living coral cover around Weizhou Island has decreased from ~ 42% in 1984 to ~ 10% in 2015 (Yu et al. 2019). The mean annual air temperature was 22.6 ± 5.1°C; the lowest and highest monthly mean temperatures occur in January (15.3 ± 2.3°C) and July (28.9 ± 2.7°C) respectively. The concentrations of DIN and dissolved inorganic phosphorus (DIP) in seawater ranged from 2.3 to 11.5 μM, and 0.02 to 0.43 μM, respectively. Thus, Weizhou Island was an area with relatively excess N, with an N-to-phosphorus ratio ranging from 12 to 350 (Ning et al. 2020).

Benthic community composition of the coral reefs was determined in earlier studies using photo quadrats (Liao et al. 2019; Yu et al. 2019). Coverage of turf algae, coral rubble, biogenic coral rock, sands, and hard corals was surveyed along transects at four sites on the reef flat of Weizhou Island. Eight 100 m transects were established at the site. On each transect, 11 quadrats (0.5 × 0.5 m) were used at 10 m intervals. Overall, a total of 88 quadrats were used. An OLYMPUS TG-4 Zoom digital waterproof camera (effective pixel density: 12 million pixels) was used to photograph each quadrat. Benthic cover and composition were analyzed using Coral Point Count with Excel extensions software that used 50 randomly placed points within each frame. Hard corals were identified to the genus level, and benthic algae were identified to the species or genus level.

The benthos of Weizhou Island consisted of 37% biogenic rock, 18% coral rubble, 16% turf algae, 9% hard coral, 3% sand, and the residual consisted of other algae or non-biological substrates (Liao et al. 2019). Weizhou Island's hard coral was mainly composed of massive corals (8%), representative of which were *Pavona*, *Porites*, *Favites*, *Galaxea fascicularis*, while cover of the branching corals such as *Acropora muricata* was < 1% (Yu et al. 2019).

Representative samples of all benthic categories, including turf algae ($n = 3$), sands, hard corals *G. fascicularis* and *A. muricata* ($n = 3$), biogenic rock ($n = 3$), and coral rubble ($n = 9$) were collected randomly from the coral reefs of Weizhou Island in July 2022. Sand sediments (0–5 cm) were collected by pushing Plexiglas tubes (6 cm diameter, 5 cm depth) into the sediment, then transferred into plastic bags and thoroughly mixed to ensure uniformity. All samples from each benthic category were cut into 9 fragments (about 50–80 cm^2, or 150 cm^3 sediment) and were then transferred into a flow-through aquarium where fresh seawater (1.9 ± 0.3 μM of NH_4^+ and 3.0 ± 0.4 μM of NO_3^-) was continuously supplied using a peristaltic pump (BT100-1L, LONGER PUMP) and allowed to acclimate under natural sunlight (average photon flux was ~ 200 μmol photons m^{-2} s^{-1}; Fig. 1, Step 1).

Incubation for measurement of NO_3^- reduction processes

Incubation was conducted in polymeric polyethylene bags (20 × 30 cm) equipped with a Teflon valve (Fig. 1, Step 2). The

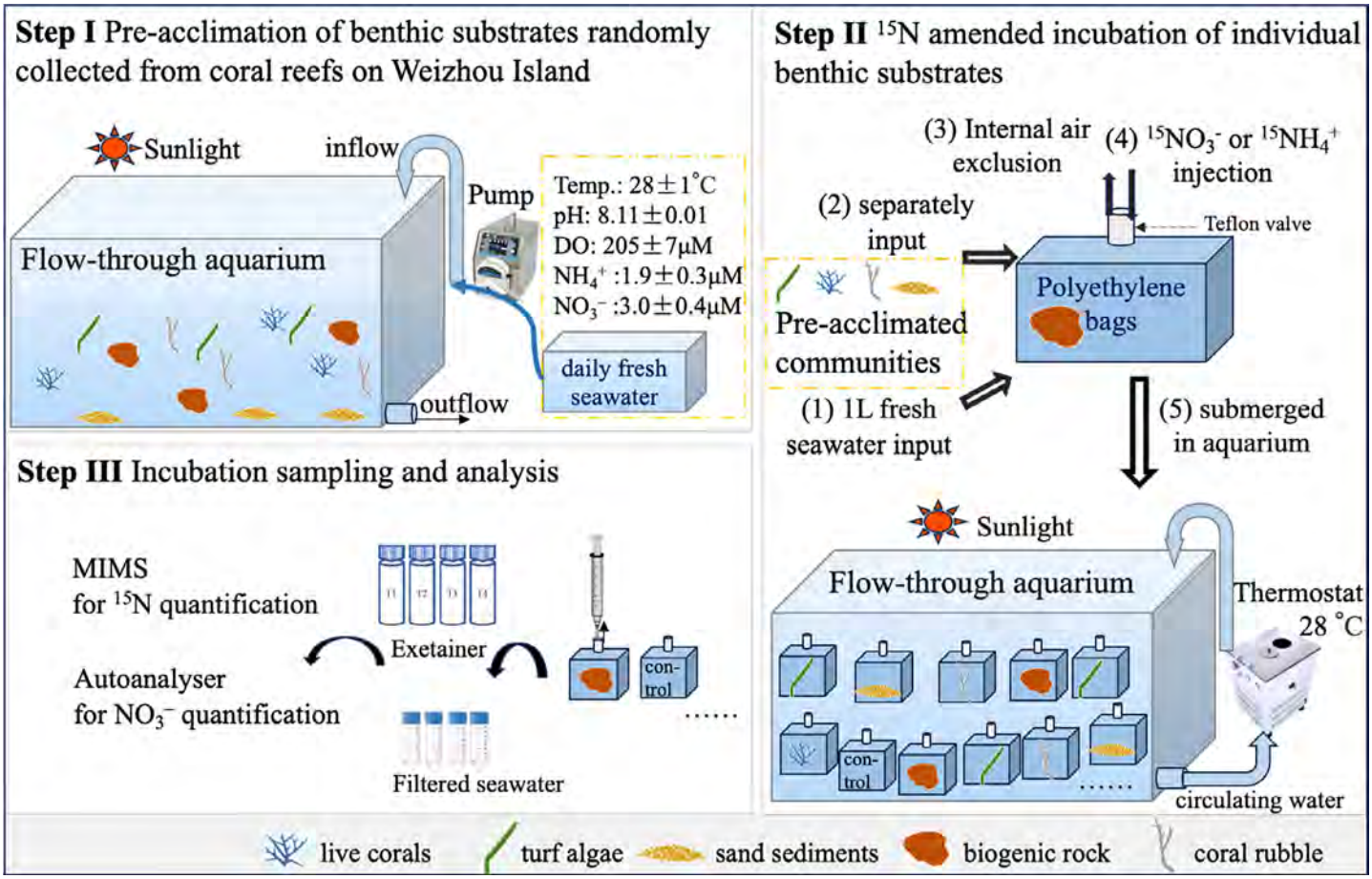


Fig. 1. Stepwise schematic of pre-acclimation, ^{15}N amended incubation, and sampling analysis.

bag was transparent and gastight. After 1 week of acclimation, all fragments from the aquarium were each transferred into separate gastight bags containing 1 L of fresh seawater. At the same time, fresh seawater without fragments served as controls to correct for planktonic background activity. After sealing the bags, the internal air was expelled through Teflon valves. In each bag of different experimental groups, 5 μM $^{15}NH_4^+$, 10 μM $^{15}NO_3^-$ or 20 μM $^{15}NO_3^-$ were added, respectively. Each experimental group included three parallel samples. Then, all bags were submerged in a flow-through aquarium, with incubation conditions consistent with those described in the previous acclimation procedure. An external thermostat regulated the temperature of the aquarium to 28 ± 0.3°C through water circulation.

All incubations lasted for 21–22 h, depending on probe (YSI ODO) monitoring of DO concentrations to validate that neither hypoxic nor hyperoxic conditions that would be detrimental to organisms, evoking physiological changes, occurred during incubations (El-Khaled et al. 2021b). Measurements of each bag were conducted four times, two during the day and the other two at night. During each sampling time (Fig. 1, Step 3), seawater in the bag was collected from the Teflon valve using 60 mL syringes. An aliquot of seawater for ^{15}N-N_2 measurement was sampled and transferred to a 12 mL Exetainer vial (Labco Ltd.) with 0.2 mL pre-added saturated mercuric chloride ($HgCl_2$). Another aliquot of seawater for nutrient measurement was filtered with 0.45 μm pore-size syringe polyethersulfone filters and then was frozen at −20°C.

Analysis methods

The concentrations of NH_4^+ and NO_3^- in seawater were determined using an autoanalyzer (QuAAtro, SEAL Analytical). The limit of detection for NH_4^+ and NO_3^- was 0.5 and 0.06 μM, respectively, with a precision of ~ 5%. The isotopic ratios of $^{29}N_2/^{28}N_2$ and $^{30}N_2/^{28}N_2$ were determined using a homemade membrane-inlet mass spectrometer (MIMS), with a precision of 1% (Xu et al. 2022). The concentration of $^{15}NH_4^+$ was determined using a hypobromite oxidation MIMS method, converting $^{15}NH_4^+$ to $^{29}N_2$ and $^{30}N_2$, after which the N_2 isotope ratios were measured using the MIMS (Song et al. 2013; Xu et al. 2022). The production rates of $^{29}N_2$ and $^{30}N_2$ were determined from the linear regression slope of their concentrations over time. The concentration of

$^{15}NH_4^+$ was derived from the concentrations of $^{29}N_2$ and $^{30}N_2$ after conversion.

Calculation and statistical analysis

Equations according to Thamdrup and Dalsgaard (2002) were used in this study without considering the minor influence of DNRA on anammox (Song et al. 2016). Thus, the potential rates of denitrification and DNRA were calculated from the production of $^{29}N_2$, $^{30}N_2$ and $^{15}NH_4^+$ in $^{15}NO_3^-$ amended incubation according to Eqs. 1 and 2, and the potential rate of anammox was calculated from the production of $^{29}N_2$ in $^{15}NH_4^+$ amended incubation according to Eq. 3. To ensure comparability between different categories, volumetric rates were normalized to surface area of the organisms/substrates according to Eq. 4.

$$\text{Denitrification rate} = P_{30}/F_N{}^2 \quad (1)$$

$$\text{DNRA rate} = P^{15}NH_4^+/F_N \quad (2)$$

$$\text{Anammox rate} = P_{29}/F_A \quad (3)$$

$$\text{Areal rate} = \text{volumetric rate}/S \times V \quad (4)$$

where F_N and F_A represented the $^{15}NO_3^-$ fraction in $^{15}NO_3^-$ amended seawater and $^{15}NH_4^+$ fraction in $^{15}NH_4^+$ amended seawater, respectively. P_{29}, P_{30}, and $P^{15}NH_4^+$ were the production rates of $^{29}N_2$, $^{30}N_2$, and $^{15}NH_4^+$, respectively. Surface areas (S) of incubated organisms/substrates were determined using the aluminum foil method (Marsh 1970). Sand surface areas were calculated using dimensions of Plexiglas tubes that were utilized for sand core sampling (surface area = $\pi \times$ radius^2). V represented the volume of seawater in the incubation bag.

The daily rates of different processes (in mmol N m^{-2} d^{-1}) represent the average rates under light and dark conditions. In this study, the reduction rate of NO_3^- was indicated by the rate of decrease of NO_3^- in $^{15}NO_3^-$ amended incubation. Thus, the total reduction rate of NO_3^- minus the sum of denitrification and DNRA rates represents the rate of other NO_3^- reduction processes such as assimilation. If the total reduction rate of NO_3^- was negative, it indicates net NO_3^- production, in which case the contribution of other NO_3^- reduction processes was considered to be nonexistent. The integrated rates of denitrification and DNRA were extrapolated by multiplying the areal rates by the cover areas of benthic categories and the corresponding 2D-to-3D conversion factor, as described by El-Khaled et al. (2021b).

The normality of the data and homogeneity of variances were tested using Shapiro–Wilk and Levene's tests, respectively. A 3-way PERMANOVA was used to test for significant differences in denitrification and DNRA rates between different benthic categories, NO_3^- dose (10 or 20 μM), or light conditions (light or dark). If significant differences were detected, pairwise t-tests accompanied by Mann–Whitney-Rank-sum tests were conducted. Type III (partial) sum of squares was utilized with an unrestricted permutation of raw data (999 permutations). A post-hoc Tukey test was used to identify which specific benthic groups significantly differed. Integrated rates of denitrification and DNRA were calculated based on the sum of means of extrapolated rates of individual benthic categories and the respective standard propagated error, with Friedman's aligned rank test checking for significant differences between 10 and 20 μM of NO_3^- amended conditions. The PERMANOVA was performed using Primer v7, and the remaining statistical analyses were performed using Statistical Package for the Social Sciences (SPSS) v26. All the statistical significance was assessed at the criterion of $p = 0.05$. SigmaPlot (Version 12.0) was used to create the figures.

Results

The potential rates of total NO_3^- reduction (−1.8–5.0 mmol N m^{-2} d^{-1}), denitrification (0.1–5.6 mmol N m^{-2} d^{-1}), DNRA (0.1–1.8 mmol N m^{-2} d^{-1}) and anammox (0.01–0.10 mmol N m^{-2} d^{-1}) for different benthic categories of the coral reefs under varying light and NO_3^- concentration conditions are listed in Supporting Information Table S1. Compared with denitrification, anammox contributed only 5% ± 3% to total N removal; therefore, 3-way PERMANOVA tests were exclusively applied to compare denitrification and DNRA processes (Supporting Information Table S2). In contrast to benthic categories, the NO_3^- reduction rate in the seawater only, as control group, was negligible (Supporting Information Fig. S1). Subsequently, integrating the 3-way PERMANOVA results with the hypotheses proposed in this study, we reveal: (1) variations in daily rates (calculated as the average of light and dark condition rates) across different categories; (2) responses to varying NO_3^- concentrations; (3) light–dark contrasts in potential denitrification and DNRA rates; and (4) integrated rates of NO_3^- reduction processes across benthic categories relative to reef areas.

Rates of NO_3^- reduction processes varied among different benthic categories

The results of the 3-way PERMANOVA indicate that the potential rates of denitrification (3-way PERMANOVA, $F_{5,48} = 10.3$, $p < 0.001$) and DNRA (3-way PERMANOVA, $F_{5,48} = 5.34$, $p < 0.001$) were statistically significantly different among different benthic categories (Supporting Information Table S2; Fig. 2). The daily rates of total NO_3^- reduction ranged from 0.07 to 2.1 mmol N m^{-2} d^{-1} (Fig. 2a). Denitrification was the predominant reduction process (0.1–3.0 mmol N m^{-2} d^{-1}), followed by DNRA (0.1–1.1 mmol N m^{-2} d^{-1}; Fig. 2). The daily rates of denitrification in turf algae, *G. fascicularis*, and biogenic rock were 2–8 times higher than those in sediments, *A. muricata*, and coral rubble (Fig. 2b). Although the daily rates of DNRA in sediments

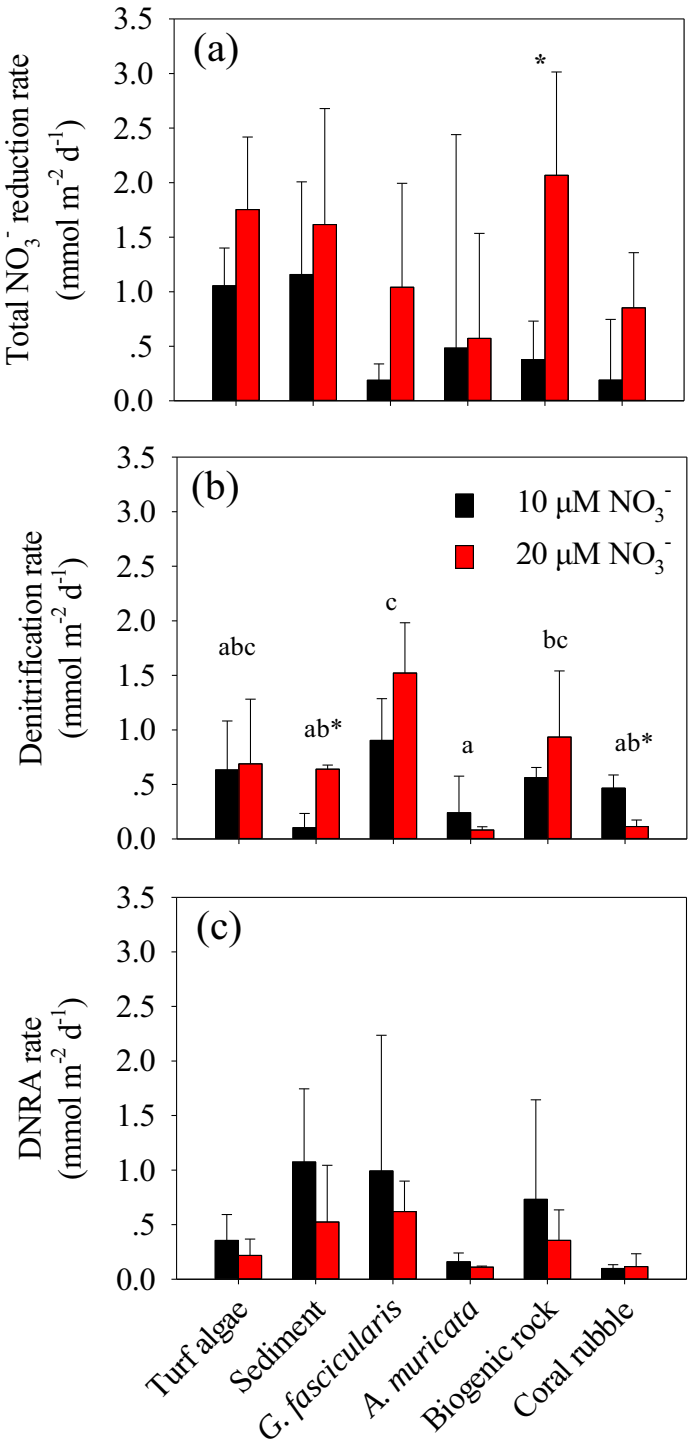


Fig. 2. The daily rates of total NO_3^- reduction (**a**), denitrification (**b**) and DNRA (**c**) of different benthic categories including turf algae, sediment, *Galaxea fascicularis*, *Acropora muricata*, biogenic rock, and coral rubble under NO_3^- amended conditions at the level of 10 and 20 μM, respectively. The error bars show standard deviation (SD). The different letters above histograms denote statistical differences between benthic categories (Tukey tests, $p < 0.05$), and asterisks indicate significant differences in each category between two NO_3^- amended groups (Mann–Whitney *U* tests, $p < 0.05$).

and *G. fascicularis* were 5–10 times higher than those in *A. muricata* and coral rubble, the high variability in DNRA between parallel samples resulted in only marginally significant differences among benthic categories (Tukey test, $p = 0.055$; Fig. 2c). The total DO consumption rate across different benthic categories ranged from 11 to 27 mmol m^{-2} d^{-1}, with the rates of *G. fascicularis* and coral rubble being the highest and lowest, respectively. At the end of the incubation, no severe hypoxic conditions were formed inside the incubation bags, with DO concentrations ranging from 51 to 110 μM (Supporting Information Table S3).

Rates of NO_3^- reduction processes under varied NO_3^- concentration

The potential rates of denitrification (3-way PERMANOVA, $F_{1,48} = 0.173$, $p = 0.869$) and DNRA (3-way PERMANOVA, $F_{1,48} = 1.65$, $p = 0.184$) did not significantly differ between 10 and 20 μM of $^{15}NO_3^-$ groups, while the interactive effect of benthic types and NO_3^- dose was significant for denitrification rates (3-way PERMANOVA, $F_{5,48} = 4.40$, $p < 0.001$; Supporting Information Table S2; Fig. 2).

The daily rates of denitrification were 0.21–2.0 and 0.12–3.0 mmol N m^{-2} d^{-1} under 10 and 20 μM NO_3^- conditions, respectively (Fig. 2b). When the NO_3^- concentration increased from 10 to 20 μM, significant changes in denitrification were observed only in sediments and coral rubble (Fig. 2b). The denitrification rate in sediments significantly increased by 6 times (Mann–Whitney *U*, $p < 0.05$), whereas the rate in coral rubble significantly decreased by 75% (Mann–Whitney *U*, $p < 0.05$). The daily rates of DNRA were 0.10–1.07 mmol N m^{-2} d^{-1} under the 10 μM NO_3^- condition and 0.11–0.62 mmol N m^{-2} d^{-1} under the 20 μM NO_3^- condition, respectively (Fig. 2c). However, no significant differences in DNRA rates were observed under different NO_3^- concentrations (Mann–Whitney *U*, $p > 0.05$).

Under the 10 μM NO_3^- condition, denitrification was the predominant NO_3^- reduction process (61%–91%) in all benthic categories of the coral reefs, except in sediments. Denitrification rates were 1.5–9.5 times higher than DNRA rates, but the DNRA rate in sediments was 5 times higher than the denitrification rate (Fig. 3a). When the NO_3^- concentrations increased to 20 μM, denitrification contributions exceeded DNRA in all categories, with ratios ranging from 1.5 to 6.3. However, the contribution of other NO_3^- reduction processes significantly increased in turf algae (9%, Mann–Whitney *U*, $p < 0.05$), *A. muricata* (52%, Mann–Whitney *U*, $p < 0.05$), and coral rubble (60%, Mann–Whitney *U*, $p < 0.05$; Fig. 3b).

Rates of NO_3^- reduction processes under light and dark conditions

Light condition had a significant effect on denitrification (3-way PERMANOVA, $F_{1,48} = 11.2$, $p < 0.001$) and DNRA (3-way PERMANOVA, $F_{1,48} = 4.41$, $p = 0.025$), and the interac-

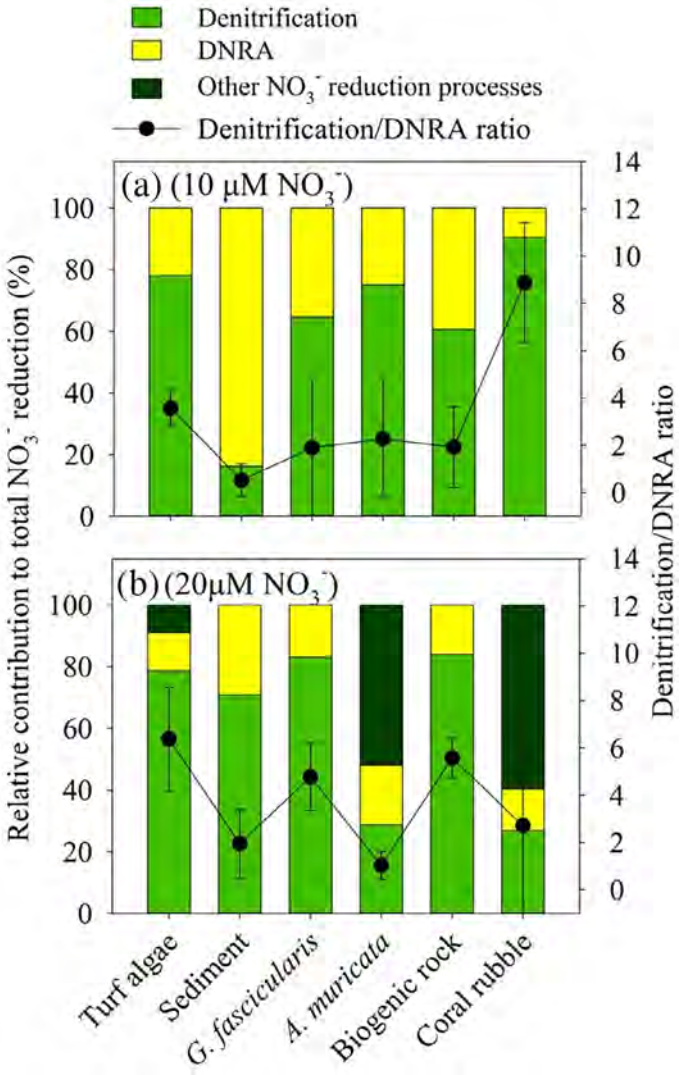


Fig. 3. Relative contribution of denitrification and DNRA to total NO_3^- reduction, and denitrification/DNRA ratios of studied benthic categories including turf algae, sediment, *Galaxea fascicularis*, *Acropora muricata*, biogenic rock, and coral rubble under 10 μM (**a**) and 20 μM (**b**) NO_3^- enriched conditions. Other NO_3^- reduction processes represented NO_3^- reduction pathways excluding denitrification and DNRA, such as assimilation, which were determined by subtracting the sum of denitrification and DNRA rates from the total NO_3^- reduction rate.

tive effect of benthic types and light was significant for both rates, while the interactive effect of light and NO_3^- dose was not significant for both rates (Supporting Information Table S3).

Under different NO_3^- concentration conditions, light affected the rates of total NO_3^- reduction, though some differences were not statistically significant due to high variability between parallel samples. In fact, the rates of total NO_3^- reduction for benthic categories such as sediments, *A. muricata*, and coral rubble were negative under light conditions (Fig. 4a,b), indicating active NO_3^- production by nitrification. The denitrification rates of benthic categories under light and dark conditions were 0.06–1.9 and 0.2–5.6 mmol N m^{-2} d^{-1}, respectively. Regardless of NO_3^- concentration, the denitrification rate in *G. fascicularis* was several times higher than that in *A. muricata* (Tukey tests, $p < 0.05$). Compared to light conditions, the denitrification rates in turf algae, sediments, *G. fascicularis*, and *A. muricata* increased 2- to 10-fold under dark conditions (Fig. 4c,d). Consequently, the contribution of denitrification to the total reduction of NO_3^- slightly increased from 53% ± 31% under light conditions to 67% ± 24% under dark conditions (Supporting Information Fig. S2).

Due to the great variability in DNRA rates under 10 μM conditions, the differences in rates among different categories were not statistically significant. However, under 20 μM conditions, the DNRA rate in *G. fascicularis* was 5 times higher than that in coral rubble and *A. muricata* (Mann–Whitney U, $p < 0.05$). Similar to denitrification, DNRA rates under dark conditions (0.07–1.8 mmol N m^{-2} d^{-1}) were higher than those under light conditions (0.01–1.3 mmol N m^{-2} d^{-1}; Fig. 4e,f).

Integrated rates of NO_3^- reduction processes in different benthic categories referred to reef areas

The integrated rates of denitrification and DNRA were extrapolated by multiplying the areal rates by the cover areas of benthic categories, with the units being mmol N m^{-2} benthic area d^{-1}, respectively, at 10 μM of NO_3^- condition, and 5.5 ± 1.6 and 1.2 ± 0.8 mmol N m^{-2} benthic area d^{-1}, respectively, at 20 μM of NO_3^- condition. The rates were similar under NO_3^- amended conditions at the level of 10 and 20 μM (Friedman's aligned rank test, $p > 0.05$; Fig. 5). However, the integrated rate of denitrification was 3–4 times higher than the DNRA rate at 20 μM NO_3^- condition (Friedman's aligned rank test, $p = 0.083$).

Biogenic rock and massive corals (representative species *G. fascicularis*) contributed the most to denitrification (27–40%), followed by turf algae (18–20%) and coral rubble (5–23%), while other categories contributed less than 5% to denitrification (Fig. 6). Similarly, massive corals and biogenic rock accounted for 34–41% of DNRA activity, followed by turf algae (13–14%) and coral rubble (6–11%), while other categories contributed less than 3% to DNRA.

Compared to N-limited coral reefs, the integrated denitrification rate of the eutrophic Weizhou Island was two orders of magnitude higher (Fig. 7). However, due to the lack of DNRA data for different categories in N-limited coral reefs in the literature (Table 1), a direct comparison of integrated DNRA rates between different reefs could not be made. When NO_3^- concentrations increased further from 10 to 20 μM, the integrated rates of denitrification and DNRA in the coral reefs of Weizhou Island did not change significantly, suggesting that the additional NO_3^- was

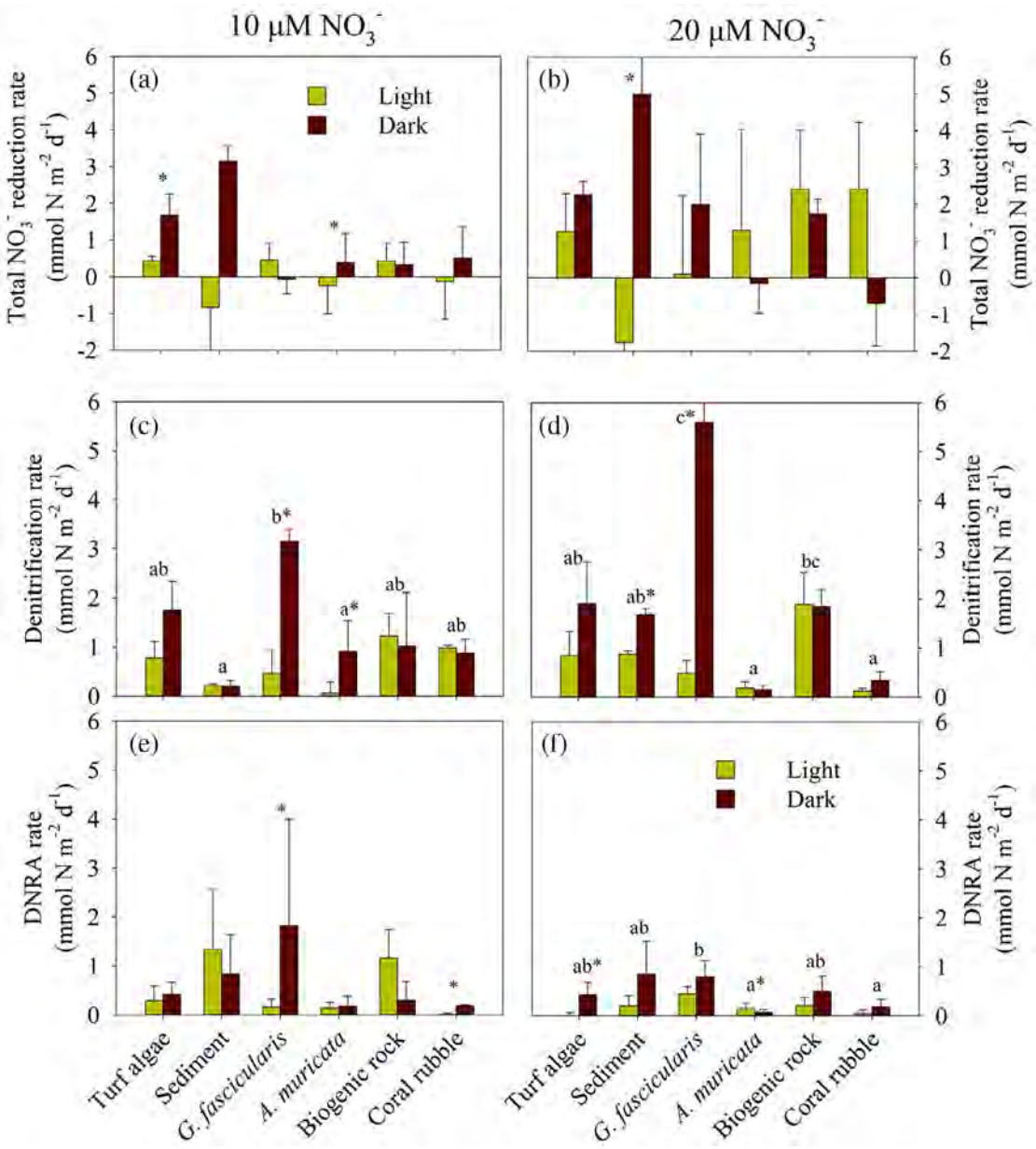


Fig. 4. Total NO_3^- reduction (**a**, **b**), denitrification (**c**, **d**) and DNRA (**e**, **f**) rates of different benthic categories, including turf algae, sediment, *Galaxea fascicularis*, *Acropora muricata*, biogenic rock, and coral rubble under light and dark conditions in the 10 μM (left panels) and 20 μM (right panels) $^{15}NO_3^-$ added groups. The error bars show standard deviation (SD). The different letters above histograms denote statistical differences between benthic categories (Tukey tests, $p < 0.05$), and asterisks indicate significant differences in each category between light and dark conditions (Mann–Whitney *U* tests, $p < 0.05$).

primarily assimilated by algae, thereby altering the structure of benthic categories (Fig. 7).

Discussion

To investigate the differences in denitrification and DNRA across different benthic categories and their response to varying NO_3^- concentrations, we utilized the ^{15}N isotope tracer techniques to measure the potential rates of denitrification and DNRA in different categories under different NO_3^- concentrations and light/dark conditions. The 3-way PERMANOVA results indicate that benthic categories, light conditions, and their interactive effects were key factors influencing the potential rates of denitrification and DNRA in benthic categories of the coral reefs. However, no significant differences were observed in denitrification and DNRA rates under 10 and 20 μM NO_3^- concentration conditions. The daily rates of denitrification and DNRA in

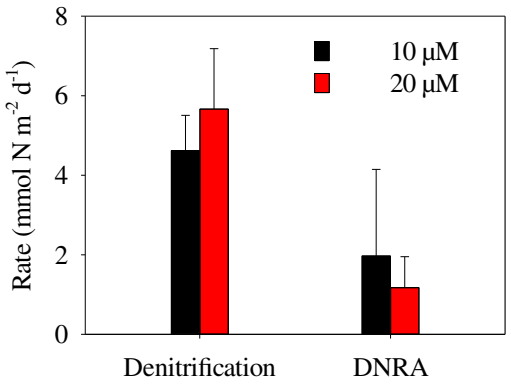


Fig. 5. Integrated rates of denitrification and DNRA (calculated as sum of means of extrapolated rates of individual benthic categories ± standard propagated error) under NO_3^- amended conditions at the level of 10 and 20 μM, respectively. No significant differences were observed by applying Friedman's aligned rank test.

G. fascicularis and biogenic rock were several times higher than those in *A. muricata* and coral rubble, with rates under dark conditions generally higher than those under light conditions. Extrapolating these findings to provide an approximate N budget for specific categories of the coral reefs, we found that biogenic rock and *G. fascicularis* contributed the most to denitrification and DNRA, followed by turf algae and coral rubble, while other categories contributed less than 5%.

Differences in dissimilatory NO_3^- reduction among benthic categories of coral reefs

Various benthic categories that make up coral reefs harbor co-associated microorganisms and can provide anaerobic environments and reactive substrates (El-Khaled et al. 2021b), thereby facilitating comprehensive denitrification and DNRA processes in the benthic categories of coral reefs. Except for the sediment, the denitrification rates of all other categories were higher than the DNRA rates. This is because the free energy required for reducing NO_3^- to NH_4^+ in the DNRA process is higher than that for reducing NO_3^- to N_2O or N_2 in the denitrification process, making denitrification more favorable. Nevertheless, some factors such as higher salinity, temperature, and carbon-to-N ratios (C : N) can favor the DNRA process (Dunn et al. 2013; Kraft et al. 2014). These differences in properties likely result in the DNRA process dominating dissimilatory NO_3^- reduction in the Weizhou Island sediments. Indeed, in our previous research on Weizhou Island (Ning et al. 2022), the C : N ratio of sediments (7.3–16) was higher than that of the coral *Acropora millepora* (6.2–9.6) and turf algae (9.0–13) (Entsch et al. 1983).

Interestingly, the contribution of anammox was negligible across benthic categories in the coral reefs of Weizhou Island, despite the widespread presence of anammox bacteria in coral reefs (Zhang et al. 2015). Similar findings have been reported in other coral reef studies (Eyre et al. 2008; Rädecker et al. 2015). This could be attributed to the abundance of

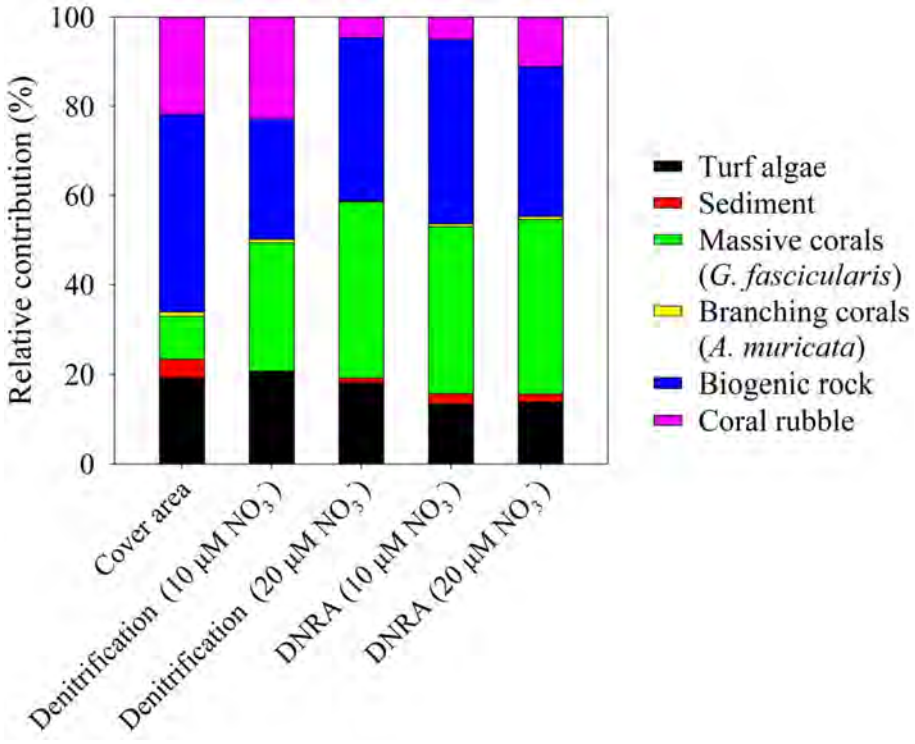


Fig. 6. Relative benthic cover and relative contribution of studied benthic categories including turf algae, sediment, *Galaxea fascicularis*, *Acropora muricata*, biogenic rock, and coral rubble to denitrification and DNRA under varied NO_3^- conditions.

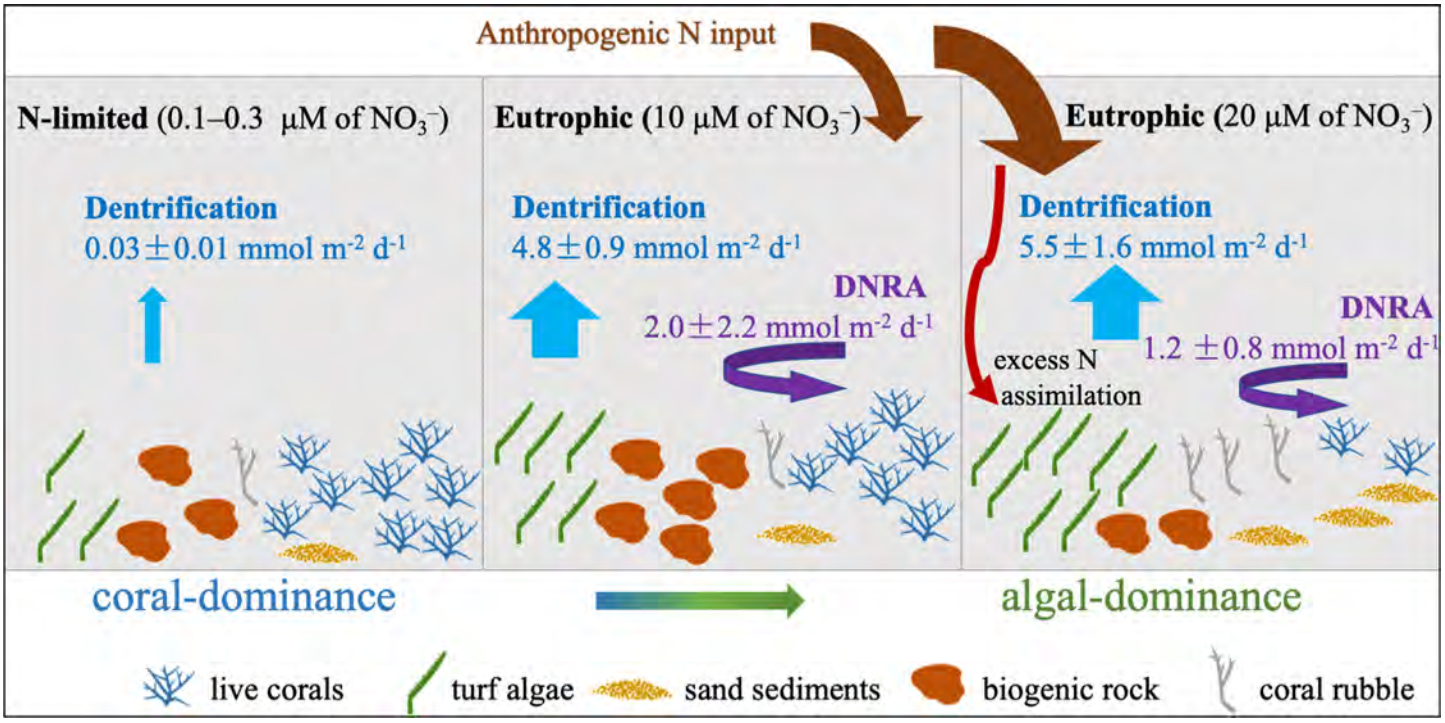


Fig. 7. Changes in the structure of benthic categories and the integrated rates of denitrification and DNRA in eutrophic (N-enriched) reef ecosystems (e.g., the coral reefs of Weizhou Island) under different N levels, including comparisons with other N-limited coral reefs (El-Khaled et al. 2021b). Due to the lack of DNRA rate data for benthic categories other than sediments and corals in N-limited coral reefs in the literature (Table 1), it is not possible to provide the integrated rate of DNRA for this area.

active organic matter in coral reefs, which interacts with microorganisms (Nelson et al. 2023). Such organic matter, serving as an energy supply and food source, favors heterotrophic denitrifying bacteria and DNRA bacteria over autotrophic anammox bacteria, whose activity is less significant (Nizzoli et al. 2010; Song et al. 2013). Additionally, high temperatures are another factor inhibiting anammox bacterial activity (Canion et al. 2014; Tan et al. 2020), making the anammox process less prominent in tropical coral reef regions.

The 3-way PERMANOVA results indicated that NO_3^- concentration was not the primary factor regulating the denitrification and DNRA rates of benthic categories of the coral reefs (Supporting Information Table S2). This suggests that the differences in organic matter content are the reason for the observed differences in the denitrification and DNRA rates of benthic categories. For instance, the organic matter produced by the photosynthesis of symbiotic zooxanthellae or captured through heterotrophic feeding by live corals provides energy for the coral holobiont (Xu et al. 2020). In contrast, the dissimilatory NO_3^- reduction in coral rubble relies solely on the organic matter adsorbed on its surface (El-Khaled et al. 2021b). Consequently, coral rubble exhibited the lowest rates of denitrification and DNRA, whereas the rates were higher in other live categories. Indeed, the rate of total DO consumption, representing organic matter activity, was the lowest in coral rubble (Supporting Information Table S3).

The DO consumption processes in benthic categories create internal anaerobic environments that facilitate anaerobic dissimilatory NO_3^- reduction processes. Simultaneously, chemical gradients develop between the internal and external environments of various benthic categories, facilitating efficient material transport (Santos et al. 2012; Babbin et al. 2021; Engelberts et al. 2021). Consequently, the consumption of dissolved oxygen leads to generally higher NO_3^- reduction rates under dark conditions compared to light conditions (Fig. 5). This is particularly evident in benthic categories with abundant algae, such as turf algae and *G. fascicularis*, where the rates differ significantly between light and dark conditions due to the influence of algal photosynthesis on dissolved oxygen levels.

The dissimilatory NO_3^- reduction rates vary significantly among different coral species, and one potential reason for this is the density of symbiotic zooxanthellae. The trophic status (i.e., autotrophy/heterotrophy) of corals may affect the activity of associated denitrifying bacteria. For corals with symbionts, the energy supply for denitrifying bacteria comes from the photosynthesis of symbiotic zooxanthellae, making denitrification in autotrophic corals stronger than that in heterotrophic corals (Tilstra et al. 2019; El-Khaled et al. 2021b). Xiang et al. (2022) also indicate that the presence of symbiotic zooxanthellae increases the abundance and alters the community structure of denitrifiers. Previous studies on 117 coral

samples from the coral reefs of Weizhou Island, including five genera, found that the zooxanthellae density, contribution of heterotrophic predation, and photosynthetic activity were higher in massive corals compared to branching corals (Xu et al. 2020). Consequently, the rates of denitrification and DNRA in the massive coral *G. fascicularis* were significantly higher than in the branching coral *A. muricata*. Additionally, the greater tissue thickness of massive corals compared to branching coral (Qin et al. 2020) helps form anaerobic environments within the corals (Babbin et al. 2021), which is another important factor contributing to the differences in NO_3^- reduction rates among different coral species. Therefore, the significant differences in denitrification and DNRA rates among benthic categories can be attributed to variations in physiological traits, C : N ratio, as well as symbiont density. However, future studies should characterize both the N cycling communities and the functional genes related to denitrification, anammox, and DNRA using tools such as 16S sequencing and qPCR. This will allow for a comprehensive analysis of the differences in denitrification mechanisms among various benthic categories and their associated microorganisms.

Response of NO_3^- reduction processes in coral reefs to different NO_3^- concentrations and its ecological implications

The total denitrification capacity and DNRA potential of the coral reefs were simultaneously influenced by the denitrification and DNRA rates of individual benthic categories and their respective coverage areas. The coral reefs of Weizhou Island, degraded by climate warming and human activities, have a significant proportion of coral rubble, accounting for 18% of the area (Liao et al. 2019). However, due to the low activity of associated denitrifying bacteria, coral rubbles contribute minimally to N removal and DNRA. In contrast, massive corals, which exhibit relatively higher tolerance to environmental stress, have become the dominant species on the coral reefs of Weizhou Island, covering 8% of the area (Yu et al. 2019). Massive corals *G. fascicularis*, with the highest individual denitrification rate, make the most substantial contribution to N removal among the six benthic categories. Biogenic rocks, which constitute the largest benthic category in this study, contribute to N removal at a level comparable to that of massive corals. However, under human influence, turf algae can rapidly take over bare substrates due to high growth rates (McManus and Polsenberg 2004; Liao et al. 2021; Roth et al. 2021), potentially weakening the total N removal capacity of the coral reef area.

Denitrification rates within a single benthic category can vary by orders of magnitude. For example, sedimentary denitrification rates differ by an order of magnitude depending on the porewater advection rate (Santos et al. 2012). However, reef sands solely cover a minor fraction of the benthic cover, so their contribution to N removal in the coral reefs of Weizhou Island remains limited, consistent with findings from other coral reef regions (El-Khaled et al. 2021b). Additionally, the denitrification rate of the same benthic category differs greatly across regions. For instance, while the coral cover is not high, denitrification rates of the corals at Weizhou Island are 1–2 orders of magnitude higher than those of Red Sea reefs (El-Khaled et al. 2021b), Caribbean reefs (Babbin et al. 2021), and the southern Great Barrier Reefs (Glaze et al. 2022). In contrast, the DIN concentrations in these regions are only 0.1–0.3 μM, whereas the DIN concentrations in the waters around Weizhou Island are 1–2 orders of magnitude higher. Such high DIN levels also inhibit N_2 fixation on the coral reefs of Weizhou Island, as the N_2 fixation rates in other coral reef regions are several times higher than those in the corals of Weizhou Island (Tilstra et al. 2019; Glaze et al. 2022; Ning et al. 2022). Therefore, the higher DIN concentrations in the coral reefs of Weizhou Island may enhance the total N removal capacity of this region. El-Khaled et al. (2021a) also found that the denitrification rates in the Red Sea reef increased 76-fold when NO_3^- concentrations were increased to 10 μM.

The overall N removal capacity of the coral reefs of Weizhou Island was two orders of magnitude higher than that of the Red Sea reefs (El-Khaled et al. 2021b). When NO_3^- concentrations were increased from 10 to 20 μM, although the ratio of denitrification to DNRA increased, changes in the integrated rates of denitrification and DNRA in the benthic categories of the coral reefs were not significant. Instead, the additional NO_3^- was utilized by algae, particularly turf algae, which used the increased NO_3^- for other processes (Fig. 7). This shift could drive the ecosystem from coral dominance to algal dominance (Holmes and Johnstone 2010; Karcher et al. 2020). Therefore, it is crucial to strictly control the discharge of anthropogenic N from land-based sources to reduce the risk of coral reef degradation due to excess N.

It should be noted that, in addition to the benthic categories focused on in this study, other common reef communities such as sponges and soft corals, which are known for their significant denitrification capabilities (Pawlik and McMurray 2020; El-Khaled et al. 2021b), were not assessed due to their scarcity in the study area. Their contributions to denitrification in response to increased NO_3^- concentrations still need to be evaluated. One limitation that should be addressed is that this study includes only one branching and one massive coral. We recommend that future studies incorporate a greater variety of coral species, as species-specific differences in denitrification rates have been documented in previous research (Tilstra et al. 2019). Additionally, the dissimilatory NO_3^- reduction rates observed in this study represent the short-term responses of benthic categories under NO_3^- enrichment. Long-term N enrichment may lead to disruptions in coral–algal symbiosis, such as coral bleaching, which would weaken denitrification (Rosset et al. 2017; Xiang et al. 2022). On the other hand, coral degradation could lead to shifts in benthic

community composition. A previous study has shown that denitrification and N_2 fixation rates exhibit no significant differences between coral-dominated and algae-dominated communities (El-Khaled et al. 2021b). However, it remains essential to conduct more extensive observations to understand the response dynamics of dissimilatory NO_3^- reduction in benthic categories under long-term N enrichment.

Conclusions

Here, we present evidence of denitrification and DNRA activities across various benthic categories, including turf algae, sediment, *G. fascicularis*, *A. muricata*, biogenic rock, and coral rubble in eutrophic coral reefs. Similar to denitrification rates, DNRA rates varied significantly among different categories. These differences can be attributed to variations in physiological morphology, C : N ratio, and the density of symbiotic algae among the benthic categories. Light availability influenced denitrification and DNRA potentials through its effect on algal photosynthesis and respiration, resulting in higher rates in turf algae, *G. fascicularis*, and *A. muricata* in the dark compared to light conditions. *G. fascicularis* exhibited significantly higher DNRA and denitrification rates than *A. muricata* due to its thicker tissue and higher density of symbiotic zooxanthellae.

Through rough estimates, the integrated rate of denitrification in the N-enriched coral reefs was two orders of magnitude higher than that in the N-limited coral reefs. However, continued anthropogenic N inputs might not enhance the integrated rates of denitrification and DNRA but could instead accelerate the growth of turf algae or other benthic macroalgae, exacerbating ecosystem degradation. Biogenic rock and massive coral species like *G. fascicularis* exhibited the highest N removal potential in the coral reefs of Weizhou Island. While it is crucial to implement strict controls on N emissions, the protection of these key benthic categories is equally important. However, it is worth noting that the potential rates observed in this study were derived from short-term N enrichment experiments. The long-term impacts on category-specific potential rates and the integrated rates of denitrification and DNRA in the reef ecosystem warrant further investigation.

Author Contributions

Zhiming Ning conceptualized the project, conducted the field work, analyzed samples and data, and wrote the manuscript. Zhijin Liu and Ronglin Xia conducted the field work and analyzed samples and data. Kefu Yu, Wei Jiang, and Bin Yang aided in conceptualizing the project, provided support, and edited the manuscript. Guodong Song conceptualized the project, provided support, analyzed samples and data, as well as edited the manuscript.

Acknowledgments

We sincerely thank the two anonymous reviewers for their insightful comments and constructive suggestions. We used the AI tool ChatGPT to refine the language of this paper, thoroughly reviewing and revising its edits to ensure they align with our intended meaning. This work was financially supported by the National Natural Science Foundation of China (Grant 42030502 and 42376044), the Guangxi Science and Technology Program (AD25069075), and the NSFC grants (42090041 and 42166002), and supported by the MCTL Visiting Fellowship Program.

Conflicts of Interest

None declared.

References

Babbin, A. R., T. Tamasi, D. Dumit, et al. 2021. "Discovery and Quantification of Anaerobic Nitrogen Metabolisms among Oxygenated Tropical Cuban Stony Corals." *The ISME Journal* 15, no. 4: 1222–1235. https://doi.org/10.1038/s41396-020-00845-2.

Canion, A., J. E. Kostka, T. M. Gihring, et al. 2014. "Temperature Response of Denitrification and Anammox Reveals the Adaptation of Microbial Communities to In Situ Temperatures in Permeable Marine Sediments that Span 50° in Latitude." *Biogeosciences* 11, no. 2: 309–320. https://doi.org/10.5194/bg-11-309-2014.

Cardini, U., V. N. Bednarz, N. van Hoytema, et al. 2016. "Budget of Primary Production and Dinitrogen Fixation in a Highly Seasonal Red Sea Coral Reef." *Ecosystems* 19, no. 5: 771–785. https://doi.org/10.1007/s10021-016-9966-1.

Dalsgaard, T., B. Thamdrup, and D. E. Canfield. 2005. "Anaerobic Ammonium Oxidation (Anammox) in the Marine Environment." *Research in Microbiology* 156: 457–464. https://doi.org/10.1016/j.resmic.2005.01.011.

Devol, A. H. 2015. "Denitrification, Anammox, and N_2 Production in Marine Sediments." *Annual Review of Marine Science* 7: 403–423. https://doi.org/10.1146/annurev-marine-010213-135040.

Dunn, R. J. K., D. Robertson, P. R. Teasdale, N. J. Waltham, and D. T. Welsh. 2013. "Benthic Metabolism and Nitrogen Dynamics in an Urbanised Tidal Creek: Domination of DNRA Over Denitrification as a Nitrate Reduction Pathway." *Estuarine, Coastal and Shelf Science* 131: 271–281. https://doi.org/10.1016/j.ecss.2013.06.027.

Eakin, C. M., H. P. A. Sweatman, and R. E. Brainard. 2019. "The 2014–2017 Global-Scale Coral Bleaching Event: Insights and Impacts." *Coral Reefs* 38, no. 4: 539–545. https://doi.org/10.1007/s00338-019-01844-2.

El-Khaled, Y. C., R. Nafeh, F. Roth, et al. 2021*a*. "High Plasticity of Nitrogen Fixation and Denitrification of Common Coral Reef Substrates in Response to Nitrate Availability." *Marine Pollution Bulletin* 168: 112430. https://doi.org/10.1016/j.marpolbul.2021.112430.

El-Khaled, Y. C., F. Roth, N. Rädecker, et al. 2020. "Simultaneous Measurements of Dinitrogen Fixation and Denitrification Associated With Coral Reef Substrates: Advantages and Limitations of a Combined Acetylene Assay." *Frontiers in Marine Science* 7: 411. https://doi.org/10.3389/fmars.2020.00411.

El-Khaled, Y. C., F. Roth, N. Rädecker, et al. 2021*b*. "Nitrogen Fixation and Denitrification Activity Differ Between Coral- and Algae-Dominated Red Sea Reefs." *Scientific Reports* 11, no. 1: 11820. https://doi.org/10.1038/s41598-021-90204-8.

Engelberts, J. P., S. J. Robbins, K. Damjanovic, and N. S. Webster. 2021. "Integrating Novel Tools to Elucidate the Metabolic Basis of Microbial Symbiosis in Reef Holobionts." *Marine Biology* 168, no. 12: 175. https://doi.org/10.1007/s00227-021-03952-6.

Entsch, B., K. Boto, R. G. Sim, and J. Wellington. 1983. "Phosphorus and Nitrogen in Coral Reef Sediments." *Limnology and Oceanography* 28, no. 3: 465–476. https://doi.org/10.4319/lo.1983.28.3.0465.

Erler, D. V., I. R. Santos, and B. D. Eyre. 2014. "Inorganic Nitrogen Transformations Within Permeable Carbonate Sands." *Continental Shelf Research* 77: 69–80. https://doi.org/10.1016/j.csr.2014.02.002.

Erler, D. V.,L. A. Trott, D. M. Alongi, and B. D. Eyre. 2013. "Denitrification, Anammox and Nitrate Reduction in Sediments of the Southern Great Barrier Reef Lagoon." *Marine Ecology Progress Series* 478: 57–70. https://doi.org/10.3354/meps10040.

Eyre, B. D., R. N. Glud, and N. Patten. 2008. "Mass Coral Spawning: A Natural Large-Scale Nutrient Addition Experiment." *Limnology and Oceanography* 53, no. 3: 997–1013. https://doi.org/10.4319/lo.2008.53.3.0997.

Fossing, H., V. A. Gallardo, B. B. Jørgensen, et al. 1995. "Concentration and Transport of Nitrate by the Mat-Forming Sulfur Bacterium *Thioploca*." *Nature* 374: 713–715. https://doi.org/10.1038/374713a0.

Glaze, T. D., D. V. Erler, and H. M. P. Siljanen. 2022. "Microbially Facilitated Nitrogen Cycling in Tropical Corals." *The ISME Journal* 16: 68–77. https://doi.org/10.1038/s41396-021-01038-1.

Holmes, G., and R. W. Johnstone. 2010. "The Role of Coral Mortality in Nitrogen Dynamics on Coral Reefs." *Journal of Experimental Marine Biology and Ecology* 387, no. 1–2: 1–8. https://doi.org/10.1016/j.jembe.2010.03.006.

Hutchins, D. A., and D. G. Capone. 2022. "The Marine Nitrogen Cycle: New Developments and Global Change." *Nature Reviews. Microbiology* 20: 401–414. https://doi.org/10.1038/s41579-022-00687-z.

Joye, S. B., S. V. Smith, J. T. Hollibaugh, and H. W. Paerl. 1996. "Estimating Denitrification Rates in Estuarine Sediments: A Comparison of Stoichiometric and Acetylene Based Methods." *Biogeochemistry* 33, no. 3: 197–215. https://doi.org/10.1007/BF02181072.

Kamp, A., D. de Beer, J. L. Nitsch, G. Lavik, and P. Stief. 2011. "Diatoms Respire Nitrate to Survive Dark and Anoxic Conditions." *Proceedings of the National Academy of Sciences of the United States of America* 108: 5649–5654. https://doi.org/10.1073/pnas.1015744108.

Karcher, D. B., F. Roth, S. Carvalho, et al. 2020. "Nitrogen Eutrophication Particularly Promotes Turf Algae in Coral Reefs of the Central Red Sea." *PeerJ* 8: e8737. https://doi.org/10.7717/peerj.8737.

Kraft, B., H. E. Tegetmeyer, R. Sharma, et al. 2014. "The Environmental Controls That Govern the End Product of Bacterial Nitrate Respiration." *Science* 345, no. 6197: 676–679. https://doi.org/10.1126/science.1254070.

Liao, Z., K. Yu, B. Chen, X. Huang, Z. Qin, and X. Yu. 2021. "Spatial Distribution of Benthic Algae in the South China Sea: Responses to Gradually Changing Environmental Factors and Ecological Impacts on Coral Communities." *Diversity and Distributions* 27, no. 5: 929–943. https://doi.org/10.1111/ddi.13243.

Liao, Z., K. Yu, Y. Wang, X. Huang, and L. Xu. 2019. "Coral–Algal Interactions at Weizhou Island in the Northern South China Sea: Variations by Taxa and the Exacerbating Impact of Sediments Trapped in Turf Algae." *PeerJ* 7: e6590. https://doi.org/10.7717/peerj.6590.

Marangoni, L. F. B., C. Ferrier-Pagès, C. Rottier, A. Bianchini, and R. Grover. 2020. "Unravelling the Different Causes of Nitrate and Ammonium Effects on Coral Bleaching." *Scientific Reports* 10, no. 1: 11975. https://doi.org/10.1038/s41598-020-68916-0.

Marsh, J. A., Jr. 1970. "Primary Productivity of Reef-Building Calcareous Red Algae." *Ecology* 51, no. 2: 255–263. https://doi.org/10.2307/1933661.

McManus, J. W., and J. F. Polsenberg. 2004. "Coral–Algal Phase Shifts on Coral Reefs: Ecological and Environmental Aspects." *Progress in Oceanography* 60, no. 2: 263–279. https://doi.org/10.1016/j.pocean.2004.02.014.

Miyajima, T., M. Suzumura, Y. Umezawa, and I. Koike. 2001. "Microbiological Nitrogen Transformation in Carbonate Sediments of a Coral-Reef Lagoon and Associated Seagrass Beds." *Marine Ecology Progress Series* 217: 273–286. https://doi.org/10.3354/meps217273.

Morris, L. A., C. R. Voolstra, K. M. Quigley, D. G. Bourne, and L. K. Bay. 2019. "Nutrient Availability and Metabolism Affect the Stability of Coral–Symbiodiniaceae Symbioses." *Trends in Microbiology* 27, no. 8: 678–689. https://doi.org/10.1016/j.tim.2019.03.004.

Morrison, T. H., T. P. Hughes, W. N. Adger, K. Brown, and M. C. Lemos. 2019. "Save Reefs to Rescue All Ecosystems." *Nature* 573, no. 7774: 333–336. https://doi.org/10.1038/d41586-019-02737-8.

Nelson, C. E., L. Wegley Kelly, and A. F. Haas. 2023. "Microbial Interactions With Dissolved Organic Matter Are Central to Coral Reef Ecosystem Function and Resilience." *Annual Review of Marine Science* 15: 431–460. https://doi.org/10.1146/annurev-marine-042121-080917.

Ning, Z., C. Fang, K. Yu, et al. 2020. "Influences of Phosphorus Concentration and Porewater Advection on Phosphorus

Dynamics in Carbonate Sands Around the Weizhou Island, Northern South China Sea." *Marine Pollution Bulletin* 160: 111668. https://doi.org/10.1016/j.marpolbul.2020.111668.

Ning, Z., K. Yu, Y. Wang, et al. 2022. "Effects of Nutrient Enrichment and Skewed N : P Ratios on Physiology of Scleractinian Corals From Weizhou Island in the Northern South China Sea." *Marine Ecology Progress Series* 682: 111–122. https://doi.org/10.3354/meps13933.

Nizzoli, D., E. Carraro, V. Nigro, and P. Viaroli. 2010. "Effect of Organic Enrichment and Thermal Regime on Denitrification and Dissimilatory Nitrate Reduction to Ammonium (DNRA) in Hypolimnetic Sediments of Two Lowland Lakes." *Water Research* 44, no. 9: 2715–2724. https://doi.org/10.1016/j.watres.2010.02.002.

Normile, D. 2009. "Bringing Coral Reefs Back From the Living Dead." *Science* 325, no. 5940: 559–561. https://doi.org/10.1126/science.325_559.

Pan, K., X. Zheng, X. Liu, and H. Jiang. 2021. "Nitrogen Cycling in a Tropical Coral Reef Ecosystem Under Severe Anthropogenic Disturbance in Summer: Insights From Isotopic Compositions." *Water Research* 207: 117824. https://doi.org/10.1016/j.watres.2021.117824.

Pawlik, J. R., and S. E. McMurray. 2020. "The Emerging Ecological and Biogeochemical Importance of Sponges on Coral Reefs." *Annual Review of Marine Science* 12: 315–337. https://doi.org/10.1146/annurev-marine-010419-010807.

Qin, Z., K. Yu, Y. Liang, B. Chen, and X. Huang. 2020. "Latitudinal Variation in Reef Coral Tissue Thickness in the South China Sea: Potential Linkage With Coral Tolerance to Environmental Stress." *Science of the Total Environment* 711: 134610. https://doi.org/10.1016/j.scitotenv.2019.134610.

Rädecker, N., C. Pogoreutz, C. R. Voolstra, J. Wiedenmann, and C. Wild. 2015. "Nitrogen Cycling in Corals: The Key to Understanding Holobiont Functioning?" *Trends in Microbiology* 23, no. 8: 490–497. https://doi.org/10.1016/j.tim.2015.03.008.

Ren, H., Y. C. Chen, X. T. Wang, et al. 2017. "21st-Century Rise in Anthropogenic Nitrogen Deposition on a Remote Coral Reef." *Science* 356, no. 6339: 749–752. https://doi.org/10.1126/science.aal3869.

Rosset, S., J. Wiedenmann, A. J. Reed, and C. D'Angelo. 2017. "Phosphate Deficiency Promotes Coral Bleaching and Is Reflected by the Ultrastructure of Symbiotic Dinoflagellates." *Marine Pollution Bulletin* 118, no. 1–2: 180–187. https://doi.org/10.1016/j.marpolbul.2017.02.044.

Roth, F., Y. C. el-Khaled, D. B. Karcher, et al. 2021. "Nutrient Pollution Enhances Productivity and Framework Dissolution in Algae—But Not in Coral-Dominated Reef Communities." *Marine Pollution Bulletin* 168: 112444. https://doi.org/10.1016/j.marpolbul.2021.112444.

Santos, I. R., B. D. Eyre, and R. N. Glud. 2012. "Influence of Porewater Advection on Denitrification in Carbonate Sands: Evidence From Repacked Sediment Column Experiments." *Geochimica et Cosmochimica Acta* 96: 247–258. https://doi.org/10.1016/j.gca.2012.08.018.

Siboni, N., E. Ben-Dov, A. Sivan, and A. Kushmaro. 2008. "Global Distribution and Diversity of Coral-Associated Archaea and their Possible Role in the Coral Holobiont Nitrogen Cycle." *Environmental Microbiology* 10, no. 11: 2979–2990. https://doi.org/10.1111/j.1462-2920.2008.01718.x.

Song, G. D., S. M. Liu, M. M. M. Kuypers, and G. Lavik. 2016. "Application of the Isotope Pairing Technique in Sediments Where Anammox, Denitrification, and Dissimilatory Nitrate Reduction to Ammonium Coexist." *Limnology and Oceanography: Methods* 14, no. 12: 801–815. https://doi.org/10.1002/lom3.10127.

Song, G. D., S. M. Liu, H. Marchant, M. M. M. Kuypers, and G. Lavik. 2013. "Anammox, Denitrification and Dissimilatory Nitrate Reduction to Ammonium in the East China Sea Sediment." *Biogeosciences* 10, no. 11: 6851–6864. https://doi.org/10.5194/bg-10-6851-2013.

Tan, E., W. Zou, Z. Zheng, et al. 2020. "Warming Stimulates Sediment Denitrification at the Expense of Anaerobic Ammonium Oxidation." *Nature Climate Change* 10, no. 4: 349–355. https://doi.org/10.1038/s41558-020-0723-2.

Thamdrup, B. 2012. "New Pathways and Processes in the Global Nitrogen Cycle." *Annual Review of Ecology, Evolution, and Systematics* 43, no. 1: 407–428. https://doi.org/10.1146/annurev-ecolsys-102710-145048.

Thamdrup, B., and T. Dalsgaard. 2002. "Production of N_2 Through Anaerobic Ammonium Oxidation Coupled to Nitrate Reduction in Marine Sediments." *Applied and Environmental Microbiology* 68, no. 3: 1312–1318. https://doi.org/10.1128/aem.68.3.1312-1318.2002.

Tilstra, A., Y. C. El-Khaled, F. Roth, et al. 2019. "Denitrification Aligns With N_2 Fixation in Red Sea Corals." *Scientific Reports* 9: 19460. https://doi.org/10.1038/s41598-019-55408-z.

Wiedenmann, J., C. D'Angelo, E. G. Smith, et al. 2013. "Nutrient Enrichment Can Increase the Susceptibility of Reef Corals to Bleaching." *Nature Climate Change* 3, no. 2: 160–164. https://doi.org/10.1038/nclimate1661.

Xiang, N., N. Rädecker, C. Pogoreutz, et al. 2022. "Presence of Algal Symbionts Affects Denitrifying Bacterial Communities in the Sea Anemone Aiptasia Coral Model." *ISME Communications* 2: 105. https://doi.org/10.1038/s43705-022-00190-9.

Xu, H., G. Song, S. Yang, R. Zhu, G. Zhang, and S. Liu. 2022. "Benthic Nitrogen Cycling in the Deep Ocean of the Kuroshio Extension Region." *Frontiers in Marine Science* 9: 997810. https://doi.org/10.3389/fmars.2022.997810.

Xu, S., K. Yu, Z. Zhang, et al. 2020. "Intergeneric Differences in Trophic Status of Scleractinian Corals From Weizhou Island, Northern South China Sea: Implication for their Different Environmental Stress Tolerance." *Journal of Geophysical Research—Biogeosciences* 125, no. 5: e2019JG005451. https://doi.org/10.1029/2019JG005451.

Yang, Q., J. Ling, Y. Zhang, et al. 2024. "Microbial Nitrogen Removal in Reef-Building Corals: A Light-Sensitive Process." *Chemosphere* 359: 142394. https://doi.org/10.1016/j.chemosphere.2024.142394.

Yu, W., W. Wang, K. Yu, et al. 2019. "Rapid Decline of a Relatively High Latitude Coral Assemblage at Weizhou Island, Northern South China Sea." *Biodiversity and Conservation* 28, no. 14: 3925–3949. https://doi.org/10.1007/s10531-019-01858-w.

Zhang, Y., J. Ling, Q. Yang, et al. 2015. "The Functional Gene Composition and Metabolic Potential of Coral-Associated Microbial Communities." *Scientific Reports* 5, no. 1: 16191. https://doi.org/10.1038/srep16191.

Supporting Information

Additional Supporting Information may be found in the online version of this article.

Submitted 03 September 2024
Revised 20 February 2025
Accepted 09 July 2025

Talanta 297 (2026) 128692

Contents lists available at ScienceDirect

Talanta

journal homepage: www.elsevier.com/locate/talanta

3D-printed SPME-based wooden-tip mass spectrometry for rapid detection of organic ultraviolet absorbers in complex matrices

Yingyuan Zhang [a,b,1], Deshuo Gao [a,1], Kefu Yu [a], Ruijie Zhang [a], Jiayu Zhang [a], Wenfeng Yu [a], Shiguo Chen [b], Jiying Pei [a,*]

[a] Guangxi Laboratory on the Study of Coral Reefs in the South China Sea, Coral Reef Research Center of China, School of Marine Sciences, Guangxi University, Nanning, 530004, China

[b] School of Resources, Environment and Materials, Guangxi University, Nanning, 530004, China

ARTICLE INFO

Keywords:
Wooden-tip ambient mass spectrometry
Solid-phase microextraction
3D printing
Organic ultraviolet absorber
Complex matrix

ABSTRACT

Organic ultraviolet absorbers (OUVs), commonly used in sunscreens and industrial products, have raised growing environmental and health concerns due to their pervasive occurrence in aquatic ecosystems. Conventional analytical techniques, such as liquid chromatography-mass spectrometry (LC-MS) and gas chromatography-mass spectrometry (GC-MS), offer high sensitivity but are constrained by labor-intensive workflows and extensive solvent use. Here, we present a rapid and portable screening method for seven priority OUVs by integrating a C_{18}-modified wooden-tip solid-phase microextraction (SPME) probe with ambient mass spectrometry (AMS). A custom-designed 3D-printed interface was designed to precisely align the ionization source with the mass spectrometer, enhancing stability, reproducibility, and operational ease. Detection limits (LODs) ranged from 0.23 μg/L to 8.17 μg/L, sufficient for high-exposure scenarios such as recreational waters (up to μg/L level) and the permitted concentration range in personal care products (typically 2–10 %, *w/w*). While the sensitivity is lower than that of LC-MS or GC-MS, the method achieves comparable extraction recoveries (81.3–119.6 %) in ultrapure water and post-cleansing facial rinses. In artificial seawater, recoveries dropped to 50.9–83.0 % due to salt and organic matter interfering with ionization. Despite this, the total analysis time was significantly reduced-from hours to minutes-without complex sample preparation. Field applications demonstrate the method's practicality: (1) OUVs in commercial sunscreens matched labeled ingredients; (2) surfactant-assisted cleansing increased OUV release from the skin by 1.58–2.31 times compared to water rinsing; and (3) benzophenone-1 (BP-1), 2-ethylhexyl-4-methoxycinnamate (EHMC), and ethylhexyl dimethyl *p*-aminobenzoic acid (ODPABA) were detected in swimming pool and coral reef waters, with concentrations up to 55.59 μg/L. This study provides an efficient, low-cost, and environmentally friendly alternative for rapid OUV screening and environmental risk assessment.

1. Introduction

Organic ultraviolet absorbers (OUVs) are synthetic compounds widely incorporated into sunscreens, cosmetics, and plastic products to shield against harmful ultraviolet (UV) radiation [1]. While they effectively prevent UV-induced skin damage and material degradation, their extensive use has raised growing environmental and human health concerns. OUVs are commonly released into aquatic environments through wastewater discharge and recreational activities, eventually reaching marine ecosystems [2]. Accumulating evidence suggests that these compounds can exert toxic effects on marine life, including coral bleaching [3], increased mortality in clownfish [4], and inhibited development in sea urchins [5]. Moreover, certain OUVs have been identified as potential endocrine disruptors, raising concerns about their long-term health impacts in humans [6]. Given their environmental persistence, ecological risks, and widespread use, there is an urgent demand for fast, high-throughput, and portable analytical platforms to support both environmental monitoring and industrial quality control. In coral reef ecosystems, where compounds such as benzophenone-3 (BP-3), 2-ethylhexyl-4-methoxycinnamate (EHMC), and

* Corresponding author.
E-mail address: pjying@gxu.edu.cn (J. Pei).
[1] The authors contributed equally to this work.

https://doi.org/10.1016/j.talanta.2025.128692
Received 28 May 2025; Received in revised form 15 July 2025; Accepted 7 August 2025
Available online 8 August 2025
0039-9140/© 2025 Elsevier B.V. All rights are reserved, including those for text and data mining, AI training, and similar technologies.

4-methylbenzylidene camphor (4-MBC) are banned in regions like Hawaii, Palau, and the U.S. Virgin Islands [7], OUV concentrations as high as 200 μg/L have still been reported in nearby waters [8]. This underscores the need for rapid, on-site screening of tourist sunscreens at entry points to help prevent further reef contamination. Similarly, in the personal care industry, fast quantification of OUVs is vital for improving analytical throughput, enabling routine product safety assessments, and ensuring compliance with regulatory limits that generally cap concentrations at 10 % (*w/w*) in cosmetic products [9].

Traditional chromatographic-mass spectrometric techniques, such as gas chromatography-mass spectrometry (GC-MS) [10] and liquid chromatography-mass spectrometry (LC-MS) [11], offer excellent sensitivity for detecting OUVs. Their detection limits (LODs) often reach ppt to ppb levels (Table 1) [12]. However, these methods are fundamentally limited by their reliance on labor-intensive and time-consuming workflows. This is primarily due to mandatory sample preparation procedures, such as solid-phase extraction (SPE) and liquid-liquid extraction (LLE) [13]. Sample preparation and chromatographic runs typically require tens of minutes to several hours per sample. In addition, large volumes of organic solvents (for LC) or carrier gases (for GC) are consumed, which increases environmental burden and operational complexity. These factors, along with the high cost of consumables like SPE cartridges and chromatographic columns, limit their practicality for high-throughput or on-site analysis.

To address these limitations, ambient mass spectrometry (AMS) has emerged as a promising alternative [14]. Techniques such as paper spray, wooden-tip (WT), and coated blade spray (CBS) enable direct analysis of complex samples with minimal or no pretreatment. For instance, low-temperature plasma ionization mass spectrometry (LTP-MS) has shown promise for the semi-quantitative screening of OUVs in personal care products [15]. Among AMS methods, the WT approach offers clear advantages for field environmental analysis. Unlike chromatographic paper, which can deform and affect spray stability and ionization [16], wooden tips provide greater mechanical strength and stability. Compared to CBS with sharp metal blades that pose handling risks [17], wooden tips are safer and easier to use on-site. Additionally, wood's hydroxyl-rich surface allows easy chemical modification without the oxide removal steps needed for metal substrates [18]. Despite these benefits, AMS is often limited by poor sensitivity, low reproducibility, and compromised quantitative accuracy [19] caused by matrix effects like ion suppression. Without sample cleanup, salts and other interferents compete with analytes during ionization, reducing signal strength.

To overcome this, solid-phase microextraction (SPME) is widely integrated with AMS [20]. SPME selectively captures and enriches target compounds while removing matrix interferences, offering both preconcentration and cleanup. This coupling substantially mitigates matrix effects, thereby improving ionization efficiency, enhancing sensitivity, and increasing quantitative reliability in AMS-based analyses. Recent developments such as CBS probes demonstrate the feasibility of SPME-AMS for detecting pharmaceuticals in complex biological samples [21]. Nevertheless, broader adoption of SPME-AMS is hindered by lack of standardized platforms and the need for manual probe alignment, which causes variability. Recent advances in 3D printing offer a solution by enabling the fabrication of modular, reproducible components tailored for AMS application [22]. For example, integration of 3D-printed interfaces in CBS-MS has enhanced portability and consistency in clinical analyses [23]. Therefore, combining 3D-printed modules with wooden-tip ambient mass spectrometry (WT-AMS) has great potential to enhance robustness, stability, and usability for OUV detection.

In this study, we present the first integration of 3D-printed SPME-based WT-AMS for the rapid detection of seven high-priority OUVs in complex samples including sunscreen and water matrices. These target compounds are benzophenone-1 (BP-1), BP-3, benzophenone-8 (BP-8), EHMC, avobenzone (AVO), 4-MBC, and ethylhexyl dimethyl *p*-aminobenzoic acid (ODPABA). These target compounds were selected based on their widespread use in commercial sunscreen formulations [24] and their frequent detection in aquatic environments, where they pose potential risks to human and ecological health. Our approach combines: (1) the simplicity and high-throughput of WT-AMS, (2) the selectivity of functionalized SPME coatings, and (3) the precision and reproducibility afforded by 3D-printed interfaces. Application to real-world samples demonstrates its potential as a portable, efficient tool for environmental monitoring and industrial quality control of OUVs.

Table 1
Summary of analytical performance of conventional OUV detection methods.

Methods	Category	Analysis time (min)	Solvent-free	Cost	On-site or LOD
Preparation	SPE	10–60	×	Tens $/col.	Limited
	LLE	10–60	× (high use)	Low-medium	Limited
Detection	GC-MS	10–30	√ (but need carrier gas)	Hundreds $/col.	ppt-ppb
	LC-MS	10–30	× (as mobile phase)	Hundreds $/col.	ppt-ppb

Note: "col." stands for column.

2. Experimental

2.1. Chemicals and materials

Dimethyloctadecyl[3-(trimethoxysilyl)propyl]ammonium chloride (DMOAP, C_{18} for SPME modification, 60 % in methanol) and anhydrous *N,N*-dimethylformamide (DMF, 99.8 %) were supplied by J&K Scientific Ltd. (Beijing, China). OUVs, including BP-1, BP-3, BP-8, AVO (>99 %), ODPABA (>98 %), and EHMC (>96 %), were obtained from TCI Chemicals (Shanghai, China). Additionally, 4-MBC (>99 %) was sourced from AccuStandard (USA). The isotopically labeled internal standard (IS), oxybenzone-d5 (BP-3-d5), was purchased from Sigma-Aldrich (St. Louis, USA). LC-MS grade methanol and acetonitrile were purchased from CNW Technologies (Germany). Ultrapure water (18.2 MΩ·cm) was produced using a Milli-Q purification system (Millipore, Bedford, USA).

Wooden toothpicks were purchased locally from a supermarket. Eight sunscreen products were acquired via Taobao (Alibaba Group, China). The 3D-printed SPME assembly including an immobilization station (using polylactic acid (PLA) filament from SUNLU, Zhuhai, China) and an aluminum alloy probe holder (using AlSi10Mg aluminum alloy powder, Dongguan, China), were fabricated with a Bambu Lab A1 mini 3D printer (Shenzhen, China) and a ZRapid Tech AFS420 metal 3D printer (Suzhou, China). Copper sheets for electrical connections were sourced locally.

2.2. Pretreatment of toothpick

The wooden toothpick tips were sharpened to a final diameter of 0.15–0.2 mm and trimmed to ~3 cm in length using a precision cutter. The sharpened tips were ultrasonically cleaned in methanol and air-dried. Surface modification was performed following Deng's protocol [25]: dried tips were dispersed in 40 mL of anhydrous DMF, followed by addition of 2 mL of DMOAP under vigorous stirring. The mixture was refluxed at 120 °C for 12 h under nitrogen to facilitate silanization. Post-reaction, the modified tips were rinsed with methanol and dried. In our current protocol, approximately 40 C_{18}-modified probes are prepared in parallel per batch. This number can be further increased by scaling up the volume of the reaction vessel. Due to their low cost and suitability for large-scale production, the SPME probes were designed for single use, eliminating the need for reuse and thereby reducing the risk of cross-contamination and variability in analytical performance.

2.3. Optimization of SPME extraction conditions and application to real samples

Stirring time and stirring speed are key parameters affecting SPME performance. Preliminary experiments were conducted to define suitable optimization ranges. Tests at 0, 30, 60, and 90 min showed that the signal decreased significantly at 60 min (Fig. S1), likely due to the establishment of a dynamic adsorption-desorption equilibrium. Therefore, the extraction time was further optimized within 0–50 min. Similarly, stirring speeds above 800 rpm led to bubble formation on the probe, forming a gas-film barrier that reduced extraction efficiency [26]. Based on this, the stirring speed was optimized within the range of 0–800 rpm.

Seawater samples were collected from two coral reef sites in Semporna, Malaysia: Timba Timba Island (4.548893°N, 118.929445°E) and Mataking Island (4.597790°N, 118.949882°E). A total of 500 mL of seawater was collected at each site and immediately filtered onboard using 4.5 μm membrane filters. After filtration, the samples were stored under refrigerated conditions until further processing in the laboratory. Swimming pool water was sampled from an outdoor pool with high swimmer activity on a Sunday and promptly transported to the laboratory for analysis. For extraction, 4 mL aliquots of seawater were enriched using C_{18}-modified probes by direct immersion under optimized conditions (30 min at 500 rpm with constant stirring). After extraction, the probes were rinsed with ultrapure water to eliminate residual matrix components prior to mass spectrometry (MS) analysis.

For sunscreen samples, approximately 0.1 g of product was mixed with 10 mL of methanol in a 15 mL glass vial and vortexed for 30 s to ensure complete homogenization. OUVs were extracted by ultrasonication, and a 5 mL portion of this extract was then diluted to 50 mL with ultrapure water and subjected to the same SPME procedure as described for seawater samples.

2.4. Mass spectrometry analysis

The C_{18}-modified probe, containing enriched OUVs, was secured in its holder and mounted onto the custom 3D-printed immobilization station for MS analysis. For each measurement, 20 μL of solvent was applied to the modified tip and allowed to equilibrate for 5 s to promote effective desorption of target analytes. Ionization was subsequently initiated by introducing an additional 30 μL of solvent under high-voltage conditions. To maximize signal intensity, key experimental parameters were systematically optimized. These included the orientation of the wooden tip relative to the MS ion transfer inlet, the applied spray voltage, the distance between the tip and the MS inlet, and the composition of the spray solvent. The tested ranges were selected based on previous studies and preliminary tests. Spray voltage (3.5–5 kV) was chosen because lower voltages could not sustain stable spray, while higher voltages caused discharge [27]. The tip-to-inlet distance (0.1–1 cm) was selected to optimize ion transmission while preventing electrical discharge and contamination of the MS inlet [28]. Spray angles (0°, 45°, 90°) represent common geometries in similar ambient ionization setups [29]. Solvent mixtures (methanol-acetonitrile from 1:0 to 0:1) were tested to cover different polarities and optimize desorption and ionization efficiency.

All experiments were performed using an LTQ mass spectrometer (Thermo Scientific, San Jose, USA). Mass spectra were acquired in positive ion mode with the inlet temperature set at 275 °C. Tandem mass spectrometry (MS/MS) was performed using helium as the collision gas, with collision-induced dissociation (CID) energy set at 35–50 %, an activation time of 30 ms, and an isolation width of m/z 1.0. All other instrument parameters were kept at their default settings.

2.5. Quality control

To ensure analytical reliability and minimize contamination risks, a comprehensive quality assurance and quality control (QA/QC) protocol was implemented throughout the sample collection and analysis processes. Procedural blanks were analyzed to verify the absence of contamination and matrix interference. Artificial seawater was employed as the blank matrix for marine samples, while commercial sunscreens containing only inorganic UV filters (titanium dioxide and zinc oxide) without any OUVs served as cosmetic blanks. None of the seven target OUVs were detected in these blanks, confirming negligible background contamination from reagents or materials.

To minimize contamination during field sampling, plastic containers were generally avoided due to the potential presence of residual OUVs. Swimming pool water samples were collected using amber glass bottles. For seawater samples, pre-cleaned polypropylene containers were used in the field for practical reasons, but potential contamination was evaluated by comparison with ultrapure water blanks and confirmed to be negligible. Field operators also avoided applying sunscreen or other personal care products prior to sampling.

Each matrix was spiked with known concentrations of the target OUVs, and recovery was evaluated by comparing the signal responses from spiked blank extracts to the corresponding nominal spike levels. Notably, glucose was added to the artificial seawater (35 ‰) at a concentration of 6.25 mg/L to better simulate real-world marine conditions. This corresponds to approximately 2.5 mg C/L of DOC, a level commonly observed in nearshore coastal waters [30], to mimic natural organic matter presence.

LODs and limits of quantitation (LOQs) were calculated using the standard deviation of eleven replicate blank measurements and the calibration curve slope. Specifically, LODs were defined as three times the standard deviation (3σ) divided by the calibration slope, while LOQs were defined as ten times the standard deviation (10σ) divided by the slope [31].

3. Result and discussion

3.1. 3D-printed assembly for SPME-based WT-AMS ionization

To ensure stable ionization and improve operational reproducibility in WT-AMS, we developed a 3D-printed assembly consisting of two modular components: a fixed base and a detachable metal holder (Fig. 1). This design aims to ensure precise spatial alignment and stable electrical contact between the SPME wooden tip and the MS inlet. The metal holder features a precision-drilled aperture that securely accommodates disposable wooden toothpicks used as SPME probes. A copper sheet is embedded at the interface between the holder and the base to facilitate reliable high-voltage transmission, ensuring consistent spray ionization during analysis. This modular configuration offers two key advantages. First, it maintains fixed spatial alignment between the probe and MS inlet, improving ionization consistency. Second, it ensures reliable electrical contact. Importantly, by isolating the replaceable holder from the fixed alignment structure, the design eliminates the need for realignment during probe replacement, which is a common issue in custom AMS systems [32].

The assembly demonstrated excellent mechanical robustness, showing no structural deformation after more than one year of repeated use. This durability stems from the minimal mechanical load during operation since the main function is simply to hold the wooden tip while the copper sheet serves as the electrode. Although PLA is known to be sensitive to organic solvents [33], this concern is mitigated in our design. The spray solvent is applied at the wooden tip, which is physically isolated from the PLA base by the metal holder and copper sheet. As a result, solvent-induced dissolution or chemical leaching from the PLA is effectively prevented [17]. Recent developments in 3D printing of sustainable materials, such as all-natural flame-retardant hydrogels, further underscore the relevance of modular, low-cost, and environmentally friendly fabrication strategies in analytical instrumentation design [34]. Consistent with this trend, our assembly produced

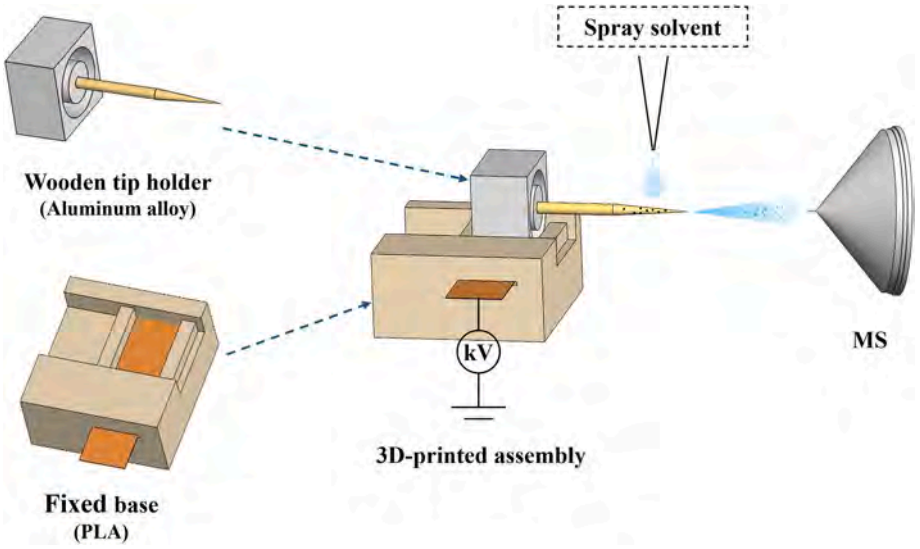


Fig. 1. Schematic diagram of the 3D-printed SPME-based WT-AMS assembly.

negligible background signals and consistent performance across repeated use. Overall, this user-friendly, low-cost, and scalable platform is well suited for laboratories developing prototype AMS systems requiring frequent probe changes.

3.2. Optimization of extraction conditions

To enhance the analytical performance of the SPME-based WT-AMS assembly, we first pretreated wooden toothpick probes with methanol prior to C_{18} surface modified. This step effectively removed surface contaminants, minimizing background noise and ion suppression during analysis [29].

As illustrated in Fig. 2a, the total ion chromatogram (TIC) obtained from the WT spray remained stable for the initial 0.6 min before gradually declining due to solvent evaporation. To ensure consistent quantification, only signal intensities within this 0.6-min window were used. For improved sensitivity and selectivity, MS/MS was employed. Characteristic fragment ions were selected based on signal strength and fragmentation specificity. As shown in Fig. 2b, the selected product ions were: *m/z* 137 for BP-1, 151 for BP-3, 121 for BP-8, 166 for ODPABA, 157 for 4-MBC, 161 for AVO, and 179 for EHMC. These ions were used for all subsequent quantification.

Given the proven efficiency of C_{18}-functionalized silica in conventional SPE [18], we evaluated the effect of C_{18} modification on our

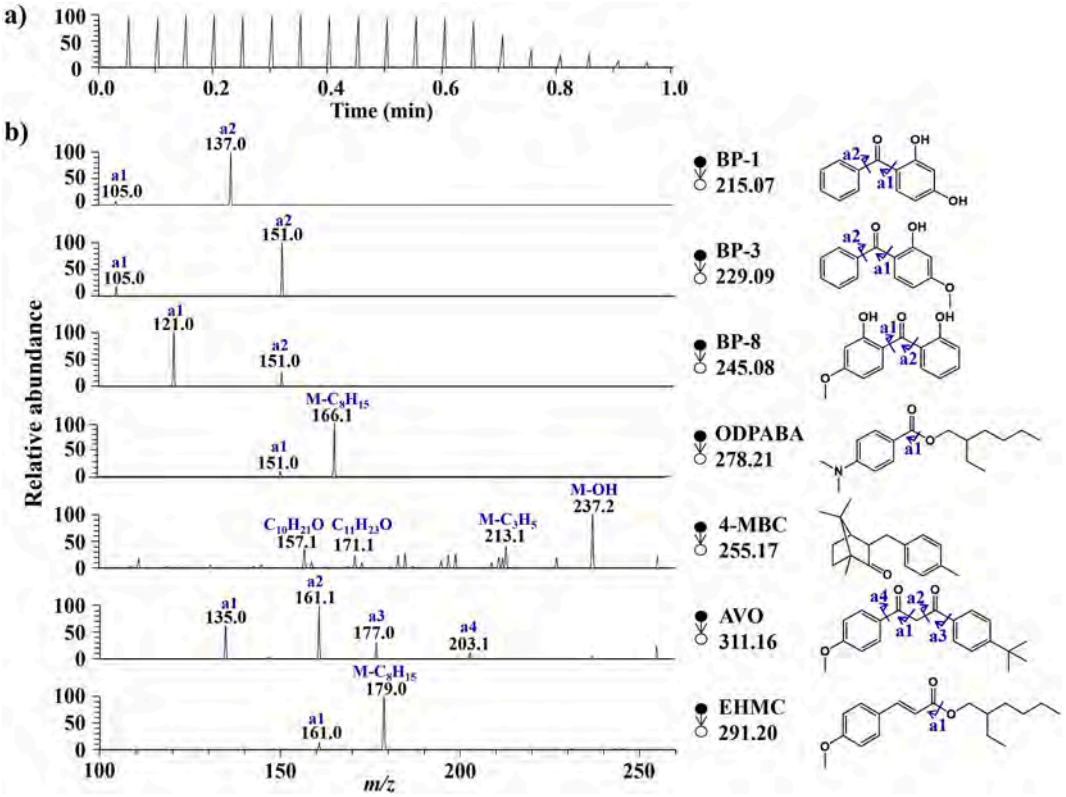


Fig. 2. a) TIC and b) MS/MS data for the seven target OUVs.

WT-AMS probes. Comparison between unmodified and C_{18}-modified wooden tips revealed significant signal enhancement across all seven analytes (Fig. 3). Enrichment factors (EFs) ranged from 2.0 for 4-MBC to 48.9 for BP-1. This variability likely reflects differences in the physicochemical properties of each compound, such as hydrophobicity, molecular weight, and steric effects [35].

Further optimization focused on extraction parameters. Extraction time and agitation speed were systematically tested. Optimal performance was achieved at 30 min extraction time and 500 rpm agitation (Fig. S2), which were applied in all subsequent experiments.

3.3. Optimization of mass spectrometry conditions

Several key parameters affecting ionization efficiency and signal quality were optimized, including the spatial orientation and distance between the wooden tip and the MS inlet, spray voltage, and spray solvent composition.

The spatial orientation of the wooden tip plays a critical role in modulating ion flow and minimizing contamination of the mass spectrometer inlet. To identify the optimal geometry, three orientations (0°, 45°, and 90° relative to the MS inlet) were tested (Fig. S3a). At 0° and 45°, mass spectra exhibited elevated background noise and poor fragmentation resolution for representative OUVs (BP-1, ODPABA, AVO, and EHMC), indicative of substantial spectral interference (Fig. S3b). In contrast, the 90° orientation yielded cleaner spectra and the highest signal intensities for all seven analytes (Fig. 4a). This improvement is likely due to the minimized entry of neutral or non-ionized species into the MS inlet, a common issue in ambient ionization techniques such as WT-AMS [29]. Therefore, the 90° configuration was adopted for all subsequent experiments.

Tip-to-inlet distance and spray voltage were further evaluated. As shown in Fig. 4b and c, optimal signal intensities for all analytes were achieved at a tip-inlet distance of 0.25 cm and a spray voltage of 4.5 kV. Distances shorter than 0.25 cm or voltages exceeding 4.5 kV led to unstable ionization due to corona discharge from localized dielectric breakdown [36,37]. Conversely, longer distances or lower voltages resulted in inefficient ion desolvation and incomplete analyte ionization, leading to diminished signal intensity [38]. Accordingly, a tip-inlet distance of 0.25 cm and a spray voltage of 4.5 kV were determined to be optimal.

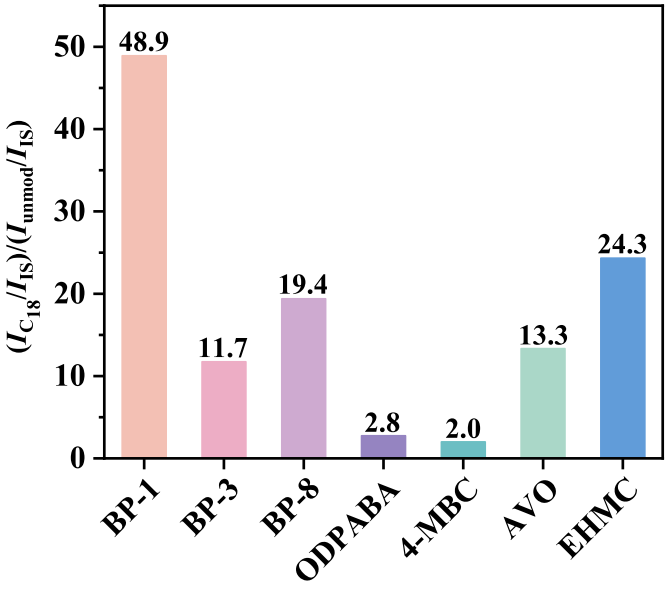


Fig. 3. EFs of seven OUVs obtained using C_{18}-modified versus unmodified SPME probes. EFs were calculated using the formula: EF = $(I_{C18}/I_{IS})/(I_{unmod}/I_{IS})$, I_{C18}/I_{IS} and I_{unmod}/I_{IS} represent the mean analyte signal intensities (n = 3) normalized to the IS for C_{18}-modified and unmodified probes, respectively.

Spray solvent composition is critical for promoting analyte desorption from the probe surface and facilitating efficient ionization. Methanol-acetonitrile mixtures were tested at varying ratios. A methanol-acetonitrile mixture of 3:7 (v/v) provided the highest signal intensities for BP-1, BP-3, BP-8, and 4-MBC, and delivered the second highest intensities for ODPABA, AVO, and EHMC (Fig. 4d). This ratio likely balances solvent polarity for efficient analyte desorption and optimal spray conditions.

3.4. Analytical performance evaluation

The analytical performance of the optimized SPME-based WT-AMS method was comprehensively evaluated in terms of reproducibility, accuracy, matrix recovery, linearity, and sensitivity. This evaluation aimed to establish the method's suitability for detecting OUVs in both environmental and cosmetic matrices.

Reproducibility is a critical parameter for AMS applications due to their susceptibility to environmental fluctuations and instrumental drift. To improve measurement stability and correct for signal variation, deuterated ISs were employed for signal normalization [19]. Following normalization, the method exhibited acceptable intermediate precision, with relative standard deviations (RSDs) ranging from 13.2 % to 23.3 % over ten replicate measurements of 0.5 mg/L samples across the seven target OUVs (Fig. S4). These values are within the acceptable range for semi-quantitative AMS methods (RSD <30 %) [39,40]. To further assess batch-to-batch consistency, we prepared three independent batches of C_{18}-modified probes, each consisting of six probes. These 18 probes were used to analyze the seven OUVs at a concentration of 0.5 mg/L. The resulting inter-batch RSDs ranged from 19.5 % to 29.9 %, demonstrating good reproducibility and minimal variability between batches (Table S1). Further improvements in reproducibility could be achieved by standardizing the WT preparation process to replace manual sharpening. Additionally, implementing an automated solvent application system would ensure more consistent solvent delivery and minimize variability caused by manual pipetting.

To evaluate potential operator bias in our SPME-based WT-AMS method, a blinded validation experiment was conducted. The operator was blinded to the true concentrations of aqueous OUV samples prepared at two levels-0 mg/L (blank) and 0.5 mg/L-with three replicates per level. As shown in Table S2, no target compounds were detected in the blank samples, confirming the absence of false positives. For the 0.5 mg/L samples, the recovery rates for the seven OUVs ranged from 94.1 % to 117.6 %, demonstrating acceptable accuracy and reliability under blinded conditions.

To assess the robustness, recovery studies were conducted using three representative media: ultrapure water, artificial seawater (simulating environmental samples) and post-cleansing facial rinse (representative of cosmetic matrices). The results showed mean recoveries ranging from 81.3 % to 119.6 % in ultrapure water and 81.4 % to 119.5 % in facial rinse (Fig. 5a). As shown in Fig. S5, the recoveries ranged from 50.9 % to 83.0 % in artificial seawater. The lower recoveries observed in artificial seawater are likely due to two contributing factors [41]: (i) the presence of dissolved organic matter, which may bind to OUVs and hinder their extraction, and (ii) high salt content, which can accumulate within the microstructures of the SPME probe and induce ion suppression during MS analysis. In comparison, both ultrapure water and facial rinse exhibited higher recoveries, suggesting minimal matrix interference and ion suppression effects in these systems. Recoveries slightly exceeding 100 % may result from pipetting variability at low volumes, matrix-induced signal enhancement [42], or trace-level background analyte residues present below the LOD in blank matrices. Despite matrix complexity, the recovery performance achieved using the WT-AMS method remains comparable to that reported for conventional SPE-based workflows [11], confirming the method's accuracy and robustness across diverse sample types.

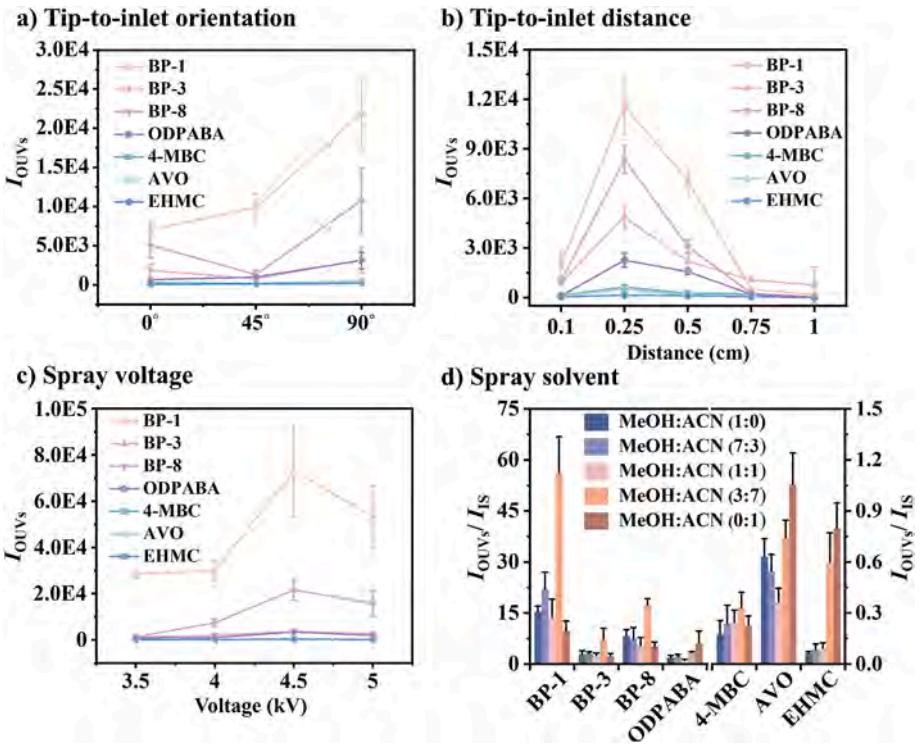


Fig. 4. Optimization of experimental parameters for the SPME-based WT-AMS method. Effect of a) tip-to-inlet orientation, b) tip-to-inlet distance, c) spray voltage, and d) spray solvent compositions on the signal intensities of the seven OUVs.

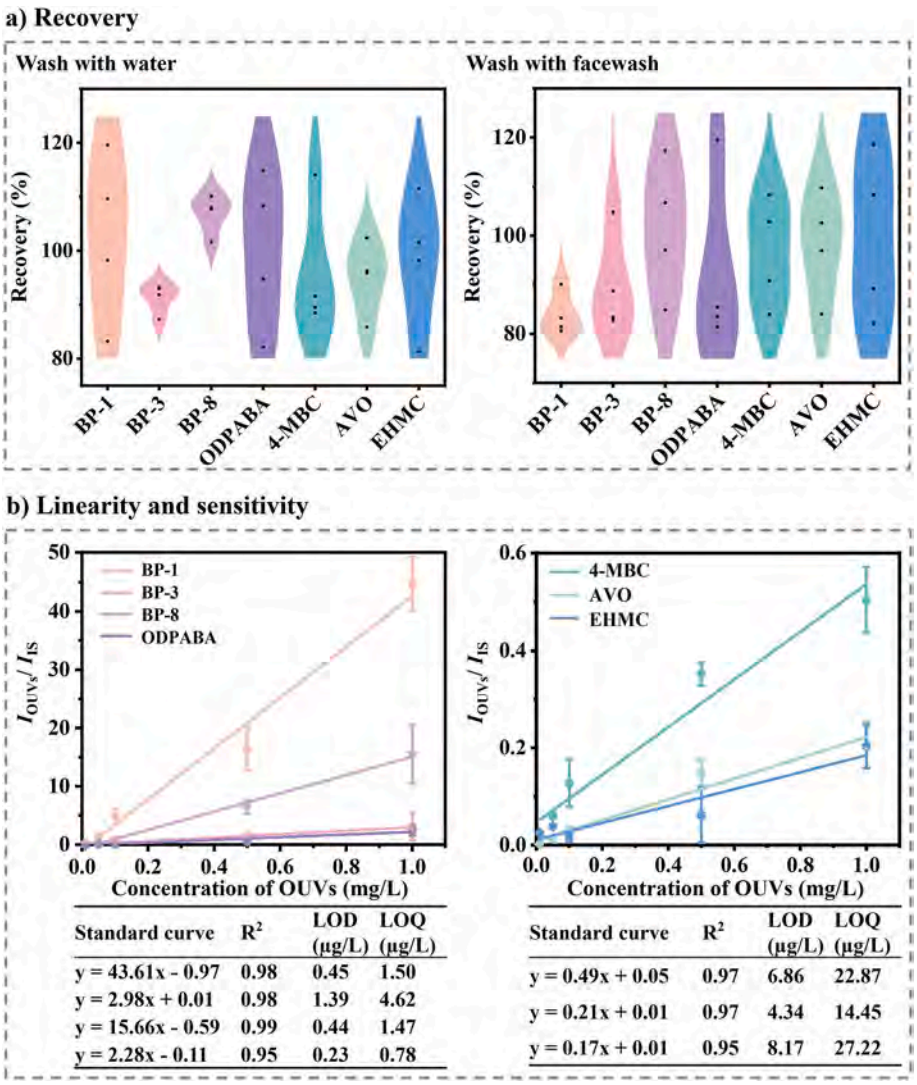
The method's quantitative capability was assessed through calibration curves constructed over a three-order-of-magnitude concentration range for each OUV (0–50 mg/L). In the 0–1 mg/L range, all analytes exhibited excellent linearity, with coefficients of determination (R^2) consistently exceeding 0.95 (Fig. 5b), indicating reliable quantification within this range. At concentrations above 1 mg/L, signal responses deviated from linearity and exhibited saturation behavior (Fig. S6), likely due to limited adsorption capacity of the SPME sorbent phase. Accordingly, the dynamic linear range for accurate quantification using this method is defined as 0–1 mg/L. The LODs were calculated to range from 0.23 μg/L to 8.17 μg/L, with corresponding LOQs between 0.78 μg/L and 27.22 μg/L. Although these LODs are higher than those typically achieved with laboratory-based LC-MS [11] or GC-MS methods [10], the trade-off is offset by significant advantages. Conventional LC-MS and GC-MS workflows require time-consuming chromatographic separation (from a few minutes to over 30 min per sample) and complex pretreatment steps such as SPE or LLE. In contrast, the SPME-based WT-AMS method provides a much simpler and faster workflow. The total analysis time is approximately 30 min per sample, primarily for the extraction step. Moreover, since extraction can be performed in parallel, the effective processing time per sample is further reduced in batch operations. By eliminating labor-intensive procedures and avoiding the use of chromatographic columns, SPE cartridges, and large volumes of organic solvents, the method not only simplifies operation but also significantly reduces costs and environmental impact. Furthermore, the portable and easy-to-assemble design enables flexible field sampling with straightforward transport back to the laboratory for analysis. Overall, the SPME-based WT-AMS method offers key advantages of speed, low cost, simplicity, and field adaptability, making it especially suitable for rapid analysis of OUVs in cosmetic and environmental samples.

3.5. Detection of real samples using our 3D-printed SPME-based WT-AMS method

To demonstrate the real-world applicability of the developed SPME-based WT-AMS method, we conducted case studies involving both commercial sunscreen products and environmental samples. These applications aim to validate the method's performance in practical scenarios and highlight its relevance for both product quality control and environmental monitoring.

Robust analytical methodologies are essential for the quality control of sunscreen products, especially given increasing regulatory restrictions on certain OUVs due to potential health risks. For example, *p*-aminobenzoic acid (PABA), a widely used UVB absorber, has been progressively banned due to its association with allergic dermatoses [43]. This highlights the need for accurate quantification of OUVs to ensure both consumer safety and regulatory compliance. To evaluate the applicability of our validated 3D-printed SPME-based WT-AMS platform, we analyzed eight commercially available sunscreen products for seven priority OUVs. As presented in Fig. 6a, EHMC, the commonly regulated UVB filter, was detected in all samples. In contrast, AVO, the broad-spectrum UVA/UVB filter, was exclusively found in Product 7. These findings aligned well with the active ingredients listed by the manufacturers. Importantly, the measured concentrations of all detected OUVs complied with current regulatory maximum allowable limits, thus confirming the platform's accuracy and suitability for product quality control and regulatory surveillance.

Beyond product composition, understanding the environmental pathways and release mechanisms of OUVs is critical, as these compounds are frequently introduced into aquatic ecosystems through domestic wastewater. A key factor influencing OUV release is consumer cleansing behavior, particularly the use of surfactant-based cleansers. Sunscreen formulations typically contain water-resistant agents such as silicones and waxes. These components make OUV residues difficult to remove by water alone [44]. Surfactants, such as sodium lauryl sulfate, facilitate the removal of these hydrophobic compounds by emulsifying



Standard curve	R^2	LOD (μg/L)	LOQ (μg/L)
y = 43.61x - 0.97	0.98	0.45	1.50
y = 2.98x + 0.01	0.98	1.39	4.62
y = 15.66x - 0.59	0.99	0.44	1.47
y = 2.28x - 0.11	0.95	0.23	0.78

Standard curve	R^2	LOD (μg/L)	LOQ (μg/L)
y = 0.49x + 0.05	0.97	6.86	22.87
y = 0.21x + 0.01	0.97	4.34	14.45
y = 0.17x + 0.01	0.95	8.17	27.22

Fig. 5. Analytical performance of the 3D-printed SPME-based WT-AMS method, including: a) recoveries across different matrices and b) linearity and sensitivity as determined from calibration curves.

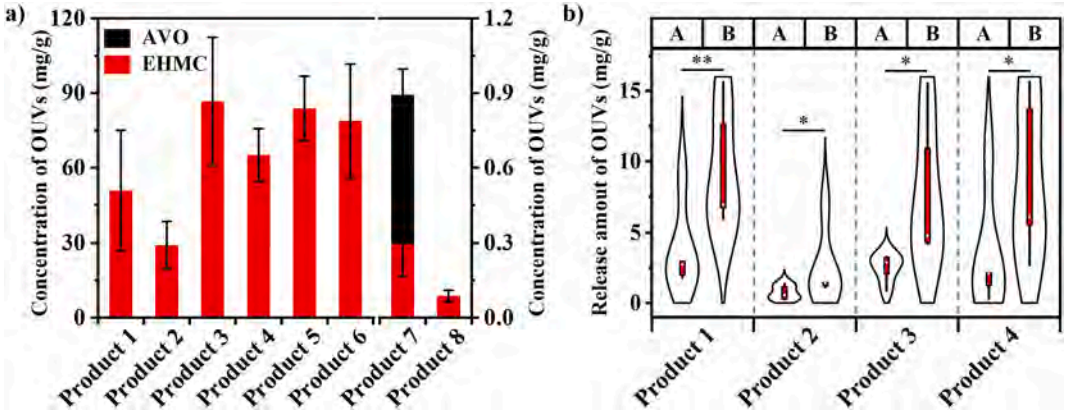


Fig. 6. a) OUV contents in eight commercially available sunscreen brands. b) Comparison of OUV release with water-only rinsing versus surfactant-assisted cleansing (**$p < 0.01$, *$p < 0.05$, ANOVA). "A" represents water-only rinsing, while "B" represents cleansing with a facial cleanser.

them. To evaluate this effect, we conducted standardized washing experiments using four representative sunscreen brands. Wastewater effluents were collected following two conditions: water-only rinsing and surfactant-assisted cleansing. As shown in Fig. 6b, surfactant use significantly increased OUV release, with concentrations 1.58 to 2.31 times higher than those from water-only rinsing ($p < 0.05$, ANOVA). These results clearly demonstrate that surfactant substantially enhance the mobilization of OUVs from the skin.

Following their release from personal care products (PCPs), OUVs are readily can be transported into aquatic environments, where they pose significant ecological and human health risks due to their potential for bioaccumulation and biomagnification [45]. In this study, both freshwater (swimming pool water) and seawater samples were analyzed to assess the presence of OUVs. In swimming pool water, BP-1 was detected at a concentration of 13.63 μg/L. Given that BP-1 is less commonly used directly in sunscreen formulations, its presence is likely attributable, at least in part, to the environmental transformation of BP-3, a widely used OUV that is known to metabolize into BP-1 [46]. Furthermore, the longer biological half-life of BP-1 relative to BP-3 indicates greater environmental persistence and a higher potential for bioaccumulation [46].

While swimming pool water represents a controlled freshwater environment with direct human input, marine ecosystems-particularly coral reefs-are more complex and vulnerable to a wider range of contaminants. To evaluate the environmental relevance of OUVs in such ecosystems, we extended our investigation to nearshore coral reef waters in Semporna, Malaysia, a region recognized as a marine biodiversity hotspot and increasingly impacted by tourism [47]. Previous studies have linked OUV contamination to adverse biological effects in corals, including bleaching, polyp retraction, impaired larval development, and increased mortality [48–50]. Seawater samples were collected from two reef sites (S1 and S2) five days after the Chinese National Day holiday (October 1–7), a period of heightened tourist activity. Analysis revealed that EHMC was present at concentrations of 25.13 μg/L at S1 and 55.59 μg/L at S2. ODPABA was also detected at 3.15 μg/L at S1 but was below the detection limit at S2. These concentrations are two to three orders of magnitude higher than typical levels reported in coastal reefs (ng/L range) and are comparable to those observed in severely impacted areas such as St. John Island, where concentrations up to 213 μg/L have been recorded [8]. In addition to OUVs released directly from recreational activities, several other sources likely contribute to the observed contamination in Semporna. Widespread plastic pollution [51,52], poor waste management [51], and weak regulatory enforcement have been reported along the coast. Degradation of vessel coatings and fishing gear may release additional OUVs, and the lack of effective wastewater treatment infrastructure leads to the discharge of untreated sewage from both coastal villages and floating settlements [53]. These findings collectively indicate a substantial anthropogenic impact on reef water quality and underscore the urgent need for coordinated monitoring and mitigation strategies to protect vulnerable marine ecosystems.

4. Conclusion

This study demonstrates the successful integration of 3D printing, SPME, and WT-AMS into a unified analytical platform for the rapid, low-cost, and environmentally friendly detection of OUVs in complex matrices. The developed method effectively overcomes key limitations of conventional chromatographic techniques-such as GC-MS and LC-MS, which typically involve costly instrumentation, labor-intensive sample pretreatment, and limited throughput. In contrast, the proposed approach offers significant advantages in operational simplicity, portability, and analytical efficiency. The optimized protocol exhibited robust analytical performance, with intermediate precision (RSD <23.3 %), satisfactory recoveries (50.9–119.6 %), and low LODs (0.23–8.17 μg/L), enabling reliable semi-quantitative analysis of seven high-priority OUVs. In addition, inter-batch RSDs of 19.5–29.9 % confirmed the method's reproducibility under varied operational conditions, while blinded recovery results between 94.1 % and 117.6 % demonstrated its accuracy and minimal operator bias. Application of the method to real-world samples provided critical insights into both product quality and environmental impact: 1) The widespread detection of regulated OUVs such as EHMC in commercial sunscreens was consistent with ingredient labels, validating the method's applicability for quality control and regulatory compliance. 2) Surfactant-assisted cleansing significantly increased OUV release into wastewater, highlighting the influence of personal hygiene practices on environmental OUV loads. 3) The detection of OUVs in real-world samples, including swimming pool water and nearshore seawater, demonstrates their environmental persistence and widespread release from PCPs. These findings underscore their potential ecological and human health risks and highlight the need for effective control and management strategies.

CRediT authorship contribution statement

Yingyuan Zhang: Writing – review & editing, Writing – original draft, Validation, Methodology, Investigation, Formal analysis, Data curation. **Deshuo Gao:** Validation, Software, Methodology, Investigation, Data curation. **Kefu Yu:** Supervision, Resources. **Ruijie Zhang:** Validation, Supervision, Resources. **Jiayu Zhang:** Validation, Investigation. **Wenfeng Yu:** Validation, Investigation. **Shiguo Chen:** Validation, Investigation. **Jiying Pei:** Writing – review & editing, Writing – original draft, Supervision, Project administration, Funding acquisition, Conceptualization.

Declaration of competing interest

The authors declare that they have no known competing financial interests or personal relationships that could have appeared to influence the work reported in this paper.

Acknowledgements

This work is supported by Guangxi Natural Science Foundation (No. 2023GXNSFAA026488), National Natural Science Foundation of China (No. 22264003), the National Innovation and Entrepreneurship Training Program for College Students (No. 202510593495).

Appendix B. Supplementary data

Supplementary data to this article can be found online at https://doi.org/10.1016/j.talanta.2025.128692.

Data availability

Data will be made available on request.

References

[1] B.R. Li, Z.Z. Yao, F. Zhao, B.Y. Meng, Z.H. Ma, C. Li, Occurrence of organic ultraviolet absorbers in the particle and gas samples from plastic greenhouses: human inhalation intake risk assessment, J. Hazard. Mater. 474 (2024) 134801, https://doi.org/10.1016/j.jhazmat.2024.134801.
[2] C.L. Mitchelmore, E.E. Burns, A. Conway, A. Heyes, I.A. Davies, A critical review of organic ultraviolet filter exposure, hazard, and risk to corals, Environ. Toxicol. Chem. 40 (2021) 967–988, https://doi.org/10.1002/etc.4948.
[3] C.M. Hansel, Sunscreens threaten coral survival, Science 376 (2022) 578–579, https://doi.org/10.1126/science.abo4627.
[4] A.N. Barone, C.E. Hayes, J.J. Kerr, R.C. Lee, D.B. Flaherty, Acute toxicity testing of TiO2-based vs. oxybenzone-based sunscreens on clownfish (Amphiprion ocellaris), Environ. Sci. Pollut. Res. 26 (2019) 14513–14520, https://doi.org/10.1007/s11356-019-04769-z.
[5] E.A. Shore, K.E. Huber, A.D. Garrett, M.H. Pespeni, Four plastic additives reduce larval growth and survival in the sea urchin Strongylocentrotus purpuratus, Mar. Pollut. Bull. 175 (2022) 113385, https://doi.org/10.1016/j.marpolbul.2022.113385.
[6] Y. Sakuragi, H. Takada, H. Sato, A. Kubota, M. Terasaki, S. Takeuchi, A. Ikeda-Araki, Y. Watanabe, S. Kitamura, H. Kojima, An analytical survey of benzotriazole UV stabilizers in plastic products and their endocrine-disrupting potential via human estrogen and androgen receptors, Sci. Total Environ. 800 (2021) 149374, https://doi.org/10.1016/j.scitotenv.2021.149374.
[7] I.B. Miller, S. Pawlowski, M.Y. Kellermann, M. Petersen-Thiery, M. Moeller, S. Nietzer, P.J. Schupp, Toxic effects of UV filters from sunscreens on coral reefs revisited: regulatory aspects for "reef safe" products, Environ. Sci. Eur. 33 (2021) 74, https://doi.org/10.1186/s12302-021-00515-w.
[8] C.A. Downs, E. Kramarsky-Winter, R. Segal, J. Fauth, S. Knutson, O. Bronstein, F. R. Ciner, R. Jeger, Y. Lichtenfeld, C.M. Woodley, P. Pennington, K. Cadenas,

A. Kushmaro, Y. Loya, Toxicopathological effects of the sunscreen UV filter, oxybenzone (benzophenone-3), on coral planulae and cultured primary cells and its environmental contamination in Hawaii and the U.S. Virgin Islands, Arch. Environ. Contam. Toxicol. 70 (2016) 265–288, https://doi.org/10.1007/s00244-015-0227-7.
[9] S.H. Mikkelsen, C. Lassen, M. Warming, E. Hansen, A. Brinch, D. Brooke, M. Crookes, E. Nielsen, J. Bredsdorff, Survey and health assessment of UV filters. Ministry of Environment and Food, DTU Food, 2015. ISBN 978-87-93352-82-7, https://i2.cdn.turner.com/cnn/2016/images/04/14/978-87-93352-82-7.pdf.
[10] K.I. Ekpeghere, U.J. Kim, O. Sung-Hee, H.Y. Kim, J.E. Oh, Distribution and seasonal occurrence of UV filters in Rivers and wastewater treatment plants in Korea, Sci. Total Environ. 542 (2016) 121–128, https://doi.org/10.1016/j.scitotenv.2015.10.033.
[11] L.N. Lyu, J. Li, Q.Y. Huang, Q. Liu, C. Yang, J.D. Dong, H.F. Su, S. Zhang, Exploring the hidden threat of organic UV filters to corals and macroalgae in coral reef ecosystem from Luhuitou, Sanya, China, Environ. Sci. Technol. 59 (2025) 8130–8139, https://doi.org/10.1021/acs.est.4c11463.
[12] S. Ramos, V. Homem, A. Alves, L. Santos, Advances in analytical methods and occurrence of organic UV-filters in the environment - a review, Sci. Total Environ. 526 (2015) 278–311, https://doi.org/10.1016/j.scitotenv.2015.04.055.
[13] J.Y. Pei, N. Liu, J.J. Hu, Y.T. Wang, K.F. Yu, R.J. Zhang, Research progress on pretreatment technique and instrumental analysis method of organic ultraviolet absorbers in environment matrices, Environmental Monitoring in China 39 (2023) 157–169, https://doi.org/10.19316/j.issn.1002-6002.2023.06.16.
[14] Z. Takáts, J.M. Wiseman, B. Gologan, R.G. Cooks, Mass spectrometry sampling under ambient conditions with desorption electrospray ionization, Science 306 (2004) 471–473, https://doi.org/10.1126/science.1104404.
[15] X. Ding, S. Gerbig, B. Spengler, S. Schulz, Reactive low temperature plasma ionization mass spectrometry for the determination of organic UV filters in personal care products, Talanta 178 (2018) 780–787, https://doi.org/10.1016/j.talanta.2017.10.021.
[16] N.E. Manicke, B.J. Bills, C.S. Zhang, Analysis of biofluids by paper spray MS: advances and challenges, Bioanalysis 8 (2016) 589–606, https://doi.org/10.4155/bio-2015-0018.
[17] W. Zhou, Q.Z. Lan, M. Dutt, J. Pawliszyn, 3D printed coated blade spray-mass spectrometry devices, Anal. Chem. 96 (2024) 16520–16524, https://doi.org/10.1021/acs.analchem.4c04613.
[18] J.W. Deng, W.Y. Li, Q.X. Yang, Y.H. Liu, L. Fang, Y.H. Guo, P.R. Guo, L. Lin, Y. Y. Yang, T.G. Luan, Biocompatible surface-coated probe for *in vivo, in situ*, and microscale lipidomics of small biological organisms and cells using mass spectrometry, Anal. Chem. 90 (2018) 6936–6944, https://doi.org/10.1021/acs.analchem.8b01218.
[19] T.H. Kuo, E.P. Dutkiewicz, J.Y. Pei, C.C. Hsu, Ambient ionization mass spectrometry today and tomorrow: embracing challenges and opportunities, Anal. Chem. 92 (2020) 2353–2363, https://doi.org/10.1021/acs.analchem.9b05454.
[20] X. Geng, Y.Q. Wang, H.L. Li, D.D.Y. Chen, Characterization of cigarette smokeomics by in situ solid-phase microextraction and confined-space direct analysis in real time mass spectrometry, Talanta 280 (2024) 126680, https://doi.org/10.1016/j.talanta.2024.126680.
[21] G.A. Gómez-Ríos, J. Pawliszyn, Development of coated blade spray ionization mass spectrometry for the quantitation of target analytes present in complex matrices, Angew. Chem. Int. Ed. 53 (2014) 14503–14507, https://doi.org/10.1002/anie.201407057.
[22] H. Guillén-Alonso, I. Rosas-Román, R. Winkler, The emerging role of 3D-printing in ion mobility spectrometry and mass spectrometry, Anal. Methods 13 (2021) 852–861, https://doi.org/10.1021/10.1039/d0ay02290j.
[23] M. Grajewski, M. Hermann, R.D. Oleschuk, E. Verpoorte, G.I. Salentijn, Leveraging 3D printing to enhance mass spectrometry: a review, Anal. Chim. Acta 1166 (2021) 338332, https://doi.org/10.1016/j.aca.2021.338332.
[24] A. Pniewska, U. Kalinowska-Lis, A survey of UV filters used in sunscreen cosmetics, Appl. Sci. 14 (2024) 3302, https://doi.org/10.3390/app14083302.
[25] J.W. Deng, Y.Y. Yang, L. Fang, L. Lin, H.Y. Zhou, T.G. Luan, Coupling solid-phase microextraction with ambient mass spectrometry using surface coated wooden-tip probe for rapid analysis of ultra trace perfluorinated compounds in complex samples, Anal. Chem. 86 (2014) 11159–11166, https://doi.org/10.1021/ac5034177.
[26] D.L. Li, H.N. Wang, L. Yang, X.K. Yan, L.J. Wang, H.J. Zhang, Intensification effects of stirred fluid on liquid–solid, gas–liquid and gas–solid interactions in flotation: a review, Chem. Eng. Process. Process Intensif. 152 (2020) 107943, https://doi.org/10.1016/j.cep.2020.107943.
[27] C. Ling, Q.F. Shi, Z.P. Wei, J.J. Zhang, J.J. Hu, J.Y. Pei, Rapid analysis of quinones in complex matrices by derivatization-based wooden-tip electrospray ionization mass spectrometry, Talanta 237 (2022) 122912, https://doi.org/10.1016/j.talanta.2021.122912.
[28] D.M. Freund, K.A. Sammons, N.P. Makunga, J.D. Cohen, A.D. Hegeman, Leaf spray mass spectrometry: a rapid ambient ionization technique to directly assess metabolites from plant tissues, J. Vis. Exp. (2018) e57949, https://doi.org/10.3791/57949.
[29] B. Hu, Z.P. Yao, Electrospray ionization mass spectrometry with wooden tips: a review, Anal. Chim. Acta 1209 (2022) 339136, https://doi.org/10.1016/j.aca.2021.339136.
[30] C. Barrón, C.M. Duarte, Dissolved organic carbon pools and export from the coastal ocean, Glob. Biogeochem. Cycles 29 (2015) 1725–1738, https://doi.org/10.1002/2014GB005056.
[31] Environmental Protection Agency, Office of science and technology, engineering and analysis division, revised assessment of detection and quantitation approaches. https://onesearch.library.northeastern.edu/permalink/01NEU_INST/fgrrp0/alma9952293931701401, 2004. (Accessed 8 July 2025).
[32] E.M. McBride, P.M. Mach, E.S. Dhummakupt, S. Dowling, D.O. Carmany, P. S. Demond, G. Rizzo, N.E. Manicke, T. Glaros, Paper spray ionization: applications and perspectives, TrAC, Trends Anal. Chem. 118 (2019) 722–730, https://doi.org/10.1016/j.trac.2019.06.028.
[33] B. Freeland, E. McCarthy, R. Balakrishnan, S. Fahy, A. Boland, K.D. Rochfort, M. Dabros, R. Marti, S.M. Kelleher, J. Gaughran, A review of polylactic acid as a replacement material for single-use laboratory components, Materials 15 (2022) 26, https://doi.org/10.3390/ma15092989.
[34] X.L. Zuo, Y. Zhou, K.G. Hao, C. Liu, R.H. Yu, A.R. Huang, C. Wu, Y.Y. Yang, 3D printed all-natural hydrogels: flame-retardant materials toward attaining green sustainability, Adv. Sci. (Weinh.) 11 (2024) e2306360, https://doi.org/10.1002/advs.202306360.
[35] P.R. Haddad, M. Taraji, R. Szücs, Prediction of analyte retention time in liquid chromatography, Anal. Chem. 93 (2021) 228–256, https://doi.org/10.1021/acs.analchem.0c04190.
[36] J.Y. Pei, C.C. Hsu, R.J. Zhang, Y.H. Wang, K.F. Yu, G.M. Huang, Unexpected reduction of iminoquinone and quinone derivatives in positive electrospray ionization mass spectrometry and possible mechanism exploration, J. Am. Soc. Mass Spectrom. 28 (2017) 2454–2461, https://doi.org/10.1007/s13361-017-1770-4.
[37] J.Y. Pei, C.C. Hsu, K.F. Yu, Y.H. Wang, G.M. Huang, Time-resolved method to distinguish protein/peptide oxidation during electrospray ionization mass spectrometry, Anal. Chim. Acta 1011 (2018) 59–67, https://doi.org/10.1016/j.aca.2018.01.025.
[38] N.B. Cech, C.G. Enke, Practical implications of some recent studies in electrospray ionization fundamentals, Mass Spectrom. Rev. 20 (2001) 362–387, https://doi.org/10.1002/mas.10008.
[39] A. Albert, J.T. Shelley, C. Engelhard, Plasma-based ambient desorption/ionization mass spectrometry: state-of-the-art in qualitative and quantitative analysis, Anal. Bioanal. Chem. 406 (2014) 6111–6127, https://doi.org/10.1007/s00216-014-7989-z.
[40] S. Gerbig, G. Stern, H.E. Brunn, R.A. Düring, B. Spengler, S. Schulz, Method development towards qualitative and semi-quantitative analysis of multiple pesticides from food surfaces and extracts by desorption electrospray ionization mass spectrometry as a preselective tool for food control, Anal. Bioanal. Chem. 409 (2017) 2107–2117, https://doi.org/10.1007/s00216-016-0157-x.
[41] J.M. Wu, X.Q. Qian, Z.G. Yang, L.F. Zhang, Study on the matrix effect in the determination of selected pharmaceutical residues in seawater by solid-phase extraction and ultra-high-performance liquid chromatography–electrospray ionization low-energy collision-induced dissociation tandem mass spectrometry, J. Chromatogr. A 1217 (2010) 1471–1475, https://doi.org/10.1016/j.chroma.2009.12.074.
[42] H. Trufelli, P. Palma, G. Famiglini, A. Cappiello, An overview of matrix effects in liquid chromatography–mass spectrometry, Mass Spectrom. Rev. 30 (2011) 491–509, https://doi.org/10.1002/mas.20298.
[43] A.J. Waters, D.R. Sandhu, G. Lowe, J. Fergson, Photocontact allergy to PABA in sunscreens: the need for continued vigilance, Contact Dermat. 60 (2009), https://doi.org/10.1111/j.1600-0536.2008.01448.x, 173-173.
[44] P.P. Agin, Water resistance and extended wear sunscreens, Dermatol. Clin. 24 (2006) 75–79, https://doi.org/10.1016/j.det.2005.08.002.
[45] J.J. Hu, C.G. Pan, F.J. Peng, H. Liang, Z.Z. Liu, K.F. Yu, An integrated multi-omics approach reveals octocrylene disrupts Tetradesmus obliquus growth by triggering a cascade of photosynthetic inhibition and metabolic dysregulation, J. Hazard. Mater. 495 (2025) 139072, https://doi.org/10.1016/j.jhazmat.2025.139072.
[46] S. Kim, K. Choi, Occurrences, toxicities, and ecological risks of benzophenone-3, a common component of organic sunscreen products: a mini-review, Environ. Int. 70 (2014) 143–157, https://doi.org/10.1016/j.envint.2014.05.015.
[47] Xinhuanet, Surge in Chinese tourist arrivals showcases strong people-to-people ties – Malaysian official. https://english.news.cn/20241001/c3690ba199d34b8da1095764dcd8f993/c.html, 2024. (Accessed 3 May 2025).
[48] D. Vuckovic, A.I. Tinoco, L. Ling, C. Renicke, J.R. Pringle, W.A. Mitch, Conversion of oxybenzone sunscreen to phototoxic glucoside conjugates by sea anemones and corals, Science 376 (2022) 644–648, https://doi.org/10.1126/science.abn2600.
[49] D. Stien, F. Clergeaud, A.M.S. Rodrigues, K. Lebaron, R. Pillot, P. Romans, S. Fagervold, P. Lebaron, Metabolomics reveal that octocrylene accumulates in pocillopora damicornis tissues as fatty acid conjugates and triggers coral cell mitochondrial dysfunction, Anal. Chem. 91 (2019) 990–995, https://doi.org/10.1021/acs.analchem.8b04187.
[50] J.Y. Pei, K. Pang, M.W. Wang, R.J. Zhang, K.F. Yu, Research progress on toxicological effects of organic ultraviolet absorbents on coral, Asian J. Ecotoxicol. 18 (2023) 51–67. https://link.cnki.net/urlid/11.5470.X.20221028.1458.008.
[51] P.L. Choo, S.R.M. Hashim, E. Saleh, R. Shapawi, Z. Waheed, Assessing anthropogenic impacts on coral reefs using local and expert knowledge in the Semporna Priority conservation area, Sabah, Malaysia, Aquat. Conserv. Mar. Freshw. Ecosyst. 35 (2025) e70108, https://doi.org/10.1002/aqc.70108.
[52] Daily Express (Malaysia), Losing the battle to plastic in semporna. https://www.dailyexpress.com.my/read/5174/losing-the-battle-to-plastic-in-semporna/, 2023. (Accessed 8 July 2025).
[53] UN Environment Programme, Enhancing wastewater, nutrient management and sanitation provision for marginalized coastal communities in Sabah, Malaysia. https://www.unep.org/topics/ocean-seas-and-coasts/ecosystem-degradation-pollution/wastewater/enhancing-wastewater?utm_source=chatgpt.com, 2024. (Accessed 8 July 2025).

Analytical Methods

ROYAL SOCIETY OF CHEMISTRY

PAPER

View Article Online
View Journal | View Issue

Check for updates

Cite this: *Anal. Methods*, 2025, **17**, 6598

Comparative evaluation of positive and negative LC-MS modes for DOM profiling†

Jiying Pei,[a] Shiguo Chen,[b] Jiayu Zhang,[a] Wenfeng Yu,[a] Weijie Qin[a] and Kefu Yu*[a]

Dissolved organic matter (DOM) in marine environments is critical for nutrient cycling and carbon storage, forming a fundamental part of the ocean's biogeochemical cycles. Traditionally, DOM analysis has utilized negative electrospray ionization (ESI−) mass spectrometry, yet positive electrospray ionization (ESI+) mode has recently gained traction. However, few studies have compared ESI+ and ESI− to understand how these modes impact the overall DOM profiling results. This study investigates DOM profiles from the Sansha Yongle Blue Hole (SYBH)—the world's deepest blue hole—using HPLC-Orbitrap-MS/MS in both ESI+ and ESI− modes. Results show that ESI+ detects a broader range of DOM ions, with a significant correlation in ion counts between the two modes across different depths. ESI+ is more effective for detecting nitrogen-rich compounds (CHN, CHON, CHONS), while ESI− is better for sulfur-rich compounds (CHOS), especially in anoxic layers. Both modes identify similar levels of carbohydrates, carboxyl-rich alicyclic molecules (CRAM), and unsaturated aliphatic compounds (UA), but ESI+ detects more highly unsaturated compounds (HU), peptides, and polyphenols. Correlations in ion counts for carbohydrates, CRAM, and UA across depths indicate consistency between modes, while differences for HU, peptides, and polyphenols suggest lower ionization efficiency in ESI−. Both modes distinguish oxic, chemocline, and anoxic layers, but molecular parameters like double bond equivalents (DBE), modified aromaticity index (AImod), and H/C ratios correlate between modes, while O/C ratios do not. These discrepancies suggest that using only one ionization mode may bias DOM interpretation. Future studies should employ multi-mode ionization to enhance DOM profiling and understanding across marine environments.

Received 24th April 2025
Accepted 24th July 2025

DOI: 10.1039/d5ay00679a

rsc.li/methods

Published on 07 August 2025. Downloaded by Guangxi University on 8/31/2025 7:18:05 AM.

1. Introduction

Dissolved organic matter (DOM) is a vital component of the marine biogeochemical cycle, serving as a reservoir of organic carbon and playing a key role in nutrient cycling and energy transfer within marine ecosystems.[1] It is integral to the oceanic food web, mediating the exchange of elements between inorganic reservoirs and the marine biosphere.[2] Additionally, DOM significantly influences microbial interactions, shaping the dynamics of microbial communities and broader ecological processes.[3] Therefore, a comprehensive understanding of DOM is essential for unraveling the complexities of oceanic processes and their connections to the global carbon cycle.

However, characterizing the composition and molecular properties of DOM presents considerable challenges due to its high complexity and heterogeneity.[4] Recent advancements in analytical techniques have facilitated more in-depth exploration of DOM's chemical complexity. Among these techniques, Fourier-transform ion cyclotron resonance mass spectrometry (FT-ICR-MS)[5] and liquid chromatography-tandem mass spectrometry (LC-MS/MS)[6] stand out for their high sensitivity, resolution, and ability to analyze complex mixtures. FT-ICR-MS is particularly valuable for its accurate mass measurements, allowing for unambiguous molecular formula assignments and providing detailed insights into the molecular diversity of DOM.[7] Despite these advantages, elucidating the molecular structure of DOM remains challenging, especially regarding isomers, which limits the ability to determine its origins and cycling pathways in the environment. In contrast, LC-MS/MS offers significant advantages for structural analysis. It enables both level 1 and level 2 structural identification through molecular annotation, thereby enhancing the understanding of DOM's composition. When combined with bioinformatics platforms like GNPS (Global Natural Products Social Molecular Networking), LC-MS/MS expands the scope of DOM structure analysis, facilitating more comprehensive profiling.[8] The incorporation of liquid chromatography (LC) as a pre-separation step further improves analysis by reducing sample complexity and minimizing ion suppression.[9] This is essential for detecting low-abundance compounds and separating isomers while yielding valuable retention time data for more

[a]*Guangxi Laboratory on the Study of Coral Reefs in the South China Sea, Coral Reef Research Center of China, School of Marine Sciences, Guangxi University, Nanning 530004, China. E-mail: kefuyu@scsio.ac.cn*

[b]*School of Resources, Environment and Materials, Guangxi University, Nanning 530004, China*

† Electronic supplementary information (ESI) available. See DOI: https://doi.org/10.1039/d5ay00679a

This journal is © The Royal Society of Chemistry 2025

Published on 07 August 2025. Downloaded by Guangxi University on 8/31/2025 7:18:05 AM.

accurate qualitative and quantitative analyses of DOM.[10] These advanced capabilities are critical for comparing compounds across samples, allowing for deeper insights into the molecular variability of DOM. By leveraging high-resolution LC-MS/MS, researchers can generate comprehensive molecular inventories from complex environmental datasets. This is vital for addressing key questions about the geochemistry of DOM.

In DOM studies, selecting the appropriate ionization mode is critical, as it significantly impacts the types and range of detectable compounds. Traditionally, the negative electrospray ionization (ESI−) mode has been preferred for targeting compounds with acidic functional groups, such as organic acids and phosphates, due to its high ionization efficiency for these species.[11] However, advancements in mass spectrometry have highlighted the increasing importance of the positive electrospray ionization (ESI+) mode. ESI+ enhances ionization efficiency for nitrogen-containing compounds and achieves higher match rates in spectral database searches.[8] For instance, ESI+ has demonstrated strong capabilities in detecting nitrogen-rich xenobiotics, including pharmaceuticals and personal care products, in marine environments.[12] In this content, ESI+ has demonstrated superior performance in compound annotation, offering broader coverage of DOM chemical space compared to ESI−. Despite the distinct advantages of both ionization modes, substantial differences in molecular formula assignments are frequently observed. Recently, several studies have focused on comparing ESI+ and ESI− modes for DOM characterization.[13–16] For example, a study on DOM in Antarctic snow revealed only 1–11% formula overlap between the two modes.[13] Similarly, a study of seawater and freshwater from New Zealand demonstrated that 30% of molecular formulas were shared between the two sample types in ESI−, while over 90% overlapped in ESI+, suggesting that ESI+ captures a broader set of molecular features common across aquatic environments.[14] This study further revealed significant discrepancies in key bulk parameters, such as double bond equivalents (DBE), the element ratios (H/C and O/C), between ionization modes. These findings underscore that each ionization mode reveals distinct aspects of DOM composition, highlighting the importance of careful mode selection to capture comprehensive molecular diversity.[15,16]

However, most existing studies comparing ESI+ and ESI− have primarily focused on general metrics, including the total number of assigned molecular formulas, formula overlap, elemental compositions, and heteroatom distributions. Comparative evaluations at a finer scale—specifically across molecular categories such as carbohydrates, carboxyl-rich alicyclic molecules (CRAM), unsaturated aliphatic compounds (UA), highly unsaturated compounds (HU), peptides, and polyphenols—remain limited. Furthermore, these investigations have largely been confined to standard reference materials,[15] surface waters,[16] or specific matrices like snow,[13] freshwater,[14] or lignin degradation products.[17] There is a notable lack of studies considering how dynamic environmental gradients, especially redox stratification, influence DOM ionization behavior across different modes.

To address this gap, the present study conducts a systematic comparison of ESI+ and ESI− for DOM analysis in the Sansha Yongle Blue Hole (SYBH)—the world's deepest marine blue hole. The SYBH presents a naturally occurring, vertically stratified water column with distinct oxic, chemocline, and anoxic layers,[18] offering an ideal setting to examine how hydrogeochemical gradients influence DOM composition and ionization behavior. By performing a depth-resolved comparison of DOM detected in both ionization modes, this study aims to evaluate the degree of consistency between ESI+ and ESI− in capturing molecular diversity, chemical space coverage, and compositional features. The outcomes will provide critical guidance for future DOM studies in complex marine environments, informing optimal ionization mode selection for comprehensive molecular characterization.

2. Materials and methods

2.1. Sample collection

SYBH is the world's deepest oceanic blue hole, reaching a depth of 300 meters and characterized by its unique vertical structure.[19] The steep walls enclose the central shaft, descending to approximately 50 meters below sea level. Below this depth, the cave's passage angle shifts from nearly vertical (90°) to a steeper slope exceeding 120°, reaching down to 150 meters. Beyond this point, the passage angle gradually returns to 90° as it narrows. This distinct topography limits water exchange between the surface and deeper layers, resulting in significant variations in physical and chemical properties at different depths. Based on oxygen content, the SYBH can be divided into three layers: the oxic layer (<50 m), the chemocline (50–150 m), and the anoxic layer (150–300 m).

In October 2019, 28 seawater samples were collected from SYBH (111.768°E, 16.525°N) (Fig. S1a and 1b†) at various depths, encompassing the oxic layer (0 m, 10 m, 20 m), the chemocline (50 m, 80 m, 85 m, 90 m, 95 m, 100 m, 110 m, 120 m, 150 m), and the anoxic layer (200 m, 250 m) (Fig. S1c†). Each depth was sampled in duplicate. Sampling techniques differed based on depth: a conductivity-temperature-depth (CTD) system with a 12-bottle rosette sampler (General Oceanics, USA) was employed for the oxic layer and chemocline. However, the complex terrain of SYBH limited the winch to a maximum depth of 190 m. To collect samples from the deeper anoxic layer, a remotely operated vehicle (ROV) equipped with GO-Flo bottles (General Oceanics, USA) was used. Environmental parameters, including temperature, salinity, DO, pH, turbidity, and chlorophyll-a (Chl-a), were measured *in situ* across the 0 to 300 m depth range using the CTD system. All seawater samples were filtered on-site using a 0.45 μm pore size membrane filter (Acropak, Pall) and stored at −20 °C for subsequent DOM analysis in the laboratory. The experimental workflow is outlined in Fig. S2.†

2.2. Solid phase extraction

The solid phase extraction (SPE) method followed the protocol developed by Dittmar *et al.*[20] Filtered seawater samples (1.2 L)

Published on 07 August 2025. Downloaded by Guangxi University on 8/31/2025 7:18:05 AM.

were acidified to a pH of 2 using hydrochloric acid (HCl) and concentrated with Agilent Bond Elut PPL cartridges (200 mg, 3 mL). Before loading the samples, the cartridges were conditioned with 8 mL of methanol, followed by 8 mL of acidified Milli-Q water (pH = 2). The seawater was then passed through the cartridges at a flow rate of 4 mL min^{-1}, followed by a rinse with 10 mL of acidified Milli-Q water. After drying the cartridges with nitrogen gas, the DOM was eluted using 8 mL of methanol. The eluent was concentrated to a final volume of 0.5 mL under nitrogen gas and reconstituted with an equal volume (0.5 mL) of Milli-Q water. The final extract was stored at −20 °C until analysis by LC-MS/MS.

2.3. LC-MS/MS data acquisition and pre-processing

The seawater extracts were analyzed using a Thermo Q-Exactive mass spectrometer coupled with a Dionex UltiMate 3000 HPLC system. Chromatographic separation was achieved using an ACQUITY CSH C18 column (2.1 × 100 mm; 1.7 μm particle size; Waters, MA, USA) at a flow rate of 200 μL min^{-1} and a temperature of 30 °C. The mobile phase consisted of H_2O with 0.1% formic acid (mobile phase A) and methanol with 0.1% formic acid (mobile phase B). The gradient profile was as follows: from 0 to 3 minutes, 5% B; from 3 to 20 minutes, a linear increase from 5% to 95% B. The system was held at 95% B for 5 minutes, then returned to 5% B over 1 minute, followed by a 4-minute equilibration before the next injection. A 2 μL injection volume was used for each sample.

Mass spectrometry data were collected using data-dependent acquisition (DDA) in both ESI+ and ESI−. The ESI source parameters were optimized as follows: sheath gas flow, 35 L min^{-1}; auxiliary gas flow, 15 L min^{-1}; auxiliary gas temperature, 250 °C. The spray voltage was set to 3.5 kV for ESI+ and 3.0 kV for ESI−. The inlet capillary temperature was maintained at 350 °C, with an S-lens RF level of 50 V applied to enhance ion transmission. The full mass spectra were scanned from *m*/*z* 100 to 1000, achieving a resolution of 35 000 at *m*/*z* 200 (R*m*/*z* 200). A maximum ion injection time of 100 ms was set, with automated gain control (AGC) configured at 3.0×10^6. In MS/MS mode, the top 10 most intense ions were selected for fragmentation. The MS/MS scans achieved a resolution of 17 500 at *m*/*z* 200 (R*m*/*z* 200), with a maximum ion injection time of 50 ms and AGC set to 1.0×10^5. The precursor selection window for MS/MS was set at *m*/*z* 1.5, with normalized collision energy gradually increasing from 15% to 30%.

Chromatographic peaks, including MS1 features and MS/MS spectra, were extracted from mass spectrometry raw data using MZmine software (version 3.4.27), an open-source tool.[21] The LC-MS/MS raw data are accessible through the Mass Spectrometry Interactive Virtual Environment (**http://massive.ucsd.edu/**) under accession number MSV000080562. Feature extraction employed an exact mass detector with signal thresholds of 70 000 for full MS spectra and 10 000 for MS/MS spectra. The Automated Data Analysis Pipeline (ADAP) chromatogram building used a minimum height of 70 000 and an *m*/*z* tolerance of 0.001 (or 5 ppm). Chromatograms were deconvoluted using the local minimum algorithm, with a peak duration range between 0.07 and 1.20 minutes and a minimum absolute height of 70 000. Isotopic peaks were grouped with an *m*/*z* tolerance of 0.003 Da (or 12 ppm) and a retention time tolerance of 0.05 minutes. Peak alignment was conducted using the Join Aligner Module, applying an *m*/*z* tolerance of 0.02 Da and a retention time tolerance of 0.02 minutes. The final peak list underwent gap filling, utilizing an intensity tolerance of 5%, an *m*/*z* tolerance of 0.001 Da (or 5 ppm), and a retention time tolerance of 0.15 minutes.

2.4. Molecular formula assignment (SIRIUS, ZODIAC) and DOM analysis

The tandem mass spectrometry data exported from MZmine software were annotated using the SIRIUS computational tool. *De novo* molecular formulas were determined using the SIRIUS module, which involved accurate mass calculation, comparison of experimental and predicted isotopic patterns, and analysis of fragmentation trees of the fragment ions.[22] To enhance the accuracy of molecular formula predictions, the ZODIAC module was applied to analyze joint fragments and losses across the fragmentation trees of various compounds in the dataset.[23] The SIRIUS parameters were configured as follows: elements were restricted to carbon (C), hydrogen (H), oxygen (O), nitrogen (N), sulfur (S) and phosphorus (P). A maximum of 10 molecular formula candidates was retained, with the computed maximum precursor ion *m*/*z* set to 600. The instrument type was specified as Orbitrap, and the maximum allowed *m*/*z* deviation was set to 5 ppm. All adducts were considered (auto-charge), and a ZODIAC threshold filter of 0.98 was applied. DOM classification was performed based on the following criteria:[24] carbohydrates, 1.6 < H/C < 2.0, 0.7 < O/C < 1.0, and $N = 0$; CRAM, 0.3 < DBE/C < 0.68, 0.2 < DBE/H < 0.95, and 0.77 < DBE/O < 1.75; UA, 1.5 ≤ H/C < 2, O/C < 0.9, and $N = 0$; HU, AI_{mod} < 0.5, H/C < 1.5, and O/C < 0.9; peptides, 1.5 < H/C < 2.0, O/C ≤ 0.9, and $N > 0$; polyphenols, 0.5 < AI_{mod} < 0.66. The bulk parameters of DOM,[7] including DBE, modified aromaticity index (AI_{mod}), H/C, and O/C, were calculated using the magnitude-weighted average of normalized peak intensities. The normalized intensity of each formula was determined by dividing the peak intensity of each formula by the total intensity of all formulas within each sample.

2.5. Quality control

To ensure the reliability and accuracy of LC-MS/MS analysis for seawater samples, a rigorous quality control protocol was implemented. First, a blank control test was performed to identify any potential contamination during the sample preparation process. In this test, 1.2 L of ultrapure water was subjected to the same extraction procedure as the seawater samples. The signal intensities obtained from the blank control were then subtracted from the corresponding seawater sample intensities to account for background interference. In addition, quality control (QC) samples were prepared by combining 50 mL of seawater from different depths of the SYBH. These pooled samples were processed using SPE, applying the same procedure used for seawater samples. QC samples were

 This journal is © The Royal Society of Chemistry 2025

Published on 07 August 2025. Downloaded by Guangxi University on 8/31/2025 7:18:05 AM.

analyzed at regular intervals, specifically after every six seawater samples, to monitor instrument performance and detect any drift or inconsistencies. The relative standard deviation (RSD) range for the remaining 9 characteristic peaks, excluding the 9th peak, is 1.8–7.3% across the five quality control samples (Fig. S3†), indicating acceptable reproducibility within the quality control framework. For data processing, chromatographic peaks exhibiting a standard deviation greater than 30% in the QC samples were excluded to ensure reliability. Prior to instrumental analysis, three consecutive blank injections were made to assess the stability of the instrument and identify any potential background contamination.

2.6. Statistical analysis

Statistical analyses were conducted using multiple software platforms. Principal Component Analysis (PCA) and Orthogonal Partial Least Squares Discriminant Analysis (OPLS-DA) were performed with SIMCA software (version 14.1, Umetrics, Umea, Sweden). Principal Coordinates Analysis (PCoA) was conducted using R packages (version 4.2.2). Statistical significance was assessed with SPSS software (version 23, IBM Corporation, New York, USA). For normally distributed data, Pearson correlation coefficients were calculated to evaluate inter-group correlations, while Spearman correlation coefficients were used for non-normally distributed data. Venn diagrams displaying overlapping compounds across different groups was generated with Venny 2.1, available online at **https://bioinfogp.cnb.csic.es/tools/venny/**. Other statistical analyses were conducted using Origin software (version 2021, OriginLab Corporation, Massachusetts, USA) for tasks not explicitly described.

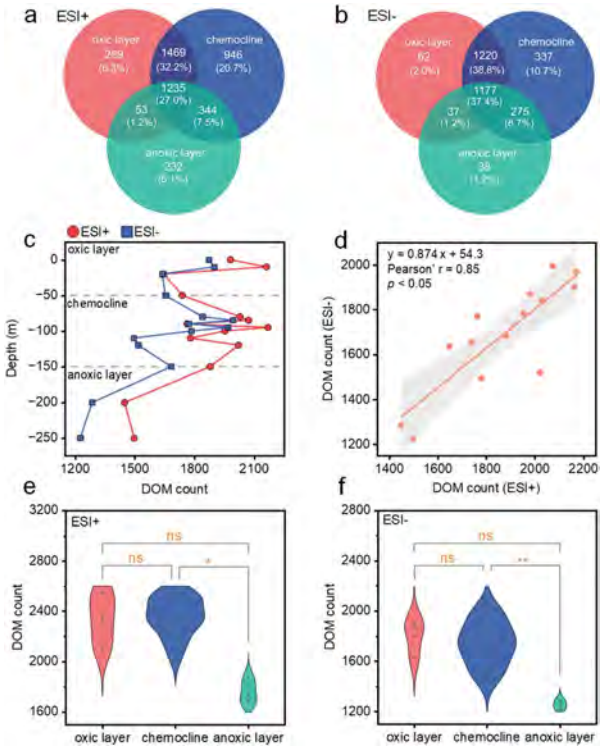


Fig. 1 Venn diagrams showing the distribution of DOM within the oxic layer, chemocline, and anoxic layer under (a) ESI+ and (b) ESI− modes. (c) Variation in DOM counts, and (d) linear correlation analysis of DOM counts, across different depths of the SYBH under ESI+ and ESI− modes. Violin plots displaying DOM counts within the oxic layer, chemocline, and anoxic layer under (e) ESI+ and (f) ESI− modes (* indicates $p < 0.05$, ** indicates $p < 0.01$).

3. Result and discussion

3.1. Comparison of ion features for DOM analysis in ESI+ and ESI− in SYBH

Analysis of DOM in the SYBH using ESI+ and ESI− mass spectrometry revealed distinct ion features across these two modes. The ESI+ mode detected a total of 4568 ions, surpassing the 3146 ions detected in the ESI− mode (Fig. 1a and b). This broader DOM mass spectrum coverage in the ESI+ can be attributed to two main factors. First, acidification with hydrochloric acid increased proton availability, enhancing protonation of organic molecules and thus improving ionization efficiency for ESI+ detection.[25] Second, to enhance the ionization efficiency in the ESI+ mode, low concentrations of acidic reagents are often added to the mobile phase. This not only facilitates protonation reactions but also promotes the formation of various cation adducts.[8] In both ionization modes, most ions were detected in at least two water layers (oxic layer, chemocline, and anoxic layer). In the ESI+, 27.0% of ions were shared across all three layers, while an additional 32.2%, 1.2%, and 7.5% were detected in at least two layers. In contrast, in the ESI−, 37.4% of ions were common across all three layers, with 38.8%, 1.2%, and 8.7% observed in at least two layers. This pattern suggests that the ESI+ has a lower proportion of ions detected across multiple layers (67.9% = 27.0% + 32.2% + 1.2% + 7.5%) than the ESI− (86.1% = 37.4% + 38.8% + 1.2% + 8.7%), resulting in a higher proportion of layer-specific ions in ESI+. For instance, in the oxic layer, 6.3% of ions were unique to the ESI+, compared to only 2.0% in the ESI−. Similarly, in the chemocline, 20.7% of ions were unique to ESI+ *versus* 10.7% in ESI−, and in the anoxic layer, 5.1% were unique to ESI+ compared to 1.2% in ESI−. The more diverse and layer-specific ions observed in ESI+ likely reflects its broader DOM coverage[12] and greater sensitivity to certain molecular classes unique to specific layers, which are less efficiently detected in ESI−.

The distribution of DOM counts across different depths in the SYBH was analyzed in both ESI+ and ESI− to evaluate consistency between the two techniques. As shown in Fig. 1c and d, both modes exhibit a similar trend in DOM counts across depths ($p < 0.05$), suggesting comparable data quality and consistency across ionization methods. This consistency between modes strengthens the reliability of the results. The average DOM counts at the three layers showed that the oxic layer and the chemocline had comparable DOM levels in both ionization modes (Fig. 1e and f). However, both layers exhibited significantly higher DOM counts compared to the anoxic layer. The reduced DOM counts in the anoxic layer can be attributed to two main factors: microbial degradation of DOM and limited water mixing between layers. In the surface layer,

Published on 07 August 2025. Downloaded by Guangxi University on 8/31/2025 7:18:05 AM.

phytoplankton and other organisms produce substantial organic material. As these organisms die, their remains settle through the water column,[26] where microbial activity induces oxidative decomposition, progressively reducing DOM levels with increasing depth.[27] However, limited vertical water mixing prevents the replenishment of DOM in the anoxic layer from the oxygen-rich surface layers. This restricted mixing, coupled with microbial degradation, contributes to the significantly lower DOM counts observed in the anoxic zone.

3.2. Elemental composition of DOM in ESI+ and ESI− in SYBH

DOM can be classified into six categories based on elemental composition: CH, CHO, CHN, CHON, CHOS, and CHONS.[28] Analysis of DOM composition in SYBH across ESI+ and ESI− reveals distinct ionization patterns. Nitrogen-containing compounds (CHN, CHON and CHONS) are more prevalent in ESI+, accounting for 36.9% of the detected compounds (2.0% for CHN, 32.4% for CHON and 2.5% for CHONS), compared to only 10.2% in ESI− (0.1% for CHN, 9.0% for CHON and 1.1% for CHONS) (Fig. 2a). Conversely, CHO and CHOS compounds are more frequently detected in ESI−, with 85.7% of CHO and 4.0% of CHOS detected, compared to 59.1% of CHO and 1.2% of CHOS in ESI+ (Fig. 2a). The absolute detection counts of these six types of DOM in each mode were shown in Fig. 2b. Specifically, CHN compounds (71), CHON compounds (1152) and CHONS compounds (88) are more abundantly detected in ESI+ than in ESI−, where only 3 CHN, 198 CHON and 25 CHONS compounds are observed. In contrast, CHOS compounds are detected more frequently in ESI− (88) than in ESI+ (44). For CH and CHO classes, CHO compounds show higher detection counts in ESI+ (2104 in ESI+ *vs.* 1892 in ESI−), while CH compounds are rare in both modes (99 in ESI+ *vs.* 1 in ESI−). These observations suggest that different ionization modes preferentially ionize specific types of compounds. Nitrogen-containing compounds, such as those with CHN, CHON and CHONS compositions, are more readily protonated in ESI+ due to the higher basicity of nitrogen atoms, which facilitates protonation.[29] In contrast, sulfur-containing compounds, such as those with $-SO_3H$, $-SO_2$, and $-SH$ are more likely to form negative ions in ESI−.[30] This is attributed to the electron-

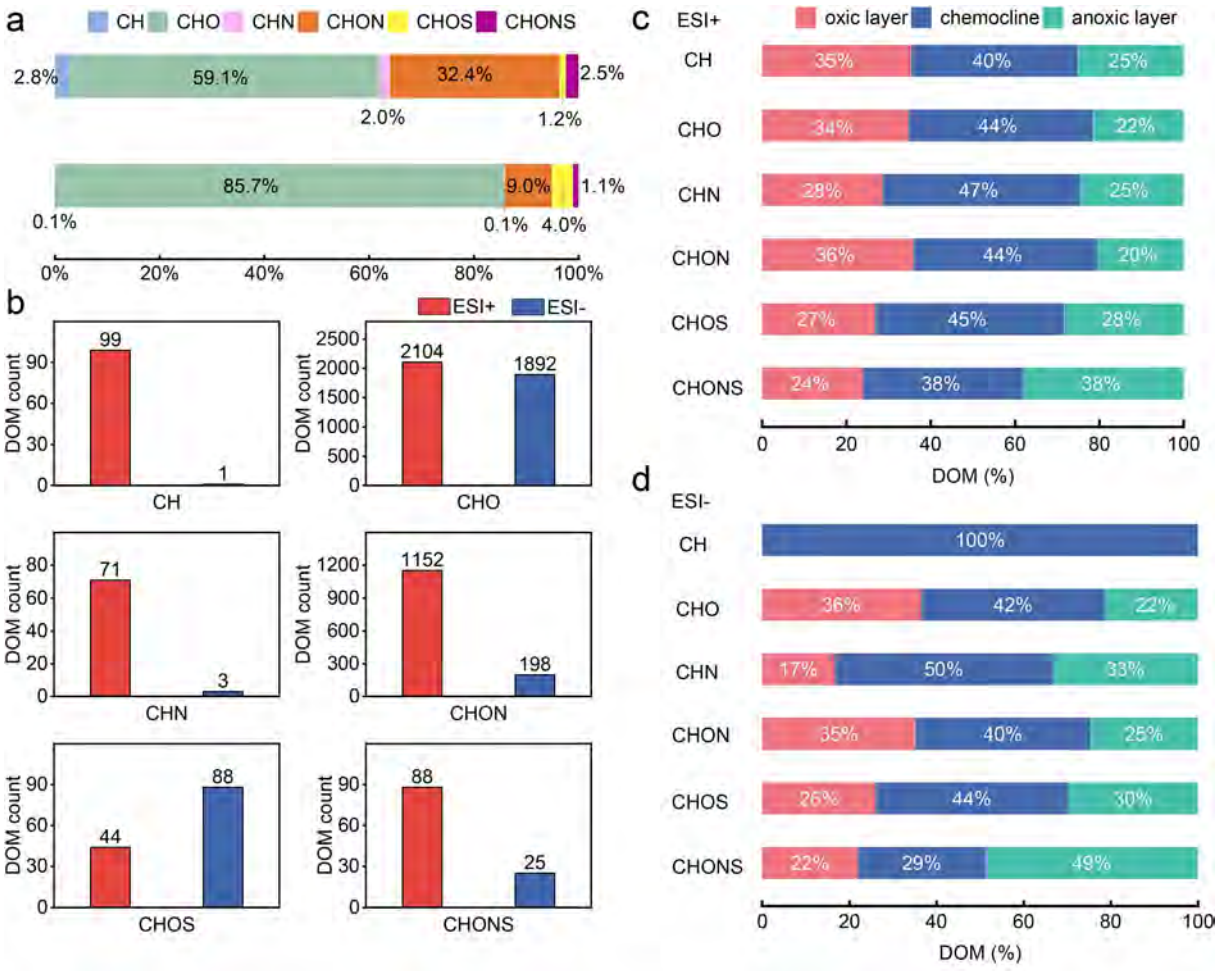


Fig. 2 (a) Molecular elemental composition of DOM in the SYBH under ESI+ and ESI− modes. (b) Count of DOM with elemental composition of CH, CHO, CHN, CHON, CHOS and CHONS under ESI+ and ESI− modes. Distribution of DOM with different elemental compositions across the oxic layer, chemocline, and anoxic layer of the SYBH under (c) ESI+, and (d) ESI− modes.

 This journal is © The Royal Society of Chemistry 2025

Published on 07 August 2025. Downloaded by Guangxi University on 8/31/2025 7:18:05 AM.

withdrawing nature of sulfur, which stabilizes negative charges on adjacent atoms and promotes deprotonation.[31] For compounds with a CHO elemental composition, their complex structural diversity leads to some being more readily detected in ESI+, while others are more efficiently ionized in ESI−. Lastly, CH-only compounds are infrequently detected in either ionization mode due to the lack of polar or ionizable functional groups. The slightly higher detection rate in ESI+ may result from alternative ionization mechanisms, such as adduct formation with NH_4^+ or Na^+,[32] or from the lower chemical background noise typically associated with ESI+.

The detection frequencies of six DOM groups (CH, CHO, CHN, CHON, CHOS, and CHONS) across different water layers were analyzed under both ESI+ and ESI− modes (Fig. 2c and d). Across both ionization modes, the chemocline of SYBH consistently showed the highest relative proportions for CH, CHO, CHN, CHON compounds. Conversely, sulfur-containing compounds (CHOS and CHONS) show their highest proportions in the chemocline or anoxic layer under both ionization modes. The elevated levels of CH, CHO, CHN and CHON compounds in the chemocline reflect their overall greater abundance in this layer. As discussed above, this enrichment is probably driven by intense biological activity at the oxic–anoxic interface, including photosynthesis and diverse microbial metabolic processes, which contribute to the generation and transformation of organic metabolites.[33] In contrast, the higher levels of CHOS and CHONS in the chemocline and anoxic layer suggest specific enrichment mechanisms favoring the accumulation of sulfur-containing DOM in oxygen-deprived conditions.[34] These mechanisms likely involve both microbial and abiotic processes. Under anoxic conditions, sulfur-reducing bacteria play a significant role in sulfur transformation, generating sulfur-containing DOM as metabolic byproducts.[35] For example, Patin *et al.* observed an abundance of reduced sulfur compounds produced by sulfur-reducing microorganisms in the oxygen-depleted zones of Amberjack Hole in the Gulf of Mexico.[36] Additionally, abiotic processes further contribute to sulfur DOM accumulation under anoxic conditions.[37] Gomez-Saez *et al.* demonstrated that abiotic reactions between reduced sulfur species and DOM are important contributors to the buildup of sulfur-rich DOM during anoxic events.[38]

It is important to note that compound-specific detection frequencies can be influenced by ionization efficiency. This efficiency may, in turn, be modulated by matrix effects such as salinity and pH gradients with depth.[39] However, these factors are unlikely to significantly affect the vertical distribution patterns observed in this study. Pre-analytical acidification to pH $\sim$ 2, followed by SPE and LC, substantially attenuates matrix-induced ion suppression, particularly those arising from ionic strength and salt composition.[40] Moreover, the vertical salinity gradient in SYBH is relatively narrow, with values ranging from 33.5‰ to 34.6‰, representing only a 3.3% relative difference (Fig. S4†), thereby further limiting the extent of matrix-driven variability in ionization efficiency across depths.

3.3. Classification of DOM in ESI+ and ESI− in SYBH

DOM in seawater consists of a complex blend of organic compounds. They are generally categorized into six primary types based on their elemental composition and structural features: carbohydrates, CRAM, HU, UA, peptides, and polyphenols.[41,42] Each category exhibits unique chemical characteristics. Carbohydrates are highly oxygenated compounds

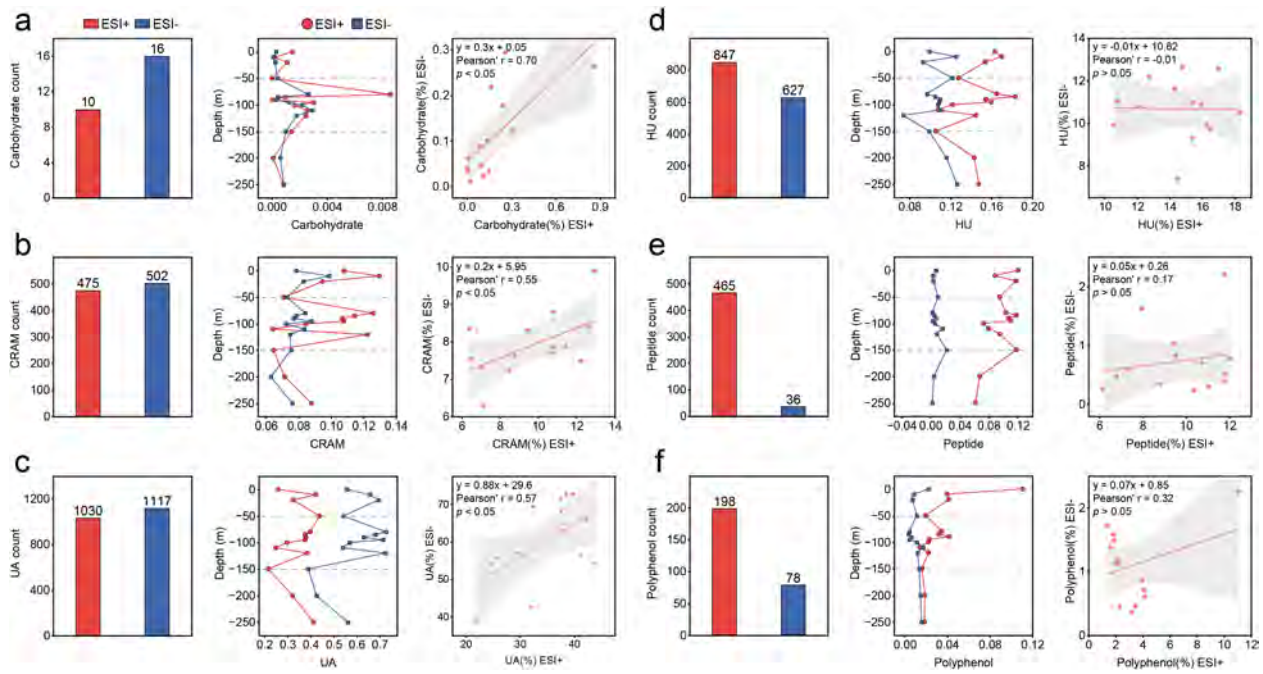


Fig. 3 The count of (a) carbohydrates, (b) CRAM, (c) UA, (d) HU, (e) peptide, and (f) polyphenol in the SYBH under ESI+ and ESI− modes, with variations in abundance at different depths and linear correlation analysis.

Published on 07 August 2025. Downloaded by Guangxi University on 8/31/2025 7:18:05 AM.

devoid of nitrogen atoms and are primarily composed of simple and complex sugars. These compounds typically ionize in ESI+ as $[M + alkali]^+$ and in ESI− as $[M - H]^-$.[43,44] However, carbohydrates have low ionization efficiency in both modes. In DOM samples from SYBH, only 10 carbohydrate ions were detected in ESI+ and 16 in ESI− (Fig. 3a). CRAM, characterized by numerous carboxyl groups, easily lose protons in ESI− due to their acidic nature. They can also gain protons in ESI+ because of the high electronegativity of oxygen atoms. As a result, CRAM showed a balanced detection frequency between the two modes, with 475 ions in ESI+ and 502 ions in ESI− (Fig. 3b). This balance aligns with findings from studies near New Zealand's South Island, where similar counts of CRAM were detected in both ionization modes.[14] UA and HU are both unsaturated compounds, which displayed comparable ion counts in ESI+ and ESI−. For UA, 1030 ions were detected in ESI+ and 1117 ions in ESI− (Fig. 3c). For HU, 847 ions were detected in ESI+ compared to 627 in ESI− (Fig. 3d). Peptides exhibited much higher ionization efficiency in ESI+. This is attributed to their high nitrogen content, particularly amine groups, which readily accept protons. As a result, 465 peptide ions were detected in ESI+, compared to only 36 ions in ESI− (Fig. 3e). Polyphenols also ionized more efficiently in ESI+. This is because their hydroxyl groups are conjugated to aromatic rings, and the electron-rich benzene rings act as electron donors, enhancing the protonation of the hydroxyl oxygen. Consequently, 198 polyphenol ions were detected in ESI+, compared to 78 ions in ESI− (Fig. 3f).

Correlation analysis between ESI+ and ESI− for the six types of DOM in the SYBH revealed distinct distribution patterns across depths. For carbohydrates, CRAM, and UA, their content trends with depth were consistent between the two ionization modes ($p < 0.05$) (Fig. 3a–c). However, no correlation was observed between ESI+ and ESI− for HU, peptides, and polyphenols ($p > 0.05$) (Fig. 3d–f). The consistent trends for the former group are likely due to their balanced detection frequencies across both ionization modes. In contrast, the lack of correlation for the latter group arises from their preferential ionization in ESI+, making ESI− detections unreliable. These findings highlight the importance of considering ionization mode biases when interpreting data, as relying solely on one mode for compounds that predominantly ionize in the other may lead to distorted conclusions about their environmental roles and interactions.

ESI+ data reveal that average concentrations of CRAM, UA, peptides, and polyphenols are lower in the anoxic layer than in the oxic layer. For CRAM and UA, similar vertical patterns were also captured in ESI− mode, consistent with their strong cross-mode correlation. These compounds likely have important ecological functions in stratified aquatic systems. Specifically, CRAM and UA, which are characterized by their chemical recalcitrance, may serve as important contributors to carbon retention in the anoxic zone.[24] Peptides, especially small or cyclic dipeptides, are increasingly recognized for their involvement in microbial signalling.[45] This is supported by our integrated metabolomics and metagenomics data, which show elevated levels of the dipeptide Glu–Phe in the anoxic layer alongside a higher abundance of anaerobic bacteria.[46] Moreover, polyphenols, with their redox activity and microbial reactivity,[47,48] likely influence microbial interactions and nutrient cycling, particularly in the oxic surface waters. Collectively, these results highlight the significant biogeochemical roles of these compound groups in stratified aquatic environments.

3.4. Bulk parameters and molecular profiling for DOM analysis in ESI+ and ESI− in SYBH

In the analysis of DOM, bulk molecular parameters such as DBE, H/C, AI_{mod}, and O/C are critical for evaluating its complexity, reactivity, and environmental significance.[49,50] These parameters offer insight into DOM's molecular structure, particularly regarding unsaturation, aromaticity, and oxidation. The results

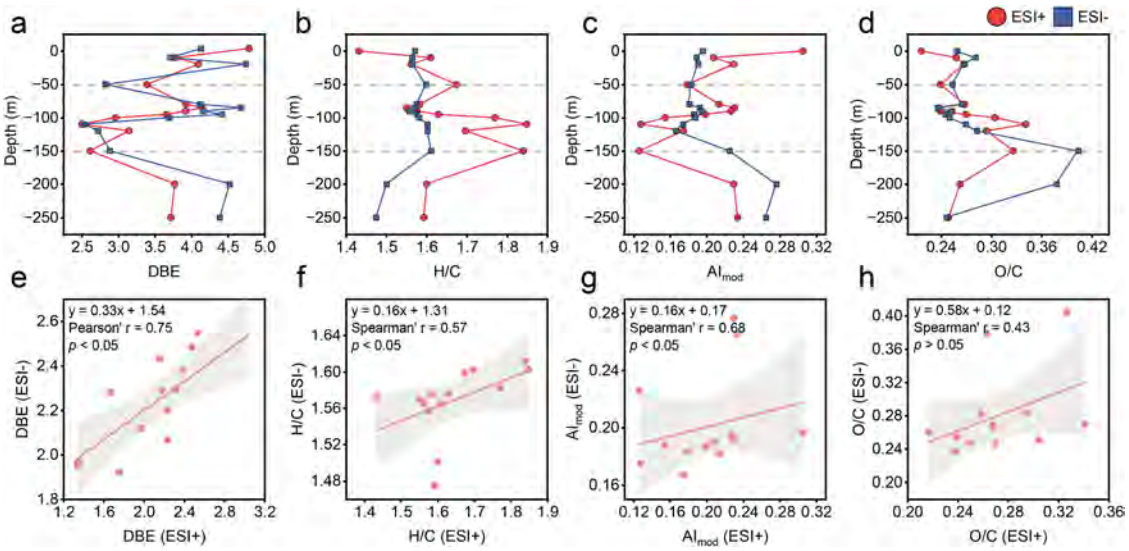


Fig. 4 (a–d) Variation in DBE, H/C, AI_{mod}, and O/C across different depths of the SYBH under ESI+ and ESI− modes. (e–h) Linear correlation analysis of these parameters across different depths of the SYBH between ESI+ and ESI− modes.

 This journal is © The Royal Society of Chemistry 2025

Published on 07 August 2025. Downloaded by Guangxi University on 8/31/2025 7:18:05 AM.

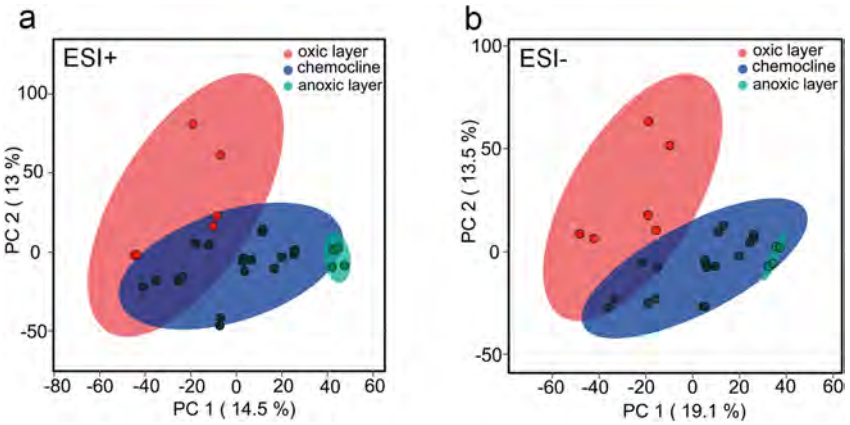


Fig. 5 PCA plots illustrating the differentiation of seawater samples from the oxic layer, chemocline, and anoxic layer of the SYBH under (a) ESI+, and (b) ESI− modes.

showed consistent correlations for DBE, H/C, and AI_{mod} between ESI+ and ESI− modes (Fig. 4a–c, and Fig. 4e–g). This consistency likely arises from the interdependence of these parameters, as they all reflect molecular unsaturation: higher DBE values typically coincide with lower H/C and higher AI_{mod} values, as shown in Fig. S5.† However, the O/C does not display the same consistency across two modes (Fig. 4d and h). It suggests that specific DOM molecular characteristics, such as O/C, may require mode-specific analysis for accurate detection and interpretation.

To explore the compositional differences of DOM across various depths in the SYBH, PCA (Fig. 5), PCoA (Fig. S6†) and OPLS (Fig. S7†) analyses were conducted. The results revealed distinct compositional variations among the oxic, chemocline, and anoxic layers in both ESI+ and ESI− modes. Despite the inherent selectivity of each ionization mode for specific DOM components, the broad molecular coverage provided by both modes enabled effective differentiation of DOM composition across these environmental layers. The vertical stratification of DOM in the SYBH appears to be influenced by the unique environmental conditions at each depth. In the oxic layer, high light availability and elevated oxygen concentrations sustain a diverse community of photosynthetic organisms, such as algae and cyanobacteria, which actively produce DOM.[51] The DOM in this layer is typically fresh, labile, and undergoes rapid biological turnover, resulting in a dynamic pool of readily cycled organic compounds. The chemocline, characterized by steep gradients in oxygen, salinity, temperature, chlorophyll concentration, turbidity, and pH (Fig. S4†), creates a transitional zone where aerobic and anaerobic microbial communities coexist.[52] This zone facilitates diverse metabolic processes, leading to the production of a more complex and heterogeneous DOM pool in the anoxic layer, the absence of oxygen creates a habitat for anaerobic microbes that utilize alternative electron acceptors for metabolism.[53] This results in a distinct DOM composition compared to the oxic layer and chemocline.

4. Conclusions

This study provides a comprehensive comparison of ESI+ and ESI− modes in HPLC-Orbitrap-MS/MS for profiling DOM in the SYBH, highlighting how ionization mode selection influences the detection and interpretation of DOM characteristics. ESI+ captured a broader range of DOM ions than ESI−, although a significant correlation was observed between ion counts detected by both modes across different layers. Elemental composition analysis revealed that nitrogen-rich compounds (CHN, CHON and CHONS) were more abundant in ESI+, while sulfur-rich compounds (CHOS) were preferentially detected in ESI−, particularly in the anoxic layers of the SYBH. Further classification of compounds showed similar detection frequencies for CRAM, UA, and HU across the two ionization modes, while peptides and polyphenols were detected more frequently in ESI+, and carbohydrates consistently showed low detection counts in both modes. Correlation analysis indicated that carbohydrates, CRAM, and UA exhibited significant consistency between ESI+ and ESI− across layers, whereas HU, peptides, and polyphenols showed no correlation. Among bulk molecular parameters, DBE, AI_{mod}, and H/C exhibited consistent correlations between ESI+ and ESI−, while O/C did not, suggesting that specific DOM molecular characteristics may require mode-specific analyses for accurate detection. Despite these discrepancies, both ionization modes effectively differentiated DOM composition across the oxic, chemocline, and anoxic layers of the SYBH. These findings emphasize the importance of using the appropriate ionization mode in DOM analysis. While some parameters yielded consistent results across both modes, others showed significant discrepancies, potentially leading to biased interpretations if only one mode is used. To ensure a more accurate and comprehensive molecular profiling of DOM, we recommend employing multi-mode ionization strategies in future research, enabling a more nuanced analysis of DOM across diverse environmental conditions.

Data availability

Data will be made available on request.

Author contributions

Jiying Pei: writing – review and editing, project administration, funding acquisition, methodology, conceptualization. Shiguo

Published on 07 August 2025. Downloaded by Guangxi University on 8/31/2025 7:18:05 AM.

Chen: writing – original draft, visualization, investigation, formal analysis, software. Kefu Yu: project administration, funding acquisition, resources. Jiayu Zhang: investigation. Wenfeng Yu: supervision. Weijie Qin: software.

Conflicts of interest

There are no conflicts to declare.

Acknowledgements

This work was supported by Guangxi Science and Technology Program (No. AD25069075), Guangxi Natural Science Foundation (No. 2023GXNSFAA026488) and National Natural Science Foundation of China (No. 22264003 and 42090041).

References

1 C. S. Hopkinson and J. J. Vallino, Efficient export of carbon to the deep ocean through dissolved organic matter, *Nature*, 2005, **433**(7022), 142–145.
2 E. B. Kujawinski, The impact of microbial metabolism on marine dissolved organic matter, *Ann. Rev. Mar. Sci.*, 2011, **3**, 567–599.
3 L. Wang, Microbial control of the carbon cycle in the ocean, *Nat. Sci. Rev.*, 2018, **5**(2), 287–291.
4 T. S. Catala, S. Shorte and T. Dittmar, Marine dissolved organic matter: a vast and unexplored molecular space, *Appl. Microbiol. Biotechnol.*, 2021, **105**(19), 7225–7239.
5 O. J. Lechtenfeld, G. Kattner, R. Flerus, S. L. McCallister, P. Schmitt-Kopplin and B. P. Koch, Molecular transformation and degradation of refractory dissolved organic matter in the Atlantic and Southern Ocean, *Geochim. Cosmochim. Acta*, 2014, **126**, 321–337.
6 C. Patriarca, J. Bergquist, P. J. R. Sjoberg, L. Tranvik and J. A. Hawkes, Online HPLC-ESI-HRMS method for the analysis and comparison of different dissolved organic matter samples, *Environ. Sci. Technol.*, 2018, **52**(4), 2091–2099.
7 P. Li, J. Tao, J. Lin, C. He, Q. Shi, X. Li, *et al.*, Stratification of dissolved organic matter in the upper 2000 m water column at the Mariana Trench, *Sci. Total Environ.*, 2019, **668**, 1222–1231.
8 D. Petras, J. J. Minich, L. B. Cancelada, R. R. Torres, E. Kunselman, M. Wang, *et al.*, Non-targeted tandem mass spectrometry enables the visualization of organic matter chemotype shifts in coastal seawater, *Chemosphere*, 2021, **271**, 129450.
9 D. Petras, I. Koester, R. Da Silva, B. M. Stephens, A. F. Haas, C. E. Nelson, *et al.*, High-resolution liquid chromatography tandem mass spectrometry enables large scale molecular characterization of dissolved organic matter, *Front. Mar. Sci.*, 2017, **4**, 405.
10 L. Wegley Kelly, C. E. Nelson, D. Petras, I. Koester, Z. A. Quinlan, M. G. I. Arts, *et al.*, Distinguishing the molecular diversity, nutrient content, and energetic potential of exometabolomes produced by macroalgae and reef-building corals, *Proc. Natl. Acad. Sci. U. S. A.*, 2022, **119**(5), e2110283119.
11 Z. Zhou, Q.-L. Fu, M. Fujii and T. D. Waite, Complementary elucidation of the molecular characteristics of groundwater dissolved organic matter using ultrahigh-resolution mass spectrometry coupled with negative– and positive-Ion electrospray ionization, *Environ. Sci. Technol.*, 2023, **57**(11), 4690–4700.
12 L. Cancelada, R. R. Torres, J. Garrafa Luna, P. C. Dorrestein, L. I. Aluwihare, K. A. Prather, *et al.*, Assessment of styrene-divinylbenzene polymer (PPL) solid-phase extraction and non-targeted tandem mass spectrometry for the analysis of xenobiotics in seawater, *Limnol. Oceanogr.: Methods*, 2021, **20**(2), 89–101.
13 R. Antony, A. M. Grannas, A. S. Willoughbys, R. L. Sleighter, M. Thamban and P. G. Hatcher, Origin and sources of dissolved organic matter in snow on the East Antarctic ice sheet, *Environ. Sci. Technol.*, 2014, **48**(11), 6151–6159.
14 M. Gonsior, B. M. Peake, W. T. Cooper, D. C. Podgorski, J. D'Andrilli, T. Dittmar, *et al.*, Characterization of dissolved organic matter across the subtropical convergence off the South Island, New Zealand, *Mar. Chem.*, 2011, **123**(1–4), 99–110.
15 S. L. Felgate, A. J. Craig, L. W. K. Moodie and J. Hawkes, Characterization of a newly available coastal marine dissolved organic matter reference material (TRM-0522), *Anal. Chem.*, 2023, **95**(16), 6559–6567.
16 D. Bergmann, J. Matarrita-Rodriguez and H. Abdulla, Toward a more comprehensive approach for dissolved organic matter chemical characterization using an Orbitrap Fusion Tribrid mass spectrometer coupled with ion and liquid chromatography techniques, *Anal. Chem.*, 2024, **96**(9), 3744–3753.
17 Y. L. Qi, P. Q. Fu, S. L. Li, C. Ma, C. Q. Liu and D. A. Volmer, Assessment of molecular diversity of lignin products by various ionization techniques and high-resolution mass spectrometry, *Sci. Total Environ.*, 2020, **713**, 136573.
18 L. Xie, B. Wang, X. Pu, M. Xin, P. He, C. Li, *et al.*, Hydrochemical properties and chemocline of the Sansha Yongle Blue Hole in the South China Sea, *Sci. Total Environ.*, 2019, **649**, 1281–1292.
19 T. Li, A. Feng, Y. Liu, Z. Li, K. Guo, W. Jiang, *et al.*, Three-dimensional (3D) morphology of Sansha Yongle Blue Hole in the South China Sea revealed by underwater remotely operated vehicle, *Sci. Rep.*, 2018, **8**(1), 17122.
20 T. Dittmar, B. Koch, N. Hertkorn and G. Kattner, A simple and efficient method for the solid-phase extraction of dissolved organic matter (SPE-DOM) from seawater, *Limnol. Oceanogr.: Methods*, 2008, **6**, 230–235.
21 S. Heuckeroth, T. Damiani, A. Smirnov, O. Mokshyna, C. Brungs, A. Korf, *et al.*, Reproducible mass spectrometry data processing and compound annotation in MZmine 3, *Nat. Protoc.*, 2024, **19**(9), 2597–2641.
22 K. Duhrkop, M. Fleischauer, M. Ludwig, A. A. Aksenov, A. V. Melnik, M. Meusel, *et al.*, SIRIUS 4: a rapid tool for turning tandem mass spectra into metabolite structure information, *Nat. Methods*, 2019, **16**(4), 299–302.

 This journal is © The Royal Society of Chemistry 2025

Published on 07 August 2025. Downloaded by Guangxi University on 8/31/2025 7:18:05 AM.

23 M. Ludwig, L.-F. Nothias, K. Dührkop, I. Koester, M. Fleischauer, M. A. Hoffmann, *et al.*, Database-independent molecular formula annotation using Gibbs sampling through ZODIAC, *Nat. Mach. Intell.*, 2020, **2**(10), 629–641.
24 P. Li, W. Liang, Y. Zhou, Y. Yi, C. He, Q. Shi, *et al.*, Hypoxia diversifies molecular composition of dissolved organic matter and enhances preservation of terrestrial organic carbon in the Yangtze River Estuary, *Sci. Total Environ.*, 2024, **906**, 167661.
25 P. Kebarle and U. H. Verkerk, Electrospray: from ions in solution to ions in the gas phase, what we know now, *Mass Spectrom. Rev.*, 2009, **28**(6), 898–917.
26 U. Alcolombri, F. J. Peaudecerf, V. I. Fernandez, L. Behrendt, K. S. Lee and R. Stocker, Sinking enhances the degradation of organic particles by marine bacteria, *Nat. Geosci.*, 2021, **14**(10), 775.
27 C. Pelikan, K. Wasmund, C. Glombitza, B. Hausmann, C. W. Herbold, M. Flieder, *et al.*, Anaerobic bacterial degradation of protein and lipid macromolecules in subarctic marine sediment, *ISME J.*, 2021, **15**(3), 833–847.
28 Z. L. Chen, H. Zhang, Y. Yi, Y. He, P. Li, Y. Wang, *et al.*, Dissolved organic matter composition and characteristics during extreme flood events in the Yangtze River Estuary, *Sci. Total Environ.*, 2024, **914**, 169827.
29 N. B. Cech and C. G. Enke, Practical implications of some recent studies in electrospray ionization fundamentals, *Mass Spectrom. Rev.*, 2001, **20**(6), 362–387.
30 E. B. Kujawinski, K. Longnecker, N. V. Blough, R. D. Vecchio, L. Finlay, J. B. Kitner, *et al.*, Identification of possible source markers in marine dissolved organic matter using ultrahigh resolution mass spectrometry, *Geochim. Cosmochim. Acta*, 2009, **73**(15), 4384–4399.
31 M. Sun, W. Dai and D. Q. Liu, Fragmentation of aromatic sulfonamides in electrospray ionization mass spectrometry: elimination of SO_2 *via* rearrangement, *J. Mass Spectrom.*, 2008, **43**(3), 383–393.
32 A. Kruve and K. Kaupmees, Adduct formation in ESI/MS by mobile phase additives, *J. Am. Soc. Mass Spectrom.*, 2017, **28**(5), 887–894.
33 J. Beardall, M. Bjork and S. Beer, *Photosynthesis in the Marine Environment*, Wiley Blackwell, 2014, p. 224.
34 H. Ibrahim and L. Tremblay, Origin of dissolved organic sulfur in marine waters and the impact of abiotic sulfurization on its composition and fate, *Mar. Chem.*, 2023, **254**, 104273.
35 E. Magnuson, I. Altshuler, N. J. Freyria, R. J. Leveille and L. G. Whyte, Sulfur-cycling chemolithoautotrophic microbial community dominates a cold, anoxic, hypersaline Arctic spring, *Microbiome*, 2023, **11**(1), 203.
36 N. V. Patin, Z. A. Dietrich, A. Stancil, M. Quinan, J. S. Beckler, E. R. Hall, *et al.*, Gulf of Mexico blue hole harbors high levels of novel microbial lineages, *ISME J.*, 2021, **15**(8), 2206–2232.
37 H. A. Abdulla, D. J. Burdige and T. Komada, Abiotic formation of dissolved organic sulfur in anoxic sediments of Santa Barbara Basin, *Org. Geochem.*, 2020, **139**, 103879.
38 G. V. Gomez-Saez, T. Dittmar, M. Holtappels, A. M. Pohlabeln, A. Lichtschlag, B. Schnetger, *et al.*, Sulfurization of dissolved organic matter in the anoxic water column of the Black Sea, *Sci. Adv.*, 2021, **7**(25), eabf6199.
39 G. Y. Li and G. M. Huang, Alleviation of ion suppression effect in sonic spray ionization with induced alternating current voltage, *J. Mass Spectrom.*, 2014, **49**(7), 639–645.
40 H. Trufelli, P. Palma, G. Famiglini and A. Cappiello, An overview of matrix effects in liquid chromatography-mass spectrometry, *Mass Spectrom. Rev.*, 2011, **30**, 491–509.
41 S. Kim, L. A. Kaplan and P. G. Hatcher, Biodegradable dissolved organic matter in a temperate and a tropical stream determined from ultra-high resolution mass spectrometry, *Limnol. Oceanogr.*, 2006, **51**(2), 1054–1063.
42 M. Seidel, M. Beck, T. Riedel, H. Waska, I. G. N. A. Suryaputra, B. Schnetger, *et al.*, Biogeochemistry of dissolved organic matter in an anoxic intertidal creek bank, *Geochim. Cosmochim. Acta*, 2014, **140**, 418–434.
43 A. Reis, M. R. Domingues, P. Domingues, A. J. Ferrer-Correia and M. A. Coimbra, Positive and negative electrospray ionisation tandem mass spectrometry as a tool for structural characterisation of acid released oligosaccharides from olive pulp glucuronoxylans, *Carbohydr. Res.*, 2003, **338**(14), 1497–1505.
44 J. Hofmann, H. S. Hahm, P. H. Seeberger and K. Pagel, Identification of carbohydrate anomers using ion mobility-mass spectrometry, *Nature*, 2015, **526**(7572), 241–244.
45 S. Sun, Y. Liu, C. Weng, S. Sun, F. Li, H. Li, *et al.*, Cyclic dipeptides mediating quorum sensing and their biological effects in *Hypsizygus marmoreus*, *Biomolecules*, 2020, **10**(2), 298.
46 J. Pei, S. Chen, K. Yu, J. Liang, R. Zhang, P. Li, *et al.*, Microbial regulation of dissolved organic matter revealed by integrated metabolomics and metagenomics in the world's deepest blue hole, *Mar. Environ. Res.*, 2025, DOI: **10.1016/j.marenvres.2025.107354**.
47 J. I. Obeme-Nmom, R. O. Abioye, S. S. R. Flores and C. C. Udenigwe, Regulation of redox enzymes by nutraceuticals: a review of the roles of antioxidant polyphenols and peptides, *Food Funct.*, 2024, **15**(22), 10956–10980.
48 L. De Rossi, G. Rocchetti, L. Lucini and A. Rebecchi, Antimicrobial potential of polyphenols: mechanisms of action and microbial responses—a narrative review, *Antioxidants*, 2025, **14**(2), 200.
49 E. Bae, I. J. Yeo, B. Jeong, Y. Shin, K. H. Shin and S. Kim, Study of double bond equivalents and the numbers of carbon and oxygen atom distribution of dissolved organic matter with negative-mode FT-ICR MS, *Anal. Chem.*, 2011, **83**(11), 4193–4199.
50 A. Hu, L. Han, X. Lu, G. Zhang and J. Wang, Global patterns and drivers of dissolved organic matter across Earth systems: insights from H/C and O/C ratios, *Fundam. Res.*, 2024, DOI: **10.1016/j.fmre.2023.11.018**.
51 C. A. Carlson, S. Liu, B. M. Stephens and C. J. English, DOM production, removal, and transformation processes in

marine systems, in, *Biogeochemistry of Marine Dissolved Organic Matter*, Academic Press, 3rd edn, 2024, pp. 137–246.
52 B. Chen, K. F. Yu, L. Fu, Y. X. Wei, J. Y. Liang, Z. H. Liao, *et al.*, The diversity, community dynamics, and interactions of the microbiome in the world's deepest blue hole: insights into extreme environmental response patterns and tolerance of marine microorganisms, *Microbiol. Spectr.*, 2023, **11**(6), e0053123.
53 C. J. Rebouche and H. Seim, Carnitine metabolism and its regulation in microorganisms and mammals, *Annu. Rev. Nutr.*, 1998, **18**, 39–61.

Published on 07 August 2025. Downloaded by Guangxi University on 8/31/2025 7:18:05 AM.

 This journal is © The Royal Society of Chemistry 2025

Marine Environmental Research 210 (2025) 107354

Contents lists available at ScienceDirect

Marine Environmental Research

journal homepage: www.elsevier.com/locate/marenvrev

Microbial regulation of dissolved organic matter revealed by integrated metabolomics and metagenomics in the World's deepest blue hole

Jiying Pei [a,1,*], Shiguo Chen [b,1], Kefu Yu [a,c,**], Jiayuan Liang [a,***], Ruijie Zhang [a], Penghui Li [d,e], Zhuanghao Hou [f], Liang Fu [g], Honglin Ma [g]

[a] Guangxi Laboratory on the Study of Coral Reefs in the South China Sea, Coral Reef Research Center of China, School of Marine Sciences, Guangxi University, Nanning, 530004, China
[b] School of Resources, Environment and Materials, Guangxi University, Nanning, 530004, China
[c] Southern Marine Science and Engineering Guangdong Laboratory (Guangzhou), Guangzhou, 511458, China
[d] School of Marine Sciences, Sun Yat-sen University, Zhuhai, 519082, China
[e] Southern Marine Science and Engineering Guangdong Laboratory (Zhuhai), Zhuhai, 519082, China
[f] School of Chemistry and Materials Science and National Synchrotron Radiation Laboratory, University of Science and Technology of China, Hefei, 230026, China
[g] Sansha Track Ocean Coral Reef Conservation Research Institute, Sansha, 573199, China

ARTICLE INFO

Keywords:
Dissolved organic matter
Metabolomics
Metagenomics
Oxygen stratification
Blue hole

ABSTRACT

Dissolved organic matter (DOM) is central to marine biogeochemical cycles, with its composition and dynamics closely linked to microbial communities. In oxygen-stratified extreme environments, however, the ecological relationships between DOM and microbes remain insufficiently explored. This study explores the dynamics of DOM and microbial communities in the Sansha Yongle Blue Hole, the world's deepest ocean blue hole, using an integrated metabolomics and metagenomics approach. Our findings elucidate significant alterations in microbial communities and DOM composition in response to variations in oxygen concentrations. Specifically, various DOM components, including dissolved organic sulfur (DOS) and dissolved organic nitrogen (DON), along with a spectrum of small molecule metabolites, were affected by microbial metabolic activities. Higher concentrations of DOS in the anoxic layer were positively correlated with increased sulfur metabolism in microbial communities, whereas lower concentrations of DON in the chemocline were associated with the coupling of nitrification and denitrification processes. Additionally, metabolites such as lipids, amino acids, isovalerylcarnitine, and peptides, associated with microbial physiological functions, energy metabolism, and signal transduction processes, varied with oxygen stratification. These findings contribute to a deeper understanding of the intricate relationships between microbial communities and DOM dynamics in extreme marine environments.

1. Introduction

Dissolved organic matter (DOM) is one of the largest pools of reduced carbon in the ocean, comprising a chemically diverse assemblage of molecules. Its complex composition encompasses thousands of distinct compounds—including amino acids, lipids, carbohydrates, phenolic compounds (Li et al., 2024a), and a wide range of heteroatom-containing molecules such as those dissolved organic sulfur (DOS) and dissolved organic nitrogen (DON) (Gomez-Saez et al., 2021). This molecular heterogeneity imparts diverse chemical reactivities and biological availabilities, allowing DOM to serve as a critical mediator in marine biogeochemical cycles (Hansell et al., 2009). Within DOM, DOS and DON occupy particularly important roles in linking carbon and nutrient cycling. DOS serves as both an energy source and a redox-active pool for microorganisms capable of sulfur oxidation and reduction (Tripp et al., 2008). Similarly, DON represents a key nitrogen source for heterotrophic and autotrophic microbes, especially in oligotrophic systems where inorganic nitrogen is limiting (Zehr and Capone, 2020). The

* Corresponding author. Guangxi Laboratory on the Study of Coral Reefs in the South China Sea, Coral Reef Research Center of China, School of Marine Sciences, Guangxi University, Nanning, 530004, China
** Corresponding author.
*** Corresponding author.
E-mail addresses: pjying@gxu.edu.cn (J. Pei), kefuyu@scsio.ac.cn (K. Yu), jyliang@gxu.edu.cn (J. Liang).
[1] Jiying Pei and Shiguo Chen are co-first authors.

https://doi.org/10.1016/j.marenvres.2025.107354
Received 19 March 2025; Received in revised form 13 June 2025; Accepted 8 July 2025
Available online 8 July 2025
0141-1136/© 2025 Elsevier Ltd. All rights are reserved, including those for text and data mining, AI training, and similar technologies.

bioavailability of DOS and DON depends not only on their molecular structure but also on the functional potential of the microbial communities that utilize them.

Microorganisms are the primary biological agents controlling the turnover and transformation of DOM. Through biosynthetic pathways, heterotrophic degradation, and redox-sensitive transformations, microbial activity modulates DOM quantity, composition, and lability (Kujawinski, 2011; Osterholz et al., 2016). These transformations are not uniform throughout the water column. Instead, they are profoundly influenced by physicochemical gradients, particularly redox conditions (Suominen et al., 2021). In oxygen-depleted or anoxic environments, such as euxinic basins, oxygen minimum zones, and marine blue holes, microbial communities adapt by expressing specialized metabolic pathways including anaerobic respiration, fermentation, sulfur and nitrogen dissimilation, and carbon fixation (Jessen et al., 2017; Patin et al., 2021). As a result, the DOM composition in these systems may reflect a fingerprint of unique microbial metabolisms not observable in surface or well-oxygenated waters. Despite advances in DOM characterization using high-resolution mass spectrometry (Petras et al., 2017), our understanding of the mechanistic links between microbial metabolism and DOM composition—especially under varying redox regimes—remains limited. DOM studies have traditionally focused on bulk measurements (e.g., total dissolved organic carbon (DOC) concentration) or general indicators of lability (e.g., fluorescence indices), which fail to capture the nuanced molecular transformations driven by microbial processes (Bachi et al., 2023; Chaichana et al., 2019).

The Sansha Yongle Blue Hole (SYBH), located in the South China Sea, represents an exceptional natural laboratory to investigate these interactions. As the world's deepest known marine blue hole (>300 m), SYBH exhibits pronounced vertical stratification in oxygen concentration, transitioning from oxygenated surface waters to anoxic and sulfidic conditions below ~90 m (Li et al., 2018; Xie et al., 2019). This strong redox gradient is accompanied by marked shifts in microbial community composition and functional gene abundance with depth (Li et al., 2024b; Zhou et al., 2023). The unique hydrogeological isolation and vertical redox zonation of SYBH make it an ideal site to examine how microbial processes regulate DOM molecular transformations across a natural, chemically stratified water column.

In recent years, advanced analytical tools have emerged to characterize both the microbial and chemical dimensions of such systems. Exometabolomics, the study of extracellular microbial metabolites, allows for direct observation of biologically derived or transformed DOM molecules (Pei et al., 2022a, 2022b, 2024). These methods can detect thousands of mass features, many of which are biologically active or traceable to specific microbial functions. In parallel, shotgun metagenomics provides insight into the taxonomic composition and functional gene repertoire of microbial communities, revealing pathways for carbon, nitrogen, and sulfur metabolism (New and Brito, 2020). While several studies have applied either metagenomics or metabolomics to marine systems, few have integrated both approaches to simultaneously map microbial metabolic potential and the resulting DOM molecular landscape (Pena-Ocana et al., 2022). Such integrative strategies are crucial for disentangling the cause-effect relationships between microbial community composition, metabolic capacity, and DOM chemistry.

In this study, we investigate the microbial regulation of DOM molecular composition across the redox-stratified water column of the SYBH by integrating high-resolution metabolomics and shotgun metagenomics. Our primary objectives are to: 1) Characterize the molecular composition of DOM—including DOS and DON—at multiple depths along the oxygen gradient; 2) Profile the microbial community structure and functional gene distribution across various depths; 3) Identify correlations between microbial metabolic pathways and specific DOM compound classes, with particular focus on sulfur and nitrogen cycling. We hypothesize that microbial communities exert depth-dependent control over DOM composition through selective degradation, transformation, and biosynthesis processes that are closely aligned with local redox conditions and nutrient availability. Specifically, we propose that the dominance of anaerobic pathways in anoxic zones will correlate with distinct signatures in DOM composition, particularly in the DOS and DON pools. Through this integrative analysis, we aim to bridge the gap between microbial ecology and DOM biogeochemistry, offering novel insights into the controls on carbon and nutrient cycling in extreme marine environments.

2. Materials and methods

2.1. Sample collection

The SYBH is situated within the intertidal reef platform of the eastern Yongle atoll in the South China Sea (111.768°E, 16.525°N) (Fig. 1a and b). In October 2019, a total of 28 seawater samples were systematically collected from different depths within the SYBH (0 m, 10 m, 20 m, 50 m, 80 m, 85 m, 90 m, 95 m, 100 m, 110 m, 120 m, 150 m, 200 m, and 250 m) (Fig. 1c). Two duplicate samples were obtained at each depth. Sampling above 190 m was conducted using a conductivity-temperature-depth (CTD) system equipped with rosette samplers, while sampling below 190 m was performed with a remotely operated vehicle (ROV) equipped with a home-made sampler. Environmental parameters, including temperature, salinity, dissolved oxygen (DO), pH, turbidity, and chlorophyll-a (Chl-a), were measured in situ across the 0–300 m depth range using the CTD system mounted on the ROV. Additionally, two additional seawater samples were collected at the reference point on the outer reef slope of Yongle Atoll (111.799°E, 16.534°N) to compare the DOM composition with that of the SYBH. Water samples for DOM analysis and metagenomic analysis were treated in situ. Further details of the sampling and in situ treatment methods can be found in Text S1.

2.2. Solid phase extraction

The solid-phase extraction (SPE)-DOM method followed the procedure developed by Dittmar (Dittmar et al., 2008). Briefly, the filtered seawater samples (1.2 L) were acidified with HCl to pH = 2 and then extracted using Agilent Bond Elut PPL cartridges (200 mg, 3 mL). The cartridges were pre-conditioned with 8 mL of methanol and 8 mL of acidified Milli-Q water (pH = 2) sequentially. Then, seawater was loaded onto the cartridges at a flow rate of 4 mL/min, followed by a wash with 10 mL of acidified Milli-Q water. The sorbents were dried using nitrogen gas, and the adsorbed DOM was eluted with 8 mL of methanol. The eluent was dried to a volume of 0.5 mL using nitrogen gas, and then reconstituted with 0.5 mL of Milli-Q water (1:1 v/v). The extract was stored at −20 °C until liquid chromatography tandem mass spectrometry (LC-MS/MS) analysis.

2.3. LC-MS/MS data acquisition and pre-processing

The DOM extracts were analyzed using a Thermo Q-Exactive mass spectrometer coupled to a Dionex Ulti-Mate 3000 UHPLC system. The chromatographic separation involved methanol and water as mobile phases, with a gradient shift from 5 % to 95 % methanol over 20 min, followed by a 5-min maintenance period. Mass spectrometry data acquisition occurred in positive electrospray ionization (ESI) mode using data-dependent acquisition (DDA). Chromatographic peak extraction from raw mass spectrometry data was conducted using the open-source MZmine software (version 3.4.27) (Heuckeroth et al., 2024). Detailed LC-MS/MS parameters and MZmine extraction parameters can be found in Text S2 and Text S3, respectively. To account for differences in total ion signal across samples, each feature was normalized by dividing its peak intensity by the total ion intensity of all features within the same sample.

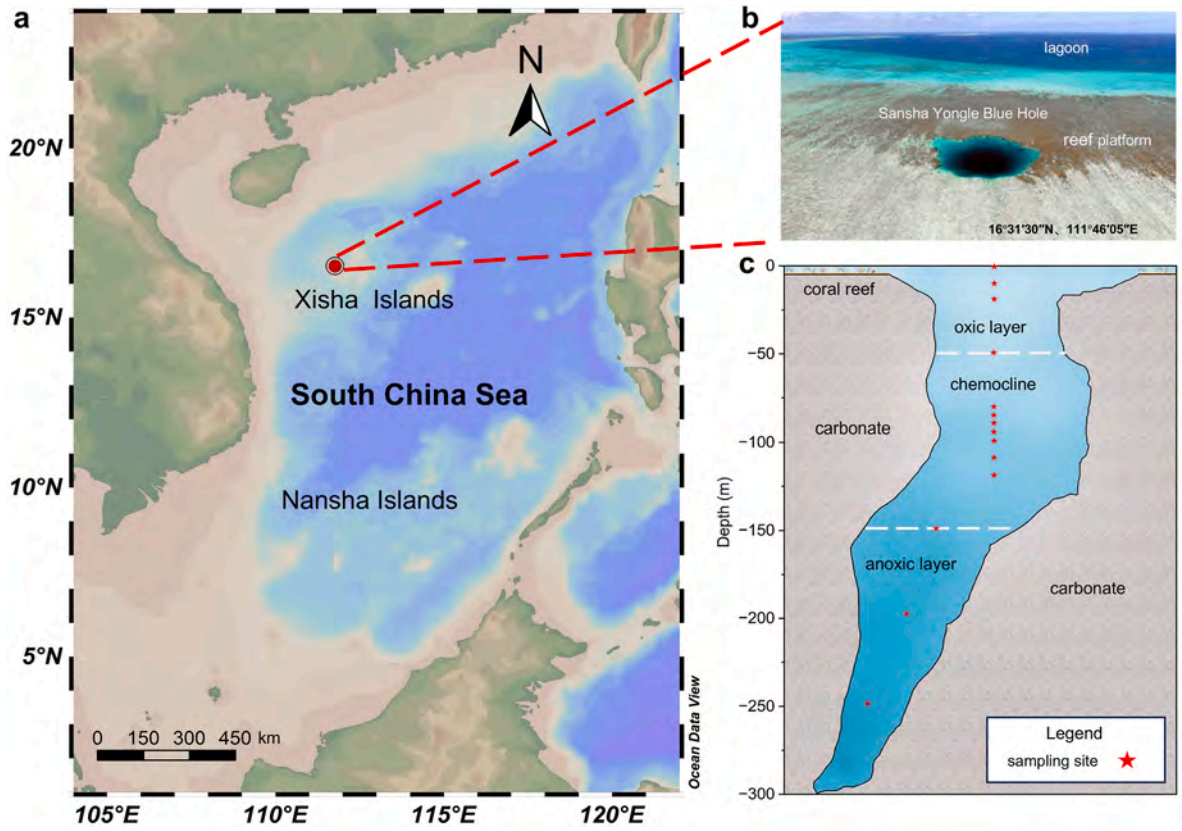


Fig. 1. (a) Map depicting the study area. (b) Realistic depiction of the SYBH located within the reef platform of Yongle Atoll, Xisha Islands. (c) Cross-sectional view of the SYBH and the sampling depths.

2.4. Molecular formula assignment and compound identification

The LC-MS/MS data, exported from MZmine software, underwent molecular formula assignment using the SIRIUS computational annotation tool (version 5.6.3) (Duhrkop et al., 2019). This annotation process involved determining molecular formulas, accurate mass calculation, matching of experimental and predicted isotopic patterns, and analysis of fragmentation trees of the fragment ions, with specific parameters detailed in Text S4. Molecules were classified as DON or DOS based on their molecular formulas, with compounds containing at least one nitrogen or sulfur atom designated as DON or DOS, respectively. Molecules containing both nitrogen and sulfur were included in both categories, reflecting their dual roles in the DOM pool. The relative concentrations of DON and DOS were estimated semi-quantitatively by summing the normalized ion intensities of all identified DON or DOS molecules within each sample. This approach expresses the abundance of each category as a proportion of total detected DOM ion intensity. To assess potential biases toward specific ionized DOM molecules, the ion feature-standardized score (z-score) was calculated. This approach minimized bias arising from variable ionization efficiencies and enabled a more accurate comparison of relative DOM concentrations across samples (Fig. S1).

Compound identification was conducted using the Feature-based Molecular Networking (FBMN) module on the Global Natural Product Social Molecular Networking (GNPS) website. Molecular networking operates on the principle that compounds with similar structures produce similar fragments in their MS/MS spectra (Chung et al., 2021). The structural similarity, quantified by cosine values in the comparison of similar MS/MS spectra (Text S5), facilitates effective inference of the structures of unknown compounds. FBMN analysis for the SYBH dataset was conducted with specific parameters outlined in Text S6. Leveraging the annotated compounds identified via the GNPS library search as "seeds", additional unknown compounds were deduced through manual interpretation. The resulting annotated compounds underwent validation by cross-checking against spectra observed in various databases, including MassBank Europe, MassBank of North America, Metlin, HMDB, and mzCloud. To visualize the output files generated from the FBMN analysis, Cytoscape was utilized (version 3.8.0) (Shannon et al., 2003).

2.5. Microbial DNA extraction and metagenomic analysis

Aseptic forceps were utilized to carefully section the filter membrane containing microorganisms from the frozen storage tube. Subsequently, the FastDNA Spin Kit for Soil was employed to extract total microbial DNA from the filter membrane, preparing it for metagenomic sequencing analysis. The DNA libraries were sequenced on the illumina platform. Subsequently, MEGAHIT software (version 1.1.2) was used for metagenome assembly, with a filter applied to contig sequences shorter than 300 bp (Li et al., 2015). Assembly results were evaluated using QUAST software (version 2.3) (Gurevich et al., 2013). To identify coding regions in the genome, MetaGeneMark software (version 3.26) available at http://exon.gatech.edu/meta_gmhmmp.cgi was utilized (Zhu et al., 2010). Redundancy was removed using cd-hit software (version 4.6.6) at http://www.bioinformatics.org/cd-hit/with a similarity threshold set at 95 % and a coverage threshold at 90 % (Fu et al., 2012). BLAST comparisons were conducted between non-redundant protein sequences and the protein sequences cataloged in the KEGG database for corresponding gene functional annotations. Additionally, sequence comparisons were performed against the species information in the Nr database to obtain insights into sample species composition and relative abundance.

2.6. Quality control

To ensure the reliability of subsequent analysis, for the LC-MS/MS analysis of seawater samples, a comprehensive quality control protocol was implemented, encompassing sample pretreatment, instrument detection, and data analysis. This protocol included a blank control experiment conducted for SPE analysis, a quality control sample prepared from the 14 seawater samples to monitor the stability of the pretreatment and instrument analysis process, a blank experiment to assess instrument pollution, and the use of internal standards to calibrate instrument fluctuations. For a detailed description of the process, refer to Text S7. Raw reads obtained from sequencing were filtered to remove low-quality sequences. This essential step was performed using the software Trimmomatic (version 0.33) (Bolger et al., 2014), which generated clean tags with improved sequencing quality. The relative standard deviation (RSD) of microbial abundance and peak area of DOM in the duplicate samples across various layers ranged from 9.3 % to 17.4 % and from 7.3 % to 13.5 %, respectively (Fig. S2).

2.7. Statistical analysis

Statistical significance was determined using SPSS software (version 23) with a significance threshold set at $p < 0.05$. Normality was assessed using the Shapiro-Wilk test, and an independent sample *t*-test was applied for data with a normal distribution. Alternatively, the Mann-Whitney *U* test was employed for non-normally distributed data. A Venn plot was generated using Venny 2.1 (https://bioinfogp.cnb.csic.es/tools/venny/). Redundancy analysis was conducted using R packages. For multi-omics analysis, Data Integration Analysis for Biomarker discovery using Latent cOmponents (DIABLO) was performed with the mixOmics package (Singh et al., 2019), diagnostic plots and sample plots from multiblock sparse partial least squares discriminant analysis (sPLS-DA) were applied to the correlation study. The microbial taxa at the order level, comprising the top 28 weighted species selected based on model accuracy, were visualized through correlation circles. Other statistical analyses, unless specified, were conducted using Origin software (version 2024).

3. Results

3.1. Physicochemical properties of the SYBH

The aquatic physicochemical parameters within the SYBH exhibited a distinct stratified structure (Fig. 2). Notably, temperature, DO and pH consistently decreased with increasing depth, while salinity and turbidity showed an upward trend. Significant fluctuations of these parameters were observed at depths of 30 m, 50 m, 90 m, and 150 m. For example, at a depth of 50 m, there was a drastic decrease in temperature, DO, and pH, accompanied by a simultaneous increase in salinity. At a depth of 90 m, the oxygen concentration dramatically dropped to zero. At the depth of 150 m, while temperature, salinity, DO, and pH showed minimal change, there was a drastic increase in turbidity. According to these physicochemical parameters, the SYBH water column could therefore be categorized into three layers: the oxic layer (<50 m), the chemocline (50–150 m), and the anoxic layer (150–300 m).

3.2. Chemical diversity and vertical distribution of DOM

A total of 4568 DOM features were extracted from the mass spectrometry dataset for water samples collected from the 14 layers. Among these, 1235 (27.03 %) were present in all three layers, while 289, 946, and 232 molecules were unique to the oxic layer, chemocline, and anoxic layer, respectively (Fig. 3a). Compared to a reference open-ocean site, SYBH exhibited 2048 additional DOM molecules. On average, 1929, 1934, and 1473 DOM molecules were detected in the oxic, chemocline, and anoxic layers, respectively, with corresponding Shannon indices of 8.59, 8.73, and 8.38 (Fig. 3b). A positive correlation was observed between molecular richness and Shannon index (Fig. 3c). Statistically significant differences in both metrics were found between the chemocline and anoxic layer ($p < 0.05$), but not between the oxic layer and chemocline ($p > 0.05$) (Fig. S3). Principal coordinates analysis (PCoA) and orthogonal partial least squares discriminant analysis (OPLS-DA) showed a clear separation of DOM profiles, especially between the anoxic layer and the other two (Fig. 3d, Fig. S4). A total of 198, 322, and 444 differential molecules were identified between the oxic vs. chemocline, oxic vs. anoxic, and chemocline vs. anoxic comparisons, respectively (Fig. S5).

Out of 4568 DOM molecules, SIRIUS predicted 3574 high-quality

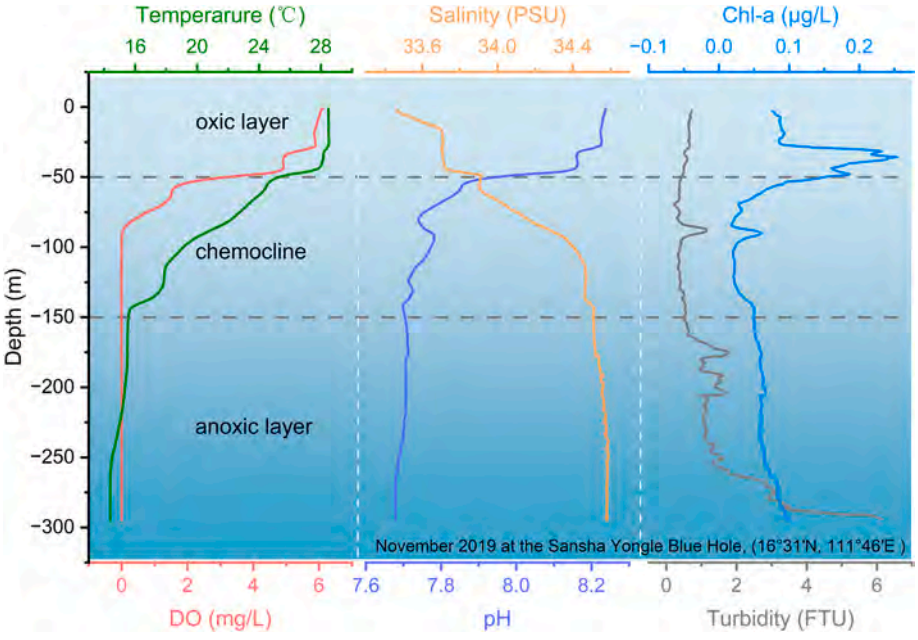


Fig. 2. Variations in physicochemical properties (temperature, DO, salinity, pH, Chl-a, and turbidity at different depths within the SYBH.

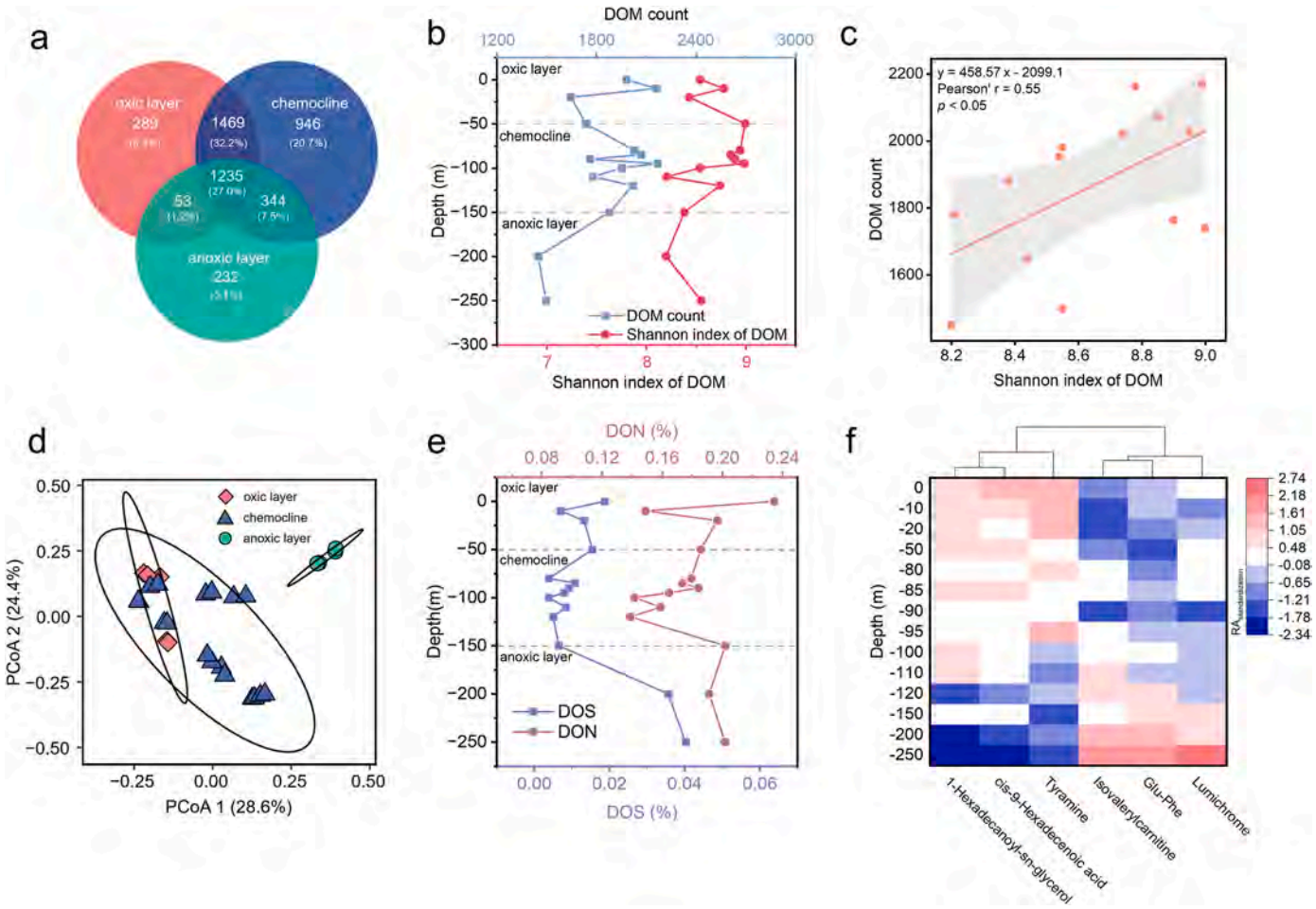


Fig. 3. (a) Venn plot illustrating the distribution of DOM within the oxic layer, chemocline, and anoxic layer of the SYBH. (b) Plot displaying the variation of the DOM count and Shannon index across different depths. (c) Linear correlation analysis between the DOM count and the Shannon index of DOM across different depths. (d) PCoA plot for distinguishing samples from the oxic, chemocline, and the anoxic layer. (e) Variation in the relative abundance of ion peak areas for DOS and DON at different depths within the SYBH. (f) Heatmap depicting the distribution of differential metabolites across different depths.

molecular formulas, including 125 DOS and 1194 DON compounds. DOS concentrations were highest in the anoxic layer, with comparable concentrations in the oxic layer and chemocline, while DON levels were comparable between the oxic and anoxic layers but lower in the chemocline (Fig. 3e). GNPS-based annotation identified 147 DOM molecules, and molecular networking deduced 128 additional structures, totaling 275 annotated compounds. The analysis of differential DOM molecules among the three layers ($p < 0.05$) revealed distinct vertical distribution patterns. Tyramine, cis-9-hexadecenoic acid, and 1-hexadecanoyl-sn-glycerol were primarily enriched in the oxic layer and chemocline, whereas lumichrome, Glu-Phe, and isovalerylcarnitine were predominant in the anoxic layer (Fig. 3f, Fig. S6). These identifications were confidently identified using spectral library matching, with cosine similarity scores ranging from 0.70 to 0.99 (Fig. S7).

3.3. Microbial community and functional analysis

Metagenomic data, described in Table S1 revealed high-quality results with Q30 (%) values exceeding 91 % across all samples. The N50 length ranged from 1006 to 4067, and gene counts varied between 330,686 and 880,209, indicating that the data were robust and suitable for further analysis. To assess microbial diversity, the Shannon index was calculated for each layer in the SYBH. The mean Shannon indices were 4.27 for the oxic layer, 5.03 for the chemocline, and 4.39 for the anoxic layer, with a significant difference observed between the oxic layer and chemocline, but no significant difference between the chemocline and anoxic layer (Fig. 4a). Multivariate statistical analyses, encompassing principal components analysis (PCA) (Fig. 4b) and OPLS-DA (Fig. S8), were employed to investigate water stratification across the 14 layers of the SYBH based on microbial profiling. The results revealed a distinct separation of samples from the oxic layer, chemocline, and anoxic layer. Redundancy analysis (RDA) indicated that DO significantly influenced microbial communities, comparable to the effects of temperature and salinity (Fig. 4c).

Microbial community composition analysis indicated that orders characterized by a higher diversity of anaerobic and microaerophilic species, such as Desulfobacterales and Thiotrichales were more abundant in the anoxic layer (Fig. 4d, Fig. S9a and b). Conversely, aerobic species orders, such as Rhodobacterales and Rhizobiales, associated with nitrogen metabolism, were more prevalent in the oxic layer (Fig. 4d). Notably, nitrifying bacteria orders and denitrifying bacteria orders, including Nitrosopumilales, Nitrosomonadales and Planctomycetales, were concentrated in the chemocline (Fig. S9c and d).

Metabolic functions of microbial communities were annotated against the KEGG metabolic pathway database, identifying 174 metabolic pathways. Statistical analysis revealed 12 pathways with significant differences between the oxic and anoxic layers ($p < 0.05$). Examination of these pathways across various depths (Fig. 4e) showed that energy metabolism and signal transduction were more abundant in the anoxic layer. Conversely, pathways related to the metabolism of cofactors and vitamins, nucleotide metabolism, amino acid metabolism, carbohydrate metabolism, xenobiotics biodegradation, lipid

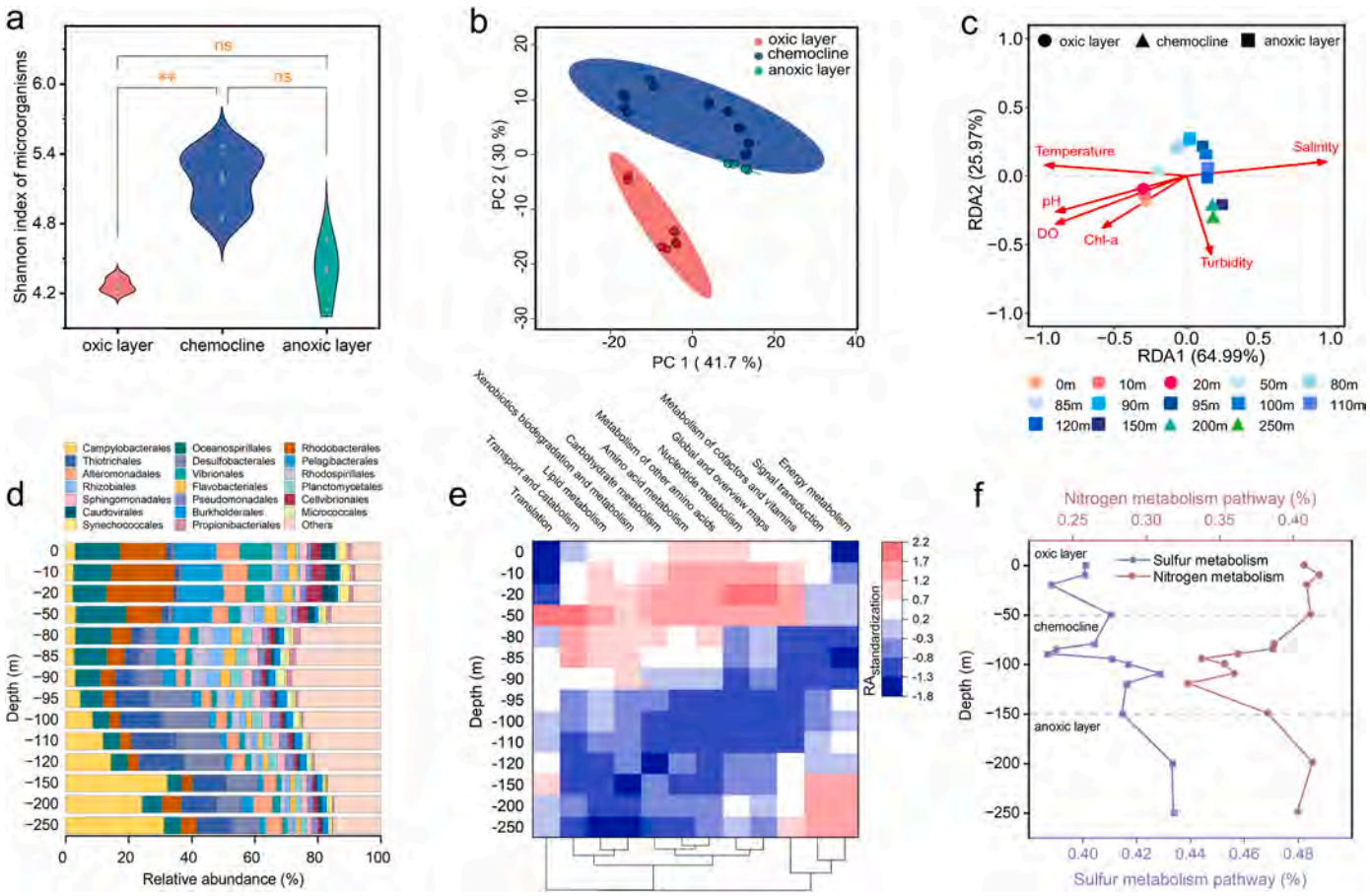


Fig. 4. (a) Violin plot depicting the Shannon index of microorganisms in the oxic layer, chemocline, and anoxic layer within the SYBH. (b) PCA plot for distinguishing samples from the oxic, chemocline, and the anoxic layer. (c) RDA plot showing the relationship between environmental factors and microbial community composition. (d) Relative abundance of microorganisms at the order level across different layers. (e) Heatmap displaying the distribution of metabolic pathways of microorganisms across different depths. (f) Variation of the relative abundance of sulfur metabolism and nitrogen metabolism across different depths.

metabolism, and translation were more prominent in the oxic layer. Sulfur metabolism exhibited a higher relative abundance in the anoxic layer compared to the oxic layer (Fig. 4f), especially in modules like assimilatory sulfate reduction (M00176) (Fig. S10a) and thiosulfate oxidation by the SOX complex (M00595) (Fig. S10b). Nitrogen metabolism's relative abundance was similar between the oxic and anoxic layers but significantly lower in the chemocline (Fig. 4f). Notably, the nitrification module, denitrification module (Fig. S11a and b) and nitrogen fixation-related genes and nifH were most prevalent in the anoxic layer (Fig. S11c and d).

3.4. Correlation analysis between DOM and microbial communities

To explore the relationship between DOM and microbial communities across redox gradients in SYBH, multivariate correlation analyses were conducted. MixOmics analysis revealed strong correlations between the distribution of DOM and microorganisms (Fig. 5a), with an R-value of 0.94. Consistently, sPLS-DA plots showed a consistent distribution trend of DOM with microorganisms across the oxic layer, chemocline, and anoxic layer (Fig. 5b and c). Further analysis showed a significant positive correlation ($p < 0.05$) between DOM molecular diversity and microbial diversity (Fig. 5d), both of which peaked in the chemocline zone (Fig. S12). This pattern indicates that redox transitions may shape both chemical and biological complexity. Furthermore, DOM elemental composition was closely linked to microbial metabolic potential: concentrations of DOS showed a significant positive correlation ($p < 0.05$) with the abundance of genes involved in sulfur metabolism, while DON was positively correlated ($p < 0.05$) with nitrogen metabolism-related gene abundance (Fig. 5e and f).

At the taxon-metabolite level, distinct associations were identified across redox zones (Fig. 5g). In the oxic layer, aerobic bacteria including Puniceicoccales, Oceanospirillales, Pelagibacterales, and Arenicellales were associated with metabolites such as 1-hexadecanoyl-sn-glycerol, cis-9-hexadecenoic acid, and tyramine. In contrast, anaerobic taxa such as Candidatus Altiarchaeares and Thermodesulfobacteriales in the anoxic layer were correlated with isovalerylcarnitine, lumichrome, and Glu-Phe. Microbial responses to different redox environments may be reflected in the activity of key metabolic enzymes. Notably, a significant negative correlation ($p < 0.05$) was observed between the relative abundance of isovaleryl-CoA dehydrogenase and the concentration of isovalerylcarnitine in the water column (Fig. 5h). This suggests that the accumulation of isovalerylcarnitine may be linked to reduced expression of its associated catabolic enzyme under anoxic conditions.

4. Discussion

4.1. Environmental influences on microbial diversity

In marine ecosystems, environmental conditions intricately shape microbial community composition. In the SYBH, a distinct thermohaline gradient forms within the chemocline, limiting upper and lower water layer mixing (Fig. 2). This gradient creates significant variations in DO, temperature, salinity, pH, Chl-a, and turbidity along the water column, creating distinct ecological niches for microbial communities. The RDA analysis (Fig. 4c) revealed that microbial community composition was significantly influenced by these environmental factors. Samples from

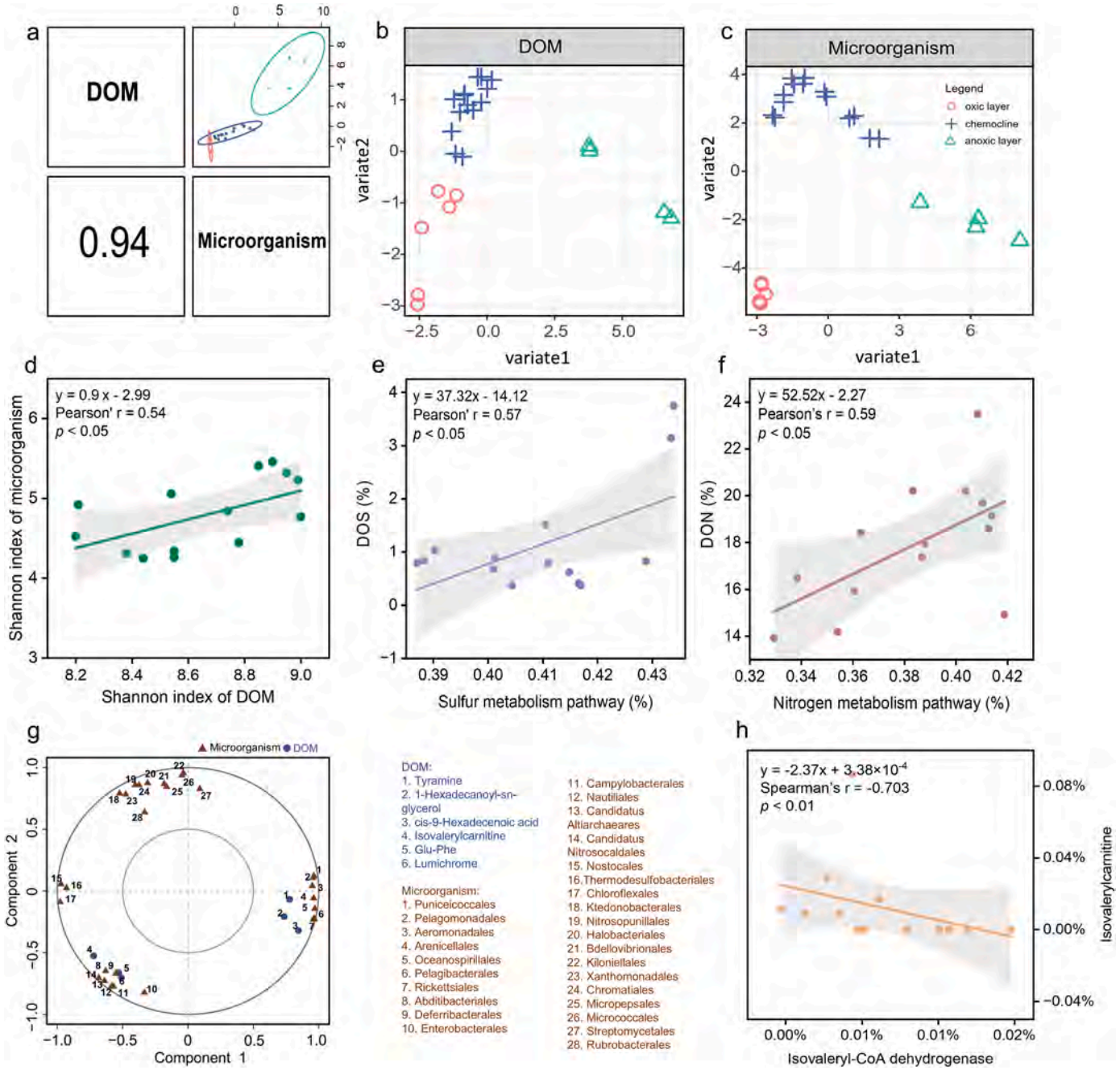


Fig. 5. (a) Score plot from DIABLO analysis. Multiblock sPLS-DA plots illustrating clear separation of samples from the oxic layer, chemocline, and anoxic layer based on (b) metabolomics and (c) metagenomics profiles. (d) Correlation between the Shannon diversity index of DOM and microbial communities, emphasizing compositional coupling across depths. Linear correlations between the relative abundance of DOM ion peaks and microbial functional groups, highlighting the associations between (e) DOS and sulfur metabolism, and (f) DON and nitrogen metabolism. (g) Correlation circle plot derived from multiblock sPLS-DA analysis conducted on DOM and microorganism datasets. (h) Positive correlation between the abundance of isovaleryl-CoA dehydrogenase and isovalerylcarnitine, suggesting microbial mediation of energy-related metabolites.

the oxic layer were positively associated with DO, pH, and Chl-a. High DO supports aerobic taxa such as Oceanospirillales, while elevated Chl-a indicates increased primary productivity, which provides organic matter to fuel heterotrophic microbial activity. In contrast, microbial communities in the anoxic layer were more strongly associated with turbidity. Elevated turbidity often reflects higher levels of suspended particles, which can serve as attachment surfaces and nutrient sources for anaerobic microbes such as Desulfobacterales (Ma et al., 2024).These patterns are consistent with findings from other marine environments. For example, Jessen et al. reported that oxygen gradients in the Black Sea significantly shaped microbial community structure and ecosystem function (Jessen et al., 2017). Abirami et al. observed that microbial communities adapt to various physicochemical factors, including temperature and nutrient availability (Abirami et al., 2021). Similarly, Zaikova et al. found increased microbial diversity in the hypoxic transition zone of Saanich Inlet compared to deeper anoxic waters (Zaikova et al., 2010). Together, these results suggest that the microbial community structure in the SYBH is shaped by environmental gradients and the adaptive responses of microbes to changing redox and physicochemical conditions across the water column.

4.2. Microorganism-regulated metabolism in SYBH

In the ocean, DOM experiences dynamic changes influenced by microorganisms through metabolic pathways such as production (LaBrie et al., 2022), degradation (Xiao et al., 2022), and transformation (Xiao et al., 2023). This microbial regulation establishes a strong correlation between DOM diversity and microbial diversity (Chen et al., 2022; Suominen et al., 2021). Moreover, even within a single microorganism, specific environmental conditions can induce diverse metabolic pathways. This adaptability and specialization of microbial species to their environmental conditions enhance the repertoire of metabolites they produce (Doi, 2018). Consequently, the varied microbial diversity and metabolic pathways in the SYBH contribute to the abundance and diversity of DOM observed in this oxygen-stratified environment.

4.2.1. Microorganism-regulated sulfur metabolism in SYBH

Microbial-regulated sulfur metabolism is integral to the biogeochemical cycles of DOS, vital for global climate regulation (Ksionzek et al., 2016). In the SYBH, DOS shows a pronounced vertical gradient, with notably lower concentrations in the oxic layer and chemocline compared to deeper layers. This depletion is likely due to enhanced microbial remineralization of DOS in oxygen-rich environments. Compared to DOC, DOS is more chemically reactive and thus more prone to microbial degradation during its vertical transport from surface to depth (Tang and Liu, 2023). This observation is consistent with patterns reported in the North Atlantic Deep Water, where aging waters exhibit a decline in total organic sulfur while DOC remains relatively stable (Longnecker et al., 2020). These findings suggest that microbial activity in surface and mid-depth waters accelerates DOS turnover, contributing to its reduced presence in the upper water column of SYBH.

In contrast, DOS concentrations increase in the anoxic bottom layers of SYBH, likely due to both microbial and abiotic processes. Microbial community analysis revealed a higher relative abundance of sulfur-reducing microorganisms in the anoxic zone compared to oxic layers, including Desulfobacterales, Desulfovibrionales, Thermodesulfobacteriales, and Desulfuromonadales (Fig. S9a). These taxa are typical sulfate-reducing bacteria (SRB), capable of using inorganic sulfate (SO_4^{2-}) as terminal electron acceptors, producing hydrogen sulfide (H_2S) as a byproduct. The dominance of Desulfobacterales, in particular, reflects strong adaptation to the anoxic conditions in SYBH. The accumulation of H_2S in the anoxic bottom waters (Yao et al., 2020) is consistent with both the elevated abundance of sulfate-reduction genes (Fig. S10a) and the activity of SRB. Furthermore, H_2S can participate in abiotic reactions with DOM, promoting the formation of new DOS compounds. This mechanism has been observed in other anoxic marine systems, such as the Black Sea and shallow hydrothermal vents, where non-biological interactions between H_2S and organic matter contribute to DOS production (Gomez-Saez et al., 2021). Together, these findings indicate that DOS dynamics in SYBH are shaped by a dual mechanism: microbial remineralization dominates in the oxygenated upper layers, while microbial sulfate reduction and H_2S-mediated DOS formation drive DOS accumulation in the anoxic bottom waters.

4.2.2. Microorganism-regulated nitrogen metabolism in SYBH

The vertical distribution of DON within the SYBH is influenced by microbial metabolism. In the oxygen-rich layers of SYBH, prevalent nitrogen-fixing bacteria convert atmospheric N_2 into bioavailable forms, primarily ammonia nitrogen. This ammonia nitrogen is further metabolized into organic nitrogen, actively contributing to DON cycling in the surface marine environment (Letscher et al., 2013; McCarthy et al., 2004). As depth increases within SYBH, organic matter undergoes oxidation and decomposition, converting organic nitrogen into ammonia (Chen et al., 2023). The chemocline of SYBH, acting as the boundary between the oxic and anoxic regions, provides conditions for the simultaneous occurrence of aerobic nitrification and anaerobic denitrification processes in its micro-oxic environment. This study suggests that the decrease in the relative abundance of DON is closely related to the coupled nitrification-denitrification process. In this process, DON is first decomposed by heterotrophic microorganisms into ammonia, which is then converted into nitrate by nitrifying bacteria. Subsequently, in local anoxic microenvironments, denitrifying bacteria reduce the nitrate to gaseous nitrogen (Ji et al., 2018). This coupled process accelerates the mineralization of DON and the removal of nitrogen through the continuous conversion pathway of "DON → ammonia → nitrate → gaseous nitrogen" ultimately causing it to escape the system in gaseous form, resulting in a decrease in DON accumulation in the chemocline, a higher relative abundance of functional genes related to nitrification and denitrification was observed (Fig. S11a and b). At the same time, a large number of nitrifying microorganisms capable of converting ammonia to nitrite were present (including Nitrosopumilales, Nitrosomonadales, Nitrospinales, Nitrospirales, and Cenarchaeales), as well as denitrifying microorganisms including Planctomycetales, Xanthomonadales, Hydrogenophilales, and Pseudomonadales (Fig. S9c and d), further confirming the above inference.

Conversely, the increase in DON concentrations in the anoxic layer of the SYBH compared to the chemocline is associated with anaerobic microbial nitrogen fixation. This is supported by the observed increase in nitrogenase content within the anoxic layer, where nitrogenase facilitates nitrogen fixation under low-oxygen conditions (Bauersachs et al., 2010; Yin et al., 2023). Additionally, the increased abundance of modules related to nitrogen fixation (Fig. S11c), along with a heightened presence of the nifH gene (Fig. S11d), associated with various nitrogen-fixing bacteria, underscores the significant role of microbial nitrogen fixation in augmenting DON concentrations in this anoxic environment. The nitrogen in the anoxic layer of the SYBH may originate from microbial denitrification or anammox processes, sustaining the availability of nitrogen for nitrogen-fixing bacteria to continue contributing to the DON pool.

4.3. Other microorganism-regulated metabolism in SYBH

The microbial community in SYBH produces a diverse array of metabolites involved in energy metabolism and signal transduction. Elevated levels of 1-hexadecanoyl-sn-glycerol and cis-9-hexadecenoic acid in the oxic layer may stem from active microbial lipid metabolism (Liu et al., 2020). Similarly, higher concentrations of tyramine in the oxic layer may suggest active microbial amino acid metabolism. In environments with limited organic carbon, microorganisms may alter their metabolic strategies to support survival. The increased concentrations of isovalerylcarnitine in the anoxic layer of SYBH may enhance microbial metabolic energy utilization efficiency. Isovalerylcarnitine, essential for fatty acid oxidation, aids in breaking down fatty acids for energy production within mitochondria (Rebouche and Seim, 1998). This process relies on the enzyme isovaleryl-CoA dehydrogenase, which is critical for mitochondrial beta-oxidation. Reduced levels of this enzyme in the anoxic layer of SYBH suggest a shift towards optimizing energy generation through enhanced mitochondrial beta-oxidation in response to oxygen depletion, potentially leading to the accumulation of isovalerylcarnitine (Fig. 5e) (Kuhn et al., 2023).

Functional annotation analysis reveals enriched signal transduction processes in the anoxic layer of SYBH (Fig. 4e), indicating the involvement of signal transduction molecules such as Glu-Phe and lumichrome in microbial communication. Previous investigations have shown that cyclic dipeptides signal the transport of peptidases in aerobic, gram-negative bacteria in deep-sea environments (Sun et al., 2020), while lumichrome contributes to biotic signal transduction during biofilm formation (van Galen et al., 2020). These findings suggest that the elevated concentrations of Glu-Phe and lumichrome in the anoxic layer of SYBH are crucial for microbial adaptation in this unique marine environment.

5. Conclusions

Leveraging an integrative approach that intertwines metabolomics and metagenomics, this study conducted an in-depth exploration of DOM diversity, the functional potential of microbial communities, and their ecological roles within the SYBH. A significant correlation between DOM distribution and microbial activity, influenced by environmental factors, notably oxygen concentrations, was observed. Various components of DOM, including DOS and DON, as well as an array of metabolites, were discernibly impacted by the metabolic activities of microorganisms, specifically bacteria associated with sulfur and nitrogen metabolism. The research provides crucial insights into global carbon cycling dynamics through detailed profiling of DOM composition. This improved understanding significantly enhances our grasp of how ecosystems operate in intricate marine environments, particularly those marked by notable fluctuations in oxygen concentration.

CRediT authorship contribution statement

Jiying Pei: Writing – review & editing, Project administration, Methodology, Funding acquisition, Conceptualization. **Shiguo Chen:** Writing – original draft, Visualization, Investigation, Formal analysis. **Kefu Yu:** Resources, Project administration, Funding acquisition. **Jiayuan Liang:** Writing – review & editing, Resources, Methodology, Data curation. **Ruijie Zhang:** Supervision. **Penghui Li:** Methodology. **Zhuanghao Hou:** Software. **Liang Fu:** Resources. **Honglin Ma:** Investigation.

Data availability statement

The raw LC-MS/MS data has been deposited in the Mass Spectrometry Interactive Virtual Environment (http://massive.ucsd.edu/) under the accession number MSV000080562. The raw metagenomic data has been submitted into the NCBI Sequence Read Archive database (https://www.ncbi.nlm.nih.gov/) under the accession numbers PRJNA1201745. The map in Fig. 1a was prepared with the software Ocean Data View (version 5.6.7) (Schlitzer, 2002). The image in Fig. 1b was reproduced from http://www.trackocean.cn/.

Declaration of competing interest

The authors declare that they have no known competing financial interests or personal relationships that could have appeared to influence the work reported in this paper.

Acknowledgments

This work was supported by Guangxi Science and Technology Program (No. AD25069075), Guangxi Natural Science Foundation (Nos. 2023GXNSFAA026488), and National Natural Science Foundation of China (Nos. 22264003 and 42090041).

Appendix A. Supplementary data

Supplementary data to this article can be found online at https://doi.org/10.1016/j.marenvres.2025.107354.

Data availability

Data will be made available on request.

References

Abirami, B., Radhakrishnan, M., Kumaran, S., Wilson, A., 2021. Impacts of global warming on marine microbial communities. Sci. Total Environ. 791, 147905. https://doi.org/10.1016/j.scitotenv.2021.147905.

Bachi, G., Morelli, E., Gonnelli, M., Balestra, C., Casotti, R., Evangelista, V., et al., 2023. Fluorescent properties of marine phytoplankton exudates and lability to marine heterotrophic prokaryotes degradation. Limnol. Oceanogr. 68 (4), 982–1000. https://doi.org/10.1002/lno.12325.

Bauersachs, T., Speelman, E.N., Hopmans, E.C., Reichart, G.J., Schouten, S., Damste, J.S., 2010. Fossilized glycolipids reveal past Oceanic N_2 fixation by heterocystous Cyanobacteria. Proc. Natl. Acad. Sci. U. S. A 107 (45), 19190–19194. https://doi.org/10.1073/pnas.1007526107.

Bolger, A.M., Lohse, M., Usadel, B., 2014. Trimmomatic: a flexible trimmer for illumina sequence data. Bioinformatics 30 (15), 2114–2120. https://doi.org/10.1093/bioinformatics/btu170.

Chaichana, S., Jickells, T., Johnson, M., 2019. Interannual variability in the summer dissolved organic matter inventory of the north sea: implications for the Continental shelf pump. Biogeosciences 16 (5), 1073–1096. https://doi.org/10.5194/bg-16-1073-2019.

Chen, L., Yao, P., Yang, Z., Fu, L., 2023. Seasonal and vertical variations of nutrient cycling in the world's deepest blue hole. Front. Mar. Sci. 10, 1172475. https://doi.org/10.3389/fmars.2023.1172475.

Chen, Q., Lønborg, C., Chen, F., Gonsior, M., Li, Y., Cai, R., et al., 2022. Increased microbial and substrate complexity result in higher molecular diversity of the dissolved organic matter pool. Limnol. Oceanogr. 67 (11), 2360–2373. https://doi.org/10.1002/lno.12206.

Chung, H., Kao, C., Wang, T., Chu, J., Pei, J., Hsu, C., 2021. Reaction tracking and high-throughput screening of active compounds in combinatorial chemistry by tandem mass spectrometry molecular networking. Anal. Chem. 93 (4), 2456–2463. https://doi.org/10.1021/acs.analchem.0c04481.

Dittmar, T., Koch, B., Hertkorn, N., Kattner, G., 2008. A simple and efficient method for the solid-phase extraction of dissolved organic matter (SPE-DOM) from seawater. Limnol Oceanogr. Methods 6, 230–235. https://doi.org/10.4319/lom.2008.6.230.

Doi, Y., 2018. Lactic acid fermentation is the main aerobic metabolic pathway in Enterococcus faecalis metabolizing a high concentration of glycerol. Appl. Microbiol. Biotechnol. 102 (23), 10183–10192. https://doi.org/10.1007/s00253-018-9351-4.

Duhrkop, K., Fleischauer, M., Ludwig, M., Aksenov, A.A., Melnik, A.V., Meusel, M., et al., 2019. Sirius 4: a rapid tool for turning tandem mass spectra into metabolite structure information. Nat. Methods 16 (4), 299–302. https://doi.org/10.1038/s41592-019-0344-8.

Fu, L., Niu, B., Zhu, Z., Wu, S., Li, W., 2012. CD-HIT: accelerated for clustering the next-generation sequencing data. Bioinformatics 28 (23), 3150–3152. https://doi.org/10.1093/bioinformatics/bts565.

Gomez-Saez, G.V., Dittmar, T., Holtappels, M., Pohlabeln, A.M., Lichtschlag, A., Schnetger, B., et al., 2021. Sulfurization of dissolved organic matter in the anoxic water column of the black sea. Sci. Adv. 7 (25), eabf6199. https://doi.org/10.1126/sciadv.abf6199.

Gurevich, A., Saveliev, V., Vyahhi, N., Tesler, G., 2013. QUAST: quality assessment tool for genome assemblies. Bioinformatics 29 (8), 1072–1075. https://doi.org/10.1093/bioinformatics/btt086.

Hansell, D.A., Carlson, C.A., Repeta, D.J., Schlitzer, R., 2009. Dissolved organic matter in the ocean a controversy stimulates new insights. Oceanography (Wash. D. C.) 22 (4), 202–211. https://doi.org/10.5670/oceanog.2009.109.

Heuckeroth, S., Damiani, T., Smirnov, A., Mokshyna, O., Brungs, C., Korf, A., et al., 2024. Reproducible mass spectrometry data processing and compound annotation in MZmine 3. Nat. Protoc. 19 (9), 2597–2641. https://doi.org/10.1038/s41596-024-00996-y.

Jessen, G.L., Lichtschlag, A., Ramette, A., Pantoja, S., Rossel, P.E., Schubert, C.J., et al., 2017. Hypoxia causes preservation of labile organic matter and changes seafloor microbial community composition (black sea). Sci. Adv. 3 (2), e1601897. https://doi.org/10.1126/sciadv.1601897.

Ji, Q., Buitenhuis, E., Suntharalingam, P., Sarmiento, J.L., Ward, B.B., 2018. Global nitrous oxide production determined by oxygen sensitivity of nitrification and denitrification. Glob. Biogeochem. Cycles 32 (12), 1790–1802. https://doi.org/10.1029/2018gb005887.

Ksionzek, K.B., Lechtenfeld, O.J., McCallister, S.L., Schmitt-Kopplin, P., Geuer, J.K., Geibert, W., et al., 2016. Dissolved organic sulfur in the ocean: biogeochemistry of a petagram inventory. Science 354 (6311), 456–459. https://doi.org/10.1126/science.aaf7796.

Kuhn, S., Williams, M.E., Dercksen, M., Sass, J.O., van der Sluis, R., 2023. The glycine N-acyltransferases, GLYAT and GLYATL1, contribute to the detoxification of isovaleryl-CoA - an in-silico and in vitro validation. Comput. Struct. Biotec. 21, 1236–1248. https://doi.org/10.1016/j.csbj.2023.01.041.

Kujawinski, E.B., 2011. The impact of microbial metabolism on marine dissolved organic matter. Ann. Rev. Mar. Sci 3, 567–599. https://doi.org/10.1146/annurev-marine-120308-081003.

LaBrie, R., Péquin, B., St-Gelais, N.F., Yashayaev, I., Cherrier, J., Gélinas, Y., et al., 2022. Deep ocean microbial communities produce more stable dissolved organic matter through the succession of rare prokaryotes. Sci. Adv. 8 (27), eabn0035. https://doi.org/10.1126/sciadv.abn0035.

Letscher, R.T., Hansell, D.A., Carlson, C.A., Lumpkin, R., Knapp, A.N., 2013. Dissolved organic nitrogen in the global surface ocean: distribution and fate. Glob. Biogeochem. Cycles 27 (1), 141–153. https://doi.org/10.1029/2012gb004449.

Li, D., Liu, C.M., Luo, R., Sadakane, K., Lam, T.W., 2015. MEGAHIT: an ultra-fast single-node solution for large and complex metagenomics assembly via succinct de Bruijn graph. Bioinformatics 31 (10), 1674–1676. https://doi.org/10.1093/bioinformatics/btv033.

Li, P., Liang, W., Zhou, Y., Yi, Y., He, C., Shi, Q., et al., 2024a. Hypoxia diversifies molecular composition of dissolved organic matter and enhances preservation of

terrestrial organic carbon in the yangtze river Estuary. Sci. Total Environ. 906, 167661. https://doi.org/10.1016/j.scitotenv.2023.167661.
Li, Q., Lei, Y., Li, T., 2024b. DNA metabarcoding reveals ecological patterns and driving mechanisms of archaeal, bacterial, and eukaryotic communities in sediments of the sansha yongle blue hole. Sci. Rep. 14 (1), 6745. https://doi.org/10.1038/s41598-024-57214-8.
Li, T., Feng, A., Liu, Y., Li, Z., Guo, K., Jiang, W., et al., 2018. Three-dimensional (3D) morphology of sansha yongle blue hole in the South China Sea revealed by underwater remotely operated vehicle. Sci. Rep. 8 (1), 17122. https://doi.org/10.1038/s41598-018-35220-x.
Liu, B., Sun, Y., Hang, W., Wang, X., Xue, J., Ma, R., et al., 2020. Characterization of a novel Acyl-ACP Delta(9) desaturase gene responsible for palmitoleic acid accumulation in a diatom Phaeodactylum tricornutum. Front. Microbiol. 11, 584589. https://doi.org/10.3389/fmicb.2020.584589.
Longnecker, K., Oswald, L., Kido Soule, M.C., Cutter, G.A., Kujawinski, E.B., 2020. Organic sulfur: a spatially variable and understudied component of marine organic matter. Limnol. Oceanogr. Lett. 5 (4), 305–312. https://doi.org/10.1002/lol2.10149.
Ma, J., Wen, L., Li, X., Dai, J., Song, J., Wang, Q., et al., 2024. Different fates of particulate matters driven by marine hypoxia: a case study of oxygen minimum zone in the Western Pacific. Mar. Environ. Res. 200, 106648. https://doi.org/10.1016/j.marenvres.2024.106648.
McCarthy, M.D., Benner, R., Lee, C., Hedges, J.I., Fogel, M.L., 2004. Amino acid carbon isotopic fractionation patterns in Oceanic dissolved organic matter: an unaltered photoautotrophic source for dissolved organic nitrogen in the ocean? Mar. Chem. 92 (1–4), 123–134. https://doi.org/10.1016/j.marchem.2004.06.021.
New, F.N., Brito, I.L., 2020. What is metagenomics teaching Us, and what is missed? Annu. Rev. Microbiol. 74, 117–135. https://doi.org/10.1146/annurev-micro-012520-072314.
Osterholz, H., Singer, G., Wemheuer, B., Daniel, R., Simon, M., Niggemann, J., et al., 2016. Deciphering associations between dissolved organic molecules and bacterial communities in a pelagic marine system. ISME J. 10 (7), 1717–1730. https://doi.org/10.1038/ismej.2015.231.
Patin, N.V., Dietrich, Z.A., Stancil, A., Quinan, M., Beckler, J.S., Hall, E.R., et al., 2021. Gulf of Mexico blue hole harbors high levels of novel microbial lineages. ISME J. 15 (8), 2206–2232. https://doi.org/10.1038/s41396-021-00917-x.
Pei, J., Chen, S., Yu, K., Hu, J., Wang, Y., Zhang, J., et al., 2022a. Metabolomics characterization of Scleractinia corals with different life-history strategies: a case study about *pocillopora Meandrina* and *Seriatopora hystrix* in the South China Sea. Metabolites 12 (11), 1079. https://doi.org/10.3390/metabo12111079.
Pei, J., Yu, W., Zhang, J., Kuo, T., Chung, H., Hu, J., et al., 2022b. Mass spectrometry-based metabolomic signatures of coral bleaching under thermal stress. Anal. Bioanal. Chem. 414 (26), 7635–7646. https://doi.org/10.1007/s00216-022-04294-y.
Pei, J., Zhou, Y., Chen, S., Yu, K., Qin, Z., Zhang, R., et al., 2024. Chemical diversity of scleractinian corals revealed by untargeted metabolomics and molecular networking. Acta Oceanol. Sin. 42 (11), 127–135. https://doi.org/10.1007/s13131-023-2173-y.
Pena-Ocana, B.A., Ovando-Ovando, C.I., Puente-Sanchez, F., Tamames, J., Servin-Garciduenas, L.E., Gonzalez-Toril, E., et al., 2022. Metagenomic and metabolic analyses of poly-extreme microbiome from an active crater volcano Lake. Environ. Res. 203, 111862. https://doi.org/10.1016/j.envres.2021.111862.
Petras, D., Koester, I., Da Silva, R., Stephens, B.M., Haas, A.F., Nelson, C.E., et al., 2017. High-resolution liquid chromatography tandem mass spectrometry enables large scale molecular characterization of dissolved organic matter. Front. Mar. Sci. 4, 405. https://doi.org/10.3389/fmars.2017.00405.
Rebouche, C.J., Seim, H., 1998. Carnitine metabolism and its regulation in microorganisms and mammals. Annu. Rev. Nutr. 18, 39–61. https://doi.org/10.1146/annurev.nutr.18.1.39.
Schlitzer, R., 2002. Interactive analysis and visualization of geoscience data with ocean data view. Comput. Geosci. 28 (10), 1211–1218. https://doi.org/10.1016/s0098-3004(02)00040-7.
Shannon, P., Markiel, A., Ozier, O., Baliga, N.S., Wang, J.T., Ramage, D., et al., 2003. Cytoscape: a software environment for integrated models of biomolecular interaction networks. Genome Res. 13 (11), 2498–2504. https://doi.org/10.1101/gr.1239303.
Singh, A., Shannon, C.P., Gautier, B., Rohart, F., Vacher, M., Tebbutt, S.J., et al., 2019. DIABLO: an integrative approach for identifying key molecular drivers from multi-omics assays. Bioinformatics 35 (17), 3055–3062. https://doi.org/10.1093/bioinformatics/bty1054.
Sun, S.J., Liu, Y.C., Weng, C.H., Sun, S.W., Li, F., Li, H., et al., 2020. Cyclic dipeptides mediating quorum sensing and their biological effects in Hypsizygus marmoreus. Biomolecules 10 (2), 298. https://doi.org/10.3390/biom10020298.
Suominen, S., Gomez-Saez, G.V., Dittmar, T., Sinninghe Damsté, J.S., Villanueva, L., 2021. Interplay between microbial community composition and chemodiversity of dissolved organic matter throughout the black sea water column redox gradient. Limnol. Oceanogr. 67 (2), 329–347. https://doi.org/10.1002/lno.11995.
Tang, K., Liu, L., 2023. Bacteria are driving the ocean's organosulfur cycle. Trends Microbiol. 31 (8), 772–775. https://doi.org/10.1016/j.tim.2023.05.003.
Tripp, H.J., Kitner, J.B., Schwalbach, M.S., Dacey, J.W., Wilhelm, L.J., Giovannoni, S.J., 2008. SAR11 marine bacteria require exogenous reduced sulphur for growth. Nature 452 (7188), 741–744. https://doi.org/10.1038/nature06776.
van Galen, C., Barnard, D.T., Stanley, R.J., 2020. Stark spectroscopy of lumichrome: a possible candidate for stand-off detection of bacterial quorum sensing. J. Phys. Chem. B 124 (52), 11835–11842. https://doi.org/10.1021/acs.jpcb.0c09498.
Xiao, S., Chen, J., Shen, Y., Chen, Q., Wang, Y., Li, Y., et al., 2023. Molecular characterization of organic matter transformation mediated by microorganisms under anoxic/hypoxic conditions. Sci. China Earth Sci. 66 (4), 894–909. https://doi.org/10.1007/s11430-022-1080-8.
Xiao, X., Powers, L.C., Liu, J., Gonsior, M., Zhang, R., Zhang, L., et al., 2022. Biodegradation of terrigenous organic matter in a stratified large-volume water column: implications of the removal of terrigenous organic matter in the coastal ocean. Environ. Sci. Technol. 56 (8), 5234–5246. https://doi.org/10.1021/acs.est.1c08317.
Xie, L., Wang, B., Pu, X., Xin, M., He, P., Li, C., et al., 2019. Hydrochemical properties and chemocline of the sansha yongle blue hole in the South China Sea. Sci. Total Environ. 649, 1281–1292. https://doi.org/10.1016/j.scitotenv.2018.08.333.
Yao, P., Wang, X.C., Bianchi, T.S., Yang, Z.S., Fu, L., Zhang, X.H., et al., 2020. Carbon cycling in the world's deepest blue hole. Journal of Geophysical Research-Biogeosciences 125 (2), e2019JG005307. https://doi.org/10.1029/2019jg005307.
Yin, M., Song, J., Duan, L., Yuan, H., Li, X., Peng, Q., 2023. North-south differences in hypoxia and nitrogen cycle of the East China Sea over the last century indicated by sedimentary bacteriohopanepolyols. Chem. Geol. 620, 121340. https://doi.org/10.1016/j.chemgeo.2023.121340.
Zaikova, E., Walsh, D.A., Stilwell, C.P., Mohn, W.W., Tortell, P.D., Hallam, S.J., 2010. Microbial community dynamics in a seasonally anoxic fjord: Saanich inlet, British Columbia. Environ. Microbiol. 12 (1), 172–191. https://doi.org/10.1111/j.1462-2920.2009.02058.x.
Zehr, J.P., Capone, D.G., 2020. Changing perspectives in marine nitrogen fixation. Science 368 (6492), eaay9514. https://doi.org/10.1126/science.aay9514.
Zhou, S., Liu, J., Yao, P., Fu, L., Yang, Z., Zhang, Y., et al., 2023. Unique bacterial communities and lifestyles in deep ocean blue holes: insights from the yongle blue hole (south China sea). Front. Mar. Sci. 10, 1086117. https://doi.org/10.3389/fmars.2023.1086117.
Zhu, W., Lomsadze, A., Borodovsky, M., 2010. Ab initio gene identification in metagenomic sequences. Nucleic Acids Res. 38 (12), e132. https://doi.org/10.1093/nar/gkq275.

sustainability

MDPI

Review

Advances in Dissolved Organic Carbon Remote Sensing Inversion in Inland Waters: Methodologies, Challenges, and Future Directions

Dandan Xu [1,†], Rui Xue [2,†], Mengyuan Luo [3], Wenhuan Wang [3,4], Wei Zhang [4,*] and Yinghui Wang [3,4,*]

[1] School of Resources, Environment and Materials, Guangxi University, Nanning 530004, China; xd@st.gxu.edu.cn
[2] Institute of Science and Technology Information, Beijing Academy of Science and Technology, Beijing 100089, China; xuer@bjast.ac.cn
[3] Institute of Green and Low Carbon Technology, Guangxi Institute of Industrial Technology, Nanning 530200, China; 15578905661@163.com (M.L.); wwhuan2202@126.com (W.W.)
[4] School of Marine Sciences, Guangxi University, Nanning 530004, China
* Correspondence: zhangwei20@gxu.edu.cn (W.Z.); wyh@gxu.edu.cn (Y.W.)
† These authors contributed equally to this work.

Abstract

Inland waters, serving as crucial carbon sinks and pivotal conduits within the global carbon cycle, are essential targets for carbon assessment under global warming and carbon neutrality initiatives. However, the extensive spatial distribution and inherent sampling challenges pose fundamental difficulties for monitoring dissolved organic carbon (DOC) in these systems. Since 2010, remote sensing has catalyzed a technological revolution in inland water DOC monitoring, leveraging its advantages for rapid, cost-effective long-term observation. In this critical review, we systematically evaluate research progress over the past two decades to assess the performance of remote sensing products and existing methodologies in DOC retrieval. We provide a detailed examination of diverse remote sensing data sources, outlining their application characteristics and limitations. By tracing uncertainties in retrieval outcomes, we identify atmospheric correction, spatial heterogeneity, and model and data deficiencies as primary sources of uncertainty. Current retrieval approaches—direct, indirect, and machine learning (ML) methods—are thoroughly scrutinized for their features, effectiveness, and application contexts. While ML offers novel solutions, its application remains nascent, constrained by limited waterbody-specific samples and model constraints. Furthermore, we discuss current challenges and future directions, focusing on data optimization, feature engineering, and model refinement. We propose that future research should (1) employ integrated satellite–air–ground observations and develop tailored atmospheric correction for inland waters to reduce data noise; (2) develop deep learning architectures with branch networks to extract DOC's intrinsic shortwave absorption and longwave anti-interference features; and (3) incorporate dynamic biogeochemical processes within study regions to refine retrieval frameworks using biogeochemical indicators. We also advocate for multi-algorithm collaborative prediction to overcome the spectral paradox and unphysical solutions arising from the single data-driven paradigm of traditional ML, thereby enhancing retrieval reliability and interpretability.

Keywords: carbon neutrality; inland waters; dissolved organic carbon; inversion methods; machine learning

check for updates

Academic Editor: Tommaso Caloiero

Received: 28 May 2025
Revised: 2 July 2025
Accepted: 18 July 2025
Published: 21 July 2025

Citation: Xu, D.; Xue, R.; Luo, M.; Wang, W.; Zhang, W.; Wang, Y. Advances in Dissolved Organic Carbon Remote Sensing Inversion in Inland Waters: Methodologies, Challenges, and Future Directions. *Sustainability* **2025**, *17*, 6652. https://doi.org/10.3390/su17146652

Copyright: © 2025 by the authors. Licensee MDPI, Basel, Switzerland. This article is an open access article distributed under the terms and conditions of the Creative Commons Attribution (CC BY) license (https://creativecommons.org/licenses/by/4.0/).

1. Introduction

Under the background of global carbon neutrality goals, dissolved organic carbon (DOC) in inland waters has become an important research subject for carbon assessment and carbon emissions. DOC in inland waters plays a critical role in global carbon cycling and global climate change. Approximately 40% of organic carbon is stored annually in inland reservoirs [1], with concentrations equivalent to 6–13% of marine organic carbon [2]. Inland rivers transport up to 400 million metric tons of organic carbon each year [3]. Statistical data indicate [4,5] that 25% to 44% of carbon in inland water bodies dominated by rivers, lakes, and reservoirs is emitted into the atmosphere as greenhouse gases. Under microbial and photochemical processes, DOC in water bodies becomes a net source of atmospheric carbon dioxide [6,7], and high DOC concentrations accelerate global warming. In turn, the positive feedback cycle of global warming further promotes biological and physicochemical changes in inland waters [8–11], altering DOC fate pathways and intensifying greenhouse gas emissions.

The DOC concentrations in inland waters directly affect drinking-water risks and water resource management difficulty [12–14]. When river water with high DOC concentrations recharges groundwater, oxidation products generated by bacterial oxidative processes significantly influence groundwater pH levels [15]. Particularly during drinking-water treatment, high DOC concentrations react with chlorine to produce substantial disinfection byproducts, increasing cancer risks [16]. Additionally, DOC in inland water bodies alters lake food web structures, exerting profound impacts on ecosystem functions and biodiversity [17].

The traditional approach for monitoring DOC in inland waters involves manual fixed-point sampling of water bodies followed by laboratory analysis. However, the distribution of inland waters is relatively scattered with extensive coverage, resulting in high sampling difficulty and prolonged sampling cycles. The dynamic processes of biogeochemical cycles persistently act upon inland water bodies, inducing spatiotemporally uncertain dynamic variations in DOC [18,19]. Traditional sampling methods are insufficient to accommodate the requirements of large-scale and long-term monitoring. Therefore, adopting advanced technologies to achieve accurate and high-frequency monitoring and assessment of inland water DOC concentrations constitutes a current imperative demand.

The variations in DOC concentration within water bodies influence the optical characteristics of dissolved organic matter, which provides a technical possibility for retrieving DOC through the responses of aquatic optical properties. However, the light absorption by DOC is relatively complex, with absorption spectra lacking characteristic peaks, resulting in often suboptimal practical application effectiveness. Colored dissolved organic matter (CDOM), the optically active component of DOC also termed "yellow substance" [20], exhibits strong absorption in ultraviolet and blue light spectral regions, demonstrating more sensitive aquatic optical responses. CDOM has emerged as an effective optical characteristic proxy for DOC inversion in specific rivers [21], lakes [22,23], and estuarine/coastal waters [24].

Remote sensing technology is a crucial method for measuring and analyzing the optical properties of water bodies. Its ability to rapidly acquire large-scale water quality data has made it a significant tool for studying DOC in inland waters, overcoming the limitations inherent in traditional ground-based monitoring methods [25–29]. This review analyzed the remote sensing literature on DOC in inland waters indexed in SCI-EXPANDED from 1 January 2005 to January 2025 through Web of Science. After deduplication and screening, the final dataset comprised 227 articles contributed by 1120 authors affiliated with 478 organizations across 47 countries. The top three productive nations were the United States (83 articles, 36.56%), China (70 articles, 30.84%), and Canada (33 articles,

14.54%). Global-scale research patterns and international collaborations are visualized in Figure 1, revealing distinct geographical distributions and cooperative networks within this scientific domain.

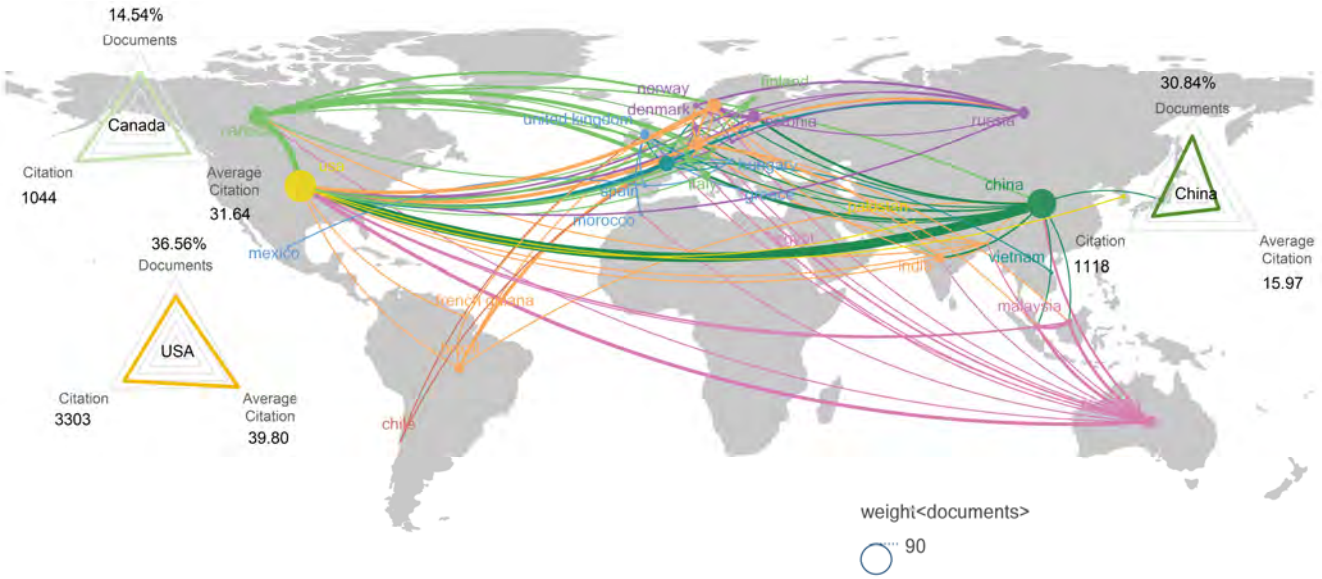


Figure 1. Global research overview of inland water DOC.

Among journals publishing more than five articles on the topic (Table 1), Remote Sensing ranked first in output (25 articles, 11.1% of total publications), followed by Remote Sensing of Environment (18 articles, 7.9%), both emphasizing satellite-based remote sensing for biogeochemical studies in inland waters and iterative advancements in DOC retrieval models. Keyword co-occurrence mapping (Figure 2) further reveals that remote sensing technology has emerged as a pivotal tool for DOC research in inland aquatic systems over the past decade, with thematic clusters highlighting its critical role in monitoring carbon cycling, water quality, and climate feedback mechanisms.

Table 1. Journals with more than 5 articles.

Source	Documents	Citation	Average Citation
Remote sensing	25	730	29.20
Remote Sensing of Environment	18	1332	74
Biogeosciences	11	380	34.54
Water Research	9	326	36.22
Science of the Total Environment	8	246	30.75
Journal of Geophysical Research: Biogeosciences	6	184	30.66
Water	6	114	19
International Journal of Applied Earth Observation and Geoinformation	5	84	16.8

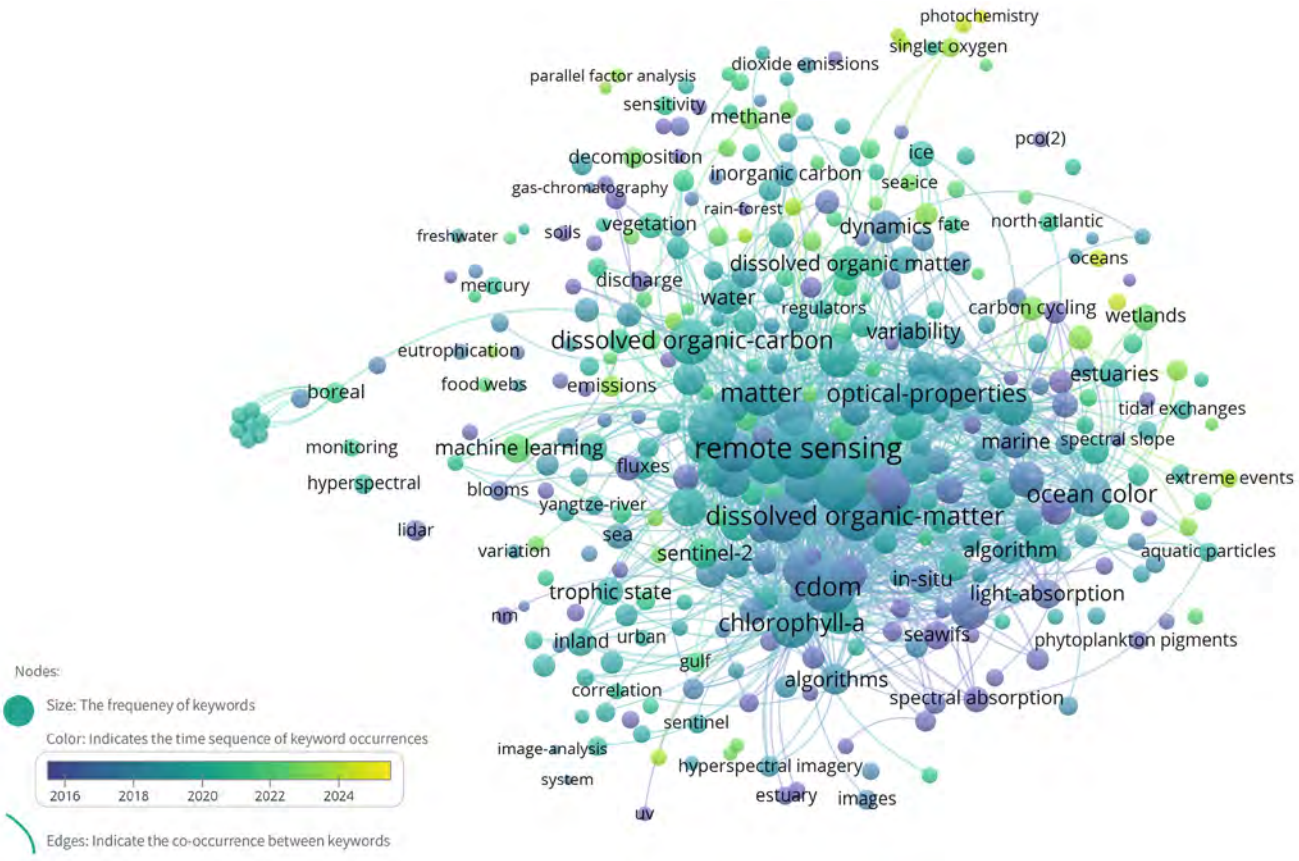


Figure 2. Inland water DOC knowledge graph (2005–2025).

Although significant progress has been made in remote sensing technology for DOC monitoring, multiple technical bottlenecks persist in the accurate inversion of CDOM in inland waters. Inland water bodies exhibit more complex optical characteristics, where their radiative transfer processes are strongly influenced by total suspended matter (TSM) and phytoplankton [30,31]. As an important optically active constituent, the spectral signals contributed by CDOM are often obscured by the scattering noise from TSM and absorption signals from phytoplankton, rendering traditional water-color remote sensing methods constructed for Case I waters inapplicable for direct implementation [32–34]. Furthermore, regional variations in DOC sources and composition pose additional challenges to the generalizability of inversion methods [24]. The current remote sensing inversion of inland water DOC reveals several critical research gaps that urgently need to be addressed:

1. How can the application effectiveness of remote sensing data in DOC inversion for inland waters be improved?
2. How can robust DOC/CDOM remote sensing inversion methods suitable for inland waters with complex optical properties be developed?
3. How can the professional efficacy of traditional machine learning in water quality inversion be specifically enhanced?

Consequently, conducting in-depth discussions to address these challenges and explore more transferable inversion methods with optimization strategies is crucial. This review synthesizes recent advances in remote sensing retrieval approaches for DOC in inland waters, systematically examines persisting technical challenges across methodological implementations, and critically discusses limitations and future priorities in current inversion frameworks. By integrating empirical findings and theoretical refinements, the analysis aims to offer guidance for next-generation DOC monitoring protocols while con-

tributing actionable insights to advance evidence-based water resource governance and ecological conservation strategies.

2. Integration of Multi-Source Data and Uncertainty Provenance Analysis

Early ocean-color satellites prioritized sensors optimized for systematic monitoring of vast Case 1 waters, employing wide-swath scanning to achieve global coverage. Owing to lower concentrations of suspended particulates and dissolved organics, marine optical signals exhibit spectral simplicity, substantially reducing the complexity of water constituent retrieval and enabling standardized model development. The 1978 launch of the U.S. coastal zone color scanner (CZCS), the first dedicated ocean-color satellite, enabled the systematic mapping of global marine chlorophyll concentrations, culminating in the inaugural global ocean primary productivity atlas. Subsequent missions, including India's IRS-P3 (1996), Japan's ADEOS-1 (1996), and others with enhanced swath-width capabilities, further advanced observational frameworks (Table 2).

Table 2. The world's leading water-color remote sensing satellites [35–38].

Source	Satellite	Sensor	Number of Bands	Band Range (nm)	Spatial Resolution (m)	Temporal Resolution (Day)
Ocean-Color Sensors	Nimbus-7	CZCS	6	433–12,500	825	1–2
	IRS-P3	MOS	18	408–1600	500	5
	ADEOS-I	OCTS	12	402–125,00	700	41
	Terra (EOS AMI)	MODIS Terra	36	405–14,385	1000	1–2
	KOMPSAT-I	OSMI	6	400–900	850	28
	HY-1A	COCTS	10:04	402–12,500	1100:250	3
	HY-1A	CZI	10:04	420–890	1100:250	3
	ENVISAT	MERIS	15	412–1050	300/1200	3
	Myriade Series	PARASOL	9	443–1020	6000	16
	Oceansat	OCM-II	12	400–900	350/4000	2
	Sentinel-3A/B	OLCI	16	400–1040	300	2
	Himawari-9	AHI	16	450–13,400	500–2000	10 min
	NOAA-20	VIIRS	22	412–2250	375, 750	0.5
	HY-1C/1D	COCTS	10	402–12,500	1100	1
	GK-2B	GOCI-II	13	380–865	500	1 h
	EOS-06	OCM-3	13	400–1010	360	2
	PACE	OCI	200	340–890	1000	2
Inland/Coastal Water Sensors	Sentinel-2	MSI	13	443–2190	10, 20, 60	5
	HJ-1A/B	CCD	4	430–900	30	4
	Landsat-8, 9	OLI	11	433–12,510	15, 30, 100	16
	Planet	PlanetScope-2	8	455–860	3	1
	Trra, Aqua	MODIS	36	402–965 3660–14,338.5	250, 500, 1000	1–2
	SPOT-6/7	HRVIR	5	450–680	10, 20	26
	GF-5	AHSI	330	400–2500	30, 60	5–16

The late 20th-century emergence of global warming and carbon cycle research propelled ocean-color remote sensing into a pivotal role in quantifying marine carbon sinks. Long-term datasets from platforms such as NASA's Terra/EOS AM-1 (1999), Korea's KOMPSAT-I (1999), China's HY-1A (2002), Argentina's SAC-C (2000), ESA's ENVISAT (2002), and France's Myriade Series (2004) became indispensable for modeling marine

primary productivity and carbon flux dynamics. Post-2000, the global carbon neutrality imperative shifted scientific attention to inland aquatic carbon sinks. However, kilometer-scale resolutions of traditional ocean-color satellites prove inherently incompatible with the fine-grained spatial heterogeneity of inland systems (e.g., rivers) [39,40]. This spatial-scale discordance—compounded by complex inland optical properties—has prompted the deployment of land/coastal sensors with enhanced spatial resolution (e.g., 10–30 m) and spectrally tailored radiometric capabilities for inland water monitoring.

2.1. Satellite–Air–Ground Synergistic Observation

High-resolution land-focused satellites (e.g., Landsat OLI, Sentinel-2 MSI) with 10–30 m spatial resolution enable the spatial differentiation of dissolved organic carbon (DOC) in medium-sized lakes [41–48]. However, their utility in high-frequency continuous monitoring is constrained by extended revisit cycles (5–16 days) and persistent cloud interference—for instance, data availability for Sentinel-2 in southern China falls below 20% [49]. High-frequency satellites like Terra/Aqua MODIS (1–2-day revisit) partially offset temporal resolution limitations, but their coarse spatial resolution and broad spectral bandwidths necessitate the integration of boundary-bandwidth correction models for radiometric optimization [50,51]. While HJ-1A/B CCD satellites offer high spatiotemporal resolution suitable for small-lake CDOM monitoring [52], their limited spectral resolution risks feature loss, requiring ground-truth data for spectral interpretation [53,54]. Commercial platforms (e.g., Planet, 3 m resolution), driven by market forces, prioritize high spatial and temporal resolution imagery as their core competitive edge. While this endows them with exceptional spatial identification capabilities for small-scale river monitoring, the inherent trade-off between spectral and spatial resolution necessitates substantial compromise in spectral resolution to maintain adequate image signal-to-noise ratios. As a result, critical UV absorption peaks (200–400 nm) from aromatic compounds and conjugated double-bond organics in DOC remain undetectable due to the limited spectral resolution of commercial systems, leading to the loss of key spectral fingerprints for DOC characterization [34].

A comprehensive analysis of inland/coastal-water-satellite-based studies concerning inland waters CDMO/DOC, spanning records from the inception of the Web of Science through 2025, was undertaken (articles failing retrieval criteria were manually screened out), as shown in Figure 3.

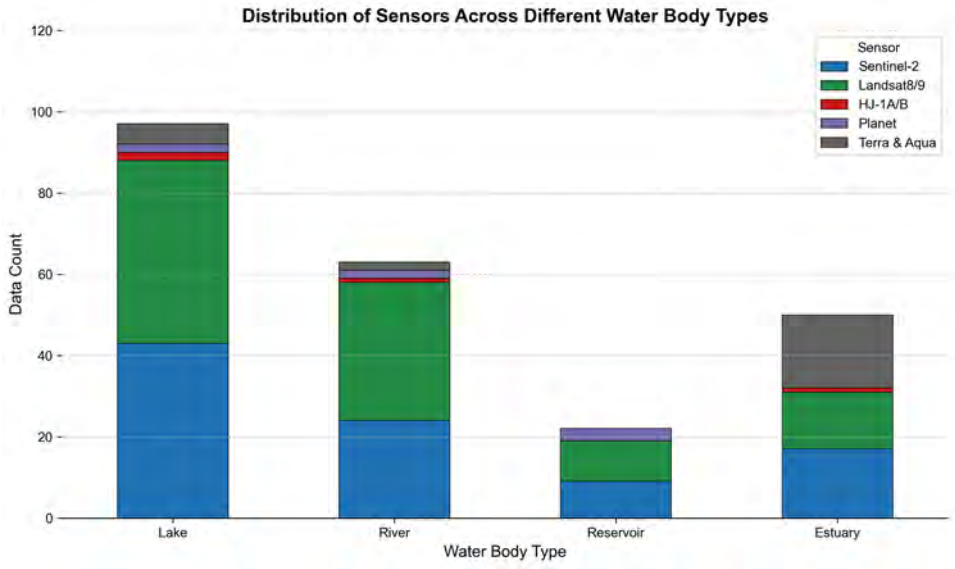


Figure 3. Overview of the application of commonly used satellites in different types of inland waters.

The Landsat 8/9 and Sentinel-2 satellites exhibit the most widespread application, attributable to their quantitatively superior numbers of spectral bands and broader band ranges. The Terra and Aqua satellites, constrained by their lower spatial resolutions, are primarily suitable for large-scale estuarine and extensive lacustrine studies. The very coarse spatial resolution of Planet satellites significantly increases computational complexity when applied to large estuaries, though they remain appropriate for river and lake investigations [55]. Table 3 presents typical application cases of remote sensing data sources in inland waters.

Table 3. Typical application cases of remote sensing data sources in inland waters.

Case	Study Area	Overview
[56]	River basins and coastal areas from the Rajang River	Using Landsat-8 data to construct band ratio combinations, perform regression based on in situ DOC, validate the model with three verification methods (simple grouping, K-fold analysis, and bootstrap), and estimate the DOC flux from April 2013 to December 2018 by using the constructed regression model (R^2 = 0.88, MAPE = 5.71%) and river discharge.
[57]	Erhai Lake	A CDOM prediction model was constructed using empirical methods based on Aqua satellite imagery and insitu measured data. The model was then used to invert the CDOM changes across the entire lake from 2013 to 2019.
[43]	Small water surface reservoirs in the Brazilian semiarid region	Based on Landsat-8 imagery and RapidEye commercial satellite imagery, a CDOM model was constructed. The results showed that the green band of Landsat-8 performed better (R^2 = 0.69 vs. RapidEye: R^2 = 0.25), especially for non-perennial reservoirs with high CDOM concentrations and without optical interference from phytoplankton.
[41]	Ganh Hao River	The MLR model developed from Sentinel-2 data demonstrated stable performance (comprehensive error value = 0.66, 0.53) across both water body types (Class 1: low aCDOM (412), Class 2: medium to high aCDOM (412)), while the Landsat-8-based MLR model achieved the highest accuracy (value = 0.15) in Class 1 but showed significant performance degradation in Class 2 (value = 0.46).

The spatial, temporal, and spectral configurations of sensors impose significant constraints on inland water research. Particularly with the growing demand for high-frequency dynamic monitoring in turbid, optically complex waters, the limitations of single-platform systems in terms of observation continuity and data utility have become increasingly apparent, highlighting the urgent need to develop an integrated multi-source data framework.

To overcome single-sensor constraints, satellite–air–ground synergistic frameworks are emerging as a paradigm [58–60]. Spatially, drone-borne hyperspectral systems (decimeter-scale resolution) resolve DOC concentration gradients in rivers [61–63], circumventing the pixel-mixing artifacts endemic to satellite data [64–66]. Temporally, when short-term extreme rainfall or snowmelt events flush terrestrial organic matter (e.g., litter, livestock manure, fertilizer residues) into water bodies as dissolved organic carbon (DOC), traditional single-platform sampling frequencies often fail to capture these event-driven DOC pulses. Models built without such high-frequency data cannot accurately reflect real condi-

tions, compromising subsequent analytical results. Therefore, implementing sub-second sampling with near-surface hyperspectral imagers enables the effective capture of DOC fluctuations following ultra-short-term events [67]. This provides critical data support for optimizing sampling frequencies and algorithm design, making monitoring and analytical methods more adaptable to complex and dynamic environmental conditions. Simultaneously, this approach allows for the effective monitoring and management of explosive "black water " events to avoid ecological catastrophes [68].

The benefits of this synergistic framework rely on a range of advanced technologies. For instance, Sentinel-2 MSI's enhanced radiometric sensitivity (e.g., Band 1 at 443 nm) successfully retrieves blue-violet signals in high-CDOM waters [69]. Spatiotemporal fusion algorithms (e.g., STARFM) harmonize multi-resolution datasets to achieve continuous coverage [70,71], complemented by tri-level validation networks (satellite-UAV-ground spectrometers) on the Google Earth Engine (GEE) platform for automated data matching and consistency assessment [60,72].

2.2. Uncertainty Provenance

Uncertainty in DOC remote sensing retrieval arises from coupled errors across the processing chain [73,74], with atmospheric correction being the dominant factor for inland waters [75,76]. The optical complexity of these systems—shaped by anthropogenic activities (e.g., industrial discharge, agricultural runoff, shipping disturbances) and heterogeneous topography (e.g., mountainous closed basins, estuarine deltas)—generates terrestrial aerosol-dominated atmospheres (enriched with organic carbon and minerals) [77]. These aerosols, compounded by strong absorption from waterborne CDOM and non-algal particles (NAP, e.g., sediments, humus) in near-infrared (NIR) bands [78], invalidate core assumptions of marine-oriented atmospheric correction models (e.g., FLAASH). For instance, post-correction blue-violet band reflectance in highly turbid, CDOM-rich inland waters often falls ≤ 0 [79,80], highlighting systemic model failures.

Targeted atmospheric correction strategies are, thus, critical for inland aquatic systems [79,81,82]. While some studies bypass correction by directly modeling raw imagery [80], such approaches lack universality due to regional environmental dependencies. Pioneering work by Fan et al. [83] demonstrated the efficacy of multilayer neural networks in correcting turbid water atmospheres, offering a scalable framework for inland applications [75,84]. Hardware advancements, such as Sentinel-2 MSI's enhanced radiative sensitivity and signal-to-noise ratio, further mitigate detection challenges for blue-violet band water-leaving radiance [69].

Spatial heterogeneity exacerbates uncertainty. Low-resolution sensors (e.g., MODIS) underestimate DOC biogeochemical gradients in inland waters due to scale mismatch [40]. For small-scale features (e.g., river meanders, lake margins), dynamic resolution selection and linear spectral mixture analysis (LSMA) are essential to disentangle land-water mixed signals [85].

Data and model structural limitations compound errors [86,87]. SPOT HRVIR's high inter-band correlation (R^2 = 0.92–0.99) reduces sensitivity to inland reservoir DOC variability [88]. GF-5's hyperspectral capability remains underutilized due to limited historical data (launched 9 May 2018), restricting its application to pilot studies [89,90]. To enhance reliability, recent efforts focus on model architecture innovation. This review systematically categorizes existing models' developmental trajectories, technical merits, and constraints (summarized in Table 4), providing a roadmap for next-generation high-fidelity DOC retrieval frameworks.

Table 4. Comparison of sources of uncertainty.

Error Source	Atmospheric Correction	Spatial Heterogeneity	Model/Data Deficiencies
Impact Nature	Fundamental, systemic errors	Regional, scale-dependent errors	Algorithmic or structural limitations
Correctability	Requires ground validation + advanced algorithms	High-resolution data + spectral unmixing	Model optimization + data fusion
Directness on DOC Retrieval	Directly determines spectral fidelity	Indirectly affects pixel purity	Dependent on input data quality + model architecture

3. Optical Principles and Methods of DOC Remote Sensing Retrieval

3.1. Optical Foundations of DOC Remote Sensing Retrieval

The principle of DOC remote sensing inversion is primarily grounded in the coupling relationship between aquatic optical properties and radiative transfer mechanisms (Figure 4).

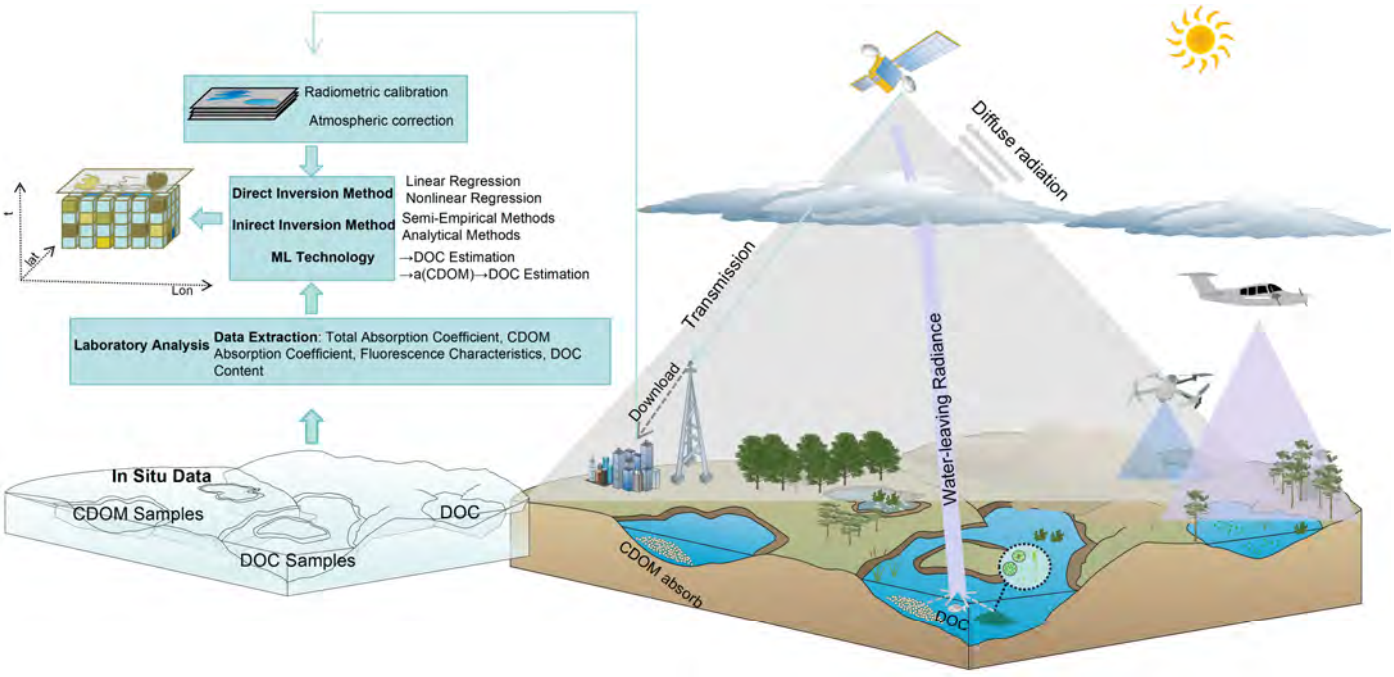


Figure 4. DOC inversion principle of remote sensing.

Specifically, the water-leaving radiance formed through solar radiation undergoing surface reflection, in-water scattering/absorption, and transmission processes penetrates the atmosphere to be captured by spaceborne sensors. The DOC remote sensing inversion is achieved through the extraction and processing of remote sensing information. The complete inversion workflow comprises three core stages: First, radiometric calibration converts raw digital number values into absolute radiance quantities; subsequently, regionally applicable atmospheric correction algorithms for inland waters are employed to isolate water-leaving radiance; and ultimately, based on corrected water surface reflectance spectra, regression models or bio-optical models incorporating DOC concentration or absorption characteristics are established to achieve the spatiotemporal inversion of DOC concentrations.

3.2. Validation and Evaluation

In model validation and evaluation, methods such as independent sample validation, K-fold cross-validation, and leave-one-out cross-validation are commonly employed [43,56,57]. For machine learning models, training and test sets are partitioned according to industry conventions like 7:3 or 8:2 [91]. Under the premise of ensuring the training set covers sufficient spectral features, an independent test set is utilized to quantify the model's generalization error. During cross-sensor validation, band matching is accomplished through the spectral response function (SRF): Measured hyperspectral data are convolved with the target sensor's SRF, converted into the corresponding satellite band reflectance characteristics, and then input into the inversion models to verify cross-platform applicability. The spectral response function (SRF) is given by Equation (1).

$$\mathrm{Band_i} = \frac{\int_{\lambda_{min}}^{\lambda_{max}} \mathrm{SRF}(\lambda) R_{rs} d\lambda}{\int_{\lambda_{min}}^{\lambda_{max}} \mathrm{SRF}(\lambda) d\lambda} \quad (1)$$

$\mathrm{Band_i}$ represents the equivalent band of the remote sensing satellite, where λ_{min} and λ_{max} are the boundary wavelengths of band i, and $\mathrm{SRF}(\lambda)$ is the spectral response of the i-th band of the sensor at wavelength λ.

The performance evaluation of remote sensing inversion models is typically based on metrics such as R^2, MAE, RMSE, and bias. Here, R^2 reflects the model's explanatory power for the variance in DOC concentration, MAE quantifies the average deviation of the retrieved values, RMSE is sensitive to errors from extreme values, and bias reveals the model's systematic tendency towards overestimation or underestimation. The commonly used performance evaluation metrics for remote sensing inversion models and their corresponding model explanatory power are presented in the Table 5.

Table 5. Main performance metrics and model explanatory power for remote sensing DOC inversion.

Evaluation Metrics	Formula	Correlation with Error
R^2	$1 - \frac{\sum_{i=1}^{n}\left(y_i - \widetilde{y}_i\right)^2}{\sum_{i=1}^{n}(y_i - \overline{y}_i)^2}$	A higher R^2 value indicates a smaller sum of squared deviations between predicted and measured values relative to the total variance, reflecting a lower overall error level of the model.
MAE	$\frac{1}{n}\sum_{i=1}^{n}\left\|y_i - \widetilde{y}_i\right\|$	The smaller the MAE, the smaller the average absolute error of the retrieved values, indicating better prediction stability of the model in regions with gradual water gradients.
RMSE	$\sqrt{\frac{1}{n}\sum_{i=1}^{n}\left(y_i - \widetilde{y}_i\right)^2}$	A larger RMSE indicates poorer model performance in handling extreme values or anomalous scenarios, where retrieved results potentially exhibit greater variability, and it is effective for identifying extreme scenarios such as estuaries and algal bloom areas.
Bias	$\frac{1}{n}\sum_{i=1}^{n}\left(y_i - \widetilde{y}_i\right)$	A large absolute bias value may result from the model's omission of atmospheric correction or radiative transfer losses, inducing systematic deviations in retrieved results; this can be addressed by refining the model with physical priors.
MAPE	$\frac{100\%}{n}\sum_{i=1}^{n}\left\|\frac{y_i - \widetilde{y}_i}{y_i}\right\|$	A MAPE of 0% indicates a perfect model. The smaller the MAPE value, the better the accuracy of the prediction model.

note: y_i is the measured value for sample i; $\widetilde{y}_i$ is the retrieved value of the model; $\overline{y}_i$ is the mean of measured samples.

3.3. Direct Inversion Methods for Remote Sensing of DOC and Physical Drivers of Their Accuracy

3.3.1. Direct Retrieval Method for DOC Remote Sensing: Spectral Matching and Concentration Quantification

The technical framework of the direct inversion method comprises three core procedures: (1) collecting spatially representative DOC in situ measurement data; (2) synchronously acquiring remote sensing imagery and extracting spectral characteristics of target water bodies (e.g., band reflectance, band ratios, or spectral indices); and (3) developing inversion equations through correlation analysis and regression modeling. As one of the earliest methodological frameworks in DOC remote sensing, Chen and Shi (2001) [92] pioneered a multivariate linear model (Equation (2)) leveraging 130 simulated spectral datasets to invert DOC concentrations from optimal band combinations of reflectance.

$$\log(\mathrm{DOC}) = 1.2419\log(\mathrm{R670}/\mathrm{R412}) - 0.2614 \quad (2)$$

Hirtle and Rencz [80] employed Landsat ETM+ Band 2 to establish a logarithmic model for DOC (log(DOC)) in Nova Scotia lakes ($R^2 = 0.72$), but it was not applicable to Finnish lakes with high DOC concentrations (>18.3 mg/L) [93], revealing the regional dependency limitation of the model. Recently, Chunhock et al. [56], through conducting a comparative analysis of 24 river DOC inversion models, identified that the exponential function model utilizing the Landsat-8 OLI B4/B3 band combination (Equation (3)) demonstrated optimal accuracy, though its applicability remains constrained to low-turbidity river systems.

$$\mathrm{DOC} = 89.86e^{\mathrm{B4}/\mathrm{B3}} \quad (3)$$

3.3.2. Physically Driven Factors Governing the Accuracy of Direct Inversion Methods

While direct methods demonstrate operational simplicity, their inversion accuracy faces inherent limitations. CDOM, constituting 10–90% of DOC [94–96], dominates spectral signals through its ultraviolet-visible absorption characteristics. However, non-chromophoric constituents such as carbohydrates and amino acids remain spectrally undetectable due to optical inertness, resulting in scale decoupling between spectral signatures and DOC concentrations as remote sensing signals only capture partial DOC components. This decoupling is partially mitigated in estuarine and coastal waters under single-salinity-driven mixing regimes, manifesting dual conservative mixing behavior through coupled "DOC-salinity" and "CDOM-salinity" relationships. As a hydrological tracer of river-ocean mixing, salinity-mediated dual conservation reflects characteristic conservative mixing patterns between terrestrial and marine water masses [97–99]. In major Arctic and subarctic rivers, including the Ob, Yenisei, and Yukon, CDOM and DOC exhibit robust, high-correlation relationships [99]. This strong covariation arises from their proximity to polar regions, where runoff and precipitation drive substantial inputs of terrestrial carbon from organic-rich soils [100], sustaining tightly coupled CDOM–DOC dynamics with minimal influence from biogeochemical alterations [101,102]. Table 6 compiles representative CDOM–DOC relationships with associated R^2 values observed across these river and other water systems.

Table 6. Regional robust relationship and R^2 between CDOM and DOC.

Number	CDOM–DOC	R^2	Reference
1	$CDOM = 0.6054 + 0.4939 \cdot DOC$	0.86	[103]
2	$\ln DOC = \alpha + \beta \ln ag(275) + \gamma \ln ag(295)$	/	[104]
3	$DOC = 55 + 357 \cdot a_{CDOM}(443)$	/	[105]
4	$DOC = 245 + 171 \cdot a_{CDOM}(443)$	/	[106]
5	$a_{CDOM}(440) = 0.5 \cdot DOC - 1.52$	0.95	[107]
6	$DOC = 32.942 \cdot a_{CDOM}(412) + 95.587$ $DOC = 95.519 \cdot a_{CDOM}(412) + 78.795$ $DOC = 213.34 \cdot a_{CDOM}(412) + 38.044$	0.78 0.81 0.72	[108]
7	$DOC = 2.13 + 1.24 \times (CDOM)$	0.84	[109]
8	$CDOM = 1.593DOC - 2.453$	0.88	[46]
9	$DOC = 1.268a_{CDOM}(440) + 3.623$	0.76	[44]
10	$DOC = 2.351 + 92.515c_{CDOM}$	0.873	[110]
11	$c_{DOC} = \alpha + \beta \cdot a_{250} + \gamma \cdot a_{365}$	/	[111]
12	$c_{DOC} = 59.1c_{CDOM}$	0.74	[112]
13	$DOC = 1.89 + 0.78a_{CDOM}(443)$	0.73	[113]

However, in the vast majority of rivers and inland water bodies, DOC–CDOM relationships exhibit diminished conservatism due to complex interactions involving photochemical degradation, heterogeneous terrestrial inputs, and microbial transformations [99]. For instance, subtropical rivers draining intensively managed agricultural watersheds (e.g., the Pearl River) display pronounced seasonal DOC–CDOM decoupling driven by accelerated microbial processing under high-temperature, high-humidity conditions [114–117], with variability exceeding that observed in temperate systems like the Yangtze River [118]. The high organic matter load of anthropogenic origin in the Nile River in Africa leads to the highest DOC concentration in autumn [119]. The Mississippi River demonstrates disrupted correlations due to autochthonous CDOM production from active phytoplankton blooms [120,121]. As a lowland river, the Murray is perennially influenced by floods. Following flood inundation, substantial phytoplankton and carbon are delivered to the Murray River, resulting in an extremely unstable correlation between CDOM and DOC [122,123]. Tidal modulation further complicates estuarine DOC dynamics, where concentrations may exhibit positive or negative correlations with tidal height depending on upstream terrestrial inputs [124] or hydraulic retention time [125]. While river discharge generally governs DOC dilution/transport, producing discharge–concentration correlations [126,127], these relationships become statistically insignificant under complex hydrological regimes [128]. Notably, DOC accumulation in mesohaline zones has been documented in nutrient-enriched inland waters [129]. Such multifaceted nonlinear behaviors collectively undermine CDOM–DOC correlations, representing a pervasive challenge across inland aquatic systems.

3.4. DOC Remote Sensing Indirect Inversion Method: Cross-Media Inference via Robust CDOM–DOC Relationships

Indirect DOC retrieval hinges on establishing cross-media predictive relationships between DOC and CDOM by leveraging the latter's optical activity, contingent upon their statistically robust correlation (Table 3). Fichot and Benner (2011) [104] developed a mul-

tiple linear regression (MLR) model using CDOM absorption coefficients at 275 nm and 295 nm across diverse global water bodies, achieving a minimal DOC retrieval error of 4.2%. However, Asmala et al. [130] identified multicollinearity among predictors (VIF > 10) in this model during validation in three Finnish rivers, proposing, instead, a simple linear regression (SLR) model based solely on 355 nm absorption to enhance robustness. Optimizing regression architecture is critical for cross-media inference accuracy. In Eutrophic Lake Ebinur (China), comparative analyses of linear, quadratic, exponential, and logarithmic models revealed the superior performance of linear regression ($R^2 > 0.74$ vs. $R^2 < 0.72$ for nonlinear models) [112], likely attributable to the salinity-mediated enhancement of linear CDOM–DOC coupling.

3.4.1. Semi-Empirical Method for CDOM: From Spectra to CDOM

CDOM retrieval from remote sensing reflectance (Rrs) predominantly employs empirical methods supplemented by semi-analytical optical parameterizations. A standard workflow is as follows: Based on the spectral absorption curve, the combination of sensitive multispectral satellite bands is selected to establish a statistical model of a_{CDOM} (the absorption coefficient of CDOM, which is often used to characterize CDOM concentration). For instance, the Kolyma River study [103] employed Landsat TM/ETM+ band ratios (Band 3 and Band 2/Band 1) to construct a linear regression model, yet the maximum accuracy reached only $R^2 = 0.7832$, which exposes the insufficient spectral resolution of broadband sensors in resolving characteristic absorption peaks of CDOM. Lai et al. [94] used Landsat B1/B3 ratios for CDOM estimation ($R^2 = 0.82$), subsequently deriving DOC concentrations via CDOM–DOC correlations with RMSE = 0.65 m^{-1} and MSE = 10.9%. Its performance is constrained by two critical bottlenecks:

- Model rigidity: Traditional least squares regression relying on static parameters (e.g., fixed band weights) struggles to adapt to spatiotemporal heterogeneity of water inherent optical properties (IOPs) [30,103,131].
- Error propagation: The "two-step" indirect inversion pathway (Rrs $\rightarrow$ a_{CDOM} $\rightarrow$ C_{DOC}) induces nonlinear amplification of errors. In the Kolyma River case [103], DOC inversion standard errors increased from $\pm$0.92 mg L^{-1} at the CDOM stage to $\pm$1.68 mg L^{-1}, representing an 82.6% error escalation.

While empirical frameworks partially incorporate IOPs, their reliance on heuristic band ratios neglects the explicit modeling of IOP component interactions (e.g., phytoplankton vs. non-algal particle absorption-scattering coupling), fundamentally limiting model generalizability.

3.4.2. Analytical Method: From Spectra to CDOM

Analytical methods offer broader applicability compared to empirical frameworks. Rooted in radiative transfer theory, these methods derive absorption and backscattering coefficients through rigorous analytical solutions. However, practical implementation remains challenging due to multiple scattering and optical heterogeneity in natural waters [132]. Semi-analytical methods bridge this gap by coupling radiative transfer equations with empirical parameterizations, preserving physical interpretability while ensuring computational feasibility. These approaches demonstrate superior parameter retrieval accuracy and generalizability over traditional empirical models [133,134]. Current mainstream semi-analytical algorithms include the quasi-analytical algorithm (QAA) [135]; the Garver–Siegel–Maritorena (GSM) algorithm [136,137]; and the generalized inherent optical Properties (GIOP) algorithm [138,139].

The widely used QAA_v6 [140] and QAA_CDOM [133,141] algorithms excel in ocean-color applications but exhibit limitations in turbid inland waters. High suspended sediment

loads induce multiple scattering and terrestrial signal interference, leading to significant errors in inherent optical property (IOP) retrievals [142]. For instance, Pan et al. [143] reported an RMSE = 1.39 m^{-1}, when applying QAA to hypereutrophic Lake Taihu. Recent advancements focus on algorithm customization: Wang et al. [144] recalibrated QAA empirical equations using in situ data, developing the QAA_cj variant for highly turbid estuaries (RMSE < 1.12 m^{-1}). Le et al. [145] proposed a phytoplankton absorption coefficient separation algorithm for Taihu Lake water bodies, successfully decoupling chlorophyll and CDOM absorption signals (similarity coefficient S = 0.97 between separated and measured spectra). However, spectral aliasing effects between CDOM and suspended particulate matter (SPM) in the blue spectral region (400–500 nm) still lead to residual spectral confounding errors (RMSE) in inversion. Notably, recent research in China's Yangtze River Estuary [146] introduced machine learning techniques, utilizing a backpropagation neural network to establish a nonlinear mapping model between the backscattering coefficient of suspended particles (b_{bp}) and the hybrid absorption coefficient a_p (sum of phytoplankton absorption coefficient a_{ph} and non-algal particle absorption coefficient a_{dg}). This data-driven approach effectively enhances the physical consistency of CDOM concentration retrieval.

Critical improvements for QAA in inland waters involve (1) the localized calibration of empirical parameters and sub-equations within QAA architectures [140,147–152], and (2) reference wavelength optimization [153]. The standard optical assumptions at default reference wavelengths (e.g., 670 nm) in QAA_v6 and QAA_CDOM algorithms mismatch actual inland water conditions dominated by elevated CDOM absorption and SPM scattering. This discrepancy necessitates dynamic wavelength adjustments tailored to site-specific water composition and constituent gradients. Empirical studies demonstrate that shifting reference wavelengths from the conventional 670 nm to 740 nm (e.g., turbid inland waters in Northeast China) [154] or near-infrared bands (e.g., Lake Taihu [155] and Chinese turbid inland lakes [156]) enhances water column penetration depth and mitigates suspended particulate interference, thereby significantly improving QAA's retrieval stability in eutrophic waters.

The GSM and GIOP frameworks employ distinct mathematical approaches for deriving CDOM absorption coefficients: GSM utilizes nonlinear equations, while GIOP relies on eigen-based matrix inversion techniques. Since GSM uses nonlinear equations to derive optical parameters such as the absorption coefficients of substances in water bodies, it is highly dependent on prior spectral libraries. It needs to rely on laboratory and in-situ measurement differences to construct accurate and comprehensive spectra covering CDOM, phytoplankton, and suspended particulate matter, so as to enable the GSM model to have better adaptability in different types of water bodies (such as oceans, lakes, and rivers). In applied research, Matsuoka et al. [157] successfully applied the GSM model to estimate CDOM absorption in coastal waters, achieving DOC retrieval through robust CDOM–DOC correlations (R^2 = 0.97). However, its efficacy in inland DOC estimation remains unvalidated due to complex optical interference. Salama et al. [158] modified the GSM model while obtaining the spectral dependence of inland waters, addressing the limitation that GSM is limited to the ocean. Both GSM and QAA exhibit significant performance degradation at high solar zenith angles [159], necessitating enhanced atmospheric correction protocols. To mitigate this, Xu et al. [160] developed a spherical-shell atmospheric vector radiative transfer model using Monte Carlo simulations, explicitly accounting for Earth curvature effects under extreme illumination conditions.

GIOP offers superior flexibility through a dynamic selection of phytoplankton absorption models (e.g., Bricaud's formulation vs. exponential decay) and region-specific parameter optimization [135,139,161,162]. Despite this adaptability, GIOP generally underperforms in retrieval accuracy compared to QAA and GSM. A comparative study in eastern

New Caledonia lagoons revealed GIOP's inferior precision [142], relegating it to niche applications despite its theoretical versatility. Table 7 summarizes the core advantages and application limitations of QAA, GSM, and GIOP.

Table 7. Comparative advantages and constraints of QAA, GSM, and GIOP.

Model	Core Advantages	Applicable Inland Water Types	Operational Constraints
QAA	• Lowest computational complexity, extremely fast processing speed • Fully transparent and traceable inversion process (no optimization black box)	• Clean lakes • Low-to-moderate turbidity reservoirs • Low-flow rivers	• Low-to-medium SZA (sensitive to angle changes) • Multispectral bands • Low computational resource demand
GSM	• Capable of rapid estimation in highly turbid waters	• Estuarine mixing zones • High-sediment rivers • Eutrophic shallow lakes	• Low-to-medium SZA • Multispectral bands • Iterative computation required, high computational resource demand
GIOP	• Multi-component IOPs spectral resolution capability • Customizable parameterization schemes with high flexibility for complex optical properties	• Urban polluted waters • Heavily eutrophic lakes • Algal bloom-dominated waters	• Medium-to-high SZA • Hyperspectral data • High-iteration computation, high computational resource demand

Although analytical methods have explicitly modeled IOPs compared to empirical frameworks, the generalization capabilities of algorithms such as QAA, GSM, and GIOP across water bodies are still constrained by drastic fluctuations in substance concentrations across different water areas. Introducing mass-specific inherent optical properties (MSIOPs) can mitigate the interference of substance concentration fluctuations on optical signals. For example, a^*_{CDOM} quantifies the CDOM absorption capacity per unit mass of DOC, while b^*_{bbp} uniformly characterizes the specific scattering efficiency of particulate matter. De Stefano et al. [163] discovered through Gaussian decomposition that there is a strong nonlinear relationship between the a_{270}:a_{320} ratio and DOC-specific absorption coefficient a^*_{355} (a(355)/DOC) and a^*_{440} (a(440)/DOC). The constructed model achieved favorable results in both deep and shallow lakes (with high R^2 and MAPD < 16%).

3.5. Enhanced Strategies for Nonstationary CDOM–DOC Relationships

In aquatic systems, CDOM and chlorophyll-a concentrations typically exhibit a weak correlation [164,165]. In contrast, DOC (dissolved organic carbon) demonstrates significant sensitivity to phytoplankton dynamics [166] and increases markedly with algal proliferation during eutrophication [167]. When chlorophyll-a concentration exceeds 0.8 μg/L, biological processes—such as algal growth and mortality—dominate DOC gradient variations. The extracellular products secreted (EPS) during vigorous algal growth and photosynthetic byproducts are predominantly low-molecular-weight colorless compounds. This causes an imbalance between the proportion of DOC components released by algae and CDOM, disrupting the DOC–CDOM correlation typically formed in natural waters from similar sources (e.g., terrestrial input and microbial metabolism). Conversely, when chlorophyll-a concentration falls below this threshold, abiotic processes dominate, and the DOC–CDOM

correlation reemerges. To address this biological decoupling phenomenon, Liu et al. [99] developed a dual-mode inversion framework. This framework employs a "conservative mixing" model to describe the linear relationship between DOC and CDOM under low chlorophyll-a conditions and utilizes a "biological disturbance" model to quantify the impact of biological processes on DOC variability during algal blooms. This approach adaptively resolves the challenge of DOC dynamics across different trophic states.

Beyond biological disturbances, photochemical processes additionally impair CDOM's capacity as a DOC proxy. Photodegradation (photobleaching), defined as the photochemical mineralization of dissolved organic matter under solar radiation, intensifies substantially in highly irradiated shallow inland waters. Within these systems, aromatic conjugated structures in CDOM experience accelerated cleavage through direct photolysis or indirect photo-oxidation mechanisms. Simultaneously, macromolecular humic substances decompose into low-molecular-weight organic acids, fundamentally restructuring their optical characteristics and critically compromising CDOM's reliability for DOC estimation.

Furthermore, given photodegradation's minimal influence on visible band absorption (>380 nm), retrieval models dependent on this spectral range cannot detect photolytic alterations in CDOM, thereby introducing systematic biases. Conversely, CDOM's ultraviolet-band optical properties demonstrate heightened sensitivity to photodegradation. Specifically, the attenuation rate of $a_{CDOM}(380)$ (indicative of conjugated double-bond systems) significantly exceeds that of $a_{CDOM}(275)$ (representing phenolic structures). This differential degradation elevates the spectral slope $S_{275–295}$, enabling its application as an optical tracer for monitoring CDOM compositional transformation. The Yangtze River Estuary model [168] incorporated the spectral slope $S_{275–295}$ as a characteristic parameter into the CDOM–DOC derivation methods, resolving non-conservative mixing issues between CDOM and DOC, with the correlation coefficient increased to $R^2 = 0.746$. Danhiez et al. [169] achieved enhanced DOC retrieval accuracy by synergistically integrating $S_{275–295}$ and $S_{320–412}$ into inversion models. Monsoon-driven observations reveal distinct CDOM dynamics: elevated high-molecular-weight fractions with lower $S_{280–500}$ during monsoon seasons, contrasting sharply with post-monsoon dominance of low-molecular-weight CDOM and higher $S_{280–500}$ [170]. In regions where stable statistical correlations between DOC and CDOM are lacking, integrating biogeochemical process indicators into remote sensing inversion frameworks offers a promising pathway to enhance model robustness.

3.6. Machine Learning-Driven DOC Retrieval

Recent advances in machine learning (ML) techniques—including neural networks, support vector machines, random forests, and deep learning—have demonstrated significant potential for DOC estimation by leveraging their capacity to model nonlinear relationships and fuse multisource data. Unlike conventional empirical approaches, ML models dynamically synthesize multispectral imagery, meteorological parameters, and environmental variables, autonomously extracting complex feature associations to map spatiotemporal DOC distributions (Figure 5). Key strengths lie in automated data processing, adaptive model optimization, and the resolution of nonlinear interactions.

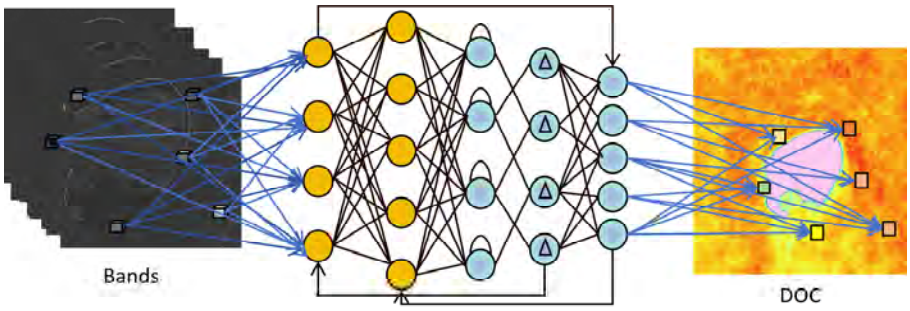


Figure 5. Schematic diagram of artificial intelligence-driven DOC remote sensing inversion in inland waters (the deep model is constructed based on a multi-level stacked deep feedforward network architecture, effectively decoupling the absorption characteristics of water quality parameters through hierarchical deduction to prevent error propagation to the DOC output layer. Internally embedded recurrent neurons enable output feedback after fixed temporal delays, capturing DOC concentration dynamics influenced by seasonal hydrological variations and spatial propagation processes. Incorporated residual structures including Update Gate and Reset Gate synchronously capture localized waterbody features and global trends, addressing spatial heterogeneity challenges in inland waterbodies.).

Early applications focused on CDOM estimation, with backpropagation (BP) neural networks outperforming traditional band-ratio models through multidimensional inputs and robust fitting [171]. Random forest (RF) algorithms addressed single-model biases by aggregating decision trees, achieving reliable CDOM retrievals in Chinese inland lakes [172]. XGBoost further advanced robustness by integrating regularization to mitigate overfitting, demonstrating superior performance in the Songhua River $\left(R^2 = 0.89, \text{testdat } R^2 = 0.85\right)$ [113], Lake Chao (spanning 40-year CDOM dynamics, $R^2 = 0.955$, RF: $R^2 = 0.924$) [91], and Pearl River Estuary ($R^2 = 0.90$) [173]. Figure 6 shows a comparative demonstration of the application performance of new ML technologies in inland waters for some typical cases, including [174,175]. Particularly for Chaohu Lake, the study cited empirical models proposed by Xu et al. [176] (2018), Olmanson et al. [177] (2020), Chen & Zhu [178] (2022), and Siswanto et al. [179] (2011). Evaluation showed that all four models had determination coefficients (R^2) below 0.01, with the MAE ranging from 0.136 to 1.71, the RMSE ranging from 0.164 to 0.219, and a maximum bias of 1.248, indicating significant estimation deviations. Similarly, when three empirical models proposed by Sun et al. [180] were validated with data from the Pearl River Estuary, the R^2 values only ranged from 0.53 to 0.57, and the MAPE was between 23.27% and 46.87%, significantly underperforming compared to ML models. These results highlight the application advantages of ML in retrieving DOC in inland waters. Emerging studies highlight ML's unique ability to abstract features and control error propagation, particularly in optically complex inland waters where empirical models oversimplify biogeochemical processes and indirect retrievals suffer accuracy loss [18,180–189]. This advantage has been validated by extensive data: After testing ML, traditional empirical models, and the QAA algorithm using 1097 samples from multiple countries including Australia and New Zealand, Pahlevan et al. [190] found that ML maintains prediction stability across three orders of magnitude of a_{CDOM} (from 10^{-2} to 10^{1} m^{-1}), whereas traditional models and QAA are only reliable at the 10^{0} absorption coefficient level. Additionally, ML exhibits superior estimation bias (slope = 0.752, RMSLD = 0.693) and uncertainty compared to empirical models (slope = 0.586, RMSLD = 1.108) and QAA (slope = 0.607, RMSLD = 1.149).

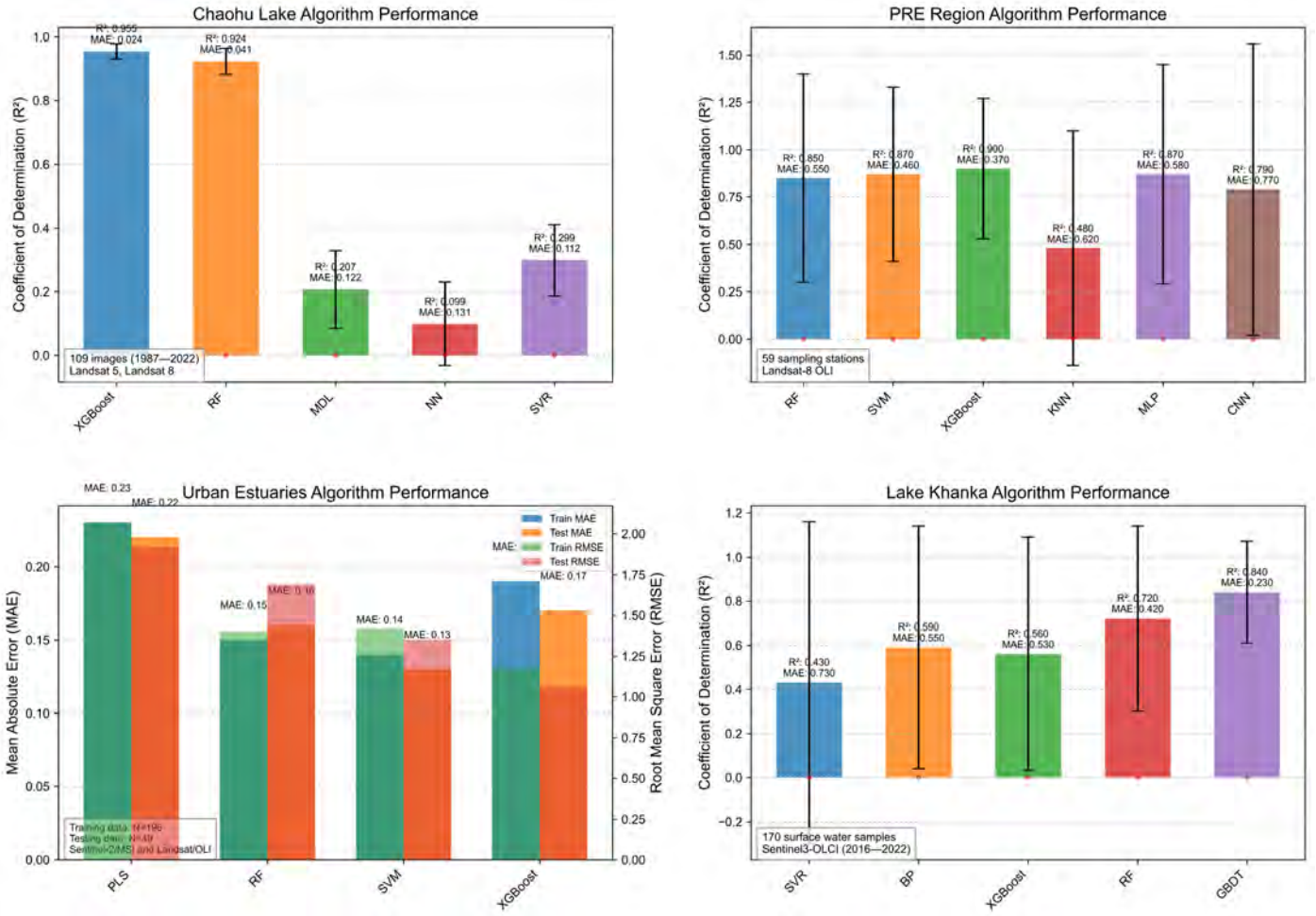


Figure 6. Performance comparison of ML algorithms in related studies.

Remote sensing inversion methods for DOC have evolved from empirical–statistical approaches to physics-informed paradigms and, more recently, artificial intelligence-driven frameworks. However, critical technical bottlenecks persist (Table 8). Direct retrieval methods remain constrained by stringent water quality requirements and limited generalizability. While deep learning architectures show potential to mitigate error propagation in indirect approaches, current efforts largely repurpose generic machine learning models rather than developing DOC-specific solutions. Such general-purpose ML approaches are subject to dual constraints arising from both data limitations and inherent model characteristics.

Table 8. Comparison of various remote sensing inversion methods.

Method/Step	Advantages	Disadvantages	Limitations	Applicability
Direct Inversion Methods	Simple model; Fast computation; Low data requirements.	High regional dependency; Ignores optical mechanisms; Poor generalization.	Only suitable for optically stable waters; Low long-term monitoring reliability.	Short-term monitoring of single water body (e.g., clear rivers).

Table 8. *Cont.*

Method/Step				Advantages	Disadvantages	Limitations	Applicability
Indirect Inversion Method	From Spectra to CDOM	Semi-Empirical Method		Relatively strong physical relevance; Moderate data needs.	Affected by CDOM sources and seasonal variations.	Effective for high CDOM waters; Large errors in low CDOM waters.	CDOM dominated eutrophic lakes/rivers.
		Semi-Analytical Method	QAA	Clear physical mechanisms; Compatible with multi-spectral satellite data.	Relies on atmospheric correction accuracy; Large errors in deep water/highly turbid waters.	Requires accurate separation of CDOM from other absorbers (e.g., phytoplankton).	Moderately turbid shallow lakes.
			GSM	Low complexity, strong global applicability; Robust for highly turbid waters.	Requires prior spectral library support.	CDOM absorption easily confounded with particulate matter in turbid waters.	Large turbid lakes/estuaries; High suspended sediment waters.
			GIOP	Highly customizable; Flexible; Adapts to complex optical properties.	Difficult parameter optimization; High result uncertainty.	Requires extensive validation data for sub-model integration.	Urban waters or eutrophic lakes with complex optical properties.
	From CDOM to DOC	Robust CDOM–DOC Relationships		Sensitive to high CDOM concentrations, captures seasonal DOC variations; Simple implementation.	Demands extensive field sampling for CDOM absorption and DOC data.	CDOM:DOC ratio affected by sources (terrestrial/autochthonous), seasonality (e.g., snowmelt), and photodegradation may cause model failure.	CDOM-dominated waters; Terrestrial input regions; Short-term monitoring needs.
	ML Method			Strong high-dimensional data processing; Integrates multi-source data (spectral + environmental factors); Superior nonlinear modeling.	Requires large labeled datasets; Poor model interpretability; High computational resources.	Weak generalization in data-scarce regions.	Complex waters with hyperspectral data support; Long-term temporal monitoring.

First, the efficacy of general models is often constrained by the data-driven paradigm: ML relies on large-scale annotated datasets for end-to-end training. However, acquiring in situ measurements of DOC in aquatic remote sensing is costly, and samples are often spatially heterogeneous. When sample sizes are insufficient, the data struggle to comprehensively capture the seasonal variations, estuarine mixing processes, algal bloom

dynamics, and periodic anthropogenic activities (e.g., fishing, agricultural runoff within watersheds) within the study area. This data scarcity significantly compromises the applicability of model inversion results in complex scenarios. Furthermore, the spectral characteristics of CDOM exhibit nonlinear distributions across diverse water bodies, which limited samples fail to fully represent within the feature space. For water areas with limited samples, strategies like transfer learning and domain adaptation can be employed. This involves initial training using marine models or samples from inland water areas with abundant data, followed by fine-tuning with a small number of samples from the target region. Domain adaptation techniques reduce the distribution discrepancy between the source domain (water areas with large samples) and the target domain (small-sample target area) through feature alignment or adversarial learning, facilitating rapid model adaptation to new scenarios. Concurrently, data augmentation techniques can be leveraged, such as using generative adversarial networks (GANs) to generate more training data from limited samples, thus enhancing data diversity.

Second, the interaction between small sample sizes and ML models further exacerbates errors: (1) Models struggle to distinguish effective signals from noise during training, easily overfitting to random fluctuations in the data, and (2) insufficient samples amplify parameter estimation errors, leading to substantially degraded generalization capability. These deficiencies are particularly pronounced in highly heterogeneous waters or lakes with strong seasonality, potentially causing biases in inversion results to exceed acceptable thresholds for practical applications. In this regard, a machine learning model can be trained based on in situ data, and a high signal-to-noise ratio model can be constructed by using the high accuracy of in situ measurement data [191,192].

Furthermore, the inherent properties of ML models impose fundamental constraints on DOC inversion accuracy. BP neural networks, optimized via gradient descent, are prone to converging to local minima within non-convex loss functions. This is especially problematic when DOC spectral features overlap with those of suspended particulate matter and chlorophyll-a, potentially causing the model to misattribute spectral signals from high-chlorophyll regions to DOC, resulting in systematic overestimation errors in algal bloom-dominated waters. For tree-based models like XGBoost, dependence on tree-depth parameters increases markedly in waters with complex compositions. Excessive tree depth induces overfitting, causing significant divergence between training and test set accuracy, particularly in optically complex zones such as estuarine mixing areas. Regarding CNNs, while pooling operations confer translational invariance, they inevitably discard fine-grained spatial location information. This leads to structural errors in inversions for small water bodies or inland lakes with steep water quality gradients. More critically, while CNNs automatically extract spectral features, they—like other deep learning approaches [193,194]—struggle to explicitly incorporate physicochemical priors, such as radiative transfer theory in water or the fluorescence properties of organic matter. This results in a lack of interpretability in the translation of spectral features to biogeochemical parameters.

4. Optimizing DOC Retrieval: From Feature Engineering to Algorithmic Synergy

4.1. Synergistic Global Exploration of Domain-Specific Hyperparameter Space via Intelligent Optimization Algorithms

The direct transplantation of generic machine learning models inherently constrains their efficacy in domain-specific applications, particularly for DOC retrieval in optically complex aquatic systems. Employing optimization algorithms as "couplers" between ML methods and domain-specific knowledge can address the limitations of general-purpose

ML systems. By establishing a parameter optimization framework under multi-objective constraints, hydrogeographic principles and the Beer–Lambert law can be transformed into mathematical constraints, thereby directing model architectures toward domain-optimal and physically reasonable solutions. Concurrently, initializing parameter weights through prior knowledge (correlation relationships) accelerates convergence while avoiding local optima and counterintuitive solutions. For instance, Abdollahi et al. [195] effectively mitigated the defect of gradient descent methods being prone to becoming trapped in local optima by introducing genetic algorithms (GA) into the parameter optimization process of backpropagation (BP) neural networks. Furthermore, Chen et al. [196] innovatively integrated GA's global exploration capability with XGBoost's regularization constraints to construct a GA-XGBoost joint optimization framework, which significantly enhanced the inversion accuracy of water quality parameters in urban rivers.

4.2. Data Optimization—Feature Engineering

Within theoretical frameworks of model fusion and optimization, advanced feature engineering is imperative to construct and enhance optical relevance in data inputs. Based on the exponential decay characteristics of CDOM in the ultraviolet-visible spectral range (e.g., contributing 50% of the absorption at 443 nm [197]), shortwave band combinations have been extensively employed for DOC inversion. Based on systematic analyses of the literature [93,94,103,110,145,172,173,176,189,198–204] (statistical results shown in Figure 7), in inland waters with high CDOM concentrations, water bodies exhibit larger absorption coefficients in blue and violet spectral regions [205]. The "red-blue", "green-blue", and "red-violet" bands demonstrate enhanced applicability. This advantage may manifest through synergistic effects in spectral response mechanisms: The blue-violet bands predominantly reflect intrinsic CDOM absorption characteristics, while the red bands, being less influenced by components like chlorophyll, effectively decouple mixed spectral signals, thereby improving the robustness of DOC inversion methods. When CDOM concentrations decrease, the red-green spectral proportions in absorption characteristics increase [22]. In such scenarios, red-green bands exhibit better performance in inland waters with non-extremely low concentrations, which aligns with the findings reported by Zhu et al. [107].

However, the inherent optical heterogeneity of inland waters [206,207] and spectral interference from complex water quality parameters [107,208] fundamentally undermine the applicability of traditional characteristic bands. This interference originates from the deep coupling of absorption signals among CDOM, NAP, and phytoplankton. By integrating in situ measurements from multiple global regions [208–221] (Argentina, Portugal, Brazil, Canada, New York State-USA, Southern Finland, Southeastern/Northeastern China, Scotland-UK, and Southwestern Sweden), a ternary diagram of non-water absorption (Figure 8e) and typical absorption spectra (Figure 8a–d) of inland waters at the characteristic wavelength of CDOM (~440 nm) were plotted. The figure reveals that the absorption of the three components forms a "mixed fingerprint" effect.

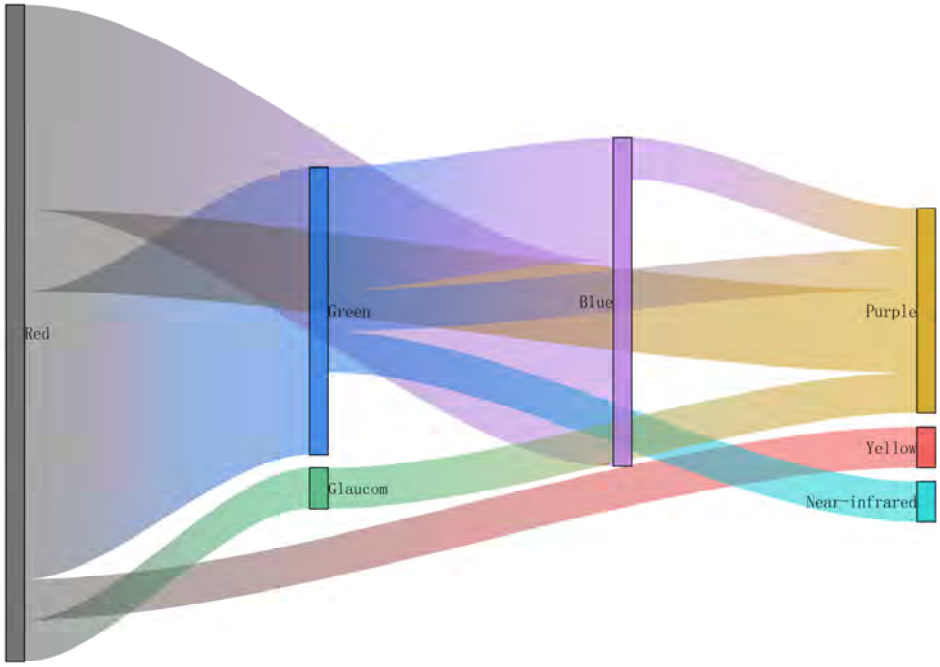


Figure 7. Sankey diagram of DOC remote sensing inversion feature (cross-sensor standardized band combinations with inter-band operation methods including algebraic operations, nonlinear transformations, and composite operations).

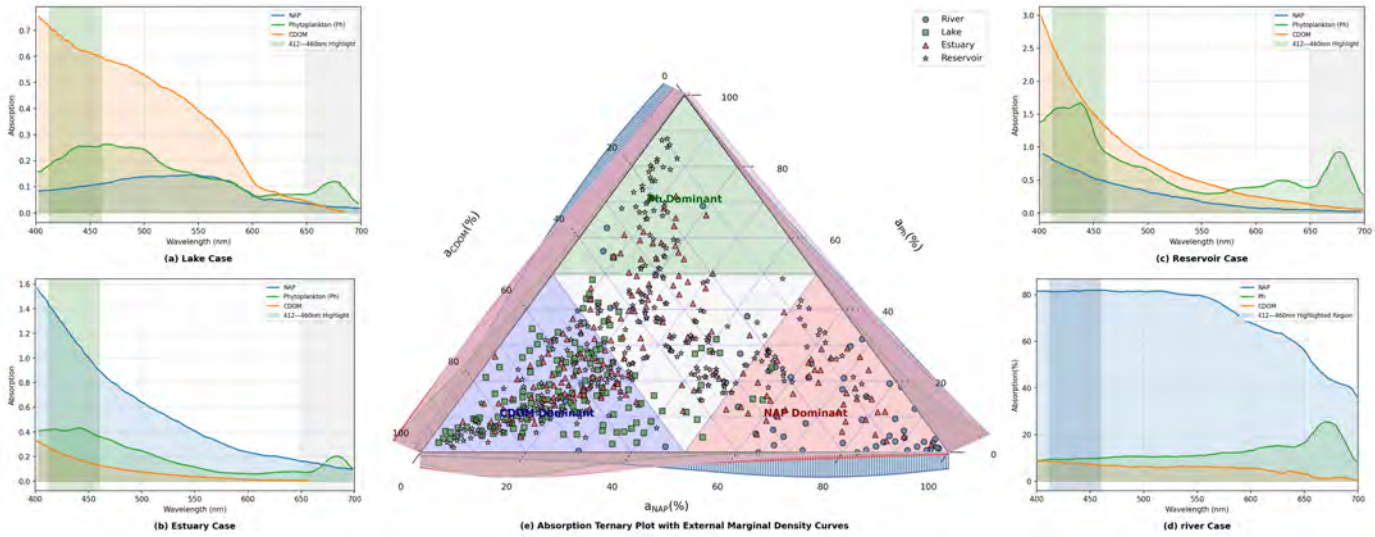


Figure 8. Non-water absorption characteristics (**a**–**d**) and ternary diagrams with marginal density curves (**e**) of inland waters.

In high-turbidity rivers, NAP dominates (mean absorption contribution: 67.19%), severely masking CDOM signals; lakes exhibit CDOM predominance (67.12%) with balanced contributions from NAP (19.74%) and Ph (18.13%); whereas reservoirs display the strongest three-component spectral mixing (CDOM: 42.69%, Ph: 31.33%, NAP: 25.97%). Scattered data points in ternary diagrams further confirm no absolute dominance of any single optical component, with spatial heterogeneity in Ph-NAP compositional ratios driving waterbody-specific CDOM interference mechanisms—exemplified by reservoirs where CDOM contribution ranges from 6.9% to 93.56% (n = 300), highlighting the challenge in selecting optical decoupling features for inland waters.

From the perspective of current research, current methodologies for retrieving DOC predominantly prioritize the selection of short-wavelength spectral bands (blue and green regions), while demonstrating limited utilization of long-wavelength bands (yellow and infrared regions). While this strategy reduces model complexity, it simultaneously sacrifices the detailed representation of CDOM characteristics in long-wavelength spectra. Experimental results from Zhu et al. further substantiate that incorporating spectral bands exceeding 600 nm can effectively enhance CDOM inversion accuracy, particularly in complex inland freshwater systems [48,107,205,222,223]. Although the incorporation of long-wavelength bands can enhance inversion accuracy, traditional band ratio processing approaches struggle to resolve their nonlinear interactions [18,224,225]. Feature optimization methods such as filter-based approaches (PCA [226], the Pearson correlation coefficient [227], the chi-square test, the distance correlation coefficient [228]), wrapper-based approaches (recursive feature elimination [229], greedy algorithms [230], and exhaustive search), and embedded approaches [231] (penalty term-based feature selection and learning model-based feature ranking) can yield highly expressive model input information. However, these methods rely on the manual construction of the feature database and fail to autonomously uncover cross-scale spectral correlations.

In comparison, large-scale deep learning models (e.g., transformer-based architectures and CNN) generally exhibit superior feature learning capabilities. Future research on DOC remote sensing inversion could leverage these large models to construct multi-scale feature fusion deep learning frameworks. A dual-branch network architecture could be designed: The shortwave branch (400–600 nm) would employ ResNet-18 to extract intrinsic absorption characteristics of CDOM, with the ResNet-18 architecture having been proven to excel in monitoring the vertical distribution of algal blooms in inland reservoirs [232], thanks to its robust feature extraction capabilities and stable training process. The longwave branch (600–900 nm) would utilize the convolution block attention module (CBAM) to decouple interference from turbid water bodies, where the CBAM mechanism has verified its effectiveness in decoupling chlorophyll content in bay waters [233], with its attention mechanism extendable to spectral signal separation tasks in turbid inland waters. However, the shortwave and longwave designs require high spatial and temporal resolution data support [234] for application in complex inland waters, further highlighting the necessity of the satellite–air–ground synergistic data collaboration discussed in Section 2.1. Ultimately, a feature pyramid could be implemented to achieve cross-band synergistic interpretation of spectral information.

5. Conclusions and Prospects

Since 2010, emerging remote sensing paradigms have fundamentally revolutionized inland water DOC monitoring, transitioning from discrete in situ sampling to remote sensing-based quantification—a transformation closely aligned with the global carbon neutrality imperative. While current inversion frameworks exhibit limitations in spatiotemporal resolution, atmospheric correction accuracy, and methodological generalizability, six convergent pathways emerge to advance this field:

- Land-observing satellites (e.g., Landsat-8 and Sentinel-2) have proven to be effective and advantageous in replacing ocean-color remote sensing for monitoring small-scale inland water bodies. However, their standalone application remains constrained by insufficient spectral granularity and temporal coverage, necessitating synergistic integration with near-surface and UAV-mounted hyperspectral platforms.
- Uncertainty mitigation requires rethinking atmospheric correction paradigms. Legacy marine-oriented models (FLAASH, 6S) prove inadequate for optically complex inland waters. While neural networks show potential, bespoke atmospheric correction proto-

cols tailored to terrestrial sensors and regional biogeochemical variability should be developed alongside next-generation sensors with enhanced radiometric sensitivity.

- Indirect DOC inversion via CDOM proxies remains viable in systems governed by salinity gradients or terrestrial carbon export via unidirectional runoff. However, the decoupling mechanism caused by the complex effects of biogeochemistry needs to be addressed using a framework of local driver optimization.
- Methodological evolution hinges on transcending the empirical–analytical dichotomy. Semi-analytical approaches coupling radiative transfer models with bio-optical mechanisms exhibit superior generalizability over their empirical counterparts, yet their inland water adaptations (QAA, GSM, and GIOP) require substantial refinement. Hybrid models integrating mechanistic constraints with data-driven calibration represent a critical frontier.
- Machine learning's nonlinear mapping capacity offers promise in circumventing error propagation in traditional methods, but its black-box nature and data dependency necessitate physics-informed architectures. Future research may employ optimization algorithms as a coupling mechanism between ML methods and domain knowledge to resolve the single data-driven paradigm of general ML.
- Advancing spectral feature engineering demands transcending heuristic feature selection. Deep learning architectures with dual-branch networks could disentangle shortwave-longwave spectral interactions, enabling cross-band synergistic analysis while suppressing sensor-specific noise.

Author Contributions: Conceptualization, D.X. and R.X.; methodology, D.X. and M.L.; software, W.W.; validation, M.L., R.X. and W.W.; formal analysis, W.Z.; investigation, R.X.; resources, Y.W.; data curation, W.Z.; writing—original draft preparation, D.X.; writing—review and editing, Y.W.; visualization, W.W. and Y.W.; supervision, Y.W.; project administration, W.W.; funding acquisition, Y.W. All authors have read and agreed to the published version of the manuscript.

Funding: This research was funded by the Guangxi Science and Technology Major Program, grant number GUIKEAA23062054; the Science and Technology Research and Development Projects of Guangxi Institute of Industrial Technology, grant number CYY-HT2023-JSJJ-0037, and Guangxi Key Research and Development Program of China, grant number GUIKEAB24010248.

Institutional Review Board Statement: Not applicable.

Informed Consent Statement: Not applicable.

Data Availability Statement: Data supporting the conclusions of this article will be made available by the authors on request.

Conflicts of Interest: The authors declare no conflicts of interest.

Abbreviations

The following abbreviations are used in this manuscript:

DOC	Dissolved Organic Carbon
CDOM	Colored Dissolved Organic Matter
TSM	Total Suspended Matter
CZCS	Coastal Zone Color Scanner
STARFM	Spatial and Temporal Adaptive Reflectance Fusion Model
GEE	Google Earth Engine
NAP	Non-Algal Particles
NIR	Near Infrared
FLAASH	Fast Line-of-sight Atmospheric Analysis of Spectral hHypercubes
SRF	Spectral Response Function

R^2	Coefficient of Determination
MAE	Mean Absolute Error
RMSE	Root Mean Square Error
MAPE	Mean Absolute Percentage Error
VIF	Variance Inflation Factor
LSMA	Linear Spectral Mixture Analysis
R_{rs}	Remote Sensing Reflectance
MLR	Multiple Linear Regression
SLR	Simple Linear Regression
IOPs	Inherent Optical Properties
a_{CDOM}	Absorption Coefficient of CDOM
QAA	Quasi-Analytical Algorithm
GSM	Garver–Siegel–Maritorena
GIOP	Generalized Inherent Optical Properties
SPM	Suspended Particulate Matter
b_{bp}	Backscattering Coefficient of Suspended Particles
a_{ph}	Phytoplankton Absorption Coefficient
a_{dg}	Non-algal Particle Absorption Coefficient
a_p	Hybrid Absorption Coefficient: aph+adg
MSIOPs	Mass-Specific Inherent Optical Properties
a^*_{CDOM}	a_{CDOM}/DOC
b^*_{bp}	b_{bp}/TSM
EPS	Extracellular Products Secreted
SZA	Solar Zenith Angles
S	Spectral Slope Parameters
PRE	Pearl River Estuary
ML	Machine Learning
RF	Random Forest
BP	backpropagation Neural Networks
XGBoost	Extreme Gradient Boosting
NN	Neural Network
SVM	Support Vector Machine
KNN	K-Nearest Neighbors
MLP	Multi-Layer Perceptron
PLS	Partial Least Squares
GBDT	Gradient Boosting Decision Tree
SVR	Support Vector Machine
RMSLD	Root Mean Square Logarithmic Deviation
GANs	Generative Adversarial Networks
CNN	Convolutional Neural Networks
GA	Genetic Algorithms
PCA	Principal Component Analysis
Ph	Phytoplankton
CBAM	Convolution Block Attention Module

References

1. Mendonça, R.; Müller, R.A.; Clow, D.; Verpoorter, C.; Raymond, P.; Tranvik, L.J.; Sobek, S. Organic carbon burial in global lakes and reservoirs. *Nat. Commun.* **2017**, *8*, 1694. [CrossRef] [PubMed]
2. Huang, S.; Pu, J.; Cao, J.; Li, J.; Zhang, T.; Jiang, F.; Li, L.; Wu, F.; Pan, M.; Bai, B. Origin and effect factors of sedimentary organic carbon in a karst groundwater-fed reservoir, South China. *Environ. Sci. Pollut. Res.* **2018**, *25*, 8497–8511. [CrossRef] [PubMed]
3. Probst, J.; Mortatti, J.; Tardy, Y. Carbon river fluxes and weathering Co_2 consumption in the Congo and Amazon river basins. *Appl. Geochem.* **1994**, *9*, 1–13. [CrossRef]
4. Holgerson, M.A.; Raymond, P.A. Large contribution to inland water Co_2 and ch4 emissions from very small ponds. *Nat. Geosci.* **2016**, *9*, 222–226. [CrossRef]

5. Stanley, E.H.; Casson, N.J.; Christel, S.T.; Crawford, J.T.; Loken, L.C.; Oliver, S.K. The ecology of methane in streams and rivers: Patterns, controls, and global significance. *Ecol. Monogr.* **2016**, *86*, 146–171. [CrossRef]
6. Tank, S.E.; Frey, K.E.; Striegl, R.G.; Raymond, P.A.; Holmes, R.M.; McClelland, J.W.; Peterson, B.J. Landscape-level controls on dissolved carbon flux from diverse catchments of the circumboreal. *Glob. Biogeochem. Cycles* **2012**, *26*, GB0E02. [CrossRef]
7. Coble, P.G. Characterization of marine and terrestrial DOM in seawater using excitation-emission matrix spectroscopy. *Mar. Chem.* **1996**, *51*, 325–346. [CrossRef]
8. Tiwari, T.; Sponseller, R.A.; Laudon, H. Extreme climate effects on dissolved organic carbon concentrations during snowmelt. *J. Geophys. Res. Biogeosci.* **2018**, *123*, 1277–1288. [CrossRef]
9. Fenner, N.; Meadham, J.; Jones, T.; Hayes, F.; Freeman, C. Effects of climate change on peatland reservoirs: A doc perspective. *Glob. Biogeochem. Cycles* **2021**, *35*, e2021GB006992. [CrossRef]
10. Hampton, S.E.; Galloway, A.W.; Powers, S.M.; Ozersky, T.; Woo, K.H.; Batt, R.D.; Labou, S.G.; O'Reilly, C.M.; Sharma, S.; Lottig, N.R. Ecology under lake ice. *Ecol. Lett.* **2017**, *20*, 98–111. [CrossRef] [PubMed]
11. Song, K.; Wen, Z.; Jacinthe, P.-A.; Zhao, Y.; Du, J. Dissolved carbon and CDOM in lake ice and underlying waters along a salinity gradient in shallow lakes of northeast China. *J. Hydrol.* **2019**, *571*, 545–558. [CrossRef]
12. Hao, R.; Ning, X.; Zhou, Y.; Ma, R.; Zhang, X.; Qiu, G.; Hu, R. Inputs of terrestrial dissolved organic matter in dam reservoirs during precipitation: Impact on water quality and management. *Nat. Hazards* **2024**, *120*, 4349–4366. [CrossRef]
13. Zhu, X.; Chen, L.; Pumpanen, J.; Ojala, A.; Zobitz, J.; Zhou, X.; Laudon, H.; Palviainen, M.; Neitola, K.; Berninger, F. The role of terrestrial productivity and hydrology in regulating aquatic dissolved organic carbon concentrations in boreal catchments. *Glob. Chang. Biol.* **2022**, *28*, 2764–2778. [CrossRef] [PubMed]
14. Hong, X.; Chen, X.; Xia, K.; Zhang, W.; Wang, Z.; Liu, D.; Li, S.; Zhang, W. Simulation of groundwater dissolved organic carbon in Yufu river basin during artificial recharge: Improving through the swat-modflow-rt3d reaction module. *Sustainability* **2024**, *16*, 6692. [CrossRef]
15. Brailsford, F.L.; Glanville, H.C.; Golyshin, P.N.; Johnes, P.J.; Yates, C.A.; Jones, D.L. Microbial uptake kinetics of dissolved organic carbon (DOC) compound groups from river water and sediments. *Sci. Rep.* **2019**, *9*, 11229. [CrossRef] [PubMed]
16. Regan, S.; Hynds, P.; Flynn, R. An overview of dissolved organic carbon in groundwater and implications for drinking water safety. *Hydrogeol. J.* **2017**, *25*, 959–967. [CrossRef]
17. Brüsecke, J.; Muotka, T.; Huttunen, K.L.; Litjo, S.; Lepo, W.P.; Jyväsjärvi, J. Drainage-induced browning causes both loss and change of benthic biodiversity in headwater streams. *Limnol. Oceanogr. Lett.* **2023**, *8*, 620–627. [CrossRef]
18. Sagan, V.; Peterson, K.T.; Maimaitijiang, M.; Sidike, P.; Sloan, J.; Greeling, B.A.; Maalouf, S.; Adams, C. Monitoring inland water quality using remote sensing: Potential and limitations of spectral indices, bio-optical simulations, machine learning, and cloud computing. *Earth-Sci. Rev.* **2020**, *205*, 103187. [CrossRef]
19. Zhang, Y.; Guo, F.; Meng, W.; Wang, X.-Q. Water quality assessment and source identification of Daliao river basin using multivariate statistical methods. *Environ. Monit. Assess.* **2009**, *152*, 105–121. [CrossRef] [PubMed]
20. Lednicka, B.; Kubacka, M.; Freda, W.; Haule, K.; Ficek, D.; Sokólski, M. Multi-parameter algorithms of remote sensing reflectance, absorption and backscattering for coastal waters of the southern Baltic sea applied to Pomeranian lakes. *Water* **2023**, *15*, 2843. [CrossRef]
21. Song, K.; Zhao, Y.; Wen, Z.; Fang, C.; Shang, Y. A systematic examination of the relationships between CDOM and DOC in inland waters in China. *Hydrol. Earth Syst. Sci.* **2017**, *21*, 5127–5141. [CrossRef]
22. Brezonik, P.L.; Olmanson, L.G.; Finlay, J.C.; Bauer, M.E. Factors affecting the measurement of CDOM by remote sensing of optically complex inland waters. *Remote Sens. Environ.* **2015**, *157*, 199–215. [CrossRef]
23. Song, K.; Wen, Z.; Xu, Y.; Yang, H.; Lyu, L.; Zhao, Y.; Fang, C.; Shang, Y.; Du, J. Dissolved carbon in a large variety of lakes across five limnetic regions in china. *J. Hydrol.* **2018**, *563*, 143–154. [CrossRef]
24. Cao, F.; Tzortziou, M.; Hu, C.; Mannino, A.; Fichot, C.G.; Del Vecchio, R.; Najjar, R.G.; Novak, M. Remote sensing retrievals of colored dissolved organic matter and dissolved organic carbon dynamics in North American estuaries and their margins. *Remote Sens. Environ.* **2018**, *205*, 151–165. [CrossRef]
25. Villota-González, F.H.; Sulbarán-Rangel, B.; Zurita-Martínez, F.; Gurubel-Tun, K.J.; Zúñiga-Grajeda, V. Assessment of machine learning models for remote sensing of water quality in lakes Cajititlán and Zapotlán, Jalisco—Mexico. *Remote Sens.* **2023**, *15*, 5505. [CrossRef]
26. Arias-Rodriguez, L.F.; Duan, Z.; Díaz-Torres, J.d.J.; Basilio Hazas, M.; Huang, J.; Kumar, B.U.; Tuo, Y.; Disse, M. Integration of remote sensing and Mexican water quality monitoring system using an extreme learning machine. *Sensors* **2021**, *21*, 4118. [CrossRef] [PubMed]
27. Wen, Z.; Song, K.; Liu, G.; Shang, Y.; Fang, C.; Du, J.; Lyu, L. Quantifying the trophic status of lakes using total light absorption of optically active components. *Environ. Pollut.* **2019**, *245*, 684–693. [CrossRef] [PubMed]

28. Joshi, I.D.; D'Sa, E.J.; Osburn, C.L.; Bianchi, T.S.; Ko, D.S.; Oviedo-Vargas, D.; Arellano, A.R.; Ward, N.D. Assessing chromophoric dissolved organic matter (CDOM) distribution, stocks, and fluxes in Apalachicola bay using combined field, VIIRS ocean color, and model observations. *Remote Sens. Environ.* **2017**, *191*, 359–372. [CrossRef]
29. Wang, W.; Guo, Q.; Du, C. Research advances in water environmental carbon cycle in the Yangtze river basin. *Chin. J. Ecol.* **2023**, *42*, 736.
30. Odermatt, D.; Gitelson, A.; Brando, V.E.; Schaepman, M. Review of constituent retrieval in optically deep and complex waters from satellite imagery. *Remote Sens. Environ.* **2012**, *118*, 116–126. [CrossRef]
31. Dierssen, H.M. Perspectives on empirical approaches for ocean color remote sensing of chlorophyll in a changing climate. *Proc. Natl. Acad. Sci. USA* **2010**, *107*, 17073–17078. [CrossRef] [PubMed]
32. Zhang, Y.; Zhou, L.; Zhou, Y.; Zhang, L.; Yao, X.; Shi, K.; Jeppesen, E.; Yu, Q.; Zhu, W. Chromophoric dissolved organic matter in inland waters: Present knowledge and future challenges. *Sci. Total Environ.* **2021**, *759*, 143550. [CrossRef] [PubMed]
33. Zhao, Y.; Wang, S.; Zhang, F.; Shen, Q.; Li, J.; Yang, F. Remote sensing-based analysis of spatial and temporal water colour variations in Baiyangdian lake after the establishment of the Xiong'an new area. *Remote Sens.* **2021**, *13*, 1729. [CrossRef]
34. Zhou, G.; Tian, G.; Liu, Q.; Li, J.; Tang, J. Uncertainty analysis of inland water quality remote sensing: A review. *Adv. Earth Sci.* **2009**, *24*, 150–158.
35. Mohseni, F.; Saba, F.; Mirmazloumi, S.M.; Amani, M.; Mokhtarzade, M.; Jamali, S.; Mahdavi, S. Ocean water quality monitoring using remote sensing techniques: A review. *Mar. Environ. Res.* **2022**, *180*, 105701. [CrossRef] [PubMed]
36. Mascarenhas, V.; Keck, T. Marine Optics and Ocean Color Remote Sensing. In *YOUMARES 8–Oceans Across Boundaries: Learning from Each Other: Proceedings of the 2017 Conference for Young Marine Researchers in Kiel, Germany*; Springer International Publishing: Berlin/Heidelberg, Germany, 2018; pp. 41–54.
37. Isada, T.; Hooker, S.B.; Taniuchi, Y.; Suzuki, K. Evaluation of retrieving chlorophyll a concentration and colored dissolved organic matter absorption from satellite ocean color remote sensing in the coastal waters of Hokkaido, Japan. *J. Oceanogr.* **2022**, *78*, 263–276. [CrossRef]
38. Mouw, C.B.; Greb, S.; Aurin, D.; DiGiacomo, P.M.; Lee, Z.; Twardowski, M.; Binding, C.; Hu, C.; Ma, R.; Moore, T. Aquatic color radiometry remote sensing of coastal and inland waters: Challenges and recommendations for future satellite missions. *Remote Sens. Environ.* **2015**, *160*, 15–30. [CrossRef]
39. Palmer, S.C.; Kutser, T.; Hunter, P.D. *Remote Sensing of Inland Waters: Challenges, Progress and Future Directions*; Elsevier: Amsterdam, The Netherlands, 2015; Volume 157, pp. 1–8.
40. Lee, Z.; Hu, C.; Arnone, R.; Liu, Z. Impact of sub-pixel variations on ocean color remote sensing products. *Opt. Express* **2012**, *20*, 20844–20854. [CrossRef] [PubMed]
41. Nguyen, V.S.; Loisel, H.; Vantrepotte, V.; Mériaux, X.; Tran, D.L. An empirical algorithm for estimating the absorption of colored dissolved organic matter from sentinel-2 (MSI) and landsat-8 (OLI) observations of coastal waters. *Remote Sens.* **2024**, *16*, 4061. [CrossRef]
42. Pahlevan, N.; Chittimalli, S.K.; Balasubramanian, S.V.; Vellucci, V. Sentinel-2/landsat-8 product consistency and implications for monitoring aquatic systems. *Remote Sens. Environ.* **2019**, *220*, 19–29. [CrossRef]
43. Coelho, C.; Heim, B.; Foerster, S.; Brosinsky, A.; De Araújo, J.C. In situ and satellite observation of CDOM and chlorophyll-a dynamics in small water surface reservoirs in the Brazilian semiarid region. *Water* **2017**, *9*, 913. [CrossRef]
44. Chen, J.; Zhu, W.; Tian, Y.Q.; Yu, Q. Monitoring dissolved organic carbon by combining landsat-8 and sentinel-2 satellites: Case study in saginaw river estuary, lake huron. *Sci. Total Environ.* **2020**, *718*, 137374. [CrossRef] [PubMed]
45. Li, J.; Yu, Q.; Tian, Y.Q.; Becker, B.L.; Siqueira, P.; Torbick, N. Spatio-temporal variations of CDOM in shallow inland waters from a semi-analytical inversion of landsat-8. *Remote Sens. Environ.* **2018**, *218*, 189–200. [CrossRef]
46. Griffin, C.; McClelland, J.; Frey, K.; Fiske, G.; Holmes, R. Quantifying CDOM and doc in major arctic rivers during ice-free conditions using landsat tm and ETM+ data. *Remote Sens. Environ.* **2018**, *209*, 395–409. [CrossRef]
47. Chen, J.; Zhu, W.-N.; Tian, Y.Q.; Yu, Q. Estimation of colored dissolved organic matter from landsat-8 imagery for complex inland water: Case study of lake Huron. *IEEE Trans. Geosci. Remote Sens.* **2017**, *55*, 2201–2212. [CrossRef]
48. Chen, J.; Zhu, W.; Tian, Y.Q.; Yu, Q.; Zheng, Y.; Huang, L. Remote estimation of colored dissolved organic matter and chlorophyll-a in lake Huron using sentinel-2 measurements. *J. Appl. Remote Sens.* **2017**, *11*, 036007. [CrossRef]
49. Chen, J.; Chen, S.; Fu, R.; Li, D.; Jiang, H.; Wang, C.; Peng, Y.; Jia, K.; Hicks, B.J. Remote sensing big data for water environment monitoring: Current status, challenges, and future prospects. *Earth's Future* **2022**, *10*, e2021EF002289. [CrossRef]
50. Cao, Z.; Ma, R.; Duan, H.; Xue, K. Effects of broad bandwidth on the remote sensing of inland waters: Implications for high spatial resolution satellite data applications. *ISPRS J. Photogramm. Remote Sens.* **2019**, *153*, 110–122. [CrossRef]
51. Kumar, A.; Mehta, M. Investigating the effect of relative spectral response on the estimation of atmospheric parameters: A case study of landsat 8 (OLI) and sentinel 2 (MSI). *J. Indian Soc. Remote Sens.* **2024**, *52*, 2115–2122. [CrossRef]
52. Chen, L.; Tian, L.; Qiu, F.; Chen, X. Water color constituents remote sensing in Wuhan Donghu lake using hj-1a/b ccd imagery. *Geomat. Inf. Sci. Wuhan Univ.* **2011**, *36*, 1280–1283.

53. Han, X.; Zhang, H.; Xue, J.-H.; Sun, W. A spectral–spatial jointed spectral super-resolution and its application to hj-1a satellite images. *IEEE Geosci. Remote Sens. Lett.* **2021**, *19*, 5505905. [CrossRef]
54. Zhou, L.; Roberts, D.A.; Ma, W.; Zhang, H.; Tang, L. Estimation of higher Chlorophylla concentrations using field spectral measurement and hj-1a hyperspectral satellite data in Dianshan lake, China. *ISPRS J. Photogramm. Remote Sens.* **2014**, *88*, 41–47. [CrossRef]
55. Cooley, S.W.; Smith, L.C.; Stepan, L.; Mascaro, J. Tracking dynamic northern surface water changes with high-frequency planet cubesat imagery. *Remote Sens.* **2017**, *9*, 1306. [CrossRef]
56. ChunHock, S.; Cherukuru, N.; Mujahid, A.; Martin, P.; Sanwlani, N.; Warneke, T.; Rixen, T.; Notholt, J.; Müller, M. A new remote sensing method to estimate river to ocean doc flux in peatland dominated Sarawak coastal regions, Borneo. *Remote Sens.* **2020**, *12*, 3380. [CrossRef]
57. Zhang, H.; Yao, B.; Wang, S.; Wang, G. Remote sensing estimation of the concentration and sources of coloured dissolved organic matter based on MODIS: A case study of Erhai lake. *Ecol. Indic.* **2021**, *131*, 108180. [CrossRef]
58. Li, X.; Liu, S.; Liu, Q.; Xiao, Q.; Che, T.; Ma, M.; Jin, R.; Ran, Y.; Wen, J.; Xu, Z. Heihe remote sensing experiments: Retrospect and prospect. *Natl. Remote Sens. Bull.* **2023**, *27*, 224–248. [CrossRef]
59. Wang, S.; Qin, B. Application of optical remote sensing in harmful algal blooms in lakes: A review. *Remote Sens.* **2025**, *17*, 1381. [CrossRef]
60. Hou, Y.; Hu, N.; Teng, C.; Zheng, L.; Zhang, J.; Gong, Y. Monitoring and evaluation of ecological restoration effectiveness: A case study of the Liaohe river estuary wetland. *Sustainability* **2025**, *17*, 2973. [CrossRef]
61. Guo, X.; Liu, H.; Zhong, P.; Hu, Z.; Cao, Z.; Shen, M.; Tan, Z.; Liu, W.; Liu, C.; Li, D. Remote retrieval of dissolved organic carbon in rivers using a hyperspectral drone system. *Int. J. Digit. Earth* **2024**, *17*, 2358863. [CrossRef]
62. Yang, Z.; Gong, C.; Ji, T.; Hu, Y.; Li, L. Water quality retrieval from zy1-02d hyperspectral imagery in urban water bodies and comparison with sentinel-2. *Remote Sens.* **2022**, *14*, 5029. [CrossRef]
63. Zeng, C.; Richardson, M.; King, D.J. The impacts of environmental variables on water reflectance measured using a lightweight unmanned aerial vehicle (uav)-based spectrometer system. *ISPRS J. Photogramm. Remote Sens.* **2017**, *130*, 217–230. [CrossRef]
64. Xiang, T.-Z.; Xia, G.-S.; Zhang, L. Mini-unmanned aerial vehicle-based remote sensing: Techniques, applications, and prospects. *IEEE Geosci. Remote Sens. Mag.* **2019**, *7*, 29–63. [CrossRef]
65. Yao, H.; Qin, R.; Chen, X. Unmanned aerial vehicle for remote sensing applications—A review. *Remote Sens.* **2019**, *11*, 1443. [CrossRef]
66. Chabot, D. Trends in drone research and applications as the journal of unmanned vehicle systems turns five. *J. Unmanned Veh. Syst.* **2018**, *6*, vi–xv. [CrossRef]
67. Sun, X.; Zhang, Y.; Shi, K.; Zhang, Y.; Li, N.; Wang, W.; Huang, X.; Qin, B. Monitoring water quality using proximal remote sensing technology. *Sci. Total Environ.* **2022**, *803*, 149805. [CrossRef] [PubMed]
68. Su, L.; Zhou, Y.; Fan, L.; Li, J.; Huang, Y. Research on remote sensing identification model of urban malodorous black water in pearl river estuary based on high-resolution image. *Pol. J. Environ. Stud.* **2023**, *32*, 731–743. [CrossRef] [PubMed]
69. Liu, G.; Li, S.; Song, K.; Wang, X.; Wen, Z.; Kutser, T.; Jacinthe, P.-A.; Shang, Y.; Lyu, L.; Fang, C. Remote sensing of CDOM and DOC in alpine lakes across the Qinghai-Tibet plateau using sentinel-2a imagery data. *J. Environ. Manag.* **2021**, *286*, 112231. [CrossRef] [PubMed]
70. Gao, F.; Masek, J.; Schwaller, M.; Hall, F. On the blending of the Landsat and MODIS surface reflectance: Predicting daily Landsat surface reflectance. *IEEE Trans. Geosci. Remote Sens.* **2006**, *44*, 2207–2218.
71. Dhillon, M.S.; Dahms, T.; Kübert-Flock, C.; Steffan-Dewenter, I.; Zhang, J.; Ullmann, T. Spatiotemporal fusion modelling using starfm: Examples of Landsat 8 and sentinel-2 NDVI in Bavaria. *Remote Sens.* **2022**, *14*, 677. [CrossRef]
72. Amani, M.; Ghorbanian, A.; Ahmadi, S.A.; Kakooei, M.; Moghimi, A.; Mirmazloumi, S.M.; Moghaddam, S.H.A.; Mahdavi, S.; Ghahremanloo, M.; Parsian, S. Google earth engine cloud computing platform for remote sensing big data applications: A comprehensive review. *IEEE J. Sel. Top. Appl. Earth Obs. Remote Sens.* **2020**, *13*, 5326–5350. [CrossRef]
73. Zhu, W.; Yu, Q.; Tian, Y.Q. Uncertainty analysis of remote sensing of colored dissolved organic matter: Evaluations and comparisons for three rivers in North America. *ISPRS J. Photogramm. Remote Sens.* **2013**, *84*, 12–22. [CrossRef]
74. Povey, A.; Grainger, R. Known and unknown unknowns: Uncertainty estimation in satellite remote sensing. *Atmos. Meas. Tech.* **2015**, *8*, 4699–4718. [CrossRef]
75. Ilori, C.O.; Pahlevan, N.; Knudby, A. Analyzing performances of different atmospheric correction techniques for Landsat 8: Application for coastal remote sensing. *Remote Sens.* **2019**, *11*, 469. [CrossRef]
76. Gilerson, A.; Herrera-Estrella, E.; Foster, R.; Agagliate, J.; Hu, C.; Ibrahim, A.; Franz, B. Determining the primary sources of uncertainty in retrieval of marine remote sensing reflectance from satellite ocean color sensors. *Front. Remote Sens.* **2022**, *3*, 857530. [CrossRef]
77. Zhao, D.; Feng, L.; He, X. Global gridded aerosol models established for atmospheric correction over inland and nearshore coastal waters. *J. Geophys. Res. Atmos.* **2023**, *128*, e2023JD038815. [CrossRef]

78. Zheng, K.; Shao, T.; Ning, J.; Zhuang, D.; Liang, X.; Ding, X. Water quality, basin characteristics, and discharge greatly affect cdom in highly turbid rivers in the yellow river Basin, China. *J. Clean. Prod.* **2023**, *404*, 136995. [CrossRef]
79. Wang, D.; Ma, R.; Xue, K.; Loiselle, S.A. The assessment of landsat-8 Oli atmospheric correction algorithms for inland waters. *Remote Sens.* **2019**, *11*, 169. [CrossRef]
80. Hirtle, H.; Rencz, A. The relation between spectral reflectance and dissolved organic carbon in lake water: Kejimkujik national park, Nova Scotia, Canada. *Int. J. Remote Sens.* **2003**, *24*, 953–967. [CrossRef]
81. Zhu, W.; Pang, S.; Chen, J.; Sun, N.; Huang, L.; Zhang, Y.; Zhang, Z.; He, S.; Cheng, Q. Spatiotemporal variations of total suspended matter in complex archipelagic regions using a sigmoid model and landsat-8 imagery. *Reg. Stud. Mar. Sci.* **2020**, *36*, 101308. [CrossRef]
82. Tan, K.; Wang, X.; Niu, C.; Wang, F.; Du, P.; Sun, D.-X.; Yuan, J.; Zhang, J. Vicarious calibration for the AHSI instrument of gaofen-5 with reference to the CRCS Dunhuang test site. *IEEE Trans. Geosci. Remote Sens.* **2020**, *59*, 3409–3419. [CrossRef]
83. Fan, Y.; Li, W.; Gatebe, C.K.; Jamet, C.; Zibordi, G.; Schroeder, T.; Stamnes, K. Atmospheric correction over coastal waters using multilayer neural networks. *Remote Sens. Environ.* **2017**, *199*, 218–240. [CrossRef]
84. Wang, D.; Ronghua, M.; Xue, K.; Li, J. Improved atmospheric correction algorithm for Landsat 8–Oli data in turbid waters: A case study for the lake Taihu, China. *Opt. Express* **2019**, *27*, A1400–A1418. [CrossRef] [PubMed]
85. Liu, H.; Yu, Z.; Shum, C.; Man, Q.; Wang, B. A new hierarchical multiplication and spectral mixing method for quantification of forest coverage changes using GAOFEN (gf)-1 imagery in Zhejiang Province, China. *IEEE Trans. Geosci. Remote Sens.* **2023**, *61*, 4407210. [CrossRef]
86. Mélin, F.; Sclep, G.; Jackson, T.; Sathyendranath, S. Uncertainty estimates of remote sensing reflectance derived from comparison of ocean color satellite data sets. *Remote Sens. Environ.* **2016**, *177*, 107–124. [CrossRef]
87. Sayer, A.M.; Govaerts, Y.; Kolmonen, P.; Lipponen, A.; Luffarelli, M.; Mielonen, T.; Patadia, F.; Popp, T.; Povey, A.C.; Stebel, K. A review and framework for the evaluation of pixel-level uncertainty estimates in satellite aerosol remote sensing. *Atmos. Meas. Tech.* **2020**, *13*, 373–404. [CrossRef]
88. Cairns, S.H.; Dickson, K.L.; Atkinson, S.F. An examination of measuring selected water quality trophic indicators with spot satellite HRV data. *Photogramm. Eng. Remote Sens.* **1997**, *63*, 263–265.
89. Zheng, Y.; Wang, J.; Kondratenko, Y.; Wu, J. Research progress in surface water quality monitoring based on remote sensing technology. *Int. J. Remote Sens.* **2024**, *45*, 2337–2373. [CrossRef]
90. Shen, F.; Zhao, H.; Zhu, Q.; Sun, X.; Liu, Y. Chinese Hyperspectral satellite missions and preliminary applications of aquatic environment. In Proceedings of the 2021 IEEE International Geoscience and Remote Sensing Symposium IGARSS, Brussels, Belgium, 11–16 July 2021; IEEE: New York, NY, USA, 2021; pp. 1233–1236.
91. Zhang, Z.; Zhang, H.; Jin, Y.; Guo, H.; Tian, S.; Huang, J.J.; Zhu, X. Analysing the spatiotemporal variation and influencing factors of lake Chaohu's CDOM over the past 40 years using machine learning. *Ecohydrology* **2024**, *17*, e2639. [CrossRef]
92. Chen, C.; Shi, P. Application of ocean color satellite remote sensing data for estimation of doc concentration. *Acta Sci. Circumstantiae* **2001**, *21*, 5.
93. Kutser, T.; Pierson, D.C.; Tranvik, L.; Reinart, A.; Sobek, S.; Kallio, K. Using satellite remote sensing to estimate the colored dissolved organic matter absorption coefficient in lakes. *Ecosystems* **2005**, *8*, 709–720. [CrossRef]
94. Lai, F.; Yang, Q.; Song, K.; Shang, Y. Remote sensing estimation of doc concentration of reservoirs in Northeast China based on cdom absorption. *J. Lake Sci.* **2023**, *35*, 224–235.
95. Song, K.; Zang, S.; Zhao, Y.; Li, L.; Du, J.; Zhang, N.; Wang, X.; Shao, T.; Guan, Y.; Liu, L. Spatiotemporal characterization of dissolved carbon for inland waters in semi-humid/semi-arid region, China. *Hydrol. Earth Syst. Sci.* **2013**, *17*, 4269–4281. [CrossRef]
96. Granskog, M.A.; Macdonald, R.W.; Mundy, C.-J.; Barber, D.G. Distribution, characteristics and potential impacts of chromophoric dissolved organic matter (CDOM) in Hudson strait and Hudson bay, Canada. *Cont. Shelf Res.* **2007**, *27*, 2032–2050. [CrossRef]
97. Al-Rubaay, H.I.A. Optical Remote Sensing of Coloured Dissolved Organic Matter (CDOM) for Better Estimation of Dissolved Organic Carbon (DOC) in South-East Queensland Water Reservoirs. Ph.D. Thesis, University of Southern Queensland, Toowoomba, Australia, 2021.
98. Jiang, X.; Liu, D.; Li, J.; Duan, H. Eutrophication and salinization elevate the dissolved organic matter content in arid lakes. *Environ. Res.* **2023**, *233*, 116471. [CrossRef] [PubMed]
99. Liu, Q.; Pan, D.; Bai, Y.; Wu, K.; Chen, C.-T.A.; Sun, J.; Zhang, L. The satellite reversion of dissolved organic carbon (DOC) based on the analysis of the mixing behavior of doc and colored dissolved organic matter: The east China sea as an example. *Acta Oceanol. Sin.* **2013**, *32*, 1–11. [CrossRef]
100. Wang, J.-J.; Lafreniere, M.J.; Lamoureux, S.F.; Simpson, A.J.; Gelinas, Y.; Simpson, M.J. Differences in riverine and pond water dissolved organic matter composition and sources in Canadian high arctic watersheds affected by active layer detachments. *Environ. Sci. Technol.* **2018**, *52*, 1062–1071. [CrossRef] [PubMed]

101. Stedmon, C.; Amon, R.; Rinehart, A.; Walker, S. The supply and characteristics of colored dissolved organic matter (CDOM) in the arctic ocean: Pan arctic trends and differences. *Mar. Chem.* **2011**, *124*, 108–118. [CrossRef]
102. Hessen, D.O.; Carroll, J.; Kjeldstad, B.; Korosov, A.A.; Pettersson, L.H.; Pozdnyakov, D.; Sørensen, K. Input of organic carbon as determinant of nutrient fluxes, light climate and productivity in the Ob and Yenisey estuaries. *Estuar. Coast. Shelf Sci.* **2010**, *88*, 53–62. [CrossRef]
103. Griffin, C.G.; Frey, K.E.; Rogan, J.; Holmes, R.M. Spatial and interannual variability of dissolved organic matter in the Kolyma river, east Siberia, observed using satellite imagery. *J. Geophys. Res. Biogeosci.* **2011**, *116*, G03018. [CrossRef]
104. Fichot, C.G.; Benner, R. A novel method to estimate doc concentrations from CDOM absorption coefficients in coastal waters. *Geophys. Res. Lett.* **2011**, *38*, L03610. [CrossRef]
105. Matsuoka, A.; Bricaud, A.; Benner, R.; Para, J.; Sempéré, R.; Prieur, L.; Bélanger, S.; Babin, M. Tracing the transport of colored dissolved organic matter in water masses of the southern Beaufort sea: Relationship with hydrographic characteristics. *Biogeosciences* **2012**, *9*, 925–940. [CrossRef]
106. Walker, S.A.; Amon, R.M.; Stedmon, C.A. Variations in high-latitude riverine fluorescent dissolved organic matter: A comparison of large arctic rivers. *J. Geophys. Res. Biogeosci.* **2013**, *118*, 1689–1702. [CrossRef]
107. Zhu, W.; Yu, Q.; Tian, Y.Q.; Becker, B.L.; Zheng, T.; Carrick, H.J. An assessment of remote sensing algorithms for colored dissolved organic matter in complex freshwater environments. *Remote Sens. Environ.* **2014**, *140*, 766–778. [CrossRef]
108. Vantrepotte, V.; Danhiez, F.-P.; Loisel, H.; Ouillon, S.; Mériaux, X.; Cauvin, A.; Dessailly, D. CDOM-doc relationship in contrasted coastal waters: Implication for doc retrieval from ocean color remote sensing observation. *Opt. Express* **2015**, *23*, 33–54. [CrossRef] [PubMed]
109. Herrault, P.-A.; Gandois, L.; Gascoin, S.; Tananaev, N.; Le Dantec, T.; Teisserenc, R. Using high spatio-temporal optical remote sensing to monitor dissolved organic carbon in the Arctic River Yenisei. *Remote Sens.* **2016**, *8*, 803. [CrossRef]
110. Liu, H.; Li, Q.; Bai, Y.; Yang, C.; Wang, J.; Zhou, Q.; Hu, S.; Shi, T.; Liao, X.; Wu, G. Improving satellite retrieval of oceanic particulate organic carbon concentrations using machine learning methods. *Remote Sens. Environ.* **2021**, *256*, 112316. [CrossRef]
111. Jiang, X.; Liu, D.; Zhong, P.; Duan, H. Estimation of doc concentration in the surface water of lake Bosten using CDOM absorption coefficient. *China Environ. Sci.* **2022**, *42*, 5824–5835.
112. Cao, N.; Lin, X.; Liu, C.; Tan, M.L.; Shi, J.; Jim, C.-Y.; Hu, G.; Ma, X.; Zhang, F. Estimation of dissolved organic carbon using sentinel-2 in the eutrophic lake Ebinur, China. *Remote Sens.* **2024**, *16*, 252. [CrossRef]
113. Feng, P.; Song, K.; Wen, Z.; Tao, H.; Yu, X.; Shang, Y. Remote sensing estimation of CDOM for Songhua river of China: Distributions and implications. *Remote Sens.* **2024**, *16*, 4608. [CrossRef]
114. Li, J.; Yu, Q.; Tian, Y.Q.; Boutt, D.F. Effects of landcover, soil property, and temperature on covariations of doc and cdom in inland waters. *J. Geophys. Res. Biogeosci.* **2018**, *123*, 1352–1365. [CrossRef]
115. Liao, Z.; Wang, Y.; Xie, K.; Xie, N.; Cai, X.; Zhou, L.; Yuan, Y. Photochemistry of dissolved organic matter in water from the Pearl river (China): Seasonal patterns and predictive modelling. *Water Res.* **2022**, *208*, 117875. [CrossRef] [PubMed]
116. Li, S.-L.; Zhang, H.; Yi, Y.; Zhang, Y.; Qi, Y.; Mostofa, K.M.; Guo, L.; He, D.; Fu, P.; Liu, C.-Q. Potential impacts of climate and anthropogenic-induced changes on DOM dynamics among the major Chinese rivers. *Geogr. Sustain.* **2023**, *4*, 329–339. [CrossRef]
117. Li, Y.; Song, G.; Massicotte, P.; Yang, F.; Li, R.; Xie, H. Distribution, seasonality, and fluxes of dissolved organic matter in the pearl river (Zhujiang) estuary, China. *Biogeosciences* **2019**, *16*, 2751–2770. [CrossRef]
118. Zhao, L.; Gao, L.; Guo, L. Seasonal variations in molecular size of Chromophoric dissolved organic matter from the lower Changjiang (Yangtze) river. *J. Geophys. Res. Biogeosci.* **2021**, *126*, e2020JG006160. [CrossRef]
119. Badr, E.-S.A. Spatio-temporal variability of dissolved organic nitrogen (don), carbon (doc), and nutrients in the Nile river, Egypt. *Environ. Monit. Assess.* **2016**, *188*, 580. [CrossRef] [PubMed]
120. Guo, J.; Liang, S.; Wang, X.; Pan, X. Distribution and dynamics of dissolved organic matter in the Changjiang estuary and Adjacent sea. *J. Geophys. Res. Biogeosci.* **2021**, *126*, e2020JG006161. [CrossRef]
121. Motard-Côté, J.; Kieber, D.J.; Rellinger, A.; Kiene, R.P. Influence of the mississippi river plume and non-bioavailable DMSP on dissolved DMSP Turnover in the Northern Gulf of Mexico. *Environ. Chem.* **2015**, *13*, 280–292. [CrossRef]
122. Nielsen, D.L.; Cook, R.A.; Ning, N.; Gawne, B.; Petrie, R. Carbon and nutrient subsidies to a lowland river following floodplain inundation. *Mar. Freshw. Res.* **2015**, *67*, 1302–1312. [CrossRef]
123. Gibbs, M.S.; Wallace, T.; Mosley, L.M. Constraining organic matter composition and dynamics as a dominant driver of hypoxic blackwater risk during river Murray floodplain inundation. *Hydrol. Process.* **2022**, *36*, e14529. [CrossRef]
124. Amaral, V.; Romera-Castillo, C.; García-Delgado, M.; Gómez-Parra, A.; Forja, J. Distribution of dissolved organic matter in estuaries of the southern Iberian Atlantic basin: Sources, behavior and export to the coastal zone. *Mar. Chem.* **2020**, *226*, 103857. [CrossRef]
125. Tan, L.-S.; Ge, Z.-M.; Fei, B.-L.; Xie, L.-N.; Li, Y.-L.; Li, S.-H.; Li, X.-Z.; Ysebaert, T. The roles of vegetation, tide and sediment in the variability of carbon in the salt marsh dominated tidal creeks. *Estuar. Coast. Shelf Sci.* **2020**, *239*, 106752. [CrossRef]

126. Lynch, L.M.; Sutfin, N.A.; Fegel, T.S.; Boot, C.M.; Covino, T.P.; Wallenstein, M.D. River channel connectivity shifts metabolite composition and dissolved organic matter chemistry. *Nat. Commun.* **2019**, *10*, 459. [CrossRef] [PubMed]
127. Letourneau, M.L.; Medeiros, P.M. Dissolved organic matter composition in a marsh-dominated estuary: Response to seasonal forcing and to the passage of a hurricane. *J. Geophys. Res. Biogeosci.* **2019**, *124*, 1545–1559. [CrossRef]
128. Ye, L.; Wu, X.; Liu, B.; Yan, D. Tidal and seasonal variation in the concentrations of the organic carbons in the tidal freshwater reach of Changjiang river. *Acta Sci. Circumstantiae* **2022**, *42*, 338–346.
129. Hansell, D.A.; Carlson, C.A. *Biogeochemistry of Marine Dissolved Organic Matter*; Academic Press: Cambridge, MA, USA, 2014.
130. Asmala, E.; Stedmon, C.A.; Thomas, D.N. Linking CDOM spectral absorption to dissolved organic carbon concentrations and loadings in boreal estuaries. *Estuar. Coast. Shelf Sci.* **2012**, *111*, 107–117. [CrossRef]
131. Jégou, F.; Jallais, G.; Salmon, E.; Guenet, B.; Herrault, P.-A.; Gogo, S.; Gandois, L.; Guimbaud, C.; Laggoun-Defarge, F.; Moulard, N. *Variability of Dissolved Organic Carbon (DOC) in the 6 Largest Arctic Rivers Estimated Using High Resolution Sentinel-2 and Landsat-8 Imageries Over the 2013–2021 Period*; EGU General Assembly: Munich, Germany, 2022; p. EGU22-9645.
132. Yang, H.; Kong, J.; Hu, H.; Du, Y.; Gao, M.; Chen, F. A review of remote sensing for water quality retrieval: Progress and challenges. *Remote Sens.* **2022**, *14*, 1770. [CrossRef]
133. Zhu, W.; Yu, Q. Inversion of chromophoric dissolved organic matter from eo-1 hyperion imagery for turbid estuarine and coastal waters. *IEEE Trans. Geosci. Remote Sens.* **2012**, *51*, 3286–3298. [CrossRef]
134. Keller, P.A. Comparison of two inversion techniques of a semi-analytical model for the determination of lake water constituents using imaging spectrometry data. *Sci. Total Environ.* **2001**, *268*, 189–196. [CrossRef] [PubMed]
135. Lee, Z.; Carder, K.L.; Arnone, R.A. Deriving inherent optical properties from water color: A multiband quasi-analytical algorithm for optically deep waters. *Appl. Opt.* **2002**, *41*, 5755–5772. [CrossRef] [PubMed]
136. Garver, S.A.; Siegel, D.A. Inherent optical property inversion of ocean color spectra and its biogeochemical interpretation: 1. Time series from the Sargasso sea. *J. Geophys. Res. Ocean.* **1997**, *102*, 18607–18625. [CrossRef]
137. Yang, C.; Ye, H. A new semianalytical model for retrieving chlorophyll a concentration and magnitude of fluorescence in the South China sea. *Bull. Mar. Sci.* **2022**, *98*, 165–184. [CrossRef]
138. Werdell, P.J.; Franz, B.A.; Bailey, S.W.; Feldman, G.C.; Boss, E.; Brando, V.E.; Dowell, M.; Hirata, T.; Lavender, S.J.; Lee, Z. Generalized ocean color inversion model for retrieving marine inherent optical properties. *Appl. Opt.* **2013**, *52*, 2019–2037. [CrossRef] [PubMed]
139. Erickson, Z.K.; McKinna, L.; Werdell, P.J.; Cetinić, I. Bayesian approach to a generalized inherent optical property model. *Opt. Express* **2023**, *31*, 22790–22801. [CrossRef] [PubMed]
140. Zhan, J.; Zhang, D.; Tan, L.; Zhang, G.; Župan, R. Performance analysis of inverting optical properties based on quasi-analytical algorithms. *Multimed. Tools Appl.* **2022**, *81*, 4693–4709. [CrossRef]
141. Zhu, W.; Yu, Q.; Tian, Y.Q.; Chen, R.F.; Gardner, G.B. Estimation of chromophoric dissolved organic matter in the Mississippi and Atchafalaya river plume regions using above-surface hyperspectral remote sensing. *J. Geophys. Res. Ocean.* **2011**, *116*, C02011. [CrossRef]
142. Najah, A.; Al-Shehhi, M.R. Performance of the ocean color algorithms: Qaa, Gsm, and Giop in inland and coastal waters. *Remote Sens. Earth Syst. Sci.* **2021**, *4*, 235–248. [CrossRef]
143. Pan, H.; Lyu, H.; Wang, Y.; Jin, Q.; Wang, Q.; Li, Y.; Fu, Q. An improved approach to retrieve IOPS based on a quasi-analytical algorithm (QAA) for turbid eutrophic inland water. *IEEE J. Sel. Top. Appl. Earth Obs. Remote Sens.* **2015**, *8*, 5177–5189. [CrossRef]
144. Wang, Y.; Shen, F.; Sokoletsky, L.; Sun, X. Validation and calibration of QAA algorithm for CDOM absorption retrieval in the changjiang (Yangtze) estuarine and coastal waters. *Remote Sens.* **2017**, *9*, 1192. [CrossRef]
145. Le Chengfeng, L.Y.; Yong, Z. Study on partitioning of phytoplankton absorption coefficient from total spectral absorption in Taihu lake. *Acta Opt. Sin.* **2010**, *30*, 3090–3096. [CrossRef]
146. Lu, S.; Jiang, J.; Zhu, W. Remote sensing inversion and daily variation of CDOM based on GOCI in the Changjiang estuary and adjacent waters. *Haiyang Xuebao* **2017**, *39*, 133–145.
147. Rodrigues, T.W.P. From Oligo to Eutrophic Inland Waters: Advancements and Challenges for Bio-Optical Modeling. 2017. Available online: http://hdl.handle.net/11449/150315 (accessed on 27 May 2025).
148. Watanabe, F.; Mishra, D.R.; Astuti, I.; Rodrigues, T.; Alcântara, E.; Imai, N.N.; Barbosa, C. Parametrization and calibration of a quasi-analytical algorithm for tropical eutrophic waters. *ISPRS J. Photogramm. Remote Sens.* **2016**, *121*, 28–47. [CrossRef]
149. Mishra, S.; Mishra, D.R.; Lee, Z. Bio-optical inversion in highly turbid and cyanobacteria-dominated waters. *IEEE Trans. Geosci. Remote Sens.* **2013**, *52*, 375–388. [CrossRef]
150. Li, L.; Li, L.; Song, K. Remote sensing of freshwater cyanobacteria: An extended IOP inversion model of inland waters (iimiw) for partitioning absorption coefficient and estimating phycocyanin. *Remote Sens. Environ.* **2015**, *157*, 9–23. [CrossRef]
151. Ogashawara, I.; Li, L.; Druschel, G.K. Retrieval of inherent optical properties from multiple aquatic systems using a quasi-analytical algorithm for several water types. *Remote Sens. Appl. Soc. Environ.* **2022**, *27*, 100807. [CrossRef]

152. Shi, L.; Mao, Z.; Zhang, Y.; Wang, Z.; Tu, Q. An extended quasi− analytical algorithm for retrieving absorption coefficient using 510–620 nm bands from OLCI and meris satellite data. *Water* **2024**, *16*, 67. [CrossRef]
153. Zeng, Z.; Tang, B.-H.; Wang, D.; Huang, L.; Chen, G.; Ge, Z. Estimation of chromophpric dissolved organic matter concentration in Erhai lake using the quasi-analytical algorithm from sentinel-3 satellite data. *IEEE Access* **2024**, *12*, 44586–44597. [CrossRef]
154. Li, S.; Song, K.; Mu, G.; Zhao, Y.; Ma, J.; Ren, J. Evaluation of the quasi-analytical algorithm (QAA) for estimating total absorption coefficient of turbid inland waters in northeast China. *IEEE J. Sel. Top. Appl. Earth Obs. Remote Sens.* **2016**, *9*, 4022–4036. [CrossRef]
155. Le, C.F.; Li, Y.M.; Zha, Y.; Sun, D.; Yin, B. Validation of a quasi-analytical algorithm for highly turbid eutrophic water of Meiliang bay in Taihu lake, China. *IEEE Trans. Geosci. Remote Sens.* **2009**, *47*, 2492–2500.
156. Chu, Q.; Zhang, Y.; Ma, R.; Hu, M.; Jing, Y. Modis-based remote estimation of absorption coefficients of an inland turbid lake in China. *Remote Sens.* **2020**, *12*, 1940. [CrossRef]
157. Matsuoka, A.; Hooker, S.; Bricaud, A.; Gentili, B.; Babin, M. Estimating absorption coefficients of colored dissolved organic matter (CDOM) using a semi-analytical algorithm for southern Beaufort sea waters: Application to deriving concentrations of dissolved organic carbon from space. *Biogeosciences* **2013**, *10*, 917–927. [CrossRef]
158. Salama, M.; Dekker, A.; Su, Z.; Mannaerts, C.; Verhoef, W. Deriving inherent optical properties and associated inversion-uncertainties in the Dutch lakes. *Hydrol. Earth Syst. Sci.* **2009**, *13*, 1113–1121. [CrossRef]
159. Li, H.; He, X.; Shanmugam, P.; Bai, Y.; Wang, D.; Huang, H.; Zhu, Q.; Gong, F. Semi-analytical algorithms of ocean color remote sensing under high solar zenith angles. *Opt. Express* **2019**, *27*, A800–A817. [CrossRef] [PubMed]
160. Xu, F.; He, X.; Jin, X.; Cai, W.; Bai, Y.; Wang, D.; Gong, F.; Zhu, Q. Spherical vector radiative transfer model for satellite ocean color remote sensing. *Opt. Express* **2023**, *31*, 11192–11212. [CrossRef] [PubMed]
161. Aguilar-Maldonado, J.A.; Santamaría-del-Ángel, E.; Gonzalez-Silvera, A.; Sebastiá-Frasquet, M.T. Detection of phytoplankton temporal anomalies based on satellite inherent optical properties: A tool for monitoring phytoplankton blooms. *Sensors* **2019**, *19*, 3339. [CrossRef] [PubMed]
162. O'Shea, R.E.; Pahlevan, N.; Smith, B.; Boss, E.; Gurlin, D.; Alikas, K.; Kangro, K.; Kudela, R.M.; Vaičiūtė, D. A hyperspectral inversion framework for estimating absorbing inherent optical properties and biogeochemical parameters in inland and coastal waters. *Remote Sens. Environ.* **2023**, *295*, 113706. [CrossRef]
163. De Stefano, L.G.; Valdivia, A.S.; Gianello, D.; Gerea, M.; Reissig, M.; Garcia, P.E.; García, R.D.; Cárdenas, C.S.; Dieguez, M.d.C.; Queimaliños, C.P. Using CDOM spectral shape information to improve the estimation of doc concentration in inland waters: A case study of Andean Patagonian lakes. *Sci. Total Environ.* **2022**, *824*, 153752. [CrossRef] [PubMed]
164. Cai, X.; Meng, J.; Yuan, C.; Liu, R.; Hou, E.; Bi, D.; Li, Y.; Qian, C.; Zhong, S. Seasonal distribution of observed colored dissolved organic matter (CDOM) in the eastern Indian ocean. *J. Ocean Univ. China* **2023**, *22*, 886–896. [CrossRef]
165. Yin, Y.; Wu, Z.; Zhang, Y.; Liu, M.; Zhou, Y.; Gao, Y.; He, J.; Yu, Z. Absorption characteristics and sources analysis of CDOM in xin'anjiang reservoir in summer. *China Environ. Sci.* **2014**, *34*, 3207–3214.
166. Estlander, S.; Horppila, J. Effects of dissolved organic carbon gradient on Epilimnetic zooplankton communities in lakes. *Hydrobiologia* **2023**, *850*, 4015–4027. [CrossRef]
167. Song, K.; Wen, Z.; Shang, Y.; Yang, H.; Lyu, L.; Liu, G.; Fang, C.; Du, J.; Zhao, Y. Quantification of dissolved organic carbon (DOC) storage in lakes and reservoirs of mainland China. *J. Environ. Manag.* **2018**, *217*, 391–402. [CrossRef] [PubMed]
168. Yu, X.; Shen, F.; Liu, Y. Light absorption properties of CDOM in the Changjiang (Yangtze) estuarine and coastal waters: An alternative approach for doc estimation. *Estuar. Coast. Shelf Sci.* **2016**, *181*, 302–311. [CrossRef]
169. Danhiez, F.; Vantrepotte, V.; Cauvin, A.; Lebourg, E.; Loisel, H. Optical properties of chromophoric dissolved organic matter during a phytoplankton bloom. Implication for doc estimates from CDOM absorption. *Limnol. Oceanogr.* **2017**, *62*, 1409–1425. [CrossRef]
170. Singh, S.; Raulo, S.; Acharyya, T.; Mishra, D.R.; Kumar, A.; Gopinath, A.; Muduli, P.R.; Rastogi, G. Dynamics and source characterization of chromophoric dissolved organic matter (CDOM) in a tropical monsoon driven lagoon. *Mar. Chem.* **2024**, *265*, 104430. [CrossRef]
171. He, Y.; Gong, Z.; Zheng, Y.; Zhang, Y. Inland reservoir water quality inversion and eutrophication evaluation using bp neural network and remote sensing imagery: A case study of Dashahe reservoir. *Water* **2021**, *13*, 2844. [CrossRef]
172. Wu, Z.; Li, J.; Wang, R.; Shi, L.; Miao, S.; Lv, H.; Li, Y. Estimation of CDOM concentration in inland lake based on random forest using sentinel-3a olci. *J. Lake Sci* **2018**, *30*, 979–991.
173. Huang, Y.; Pan, J.; Devlin, A.T. Enhanced estimate of chromophoric dissolved organic matter using machine learning algorithms from landsat-8 Oli data in the pearl river estuary. *Remote Sens.* **2023**, *15*, 1963. [CrossRef]
174. Menendez, A.; Tzortziou, M. Augmenting estuary monitoring from space: New retrievals of fine-scale CDOM quality and doc exchange. *Int. J. Appl. Earth Obs. Geoinf.* **2025**, *137*, 104389. [CrossRef]
175. Qiang, S.; Song, K.; Shang, Y.; Lai, F.; Wen, Z.; Liu, G.; Tao, H.; Lyu, Y. Remote sensing estimation of CDOM and doc with the environmental implications for lake Khanka. *Remote Sens.* **2023**, *15*, 5707. [CrossRef]

176. Xu, J.; Fang, C.; Gao, D.; Zhang, H.; Gao, C.; Xu, Z.; Wang, Y. Optical models for remote sensing of chromophoric dissolved organic matter (CDOM) absorption in Poyang lake. *ISPRS J. Photogramm. Remote Sens.* **2018**, *142*, 124–136. [CrossRef]
177. Olmanson, L.G.; Page, B.P.; Finlay, J.C.; Brezonik, P.L.; Bauer, M.E.; Griffin, C.G.; Hozalski, R.M. Regional measurements and spatial/temporal analysis of CDOM in 10,000+ optically variable Minnesota lakes using Landsat 8 imagery. *Sci. Total Environ.* **2020**, *724*, 138141. [CrossRef] [PubMed]
178. Chen, J.; Zhu, W. Consistency evaluation of landsat-7 and landsat-8 for improved monitoring of colored dissolved organic matter in complex water. *Geocarto Int.* **2022**, *37*, 91–102. [CrossRef]
179. Siswanto, E.; Tang, J.; Yamaguchi, H.; Ahn, Y.-H.; Ishizaka, J.; Yoo, S.; Kim, S.-W.; Kiyomoto, Y.; Yamada, K.; Chiang, C. Empirical ocean-color algorithms to retrieve chlorophyll-a, total suspended matter, and colored dissolved organic matter absorption coefficient in the yellow and east China seas. *J. Oceanogr.* **2011**, *67*, 627–650. [CrossRef]
180. Sun, X.; Zhang, Y.; Zhang, Y.; Shi, K.; Zhou, Y.; Li, N. Machine learning algorithms for chromophoric dissolved organic matter (CDOM) estimation based on landsat 8 images. *Remote Sens.* **2021**, *13*, 3560. [CrossRef]
181. Toming, K.; Liu, H.; Soomets, T.; Uuemaa, E.; Nõges, T.; Kutser, T. Estimation of the biogeochemical and physical properties of lakes based on remote sensing and artificial intelligence applications. *Remote Sens.* **2024**, *16*, 464. [CrossRef]
182. Li, S.; Song, K.; Wang, S.; Liu, G.; Wen, Z.; Shang, Y.; Lyu, L.; Chen, F.; Xu, S.; Tao, H. Quantification of chlorophyll-a in typical lakes across China using sentinel-2 MSI imagery with machine learning algorithm. *Sci. Total Environ.* **2021**, *778*, 146271. [CrossRef] [PubMed]
183. Cao, Z.; Ma, R.; Duan, H.; Pahlevan, N.; Melack, J.; Shen, M.; Xue, K. A machine learning approach to estimate chlorophyll-a from landsat-8 measurements in inland lakes. *Remote Sens. Environ.* **2020**, *248*, 111974. [CrossRef]
184. Pahlevan, N.; Smith, B.; Schalles, J.; Binding, C.; Cao, Z.; Ma, R.; Alikas, K.; Kangro, K.; Gurlin, D.; Hà, N. Seamless retrievals of chlorophyll-a from sentinel-2 (MSI) and sentinel-3 (OLCI) in inland and coastal waters: A machine-learning approach. *Remote Sens. Environ.* **2020**, *240*, 111604. [CrossRef]
185. Ye, H.; Tang, S.; Yang, C. Deep learning for chlorophyll-a concentration retrieval: A case study for the pearl river estuary. *Remote Sens.* **2021**, *13*, 3717. [CrossRef]
186. Keller, S.; Maier, P.M.; Riese, F.M.; Norra, S.; Holbach, A.; Börsig, N.; Wilhelms, A.; Moldaenke, C.; Zaake, A.; Hinz, S. Hyperspectral data and machine learning for estimating CDOM, chlorophyll a, diatoms, green algae and turbidity. *Int. J. Environ. Res. Public Health* **2018**, *15*, 1881. [CrossRef] [PubMed]
187. Tian, D.; Zhao, X.; Gao, L.; Liang, Z.; Yang, Z.; Zhang, P.; Wu, Q.; Ren, K.; Li, R.; Yang, C. Estimation of water quality variables based on machine learning model and cluster analysis-based empirical model using multi-source remote sensing data in inland reservoirs, south China. *Environ. Pollut.* **2024**, *342*, 123104. [CrossRef] [PubMed]
188. Ruescas, A.B.; Hieronymi, M.; Mateo-Garcia, G.; Koponen, S.; Kallio, K.; Camps-Valls, G. Machine learning regression approaches for colored dissolved organic matter (CDOM) retrieval with s2-msi and s3-olci simulated data. *Remote Sens.* **2018**, *10*, 786. [CrossRef]
189. Wu, M.; Huang, J.; Gong, L.; Jiang, T. Analysis of doc concentration variation and driving forces in the arctic river Lena based on long-term landsat time series. *Natl. Remote Sens. Bull.* **2021**, *25*, 830–845. [CrossRef]
190. Pahlevan, N.; Smith, B.; Alikas, K.; Anstee, J.; Barbosa, C.; Binding, C.; Bresciani, M.; Cremella, B.; Giardino, C.; Gurlin, D. Simultaneous retrieval of selected optical water quality indicators from landsat-8, sentinel-2, and sentinel-3. *Remote Sens. Environ.* **2022**, *270*, 112860. [CrossRef]
191. Marinho, R.R.; Harmel, T.; Martinez, J.-M.; Filizola Junior, N.P. Spatiotemporal dynamics of suspended sediments in the negro river, amazon basin, from in situ and sentinel-2 remote sensing data. *ISPRS Int. J. Geo-Inf.* **2021**, *10*, 86. [CrossRef]
192. Freire da Silva, E.F.; Leao de Moraes Novo, E.M.; Lobo, F.d.L.; Faria Barbosa, C.C.; Cairo, C.T.; Noernberg, M.A.; da Silva Rotta, L.H. A machine learning approach for monitoring Brazilian optical water types using sentinel-2 MSI. *REMOTE Sens. Appl. Soc. Environ.* **2021**, *23*, 100577. [CrossRef]
193. Castelvecchi, D. Can we open the black box of ai? *Nat. News* **2016**, *538*, 20. [CrossRef] [PubMed]
194. Voosen, P. How AI detectives are craking open the black box of deep learning. *Science*, 6 July 2017.
195. Abdollahi, H.; Noaparast, M.; Shafaei, S.Z.; Akcil, A.; Panda, S.; Kashi, M.H.; Karimi, P. Prediction and optimization studies for bioleaching of molybdenite concentrate using artificial neural networks and genetic algorithm. *Miner. Eng.* **2019**, *130*, 24–35. [CrossRef]
196. Chen, B.; Mu, X.; Chen, P.; Wang, B.; Choi, J.; Park, H.; Xu, S.; Wu, Y.; Yang, H. Machine learning-based inversion of water quality parameters in typical reach of the urban river by UAV multispectral data. *Ecol. Indic.* **2021**, *133*, 108434. [CrossRef]
197. Gholizadeh, M.H.; Melesse, A.M.; Reddi, L. A comprehensive review on water quality parameters estimation using remote sensing techniques. *Sensors* **2016**, *16*, 1298. [CrossRef] [PubMed]
198. Kutser, T. The possibility of using the landsat image archive for monitoring long time trends in coloured dissolved organic matter concentration in lake waters. *Remote Sens. Environ.* **2012**, *123*, 334–338. [CrossRef]

199. Cherukuru, N.; Ford, P.W.; Matear, R.J.; Oubelkheir, K.; Clementson, L.A.; Suber, K.; Steven, A.D. Estimating dissolved organic carbon concentration in turbid coastal waters using optical remote sensing observations. *Int. J. Appl. Earth Obs. Geoinf.* **2016**, *52*, 149–154. [CrossRef]
200. Chen, C.; Pan, Z.; Shi, P. Simulation of seawater reflection and its application in retrieval of yellow substances by sensing data. *J. Trop. Oceanogr.* **2003**, *22*, 33–39.
201. Slonecker, E.T.; Jones, D.K.; Pellerin, B.A. The new landsat 8 potential for remote sensing of colored dissolved organic matter (cdom). *Mar. Pollut. Bull.* **2016**, *107*, 518–527. [CrossRef] [PubMed]
202. Kutser, T.; Herlevi, A.; Kallio, K.; Arst, H. A hyperspectral model for interpretation of passive optical remote sensing data from turbid lakes. *Sci. Total Environ.* **2001**, *268*, 47–58. [CrossRef] [PubMed]
203. Olmanson, L.G.; Brezonik, P.L.; Bauer, M.E. Remote sensing for regional lake water quality assessment: Capabilities and limitations of current and upcoming satellite systems. *Adv. Watershed Sci. Assess.* **2015**, *33*, 111–140.
204. Brando, V.E.; Dekker, A.G. Satellite hyperspectral remote sensing for estimating estuarine and coastal water quality. *IEEE Trans. Geosci. Remote Sens.* **2003**, *41*, 1378–1387. [CrossRef]
205. Kutser, T.; Paavel, B.; Verpoorter, C.; Ligi, M.; Soomets, T.; Toming, K.; Casal, G. Remote sensing of black lakes and using 810 nm reflectance peak for retrieving water quality parameters of optically complex waters. *Remote Sens.* **2016**, *8*, 497. [CrossRef]
206. Zhang, L.; Fang, Y.; Cai, H.; Zhang, S. Spatio-temporal heterogeneities in water quality and their potential drivers in lake Chaohu (China) from 2001 to 2017. *Ecohydrology* **2021**, *14*, e2333. [CrossRef]
207. Zhao, Y.; He, X.; Pan, S.; Bai, Y.; Wang, D.; Li, T.; Gong, F.; Zhang, X. Satellite retrievals of water quality for diverse inland waters from sentinel-2 images: An example from Zhejiang province, China. *Int. J. Appl. Earth Obs. Geoinf.* **2024**, *132*, 104048. [CrossRef]
208. Shi, L.; Mao, Z.; Wu, J.; Liu, M.; Zhang, Y.; Wang, Z. Variations in spectral absorption properties of phytoplankton, non-algal particles and Chromophoric dissolved organic matter in lake Qiandaohu. *Water* **2017**, *9*, 352. [CrossRef]
209. Li, S.; Zhang, J.; Mu, G.; Ju, H.; Wang, R.; Li, D.; Shabbir, A.H. Spatiotemporal characterization of chromophoric dissolved organic matter (CDOM) and CDOM-doc relationships for highly polluted rivers. *Water* **2016**, *8*, 399. [CrossRef]
210. Wang, B.; Axe, L.; Michalopoulou, Z.-H.; Riman, R.E.; Tan, M.C.; Wei, L. Light absorption properties of the New York/New Jersey Harbor estuary. *Hydrobiologia* **2016**, *766*, 173–188. [CrossRef]
211. Shao, T.; Zheng, H.; Song, K.; Zhao, Y.; Zhang, B. Influence of environmental factors on absorption characteristics of suspended particulate matter and CDOM in Liaohe river watershed, northeast China. *Environ. Sci. Pollut. Res.* **2017**, *24*, 19322–19337. [CrossRef] [PubMed]
212. Ylöstalo, P.; Kallio, K.; Seppälä, J. Absorption properties of in-water constituents and their variation among various lake types in the boreal region. *Remote Sens. Environ.* **2014**, *148*, 190–205. [CrossRef]
213. Rodrigues, T.; Alcantara, E.; Rotta, L.; Bernardo, N.; Watanabe, F. An investigation into the relationship between light absorption budget and trophic status in inland waters. *Ecol. Indic.* **2020**, *115*, 106410. [CrossRef]
214. Araújo, C.A.; Bélanger, S. Variability of bio-optical properties in nearshore waters of the estuary and gulf of st. Lawrence: Absorption and backscattering coefficients. *Estuar. Coast. Shelf Sci.* **2022**, *264*, 107688. [CrossRef]
215. Watanabe, F.; Alcântara, E.; Curtarelli, M.; Kampel, M.; Stech, J. Landsat-based remote sensing of the colored dissolved organic matter absorption coefficient in a tropical oligotrophic reservoir. *Remote Sens. Appl. Soc. Environ.* **2018**, *9*, 82–90. [CrossRef]
216. Bernardo, N.; Alcântara, E.; Watanabe, F.; Rodrigues, T.; Carmo, A.d.; Gomes, A.C.C.; Andrade, C. Light absorption budget in a reservoir cascade system with widely differing optical properties. *Water* **2019**, *11*, 229. [CrossRef]
217. Rodrigues, T.; Mishra, D.R.; Alcântara, E.; Astuti, I.; Watanabe, F.; Imai, N. Estimating the optical properties of inorganic matter-dominated oligo-to-mesotrophic inland waters. *Water* **2018**, *10*, 449. [CrossRef]
218. Hao, Y.; Cui, T.; Singh, V.P.; Zhang, J.; Yu, R.; Zhao, W. Diurnal variation of light absorption in the yellow river estuary. *Remote Sens.* **2018**, *10*, 542. [CrossRef]
219. Sent, G.; Biguino, B.; Favareto, L.; Cruz, J.; Sá, C.; Dogliotti, A.I.; Palma, C.; Brotas, V.; Brito, A.C. Deriving water quality parameters using sentinel-2 imagery: A case study in the Sado estuary, Portugal. *Remote Sens.* **2021**, *13*, 1043. [CrossRef]
220. Arena, M.; Delgado, A.L.; Celleri, C.; Pratolongo, P.D. Preliminary assessment of spatial and short-term variability of bio-optical properties in a tidal dominated estuary (Bahía Blanca, Argentina). *Reg. Stud. Mar. Sci.* **2019**, *29*, 100639. [CrossRef]
221. Werther, M.; Odermatt, D.; Simis, S.G.; Gurlin, D.; Jorge, D.S.; Loisel, H.; Hunter, P.D.; Tyler, A.N.; Spyrakos, E. Characterising retrieval uncertainty of chlorophyll-a algorithms in oligotrophic and mesotrophic lakes and reservoirs. *ISPRS J. Photogramm. Remote Sens.* **2022**, *190*, 279–300. [CrossRef]
222. Yu, Q.; Tian, Y.Q.; Chen, R.F.; Liu, A.; Gardner, G.B.; Zhu, W. Functional linear analysis of in situ hyperspectral data for assessing cdom in rivers. *Photogramm. Eng. Remote Sens.* **2010**, *76*, 1147–1158. [CrossRef]
223. Cai, X.; Li, Y.; Lei, S.; Zeng, S.; Zhao, Z.; Lyu, H.; Dong, X.; Li, J.; Wang, H.; Xu, J. A hybrid remote sensing approach for estimating chemical oxygen demand concentration in optically complex waters: A case study in inland lake waters in eastern China. *Sci. Total Environ.* **2023**, *856*, 158869. [CrossRef] [PubMed]

224. Attila, J.; Koponen, S.; Kallio, K.; Lindfors, A.; Kaitala, S.; Ylöstalo, P. Meris case ii water processor comparison on coastal sites of the northern Baltic sea. *Remote Sens. Environ.* **2013**, *128*, 138–149. [CrossRef]
225. Sun, Y.; Wang, D.; Li, L.; Ning, R.; Yu, S.; Gao, N. Application of remote sensing technology in water quality monitoring: From traditional approaches to artificial intelligence. *Water Res.* **2024**, *267*, 122546. [CrossRef] [PubMed]
226. Pandi, S.R.; Sarma, N.S.; Gundala, C.; Naroju, V.H.; Lotliker, A.A.; Bajish, C.C.; Tripathy, S.C. Chromophoric dissolved organic matter traces seasonally changing coastal processes in a river-influenced region of the western bay of Bengal. *Environ. Sci. Pollut. Res.* **2024**, *31*, 49372–49392. [CrossRef] [PubMed]
227. Chen, J.; Zhu, W.; Zheng, Y.; Tian, Y.Q.; Yu, Q. Monitoring seasonal variations of colored dissolved organic matter for the saginaw river based on landsat-8 data. *Water Supply* **2019**, *19*, 274–281. [CrossRef]
228. Ratnasingam, S.; Muñoz-Lopez, J. Distance correlation-based feature selection in random forest. *Entropy* **2023**, *25*, 1250. [CrossRef] [PubMed]
229. Fan, W.; Xu, Z.; Liu, Y.; Dong, Q.; Zhang, S.; Zhu, Z.; Yang, Z. Satellite-based estimation of nitrous oxide concentration and emission in a large estuary. *Environ. Sci. Technol.* **2025**, *59*, 5012–5020. [CrossRef] [PubMed]
230. Sadaiappan, B.; Balakrishnan, P.; CR, V.; Vijayan, N.T.; Subramanian, M.; Gauns, M.U. Applications of machine learning in chemical and biological oceanography. *ACS Omega* **2023**, *8*, 15831–15853. [CrossRef] [PubMed]
231. Cardall, A.C.; Hales, R.C.; Tanner, K.B.; Williams, G.P.; Markert, K.N. Lasso (l1) regularization for development of sparse remote-sensing models with applications in optically complex waters using gee tools. *Remote Sens.* **2023**, *15*, 1670. [CrossRef]
232. Hong, S.M.; Baek, S.-S.; Yun, D.; Kwon, Y.-H.; Duan, H.; Pyo, J.; Cho, K.H. Monitoring the vertical distribution of HABS using hyperspectral imagery and deep learning models. *Sci. Total Environ.* **2021**, *794*, 148592. [CrossRef] [PubMed]
233. Yu, D.; Jiang, G.; Gao, H.; Ren, L.; Chen, C.; Yang, L.; Zhou, M.; Pan, S. Optimization of convolutional neural network with dual attention mechanism: Estimation of chlorophyll-a concentration in the Taiwan strait using MODIS data. *Estuar. Coast. Shelf Sci.* **2024**, *300*, 108729. [CrossRef]
234. Xu, J.; Pan, J.; Devlin, A.T. Variations in chlorophyll-a concentration in response to hydrodynamics in a flow-through lake: Remote sensing and modeling studies. *Ecol. Indic.* **2023**, *148*, 110128. [CrossRef]

Disclaimer/Publisher's Note: The statements, opinions and data contained in all publications are solely those of the individual author(s) and contributor(s) and not of MDPI and/or the editor(s). MDPI and/or the editor(s) disclaim responsibility for any injury to people or property resulting from any ideas, methods, instructions or products referred to in the content.

sustainability

MDPI

Article

Estimation of Mangrove Aboveground Carbon Using Integrated UAV-LiDAR and Satellite Data

Xuzhi Mai [1,†], Quan Li [2,†], Weifeng Xu [3], Songwen Deng [1], Wenhuan Wang [1,4], Wenqian Wu [4], Wei Zhang [1,*] and Yinghui Wang [1,4,*]

[1] School of Marine Sciences, Guangxi University, Nanning 530004, China; jrsx@st.gxu.edu.cn (X.M.); 2427401423@st.gxu.edu.cn. (S.D.); wwhuan2202@126.com (W.W.)
[2] Guangxi-ASEAN Technology Transfer Center, Nanning 53001, China; lqgattc@163.com
[3] School of Resources, Environment and Materials, Guangxi University, Nanning 530004, China; xwf@st.gxu.edu.cn
[4] Institute of Green and Low Carbon Technology, Guangxi Institute of Industrial Technology, Nanning 530200, China; wuwq1@foxmail.com
* Correspondence: zhangwei20@gxu.edu.cn (W.Z.); wyhgxu@126.com (Y.W.)
† These authors contributed equally to this work.

Abstract

Mangroves are critical blue carbon ecosystems, yet accurately estimating their aboveground carbon (AGC) stocks remains challenging due to structural complexity and spectral saturation in dense canopies. This study aims to develop a scalable AGC estimation framework by integrating high-resolution canopy height (CH) data from UAV-LiDAR with multi-source satellite features from Sentinel-1, Sentinel-2, and ALOS PALSAR-2. Using the Maowei Sea mangrove zone in Guangxi, China, as a case study, we extracted structural, spectral, and textural features and applied Random Forest regression with Recursive Feature Elimination (RFE) to optimize feature combinations. Results show that incorporating UAV-derived CH significantly improves model accuracy (R^2 = 0.75, RMSE = 14.18 Mg C ha^{-1}), outperforming satellite-only approaches. CH was identified as the most important predictor, effectively mitigating saturation effects in high-biomass stands. The estimated total AGC in the study area was 88,363.73 Mg, with a mean density of 53.01 Mg C ha^{-1}. This study highlights the advantages of cross-scale UAV–satellite data fusion for accurate, regionally scalable AGC mapping, offering a practical tool for blue carbon monitoring and coastal ecosystem management under global change.

Keywords: aboveground carbon estimation; UAV-LiDAR; multi-source data fusion; mangrove ecosystems; canopy height modeling; Pinglu Canal

check for updates

Academic Editors: Zhaohui Xue, Lina Ke, Xiyong Hou, Guangshuai Zhang, Wenting Wu and Antonio Miguel Martínez-Graña

Received: 3 June 2025
Revised: 4 August 2025
Accepted: 15 August 2025
Published: 12 September 2025

Citation: Mai, X.; Li, Q.; Xu, W.; Deng, S.; Wang, W.; Wu, W.; Zhang, W.; Wang, Y. Estimation of Mangrove Aboveground Carbon Using Integrated UAV-LiDAR and Satellite Data. *Sustainability* **2025**, *17*, 8211. https://doi.org/10.3390/su17188211

Copyright: © 2025 by the authors. Licensee MDPI, Basel, Switzerland. This article is an open access article distributed under the terms and conditions of the Creative Commons Attribution (CC BY) license (https://creativecommons.org/licenses/by/4.0/).

1. Introduction

Blue carbon ecosystems, particularly mangroves, play a critical role in global climate regulation. Despite covering less than 1% of Earth's terrestrial area, mangroves are among the most carbon-rich forest types on the planet and possess exceptional capacity for carbon sequestration and long-term storage [1,2]. By efficiently absorbing atmospheric CO_2 through photosynthesis and storing carbon in biomass and organic-rich soils, mangroves are increasingly recognized as a nature-based solution to mitigate climate change. Typically distributed along tropical and subtropical coastlines, mangrove forests are unique intertidal wetlands characterized by high productivity and ecological value. They deliver diverse ecosystem services, including coastal protection, shoreline stabilization, and biodiversity

conservation [3]. Dense root systems dissipate wave energy, reducing storm surge and tsunami impacts, while also providing critical nursery and breeding habitats for economically and ecologically important aquatic species. However, mangrove ecosystems have suffered significant degradation in recent decades. According to the World Mangrove Report 2022, global mangrove area has declined by more than 5200 km^2 since 1996, primarily driven by aquaculture expansion and unsustainable coastal development. This habitat loss not only undermines ecosystem services but also results in the release of previously sequestered blue carbon, contributing to increased greenhouse gas emissions. In response, China's Ministry of Natural Resources and National Forestry and Grassland Administration jointly launched the Mangrove Conservation and Restoration Action Plan (2020–2025) in August 2020. The plan prioritizes mangrove protection, restoration, and carbon sink research as part of the nation's strategy to peak carbon emissions before 2030. These policy initiatives underscore the urgent need for accurate mangrove carbon stock assessment to support sustainable ecosystem management and climate mitigation.

Despite increased conservation efforts, large-scale coastal engineering projects continue to pose risks to mangrove carbon stocks and ecological functions. One such case is the construction of the Pinglu Canal in Guangxi, China—a 140 km waterway whose estuarine outlet intersects the Maowei Sea mangrove zone. According to the project's environmental impact assessment, canal development will result in the permanent loss of approximately 13.87 hectares of mangroves and affect more than 250,000 individual mangrove trees. The excavation and navigation operations will alter sediment transport and tidal hydrodynamics, potentially disrupting the sedimentary and hydrological conditions essential for mangrove survival. This case highlights the need for quantitative assessment of how large infrastructure projects affect mangrove carbon storage and ecosystem service provision [4].

Accurate estimation of mangrove carbon stocks is fundamental for scientific management and environmental impact evaluation. Traditional approaches typically rely on ground plot surveys and empirical biomass models, which are labor-intensive and difficult to implement in muddy, inaccessible mangrove environments. In contrast, remote sensing offers a more efficient means of large-scale monitoring. Optical remote sensing, in particular, enables wide-area coverage and high temporal resolution. Early studies used moderate-resolution imagery (e.g., Landsat and MODIS) to estimate mangrove biomass [5,6]. However, passive optical sensors are susceptible to atmospheric interference and can only capture surface reflectance of the canopy, failing to penetrate dense vegetation to retrieve structural detail. In high-biomass forests, vegetation indices such as the NDVI often exhibit saturation—reflectance values plateau beyond a certain biomass threshold—thus reducing estimation accuracy [7,8]. Similarly, synthetic aperture radar (SAR) data from systems like Sentinel-1 or ALOS PALSAR are limited by their wavelength and polarization, resulting in saturation at 50–150 Mg/ha, depending on the band (C or L) [9,10]. Furthermore, while textural metrics can supplement spectral and SAR data by capturing spatial heterogeneity, their effectiveness also diminishes in structurally homogeneous canopies [11,12]. As such, traditional optical and SAR-based methods face challenges in accurately assessing biomass in high-carbon-density mangrove stands [13].

To overcome these challenges, structural variables—particularly canopy height (CH)—have increasingly been employed. Satellite-based LiDAR missions, such as the Global Ecosystem Dynamics Investigation (GEDI) and the Ice, Cloud, and land Elevation Satellite-2 (ICESat-2), have improved forest structure retrieval globally by providing vertical vegetation metrics [14,15]. However, these systems generate sparse and discontinuous samples, struggling with the vertical complexity of coastal mangrove ecosystems due to limited spatial resolution, sampling density, and tidal influences. Airborne LiDAR systems offer improved vertical accuracy, but most prior studies—such as Shang et al. [16],

which utilized a full-waveform UV LiDAR mounted on an ultralight aircraft—focused on temperate deciduous forests and operated at relatively coarse ground footprints (~2.2 m) with point spacing of ~1 m. While these systems are capable of capturing general forest structure, their limited flexibility, lower point density, and coarser spatial detail make them less suitable for resolving the fine-scale heterogeneity of mangrove canopies.

Conversely, UAV-LiDAR systems generate dense point clouds, enabling detailed characterization of canopy structure and accurate extraction of vegetation attributes [17]. Recent studies confirm that UAV-derived canopy height models (CHMs) achieve high accuracy in dense mangroves [18]. UAV-LiDAR serves as a valuable intermediary between ground surveys and satellite data, providing reliable references for canopy height estimation [19]. However, UAV-LiDAR's high operational cost and limited spatial coverage restrict its use for regional AGC mapping. Recently, attempts have been made to integrate UAV-LiDAR and satellite remote sensing data, supporting canopy height interpolation at regional scales [20]. The effectiveness of such integration for regional AGC estimation remains to be thoroughly investigated.

In recent years, machine learning (ML) techniques have become indispensable tools for estimating aboveground carbon (AGC), owing to their ability to capture complex and nonlinear relationships between vegetation characteristics and biomass. Among various ML algorithms, the tree-based ensemble model Random Forest (RF) has consistently demonstrated robust predictive performance across a wide range of ecological applications [21]. Its ensemble structure, which integrates multiple decision trees, enhances generalization capability and effectively mitigates overfitting [22,23]—an advantage particularly critical when modeling heterogeneous and high-biomass environments such as mangrove forests. In the context of remote sensing-based AGC estimation, recent advances have focused on cross-scale integration of multi-source data and fusion of diverse vegetation features to improve model performance [24]. However, stacking a large number of input variables into machine learning models may lead to redundancy, increased computational cost, and diminished marginal returns in accuracy. Empirical studies have shown that while multi-feature fusion can initially enhance predictive performance, its effectiveness tends to plateau once the feature set exceeds a certain threshold [15,25]. Therefore, optimizing feature selection is critical to constructing parsimonious and interpretable AGC estimation models. In this study, we employed Recursive Feature Elimination (RFE), a wrapper-based feature selection method, to systematically identify a subset of the most informative predictors from the multi-source remote sensing dataset. By iteratively removing the least important features based on model performance, RFE enables the reduction in dimensionality while retaining key structural and spectral information relevant to AGC. This is especially important for mangrove ecosystems, where high canopy density and spectral saturation present additional challenges for remote sensing-based modeling.

The Maowei Sea mangrove ecosystem in Guangxi, China, was selected as the study area due to its ecological representativeness, high biomass density, and exposure to active coastal development pressures. It is one of the largest and most biodiverse mangrove zones in southern China, consisting of both natural and planted stands with varying canopy structures. Moreover, it is directly affected by large-scale infrastructure projects such as the Pinglu Canal, making it an ideal site for assessing blue carbon dynamics under anthropogenic disturbance.

Building on this foundation, the present study targets the Maowei Sea mangrove ecosystem in Guangxi as a representative high-biomass coastal wetland, aiming to develop a scalable and accurate AGC estimation framework through the integration of UAV-LiDAR-derived canopy height and multi-source satellite remote sensing features (Sentinel-1, Sentinel-2, and PALSAR-2). Unlike previous approaches that rely solely on

sparse spaceborne LiDAR footprints or traditional optical/SAR indices, our method leverages dense structural information acquired from UAV-LiDAR as a foundation for cross-scale feature interpolation and model training. The central hypothesis of this study is that fusing UAV-derived structural metrics with spectral and radar-based vegetation indices will enhance AGC prediction performance by mitigating saturation effects and enhancing structural sensitivity.

Specifically, we investigate two key aspects: (1) how the fusion of UAV-LiDAR and satellite remote sensing features can enhance AGC model accuracy and generalization capability at regional scales and (2) how the number and composition of vegetation features affect model performance, particularly under high-biomass conditions. Through RFE and comparative modeling, we demonstrate that an optimal subset of features—including canopy height, spectral features, and textural features—can maximize model efficiency without sacrificing accuracy. These findings contribute a methodological basis for scalable, interpretable blue carbon monitoring and provide critical insights for ecosystem impact assessments in regions undergoing large-scale coastal development.

2. Materials

2.1. Study Area and Field Data Collection

The Maowei Sea is located in the southern part of Guangxi Zhuang Autonomous Region, along the northern coastline of Qinzhu Bay (Longitude: 108°28′–108°37′ E; Latitude: 21°48′–21°55′ N), and serves as a critical estuarine outlet for the Pinglu Canal. Situated near the Beibu Gulf, it lies at the transitional zone between tropical and subtropical climates, representing a typical coastal wetland ecosystem. The region spans approximately 15 km from east to west and 17 km from north to south, with a total area of about 135 km^2. The landscape is characterized by extensive shallow tidal flats, estuarine mangrove wetlands, and nearshore marine environments. Among these, the mangrove-covered area accounts for approximately 19.97 km^2. Figure 1 provides a high-resolution overview of the Maowei Sea mangrove estuary, including the delineated study area boundary, spatial distribution of mangroves (in red), and the locations of field plots (yellow). The figure also includes a regional locator map and field photographs to contextualize sampling activities and site conditions. The terrain is flat, with an average elevation of less than 5 m above sea level. The climate is characterized as a South Asian monsoon climate, with an average annual temperature of about 22 °C and annual precipitation of approximately 1800 mm, mostly concentrated between May and September during the rainy season. Mangroves are the dominant vegetation type in this region, with species such as *Aegiceras corniculatum*, *Kandelia candel*, and *Sonneratia apetala* being common [26]. These mangroves play a significant ecological role, including carbon sequestration, coastal protection, and maintaining biodiversity. Additionally, the Maowei Sea area experiences significant sediment deposition and is strongly influenced by tidal actions, which provide abundant nutrients for mangrove growth [27].

The Maowei Sea mangrove area, located in the northeastern Beibu Gulf of Guangxi, China, was selected as the study site due to its ecological representativeness, spatial heterogeneity, and significance in regional blue carbon assessment. As one of the largest and most biodiverse estuarine mangrove ecosystems in southern China, Maowei Sea is situated at the transitional zone between tropical and subtropical climates, where complex hydrological dynamics, seasonal tidal regimes, and anthropogenic disturbances converge. In recent years, the Maowei Sea has also become a hotspot for coastal infrastructure expansion, notably serving as the estuarine outlet of the Pinglu Canal—one of China's major inland waterway projects. This has led to increased land-use pressure, habitat fragmentation, and salinity fluctuations, making it an ideal natural laboratory for testing AGC estimation

frameworks under real-world environmental stressors. Given its ecological importance, policy relevance, and representativeness of subtropical Asian mangrove systems, the Maowei Sea offers valuable insights for scalable blue carbon monitoring and coastal management in the context of global change [28,29].

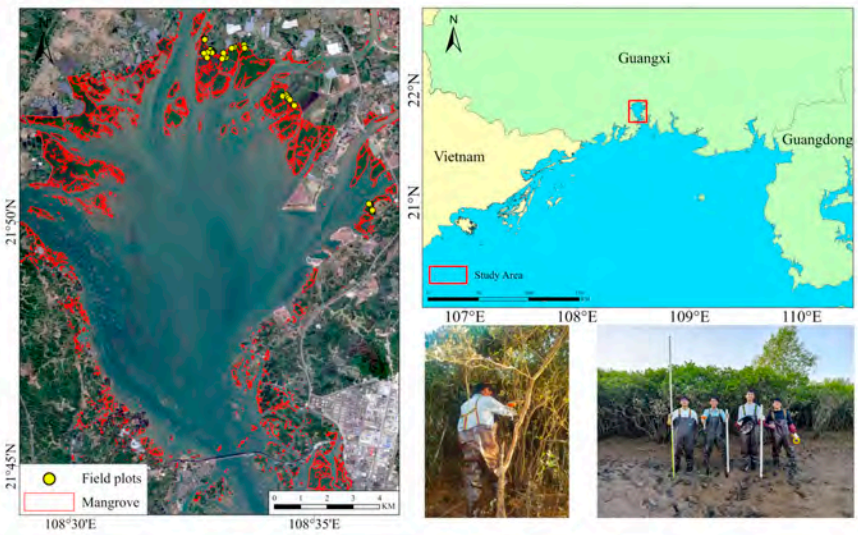


Figure 1. Study area location, mangrove distribution, and field sampling in the Maowei Sea region.

Before conducting the field surveys, we meticulously investigated the distribution ranges of mangrove species, tidal fluctuations, and low-tide timings in the study area. The research team conducted field investigations in the Maowei Sea region from 30 November to 4 December 2024. Survey points were chosen in accessible and safe areas according to the spatial distribution patterns of mangrove species. A total of 40 sample plots were evenly distributed throughout the study area. The dominant species in the study area are primarily *S. apetala*, *K. candel*, and *A. corniculatum*, and these sample plots were mainly located within the communities dominated by these species.

Due to significant variation in mangrove species composition, community succession stages, and plot accessibility, we tailored the size and shape of each sample plot to the characteristics of the respective communities [30]. In areas dominated by *S. apetala* and *K. candel*, where the distribution was relatively sparse, sample plots were set at 10 m × 10 m, aligning with the pixel size of Sentinel-2 imagery. Conversely, in areas with denser distributions of *A. corniculatum*, initial plot size was set at 5 m × 5 m and subsequently adjusted (multiplied by 4) to match the 10 m × 10 m scale of Sentinel data.

Within each sample plot, tree height was measured using a telescopic measuring pole and a handheld laser rangefinder. Meanwhile, the geographic coordinates (latitude and longitude) of each tree, along with the tree species, were recorded using RTK (Real-Time Kinematic) equipment. For *S. apetala* and *K. candel*, the diameter at breast height (DBH) was measured at 1.3 m and 0.5 m, respectively. For *A. corniculatum*, canopy diameter (CD), including the long and short radii of the canopy projection, was measured, assuming the canopy shape to be either circular or elliptical. In the field survey data, *S. apetala* exhibited relatively high tree heights, with a maximum of 9.1 m and an average of 4.55 m. *A. corniculatum* showed an average tree height of 2.82 m (range: 1.45–5.6 m) and an average crown width of 1.9 m (range: 0.56–4.36 m). For *K. candel*, the average tree height was 2.95 m (range: 1.53–5.7 m), and the average DBH was 7.99 (range: 1.9–19.7 cm). The mean tree density was 70 trees per 100 m^2, with a range of 17–132 trees per 100 m^2. The average AGC density from the field survey was 61.2 Mg C/ha. The maximum AGC density was 200.12 Mg C/ha, and the minimum AGC was 7.74 Mg C/ha.

2.2. Calculation of Mangrove Aboveground Carbon Stocks

Aboveground biomass (AGB) was estimated using species-specific allometric equations. Due to variations in the size, shape, and anatomical structure of mangrove species, as well as differences between the species for which the allometric equations were originally developed, the AGB of many mangrove species is often estimated using generalized allometric equations (Supplementary Table S2). To quantify the AGC stock in mangrove biomass, the AGB was multiplied by a carbon concentration factor. This factor is typically determined through compositional analysis of individual samples, using the dry combustion method (e.g., elemental analyzer). However, due to strict conservation policies in many areas, it is not feasible to fell trees for direct analysis. As such, the AGB of mangroves is commonly converted to carbon by applying a carbon conversion factor, which typically ranges from 0.46 to 0.50. In this study, the carbon concentration ratio for the AGB of mangroves was set at 0.48 [31].

2.3. Remote Sensing Data Collection and Processing

2.3.1. UAV-LiDAR Data

UAV-LiDAR point cloud data were acquired over the sampling area using a LiAir H800 (GreenValley, Beijing, China) laser scanner mounted on a DJI M350 RTK (DJI, Shenzhen, China) Unmanned Aerial Vehicle (UAV). The LiAir H800 operates at a wavelength of 905 nm, features 32 laser channels, and is capable of recording up to 640,000 points per second. The system supports up to 7 returns per pulse, with an estimated laser footprint diameter of approximately 5 cm at the flight altitude of 100 m. Data acquisition was conducted at a flight altitude of 100 m and a flight speed of 10 m/s. To ensure data quality and minimize interference, surveys were performed on 30 November 2024, at 3:00 PM, under clear weather conditions, avoiding persistent winds, and timed during low to mid-tide periods. All LiDAR data processing was conducted using LiDAR360 8.0 (GreenValley, Beijing, China) following a standardized workflow. Initially, noise points were filtered to remove outliers and erroneous returns. The denoised point cloud was subsequently classified into ground and non-ground points using an improved progressive Triangulated Irregular Network (TIN) densification filtering algorithm. Given the relatively flat topography of the mangrove site, the TIN ground filtering algorithm was configured with conservative parameters to enhance ground classification accuracy. Specifically, the maximum iteration angle was set to 6° and the maximum iteration distance to 1.2 m, as recommended for low-relief and vegetated terrain in the LiDAR360 8.0 User Guide. These settings help avoid over-interpolation across non-ground objects such as exposed roots or low-lying vegetation. Accurate ground classification is essential for generating a reliable Digital Elevation Model (DEM), which directly influences the precision of the Canopy Height Model (CHM). By optimizing the TIN parameters, we minimized topographic distortion and ensured that CHM values more accurately reflected true vegetation height. To further improve classification accuracy, ground points were manually reviewed and refined based on visual inspection of cross-sectional profiles, point cloud elevation consistency, and local terrain continuity. Misclassified vegetation or structure points (e.g., low shrubs, roots, or elevated boardwalks) were identified and corrected by referencing intensity values and spatial context. Based on the classified point cloud, a Digital Elevation Model (DEM) was generated from ground points to represent the bare-earth surface. The non-ground points were then normalized using the DEM to remove topographic effects. Subsequently, a Digital Surface Model (DSM) was derived from the normalized non-ground points to capture surface features, including vegetation canopies. To ensure consistency in height calculations, both the DEM and DSM were resampled to a spatial resolution of 10 × 10 m, which corresponds to the CHM grid size and matches the resolution of the satellite imagery. Using consistent

resolution between DEM and DSM is critical for minimizing spatial misalignment and ensuring reliable canopy height extraction. The CHM was then calculated using the Raster Calculator tool within LiDAR360 8.0, based on the equation CHM = DSM − DEM, representing vegetation height above the ground surface. All processing steps—including noise filtering, point cloud classification, DEM/DSM generation, and CHM extraction—were completed within a single software environment to ensure methodological consistency and analytical accuracy. All data processing procedures—including noise filtering, ground classification, DEM/DSM generation, and CHM calculation—were conducted in accordance with standard practices outlined in the LiDAR360 User Guide (https://www.lidar360.com/gvi/web/us/file/EN-LiDAR360UserGuide-ZH.pdf) (accessed on 9 January 2025), which provides detailed descriptions of the software tools and parameter settings.

2.3.2. Satellite RS Data

The remote sensing data utilized in this study include Sentinel-2 multispectral imagery, Sentinel-1 C-band synthetic aperture radar (SAR) data, and L-band PALSAR imagery. Given that the sample points were collected during 2024, remote sensing imagery from the same time period in 2024 was selected for analysis to ensure temporal consistency.

Sentinel-2 data were acquired from the Copernicus Open Access Hub (https://dataspace.copernicus.eu/explore-data) (accessed on 1 January 2025), specifically using Level-1C products of the Multispectral Instrument (MSI) from 30 November 2024. The data, provided as Top-of-Atmosphere Reflectance (TOA), were atmospherically corrected using the Sen2Cor processor (version 2.5.5) to produce Bottom-of-Atmosphere Reflectance (BOA) products. To maintain consistency in spatial resolution, the Sen2Res 1.1 plugin developed by the European Space Agency (ESA) was employed to resample all bands to a unified resolution of 10 m. The Sentinel-2 satellite provides 13 spectral bands, including red-edge bands that are particularly sensitive to vegetation characteristics such as mangrove species height, making them ideal for ecosystem monitoring. Moreover, the 5-day revisit cycle of Sentinel-2 enhances the probability of obtaining cloud-free images, which is particularly advantageous for monitoring tropical mangrove areas, often subject to persistent cloud cover [32].

In addition, Sentinel-1 C-band SAR data were used, acquired as part of the "Sentinel-1 SAR GRD" dataset. The data underwent several preprocessing steps, including the application of orbit files, removal of GRD boundary noise, thermal noise reduction, radiometric calibration, and terrain correction (orthorectification), yielding backscatter coefficients (σ°) in decibels (dB). SAR data are notably less sensitive to cloud cover, providing stable and complete imagery for the study area. Dual-polarized (VV + VH) data, from 5 December 2024, were selected for this study, with resampling to a 10 m resolution using the nearest neighbor method to ensure data accuracy.

Finally, PALSAR-2 data were obtained from the Google Earth Engine (GEE) platform. The PALSAR-2 ScanSAR Level 2.2 data had already undergone orthorectification and terrain radiometric correction, ensuring geometric accuracy. The geometric correction process ensured the spatial registration of the PALSAR-2 images, allowing them to align with other remote sensing datasets (e.g., Sentinel-1 and Sentinel-2) within the same coordinate system. This facilitated the accurate fusion of multi-source data. The dual-polarized (HH + HV) data, from 20 November 2024, were selected, and the data were resampled to 10 m using the nearest neighbor method to ensure consistency and suitability for analysis.

To ensure temporal consistency across multi-source datasets, all remote sensing data were selected based on the field sampling date, which was conducted on 30 November 2024. UAV-LiDAR and Sentinel-2 data were acquired on the same day, while PALSAR-2

and Sentinel-1 imagery were selected within a short time window (20 November and 5 December, respectively), thereby minimizing phenological and environmental variations.

For spatial alignment, all datasets—including UAV-LiDAR-derived CHM, Sentinel-1/2, and PALSAR-2 imagery—were reprojected to a unified coordinate system (WGS 84/UTM Zone 49N). Raster matching and alignment were then performed using the "Snap Raster" function in ArcGIS Pro 3.0.2 to ensure strict pixel-to-pixel correspondence among input layers.

To address resolution differences between sensors, all datasets were resampled to a common spatial resolution of 10 m. Bilinear interpolation was applied to continuous variables such as Sentinel-2 spectral reflectance and UAV-LiDAR canopy height, ensuring smooth spatial transitions and reducing pixelation artifacts. For radar backscatter layers from Sentinel-1 and PALSAR-2, nearest neighbor interpolation was used to preserve the physical integrity of the original backscatter values, which are sensitive to interpolation distortion. This tailored resampling strategy, along with consistent temporal and spatial alignment, ensures data compatibility and integrity for subsequent feature extraction and AGC model development. The details of all remote sensing datasets used in this study are summarized in Table 1.

Table 1. Spectral and textural features used for aboveground carbon (AGC) estimation and their definitions.

Feature Type	Variables	Definition	Reference
Spectral feature	Multispectral Bands	B2, B3, B4, B5, B6, B7, B8, B8a, B11, B12	[33]
	Normalized difference vegetation index (NDVI)	(B8 − B4)/(B8 + B4)	[34]
	Green normalized difference vegetation index (GNDVI)	(B8 − B3)/(B8 + B3)	[35]
	Enhanced vegetation index (EVI)	2.5 [(B8 − B4)/B8 + 6B4 − 7.5B2 + 1]	[36]
	Ratio Vegetation Index (RVI)	B8/B4	[37]
	Normalized Difference Water Index (NDWI)	(B3 − B8)/(B3 + B8)	[31]
	Modified Normalized Difference Water Index (MNDWI)	(B3 − B11)/(B3 + B11)	[38]
	Difference Vegetation Index (DVI)	B8 − B4	[39]
	Forest Discrimination Index (FDI)	B8 − B3 − B4	[40]
	Canopy leaf greenness index (Clg)	B8/B3 − 1	[41]
	Canopy Leaf Greenness—Red Edge 1 (Clg-re1)	B5/B3 − 1	[41]
	Canopy Leaf Greenness—Red Edge 2 (Clg-re2)	B6/B3 − 1	[41]
	Canopy Leaf Greenness—Red Edge 3 (Clg-re3)	B7/B3 − 1	[41]
	Inverted Red-Edge Chlorophyll Index (IRECI)	(B7 − B4)/(B5/B6)	[42]
	Medium Resolution Imaging Spectrometer (MERIS) terrestrial chlorophyll index (MTCI)	(B6 − B5)/(B5 − B4)	[43]
	Red-edge Normalized Difference Vegetation Index 1 (NDVIre1)	(B8 − B5)/(B8 + B5)	[44]
	Red-edge Normalized Difference Vegetation Index 2 (NDVIre2)	(B8 − B6)/(B8 + B6)	[44]
	Red-edge Normalized Difference Vegetation Index 3 (NDVIre3)	(B8 − B7)/(B8 + B7)	[44]
	Pigment Specific Simple Ratio (PSSRa)	B7/B4	[45]
	VV, VH, VV + VH, VV–VH	Polarization backscatter coefficients and indices calculated based on the dual-polarization SAR data (VV, VH) from Sentinel-1.	[21]
	HH, HV, HH + HV, HH–HV	Polarization backscatter coefficients and indices calculated based on the dual-polarization SAR data (HH, HV) from ALOS PALSAR-2.	[21]

Table 1. *Cont.*

Feature Type	Variables	Definition	Reference
Textural feature	Co-occurrence measures mean (CMM) Co-occurrence measures variance (CMV) Co-occurrence measures homogeneity (CMH) Co-occurrence measures contrast (CMC) Co-occurrence measures dissimilarity (CMD) Co-occurrence measures entropy (CME) Co-occurrence measures second moment (CMSM) Co-occurrence measures correlation (CMC)	Haralick textural variables derived from Sentinel-2 bands (B2, B3, B4, B5, B6, B7, B8, B8a, B11, B12), Sentine-1(VH, VV), and PALSAR-2(HH, HV).	[31]

3. Methods

The overall workflow of the AGC estimation framework is illustrated in Figure 2.

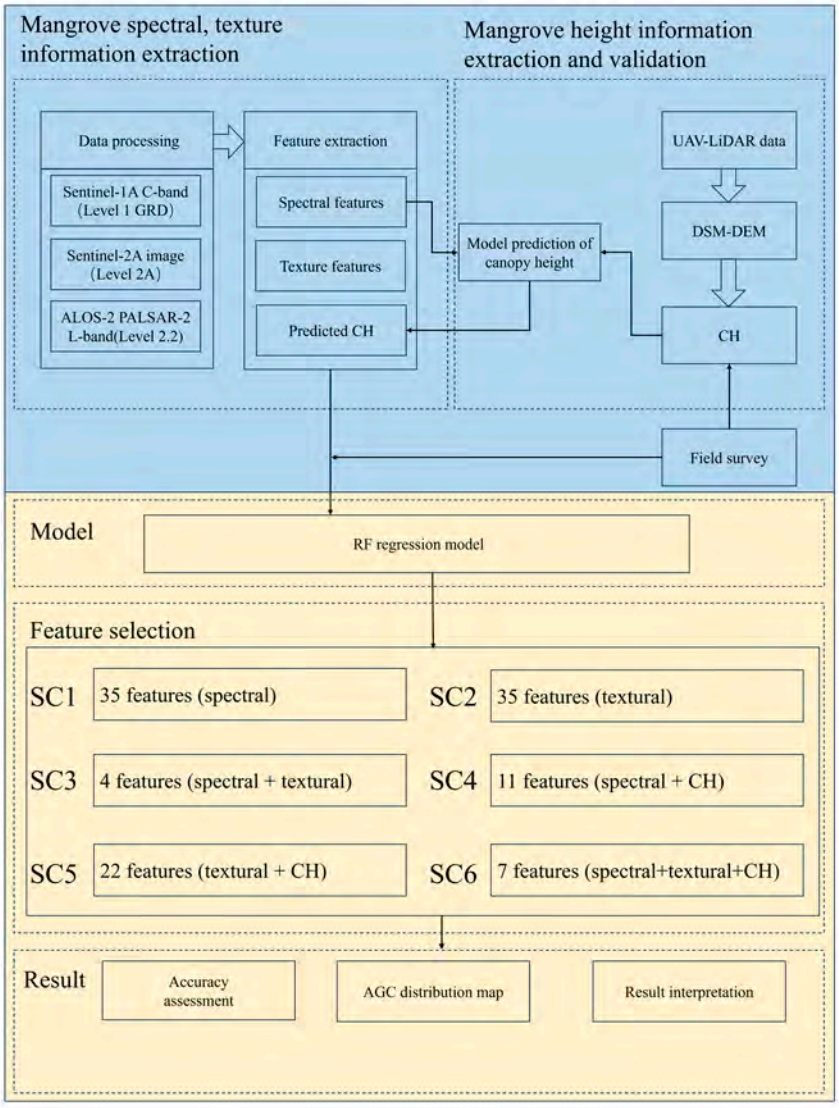


Figure 2. Workflow of AGC estimation in mangroves using UAV-LiDAR and multi-source satellite data fusion.

3.1. Mangrove Extent Extraction

To delineate the mangrove distribution within the Maowei Sea area, we adopted the Improved Mangrove Mapping Algorithm (IMMA) proposed by Zhao et al. [46], which extracts classification rules from trained RF models to produce transparent and reproducible mangrove maps. This method identifies mangrove extents based on a combination of Sentinel-2-derived spectral indices (e.g., MVI, NDI4, B8/B2) and elevation constraints. The rule set used (e.g., B12 < 0.06 and B8/B2 > 3.50 and elevation < 4.70 and MVI > 2.92 and NDI4 < 0.07) was derived from knowledge distillation of high-accuracy black-box models. The IMMA method achieved an overall accuracy of 82.3% for the coastal region of China and has demonstrated excellent generalization capability and robustness against false positives in complex land cover mosaics. Importantly, the IMMA algorithm has also been shown to mitigate the influence of mixed pixels, particularly in transitional zones such as mangrove–water or mangrove–mudflat boundaries. By utilizing interpretable rule sets and carefully selected spectral ratios (e.g., B8/B2 > 3.5), the IMMA reduces misclassification caused by spectral confusion between mangroves and spectrally similar surrounding land cover types. This advantage has been explicitly demonstrated in the original study, where the IMMA exhibited greater robustness than black-box models in ecologically complex or fragmented coastal areas. Based on this method, we generated a binary mangrove mask at 10 m resolution and subsequently validated and refined the results through visual inspection and reference to high-resolution imagery.

3.2. Extraction of Vegetation Feature

3.2.1. Spectral Feature

To characterize the spectral properties of mangrove canopies, a total of 36 features were extracted, including multispectral reflectance bands and vegetation indices from Sentinel-2 imagery, as well as backscatter coefficients from Sentinel-1 and PALSAR-2 SAR data. Specifically, visible, red-edge, and near-infrared bands (e.g., B2–B8A), along with indices such as the normalized difference vegetation index (NDVI) and Modified Vegetation Index (MVI), were employed to capture information related to chlorophyll content, canopy density, and water stress. Additionally, VV and VH polarizations from Sentinel-1, and HH and HV polarizations from PALSAR-2, were used to infer canopy moisture and structural characteristics [47]. These spectral variables were selected based on their documented relevance to vegetation structure and biomass in mangrove ecosystems, thereby supporting species differentiation, canopy condition assessment, and improved AGC estimation (Table 1).

3.2.2. Textural Feature

To capture spatial heterogeneity within mangrove canopies, textural metrics were calculated from Sentinel-1, Sentinel-2, and PALSAR-2 imagery using the Gray Level Co-occurrence Matrix (GLCM) approach, following standard protocols [48]. These features are particularly valuable in distinguishing structural variation in dense vegetation, where spectral responses may saturate. By encoding canopy roughness, spatial arrangement, and internal texture, GLCM metrics provide complementary structural information that enhances AGC modeling accuracy, especially in mixed-species or structurally diverse mangrove stands (Table 1).

3.2.3. Canopy Height

CH was derived from UAV-based LiDAR data, which provides high-density point clouds for precise vegetation structure characterization. The CH was calculated by subtracting the DEM from the DSM. To ensure the reliability of the LiDAR-derived CH, we

validated it using ground measurements (Figure 3). All of the LiDAR point clouds were first tessellated into grids with a cell size of 10 × 10 m, maintaining the same original point as that of the Sentinel-1 and Sentinel-2 imagery. We finally obtained 10,000 candidate LiDAR samples with a size of 10 × 10 m. For enhanced regional CH estimation, we integrated canopy spectral features, dual-polarization synthetic aperture radar (SAR) data (VV and VH polarizations), and employed an RF regression model. This approach follows established methodologies to ensure both the robustness and comparability of CH data for accurate AGC estimation. The performance of the CH model was evaluated with R^2 = 0.71 and RMSE = 1.84 m (Supplementary Figure S2), indicating good predictive accuracy. Further details are provided in the Supplementary Materials.

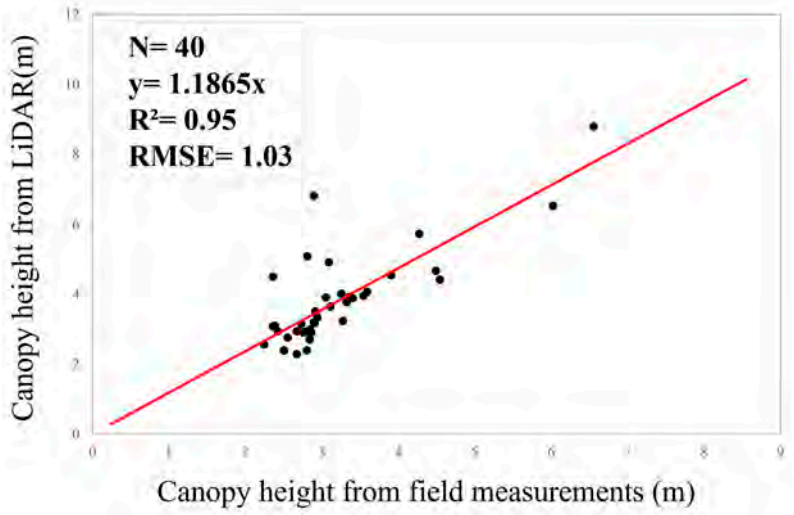


Figure 3. Comparison of canopy height (CH) from LiDAR and field measurements. The black dots represent individual sample plots, and the red line indicates the fitted linear regression between LiDAR-derived and field-measured canopy height.

3.3. AGC Estimation Model

In this study, AGC estimation was performed using an RF regression model, integrating spectral, textural, and canopy height features derived from Sentinel-1, Sentinel-2, PALSAR-2, and UAV-LiDAR data. The model was trained and optimized using grid search and cross-validation to fine-tune key hyperparameters, ensuring robust performance. Feature importance analysis was conducted to assess the contribution of different variables to AGC prediction (Figure 2).

3.3.1. Feature Selection and Machine Learning Algorithms

The selection of appropriate variables is essential for constructing accurate AGC models. Initial variable selection was based on previous research and domain expertise, with a summary of potentially effective features. However, due to geographical and vegetation differences across study areas, feature selection within a machine learning framework can enhance model efficiency and improve predictive accuracy. In this study, RFE was used for variable selection [49,50]. During the RFE process, an external estimator assigns weights to the features and trains on the initial feature set to assess their importance. The least important feature is removed, and the process is repeated on the pruned set until optimal feature selection is achieved. RF was chosen as the estimator. Feature selection was optimized through cross-validation, and the optimal subset was determined using the coefficient of determination (R^2) and root mean square error (RMSE) metrics derived from five-fold cross-validation.

RFE was selected in this study for several reasons. First, it is capable of handling high-dimensional input data and is particularly effective at reducing feature redundancy, which is common in multi-source remote sensing datasets. Second, unlike filter-based or univariate selection methods, RFE considers feature interactions and nonlinear relationships, which are crucial when modeling AGC using spectral, textural, and structural variables. Third, RFE is model-agnostic and integrates well with tree-based learning algorithms such as RF, which provide reliable internal feature importance rankings. These advantages make RFE particularly well suited for identifying robust and compact feature subsets in ensemble-based regression models such as RF.

RF was employed to estimate AGC in mangrove ecosystems. As an ensemble learning method, RF excels in handling high-dimensional datasets and modeling complex relationships between predictor variables [51]. RF has demonstrated strong predictive performance and stability in biomass modeling tasks. The model works by generating multiple decision trees through bootstrap resampling and aggregating their results, which enhances the model's generalization ability and reduces overfitting. To optimize RF model performance, grid search was used for hyperparameter tuning. This method explores a predefined range of hyperparameters and evaluates different combinations using cross-validation, ensuring that the optimal parameter set is selected. This process improves the model's predictive accuracy and its ability to reliably estimate AGC in mangroves.

3.3.2. Accuracy Assessment

In this study, all 40 samples were randomly divided into a training set (80%) and a testing set (20%) and applied to the RF model. Although the overall sample size is relatively small, this 80/20 partition strategy is widely adopted in mangrove carbon estimation studies [24,52,53]. To further mitigate the limitations associated with a small testing set, a five-fold cross-validation (CV) approach was employed during the training process to optimize the model's hyperparameters and assess generalization performance. This strategy ensures that each sample is used for both training and validation across multiple iterations, thereby enhancing the robustness of model evaluation and minimizing overfitting risk. As noted by Pedregosa et al. [54], cross-validation is an essential tool in small-sample scenarios, offering reliable performance estimation by generating multiple train/test splits from limited data. The Scikit-Learn library was utilized to fine-tune the optimal parameters of the machine learning model. Model performance was assessed using the coefficient of determination (R^2) and RMSE metrics to compare the effectiveness of different feature combinations. The R^2 metric evaluates how well the model's predictions fit the observed values, while RMSE quantifies the prediction error. The consistent improvements observed across various feature combinations further support the validity and stability of the evaluation results despite the relatively small testing set.

$$R^2 = 1 - \frac{(y_i - \hat{y}_i)^2}{(y_i - \overline{y})^2} \quad (1)$$

$$RMSE = \sqrt{\frac{\sum_{i=1}^{n}(y_i - \hat{y}_i)^2}{n}} \quad (2)$$

where y_i and $\overline{y_i}$ represent the observed values and the mean of the AGC, respectively, while $\hat{y}_i$ denotes the predicted values. To further analyze the impact of different vegetation feature combinations and machine learning approaches on the estimation of AGC, we computed the average R^2 values for different feature subsets. All analyses were conducted using Python software (version 3.9).

4. Results

4.1. Modeling Results Comparison Between Different Features

In this research, features were screened using RFE, and five-fold cross-validation was employed to evaluate the accuracy of different data combinations. The features used are derived from three types of data: spectral features, textural features, and canopy height. The estimation capabilities of the three types of data and the changes in model accuracy before and after performing RFE were assessed separately by performing AGC estimation with single or multiple data combinations. The results are summarized in Table 2 and illustrated by scatterplots in Figure 4.

Table 2. Test results for various feature combinations and their number of features calculated based on Recursive Feature Elimination (RFE) feature selection.

Data Combinations	ALL Features			Selected Features		
	R^2	RMSE (Mg/ha)	Number	R^2	RMSE (Mg/ha)	Number
Spectral	0.49	17.16	36	0.50	17.17	35
Textural	0.14	47.23	40	0.15	47.77	35
Spectral + Textural	0.62	17.81	76	0.64	14.59	4
Spectral + CH	0.56	19.16	37	0.63	14.77	11
Textural + CH	0.23	19.03	41	0.24	21.12	22
Spectral + Textural + CH	0.72	17.33	77	0.75	14.18	7

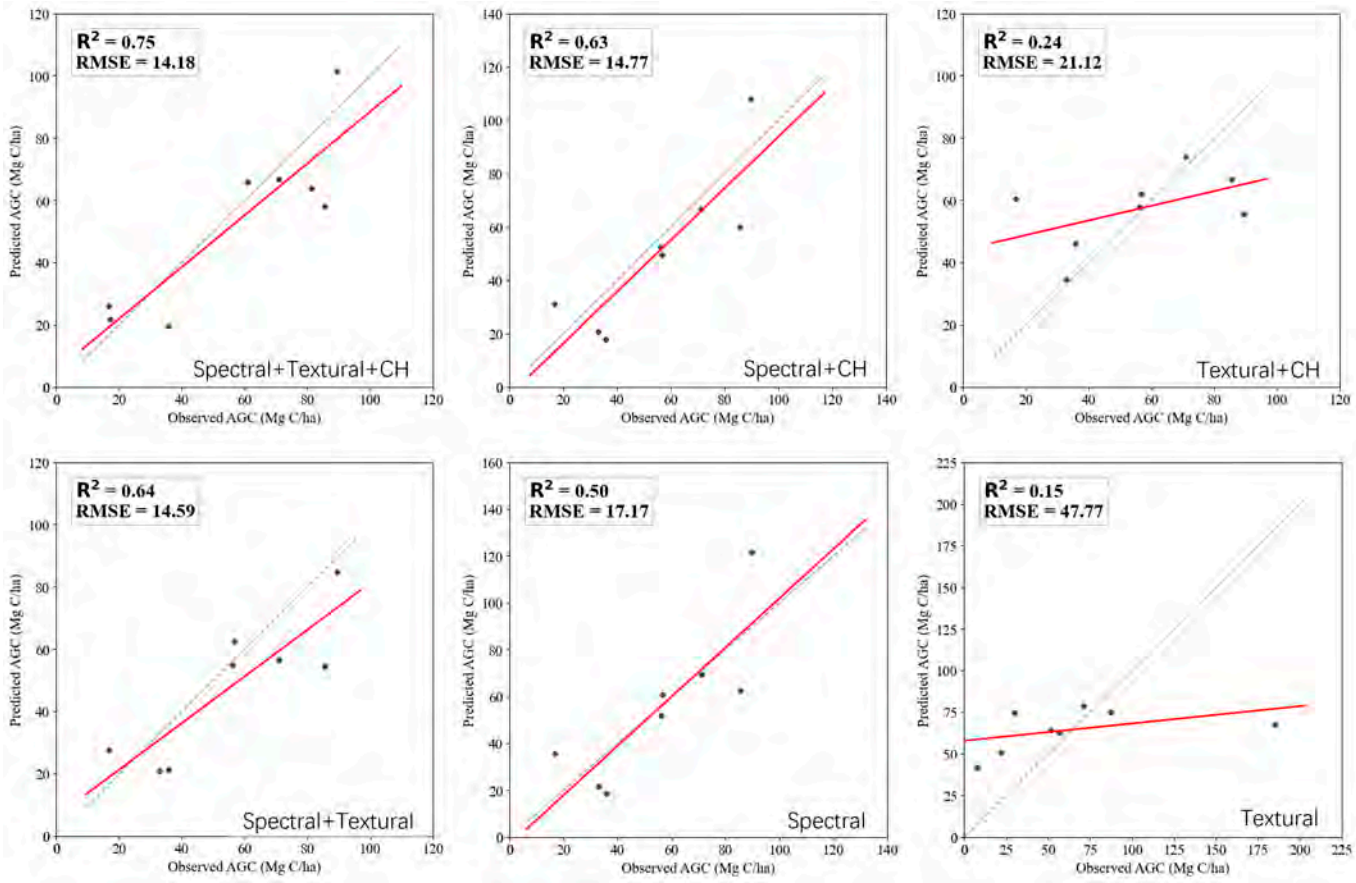


Figure 4. Comparison of AGC prediction models using different combinations of predictor variables. The black dots represent the testing samples, the red line indicates the fitted regression line between predicted and observed AGC, and the dotted line represents the 1:1 reference line.

Among all tested feature combinations, the integration of spectral and textural features yielded notable improvements in model performance compared to individual sources. For instance, the spectral + textural model achieved an R^2 of 0.64 and an RMSE of 14.59 Mg/ha after RFE, outperforming the use of spectral features alone (R^2 = 0.50, RMSE = 17.17 Mg/ha) or textural features alone (R^2 = 0.15, RMSE = 47.77 Mg/ha). This suggests that incorporating spatial variability through texture metrics enhances the sensitivity of spectral-based models to vegetation structure. While the improvement from spectral to spectral + CH in terms of R^2 (from 0.50 to 0.63) might appear moderate, the RMSE significantly decreased from 17.17 to 14.77 Mg/ha, clearly indicating a meaningful enhancement in prediction accuracy. Moreover, this model required fewer features (11 features) after RFE, improving model simplicity and generalization. The addition of CH led to further substantial improvements. The model integrating spectral, textural, and CH features achieved the best performance (R^2 = 0.75, RMSE = 14.18 Mg/ha) with only seven RFE-selected features. This indicates that CH, as a structural variable directly related to vertical biomass distribution, plays a dominant role in improving AGC prediction. Notably, even though texture or CH alone contributed limitedly when used in isolation (e.g., CH + texture yielded R^2 = 0.24), their synergistic effect with spectral data significantly enhanced model accuracy. Figure 4 provides a visual comparison of predicted vs. observed AGC values across different feature combinations. Models incorporating CH demonstrated a closer alignment with the 1:1 reference line, smaller dispersion, and notably lower prediction errors, further confirming the robustness and reliability of CH as a critical variable.

In summary, these results underscore the crucial role of structural metrics, especially canopy height, in addressing signal saturation issues in high-biomass mangrove forests. The integration of spectral, textural, and structural features provides a more comprehensive depiction of canopy heterogeneity, enabling improved AGC estimation and greater generalization capability across spatially diverse regions.

4.2. Mangrove AGC Map of Maowei Sea

The total AGC of the Maowei Sea mangroves is estimated at 88,363.73 metric tons, with a mean AGC density of 53.01 Mg C/ha (Figure 5). Spatial distribution analysis reveals that higher AGC values are concentrated in the northwestern coastal zones, particularly in Kangxiling and Tuanhe Island, where mature, planted *S. apetala* stands with well-developed canopy structures dominate, contributing significantly to the carbon stock. In contrast, the *S. apetala* communities in the northwestern part of Jianxinwei have mainly been established through natural regeneration from propagules dispersed by tidal currents from Kangxiling. These younger and more sparsely distributed stands exhibit relatively lower AGC. Meanwhile, the eastern part of Jianxinwei is primarily occupied by mature *A. corniculatum* communities, interspersed with scattered *K. candel*, resulting in higher AGC values due to well-structured canopy layers and substantial biomass accumulation. Compared to existing regional or global AGC datasets derived from moderate-resolution satellite imagery (e.g., 30 m or coarser), our final AGC map offers improved spatial detail (10 m resolution) and enhanced structural sensitivity by incorporating UAV-LiDAR-derived canopy height. This fine-scale mapping allows better identification of intra-patch variability and supports localized ecosystem management and impact assessment.

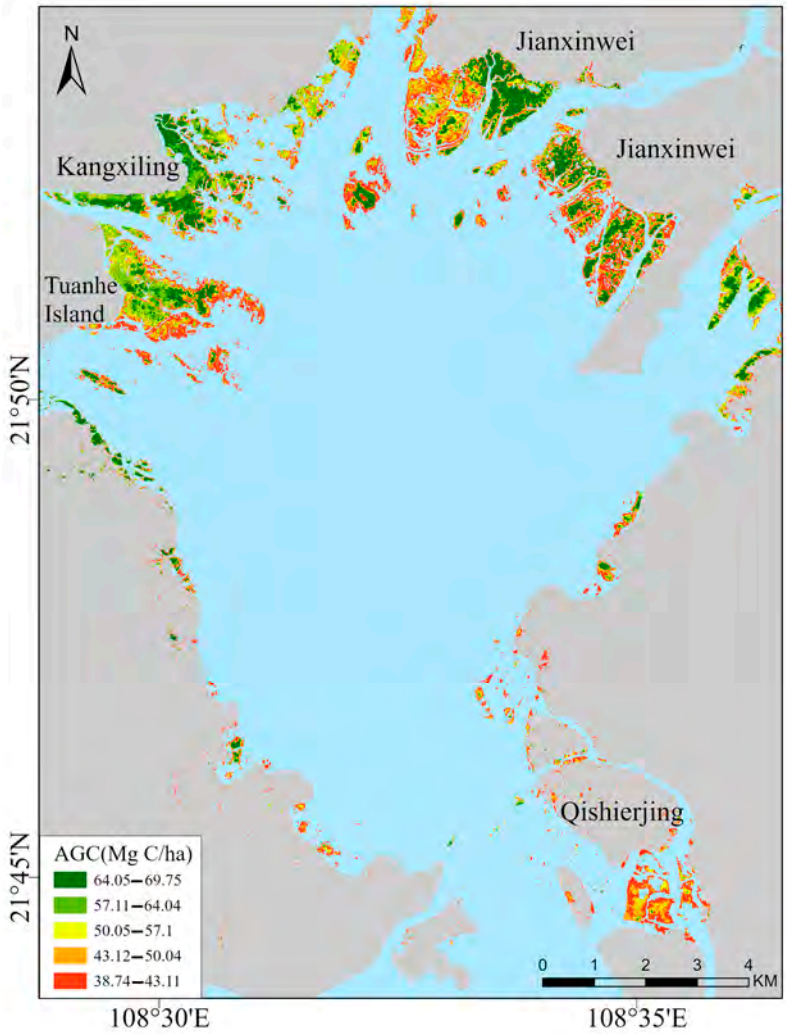


Figure 5. Mangrove AGC map of Maowei Sea.

5. Discussion

5.1. Contribution of Canopy Height from UAV-LiDAR to Multi-Source AGC Modeling in Mangroves

Optical and SAR remote sensing have been widely applied in forest biomass estimation, but both suffer from signal saturation effects in high-biomass regions due to their inherent physical limitations. Optical sensors (e.g., Landsat and Sentinel-2) estimate biomass through empirical relationships between spectral reflectance and vegetation indices such as the NDVI. However, in dense canopy forests where the crown is fully closed, the reflectance signal becomes saturated, weakening its responsiveness to variations in canopy structure [55]. Similarly, SAR sensors (e.g., Sentinel-1 and ALOS PALSAR) use backscatter intensity to estimate biomass but are constrained by limited penetration capabilities: the C-band saturates around 50–80 Mg/ha and the L-band around 100–150 Mg/ha, failing to resolve structural complexity in high-biomass stands [56]. Although texture features derived from GLCM, such as contrast and entropy, can partially compensate for spectral and radar limitations—especially in low-to-moderate biomass forests—their sensitivity also diminishes in highly homogeneous closed canopies [57,58]. As such, biomass estimation methods that rely solely on spectral or SAR data often encounter accuracy bottlenecks in mangrove ecosystems with high biomass density.

To address these limitations, recent studies have incorporated structural parameters—especially canopy height—to enhance model responsiveness to biomass varia-

tion. Satellite LiDAR systems such as GEDI have made it possible to acquire canopy height measurements at global scales for AGC estimation. For instance, Zhao et al. integrated GEDI-derived canopy height with Sentinel-2 spectral features to estimate urban biomass, achieving an R^2 of 0.58 and RMSE of 14.25 Mg/ha [59]; Tian et al. reported improved accuracy (R^2 = 0.75, RMSE = 17.34 Mg/ha) in a similar fusion framework over forested regions in Fujian, China [60]. However, GEDI's spatial sampling is limited by its orbital characteristics: with a footprint diameter of ~25 m and inter-track spacing exceeding 600 m, GEDI provides discrete observations that are insufficient to capture the structural heterogeneity of mangrove forests. In areas with rapid structural variation or mixed-species assemblages, the performance of GEDI-based estimation can be suboptimal. Furthermore, in forests with canopy heights exceeding 20 m, multiple scattering effects and attenuated ground returns can introduce uncertainty in height retrieval [15,61]. In contrast, UAV-based remote sensing offers centimeter-level spatial resolution and can capture fine-scale canopy structure and height variation. In the Maowei Sea region, Tian et al. achieved an AGB estimation accuracy of R^2 = 0.83 (RMSE = 22.76 Mg/ha) by integrating UAV-derived spectral, structural, and texture features [24]. Dhakal et al. reported even higher accuracy in agricultural applications (R^2 = 0.93, RMSE% = 15.97%) [62]. UAV-LiDAR generates dense point clouds capable of accurately delineating both terrain and canopy heights, thereby complementing the limitations of spectral and SAR data in densely vegetated environments. Nevertheless, due to limited flight efficiency and coverage, UAV approaches alone are insufficient for large-scale carbon stock mapping.

To achieve both high estimation accuracy and spatial generalization, this study integrates UAV-LiDAR-derived CH with multi-source satellite data (Sentinel-1, Sentinel-2, and ALOS PALSAR-2) for regional-scale modeling of AGC in the Maowei Sea mangrove ecosystem. Unlike conventional upscaling frameworks that propagate AGB estimates sequentially from field plots to UAV data and subsequently to satellite imagery [63,64], this study adopts a structure-oriented approach. High-resolution CH data obtained from UAV-LiDAR in representative subregions are fused with spectral features to establish predictive models, enabling the interpolation of canopy height across the broader mangrove landscape.

Rather than transferring biomass estimates across scales, our framework leverages canopy height—a physiologically meaningful and directly observable structural variable—as the core modeling input (Figure 6). CH was a key structural parameter in allometric equations—the model maintains sensitivity to biomass variation even in high-biomass mangrove stands, thus mitigating the saturation effects commonly observed in NDVI-based optical methods and polarization backscatter coefficients. By incorporating CH, the model maintains sensitivity to vertical structural variation, which is often lost in traditional reflectance- or backscatter-driven approaches. The contribution of UAV-derived CH is threefold: (1) it remains responsive in optically saturated or SAR-penetration-limited zones; (2) it bridges the scale gap between ground plots and coarse-resolution satellite data; and (3) it enhances model robustness across heterogeneous canopy conditions.

Our fusion-based model achieved an R^2 of 0.75 and RMSE of 14.18 Mg/ha, outperforming satellite-only approaches, such as the approach of Pham et al., who reported R^2 = 0.63 and RMSE = 25.08 Mg/ha. While prior studies integrating UAV and satellite data [63,64] (Niu et al., 2024: R^2 = 0.74; Wang et al., 2019: R^2 = 0.67) demonstrated improved accuracy, they relied on multi-level AGB regression, which may introduce cumulative uncertainty. In contrast, our approach reduces such error propagation by directly modeling canopy structure rather than AGB, thus improving generalizability and resilience to ecological heterogeneity. Table 3 summarizes the performance and scale applicability of three typical modeling strategies: (1) satellite-only models (R^2 = 0.58–0.75), (2) UAV-only approaches with high local accuracy (R^2 up to 0.93) but limited spatial extent, and (3) UAV–satellite fu-

sion methods, which offer an effective compromise between accuracy and scalability. These results underscore the advantages of structure-driven, cross-scale modeling for reliable estimation of AGC in mangrove ecosystems.

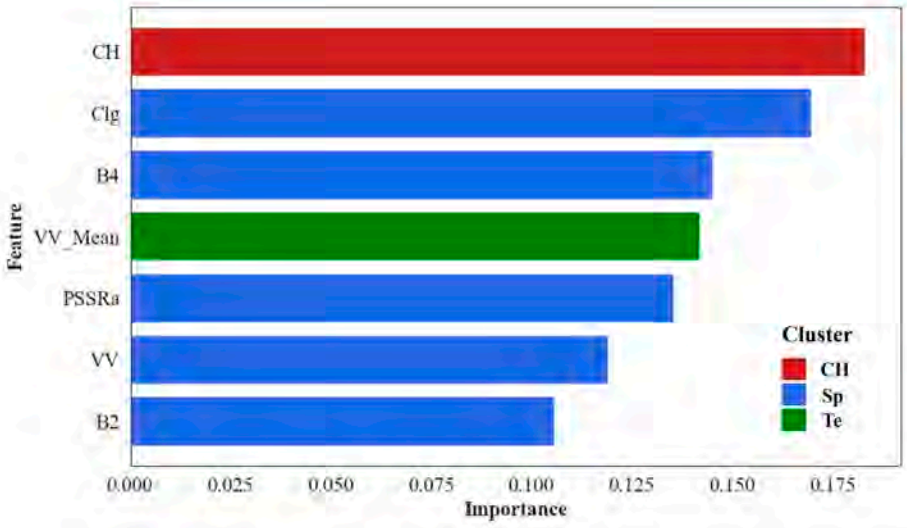


Figure 6. Feature importance for AGC estimation in mangroves.

Table 3. Comparison of sensor types in terms of accuracy and spatial scale for estimating aboveground biomass across vegetation types.

Sensor Type	Scale	Accuracy	Reference
Satellite	Regional	R^2 = 0.58; RMSE = 14.25 Mg/Ha	Zhao et al. [59]
		R^2 = 0.75; RMSE = 17.34 Mg/Ha	Tian et al. [60]
UAV	Local	R^2 = 0.83; RMSE = 22.76 Mg/Ha	Tian et al. [24]
		R^2 = 0.93; RMSE% = 15.97%	Dhakal et al. [62]
Satellite + UAV Fusion	Regional	R^2 = 0.74; RMSE = 1.84 Mg/Ha	Niu et al. [53]
		R^2 = 0.62; RMSE = 50.36 Mg/Ha	Wang et al. [64]

The differences in model accuracy across studies can be attributed to several key factors. First, satellite-only models often suffer from signal saturation in dense mangrove canopies due to limited sensitivity of spectral indices and radar backscatter at high biomass levels, particularly in monospectral NDVI-based approaches or C-band SAR applications. Second, while UAV-only methods yield high local accuracy, they are constrained by limited spatial coverage and lack of regional generalizability. Third, many UAV–satellite fusion studies adopt hierarchical regression frameworks that estimate AGB in stages (e.g., field-to-UAV and UAV-to-satellite), which can compound uncertainty at each step due to error propagation and scaling mismatch.

In contrast, our structure-oriented modeling approach directly integrates UAV-derived CH into satellite-scale models, using canopy height as a physiologically grounded proxy that is less prone to saturation and more robust to interspecies variation. This allows for continuous, spatially coherent AGC estimation across structurally heterogeneous mangrove landscapes. Moreover, the use of RFE for feature selection minimizes collinearity and redundancy, further enhancing model robustness compared to conventional fusion frameworks. These methodological distinctions help explain the improved performance of our model (R^2 = 0.75, RMSE = 14.18 Mg/ha) relative to existing approaches.

While the proposed UAV–satellite fusion framework demonstrates strong performance at the regional scale, its scalability to national or continental levels requires further consideration, particularly in light of the limited spatial coverage of UAV platforms. One promising pathway is to use UAV-LiDAR as a source of calibration data to support the training and

validation of large-scale models built upon wall-to-wall satellite observations. In this context, UAV-derived canopy height samples collected from representative ecological zones can serve as structural references for extrapolating forest metrics across broader extents. This concept has been increasingly recognized in recent studies, where UAV or airborne LiDAR data are used to calibrate or guide satellite-based forest structure modeling. For example, Jian et al. demonstrated that UAV-LiDAR data could effectively calibrate stereo optical satellite imagery (ZY-3) for accurate canopy height estimation, underscoring the value of UAV data as local reference sources in large-scale applications [65]. Similarly, Wang et al. integrated airborne LiDAR and GEDI waveform data to calibrate large-area canopy height models using Sentinel-2 spectral features [66]. In a national-scale application, Li et al. utilized airborne LiDAR-derived canopy height data from the Japan Forestry Agency, in combination with multi-source satellite inputs (Sentinel-2, ALOS-2 PALSAR, and SRTM), to train RF models and generate a 10 m resolution canopy height map across Japan [67]. These studies collectively highlight how high-resolution structural references, even if spatially sparse, can be effectively leveraged to enable scalable and accurate forest structure estimation. With the growing availability of high-quality satellite and airborne datasets, such hybrid frameworks offer a promising foundation for extending AGC monitoring to national or even continental scales in mangrove and other forest ecosystems.

Nevertheless, the broader application of this UAV–satellite fusion framework is subject to several spatial, logistical, and economic constraints. First, the spatial applicability of the current model is primarily limited to coastal mangrove zones with relatively similar species composition, canopy structures, and tidal regimes as the training region (e.g., Maoweihai in Guangxi). Extrapolating the model to ecologically distinct mangrove systems—such as those in tropical Southeast Asia or arid coastal regions—may require re-calibration or re-training with locally representative data. Second, UAV-LiDAR campaigns, though cost-effective at small scales, remain logistically demanding and expensive for large-scale deployment, especially in remote or protected areas where flight permissions are restricted. The acquisition cost and time investment for UAV-based canopy height mapping may pose practical barriers to widespread adoption. Furthermore, harmonizing datasets from different satellite sensors and UAV platforms across seasons introduces additional technical complexity. Therefore, while the proposed framework is promising in regional applications and scalable with proper calibration, its broader implementation necessitates careful consideration of ecological representativeness, cost-efficiency, and data integration feasibility. Future work could explore semi-automated UAV data acquisition pipelines, cross-region transfer learning, and integration of sensors (e.g., LiDAR-equipped satellites) to further reduce these bottlenecks and enhance model generalizability.

5.2. Contributions of Multidimensional Features to Mangrove AGC Estimation and Implications of Feature Selection

While CH plays a dominant role in AGC estimation, spectral and textural features remain indispensable for capturing complementary information on vegetation composition, physiological status, and surface structure—particularly under species-specific ecological conditions. As shown in the feature importance analysis (Figure 6), several spectral indices and texture metrics make non-negligible contributions to AGC prediction when used in conjunction with CH, offering a multidimensional representation of mangrove canopy properties. However, the predictive influence of these features varies with canopy density, species-specific traits, and structural heterogeneity.

In this study, the B4 band, B2band, and VV band have relatively small direct impacts on mangrove carbon stock and generally exhibit negative correlations (Figure 7). The B4 primarily reflects vegetation's photosynthetic activity, and its reflectance is closely related to chlorophyll content [68]. Healthy vegetation typically absorbs more red light, while

vegetation in poorer health reflects more red light, resulting in lower carbon stock. Therefore, this band shows a negative correlation with carbon stock. The B2 band, located in the blue region of the visible spectrum, is strongly affected by chlorophyll absorption and atmospheric or surface water scattering, which limits its reliability in vegetated and coastal environments [69]. In mangrove ecosystems, the combination of intensified specular reflection from tidal waters and high chlorophyll absorption further attenuates blue reflectance, limiting the utility of B2 in estimating AGC, contributing less to AGC estimation, and negatively correlating with AGC (Figure 6). The VV band from SAR data captures canopy density and surface roughness, offering useful structural insights for AGC estimation. However, its limited penetration capability in high-biomass forests results in saturation effects, reducing its standalone predictive power. Despite this, VV-based features remain valuable when integrated with spectral and canopy height metrics, contributing to improved AGC modeling under multi-source data frameworks [70]. In low-density mangrove forests, radar wave reflectance is typically enhanced, thus showing a negative correlation with carbon stock. However, despite the small contribution of these bands to carbon stock estimation individually, they still provide supplementary information in the fusion of multi-source data [71], particularly within different mangrove species' growth environments (Figure 7). This indicates that, although spectral and radar bands contribute limitedly in certain environments, under specific ecological conditions, they remain valuable in enhancing the reliability of carbon stock estimation.

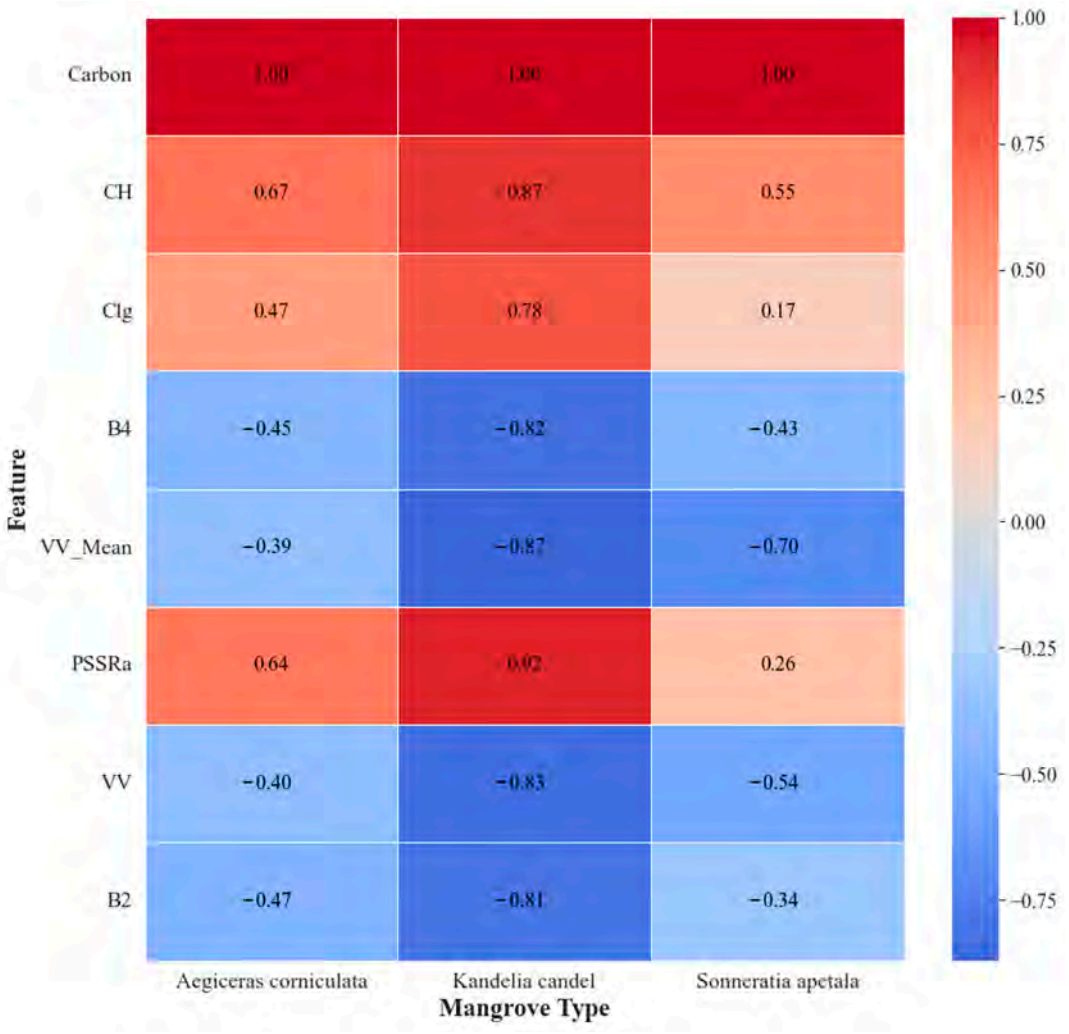


Figure 7. Correlation between features and mangrove types for AGC.

As shown in Figure 7, different mangrove species exhibit distinct correlation patterns with key predictive features, indicating species-specific sensitivities in AGC estimation. For instance, *K. candel* shows strong positive correlations with CH (0.87), Clg (0.78), and PSSRa (0.92), highlighting the effectiveness of canopy height and chlorophyll-related indices for this species. In contrast, *S. apetala* demonstrates a weak positive correlation with Clg (0.17) but a strong negative correlation with VV_Mean (–0.70), suggesting that increased radar texture variability corresponds to lower AGC in dense, structurally uniform stands. This may reflect signal saturation and reduced canopy heterogeneity in *S. apetala*-dominated areas, limiting the utility of conventional spectral and textural features. In monoculture zones where a single species dominates, the discriminative capacity of texture-based metrics (e.g., CMV and CMSM) is likely reduced due to the lack of inter-species structural variability. Previous studies have shown that texture features are more effective in mixed-species mangrove stands with varying leaf morphology and branching complexity [72]. Therefore, species homogeneity may constrain the effectiveness of textural features, underscoring the importance of integrating structural and physiological indicators in AGC modeling for such environments.

Previous studies have typically employed extensive sets of multi-source features—including spectral, textural, and structural parameters—to maximize the predictive potential for estimating mangrove AGC [25,73]. However, these studies consistently encountered significant redundancy due to high collinearity among selected variables, limiting the effective utilization of the information embedded within these datasets. Consequently, only a small subset of features genuinely contributed to accurate AGC estimation, with many others offering minimal incremental value. In contrast, our study systematically addressed this limitation by employing RFE to rigorously evaluate and reduce redundancy among multi-source variables. This methodological refinement effectively identified a concise yet powerful subset of predictors that substantially improved both accuracy and interpretability of the AGC estimation model. Notably, the inclusion of UAV-derived CH emerged as a critical structural predictor, markedly enhancing model performance and demonstrating that carefully selected, structurally representative variables significantly outperform more extensive but redundant feature sets. Therefore, our findings emphasize that strategic selection and integration of complementary and structurally meaningful predictors, particularly canopy height, are essential for constructing robust, reliable, and parsimonious AGC estimation models in mangrove ecosystems.

Note: CH = canopy height; Clg = canopy leaf greenness index; B4, B2 = Sentinel-2 bands (Red and Blue); VV_Mean = Texture feature (GLCM mean) from Sentinel-1 VV polarization; PSSRa = Pigment Specific Simple Ratio; VV = Sentinel-1 VV polarization backscatter; see Table 1 for full definitions and formulas.

5.3. Comparison of Mangrove Height and AGB in Maowei Sea and Other Regions

The comparison of mangrove structural characteristics across different regions reveals significant spatial variability in canopy height and AGB. In China, mangrove vegetation exhibits a clear latitudinal gradient. For instance, in subtropical zones such as the Zhangjiang Estuary in Fujian (~24° N), mangroves are typically stunted, with an average height of only ~3.1 m and AGB values ranging between 80 and 90 Mg/ha [74,75]. In contrast, warmer southern areas such as the Maowei Sea in Guangxi and Hainan Island (~18–20° N) support taller mangroves with mean heights of 6–7 m and AGB values exceeding 100 Mg/ha [64]. Specifically, the mangroves in Hainan exhibit an average canopy height of 6.99 m and an AGB of 128 Mg/ha, significantly higher than those in other Chinese provinces. For example, the average AGB in the Jiulong River Estuary, Fujian, is ~79 Mg/ha [75] and ~55 Mg/ha in Shenzhen Bay, Guangdong [76], both markedly lower than the values ob-

served in Hainan. These regional differences demonstrate that, even within a relatively narrow latitudinal range, varying ecological conditions can lead to significant differences in mangrove structure and carbon storage capacity.

Regional differences in mangrove canopy height and AGB are driven by multiple factors, among which latitude and climate are primary determinants. It is well established that mangrove height generally decreases with increasing latitude—a global pattern whereby the tallest mangrove stands are found in equatorial regions, while subtropical mangroves tend to be shorter [77]. In China, mangroves are primarily located near the tropical–subtropical transition zone (~18–28° N). In regions such as Fujian and Guangdong, colder winter temperatures and occasional frost events can inhibit mangrove growth. In contrast, the tropical climate of Hainan—with year-round warmth and a prolonged growing season—provides more favorable conditions for mangrove development [78].

Species composition is another critical factor affecting mangrove structure and carbon storage potential. In tropical southern China, particularly in Hainan and parts of Guangxi, mangrove communities contain large-canopy species such as Bruguiera sexangula and *S. apetala*, which often exceed 8 m in height and exhibit high biomass accumulation potential. These species are key contributors to the higher canopy height and AGB observed in Hainan. In the present study area, the Maowei Sea, *S. apetala* is also a dominant species, widely distributed in Kangxiling Town and surrounding zones, and exhibits relatively high canopy structure and biomass. Conversely, in higher-latitude subtropical regions such as Fujian and Guangdong, mangrove communities are typically dominated by cold-tolerant, low-stature species, including *K candel*, *Avicennia marina*, and *A. corniculatum*, with typical heights ranging from 2 to 4 m [79]. This compositional limitation directly constrains the maximum attainable canopy height and AGB in high-latitude mangrove ecosystems, thereby contributing to the observed discrepancies in carbon stock estimates across regions [64].

Beyond biogeography, hydrothermal conditions and geomorphological settings also play essential roles in mangrove development. River deltas and regions with high rainfall provide ample freshwater and nutrients, enhancing mangrove productivity [80]. Freshwater input effectively mitigates salinity stress and promotes canopy development and is regarded as a critical factor in vertical structural formation [81]. In contrast, arid or hypersaline environments restrict growth and often result in low-stature shrub-like mangrove communities with reduced productivity. For example, in the semi-arid coastal zone of northwestern Australia (~22° S), the average mangrove height is only ~3 m, with AGB levels around 70 Mg/ha—conditions largely attributed to the region's harsh, dry climate [82,83].

To further contextualize China's mangrove forests at a global scale, we compared average canopy height and AGB values across representative regions (Table 4). Results indicate that the Maowei Sea mangroves (mean height ~6.08 m, AGB ~108 Mg/ha) outperform higher-latitude counterparts such as Florida, USA (~25° N, ~5 m height, AGB 30–40 Mg/ha) [84] and northwestern Australia (~22° S, ~3 m height, AGB ~70 Mg/ha) [83]. However, these values remain lower than those of equatorial tropical mangroves, such as those in coastal Africa (mean height ~7.5 m, AGB ~116 Mg/ha) [85] and Papua, Indonesia, where average tree height reaches ~21 m and AGB density climbs to 293 Mg/ha [86]. These exceptionally high-biomass mangrove stands, found in humid tropical estuaries with abundant freshwater and nutrient supply, represent some of the tallest and most carbon-rich mangroves globally.

Table 4. Comparison of tree height and aboveground biomass (AGB) of mangroves in different regions.

Region	Latitude Range	Mean Tree Height (m)	AGB (Mg/ha)
Florida, USA	25°03′ N	~5.0	38.77
Zhanjiang, China	20°~22° N	2.81	89.29
Maowei Sea, China	21°50′ N	6.08	108.18
Hainan, China	18°~20° N	6.99	128.27
Papua, Indonesia	4°30′ S	~21	292.72
Africa	19° N~10° S	7.5	116
Northwestern Australia	21°58′ S	3.2	70

These findings underscore the necessity of mapping mangrove canopy height and AGB distributions at large spatial scales. Traditional mangrove maps typically focus only on spatial extent and fail to capture structural variation. For instance, two mangrove areas of equal size may differ significantly in ecosystem functioning: one being a tall, mature forest and the other a low-stature shrubland. Taller mangrove stands generally store more AGC and provide more complex vertical habitat structures that support greater biodiversity. Therefore, generating high-resolution maps of mangrove canopy height and AGB is essential for precise carbon accounting, identifying blue carbon conservation hotspots, and guiding restoration and sustainable management strategies.

5.4. Method Uncertainty Considerations and Future Perspectives

The estimation of AGC in mangrove ecosystems using multi-source remote sensing and field data is inherently affected by various sources of uncertainty. These uncertainties originate primarily from (1) remote sensing data acquisition and processing, (2) field measurement quality, and (3) statistical modeling procedures. First, multi-source satellite data—such as Sentinel-1, Sentinel-2, and PALSAR-2—possess intrinsic differences in sensor characteristics (e.g., spectral bandwidth, polarization, and incidence angle) and spatial resolutions. Additionally, the preprocessing procedures involved, including radiometric calibration, geometric registration, and atmospheric correction, may introduce systematic or random errors. These inconsistencies could affect the comparability and accuracy of extracted features, thereby propagating error into the AGC estimation model. Second, the 10 m spatial resolution used in this study, though widely adopted in mangrove mapping, may not sufficiently resolve fine-scale canopy heterogeneity. In particular, at mangrove fringe zones or tidal creek edges, the presence of mixed pixels containing water, mudflats, and vegetation complicates spectral signal interpretation. Seasonal changes in vegetation phenology and water level dynamics further increase the spectral variability, introducing temporal uncertainty in reflectance-based indicators. Third, field measurements of canopy height, canopy diameter, and diameter at breast height—used to calibrate and validate AGC models—are subject to observer bias, instrumental limitations, and ecological constraints. In dense mangrove stands, difficult terrain and high vegetation density often prevent accurate and consistent measurements. Errors in DBH and height can be significantly amplified when propagated through nonlinear allometric equations, resulting in biased AGC estimations. In addition, species misidentification or geolocation errors during field surveys may also introduce noise in the ground truth dataset. Finally, the machine learning algorithm itself (RF, in this case) is another source of uncertainty. Model performance can be influenced by sample representativeness, overfitting or underfitting due to hyperparameter settings, and randomness in feature selection during model training. These factors may limit model generalizability, particularly when applied beyond the original sampling zones.

To address the above-mentioned sources of uncertainty, future research should pursue targeted strategies to improve model generalizability, robustness, and ecological interpretability. First, to mitigate the impact of sensor inconsistencies and preprocessing errors

across multi-source satellite data (e.g., Sentinel-1/2, PALSAR-2), future studies could explore the use of sensor-specific correction models, radiometric normalization techniques, or cross-sensor feature harmonization frameworks. Additionally, the incorporation of physics-informed machine learning approaches—such as Physics-Informed Neural Networks (PINNs)—can help reduce the reliance on empirically extracted features by embedding ecological principles (e.g., allometric equations) into model structure, thereby improving consistency across sensors and time periods [87,88]. Second, to compensate for spatial resolution limitations and mixed-pixel effects, particularly in fringe zones and tidal interfaces, future work could integrate higher-resolution satellite data sources (e.g., GF-2, Pléiades Neo, and WorldView) as reference layers for downscaling or super-resolution learning, particularly when combined with UAV-LiDAR-derived structural features. Time-series modeling may also help capture phenological dynamics and tidal fluctuations, reducing temporal uncertainty in reflectance-based indicators. Such spatiotemporal integration is especially valuable in environments characterized by seasonal or sub-daily variability. Third, to reduce field-based measurement error and ecological sampling bias, future research should adhere strictly to standardized forest inventory protocols and invest in enhanced training for field personnel. Expanding the number and spatial representativeness of ground plots—particularly in structurally complex or difficult-to-access zones—and increasing their temporal sampling frequency (e.g., seasonal or annual remeasurements) can improve ground-truth data quality and support the detection of AGC dynamics over time. In parallel, efforts should be made to minimize species misidentification and geolocation inaccuracies, including the use of GPS post-correction, botanical verification, and digital field mapping systems. To further enhance the ecological interpretability and accuracy of AGC estimation, future work will consider incorporating additional biometric variables. Tree age can serve as an indicator of stand development and long-term growth dynamics, while wood density is a key factor influencing carbon accumulation, especially among trees with similar canopy height. Integrating these complementary parameters may help reduce residual uncertainty and improve model performance across heterogeneous mangrove structures. Finally, to address uncertainty stemming from the modeling process itself, future work should implement formal sensitivity analysis (e.g., Sobol or variance decomposition methods) to quantify the influence of input variables such as CH, VV_Mean, or Clg. Such analysis can guide feature selection, reduce redundancy, and improve model parsimony [89–91]. Additionally, incorporating ancillary non-remote sensing variables—such as soil salinity, elevation, organic matter content, or local climate (e.g., rainfall and temperature)—may significantly enhance model performance by capturing ecological gradients not observable from spectral or structural data alone. These improvements can collectively enhance model applicability across different mangrove types and biogeographic contexts.

Looking ahead, several additional research avenues warrant further exploration to enhance the ecological interpretability of AGC estimation in mangrove ecosystems. First, the coupling between aboveground and belowground carbon pools remains insufficiently understood. While this study focused on AGC, future field campaigns will incorporate soil organic carbon (SOC) sampling and spatial analysis to investigate its correlation with UAV-derived canopy metrics, aiming to uncover structural linkages between aboveground and belowground carbon stocks.

Second, although CH was employed as the primary structural parameter in this study due to its stability and transferability, the high-density UAV-LiDAR point clouds collected provide a valuable opportunity to derive more detailed three-dimensional canopy metrics—such as porosity, clumping index, and foliage distribution. These structural attributes are known to modulate light interception and photosynthetic light use

efficiency (LUE), particularly in complex mangrove canopies. Future localized analyses will explore these metrics to improve the mechanistic understanding of canopy structure–function interactions.

Finally, the explicit inclusion of photosynthetically active radiation (PAR) in AGC modeling represents a promising direction. While PAR was not incorporated in the current study due to the lack of co-temporal in situ observations and the coarse spatial resolution of existing satellite products, several spectral variables used—such as Sentinel-2 red-edge bands and the canopy leaf greenness index—are physiologically linked to chlorophyll content and light absorption and thus may serve as indirect indicators of LUE. Future efforts will consider integrating modeled or measured PAR datasets (e.g., from GLASS, MODIS, or ground-based quantum sensors) with UAV-derived structural traits to more accurately characterize LUE and its influence on AGC variation across heterogeneous mangrove landscapes.

6. Conclusions

This study demonstrates the effectiveness of integrating UAV-derived LiDAR with multi-source satellite imagery (Sentinel-1, Sentinel-2, and PALSAR-2) for accurate estimation of mangrove CH and AGC. Canopy height emerged as a key structural feature that mitigates spectral saturation and significantly improves AGC model performance. The fusion of spectral, textural, and structural variables yielded optimal results (R^2 = 0.75, RMSE = 14.18 Mg C/ha), confirming the value of multi-dimensional feature integration. While previous studies have advanced satellite-based carbon mapping through machine learning or multi-temporal fusion, they are often limited in retrieving fine-scale structural indicators such as CH. UAV-based LiDAR offers precise vertical structure information that bridges this resolution gap, making it a critical complement to satellite observations. The Maowei Sea mangroves exhibited a mean canopy height of 6.08 m and an average AGC density of 53.01 Mg C/ha, with a total regional AGC stock of 88,363.73 Mg. These findings underscore the potential of UAV–satellite fusion frameworks for scalable, accurate blue carbon monitoring in structurally complex ecosystems. The methodology presented here contributes to improving regional carbon accounting and supports climate mitigation, coastal ecosystem resilience, and the sustainable management of blue carbon resources in the context of global environmental change.

Supplementary Materials: The following supporting information can be downloaded at: https://www.mdpi.com/article/10.3390/su17188211/s1, Figure S1: Mangrove CH map of Maowei Sea; Figure S2: Scatterplot of predicted vs. observed CH from the RF model; Figure S3: Feature importance for CH prediction in the RF model; Table S1: Mangrove plot characteristics (data are presented as mean); Table S2: Allometric growth equations of different mangrove communities; Table S3: Indicators for predicting CH based on random forest (RF). References [92–94] has been cited to in the supplementary material.

Author Contributions: Conceptualization, methodology, software, validation, X.M. and Q.L.; formal analysis, X.M., W.X. and Q.L.; investigation, W.X., X.M., W.W. (Wenqian Wu), S.D. and W.W. (Wenhuan Wang); data curation, X.M., S.D. and W.X.; writing—original draft preparation, X.M.; writing—review and editing, W.Z. and Y.W.; visualization, S.D., W.W. (Wenqian Wu) and W.W. (Wenhuan Wang); supervision, W.Z. and Y.W.; funding acquisition, Y.W. All authors have read and agreed to the published version of the manuscript.

Funding: This research was funded by the Guangxi Science and Technology Major Program, grant number GUIKEAA23062054; the Science and Technology Research and Development Projects of Guangxi Institute of Industrial Technology, grant number CYY-HT2023-JSJJ-0037; and the Guangxi Key Research and Development Program, grant number GUIKEAB24010248.

Institutional Review Board Statement: Not applicable.

Informed Consent Statement: Not applicable.

Data Availability Statement: The data presented in this study are available on request from the corresponding author.

Conflicts of Interest: The authors declare no conflicts of interest.

Abbreviations

The following abbreviations are used in this manuscript:

Abbreviation	Full Term
AGC	Aboveground Carbon
AGB	Aboveground Biomass
GEE	Google Earth Engine
GLCM	Gray Level Co-occurrence Matrix
DEM	Digital Elevation Model
DSM	Digital Surface Model
RF	Random Forest
RFE	Recursive Feature Elimination
R^2	Coefficient of determination
RMSE	Root mean square error
CH	Canopy Height
UAV	Unmanned Aerial Vehicle
LiDAR	Light Detection and Ranging
RTK	Real-Time Kinematic
TIN	Triangulated Irregular Network
SAR	Synthetic Aperture Radar
GEDI	Global Ecosystem Dynamics Investigation
ICESat-2	Ice, Cloud, and Land Elevation Satellite-2

References

1. Donato, D.C.; Kauffman, J.B.; Murdiyarso, D.; Kurnianto, S.; Stidham, M.; Kanninen, M. Mangroves among the most carbon-rich forests in the tropics. *Nat. Geosci.* **2011**, *4*, 293–297. [CrossRef]
2. Atwood, T.B.; Connolly, R.M.; Almahasheer, H.; Carnell, P.E.; Duarte, C.M.; Lewis, C.J.E.; Irigoien, X.; Kelleway, J.J.; Lavery, P.S.; Macreadie, P.I.; et al. Global patterns in mangrove soil carbon stocks and losses. *Nat. Clim. Change* **2017**, *7*, 523–528. [CrossRef]
3. Campbell, A.D.; Fatoyinbo, T.; Charles, S.P.; Bourgeau-Chavez, L.L.; Goes, J.; Gomes, H.; Halabisky, M.; Holmquist, J.; Lohrenz, S.; Mitchell, C.; et al. A review of carbon monitoring in wet carbon systems using remote sensing. *Environ. Res. Lett.* **2022**, *17*, 25009. [CrossRef]
4. Yi, X.; Jie, L.; Shengfa, Y.; Wenjie, L. Impact of channel deepening on the saltwater intrusion process in the Qinjiang River estuary, Southeast China. *Estuar. Coast. Shelf Sci.* **2024**, *300*, 108718. [CrossRef]
5. Xu, H.; He, B.; Guo, L.; Yan, X.; Zeng, Y.; Yuan, W.; Zhong, Z.; Tang, R.; Yang, Y.; Liu, H.; et al. Global forest plantations mapping and biomass carbon estimation. *J. Geophys. Res. Biogeosci.* **2024**, *129*, e2023JG007441. [CrossRef]
6. Chen, H.; Qin, Z.; Zhai, D.L.; Ou, G.; Li, X.; Zhao, G.; Fan, J.; Zhao, C.; Xu, H. Mapping forest aboveground biomass with MODIS and Fengyun-3C VIRR imageries in Yunnan Province, Southwest China using linear regression, k-nearest neighbor and random forest. *Remote Sens.* **2022**, *14*, 5456. [CrossRef]
7. Mutanga, O.; Adam, E.; Cho, M.A. High density biomass estimation for wetland vegetation using WorldView-2 imagery and random forest regression algorithm. *Int. J. Appl. Earth Obs. Geoinf.* **2012**, *18*, 399–406. [CrossRef]
8. Zhao, P.; Lu, D.; Wang, G.; Wu, C.; Huang, Y.; Yu, S. Examining spectral reflectance saturation in Landsat imagery and corresponding solutions to improve forest aboveground biomass estimation. *Remote Sens.* **2016**, *8*, 469. [CrossRef]
9. Sinha, S.; Santra, A.; Sharma, L.; Jeganathan, C.; Nathawat, M.S.; Das, A.K.; Mohan, S. Multi-polarized Radarsat-2 satellite sensor in assessing forest vigor from above ground biomass. *J. For. Res.* **2018**, *29*, 1139–1145. [CrossRef]
10. Michelakis, D.; Stuart, N.; Brolly, M.; Woodhouse, I.H.; Lopez, G.; Linares, V. Estimation of woody biomass of pine savanna woodlands from ALOS PALSAR imagery. *IEEE J. Sel. Top. Appl. Earth Obs. Remote Sens.* **2014**, *8*, 244–254. [CrossRef]

11. Ehlers, D.; Wang, C.; Coulston, J.; Zhang, Y.; Pavelsky, T.; Frankenberg, E.; Woodcock, C.; Song, C. Mapping forest aboveground biomass using multisource remotely sensed data. *Remote Sens.* **2022**, *14*, 1115. [CrossRef]
12. Singh, C.; Karan, S.K.; Sardar, P.; Samadder, S.R. Remote sensing-based biomass estimation of dry deciduous tropical forest using machine learning and ensemble analysis. *J. Environ. Manag.* **2022**, *308*, 114639. [CrossRef]
13. Mutanga, O.; Masenyama, A.; Sibanda, M. Spectral saturation in the remote sensing of high-density vegetation traits: A systematic review of progress, challenges, and prospects. *ISPRS J. Photogramm. Remote Sens.* **2023**, *198*, 297–309. [CrossRef]
14. Silva, C.A.; Duncanson, L.; Hancock, S.; Neuenschwander, A.; Thomas, N.; Hofton, M.; Fatoyinbo, L.; Simard, M.; Marshak, C.Z.; Armston, J.; et al. Fusing simulated GEDI, ICESat-2 and NISAR data for regional aboveground biomass mapping. *Remote Sens. Environ.* **2021**, *253*, 112234. [CrossRef]
15. Dubayah, R.; Blair, J.B.; Goetz, S.; Fatoyinbo, L.; Hansen, M.; Healey, S.; Hofton, M.; Hurtt, G.; Kellner, J.; Luthcke, S.; et al. The Global Ecosystem Dynamics Investigation: High-resolution laser ranging of the Earth's forests and topography. *Sci. Remote Sens.* **2020**, *1*, 100002. [CrossRef]
16. Shang, X.; Chazette, P. Interest of a full-waveform flown UV lidar to derive forest vertical structures and aboveground carbon. *Forests* **2014**, *5*, 1454–1480. [CrossRef]
17. Zhao, X.; Su, Y.; Hu, T.; Cao, M.; Liu, X.; Yang, Q.; Guan, H.; Liu, L.; Guo, Q. Analysis of UAV lidar information loss and its influence on the estimation accuracy of structural and functional traits in a meadow steppe. *Ecol. Indic.* **2022**, *135*, 108515. [CrossRef]
18. Liu, K.; Shen, X.; Cao, L.; Wang, G.; Cao, F. Estimating forest structural attributes using UAV-LiDAR data in Ginkgo plantations. *ISPRS J. Photogramm. Remote Sens.* **2018**, *146*, 465–482. [CrossRef]
19. Mao, P.; Ding, J.; Jiang, B.; Qin, L.; Qiu, G.Y. How can UAV bridge the gap between ground and satellite observations for quantifying the biomass of desert shrub community? *ISPRS J. Photogramm. Remote Sens.* **2022**, *192*, 361–376. [CrossRef]
20. Wang, S.; Liu, C.; Li, W.; Jia, S.; Yue, H. Hybrid model for estimating forest canopy heights using fused multimodal spaceborne LiDAR data and optical imagery. *Int. J. Appl. Earth Obs. Geoinf.* **2023**, *122*, 103431. [CrossRef]
21. Li, J.; Bao, W.; Wang, X.; Song, Y.; Liao, T.; Xu, X.; Guo, M. Estimating Aboveground Biomass of Boreal Forests in Northern China Using Multiple Data sets. *IEEE Trans. Geosci. Remote Sens.* **2024**, *62*, 1–10.
22. Liu, B.; Liu, P.; Wang, Y.; Li, Z.; Lv, H.; Lu, W.; Olofsson, T.; Rabczuk, T. Explainable machine learning for multiscale thermal conductivity modeling in polymer nanocomposites with uncertainty quantification. *Compos. Struct.* **2025**, *307*, 119292. [CrossRef]
23. Liu, B.; Lu, W.; Olofsson, T.; Zhuang, X.; Rabczuk, T. Stochastic interpretable machine learning based multiscale modeling in thermal conductivity of Polymeric graphene-enhanced composites. *Compos. Struct.* **2024**, *327*, 117601. [CrossRef]
24. Tian, Y.; Huang, H.; Zhou, G.; Zhang, Q.; Tao, J.; Zhang, Y.; Lin, J. Aboveground mangrove biomass estimation in Beibu Gulf using machine learning and UAV remote sensing. *Sci. Total Environ.* **2021**, *781*, 146816. [CrossRef]
25. Maimaitijiang, M.; Sagan, V.; Sidike, P.; Hartling, S.; Esposito, F.; Fritschi, F.B. Soybean yield prediction from UAV using multimodal data fusion and deep learning. *Remote Sens. Environ.* **2020**, *237*, 111599. [CrossRef]
26. Huang, Z.; Tian, Y.; Zhang, Q.; Huang, Y.; Liu, R.; Huang, H.; Zhou, G.; Wang, J.; Tao, J.; Yang, Y.; et al. Estimating mangrove above-ground biomass at Maowei Sea, Beibu Gulf of China using machine learning algorithm with Sentinel-1 and Sentinel-2 data. *Geocarto Int.* **2022**, *37*, 15778–15805. [CrossRef]
27. Tian, Y.; Huang, H.; Zhou, G.; Zhang, Q.; Xie, X.; Ou, J.; Zhang, Y.; Tao, J.; Lin, J. Mangrove biodiversity assessment using UAV LiDAR and hyperspectral data in China's Pinglu canal estuary. *Remote Sens.* **2023**, *15*, 2622. [CrossRef]
28. Xiao, Y.; Li, D.; Yang, S.; Hu, J.; Li, W. Response of salt water intrusion to a huge navigation project construction in the Qinjiang River Estuary, Southeast China. *J. Coast. Conserv.* **2023**, *27*, 69. [CrossRef]
29. Deng, S.; Luo, M.; Wang, W.; Lan, S.; Xu, W.; Mai, X.; Zhang, W. Assessment of biodiversity and landscape changes during the Pinglu Canal construction and the benefits of ecological restoration based on Rao's Q index. *Ecol. Eng.* **2025**, *219*, 107709. [CrossRef]
30. Wang, D.; Wan, B.; Qiu, P.; Tan, X.; Zhang, Q. Mapping mangrove species using combined UAV-LiDAR and Sentinel-2 data: Feature selection and point density effects. *Adv. Space Res.* **2022**, *69*, 1494–1512. [CrossRef]
31. Meng, Y.; Gou, R.; Bai, J.; Moreno-Mateos, D.; Davis, C.C.; Wan, L.; Song, S.; Zhang, H.; Zhu, X.; Lin, G. Spatial patterns and driving factors of carbon stocks in mangrove forests on Hainan Island, China. *Glob. Ecol. Biogeogr.* **2022**, *31*, 1692–1706. [CrossRef]
32. Kalinaki, K.; Malik, O.A.; Lai, D.T.C. FCD-AttResU-Net: An improved forest change detection in Sentinel-2 satellite images using attention residual U-Net. *Int. J. Appl. Earth Obs. Geoinf.* **2023**, *122*, 103453. [CrossRef]
33. Wang, D.; Wan, B.; Liu, J.; Su, Y.; Guo, Q.; Qiu, P.; Wu, X. Estimating aboveground biomass of the mangrove forests on northeast Hainan Island in China using an upscaling method from field plots, UAV-LiDAR data and Sentinel-2 imagery. *Int. J. Appl. Earth Obs. Geoinf.* **2020**, *85*, 101986. [CrossRef]
34. Valderrama-Landeros, L.; Flores-de-Santiago, F.; Kovacs, J.M.; Flores-Verdugo, F. An assessment of commonly employed satellite-based remote sensors for mapping mangrove species in Mexico using an NDVI-based classification scheme. *Environ. Monit. Assess.* **2018**, *190*, 23. [CrossRef] [PubMed]

35. García Cárdenas, D.A.; Ramón Valencia, J.A.; Alzate Velásquez, D.F.; Palacios Gonzalez, J.R. Dynamics of the indices NDVI and GNDVI in a rice growing in its reproduction phase from multi-spectral aerial images taken by drones. In *Advances in Information and Communication Technologies for Adapting Agriculture to Climate Change II, Proceedings of the International Conference of ICT for Adapting Agriculture to Climate Change, Popayán, Colombia, 22–24 November 2017*; Springer: Berlin/Heidelberg, Germany, 2018; pp. 106–119.
36. Huete, A.; Didan, K.; Miura, T.; Rodriguez, E.P.; Gao, X.; Ferreira, L.G. Overview of the radiometric and biophysical performance of the MODIS vegetation indices. *Remote Sens. Environ.* **2002**, *83*, 195–213. [CrossRef]
37. Tran, T.V.; Reef, R.; Zhu, X. A review of spectral indices for mangrove remote sensing. *Remote Sens.* **2022**, *14*, 4868. [CrossRef]
38. Ji, L.; Zhang, L.; Wylie, B. Analysis of dynamic thresholds for the normalized difference water index. *Photogramm. Eng. Remote Sens.* **2009**, *75*, 1307–1317. [CrossRef]
39. Zhu, Y.; Liu, K.; Liu, L.; Wang, S.; Liu, H. Retrieval of mangrove aboveground biomass at the individual species level with worldview-2 images. *Remote Sens.* **2015**, *7*, 12192–12214. [CrossRef]
40. Kamal, M.; Phinn, S.; Johansen, K. Object-based approach for multi-scale mangrove composition mapping using multi-resolution image datasets. *Remote Sens.* **2015**, *7*, 4753–4783. [CrossRef]
41. Gitelson, A.A.; Gritz, Y.; Merzlyak, M.N. Relationships between leaf chlorophyll content and spectral reflectance and algorithms for non-destructive chlorophyll assessment in higher plant leaves. *J. Plant Physiol.* **2003**, *160*, 271–282. [CrossRef]
42. Castillo, J.A.A.; Apan, A.A.; Maraseni, T.N.; Salmo, S.G., III. Estimation and mapping of above-ground biomass of mangrove forests and their replacement land uses in the Philippines using Sentinel imagery. *ISPRS J. Photogramm. Remote Sens.* **2017**, *134*, 70–85. [CrossRef]
43. Dash, J.; Curran, P.J. The MERIS terrestrial chlorophyll index. *Int. J. Remote Sens.* **2004**, *25*, 5403–5413. [CrossRef]
44. Shoko, C.; Mutanga, O. Examining the strength of the newly-launched Sentinel 2 MSI sensor in detecting and discriminating subtle differences between C3 and C4 grass species. *ISPRS J. Photogramm. Remote Sens.* **2017**, *129*, 32–40. [CrossRef]
45. Blackburn, G.A. Spectral indices for estimating photosynthetic pigment concentrations: A test using senescent tree leaves. *Int. J. Remote Sens.* **1998**, *19*, 657–675. [CrossRef]
46. Zhao, C.; Jia, M.; Wang, Z.; Mao, D.; Wang, Y. Identifying mangroves through knowledge extracted from trained random forest models: An interpretable mangrove mapping approach (IMMA). *ISPRS J. Photogramm. Remote Sens.* **2023**, *201*, 209–225. [CrossRef]
47. Zhang, L.; Han, W.; Niu, Y.; Chávez, J.L.; Shao, G.; Zhang, H. Evaluating the sensitivity of water stressed maize chlorophyll and structure based on UAV derived vegetation indices. *Comput. Electron. Agric.* **2021**, *185*, 106174. [CrossRef]
48. Haralick, R.M.; Shanmugam, K.; Dinstein, I.H. Textural Features for Image Classification. *IEEE Trans. Syst. Man Cybern.* **1973**, *SMC-3*, 610–621. [CrossRef]
49. Guyon, I.; Elisseeff, A. An introduction to variable and feature selection. *J. Mach. Learn. Res.* **2003**, *3*, 1157–1182.
50. Guyon, I.; Weston, J.; Barnhill, S.; Vapnik, V. Gene selection for cancer classification using support vector machines. *Mach. Learn.* **2002**, *46*, 389–422. [CrossRef]
51. Breiman, L. Random forests. *Mach. Learn.* **2001**, *45*, 5–32. [CrossRef]
52. Pham, T.D.; Yokoya, N.; Xia, J.; Ha, N.T.; Le, N.N.; Nguyen, T.T.T.; Dao, T.H.; Vu, T.T.P.; Pham, T.D.; Takeuchi, W. Comparison of machine learning methods for estimating mangrove above-ground biomass using multiple source remote sensing data in the red river delta biosphere reserve, Vietnam. *Remote Sens.* **2020**, *12*, 1334. [CrossRef]
53. Wang, Z.; Zhang, Y.; Li, F.; Gao, W.; Guo, F.; Li, Z.; Yang, Z. Regional mangrove vegetation carbon stocks predicted integrating UAV-LiDAR and satellite data. *J. Environ. Manag.* **2024**, *368*, 122101. [CrossRef]
54. Pedregosa, F.; Varoquaux, G.; Gramfort, A.; Michel, V.; Thirion, B.; Grisel, O.; Blondel, M.; Prettenhofer, P.; Weiss, R.; Dubourg, V.; et al. Scikit-learn: Machine learning in Python. *J. Mach. Learn. Res.* **2011**, *12*, 2825–2830.
55. Lu, D. The potential and challenge of remote sensing-based biomass estimation. *Int. J. Remote Sens.* **2006**, *27*, 1297–1328. [CrossRef]
56. Mitchard, E.T.A.; Saatchi, S.S.; Woodhouse, I.H.; Nangendo, G.; Ribeiro, N.S.; Williams, M.; Ryan, C.M.; Lewis, S.L.; Feldpausch, T.R.; Meir, P. Using satellite radar backscatter to predict above-ground woody biomass: A consistent relationship across four different African landscapes. *Geophys. Res. Lett.* **2009**, 36. [CrossRef]
57. Le Toan, T.; Quegan, S.; Davidson, M.W.J.; Balzter, H.; Paillou, P.; Papathanassiou, K.; Plummer, S.; Rocca, F.; Saatchi, S.; Shugart, H.; et al. The BIOMASS mission: Mapping global forest biomass to better understand the terrestrial carbon cycle. *Remote Sens. Environ.* **2011**, *115*, 2850–2860. [CrossRef]
58. Hyde, P.; Dubayah, R.; Walker, W.; Blair, J.B.; Hofton, M.; Hunsaker, C. Mapping forest structure for wildlife habitat analysis using multi-sensor (LiDAR, SAR/InSAR, ETM+, Quickbird) synergy. *Remote Sens. Environ.* **2006**, *102*, 63–73. [CrossRef]
59. Zhao, X.; Hu, W.; Han, J.; Wei, W.; Xu, J. Urban Above-Ground Biomass Estimation Using GEDI Laser Data and Optical Remote Sensing Images. *Remote Sens.* **2024**, *16*, 1229. [CrossRef]
60. Tian, C.S.; Zhou, X.; Hao, Y.; Tan, F.; Wang, Y.; Wu, S.; Lin, H. Optimization model of forest aboveground biomass based on GEDI canopy height: A case study in Fujian, China. *Acta Ecol. Sin.* **2024**, *44*, 7264–7277.

61. Hancock, S.; Armston, J.; Hofton, M.; Sun, X.; Tang, H.; Duncanson, L.I.; Kellner, J.R.; Dubayah, R. The GEDI simulator: A large-footprint waveform lidar simulator for calibration and validation of spaceborne missions. *Earth Space Sci.* **2019**, *6*, 294–310. [CrossRef] [PubMed]
62. Dhakal, R.; Maimaitijiang, M.; Chang, J.; Caffe, M. Utilizing spectral, structural and textural features for estimating oat above-ground biomass using UAV-based multispectral data and machine learning. *Sensors* **2023**, *23*, 9708. [CrossRef] [PubMed]
63. Niu, X.; Chen, B.; Sun, W.; Feng, T.; Yang, X.; Liu, Y.; Liu, W.; Fu, B. Estimation of coastal wetland vegetation aboveground biomass by integrating UAV and satellite remote sensing data. *Remote Sens.* **2024**, *16*, 2760. [CrossRef]
64. Wang, D.; Ban, W.; Qiu, P.; Zuo, Z.; Wang, R.; Wu, X. Mapping height and aboveground biomass of mangrove forests on Hainan Island using UAV-LiDAR sampling. *Remote Sens.* **2019**, *11*, 2156. [CrossRef]
65. Jian, K.; Du, L.; Yu, Y.; Li, G. Improving Forest Canopy Height Mapping in Wuyishan National Park Through Calibration of ZiYuan-3 Stereo Imagery Using Limited Unmanned Aerial Vehicle LiDAR Data. *Forests* **2025**, *16*, 125. [CrossRef]
66. Wang, J.; Shen, X.; Cao, L. Upscaling forest canopy height estimation using waveform-calibrated GEDI spaceborne LiDAR and Sentinel-2 data. *Remote Sens.* **2024**, *16*, 2138. [CrossRef]
67. Li, H.; Hiroshima, T.; Li, X.; Hayashi, M.; Kato, T. High-resolution mapping of forest structure and carbon stock using multi-source remote sensing data in Japan. *Remote Sens. Environ.* **2024**, *312*, 114322. [CrossRef]
68. Datt, B. Remote sensing of chlorophyll a, chlorophyll b, chlorophyll a + b, and total carotenoid content in eucalyptus leaves. *Remote Sens. Environ.* **1998**, *66*, 111–121. [CrossRef]
69. Lee, Z.P.; Carder, K.; Amone, R.; He, M.X. Determination of primary spectral bands for remote sensing of aquatic environments. *Sensors* **2007**, *7*, 3428–3441. [CrossRef] [PubMed]
70. Zhang, Y.; Zou, Y.; Wang, Y. Remote Sensing of Forest Above-Ground Biomass Dynamics: A Review. *Forests* **2025**, *16*, 821. [CrossRef]
71. Xu, W.; Cheng, Y.; Luo, M.; Mai, X.; Wang, W.; Zhang, W.; Wang, Y. Progress and Limitations in Forest Carbon Stock Estimation Using Remote Sensing Technologies: A Comprehensive Review. *Forests* **2025**, *16*, 449. [CrossRef]
72. Wang, T.; Zhang, H.; Lin, H.; Fang, C. Textural–spectral feature-based species classification of mangroves in Mai Po Nature Reserve from Worldview-3 imagery. *Remote Sens.* **2015**, *8*, 24. [CrossRef]
73. Tian, Y.; Zhang, Q.; Huang, H.; Huang, Y.; Tao, J.; Zhou, G.; Zhang, Y.; Yang, Y.; Lin, J. Aboveground biomass of typical invasive mangroves and its distribution patterns using UAV-LiDAR data in a subtropical estuary: Maoling River estuary, Guangxi, China. *Ecol. Indic.* **2022**, *136*, 108694. [CrossRef]
74. Zhu, X.; Hou, Y.; Weng, Q.; Chen, L. Integrating UAV optical imagery and LiDAR data for assessing the spatial relationship between mangrove and inundation across a subtropical estuarine wetland. *ISPRS J. Photogramm. Remote Sens.* **2019**, *149*, 146–156. [CrossRef]
75. Wang, M.; Cao, W.; Guan, Q.; Wu, G.; Wang, F. Assessing changes of mangrove forest in a coastal region of southeast China using multi-temporal satellite images. *Estuar. Coast. Shelf Sci.* **2018**, *207*, 283–292. [CrossRef]
76. Jiang, L.Z.; Yang, D.D.; Mei, L.Y.; Yang, X.M. The Remote Sensing Estimation of Carbon Storage in Mangrove Plant Communities in Shenzhen City. *Wetl. Sci.* **2018**, *16*, 618–625.
77. Aslan, A.; Aljahdali, M.O. Characterizing global patterns of mangrove canopy height and aboveground biomass derived from SRTM data. *Forests* **2022**, *13*, 1545. [CrossRef]
78. Shi, X.; Nie, T.Z.; Xiong, Q.; Liu, Z.X.; Zhang, J.Y.; Liu, W.J.; Wu, L.; Cui, W.; Sun, Z.Y. Carbon Stock Increment Projection of Mangrove Ecosystems on Hainan Island Based on InVEST and MaxEnt Models. *J. Trop. Biol.* **2023**, *14*, 298–306.
79. Peng, Y.L.; Wang, Y.S.; Fei, J.; Sun, C.C.; Cheng, H. Ecophysiological differences between three mangrove seedlings (*Kandelia obovata*, *Aegiceras corniculatum*, and *Avicennia marina*) exposed to chilling stress. *Ecotoxicology* **2015**, *24*, 1722–1732. [CrossRef] [PubMed]
80. Hayes, M.A.; Jesse, A.; Welti, N.; Tabet, B.; Lockington, D.; Lovelock, C.E. Groundwater enhances above-ground growth in mangroves. *J. Ecol.* **2019**, *107*, 1120–1128. [CrossRef]
81. Perri, S.; Detto, M.; Porporato, A.; Molini, A. Salinity-induced limits to mangrove canopy height. *Glob. Ecol. Biogeogr.* **2023**, *32*, 1561–1574. [CrossRef]
82. Adame, M.F.; Reef, R.; Santini, N.S.; Najera, C.; Turschwell, M.P.; Hayes, M.A.; Masque, P.; Lovelock, C.E. Mangroves in arid regions: Ecology, threats, and opportunities. *Estuar. Coast. Shelf Sci.* **2021**, *248*, 106796. [CrossRef]
83. Hickey, S.M.; Callow, N.J.; Phinn, S.; Lovelock, C.E.; Duarte, C.M. Spatial complexities in aboveground carbon stocks of a semi-arid mangrove community: A remote sensing height-biomass-carbon approach. *Estuar. Coast. Shelf Sci.* **2018**, *200*, 194–201. [CrossRef]
84. Simard, M.; Zhang, K.; Rivera-Monroy, V.H.; Ross, M.S.; Ruiz, P.; Castaneda-Moya, E.; Twilley, R.R.; Rodriguez, E. Mapping height and biomass of mangrove forests in Everglades National Park with SRTM elevation data. *Photogramm. Eng. Remote Sens.* **2006**, *72*, 299–311. [CrossRef]

85. Fatoyinbo, T.E.; Simard, M. Height and biomass of mangroves in Africa from ICESat/GLAS and SRTM. *Int. J. Remote Sens.* **2013**, *34*, 668–681. [CrossRef]
86. Aslan, A.; Rahman, A.F.; Warren, M.W.; Robeson, S.M. Mapping spatial distribution and biomass of coastal wetland vegetation in Indonesian Papua by combining active and passive remotely sensed data. *Remote Sens. Environ.* **2016**, *183*, 65–81. [CrossRef]
87. Wang, C.; Bentivegna, E.; Zhou, W.; Klein, L.; Elmegreen, B. Physics-informed neural network super resolution for advection-diffusion models. *arXiv* **2020**, arXiv:2011.02519.
88. Liu, B.; Wang, Y.; Rabczuk, T.; Olofsson, T.; Lu, W. Multi-scale modeling in thermal conductivity of polyurethane incorporated with phase change materials using physics-informed neural networks. *Renew. Energy* **2024**, *220*, 119565. [CrossRef]
89. Liu, B.; Vu, N.; Zhuang, X.; Rabczuk, T. Stochastic multiscale modeling of heat conductivity of Polymeric clay nanocomposites. *Mech. Mater.* **2020**, *142*, 103280. [CrossRef]
90. Liu, B.; Penaka, S.R.; Lu, W.; Feng, K.; Rebbling, A.; Olofsson, T. Data-driven quantitative analysis of an integrated open digital ecosystems platform for user-centric energy retrofits: A case study in northern Sweden. *Technol. Soc.* **2023**, *75*, 102347. [CrossRef]
91. Liu, B.; Liu, P.; Lu, W.; Olofsson, T. Explainable Artificial Intelligence (XAI) for Material Design and Engineering Applications: A Quantitative Computational Framework. *Int. J. Mech. Syst. Dyn.* **2025**, *5*, 236–265. [CrossRef]
92. Hu, Y.; Xu, Y.; Xue, C.; Luo, Y.; Liao, B.; Zhu, N. Studies on carbon storages of Sonneratia apetala forest vegetation and soil in Guangdong Province. *J. South China Agric. Univ.* **2019**, *40*, 95–103.
93. Fu, W.; Wu, Y. Estimation of aboveground biomass of different mangrove trees based on canopy diameter and tree height. *Procedia Environ. Sci.* **2011**, *10*, 2189–2194. [CrossRef]
94. Tam, N.; Wong, Y.; Lan, C.; Chen, G. Community structure and standing crop biomass of a mangrove forest in Futian Nature Reserve, Shenzhen, China. *Hydrobiologia* **1995**, *295*, 193–201. [CrossRef]

Disclaimer/Publisher's Note: The statements, opinions and data contained in all publications are solely those of the individual author(s) and contributor(s) and not of MDPI and/or the editor(s). MDPI and/or the editor(s) disclaim responsibility for any injury to people or property resulting from any ideas, methods, instructions or products referred to in the content.

Bulletin of Environmental Contamination and Toxicology (2025) 114:57
https://doi.org/10.1007/s00128-025-04034-9

Influence of Air, Water, Light, and Salinity on Release of Plasticizers, Flame Retardants, and Ultraviolet Absorbents from Polystyrene Plastic

Hongshuang Shen[1,2] · Fang Liu[1,2] · Ruijie Zhang[1,2] · Annan Yan[2] · Yaru Kang[2] · Jingyu Wang[1] · Kefu Yu[2,3]

Received: 19 December 2024 / Accepted: 11 March 2025
© The Author(s), under exclusive licence to Springer Science+Business Media, LLC, part of Springer Nature 2025

Abstract
This study investigated how air, water, light, and salinity influence the release of three additives—phthalic acid esters (PAEs), organophosphate esters (OPEs), and organic ultraviolet absorbents (OUVAs)—from expanded polystyrene plastic (EPS). GC-MS/MS was used to quantify the concentrations of the three additives. The release kinetics and mechanisms under different conditions and the effects of various factors were analyzed. The release of PAEs and OPEs was more consistent with the first-order kinetics, while the release fitting of OUVAs was more in line with the second-order kinetics. Among all conditions, air exposure led to the highest release rates of PAEs ($\sum_{16}$PAEs: k = 0.868 ng/g·day) and OPEs ($\sum_{11}$OPEs: k = 0.927 ng/g·day). Compared to freshwater, seawater moderately inhibited EPS aging and additive release due to ion effects. Light significantly influenced both the rate and amount of additive release. Finally, the global release of plastic additives from EPS waste was estimated at 33.5k tons for PAEs, 646 tons for OPEs, and 420 tons for OUVAs.

Keywords Expanded polystyrene (EPS) aging · PAEs · OPEs · OUVAs · Additives leaching

Plastic, widely used in packaging, textiles, and construction due to its durability and affordability (Hahladakis et al. 2018), saw global production soar from 1.5 million tons in 1950 to 400 million tons by 2022 (Barlucchi et al. 2024). However, less than 20% of plastic waste is recycled, leaving large amounts to enter natural ecosystems (Rakib et al. 2021, 2022). Annual riverine plastic flux into marine environments is estimated at 1.15–2.41 million tons (Rakib et al. 2023a), representing 67% of total river-borne plastic pollution (Mehta et al. 2025). Though non-biodegradable, plastics undergo fragmentation into microplastics due to ultraviolet radiation (Liu et al. 2023), temperature fluctuations (Ding et al. 2020), and salinity fluctuations (Wen et al. 2023). Plastic degradation generates microplastics and induces surface cracking, which accelerates additive leaching into the environment, thereby amplifying ecotoxicological risks (Wang et al. 2024).

Most chemicals used in plastic manufacturing demonstrate toxicity to both non-human organisms and humans, with endocrine disruptors and carcinogenic compounds representing the predominant hazards (Rakib et al. 2023b). Phthalates (PAEs), common plasticizers that enhance flexibility and durability in plastics, are widely used. According to studies, the global annual consumption of phthalates (PAEs) reached 7.5 million tons in 2018 (Pradhan et al. 2018), accounting for 95% of the entire plasticizer market. Phthalates are endocrine disruptors that are teratogenic, neurotoxic, and reproductively toxic (Poopal et al. 2020). In addition to phthalates, other plastic additives such as organophosphates and UV absorbers also pose significant risks. In 2018, organophosphate production reached more than 1 million tons (Fernandez-Arribas et al. 2023). A growing number of studies have shown that OPEs have adverse effects on biological and human health, including reproductive developmental toxicity, endocrine disruption toxicity, and neurotoxicity (Klose et al. 2022). According to data, the annual global production of UV absorbers is up to 10,000 tons (Carve et al. 2021). Some benzotriazoles have

✉ Ruijie Zhang
rjzhang@gxu.edu.cn

[1] School of Resources, Environment, and Materials, Guangxi University, Nanning 530004, China

[2] Guangxi Laboratory on the Study of Coral Reefs in the South China Sea, Coral Reef Research Center of China, School of Marine Sciences, Guangxi University, Nanning 530004, China

[3] Southern Marine Science and Engineering Guangdong Laboratory (Guangzhou), Guangzhou 511458, China

Published online: 27 March 2025

been classified as high-yield chemicals by the Organization for Economic Cooperation and Development (Wick et al. 2016).

Expanded polystyrene (EPS), a low-cost and lightweight material with thermal insulation properties, was selected for this study due to its widespread use in packaging, construction, and fishing. However, its lightweight property also makes it prone to floating on water surfaces, increasing its exposure to environmental factors such as sunlight and rain.

Understanding the release behavior of plastic additives is essential for controlling co-existing contaminants and assessing environmental health risks. This study focuses on polystyrene plastics and aims to: (i) analyze the content and composition of three plastic additives in polystyrene materials; (ii) investigate the impact of different simulated environments on additive release; and (iii) estimate the mass loadings of these additives in polystyrene plastics.

Materials and Methods

Standards and Materials

In this study, 11 OPEs, 16 PAEs, and 13 OUVAs, which are widely used in the market, were measured and analyzed. Quantitative recovery indicators, D_4-DMP, D_4-BBP, and D_4-DEHP (to monitor PAEs), D_{27}-TNBP and D_{15}-TPHP (to monitor OPEs), and D_5-BP-3 (to monitor OUVAs), were added to each sample to monitor the recovery of the target compounds. Detailed information on the above 40 standardized products is provided in the Supplementary materials (Tables S1-S3). The EPS plastic used in the simulation experiment was purchased from an online shopping platform.

Experimental Setup

Brand-new EPS foam plastics were divided into five groups (T_1-T_5), each consisting of 8 replicates, with each replicate weighing 0.3 g. The T_1 group was designated as the air-exposed group, with plastic samples placed uncovered on stainless steel screens and exposed to simulated rainfall and ultraviolet irradiation generated by the aging device. A beaker was placed at the bottom of group T_1 to collect leachate produced during aging. For groups T_2 and T_4, 300 mL of ultrapure water was added to each group. For groups T_3 and T_5, 300 mL of artificial seawater (salinity 32‰, prepared with sea salt and ultrapure water) was used. The groups T_4 and T_5 were wrapped in tin foil, and protected from light. All vials were sealed with glass stoppers. The specific experimental setup is shown in Fig. 1. All samples were placed in the UV-accelerated aging chamber. The samples were exposed for 2, 4, 6, 8, 10, 12, 14, and 16 days. We collected EPS samples after aging for subsequent analysis. EPS samples were collected after aging for subsequent analysis. Simultaneously, the additive content in the brand-new foam was measured. The parameters of the UV-accelerated aging chamber are provided in Text S2.

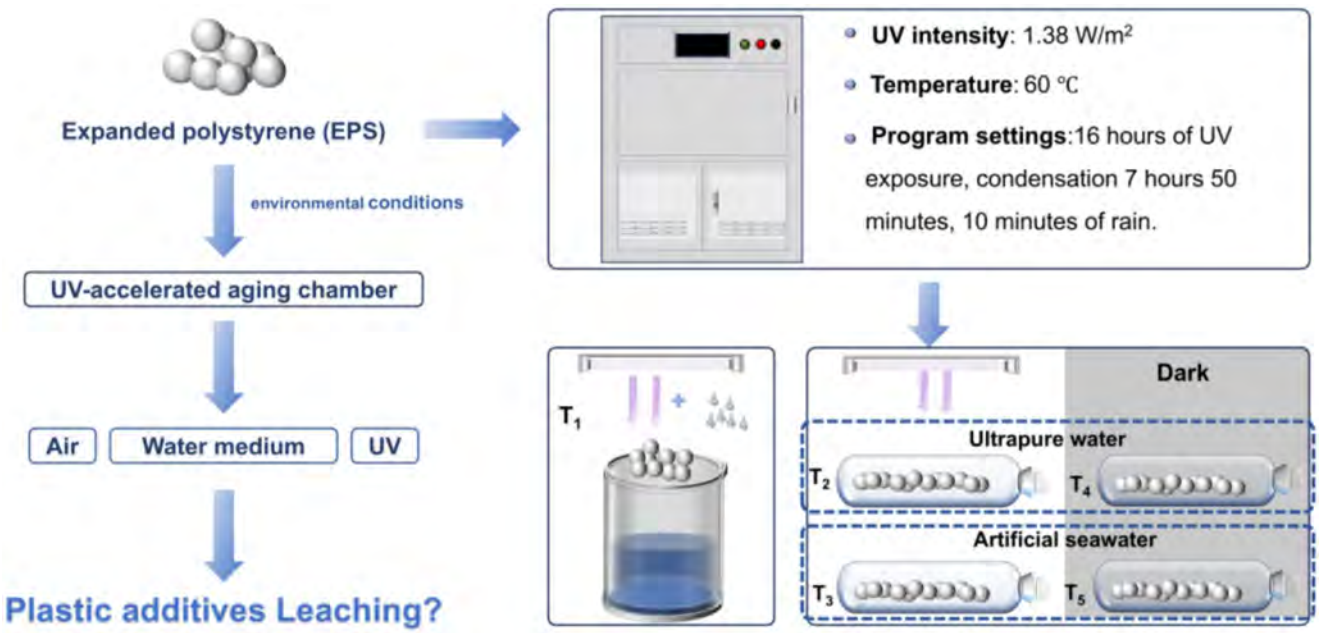


Fig. 1 The experimental setup of EPS expose to different environments

Extraction of Additives from Plastic Samples

Each plastic sample was placed in a 50-mL brown vial with 30 mL of dichloromethane as the extractant. To each vial, 60 ng of D_4-DMP, D_4-BBP, and D_4-DEHP, and 20 ng of D_{27}-TNBP, D_{15}-TPHP, and D_5-BP-3 were added as recovery rate indicators. The vials were then subjected to ultrasonic extraction in an ultrasonic cleaner (25 ℃, 300 W, 40 kHz) for 30 min. The extracts from each sample were combined into a 250-mL Florence flask, and the extraction process was repeated three times. The combined extracts were concentrated to near dryness using a rotary evaporator (1000 rpm, 40 ℃). Solvent displacement was then performed by adding 3–4 mL of ethyl acetate in two batches. Finally, the resulting solution was transferred into a 1.5-mL brown injection vial using ethyl acetate. Identification and quantification of all additives were conducted using an Agilent 7890 gas chromatography-tandem 7000C triple quadrupole mass spectrometry (GC-MS/MS, Agilent Technologies, Palo Alto, USA) in Multiple Reaction Monitoring (MRM) mode. Detailed information about mass spectral parameters is provided in Text S1 and Tables S4-S6.

Quality Assurance/Quality Control (QA/QC)

Strict quality control procedures were employed throughout all experimental operations to minimize the influence of external environmental contamination. Metal products used in sample processing underwent washing with hexane, methylene chloride, and ultrapure water to remove residual contaminants from their surfaces. During GC-MS/MS measurements, the samples were spiked with ethyl acetate as a procedural blank. Additionally, one quality control (QC) point was included for every 10 samples to monitor instrument performance. The final concentrations of target compounds in all measured samples were obtained by subtracting the concentrations of target compounds found in the blank samples.

Data Analysis

During the experiment, the release of additives from plastics into water was determined by subtracting the additive concentrations in aged samples from their initial concentrations in the plastics. Additives with relatively high concentrations were analyzed using kinetic fitting, and their leaching behavior was modeled with both first-order and second-order kinetic equations, fitted using Origin software.

The first-order kinetic model:

$$Q_t = Q_e(1 - e^{-k_1 t}) \quad (1)$$

The second-order kinetic model:

$$\frac{1}{(Q_e - Q_t)} = \frac{1}{Q_e} + k_2 t \quad (2)$$

Where Q_t is the amount of plastic additive leached at moment t. Q_e is the amount of additive at the leaching equilibrium; k_1 is the rate constant of the first-order kinetic model, and k_2 is the rate constant of the second-order kinetic model.

Results and Discussion

Composition of Additives in Virgin EPS Foam

As shown in Fig. 2, the content of the three additives in the original EPS plastic decreases sequentially from high to low as PAEs ($\sum_{16}$PAEs: 4.64×10^4 ng/g), OPEs ($\sum_{11}$OPEs: 695 ng/g), and OUVAs ($\sum_{13}$OUVAs: 461 ng/g). The detection results for 16 PAEs are consistent with previous studies, with DEHP (84%) and DPHP (11%) identified as the main detected compounds (Fig. 2a). Among the 11 OPEs, the chlorinated OPEs, TCIPPs, and TCEP dominate (Fig. 2b). Due to the varied physicochemical properties of OPEs, their distribution behaviors in aquatic environments differ.

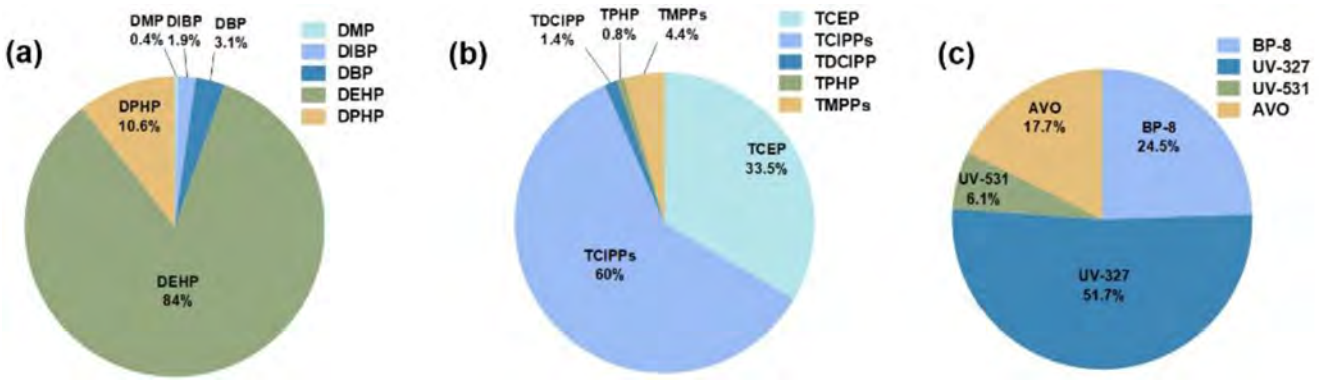


Fig. 2 Percentage of PAEs, OPEs and OUVAs in unaged EPS. (The figure shows the percentage of compounds detected and does not show the detection of 0.)

Generally, chlorinated OPEs exhibit greater hydrophilicity compared to other OPEs (Wang et al. 2023). Among the 13 OUVAs, UV-327 (55%) and BP-8 (26%) also have relatively high concentrations (Fig. 2c). However, the additive concentrations vary across plastic types and production formulations, leading to observed discrepancies in reported values.

Release Characteristics of Additives Under Different Environmental Conditions

As shown in Fig. 3, the additive content in the plastic did not consistently decrease across the five environmental simulation exposure modes. Instead, additive content showed an initial rapid decline, followed by slow fluctuations (increase and/or decrease) over time, indicating a transition from fast release to dynamic adsorption-desorption processes. This trend may arise from aging-induced changes in EPS particle properties (e.g., surface morphology, crystallinity), which alter additive migration under environmental stressors (Liu et al. 2023).

Air Exposure Conditions

The levels of the three additives in EPS foam pellets decreased rapidly under air exposure, with reductions of 74.3% for PAEs within the first 6 days, 98.1% for OPEs within 8 days, and 95.9% for OUVAs within 2 days.

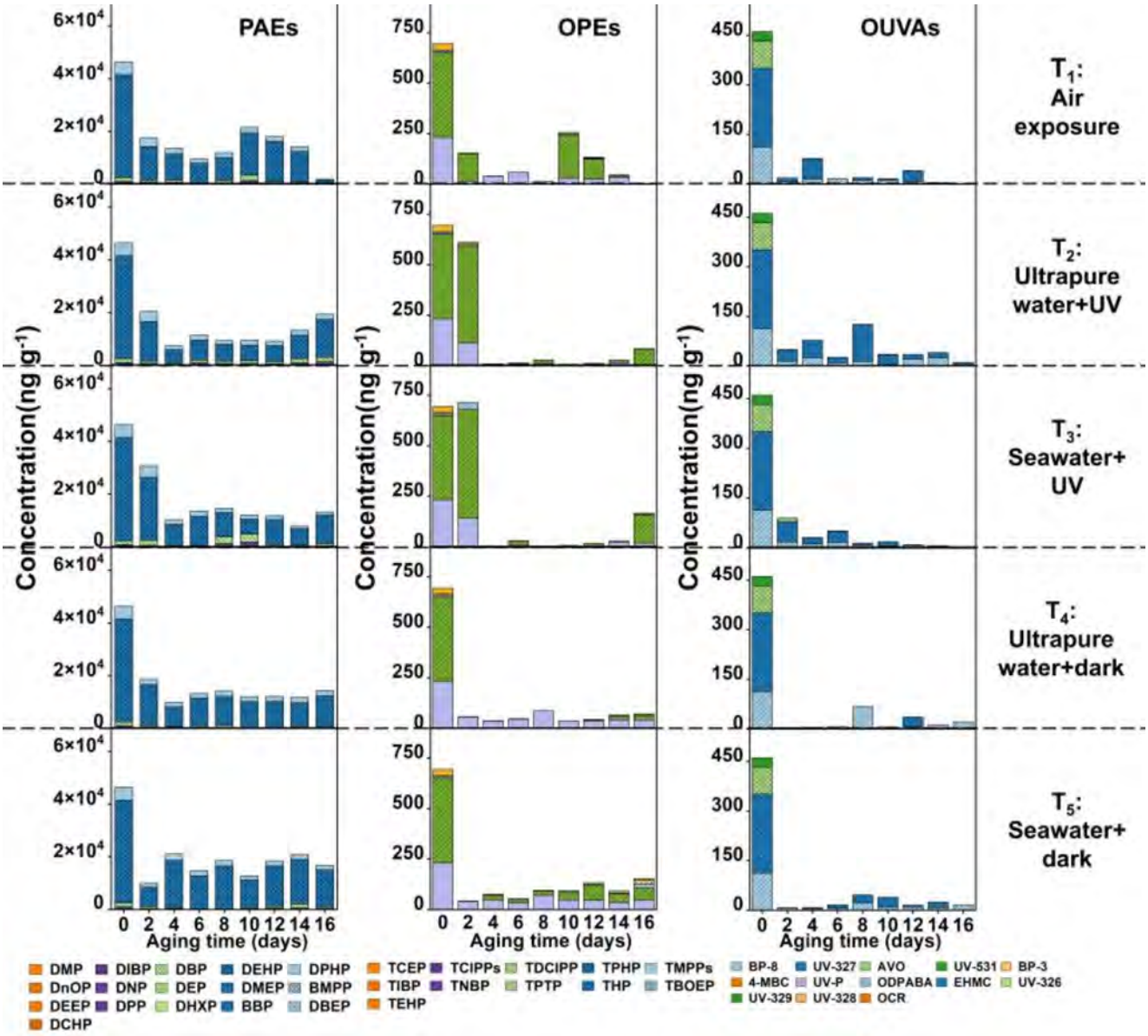


Fig. 3 Dynamic changes in the content of PAEs, OPEs, and OUVAs additives in the EPS particles after their exposure to different environments

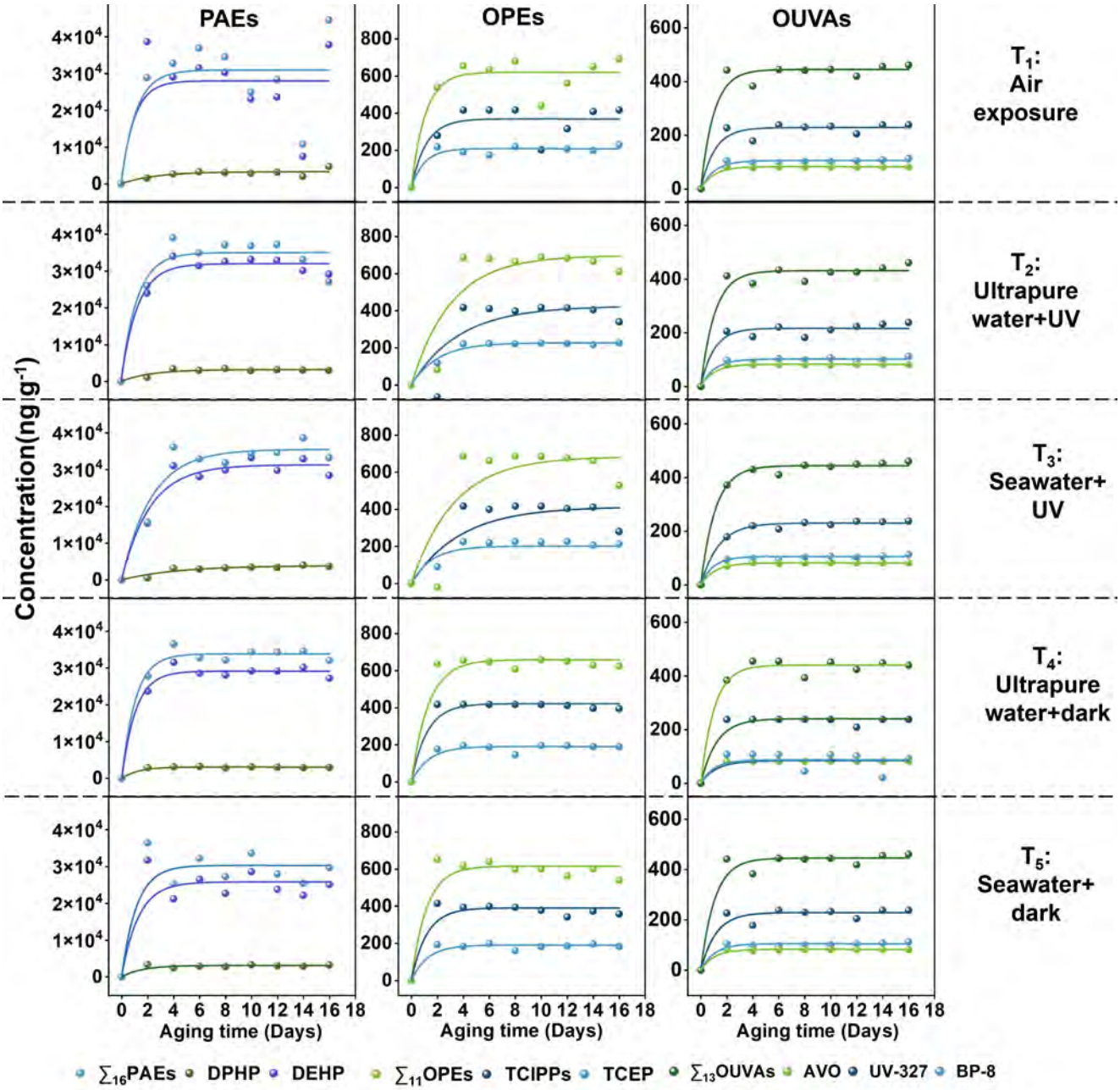


Fig. 4 The first-order kinetic model of the release of PAEs, OPEs, and OUVAs in the EPS particles under different environments

Following this initial decline, all three additives exhibited a transient increase, with PAEs, OPEs, and OUVAs rising by 20.6%, 34.9%, and 12.8%, respectively (Fig. 3). This re-adsorption phase was more pronounced under air exposure than other conditions, which suggests that additives released from EPS foam can re-adsorb onto the plastic surface under specific environmental factors. Additive levels then declined steadily, reaching their lowest concentrations on day 16 ($\sum_{16}$PAEs: 1.88×10^3 ng/g; $\sum_{11}$OPEs: 2.86 ng/g; $\sum_{13}$OUVAs: undetectable).

Compared to water exposure, air exposure exhibited more dynamic adsorption and release patterns, likely due to increased susceptibility to UV radiation, temperature fluctuations, and rainfall. The first-order kinetic fit plots align more closely with the experimental release results, consistent with findings from other studies (Zhong et al. 2023). The kinetic analysis supports these observations, with first-order kinetic models fitting the release of PAEs and OPEs better than second-order models (Fig. S4 and S5, Tables S7 and S8). The release rates under air exposure were the highest across all scenarios ($\sum_{16}$PAEs: k = 0.868 ng/g·day;

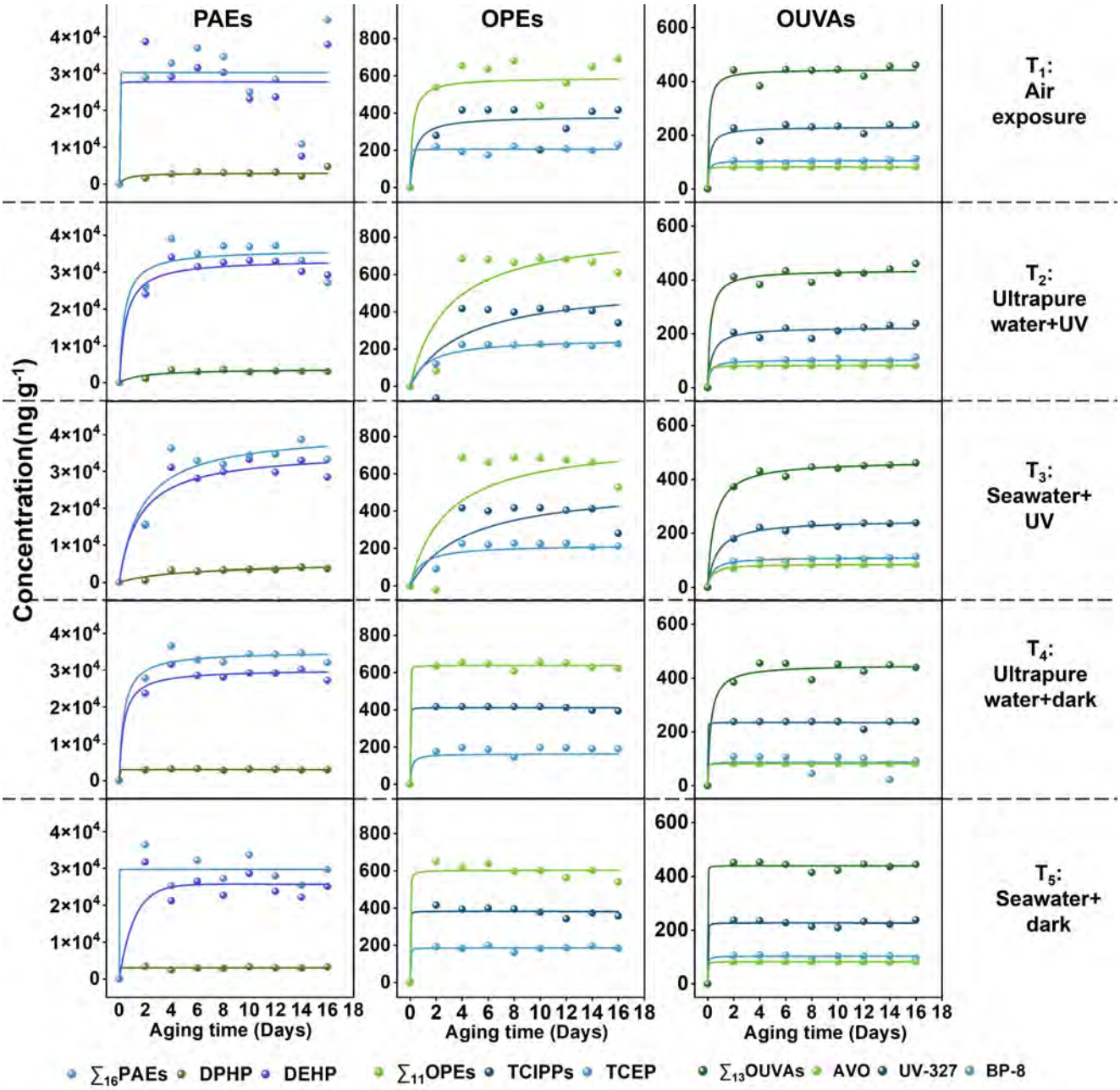


Fig. 5 The second-order kinetic model of the release of PAEs, OPEs, and OUVAs in the EPS particles under different environments

$\sum_{11}$OPEs: k = 0.927 ng/g·day), reinforcing the role of environmental factors in accelerating additive release under air exposure conditions. The initial rapid release of additives under air exposure is driven not only by physical desorption but also by photo-oxidation and thermal degradation of the EPS matrix. This suggests that environmental factors act as 'catalysts' for aging-induced additive release.

Among the three additives, OUVAs exhibited a distinct release pattern under air exposure, with a clear outward release trend and complete disappearance by day 16 (Fig. 3). This behavior is likely due to prolonged UV exposure, which facilitates the release of OUVAs from EPS foams into the environment. Furthermore, the ability of OUVAs to absorb UV rays may lead to the cleavage of chemical bonds and their degradation into non-UV-active compounds (Vila et al. 2017).

Effect of Salinity on the Release of Plastic Additives Under Water Exposure

As shown in Fig. 3, additive levels in EPS foam pellets decreased rapidly during the initial exposure to ultrapure

water. Significant reductions were observed for $\sum_{16}$PAEs and $\sum_{11}$OPEs from day 0 to day 4, with peak release levels on day 4 ($\sum_{16}$PAEs: 7.38×10^3 ng/g; $\sum_{11}$OPEs: 9.74 ng/g). While both additives displayed strong release properties initially, their behavior diverged afterward. $\sum_{16}$PAEs showed a slight increase on day 6, stabilized from days 6 to 12, and then rose significantly. Conversely, $\sum_{11}$OPEs exhibited adsorption after day 4, reaching a maximum concentration on day 16 ($\sum_{11}$OPEs: 84.8 ng/g). These trends align with prior studies on brominated flame retardants (BFRs) and PAEs, which showed rapid release followed by gradual equilibrium (Zuo et al. 2023). Plastic additives, incorporated into polymers through non-covalent bonding, are released upon contact with a liquid matrix. However, their hydrophobicity often leads to re-adsorption onto the polymer surface (Dhavamani et al. 2022). Over time, the EPS plastic adsorption capacity may increase due to environmental factors, further facilitating additive uptake. This explains why additive levels do not always consistently decline during exposure, though aged plastics still release additives more readily than unaged ones (Chen et al. 2023).

In seawater, $\sum_{16}$PAEs and $\sum_{11}$OPEs exhibited a similar initial release trend to ultrapure water during days 0 to 4. However, from days 6 to 16, their concentrations were slightly higher than under ultrapure water exposure. The presence of inorganic ions in seawater likely inhibited additive release by reducing the solubility and diffusion of non-ionic compounds (Dhavamani et al. 2022). Additionally, salinity and dissolved organic matter (DOM) enhanced the adsorption of additives onto plastics (Chen et al. 2019). The aging process in seawater may also be suppressed due to the presence of photochemically active ions (e.g., bromide, chloride, nitrate, carbonate). These ions can indirectly or directly affect free radical reactions involved in plastic aging, thereby limiting additive release. Kinetic simulations confirm this: the equilibrium release (Q_e) and release rates of DEHP and OPEs were significantly lower in seawater than in ultrapure water (DEHP: 31315 ng/g < 31990 ng/g; OPEs: 684 ng/g < 698 ng/g).

The OUVAs behaved differently from the PAEs and OPEs. When exposed to ultrapure water, OUVAs showed a decrease followed by an increasing trend from 0 to 8 days, reaching a maximum on day 8 ($\sum_{13}$OUVAs: 125.76 ng/g). They then reached a release-adsorption equilibrium from days 10 to 14 and achieved a minimum concentration on day 16 ($\sum_{13}$OUVAs: 10.9 ng/g) (Fig. 3). Analysis of individual OUVAs revealed that AVO was almost entirely released within the first day and almost a very small amount is adsorbed during the subsequent releases. It can also be seen in the accompanying table that AVO is the substance with the highest release rate (Table S9). UV-327, which accounted for the highest proportion, showed a significant decreasing trend on days 0–6 and 8–16. In contrast, BP-8 exhibited an increasing trend in the later stages of aging. This difference may be related to the inherent properties of these compounds. Under seawater exposure, $\sum_{13}$OUVAs in EPS foam particles showed a significant decreasing trend on days 0–4 and reached the lowest value on day 4 ($\sum_{13}$OUVAs: 30.5 ng/g), and also showed a significant decreasing trend on days 6–16 and completely disappeared on day 16 ($\sum_{13}$OUVAs: 0 ng/g), which was different from PAEs and OPEs. Unlike PAEs and OPEs in EPS foam particles, UV irradiation both promotes additive release through EPS fragmentation and photodegrades OUVAs. This aligns with the observed OUVAs decline in UV-exposed samples (Fig. 3), where aging enhanced additive migration (Xu et al. 2025).

Effect of Light on the Release of Plastic Additives Under Water Exposure

Under light-avoidance conditions, the release of $\sum_{16}$PAEs and $\sum_{11}$OPEs from EPS foam particles reached minimum levels on day 4 ($\sum_{16}$PAEs: 7.44×10^3 ng/g; $\sum_{11}$OPEs: 38.51 ng/g) and day 2 ($\sum_{16}$PAEs: 7.28×10^3 ng/g; $\sum_{11}$OPEs: 42.50 ng/g), respectively, before gradually equilibrating. A comparison between light-avoidance and UV-exposure groups revealed that while both conditions exhibited high initial release rates, the release levels in light-avoidance groups were consistently lower (Tables S7 and S8). As shown in Fig. 3, after reaching maximum release levels, no significant adsorption or release occurred, with equilibrium levels remaining lower than those under UV exposure. This indicates that UV absence significantly slowed both the rate and extent of EPS aging. Under light-avoidance conditions in seawater, the additive release was more pronounced than in ultrapure water under the same conditions, likely due to the effects of salinity, which influences solubility and diffusion.

Under light-avoidance conditions, $\sum_{13}$OUVAs in EPS foam particles exhibited similar trends across both ultrapure water and seawater. A significant decrease was observed on day 2 (ultrapure water: 4.45 ng/g; seawater: 7.59 ng/g), followed by a gradual increase from days 2 to 8, reaching maximum values on day 8 (ultrapure water: 67.6 ng/g; seawater: 46.5 ng/g). From days 8 to 16, OUVAs levels decreased slightly, with final concentrations of 21.3 ng/g (ultrapure water) and 16.6 ng/g (seawater) on day 16. These levels were significantly higher than those observed in the UV-exposure groups on day 16, suggesting that UV irradiation accelerates the degradation of OUVAs in EPS foam particles. The difference highlights the pivotal role of UV exposure in promoting additive degradation, especially for OUVAs, compared to light-avoidance conditions.

Estimation of Total Release Quantity of Plastic Additives in the Marine EPS Waste

According to previous literature calculations, the cumulative mass of floating microplastics in the ocean ranges from 0.093 to 23.6 million tons (van Sebille et al. 2015). Polystyrene is one of the common polymers found in the marine environment, comprising approximately 4% of marine microplastics (Erni-Cassola et al. 2019).

It is estimated that the amount of additives that enter the ocean each year from EPS plastic is calculated by the following formula:

$$Q_{Total} = C_i \times M_{microplastics} \times P_{EPS} \times 10^{-6} \quad (3)$$

Where Q_{Total} is the total amount of additives released from EPS plastics per year; C_i is defined as the equilibrium release of the additive from the EPS; $M_{microplastics}$ is the weight of microplastics entering the oceans each year. P_{EPS} is the percentage of EPS plastics in the total plastics.

Based on calculations, the estimated release of the three additives into the ocean is 33.5k tons for PAEs, 646 tons for OPEs, and 420 tons for OUVAs. The massive release of these additives highlights the urgency of addressing the issue of EPS waste management. Understanding the dynamics and pathways of additive release during EPS aging is critical to assessing long-term environmental pollution risks, particularly in landfills and marine ecosystems. Due to their lightweight and buoyant properties, EPS plastics tend to float on the ocean surface, where they are exposed to complex environmental factors from both water and air. This increases the potential for additive release, posing a significant threat to the marine environment. However, this estimation is simplified, as EPS foam in the ocean is also affected by additional natural factors, such as waves. More precise calculations require further detailed research. Despite this, the environmental risks associated with EPS plastics remain undeniable.

Conclusions

The release of plastic additives is primarily driven by their migration and diffusion within the plastic matrix. However, external environmental conditions, such as air exposure, seawater immersion, and light, alter the surface properties of EPS plastics, indirectly influencing this process. In this study, the additive release characteristics under the interaction of several environmental conditions were investigated. However, it is difficult for laboratory simulation to fully reproduce complex environmental parameters, and field studies should be strengthened to establish dynamic release models in future studies. The environmental persistence of EPS and the release of additives pose a risk to the ecosystem. In the future, biodegradable alternatives to EPS should be developed and bio-based additives should be explored to replace traditional toxic plasticizers/flame retardants. At the same time, more comprehensive recycling technologies should be designed to reduce the generation of EPS waste.

Acknowledgements This work was supported by the Guangxi Natural Science Foundation (2020GXNSFDA297005).

Declarations

Competing Interests The authors declare no competing interests.

References

Barlucchi L, Biale G, La Nasa J, Mattonai M, Pezzini S, Corti A, Castelvetro V, Modugno F (2024) Abiotic degradation and accelerated ageing of microplastics from biodegradable and recycled materials in artificial seawater. Sci Total Environ 954:176832. https://doi.org/10.1016/j.scitotenv.2024.176832

Carve M, Nugegoda D, Allinson G, Shimeta J (2021) A systematic review and ecological risk assessment for organic ultraviolet filters in aquatic environments. Environ Pollut 268(Pt B):115894. https://doi.org/10.1016/j.envpol.2020.115894

Chen C, Chen L, Yao Y, Artigas F, Huang Q, Zhang W (2019) Organotin release from Polyvinyl chloride microplastics and concurrent photodegradation in water: impacts from salinity, dissolved organic matter, and light exposure. Environ Sci Technol 53(18):10741–10752. https://doi.org/10.1021/acs.est.9b03428

Chen X, Chen C-E, Guo X, Sweetman AJ (2023) Sorption and desorption of bisphenols on commercial plastics and the effect of UV aging. Chemosphere 310:136867. https://doi.org/10.1016/j.chemosphere.2022.136867

Dhavamani J, Beck AJ, Gledhill M, El-Shahawi MS, Kadi MW, Ismail IMI, Achterberg EP (2022) The effects of salinity, temperature, and UV irradiation on leaching and adsorption of phthalate esters from polyethylene in seawater. Sci Total Environ 838:155461. https://doi.org/10.1016/j.scitotenv.2022.155461

Ding L, Mao R, Ma S, Guo X, Zhu L (2020) High temperature depended on the ageing mechanism of microplastics under different environmental conditions and its effect on the distribution of organic pollutants. Water Res 174:115634. https://doi.org/10.1016/j.watres.2020.115634

Erni-Cassola G, Zadjelovic V, Gibson MI, Christie-Oleza JA (2019) Distribution of plastic polymer types in the marine environment; A meta-analysis. J Hazard Mater 369:691–698. https://doi.org/10.1016/j.jhazmat.2019.02.067

Fernandez-Arribas J, Moreno T, Eljarrat E (2023) Human exposure to organophosphate esters in water and packed beverages. Environ Int 175:107936. https://doi.org/10.1016/j.envint.2023.107936

Hahladakis JN, Velis CA, Weber R, Iacovidou E, Purnell P (2018) An overview of chemical additives present in plastics: migration, release, fate and environmental impact during their use, disposal and recycling. J Hazard Mater 344:179–199. https://doi.org/10.1016/j.jhazmat.2017.10.014

Klose J, Pahl M, Bartmann K, Bendt F, Blum J, Dolde X, Forster N, Holzer AK, Hubenthal U, Kessel HE, Koch K, Masjosthusmann S, Schneider S, Sturzl LC, Woeste S, Rossi A, Covaci A, Behl M, Leist M, Tigges J, Fritsche E (2022) Neurodevelopmental toxicity

assessment of flame retardants using a human DNT in vitro testing battery. Cell Biol Toxicol 38(5):781–807. https://doi.org/10.1007/s10565-021-09603-2

Liu H, Zhang X, Ji B, Qiang Z, Karanfil T, Liu C (2023) UV aging of microplastic polymers promotes their chemical transformation and byproduct formation upon chlorination. Sci Total Environ 858. https://doi.org/10.1016/j.scitotenv.2022.159842

Mehta J, Dilbaghi N, Deep A, Hai FI, Hassan AA, Kaushik A, Kumar S (2025) Plastic waste upcycling into carbon nanomaterials in circular economy: synthesis, applications, and environmental aspects. Carbon 234. https://doi.org/10.1016/j.carbon.2024.119969

Poopal RK, Zhang J, Zhao R, Ramesh M, Ren Z (2020) Biochemical and behavior effects induced by diheptyl phthalate (DHPP) and diisodecyl phthalate (DIDP) exposed to zebrafish. Chemosphere 252:126498. https://doi.org/10.1016/j.chemosphere.2020.126498

Pradhan A, Olsson PE, Jass J (2018) Di(2-ethylhexyl) phthalate and diethyl phthalate disrupt lipid metabolism, reduce fecundity and shortens lifespan of caenorhabditis elegans. Chemosphere 190:375–382. https://doi.org/10.1016/j.chemosphere.2017.09.123

Rakib MRJ, De-la-Torre GE, Pizarro-Ortega CI, Dioses-Salinas DC, Al-Nahian S (2021) Personal protective equipment (PPE) pollution driven by the COVID-19 pandemic in Cox's Bazar, the longest natural beach in the world. Mar Pollut Bull 169. https://doi.org/10.1016/j.marpolbul.2021.112497

Rakib MRJ, Ertaş A, Walker TR, Rule MJ, Khandaker MU, Idris AM (2022) Macro marine litter survey of sandy beaches along the Cox's Bazar Coast of Bay of Bengal, Bangladesh: Land-based sources of solid litter pollution. Mar Pollut Bull 174. https://doi.org/10.1016/j.marpolbul.2021.113246

Rakib MRJ, Al Nahian S, Madadi R, Haider SMB, De-la-Torre GE, Walker TR, Jonathan MP, Cowger W, Khandaker MU, Idris AM (2023a) Spatiotemporal trends and characteristics of microplastic contamination in a large river-dominated estuary. Environ Sci Processes Impacts 25(5):929–940. https://doi.org/10.1039/d3em00014a

Rakib MRJ, Sarker A, Ram K, Uddin MG, Walker TR, Chowdhury T, Uddin J, Khandaker MU, Rahman MM, Idris AM (2023b) Microplastic toxicity in aquatic organisms and aquatic ecosystems: a review. Water Air Soil Pollut 234(1). https://doi.org/10.1007/s11270-023-06062-9

van Sebille E, Wilcox C, Lebreton L, Maximenko N, Hardesty BD, van Franeker JA, Eriksen M, Siegel D, Galgani F, Law KL (2015) A global inventory of small floating plastic debris. Environ Res Lett 10(12):124006. https://doi.org/10.1088/1748-9326/10/12/124006

Vila M, Celeiro M, Lamas JP, Garcia-Jares C, Dagnac T, Llompart M (2017) Simultaneous in-vial acetylation solid-phase Microextraction followed by gas chromatography tandem mass spectrometry for the analysis of multiclass organic UV filters in water. J Hazard Mater 323:45–55. https://doi.org/10.1016/j.jhazmat.2016.06.056

Wang Y, Zhao Y, Han X, Wang J, Wu C, Zhuang Y, Liu J, Li W (2023) A review of organophosphate esters in aquatic environments: levels, distribution, and human exposure. Water 15(9). https://doi.org/10.3390/w15091790

Wang Y, Zhao J, Fu Z, Guan D, Zhang D, Zhang H, Zhang Q, Xie J, Sun Y, Wang D (2024) Innovative overview of the occurrence, aging characteristics, and ecological toxicity of microplastics in environmental media. Environ Pollut 346. https://doi.org/10.1016/j.envpol.2024.123623

Wen Q, Liu N, Qu R, Ge F (2023) High salinity promotes the Photoaging of polystyrene microplastics with humic acid in seawater. Sci Total Environ 901:165741. https://doi.org/10.1016/j.scitotenv.2023.165741

Wick A, Jacobs B, Kunkel U, Heininger P, Ternes TA (2016) Benzotriazole UV stabilizers in sediments, suspended particulate matter and fish of German rivers: new insights into occurrence, time trends and persistency. Environ Pollut 212:401–412. https://doi.org/10.1016/j.envpol.2016.01.024

Xu Z, Zhang J, Qi R, Liu Q, Cao H, Wen F, Liao Y, Shih K, Tang Y (2025) Complex release dynamics of microplastic additives: an interplay of additive degradation and microplastic aging. J Hazard Mater. https://doi.org/10.1016/j.jhazmat.2025.137711

Zhong X, Yi X, Cheng F, Tong H, Xu W, Yang X (2023) Leaching of di-2-ethylhexyl phthalate from biodegradable and conventional microplastics and the potential risks. Chemosphere 311. https://doi.org/10.1016/j.chemosphere.2022.137208

Zuo L, Li Y, Hou W, Wang F, Feng Y, Zhang Z (2023) Leaching of Triphenyl phosphate and tri-n-butyl phosphate from polystyrene microplastics: influence of plastic properties and simulated digestive fluids. Environ Sci Pollut Res 30(53):114659–114666. https://doi.org/10.1007/s11356-023-30229-w

Publisher's Note Springer Nature remains neutral with regard to jurisdictional claims in published maps and institutional affiliations.

Springer Nature or its licensor (e.g. a society or other partner) holds exclusive rights to this article under a publishing agreement with the author(s) or other rightsholder(s); author self-archiving of the accepted manuscript version of this article is solely governed by the terms of such publishing agreement and applicable law.

Desalination and Water Treatment 321 (2025) 101007

Contents lists available at ScienceDirect

Desalination and Water Treatment

journal homepage: www.sciencedirect.com/journal/desalination-and-water-treatment/

Research progress on fungi and their spore inactivation in different water bodies

Fangyu Liang [a,b], Yuanyuan Zhang [b,*]

[a] School of Resources, Environment and Materials, Guangxi University, Nanning 530004, China
[b] School of Marine Sciences, Guangxi Laboratory on the Study of Coral Reefs in the South China Sea, Guangxi University, Nanning 530004, China

ARTICLE INFO

Keywords:
Fungi
Fungal spore
Inactivation technology
Disinfection
Research status

ABSTRACT

The presence of fungi and their spores in aquatic environments constitutes an increasingly important environmental and public health issue, with potential impacts ranging from alterations in water quality to health risks for both humans and animals. This review summarizes the latest advancements in the inactivation of fungi and their spores in various types of water bodies, including surface water, drinking water, and seawater. The paper provides a systematic review of the distribution characteristics of fungi and spores in aquatic environments, commonly used fungal identification methods, and the progress made in inactivation technologies. By critically analyzing the limitations of existing research, we offer perspectives on future research directions, aiming to provide theoretical guidance and support for the optimization and development of fungal contamination control and novel inactivation technologies. Given the strong resistance of fungal spores to conventional disinfection methods, this review systematically evaluates the limitations of current approaches and seeks to lay the necessary knowledge foundation for improving the effectiveness of fungal control strategies and inactivation technologies.

1. Introduction

The rapid development of the social economy has led to corresponding environmental problems[1–3]. As one of the most common substances on Earth, water is an important resource for all life, including human beings. It is one of the most critical components of living things and is often the first to be polluted. Water pollution is not only harmful to human health, but also directly affects economic development and social stability. Ebenstein et al. [4] found that the pollution has significantly impeded health improvement in China over the past two decades. One major factor contributing to the country's high cancer rates is the worsening water quality [5]. The deterioration in water quality will increase the incidence rate of gastrointestinal cancer by 9.7 % [6]. Ling et al. [7] studied the quantitative method of environmental value loss of water pollution based on emergy theory. Taking Zhengzhou city as a case study, the findings revealed that the average economic loss due to water pollution from 2000 to 2015 amounted to 5.948 billion yuan, which represented 1.28 % of gross domestic product. It is reported that the frequency of sudden biological pollution incidents in public water systems is much higher than that of chemical pollution incidents[8]. Biological pollution of water refers to the phenomena where various organisms, especially parasites, bacteria, viruses, and fungi, contaminate aquatic environment and drinking water, potentially leading to human diseases[9–12]. In recent years, people have been paying more and more attention to the potential harm of biological pollutants in water to human health and even environmental health[13–15]. However, because waterborne fungi do not typically cause acute toxicity in water in the same way that viruses and bacteria do, they have not received as much attention in water quality studies and have often been overlooked in past research [16]. There is growing evidence that chronic exposure to waterborne fungi, particularly those producing mycotoxins, can lead to long-term health effects. These include respiratory disorders, allergic reactions, and potential systemic toxicity such as liver damage or immunosuppression[17–19]. A total of 98,656 articles on the theme of "fungi" and "water" and 7722 articles on the theme of "fungal spores" and "water" were recorded on the Web of Science. Judging from the number of articles, since 2000, the attention of fungi in water has increased obviously, as shown in Fig. 1, especially in the last five years. Compared with bacteria, fungi have a more complex cell structure and exist in forms such as dormancy, germination, aggregation, and biofilm

* Corresponding author.
E-mail address: yyzhang@gxu.edu.cn (Y. Zhang).

https://doi.org/10.1016/j.dwt.2025.101007
Received 17 October 2024; Received in revised form 5 January 2025; Accepted 14 January 2025
Available online 16 January 2025
1944-3986/© 2025 The Authors. Published by Elsevier Inc. This is an open access article under the CC BY-NC-ND license (http://creativecommons.org/licenses/by-nc-nd/4.0/).

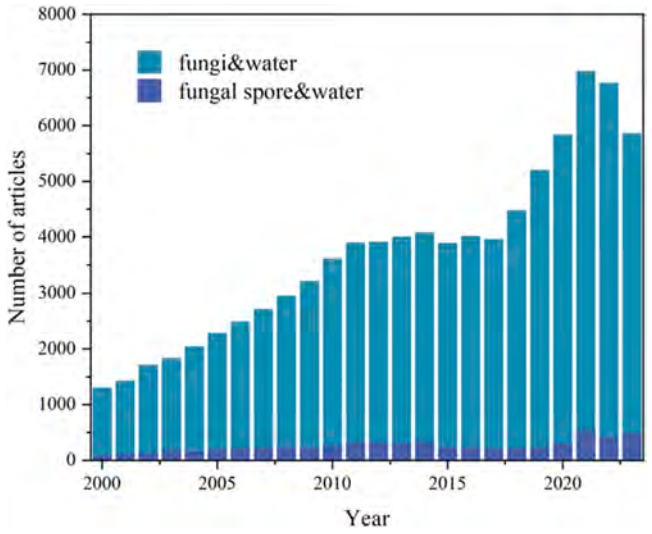


Fig. 1. Annual publications of fungi in water.

in water. They are difficult to control and disinfect. Water with high organic matter and phosphorus content poses a higher risk of fungal outbreaks [20]. At present, most research focuses on bacteria and viruses, with less emphasis on fungi [21]. At present, China's " Standards for drinking water quality" (GB 5749–2022) has not clearly stipulated the detection standard for fungi. On a global scale, only Sweden has formulated relevant laws and regulations on fungal pollution in drinking water, and its standard stipulates that the number of fungi should not exceed 100 CFU/100 mL [22].

Fungal pollution should not be underestimated. Studies in recent decades have shown that fungal pollution in water is a serious issue, causing significant harm to both the environment and human health [20]. On the one hand, fungal pollution affects water quality, mainly manifesting in the color, smell, and taste of drinking water [23]; On the other hand, fungal pollution can also pose a threat to human health, especially for individuals with compromised immune systems, and such infections can be fatal [24]. According to previous studies, fungi are everywhere in water [25–28]. Because the growth of fungi is influenced by various water quality conditions and the specific environmental characteristics of each water body, the species and quantity of fungi vary significantly across different water bodies and regions [29]. At present, many countries and regions usually use fecal pollution indicator bacteria (e.g., *Escherichia coli*) to assess the risk of potentially pathogenic microorganisms in water[30–32].However, some studies show that the presence of fecal contamination indicator bacteria in water does not necessarily mean the presence of fungal pollution, and there is no direct correlation between them [22,33–35]. When evaluating water quality safety, the existence and risk of fungi and microorganisms in water cannot be fully reflected only by the indicator bacteria index.

Currently, detection methods can be broadly categorized into three groups: culture-based methods, biochemical-based methods, and molecular biology-based methods. Each method possesses inherent strengths and limitations, necessitating the optimization of current methodologies and the integration of various detection techniques. In order to effectively control fungal populations in aquatic environments, researchers have developed various methods for fungal inactivation following qualitative and quantitative assessments. These methods can be broadly categorized into biological, chemical, and physical approaches. However, each method has its own limitations in practical applications, such as cost, efficacy, and potential environmental impacts. Therefore, it is of great significance to explore efficient fungal detection methods and environmentally friendly fungal inactivation techniques to control biological pollution and develop effective inactivation methods.

While several studies have explored individual aspects of fungal inactivation or detection, there is a lack of comprehensive reviews that integrate recent advancements, evaluate the effectiveness of various methods. This review provides a comprehensive analysis of current fungal inactivation technologies and, importantly, presents the first comparative evaluation of fungal detection methods, highlighting their applicability and limitations. The current research deficiencies in this field are analyzed, and future prospects are discussed. This paper aims to provide a theoretical basis for future research on controlling fungal pollution and developing fungal inactivation technology.

2. Investigation and research status of fungi and spores in water

Microbial contamination in water bodies not only affects the quality of life but can even lead to disease outbreaks that threaten human health, and therefore has received widespread attention. According to the survey data of the World Health Organization, about 80 % of human diseases are related to water[36]. Water pollution mainly involves biological contamination and chemical contamination, with biological contamination being the primary concern[37]. In the past, water quality safety research primarily focused on pathogenic microorganisms such as viruses and bacteria, which can cause acute diseases or epidemics, while research on fungi has been relatively limited.

2.1. Investigation and research status of fungi in water

Fungi, including molds, yeasts, and mushroom, are eukaryotic organisms producing conidia (spores) that are easy to disperse in and contaminate the surrounding environments[38]. Fungi can survive in various natural, man-made, and extreme environments, and some fungi can develop strong physiological adaptability under certain conditions, which may change with variations in seawater parameters [39].

Fungal contamination occupies a large portion of urban water supply systems[40]. Fungal contamination of water has significant implications for hospitals and health institutions, particularly for immunocompromised patients[41]. With the sustainable development of China's social economy, the problem of water pollution has become increasingly serious, significantly impacting drinking water quality. This issue requires urgent attention.

In addition to drinking water sources, aquatic ecosystems, such as lakes and ponds, also serve as significant habitats for fungal diversity. For example, a large number of fungi in lakes and ponds across northeastern Germany and Scandinavia have yet to be fully characterized[42,43]. Although these microorganisms have not been isolated in culture, they may be highly abundant and could play a dominant role in the functioning of natural ecosystems[44]. In contrast to research on terrestrial and wetland fungi, the exploration and understanding of most aquatic fungi and their ecological functions are still limited, with studies primarily concentrated on specific habitats within lotic (flowing-water) ecosystems[45–47].

Relative to the finite freshwater resources, which constitute approximately 2.5 % of the Earth's total hydrosphere, the Earth's surface is 71 % covered by oceans, encompassing a total area of approximately 360 million square kilometres. It holds about 1.3 billion cubic kilometres of water, constituting roughly 97 % of the total water on Earth. Recent studies have revealed the presence of a diverse range of fungal species in marine environments. Some studies estimate that there are 1692 species of fungi in the ocean [48]. Jones et al. [49] show that In marine environments, mangrove substrata are dominated by *Dothideomycetes*, while submerged woody substrata in coastal waters host a high abundance of halosphaeriaceous species. Fungi in seawater are an important and diverse microbial community, which plays a key role in marine ecosystems [50–52]. Fungi in seawater grow on a variety of substrates, including wood, sediments, mud, soil, sand, algae, corals, rotting leaves of mangroves, intertidal weeds, and even on crustaceans [53–56].

Many studies show that the potential harm caused by fungi in seawater can not be ignored. Sallenave-Namont et al. [57] isolated and identified toxic saprophytic fungi from shellfish, sediments and seawater samples in marine shellfish culture areas. They identified 456 strains, including 12 different genera, with *Penicillium*, *Aspergillus*, *Trichoderma* and *Cladosporium* being obviously dominant. Their research shows that filter-feeding shellfish accumulate toxic metabolites from fungi, indicating that consuming contaminated shellfish poses a risk of poisoning. At the same time, seawater has an important influence on the formation and toxicity of fungal metabolites. Song et al. [58] found that seawater factors can promote many fungal strains to produce bioactive metabolites, including plant pathogens, marine phytoplankton inhibitors and toxic substances of marine animals. Kerzaon et al. [59] research shows that although the secretion of marine strains seems to be less affected by seawater salinity compared to terrestrial strains, seawater salinity increases the secretion of *Aspergillus fumigatus* and the excretion of colloid toxins. This may exacerbate the toxicity of *Aspergillus fumigatus* in the marine environment. Reich et al. [60] found that some fungal species that dominate the microbial community with low pH value are known pathogenic fungi.

Despite the increasing number of fungal species identified in aquatic systems, global fungal diversity is estimated to lie between 1.5 and 1.6 million species [61]. However, the study and detection of marine fungi by both domestic and international researchers remain constrained by methodological limitations [21,56]. Therefore, the exploration of new methodologies and technologies for investigating marine fungi is imperative, offering significant scientific and practical value for the advancement of marine science and the conservation of marine environments.

2.2. Investigation and research status of spores in water

Fungi primarily reproduce through spores, which are typically highly resistant to chlorine. Fungal spores are at the end of the reproductive development cycle of fungi and possess the ability to develop into a new generation, making them crucial in fungal propagation. Most studies on the fungi disinfection in water focus on dispersed spores [20].

In potable water systems, fungi are present both as individual, dispersed spores and in aggregated forms, where they grow, germinate into hyphae, and ultimately create biofilms[62]. Zhang et al. [63] found that fungal spores easily form aggregates under neutral or slightly alkaline conditions. Furthermore, the resistance of these aggregates to disinfectants increases with their degree of aggregation. Cao et al. [64] found that fungal spores exhibit significant germination potential in natural water environments. Most fungi isolated from drinking water by Zhao et al. [65] belong to *Ascomycota*, which are capable of forming conidia. Studies have shown that fungal spores with relatively high chlorine tolerance can become natural components of microorganisms in drinking water distribution systems. This phenomenon may contribute to an increased fungal content in tap water or water storage tanks.

The cell wall of fungal spores serves as a robust defense mechanism against adverse environments until conditions become suitable for germination and reproduction. Compared to bacterial cell walls, fungal spore walls are structurally more complex and composed of stronger materials. Direct exposure to the environment endows fungal spores with the ability to tolerate extreme conditions such as oxidative environments, ultraviolet (UV) radiation, high temperatures, osmotic pressure variations, and a wide range of pH levels [66,67]. As a result, fungal spores are able to persist in the high osmotic pressure and wide range of pH conditions found in the ocean.

Researchers conducted experiments to investigate the survival rates of fungal spores from the Dead Sea under various salinity conditions [68]. Results showed that both mycelia and spores of Dead Sea isolates exhibited remarkable tolerance to high salt concentrations, with some mycelia surviving for weeks in undiluted Dead Sea water. While spores of terrestrial isolates generally showed poor survival in undiluted Dead Sea water, those from the Dead Sea demonstrated significantly higher viability. These findings suggest the presence of adapted halotolerant or halophilic fungi within the Dead Sea ecosystem.

The germination of spores can lead many fungi to cause diseases to humans, animals, and plants. Once germinated, fungal spores start growing on their host. Due to their high metabolic activity, germinated spores produce more toxic factors, and the release of toxins, pathogenic factors, or immunostimulating components (such as cell wall components) can harm to host. Previous studies have shown that fungal conidia with a diameter less than 5 μm can enter the alveoli, causing fungal lung infections, while conidia with a diameter of 5–50 μm may enter the respiratory system and remain in the throat, leading to diseases like sinusitis. Historically, research on water disinfection has mainly focused on bacteria and viruses, often overlooking fungal and spore contamination. However, studies in recent decades have revealed fungal contamination in various water sources, posing environmental and health risks. Therefore, urgent measures are needed to control fungal contamination and ensure water safety.

3. Common fungi and spore detection methods

At present, detection methods are mainly divided into three categories: traditional methods based on culture, microbial detection methods based on biochemistry, and molecular biology-based methods. Traditional culture methods primarily rely on direct observation of the physiological behaviors of cultivated fungi and spores. Biochemistry-based methods detect microorganisms through specific biochemical reactions or biomolecular characteristics, utilizing the structural and functional features of different molecules in microorganisms.

Heterotrophic plate count (HPC), categorized by different inoculation techniques, include pour plate (PP), spread plate (SP) and membrane filter (MF)[69]. The PP method is simple, convenient and cost-effective, but has limitations such as difficulty in counting colonies in agar and a maximum sample volume of 1.0 mL. The SP method, while also simple, exposes colonies to aerobic conditions on the agar surface, resulting in higher bacterial counts compared to the PP method. However, it requires preparation of Petri dishes and sterile glass rods beforehand, and a pollution-free environment during handling, with a maximum sample size of 1.0 mL and an optimal inoculation amount of 0.1–0.5 mL. The MF method is the most versatile, capable of processing sample volumes ranging from less than 1.0 mL to as much as 10.0 L. However, it requires more equipment, is more expensive, and counting colonies can be more challenging compared to the other two methods.

Biochemical methods include defined substrate technology (DST), flow cytometry (FCM), and adenosine triphosphate (ATP) bioluminescence. DST is a biochemical method that utilizes the metabolic characteristics of microorganisms. By adding indicators or chemical reagents, it can rapidly and sensitively detect microorganisms. Nevertheless, the test reagents are primarily imported, resulting in higher costs. FCM, which employs specific staining for rapid and accurate fungal quantification, is widely used in fungal detection. However, it requires pretreatment to disrupt the cell wall and cannot differentiate between fungal species, demanding certain operational experience. The ATP method labels viable cells with luciferase and uses a bioluminescence detector to quickly measure fluorescence. It is simple to operate, but the optimal conditions for the reaction system are not yet well-defined, and interference from cells and free ATP in natural water bodies is difficult to eliminate.

The methods based on molecular biology rely on the continuous advancement of DNA and RNA research technologies, including the polymerase chain reaction (PCR), fingerprinting and high - throughput sequencing (HTS). PCR rapidly amplifies specific DNA fragments through enzymatic reactions, demonstrating high specificity and reproducibility. It is simple to operate, cost-effective, and widely applied. However, the intercalating dyes used are toxic, and it cannot

distinguish between live and dead bacteria. qPCR, by extracting total DNA and employing specific primers, enables real-time quantitative analysis of fungal species and abundance in water bodies. It is particularly adept at detecting toxin-producing fungi, but it comes with higher costs and a risk of false positive results. dPCR enables absolute quantification of target molecules by directly counting fluorescent signals within individual PCR reaction units. This method is less susceptible to inhibition, but requires high-quality templates, specialized equipment, and highly specific primers. Furthermore, dPCR can be costly and may generate false positives. Fingerprint method is a method to obtain chemical characteristic map of substance by special analysis method. It has high reliability, but it is easy to be affected by sample complexity. It is highly specific, highly dependent on standard libraries, and requires standardized operating procedures. HTS is a high-throughput experimental technique that analyzes microbial populations at the molecular and cellular levels. It utilizes automated systems for rapid, large-scale sequencing but is limited by relatively short read lengths.

Table 1 offers a detailed comparison of all the aforementioned detection methods. [20]. The increasing number of asterisks (※) in the table indicates a corresponding increase in the severity of the technical limitations or defects.

Each method has its own advantages and disadvantages, so there is urgent need to optimize these methods and integrate various detection techniques for comparing and referencing research results from different regions and countries. Additionally, it is crucial to develop rapid detection methods that are easy to implement, thereby enhancing the efficiency and accuracy of fungal detection in water.

4. Common fungi and spore inactivation technology

Methods for controlling fungal contamination encompass both physical and chemical disinfection techniques. Physical disinfection methods include ultraviolet light-emitting diode (UV-LED) and solar disinfection, while chemical disinfection methods involve the use of agents such as chlorine, chloramine, chlorine dioxide, and ozone [70–75]. The inactivation mechanisms of physical and chemical disinfectants differ significantly. Physical methods induce DNA damage, primarily through the formation of pyrimidine dimers, whereas chemical agents often target cell membranes, leading to alterations in permeability and ultimately cell death[74]. The characteristics of chemical and physical disinfection are combined by advanced disinfection processes (ADPs) (Fig. 2), which not only destroy the integrity of the cell membrane but also damage DNA and enhance the levels of intracellular Reactive oxygen species (ROS). This ultimately leads to the destruction and inactivation of fungi.

Various methods have been employed to inactivate fungi and spores, including biological, chemical, and physical approaches such as antifungal agents, photodynamic therapy, UV sterilizers, and plasma treatment [76,77]. However, each method has its own set of advantages and disadvantages. Currently, there is no systematic review on the technical efficacy of fungal spore inactivation in water [65]. Additionally, fungi may enter a dormant state in low temperatures, limiting their susceptibility to bactericidal treatments [78,79],thus posing a challenge to complete fungi inactivation.

4.1. UV inactivation technology

UV irradiation is a physical disinfection technology distinct from chemical disinfectants. UV irradiation does not produce teratogenic or carcinogenic disinfection by-products and generally does not alter the physical and chemical properties of water. UV light is categorized into four parts based on wavelength: (1) UV-A, ranging from 315 to 400 nm; (2) UV-B, ranging from 280 to 315 nm; (3) UV-C, ranging from 200 to 280 nm; and (4) vacuum UV light, ranging from 100 to 200 nm. UV irradiation in the UV-C wavelength range has become the preferred method for disinfecting supply water and is commonly employed in most recirculating aquaculture systems. This technique is highly regarded for its efficacy in inactivating fish pathogenic bacteria and certain viruses[80].

Nourmoradi et al. [81] evaluated the efficiency of UV(254 nm) irradiation in inactivating *Aspergillus* in water. The results showed the 4 log inactivation for *A. fumigatus*, *A. niger* and *A. flavus* at a density of 1000 CFU/mL was achieved at UV fluences of 12.45 mJ/cm^2, 16.6 mJ/cm^2 and 20.75 mJ/cm^2, respectively. Sisti et al. [82] investigated *Aspergillus* contamination in tap water, finding that spores at a concentration of 10^6 CFU/mL achieved 1.38–2.67 log inactivation after just 10 s of UV-C (254 nm) irradiation at a fluence of 32 mJ/cm^2. *Aspergillus flavus* and *Aspergillus Niger*, which were the most resistant, achieved 2.37 log inactivation after 40 s of irradiation at 128 mJ/cm^2. Therefore, it can be concluded.

Reactivation of pathogenic microorganisms occurs under UV irradiation, including both light reactivation and dark repair mechanisms. Wen et al. [83] found that fungal spores, with a concentration of 10^6 CFU/mL and exposed to UV radiation (254 nm) at an average fluence rate of 0.112 mW/cm^2, exhibit resistance to UV radiation in real groundwater, displaying a higher degree of photo-revival compared to phosphate buffer solution (PBS). Both light reactivation and dark repair mechanisms weaken the effectiveness of UV disinfection, posing potential risks to water safety. Furthermore, the UV disinfection method exhibits certain limitations. Notably, fungal spores can demonstrate varying degrees of resistance to UV radiation. Wen et al. [75] found that four fungal spores, with an initial concentration ranging from (2–7) $\times$ 10^5 CFU/mL and exposed to UV radiation at 254 nm with a fluence rate of 0.109 mW/cm^2, exhibited varying degrees of resistance to UV radiation, in the order: *Cladosporium* sp.> *Penicillium* sp.> *Acroporium* sp.> *Trichoderma* sp. In practical applications, UV lamp have a finite lifespan and necessitate significant maintenance. Moreover, the continuous disinfection capacity of UV systems is often limited, and their efficacy can be adversely affected by variations in water quality parameters such as flow rate, turbidity, and the presence of particulate matter.

In addition to using UV alone, studies have explored combinations of UV inactivation with other inactivation technologies. Sichel et al. [84] deactivated the pathogenic fungus *Fusarium* by combining sunlight (UV-A) with H_2O_2.They found that *Fusarium* was effectively deactivated in both distilled water and actual well water, achieving a great inactivation effect compared H_2O_2 alone in the absence of sunlight.

Table 1
Common fungi and spore detection methods.

Testing method	Quantified but qualitatively uncertain			Qualitative but not quantitative	Qualitative and quantitative				
	HPC	FCM	ATP	finger-print	DST	PCR	qPCR	dPCR	HTS
Testing time	※※※	※	※	※※	※※	※	※	※	※
Testing cost	※	※※	※※	※※※	※※	※	※	※※※	※
Personnel professionalism	※	※	※	※※※	※	※※※	※※※	※※※	※※※
Other factors influence	※※※	※	※※	※※	※※	※※	※※	※	※※
Error	※※※	※	※※	※※	※	※※	※※	※	※※
Sensitivity	※※※	※	※	※※	※	※	※	※	※

Note: "※" - low, "※※" - medium, "※※※" - high

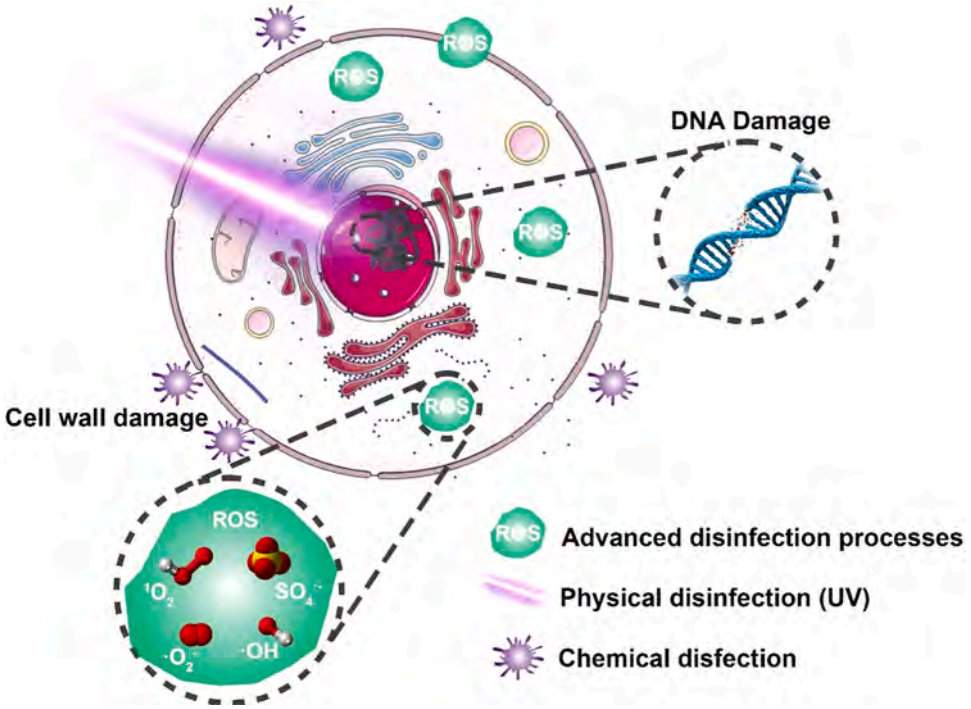


Fig. 2. The attacking targets of chemical disinfection, physical disinfection and advanced disinfection processes.

4.2. Chlorination inactivation technology

The chlorination inactivation method uses chlorine as a disinfectant for water supply and sewage. It is known for its low cost, effective disinfection, and ease of use, making it widely utilized in water treatment. Chlorine exhibits broad-spectrum antimicrobial properties, effectively targeting a wide range of microorganisms, including fungi [85]. Xu et al. [86] confirmed that chlorine-based disinfectants have different inactivation mechanisms for fungal spores. Chlorine and chlorine dioxide destroy cell walls and cell membranes, inactivate spores, and lead to intracellular material leakage and cell death. Wen et al. [87] studied the spores of three dominant fungi in underground water sources, revealing that these fungi exhibit varying degrees of chlorine tolerance: *Trichoderma*>*Penicillium*>*Cladosporium*. The study also observed that larger fungal spores tend to have stronger hydrophilicity, which enhances their susceptibility to inactivation.

However, currently, water bodies are severely polluted by organic matter. When disinfectants react with dissolved organic matter (DOM) in source water, they can form disinfection by-products (DBPs), some of which have been shown to exhibit high mutagenic and carcinogenic effects in animals[88]. Several epidemiological studies have shown that prolonged consumption of chlorinated water may raise the risk of urinary bladder cancer[89]. In response to the health risks associated with DBPs, numerous countries and organizations have put in place regulations and guidelines for DBPs in drinking water, primarily focusing on THMs and HAAs (known as regulated-DBPs)[90]. Recent studies on seawater disinfection have demonstrated that significant quantities of brominated disinfection by-products (Br-DBPs) are formed in chlorinated seawater, most of which contain aromatic ring structures[91,92]. Notably, DBPs with aromatic structures are more lipophilic, exhibiting higher log *P* values (2.40–5.01) compared to their aliphatic halogenated counterparts (0.43–1.79) [93,94]. This increased lipophilicity enhances their ability to permeate cell membranes and accumulate in marine organisms[93,95,96]. For example, elevated levels of polybrominated diphenyl ethers and brominated phenolic compounds have been detected in the blood of fish and wildlife from the Baltic Sea [96] as well as in seafood[95]. Additionally, some microorganisms that are resistant to chlorination disinfection remain difficult to inactivate. Therefore, the primary focus now is to identify a more effective disinfection method.

4.3. Chloramine inactivation technology

The chloramine inactivation method involves producing monochloramine and dichloramine through the reaction of chlorine and ammonia, aiming to achieve oxidation and disinfection. This method is widely favored for its prolonged efficacy and minimal impact. Chloramine is extensively utilized for the inactivation of bacteria, viruses and protozoa. Ma et al. [26] analyzed hot water samples before and after using monochloramine as a field disinfectant in a hospital hot water system. The results indicated that the use of chloramine for secondary disinfection did not alter the structure of fungal community. Subsequently, Ma et al. [72] further investigated the inactivation effect of mono-chloramine on fungal spores of *Aspergillus* and *Penicillium*. They found that the inactivation data followed the delayed Chick-Watson model, and the required Ct value achieve 99.9 % inactivation ranged from 90.33 to 531.3 mg min/L. Furthermore, some researchers have compared the inactivation of fungal spores by chloramine in laboratory-grade water and settled water at the laboratory scale. The results indicated that under the same concentration of chloramine, the inactivation of several fungal spores was more effective in laboratory-grade water. In contrast, the inactivation rate constants were lower in settled water. However, for *Penicillium* species, there was no significant difference in the inactivation rate constants between laboratory-grade water and settled water[97].

Monochloramine inactivates spores by penetrating cells and damaging their DNA. Similarly, Cao et al. [74] discovered that chloramines primarily target the cellular DNA of fungal spores rather than the cell membrane, in contrast to chlorine and chlorine dioxide.

4.4. Chlorine dioxide inactivation technology

Chlorine dioxide is a potent disinfectant developed in the United States in the 1980 s. Wei et al. [98] studied the inactivation of *Candida albicans* by chlorine dioxide, finding that the removal rate could reach

99.12 % when treated with 15 mmol/L chlorine dioxide for 5 min. Additionally, Ma et al. [99] discovered that a 20 ppm chlorine dioxide treatment for 10 min achieved a removal rate of more than 99.9 % for *candida*, and a removal rate of 98.2 % for *Penicillium*.

There has been relatively little research on inactivation of fungal spores by chlorine dioxide. The use of in-line biocides during ballast water uptake is an effective strategy for mitigating the introduction of potential invasive species in marine platforms. Chlorine dioxide is a highly effective treatment, capable of eliminating a broad range of organisms, including various microbial and fungal species. It can be applied at an effective dose under real-world operational conditions and degrades rapidly to safe, undetectable levels. This makes it a promising approach for controlling bioinvasions while minimizing environmental risks[100]. Vandekinderen et al. [101] studied the effect of gaseous chlorine dioxide on microorganisms, finding that at a concentration of 0.08 mg/L and 1 min exposure, it had minimal impact on fungal spores, reducing *Aspergillus* by an average of 0.1 log and *Penicillium* by 0.4 log. Subsequently, Wen et al. [87] investigated the inactivation mechanism of fungal spores by chlorine dioxide, revealing that it follows the Chick-Watson model due to its strong oxidation capabilities, which disrupt the cell walls and membranes of fungal spores, rendering them inactive. Further experiments by Wen et al. [34] with chlorine on spores from three genera demonstrated that during chlorine disinfection, spores lost culturability initially followed by membrane destruction. The membrane failure rate was found to be higher with chlorine dioxide›chlorine gas›chloramine. ROS are critical metabolic indicators and signaling molecules in the development and physiological responses of fungal organisms[102]. The production of ROS in fungi is enhanced under various stress conditions, including nutrient deprivation, exposure to light, and interactions with other organisms[102]. Elevated intracellular ROS levels can lead to significant cellular damage, adversely affecting DNA integrity (promoting protein oxidation, double-strand breaks, and damage to other intracellular components), and contributing to membrane instability[103]. In another study, Zhang et al. [63] observed that chlorine dioxide was more effective than monochloramine and chlorine in disinfecting fungi with different levels of aggregation. Their findings indicated higher membrane permeability and a greater proportion of cells with elevated intracellular ROS levels, with the efficacy ranking as chlorine dioxide›monochloramine›chlorine. Chlorine dioxide disinfection is widely favored due to several advantages: it reduces chlorinated by-products in water, is unaffected by water pH, and prevents secondary pollution effectively. However, challenges include safety concerns and high costs associated with storing and transporting disinfectant materials.

4.5. Comparison of inactivation efficacy under similar conditions

Nowadays, advanced UV-based disinfection technologies are being explored as key alternatives. These methods generate a range of highly reactive radicals—such as sulfate radicals (SO4•−), hydroxyl radicals (•OH), chlorine radicals (•Cl), and chlorinated radicals (Cl2•−)—which are effective at removing various contaminants and microorganisms.

This paper summarizes the rate constants for the inactivation of fungal spores by different oxidants or UV disinfection processes under similar conditions, as shown in Fig. 3.

4.6. Other inactivation technologies

Ozone (O_3) is a type of sterilization technology widely used in water treatment, air purification, food processing, medical treatment, and other fields. Its sterilization speed is more than twice that of chlorine. O_3 sterilization leaves no residue and causes no secondary pollution, making it a green environmental protection element. Previously, researchers utilized O_3 to control the growth of fungal spores and reduce toxin pollution in the laboratories. Foreign researchers have evaluated the antifungal ability of O_3 gas against toxic fungal spores (*Fusarium*, *Aspergillus*, and *Penicillium*) in laboratory-scale treatment experiments. They found that the growth of fungal colonies, particularly *Fusarium* and *Penicillium*, could be effectively inhibited with varying exposure times under 60 mol/mol O_3 gas. Moreover, exposure to O_3 gas can inhibit conidia germination and induce change in hyphal morphology, leading to the death of fungal spores and the release of reactive oxygen species. The inactivation of fungal spores by ozone occurs in two distinct stages: first, the survival rate decreases rapidly, followed by slower inactivation. Studies examining the effects of ozone on juvenile turbot physiology highlight the potential for its controlled use in aquaculture. Such applications may provide an effective strategy for pathogen management while minimizing negative impacts on fish health[104]. O_3 demonstrates an efficient inactivation effect on fungal spores and can potentially replace other disinfectants for treating fungi-contaminated water [105].

In addition to the traditional sterilization technology, there are several new inactivation methods, including photocatalysis, graphite adsorbent combined with electrochemistry, curcumin-induced photosensitive treatment, gamma radiation, and others. Hussain et al. [106] studied the inactivation effect of graphite adsorbent combined with electrochemical regeneration on various microorganisms in water. Their research using mini-SBR (sequential batch reactor) for sequential adsorption and electrochemical regeneration experiments demonstrated that fungal spores were completely removed from the solution due to indirect oxidation, achieving a regeneration efficiency higher than 96 %. Curcumin exhibits photosensitivity, leading to photochemical reactions upon excitation, thereby enhancing its antibacterial effectiveness. Al-Asmari et al. [107] investigated curcumin-mediated photosensitization effects on spores of *Aspergillus Niger*, *Aspergillus flavus*, *Penicillium griseofulvum*, and other fungi using three methods. Their findings indicated that expose to a light dose of 360 J/cm^2 and 800 μM curcumin completely inhibited *Aspergillus Niger*, inhibited *Aspergillus flavus* by 75 %, and inhibited *Penicillium griseofulvum* by 80.4 %. The peracetic acid (PFA) method is known for its high disinfection efficiency and minimal disinfection by-products, widely applied in water disinfection. Lin et al. [108] observed that the inactivation effectiveness of PFA was highest for *Escherichia coli*, followed by *Aspergillus Niger* and *Aspergillus flavus*. Moreover, they found significantly enhanced inactivation efficiency of PFA under acidic conditions compared to neutral pH, with further improvements noted with increased temperature and concentration. Their results demonstrated that PFA disrupts cell membranes and reduces fungal spore regeneration ability substantially post-inactivation, albeit with partial effectiveness in actual water scenarios. Wen et al. [109] utilized BCDMH (bromine-chlorine-dimethylhydantoin) powder disinfectant to inactivate fungal spores from two genera. They observed that the inactivation efficiency of fungal spores increased with higher BCDMH concentration. Acidic conditions and elevated temperature were found to promote BCDMH effectiveness against fungal spores; while the addition of halide ions (Br- and I-) notably improve its. However, further studies are required to explore the formation, persistence, and degradation mechanism of BCDMH by-products.

For the inactivation effect of the aforementioned technologies on fungi and their spores, current research primarily focuses on assessing inactivation efficiency and understanding inactivation mechanics. However, there remains a relative scarcity of research on the specific inactivation mechanism of fungi and their spores by these techniques.

5. Summary and prospect

In the past few decades, China's economy has developed rapidly, but this growth has also caused significant damage to the ecological environment, particularly to water bodies. As public awareness of environmental protection and concerns about health have increased, there is growing attention to water quality safety. Currently, among the common methods for detecting fungi, the plate method is the most widely

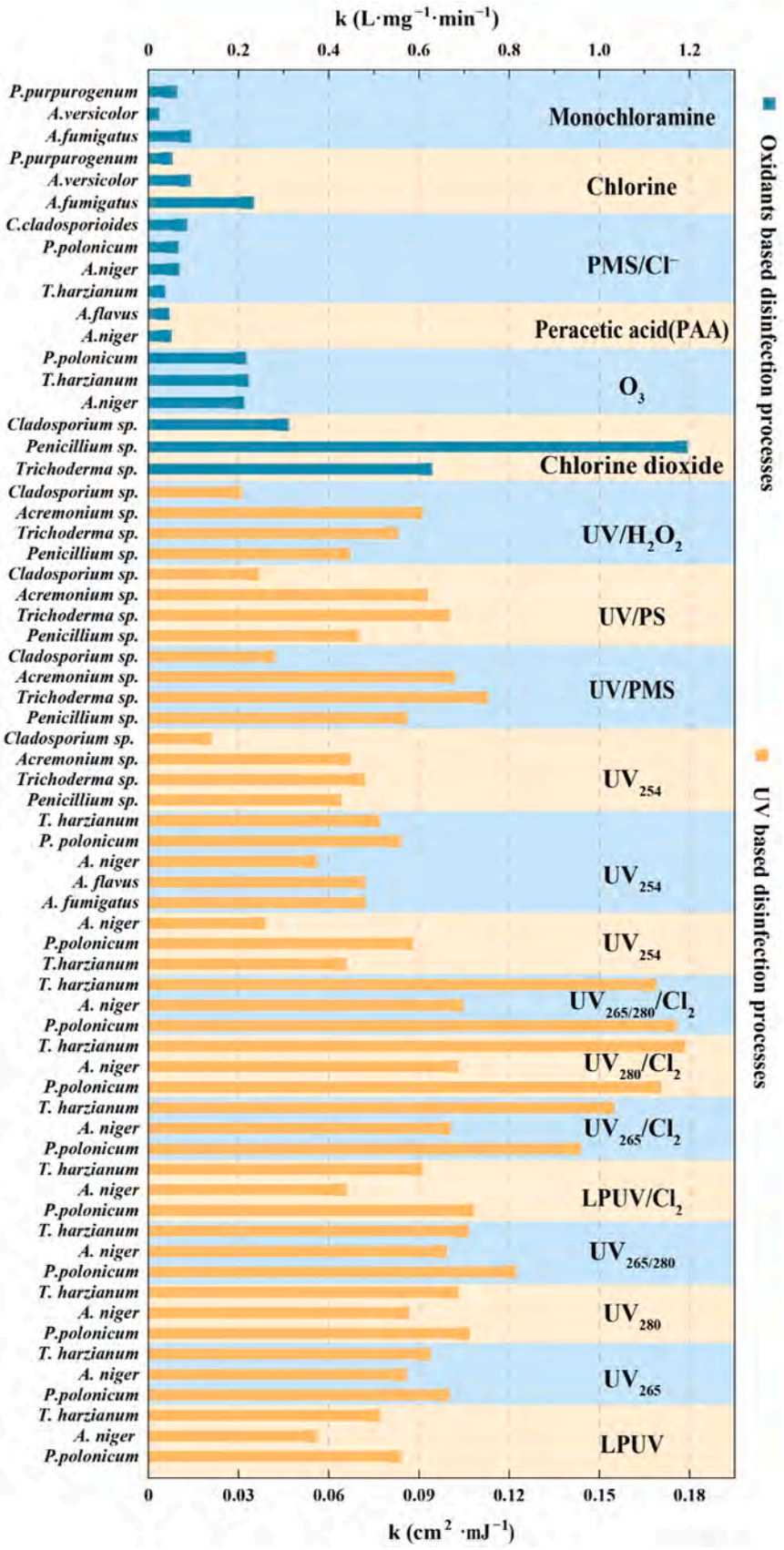


Fig. 3. Inactivation rate constants for oxidants or UV based disinfection processes on fungal spores under similar conditions.

used. It is noteworthy that while flow cytometry (FCM) has been extensively applied to characterize bacteria in water treatment and assess their viability during disinfection processes, its use in detecting fungal spores remains relatively uncommon. However, combining FCM technology with various fluorescent dyes shows potential as an effective approach to evaluate disinfection mechanisms, warranting further exploration [74,110,111]. There is a need for other rapid and more effective detection methods as well.

Given the evident structural differences between fungi and bacteria, understanding the disinfection effects and mechanism of disinfectants on fungal spores is crucial. This understanding can establish a theoretical foundation and provide scientific guidance for fungal control. In recent years, both domestic and international scholars have systematically studied methods for controlling inactivation, as well as the mechanics and mechanisms of fungal inactivation. However, further research is needed on the germination, aggregation, and biofilm formation of fungi from spores, along with the disinfection of fungal biofilm and bacterial-fungal composite biofilms. Existing fungal inactivation technologies often fail to fully meet modern societal needs. Addressing current shortcomings and developing new fungal inactivation technologies could greatly enhance the prospects for fungi and their spores in water [64,108,112]. Currently, most research on fungal disinfection in water focuses on the inactivation effects and mechanisms of dormant fungal spores. However, there remains a significant gap in understanding the inactivation laws and mechanisms of germinated fungal spores, warranting further investigation [113]. Therefore, to safeguard public health comprehensively, it is imperative to deeply investigate the growth and reproductive patterns of fungi and their spores, identify factors triggering fungal outbreaks, and develop easily deployable, rapid, and accurate detection methods alongside effective disinfection technologies.

CRediT authorship contribution statement

Yuanyuan Zhang: Writing – review & editing, Supervision, Funding acquisition, Conceptualization. **Fangyu Liang:** Writing – original draft, Visualization, Investigation.

Declaration of Competing Interest

The whole or part of the work involved in this paper has not been published previously, and the publication of this manuscript is approved by all authors.

Acknowledgements

This study was supported by the Guangxi Natural Science Foundation (2024JJA160306) and the Guangxi Higher Education Undergraduate Teaching Reform Project (2023JGB111).

Data availability

Data will be made available on request.

References

[1] Zhang Q, Zhu J, Mulder J, Wang Q, Liu C, He N. High environmental costs behind rapid economic development: Evidence from economic loss caused by atmospheric acid deposition. J Environ Manag 2023;334:117511.
[2] Feng S, Mohd Shafiei MW, Ng TF, Ren J, Jiang Y. The intersection of economic growth and environmental sustainability in China: Pathways to achieving SDG. Energy Strategy Rev 2024;55:101530.
[3] Liang L, Wang Z, Li J. The effect of urbanization on environmental pollution in rapidly developing urban agglomerations. J Clean Prod 2019;237:117649.
[4] Ebenstein A, Fan M, Greenstone M, He G, Yin P, Zhou M. Growth, Pollution, and Life Expectancy: China from 1991-2012. Am Econ Rev 2015;105:226–31.
[5] Chen W, Zheng R, Baade PD, Zhang S, Zeng H, Bray F, Jemal A, Yu XQ, He J. Cancer statistics in China, 2015. CA: A Cancer J Clin 2016;66:115–32.
[6] Ebenstein A. The Consequences of Industrialization: Evidence from Water Pollution and Digestive Cancers in China. Rev Econ Stat 2012;94:186–201.
[7] Ling M, Lv C, Guo X. Quantification method of water environmental value loss caused by water pollution based on emergy theory. Desalin Water Treat 2018; 129:299–303.
[8] Craun GF, Brunkard JM, Yoder JS, Roberts VA, Carpenter J, Wade T, Calderon RL, Roberts JM, Beach MJ, Roy SL. Causes of Outbreaks Associated with Drinking Water in the United States from 1971 to 2006. Clin Microbiol Rev 2010.
[9] Olenin S, Elliott M, Minchin D, Katsanevakis S. Marine ecosystem health and biological pollution: Reconsidering the paradigm. Mar Pollut Bull 2024;200: 116054.
[10] Babič MN, Gunde-Cimerman N, Vargha M, Tischner Z, Magyar D, Veríssimo C, Sabino R, Viegas C, Meyer W, Brandão J. Fungal Contaminants in Drinking Water Regulation? A Tale of Ecology, Exposure, Purification and Clinical Relevance. Int J Environ Res Public Health 2017;14:636.
[11] Sylvestre É , Prévost M, Burnet J-B, Smeets P, Medema G, Hachad M, Dorner S. Using surrogate data to assess risks associated with microbial peak events in source water at drinking water treatment plants. Water Res 2021;200:117296.
[12] Xu H, Pang Y, Li Y, Zhang S, Pei H. Using sodium percarbonate to suppress vertically distributed filamentous cyanobacteria while maintaining the stability of microeukaryotic communities in drinking water reservoirs. Water Res 2021; 197:117111.
[13] Wang D, Chan BC-L, Zhang B, Wong KC-Y, Kan LL-Y, Wong C-K. Dark under the Lamp: Neglected Biological Pollutants in the Environment Are Closely Linked to Lung Cancer. Int J Mol Sci 2024;25:3081.
[14] Feng L, Wang Y, Hou X, Qin B, Kutser T, Qu F, Chen N, Paerl HW, Zheng C. Harmful algal blooms in inland waters. Nat Rev Earth Environ 2024;5:631–44.
[15] Dolah FMV, Roelke D, Greene RM. Health and Ecological Impacts of Harmful Algal Blooms: Risk Assessment Needs. Hum Ecol Risk Assess: Int J 2001;7: 1329–45.
[16] Hageskal G, Lima N, Skaar I. The study of fungi in drinking water. Mycol Res 2009;113:165–72.
[17] Ayofemi Olalekan Adeyeye S. Aflatoxigenic fungi and mycotoxins in food: a review. Crit Rev Food Sci Nutr 2020;60:709–21.
[18] Moretti A, Susca A, Mulé G, Logrieco AF, Proctor RH. Molecular biodiversity of mycotoxigenic fungi that threaten food safety. Int J Food Microbiol 2013;167: 57–66.
[19] Mhlongo TN, Ogola HJO, Selvarajan R, Sibanda T, Kamika I, Tekere M. Occurrence and diversity of waterborne fungi and associated mycotoxins in treated drinking water distribution system in South Africa: implications on water quality and public health. Environ Monit Assess 2020;192:519.
[20] Wan Q, Wen G, Cui Y, Cao R, Xu X, Wu G, Wang J, Huang T. Occurrence and control of fungi in water: New challenges in biological risk and safety assurance. Sci Total Environ 2023;860:160536.
[21] Hassett BT, Borrego EJ, Vonnahme TR, Rämä T, Kolomiets MV, Gradinger R. Arctic marine fungi: biomass, functional genes, and putative ecological roles. ISME J 2019;13:1484–96.
[22] Göttlich E, van der Lubbe W, Lange B, Fiedler S, Melchert I, Reifenrath M, Flemming H-C, de Hoog S. Fungal flora in groundwater-derived public drinking water. Int J Hyg Environ Health 2002;205:269–79.
[23] Kikuchi T, Kadota S, Suehara H, Nishi A, Tsubaki K. Odorous metabolites of a fungus, Chaetomium globosum Kinze ex Fr. Identification of geosmin, a musty-smelling compound. Chem Pharm Bull 1981;29:1782–4.
[24] VandenBergh MFQ, Verweij PE, Voss A. Epidemiology of nosocomial fungal infections: invasive aspergillosis and the environment. Diagn Microbiol Infect Dis 1999;34:221–7.
[25] Hageskal G, Gaustad P, Heier BT, Skaar I. Occurrence of moulds in drinking water. J Appl Microbiol 2007;102:774–80.
[26] Ma X, Baron JL, Vikram A, Stout JE, Bibby K. Fungal diversity and presence of potentially pathogenic fungi in a hospital hot water system treated with on-site monochloramine. Water Res 2015;71:197–206.
[27] Kanzler D, Buzina W, Paulitsch A, Haas D, Platzer S, Marth E, Mascher F. Occurrence and hygienic relevance of fungi in drinking water. Mycoses 2008;51: 165–9.
[28] Pereira VJ, Basílio MC, Fernandes D, Domingues M, Paiva JM, Benoliel MJ, Crespo MT, San Romão MV. Occurrence of filamentous fungi and yeasts in three different drinking water sources. Water Res 2009;43:3813–9.
[29] Grabińska-Łoniewska A, Konieczkowicz-Kowalska T, Wardzyńska G, Boryn K. Occurrence of fungi in water distribution system. Pol J Environ Stud 2007;16: 539–47.
[30] Saingam P, Li B, Yan T. Fecal indicator bacteria, direct pathogen detection, and microbial community analysis provide different microbiological water quality assessment of a tropical urban marine estuary. Water Res 2020;185:116280.
[31] Devane ML, Moriarty E, Weaver L, Cookson A, Gilpin B. Fecal indicator bacteria from environmental sources; strategies for identification to improve water quality monitoring. Water Res 2020;185:116204.
[32] Paule-Mercado MA, Ventura JS, Memon SA, Jahng D, Kang J-H, Lee C-H. Monitoring and predicting the fecal indicator bacteria concentrations from agricultural, mixed land use and urban stormwater runoff. Sci Total Environ 2016;550:1171–81.
[33] Tallon P, Magajna B, Lofranco C, Leung KT. Microbial Indicators of Faecal Contamination in Water: A Current Perspective. Water Air Soil Pollut 2005;166: 139–66.
[34] Field KG, Samadpour M. Fecal source tracking, the indicator paradigm, and managing water quality. Water Res 2007;41:3517–38.

[35] Li E, Saleem F, Edge TA, Schellhorn HE. Biological Indicators for Fecal Pollution Detection and Source Tracking: A Review. Processes 2021;9:2058.
[36] Lin L, Yang H, Xu X. Effects of Water Pollution on Human Health and Disease Heterogeneity: A Review. Front Environ Sci 2022;10.
[37] Alygizakis NA, Urík J, Beretsou VG, Kampouris I, Galani A, Oswaldova M, Berendonk T, Oswald P, Thomaidis NS, Slobodnik J, Vrana B, Fatta-Kassinos D. Evaluation of chemical and biological contaminants of emerging concern in treated wastewater intended for agricultural reuse. Environ Int 2020;138:105597.
[38] Stajich JE, Berbee ML, Blackwell M, Hibbett DS, James TY, Spatafora JW, Taylor JW. The Fungi. Curr Biol 2009;19:R840–5.
[39] Capello M, Carbone C, Cecchi G, Consani S, Cutroneo L, Di Piazza S, Greco G, Tolotti R, Vagge G, Zotti M. A mycological baseline study based on a multidisciplinary approach in a coastal area affected by contaminated torrent input. Mar Pollut Bull 2017;119:446–53.
[40] Gonçalves AB, Paterson RRM, Lima N. Survey and significance of filamentous fungi from tap water. Int J Hyg Environ Health 2006;209:257–64.
[41] Oliveira HMB, Santos C, Paterson RRM, Gusmão NB, Lima N. Fungi from a Groundwater-Fed Drinking Water Supply System in Brazil. Int J Environ Res Public Health 2016;13:304.
[42] Khomich M, Davey ML, Kauserud H, Rasconi S, Andersen T. Fungal communities in Scandinavian lakes along a longitudinal gradient. Fungal Ecol 2017;27:36–46.
[43] Heeger F, Bourne EC, Baschien C, Yurkov A, Bunk B, Spröer C, Overmann J, Mazzoni CJ, Monaghan MT. Long-read DNA metabarcoding of ribosomal RNA in the analysis of fungi from aquatic environments. Mol Ecol Resour 2018;18:1500–14.
[44] Giner CR, Forn I, Romac S, Logares R, de Vargas C, Massana R. Environmental Sequencing Provides Reasonable Estimates of the Relative Abundance of Specific Picoeukaryotes. Appl Environ Microbiol 2016.
[45] Wurzbacher CM, Bärlocher F, Grossart H-P. Fungi in lake ecosystems. Aquat Microb Ecol 2010;59:125–49.
[46] Reich M, Labes A. How to boost marine fungal research: A first step towards a multidisciplinary approach by combining molecular fungal ecology and natural products chemistry. Mar Genom 2017;36:57–75.
[47] Grossart H-P, Van den Wyngaert S, Kagami M, Wurzbacher C, Cunliffe M, Rojas-Jimenez K. Fungi in aquatic ecosystems. Nat Rev Microbiol 2019;17:339–54.
[48] Jones EBG, Pang K-L, Abdel-Wahab MA, Scholz B, Hyde KD, Boekhout T, Ebel R, Rateb ME, Henderson L, Sakayaroj J, Suetrong S, Dayarathne MC, Kumar V, Raghukumar S, Sridhar KR, Bahkali AHA, Gleason FH, Norphanphoun C. An online resource for marine fungi. Fungal Divers 2019;96:347–433.
[49] Jones EBG, Pang K-L. Tropical aquatic fungi. Biodivers Conserv 2012;21:2403–23.
[50] Blackwell M. The Fungi: 1, 2, 3 … 5.1 million species? Am J Bot 2011;98:426–38.
[51] Wang Z-P, Liu Z-Z, Wang Y-L, Bi W-H, Liu L, Wang H-Y, Zheng Y, Zhang L-L, Hu S-G, Xu S-S, Zhang P. Fungal community analysis in seawater of the Mariana Trench as estimated by Illumina HiSeq. RSC Adv 2019;9:6956–64.
[52] Samuel P, Prince Prabakaran. Antibacterial Activity of Marine derived Fungi Collected from South East Coast of Tamilnadu. India 2011;1:86–94.
[53] Hyde KD, Jones EBG, Leaño E, Pointing SB, Poonyth AD, Vrijmoed LLP. Role of fungi in marine ecosystems. Biodivers Conserv 1998;7:1147–61.
[54] De Leo F, Lo Giudice A, Alaimo C, De Carlo G, Rappazzo AC, Graziano M, De Domenico E, Urzì C. Occurrence of the black yeast Hortaea werneckii in the Mediterranean Sea. Extremophiles 2019;23:9–17.
[55] Berbee ML, James TY, Strullu-Derrien C. Early Diverging Fungi: Diversity and Impact at the Dawn of Terrestrial Life. Annu Rev Microbiol 2017;71:41–60.
[56] Nguyen MTHD, Thomas T. Diversity, host-specificity and stability of sponge-associated fungal communities of co-occurring sponges. PeerJ 2018;6:e4965.
[57] Sallenave-Namont C, Pouchus YF, Robiou du Pont T, Lassus P, Verbist JF. Toxigenic saprophytic fungi in marine shellfish farming areas. Mycopathologia 2000;149:21–5.
[58] Song Y, Miao F, Liu X, Ji N. Responses of marine-derived Trichoderma fungi to seawater and their potential antagonistic behaviour. J Ocean Limnol 2019;37:525–34.
[59] Kerzaon I, Grovel O, Robiou Du Pont T, Le Pape P, Pouchus Y-F. Effects of seawater on growth and gliotoxin excretion of marine strains of Aspergillus fumigatus Fres. Toxicon 2008;51:398–405.
[60] Reich M, Wichels A, Panzer K, Krause E, Giménez L, Gerdts G. Impacts of a reduction in seawater pH mimicking ocean acidification on the structure and diversity of mycoplankton communities. Aquat Microb Ecol 2017;79:221–33.
[61] Hawksworth DL. The fungal dimension of biodiversity: magnitude, significance, and conservation. Mycol Res 1991;95:641–55.
[62] Harding MW, Marques LLR, Howard RJ, Olson ME. Can filamentous fungi form biofilms? Trends Microbiol 2009;17:475–80.
[63] Zhang H, Xu X, Tan L, Liang Z, Cao R, Wan Q, Xu H, Wang J, Huang T, Wen G. The aggregation of Aspergillus spores and the impact on their inactivation by chlorine-based disinfectants. Water Res 2021;204:117629.
[64] Cao R, Tan L, Li K, Wan Q, Wu G, Wang J, Tian W, Huang T, Wen G. The germination of fungal spores in water and enhanced their resistance to chlor(am)ine: Characteristics and mechanisms. Chem Eng J 2023;454:140184.
[65] Zhao H-X, Zhang T-Y, Wang H, Hu C-Y, Tang Y-L, Xu B. Occurrence of fungal spores in drinking water: A review of pathogenicity, odor, chlorine resistance and control strategies. Sci Total Environ 2022;853:158626.
[66] Ulanowski Z, Ludlow IK. Water distribution, size and wall thickness in Lycoperdon pyriforme spores. Mycol Res 1989;93:28–32.
[67] Peberdy JF. Fungal Cell Walls — A Review. In: Kuhn PJ, Trinci APJ, Jung MJ, Goosey MW, Copping LG, editors. Biochemistry of Cell Walls and Membranes in Fungi. Berlin, Heidelberg: Springer; 1990. p. 5–30.
[68] Kis-Papo T, Oren A, Wasser SP, Nevo E. Survival of Filamentous Fungi in Hypersaline Dead Sea Water. Micro Ecol 2003;45:183–90.
[69] Reasoner DJ. Heterotrophic plate count methodology in the United States. Int J Food Microbiol 2004;92:307–15.
[70] Hageskal G, Tryland I, Liltved H, Skaar I. No simple solution to waterborne fungi: various responses to water disinfection methods. Water Supply 2012;12:220–6.
[71] Luo X, Xu X, Cao R, Wan Q, Wang J, Xu H, Lin Y, Wen G, Huang T. The formation kinetics and control of biofilms by three dominant fungi species isolated from groundwater. J Environ Sci 2021;109:148–60.
[72] Ma X, Bibby K. Free chlorine and monochloramine inactivation kinetics of Aspergillus and Penicillium in drinking water. Water Res 2017;120:265–71.
[73] Pereira VJ, Marques R, Marques M, Benoliel MJ, Barreto Crespo MT. Free chlorine inactivation of fungi in drinking water sources. Water Res 2013;47:517–23.
[74] Cao R, Wan Q, Xu X, Tian S, Wu G, Wang J, Huang T, Wen G. Differentiation of DNA or membrane damage of the cells in disinfection by flow cytometry. J Hazard Mater 2022;435:128924.
[75] Wen G, Xu X, Zhu H, Huang T, Ma J. Inactivation of four genera of dominant fungal spores in groundwater using UV and UV/PMS: Efficiency and mechanisms. Chem Eng J 2017;328:619–28.
[76] Madugundu GS, Park Y, Sanche L, Wagner JR. Radiation-Induced Formation of 2′,3′-Dideoxyribonucleosides in DNA: A Potential Signature of Low-Energy Electrons. J Am Chem Soc 2012;134:17366–8.
[77] Dobrynin D, Fridman G, Friedman G, Fridman A. Physical and biological mechanisms of direct plasma interaction with living tissue. N J Phys 2009;11:115020.
[78] Keller R, Tetro JA, Susan Springthorpe V, Sattar SA. The Influence of Temperature on Norovirus Inactivation by Monochloramine in Potable Waters: Testing with Murine Norovirus as a Surrogate for Human Norovirus. Food Environ Virol 2010;2:97–100.
[79] Ran Z, Li S, Huang J, Yuan Y, Cui C, Williams CD. Inactivation of Cryptosporidium by ozone and cell ultrastructures. J Environ Sci 2010;22:1954–9.
[80] Øye AK, Rimstad E. Inactivation of infectious salmon anaemia virus, viral haemorrhagic septicaemia virus and infectious pancreatic necrosis virus in water using UVC irradiation. Dis Aquat Org 2001;48:1–5.
[81] Nourmoradi H, Nikaeen M, Stensvold CR, Mirhendi H. Ultraviolet irradiation: An effective inactivation method of Aspergillus spp. in water for the control of waterborne nosocomial aspergillosis. Water Res 2012;46:5935–40.
[82] M. Sisti, G.F. Schiavano, M.D. Santi, G. Brandi, Ultraviolet germicidal irradiation in tap water contaminated by Aspergillus spp, (n.d.).
[83] Wen G, Wan Q, Deng X, Cao R, Xu X, Chen Z, Wang J, Huang T. Reactivation of fungal spores in water following UV disinfection: Effect of temperature, dark delay, and real water matrices. Chemosphere 2019;237:124490.
[84] Sichel C, Fernández-Ibáñez P, De Cara M, Tello J. Lethal synergy of solar UV-radiation and H2O2 on wild Fusarium solani spores in distilled and natural well water. Water Res 2009;43:1841–50.
[85] Ekundayo TC, Igwaran A, Oluwafemi YD, Okoh AI. Global bibliometric meta-analytic assessment of research trends on microbial chlorine resistance in drinking water/water treatment systems. J Environ Manag 2021;278:111641.
[86] Xu X, Cao R, Li K, Wan Q, Wu G, Lin Y, Huang T, Wen G. The protective role and mechanism of melanin for Aspergillus niger and Aspergillus flavus against chlorine-based disinfectants. Water Res 2022;223:119039.
[87] Wen G, Xu X, Huang T, Zhu H, Ma J. Inactivation of three genera of dominant fungal spores in groundwater using chlorine dioxide: Effectiveness, influencing factors, and mechanisms. Water Res 2017;125:132–40.
[88] Liu X, Chen L, Yang M, Tan C, Chu W. The occurrence, characteristics, transformation and control of aromatic disinfection by-products: A review. Water Res 2020;184:116076.
[89] Villanueva C, Fernandez F, Malats N, Grimalt J. M. Kogevinas, Meta-analysis of studies on individual consumption of chlorinated drinking water and bladder cancer. J Epidemiol Community Health 2003;57:166–73.
[90] Federal Register; 2006.
[91] Qiang Z, Zhang H, Dong H, Adams C, Luan G, Wang L. Formation of disinfection byproducts in a recirculating mariculture system: emerging concerns. Environ Sci Process Impacts 2015;17:471–7.
[92] Zhang H, Zhang Y, Shi Q, Zheng H, Yang M. Characterization of Unknown Brominated Disinfection Byproducts during Chlorination Using Ultrahigh Resolution Mass Spectrometry. Environ Sci Technol 2014;48:3112–9.
[93] Yang M, Zhang X. Comparative Developmental Toxicity of New Aromatic Halogenated DBPs in a Chlorinated Saline Sewage Effluent to the Marine Polychaete Platynereis dumerilii. Environ Sci Technol 2013;47:10868–76.
[94] Pan Y, Zhang X. Four Groups of New Aromatic Halogenated Disinfection Byproducts: Effect of Bromide Concentration on Their Formation and Speciation in Chlorinated Drinking Water. Environ Sci Technol 2013;47:1265–73.
[95] Whitfield FB, Drew M, Helidoniotis F, Svoronos D. Distribution of Bromophenols in Species of Marine Polychaetes and Bryozoans from Eastern Australia and the Role of Such Animals in the Flavor of Edible Ocean Fish and Prawns (Shrimp). J Agric Food Chem 1999;47:4756–62.
[96] Marsh G, Athanasiadou M, Bergman Å, Asplund L. Identification of Hydroxylated and Methoxylated Polybrominated Diphenyl Ethers in Baltic Sea Salmon (Salmo salar) Blood. Environ Sci Technol 2004;38:10–8.
[97] Pereira VJ, Marques M, Marques R, Benoliel MJ, Barreto Crespo MT. Inactivation of Fungi in Treated Surface Water by Chloramination. J AWWA 2017;109.

[98] Wei M-K, Wu Q-P, Huang Q, Wu J-L, Zhang J-M. Plasma membrane damage to *Candida albicans* caused by chlorine dioxide (ClO_2). Lett Appl Microbiol 2008;47:67–73.
[99] Ma J-W, Huang B-S, Hsu C-W, Peng C-W, Cheng M-L, Kao J-Y, Way T-D, Yin H-C, Wang S-S. Efficacy and Safety Evaluation of a Chlorine Dioxide Solution. IJERPH 2017;14:329.
[100] Maranda L, Cox AM, Campbell RG, Smith DC. Chlorine dioxide as a treatment for ballast water to control invasive species: Shipboard testing. Mar Pollut Bull 2013;75:76–89.
[101] Vandekinderen I, Devlieghere F, Van Camp J, Kerkaert B, Cucu T, Ragaert P, De Bruyne J, De Meulenaer B. Effects of food composition on the inactivation of foodborne microorganisms by chlorine dioxide. Int J Food Microbiol 2009;131:138–44.
[102] pollu
[103] none
[104] Reiser S, Schroeder JP, Wuertz S, Kloas W, Hanel R. Histological and physiological alterations in juvenile turbot (*Psetta maxima*, L.) exposed to sublethal concentrations of ozone-produced oxidants in ozonated seawater. Aquaculture 2010;307:157–64.
[105] Wen G, Liang Z, Xu X, Cao R, Wan Q, Ji G, Lin W, Wang J, Yang J, Huang T. Inactivation of fungal spores in water using ozone: Kinetics, influencing factors and mechanisms. Water Res 2020;185:116218.
[106] Hussain SN, Trzcinski AP, Asghar HMA, Sattar H, Brown NW, Roberts EPL. Disinfection performance of adsorption using graphite adsorbent coupled with electrochemical regeneration for various microorganisms present in water. J Ind Eng Chem 2016;44:216–25.
[107] Al-Asmari F, Mereddy R, Sultanbawa Y. A novel photosensitization treatment for the inactivation of fungal spores and cells mediated by curcumin. J Photochem Photobiol B: Biol 2017;173:301–6.
[108] Lin Y, Xu X, Tian S, Wang J, Cao S, Huang T, Xie W, Ran Z, Wen G. Inactivation of fungal spores by performic acid in water: Comparisons with peracetic acid. J Hazard Mater 2023;458:131929.
[109] Wen G, Tan L, Cao R, Wan Q, Xu X, Wu G, Wang J, Huang T. Inactivation of waterborne fungal spores by 1-bromo-3-chloro-5,5-dimethylhydantoin: Kinetics, influencing factors and mechanisms. Chemosphere 2021;274:129764.
[110] Wen G, Cao R, Wan Q, Tan L, Xu X, Wang J, Huang T. Development of fungal spore staining methods for flow cytometric quantification and their application in chlorine-based disinfection. Chemosphere 2020;243:125453.
[111] Cao R, Wan Q, Tan L, Xu X, Wu G, Wang J, Xu H, Huang T, Wen G. Evaluation of the vital viability and their application in fungal spores' disinfection with flow cytometry. Chemosphere 2021;269:128700.
[112] Wan Q, Wen G, Cao R, Xu X, Zhao H, Li K, Wang J, Huang T. Comparison of UV-LEDs and LPUV on inactivation and subsequent reactivation of waterborne fungal spores. Water Res 2020;173:115553.
[113] Wan Q, Cao R, Wen G, Xu X, Xia Y, Wu G, Li Y, Wang J, Lin Y, Huang T. Sequential use of UV-LEDs irradiation and chlorine to disinfect waterborne fungal spores: Efficiency, mechanism and photoreactivation. J Hazard Mater 2022;423:127102.

Materials Chemistry and Physics 334 (2025) 130478

Contents lists available at ScienceDirect

Materials Chemistry and Physics

journal homepage: www.elsevier.com/locate/matchemphys

Effects of dissolved oxygen accelerated *P. aeruginosa* on the corrosion mechanism of X70 steel in simulated marine environments

Riguang Zhu [a,b], Guiyuan Xie [a,b], Zu-an Qin [a,b], Xingying Tang [a,b,*], Jianjun Cai [c], Jianqiao Yang [d]

[a] Guangxi Laboratory on the Study of Coral Reefs in the South China Sea, Coral Reef Research Center of China, Nanning, 530004, China
[b] School of Marine Sciences, Guangxi University, Nanning, 530004, China
[c] Guilin University of Electronic Technology, Guilin, 541004, China
[d] Xi'an Jiaotong University, Xi'an, 710049, China

HIGHLIGHTS

- Dissolved oxygen affects corrosion of X70 steel by altering the respiration of *P. aeruginosa*.
- Accelerated corrosion of X70 steel by *P. aeruginosa* in aerobic environments.
- *P. aeruginosa* under the biofilm accelerated localised corrosion of X70 steel causing severe pitting.
- Aerobic *P. aeruginosa* is more corrosive than anaerobic *P. aeruginosa*.

ARTICLE INFO

Keywords:
MIC
P. aeruginosa
Dissolved oxygen
Localized corrosion
Uniform corrosion
Biofilm

ABSTRACT

Dissolved oxygen exerts a complex influence on microbial corrosion in marine environments. This paper investigates the effects of dissolved oxygen on the corrosion behavior of X70 steel in seawater, both in the presence and absence of *P. aeruginosa*, through electrochemical testing, surface morphology observation, corrosion weight loss analysis, and elemental analysis of corrosion products. The findings reveal that the uniform corrosion rate in the anaerobic *P. aeruginosa* seawater environment was lower than that in sterile seawater; however, localized corrosion was markedly severe, with pitting pits reaching a maximum width of 578.38 μm and a maximum depth of 49.938 μm—significantly greater than the maximum depth of 29.606 μm observed under sterile conditions. *P. aeruginosa* formed a biofilm on the steel substrate, which promoted localized corrosion. The introduction of dissolved oxygen accelerated the overall corrosion of X70 steel in the presence of marine *P. aeruginosa*, yielding a maximum corrosion rate of 45.62 mpy after 7 days of immersion, approximately two orders of magnitude greater than the corrosion rate under anaerobic conditions. The presence of dissolved oxygen enhanced the metabolic activity of *P. aeruginosa*, facilitated redox reactions in the steel matrix, and resulted in the formation of extensive metal oxide and microbial films. These metal oxides, primarily consisting of Fe_3O_4, FeOOH, and Fe_2O_3, combined with microbial cinema to create a composite product layer, significantly impacting the overall corrosion of X70 steel and promoting localized corrosion to a considerable extent.

1. Introduction

With the rapid development of the economy, China is confronting a significant energy shortage, prompting a pressing need to harness the abundant resources of the ocean to address ongoing developmental challenges [1]. X70 pipeline steel boasts exceptional properties, including high strength, toughness, good weldability, excellent forming characteristics, and resistance to corrosion and cracking, all at a low production cost. It is widely employed in the oil and gas industry, particularly for the transport of marine oil and gas [2–4], However, the extreme complexity of the marine natural environment makes metal materials particularly vulnerable to various factors, including biological influences [4], flow scour [5], temperature [6], pressure [7], dissolved oxygen [5–8], pH, and more. These harsh marine conditions can corrode

* Corresponding author. Guangxi Laboratory on the Study of Coral Reefs in the South China Sea, Coral Reef Research Center of China, Nanning, 530004, China.
E-mail address: tangxingying@gxu.edu.cn (X. Tang).

https://doi.org/10.1016/j.matchemphys.2025.130478
Received 16 November 2024; Received in revised form 7 January 2025; Accepted 28 January 2025
Available online 30 January 2025
0254-0584/© 2025 Elsevier B.V. All rights are reserved, including those for text and data mining, AI training, and similar technologies.

oil and gas transport pipeline steel, leading to potential damage, oil and gas leaks, and even severe explosions on oil and gas platforms [9].

Global statistics show that microbiologically influenced corrosion (MIC) leads to significant economic losses each year, accounting for approximately 20 % of the cost of corrosion of metallic materials [10,11]. MIC is influenced either directly by microbial activity or indirectly by microbial metabolites [12–15]. *Pseudomonas aeruginosa* is a common Gram-negative, motile, rod-shaped bacterium found abundantly in soils, marshes, and coastal marine environments [16]. It has been successfully isolated and characterized in coastal waters at various global locations and has frequently been implicated in cases of steel material failure in marine engineering [17–22]. *P. aeruginosa* is a representative marine electroactive bacterium that facilitates electron transfer on metal surfaces, accelerating the electrochemical corrosion reactions of metals and triggering localized corrosion phenomena [18,23]. Additionally, the electroactive properties of *P. aeruginosa* enable metal surfaces to exchange electrons, a mechanism that differs significantly from traditional chemical corrosion processes. Furthermore, *P. aeruginosa* can form biofilms on metal surfaces. On one hand, biofilms can shield corrosive factors, such as oxygen, from direct contact with the metal surface, thus slowing down corrosion [24,25]. On the other hand, biofilms alter corrosion kinetics on metal surfaces, and the metabolism of microorganisms within the biofilm can contribute to microbial corrosion through indirect effects, such as the secretion of acidic substances [26,27]. Recent studies [19,28,29] have shown that *P. aeruginosa* induces extracellular electron transfer to initiate corrosion by utilizing electrons generated from the oxidation of elemental iron (an electron donor) to reduce terminal electron acceptors like oxygen and nitrate [30,31]. These studies highlight the complex and multifaceted role of *P. aeruginosa* in marine corrosion, underscoring the need for further in-depth research into its corrosion behavior in marine environments.

The marine environment is highly complex, with varying dissolved oxygen (DO) concentrations across different regions [32]. The role of DO in metal dissolution kinetics is crucial, as it not only influences the corrosion process but also affects the formation and stability of oxide films on metal surfaces. High DO concentrations promote the formation of passivation films on metal surfaces [33], which help inhibit corrosion. In contrast, low DO concentrations can lead to the breakdown of passivation films, making metal surfaces more susceptible to localized corrosion [34,35]. Additionally, DO levels can influence microorganisms' growth and metabolic properties, thereby impacting surface biofilms' structure and physiological activity [33,36].

While significant research has focused on the effect of dissolved oxygen on metal corrosion, there is still a lack of systematic investigation into the specific mechanisms by which dissolved oxygen influences microbial metabolism and corrosion, particularly the corrosion behavior of *P. aeruginosa* under varying dissolved oxygen conditions. Therefore, studying the combined effects of dissolved oxygen and *P. aeruginosa* on the corrosion of X70 pipeline steel is crucial for controlling and preventing microbial corrosion in complex marine environments and assessing equipment safety. This study investigates the corrosion characteristics and mechanisms of X70 steel in the presence and absence of *P. aeruginosa*, with varying dissolved oxygen levels. The corrosion process of X70 steel induced by *P. aeruginosa* is analyzed through electrochemical testing, surface morphology observation, and other methods. The findings provide valuable insights into the practical application and corrosion protection of X70 pipeline steel in marine environments.

2. Methodology

2.1. Material and specimen

The corrosion material utilized in this experiment is X70 pipeline steel, sourced from Anshan Iron and Steel Works of China. The primary chemical composition of this steel is detailed in Table 1.

X70 pipeline steel was cut into specimen blocks measuring 10 mm × 10 mm × 3 mm for electrochemical testing using wire-cutting techniques. A copper wire was soldered to the backside of each specimen to serve as an electrochemical test electrode, while the non-working surfaces were sealed with epoxy resin within a polyethylene sample holder to prevent crevice corrosion, leaving a 1 cm^2 corrosion area exposed. The working surfaces were polished sequentially with 400#, 800#, 1200#, and 2000# SiC sandpaper, achieving a mirror finish with 1 μm diamond suspension on a polishing machine. The specimens were then ultrasonically rinsed, degreased, and dehydrated using sterile distilled water, acetone, and anhydrous ethanol, followed by nitrogen blow-drying before being stored in a drying dish for later use. For morphological analysis, samples were processed to dimensions of 30 mm × 20 mm × 3 mm, with a round hole of 3 mm diameter punched at the top center for easy fixation in the reactor. The surfaces were ground and polished step by step using the aforementioned SiC sandpaper until smooth and even. The specimens underwent ultrasonic rinsing, degreasing, and dehydration with sterile distilled water, acetone, and anhydrous ethanol, followed by nitrogen blow-drying and weighing. The samples were stored in a drying box prior to corrosion testing. Each specimen was sterilized in a 75 % ethanol solution for 60 min and subsequently irradiated with UV light for at least 30 min to eliminate any microbial contamination before the corrosion tests were conducted.

2.2. Bacterial cultures and corrosive environments

The corrosive microorganism used in this study was *Pseudomonas aeruginosa* strain 1A05429, isolated from offshore seawater in the South China Sea and provided by the South China Sea Institute of Oceanography, Chinese Academy of Sciences. The bacterium was genomically characterized through 16S rDNA sequencing, confirmed as *P. aeruginosa*, and preserved in the laboratory. The bacteria were cultured in an enrichment medium consisting of LB broth, which contained 0.5 g/L K_2HPO_4, 0.5 g/L $NaNO_3$, 0.2 g/L $CaCl_2$, 0.5 g/L $MgSO_4{\cdot}7H_2O$, 0.5 g/L $(NH_4)_2SO_4$, and 10 g/L ferric ammonium citrate. To simulate a marine environment, artificial seawater was prepared as the test solution according to the ASTM D 1141-98 standard. The composition of the artificial seawater included 24.48 g/L NaCl, 3.916 g/L Na_2SO_4, 1.16 g/L $CaCl_2$, 0.695 g/L KCl, 5.2 g/L $MgCl_2$, 0.201 g/L $NaHCO_3$, 0.027 g/L H_3BO_3, 0.025 g/L $SrCl_2$, 0.101 g/L KBr, and 0.003 g/L NaF. The pH of the artificial seawater was adjusted to between 7.2 and 7.5 using sodium hydroxide (1 mol/L) and autoclaved at 121 °C for 30 min to prevent contamination by other microorganisms. After 24 h of incubation, 3000 mL of LB medium containing 10 % *P. aeruginosa* was added to the sterilized reactor, resulting in an inoculated experimental medium with a *P. aeruginosa* concentration of 10^5–10^7 CFU/mL. For the sterile group, 3000 mL of sterile artificial seawater with 10 % sterile LB broth was utilized, while the constant dissolved oxygen (DO) group consisted of 3000 mL of artificial seawater with 10 % *P. aeruginosa* LB liquid medium. The dissolved oxygen concentration in the solution was maintained at approximately 2 ppm using an air cylinder. All corrosion tests were conducted under airtight conditions, with the reactor immersed in a thermostatic water bath at a controlled temperature of 25 °C. The

Table 1
Chemical composition of X70 pipeline steel (wt.%).

C	Si	Mn	P	S	Cr	Ti	Nb	Al	Cu	Ni	Fe
0.06	0.08	1.42	0.012	0.02	0.03	0.102	0.029	0.03	0.02	0.01	Bal

population of *P. aeruginosa* was determined via plate counting, and the bacterial growth curve during the corrosion of X70 steel was plotted based on changes in bacterial numbers. The pH of the solution was measured and recorded using a pH meter, and variations in dissolved oxygen levels over time were monitored with a dissolved oxygen meter.

2.3. Electrochemical tests

Electrochemical tests were conducted using a CHI660D electrochemical workstation, employing a three-electrode test system. The working electrode (WE) was an epoxy-sealed X70 pipeline steel specimen with a 1 cm^2 exposed surface area. An Ag/AgCl electrode served as the reference electrode (RE), while a platinum electrode functioned as the auxiliary electrode (CE). All electrodes were sterilized with 75 % alcohol and subsequently exposed to ultraviolet light for over 3 h. The electrochemical experiments included measurements of open circuit potential (OCP), electrochemical impedance spectroscopy (EIS), linear polarization resistance (LPR), and potentiodynamic polarization (PDP) at various time intervals. The EIS was performed at OCP, with potential fluctuations not exceeding 5 mV over 500 s. The frequency measurement range was set from 10^5 to 10^{-2} Hz, with an AC perturbation amplitude of 5 mV, collecting 10 data points for each order of magnitude. The electrochemical impedance data were analyzed and fitted using ZSimpWin software. The kinetic polarization curve was tested within a potential range of −0.5 V–0.5 V (vs OCP), with the scan progressing from cathodic to anodic potentials at a rate of 1 mV/s. A scanning range of ±10 mV relative to the open-circuit potential was selected to closely represent the true state of the system. The polarization resistance (R_p) was derived by calculating the slope of the potential versus current plot, while the corrosion current (I_{corr}) obtained from the PDP analysis provided insights into the material transport and corrosion mechanisms on the electrode surface, allowing for the conversion to an intuitive corrosion rate.

2.4. Surface morphology analysis

The corrosion morphology of the specimens was meticulously examined using a metallurgical microscope (Nikon Eclipse LV150NL, Japan) and a scanning electron microscope (SEM, Hitachi SU5000, Japan). Following the experiments conducted in the bacterial-containing reactor, the corroded specimens were immersed in a 2.5 % (v/v) glutaraldehyde solution for 8 h at 4 °C to fix the biofilm. They were then rinsed twice (5 min each) with phosphate-buffered saline (PBS) and deionized water, followed by rinsing with 25 %, 50 %, 75 %, and 100 % (v/v) ethanol solutions for 10 min at each concentration. The specimens were subsequently dried under nitrogen flow [37] and stored in a desiccator. Corrosion specimens prepared under aseptic conditions underwent similar washing and drying procedures. The scanning electron microscope was employed to observe the morphology of the bacteria and biofilm at a beam voltage of 15 kV, while the morphology of the oxide film was analyzed in the sterile control group. Additionally, scanning X-ray energy dispersive spectroscopy (EDS, FEI TeN-Cai G2 F20 S-Twin, USA) was utilized to assess the elemental composition, distribution, and relative content of the corrosion products at an accelerating voltage of 200 kV.

2.5. Pit morphology and depth analysis

The contour and depth of the corrosion pits were observed and measured using a confocal laser scanning microscope (CLSM Model C2 Plus, Nikon, Japan) focusing on the largest corrosion pits. Prior to this experiment, adhering biofilm and corrosion products were removed from the specimen surface following ASTM Standard G1-03. The maximum pit depth was determined by randomly selecting five areas on the X70 steel specimen and measuring the depth of each pit.

2.6. Weight loss

To determine the corrosion rate, the length, width, and height of the corrosion loss samples were accurately measured and recorded using vernier calipers to calculate the effective surface area prior to the corrosion test. A high-precision electronic analytical balance (model MCE125P–2CCN–U, with a measurement accuracy of 0.01 mg) was employed for weighing, with each sample weighed at least four times to establish its initial weight. After the reaction was completed under the specified experimental conditions, the samples were removed and rinsed with deionized water. A descaling agent was then utilized in an ultrasonic bath for 30–60 s to eliminate corrosion products from the sample surfaces. According to GB/T 16545-2015, the descaling agent solution was prepared by mixing 50 mL of 36 % hydrochloric acid, 50 mL of deionized water, and 0.346 g of hexamethylenetetramine. The samples were subsequently rinsed with distilled water and anhydrous alcohol, dried with nitrogen, and then weighed again using the electronic balance. The corrosion rate was calculated using the specified formula (1), with three parallel samples set up in each corrosion system to derive an average value.

$$v = (m_0 - m_1) / St \quad (1)$$

where v is the corrosion rate in $g{\cdot}m^{-2}{\cdot}h^{-1}$, m_0, and m_1 are the original and final weight of the samples in g, respectively, t is the immersion time in hours, and S is the exposed surface area in m^2.

3. Result and discussion

3.1. Parametric analysis of corrosive media

Fig. 1 illustrates the changes in *P. aeruginosa* concentration, dissolved oxygen levels, and the pH of the solution after immersing X70 steel in seawater with or without *P. aeruginosa* for different durations. In the absence of exogenous dissolved oxygen, *P. aeruginosa* proliferates and consumes oxygen through respiration. The bacterial concentration peaks after 1 day and then declines as the bacteria die from overpopulation. The dissolved oxygen concentration gradually decreases and almost disappears after 2 days. In sterile seawater, X70 steel slightly increases the solution's pH over time due to the redox reactions occurring at the anode (where Fe dissolves) and the cathode (where oxygen is reduced, producing OH^- ions). These hydroxide ions contribute to a gradual pH increase [38]. However, After immersion in seawater containing *P. aeruginosa* for different times, the pH first decreased and then slightly increased with the prolongation of the reaction time because *P. aeruginosa* reproduced in large quantities and respiration to produce CO_2 dissolved in the system, which decreased the pH of the solution and another reason was that *P. aeruginosa* secreted a large amount of acidic extracellular substances in anaerobic or low-oxygen conditions [20,39], which decreased the pH of the system. In *P. aeruginosa* seawater with added dissolved oxygen, due to the addition of dissolved oxygen, *P. aeruginosa* participates in the redox reaction, which makes the redox reaction more intense, and the cathode undergoes an oxygen uptake reaction to produce more OH^-, so the system pH increases. On the one hand, due to the continuous aeration of the corrosion system, the solubility of CO_2 produced by bacterial respiration is reduced, on the other hand, the extracellular substances secreted by *P. aeruginosa* under aerobic conditions are mainly neutral or weakly alkaline [20]. In summary, the corrosion of X70 steel in *P. aeruginosa* seawater with added dissolved oxygen is mainly weakly alkaline.

3.2. Surface morphology analysis

Using metallographic microscopy, the morphology of X70 steel specimens immersed for varying durations was examined, as depicted in Fig. 2. Panels (a) to (e) show the metallographic morphology of X70 steel

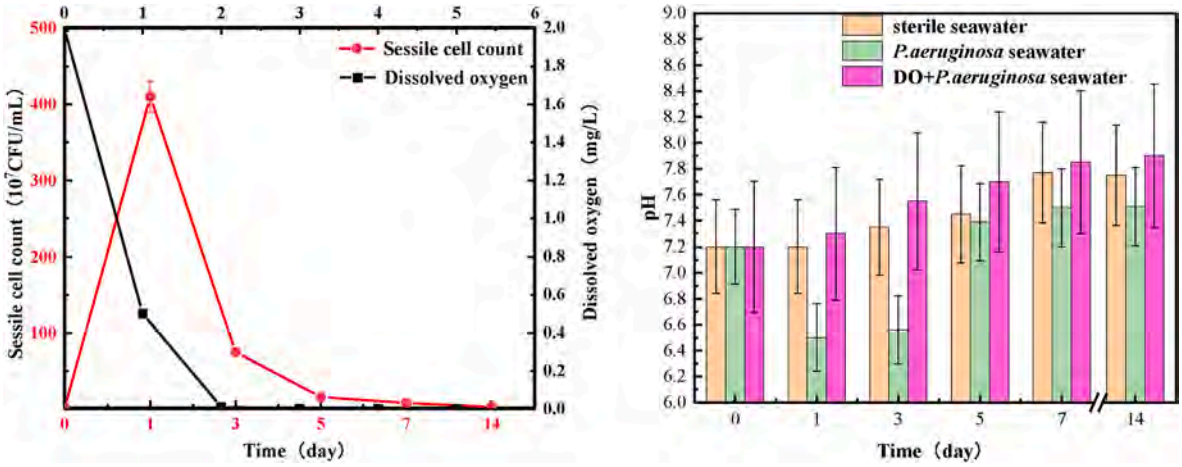


Fig. 1. Parameters of corrosive medium. (a)Sessile cell count and DO, (b)pH.

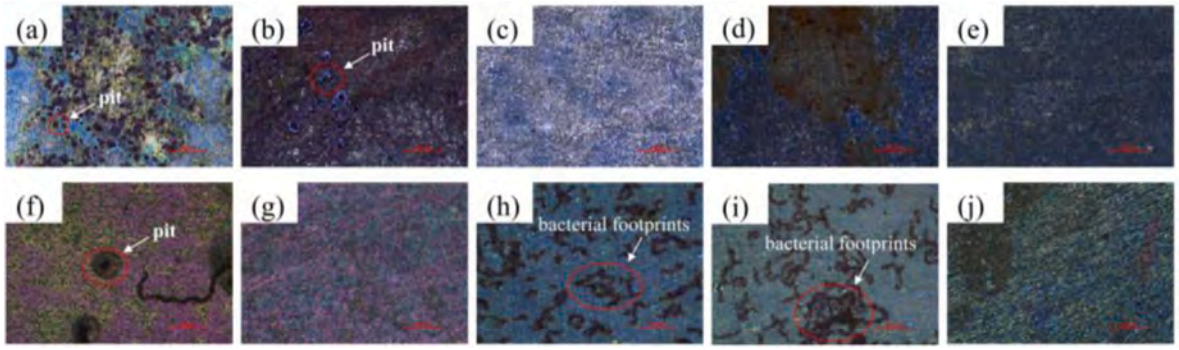


Fig. 2. Metallographic microscopy of corrosion patterns on X70 steel immersed in sterile seawater and anaerobic *P. aeruginosa*-contaminated seawater over time. (a–e) Sterile seawater after 1, 3, 5, 7, and 14 days; (f–j) anaerobic *P. aeruginosa* seawater at 1, 3, 5, 7, and 14 days.

in sterile seawater. After one day of immersion, numerous uniformly distributed pitting pits were evident on the surface. By three days, the corrosion product film began to cover these pits, although larger pits remained exposed. After five days, few corrosion pits were observable, indicating that the corrosion product film had thickened significantly. This gradual buildup of the passivation film likely hindered seawater access to the X70 steel, resulting in a reduced corrosion rate.

Panels (f) to (j) illustrate the metallographic morphology of X70 steel immersed in anaerobic *P. aeruginosa* seawater over different time intervals. After one day, the specimen surface exhibited fewer corrosion craters and a flatter profile compared to the sterile seawater sample. However, with prolonged immersion—particularly after five and seven days—the surface showed an increase in irregular scratches. This phenomenon was attributed to the presence of dead cells on the substrate surface, creating voids that resembled 'bacterial footprints' [40]. After fourteen days of immersion, the surface appeared smooth due to biofilm coverage secreted by *P. aeruginosa*. Despite a reduction in bacterial numbers in the seawater, the increasing biofilm thickness rendered the X70 steel more resistant to corrosive factors, resulting in a higher corrosion rate in the *P. aeruginosa* environment compared to sterile seawater.

Fig. 3 illustrates the metallographic appearance of X70 steel immersed in *P. aeruginosa* seawater with 2 ppm dissolved oxygen over time. The addition of dissolved oxygen led to observable delamination of the corrosion product film, with increased accumulation of corrosion products on the surface. Additionally, more irregularly distributed pits and pronounced irregular scratches were evident, highlighting the impact of dissolved oxygen on corrosion behavior.

Fig. 4 illustrates the SEM morphology of X70 steel after immersion in sterile seawater for varying durations. Panels (a) to (e) depict the

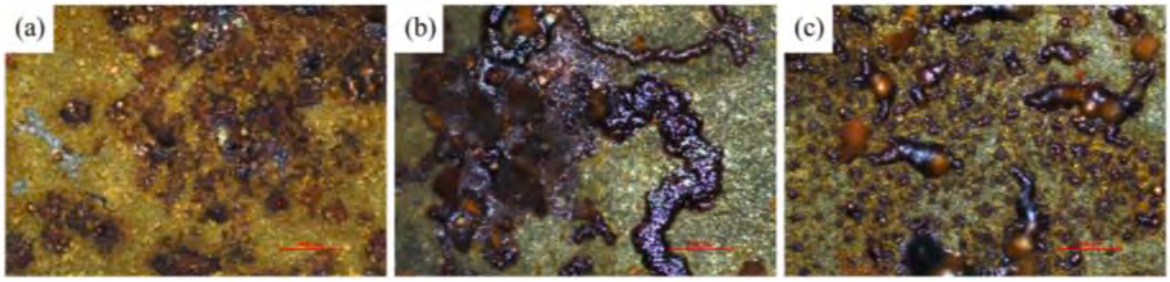


Fig. 3. Metallographic microscopic morphology of X70 steel immersed in *P. aeruginosa* seawater containing 2 ppm dissolved oxygen over time. (a) 3 days, (b) 7 days, (c) 14 days.

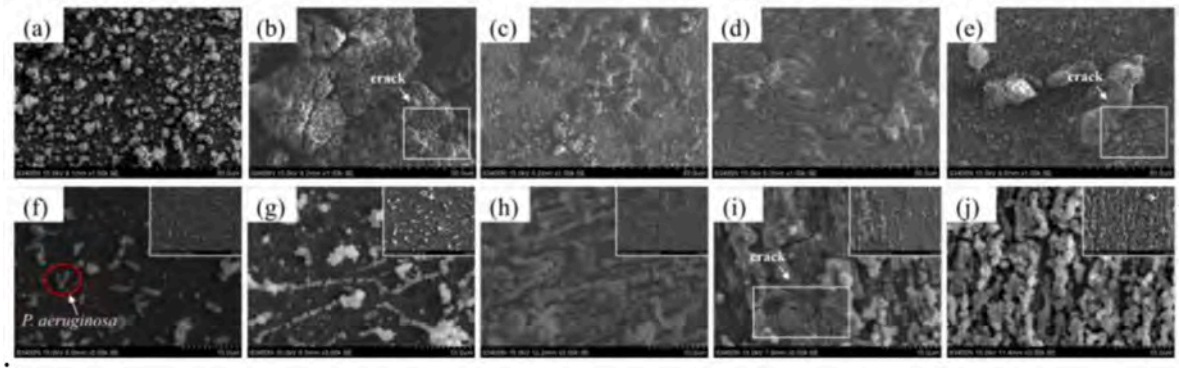


Fig. 4. SEM morphology of X70 steel immersed in seawater for varying durations, with and without *P. aeruginosa.* (a–e) Sterile seawater at 1, 3, 5, 7, and 14 days. (f–j) Anaerobic *P. aeruginosa* seawater at 1, 3, 5, 7, and 14 days.

progression of corrosion. After 1 day, numerous granular corrosion products were evident on the surface, loosely distributed and not fully covering the observation area, indicating early-stage corrosion. By 3 days, these products had formed a dense membrane characterized by noticeable crack demarcation. As immersion continued, the accumulation of corrosion products on the membrane surface led to a thickening of the passivation film, suggesting enhanced corrosion resistance over time.

Fig. 4 f ~ j shows the SEM morphology of X70 steel in anaerobic *P. aeruginosa* seawater after immersion for different days. After 1 day of immersion in seawater of anaerobic *P. aeruginosa*, granular corrosion products were also formed on the surface of X70 steel, but the corrosion products formed were less than those immersed in sterile seawater, the granular corrosion products formed were smaller, and rod-shaped microorganisms could be observed adhering to the surface, and after 3 d of immersion, the surface of X70 steel was covered with a layer of rod-shaped microorganisms composed of a biofilm, distributed in clusters [22], and with the prolongation of the immersion time, the biofilm covered an increasing area, and the formed biofilm was thicker and thicker, with a uniform film distribution, and *P. aeruginosa* formed a prominent loose multicellular biofilm structure through the accumulation of itself and its extracellular material, in general, microbial membranes in nature have a high degree of mechanical stability and viscoelasticity [41], and once formed, it can largely resist external perturbations and play a certain role in isolation [41,42].

Fig. 5 illustrates the SEM morphology of X70 steel immersed in *P. aeruginosa* seawater with 2 ppm dissolved oxygen over various periods. After 3 days, the corrosion products consisted of a composite film made of both biofilm and oxide film from *P. aeruginosa*, creating a loose and porous structure in cluster formations [43]. By 7 days, a significant accumulation of corrosion products was observed; compared to day three, the product film appeared flatter with visible surface cracks, suggesting instability in the film's formation. By 14 days, the cracks had vanished, and the corrosion products transitioned to a filamentous distribution, indicating ongoing changes in the corrosion dynamics influenced by microbial activity and environmental conditions.

3.3. Elemental composition and structure analysis

Fig. 6 presents the EDS (Energy Dispersive X-ray Spectroscopy) analysis of X70 steel after 14 days of immersion in seawater, both with and without *P. aeruginosa*. In the sterile seawater environment, the highest elemental contents of Fe and O suggest that the primary corrosion products are iron oxides or hydroxides. In contrast, the anaerobic seawater environment containing *P. aeruginosa* showed lower levels of Fe and O but higher concentrations of C and N. This indicates the presence of bacterial activity and the secretion of extracellular polymers and other biologically active substances, which contribute to the corrosion process. The reduced iron oxidation products in this environment imply that microbial activity significantly influences the corrosion mechanisms and the nature of the corrosion products formed.

Fig. 7 displays the EDS plots of X70 steel immersed in *P. aeruginosa* seawater with 2 ppm dissolved oxygen over different immersion times. Compared to the results shown in Fig. 6, the corrosion products in this environment not only consist of bacteria and their secreted extracellular polymers but also exhibit a significantly higher presence of iron oxidation products. This indicates that the addition of dissolved oxygen influences the corrosion process by enhancing the formation of iron oxides, while still allowing for microbial contributions to the corrosion mechanism. The presence of both biological and inorganic components in the corrosion products underscores the complex interactions occurring in the marine environment.

To further analyze the elemental composition and distribution on the surface of X70 steel, high-resolution X-ray photoelectron spectroscopy (XPS) was performed, as illustrated in Fig. 8. The surface C 1s spectra for X70 steel after immersion in different environments are presented in panels (a), (d), and (g), corresponding to sterile seawater, anaerobic *P. aeruginosa* seawater, and *P. aeruginosa* seawater containing 2 ppm dissolved oxygen, respectively. The fitted peaks include C–C (284.8 eV), C═O (289.0 ± 0.2 eV), C–O (286.0 ± 0.1 eV), and O–C═O (288.5 ± 0.3 eV). It was observed that the corrosion products of X70 steel in sterile seawater contained only inorganic carbon and oxygen compounds. In contrast, the corrosion products in *P. aeruginosa*-containing seawater also included organic carbon and oxygen compounds. These

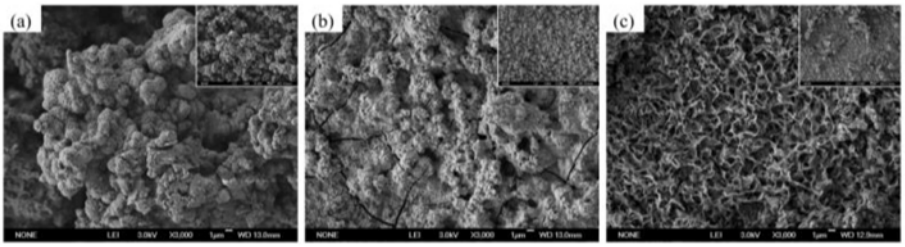


Fig. 5. SEM morphology of X70 steel immersed in *P. aeruginosa* seawater containing 2 ppm dissolved oxygen over time. (a) 3 days, (b) 7 days, (c) 14 days.

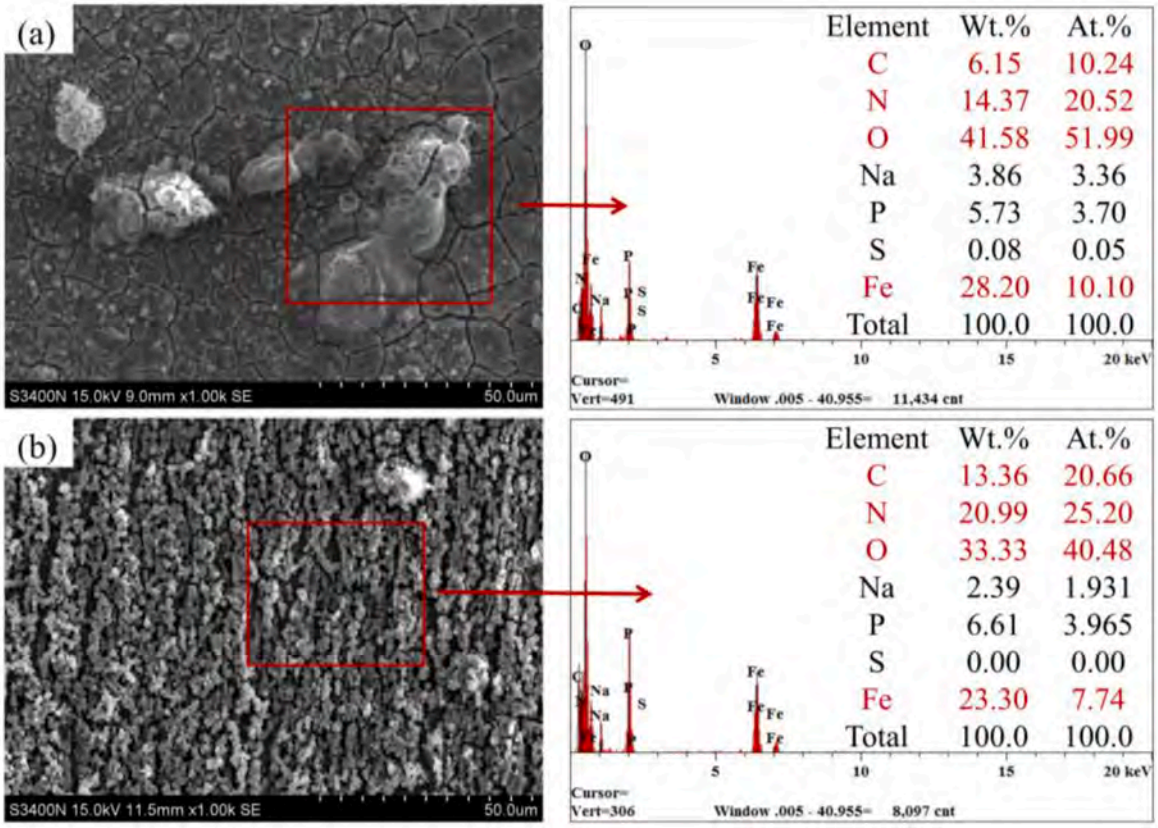


Fig. 6. Elemental content of X70 steel immersed for 14 days in seawater with and without *P. aeruginosa*. (a) sterile seawater, (b) anaerobic *P. aeruginosa* seawater.

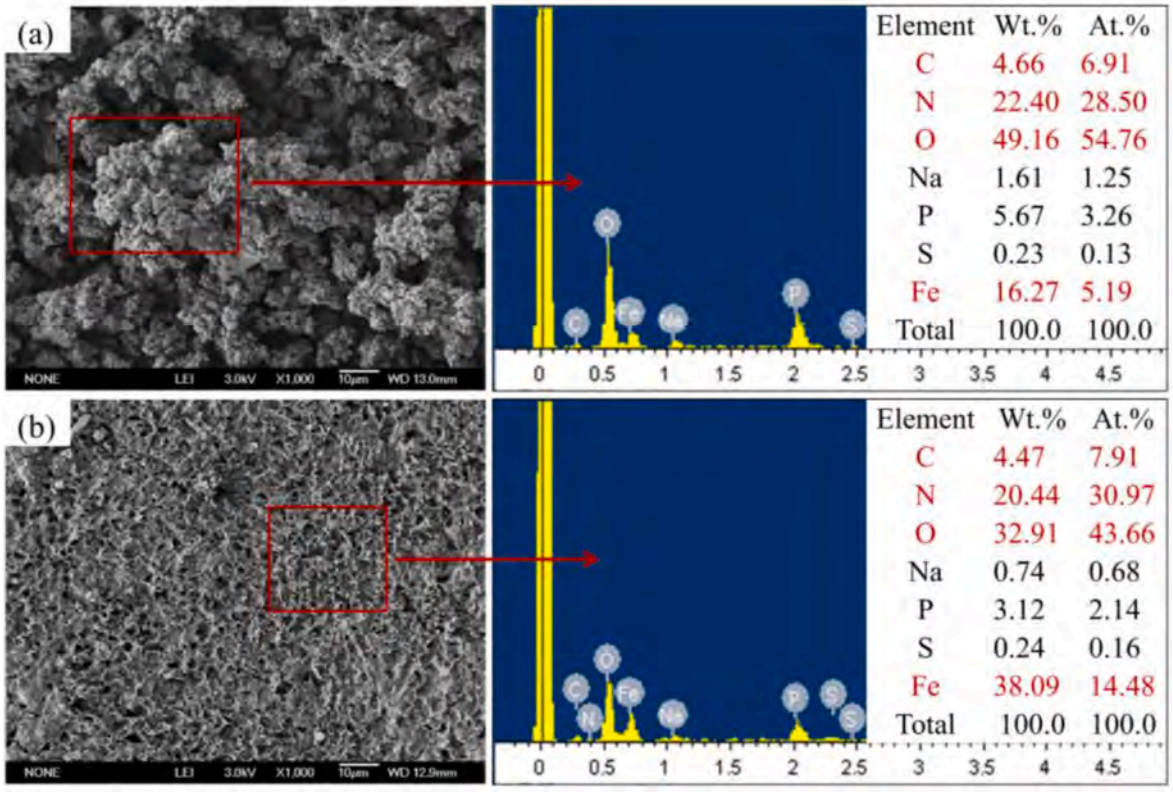


Fig. 7. Elemental content of X70 steel immersed in *P. aeruginosa* seawater containing 2 ppm dissolved oxygen for different time periods. (a) 3days, (b) 14days.

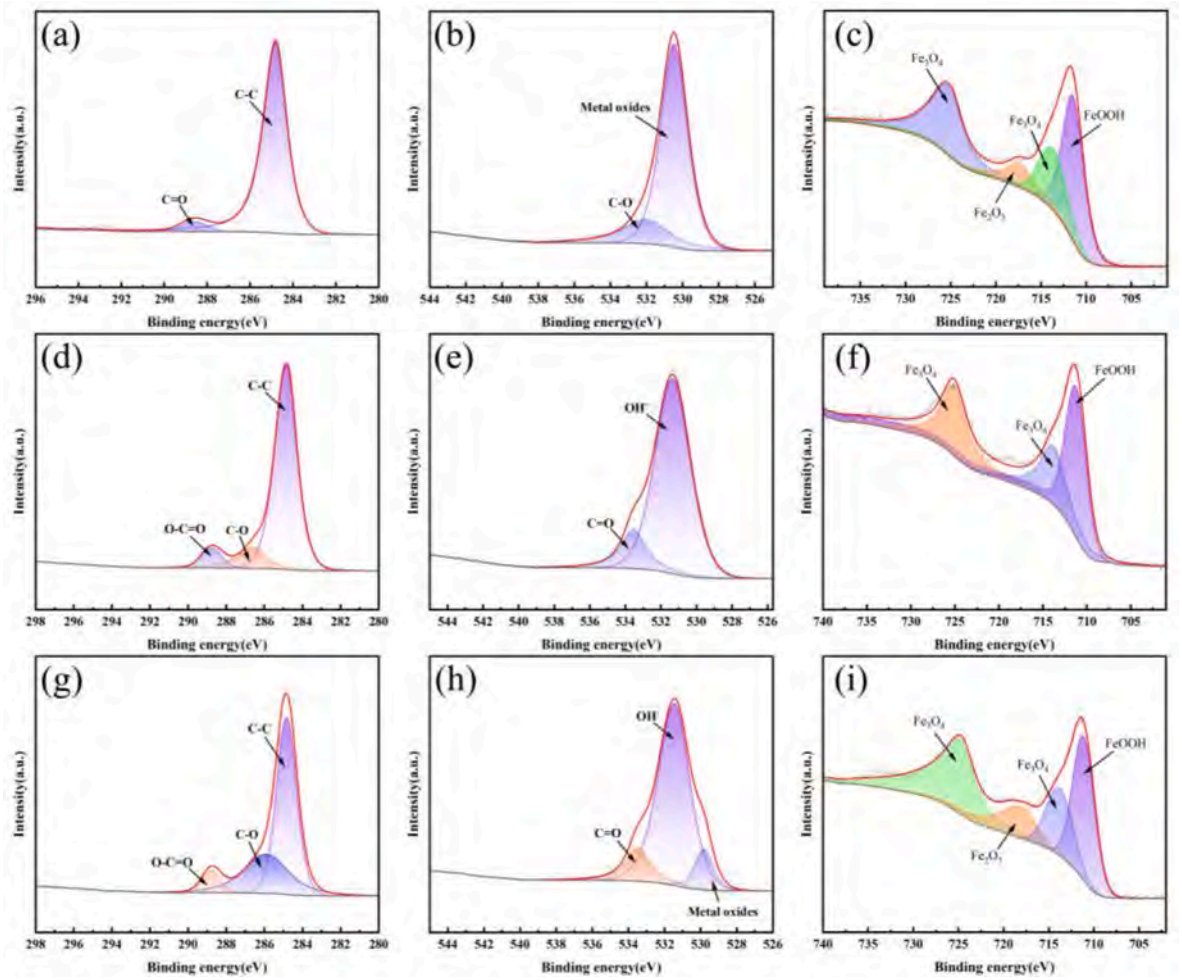


Fig. 8. High-resolution XPS maps of different elements of X70 steel after 14 days of immersion in seawater, with and without *P. aeruginosa*. (a–c) Sterile seawater, (d–f) Anaerobic *P. aeruginosa* seawater, (g–i) DO + *P. aeruginosa* seawater.

organic compounds were identified as extracellular polymers, such as polysaccharides, lipoproteins, and cell-surface proteins, indicating that extracellular polymers on the specimen's surface may participate in the corrosion process. Additionally, the organic content was higher in seawater with *Pseudomonas aeruginosa* and 2 ppm of dissolved oxygen, suggesting that the presence of both the bacteria and dissolved oxygen enhances the organic matter accumulation, analysis reveals that only inorganic carbon and oxygen compounds were present in the corrosion products of X70 steel immersed in sterile seawater. In contrast, both organic carbon and oxygen compounds were detected in the corrosion products formed in anaerobic *P. aeruginosa* seawater, with an increased presence of organic matter observed in the samples immersed in seawater containing 2 ppm dissolved oxygen. This highlights that the corrosion process in anaerobic *P. aeruginosa* seawater leads to the formation of biofilms, with greater accumulation occurring under oxygenated conditions. The O 1s spectra (shown in panels (b), (e), and (h)) corroborate this finding, indicating a higher concentration of hydroxyl groups (OH^-) at approximately 531.2 eV ± 0.1 eV following corrosion [44], suggesting a more complex corrosion environment influenced by microbial activity. Panels (c), (f), and (i) illustrate the relative content and distribution of metal oxides on the X70 steel surface after immersion in various environments. Notably, higher concentrations of Fe_3O_4 (714.0 ± 0.1 eV) [45] and FeOOH (711.5 ± 0.1 eV) [46–49]were detected after corrosion in sterile seawater and in *P. aeruginosa* seawater containing 2 ppm dissolved oxygen. Both environments exhibited the presence of Fe_2O_3 in the corrosion products [50], contributing to the reddish-brown appearance of the corrosion layer. Conversely, no Fe_2O_3 was detected in the corrosion products from anaerobic *P. aeruginosa* seawater, aligning with previous analyses indicating a diminished presence of metal oxides in this environment. The minimal formation of metal oxides suggests that any oxides detected resulted from redox reactions involving oxygen present in the water. Thus, the surface of X70 steel in anaerobic *P. aeruginosa* seawater is predominantly covered by biofilms, whereas in sterile seawater, a metal oxide film forms. In the presence of 2 ppm dissolved oxygen, the corrosion products represent a composite of both metal oxide films and microbial films. In all three corrosive environments, the corrosion products showed a high concentration of FeOOH, which is commonly attributed to the high Cl^- concentration in seawater [51]. The presence of Cl^- significantly increases the tendency for pitting corrosion in the rust layer, creating numerous attachment sites for *P. aeruginosa*, thereby accelerating the material's corrosion.

3.4. Pit morphology and depth analysis

To assess whether biofilm growth on the surface of X70 steel contributed to pitting corrosion, the corrosion morphology following the removal of biofilm and corrosion products was examined. Fig. 9 illustrates the maximum pitting pit metallographies of X70 steel after immersion in seawater environments with and without *P. aeruginosa* over varying durations. The morphology of the deepest pit is depicted in Fig. 11. The results show that the diameter of the maximum pitting pits on X70 steel increases with immersion time in both seawater conditions. Notably, the presence of *P. aeruginosa* significantly exacerbates local

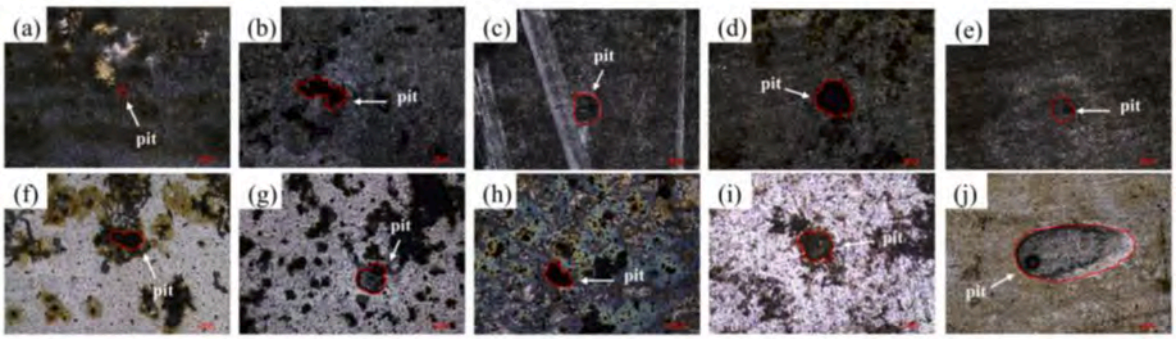


Fig. 9. Corrosion pit morphology of X70 steel after immersion in seawater, with and without *P. aeruginosa*, for different durations to remove corrosion products. (a–e) Sterile seawater: (a) 1 day, (b) 3 days, (c) 5 days, (d) 7 days, (e) 14 days. (f–j) Anaerobic *P. aeruginosa* seawater: (f) 1 day, (g) 3 days, (h) 5 days, (i) 7 days, (j) 14 days.

corrosion, leading to a greater increase in both the size and depth of the pitting pits. In anaerobic *P. aeruginosa* seawater, the uneven distribution of bacterial colonies on the X70 steel surface causes localized metabolic activity, intensifying electrochemical corrosion in areas where bacteria aggregate. This bacterial concentration not only accelerates metal dissolution but also creates more space for pitting to develop, resulting in more severe localized corrosion. Specifically, the maximum depth of corrosion pits in the presence of *P. aeruginosa* was recorded at 49.938 μm (Fig. 11 d), which is considerably deeper than the maximum depth of 29.606 μm observed under sterile seawater conditions (Fig. 11 b). The increase in active sites on X70 steel in sterile seawater, due to the presence of chloride ions (Cl^-), facilitates pitting corrosion [52]. However, the formation of a dense passivation film diminishes the likelihood of pitting, leading to predominantly uniform corrosion in that environment. In contrast, in *P. aeruginosa* seawater containing 2 ppm dissolved oxygen (Fig. 10), two primary phenomena were observed first, *P. aeruginosa* disrupts the passivation film on the X70 steel surface, leading to pronounced pitting corrosion; second, the presence of dissolved oxygen encourages the formation of a metal oxide film, which partially covers the pitting craters, thereby reducing the extent of localized corrosion. The maximum pit depth in this scenario was measured at 46.572 μm (Fig. 11 f). As a result, both uniform and localized corrosion coexist in *P. aeruginosa* seawater with dissolved oxygen, resulting in a more severe overall corrosion effect on the X70 steel.

3.5. Electrochemical tests

3.5.1. EIS spectra

Fig. 13 presents the electrochemical impedance spectroscopy (EIS) spectra and Bode-phase plots for X70 steel immersed in seawater environments with and without *P. aeruginosa* over various time periods. The radius of the capacitive arc in the EIS spectrum indicates the resistance to electrochemical reactions on the electrode surface, with a larger arc signifying greater resistance. As immersion time increases, the impedance spectral radius for X70 steel in both sterile seawater and anaerobic *P. aeruginosa* environments grows larger, suggesting that the overall resistance of the system increases and the metal corrosion reaction becomes more challenging, leading to a reduced corrosion rate. Specifically, Fig. 13a and (c) show that during the first 3 days of immersion, the impedance spectral radius enlarges, indicating a gradual decrease in the corrosion rate. However, a notable decrease in this radius occurs at 7 days, likely due to the detachment of the corrosion product film, which leads to an increase in the corrosion rate. When X70 steel is immersed in *P. aeruginosa* seawater containing 2 ppm dissolved oxygen, two semicircles are observed in both the high-frequency and low-frequency regions, with their radii displaying opposite trends over time. Notably, the impedance spectral radius in this oxygenated environment is significantly smaller than that in sterile and anaerobic environments, indicating more aggressive corrosion activity. The Bode plots further illustrate this behavior, with the impedance modulus in the low-frequency region ($|Z|$ at 0.01 Hz) reflecting the changes in the capacitive loop [22]. As depicted in Fig. 13b–(d), and (f), the low-frequency region's impedance modulus is highest for X70 steel samples in anaerobic *P. aeruginosa* seawater, followed by sterile seawater, and lowest in the *P. aeruginosa* seawater with 2 ppm dissolved oxygen. This pattern indicates that corrosion resistance is greatest in the anaerobic environment, making the corrosion reaction more difficult, while the most aggressive corrosion occurs in the presence of dissolved oxygen.

Based on the results of the Bode-phase diagram, it was observed that X70 steel, irrespective of the immersion conditions with or without *P. aeruginosa*, exhibited a single time constant in the low-frequency region. Consequently, the equivalent circuit of R(QR) was selected to simulate the corrosion process [53]. In contrast, the Bode diagram for X70 steel immersed in *P. aeruginosa* seawater containing 2 ppm dissolved oxygen displayed two-time constants; thus, the equivalent circuit of R(Q(R(QR))) was employed for simulating the corrosion process. Fig. 12 shows the equivalent circuits used to fit EIS data. All the EIS data

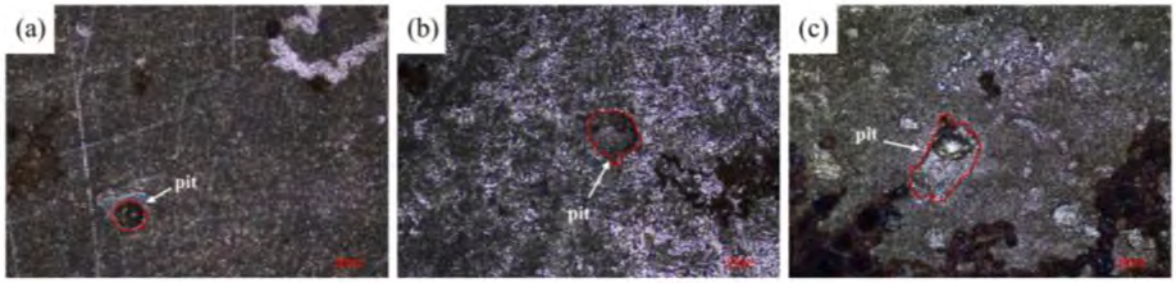


Fig. 10. Corrosion pit morphology of X70 steel after immersion in *P. aeruginosa* seawater containing 2 ppm dissolved oxygen for different times to remove corrosion products. (a) 3 days, (b) 7 days, (c) 14 days.

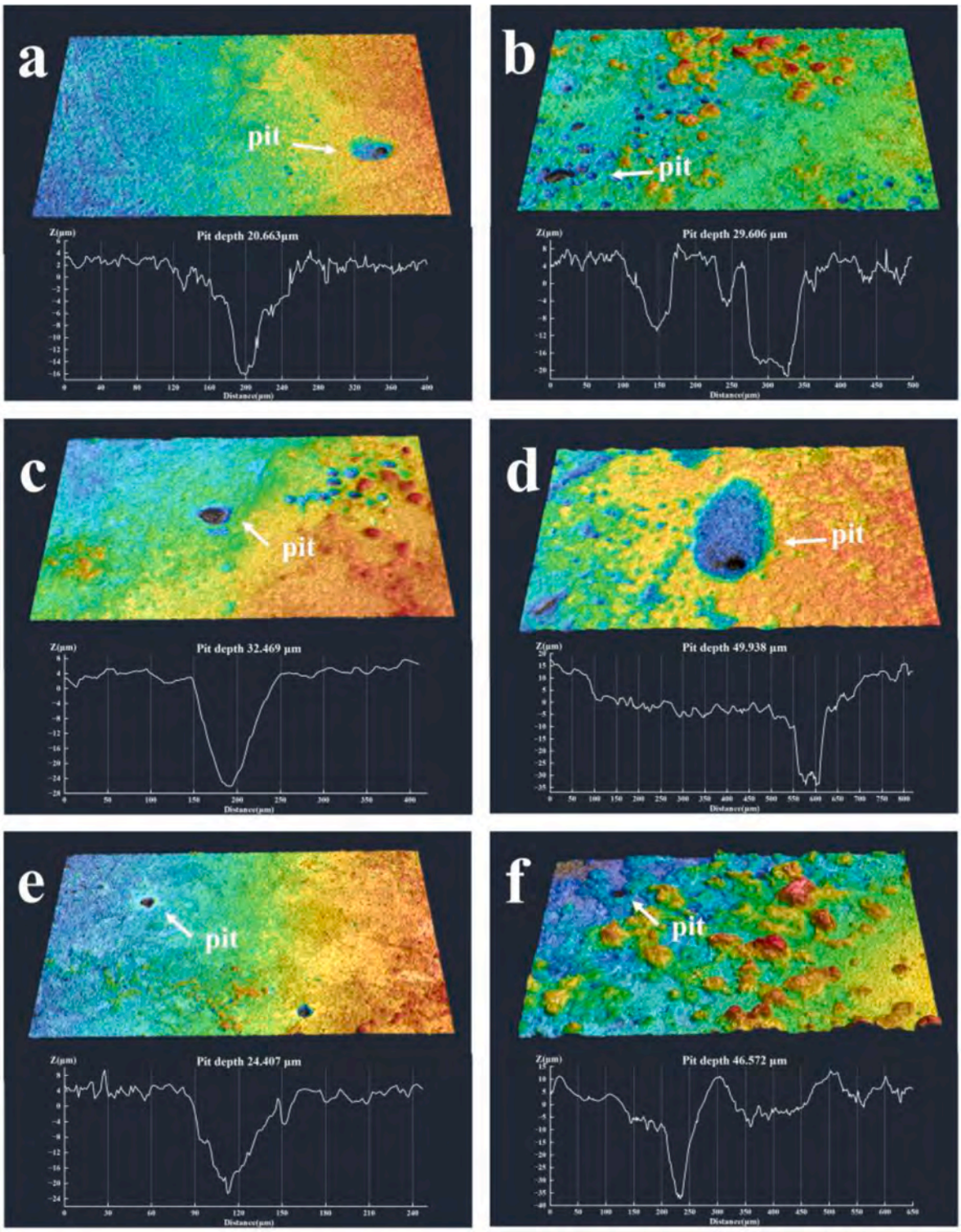


Fig. 11. CLSM 3-D images of the deepest pits on X70 steel after different immersion durations. (a) Sterile seawater: 7 days, (b) 14 days. (c) Anaerobic *P. aeruginosa* seawater: 7 days, (d) 14 days. (e) DO + *P. aeruginosa* seawater: 7 days, (f) 14 days.

were fitted well (Fig. 13) with a smaller fitted error (<10 %). The resistance value of the specimen is represented by the following equation:

$$Z = R_S + \frac{R_f}{(jw)^{n_1} Q_f + \frac{1}{R_f + \frac{1}{(jw)^{n_2} Q_{dl} + \frac{1}{R_{ct}}}}} \quad (2)$$

Where R_s is the solution resistance between the reference electrode and the working electrode, Ω; R_f is the resistance of the corrosion product layer, R_{ct} is the charge transfer resistance of the oxidation reaction at the metal/rust layer interface, which represents the resistance to the charge crossing the double layer; ω is the angular frequency of the potential sine wave, j is an imaginary unit, and Q_f and Q_{dl} are the constant-phase angular components reflecting the capacitance of the product layer and the double layer, respectively. Here Q is used instead of the pure capacitance C because in the actual electrode process, the generated

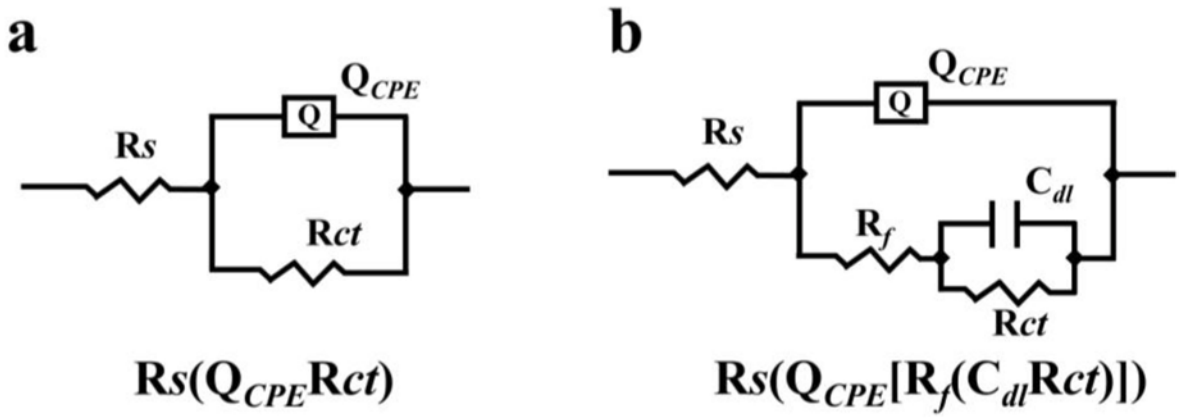


Fig. 12. Equivalent circuits used for fitting the impedance spectra of X70 steel: (a) in the Sterile seawater and anaerobic *P. aeruginosa* seawater, and (b) in the DO + *P. aeruginosa* seawater.

corrosion products change, as well as the existence of porous, rough morphology and adsorption phenomena on the electrode surface, which makes the pure capacitance characteristics deviate from the pure capacitance characteristics, and therefore the constant phase element *Q* is used [54]. It is shown in the following equation [55].

$$Q = Y_0^{-1} / (j \bullet \omega)^n \quad (3)$$

Y_0 is a constant that characterizes the magnitude of the capacitance, while n indicates the roughness of the electrode surface, reflecting the unevenness of the corrosion current density distribution and the degree of deviation from ideal capacitance, thus illustrating the strength of the dispersion effect [56]. Table 2 presents the parameters obtained by fitting the equivalent circuit using Zsimp-Win software, revealing that R_{ct} and R_f exhibit significant changes with increased immersion time. By correlating the concentration of *P. aeruginosa* with the trend of Y_0, it is evident that the bacterial concentration follows a similar pattern to the changes in the active sites on the surface of X70 steel. This suggests that the presence of *P. aeruginosa* directly influences the electrochemical corrosion of X70 steel. In all three corrosive environments, the values of R_{ct} progressively increase as corrosion advances, indicating enhanced resistance to charge transfer across the bilayer and an overall increase in corrosion resistance. For equivalent immersion durations, the order is R_{ct} in anaerobic *P. aeruginosa* seawater > R_{ct} in sterile seawater > R_{ct} in *P. aeruginosa* seawater with 2 ppm dissolved oxygen. Regarding the immersion roughness of the electrode surface at different time points, n indicates that the presence of *P. aeruginosa* promotes localized corrosion of X70 steel during the first 3 days of immersion. After this period, in the sterile seawater environment, the surface of X70 steel primarily forms an oxide passivation film, which densely covers the corrosion pits, leading to a flat electrode. In the anaerobic *P. aeruginosa* seawater environment, the metabolic activities of *P. aeruginosa* produce extracellular substances that form a biofilm, with bacteria aggregating in the corrosion pits, reducing the electrode roughness. In the oxygenated *P. aeruginosa* seawater environment, the roughness increases, with a low 'n' value of 0.67, indicating a more uneven surface. This may be due to the formation of both oxide and biofilm layers on the porous electrode. The presence of dissolved oxygen leads to a loosening of these layers due to CO_2 produced by bacterial respiration, making the material more vulnerable to microbial and seawater corrosion. Additionally, *P. aeruginosa* accumulates in the pores, further accelerating local corrosion. The dissolved oxygen not only drives electrochemical corrosion but also significantly affects microbial activity [24].

3.5.2. OCP, LPR and potentiodynamic polarization analysis

The polarization curves of X70 steel immersed for varying durations in seawater environments, both with and without *P. aeruginosa*, are depicted in Fig. 14 (a, b, c). The differences between the polarization curves for X70 steel in sterile seawater and anaerobic *P. aeruginosa* seawater are minimal, yet they are lower in magnitude compared to those observed in *P. aeruginosa* seawater containing 2 ppm dissolved oxygen. The shapes of the anodic and cathodic polarization curves clearly indicate that the polarization process is predominantly governed by the anodic response, attributed to the formation of biofilms and passivation films. Immersion in *P. aeruginosa* seawater with 2 ppm dissolved oxygen results in a more negatively skewed open circuit potential (OCP) due to the substantial CO_2 production from aerobic respiration by *P. aeruginosa*. Conversely, the electrode surfaces in high dissolved oxygen (DO) conditions are replenished with oxygen, leading to an increase in the partial pressure of oxygen and a corresponding negative shift in the corrosion potential, suggesting that biofilm formation concurrently influences the cathodic process [57]. X70 steel immersed in aseptic seawater for varying durations exhibits a critical potential at which the current density experiences a sudden increase, defined as the pitting potential [58]. This pitting potential is more negative in anaerobic *P. aeruginosa* seawater, indicating a heightened likelihood of pitting corrosion in this environment. The Tafel extrapolation method was employed to analyze the polarization curves, from which the self-corrosion potential (E_{corr}) and corrosion current density (I_{corr}) were measured. The polarization resistance (R_P) was then calculated by integrating the anodic and cathodic polarization Tafel constants, namely the anodic and cathodic slopes (β_a and β_c), using the following equations.

$$R_p = \frac{\beta_a \cdot \beta_c}{2.303 \cdot (\beta a + \beta c) \cdot I_{corr}} \quad (4)$$

The polarization curve parameters obtained through fitting are illustrated in Fig. 14 (d, e, f), which serve as indicators of the instantaneous corrosion rate of the material, given that the reciprocal of the polarization resistance ($1/R_P$) is directly proportional to the corrosion rate [59]. With prolonged immersion time, both I_{corr} and $1/R_P$ for X70 steel in sterile seawater decreased, signifying a gradual decline in the electrochemical corrosion rate, which reduced from 7.43 mpy to 1.12 mpy. This reduction is attributed to the accumulation of corrosion products on X70 steel when exposed to corrosive factors in seawater, leading to the formation of a passivation film that obstructs the ingress of corrosive elements, thereby inhibiting uniform corrosion and resulting in a lower corrosion rate. In contrast, I_{corr} and $1/R_P$ for X70 steel in seawater containing *P. aeruginosa* initially increased and subsequently decreased, indicating an initial rise in the electrochemical corrosion rate, peaking at 2.62 mpy after 3 days of immersion, before dropping to a minimum of 0.78 mpy after 14 days. This trend can be explained by the rapid proliferation of *P. aeruginosa* during the first 3 days, which increased bacterial concentration and facilitated electron loss, thereby elevating the corrosion rate. As the concentration of *P. aeruginosa* rose,

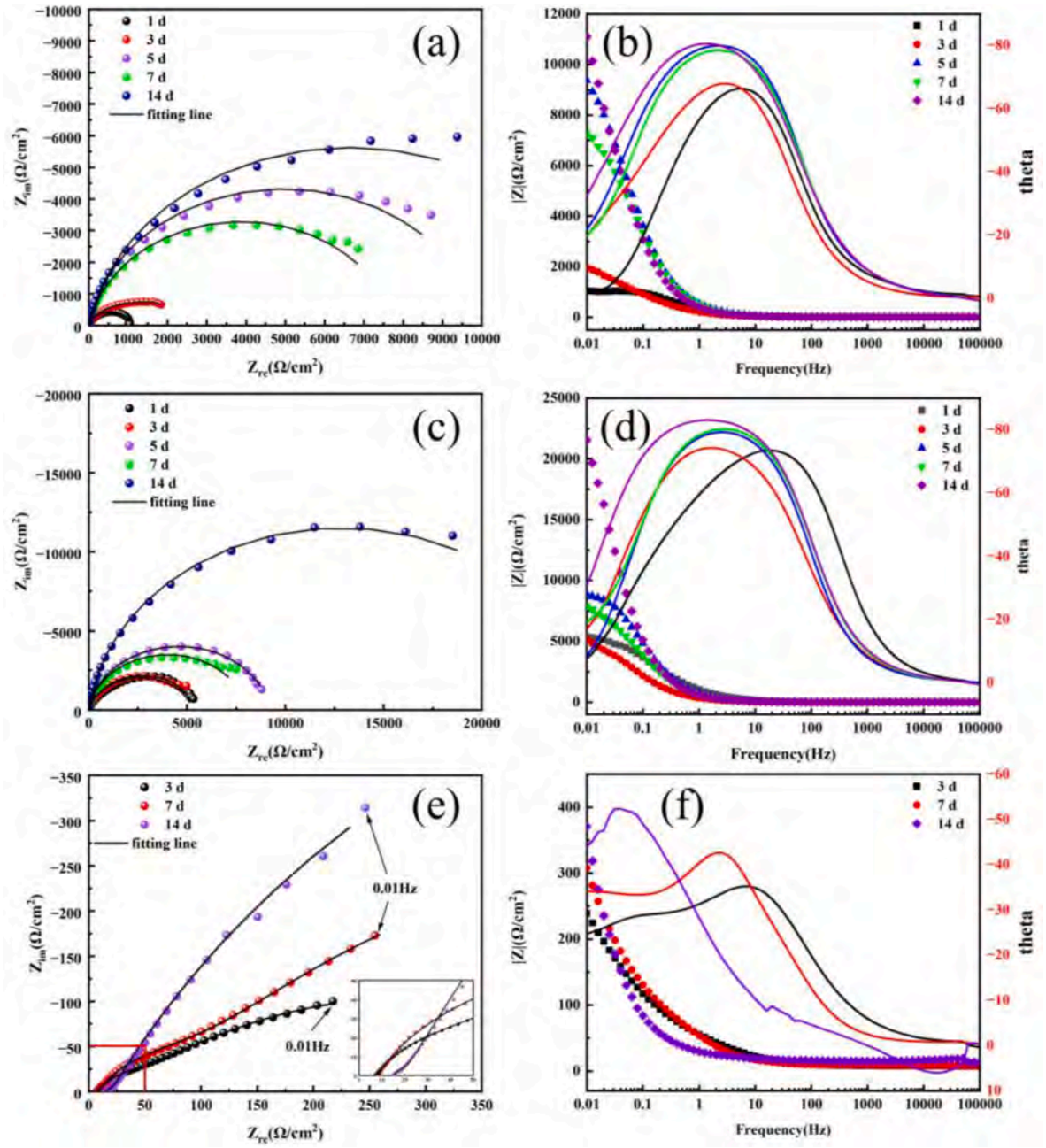


Fig. 13. Nyquist and Bode-phase plots of X70 steel. (a) Nyquist plot in sterile seawater, (b) Bode phase plot in sterile seawater, (c) Nyquist plot in anaerobic *P. aeruginosa* seawater, (d) Bode phase plot in anaerobic *P. aeruginosa* seawater, (e) Nyquist plot in DO + *P. aeruginosa* seawater, (f) Bode phase plot in DO + *P. aeruginosa* seawater.

the rates of electron gain and loss accelerated, intensifying the electrode reactions on the X70 steel surface. Furthermore, the presence of *P. aeruginosa* compromised the integrity of the passivation film, diminishing its protective capabilities and leading to a rise in the corrosion rate during the initial immersion period. However, with continued immersion, the thickness of the biofilm on the surface of X70 steel increased, primarily comprising a gel-like biofilm formed by *P. aeruginosa* and its secretions [60]. This biofilm effectively obstructed Cl^- in the environment and became densely packed, limiting the replenishment of *P. aeruginosa* on the X70 steel surface as bacterial death occurred, resulting in a reduction in the corrosion rate [22]. For equivalent immersion durations, the corrosion rate of X70 steel in the *P. aeruginosa*-containing seawater was lower than that in sterile seawater, attributed to the dominance of *P. aeruginosa* in corroding the steel, leading to fewer corrosion products on the surface. In contrast, in *P. aeruginosa* seawater with 2 ppm dissolved oxygen, the presence of dissolved oxygen, combined with local variations in oxygen concentration on the X70 steel surface due to the metabolic activities of *P. aeruginosa* and the presence of metal cations from metal dissolution, resulted in more vigorous redox reactions [61]. Consequently, the electrode reactions were more intense than those observed under other conditions, with a maximum corrosion electrochemical rate of 45.62 mpy, significantly exceeding the combined corrosion rates in sterile seawater and anaerobic *P. aeruginosa* environments.

3.6. Weight loss

The results of corrosion weight loss for X70 steel specimens

Table 2
Fitting results of EIS spectra under different conditions.

Time(day)	R_S(ohm cm^2)	Q,Y_0(S·sn·cm^{-2})	n_1	R_f(ohm cm^2)	Q,Y_0(S·sn·cm^{-2})	n_2	R_{ct}(ohm cm^2)
sterile seawater							
1	10.35	5.52×10^{-4}	0.85				1087
3	8.08	5.23×10^{-4}	0.84				1410
5	9.25	3.69×10^{-4}	0.91				9911
7	8.80	3.82×10^{-4}	0.89				7760
14	7.32	4.82×10^{-4}	0.89				13296
anaerobic *P. aeruginosa* seawater							
1	6.99	1.92×10^{-4}	0.83				5301
3	7.51	5.73×10^{-4}	0.85				5453
5	10.55	2.46×10^{-4}	0.91				9165
7	7.12	3.13×10^{-4}	0.91				8020
14	6.88	2.95×10^{-4}	0.93				25703
DO + *P. aeruginosa* seawater							
3	7.28	3.15×10^{-3}	0.67	64.1	1.28×10^{-2}	0.50	451.4
7	8.41	4.54×10^{-3}	0.70	128.6	1.70×10^{-2}	0.61	927.7
14	15.22	5.92×10^{-3}	0.72	10.38	1.23×10^{-2}	0.71	1757

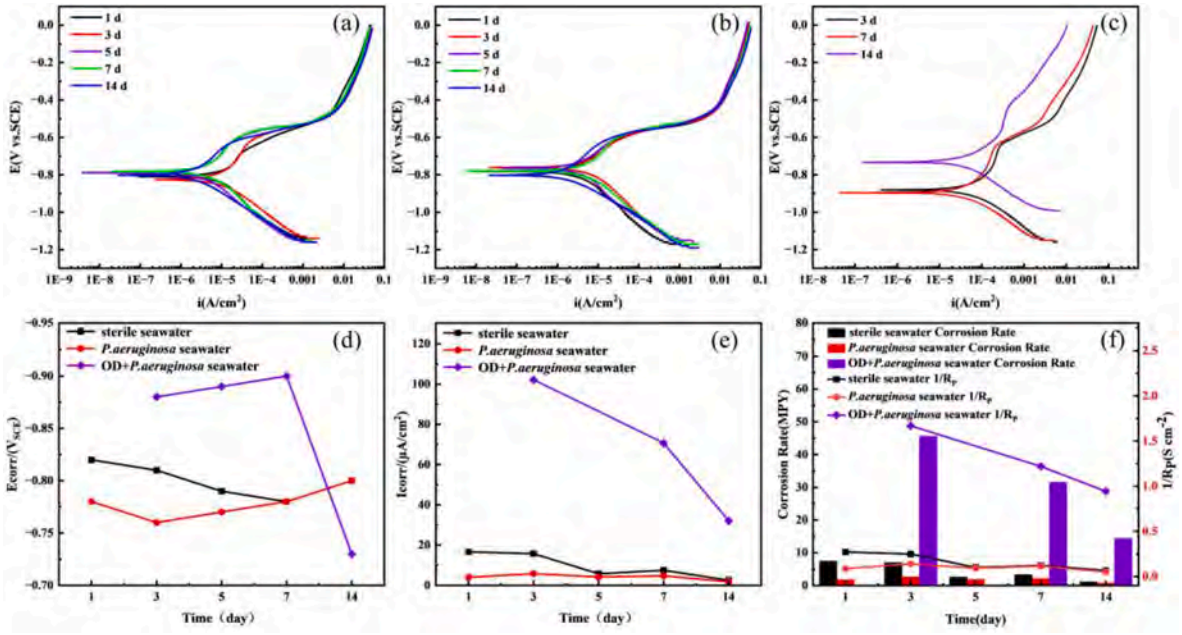


Fig. 14. Kinetic potential polarization curves and fitting parameters for X70 steel immersed for different durations in seawater with or without *P. aeruginosa*. (a) Sterile seawater, (b) Anaerobic *P. aeruginosa*, (c) DO + *P. aeruginosa*, (d) Corrosion potential (E_{corr}), (e) Corrosion current (I_{corr}), (f) Corrosion rate and $1/R_P$.

immersed in seawater, both with and without *P. aeruginosa*, over varying durations are depicted in Fig. 15. In the sterile seawater environment, the corrosion weight loss rate progressively diminished from 34.58 g m^{-2} h^{-1}–8.30 g m^{-2} h^{-1} as immersion time increased. Conversely, in anaerobic *P. aeruginosa* seawater, the corrosion weight loss rate decreased from 11.67 g m^{-2} h^{-1}–2.29 g m^{-2} h^{-1} with extended immersion, revealing an inverse relationship with time; notably, the corrosion weight loss rate of X70 steel in sterile seawater was approximately three to five times greater than that in anaerobic *P. aeruginosa* seawater. This alteration in corrosion weight loss rate aligns with the trends observed in corrosion current density and electrochemical corrosion rate during electrochemical analysis. In *P. aeruginosa* seawater containing 2 ppm dissolved oxygen, the combined effects of dissolved oxygen and microbial corrosion resulted in a peak corrosion weight loss rate of 94.88 g m^{-2} h^{-1} after seven days, surpassing the rates recorded under other conditions. Thus, the presence of dissolved oxygen significantly accelerated the corrosion of X70 steel by *P. aeruginosa* in the seawater solution.

3.7. Discussion

Integrating the simulated equivalent circuit of electrochemical impedance spectroscopy reveals the corrosion mechanism illustrated in Fig. 16. In a sterile seawater environment, X70 steel primarily forms a metal oxide film during corrosion. In contrast, in anaerobic *P. aeruginosa* seawater, corrosion predominantly results in the formation of a biofilm. Notably, in *P. aeruginosa* seawater containing 2 ppm dissolved oxygen, the corrosion products consist of a combination of both the metal oxide film and the microbial membrane.

In a sterile seawater environment (Fig. 16a), X70 steel undergoes corrosion during the pre-corrosion period, and the steel substrate is exposed to the seawater environment, where O_2 and Cl^- contribute to its corrosion [62]. These factors primarily promote the cathodic reaction in the corrosion cell, leading to oxygen depletion on the steel surface. The formation of OH^- reacts with anodically dissolved Fe^{2+} [63,64], resulting in the generation of a significant amount of oxide that covers the steel surface. The reddish-brown Fe_2O_3 particles produced in this stage are sparsely distributed, forming a loose and porous layer [65], which offers no protective effect (Formula 8). In contrast, FeOOH and

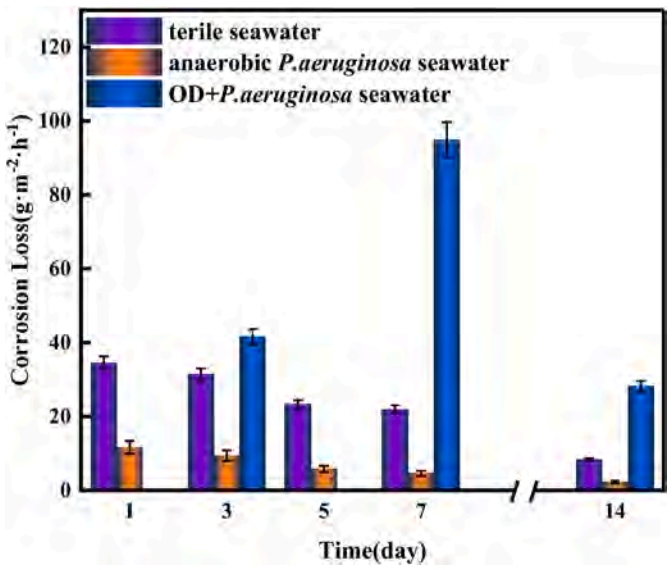


Fig. 15. Corrosion weight loss rate of X70 steel immersed in seawater under different conditions.

Fe_3O_4 particles are more densely distributed and serve as the main components of the passivation film, providing protection to the steel substrate [66] (Formula 9). As corrosion progresses, the protective oxide film gradually thickens, reducing the corrosion rate. However, due to the sparse distribution of reddish-brown Fe_2O_3 particles and erosion by Cl^-, the surface corrosion film of the steel substrate shows noticeable cracks [67] (Fig. 6). Cl^- significantly enhances the tendency for pitting corrosion in the rust layer, leading to the formation of numerous pitting craters, which act as channels for the transport of corrosive media. The maximum depth of the pitting crater reaches 29.606 μm (Fig. 11b).

The diverse respiratory patterns of *P. aeruginosa* result in lower biofilm coverage on the X70 steel surface in anaerobic conditions compared to *P. aeruginosa* seawater supplemented with 2 ppm dissolved oxygen. An analysis of corrosion electrochemistry and pit formation reveals that the corrosion rate of X70 steel in *P. aeruginosa* seawater with 2 ppm dissolved oxygen is the highest, while that in anaerobic *P. aeruginosa* seawater is the lowest. However, the size and depth of corrosion pits in anaerobic conditions exceed those in oxygenated seawater. In sterile seawater, pitting corrosion is not prominent (Figs. 9 and 10), and uniform corrosion predominates. When the dissolved oxygen concentration is low, *P. aeruginosa* primarily carries out anaerobic respiration, obtaining electrons through the oxidation of Fe on the material surface. These electrons are then transferred intracellularly for biometabolic activities. *P. aeruginosa* aggregates in the dissolution pits, creating a concentration difference that leads to localized corrosion [68]. The maximum depth of the corrosion pits reaches 49.938 μm (Fig. 11d). An extracellular biofilm forms over the X70 steel surface, which has a viscoelastic nature that provides an insulating effect, preventing Cl^- in seawater from directly contacting the steel substrate. This reduces the corrosion rate [41]. Additionally, the formation of FeOOH and Fe_3O_4 passivation films on the steel surface (Formula 5) provides protective effects. As the immersion time increases, the biofilm thickens, while the concentration of *P. aeruginosa* decreases, leading to a minimum corrosion rate of 0.78 mpy after 14 days of immersion, although localized corrosion remains the most severe. In seawater containing 2 ppm constant dissolved oxygen, *P. aeruginosa* proliferates extensively on X70 steel. The bacterial colonies compete for oxygen through aerobic respiration, and the biofilm is unevenly distributed, which easily leads

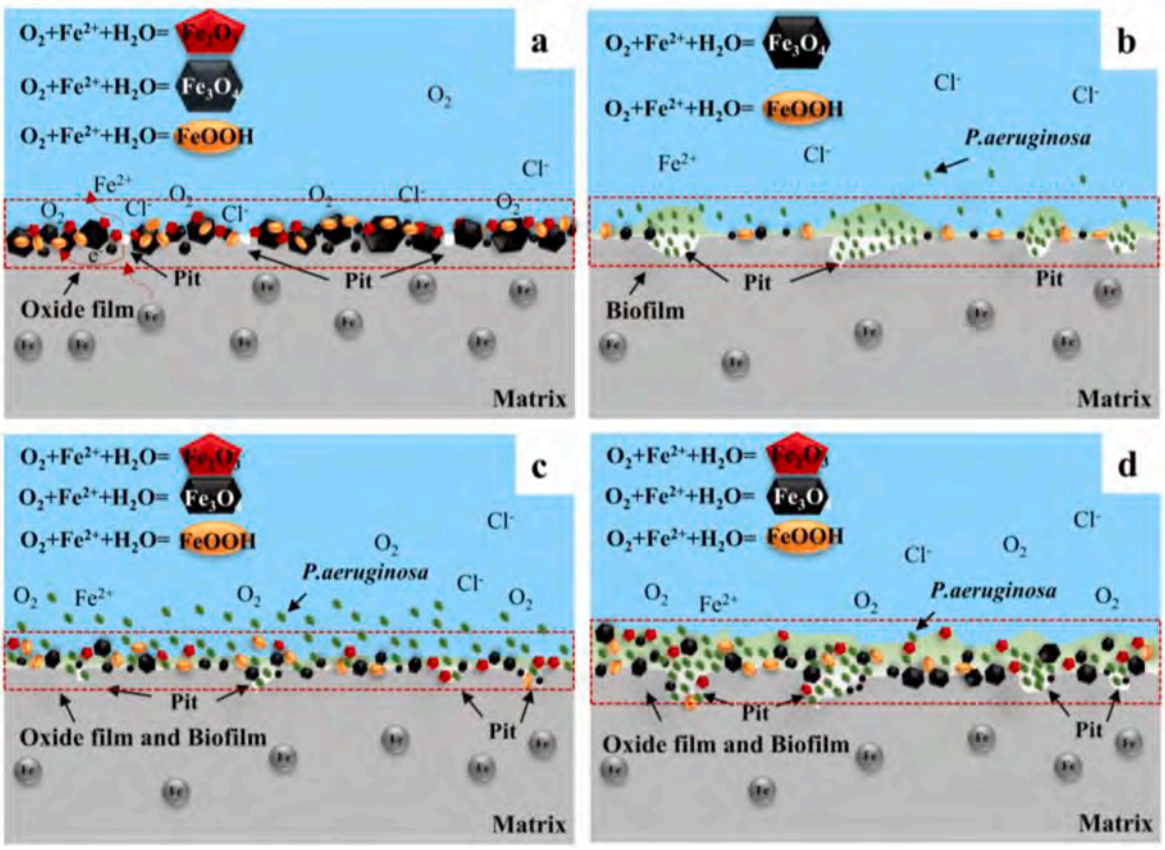


Fig. 16. Corrosion mechanism of X70 steel in different media. (a) sterile seawater, (b) anaerobic *P. aeruginosa*, (c) DO + *P. aeruginosa* 3 days, (d) DO + *P. aeruginosa* 7 days.

to the formation of oxygen concentration gradients. In the biofilm region, the oxygen concentration is low, acting as the cathode in a corrosion cell, where reduction reactions occur. The steel substrate functions as the anode, where oxidation reactions take place, accelerating the electrochemical reaction rate [69]. This increases the dissolution rate of iron ions and leads to the formation of a significant amount of metal oxides covering the steel surface. Aerobic respiration by *P. aeruginosa* produces gases, making the oxide layer loose and porous [70], primarily composed of Fe_2O_3 (Formula 4). This structure provides pathways for bacterial renewal and substance transport in the seawater. Fe_2O_3 exhibits high electrochemical activity. On one hand, organic acids secreted by *P. aeruginosa*, such as acetic acid and lactic acid, can react with Fe_2O_3, reducing it to Fe^{2+} or converting it into other oxides, causing the oxide to peel off. On the other hand, the bacterial metabolic process induces changes in the surface potential, enhancing electron transfer reactions and accelerating the reduction of Fe_2O_3 to Fe^{2+}. These transformations disrupt the stability of Fe_2O_3, increasing the surface reactivity of X70 steel, which in turn intensifies the corrosion process. Sufficient DO concentration allows microorganisms to adhere to and grow in the biofilm, forming bioaggregates [71]. Thus, the oxide layer and biofilm continue to accumulate, forming a composite product film. The corrosion products on the steel surface are continually renewed, and iron is progressively dissolved from the substrate, leading to an accelerated local and uniform corrosion rate. The maximum corrosion rate reaches 45.62 mpy, which is approximately two orders of magnitude higher than the corrosion rate of *P. aeruginosa* in the absence of added oxygen. In the first 3 days of immersion (Fig. 16c), the biofilm exhibits low thickness yet substantial biomass, with a random distribution and rapid metabolic activity, creating a significant concentration gradient of the corrosion medium. The corrosion weight loss rate of X70 steel due to dissolved oxygen and *P. aeruginosa* is less than the sum of the corrosion weight loss rates from immersion in sterile seawater and anaerobic *P. aeruginosa*, indicating that corrosion is primarily uniform. After 7 days of immersion, as nutrient levels decline and attachment sites shift, bacteria predominantly cluster in pitting pits and their vicinity, deepening the degree of pitting corrosion. Consequently, the corrosion weight loss rate of X70 steel due to dissolved oxygen and *P. aeruginosa* surpasses the sum of the corrosion weight loss rates from sterile seawater and separate anaerobic *P. aeruginosa* immersion, signifying that corrosion is primarily localized and bacteria-induced.

The main corrosion electrochemical and chemical reactions were as follows [72].

Anodic reaction

$$Fe \rightarrow Fe^{2+} + 2e^- \quad (5)$$

Cathodic reaction

$$O_2 + 2H_2O + 4e^- \rightarrow 4OH^- \quad (6)$$

Formation of corrosion products

$$2Fe^{2+} + 4OH^- + 1/2O_2 \rightarrow 2FeOOH + H_2O \quad (7)$$

$$2FeOOH \rightarrow Fe_2O_3 + H_2O \quad (8)$$

$$6FeOOH \rightarrow 2Fe_3O_4 + 3H_2O + 1/2O_2 \quad (9)$$

$$Cl^- + Fe_2O_3nH_2O \rightarrow [FeCl] + nOH^- \quad (10)$$

4. Conclusions

MIC arises from the metabolic activities of microorganisms and their interactions with metals. As a facultative aerobic bacterium, the metabolic activity of *P. aeruginosa* is significantly influenced by the concentration of dissolved oxygen. In this experiment, we investigated the corrosion of X70 steel in seawater, both with and without *P. aeruginosa*, by varying the presence of exogenous dissolved oxygen in the corrosion environment. The primary conclusions are as follows

(1) The corrosion rate of X70 steel in seawater, regardless of the presence of *P. aeruginosa*, diminishes with extended immersion time. At equivalent immersion durations, the overall corrosion rate of X70 steel in seawater containing *P. aeruginosa* is lower than that observed in sterile seawater; however, localized corrosion is pronounced, characterized by numerous corrosion pits, which exhibit greater depth and width. Notably, the maximum corrosion pit depth reaches 49.938 μm, significantly exceeding the maximum pitting depth of 29.606 μm recorded under sterile conditions.
(2) X70 steel primarily experiences uniform corrosion in sterile seawater, whereas, in anaerobic *P. aeruginosa* seawater, localized corrosion predominates, characterized by a high local corrosion rate and significant pitting. In *P. aeruginosa* seawater containing 2 ppm of dissolved oxygen, uniform corrosion is observed during the first 3 days of immersion; however, following this period, localized corrosion driven by microbial activity becomes the dominant mechanism.
(3) Dissolved oxygen enhanced the physiological activity of *P. aeruginosa* by altering its respiration mode, leading to an increased corrosion rate. The maximum corrosion rate reached 45.62 mpy, accompanied by a peak corrosion weight loss rate of 94.88 g m^{-2} h^{-1} after 7 d of immersion. Conversely, in the absence of applied oxygen, the minimum corrosion rate was 0.78 mpy, with a corrosion weight loss rate of 2.29 g m^{-2} h^{-1}. This indicates that the corrosion rate with dissolved oxygen was approximately two orders of magnitude greater than that observed under anaerobic conditions.
(4) The introduction of dissolved oxygen alters the corrosion products on the surface of X70 steel. In aerobic environments with *P. aeruginosa*, the corrosion products consist of a composite film formed by metal oxides and microbial films, primarily including Fe_3O_4, FeOOH, and Fe_2O_3. The presence of loose Fe_2O_3 renders X70 steel more vulnerable to corrosion by *P. aeruginosa*. Conversely, in the absence of applied oxygen, *P. aeruginosa* primarily forms biofilms, accompanied by a limited quantity of metal oxides, predominantly Fe_3O_4 and FeOOH.

CRediT authorship contribution statement

Riguang Zhu: Writing – review & editing, Writing – original draft, Investigation, Data curation. **Guiyuan Xie:** Writing – review & editing, Validation. **Zu-an Qin:** Writing – review & editing, Validation. **Xingying Tang:** Writing – review & editing, Writing – original draft, Validation, Project administration, Methodology, Funding acquisition. **Jianjun Cai:** Writing – review & editing, Validation, Methodology. **Jianqiao Yang:** Writing – review & editing, Validation, Methodology.

Ethical approval

Not applicable.

Declaration of competing interest

The authors declare the following financial interests/personal relationships which may be considered as potential competing interests: Xingying Tang reports financial support was provided by National Natural Science Foundation of China. If there are other authors, they declare that they have no known competing financial interests or personal relationships that could have appeared to influence the work reported in this paper.

Acknowledgements

The authors gratefully acknowledge the financial support from the National Natural Science Foundation of China (No. 22068003).

Data availability

Data will be made available on request.

References

[1] M. Visbeck, Ocean science research is key for a sustainable future, Nat. Commun. 9 (1) (2018) 690.
[2] Z. Xu, P. Zhang, B. Zhang, et al., Effect of tensile stress on the hydrogen adsorption of X70 pipeline steel, Int. J. Hydrogen Energy 47 (50) (2022) 21582–21595.
[3] D. Sun, D. Wang, L. Li, et al., Study on stress corrosion behavior and mechanism of X70 pipeline steel with the combined action of sulfate-reducing bacteria and constant load, Corrosion Sci. (2023) 213.
[4] F. Sun, S. Ren, Z. Li, et al., Comparative study on the stress corrosion cracking of X70 pipeline steel in simulated shallow and deep sea environments, Mater. Sci. Eng. Structural Mater. Propert. Microstruct. Process. 685 (2017) 145–153.
[5] L. Zhang, J. Wang, Effect of dissolved oxygen content on stress corrosion cracking of a cold worked 316L stainless steel in simulated pressurized water reactor primary water environment, J. Nucl. Mater. 446 (1–3) (2014) 15–26.
[6] H. Su, Y. Liang, Y. Wang, et al., Effect of dissolved oxygen on pitting corrosion behavior of low-alloy steel under hydrostatic pressure, Int. J. Electrochem. Sci. 14 (5) (2019) 4812–4827.
[7] T. Duan, W. Peng, K. Ding, et al., Long-term field exposure corrosion behavior investigation of 316L stainless steel in the deep sea environment, Ocean Eng. 189 (2019) 106405.
[8] J. Feng, Z.M. Wang, D. Zheng, et al., Influence of dissolved oxygen on the corrosion of mild steel in a simulated cement pore solution under supercritical carbon dioxide, Construct. Build. Mater. 311 (2021) 125270.
[9] X. Li, D. Zhang, Z. Liu, et al., Materials science : share corrosion data, Nature 527 (7579) (2015) 441–442.
[10] I.N. Etim, D.I. Njoku, P.C. Uzoma, et al., Microbiologically influenced corrosion: a concern for oil and gas sector in africa, Chem. Africa-A J. Thtunisian Chem. Soc. 6 (2) (2023) 779–804.
[11] Di Wang, E. Zhou, D. Xu, et al., Burning question: are there sustainable strategies to prevent microbial metal corrosion ? Microb. Biotechnol. 16 (11) (2023) 2026–2035.
[12] E. Puentes-Cala, V. Tapia-Perdomo, D. Espinosa-Valbuena, et al., Microbiologically influenced corrosion : the gap in the field, Front. Environ. Sci. 10 (2022).
[13] D. Xu, T. Gu, D.R. Lovley, Microbially mediated metal corrosion, Nat. Rev. Microbiol. 21 (11) (2023) 705–718.
[14] Y. Zhang, T. Zhang, H. Wan, et al., Mechanism of microbiologically induced anaerobic water-line corrosion of 980 high strength steel in nutrient-rich artificial seawater, Corrosion Sci. 220 (2023).
[15] T. Zhang, Z. Xu, H. Wan, et al., Dual corrosion promotion of pipeline steel in sea mud induced by sulfate reducing bacteria: bacteria concentration cell and electronic conduction of the biofilms covered sand grains, Corrosion Sci. 232 (2024).
[16] C.K. Stover, X.Q. Pham, A.L. Erwin, et al., Complete genome sequence of Pseudomonas aeruginosa PAO1, an opportunistic pathogen, Nature 406 (6799) (2000) 959–964.
[17] H. Li, E. Zhou, D. Zhang, et al., Microbiologically influenced corrosion of 2707 hyper-duplex stainless steel by marine Pseudomonas aeruginosa biofilm, Sci. Rep. 6 (1) (2016).
[18] L. Huang, Y. Huang, Y. Lou, et al., Pyocyanin-modifying genes phzM and phzS regulated the extracellular electron transfer in microbiologically-influenced corrosion of X80 carbon steel by Pseudomonas aeruginosa, Corrosion Sci. 164 (2020) 108355.
[19] B. Chugh, Singh M. Sheetal, et al., Extracellular electron transfer by Pseudomonas aeruginosa in biocorrosion: a review, ACS Biomater. Sci. Eng. 8 (3) (2022) 1049–1059.
[20] J. Tang, R. Guo, X. Zhang, et al., Effect of Pseudomonas aeruginosa on corrosion of X65 pipeline steel, Heliyon 8 (12) (2022) e12588.
[21] D. Liu, Z. Hu, M. Li, et al., Synergistic effect on corrosion behavior of X80 steel influenced by Pseudomonas aeruginosa and Acetobacter aceti, Separ. Purif. Technol. 351 (2024) 128135.
[22] Z. Shao, R. Guo, J. Tang, et al., Effect of Pseudomonas aeruginosa on corrosion behavior of X65 carbon steel, Materials 17 (10) (2024) 2428.
[23] A. Abdolahi, E. Hamzah, Z. Ibrahim, et al., Microbially influenced corrosion of steels by Pseudomonas aeruginosa, Corrosion Rev. 32 (3–4) (2014) 129–141.
[24] J. Luo, R. Jia, R. Yu, et al., Influence of dissolved oxygen on biofilm microbial community structure and effluent water quality in aqueduct, J. Harbin Inst. Technol. 48 (8) (2016) 24–30.
[25] H.C. Flemming, J. Wingender, The biofilm matrix, Nat. Rev. Microbiol. 8 (9) (2010) 623–633.
[26] C. Zhuo, H. Zhang, Y. Liu, et al., Effect of Pseudomonas aeruginosa on the corrosion behaviour of 2205 duplex stainless steel, J. Mater. Res. 33 (5) (2019) 321–330.
[27] E. Zhou, M. Zhang, Y. Huang, et al., Accelerated biocorrosion of stainless steel in marine water via extracellular electron transfer encoding gene phzH of Pseudomonas aeruginosa, Water Res. 220 (2022) 118634.
[28] D. Liu, H. Yang, J. Li, et al., Electron transfer mediator PCN secreted by aerobic marine Pseudomonas aeruginosa accelerates microbiologically influenced corrosion of TC4 titanium alloy, J. Mater. Sci. Technol. 79 (2021) 101–108.
[29] L. Huang, W. Chang, D. Zhang, et al., Acceleration of corrosion of 304 stainless steel by outward extracellular electron transfer of Pseudomonas aeruginosa biofilm, Corrosion Sci. 199 (2022).
[30] Y. Jin, E. Zhou, T. Ueki, et al., Accelerated microbial corrosion by magnetite and electrically conductive pili through direct Fe^0-to-Microbe electron transfer, Angew. Chem. Int. Ed. 62 (38) (2023).
[31] E. Zhou, Y. Lekbach, T. Gu, et al., Bioenergetics and extracellular electron transfer in microbial fuel cells and microbial corrosion, Curr. Opin. Electrochem. 31 (2022).
[32] J. Li, Y. Jin, J. Li, et al., The effect of dissolved oxygen and Shewanella algae on the corrosion mechanism of titanium in a simulated marine environment, Corrosion Sci. 239 (2024) 112400.
[33] K.S. Raja, D.A. Jones, Effects of dissolved oxygen on passive behavior of stainless alloys, Corrosion Sci. 48 (7) (2006) 1623–1638.
[34] L. Chen, B. Dong, W. Liu, et al., Failure analysis of corrosion products formed during CO 2 pre-corrosion of X70 and 3Cr steels: effect of oxygen contamination, Eng. Fail. Anal. 140 (2022).
[35] Xu Di, T. Chen, G. Yang, et al., Insight into the effect of oxygen content on the corrosion behavior of X70 pipeline steel in a typical simulated soil solution by dissolution-diffusion-deposition model, Corrosion Sci. 240 (2024).
[36] H. Zeng, Y. Yang, M. Zeng, et al., Effect of dissolved oxygen on electrochemical corrosion behavior of 2205 duplex stainless steel in hot concentrated seawater, J. Mater. Sci. Technol. 66 (2021) 177–185.
[37] L.C. Xu, K.Y. Chan, H. Fang, Application of atomic force microscopy in the study of microbiologically influenced corrosion, Mater. Char. 48 (2–3) (2002) 195–203.
[38] C. Tan, N.K. Elumalai, K.N. Krishnan, Preliminary study of microbiologically influenced corrosion by Pseudomonas aeruginosa on high Chromium white iron, PLoS One 19 (8) (2024).
[39] F.M.L. Bushell, P.D. Tunner, S. Jabbari, et al., Synergistic impacts of organic acids and pH on growth of Pseudomonas aeruginosa : a comparison of parametric and bayesian non-parametric methods to model growth, Front. Microbiol. 9 (2019).
[40] O. Lieleg, M. Caldara, R. Baumgaertel, et al., Mechanical robustness of Pseudomonas aeruginosa biofilms, Soft Matter 7 (7) (2011) 3307–3314.
[41] M.S. Suma, R. Basheer, B.R. Sreelekshmy, et al., Pseudomonas putida RSS biopassivation of mild steel for long term corrosion inhibition, Int. Biodeterior. Biodegrad. 137 (2019) 59–67.
[42] M. Moradi, S. Ye, Z. Song, Dual role of Psudoalteromonas piscicida biofilm for the corrosion and inhibition of carbon steel in artificial seawater, Corrosion Sci. 152 (2019) 10–19.
[43] L. Huang, Corrosion Behaviour and Extracellular Electron Transfer Mechanism of Marine Pseudomonas aeruginosa on Typical Steel Materials, University of Science and Technology Beijing, 2021.
[44] M. Chellouli, D. Chebabe, A. Dermaj, et al., Corrosion inhibition of iron in acidic solution by a green formulation derived from Nigella sativa L, Electrochim. Acta 204 (2016) 50–59.
[45] M. Zhao, J. Wang, Y. Ma, et al., Electroactive Shewanella algae accelerates the crevice corrosion of X70 pipeline steel in marine environment, Corrosion Sci. 235 (2024).
[46] S. Guo, L. Xu, L. Zhang, et al., Characterization of corrosion scale formed on 3Cr steel in CO 2 -saturated formation water, Corrosion Sci. 110 (2016) 123–133.
[47] Z. Li, Y. Xu, J. Zhang, et al., Living marine bacterium Tenacibaculum mesophilum D-6 inhibits crevice corrosion of X70 carbon steel, Corrosion Sci. 215 (2023).
[48] M.S. Khan, C. Yang, Y. Zhao, et al., An induced corrosion inhibition of X80 steel by using marine bacterium Marinobacter salsuginis, Colloids Surf. B Biointerfaces (2020) 189.
[49] X. Chen, W. Cui, Y. Wang, et al., Effects of cathodic protection potential on microbiologically induced corrosion behavior of X70 steel in a near-neutral pH solution, Mater. Res. Express 10 (6) (2023).
[50] X. Wang, X. Song, Y. Chen, et al., Corrosion behavior of X70 and X80 pipeline steels in simulated soil solution, Int. J. Electrochem. Sci. 13 (7) (2018) 6436–6450.
[51] Y. Ma, Y. Li, F. Wang, Corrosion of low carbon steel in atmospheric environments of different chloride content, Corrosion Sci. 51 (5) (2009) 997–1006.
[52] W. Zhou, W. Lan, X. Cao, et al., Effect of a high concentration of chloride ions on the corrosion behaviour of X80 pipeline steel in 0.5 mol L-1 NaHCO3 solutions, Int. J. Electrochem. Sci. 13 (2) (2018) 1283–1292.
[53] R.O. Rihan, Electrochemical corrosion behavior of X52 and X60 steels in carbon dioxide containing saltwater solution, Mater. Res. IBERO-Am. J. Mater. 16 (1) (2013) 227–236.
[54] K. Gong, M. Wu, G. Liu, Comparative study on corrosion behaviour of rusted X100 steel in dry/wet cycle and immersion environments, Construct. Build. Mater. 235 (2020).
[55] S. Wang, D. Liu, N. Du, et al., Corrosion behavior of X80 pipeline steel under thin electrolyte layer of acidic soil simulated solution, Int. J. Electrochem. Sci. 11 (4) (2016) 2534–2549.
[56] C.C. Pan, X. Zhang, F. Yang, et al., Corrosion and cavitation erosion behavior of GLNN/Cu composite in simulated seawater, Acta Metall. Sin. 58 (5) (2022) 599–609.
[57] Z. Cui, S. Chen, Y. Dou, et al., Passivation behavior and surface chemistry of 2507 super duplex stainless steel in artificial seawater : influence of dissolved oxygen and pH, Corrosion Sci. 150 (2019) 218–234.

[58] Y. Wang, G. Cheng, W. Wu, et al., Effect of pH and chloride on the micro-mechanism of pitting corrosion for high strength pipeline steel in aerated NaCl solutions, Appl. Surf. Sci. 349 (2015) 746–756.
[59] Q. Hu, T. Zhang, S. Chen, et al., An instantaneous corrosion monitoring technique based on combining modified electrochemical noise and artificial neural network for determination of corrosion type and 2014 aluminium alloy corrosion rate in NaCl and Ce (NO 3) 3 solutions, Int. J. Electrochem. Sci. 17 (2) (2022).
[60] E.Q.A. Nwoko, I.N. Okeke, Bacteria autoaggregation: how and why bacteria stick together, Biochem. Soc. Trans. 49 (3) (2021) 1147–1157.
[61] J. Telegdi, A. Shaban, L. Trif, Review on the microbiologically influenced corrosion and the function of biofilms, Int. J. Corr. Scale Inhibit. 9 (1) (2020) 1–33.
[62] S. Zhang, J. Yan, L. Zheng, et al., Effect of alternating current and Cl- ions on corrosion behavior of X70 steel in NaCl solution, Int. J. Electrochem. Sci. 18 (2) (2023) 49–58.
[63] Z.Y. Liu, X.G. Li, C.W. Du, et al., Effect of dissolved oxygen on stress corrosion cracking of X70 pipeline steel in near-neutral pH solution, Corrosion 66 (1) (2010).
[64] W. Wu, Y. Pan, Z. Liu, et al., Electrochemical and stress corrosion mechanism of submarine pipeline in simulated seawater in presence of different alternating current densities, Materials 11 (7) (2018) 1074.
[65] X. Zhong, W. Lu, H. Yang, et al., Oxygen corrosion of N80 steel under laboratory conditions simulating high pressure air injection: analysis of corrosion products, J. Petrol. Sci. Eng. 172 (2019) 162–170.
[66] L. Zhou, S. Yang, Atmospheric corrosion of offshore steel and development of weathering steel, China Metallurgy 32 (8) (2022) 7–24.
[67] Y. Wan, J. Tan, S. Zhu, et al., Insight into atmospheric pitting corrosion of carbon steel via a dual-beam FIB/SEM system associated with high-resolution TEM, Corrosion Sci. 152 (2019) 226–233.
[68] T. Gu, R. Jia, T. Unsal, et al., Toward a better understanding of microbiologically influenced corrosion caused by sulfate reducing bacteria, J. Mater. Sci. Technol. 35 (4) (2019) 631–636.
[69] M.F. Hamad, H.D. Abdul Kader, H.A. Alabdly, et al., Corrosion of carbon steel in oxygen and NaCl concentration cells: the influence of solution temperature and aeration, Iraqi J. Chem. Petrol. Eng. (Online) 20 (3) (2019) 49–57.
[70] J. Duan, S. Wu, X. Zhang, et al., Corrosion of carbon steel influenced by anaerobic biofilm in natural seawater, Electrochim. Acta 54 (1) (2008) 22–28.
[71] B.T. Hargrave, Epibenthic algal production and community respiration in the sediments of marion lake, J. Fish. Res. Board Can. 26 (8) (1969) 2003–2026.
[72] X. Zhou, Q. Wang, H. Su, et al., Marine tidal corrosion of X80 pipeline steel under federative action of Pseudomonas sp. and Desulfovibrio desulfuricans, Int. Biodeterior. Biodegrad. 187 (2024) 105732.

The Journal of Supercritical Fluids 218 (2025) 106495

Contents lists available at ScienceDirect

The Journal of Supercritical Fluids

journal homepage: www.elsevier.com/locate/supflu

Comparative study of the corrosion behavior of Inconel 625 in supercritical water containing dissolved and molten phosphates

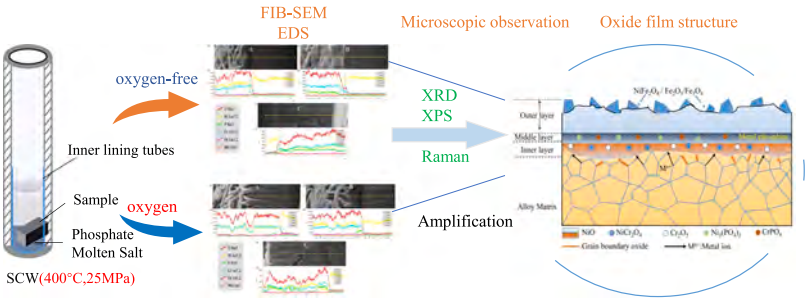
Jiquan Chen [a,b], Zitao Lin [c,d], Xingying Tang [b,*], Ke Li [a], Riguang Zhu [b], Jianqiao Yang [e]

[a] School of Resources, Environment, and Materials, Guangxi University, Nanning 530004, China
[b] School of Marine Sciences, Guangxi University, Nanning 530004, China
[c] Guangxi Road and Bridge Engineering Group Co., Ltd., Nanning, Guangxi 530200, China
[d] Guangxi Highway Detect Co Ltd, Nanning 530200, China
[e] School of Energy and Power Engineering, Xi'an Jiaotong University, Xi'an, China

HIGHLIGHTS

- A dynamic competition exists between phosphate ions and oxygen-containing ions.
- The existence of metallic phosphate passivation layers that inhibit ion diffusion.
- The phosphate molten salt is extremely corrosive.
- Phosphate molten salt dissolve Cr in chromium oxide directly as Cr^{3+}.

GRAPHICAL ABSTRACT



ARTICLE INFO

Keywords:
Supercritical water oxidation
Inconel 625
Phosphate
Corrosion

ABSTRACT

This paper presents a comparative study of the corrosion behavior of Inconel 625 in supercritical water with different oxygen contents and phosphate phases. The results showed that the dissolved phosphate phase could compete with oxygen and that the addition of oxygen converted Cr_2O_3 to Cr^{6+}, resulting in a reduction in the thickness of the oxide film. The oxide film formed consisted of three distinct layers. The outer layer consists of NiO, Fe_2O_3, and $NiFe_2O_4$, which were formed by the diffusion of metal cations outward. The middle layer was a metal phosphate passivation layer which could prevent the diffusion of Fe, Ni, etc. and retard corrosion. The inner layer was formed by inward oxidation of oxygen ions with Cr to form Cr_2O_3. Phosphate molten salt were highly corrosive and can directly dissolve Cr_2O_3 into soluble Cr^{3+}, a process accelerated by oxygen, increasing the Cr^{3+} content from 59.63 % to 77.54 %.

1. Introduction

Supercritical water (SCW, T = 374.1 ℃, P = 22.1 MPa) has excellent mass and heat transfer properties due to its low polarity, low dielectric constant, and high diffusion coefficients [1]. Supercritical water oxidation (SCWO) is an advanced oxidation treatment technology that utilizes SCW to treat recalcitrant, high-concentration organic wastewater, organic waste, sludge, and other challenging materials [2–4]. The

* Corresponding author.
E-mail address: tangxingying@gxu.edu.cn (X. Tang).

https://doi.org/10.1016/j.supflu.2024.106495
Received 2 October 2024; Received in revised form 8 December 2024; Accepted 10 December 2024
Available online 12 December 2024
0896-8446/© 2024 Elsevier B.V. All rights are reserved, including those for text and data mining, AI training, and similar technologies.

treatment process generates no secondary pollutants like NOx or SOx. But SCWO reactor materials may corrode due to the acidic solution from oxidizing heteroatom-containing organic materials. Alkali is usually added to neutralize the acid, yet this forms inorganic salts [5]. Inorganic salts in SCWO crystallize and deposit on the heat exchanger and reactor due to insolubility, thus reduces system pressure, decreases heat transfer efficiency, increases the risk of plugging, and may exacerbate corrosion [6–11]. Nevertheless, recent studies have found that in SCW treatment environments, hydrothermal molten salts (HyMoS) with melting points below 400 ℃ can generate solvent-dissolved solid salts in-situ and can reduce the salt deposition problem, and this system of HyMoS brings more applications as well as possibilities for sustainable manufacturing, materials synthesis, and others [12,13].

However, the majority of people fail to recognize that HyMoS can induce severe corrosion of alloys, which will be a major problem to hinder its development. While Zhang et al. [13] utilised the Na_2HPO_4 hydrothermal molten salt generated during the SCW threatment of glyphosate wastewater, whereas most of the previous studies have focused on the role of phosphate as an additional solvent. Moreover, our previous research had confirmed that the corrosion rate was reduced by the addition of PO_4^{3-} to SCW environments containing oxygen and Cl^-, indicating that the addition of phosphate ions can inhibit corrosion [14]. Ma et al. [15] studied the corrosion behavior of different alloys in SCWO environments containing Na_3PO_4, Na_2SO_4, and NaCl. They found that the addition of Na_2SO_4 or NaCl could accelerate the corrosion rate of the alloy in SCW with oxygen and phosphate ions. The simultaneous presence of SO_4^{2-} and Cl^- disrupted the formation of insoluble metal phosphates on the oxide film of the alloy. Guo et al. [16] investigated the corrosion behavior of Inconel 625 in SCW containing sulfate and phosphate ions. The corrosion rate decreased after the alloy was passivated with sodium phosphate, indicating improved corrosion resistance. Metal phosphates could exist stably on the alloy surface and inhibit the diffusion of metal cations and oxygen anions near the interface. Xu et al. [17] investigated the corrosion behavior of alloy 600 in SCW with Cl^-, SO_4^{2-}, and PO_4^{3-}. Researchers discovered that phosphates precipitated from SCW could exist in a molten state, and that some oxides could be soluble in the ionic melt of low-melting-point phosphate salts, to form a eutectic melt consisting of $FePO_4$-$Ni_3(PO_4)_2$-Na_3PO_4-Na_2HPO_4.

Much of the research to date has focused on the addition of phosphates to systems containing one or more aggressive ions, with the aim of elucidating the role of phosphates in corrosion inhibition. In SCW, phosphates can form HyMoS, which precipitates at a temperature above the melting temperature, combines with the deposited salts in the SCWO system and carries the deposited salts out of the system by cooling. In this way, salt deposition can be handled efficiently and without contamination, and the solution can be recycled. However, in recent experiments, it was found that the oxide film formed on the alloy surface would dissolve and fail in the hydrothermal phosphate molten salt environment, while there was no focus on the corrosion behavior and mechanism, so the safety of using phosphate molten salt to handle salt deposition in the SCWO system needs to be further investigated. Therefore, in this paper, the corrosion phenomenon of phosphate molten salt on alloys in the field of supercritical water oxidation is of great significance to safely solve the salt deposition problem. And in the field of HyMoS corrosion, it is of pioneering significance, which will lay an important foundation for the subsequent related research and technology development, and provide new ideas and directions.

Based on the considerations above, in this study, Inconel 625 was used as the experimental material, and Na_2HPO_4, which is abundant in glyphosate wastewater, was chosen as the reagent to investigates the influence of the presence of different phosphate phases (dissolved/molten salt phase) and oxygen on the corrosion behavior of Inconel 625 in SCW.

Table 1
Main elemental composition (wt%) of tested Inconel 625.

Alloy	Ni	Cr	Fe	Mo	Nb	Mn	C
625	58.3	23.0	5.0	9.0	3.15	0.5	0.08

2. Experimental

2.1. Material

The material used in this study was Inconel 625, purchased from Dongguan Ruichang Metal Co. Ltd. in China, and its elemental composition by weight percentage is presented in Table 1. The material was cut into specimens with dimensions of 5 mm × 5 mm × 2 mm using wire cutting. In order to obtain continuous and uniform corrosion samples, the specimens were polished sequentially with 240#, 600#, 1200#, and 2000# water sandpaper and finally with 1 μm diamond suspension. Na_2HPO_4 (melting point 245 °C) purchased from Tianjin Komeo Chemical Reagent Co. ltd. in China was used as the solution to achieve the predetermined corrosion level, with total phosphorus (as PO_4^{3-}) levels of 500 mg/L (dissolved phase), 1000 mg/L (near-saturated phase) and 5000 mg/L (molten salt phase), respectively, as calculated [17,18].

2.2. Apparatus and methodology

The experiments were carried out using a high-temperature intermittent reaction tube apparatus made of 316 L stainless steel, with a maximum operating temperature of 600 ℃, a pressure resistance of 30 MPa, and a reactor volume of 20 mL. The apparatus consists of a pressurized reaction tube and two lined tubes. As shown in Fig. 1, ultrathin quartz liner tubes and Inconel 625 liner tubes were used in the corrosion test environment to mitigate the potential interference of hydrothermal salt phase electrochemical corrosion [6,19]. The corrosion test conditions are summarized in Table 2, the exposure temperature, pressure, and time duration for each test is 400 ℃, 25 MPa, and 60 h, respectively. To ensure the accuracy of the experimental data, three parallel samples were used for each set of tests. A run of blank tests was also done, and the weight changes during the temperature rise and fall process (SCW exposure for 0 h) were calculated in the blank tests to ensure the accuracy of the experimental data. Prior to conducting the experiments, a series of pre-corrosion passivation experiments were performed on the reaction tubes using phosphate solutions to exclude any potential interference with the alloy reaction tube setup. Subsequently, the temperature was ramped up to 400 ℃ at a rate of 1 ℃/s, and the autogenous pressure at this temperature was the experimental pressure. In the oxygenation experiments, oxygen was passed at room temperature (25 ℃) and the oxygen content was the volume of the reactor filled with oxygen at room temperature plus the volume of oxygen dissolved in solution, the oxygen concentration to meet the conditions of the phosphorus-containing wastewater with a COD concentration of 10,000 mg/L. The oxygen concentration was calculated to be 1400 mg/L. The reaction was terminated after 60 h. The specimens were then cooled to room temperature and cleaned via ultrasonication in deionized water and acetone for 20 minutes. Subsequently, the specimens were subjected to a vacuum drying process for a duration of 30 minutes.

The surface morphology of the oxide film on the specimens was examined using a scanning electron microscope (SEM, Sigma 500, Carl Zeiss. USA), operating at an accelerating voltage of 3 kV. For characterizing the cross-sectional morphology and composition of the specimens, a focused ion beam scanning electron microscope (FIB-SEM, FEI Scios 2 HiVac. USA) was employed, and it operated at 5 kV. EDS line scans were conducted at 5 kV to analyze the oxide film's structure, element distribution, and growth patterns. XRD (BRUKER AXS D8 Discover. DEU) analyses were measured in the 2θ range from −10° to 160° in steps of 0.0001°. To further investigate the oxide film, a Raman

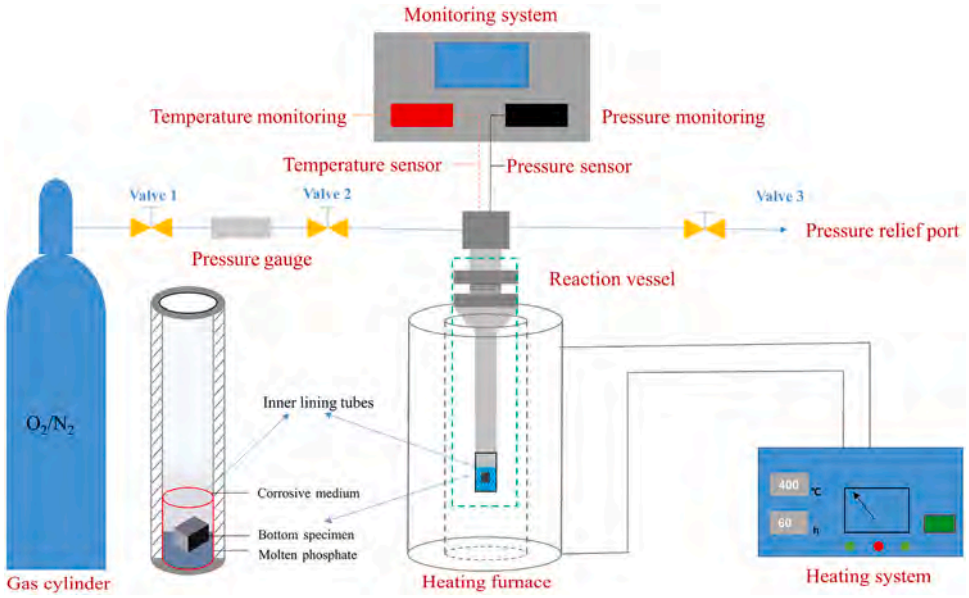


Fig. 1. Experimental device diagram.

Table 2
Test conditions for corrosion.

Run	1	2	3	4	5	6
PO_4^{3-} (mg/L)	500	1000	5000	500	1000	5000
O_2 (mg/L)	0	0	0	1400	1400	1400

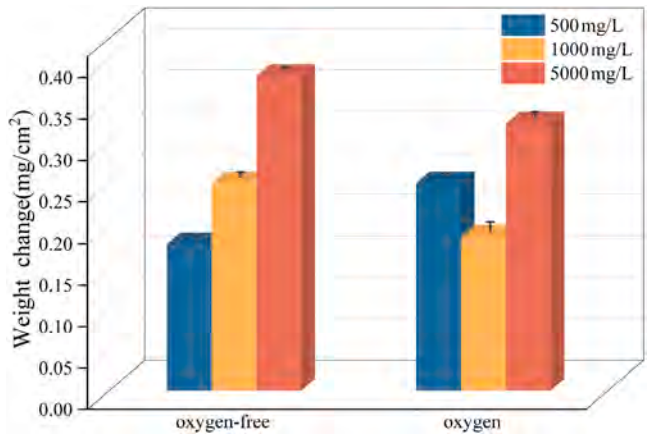


Fig. 2. Weight change of Inconel 625 after 60 h of exposure to SCW with different oxygen and phosphate concentrations.

spectroscopy system (Renishaw inVia, UK) was employed with a 532 nm excitation wavelength. Spectra were collected in the wavenumber range of 100–1500 cm^{-1}, with an exposure time of 10 seconds. During scanning, multiple scan points were selected on the specimen's surface. The surface composition and chemical state of the oxide films were analysed using an X-ray photoelectron spectrometer (XPS, ESCALAB 250XI. USA) with an Al target as the X-ray excitation source. Sampling depths ranged from 0.5 nm to 2 nm and information detection depths ranged from 1.5 nm to 6 nm.

3. Results

3.1. Weight changes

Fig. 2 presents the weight change of Inconel 625 after 60 h of exposure to SCW with different oxygen and phosphate concentrations. The results show that the corrosion weight gain of Inconel 625 gradually increased with increasing phosphate ion concentrations under oxygen-free conditions. In Run 5 and Run 6, the introduction of oxygen did not increase the weight gain of the alloy. This means that there may be competition between phosphate and oxygenated radicals in SCW, which weakening the interaction with aggressive anions as the metal cations diffuse outward from the alloy. In addition, a reduction in weight gain may be attributed to the fact that the oxide film formed on Inconel 625 is not compact and is susceptible to shedding.

3.2. Oxidation morphology

Fig. 3 presents the SEM images of Inconel 625 after 60 h exposure to SCW with different oxygen and phosphate concentrations. As shown in Fig. 3(a-1), a complete oxide film is evident, characterized by relatively small oxide particles, primarily composed of needle-like oxides dominated by O and Cr [19]. In Fig. 3(b-1), the needle-like oxide changes to a plate-like structure and the size of the oxide particles becomes larger, resulting in the formation of a denser oxide film. It can be seen that the higher concentration of phosphate at saturation solubility leads to the formation of a more protective oxide film. In Fig. 3(c-1), the oxide particle size further increases due to the higher phosphate concentration.

In contrast, under oxygenated conditions, Fig. 3(a-2) shows that the size of the oxides is significantly larger than that in Fig. 3(a-1). The morphology of the oxide in Fig. 3(b-2) is essentially the same as that in Fig. 3(c-1), suggesting that the presence of oxygen accelerates the formation of the oxide film. The massive oxides in Fig. 3(c-2) may be sodium phosphate salt deposits or spinel oxides.

In order to gain further insight into the evolution of the Inconel 625 oxide film in SCW containing phosphate molten salt, Fig. S1 presents SEM images of the film growth of Inconel 625 in SCW under oxygen-free conditions, with a phosphate concentration of 5000 mg/L. The inner oxide film can be observed in Fig. S1(a-b), where oxygen exhibits a certain degree of solubility in the oxide film. The formation of the inner

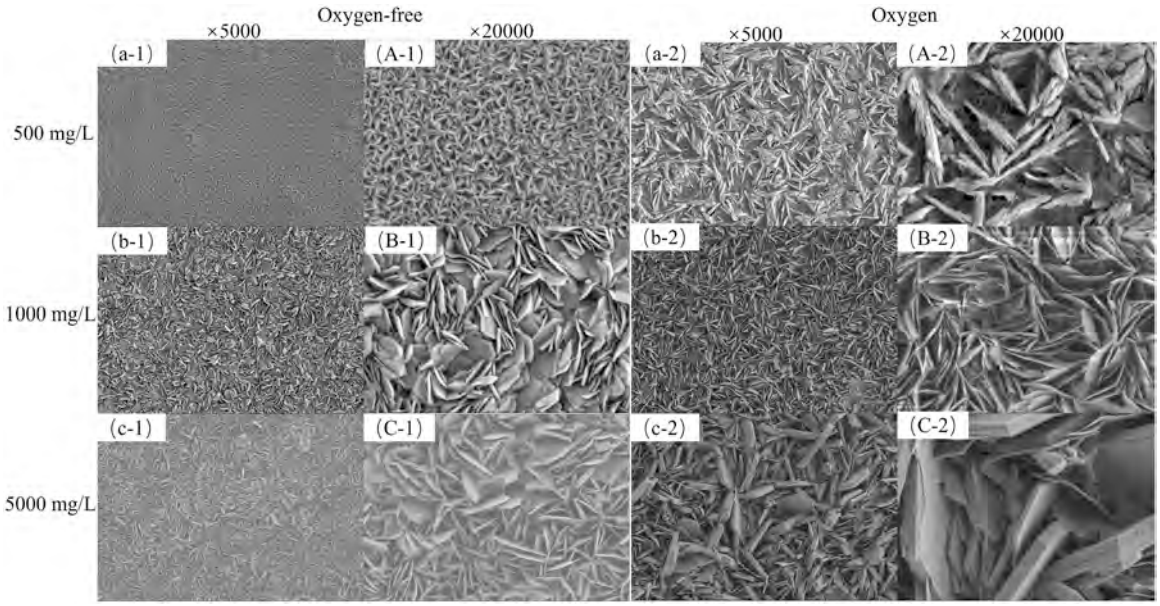


Fig. 3. SEM images of Inconel 625 after 60 h exposure to SCW with different oxygen and phosphate concentrations, (A) 500 mg/L phosphate (B) 1000 mg/L phosphate (C) 5000 mg/L phosphate; 1-oxygen-free, 2-oxygen.

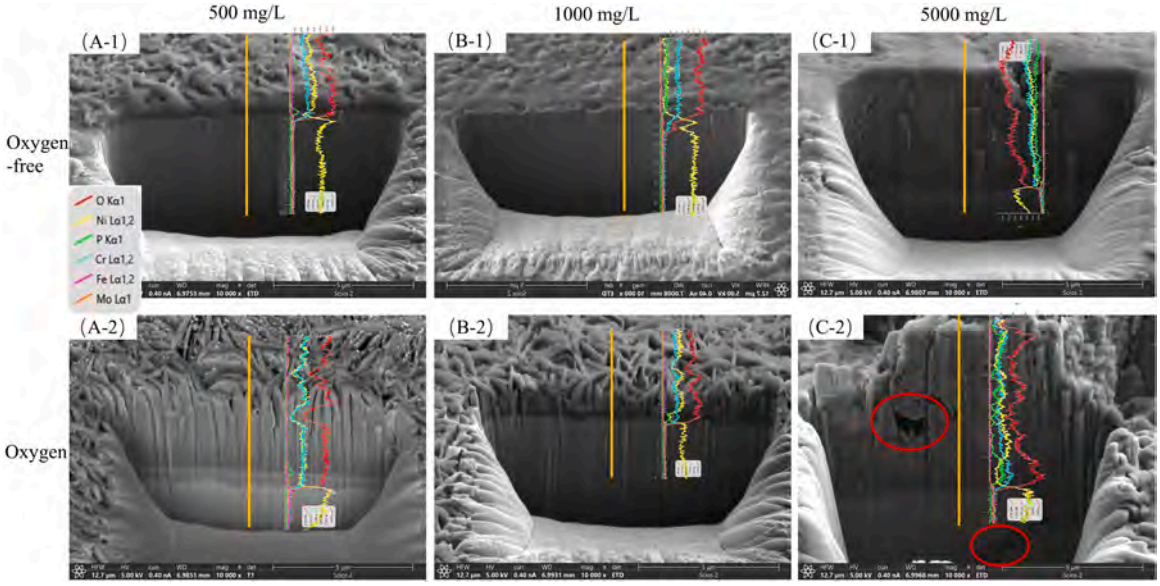


Fig. 4. FIB-SEM images and EDS line scans of Inconel 625 exposed to SCW for 60 h in oxygen/oxygen-free and at three different phosphate concentrations, A-500 mg/L, B-1000 mg/L, C-5000 mg/L, 1-oxygen-free, 2-oxygen.

oxide was attributed to the diffusion of H_2O and O_2 into the matrix and inward transport of oxygen ions. However, as shown Fig. S1(c-e), there is large undulations on the surface, which indicates the presence of oxide film dissolution, flaking, and dissolution precipitation of corrosion product. Fig. S1(e) shows the existence of pitting, indicating faster precipitation of phosphate molten salt droplet. This phosphate molten salt caused more severe penetration corrosion of the alloy substrate. The growth of lamellar oxides along grain boundaries can be observed in Figs. S1(f) and S2, and it is presumed that Mn(Ni) precipitated along the grain boundaries to form oxides, and the intergranular oxides continued to grow with time. It also indicates that phosphate deposition accelerated the dissolution and diffusion rate of metal elements in the alloy matrix along the grain boundaries.

Fig. S3 presents SEM images of Inconel 625 in SCW at different exposure times under an oxygen concentration of 1400 mg/L and a phosphate concentration of 5000 mg/L. As shown in Fig. S3(a) and (b), it is evident that the surface of the specimen exhibits noticeable scratches, indicating a slight degree of corrosion. Further corrosion products were observed on the surface, probably deposited during the corrosion process. These products may have been formed as a result of the unwashed phosphate depositing on the surface. From Fig. S3(c), it can be seen that part of the oxide film has been removed, which may have been caused by the corrosion process. The surfaces of Fig. S3 (d-f) formed of a lumpy oxide layer, which became flatter and denser with time. The surface oxides may be spinel and metal phosphates.

3.3. Cross-section analysis

Fig. 4 shows FIB-SEM images and EDS line scans of Inconel 625 exposed for 60 h to SCW at three different phosphate concentrations. In

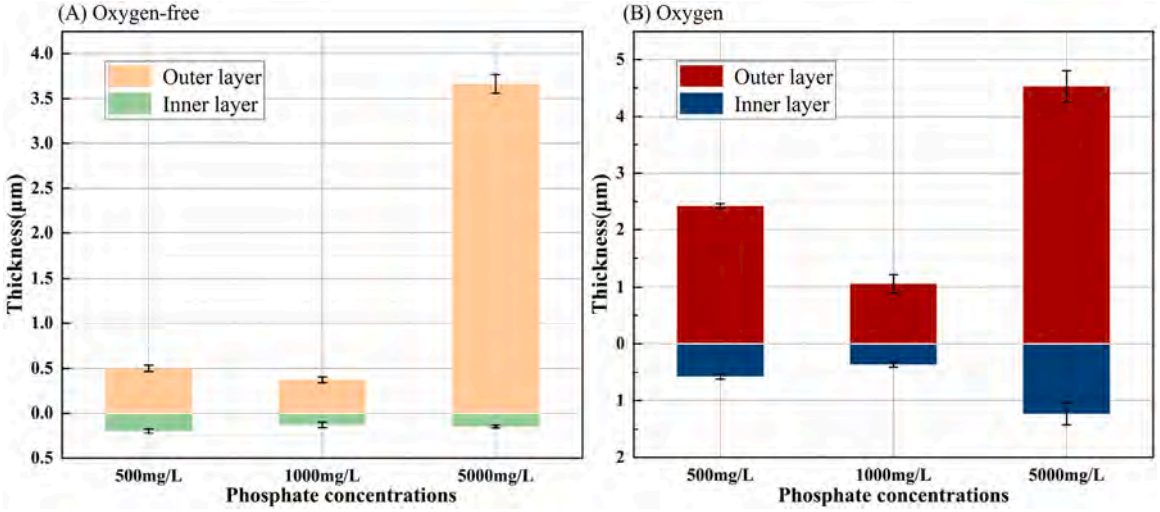


Fig. 5. Oxide film thickness of Inconel 625 exposed to SCW at three phosphate concentrations for 60 h, A-oxygen-free, B-oxygen.

Fig. 4 (A-1,2), the oxide film on the surface of the sample shows a continuous smooth cross-section, and it was found from EDS that the Ni was continuously diffusing outwards and enriched near the oxide layer, resulting in an increase and then a decrease in the nickel content from the substrate to the oxide film. Additionally, and it was also found that the Phosphorus(P) content showed a peak at the darker inner and outer junctions. In Fig. 4(B-1), the shape of corrosion products in the oxide film gradually disappears, and the oxide layer is thin. This may be due to pitting corrosion leading to localized dissolution and stripping of the oxide film. The oxide film is observed to be a phosphate-containing corrosion film. In Fig. 4(B-2) also shows the highest P content at the junction of the inner and outer layers, which is consistent with Figs. 4(A-1,2), but P was not found in the oxide film, which may be due to the competition between phosphate and oxygen, and the oxygen was dominant, giving preference to the formation of the oxide film rather than the phosphide film. As shown in Fig. 4(C-1), there is a thick and dense phosphorus-containing oxide film on the surface of the displayed sample, but there are corrosion pits on the surface. However, in Fig. 4(C-2), there are corrosion pits on the surface of the oxide film, and holes in the outer oxide film, suggesting that the molten salt may have the effect of corrosion penetration. Whereas, the highest chromium content was observed at the junction of inner and outer layers in Fig. 4 (A-1) by oxygen-free EDS line scanning, which indicated that the phosphate passivation film hindered the diffusion of Cr to the outside. However, as the concentration of phosphate ions increased, chromium diffused into the outer oxide film and may even diffuse into it. This suggests that Cr_2O_3 and other chromium oxides in the inner oxide film may dissolve in the molten phosphate during phosphate deposition. However, under oxygenated conditions, the inner oxide film thickened significantly. Metal cations diffused outward through the metal phosphate layer to form the external oxide film. In contrast, O^{2-} anions diffused inwards through the metal phosphate layer to form an internal oxide film. The dissolution of phosphate into the oxide film under the conditions of Fig. 4(B-1), but not under the conditions of Fig. 4(B-2), confirms the competitive role of phosphate and O^{2-}. The EDS results in Fig. 5(B-1) and Fig. 5(C) show that element P was uniformly distributed throughout the oxide layer. This observation suggests that the phosphate molten salt is present during the growth of the oxide film. As illustrated in Fig. 4(C-2), the metal phosphates were mainly present in the form of stable $Ni_3(PO_4)_2$ and $CrPO_4$. During the initial phase of corrosion, metal cations in the sample formed stable metal phosphate deposits at the original interface between the sample and the Na_2HPO_4 corrosion solution [20, 21].

Fig. 5 shows the oxide film thickness of Inconel 625 exposed to SCW at three phosphate concentrations for 60 h. Fig. 5A shows that the thickness of the internal oxide layer became progressively smaller as the phosphate concentration increased. The thinnest oxide film was observed in Fig. 5B, which may be attributed to the strong competition between oxygen and phosphate as well as the dissolution and precipitation of the oxide film in this condition, while in the molten salt condition, a thicker outer oxide film was formed due to the deposition of molten salt. The results obtained in oxygen-free/oxygen conditions are almost the same and the thickness of the inner oxide layer was found to be significantly smaller, suggesting that the metal phosphate layer prevented the internal oxidation process of anions such as O^{2-} and this result was confirmed in the EDS line scans.

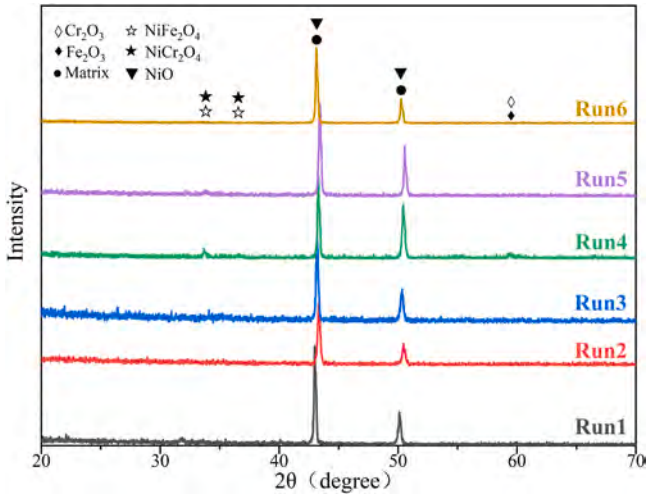


Fig. 6. XRD images of Inconel 625 in SCW with different phosphate concentrations under oxygen-free/oxygen conditions for an exposure time of 60 h.

3.4. Oxide analysis

3.4.1. XRD analysis

Fig. 6 presents the XRD patterns of Inconel 625 after 60 h of exposure in SCW with different phosphate concentrations under both oxygen-free/oxygen conditions. The ICSD standard card data indicates that peaks corresponding to Fe_2O_3 (33–0664) and Cr_2O_3 (70–3765) were detected on the surface during Run 1. However, due to the presence of various substances on the alloy surface and the intrinsic noise of the

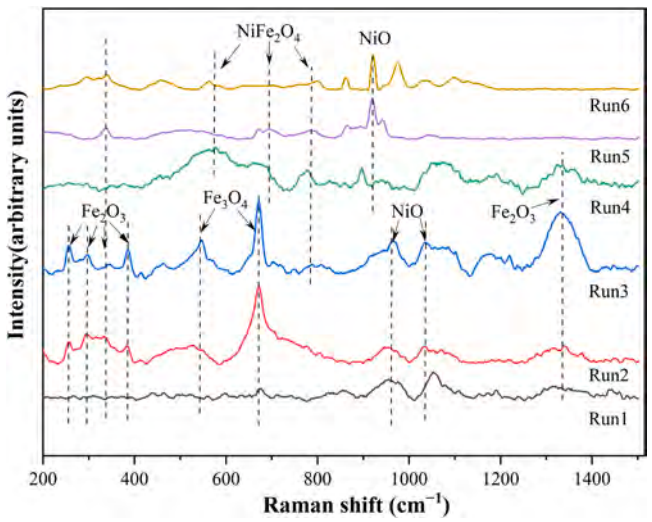


Fig. 7. Raman spectra of Inconel 625 in SCW under oxygen-free/oxygen conditions with different phosphate concentrations for 60 h exposure time.

instrument, the XRD spectrum was unable to distinguish weak peaks between Fe_2O_3 and Cr_2O_3. Further validation results will be analyzed through XPS. In Runs 2, 3, and 6, no characteristic peaks were detected except for the background. In Runs 4 and 5, peaks corresponding to $NiCr_2O_4$ and $NiFe_2O_4$ were identified on the surface. The solid-phase reaction between NiO and oxides, such as Cr_2O_3 and Fe_2O_3 was accelerated by the introduction of oxygen, resulting in more pronounced spinel peaks. During the deposition of molten phosphate salts, oxides such as NiO dissolve faster in the SCW than towards the substrate side of the alloy, causing the spinel peak attenuation to be undetectable in Run 6. Spinel was mainly present in the outer oxide film facing the interior, while the outer oxide film under the dissolved salt phase was thicker, rendering the spinel phase cannot be detected at the surface.

3.4.2. Raman analysis

The SEM analysis revealed that the surface morphology of Inconel 625 was covered in sediment, and the XRD analysis showed characteristic peaks that were limited. To further investigate, Raman spectroscopy was employed as an additional detection method [22]. Fig. 7 shows the Raman spectra of Inconel 625 samples after 60 h of exposure in SCW with different phosphate concentrations under oxygen-free/oxygen conditions. The spectra from the sample surface reveal peaks corresponding to Fe_2O_3, Fe_3O_4, NiO, and a spinel structure [23–25]. It is noteworthy that the characteristic peaks do not show any significant shift as the phosphate concentration increases. However, the formation of the $NiFe_2O_4$ spinel structure from Fe_2O_3 and oxygen under oxygenated conditions indicates that oxygen accelerated solid-phase formation.

3.4.3. XPS analysis

Fig. 8 shows the characteristic XPS spectra of Inconel 625 exposed for 60 h in SCW with oxygen-free and at three different phosphate concentrations. Since the content of Ni and Cr in Inconel 625 is more than 80 %, the spectra of Ni 2p3/2, 2p1/2, and Cr 2p3/2, 2p1/2 energy levels were examined. The Ni 2p3/2 peak in the dissolved phase of phosphates is attributed to $Ni(OH)_2$ [26] and $Ni_3(PO_4)_2$ [27]. The three binding energies of Ni 2p3/2 in phosphate molten salt correspond to NiO, $Ni(OH)_2$ and $Ni_3(PO_4)_2$ at 854.6 eV, 856.3 eV and 857.5 eV, respectively. The Cr 2p3/2 peak in the dissolved phase of phosphates corresponds to Cr^{3+} and Cr_2O_3 with binding energies of 577.3 ± 0.2 eV and 575.7 ± 0.2 eV, respectively. The peak of the metal Cr^0 was detected at 574.3 eV at a phosphate concentration of 1000 mg/L due to the stripping of the surface oxide film, and the ratios of Cr^0 to Cr^{3+} were semi-quantitatively calculated to be 38.92 % and 61.09 %, respectively.

In phosphate molten salt conditions, peaks of Cr^{3+} and Cr_2O_3 shift to binding energies of 577.9 eV and 576.4 eV. This shift is attributed to the chemical displacement of Cr 2p3/2 to higher binding energies with increasing phosphate concentration. XPS valence analysis showed that the oxidation products were dominated by NiO and Cr_2O_3. This is in general agreement with the XRD results.

Fig. 9 shows the characteristic XPS spectra of Inconel 625 exposed for 60 h in SCW with an oxygen concentration of 1400 mg/L and at three different phosphate concentrations. The Ni 2p3/2 exhibits two peaks in the dissolved phase, attributed to $Ni(OH)_2$ and $Ni_3(PO_4)_2$, with binding energies at 855.6 ± 0.2 eV and 856.7 ± 0.2 eV, respectively. In phosphate molten salt conditions, three binding energies at 854.1 eV, 856.1 eV, and 857.1 eV are assigned to NiO, $Ni(OH)_2$, and $Ni_3(PO_4)_2$, respectively. The increase in phosphate concentration causeed a chemical shift in Ni 2p3/2 peak to undergo a chemical shift toward a lower binding energy, indicating the oxidation of Ni. This explains why NiO was detected on the surface of samples under phosphate molten salt conditions, which coincides the results obtained under oxygen-free conditions.

The binding energies of the Cr 2p3/2 peaks corresponding to the Cr^0, Cr_2O_3, Cr^{3+}, and Cr^{6+} peaks at the three concentrations were 574.3 ± 0.2 eV, 576.5 ± 0.2 eV, 578.0 ± 0.2 eV, and 579.5 ± 0.1 eV, respectively. Semi-quantitative calculations showed that in (a) the proportions of Cr^0, Cr^{3+}, and Cr^{6+} were 6.97 %, 27.85 % and 65.18 % respectively. In (b) the proportions of Cr^{3+} and Cr^{6+} were 59.63 % and 40.37 % respectively. Comparison with (a) showed that the proportion of Cr^{6+} decreased but the oxygen content remained unchanged, further confirming the existence of competition between phosphate and oxygen. In (c) the proportions of Cr^0 and Cr^{3+} were 22.46 % and 77.54 % respectively. Under phosphate conditions, alloys in SCW corroded faster when exposed to oxygen in the dissolved phase, causing the oxidation state of chromium to change from Cr^{3+} to Cr^{6+} [28–30]. However, However, in the phosphate molten salt conditions, Cr_2O_3 can be directly dissolved to form Cr^{3+}, limiting the conversion to Cr^{6+} and resulting in an insignificant Cr^{6+} peak.

4. Discussion

4.1. Formation of oxide films on alloys under dissolved-phase phosphate corrosion

In previous studies, the mechanisms of oxide film growth, metal dissolution, and metal salt precipitation have been widely accepted by researchers as typical mechanisms [31–33]. The corrosion resistance of alloyed materials often depends on the stability of surface metal oxides. In SCW containing unsaturated phosphates, the formation of oxide films can be explained by a similar dissolution-precipitation mechanism [32, 34,35]. During the initial stages of corrosion, phosphate ions react with Cr, Fe, and Ni, resulting in the formation of corresponding metal phosphates ($CrPO_4$, $FePO_4$, and $Ni_3(PO_4)_2$) that deposit on the original surface of the alloy. This reaction competes with oxygen radicals in SCW, which weakens the contact between corrosive anions and metal cations that diffused outward in the alloy. This process results in the formation of a barrier film on the alloy surface [16,36,37]. Additionally, it has been demonstrated that the dissolution of oxide films in SCW is reduced. The addition of a phosphate passivation layer between the alloy matrix and the solution can impede the transfer of substances in the vicinity of the alloy interface [38], inhibit the electrochemical reactions of the alloy matrix, and decelerate corrosion [16,39]. In addition, the size of the oxide film increases with increasing phosphate concentration, while the surface of the oxide film becomes denser.

As the reaction progresses, Fe, Cr, and Ni diffuse outward through the phosphate passivation layer to form an outer oxide film. Due to the differing diffusion rates of the constituent elements (Fe>Ni>Cr) [40], the Fe oxide was located at the outermost layer of the film, where Fe^{2+} and Fe^{3+} react with O_2 and oxygen ions to form Fe_2O_3 and Fe_3O_4, which

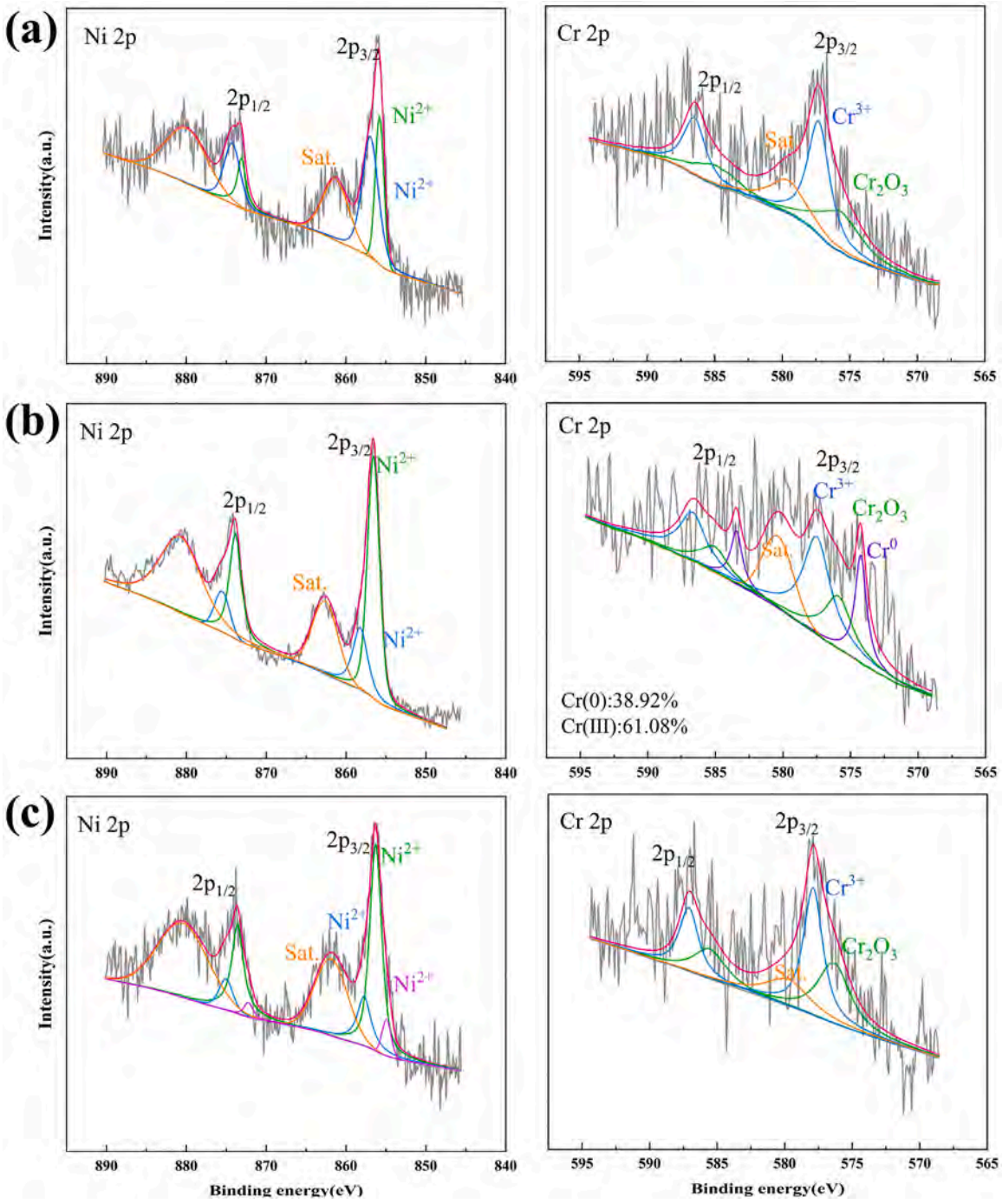


Fig. 8. XPS spectra of Inconel 625 exposed to three phosphate concentrations of SCW for 60 h, (a) 500 mg/L, (b) 1000 mg/L, (c) 5000 mg/L.

explains the prominent peaks of iron oxides observed in Raman spectroscopy. Ni existed in SCW mainly as NiO and $Ni(OH)_2$, and NiO can be hydrolyzed to $Ni(OH)_2$ [41]. In addition, solid-phase reactions between Ni and Cr oxides and their hydroxides occur near the original alloy interface, resulting in the formation of $NiCr_2O_4$. This compound is then incorporated into Cr_2O_3, NiO, and $Ni(OH)_2$ [42]. Over time, the outermost NiO and $Ni(OH)_2$ react with the outermost Fe_2O_3 through solid-phase reactions to form $NiFe_2O_4$. As the Cr content accumulates in the oxide film, and Fe and Ni gradually diffuse outward, the spinel structure of $NiFe_2O_4$ is transformed into $FeCr_2O_4$.

The inner oxide film is composed of NiO and Cr_2O_3. Initially, oxygen and water molecules adsorb onto the alloy surface and dissolve in the inner oxide film, reacting with diffusing metal cations to form oxides. In the early stages of corrosion, a mixed oxide of Ni and Cr forms on the material surface. Due to the higher growth rate of Ni-containing oxides compared to Cr_2O_3, large amounts of NiO and $NiCr_2O_4$ oxides form before the continuous formation of Cr_2O_3 oxide film. Simultaneously, phosphate ions reacted with the alloy matrix to form deposited metal phosphates on the surface. Furthermore, O_2 and H_2O adsorb on the outer oxide film through the cracks between needlelike and platelike oxides. Subsequently, they are dissolved into the oxide film and diffuse into the inner oxide film, passing through the original interface barrier layer of metal phosphates. The reaction of diffusing Cr and Ni with oxygen results in the formation of oxides. Oxygen ions are transported inward through vacancies in the inner layer [43]. As the outer oxide film grows towards the substrate, Cr_2O_3 and NiO in the outer oxide film react

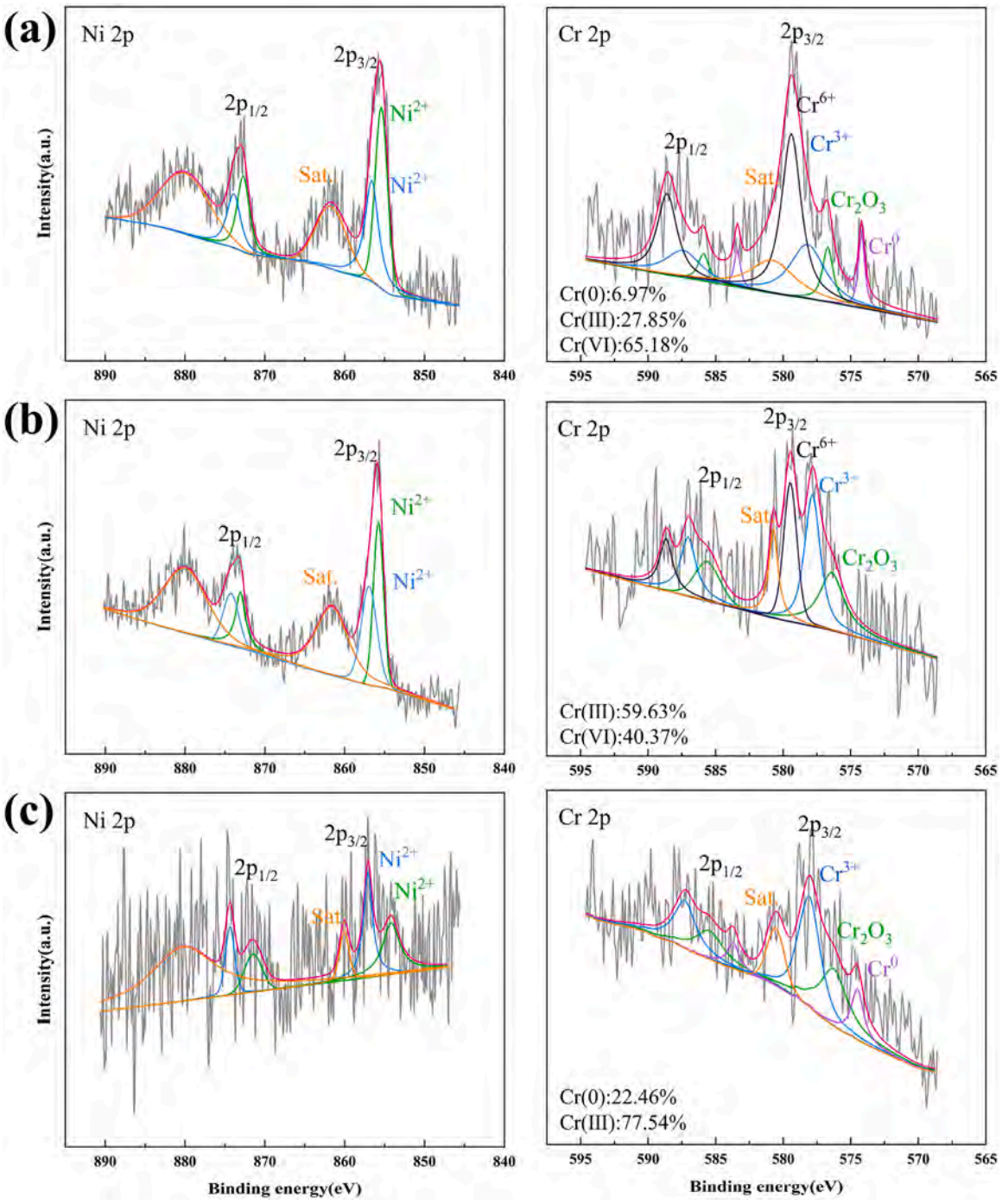


Fig. 9. XPS spectra of Inconel 625 exposed for 60 hours to SCW at an oxygen concentration of 1400 mg/L and three different phosphate concentrations, (a) 500 mg/L, (b)1000 mg/L, (c)5000 mg/L.

through solid-phase reactions to form $NiCr_2O_4$.

In SCW containing oxygen and phosphate, the higher oxygen partial pressure on the SCW side causes a significant amount of oxygen to dissolve in the oxide film. The combination of these factors leads to the formation of oxides, with the mechanism of oxide film formation being mainly dominated by solid-phase growth. As the concentration of phosphate increases, competition between phosphate and oxygen takes place. The presence of phosphate in the system results in the occupation of vacancies left by metal cations diffusing outward, thereby weakening the solid-phase growth mechanism of oxides, leading to a thinning of the oxide film, especially in the inner layer, and makes it difficult to form a thicker Cr_2O_3 layer. This also results in the absence of a stable oxide layer to protect the substrate and also causes the oxide film produced to flake off, which can also explain the quality change of the alloy at 1000 mg/L is reduced. Thus the composition of the oxide layer of the alloy under dissolved phase conditions is as follows: the inner layer consists of nickel and chromium oxides, the intermediate layer consists of metal phosphates, and the outermost layer probably consists of Ni and Fe oxides as well as spinel. The structure diagram of the oxide film is presented in Fig. 11.

4.2. Corrosion mechanism of alloys under phosphate molten salt

In the conditions of phosphate molten salt, the corrosion of nickel-

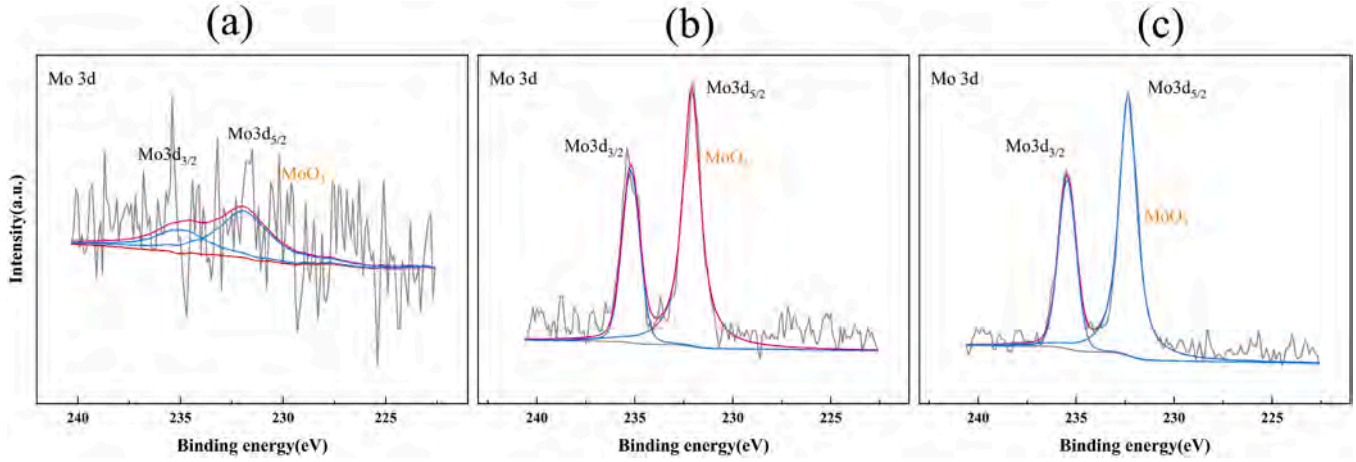


Fig. 10. XPS spectra of Inconel 625 after 60 h of exposure to SCW with oxygen concentration of 1400 mg/L and three different phosphate concentrations, (a) 500 mg/L, (b)1000 mg/L, (c)5000 mg/L.

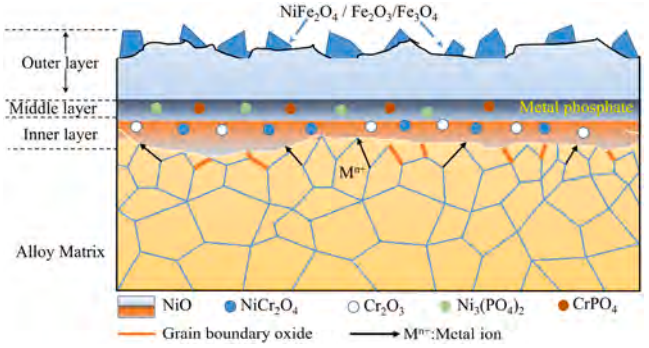


Fig. 11. Schematic diagram of the oxide film structure on the surface of Inconel 625 in SCW containing phosphates.

based alloy is mainly completed by dissolving the oxide film through molten salt. Phosphate molten salt have a strong ion transfer capability, which accelerates the diffusion of metal elements and corrosive ions, as well as facilitate the completion of oxidation reactions through a high diffusion rate. In the unsaturated phosphate environment, phosphate ions can compete with oxygen and impede the diffusion of oxygen into the interior of alloy matrix. However, when exposed to phosphate molten salts, the presence of H_2O alters the redox state of the molten salts and can enhance the corrosion of Inconel 625 [44]. Moreover, molten salt can also adsorb oxygen and oxides, which act as an accelerating force for corrosion [45,46]. The corrosion in phosphate molten salt is therefore more severe than that of conventional phosphate salt.

In the initial stages of corrosion, water or oxygen acts as an oxygen donor and oxygen ions are adsorbed into the matrix to form oxides with metal ions [8]. An optimal oxygen concentration can expedite the formation of a protective oxide film, while an excessively high oxygen concentration can cause severe damage to the oxide layer [47]. Thus, the presence of oxygen has a significant impact on the entire molten salt passivation mechanism [48]. Under high-temperature molten salt conditions, molten salt conducts charges in an ionic manner, separating the alloy from the gas phase. In the presence of SCW, molten salt reacts to form corresponding acids and hydroxides, which accelerate corrosion [49–51]. While phosphate molten salt can undergo hydrolysis, the extent of hydrolysis is low in SCW [52], and the resulting oxides are soluble in phosphate molten salt [17]. Therefore, in phosphate molten salt conditions, the corrosion of the alloy is primarily dominated by the metal's thermal corrosion. In the second stage of corrosion, due to the immiscibility of phosphate molten salt and SCW, in the microenvironment of the alloy surface and the deposition of phosphate molten salt, H_2O adsorbed in molten salt transports oxygen ions, forming oxides with metal ions that outwardly diffuse from the alloy matrix. Additionally, H_2O reacts with outwardly diffusing metal cations such as Ni^{2+}, forming $Ni(OH)_2$ precipitates [53]. Subsequently, oxides and hydroxides react with Na_2HPO_4, producing metal phosphates and H_2O. The formed metal phosphates re-enter the molten salt, creating a eutectic salt of $FePO_4$-$Ni_3(PO_4)_2$-Na_3PO_4-Na_2HPO_4, which further promotes corrosion. Furthermore, under molten salt conditions, regardless of the presence of oxygen, NaO_2 reacts with NiO to form Na_2NiO_2 [54,55]. Taking Ni as an example,

$$Ni + H_2O(SCW) \rightarrow NiO + H_2 \quad (1)$$

$$NiO \rightarrow Ni^{2+} + O^{2-} \quad (2)$$

$$Ni^{2+} + 2H_2O \rightarrow Ni(OH)_2 + 2H^+ \quad (3)$$

$$2HPO_4^{2-} + 3Ni^{2+} + H_2O \rightarrow Ni_3(PO_4)_2 + 2OH^- \quad (4)$$

The corrosion process under molten salt deposition is as follows:

$$Ni + PO_4^{3-} \rightarrow NiO + Ni_3P + O^{2-} \quad (5)$$

$$NiO + Na_2O \rightarrow Na_2NiO_2 \quad (6)$$

$$NiO + O^{2-} \leftrightarrow NiO_2^{2-} \quad (7)$$

$$2NiO + Na_2O + O^{2-} \rightarrow Na_2NiO_2 \quad (8)$$

The electrochemical reaction arises from the inherent instability of the base metal upon contact with phosphate molten salt. Corrosion is initiated by the penetration of the protective oxide layer, which leads to intergranular corrosion and microcracking. As the protective oxide film dissolves, molten salt infiltrates into the matrix through the porous oxide layer (as shown in Fig. 4C-2). Intergranular corrosion occurs under phosphate molten salt deposition. In the conditions of this study, intergranular corrosion of nickel-based alloys may be carbide precipitation [56,57]. Additionally, in the SCW environment, the selective precipitation of certain metal compounds, such as sigma-phase FeCr, may occur along the grain boundaries. Fig. 10 illustrates the presence of Mo oxides on the surface oxide layer. As Mo dissolves and diffuses slowly, it is predominantly observed in the inner layer, implying that Mo's presence could be attributed to intergranular precipitation [58–60].

In SCW, metal ions outwardly diffuse and react with SCW to form oxides. Subsequently, phosphate molten salt dissolves the oxide film and

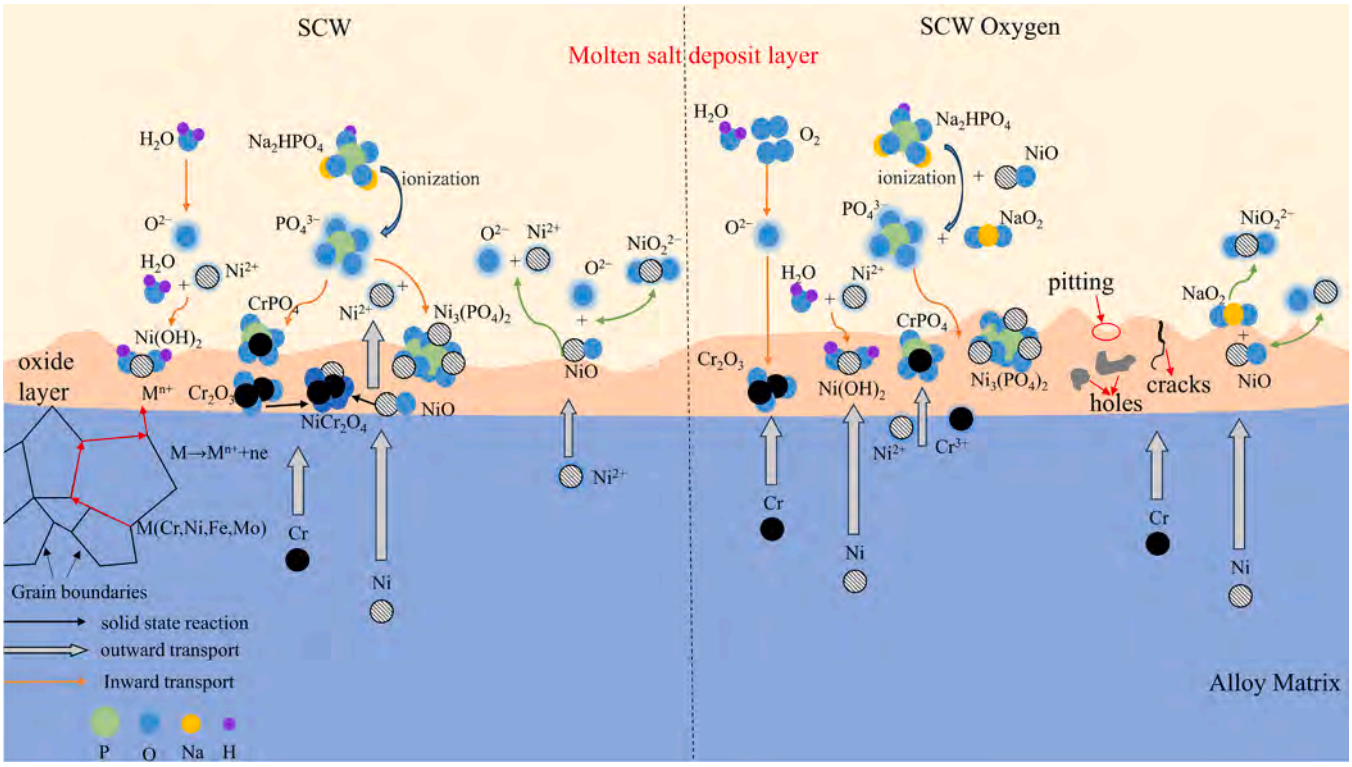


Fig. 12. Schematic diagram of corrosion mechanism of Inconel 625 in SCW containing phosphate and phosphate molten salt.

further reacts with it to generate metal phosphides. Under molten salt conditions, the composition of the alloy oxide layer mainly comprises metal phosphates, nickel oxides, and chromium oxides. The loose metal phosphate corrosion products deposited on the surface are unstable and can be easily stripped away along with other readily removable oxides, thereby exposing the inner oxide layer. However, the Cr_2O_3 within the inner layer is unstable in a highly oxygenated SCW environment. This instability arises from the accelerated conversion of Cr^{3+} to Cr^{6+} in the presence of oxygen and its subsequent dissolution in SCW [21,61–63]. Interestingly, in the present study, phosphate was found to inhibit the oxygen-mediated conversion of Cr^{3+} to Cr^{6+} [64]. As a result, Cr is directly dissolved into supercritical water and phosphate molten salts as Cr^{3+}. XPS analyses showed the absence of Cr^{6+} in oxygenated phosphates. In addition, nickel oxide is less stable than chromium oxide and oxides with spinel structure. Under SCW conditions, NiO tends to dissolve, flake or form cavities. Hence, the corrosion losses occurring under phosphate molten salt conditions are primarily ascribed to the dissolution and stripping of nickel oxides and the loss of Cr^{3+}. Fig. 12 illustrates the corrosion mechanism of Inconel 625 in SCW containing phosphate.

5. Conclusion

This study investigates the corrosion behavior of Inconel 625 in SCW (400℃, 25 MPa) under various conditions: oxygen-free, oxygen concentration of 1400 mg/L, and different phosphate concentrations (500 mg/L, 1000 mg/L, 5000 mg/L). Additionally, the inhibitory effect of phosphate passivation layers on oxide film formation is examined. The corrosion mechanisms of phosphate in different phases are analyzed. The main conclusions are as follows:

1) In the dissolved phase of phosphate salts under SCW conditions, as phosphate concentration increases, the thickness of the inner oxide film on the alloy surface decreases. Phosphate ions compete with oxygen-containing ions, thereby retarding the extent of oxidation corrosion.
2) The inner and outer oxide films are the results of inward oxidation by oxygen ions and outward diffusion of metal cations. The presence of a metallic phosphate passivation layer at the interface impedes the corrosion of Fe, Ni and other metals. The outer oxide film is composed of oxides such as Fe_3O_4, Fe_2O_3, $NiFe_2O_4$, NiO, $Ni(OH)_2$, and metal phosphates. The inner layer consists of spinels such as NiO, Cr_2O_3, and $NiCr_2O_4$.
3) SCW, oxygen, and phosphate molten salt exhibit strong synergistic effects. In the presence of dissolved phosphate, oxygen converts insoluble Cr^{3+} to soluble Cr^{6+} in the alloy. However, in the presence of molten phosphate salt, insoluble Cr^{3+} directly dissolves in SCW.
4) It was found that the growth of oxide films under dissolved phosphate conditions consists of dissolved precipitation in the outer layer, blocked diffusion in the intermediate passivation layer and internal oxidation in the inner layer. Under phosphate molten salt conditions, the entire oxide film growth process is accompanied by both oxide melting and metal phosphide growth.

CRediT authorship contribution statement

Jiquan Chen: Validation, Data curation, Conceptualization. **Zitao Lin:** Writing – review & editing, Writing – original draft, Methodology, Data curation, Conceptualization. **Jianqiao Yang:** Writing – review & editing, Validation. **Riguang Zhu:** Validation, Formal analysis. **Ke Li:** Data curation, Conceptualization. **Xingying Tang:** Writing – review & editing, Writing – original draft, Visualization, Validation, Investigation.

Declaration of Competing Interest

The authors declare that they have no known competing financial interests or personal relationships that could have appeared to influence the work reported in this paper.

Acknowledgment

This work was supported by the National Natural Science Foundation of China (22068003).

Appendix A. Supporting information

Supplementary data associated with this article can be found in the online version at doi:10.1016/j.supflu.2024.106495.

Data Availability

Data will be made available on request.

References

[1] P.A. Marrone, Supercritical water oxidation—current status of full-scale commercial activity for waste destruction, J. Supercrit. Fluids 79 (2013) 283–288, https://doi.org/10.1016/j.supflu.2012.12.020.
[2] S.V.P. Mylapilli, S.N. Reddy, Sub and supercritical water oxidation of pharmaceutical wastewater, J. Environ. Chem. Eng. 7 (2019) 103165, https://doi.org/10.1016/j.jece.2019.103165.
[3] Z. Yan, B. örmeci, Y. Han, J. Zhang, Supercritical water oxidation for treatment of wastewater sludge and recalcitrant organic contaminants, Environ. Technol. Innov. 18 (2020) 100728, https://doi.org/10.1016/j.eti.2020.100728.
[4] G.B.M. de Souza, M.B. Pereira, L.C. Mourão, M.P. Dos Santos, J.A. de Oliveira, I.A. A. Garde, C.G. Alonso, V. Jegatheesan, L. Cardozo-Filho, Supercritical water technology: an emerging treatment process for contaminated wastewaters and sludge, Rev. Environ. Sci. Bio. 21 (2022) 75–104, https://doi.org/10.1007/s11157-021-09601-0.
[5] M.D. Bermejo, M.J. Cocero, Supercritical water oxidation: a technical review, AICHE J. 52 (2006) 3933–3951, https://doi.org/10.1002/aic.10993.
[6] J. Yang, Y. Ding, F. Zhao, S. Wang, Y. Li, D. Xu, Under-deposit corrosion of Cr-coated Ni-based alloys in supercritical water oxidation environment at 500 °C, J. Supercrit. Fluids 208 (2024) 106213, https://doi.org/10.1016/j.supflu.2024.106213.
[7] P. Feng, W. Yang, D. Xu, M. Ma, Y. Guo, Z. Jing, Characteristics, mechanisms and measurement methods of dissolution and deposition of inorganic salts in sub-/supercritical water, Water Res 225 (2022) 119167, https://doi.org/10.1016/j.watres.2022.119167.
[8] J.H. Wang, D.G. Li, T.M. Shao, Electrochemical study on the hot corrosion behavior of Ni16Cr13Co4Mo alloy in molten NaCl-KCl and NaCl-KCl-Na_2SO_4, Corros. Sci. 200 (2022) 110247, https://doi.org/10.1016/j.corsci.2022.110247.
[9] D. Xu, C. Huang, S. Wang, G. Lin, Y. Guo, Salt deposition problems in supercritical water oxidation, Chem. Eng. J. 279 (2015) 1010–1022, https://doi.org/10.1016/j.cej.2015.05.040.
[10] M. Hodes, P. Griffith, K.A. Smith, W.S. Hurst, W.J. Bowers, K. Sako, Salt solubility and deposition in high temperature and pressure aqueous solutions, AICHE J. 50 (2004) 2038–2049, https://doi.org/10.1002/aic.10238.
[11] M. Hodes, P.A. Marrone, G.T. Hong, K.A. Smith, J.W. Tester, Salt precipitation and scale control in supercritical water oxidation—part A: fundamentals and research, J. Supercrit. Fluids 29 (2004) 265–288, https://doi.org/10.1016/S0896-8446(03)00093-7.
[12] T. Voisin, A. Erriguible, C. Aymonier, A new solvent system: hydrothermal molten salt, Sci. Adv. 6 (2020), https://doi.org/10.1126/sciadv.aaz7770.
[13] Y. Zhang, S. Wang, Z. Gao, Y. Li, T. Xu, J. Li, D. Xu, J. Yang, Hydrothermal molten salt: a hydrothermal fluid in SCWO treatment of hypersaline wastewater, Chem. Eng. J. 421 (2021) 129589, https://doi.org/10.1016/j.cej.2021.129589.
[14] X. Tang, S. Wang, D. Xu, Y. Gong, J. Zhang, Y. Wang, Corrosion behavior of Ni-based alloys in supercritical water containing high concentrations of salt and oxygen, Ind. Eng. Chem. Res. 52 (2013) 18241–18250, https://doi.org/10.1021/ie401258k.
[15] Z. Ma, D. Xu, S. Guo, Y. Wang, S. Wang, Z. Jing, Y. Guo, Corrosion properties and mechanisms of austenitic stainless steels and Ni-base alloys in supercritical water containing phosphate, sulfate, chloride and oxygen, Oxid. Met. 90 (2018) 599–616, https://doi.org/10.1007/s11085-018-9855-4.
[16] S. Guo, D. Xu, G. Jiang, Y. Guo, Z. Jing, Sulfate corrosion and phosphate passivation of Ni-based alloy in supercritical water, J. Supercrit. Fluids 184 (2022) 105564, https://doi.org/10.1016/j.supflu.2022.105564.
[17] T. Xu, S. Wang, X. Tang, Y. Li, J. Yang, J. Li, Y. Zhang, Corrosion mechanism of Inconel 600 in oxidizing supercritical aqueous systems containing multiple salts, Ind. Eng. Chem. Res. 58 (2019) 23046–23056, https://doi.org/10.1021/acs.iecr.9b04527.
[18] X. Ding, J.D. Sheehan, T. Zhang, Z. Shen, Y. Wang, Z. Jiang, T. Fang, Experimental-computational approach for elucidating the dissolution behavior of potassium phosphates in near- and supercritical water, J. Supercrit. Fluids 181 (2022) 105488, https://doi.org/10.1016/j.supflu.2021.105488.
[19] J. Yang, S. Wang, Y. Li, D. Xu, Under-deposit corrosion of Ni-based alloy 825 and Fe-Ni based alloy 800 in supercritical water oxidation environment, Corros. Sci. 167 (2020) 108493, https://doi.org/10.1016/j.corsci.2020.108493.
[20] M.C. Sun, X.Q. Wu, Z.E. Zhang, E.H. Han, Analyses of oxide films grown on Alloy 625 in oxidizing supercritical water, J. Supercrit. Fluids 47 (2008) 309–317, https://doi.org/10.1016/j.supflu.2008.07.010.
[21] K. Chang, S. Chen, T. Yeh, J. Kai, Effect of dissolved oxygen content on the oxide structure of Alloy 625 in supercritical water environments at 700 °C, Corros. Sci. 81 (2014) 21–26, https://doi.org/10.1016/j.corsci.2013.11.034.
[22] J. Yang, S. Wang, D. Xu, Y. Guo, C. Yang, Y. Li, Effect of ammonium chloride on corrosion behavior of Ni-based alloys and stainless steel in supercritical water gasification process, Int. J. Hydrog. Energy 42 (2017) 19788–19797, https://doi.org/10.1016/j.ijhydene.2017.05.078.
[23] X. Zhong, F. Hamdani, J. Xu, T. Shoji, T. Tatsuki, J. Morii, W. Sasaki, Y. Ishii, Effects of dissolved oxygen on the oxide scales formed on ferritic-martensitic steel T12 exposed to supercritical water, Corros. Sci. 167 (2020) 108516, https://doi.org/10.1016/j.corsci.2020.108516.
[24] C. Liu, T. Shen, C. Yao, H. Chang, K. Wei, L. Niu, Z. Ma, Z. Wang, Corrosion behavior of ferritic–martensitic steels SIMP and T91 in fast-flowing steam, Corros. Sci. 187 (2021) 109474, https://doi.org/10.1016/j.corsci.2021.109474.
[25] Z. Zhu, Y. Li, C. Ma, X. Liu, G. Liu, S. Wang, H. Xu, N. Zhang, The corrosion behavior of Nickel-based alloy Inconel 740H in supercritical water, Corros. Sci. 192 (2021) 109848, https://doi.org/10.1016/j.corsci.2021.109848.
[26] D.W.K.A.K.K. Lian, Investigation of a “two - state” tafel phenomenon for the oxygen evolution reaction on an amorphous Ni - Co alloy, J. Electrochem. Soc. 142 (1995).
[27] X. Xu, X. Song, X. Liu, H. Wang, Y. Hu, J. Xia, J. Chen, M. Shakouri, Y. Guo, Y. Wang, A highly efficient nickel phosphate electrocatalyst for the oxidation of 5-hydroxymethylfurfural to 2,5-furandicarboxylic acid, ACS Sustain. Chem. Eng. 10 (2022) 5538–5547, https://doi.org/10.1021/acssuschemeng.2c00121.
[28] T.M. Hayward, I.M. Svishchev, R.C. Makhija, Stainless steel flow reactor for supercritical water oxidation: corrosion tests, J. Supercrit. Fluids 27 (2003) 275–281, https://doi.org/10.1016/S0896-8446(02)00264-4.
[29] S. Mahboubi, Y. Jiao, W. Cook, W. Zheng, D.A. Guzonas, G.A. Botton, J.R. Kish, Stability of chromia (Cr_2O_3)-based scales formed during corrosion of austenitic Fe-Cr-Ni alloys in flowing oxygenated supercritical water, Corrosion 72 (2016) 1170–1180, https://doi.org/10.5006/1982.
[30] D. Xu, Z. Ma, S. Guo, X. Tang, Y. Guo, S. Wang, Corrosion characteristics of 316L as transpiring wall material in supercritical water oxidation of sewage sludge, Int. J. Hydrog. Energy 42 (2017) 19819–19828, https://doi.org/10.1016/j.ijhydene.2017.05.245.
[31] P. Kritzer, Corrosion in high-temperature and supercritical water and aqueous solutions: A review, J. Supercrit. Fluids 29 (2004) 1–29, https://doi.org/10.1016/S0896-8446(03)00031-7.
[32] H. Kim, D.B. Mitton, R.M. Latanision, Corrosion behavior of Ni-base alloys in aqueous HCl solution of pH 2 at high temperature and pressure, Corros. Sci. 52 (2010) 801–809, https://doi.org/10.1016/j.corsci.2009.10.042.
[33] Y. Li, T. Xu, S. Wang, J. Yang, J. Li, T. Xu, D. Xu, Characterization of oxide scales formed on heating equipment in supercritical water gasification process for producing hydrogen, Int. J. Hydrog. Energy 44 (2019) 29508–29515, https://doi.org/10.1016/j.ijhydene.2019.01.284.
[34] X. Gao, X. Wu, Z. Zhang, H. Guan, E. Han, Characterization of oxide films grown on 316L stainless steel exposed to H_2O_2-containing supercritical water, J. Supercrit. Fluids 42 (2007) 157–163, https://doi.org/10.1016/j.supflu.2006.12.020.
[35] Z. Deng, P. Yang, Z. Huo, L. Zou, Y. Wang, Comparison and mechanism research of corrosion behavior of materials used in supercritical water-cooled reactors, J. Supercrit. Fluids 207 (2024) 106192, https://doi.org/10.1016/j.supflu.2024.106192.
[36] L. Hou, N. Dang, H. Yang, B. Liu, Y. Li, Y. Wei, X. Chen, A combined inhibiting effect of sodium alginate and sodium phosphate on the corrosion of magnesium alloy AZ31 in NaCl solution, J. Electrochem. Soc. 163 (2016) C486–C494, https://doi.org/10.1149/2.0941608jes.
[37] J. Wang, H. Yang, M. Du, J. Hou, W. Peng, C. Lin, Corrosion mechanism of 5083 aluminum alloy in seawater containing phosphate, J. Ocean U. China 20 (2021) 372–382, https://doi.org/10.1007/s11802-021-4545-2.
[38] X. Tang, S. Wang, L. Qian, Y. Li, Z. Lin, D. Xu, Y. Zhang, Corrosion behavior of nickel base alloys, stainless steel and titanium alloy in supercritical water containing chloride, phosphate and oxygen, Chem. Eng. Res. Des. 100 (2015) 530–541, https://doi.org/10.1016/j.cherd.2015.05.003.
[39] S.L. Zhang, X.L. Zhang, H.H. Chen, M.M. Zhang, Corrosion and protection characteristics of phosphate coatings: effect of yttrium oxide as additive, Trans. Inst. Met. Finish 86 (2013) 167–171, https://doi.org/10.1179/174591908X304207.
[40] L. Zhong, B. Xiao, C. Su, H.I. Khan, H. Xu, N. Zhang, Z. Zhu, The oxidation behavior of Nickel-based alloy Inconel 617 in supercritical water, Mater. Corros. 73 (2022) 1132–1143, https://doi.org/10.1002/maco.202112948.
[41] J. Yang, S. Wang, Y. Li, X. Tang, Y. Wang, D. Xu, Y. Guo, Effect of salt deposit on corrosion behavior of Ni-based alloys and stainless steels in supercritical water, J. Supercrit. Fluids 152 (2019) 104570, https://doi.org/10.1016/j.supflu.2019.104570.
[42] X. Zhong, E. Han, X. Wu, Corrosion behavior of Alloy 690 in aerated supercritical water, Corros. Sci. 66 (2013) 369–379, https://doi.org/10.1016/j.corsci.2012.10.001.
[43] S. Sharifi-Asl, M.L. Taylor, Z. Lu, G.R. Engelhardt, B. Kursten, D.D. Macdonald, Modeling of the electrochemical impedance spectroscopic behavior of passive iron using a genetic algorithm approach, Electrochim. Acta 102 (2013) 161–173, https://doi.org/10.1016/j.electacta.2013.03.143.

[44] Y.L. Wang, Q. Wang, H.J. Liu, C.L. Zeng, Effects of the oxidants H_2O and CrF_3 on the corrosion of pure metals in molten (Li, Na, K)F, Corros. Sci. 103 (2016) 268–282, https://doi.org/10.1016/j.corsci.2015.11.032.
[45] J. Qiu, Y. Zou, G. Yu, H. Liu, Y. Jia, Z. Li, P. Huai, X. Zhou, H. Xu, Compatibility of container materials with Cr in molten FLiNaK salt, J. Fluor. Chem. 168 (2014) 69–74, https://doi.org/10.1016/j.jfluchem.2014.09.010.
[46] J. Luo, C.K. Deng, N.U.H. Tariq, N. Li, R.F. Han, H.H. Liu, J.Q. Wang, X.Y. Cui, T. Y. Xiong, Corrosion behavior of ss316L in ternary Li_2CO_3–Na_2CO_3–K_2CO_3 eutectic mixture salt for concentrated solar power plants, Sol. Energy Mater. Sol. Cells 217 (2020) 110679, https://doi.org/10.1016/j.solmat.2020.110679.
[47] L. Ai, Y. Zhou, M. Chen, Role of dissolved oxygen in iron oxidation in supercritical water: insights from reactive dynamics simulations, J. Phys. Chem. C. 123 (2019) 15009–15016, https://doi.org/10.1021/acs.jpcc.9b01936.
[48] C. Frayret, P. Botella, T. Jaszay, M.H. Delville, Titanium dissolution-passivation in highly chloridic and oxygenated aqueous solutions, J. Electrochem. Soc. 151 (2004) B543, https://doi.org/10.1149/1.1787171.
[49] M. Lee, O. Muránsky, I. Karatchevtseva, H. Huang, K.J. Laws, Corrosion performance of Ni-based structural alloys for applications in molten-salt based energy systems: experiment & numerical validation, Corros. Sci. 190 (2021) 109607, https://doi.org/10.1016/j.corsci.2021.109607.
[50] A. Sobolev, D. Bograchev, K. Borodianskiy, M. Zinigrad, Kinetics and mechanism of corrosion of oxide coating fabricated on aluminum alloy by the plasma electrolytic oxidation in molten salt, Corros. Sci. 208 (2022) 110604, https://doi.org/10.1016/j.corsci.2022.110604.
[51] Z. Xu, J.C. Wang, Z. Liang, H. Zhu, Z.H. Yang, Influence of Nb on the hot corrosion behaviors of a Fe–Cr–Ni heat-resistant steel weld metal in the Na_2SO_4–NaCl molten salt at 700 °C, Met. Mater. Int. 29 (2023) 3645–3654, https://doi.org/10.1007/s12540-023-01468-w.
[52] W.T. Wofford, E.F. Gloyna, Solubility of potassium hydroxide and potassium phosphate in supercritical water, J. Chem. Eng. Data 40 (1995) 968–973, https://doi.org/10.1021/je00020a052.
[53] S. Rong, L. Huang, R. Wang, J. Xu, Z. Peng, Y. Chen, H. Jin, L. Guo, Corrosion behaviors of Ni-based and Fe-based alloys in supercritical water gasification with inorganic chloride salt, Corros. Sci. 219 (2023) 111241, https://doi.org/10.1016/j.corsci.2023.111241.
[54] M. Zhu, H. Ma, M. Wang, Z. Wang, A. Sharif, Effects of cations on corrosion of Inconel 625 in molten chloride salts, High. Temp. Mater. Process. 35 (2016) 337–345, https://doi.org/10.1515/htmp-2014-0225.
[55] S. Zhang, H. Li, Z. Jiang, B. Zhang, Z. Li, J. Wu, H. Feng, H. Zhu, F. Duan, Chloride- and sulphate-induced hot corrosion mechanism of super austenitic stainless steel S31254 under dry gas environment, Corros. Sci. 163 (2020) 108295, https://doi.org/10.1016/j.corsci.2019.108295.
[56] A. Sehgal, B.G. Ateya, H.W. Pickering, Synergistic effects of chromium depletion and ohmic potential drop on the susceptibility to intergranular corrosion and hydrogen embrittlement of sensitized stainless steel, Acta Mater. 45 (1997) 3389–3399, https://doi.org/DOI:10.1016/S1359-6454(97)00001-3.
[57] C.J. Van Niekerk, M. Du Toit, M.W. Erwee, Sensitization of Aisi 409 ferritic stainless steel during low heat input arc welding, Weld. World 56 (2012) 54–64, https://doi.org/DOI:10.1007/BF03321350.
[58] S. Zhang, H. Li, Z. Jiang, B. Zhang, Z. Li, J. Wu, S. Fan, H. Feng, H. Zhu, Effects of Cr and Mo on precipitation behavior and associated intergranular corrosion susceptibility of superaustenitic stainless steel s32654, Mater. Charact. 152 (2019) 141–150, https://doi.org/10.1016/j.matchar.2019.04.010.
[59] J. Ma, S. Zhang, J. Ma, Y. Li, X. Liang, P. Han, An efficient strategy for enhancing the corrosion resistance of S31254 super austenitic stainless steel through slight Mo segregation, J. Mater. Res. Technol. 25 (2023) 647–656, https://doi.org/10.1016/j.jmrt.2023.05.264.
[60] J. Zhu, H. Kokawa, K. Feng, Z. Li, Unexpectedly high corrosion susceptibility near fusion boundaries of Inconel 625 manufactured by laser powder bed fusion, Corros. Sci. 223 (2023) 111432, https://doi.org/10.1016/j.corsci.2023.111432.
[61] T. Fujii, K. Sue, S. Kawasaki, Effect of pressure on corrosion of Inconel 625 in supercritical water up to 100 MPa with acids or oxygen, J. Supercrit. Fluids 95 (2014) 285–291, https://doi.org/10.1016/j.supflu.2014.09.017.
[62] K.I. Choudhry, D.A. Guzonas, D.T. Kallikragas, I.M. Svishchev, On-line monitoring of oxide formation and dissolution on Alloy 800H in supercritical water, Corros. Sci. 111 (2016) 574–582, https://doi.org/10.1016/j.corsci.2016.05.042.
[63] J.Q. Yang, S.Z. Wang, X.Y. Tang, Y.Z. Wang, Y.H. Li, Effect of low oxygen concentration on the oxidation behavior of Ni-based alloys 625 and 825 in supercritical water, J. Supercrit. Fluids 131 (2018) 1–10, https://doi.org/10.1016/j.supflu.2017.07.008.
[64] Y. Li, S. Wang, P. Sun, J. Yang, X. Tang, D. Xu, Y. Guo, J. Yang, D.D. Macdonald, Investigation on early formation and evolution of oxide scales on ferritic–martensitic steels in supercritical water, Corros. Sci. 135 (2018) 136–146, https://doi.org/10.1016/j.corsci.2018.02.036.

Marine Environmental Research 213 (2026) 107643



Contents lists available at ScienceDirect

Marine Environmental Research

journal homepage: www.elsevier.com/locate/marenvrev



Microplastic in tropical island estuaries in China: Source identification and management framework development

Bin Chen [a,b], Yang Zhou [c], Kazi Belayet Hossain [d], Yixin Chen [d], Xiaoshan Zhu [f], Hengxiang Li [g], Xiangrong Xu [h,*], Minggang Cai [c,d,e,**]

[a] Key Laboratory of Estuarine Ecological Security and Environmental Health, Education Department of Fujian, Tan Kah Kee College, Xiamen University, Zhangzhou, 363105, China
[b] Department of Environmental Science and Engineering, Tan Kah Kee College, Xiamen University, Zhangzhou, 363105, China
[c] College of the Environment & Ecology, Xiamen University, Xiamen, 361102, China
[d] College of the Ocean & Earth Science, Xiamen University, Xiamen, 361102, China
[e] State Key Laboratory of Marine Environmental Science, Xiamen University, Xiamen, 361102, China
[f] School of Ecology, Hainan University, Haikou, 570228, China
[g] South China Sea Institute of Oceanology, Chinese Academy of Sciences, Guangzhou, 510301, China
[h] Guangxi Laboratory on the Study of Coral Reefs in the South China Sea, Coral Reef Research Center of China, School of Marine Sciences, Guangxi University, Nanning, 530004, China

ARTICLE INFO

Keywords:
Microplastics
Estuary
Tropical region
Policy framework
Hainan island
South China Sea

ABSTRACT

This study investigates a comprehensive assessment of microplastic (MP) pollution in the contrasting estuarine systems of Hainan Island, China: the urbanized Nandu River Estuary and the less-developed Wanquan River Estuary. Analysis of surface water samples revealed an overall MP abundance ranging from 0.05 to 0.60 particles/m^3. A notable finding was the significantly higher concentration in the Wanquan Estuary (0.32 ± 0.13 particles/m^3) compared to the Nandu Estuary (0.17 ± 0.10 particles/m^3), suggesting that tourism and agricultural activities may be more significant contributors than urbanisation alone in this context. Morphologically, MPs were predominantly linear and fibrous, with white and blue being the most common colors, and a size distribution concentrated in the 500–2000 μm range. Polymer composition analysis identified Polyolefins, polyester, and polyethylene as dominant, with signatures pointing to distinct anthropogenic sources for each estuary: packaging, textiles, and fisheries for the Nandu, and agricultural films and tourism-related waste for the Wanquan. Statistical correlations indicated that water temperature and pH enhanced MP suspension, while turbidity facilitated sedimentation. Source apportionment via Principal Component Analysis and Multiple Linear Regression confirmed these links, highlighting tourism (wet wipes, textiles), fisheries (abandoned gear), and inadequate waste management as primary pathways. The relatively low abundances, compared to global estuaries, potentially reflect the positive impact of Hainan's stringent plastic bans. However, the persistence of specific polymers underscores the need for continued, targeted management strategies. This research establishes a critical baseline for MP pollution in tropical estuaries and offers valuable insights for policy-making aimed at mitigating marine plastic pollution.

1. Introduction

Microplastics (MPs), synthetic polymer particles <5 mm, are a pervasive environmental contaminant first formally identified in marine ecosystems by Thompson et al. (2004). These particles originate from diverse sources, categorized as primary, such as microbeads from personal care products and industrial pellets, and secondary, resulting from the fragmentation of larger plastic debris (Cole, 2016; Cai et al., 2018; Cai et al., 2022). The scale of the issue is monumental; global plastic production reached approximately 400.3 million metric tons in 2022 (Plastics Europe, 2023), with a disconcertingly low recycling rate, leading to significant environmental accumulation. MPs have been

* Corresponding author.
** Corresponding author. College of the Environment & Ecology, Xiamen University, Xiamen, 361102, China.
E-mail addresses: xuxr@gxu.edu.cn (X. Xu), mgcai@xmu.edu.cn (M. Cai).

https://doi.org/10.1016/j.marenvres.2025.107643
Received 15 August 2025; Received in revised form 27 September 2025; Accepted 20 October 2025
Available online 21 October 2025
0141-1136/© 2025 Elsevier Ltd. All rights are reserved, including those for text and data mining, AI training, and similar technologies.

detected in virtually every ecosystem on Earth, from the deepest ocean trenches to remote mountain air (Huang et al., 2021; Trainic et al., 2020), and have even been documented in human tissues, raising substantial public health concerns (Leslie et al., 2022). Their persistence, capacity for long-range transport, and ability to adsorb and concentrate toxic pollutants have led to comparisons with other persistent organic pollutants (Ahmed et al., 2022; Rochman et al., 2013; Wang et al., 2024).

The environmental and biological impacts of MPs are profound. In marine environments, they pose a direct threat to biota through ingestion and entanglement, leading to physical harm, oxidative stress, and potential trophic transfer through food webs (Chen et al., 2025; Wright et al., 2013; Pegado et al., 2018). Furthermore, they can alter sediment properties and disrupt microbial communities essential for ecosystem functioning (Malla-Pradhan et al., 2022). The discovery of airborne MPs has expanded concerns to include potential respiratory risks for both humans and terrestrial animals (Qi et al., 2022). With estimates suggesting that 75 to 199 million tons of plastic are currently in the ocean and inputs could nearly triple by 2040 without urgent action (UNEP, 2021), MPs represent a critical threat to global biodiversity, ecosystem services, and food security.

Rivers are recognized as major pathways for transporting land-based plastics to the oceans, contributing over 80 % of marine plastic pollution (Lebreton et al., 2017). Estuaries, the dynamic transition zones between rivers and seas, act as temporary sinks and hotspots for MP accumulation. While significant research has focused on large temperate river systems like the Yangtze and Pearl River estuaries in China (Zhao et al., 2014; Mai et al., 2019), tropical estuaries, particularly those surrounding islands, remain critically understudied (Xia et al., 2021; Wang et al., 2023). These systems are often characterized by unique hydrological regimes, high biodiversity, and economies heavily reliant on tourism and fisheries, making them vulnerable to MP pollution.

Hainan Island, China's largest tropical island, exemplifies this research gap. Its two principal river systems, the Nandu River and the Wanquan River, drain distinct landscapes and empty into estuaries with contrasting anthropogenic pressures. The Nandu River Estuary, located on the northern coast near the urban center of Haikou, is influenced by urbanization, port activities, and dense population. In contrast, the Wanquan River Estuary on the eastern coast is renowned for its scenic beauty near Bo'ao, a site of international conferences, but faces growing pressures from tourism and agricultural runoff. Understanding MP pollution in these contrasting tropical estuaries is essential for developing targeted mitigation strategies.

Therefore, this study aims to investigate the abundance, distribution, and characteristics of MPs in the Nandu and Wanquan River Estuaries of Hainan Island. The specific objectives are to: (1) quantify and compare the spatial distribution of MP abundance between the two estuaries; (2) characterize the physical (size, shape, color) and chemical (polymer type) properties of the collected MPs; (3) identify potential pollution sources through correlation with environmental factors and statistical source apportionment; and (4) discuss the findings in the context of local plastic waste management policies. The results will provide a crucial baseline for MP pollution in tropical island estuaries and inform effective conservation and policy measures for these vulnerable ecosystems.

2. Materials and methods

2.1. Study area

This study analyzed water samples from the two principal river systems of Hainan Island: the Nandu River Estuary and the Wanquan River Estuary. The Nandu River, the island's longest, drains a large basin, and its estuary on the northern coast discharges into the Qiongzhou Strait. This area is characterized by a highly urbanized environment surrounding Haikou, the provincial capital. In contrast, the Wanquan River Estuary is located on the eastern coast and flows into the South China Sea. It is renowned for a scenic, less-developed landscape near Bo'ao, where a distinctive sandbar forms a "jade belt." Sampling was conducted across 12 stations in the Nandu River Estuary and 13 in the Wanquan River Estuary during April 2023 to compare the geophysically influenced water quality of these distinct systems (Fig. 1).

2.2. Sample collection

In this study, Manta trawl nets were used to collect MPs in surface water. The network ports were 1m in length and 0.5 m in width. Hollow stainless steel structures on both sides enabled the net frame to float on the water surface. The mesh length is 4 m, the aperture is 330 μm, and the bottom connects to a stainless steel mesh tube. The volume of filtered water is calculated using a network port flow meter. Trawl collection will be carried out in sea conditions below Level 3, trawling on the left side of the ship at a speed of 1.5 knots (2.78 km/h) for 15 min. After trawling, the samples were washed from the outside to the bottom tube, collected in a 500 mL brown wide-mouth glass bottle, and brought back to the laboratory for storage at 4 °C for further analysis.

2.3. Sample pretreatment

First, the sample in the brown wide-mouth glass bottle is washed onto a 5 mm metal mesh screen for filtration, discarding any large debris trapped in the screen. Rinse the filtered sample again to a metal mesh screen of 330 μm, rinse the screen with appropriate amount of pure water, transfer all the trapped substances on the screen to a 1 L beaker, cover the beaker mouth with aluminum foil, leave a small mouth for easy drying, and place the beaker in the oven at 65 °C to dry. After drying, add 30 ml 0.05 mol/L Divalent iron solution and 30 ml 30 % hydrogen peroxide solution to the beakers to dissolve organic matter, seal the beakers with aluminum foil and leave for about 10 min. If the reaction is very violent, immediately place it in a cold bath. If the organic matter can still be observed, continue to add an appropriate amount of 30 % hydrogen peroxide solution until the organic matter is completely dissolved. Then, let the reaction stand for 24 h 7 g sodium chloride is added to the above mixed solution every 20 ml, and the sodium chloride is stirred to completely dissolve in the mixed solution to form a saturated sodium chloride solution with a density of 1.2 g/cm^3. The mixed solution after dissolved sodium chloride is left to stand for 24 h for flotation to obtain a microplastic suspension. A vacuum pump and a sand core device were used to filter the suspension of the flotation solution onto a nylon membrane (20 μm; 47 mm), using pure water to rinse the beaker and sand core device several times, so that the sample is completely transferred to the filter membrane. Remove the filter film and place it in a clean glass dish. Dry it in an oven at 50 °C for 24 h.

2.4. Visual examination and identification

The nylon membrane (Aperture: 20 μm, diameter 47 mm, Millipore) is placed under a microscope(Leica,DM750,Germany), using the Z-shape method, a photograph is taken from the top left corner of the membrane to record the size, shape and color of all suspicious microplastic particles until the entire membrane is completely covered. Samples of MPs are identified by Fourier Transform micro infrared spectrometer (Thermo Fisher Scientific Nicolet iN10, U.S.A.), using an Auto IMAGE-microscope attached to a PerkinElmer Spectrum GX spectrometer equipped with a nitrogen-cooled Mercury cadmium telluride detector and processed by MONIC™ Picta™ software and compared with the OMNIC polymer reference spectra library (Hossain et al., 2023). The spectral detector range was 7600–450 cm^{-1}, with 16 scans at a resolution of 4 cm^{-1} (Detector DTGS). The samples are only identified as MPs if they match more than 70 % of the plastic components in the database. Less than 70 % of the samples are excluded.

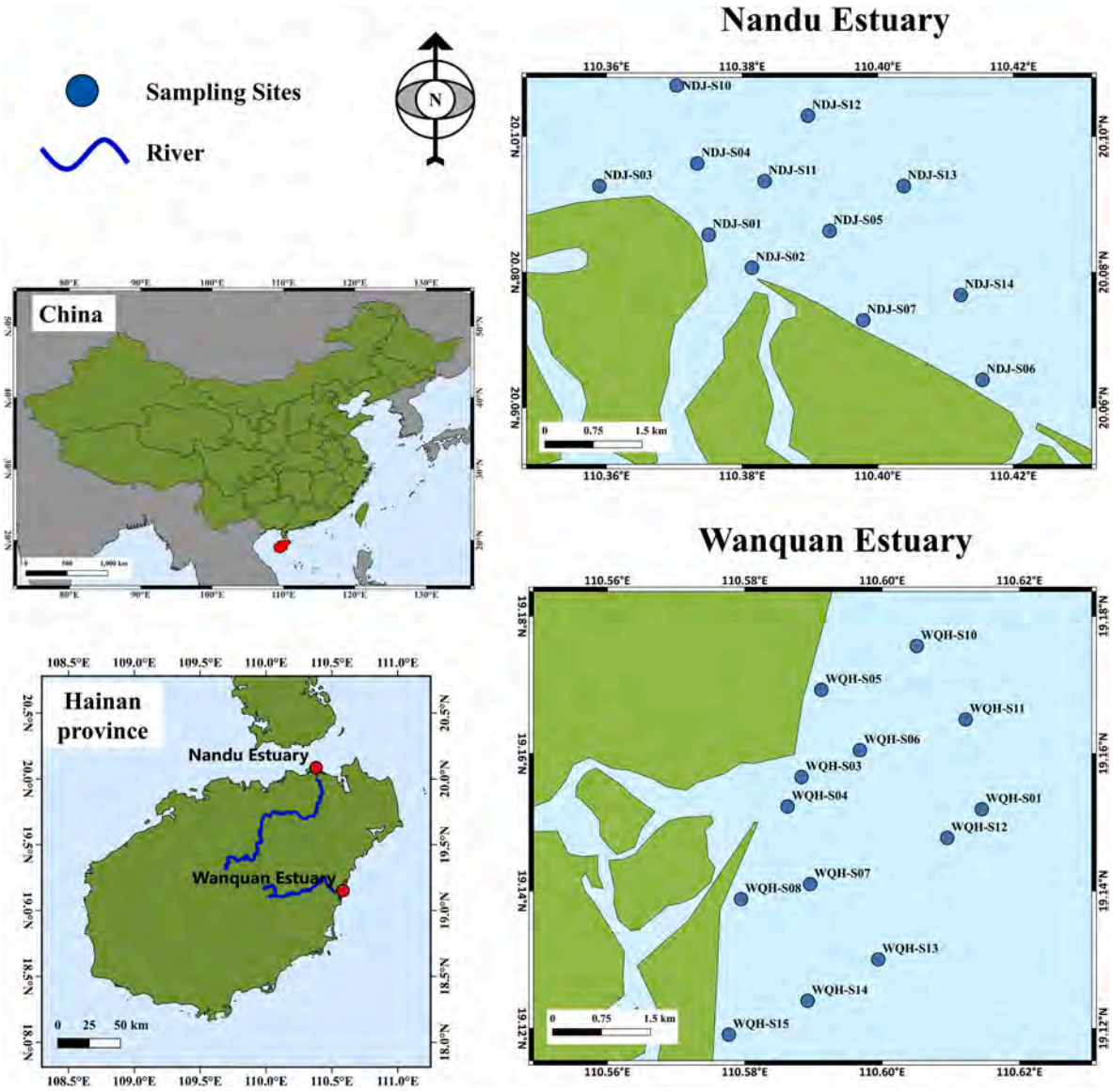


Fig. 1. Sampling stations at the Estuaries of Nandu Estuary and Wanquan Estuary (a) The location of Hainan Island in China; (b) The locations of Nandu Estuary and Wanquan Estuary on Hainan Island; (c) Sampling station at the estuary of Nandu Estuary; (d) Sampling station at the estuary of Wanquan Estuary.

2.5. Quality assurance and quality control

To ensure data accuracy, comprehensive contamination control measures were implemented throughout the study. The laboratory was maintained under semi-closed conditions with restricted airflow to minimize airborne microplastic deposition. All glassware and equipment including beakers, filtration units, and sampling tools were meticulously rinsed three times with ultrapure water to eliminate residual plastics. During sample processing, containers were sealed with acid washed aluminum foil to prevent external particulate contamination.

Researchers wore 100 % cotton lab coats and nitrile gloves to avoid synthetic fiber shedding. A multi-tiered blank control system was employed: (1) field blanks accompanied each sampling campaign, (2) laboratory blanks using ultrapure water replicated analytical procedures, and (3) process blanks were integrated into every 10-sample batch. The average blank contamination (8 ± 3 particles/sample) was subtracted from raw data, representing <5 % of the lowest sample concentrations, ensuring minimal interference.

Additional quality checks included microscopic inspection of blank filters and polymer characterization of contaminant particles to trace and mitigate contamination sources. These protocols adhered to standardized microplastic research guidelines, ensuring methodological consistency and data reliability. By systematically addressing potential contamination pathways from airborne fibers to reagent impurities this study maintains high confidence in reported microplastic abundances, supporting robust environmental assessments. Such rigorous controls are critical for accurate microplastic monitoring, particularly in regions with low ambient microplastic levels.

2.6. Data analysis

The MPs abundance (C, particles/m^3) in surface water is calculated as follows:

$$C = n/v \times t \times w \times h$$

In the formula, C is the abundance of MPs, expressed in (particles/m^3); n is the quantity of MPs, expressed in (particles); v is the drag speed of manta net on the surface of water, expressed in (m/s); t is the drag time of manta net on the surface of water, expressed in (s); w indicates the

width of the manta network port (m), and h indicates the height of the manta network port (m). The abundance of MPs was shown in the form of "Abundance ± Standard deviation particles/m^3".

Microsoft Excel 2019 was used for data analysis, and SPSS 25.0.0 was used for statistical analysis, with $p < 0.05$ indicating statistical significance. Origin 2023b and R 4.2.1 were used to draw the diagram, and Surfer 20 and ArcMap 10.7 were used to draw the sampling station map.

2.7. Potential sources analysis of microplastics

To investigate the potential sources of microplastics in the Nandu and Wanquan Estuaries, separately, Principal Component Analysis (PCA) was performed on polymer composition data. The optimal number of principal components (PCs) was determined using two established criteria: (1) the Kaiser criterion (retaining PCs with eigenvalues >1) and (2) cumulative variance explanation (selecting the minimum number of PCs required to explain ≥80 % of total variance). The more conservative estimate (higher number of PCs) from these two methods was adopted for subsequent analysis (Zhu et al., 2023).

Afterward, multiple linear regression (MLR) was applied to assess the relationship between microplastic abundance and the retained PC scores. Only PCs demonstrating statistically significant associations ($p < 0.05$) were considered for further interpretation (Zhang et al., 2022). To identify the most relevant polymers within these significant PCs, we applied a loading threshold of |0.5|, ensuring that only contributing polymers were included (Peng et al., 2022).

This integrated analytical approach combining PCA dimensionality reduction, MLR-based significance testing, and loading threshold filtering revealed key polymer markers, including polyethylene (PE), polypropylene (PP), polystyrene (PS), polyethylene terephthalate (PET), and polyvinyl chloride (PVC). Each polymer type was linked to specific anthropogenic sources and environmental pathways. All analyses were conducted using R version 4.2.1.

3. Results and discussions

3.1. MPs abundance and spatial distribution

3.1.1. Temporal trends of MPs

This study detected a total of 2115.80 MP particles across all samples, with abundances ranging from 0.05 to 0.60 particles/m^3 (mean: 0.24 ± 0.14 particles/m^3). The Nandu Estuary showed lower abundances (0.05–0.35 particles/m^3, mean: 0.17 ± 0.10 particles/m^3) compared to Wanquan Estuary (0.17–0.60 particles/m^3, mean: 0.32 ± 0.13 particles/m^3) (Table S2). These findings align with historical data from the Hainan Ecological Environment Monitoring Center, which reported means of 0.42–0.53 particles/m^3 between 2021 and 2022 (Department of Ecology and Environment of Hainan Province, 2022, 2023), and according to a previous study the MPs levels in three major rivers in Hainan province were 0.42–0.44 particles/m^3 (Xie et al., 2023). While methodological differences exist, the consistent order of magnitude suggests stable MP pollution levels in recent years, potentially reflecting the efficacy of Hainan's plastic bans. Notably, our April 2023 data show lower abundances than previous years, possibly indicating seasonal variations or declining trends in MP abundance.

3.1.2. Comparative abundance level of MPs

To assess the Microplastic levels in Nandu Estuary and Wanquan Estuary estuaries, the results of other studies using trawl sampling can be compared with our data. The abundance of MPs in two estuaries was studied lower than the Bohai Sea (0.74 particles/m^3), the Yellow Sea (0.54 particles/m^3) slightly higher than the East China Sea (0.22 particles/m^3) and close to the northern South China Sea (0.29 particles/m^3) (Ministry of Ecology and Environment of the People's Republic of China, 2022). Compared with some major bays and estuaries in China, Including Laizhou Bay(1.70 ± 1.50 particles/m^3)(Teng et al., 2020), Hangzhou Bay (0.14 ± 0.12 particles/m^3) (Wang et al., 2020), Xiangshan Bay (8.90 ± 4.70 particles/m^3) (Chen et al., 2018), Xiamen Bay (514 ± 520 particles/m^3) (Tang et al., 2018), Haikou Bay (0.44 ± 0.21 particles/m^3) (Qi et al., 2020), Yangtze Estuary (0.167 ± 0.138 particles/m^3) (Zhao et al., 2014), Pearl River Delta (0.005–0.7 particles/m^3) (Mai et al., 2019), The abundance of MPs in this study was at a low to medium level (Table S1).

Compared with other international research, Our abundance data is much lower than Offshore Japan (3.74 ± 10.40 particles/m^3) (Isobe et al., 2015), Nakdong River Estuary in the Southeastern Sea of Korea (0.62–57 particles/m^3) (Kang et al., 2015), South San Francisco Bay, USA (7.25 particles/m^3) (Sutton et al., 2016). Due to differences between different research methods (sample collection, processing, and analysis), there are significant differences in microplastic abundance levels even within the same study area. This study mainly focuses on the large particle size microplastic particles obtained by trawl sampling method, which has a certain comparability with the above domestic and foreign studies. In general, the level of Microplastic in Wanquan Estuary and Nandu Estuary is low in both international and domestic estuaries and offshore environments.

3.1.3. Spatial distribution patterns

Spatial analysis revealed distinct distribution patterns between estuaries (Fig. 2). In the Nandu Estuary, MP abundance generally decreased with offshore distance, though peaks occurred at mid-distance stations (NDJ-S03, NDJ-S14). This anomaly may stem from tidal dynamics and estuarine frontal systems that trap MPs offshore (Wang et al., 2022). Conversely, the Wanquan Estuary exhibited uniform spatial distribution, with minimal variation among stations. This homogeneity likely reflects the combined influence of the southeast monsoon and coastal currents during the April sampling period, which may promote broader dispersion of MPs throughout the estuary.

3.1.4. Comparative assessment and implications

When compared with Xie et al. (2023)'s data, our study recorded lower maximum abundances at both estuaries, particularly in the Nandu Estuary. This discrepancy may arise from: (1) seasonal differences (November vs. April sampling), (2) methodological variations in sampling/analysis, or (3) actual declines in MP pollution due to policy interventions. The consistent finding of higher MP loads in Wanquan Estuary across studies suggests persistent pollution sources, possibly linked to its tourism-driven economy. These spatial-temporal patterns highlight the need for standardized monitoring protocols and targeted management strategies based on estuary-specific hydrodynamic and anthropogenic factors.

3.2. Morphological characteristics of MPs

3.2.1. Shape and color of MPs

Microplastics (MPs) in the Nandu and Wanquan Estuary estuaries exhibited six distinct morphological types: line, fiber, fragment, film, pellet, and foam. Linear MPs dominated both estuaries (Nandu: 59.6 %; Wanquan: 49.0 %), followed by fibrous forms (Nandu: 19.9 %; Wanquan: 27.1 %). Fragmentary MPs accounted for 12.8 % and 13.8 % in Nandu and Wanquan Estuaries, respectively, displaying characteristic surface weathering features that enhance their potential for toxicant adsorption (Naqash et al., 2020). The predominance of fibrous/linear morphologies aligns with national studies, suggesting origins from municipal wastewater, textile degradation, and fisheries operations (Wang et al., 2019). Comparative data from Chinese coastal systems show similar patterns: Laizhou Bay (96.08 % fibers; Teng et al., 2020), Yellow Sea (75.4 % fibers; Sun et al., 2018), and Haikou Bay (83.12 % fibers; Qi et al., 2020). Film MPs (Nandu: 5.0 %; Wanquan: 7.0 %) likely derived from packaging materials and agricultural mulch (Yang et al., 2022), while foam particles (1.9–2.4 %) reflected insulation and aquaculture applications (Zhang et al., 2021). It is noted that 'line' and 'fiber'

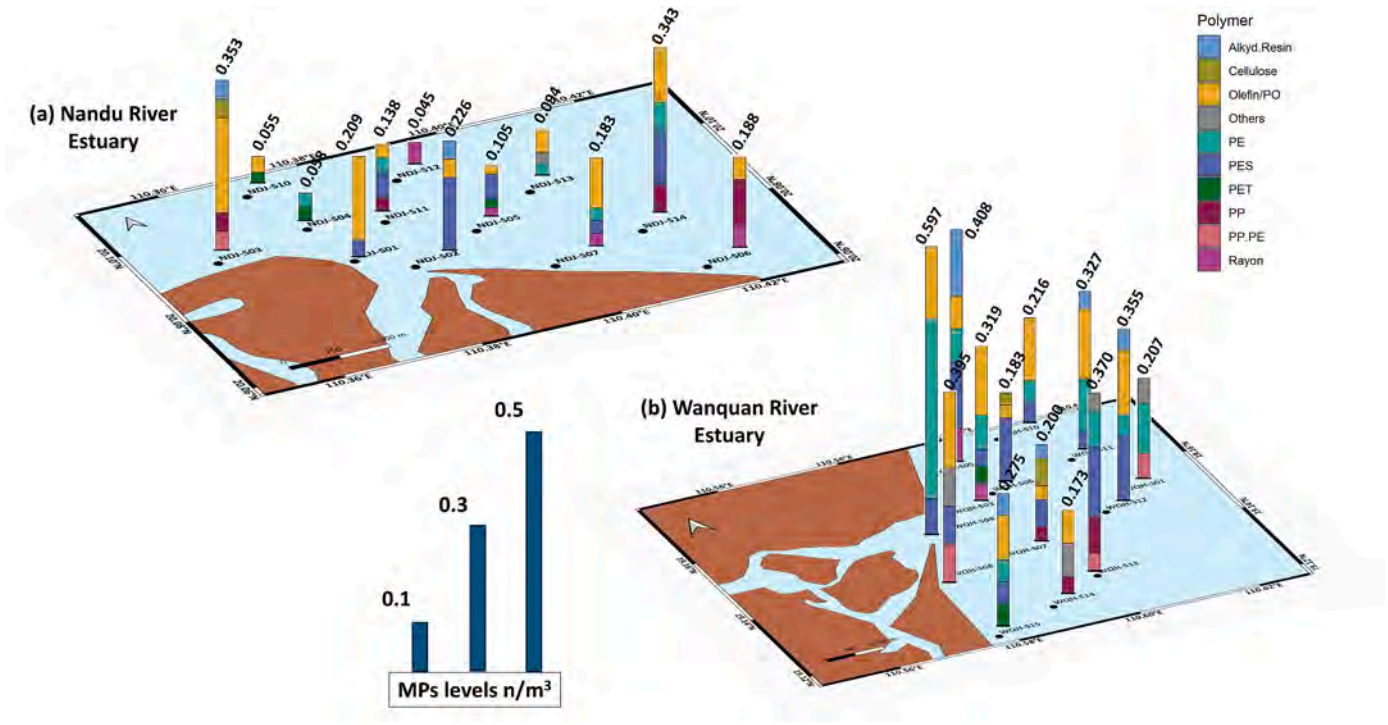


Fig. 2. Abundance and distribution of MPs at the Estuaries of (a) Nandu Estuary and (b) Wanquan Estuary.

are distinguished as separate categories in this study, where 'line' refers to rigid, brittle filaments often from fishing gear, and 'fiber' denotes flexible, thread-like particles typically from textiles (Peng et al., 2022; Wu et al., 2021).

Color analysis revealed white as the predominant hue (Nandu: 37.1 %; Wanquan: 41.6 %), with blue (24.9 %, 21.3 %) and transparent (13.0 %, 21.3 %) as secondary colors. The chromatic distribution reflects both production patterns of consumer plastics (Li et al., 2018) and environmental weathering processes (Zhao et al., 2022). Notably, Wanquan Estuary showed higher transparent MPs, potentially indicating different pollution sources. Blue MPs were associated with marine activities, particularly fishing gear degradation (Kasamesiri et al., 2021), while the prevalence of light-colored particles corresponds to disposable product fragmentation in coastal environments.

3.2.2. Size of MPs

In this study, the particle size range of MPs detected was 330 μm–5000 μm, and the particle size range of MPs in the Nandu Estuary and Wanquan Estuary was mainly 500–1000 μm and 1000–2000 μm (Fig. 3). The contribution of MPs in different particle sizes was similar between the two estuaries, with 330–500 μm (8.9 %), 500–1000 μm (31.6 %), 1000–2000 μm (39.7 %) and 2000–5000 μm (19.8 %) in Nandu Estuary. At the mouth of Wanquan Estuary, the detected MPs were 330–500 μm (10.2 %), 500–1000 μm (33.4 %), 1000–2000 μm (37.2 %), and 2000–5000 μm (19.2 %). Due to the characteristics of the sampling method, this study ignored MPs below 330 μm, but within the range above 330 μm, large particle size MPs dominated the two estuaries, which may be due to the proximity of the study area to the source of plastic. MPs undergo the breaking process for a short time.

3.2.3. Composition of MPs

Micro-FTIR spectroscopy identified eleven polymer types, with PolyOlefins (Olefin/PO: Nandu 40.0 %, Wanquan 27.9 %), polyester (PES: 21.7 %, 22.5 %), and polyethylene (PE: Wanquan 22.8 %) as dominant components. The Nandu Estuary's industrial character was reflected in higher PP (10.9 %) and Olefin/PO loads, associated with packaging and manufacturing sectors (Ramasamy and Subramanian, 2023). Wanquan's agricultural influence manifested in elevated PE from plastic mulch degradation (Piehl et al., 2018). Textile derived PES represented significant proportions in both systems, underscoring laundry wastewater contributions.

Notable secondary components included PET (beverage containers), alkyd resins (marine coatings), and cellulose-based fibers. The polymer signatures distinguish the estuaries' anthropogenic profiles: Nandu's urban-industrial inputs versus Wanquan's agro-tourism sources. This compositional analysis provides critical baseline data for source apportionment and highlights the need for sector-specific mitigation strategies in tropical estuarine systems.

3.3. Correlation analysis between MPs and water physicochemical factors

Pearson correlation analysis revealed significant relationships between microplastic (MP) abundance and key water quality parameters, with underlying mechanisms likely driven by the unique hydrodynamics of tropical estuaries. The positive correlation with temperature ($R = 0.56$, $p < 0.01$) may be attributed to reduced water viscosity in warmer conditions, which decreases settling velocity (Luo et al., 2022) and enhances MP suspension in the water column (Al-Zawaidah et al., 2023). Concurrently, the positive correlation with pH ($R = 0.66$, $p < 0.001$) suggests that more alkaline conditions alter the dissociation state of surface functional groups on MPs and natural particles, increasing negative surface charges and enhancing electrostatic repulsion (Oriekhova and Stoll, 2018). This reduces MP adsorption to suspended sediments, counteracting sedimentation (Soler et al., 2025). Conversely, the negative correlation with turbidity ($R = -0.44$, $p < 0.01$) indicates that high sediment loads provide abundant sites for MP adsorption and aggregation, promoting settlement despite the conditions that favor suspension (Ding et al., 2025). These findings highlight a complex interplay where monsoon-driven hydrological changes in tropical systems like Hainan's estuaries critically control MP fate by modulating these competing mechanisms, with direct implications for seasonal monitoring and mitigation (Fig. 4).

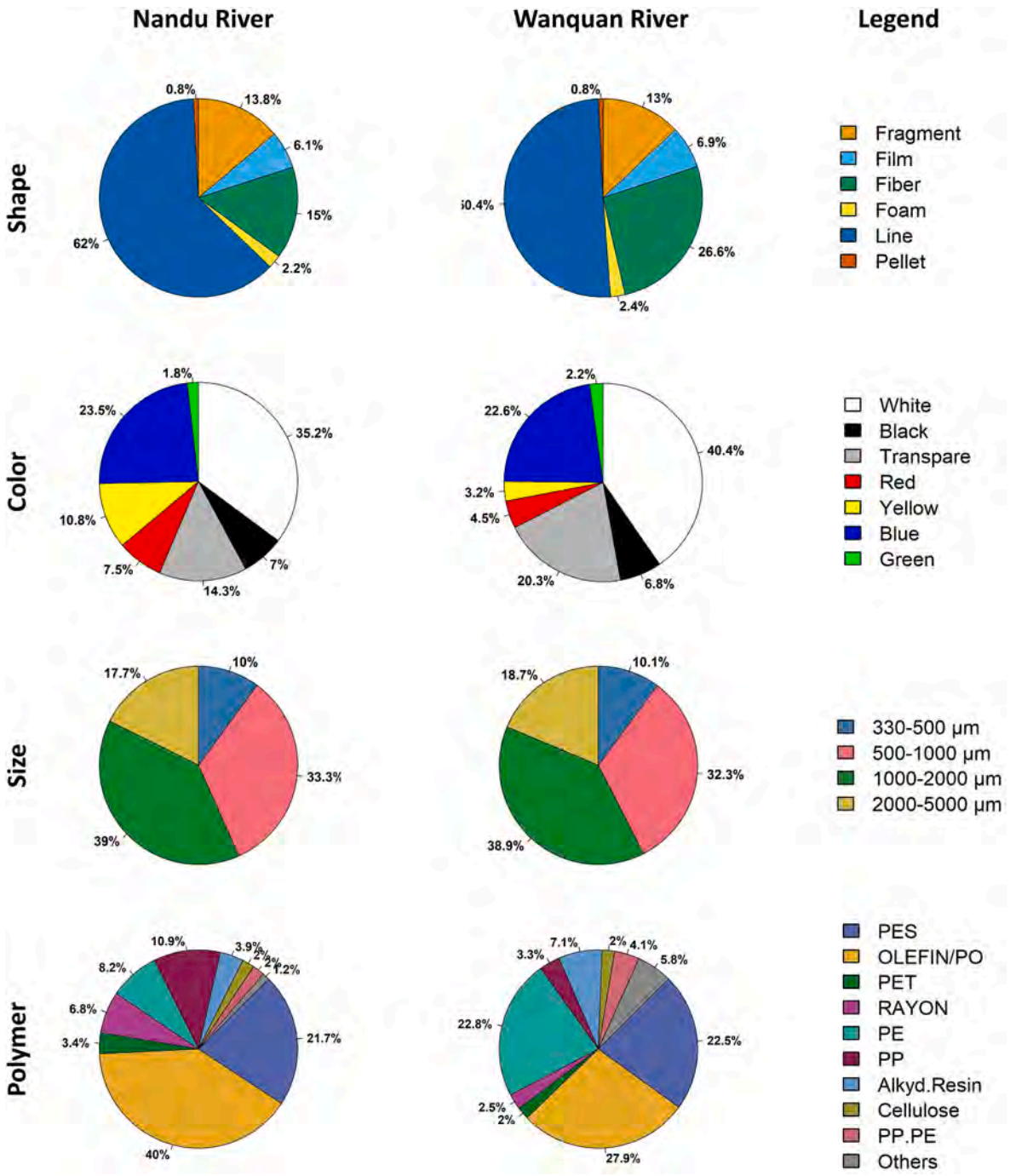


Fig. 3. Characteristics of MPs at the estuaries of the Nandu Estuary and the Wanquan Estuary.

3.4. Potential sources of MPs in Nandu and Wanquan Estuary

3.4.1. Source apportionment of MPs

Principal Component Analysis (PCA) was performed on the polymer composition data from the Nandu and Wanquan Estuaries to identify the key sources of microplastics. Initially, 10 principal components (PCs) were extracted for both the Nandu Estuary and the Wanquan Estuary. The optimal number of PCs was determined using the Kaiser criterion (eigenvalues >1) and cumulative variance explanation (≥80 % of total variance). The more conservative estimate yielded 5 PCs for both rivers (Table S4).

Then, multiple linear regression (MLR) was conducted to assess the relationship between microplastic abundance and the retained PC scores. For the Nandu Estuary, PC-1, PC-2, and PC-3 exhibited statistically significant associations ($p < 0.05$). In the Wanquan Estuary, significant associations were observed for PC-1 and PC-4 ($p < 0.05$) (Table S5).

3.4.2. Dominant sources of MPs in the Nandu and Wanquan Estuary

The Nandu Estuary has multiple sources of microplastics, according to the analysis of polymer loadings (|>0.5|). The high association (Table 1) between cellulose (PC-1: 0.515) and textile and paper pollution suggests that laundry discharges, wet wipes used by tourists, and agricultural runoff are the main causes. The abundance of cellulose-based MPs may be a result of inadvertent waste disposal from hotels, resorts, and leisure activities, given Hainan's reliance on tourism.

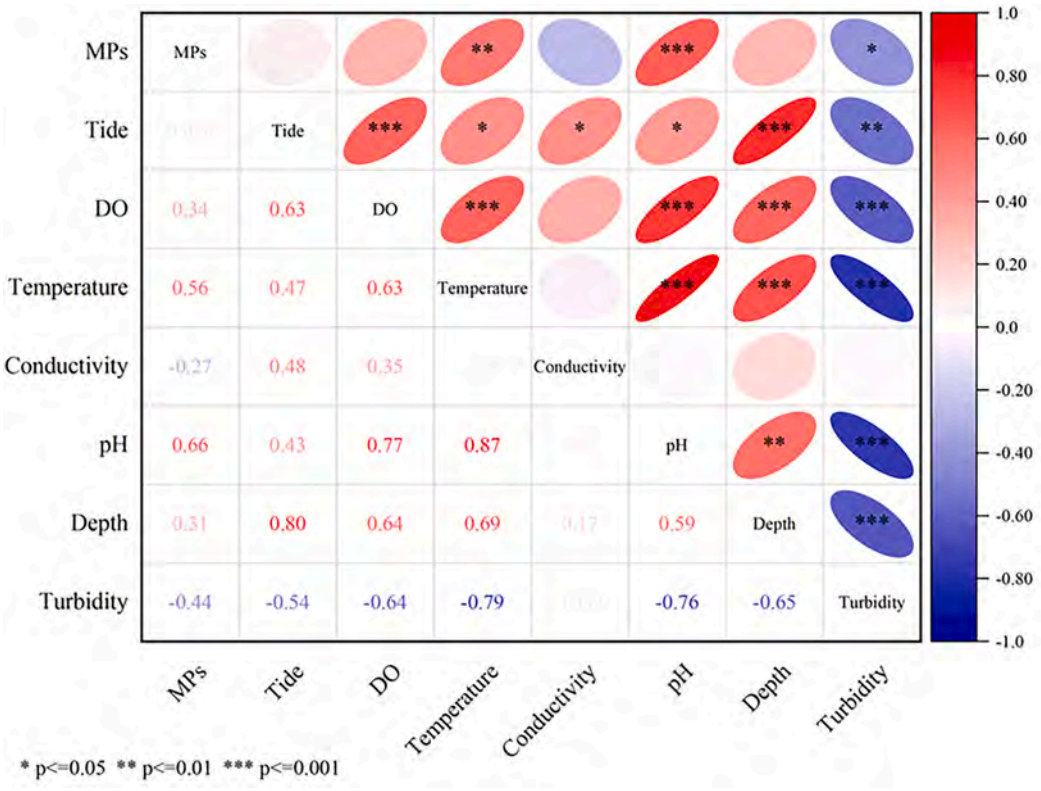


Fig. 4. Correlation between microplastic abundance and physical and chemical properties of water bodies.

Table 1
PCA loading of different polymers grouped by Nandu and Wanquan Estuary.

	Nandu Estuary			Wanquan Estuary	
	PC1	PC2	PC3	PC1	PC4
PES	0.004228	**0.585942**	0.192163	0.168593	−0.47326
Olefin/PO	0.415845	0.144919	0.133567	0.366414	−0.25168
PET	−0.20628	−0.13224	−0.24244	0.228853	**0.504849**
Rayon	−0.12753	−0.35416	0.424414	0.443868	0.124967
PE	−0.13425	0.483897	0.214331	**0.516657**	−0.43999
PP	0.149745	−0.11411	**0.598178**	−0.31949	−0.18863
Alkyd.Resin	0.43542	0.134348	−0.13171	0.44728	0.101022
Cellulose	**0.515782**	−0.12354	−0.1244	−0.16995	0.31124
PP.PE	0.315782	−0.12354	−0.1244	−0.35884	−0.22299
Others	−0.07833	0.123838	−0.13717	−0.33843	0.237106

Likewise, the significance of synthetic textiles is highlighted by the significant loading of polyester (PES, PC-2: 0.586), which is probably caused by laundry effluents. The significant presence of polypropylene (PP, PC-3: 0.598) further implicates packaging debris and industrial nurdle spills, abandoned fishing gear, suggesting urban runoff, fishery operations and waste management as major pathways (Zhang et al., 2022; Zhu et al., 2023).

In contrast, the Wanquan Estuary showed a stronger influence from polyethylene (PE, PC-1: 0.517), mainly linked to plastic bags and films from industrial pellet losses and stormwater runoff. The high loading of polyethylene terephthalate (PET, PC-4: 0.505) indicates contributions from beverage containers and food packaging, likely exacerbated by tourism-related litter (e.g., single-use bottles) and laundry derived synthetic fibers (Fig. 5). These findings align with global studies identifying urbanization, poor waste management, and tourism as dominant MP sources in estuarine systems (Li et al., 2021; Wang et al., 2022).

3.5. Policy implications and comparative assessment of microplastic sources

3.5.1. Policy effectiveness and remaining challenges

Hainan's progressive plastic control measures, initiated with the 2016 amendment of the "Hainan Provincial Marine Environmental Protection Regulations" (Standing Committee of Hainan Provincial People's Congress, 2016) and intensified through the 2019 ban on non-degradable plastics, have achieved 78–80 % adoption of alternatives by 2023 (General Office of Hainan Provincial Government, 2024), completely prohibiting the production, sale, and use of non-degradable single-use plastic products. This is more thorough than the "plastic restriction" policies in most other provinces (such as partial restrictions in Guangdong and Shanghai). The 2021–2023 monitoring program across key bays in Hainan, including Sanya Bay and Haikou Bay, documented dramatic declines in floating litter (83.2 %) and seabed litter (81.7 %). These figures strongly validate the effectiveness of Hainan's comprehensive plastic ban policy. However, to objectively assess the policy's impact, it is crucial to consider other contributing factors that create a

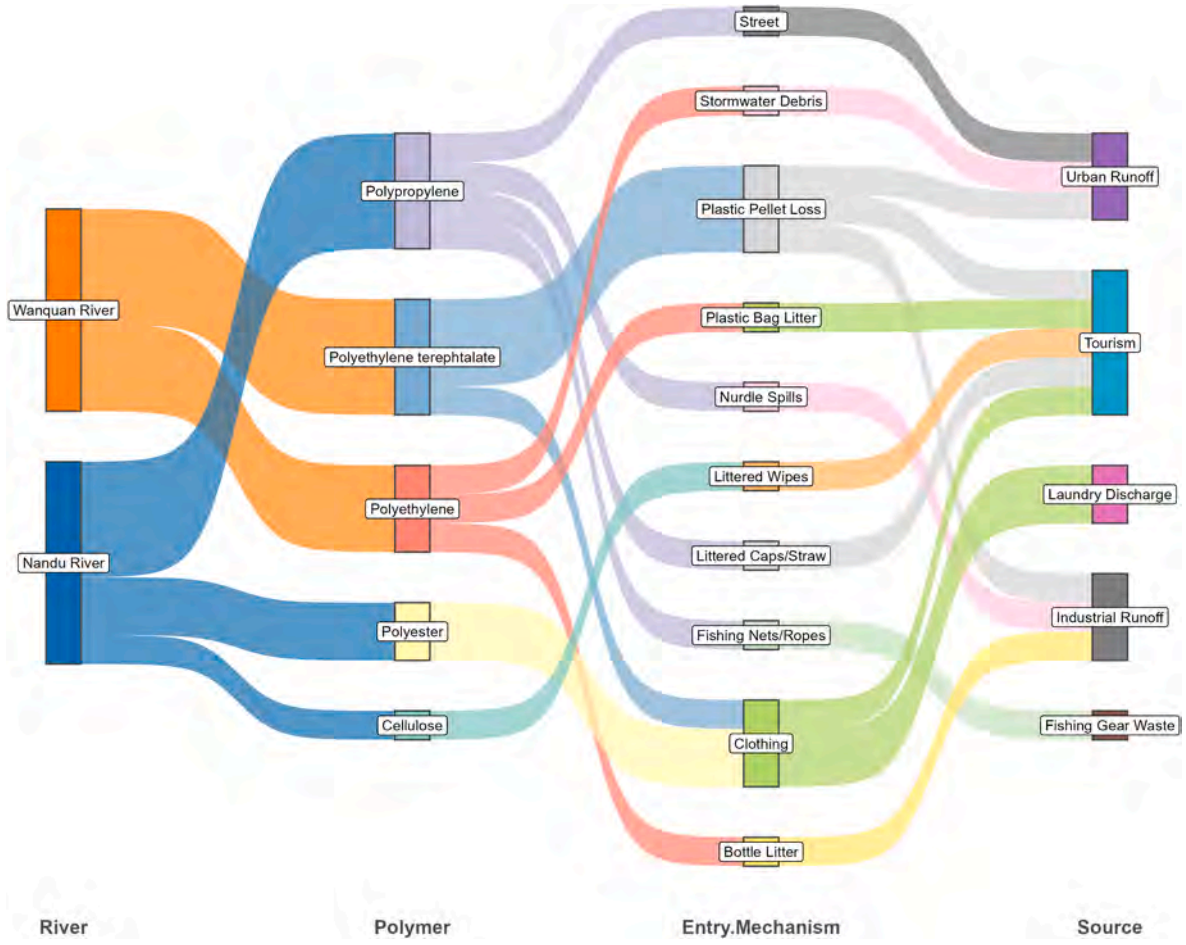


Fig. 5. Microplastics sources in Nandu and Wanquan Estuary.

favorable baseline for pollution control on the island.

Several inherent conditions differentiate Hainan from more densely populated and industrialized mainland provinces. Firstly, Hainan's population density is significantly lower than that of major coastal economic centers like Shanghai and Guangdong, implying less pressure from per capita plastic consumption and waste generation. Secondly, its economy is dominated by tourism and agriculture, lacking the large-scale manufacturing sectors that are significant sources of primary microplastic pollution elsewhere. Geographically, Hainan's isolation as an island and the hydrological barrier of the Qiongzhou Strait, combined with strict transport controls, drastically reduce the cross-border influx of plastic waste from the mainland. Furthermore, the island's rivers, characterized by fast flow rates and high seasonal runoff, may facilitate the transport of pollutants to the open ocean rather than allowing them to accumulate in estuaries.

Despite these advantageous pre-existing conditions, the stringency and systematic nature of Hainan's policy itself remain a critical factor. The province has established a comprehensive institutional framework, including local regulations, negative lists, traceability management platforms, and support for alternative industries, creating a closed-loop management system across the entire plastic lifecycle. The strictness and extensive coverage of this governance system surpass the measures in place in many mainland provinces, solidifying its role as a decisive factor in achieving the observed significant reduction in marine plastic litter. However, persistent detection of PES, PP, and PET reveals three unresolved pathways (Table S6):

1. **Tourism & Hospitality:** Despite the 2022 "Third Batch Catalog" banning non-woven bags containing PE/PP/PET (Hainan Ecology and Environment Department, 2022), high-traffic zones such as Sanya still need to strengthen the source control of wet wipes and beverage containers.
2. **Fisheries & Aquaculture:** The 2022–2024 Nandu Estuary fishing ban enforcement (Hainan Provincial Department of Ecology and Environment, 2024; 2024) has not fully addressed abandoned gear (PES/PP), highlighting the need for gear-marking systems (as Norway implements) and expanded biodegradable alternatives (current capacity: 40,400 tons of films/bags).
3. **Urban/Industrial:** Qionghai's 2022–2025 marine restoration projects (Qionghai Government, 2025) improved habitats.In this period 2023 Qiongzhou Strait transport bans enhanced the filtration system and strictly prevented the input and leakage of PE/PP particulate materials into the island (*Hainan Provincial Government, 2023*; Hainan Government, 2023).

3.5.2. *Comparative analysis with global estuarine systems*

Hainan's strict 2019 plastic ban is probably the reason why the Nandu-Wanquan system in Hainan has much lower microplastic concentrations than other heavily polluted estuaries, such as the Pearl River Delta (0.005–0.7 particles/m^3; Mai et al., 2019) and the Yangtze Estuary (0.167 ± 0.138 particles/m^3; Zhao et al., 2014). Three key interventions emerge from global best practices:

1. **Textile Controls:** Adopting the EU's washing machine filter mandate (EU Commission, 2022) could address persistent polyester (PES) microfibers, complementing Hainan's existing 2022 textile restrictions (Hainan Provincial Department of Ecology and Environment, 2022).

2. **Fisheries Management:** Implementing Norway's Extended Producer Responsibility schemes (MCEN, 2021) for fishing gear would enhance the ecological benefits of Haikou's 2021 Longtang Dam Hub renovations (The People's Government of Haikou, 2021).
3. **Tourism Governance**: Integrating Bali's awareness-penalty system (Bali Provincial Government, 2023) aligns with Hainan Provincial Department of Ecology and Environment, 2022 tourism-focused regulations (Article 6) to reduce single-use plastic litter (Standing Committee of Hainan Provincial People's Congress, 2024).

These strategic comparisons demonstrate that while Hainan's policies have reduced MP loads below heavily industrialized estuaries, targeted adoption of international best practices could further improve management outcomes.

3.5.3. *Future directions for MPs source control*

Hainan's experience suggests potential pathways for reconciling economic development with environmental protection through plastic pollution control measures. The temporal correlation between policy implementation and improved environmental metrics indicates that well-designed regulations may contribute to reducing plastic pollution while maintaining economic growth. Microplastic management in Hainan remains a long-term challenge that requires comprehensive monitoring programs, particularly for persistent polymers like PET and PES that continue to appear in coastal environments. In the process of economic development, industrial structure upgrading, and population growth, Hainan has successfully achieved the coordinated progress of environmental benefits and socio-economic development through the implementation of scientific and effective microplastic control policies. Microplastics in Hainan presents a long-term and complex challenge that demands comprehensive monitoring programs, particularly for persistent polymers like PET and PES that dominate coastal pollution. As shown in Fig. 6, the tourism sector contributes significantly through wet wipes (cellulose), beverage containers (PET), and single-use plastics (PE, PET), while fisheries generate pollution from abandoned fishing gear (PP) and synthetic rope (PP). Urban areas contribute to the problem by adding industrial pellets (PE, PP), laundry fibers (PES), and street runoff (PE). Current policy measures, including the 2019 plastic ban, have achieved 70–80 % alternative adoption and 83 % litter reduction, with monitoring programs tracking river and estuary microplastics since 2021. The General Office of the People's Government of Hainan Province (2023) reports that Hainan's biodegradable materials industry produced 40,400 tons of films and bags in 2023, representing a significant resource for replacing conventional plastics in high-risk sectors.

To address remaining gaps in persistent polymer management and circular economy implementation, Fig. 6 proposes a multi-pronged approach. Technological solutions include washing machine filters, stormwater capture systems, and drone monitoring. Policy enhancements involve gear marking systems, extended producer responsibility (EPR) schemes, and tourism waste penalties. Industrial shifts focus on biodegradable alternatives and green packaging incentives. These integrated measures aim to reduce microplastic loads and improve coastal ecosystem health, while addressing current limitations in stormwater filtration and polymer identification. The framework emphasizes coordinated action across all pollution sources to strengthen Hainan's marine protection framework, with the biodegradable materials production capacity serving as a key resource for sustainable alternatives.

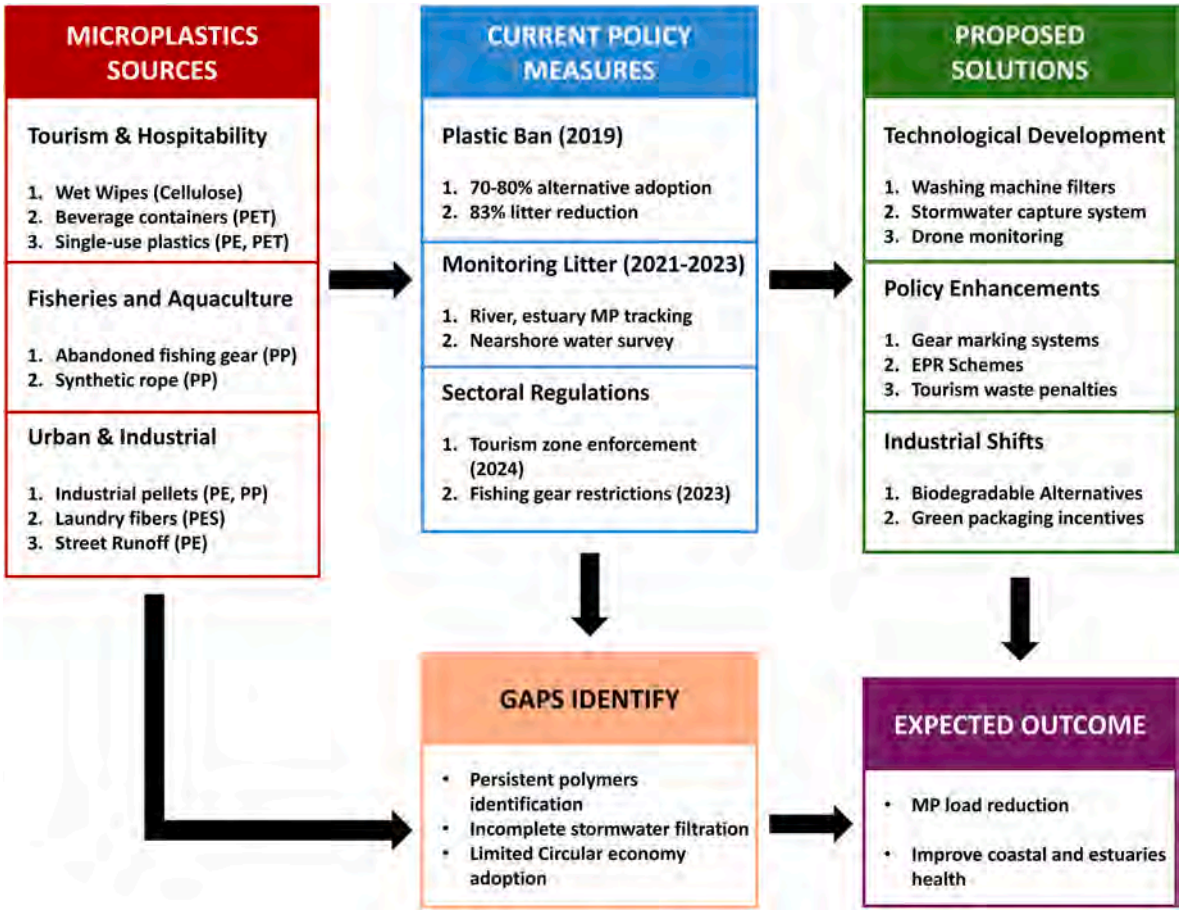


Fig. 6. Microplastics pollution management framework in coastal and estuarine environments.

3.6. Limitations of study

This study offers a critical baseline assessment of microplastic pollution; however, its primary limitation is the single sampling event conducted during the dry season (April). Consequently, the reported concentrations are highly likely to represent a lower-bound estimate of annual MP loads, as wet-season rainfall and associated riverine runoff are known to significantly increase the transport of land-based plastics into estuaries. This sampling constraint directly impacts the generalizability of our findings, as we cannot capture seasonal variations in polymer composition that may be linked to specific wet-weather activities (e.g., intensified agricultural runoff or tourism peaks). The data presented here thus provide a snapshot of dry-season conditions and should not be extrapolated to represent annual averages or peak pollution events. Future research must prioritize multi-seasonal sampling, particularly during the wet season (August–October), to fully elucidate seasonal dynamics and establish a truly representative annual baseline.

A further methodological consideration is the use of a 330 μm mesh, which biases the results toward larger MPs. Therefore, the reported values are strictly representative of the ≥330 μm fraction and are most comparable to studies using similar methodology. Comparisons with research employing finer mesh sizes should be made with caution, as those methodologies capture a greater abundance of smaller particles. To build upon these findings, future work should employ a multi-mesh sampling strategy to characterize the full size spectrum of MP pollution.

To build upon these findings, future work should implement multi-seasonal sampling at the river mouths. This approach would provide a more comprehensive understanding of temporal trends and yield more robust baseline data for the region. Additionally, employing a multi-mesh sampling strategy would help characterize the full size spectrum of MP pollution.

4. Conclusion

This study provides a comprehensive assessment of microplastic (MP) pollution in the tropical estuaries of Hainan Island, revealing significantly lower MP concentrations in the Nandu (0.17 ± 0.10 particles/m^3) and Wanquan Estuaries (0.32 ± 0.13 particles/m^3) compared to heavily polluted systems like the Yangtze River. The dominance of fibrous/linear MPs (49–60 %) and white-colored particles (37–42 %) points to textile degradation and urban wastewater as major sources, while Olefin/PO (Nandu Estuary) and polyethylene (Wanquan Estuary) highlight distinct industrial and agricultural inputs. Spatial patterns differed markedly, with Nandu's offshore-decreasing concentrations reflecting tidal dynamics, while Wanquan's uniform dispersion suggests monsoon-driven mixing. Strong correlations with temperature ($R = 0.56$) and pH ($R = 0.66$) underscore the influence of environmental factors on MP distribution. These findings demonstrate the efficacy of Hainan's 2019 plastic ban, evidenced by declining MP levels, yet persistent polymers like PET and PES indicate unresolved pathways from tourism, fisheries, and urban runoff.

While the findings demonstrate progress consistent with Hainan's plastic ban, it is crucial to interpret them within the key limitation of dry-season sampling. The concentrations reported likely underestimate peak wet-season loads, and the identified sources and patterns may not fully represent annual cycles. Therefore, the management framework proposed, including targeted interventions like stormwater filtration and biodegradable gear should be viewed as a foundational step. A critical priority for future research is multi-seasonal monitoring to validate these findings, accurately quantify annual loads, and refine mitigation strategies to account for seasonal variability. By establishing this baseline and highlighting the necessity of temporal data, this work provides an essential foundation for managing tropical estuaries, emphasizing the importance of adaptive, region-specific strategies to protect these ecologically sensitive ecosystems.

The study underscores the need for targeted interventions, such as enhanced stormwater filtration and biodegradable fishing gear, to address lingering pollution sources. Seasonal sampling limitations suggest future research should incorporate multi-temporal assessments to capture monsoon-driven variability. By establishing baseline data and linking MP dynamics to local policies, this work provides a framework for managing tropical estuaries, emphasizing the importance of region-specific strategies. Continued monitoring and adoption of global best practices, like the EU's washing machine filters, will be critical to sustaining Hainan's progress in mitigating MP pollution and protecting these ecologically sensitive ecosystems.

CRediT authorship contribution statement

Bin Chen: Writing – original draft, Resources, Investigation, Data curation. **Yang Zhou:** Writing – review & editing, Visualization, Formal analysis. **Kazi Belayet Hossain:** Writing – review & editing, Visualization, Formal analysis. **Yixin Chen:** Writing – review & editing, Resources. **Xiaoshan Zhu:** Resources, Investigation. **Hengxiang Li:** Writing – review & editing. **Xiangrong Xu:** Conceptualization. **Minggang Cai:** Supervision, Methodology, Conceptualization.

Declaration of competing interest

The authors declare that they have no known competing financial interests or personal relationships that could have appeared to influence the work reported in this paper.

Acknowledgements

This study was supported by the Hainan Province Science and Technology Special Fund (ZDYF2022SHFZ317), National Natural Science Foundation of China (42576044), University-Industry-Research Joint Innovation Program of Fujian Province (2025Y4002), Guangxi Science and Technology Program (AB25069113), Social Science Foundation of Fujian Province (FJ2024BF047), and Natural Science Foundation of Xiamen (3502Z20227322).

Appendix A. Supplementary data

Supplementary data to this article can be found online at https://doi.org/10.1016/j.marenvres.2025.107643.

Data availability

Data will be made available on request.

References

Ahmed, R., Hamid, A.K., Krebsbach, S.A., He, J.Z., Wang, D.J., 2022. Critical review of microplastics removal from the environment. Chemosphere 293.

Al-Zawaidah, H., Vermeulen, B., Waldschläger, K., 2023. The vertical distribution of riverine microplastics: the role of turbulence. In: Cocca, M., Ambrogi, V., Avolio, R., Castaldo, R., Errico, M.E., Gentile, G. (Eds.), Proceedings of the 3rd International Conference on Microplastic Pollution in the Mediterranean Sea. Springer Water. Springer, Cham, pp. 215–222.

Bali Provincial Government, 2023. Governor Regulation No. 47 of 2023 Concerning the Reduction of single-use Plastics* [Peraturan Gubernur Bali Nomor 47 Tahun 2023 Tentang Pengurangan Penggunaan Plastik Sekali Pakai].

Cai, M.G., He, H.X., Liu, M.Y., Li, S.W., Tang, G.W., Wang, W.M., Huang, P., Wei, G., Lin, Y., Chen, B., Hu, J.H., Cen, Z.N., 2018. Lost but can't be neglected: huge quantities of small microplastics hide in the South China Sea. Sci. Total Environ. 633, 1206–1216.

Cai, M.G., Liu, M.Y., Qi, H.Y., Cui, Y.Z., Zhang, M.Y., Huang, P., Wang, L.R., Xie, M.J., Li, Y.F., Wang, W.M., Ke, H.W., Liu, F.J., 2022. Transport of microplastics in the South China Sea: a review. Gondwana Res. 108, 49–59.

Chen, B., Hossain, K.B., Kang, R.Y., Zhou, Y., Wang, J., Cai, M.G., 2025. Assessment of microplastic hazards in Penaeus vannamei shrimp in a typical estuary of China: polymer composition, risk assessment, and health implications. J. Oceanol. Limnol. 43 (2), 572–588.

Chen, M.L., Jin, M., Tao, P.R., Wang, Z., Xie, W.P., Yu, X.B., Wang, K., 2018. Assessment of microplastics derived from mariculture in Xiangshan Bay, China. Environ. Pollut. 242, 1146–1156.
Cole, M., 2016. A novel method for preparing microplastic fibers. Sci. Rep. 6.
Department of Ecology and Environment of Hainan Province, 2022. Hainan ecological and environmental bulletin, 2021. https://hnsthb.hainan.gov.cn/xxgk/0200/0202/hjzl/hjzkgb/202206/t20220602_3205707.html.
Department of Ecology and Environment of Hainan Province, 2023. Hainan ecological and environmental bulletin, 2022. https://hnsthb.hainan.gov.cn/xxgk/0200/0202/hjzl/hjzkgb/202306/t20230602_3428656.html.
Ding, Y., Sha, C., Wang, T., 2025. Seasonal dynamics of microplastics in the central South China Sea: abundance, sources, influencing factors, and ecological risks. J. Environ. Chem. Eng. 13 (2), 115937.
European Commission, 2022. Commission delegated regulation (EU) 2022/1616 of 8 June 2022 supplementing Regulation (EU) 2019/1020 of the European Parliament and of the Council with regard to requirements on the release of synthetic microfibers from textile products. Off. J. Eur. Union L 242, 1–7. https://eur-lex.europa.eu/eli/reg_del/2022/1616/oj.
General Office of the People's Government of Hainan Province, 2023. Our province actively promotes the full chain plastic pollution control. https://www.hainan.gov.cn/hainan/5309/202312/5a825ea8091b4307a6061d63b7e436c0.shtml.
General Office of the People's Government of Hainan Province, 2024a. Hainan steadily promotes the protection, restoration, and pollution prevention of marine ecosystems, and explores the path to realizing the ecological value of marine natural resources. https://www.hainan.gov.cn/hainan/hjzf/202408/d6169ed76afe4de3b42feea5cd0e5e76.shtml.
General Office of the People's Government of Hainan Province, 2024b. Our Province has Established a full-chain closed-loop "Plastic Ban" System.
General Office of the People's Government of Hainan Province, 2024c. The Annual Production Capacity of Biodegradable Substitutes in Hainan has Reached 133,000 Tons, and the Substitute Technology has Reached the International Advanced Level.
Hainan Provincial Department of Ecology and Environment, 2022. Our province will 'update' the list of banned plastics. https://www.hainan.gov.cn/hainan/hjzf/202212/f405059638f44931b905d95581345826.shtml.
Hainan provincial department of ecology and environment. https://www.hainan.gov.cn/hainan/5309/202410/d99695bc27444012bee6e9d3eae5cc99.shtml, 2024.
Hossain, K.B., Lin, Y., Chen, K., Zhang, M., Liu, M., Zhao, W., Ke, H., Liu, F., Wang, C., Cai, M., 2023. Policy impact on microplastic reduction in China: observation and prediction using statistical model in an itensive mariculture Bay. Sci. Total Environ. 858 (3), 160075.
Huang, B., Sun, L.Y., Liu, M.R., Huang, H.Y., He, H., Han, F.X., Wang, X.X., Xu, Z.X., Li, B., Pan, X.J., 2021. Abundance and distribution characteristics of microplastic in plateau cultivated land of Yunnan Province, China. Environ. Sci. Pollut. Control Ser. 28 (2), 1675–1688.
Isobe, A., Uchida, K., Tokai, T., Iwasaki, S., 2015. East Asian seas: a hot spot of pelagic microplastics. Mar. Pollut. Bull. 101 (2), 618–623.
Kang, J.H., Kwon, O.Y., Lee, K.W., Song, Y.K., Shim, W.J., 2015. Marine neustonic microplastics around the southeastern coast of Korea. Mar. Pollut. Bull. 96 (1–2), 304–312.
Kasamesiri, P., Meksumpun, C., Meksumpun, S., Ruengsorn, C., 2021. Assessment on microplastics contamination in freshwater FISH: a case study of the Ubolratana reservoir, Thailand. Int. J. GEOMATE 20 (77), 62–68.
Lebreton, L.C.M., Van der Zwet, J., Damsteeg, J.W., Slat, B., Andrady, A., Reisser, J., 2017. River plastic emissions to the world's oceans. Nat. Commun. 8.
Leslie, H.A., van Velzen, M.J.M., Brandsma, S.H., Vethaak, A.D., Garcia-Vallejo, J.J., Lamoree, M.H., 2022. Discovery and quantification of plastic particle pollution in human blood. Environ. Int. 163.
Li, H.X., Ma, L.S., Lin, L., Ni, Z.X., Xu, X.R., Shi, H.H., Yan, Y., Zheng, G.M., Rittschof, D., 2018. Microplastics in oysters &ITSaccostrea cucullata&IT along the Pearl River Estuary, China. Environ. Pollut. 236, 619–625.
Li, Y.F., Liu, S.G., Liu, M.Y., Huang, W., Chen, K., Ding, Y.C., Wu, F.Z., Ke, H.W., Lou, L. H., Lin, Y., Zhang, M.Y., Liu, F.J., Wang, C.H., Cai, M.G., 2021. Mid-level riverine outflow matters: a case of microplastic transport in the Jiulong River, China. Front. Mar. Sci. 8.
Luo, H., Liu, C., He, D., Xu, J., Sun, J., Li, J., Pan, X., 2022. Environmental behaviors of microplastics in aquatic systems: a systematic review on degradation, adsorption, toxicity and biofilm under aging conditions. J. Hazard Mater. 423 (Part A), 126915.
Mai, L., You, S.N., He, H., Bao, L.J., Liu, L.Y., Zeng, E.Y., 2019. Riverine microplastic in the Pearl River Delta, China: are modeled estimates accurate? Environ. Sci. Technol. 53 (20), 11810–11817.
Malla-Pradhan, R., Suwunwong, T., Phoungthong, K., Joshi, T.P., Pradhan, B.L., 2022. Microplastic in urban Lake Phewa, Nepal: the first report on abundance and composition in surface water of lake in different seasons. Environ. Sci. Pollut. Control Ser. 29 (26), 39928–39936.
Ministry of Ecology and Environment of the People's Republic of China, 2022. 2021 bulle¬tin on the State of China's marine ecology and environment. https://www.mee.gov.cn/hjzl/sthjzk/jagb/202205/P020220527579939593049.pdf.
Naqash, N., Prakash, S., Kapoor, D., Singh, R., 2020. Interaction of freshwater microplastics with biota and heavy metals: a review. Environ. Chem. Lett. 18 (6), 1813–1824.
Oriekhova, O., Stoll, S., 2018. Heteroaggregation of nanoplastic particles in the presence of inorganic colloids and natural organic matter. Environ. Sci. Nano 5 (3), 792–799.
Pegado, T., Schmid, K., Winemiller, K.O., Chelazzi, D., Cincinelli, A., Dei, L., Giarrizzo, T., 2018. First evidence of microplastic ingestion by fishes from the Amazon River estuary. Mar. Pollut. Bull. 133, 814–821.
Peng, B., Hossain, K.B., Lin, Y., Zhang, M., Zheng, H., Yu, J., Meng, X., Wang, J., Cui, Y., Wu, B., Lou, L., Cai, M., 2022. Assessment and sources identification of microplastics, PAHs and OCPs in the Luoyuan Bay, China: based on multi-statistical analysis. Mar. Pollut. Bull. 175 (11), 113351.
Piehl, S., Leibner, A., Löder, M.G.J., Dris, R., Bogner, C., Laforsch, C., 2018. Identification and quantification of macro- and microplastics on an agricultural farmland. Sci. Rep. 8.
Qi, H.Y., Fu, D.D., Wang, Z.Z., Gao, M.Y., Peng, L.C., 2020. Microplastics occurrence and spatial distribution in water and sediment of Haikou Bay in the northern South China Sea. Estuar. Coast Shelf Sci. 239.
Qi, H.Y., Li, H.L., Meng, X.L., Peng, L.C., Zheng, H.W., Wang, L.R., Wang, W.M., Chen, K., Zhang, J.J., Zhang, H.F., Cai, M.G., 2022. Fate of microplastics in deep-sea sediments and its influencing factors: evidence from the Eastern Indian Ocean. Sci. Total Environ. 828.
Ramasamy, R., Subramanian, R.B., 2023. Microfiber mitigation from synthetic textiles - impact of combined surface modification and finishing process. Environ. Sci. Pollut. Control Ser. 30 (17), 49136–49149.
Soler, M., Colomer, J., Pohl, F., Serra, T., 2025. Transport and sedimentation of microplastics by turbidity currents: dependence on suspended sediment concentration and grain size. Environ. Int. 195, 109271.
Standing Committee of Hainan Provincial People's Congress, 2016. Regulations on marine environmental protection. In: Hainan Province. https://www.hainan.gov.cn/hainan/dfxfg/202203/ac805a40c4954a0ebd9a50b44b6c5867.shtml.
Standing Committee of Hainan Provincial People's Congress, 2024. Regulations on prohibiting disposable non-degradable plastic products in Hainan Special Economic Zone. https://www.hainan.gov.cn/hainan/dfxfg/202412/9436e38f2b364b888436908132ac209b.shtml.
Sun, X.X., Liang, J.H., Zhu, M.L., Zhao, Y.F., Zhang, B., 2018. Microplastics in water and zooplankton from the Yellow Sea. Environ. Pollut. 242, 585–595.
Sutton, R., Mason, S.A., Stanek, S.K., Willis-Norton, E., Wren, I.F., Box, C., 2016. Microplastic contamination in the San Francisco Bay, California, USA. Mar. Pollut. Bull. 109 (1), 230–235.
Tang, G.W., Liu, M.Y., Zhou, Q., He, H.X., Chen, K., Zhang, H.B., Hu, J.H., Huang, Q.H., Luo, Y.M., Ke, H.W., Chen, B., Xu, X.R., Cai, M.G., 2018. Microplastics and polycyclic aromatic hydrocarbons (PAHs) in Xiamen coastal areas: implications for anthropogenic impacts. Sci. Total Environ. 634, 811–820.
Teng, J., Zhao, J.M., Zhang, C., Cheng, B., Koelmans, A.A., Wu, D., Gao, M., Sun, X.Y., Liu, Y.L., Wang, Q., 2020. A systems analysis of Microplastic in Laizhou Bay. China. Sci. Total Environ. 745.
The People's Government of Haikou, 2021. Notice from the Office of the People's Government of Haikou City on issuing the management measures for Haikou marine ranch. http://www.haikou.gov.cn/xxgk/szfbjxxgk/zcfg/szfxzgfxwj/202109/t410981.shtml.
Thompson, R.C., Olsen, Y., Mitchell, R.P., Davis, A., Rowland, S.J., John, A.W.G., McGonigle, D., Russell, A.E., 2004. Lost at sea: where is all the plastic? Science 304 (5672), 838-838.
Trainic, M., Flores, J.M., Pinkas, I., Pedrotti, M.L., Lombard, F., Bourdin, G., Gorsky, G., Boss, E., Rudich, Y., Vardi, A., Koren, I., 2020. Airborne microplastic particles detected in the remote marine atmosphere. Commun. Earth Environ. 1 (1).
United Nations Environment Programme, 2021. From Pollution to Solution:A Global Assessment of Marine Litter and Plastic Pollution. Nairobi.
Wang, F., Xiang, L.L., Leung, K.S.Y., Elsner, M., Zhang, Y., Guo, Y.M., Pan, B., Sun, H.W., An, T.C., Ying, G.G., Brooks, B.W., Hou, D.Y., Helbling, D.E., Sun, J.Q., Qiu, H., Vogel, T.M., Zhang, W., Gao, Y.Z., Simpson, M.J., Luo, Y., Chang, S.X., Su, G.Y., Wong, B.M., Fu, T.M., Zhu, D., Jobst, K.J., Ge, C.J., Coulon, F., Harindintwali, J.D., Zeng, X.K., Wang, H.J., Fu, Y.H., Wei, Z., Lohmann, R., Chen, C., Song, Y., Sanchez-Cid, C., Wang, Y., El-Naggar, A., Yao, Y.M., Huang, Y.R., Law, J.C.F., Gu, C.G., Shen, H.Z., Gao, Y.P., Qin, C., Li, H., Zhang, T., Corcoll, N., Liu, M., Alessi, D.S., Li, H., Brandt, K.K., Pico, Y., Gu, C., Guo, J.H., Su, J.Q., Corvini, P., Ye, M., Rocha-Santos, T., He, H., Yang, Y., Tong, M.P., Zhang, W.N., Suanon, F., Brahushi, F., Wang, Z.Y., Hashsham, S.A., Virta, M., Yuan, Q.B., Jiang, G.F., Tremblay, L.A., Bu, Q. W., Wu, J.C., Peijnenburg, W., Topp, E., Cao, X.D., Jiang, X., Zheng, M.H., Zhang, T. L., Luo, Y.M., Zhu, L.Z., Li, X.D., Barceló, D., Chen, J.M., Xing, B.S., Amelung, W., Cai, Z.W., Naidu, R., Shen, Q.R., Pawliszyn, J., Zhu, Y.G., Schaeffer, A., Rillig, M.C., Wu, F.C., Yu, G., Tiedje, J.M., 2024. Emerging contaminants: a one Health perspective. Innovation 5 (4).
Wang, T., Hu, M.H., Song, L.L., Yu, J., Liu, R.J., Wang, S.X., Wang, Z.F., Sokolova, I., Huang, W., Wang, Y.J., 2020. Coastal zone use influences the spatial distribution of microplastics in Hangzhou Bay, China. Environ. Pollut. 266.
Wang, T., Zha, S.Y., Zhu, L.X., McWilliams, J.C., Galgani, L., Amin, R.M., Nakajima, R., Jiang, W.S., Chen, M.L., 2022. Accumulation, transformation and transport of microplastics in estuarine fronts. Nat. Rev. Earth Environ. 3 (11), 795–805.
Wang, T., Zou, X.Q., Li, B.J., Yao, Y.L., Zang, Z., Li, Y.L., Yu, W.W., Wang, W.Z., 2019. Preliminary study of the source apportionment and diversity of microplastics: taking floating microplastics in the South China Sea as an example. Environ. Pollut. 245, 965–974.
Wang, T.T., Tang, W.Q., Wu, D.H., Yu, X.R., Wang, G.Y., Cai, X.W., Shao, S., Wang, S., Mo, L., Liu, Y.S., Ying, G.G., Chen, Z.B., 2023. Abundance and characteristics of microplastics in the Wanquan Estuary, Hainan Island. Mar. Pollut. Bull. 189.
Wu, Q., Liu, S., Chen, P., Liu, M., Cheng, S.Y., Ke, H., Huang, P., Ding, Y., Cai, M., 2021. Microplastics in seawater and two sides of the Taiwan Strait: reflection of the socialeconomic development. Mar. Pollut. Bull. 169, 112588.
Xia, B., Sui, Q., Sun, X.M., Zhu, L., Wang, R.Y., Cai, M.G., Chen, B.J., Qu, K.M., 2021. Microplastic in surface water of Sanggou Bay, China: occurrence, source and inventory. Mar. Pollut. Bull. 162.

Xie, F.W., Wang, S.L., Wu, S.Y., Lei, Y., Feng, Y., Mo, S.W., He, S.H., 2023. Microplastic in the estuaries of three major rivers in Hainan during autumn. J. Guangdong Ocean Univ. 43 (4), 137–144.
Yang, Y., Li, Z., Yan, C.R., Chadwick, D., Jones, D.L., Liu, E.K., Liu, Q., Bai, R.H., He, W. Q., 2022. Kinetics of microplastic generation from different types of mulch films in agricultural soil. Sci. Total Environ. 814.
Zhang, M., Lin, Y., Booth, A.M., Song, X., Cui, Y., Xia, B., Gu, Z., Li, Y., Liu, F., Cai, M., 2022. Fate, source and mass budget of sedimentary microplastics in the Bohai Sea and the Yellow Sea. Environ. Pollut. 294, 118640.
Zhang, T., Lin, L., Li, D.Q., Wu, S.N., Kong, L., Wang, J.C., Shi, H.T., 2021. The Microplastic in beaches that served as historical nesting grounds for green turtles on Hainan Island, China. Mar. Pollut. Bull. 173.
Zhao, S.Y., Zhu, L.X., Wang, T., Li, D.J., 2014. Suspended microplastics in the surface water of the Yangtze Estuary System, China: first observations on occurrence, distribution. Mar. Pollut. Bull. 86 (1–2), 562–568.
Zhao, X.L., Wang, J.Y., Leung, K.M.Y., Wu, F.C., 2022. Color: an important but overlooked factor for plastic photoaging and microplastic formation. Environ. Sci. Technol.
Zhu, Z., Hossain, K.B., Wei, H., Jia, R., Gao, X., Jin, H., Cai, M., 2023. Distribution and sources of microplastics in the Beibu Gulf using in-situ filtration technique. Mar. Pollut. Bull. 188.

animals

MDPI

Article

Protective Effect of Nanobodies Targeting Sip Protein Against *Streptococcus agalactiae* Infection in Tilapia (*Oreochromis niloticus*)

Zhishen Wang [1,†], Huiling Wu [2,†], Weihao He [1], Shunqiang Wei [1], Xuemin Wei [1], Chaoshuai Wei [1], Yinghui Wang [1,2,*] and Aiguo Huang [1,*]

[1] Guangxi Laboratory on the Study of Coral Reefs in the South China Sea, Coral Reef Research Center of China, School of Marine Sciences, Guangxi University, Nanning 530004, China; 2227301031@st.gxu.edu.cn (Z.W.); scauheweihao@163.com (W.H.); 18577889437@163.com (S.W.); 2327301032@st.gxu.edu.cn (X.W.); wcs@gxu.edu.cn (C.W.)

[2] Institute of Green and Low Carbon Technology, Guangxi Institute of Industrial Technology, Nanning 530000, China; whl415899@126.com

* Correspondence: wyh@gxu.edu.cn (Y.W.); aiguo_200891@126.com (A.H.)

† These authors contributed equally to this work.

Simple Summary

Antibiotics remain the primary method for controlling *Streptococcus agalactiae* (GBS) in aquaculture environments. However, while antibiotics can eliminate GBS, they may also lead to the release of virulence factors and the emergence of drug-resistant strains. Additionally, GBS can breach the blood–brain barrier in fish and damage the nervous system, accelerating fish mortality. Therefore, this study aims to explore green, virulence-neutralizing, and blood–brain barrier-penetrating strategies for preventing GBS infection. Nanobodies (Nbs), currently the smallest genetically engineered antibodies, possess potential for rapid degradation, toxin neutralization, and barrier system penetration, making them a crucial source for new drug development. Notably, this study utilized phage display technology to screen and obtain a nanobody Nb30 from a camel-derived nanobody phage library, which can target surface immunogenic (Sip) protein and inhibit GBS infection in tilapia (*Oreochromis niloticus*) tissues, and improve survival rates in infected fish. In summary, Nb30 is a sustainable, effective neutralizing antibody with promising application potential.

Abstract

Streptococcus agalactiae (GBS) has emerged as one of the most prevalent bacterial pathogens causing severe economic losses in tilapia aquaculture due to its highly contagious and lethal nature. Nanobodies (Nbs), characterized by their small molecular size, enhanced tissue penetration, high tolerance, and exceptional antigen-binding affinity, represent a promising green alternative to conventional antibiotics. In the present study, the objective was to explore the potential of specific Nbs in the treatment of tilapia GBS disease. We first screened specific Nbs targeting the surface immunogenic (Sip) protein of GBS from a naïve phage display library, and a novel nanobody Nb30 was obtained. Nb30 was expressed in *Escherichia coli* and purified using the Ni-NTA Agarose column. Indirect ELISA showed that Nb30 had a high affinity against Sip and GBS in vitro. Moreover, Nb30 significantly reduced GBS colonization in the liver, spleen, and brain of GBS-infected tilapia. The survival rate in the control groups was 53%, whereas it was increased to 86% after treatment with 100 mg/kg Nb30. Transcriptome profiling revealed that Nb30 could modulate critical biological processes, including antioxidant defense, immune regulation, amino acid/protein synthesis, and energy metabolism in the liver tissues of GBS-infection tilapia. Notably, the

check for updates

Academic Editor: Miroslava Kačániová

Received: 10 October 2025
Revised: 30 October 2025
Accepted: 1 November 2025
Published: 4 November 2025

Citation: Wang, Z.; Wu, H.; He, W.; Wei, S.; Wei, X.; Wei, C.; Wang, Y.; Huang, A. Protective Effect of Nanobodies Targeting Sip Protein Against *Streptococcus agalactiae* Infection in Tilapia (*Oreochromis niloticus*). *Animals* **2025**, *15*, 3207. https://doi.org/10.3390/ani15213207

Copyright: © 2025 by the authors. Licensee MDPI, Basel, Switzerland. This article is an open access article distributed under the terms and conditions of the Creative Commons Attribution (CC BY) license (https://creativecommons.org/licenses/by/4.0/).

expression levels of antioxidant enzymes (*cat* and *gpx*) were significantly up-regulated, and the TLR/MyD88/NF-κB pathway-related genes (*tlr5*, *myd88*, *irak4*, *traf6*, *Rela*, and *NF-κB2*) were significantly down-regulated after treatment with Nb30. Collectively, these findings establish a novel therapeutic strategy for controlling GBS infection in tilapia and provide evidence supporting the application of nanobodies as sustainable alternatives to antibiotics in aquaculture disease management.

Keywords: nanobodies; *Streptococcus agalactiae*; surface immunogenic protein; *Oreochromis niloticus*; antibacterial activity

1. Introduction

Tilapia is one of the most important aquaculture species recommended by the Food and Agriculture Organization of the United Nations (FAO) to the world [1]. However, in recent years, with the expansion of aquaculture scale and the increase in aquaculture density, the prevalence of bacterial infections, primarily caused by *Streptococcus agalactiae,* has posed a significant threat in major tilapia farming regions globally [2,3]. *S. agalactiae*, also referred to as Group B *Streptococcus* (GBS), can be categorized into 10 serotypes, Ia, Ib, and II-IX depending on the capsule polysaccharide [4]. The main signs of GBS infection in tilapia are septicemia and meningitis, resulting in melanosis, exophthalmia and erratic swimming [5,6]. In the past, broad-spectrum antibiotics have been used commercially for the treatment of GBS infection in tilapia, but the misuse of antibiotics has resulted in the widespread occurrence of bacterial resistance, which affects their therapeutic efficacy and contributes to environmental pollution [7,8]. Therefore, there is an urgent need for the development of a novel environmentally friendly alternative to antibiotics for GBS infection.

In the 1990s, Hamers and his colleagues identified a naturally occurring monoclonal antibody in camelid serum that lacked the light chain. The cloning of the variable region of the heavy chain antibody resulted in the generation of a single-domain antibody, also referred to as a nanobody (Nb), which was constituted exclusively of heavy chains [9]. Nbs are the smallest antigen-binding fragments known to exist naturally, and they have the advantages of small molecular weight, high tissue penetration, high tolerance, high affinity, and ease of production. The excellent properties of Nbs have promoted their applications in the fields of neutralizing viruses and pathogenic bacteria [10–12]. For example, Nbs could target the virulence factor FliC protein against *Salmonella enteritidis* infection in chicken [13]. In addition, Nbs could effectively interact with lipopolysaccharides and neutralize *Vibrio cholerae* infection in vitro and in vivo [14]. These studies suggest that the development of Nbs against virulence proteins or surface components of pathogenic bacteria can prevent and treat pathogen infection. Therefore, Nbs may be a new alternative to antibiotic treatment.

Adhesins play a key role in the process of bacterial invasion into the host by interacting with corresponding receptors on the host cell to achieve bacterial attachment [15]. Studies have shown the presence of a variety of adhesins on the surface of GBS, including fibrinogen-binding proteins (Fbs), laminin-binding proteins (Lmb), C5a peptidase (ScpB), and surface immunogenic protein (Sip) [16]. Sip, as a major adhesin of GBS, exhibits high homology across different serotypes of GBS and is involved in bacterial adhesion and host tissue colonization. It has been noted that by knocking out the gene encoding Sip, the virulence of the obtained GBS strains was significantly reduced [17]. Thus, the Sip has become a main target for therapeutic development. Sip protein has been shown to a strong immunogenicity in a variety of animal models for immune experiments. An animal

model demonstrated that specific antibodies against Sip could cross the placenta to confer protection to newborns against diseases caused by GBS [18].

In this study, we aimed to screen Sip-targeting nanobodies (Nbs) from a naïve phage-displayed nanobody library through three rounds of panning-elution-amplification cycles. The selected Nbs were subsequently expressed and purified. In vitro experiments were used to demonstrate the binding capability of purified Nbs to Sip and GBS. Furthermore, the GBS-infected tilapia (*O. niloticus*) model was utilized to evaluate the in vivo antibacterial activity of Nbs. The mechanisms underlying their anti-GBS effects and protective roles in tilapia were systematically investigated. This study would provide a novel strategy for disease prevention and control of GBS infections in aquaculture.

2. Materials and Methods

2.1. Fish and Bacteria

Healthy tilapia (9 ± 0.5 g) were purchased from a tilapia farm in Nanning, Guangxi, China. Throughout the study, these fish were kept in 100 L aeration tanks and fed a commercial diet twice a day. The water was partially changed daily and the temperature was maintained at 30 ± 1.0 °C. The animal use protocol was approved by the Animal Care and Welfare Committee of Guangxi University (GXU-2023-0134). The Ia-type GBS isolated from the tilapia fish farm in Nanning, Guangxi was generously donated by Dr. Song Zhu from Southwest University. The *Escherichia coli* SS320 strain and the helper phage M13K07 were obtained from Kangti Life (Shenzhen, China).

2.2. Biopanning of Sip-Specific Nbs from Phage Display Libraries

The purified Sip protein of GBS was previously prepared and stored in our laboratory according to methods described by previous researchers [19]. The selection process of nanobodies, as previously described [20], can be summarized as follows: the immunotubes are coated with purified Sip protein (50 μg per tube) at 4 °C overnight, and a negative blank control was established to account for nonspecific binding. Immunization tubes were washed 3 times with PBS, followed by the addition of 2 mL of blocking solution (5% skimmed milk powder) and spin blocking for 2 h. Naïve phage-displayed Nb libraries (1×10^{12} pfu/tube) were added to the immunization tubes and incubated at room temperature with spinning for 1 h. The tubes were washed 20 times by the addition of 2 mL of PBST (1× PBS, containing 0.05% Tween 20 (Solarbio, Beijing, China)). The remaining bound phage particles were eluted with 1 mL of 0.25 mg/mL Trypsin (Sangon Biotech, Shanghai, China) solution for 30 min and terminate the elution by adding 10 μL of 10% AEBSF (Sangon Biotech, Shanghai, China). *E. coli* SS320 was infected with the eluted phage with M13K07 helper phage and subsequently amplified overnight at 37 °C. The amplified phage was finally purified using PEG 4000/2.5 M NaCl (Solarbio, Beijing, China) precipitation for the next round of selection. The purified phages were identified using Phage ELISA as previously reported [20]. In brief, the recombinant Sip (approximately 400 ng/well) was coated on a 96-well plate at 4 °C. After washing three times with PBST, the plate was blocked with 1.5% skim milk at 37 °C for 1 h. The plate was then washed and the amplified phage was added to each well, followed by incubation at 37 °C for 2 h. The plate was washed six times with PBST, and then the HRP-conjugated anti-M13 mouse monoclonal antibody (Santa Cruz, Shanghai, China) was added, incubated at 37 °C for 1 h. Subsequently, 100 μL of TMB two-component color development solution (Solarbio, Beijing, China) was added, and the reaction was allowed to develop. The reaction was stopped by adding 50 μL of ELISA stop solution (Solarbio, Beijing, China), and the absorbance was measured at 450 nm using a microplate reader. The sequencing of clones that yield a

positive reaction with phiS3/psiR3 primers (Table S1), and the grouping of Nbs based on differences in the CDR regions.

2.3. Expression and Purification of Nanobody Nb30

A pair of primers Nbs-F/Nbs-R (Table S1) was designed based on the gene sequence of Nb30, and PCR amplification was performed to amplify the Nb30 gene. The amplified product was cloned into the EcoRI and HindIII sites of the pET-28a (+) vector. The recombinant plasmid pET28a-Nb30 was then transformed into *Escherichia coli* BL21(DE3) (Sangon Biotech, Shanghai, China). Expression of the recombinant protein Nb30 was induced with 0.8 mM IPTG (Sangon Biotech, Shanghai, China) at 37 °C for 6 h. Cells were disrupted using a cell disruptor, and the supernatant and pellet fractions were analyzed by SDS-PAGE. The inclusion body protein was solubilized in 8 M urea and purified using a Ni-NTA affinity chromatography column (CWBIO, Taizhou, China). The refolding of the denatured protein was performed according to the manufacturer's protocol. Briefly, the inclusion body protein was dialyzed against 8 M→6 M→4 M→2 M→0 M urea solutions at 4 °C for 12 h each step, with the final dialysis in PBS buffer. The refolded protein was concentrated using a centrifugal filter and the concentration was determined using a BCA protein assay kit (CWBIO, Taizhou, China).

2.4. In Vitro Affinity Validation

To detect the binding activity of purified Nb30 to Sip and GBS, an indirect ELISA was performed as described in a previous report [20]. Briefly, 96-well plates were immobilized with purified Sip protein (400 ng per well) or inactivated GBS (about 1×10^8 CFU/mL). Then a series of purified recombinant protein Nb30 (0.05 to 10 mg/L) was added to the plates and incubated with Sip or GBS. Finally, an anti-His tag monoclonal antibody (Solarbio, Beijing, China) was used to detect the bound Nb30.

2.5. Anti-GBS Activity of Nb30 in Tilapia

The anti-GBS activity of Nbs was tested by analyzing the bacterial copy number in tilapia tissues and the survival rate of GBS-infected tilapia. Tilapia were randomly divided into three groups: control groups, low-dose treatment groups and high-dose treatment groups. The control groups were injected intraperitoneally with 100 μL of GBS solution (about 3×10^8 CFU/mL), the low-dose groups were injected with 100 μL of mixtures containing GBS and 50 mg/kg of Nb, and the high-dose groups were injected with GBS and 100 mg/kg of Nb. Each group was performed in triplicate, and each replicate contained 15 fish. After 24 h of treatment, tilapia were euthanized and the liver, spleen, and brain tissues were sampled and stored at −80 °C for subsequent experiments. The same treatment was performed to evaluate the protective effects of Nb30 on GBS-infected tilapia.

2.6. Genomic DNA Extraction and Absolute Quantification of GBS Copy Numbers

Using a tissue grinder to perform physical grinding on the tilapia tissue, and total genomic DNA was extracted using the TIANamp Bacteria DNA Kit (Tiangen, Beijing, China) according to the manufacturer's instructions. GBS genomic DNA was quantified by real-time qPCR (qPCR) as described in a previous study [20]. Briefly, the *cfb* gene encoding the CAMP factor was selected as the target gene and cloned into the pMD19-T vector (Takara, Beijing, China) by using cfb primers (Table S1). The copy number of the target amplicon was quantified by measuring the concentration using a NanoDrop spectrophotometer (Analytik Jena, Jena, Germany). The target amplicon was diluted into a 10-fold series and used as a template for qPCR. qPCR was performed in a Rapid Real-Time Fluorescence Quantitative PCR System (ABI 7500, Thermo Fisher, Waltham, MA, USA) using UltraSYBR mixtures (CWBIO, Taizhou, China). qPCR cycling conditions were 95 °C

for 10 min, followed by 40 cycles of denaturation at 95 °C for 15 s, and then annealing at 60 °C for 1 min. To verify the amplification of individual products, melt curves were analyzed at the end of each PCR thermal profile from 65 °C to 95 °C in 5 s steps. The logarithm of the *cfb* gene copy number and the corresponding cycling threshold (Ct) value were regressed as a standard curve to determine the copy number of GBS.

2.7. RNA Extraction and Relative Quantification of Tilapia Gene Expression

Total RNA was extracted from the tilapia liver tissues using TRIzon reagent (CWBIO, Taizhou, China). The mass and concentration of extracted RNA were determined using 1.5% agarose gel electrophoresis and a NanoDrop spectrophotometer. The extracted RNA was then reverse transcribed into cDNA using HiFiScript cDNA synthesis kit (CWBIO, Taizhou, China). The expression levels of *tlr5*, *myd88*, *irak4*, *traf6*, *Rela*, *NF-κb2*, *cat*, *gpx* and *c-type lysozyme* were detected by qPCR. *β-actin* was chosen as the reference gene in this study. The primers for qPCR in this study are shown in Table S1. The fold changes of gene expression levels were performed by the $2^{-\Delta\Delta Ct}$ method.

2.8. Library Construction and Transcriptome Sequencing

From the control group and high-dose treatment groups, 9 fish were randomly selected from each group. The liver tissue of these fish was isolated, and the liver tissue of 3 fish was mixed to form one sample. All samples were immediately frozen in liquid nitrogen and stored at −80 °C ultra-low temperature refrigerator. After the collection was completed, the samples were sent to Shanghai Meiji Biomedical Technology Co., Ltd. (Shanghai, China). for sample preparation and library construction to ensure the accuracy and reliability of the data. Total RNA was extracted from the liver tissue of the Nile tilapia using Trizol reagent and the RNA Purification Kit. First-strand cDNA was synthesized using random primers and reverse transcriptase, followed by second-strand cDNA synthesis using DNA polymerase and RNase H. The purified cDNA was end-repaired and A-tailed, and specific adapters were ligated to construct the sequencing library. The library was amplified and screened by PCR to verify appropriate fragment size and concentration. After quality control, high-throughput sequencing was performed on the Illumina NovaSeq X Plus sequencer (San Diego, CA, USA) [21].

Raw data were processed using Fastp (Version 0.23.4) to obtain high-quality clean data. The filtered data were aligned to the reference genome (GenBank: GCF_001858045.2) using appropriate parameters. Differential expression genes (DEGs) were identified using DESeq2 (Version 1.42.0) with default settings and thresholds of p-adjust < 0.05 and $|\log_2 FC| > 1$. GO and KEGG enrichment analysis of DEGs was performed on the Majorbio Cloud Platform (https://www.majorbio.com/tools, accessed on 9 January 2025).

2.9. Statistical Analysis

Statistical analyses were performed using SPSS 18.0 statistical software (SPSS Inc., Chicago, IL, USA). Data were expressed as mean ± standard deviation (SD). The significance determined by analyzing the data was using one-way analysis of variance (ANOVA) and post hoc Tukey test. Significant differences were defined as $p < 0.05$ (*), $p < 0.01$ (**).

3. Results

3.1. Biopanning and Identification of Sip-Specific Nbs

The purification of the Sip protein was obtained using a Ni-NTA affinity column (Figure S1), and used as a target protein for biopanning of Nbs. After three rounds of panning-elution-amplification, 48 positive clone strains were identified using phage ELISA, and three Nb clones with different sequences, named Nb12, Nb30, and Nb41, were obtained

after sequence alignment (Figure 1A). These Nb clones were similar in four framework regions, and differed significantly only in three CDR regions (Figure 1B). In the study, Nb30 was selected for further investigation based on its in vitro affinity activity.

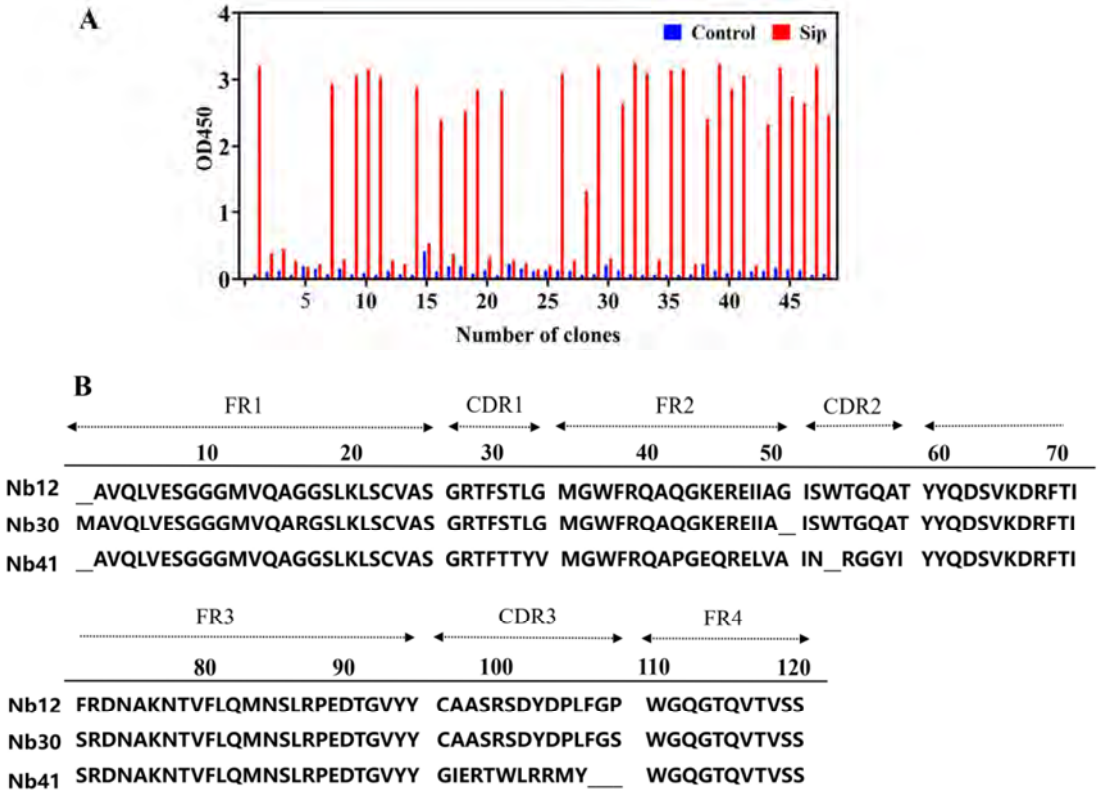


Figure 1. Identification of nanobodies (Nbs) targeting Sip. (**A**) Identification of specific Nbs by indirect phage ELISA; (**B**) Analysis of the amino acid sequence of positive Nbs.

3.2. Prokaryotic Expression, Purification and In Vitro Affinity Test of Nb30

The results of SDS-PAGE showed that Nb30 was mainly expressed as inclusion bodies in BL21 cells, and its molecular weight was about 20 kDa (Figure 2A). Recombinant protein Nb30 was further purified using a Ni-NTA affinity column (Figure 2B). Subsequently, the binding activity of Nb30 to Sip or GBS was detected using ELISA. The results indicate that the in vitro-expressed Nb30 maintains binding activity with Sip and GBS, and its binding capacity increases with increasing concentrations of Nb30, exhibiting a clear dose-dependent effect (Figure 2C,D).

3.3. Nb30 Improves Survival Rate and Inhibits GBS Infection in Tilapia

As shown in Figure 3A–C, Nb30 significantly inhibited GBS infection in different tissues of tilapia within 24 h at concentrations of 50 and 100 mg/kg. Compared with the control groups, the GBS copy numbers in spleen, liver and brain tissues of GBS-infected tilapia, respectively, decreased by 29.43, 7.62 and 5.84-fold after treatment with 50 mg/kg Nb30, and decreased by 45.84, 25.78 and 11.52-fold after treatment with 100 mg/kg Nb30. To investigate the protective effect of Nb30 on GBS-infected tilapia, a 7-day cumulative survival rate experiment was conducted. As shown in Figure 3D, there was a difference in the survival rate of GBS-infected tilapia between the control groups and treatment groups. The survival rate in the control groups was 53%, whereas the survival rate was increased to 73% ($p > 0.05$) and 86% ($p > 0.05$) after treatment with 50 mg/kg and 100 mg/kg Nb30.

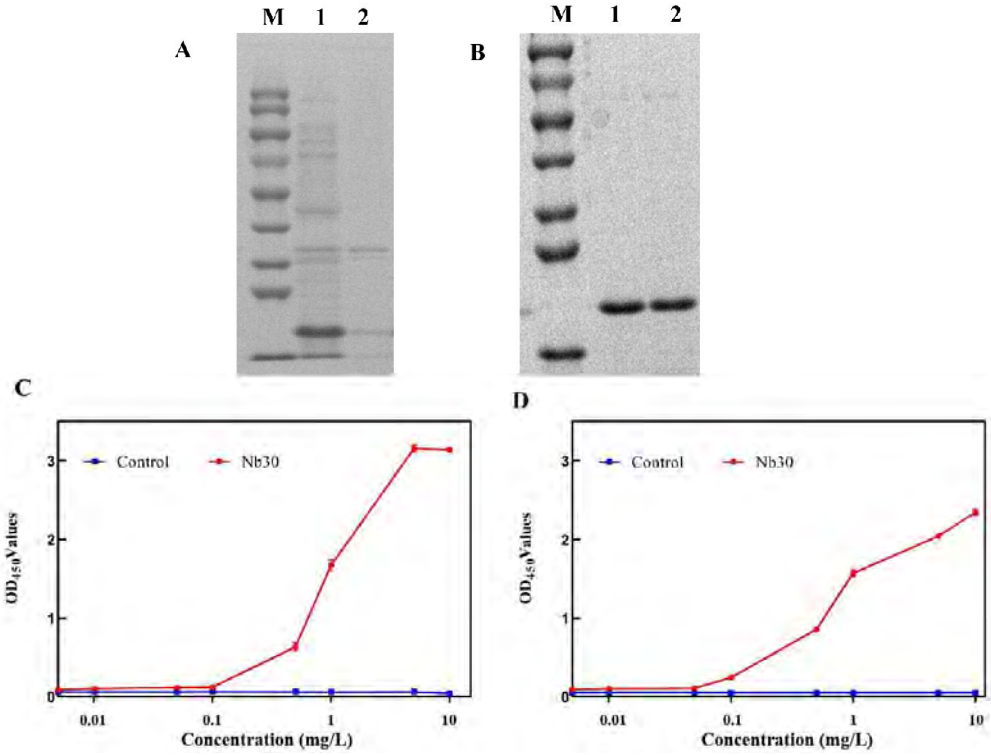


Figure 2. Expression and purification of nanobody Nb30. (**A**) SDS-PAGE analysis of the expression of Nb30. M: protein marker, lane 1: precipitation of Nb30 expression, lane 2: supernatant of Nb30 expression; (**B**) SDS-PAGE analysis of the purified Nb30; (**C**,**D**) Detection of the binding ability of Nb30 to (**C**) Sip and (**D**) GBS by indirect ELISA.

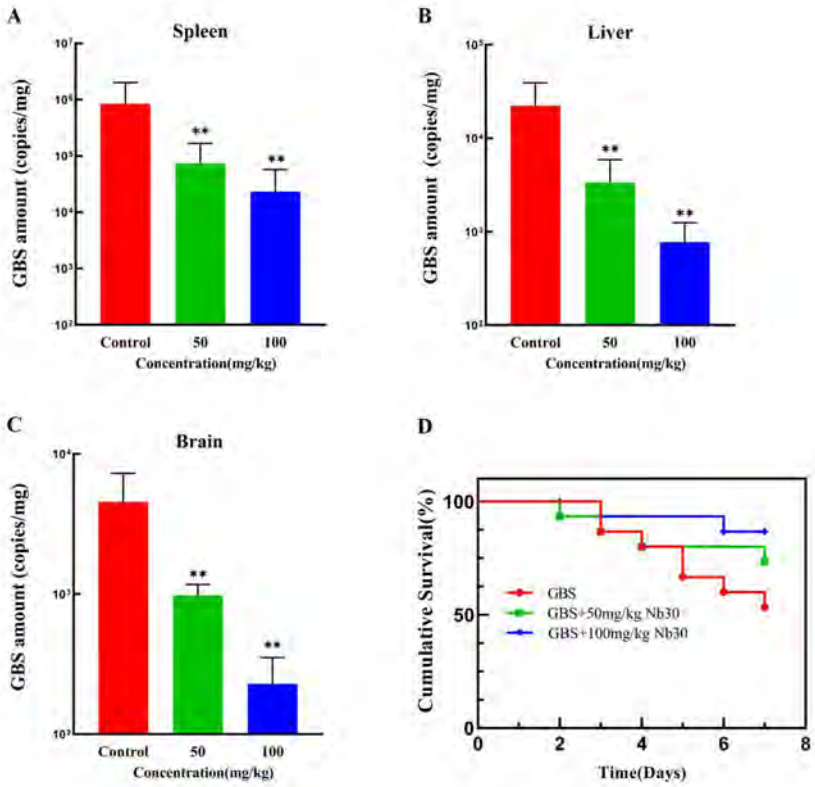


Figure 3. Antibacterial activity of Nb30 against GBS in tilapia. Copy numbers of GBS in (**A**) spleen, (**B**) liver, and (**C**) brain tissues of tilapia after 24 hpi; (**D**) Survival curves of GBS-infected tilapia treated with different concentrations of Nb30. Mortality in each group was recorded continuously for 7 days. ** $p < 0.01$, compared to control.

3.4. Transcriptome Changes in the Liver of GBS-Infected Tilapia Under Nb30 Treatment

To further investigate the protective mechanism of Nb30 against GBS in tilapia, transcriptomic sequencing was performed between the control groups and high-dose groups (Figure 4). As shown in Figure 4A, a total of 637 significantly differential genes (DEGs) were identified, of which 161 genes were up-regulated and 476 genes were down-regulated. To predict the relevant biological functions and corresponding pathways of these important DEGs, GO and KEGG enrichment analyses were performed. GO functional enrichment analysis classified DEGs into three functional groups, and the top 20 DEGs that were significantly enriched in BP (Biological Processes), CC (Cellular components), and MF (Molecular Function) (Figure 4B). In the context of BP, DEGs were found to be enriched in "oxygen carrier activity", "chemokine receptor", "chemokine activity", "molecular carrier activity", "G protein-coupled receptor binding" and "heme binding". About CC, DEGs were predominantly found to belong to the "hemoglobin complex" and "extracellular region". In the MF, DEGs were mainly enriched in "immune system processes", "immune response" and "cell adhesion". KEGG analysis showed that the top 20 KEGG pathways were significantly enriched in "Ascorbate and aldarate metabolism", "Pentose and glucuronate interconversions", "Histidine metabolism", "Retinol metabolism", "beta-Alanine metabolism", "Cytokine-cytokine receptor interaction", "Drug metabolism-cytochrome P450", "Metabolism of xenobiotics by cytochrome P450" and "PPAR signaling pathway", the majority of which are associated with immune-related functions (Figure 4C).

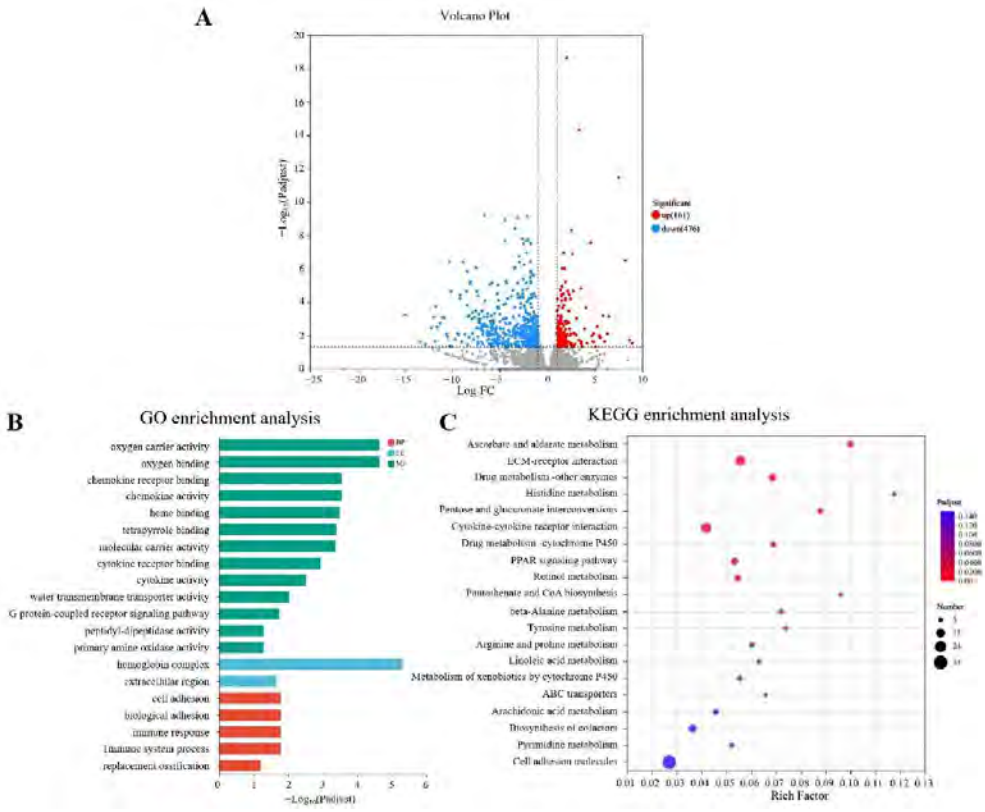


Figure 4. Integration diagram of multidimensional transcriptome analysis of tilapia liver tissue after treatment with Nb30 for 24 h. (**A**) Volcano plot of the comparison between the control group and high-dose treatment groups; (**B**) GO enrichment analysis of the differentially expressed genes (DEGs) in comparison of the control group and high-dose treatment groups; (**C**) KEGG enrichment analysis of the DEGs in comparison of the control group and high-dose treatment groups.

3.5. Analysis of the Gene Expression of TLR/NF-κB Pathway, Antioxidant and Immune Levels in Tilapia

Differences in the gene expressions involved in the TLR/MyD88/NF-κB inflammatory pathway were investigated in the liver tissues of tilapia in this study. As shown in Figure 5A–F, the transcriptional levels of genes *tlr5*, *myd88*, *irak4*, *traf6*, *Rela*, and *NF-kB2* within TLR/NF-κB pathway in high-dose groups were significantly down-regulated ($p < 0.01$) compared with those in the control groups. Moreover, the antioxidant genes *cat* and *gpx*, and the immune gene *c-type lysozyme* were significantly up-regulated ($p < 0.01$) after Nb30 treatment (Figure 5G–I).

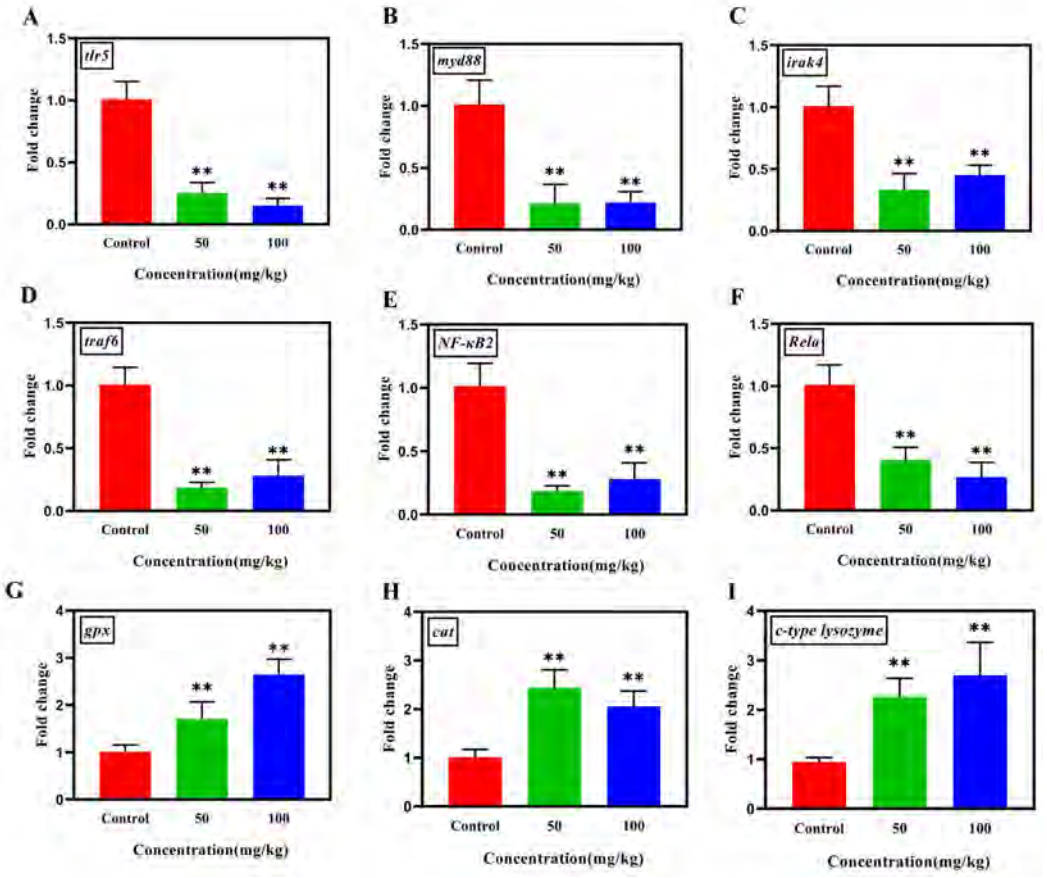


Figure 5. The effect of Nb30 on the expressions of TLR/MyD88/NF-κB inflammatory pathway, antioxidant and immune genes (**A**) *tlr5*, (**B**) *myd88*, (**C**) *irak4*, (**D**) *traf6*, (**E**) *Nf-kB2*, (**F**) *Rela*, (**G**) *gpx*, (**H**) *cat*, and (**I**) *c-type lysozyme* in the liver tissues of GBS-infected tilapia after 24 hpi. ** $p < 0.01$, compared to control.

4. Discussion

GBS, a serious pathogen, poses a major threat to the tilapia aquaculture industry. In the context of diminishing effectiveness of antibiotic treatments, the development of new prevention and control strategies is particularly urgent. Vaccination has received much attention as an emerging effective tool [22,23]. However, due to the diversity of GBS serotypes, designing and preparing vaccines that offer broad protection has become a major challenge in vaccine development. Sip protein, one of the key adhesion proteins for the invasion of host cells by GBS, is highly conserved, making the Sip proteins a popular target for the development of vaccines or drugs against GBS. Currently, delivery of purified Sip proteins to tilapia in a variety of ways to stimulate the production of specific antibodies is an effective method against GBS infestation [24,25]. However, the method has the limitation that inoculation is time-consuming. Nanobodies have great advantages

in the diagnosis and treatment of bacterial and viral diseases because their elongated CDR3 loop provides sufficient antigen-binding sites and can extend to hidden epitopes of antigens [26], making the development of nanobodies targeting Sip proteins a promising new antibacterial strategy.

Phage display technology is currently the mainstream technique for screening nanobodies (Nbs) against target antigens, which allows Nbs to be displayed on the phage surface and maintain their spatial structure and bioactivity, and this approach greatly improves the efficiency of screening [27,28]. Currently, the main mechanism of Nbs against pathogens is by blocking the binding of pathogens to host cells [29,30]. For example, researchers screened four Nbs against Shiga toxin-producing *Escherichia coli* (STEC) and enterotoxin-producing *E. coli* (ETEC) bacterial trichomonas protein F18, which competitively interfered with the binding of F18 to the blood group antigen receptor, thereby inhibiting the pathogen's adherent infection in piglets [31]. A high-affinity Nb Abi-Se07 targeted virulence factor FliC of *Salmonella* was screened from an Nb phage library and was specific to adhere to the surface of *Salmonella* and inhibit its invasion into host cells [32]. In this study, we screened three specific Nbs from a naïve phage library using Sip proteins as targets. Among these, Nb30 demonstrated excellent Sip-binding activity in in vitro binding assays and was able to bind to GBS. To further validate the inhibitory activity, we evaluated the antibacterial activity of Nb30 by employing a GBS-infected tilapia model and quantified the copy number changes of GBS in spleen, liver and brain tissues of tilapia by qPCR. The results demonstrated that Nb30 significantly inhibited the proliferation of GBS in various tissues of tilapia. This inhibition may be attributed to the ability of Nb30 to bind to the Sip protein on GBS, thereby blocking the interaction between the Sip protein and the host receptor cells. Consequently, this hinders the adhesion of GBS to the host cells, which ultimately leads to the differences in survival rates of tilapia [33].

The TLR/MyD88/NF-κB signaling pathway is a key pathway in the inflammatory response system of fish, and it is widely present in a wide range of fish tissue cells and is involved in the pathogenesis and regulation of inflammatory and infectious diseases [34,35]. Toll-like receptors (TLRs) are a class of pattern-recognition receptors capable of triggering inflammatory immune responses in the body. All TLR proteins activate the MyD88-dependent pathway and generate a signaling cascade reaction with MyD88, during which the body will release a series of intermediate factors, such as irak4, traf6, etc., and ultimately activate the production of NF-κB family proteins involved in inflammatory response and cytotoxicity factors (Rela, NF-κB2, etc.) [36]. It has been shown that the expression of genes related to the TLR/MyD88/NF-κB signaling pathway is significantly up-regulated in tilapia after GBS infestation, leading to a severe inflammatory response in the fish [37–39]. Interestingly, the expression of genes related to the TLR/MyD88/NF-κB signaling pathway was down-regulated when Nb30 acted. In conclusion, Nb30 may attenuate the inflammatory response induced by GBS by inhibiting the TLR/MyD88/NF-κB signaling pathway.

It is well known that redox balance in the organism is essential for maintaining normal cellular activity and is closely related to a variety of physiopathological responses. However, when tilapia are infected with GBS, the attack of pathogenic bacteria induces cellular damage and a strong inflammatory response, leading to an imbalance between the oxidative and antioxidant systems caused by excessive production or insufficient removal of reactive oxygen species (ROS) [40]. Catalase (cat) and glutathione peroxidase (gpx) are important components of the antioxidant defense system in fish and play a key role in the balance between ROS production and antioxidants. When tilapia were infected with GBS, the gene expression levels of *cat* and *gpx* were significantly down-regulated [40]. Our study showed that Nb30 significantly improved the expression level of *cat*, *gpx* in tilapia, which is similar to the previous findings that specific antibodies could attenuate the oxidative

damage caused by pathogenic bacterial invasion [41]. Lysozyme activity is an important marker of innate immunity in fish, and the innate immune response is characterized by its rapid response to the presence of pathogens, activation of cellular defense mechanisms and networks of action, including production of antimicrobial substances and proteins, and activation of nonclassical complement to help fish resist invasion by pathogens [42]. Bacteria often adhere to host cell receptors through surface structures, transforming into a state that allows them to form biofilms, thereby resisting antibody and complement penetration and evading phagocytosis by phagocytes. Therefore, developing drugs that target adhesins is a crucial measure in preventing and treating bacterial diseases [43]. Nb30 primarily targets the adhesin Sip of GBS. When Nb30 binds to GBS, it may interfere with GBS adhesion to tilapia tissues, causing GBS to become a free-floating state. This transformation facilitates the initiation of the host's immune defense mechanisms, as free-floating bacteria lack physical barriers and are more easily phagocytosed by phagocytes such as neutrophils and macrophages [44,45]. Additionally, antibodies acting on the bacteria can activate the host's complement system, enhancing immune clearance through opsonization [46]. Therefore, we speculate that Nb30 blocks GBS adhesion to host cell receptors, enhances the tilapia's ability to capture free-floating bacteria, thereby promoting immune function and increased the expression of *c-type lysozyme* in GBS-infected tilapia, which helped tilapia to clear GBS from the body.

Cytochrome P450, a large superfamily of enzymes with heme as a cofactor, acts as a multifunctional biocatalyst and plays a key role in the detoxification of xenobiotics, the metabolism of exogenous and endogenous compounds, and homeostasis in vivo. In addition, several studies have shown that cytochrome P450 also plays an important role in immune defense. For instance, Zhang et al. identified a substantial number of cytochrome P450 genes from spotted catfish subjected to bacterial attack using RNA-seq, suggesting that these genes may play a significant role in defense against bacteria [47]. Reynaud et al. demonstrated that the expression of microsomal cytochrome P450 and related enzymes can be regulated when fish defense mechanisms are activated [48]. In the present study, Nb30 enhanced drug metabolism-cytochrome P450 and cytochrome P450 metabolic pathways to exogenous drugs in tilapia liver tissues, which may enhance the body's immune response against GBS, thus exerting the biotransformation function and detoxification capacity of liver tissues.

A transcriptome analysis was conducted on the high-concentration treatment groups and the control groups, which yielded 637 differentially expressed genes (DEGs). Subsequent results revealed a series of DEGs implicated in substance metabolism and immune-related pathways, encompassing A scorbate and aldarate metabolism, Drug metabolism-cytochrome P450, Metabolism of xenobiotics by cytochrome P450 and chemokine signaling pathways. Ascorbate and aldarate metabolism represent a significant carbohydrate metabolic pathway in living organisms, with the capacity to protect cells from oxidative damage caused by aerobic metabolism and a range of pollutants. It has been found that ascorbate and aldarate metabolism were significantly inhibited when mud crabs were infected with mud crab diademovirus-1 (MCDV-1), which may facilitate the pathogen's ability to infect the host [49]. In the present study, the expression of genes associated with ascorbic acid and aldaric acid metabolism was found to be significantly enhanced following the action of Nb30, a finding that aligns with previous studies that observed the up-regulation of antioxidant genes.

Chemokines are a class of signaling proteins or small cellular factors. In organisms, chemokines regulate leukocyte migration, influencing T cell secretion and are pivotal factors between innate and adaptive immunity [50]. A variety of CC-like and CXC-like factors, including CCL3, CCL19 & CXC14, were identified in our study, and there were

different degrees of upward or downward trends of these chemokines, suggesting that the role of Nb30 for promoting immune responses in tilapia is complex. Interestingly, the present study revealed that GO enrichment analysis of immune response pathways identified multiple genes associated with antigen presentation and antimicrobial peptide expression, including mamu class II histocompatibility antigen, proteasome subunit beta type-9 (PSMB9), transmembrane protein 173 (TMEM173), and moronecidin. Notably, these genes exhibited significant downregulation in the control group compared to the treatment group. This phenomenon may be attributable to Nb30's inhibitory effect on GBS adhesion to host cells, thereby enhancing the immune system's capacity to capture free bacterial antigens. These findings are corroborated by the concomitant upregulation of c-type lysozyme expression, collectively supporting the critical role of Nb30 in activating both innate and adaptive immune responses in tilapia. In conclusion, transcriptomic analysis further demonstrated that Nb30 modulates multiple physiological processes in Nile tilapia, including antioxidant stress response, immune function, amino acid and protein synthesis, as well as energy metabolism. These comprehensive molecular changes collectively contribute to the improved survival and physiological homeostasis of fish under GBS challenge, highlighting Nbs' multifaceted regulatory functions in enhancing fish disease resistance.

5. Conclusions

In this study, we focused on using the highly conserved adhesin Sip of GBS as a specific protein target, rather than the whole GBS bacterium, which may improve the antibacterial activity of nanobodies against GBS serum type variations. In a tilapia infection model, Nb30 effectively reduced GBS colonization in the liver, spleen, and brain of Nile tilapia, accompanied by a downregulation of TLR/MyD88/NF-κB pathway-related inflammatory genes and improved survival rates of infected fish. We also used transcriptomics to analyze the metabolic and immune functions of Nile tilapia, confirming that Nb30 alleviates oxidative stress, regulates immune responses, enhances amino acid/protein synthesis, and energy metabolism. In summary, this manuscript advances the study of nanobodies' antibacterial mechanisms and provides a potential broad-spectrum protective nanobody against multiple GBS serotypes. Our findings offer a strategy for controlling GBS infection in tilapia and further validate the use of nanobodies as a sustainable antibiotic alternative for managing bacterial diseases in aquaculture. However, how to efficiently deliver Nbs into fish bodies is a problem that needs to be addressed in the future.

Supplementary Materials: The following supporting information can be downloaded at: https://www.mdpi.com/article/10.3390/ani15213207/s1. Figure S1: Plasmid construction and protein expression of pET28a-Sip; Table S1: Sequences of primers for this study.

Author Contributions: Methodology, Z.W., W.H., S.W., X.W., C.W. and A.H.; software, Z.W., H.W., W.H. and S.W.; validation, Z.W., H.W., W.H. and C.W.; data curation, Z.W. and H.W.; writing—original draft, Z.W. and W.H.; writing—review & editing, H.W., S.W., X.W., Y.W. and A.H.; supervision, Y.W. and A.H.; project administration, Y.W. and A.H.; funding acquisition, H.W., Y.W. and A.H. All authors have read and agreed to the published version of the manuscript.

Funding: This work was funded by Natural Science Foundation of Guangxi (2021GXNSFBA075008), Guangxi Science and Technology Program (No. AD22080029, AD25069075), National Natural Science Foundation of China (No. 42106133), and Green and Low Carbon Technology Program of Guangxi Institute of Industrial Technology (DTS-202305001, DTS-202503001).

Institutional Review Board Statement: The animal use protocol was approved by the Animal Care and Welfare Committee of Guangxi University (GXU-2023-0134, approved by 5 January 2023).

Informed Consent Statement: Written informed consent was obtained from the owner of the animals involved in this study.

Data Availability Statement: The data supporting the findings of the study are available from the corresponding author upon reasonable request.

Acknowledgments: We sincerely thank Song Zhu from Southwest University for providing the GBS strain.

Conflicts of Interest: The authors declare no competing interests in this manuscript.

References

1. Sakyi, M.E.; Cai, J.; Tang, J.; Abarike, E.D.; Xia, L.; Li, P.; Kuebutornye, F.K.A.; Zou, Z.; Liang, Z.; Jian, J. Effects of starvation and subsequent re-feeding on intestinal microbiota, and metabolic responses in Nile tilapia, *Oreochromis niloticus*. *Aquac. Rep.* **2020**, *17*, 100370. [CrossRef]
2. Mian, G.F.; Godoy, D.T.; Leal, C.A.G.; Yuhara, T.Y.; Costa, G.M.; Figueiredo, H.C.P. Aspects of the natural history and virulence of *S. agalactiae* infection in Nile tilapia. *Vet. Microbiol.* **2009**, *136*, 180–183. [CrossRef]
3. Sirimanapong, W.; Phuoc, N.N.; Crestani, C.; Chen, S.E.; Zadoks, R.N. Geographical, Temporal and Host-Species Distribution of Potentially Human-Pathogenic Group B *Streptococcus* in Aquaculture Species in Southeast Asia. *Pathogens* **2023**, *12*, 525. [CrossRef] [PubMed]
4. Slotved, H.C.; Kong, F.; Lambertsen, L.; Sauer, S.; Gilbert, G.L. Serotype IX, a proposed new *Streptococcus agalactiae* serotype. *J. Clin. Microbiol.* **2007**, *45*, 2929–2936. [CrossRef] [PubMed]
5. Zhang, Z. Research Advances on Tilapia Streptococcosis. *Pathogens* **2021**, *10*, 558. [CrossRef]
6. Osman, K.M.; Al-Maary, K.S.; Mubarak, A.S.; Dawoud, T.M.; Moussa, I.M.I.; Ibrahim, M.D.S.; Hessain, A.M.; Orabi, A.; Fawzy, N.M. Characterization and susceptibility of streptococci and enterococci isolated from Nile tilapia (*Oreochromis niloticus*) showing septicaemia in aquaculture and wild sites in Egypt. *BMC Vet. Res.* **2017**, *13*, 357. [CrossRef]
7. Zhang, Y.; Du, X.S.; Deng, S.; Li, C.H.; He, Q.; He, G.P.; Zhou, M.; Wang, H.B.; Deng, R.J. Dual Triple Helix-Aptamer Probes for Mix-and-Read Detecting Antibiotics in Fish and Milk. *J. Agric. Food Chem.* **2020**, *68*, 9524–9529. [CrossRef]
8. Mohammed, E.A.H.; Kovacs, B.; Kuunya, R.; Mustafa, E.O.A.; Abbo, A.S.H.; Pal, K. Antibiotic Resistance in Aquaculture: Challenges, Trends Analysis, and Alternative Approaches. *Antibiotics* **2025**, *14*, 598. [CrossRef]
9. Ghahroudi, M.A.; Desmyter, A.; Wyns, L.; Hamers, R.; Muyldermans, S. Selection and identification of single domain antibody fragments from camel heavy-chain antibodies. *Febs Lett.* **1997**, *414*, 521–526. [CrossRef]
10. Barta, M.L.; Shearer, J.P.; Arizmendi, O.; Tremblay, J.M.; Mehzabeen, N.; Zheng, Q.; Battaile, K.P.; Lovell, S.; Tzipori, S.; Picking, W.D.; et al. Single-domain antibodies pinpoint potential targets within *Shigella* invasion plasmid antigen D of the needle tip complex for inhibition of type III secretion. *J. Biol. Chem.* **2017**, *292*, 16677–16687. [CrossRef]
11. Ebrahimizadeh, W.; Gargari, S.M.; Rajabibazl, M.; Ardekani, L.S.; Zare, H.; Bakherad, H. Isolation and characterization of protective anti-LPS nanobody against *V. cholerae O1* recognizing Inaba and Ogawa serotypes. *Appl. Microbiol. Biotechnol.* **2013**, *97*, 4457–4466. [CrossRef]
12. Chi, X.; Zhang, X.; Pan, S.; Yu, Y.; Shi, Y.; Lin, T.; Duan, H.; Liu, X.; Chen, W.; Yang, X.; et al. An ultrapotent RBD-targeted biparatopic nanobody neutralizes broad SARS-CoV-2 variants. *Signal Transduct. Target. Ther.* **2022**, *7*, 780–789. [CrossRef]
13. Yang, M.; Gu, K.; Xu, Q.; Wen, R.Q.; Li, J.P.; Zhou, C.Y.; Zhao, Y.; Shi, M.W.; Weng, Y.; Guo, B.Y.; et al. Recombinant *Lactococcus lactis* secreting FliC protein nanobodies for resistance against *Salmonella* enteritidis invasion in the intestinal tract. *J. Nanobiotechnology* **2024**, *22*, 629. [CrossRef]
14. Vanmarsenille, C.; del Olmo, I.D.; Elseviers, J.; Ghassabeh, G.H.; Moonens, K.; Vertommen, D.; Martel, A.; Haesebrouck, F.; Pasmans, F.; Hernalsteens, J.P.; et al. Nanobodies targeting conserved epitopes on the major outer membrane protein of *Campylobacter* as potential tools for control of *Campylobacter* colonization. *Vet. Res.* **2017**, *48*, 86. [CrossRef]
15. Jacques, M.; Paradis, S.E. Adhesin-receptor interactions in *Pasteurellaceae*. *Fems Microbiol. Rev.* **1998**, *22*, 45–59. [CrossRef]
16. Shabayek, S.; Spellerberg, B. Group B Streptococcal Colonization, Molecular Characteristics, and Epidemiology. *Front. Microbiol.* **2018**, *9*, 437. [CrossRef] [PubMed]
17. Li, L.P.; Liu, Y.; Huang, T.; Liang, W.W.; Chen, M. Development of an attenuated oral vaccine strain of tilapia Group B Streptococci serotype Ia by gene knockout technology. *Fish Shellfish. Immunol.* **2019**, *93*, 924–933. [CrossRef]
18. Martin, D.; Rioux, S.; Gagnon, E.; Boyer, M.; Hamel, J.; Charland, N.; Brodeur, B.R. Protection from group B streptococcal infection in neonatal mice by maternal immunization with recombinant Sip protein. *Infect. Immun.* **2002**, *70*, 4897–4901. [CrossRef]
19. Díaz-Dinamarca, D.A.; Jerias, J.I.; Soto, D.A.; Soto, J.A.; Díaz, N.V.; Leyton, Y.Y.; Villegas, R.A.; Kalergis, A.M.; Vásquez, A.E. The Optimisation of the Expression of Recombinant Surface Immunogenic Protein of Group B Streptococcus in *Escherichia coli* by Response Surface Methodology Improves Humoral Immunity. *Mol. Biotechnol.* **2018**, *60*, 215–225. [CrossRef]

20. Huang, A.-G.; He, W.-H.; Su, L.-J.; Zhang, F.-L.; Wang, Y.-H. Identification of a camelid-derived nanobody as a potential therapeutic agent against *Streptococcus agalactiae* infection. *Aquaculture* **2022**, *561*, 738725. [CrossRef]
21. Sun, W.; Li, C.; Jiang, L.; Pan, Z.; Qiao, G.; Chen, J. Complete genome sequence of the obligate endosymbiont *Buchnera aphidicola* of the poplar bark aphid *Pterocomma populeum*. *Microbiol. Resour. Announc.* **2025**, *14*, e00379-00325. [CrossRef]
22. de Queiróz, G.A.; Silva, T.M.F.E.; Leal, C.A.G. Duration of Protection and Humoral Immune Response in Nile Tilapia (*Oreochromis niloticus* L.) Vaccinated against *Streptococcus agalactiae*. *Animals* **2024**, *14*, 1744.
23. Nurani, F.S.; Sukenda, S.; Nuryati, S. Maternal immunity of tilapia broodstock vaccinated with polyvalent vaccine and resistance of their offspring against *Streptococcus agalactiae*. *Aquac. Res.* **2020**, *51*, 1513–1522. [CrossRef]
24. Liu, J.; Liu, G.Y.; Cao, Y.; Du, H.; Liu, T.Q.; Liu, M.Z.; Li, P.F.; He, Y.; Wang, G.X.; Yu, Q.; et al. BNC-rSS, a bivalent subunit nanovaccine affords the cross-protection against *Streptococcus agalactiae and Streptococcus iniae* infection in tilapia. *Int. J. Biol. Macromol.* **2023**, *253*, 126670. [CrossRef]
25. Cai, Y.Z.; Liu, Z.G.; Lu, M.X.; Ke, X.L.; Zhang, D.F.; Gao, F.Y.; Cao, J.M.; Wang, M.; Yi, M.M. Oral immunization with surface immunogenic protein from *Streptococcus agalactiae* expressed in *Lactococcus lactis* induces protective immune responses of tilapia (Oreochromis niloticus). *Aquac. Rep.* **2020**, *18*, 100538. [CrossRef]
26. Muyldermans, S. Nanobodies: Natural Single-Domain Antibodies. *Ann. Rev. Biochem.* **2013**, *82*, 775–797. [CrossRef]
27. Reader, R.H.; Workman, R.G.; Maddison, B.; Gough, K.C. Advances in the Production and Batch Reformatting of Phage Antibody Libraries. *Mol. Biotechnol.* **2019**, *61*, 801–815. [CrossRef] [PubMed]
28. Hsu, C.-Y.; Jasim, S.A.; Rodrigues, P.; Rizaev, J.A.; Malathi, H.; Ashraf, A.; Thakur, R.; Arya, R.; Jawad, M.A.; Gabble, B.C. Recent progress on phage display-based biosensing systems for detection of pathogenic bacteria in food and water. *Microchem. J.* **2025**, *208*, 112356. [CrossRef]
29. Sanaei, M.; Setayesh, N.; Sepehrizadeh, Z.; Mahdavi, M.; Yazdi, M.H. Nanobodies in Human Infections: Prevention, Detection, and Treatment. *Immunol. Investig.* **2020**, *49*, 875–896. [CrossRef]
30. Pradhan, S.; Swanson, C.J.; Leff, C.; Tengganu, I.; Bergeman, M.H.; Wisna, G.B.M.; Hogue, I.B.; Hariadi, R.F. Viral Attachment Blocking Chimera Composed of DNA Origami and Nanobody Inhibits Pseudorabies Virus Infection In Vitro. *Acs Nano* **2023**, *17*, 23317–23330. [CrossRef] [PubMed]
31. Moonens, K.; De Kerpel, M.; Coddens, A.; Cox, E.; Pardon, E.; Remaut, H.; De Greve, H. Nanobody Mediated Inhibition of Attachment of F18 Fimbriae Expressing *Escherichia coli*. *PLoS ONE* **2014**, *9*, e114691. [CrossRef] [PubMed]
32. Huen, J.; Yan, Z.; Iwashkiw, J.; Dubey, S.; Gimenez, M.C.; Ortiz, M.E.; Patel, S.; Jones, M.D.; Riazi, A.; Terebiznik, M.; et al. A Novel Single Domain Antibody Targeting FliC Flagellin of *Salmonella enterica* for Effective Inhibition of Host Cell Invasion. *Front. Microbiol.* **2019**, *10*, 2665. [CrossRef]
33. Zhang, L.P.; Hong, Y.C.; Sun, K.H.; Zhao, S.Y.; Bai, Y.H.; Yang, S.Y.; Tao, J.J.; Shi, F.; Zhan, F.B.; Lin, L.; et al. Passive protection of chicken egg yolk immunoglobulin (IgY) against Streptococcus agalactiae infection in Nile tilapia (*Oreochromis* niloticus). *Fish Shellfish. Immunol.* **2024**, *154*, 109923. [CrossRef] [PubMed]
34. Guo, S.T.; Gao, W.X.; Zeng, M.S.; Liu, F.L.; Yang, Q.Z.M.; Chen, L.; Wang, Z.S.; Jin, Y.J.; Xiang, P.; Chen, H.X.; et al. Characterization of *TLR1* and expression profiling of TLR signaling pathway related genes in response to *Aeromonas hydrophila* challenge in hybrid yellow catfish (*Pelteobagrus fulvidraco* ♀x *P. vachelli* ♂>). *Front. Immunol.* **2023**, *14*, 1163781. [CrossRef]
35. Zhang, J.; Kong, X.H.; Zhou, C.J.; Li, L.; Nie, G.X.; Li, X.J. Toll-like receptor recognition of bacteria in signal pathways fish: Ligand specificity and signal pathways. *Fish Shellfish. Immunol.* **2014**, *41*, 380–388. [CrossRef]
36. Kumar, H.; Kawai, T.; Akira, S. Toll-like receptors and innate immunity. *Biochem. Biophys. Res. Commun.* **2009**, *388*, 621–625. [CrossRef]
37. Nguyen Bao, T.; Lee, P.-T. Functional characterization of myeloid differentiation factor 88 in Nile tilapia (*Oreochromis niloticus*). *Comp. Biochem. Physiol. B-Biochem. Mol. Biol.* **2020**, *250*, 110485.
38. Han, X.Q.; Gao, F.Y.; Lu, M.X.; Liu, Z.G.; Wang, M.; Ke, X.L.; Yi, M.M.; Cao, J.M. Molecular characterization, expression and functional analysis of IRAK1 and, Cheek for IRAK4 in Nile tilapia (*Oreochromis niloticus*). *Fish Shellfish. Immunol.* **2020**, *97*, 135–145. [CrossRef] [PubMed]
39. Gao, F.Y.; Liu, J.; Lu, M.X.; Liu, Z.G.; Wang, M.; Ke, X.L.; Yi, M.M.; Cao, J.M. Nile tilapia Toll-like receptor 7 subfamily: Intracellular TLRs that recruit MyD88 as an adaptor and activate the NF-κB pathway in the immune response. *Dev. Comp. Immunol.* **2021**, *125*, 104173. [CrossRef] [PubMed]
40. Du, J.L.; Cao, L.P.; Jia, R.; Gu, Z.Y.; He, Q.; Xu, P.; Jeney, G.; Ma, Y.Z.; Yin, G.J. Analysis of *Streptococcus agalactiae*-induced liver injury in tilapia (*Oreochromis niloticus*). *Aquac. Res.* **2020**, *51*, 1398–1405. [CrossRef]
41. Li, Y.K.; Huang, B.Z.; Sun, S.J.; Liu, N.Y.; Li, Y.Q.; Lan, M.W.; Wang, X.A.; Zhang, Y.W.; Wu, A.L.; Yang, S.Y.; et al. Immunoprotection effects of chicken egg yolk immunoglobulins (IgY) against Aeromonas veronii infection in Sinocyclocheilus grahami. *Aquaculture* **2023**, *563*, 738935. [CrossRef]

42. Biller, J.D.; Polycarpo, G.D.; Moromizato, B.S.; Sidekerskis, A.P.D.; da Silva, T.D.; dos Reis, I.C.; Fierro-Castro, C. Lysozyme activity as an indicator of innate immunity of tilapia (*Oreochromis niloticus*) when challenged with LPS and *Streptococcus agalactiae*. *Rev. Bras. Zootec.-Braz. J. Anim. Sci.* **2021**, *50*, e20210053. [CrossRef]
43. Klemm, P.; Vejborg, R.M.; Hancock, V. Prevention of bacterial adhesion. *Appl. Microbiol. Biotechnol.* **2010**, *88*, 451–459. [CrossRef] [PubMed]
44. Krachler, A.M.; Orth, K. Targeting the bacteria-host interface: Strategies in anti-adhesion therapy. *Virulence* **2013**, *4*, 284–294. [CrossRef]
45. Ghosh, S.; Chakraborty, K.; Nagaraja, T.; Basak, S.; Koley, H.; Dutta, S.; Mitra, U.; Das, S. An adhesion protein of *Salmonella enterica* serovar Typhi is required for pathogenesis and potential target for vaccine development. *Proc. Natl. Acad. Sci. USA* **2011**, *108*, 3348–3353. [CrossRef]
46. Dalia, A.B.; Weiser, J.N. Minimization of Bacterial Size Allows for Complement Evasion and Is Overcome by the Agglutinating Effect of Antibody. *Cell Host Microbe* **2011**, *10*, 486–496. [CrossRef]
47. Zhang, J.R.; Yao, J.; Wang, R.J.; Zhang, Y.; Liu, S.K.; Sun, L.Y.; Jiang, Y.L.; Feng, J.B.; Liu, N.N.; Nelson, D.; et al. The cytochrome P450 genes of channel catfish: Their involvement in disease defense responses as revealed by meta-analysis of RNA-Seq data sets. *Biochim. Biophys. Acta-Gen. Subj.* **2014**, *1840*, 2813–2828. [CrossRef] [PubMed]
48. Reynaud, S.; Marrionet, D.; Taysse, L.; Deschaux, P. Interleukin-1α and tumor necrosis factor α modulate cytochrome P450 activities in carp (*Cyprinus carpio*). *Ecotoxicol. Environ. Saf.* **2005**, *62*, 355–362. [CrossRef] [PubMed]
49. Liao, M.Z.; Cheng, C.H.; Li, G.Y.; Ma, H.L.; Liu, G.X.; Fan, S.G.; Deng, Y.Q.; Jiang, J.J.; Feng, J.; Guo, Z.X. Transcriptome analysis of *Scylla paramamosain* hepatopancreas response to mud crab dicistrovirus-1 infection. *Fish Shellfish. Immunol.* **2024**, *154*, 109872. [CrossRef]
50. Wong, M.M.; Fish, E.N. Chemokines: Attractive mediators of the immune response. *Semin. Immunol.* **2003**, *15*, 5–14. [CrossRef]

Disclaimer/Publisher's Note: The statements, opinions and data contained in all publications are solely those of the individual author(s) and contributor(s) and not of MDPI and/or the editor(s). MDPI and/or the editor(s) disclaim responsibility for any injury to people or property resulting from any ideas, methods, instructions or products referred to in the content.

forests

MDPI

Article

High-Resolution Mapping and Impact Assessment of Forest Aboveground Carbon Stock in the Pinglu Canal Basin: A Multi-Sensor and Multi-Model Machine Learning Approach

Weifeng Xu [1], Xuzhi Mai [2], Songwen Deng [2], Wenhuan Wang [2,3], Wenqian Wu [3], Wei Zhang [2,*] and Yinghui Wang [2,3]

[1] School of Resources, Environment and Materials, Guangxi University, Nanning 530004, China; xwf@st.gxu.edu.cn
[2] School of Marine Sciences, Guangxi University, Nanning 530004, China; 2327301019@st.gxu.edu.cn (X.M.); dsw591603897@gmail.com (S.D.); wwhuan2202@126.com (W.W.); wyh@gxu.edu.cn (Y.W.)
[3] Institute of Green and Low Carbon Technology, Guangxi Institute of Industrial Technology, Nanning 530200, China; wuwq1@foxmail.com
* Correspondence: zhangwei20@gxu.edu.cn

Abstract

Accurate estimation of forest aboveground carbon stock (AGC) is critical for climate change mitigation and ecological management. This study develops a high-resolution AGC estimation workflow for the Pinglu Canal basin, integrating Sentinel-2, Sentinel-1, ALOS PALSAR, and SRTM data with field survey measurements. Feature selection via Recursive Feature Elimination and modeling with a Random Forest algorithm—optimized through hyperparameter tuning—yielded high predictive accuracy under the ***ALL*** data combination (R^2 = 0.818, RMSE = 11.126 tC/ha), enabling the generation of a 10 m-resolution AGC map. The total AGC in 2024 was estimated at 2.26 × 10^6 tC. To evaluate human-induced changes, we established a baseline scenario based on historical AGC trends (2002–2021) and climate data. Comparisons revealed that afforestation and vegetation restoration during canal construction led to higher AGC values than projected under natural conditions. This positive deviation highlights the effectiveness of targeted ecological interventions in mitigating carbon loss and promoting forest recovery. Our results demonstrate a cost-effective, scalable method for AGC mapping using freely accessible remote sensing data and machine learning. The findings also provide insights into balancing large-scale infrastructure development with ecosystem conservation.

Keywords: multi-source remote sensing data; forest aboveground carbon stock; Recursive Feature Elimination; machine learning; Pinglu Canal basin; forest ecosystem dynamics

check for updates

Academic Editor: Yunjun Yao

Received: 12 June 2025
Revised: 2 July 2025
Accepted: 7 July 2025
Published: 9 July 2025

Citation: Xu, W.; Mai, X.; Deng, S.; Wang, W.; Wu, W.; Zhang, W.; Wang, Y. High-Resolution Mapping and Impact Assessment of Forest Aboveground Carbon Stock in the Pinglu Canal Basin: A Multi-Sensor and Multi-Model Machine Learning Approach. *Forests* **2025**, *16*, 1130. https://doi.org/10.3390/f16071130

Copyright: © 2025 by the authors. Licensee MDPI, Basel, Switzerland. This article is an open access article distributed under the terms and conditions of the Creative Commons Attribution (CC BY) license (https://creativecommons.org/licenses/by/4.0/).

1. Introduction

The current climate and biodiversity crises pose significant risks to ecosystems and human societies [1]. As highlighted by the IPCC and the Paris Agreement, forests are vital for maintaining ecosystem stability and mitigating climate change [2]. Forests, the primary carbon sinks within terrestrial ecosystems, are pivotal to the global carbon cycle due to their ability to absorb and retain carbon, thereby contributing significantly to climate regulation [3,4]. Therefore, precise monitoring of forests is crucial for developing informed climate policies, safeguarding biodiversity, and ensuring sustainable development [5,6]. In particular, understanding the spatial dynamics of forest carbon stock and

evaluating its responses to large-scale anthropogenic disturbances—such as major infrastructure development—has become increasingly important in both ecological research and environmental management.

China, recognizing the urgency of climate change, has set dual carbon goals: peaking carbon emissions by 2030 and achieving carbon neutrality by 2060. To meet these targets, China has implemented comprehensive strategies, including the promotion of renewable energy, emissions reduction, and enhanced carbon sequestration through forest conservation and afforestation programs [7]. China's forests, covering approximately 23% of the country's land area, are fundamental to carbon sequestration and ecosystem stability, contributing significantly to the nation's dual carbon goals [8]. In particular, Guangxi province, with its diverse and abundant forest resources, is a key region in supporting these national objectives through sustainable forest management and carbon storage efforts [9]. At the same time, the region is undertaking the construction of the Pinglu Canal, a major infrastructure project designed to enhance water transportation efficiency and stimulate regional economic growth. However, despite the anticipated economic and logistical benefits, the project is likely to exert considerable pressure on the ecosystems along its route. The Environmental Impact Assessment results indicate that the canal construction project will occupy 3276.7 ha of forest, with a permanently occupied area of 987.12 ha. Consequently, it is essential to carefully evaluate and mitigate the environmental impacts, particularly on the forests within the canal's watershed. Integrating conservation efforts into the planning and implementation phases will be crucial to minimizing the ecological footprint of this development [10].

Currently, research on the canal basin ecosystems primarily focuses on the Panama Canal [11–13], which is in operation. Monitoring projects conducted by the Smithsonian Tropical Research Institute and the Panama Environmental Authority indicate that the forests in the Panama Canal watershed play a vital role in biodiversity and water resource protection. However, these ecosystems are facing increasing pressures due to human activities [14]. Moreover, the forests in the Panama Canal watershed are closely linked to canal operations, and reforestation affects ecosystem services in complex ways. Under different conditions, reforestation has both positive impacts and trade-offs concerning water flow, carbon sequestration, and timber production [15]. Additionally, the Panama Canal provides valuable reference points for forest ecosystem protection measures during the construction phase of large-scale infrastructure projects. During the early stages of the canal's construction, the United States, for security and water supply reasons, protected the forests along a 660 km corridor on both sides of the canal. Today, after the Panama Canal was handed over to Panama, the surrounding forests remain intact and have been incorporated into national parks and nature reserves [16]. This experience provides valuable lessons for the development of new canals, demonstrating the potential for achieving a balance between environmental and social benefits. Despite the valuable insights from existing studies, research on the ecological impacts during the construction phase of canal projects remains limited. This gap is particularly evident in understanding how large-scale infrastructure affects forest ecosystems in both the short and the long term. As such, targeted research is urgently needed to fill this knowledge gap and support more informed environmental management in future canal projects.

Reliable quantification of aboveground carbon stock (AGC) in forests is critical for evaluating ecosystem functioning and informing strategies for climate change mitigation [17]. Traditional methods based on field inventories and biomass models offer high precision but are constrained by limited spatial coverage and high labor costs [18]. With advances in remote sensing, satellite-based AGC estimation has become a practical solution for large-scale monitoring [19]. Optical and Synthetic Aperture Radar (SAR) data provide

complementary information: optical sensors capture canopy structure in clear conditions, while SAR enables observations under clouds and in complex terrain [20–23]. However, single-source data face limitations. Optical sensors suffer from cloud contamination and canopy saturation, while SAR is prone to signal saturation and environmental sensitivity to factors like precipitation and soil moisture [24]. Integrating data from multiple sources has proven to be an effective approach for addressing these challenges. Integrating spectral, structural, and topographic features from multiple sensors significantly improves AGC estimation accuracy and robustness, especially in heterogeneous landscapes [25,26]. This approach has shown strong applicability in complex ecological settings [27,28]. Modeling methods have also evolved. Linear regression is widely used but often fails to capture non-linear relationships between variables and AGC [29,30]. Machine learning models—such as Support Vector Regression (SVR), Random Forest (RF), and Extreme Gradient Boosting (XGBoost)—offer enhanced performance, particularly when combined with feature selection and hyperparameter tuning [31–33]. Accurate spatial alignment between remote sensing pixels and field plots is also critical to reduce uncertainty and improve model reliability [34]. In summary, combining multi-sensor remote sensing data with robust machine learning models provides a scalable and reliable framework for accurate AGC estimation. Recent research has confirmed that combining field inventory data with machine learning algorithms is a feasible approach for estimating AGC across different spatial scales [35–37].

To address the research gap concerning the effects of canal construction on forest ecosystems during the construction period, this study employs multi-source remote sensing data combined with machine learning methods to estimate forest AGC in the Pinglu Canal basin for the year 2024 at a 10 m resolution. Additionally, historical data are utilized to assess the construction-related impacts on forest dynamics within the basin. The objectives of this study are (1) to combine tree-level measurements with remote sensing data at a fine scale to obtain accurate pixel-level AGC datasets; (2) to use Recursive Feature Elimination (RFE) for feature selection and assess the effectiveness of different data types or combinations of data in AGC modeling predictions; (3) to optimize the parameters of RF and XGBoost models through grid search and evaluate their estimation capabilities for AGC in comparison with Multiple Linear Regression (MLR) and SVR, and then use the best-performing model to predict AGC and produce a spatial distribution map of AGC at a 10 m resolution for the Pinglu Canal basin; and (4) to analyze the impact of the canal construction on the forest ecosystem by examining the interannual variations in forest area and AGC. This study represents the first attempt to estimate forest AGC in the Pinglu Canal basin using high-resolution remote sensing data, while also examining the ecological impacts of the canal by analyzing temporal changes in forest area and AGC. It provides valuable insights into the relationship between large-scale infrastructure projects and forest ecosystems, contributing to the understanding of how canal construction affects forest AGC.

2. Materials and Methods

2.1. Study Area

The Pinglu Canal, spanning a total length of 135 km, is located in Guangxi Province, China (Figure 1). The canal basin experiences an annual average rainfall exceeding 1800 mm and a mean temperature of 21.7 °C, reflecting the characteristics of a subtropical monsoon climate. The topography is highly diverse, ranging from low-lying plains to high-altitude mountainous regions, with elevations spanning from −2 m to 371 m above sea level. This varied terrain supports a range of ecosystems, including forests that play a critical role in carbon stock and maintaining ecological stability, consisting primarily of evergreen broadleaf forests and mixed coniferous forests. Notably, plantations are the predominant

forest type in the basin, featuring key species such as Chinese fir (*Cunninghamia lanceolata*), eucalyptus (*Eucalyptus* spp.), masson pine (*Pinus massoniana*), and slash pine (*Pinus elliottii*).

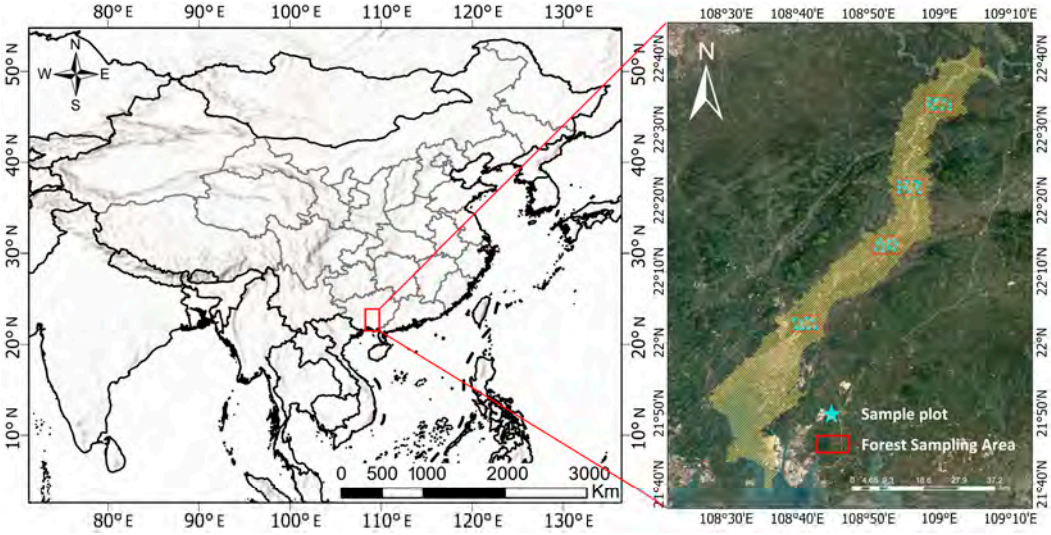


Figure 1. Study area and sample plot distribution.

The Pinglu Canal project, a significant waterway construction initiative in southern China, has substantially transformed local land use and ecological patterns. This study aims to assess the potential impacts of canal construction on forest ecosystems, with a particular focus on the dynamics of forest AGC.

2.2. Data and Methodology

To obtain an accurate spatial distribution of forest carbon stock in the Pinglu Canal basin for 2024, a systematic workflow was developed, integrating field survey data, remote sensing data preprocessing, feature selection, and machine learning-based modeling. This workflow combines multi-source data, including SAR, optical data, and terrain data, to extract essential variables such as backscatter coefficients, vegetation indices, texture features, and topographic parameters. The field survey data were transformed into pixel-level AGC values, which were then combined with remote sensing-derived features for model training. RFE was employed to select the most relevant predictors, which were subsequently used in a Random Forest regression framework. The final model was validated against field survey data to ensure accuracy, leading to the generation of a comprehensive forest AGC map for the Pinglu Canal basin in 2024. The workflow is illustrated in Figure 2, providing a detailed representation of the methodological approach adopted in this study.

2.2.1. Field Sampling and Plot Inventory

To obtain field data on forest carbon stock within the study area, we conducted a plot survey in four regions of the watershed, covering the area from the upstream of the canal to the estuary, from September to October 2024. Prior to the field survey, we selected representative vegetation types based on imagery and forestry reports. A survey plan was then formulated to ensure that the selected sample plots represented the full spectrum of vegetation diversity across the study area. Ultimately, due to practical considerations such as road accessibility, we established 37 square sample plots, each measuring 25 m $\times$ 25 m. Trees with a diameter at breast height (DBH) $\geq$ 5 cm were measured, and the surveyed characteristics included the DBH, tree height, and species of all trees within the plots. In addition, the coordinates of each individual tree within the sample plots were recorded using a handheld Real-Time Kinematic (RTK) device. These high-precision spatial data

were used to accurately locate each tree, enabling detailed analysis and integration with remote sensing data for subsequent AGC estimation.

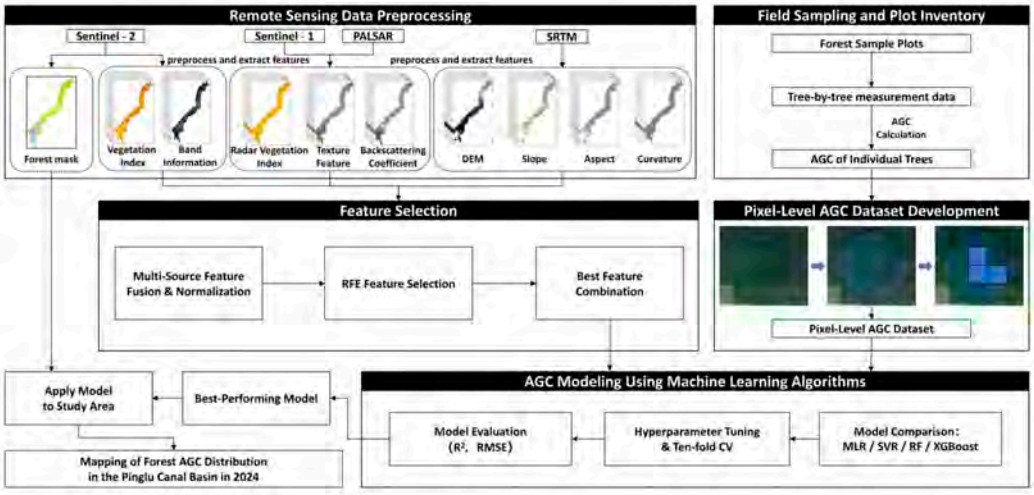


Figure 2. Flowchart showing the overall workflow for data preprocessing, modeling, and forest AGC mapping in the Pinglu Canal basin in 2024.

Based on the field survey, a total of 4038 trees were recorded across all sample plots. Among these, the dominant tree species was eucalyptus, with 3069 individuals, followed by slash pine (*Pinus elliottii*), with 610 individuals; masson pine (*Pinus massoniana*), with 149 individuals; and other species, accounting for 210 individuals. This species composition reflects the diversity of vegetation within the study area and serves as a critical foundation for constructing accurate AGC models. These data were further processed and integrated with remote sensing features to derive pixel-level AGC estimates for the study region.

2.2.2. Pixel-Level AGC Dataset Development

Accurately estimating forest AGC at the pixel level requires the precise integration of field data and remote sensing imagery. To better capture spatial heterogeneity within sample plots, we adopted and refined a method that integrates high-precision tree-level coordinate data with the Sentinel-2 pixel grid. While similar methods have been applied in forest structure inversion and individual tree segmentation studies based on UAV data [38,39], this study advances the approach by incorporating tree-level RTK data, handling missing pixels, and ensuring alignment with the spatial resolution of Sentinel-2 imagery. These improvements enhance the application of this method in integrating satellite pixel data with field plot measurements.

This methodology provides a more accurate and robust framework for generating pixel-level AGC datasets. The precise tree-level coordinates collected during the field survey were used to delineate the boundaries of each sample plot, which were then mapped onto the Sentinel-2 pixel grid (10 m × 10 m). Subsequently, pixels within the boundaries of each sample plot were extracted, while pixels with missing data were excluded [40] to ensure the completeness and accuracy of the training dataset (Figure 3).

Building upon this framework, the next step was to calculate the AGC for each selected pixel. Using species-specific allometric equations, the aboveground biomass (AGB) of each tree was computed as follows:

$$\mathrm{AGB} = a \times (\mathrm{DBH})^b \times (\mathrm{H})^c \quad (1)$$

where a, b, and c are species-specific parameters derived from allometric models; DBH is the diameter at breast height (cm); and H is the tree height (m).

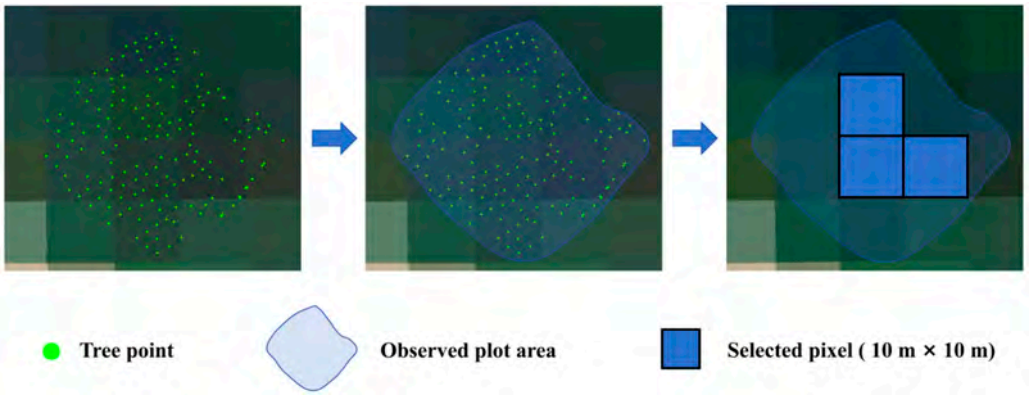


Figure 3. The flowchart illustrates the process of converting field-measured individual tree data into Sentinel-2 pixel-level carbon storage for subsequent training. Ultimately, only pixels with no missing data were included in the dataset.

The AGC of each individual tree was then calculated by applying a carbon conversion factor (CF), which quantifies the proportion of biomass attributable to carbon:

$$\mathrm{AGC(tree)} = \mathrm{AGB} \times \mathrm{CF} \tag{2}$$

Typically, CF values range between 0.47 and 0.50. In this study, to achieve more accurate forest AGC distribution estimates, the CF for all sampled tree species was obtained from national standards. For tree species without specified CF values in the standards, they were categorized into soft broadleaf and hard broadleaf forest types, and the corresponding CF values were applied accordingly.

Finally, the total AGC for each pixel was derived by aggregating the AGC of all individual trees within the corresponding plot boundary:

$$\text{Total AGC(pixel)} = \sum_{i=1}^{n} \mathrm{AGC}_i \tag{3}$$

where n is the number of trees within the plot, and AGC_i is the AGC of the i-th tree.

This methodological approach enabled the integration of fine-scale, tree-level measurements with remote sensing data, ensuring that the resulting pixel-level AGC estimates were accurate and compatible with the spatial resolution of multi-source remote sensing data. However, it should be noted that this approach may still be subject to certain limitations, such as data loss caused by mixed pixels or imperfect alignment between ground plots and remote sensing grids, which are further discussed in the Section 4.

2.2.3. Remote Sensing Data Preprocessing

1. Optical Data

Optical data can be used to estimate forest AGC because they capture key spectral information related to vegetation structure, canopy characteristics, and biochemical properties, which are closely correlated with biomass. The free accessibility, global coverage, high temporal and spatial resolution, and long temporal scale of Sentinel-2 data make them a valuable resource for monitoring forest carbon dynamics over time. The dataset used in this study is the Sentinel-2 L2A surface reflectance product, which has undergone atmospheric correction and orthorectification to provide high-quality, geometrically aligned surface reflectance data. To account for the effects of cloud cover, we used imagery acquired on 31 October 2024, which closely aligns with the timing of field surveys. In this study, we utilized bands with a 10 m resolution (blue, green, red, and near-infrared 1) and a

20 m resolution (red edge 1, red edge 2, red edge 3, near-infrared 2, shortwave infrared 1, and shortwave infrared 2). All bands were resampled to a 10 m resolution using the Sen2Res processor in SNAP 11.0.0. Furthermore, previous studies have demonstrated that spectral vegetation indices carry significant information for biomass estimation. Based on the processed Sentinel-2 imagery, we calculated 18 commonly used vegetation indices for biomass estimation (Table 1).

Table 1. Bands, indices, and features extracted from Sentinel-2, Sentinel-1, PALSAR, and SRTM data.

Sensor		Bands, Indices or Texture Features	Description
Sentinel-2	Multispectral bands	B2	490 nm, blue
		B3	560 nm, green
		B4	665 nm, red
		B5	705 nm, red edge1
		B6	740 nm, red edge2
		B7	783 nm, red edge3
		B8	842 nm, NIR
		B8A	865 nm, red edge4
		B11	1610 nm, SWIR
		B12	2190 nm, SWIR
	Vegetation indices	ARVI, CVI, DVI, EVI, GNDVI, GRVI, IPVI, LAI, MSAVI, MTCI, NBR, NBR2, NDI45, NDVI, NDWI, REIP, SAVI, WDVI	All 18 vegetation indices are calculated based on multispectral bands.
Sentinel-1	Polarization	VV	Vertical–vertical polarization
		VH	Vertical–horizonal polarization
	Indices	VV + VH	All 5 indices are calculated based on the dual-polarization backscatter coefficient (VV and VH).
		VV − VH	
		VV/VH	
		VH/VV	
		(VV − VH)/(VV + VH)	
	Texture feature	Mean	Texture features are extracted from dual-polarization backscatter coefficients (VV and VH) using GLCM with a 7×7 pixel window.
		Variance	
		Homogeneity	
		Contrast	
		Dissimilarity	
		Entropy	
		Second moment	
		Correlation	
PALSAR	Polarization	HH	Horizontal–horizontal polarization
		HV	Horizontal–vertical polarization
	Indices	HH + HV	All 5 indices are calculated based on the dual-polarization backscatter coefficient (HH and HV).
		HH − HV	
		HH/HV	
		HV/HH	
		(HH − HV)/(HH + HV)	
	Texture feature	Same as Sentinel-1	Texture features are extracted from dual-polarization backscatter coefficients (HH and HV) using GLCM with a 7×7 pixel window.
SRTM	DEM	Elevation	Height above sea level
	Indices	Slope	All 5 indices are all calculated using standard terrain analysis algorithms in GIS software (ArcGIS Pro, version 3.0.1).
		Aspect	
		Curvature	
		Plan curvature	
		Profile curvature	

2. SAR Data

SAR data, renowned for their capability to penetrate vegetation and capture structural information under all-weather conditions, represent a critical resource for forest AGC estimation. In this study, SAR datasets from Sentinel-1 and ALOS-2 PALSAR-2 were employed. To ensure consistency with Sentinel-2 data, the Sentinel-1 and PALSAR data were resampled to a 10 m spatial resolution. Sentinel-1 data, consisting of two scenes corresponding to the field sampling period, were acquired through the European Space Agency data portal. The data underwent preprocessing in SNAP 11.0.0 to derive VV and VH polarized backscatter coefficients, expressed in decibels (dB). Subsequently, five dual-polarization indices were computed based on these backscatter coefficients. Additionally, a suite of texture features, including mean, variance, homogeneity, contrast, dissimilarity, entropy, second moment, and correlation, was extracted using the gray-level co-occurrence matrix method with a 7×7 pixel window. Due to maintenance on the official platform, PALSAR data were obtained from Google Earth Engine (GEE). The imagery acquisition date was selected as the closest available scene covering the Pinglu Canal Basin to the field sampling period (30 August). The dataset provided HH and HV polarized backscatter coefficients directly. Utilizing these coefficients, the same five dual-polarization indices were calculated, and the same set of texture features was extracted. The integration of these polarization indices and texture features offered detailed insights into vegetation structure and heterogeneity, significantly enhancing the precision of forest AGC estimation across the study area.

3. Topographic Data

Topographic factors, including elevation and terrain variability, are essential in forest AGC estimation due to their impact on vegetation distribution, growth conditions, and biomass accumulation. In this study, we utilized the Shuttle Radar Topography Mission (SRTM) Digital Elevation Model (DEM), which provides global elevation data at a spatial resolution of 30 m. The SRTM DEM has been widely validated for its high accuracy and reliability in representing topographic features. To ensure consistency with other datasets, the SRTM data were resampled to a 10 m resolution. Furthermore, topographic variables such as slope, aspect, and curvature were derived from the resampled DEM and incorporated into the analysis to account for the effects of terrain on forest biomass distribution.

4. Forest Mask

The forest mask is a critical element for understanding the spatial distribution and dynamic changes of forest cover, playing a key role in AGC estimation, biodiversity assessment, and the monitoring of land use changes. In this study, the forest mask was generated using the deep learning-based Dual-Net framework proposed by Liu et al. [41]. This algorithm integrates dual-date Sentinel-2 imagery, multimodal information fusion (which combines spatial and temporal features), and low-level attention constraints to enhance classification accuracy. By effectively capturing spectral, textural, and temporal characteristics, it enables precise differentiation of land cover types. The classification results produced by this algorithm outperform those of commonly used land cover products, achieving superior accuracy and enabling the generation of more refined and precise forest masks.

In this study, land cover classification for the Pinglu Canal basin from 2021 to 2024 was conducted using the Dual-Net framework. This framework, based on Sentinel-2 imagery, was implemented on the AI Earth platform developed by Alibaba DAMO Academy [42]. The classification outputs were further processed to extract a forest mask. Additionally, the mangrove areas within the mask were removed using the mangrove identification algorithm proposed by Zhao et al. [43] in their study, with the corresponding code made

available as open-source on GEE. This approach accurately delineated forested and non-forested areas, providing a reliable dataset for subsequent analyses of forest carbon stock and the spatiotemporal dynamics of forest cover.

5. Historical Forest AGC Data

This study utilizes the forest AGC data for China from 2002 to 2021, provided by Chen et al. [44]. This dataset was generated at a 1 km resolution by integrating multiple remote sensing observations, such as SAR backscatter, optical data, and passive microwave data, with extensive field measurements and machine learning models. The dataset includes both aboveground and belowground carbon pools, offering comprehensive and spatially explicit information on forest carbon stock changes over the past two decades.

The AGC data were calibrated against field measurements to ensure high accuracy and extended temporally using regression models incorporating vegetation cover and other biophysical predictors. This dataset provides a reliable foundation for understanding long-term trends in forest carbon dynamics, including regional differences in forest biomass allocation and carbon sequestration. It, together with historical temperature and precipitation data obtained from the ERA5_Land dataset on GEE, was instrumental in establishing a historical baseline for analyzing the forest AGC in the Pinglu Canal basin.

2.2.4. Feature Selection

Selecting appropriate variables is crucial for constructing AGC models. Most initial variables are chosen based on previous research findings and relevant academic experience, followed by a summary of variables that may be effective for modeling. However, due to differences in geographical and vegetation characteristics, the variables used for AGC modeling often vary between different study areas. Meanwhile, in the context of machine learning, the variable selection process is expected to improve the efficiency of the modeling process and enhance the robustness of prediction accuracy [45]. Feature selection not only helps reduce the complexity of the model by eliminating irrelevant or redundant variables but also mitigates the risk of overfitting, particularly when working with high-dimensional datasets.

In this study, a feature-level data fusion strategy was applied before feature selection to integrate multi-source remote sensing inputs. Spectral indices (e.g., NDVI, EVI) from Sentinel-2, radar backscatter metrics (e.g., VV, VH, entropy, second moment) from Sentinel-1 and ALOS PALSAR-2, and topographic features (e.g., elevation, slope, curvature) from SRTM were extracted as primary variables.

Prior to fusion, all layers underwent radiometric correction, geometric alignment, and spatial resampling to a unified 10 m resolution using nearest-neighbor interpolation, ensuring pixel-level co-registration across data sources. After preprocessing, variables were min–max normalized to ensure comparability and minimize scaling bias [46]. These standardized features were then stacked at the pixel level to form a unified multivariate feature set. This approach allows for the synergistic use of spectral, structural, and topographic information, capturing the complementary characteristics of each sensor type.

Unlike raw stacking, the fusion process in this study emphasizes cross-source consistency and physical interpretability of features. Similar feature-level fusion strategies have been widely applied and validated in previous studies for enhancing forest biomass and carbon estimation accuracy [28,40,47,48].

To achieve these benefits, this study employed the RFE method to perform variable selection. In the RFE process, an external estimator is provided to assign weights to the features [49]. The estimator is first trained on the initial feature set to determine the importance of each feature. Subsequently, the least important feature is removed from the current feature set. This process is recursively repeated on the pruned feature set

to perform feature selection. In this study, RF was used as the feature estimator [50]. RF is highly appropriate for this application, given its capacity to model complex nonlinear relationships and variable interactions, along with its resistance to multicollinearity issues. The number of selected features was determined through automated tuning via cross-validation. The optimization and comparison of feature subsets were based on the coefficient of determination (R^2) and root mean square error (RMSE) obtained from ten-fold cross-validation.

By systematically identifying the most important features, this approach ensures that the final model is not only accurate but also computationally efficient. Additionally, focusing on the most relevant variables allows for better generalization to unseen data, further enhancing the applicability and reliability of the AGC estimation model across different study areas.

2.2.5. Machine Learning Algorithms

To evaluate the suitability and predictive performance of different modeling approaches for AGC estimation, four representative machine learning algorithms were tested:

MLR is a fundamental statistical technique used to characterize the relationship between a dependent variable and several independent predictors [51]. It assumes that the dependent variable is a linear combination of the predictors. MLR is computationally efficient and interpretable, making it useful for initial analysis when relationships are expected to be linear. However, it may not capture complex nonlinearities, which limits its performance in more intricate datasets.

SVR extends the concept of Support Vector Machines to regression tasks [52]. SVR aims to find a function that fits the data while allowing for some error within a specified margin. By using kernel functions, such as the radial basis function kernel, SVR can effectively capture nonlinear relationships. This makes SVR particularly suitable for modeling complex patterns in high-dimensional data, as is common in remote sensing applications.

RF is an ensemble learning method that constructs multiple decision trees and aggregates their outputs to improve prediction accuracy and reduce overfitting. It handles high-dimensional and nonlinear data effectively and is robust to noise and multicollinearity. RF has been widely applied in remote sensing studies due to its interpretability, resistance to overfitting, and ability to estimate variable importance.

Extreme Gradient Boosting is a powerful ensemble algorithm based on gradient boosting decision trees [53]. It builds models sequentially, with each new tree correcting errors made by the previous ones. XGBoost is known for its high predictive performance, regularization capabilities, and computational efficiency. It has gained popularity in environmental modeling tasks for its ability to handle complex feature interactions and large datasets.

These methods represent both linear and nonlinear regression techniques commonly used in remote sensing and environmental modeling. Each algorithm was selected and handled based on its characteristics and typical usage in similar tasks [54].

MLR, as a classical linear baseline, does not involve hyperparameters, but RFE was applied beforehand to address multicollinearity and improve model robustness. SVR was implemented with a radial basis function kernel, commonly used for capturing nonlinear patterns [55]. Grid search was performed to select the penalty parameter $C \in \{0.1, 1, 10, 100\}$ and kernel coefficient $\gamma \in \{0.01, 0.1, 1\}$, based on prior studies and empirical testing.

For the tree-based ensemble methods, RF and XGBoost, hyperparameter tuning was essential due to their flexible structure and potential to overfit [36]. For RF, the following parameters were tuned via grid search: number of trees (n_estimators $\in$ {100, 200, 300}), maximum tree depth (max_depth $\in$ {3, 6, 9}), tree depth (max_depth $\in$ {10, 20, None}), minimum samples required at a leaf node (min_samples_leaf $\in$ {1, 2, 3, 4, 5}), minimum

samples to split a node (min_samples_split ∈ {2, 4, 6, 8, 10}), and number of features considered at each split (max_features ∈ {'auto', 'sqrt', 'log2'}). Similarly, XGBoost was tuned over key parameters: learning rate (eta ∈ {0.01, 0.05, 0.1}), number of boosting rounds (n_estimators ∈ {100, 200, 300}), tree depth (max_depth ∈ {1, 2, 3, 4, 5, 6, 7, 8, 9}), and subsampling ratio (subsample ∈ {0.6, 0.8, 1.0}). These configurations allowed for a comprehensive search of the model space, enhancing both prediction accuracy and generalizability [56].

All models were trained and validated using ten-fold cross-validation, which partitions the dataset into ten equal parts and iteratively uses one for validation and the rest for training [57]. This approach helps reduce overfitting and ensures a fair and robust comparison across models. Performance was evaluated using R^2 and RMSE.

Among all tested algorithms, the RF model—combined with RFE and hyperparameter tuning—demonstrated the best predictive performance and was therefore selected for high-resolution, pixel-level AGC mapping. This selection is supported by the quantitative comparison presented in Section 3.2, where RF achieved the highest R^2 and lowest RMSE among all models.

2.2.6. Model Evaluation

To evaluate the performance of the selected feature and machine learning models, we split the dataset into a training set (70%) and a test set (30%). This study employed 10-fold cross-validation to test model hyperparameters and address issues such as overfitting. The models were assessed using two primary metrics: RMSE and R^2. RMSE provides a measure of the average prediction error, with lower values indicating better model performance. The R^2 value quantifies the proportion of variance in the target variable explained by the model, with higher values indicating a better fit. The formulas for RMSE and R^2 are defined as follows:

$$\mathrm{RMSE} = \sqrt{\frac{1}{n}\sum_{i=1}^{n}(y_i - \hat{y}_i)^2} \quad (4)$$

$$R^2 = 1 - \frac{\sum_{i=1}^{n}(y_i - \hat{y}_i)^2}{\sum_{i=1}^{n}(y_i - \overline{y})^2} \quad (5)$$

where n is the observed sample size, y_i is the observed value for observation i, $\hat{y}_i$ is the predicted value i, and $\overline{y}$ is the mean of the observed values.

3. Results

3.1. Data Collection Comparison and Feature Selection

This study employed RFE to identify the most relevant input variables and utilized ten-fold cross-validation to evaluate the prediction performance across different feature set combinations. The input variables were derived from three main sources: optical data (Sentinel-2), Synthetic Aperture Radar imagery (Sentinel-1 and ***PALSAR***), and topographic attributes (***SRTM***). Random Forest was used as the modeling framework to assess the effectiveness of individual and fused datasets, both prior to and following feature selection.

For models trained on individual datasets, Sentinel-1 (***S1***) outperformed the others in estimation accuracy, followed by Sentinel-2 (***S2***). ***PALSAR*** and ***SRTM*** yielded comparatively lower accuracy, which may be attributed to their coarser spatial resolution and the mismatch in acquisition time between the remote sensing imagery and field data collection. Among the pairwise data combinations, the ***S1*** and ***SRTM*** duo produced the best results, followed by the ***S1*** and ***S2*** combination. When three datasets were used, the integration of ***S2***, ***S1***, and

SRTM showed the most reliable performance. Finally, when all four datasets were combined (***ALL***), the accuracy was slightly higher than the ***S2 + S1 + SRTM*** configuration, making it the best-performing combination overall. These findings indicate that incorporating a greater diversity of data sources generally enhances estimation accuracy.

Table 2 reveals that removing ***S1*** data from any two- or three-source combination led to a substantial decline in accuracy. This emphasizes the unique contribution of ***S1***, which offers the ability to penetrate cloud cover and forest canopies, capturing critical structural details such as canopy density and vegetation type. Such structural insights are vital for AGC estimation, particularly in ecologically complex or topographically varied regions. Furthermore, ***S1*** complements other datasets by supplying information that cannot be obtained through optical or topographic sources alone, thus strengthening model robustness.

Table 2. Comparison of forest AGC estimation models using different remote sensing data combinations.

Sensor	Number	R^2	RMSE	Selected	R^2	RMSE
S2	28	0.441	19.370	24	0.446	19.281
S1	23	0.577	17.723	22	0.580	17.662
PALSAR	23	0.356	19.113	11	0.360	19.053
SRTM	6	0.342	24.017	4	0.361	21.696
S2 + S1	51	0.601	16.361	42	0.610	16.190
S2 + PALSAR	51	0.494	19.217	28	0.503	19.063
S2 + SRTM	34	0.495	18.160	14	0.506	17.949
S1 + PALSAR	46	0.601	17.482	45	0.608	17.555
S1 + SRTM	29	0.615	16.897	22	0.630	16.569
PALSAR + SRTM	29	0.422	20.130	28	0.431	19.979
S2 + S1 + PALSAR	74	0.621	12.634	50	0.658	11.999
S2 + S1 + SRTM	57	0.640	13.373	37	0.655	13.090
S2 + PALSAR + SRTM	57	0.499	19.298	41	0.520	18.887
S1 + PALSAR + SRTM	52	0.616	14.067	51	0.632	13.613
ALL	80	0.647	12.191	21	0.659	11.980

Post-RFE, the number of retained features differed significantly across data combinations. However, there was no clear linear relationship between the number of features and the overall model performance. Although feature reduction varied, the relative ranking of each combination in terms of prediction accuracy remained stable. As detailed in Table 2, the combinations of ***S2 + S1 + PALSAR***, ***S2 + S1 + SRTM***, and ***ALL*** yielded favorable results, with the ***ALL*** set producing the highest accuracy and the fewest features. When model accuracy was comparable, the dataset with fewer selected features offered greater computational efficiency in prediction tasks.

3.2. Model Validation

Using the optimized subsets of selected features, we developed models based on MLR, SVR, and RF and XGBoost algorithms with hyperparameters fine-tuned via grid search. The generalization performance of each model was then assessed using the reserved test dataset.

To facilitate comparison, three data combinations were chosen—***S2 + S1 + PALSAR***, ***S2 + S1 + SRTM***, and the comprehensive ***ALL*** dataset—as they had shown similar potential during the feature selection stage. Figure 4 illustrates the model accuracies across all four algorithms for these combinations.

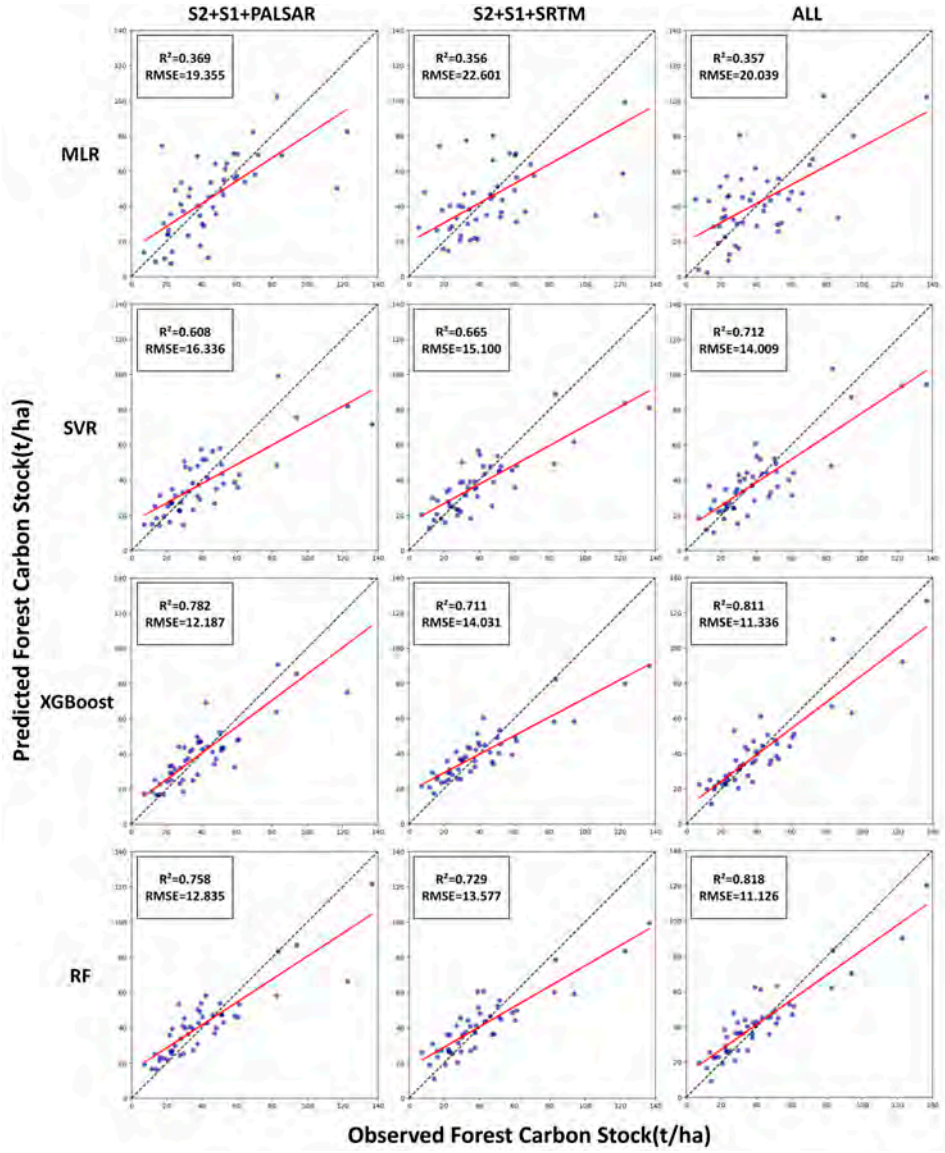


Figure 4. Comparison of forest AGC estimation using different algorithms and data combinations.

Validation outcomes demonstrate that model performance varied notably depending on the data inputs, with the ***ALL*** dataset (integrating ***S1***, ***S2***, ***PALSAR***, and ***SRTM***) yielding the highest accuracy overall. Among the modeling approaches, the grid-search-optimized RF and XGBoost algorithms consistently outperformed the others. In contrast, MLR produced the poorest results regardless of the input combination, likely due to its inability to effectively model the complex nonlinear patterns associated with forest AGC. Although SVR performed better than MLR, it still struggled to accommodate the intricate nature of the multi-source dataset. Comparatively, RF and XGBoost, with their enhanced nonlinear learning capabilities, achieved superior performance, with RF delivering the highest accuracy under the ***ALL*** configuration (R^2 = 0.818, RMSE = 11.126 tC/ha).

These results underscore the advantages of integrating diverse remote sensing datasets for improved AGC estimation. The RF model in particular emerged as the most effective method due to its robustness and adaptability to nonlinear relationships. Consequently, the RF model optimized with grid search under the ***ALL*** data configuration was selected as the final estimation model for forest AGC in the Pinglu Canal basin. This model not only achieved the best predictive performance but also benefited from using a minimal subset of features, thus enhancing computational efficiency while maintaining high estimation relia-

bility. Its effectiveness makes it particularly well suited for the spatiotemporal assessment of AGC within the study area.

3.3. Spatial Distribution of Forest AGC in the Pinglu Canal Basin

Based on the optimized Random Forest model under the ***ALL*** data combination, the estimated forest AGC values are shown in Figure 5. The figure reveals significant spatial variability in the AGC across the Pinglu Canal basin. Overall, high-carbon-stock areas are primarily distributed in the northern upstream and central regions, particularly in areas with dense forest coverage, where the AGC values can reach up to 66.85 tC/ha. In contrast, the downstream regions, especially near river corridors, exhibit noticeably lower carbon stock, with most values ranging from 6.37 to 25.58 tC/ha, represented by lighter colors. The trend of decreasing carbon stock from north to south is attributed to the dense vegetation and extensive forest coverage in the northern and central regions, whereas the downstream areas have reduced vegetation coverage due to agricultural activities, urban expansion, or infrastructure development. Statistical analysis of all pixels indicates that the average aboveground carbon density in the study area is 37.38 tC/ha. The statistical histogram of the pixel values shows that the majority of aboveground carbon density values in the study area fall within the range of 28 to 52 tC/ha. Furthermore, based on the forest area of the study region (6.07×10^4 ha), the total aboveground carbon stock is calculated to be 2.26×10^6 tC.

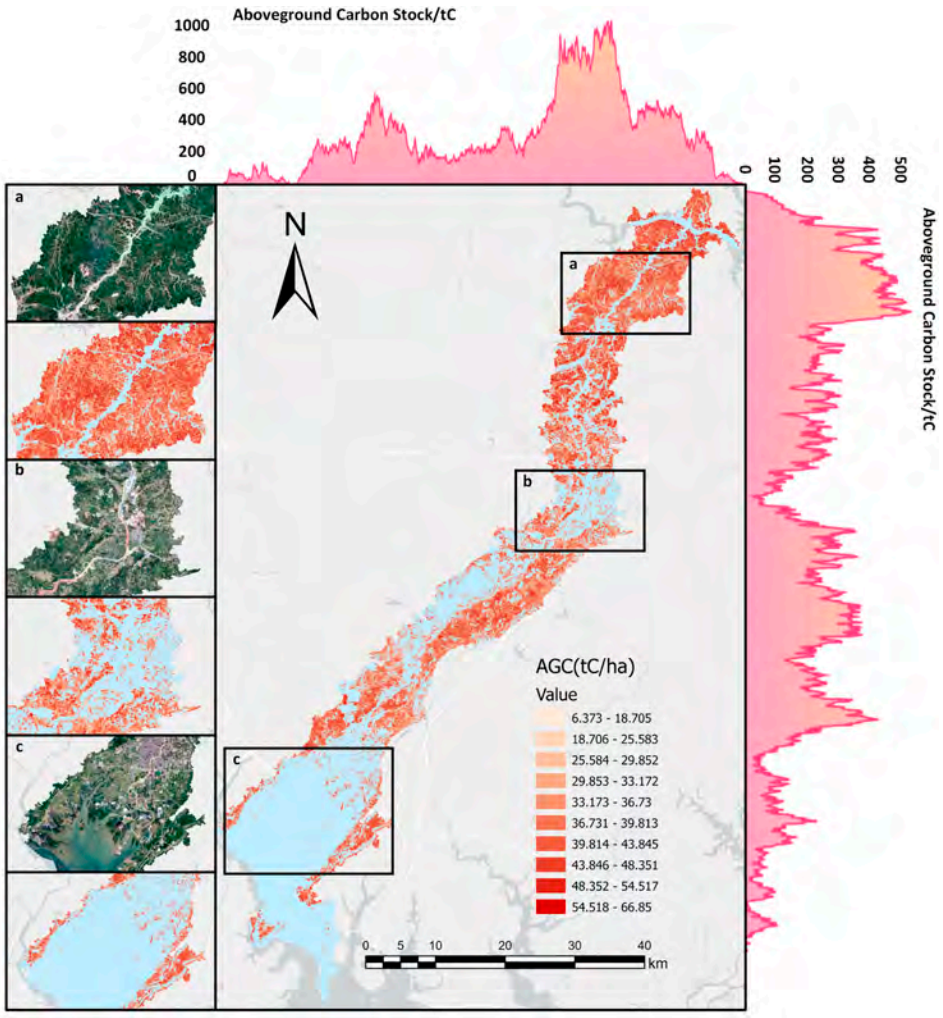


Figure 5. Spatial distribution and profile statistics of AGC in the Pinglu Canal basin. Panels a–c show representative high- and low-carbon-density areas corresponding to real land cover conditions.

4. Discussion

4.1. Addressing Spatial Heterogeneity in AGC Estimation with Advanced Sampling Methods

Accurate estimation of forest AGC largely depends on the precise alignment between field measurements and remote sensing data. Traditional methods typically rely on matching sample plots to satellite pixels by recording the plot's central coordinates or corner coordinates and aggregating plot-level attributes [58,59]. However, these methods assume uniform distribution of attributes within plots, neglecting spatial heterogeneity, and often result in misalignment with pixel grids, leading to inaccuracies in AGC estimation.

To address these limitations, we adopted a sampling method inspired by UAV studies, utilizing handheld RTK devices to record precise coordinates for each tree, enabling accurate alignment of tree point data with Sentinel-2 pixel grids. Unlike traditional methods, this approach accurately maps individual tree positions to corresponding pixel grids, capturing the spatial heterogeneity within sample plots. Pixels with missing or incomplete data were excluded, ensuring that only fully representative pixels were used for AGC estimation. This preserves the variability of forest attributes while avoiding the assumption of uniform distribution. Additionally, the alignment with Sentinel-2 grids minimizes errors caused by misregistration between field plots and remote sensing data, significantly enhancing the accuracy of pixel-level AGC estimation [60]. By accounting for within-plot variability, excluding incomplete pixels, and ensuring precise correspondence between field data and satellite imagery, our method establishes a more reliable foundation for AGC modeling and spatial analysis. To further validate this, we conducted a global spatial autocorrelation analysis using Moran's I [61]. It would provide further insights into the spatial structure of carbon storage and could help evaluate the effectiveness of different sampling or modeling strategies in representing spatial variability [62]. The result yielded a value of 0.77 ($p < 0.01$), indicating strong and statistically significant positive spatial autocorrelation. In addition, a local spatial clustering analysis was conducted to further examine the distribution pattern of AGC values (Figure 6).

As shown in Figure 6, significant high–high clusters were mainly concentrated in the central and northern areas of the forested region, where vegetation is denser and more continuous. In contrast, low–low clusters appeared along the southern and peripheral zones, which may reflect more fragmented or sparse forest stands. These spatial patterns emphasize the non-random distribution of forest carbon and further demonstrate the capacity of our pixel-level modeling framework to capture ecological spatial variability.

An additional advantage of our approach is its ability to significantly increase the number of modeling-ready AGC pixels derived from field data. Using 37 sample plots, we were able to obtain 158 forest AGC pixels for modeling, compared to traditional survey methods, where typically only one AGC pixel can be generated per sample plot [63]. This substantial increase in pixel-level data density enhances the robustness of AGC modeling by providing a more comprehensive representation of spatial variability, ultimately improving model performance and reliability.

A major limitation of our approach is the reduced utilization of field data due to the exclusion of incomplete pixels. As a result, many individual tree data points were not incorporated into the current analysis. Specifically, approximately 43% of individual tree data were excluded from this study. For 10 sample plots, the utilization rate of individual tree data was even below 45%, highlighting the limitations of the current approach in fully leveraging available data.

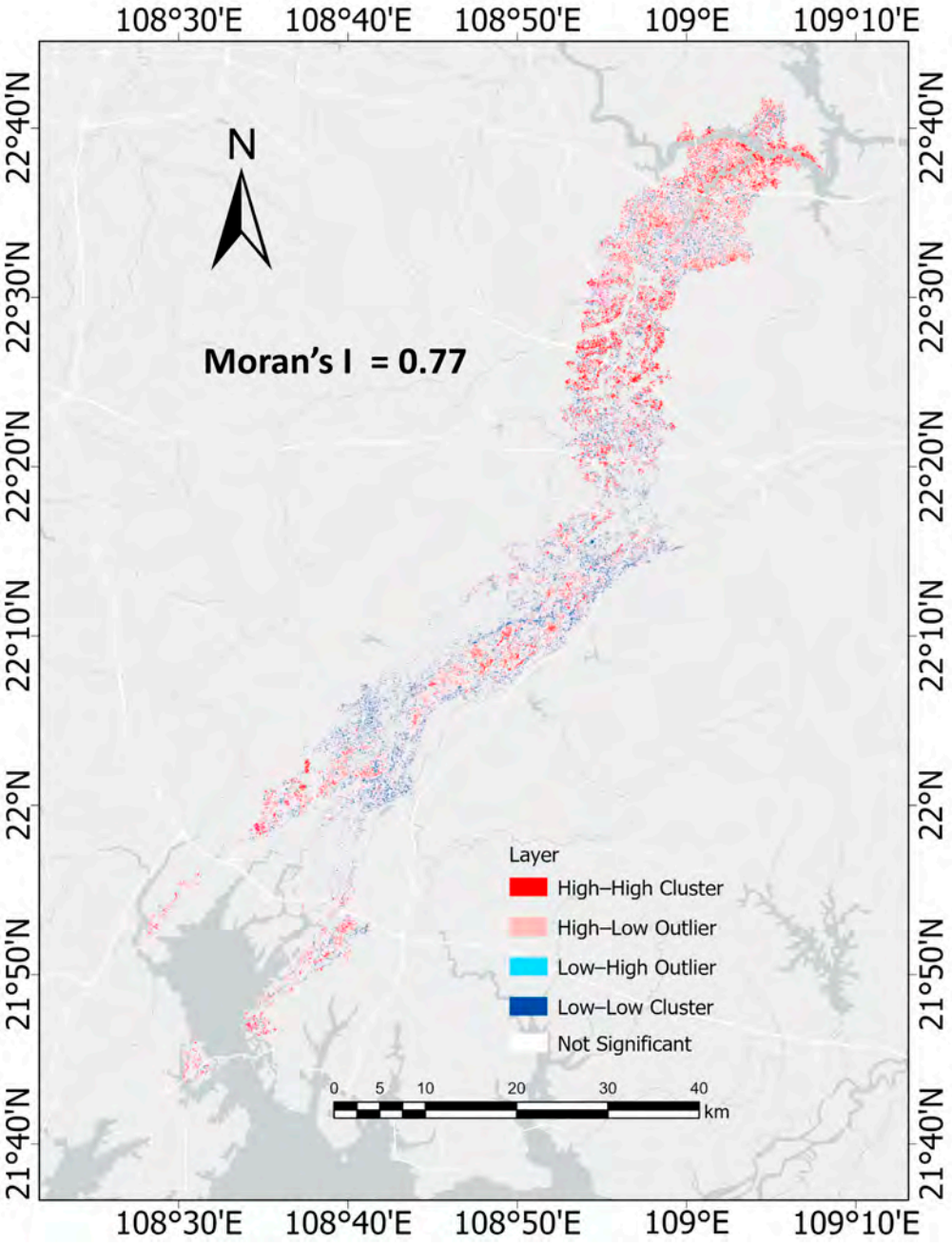


Figure 6. Local Moran's I cluster map of forest aboveground carbon stock in the Pinglu Canal basin.

To address this issue in future work, we plan to integrate UAV LiDAR data for individual tree biomass estimation, allowing for the full utilization of all individual tree data [64,65]. This integration would enable the generation of additional forest AGC pixels, further enhancing data density and improving the overall robustness of AGC modeling.

4.2. Relationship Between Multiple Source Factors and AGC

Analyzing the interplay between various data sources and AGC underscores the critical value of integrating multi-source remote sensing inputs for improving AGC prediction accuracy [66]. This study offers an in-depth evaluation of feature importance rankings alongside correlation analyses between selected variables and AGC, highlighting how inputs from diverse datasets contribute to model performance.

As shown in Figure 7, features derived from ***S1***, ***S2***, ***PALSAR***, and ***SRTM*** exhibit varying degrees of influence in the AGC estimation model. Among them, S1 features—

particularly VH-based entropy and second moment—emerge as the most influential, primarily due to their effectiveness in capturing vegetation structural complexity and texture [67]. S2-derived indices, such as the Normalized Burn Ratio (NBR) and Red-Edge Inflection Point (REIP), also rank highly, underscoring the role of spectral metrics in reflecting canopy condition and health [68]. Although variables from ***PALSAR*** and ***SRTM*** like variance (HH) and profile curvature demonstrate lower importance scores, they provide supplementary information related to terrain and surface structure. These outcomes reveal the complementary benefits of combining datasets: ***S1*** and ***S2*** serve as the primary contributors to AGC prediction, while ***PALSAR*** and ***SRTM*** reinforce model stability by offering structural and topographic context.

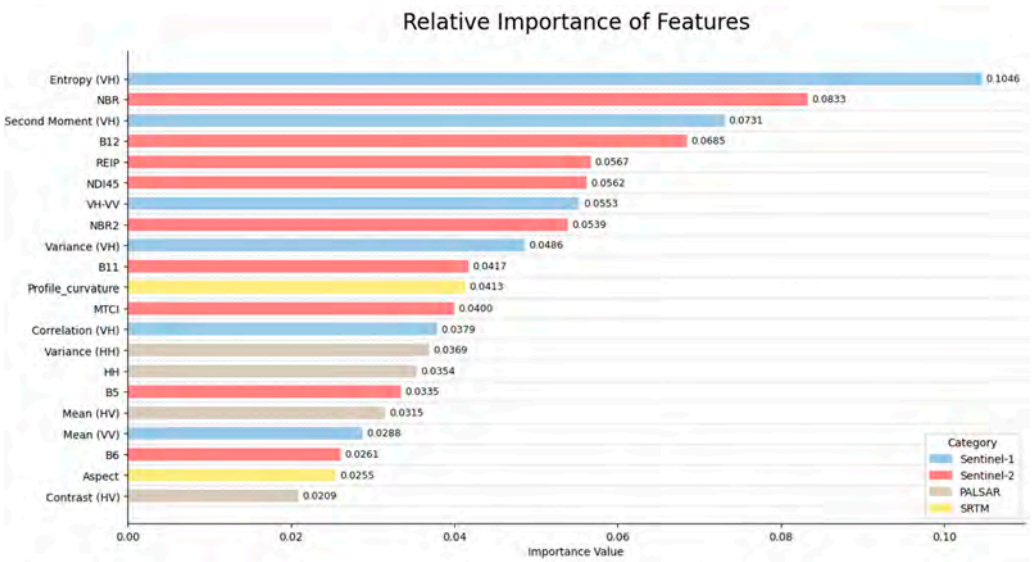


Figure 7. Relative importance ranking of multi-source remote sensing features in the random forest model optimized by grid search.

Further insights are provided in Figure 8, which displays the relationships between AGC and selected variables across different forest categories. In the aggregated dataset (***ALL***), moderate positive correlations are observed between AGC and ***S1*** variables such as VH-VV and VH entropy, highlighting the relevance of SAR-derived structural features. ***S2*** metrics consistently show absolute correlation coefficients exceeding 0.4, reflecting their importance in representing vegetation properties and spatial carbon distribution, especially in regions with lower to medium biomass levels. Conversely, terrain attributes (e.g., SRTM-derived profile curvature) and specific ***PALSAR*** variables (e.g., HV contrast and HH variance) display weaker correlations with AGC.

Distinct forest types exhibit unique patterns in feature relevance. For eucalyptus stands, ***S2*** variables like NBR and B12 are strongly associated with AGC, indicating spectral indices' sensitivity to eucalyptus canopy and biomass dynamics [69]. Slash pine, on the other hand, responds more to structural inputs from ***S1*** and PALSAR, as reflected by stronger correlations with VH correlation and HV mean. Masson pine AGC correlates robustly with all ***S1***-derived metrics, suggesting its structural characteristics are well captured by radar data. In mixed forests, a notable positive relationship is observed between AGC and the HV mean from PALSAR, signifying the value of SAR data in detecting structural heterogeneity. Interestingly, AGC in these mixed stands is negatively correlated with terrain variables from SRTM, indicating that complex topography, such as steep slopes, may inhibit forest growth and reduce carbon accumulation [70,71]. A summary comparison of the key variables from each data source and their relevance to AGC modeling across forest types is provided in Table 3.

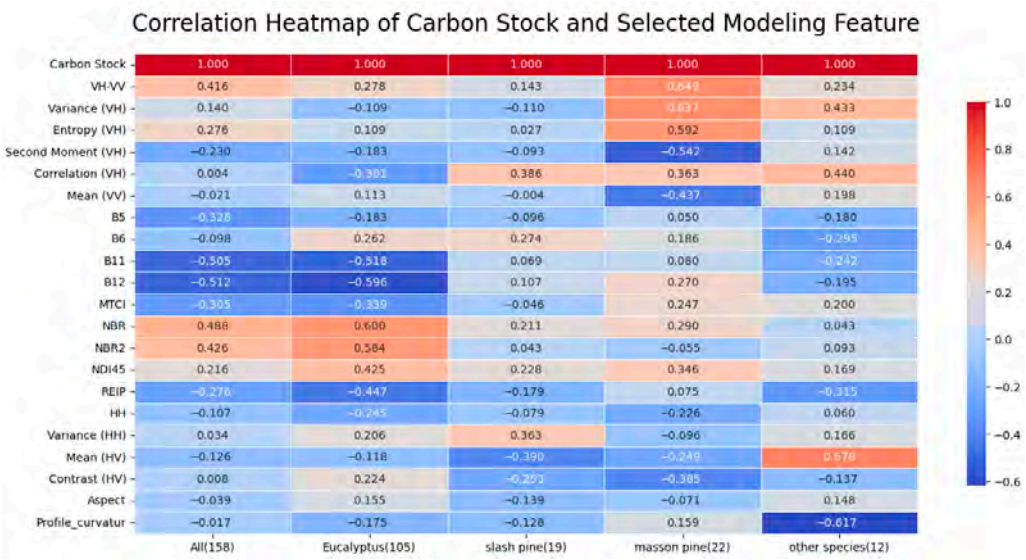


Figure 8. Correlation heatmap of AGC and modeling features across different tree species.

Table 3. Summary of Key Variables from Multi-Source Datasets and Their Relationship with AGC.

Data Source	Key Variables	Importance/ Feature Role	Typical Forest Types	Correlation with AGC	Notes/ Interpretation
Sentinel-1	Entropy (VH), VH-VV, second moment (VH)	High—captures structure and texture	Masson pine	Moderate to high	Key radar variables for structure; performs well in high-biomass and coniferous areas
Sentinel-2	NBR, REIP, B12	High—spectral condition indicators	Eucalyptus	Moderate to high	Sensitive to canopy health and chlorophyll; good in low–medium biomass zones
PALSAR	Variance (HH), HH, mean (HV)	Medium—supplementary structure	Mixed forests	Low to moderate	Adds heterogeneity info, useful in mixed stands
SRTM	Profile_curvature, aspect	Low—topographic background	Mixed forests	Weak	Reflects terrain influence; steep areas may limit carbon accumulation

Collectively, these results emphasize the significance of fusing multi-source datasets in AGC modeling. Sentinel-1 plays a crucial role by providing structural and textural details; Sentinel-2 offers rich spectral indicators of canopy health; and both PALSAR and SRTM add contextual information related to elevation and landscape complexity. The integration of these complementary data sources enables comprehensive and accurate carbon stock estimation across varied forest ecosystems [72].

4.3. Analysis of Interannual Variation of AGC and Area Change in the Pinglu Canal Basin Forest

To better evaluate the impact of canal construction on the forest ecosystem within the basin, analyses were conducted at two spatial scales [73]: the entire basin and a 1 km buffer zone around the river channels, which represents the Environmental Impact Assessment (EIA) area. Figure 9 illustrates the forest area dynamics in the Pinglu Canal basin from 2021 to 2024, based on forest masks generated in this study. The figure reveals significant interannual variations in forest area, driven by both canal construction activities and subsequent ecological restoration measures.

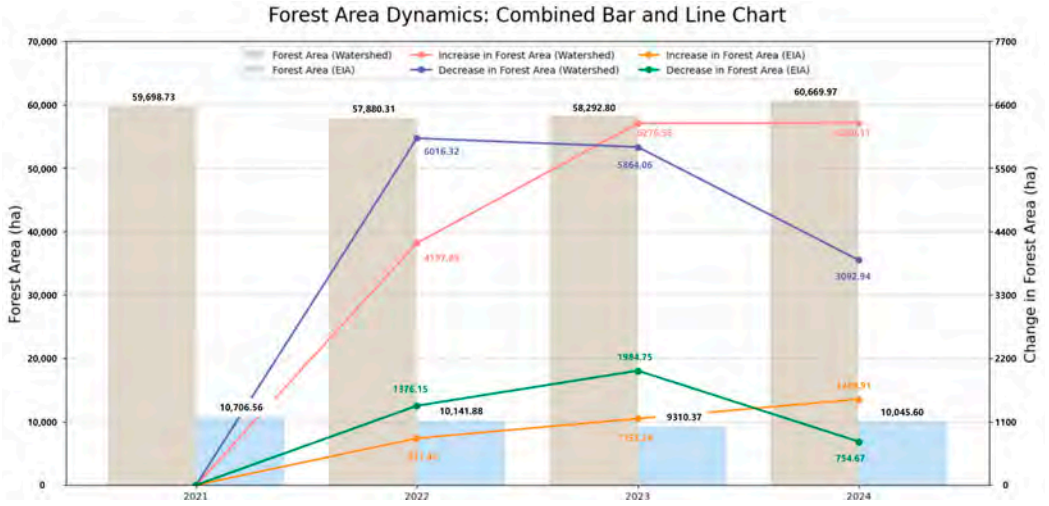


Figure 9. Annual forest area dynamics: increase and decrease.

In the EIA area, where construction activities were most concentrated, the forest area experienced a significant decline in 2022 due to land clearing for canal construction. Although reforestation measures improved forest cover in 2023 and 2024, the forest area in the EIA zone had not yet returned to 2021 levels by 2024. This is primarily due to the ongoing construction of the Pinglu Canal, as several areas within the 1 km buffer zone remain occupied by engineering projects, limiting the extent of forest recovery. In contrast, the entire watershed showed a more balanced trend. The forest area initially decreased from 59,683.73 ha in 2021 to 57,880.31 ha in 2022, reflecting the broader deforestation impact of construction activities. However, from 2023 onwards, forest recovery efforts led to a steady increase, culminating in 60,669.97 ha by 2024, demonstrating the effectiveness of large-scale conservation and reforestation initiatives [74]. These findings indicate that, although ongoing construction activities within the EIA area continue to hinder the complete recovery of forests to pre-construction levels, proactive conservation and reforestation measures have significantly increased forest area across the entire watershed.

Furthermore, a historical baseline scenario for the Pinglu Canal basin was established using historical AGC data from 2002 to 2021 and precipitation and temperature data obtained from the ERA5_Land dataset on GEE. A linear model was employed for fitting and prediction, yielding the predicted 2024 forest AGC with $R^2 = 0.76$ and RMSE = 184,137.79 tC for the entire basin, and $R^2 = 0.70$ and RMSE = 34,188.66 tC for the EIA area. The predicted values were then compared with the AGC estimates for 2024 derived in this study using multi-source remote sensing data. For the entire basin, the baseline scenario predicts a carbon stock of 2,079,631.86 tC, while the estimate based on multi-source remote sensing data is higher, at 2,260,779.61 tC, reflecting the positive impact of reforestation and conservation measures implemented during the canal construction period. Similarly, in the EIA area, the baseline scenario predicts 359,349.23 tC, whereas the estimated value reaches 370,767.55 tC, despite ongoing construction activities. These findings highlight the effectiveness of targeted vegetation restoration and protection efforts in enhancing carbon sequestration, even under the constraints of large-scale infrastructure projects [75].

Since the construction of the Pinglu Canal began in July 2022, afforestation efforts along the canal's route, as reported by the Guangxi Forestry Bureau, have resulted in the completion of 19,063 ha of new forest plantations. These efforts have significantly strengthened ecological restoration in the counties and districts traversed by the canal. While the construction activities have inevitably impacted the forest ecosystems along the canal, proactive forest conservation and vegetation restoration measures have substantially mitigated these effects. The overall forest area in the basin has increased, and

carbon stock estimates for both the entire basin and the EIA zone in 2024 exceed baseline scenario predictions. These efforts have not only enhanced carbon sequestration capacity but also improved the resilience and stability of the forest ecosystems. Such findings highlight the importance of embedding ecological compensation and vegetation recovery into infrastructure planning frameworks. Their demonstrated effectiveness suggests that large-scale projects like the Pinglu Canal can serve as models for integrating development with environmental goals, including carbon neutrality targets and land-use policy. Additionally, the use of multi-source remote sensing offers a scalable, cost-effective approach for tracking ecological impacts and restoration effectiveness, thereby supporting data-driven environmental governance. This case demonstrates that, with well-planned restoration initiatives, development and ecological protection are not mutually exclusive, but can be jointly pursued within a sustainable planning framework [76].

4.4. Method Comparison and Applicability

Recent advances in AGC estimation have focused on multi-source remote sensing integration and machine learning techniques. Current mainstream approaches can be broadly categorized as follows:

(1) Spaceborne LiDAR-based modeling using GEDI or ICESat-2

These methods utilize LiDAR observations to extract forest vertical structure features such as canopy height and layering [77]. They are effective in alleviating spectral saturation in high-biomass areas and are widely used for global-scale AGC estimation. However, due to sparse sampling density and discontinuous spatial distribution, they are not suitable for pixel-level wall-to-wall mapping. This limits their applicability in local-scale ecological engineering assessments, where a trade-off exists between accuracy and spatial coverage.

(2) High-resolution remote sensing modeling based on deep learning (e.g., CNN, Transformer)

Deep learning has been increasingly applied in remote sensing, enabling end-to-end AGC estimation using high-resolution imagery. These models can achieve excellent prediction accuracy in regions with abundant training data and stable land cover [78]. However, they require large volumes of high-quality labeled samples, lack interpretability, and are sensitive to data imbalance or domain shifts. These limitations restrict their generalizability in ecologically heterogeneous regions.

(3) Empirical regression models based on vegetation indices or topographic variables

Traditional regression models use vegetation indices such as NDVI or EVI to establish empirical relationships with AGC [79]. These methods are simple to implement and scalable, making them suitable for broad regional assessments. However, they are vulnerable to saturation effects and terrain-induced distortion, and are limited in estimating AGC in structurally complex or data-sparse environments.

This study proposes a practical alternative that combines open-access data from Sentinel-2, Sentinel-1, ALOS PALSAR, and SRTM with a Random Forest model optimized by RFE and hyperparameter tuning. The resulting model achieves 10 m-resolution AGC mapping with high accuracy. Unlike approaches that rely on LiDAR or complex neural networks, this method balances accuracy, interpretability, and cost-efficiency, making it suitable for regions with complex ecosystems and limited ground data.

All remote sensing data used in this study are freely available through the GEE and Copernicus platforms, enabling scalable applications. Importantly, although the model requires representative ground samples for training, it does not rely on extensive or updated forest inventories. Once trained, the model can be applied across larger areas using only

remote sensing features, offering a practical solution for regions with limited field data but adequate satellite coverage.

This approach is particularly applicable in developing regions, coastal ecosystems, and infrastructure corridors, where field surveys are often constrained. To further improve model automation and accuracy, future work may integrate UAV-based LiDAR data with remote sensing variables to obtain detailed structural information while reducing the labor cost of field campaigns.

Nevertheless, three limitations remain. First, the model lacks explicit structural metrics such as canopy height, which may lead to underestimation in dense forests. Second, the absence of time-series features limits the capacity to capture seasonal and interannual dynamics. Third, the model still depends on ground plot data for training, and performance may decline if plot distribution or quality is insufficient.

To establish a baseline scenario, we used a simple linear regression model based on AGC trends from 2002 to 2021. While straightforward, this approach may oversimplify complex ecological processes. Future studies could explore more robust time-series models such as ARIMA [80] or LSTM [81] to better account for nonlinear drivers of AGC change.

5. Conclusions

The accurate estimation of forest AGC is critical for addressing climate change and achieving sustainable development. In this study, we integrated high-resolution remote sensing data with machine learning techniques to explore the application of multi-source remote sensing data and model optimization in AGC estimation, focusing on evaluating the impact of the Pinglu Canal construction on the forest ecosystem. The main contributions of this study are as follows:

- By integrating high-precision tree-level coordinate data obtained from RTK with Sentinel-2 imagery, this study developed a high-quality, pixel-level AGC dataset for the Pinglu Canal basin in 2024. This approach effectively addressed key challenges, including aligning field measurements with satellite data resolution and capturing spatial heterogeneity, thereby providing a robust foundation for accurate carbon stock estimation.
- Using RFE, we conducted effective feature selection and compared the estimation capabilities of different machine learning models. Among all tested data combinations and models, the hyperparameter-optimized RF model demonstrated the best performance in AGC estimation. Based on this, we generated a 10 m-resolution AGC spatial distribution map for the Pinglu Canal basin, offering a visual tool for carbon stock monitoring.
- By comparing the predicted 2024 AGC under a baseline scenario with the estimated AGC derived from multi-source remote sensing data and field survey data under actual conditions, we found that active forest conservation and vegetation restoration measures during the Pinglu Canal construction period resulted in better forest growth than natural growth scenarios. This highlights the potential for large-scale infrastructure projects to achieve a certain degree of harmony between construction and forest ecosystem protection.

Our methodology, relying on freely accessible remote sensing data as predictors for machine learning models, combined with high spatial and temporal resolution satellite imagery, proved to be cost-effective, scalable, and highly reliable for AGC estimation in the Pinglu Canal basin. To further enhance data utility and improve AGC estimation accuracy, future work will integrate UAV-based LiDAR data with multi-source remote sensing datasets.

Author Contributions: Conceptualization, methodology, software, validation, W.X.; formal analysis, W.X. and X.M.; investigation, W.X., W.W. (Wenqian Wu), X.M., S.D. and W.W. (Wenhuan Wang); data curation, W.X., S.D. and X.M.; writing—original draft preparation, W.X.; writing—review and editing, W.Z.; visualization, S.D., W.W. (Wenqian Wu) and W.W. (Wenhuan Wang); supervision, W.Z.; funding acquisition, Y.W. All authors have read and agreed to the published version of the manuscript.

Funding: This research was funded by the Guangxi Science and Technology Major Program, grant number GUIKEAA23062054; the Science and Technology Research and Development Projects of Guangxi Institute of Industrial Technology, grant number CYY-HT2023-JSJJ-0037; and the Guangxi Key Research and Development Program, grant number GUIKEAB24010248.

Data Availability Statement: The data presented in this study are available on request from the corresponding author.

Acknowledgments: During the preparation of this manuscript, the authors used OpenAI's ChatGPT (GPT-4, March 2025 version) for the purposes of improving language clarity, refining logical flow, and assisting in information and literature retrieval. The authors have reviewed and edited all AI-generated content and take full responsibility for the integrity and accuracy of the final manuscript.

Conflicts of Interest: The authors declare no conflicts of interest.

Abbreviations

The following abbreviations are used in this manuscript:

AGC	Aboveground carbon stock
SAR	Synthetic Aperture Radar
SVR	Support Vector Regression
RF	Random Forest
RFE	Recursive Feature Elimination
MLR	Multiple Linear Regression
RTK	Real-Time Kinematic
GEE	Google Earth Engine
SRTM	Shuttle Radar Topography Mission
DEM	Digital Elevation Model
AGB	Aboveground biomass
R^2	Coefficient of determination
RMSE	Root mean square error
SVM	Support Vector Machine
EIA	Environmental Impact Assessment

References

1. Malhi, Y.; Franklin, J.; Seddon, N.; Solan, M.; Turner, M.G.; Field, C.B.; Knowlton, N. Climate change and ecosystems: Threats, opportunities and solutions. *Philos. Trans. R. Soc. B Biol. Sci.* **2020**, *375*, 20190104. [CrossRef] [PubMed]
2. Pörtner, H.-O.; Scholes, R.J.; Agard, J.; Archer, E.; Arneth, A.; Bai, X.; Barnes, D.; Burrows, M.; Chan, L.; Cheung, W.L.W. *Scientific Outcome of the IPBES-IPCC Co-Sponsored Workshop on Biodiversity and Climate Change*; Intergovernmental Science-Policy Platform on Biodiversity and Ecosystem Services (IPBES): Bonn, Germany, 2021.
3. Falkowski, P.; Scholes, R.J.; Boyle, E.; Canadell, J.; Canfield, D.; Elser, J.; Gruber, N.; Hibbard, K.; Högberg, P.; Linder, S. The global carbon cycle: A test of our knowledge of earth as a system. *Science* **2000**, *290*, 291–296. [CrossRef] [PubMed]
4. Lorenz, K. *Carbon Sequestration in Forest Ecosystems*; Springer: Berlin/Heidelberg, Germany, 2010.
5. Goetz, S.J.; Hansen, M.; Houghton, R.A.; Walker, W.; Laporte, N.; Busch, J. Measurement and monitoring needs, capabilities and potential for addressing reduced emissions from deforestation and forest degradation under REDD+. *Environ. Res. Lett.* **2015**, *10*, 123001. [CrossRef]
6. Jenkins, M.; Schaap, B. Forest ecosystem services. In *Background Analytical Study*; United Nations Forum on Forests: New York, NY, USA, 2018; Volume 1.
7. Wang, Y.; Guo, C.-H.; Chen, X.-J.; Jia, L.-Q.; Guo, X.-N.; Chen, R.-S.; Zhang, M.-S.; Chen, Z.-Y.; Wang, H.-D. Carbon peak and carbon neutrality in China: Goals, implementation path and prospects. *China Geol.* **2021**, *4*, 720–746. [CrossRef]

8. FAO. *Global Forest Resources Assessment 2020: Main Report*; Food and Agriculture Organization of the United Nations: Rome, Italy, 2020.
9. Zhou, Q.; Wang, L.; Tang, F.; Zhao, S.; Huang, N.; Zheng, K. Mapping spatial and temporal distribution information of plantations in Guangxi from 2000 to 2020. *Front. Ecol. Evol.* **2023**, *11*, 1201161. [CrossRef]
10. Carse, A. Nature as infrastructure: Making and managing the Panama Canal watershed. *Soc. Stud. Sci.* **2012**, *42*, 539–563. [CrossRef]
11. Condit, R.; Robinson, W.D.; Ibáñez, R.; Aguilar, S.; Sanjur, A.; Martínez, R.; Stallard, R.F.; García, T.; Angehr, G.R.; Petit, L. The Status of the Panama Canal Watershed and Its Biodiversity at the Beginning of the 21st Century: Long-term ecological studies reveal a diverse flora and fauna near the Panama Canal, harbored within a corridor of forest stretching from the Caribbean to the Pacific, but deforestation, land degradation, erosion, and overhunting remain threats. *Bioscience* **2001**, *51*, 389–398.
12. Moreno, S.H. Impact of development on the Panama Canal environment. *J. Interam. Stud. World Aff.* **1993**, *35*, 129–150. [CrossRef]
13. Wallander, S.; Lauterbach, S.; Anderson, K.; Chou, F.; Grossman, J.M.; Schloegel, C. Existing markets for ecosystem services in the Panama canal watershed. In *Emerging Markets for Ecosystem Services*; CRC Press: Boca Raton, FL, USA, 2021; pp. 311–336.
14. Ibáñez, R.; Condit, R.; Angehr, G.; Aguilar, S.; GarcÍa, T.; MartÍnez, R.; Sanjur, A.; Stallard, R.; Wright, S.J.; Rand, A.S. An ecosystem report on the Panama Canal: Monitoring the status of the forest communities and the watershed. *Environ. Monit. Assess.* **2002**, *80*, 65–95. [CrossRef]
15. Simonit, S.; Perrings, C. Bundling ecosystem services in the Panama Canal watershed. *Proc. Natl. Acad. Sci. USA* **2013**, *110*, 9326–9331. [CrossRef]
16. Condit, R. Extracting environmental benefits from a new canal in Nicaragua: Lessons from Panama. *PLoS Biol.* **2015**, *13*, e1002208. [CrossRef]
17. Gibbs, H.K.; Brown, S.; Niles, J.O.; Foley, J.A. Monitoring and estimating tropical forest carbon stocks: Making REDD a reality. *Environ. Res. Lett.* **2007**, *2*, 045023. [CrossRef]
18. Segura, M.; Kanninen, M. Allometric models for tree volume and total aboveground biomass in a tropical humid forest in Costa Rica 1. *Biotropica* **2005**, *37*, 2–8. [CrossRef]
19. Lu, D.; Chen, Q.; Wang, G.; Liu, L.; Li, G.; Moran, E. A survey of remote sensing-based aboveground biomass estimation methods in forest ecosystems. *Int. J. Digit. Earth* **2016**, *9*, 63–105. [CrossRef]
20. Halme, E.; Pellikka, P.; Mottus, M. Utility of hyperspectral compared to multispectral remote sensing data in estimating forest biomass and structure variables in Finnish boreal forest. *Int. J. Appl. Earth Obs. Geoinf.* **2019**, *83*, 101942. [CrossRef]
21. Li, W.; Zhang, Y.; Zhang, J.; Chen, H.; Chen, E.; Zhao, L.; Zhao, D. Tropical forest AGB estimation based on structure parameters extracted by TomoSAR. *Int. J. Appl. Earth Obs. Geoinf.* **2023**, *121*, 103369. [CrossRef]
22. Puliti, S.; Breidenbach, J.; Schumacher, J.; Hauglin, M.; Klingenberg, T.F.; Astrup, R. Above-ground biomass change estimation using national forest inventory data with Sentinel-2 and Landsat. *Remote Sens. Environ.* **2021**, *265*, 112644. [CrossRef]
23. Verly, O.M.; Leite, R.V.; da Silva Tavares-Junior, I.; da Rocha, S.J.S.S.; Leite, H.G.; Gleriani, J.M.; Rufino, M.P.M.X.; de Fatima Silva, V.; Torres, C.M.M.E.; Plata-Rueda, A. Atlantic forest woody carbon stock estimation for different successional stages using Sentinel-2 data. *Ecol. Indic.* **2023**, *146*, 109870. [CrossRef]
24. Schmitt, M.; Zhu, X.X. Data fusion and remote sensing: An ever-growing relationship. *IEEE Geosci. Remote Sens. Mag.* **2016**, *4*, 6–23. [CrossRef]
25. Sinha, S.; Mohan, S.; Das, A.; Sharma, L.; Jeganathan, C.; Santra, A.; Santra Mitra, S.; Nathawat, M. Multi-sensor approach integrating optical and multi-frequency synthetic aperture radar for carbon stock estimation over a tropical deciduous forest in India. *Carbon Manag.* **2020**, *11*, 39–55. [CrossRef]
26. Yang, Q.; Niu, C.; Liu, X.; Feng, Y.; Ma, Q.; Wang, X.; Tang, H.; Guo, Q. Mapping high-resolution forest aboveground biomass of China using multisource remote sensing data. *GISci. Remote Sens.* **2023**, *60*, 2203303. [CrossRef]
27. Kanga, S. Advancements in remote sensing tools for forestry analysis. *Sustain. For.* **2023**, *6*, 2269. [CrossRef]
28. Li, J.; Bao, W.; Wang, X.; Song, Y.; Liao, T.; Xu, X.; Guo, M. Estimating Aboveground Biomass of Boreal Forests in Northern China Using Multiple Data sets. *IEEE Trans. Geosci. Remote Sens.* **2024**, *62*, 4408410.
29. Cosenza, D.N.; Korhonen, L.; Maltamo, M.; Packalen, P.; Strunk, J.L.; Næsset, E.; Gobakken, T.; Soares, P.; Tomé, M. Comparison of linear regression, k-nearest neighbour and random forest methods in airborne laser-scanning-based prediction of growing stock. *Forestry* **2021**, *94*, 311–323. [CrossRef]
30. Mohammadi, J.; Shataee, S.; Babanezhad, M. Estimation of forest stand volume, tree density and biodiversity using Landsat ETM+ Data, comparison of linear and regression tree analyses. *Procedia Environ. Sci.* **2011**, *7*, 299–304. [CrossRef]
31. Georgopoulos, N.; Gitas, I.Z.; Stefanidou, A.; Korhonen, L.; Stavrakoudis, D. Estimation of Individual Tree Stem Biomass in an Uneven-Aged Structured Coniferous Forest Using Multispectral LiDAR Data. *Remote Sens.* **2021**, *13*, 4827. [CrossRef]
32. Singh, C.; Karan, S.K.; Sardar, P.; Samadder, S.R. Remote sensing-based biomass estimation of dry deciduous tropical forest using machine learning and ensemble analysis. *J. Environ. Manag.* **2022**, *308*, 114639. [CrossRef]

33. Bergstra, J.; Bardenet, R.; Bengio, Y.; Kégl, B. Algorithms for hyper-parameter optimization. In Proceedings of the 25th International Conference on Neural Information Processing Systems, Granada, Spain, 12–15 December 2011; Volume 24.
34. Jung, J.; Kim, S.; Hong, S.; Kim, K.; Kim, E.; Im, J.; Heo, J. Effects of national forest inventory plot location error on forest carbon stock estimation using k-nearest neighbor algorithm. *ISPRS J. Photogramm. Remote Sens.* **2013**, *81*, 82–92. [CrossRef]
35. Urbazaev, M.; Thiel, C.; Cremer, F.; Dubayah, R.; Migliavacca, M.; Reichstein, M.; Schmullius, C. Estimation of forest aboveground biomass and uncertainties by integration of field measurements, airborne LiDAR, and SAR and optical satellite data in Mexico. *Carbon Balance Manag.* **2018**, *13*, 5. [CrossRef]
36. Huang, L.; Huang, Z.; Zhou, W.; Wu, S.; Li, X.; Mao, F.; Song, M.; Zhao, Y.; Lv, L.; Yu, J. Landsat-based spatiotemporal estimation of subtropical forest aboveground carbon storage using machine learning algorithms with hyperparameter tuning. *Front. Plant Sci.* **2024**, *15*, 1421567. [CrossRef]
37. Zhang, Y.; He, B.; Chen, R.; Zhang, H.; Fan, C.; Yin, J.; Li, Y. The potential of optical and SAR time-series data for the improvement of aboveground biomass carbon estimation in Southwestern China's evergreen coniferous forests. *GISci. Remote Sens.* **2024**, *61*, 2345438. [CrossRef]
38. Ecke, S.; Stehr, F.; Frey, J.; Tiede, D.; Dempewolf, J.; Klemmt, H.-J.; Endres, E.; Seifert, T. Towards operational UAV-based forest health monitoring: Species identification and crown condition assessment by means of deep learning. *Comput. Electron. Agric.* **2024**, *219*, 108785. [CrossRef]
39. Qin, H.; Zhou, W.; Yao, Y.; Wang, W. Individual tree segmentation and tree species classification in subtropical broadleaf forests using UAV-based LiDAR, hyperspectral, and ultrahigh-resolution RGB data. *Remote Sens. Environ.* **2022**, *280*, 113143. [CrossRef]
40. Li, H.; Hiroshima, T.; Li, X.; Hayashi, M.; Kato, T. High-resolution mapping of forest structure and carbon stock using multi-source remote sensing data in Japan. *Remote Sens. Environ.* **2024**, *312*, 114322. [CrossRef]
41. Liu, S.; Wang, H.; Hu, Y.; Zhang, M.; Zhu, Y.; Wang, Z.; Li, D.; Yang, M.; Wang, F. Land use and land cover mapping in China using multimodal fine-grained dual network. *IEEE Trans. Geosci. Remote Sens.* **2023**, *61*, 4405219. [CrossRef]
42. Xu, H.; Man, Y.; Yang, M.; Wu, J.; Zhang, Q.; Wang, J. Analytical Insight of Earth: A Cloud-Platform of Intelligent Computing for Geospatial Big Data. *arXiv* **2023**, arXiv:2312.16385.
43. Zhao, C.; Qin, C.-Z. 10-m-resolution mangrove maps of China derived from multi-source and multi-temporal satellite observations. *ISPRS J. Photogramm. Remote Sens.* **2020**, *169*, 389–405. [CrossRef]
44. Chen, Y.; Feng, X.; Fu, B.; Ma, H.; Zohner, C.M.; Crowther, T.W.; Huang, Y.; Wu, X.; Wei, F. Maps with 1 km resolution reveal increases in above-and belowground forest biomass carbon pools in China over the past 20 years. *Earth Syst. Sci. Data* **2023**, *15*, 897–910. [CrossRef]
45. Li, Y.; Li, C.; Li, M.; Liu, Z. Influence of variable selection and forest type on forest aboveground biomass estimation using machine learning algorithms. *Forests* **2019**, *10*, 1073. [CrossRef]
46. Cabello-Solorzano, K.; Ortigosa de Araujo, I.; Peña, M.; Correia, L.; Tallón-Ballesteros, A.J. The impact of data normalization on the accuracy of machine learning algorithms: A comparative analysis. In Proceedings of the International Conference on Soft Computing Models in Industrial and Environmental Applications, Salamanca, Spain, 5–7 September 2023; pp. 344–353.
47. Wang, C.; Zhang, W.; Ji, Y.; Marino, A.; Li, C.; Wang, L.; Zhao, H.; Wang, M. Estimation of Aboveground Biomass for Different Forest Types Using Data from Sentinel-1, Sentinel-2, ALOS PALSAR-2, and GEDI. *Forests* **2024**, *15*, 215. [CrossRef]
48. Wang, Z.; Zhang, Y.; Li, F.; Gao, W.; Guo, F.; Li, Z.; Yang, Z. Regional mangrove vegetation carbon stocks predicted integrating UAV-LiDAR and satellite data. *J. Environ. Manag.* **2024**, *368*, 122101. [CrossRef]
49. Guyon, I.; Weston, J.; Barnhill, S.; Vapnik, V. Gene selection for cancer classification using support vector machines. *Mach. Learn.* **2002**, *46*, 389–422. [CrossRef]
50. Breiman, L. Random forests. *Mach. Learn.* **2001**, *45*, 5–32. [CrossRef]
51. Uyanık, G.K.; Güler, N. A study on multiple linear regression analysis. *Procedia Soc. Behav. Sci.* **2013**, *106*, 234–240. [CrossRef]
52. Awad, M.; Khanna, R.; Awad, M.; Khanna, R. Support vector regression. In *Efficient Learning Machines: Theories, Concepts, and Applications for Engineers and System Designers*; Apress: New York, NY, USA, 2015; pp. 67–80.
53. Chen, T.; Guestrin, C. Xgboost: A scalable tree boosting system. In Proceedings of the 22nd ACM SIGKDD International Conference on Knowledge Discovery and Data Mining, San Francisco, CA, USA, 13–17 August 2016; pp. 785–794.
54. Cheng, F.; Ou, G.; Wang, M.; Liu, C. Remote sensing estimation of forest carbon stock based on machine learning algorithms. *Forests* **2024**, *15*, 681. [CrossRef]
55. Ding, X.; Liu, J.; Yang, F.; Cao, J. Random radial basis function kernel-based support vector machine. *J. Frankl. Inst.* **2021**, *358*, 10121–10140. [CrossRef]
56. Jiang, W.; Zhang, L.; Zhang, X.; Gao, S.; Gao, H.; Sun, L.; Yan, G. Multi-Decision Vector Fusion Model for Enhanced Mapping of Aboveground Biomass in Subtropical Forests Integrating Sentinel-1, Sentinel-2, and Airborne LiDAR Data. *Remote Sens.* **2025**, *17*, 1285. [CrossRef]
57. Kohavi, R. A study of cross-validation and bootstrap for accuracy estimation and model selection. In Proceedings of the International Joint Confeence on Artificial Intelligence, Montreal, QC, Canada, 20–25 August 1995; pp. 1137–1145.

58. Wang, X.; Jiao, H. Spatial scaling of forest aboveground biomass using multi-source remote sensing data. *IEEE Access* **2020**, *8*, 178870–178885. [CrossRef]
59. Yan, X.; Li, J.; Smith, A.R.; Yang, D.; Ma, T.; Su, Y.; Shao, J. Evaluation of machine learning methods and multi-source remote sensing data combinations to construct forest above-ground biomass models. *Int. J. Digit. Earth* **2023**, *16*, 4471–4491. [CrossRef]
60. Yan, L.; Roy, D.; Li, Z.; Zhang, H.; Huang, H. Sentinel-2A multi-temporal misregistration characterization and an orbit-based sub-pixel registration methodology. *Remote Sens. Environ.* **2018**, *215*, 495–506. [CrossRef]
61. Dai, W.; Fu, W.; Jiang, P.; Zhao, K.; Li, Y.; Tao, J. Spatial pattern of carbon stocks in forest ecosystems of a typical subtropical region of southeastern China. *For. Ecol. Manag.* **2018**, *409*, 288–297. [CrossRef]
62. Lin, Z.; Chao, L.; Wu, C.; Hong, W.; Hong, T.; Hu, X. Spatial analysis of carbon storage density of mid-subtropical forests using geostatistics: A case study in Jiangle County, southeast China. *Acta Geochim.* **2018**, *37*, 90–101. [CrossRef]
63. Fuchs, H.; Magdon, P.; Kleinn, C.; Flessa, H. Estimating aboveground carbon in a catchment of the Siberian forest tundra: Combining satellite imagery and field inventory. *Remote Sens. Environ.* **2009**, *113*, 518–531. [CrossRef]
64. Xu, D.; Wang, H.; Xu, W.; Luan, Z.; Xu, X. LiDAR applications to estimate forest biomass at individual tree scale: Opportunities, challenges and future perspectives. *Forests* **2021**, *12*, 550. [CrossRef]
65. Liao, K.; Li, Y.; Zou, B.; Li, D.; Lu, D. Examining the role of UAV Lidar data in improving tree volume calculation accuracy. *Remote Sens.* **2022**, *14*, 4410. [CrossRef]
66. Mohammed, K.; Kpienbaareh, D.; Wang, J.; Goldblum, D.; Luginaah, I.; Lupafya, E.; Dakishoni, L. Synthesizing Local Capacities, Multi-Source Remote Sensing and Meta-Learning to Optimize Forest Carbon Assessment in Data-Poor Regions. *Remote Sens.* **2025**, *17*, 289. [CrossRef]
67. Cheekhooree, K. Canopy Height Assessment in South Australian Pinus Radiata Plantations Using Sentinel-1: A Comparative Analysis Between INSAR and Machine Learning Algorithms. Master's Thesis, Flinders University, College of Science and Engineering, Bedford Park, Australia, 2024.
68. Lausch, A.; Erasmi, S.; King, D.J.; Magdon, P.; Heurich, M. Understanding forest health with remote sensing-part I—A review of spectral traits, processes and remote-sensing characteristics. *Remote Sens.* **2016**, *8*, 1029. [CrossRef]
69. Datt, B. Remote Sensing of Foliar Biochemistry and Biophysical Properties in Eucalyptus Species: Application of High Spectral Resolution Reflectance Measurements. Ph.D. Thesis, UNSW Sydney, Sydney, Australia, 1999.
70. Sharma, C.; Gairola, S.; Baduni, N.; Ghildiyal, S.; Suyal, S. Variation in carbon stocks on different slope aspects in seven major forest types of temperate region of Garhwal Himalaya, India. *J. Biosci.* **2011**, *36*, 701–708. [CrossRef]
71. Singh, S. Understanding the role of slope aspect in shaping the vegetation attributes and soil properties in Montane ecosystems. *Trop. Ecol.* **2018**, *59*, 417–430.
72. Xu, W.; Cheng, Y.; Luo, M.; Mai, X.; Wang, W.; Zhang, W.; Wang, Y. Progress and Limitations in Forest Carbon Stock Estimation Using Remote Sensing Technologies: A Comprehensive Review. *Forests* **2025**, *16*, 449. [CrossRef]
73. Zhang, X.; Shen, J.; Sun, F.; Wang, S. Spatial-temporal evolution and influencing factors analysis of ecosystem services value: A case study in sunan canal basin of jiangsu province, eastern China. *Remote Sens.* **2022**, *15*, 112. [CrossRef]
74. Zhao, H.; Wu, C.; Wang, X. Large-scale forest conservation and restoration programs significantly contributed to land surface greening in China. *Environ. Res. Lett.* **2022**, *17*, 024023. [CrossRef]
75. Lu, F.; Hu, H.; Sun, W.; Zhu, J.; Liu, G.; Zhou, W.; Zhang, Q.; Shi, P.; Liu, X.; Wu, X. Effects of national ecological restoration projects on carbon sequestration in China from 2001 to 2010. *Proc. Natl. Acad. Sci. USA* **2018**, *115*, 4039–4044. [CrossRef]
76. Mitra, S.; Madhuvanthi, S.; Sabumon, P. Integrating Green Infrastructure. In *Nature-Based Solutions in Achieving Sustainable Development Goals*; Springer: Cham, Switzerland, 2024; p. 167.
77. Neuenschwander, A.; Duncanson, L.; Montesano, P.; Minor, D.; Guenther, E.; Hancock, S.; Wulder, M.; White, J.C.; Purslow, M.; Thomas, N. Towards global spaceborne lidar biomass: Developing and applying boreal forest biomass models for ICESat-2 laser altimetry data. *Sci. Remote Sens.* **2024**, *10*, 100150. [CrossRef]
78. Zhang, F.; Tian, X.; Zhang, H.; Jiang, M. Estimation of aboveground carbon density of forests using deep learning and multisource remote sensing. *Remote Sens.* **2022**, *14*, 3022. [CrossRef]
79. Poudel, A.; Shrestha, H.L.; Mahat, N.; Sharma, G.; Aryal, S.; Kalakheti, R.; Lamsal, B. Modeling and Mapping of Aboveground Biomass and Carbon Stock Using Sentinel-2 Imagery in Chure Region, Nepal. *Int. J. For. Res.* **2023**, *2023*, 5553957. [CrossRef]
80. Shumway, R.H.; Stoffer, D.S.; Shumway, R.H.; Stoffer, D.S. ARIMA models. In *Time Series Analysis and Its Applications: With R Examples*; Springer: Berlin/Heidelberg, Germany, 2017; pp. 75–163.
81. Greff, K.; Srivastava, R.K.; Koutník, J.; Steunebrink, B.R.; Schmidhuber, J. LSTM: A search space odyssey. *IEEE Trans. Neural Netw. Learn. Syst.* **2016**, *28*, 2222–2232. [CrossRef]

Disclaimer/Publisher's Note: The statements, opinions and data contained in all publications are solely those of the individual author(s) and contributor(s) and not of MDPI and/or the editor(s). MDPI and/or the editor(s) disclaim responsibility for any injury to people or property resulting from any ideas, methods, instructions or products referred to in the content.

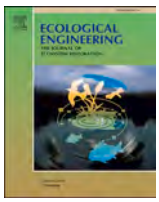
Ecological Engineering 219 (2025) 107709



Contents lists available at ScienceDirect

Ecological Engineering

journal homepage: www.elsevier.com/locate/ecoleng





Assessment of biodiversity and landscape changes during the Pinglu Canal construction and the benefits of ecological restoration based on Rao's Q index☆

Songwen Deng [a,1], Mengyuan Luo [b,1], Wenhuan Wang [a,b], Sixiang Lan [b], Weifeng Xu [c], Xuzhi Mai [a], Wei Zhang [a,*]

[a] School of Marine Science, Guangxi University, Nanning 530004, China
[b] Institute of Green and Low Carbon Technology, Guangxi Institute of Industrial Technology, Nanning 530200, China
[c] School of Resources, Environment and Materials, Guangxi University, Nanning 530004, China

ARTICLE INFO

Keywords:
Biodiversity assessment
Landscape fragmentation
Ecological restoration
Remote sensing
Rao's Q index
Urban and infrastructure impact

ABSTRACT

Assessing biodiversity change is crucial for evaluating the ecological impacts of infrastructure development. Taking the Pinglu Canal as an example, this study integrates Rao's Q index, remote sensing data, and landscape metrics to analyze the ecological pattern changes and restoration benefits before and after canal construction from 2015 to 2024. Results indicated that canal construction significantly intensified fragmentation of forests, wetlands, and farmlands, resulting in about a 25 % decrease in Rao's Q index during the initial construction phase (2022), reflecting notable biodiversity loss. Following ecological restoration measures (such as afforestation compensation and wetland restoration) implemented in 2023–2024, Rao's Q showed differentiated recoveries across ecosystems, with forest ecosystems recovering by approximately 20 %, respectively. This research confirms that the Rao's Q index is suitable for evaluating biodiversity changes in heterogeneous landscapes but may overestimate biodiversity in homogeneous ecosystems like mangroves, thus necessitating correction through complementary metrics. The findings provide important theoretical support and practical references for ecological restoration planning in infrastructure projects.

1. Introduction

Modern canals, as essential waterway infrastructure, are widely utilized in shipping, irrigation, drainage, energy production, and ecological management(Lin et al., 2020). Globally, canals play a pivotal role in promoting regional economic development and optimizing resource allocation, particularly in connecting inland areas with the ocean, improving transportation efficiency, and reducing transport costs, making them irreplaceable in these domains. Despite their significant contributions to economic and social development, the construction and operation of modern canals pose potential threats to local ecosystems and biodiversity(Condit et al., 2001). Canal construction often involves large-scale land excavation and modification, leading to the destruction or fragmentation of natural ecosystems such as wetlands, forests, and grasslands(Han et al., 2024). This fragmentation effect is particularly concerning when canals traverse biodiversity-rich areas, as it may severely disrupt habitats, thereby affecting species survival and reproduction(Tang et al., 2021). For instance, canals can sever migration corridors, resulting in population isolation, reduced genetic diversity, and an increased risk of species extinction. Such ecological disturbances underscore the need for comprehensive environmental assessments and mitigation strategies to balance the benefits of canal development with biodiversity conservation(Zhao et al., 2025). As a flagship project of China's "New Western Land-Sea Corridor", the Pinglu Canal exemplifies the intersection of large-scale artificial construction and ecologically sensitive zones, making it a representative case for

☆ This research was funded by the Guangxi Science and Technology Major Program, grant number GUIKEAA23062054; the Science and Technology Research and Development Projects of Guangxi Institute of Industrial Technology, grant number CYY-HT2023-JSJJ-0037; and the Guangxi Key Research and Development Program, grant number GUIKEAB24010248.

* Corresponding author.
E-mail address: zhangwei20@gxu.edu.cn (W. Zhang).

[1] These authors contributed equally to this work.

https://doi.org/10.1016/j.ecoleng.2025.107709
Received 13 April 2025; Received in revised form 31 May 2025; Accepted 14 June 2025
Available online 18 June 2025
0925-8574/© 2025 Elsevier B.V. All rights are reserved, including those for text and data mining, AI training, and similar technologies.

evaluating the ecological impacts of infrastructure development on biodiversity and landscape patterns.

Landscape metrics are scientific indicators used to quantify landscape spatial patterns, primarily describing the composition, shape, spatial distribution, and ecological functions of landscape patches (Schindler et al., 2015). The concept of landscape metrics can be traced back to the 1980s when ecologists and geographic information science researchers began to explore the influence of landscape spatial structure on ecosystem functions(Turner, 1989). In recent years, with advancements in remote sensing technology and GIS(geographic information systems), landscape metrics have played a crucial role in studying the relationships between landscape patterns and ecological processes (Arekhi et al., 2017; Li and Wu, 2004; Turner, 2014). They have become essential tools for analyzing land-use change, ecosystem services, species habitat patterns, and environmental management. Landscape metrics are widely applied in ecological conservation, urban planning, agricultural landscape management, and ecosystem assessment(Reddy, 2021; Ricotta et al., 2016).

Biodiversity refers to the diversity of all life forms on Earth, encompassing multiple levels from genes to ecosystems(Bullock et al., 2011; Jorgensen, 2015). Species diversity, a fundamental component of biodiversity, specifically denotes species richness, evenness, and interspecies relationships within a given region(Atkinson et al., 2022). It serves as a critical indicator of ecosystem health and stability, playing a pivotal role in ecosystem productivity, nutrient cycling, soil and water conservation, and climate regulation(Hernández-Stefanoni et al., 2012). Species diversity not only considers the number of species but also accounts for the distribution, population size, and functional roles of species within an ecosystem(Benayas et al., 2009; Borges-Matos et al., 2023). Ecosystems with high species diversity provide diverse habitats, facilitate the survival of various organisms, and enhance ecosystem resilience and resistance to environmental disturbances(Chen et al., 2024; Graham et al., 2019; Vihervaara et al., 2017).

Although traditional biodiversity indices like Shannon and Simpson indices are commonly utilized to assess ecological impacts of infrastructure development, these approaches often exhibit biases in biodiversity estimation within homogeneous vegetation systems and fail to adequately capture ecosystem structural complexity and heterogeneity (Aue et al., 2012; Malavasi et al., 2021). Rao's Q (Rao's Quadratic Entropy Index) is a landscape metric used to measure species diversity and evenness within an ecosystem. Originally proposed by (Rao, 1982), this index has been widely applied in ecological studies. Unlike traditional species richness or the Shannon-Wiener Diversity Index, Rao's Q not only accounts for species richness but also incorporates species similarity, reflecting species distribution and relative abundance.(Rocchini et al., 2017) was the first to use multidimensional remote sensing data to estimate Rao's Q index, highlighting its advantages over remotely sensed Shannon diversity indices. Rao's Q index, capable of simultaneously considering species richness and functional dissimilarity, has been gradually applied in remote sensing-based biodiversity assessment in complex ecosystems, demonstrating potential advantages over traditional indices(Gillespie et al., 2008; Rocchini et al., 2010; Khare et al., 2021). However, studies focusing on ecosystem heterogeneity changes during the construction of large-scale artificial canals are limited, and the applicability of Rao's Q in homogeneous ecosystems like wetlands has not been systematically validated (Rocchini et al., 2019; Rocchini et al., 2024).

This study addresses the following questions: How does large-scale canal construction impact regional ecological diversity and landscape heterogeneity? Can Rao's Q index reflect these changes more accurately than traditional indices? Taking the under-construction Pinglu Canal as a case, this research integrates Rao's Q index, remote sensing data, and landscape metrics to explore the ecological impact of canal construction, validate the effectiveness of Rao's Q in biodiversity assessment, and identify ecosystem-specific responses to construction and restoration activities. The findings aim to provide a scientific basis and management recommendations for future infrastructure development and ecological restoration planning.

2. Materials and methods

2.1. Study area

The Pinglu Canal (108°35′ E-109°04′ E, 21°44′ N-22°38′ N) is an under-construction canal located in Guangxi, China (Fig. 1). It has a total length of 135 km, a width ranging from 80 to 145 m, and a water depth of 6.0–6.5 m, allowing navigation for 5000-ton inland vessels. The canal features three cascade ship locks along its course and commenced construction in March 2022.Unlike natural rivers, the Pinglu Canal is a completely newly constructed artificial waterway, rather than an expansion or dredging of an existing river. Consequently, its construction has caused greater disturbances to the original ecosystem, resulting in more pronounced fragmentation effects. The project involves large-scale deforestation, wetland transformation, and farmland acquisition, significantly impacting ecosystem integrity, biodiversity, and ecological services within the watershed. In the short term, these changes have led to habitat loss, alterations in ecological functions, and a potential decline in biodiversity(Cao et al., 2025).

The canal region is characterized by a typical karst landscape, with complex terrain, highly heterogeneous ecosystems, and rapid land-use transitions(Peel et al., 2007). The biotic communities in this region exhibit a high degree of local adaptation. Against this backdrop, traditional biodiversity metrics such as the Shannon index and Simpson index may fail to fully capture changes in landscape structural complexity and ecological heterogeneity. In contrast, the Rao's Q index, by integrating species richness and functional dissimilarity, provides a more precise assessment of landscape fragmentation, declines in ecological connectivity, and habitat diversity dynamics before and after canal construction.

Based on the land use scope of the Pinglu Canal and relevant Chinese policies on river ecological protection, this study examines the Pinglu Canal Basin at two spatial scales:

1) Occupied area of the canal project: Defined according to the official construction planning boundaries.
2) Canal watershed: Delineated using China's administrative divisions, the HydroSHEDS watershed dataset (hybas_as_lev12_v1c), and the pour point dataset (hybas_pour_lev12_v1_shp). The watershed boundaries were extracted using the Watershed Tool in ArcGIS Pro.

The construction of the Pinglu Canal involves multiple ecological restoration projects (Table 1), which are implemented concurrently with canal development. As of October 2024, approximately 50 % of the ecological restoration projects have been completed, with major achievements including ecological slope protection, landscape greening, mangrove compensation, and farmland creation projects.

2.2. Field data

In October 2024, a vegetation species diversity survey was conducted across 77 sampling plots within the study area, covering most of the major natural ecosystems in the Pinglu Canal Basin (natural forests, plantations, and mangroves). RTK equipment (spatial error < 2 cm) was used to obtain the geographic coordinates of the four corners and the center of each plot. All vegetation species and plant parameters within the plots were recorded.

Among the sampling plots, 37 were forest plots, with *Eucalyptus grandis* × urophylla as the dominant species, followed by *Pinus elliottii*, *Pinus massoniana*, and *Bambusa chungii*. 40 were mangrove plots, primarily dominated by *Excoecaria agallocha*, followed by *Sonneratia apetala* and *Kandelia obovata*. The species richness across plots varied between 3 and 25 species. Plantations and mangrove plots generally

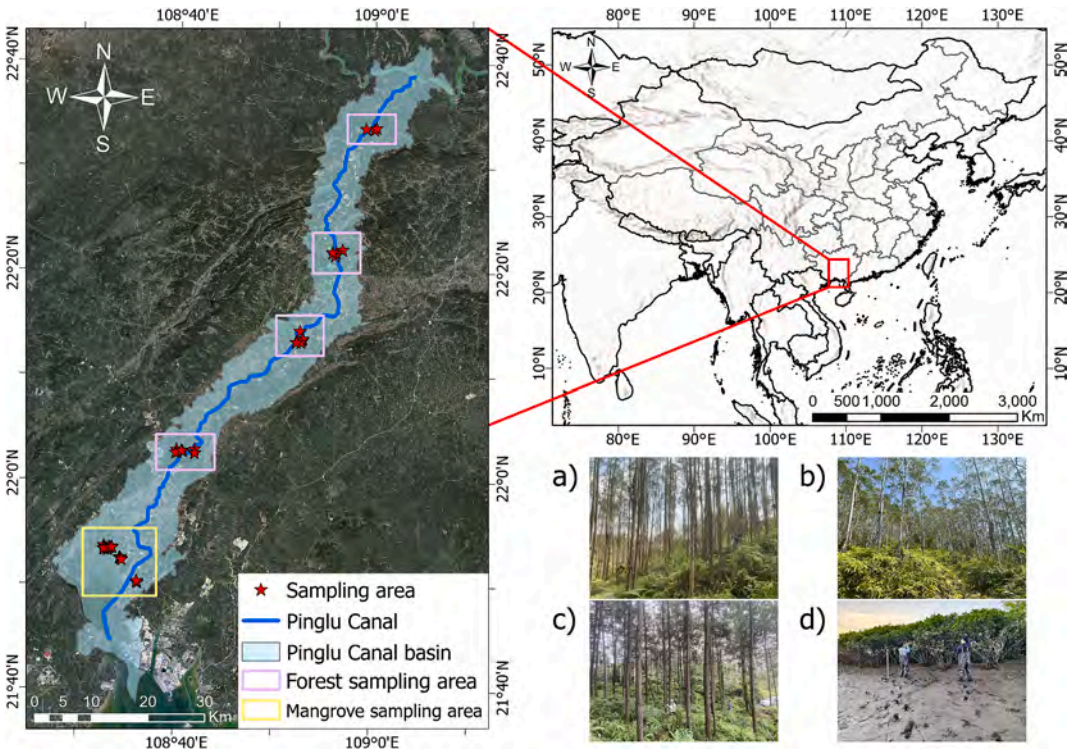


Fig. 1. A schematic map of the study area and sampling locations based on Landsat 9 true-color composite imagery. (a), (b), and (c) represent forest sampling sites, while (d) represents a mangrove sampling site.

Table 1
The area and spatial distribution of ecological restoration projects in the Pinglu Canal.

Ecological Restoration Project	Area (ha)	Location
Submerged Ecological Bank Protection	107.89	Occupied area
Ecological Slope Protection	322.78	Occupied area
Landscape Greening	22.42	Occupied area
Wetland Ecological Conservation Zone	333.80	Within the watershed
Farmland Creation	5788.36	Within the watershed
Forest Compensation	2884.66	Within the watershed, off-site restoration
Mangrove Compensation	32.86	Within the watershed, off-site restoration

exhibited lower species richness (<10 species), with the mangrove communities in this region being particularly simplified (<3 species). In contrast, natural forests demonstrated higher species diversity (>10 species).

2.3. Remote sensing data

This study utilized Landsat 8/9 OLI Level-2 imagery from October of each year (2015–2024), obtained from the USGS (United States Geological Survey). The images underwent radiometric calibration, atmospheric correction, and geometric correction, with a spatial resolution of 30 m. Radiometric calibration was conducted using the metadata provided by the USGS, converting digital number (DN) values to top-of-atmosphere (TOA) reflectance. Atmospheric correction was performed using the LEDAPS (Landsat Ecosystem Disturbance Adaptive Processing System) algorithm, which employs the 6S radiative transfer model to remove atmospheric effects and retrieve surface reflectance. Geometric correction ensured co-registration accuracy within 0.5 pixels by referencing ground control points and terrain data.

Based on the imagery, a 10-year NDVI(Normalized Difference Vegetation Index) time series was computed to derive the remotely sensed Shannon diversity index and Rao's Q index. NDVI is one of the most widely used remote sensing-based vegetation indices. NDVI exhibits high compatibility with Rao's Q index in remote sensing-based biodiversity assessments. Emphasizing canopy greenness and photosynthetic activity, NDVI effectively reflects primary productivity and spectral heterogeneity. Compared to indices such as EVI and SAVI, NDVI is less dependent on algorithmic parameter settings and assumptions regarding soil background, making it more suitable for regions characterized by complex and diverse surface types.(Madonsela et al., 2017; Verbesselt et al., 2010). Previous studies have demonstrated that NDVI variations are associated with ecosystem energy exchange and primary productivity, making it an effective indicator for assessing regional biodiversity(Hauser et al., 2021; Skidmore et al., 2021).

A SVM (Support Vector Machine) classification method was applied to the imagery for supervised land cover classification. Training datasets were established for six land cover types: forest, farmland, soil, buildings, waters, and wetland. Using a visual interpretation validation set derived from GEE (Google Earth Engine) and a statistical validation set collected from official land survey reports in 2022, accuracy assessment was conducted through a confusion matrix approach, yielding an overall accuracy of 83.61 %. Land-use change maps for the study area from 2015 to 2024 were generated to facilitate further analysis of landscape metrics across different land cover types.

2.4. Biodiversity assessment indicators

The SHDI is a biodiversity metric based on information theory, widely applied in ecological studies. This index reflects landscape heterogeneity and is particularly sensitive to the uneven distribution of species, emphasizing the contribution of rare species to overall biodiversity. Its calculation formula is:

$$SHDI = -\sum_{i=1}^{S} p_i \ln p_i$$

where S represents the total number of species, and p_i denotes the proportion of the i-th species in the total population. When a community consists of only one species, SHDI reaches its minimum value of 0. As SHDI increases, it indicates an increase in species richness or a trend toward a more even species distribution within the landscape. When a community comprises two or more species with equal abundance, the Shannon index reaches its maximum value, ln(S).

The Rao's Q index was originally introduced by (Rao, 1982) and later applied to species diversity assessment by (Botta-Dukát, 2005). (Rocchini et al., 2017) further developed a remote sensing-based model for calculating Rao's Q index, with the following formula:

$$Q_{rs} = \sum_{i=1}^{C-1} \sum_{j=i1}^{C} d_{ij} \times p_i \times p_j$$

where:Q_{rs} = Remote sensing−based Rao's Q diversity index, p = Relative abundance of pixel values in the input image, d_{ij} = Spectral distance between pixel i and pixel j, i and j = Indexes of pixels i and j.

Using NDVI imagery as the input data source, Rao's Q index was computed for each pixel via linear regression and validated against field survey data. Additionally, the H′ (Shannon entropy index) was calculated to compare its performance with the Rao's Q diversity index.

2.5. Landscape metrics

Landscape metrics are essential indicators for quantitatively describing landscape spatial patterns, widely applied in ecology, land-use change analysis, and environmental management. These metrics mathematically quantify the shape, size, distribution, and spatial interactions of landscape patches, providing insights into how landscape patterns influence ecological processes across different spatial scales. Based on continuous land-use data from 2015 to 2024, a time series of 11 landscape metrics was constructed. These metrics were categorized into four major groups according to the specific landscape characteristics they represent (Table 2).

The selection of landscape metrics in this study was based on their ecological relevance to biodiversity and landscape fragmentation processes. Specifically, PD (Patch Density) was used to quantify the degree of fragmentation by measuring the number of patches per unit area, which reflects habitat discontinuity and edge proliferation. LSI (Landscape Shape Index) captures the complexity of patch shapes, often associated with human disturbance and ecological edge effects. COHESION(Patch Cohesion Index) and AI (Aggregation Index) reflect landscape connectivity and aggregation, critical for evaluating ecological corridors and species movement pathways. SPLIT (Splitting Index) and MESH (Effective Mesh Size) describe landscape division and effective habitat size, indicating the degree of isolation among habitat patches. Together, these indices offer a comprehensive assessment of spatial patterns and ecological processes across heterogeneous land-use types, which is essential for understanding the biodiversity impacts of large-scale infrastructure projects(Fahrig, 2003; Herold et al., 2005; Schindler et al., 2008; Sha and Tian, 2010; Walz and Syrbe, 2013).

2.6. Technology path

The technology path of this study is illustrated in Fig. 2 and comprises six main steps. First, Landsat 8/9 imagery from 2015 to 2024 was acquired and preprocessed through radiometric correction, geometric correction, cloud removal, and cropping. Second, NDVI was computed, and supervised classification was conducted to extract land use information, resulting in vegetation index and land use classification maps. Third, the Rao's Q index and various landscape metrics were calculated independently. Next, a joint analytical framework was constructed to examine the relationships between Rao's Q and landscape structure, assessing the index's responsiveness to fragmentation and heterogeneity. Finally, the study evaluated the applicability and effectiveness of Rao's Q in characterizing landscape patterns, supporting biodiversity monitoring using remote sensing techniques.

3. Results

3.1. Trends in biodiversity in the Pinglu Canal Basin from 2015 to 2024

Table 3 presents the R (correlation coefficient) and RMSE (root mean square error) between the H′ index calculated from field data and the

Table 2
Categories of Landscape Metrics, Calculation Formulas, and Their Implications for Landscape Issues. This table categorizes landscape metrics based on their ecological significance, illustrating their mathematical formulations and their relevance to landscape pattern analysis, habitat fragmentation, and ecosystem connectivity.

Category	Metric	Formula	Landscape Issues Represented
Patch Composition and Structure	PLAND (Percentage of Landscape)	$\text{PLAND} = \left(\frac{\sum A_{ij}}{A}\right) \times 100$	Landscape scale, total habitat area
	PD (Patch Density)	$\text{PD} = \frac{NP}{TA} \times 10^4$	
	TE (Total Edge Length)	$\text{TE} = \sum P_{ij}$	
Shape Complexity	LSI (Landscape Shape Index)	$\text{LSI} = \frac{0.25E}{\sqrt{TA}}$	Edge effects, degree of human disturbance
	PAFRAC (Perimeter-Area Fractal Dimension)	$\text{PAFRAC} = \frac{2}{\beta}$	
Spatial Distribution and Connectivity	CLUMPY (Clumpiness Index)	$\text{CLUMPY} = \frac{G_i - E_i}{G_{i,max} - E_i}$	Species migration resistance, ecological connectivity, interaction between patch types
	IJI (Interspersion and Juxtaposition Index)	$\text{IJI} = -\frac{\sum_{i=1}^{m}\sum_{k=i1}^{m}\left(\frac{e_{ik}}{E}\ln\frac{e_{ik}}{E}\right)}{\ln\left(\frac{m(m-1)}{2}\right)} \times 100$	
	AI (Aggregation Index)	$\text{AI} = \left(\frac{g_{ii}}{\max g_{ii}}\right) \times 100$	
	COHESION (Patch Cohesion Index)	$\text{COHESION} = \left(1 - \frac{\sum_{i=1}^{n} p_i}{\sum_{i=1}^{n} p_i\sqrt{a_i}}\right) \times 100$	
Landscape Fragmentation and Isolation	MESH (Effective Mesh Size)	$\text{MESH} = \frac{\sum_{i=1}^{n} a_i^2}{TA}$	Habitat isolation risk, biodiversity maintenance capacity
	SPLIT (Splitting Index)	$\text{SPLIT} = \frac{TA}{\sum_{i=1}^{n} a_i^2}$	

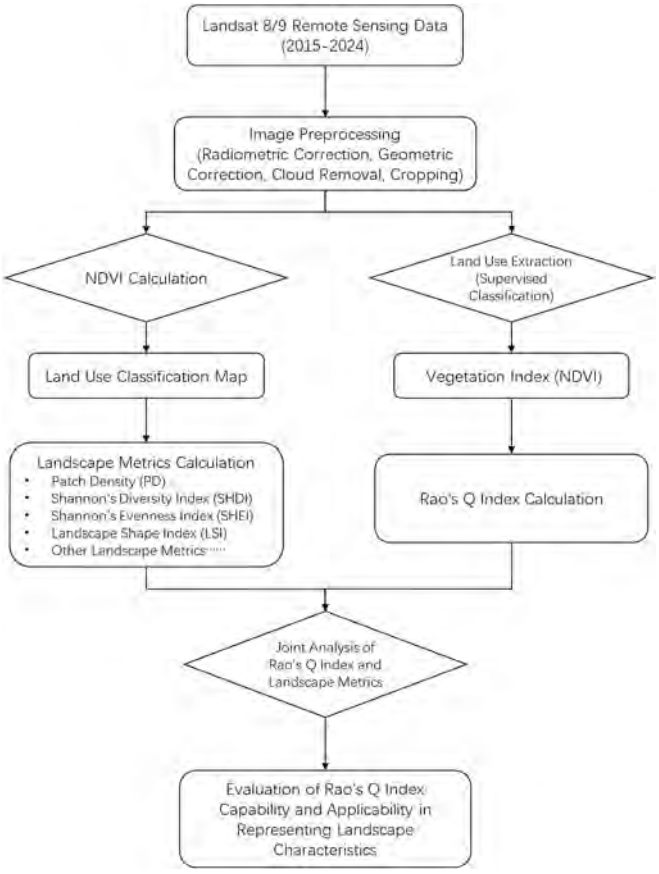


Fig. 2. The technology path for joint analysis of Rao's Q index and landscape metrics using remote sensing data.

Table 3.
Validation of Rao's Q and H' against observed Shannon diversity using all sampling data, as well as grouped forest and mangrove sampling data. The table reports the coefficient of determination (R) and root mean square error (RMSE), with significance level: $*P < 0.001$.

	Biodiversity Index	R	RMSE
All data	Rao's Q	0.21	0.56
	H′	0.19	0.55
Forest	Rao's Q	0.64*	0.29
	H′	0.55*	0.32
Wetland	Rao's Q	0.05	0.36
	H′	0.09	0.36

Rao's Q index and H′ index derived from Landsat 8/9 imagery. When validated using all sampling data, the correlation between the two indices was relatively weak. To further investigate this, we separately analyzed the correlation using field data from forests and wetland. The results indicate that Rao's Q index demonstrated a stronger correlation ($R > 0.64$) and a significant relationship ($P < 0.001$) in evergreen broadleaf forests. Moreover, Rao's Q exhibited higher correlation than the H′ index in this ecosystem. However, in wetland, both indices showed relatively low correlation.

Fig. 3 illustrates the time series of Rao's Q index and H′ index from 2015 to 2024. The analysis is divided into two periods: pre-construction phase (2015–2021) and construction phase (2022–2024).Before construction, both Rao's Q index and H′ index exhibited stable and relatively low values over large forested and farmland areas. This is primarily due to the homogeneous canopy composition of forests and farmlands, where a single dominant species results in low spectral heterogeneity within their core areas. In contrast, higher index values were observed in land-use complex regions, mainly due to the high fragmentation of different land-use types, including buildings, soil, farmland, forest, and waters, which increases spectral heterogeneity. Along natural riverbanks, particularly in the Qinjiang River channel, the indices exhibited the highest values. This may be attributed to the narrow width of the Qinjiang River, which occupies only 2–3 pixels in Landsat 8/9 imagery, leading to high spectral heterogeneity between these water pixels and the surrounding land pixels. Conversely, in larger water bodies, such as the upstream Xijiang River system and the coastal Maowei Sea, both indices effectively distinguished the biodiversity contrast between water bodies and shorelines.

During the construction phase of the Pinglu Canal, both Rao's Q index and H′ index within the occupied area exhibited a decline-increase trend. In early 2022, the initial construction phase involved large-scale land occupation of forests and farmlands, leading to a sharp decline in vegetation indices. These areas were converted into bare soil landscapes, resulting in reduced spectral heterogeneity, which contributed to the decrease in both indices. In 2023–2024, although the area of developed land and bare soil continued to expand, the simultaneous implementation of ecological restoration projects increased spectral heterogeneity within the occupied area. Consequently, the spatial distribution of biodiversity within the construction zone followed a high-low-high pattern over time.

3.2. The time series of Rao's Q index and the changes in the area of different land cover types

Fig. 4 illustrates the time series changes in Rao's Q index from 2015 to 2024 at both the occupied area of the Pinglu Canal (Fig. 4a) and the watershed scale (Fig. 4b). Overall, Rao's Q index remained relatively stable at both spatial scales throughout 2015–2024. However, in 2022, the range of the index narrowed, indicating a decline in landscape heterogeneity, which may be attributed to the disappearance or reduction of certain landscape types. In 2023–2024, Rao's Q index reached relatively high values at both scales, suggesting an increased degree of landscape mixing during this period. This trend may reflect the initial impact of canal construction, as land-use changes were more pronounced in response to large-scale infrastructure development.

In terms of area change trends across different land cover types, we first examine the changes within the occupied area of the canal construction zone. Forest area remained relatively stable before 2020, but declined sharply from 2022 onward, nearing complete disappearance by 2024, indicating a significant impact of canal construction on forests. Built-up land increased rapidly after 2021, particularly peaking between 2022 and 2023, aligning with urban expansion associated with canal development. Soil was relatively sparse before 2022 but increased significantly afterward, reflecting large-scale land clearing and development activities due to canal construction. Farmland and wetland areas also declined notably after 2022, suggesting that the canal construction negatively impacted agricultural and wetland ecosystems.

At the watershed scale, forest area exhibited a gradual decline after 2017, indicating that forest landscape changes were influenced by broader, long-term factors at a larger spatial scale. Farmland area dropped sharply in 2017 but showed gradual recovery after 2018, likely reflecting adaptive land-use changes, where some agricultural areas were relocated or converted. Built-up land area grew gradually after 2019, indicating urban expansion within the watershed, though at a moderate rate. However, its growth rate increased significantly in 2022, mirroring the trends observed at the occupied area scale, further confirming the impact of large-scale canal construction. Water body area exhibited a slight decline after 2022, which may be attributed to temporary river closures during canal construction and an increase in suspended sediment concentration, reducing the visible water surface area.

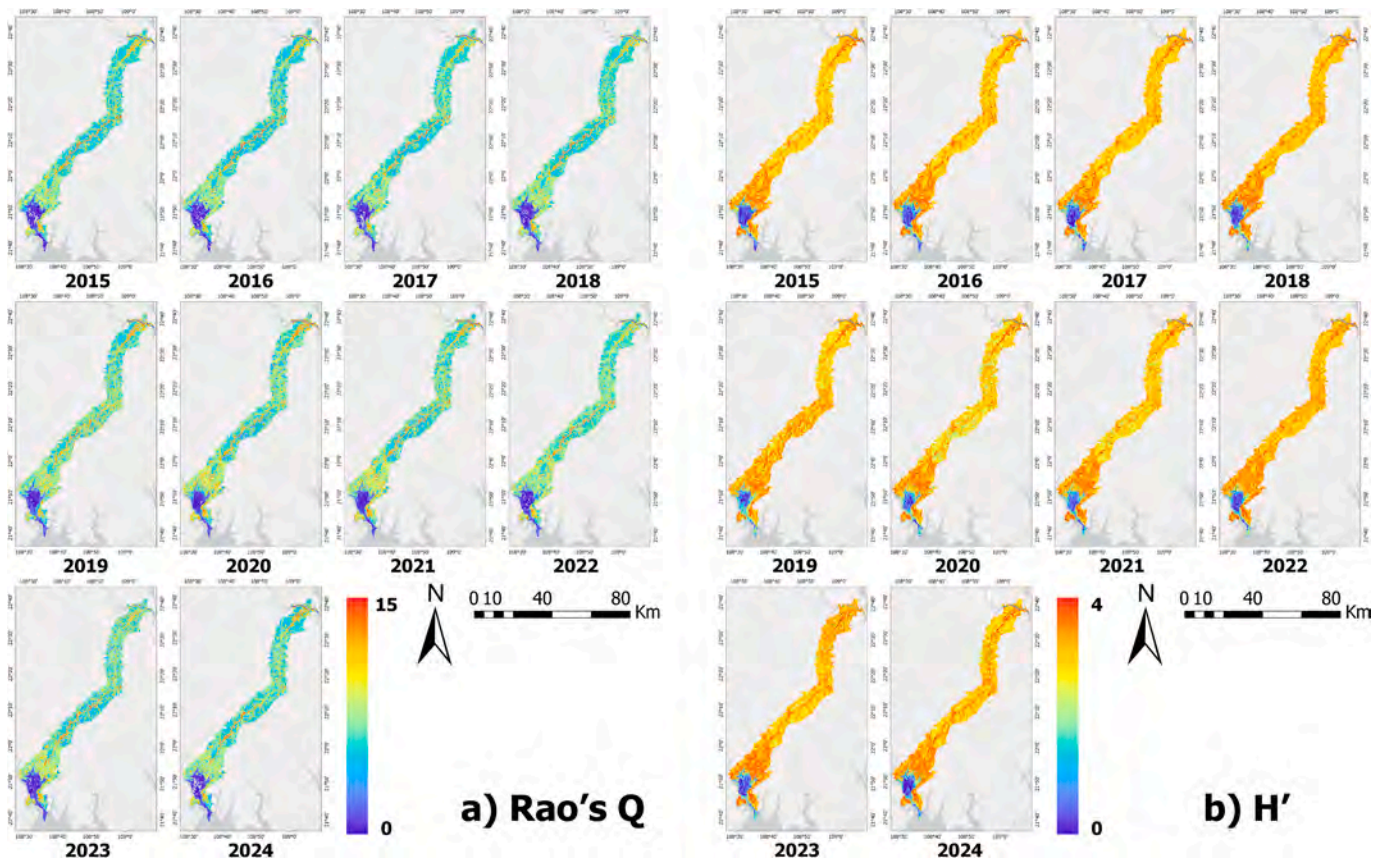


Fig. 3. Time series of the spatial distribution of Rao's Q and H′ indices in the study area for October of each year from 2015 to 2024. (a) Rao's Q index, (b) H′ diversity index.

3.3. The time series of changes in landscape indices

During the construction of the Pinglu Canal, landscape structure underwent significant changes, particularly in the dynamic transitions between forests, wetlands, and built-up land. To quantify these changes, we constructed time series of 11 landscape metrics at two spatial scales (Fig. 5, Fig. 6, and supplementary materials). Among these metrics, PD, LSI, TE, COHESION, and SPLIT exhibited the most significant changes, reflecting the profound impact of canal construction on regional landscape patterns.

PD index reflects the degree of landscape fragmentation. The study found that PD values for forests and wetlands increased significantly after 2022, indicating that canal construction had a substantial impact on the fragmentation of these ecosystems. Additionally, PD values for built-up land and bare soil also increased rapidly, reflecting accelerated urbanization along the canal corridor. Correspondingly, the TE index increased sharply after 2022, suggesting that landscape patch boundaries became more complex. This trend was primarily driven by large-scale land-use transitions, such as forest fragmentation, wetland reduction, and the conversion of farmland to built-up land. The LSI measures the complexity of landscape patch shapes. The results indicate that LSI values in the canal construction area increased significantly after 2022, suggesting that newly formed landscape patches tended to be more irregular in shape. This trend is closely related to ecosystem fragmentation caused by human intervention, particularly in wetland and mangrove areas, where newly fragmented wetland patches exhibited irregular and complex boundaries. The COHESION index, which represents overall landscape connectivity, declined markedly for forests and wetlands after 2022, indicating that connectivity within these ecosystems was disrupted. This decline is directly linked to landscape fragmentation and habitat loss caused by canal construction. At the same time, the SPLIT, which quantifies the degree of landscape division, increased significantly after 2022, particularly in forest areas, indicating further ecosystem fragmentation. This suggests that biodiversity and ecological functions may have been more severely impacted due to habitat isolation and disruption.

In addition to the indices mentioned above, changes were also observed in the AI and Interspersion and IJI for farmland, wetlands, and bare soil, indicating an increase in spatial interspersion among different land-use types. However, these changes were relatively minor compared to the significant variations in PD, LSI, and COHESION indices.

Overall, canal construction has intensified the fragmentation of forests and wetlands, expanded built-up areas, and increased landscape heterogeneity. The variations in landscape metrics suggest that ecosystem integrity has been affected, though ecological restoration measures implemented in 2023–2024 have provided some mitigation. Future research should integrate ecological monitoring data to further explore the long-term impacts of landscape changes on biodiversity and optimize ecological restoration strategies to minimize the long-term negative effects of canal construction on regional ecosystems.

Since the implementation of large-scale ecological restoration policies in 2022, changes in landscape metrics across land cover types indicate varying levels of benefit among different ecosystems, with forest and wetland ecosystems showing particularly significant recovery effects.

At the basin scale, wetlands exhibited positive changes across multiple indicators: TE increased by 20.0 %, PD rose by 28.6 %, and the LSI improved by 10.0 %. These changes suggest a more complex spatial structure and enhanced ecological connectivity of wetland ecosystems. Although the PLAND of forests slightly decreased by 10.5 %, the stability in shape and aggregation metrics (LSI decreased by only 3.8 %) indicates that restoration measures have effectively curbed further fragmentation.

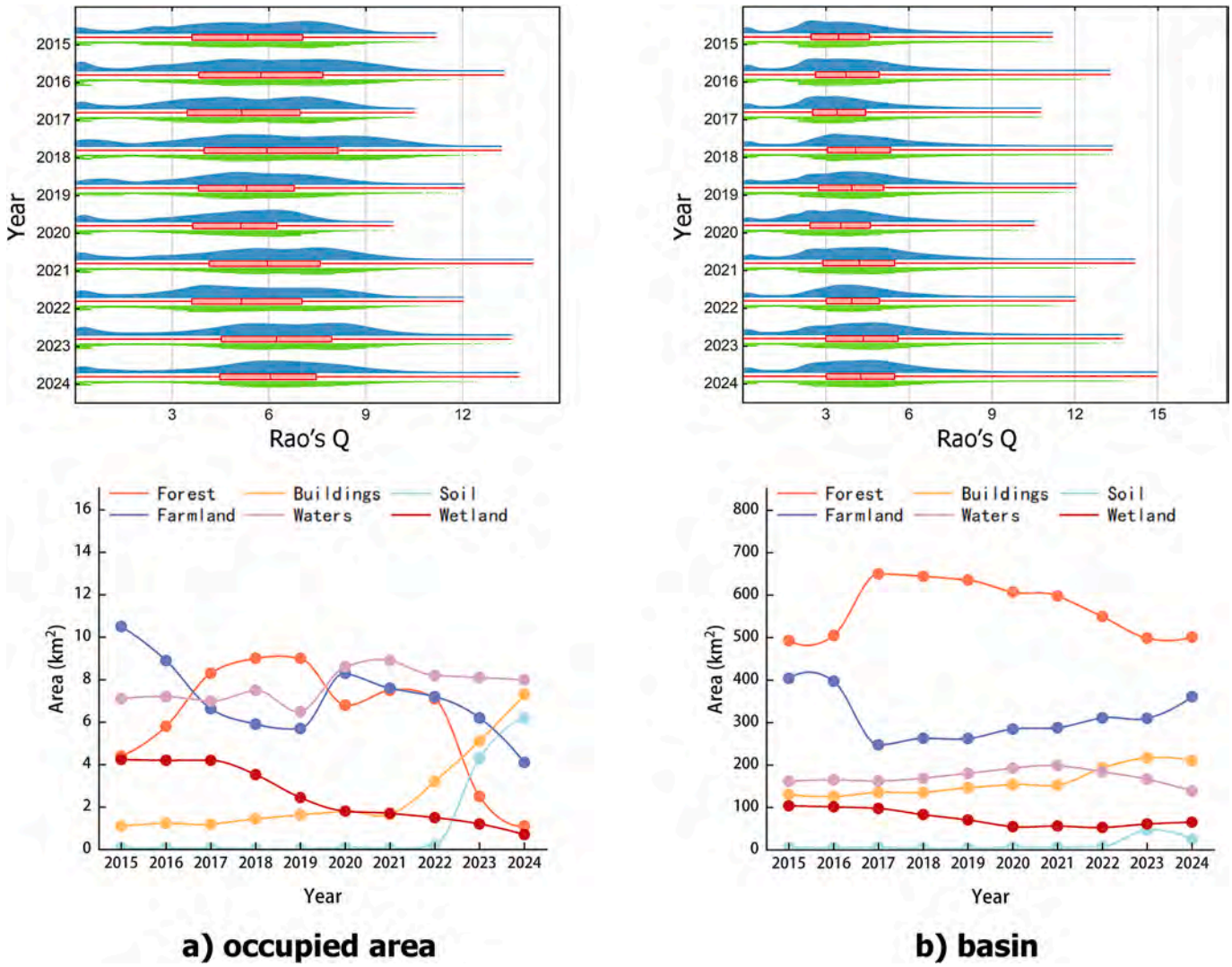


Fig. 4. Time series of the mean Rao's Q index and its spatial distribution within the occupied area and watershed, along with the land cover area change trends for different land-use types within these regions.

Within the occupied area of canal construction, forests and wetlands experienced inevitable loss; however, the PD values for bare soil and built-up land more than doubled—far exceeding the decline rates of forest and wetland areas—indicating that forest boundaries may have been subject to redline management or deliberate protection during construction, thereby avoiding more severe disturbance. Wetland TE decreased by 12.5 %, which is lower than that of farmland (53.6 %) and forest (14.3 %), while the CLUMPY index remained stable. This suggests that wetlands may have been preserved or artificially reconstructed as ecological buffers during the restoration process.

Notably, bare soil and built-up areas experienced the most intense landscape disturbances. The PLAND of bare soil increased from 0 to 5 % at the basin level and reached 12 % in the occupied area, confirming the extensive land exposure caused by construction activities. Nevertheless, the relative improvement trends observed in forest and wetland ecosystems after 2022 indicate that these two ecosystems were the primary beneficiaries of this round of ecological restoration efforts, particularly in terms of spatial continuity and patch aggregation.

4. Discussion

4.1. Advantages of Rao's Q Index in remote sensing-based biodiversity monitoring

Current studies on Rao's Q index have been limited to terrestrial ecosystems(Khare et al., 2021). This study represents the first attempt to apply an NDVI-based Rao's Q index to evaluate species diversity in large-scale complex ecosystems(Randin et al., 2020). Overall, the construction of the Pinglu Canal has significantly altered landscape composition and ecological patterns along its corridor. In the construction zone, forest and wetland areas sharply declined, while bare and built-up lands expanded, resulting in a notable drop in Rao's Q index in 2022 and indicating increased landscape homogenization. With the implementation of ecological restoration projects during 2023–2024, landscape heterogeneity and biodiversity showed partial recovery, although responses varied by ecosystem type. At the watershed scale, changes were more moderate, but long-term declines in forest cover and urban land expansion remain pressing concerns, potentially affecting regional carbon storage and hydrological regulation functions(Wang et al., 2021).

Although the Rao's Q index proved effective in capturing spectral heterogeneity and ecosystem complexity, its application also presents limitations that warrant critical reflection. Notably, in homogeneous

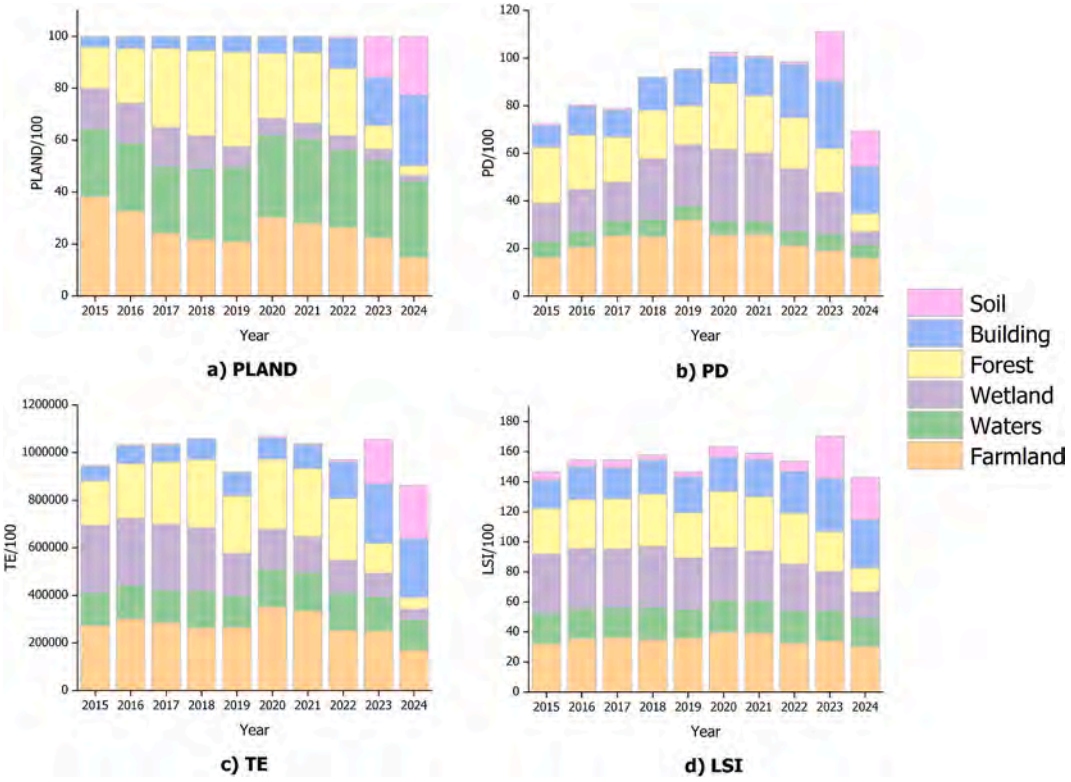


Fig. 5. Changes in four landscape metrics (PD, LSI, TE, and PLAND) within the occupied area of the Pinglu Canal from 2015 to 2024.

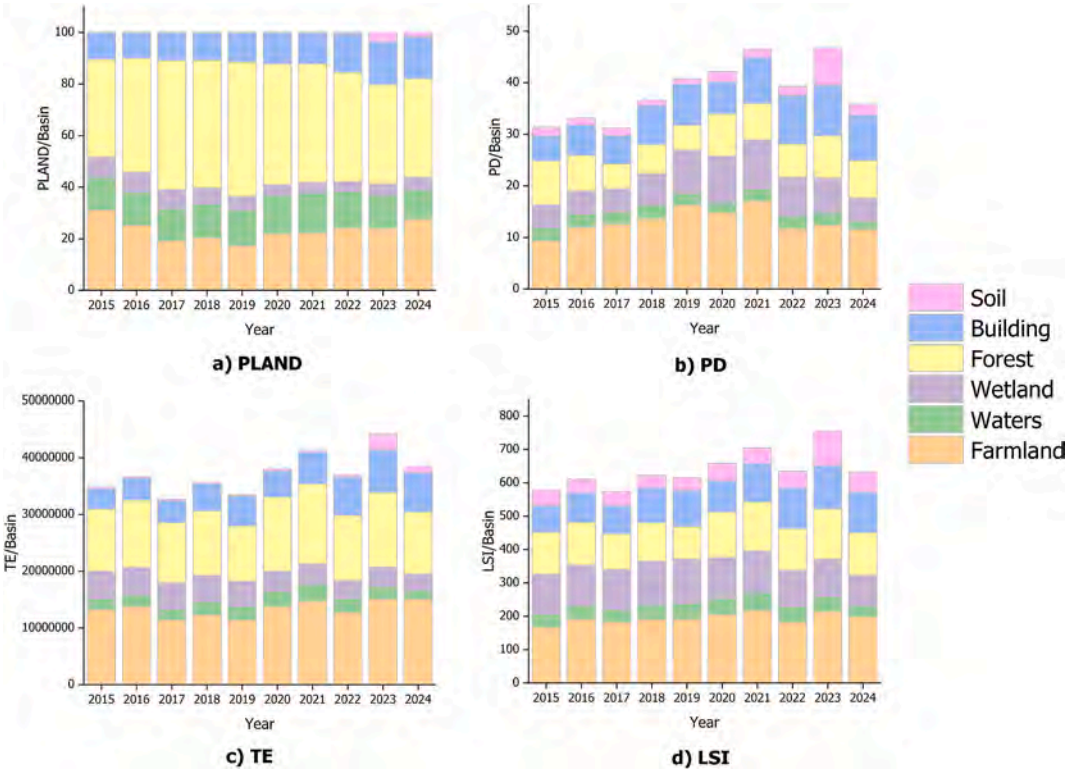


Fig. 6. Changes in four landscape metrics (PD, LSI, TE, and PLAND) in the Pinglu Canal watershed from 2015 to 2024.

ecosystems such as mangroves or monoculture plantations, high edge contrast may inflate Rao's Q values despite low species richness—particularly problematic given that remote sensing primarily reflects canopy structure and fails to capture understory or microhabitat diversity. Mangrove communities in the study area exhibit structural simplicity and lower observed Shannon diversity values. However, based on remote sensing data, the Rao's Q index for mangroves appears higher than that for forests, primarily due to the calculation method of

Rao's Q. This index is derived from remote sensing spectral heterogeneity theory, accounting for pixel values and inter-pixel differences (Wang et al., 2022). Furthermore, the index is sensitive to spatial resolution and vegetation density, potentially introducing bias in densely vegetated or early-successional systems due to pixel saturation or limited within-pixel variability(Fig. 7).

During the Pinglu Canal construction, both Rao's Q and H′ indices exhibited a decline followed by a rise; however, Rao's Q more effectively reflected spectral heterogeneity changes associated with ecological restoration. The study results indicate that the Rao's Q index exhibits a higher correlation in the study area ($R = 0.64$, $P < 0.001$), suggesting that it better captures biodiversity characteristics within the ecosystem. In contrast, the H′ performs relatively weakly($R = 0.55$, $P < 0.001$), likely because H′ primarily emphasizes species evenness and struggles to effectively distinguish spectral characteristics of different vegetation types. While both indices decreased with the expansion of bare soil, Rao's Q showed a more sensitive response during the 2023–2024 restoration phase, highlighting its suitability for dynamic biodiversity monitoring. Restoration measures—such as ecological slope protection, landscape greening, and farmland creation—were implemented alongside construction(Watts et al., 2010). As shown in Fig. 8, Rao's Q increased along restored riverbanks and newly created soil-filled areas, especially in canal lock and diversion zones. In contrast, biodiversity declined along original riverbanks during construction but rebounded following restoration efforts. By 2024, biodiversity was notably enhanced in the excavation areas due to ongoing slope protection, afforestation, and land cover transformation. Overall, these trends indicate that simultaneous restoration contributed to partial biodiversity recovery after the 2022 decline.

To improve the robustness of biodiversity assessment in future studies, it is recommended to incorporate complementary indicators such as functional diversity indices (e.g., FRic, FEve), β-diversity measures (e.g., Sørensen Index, Bray–Curtis), species-habitat models (e.g., MaxEnt), and time-series variability analysis. These additions can help construct a multidimensional and ecologically grounded biodiversity monitoring framework, addressing the limitations of single-index approaches like Rao's Q, and better guiding future conservation and restoration planning in large-scale infrastructure contexts.

4.2. *Rao's Q has a higher correlation with landscape indices in areas with complex land cover types*

The Rao's Q index, as a functional diversity metric for assessing biodiversity, is fundamentally designed to account for both species richness and functional dissimilarity among species. At the regional scale, Rao's Q not only reflects community-level heterogeneity but is also indirectly influenced by habitat structure and spatial configuration. Landscape metrics such as PD, LSI, and COHESION describe the spatial distribution patterns and fragmentation levels of different land-use types.From an ecological mechanism perspective, landscapes characterized by greater structural complexity and higher connectivity can provide more microhabitats and ecological niches for various species, thereby enhancing functional diversity and increasing Rao's Q values. In contrast, highly fragmented or homogeneous landscapes may restrict

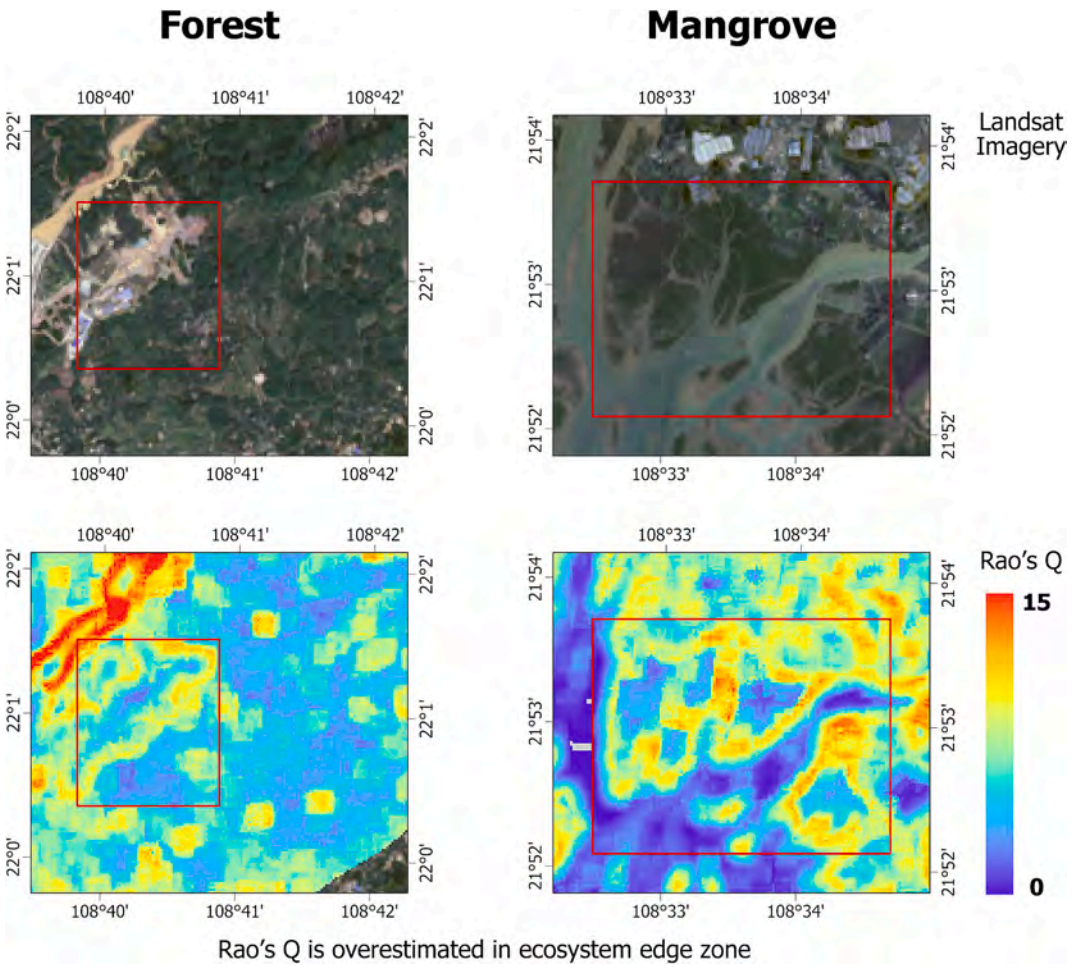


Fig. 7. Abnormally high Rao's Q index values at the edges of forests and mangroves. The spectral heterogeneity differences between forests/mangroves and their surrounding areas result in an overestimation of biodiversity in mangrove regions by the Rao's Q index.

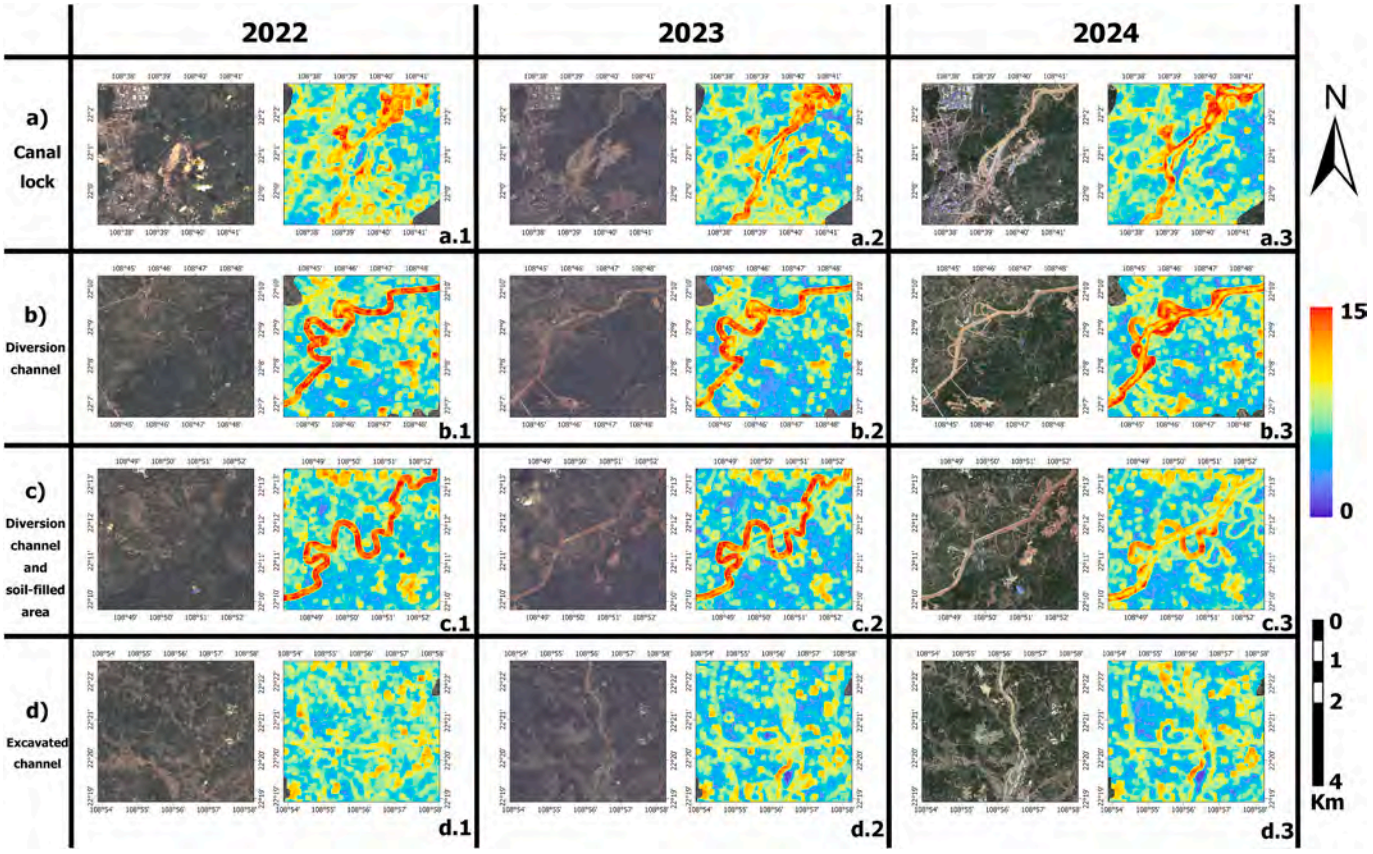


Fig. 8. Changes in Rao's Q values within ecological restoration areas. (a) Canal lock; (b) Diversion channel; (c) Diversion channel and soil-filled area; (d) Excavated channel.

species movement and resource accessibility, leading to lower Rao's Q values. Thus, a potential positive correlation exists between landscape complexity and functional diversity, which tends to be more pronounced in ecologically sensitive systems such as wetlands and forests.

This section examines the temporal dynamics between Rao's Q and key landscape metrics across different land cover types, aiming to further elucidate how landscape patterns drive changes in regional ecological diversity.

Landscape indices that exhibit strong correlations with Rao's Q can reveal the ecological characteristics of landscape structures (Fig. 9). The study found that Rao's Q increased with higher PLAND for bare soil and built-up land but declined with higher forest PLAND, indicating that mixed or heterogeneous landscapes support greater biodiversity than those dominated by a single land type (e.g., forests or farmlands). This aligns with the ecological principle that habitat homogeneity reduces niche availability (Pangtey et al., 2023).

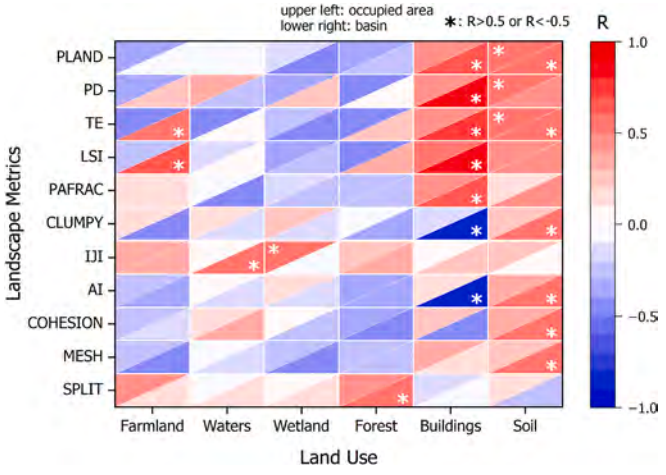


Fig. 9. Correlation coefficients (R) between landscape indices of different land cover types and Rao's Q index at different spatial scales. The upper left value in each cell represents the correlation within the occupied area, while the lower right value represents the correlation within the watershed.

Patch Density (PD) and Total Edge (TE), both indicators of fragmentation, showed positive correlations with Rao's Q in urban and bare soil areas. High patch density and edge complexity suggest diverse microhabitats and ecological transition zones, promoting species richness, especially for edge-adapted species. These transition areas can enhance species diversity, particularly for edge species, while also facilitating ecological processes, such as nutrient flow between different habitats (Kumar et al., 2006). The positive correlation between Rao's Q and edge indices suggests that this index effectively reflects ecological complexity within landscapes. When the interspersion between different ecosystems increases, landscape diversity also increases.

Similarly, the Landscape Shape Index (LSI) was positively associated with Rao's Q in urban areas, as irregular patch shapes reflect high interspersion of land-use types, enhancing ecological complexity. However, excessive fragmentation can harm interior species, highlighting the need for complementary metrics. For instance, CLUMPY and AI showed that while compact urban zones reduce diversity, contiguous forests—though beneficial to some taxa—also decrease overall heterogeneity (Schooley & Branch, 2011; Torresani et al., 2019). Conversely, forest aggregation was negatively correlated with Rao's Q, suggesting that while extensive contiguous forests benefit certain species, they reduce overall landscape heterogeneity. Thus, the interpretation of Rao's Q should be integrated with landscape connectivity metrics to comprehensively assess ecological complexity.

In forested areas, the correlation between Rao's Q and landscape metrics is generally low or negative, due to the homogeneous structure, low fragmentation, and limited edge effects of forests. For instance, forest PLAND shows a correlation of −0.38 with Rao's Q, while PD and TE range from −0.41 to −0.44, suggesting that extensive, contiguous forest cover tends to reduce landscape heterogeneity. However, when fragmentation increases or restoration enhances spatial complexity, Rao's Q rises, indicating its sensitivity to structural changes. SPLIT is positively correlated with Rao's Q ($R = 0.43$), supporting its effectiveness in capturing diversity in fragmented forest ecosystems(Saura et al., 2006).

In contrast, built-up and bare land areas typically exhibit high heterogeneity.(Purdon et al., 2022). Urban areas, with diverse materials and spatial layouts, produce complex boundaries and spectral variability, while bare lands—shaped by development or erosion—show similar irregularity(Nakamura et al., 2020). A positive correlation is observed between urban and bare land landscape indices and Rao's Q. The correlation coefficient between built-up land PLAND and Rao's Q is approximately 0.43, while built-up land patch density and edge length exhibit correlations of around 0.48. Notably, the urban LSI has the highest correlation with Rao's Q, at approximately 0.51. Similarly, bare land cover and its fragmentation indices also show strong correlations ($R_{PLAND} = 0.50$, $R_{PD} = 0.53$, $R_{TE} = 0.52$). These strong correlations suggest that the introduction of scattered built-up or bare land patches into the landscape significantly increases overall landscape diversity. This finding highlights the sensitivity of Rao's Q to heterogeneous landscapes, making it a valuable metric for assessing urban expansion, land-use changes, and ecological disturbances.

As a second-order entropy metric, Rao's Q reflects both the abundance and ecological dissimilarity of landscape types(Rocchini et al., 2024). Unlike traditional indices, it captures functional differences—e.g., between diverse habitats vs. uniform farmlands—yielding higher values when distinct land-cover types coexist. It is especially sensitive to ecological transition zones, where species richness is often elevated. High Rao's Q values indicate a mosaic of habitats, which supports biodiversity and ecosystem resilience through services like pollination and buffering.

In summary, Rao's Q is elevated in landscapes with fine-scale heterogeneity and diverse cover types, and lower in uniform land covers. It correlates most strongly with patch density, edge length, shape complexity, and interspersion—particularly in urban, bare land, and wetland contexts. These results affirm Rao's Q as a robust indicator of landscape complexity and ecological diversity. Future studies should integrate field-based biodiversity data to further validate its ecological relevance.

4.3. Ecological protection benefits and management strategies of ecological restoration projects during the construction of the Pinglu Canal

Despite progress in remote sensing-based biodiversity assessment, several limitations remain in the context of large-scale infrastructure projects. Traditional indices like Shannon and Simpson fail to capture ecosystem heterogeneity, especially in homogeneous landscapes such as mangroves and monoculture plantations. Although Rao's Q offers theoretical advantages by integrating species richness and dissimilarity, its use in anthropogenically disturbed systems—particularly during construction and ecological restoration—is still underexplored. Moreover, current approaches often neglect the role of landscape configuration, failing to link biodiversity dynamics with patch fragmentation, connectivity, or spatial isolation. Additionally, biodiversity assessments are frequently cross-sectional, overlooking dynamic shifts over construction-restoration periods. These gaps hinder effective monitoring and limit the application of biodiversity metrics in supporting ecological planning.

Large-scale infrastructure projects inevitably impact regional ecosystems. Forest and wetland fragmentation reduces carbon storage and biodiversity, while urbanization and agriculture accelerate wetland loss and disrupt hydrological cycles(Doxa et al., 2022). Although built-up land may enhance infrastructure connectivity, it increases ecological pressure. Urban sprawl and farmland loss can create short-term microhabitats, yet long-term effects include landscape homogenization and wetland degradation(Walz et al., 2016). High urban density (PLAND >25 %) threatens habitat-dependent species(Jalkanen et al., 2020), and declining wetland aggregation may impair hydrological regulation and migratory pathways(Kim and Pauleit, 2007). Therefore, using Rao's Q alone may overlook key species loss, calling for field validation and indicator species monitoring(Marshall et al., 2020).

During the Pinglu Canal construction, quantifying biodiversity and landscape indices helped guide precise conservation strategies(Torras et al., 2009). Biodiversity thresholds (e.g., built-up land >5 %/year) can define ecological redlines(Turner et al., 2013). Suggested strategies include embedding ecological patches into urban zones, protecting highly connected ecosystems (COHESION >98), building corridors in fragmented areas (high SPLIT), and regulating land expansion. (Li et al., 2022; Zhao et al., 2021; Kerr and Remmel, 2024; Wu et al., 2016). Long-term priorities include wetland/forest restoration and ecological compensation mechanisms(Jellinek et al., 2019; Tian et al., 2016).

While the ecological restoration measures implemented during the Pinglu Canal construction have demonstrated short-term biodiversity benefits, their long-term sustainability remains uncertain under ongoing urbanization and land-use pressures. Continuous expansion of built-up areas may gradually erode restored habitats, increase edge effects, and fragment newly established ecological patches, reducing their ecological resilience and connectivity. Additionally, without proper maintenance and ecological management, artificial restoration zones—such as greening belts and ecological slopes—may degrade due to invasive species, soil erosion, or hydrological changes.

To maintain biodiversity under development pressure, adaptive strategies should be prioritized. These include establishing buffer zones between urban and ecological areas to reduce anthropogenic disturbances, enhancing connectivity through ecological corridors to facilitate species movement, and implementing dynamic monitoring systems using time-series remote sensing to detect early signs of ecosystem degradation. Moreover, integrating nature-based solutions (NbS) and community-based management can increase social acceptance and long-term stewardship of restored landscapes. These strategies are critical for aligning short-term restoration outcomes with broader goals of ecological resilience and urban sustainability, especially in rapidly developing regions like the Pinglu Canal corridor.

5. Conclusion

This study systematically assessed biodiversity changes before and after the construction of the Pinglu Canal (2015–2024) using the Rao's Q index, remote sensing data, and landscape metrics. The results revealed the following: The Rao's Q index, based on NDVI data, outperformed the Shannon diversity index in the study area, with a stronger correlation to field-measured biodiversity ($R = 0.64$, RMSE = 0.29). Rao's Q showed strong correlations with fragmentation indices such as PD, ED, LSI, and SPLIT, making it an effective tool to assess biodiversity responses to large-scale land disturbances. The canal construction phase (2022) significantly reduced biodiversity, while ecological restoration from 2023 to 2024 led to partial recovery, with forests and wetlands showing varied effectiveness. The Rao's Q index may overestimate biodiversity in homogeneous ecosystems (e.g., mangroves), suggesting the need for multi-index integration in such environments. This study is the first to quantify the impact of canal construction on landscape fragmentation and biodiversity using Rao's Q index and landscape metrics, addressing a research gap regarding the effects of large-scale artificial canal construction on biodiversity. The findings highlight the effectiveness of Rao's Q index in assessing multi-ecosystem fragmentation, while also identifying its limitations in homogeneous vegetation systems such as

wetlands and mangroves. This provides new theoretical support for applying Rao's Q index in ecological conservation and landscape planning.

These findings offer valuable insights for ecological planning and national policy: The integration of Rao's Q and landscape metrics supports green infrastructure planning, allowing early identification of ecologically sensitive zones and embedding ecological restoration in project design. The fragmentation and connectivity indices provide a scientific basis for delineating and managing ecological redlines, helping to maintain landscape integrity amid development. The observed restoration effectiveness aligns with the objectives of China's 14th Five-Year Plan for Ecological and Environmental Protection and the carbon neutrality strategy, especially in enhancing ecosystem carbon sinks and biodiversity co-benefits. The approach proposed in this study can serve as a monitoring and evaluation tool for future ecological projects, contributing to the construction of a long-term national ecological security system. Building on this research, future directions may include incorporating multi-source remote sensing to improve the identification accuracy of homogeneous ecosystems such as mangroves, establishing quantitative linkages between biodiversity and ecosystem services, and constructing a cross-scale ecological monitoring and assessment framework.

CRediT authorship contribution statement

Songwen Deng: Writing – review & editing, Writing – original draft, Visualization, Validation, Resources, Project administration, Methodology, Investigation, Formal analysis, Data curation, Conceptualization. **Mengyuan Luo:** Writing – original draft, Methodology. **Wenhuan Wang:** Data curation. **Sixiang Lan:** Data curation. **Weifeng Xu:** Data curation. **Xuzhi Mai:** Data curation. **Wei Zhang:** Supervision, Funding acquisition.

Declaration of competing interest

The authors declare that they have no known competing financial interests or personal relationships that could have appeared to influence the work reported in this paper.

Appendix A. Supplementary data

Supplementary data to this article can be found online at https://doi.org/10.1016/j.ecoleng.2025.107709.

Data availability

Data will be made available on request.

References

Arekhi, M., Yilmaz, O.Y., Yilmaz, H., Akyüz, Y.F., 2017. Can tree species diversity be assessed with Landsat data in a temperate forest? [Article]. Environ. Monit. Assess. 189 (11), 14. Article 586. https://doi.org/10.1007/s10661-017-6295-6.

Atkinson, J., Brudvig, L.A., Mallen-Cooper, M., Nakagawa, S., Moles, A.T., Bonser, S.P., 2022. Terrestrial ecosystem restoration increases biodiversity and reduces its variability, but not to reference levels: a global meta-analysis [Article]. Ecol. Lett. 25 (7), 1725–1737. https://doi.org/10.1111/ele.14025.

Aue, B., Ekschmitt, K., Hotes, S., Wolters, V., 2012. Distance weighting avoids erroneous scale effects in species-habitat models [Article]. Methods Ecol. Evol. 3 (1), 102–111. https://doi.org/10.1111/j.2041-210X.2011.00130.x.

Benayas, J.M.R., Newton, A.C., Diaz, A., Bullock, J.M., 2009. Enhancement of biodiversity and ecosystem services by ecological restoration: a meta-analysis [Article]. Science 325 (5944), 1121–1124. https://doi.org/10.1126/science.1172460.

Borges-Matos, C., Maron, M., Metzger, J.P., 2023. A review of condition metrics used in biodiversity offsetting [Review]. Environ. Manag. 72 (4), 727–740. https://doi.org/10.1007/s00267-023-01858-1.

Botta-Dukát, Z., 2005. Rao's quadratic entropy as a measure of functional diversity based on multiple traits [Article]. J. Veg. Sci. 16 (5), 533–540. https://doi.org/10.1111/j.1654-1103.2005.tb02393.x.

Bullock, J.M., Aronson, J., Newton, A.C., Pywell, R.F., Rey-Benayas, J.M., 2011. Restoration of ecosystem services and biodiversity: conflicts and opportunities [Review]. Trends Ecol. Evol. 26 (10), 541–549. https://doi.org/10.1016/j.tree.2011.06.011.

Cao, Y., Su, K., You, Y.F., Jiang, X.B., Li, C., Chen, J.J., 2025. Pinglu Canal Construction and its Impact on Wildlife Habitat Connectivity: a Multi-Species Network Analysis and Ecological Restoration Strategy [Article]. Land 14 (1), 24. Article 150. https://doi.org/10.3390/land14010150.

Chen, Y., Cheng, C., Xiong, K.N., Rong, L., Zhang, S.H., 2024. Quantifying the biodiversity and ecosystem service outcomes of karst ecological restoration: a meta-analysis of South China Karst [Article]. Catena 245, 9. Article 108278. https://doi.org/10.1016/j.catena.2024.108278.

Condit, R., Robinson, W.D., Ibáñez, R., Aguilar, S., Sanjur, A., Martínez, R., Stallard, R.F., García, T., Angehr, G.R., Petit, L., Wright, S.J., Robinson, T.R., Heckadon, S., 2001. The status of the Panama Canal watershed and its biodiversity at the beginning of the 21st century [Article]. Bioscience 51 (5), 389–398. https://doi.org/10.1641/0006-3568(2001)051[0389:Tsotpc]2.0.Co;2.

Doxa, A., Almpanidou, V., Katsanevakis, S., Queirós, A.M., Kaschner, K., Garilao, C., Kesner-Reyes, K., Mazaris, A.D., 2022. 4D marine conservation networks: Combining 3D prioritization of present and future biodiversity with climatic refugia [Article]. Glob. Chang. Biol. 28 (15), 4577–4588. https://doi.org/10.1111/gcb.16268.

Fahrig, L., 2003. Effects of habitat fragmentation on biodiversity. Annu. Rev. Ecol. Evol. Syst. 34 (1), 487–515.

Gillespie, T.W., Foody, G.M., Rocchini, D., Giorgi, A.P., Saatchi, S., 2008. Measuring and modelling biodiversity from space [Review]. Prog. Phys. Geogr.-Earth Environ. 32 (2), 203–221. https://doi.org/10.1177/0309133308093606.

Graham, L.J., Spake, R., Gillings, S., Watts, K., Eigenbrod, F., 2019. Incorporating fine-scale environmental heterogeneity into broad-extent models [Article]. Methods Ecol. Evol. 10 (6), 767–778. https://doi.org/10.1111/2041-210x.13177.

Han, Z.X., Yin, D.K., Zhao, R.X., Liu, Z.J., Cheng, R.H., Lin, G.W., Jia, H.F., 2024. The ecological effect of ship canals on wetlands [Review]. Water 16 (22), 21. Article 3324. https://doi.org/10.3390/w16223324.

Hauser, L.T., Feret, J.B., Binh, N.A., van der Windt, N., Sil, A.F., Timmermans, J., Soudzilovskaia, N.A., van Bodegom, P.M., 2021. Towards scalable estimation of plant functional diversity from Sentinel-2: In-situ validation in a heterogeneous (semi-)natural landscape [Article]. Remote Sens. Environ. 262, 14. Article 112505. https://doi.org/10.1016/j.rse.2021.112505.

Hernández-Stefanoni, J.L., Gallardo-Cruz, J.A., Meave, J.A., Rocchini, D., Bello-Pineda, J., López-Martínez, J.O., 2012. Modeling α- and β-diversity in a tropical forest from remotely sensed and spatial data [Article]. Int. J. Appl. Earth Obs. Geoinf. 19, 359–368. https://doi.org/10.1016/j.jag.2012.04.002.

Herold, M., Couclelis, H., Clarke, K.C., 2005. The role of spatial metrics in the analysis and modeling of urban land use change. Comput. Environ. Urban. Syst. 29 (4), 369–399.

Jalkanen, J., Vierikko, K., Moilanen, A., 2020. Spatial prioritization for urban Biodiversity Quality using biotope maps and expert opinion [Article]. Urban For. Urban Green. 49, 11. Article 126586. https://doi.org/10.1016/j.ufug.2020.126586.

Jellinek, S., Wilson, K.A., Hagger, V., Mumaw, L., Cooke, B., Guerrero, A.M., Erickson, T. E., Zamin, T., Waryszak, P., Standish, R.J., 2019. Integrating diverse social and ecological motivations to achieve landscape restoration [Editorial Material]. J. Appl. Ecol. 56 (1), 246–252. https://doi.org/10.1111/1365-2664.13248.

Jorgensen, D., 2015. Ecological restoration as objective, target, and tool in international biodiversity policy [Article]. Ecol. Soc. 20 (4), 5. Article 43. https://doi.org/10.5751/es-08149-200443.

Kerr, B., Remmel, T.K., 2024. Activity-based measures of landscape fragmentation [Article]. Landsc. Ecol. 39 (12), 18. Article 198. https://doi.org/10.1007/s10980-024-01987-w.

Khare, S., Latifi, H., Rossi, S., 2021. A 15-year spatio-temporal analysis of plant β-diversity using Landsat time series derived Rao's Q index [Article]. Ecol. Indic. 121, 12. Article 107105. https://doi.org/10.1016/j.ecolind.2020.107105.

Kim, K.H., Pauleit, S., 2007. Landscape character, biodiversity and land use planning: the case of Kwangju City Region, South Korea [Article]. Land Use Policy 24 (1), 264–274. https://doi.org/10.1016/j.landusepol.2005.12.001.

Li, H., Wu, J., 2004. Use and misuse of landscape indices. Landsc. Ecol. 19, 389–399.

Li, P.S., Li, D., Sun, X.Q., Chu, Z.S., Xia, T., Zheng, B.H., 2022. Application of ecological restoration technologies for the improvement of biodiversity and ecosystem in the River [Review]. Water 14 (9), 16. Article 1402. https://doi.org/10.3390/w14091402.

Lin, H.Y., Cooke, S.J., Wolter, C., Young, N., Bennett, J.R., 2020. On the conservation value of historic canals for aquatic ecosystems [Article]. Biol. Conserv. 251, 33. Article 108764. https://doi.org/10.1016/j.biocon.2020.108764.

Madonsela, S., Cho, M.A., Ramoelo, A., Mutanga, O., 2017. Remote sensing of species diversity using Landsat 8 spectral variables [Article]. ISPRS J. Photogramm. Remote Sens. 133, 116–127. https://doi.org/10.1016/j.isprsjprs.2017.10.008.

Malavasi, M., Bazzichetto, M., Komárek, J., Moudry, V., Rocchini, D., Bagella, S., Acosta, A.T.R., Carranza, M.L., 2021. Unmanned aerial systems-based monitoring of the eco-geomorphology of coastal dunes through spectral Rao's Q [Article]. Appl. Veg. Sci. 24 (1), 10. Article e12567. https://doi.org/10.1111/avsc.12567.

Marshall, E., Wintle, B.A., Southwell, D., Kujala, H., 2020. What are we measuring? A review of metrics used to describe biodiversity in offsets exchanges [Review]. Biol. Conserv. 241, 8. Article 108250. https://doi.org/10.1016/j.biocon.2019.108250.

Nakamura, G., Gonçalves, L.O., Duarte, L.D., 2020. Revisiting the dimensionality of biological diversity [Article]. Ecography 43 (4), 539–548. https://doi.org/10.1111/ecog.04574.

Peel, M.C., Finlayson, B.L., McMahon, T.A., 2007. Updated world map of the Koppen-Geiger climate classification [Article]. Hydrol. Earth Syst. Sci. 11 (5), 1633–1644. https://doi.org/10.5194/hess-11-1633-2007.

Purdon, A., Mole, M.A., Selier, J., Kruger, J., Mafumo, H., Olivier, P.I., 2022. Using the Rao's Q diversity index as an indicator of protected area effectiveness in conserving biodiversity. Eco. Inform. 72, 101920.

Randin, C.F., Ashcroft, M.B., Bolliger, J., Cavender-Bares, J., Coops, N.C., Dullinger, S., Dirnböck, T., Eckert, S., Ellis, E., Fernández, N., Giuliani, G., Guisan, A., Jetz, W., Joost, S., Karger, D., Lembrechts, J., Lenoir, J., Luoto, M., Morin, X., Payne, D., 2020. Monitoring biodiversity in the Anthropocene using remote sensing in species distribution models [Article]. Remote Sens. Environ. 239, 18. Article 111626. https://doi.org/10.1016/j.rse.2019.111626.

Rao, C.R., 1982. Diversity and dissimilarity coefficients: a unified approach. Theor. Popul. Biol. 21 (1), 24–43.

Reddy, C.S., 2021. Remote sensing of biodiversity: what to measure and monitor from space to species? [Review]. Biodivers. Conserv. 30 (10), 2617–2631. https://doi.org/10.1007/s10531-021-02216-5.

Ricotta, C., de Bello, F., Moretti, M., Caccianiga, M., Cerabolini, B.E.L., Pavoine, S., 2016. Measuring the functional redundancy of biological communities: a quantitative guide [Article]. Methods Ecol. Evol. 7 (11), 1386–1395. https://doi.org/10.1111/2041-210x.12604.

Rocchini, D., Balkenhol, N., Carter, G.A., Foody, G.M., Gillespie, T.W., He, K.S., Kark, S., Levin, N., Lucas, K., Luoto, M., Nagendra, H., Oldeland, J., Ricotta, C., Southworth, J., Neteler, M., 2010. Remotely sensed spectral heterogeneity as a proxy of species diversity: recent advances and open challenges [Article]. Eco. Inform. 5 (5), 318–329. https://doi.org/10.1016/j.ecoinf.2010.06.001.

Rocchini, D., Marcantonio, M., Ricotta, C., 2017. Measuring Rao's Q diversity index from remote sensing: an open source solution [Article]. Ecol. Indic. 72, 234–238. https://doi.org/10.1016/j.ecolind.2016.07.039.

Rocchini, D., Marcantonio, M., Da Re, D., Chirici, G., Galluzzi, M., Lenoir, J., Ricotta, C., Torresani, M., Ziv, G., 2019. Time-lapsing biodiversity: an open source method for measuring diversity changes by remote sensing [Article]. Remote Sens. Environ. 231, 7. Article 111192. https://doi.org/10.1016/j.rse.2019.05.011.

Rocchini, D., Torresani, M., Ricotta, C., 2024. On the mathematical properties of spatial Rao's Q to compute ecosystem heterogeneity. Theor. Ecol. 17 (3), 247–254.

Saura, S., Torras, O., Gil-Tena, A., Pascual-Hortal, L., 2006 Sep. Shape irregularity as an indicator of forest biodiversity and guidelines for metric selection. In: Patterns and Processes in Forest Landscapes: Multiple Use and Sustainable Management. IUFRO Landscape Ecology Workshop, Locorotondo, ITALY.

Schindler, S., Poirazidis, K., Wrbka, T., 2008. Towards a core set of landscape metrics for biodiversity assessments: a case study from Dadia National Park, Greece [Article]. Ecol. Indic. 8 (5), 502–514. https://doi.org/10.1016/j.ecolind.2007.06.001.

Schindler, S., von Wehrden, H., Poirazidis, K., Hochachka, W.M., Wrbka, T., Kati, V., 2015. Performance of methods to select landscape metrics for modelling species richness [Article]. Ecol. Model. 295, 107–112. https://doi.org/10.1016/j.ecolmodel.2014.05.012.

Sha, M., Tian, G., 2010. An analysis of spatiotemporal changes of urban landscape pattern in Phoenix metropolitan region. Procedia Environ. Sci. 2, 600–604.

Skidmore, A.K., Coops, N.C., Neinavaz, E., Ali, A., Schaepman, M.E., Paganini, M., Kissling, W.D., Vihervaara, P., Darvishzadeh, R., Feilhauer, H., Fernandez, M., Fernández, N., Gorelick, N., Geizendorffer, I., Heiden, U., Heurich, M., Hobern, D., Holzwarth, S., Muller-Karger, F.E., Wingate, V., 2021. Priority list of biodiversity metrics to observe from space [Article]. Nat. Ecol. Evol. 5 (7), 896–906. https://doi.org/10.1038/s41559-021-01451-x.

Tang, F., Zhou, X., Li, W., Zhang, Y.J., Fu, M.C., Zhang, P.T., 2021. Linking ecosystem service and MSPA to construct landscape ecological network of the huaiyang section of the grand canal [Article]. Land 10 (9), 23. Article 919. https://doi.org/10.3390/land10090919.

Tian, Y., Guo, Z.Q., Zhong, W., Qiao, Y.C., Qin, J.X., 2016. A design of ecological restoration and eco-revetment construction for the riparian zone of Xianghe Segment of China's Grand Canal [Article]. Int J Sust Dev World 23 (4), 333–342. https://doi.org/10.1080/13504509.2015.1127862.

Torras, O., Martín-Queller, E., Saura, S., 2009. Relating landscape structure, environment and management to biodiversity indicators estimated from forest inventory data in Catalonia (NE Spain) [Article]. Invest. Agrar.-Sist. Recur. For. 18 (3), 322–337. <Go to ISI>://WOS:000273698300008.

Torresani, M., Rocchini, D., Sonnenschein, R., Zebisch, M., Marcantonio, M., Ricotta, C., Tonon, G., 2019. Estimating tree species diversity from space in an alpine conifer forest: the Rao's Q diversity index meets the spectral variation hypothesis [Article]. Eco. Inform. 52, 26–34. https://doi.org/10.1016/j.ecoinf.2019.04.001.

Turner, M.G., 1989. Landscape ecology: the effect of pattern on process. Annu. Rev. Ecol. Evol. Syst. 171–197. https://doi.org/10.1146/annurev.es.20.110189.001131.

Turner, W., 2014. Sensing biodiversity [Editorial Material]. Science 346 (6207), 301–302. https://doi.org/10.1126/science.1256014.

Turner, M.G., Donato, D.C., Romme, W.H., 2013. Consequences of spatial heterogeneity for ecosystem services in changing forest landscapes: priorities for future research [Article]. Landsc. Ecol. 28 (6), 1081–1097. https://doi.org/10.1007/s10980-012-9741-4.

Verbesselt, J., Hyndman, R., Newnham, G., Culvenor, D., 2010. Detecting trend and seasonal changes in satellite image time series [Article]. Remote Sens. Environ. 114 (1), 106–115. https://doi.org/10.1016/j.rse.2009.08.014.

Vihervaara, P., Auvinen, A.P., Mononen, L., Törmä, M., Ahlroth, P., Anttila, S., Böttcher, K., Forsius, M., Heino, J., Heliölä, J., Koskelainen, M., Kuussaari, M., Meissner, K., Ojala, O., Tuominen, S., Viitasalo, M., Virkkala, R., 2017. How Essential Biodiversity Variables and remote sensing can help national biodiversity monitoring [Article]. Glob. Ecol. Conserv. 10, 43–59. https://doi.org/10.1016/j.gecco.2017.01.007.

Walz, U., Syrbe, R.U., 2013. Linking landscape structure and biodiversity [Editorial Material]. Ecol. Indic. 31, 1–5. https://doi.org/10.1016/j.ecolind.2013.01.032.

Walz, U., Hoechstetter, S., Dragut, L., Blaschke, T., 2016. Integrating time and the third spatial dimension in landscape structure analysis [Article]. Landsc. Res. 41 (3), 279–293. https://doi.org/10.1080/01426397.2015.1078455.

Wang, M., Liu, Q.H., Pang, X.Y., 2021. Evaluating ecological effects of roadside slope restoration techniques: a global meta-analysis [Article]. J. Environ. Manag. 281, 10. Article 111867. https://doi.org/10.1016/j.jenvman.2020.111867.

Wang, D.Z., Qiu, P.H., Wan, B., Cao, Z.X., Zhang, Q.F., 2022. Mapping α- and β-diversity of mangrove forests with multispectral and hyperspectral images [Article]. Remote Sens. Environ. 275 (14). https://doi.org/10.1016/j.rse.2022.113021. Article 113021.

Watts, K., Eycott, A.E., Handley, P., Ray, D., Humphrey, J.W., Quine, C.P., 2010. Targeting and evaluating biodiversity conservation action within fragmented landscapes: an approach based on generic focal species and least-cost networks [Article]. Landsc. Ecol. 25 (9), 1305–1318. https://doi.org/10.1007/s10980-010-9507-9.

Wu, G., Tan, L.B., Yan, Y., Tian, Y., Shen, Y., Cao, H.M., Dong, M.T., 2016. Measures and planning for wetland restoration of Xianghe Segment of China's Grand Canal [Article]. Int J Sust Dev World 23 (4), 326–332. https://doi.org/10.1080/13504509.2015.1136856.

Zhao, H.Z., Liu, D.F., Li, F.X., Liu, X.J., Niu, J.Q., He, J.H., Liu, Y.L., 2021. Incorporating spatio-temporal connectivity for prioritized conservation of individual habitat patches in a dynamic landscape [Article]. Ecol. Indic. 124, 10. Article 107414. https://doi.org/10.1016/j.ecolind.2021.107414.

Zhao, J.Y., Fu, X., Sa, N., Kou, X.Y., He, X.J., Zheng, S.N., Lu, Z.H., Wu, G., Sang, W.G., 2025. Forest eco-function restoration and its positive effects on biodiversity improvement in China's ecological conservation programs [Article]. Ecol. Eng. 212, 9. Article 107530. https://doi.org/10.1016/j.ecoleng.2025.107530.

Biomass and Bioenergy 205 (2026) 108536

Contents lists available at ScienceDirect

Biomass and Bioenergy

journal homepage: www.elsevier.com/locate/biombioe

Synergistic hydrothermal carbonization and wet oxidation for sustainable sewage sludge valorization and process waters toxicity mitigation

Geng Yang [a], Xingying Tang [e,*], Xingtao Wang [a], You Wu [d], Hui Ma [a], Shengyan Pu [a,b,c,**]

[a] State Key Laboratory of Geohazard Prevention and Geoenvironment Protection, Chengdu University of Technology, Chengdu, 610059, PR China
[b] Tianfu Jiangxi Laboratory, Chengdu, Sichuan, 610059, PR China
[c] State Key Laboratory of Environmental Criteria and Risk Assessment, Chinese Research Academy of Environmental Sciences, Beijing, 100012, PR China
[d] School of Human Settlements and Civil Engineering, Xi'an Jiaotong University, 28#, Xianning West Road, Xi'an, Shaanxi, 710049, PR China
[e] Guangxi Laboratory on the Study of Coral Reefs in the South China Sea, Coral Reef Research Centre of China, School of Marine Sciences, Guangxi University, Nanning, 530004, PR China

ARTICLE INFO

Keywords:
Hydrothermal carbonization
Wet oxidation
Sewage sludge valorization
Sustainable sludge management

ABSTRACT

This study evaluates the integration of hydrothermal carbonization (HTC, 150–250 °C) and wet oxidation (WO, 250 °C) for sewage sludge treatment, focusing on hydrochar (HC) properties, phosphorus recovery, and process waters (PWs) impacts on biological systems. HTC increased HC's specific surface area from 17.83 to 61.54 m^2/g (250 °C) and enriched total phosphorus (TP) by 79–96.5 %, while WO further stabilized HC by reducing volatile content from ~30 % to <10 % and converting non-apatite inorganic phosphorus (NAIP) to apatite phosphorus (AP). Direct addition of HTC PWs to an AAO system reduced COD, NH_4^+-N, and TN removal rates by 24.7 %, 36.4 %, and 34.9 % (5 % dosage), respectively, due to recalcitrant organics (phenols, nitrogenous heterocycles) and elevated nitrogen loads (TN > 1200 mg/L). In contrast, WO pretreatment decomposed organics into bioavailable small molecules, maintaining COD removal rates at ~86 % (5 % dosage) and mitigating microbial inhibition. Microbial analysis revealed HTC PWs suppressed Proteobacteria (42.99 %→31.78 %) and Firmicutes (22.79 %→5.69 %), while enriching stress-tolerant Actinobacteria (>25 % abundance). However, high WO oxidant doses (>10 %) reduced HC yield (49.67 %) and phosphorus recovery (69.23 %), highlighting the need for parameter optimization. This work demonstrates the HTC-WO synergy as a viable strategy for sludge valorization and PW detoxification, balancing resource recovery (e.g., stabilized HC, 45.59 mg/g TP) with biological system compatibility, while underscoring the critical role of oxidant dosage in process scalability.

1. Introduction

Biological treatment is one of the simplest and most effective methods for municipal wastewater treatment. However, it generates large amounts of sewage sludge (SS). In China, approximately 10 tonnes of sludge (on a dry basis) are produced for every 10,000 tonnes of sewage treated [1]. Sewage sludge has a complex composition, high water content, and contains heavy metals and recalcitrant organic pollutants [2,3]. Therefore, it is crucial to develop efficient and sustainable sludge treatment methods.

Currently, typical sludge treatment and disposal methods in China include dry incineration, aerobic composting, or land application following anaerobic digestion [4,5]. However, the high moisture content of SS can hinder the efficiency of these processes [6]. Hydrothermal carbonization (HTC) is a highly efficient thermochemical process for treating wet biomass and is considered a promising method for SS treatment. Operating at relatively low temperatures (~130–250 °C) and autogenous pressures (~1–5 MPa) [7,8], HTC is more effective than slow pyrolysis for moisture-containing feeds (e.g., sludge) due to the lack of dewatering requirements and better heat transfer from water [9].

The main products of HTC are solid hydrochar (HC), a small amount of gas, and HTC process waters (PWs). HC has promising applications as a solid fuel and carbonaceous material in various fields, including environmental remediation and agriculture [10–12]. In contrast, HTC PWs are by-products, especially when treating high-moisture biomass feedstocks such as SS. During the HTC process, chemical reactions such

* Corresponding author.
** Corresponding author. State Key Laboratory of Geohazard Prevention and Geoenvironment Protection (Chengdu University of Technology), Chengdu, 610059, PR China.
E-mail addresses: tangxingying@gxu.edu.cn (X. Tang), pushengyan@gmail.com, pushengyan13@cdut.edu.cn (S. Pu).

https://doi.org/10.1016/j.biombioe.2025.108536
Received 20 July 2025; Received in revised form 13 October 2025; Accepted 23 October 2025
Available online 2 November 2025
0961-9534/© 2025 Published by Elsevier Ltd.

as hydrolysis, dehydration, decarboxylation, condensation, and liquid isomerization occur [13]. As a result, HTC PWs contain a large number of water-soluble organic compounds, including organic acids, furfural, 5-hydroxymethylfurfural (5-HMF), phenols, nitrogen-containing heterocyclic compounds, and phenolic derivatives [14,15], resulting in high levels of total organic carbon (TOC), chemical oxygen demand (COD) and NH_4^+-N.

The most straightforward approach for treating HTC PWs is to process them through the biochemical system of a wastewater treatment plant prior to discharge; however, it remains uncertain whether HTC PWs will inhibit the biochemical system of the wastewater treatment plant. In recent years, several studies have explored suitable treatment methods for HTC PWs, including the use of HTC PWs as liquid fertilisers, the employment of microorganisms to degrade organic constituents, and the application of thermal treatments. For instance, Shan et al. evaluated the potential of the liquid phase from the co-hydrothermal carbonization of agricultural waste and SS as a liquid fertilizer [16], concluding that co-hydrothermal carbonization wastewater could replace up to 60 % of chemical fertilizers. Although using HTC PWs as a liquid fertilizer is promising, some reports have suggested that the complex organic matter in HTC PWs can inhibit seed germination [17,18]. Anaerobic digestion (AD) is another effective treatment method for HTC PWs. Langone et al. demonstrated that AD could degrade 83 % of the COD in HTC PWs, with the resulting products potentially serving as a carbon source for wastewater treatment [19]. The potential methane yields of the HTC-AD process were explored by Aragón-Briceño et al. [20], with results showing methane yields ranging from 20.3 to 67.5 m^3/tonne of sludge, depending on process parameters. Despite numerous studies showing the effectiveness of AD for sludge treatment, its application is limited by feedstock and reaction parameter requirements for HTC [21]. Process parameters of HTC directly affect methane yield, and larger reactor sizes and slower reaction processes further restrict its application [22].

Wet oxidation (WO) is a thermal process with significant potential for organic degradation. WO involves adding oxidants at high temperatures (120–320 °C) and pressures (0.5–20 MPa) to degrade organics in water, especially those difficult for microorganisms to handle [23]. Compared to AD, WO has a faster reaction process and is more suitable for small-scale sludge disposal than anaerobic digestion. The HTC-WO combination has good potential for heat generation, with the heat produced by WO sustaining the HTC process [24,25]. HTC thermochemically dewaters sludge to produce a carbonaceous HC and PWs—retaining part of the organic carbon in the solid while partitioning soluble and more recalcitrant compounds to the liquid. WO then supplies oxidation (and recoverable heat) to abate those recalcitrant compounds in the liquor. Treating the entire slurry under unified conditions simplifies the flowsheet, reduces reagents and footprint, and improves downstream biological compatibility compared with liquid-only polishing. Reza et al. applied WO to treat the liquid phase produced after HTC of dairy manure and sludge, achieving a COD reduction of approximately 70 % at 200 °C [13,14]. Despite these advantages, most WO-after-HTC studies have treated only the HTC PWs, aiming at COD polishing while decoupling detoxification from the fate and value of the HC. This leaves key gaps: the solid–liquid trade-offs are not quantified under one process envelope; phosphorus speciation and mineral binding are seldom mapped beyond bulk TP [26]; and the biological compatibility of treated waters with downstream reactors remains insufficiently addressed.

In this work, we instead apply WO to the entire HTC slurry (HC + PWs) to maintain a system-level perspective, explicitly linking (i) solid–liquid co-evolution relevant to valorization, (ii) mechanistic P pathways by coupling SMT fractions with XRD phases (e.g., NAIP→AP transitions), and (iii) downstream relevance by considering compatibility with AAO operation. This integrated framing also clarifies an oxidant-dosage design space that can guide co-optimization of detoxification and resource recovery, rather than focusing on PWs polishing alone.

2. Materials and methods

2.1. Hydrothermal carbonization

SS was collected from the Ximingjiang Wastewater Treatment Plant, Nanning, China, which utilizes the AAO fabrication process. The moisture content of dewatered sewage sludge was 62.95 %; pH value, 7.31. To minimize fermentation, the undried sludge was kept refrigerated at 4 °C in sealed containers and used promptly; immediately before each run, DI water was added to re-adjust the moisture content to 90 % (w/w). HTC experiments were performed in an intermittent reactor made of 304 stainless steel. For each experiment, 10 g raw SS were added to the reactor,The reactor was purged with nitrogen gas and sealed. The reactor was placed in a tube furnace for heating. The HTC temperatures were 150,175,200,225, and 250 °C, with a heating rate of 10 °C/min^{-1}, and the residence time was 60 min whereas residence times of 30, 60, or 90 min were tested with an HTC temperature of 250 °C. The pressure depended predominantly on the saturation vapor pressure of water at each reaction temperature. After the reaction,as the reactor reached room temperature, the products was removed and vacuum filtered for 15 min using medium-rate qualitative filter paper to separate the PWs and hydrochar. The dewatered HC was dried at 105 °C for 24 h prior to characterization, HC and PWs were kept refrigerated for chemical characterization. Each experiment was conducted in triplicate, and the results are shown as mean values.

2.2. Wet oxidation

WO was carried out in the same 304-stainless-steel batch reactor used for HTC. Unless otherwise stated, the entire HTC product obtained at 250 °C for 60 min (i.e., HC plus its corresponding PWs, without washing or drying) was used as the WO feed to preserve the original solid–liquid composition produced by HTC. Oxidant and dosage. Analytical-grade 30 % (w/w) H_2O_2 was used as the sole oxidant. Four dosage levels were tested: 5, 10, 15, and 20 % (v/v), defined as the volume of 30 % H_2O_2 added per 100 mL of HTC slurry at room temperature prior to sealing the reactor. The four conditions are hereafter denoted WO-5 %, WO-10 %, WO-15 %, and WO-20 %. The pre-measured volume of 30 % H_2O_2 was added dropwise into the HTC slurry with gentle manual swirling at ambient temperature. The reactor was then purged with N_2 for 1 min to remove air, sealed, and placed horizontally in a tube furnace. The temperature was ramped at 10 °C min^{-1} to 250 °C and held for 60 min. No external gas was supplied during WO; the system pressure was autogenous, arising from water vapor and the decomposition of H_2O_2. After the isothermal hold, the reactor was rapidly cooled to room temperature in a water bath, slowly vented to release internal pressure.

2.3. Characterization of HC

Hydrochar (HC) yield was calculated on a dry-mass basis as:

$$HC_{Yield} = \frac{mHC_{Dry}}{mSS_{Dry}} \times 100\% \quad (1)$$

where mHC_{Dry} is the oven-dry mass of HC after solid–liquid separation and drying (105 °C, 24 h), and mSS_{Dry} is the oven-dry mass of the SS charged to the reactor. Unless otherwise stated, all HC-related metrics are reported on a dry-weight basis.

Proximate analysis of SS and HC—including ash (Ash), volatile matter (VM), and fixed carbon (FC)—was performed following GB/T 212–2008 using a programmable muffle furnace. Briefly, VM was determined by heating the oven-dried sample at 900 ± 10 °C for 7 min under an inert atmosphere; Ash was determined by oxidizing the residue at 750 ± 10 °C in air to constant mass; FC was calculated by difference: FC (%) = 100 − Ash (%) − VM (%). All measurements were conducted in

triplicate and reported as mean ± SD.

Morphological characterization of HC observed by field emission scanning electron microscopy (SEM, Hitachi, Regulus 8100). The thermal stability of HC was observed by the thermogravimetric analyzer (TGA, NETZSCH, STA 499C), The BET specific surface area was determined by nitrogen adsorption (Micrometer, ASAP2020). HC surface functional groups were identified using Fourier transform infrared spectroscopy (FT-IR, Shimadzu, IRTracer-100), X-ray diffraction (XRD, RIGAKU, Ultima IV) instrument identified the oxide crystal structure.

2.4. AAO system simulation

In order to investigate the potential effects of HTC PWs and WO PWs on the biochemical system of the WWTP, the AAO process was selected in this study to simulate the biochemical system of the WWTP, as shown in Fig. 1. The influent was domestic wastewater and domestic wastewater with added HTC PWs and WO PWs, respectively, and the effluent NH_4^+-N, COD and TN were measured for comparison. Domestic wastewater and sludge were obtained from Ximingjiang Wastewater Treatment Plant in Nanning City, China. The effective volumes of the anaerobic, anoxic and oxygen tanks were 1 L, 1 L and 3 L, respectively. The influent flow rate was set at 0.1 L/h and the temperature was maintained at 25 °C. The dissolved oxygen (DO) concentration in the oxygenated tank was maintained within the range of 3.0 mg/L to 4.0 mg/L.

2.5. Analytical methods for PWs and phosphorus

The samples were analyzed for TOC, COD, TN and NH_3-N. TOC was measured in PWs using a total organic carbon analyzer (Shimadzu, TOC-L CPN), and NH_4^+-N, COD and TN were measured in PWs using a water quality analyzer (HACH, DR 3900).

Phosphorus fractions in sludge and HC samples were analyzed using the SMT method, as illustrated in Fig. S1., the process is delineated in meticulous detail. Phosphorus was categorized into five groups: total phosphorus (TP), inorganic phosphorus (IP), organic phosphorus (OP), non-apatite state inorganic phosphorus (NAIP), and apatite state inorganic phosphorus (AP). The extracted phosphate content was measured using molybdenum blue spectrophotometry.

2.6. Microbial sequencing

Microbial genomic DNA was extracted from samples with the E.Z.N.A.® DNA Kit (Omega Bio-tek) according to the manufacturer's instructions. Quality and concentration were verified by agarose gel electrophoresis (1.0 %) and NanoDrop2000 spectrophotometry (Thermo Scientific), then stored at −80 °C. The V3-V4 region of the bacterial 16S rRNA gene was amplified using primers ACTCCTACGGGAGGCAGCAG and GGACTACHVGGGTWTCTAAT in a T100 Thermal Cycler (BIO-RAD). The 20 μL PCR reaction comprised: 4 μL 5 × Fast Pfu buffer, 2 μL 2.5 mM dNTPs, 0.8 μL each primer (5 μM), 0.4 μL Fast Pfu polymerase, 10 ng template DNA, and ddH_2O. Thermocycling included: 95 °C for 3 min; 27 cycles of 95 °C (30 s), 55 °C (30 s), 72 °C (45 s); 72 °C for 10 min; hold at 4 °C PCR products were purified from 2 % agarose gels (PCR Clean-Up Kit, YuHua) and quantified (Qubit 4.0, Thermo Fisher). Purified amplicons were pooled equimolarly and paired-end sequenced (Illumina PE300/PE250 platform) by Majorbio Bio-Pharm Technology Co. Ltd. under standard protocols. Raw reads were deposited in the NCBI SRA database.

3. Results and discussion

3.1. HC characteristics

3.1.1. Yield

The HTC process is mainly influenced by residence time and hydrothermal process temperature, which determine the reaction intensity and the degree of sludge carbonization. Table 1 shows that the HC yield (ratio of hydrocar mass to raw sludge dry mass) decreases with increasing residence time and hydrothermal process temperature. As the

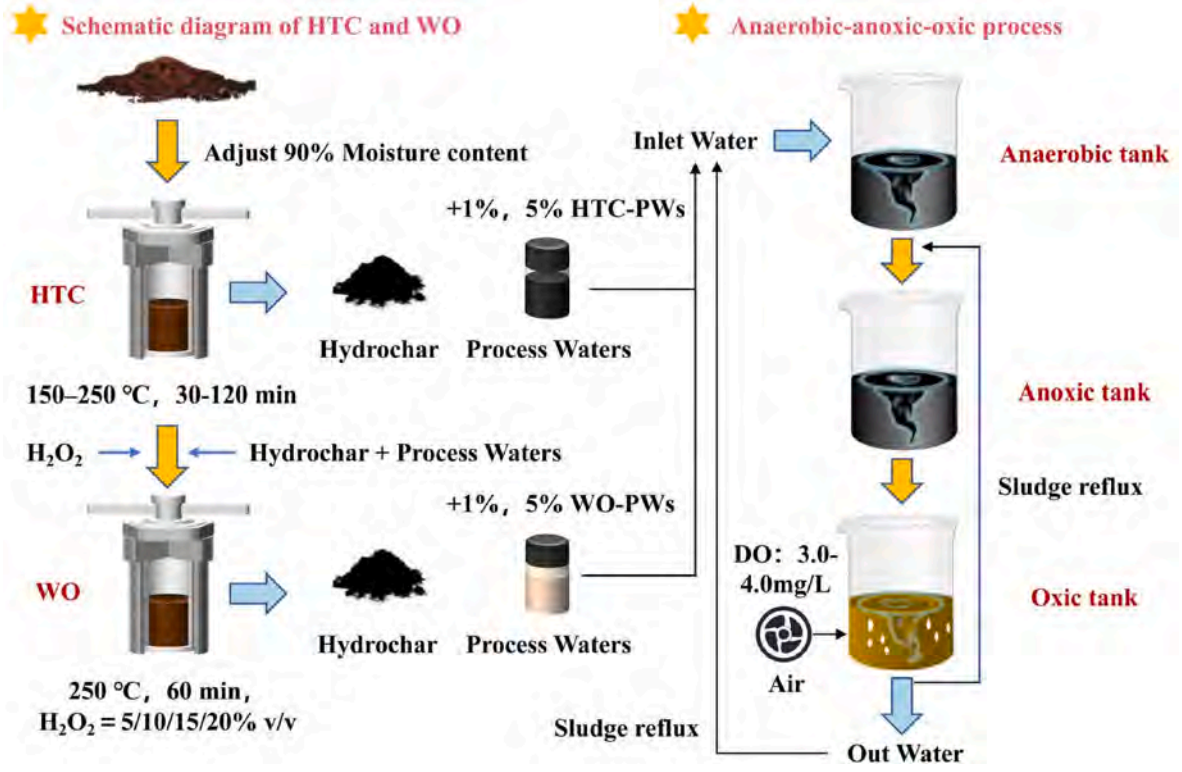


Fig. 1. Experimental flowchart.

Table 1
Yield, specific surface area and industrial analysis of hydrochar under different HTC and WO conditions.

Sample	BET surface area/(m^2/g)	Yield/ %	Ash/ %	VM/ %	FC/ %
SS	17.8255 ± 0.1697	–	46.35	49.98	3.67
HTC-150-60	42.6302 ± 0.2582	72.95	58.73	39.42	1.85
HTC-175-60	45.1692 ± 0.1449	67.63	64.76	33.31	1.93
HTC-200-60	52.7332 ± 0.5603	63.33	66.13	31.25	2.62
HTC-225-60	56.3193 ± 0.2644	61.14	68.02	28.95	3.03
HTC-250-60	61.5408 ± 0.3028	59.71	68.11	28.77	3.12
HTC-250-30	57.0071 ± 0.7545	62.39	66.40	30.62	2.98
HTC-250-90	63.4966 ± 0.4648	58.77	68.33	28.48	3.19
HTC-250-120	55.3844 ± 0.3379	57.21	67.46	29.27	3.27
WO-5 %	56.1916 ± 0.2164	58.11	81.18	11.63	7.19
WO-10 %	54.7135 ± 0.3314	57.19	82.33	9.45	8.22
WO-15 %	47.1613 ± 0.3649	51.08	81.92	9.52	8.56
WO-20 %	43.2031 ± 0.4590	49.67	82.53	9.09	8.38

(1) Yield (%) = mHC,dry/mSS,dry × 100.
(2) Ash, volatile matter (VM), and fixed carbon (FC) are reported as mass percentages on a dry basis determined by proximate analysis.
(3) Process temperature refers to HTC or WO setpoint; residence time is the isothermal hold time.

hydrothermal process temperature increased from 150 °C to 250 °C, the HC yield (dry basis) decreased from 72.95 % to 59.71 %. Hydrolysis is the first step in the HTC process. As this process takes place in the subcritical zone, an increase in temperature changes the viscosity of the water [28], facilitating its penetration into the porous medium and the decomposition of the biomass [29]. Higher temperatures and longer residence times enhance HC dissolution, which is the primary cause of HC yield variation [9]. Although less significant than the hydrothermal process temperature, the residence time also affects the yield; for example, the yield decreased from 62.39 % to 57.21 % as the residence time increased from 30 to 120 min.

After HTC, the product was subjected to WO. The WO further reduced the HC yield. Table 1 shows that the addition of 20 % hydrogen peroxide reduced the HC yield to 49.67 %. The WO process maintains a high temperature and increases the residence time, which promotes HC polymerisation. The presence of an oxidant intensifies the WO reaction, causing partial HC oxidation and dissolution, which is the main reason for the reduced yield.

3.1.2. Specific surface area

As shown in Tables 1 and In comparison with the original SS, the specific surface area of HC exhibited a significant increase following HTC, with this increase being gradual and proportionate to the hydrothermal process temperature. The surface area rose from 17.83 m^2/g to 61.54 m^2/g at 250 °C for 60 min, indicating enhanced adsorption and reactivity [30,31]. This phenomenon is primarily attributed to the release of organic components at elevated temperatures, which leads to the formation of additional micro-pores. Within the experimental temperature range of 150–250 °C, a consistent increase in specific surface area was observed, suggesting that it is predominantly determined by the inherent nature of the raw material. However, an increase in residence time from 90 to 120 min led to a decrease in specific surface area from 63.4966 m^2/g to 55.3844 m^2/g, suggesting that an extended residence time hinders the formation of pores, thereby reducing the specific surface area. Fig. S2 demonstrates that the SS surface became more smooth, with no visible pores or cracks, and the particles became larger and more dispersed. Following HTC, the presence of discernible pores became evident on the HC surface, and as the temperature increased, the surface exhibited increased roughness with a greater prevalence of pore cracks, thereby confirming the observed trend in specific surface area.

Table 1 demonstrates that the specific surface area of HC diminished after WO and exhibited a significant decline with increasing hydrogen peroxide addition, suggesting that the WO process induced damage to the HC's surface structure and led to the collapse of pore walls. Scanning electron microscopy revealed that 10 % hydrogen peroxide formed irregular grooves on the charcoal surface, damaging porosity and fracture characteristics; 20 % hydrogen peroxide made the surface smoother and further eliminated the porous structure. This demonstrates that the WO process first destroys the HC's surface structure and then repolymerises it, with more added oxidant leading to more severe destruction and higher polymerisation degree.

3.1.3. Surface functional groups

As illustrated in Fig. 2(a), the FTIR spectra of HC after HTC and WO treatment remained largely unchanged, indicating that WO exerted minimal influence on the functional groups of HC. The 3600-3200 cm^{-1} peak intensity was attributed to the -OH telescopic vibration, and it was observed that the -OH peak exhibited a significant decrease after HTC and WO, suggesting that the performance of sludge dewatering was considerably enhanced [32]. The 2800-3000 cm^{-1} peak was identified as an aliphatic CH group, and it was found that WO exerted minimal influence on this peak. The 2800-3000 cm^{-1} peak is an aliphatic CH group, which is almost unaffected by WO. Following the addition of WO [33], there was an observed enhancement in the intensity of vibrational absorption peaks attributed to C=O stretching at 1734-1730 cm^{-1} [34], accompanied by an increase in the intensity of vibrational absorption peaks linked to phenolic -OH bending near 1300 cm^{-1} [35]. These observations suggest that WO promotes the development of oxygen-containing functional groups on the surface of hydrocarbon. The 830 cm^{-1} peaks increased, and the intensity of the -OH bending peaks increased, which meant that the performance of sludge dewatering was improved.The 830 cm^{-1} vibrational absorption peak is enhanced and is related to the aromatic C-H bending vibration, suggesting that WO promotes the formation of aromatic structures in HC. The peak at approximately 1000 cm^{-1} is attributed to the Si-O stretching vibration, which is predominantly attributable to the presence of silica in SS, a component that remains after HTC and WO.

3.1.4. Thermal stability

Thermogravimetric analysis was conducted under an air atmosphere (oxidative combustion. Fig. 2(c) and (d) present the TG-DTG curves for HC following HTC (250 °C, 60 min) and WO (10 % H_2O_2), respectively. The pyrolysis of HC is characterised by three distinct stages: namely, dehydration, volatile combustion, and fixed carbon combustion [32]. Following HTC, the dehydration stage of HC occurs between 30 °C and 150 °C, with mass loss primarily attributable to bound water elimination [36]. Aliphatic compounds and other small molecules begin to volatilise around 225 °C, while larger molecules and heavier volatiles commence decomposition around 325 °C. The DTG curve indicates a peak in the mass loss rate around 350 °C, suggesting that HTC retains more heavy volatiles in the HC [37]. The fixed carbon combustion stage occurs between 650 °C and 750 °C, with the TG curve initially flat before steepening, indicating the burning of residual volatiles until complete combustion when oxygen fully contacts the fixed carbon [38].

Table 1 lists the volatile and fixed carbon contents of SS and HC. A comparison of the TG-DTG curves reveals that WO significantly enhances the thermal stability of HC, reducing its mass loss during the dehydration stage, which correlates with the hydrophobicity of HC. Unlike HTC, the post-WO HC shows no significant mass loss between 230 °C and 550 °C, indicating that WO removes most volatiles from the HC. The slight DTG fluctuations between 450 °C and 500 °C may be attributed to the presence of volatiles formed during WO that differ from those in the HTC product. The fixed carbon combustion stage also occurs at 650 °C–750 °C, but with higher mass loss, which is consistent with industrial analyses showing reduced volatiles and increased fixed carbon and ash after WO. This decline in volatiles signifies enhanced handling, storage, and transport safety for the HC [39], while the augmented fixed carbon points to stable sludge carbonization by WO.

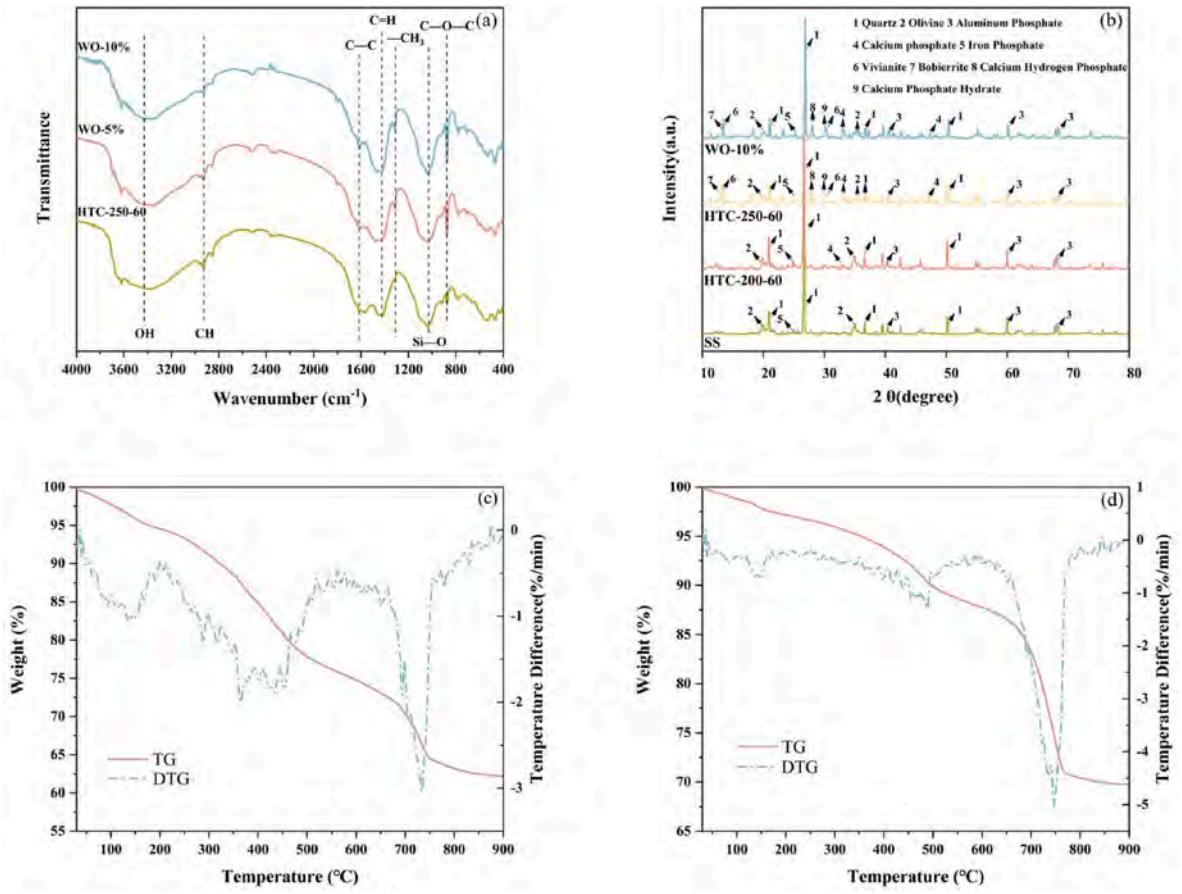


Fig. 2. (a). FTIR spectral results (b). XRD of SS and hydrochar (c). TG-DTG curves for hydrochar (250 °C, 60 min) (d). TG-DTG curves for hydrochar (WO-10 %).

The increased ash suggests some HC dissolution into the sludge.

3.2. The occurrence pattern and transformation mechanism of phosphorus

3.2.1. Distribution and enrichment characteristics of phosphorus forms

As illustrated in Fig. 3., the recovery of phosphorus is presented under varying HTC and WO conditions. It is evident that as the

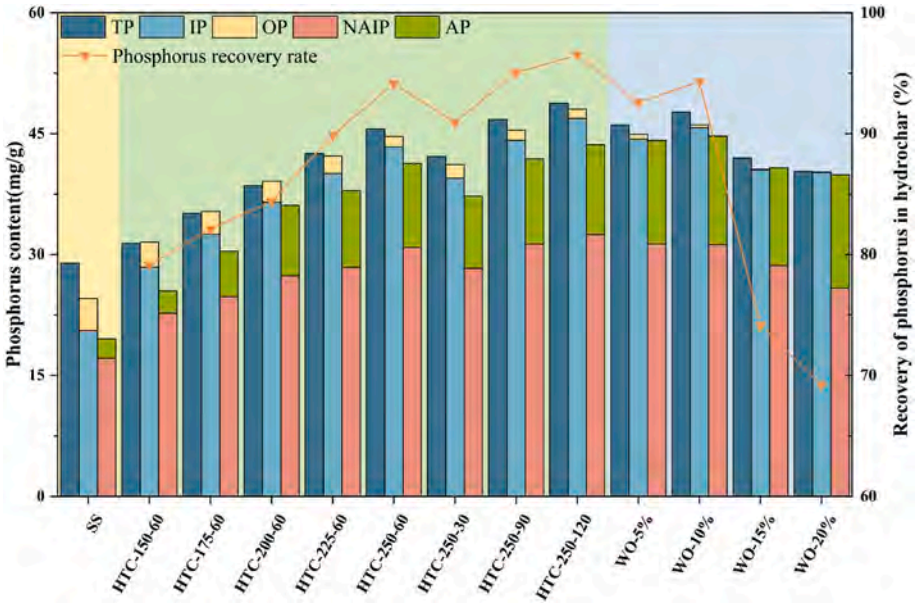


Fig. 3. Content of different forms of phosphorus in hydrochar under different HTC and WO conditions.

hydrothermal process temperature and residence time increased, the TP content in the HC increased from 28.92 mg/L in SS to 31.37–45.59 mg/L (150–250 °C, 60 min), indicating significant phosphorus enrichment and recovery (79.13 %–96.5 %). This observation is consistent with the findings of previous studies [27], which demonstrated that phosphorus conversion is influenced by temperature, duration, and the nature of the feedstock. Following sludge hydrothermal treatment, a significant proportion of phosphorus was retained in HC, contrasting with the behaviour observed in algae, where the majority of phosphorus entered the liquid phase. This variation can be attributed to the composition of the feedstock, particularly the presence of precipitated phosphate [40].

Following HTC (150 °C for 1 h or 250 °C for 1 h), TP in HC increased to 31.37 mg/g and 45.49 mg/g from SS's 28.92 mg/g. High temperatures hydrolysed organic phosphorus in SS to orthophosphate, thereby boosting IP and driving organic-to-inorganic conversion. In addition, both NAIP and AP exhibited a gradual increase, with AP's proportion rising, indicating NAIP transformation to more stable AP [41–43]. WO treatment slightly boosted phosphorus recovery at low hydrogen peroxide doses but reduced it significantly above 10 %, to 69.23 % at 20 %. It was observed that excess hydrogen peroxide intensifies the WO reaction, leading to the dissolution of some HC and the movement of phosphorus to the liquid phase. The results also indicate a decrease in TP in HC, a near-vanishing of OP, and an increase in AP's proportion, suggesting that WO converted phosphorus to a more stable form.In summary, WO markedly affected phosphorus recovery in HC, with low doses having minimal effects but high doses causing significant recovery drops, and WO promoting NAIP - to - AP conversion.

3.2.2. Phosphorus transformation pathways

XRD analyses were conducted to determine the phosphorus-metal binding in HC under different conditions (Fig. 2(b)). The results of the XRD analysis of SS with HC generated by HTC and WO reactions are presented in Fig. 2(b). All samples contain SiO_2, olivine ($MgFeSiO_4$) and aluminium phosphate, consistent with previous studies [44]. Aluminium phosphate has been identified as the predominant form of P bound to metals, thereby corroborating the hypothesis that NAIP in SS is predominantly Fe-P and Al-P. In the SMT framework used here, NAIP operationally covers Fe–P and Al–P pools, whereas AP represents Ca-bound phosphates. Thus, the persistent aluminium phosphate signal in XRD is consistent with the NAIP fraction measured by SMT. It has been demonstrated that the Ca-P - bound form emerges in conjunction with an increase in reaction temperature, and the emergence of novel peaks such as vivianite and bobierrite post - HTC serves to indicate that HTC converts pyrophosphate to orthophosphate, which exhibits a weak binding affinity to Mg^{2+} and Ca^{2+} and consequently forms stable P compounds [45]. These vivianite-/bobierrite-type phases fall within NAIP in SMT, providing a mineralogical counterpart to the NAIP fraction at higher HTC temperatures.

Following the occurrence of WO, an increase in AP was observed, as evidenced by the presence of additional Ca-related compounds. The advent of new peaks, such as calcium hydrogen phosphate ($CaH_2P_2O_7$) and hydrated calcium phosphate ($Ca(PO_3)_2{\cdot}2H_2O$), was accompanied by a gradual intensification of their peak intensities. This strengthening of Ca–P signals aligns with the SMT-observed rise in AP, indicating a shift from Fe/Al-bound P (NAIP) toward Ca-bound P (AP) during HTC and more clearly after WO. The potential P transformation pathways during the reaction are illustrated in Fig. 4, Fe-P and Al-P partially transform to Ca-P as the temperature rises, and this phenomenon is more pronounced after WO, corresponding to the increase in AP. XRD results indicate that aluminium phosphate is the predominant P-bearing mineral across all HC samples.Raising the temperature promotes the conversion of Fe-P and Al-P to Ca-P, a process further catalyzed by WO. We note that some phosphorus can remain poorly crystalline or surface-bound (e.g., thin Ca/Fe/Al phosphate coatings), which contributes to SMT fractions without producing distinct XRD peaks [46]; this explains minor differences between SMT proportions and XRD peak intensities.

3.3. Evolution law of pollutants in PWs

As shown in Fig. 5., the variation in wastewater pollutant indicators during HTC and WO treatment is illustrated. Experimentally, the HTC process temperature exerted a strong influence on PWs quality: as temperature increased from 150 to 250 °C, COD rose from 5106 to 19,189 mg/L, TOC showed the same upward trend, and NH_4^+-N markedly increased. This phenomenon can be attributed to the EPS, which constitutes the primary form of sludge organic matter (50–90 %) [47], and which undergoes dissociation of its polymer mesh structure at elevated temperatures, resulting in the dissolution of macromolecules such as intracellular polysaccharides and proteins [48,49]. The observed change in wastewater colour with increasing temperature can be

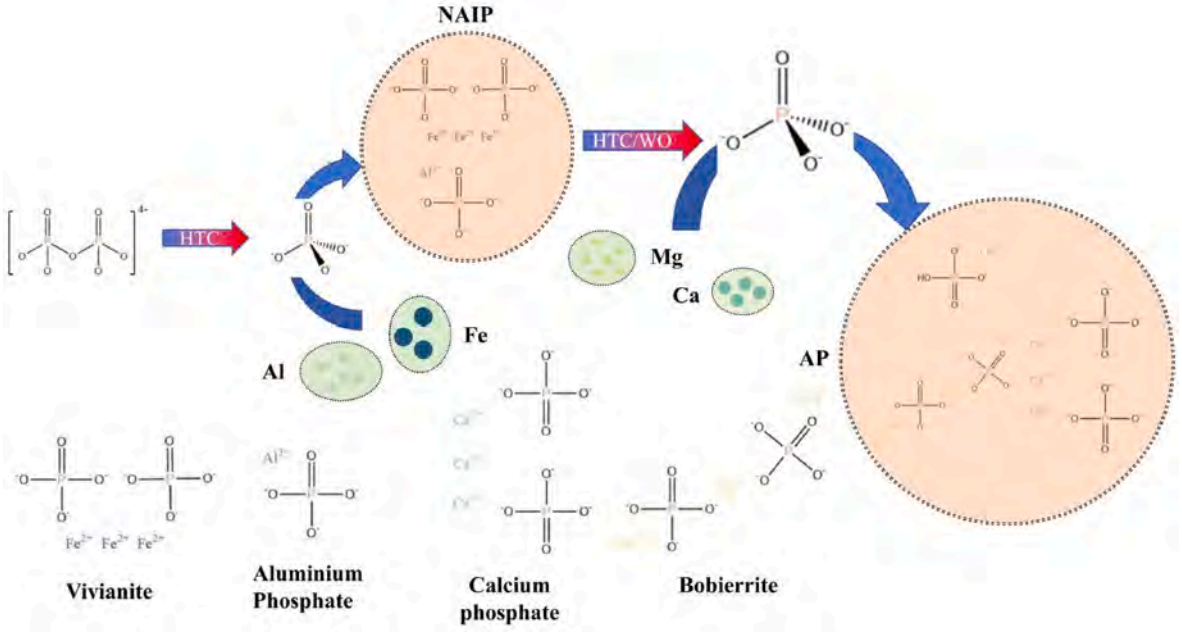


Fig. 4. Mechanism of phosphorus transformation.

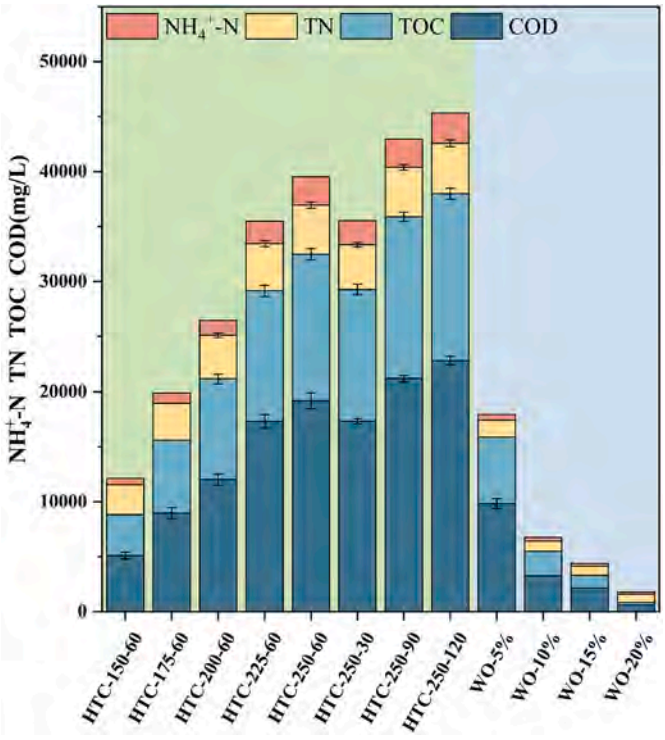


Fig. 5. Concentrations of COD, TOC, NH4+-N, and TN in PWs under different HTC and WO conditions.

elucidated by this process. At 200 °C, the solution is slightly yellow and transparent; however, it becomes darker at higher temperatures, due to an increased maillard reaction product.

The evolution of nitrogenous compounds in sludge exhibited staged characteristics, with TN increasing linearly with temperature between 150 and 200 °C (714 - 1651 mg/L), primarily from organic nitrogen (Org-N) produced by protein hydrolysis and NH_4^+-N formed by its deamidation (324 - 1047 mg/L) [50]. However, at temperatures above 200 °C, condensation reactions became the predominant process, with amino acids and reducing sugars generating pyrrole/pyridine-like heterocyclic compounds via the maillard reaction and sequestering in the HC. High-temperature-induced ring-opening reactions partially released NH_4^+-N, thereby slowing the TN increase rate [51,52]. The data show that temperature had a stronger effect on nitrogen conversion than residence time.

In the wet oxidation system, the hydroxyl radical (·OH) generated by H_2O_2 thermal catalysis preferentially cleaves macromolecular organics through hydrogen extraction and electron transfer. The degradation pathway occurs in two stages: initially, complex organics are decomposed into small molecule intermediates, and subsequently, they are ultimately mineralised into CO_2 and H_2O via decarboxylation/dehydrogenation [53]. It is noteworthy that the efficiency of WO in removing nitrogen-containing pollutants exhibits significant variations. During WO (250 °C, 60 min), organic-nitrogen compounds are rapidly oxidized/deaminated to NH_4^+-N, so the NH_4^+-N concentration in the PWs increases with reaction time. However, the electrophilic nature of ·OH makes it difficult to attack NH_4^+'s inert electronic structure, resulting in a near-conserved total nitrogen in the system [54].

Taken together, the results show that oxidant dosage matters a lot. At low H_2O_2 levels (<~5 %), the process waters are not cleaned enough and stubborn organics remain. At middle levels (~5–10 %), wet oxidation cleans the water well while keeping the downsides for the solid small (HC yield, surface area) and keeping phosphorus in more stable forms. This range is a practical operating window that balances purification and valorization. At high levels (≥~15–20 %), the solid starts to dissolve more, extra cleaning of the water brings smaller gains, and phosphorus left in the solid drops—so the overall benefits decline. From a design point of view, we suggest starting with a mid H_2O_2 dose (~5–10 % v/v of the slurry) and then adjusting on site. Tune it to: (i) how clean you need the process water (COD/TOC goals), (ii) how much you want to protect the hydrochar (yield, surface area), and (iii) how much phosphorus you aim to keep and in what form.

3.4. Impact of PWs recharge on the AAO system

HTC PWs treated with WO reduced COD and TOC concentrations, but TN and ammonia levels remained high, which would increase the load on the biochemical system when added to the influent. To assess this impact, HTC PWs and WO PWs were added to the AAO system influent in different proportions. Fig. 6 shows that over 30 days of operation, the average removal rates of COD, ammonia, and TN from the raw effluent were 85.86 %, 85.78 %, and 82.79 %, respectively. After the addition of HTC PWs, the removal rate decreased with the increase of the addition ratio. Specifically, 1 % and 5 % additions reduced the COD removal rate to 79.23 % and 64.52 %, respectively. Even at the low addition rate, the average COD in the effluent was 109.64 mg/L, exceeding the Chinese emission standard. This is because HTC PWs contain complex, hard - to - degrade and toxic organic matter, increasing the influent load. The microbial metabolic load becomes too high, while the hydraulic retention time remains unchanged, making it difficult for microbes to fully degrade the organic matter. These organics reduce the wastewater's biodegradability and inhibit microbial activity, especially at high addition ratios, resulting in a significant decrease in COD removal rate. In contrast, the COD removal rate was not affected by the addition of WO PWs, remaining at 86.46 % and 86.38 % for 1 % and 5 % additions, respectively. WO removed most of the organic matter, reducing the influent load and lessening the impact on the biochemical system. WO decomposed the macromolecules of organic matter into small molecules easily utilised by microorganisms at high temperature and pressure, improving the influent's biodegradability and enhancing the degradation efficiency.

Here, we note that the 5 % HTC PWs phase likely did not reach a new steady state within the ~30-day window. The high loading introduced a strong shock to the AAO system—elevating organic and nitrogen loads and introducing inhibitory compounds—so acclimation was incomplete and COD removal continued to decline. Accordingly, we interpret the 5 % HTC PWs results as a transient shock-response rather than steady performance, and use them to illustrate the system's limited short-term resilience under high HTC PWs dosing. Longer operation or gradual ramping would be required to determine the true steady state at this loading.

The effect of 1 % addition of HTC PWs on ammonia and TN removal was not significant, with removal rates of 84.21 % and 74.29 %, respectively. At small additions, the influent NH_4^+-N and TN loads did not increase significantly. The NH_4^+-N removal rate was higher than that of TN because the organic nitrogen in HTC PWs was difficult to remove directly by the traditional biochemical system. However, at 5 % dosage, the removal rate decreased to 54.53 % and 53.83 %. HTC PWs inhibited the nitrification and denitrification process, especially at high concentrations, by inhibiting key enzyme activities. For example, phenolic compounds inhibit AMO activity and block ammonia oxidation; nitrogen - containing heterocyclic compounds interfere with nitrite oxidation [55–57].

After adding WO PWs, the ammonia and TN removal rates were stable. The WO products contained easily degradable small molecular organic matter, providing a carbon source for denitrifying bacteria and promoting nitrate reduction. However, at 5 % addition, the effluent NH_4^+-N and TN levels increased, sometimes exceeding the discharge standard. Although WO reduces the inhibition of key enzymes by toxic organic matter, the high proportion of addition makes the concentration of NH_4^+-N and TN in the influent water too high, exceeding the

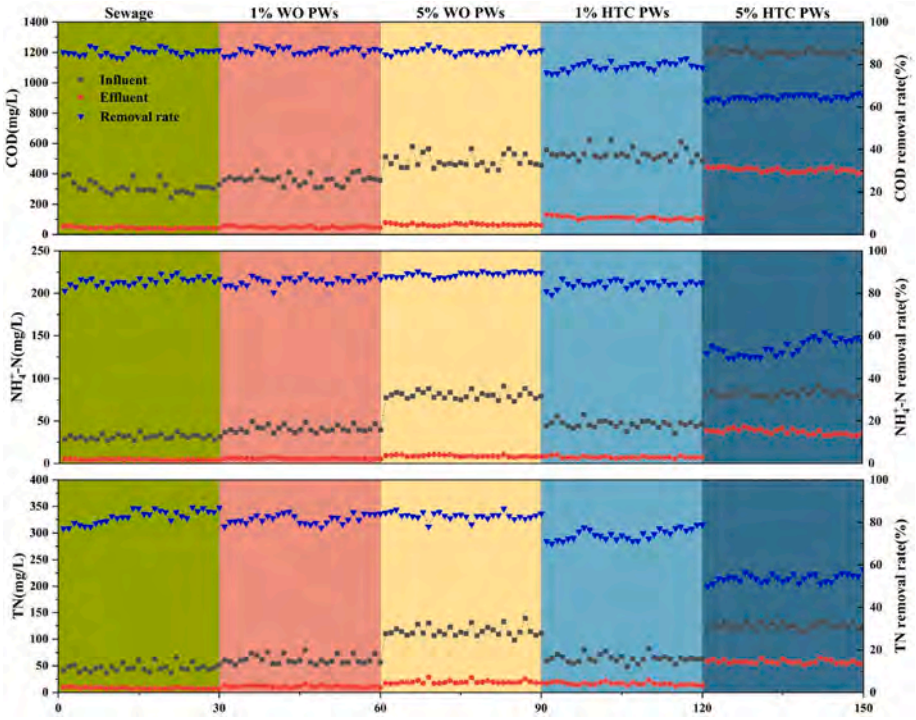


Fig. 6. Effects on COD, ammonia and TN removal with addition of HTC PWs and WO PWs.

processing capacity of nitrifying bacteria. This results in incomplete nitrification and denitrification, and the effluent water level rises. In summary, a high proportion of HTC PWs and WO PWs will impact the biochemical system, but HTC PWs may cause the effluent to exceed the standard even in small doses, while WO PWs have a smaller impact and can digest more volume in engineering applications, but attention should be paid to the addition proportion.

3.5. Impact of microbial communities

The addition of HTC PWs was shown to affect the effluent treatment effect of the biochemical system, compared to WO PWs, which produced less effect. This suggests that HTC PWs are not suitable for direct entry into the biochemical system. The effect of HTC PWs on the biochemical system was mainly due to the alteration of the microbial community structure in the system. To further test this hypothesis, this study was carried out by 16S rRNA high-throughput sequencing to understand the changes in microbial community structure in the AAO system. The Coverage index was above 0.99 in all six groups of samples (Fig. 7.), which indicated that the data provided were sufficient to reflect the distribution of microbial communities [58–60]. The sludge samples in the anaerobic, anoxic and aerobic tanks exhibited a similar trend following the introduction of HTC PWs. The Ace and Chao1 indices of the six groups of samples decreased, indicating a decline in the

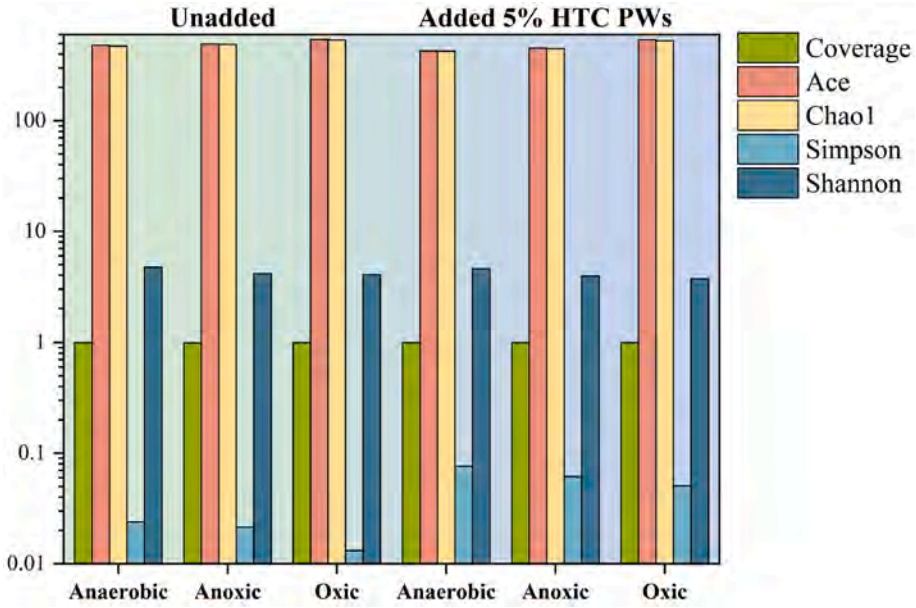


Fig. 7. Microbial abundance and diversity after addition of HTC PWs.

abundance of microorganisms. The Simpson and Shannon indices are utilised to reflect microbial diversity, and the Simpson index increased after the addition of the HTC PWs, reflecting the increased concentration of dominant species and decreased diversity of the microbial community. This phenomenon is further elucidated by the changes in the Shannon index, which decreased after the addition of the HTC PWs, indicating a decline in the combined diversity. The introduction of HTC PWs was associated with enrichment of a few dominant taxa and may have reduced functional bacterial activity, which is consistent with the observed decreases in COD, ammonia, and TN removal rates.

In order to further investigate the effect of the addition of HTC PWs on the AAO system, the microbial community structure was analyzed. Fig. 8 shows the microbial community composition at the gate level in the AAO system with and without the addition of HTC PWs. To aid interpretation, we also present low-abundance phyla (<1–2 % relative abundance) in Fig. 8. Although numerically minor, these groups can contribute to community resilience and stress response, and may modulate key functions under inhibitory loads (e.g., phenolics and N-heterocycles from HTC PWs). The predominant bacterial phyla observed in the anaerobic tank in the absence of HTC PW addition were Proteobacteria, Firmicutes, and Bacteroidetes. In contrast, the dominant bacterial phyla in the anoxic tank were Proteobacteria, Bacteroidetes, and Chloroflexi in the anaerobic pools, and Proteobacteria, Bacteroidetes, and Actinobacteria in the aerobic pools. The relative abundance of Prote Proteobacteria and Firmicutes in the anaerobic pools was significantly reduced by the addition of HTC PWs from 42.99 % to 22.79 %–31.78 % and 5.69 %, respectively, while the relative abundance of Actinobacteria increased significantly, which was mainly due to the fact that Actinobacteria were more tolerant to the complex organics in the HTC PWs. The decline in the relative abundance of Proteobacteria and Firmicutes may indicate that inhibitory compounds in HTC PWs contributed to reduced hydrolytic/heterotrophic capacity. The enrichment of tolerant flora (Actinobacteria, Armatimonadetes) has been unable to compensate for this part of the functionality loss, which is consistent with the phenomenon of decreasing the removal efficiency of COD.

In the anoxic tank, the relative abundance of Proteobacteria also decreased significantly from 57.74 % to 41.41 % with the addition of HTC PWs, while there was a small decrease in the relative abundance of Bacteroidetes. Actinobacteria and Chloroflexi became the dominant flora in the anoxic tank. Actinobacteria are implicated in denitrification; however, their abundance decreased, possibly due to toxicity and/or competition for carbon sources. Conversely, the abundance of Actinobacteria and Chloroflexi increased due to enhanced tolerance to toxic substances.The addition of HTC PWs resulted in an imbalance of influent C/N, leading to the inhibition of functional bacteria due to an increase in toxic substances, thereby impairing nitrogen removal in the system. In the aerobic pool, the relative abundance of Proteobacteria also decreased to some extent, from 62.74 % to 47.73 %, and the relative magnitude of Actinobacteria increased sharply, from 8.96 % to 25.43 %, while the relative abundance of Nitrospirae, the main functional bacterial phylum in the aerobic pool, also decreased more, from 5.67 % to 2.83 %. Heterotrophic taxa such as Actinobacteria may compete with nitrifiers for dissolved oxygen; such competition could help explain the lower ammonia removal observed. In conclusion, the performance of the system was found to be inhibited overall following the addition of HTC PWs, with the functional flora being suppressed, tolerant bacteria being enriched, and the metabolic capacity being inadequate. Consequently, the system's COD and nitrogen removal efficiencies were found to be significantly reduced.

4. Conclusion

This study demonstrates that integrating HTC and WO effectively addresses the dual challenges of SS valorization and PWs management. HTC converted sludge into HC with enhanced specific surface area (61.54 m^2/g at 250 °C) and enriched phosphorus content (TP recovery: 79–96.5 %), while subsequent WO treatment further stabilized HC by reducing volatile matter (from ~30 % to <10 %) and converting NAIP into AP, improving its suitability for resource recovery. However, direct addition of HTC PWs to the AAO system severely inhibited microbial activity, reducing COD, NH_4^+-N, and TN removal rates by up to 24.7 %, 36.4 %, and 34.9 %, respectively, due to recalcitrant organics (e.g., phenols, nitrogenous heterocycles) and elevated nitrogen loads. In contrast, WO pretreatment decomposed complex organics into bioavailable small molecules (e.g., short-chain acids), maintaining COD removal rates at ~86 % even at 5 % dosage and mitigating toxicity to nitrifying and denitrifying bacteria. Microbial community analysis revealed that HTC PWs simplified functional diversity, suppressing Proteobacteria and Firmicutes (critical for organic hydrolysis) while enriching stress-tolerant Actinobacteria, whereas WO preserved key taxa (e.g., Nitrospirae) essential for nitrogen removal. Despite the benefits of the HTC-WO tandem process, high oxidant doses (>10 %) reduced HC yield (49.67 % at 20 % H_2O_2) and phosphorus recovery (69.23 %), highlighting the need for parameter optimization. These

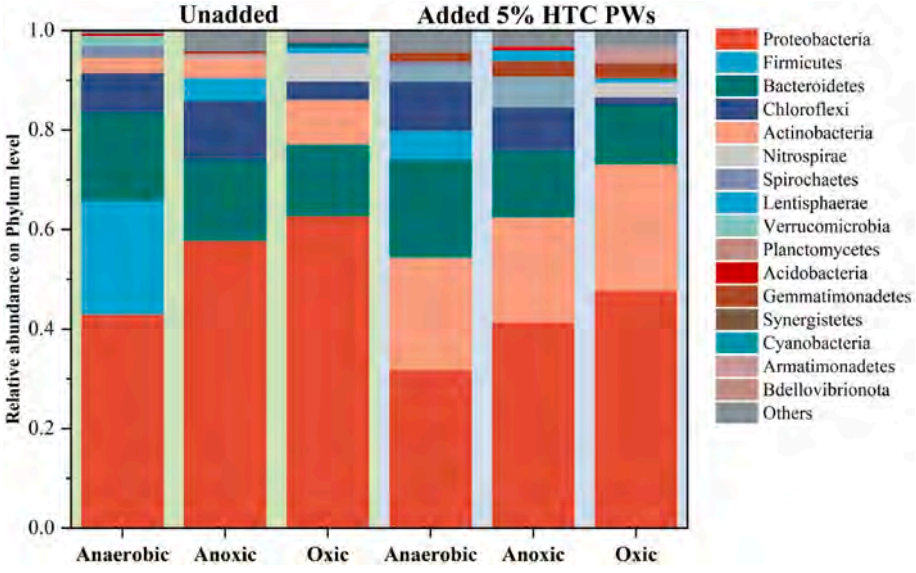


Fig. 8. Microbial community compositions at the phylum level.

findings underscore the potential of HTC-WO integration to reconcile sludge-derived resource recovery with environmental safety, though future work should prioritize catalytic WO systems for enhanced mineralization, cost-effective oxidant utilization, and long-term impacts on full-scale bioreactors. This research provides a scientific foundation for sustainable sludge management aligned with circular economy principles. Future study should (i) evaluate fuel-related properties of HC (e.g., HHV and combustion behavior) under representative HTC-WO conditions, and (ii) refine the oxidant-dosage strategy to balance process-water detoxification with preservation of HC quality and phosphorus recovery, exploring catalytic or staged dosing could help minimize oxidant demand while maintaining co-benefits.

CRediT authorship contribution statement

Geng Yang: Writing – original draft, Visualization, Formal analysis, Data curation. **Xingying Tang:** Writing – review & editing, Formal analysis, Data curation. **Xingtao Wang:** Visualization, Data curation. **You Wu:** Visualization, Data curation. **Hui Ma:** Writing – review & editing, Conceptualization. **Shengyan Pu:** Writing – review & editing, Investigation, Funding acquisition, Conceptualization.

Declaration of competing interest

The authors declare that there is no conflict of interest regarding the publication of this paper.

Acknowledgment

This research was supported by the National Natural Science Foundation of China (U22A20591, 42077185), the National Key Research and Development Program of China (2024YFC3712700), and the Research Fund of State Key Laboratory of Geohazard Prevention and Geoenvironment Protection (SKLGP2020Z002).

Appendix A. Supplementary data

Supplementary data to this article can be found online at https://doi.org/10.1016/j.biombioe.2025.108536.

Data availability

Data will be made available on request.

References

[1] L. Wei, F. Zhu, Q. Li, C. Xue, X. Xia, H. Yu, Q. Zhao, J. Jiang, S. Bai, Development, current state and future trends of sludge management in China: based on exploratory data and CO2-equivaient emissions analysis, Environ. Int. 144 (2020) 106093.
[2] X. Zheng, T. Liu, M. Guo, D. Li, N. Gou, X. Cao, X. Qiu, X. Li, Y. Zhang, G. Sheng, B. Pan, A.Z. Gu, Z. Li, Impact of heavy metals on the formation and properties of solvable microbiological products released from activated sludge in biological wastewater treatment, Water Res. 179 (2020) 115895.
[3] J.C. Steele, X. Meng, A.K. Venkatesan, R.U. Halden, Comparative meta-analysis of organic contaminants in sewage sludge from the United States and China, Sci. Total Environ. 821 (2022) 153423.
[4] Y. Liang, D. Xu, P. Feng, B. Hao, Y. Guo, S. Wang, Municipal sewage sludge incineration and its air pollution control, J. Clean. Prod. 295 (2021) 126456.
[5] H. Lü, X. Chen, C. Mo, Y. Huang, M. He, Y. Li, N. Feng, A. Katsoyiannis, Q. Cai, Occurrence and dissipation mechanism of organic pollutants during the composting of sewage sludge: a critical review, Bioresource Technol 328 (2021) 124847.
[6] H. Xiao, K. Li, D. Zhang, Z. Tang, X. Niu, L. Yi, Z. Lin, M. Fu, Environmental, energy, and economic impact assessment of sludge management alternatives based on incineration, Journal of Environmental Management 321 (2022) 115848.
[7] B. Zhang, B.K. Biswal, J. Zhang, R. Balasubramanian, Hydrothermal treatment of biomass feedstocks for sustainable production of chemicals, fuels, and materials: progress and perspectives, Chem. Rev. 123 (2023) 7193–7294.
[8] M. Malhotra, A. Garg, Hydrothermal carbonization of sewage sludge: optimization of operating conditions using design of experiment approach and evaluation of resource recovery potential, J. Environ. Chem. Eng. 11 (2023) 109507.
[9] G. Brunner, Hydrothermal and supercritical water processing of inorganic substances, Supercritical Fluid Science and Technology 5 (2014) 573–589.
[10] H. Liu, I.A. Basar, A. Nzihou, C. Eskicioglu, Hydrochar derived from municipal sludge through hydrothermal processing: a critical review on its formation, characterization, and valorization, Water Res. 199 (2021) 117186.
[11] M.N. Mahmood Al-Nuaimy, N. Azizi, Y. Nural, E. Yabalak, Recent advances in environmental and agricultural applications of hydrochars: a review, Environ. Res. 250 (2024) 117923.
[12] C. Wang, X. Ling, W. Sun, X. Sun, C. He, Elaboration of cost-effective adsorbents derived from sewage sludge through hydrothermal carbonization: influence of process parameters and feedstock components on the adsorption performance, J. Clean. Prod. 434 (2024) 140358.
[13] M.T. Reza, J. Andert, B. Herklotz, D. Busch, J. Pielert, J. Lynam, J. Mumme, Review article: hydrothermal carbonization of biomass for energy and crop production, Appl. Bioenergy 1 (2014).
[14] M.T. Reza, A. Freitas, X. Yang, C.J. Coronella, Wet air oxidation of hydrothermal carbonization (HTC) process liquid, ACS. Sustain. Chem. Eng. 4 (2016) 3250–3254.
[15] L. Liu, Y. Zhai, X. Liu, X. Liu, Z. Wang, Y. Zhu, M. Xu, Features and mechanisms of sewage sludge hydrothermal carbonization aqueous phase after ferrous/persulfate-based process: the selective effect of oxidation and coagulation, J. Clean. Prod. 366 (2022) 132831.
[16] G. Shan, W. Li, S. Bao, Y. Li, W. Tan, Co-hydrothermal carbonization of agricultural waste and sewage sludge for product quality improvement: fuel properties of hydrochar and fertilizer quality of aqueous phase, Journal of Environmental Management 326 (2023) 116781.
[17] S. Novianti, A. Nurdiawati, I.N. Zaini, H. Sumida, K. Yoshikawa, Hydrothermal treatment of palm oil empty fruit bunches: an investigation of the solid fuel and liquid organic fertilizer applications, Biofuels 7 (2016) 627–636.
[18] L.G. Fregolente, T.B.A.R. Miguel, E. de Castro Miguel, C. de Almeida Melo, A. B. Moreira, O.P. Ferreira, M.C. Bisinoti, Toxicity evaluation of process water from hydrothermal carbonization of sugarcane industry by-products, ENVIRON SCI POLLUT R 26 (2019) 27579–27589.
[19] M. Langone, G. Sabia, L. Petta, L. Zanetti, P. Leoni, D. Basso, Evaluation of the aerobic biodegradability of process water produced by hydrothermal carbonization and inhibition effects on the heterotrophic biomass of an activated sludge system, Journal of Environmental Management 299 (2021) 113561.
[20] C.I. Aragón-Briceño, A.B. Ross, M.A. Camargo-Valero, Mass and energy integration study of hydrothermal carbonization with anaerobic digestion of sewage sludge, Renew. Energ. 167 (2021) 473–483.
[21] R.Z. Gaur, O. Khoury, M. Zohar, E. Poverenov, R. Darzi, Y. Laor, R. Posmanik, Hydrothermal carbonization of sewage sludge coupled with anaerobic digestion: integrated approach for sludge management and energy recycling, Energ. Convers. Manage 224 (2020) 113353.
[22] M.T. Reza, X. Yang, C.J. Coronella, H. Lin, U. Hathwaik, D. Shintani, B.P. Neupane, G.C. Miller, Hydrothermal carbonization (HTC) and pelletization of two arid land plants bagasse for energy densification, ACS. Sustain. Chem. Eng. 4 (2016) 1106–1114.
[23] L.B. Silva Thomsen, K. Anastasakis, P. Biller, Wet oxidation of aqueous phase from hydrothermal liquefaction of sewage sludge, Water Res. 209 (2022) 117863.
[24] G. Riedel, R. Koehler, J. Poerschmann, F. Kopinke, B. Weiner, Combination of hydrothermal carbonization and wet oxidation of various biomasses, Chem. Eng. J. 279 (2015) 715–724.
[25] I. Baskyr, B. Weiner, G. Riedel, J. Poerschmann, F.D. Kopinke, Wet oxidation of char–water-slurries from hydrothermal carbonization of paper and brewer's spent grains, Fuel Process. Technol. 128 (2014) 425–431.
[26] S. McIntosh, R.V. Padilla, T. Rose, A.L. Rose, E. Boukaka, D. Erler, Crop fertilisation potential of phosphorus in hydrochars produced from sewage sludge, Sci. Total Environ. 817 (2022) 153023.
[27] G. Boniardi, L. Sessolo, E. Gelmi, A. Turolla, R. Canziani, Targeting phosphorus recovery from sewage sludge while preventing contaminant spread via combined hydrothermal carbonization and wet chemical extraction, Sep. Purif. Technol. 339 (2024) 126620.
[28] P.D. Tembhekar, K.V. Padoley, S.L. Mudliar, S.N. Mudliar, Kinetics of wet air oxidation pretreatment and biodegradability enhancement of a complex industrial wastewater, J. Environ. Chem. Eng. 3 (2015) 339–348.
[29] J.C. Martins-Vieira, P.C. Torres-Mayanga, D. Lachos-Perez, Hydrothermal processing of lignocellulosic biomass: an overview of subcritical and supercritical water hydrolysis, Bioenerg. Res. 16 (2023) 1296–1317.
[30] K. Yu, W. Huan, H. Teng, J. Guo, B. Li, Effect of oxygen-containing functional group contents on sorption of lead ions by acrylate-functionalized hydrochar, Environ. Pollut. 349 (2024) 123921.
[31] J. Fan, F. Li, D. Fang, Q. Chen, Q. Chen, H. Wang, B. Pan, Effects of hydrophobic coating on properties of hydrochar produced at different temperatures: specific surface area and oxygen-containing functional groups, Bioresource Technol 363 (2022) 127971.
[32] C. Peng, Y. Zhai, Y. Zhu, B. Xu, T. Wang, C. Li, G. Zeng, Production of char from sewage sludge employing hydrothermal carbonization: char properties, combustion behavior and thermal characteristics, Fuel 176 (2016) 110–118.
[33] Y. Lin, D. Wang, T. Wang, Ethanol production from pulp & paper sludge and monosodium glutamate waste liquor by simultaneous saccharification and fermentation in batch condition, Chem. Eng. J. 191 (2012) 31–37.
[34] J. Yu, L. Tang, Y. Pang, G. Zeng, J. Wang, Y. Deng, Y. Liu, H. Feng, S. Chen, X. Ren, Magnetic nitrogen-doped sludge-derived biochar catalysts for persulfate activation: internal electron transfer mechanism, Chem. Eng. J. 364 (2019) 146–159.
[35] S. Oh, J. Son, P. Chiu, Biochar-mediated reductive transformation of nitro herbicides and explosives, Environ. Toxicol. Chem./SETAC 32 (2013).

[36] A.L. Pauline, K. Joseph, Hydrothermal carbonization of oily sludge for solid fuel recovery – investigation of chemical characteristics and combustion behaviour, J. Anal. Appl. Pyrolysis 157 (2021) 105235.
[37] T. Liu, Q. Lang, Y. Xia, Z. Chen, D. Li, J. Ma, C. Gai, Z. Liu, Combination of hydrothermal carbonization and oxy-fuel combustion process for sewage sludge treatment: combustion characteristics and kinetics analysis, Fuel 242 (2019) 265–276.
[38] H. Zhang, G. Xue, H. Chen, X. Li, S. Chen, Revealing the heating value characteristics of sludge-based hydrochar in hydrothermal process: from perspective of hydrolysate, Water Res. 198 (2021) 117170.
[39] C. He, A. Giannis, J. Wang, Conversion of sewage sludge to clean solid fuel using hydrothermal carbonization: hydrochar fuel characteristics and combustion behavior, Appl. Energ. 111 (2013) 257–266.
[40] X. Zheng, Z. Jiang, Z. Ying, Y. Ye, W. Chen, B. Wang, B. Dou, Migration and transformation of phosphorus during hydrothermal carbonization of sewage sludge: focusing on the role of pH and calcium additive and the transformation mechanism, Acs. Sustain. Chem. Eng. 8 (2020) 7806–7814.
[41] Y. Xu, F. Yang, L. Zhang, X. Wang, Y. Sun, Q. Liu, G. Qian, Migration and transformation of phosphorus in municipal sludge by the hydrothermal treatment and its directional adjustment, Waste Manage. (Tucson, Ariz.) 81 (2018) 196–201.
[42] T. Wang, Y. Zhai, Y. Zhu, C. Peng, T. Wang, B. Xu, C. Li, G. Zeng, Feedwater pH affects phosphorus transformation during hydrothermal carbonization of sewage sludge, Bioresource Technol 245 (2017) 182–187.
[43] M. Gong, H. Chu, J. Feng, Y. Su, Regulating the distribution of phosphorus in sewage sludge hydrothermal carbonization products by complexation pretreatment, J. Environ. Chem. Eng. 12 (2024) 111921.
[44] T. Qian, H. Jiang, Migration of phosphorus in sewage sludge during different thermal treatment processes, ACS. Sustain. Chem. Eng. 2 (2014) 1411–1419.
[45] R. Huang, C. Fang, X. Lu, R. Jiang, Y. Tang, Transformation of phosphorus during (hydro)thermal treatments of solid biowastes: reaction mechanisms and implications for P reclamation and recycling, Environ. Sci. Technol. 51 (2017) 10284–10298.
[46] R.W. McDowell, L.M. Condron, Chemical nature and potential mobility of phosphorus in fertilized grassland soils, Nutr. Cycl.Agroecosys 57 (2000) 225–233.
[47] T.T. More, J.S.S. Yadav, S. Yan, R.D. Tyagi, R.Y. Surampalli, Extracellular polymeric substances of bacteria and their potential environmental applications, Journal of Environmental Management 144 (2014) 1–25.
[48] S. Peng, A. Hu, J. Ai, W. Zhang, D. Wang, Changes in molecular structure of extracellular polymeric substances (EPS) with temperature in relation to sludge macro-physical properties, Water Res. 201 (2021) 117316.
[49] K. Wu, Y. Gao, G. Zhu, J. Zhu, Q. Yuan, Y. Chen, M. Cai, L. Feng, Characterization of dairy manure hydrochar and aqueous phase products generated by hydrothermal carbonization at different temperatures, J. Anal. Appl. Pyrolysis 127 (2017) 335–342.
[50] X. Zhuang, Y. Huang, Y. Song, H. Zhan, X. Yin, C. Wu, The transformation pathways of nitrogen in sewage sludge during hydrothermal treatment, Bioresource Technol 245 (2017) 463–470.
[51] Y. Chen, L. Tian, T. Liu, Z. Liu, Z. Huang, H. Yang, L. Tian, Q. Huang, W. Li, Y. Gao, Z. Zhang, Speciation and transformation of nitrogen for sewage sludge hydrothermal carbonization-influence of temperature and carbonization time, Waste Manage. (Tucson, Ariz.) 162 (2023) 8–17.
[52] A. Dimitriadis, S. Bezergianni, Hydrothermal liquefaction of various biomass and waste feedstocks for biocrude production: a state of the art review, Renew. Sustain. Energy Rev. 68 (2017) 113–125.
[53] R.S. Dhamorikar, V.G. Lade, P.V. Kewalramani, A.B. Bindwal, Review on integrated advanced oxidation processes for water and wastewater treatment, J. Ind. Eng. Chem. (2024).
[54] X. Liu, J. Wang, Selective oxidation of ammonium to nitrogen gas by advanced oxidation processes: reactive species and oxidation mechanisms, J. Environ. Chem. Eng. 11 (2023) 110263.
[55] A.D. Romero, J.V. Poli, S. Larson, S. Stagg-Williams, R. Carter, B.S.M. Sturm, Inhibition of nitrifying bacteria from heterocyclic N-containing organic compounds from municipal sludge hydrothermal liquefaction, Frontiers in Chem. Eng. 7 (2025).
[56] W. Li, S. Liu, F. Sun, C. Wang, Y. Wang, C. Chen, Phenol inhibition and recovery strategies of anaerobic ammonium oxidation (anammox) in wastewater: mechanisms and practical implications, Chem. Eng. J. 500 (2024) 157019.
[57] D. Luo, J. Qian, X. Jin, L. Zhang, K. You, P. Yu, J. Fu, How phenol stresses anammox for the treatment of ammonia-rich wastewater: Phenomena, microbial community evolution and molecular modeling, Bioresource Technol 347 (2022) 126747.
[58] J. Chen, H. Luo, D. Luo, Y. Chen, J. Tang, H. Ma, S. Pu, New insights into the degradation of nitrobenzene by activated persulfate with sulfidated nanoscale zero-valent iron: synergistic effects of reduction and reactive oxygen species oxidation, Separ. Purif. Technol. (2023) 322.
[59] G. Hou, X. Zhao, T. Zhao, X. Wu, S. Pu, The adsorption of PAHs on microplastics and desorption in the simulated human digestivesystem, Chem. Eng. J. 473 (2023) 145157.
[60] C. Chang, Q. Wang, Q. Xue, F. Liu, L. Hou, S. Pu, Highly efficient detection of chloramphenicol in water using Ag and Ti02 nanoparticlesmodified laser-induced graphene electrode, Microchem. J. 173 (2022) 107037.

Biochemical Engineering Journal 216 (2025) 109662

Contents lists available at ScienceDirect

Biochemical Engineering Journal

journal homepage: www.elsevier.com/locate/bej

Advancements of the *Vibrio coralliilyticus* eDNA detection based on Co-Fe PBA-assisted biosensors for the rapid coral-disease warning

Yibo Zhang [a,1], Hongjie Liu [b,1], Shaopeng Wang [a,b,c,d,*], Hao Fu [b], Yuanyu Xie [c], Chaoxin Zhang [b], Man Zhang [d], Jie Lu [c], Liwei Wang [d,e,**], Kefu Yu [d,e]

[a] School of Resources, Environment and Materials, Guangxi University, Nanning 530004, PR China
[b] School of Chemistry and Chemical Engineering, Guangxi University, Nanning 530004, PR China
[c] College of Life Science and Technology, Guangxi University, Nanning 530004, PR China
[d] Guangxi Laboratory on the Study of Coral Reefs in the South China Sea, Coral Reef Research Center of China, School of Marine Sciences, Guangxi University, Nanning 530004, PR China
[e] Southern Marine Science and Engineering Guangdong Laboratory (Guangzhou), Guangzhou 511458, PR China

ARTICLE INFO

Keywords:
Vibrio coralliilyticus
eDNA
Portable biosensor
On-site detection
Coral disease diagnosis

ABSTRACT

Vibrio coralliilyticus (*V. coralliilyticus*) can lead to severe coral diseases and is one of the main causes of coral bleaching. However, there is still a lack of convenient, and non-invasive detection methods for *V. coralliilyticus*, which brings inconvenience to coral health management. Here, a portable electrochemical biosensor was developed based on environmental DNA (eDNA) and cobalt-iron Prussian Blue Analogue (Co-Fe PBA) electrode material for detecting *V. coralliilyticus*. Notably, this sensor identified and quantified *V. coralliilyticus* eDNA in water through specific DNA probes, overcoming the previously reported complex and destructive pretreatment processes. Additionally, thanks to the high specific surface area of Co-Fe PBA, which provided abundant sites for probe anchoring, the constructed portable biosensor exhibited excellent detection performances. Specifically, the detection limit was as low as 19.0 fM, and the linear range was from 100 fM to 100 nM. In subsequent coral infection experiments, the eDNA of *V. coralliilyticus* increased on the eve of coral bleaching. Based on this change, the occurrence of coral bleaching was successfully predicted. Therefore, this portable biosensor is suitable for dynamic monitoring of *V. coralliilyticus*, helping to reveal the potential risks to coral health and providing a reference for ecological decision-making for coral reef protection.

1. Introduction

Coral reef ecosystems are highly concerned for their rich biodiversity and complex ecological structure, and their ecological, economic, and social significance is widely recognized [1,2]. However, coral reefs belong to the most fragile ecosystems. Due to human activities and environmental changes, nearly half of the world's reef-building corals have been disappearing since the 1950s [3], wherein about 30 % of these losses are attributed to diseases [4]. While the global extinction risk of most coral species is lower than previously estimated, local depletions pose imminent threats that can have ecologically devastating impacts on coral reefs [5,6].

Currently, only a few pathogenic bacteria have been confirmed as coral pathogens according to Koch's postulates, with *Vibrio coralliilyticus* (*V. coralliilyticus*) being one of the primary pathogens responsible for coral bleaching syndrome in *Pocillopora damicornis* (*P. damicornis*) [7,8]. Generally speaking, *V. coralliilyticus* maintains a symbiotic relationship with *P. damicornis* under normal temperatures. However, rising temperatures can induce behavioral switches in *V. coralliilyticus* due to global warming, leading to tissue dissolution, expulsion of symbiotic algae, and eventual death of the coral [9–11]. Presently, coral disease diagnosis mainly relies on the on-site observation of macroscopic lesions, which results in the misidentification of diseases in different environments. Moreover, the disease has already affected the corals before

* Corresponding author at: School of Resources, Environment and Materials, Guangxi University, Nanning 530004, PR China.
** Corresponding author at: Guangxi Laboratory on the Study of Coral Reefs in the South China Sea, Coral Reef Research Center of China, School of Marine Sciences, Guangxi University, Nanning 530004, PR China.
E-mail addresses: wsp@gxu.edu.cn (S. Wang), wangliwei0427@163.com (L. Wang).
[1] These authors contributed equally to this work.

https://doi.org/10.1016/j.bej.2025.109662
Received 26 December 2024; Received in revised form 27 January 2025; Accepted 2 February 2025
Available online 6 February 2025
1369-703X/© 2025 Elsevier B.V. All rights are reserved, including those for text and data mining, AI training, and similar technologies.

the symptoms can be observed, delaying the appropriate treatment [4,12]. In addition, there have been several research reports on the detection of *V. coralliilyticus* based on DNA technology, such as polymerase chain reaction (PCR) [13,14]. Nevertheless, all existing methods require cutting down corals and transporting them to the laboratory for testing. This operation has significant drawbacks. On one hand, the cutting behavior directly causes physical damage to the corals, disrupting their ecological structure and integrity. On the other hand, from coral collection and long-distance transportation to the final laboratory testing, there are numerous uncertainties in the entire process. These uncertainties may interfere with the physiological state of the corals, and at the same time, affect *V. coralliilyticus*, leading to deviations in the detection results and making it difficult to accurately reflect the true condition of corals in the natural environment.

Compared with traditional detection methods, environmental DNA (eDNA) technology, with its outstanding advantages of high sensitivity, accurate results, and non-invasiveness to organisms, offers a new perspective in the field of coral pathogen detection [15,16]. eDNA represents the DNA that organisms release into the surrounding environment through shedding or excretion. It has now been widely applied in species diversity analysis, particularly achieving remarkable results in the study of aquatic ecological environments [17]. This technology eliminates the need to cut down corals, thus avoiding secondary damage to them, and meets the demand for efficient detection of coral pathogens [18].

However, current eDNA-based detection methods generally rely on large-scale instruments, making on-site detection difficult. Additionally, since the activity of eDNA samples can be limited by complex environments and transportation and storage conditions, the on-site detection method is quite essential [19,20]. Electrochemical DNA biosensors have emerged as one of the ideal solutions due to their sensitivity, rapidity, and portability [21], which rely on the hybridization of capture probes and target sequences to generate electrical signals, allowing for quick and effective identification of targets based on the 'Watson-Crick pairing principle'[22], and have been widely used in detecting food-borne bacteria, antibodies, viruses, and so on [23–25]. Meanwhile, electrochemical biosensors do not require large-scale instruments and can be operated without the need for professional personnel. Additionally, nanomaterials significantly improve biosensors' performances due to their electrochemical properties when used as electrodes [26]. Thereinto, Prussian Blue Analogue (PBA), with its special tunable structure and good conductivity, can enhance the DNA loading and signal transmission remarkably [27,28]. Therefore, electrochemical DNA biosensors can be used for large-scale monitoring of the abundance changes for coral disease pathogens, thus enabling early warnings of coral diseases and providing a theoretical basis for the protection work against coral diseases.

In this work, Co-Fe PBA nanoframes (Co-Fe PBA NFs) were employed as the electrode material, and connected with oligonucleotide probes of high-specificity sequences to construct an efficient portable sensor on a Screen-Printed Electrode (SPE) for the on-site detection of *V. coralliilyticus*. Additionally, a coral infection experiment on *P. damicornis* verified the correlation between the biosensor detection results and the risk of coral disease. It is worth noting that when the concentration of *V coralliilyticus* reached 645 copies/μL, the coral exhibited bleaching symptoms. Verification through traditional methods and droplet digital PCR (ddPCR) proved that the biosensor is accurate and reliable. It can be seen that the electrochemical biosensor can play a role in large-scale monitoring of the abundance changes of coral disease pathogens, realizing the early-warning function for coral diseases, and thus laying a theoretical foundation for the protection work of coral diseases.

2. Experiment

2.1. Material and methods

All the Material and methods details can be found in Supporting Information S1.1, S1.2, and **S1.3.**

2.2. Probes design

Specific probes targeting the gene were designed with NCBI online; the corresponding ssDNA were synthesized by Shanghai Sangon (Shanghai, China). The sequences of ssDNA could be found in Table S1, Supporting Information.

2.3. DNA preparation

Conduct bacterial culturing and DNA preparation as required (Supporting Information S1.4).

2.4. Construction of biosensor

First, a sensor was constructed using a glassy carbon electrode (GCE) to evaluate the feasibility of the construction method. Then, the process of the portable biosensor was similar to that on GCE, which was shown in Fig. 1. Firstly, drop 10 μL of the Co-Fe PBA NFs solution containing 1 % chitosan onto the treated surface of the GCE (Supporting Information S1.5) and then dried for 30 min at room temperature, recorded as GCE/PBA. Next, 10 μL glutaraldehyde solution (2.5 %) was incubated on the surface of the modified electrode for 30 min at room temperature. After that 10 μL of capture probe (noted as CP, 1 μM) was added onto the surface of the modified electrode for 1 h at room temperature, recorded as GCE/PBA/CP. Afterward, 10 μL of Bovine Serum Albumin (BSA) was added onto the surface of the modified electrode to block nonspecific active sites. Before commencing the experiment, the modified electrode was stored at 4°C. Finally, 10 μL of the Target DNA with adsorbed Methylene Blue (MB) was dropped onto the modified electrode and incubated for 1 h at room temperature. MB was intercalated into dsDNA, and its signal changes can be detected by electrochemical methods. The modified electrode surface was washed with PBS buffer and deionized water, dried, and then stored at 4°C, respectively, recorded as GCE/PBA/CP/Target. Then, the same construction process was conducted on Screen-Printed Electrodes (SPE) as a portable chip in building a portable biosensor. Subsequently, electrochemical tests were carried out (Supporting Information S1.6). After the test is completed, rinse the surface of the electrode with water and ethanol, and then conduct physical polishing again (More details were provided in Supporting Information S1.5).

2.5. Infection experiment of P. damicornis

As shown in Fig. S1, the four experimental groups were named as C25 (Fig. S1a), C30 (Fig. S1b), T25 (Fig. S1c), and T30 (Fig. S1d), respectively, where C/T represented the absence/presence of *V. coralliilyticus* inoculation (1 mL, 10^7 CFU/mL), and 25/30 represented the coral culture water temperature of 25°C /30°C. More coral experimental details were provided in Supporting Information S1.7, S1.8, and S1.9.

The blank test and data analysis can be found in the Supporting Information S1.10 and S1.11.

3. Results and discussion

3.1. Characterization of electrode material

SEM was used to characterize the morphological characteristics of Co-Fe PBA NFs, which possessed a hollow, open cubic framework

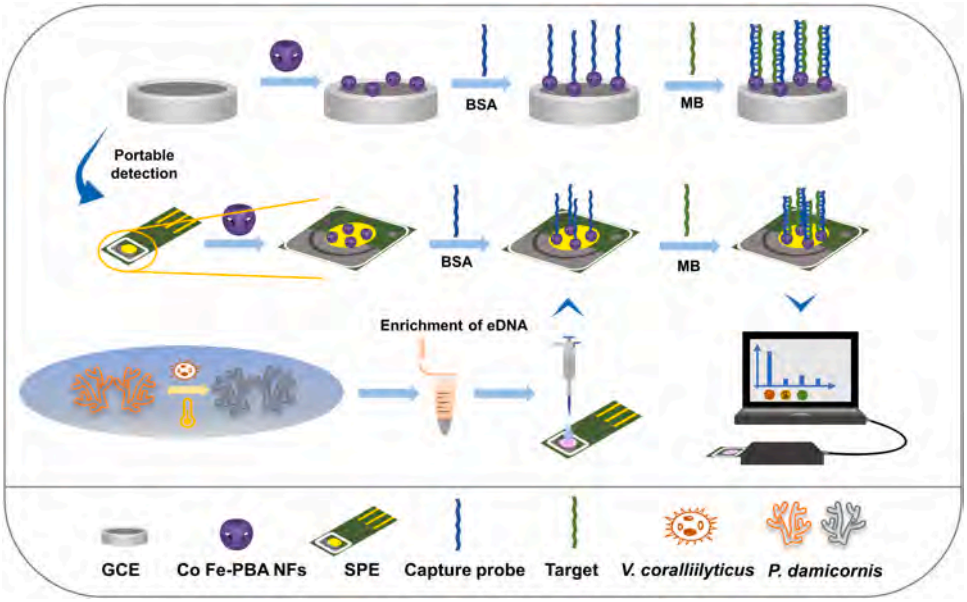


Fig. 1. Construction and detection process of the biosensor.

structure with a size of approximately 280 nm (Fig. 2**a**). The elemental composition of Co-Fe PBA NFs was analyzed by XPS (Fig. 2**b** and Fig. S2a, **b**), proving the existing elements such as Co, Fe, O, N, and C. Besides, in the XRD pattern (Fig. 2**c**), the peaks appearing at $2\theta = 17.6$, 24.5, 35.6, 43.9, 51.2, and 57.8 corresponded to the (200), (220), (400), (420), (440), and (620) crystal planes respectively. They all originated from PBA and were closely related to their structures, which also indicated the successful synthesis of Co-Fe PBA NFs [29–31]. In addition, Raman spectroscopy (Fig. S2c) also show spectral bands of Fe-Co, Fe-C, and C≡N at 228, 565, and 2129 cm^{-1}. These spectral bands were also associated with the specific structural characteristics of reported PBA, proving the successful synthesis of Co-Fe PBA NFs [32–34]. This also corresponds to the XRD results (Fig. 2**c**).

Then, the specific surface area was determined by N_2 isotherm adsorption-desorption (Fig. 2**d**) to be 71.990 m^2/g, and gave the pore distribution of Co-Fe PBA NFs (Fig. 2**d, inset**), obtaining a pore size of 9.355 nm, which belonged to the mesopores. A larger specific surface area could provide more active sites for the hybridization reaction at the electrode interface. At the same time, it was conducive to the transfer of charges, thereby enhancing the sensitivity and improving the detection performance of the biosensor [35].

In order to explore the contribution of the special structure of elec-

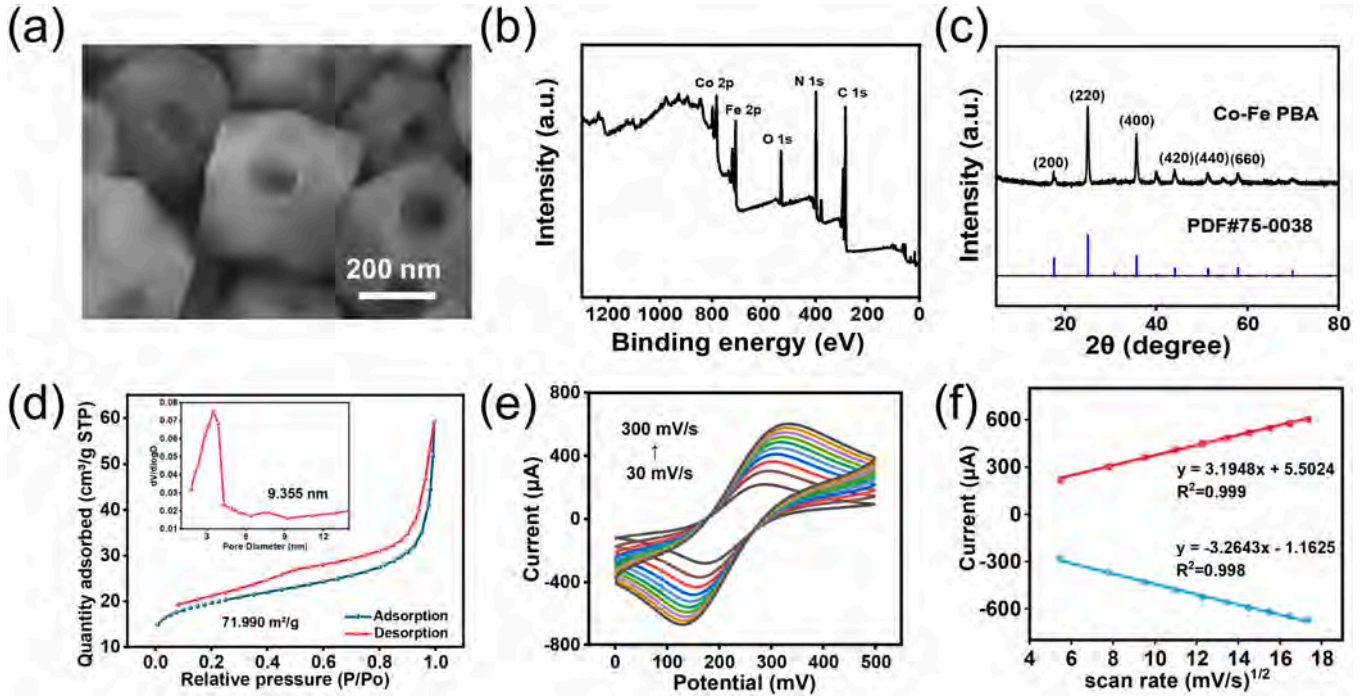


Fig. 2. Characterization of Co-Fe PBA NFs: (a) SEM, (b) XPS, (c) XRD, and (d) N_2 isotherm adsorption-desorption of Co-Fe PBA NFs; (e) redox behavior of Co-Fe PBA NFs electrodes using CV at scan rates between 30 and 300 mV/s; (f) the linear regression plot between the current and square root of scan-rates based on the Co-Fe PBA NFs electrode.

trode materials to electrochemical sensing performances, Co-Fe PBA NFs were tested by cyclic voltammetry (CV) at different scan rates (Fig. 2**e**), and then a linear relationship was found between the redox peak current and the square root of the scan rate (Fig. 2**f**). According to the calculation of formulas (1) [36,37], the electrochemically surface areas (ECSA) of the bare or PBA modified electrodes were 0.178 and 0.290 cm^2, respectively, as shown in Fig. S3. Obviously, the ECSA was improved by 62.9 % for the latter electrode. (I_{pa}: oxidation current, A: the electroactive surface area, D: the diffusion coefficient of 7.60 $\times 10^{-6}$ cm^2 s^{-1}, n: the electron transfer number of 1, C: the concentration of $[Fe(CN)_6]^{3-/4-}$, ν: the scanning rate, respectively.)

$$I_{pa} = 2.69 \times 10^5 \times A \times D^{1/2} \times n^{3/2} \times C \times \nu^{1/2} \quad (1)$$

3.2. Construction of portable biosensor

Electrochemical impedance spectroscopy (EIS) was used to characterize impedance changes during the construction of electrochemical biosensors [37]. The Nyquist plot obtained from the EIS result typically formed a semicircular arc, where the diameter reflected the resistive properties of the electrochemical system. The feasibility verification shown in Fig. 3 corresponded to the previous biosensor construction processes. As shown in Fig. 3**a**, when the surface of the GCE was modified by Co-Fe PBA NFs as GCE/PBA, a semicircle with a smaller radius (68 Ω) than that of the bare GCE (81 Ω) was observed, indicating the successful combination of Co-Fe PBA NFs and the electrode, which was beneficial to electron transfer and further improved the detection ability of the biosensor. After further adding CP on the surface of GCE/PBA, the diameter of the semicircle increased, indicating that the amide reaction occurred and amino was successfully introduced at the end of the CP on the GCE/PBA/CP electrode [38]. The increase in impedance value came from the electrostatic repulsion between the negative charge pair of $[Fe(CN)_6]^{3-/4-}$ on the electrode surface and the probe DNA [39]. Then, the semicircle increased sharply when Bovine Serum Albumin (BSA) was introduced on the surface of GCE/PBA/CP. Since BSA could block the non-specific active sites on the electrode surface and reduce the generation of false positive results, it could also hinder the electron transfer efficiency at the electrode interface as a macromolecular substance. In the next step, the addition of Target DNA greatly reduced the diameter of the semicircle. This was because Target DNA and CP formed dsDNA based on the complementary base pairing hybridization and the signals were enlarged by the adsorbed MB molecules, enhancing the electron transfer rate at the electrode interface [40,41].

Correspondingly, in Fig. 3**b**, CV was also used to test and characterize each stage of the biosensor construction process, and the results were consistent with the changing trend shown by EIS (Fig. 3**a**), indicating the successful construction of the biosensor. Then, the same construction method was applied to SPE (Fig. 3**c**), and the CA results showed similar variation trends as those on GCE, indicating such a method actually could be feasible to build a portable platform for the detection of *V. coralliilyticus*. In addition, more detailed experiments were also carried out to obtain the optimal detection parameters (shown in Fig. S4), and the subsequent testing was executed under the above-optimized conditions.

More importantly, chronocoulometry (CC) was used to study the CP density. As shown in Fig. 3**d**, Q_{total} and Q_{dl} were 5.053 and 1.495, respectively. Quantitative calculation of Γ_{ss} yielded a CP density of 8.84 $\times 10^{11}$ molecules cm^{-2} by using formulas (2) and (3) [42,43]. (N_A: Avogadro's number, n: electrons number, F is the Faraday constant (96, 487 C $equiv^{-1}$), z: charge of the redox molecule (for RuHex, z is 3), A: the electrochemically surface areas (0.290 cm^2), m: number of nucleotides in the DNA (in this study, m is 26).)

$$\Gamma_{ss} = (Q_{ss} \quad N_A/nF\ A)(z/m) \quad (2)$$

$$Q_{ss} = \quad Q_{total} - Q_{dl} \quad (3)$$

As shown in Fig. 1, when the target system containing

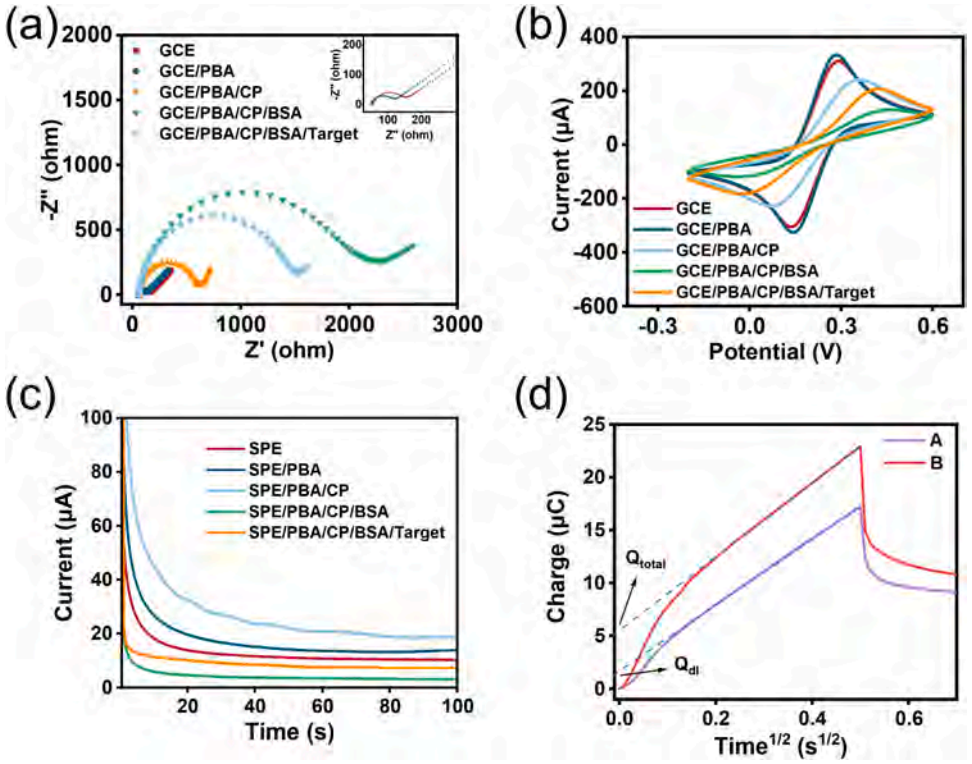


Fig. 3. Feasibility of the construction method. (a) EIS, (b) CV of the biosensor constructed on GCE, and (c) CA of the biosensor constructed on SPE at different modification stages. (d) Chronocoulometric curves of SPE/PBA/BSA/CP: (A) in Tris-HCl (10 mM, pH 7.4) and (B) in Tris-HCl (10 mM, pH 7.4) containing 50 μM of RuHex. Target concentration is 100 pM.

V. coralliilyticus eDNA is dropped onto the electrode surface, due to the presence of capture probes on the electrode surface that are highly specific and complementary to *V. coralliilyticus* eDNA, base-complementary pairing occurs at the electrode interface. A large amount of target DNA adsorbed with MB is immobilized on the electrode surface. Since MB is an electrochemically active substance, it can enhance the electron transfer rate at the electrode interface, leading to an increase in the electrochemical signal. Thus, the concentration of *V. coralliilyticus* eDNA can be quantified by the magnitude of the change in the electrochemical signal.

3.3. Performance evaluation of the portable biosensor

The electrochemical properties of the portable biosensor were evaluated as shown in the schematic illustration in Fig. 4**a**. Specifically, the portable biosensor was tested with different concentrations of Target DNA by the CA method. As shown in Fig. 4**b**, the target concentration was reflected by measuring the current response of the Target DNA. An excellent linear relationship could be fitted between the peak current and the logarithm of the Target DNA concentration (Fig. 4**c**) according to formula (4). Besides, the limit of detection (LOD) was calculated as 19.0 fM using formula (5) and the Limit of Quantitation (LOQ) was calculated as 71.25 fM using formula (6), where σ is the standard deviation of the blank response (n = 8), and S is the slope of the calibration curve obtained from three independent devices (n = 3) [44]. Compared to the reported technology for detecting bacterium (Table S2), the biosensor had a lower detection limit, indicating its superior performance.

$$y = 3.608x + 64.589 \quad (4)$$

$$\mathrm{LOD} = 3\sigma/S \quad (5)$$

$$\mathrm{LOQ} = 10\sigma/S \quad (6)$$

Moreover, such a wide detection range should be attributed to the hollow, open structure of Co-Fe PBA NFs, which brought a larger sensing area to the electrode, thus loading more capture probes. The result was also reflected in Fig. 2**f**: the ECSA of the GCE/PBA electrode was increased by 62.9 % compared to the bare GCE. The above results showed that the biosensor could perform accurate quantification of the Target DNA at certain concentrations, thereby indirectly reflecting the abundance changes of *V. coralliilyticus* in the coral-living area and providing a basis for coral health assessment.

Besides, a series of tests were conducted to verify the performance of the portable biosensor. First, the reproducibility of the portable biosensor was tested. As shown in Fig. 5**a**, it could be observed that all of the different batches of biosensors displayed good reproducibility when detecting 10, 0.1, and 0.001 nM of *V. coralliilyticus* DNA. The RSD was lower than 3.9 %, indicating that the construction method realized accurate and repeated detection [45,46]. In addition, specificity is a crucial characteristic of biosensors related to their reliability. In Fig. 5**b**, the portable biosensor presented relatively low current responses in other interfering species or blank samples, and the response to *V. coralliilyticus* was the highest and almost equal to the mixed group (Mix) of all the above species. The current response displayed a significant difference ($P < 0.001$). At the same time, the specificity was further verified by the target with sequence mismatch. As shown in Fig. 5**c**, the mismatched target also only possessed a low current response ($P < 0.001$) [47]. The results showed that compared with other interferences, the portable biosensor exhibited excellent specific recognition capability for *V. coralliilyticus* and also recognized the target in the mixture, indicating its excellent anti-interference property in a complex environment.

Finally, long-term stability is also an important property of biosensors, which has a decisive influence on the practical application effect and reliability. As shown in Fig. 5**d**, the portable biosensor only lost 12.2 % of the electrical signal after being placed for one week, which met the actual requirements, indicating that the portable biosensor possessed good long-term stability. The above test results comprehensively proved that the biosensor with good performance could support the needs of coral health assessment.

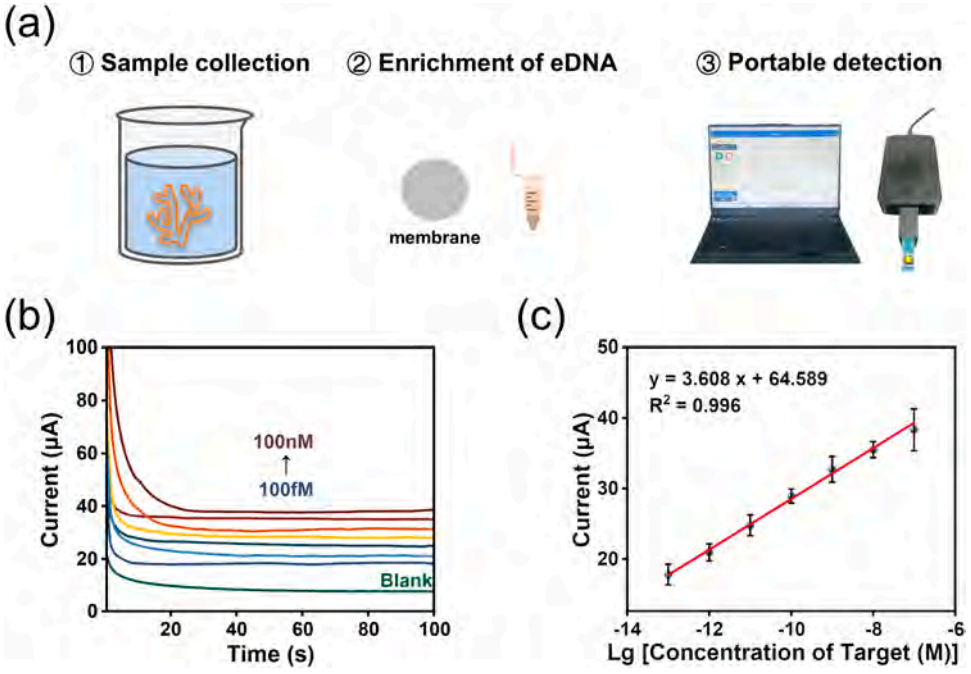


Fig. 4. Electrochemical property evaluation of the portable biosensor: (a) sample detection process including sample collection, eDNA enrichment, and portable detection, (b) CA test with Target DNA concentrations ranging from 100 fM to 100 nM, and (c) the linear fitting of the current *vs.* the concentration of Target DNA. Error bars represent the standard deviation (SD) of three parallel experiments.

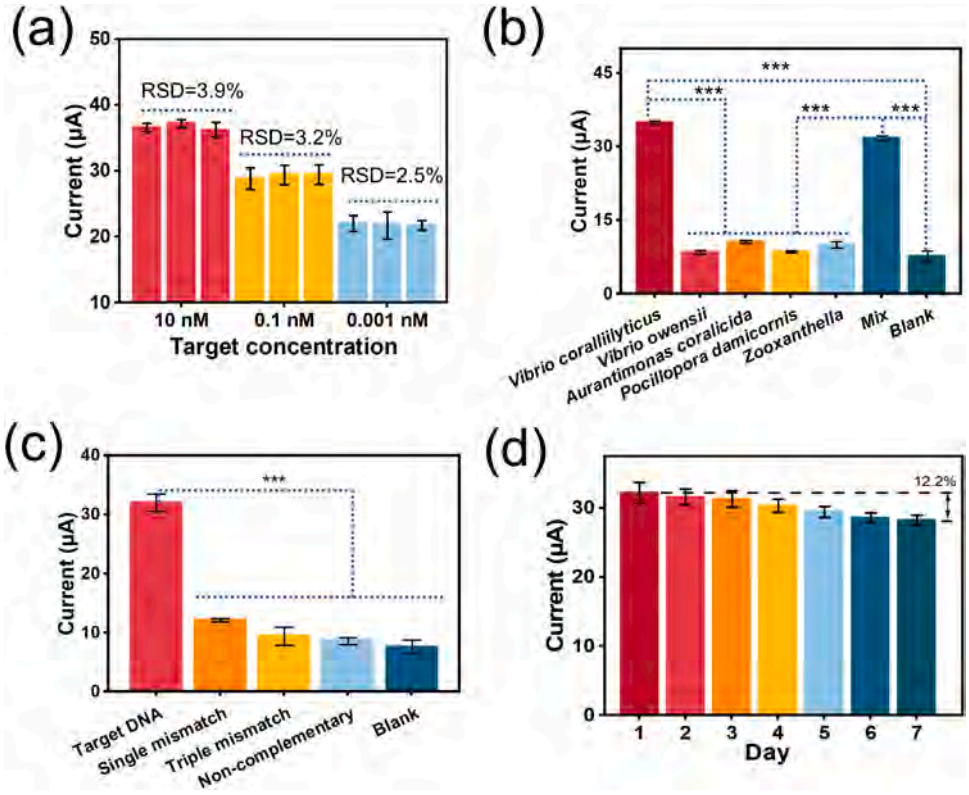


Fig. 5. Various performances of the portable biosensor: (a) reproductivity (Num. = 3), (b) selectivity to the DNA (10 nM) of other species, (c) specificity to Target DNA (1 nM) with different mismatch types in sequence, and (d) stability after restoring under −20°C for seven days. Error bars represent the standard deviation (SD) of three parallel experiments. * : $P < 0.05$, * *: $0.001 < P < 0.01$, * ** : $P < 0.001$.

3.4. Applicability

Upon the successful accomplishment of the preliminary performance assessment of the portable biosensor, subsequent coral infection experiments were further executed within the aquarium environment. This was achieved by simulating the elevation of seawater temperature triggered by global warming phenomena. In this specific experimental setup, *P. damicornis* was deliberately selected as the target coral for the study. The particular pathogen, *V. coralliilyticus*, which had been positively identified on the surface of the chosen coral, was strategically utilized to mimic the real-world presence of such pathogens within the natural marine ecosystem (Fig. S1). Through this approach, the objective was to meticulously observe the impact of *V. coralliilyticus* on corals within a relatively warmer environment and to rigorously verify the applicability of the portable biosensor during the entire process of coral infection. After two weeks of incubation and regular sampling, the results were shown in Figs. 6 and 7. Wherein, Fig. 6**a** reflected the color change of such coral during the warming experiment, the main color of each group of corals in Fig. 6**a** was further processed to clarify the process of color shift for each coral, shown in Fig. 6**b**, where the relative luminance was the result of the calculation of the Red Green Blue (RGB) values of the main color of the corals, with the formula (6) [48].

$$Y = 0.212\ R + 0.715\ G + 0.072\ B \quad (6)$$

Relative luminance is used to simulate the human eye's perception of white light: the larger the value is, the more seriously the coral's main body is biased toward white, and the deeper the coral's bacterial bleaching occurs due to infection by pathogenic bacteria. It could be clearly observed that before and after the incubation, there was no obvious change between the C25 and T25 groups, which might be due to

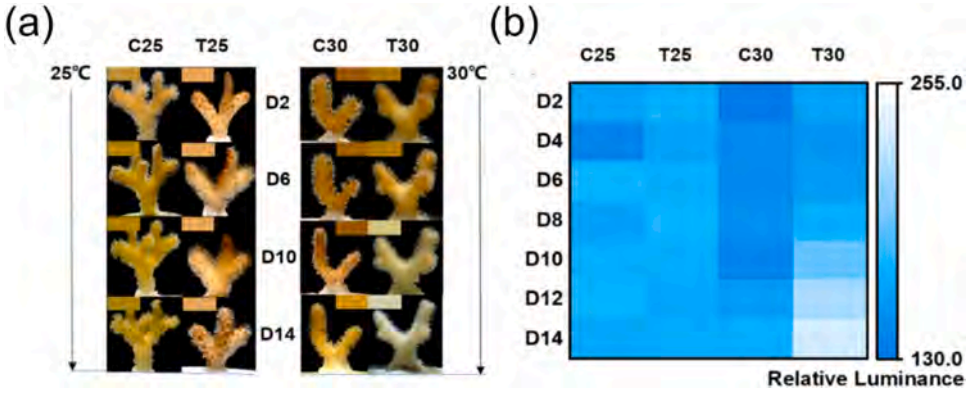


Fig. 6. Morphological changes of *P. damicornis* during infection experiment: (a) photographs, and (b) the thermal graphs of corals in four groups (C25, T25, C30, T30) with respective relative luminance.

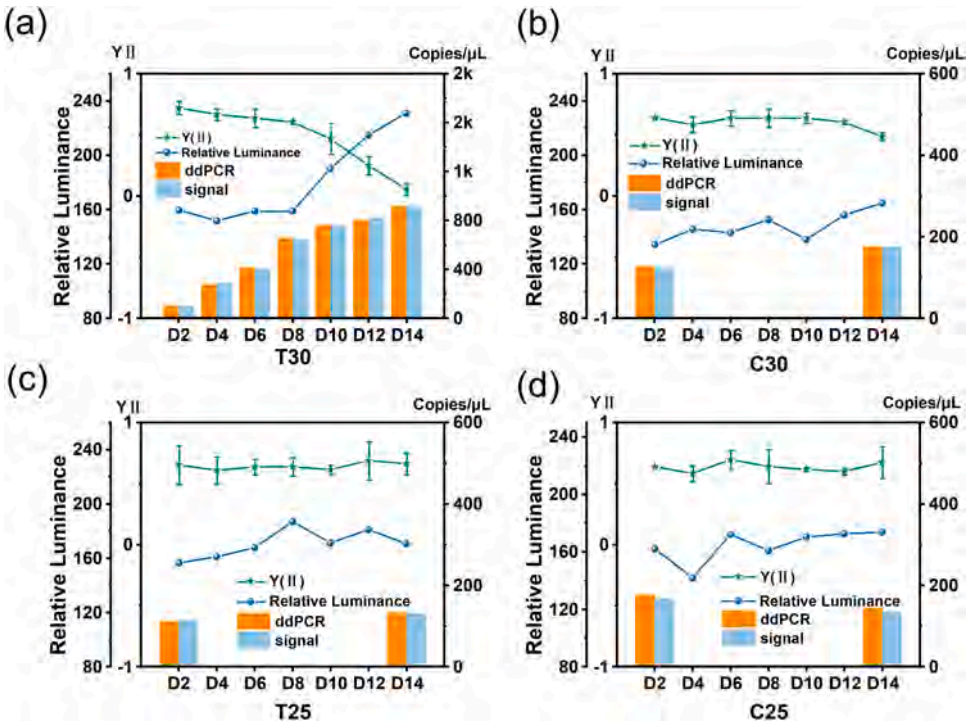


Fig. 7. Summary charts of the changes in the coral health index: (a) T30, (b) C30 (c) T25, and (d) C25. Error bars represent the standard deviation (SD) of three parallel experiments.

that *V. coralliilyticus* is a conditionally pathogenic bacteria affected by temperature. Its pathogenicity is very weak at a normal water temperature of 25°C and almost harmless for the coral. Therefore, there was no apparent difference in the coral morphology, no matter whether *V. coralliilyticus* was inoculated. In contrast, coral color in the warming group T30 significantly changed to lighter and then tended to be white, indicating that the group of corals inoculated with *V. coralliilyticus* was indeed attacked by the pathogen, and there was a significant tendency to bleaching. But for C30, although the corals were not inoculated with *V. coralliilyticus*, there was still a slight tendency to lighten. The reason might be that the experimental seawater sample was obtained from the coral aquarium. It was inevitable that a trace amount of *V. coralliilyticus* would be introduced due to the wide distribution of *V. coralliilyticus* when the coral samples were brought back from the field to the aquarium, which was also verified in the subsequent experimental data (Fig. 7).

Samples obtained periodically during the coral infection experiments were analyzed by different methods, as shown in Fig. 7, where Y(II) indicated the maximal photosynthetic efficiency of the corals, reflecting the ability of the coral to carry out photosynthetic reactions, thus could be regarded as a traditional indicator of the coral health status [49]; the relative luminance was calculated in the same way as in the previous text, reflecting the ability of the human eye to recognize the whitening of the coral's color; signal and ddPCR indicated the test results of Target DNA concentration in water samples by portable sensor and Gold standard method (ddPCR), respectively. It could be observed that the relative luminance of the T30 group increased dramatically with the increase of incubation time (Fig. 7**a**), which was accompanied by the gradual decrease of Y(II) in the process, indicating that the T30 corals showed a tendency to bleach in the warming environment, and the level of coral health was decreasing. Eventually, the corals were completely bleached, proving the preceding judgment that the virulence of *V. coralliilyticus* in corals was temperature-dependent.

Besides, the concentration of *V. coralliilyticus* eDNA was tested by the portable biosensor during the experiment (Fig. 7**a**), which increased slowly in the first two days after inoculation. The reason might be that the pathogen might need time to adapt to the new environment at the early stage of infection, hence its virulence was not obvious; then the eDNA concentration increased rapidly after D2, which indicated that *V. coralliilyticus* had successfully infected the coral, and proliferated in large quantities under the suitable environmental conditions; afterward, when the eDNA concentration of *V. coralliilyticus* reached 645 copies/μL (D8), it was found that the coral health level was declining significantly including both the obvious shift in coral color and the decrease in photosynthetic level. Importantly, the biosensor showed the same trend of change as the above traditional methods throughout the infection experiment. The results suggested that the electrochemical DNA biosensor could also reflect the health level of corals and further diagnose coral disease pathogens compared to the traditional methods of visual observation and photosynthetic indicators.

It was also noted that there was a time lag between the large increase in relative luminance, or the large decrease in photosynthetic efficiency of the corals, and the increase in eDNA concentration, indicating that the attack of *V. coralliilyticus* on the corals was not apparent until it proliferated up to a certain threshold. Therefore, it was not reliable to determine whether the corals were infected with *V. coralliilyticus* just based on the coral's appearance in the early stage of the infection or from the traditional methods, such as photosynthesis indicators, or when the coral had been infected but could not determine how severe the infection was. Therefore, the portable biosensor in this study could detect *V. coralliilyticus* eDNA rapidly and accurately, which had the potential to detect the potential risk of coral bleaching before the coral presented obvious symptoms, thus taking effective measures to protect the coral in advance.

Meanwhile, the accuracy of the biosensor results was verified by ddPCR after each portable biosensor detection of eDNA concentration in water samples (Fig. 7). After calculation, there was no significant difference between the results of ddPCR and the portable biosensor ($P > 0.05$), which indicated that the biosensor was accurate and reliable enough to be practically applied in the field detection of *V. coralliilyticus*, providing new ideas for the on-site diagnosis of coral diseases.

In addition, the curve changes in group C30 (Fig. 7**b**) were similar to

those of T25 (Fig. 7**c**) and C25 (Fig. 7**d**) in the first and middle stages before D10, but differences appeared in the later stages after D10, where a small increase in the eDNA concentration was observed, and accordingly, relative luminance and photosynthetic efficiency were slightly increased and reduced, respectively as a result of the infection. The results of Fig. 7**b** corresponded to the aforementioned trend of changes in group C30 (Fig. 6). Moreover, neither of the *V. coralliilyticus* was active in group T25 or C25 (Fig. 7**c**, **d**) since the temperature did not reach the condition of pathogenicity, so the inoculation did not have a significant effect on the corals, and the overall trend of the curves was stable without large fluctuations.

It was also noted in Fig. 7 that *V. coralliilyticus* eDNA was detected in D0 through the biosensor in the four experimental groups, and ddPCR also proved its existence. The results showed that a trace amount of *V. coralliilyticus* usually existed in naturally fresh seawater and had the potential to cause coral disease outbreaks, even in small amounts. Therefore, it was concluded that *V. coralliilyticus* existed in the sea areas, and the coral growth therein was accompanied by the potential threat of disease. The present study has the potential to predict coral disease outbreaks by extensively monitoring *V. coralliilyticus* eDNA in the event of seawater warming, thus providing an on-site and rapid response to prevent disease outbreaks and protect coral ecosystems.

In addition, a blank test was conducted in order to prevent the introduction of external contamination due to artificial sampling operations in the coral culture experiment, and the results were shown in Fig. S5. Significantly, there was almost no signal corresponding in all steps of sampling, and it was in contrast with the obtained sample in biosensor performances. These results showed that no external contamination was introduced during the sampling and testing process to interfere with the test results.

4. Conclusion

In conclusion, a novel, highly sensitive and selective portable biosensor was developed for detecting *V. coralliilyticus* eDNA by using Co-Fe PBA NFs as electrode material and the ssDNA probe to specifically identify *V. coralliilyticus*. The constructed biosensor possessed a wide detection range from 100 fM to 100 nM, and an exceptionally lower detection limit of 19.0 fM. In addition, a coral infection experiment by simulating seawater warming proved that the coral got to bleach when the *V. coralliilyticus* eDNA increased to 645 copies/μL at the temperature of 30°C. It was further verified that the biosensor could dynamically track the changes of eDNA abundance in the seawater and showed the potential to evaluate the health status of corals and help the early warning of coral pathogens of infection. The results were also compared with traditional methods and ddPCR, confirming the portable biosensor's validity and reliability, demonstrating that the constructed biosensor is promising for the on-site detection of coral pathogenic bacteria. In summary, the electrochemical biosensor has demonstrated remarkable performance in detecting *V. coralliilyticus*, showing high efficiency and notable sensitivity. However, a drawback lies in the current water sample pretreatment, which is both time-consuming and labor-intensive, impeding the sensor's ability to conduct rapid detection. To surmount this hurdle, our research team is actively delving into the application of microfluidic devices. These devices are expected to simplify and expedite the extraction process. By integrating microfluidics, we anticipate achieving real-time, on-site detection of *V. coralliilyticus*. Such an achievement will lay a solid foundation for early warning of coral bleaching. Moreover, it will enhance comprehensive ecological monitoring in marine environments, providing critical data for conservation efforts and ecological research.

CRediT authorship contribution statement

Xie Yuanyu: Investigation. **Zhang Chaoxin:** Investigation. **Zhang Yibo:** Writing – review & editing, Writing – original draft, Investigation, Data curation. **Liu Hongjie:** Writing – original draft, Investigation. **Wang Shaopeng:** Software, Investigation. **Fu Hao:** Investigation. **Lu Jie:** Investigation. **Yu Kefu:** Writing – review & editing. **Wang Liwei:** Conceptualization. **Zhang Man:** Investigation.

Declaration of Competing Interest

The authors declare that they have no known competing financial interests or personal relationships that could have appeared to influence the work reported in this paper.

Acknowledgments

This work was funded by the National Science Foundation of China (42090041, 42030502); Key Projects of Guangxi Natural Science Foundation (No. 2020GXNSFDA297015), China; Natural Science Foundation of Guangxi Province (No. 2022GXNSFAA035565), China; Self-Topic Project of Guangxi Laboratory on the Study of Coral Reefs in the South China Sea, Nanning 530004, China (No. GXLSCRSCS2023102).

Appendix A. Supporting information

Supplementary data associated with this article can be found in the online version at doi:10.1016/j.bej.2025.109662.

Data Availability

Data will be made available on request.

References

[1] W. Zhang, Y. Sik Ok, M.S. Bank, C. Sonne, Macro- and microplastics as complex threats to coral reef ecosystems, Environ. Int. 174 (2023) 107914, https://doi.org/10.1016/j.envint.2023.107914.
[2] P. Smallhorn-West, S. Gordon, K. Stone, D. Ceccarelli, S. Malimali, T. Halafihi, M. Wyatt, T. Bridge, R. Pressey, G. Jones, Biophysical and anthropogenic influences on the status of Tonga's coral reefs and reef fish fishery, PLoS One 15 (2020) e0241146, https://doi.org/10.1371/journal.pone.0241146.
[3] T.D. Eddy, V.W.Y. Lam, G. Reygondeau, A.M. Cisneros-Montemayor, K. Greer, M.L. D. Palomares, J.F. Bruno, Y. Ota, W.W.L. Cheung, Global decline in capacity of coral reefs to provide ecosystem services, One Earth 4 (2021) 1278–1285, https://doi.org/10.1016/j.oneear.2021.08.016.
[4] T. Moriarty, W. Leggat, M.J. Huggett, T.D. Ainsworth, Coral disease causes, consequences, and risk within coral restoration, Trends Microbiol 28 (2020) 793–807, https://doi.org/10.1016/j.tim.2020.06.002.
[5] C.R. Voolstra, J.B. Raina, M. Dorr, A. Cardenas, C. Pogoreutz, C.B. Silveira, A. R. Mohamed, D.G. Bourne, H. Luo, S.A. Amin, R.S. Peixoto, The coral microbiome in sickness, in health and in a changing world, Nat. Rev. Microbiol. 22 (2024) 460–475, https://doi.org/10.1038/s41579-024-01015-3.
[6] A. Dietzel, M. Bode, S.R. Connolly, T.P. Hughes, The population sizes and global extinction risk of reef-building coral species at biogeographic scales, Nat. Ecol. Evol. 5 (2021) 663–669, https://doi.org/10.1038/s41559-021-01393-4.
[7] Y. Ben-Haim, M. Zicherman-Keren, E. Rosenberg, Temperature-regulated bleaching and lysis of the coral *Pocillopora damicornis* by the novel pathogen *Vibrio coralliilyticus*, Appl. Environ. Microbiol. 69 (2003) 4236–4242, https://doi.org/10.1128/AEM.69.7.4236-4242.2003.
[8] D.S. Beatty, C.S. Clements, J.M. Valayil, S.Y. Jarvis, K.B. Ritchie, F.J. Stewart, M. E. Hay, Variance of coral anti-pathogen defense in response to transplantation between coral- and macroalgal-dominated reefs, Coral Reefs 41 (2022) 1417–1431, https://doi.org/10.1007/s00338-022-02291-2.
[9] M. Garren, K. Son, J. Tout, J.R. Seymour, R. Stocker, Temperature-induced behavioral switches in a bacterial coral pathogen, ISME J. 10 (2016) 1363–1372, https://doi.org/10.1038/ismej.2015.216.
[10] Z. Zhou, S. Zhao, J. Tang, Z. Liu, Y. Wu, Y. Wang, S. Lin, Altered immune landscape and disrupted coral-symbiodinium symbiosis in the scleractinian coral *Pocillopora damicornis* by *Vibrio coralliilyticus* challenge, Front. Physiol. 10 (2019) 366, https://doi.org/10.3389/fphys.2019.00366.
[11] B. Ushijima, J.L. Meyer, S. Thompson, K. Pitts, M.F. Marusich, J. Tittl, E. Weatherup, J. Reu, R. Wetzell, G.S. Aeby, C.C. Hase, V.J. Paul, Disease diagnostics and potential coinfections by *Vibrio coralliilyticus* during an ongoing coral disease outbreak in Florida, Front. Microbiol. 11 (2020) 569354, https://doi.org/10.3389/fmicb.2020.569354.
[12] D. Sharma, C. Ravindran, Diseases and pathogens of marine invertebrate corals in Indian reefs, J. Invertebr. Pathol. 173 (2020) 107373, https://doi.org/10.1016/j.jip.2020.107373.

[13] L.A. Chimetto Tonon, J.R. Thompson, A.P.B. Moreira, G.D. Garcia, K. Penn, R. Lim, R.G.S. Berlinck, C.C. Thompson, F.L. Thompson, Quantitative detection of active *Vibrios* associated with white plague disease in *Mussismilia braziliensis* Corals, Front. Microbiol. 8 (2017) 2272, https://doi.org/10.3389/fmicb.2017.02272.
[14] R. Li, Y. Huang, J. Wu, H. Dang, L. Wang, W. Zhang, J. Ding, Whole genome analysis and specific PCR primer development for *Vibrio coralliilyticus*, combined with transcription and metabolome analysis of red spotting disease in the sea urchin, Strongylocentrotus intermedius, Aquac. Rep. 22 (2022) 100957, https://doi.org/10.1016/j.aqrep.2021.100957.
[15] R. Zeng, H. Gong, Y. Li, Y. Li, W. Lin, D. Tang, D. Knopp, CRISPR-Cas12a-derived photoelectrochemical biosensor for point-of-care diagnosis of nucleic acid, Anal. Chem. 94 (2022) 7442–7448, https://doi.org/10.1021/acs.analchem.2c01373.
[16] H. Gong, Y. Wu, R. Zeng, Y. Zeng, X. Liu, D. Tang, CRISPR/Cas12a-mediated liposome-amplified strategy for the photoelectrochemical detection of nucleic acid, 8977-8898, Chem. Commun. 57 (2021), https://doi.org/10.1039/d1cc03743a.
[17] E.A. Didaskalou, K.B. Trimbos, K.A. Stewart, Environmental DNA, Curr. Biol. 32 (2022) R1250–R1252, https://doi.org/10.1016/j.cub.2022.09.052.
[18] L. Wang, Q. Bin, H. Liu, Y. Zhang, S. Wang, S. Luo, Z. Chen, M. Zhang, K. Yu, New insights into the on-site monitoring of probiotics eDNA using biosensing technology for heat-stress relieving in coral reefs, Biosens. Bioelectron. 243 (2024) 115790, https://doi.org/10.1016/j.bios.2023.115790.
[19] H. Gong, X. Hu, R. Zeng, Y. Li, J. Xu, M. Li, D. Tang, CRISPR/Cas12a-based photoelectrochemical sensing of microRNA on reduced graphene oxide-anchored Bi_2WO_6 coupling with catalytic hairpin assembly, Sens. Actuators B Chem. 369 (2022) 132307, https://doi.org/10.1016/j.snb.2022.132307.
[20] R. Zeng, J. Xu, L. Lu, Q. Lin, X. Huang, L. Huang, M. Li, D. Tang, Photoelectrochemical bioanalysis of microRNA on yolk-in-shell Au@CdS based on the catalytic hairpin assembly-mediated CRISPR-Cas12a system, Chem. Commun. 58 (2022) 7562–7565, https://doi.org/10.1039/d2cc02821b.
[21] B. Rafique, M. Iqbal, T. Mehmood, M.A. Shaheen, Electrochemical DNA biosensors: a review, Sens. Rev. 39 (2019) 34–50, https://doi.org/10.1108/Sr-08-2017-0156.
[22] Z. Zeng, R. Zhou, R. Sun, X. Zhang, Z. Cheng, C. Chen, Q. Zhu, Nonlinear hybridization chain reaction-based functional DNA nanostructure assembly for biosensing, bioimaging applications, Biosens. Bioelectron. 173 (2021) 112814, https://doi.org/10.1016/j.bios.2020.112814.
[23] B. Meshram, A. Agrawal, S. Adil, S. Ranvir, K. Sande, Biosensor and its application in food and dairy industry: a review, Int. J. Curr. Microbiol. Appl. Sci. 7 (2018) 3305–3324, https://doi.org/10.20546/ijcmas.2018.702.397.
[24] K. Mao, H. Zhang, F. Ran, H. Cao, R. Feng, W. Du, X. Li, Z. Yang, Portable biosensor combining CRISPR/Cas12a and loop-mediated isothermal amplification for antibiotic resistance gene ermB in wastewater, J. Hazard. Mater. 462 (2024) 132793, https://doi.org/10.1016/j.jhazmat.2023.132793.
[25] R. Gupta, N. Raza, S.K. Bhardwaj, K. Vikrant, K.H. Kim, N. Bhardwaj, Advances in nanomaterial-based electrochemical biosensors for the detection of microbial toxins, pathogenic bacteria in food matrices, J. Hazard. Mater. 401 (2021) 123379, https://doi.org/10.1016/j.jhazmat.2020.123379.
[26] K. Jiao, Z. Kang, B. Wang, S. Jiao, Y. Jiang, Z. Hu, Applying Co_3O_4@nanoporous carbon to nonenzymatic glucose biofuel cell and biosensor, Electroanalysis 30 (2018) 525–532, https://doi.org/10.1002/elan.201700719.
[27] X. Hua, T. Zhao, X. Gui, B. Jin, A NiFe PBA/AuNPs nanocomposite sensitive immunosensor for electrochemical detection of PSA, Anal. Methods 16 (2024) 1923–1933, https://doi.org/10.1039/d3ay02184j.
[28] T. Liu, C. Chen, D.K. Xiong, J. Wang, C.X. Lu, S.L. Ying, Y.X. Kong, F.Y. Yi, The facile fabrication and high-performance sensing of glucose of sea-urchin-like CoFeLDH/PBA/NF heterojunction, N. J. Chem. 45 (2021) 22564–22568, https://doi.org/10.1039/d1nj04598a.
[29] L.J. Yang, S.Z. Feng, G.C. Xu, B. Wei, L. Zhang, Electrospun MOF-based FeCo nanoparticles embedded in nitrogen-doped mesoporous carbon nanofibers as an efficient bifunctional catalyst for oxygen reduction and oxygen evolution reactions in zinc-air batteries, ACS Sustain Chem. Eng. 7 (2019) 5462–5475, https://doi.org/10.1021/acssuschemeng.8b06624.
[30] J. Kim, S.B. Lee, S.K. Lee, K.H. Kim, Magnetic thermal dissipations of FeCo hollow fibers filled in composite sheets under alternating magnetic field, Appl. Surf. Sci. 415 (2017) 114–118, https://doi.org/10.1016/j.apsusc.2016.10.170.
[31] S. Qiu, Y.K. Xu, X.Y. Wu, X.L. Ji, Prussian blue analogues as electrodes for aqueous monovalent ion batteries, Electrochem. Energy Rev. 5 (2022) 242–262, https://doi.org/10.1007/s41918-020-00088-x.
[32] L.Y. Wang, X.X. Cheng, Z.Q. Wang, C.Y. Ma, Y.K. Qin, Investigation on Fe-Co binary metal oxides supported on activated semi-coke for NO reduction by CO, Appl. Catal. B 201 (2017) 636–651, https://doi.org/10.1016/j.apcatb.2016.08.021.
[33] J.Z. Zhang, Z. Zhang, H.B. Zhang, Y. Mei, F. Zhang, P.X. Hou, C. Liu, H.M. Cheng, J. C. Li, Prussian-blue-analogue-derived ultrathin Co_2P-Fe_2P nanosheets for universal-pH overall water splitting, Nano Lett. 23 (2023) 8331–8338, https://doi.org/10.1021/acs.nanolett.3c02706.
[34] H. Guan Xu, C. Zhu, H. Yang Lin, J. Kai Liu, Y. Xiao Wu, H. Qin Fu, X. Yu Zhang, F. Mao, H. Yang Yuan, C. Sun, P. Fei Liu, H. Gui Yang, Oxygen plasma triggered Co-O-Fe motif in prussian blue analogue for efficient and robust alkaline water oxidation, Angew. Chem. Int. Ed. Engl. (2024) e202415423, https://doi.org/10.1002/anie.202415423.
[35] Y.X. Xu, Q. Li, H.G. Xue, H. Pang, Metal-organic frameworks for direct electrochemical applications, Coord. Chem. Rev. 376 (2018) 292–318, https://doi.org/10.1016/j.ccr.2018.08.010.
[36] F.X. Hu, T. Hu, S. Chen, D. Wang, Q. Rao, Y. Liu, F. Dai, C. Guo, H.B. Yang, C.M. Li, Single-atom cobalt-based electrochemical biomimetic uric acid sensor with wide linear range and ultralow detection limit, Nanomicro Lett. 13 (2020) 7, https://doi.org/10.1007/s40820-020-00536-9.
[37] X.L. Zhang, S.S. Li, Y.J. Liu, W.W. Liu, L.Q. Kong, Y.Q. Chai, X.L. Luo, R. Yuan, High-efficiency 3D DNA walker immobilized by a DNA tetrahedral nanostructure for fast and ultrasensitive electrochemical detection of MiRNA, Anal. Chem. 95 (2023) 4077–4085, https://doi.org/10.1021/acs.analchem.2c04847.
[38] B. Zhang, P. Tian, H. Zhu, L. Xie, P. Dai, B. He, Ultrasensitive detection of PCB77 based on exonuclease III-powered DNA walking machine, J. Hazard. Mater. 416 (2021) 125831, https://doi.org/10.1016/j.jhazmat.2021.125831.
[39] L. Fan, G. Wang, W. Liang, W. Yan, Y. Guo, S. Shuang, C. Dong, Y. Bi, Label-free and highly selective electrochemical aptasensor for detection of PCBs based on nickel hexacyanoferrate nanoparticles/reduced graphene oxides hybrids, Biosens. Bioelectron. 145 (2019) 111728, https://doi.org/10.1016/j.bios.2019.111728.
[40] D. Long, M. Li, H. Wang, H. Wang, Y. Chai, R. Yuan, A photoelectrochemical biosensor based on fullerene with methylene blue as a sensitizer for ultrasensitive DNA detection, Biosens. Bioelectron. 142 (2019) 111579, https://doi.org/10.1016/j.bios.2019.111579.
[41] R. Zhuravel, H. Huang, G. Polycarpou, S. Polydorides, P. Motamarri, L. Katrivas, D. Rotem, J. Sperling, L.A. Zotti, A.B. Kotlyar, J.C. Cuevas, V. Gavini, S.S. Skourtis, D. Porath, Backbone charge transport in double-stranded DNA, Nat. Nanotechnol. 15 (2020) 836–840, https://doi.org/10.1038/s41565-020-0741-2.
[42] Z. Wei, X. Zhang, Y. Chen, H. Liu, S. Wang, M. Zhang, H. Ma, K. Yu, L. Wang, A new strategy based on a cascade amplification strategy biosensor for on-site eDNA detection and outbreak warning of crown-of-thorns starfish, Sci. Total Environ. 927 (2024) 172258, https://doi.org/10.1016/j.scitotenv.2024.172258.
[43] X.L. Zhang, S.S. Li, Y.J. Liu, W.W. Liu, L.Q. Kong, Y.Q. Chai, X.L. Luo, R. Yuan, High-efficiency 3D DNA walker immobilized by a DNA tetrahedral nanostructure for fast and ultrasensitive electrochemical detection of MiRNA, Anal. Chem. 95 (2023) 4077–4085, https://doi.org/10.1021/acs.analchem.2c04847.
[44] Y. Chen, Y. Gu, X. Yi, H. Huang, Y. Li, B. Yang, S. Guo, L. Bai, Conductive nano-gold self-assembled MXene@hemin with high catalytic activity achieved by strong metal-support interactions: a powerful nanozyme for development of electrochemical aptasensor in tuberculosis diagnosis, Chem. Eng. J. 466 (2023) 143112, https://doi.org/10.1016/j.cej.2023.143112.
[45] R. Zeng, M. Qiu, Q. Wan, Z. Huang, X. Liu, D. Tang, D. Knopp, Smartphone-based electrochemical immunoassay for point-of-care detection of SARS-CoV-2 nucleocapsid protein, Anal. Chem. 94 (2022) 15155–15161, https://doi.org/10.1021/acs.analchem.2c03606.
[46] D. Wu, J. Tang, Z. Yu, Y. Gao, Y. Zeng, D. Tang, X. Liu, Pt/Zn-TCPP nanozyme-based flexible immunoassay for dual-mode pressure–temperature monitoring of low-abundance proteins, Anal. Chem. 96 (2024) 8740–8746, https://doi.org/10.1021/acs.analchem.4c01059.
[47] E. Rubio-Portillo, S. Robertson, J. Anton, Coral mucus as a reservoir of bacteriophages targeting *Vibrio* pathogens, ISME J. 18 (2024), https://doi.org/10.1093/ismejo/wrae017.
[48] S. Yin, M.N. Hossain, Y. Li, C. Sun, H.-B. Kraatz, Development of a novel electrochemical aptasensor based on catalytic hairpin assembly and DNA tetrahedron for the detection of 25-hydroxyvitamin D3, Sens. Actuators B Chem. 354 (2022) 131217, https://doi.org/10.1016/j.snb.2021.131217.
[49] W. He, G. Yoo, Y. Ryu, Evaluation of effective quantum yields of photosystem II for CO_2 leakage monitoring in carbon capture and storage sites, PeerJ 9 (2021) e10652, https://doi.org/10.7717/peerj.10652.

forests

MDPI

Review

Progress and Limitations in Forest Carbon Stock Estimation Using Remote Sensing Technologies: A Comprehensive Review

Weifeng Xu [1,†], Yaofei Cheng [2,†], Mengyuan Luo [3], Xuzhi Mai [4], Wenhuan Wang [3,4], Wei Zhang [4,*] and Yinghui Wang [3,4,*]

[1] School of Resources, Environment and Materials, Guangxi University, Nanning 530004, China; xwf@st.gxu.edu.cn
[2] Guangxi Pinglu Canal Constriction Co., Ltd., Nanning 530022, China; cyf2004cd@163.com
[3] Institute of Green and Low Carbon Technology, Guangxi Institute of Industrial Technology, Nanning 530200, China; lvseditansuolmy@126.com (M.L.); wwhuan2202@126.com (W.W.)
[4] School of Marine Sciences, Guangxi University, Nanning 530004, China; 2327301019@st.gxu.edu.cn
* Correspondence: zhangwei20@gxu.edu.cn (W.Z.); wyh@gxu.edu.cn (Y.W.)
† These authors contributed equally to this work.

Abstract: Forests play a key role in carbon sequestration and oxygen production. They significantly contribute to carbon peaking and carbon neutrality goals. Accurate estimation of forest carbon stocks is essential for a precise understanding of the carbon sequestration capacity of forest ecosystems. Remote sensing technology, with its wide observational coverage, strong timeliness, and low cost, is essential for carbon stock estimation research. However, challenges in data acquisition and processing include data variability, signal saturation in dense forests, and environmental limitations. These factors hinder accurate carbon stock estimation. This review summarizes the current state of research on forest carbon stock estimation from two aspects, namely remote sensing data and estimation methods, highlighting both the advantages and the limitations of various data sources and models. It also explores technological innovations and cutting-edge research in the field, focusing on deep learning techniques, optical vegetation thickness estimation methods, and the impact of forest–climate interactions on carbon stock estimation. Finally, the review discusses the current challenges in the field, including issues related to remote sensing data quality, model adaptability, forest stand complexity, and uncertainties in the estimation process. Based on these challenges, the paper looks ahead to future trends, proposing potential technological breakthroughs and pathways. The aim of this study is to provide theoretical support and methodological guidance for researchers in related fields.

Keywords: data source synergy; estimation methods; deep learning; AI-driven innovation

Academic Editor: Nikolay S. Strigul

Received: 24 January 2025
Revised: 28 February 2025
Accepted: 28 February 2025
Published: 2 March 2025

Citation: Xu, W.; Cheng, Y.; Luo, M.; Mai, X.; Wang, W.; Zhang, W.; Wang, Y. Progress and Limitations in Forest Carbon Stock Estimation Using Remote Sensing Technologies: A Comprehensive Review. *Forests* **2025**, *16*, 449. https://doi.org/10.3390/f16030449

Copyright: © 2025 by the authors. Licensee MDPI, Basel, Switzerland. This article is an open access article distributed under the terms and conditions of the Creative Commons Attribution (CC BY) license (https://creativecommons.org/licenses/by/4.0/).

1. Introduction

Since the Industrial Age, the increased use of fossil fuels has led to a significant rise in greenhouse gas emissions, particularly carbon dioxide (CO_2), a key driver of global warming [1]. This disruption to the ecological balance poses a threat to human living conditions. In 2024, global CO_2 emissions are projected to reach 41.6 billion tons, exceeding

the 40.6 billion tons recorded in 2023, according to the "Global Carbon Project" in their Global Carbon Budget report [2]. Achieving the Paris Agreement's target of limiting the global temperature rise to well below 1.5 °C and implementing China's dual carbon strategy, which aims to peak carbon emissions by 2030 and achieve carbon neutrality by 2060, remain major challenges. Addressing global climate change requires not only reducing carbon emissions but also enhancing carbon sinks. Strengthening the resilience and stability of ecosystems is crucial to increasing their carbon sequestration capacity [3].

Forests, as the largest and most biologically diverse terrestrial ecosystems, have a unique capacity for carbon sequestration and oxygen production [4]. Through photosynthesis, trees absorb atmospheric CO_2 and store it in forest biomass, making them one of the most effective and economically viable methods to reduce atmospheric CO_2 levels [5]. However, forest carbon sequestration is influenced by forest dynamics and human activities. Forest carbon stocks and the carbon cycle are critical to understanding the role of terrestrial ecosystems in global carbon cycling and climate change [6]. Monitoring carbon stocks and their temporal changes is essential for reducing uncertainties in broader ecosystem carbon cycle models.

Traditional forest inventory methods, which measure tree height, diameter at breast height (DBH), and crown width within sample plots, provide accurate data on forest characteristics. These inventories have been used to develop and validate carbon stock estimation models [7]. For instance, Fang Jingyun et al. [8] utilized fifty years of China's continuous forest inventory data to assess changes in the country's forest carbon stocks from 1949 to 1998. Similarly, Andreas Margerl et al. [9] employed the United States' national, historical, and recent forest inventory data spanning from 1907 to 2012 to evaluate the dynamic variations in carbon content within the native forest ecosystems of the United States during this period. Despite their high accuracy, these traditional methods are time-consuming, labor-intensive, and require tree felling, which can damage ecosystems. Thus, these methods are not scalable or cost-effective for meeting growing demands for forest data.

With the widespread adoption of satellite remote sensing technology and the commercialization of geospatial data in the 1980s, this field has rapidly advanced [10]. However, beyond satellites, other platforms, like aircraft and unmanned aerial vehicles (UAVs), have also emerged as powerful tools in forest monitoring. Aircraft-based observational platforms provide higher spatial resolution and more flexible observation schedules compared to satellites, making them particularly useful for monitoring forest dynamics on a regional scale. UAVs, with their ability to fly at low altitudes, enable highly detailed measurements of forest structure and biomass, offering a cost-effective solution for local-scale monitoring and dynamic changes in forest carbon stocks. These platforms complement satellite data by filling gaps in spatial and temporal resolution, providing more accurate and timely estimates of carbon stocks [11]. Compared to traditional ground-based inventories, which are labor-intensive, time-consuming, and require tree felling, remote sensing platforms provide a more efficient and less invasive method for assessing forest structure and carbon content. Figure 1 illustrates this comparison, highlighting the strengths and limitations of both traditional and remote sensing methods in mapping forest carbon storage distribution.

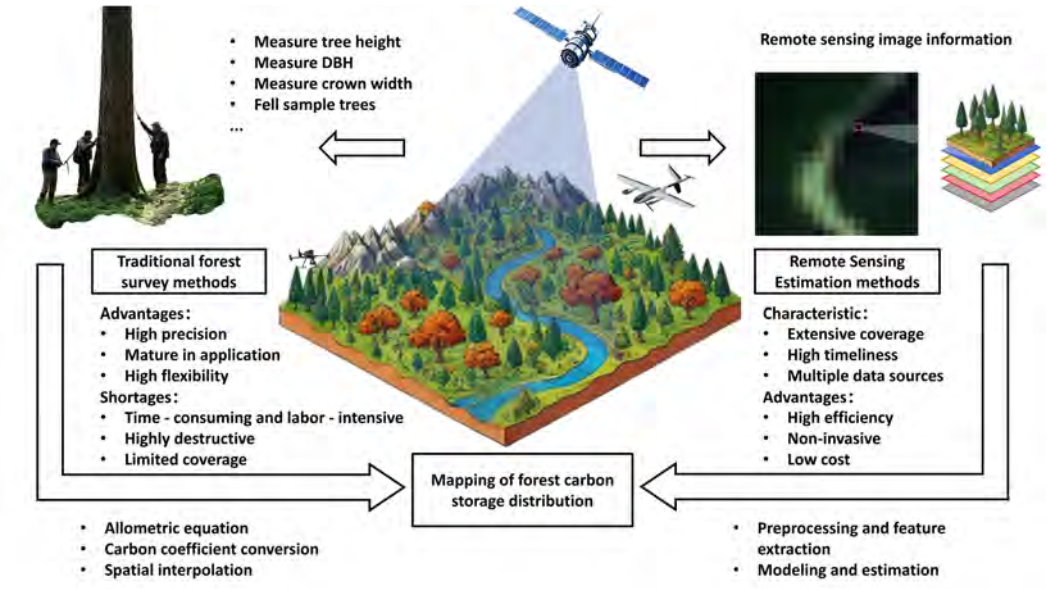


Figure 1. Comparison of traditional forest survey methods and remote sensing estimation methods for forest carbon storage mapping.

To comprehensively evaluate the estimation methodologies of carbon stocks utilizing observational technology, an extensive literature search was conducted on 10 December 2024 within the Web of Science Core Collection database. The search employed the keywords "forest carbon stocks" and "remote sensing". A total of 2191 publications, encompassing scientific research articles and other relevant online media literature published between 1999 and 2024, were systematically reviewed and analyzed. The findings were subsequently synthesized, highlighting the annual publication trends, the geographical distribution of research outputs, and the distribution across various academic journals, as illustrated in Figure 2.

Figure 2a illustrates a significant increase in both the number of studies and article citations concerning the estimation of forest carbon stocks using remote sensing technology from 2000 to 2024. Notably, since 2022, the annual publication count has exceeded 400 papers for three consecutive years, and the cumulative citation count has surpassed 15,000. This trend reflects the heightened global research activities related to forest aboveground biomass (AGB), driven by the emergence of environmental protection initiatives, such as the Paris Agreement and China's commitments to carbon peak and carbon neutrality. Figure 2b depicts the distribution of publications based on the country of the first author's institutional affiliation. The United States, China, and Germany are the leading contributors, with 1126, 1079, and 269 papers, respectively. Figure 2c presents the top 10 journals ranked by publication volume in this domain, highlighting highly esteemed journals in the field of remote sensing, including *Remote Sensing* (690 papers) and *Remote Sensing of Environment* (344 papers). These journals are recognized as primary platforms for disseminating research on forest carbon stock estimation and related remote sensing applications. These trends clearly demonstrate the critical role of remote sensing technology in advancing forest carbon monitoring.

With the advent of the era of big geospatial data and the advancement of sensor technologies, the volume of remote sensing data applicable to the estimation of forest carbon stocks is increasing exponentially [12]. Concurrently, developments in computer science have introduced novel methodologies for constructing estimation models [13,14]. Remote sensing data serve as the foundational observational information, while estimation techniques are employed to analyze and infer carbon stocks based on this data.

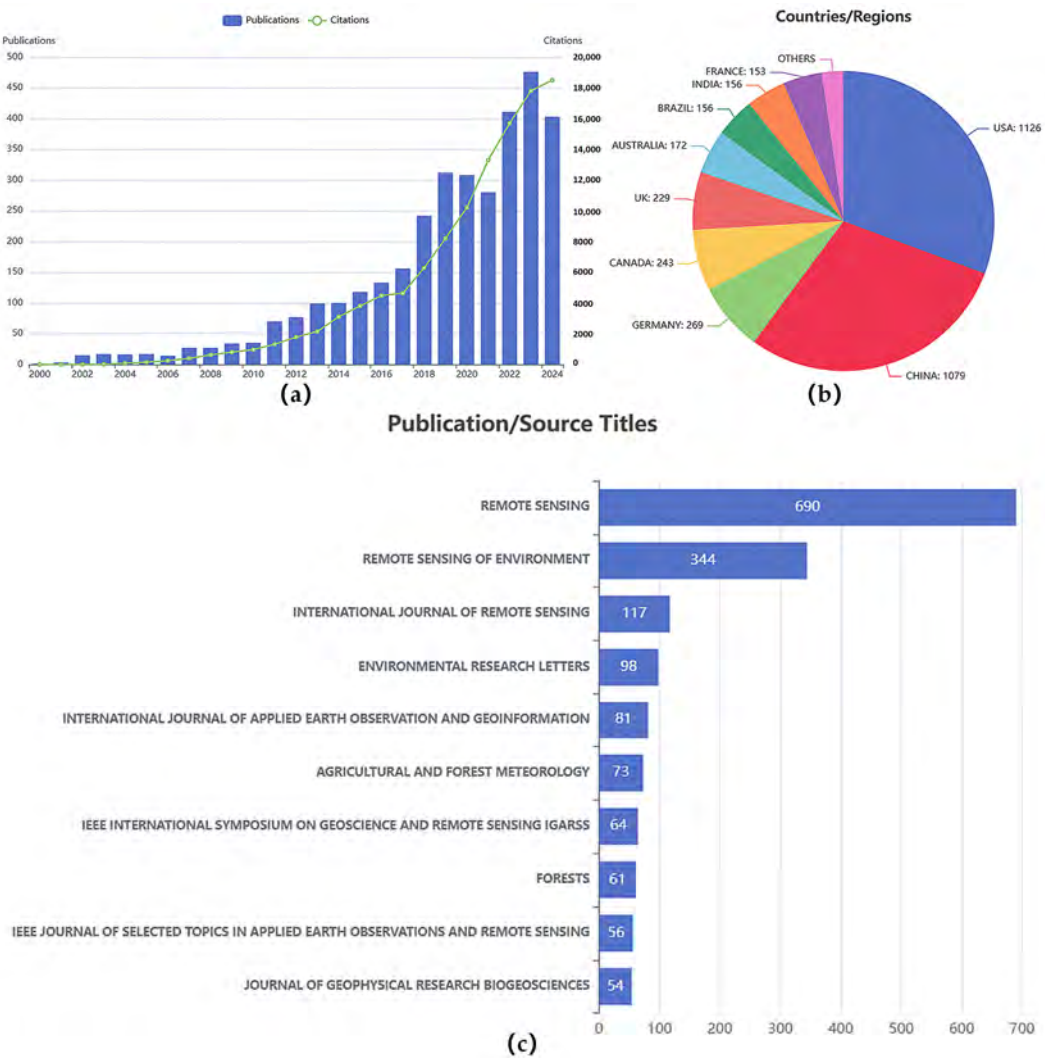


Figure 2. Trends, geographic distribution of the authors or research institutions, and source titles of publications on forest carbon stock estimation using remote sensing. (**a**) Annual number of publications and citations from 2000 to 2024, showing a significant increase in both over time. (**b**) Distribution of publications by country/region, highlighting major contributing countries such as the USA and China. (**c**) Top publication sources, listing the most frequently appearing journals in this research field, with "Remote Sensing" leading the count.

This paper aims to fill gaps in the current literature by providing a comprehensive review of remote sensing-based forest carbon storage estimation, focusing on technological advances and the limitations inherent in current methodologies. Furthermore, the paper will discuss how current methods can be better applied in real-world contexts, such as climate policy formulation and forest management practices, where precise carbon stock data are crucial for informed decision-making. By presenting an in-depth overview of these areas, this study seeks to supplement existing knowledge and provide insights into future research directions. The ultimate goal is to offer a more nuanced understanding of the challenges in remote sensing-based carbon stock estimation and to propose potential solutions that could advance both theoretical and practical applications of this field.

2. Remote Sensing Data Sources

Remote sensing data can be categorized into optical, synthetic aperture radar (SAR), and light detection and ranging (LiDAR) data based on the sensor type used [15]. These

datasets, with varying spatial resolutions and spectral bands, support the estimation of forest carbon stocks.

2.1. Optical Data

Optical remote sensing data are crucial for estimating forest carbon stocks due to variations in reflectance spectral curves across plant species in the visible and near-infrared (NIR) bands. Even within a single species, reflectance can fluctuate based on environmental conditions and phenological stages [16]. These spectral characteristics enable continuous monitoring of plant growth and accurate carbon stock estimation, establishing optical data as a widely used modality in forest carbon stock research. Common reflectance indices, such as the normalized difference vegetation index (NDVI), are used to assess vegetation health and biomass [17], while the enhanced vegetation index (EVI) improves upon the NDVI by reducing atmospheric and soil noise. The photochemical reflectance index (PRI) offers insights into plant photosynthetic activity, further enhancing carbon stock estimation accuracy. Optical data are primarily categorized into multispectral and hyperspectral data.

2.1.1. Multispectral Data

The use of optical remote sensing for carbon stock estimation began in the 1970s, initially with single-band imagery. However, the accuracy of early methods was impacted by atmospheric conditions, soil characteristics, and sensor performance. The use of multispectral data, combining multiple spectral bands, improved accuracy by better correlating with forest biomass and carbon stocks [18]. Today, multispectral datasets, such as Landsat, WorldView, and the GF series, are widely used in forest carbon stock estimation. These datasets are commonly processed using regression techniques that model relationships between carbon stocks and spectral, terrain, and texture variables.

Advancements in sensor technology have led to higher spatial resolution imagery, which aids in classification tasks, such as tree species identification, improving carbon stock estimations [19]. However, high-resolution imagery often lacks comprehensive spectral information, and its higher cost and susceptibility to weather conditions present challenges in practical applications [20].

2.1.2. Hyperspectral Data

Hyperspectral data capture biophysical and chemical characteristics more precisely than multispectral data, making them valuable for carbon stock estimation. Hyperspectral technology originated from the imaging spectrometer research program in the United States. It was first proposed by researchers at the Jet Propulsion Laboratory of the California Institute of Technology and has since made significant advancements with the support of NASA [21]. Compared to multispectral data, hyperspectral data offer the capability to capture biophysical and chemical characteristics across various temporal and spatial scales, utilizing finer spectral resolution bands and providing more comprehensive spectral information [22]. Additionally, the utilization of narrow-band vegetation indices derived from hyperspectral data can mitigate the effects of atmospheric and water absorption, as well as address the saturation issues associated with broadband vegetation indices [23].

However, the large number of spectral bands in hyperspectral data can lead to redundancy, increasing processing and storage costs. Additionally, hyperspectral sensors are more susceptible to atmospheric conditions, requiring rigorous correction techniques to ensure accurate data [22]. Despite these challenges, hyperspectral data provide significant potential for enhancing carbon stock estimates.

2.1.3. Progress in Forest Carbon Stock Estimation Based on Optical Data

Optical data were first applied to the estimation of biomass and carbon stocks, extracting vegetation parameters from images, generating values indicative of biomass through band calculations, and using this information to estimate aboveground biomass of forests (Table 1). This approach is widely used because of its simplicity and high estimation accuracy.

Table 1. Recent studies on forest carbon stock estimation using optical data.

Study	Study Area	Data Source	Highlight	Accuracy	Mothed
Halme et al. [24]	Hyytialä Station, Finland (*boreal coniferous forest*)	AISA: 0.7 m; Sentinel-2: 10 m	Hyperspectral data improve LAI estimates, while Sentinel-2 provides similar accuracy for height, basal area, and biomass.	R^2 = 0.63 RMSE = 21.46	SVR, GPR, 120 plots, 5-fold cv
Verly et al. [25]	Federal University of Viçosa, Brazil (*montane semi-deciduous forest*)	Sentinel-2: 10 m	Vegetation indices did not improve carbon prediction, but rainy-season spectral variables (blue, green, red, NIR) enhanced accuracy.	R = 0.9871 RMSE = 4.1696	Artificial neural networks selection, 30 plots
Li et al. [26]	Hunan Province, China (*subtropical evergreen broadleaf forest*)	Landsat 8 OLI: 30 m	Seasonal Landsat 8 imagery yielded varied forest AGB estimates and highlighted uncertainties in biomass estimation.	R^2 = 0.55 RMSE = 19.45	Stepwise regression, 5-fold cv, 303 plots
Sa et al. [27]	Saihanba Forest, Hebei, China (t*emperate coniferous forest*)	Sentinel-2: 10 m; Landsat 8 OLI: 30 m	The new vegetation and texture ratio indices outperform traditional methods in accurately reflecting forest changes and estimating canopy closure, basal area, and AGB.	R^2 = 0.6991 RMS = 3.2687	Linear regression, 65 plots

However, there are still certain limitations in the application of optical data in the study of forest carbon stock estimation. Firstly, optical images may experience a decline in image quality and data loss due to differences in sunlight and cloud interference. Secondly, optical data mainly acquire spectral information within the ground area covered by the image, only providing information on the horizontal distribution of the forest, but do not offer vertical distribution information. Finally, in areas with high forest canopy density and accumulation, optical data may exhibit oversaturation, resulting in a lower estimation of carbon stocks.

2.2. SAR Data

SAR data offer advantages over optical data, including a broader wavelength range, enhanced penetration, and reduced susceptibility to weather conditions, making them valuable for forest carbon stock estimation [28]. SAR data allow for the acquisition of vertical structural information about forests, which is critical for accurate carbon stock calculations [29].

2.2.1. Classification of SAR Data

SAR data can be classified based on polarization modes, frequency bands, and scattering mechanisms [30], with each offering distinct benefits for carbon stock estimation.

- Polarization mode: Single polarization provides basic forest coverage and structural classification. Dual polarization improves vegetation type differentiation and biomass estimation, while full polarization enables precise biomass and carbon stock estimation, particularly in complex forests. Cross-polarization increases sensitivity to volume scattering, beneficial for dense forest structures [31].

- Frequency bands: The P-band and L-band are best for estimating biomass and tree trunk data due to their strong penetration capabilities [32]. The C-band and X-band are used for monitoring forest canopy structures [33], while the Ku-band and Ka-band, which are more suited for monitoring forest health, are less effective for direct carbon stock estimation [34].
- Scattering mechanisms: Volume scattering is key for evaluating forest density and biomass, while double scattering helps estimate trunk density in densely vegetated areas. The backscattering coefficient, influenced by forest structure, aids in inferring biomass and forest health [35].

By utilizing these different classifications, SAR data provide a comprehensive approach to estimating forest carbon stocks, offering detailed insights into forest structure and biomass.

2.2.2. Estimation of Forest Carbon Stocks Using Multi-Frequency SAR Data Synergy

Recent advancements in SAR technology allow for multi-frequency data integration, enhancing the accuracy of forest carbon stock estimations. Polarimetric interferometric SAR, when combined with interferometric phase data, helps delineate the three-dimensional structure of forests, particularly the vertical distribution of tree heights [36]. These 3D structural data are essential for precise biomass and carbon stock estimation [37].

The use of multi-frequency SAR data also addresses the limitations of optical data, which struggles under rainy or cloudy conditions, enhancing the reliability of forest carbon estimates. Additionally, the robustness of SAR data against atmospheric disturbances allows for continuous, reliable monitoring of forest ecosystems, improving long-term forest management and climate mitigation efforts.

2.2.3. Progress in Forest Carbon Stock Estimation Based on SAR Data

SAR data can provide high-quality surface cover information under various weather conditions and is unaffected by cloud cover and precipitation, making it particularly suitable for estimating forest carbon stocks. Through multi-temporal analysis of SAR data, it is possible to effectively monitor changes in forest structure, improving the accuracy and timeliness of carbon stock estimation. Table 2 summarizes recent studies on forest carbon stock estimation using SAR data.

Table 2. Recent studies on forest carbon stock estimation using SAR data.

Study	Study Area	Data Source	Accuracy	Highlight	Parameters	Verification
Li et al. [38]	Monda test site near the equator	F-SAR	$R^2 = 0.947$	Developed a TomoSAR-based approach to estimate tropical forest AGB by extracting vertical structural parameters, including under-canopy terrain, vertical backscatter power, canopy height, and total canopy backscatter power.	HH, HV, VV	Existing inventory data
Hu et al. [39]	Saihanba Forest, Hebei, China	GF-3, ALOS-PALSAR	$R^2 = 0.93$	Combining C- and L-band data provides a more comprehensive representation of forest canopy information, enhancing the saturation point in biomass estimation.	HH, HV, VH, VV; wavelength = 5.5 cm, incidence angle = 21.3°; wavelength = 23.6 cm, incidence angle = 27.8°	Field data from 50 plots
Ali et al. [40]	Hardevan Forest, India	TanDEM-X, ALOS-PALSAR	$R^2 = 0.704$	Utilized time series L-band backscatter data to assess the impact of different polarizations on the accuracy of AGB	HH, HV, VH, VV	Field data from 60 plots

Ramachandran et al. [41]	Palaku Moist Tropical Forest, French Guiana	TropiSAR	$R^2 = 0.89$	and forest height estimates, enabling their joint inversion. TomoSAR is promising for AGB estimation compared to LiDAR; their combination facilitates regional and global AGB mapping.	HH, HV, VH, VV; wavelength = 0.75 cm, incidence angle = 24–62°	Airborne LiDAR and inventory data

Despite the advantages of SAR images in data acquisition and carbon stock estimation, the associated data processing procedures are complex. SAR data also show limited sensitivity to vegetation type variations. In areas with complex terrain, such as mountainous regions, radar signals are affected by terrain undulations, leading to terrain-induced deviations in radar echo intensity. These effects can hinder the accurate estimation of forest structure and biomass, especially in steep regions. Furthermore, the backscattering coefficient, commonly used in SAR data applications, can produce inaccurate results due to its sensitivity to changes in forest structure and aboveground biomass. While SAR performs well in estimating carbon stocks in low-density forests, its effectiveness diminishes in high-density forests, where the correlation between radar backscatter and biomass weakens, leading to saturation effects. These challenges highlight the need for advanced processing techniques and integrated approaches to improve the accuracy and reliability of SAR-based forest carbon stock estimations, especially in dense and topographically complex forest ecosystems.

2.3. LiDAR Data

LiDAR is an active remote sensing technology that efficiently captures precise three-dimensional spatial data by emitting laser pulses and detecting their reflected signals [42]. It is particularly advantageous for estimating forest carbon stocks due to its ability to accurately capture vertical forest structure and overcome signal saturation issues typical of optical and SAR data. These capabilities significantly improve biomass and carbon sequestration assessments, providing more reliable and detailed information. LiDAR's high spatial resolution aids in developing advanced models for forest structure analysis, making it a key tool in forest management and climate change mitigation strategies [43].

2.3.1. Airborne LiDAR

Airborne LiDAR, deployed on aircraft or UAVs, offers high-precision three-dimensional measurements of forest ecosystems [44]. It has become an essential tool for estimating forest carbon stocks due to its superior spatial resolution and coverage compared to traditional methods. Airborne LiDAR efficiently surveys inaccessible areas, capturing detailed structural information, such as canopy height, density, and understory terrain. This enables accurate biomass estimation, differentiation of forest types, and analysis of forest gaps and edges, which often have significantly different carbon stock values [45]. Furthermore, UAV technology advancements and reduced laser costs have made airborne LiDAR more accessible, expanding its application in complex, large-scale terrains [46].

2.3.2. Spaceborne LiDAR

Spaceborne LiDAR, mounted on satellites, provides large-scale, high-precision measurements of the Earth's surface, including forest vertical structures [47]. Its ability to cover vast areas from orbit makes it ideal for regional and global carbon stock monitoring. Spaceborne LiDAR can measure parameters, such as canopy height and area, helping to distinguish between forest types and estimate biomass [48]. This technology supports global carbon stock assessments, especially in remote or difficult-to-reach areas, like tropical rainforests [49]. Notable missions, such as NASA's GEDI and ICESat-2, are advancing

forest structure data acquisition, refining global carbon cycle models, and enhancing our understanding of forests' role in climate regulation.

2.3.3. Progress in Forest Carbon Stock Estimation Based on LiDAR Data

LiDAR, as an advanced active remote sensing detection method, operates by independently emitting laser pulses toward target ground objects and analyzing the returned signals to obtain precise measurements of stand height and vertical forest structure. This capability distinguishes LiDAR from other remote sensing technologies, enabling the acquisition of detailed three-dimensional information that is unattainable through alternative methods. Table 3 presents recent studies on forest carbon stock estimation using LiDAR data.

Table 3. Recent Studies on Forest Carbon Stock Estimation Using LiDAR Data.

Study	Study Area	Data Source	Accuracy	Highlight	LiDAR Parameters	LiDAR-Derived Metrics
Bazezew et al. [50]	Aye Xitan Tropical Rainforest Reserve, Malaysia	ALS, TLS	$R^2 = 0.96$	Integrating ALS and TLS data estimates tropical forest AGB more accurately than traditional field methods, reducing underestimation and improving carbon stock assessments.	Pulse rate = 70 kHz and 240 kHz, scan angle = 60°, laser points/m² = 5 to 6 points with 808 m to 1155 swath width	CHM
Zhou et al. [51]	Zhejiang A&F University, China	ULS	$R^2 = 0.85$	Proposed a voxel-coupled convex hull slicing algorithm to calculate individual tree 3D foliage volume by splitting crown point clouds by height and applying distinct volume calculations, enhancing estimation accuracy.	----------	Height-related metrics, density-related metrics, canopy-related metrics
Beyene et al. [52]	Pudu, Selangor, Malaysia	TLS	$R^2 = 0.98$	TLS surpasses optical remote sensing and traditional methods in acquiring tropical forest parameters by offering higher tree detection rates, precise DBH and tree height measurements, and reliable AGB estimations.	Laser wavelengths (1550 nm) and has a measurement ranging from 1.5 to 600 m.	CHM,DBH
Tian et al. [53]	Ejina Banner, Inner Mongolia, China	ICESat, Geoscience Laser Altimeter System	$R^2 = 0.741$	Developed the CHL-BEM biomass estimation model, which integrates vertical canopy structure and horizontal canopy cover information, outperforming traditional models that use only average or maximum tree height.	Laser wavelengths = 1064 nm (near-infrared, NIR), 532 nm (green light); pulse repetition rate: 40 Hz	CTH,CC

However, LiDAR also presents certain limitations in its application. Typically, LiDAR data acquisition is conducted via airborne platforms (such as aircraft and unmanned aerial vehicles) or ground-based systems, resulting in relatively limited coverage and posing challenges for large-scale, rapid monitoring of extensive forested areas. Even with spaceborne LiDAR platforms, like NASA's GEDI, the spatial resolution remains insufficient for high-precision forest carbon stock estimations. Additionally, LiDAR data are inherently high-precision three-dimensional point clouds, which entail substantial data volumes. The processing and analysis of such data are complex and necessitate specialized software and significant computational resources for tasks including data preprocessing, feature extraction, and modeling. This complexity is particularly pronounced when handling large-scale datasets, making the processing time-consuming and resource-intensive. Consequently, while LiDAR offers unparalleled accuracy and detail in forest structure measurements, its limitations in coverage, spatial resolution, and data processing complexity must be addressed to fully leverage its potential in forest carbon stock estimation.

2.4. Multi-Source Remote Sensing Data

The application of remote sensing data sources—optical, SAR, and LiDAR—has proven effective in forest carbon stock estimation, with each offering distinct advantages. However, each approach also has limitations that can impact the accuracy and comprehensiveness of carbon stock models. To overcome these challenges, integrating multi-source remote sensing data has emerged as a promising solution. By combining the complementary strengths of these data types, it provides more robust and reliable carbon stock estimates. The following table compares the three data types, highlighting their suitability for different forest types and the technical considerations involved in carbon estimation. A comparative analysis of optical, SAR, and LiDAR data for forest carbon stock estimation is presented in Table 4.

Table 4. Comparison of optical, SAR, and LiDAR data for forest carbon stock estimation.

Feature	Optical Data	SAR Data	LiDAR Data
Strengths	High spatial resolution, suitable for capturing spectral information and vegetation indices	Effective in all weather conditions, can penetrate clouds, suitable for nighttime	Provides accurate 3D forest structure measurements, including canopy height and density
Limitations	Limited penetration ability, struggles with dense vegetation, affected by atmospheric conditions (e.g., clouds)	Lower spatial resolution, data interpretation is challenging, less effective in dense forests	High data acquisition cost, limited by scanning angles, requires specialized equipment
Sensitivity to vegetation structure	Sensitive to canopy characteristics (e.g., leaf area index, canopy coverage, and biomass)	Sensitive to surface roughness and vegetation structure, including biomass	Sensitive to canopy height, vertical structure, and topography
Applicable forest types	Suitable for open woodlands, low-density forests, grasslands, and agricultural areas (e.g., tropical and temperate forests)	Suitable for dense forests, wetlands, forest edges, humid regions, effective in subtropical and high-latitude forests	Suitable for high-density forests, tropical rainforests, coniferous forests, and regions with complex forest structures
Technical requirements	Moderate, typically requires image processing and atmospheric correction	High, requires radar signal processing, polarization handling, and efficient interpretation techniques	High, requires LiDAR equipment, point cloud processing, and 3D modeling software
Data acquisition cost	Low, many satellite data available for free (e.g., Landsat, Sentinel)	Moderate, mainly relies on satellite or dedicated radar platforms, some data available publicly	High, requires specialized equipment (airborne or satellite LiDAR), high data acquisition and processing costs

Data fusion techniques, such as pixel-level fusion, feature-level fusion, and decision-level fusion, combine multiple remote sensing data sources into a single, integrated model. This approach enhances the ability to estimate forest carbon stocks by leveraging the unique strengths of each data type simultaneously [54]. Pixel-level fusion merges raw image data from different sensors, allowing for the creation of higher-dimensional data that captures more detailed information on forest structure and biomass. Feature-level fusion, on the other hand, integrates specific features or attributes extracted from each dataset, providing a more comprehensive view of forest dynamics. Decision-level fusion synthesizes the results from separate models, producing a final estimation of forest carbon stocks that incorporates the diverse perspectives offered by each dataset. The integration of these data sources allows for a more accurate and robust estimation of carbon stocks by incorporating complementary information on forest structure, vegetation cover, and environmental conditions. For example, while LiDAR data excel at capturing vertical structure and canopy height, optical data can provide rich spectral information for vegetation classification, and SAR data can offer insights into forest moisture and roughness. The fusion of these datasets creates a more complete representation of forest ecosystems, addressing gaps left by individual sensors. This approach not only improves the precision of biomass and carbon stock estimates but also enhances the adaptability of models to

varying forest types and environmental conditions. By synthesizing the strengths of each sensor type, data fusion techniques significantly contribute to more reliable and scalable remote sensing-based assessments of forest carbon stocks.

To systematically investigate the utilization of multi-source remote sensing data in forest carbon stock estimation, an online scientific literature search was conducted in the Web of Science Core Collection using the keywords "forest carbon stocks", "remote sensing", and "multi-source data". These search terms were specifically chosen to identify studies that employed combinations of different remote sensing data sources for mapping forest carbon stocks or biomass. From this search, 31 papers published between 2019 and 2024 were selected [55–85], focusing on the data sources utilized in multi-source remote sensing-based forest carbon stock estimations. The distribution and usage patterns of various remote sensing data types in these studies are illustrated in Figure 3.

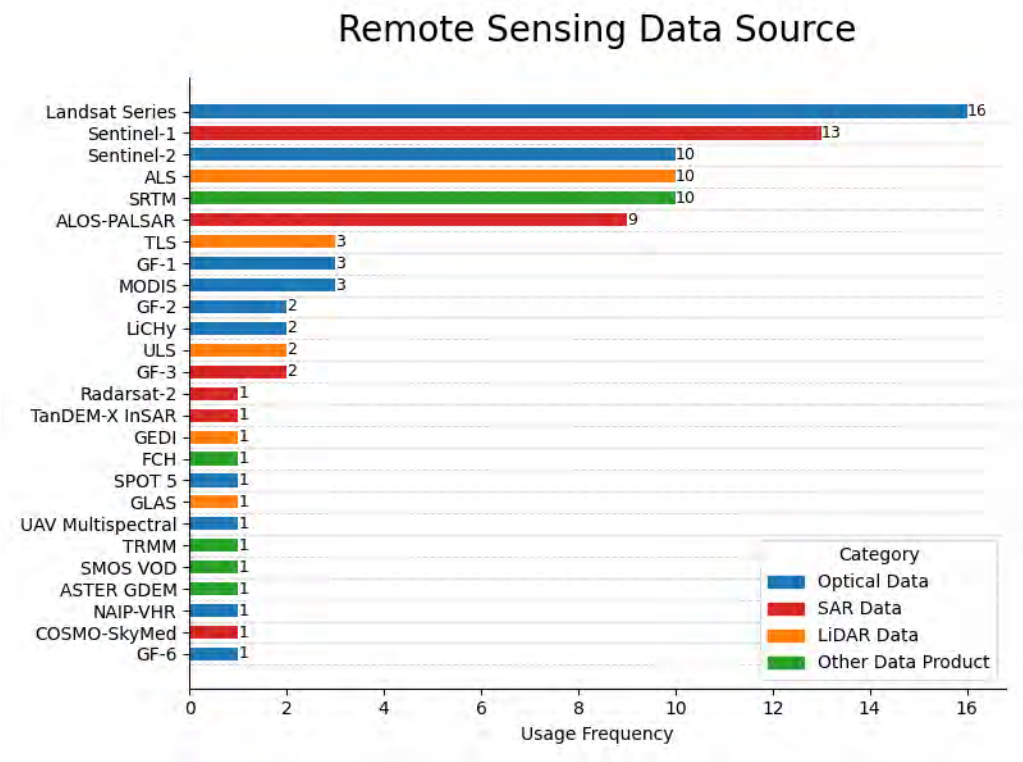


Figure 3. Frequency of remote sensing data sources used in forest carbon stock estimation studies.

According to the statistical analysis of the reviewed literature, among the 31 selected studies, Landsat 8, Sentinel-1, Sentinel-2, airborne laser scanning (ALS), Shuttle Radar Topography Mission (SRTM) and ALOS-PALSAR data sources exhibit high occurrence frequencies. Notably, Landsat series satellite data (such as Landsat 8), Sentinel series satellite data (Sentinel-1 and Sentinel-2), advanced land observing satellite phased-array-type L-band synthetic aperture radar (ALOS-PALSAR), and SRTM data are primarily provided by governmental agencies or related institutions, allowing free access to users and thereby reducing research costs. The maturity of the data processing methods and the availability of supporting software further facilitate widespread utilization among researchers. Additionally, these data sources offer extensive coverage suitable for global or large-area forest carbon stock estimation studies across various scales.

ALS is extensively employed in numerous studies due to its ability to directly acquire three-dimensional spatial information of forests, including tree height, canopy height, and canopy volume. These detailed structural parameters are essential for accurately estimat-

ing forest biomass. With the ongoing advancements in remote sensing technology, an increasing number of sensors and data sources have become available. For instance, China's Gaofen series satellites, which encompass multiple satellite types with high spatial, temporal, and spectral resolutions, such as GF-1, GF-2, and GF-3, have been utilized in many studies [86,87]. Additionally, terrestrial laser scanning (TLS), unmanned laser scanning (ULS), and ALS are employed to collect LiDAR data, thereby enhancing the acquisition of comprehensive forest parameters. TLS provides detailed information on lower forest structures, while ALS or ULS offers large-scale forest canopy data [88]. The integration of these three LiDAR technologies enables a more comprehensive description of forest structures and mitigates the limitations associated with lower canopy point cloud deficiencies. This comprehensive approach is suitable for forest areas of varying scales and complexities, meeting the requirements for high-precision estimations in localized regions as well as large-scale forest monitoring. Despite their unique advantages, these new data sources may present challenges related to data acquisition difficulty, higher costs, processing complexity, and lower application maturity, resulting in limited widespread usage. In contrast, the aforementioned commonly used data sources strike an optimal balance between technical feasibility, data quality, and accessibility, thereby dominating current research endeavors.

Among the collected studies on forest carbon stock estimation based on multi-source remote sensing data, the studies summarized in Table 5 have achieved commendable results.

Table 5. Recent studies on forest carbon stock estimation using multi-source remote sensing data.

Study	Study Area	Data Source	Accuracy	Highlight	Fusion Method	Verification
Han et al. [56]	Dabie Mountain Region, China	GF-1, Sentinel-1, SRTM	$R^2 = 0.70$	GF1's NDVI, blue band, and red band texture were significantly correlated with AGB, and elevation was significantly positively correlated with AGB.	Feature-level integration	10-fold cv
Mohite et al. [69]	Forest of India	GEDI, Sentinel-2, Sentinel-1, SRTM	$R^2 = 0.74$	Combined GEDI LiDAR with multi-source satellite and forest soil data to achieve large-scale spatial mapping of forest AGB in India, enhancing forest carbon stock monitoring.	Feature-level integration	5-fold cv
Li et al. [72]	Daxinganling Region, China	Sentinel-1, Sentinel-2, ALOS-PALSAR, SRTM	$R^2 = 0.67$	Compared four data types and their combinations. Found that combining optical and microwave remote sensing with terrain data were most effective for AGB estimation.	Feature-level integration	10-fold cv
Ayushi et al. [73]	Tropical forests of the BRT Tiger Reserve, Indian	Sentinel-1, Sentinel-2, SRTM	$R^2 = 0.82$	Emphasized integrating multi-source auxiliary datasets, providing new approaches for biomass mapping in heterogeneous landscapes.	Feature-level integration	10-fold cv

It is evident that the fusion of multi-source remote sensing data positively enhances the accuracy of forest carbon stock estimations. However, the integration of diverse data types poses several challenges. One of the primary issues is the disparity in spatial and temporal resolution across different data sources, which can lead to misalignment and inconsistencies during fusion [89]. Additionally, the varying data processing techniques and calibration requirements for each data type further complicate the fusion process, leading to potential errors in the final carbon stock estimations. To address these challenges, advanced data preprocessing and normalization methods can align datasets, while machine learning techniques can automate the fusion process. Calibration with ground-

truth data and the use of robust fusion algorithms further improve accuracy and reliability in forest carbon stock estimations.

3. Estimation Methods of Forest Carbon Stocks Based on Remote Sensing Technology

The choice of estimation methodology is critical for forest carbon stock estimation, impacting both the accuracy and applicability of models. Estimation methods can be broadly categorized into two types: empirical models and process-based models [90]. Empirical models use statistical relationships between remote sensing data and measured carbon stocks [91], while process-based models simulate biological and physical carbon dynamics within forest ecosystems [92].

3.1. Empirical Models

Empirical models offer an efficient approach for estimating forest carbon stocks, leveraging remote sensing data to establish statistical correlations with biomass and carbon stock measurements [93]. These models are particularly useful for large-scale carbon stock assessments, providing a broad overview of carbon distribution. The key variables used for estimation vary depending on the type of remote sensing data:

- Optical data: Vegetation indices (e.g., NDVI, EVI) and band reflectance are commonly used to estimate biomass [94]. Band combinations and spectral texture features help identify relationships between spectral properties and forest biomass [95].
- SAR data: The backscattering coefficient is a critical variable, providing insights into forest structure and biomass. Polarization modes (e.g., HH, HV, and VV) offer information about different canopy layers and forest density.
- LiDAR data: Key variables, such as canopy height, density, and three-dimensional structural metrics (from LiDAR point clouds) are used to estimate forest biomass and carbon stocks [96]. LiDAR data's ability to capture detailed vertical and horizontal forest structure enhances the accuracy of these estimates [97].

Traditional empirical regression models and machine learning models are two prominent methods used for these estimations. Regression models, including linear, polynomial, and stepwise regressions, assume fixed relationships between variables and are easy to implement, but they may struggle with complex, nonlinear forest dynamics. Machine learning approaches, such as decision trees and neural networks, capture more complex relationships and offer higher accuracy but require large datasets and careful tuning.

3.1.1. Traditional Empirical Regression Model Methods

Traditional empirical regression models—such as linear regression, polynomial regression, ridge regression, LASSO regression, stepwise regression, and geographically weighted regression (GWR)—are widely used for forest carbon stock estimation. These models offer simplicity and efficiency, particularly in environments with extensive ground-truth data.

- Linear regression establishes a direct relationship between dependent and independent variables, but struggles with nonlinear relationships [98].
- Polynomial regression extends linear models to capture nonlinear patterns but may overfit with higher polynomial degrees [99].
- Ridge and LASSO regression introduce regularization to improve model robustness by preventing overfitting [100,101].
- Stepwise regression automates variable selection, improving simplicity and explanatory power [102].

- GWR accounts for spatial heterogeneity by allowing local variations in regression coefficients, enhancing model accuracy in spatially diverse environments [103].

While traditional empirical regression models offer efficiency, they have limitations. They generally assume fixed relationships between variables, which are insufficient for capturing the complex, nonlinear dynamics in forest ecosystems. Additionally, they are sensitive to data quality and outliers, reducing model reliability. The generalizability of these models is also limited, requiring recalibration for different regions or forest types.

3.1.2. Machine Learning Methods

The advancement of computer science has facilitated the emergence of novel methodologies for establishing carbon stock estimation models, with machine learning (ML) standing out as a prominent branch of artificial intelligence dedicated to developing algorithms that autonomously learn and improve from data [104]. To better understand the key differences between traditional empirical regression models and machine learning-based approaches, a comparison of their main features is presented in Table 6.

Table 6. Comparison of traditional empirical regression models and machine learning models for forest carbon stock estimation.

Feature	Traditional Empirical Regression Models	Machine Learning Models
Model assumptions	Assumes fixed relationships between independent and dependent variables, usually linear or simple nonlinear	Does not require explicit assumptions about the relationship between variables, capable of capturing complex nonlinearities
Flexibility and adaptability	Less flexible, inadequate for capturing complex, nonlinear dynamics in forest ecosystems	Highly flexible, adaptable to complex, dynamic data, capable of modeling nonlinear and time-varying patterns
Data requirements	High-quality data required, sensitive to outliers	Lower data quality requirements, can handle missing values and outliers
Computational complexity	Relatively low, simple computation, suitable for small datasets	High computational complexity, especially when dealing with large datasets, may require more computational resources
Applicability	Typically suited for smaller datasets or simpler scenarios, often used for standard forest carbon stock estimation	More suitable for large datasets and complex problems, such as multi-source remote sensing data and varying forest types

Among the various ML algorithms, random forest regression and extreme gradient boosting (XGBoost) are particularly prominent in forest carbon stock estimation.

Random forest regression is an ensemble method that constructs multiple decision trees and aggregates their predictions [105]. This algorithm excels at handling complex, nonlinear relationships and is robust to data noise, missing values, and high-dimensional feature spaces. It is highly generalizable, making it suitable for diverse forest carbon stock estimation scenarios. Recent advancements, such as geographically weighted random forest regression [106] and Bayesian kriging integrations [107], have further improved its accuracy in carbon stock estimation.

XGBoost, another powerful ML algorithm, is based on ensemble learning and gradient boosting principles [108]. It builds multiple decision trees and combines them through weighted summation, while regularization techniques control model complexity. XGBoost is particularly effective at managing nonlinear relationships between carbon stocks and forest structural features, offering high estimation accuracy and strong potential for forest carbon stock applications [109].

Additionally, other machine learning algorithms have been successfully applied to forest carbon stock estimation, achieving commendable results alongside the previously mentioned random forest and XGBoost algorithms, as summarized in Table 7.

Table 7. Recent studies on forest carbon stock estimation using machine learning methods.

Study	Study Area	Algorithm	Accuracy	Highlight	Verification
Singh et al. [110]	Dhanbad Region, Jharkhand, India	GAMM, K-NN, SVM, ANN, RF	RF: adjusted $R^2 = 0.91$	Integrated machine learning and field surveys enable finer-scale AGB estimation, highlighting new spectral bands' benefits and the importance of uncertainty mapping for enhanced prediction accuracy.	Field data from 106 plots, 5-fold CV
Fararoda et al. [111]	Forests of India	RF	$R^2 = 0.89$	First use of multi-source data and machine learning to estimate aboveground biomass in Indian forests, overcoming single-sensor saturation in high biomass areas and improving accuracy.	Inventory data, 10-fold CV
Qadeer et al. [112]	Diamir District, Gilgit-Baltistan, Pakistan	RF, GTB, CatBoost, LightGBM, XGBoost	LightGBM: $R^2 = 0.734$	Assessed ML algorithms for AGB prediction in complex terrains. LightGBM and XGBoost performed best with specific datasets, handling nonlinearities and improving accuracy.	Field data from 171 plots
Li et al. [113]	Chenzhou, Hunan, China	LR, RF, XGBoost	XGBoost: $R^2 = 0.75$	Examined the importance of parameter optimization in machine learning algorithms.	Inventory data, 10-fold CV

Despite the proven potential of ML methods in forest carbon stock estimation, their application is often limited to specific regions and forest types [114]. A major challenge is the lack of calibrated data across different environmental conditions, which hinders the transferability of models. This makes it difficult to apply models trained in one region to others with different ecological contexts. Additionally, ML models face issues, such as overfitting, where models become overly complex and fit data noise rather than underlying trends. Data bias, arising from limited or unrepresentative training datasets, can further degrade model performance in diverse ecological settings. Moreover, the high computational costs of training sophisticated ML models, especially with large-scale, high-resolution datasets, can pose barriers. To improve model generalization, future research should focus on developing more versatile ML models that can better adapt to varying environmental conditions, address data calibration challenges, and mitigate overfitting and bias [115]. These improvements would enhance the scalability and applicability of ML models for global forest carbon stock estimation.

3.1.3. Limitations of Empirical Models

Empirical models, including traditional regression models and machine learning approaches, are effective in directly estimating forest carbon stocks by capturing statistical relationships between explanatory variables and observed carbon stocks from sample plots. These models can be used to estimate carbon stocks in unmeasured areas, often providing satisfactory fitting accuracy. However, their performance is limited by the inherent challenges of remote sensing data, such as climatic conditions, sensor calibration, and viewing angles. Issues, like cloud cover, atmospheric disturbances, and image noise, can degrade data quality, affecting the precision of model inversions. Additionally, direct inversion models, which rely on statistical correlations, lack a mechanistic understanding of the biophysical processes driving carbon cycling. This limits their ability to explain the

factors influencing carbon stock changes or predict future trends accurately. The applicability of these models is also constrained by the availability of observational data, making them less effective in regions or time periods outside the scope of the training datasets. Consequently, the extrapolation performance of these models decreases when applied to different forest types or regions with varying climatic conditions, limiting their generalizability and predictive accuracy.

3.2. Estimation of Forest Carbon Stocks Using Process Models

While direct estimation methods, such as field-based measurements of DBH, height, and stand density, are straightforward, they are often limited by spatial heterogeneity and measurement errors. Furthermore, these methods struggle to capture the dynamic ecological processes that govern forest ecosystems.

To address these limitations, process-based models have emerged. Unlike empirical models, process-based models simulate carbon cycling within forest ecosystems, considering interactions between climate, soil, and forest management practices [116]. These models offer more detailed and long-term estimates of carbon stocks, making them particularly useful for large-scale regions or areas with sparse field data.

3.2.1. Principles of Process Models

As understanding of biophysical and chemical processes evolves, studies increasingly focus on key factors, such as solar radiation, photosynthesis, respiration, and nutrient cycling [117]. Parameters, like leaf area index, canopy coverage, photosynthetically active radiation, and chlorophyll content, are integrated into mechanistic models to simulate carbon dynamics [118]. Radiation transfer models, which simulate how solar radiation is absorbed by the canopy, are crucial for predicting carbon fluxes. These models provide critical insights into forest productivity and carbon sequestration, though they represent only one aspect of broader process-based models, which incorporate various ecological and environmental factors.

3.2.2. Common Process Models Applied in Forest Carbon Stock Estimation

Several widely used process-based models are employed in forest carbon stock estimation, including the Biome-BGC (biogeochemical cycles), CASA (Carnegie–Ames–Stanford approach), DGVM (dynamic global vegetation model), and CLM (community land model). Each model has its strengths, limitations, and unique features suited for different research scenarios, as follows:

- Biome-BGC: Simulates carbon, nitrogen, and water cycles, providing a detailed model for carbon storage in forest ecosystems [119]. It is especially useful for modeling carbon dynamics under extreme environmental conditions, like drought or excess moisture [120].
- CASA: Focuses on vegetation photosynthesis and estimates net primary productivity from remote sensing data [121]. It has shown good performance in large-scale carbon stock estimation, incorporating biomass density and carbon stock calculations [122].
- DGVM: Models dynamic interactions between vegetation and the environment, simulating processes, like photosynthesis, respiration, and carbon transfer [123]. It is particularly effective for predicting forest carbon stock changes due to climate change [124].
- CLM: A terrestrial ecosystem model that simulates energy, carbon, and water cycling [125]. It provides essential insights for climate change studies and forest carbon modeling at regional and global scales, supporting forest management and policy decisions [126].

In addition to these models, various other process-based models have been applied to forest carbon stock estimation. A summary of recent research using process models for forest carbon stock estimation is presented in Table 8.

Table 8. Recent studies on forest carbon stock estimation using process models.

Study	Study Area	Model	Highlight	Input Parameters	Scale of Study Area
Gao et al. [127]	Global vegetation	IAP-DVGM	Simulated global vegetation and carbon flux responses to warming. Analysis indicates that carbon flux is influenced by leaf area index, temperature, and precipitation.	Meteorological data, vegetation data	Global
Srinet et al. [128]	Himalayan Foothills, India	Biome-BGC	Studied climate impacts on carbon flux and showed forest carbon sink potential.	Meteorological data, site characteristics, ecophysiological parameters	Regional
Bai et al. [129]	Mengjiagang Forest Farm, Heilongjiang Province, China	3-PG	Used a 3-PG model and remote sensing to predict larch DBH and biomass, generating carbon storage maps for artificial plantations.	Meteorological data, soil data, vegetation data	Regional
Wang et al. [130]	Shenzhen, China	CASA	CASA outperforms InVEST spatially. From 2008–2022, Shenzhen's construction land increased, green and other land uses decreased, and green carbon storage declined.	Meteorological data, NDVI, SR, vegetation data	Regional

3.2.3. Limitations of Process Models

Estimating forest carbon stocks with process-based models offers a dynamic method to simulate carbon changes, incorporating factors, such as climate, environmental conditions, and management practices. These models can adapt to different spatial and temporal scales, providing valuable insights for decision-making and scenario prediction. However, they require large datasets, including meteorological variables, soil properties, and vegetation parameters, which may be difficult to obtain or lack accuracy. Data quality issues can significantly impact model reliability.

Additionally, the complex ecological processes these models simulate, such as soil carbon release and root carbon input, are challenging to measure directly, complicating model validation. While process models are useful for predicting the impacts of climate and land-use changes on carbon stocks, they are subject to high uncertainty, especially when forecasting future scenarios. Uncertainties in climate projections, vegetation responses, and other variables can significantly increase error margins in predictions.

3.3. Advancing Empirical and Process Models: Comparison, Uncertainty, and the Role of Artificial Intelligence

To fully appreciate the strengths and limitations of empirical and process-based models, it is important to consider their sensitivity to different forest types, the uncertainties inherent in each approach, and how artificial intelligence is increasingly shaping their development.

3.3.1. Comparison of Empirical and Process Models

The suitability of forest carbon stock estimation models varies depending on the forest type, as each model's strengths and limitations align differently with forest structure and environmental conditions. Both empirical and process models have their advantages and challenges when applied to different forest ecosystems, making the choice of model crucial for accurate carbon stock estimation. Table 9 summarizes the sensitivity of each model type to different forest types, as well as their respective strengths, limitations, and the data required for each approach.

Table 9. Comparison of empirical and process-based models for forest carbon stock estimation.

Model Type	Required Data	Strengths	Limitations	Forest Type Sensitivity
Empirical models	- Remote sensing data (e.g., optical, SAR, LiDAR); - Ground-truth data (e.g., biomass samples, field surveys).	High efficiency and simplicity in biomass and carbon stock estimations.	Limited adaptability to complex and heterogeneous forest ecosystems.	- Sensitive to forest structure and spectral characteristics; - Performance may vary across different forest types due to spectral homogeneity.
Process models	- Remote sensing data; - Meteorological data (e.g., temperature, precipitation); - Soil and vegetation data (e.g., nutrient content, leaf area index).	Provide a more holistic, dynamic understanding of carbon cycling.	Require more detailed input data and complex simulations, which may not always be available.	- Better suited for forests with diverse ecological conditions (e.g., tropical, boreal); - More sensitive to environmental variables (e.g., climate, soil, nutrient cycles) compared to empirical models.

Empirical models tend to perform well in relatively homogeneous forest types, such as temperate forests or plantation forests, where spectral characteristics remain consistent and can be easily linked to carbon stocks [131]. These models are advantageous in terms of speed and efficiency, especially in regions with extensive ground-truth data. However, their applicability may be limited in forests with high ecological complexity, where spectral signals are more variable.

Conversely, process-based models are particularly effective in forests with diverse ecological conditions, such as tropical rainforests or boreal forests, where there are significant variations in species composition, canopy structure, and environmental factors [132]. These models take into account various biophysical processes and climate interactions, making them better suited for capturing the dynamic nature of carbon cycling in complex forest environments. However, their reliance on extensive data and complex simulations can make them more resource-intensive compared to empirical models.

In summary, while empirical models offer simplicity and efficiency, they may fall short in complex forest ecosystems, where process-based models excel. The choice between these two approaches should be guided by the forest type, data availability, and the level of detail required for the study.

3.3.2. Model Validation in Empirical and Process Models

Model validation is essential for ensuring the accuracy and reliability of forest carbon stock estimations [133]. In empirical models, validation typically involves comparing predictions with ground-truth data, such as biomass samples or field surveys. Cross-validation techniques are often used to assess the model's generalizability by splitting the dataset into training and validation subsets, helping to avoid overfitting. For process-based models, validation requires long-term field data to assess the accuracy of carbon dynamics simulations, ensuring they reflect real-world processes, like photosynthesis and nutrient cycling.

However, validation faces challenges, particularly in regions with limited ground-truth data. In areas with complex ecological conditions, such as tropical or boreal forests, the scarcity of detailed data on forest structure and climate factors can hinder validation efforts. Furthermore, models trained in one region may perform poorly when transferred to another, underscoring the need for careful calibration to specific regions.

To improve model validation, future research should focus on obtaining more region-specific ground-truth data, particularly in understudied areas. Advanced technologies, like UAVs and high-resolution satellite imagery, can assist in overcoming data gaps.

Additionally, employing multi-source data and integrating uncertainty analysis will enhance validation, improving the accuracy and applicability of forest carbon stock estimations across diverse ecosystems.

3.3.3. Uncertainty in Empirical and Process Models

Uncertainty is a key challenge in forest carbon stock estimation, impacting both empirical and process-based models.

In empirical models, uncertainty mainly arises from the quality and availability of ground-truth data [134]. The accuracy of these models depends on how well the calibration data represent the studied area. In regions with limited field data, carbon stock estimates may be less reliable, as empirical models often assume fixed relationships between input variables, which may not apply across different forest types or environmental conditions.

Process models also face uncertainty, particularly due to their reliance on numerous input variables, such as climate data, soil characteristics, and vegetation parameters [135]. The accuracy of these models depends on the precision and availability of these factors, and gaps in data, such as unreliable or missing meteorological information, can lead to errors. The complexity of these models and their numerous interacting processes also introduce additional uncertainties, especially when simulating long-term carbon dynamics under varying environmental conditions.

Both model types are affected by uncertainty, but the nature of these uncertainties differs. While empirical models struggle with data representativeness, process-based models face challenges in the availability and precision of ecological data. To reduce these uncertainties, improvements in data quality and advancements in modeling techniques are essential. Integrating multiple data sources and refining parameterization can enhance the reliability of carbon stock estimations. Overall, empirical models are limited by gaps in ground-truth data, while process models rely on complex, often incomplete ecological data. Overcoming these challenges requires enhanced data collection and improved modeling methods.

3.3.4. The Growing Importance of Artificial Intelligence in Both Model Types

Artificial intelligence (AI) is playing an increasingly important role in enhancing forest carbon stock estimation methods [136], particularly in empirical and process-based models. In empirical models, machine learning techniques, like random forest approaches and deep learning, are improving predictive accuracy by capturing complex, nonlinear relationships in large datasets. AI allows these models to adapt better to diverse forest types and environmental conditions, boosting reliability and precision.

For process-based models, AI can optimize parameterization and simulate ecological processes with higher accuracy [137]. AI algorithms can help refine complex models by learning from observed data, reducing computational costs, and improving simulations of carbon dynamics under varying environmental conditions.

AI's integration into both model types significantly enhances scalability, adaptability, and accuracy, offering new opportunities for better forest carbon stock estimations. As AI advances, it will continue to improve the precision and efficiency of these models, supporting forest management and climate change mitigation strategies. In conclusion, AI is revolutionizing both empirical and process-based models by improving their predictive capabilities, reducing uncertainty, and making them more applicable across different forest types and conditions.

4. Technological Innovation and the Latest Research Progress

Technological advancements are revolutionizing the use of remote sensing for forest carbon stock estimation. The integration of deep learning techniques has significantly improved both the efficiency and accuracy of carbon stock estimations, particularly in processing large-scale datasets and enhancing pattern recognition capabilities [138]. Research on vegetation optical depth (VOD) has also introduced new ways to capture forest structural characteristics, refining the carbon stock estimation process [139]. Moreover, growing recognition of the bidirectional relationship between forests and climate change is enhancing methods for forecasting future carbon dynamics and informing climate change mitigation strategies [140]. Collectively, these innovations are broadening the applications of remote sensing in forest carbon stock estimation.

4.1. Deep Learning

Deep learning, a subset of machine learning based on artificial neural networks, has shown promise for forest carbon stock estimation, especially in processing complex data, like remote sensing images and time-series data [141]. It excels at capturing intricate patterns in large datasets [142], offering a solution where traditional methods may fall short.

4.1.1. Introduction of Related Algorithms

Deep learning encompasses various classic neural network architectures, each with distinct structures and functions tailored to different types of data and tasks [143]. Among these, two deep learning architectures are particularly well-suited for estimating forest carbon stocks due to their ability to handle complex and high-dimensional data, such as remote sensing imagery and time-series observations.

- Convolutional Neural Networks (CNNs)
- CNNs are particularly effective for processing high-resolution optical images [144]. By automatically extracting features, like tree edges and crown shapes, CNNs enhance the accuracy of carbon stock estimations across various forest types[145]. Their ability to process large-scale, high-resolution images makes them adaptable for diverse environmental conditions and vital for forest management and carbon cycle research [146].
- Recurrent Neural Networks (RNNs) and Long Short-Term Memory Networks (LSTMs).

RNNs and LSTMs excel at handling time-series data, such as monitoring tree growth and climate variations [147]. These models help predict dynamic changes in forest carbon stocks over time by capturing temporal dependencies [148]. LSTMs address issues in traditional RNNs, like the vanishing gradient problem, by improving memory retention [149], which is crucial for modeling long-term climate influences on carbon stocks.

4.1.2. Applications and Limitations of Deep Learning in the Field of Forest Carbon Stocks

Deep learning has become a powerful tool for estimating forest carbon stocks, providing innovative approaches to process large and complex datasets, such as remote sensing imagery and time-series data [150]. By leveraging its ability to automatically learn intricate features, deep learning models can address the complexities of forest carbon estimation that traditional methods struggle with.

In terms of applications, deep learning techniques, like CNNs and RNNs, are particularly effective in specific scenarios. For instance, in tropical reforestation projects, a deep learning-based end-to-end model utilizing individual tree detection from low-cost RGB-

only drone imagery has been shown to accurately estimate forest carbon stock within official carbon offsetting certification standards [151]. Additionally, deep learning models have been applied to estimate forest biomass from airborne LiDAR point clouds, providing more accurate estimates compared to traditional methods [152]. These models are also well-suited for large-scale forest carbon monitoring, where they can efficiently process vast datasets, providing timely and accurate carbon stock estimates that traditional methods cannot easily achieve.

However, deep learning models come with several limitations. One major challenge is the high demand for large, high-quality labeled datasets, which are often difficult and expensive to obtain, especially in remote regions. Additionally, these models are highly dependent on the quality and representativeness of training data, and poor generalization to new or diverse forest types can lead to unreliable estimates. Another limitation is the lack of interpretability—deep learning models are often seen as "black boxes", making it difficult to understand how predictions are made, which poses challenges for validation and practical application in forest management. Lastly, deep learning models require significant computational resources, making them less accessible in areas with limited access to high-performance computing infrastructure [153].

In conclusion, while deep learning offers considerable potential to enhance forest carbon stock estimation, addressing the challenges of data availability, model transparency, and computational demands is crucial for fully realizing its benefits. Continued research into improving model generalization and reducing data dependency will help unlock the full potential of deep learning in forest carbon monitoring.

4.2. VOD

VOD is a critical remote sensing indicator used in forest carbon stock estimation, providing valuable insights into vegetation biomass, water content, and structural characteristics [154]. VOD captures the interaction between vegetation and microwave radiation, making it a crucial tool for forest carbon monitoring and climate change assess men. It enhances the accuracy of carbon stock estimates by offering a clearer understanding of forest biomass and moisture content [155], both of which are tightly linked to carbon sequestration processes.

4.2.1. Acquisition Methods

VOD is derived from microwave sensors operating at various frequencies, such as the SMOS satellite in the L-band and AMSR-E in the C-band and X-band. These sensors enable large-area VOD estimation, which is vital for monitoring forest ecosystems. The inversion process typically utilizes the 0-order Tau-Omega radiative transfer model, which simulates the brightness temperature of the vegetation layer. To improve accuracy, environmental parameters, like soil temperature, surface roughness, and effective scattering albedo are considered, as they significantly impact the VOD estimation process.

4.2.2. Applications of VOD in Forest Monitoring

VOD has proven to be especially useful in the following specific forest environments, where its unique advantages become evident:

- Tropical forests: VOD correlates strongly with forest biomass, particularly in high-biomass areas, offering a more reliable estimate than optical indices. In some regions, like the Amazon and African tropical forests, L-band VOD has been validated as a key tool for biomass estimation.
- Boreal forests: In snow-covered areas where optical data are often compromised, VOD provides consistent measures of forest moisture, enabling year-round monitoring of forest health.

- Dryland ecosystems: VOD also serves as an indicator of drought stress and recovery, tracking changes in vegetation moisture to assess the impacts of water scarcity on forest ecosystems.

Key advancements include the following:

- Relationship with forest biomass: VOD, particularly at L-band, shows a strong linear relationship with AGB, making it an effective tool for biomass estimation in regions with high forest density [156].
- Monitoring forest ecosystem functions: VOD is closely related to ecological processes, like photosynthesis and water-use efficiency [157]. Studies have demonstrated that VOD can be linked with metrics, such as primary productivity and light-use efficiency, enhancing the understanding of forest ecosystems' response to climate change.
- Forest disturbance and restoration: VOD enables the detection of forest disturbances (e.g., fires, droughts) and the tracking of restoration efforts [158]. It provides real-time updates on vegetation recovery, making it invaluable for ecological restoration practices and forest management.
- Despite its promise, challenges remain with VOD usage. The complexity of inversion algorithms and varying results from different methods highlight the need for optimization and standardization. Additionally, VOD is influenced by various factors, like soil moisture, vegetation type, and topography, complicating its interpretation. To improve the reliability of VOD, future research should focus on refining algorithms, integrating multi-source data, and incorporating machine learning techniques to enhance its utility in forest carbon stock monitoring.

4.3. Bidirectional Influences Between Climate and Forest Carbon Stocks

The relationship between forest carbon stocks and climate is a dynamic feedback loop [159], where forests regulate atmospheric CO_2 concentrations through carbon sequestration, while climate change influences forest health, structure, and carbon storage capacity. Understanding these intricate interactions is crucial for developing effective strategies to mitigate climate change and enhance forest-based carbon sequestration.

4.3.1. The Impact of Climate on Changes in Forest Carbon Stocks

Climate factors, especially temperature and precipitation [160], are key drivers of forest carbon dynamics. Favorable conditions, such as warm and moist climates, enhance photosynthesis and forest productivity, enabling forests to absorb more CO_2 and increase carbon storage.

Conversely, extreme climate events—such as drought, wildfires, and storms—can drastically reduce forest carbon stocks by causing tree mortality, disrupting photosynthesis, and damaging forest structure [161]. Over time, climate change is leading to shifts in species distribution, further impacting carbon sequestration potential [162]. These changes highlight the need for models that account for both current and future climate impacts on forest carbon stocks.

4.3.2. The Impact of Forest Carbon Stocks on Changes in Climate

Forests are essential for regulating the climate through carbon sequestration. By absorbing CO_2 and storing it in vegetation and soil, forests help mitigate global warming [163]. This "climate regulation" role is vital for reducing atmospheric CO_2 concentrations, thereby stabilizing climate systems. Forests also provide vital ecosystem services, including water conservation and soil protection, contributing to ecological balance and climate stability [164]. Their ability to influence surface properties (e.g., albedo and roughness)

and the water cycle further supports regional climate regulation, affecting water availability and precipitation patterns.

Forest vegetation plays a critical role in regulating the climate through its structure and function [165]. Vegetation structure influences surface properties, like albedo and roughness. Dense forests increase surface roughness, reduce solar radiation reflection, and raise surface temperatures, while sparse forests have the opposite effect, enhancing radiation reflection and lowering temperatures. This temperature regulation is crucial in regional climate models. In addition, forests influence the water cycle by releasing water into the atmosphere through transpiration, increasing atmospheric water vapor. This not only promotes precipitation but also helps regulate its distribution and intensity. Forests play a key role in redistributing precipitation, which impacts river runoff, groundwater reserves, and regional climate patterns [166].

In conclusion, the relationship between forest carbon stocks and climate is bidirectional, with each influencing the other. Understanding and preserving forest ecosystems is essential for accurate carbon stock estimation and effective climate change mitigation.

5. Discussion

5.1. Challenges

The estimation of forest carbon stocks encounters a range of challenges in both scientific research and practical applications. These challenges are primarily related to data acquisition, model development, forest stand characteristics, and the uncertainties inherent in the estimation process.

5.1.1. Data and Models

Accurately estimating forest carbon stocks using remote sensing data presents several challenges, stemming from both the characteristics of the data and the methods used for analysis. One primary issue is signal saturation, particularly in dense vegetation areas, which can lead to underestimations of carbon stock. For optical data, atmospheric disturbances, such as cloud cover and varying sunlight, can degrade image quality. Radar data are less affected by weather but can still suffer from signal degradation due to rain or surface interference, reducing reliability.

To address these challenges, data fusion techniques that combine optical, radar, and LiDAR data have proven effective. These approaches compensate for the limitations of each data source—radar provides structural data unaffected by weather, optical data offer spectral information, and LiDAR captures vertical structure with high precision. Combining these data types enhances the overall accuracy of carbon stock estimates. Moreover, atmospheric correction and time-series analysis can further improve data reliability across varying conditions.

Another significant challenge is the temporal and spatial resolution of remote sensing data. In complex ecosystems, fine-scale variations in forest structure can greatly influence carbon storage, yet satellite data may not have the spatial resolution needed to capture these changes. High-resolution LiDAR and UAV imagery can help address this challenge by providing detailed structural data. Time-series analysis of multi-temporal satellite data can also track carbon stock changes over time.

Despite advances in data fusion and high-resolution technologies, data gaps and a lack of field validation data remain obstacles. These gaps can be filled using gap-filling algorithms and global datasets that complement local observations. Additionally, machine learning techniques can enhance data continuity and optimize the gap-filling process.

Regarding estimation methods, empirical models, including traditional regression and machine learning approaches, have been widely used to establish statistical relationships between remote sensing data and measured carbon stocks. While these models are efficient, they are limited by data resolution, processing techniques, and the availability of reliable ground data. Moreover, they may lack ecological interpretability, reducing their generalizability to other forest types or environmental conditions.

In contrast, process-based models, which simulate carbon dynamics through ecological parameters, such as photosynthesis, respiration, and nutrient cycling, provide a more comprehensive understanding of carbon sequestration. However, these models require large amounts of high-quality data and significant computational resources. Their accuracy is compromised if input data are insufficient or inaccurate.

Ultimately, the choice between empirical and process-based models depends on the research objectives and data availability. Hybrid models, combining the efficiency of empirical methods with the ecological depth of process-based models, offer a more reliable framework for forest carbon stock estimation across different ecosystems.

In conclusion, while challenges in data and modeling exist, they can be overcome through the integration of multiple data sources, advanced processing techniques, and hybrid models, enhancing the precision and applicability of forest carbon stock estimations.

5.1.2. Forest Stand

The intricate structure of global forest stands presents numerous formidable challenges to the accurate estimation of forest carbon stocks, primarily manifested in the following aspects.

Firstly, the diversity in stand structures results in a wide variety of forest types. Distinct forest ecosystems, such as tropical rainforests, temperate broadleaf forests, and boreal coniferous forests, exhibit significant variations in tree species composition, age distribution, and stand architecture [167]. These differences cause variations in signal reflection, such as differences in how various tree species or forest layers reflect light, making it difficult to develop universal carbon stock estimation models. For instance, certain tree species may have different spectral signatures due to leaf structure or canopy density, which complicates the use of remote sensing data for biomass estimation. This heterogeneity not only complicates model development but also reduces the accuracy and generalizability of the estimations.

Secondly, significant intraspecific variability exists among individual trees within the same stand [168]. Trees within a given stand vary in their morphological characteristics, such as height, diameter at breast height (DBH), and crown width, as well as in their growth rates. This variability increases the complexity of assessing forest biomass and carbon stocks. In particular, some methods, like averaging or using simple statistical models, may not accurately represent the diversity in tree structures. Machine learning approaches, such as random forest or neural networks, may improve this by capturing complex relationships between tree characteristics and carbon storage, but their sensitivity to tree crown closure and vertical stratification changes must be carefully validated.

Moreover, the vertical stratification of stands is complex, comprising multiple layers, such as the canopy, shrub, and herb layers. The interactions among these layers and their respective contributions to carbon storage are difficult to quantify precisely [169]. For example, estimating the contribution of understory vegetation or shrubs to the overall carbon stock is challenging due to their small size and limited biomass relative to the overstory. Multi-source data fusion, combining optical, radar, and LiDAR data, can help estimate biomass across these different layers more effectively. However, integrating these

data sources requires advanced algorithms and robust calibration methods to ensure accurate and consistent results.

Additionally, the spatial distribution of forests is often heterogeneous, with such features as forest gaps and edges [170]. Carbon stocks and ecological processes in these regions can differ markedly from those within the interior of the stand. Accurately capturing this spatial heterogeneity, particularly in large-scale estimations, requires scaling models that can account for micro-environments within forest stands. Process-based models and data assimilation techniques have shown promise in capturing this spatial variability, yet their scalability and applicability to large, heterogeneous forest complexes remain a key challenge.

Finally, forest ecosystems are subject to various natural and anthropogenic disturbances, including fires, pests, diseases, and logging activities [171]. These disturbances alter stand structure, impede forest growth, and disrupt carbon cycling processes, adding another layer of complexity to carbon stock estimation. Addressing these challenges requires dynamic models that account for disturbance impacts, such as the effect of pest infestations on carbon dynamics or the recovery of carbon stocks after forest fires. The integration of disturbance models with remote sensing data and long-term field observation can enhance the accuracy of carbon estimates, but the lack of widely accepted scalable procedures for these dynamic adjustments remains a significant gap.

In conclusion, the complex structure of global stands imposes numerous severe challenges on the estimation of forest carbon stocks. However, solutions to overcome these challenges are emerging. Advanced methods, such as machine learning algorithms, multi-source data fusion, and process-based models, offer promising pathways for improving the accuracy and reliability of estimations. By combining long-term field observation data with these innovative modeling techniques, future efforts can address the complexities of forest heterogeneity, ultimately enhancing the precision of carbon stock estimates. Further research into scaling and applying these models to larger, more heterogeneous forest complexes is critical for advancing forest carbon monitoring and management.

5.1.3. Uncertainty

The estimation of forest carbon stocks is pivotal for elucidating the role of forest ecosystems within the global carbon cycle; however, numerous uncertainties inherent in the estimation process significantly challenge the accuracy of these assessments.

One primary source of uncertainty arises from the characteristics of remote sensing data [172]. For instance, utilizing remote sensing imagery of varying resolutions—such as National Agriculture Imagery Program images and LiDAR point clouds—introduces variability in resolution and point cloud density, which can substantially influence estimation outcomes. The variability in these datasets necessitates careful consideration of calibration and validation techniques, particularly in multi-source datasets. Calibration procedures, such as adjusting for sensor differences, are essential to mitigate inconsistencies across different sensors, like Landsat OLI and Landsat ETM+, while validation processes, particularly cross-validation, can help assess model performance under diverse conditions, improving reliability. Additionally, the preprocessing of data from disparate sensors, including radiometric calibration, atmospheric correction, and topographic correction, introduces potential sources of error. Identifying and standardizing preprocessing methods are crucial to minimizing uncertainties across datasets and ensuring harmonization.

Furthermore, the selection of sample plots is often subject to subjective biases, and the measurement of tree parameters—such as tree height and DBH—is prone to errors stemming from measurement tools and methodologies [173]. These errors can be reduced by applying robust statistical validation methods, such as bootstrapping or Bayesian approaches, to quantify and correct for biases in field measurements and sample selection.

Human-induced disturbances, including logging, grazing, and tourism, vary across regions and forest types, adding layers of complexity and uncertainty. Quantifying these disturbances, particularly their temporal variability, can be improved through uncertainty propagation methods, such as Monte Carlo simulations, which incorporate disturbance effects into uncertainty models. This will enable more accurate predictions of their impact on forest structure and carbon stocks.

Spatial scale conversion also introduces uncertainty; transitioning from local to regional or global scales alters the relationship between forest structure and carbon stocks, resulting in discrepancies in estimation accuracy as pixel size increases [174]. This scale effect complicates the direct comparison and integration of estimation results across different studies and applications. To reduce scale-related uncertainty, multi-scale modeling approaches and hierarchical Bayesian models can be employed to account for scale effects and provide more accurate results when aggregating data at various spatial resolutions. These methods allow for the incorporation of varying levels of uncertainty depending on the spatial scale of analysis, improving both the consistency and applicability of carbon stock estimates.

Collectively, these intertwined uncertainty factors impede the determination of optimal remote sensing data resolutions and preprocessing techniques, hinder the development of unified estimation models, and elevate the complexity and difficulty of carbon stock estimations. However, addressing these uncertainties through statistical methods, model calibration, and rigorous validation procedures is critical for improving the accuracy and reliability of carbon stock estimates. In the context of climate policy or forest resource management, where accurate data are essential for decision-making, quantifying and controlling uncertainty is indispensable. The application of comprehensive uncertainty analysis and robust statistical frameworks will enhance the practical utility of these estimates and facilitate their integration into policy and management strategies.

5.2. Future Prospects

The future of forest carbon stock estimation via remote sensing will be driven by advancements in artificial intelligence, multi-source data integration, and methodological standardization. This section outlines both short-term implementable solutions and long-term research directions, emphasizing practical adoption and scalability.

5.2.1. Short-Term Implementable Solutions

AI-driven automation for carbon stock estimation: AI enhances efficiency and accuracy by automating feature extraction and classification [175]. Deep learning models, such as convolutional neural networks and transformers, improve high-resolution image processing. Future efforts should focus on transfer learning for model adaptation across forest types and self-supervised learning to reduce reliance on labeled training data [176].

Improved multi-source data fusion and calibration: Integrating optical, SAR, LiDAR, and microwave-based data improves estimation accuracy but requires addressing discrepancies in spatial resolution, acquisition timing, and sensor characteristics [177]. Standardized correction algorithms, refined data assimilation techniques, and advancements in VOD-based biomass estimation will help overcome these challenges.

Pilot projects for AI-driven multi-source remote sensing: Pilot projects should target data-rich forest regions, combining multi-source remote sensing with machine learning to develop tailored carbon stock estimation models. Once validated, these models can be scaled to diverse forest ecosystems, providing a structured roadmap for AI-driven forest carbon assessments [175].

Standardization and open data policies for carbon accounting: A lack of standardized methodologies and open-access datasets hinders practical implementation. Immediate efforts should focus on benchmark datasets integrating field inventory and remote sensing data, metadata standardization for seamless integration into carbon reporting systems, and expanding open-access platforms with preprocessed biomass layers [178].

5.2.2. Long-Term Research Directions

AI-augmented process-based models for dynamic carbon accounting: Hybrid AI-process models integrating machine learning with ecosystem simulations will refine carbon flux estimation and improve climate-adaptive assessments [175,179]. Incorporating real-time environmental data will enhance predictive capabilities, enabling better forest response modeling under changing climate conditions.

High-frequency, high-resolution carbon monitoring: Next-generation satellites will provide near-continuous monitoring at unprecedented scales [180]. Expanding LiDAR-based global carbon mapping, leveraging geostationary satellites for sub-daily productivity measurements, and integrating CubeSat and UAV-based monitoring will enable localized, high-resolution assessments.

Climate-responsive carbon stock estimation and policy integration: Long-term carbon stock estimation must account for climate-forest feedback mechanisms. Refining models to assess forest resilience under extreme climate events and aligning remote sensing with policy frameworks will enhance decision-making relevance [181]. Standardized carbon offset indicators will ensure integration into international climate agreements.

The future of remote sensing-based forest carbon stock estimation hinges on AI-driven automation, multi-source data integration, and methodological standardization. Short-term efforts should prioritize data harmonization and algorithm improvements, while long-term research must address climate adaptation, dynamic modeling, and policy integration. Collaboration between researchers, policymakers, and space agencies is essential to bridge theory and practical implementation, ensuring that remote sensing plays a central role in sustainable forest management and carbon mitigation.

6. Conclusions

Accurate forest carbon stock estimation is crucial for understanding carbon cycles and supporting climate policies. This review emphasizes key advancements in remote sensing-based carbon assessment, particularly in deep learning models, multi-source data integration, and AI-driven large-scale monitoring. Deep learning models, such as CNNs and transformers, enhance estimation accuracy by capturing complex patterns in spatial and spectral data. Multi-source data fusion, integrating optical, SAR, and LiDAR data, improves precision, especially in high-biomass forests. Despite these advancements, further work is needed to refine model adaptability and address sensor harmonization challenges.

Improved forest carbon estimation has significant policy implications, enhancing carbon inventory accuracy and supporting international frameworks, like the Paris Agreement and REDD+. AI-driven monitoring facilitates real-time tracking of forest changes, enabling more responsive management. Expanding AI-assisted databases will increase transparency and scalability in global carbon monitoring efforts. Future research should focus on bridging the gap between high-resolution research and practical implementation. Collaboration among researchers, policymakers, and global organizations is essential to develop robust and actionable carbon estimation frameworks. Through the integration of AI, remote sensing, and standardized protocols, remote sensing will play a pivotal role in advancing climate action.

Author Contributions: Conceptualization, W.X. and Y.C.; methodology, W.X.; software, W.X.; validation, Y.C. and W.Z.; investigation, W.X., M.L., X.M. and W.W.; writing—review and editing, W.X., Y.C. and W.Z.; visualization, W.X.; supervision, W.Z.; funding acquisition, Y.W. All authors have read and agreed to the published version of the manuscript.

Funding: This research was funded by the Guangxi Science and Technology Major Program, grant number GUIKEAA23062054; the Science and Technology Research and Development Projects of Guangxi Institute of Industrial Technology, grant number CYY-HT2023-JSJJ-0037; and the Guangxi Key Research and Development Program, grant number GUIKEAB24010248.

Data Availability Statement: The data presented in this study are available on request from the corresponding author.

Conflicts of Interest: The authors declare no conflicts of interest.

Abbreviations

The following abbreviations are used in this manuscript:

GCP	Global Carbon Project
AGB	Aboveground biomass
DBH	Tree diameter at breast height
SAR	Synthetic aperture radar
LiDAR	Light laser detection and ranging
NIR	Near-infrared
GF	China's Gaofen series satellites
NASA	National Aeronautics and Space Administration
GEDI	Global Ecosystem Dynamics Investigation
ICESat-2	Ice, Cloud, and Land Elevation Satellite-2
SRTM	Shuttle Radar Topography Mission
TLS	Terrestrial LiDAR system
ULS	Unmanned Lidar system
ALS	Airborne LiDAR system
NDVI	Normalized difference vegetation index
EVI	Enhanced vegetation index
LASSO	Least absolute shrinkage and selection operator
GWR	Geographically weighted regression
ML	Machine learning
XGBoost	Extreme gradient boosting
PAR	Photosynthetically active radiation
Biome-BGC	Biogeochemical cycles
CASA	Carnegie–Ames–Stanford approach
NPP	Net primary productivity
DGVM	Dynamic global vegetation model
CLM	Community land model
NCAR	National Center for Atmospheric Research
CNN	Convolutional neural network
RNN	Recurrent neural network
LSTM	Long short-term memory network
VOD	Vegetation optical depth
AI	Artificial intelligence

References

1. Yoro, K.O.; Daramola, M.O. CO_2 emission sources, greenhouse gases, and the global warming effect. In *Advances in Carbon Capture*; Elsevier: Amsterdam, The Netherlands, 2020; pp. 3–28.
2. Friedlingstein, P.; O'Sullivan, M.; Jones, M.W.; Andrew, R.M.; Hauck, J.; Landschützer, P.; Le Quéré, C.; Li, H.; Luijkx, I.T.; Olsen, A. Global Carbon Budget 2024. *Earth Syst. Sci. Data Discuss.* **2024**, *2024*, 1–133.

3. Anderegg, W.R.; Trugman, A.T.; Badgley, G.; Anderson, C.M.; Bartuska, A.; Ciais, P.; Cullenward, D.; Field, C.B.; Freeman, J.; Goetz, S.J. Climate-driven risks to the climate mitigation potential of forests. *Science* **2020**, *368*, eaaz7005.
4. Malhi, Y.; Meir, P.; Brown, S. Forests, carbon and global climate. *Philos. Trans. R. Soc. Lond. Ser. A Math. Phys. Eng. Sci.* **2002**, *360*, 1567–1591.
5. Musselman, R.C.; Fox, D.G. A review of the role of temperate forests in the global CO2 balance. *J. Air Waste Manag. Assoc.* **1991**, *41*, 798–807.
6. Bloom, A.A.; Exbrayat, J.-F.; Van Der Velde, I.R.; Feng, L.; Williams, M. The decadal state of the terrestrial carbon cycle: Global retrievals of terrestrial carbon allocation, pools, and residence times. *Proc. Natl. Acad. Sci. USA* **2016**, *113*, 1285–1290.
7. Xie, X.; Wang, Q.; Dai, L.; Su, D.; Wang, X.; Qi, G.; Ye, Y. Application of China's national forest continuous inventory database. *Environ. Manag.* **2011**, *48*, 1095–1106.
8. Fang, J.; Chen, A.; Peng, C.; Zhao, S.; Ci, L. Changes in forest biomass carbon storage in China between 1949 and 1998. *Science* **2001**, *292*, 2320–2322.
9. Magerl, A.; Le Noë, J.; Erb, K.-H.; Bhan, M.; Gingrich, S. A comprehensive data-based assessment of forest ecosystem carbon stocks in the US 1907–2012. *Environ. Res. Lett.* **2019**, *14*, 125015.
10. Navalgund, R.R.; Jayaraman, V.; Roy, P. Remote sensing applications: An overview. *Curr. Sci.* **2007**, 1747-1766.
11. Gong, Z.; Ge, W.; Guo, J.; Liu, J. Satellite remote sensing of vegetation phenology: Progress, challenges, and opportunities. *ISPRS J. Photogramm. Remote Sens.* **2024**, *217*, 149–164.
12. Goetz, S.; Dubayah, R. Advances in remote sensing technology and implications for measuring and monitoring forest carbon stocks and change. *Carbon Manag.* **2011**, *2*, 231–244.
13. Liu, Z.; Peng, C.; Work, T.; Candau, J.-N.; DesRochers, A.; Kneeshaw, D. Application of machine-learning methods in forest ecology: Recent progress and future challenges. *Environ. Rev.* **2018**, *26*, 339–350.
14. Zhao, Q.; Yu, S.; Zhao, F.; Tian, L.; Zhao, Z. Comparison of machine learning algorithms for forest parameter estimations and application for forest quality assessments. *For. Ecol. Manag.* **2019**, *434*, 224–234.
15. Panda, S.S.; Rao, M.N.; Thenkabail, P.S.; Misra, D.; Fitzgerald, J.P. Remote Sensing Systems—Platforms and Sensors: Aerial, Satellite, UAV, Optical, Radar, and LiDAR. In *Remote Sensing Handbook, Volume I*; CRC Press: Boca Raton, FL, USA, 2016; pp. 3–86.
16. Teillet, P.; Staenz, K.; William, D. Effects of spectral, spatial, and radiometric characteristics on remote sensing vegetation indices of forested regions. *Remote Sens. Environ.* **1997**, *61*, 139–149.
17. Gao, S.; Yan, K.; Liu, J.; Pu, J.; Zou, D.; Qi, J.; Mu, X.; Yan, G. Assessment of remote-sensed vegetation indices for estimating forest chlorophyll concentration. *Ecol. Indic.* **2024**, *162*, 112001.
18. Tsitsi, B. Remote sensing of aboveground forest biomass: A review. *Trop. Ecol.* **2016**, *57*, 125–132.
19. Li, D.; Wang, M.; Jiang, J. China's high-resolution optical remote sensing satellites and their mapping applications. *Geo-Spat. Inf. Sci.* **2021**, *24*, 85–94.
20. Dalla Mura, M.; Prasad, S.; Pacifici, F.; Gamba, P.; Chanussot, J.; Benediktsson, J.A. Challenges and opportunities of multimodality and data fusion in remote sensing. *Proc. IEEE* **2015**, *103*, 1585–1601.
21. ElMasry, G.; Sun, D.-W. Principles of hyperspectral imaging technology. In *Hyperspectral Imaging for Food Quality Analysis and Control*; Elsevier: Amsterdam, The Netherlands, 2010; pp. 3–43.
22. Bioucas-Dias, J.M.; Plaza, A.; Camps-Valls, G.; Scheunders, P.; Nasrabadi, N.; Chanussot, J. Hyperspectral remote sensing data analysis and future challenges. *IEEE Geosci. Remote Sens. Mag.* **2013**, *1*, 6–36.
23. Thenkabail, P.S.; Lyon, J.G.; Huete, A. Advances in hyperspectral remote sensing of vegetation and agricultural crops. In *Fundamentals, Sensor Systems, Spectral Libraries, and Data Mining for Vegetation*; CRC Press: Boca Raton, FL, USA, 2018; pp. 3–37.
24. Halme, E.; Pellikka, P.; Mõttus, M. Utility of hyperspectral compared to multispectral remote sensing data in estimating forest biomass and structure variables in Finnish boreal forest. *Int. J. Appl. Earth Obs. Geoinf.* **2019**, *83*. https://doi.org/10.1016/j.jag.2019.101942.
25. Verly, O.M.; Vieira Leite, R.; da Silva Tavares-Junior, I.; José Silva Soares da Rocha, S.; Garcia Leite, H.; Marinaldo Gleriani, J.; Paula Miranda Xavier Rufino, M.; de Fatima Silva, V.; Moreira Miquelino Eleto Torres, C.; Plata-Rueda, A.; et al. Atlantic forest woody carbon stock estimation for different successional stages using Sentinel-2 data. *Ecol. Indic.* **2023**, *146*. https://doi.org/10.1016/j.ecolind.2023.109870.
26. Li, C.; Li, M.; Liu, J.; Li, Y.; Dai, Q. Comparative Analysis of Seasonal Landsat 8 Images for Forest Aboveground Biomass Estimation in a Subtropical Forest. *Forests* **2019**, *11*, 45. https://doi.org/10.3390/f11010045.

27. Sa, R.; Fan, W. Estimation of Forest Parameters in Boreal Artificial Coniferous Forests Using Landsat 8 and Sentinel-2A. *Remote Sens.* **2023**, *15*, 3605. https://doi.org/10.3390/rs15143605.
28. Treuhaft, R.N.; Law, B.E.; Asner, G.P. Forest attributes from radar interferometric structure and its fusion with optical remote sensing. *BioScience* **2004**, *54*, 561–571.
29. Sinha, S.; Jeganathan, C.; Sharma, L.K.; Nathawat, M.S. A review of radar remote sensing for biomass estimation. *Int. J. Environ. Sci. Technol.* **2015**, *12*, 1779–1792.
30. Beaudoin, A.; Le Toan, T.; Goze, S.; Nezry, E.; Lopes, A.; Mougin, E.; Hsu, C.; Han, H.; Kong, J.; Shin, R. Retrieval of forest biomass from SAR data. *Int. J. Remote Sens.* **1994**, *15*, 2777–2796.
31. Frey, O.; Meier, E. Analyzing tomographic SAR data of a forest with respect to frequency, polarization, and focusing technique. *IEEE Trans. Geosci. Remote Sens.* **2011**, *49*, 3648–3659.
32. Neumann, M.; Saatchi, S.S.; Ulander, L.M.; Fransson, J.E. Assessing performance of L-and P-band polarimetric interferometric SAR data in estimating boreal forest above-ground biomass. *IEEE Trans. Geosci. Remote Sens.* **2012**, *50*, 714–726.
33. Stofan, E.R.; Evans, D.L.; Schmullius, C.; Holt, B.; Plaut, J.J.; van Zyl, J.; Wall, S.D.; Way, J. Overview of results of spaceborne imaging radar-C, X-band synthetic aperture radar (SIR-C/X-SAR). *IEEE Trans. Geosci. Remote Sens.* **1995**, *33*, 817–828.
34. Song, A.H.; Cheng, Y.J. Shared-aperture dual-polarized Ku-band and single-polarized Ka-band phased array antenna with scanning coverage enhancement. *IEEE Trans. Antennas Propag.* **2022**, *70*, 10426–10435.
35. Moghaddam, M.; Saatchi, S. Analysis of scattering mechanisms in SAR imagery over boreal forest: Results from BOREAS'93. *IEEE Trans. Geosci. Remote Sens.* **1995**, *33*, 1290–1296.
36. Balzter, H. Forest mapping and monitoring with interferometric synthetic aperture radar (InSAR). *Prog. Phys. Geogr.* **2001**, *25*, 159–177.
37. Englhart, S.; Keuck, V.; Siegert, F. Modeling aboveground biomass in tropical forests using multi-frequency SAR data—A comparison of methods. *IEEE J. Sel. Top. Appl. Earth Obs. Remote Sens.* **2011**, *5*, 298–306.
38. Li, W.; Zhang, Y.; Zhang, J.; Chen, H.; Chen, E.; Zhao, L.; Zhao, D. Tropical forest AGB estimation based on structure parameters extracted by TomoSAR. *Int. J. Appl. Earth Obs. Geoinf.* **2023**, *121*, 103369. https://doi.org/10.1016/j.jag.2023.103369.
39. Hu, Y.; Nie, Y.; Liu, Z.; Wu, G.; Fan, W. Improving the Potential of Coniferous Forest Aboveground Biomass Estimation by Integrating C- and L-Band SAR Data with Feature Selection and Non-Parametric Model. *Remote Sens.* **2023**, *15*, 4194. https://doi.org/10.3390/rs15174194.
40. Ali, N.; Khati, U. Forest Aboveground Biomass and Forest Height Estimation Over a Sub-tropical Forest Using Machine Learning Algorithm and Synthetic Aperture Radar Data. *J. Indian Soc. Remote Sens.* **2024**, *52*, 771–786. https://doi.org/10.1007/s12524-024-01821-5.
41. Ramachandran, N.; Saatchi, S.; Tebaldini, S.; d'Alessandro, M.M.; Dikshit, O. Mapping tropical forest aboveground biomass using airborne SAR tomography. *Sci. Rep.* **2023**, *13*, 6233. https://doi.org/10.1038/s41598-023-33311-y.
42. Dong, P.; Chen, Q. *LiDAR Remote Sensing and Applications*; CRC Press: Boca Raton, FL, USA, 2017.
43. Camarretta, N.; Harrison, P.A.; Bailey, T.; Potts, B.; Lucieer, A.; Davidson, N.; Hunt, M. Monitoring forest structure to guide adaptive management of forest restoration: A review of remote sensing approaches. *New For.* **2020**, *51*, 573–596.
44. Li, X.; Liu, C.; Wang, Z.; Xie, X.; Li, D.; Xu, L. Airborne LiDAR: State-of-the-art of system design, technology and application. *Meas. Sci. Technol.* **2020**, *32*, 032002.
45. Shugart, H.; Saatchi, S.; Hall, F. Importance of structure and its measurement in quantifying function of forest ecosystems. *J. Geophys. Res. Biogeosci.* **2010**, *115*, https://doi.org/10.1016/j.rse.2006.07.001.
46. Tian, L.; Wu, X.; Tao, Y.; Li, M.; Qian, C.; Liao, L.; Fu, W. Review of remote sensing-based methods for forest aboveground biomass estimation: Progress, challenges, and prospects. *Forests* **2023**, *14*, 1086.
47. Hancock, S.; McGrath, C.; Lowe, C.; Davenport, I.; Woodhouse, I. Requirements for a global lidar system: Spaceborne lidar with wall-to-wall coverage. *R. Soc. Open Sci.* **2021**, *8*, 211166.
48. Simard, M.; Pinto, N.; Fisher, J.B.; Baccini, A. Mapping forest canopy height globally with spaceborne lidar. *J. Geophys. Res. Biogeosciences* **2011**, *116*, 4021.
49. Fatoyinbo, T.; Armston, J.; Simard, M.; Saatchi, S.; Denbina, M.; Lavalle, M.; Hofton, M.; Tang, H.; Marselis, S.; Pinto, N. The NASA AfriSAR campaign: Airborne SAR and lidar measurements of tropical forest structure and biomass in support of current and future space missions. *Remote Sens. Environ.* **2021**, *264*, 112533.
50. Bazezew, M.N.; Hussin, Y.A.; Kloosterman, E.H. Integrating Airborne LiDAR and Terrestrial Laser Scanner forest parameters for accurate above-ground biomass/carbon estimation in Ayer Hitam tropical forest, Malaysia. *Int. J. Appl. Earth Obs. Geoinf.* **2018**, *73*, 638–652. https://doi.org/10.1016/j.jag.2018.07.026.

51. Zhou, L.; Li, X.; Zhang, B.; Xuan, J.; Gong, Y.; Tan, C.; Huang, H.; Du, H. Estimating 3D Green Volume and Aboveground Biomass of Urban Forest Trees by UAV-Lidar. *Remote Sens.* **2022**, *14*, 5211. https://doi.org/10.3390/rs14205211.
52. Beyene, S.M.; Hussin, Y.A.; Kloosterman, H.E.; Ismail, M.H. Forest Inventory and Aboveground Biomass Estimation with Terrestrial LiDAR in the Tropical Forest of Malaysia. *Can. J. Remote Sens.* **2020**, *46*, 130–145. https://doi.org/10.1080/07038992.2020.1759036.
53. Tian, J.; Wang, L.; Li, X.; Yin, D.; Gong, H.; Nie, S.; Shi, C.; Zhong, R.; Liu, X.; Xu, R. Canopy Height Layering Biomass Estimation Model (CHL-BEM) with Full-Waveform LiDAR. *Remote Sens.* **2019**, *11*, 1446. https://doi.org/10.3390/rs11121446.
54. Shiney, S.A.; Geetha, R. Estimation of Above Ground Biomass Using Machine Learning and Deep Learning Algorithms: A Review. In *International Conference on Advances in Artificial Intelligence and Machine Learning in Big Data Processinging*; Springer: Cham, Switzerland, 2023; pp. 181–196.
55. Li, H.; Kato, T.; Hayashi, M.; Wu, L. Estimation of Forest Aboveground Biomass of Two Major Conifers in Ibaraki Prefecture, Japan, from PALSAR-2 and Sentinel-2 Data. *Remote Sens.* **2022**, *14*, 468. https://doi.org/10.3390/rs14030468.
56. Han, H.; Wan, R.; Li, B. Estimating Forest Aboveground Biomass Using Gaofen-1 Images, Sentinel-1 Images, and Machine Learning Algorithms: A Case Study of the Dabie Mountain Region, China. *Remote Sens.* **2021**, *14*, 176. https://doi.org/10.3390/rs14010176.
57. Qian, C.; Qiang, H.; Wang, F.; Li, M. Estimation of Forest Aboveground Biomass in Karst Areas Using Multi-Source Remote Sensing Data and the K-DBN Algorithm. *Remote Sens.* **2021**, *13*, 5030. https://doi.org/10.3390/rs13245030.
58. Zhang, L.; Shao, Z.; Liu, J.; Cheng, Q. Deep Learning Based Retrieval of Forest Aboveground Biomass from Combined LiDAR and Landsat 8 Data. *Remote Sens.* **2019**, *11*, 1459. https://doi.org/10.3390/rs11121459.
59. Sinha, S.; Mohan, S.; Das, A.K.; Sharma, L.K.; Jeganathan, C.; Santra, A.; Santra Mitra, S.; Nathawat, M.S. Multi-sensor approach integrating optical and multi-frequency synthetic aperture radar for carbon stock estimation over a tropical deciduous forest in India. *Carbon Manag.* **2019**, *11*, 39–55. https://doi.org/10.1080/17583004.2019.1686931.
60. Yang, Q.; Niu, C.; Liu, X.; Feng, Y.; Ma, Q.; Wang, X.; Tang, H.; Guo, Q. Mapping high-resolution forest aboveground biomass of China using multisource remote sensing data. *GIScience Remote Sens.* **2023**, *60*. https://doi.org/10.1080/15481603.2023.2203303.
61. Wang, L.; Ju, Y.; Ji, Y.; Marino, A.; Zhang, W.; Jing, Q. Estimation of Forest Above-Ground Biomass in the Study Area of Greater Khingan Ecological Station with Integration of Airborne LiDAR, Landsat 8 OLI, and Hyperspectral Remote Sensing Data. *Forests* **2024**, *15*, 1861. https://doi.org/10.3390/f15111861.
62. Hong, Y.; Xu, J.; Wu, C.; Pang, Y.; Zhang, S.; Chen, D.; Yang, B. Combining Multisource Data and Machine Learning Approaches for Multiscale Estimation of Forest Biomass. *Forests* **2023**, *14*, 2248. https://doi.org/10.3390/f14112248.
63. Su, R.; Du, W.; Ying, H.; Shan, Y.; Liu, Y. Estimation of Aboveground Carbon Stocks in Forests Based on LiDAR and Multispectral Images: A Case Study of Duraer Coniferous Forests. *Forests* **2023**, *14*, 992. https://doi.org/10.3390/f14050992.
64. Huang, H.; Wu, D.; Fang, L.; Zheng, X. Comparison of Multiple Machine Learning Models for Estimating the Forest Growing Stock in Large-Scale Forests Using Multi-Source Data. *Forests* **2022**, *13*, 1471. https://doi.org/10.3390/f13091471.
65. Xiao, J.; Chen, L.; Zhang, T.; Li, L.; Yu, Z.; Wu, R.; Bai, L.; Xiao, J.; Chen, L. Identification of Urban Green Space Types and Estimation of Above-Ground Biomass Using Sentinel-1 and Sentinel-2 Data. *Forests* **2022**, *13*, 1077. https://doi.org/10.3390/f13071077.
66. Zhu, Y.; Feng, Z.; Lu, J.; Liu, J. Estimation of Forest Biomass in Beijing (China) Using Multisource Remote Sensing and Forest Inventory Data. *Forests* **2020**, *11*, 163. https://doi.org/10.3390/f11020163.
67. Bourgoin, C.; Blanc, L.; Bailly, J.-S.; Cornu, G.; Berenguer, E.; Oszwald, J.; Tritsch, I.; Laurent, F.; Hasan, A.F.; Sist, P.; et al. The Potential of Multisource Remote Sensing for Mapping the Biomass of a Degraded Amazonian Forest. *Forests* **2018**, *9*, 303. https://doi.org/10.3390/f9060303.
68. Wu, Y.; Mao, Z.; Guo, L.; Li, C.; Deng, L. Forest Volume Estimation Method Based on Allometric Growth Model and Multisource Remote Sensing Data. *IEEE J. Sel. Top. Appl. Earth Obs. Remote Sens.* **2023**, *16*, 8900–8912. https://doi.org/10.1109/jstars.2023.3313251.
69. Mohite, J.; Sawant, S.; Pandit, A.; Sakkan, M.; Pappula, S.; Parmar, A. Forest aboveground biomass estimation by GEDI and multi-source EO data fusion over Indian forest. *Int. J. Remote Sens.* **2024**, *45*, 1304–1338. https://doi.org/10.1080/01431161.2024.2307944.
70. Yan, X.; Li, J.; Smith, A.R.; Yang, D.; Ma, T.; Su, Y.; Shao, J. Evaluation of machine learning methods and multi-source remote sensing data combinations to construct forest above-ground biomass models. *Int. J. Digit. Earth* **2023**, *16*, 4471–4491. https://doi.org/10.1080/17538947.2023.2270459.

71. Goïta, K.; Mouloungou, J.; Bénié, G.B. Estimation of aboveground biomass and carbon in a tropical rain forest in Gabon using remote sensing and GPS data. *Geocarto Int.* **2017**, *34*, 243–259. https://doi.org/10.1080/10106049.2017.1386720.
72. Li, J.; Bao, W.; Wang, X.; Song, Y.; Liao, T.; Xu, X.; Guo, M. Estimating Aboveground Biomass of Boreal Forests in Northern China Using Multiple Datasets. *IEEE Trans. Geosci. Remote Sens.* **2024**, *62*, 4408410. https://doi.org/10.1109/tgrs.2024.3408316.
73. Ayushi, K.; Babu, K.N.; Ayyappan, N.; Nair, J.R.; Kakkara, A.; Reddy, C.S. A comparative analysis of machine learning techniques for aboveground biomass estimation: A case study of the Western Ghats, India. *Ecol. Inform.* **2024**, *80*, 102479. https://doi.org/10.1016/j.ecoinf.2024.102479.
74. Qi, W.; Saarela, S.; Armston, J.; Ståhl, G.; Dubayah, R. Forest biomass estimation over three distinct forest types using TanDEM-X InSAR data and simulated GEDI lidar data. *Remote Sens. Environ.* **2019**, *232*, 111283. https://doi.org/10.1016/j.rse.2019.111283.
75. Du, Y.; Chen, D.; Li, H.; Liu, C.; Liu, S.; Zhang, N.; Fan, J.; Jiang, D. Research on Estimating and Evaluating Subtropical Forest Carbon Stocks by Combining Multi-Payload High-Resolution Satellite Data. *Forests* **2023**, *14*, 2388. https://doi.org/10.3390/f14122388.
76. Li, H.; Kato, T.; Hayashi, M.; Liu, J. Using multisource satellite products to estimate forest aboveground biomass in Oita prefecture: A novel approach with improved accuracy and computational efficiency. *Geocarto Int.* **2022**, *38*, 1–20. https://doi.org/10.1080/10106049.2022.2134466.
77. Wang, X.; Jiao, H. Spatial Scaling of Forest Aboveground Biomass Using Multi-Source Remote Sensing Data. *IEEE Access* **2020**, *8*, 178870–178885. https://doi.org/10.1109/access.2020.3027361.
78. Zhang, D.; Ni, H. Inversion of Forest Biomass Based on Multi-Source Remote Sensing Images. *Sensors* **2023**, *23*, 9313. https://doi.org/10.3390/s23239313.
79. Ometto, J.P.; Gorgens, E.B.; de Souza Pereira, F.R.; Sato, L.; de Assis, M.L.R.; Cantinho, R.; Longo, M.; Jacon, A.D.; Keller, M. A biomass map of the Brazilian Amazon from multisource remote sensing. *Sci. Data* **2023**, *10*, 668. https://doi.org/10.1038/s41597-023-02575-4.
80. Sa, R.; Nie, Y.; Chumachenko, S.; Fan, W. Biomass Estimation and Saturation Value Determination Based on Multi-Source Remote Sensing Data. *Remote Sens.* **2024**, *16*, 2250. https://doi.org/10.3390/rs16122250.
81. Fan, W.; Tian, J.; Knoke, T.; Yang, B.; Liang, F.; Dong, Z. Investigating Dual-Source Satellite Image Data and ALS Data for Estimating Aboveground Biomass. *Remote Sens.* **2024**, *16*, 1804. https://doi.org/10.3390/rs16101804.
82. Lyu, G.; Wang, X.; Huang, X.; Xu, J.; Li, S.; Cui, G.; Huang, H. Toward a More Robust Estimation of Forest Biomass Carbon Stock and Carbon Sink in Mountainous Region: A Case Study in Tibet, China. *Remote Sens.* **2024**, *16*, 1481. https://doi.org/10.3390/rs16091481.
83. Li, X.; Ye, Z.; Long, J.; Zheng, H.; Lin, H. Inversion of Coniferous Forest Stock Volume Based on Backscatter and InSAR Coherence Factors of Sentinel-1 Hyper-Temporal Images and Spectral Variables of Landsat 8 OLI. *Remote Sens.* **2022**, *14*, 2754. https://doi.org/10.3390/rs14122754.
84. Zhang, W.; Zhao, L.; Li, Y.; Shi, J.; Yan, M.; Ji, Y. Forest Above-Ground Biomass Inversion Using Optical and SAR Images Based on a Multi-Step Feature Optimized Inversion Model. *Remote Sens.* **2022**, *14*, 1608. https://doi.org/10.3390/rs14071608.
85. Chen, X.; Guo, Y.; Chen, Z.; Luo, X.; Wang, P.; Shi, M.; Wang, X. A new method for estimating forest stand carbon stock: Segmentation and modeling based on forest aboveground imagery., *Ecol. Indic.*, **2024**, *167*, p. 112697.
86. Liu, J.; Yang, B.; Li, M.; Xu, D. Assessing Forest-Change-Induced Carbon Storage Dynamics by Integrating GF-1 Image and Localized Allometric Growth Equations in Jiangning District, Nanjing, Eastern China (2017–2020). *Forests* **2024**, *15*, 506.
87. Yang, F.; Marino, A.; Ji, Y.; Shi, J.; Zhao, H.; Zhang, W. Component and Total Forest Aboveground Biomass Estimation Using GF-1/3 Images. In Proceedings of the IGARSS 2024-2024 IEEE International Geoscience and Remote Sensing Symposium, Athens, Greece, 7–12 July 2024; pp. 4899–4902.
88. Vandendaele, B.; Fournier, R.A.; Vepakomma, U.; Pelletier, G.; Lejeune, P.; Martin-Ducup, O. Estimation of northern hardwood forest inventory attributes using UAV laser scanning (ULS): Transferability of laser scanning methods and comparison of automated approaches at the tree-and stand-level. *Remote Sens.* **2021**, *13*, 2796.
89. Karim, S.; Tong, G.; Li, J.; Qadir, A.; Farooq, U.; Yu, Y. Current advances and future perspectives of image fusion: A comprehensive review. *Inf. Fusion* **2023**, *90*, 185–217.
90. Miehle, P.; Battaglia, M.; Sands, P.J.; Forrester, D.I.; Feikema, P.M.; Livesley, S.J.; Morris, J.D.; Arndt, S.K. A comparison of four process-based models and a statistical regression model to predict growth of Eucalyptus globulus plantations. *Ecol. Model.* **2009**, *220*, 734–746.
91. Vicharnakorn, P.; Shrestha, R.P.; Nagai, M.; Salam, A.P.; Kiratiprayoon, S. Carbon stock assessment using remote sensing and forest inventory data in Savannakhet, Lao PDR. *Remote Sens.* **2014**, *6*, 5452–5479.

92. Newell, J.P.; Vos, R.O. Accounting for forest carbon pool dynamics in product carbon footprints: Challenges and opportunities. *Environ. Impact Assess. Rev.* **2012**, *37*, 23–36.
93. Rodríguez-Veiga, P.; Wheeler, J.; Louis, V.; Tansey, K.; Balzter, H. Quantifying forest biomass carbon stocks from space. *Curr. For. Rep.* **2017**, *3*, 1–18.
94. Bannari, A.; Morin, D.; Bonn, F.; Huete, A. A review of vegetation indices. *Remote Sens. Rev.* **1995**, *13*, 95–120.
95. Ouma, Y.O.; Tetuko, J.; Tateishi, R. Analysis of co-occurrence and discrete wavelet transform textures for differentiation of forest and non-forest vegetation in very-high-resolution optical-sensor imagery. *Int. J. Remote Sens.* **2008**, *29*, 3417–3456.
96. Mohan, M.; Silva, C.A.; Klauberg, C.; Jat, P.; Catts, G.; Cardil, A.; Hudak, A.T.; Dia, M. Individual tree detection from unmanned aerial vehicle (UAV) derived canopy height model in an open canopy mixed conifer forest. *Forests* **2017**, *8*, 340.
97. Ayrey, E.; Fraver, S.; Kershaw Jr, J.A.; Kenefic, L.S.; Hayes, D.; Weiskittel, A.R.; Roth, B.E. Layer stacking: A novel algorithm for individual forest tree segmentation from LiDAR point clouds. *Can. J. Remote Sens.* **2017**, *43*, 16–27.
98. Poole, M.A.; O'Farrell, P.N. The assumptions of the linear regression model. *Trans. Inst. Br. Geogr.* **1971**, 145-158.
99. Ostertagová, E. Modelling using polynomial regression. *Procedia Eng.* **2012**, *48*, 500–506.
100. Ranstam, J.; Cook, J.A. LASSO regression. *J. Br. Surg.* **2018**, *105*, 1348.
101. McDonald, G.C. Ridge regression. *Wiley Interdiscip. Rev. Comput. Stat.* **2009**, *1*, 93–100.
102. Derksen, S.; Keselman, H.J. Backward, forward and stepwise automated subset selection algorithms: Frequency of obtaining authentic and noise variables. *Br. J. Math. Stat. Psychol.* **1992**, *45*, 265–282.
103. Brunsdon, C.; Fotheringham, A.S.; Charlton, M.E. Geographically weighted regression: A method for exploring spatial nonstationarity. *Geogr. Anal.* **1996**, *28*, 281–298.
104. Dunjko, V.; Briegel, H.J. Machine learning & artificial intelligence in the quantum domain: A review of recent progress. *Rep. Prog. Phys.* **2018**, *81*, 074001.
105. Breiman, L. Random forests. *Mach. Learn.* **2001**, *45*, 5–32.
106. Santos, F.; Graw, V.; Bonilla, S. A geographically weighted random forest approach for evaluate forest change drivers in the Northern Ecuadorian Amazon. *PLoS ONE* **2019**, *14*, e0226224.
107. Wu, Z.; Yao, F.; Zhang, J.; Liu, H. Estimating Forest Aboveground Biomass Using a Combination of Geographical Random Forest and Empirical Bayesian Kriging Models. *Remote Sens.* **2024**, *16*, 1859.
108. Chen, T.; Guestrin, C. Xgboost: A scalable tree boosting system. In Proceedings of the 22nd ACM SIGKDD International Conference on Knowledge Discovery and Data Mining, San Francisco, CA, USA, 13–17 August 2016; pp. 785–794.
109. Li, Y.; Li, C.; Li, M.; Liu, Z. Influence of variable selection and forest type on forest aboveground biomass estimation using machine learning algorithms. *Forests* **2019**, *10*, 1073.
110. Singh, C.; Karan, S.K.; Sardar, P.; Samadder, S.R. Remote sensing-based biomass estimation of dry deciduous tropical forest using machine learning and ensemble analysis. *J. Environ. Manag.* **2022**, *308*, 114639. https://doi.org/10.1016/j.jenvman.2022.114639.
111. Fararoda, R.; Reddy, R.S.; Rajashekar, G.; Chand, T.R.K.; Jha, C.S.; Dadhwal, V.K. Improving forest above ground biomass estimates over Indian forests using multi source data sets with machine learning algorithm. *Ecol. Inform.* **2021**, *65*, 101392. https://doi.org/10.1016/j.ecoinf.2021.101392.
112. Qadeer, A.; Shakir, M.; Wang, L.; Talha, S.M. Evaluating machine learning approaches for aboveground biomass prediction in fragmented high-elevated forests using multi-sensor satellite data. *Remote Sens. Appl. Soc. Environ.* **2024**, *36*, 101291. https://doi.org/10.1016/j.rsase.2024.101291.
113. Li, Y.; Li, M.; Li, C.; Liu, Z. Forest aboveground biomass estimation using Landsat 8 and Sentinel-1A data with machine learning algorithms. *Sci. Rep.* **2020**, *10*, 9952. https://doi.org/10.1038/s41598-020-67024-3.
114. Ahirwal, J.; Nath, A.; Brahma, B.; Deb, S.; Sahoo, U.K.; Nath, A.J. Patterns and driving factors of biomass carbon and soil organic carbon stock in the Indian Himalayan region. *Sci. Total Environ.* **2021**, *770*, 145292.
115. Tamayo-Vera, D.; Wang, X.; Mesbah, M. A review of machine learning techniques in agroclimatic studies. *Agriculture* **2024**, *14*, 481.
116. Luckai, N.; Larocque, G.R. Challenges in the application of existing process-based models to predict the effect of climate change on C pools in forest ecosystems. *Clim. Change* **2002**, *55*, 39–60.
117. Ciais, P.; Dolman, A.J.; Bombelli, A.; Duren, R.; Peregon, A.; Rayner, P.J.; Miller, C.; Gobron, N.; Kinderman, G.; Marland, G. Current systematic carbon-cycle observations and the need for implementing a policy-relevant carbon observing system. *Biogeosciences* **2014**, *11*, 3547–3602.

118. Wu, R.-Q.; Jia, J.-B.; Yan, W.-D.; Hu, L.; Wang, Y.-F.; Chen, Y. Characteristics of canopy conductance and environmental driving mechanism in three monsoon climate regions of China. *Front. Environ. Sci.* **2022**, *10*, 935926.
119. White, M.A.; Thornton, P.E.; Running, S.W.; Nemani, R.R. Parameterization and sensitivity analysis of the BIOME–BGC terrestrial ecosystem model: Net primary production controls. *Earth Interact.* **2000**, *4*, 1–85.
120. Bond-Lamberty, B.; Gower, S.T.; Ahl, D.E. Improved simulation of poorly drained forests using Biome-BGC. *Tree Physiol.* **2007**, *27*, 703–715.
121. Potter, C.S.; Randerson, J.T.; Field, C.B.; Matson, P.A.; Vitousek, P.M.; Mooney, H.A.; Klooster, S.A. Terrestrial ecosystem production: A process model based on global satellite and surface data. *Glob. Biogeochem. Cycles* **1993**, *7*, 811–841.
122. Liu, Z.; Hu, M.; Hu, Y.; Wang, G. Estimation of net primary productivity of forests by modified CASA models and remotely sensed data. *Int. J. Remote Sens.* **2018**, *39*, 1092–1116.
123. Purves, D.; Pacala, S. Predictive models of forest dynamics. *Science* **2008**, *320*, 1452–1453.
124. Wu, L.; Kato, T.; Sato, H.; Hirano, T.; Yazaki, T. Sensitivity analysis of the typhoon disturbance effect on forest dynamics and carbon balance in the future in a cool-temperate forest in northern Japan by using SEIB-DGVM. *For. Ecol. Manag.* **2019**, *451*, 117529.
125. Lawrence, P.J.; Chase, T.N. Representing a new MODIS consistent land surface in the Community Land Model (CLM 3.0). *J. Geophys. Res. Biogeosci.* **2007**, *112*, G01023.
126. Dos Santos, T.; Keppel-Aleks, G.; De Roo, R.; Steiner, A. Can land surface models capture the observed soil moisture control of water and carbon fluxes in temperate-to-boreal forests? *J. Geophys. Res. Biogeosci.* **2021**, *126*, e2020JG005999.
127. Gao, X.; Zhu, J.; Zeng, X.; Zhang, M.; Dai, Y.; Ji, D.; Zhang, H. Changes in Global Vegetation Distribution and Carbon Fluxes in Response to Global Warming: Simulated Results from IAP-DGVM in CAS-ESM2. *Adv. Atmos. Sci.* **2022**, *39*, 1285–1298. https://doi.org/10.1007/s00376-021-1138-3.
128. Srinet, R.; Nandy, S.; Patel, N.R.; Padalia, H.; Watham, T.; Singh, S.K.; Chauhan, P. Simulation of forest carbon fluxes by integrating remote sensing data into biome-BGC model. *Ecol. Model.* **2023**, *475*, 110185. https://doi.org/10.1016/j.ecolmodel.2022.110185.
129. Bai, Y.; Pang, Y.; Kong, D. Integrating remote sensing and 3-PG model to simulate the biomass and carbon stock of Larix olgensis plantation. *For. Ecosyst.* **2024**, *11*, 100213. https://doi.org/10.1016/j.fecs.2024.100213.
130. Wang, R.-Y.; Mo, X.; Ji, H.; Zhu, Z.; Wang, Y.-S.; Bao, Z.; Li, T. Comparison of the CASA and InVEST models' effects for estimating spatiotemporal differences in carbon storage of green spaces in megacities. *Sci. Rep.* **2024**, *14*, 5456. https://doi.org/10.1038/s41598-024-55858-0.
131. Pretzsch, H.; Hilmers, T. Structural diversity and carbon stock of forest stands: Tradeoff as modified by silvicultural thinning. *Eur. J. For. Res.* **2024**, 1–22.
132. Larocque, G.R.; Komarov, A.; Chertov, O.; Shanin, V.; Liu, J.; Bhatti, J.S.; Wang, W.; Peng, C.; Shugart, H.H.; Xi, W. Process-Based Models: A Synthesis of Models and Applications to Address Environmental and Management Issues 1. In *Ecological Forest Management Handbook*; CRC Press: Boca Raton, FL, USA, 2024; pp. 209–246.
133. Adhikari, D.; Singh, P.P.; Tiwary, R.; Barik, S.K. Forest carbon stock-based bioeconomy: Mixed models improve accuracy of tree biomass estimates. *Biomass Bioenergy* **2024**, *183*, 107142.
134. García-Soria, J.L.; Morata, M.; Berger, K.; Pascual-Venteo, A.B.; Rivera-Caicedo, J.P.; Verrelst, J. Evaluating epistemic uncertainty estimation strategies in vegetation trait retrieval using hybrid models and imaging spectroscopy data. *Remote Sens. Environ.* **2024**, *310*, 114228.
135. Lei, Q.; Zhang, T.; An, M.; Luo, J.; Qin, L.; Zhu, A.-X.; Qiu, W.; Du, X.; Liu, H. Sensitivity analysis of SWAT streamflow and water quality to the uncertainty in soil properties generated by the SoLIM model. *J. Hydrol.* **2024**, *642*, 131879.
136. Güler, S. The role of artificial intelligence and remote sensing technologies in forest ecosystems and their importance in determining carbon capture potential. *SilvaWorld* **2024**, *3*, 44–51.
137. Schneider, T.; Leung, L.R.; Wills, R.C. Opinion: Optimizing climate models with process knowledge, resolution, and artificial intelligence. *Atmos. Chem. Phys.* **2024**, *24*, 7041–7062.
138. Yuan, Q.; Shen, H.; Li, T.; Li, Z.; Li, S.; Jiang, Y.; Xu, H.; Tan, W.; Yang, Q.; Wang, J. Deep learning in environmental remote sensing: Achievements and challenges. *Remote Sens. Environ.* **2020**, *241*, 111716.
139. Liu, Y.Y.; De Jeu, R.A.; McCabe, M.F.; Evans, J.P.; Van Dijk, A.I. Global long-term passive microwave satellite-based retrievals of vegetation optical depth. *Geophys. Res. Lett.* **2011**, *38*, L18402.
140. Du, X.; Lei, X.; He, X.; Lan, J.; Guo, H.; Xu, Q. Ecosystem service multifunctionality of mixed conifer-broad-leaved forests under climate change and forest management based on matrix growth modelling. *For. Ecosyst.* **2024**, *11*, 100231.

141. Sarker, I.H. Deep learning: A comprehensive overview on techniques, taxonomy, applications and research directions. *SN Comput. Sci.* **2021**, *2*, 420.
142. Längkvist, M.; Karlsson, L.; Loutfi, A. A review of unsupervised feature learning and deep learning for time-series modeling. *Pattern Recognit. Lett.* **2014**, *42*, 11–24.
143. Alom, M.Z.; Taha, T.M.; Yakopcic, C.; Westberg, S.; Sidike, P.; Nasrin, M.S.; Hasan, M.; Van Essen, B.C.; Awwal, A.A.; Asari, V.K. A state-of-the-art survey on deep learning theory and architectures. *Electronics* **2019**, *8*, 292.
144. Kattenborn, T.; Leitloff, J.; Schiefer, F.; Hinz, S. Review on Convolutional Neural Networks (CNN) in vegetation remote sensing. *ISPRS J. Photogramm. Remote Sens.* **2021**, *173*, 24–49.
145. Zhao, H.; Morgenroth, J.; Pearse, G.; Schindler, J. A systematic review of individual tree crown detection and delineation with convolutional neural networks (CNN). *Curr. For. Rep.* **2023**, *9*, 149–170.
146. Salcedo-Sanz, S.; Ghamisi, P.; Piles, M.; Werner, M.; Cuadra, L.; Moreno-Martínez, A.; Izquierdo-Verdiguier, E.; Muñoz-Marí, J.; Mosavi, A.; Camps-Valls, G. Machine learning information fusion in Earth observation: A comprehensive review of methods, applications and data sources. *Inf. Fusion* **2020**, *63*, 256–272.
147. Banskota, A.; Kayastha, N.; Falkowski, M.J.; Wulder, M.A.; Froese, R.E.; White, J.C. Forest monitoring using Landsat time series data: A review. *Can. J. Remote Sens.* **2014**, *40*, 362–384.
148. Mienye, I.D.; Swart, T.G.; Obaido, G. Recurrent neural networks: A comprehensive review of architectures, variants, and applications. *Information* **2024**, *15*, 517.
149. Zhou, Z.; Wu, X.; Peng, B. An Approach to Predicting Urban Carbon Stock Using a Self-Attention Convolutional Long Short-Term Memory Network Model: A Case Study in Wuhan Urban Circle. *Remote Sens.* **2024**, *16*, 4372.
150. Tian, X.; Li, J.; Zhang, F.; Zhang, H.; Jiang, M. Forest Aboveground Biomass Estimation Using Multisource Remote Sensing Data and Deep Learning Algorithms: A Case Study over Hangzhou Area in China. *Remote Sens.* **2024**, *16*, 1074. https://doi.org/10.3390/rs16061074.
151. Reiersen, G.; Dao, D.; Lütjens, B.; Klemmer, K.; Amara, K.; Steinegger, A.; Zhang, C.; Zhu, X. ReforesTree: A dataset for estimating tropical forest carbon stock with deep learning and aerial imagery. *Proc. AAAI Conf. Artif. Intell.* **2022**, *36*, 12119–12125.
152. Oehmcke, S.; Li, L.; Revenga, J.C.; Nord-Larsen, T.; Trepekli, K.; Gieseke, F.; Igel, C. Deep learning based 3D point cloud regression for estimating forest biomass. In Proceedings of the 30th International Conference on Advances in Geographic Information Systems, Seattle, WA, USA, 1–4 November 2022; pp. 1–4.
153. Sudha, S.; Aji, S. Exploring the advancements in high-performance computing paradigm for remote sensing big data analytics. *Cloud Comput. Data Sci.* **2024**, *5*, 50–61.
154. Frappart, F.; Wigneron, J.-P.; Li, X.; Liu, X.; Al-Yaari, A.; Fan, L.; Wang, M.; Moisy, C.; Le Masson, E.; Aoulad Lafkih, Z. Global monitoring of the vegetation dynamics from the Vegetation Optical Depth (VOD): A review. *Remote Sens.* **2020**, *12*, 2915.
155. Chaparro, D.; Duveiller, G.; Piles, M.; Cescatti, A.; Vall-llossera, M.; Camps, A.; Entekhabi, D. Sensitivity of L-band vegetation optical depth to carbon stocks in tropical forests: A comparison to higher frequencies and optical indices. *Remote Sens. Environ.* **2019**, *232*, 111303. https://doi.org/10.1016/j.rse.2019.111303.
156. Vittucci, C.; Laurin, G.V.; Tramontana, G.; Ferrazzoli, P.; Guerriero, L.; Papale, D. Vegetation optical depth at L-band and above ground biomass in the tropical range: Evaluating their relationships at continental and regional scales. *Int. J. Appl. Earth Obs. Geoinf.* **2019**, *77*, 151–161.
157. Wang, H.; Wigneron, J.-P.; Ciais, P.; Yao, Y.; Fan, L.; Liu, X.; Li, X.; Green, J.K.; Tian, F.; Tao, S.; et al. Seasonal variations in vegetation water content retrieved from microwave remote sensing over Amazon intact forests. *Remote Sens. Environ.* **2023**, *285*, 113409. https://doi.org/10.1016/j.rse.2022.113409.
158. Li, F.; Diop, S.; Hirwa, H.; Maesho, S.; Ning, X.; Tian, C.; Qiao, Y.; Faye, C.; Cissé, B.; Guisse, A. Dryland Social-Ecological Systems in Africa. In *Dryland Social-Ecological Systems in Changing Environments*; Springer Nature: Singapore: 2024; pp. 273–323.
159. Anderson-Teixeira, K.J.; Miller, A.D.; Mohan, J.E.; Hudiburg, T.W.; Duval, B.D.; DeLucia, E.H. Altered dynamics of forest recovery under a changing climate. *Glob. Change Biol.* **2013**, *19*, 2001–2021.
160. Benzing, D.H. Vulnerabilities of tropical forests to climate change: The significance of resident epiphytes. *Clim. Change* **1998**, *39*, 519–540.
161. Frank, D.; Reichstein, M.; Bahn, M.; Thonicke, K.; Frank, D.; Mahecha, M.D.; Smith, P.; Van der Velde, M.; Vicca, S.; Babst, F. Effects of climate extremes on the terrestrial carbon cycle: Concepts, processes and potential future impacts. *Glob. Change Biol.* **2015**, *21*, 2861–2880.
162. Aitken, S.N.; Yeaman, S.; Holliday, J.A.; Wang, T.; Curtis-McLane, S. Adaptation, migration or extirpation: Climate change outcomes for tree populations. *Evol. Appl.* **2008**, *1*, 95–111.

163. Jarvis, P.G. Atmospheric carbon dioxide and forests. *Philos. Trans. R. Soc. Lond. B Biol. Sci.* **1989**, *324*, 369–392.
164. Jenkins, M.; Schaap, B. Forest ecosystem services. *Backgr. Anal. Study* **2018**, *1*.
165. Thom, D.; Rammer, W.; Seidl, R. The impact of future forest dynamics on climate: Interactive effects of changing vegetation and disturbance regimes. *Ecol. Monogr.* **2017**, *87*, 665–684.
166. Sheil, D. Forests, atmospheric water and an uncertain future: The new biology of the global water cycle. *For. Ecosyst.* **2018**, *5*, 19.
167. Barbier, S.; Gosselin, F.; Balandier, P. Influence of tree species on understory vegetation diversity and mechanisms involved—A critical review for temperate and boreal forests. *For. Ecol. Manag.* **2008**, *254*, 1–15.
168. Kobe, R.K. Intraspecific variation in sapling mortality and growth predicts geographic variation in forest composition. *Ecol. Monogr.* **1996**, *66*, 181–201.
169. Aminu, M.D.; Nabavi, S.A.; Rochelle, C.A.; Manovic, V. A review of developments in carbon dioxide storage. *Appl. Energy* **2017**, *208*, 1389–1419.
170. Harper, K.A.; Macdonald, S.E.; Burton, P.J.; Chen, J.; Brosofske, K.D.; Saunders, S.C.; Euskirchen, E.S.; Roberts, D.; Jaiteh, M.S.; Esseen, P.A. Edge influence on forest structure and composition in fragmented landscapes. *Conserv. Biol.* **2005**, *19*, 768–782.
171. Seidl, R.; Fernandes, P.M.; Fonseca, T.F.; Gillet, F.; Jönsson, A.M.; Merganičová, K.; Netherer, S.; Arpaci, A.; Bontemps, J.-D.; Bugmann, H. Modelling natural disturbances in forest ecosystems: A review. *Ecol. Model.* **2011**, *222*, 903–924.
172. Fassnacht, F.E.; White, J.C.; Wulder, M.A.; Næsset, E. Remote sensing in forestry: Current challenges, considerations and directions. *For. Int. J. For. Res.* **2024**, *97*, 11–37.
173. Nehrbass-Ahles, C.; Babst, F.; Klesse, S.; Nötzli, M.; Bouriaud, O.; Neukom, R.; Dobbertin, M.; Frank, D. The influence of sampling design on tree-ring-based quantification of forest growth. *Glob. Change Biol.* **2014**, *20*, 2867–2885.
174. Rejou-Mechain, M.; Muller-Landau, H.C.; Detto, M.; Thomas, S.C.; Le Toan, T.; Saatchi, S.S.; Barreto-Silva, J.S.; Bourg, N.A.; Bunyavejchewin, S.; Butt, N. Local spatial structure of forest biomass and its consequences for remote sensing of carbon stocks. *Biogeosciences* **2014**, *11*, 6827–6840.
175. Sengupta, A. FOREST: Future-Oriented AI Systems for Enhancing Plant Health Monitoring and Sustainable Treatments in Precision Agriculture. In Proceedings of the 2024 IEEE International Symposium on Technology and Society (ISTAS), Puebla, Mexico, 18–20 September 2024; pp. 1–8.
176. Kuzu, R.S.; Antropov, O.; Molinier, M.; Dumitru, C.O.; Saha, S.; Zhu, X.X. Forest disturbance detection via self-supervised and transfer learning with sentinel-1&2 images. *IEEE J. Sel. Top. Appl. Earth Obs. Remote Sens.* **2024**, *17*, 4751–4767.
177. Samadzadegan, F.; Toosi, A.; Dadrass Javan, F. A critical review on multi-sensor and multi-platform remote sensing data fusion approaches: Current status and prospects. *Int. J. Remote Sens.* **2024**, *46*, 1327–1402.
178. Schlickmann, M.B.; Bueno, I.T.; Valle, D.; Hammond, W.M.; Prichard, S.J.; Hudak, A.T.; Klauberg, C.; Karasinski, M.A.; Brock, K.M.; Rocha, K.D.; et al. Statewide Forest Canopy Cover Mapping of Florida Using Synergistic Integration of Spaceborne LiDAR, SAR, and Optical Imagery. *Remote Sens.* **2025**, *17*, 320.
179. Cheng, M.; Liu, K.; Liu, Z.; Xu, J.; Zhang, Z.; Sun, C. Combination of Multiple Variables and Machine Learning for Regional Cropland Water and Carbon Fluxes Estimation: A Case Study in the Haihe River Basin. *Remote Sens.* **2024**, *16*, 3280.
180. Zhu, J.; Xie, Y.; Fu, H.; Wang, C. Penetration Mapping of Forest Cover Using Spaceborne P-band SAR: A Review of the European Space Agency's BIOMASS Mission. *Geomat. Inf. Sci. Wuhan Univ.* **2024**.
181. O'Mara, T.; Meador, A.S.; Colavito, M.; Waltz, A.; Barton, E. Navigating the evolving landscape of wildfire management: A systematic review of decision support tools. *Trees For. People* **2024**, *16*, 100575.

Disclaimer/Publisher's Note: The statements, opinions and data contained in all publications are solely those of the individual author(s) and contributor(s) and not of MDPI and/or the editor(s). MDPI and/or the editor(s) disclaim responsibility for any injury to people or property resulting from any ideas, methods, instructions or products referred to in the content.



质谱学报
Journal of Chinese Mass Spectrometry Society
ISSN 1004-2997,CN 11-2979/TH

《质谱学报》网络首发论文

题目：基于单细胞质谱组学研究珊瑚共生虫黄藻的化学多样性
作者：张佳宇，陈仕国，余克服，梁甲元，侯壮豪，裴继影
收稿日期：2025-05-27
网络首发日期：2025-08-12
引用格式：张佳宇，陈仕国，余克服，梁甲元，侯壮豪，裴继影．基于单细胞质谱组学研究珊瑚共生虫黄藻的化学多样性[J/OL]．质谱学报.
https://link.cnki.net/urlid/11.2979.TH.20250812.1603.003



网络首发：在编辑部工作流程中，稿件从录用到出版要经历录用定稿、排版定稿、整期汇编定稿等阶段。录用定稿指内容已经确定，且通过同行评议、主编终审同意刊用的稿件。排版定稿指录用定稿按照期刊特定版式（包括网络呈现版式）排版后的稿件，可暂不确定出版年、卷、期和页码。整期汇编定稿指出版年、卷、期、页码均已确定的印刷或数字出版的整期汇编稿件。录用定稿网络首发稿件内容必须符合《出版管理条例》和《期刊出版管理规定》的有关规定；学术研究成果具有创新性、科学性和先进性，符合编辑部对刊文的录用要求，不存在学术不端行为及其他侵权行为；稿件内容应基本符合国家有关书刊编辑、出版的技术标准，正确使用和统一规范语言文字、符号、数字、外文字母、法定计量单位及地图标注等。为确保录用定稿网络首发的严肃性，录用定稿一经发布，不得修改论文题目、作者、机构名称和学术内容，只可基于编辑规范进行少量文字的修改。

出版确认：纸质期刊编辑部通过与《中国学术期刊（光盘版）》电子杂志社有限公司签约，在《中国学术期刊（网络版）》出版传播平台上创办与纸质期刊内容一致的网络版，以单篇或整期出版形式，在印刷出版之前刊发论文的录用定稿、排版定稿、整期汇编定稿。因为《中国学术期刊（网络版）》是国家新闻出版广电总局批准的网络连续型出版物（ISSN 2096-4188，CN 11-6037/Z），所以签约期刊的网络版上网络首发论文视为正式出版。

网络首发时间：2025-08-12 18:04:14　网络首发地址：https://link.cnki.net/urlid/11.2979.TH.20250812.1603.003

基于单细胞质谱组学研究珊瑚共生虫黄藻的化学多样性

张佳宇[1]，陈仕国[1]，余克服[1]，梁甲元[1]，侯壮豪[2]，裴继影[1]

（1. 广西大学，广西南海珊瑚礁研究重点实验室，广西大学珊瑚礁研究中心，广西大学海洋学院，广西 南宁 530004；
2. 中国科学技术大学化学与材料科学学院，安徽 合肥 230000）

摘要：虫黄藻（Symbiodiniaceae）作为珊瑚共生体的重要组成部分，其生态特征在决定珊瑚对环境胁迫的响应中发挥着关键作用。然而，目前尚不清楚不同生态类型虫黄藻的代谢多样性是否与其环境适应能力密切相关。为揭示二者之间的关联，本研究基于单细胞质谱组学技术，系统解析了耐光照的 *Symbiodinium* 属（A 型）、广泛分布的 *Cladocopium* 属（C 型）及耐热的 *Durusdinium* 属（D 型）3 种不同生态类型的虫黄藻代谢特征。结果表明，A 型虫黄藻的亮氨酸含量显著低于 C 型和 D 型，C 型虫黄藻富集缬氨酸，而 D 型虫黄藻特异性积累二甲基巯基丙酸内盐（dimethylsulfoniopropionate, DMSP）。高分辨串联质谱（HRMS/MS）碎片离子匹配进一步验证了代谢物鉴定的可靠性。因此，推测 A 型虫黄藻可能通过调控还原型辅酶 I（reduced nicotinamide adenine dinucleotide, NADH）再生途径增强光保护能力，C 型虫黄藻通过调节宿主氨基酸代谢维持共生稳态，而 D 型虫黄藻依赖抗氧化防御系统提升对环境胁迫的耐受性。本研究为珊瑚共生虫黄藻的适应机制提供了新的分子视角，有助于深入理解珊瑚-虫黄藻共生体系在全球气候变化背景下的响应机制。

关键词：单细胞；质谱；虫黄藻；代谢组学

中图分类号： **O657.63**　　**文献标识码：**A

DOI: 10.7538/zpxb.2025.0069　　**CSTR:** 32365.14. zpxb.2025.0069

Study on Chemical Diversity of Coral-Symbiotic Symbiodiniaceae Based on Single-Cell Mass Spectrometry

ZHANG Jia-yu[1], CHEN Shi-guo[1], YU Ke-fu[1], LIANG Jia-yuan[1], HOU Zhuang-hao[2], PEI Ji-ying[1]

(1. *School of Marine Sciences, Coral Reef Research Center of China, Guangxi Laboratory on the Study of Coral Reefs in the South China Sea, Guangxi University, Nanning* 530004*, China;*
2. *School of Chemistry and Materials Science, University of Technology and Science of China, Hefei 230000, China*)

Abstract: Coral reefs, often referred to as the ‘tropical rainforests of the sea’, are among the most ecologically diverse and productive marine ecosystems on Earth. However, climate change—especially global ocean warming—has triggered widespread coral bleaching events, posing a severe threat to reef biodiversity, structure, and their function. Central to coral resilience is the symbiotic relationship with Symbiodiniaceae, a family of photosynthetic dinoflagellates that provide essential nutrients to the coral host. The environmental adaptability of this symbiosis is strongly influenced by the physiological and metabolic traits of the symbionts. While extensive research has characterized Symbiodiniaceae diversity and abundance at the population level, relatively little is known about the metabolic and functional heterogeneity that exists at the level of individual cells—particularly across phylogenetically distinct clades. To address this gap, a custom-built induced nano-electrospray ionization (Induced nanoESI) single-cell mass spectrometry platform was developed and applied. This platform enables high-sensitivity, label-free profiling of intracellular metabolites from individual Symbiodiniaceae cells, facilitating a more detailed

国家自然科学基金项目（22264003）；广西科技基地与人才专项（桂科 AD25069075）；广西自然科学基金项目（2023GXNSFAA026488）；广西大学大学生创新创业训练计划（202410593445）；广西大学大学生创新创业训练计划（202410593442）
本文通信作者裴继影、侯壮豪

understanding of their functional and metabolic diversity. This platform was applied to characterize the metabolic profiles of three ecologically divergent Symbiodiniaceae clades, including the light-tolerant *Symbiodinium* (Clade A), the broadly distributed *Cladocopium* (Clade C), and the thermotolerant *Durusdinium* (Clade D). The method demonstrated good reproducibililty and sensitivity in single-cell metabolomics. Using multivariate statistical analyses—including principal coordinate analysis (PCoA) and orthogonal partial least squares discriminant analysis (OPLS-DA)—we observed clear metabolic differentiation among the three clades. Clear metabolic differentiation among the three clades was observed using multivariate statistical analyses, including principal coordinate analysis (PCoA) and orthogonal partial least squares discriminant analysis (OPLS-DA). A total of 14 differential metabolites were identified through high-resolution mass spectrometry (HRMS) and further confirmed by liquid chromatography coupled to hybrid high-resolution mass spectrometry (LC-HRMS/MS) spectral matching. Among these, leucine was found to be significantly depleted in Clade A relative to Clades C and D; valine was highly enriched in Clade C; and dimethylsulfoniopropionate (DMSP), a well-known osmoprotectant and antioxidant, was specifically accumulated in Clade D. These results suggest distinct clade-specific metabolic strategies. It is proposed that leucine biosynthesis is downregulated by Clade A to reduce acetyl-CoA accumulation, thereby promoting reduced nicotinamide adenine dinucleotide (NADH) regeneration and enhancing cyclic electron flow under high-light stress. Clade C's elevated valine levels may aid in host nutritional support and symbiotic stability. Clade D's high DMSP production likely contributes to oxidative stress resistance and thermal tolerance. In conclusion, this study highlights the power of single-cell metabolomics in uncovering functional diversity within symbiodiniaceae. New molecular insights into coral-symbiont interactions are provided by our findings, and a foundation is established for understanding how clade-specific metabolic adaptations contribute to coral reef resilience in a changing climate.
Key words: single-cell; mass spectrometry; symbiodiniaceae; metabolomics

珊瑚礁作为海洋生态系统的重要组成部分，凭借其丰富的生物多样性和较高的初级生产力，被誉为“海洋中的热带雨林”[1]。除提供渔业资源和天然药物原料外，珊瑚礁还在旅游服务、海岸防护等方面发挥着不可替代的生态与经济功能[2-4]。然而，近年来全球气候变化导致珊瑚礁大规模白化，例如 1997~1998 年、2009~2010 年以及 2015~2017 年发生的 3 次全球性“珊瑚白化”事件，波及了全球 70%以上的珊瑚礁区[5-7]。珊瑚白化是指珊瑚宿主通过胞吐作用主动排出共生虫黄藻（Symbiodiniaceae），导致光合色素丧失、骨骼显现白色的现象，其中海表温度异常升高被认为是主要的诱因[8]。高温引发的珊瑚白化威胁着珊瑚礁的存活，并影响其生长、繁殖和生态功能。

近年来，适应性白化假说提出，珊瑚能够通过调节体内共生虫黄藻的群落结构，来提升对环境胁迫的耐受性。研究表明，珊瑚在经历热胁迫后，可通过改变优势虫黄藻类型以增强热耐受性。例如，Berkelmans 等[9]通过将鹿角珊瑚（*Acropora millepora*）移植至高温海域发现，其体内主要共生藻型由热敏感的 *Cladocopium* 属转变为耐热性更强的 *Durusdinium* 属，珊瑚的热耐受阈值提高了 1~1.5 ℃。同样，Baker 等[10]在 1997~1998 年 ENSO 事件前后对巴拿马海域 *Pocillopora* 属珊瑚的跟踪研究发现，含 *Durusdinium* 属虫黄藻的珊瑚比例由 43%升至 63%，且几乎未发生白化，而以 *Cladocopium* 属共生的珊瑚则出现严重白化。系统发育分析显示，虫黄藻科已被鉴定出 11 个属，其中与珊瑚形成稳定共生关系的主要包括 *Symbiodinium*（A 型）、*Breviolum*（B 型）、*Cladocopium*（C 型）和 *Durusdinium*（D 型）等[11-14]。不同属虫黄藻在生理生态特性上存在显著差异：A 型耐高光环境，C 型物种丰富且生态位广泛，D 型则在高温波动及高浊度环境中表现出更强的耐受性[11]。可见，珊瑚对环境胁迫的耐受性在很大程度上取决于其共生虫黄藻群落的组成与结构。然而，目前多数研究主要集中在群体水平，对珊瑚组织中虫黄藻的整体种类和丰度进行分析，忽略了单细胞层面上虫黄藻细胞间潜在的功能和代谢异质性[15]。细胞间代谢差异可能在珊瑚应对环境变化、帮助

珊瑚白化恢复等过程中发挥关键作用。因此，为深入揭示不同属虫黄藻在珊瑚-虫黄藻共生关系中的功能异质性，有必要引入具备单细胞分辨率的代谢组学等高通量分析技术，以解析不同虫黄藻个体间的代谢差异及其在环境适应中的潜在作用。

单细胞分析技术以单个细胞为研究单位，能够独立、精准地解析珊瑚共生虫黄藻的代谢特征，揭示被群体平均效应掩盖的细胞特异性机制。目前，单细胞分析常用的方法包括荧光检测、超微电极电化学检测、色谱分析与质谱分析等，其中，质谱技术凭借高灵敏度和高分辨率的优点，已成为单细胞代谢组学研究的核心手段[16]。纳升电喷雾离子化（nano-electrospray ionization, nano-ESI）作为广泛应用的单细胞质谱离子化方式，在单细胞分子分析中发挥着重要作用[17]。传统 nano-ESI 技术通过将金属丝插入毛细管并施加高电压实现样品离子化，但其操作复杂，且金属电极直接接触样品溶液易引发电化学干扰，导致代谢物氧化或其他变化。为此，感应电喷雾离子化（Induced nano-electrospray ionization, Induced nanoESI）技术应运而生。该方法避免了电极与样品溶液的直接接触，不仅简化了电压施加流程，还显著降低了电化学副反应对代谢物信号的干扰[18]。Induced nanoESI 技术已成功应用于神经元、肿瘤细胞及溶酶体等多种单细胞或细胞器的代谢组学研究，展现出优异的灵敏度和良好的重复性[19-22]。

本研究基于 Induced nanoESI 质谱技术，针对 A、C、D 三属珊瑚共生虫黄藻进行单细胞代谢组学分析。通过多元统计分析系统地比较三属虫黄藻在单细胞水平的代谢指纹特征，筛选具有属特异性的标志性代谢物，并结合液相色谱-高分辨质谱串联（liquid chromatography coupled to hybrid high-resolution mass spectrometry, LC-HRMS/MS）技术进行验证。进一步探讨关键代谢物在珊瑚-虫黄藻共生体系中参与化学生态适应机制的潜在作用，旨在为揭示珊瑚礁生态系统应对环境变化的代谢调控策略提供新的单细胞代谢学证据与理论支撑。

1 实验部分

1.1 主要仪器与装置

Exactive Plus Orbitrap 质谱仪、UPLC-Q-Exactive Orbitrap 质谱仪：美国 Thermo Fisher Scientific 公司产品；Olympus CK2 倒置显微镜：日本 Olympus 公司产品；Burleigh 显微操作平台、Sutter Instruments P-2000 激光微移液器：美国 Novato 公司产品；Sigma 3-18K 高速冷冻离心机：德国 SIGMA 公司产品。

1.2 主要材料与试剂

Reef Crystals 人工海盐：美国 Instant Ocean 公司产品；硼硅玻璃毛细管（外径 1.2 mm，内径 0.9 mm）：美国 SUTTER INSTRUMENT 公司产品；L1 培养基：上海光语生物科技有限公司产品；甲醇：德国 Merck 公司产品；卡那霉素、氨苄青霉素、链霉素、两性霉素 B：德国 BIOFROX 公司产品。

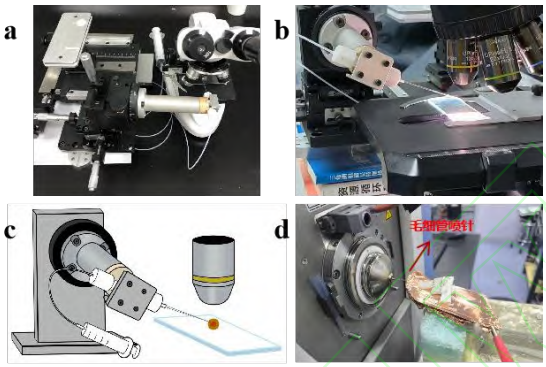
1.3 虫黄藻的培养

使用人工海盐配制盐度为 35‰的人工海水，初始 pH 值调至 8.2。海水经 0.22 μm 孔径微孔滤膜，通过真空抽滤系统预过滤后，置于高压蒸汽灭菌器中，在 121 ℃下灭菌 15 min，冷却至室温，备用。以灭菌后的人工海水为基质，配制含抗生素的 L1 培养基，抗生素添加浓度为 50 mg/L 卡那霉素、100 mg/L 氨苄青霉素、50 mg/L 链霉素、2.5 mg/L 两性霉素 B。A、C 和 D 型虫黄藻在盐度 35‰、温度（25±1）℃、光照强度 90 μmol/(m²·s)、明暗周期为 14 h 光照/10 h 黑暗的培养条件下生长。

1.4 单细胞质谱分析

1.4.1 样品制备　取 2 μL 初始浓度为 6.1×10^5 cells/mL 的虫黄藻细胞悬液，均匀滴加在载玻片表面。为便于在显微镜下快速定位目标细胞，先使用马克笔在载玻片上划定 1 个圆形区

域，然后将细胞悬液滴加在该区域内。随后在 25 ℃恒温条件下静置 5 min，以使细胞沉底。使用拉制仪制备尖端孔径约为 1.0 μm 的硼硅玻璃毛细管，其拉制参数设定如下：加热强度（heat）=550，加热线圈类型（filament）=4，拉伸速度（velocity）=23，延迟时间（delay）=130，拉力强度（pull）=50。毛细管内预先注入超纯水作为电极内液。将装载溶剂的毛细管连接至气压控制装置，随后固定在显微操作平台上。实验中，将毛细管尖端接触目标单细胞膜表面，并将针尖插入细胞，通过气压系统实现对单细胞内容物的抽取。取样平台的构建及操作示意图示于图 1a~1c。



注：a, b. 单细胞取样实验装置实物图；c. 单细胞取样示意图；d. 单细胞质谱分析平台

图 1　实验装置图

Fig.1　Experimental setup

1.4.2　质谱分析　　单细胞质谱分析平台示于图 1d，将装载有样品的毛细管尖端对准质谱锥口，并保持约 5 mm 的距离。在感应电极上施加幅值 10 kV、频率 1 000 Hz 的交流电压，在感应电场作用下，实现毛细管内液体的电喷雾与离子化，从而获得单细胞的质谱信号。质谱采集采用正离子模式，因其具有较高的离子化效率和信噪比，可实现灵敏且稳定的检测效果，因此广泛应用于单细胞质谱分析中[21, 23-26]。相比之下，负离子模式在 Induced nanoESI 过程中更易发生放电，降低喷雾稳定性，进而影响信号质量。在相同条件下，分别采集 A、C、D 三属虫黄藻各 24 个单细胞数据。质谱参数设置如下：S 型离子透镜的 s-lens 设为 50%（正离子模式），毛细管温度 275 ℃，质量分辨率 140 000，微扫描数量设置为 1，最大离子注入时间 10 ms。

1.4.3　数据分析　　原始质谱数据通过 Thermo Fisher Xcalibur 软件导出，并在 MATLAB 2016b 平台上进行处理，包括峰位对齐与峰强度提取。为减少因盐基质抑制、仪器敏感度变化及喷雾效率波动所带来的系统误差，本实验采用总离子流归一化方法。具体而言，将每个代谢物峰面积标准化到其所属样本的总离子流强度上[27]。归一化后的数据用于后续的多维统计分析和差异筛选，以此提高数据的稳定性、可比性与分析的可靠性。

1.4.4　代谢物鉴定　　单细胞质谱分析得到的数据基于 PlantCy 代谢物库，通过精确的质量数进行代谢物鉴定。检索的物质以质子化形式（$[M+H]^+$），钠、钾、NH_3 加合物的形式（$[M+Na]^+$、$[M+K]^+$、$[M+NH_4]^+$），脱水形式（$[M+H—H_2O]^+$、$[M+H—2H_2O]^+$）的理论分子质量为基准，当质量数的误差小于 10^{-5} 时，即认为其为同一代谢物。

1.5　LC-HRMS/MS 分析

1.5.1　样品制备　　取 50 mL 虫黄藻细胞悬液，在 4 ℃下以 2 500×g 离心 5 min，弃除上清液，保留细胞沉淀。向细胞沉淀中加入 1 mL 体积分数为 70%的甲醇水溶液，摇晃均匀。将混合液超声处理 20 min 后，再次在 4 ℃下以 2 500×g 离心 5 min，收集上清液。随后，使用孔径为 0.22 μm 的有机系针式过滤器对上清液进行过滤，并转移至色谱小瓶中。A、C、D 属

虫黄藻每种样品均制备 4 个生物学重复，最后对提取物进行 LC-HRMS/MS 分析。

1.5.2 仪器分析　使用 ACQUITY CSH C18 色谱柱（2.1 mm×100 mm，1.7 μm）进行色谱分离，流速 200 μL/min，温度 30 ℃。流动相为含 0.1%甲酸的水溶液（A 相）和含 0.1%甲酸的甲醇溶液（B 相）；梯度为 0~3 min（5%B），3~20 min（5%~95%B），系统随后在 95%B 下维持 5 min，然后在 1 min 内切换到 5%B，并在下次进样前进行 4 min 平衡，每个样品的进样体积为 2 μL。采用数据依赖采集模式，鞘气流速 35 L/min，辅助气体流速 15 L/min，扫气流速 0 L/min，辅助气体温度 250 ℃。喷雾电压设置为 3.5 kV，进样毛细管温度 350 ℃，S-lens 射频电压设置为 50 V。在全扫描模式下，质量扫描范围 *m/z* 100~1 000，分辨率 35 000（$R_{m/z}$ 200）。最大离子注入时间设为 100 ms，自动增益控制（automatic gain control, AGC）目标值为 3.0×10^6。在 MS/MS 模式下，每次采集选择最强的前 10 个母离子进行碎片化。碎片扫描分辨率设为 17 500（$R_{m/z}$ 200），最大离子注入时间 50 ms，AGC 目标值设为 1.0×10^5。母离子隔离窗口宽度为 *m/z* 1.5，归一化碰撞能量按 15%~30%逐步递增。

1.5.3 质谱数据预处理　使用 MZmine 4.3.0 软件对原始质谱数据进行预处理，以提取代谢物特征信息。预处理流程包括以下 9 个步骤：1）进行质谱峰检测，提取 *m/z* 特征信号；2）采用自动化数据分析工作流算法进行色谱峰构建；3）通过局部最小特征解析进行解卷积；4）使用 ^{13}C 同位素过滤以去除同位素干扰；5）通过峰对齐匹配不同样本中的特征峰；6）进行峰识别；7）应用重复特征过滤去除冗余信号；8）利用特征筛选剔除低质量峰；9）最后进行线性归一化以校正样本间的信号偏差。

1.5.4 代谢物鉴定　将 MZmine 软件导出的 mgf 格式文件与特征量化表上传至 GNPS 平台，用于代谢物鉴定分析。参数设置中，母离子质量容差和碎片离子质量容差均设置为 0.02 u，其余参数保持默认值。

1.6 统计学分析

鉴于单细胞质谱数据的稀疏性、强非正态分布及复杂非线性结构，本文采用主坐标分析（principal coordinate analysis, PCoA）对单细胞数据进行无监督统计学分析。PCoA 在 RStudio（R for Windows 4.4.3）中进行，基于 vegan 包的 vegdist（）函数计算 Bray-Curtis 距离矩阵，随后使用 adonis（）函数（置换次数设为 999）进行置换多元方差分析（permutational multivariate analysis of variance, PERMANOVA）检验，以评估组间差异。为进一步识别潜在差异代谢物，在 SIMCA-P v14.1 软件中进行正交偏最小二乘判别分析（orthogonal partial least squares discriminant analysis, OPLS-DA），并计算变量投影重要性（variable importance in projection, VIP）值。VIP 值大于 1.0 的代谢物被认为是具有显著区分贡献的候选差异标志物。数据正态性通过 Shapiro-Wilk 检验评估，符合正态分布时采用独立样本 *t* 检验，非正态分布时采用非参数检验。$p<0.05$ 被认为具有统计学差异，$p<0.01$ 表示具有高度统计学差异。

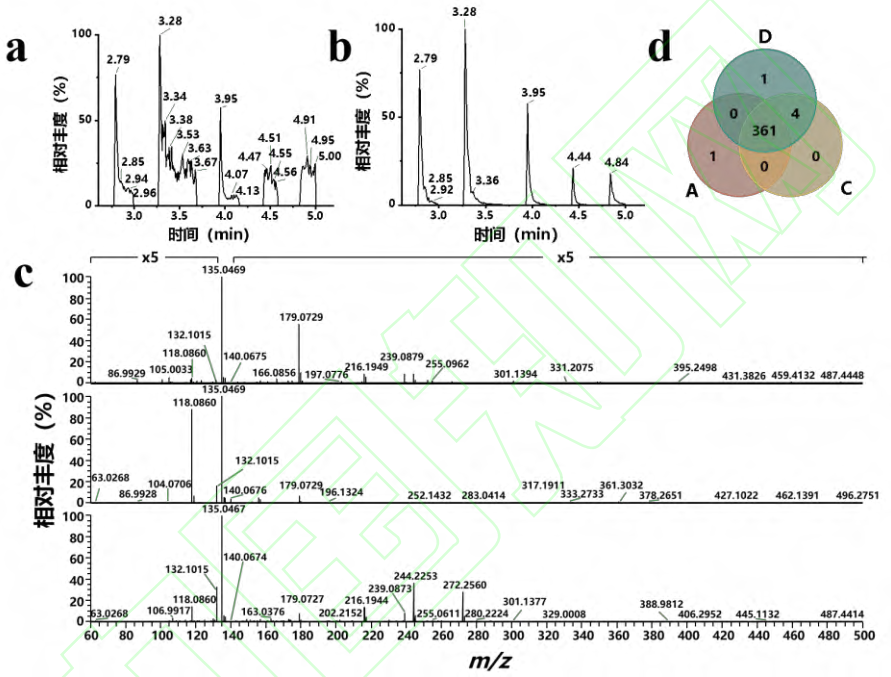
2 结果与讨论

2.1 虫黄藻单细胞质谱分析的性能表征

本研究基于自建的单细胞质谱分析平台，对虫黄藻细胞进行系统的分析性能评估。在连续 5 次测试中，单个虫黄藻细胞的信号持续时间稳定在 0.15~0.42 min 之间，表明该方法在重复性方面表现良好，示于图 2a。以 *m/z* 135.046 9 的代谢物为代表，其信号在 0.20 min 内迅速达到峰值并迅速衰减至基线，提示细胞内代谢物在极短时间内完成释放与电离过程，示于图 2b。这一特征可归因于虫黄藻细胞体积较小（细胞直径为 8~11 μm，体积估算约为 512~1 331 μm^3），导致其胞内代谢物总量有限。当施加电压引发电喷雾过程后，代谢物立即释放至电喷雾区域，在毛细管末端形成瞬时强信号。随着胞内物质耗尽，后续信号主要来源于毛细管中残余溶剂和背景离子。

质谱分析结果表明，该平台对低分子质量代谢物（*m/z*<300）具有良好的检测灵敏度，

而高分子质量代谢物的检出率较低，示于图 2c。可能原因是单细胞样本基质复杂，抑制了大分子代谢物的电离效率与挥发能力，限制其被质谱捕获。值得注意的是，*m/z* 135.046 9 的代谢物在所有检测信号中表现出最强的相对丰度，推测其可能为虫黄藻中一种重要的胞内代谢物，在后续的结构鉴定和功能解析中需给予重点关注。为评估不同属虫黄藻代谢组组成的一致性，本实验对三属虫黄藻样品（A、C、D 型）进行代谢物的韦恩图分析，示于图 2d。结果显示，共检出的代谢物中有 361 种为三者共有，所占比例显著，说明这三属虫黄藻在基础代谢组成上高度一致。同时，仅在 A 型和 D 型中各检出 1 种特异性代谢物，而在 C 型中未检出特异性成分，表明其核心代谢物组成差异极小，仅存在有限的种属特异性表达。进一步基于 PlantCyc 代谢物数据库和 LC-HRMS/MS 二级质谱图，对所有检测到的代谢物进行比对鉴定，最终确认了 14 种代谢物，具体信息列于表 1。



注：a. 连续 5 次单细胞分析的总离子流图；b. 最强信号代谢物（*m/z* 135.046 9）的提取离子流图；c. 三属虫黄藻（A、C、D）典型的单细胞分析质谱图；d. 三属虫黄藻（A、C、D）代谢产物的韦恩图

图 2　虫黄藻单细胞的质谱分析

Fig.2　Single-cell mass spectrometry analysis of Symbiodiniaceae

表 1　虫黄藻代谢物鉴定结果

Table 1　Identification results of Symbiodiniaceae metabolites

中文名 Chinese name	英文名 English name	实测 *m/z* Experimental *m/z*	加合离子类型 Adduct type	理论 *m/z* Theoretical *m/z*	误差/10^{-6} Error/10^{-6}
3-氨基丙醛	3-Aminopropionaldehyde	74.0603	$[M+H]^+$	74.0606	-4.05
戊内酯	Valerolactone	101.0595	$[M+H]^+$	101.0603	-7.92
阿拉伯糖醇	Arabitol	117.0545	$[M+H-2H_2O]^+$	117.0552	-5.98
缬氨酸	Valine	118.0866	$[M+H]^+$	118.0868	-1.69
烟酰胺	Nicotinamide	123.0551	$[M+H]^+$	123.0558	-5.69
焦谷氨酸	Pyroglutamic acid	130.0495	$[M+H]^+$	130.0504	-6.92
亮氨酸	Leucine	132.1021	$[M+H]^+$	132.1025	-3.03
二甲基巯基丙酸内盐（DMSP）	Dimethylsulfoniopropionate (DMSP)	135.0469	$[M+H]^+$	135.0480	-8.15
2-氨基苯甲酸	2-Aminobenzoic acid	138.0546	$[M+H]^+$	138.0555	-6.52
甜菜碱	Betaine	140.0676	$[M+Na]^+$	140.0687	-7.85
三羟基丁烷	Trihydroxybutane	145.0254	$[M+K]^+$	145.0267	-8.96
谷氨酰胺	Glutamine	147.0760	$[M+H]^+$	147.0770	-6.80
N-氨甲酰腐胺	*N*-Carbamoylputrescine	170.0681	$[M+K]^+$	170.0696	-8.82
精氨酸	Arginine	175.1183	$[M+H]^+$	175.1195	-6.85

2.2 差异代谢物筛选

为深入解析不同虫黄藻种属间的代谢组差异，本实验结合无监督的 PCoA 与有监督的 OPLS-DA 方法，对三属虫黄藻样品的代谢轮廓进行系统分析。PCoA 结果显示，三类样品在二维空间中显著分离，第一主坐标（principal coordinate 1, PCo1）和第二主坐标（principal coordinate 2, PCo2）分别解释了 41.5%和 14.2%的变异，总体累计解释变异达 55.7%，示于图 3a。PERMANOVA 检验进一步证实了组间差异具有统计学显著性（R^2=0.17，p=0.001），说明 3 种虫黄藻在代谢层面存在显著差异。OPLS-DA 模型进一步验证了该分离趋势，模型的拟合优度和预测能力分别为 R^2X=0.624、R^2Y=0.754 和 Q^2=0.594，显示出良好的分类性能，示于图 3b。200 次置换检验结果（p<0.01）排除了模型过拟合的可能性，表明 OPLS-DA 模型稳定可靠，可用于筛选虫黄藻间的差异代谢物。

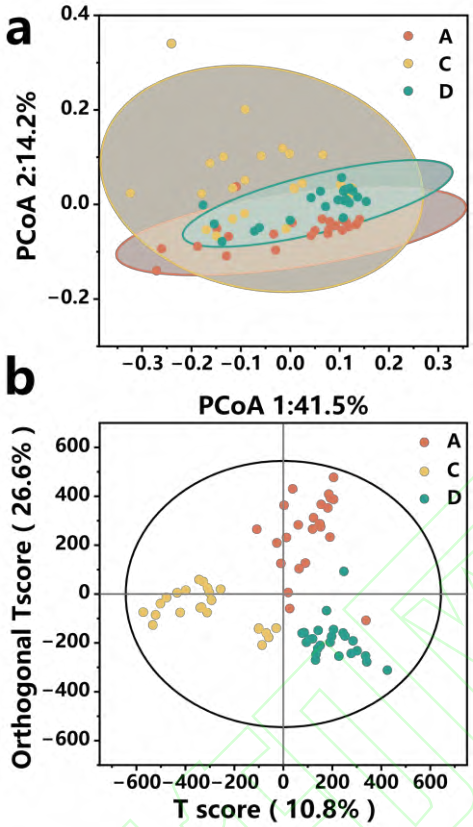
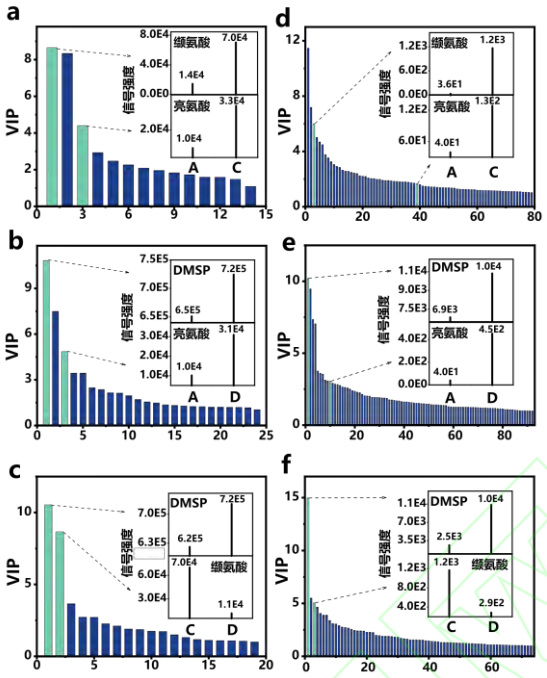


图 3　三属虫黄藻单细胞代谢物的 PCoA（a）和 OPLS-DA（b）得分图

Fig.3　PCoA (a) and OPLS-DA (b) score plots of single-cell metabolites of three clades of Symbiodiniaceae

基于三属虫黄藻单细胞代谢物 OPLS-DA 的结果，以变量重要性投影值（VIP>1.0）和显著性检验（p<0.05）为标准，筛选出具有显著差异的特征代谢物。从图 4a~4c 可见，在不同虫黄藻属间的比较中，A 型与 C 型：缬氨酸（VIP=8.660，p<0.001）和亮氨酸（VIP=4.405，p<0.001）在 C 型中含量显著高于 A 型；A 型与 D 型：DMSP（VIP=10.844，p=0.004）和亮氨酸（VIP=4.863，p<0.001）在 D 型中含量更高；C 型与 D 型：DMSP（VIP=10.544，p=0.011）在 D 型中富集，而缬氨酸（VIP=8.668，p<0.001）在 C 型中显著富集。综上，亮氨酸在所有比较组中以 A 型虫黄藻含量最低，缬氨酸在 C 型中最为富集，而 DMSP 在 D 型中含量最高。各差异代谢物在 3 种虫黄藻中的丰度分布情况示于图 5。同时，这些代谢物的 HRMS/MS 二级谱图与标准谱图的余弦相似度（cosine）相似度在 0.88~0.99 之间，表明匹配良好，示于图 6。此外，2 种平台下差异代谢物的丰度变化趋势一致，显著性水平相符，进一步证明了单细胞质谱方法在代谢物定性和定量分析中的稳定性和可靠性，示于图 4d~4f。



注：a、d 为 A、C 两属虫黄藻；b、e 为 A、D 两属虫黄藻；c、f 为 C、D 两属虫黄藻

图 4　三属虫黄藻单细胞质谱分析（a、b、c）和 LC-HRMS/MS 分析（d、e、f）的 VIP 图

Fig.4　VIP figures of single-cell mass spectrometry (a, b, c) and LC-HRMS/MS (d, e, f) of three clades of Symbiodiniaceae

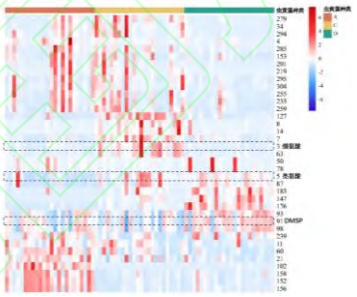


图 5　三属虫黄藻单细胞质谱中差异代谢物的丰度热图

Fig.5　Heatmap of differential metabolite abundances in single-cell mass spectrometry of three Symbiodiniaceae clades

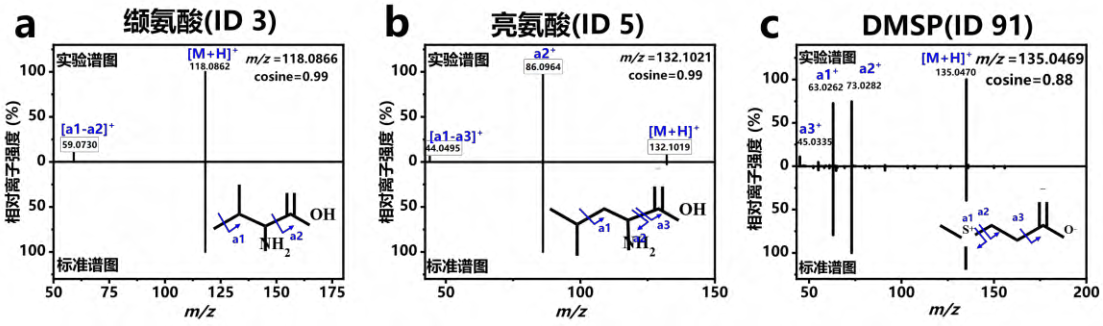


图 6　3 种差异代谢物的二级质谱图

Fig.6　LC-HRMS/MS spectra of three differential metabolites

2.3 差异代谢物功能分析

本实验进一步探讨了基于上述筛选获得的缬氨酸、亮氨酸和 DMSP 等 3 种关键差异代谢物在不同虫黄藻种属中的潜在生理功能，这些代谢物的差异分布模式与各虫黄藻的生态适应特征表现出一致性，提示它们可能在虫黄藻的环境适应和共生关系中发挥重要作用。

A 型虫黄藻表现出独特的亮氨酸代谢特征，其细胞内亮氨酸含量显著低于 C 型和 D 型虫黄藻，这一现象可能与其典型的高光环境适应性相关。A 型虫黄藻主要分布于浅海高光强的环境中，表现出显著的循环电子传递（cyclic electron flow, CEF）活性，以缓解高光胁迫下叶绿体内腺嘌呤核苷三磷酸/还原型辅酶 II （adenosine triphosphate/reduced nicotinamide adenine dinucleotide phosphate, ATP/NADPH）的代谢失衡[28]。根据现有研究并结合系统进化特征推测：A 型虫黄藻极可能依赖 II 型 NADH 脱氢酶（type II NADH dehydrogenase, NDH-2）介导的还原型辅酶I（reduced nicotinamide adenine dinucleotide, NADH）代谢途径来调节 CEF[29-30]。在代谢层面，亮氨酸首先降解形成 3-羟基-3-甲基戊二酰辅酶 A，然后在酶的作用下生成乙酰辅酶 A 和乙酰乙酸[31]。已有研究表明，乙酰辅酶 A 能通过反馈机制抑制 NADH 的再生[32]。因此，推测 A 型虫黄藻通过降低亮氨酸含量来减少乙酰辅酶 A 的生成，缓解其对 NADH 再生的抑制作用。这一代谢调控策略可能促进 NADH 的积累，进而增强依赖 NDH-2 的 CEF 活性，最终提高其对高光环境的适应能力。

作为目前分布最广泛的虫黄藻类型之一，C 型虫黄藻表现出显著的缬氨酸代谢特征，其细胞内缬氨酸含量显著高于 A 型和 D 型虫黄藻。这一代谢特征可能与其共生适应性密切相关。缬氨酸作为一种必需氨基酸，多数后生动物宿主无法自行合成，需通过外源性补充。相关研究表明，在刺胞动物中（如海葵和有孔虫），携带共生虫黄藻的个体体内缬氨酸水平显著高于无共生或去除共生体的对照组，表明共生虫黄藻可能在一定程度上弥补宿主在缬氨酸合成方面的不足[33-34]。因此，C 型虫黄藻中缬氨酸的富集可能增强其为宿主提供必需氨基酸的能力，从而提高共生的稳定性，促进其在多种宿主中的广泛分布和持久共生关系。这一代谢补偿机制可能是 C 型虫黄藻适应广泛生态环境的重要基础之一。

D 型虫黄藻表现出显著的环境适应特性，其细胞内 DMSP 含量显著高于其他 2 种虫黄藻。这一特征可能与其在温度和浊度波动较大环境中的生存策略直接相关。DMSP 及其裂解产物二甲基硫醚（dimethylsulphide, DMS）和丙烯酸酯在极端环境条件下发挥重要的抗氧化防御功能。它们能够与羟基自由基（·OH）等反应活性氧（reactive oxygen species, ROS）迅速反应，从而有效清除细胞内的自由基，特别是 DMS 和丙烯酸酯的反应活性可达到 DMSP 的 20~60 倍[35]。此外，DMSP 也参与浮游植物和大型海藻细胞内多种保护性生理机制，包括渗透压调节和低温适应[36-37]。基于这些发现，我们认为 D 型虫黄藻可能通过维持高水平的 DMSP，构建了 1 个包含抗氧化防御、渗透调节和温度适应在内的多层次保护系统，这为其在环境波动剧烈的生境中生存提供了重要的代谢保障。

3 结论

本研究通过自建的单细胞质谱分析平台，对不同属的虫黄藻进行了系统的代谢组学分析，并评估了该方法的重复性和灵敏度。结果表明，该平台在低分子质量代谢物检测中表现出良好的灵敏度，且具有较高的重复性，适用于虫黄藻细胞的代谢组学研究。基于 PCoA 和 OPLS-DA 的结果，发现不同属虫黄藻在整体代谢轮廓上存在显著差异，提示其在长期进化中可能形成了独特的代谢适应策略：A 型虫黄藻在高光强环境中可能通过调控亮氨酸代谢来缓解叶绿体内 ATP/NADPH 的代谢失衡；C 型虫黄藻可能通过为宿主提供缬氨酸来维持其与宿主的稳定共生关系；而 D 型虫黄藻则通过合成 DMSP 构建高效的抗氧化防御体系，从而提升其对极端环境的耐受能力。总体而言，本研究以单细胞代谢组学为手段，从分子水平揭示了不同属虫黄藻的代谢适应机制。该研究不仅为理解虫黄藻的环境响应和宿主共生策略提供了

思路，也为进一步探索珊瑚共生体的功能协同及其生态意义奠定了理论基础。

参考文献：

[1] 赵美霞, 余克服, 张乔民. 珊瑚礁区的生物多样性及其生态功能[J]. 生态学报, 2006, 26(1): 186-194.
ZHAO Meixia, YU Kefu, ZHANG Qiaomin. Review on coral reefs biodiversity and ecological function[J]. Acta Ecologica Sinica, 2006, 26(1): 186-194(in Chinese).
[2] SMITH S V. Coral-reef area and the contributions of reefs to processes and resources of the world's oceans[J]. Nature, 1978, 273(5 659): 225-226.

[3] WOODHEAD A J, HICKS C C, NORSTRÖM A V, WILLIAMS G J, GRAHAM N A J. Coral reef ecosystem services in the anthropocene[J]. Functional Ecology, 2019, 33(6): 1 023-1 034.
[4] PEIXOTO R S, SWEET M, BOURNE D G. Customized medicine for corals[J]. Frontiers in Marine Science, 2019, 6: 686.
[5] HUGHES T P, KERRY J T, ÁLVAREZ-NORIEGA M, ÁLVAREZ-ROMERO J G, ANDERSON K D, BAIRD A H, BABCOCK R C, BEGER M, BELLWOOD D R, BERKELMANS R, BRIDGE T C, BUTLER I R, BYRNE M, CANTIN N E, COMEAU S, CONNOLLY S R, CUMMING G S, DALTON S J, DIAZ-PULIDO G, MARK EAKIN C, FIGUEIRA W F, GILMOUR J P, HARRISON H B, HERON S F, HOEY A S, HOBBS J A, HOOGENBOOM M O, KENNEDY E V, KUO C Y, LOUGH J M, LOWE R J, LIU G, McCULLOCH M T, MALCOLM H A, McWILLIAM M J, PANDOLFI J M, PEARS R J, PRATCHETT M S, SCHOEPF V, SIMPSON T, SKIRVING W J, SOMMER B, TORDA G, WACHENFELD D R, WILLIS B L, WILSON S K. Global warming and recurrent mass bleaching of corals[J]. Nature, 2017, 543(7 645): 373-377.
[6] FENG M, McPHADEN M J, XIE S P, HAFNER J. La Niña forces unprecedented leeuwin current warming in 2011[J]. Scientific Reports, 2013, 3(1): 1 277.
[7] HUGHES T P, ANDERSON K D, CONNOLLY S R, HERON S F, KERRY J T, LOUGH J M, BAIRD A H, BAUM J K, BERUMEN M L, BRIDGE T C, CLAAR D C, MARK EAKIN C, GILMOUR J P, GRAHAM N A J, HARRISON H, HOBBS J A, HOEY A S, HOOGENBOOM M, LOWE R J, McCULLOCH M T, PANDOLFI J M, PRATCHETT M, SCHOEPF V, TORDA G, WILSON S K. Spatial and temporal patterns of mass bleaching of corals in the Anthropocene[J]. Science, 2018, 359(6 371): 80-83.
[8] DOUGLAS A E. Coral bleaching— how and why?[J]. Marine Pollution Bulletin, 2003, 46(4): 385-392.
[9] BERKELMANS R, van OPPEN M J H. The role of zooxanthellae in the thermal tolerance of corals: a 'nugget of hope' for coral reefs in an era of climate change[J]. Proceedings Biological Sciences, 2006, 273(1 599): 2 305-2 312.
[10] BAKER A C, STARGER C J, McCLANAHAN T R, GLYNN P W. Corals' adaptive response to climate change[J]. Nature, 2004, 430(7 001): 741.
[11] LaJEUNESSE T C, PARKINSON J E, GABRIELSON P W, JEONG H J, REIMER J D, VOOLSTRA C R, SANTOS S R. Systematic revision of Symbiodiniaceae highlights the antiquity and diversity of coral endosymbionts[J]. Current Biology, 2018, 28(16): 2 570-2 580.
[12] POCHON X, LaJEUNESSE T C. *Miliolidium* n. gen, a new symbiodiniacean genus whose members associate with soritid foraminifera or are free-living[J]. Journal of Eukaryotic Microbiology, 2021, 68(4): e12856.
[13] NITSCHKE M R, CRAVEIRO S C, BRANDÃO C, FIDALGO C, SERÔDIO J, CALADO A J, FROMMLET J C. Description of *Freudenthalidium* gen. nov. and *Halluxium* gen. nov. to Formally Recognize Clades Fr3 and H as Genera in the Family Symbiodiniaceae (Dinophyceae)[J]. Journal of Phycology, 2020, 56(4): 923-940.
[14] LaJEUNESSE T C, WIEDENMANN J, CASADO-AMEZÚA P, D'AMBRA I, TURNHAM K E, NITSCHKE M R, OAKLEY C A, GOFFREDO S, SPANO C A, CUBILLOS V M, DAVY S K, SUGGETT D J. Revival of

Philozoon Geddes for host-specialized dinoflagellates, 'zooxanthellae', in animals from coastal temperate zones of northern and southern hemispheres[J]. European Journal of Phycology, 2022, 57(2): 166-180.
[15] CHEN B, WEI Y, YU K, LIANG Y, YU X, LIAO Z, QIN Z, XU L, BAO Z. The microbiome dynamics and interaction of endosymbiotic *Symbiodiniaceae* and fungi are associated with thermal bleaching susceptibility of coral holobionts[J]. Applied and Environmental Microbiology, 2024, 90(4): e0193923.
[16] ZHU Y, LIU R, YANG Z. Redesigning the T-probe for mass spectrometry analysis of online lysis of non-adherent single cells[J]. Analytica Chimica Acta, 2019, 1 084: 53-59.
[17] 尤穆英楠, 刘心昱, 石先哲, 许国旺. 基于质谱的单细胞分析技术研究新进展[J]. 质谱学报, 2024, 45(3): 316-331.
YOU Muyingnan, LIU Xinyu, SHI Xianzhe, XU Guowang. New advances of single-cell analysis based on mass spectrometry[J]. Journal of Chinese Mass Spectrometry Society, 2024, 45(3): 316-331(in Chinese).
[18] PEI J, ZHOU X, WANG X, HUANG G. Alleviation of electrochemical oxidation for peptides and proteins in electrospray ionization: obtaining more accurate mass spectra with induced high voltage[J]. Analytical Chemistry, 2015, 87(5): 2 727-2 733.
[19] ZHU H, WANG N, YAO L, CHEN Q, ZHANG R, QIAN J, HOU Y, GUO W, FAN S, LIU S, ZHAO Q, DU F, ZUO X, GUO Y, XU Y, LI J, XUE T, ZHONG K, SONG X, HUANG G, XIONG W. Moderate UV exposure enhances learning and memory by promoting a novel glutamate biosynthetic pathway in the brain[J]. Cell, 2018, 173(7): 1 716-1 727.
[20] ZHU H, ZOU G, WANG N, ZHUANG M, XIONG W, HUANG G. Single-neuron identification of chemical constituents, physiological changes, and metabolism using mass spectrometry[J]. Proceedings of the National Academy of Sciences of the United States of America, 2017, 114(10): 2 586-2 591.
[21] ZHENG X, HOU Z, QIAN Y, ZHANG Y, CUI Q, WANG X, SHEN Y, LIU Z, ZHOU Y, FU B, SUN R, TIAN Z, HUANG G, WEI H. Tumors evade immune cytotoxicity by altering the surface topology of NK cells[J]. Nature Immunology, 2023, 24(5): 802-813.
[22] ZHU H, LI Q, LIAO T, YIN X, CHEN Q, WANG Z, DAI M, YI L, GE S, MIAO C, ZENG W, QU L, JU Z, HUANG G, CANG C, XIONG W. Metabolomic profiling of single enlarged lysosomes[J]. Nature Methods, 2021, 18(7): 788-798.
[23] ZHUANG M, HOU Z, CHEN P, LIANG G, HUANG G. Introducing charge tag *via* click reaction in living cells for single cell mass spectrometry[J]. Chemical Science, 2020, 11(28): 7308-7312.
[24] HOU Z, LUAN M, ZHAN L, WANG X, YUAN S, CAO K, SHENG Y, YIN H, LIU Y, HUANG G. Native mass spectrometry for peptide-metal interaction in picoliter cell lysate[J]. Analytical Chemistry, 2022, 94(40): 13 829-13 833.
[25] ONJIKO R M, MOODY S A, NEMES P. Single-cell mass spectrometry reveals small molecules that affect cell fates in the 16-cell embryo[J]. Proceedings of the National Academy of Sciences of the United States of America, 2015, 112(21): 6 545-6 550.
[26] LORENZO TEJEDOR M, MIZUNO H, TSUYAMA N, HARADA T, MASUJIMA T. *In situ* molecular analysis of plant tissues by live single-cell mass spectrometry[J]. Analytical Chemistry, 2012, 84(12): 5 221-5 228.
[27] LIU R, YANG Z. Single cell metabolomics using mass spectrometry: techniques and data analysis[J]. Analytica Chimica Acta, 2021, 1 143: 124-134.
[28] REYNOLDS J M, BRUNS B U, FITT W K, SCHMIDT G W. Enhanced photoprotection pathways in symbiotic dinoflagellates of shallow-water corals and other cnidarians[J]. Proceedings of the National Academy of Sciences of the United States of America, 2008, 105(36): 13 674-13 678.
[29] SHOGUCHI E, SHINZATO C, KAWASHIMA T, GYOJA F, MUNGPAKDEE S, KOYANAGI R, TAKEUCHI T, HISATA K, TANAKA M, FUJIWARA M, HAMADA M, SEIDI A, FUJIE M, USAMI T, GOTO H, YAMASAKI

S, ARAKAKI N, SUZUKI Y, SUGANO S, TOYODA A, KUROKI Y, FUJIYAMA A, MEDINA M, COFFROTH M A, BHATTACHARYA D, SATOH N. Draft assembly of the symbiodinium minutum nuclear genome reveals dinoflagellate gene structure[J]. Current Biology, 2013, 23(15): 1 399-1 408.

[30] PELTIER G, ARO E M, SHIKANAI T. NDH-1 and NDH-2 plastoquinone reductases in oxygenic photosynthesis[J]. Annual Review of Plant Biology, 2016, 67(1): 55-80.

[31] DÍAZ-PÉREZ A L, DÍAZ-PÉREZ C, CAMPOS-GARCÍA J. Bacterial *l*-leucine catabolism as a source of secondary metabolites[J]. Reviews in Environmental Science and Bio/Technology, 2016, 15(1): 1-29.

[32] TAKEUCHI M, AMAO Y. Inhibitory effect of acetyl-CoA on a visible light-driven NADH regeneration system composed a of water-soluble zinc porphyrin and a rhodium complex[J]. Chemistry Letters, 2024, 53(3): upae014.

[33] WANG J T, DOUGLAS A E. Essential amino acid synthesis and nitrogen recycling in an alga-invertebrate symbiosis[J]. Marine Biology, 1999, 135(2): 219-222.

[34] UHLE M E, MACKO S A, SPERO H J, ENGEL M H, LEA D W. Sources of carbon and nitrogen in modern planktonic foraminifera: the role of algal symbionts as determined by bulk and compound specific stable isotopic analyses[J]. Organic Geochemistry, 1997, 27(3/4): 103-113.

[35] SUNDA W, KIEBER D J, KIENE R P, HUNTSMAN S. An antioxidant function for DMSP and DMS in marine algae[J]. Nature, 2002, 418(6 895): 317-320.

[36] STEFELS J. Physiological aspects of the production and conversion of DMSP in marine algae and higher plants[J]. Journal of Sea Research, 2000, 43(3/4): 183-197.

[37] TREVENA A J, JONES G B, WRIGHT S W, van den ENDEN R L. Profiles of DMSP, algal pigments, nutrients and salinity in pack ice from eastern Antarctica[J]. Journal of Sea Research, 2000, 43(3/4): 265-273.

（收稿日期：2025-05-27；修回日期：2025-07-09）

陈思思,薛宇阳,唐兴颖,等.液相循环对制糖固废共水热碳化影响机制研究 [J]. 中国环境科学, 2025,45(3):1364-1374.
Chen S S, Xue Y Y, Tang X Y, et al. Study on the mechanism of liquid-phase cycling on the co-hydrothermal carbonation of sugar solid waste [J]. China Environmental Science, 2025,45(3):1364-1374.

液相循环对制糖固废共水热碳化影响机制研究

陈思思[1],薛宇阳[1],唐兴颖[2*],王智洁[1],张莹莹[2],钱黎黎[3],李尚泽[1],王英辉[2,4] (1.广西大学资源环境与材料学院,广西 南宁 530004；2.广西大学海洋学院,广西南海珊瑚礁研究重点实验室/珊瑚礁研究中心,广西 南宁 530004；3.江苏大学能源与动力工程学院,江苏 镇江 212000；4.广西产研院绿色低碳技术研究所有限公司,广西 南宁 530022)

摘要：本研究以糖厂滤泥和甘蔗渣为原料,在 240℃-60min-质量比 5:1 条件下共水热碳化,研究液相循环对共水热碳化固液相产物影响,并探究其反应路径.结果表明,液相循环促进了共水热碳化的反应进程,水热炭性质明显改善.随着液相循环进行,水热炭产率和高热值(HHV)大幅提高,灰分含量显著降低,其表面微球结构数量增多,第二次循环后水热炭获得最大比表面积 31.2m^2/g,基团 CH_X,C-C/C=C 和-C-OR/-C-NR 含量呈上升趋势,而 C=O/C=N 和-COOR 含量明显减少;液相产物中有机酸和酮类含量增多,芳香族化合物从 0.31%增加到 13.75%,碳氢化合物、酰胺类和酯类减少.液相循环下,有机酸积累形成的酸性环境催化了水解等反应的发生,并促进美拉德反应的进行,有效提高水热炭的芳构化程度,有利于强化水热炭表面的含氧官能团,使其提供更多的化学位点,赋予了水热炭更优异的吸附性能,提高其土地利用潜力.

关键词：液相循环；共水热碳化；水热炭；糖厂滤泥；甘蔗渣
中图分类号：X705 **文献标识码**：A **文章编号**：1000-6923(2025)03-1364-11
DOI:10.19674/j.cnki.issn1000-6923.2025.0044

Study on the mechanism of liquid-phase cycling on the co-hydrothermal carbonation of sugar solid waste. CHEN Si-si[1], XUE Yu-yang[1], TANG Xing-ying[2*], WANG Zhi-jie[1], ZHANG Ying-ying[2], QIAN Li-li[3], LI Shang-ze[1], WANG Ying-hui[2,4] (1.School of Resources, Environment and Materials, Guangxi University, Nanning 530004, China；2.Guangxi Laboratory on the Study of Coral Reefs in the South China Sea/Coral Reef Research Center of China, School of Marine Sciences, Guangxi University, Nanning 530004, China；3.School of Energy and Power Engineering, Jiangsu University, Zhenjiang 212000, China；4.Guangxi Institute of Green and Low Carbon Technology Co, Ltd, Nanning 530022, China). *China Environmental Science*, 2025,45(3)：1364~1374

Abstract：The study utilized filter mud and bagasse as raw materials for the co-hydrothermal carbonization process at 240℃-60min-5:1. The primary objective of this study was to investigate the impact of liquid-phase cycling on the solid-liquid phase products of the co-hydrothermal carbonization process and to elucidate the reaction pathways. The experimental findings demonstrated that liquid-phase cycling significantly enhanced the reaction process of co-hydrothermal carbonization, resulting in substantial improvements in the hydrochar properties. In the liquid-phase cycling process, there was a substantial increase in the hydrochar yield and higher heating value (HHV), accompanied by a significant decrease in ash content and an increase in microsphere structures on the surface. Following the second cycling, the hydrochar obtained a maximum specific surface area of 31.2m^2/g, and the contents of the groups CHX, C-C/C=C, and -C/OR/-C-NR exhibited a tendency to increase, while the contents of C=O/C=N and -COOR decreased significantly; In the liquid-phase products, the contents of organic acids and ketones increased. Concurrently, the proportion of aromatic compounds remarkably rose from 0.31% to 13.75%, and hydrocarbons, amides, and esters decreased. Within the liquid-phase cycle, the acidic environment generated by the accumulation of organic acids served as a catalyst for hydrolysis and other reactions, and simultaneously facilitated the Maillard reaction, which effectively enhanced the degree of aromatization of the hydrochar. Moreover, it was beneficial for fortifying the oxygen-containing functional groups on the surface of the hydrothermal carbon, thereby creating more chemically active sites. Consequently, the hydrochar was bestowed with enhanced adsorption capabilities and its potential for land application was elevated.

Key words：liquid phase recycling；co-hydrothermal carbonization；hydrochar；filter mud；bagasse

广西是我国甘蔗的主产地,其蔗糖产量约占全国总产量的三分之二.制糖工艺的副产物主要为滤泥、蔗渣、蔗梢叶和糖蜜,其中蔗梢叶是良好的饲料资源,直接或经简单处理后作为粗饲料喂养畜禽动

收稿日期：2024-08-05
基金项目：国家自然科学基金资助项目(22068003);广西科技重大专项项目(AA22117014)
* 责任作者, 讲师, tangxingying@gxu.edu.cn

中国知网 https://www.cnki.net

物;糖蜜主要可用于制作酒精和酵母,均可满足产业化要求;而糖厂滤泥通常施肥于肥沃田地或随意置放,除占用大面积土地资源外,还因其含水率高、富含有机物和糖类等,极易导致腐烂发臭、滋生细菌、污染空气,对环境造成严重影响[1];甘蔗渣经加工后可以作为糖厂燃料或用于制作动物饲料,但存在利用率和附加值低等问题,难以高效资源化利用.因此,开发新型处置方法,对糖厂滤泥及甘蔗渣进行有效的无害化处理和资源化利用势在必行.

共热碳化技术作为一种绿色、低碳、高效的热化学技术,是指在水热碳化过程中两种或者多种原料进行热化学转化,降低预处理能耗成本的同时,有效改善水热碳化反应的效率和产物的性质,并且获得的水热炭具有灰分低、热值高、比表面积大,含有丰富的官能团和发达的孔隙结构,应用于能源、土壤改良、吸附基质等领域[2-6].然而,水热碳化过程会产生大量的液相副产品,主要由有机酸、糖类、酚类等有机物组成,直接排放到环境中可能对生态系统的健康构成严重威胁,浪费工业化学资源;同时,液相处理成本占水热处置废物总成本的 90%,影响经济可行性,亟需一种对环境、经济友好的方法处理水热碳化液相产物[7-9].

液相循环作为一种高效的处理策略,是将水热过程中获得的液相物质回收并与原料混合,重新进行水热碳化的处理方法,不仅能显著降低淡水消耗,还有效削减了废液处理成本,提高水热碳化系统的整体效率.Sharma 等[10]将食品和庭院垃圾共水热碳化,经过 5 次液相循环发现再循环液中高有机物和离子物质的存在促进了整个碳化过程,增加了水热炭的能量产率(86%~92%)、碳含量(68%~71%)和 HHV (20~27MJ/kg),并且还增强了水热炭的整体燃烧特性,促进了共水热碳化反应.Li 等[11]利用聚氯乙烯和玉米芯共水热碳化并循环 4 次,观察到液相循环逐步增强原料的水解,并产生具有更丰富的活性表面官能团、更多孔结构和更高产率的水热炭.针对糖业副产物所产生的环境影响和资源化利用水平低等问题,考虑利用共水热碳化及液相循环技术对糖厂滤泥和甘蔗渣进行处理,减少环境污染,得到更加优质的资源化产物.但是糖厂滤泥和甘蔗渣的共水热碳化及液相循环的反应机制尚不明确,仍需进行更为深入的研究,为水热炭产品增值提供新的思路.

本文以糖厂滤泥和甘蔗渣作为原料进行共水热碳化,研究 4 次液相再循环对水热炭的理化性质、产率、微观形貌、比表面积和含 C 官能团含量的影响,分析循环下液相产物的性质和组分变化情况,揭示其中的反应机理,解析液相循环下糖厂滤泥和甘蔗渣共水热碳化的反应路径.本研究开拓了糖厂滤泥和甘蔗渣高效利用的新方向,可为糖业副产物开发高附加值产品提供理论依据和数据支撑.

1　材料与方法

1.1　实验原料

本实验所用糖厂滤泥和甘蔗渣均取自广西农垦糖厂,所采用的工艺为磷酸亚硫酸法;其中,甘蔗渣为甘蔗压榨提汁后的固体残渣,滤泥取自糖汁硫熏中和后二次加热沉降的污泥,糖厂滤泥和甘蔗渣的主要理化性质如表 1 所示.将滤泥与甘蔗渣置于真空干燥箱中 105℃干燥 24h,使用粉碎机对其粉碎并过 100 目筛,粉碎后的样品用密封袋封装后避光储存.

表 1　糖厂滤泥和甘蔗渣的主要理化性质

Table 1　The main physicochemical properties of filter mud and sugarcane bagasse

样品名称	元素分析(wt. %)					C/N	ASH (%)	HHV (MJ/kg)	pH 值	EC (mS/cm)
	C	H	O	N	S					
糖厂滤泥	19.59	3.94	16.52	1.10	3.58	17.80	56.13	8.93	6.82	1.38
甘蔗渣	44.16	5.78	47.96	0.55	0.23	80.79	1.32	17.26	4.67	—

1.2　实验设计及运行

采用高温间歇式反应管装置进行共水热及液相循环实验,管式炉作为反应的温控装置.如图 1 所示,高温间歇式反应管采用 316L 不锈钢材质,容积为 20mL,最高反应温度 600℃,压力耐受 30MPa.

本实验前期所做的研究根据水热炭吸附性能和土地适用等因素,已确定糖厂滤泥与甘蔗渣共水热的最优反应条件为:反应温度 240℃,停留时间

中国知网　https://www.cnki.net

60min,滤泥蔗渣质量比 5:1;因此,以此最佳条件为本次实验的基础条件,进行液相循环实验.

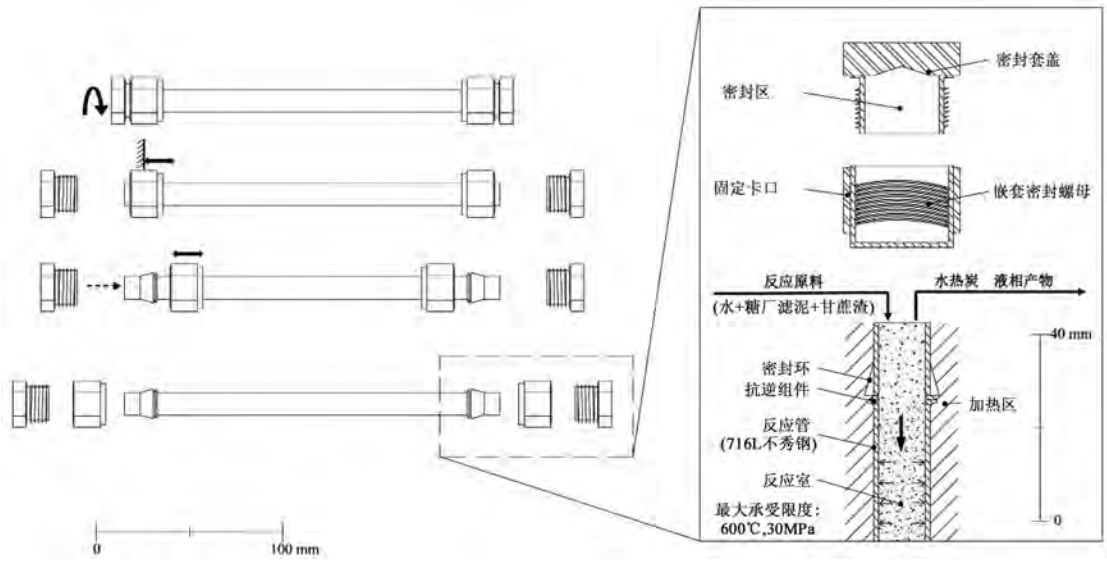


图 1 水热碳化反应装置管式炉及间歇式反应管

Fig.1 Hydrothermal carbonization batch reactor tube

将破碎后的滤泥和甘蔗渣按照 5:1 的质量比混合后均质处理,均质后的混合粉末作为反应原料.将原料和去离子水按 1:9 (*W*:*V*)的比例加入反应管中混合,设置以 5℃/min 的速率升温至 240℃,停留时间 60min.反应结束后,待反应管冷却至室温,取出水热碳化固液混合产物,采用真空泵抽滤进行固液分离.将获得的固相产物在 105℃下真空干燥 24h,研磨后过 100 目筛,所得固相产物即为水热炭,称量后放密封袋避光储存;抽滤后得到的液相产物即为水热碳化液,置于棕色玻璃瓶中,于 0~4℃冰箱中冷藏储存.

考虑到水热炭中保留的水分和分析中所需要的水分,每次进行液相循环时,将 90%的水热碳化液再次循环利用,并补充 10%的去离子水,替代下一次反应的去离子水,剩余步骤与共水热碳化实验相同.第一次共水热碳化后获得的固相产物和液相产物分别命名为 HC-R0 和 HL-R0,后续根据液相循环次数将固相产物分别命名为 HC-R1、HC-R2、HC-R3、HC-R4;液相产物分别命名为 HL-R1、HL-R2、HL-R3、HL-R4.

1.3 分析测试方法

水热炭的产率为水热炭质量与原料质量之比;pH 值和 EC 值采用雷磁 E-201-L 型 pH 计和 DJS-1-L 型 EC 计测量.

原料和水热炭的 C、H、N、S 元素质量百分比使用元素分析仪(Vario EL cube, Elementar, Germany)测定,元素 O 含量通过差减法公式(式(1))计算.

$$O\%=100\%-(C\%+H\%+N\%+S\%+Ash\%) \quad (1)$$

灰分含量根据《煤的工业分析方法测定》(GB/T 212-2008)[12]进行测定;高热值含量与元素组成含量相关,根据式 2 计算水热炭的 HHV.

$$HHV=0.3491C+1.1783H+0.1005S-0.1034O-0.015N-0.0211A \quad (2)$$

水热炭的表面形貌表征采用扫描电子显微镜(Sigma500, Zeiss, Germany)观察,加速电压 5.0kV;采用比表面积及孔径分析仪(AUTOSORB-IQ-MP, Quantachrome, USA)进行水热炭比表面积、孔容积及孔径分布的测定.

水热炭的 N_2 吸附-脱附等温曲线由全自动气体吸附仪在-196℃(77K)下测定吸附剂对高纯液氮的吸附作用,并且样品在测定前,先在 100℃温度条件下真空脱气处理 12h.通过多点 Brunauer-Emmett-Teller(BET)法计算比表面积,孔径分布采用 Barret-Joyner-Halenda(BJH)模型计算[13].

水热炭的表面官能团由傅里叶红外光谱仪(IRTrace-100, Shimadzu, Japan)分析,扫描范围在 400~4000cm^{-1} 范围内,共扫描 32 次,根据光谱中的吸收峰位置和形状判断水热炭的结构.

通过 X 射线光电子能谱仪(K-Alpha, Thermo,

中国知网 https://www.cnki.net

USA)分析水热炭表面元素的存在形态,使用 Al Kα X 射线辐射源 (hv=1486.6eV)对水热炭表面 C、N、O 元素组分进行研究,结合能使用 284.6eV 的 C1s 峰值校准测定,含 C 官能团相对百分比含量分布采用归一化法进行统计,且含量低于 1%含量的官能团不列入统计范围.

液相产物成分由气相色谱质谱联用仪(8860/5977b, Aglient, USA) 通过 HP-5MS 色谱柱测定,初始温度为 40℃,保持 3min,以 5℃/min 升温至 200℃,然后以 10℃/min 升温至 280℃,停留 3min.进样量为 0.6μL,使用 He 气作为载气气体,流量为 1.2mL/min,进样器和检测器均保持在 325℃.

液相产物的 COD 值由哈希标准 COD 试剂(2125915-CN)通过消解比色法测定, NH_3-N 浓度由哈希氨氮试剂(2606945-CN),通过水杨酸法测定.pH 和 EC 值使用 pH 计和 EC 计测量,重复测量结果 3 次取平均值,通过 Excel 记录整理实验数据,Origin 2023 分析数据、作图和拟合曲线.

2　结果与讨论

2.1　水热炭特性分析

2.1.1　理化性质与产率　表 2 为液相循环后水热炭的理化性质和产率.液相循环后,水热炭的 C 元素和 N 元素含量均显著增加, C 元素含量由 19.64wt.%(HC-R0)提升至 22.82wt.%(HC-R4),N 元素含量由 0.73wt.%(HC-R0)提升至 0.95wt.%(HC-R4).水热炭 C 元素与 N 元素含量增加是由于液相循环中一定量的可溶性蛋白质由液相转移至水热炭中[14],表明共水热碳化和再循环加剧了美拉德反应和曼尼希反应的发生[10].

表 2　水热炭的理化性质和产率

Table 2　Physicochemical properties and yield of hydrochar

样品	元素分析(wt.%)					C/N	ASH (wt.%)	HHV (MJ/kg)	pH 值	EC (mS/cm)	产率(%)
	C	H	O	N	S						
HC-R0	19.64	3.20	9.89	0.73	1.93	26.85	64.61	8.42	6.35	1.43	62.38
HC-R1	21.66	2.69	14.22	0.84	3.56	25.79	57.03	8.40	6.35	0.31	64.10
HC-R2	22.19	2.64	18.02	0.89	3.44	24.93	52.82	8.21	6.43	0.35	63.75
HC-R3	22.31	3.12	15.53	0.88	3.22	25.35	54.94	9.01	6.48	0.39	68.00
HC-R4	22.82	3.41	13.65	0.95	2.82	24.02	56.35	9.65	6.55	0.44	66.41

由于可溶性盐的流失,无机离子向液相中转移,水热炭的灰分含量由 64.61wt.%(HC-R0)下降至 52.82wt.%(HC-R2),随后上升到 56.35wt.%(HC-R4),相较于 HC-R0,液相循环后的水热炭(HC-R1~HC-R4)灰分含量显著降低;而水热炭灰分先降低后升高则可能是由于液相中溶解的灰分被水热炭重新吸收,导致水热炭中无机物浓度增加[15],从而灰分含量上升.

随着液相循环的进行,水热炭 HHV 由未进行循环时(HC-R0)的 8.42MJ/kg 增大到了 4 次循环后(HC-R4)的 9.65MJ/kg,水热炭 HHV 提高了 1.23MJ/kg.据 Sharma 等[10]的研究,水热炭 HHV 的提高是由于原料中的纤维素和半纤维素降解,产生的中间产物溶解到液相中,例如糠醛和 HMF(HHV 约为 22MJ/kg),部分中间产物随着反应的进行被转化为有机酸并在液相中不断累积,液相循环中这部分有机酸催化并加速了整个水热碳化进程,从而增大了水热炭 HHV;此外,液相中的有机酸加速了原料的转化速率,尤其是半纤维素和纤维素的水解,形成了水溶性中间体,这些物质聚合并形成具有高能量密度的固体微粒,导致水热炭中的 C 含量增加,从而增加了其能量含量[16].液相循环后的水热炭 pH 值略有上升,可能是有机酸等酸性物质向液相中转移,导致水热炭 pH 值总体有小幅度升高.

经过多次液相循环后,水热炭的产率有了显著的提高,由最初的 62.38%(HC-R0)提高到 68.00%(HC-R3),在第 3 次液相循环后(HC-R3)水热炭产率达到最大值,随后降低至 66.41%.水热炭产率的整体提高主要是因为在整个共水热碳化过程中,纤维素、半纤维素和木质素的水解,生成的化合物发生一系列脱水、脱羧反应后形成的有机酸和中间产物(如糠醛、5-HMF 和呋喃等)在液相中不断累积,形成了有机酸环境,这促进了生物质聚合物的进一步水解和分解,导致可溶性物质的浓度增加,加快了缩

中国知网　https://www.cnki.net

合和聚合反应的进行,生成更多的芳香族化合物,更有利于水热炭的形成[7,9,17];而水热炭产率第 3 次液相循环后(HC−R3)达到最大值,而第 4 次液相循环后(HC−R4)相比 HC−R3 略有降低,表明液相循环对共水热碳化中水热炭的产生具有促进作用,但这种促进作用会随着液相循环次数的增加而趋于平稳,这可能是液相中积累的有效组分达到饱和状态所致[18].

2.1.2 微观形貌与比表面积 利用扫描电子显微镜对液相循环前后的水热炭进行观察,其微观结构如图 2 所示.对比未进行液相循环(HC−R0)的水热炭较为平整的表面结构,液相循环后的水热炭(HC−R1~HC−R4)表面更加粗糙,产生了密集堆积的微球结构,尤其是 HC−R2,微球结构的数量与密度明显增多.这些微球是在有机酸的催化下,由纤维素、半纤维素和木质素分解后的中间体重新缩合和聚合而成,附着在水热炭的表面,源自单糖和含氮基团的水热炭也会出现类似的现象[15].证明了液相循环过程对水热炭产生有着促进作用[10, 19],可以促进水热炭表面微球结构的形成.

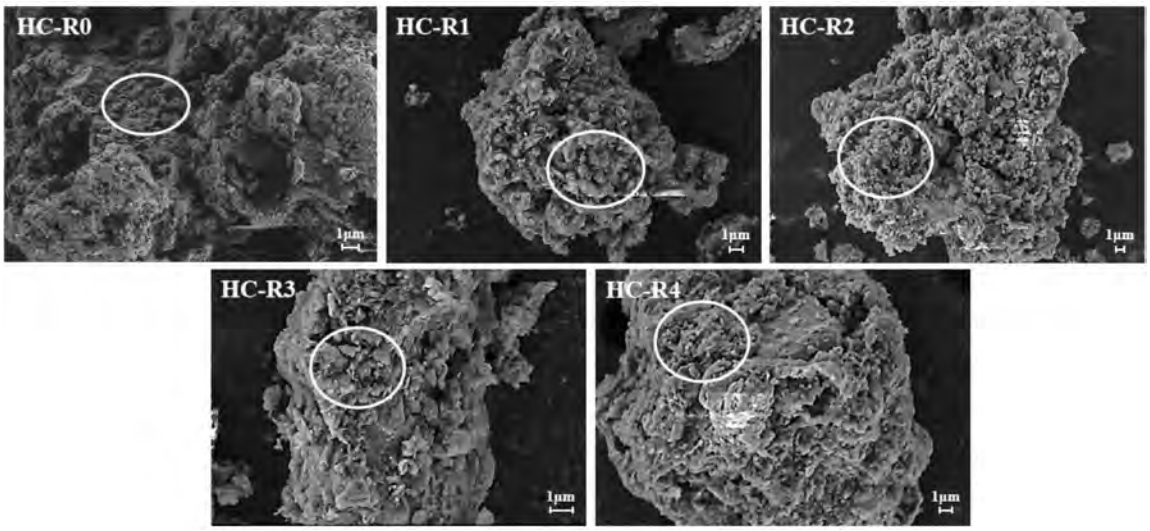


图 2 水热炭的扫描电子显微镜(SEM)图像

Fig.2 Scanning electron microscope (SEM) images of hydrochars

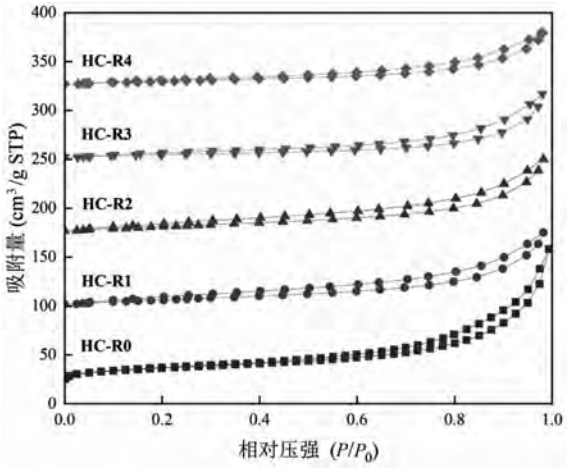


图 3 液相循环下水热炭的 N_2 吸附/脱附曲线

Fig.3 N_2 adsorption/desorption curves for hydrochar under liquid phase cycling

图 3 为液相循环下水热炭的 N_2 吸附/脱附曲线.依据 IUPAC(International Union of Pure and Applied Chemistry)分类,水热炭的吸附/脱附等温曲线均符合Ⅳ型等温线,且呈现出一定的 H4 型滞后环.表明液相循环会促进水热炭内部形成介孔,使得水热炭具有更加丰富的介孔结构.

由表 3 可知,随着液相循环进一步的进行,水热炭的比表面积有所降低,从最初的 45.92m^2/g 下降至 20.2m^2/g;孔体积也由 0.205cm^3/g 降低至 0.085cm^3/g.结合 SEM 图像分析,这种现象是因为液相循环促进了微球结构的增加,产生的微球吸附在水热炭表面,从而堵塞水热炭表面孔隙,导致水热炭比表面积减小[11].

尽管液相循环后水热炭比表面积有所下降,但经过实际对比发现,在液相循环过程中,糖厂滤泥和甘蔗渣共水热炭的比表面积仍明显优于聚氯乙烯和玉米芯共水热炭(1.17~1.75m^2/g)[11]以及稻草水热炭(8.21~12.18m^2/g)[14]等水热炭.因此,糖厂滤泥和甘蔗渣在液相循环下的共水热炭具有较强的吸附能力.

中国知网 https://www.cnki.net

表 3　液相循环下水热炭的比表面积、孔体积和孔径

Table 3　Specific surface area, pore volume, and pore size of hydrochar under liquid phase cycling

样品	比表面积(m^2/g)	孔体积(cm^3/g)	平均孔径(nm)
HC−R0	45.9	0.205	2.972
HC−R1	22.9	0.123	7.684
HC−R2	31.2	0.117	3.396
HC−R3	18.5	0.104	12.236
HC−R4	20.2	0.085	7.734

2.1.3　表面官能团　液相循环下水热炭的傅里叶变换红外光谱如图 4 所示,可以观察到有 5 组明显的吸收峰,分别代表 5 种典型的基团.

在 3402cm^{-1} 处的吸收峰为 O−H 拉伸振动引起,随着循环次数的增加,该峰显著增强,证明在液相循环下,水热炭表面 O−H 基团数量逐渐提升.这可能是由于原料中存在大量的纤维素和半纤维素,共水热过程中分解形成有机化合物,随着液相循环的进行,液相中的有机物增加了水热炭表面的 O−H 基团[20].

2922cm^{-1}和2855cm^{-1}的吸收峰则是脂肪族亚甲基的对称和不对称 C−H 拉伸引起,相比 HC−R0,HC−R1、HC−R2 和 HC−R3 的特征峰略有降低,但在 HC−R4 时有着明显提升.特征峰初始略有降低是由于液相中的糖类和脂肪族化合物在液相循环下进一步分解,并参与了芳构化反应,从而降低了水热炭 C−H 含量;随后纤维素和木质素在水热碳化循环过程中生成许多糖类和脂肪族化合物,产生了更多的甲基或亚甲基,C−H 含量提升.这也表明重复循环液相能够促进生物质原料的分解[15,21].

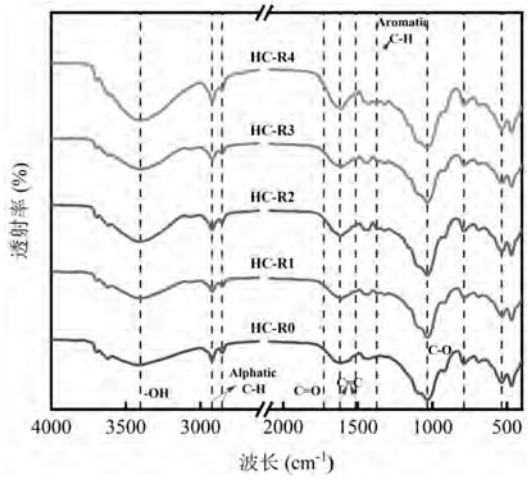


图 4　液相循环下水热炭的傅里叶变换红外光谱

Fig.4　FT−IR of hydrochar generated under liquid phase cycling

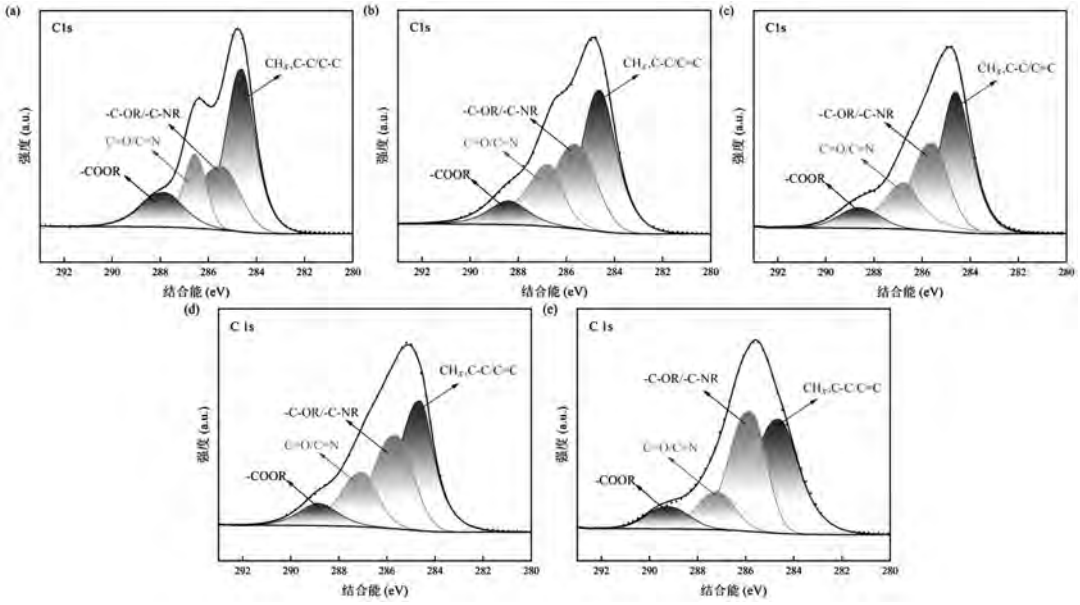


图 5　水热炭的 XPS C1s 光谱图:((a)HC−R0;(b)HC−R1;(c)HC−R2;(d)HC−R3;(e)HC−R4)

Fig.5　XPS C1s spectra of hydrochars: ((a) HC−R0; (b) HC−R1; (c) HC−R2; (d) HC−R3; (e) HC−R4)

位于 1728cm^{-1} 为羰基 C=O 的拉伸振动引起的吸收峰.在前两次液相循环中,该峰值强度表现的并不明显,但随循环次数的增加,该处特征峰在第四次循环时略有波动,这是由于共水热过程中单糖脱水脱羧生成糠醛、呋喃并进一步反应生成酮类化合物,这些物质在液相中的浓度增加,吸附在水热炭表面,

中国知网　https://www.cnki.net

导致其吸收峰略有增加.

以 1620cm^{-1} 和 1514cm^{-1} 为中心的是芳香族 C=C 拉伸振动的吸收峰.随着液相循环的进行,这两处吸收峰逐渐增强,表明液相中的有机化合物在水热碳化过程中的发生了脱水反应和芳构化反应,并在液相循环下促进了反应的进行.

位于 1035cm^{-1} 的吸收峰为糖类化合物中 C—O 拉伸振动引起的,随液相循环的增加该峰显著减弱,主要是原料中纤维素和半纤维素分解所致[14,22],液相循环有效促进了这一进程.

X 射线光电子能谱(XPS)是一种可以提供表面材料元素化合价和化学键信息的分析工具,通过 XPS 表征以及 XPS Peak 分峰拟合软件揭示水热炭结构和含量演变规律[23].水热炭的 XPS C1s 谱图如图 5 所示,主要包括脂肪族/芳香族炭基团(CH_x,C—C/C=C),结合能为 284.6eV;羟基/氨基(—C—OR/—C—NR),结合能为(285.6±0.3)eV;羰基/亚胺基(C=O/C=N),结合能为(287.0±0.4)eV;羧基、酯或内酯(—COOR),结合能为(288.6±0.2)eV[18,24].

图 6 比较了 4 组含 C 官能团相对百分比含量分布.与 HC−R0 相比,液相循环下 HC−R1~HC−R4 水热炭的 CH_x、C−C/C=C 基团减少,但随着液相循环次数的增加,有机酸的催化作用,加速了水热炭的芳构化程度,使得水热炭的 CH_x,C−C/C=C 含量增加,这一现象也验证了 FT−IR 分析中脂肪族 C−H 的变化情况.−C−OR/−C−NR 含量从 24.19%(HC−R0)显著增加至 37.83%(HC−R4),说明液相循环下,水热炭表面聚集了大量含氧官能团[23,25],同时糖类和蛋白质之间发生了美拉德反应,形成了 N−杂环化合物.C=O/C=N 的含量先呈现上升趋势,但在 HC−R4 时相比 HC−R0 有着明显的下降,−COOR 则一直呈下降趋势,这是由于液相循环促进了共水热碳化过程中的脱水和脱羧反应,导致 C=O/C=N 和−COOR 含量明显减少.

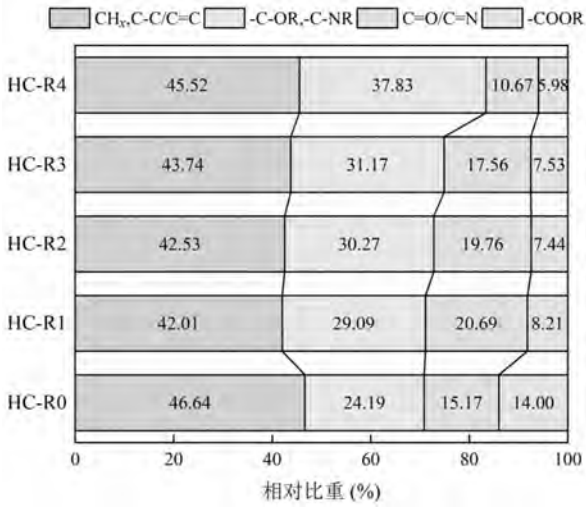


图 6 水热炭的含 C 官能团分布

Fig.6 Distribution of C−containing functional groups in hydrochars

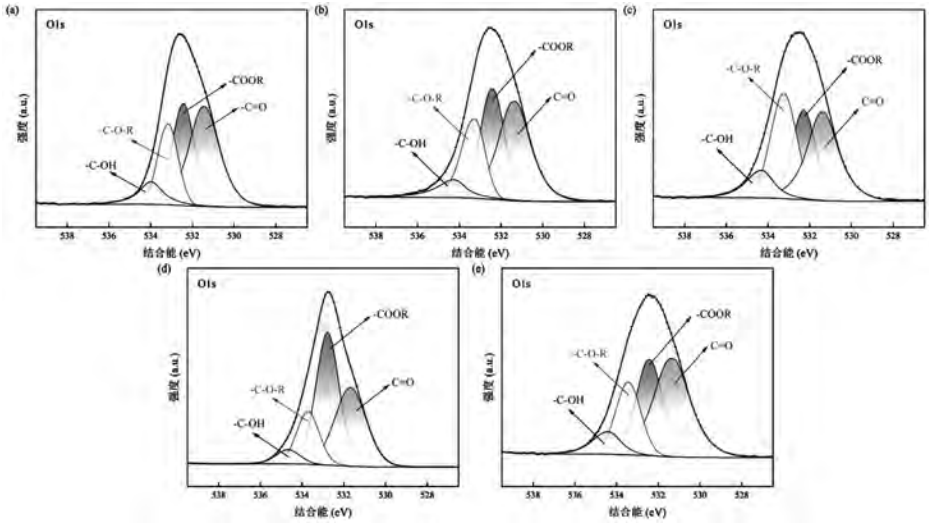


图 7 水热炭的 XPS O1s 光谱

Fig.7 XPS O1s spectra of hydrochars

(a) HC−R0; (b) HC−R1; (c) HC−R2; (d) HC−R3; (e) HC−R4

图 7 为液相循环下水热炭的 O1s 光谱,主要分为 4 种:C=O 呋喃或酮基团(结合能为 531.3eV)、—COOR

中国知网 https://www.cnki.net

羧基或酯基团(532.4eV)、—C—O—R 醚基团(533.3eV)和—C—OH 羟基(534.3eV)[18].其中 HC- R0、HC-R1 和 HC-R2 的 C=O 变化不明显,在第 3 次循环时有所下降,而后随着液相循环次数的增加,峰面积增大,这与 FT-IR 分析结果相符合,表明液相中积累的有机酸参与水热炭形成.值得注意的是,在 HC-R2 中—COOR 基团含量最少,这是脱水、脱羧反应发生剧烈的表现,并且此时—C—O—R 基团含量较多,可能是由于第二次循环加速了水解反应的发生,促使生成更多的醚键[26-27].总体来看,随着液相循环反应的进行,各含氧基团的含量均有所增加,水热炭表面官能团的种类及数量得到提高.

通过上述 FT-IR 和 XPS 的分析结果表明,液相循环下水热炭表面仍具有丰富的官能团,这一特点有助于其在环境修复和土壤调节上的应用,尤其是含氧官能团的存在起到了关键作用,相比单一组分的水热炭,本研究的糖厂滤泥和甘蔗渣共水热炭提供更多的化学位点,赋予了水热炭更优异的吸附性能,增加了水热炭的土地应用的潜力.

2.2　液相产物特性分析

2.2.1　理化性质　液相循环下共水热碳化液相产物的 pH 值、EC、NH_3-N 和 COD 值如表 4 所示.在整个循环期间,液相的 pH 值在酸性范围内略有变化(3.99~4.54),液相产物 pH 值随循环次数的增加呈下降趋势,原料中的纤维素和半纤维素分解产生的有机酸在液相中富集是水热转化过程中循环液呈酸性的主要原因,循环液的酸性环境在共水热碳化过程中起到了催化剂的作用,促进糖厂滤泥和甘蔗渣的热水解,提高水热炭产量和质量.然而,对于原料含有丰富的蛋白质生物质(如污泥、家禽肥料等)来说,液相产物的 pH 值变化与之相反,呈上升趋势,因为在循环期间有机酰胺转化为胺,促使 pH 值呈碱性[7].在第 4 次循环后,HL-R4 的 pH 值比 HL-R3 的略微增大,可能是因为糖厂滤泥中含有的少量蛋白质在反应过程中脱氨,从而使得其 pH 值增加.另外,随着循环次数的增加,液相产物的电导率也逐渐增大,表明金属盐离子和羧酸根离子在液相中聚集[14].

液相产物的 NH_3-N 含量随着循环次数的增加先减少后增加,COD 浓度从 5.48g/L(HL-R0)增加至 10.56g/L(HL-R4),主要是因为糖厂滤泥和甘蔗渣中部分有机物分解转化形成水热炭,而蛋白质这类难转化的物质先被水解为可溶性蛋白和氨基酸,进一步转化为不饱和脂肪酸、胺类或其他难降解的有机物,不断向液相中转移并聚集,从而使 COD 浓度在循环过程中逐渐升高[28].Sharma 等[10]研究了食品和庭院垃圾共水热碳化,发现了与本研究相同的现象,经过 5 次液相循环过程后,液相中的 COD 从首次运行时的 58.30g/L 增加到 96.40g/L,并随着再循环周期的增加而增大.Zhang 等[29]研究水葫芦与污泥共水热碳化经过 4 次液相循环后,循环液 COD 在 30.58~49.39g/L 范围内变化.对比发现,液相循环下糖厂滤泥和甘蔗渣共水热碳化的液相 COD 浓度显著低于其它木质纤维素生物质为原料共水热碳化液相产物的 COD 浓度,可以考虑将再循环工艺作为水热碳化液相产物的潜在处理方法,是实现有机废弃生物质更清洁、更具成本效益的双赢策略.

表 4　液相产物的 pH 值、EC、NH_3-N 和 COD

Table 4　pH、EC、NH_3-N and COD of liquid phase products

样品	pH 值	EC(mS/cm)	NH_3-N(g/L)	COD(g/L)
HL-R0	4.54	12.8	180.03	5.48
HL-R1	4.15	24.9	150.67	7.13
HL-R2	4.03	32.9	190.41	9.10
HL-R3	3.99	36.2	270.74	10.68
HL-R4	4.06	38.9	340.98	10.56

2.2.2　有机物组分　共水热碳化是一系列复杂的反应,包括了水解、脱水、脱羧、脱氨、聚合和再缩合等.为进一步分析液相的性质,采用 GC-MS 检测共水热后液相中的有机物组成成分.图 8 为液相循环过程部分有机组分的变化趋势,主要分为碳氢化合物、酰胺类、酯类、环二肽类、N-杂环化合物、酚类、酮类、芳香族化合物和有机酸.

经过对比 HL-R0 和 HL-R1 发现,液相中的碳氢化合物含量显著降低,液相循环中碳氢化合物和氨基酸发生美拉德反应生成环状二肽(氨基酸衍生物),环状二肽含量有所增加.这证明了液相循环工艺加速了美拉德反应的发生,使其产生更多的环状二肽,并主要以环二肽(D-亮氨酸-L-脯氨酸)的形式存在[30-31].

对比发现,共水热碳化过程中,有机酸含量有着较为明显的提升,在 HL-R2 达到最高含量.液相中的有机酸主要是由木质纤维组分的降解产生的,并导

中国知网　https://www.cnki.net

致液相 pH 值呈酸性.经过再循环,木质纤维降解产生的有机酸在液相中富集,提供了酸性介质环境,进一步催化了水热碳化反应,促进了脱水、脱羧等反应的进行.此外,Li 等[11]认为,部分碳链骨架的裂解形成碳氢化合物,并反应形成有机酸,这部分有机酸会与醇类化合物发生酯化反应,这可能是 HL-R3 有机酸含量降低的原因.

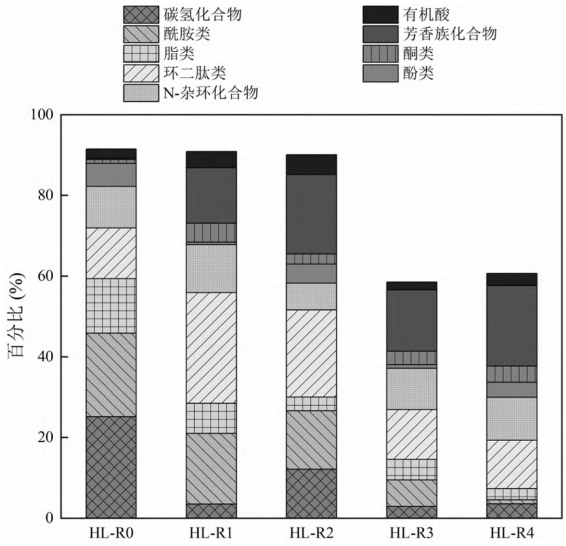


图 8 液相产物的有机物组成成分

Fig.8 Organic composition of the liquid phase products

液相中的 N-杂环化合物主要来源于蛋白质的不完全水解以及木质纤维素和蛋白质之间交互作用发生美拉德和曼尼希反应[29],并在 HL-R2 时达到最小值.另外,由于脱氨反应,蛋白质水解产生的氨基酸会转化为氨,并进一步形成酰胺;但根据 GC-MS 分析,HL-R0~HL-R4 产物中酰胺类含量随着液相循环次数的增多而明显下降,证明液相循环下更多酰胺类物质再次参与了水热碳化反应,从而使其含量减少[32].

与 HL-R0 对比,经过循环后的液相中酮类化合物含量增长明显,这些酮类化合物主要是由 5-HMF 和木糖水解生成,而液相成分中并未发现 5-HMF 等呋喃类和糠醛类化合物,这些化合物在该水热碳化条件下不稳定,被反应消耗并转化为芳香族物质[11,33].芳香族化合物不仅来源于呋喃类和糠醛类化合物的反应,还有可溶性木质素等有机物的形成[34].GC-MS 分析证明了上述结论,液相循环显著增加了芳香族化合物的含量,从 0.31%(HL-R0)增加到 13.75%(HL-R1),并在 HL-R2 时达到最大值(19.68%),这一现象也验证了前文 SEM 水热炭在液相循环后表面出现密集堆积的微球结构的分析结果.

2.3 液相循环下共水热碳化反应路径

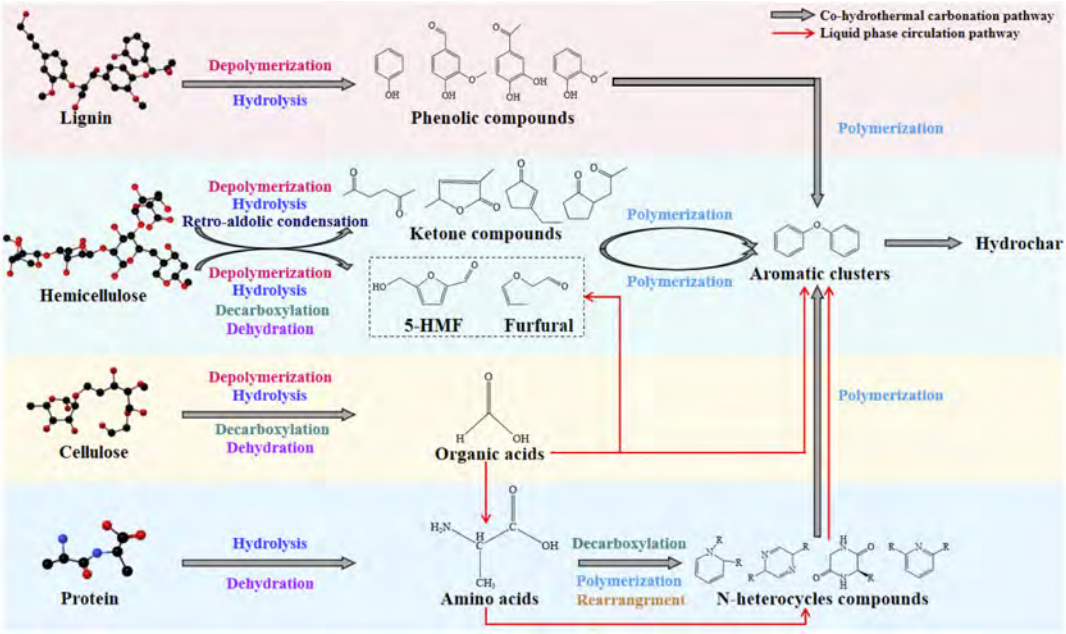


图 9 液相循环下糖厂滤泥和甘蔗渣共水热碳化反应路径

Fig.9 Reaction pathway for the co-hydrothermal carbonization process of filter mud and bagasse under liquid phase cycling

图 9 为液相循环下主要中间产物及其共水热碳化反应路径.糖厂滤泥和甘蔗渣两种原料成分主要

中国知网 https://www.cnki.net

为纤维素、半纤维素、木质素和蛋白质.在水热碳化期间,糖厂滤泥和甘蔗渣中的半纤维素先发生解聚,分解为多糖,然后水解生成木聚糖,并在异构化作用下产生戊糖或己糖.木质纤维素基质的键断裂导致纤维素形成纤维二糖等低聚物,多糖(淀粉)和二糖(蔗糖)分别转化为葡萄糖和果糖,同样异构化为戊糖和己糖[18,24].获得的单糖通过脱水、脱羧反应生成糠醛、5-HMF 等物质,并经过逆羟醛缩合反应产生醛酮类化合物;同时,葡萄糖和醛酮类化合物还发生了一系列脱水、脱羧反应生成有机酸.糖厂滤泥中的蛋白质水解后产生氨基酸,脱羧后得到的有机胺可以转化为 N-杂环化合物[35].在美拉德反应中,葡萄糖和氨基酸结合生成 Amadori 化合物,经过脱水反应形成 N-杂环化合物,并进一步转化为芳香族化合物.木质素中的可溶性木质素先水解为芳香族低聚物,后进一步水解得到酚、醛等化合物,而未分解的木质素可直接碳化成水热炭基体[36].

在液相循环期间,有机酸的积累对水热炭的形成起到重要作用,使整体反应处于酸性环境中,催化水解、脱水、重排等反应的发生[16].液相中的氨基酸在酰化作用下会被不断累积的有机酸转化为 N-杂环化合物和胺等有机相;在液相循环过程中,氨基酸、N-杂环化合物、胺等物质可以直接促进水热炭的形成[7,16],糠醛、5-HMF、苯衍生物、酚类、醛类、酮类化合物和 N-杂环化合物通过聚合转化为芳香族团簇,并进一步聚合形成水热炭[37].此外,作为水热炭生成的主要反应之一,有机酸的积累可以促进美拉德反应的进行,从而形成更多的芳香族化合物,进而转化为水热炭,这也是水热炭产率增加的主要原因.

3　结论

3.1　液相循环显著提高了水热炭的性能.液相循环下,水热炭产率大幅增高,HHV 增大了 1.23MJ/kg,表面微球结构数量增加.液相循环还促进了生物质的分解与脱水、脱羧等反应的进行,丰富了水热炭表面的含氧官能团,提供更多的化学位点,赋予了水热炭更优异的吸附性能,提高其土地利用潜力.

3.2　液相循环对液相产物的理化性质和有机质含量产生了影响.EC、NH_3-N 和 COD 值均随循环次数增多而大幅增加,pH 值则呈相反趋势;对比液相循环前后,碳氢化合物、酰胺类和酯类物质含量减少,而有机酸、芳香族化合物和酮类含量明显增多;尤其是芳香族化合物,从 0.31%(HL-R0)增大到 19.68%(HL-R2).

3.3　在液相循环中,生物大分子先通过解聚、水解、脱水脱羧等反应转化为小分子有机相,由积累的有机酸催化加速了有机质的转化,促进了美拉德反应的进行,促使更多的中间产物经过芳构化作用聚合成芳香族化合物,并最终转化成水热炭.

参考文献:

[1] 刘法球.亚法糖厂滤泥制备生物炭及其缓释肥料的初步研究 [D]. 广西大学制糖工程, 2019.
Fa Q L. Preliminary study on preparation of biochar and its slow-release fertilizer by sulfidation method sugar filter mud [D]. Guangxi University Sugar Engineering, 2019.

[2] Nguyen T A H, Bui T H, Guo W S, et al. Valorization of the aqueous phase from hydrothermal carbonization of different feedstocks: Challenges and perspectives [J]. Chemical Engineering Journal, 2023, 472:144802.

[3] Djandja O S, Liew R K, Liu C, et al. Catalytic hydrothermal carbonization of wet organic solid waste: A review [J]. Science of The Total Environment, 2023,873:162119.

[4] Wang Q, Wu S, Cui D, et al. Co-hydrothermal carbonization of organic solid wastes to hydrochar as potential fuel: A review [J]. Science of The Total Environment, 2022,850:158034.

[5] Chen Q, Liu H, Ko J, et al. Structure characteristics of bio-char generated from co-pyrolysis of wooden waste and wet municipal sewage sludge [J]. Fuel Processing Technology, 2019,183:48-54.

[6] 钱黎黎,王彦鑫,倪　俊,等.生物质水热炭改性方法及应用研究进展 [J]. 煤炭学报, 2023,48(6):2279-2290.
Li L Q, Yan X W, Jun N, et al. Research progress of modification method and application of biomass hydrochar [J]. Journal of China Coal Society, 2023,48(6):2279-2290.

[7] Leng S, Leng L, Chen L, et al. The effect of aqueous phase recirculation on hydrothermal liquefaction/carbonization of biomass: A review [J]. Bioresource Technology, 2020,318:124081.

[8] Picone A, Volpe M, Codignole Lùz F, et al. Co-hydrothermal carbonization with process water recirculation as a valuable strategy to enhance hydrochar recovery with high energy efficiency [J]. Waste Management, 2024,175:101-109.

[9] Picone A, Volpe M, Giustra M, et al. Hydrothermal carbonization of lemon peel waste: Preliminary results on the effects of temperature during process water recirculation [J]. Applied System Innovation, 2021,4(1):19.

[10] Sharma H B, Panigrahi S, Vanapalli K R, et al. Study on the process wastewater reuse and valorisation during hydrothermal co-carbonization of food and yard waste [J]. Science of The Total Environment, 2022,806:150748.

[11] Li Z, Niu S, Liu J, et al. Solid fuel production from co-hydrothermal

中国知网　https://www.cnki.net

carbonization of polyvinyl chloride and corncob: Higher dechlorination efficiency and process water recycling [J]. Science of The Total Environment, 2022,843:157082.

[12] GB/T 212−2008 煤的工业分析方法测定 [S].
GB/T 212−2008 Proximate analysis of coal [S].

[13] Li Y, Li K, Su M, et al. Fabrication of carbon/SiO_2 composites from the hydrothermal carbonization process of polysaccharide and their adsorption performance [J]. Carbohydrate Polymers, 2016,153:320−328.

[14] Fang X, Zhang D, Feng Y, et al. Directional regulation and mechanism analysis of the surface properties of hydrothermal carbon by circulating liquid in the hydrothermal carbonization procedure [J]. Environmental Research, 2023,229:116003.

[15] Leng S, Li W, Han C, et al. Aqueous phase recirculation during hydrothermal carbonization of microalgae and soybean straw: A comparison study [J]. Bioresource Technology, 2020,298:122502.

[16] Picone A, Volpe M, Messineo A. Process water recirculation during hydrothermal carbonization of waste biomass: Current knowledge and challenges [J]. Energies, 2021,14(10):2962.

[17] Wu S, Wang Q, Wu D, et al. Influence of temperature and process water circulation on hydrothermal carbonization of food waste for sustainable fuel production [J]. Journal of the Energy Institute, 2024, 112:101459.

[18] Liu T, Jiao H, Yang L, et al. Co−hydrothermal carbonization of cellulose, hemicellulose, and protein with aqueous phase recirculation: Insight into the reaction mechanisms on hydrochar formation [J]. Energy, 2022,251:123965.

[19] Ding Y, Li D, Lv M, et al. Influence of process water recirculation on hydrothermal carbonization of rice husk at different temperatures [J]. Journal of Environmental Chemical Engineering, 2023,11(2):109364.

[20] Xiao K, Liu H, Li Y, et al. Correlations between hydrochar properties and chemical constitution of orange peel waste during hydrothermal carbonization [J]. Bioresource Technology, 2018,265:432−436.

[21] Ning X, Teng H, Wang G, et al. Physiochemical, structural and combustion properties of hydrochar obtained by hydrothermal carbonization of waste polyvinyl chloride [J]. Fuel, 2020,270:117526.

[22] Ghaziaskar A, McRae G A, Mackintosh A, et al. Catalyzed hydrothermal carbonization with process liquid recycling [J]. Energy & Fuels, 2019,33(2):1167−1174.

[23] Zhang L, Wang Q, Xu F, et al. Insights into the evolution of chemical structures in hydrochars from hydrothermal carbonization of PVC [J]. Journal of the Energy Institute, 2022,105:323−333.

[24] Yang X, Wang B, Song X, et al. Co−hydrothermal carbonization of sewage sludge and coal slime with sulfuric acid for N, S doped hydrochar [J]. Journal of Cleaner Production, 2022,354:131615.

[25] Wang R, Jin Q, Ye X, et al. Effect of process wastewater recycling on the chemical evolution and formation mechanism of hydrochar from herbaceous biomass during hydrothermal carbonization [J]. Journal of Cleaner Production, 2020,277:123281.

[26] Lachos−Perez D, César Torres−Mayanga P, Abaide E R, et al. Hydrothermal carbonization and Liquefaction: differences, progress, challenges, and opportunities [J]. Bioresource Technology, 2022,343: 126084.

[27] Fang J, Zhan L, Ok Y S, et al. Minireview of potential applications of hydrochar derived from hydrothermal carbonization of biomass [J]. Journal of Industrial and Engineering Chemistry, 2018,57:15−21.

[28] Xu Z, Ma X, Zhou J, et al. The influence of key reactions during hydrothermal carbonization of sewage sludge on aqueous phase properties: A review [J]. Journal of Analytical and Applied Pyrolysis, 2022,167:105678.

[29] Zhang C, Ma X, Zheng C, et al. Co−hydrothermal carbonization of water hyacinth and sewage sludge: Effects of aqueous phase recirculation on the characteristics of hydrochar [J]. Energy & Fuels, 2020,34(11):14147−14158.

[30] Xu Z, Ma X, Zhou J, et al. The influence of key reactions during hydrothermal carbonization of sewage sludge on aqueous phase properties: A review [J]. Journal of Analytical and Applied Pyrolysis, 2022,167:105678.

[31] Jabeen S, Gao X, Hayashi J, et al. Systematic characterization of biocrude and aqueous phase from hydrothermal carbonization of algal biomass [J]. Journal of Environmental Chemical Engineering, 2022, 10(3):107953.

[32] Matayeva A, Bianchi D, Chiaberge S, et al. Elucidation of reaction pathways of nitrogenous species by hydrothermal liquefaction process of model compounds [J]. Fuel, 2019,240:169−178.

[33] Borrero−López A M, Masson E, Celzard A, et al. Modelling the reactions of cellulose, hemicellulose and lignin submitted to hydrothermal treatment [J]. Industrial Crops and Products, 2018,124: 919−930.

[34] Wang F, Wang J, Gu C, et al. Effects of process water recirculation on solid and liquid products from hydrothermal carbonization of Laminaria [J]. Bioresource Technology, 2019,292:121996.

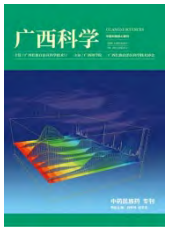
[35] Li Q, Lin H, Zhang S, et al. Co−hydrothermal carbonization of swine manure and cellulose: Influence of mutual interaction of intermediates on properties of the products [J]. Science of The Total Environment, 2021,791:148134.

[36] Wang Q, Wu S, Cui D, et al. Co−hydrothermal carbonization of corn stover and food waste: Characterization of hydrochar, synergistic effects, and combustion characteristic analysis [J]. Journal of Environmental Chemical Engineering, 2022,10(6):108716.

[37] Wang R, Lin Z, Meng S, et al. Effect of lignocellulosic components on the hydrothermal carbonization reaction pathway and product properties of protein [J]. Energy, 2022,259:125063.

作者简介：陈思思(1999−),女,安徽池州人,广西大学硕士研究生,主要研究方向为环境污染物处置技术.发表论文 6 篇.Hesterc827@163.com.

中国知网 https://www.cnki.net



广西科学
Guangxi Sciences
ISSN 1005-9164,CN 45-1206/G3

《广西科学》网络首发论文

题目：氮磷限制条件下球形棕囊藻生理生化响应及转录组学研究
作者：邢政，王佳乐，赖俊翔，王英辉，李杰
DOI：10.13656/j.cnki.gxkx.20250103.001
收稿日期：2024-02-04
网络首发日期：2025-01-06
引用格式：邢政，王佳乐，赖俊翔，王英辉，李杰．氮磷限制条件下球形棕囊藻生理生化响应及转录组学研究[J/OL]．广西科学.
https://doi.org/10.13656/j.cnki.gxkx.20250103.001



网络首发：在编辑部工作流程中，稿件从录用到出版要经历录用定稿、排版定稿、整期汇编定稿等阶段。录用定稿指内容已经确定，且通过同行评议、主编终审同意刊用的稿件。排版定稿指录用定稿按照期刊特定版式（包括网络呈现版式）排版后的稿件，可暂不确定出版年、卷、期和页码。整期汇编定稿指出版年、卷、期、页码均已确定的印刷或数字出版的整期汇编稿件。录用定稿网络首发稿件内容必须符合《出版管理条例》和《期刊出版管理规定》的有关规定；学术研究成果具有创新性、科学性和先进性，符合编辑部对刊文的录用要求，不存在学术不端行为及其他侵权行为；稿件内容应基本符合国家有关书刊编辑、出版的技术标准，正确使用和统一规范语言文字、符号、数字、外文字母、法定计量单位及地图标注等。为确保录用定稿网络首发的严肃性，录用定稿一经发布，不得修改论文题目、作者、机构名称和学术内容，只可基于编辑规范进行少量文字的修改。

出版确认：纸质期刊编辑部通过与《中国学术期刊（光盘版）》电子杂志社有限公司签约，在《中国学术期刊（网络版）》出版传播平台上创办与纸质期刊内容一致的网络版，以单篇或整期出版形式，在印刷出版之前刊发论文的录用定稿、排版定稿、整期汇编定稿。因为《中国学术期刊（网络版）》是国家新闻出版广电总局批准的网络连续型出版物（ISSN 2096-4188，CN 11-6037/Z），所以签约期刊的网络版上网络首发论文视为正式出版。

DOI：10.13656/j.cnki.gxkx.20250103.001 网络首发时间：2025-01-06 11:21:32 网络首发地址：https://link.cnki.net/urlid/45.1206.G3.20250103.1720.002

氮磷限制条件下球形棕囊藻生理生化响应及转录组学研究*

邢 政[1]，王佳乐[1]，赖俊翔[2,3**]，王英辉[1,4**]，李 杰[2,3]

（1.广西大学海洋学院，广西南宁 530004；2.广西科学院广西海洋科学院，广西近海海洋环境科学重点实验室，广西南宁 530007；3.北部湾海洋产业研究院，广西防城港 538000；4.广西产研院绿色低碳技术研究所，广西南宁 530001）

摘要：氮磷营养限制对球形棕囊藻（*Phaeocystis globosa*）生长能够产生显著的抑制作用，但其内在作用机理仍不清晰。为从细胞生理生化及转录组层面全面解析球形棕囊藻在氮磷限制下的响应机制，本研究分别设置氮限制组（N:P=4:1）、磷限制组（N:P=64:1）与对照组（N:P=16:1），测定其生理生化指标并结合转录组学分析，通过比对得到差异表达 unigene 14 272 个，其中氮限制组上调基因 4 397 个，下调基因 3 679 个；磷限制组上调基因 4 963 个，下调基因 5 079 个。研究表明氮限制对球形棕囊藻光合作用抑制效果最显著，细胞由结构型多糖合成向储能代谢型糖类物质合成转变；磷限制条件下，部分光反应蛋白合成基因上调，细胞增殖被显著抑制，囊体更薄，细胞内糖胺聚糖及脂肪酸合成相关基因均上调表达。此外，氮磷限制均会提高细胞转运蛋白的表达，抑制蛋白酶体合成。结果认为球形棕囊藻代谢活动受氮限制影响较大，生长增殖及囊体强度受磷限制影响更大。本研究从表观及分子层面初步阐释了球形棕囊藻在氮磷限制下的响应机制，为进一步揭示其生理代谢及成囊过程的内在机理提供参考，同时为相关部门制定有害藻华防治策略提供依据。

关键词：球形棕囊藻；氮磷限制；生理生化；转录组

中图分类号：Q494; X55

球形棕囊藻隶属于定鞭藻纲（Haptophyceae/Prymnesiophyceae）棕囊藻属，其异型生活史存在游离单细胞和多细胞囊体两种形态[1]。近十几年来随着广西北部湾近岸海域经济快速发展，水体富营养化加剧[2]，2011 年以来几乎每年都会暴发球形棕囊藻藻华[3]，其囊体甚至导致滨海核电站冷却水系统堵塞[4]。正因为球形棕囊藻囊体大量暴发并聚集会对生态环境及工业设施造成危害，所以对其藻华的防治也一直是海洋环境保护领域的研究重点。

水体中的营养物质是调节海洋赤潮发生的关键环境因素[5]，其中氮磷元素对海洋微藻的生长至关重要[6]。氮元素是构成藻细胞蛋白质、叶绿素、酶等物质的重要组分，是影响微藻生长的重要营养元素[7]。磷元素是藻细胞内核酸和磷脂的主要成分，同时参与能量传递、信号传导和细胞膜构建等各项代谢活动[8]。研究表明，硝酸盐和磷酸盐均为球形棕囊藻生长的主要限制因子[9]，两种营养盐的缺乏会抑制其生长及生活史转化[10]。在寡硝酸盐水体中，仅单细胞存在而没有棕囊藻囊体[11]；磷限制条件下，球形棕囊藻生长速率、囊体的数量、形态以及成囊持续时间都会受到明显抑制[9]。以广西北部湾为例，近海水体氮磷比值长期大于 Redfield 比值（16：1）[2]，为磷限制状态[12]，而磷限制缓解常伴随球形棕囊藻赤潮暴发[2]。由此可见，氮磷限制是控制球形棕囊藻藻华暴发的重要因素。因此，从控制氮磷的角度出发，全面而深入地解析氮磷限制对其藻华发展的影响及内在作用机制，对于制定更全面、更科学、

收稿日期：2024-02-04 修回日期：2024-03-16

* 国家自然科学基金项目（42266007），中央引导地方科技发展资金项目（桂科 ZY21195027）和广西科技重大专项（桂科 AA17202020）资助。

【第一作者简介】

邢 政（1997-），男，在读硕士研究生，主要从事海洋生物生态学研究，E-mail: 17756227289@163.com。

【**通信作者简介】

赖俊翔（1984-），男，研究员，主要从事海洋环境科学研究，E-mail: jxlai@gxas.cn。

王英辉（1970-），女，教授，主要从事海洋生态环境研究，E-mail: wyh@gxu.edu.cn。

更合理的藻华防治决策具有重要指导意义。然而，目前有关氮磷限制对球形棕囊藻生理生化的影响多集中于表观生理指标的测定，其内在作用机理尚不清晰，因而迫切需要从分子层面对其进行研究。

随着高通量测序技术快速发展，如今该技术已成为获取物种关键功能基因，预测其代谢通路并表征生物学过程的重要手段之一[13]。目前转录组学在棕囊藻上已取得了一些成功的应用，例如，Zhang 等[14]揭示了球形棕囊藻成囊的内在机制；Mars Brisbin 等[15]发现球形棕囊藻囊体形成过程中细胞内资源得到再分配；通过比较两种球形棕囊藻株系，Liang 等[16]发现其囊体形成过程的代谢差异；针对环境胁迫，Issak[17]发现铁富加有助于南极棕囊藻（*Phaeocystis antarctica*）囊体形成并促进其叶绿素 *a* 含量、光合效能以及颗粒有机碳和氮含量的恢复； Ren 等[18]发现聚合氯化铝改性粘土（PAC-MC）在球形棕囊藻细胞中诱导氧化应激、光合抑制和 DNA 损伤。

为从分子层面揭示氮磷限制对球形棕囊藻生理生化的影响机制，本研究对不同氮磷限制条件下囊体细胞进行转录组测序分析，通过获得的差异表达基因对其参与的代谢通路进行研究，分析结果为研究氮磷限制条件下球形棕囊藻生长成囊调控机制以及相关代谢途径奠定基础，并为采用营养盐控制调控其囊体生长及赤潮暴发提供理论依据。

1 材料与方法

1.1 培养条件

本研究中球形棕囊藻分离自广西北部湾近海海域，由广西北部湾海洋研究中心藻种室提供。采用盐度为（30±1）psu 的人工海水，添加 f/10 培养基进行预培养，培养温度为（20±1）℃，光照强度设定为 50 μmol photons·m^{-2}·s^{-1}，光照周期为 12 h:12 h。接种前将囊体摇碎，经 10 μm 筛绢过滤 2 次得到游离单细胞，初始密度为 0.5×10^4 cells·ml^{-1}，培养体积为 800 mL。设置氮限制组（4:1），对照组（16:1），磷限制组（64:1），如表 1 所示，每组设置 3 个平行，按比例定量加入氮、磷，其余按 f/10 培养基添加微量元素和维生素。实验条件与预培养条件保持一致，无菌培养周期 25 d。为防止细胞沉底贴壁死亡，每天定时摇匀 3 次，间隔 3 d 并固定时间取样测定其生理生化指标。

表 1　实验组营养盐设置浓度

Table 1　Design of nutrition concentration in each experimental group

组别 Group	NO_3^-/(μmol·L^{-1})	PO_4^{3-}/(μmol·L^{-1})	N/P ratio	初始密度/ (cells·mL^{-1}) Initial density/ (cells·mL^{-1})
N-limited group	44.10	11.00	4:1	0.5×10^4
Control group	176.40	11.00	16:1	0.5×10^4
P-limited group	176.40	2.75	64:1	0.5×10^4

1.2 生理生化指标的测定及方法

1.2.1 营养盐浓度及叶绿素 *a* 含量

采用 Whatman GF/F 滤膜过滤采集的藻液（25 mL），并将滤液保存在-20℃直至分析。按照 Hansen 和 Koroleff 的方法[19]，使用营养盐自动分析仪测定营养盐的浓度。

将所得滤膜浸泡在 6 mL 90%丙酮中，放置 4℃下黑暗萃取 24 h。离心 15 min 后，取 3 mL 上清液，用紫外分光光度计（Agilent, Cary 100）测定在波长为 630、647、664、750 nm 下的吸光值，计算叶绿素 *a* 含量[20]。

1.2.2 细胞丰度及囊体直径

采集 1 mL 藻液，用 10 μm 筛绢自然过滤收集游离单细胞，运用流式细胞仪（BD Accuri C6, BD, 美国）在荧光检测波长为（675±25）nm 的 FL 4 通道对单细胞丰度进行计数。同时取 1 mL 藻液于 24 孔板，运用倒置显微镜（Nikon, Eclipse Ti）对囊体数量、囊体内细胞数

进行计数并测量囊体直径，每个样本随机选择 30 个囊体进行测定，少于 30 个则全部计数。

1.2.3 PSII 最大量子产量（F_v/F_m）

采集藻液 5 mL，以浮游植物荧光仪（Phyto-PAM，Walz，德国）测定叶绿素荧光诱导动力学参数初始荧光（F_0）和最大荧光产量（F_m），PSII 最大量子产量（F_v/F_m）由（F_m - F_0）/F_m 计算。测定前，样品先经 10 min 暗处理，测定方法参照仪器使用说明书进行。

1.3 无参转录组分析

1.3.1 总 RNA 提取、cDNA 文库构建及测序

培养第 12 d 进行取样，每份样本取藻液 400 mL，每个处理条件取 3 份平行，4 ℃低温离心后用液氮速冻并快速研磨，按 TRIzol 试剂盒提取总 RNA，利用 Nanodrop 2000 对所提 RNA 的浓度和纯度进行检测，琼脂糖凝胶电泳检测 RNA 完整性，Agilent 5300 测定 RQN(RNA Quality Number)值。质量检测合格（OD_{260}/ OD_{280} 比值在 1.8-2.2，RQN 值≥6.7）的 RNA 样本用反转录试剂盒进行反转录，将合格样本送至上海美吉生物医药科技有限公司进行 cDNA 文库构建并在 Illumina NovaSeq 6000 测序平台进行转录组测序。

1.3.2 测序数据分析及片段组装

使用 fastp 软件过滤低质量 reads，具体操作为：去除 reads 中的接头序列，将序列末端（3'端）低质量（质量值小于 20）的碱基修剪掉，去除含 N（模块碱基）的 reads 即测序片段 5'和 3'端含接头，舍弃去 adapter 及质量修剪后长度小于 30 bp 的序列。将筛选获得的 clean reads 利用 Trinity 软件对进行 *de novo* 从头组装。运用 TransRate 和 CD-HIT 软件对组装结果进行优化过滤，再利用 BUSCO 软件评估组装质量。

1.3.3 转录组数据注释

将转录测序获得的 Unigene 与 GO (Gene Ontology)、NR (Non-Redundant Protein Sequence Database)、Swiss-Port、Pfam、KEGG (Kyoto Encyclopedia of Genes and Genomes) 及 eggNOG (Evolutionary Genealogy of Genes: Non-supervised Orthologous Groups) 数据库分别进行比对，获得在各数据库的注释信息，使用 Diamond 与 HMMER 软件对各数据库注释情况进行统计及预测。

1.3.4 表达量分析

使用软件 RSEM 分别对基因和转录本的表达水平进行定量分析，利用 DEseq2 软件构建 DEGs 分布火山图（Fold change≥|2.00|，Q 值≤0.05），显著差异基因采用 Fold change≥|2^5|，Q 值≤0.01 的标准进行筛选。使用 Limma 软件比较分析两者共有 DEGs 筛选结果及其基因表达相关性，利用层次聚类法构建不同处理组间的 DEGs 聚类热图。

1.3.5 GO 与 KEGG 通路富集分析

使用软件 Goatools 对功能基因进行 GO 富集分析（FDR≤0.05），使用 KOBAS 进行 KEGG 通路富集分析（FDR≤0.05）。

1.4 数据处理

运用 SPSS 26.0 软件对生理生化指标的数据进行单因素方差（one-way ANOVA）分析与最小差异（LSD）检验，显著性水平设置为 0.05。

2 结果与分析

2.1 培养液中营养盐浓度变化

球形棕囊藻培养液中氮磷营养盐浓度变化如图 1 所示。氮限制组中，氮磷营养盐均在第 8 天下降至最低值（氮消耗 98.43%，磷消耗 26.63%）。对照组硝酸盐浓度和磷酸盐均在第 12 天达到最低值（氮消耗 95.86%，磷消耗 87.73%），其中磷酸盐浓度有小幅度上升。磷限制组中硝酸盐浓度在第 4-8 d 下降幅度最为显著，随后下降速度放缓，实验结束时达最低（氮消耗 86.03%）；磷酸盐浓度在 0-8 d 下降速率稳定，第 8 天达最低值（磷消耗 93.10%）。

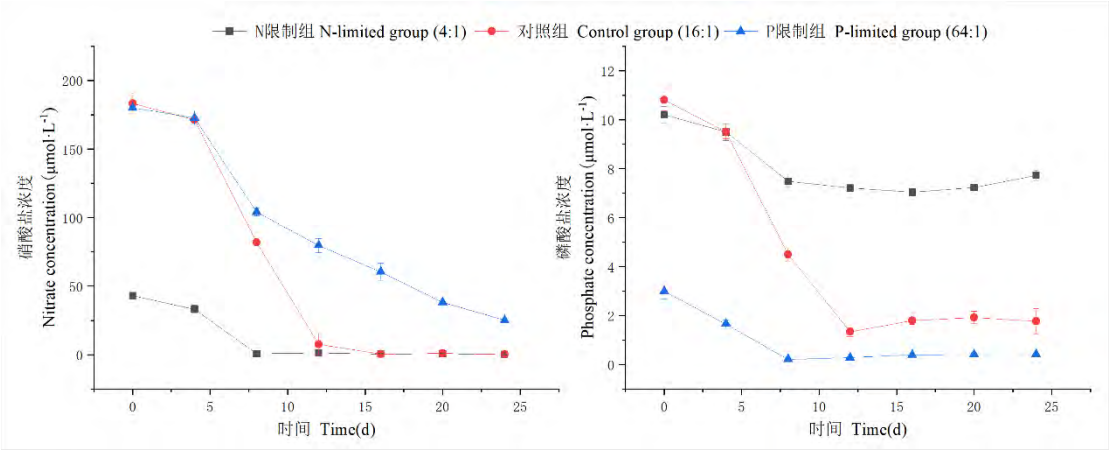
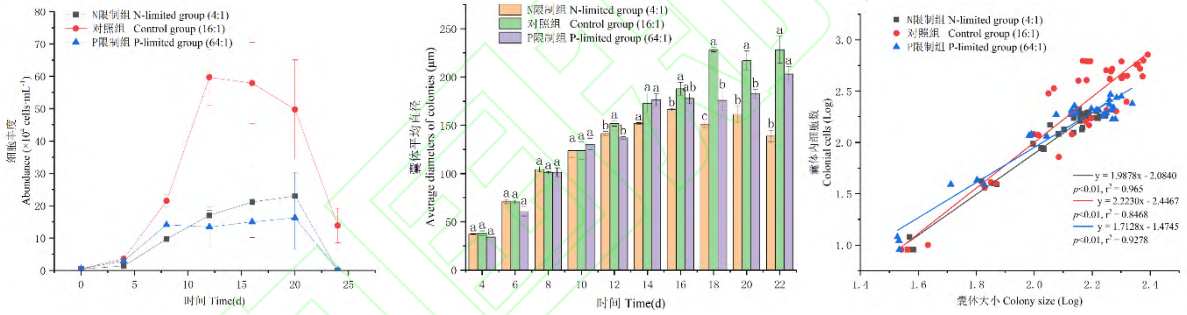


图 1　氮、磷限制条件下球形棕囊藻培养实验中溶解性无机盐的浓度变化

Fig.1　Variation in dissolved inorganic nutrients in culture of *Phaeocystis globosa* under N-limited and P-limited conditions

2.2 细胞生长曲线及囊体平均直径

细胞生长曲线如图 2（a）所示，在 0-8 d，对照组细胞生长速度最高，其次为磷限制组，氮限制组最低。对照组细胞密度在第 12 天达到峰值，随后开始缓慢下降；氮限制组细胞密度缓慢上升，在第 20 天达到峰值；磷限制组细胞密度在第 8 天达到峰值，随后趋于平稳。3 个实验组细胞密度都从第 20 天开始加速凋亡。



(a)　(b)　(c)

Different lowercase letters indicate significant differences (P<0.05) among the different nutrient limitation groups at the same time, and the same lowercase letters indicate no significant differences (P>0.05) .

图 2　氮、磷限制条件下球形棕囊藻细胞增殖及囊体生长

Fig.2　Cell proliferation and colonies growth of *Phaeocystis globosa* under N-limited and P-limited conditions

细胞囊体平均直径如图 2（b）所示，在第 4-10 d，其组间囊体平均直径差异不显著（P>0.05）。在第 12 天，对照组与氮磷限制组之间差异显著（P<0.05），而营养盐限制组之间差异不显著（P>0.05）。第 16 天，对照组与氮限制组之间差异显著（P<0.05）。第 18 天，3 个实验组间差异最为显著（P<0.05），其中对照组囊体平均直径最大，为（228.29±2.10）μm；磷限制组次之，为（175.78±10.15）μm；氮限制组平均囊体直径最低，为（150.49±2.74）μm。随后对照组和磷限制组间差异开始减小，但对照组和氮限制组间差异显著（P<0.05），表明氮限制条件下囊体平均直径最小。

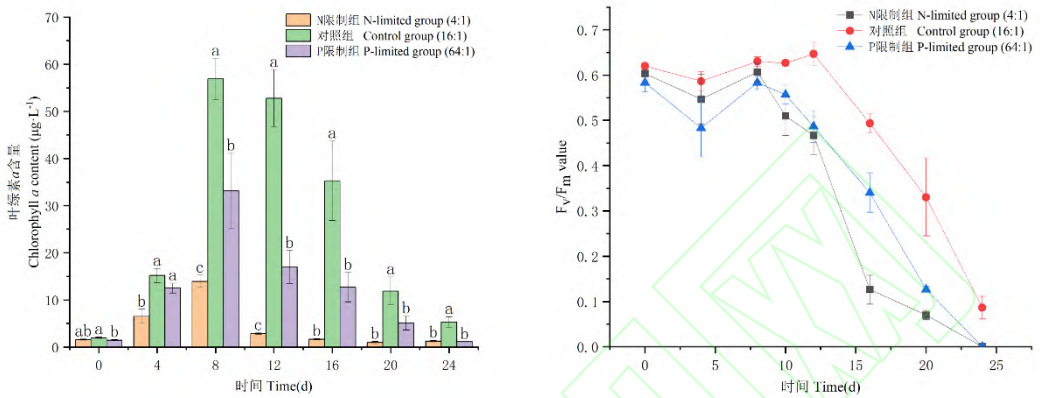
图 2（c）为氮、磷限制条件下囊体大小（log）与每个囊体内细胞数（log）之间的关系，各限制条件下囊体大小（log）与囊体细胞数量（log）呈显著的线性相关（P<0.01）。其中磷限制组回归线斜率显著低于另外两组（P<0.05），表明磷限制条件下囊体内细胞密度最低。

2.3 叶绿素 *a* 含量及 F_v/F_m

球形棕囊藻叶绿素 *a* 含量受氮磷营养盐限制影响较大，图 3（a）显示叶绿素 *a* 含量组

间差异在第 8 天和第 12 天最为显著（$P<0.05$），对照组叶绿素 *a* 含量始终保持最高。除了第 0 天和第 24 天，氮限制组叶绿素 *a* 含量略高于磷限制组外，其余时间都显著低于其他组。结果表明氮限制对球形棕囊藻叶绿素 *a* 含量抑制效果显著。

在不同营养盐限制条件下，球形棕囊藻 PSII 的最大量子产量（F_v/F_m）的变化如图 3（b）所示。在第 10 天之前，3 个组别的 F_v/F_m 差异并不显著（$P>0.05$）。从第 10 天开始，氮磷限制组 F_v/F_m 值开始显著低于对照组（$P<0.05$）。在第 16 天，组别间差异性最为显著（$P<0.05$），其中氮限制组 F_v/F_m 最低。随后氮磷限制组间差异开始缩小，但都显著低于对照组。表明在无机氮消耗殆尽后，球形棕囊藻光电子传输效率受到显著抑制。



(a) (b)

Different lowercase letters indicate significant differences ($P<0.05$) among the different nutrient limitation groups at the same time, and the same lowercase letters indicate no significant differences ($P>0.05$) .

图 3　氮、磷限制条件下球形棕囊藻叶绿素 *a* 含量及 PSII 最大量子产量（F_v/F_m）的变化

Fig.3　Variation in chlorophyll *a* content and the maximum PSII quantum yield (F_v/F_m) of *P. globosa* under N-limited and P-limited conditions

2.4 RNA 测序及 *De novo* 组装分析

球形棕囊藻 RNA 平均浓度为 214 ng/μL，OD_{260}/OD_{280} 比值在 2.0-2.2（平均值为 2.11），RQN 平均值为 7.9，符合转录组测序标准。3 个实验处理组共 9 个生物学样本的原始测序数据 62.8 Gb，各样本原始数据均达到 6.25 Gb。通过组装并去除冗余后在测序文库共鉴定 Unigene 43 793 个，总长度为 42 407 013 bp，平均长度为 968 bp，N50 长度为 1 408 bp，GC 含量 67.08%。采用 TransDecoder 识别转录本序列中候选的编码区域（即 CDS 区）得到 CDS 36 629 个，并且检测得到 19 625 条 SSR 分布于 13 567 个 Unigene 中。测序结果中 Q20 和 Q30 百分比平均值结果分别为 97.94%与 94.15%，样本测序质量可用于后续注释分析。

2.5 基因注释与功能预测

3 个实验组转录组测序获得的 Unigene 与 6 大生物信息数据库进行比对和功能注释，其中有 18 993 个 Unigene 得到注释，占比为 43.37%，具体功能注释数见表 2。NR 数据库注释物种分布如图 4 所示，其中 57.11%的 Unigene 注释到藻类物种（*Klebsormidium nitens*、*Micromonas commoda*、*Pycnococcus provasolii*、*Chara braunii*、*Micromonas pusilla*、*Chloropicon primus*、*Ostreococcus tauri*、*Chlorella sorokiniana*、*Ostreococcus* sp. *'lucimarinus'*、*Raphidocelis subcapitata*、*Coccomyxa subellipsoidea*、*Micractinium conductrix*、*Ostreobium quekettii*），剩余 42.89%数据未能在已知藻类物种基因信息库中得到相应注释。EggNOG 功能注释结果如表 3 所示，其中 Unigene 注释数目最多的功能分类是“翻译后修饰、蛋白折叠、伴侣”（1 316 条），其次为“信号转导机制”（785 条），然后是“复制、重组和修复”（659 条）和“糖类转运和代谢”（609 条）。注释到“细胞运动”（5 条）和“核结构”（2 条）功能分类的基因最少，此外，5 799 条 Unigene 未被注释其功能未知。

表 2　球形棕囊藻 Unigene 注释信息

Table 2　Unigene annotation of *P. globosa*

数值 Values	总数 Total	GO	KEGG	eggNOG	NR	SwissProt	Pfam	交集 Intersection	并集 Union
Number	43 793	11 351	8 996	12 412	12 783	10 324	16 539	6 388	18 993
Percentage	100%	25.92%	20.54%	28.34%	29.19%	23.57%	37.77%	33.63%	43.37%

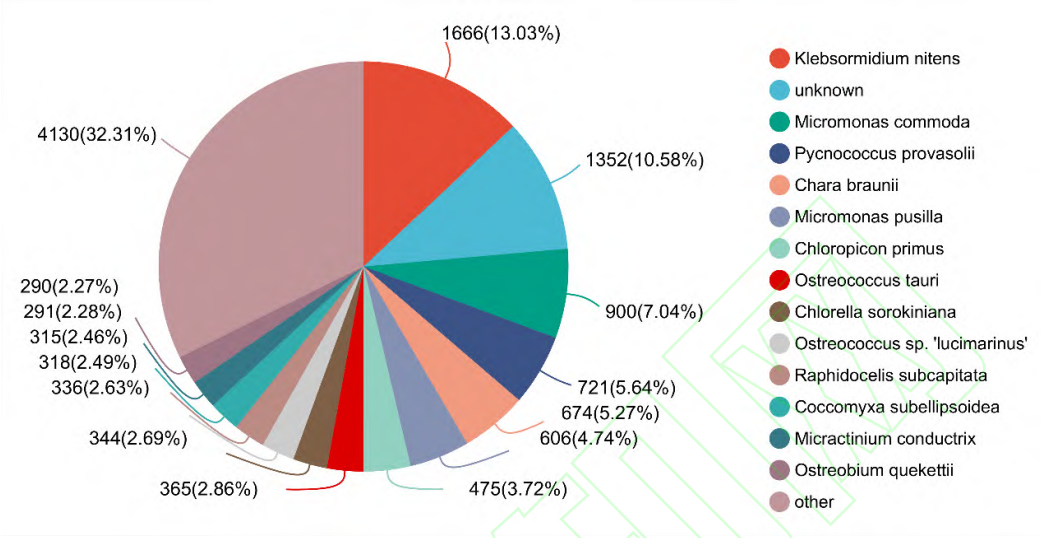


图 4　球形棕囊藻 Unigene 物种分布注释

Fig.4　Unigene annotation of *P. globosa* in species distribution

表 3　EggNOG 功能注释

Table 3　EggNOG functional annotation

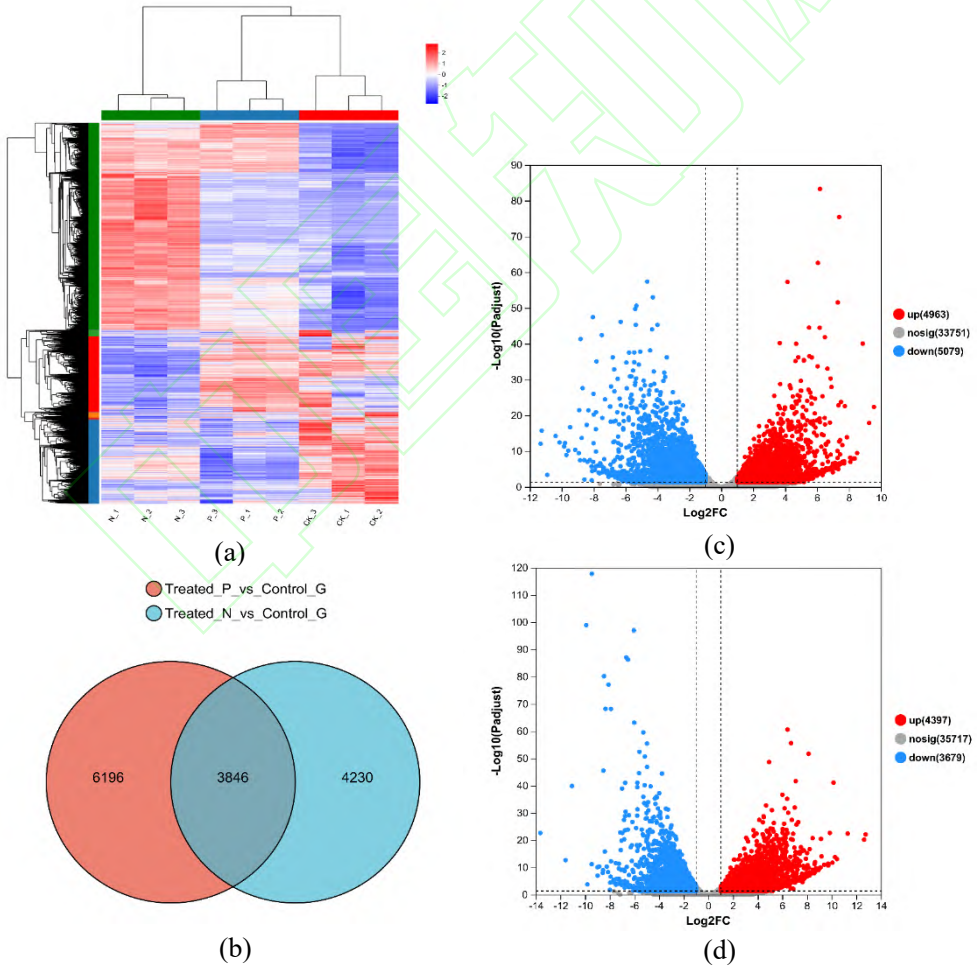
类型 Type	功能分类 Functional Categories	数目 Number
Metabolism	Energy production and conversion	326
	Amino acid transport and metabolism	470
	Nucleotide transport and metabolism	104
	Carbohydrate transport and metabolism	609
	Coenzyme transport and metabolism	175
	Lipid transport and metabolism	281
	Inorganic ion transport and metabolism	352
	Secondary metabolites biosynthesis, transport and catabolism	256
Cellular processes and signaling	Cell cycle control, cell division, chromosome partitioning	248
	Cell wall/membrane/envelope biogenesis	202
	Cell motility	5
	Posttranslational modification, protein turnover, chaperones	1 316
	Signal transduction mechanisms	785
	Intracellular trafficking, secretion, and vesicular transport	554
	Defense mechanisms	124
	Nuclear structure	2
	Cytoskeleton	379

	RNA processing and modification	108
	Chromatin structure and dynamics	116
Information storage	Translation, ribosomal structure and biogenesis	527
and processing	Transcription	384
	Replication, recombination and repair	659
Others	Function unknown	5 799

2.6 基因差异表达分析

基于 FPKM 值，利用软件 RSEM 构建球形棕囊藻 3 个处理组 Unigene 表达聚类热图，如图 5（a）所示。红色表示基因表达量较高，蓝色表示表达量较低，左侧为 Unigene 聚类树状图，其分支距离越近表示基因表达量越接近；上方为样本聚类树状图，分支距离越近表明样本表达模式越接近。球形棕囊藻中磷限制组（P）与对照组（CK）的基因集聚为一类表明两者基因具备相似的表达模式，氮限制组（N）单独为一簇说明其与两组基因表达趋势差异较大，左侧树状图显全部基因集可划分为两大簇。

以 CK 作为对照，总共检测出差异表达基因 14 272 条，图 5（b）所示，其中磷限制（P）差异表达基因 10 042 条，氮限制组（N）差异表达基因 8 076 条，共同差异表达基因 3 846 条。图 5（c）、（d）显示，磷限制组（P）相比对照（CK）上调表达基因 4 963 条，下调基因 5 079 条；氮限制组（N）上调基因 4 397 条，下调基因 3 679 条。



(a) Gene cluster expression heatmap; (b) Venn diagram of differentially expressed genes; (c) Differential gene expression volcano plot (P-limited group vs. Control group); (d) Differential gene expression volcano plot (N-limited group vs. Control group).

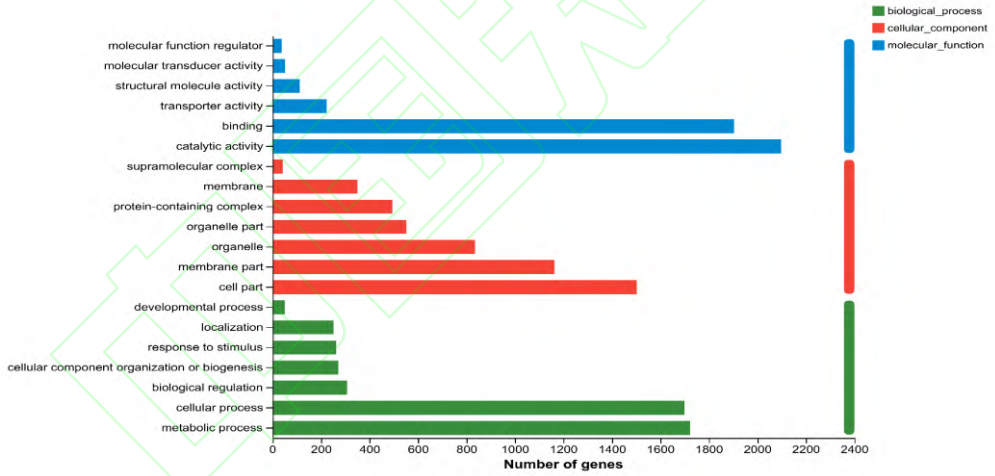
图 5　球形棕囊藻不同组别之间差异表达基因分析

Fig.5　Analysis of differentially expressed genes among different *P. globosa* comparison groups

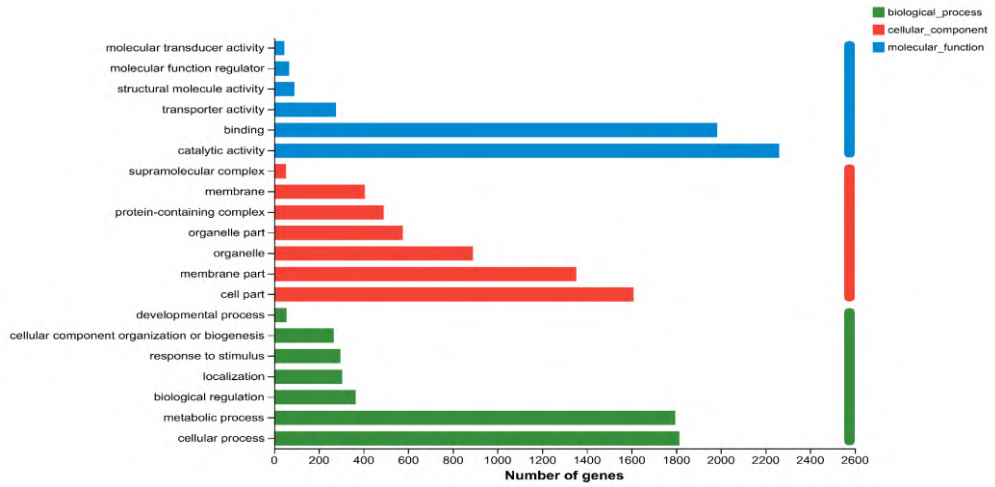
2.7 GO 与 KEGG 分类富集分析

2.7.1 GO 分类富集分析

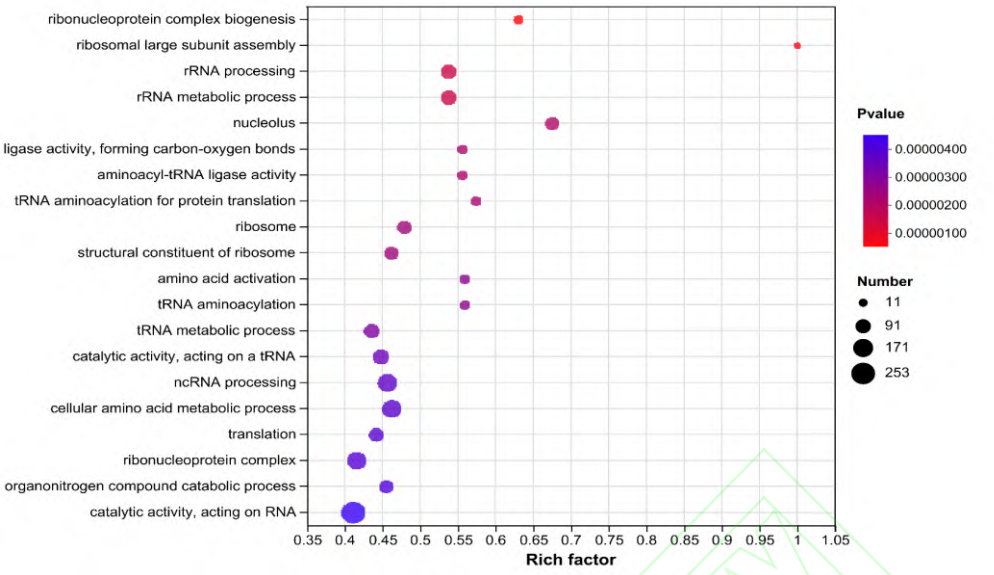
由图 6（a）和（b）可知，在分子功能（Molecular function）类别中，催化活性（Catalytic activity）所包含的 GO 条目最多（氮限制组与对照组间差异基因数是 2 098，磷限制组与对照组间差异基因数是 2 262），其次为结合（Binding）（氮限制组与对照组间差异基因数是 1 904 个，磷限制组与对照组间差异基因数是 1 985）；在细胞组分（Cellular component）类别中，GO 条目最多的是细胞组分（Cell part）（氮限制组与对照组间差异基因数是 1 503，磷限制组与对照组间差异基因数是 1 609），其次为膜组分（Membrane part）（氮限制组与对照组间差异基因数是 1 163，磷限制组与对照组间差异基因数是 1 353）；在生物学过程（Biological process）类别中，氮限制组与对照组比较中 GO 条目最多的是代谢过程（Metabolic process）（基因数为 1 722）其次为细胞过程（Cellular process）（基因数为 1 699），磷限制组与对照组比较中条目最多的是细胞过程（Cellular process）（基因数为 1 815）其次为代谢过程（Metabolic process）（基因数为 1 797）。图 6（c）和（d）为两个比较组差异基因 GO 富集 top 20 的结果，在氮限制组和对照组的比较中，富集程度较高的条目有核糖体大亚基的组装（基因数 11，富集比为 1）、细胞核条目（基因数 85，富集比 0.67）、核糖核蛋白复合体生物发生条目（基因数 34，富集比 0.63）。在磷限制组和对照组的比较中，富集程度较高的条目有 3-羟基癸醇[酰基载体蛋白]脱水酶活性（基因数 29，富集比 0.74）、S-乙酰转移酶活性（基因数 30，富集比 0.68）、脂肪酸合成酶活性（基因数 48，富集比 0.57）。



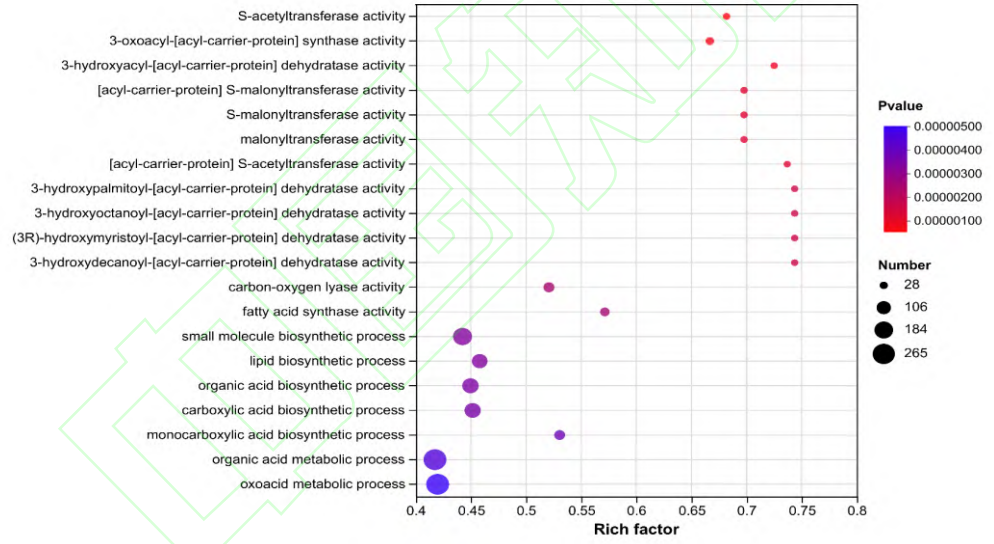
(a)



(b)


ribonucleoprotein complex biogenesis
ribosomal large subunit assembly
rRNA processing
rRNA metabolic process
nucleolus
ligase activity, forming carbon-oxygen bonds
aminoacyl-tRNA ligase activity
tRNA aminoacylation for protein translation
ribosome
structural constituent of ribosome
amino acid activation
tRNA aminoacylation
tRNA metabolic process
catalytic activity, acting on a tRNA
ncRNA processing
cellular amino acid metabolic process
translation
ribonucleoprotein complex
organonitrogen compound catabolic process
catalytic activity, acting on RNA
0.35 0.4 0.45 0.5 0.55 0.6 0.65 0.7 0.75 0.8 0.85 0.9 0.95 1 1.05
Rich factor
Pvalue
0.00000400
0.00000300
0.00000200
0.00000100
Number
11
91
171
253

(c)


S-acetyltransferase activity
3-oxoacyl-[acyl-carrier-protein] synthase activity
3-hydroxyacyl-[acyl-carrier-protein] dehydratase activity
[acyl-carrier-protein] S-malonyltransferase activity
S-malonyltransferase activity
malonyltransferase activity
[acyl-carrier-protein] S-acetyltransferase activity
3-hydroxypalmitoyl-[acyl-carrier-protein] dehydratase activity
3-hydroxyoctanoyl-[acyl-carrier-protein] dehydratase activity
(3R)-hydroxymyristoyl-[acyl-carrier-protein] dehydratase activity
3-hydroxydecanoyl-[acyl-carrier-protein] dehydratase activity
carbon-oxygen lyase activity
fatty acid synthase activity
small molecule biosynthetic process
lipid biosynthetic process
organic acid biosynthetic process
carboxylic acid biosynthetic process
monocarboxylic acid biosynthetic process
organic acid metabolic process
oxoacid metabolic process
0.4 0.45 0.5 0.55 0.6 0.65 0.7 0.75 0.8
Rich factor
Pvalue
0.00000500
0.00000400
0.00000300
0.00000200
0.00000100
Number
28
106
184
265

(d)

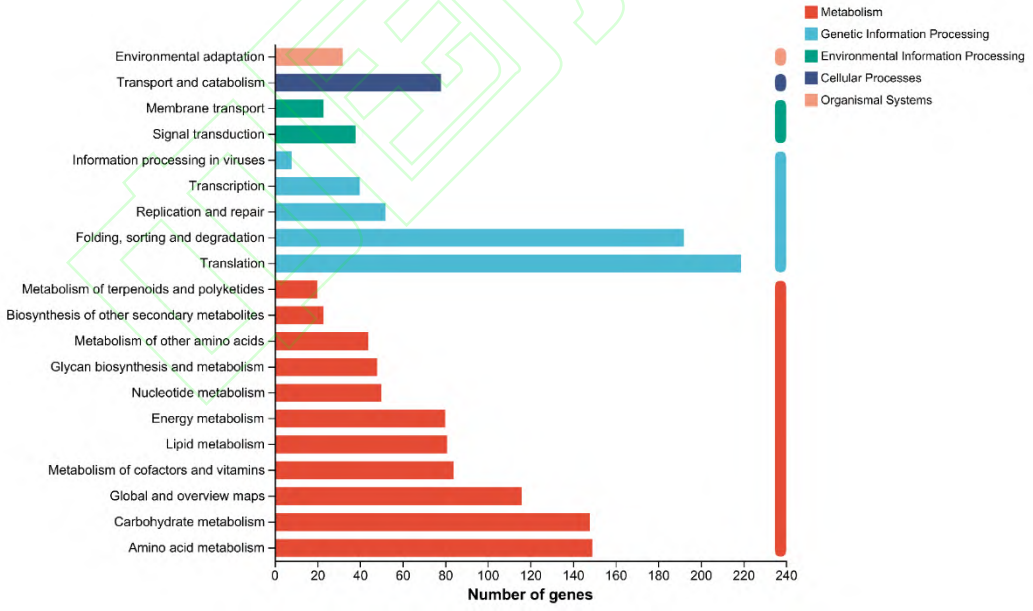
(a) GO classification (N-limited group vs. Control group); (b) GO classification (P-limited group vs. Control group); (c) GO enrichment (N-limited group vs. Control group); (d) GO enrichment (P-limited group vs. Control group).

图 6　球形棕囊藻不同比较组间的差异基因 GO 分类与富集

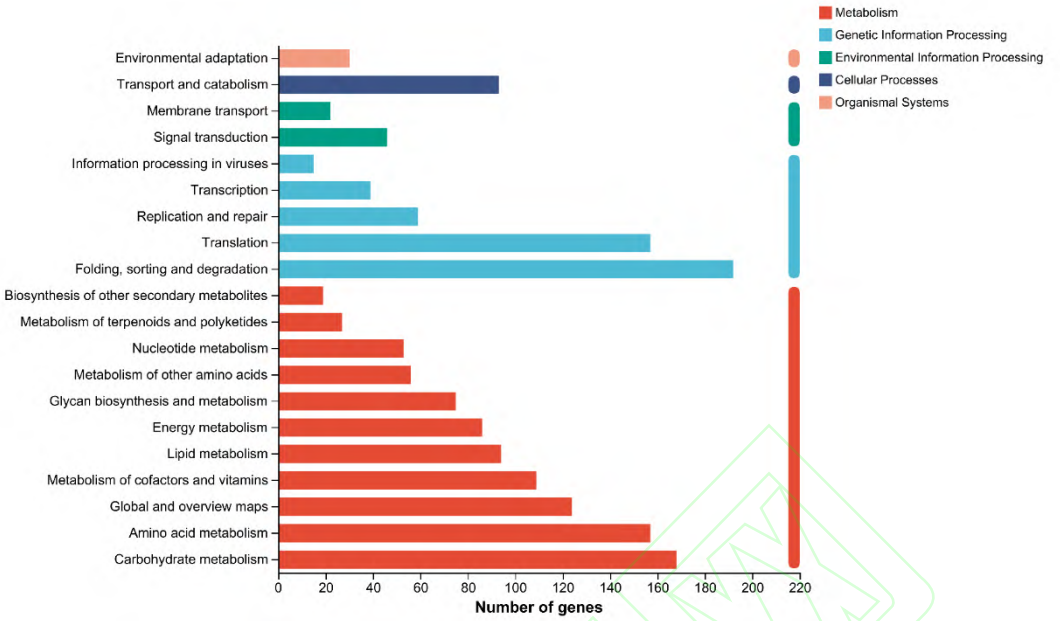
Fig.6　GO classification and enrichment of differentially expressed genes among different *P. globosa* comparison groups

2.7.2 KEGG 分类富集分析

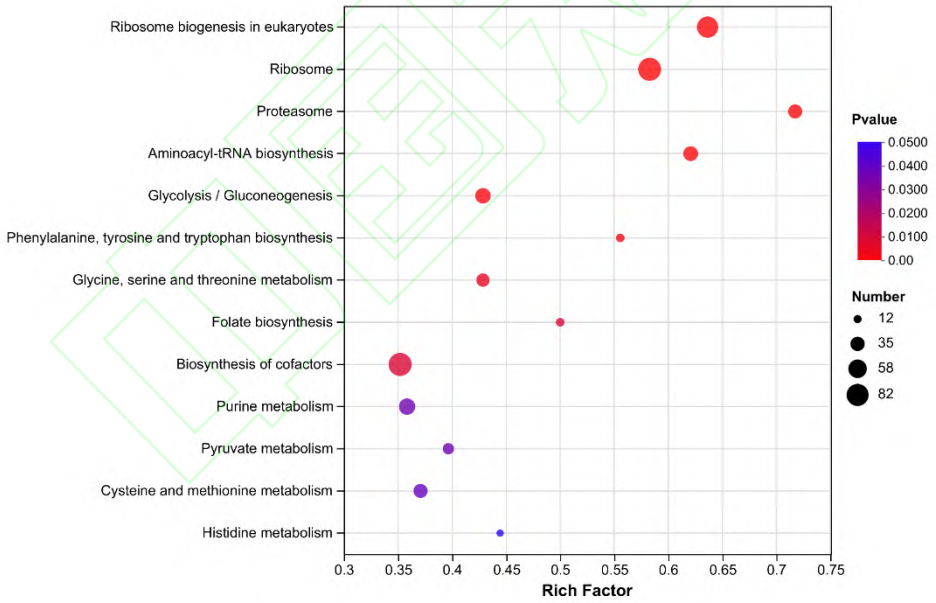
KEGG 代谢通路可分为 5 大类：代谢（Metabolism），遗传信息处理（Genetic Information Processing），环境信息处理（Environmental Information Processing），细胞过程（Cellular Processes），生物体系统（Organismal Systems）。图 7（a）和（b）显示，在氮限制组与对照组间差异基因比较中，翻译（Translation）通路所包含基因条目最多，为 219 条；在磷限制组与对照组间差异基因比较中，在通路折叠、分类和降解（Folding, sorting and degradation）中包含的基因条目最多，有 192 条。在两对比较组的差异基因 KEGG 通路富集分析中，如图 7（c）（d）所示，以 *P*-value＜0.05 作为筛选条件，top 20 结果显示，在氮限制组与对照组间差异基因比较中，富集程度最高的通路是蛋白酶体（Proteasome）通路（基因数 33，富集率 0.72），其次为真核生物中的核糖体生物发生（Ribosome biogenesis in eukaryotes）通路（基因数 70，富集率 0.64），氨酰 tRNA 生物合成（Aminoacyl-tRNA biosynthesis）通路（基因数 36，富集率 0.62）；在磷限制与对照组的比较中，富集程度最高的是类胡萝卜素生物合成（Carotenoid biosynthesis）通路（基因数 13，富集率 0.68），其次为苯丙氨酸、酪氨酸和色氨酸的生物合成（Phenylalanine, tyrosine and tryptophan biosynthesis）通路（基因数 17，富集率 0.63），然后是光合作用-天线蛋白（Photosynthesis - antenna proteins）通路（基因数 25，富集率 0.53）。



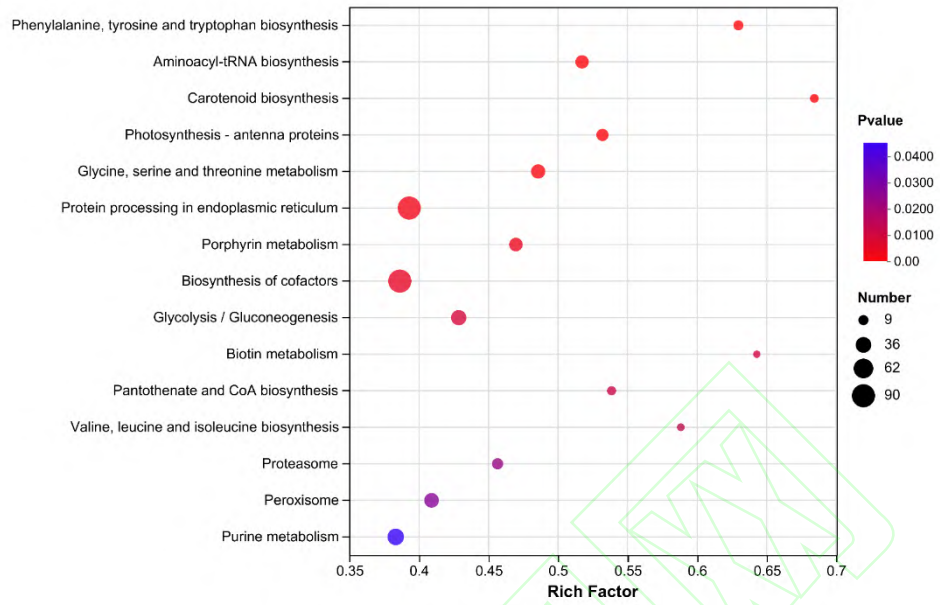
(a)


Metabolism
Genetic Information Processing
Environmental Information Processing
Cellular Processes
Organismal Systems
Environmental adaptation
Transport and catabolism
Membrane transport
Signal transduction
Information processing in viruses
Transcription
Replication and repair
Translation
Folding, sorting and degradation
Biosynthesis of other secondary metabolites
Metabolism of terpenoids and polyketides
Nucleotide metabolism
Metabolism of other amino acids
Glycan biosynthesis and metabolism
Energy metabolism
Lipid metabolism
Metabolism of cofactors and vitamins
Global and overview maps
Amino acid metabolism
Carbohydrate metabolism
0 20 40 60 80 100 120 140 160 180 200 220
Number of genes

(b)


Ribosome biogenesis in eukaryotes
Ribosome
Proteasome
Aminoacyl-tRNA biosynthesis
Glycolysis / Gluconeogenesis
Phenylalanine, tyrosine and tryptophan biosynthesis
Glycine, serine and threonine metabolism
Folate biosynthesis
Biosynthesis of cofactors
Purine metabolism
Pyruvate metabolism
Cysteine and methionine metabolism
Histidine metabolism
0.3 0.35 0.4 0.45 0.5 0.55 0.6 0.65 0.7 0.75
Rich Factor
Pvalue
0.0500
0.0400
0.0300
0.0200
0.0100
0.00
Number
12
35
58
82

(c)



(d)

(a) KEGG pathway classification (N-limited group vs. Control group); (b) KEGG pathway classification (P-limited group vs. Control group); (c) KEGG pathway enrichment (N-limited group vs. Control group); (d) KEGG pathway enrichment (P-limited group vs. Control group).

图 7　球形棕囊藻不同比较组间的差异基因 KEGG 通路分类与富集

Fig.7　KEGG pathway classification and enrichment of differentially expressed genes among different *P. globosa* comparison groups

2.8 光合作用及光合天线蛋白相关差异表达基因

通过对 KEGG 通路进行分析，发现氮磷限制对球形棕囊藻光合作用及合成光合天线蛋白的相关基因表达具有显著影响。在氮限制处理组中，PSII 光合作用复合物编码基因 *psbM*、*psbO*、*psbQ*、*psbS*、*psbU*、*psbZ*、*psb27*、*psb28* 以及 PSI 蛋白复合物编码基因 *psaE*、*psaK* 的表达都显著下调，此外光电子传输编码基因 *petH*、*petJ* 也下调表达，编码 ATP 合成酶 α、γ 亚基的基因上调表达。在光合天线蛋白通路中编码光捕获复合物叶绿素的基因 *lhca1*、*lhca3* 和 *lhcb3* 表达显著下调。这些基因对于光合作用中电子传递以及 ATP 合成都起到非常重要的作用，结果表明氮限制会显著抑制球形棕囊藻光合作用效能，编码 ATP 合成酶 α、γ 亚基的基因上调表达是对整体光合作用复合物合成抑制影响下的一种补偿机制。在磷限制组中，PS Ⅱ光合作用复合物编码基因 *psbS*、*psbU* 和 PS Ⅰ蛋白复合物编码基因 *psaK* 的表达都显著上调，此外编码细胞色素 b6/f 复合物亚基基因 *petC* 以及编码 *petH*、*petF* 的基因表达也上调，编码 ATP 合成酶 γ 亚基的基因同样上调表达，说明磷限制在很一定程度上可能会促进细胞的光合蛋白的合成，补偿磷缺乏对光合反应的限制作用。

2.9 糖酵解和糖异生、N 连接葡萄糖的生物合成以及脂肪酸合成相关差异表达基因

在糖酵解和糖异生代谢通路中，氮限制组和磷限制在一定程度会促进糖类的合成，葡萄糖 6 磷酸异构酶（GPI）、葡萄糖激酶（GCK）、醛糖 1-差向异构酶（galM）、二磷酸依赖型磷酸果糖激酶（PFP）以及 PGK、gpmI、PK、aceE、DLAT 等相关基因均显著上调。

N 连接葡萄糖的生物合成通路中，氮限制条件下，多萜醇磷酸甘露糖基转移酶（DMP1）

下调表达；磷限制条件下，糖胺聚糖链的聚合中鉴定到糖基转移酶（GTases）α-1,3-葡萄糖基转移酶（ALG6、ALG8）显著上调，α-1,6-甘露糖基转移酶（ALG12）下调。

磷限制条件下，细胞内脂肪酸合成及脂肪链延长的代谢通路中相关作用酶 FabD、FabH、FabF、FabG、FabZ、FabI、MECR 编码基因均显著上调，而在氮限制条件下，FabD 与 FabZ 显著下调，仅有 FabF 和 MECR 上调表达。

2.10 离子转运蛋白及蛋白酶体相关差异表达基因

离子转运通路中，氮限制条件会使细胞内 ABCA 超家族中 ABCA3，ABCC 超家族中 ABCC1、ABCC2、ABCC3、ABCC4、ABCC5、ABCC10，以及其他 ABC 转运体 YddA 基因表达上调。磷限制组，除了细胞内调控 ABCB 超家族 ABCB1 以及 ABCC 超家族 CydD 的基因下调，ABCC 超家族中多个基因 ABCC2、ABCC4、ABCC5、ABCC10 表达上调。氮磷限制在一定程度会促进细胞对磷元素的转运吸收，特别是氮限制对其影响最为显著。

在氮限制组中蛋白酶体 19s 调控组分顶部结构中亚基 Rpn5、Rpn6、Rpn7、Rpn8、Rpn9、Rpn10、Rpn11、Rpn12，基部结果中亚基 Rpn1、Rpn2、Rpn13、Rpt2、Rpt3、Rpt4、Rpt5，以及 20s 核心组分中亚基 α1、α2、α3、α4、α5、α6、α7 和 β1、β2、β3、β4、β5、β6、β7 相关基因表达都显著下调，在磷限制组中部分亚基的基因如 Rpn4、Rpn5、Rpn6、Rpn8 也下调表达。表明氮磷限制均会显著抑制细胞蛋白酶体的合成，从而影响细胞对废弃或者受损蛋白的降解利用，进一步影响细胞生长代谢。

3 讨论

3.1 营养盐限制对球形棕囊藻光合作用的影响

氮元素是藻类合成叶绿素的基本元素，氮缺乏会造成细胞光合色素合成减少，限制 PSI 和 PSII 反应中心蛋白合成，从而影响藻细胞对光能的吸收和转换效率[21]。氮限制条件下，随着硝酸氮迅速消耗，细胞叶绿素 *a* 含量（图 3（a））迅速下降；磷限制组叶绿素 *a* 含量下降相对缓慢。说明营养盐限制会抑制球形棕囊藻叶绿素 *a* 的合成，其中氮限制的影响最大，细胞叶绿素 *a* 合成对氮元素的需求要大于对磷的需求。同时 PSII 的最大量子产量（F_v/F_m）结果（图 3（b））显示，氮限制组 F_v/F_m 显著低于其他组（$P<0.05$），同样表明氮限制对球形棕囊藻光合效能的抑制效果大于磷限制。Loebl 等[22]研究发现，在氮限制条件下培养的海洋硅藻与颗石藻其叶绿素 *a* 含量以及 PSII 活性均显著降低。本研究也发现在氮限制条件下，PSI、PSII 蛋白复合物编码基因、光电子传输编码基因以及光合天线蛋白通路中编码光捕获复合物叶绿素的基因均显著下调，表明缺氮会导致球形棕囊藻光合作用相关蛋白的合成减少，从而降低其光合作用效能。此外发现氮限制条件下编码 ATP 合成酶 α、γ 亚基的基因上调表达，这可能是细胞为应对光捕获蛋白减少而产生的一种补偿机制。

磷限制组细胞叶绿素 *a* 含量以及 F_v/F_m 值也低于对照组，但转录组结果显示，多个 PSII 光合作用复合物编码基因上调表达，此外编码细胞色素 b6/f 复合物亚基基因以及 ATP 合成酶亚基基因也上调表达，这表明磷缺乏对细胞光合反应的抑制效果可能主要涉及光合磷酸化以及碳同化等光合反应相关的下属通路，而并非仅针对光合反应本身，这一点将是我们下一步的研究方向。由于整体光合反应及能量代谢效率低下，细胞为补偿这部分损失提高了细胞光合反应相关蛋白、色素和酶的合成，虽然相比于对照组其光反应效率仍较低，但明显高于氮限制组。

3.2 营养盐限制对球形棕囊藻生长调亡以及囊体形成的影响

营养盐限制条件下，球形棕囊藻细胞密度峰值显著低于对照组（$P<0.05$），且细胞存活期更短，调亡期更早。据转录组分析发现，氮磷限制条件下，球形棕囊藻合成蛋白酶体的多个亚基的相关基因均明显下调。蛋白酶体的主要功能是降解细胞不需要或受到损伤的蛋白质[23]，细胞对胞内废弃蛋白的降解效率下降，一方面会减弱细胞对氨基酸类物质的循环利用，

减少新蛋白的合成；另一方面也会使细胞积累大量废弃无用的蛋白，对其本身产生一定危害。这些影响会加速细胞衰亡，限制细胞自我修复能力，进而抑制细胞正常生长增殖以及代谢活动。

在球形棕囊藻囊体形成时期，细胞会分泌大量糖胺聚糖组成囊体基质[24]，在这个过程中葡萄糖基和甘露糖基转移酶至关重要，会将合成的 UDP-糖连接到多糖链中，形成聚糖[25]。氮限制条件下细胞平均囊体直径最小，这是由于在 N 连接葡萄糖的生物合成通路中，细胞多萜醇磷酸甘露糖基转移酶（DPM1）下调表达，致使糖胺聚糖合成减少，加上细胞丰度较低，因此细胞囊体直径最小。

磷限制组细胞密度峰值最低且显著低于对照组（$P<0.05$），说明磷是其生长增殖的首要限制因子[26]，磷缺乏会抑制藻细胞的正常增殖[27]。此外其囊体直径接近对照组，但由于磷限制抑制了细胞增殖，其囊体内细胞密度最低[图 2（c）]，囊体基质多而细胞少，从而更易破裂。通过转录组分析发现，在磷限制条件下，α-1,3-葡萄糖基转移酶（ALG6、ALG8）均显著上调，说明细胞会合成更多糖胺聚糖以稳定囊体结构，避免细胞密度过低引起囊体破裂。球形棕囊藻囊体扩大的过程是先通过胞吐作用释放糖胺聚糖以构建囊体结构，随后细胞生长增殖并不断进行填充[28]。此外发现 α-1,6-甘露糖基转移酶（ALG12）下调，这可能是由于磷限制导致细胞内葡萄糖和甘露糖两种糖的合成量存在差异从而影响其表达，这点仍需要进一步研究。

3.3 营养盐限制下球形棕囊藻糖类及脂肪酸合成表达

有研究表明，在氮限制条件下铜绿微囊藻（*Microcystis aeruginosa*）主要存储碳水化合物[29]，而绿藻（*Heterochlorella luteoviridis*）则主要合成油脂并存储[30]。在糖酵解和糖异生代谢通路中，发现氮缺乏会使球形棕囊藻中多个与糖类合成相关的酶基因上调表达，而脂肪酸合成的相关基因表达变化并不显著，结合上述中其糖胺聚糖合成降低，表明球形棕囊藻在应对氮胁迫时会从结构型多糖的生物合成转向对储能糖类物质的合成。

在磷限制条件下，球形棕囊藻脂肪酸合成及脂肪链延长的代谢通路中相关作用酶的基因表达显著上调，说明细胞会提高脂肪酸储量以应对磷缺乏。据相关研究表明，磷限制条件会提高缺刻缘绿藻（*Parietochloris incisa*）细胞中总脂的含量[31]，而钝顶螺旋藻（*Spirulina Platensis*）则会显著提高胞内总糖产量[32]。可见在低氮磷条件下，微藻细胞内总碳水化合物以及总脂含量的提高，是一种应对不良环境胁迫的适应机制。

本研究中球形棕囊藻通过降低生长增殖效率以及相关代谢耗能，将更多能量存储到糖类和脂质中，从而帮助细胞更好应对营养盐胁迫。

3.4 营养盐限制对球形棕囊藻氮磷吸收及转运蛋白的影响

研究表明，一些微藻细胞例如小定鞭金藻（*Prymnesium parvum*）在缺磷条件下，会增强对磷的吸收来满足其正常的生长和代谢活动，细胞内磷转运系统相关基因上调表达，磷酸盐转运蛋白大量合成[33]。本研究发现氮限制组中细胞 ABC 转运蛋白中多个基因同样上调表达甚至较磷限制更多，但对无机磷酸盐的吸收率却最低（图 1），由于氮缺乏会严重抑制细胞光合反应效能并影响蛋白以及酶的合成[7]，细胞一方面对离子转运蛋白的供能减少，另一方面缺乏对磷利用和转化过程中所需的重要酶，从而使整体转运效率下降。由于氮缺乏减少了细胞对无机磷酸盐的吸收率，细胞通过反馈机制继续提高转运蛋白的合成以补偿这种低吸收利用效率。相比于氮限制对磷酸盐吸收的影响，磷限制对细胞硝酸氮吸收率的影响较小，这说明球形棕囊藻对氮的需求量较高[34]。

4 结论

营养盐限制会显著影响球形棕囊藻光合反应、细胞生长以及囊体形成。其中氮限制对细胞代谢活动影响较大，对光合作用抑制效果突出，细胞由结构型多糖合成向储能代谢型糖类

物质合成转变。磷限制条件下，球形棕囊藻部分光反应蛋白合成基因上调表达以补偿光反应不足，此外细胞生长增殖被显著抑制，囊体内细胞丰度最低，囊体更薄，细胞内糖胺聚糖及脂肪酸合成相关基因均上调表达。另外，氮磷限制均会促进细胞转运蛋白的表达，并抑制细胞内蛋白酶体的合成。本研究发现在控氮和控磷的条件下，球形棕囊藻生理代谢及成囊过程的响应机制不同，因此对于控制其藻华暴发可依据不同海域实际氮磷限制的情况来考量。以广西北部湾海域为例，因其长期处于磷限制状态[2]，加上海洋中磷主要来源于人类活动[35]，其自然补充十分缓慢[36]，因此该海域我们认为加强磷营养盐的排放控制将有助于防控球形棕囊藻藻华的暴发。

参考文献：

[1] 陈菊芳, 徐宁, 江天久, 等. 中国赤潮新记录种: 球形棕囊藻(*Phaeocystis globosa*)[J]. 暨南大学学报(自然科学与医学版), 1999, 20(3): 124-129.

[2] 杨静, 张仁铎, 赵庄明, 等. 近 25 年广西北部湾海域营养盐时空分布特征[J]. 生态环境学报, 2015, 24(9): 1493-1498.

[3] 覃仙玲, 赖俊翔, 陈波, 等. 棕囊藻北部湾株的 18S rDNA 分子鉴定[J]. 热带亚热带植物学报, 2016, 24(2): 176-181.

[4] 曹西华, 俞志明, 邱丽霞. 改性黏土法消除球形棕囊藻赤潮的现场实验与效果评估[J]. 海洋与湖沼, 2017, 48(4): 753-759.

[5] 2020 年中国海洋生态环境状况公报(摘录)[J]. 环境保护, 2021, 49(12): 59-75.

[6] 田晶晶. 环境因子对球形棕囊藻细胞群体形成的影响[D]. 广州: 暨南大学, 2010.

[7] 郑和龙. 不同氮素浓度对 5 株微藻生长及其生化组成特征的影响[D]. 广州: 暨南大学, 2019.

[8] 闫少凯. 氮磷条件和培养模式对微藻生长及油脂含量影响的研究[D]. 芜湖: 安徽师范大学, 2019.

[9] 沈萍萍, 齐雨藻, 欧林坚. 中国沿海球形棕囊藻(*Phaeocystis globosa*)的分类、分布及其藻华[J]. 海洋科学, 2018, 42(10): 146-162.

[10] WANG X D, WANG Y, SMITH W O JR. The role of nitrogen on the growth and colony development of *Phaeocystis globosa* (Prymnesiophyceae) [J]. European Journal of Phycology, 2011, 46(3): 305-314.

[11] SMITH W O, CODISPOTI L A, NELSON D M, et al. Importance of *Phaeocystis* blooms in the high-latitude ocean carbon cycle [J]. Nature, 1991, 352: 514-516.

[12] REDFIELD A C, KETCHUM B H, RICHARDS F A. The influence of organisms on the composition of sea-water [M]// HILL M N, MAXWELL A E, GOLDBERG E D, et al. The sea: ideas and observations on progress in the study of the seas. New York: [S. n.], 1963.

[13] HONG L, LIU J L, MIDOUN S Z, et al. Transcriptome sequencing and annotation of the halophytic microalga *Dunaliella salina* [J]. Journal of Zhejiang University: Science B, 2017, 18(10): 833-844.

[14] ZHANG S F, ZHANG K, CHENG H M, et al. Comparative transcriptomics reveals colony formation mechanism of a harmful algal bloom species *Phaeocystis globosa* [J]. Science of the Total Environment, 2020, 719: 137454.

[15] MARS BRISBIN M, MITARAI S. Differential gene expression supports a resource-intensive, defensive role for colony production in the bloom-forming haptophyte, *Phaeocystis globosa* [J]. Journal of Eukaryotic Microbiology, 2019, 66(5): 788-801.

[16] LIANG D Y, WANG X D, HUO Y P, et al. Differences in the formation mechanism of giant colonies in two *Phaeocystis globosa* strains [J]. International Journal of Molecular Sciences, 2020, 21(15): 5393.

[17] ISSAK M R R. Transcriptomics of iron limitation in *Phaeocystis antarctica* [D]. Cairo, American: American University in Cairo, 2014.

[18] REN X, YU Z, SONG X, et al. Effects of modified clay on the formation of *Phaeocystis globosa* colony revealed

by physiological and transcriptomic analyses [J]. Science of the Total Environment, 2022, 838: 155985.
[19] HANSEN H P, KOROLEFF F. Determination of nutrients [M]// GRASSHOFF K, KREMLING K, EHRHARDT M. Methods of seawater analysis. [S. l: s. n.], 1999.
[20] 国家质量监督检验检疫总局, 中国国家标准化管理委员会. 海洋调查规范 第 6 部分: 海洋生物调查: GB/T 12763.6-2007[S]. 北京: 中国标准出版社, 2008.
[21] GEIDER R J, LA ROCHE J, GREENE R M, et al. Response of the photosynthetic apparatus of *Phaeodactylum tricornutum* (Bacillariophyceae) to nitrate, phosphate, or iron starvation [J]. Journal of Phycology, 1993, 29(6): 755-766.
[22] LOEBL M, COCKSHUTT A M, CAMPBELL D A, et al. Physiological basis for high resistance to photoinhibition under nitrogen depletion in *Emiliania huxleyi*[J]. Limnology and Oceanography, 2010, 55(5): 2150-2160.
[23] 宫雪. 不同氮磷条件下渤海异帽藻的生长和分子响应[D]. 大连: 大连理工大学, 2022.
[24] VAN RIJSSEL M, HAMM C E, GIESKES W W C. *Phaeocystis globosa* (Prymnesiophyceae) colonies: hollow structures built with small amounts of polysaccharides [J]. European Journal of Phycology, 1997, 32(2): 185-192.
[25] SHRESTHA R P, TESSON B, NORDEN-KRICHMAR T, et al. Whole transcriptome analysis of the silicon response of the diatom *Thalassiosira pseudonana* [J]. BMC Genomics, 2012, 13(1): 499.
[26] 王艳, 齐雨藻, 李韶山. 球形棕囊藻生长的营养需求研究[J]. 水生生物学报, 2007, 31(1): 24-29.
[27] 易文利, 金相灿, 储昭升, 等. 不同质量浓度的磷对铜绿微囊藻生长及细胞内磷的影响[J]. 环境科学研究, 2004, 17(S1): 58-61.
[28] CHIN W C, ORELLANA M V, QUESADA I, et al. Secretion in unicellular marine phytoplankton: demonstration of regulated exocytosis in *Phaeocystis globosa* [J]. Plant and Cell Physiology, 2004, 45(5): 535-542.
[29] ZUO Z, NI B, YANG L. Production of primary metabolites in *Microcystis aeruginosa* in regulation of nitrogen limitation [J]. Bioresource Technology, 2018, 270: 588-595.
[30] MENEGOL T, DIPRAT A B, RODRIGUES E, et al. Effect of temperature and nitrogen concentration on biomass composition of *Heterochlorella luteoviridis* [J]. Food Science and Technology, 2017, 37: 28-37.
[31] 童牧, 于水燕, 欧阳珑玲, 等. 氮饥饿与磷饥饿促使缺刻缘绿藻花生四烯酸含量增加的比较[J]. 水产学报, 2011, 35(5): 763-773.
[32] 陈浩, 杨冰洁, 李涛, 等. 磷浓度对海水钝顶螺旋藻生长代谢的影响[J]. 生物技术通报, 2019, 35(8): 103-110.
[33] BESZTERI S, YANG I, JAECKISCH N, et al. Transcriptomic response of the toxic prymnesiophyte *Prymnesium parvum* (N. Carter) to phosphorus and nitrogen starvation [J]. Harmful Algae, 2012, 18: 1-15.
[34] 徐宁, 齐雨藻, 陈菊芳, 等. 球形棕囊藻(*Phaeocystis globosa* Scherffel)赤潮成因分析[J]. 环境科学学报, 2003, 23(1): 113-118.
[35] 何玉新, 黄小平, 黄良民, 等. 大亚湾养殖海域营养盐的周年变化及其来源分析[J]. 海洋环境科学, 2005, 24(4): 20-23.
[36] VAN BOEKEL W. *Phaeocystis* colony mucus components and the importance of calcium ions for colony stability [J]. Marine Ecology Progress Series, 1992, 87(3): 301-305.

Study on Physiological and Biochemical Response and Transcriptomics of *Phaeocystis globosa* Under N- or P-limitation

XING Zheng[1], WANG Jiale[1], LAI Junxiang[2,3**], WANG Yinghui[1,4**], LI Jie[2,3]

（1. School of Marine Sciences, Guangxi University, Nanning, Guangxi, 530004, China; 2. Guangxi Key Laboratory of Marine Environmental Science, Guangxi Academy of Marine Sciences, Guangxi Academy of Sciences, Nanning, Guangxi, 530007, China; 3. Beibu Gulf Marine Industry Research Institute, Fangchenggang, Guangxi, 538000, China; 4. Green and Low-Carbon Technology Research Institute, Guangxi Institute of Industrial, Nanning, Guangxi, 530001, China）

Abstract: Nitrogen or phosphorus nutrient limitation can significantly inhibit the growth of *Phaeocystis globosa*, but its internal mechanism is still unclear. In order to comprehensively analyze the response mechanism of *P.globosa* under N- or P-limitation from the aspects of cell physiology, biochemistry and transcriptome, we set up N-limitation group (N:P=4:1), P-limitation group (N:P= 64:1) and control group (N:P=16:1) in this experiment. The physiological and biochemical indexes were determined and combined with transcriptome analysis. Through comparison, 14 272 differentially expressed unigenes were obtained, including 4 397 up-regulated genes and 3 679 down-regulated genes in the N-limitation group. In the P-limitation group, 4 963 genes were up-regulated and 5 079 genes were down-regulated. The study showed that N-limitation had the most significant inhibitory effect on photosynthesis of *P.globosa*, and the cells changed from structural polysaccharide synthesis to energy storage metabolic carbohydrate synthesis. Under the condition of P-limitation, some genes related to photosynthesis protein synthesis were up-regulated, cell proliferation was significantly inhibited, colonies were more fragile, and genes related to glycosaminoglycan and fatty acid synthesis in cells were up-regulated. In addition, N- or P-limitation can increase the expression of cell transporters and inhibit the synthesis of proteasome. The results showed that the metabolic activity of *P.globosa* was greatly affected by N-limitation, and the growth, proliferation and colony strength of *P.globosa* were more affected by P-limitation. In this study, the response mechanism of *P.globosa* under N- or P-limitation was preliminarily explained from the apparent and molecular levels, which provided a reference for further revealing the internal mechanism of its physiological metabolism and colony formation process, and provided a basis for relevant departments to formulate prevention and treatment strategies for algal bloom.
Key words: *Phaeocystis globosa*; N- or P-limitation; physiology and biochemistry; transcriptome

生态毒理学报
Asian Journal of Ecotoxicology
第 20 卷 第 2 期 2025 年 4 月
Vol. 20, No.2 Apr. 2025

DOI: 10.7524/AJE.1673-5897.20250227004 CSTR: 32062.14.AJE.1673-5897.20250227004
韦丽妮, 刘珊, 赵建亮, 等. 不同类型城市受纳河涌大型底栖动物多样性及其对水环境因子的响应[J]. 生态毒理学报,2025, 20(2): 92-104.
WEI L N, LIU S, ZHAO J L, et al. Diversity of macroinvertebrates in urban receiving streams adjacent to different road types and their responses to water environmental factors [J]. Asian journal of ecotoxicology, 2025, 20(2): 92-104.

不同类型城市受纳河涌大型底栖动物多样性及其对水环境因子的响应

韦丽妮[1], 刘珊[2,4,#], 赵建亮[1,3,*], 吴念念[5], 徐茹[5], 刘源[6]

1. 华南师范大学环境学院,广州 510006
2. 广西大学海洋学院,南宁 530004
3. 广东省化学品污染与环境安全重点实验室 & 环境理论化学教育部重点实验室,华南师范大学,广州 510006
4. 广西南海珊瑚礁研究重点实验室,南宁 530004
5. 中国科学院南海海洋研究所热带海洋生物资源与生态重点实验室,广州 510301
6. 山东大学海洋学院,威海 264209

收稿日期:2025-02-27 **录用日期**:2025-04-19

摘要: 随着城市化进程的加快,道路地表径流所引发的面源污染问题日益严重。城市河涌作为道路径流的主要受纳水体,正面临着显著的污染输入压力,对其生态系统构成了潜在威胁。大型底栖动物因对环境变化的高敏感性,常被作为水体生态健康状况的指示生物,能够有效反映城市河涌的生态扰动水平。本研究以广州市 3 类典型道路类型(城中村道路、高速公路、普通道路)所对应的受纳河涌为研究对象,分别于 2022 年 9 月(平水期)、2023 年 2 月(枯水期)、2023 年 7 月(丰水期)和 2023 年 10 月(平水期)开展了大型底栖动物的调查。通过分析不同道路类型受纳河涌中底栖动物的物种组成、群落结构与多样性的时空变化特征,进一步探讨了其与水环境因子的关系。调查共鉴定出大型底栖动物 22 种,隶属于 3 门 6 纲 10 目 15 科,其中节肢动物门占据优势地位,其次为环节动物和软体动物。摇蚊科与颤蚓科等典型耐污种在样点中广泛分布,说明研究区域河涌普遍受到一定程度的污染胁迫。从季节变化来看,底栖动物的物种数和平均丰度在平水期相对较高,而在丰水期和枯水期则明显下降,这一趋势可能与水动力条件及摇蚊属季节性丰度变化相关,平均生物量则受软体动物门的影响,在丰水期达到最高值。在空间分布上,城中村道路受纳河涌的物种数、平均丰度和生物量均高于高速公路和普通道路所对应的河涌,这可能与其周边土地利用方式和污水处理措施较为合理有关。多样性评价结果显示,Shannon-Wiener 指数(H')、Margalef 丰富度指数(d_M)和 Pielou 均匀度指数(J')在 2022 年平水期表现出较好生态状况,但随后呈下降趋势,反映出河涌生态系统可能正面临持续退化。不同河涌间的比较显示,城中村受纳河涌的多样性相对较高。生物完整性指数(BI)与 Goodnight-Whitley 修正指数(GBI)均表明研究区域的总体水质状况不佳,表明污染问题依然严重。冗余分析(RDA)表明,溶解氧(DO)、pH 和总磷(TP)是影响底栖动物丰度的主要水环境因子,其中 DO 的解释贡献率最高(36.9%),表明其在调控底栖动物群落结构中具有核心作用。相比之下,水环境因子对生物量的解释并不显著,说明生物量变化可能更多受到种间关系、栖息地结构或其他未监测因素的共同作用。本研究揭示了不同道路类型所驱动的城市地表径流对受纳河涌生态系统结构与功能的显著影响,强调了土地利用方式与污染控制措施在河涌生态保护中的关键作用,为城市水体生态修复与管理策略提供了科学依据与数据支持。

关键词: 受纳河涌;底栖生物;群落结构多样性;道路类型
文章编号: 1673-5897(2025)2-092-13 **中图分类号**: X171.5 **文献标识码**: A

基金项目:国家自然科学基金联合基金项目(U21A2036)
第一作者:韦丽妮(1999—),女,硕士研究生,研究方向为生态毒理学,E-mail: weilini1999@163.com
* **通信作者**(Corresponding author), E-mail: jianliang.zhao@m.scnu.edu.cn
\# **共同通信作者**(Co-corresponding author), E-mail: liushan@gxu.edu.cn

Diversity of Macroinvertebrates in Urban Receiving Streams Adjacent to Different Road Types and Their Responses to Water Environmental Factors

WEI Lini[1], LIU Shan[2,4,#], ZHAO Jianliang[1,3,*], WU Niannian[5], XU Ru[5], LIU Yuan[6]

1. School of Environment, South China Normal University, Guangzhou 510006, China

2. School of Marine Sciences, Guangxi University, Nanning 530004, China

3. Guangdong Provincial Key Laboratory of Chemical Pollution and Environmental Safety & MOE Key Laboratory of Theoretical Chemistry of Environment, South China Normal University, Guangzhou 510006, China

4. Guangxi Laboratory on the Study of Coral Reefs in the South China Sea, Nanning 530004, China

5. Key Laboratory of Tropical Marine Bio-resources and Ecology, South China Sea Institute of Oceanology, Chinese Academy of Sciences, Guangzhou 510301, China

6. Marine College, Shandong University, Weihai 264209, China

Received 27 February 2025　　**accepted** 19 April 2025

Abstract: With the rapid acceleration of urbanization, nonpoint source pollution originating from road surface runoff has emerged as an increasingly pressing environmental issue. Urban receiving streams, which function as the primary recipients of road runoff, are under substantial pollution pressure, thereby posing a potential threat to their ecosystems. Macroinvertebrates, which are highly sensitive to environmental changes, are extensively employed as bioindicators of aquatic ecosystem health and can effectively reflect the extent of ecological disturbance in urban streams. This study investigated macroinvertebrate communities in receiving streams associated with three distinct types of roads (village-in-city roads, highways, and regular roads) in Guangzhou, China, across four sampling periods: September 2022 (normal season), February 2023 (dry season), July 2023 (wet season), and October 2023 (normal season). The study analyzed the composition of species, community structure, and spatiotemporal variations in macroinvertebrate diversity and further explored their intricate relationships with water environmental factors. A total of 22 macroinvertebrate species were identified, encompassing 3 phyla, 6 classes, 10 orders, and 15 families, with Arthropoda emerging as the dominant phylum, followed by Annelids and Mollusca. Typical pollution-tolerant species, such as Chironomidae and Tubificidae, were ubiquitously distributed across sample sites, thereby indicating that the study streams were subjected to a certain degree of pollution stress. Seasonal variation revealed higher species richness and average abundance during the normal season, while these metrics experienced a significant decline during the wet and dry seasons, likely influenced by hydrodynamic conditions and seasonal fluctuations in *Chironomus* abundance. The average biomass, which was influenced by Mollusca, peaked during the wet season. Spatially, receiving streams near village-in-city roads exhibited higher species richness, average abundance, and biomass compared to those near highways and regular roads. This phenomenon may be attributed to more rational land-use patterns and wastewater treatment measures in their surrounding areas. Diversity indices, including the Shannon-Wiener index (H'), Margalef richness index (d_M), and Pielou evenness index (J'), exhibited relatively better ecological conditions during the normal season in 2022 but subsequently exhibited a downward trend, thereby reflecting that the stream ecosystems may be undergoing continuous degradation. Among the streams, those near village-in-city roads demonstrated relatively higher diversity. Both the Biotic Integrity Index (BI) and Goodnight-Whitley Modified Index (GBI) unveiled poor overall water quality in the study area, thereby highlighting the severity of pollution. Redundancy analysis (RDA) demonstrated that dissolved oxygen (DO), pH, and total phosphorus (TP) were the primary water environment factors influencing macroinvertebrate abundance, with DO having the highest explained contribution (36.9%), thereby underscoring its pivotal role in shaping community structure. In contrast, the explanatory power of water environmental factors on biomass was not significant, suggesting that bio-

mass changes may be more influenced by a complex interplay of interspecific relationships, habitat structure, or other unmonitored factors. This study elucidates the significant effects of urban surface runoff, driven by different road types, on the structure and function of the ecosystems of the receiving streams, emphasizes the crucial roles of land-use patterns and pollution control measures in the ecological protection of streams, and provides robust scientific evidence and data support for the ecological restoration and management strategies of urban water bodies.
Keywords: receiving streams; macroinvertebrates; community structure diversity; road types

0 引言

随着城市化进程的加速,地表径流已成为城市水体重要面源污染源之一[1-2]。地表径流中的污染物主要来源于大气干湿沉降和道路交通污染等[3-4],其中道路交通污染贡献最为显著。汽车尾气排放、轮胎与路面磨损、机油泄漏以及道路材料老化等过程会释放大量悬浮颗粒、重金属和多环芳烃等污染物,这些污染物在降雨期间被径流冲刷或淋溶直接或间接排入受纳水体,导致水质恶化进而对水生生态系统造成负面影响[5-9]。城市河涌通常指城市水系中连通主要河流的小型支流,一般是构成城市水体的重要组成部分。其不仅具有提供水源、防洪排涝、调节气候和净化环境的功能,还在维持城市生态平衡方面发挥着重要作用[10-12]。然而,地表径流直接排放或经雨水管道排入河涌,会不同程度影响河涌生态系统。尽管已有研究表明地表径流对河涌水质和生态系统具有显著影响,但不同道路类型所驱动地表径流对受纳河涌的影响是否存在差异,及其季节动态如何变化仍需进一步探究。因此,研究不同道路地表径流对受纳河涌的影响机制,对于城市水环境治理和生态修复具有重要意义。

广州作为中国南方快速发展的超大城市,河网发达,道路纵横,其城市化进程对水环境的影响尤为显著[13]。研究表明,城市河涌的污染主要表现为水质恶化、底泥污染及生物多样性损失等方面[14]。例如,重金属和有机污染物在河涌底泥中的积累对水生生物群落结构产生了显著影响[15-16]。大型底栖动物作为淡水生态系统中的重要类群,因其分布广泛、环境耐受性强以及对水质变化敏感,常被用作评估水生态系统健康状况的生物指标[17-18]。这类生物通过长期暴露于水体污染物中,其群落结构和组成能够直观反映水体的环境压力和水质状况[19-20]。因此,研究大型底栖动物群落的结构特征及其与水环境因子的关系,对于揭示城市地表径流对河涌生态系统的具体影响具有重要意义。

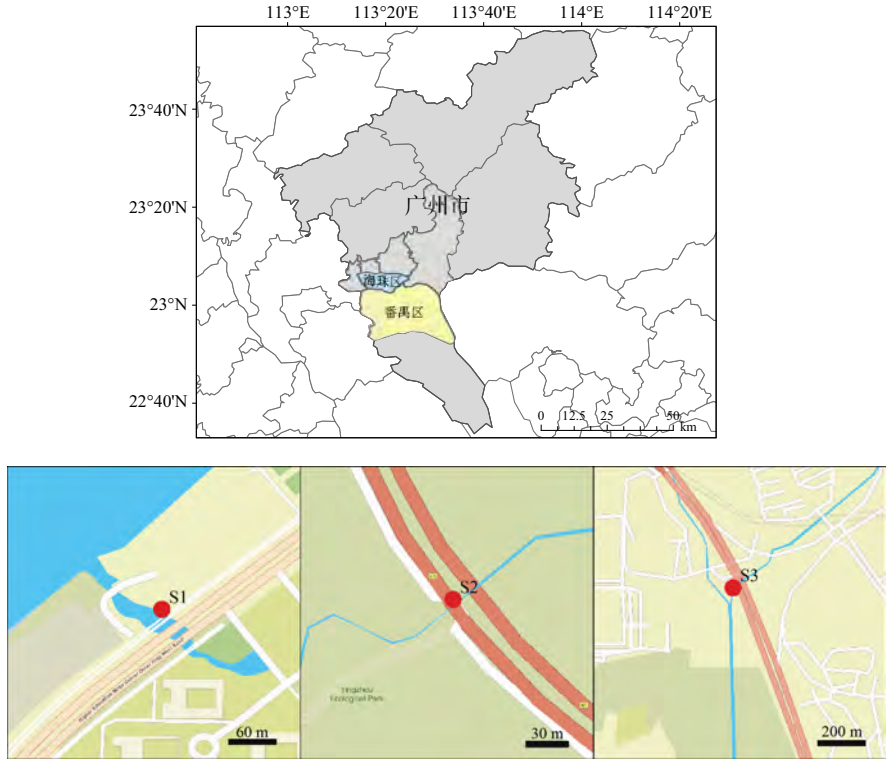
本研究以广州典型道路(包括普通道路、高速公路及城中村道路)周边受纳河涌为研究对象,系统分析了大型底栖动物群落的时空变化特征、多样性差异及其与水环境因子的关联性,深入探讨地表径流对河涌生态系统的具体影响机制。该研究有助于揭示城市道路地表径流对河涌生态系统的潜在风险,为城市水体生态修复与污染防控提供科学依据。

1 材料与方法

1.1 研究区域与采样点选取

广州市位于珠江三角洲北缘(112°57′~114°03′E,22°26′~23°56′N),是西江,北江和东江 3 条主要河流的流经地。全市河流纵横,水道密布,水域面积 744 km^2,约占全市土地面积的 10%。广州市气候类型属于亚热带季风气候,年平均气温在 21.7~23.1 ℃之间,年降水量丰富,2023 年年平均降水量为 1 923 mm,年降水日数约为 149 d[21]。作为经济高速发展的南方特大城市,2023 年广州市城镇化率高达 86.8%,道路总面积为 225.08 km^2,约占全市土地面积的 3%[22]。随着城市化进程的不断推进,道路面积持续扩张,路面携带的污染物种类和浓度也日趋复杂。降雨通常会冲刷道路表面形成径流,携带污染物进入受纳河涌,对水质和生态系统健康造成显著影响。

本研究聚焦于不同道路类型地表径流对受纳河涌大型底栖动物的贡献机制,在广州市市区,依据道路类型差异,选取了 3 种典型道路地表径流的受纳河涌作为研究对象,分别对应普通道路、高速公路以及城中村道路周边的受纳河涌,各采样点具体位置详见图 1 所示。各采样点选址依据及土地利用类型特征如下:S1 采样点为普通道路受纳河涌,位于广州大学城主要道路(外环西路)旁,代表普通道路的污染模式,周围以高校和科研机构为主,土地利用类型主要为校园居住用地,下垫面硬化程度较高,路面主要以小型汽车为主,车流量和人流量适中,该受纳河涌的最大污染源可能来自普通道路地表径流,同时伴随一些校园污水。S2 采样点为高速公路受纳河涌,代表高速公路高强度的交通污染特征。该河



注:审图号为 GS(2024)0650 号。

图 1　研究区域及采样站位

Fig. 1　Study area and sampling sites

涌贯穿于一个湿地公园,土地利用类型主要以绿地为主,其下垫面硬化面积较低,河涌上方为南沙快速港高速公路,车流量较高,主要以小型汽车和大型货车为主。高速公路的排污口直接排入该受纳河涌,形成集中排放,主要反应高速公路地表径流的污染特征。S3 采样点为城中村道路受纳河涌,位于一个城中村外围,代表城中村道路的污染模式。土地利用类型以居住区和商业区为主,人类活动频繁,下垫面的硬化程度较高,车流量适中。该区域受纳河涌除了道路地表径流的输入,同时伴随着周围的生活污水,餐饮废水的排放。这 3 个采样点均能代表广州市不同类型道路受纳河涌的一般情况,具有一定的代表性。

1.2　样品采集与分析

本研究于 2022 年 9 月(平水期)、2023 年 2 月(枯水期)、2023 年 7 月(丰水期)和 2023 年 10 月(平水期)进行了为期 1 年的底栖生物样品采集。采样期间,采用多功能水质检测仪(YSI 556MPS,美国 YSI)现场测定水温(T)、pH 和溶解氧(DO)。同时,采集 500 mL 水样至聚乙烯瓶中,24 h 内带回实验室,依据国家标准《地表水环境质量标准》(GB 3838—2002)测定水样中的硝氮(NO_3-N)、氨氮(NH_3-N)和总磷(TP)等化学指标。

根据《生物多样性观测技术导则 淡水底栖大型无脊椎动物》[23]指导准则,大型底栖动物的采集则根据采样站点的水深条件,采用不同的采样方法:普通道路受纳河涌(S1)和高速公路受纳河涌(S2)由于水深超过 3 m,属于不可涉水河段,使用彼得森采泥器(采样面积 1/32 m^2)在河涌中间进行底泥采集,具体操作为将采泥器匀速放下,触底后静置 30 s 后快速提拉绳子,保证底泥采样的完整性,重复采集 4 次后将上述样品合并成一个样品。城中村道路受纳河涌(S3)水深小于 3 m,属于可涉水河段,使用 D 型网(采样面积 0.25 m×0.25 m)在河岸随机进行拖网,具体操作为将 D 型网放置于准备采样的河底,抄网的直边紧贴河流底部,逆水流方向拖动 D 型网 1 m,并搅动网口进行样品收集,重复采集 3 次后将上述样品合并成一个样品[24-25]。现场将采集到的样品经过 40 目尼龙网筛选后,置于白磁盘中进行底栖生物的初步挑选。将挑选到的大型底栖动物置于 75% 乙醇中保存,当天带回实验室保存于低温条件下,以便进一步分析,所有采样过程、样品的挑选和保存过程

均为同一批次人员,以减少人为因素的不确定性。大型底栖动物的实验室鉴定主要通过体视显微镜(ZEISS Stemi 508,德国)进行形态学鉴定,而小型生物则需将关键鉴定部位制片,并在光学显微镜(奥林巴斯 CX-23,日本)下进行鉴定。所有底栖生物均鉴定至最低分类阶元,物种鉴定参考《中国经济动物志》《中国北方摇蚊幼虫》《中国小蚓类研究》和《大型底栖无脊椎动物水质生物评价研究》[26-29]。

1.3 数据分析

大型底栖动物的优势种采用相对重要性指数(IRI)进行分析,计算公式如下:

$$IRI=(W+N)\times F\times 10^4$$

式中:W 为每种底栖动物的生物量占总生物量的百分比,N 为每种底栖动物的丰度占总丰度的百分比,F 为每种底栖动物的出现频率占总频率的百分比。其中,IRI 值大于 1 000 为优势种,IRI 在 100 ~ 1 000 范围为重要种,IRI 在 10 ~ 100 为常见种,小于 10 为少见种。

大型底栖动物的多样性采用 Shannon-Wiener 指数(H')、均匀度(Pielou)指数(J')、物种丰富度 Margalef 指数(d_M)、生物指数(BI)和 Goodnight-Whitley 修正指数(GBI)进行分析,计算公式如下:

$$H'=-\sum_{i=1}^{s}(n_i/N)\ln(n_i/N)$$

$$d_M=(S-1)/\ln(N)$$

$$J'=H'/\log_2(S)$$

$$BI=\sum_{i=1}^{s}\frac{n_i}{N}t_i$$

$$GBI=(N-N_{oil})/N$$

式中:S 为样品的种类总数,n_i 为第 i 种的个体数,N 为总个体数,t_i 为物种 i 的耐污值,N_{oil} 为样品中寡毛类个体总数。

采用 Kruskal-Wallis 非参数检验方法检验不同类型受纳河涌生物丰度和生物量差异的显著性。采用冗余分析(RDA),利用方差膨胀因子过滤存在共线性的水环境因子(VIF>10),利用蒙特卡洛方法对水环境因子进行检验分析。

2 结果

2.1 大型底栖动物种类及优势物种

本研究对广州市 3 种类型道路地表径流的受纳河涌进行了为期 1 年的调查,共鉴定出大型底栖动物 22 种,隶属于 3 门、6 纲、10 目和 15 科。如图 2 所示,节肢动物门为优势类群,占总物种数的 50.00%,其次为环节动物门(27.27%)和软体动物门(22.73%)。就纲水平而言,昆虫纲物种最为丰富,占总物种数的 40.91%,而蛭纲和双壳纲物种较少,仅出现一次,占总物种数的 4.55%。2022 年平水期,2023 年枯水期、丰水期和平水期分别共检测到 15 种,5 种、7 种和 7 种底栖动物(表 1)。具体而言,2022 年平水期的物种数最大,而 2023 年枯水期的物种数最少,2023 年丰水期和平水期所检测到的物种数相等。对于不同道路类型受纳河涌,普通道路河涌中检出的物种数最少,仅鉴定出霍甫水丝蚓(*Limnodrilus hoffmeisteri*)和苏氏尾鳃蚓(*Branchiura sowerbyi*)2 种,特别是在 2023 年平水期,普通道路河涌未采集到任何底栖动物,表明其生境条件可能极度恶化。城中村道路受纳河涌中检出的物种数量高于其他河涌,共鉴定出 20 种大型底栖动物。在所有采样时期,城中村河涌的物种数均高于普通道路和高速公路河涌。城中村道路受纳河涌在 2022 年平水期表现出较高的物种丰富度,共采集到 14 种大型底栖动物,约为其他 3 个时期的 2 倍。而在 2023 年枯水期、丰水期和平水期,城中村河涌的物种数分别为 5 种、6 种和 5 种,物种数变化相对稳定,表明其生态系统可能具有相对较强的恢复力和稳定性。

在 2022—2023 年研究期间,对受纳河涌中大型底栖动物的优势种和重要种及其组成进行研究调查共鉴定出 3 科 5 属 5 种。如表 2 所示,2022 年平水期的优势种为德永雕翅摇蚊(*Glyptotendipes tokunagai*)和霍甫水丝蚓(*Limnodrilus hoffmeisteri*),2023 年丰水期则以黄色羽摇蚊(*Chironomus flaviplumus*)和苏氏尾鳃蚓(*Branchiura sowerbyi*)为主。至 2023 年平水期,黄色羽摇蚊(*Chironomus flaviplumus*)成为单一优势种。然而,2022 年枯水期的优势种组成与其他时期略有不同,主要以霍甫水丝蚓(*Limnodrilus hoffmeisteri*)和一种未鉴定的双翅目昆虫(*Diptera* sp.)为主。结果表明,4 个采样时期的优势种主要为摇蚊科(Chironomidae)和颤蚓科(Tubificidae)物种,其组成相对单一且均为典型的耐污种。此外,除 2023 年枯水期外,凸旋螺(*Gyraulus convexiusculus*)在其他 3 个采样时期均表现为重要种。值得注意的是,每个采样时期均存在独有的重要种。例如,2022 年平水期未鉴定的钩虾科一种(*Gammaridae* sp.),2023 年枯水期的卷甲虫属一种,2023 年丰水期的福寿螺(*Pomacea canaliculata*)和泉膀胱螺(*Physa fontinalis*),

以及 2023 年平水期的舌蛭科一种(*Glossiphoniidae* sp.)和闪蚬(*Corbicula nitens*)。

2.2　大型底栖动物生物量和生物丰度

本次调查结果显示,所有站点的总生物量为 67.71 g·m^{-2},平均生物量为 0.71 g·m^{-2}。其中,软体动物门的平均生物量最高(2.41 g·m^{-2}),占总生物量的 85.66%。环节动物门和节肢动物门的平均生物量分别为 0.21 g·m^{-2}和 0.20 g·m^{-2},分别占总生物量的 7.65%和 6.98%。从不同采样时期来看,2023 年丰水期的平均生物量最高(1.52 g·m^{-2}),其次是 2022

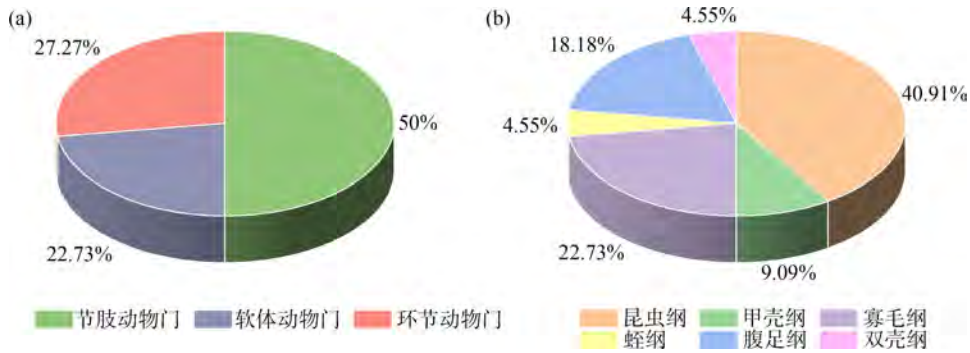


图 2　大型底栖动物门水平(a)和纲水平(b)种类百分比

Fig. 2　Composition of species at the macrobenthic phylum level (a) and order level (b)

表 1　不同采样时期平均物种数、生物量、生物丰度的组成

Table 1　Composition of average species number, biomass, and abundance in different sampling periods

采样时期	物种数(种)	平均生物量/(g·m^{-2})	平均生物丰度/(ind·m^{-2})
2022 年平水期	15	0.67	132
2023 年枯水期	5	0.04	22.4
2023 年丰水期	7	1.52	14.5
2023 年平水期	7	0.35	50.3

表 2　不同采样时期优势种和重要种的组成

Table 2　Composition of dominant and important species in different sampling periods

采样时期	优势种		重要种	
	种名	拉丁学名	种名	拉丁学名
2022 年平水期	德永雕翅摇蚊	*Glyptotendipes tokunagai*	黄色羽摇蚊	*Chironomus flaviplumus*
	霍甫水丝蚓	*Limnodrilus hoffmeisteri*	钩虾科一种	*Gammaridae* sp.
			凸旋螺	*Gyraulus convexiusculus*
2023 年枯水期	霍甫水丝蚓	*Limnodrilus hoffmeisteri*	黄色羽摇蚊	*Chironomus flaviplumus*
	昆虫纲一种	*Insecta* sp.	德永雕翅摇蚊	*Glyptotendipes tokunagai*
			卷甲虫属一种	*Armadillidium* sp.
2023 年丰水期	黄色羽摇蚊	*Chironomus flaviplumus*	霍甫水丝蚓	*Limnodrilus hoffmeisteri*
	苏氏尾鳃蚓	*Branchiura sowerbyi*	颤蚓	*Tubifex* sp.
			福寿螺	*Pomacea canaliculata*
			泉膀胱螺	*Physa foncinalis*
			凸旋螺	*Gyraulus convexiusculus*
2023 年平水期	黄色羽摇蚊	*Chironomus flaviplumus*	水丝蚓	*Limnodrilus* sp.
			舌蛭科一种	*Glossiphoniidae* sp.
			凸旋螺	*Gyraulus convexiusculus*
			闪蚬	*Corbicula nitens*

年平水期(0.67 g·m^{-2})、2023 年平水期(0.35 g·m^{-2})和 2023 年枯水期(0.04 g·m^{-2})(表 1)。2023 年丰水期的高生物量主要得益于福寿螺(*Pomacea canaliculata*)其个体较大的显著贡献。从受纳河涌的类型来看,城中村道路受纳河涌的平均生物量最高(1.86 g·m^{-2}),而高速公路受纳河涌和普通道路受纳河涌的平均生物量较低,分别为 0.10 g·m^{-2}和 0.05 g·m^{-2}。基于 Kruskal-Wallis 非参数检验的结果分析表明,普通道路受纳河涌与高速公路受纳河涌的生物量无统计学显著差异(P>0.05)。然而,两者与城中村受纳河涌的生物量存在显著性差异(P<0.001),该结果表明,道路类型对受纳河涌生态系统的影响存在空间异质性。

本次调查所有站点的总丰度为 7 618 ind·m^{-2},平均丰度为 80.19 ind·m^{-2},其中节肢动物门平均丰度最高(107 ind·m^{-2}),占总丰度 50.47%,且几乎在所有站点中均有分布。环节动物门和软体动物门的平均丰度分别为 82.4 ind·m^{-2}和 22.6 ind·m^{-2},分别占总丰度的 38.89%和 10.64%。底栖生物的平均丰度按采样时期的不同顺序排列:2022 年平水期(132 ind·m^{-2})> 2023 年平水期(50.3 ind·m^{-2})> 2023 年枯水期(22.4 ind·m^{-2})> 2023 年丰水期(14.5 ind·m^{-2})(表 1)。这一变化趋势主要由于平水期存在较多的摇蚊属(*Chironomus* sp.)生物的影响。从受纳河涌的类型来看,大型底栖动物的平均丰度依次为:城中村道路受纳河涌(161 ind·m^{-2})>高速公路受纳河涌(38.2 ind·m^{-2})>普通道路受纳河涌(35.5 ind·m^{-2})(图 3)。城中村道路受纳河涌的高丰度主要归因于软体动物门的显著贡献,软体动物在城中村道路受纳河涌中普遍分布,而在高速公路受纳河涌中仅于 2023 年平水期检出一种软体动物(闪蚬,*Corbicula nitens*),普通道路受纳河涌则未检出任何软体动物。另外采用 Kruskal-Wallis 非参数检验分析不同类型的河涌的生物丰度是否存在显著性差异,结果表明,普通道路受纳河涌与高速公路受纳河涌的丰度差异性较小(P>0.05),普通道路、高速公路受纳河涌与城中村受纳河涌的丰度存在显著性差异(P<0.001)。底栖生物平均丰度在 2022 年平水期的城中村道路受纳河涌达到最大值,为 258 ind·m^{-2}。然而,普通道路受纳河涌的平均丰度随时间推移呈递减趋势,至 2023 年丰水期甚至未采集到底栖生物样品,表明其环境可能受到持续干扰,自净能力较差。相比之下,高速公路和城中村道路受纳河涌的平均丰度变化相对稳定,依次为 2022 年平水期(分别为 80.0 ind·m^{-2}和 258 ind·m^{-2})>2023 年平水期(分别为 6.86 ind·m^{-2}和 144 ind·m^{-2})>2023 年枯水期(分别为 3.20 ind·m^{-2}和 41.6 ind·m^{-2})>2023 年丰水期(分别为 2.29 ind·m^{-2}和 34.3 ind·m^{-2})。与底栖生物的平均生物量变化趋势相似,普通道路受纳河涌的平均丰度也随采样时间呈现递减趋势,表明其环境可能受到持续干扰。高速公路受纳河涌和城中村道路受纳河涌的最高平均丰度分别出现在 2023 年平水期和 2023 年丰水期,而两者的最低平均生物量均出现在 2023 年枯水期。

2.3 大型底栖动物的多样性指数

所有站点的 H' 指数范围为 0 ~ 1.53,平均值为 0.52;d_M 指数范围为 0 ~ 1.57,平均值为 0.36;J' 指数范围为 0 ~ 0.69,平均值为 0.23。如表 3 所示,从不同时期来看,H' 指数和 d_M 指数的平均值均呈现以下

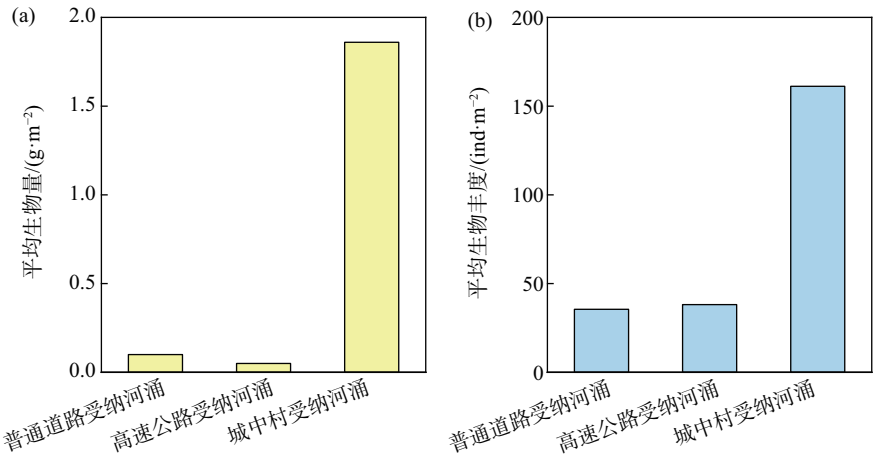


图 3 不同类型道路受纳河涌的平均生物量(a)和平均生物丰度(b)

Fig. 3 Average biomass (a) and average abundance (b) of receiving streams adjacent to different road types

趋势:2022 年平水期(H':0.83, d_M:0.62)>2023 年平水期(H':0.74, d_M:0.55)>2023 年丰水期(H':0.50, d_M:0.30)>2023 年枯水期(H':0.28, d_M:0.25)。J'指数平均值的变化趋势略有不同,其在 2023 年平水期达到最高值,为 0.43。值得注意的是,2023 年枯水期的 3 种多样性指数均为最低值,表明该时期受纳河涌的生态系统稳定性较差,可能受到环境压力或水文条件的影响。而平均 BI 和 GBI 指数均在 2023 年平水期最高,BI 在 2022 年平水期和 GBI 在 2023 年枯水期分别表现出最低值,意味着在 2023 年平水期受纳河涌环境受损严重。

从受纳河涌的类型来看,城中村道路受纳河涌的多样性指数显著高于其他类型,其 H'指数、d_M 指数和 J'指数平均值分别为 1.06、0.84 和 0.38(图 4)。相比之下,普通道路受纳河涌的 3 种多样性指数均为 0,表明其生态环境极差,可能受到严重污染或生境退化的影响。3 种指数均表现出相同的趋势,即普通道路受纳河涌生物多样性最低,城中村受纳河涌的生态系统稳定性相对较高。在单个时期的站点中,2022 年平水期的城中村道路受纳河涌表现出最高的 H'指数(1.53)和 d_M 指数(1.57),而 2023 年平水期的高速公路受纳河涌则表现出最高的 J'指数(0.69)。而 BI 和 GBI 指数所表示的结果略微不同,BI 指数是通过大型的底栖动物耐污值的不同来进行表征,其数值在城中村道路受纳河涌最高,却在高速公路受纳河涌表现出最低值。GBI 指数根据寡毛类密度来反映水体污染程度,结果在城中村受纳河涌表现出最大值,而在普通道路受纳河涌表现出最低值。从 BI 和 GBI 指数分析,城中村受纳河涌似乎是受污染程度最严重的。

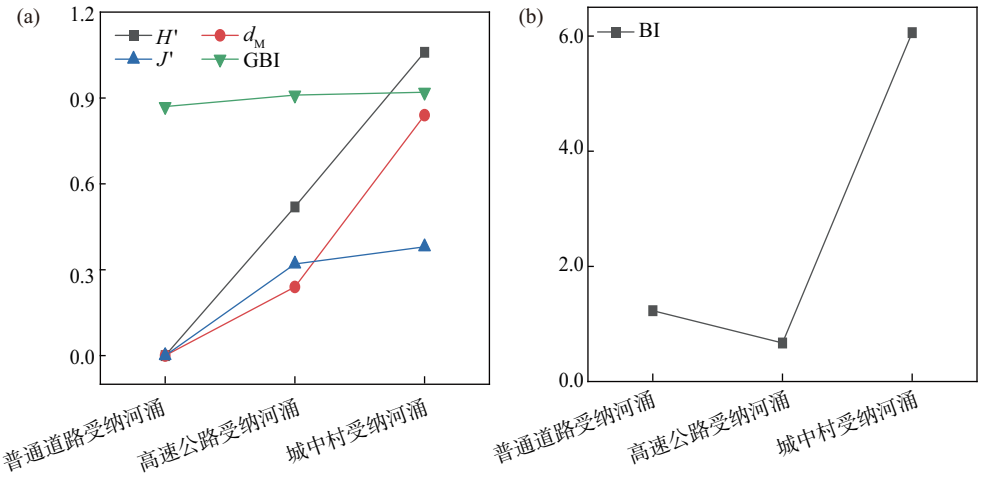


图 4　不同类型道路受纳河涌的平均 Shannon-Wiener 指数(H')、均匀度(Pielou)指数(J')、物种丰富度 Margalef 指数(d_M)、Goodnight-Whitley 修正指数(GBI) (a)和生物指数(BI) (b)

Fig. 4　Composition of average Shannon-Wiener Index (H'), Pielou Evenness Index (J'), Margalef Richness Index (d_M), Goodnight-Whitley Index (GBI) (a), and Biological Index (BI) (b), in receiving streams adjacent to different road types

表 3　不同采样时期的平均 Shannon-Wiener 指数(H')、均匀度(Pielou)指数(J')、物种丰富度 Margalef 指数(d_M)、生物指数(BI)和 Goodnight-Whitley 修正指数(GBI)组成

Table 3　Composition of average Shannon-Wiener Index (H'), Pielou Evenness Index (J'), Margalef Richness Index (d_M), Biological Index (BI), and Goodnight-Whitley Index (GBI) in different sampling periods

采样时期	H'	d_M	J'	BI	GBI
2022 年平水期	0.83	0.62	0.33	7.38	0.66
2023 年枯水期	0.28	0.25	0.12	7.55	0.60
2023 年丰水期	0.50	0.30	0.19	8.27	0.63
2023 年平水期	0.74	0.55	0.43	9.65	0.94

2.4 群落组成与水环境因子的关系

基于底栖动物群落结构、生物多样性及水环境因子的空间分布特征，本研究在科的水平上对底栖生物的生物量和生物丰度与水环境因子进行冗余(RDA)分析(图 5)，基于蒙特卡洛置换(Monte Carlo)检验筛选出对底栖动物群落组成影响较强的水环境因子。结果表明，DO(P = 0.014)、pH(P = 0.036)和TP(P = 0.024)与底栖动物群落生物丰度显著相关，是主要影响的水环境因子。其中，DO 的解释贡献率最高，达到了 36.9%，表明其对底栖动物群落的影响是显著的。其次，pH 和 TP 的解释贡献率分别为 23.8% 和 15.5%。相比之下，NH_3-N，NO_3-N 和 T 对底栖动物丰富的影响较小(P>0.05)，说明它们对底栖动物的分布影响不显著。此外，NH_3-N 和 NO_3-N 与一些底栖动物(如颤蚓科等)呈正相关，而 DO、pH 和 TP 则与其他种类的底栖动物(如摇蚊科和膀胱螺科等)呈正相关关系。而底栖生物的平均生物量与水环境因子的 RDA 分析显示，水环境因子与平均生物量未存在显著相关性(P>0.05)。

3 讨论

3.1 大型底栖动物结构与种类组成

本研究发现，节肢动物门在所有河涌中均为优势类群，尤其是摇蚊科(Chironomidae)和颤蚓科(Tubificidae)物种广泛分布并占据主导地位，群落结构呈现出物种组成单一、耐污种占优的典型特征。这一格局与在东莞、西安和北京城市河流的调查结果相一致，可能是因为城市化进程使得河涌生境单一化和碎片化[24, 30−32]。城市河流似乎都是以耐污种为优势种群，这可能是由其特殊生境所决定的，高度渠化的河道结构导致水体流动性降低，污染物持续累积难以稀释，形成高污染负荷的胁迫环境。在此条件下，具备较强环境耐受力的摇蚊科和颤蚓科显示出竞争优势[31]。先前研究表明相比于自然河流来说，城市河涌底栖生物群落主要是由无明显季节性变化的耐污种所决定的，所以其季节性变化较弱，因此探究城市河流大型底栖动物群落季节性变化应当更加注意物种丰度上的变化[33]。就其季节变化排列而言，底栖生物的平均丰度按以下顺序排列：2022 年平水期(132 ind·m^{-2})> 2023 年平水期(50.3 ind·m^{-2})> 2023 年枯水期(22.4 ind·m^{-2})> 2023 年丰水期(14.5 ind·m^{-2})，这一变化趋势可能是由于平水期适中的水流量所决定的，水体扰动较小，有利于底栖生物的栖息和觅食，从而表现出较高的丰度。而在枯水期，水位下降，水流量较弱及河床裸露导致底栖动物栖息地缩减，同时污染物浓度因河涌流量降低而增加，对群落形成明显胁迫[34]。在丰水期，由于大量降雨导致水流量剧增，这种强水动力条件对底栖生物群落的稳定性造成了显著冲击，导致底栖生物的平均丰度相对较低。但我们的研究结果与王强等[35]提出的以摇蚊为优势类群的城市河流大型底栖动物群落一般在冬春季达到密度峰值并不一致，这可能是区域特异性和采样时间的单一性造成的。而就平均生物量而言，2023 年丰水期达最高值(1.52 g·m^{-2})，而 2023 年枯水期最低(0.04 g·m^{-2})，主要是由于软体动物(如福寿螺)的季节性出现：丰水期大量检出，而在枯水期完全未见，显著拉高了群体生物量。此类差异进一步强调了降雨强度、水流扰动及水位变动在底栖动物季节性变化中的核心作用。尽

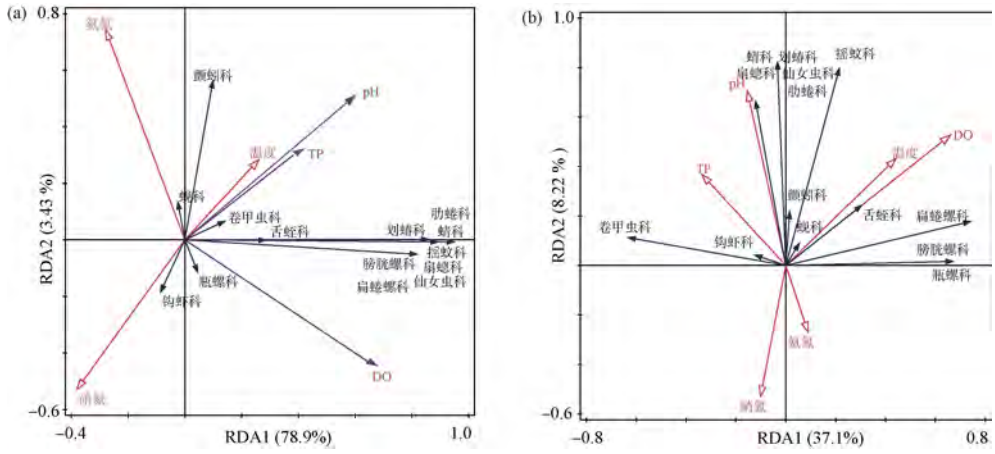


图 5 底栖动物生物丰度(a)和生物量(b)与水环境因子 RDA 分析

Fig. 5 Redundancy analysis (RDA) of benthic macroinvertebrate abundance (a) and biomass (b) with water environmental factors

管本研究采样阶段覆盖了广州市底栖生物不同的活动时期,但仍存在一些不确定性,如台风、强降雨等极端水文事件的干扰,未来研究需通过多季节连续监测验证群落结构的动态响应机制。

就不同类型道路受纳河涌而言,我们研究发现普通道路受纳河涌的物种数、生物量和丰度均最低,而城中村道路最高,高速公路居中。造成这种差异的原因可能与周围的土地利用类型和污染特征有关,普通道路受纳河涌周边土地利用类型主要以科研单位和校园为主,下垫面硬化程度高,存在生活污水和实验废水等高风险点源污染,且部分河涌缺乏完善治理设施,污染物(如重金属、多环芳烃等)易富集,直接威胁底栖生物生存[5-9]。高速公路受纳河涌周围土地利用类型主要以绿地为主,其下垫面硬化面积较低,河岸植被覆盖度高,但主要污染源为高速公路地表径流排水管的直接排入,对受纳河涌大型底栖动物还是会造成一定的影响。相比之下,城中村道路受纳河涌表现出较高的生物多样性与丰度,可能得益于适度的污染输入与部分初级污水治理措施的叠加效应:首先,受纳河涌食物链偏短,食物的丰富度几乎直接影响群落的多样性,城中村生活污水中含有较高的有机质,这些有机质可作为底栖生物的重要食物来源,缓解了食物竞争压力,促进了底栖动物的生长和繁殖[35-37]。其次就污水处理系统而言,城中村区域可能配备了初步的污水处理系统,地表径流经过管道处理后排放,减少了污染物直接进入河涌的量,从而改善了水质[34];而与大多数河涌采用合流制的污水处理方式不同,城中村则采用分流制的处理方式,通过雨污分流实现污染物高效截留,使其污水处理处理效率更高[38],此外,广州市河涌整治行动的推进和当地居民环保意识的提高也可能对改善底栖生境起到积极作用[39-41]。

群落主导物种的结构可以反映了河涌的生态稳定性。其中霍甫水丝蚓(*Limnodrilus hoffmeisteri*)和黄色羽摇蚊(*Chironomus flaviplumus*)在所有时期均为主导物种,均属典型耐污类群。优势种密度与群落总密度呈高度一致性,验证了底栖群落结构受核心物种主导的特性[42]。所有样点生态状况评估均表明水体处于中度及以上污染水平,体现出城市受纳水体典型的生态胁迫特征。

3.2　大型底栖动物群落变化特征

本研究通过 Shannon-Wiener 多样性指数(H')、Margalef 丰富度指数(d_M)和 Pielou 均匀度指数(J')对广州市不同类型受纳河涌大型底栖动物群落多样性进行了评估。结果表明,所有采样点的 H'、d_M 和 J' 值分别在 0 ~ 1.53、0 ~ 1.57 和 0 ~ 0.69 之间,整体反映出受纳河涌生态系统普遍存在中度至重度污染。其中 H' 指数在 2022 年平水期,2023 年丰水期的城中村道路受纳河涌和 2023 年平水期高速公路受纳河涌表现中度污染,d_M 指数在 2022 年平水期城中村道路受纳河涌表现出最大值为 1.57,表示水质重度污染,而其他时期不同采样点的 d_M 指数均小于 1,意味着水质严重污染。相比之下,J' 指数对部分站点表现出中度至轻度污染,提示群落分布存在一定程度的均匀性。结合生物完整性指数(BI)和 Goodnight-Whitley 指数(GBI)进一步分析水质状况,结果表明,2022 年平水期至 2023 年平水期 4 个时段的 BI 值依次为 7.38、7.55、8.27 和 9.65,GBI 值分别为 0.66、0.60、0.63 和 0.94,呈逐年升高趋势。根据生物评估分级标准,前 3 个时期的水体环境均属较差水平,而 2023 年平水期进一步恶化,反映出研究区域水生态质量在近 2 年间持续下降的趋势。

值得注意的是,由于多样性指数本身的算法机制与敏感性不同,在部分站点对水质评价结果存在一定差异,因此只用一种或几种多样性指数表征某一个站点水体质量可能存在一些不确定性[43]。如,H'、d_M 与 J' 三者在不同道路类型河涌中均表现为城中村道路受纳河涌>高速公路受纳河涌>普通道路受纳河涌,说明城中村河涌生境条件相对较优,群落结构多样性较高,而普通道路河涌水体质量最差。相较而言,BI 指数呈现出高速公路受纳河涌>普通道路受纳河涌>城中村受纳河涌的趋势,而 GBI 指数则为普通道路受纳河涌>高速公路受纳河涌>城中村受纳河涌,这是由于算法不同导致的,BI 指数不仅考虑生物种类和数量,还考虑物种对水体环境的耐受程度,普通道路受纳河涌中鉴定到的物种较少,算计出来的 BI 值较低,但不表示该站点耐污程度高。而 GBI 主要以寡毛类生物作为主要指标,先前在湖南大通湖的研究表明,当耐污类群为主要底栖生物类群时,应当谨慎使用 GBI 指标,这意味着在面对城市受纳河涌中底栖生物多样性评价时,需要更加谨慎且全面的选择参数[44]。

3.3　大型底栖动物群落特征变化与水环境因子的关系

水环境因子在调控大型底栖动物群落结构的组成和变化具有重要影响。已有研究广泛认为溶解氧

(DO)是影响底栖动物群落构建的关键环境变量之一。DO 不仅反映河流水质的变化,还通过满足底栖动物的新陈代谢活动,间接或直接影响大型底栖动物群落。由于不同生物类群对 DO 的需求不一样,DO 含量的变化往往引起物种组成的选择性筛选,从而影响群落多样性和功能特征[37,45]。在本研究中,与 DO 呈正相关的物种主要为瓶螺科和钩虾科,这些物种的生长和繁殖通常依赖于较高的氧气,而耐污性较强的颤蚓科则表现出与 DO 的负相关性,这类物种更适应低氧或缺氧环境,在有机污染较重、底泥还原性强的水体中仍能保持一定数量的种群分布。先前在河西内陆河流也观察到相似的现象[46]。其次,pH 和 TP 也被认为是显著影响底栖动物群落的水环境因子,分别对底栖动物群落结构的解释贡献率为 23.8% 和 15.5%。pH 值作为水体酸碱环境的直接反映,影响着底栖动物的生理代谢和繁殖行为,而在本研究中,pH 与一些底栖动物如颤蚓科和卷甲虫科呈正相关,表明这些物种在中性或稍偏碱性的水体中更为适宜。TP 作为表征水体富营养化程度的重要指标,其升高常伴随着浮游植物的大量繁殖,进而影响底栖动物食物结构与栖息环境。张莹等[47]对山东半岛南部海湾的大型底栖动物进行调查研究,结果表明水体营养盐物质的增加会导致大型底栖动物多样性降低。

尽管水环境因子对底栖动物群落多样性和分布具有显著影响,但在生物量变化方面,本研究 RDA 结果显示相关性不显著(P>0.05)。这一现象提示,底栖动物生物量可能受多种综合因子共同驱动,如栖息地结构复杂性、底质类型、种间竞争关系、人为干扰强度等,单一水质因子难以充分解释其变化模式。但本研究所检测的水质参数较为有限,城市河涌中存在复杂的污染效应,这些可能导致在解释水环境因子对大型底栖动物的群落多样性时出现一定的偏差。

4 结束语

本研究通过对广州市不同类型道路受纳河涌的大型底栖动物进行采样分析,揭示了其物种组成、群落结构和多样性特征。结果显示,研究区域河涌的底栖动物以耐污种为主,表明河涌受到显著的环境压力。底栖动物的丰度在平水期较高,而丰水期和枯水期较低,且城中村道路受纳河涌的底栖动物平均丰度和生物量最高,普通道路河涌最低。多样性指数和生物完整性指数均表明河涌受到严重污染。冗余分析(RDA)显示,溶解氧(DO)、pH 和总磷(TP)是影响底栖动物平均丰度的主要水环境因子,其中 DO 的解释贡献率最高。本研究明确了道路类型对城市受纳河涌生态系统的显著影响,为城市水环境治理和生态修复提供了科学依据。

通信作者简介:赵建亮(1979—),男,博士,研究员,主要研究方向为新型有机污染物化学与生态毒理学。

共同通信作者简介:刘珊(1986—),女,博士,教授,主要研究方向为新污染物的环境地球化学。

5 参考文献

[1] 马学琳, 李洪波, 罗宁, 等. 城市地表径流污染研究[J]. 中国资源综合利用, 2021, 39(5): 112-114.
MA X L, LI H B, LUO N, et al. Research on urban surface runoff pollution[J]. China resources comprehensive utilization, 2021, 39(5): 112-114.

[2] 张蕾, 周启星. 城市地表径流污染来源的分类与特征[J]. 生态学杂志, 2010, 29(11): 2272-2279.
ZHANG L, ZHOU Q X. Research advances on source classification and characteristics of contaminative urban surface runoff[J]. Chinese journal of ecology, 2010, 29(11): 2272-2279.

[3] 陈玉成, 李章平, 李章成, 等. 城市地表径流污染及其全过程削减[J]. 水土保持学报, 2004, 18(3): 133-136.
CHEN Y C, LI Z P, LI Z C, et al. Contamination of urban surface runoff and its whole course minimization[J]. Journal of soil water conservation, 2004, 18(3): 133-136.

[4] 侯思宇, 邱晨晨, 丁铖, 等. 西安市降水化学组成及来源解析[J]. 环境化学, 2020, 39(9): 2384-2394.
HOU S Y, QIU C C, DING C, et al. Analysis on chemical composition of precipitation and its source apportionment in Xi'an City[J]. Environmental chemistry, 2020, 39(9): 2384-2394.

[5] 王翔, 聂湘平, 黄卓尔, 等. 广州城市河涌沉积物浸出液对水生生物的急性毒性[J]. 生态毒理学报, 2006, 1(2): 180-185.
WANG X, NIE X P, HUANG Z E, et al. Toxicity of the lixivium of the sediment from 6 streams of Guangzhou to aquatic organisms[J]. Asian journal of ecotoxicology, 2006, 1(2): 180-185.

[6] CALVILLO S J, SPENCER WILLIAMS E, BROOKS B W. Street dust: implications for stormwater and air quality, and environmental through street sweeping[J]. Reviews of environmental contamination and toxicology, 2015, 233: 71-128.

[7] NOVOTNY V, BARTOŠOVÁ A, O'REILLY N, et al.

Unlocking the relationship of biotic integrity of impaired waters to anthropogenic stresses[J]. Water research, 2005, 39(1): 184-198.

[8] JOHNSON K A, STEINMAN A D, KEIPER W D, et al. Biotic responses to low-concentration urban road runoff [J]. Journal of the North American Benthological Society, 2011, 30(3): 710-727.

[9] SMUCKER N J, DETENBECK N E. Meta-analysis of lost ecosystem attributes in urban streams and the effectiveness of out-of-channel management practices[J]. Restoration ecology, 2014, 22(6): 741-748.

[10] 赵志良. 城市河涌水污染特征及治理措施分析[J/OL]. 城市建设理论研究(电子版), 2024(27): 184-186.
ZHAO Z L. Characteristics of urban river water pollution and its control measures[J/OL]. Theoretical research in urban construction, 2024(27): 184-186.

[11] 潘建非. 广州城市水系空间研究[D]. 北京: 北京林业大学, 2013: 1-4.

[12] 甘华阳, 卓慕宁, 李定强, 等. 广州城市道路雨水径流的水质特征[J]. 生态环境, 2006, 15(5): 969-973.
GAN H Y, ZHUO M N, LI D Q, et al. Water quality characteristics of road runoff from urban area of Guangzhou [J]. Ecology and environment, 2006, 15(5): 969-973.

[13] 郝璐, 孙阁. 城市化对流域生态水文过程的影响研究综述[J]. 生态学报, 2021, 41(1): 13-26.
HAO L, SUN G. Impacts of urbanization on watershed ecohydrological processes: progresses and perspectives[J]. Acta ecologica sinica, 2021, 41(1): 13-26.

[14] 周广宇, 龚道孝, 刘广奇, 等. 城市水环境治理工程的评估与选择——以中南地区某城市为例[J]. 给水排水, 2021, 57(4): 82-86.
ZHOU G Y, GONG D X, LIU G Q, et al. The assessment and arrangement of urban water environment treatment projects: a case study of a city in South-Central China[J]. Water & wastewater engineering, 2021, 57(4): 82-86.

[15] 王春凤, 方展强, 郑思东, 等. 广州市河涌沉积物及底栖生物体内的重金属含量及分布[J]. 安全与环境学报, 2003, 3(2): 40-43.
WANG C F, FANG Z Q, ZHENG S D, et al. Concentrations and distribution of heavy metals in sediments and benthic organisms from sewage stream in Guangzhou City [J]. Journal of safety and environment, 2003, 3(2): 40-43.

[16] VAN HASSEL J H, NEY J J, GARLING D L Jr. Heavy metals in a stream ecosystem at sites near highways[J]. Transactions of the American Fisheries Society, 1980, 109 (6): 636-643.

[17] JORDAN S J, SMITH L M. Indicators of ecosystem integrity for estuaries[M]// Estuarine Indicators. CRC Press, 2004: 467-480.

[18] RICO A, VAN DEN BRINK P J, LEITNER P, et al. Relative influence of chemical and non-chemical stressors on invertebrate communities: a case study in the Danube River[J]. Science of the total environment, 2016, 571: 1370-1382.

[19] COOK S E K. Quest for an index of community structure sensitive to water pollution[J]. Environmental pollution, 1976, 11(4): 269-288.

[20] 姚樱. 雨水口对城市道路路面雨水排放的影响[J]. 智能建筑与智慧城市, 2023(3): 169-171.
YAO Y. Influence of rainwater gully on rainwater discharge of urban road pavement[J]. Intelligent building & smart city, 2023(3): 169-171.

[21] 广州市统计局, 国家统计局广州调查队. 2024 广州统计年鉴[R]. 广州: 广州市统计局, 2024: 2-4.

[22] 广州市统计局, 国家统计局广州调查队. 2024 年广州市国民经济和社会发展统计公报[R]. 广州: 广州市统计局, 2024: 7-8.

[23] 中华人民共和国环境保护部. 生物多样性观测技术导则 淡水底栖大型无脊椎动物: HJ 710.8—2014[S]. 北京: 中国环境科学出版社, 2014: 1-28.

[24] 李晴, 张梦悦, 于明乔, 等. 东莞城市河流大型底栖动物群落结构及影响因子[J]. 生态环境学报, 2024, 33(1): 101-110.
LI Q, ZHANG M Y, YU M Q, et al. Community structure and influencing factors of macroinvertebrate in urban rivers of Dongguan[J]. Ecology and environmental sciences, 2024, 33(1): 101-110.

[25] 姜海霞. 河溪生态系统浮游生物和底栖动物多样性及交互影响研究[D]. 哈尔滨: 东北林业大学, 2024: 4-6.

[26] 王俊才, 王新华. 中国北方摇蚊幼虫[M]. 北京: 中国言实出版社, 2011: 1-291.

[27] 刘月英, 张文珍, 王跃先, 等. 中国经济动物志: 淡水软体动物[M]. 北京: 科学出版社, 1979: 1-134.

[28] 王洪铸. 中国小蚓类研究: 附中国南极长城站附近地区两新种[M]. 北京: 高等教育出版社, 2002: 1-228.

[29] 王备新. 大型底栖无脊椎动物水质生物评价研究[D]. 南京: 南京农业大学, 2003: 20-21.

[30] 廖依琳, 严雪溶, 杨涛, 等. 西安市典型河流底栖生物群落结构及影响因子[J]. 干旱区资源与环境, 2024, 38 (10): 101-110.
LIAO Y L, YAN X R, YANG T, et al. Community structure of benthic organisms in typical rivers of Xi'an and influencing factors[J]. Journal of arid land resources and environment, 2024, 38(10): 101-110.

[31] 张宇航, 张敏, 张海萍, 等. 北京河流大型底栖动物空间格局及其环境响应研究[J]. 生态毒理学报, 2018, 13

(4): 101-110.
ZHANG Y H, ZHANG M, ZHANG H P, et al. Study on the spatial pattern of macroinvertebrate and their responses to environmental changes in Beijing rivers[J]. Asian journal of ecotoxicology, 2018, 13(4): 101-110.

[32] 李斌, 李先福, 唐涛, 等. 基于大型底栖动物完整性指数评价深圳茅洲河生态状况[J]. 水生态学杂志, 2021, 42(5): 62-68.
LI B, LI X F, TANG T, et al. Ecological condition assessment of Maozhou River at Shenzhen City based on the benthic index of biological integrity[J]. Journal of hydroecology, 2021, 42(5): 62-68.

[33] JOHNSON R C, CARREIRO M M, JIN H S, et al. Within-year temporal variation and life-cycle seasonality affect stream macroinvertebrate community structure and biotic metrics[J]. Ecological indicators, 2012, 13(1): 206-214.

[34] 黄艺兰. 东江惠州段主要城市河涌水质评价及污染防治对策分析[J]. 广东水利水电, 2021(7): 27-30.
HUANG Y L. Water quality evaluation and control countermeasures of main urban rivers in Huizhou Section of Dongjiang River[J]. Guangdong water resources and hydropower, 2021(7): 27-30.

[35] 王强, 庞旭, 王志坚, 等. 城市化对河流大型底栖动物群落的影响研究进展[J]. 生态学报, 2017, 37(18): 6275-6288.
WANG Q, PANG X, WANG Z J, et al. Advances in research on the influence of urbanization on stream benthic macroinvertebrate communities[J]. Acta ecologica sinica, 2017, 37(18): 6275-6288.

[36] 任海庆, 袁兴中, 刘红, 等. 环境因子对河流底栖无脊椎动物群落结构的影响[J]. 生态学报, 2015, 35(10): 3148-3156.
REN H Q, YUAN X Z, LIU H, et al. The effects of environment factors on community structure of benthic invertebrate in rivers[J]. Acta ecologica sinica, 2015, 35(10): 3148-3156.

[37] 田伟, 徐兆礼, 周进, 等. 椒江口海域大型底栖动物群落结构的研究[J]. 复旦学报(自然科学版), 2013, 52(2): 271-277.
TIAN W, XU Z L, ZHOU J, et al. The study on macrobenthos community structure in Jiaojiang Estuary[J]. Journal of Fudan University (natural science), 2013, 52(2): 271-277.

[38] 谢卓健. 广州市某河涌流域污水现状及综合整治措施[J]. 工程技术研究, 2022, 7(11): 129-131.
XIE Z J. Current situation and comprehensive treatment measures of sewage in a river flow basin in Guangzhou [J]. Engineering and technological research, 2022, 7(11): 129-131.

[39] 广州市人民政府. 广州市水环境治理行动计划(2017-2020 年)[R]. 广州: 广州市人民政府, 2017: 1-9.

[40] 广州市水务局. 广州市城市黑臭水体治理攻坚战实施方案[R]. 广州: 广州市水务局, 2018: 1-12.

[41] 广州市规划和自然资源局. 广州市生态修复专项规划(2020-2035 年)[R]. 广州: 广州市规划和自然资源局, 2020: 1-48.

[42] SHIEH S H, KONDRATIEFF B C, WARD J V. Longitudinal changes in benthic organic matter and macroinvertebrates in a polluted Colorado Plains stream[J]. Hydrobiologia, 1999, 411: 191-209.

[43] HAN B P, LIU Z W. Tropical and sub-tropical reservoir limnology in China[M]// HU Z J, WU H, LIU Q G. The ecology of zoobenthos in reservoirs of China: a mini-review. Springer, 2012: 155-165.

[44] 卢鑫, 梁婷, 徐菁, 等. 湖南大通湖大型底栖动物群落结构特征与水质评价[J]. 生态科学, 2023, 42(3): 8-16.
LU X, LIANG T, XU J, et al. Characteristics of macrofauna community and bioassessment of water quality in the Datong Lake, Hunan, China[J]. Ecological science, 2023, 42(3): 8-16.

[45] BUSS D F, BAPTISTA D F, SILVEIRA M P, et al. Influence of water chemistry and environmental degradation on macroinvertebrate assemblages in a river basin in South-East Brazil[J]. Hydrobiologia, 2002, 481(1): 125-136.

[46] 王昱, 信雅玲, 李浩霖, 等. 河西内陆河流域大型底栖动物群落结构及生物多样性特征[J/OL]. 生态与农村环境学报. [2025-02-25]. https://doi.org/10.19741/j.issn.1673-4831.2024.0675.
WANG Y, XIN Y L, LI H L, et al. Community structure and biodiversity characteristics of macroinvertebrates in the Hexi Inland River Basin[J/OL]. Journal of ecology and rural environment. [2025-02-25]. https://doi.org/10.19741/j.issn.1673-4831.2024.0675.

[47] 张莹, 吕振波, 徐宗法, 等. 山东半岛南部海湾底栖动物群落生态特征及其与水环境的关系[J]. 生态学报, 2011, 31(15): 4455-4467.
ZHANG Y, LYU Z B, XU Z F, et al. Ecological characteristics of macrobenthic communities and their relation to water environmental factors in four bays of southern Shandong Peninsula[J]. Acta ecologica sinica, 2011, 31(15): 4455-4467. ◆

大气中 ^{7}Be 和 ^{210}Pb 时空分布特征差异和机制解析

黄思宇[1]　林武辉[2]　何贤文[3]　林晓东[4]

1（广西大学 海洋学院　南宁 530004）

2（集美大学 港口与海岸工程学院　厦门 361021）

3（生态环境部 华南核与辐射安全监督站　深圳 518026）

4（福建省辐射环境监督站　福州 350013）

摘要　对南宁市 6 a 内采集的 75 个气溶胶样品进行观测，其中 ^{7}Be 和 ^{210}Pb 活度浓度分别为 0.27~11.95 mBq·m^{-3}、（3.68±0.51）mBq·m^{-3} 和 0.23~4.33 mBq·m^{-3}、（1.51±0.13）mBq·m^{-3}，^{7}Be 和 ^{210}Pb 呈现“冬春高、夏秋低”季节特征，^{7}Be 最高值出现在春季，^{210}Pb 最高值则在冬季。^{7}Be、^{210}Pb 与 $PM_{2.5}$、PM_{10} 的同相位季节特征和较强正相关说明颗粒物载带 ^{7}Be 和 ^{210}Pb 在大气中传输；^{7}Be 与 O_3 的强相关性证实“春季泄漏”引起 ^{7}Be 自上而下从平流层进入对流层并导致 ^{7}Be 春季最高值；大气逆轨迹聚类分析指示东亚季风导致 ^{210}Pb 冬季最高值。整合全国 17 个不同地区大量数据发现，^{210}Pb 存在纬度效应，即 40°N 以北 ^{210}Pb 活度均值约为 40°N 以南的 2.2 倍；^{7}Be 存在纬度效应和高度效应，即 35°N 以北 ^{7}Be 浓度均值约为以南的 1.9 倍，^{7}Be 自上而下从平流层输入对流层过程导致高海拔地区的高 ^{7}Be 效应。^{7}Be 和 ^{210}Pb 时空分布差异导致二者冬春季有效剂量约为夏秋季的 1.4 倍，40°N 以北地区有效剂量约为 35°N 以南的 2.0 倍。

关键词　气溶胶，^{7}Be，^{210}Pb，放射性核素，辐射剂量，东亚季风

中图分类号　X831

DOI: 10.11889/j.0253-3219.2025.hjs.48.240348

CSTR: 32193.14.hjs.CN31-1342/TL.2025.48.240348

Spatiotemporal characteristics and mechanisms of ^{7}Be and ^{210}Pb in the atmosphere

HUANG Siyu[1]　LIN Wuhui[2]　HE Xianwen[3]　LIN Xiaodong[4]

1(*School of Marine Sciences, Guangxi University, Nanning 530004, China*)

2(*College of Harbour and Coastal Engineering, Jimei University, Xiamen 361021, China*)

3(*South China Nuclear and Radiation Safety Supervision Station, Ministry of Ecology and Environment, Shenzhen 518026, China*)

4(*Fujian Radiation Environment Supervision Station, Fuzhou 350013, China*)

国家自然科学基金(No.42276044)、广西自然科学基金(No.2021GXNSFBA196001, No.2024GXNSFAA010449)、福建省环保科技计划项目(No.2025R004)、中国辐射防护研究院平台开放基金(No. ZFYHHJMN-2024003)、广西南海珊瑚礁研究重点实验室开放基金(No. GXLSCRSCS2023003)资助

第一作者：黄思宇，男，1999年出生，2022年毕业于成都理工大学，现为硕士研究生，研究领域为大气放射性观测与评价

通信作者：林武辉，E-mail：linwuhui8@163.com；何贤文，E-mail：2571066576@qq.com

收稿日期：2024-08-26，修回日期：2024-10-23

Supported by National Natural Science Foundation of China (No.42276044), the Guangxi Natural Science Foundation (No.2021GXNSFBA196001, No.2024GXNSFAA010449), Fujian Environmental Protection Plan Project (No.2025R004), CIRP Open Fund of Radiation Protection Laboratories (No. ZFYHHJMN-2024003), and the Open Fund of Guangxi Key Laboratory for Coral Reef Research in the South China Sea (No. GXLSCRSCS2023003)

First author: HUANG Siyu, male, born in 1999, graduated from Chengdu University of Technology in 2022, master student, focusing on observation and evaluation of atmospheric radioactivity

Corresponding author: LIN Wuhui, E-mail: linwuhui8@163.com; HE Xianwen, E-mail: 2571066576@qq.com

Received date: 2024-08-26, revised date: 2024-10-23

中国知网　https://www.cnki.net

Abstract **[Background]** ^{7}Be and ^{210}Pb are the main radionuclides for monitoring the quality of the radiation environment of atmospheric aerosols, and the internal irradiation caused by their adsorption into aerosols and entry into the human body will be harmful to the human body, so it is of great significance to explore the characteristics and mechanisms of their spatial and temporal distribution and dose contribution. **[Purpose]** This study aims to investigate the differences in the spatial and temporal distributions of atmospheric ^{7}Be and ^{210}Pb and the mechanisms of these differences. **[Methods]** In this paper, 75 aerosol samples were collected from Nanning city, from January 2015 to December 2017 and from January 2019 to May 2022 using an ultra-high-flow air aerosol sampler, and the activity concentrations of ^{7}Be and ^{210}Pb in the aerosol were measured and analyzed using a high-purity germanium (HPGe) γ-spectrometer. The activity concentration data of ^{7}Be and ^{210}Pb were systematically collected in 17 areas of our country, as well as $PM_{2.5}$, PM_{10} and O_3 air concentration data from January 2014 to November 2023 in Nanning city. Finally, the Lagrangian inverse trajectory analysis technique based on the Hybrid Single-Particle Lagrangian Integrated Trajectory (HYSPLIT) model, combined with the clustering analysis method based on MeteoInfo software, was employed to analyze the seasonal characteristic control mechanism of ^{7}Be and ^{210}Pb. **[Results]** The activity concentrations of ^{7}Be in 41 aerosol samples from January 2019 to May 2022 ranges from 0.27 mBq·m^{-3} to 11.95 mBq·m^{-3}, with a mean value of (3.68±0.51) mBq·m^{-3}; the activity concentrations of ^{210}Pb in 60 aerosol samples from January 2015 to December 2017 and from January 2019 to February 2021 ranges from 0.23 mBq·m^{-3} to 4.33 mBq·m^{-3}, with a mean value of (1.51±0.13) mBq·m^{-3}. Combining the ^{7}Be and ^{210}Pb activity concentration data in 17 areas of China, the seasonal distribution of ^{7}Be and ^{210}Pb activity concentrations in the atmosphere of China is characterized by an overall high in winter and spring, and a low in summer and autumn, but ^{7}Be reaches its maximum value in spring while ^{210}Pb in winter. The correlation analysis shows that ^{7}Be has a significant positive correlation with $PM_{2.5}$, PM_{10}, O_3, and has the best correlation with PM_{10}. ^{210}Pb has a significant positive correlation with $PM_{2.5}$ and PM_{10} and has the best correlation with $PM_{2.5}$, while it is not correlated with O_3. The traceability analysis of air masses in Nanning city of the 2021 shows that the summer air masses mainly come from the oceanic air masses in the south with lower particle concentration, and the winter air masses mainly come from the continental air masses in the north with higher particle concentration. Combining the ^{7}Be and ^{210}Pb activity concentration data in 17 areas of China, there are effects in the spatial distribution of ^{7}Be and ^{210}Pb activity concentrations. The latitudinal effects: the mean ^{210}Pb activity concentration in the area north of about 40°N (3.20±0.24) mBq·m^{-3} is about 2.2 times higher than that in the area south of about 40° N (1.48±0.06) mBq·m^{-3}; the mean value of ^{7}Be activity concentration in the area north of about 35°N (7.44±0.26) mBq·m^{-3} is about 1.9 times of that in the area south of about 35°N (3.92±0.19) mBq·m^{-3}. The altitudinal effect: the ^{7}Be activity concentration is greater at high altitude than at low altitude. Based on the average of winter-spring and summer-autumn activity concentrations of ^{7}Be and ^{210}Pb in 17 regions of the country, it can be estimated that the radiation dose due to ^{7}Be and ^{210}Pb in winter-spring (42.08 μSv·a^{-1}) is about 1.4 times higher than that in summer-autumn (31.00 μSv·a^{-1}). Integration of monitoring data on activity concentrations of ^{7}Be and ^{210}Pb in 17 regions of the country reveals that the annual effective dose due to ^{7}Be and ^{210}Pb in the area north of 40° N (65.48 μSv·a^{-1}) is about 2.0 times higher than that in the area south of 35° N (32.75 μSv·a^{-1}). The mean annual pending effective doses due to ^{7}Be and ^{210}Pb are 2.47×10^{-3} μSv·a^{-1} and 33.57 μSv·a^{-1}, respectively. **[Conclusions]** ^{7}Be and ^{210}Pb are adsorbed on the particulate matter and transported in the atmosphere, and the $PM_{2.5}$ and PM_{10} concentrations are low in summer and autumn while high in winter and spring due to the monsoon regulation, so the ^{7}Be and ^{210}Pb show the seasonal distribution characteristics of low in summer and autumn and high in winter and spring. The highest ^{7}Be activity concentration in spring is related to the "spring leakage", while the highest ^{210}Pb activity concentration in winter is mainly influenced by the Eurasian land-based air masses in the north. The latitudinal effect of ^{210}Pb is probably related to the large amount of particulate matter brought by the northwest land-source winds in winter and the combustion process in winter heating system. The latitudinal effect of ^{7}Be may be attributed to the "spring leakage" of ^{7}Be that occurs in mid-latitudes in the spring. The altitudinal effect of ^{7}Be is controlled by the top-down transport of ^{7}Be from the stratosphere to the troposphere.

Key words Aerosol, ^{7}Be, ^{210}Pb, Radionuclide, Radiation dose, Asian monsoon

中国知网 https://www.cnki.net

大气气溶胶颗粒物可吸附多种放射性核素，这些核素通过呼吸道进入人体后产生内照射，对人体健康造成潜在危害[1-4]。^{7}Be是宇宙射线同平流层中的氮和氧原子相互作用的产物；^{210}Pb主要是由土壤释放到大气中的^{222}Rn经过衰变产生。^{7}Be和^{210}Pb一旦形成后很快被吸附在亚微米尺度气溶胶表面，并随大气过程发生迁移[5-6]。大气中含有多种放射性物质，包括原生放射性核素、宇生放射性核素和人工放射性核素。现如今，大气中人工放射性核素因长时间衰变含量甚微，对人体的影响几乎可忽略不计，因此，原生和宇生来源放射性对人体剂量的贡献情况长期以来受到人们的关注，特别是气溶胶中关键的宇生放射性核素^{7}Be和原生放射性核素^{210}Pb对人体的剂量贡献情况。

在我国，^{7}Be和^{210}Pb是大气气溶胶辐射环境质量监测的主要核素，观测其长期变化具有重要意义。我国大多数城市地区气溶胶样品中^{7}Be和^{210}Pb活度浓度季节分布特征一致，呈现出冬春高、夏秋低的特点，前人研究多将这种季节分布的原因归结于降雨的影响，鲜有研究报道造成^{7}Be和^{210}Pb冬春高、夏秋低的季节分布特点的其他影响因素以及两者在季节尺度时间分布上是否存在差异。从北半球纬度向上看，^{7}Be和^{210}Pb的活度浓度在中纬度地区达到峰值，往赤道和北极方向活度浓度不断降低[7]。对比国外，我国^{7}Be和^{210}Pb的数据较为匮乏，前人研究大多局限于某个地区，鲜有研究讨论^{7}Be和^{210}Pb在我国的空间分布上是否存在差异。

基于上述现状，本研究在观测了南宁市75个月近地面气溶胶样品中^{7}Be和^{210}Pb的活度浓度的基础上，整合全国17个地区数据，分析在时间分布上大气中^{7}Be和^{210}Pb活度浓度存在的季节特征，通过将^{7}Be和^{210}Pb活度浓度与$PM_{2.5}$、PM_{10}以及O_3浓度进行相关性分析，结合基于混合单粒子拉格朗日积分轨迹（Hybrid Single-Particle Lagrangian Integrated Trajectory Model，HYSPLIT）模型的拉格朗日逆轨迹分析技术以及基于MeteoInfo软件的聚类分析方法，解析了^{7}Be和^{210}Pb的季节特征调控机制。研究在空间分布上，指出了^{7}Be和^{210}Pb活度浓度存在纬度和高度效应并解析了产生效应的机制。此外，本研究系统评估了全国17个地区的^{7}Be和^{210}Pb吸入内照射所致年待积有效剂量，指出^{7}Be和^{210}Pb所致辐射剂量在时空分布上存在的差异。

1 样品采集与研究方法

1.1 样品采集与制备

采样地点位于南宁市广西壮族自治区辐射环境监督管理站（108.45°E，22.80°N），采样设备为华瑞核安超大流量空气气溶胶采样器（HRHA01-SFS1000/A），采样流量为600 $m^3 \cdot h^{-1}$，每个样品采集一天左右，平均一个月采集一个样品，样品采样日期为2015年1月~2017年12月以及2019年1月~2022年5月，除去法定节假日，共采集并分析75个气溶胶样品。采样滤膜为聚丙烯滤膜，尺寸为47 cm×57 cm。采样方法如下：取一张干净的滤膜，将滤膜受尘面朝向进气方向，平放在滤膜支持网上，连续采样1~2 d，保证采样体积在标准状态下大于10 000 m^3，后将采集的滤膜放入干燥设备中进行氡子体衰变，在采样结束5 d后取出滤膜，立即用天平称量，在用酒精棉清洁压片机模具和工作台之后打开滤膜，将受尘面向上平放在工作台上折叠，折叠后的滤膜塞入压片机模具底部，使用压片机将其压制成∅75 mm圆形薄片，在压片后的样品表面标识滤膜编号，装入干净的样品袋中等待上机测量。

1.2 样品测量

测量仪器设备为美国ORTEC公司生产的高纯锗γ能谱仪（GEM-C94100-LB-C和GEM-C7080-LB-C），相对探测效率分别为175%和66%，设备由上海市计量测试技术研究院/华东国家计量测试中心检定并合格。使用中国计量研究院生产的滤膜监测效率校准源对高纯锗γ能谱分析系统进行能量刻度和效率刻度。样品产生的γ射线会与高纯锗晶体产生电子-空穴对，在高压电场作用下，电子-空穴对被收集经并放大器放大形成脉冲信号，其峰值和计数率与γ射线强度呈正相关，经脉冲幅度分析器（Multi-Channel Analyzer，MCA）及模数转换器（Analoge-Digital Converter，ADC）数据前处理后送入计算机，经软件处理后形成γ能谱。利用γ能谱，通过识别^{7}Be、^{210}Pb仅有的特征峰并进行记录，以得到其放射性活度浓度数据。

1.3 年待积有效剂量估算方法

人体吸入的大气放射性核素所致年待积有效剂量估算方法参考《电离辐射防护与辐射源安全基本标准》[8]，计算公式如式（1）：

$$E_{j,\mathrm{inh}}=I_{\mathrm{inh}}\times \mathrm{DCF}_{\mathrm{inh}}=C_{\mathrm{air}}\times V\times \mathrm{DCF}_{\mathrm{inh}} \quad (1)$$

式中：$E_{j,\mathrm{inh}}$为放射性核素j所致人体年待积有效剂量，Sv·a^{-1}；I_{inh}为吸入途径的放射性核素年摄入量，Bq；C_{air}为大气中放射性核素活度浓度，Bq·m^{-3}；V为

中国知网 https://www.cnki.net

人体年呼吸总量，m^3，取自国家标准《核事故应急情况下公众受照剂量估算的模式和参数》[9]中成人（男）呼吸率典型值22.2 $m^3 \cdot d^{-1}$；DCF_{inh}为摄入单位活度放射性核素所致待积有效剂量的转化系数，$Sv \cdot Bq^{-1}$，取自《电离辐射防护与辐射源安全基本标准》[8]，具体为：对于成人（男，>17岁）来说，^{7}Be在M类（中速）吸收情况下转化系数为5.0×10^{-11} $Sv \cdot Bq^{-1}$，在S类（慢速）情况下为5.5×10^{-11} $Sv \cdot Bq^{-1}$；^{210}Pb在F类（快速）吸收情况下转化系数为9.0×10^{-7} $Sv \cdot Bq^{-1}$，在M类（中速）情况下为1.1×10^{-6} $Sv \cdot Bq^{-1}$，在S类（慢速）情况下为5.6×10^{-6} $Sv \cdot Bq^{-1}$。

1.4 PM_{10}、$PM_{2.5}$和O_3数据来源和气团逆轨迹聚类分析方法

南宁市的PM_{10}、$PM_{2.5}$以及O_3数据引用自中国空气质量在线监测分析平台（网址：https://www.aqistudy.cn/historydata/）；逆轨迹溯源分析方法采用美国国家大气与海洋管理局（National Oceanic and Atmospheric Administration，NOAA）的混合单粒子拉格朗日集合轨迹模型（Hybrid Single-Particle Lagrangian Integrated Trajectory Model，HYSPLIT）[10]；逆轨迹的聚类分析采用MeteoInfo软件中的角度聚类分析方法。本文选取南宁市地面高度100 m位置作为逆轨迹终点，使用自NOAA的GDAS（Global Data Assimilation System）气象学资料进行模拟，逆轨迹的反演起始时间选取北京时间0点、6点、12点以及18点整，反演用时168 h，每6 h进行一次逆轨迹计算，故一天可以得到4条逆轨迹，最后得到2021年冬夏季（冬季为2021年12月~2022年1月，夏季为2021年6~8月）共计728条逆轨迹，之后利用MeteoInfo软件对所有轨迹进行整合后再使用角度聚类的方法进行聚类分析，最后得到2021年南宁市冬夏季气团来源逆轨迹聚类图[11]。

2 结果与讨论

2.1 ^{7}Be和^{210}Pb季节特征

南宁市2019年1月~2022年5月采集的41份气溶胶样品中^{7}Be的活度浓度范围为0.27~11.95 $mBq \cdot m^{-3}$，均值为（3.68±0.51）$mBq \cdot m^{-3}$。2015年1月~2017年12月，2019年1月~2021年2月采集的60份气溶胶样品中^{210}Pb的活度浓度范围为0.23~4.33 $mBq \cdot m^{-3}$，均值（1.51±0.13）$mBq \cdot m^{-3}$。南宁市大气气溶胶样品中^{7}Be和^{210}Pb活度浓度季节变化趋势如图1所示，可以明显看出，^{7}Be和^{210}Pb冬春季活度浓度大于夏秋季（2018年12月~2019年5月期间由于缺少12月份数据不纳入统计）。南宁市6 a内^{7}Be冬春季活度浓度均值（4.61±0.72）$mBq \cdot m^{-3}$约为夏秋季（2.22±0.60）$mBq \cdot m^{-3}$的2.1倍。^{210}Pb冬春季活度浓度均值（1.84±0.17）$mBq \cdot m^{-3}$，约为夏秋季（1.13±0.19）$mBq \cdot m^{-3}$的1.6倍。南宁市^{7}Be和^{210}Pb活度浓度季节时间分布呈现出冬春高、夏秋低的特点。

南宁市气溶胶样品中^{7}Be和^{210}Pb活度浓度季节变化箱型图如图2所示，^{7}Be活度浓度季度均值由高到低为春季、冬季、秋季、夏季，分别为（4.99±1.11）$mBq \cdot m^{-3}$、（4.20±0.93）$mBq \cdot m^{-3}$、（3.30±1.02）$mBq \cdot m^{-3}$、（1.02±0.11）$mBq \cdot m^{-3}$；^{210}Pb活度浓度季度均值由高到低为冬季、秋季、春季、夏季，分别为（2.29±0.23）$mBq \cdot m^{-3}$、（1.67±0.28）$mBq \cdot m^{-3}$、（1.33±0.17）$mBq \cdot m^{-3}$、（0.51±0.06）$mBq \cdot m^{-3}$。南宁市^{7}Be在春季达到最大值，而^{210}Pb在冬季达到最大值。

全国17个^{7}Be和^{210}Pb采样地点分布情况如图3所示，整合这17个地区的^{7}Be和^{210}Pb活度浓度得到的季节变化箱型图如图4所示，^{7}Be活度浓度季度均值由高到低为春季、冬季、秋季、夏季，分别为（6.60±1.04）$mBq \cdot m^{-3}$、（6.23±0.87）$mBq \cdot m^{-3}$、（5.65±0.88）$mBq \cdot m^{-3}$、（4.36±1.00）$mBq \cdot m^{-3}$；^{210}Pb活度浓度季度均值由高到低为冬季、秋季、春季、夏季，分别为（2.59±0.25）$mBq \cdot m^{-3}$、（1.98±0.19）$mBq \cdot m^{-3}$、（1.50±0.16）$mBq \cdot m^{-3}$、（1.04±0.16）$mBq \cdot m^{-3}$。^{7}Be冬春季活度浓度均值（6.41±0.66）$mBq \cdot m^{-3}$，约为夏秋季（5.01±0.66）$mBq \cdot m^{-3}$的1.3倍。^{210}Pb冬春季活度浓度均值（2.05±0.19）$mBq \cdot m^{-3}$，约为夏秋季（1.51±0.16）$mBq \cdot m^{-3}$的1.4倍。大气中^{7}Be和^{210}Pb的整体季节时间分布呈现出冬春高、夏秋低的特点，但^{7}Be在春季达到最大值，而^{210}Pb在冬季达到最大值。前人研究表明，春季中纬度平流层变低，对流层变窄，平流层中^{7}Be更容易向对流层泄漏[11]（以下简称“春季泄漏”），这是^{7}Be在春季达到最大值的可能原因。冬季来源于欧亚大陆气团中的^{210}Pb母体^{222}Rn含量较高[11]，这是^{210}Pb在冬季达到最大值的可能原因。

2.2 ^{7}Be和^{210}Pb季节特征调控机制

南宁市2014年2月~2023年11月，$PM_{2.5}$、PM_{10}每月的活度浓度变化如图5所示，南宁市$PM_{2.5}$冬季均值为（45.93±2.56）$\mu g \cdot m^{-3}$，春季均值为（30.53±1.39）$\mu g \cdot m^{-3}$，夏季均值为（19.43±0.91）$\mu g \cdot m^{-3}$，秋季均值为（32.97±2.11）$\mu g \cdot m^{-3}$；PM_{10}冬季均值为（69.48±4.13）$\mu g \cdot m^{-3}$，春季均值为（53.57±2.30）$\mu g \cdot m^{-3}$，夏季均值为（38.23±1.88）$\mu g \cdot m^{-3}$，秋季均值为（57.77±3.60）$\mu g \cdot m^{-3}$。$PM_{2.5}$冬春季均值为（40.00±

中国知网 https://www.cnki.net

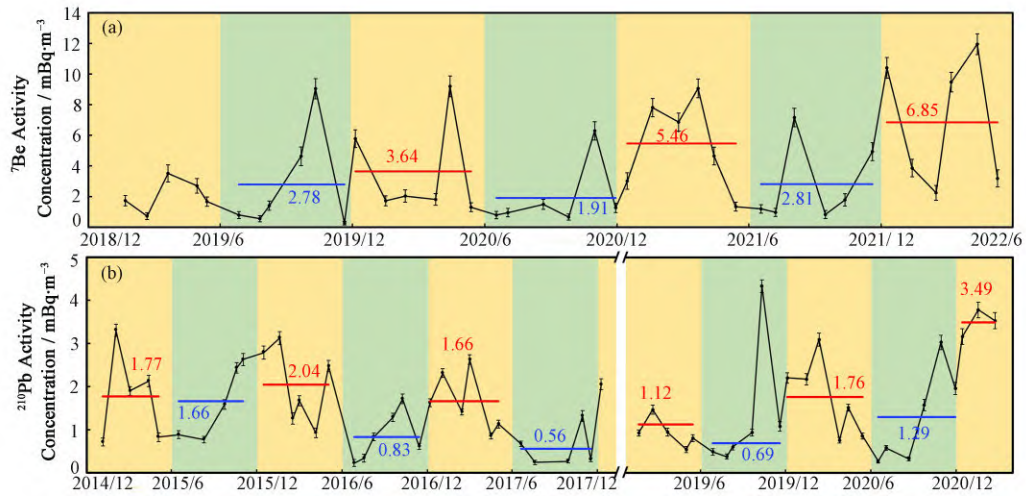


图1 (a) 南宁市^{7}Be活度浓度季节变化趋势图;(b) 南宁市^{210}Pb活度浓度季节变化趋势图(黄色区域:冬春季,12~5月;绿色区域:夏秋季,6~11月;红色实线:冬春季均值;蓝色实线:夏秋季均值)(彩图见网络版)

Fig.1 Seasonal variation trends of ^{7}Be activity concentration (a) and ^{210}Pb activity concentration (b) in Nanning city (yellow area: winter-spring, December-May; green area: summer-autumn, June-November; red solid line: winter-spring average; blue solid line: summer-autumn average) (color online)

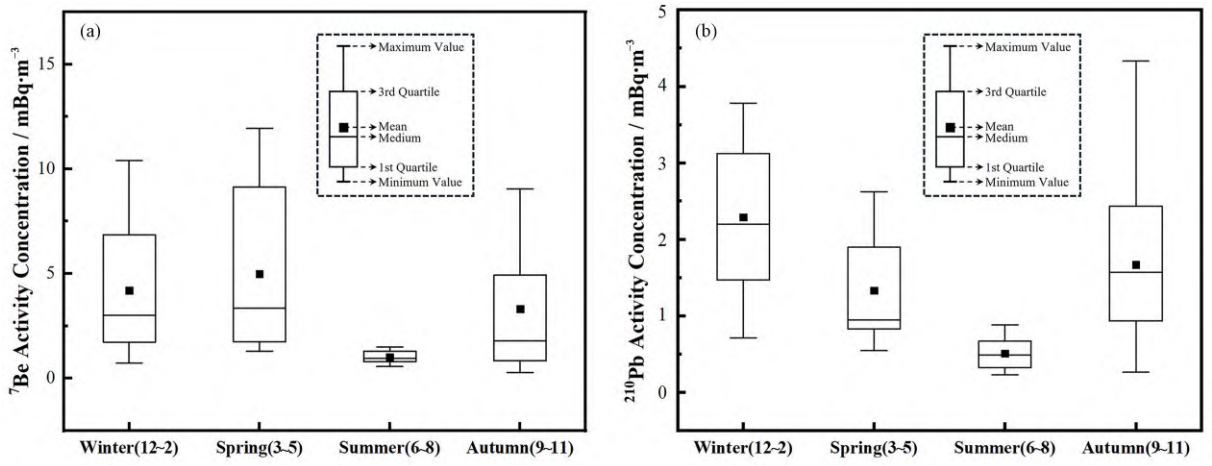


图2 南宁市^{7}Be (a)和^{210}Pb (b)活度浓度的季节变化箱型图(^{7}Be和^{210}Pb的最高值分别在春季和冬季)

Fig.2 Box plots of seasonal variations in activity concentrations of ^{7}Be (a) and ^{210}Pb (b) in Nanning city (The highest values of ^{7}Be and ^{210}Pb are in spring and winter, respectively)

1.60) μg·m^{-3},约为夏秋季均值(24.33±1.26) μg·m^{-3}的1.6倍。PM_{10}冬春季均值(64.10±2.38) μg·m^{-3},约为夏秋季均值(45.28±2.15) μg·m^{-3}的1.4倍。南宁市$PM_{2.5}$和PM_{10}浓度整体呈现出冬春高、夏秋低的特点,这一特点与^{7}Be和^{210}Pb活度浓度整体季节特征相同。

南宁市^{7}Be、^{210}Pb活度浓度分别与$PM_{2.5}$、PM_{10}浓度的相关性分析如图6所示。^{7}Be与$PM_{2.5}$和PM_{10}回归性整体较好,且与PM_{10}相关性最好,在不确定范围内差距也不是很明显,说明^{7}Be相对可能主要吸附到较粗颗粒物上随大气进行传输,这一点与部分前人的研究有些许差别[28-30]。^{210}Pb与$PM_{2.5}$和PM_{10}回归性整体较好,在不确定范围内差距不明显且与$PM_{2.5}$的相关性最好,说明相较于粒径较大的粗颗粒,^{210}Pb主要吸附在相对细颗粒物表面并随大气进行迁移传输,这一点与前人研究结果相符[29-31]。总之,相关性分析结果表明,^{7}Be和^{210}Pb都会吸附在颗粒物上随大气进行长距离输运,而$PM_{2.5}$和PM_{10}受东亚季风调控具有冬春高、夏秋低的特点,所以^{7}Be和^{210}Pb整体上也具有冬春高、夏秋低的时间分布特征。

图7展示了^{7}Be和^{210}Pb的活度浓度与O_3浓度之间的相关性分析,回归分析结果显示,^{7}Be和O_3浓度之间相关系数为0.65,p值小于0.01,表明^{7}Be与O_3浓度之间有显著的正相关。^{210}Pb与O_3浓度之间的相关性较弱,相关系数为0.22,p值为0.09,表明^{210}Pb

中国知网 https://www.cnki.net

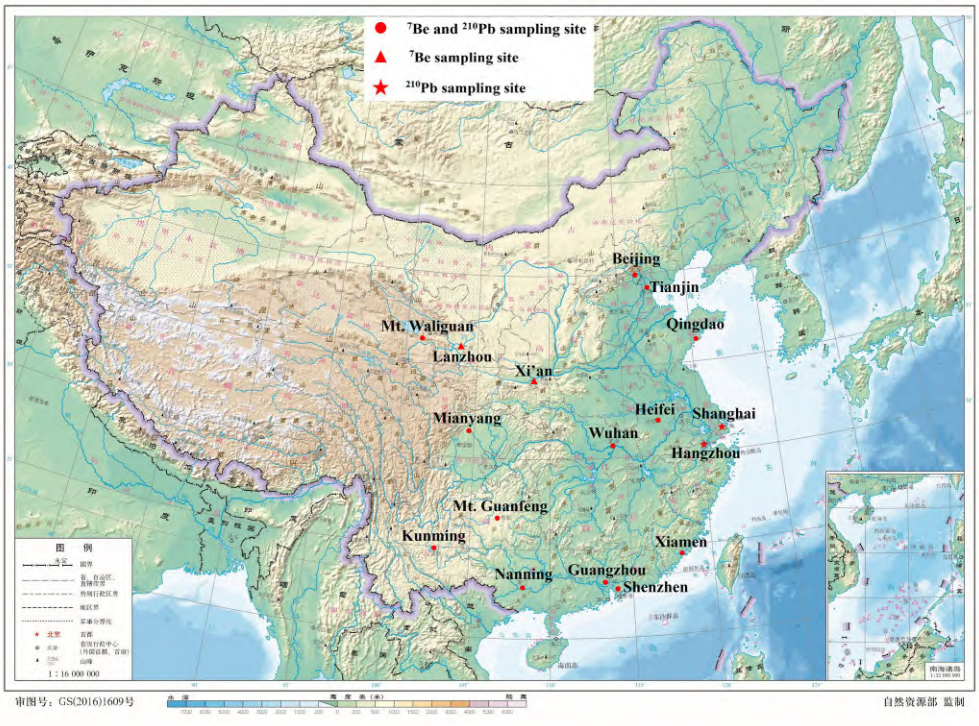


图3 中国17个地区 ^{7}Be 和 ^{210}Pb 采样位置分布示意图[审图号GS(2016)1609]

Fig.3 Distribution of ^{7}Be and ^{210}Pb sampling sites in 17 areas of China [Revision Number: GS(2016)1609]

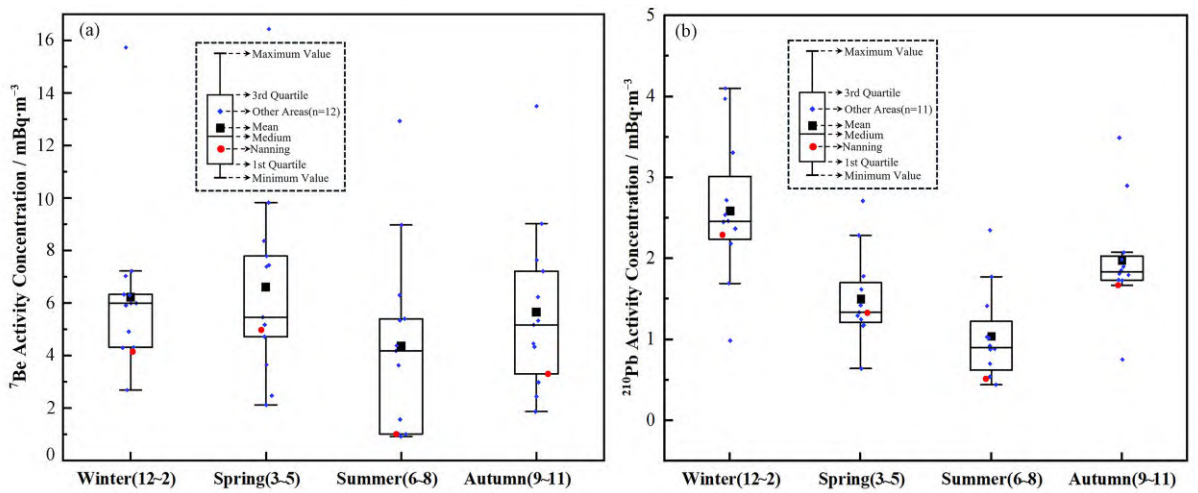


图4 中国17个地区 ^{7}Be (a)和 ^{210}Pb (b)活度浓度季节均值箱型图（^{7}Be均值来源地区包括瓦里关山[12]、观凤山[13]、绵阳[14]、北京[15]、青岛[16]、兰州[17]、西安[18]、合肥[19]、武汉[20]、昆明[21]、广州[22]、深圳[23]、南宁；^{210}Pb均值来源地区包括瓦里关山[24]、观凤山[13]、北京[15]、合肥[19]、绵阳[14]、上海[25]、武汉[20]、杭州[26]、昆明[21]、广州[22]、深圳[27]、南宁；^{7}Be 和 ^{210}Pb 的最高值分别在春季和冬季）

Fig.4 Box plots of seasonal averages of ^{7}Be (a) and ^{210}Pb (b) activity concentrations in 17 areas of China (source areas for the ^{7}Be mean include Mt. Waliguan[12], Mt. Guanfeng[13], Mianyang[14], Beijing[15], Qingdao[16], Lanzhou[17], Xi'an[18], Hefei[19], Wuhan[20], Kunming[21], Guangzhou[22], Shenzhen[23], Nanning; source areas for the ^{210}Pb mean include Mt. Waliguan[24], Mt. Guanfeng[13], Beijing[15], Hefei[19], Mianyang[14], Shanghai[25], Wuhan[20], Hangzhou[26], Kunming[21], Guangzhou[22], Shenzhen[27], Nanning; the highest values of ^{7}Be and ^{210}Pb are in spring and winter, respectively)

活度浓度与 O_3 浓度之间没有显著的线性关系，两者之间没有相关性。^{7}Be 活度浓度与 O_3 呈显著正相关，而 ^{210}Pb 与 O_3 不相关，说明 ^{7}Be 的来源与 O_3 相同，与春季平流层气团向对流层气团自上而下的垂直输送，即“春季泄漏”有关，而 ^{210}Pb 主要来源于地表土壤中释放的 ^{222}Rn 在大气中的衰变，是一个自下而上的过程，与 O_3 来源的不同造成相关性极差。所以，^{7}Be 在春季达到最高值主要是受自上而下的“春季泄漏”的影响。

2021年南宁市冬夏季的气团来源逆轨迹聚类结果如图8所示，冬季气团主要是北方的陆源气团，其中，30.95%的气团来源于西北方向的中亚地区，69.05%来源于华中地区。夏季气团主要是南方的海源气团，其中，63.89%来自印度洋，36.11%来自太

中国知网 https://www.cnki.net

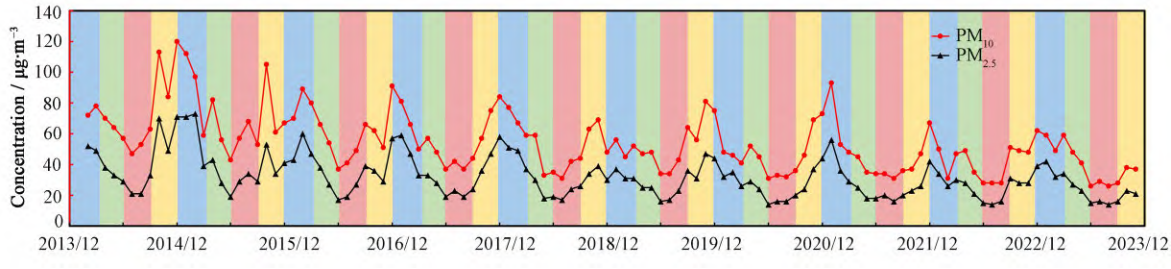


图5 南宁市2014年2月~2023年11月$PM_{2.5}$、PM_{10}月均活度浓度变化情况(蓝色区域:冬季,12~2月;绿色区域:春季,3~5月;红色区域:夏季,6~8月;黄色区域:秋季,9~11月)(彩图见网络版)

Fig.5 Changes of monthly mean activity concentrations of $PM_{2.5}$ and PM_{10} in Nanning city from February 2014 to November 2023 (blue area: winter, December-February; green area: spring, March-May; red area: summer, June-August; yellow area: autumn, September-November) (color online)

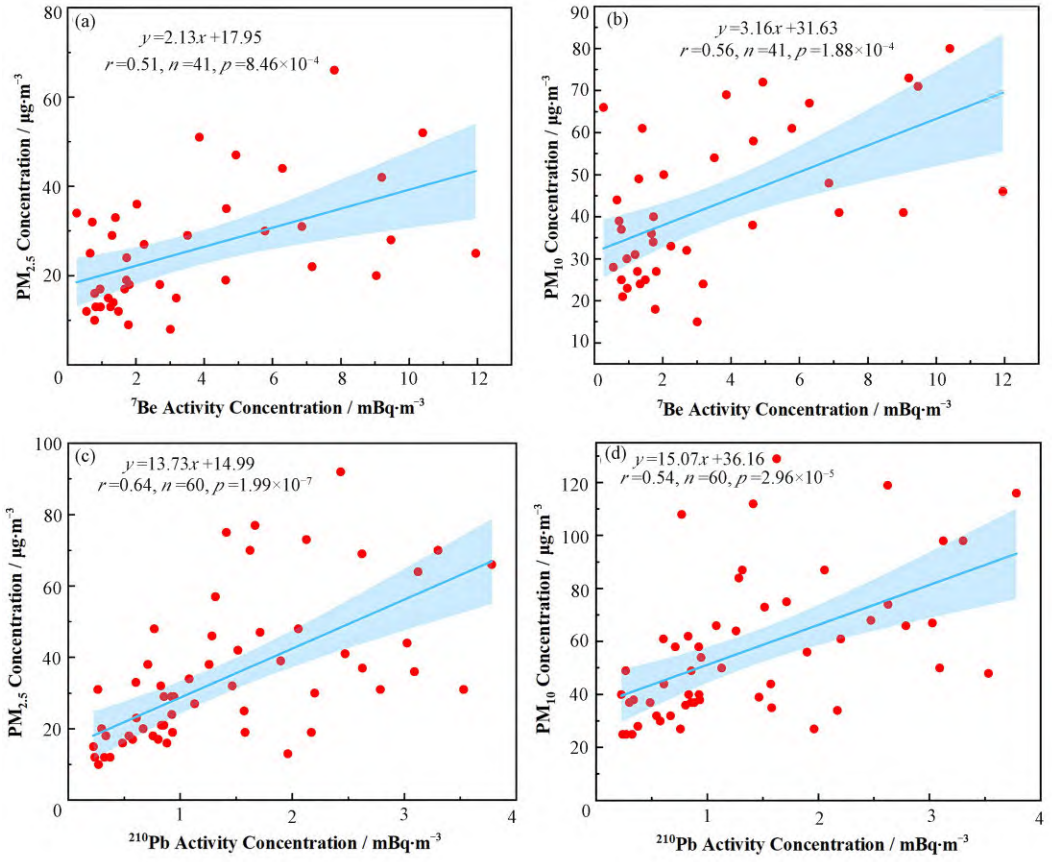


图6 ^{7}Be与$PM_{2.5}$ (a),^{7}Be与PM_{10} (b),^{210}Pb与$PM_{2.5}$ (c),^{210}Pb与PM_{10} (d)的相关性分析(彩图见网络版)

Fig.6 Correlation analyses between ^{7}Be and $PM_{2.5}$ (a), ^{7}Be and PM_{10} (b), ^{210}Pb and $PM_{2.5}$ (c), ^{210}Pb and PM_{10} (d) (color online)

平洋。^{210}Pb来源于自下而上从土壤中释放到大气中的^{222}Rn衰变,而大陆气团相比于海洋气团拥有更高的^{222}Rn含量[11],且^{210}Pb形成后会吸附在$PM_{2.5}$、PM_{10}气溶胶上随大气进行长距离输运,而南宁市$PM_{2.5}$、PM_{10}浓度冬季最高、夏季最低。因此,冬季陆地来源气团中的^{222}Rn含量和颗粒物浓度都高于夏季的海源气团,这导致^{210}Pb活度浓度呈现冬季最高、夏季最低的特征。所以,^{210}Pb冬季最高、夏季最低,与东亚季风调控下的气溶胶长距离输运有关,^{210}Pb冬季的最高值主要是受北方的欧亚大陆陆源气团影响。

大气气溶胶中的^{7}Be接近70%在平流层形成,30%在对流层上部形成,大气气溶胶中^{7}Be的活度浓度主要受"春季泄漏"、水平方向的大气输送以及降雨的影响[32-33];^{210}Pb活度浓度主要受温度、降雨和气流运动等因素影响[32]。过去大量文献表明,降雨的淋洗作用,使得大气中^{7}Be和^{210}Pb的活度浓度在多雨的季节比在少雨的季节低[22-23,34-35]。广西的汛期大概是在每年的4~9月,占全年降水量的73%[36],而南宁市大气气溶胶中放射性核素^{7}Be和^{210}Pb活度浓度低值却可以出现在每年的6、7、8、11和12月,显然小时尺度的降雨不能充分解释^{7}Be和^{210}Pb的浓度的季节分布特点,降雨不是最终的影响因素。据林武

中国知网 https://www.cnki.net

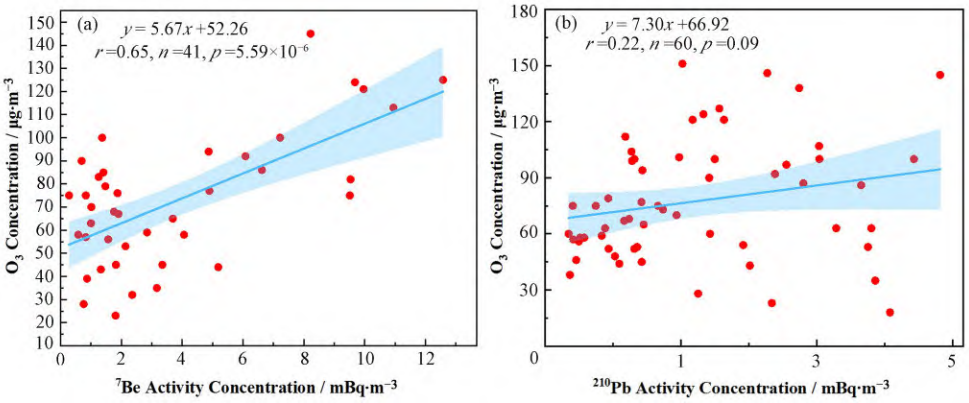


图7 ^{7}Be与O_3 (a)，^{210}Pb与O_3 (b)相关性分析（彩图见网络版）

Fig.7 Correlation analyses between ^{7}Be and O_3 (a), ^{210}Pb and O_3 (b) (color online)

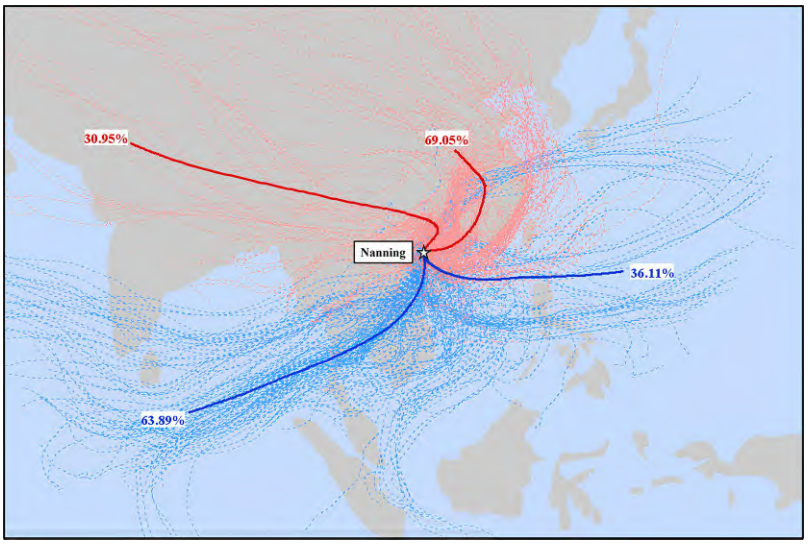


图8 2021年南宁市冬夏季气团来源7天逆轨迹聚类图（虚线为逆轨迹；实线为聚类分析结果；红色为2021年12月~2022年1月冬季；蓝色为2021年6~8月夏季）（彩图见网络版）

Fig.8 7-day inverse trajectory clustering map of winter and summer air mass sources in Nanning City in 2021 (dashed line is the inverse trajectory; solid line is the result of clustering analysis; red is the winter from December 2021 to January 2022; blue is the summer from June to August 2021) (color online)

辉等[37]提出的影响γ辐射空气吸收剂量出现“夏低冬高”的季节特征的主要因素是东亚季风影响下的海洋气团和大陆气团不同来源转换，本研究认为^{7}Be和^{210}Pb出现冬春高、夏秋低的季节特征可能主要受季风的调控。

引起南宁市^{7}Be活度浓度出现季节性分布差异的因素主要包括“春季泄漏”，季风调控下的陆、海源气团转换，而^{210}Pb的机制主要是季风调控下的陆、海源气团转换。^{7}Be和^{210}Pb都会吸附在颗粒物上随大气进行传输，而大气颗粒物浓度受控于季风调控下的陆源和海源气团转换。夏季气团来源于南方的海源气团，这导致^{7}Be和^{210}Pb活度浓度在夏季最低。冬季气团来源于北方的陆源气团，这导致^{210}Pb活度浓度在冬季最高，^{7}Be虽然也受气团来源的影响，但由于“春季泄漏”，其浓度会在春季达到最高值。季风调控下的颗粒物浓度的季节变化特征导致^{7}Be和^{210}Pb整体表现出夏秋低，冬春高的季节分布特征。^{7}Be与O_3的良好相关性佐证了^{7}Be在春季达到最大值的原因可能是春季发生在中纬度地区的“春季泄漏”，而造成^{210}Pb在冬季达到最大值的原因可能是冬季来源于北方大陆气团中的^{210}Pb母体^{222}Rn含量较高。

2.3 ^{7}Be和^{210}Pb纬度和高度效应

从北半球纬向上看，前人研究表明，^{7}Be和^{210}Pb活度浓度在中纬度地区达到峰值（^{7}Be在40°N~60°N[38-39]达到峰值），往赤道和北极地区浓度不断降低[7]。本研究在测量南宁市^{7}Be和^{210}Pb活度浓度的基础上，整合全国17个地区的^{7}Be和^{210}Pb活度浓度数据对比发现，^{210}Pb在我国空间分布上存在纬度效应，^{7}Be在我国空间分布上存在纬度和高度效应。

如图9所示，受纬度效应影响，地处40°N左右

中国知网 https://www.cnki.net

以北的北京地区^{210}Pb活度浓度均值（3.20±0.24）mBq·m^{-3}，为40°N左右以南地区（青岛、瓦里关山、合肥、绵阳、上海、武汉、杭州、观凤山、昆明、厦门、广州、深圳以及南宁）均值（1.48±0.06）mBq·m^{-3}的2.2倍，这是由于^{210}Pb主要来源于土壤析出的^{222}Rn在大气中的衰变，其吸附在颗粒物上随近地表大气进行水平迁移，这是一个自下而上的过程。故大气中颗粒物浓度是大气中^{210}Pb活度浓度的一个主要影响因素，受东亚季风的影响，冬季气团裹挟的颗粒物会从高纬度地区扩散到低纬度地区，高纬度地区受到欧亚大陆气团的影响会比低纬度地区更加显著，高纬度地区颗粒物的浓度相对于低纬度地区也会更高，此外，高纬度地区由于气候寒冷，冬季供暖系统燃烧产生的颗粒物也会相比于低纬度地区更多。所以，高纬度地区相较于低纬度地区会更多地受到冬季西北陆源风带来的大量颗粒物以及冬季供暖系统的燃烧产生的大量颗粒物的影响[39]，40°N左右以北地区^{210}Pb活度浓度会显著高于40°N左右以南地区。观凤山地区土壤中U-Ra系含量较高[13]，^{210}Pb的母体^{222}Rn释放量大，这可能导致观凤山地区^{210}Pb活度浓度较其他40°N左右以南地区更高。

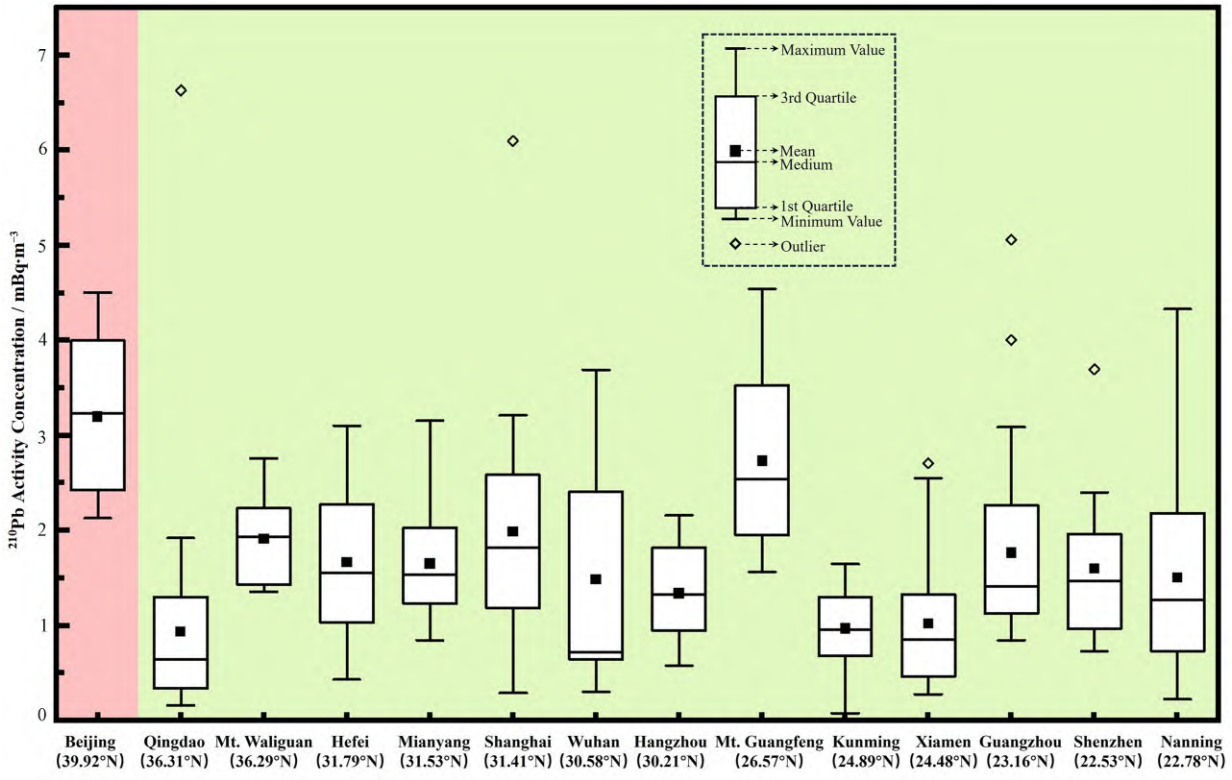


图9　中国14个地区（北京[15]、青岛[40]、瓦里关山[24]、合肥[19]、绵阳[14]、上海[25]、武汉[20]、杭州[26]、观凤山[13]、昆明[21]、厦门[35]、广州[22]、深圳[27]、南宁）^{210}Pb活度浓度水平箱型图（红色区域：40°N左右以北地区；绿色区域：40°N左右以南地区）（彩图见网络版）

Fig.9　Box plots of ^{210}Pb activity levels in 14 areas (Beijing[15], Qingdao[40], Mt. Waliguan[24], Hefei[19], Mianyang[14], Shanghai[25], Wuhan[20], Hangzhou[26], Mt. Guanfeng[13], Kunming[21], Xiamen[35], Guangzhou[22], Shenzhen[27], Nanning) of China (red area: area north of about 40°N; green area: areas south of about 40°N) (color online)

如图10（a）所示，受纬度效应的影响，35°N左右以北地区（北京、青岛和西安）近地表空气中^{7}Be活度浓度均值（7.44±0.26）mBq·m^{-3}，为35°N左右以南地区（合肥、武汉、昆明、厦门、广州、深圳以及南宁）均值（3.92±0.19）mBq·m^{-3}的1.9倍，这是因为春季中高纬度地区大气环流变化，平流层和对流层之间的交换加剧，使得更多的^{7}Be从平流层进入对流层。这种发生在中高纬度地区的“春季泄漏”现象导致了^{7}Be在40°N~60°N[38-39]达到最高值，所以35°N左右以北地区近地表空气中^{7}Be活度浓度会显著高于35°N左右以南地区。如图10（b）所示，受高度效应的影响，^{7}Be活度浓度：瓦里关山（（14.65±0.67）mBq·m^{-3}，海拔3 810 m）>兰州地区（（8.52±0.32）mBq·m^{-3}，海拔1 572 m）>观凤山地区（（4.83±0.26）mBq·m^{-3}，海拔1 080 m）>绵阳地区（（1.90±0.32）mBq·m^{-3}，海拔511 m），这是因为高海拔地区大气中的宇宙射线更强，而^{7}Be主要来源于平流层中经宇宙射线照射后高能粒子的裂解，形成的^{7}Be通过“春季泄漏”从平流层进入对流层，随后通过干湿沉降迁移至地表。这是一个自上而下的迁移过程，所以高海拔地区^{7}Be活度浓度较低海拔地区更高。

中国知网　https://www.cnki.net

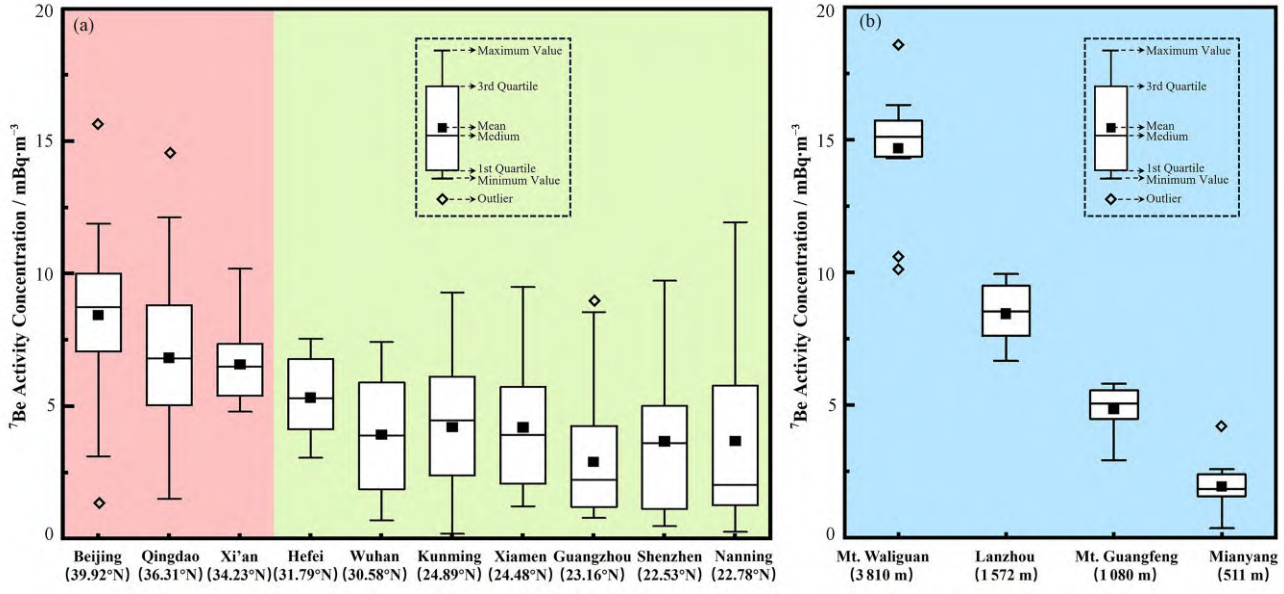


图10 中国14个地区（瓦里关山[41]、观凤山[13]、绵阳[14]、北京[42]、青岛[16]、兰州[17]、西安[18]、合肥[19]、武汉[20]、昆明[21]、厦门[35]、广州[22]、深圳[23]、南宁）^{7}Be活度浓度水平箱型图：(a) 受纬度效应影响地区的^{7}Be活度浓度水平箱型图；(b) 受高度效应影响地区的^{7}Be活度浓度水平箱型图（红色区域：35°N左右以北地区；绿色区域：35°N左右以南地区；蓝色区域：高度效应影响地区）（彩图见网络版）

Fig.10 Box plots of ^{7}Be activity levels in 14 areas (Mt. Waliguan[41], Mt. Guanfeng[13], Mianyang[14], Beijing[42], Qingdao[16], Lanzhou[17], Xi'an[18], Hefei[19], Wuhan[20], Kunming[21], Xiamen[35], Guangzhou[22], Shenzhen[23], Nanning) of China: (a) Box plot of ^{7}Be activity levels in areas subject to latitudinal effects; (b) Box plot of ^{7}Be activity levels in areas subject to altitudinal effects (red areas: areas north of about 35°N; green areas: areas south of about 35°N; blue areas: areas subject to altitudinal effects) (color online)

2.4 ^{7}Be和^{210}Pb辐射剂量时空分布差异评估

通过呼吸进入到人体的放射性核素会在人体内部发生内照射，产生辐射剂量。根据全国17个地区的^{7}Be和^{210}Pb冬春季和夏秋季活度浓度均值可估算出冬春季^{7}Be和^{210}Pb所致年待积有效剂量均值分别为2.73×10^{-3} μSv·a^{-1}、42.08 μSv·a^{-1}，夏秋季^{7}Be和^{210}Pb所致年待积有效剂量均值分别为2.37×10^{-3} μSv·a^{-1}、31.00 μSv·a^{-1}，冬春季^{7}Be和^{210}Pb所致的辐射剂量约为夏秋季的1.4倍。整合全国17个地区的^{7}Be和^{210}Pb的活度浓度监测数据对暴露于这两种放射性核素的年待积有效剂量进行估算，结果如表1和表2所示。40°N左右以北地区^{7}Be和^{210}Pb所致年待积有效剂量均值分别为3.57×10^{-3} μSv·a^{-1}、65.48 μSv·a^{-1}，35°N左右以南地区分别为1.78×10^{-3} μSv·a^{-1}、32.75 μSv·a^{-1}，北部地区^{7}Be和^{210}Pb的剂量约为南部地区的2.0倍。

据2020年中华人民共和国生态环境部全国辐射环境质量报告给出的^{7}Be和^{210}Pb活度浓度范围[43]可大致估算出全国^{7}Be所致年待积有效剂量范围为（1.62×10^{-5}~9.36×10^{-3}）μSv·a^{-1}，^{210}Pb所致年待积有效剂量范围为0.80~381.17 μSv·a^{-1}。据表1可计算出17个地区的^{7}Be和^{210}Pb平均活度浓度分别为（5.81±0.17）mBq·m^{-3}、（1.64±0.04）mBq·m^{-3}，两者所致年待积有效剂量均值分别为2.47×10^{-3} μSv·a^{-1}、33.57 μSv·a^{-1}。^{7}Be的活度浓度约为^{210}Pb的3.5倍，但^{210}Pb所致年待积有效剂量比^{7}Be大4个数量级。

3 结语

1）时间分布上^{7}Be和^{210}Pb活度浓度整体冬春高、夏秋低，但^{7}Be最高值出现在春季，而^{210}Pb出现在冬季。^{7}Be和^{210}Pb会吸附在颗粒物上随大气进行传输，季风调控下的颗粒物浓度的季节性变化导致^{7}Be和^{210}Pb整体呈现出冬春高、夏秋低的季节分布特征。宇生放射性核素^{7}Be与O_3的具有良好相关性，佐证了自上而下的“春季泄漏”现象是造成^{7}Be在春季达到最高值的主要原因，而^{210}Pb主要来源于自下而上从土壤中释放的^{222}Rn在大气中的衰变过程，与地表气团的水平输送有关，其在冬季的最高值受北方的欧亚大陆陆源气团影响。

2）^{7}Be和^{210}Pb活度浓度在空间分布上存在差异：纬向上，40°N左右以北地区的^{210}Pb活度浓度均值（3.20±0.24）mBq·m^{-3}，为40°N左右以南地区（1.48±0.06）mBq·m^{-3}的2.2倍，可能与冬季西北陆源气团带来的大量颗粒物和冬季供暖系统的燃烧过程释放^{222}Rn并载带子体^{210}Pb有关；35°N左右以北地区^{7}Be活度浓度均值（7.44±0.26）mBq·m^{-3}，为35°N左右以南地区均值（3.92±0.19）mBq·m^{-3}的1.9倍，这是由于春季发生在中纬度地区^{7}Be的“春季泄

中国知网 https://www.cnki.net

表1 中国17个地区^{7}Be对人体产生的年待积有效剂量
Table 1 Annual cumulative effective doses of ^{7}Be to humans in 17 areas of China

城市 City	呼吸类型 Respiration type	^{7}Be年待积有效剂量 ^{7}Be annual cumulative effective doses / μSv·a^{-1}
瓦里关山 Mt. Waliguan[41]	M	5.96×10^{-3}
	S	6.55×10^{-3}
北京 Beijing[42]	M	3.40×10^{-3}
	S	3.74×10^{-3}
天津 Tianjin[33]	M	2.73×10^{-3}
	S	3.00×10^{-3}
青岛 Qingdao[16]	M	2.77×10^{-3}
	S	3.04×10^{-3}
兰州 Lanzhou[17]	M	3.46×10^{-3}
	S	3.81×10^{-3}
西安 Xi'an[18]	M	2.71×10^{-3}
	S	2.98×10^{-3}
观凤山 Mt. Guanfeng[13]	M	1.94×10^{-3}
	S	2.14×10^{-3}
合肥 Hefei[19]	M	2.16×10^{-3}
	S	2.38×10^{-3}
绵阳 Mianyang[14]	M	7.70×10^{-4}
	S	8.47×10^{-4}
武汉 Wuhan[20]	M	1.59×10^{-3}
	S	1.75×10^{-3}
昆明 Kunming[21]	M	1.75×10^{-3}
	S	1.92×10^{-3}
厦门 Xiamen[35]	M	1.71×10^{-3}
	S	1.88×10^{-3}
广州 Guangzhou[22]	M	1.17×10^{-3}
	S	1.29×10^{-3}
深圳 Shenzhen[23]	M	1.70×10^{-3}
	S	1.87×10^{-3}
南宁 Nanning	M	1.49×10^{-3}
	S	1.64×10^{-3}

注：新呼吸道模型中给出的缺省肺呼吸类型，可分为中速（moderate[M]）和慢速（slow[S]）
Notes: The default lung respiration types given in the new respiratory model, which can be categorised as moderate[M] and slow[S]

表2 中国17个地区^{210}Pb对人体产生的年待积有效剂量
Table 2 Annual cumulative effective doses of ^{210}Pb to humans in 17 areas of China

城市 City	呼吸类型 Respiration type	^{210}Pb年待积有效剂量 ^{210}Pb annual cumulative effective doses / μSv·a^{-1}
瓦里关山 Mt. Waliguan[24]	F	13.13
	M	16.04
	S	81.68
北京 Beijing[15]	F	23.26
	M	28.43
	S	144.75
天津 Tianjin[33]	F	7.73
	M	9.45
	S	48.10
青岛 Qingdao[40]	F	6.78
	M	8.29
	S	42.20
观凤山 Mt. Guanfeng[13]	F	20.42
	M	24.96
	S	127.06
合肥 Hefei[19]	F	12.11
	M	14.80
	S	75.33
绵阳 Mianyang[14]	F	12.03
	M	14.71
	S	74.87
上海 Shanghai[25]	F	14.51
	M	17.74
	S	90.30
武汉 Wuhan[20]	F	10.87
	M	13.28
	S	67.61
杭州 Hangzhou[26]	F	9.55
	M	11.68
	S	59.44
昆明 Kunming[21]	F	6.86
	M	8.38
	S	42.65
厦门 Xiamen[35]	F	6.20
	M	7.58
	S	38.57
广州 Guangzhou[22]	F	12.91
	M	15.78
	S	80.32
深圳 Shenzhen[27]	F	11.52
	M	14.08
	S	71.70
南宁 Nanning	F	11.01
	M	13.46
	S	68.52

注：新呼吸道模型中给出的缺省肺呼吸类型，可分为快速（fast[F]）、中速（moderate[M]）和慢速（slow[S]）
Notes: The default lung respiration types given in the new respiratory model, which can be categorised as fast[F],moderate[M], and slow[S]

漏”。高度上，高海拔地区^{7}Be活度浓度大于低海拔地区，这是因为^{7}Be自上而下从平流层到对流层的迁移过程使得高海拔地区浓度较低海拔地区更高。

3）冬春季^{7}Be和^{210}Pb所致的辐射剂量（42.08 μSv·a^{-1}）约为夏秋季（31.00 μSv·a^{-1}）的1.4倍。40°N左右以北地区^{7}Be和^{210}Pb所致年待积有效剂量（65.48 μSv·a^{-1}）为35°N左右以南地区（32.75 μSv·a^{-1}）的2.0倍。^{7}Be和^{210}Pb所致年待积有

中国知网 https://www.cnki.net

效剂量均值分别为2.47×10^{-3} μSv·a^{-1}、33.57 μSv·a^{-1}。

作者贡献声明 黄思宇负责数据分析、数据处理和稿件撰写；林武辉负责提供数据的分析指导和论文的理论指导与撰写；何贤文负责实验样品的采集制备，数据收集整理；林晓东负责提供数据的分析指导。

参考文献

1 Lin W, Chen L, Yu W, *et al*. Radioactivity impacts of the Fukushima Nuclear Accident on the atmosphere[J]. Atmospheric Environment, 2015, **102**: 311 – 322. DOI: 10.1016/j.atmosenv.2014.11.047.

2 林武辉, 杜金秋, 拓飞, 等. 基于海洋放射性核素时空演化体系的海洋核安全评估技术[J]. 核安全, 2024, **23**(3): 37 – 44. DOI: 10.16432/j.cnki.1672-5360.2024.03.018.
LIN Wuhui, DU Jinqiu, TUO Fei , *et al*. Marine nuclear safety assessment technology based on the spatial and temporal evolution system of marine radionuclides[J]. Nuclear Safety, 2024, **23**(3): 37 – 44. DOI: 10.16432/j.cnki.1672-5360.2024.03.018.

3 陈文, 宋宏涛, 魏洪源, 等. 意外吸入核素的促排现状概述[J]. 辐射研究与辐射工艺学报, 2012, **30**(1): 8 – 13.
CHEN Wen, SONG Hongtao, WEI Hongyuan, *et al*. An overview of the current status of nuclide excretion by accidental inhalation[J]. Journal of Radiation Research and Radiation Processing, 2012, **30**(1): 8 – 13.

4 闵锐. 辐射危害流行病学调查与医源性辐射危害评估[J]. 辐射研究与辐射工艺学报, 2011, **29**(2): 77 – 83.
MIN Rui. Epidemiological investigation of radiation hazards and assessment of medical radiation hazards[J]. Journal of Radiation Research and Radiation Processing. 2011, **29**(2): 77 – 83.

5 Dibb J E, Talbot R W, Gregory G L. Beryllium 7 and lead 210 in the western hemisphere Arctic atmosphere: Observations from three recent aircraft-based sampling programs[J]. Journal of Geophysical Research: Atmospheres, 1992, **97**(D15): 16709 – 16715. DOI: 10.1029/91jd01807.

6 Koch D M, Jacob D J, Graustein W C. Vertical transport of tropospheric aerosols as indicated by ^{7}Be and ^{210}Pb in a chemical tracer model[J]. Journal of Geophysical Research: Atmospheres, 1996, **101**(D13): 18651 – 18666. DOI: 10.1029/96jd01176.

7 Zhang F L, Wang J L, Baskaran M, *et al*. A global dataset of atmospheric ^{7}Be and ^{210}Pb measurements: annual air concentration and depositional flux[J]. Earth System Science Data, 2021, **13**(6): 2963 – 2994. DOI: 10.5194/essd-13-2963-2021.

8 中华人民共和国国家质量监督检验检疫总局. 电离辐射防护与辐射源安全基本标准: GB 18871—2002[S]. 北京: 中国标准出版社, 2002.
General Administration of Quality Supervision, Inspection and Quarantine of the People's Republic of China. Basic standards for protection against ionizing radiation and for the safety of radiation sources: GB 18871—2002[S]. Beijing: Standards Press of China, 2002.

9 国家市场监督管理总局. 核事故应急情况下公众受照剂量估算的模式和参数: GB/T 17982—2018[S]. 北京: 中国标准出版社, 2018.
State Administration for Market Regulation. Models and parameters for calculating radiation doses to the public in the emergency of a nuclear accident: GB/T 17982—2018 [S]. Beijing: Standards Press of China, 2018.

10 Stein A F, Draxler R R, Rolph G D, *et al*. NOAA's HYSPLIT atmospheric transport and dispersion modeling system[J]. Bulletin of the American Meteorological Society, 2015, **96**(12): 2059 – 2077. DOI: 10.1175/bams-d-14-00110.1.

11 Chen X X, Lin W H, He X W, *et al*. Beryllium-7 and lead-210 are associated with an increase in the Arctic oscillation: evidence from atmospheric aerosols in a remote tropical region in East Asia[J]. Asia-Pacific Journal of Atmospheric Sciences, 2022, **58**(1): 65 – 82. DOI: 10.1007/s13143-021-00237-2.

12 万国江, 郑向东, Lee H N, 等. 瓦里关山与观风山近地面空气^{7}Be浓度季节性变化对比[J]. 地球化学, 2006, **35**(3): 257 – 264. DOI: 10.3321/j. issn: 0379-1726.2006.03.005.
WAN Guojiang, ZHENG Xiangdong, Lee H N, *et al*. Comparison of seasonal variations of near-surface air ^{7}Be concentrations in the Valiguan and Guanfeng mountains [J]. Geochimica, 2006, **35**(3): 257 – 264. DOI: 10.3321/j. issn:0379-1726.2006.03.005.

13 万国江, 郑向东, Lee H N, 等. 黔中气溶胶传输的^{210}Pb和^{7}Be示踪: II.月及年时间尺度的剖析[J]. 地球科学进展, 2010, **25**(5): 505 – 514.
WAN Guojiang, ZHENG Xiangdong, Lee H N, *et al*. ^{210}Pb and ^{7}Be tracing of aerosol transport in Qianzhong: II. Monthly and annual time scale profiles[J]. Advances in Earth Sciences, 2010, **25**(5): 505 – 514.

14 刘宇航, 黄英, 古川, 等. 绵阳地区近地面气溶胶中^{7}Be和^{210}Pb分布特征及其对O_3的示踪[J]. 辐射防护, 2020,

中国知网 https://www.cnki.net

40(6): 587 – 592.
LIU Yuhang, HUANG Ying, GU Chuan, *et al*. Distribution characteristics of ^{7}Be and ^{210}Pb in near surface aerosols in Mianyang area and their tracing of O_3 [J]. Radiation Protection, 2020, **40**(6): 587 – 592.

15 王欢, 孟庆华, 马永忠, 等. 2017~2020年北京地区大气气溶胶中^{7}Be和^{210}Pb放射性活度浓度监测与分析[J]. 中华放射医学与防护杂志, 2021, **41**(9): 690 – 694. DOI: 10.3760/cma.j.issn.0254-5098.2021.09.009.
WANG Huan, MENG Qinghua, MA Yongzhong, *et al*. Monitoring and analysis of activity concentrations of ^{7}Be and ^{210}Pb in atmospheric aerosol in Beijing from 2017 to 2020[J]. Chinese Journal of Radiological Medicine and Protection, 2021, **41**(9): 690 – 694. DOI: 10.3760/cma.j.issn.0254-5098.2021.09.009.

16 Yang Y L, Gai N, Geng C Z, *et al*. East Asia monsoon's influence on seasonal changes of beryllium-7 and typical POPs in near-surface atmospheric aerosols in mid-latitude City Qingdao, China[J]. Atmospheric Environment, 2013, **79**: 802 – 810. DOI: 10.1016/j.atmosenv.2013.07.021.

17 邬家龙, 孙卫, 王赟, 等. 兰州地区大气气溶胶中^{7}Be浓度[J]. 中国辐射卫生, 2011, **20**(3): 333 – 334. DOI: 10.13491/j.cnki.issn.1004-714x.2011.03.014.
WU Jialong, SUN Wei, WANG Yun, *et al*. Concentration of ^{7}Be in atmospheric aerosols in Lanzhou area[J]. Chinese Journal of Radiological Health, 2011, **20**(3): 333 – 334. DOI: 10.13491/j. cnki. issn. 1004-714x. 2011. 03.014.

18 常印忠, 王旭辉, 王世联, 等. 西安地区大气环境气溶胶样品中放射性核素监测[J]. 核技术, 2008, **31**(10): 796 – 800.
CHANG Yinzhong, WANG Xuhui, WANG Shilian, *et al*. Radionuclides monitoring in atmospheric aerosol samples in Xi'an[J]. Nuclear Techniques, 2008, **31**(10): 796 – 800.

19 杜勤, 顾先宝, 陈志, 等. 合肥市TSP和$PM_{2.5}$中^{7}Be和^{210}Pb浓度及变化研究[J]. 中国辐射卫生, 2020, **29**(5): 510 – 514. DOI: 10.13491/j.issn.1004-714X.2020.05.017.
DU Qin, GU Xianbao, CHEN Zhi, *et al*. Study on concentrations and changes of ^{7}Be and ^{210}Pb in TSP and $PM_{2.5}$ in Hefei[J]. Chinese Journal of Radiological Health, 2020, **29**(5): 510 – 514. DOI: 10.13491/j.issn.1004-714X.2020.05.017.

20 李少婷, 高雅, 卢奕夫, 等. 湖北部分地区气溶胶中放射性核素监测研究[J]. 核电子学与探测技术, 2019, **39**(6): 687 – 691.
LI Shaoting, GAO Ya, LU Yifu, *et al*. Study on the radionuclide monitoring of aerosol in some areas of Hubei [J]. Nuclear Electronics & Detection Technology, 2019, **39** (6): 687 – 691.

21 武荣国. 云南省三城市气溶胶中^{210}Pb、^{7}Be的长期变化趋势及与$PM_{2.5}$、PM_{10}和O_3关系研究[J]. 世界核地质科学, 2022, **39**(1): 130 – 138. DOI: 10.3969/j. issn. 1672-0636.2022.01.014.
WU Rongguo. Long-term trends of ^{210}Pb and ^{7}Be in aerosols from three cities in Yunnan Province and their relationship with $PM_{2.5}$, PM_{10} and O_3[J]. World Nuclear Geoscience, 2022, **39**(1): 130 – 138. DOI: 10.3969/j.issn. 1672-0636.2022.01.014.

22 吴家堡. 广州市大气^{7}Be和^{210}Pb含量分布、沉降通量和沉积速率研究[D]. 深圳: 深圳大学, 2020.
WU Jiabao. Study on atmospheric ^{7}Be and ^{210}Pb content distribution, sedimentation flux and sedimentation rate in Guangzhou[D]. Shenzhen: Shenzhen University, 2020.

23 丁敏霞, 苏玲玲, 刘国卿, 等. 深圳市大气^{7}Be沉降通量与气溶胶沉积速率[J]. 地球化学, 2017, **46**(1): 81 – 86. DOI: 10.3969/j.issn.0379-1726.2017.01.007.
DING Minxia, SU Lingling, LIU Guoqing, *et al*. Atmospheric depositional fluxes of ^{7}Be and depositional velocities of aerosols in Shenzhen[J]. Geochimica, 2017, **46**(1): 81 – 86. DOI: 10.19700/j.0379-1726.2017.01.007.

24 Zheng X D, Wan G J, Chen Z Y, *et al*. Measurement and meteorological analysis of ^{7}Be and ^{210}Pb in aerosol at Waliguan Observatory[J]. Advances in Atmospheric Sciences, 2008, **25**(3): 404 – 416. DOI: 10.1007/s00376-008-0404-y.

25 Deng B B, Zhong Q Q, Wang Q G, *et al*. Temporal variation of ^{210}Pb concentration in the urban aerosols of Shanghai, China[J]. Journal of Radioanalytical and Nuclear Chemistry, 2020, **323**(3): 1135 – 1143. DOI: 10.1007/s10967-020-07027-6.

26 曹钟港, 杨阳, 王莉莉, 等. 杭州地区大气^{210}Pb与^{210}Po水平及所致公众剂量评价[J]. 辐射防护, 2018, **38**(1): 8 – 14.
CAO Zhonggang, YANG Yang, WANG Lili, *et al*. The activity concentraction of ^{210}Pb and ^{210}Po in Hangzhou atmosphere and induced public dose assessment[J]. Radiation Protection, 2018, **38**(1): 8 – 14.

27 吴家堡, 李涌, 刘国卿, 等. 深圳市大气^{210}Pb的活度浓度、沉降通量和沉积速率研究[J]. 地球化学, 2021, **50** (2): 219 – 225. DOI: 10.19700/j.0379-1726.2021.02.008.
WU Jiabao, LI Yong, LIU Guoqing, *et al*. Activity concentrations, depositional fluxes and deposition

中国知网 https://www.cnki.net

velocities of ^{210}Pb in atmospheric aerosols of Shenzhen[J]. Geochimica, 2021, **50**(2): 219 – 225. DOI: 10.19700/j.0379-1726.2021.02.008.

28 Narazaki Y, Sakoda A, Takahashi S, *et al*. Cosmogenic ^{7}Be: Particle size distribution and chemical composition of ^{7}Be-carrying aerosols in the atmosphere in Japan[J]. Journal of Environmental Radioactivity, 2021, **237**: 106690. DOI: 10.1016/j.jenvrad.2021.106690.

29 Ismaeel A, Aba A, Al-Shammari H, *et al*. Activity size distributions of radioactive airborne particles in an arid environment: a case study of Kuwait[J]. Environmental Science and Pollution Research International, 2020, **27**(26): 33032 – 33041. DOI: 10.1007/s11356-020-09367-y.

30 覃连敬, 李美丽, 蒋岚, 等. 广州地区大气环境气溶胶样品放射性特征[J]. 核技术, 2016, **39**(9): 090501. DOI: 10.11889/j.0253-3219.2016.hjs.39.090501.
QIN Lianjing, LI Meili, JIANG Lan, *et al*. Radioactivity characteristics of atmospheric aerosol samples in Guangzhou[J]. Nuclear Techniques, 2016, **39**(9): 090501. DOI: 10.11889/j.0253-3219.2016.hjs.39.090501.

31 Marley N A, Gaffney J S, Drayton P J, *et al*. Measurement of ^{210}Pb, ^{210}Po, and ^{210}Bi in size-fractionated atmospheric aerosols: an estimate of fine-aerosol residence times[J]. Aerosol Science and Technology, 2000, **32**(6): 569 – 583. DOI: 10.1080/027868200303489.

32 Sambayev Y K, Zhumalina A G, Zhumadilov K S, *et al*. Temporal variation of atmospheric ^{7}Be and ^{210}Pb concentrations and their activity size distributions at Astana, Kazakhstan in Central Asia[J]. Journal of Radioanalytical and Nuclear Chemistry, 2020, **323**(1): 663 – 674. DOI: 10.1007/s10967-019-06968-x.

33 崔明, 于川, 高建政. 天津市大气气溶胶中^{7}Be、^{210}Pb和^{210}Po活度浓度水平及辐射剂量评估[J]. 辐射防护, 2023, **43**(5): 495 – 500.
CUI Ming, YU Chuan, GAO Jianzheng. A study of ^{7}Be, ^{210}Pb and ^{210}Po in the atmosphere of Tianjin and the committed effective dose from 2018 to 2020[J]. Radiation Protection, 2023, **43**(5): 495 – 500.

34 刘国卿, 罗奇, 潘远海, 等. 深圳市大气^{7}Be含量分布及其示踪意义[J]. 地球化学, 2014, **43**(1): 32 – 38. DOI: 10.19700/j.0379-1726.2014.01.004.
LIU Guoqing, LUO Qi, PAN Yuanhai, *et al*. Variations of airborne ^{7}Be in Shenzhen and its implication for atmospheric transport[J]. Geochimica, 2014, **43**(1): 32 – 38. DOI: 10.19700/j.0379-1726.2014.01.004.

35 门武, 林静, 王芬芬, 等. 基于^{7}Be、^{210}Pb和^{210}Po的厦门岛沿岸地区大气过程示踪研究及辐射剂量评估[J]. 应用海洋学学报, 2016, **35**(2): 266 – 274. DOI: 10.3969/J.ISSN.2095-4972.2016.02.016.
MEN Wu, LIN Jing, WANG Fenfen, *et al*. Atmospheric processes studies and radiation dose assessment based on ^{7}Be, ^{210}Pb and ^{210}Po around Xiamen Island[J]. Journal of Applied Oceanography, 2016, **35**(2): 266 – 274. DOI: 10.3969/J.ISSN.2095-4972.2016.02.016.

36 秦川, 何洁琳, 李艳兰, 等. 2021年广西气候概况[J]. 气象研究与应用, 2022, **43**(1): 84 – 89. DOI: 10.19849/j.cnki.CN45-1356/P.2022.1.15.
QIN Chuan, HE Jielin, LI Yanlan, *et al*. Climate overview of Guangxi in 2021[J]. Journal of Meteorological Research and Application, 2022, **43**(1): 84 – 89. DOI: 10.19849/j.cnki.CN45-1356/P.2022.1.15.

37 林武辉, 王诗玥, 黄亚萍, 等. 大气中γ辐射空气吸收剂量率的波动机制[J]. 中国环境科学, 2022, **42**(3): 1097 – 1103. DOI: 10.3969/j.issn.1000-6923.2022.03.013.
LIN Wuhui, WANG Shiyue, HUANG Yaping, *et al*. Mechanism of the variable γ radiation air absorbed dose rate in the atmosphere[J]. China Environmental Science, 2022, **42**(3): 1097 – 1103. DOI: 10.3969/j.issn.1000-6923.2022.03.013.

38 Gai N, Pan J, Yin X C, *et al*. Latitudinal distributions of activities in atmospheric aerosols, deposition fluxes, and soil inventories of ^{7}Be in the East Asian monsoon zone[J]. Journal of Environmental Radioactivity, 2015, **148**: 59 – 66. DOI: 10.1016/j.jenvrad.2015.06.011.

39 Wang H, Meng Q H, Ma Y Z, *et al*. Temporal variations of ^{7}Be and ^{210}Pb activity concentrations in the atmospheric aerosols during 2018 – 2019 in Beijing, China and their correlations with meteorological parameters[J]. Journal of Environmental Radioactivity, 2023, **262**: 107162. DOI: 10.1016/j.jenvrad.2023.107162.

40 Modibo O B, Tokonami S, Hosoda M, *et al*. ^{210}Pb and major ion concentrations in aerosols collected in Qingdao, a seaside area of China[J]. Radiation Environment and Medicine, 2021, **10**(1): 18 – 25. DOI: 10.51083/radiatenvironmed.10.1_18.

41 郑向东, 万国江, 汤洁, 等. 瓦里关山近地面气溶胶中^{7}Be和^{210}Pb的观测及其对O_3浓度变化的示踪[J]. 科学通报, 2005, **50**(1): 72 – 76. DOI: 10.3321/j.issn:0023-074X.2005.01.014.
ZHENG Xiangdong, WAN Guojiang, TANG Jie, *et al*. Observations of ^{7}Be and ^{210}Pb in near-surface aerosols in the Wariguan Mountains and their tracing of ozone

中国知网 https://www.cnki.net

concentration changes[J]. Chinese Science Bulletin, 2005, **50**(1): 72 – 76. DOI: 10.3321/j. issn: 0023-074X. 2005. 01.014.

42 Tan K Y, Yang Y L, Zhu X H, *et al*. Beryllium-7 in near-surface atmospheric aerosols in mid-latitude (40° N) City Beijing, China[J]. Journal of Radioanalytical and Nuclear Chemistry, 2013, **298**(2): 883 – 891. DOI: 10.1007/s10967-013-2524-9.

43 中华人民共和国生态环境部. 2020 全国辐射环境质量报告[R]. 北京, 2020: 25.
Ministry of Ecology and Environment of the People's Republic of China. 2020 annual report of the national radiation environment[R]. Beijing, 2020: 25.

中国知网 https://www.cnki.net

文章编号：1674-5566(2025)04-0887-09 DOI：10. 12024/jsou. 20241204725

涠洲岛珊瑚礁区有机氯农药的污染水平、来源和生物富集特征研究

秦贵帮[1,2,3]，张瑞杰[1,2,3]，王煜轩[1,2,3]，康亚茹[1,2,3]，史敬文[1,2,3]，王辰燕[1,2,3]，韩民伟[1,2,3]，余克服[1,2,3,4]

(1. 广西大学 海洋学院，广西 南宁 530004；2. 广西南海珊瑚礁研究重点实验室，广西 南宁 530004；3. 广西大学珊瑚礁研究中心，广西 南宁 530004；4. 南方海洋科学与工程广东省实验室(广州)，广东 广州 511458)

摘 要：为探究广西涠洲岛珊瑚礁区有机氯农药（Organochlorine pesticides，OCPs）的暴露情况，使用气相色谱串联三重四极杆质谱(GC-MS/MS)对涠洲岛周围西北、西南和东面3个方位的珊瑚礁区海水、沉积物、珊瑚宿主(珊瑚虫)组织和共生虫黄藻中7种OCPs的污染水平、来源和生物富集特征进行了研究。结果显示，涠洲岛珊瑚礁区海水普遍存在OCPs，滴滴涕(DDTs)是OCPs中的主要成分，其中海水$\sum_7$OCPs的含量为(119±118) pg/L，$\sum_6$DDTs的含量为(84.1±82.3) pg/L，沉积物、珊瑚宿主组织和虫黄藻中$\sum_7$OCPs的含量分别为(0.27±0.22) ng/g dw、(1.90±2.04) ng/g dw和(17.70±7.29) ng/g dw。珊瑚宿主组织和共生虫黄藻中7种目标OCPs的lgBAFs的平均值为2.04~3.44和2.25~4.06，表明共生虫黄藻比珊瑚宿主对OCPs具有更强的富集能力，这种更高的富集能力是否会带来更高的生态风险值得深入研究。生态风险评价结果显示，当前涠洲岛珊瑚礁区沉积物和海水中7种目标OCPs的生态风险都处于较低水平。来源解析结果显示，历史残留物质是涠洲岛珊瑚礁区DDTs的主要来源，其中以三氯杀螨醇产品为主。

关键词：珊瑚；有机氯农药；来源解析；生态风险评价；生物富集

中图分类号：X 592 **文献标志码：**A

珊瑚礁生态系统被誉为“海底热带雨林”和“海底花园”，其面积仅占整个海洋的不到0.2%，却为超过25%的海洋生物提供了生存空间，是海洋中最具生物生产力和多样性的生态系统。

但同时珊瑚礁生态系统也是敏感脆弱的[1]，人为对珊瑚礁的压力已经超过了珊瑚的再生能力，造成物种组成的急剧变化和严重的生态及经济损失[2]。在南海，由于过度捕捞、污染、疾病和气候变化等，活珊瑚覆盖率出现了急剧下降的问题[3-4]。由有毒物质(如农用化学品、工业毒素和生活垃圾等)引起的水质退化往往对近岸珊瑚造成更大程度的影响[4-5]。

化学污染物可以通过各种途径进入珊瑚礁系统，被认为是导致珊瑚礁系统衰退的重要因素之一。持久性有机污染物(Persistent organic pollutants，POPs)具有长距离运输、持久性、生物蓄积性和生物毒性等特点而备受关注。有机氯农药(Organochlorine pesticides，OCPs)是一种典型的POPs，可通过长距离大气输送、洋流和动物迁移等各种途径在局部和全球范围内传播，导致其在空气、海水、湖泊、沉积物和生物体内普遍存在[6-8]。现有数据表明，近年来由于与生产和使用有关的OCPs主要来源的减少，大多数OCPs的环境水平都有所下降。然而，由于二次排放，如旧库存(沉积物、土壤和水等)中的释放、少数含有OCPs的旧类型设备仍在使用，OCPs污染仍然值得进一步关注[9]。

涠洲岛位于北部湾东北部，是广西沿岸最大的岛屿，拥有典型的滨海珊瑚礁生态系统。在珊瑚生存严重受全球变暖影响的大背景下，涠洲岛拥有较高纬度的地理位置，是中国最高纬度的大面积珊瑚礁生长区域，可以为珊瑚生存提供一个

收稿日期：2024-12-10 **修回日期：**2025-04-30

基金项目：国家自然科学基金（42030502，42090041）；广西科技基地和人才专项（桂科AD25069075）

作者简介：秦贵帮(1998—)，男，硕士研究生，研究方向为海洋科学。E-mail：qguibang@163.com

通信作者：张瑞杰，E-mail：rjzhang@gxu.edu.cn

版权所有 ©《上海海洋大学学报》编辑部(CC BY-NC-ND 4.0)
Copyright © Editorial Office of Journal of Shanghai Ocean University (CC BY-NC-ND 4.0)

拥有较低温度海水的“避难所”,研究涠洲岛珊瑚生境对未来珊瑚向高纬度扩散生长的适应性有重要意义。然而有机污染物也在威胁着涠洲岛珊瑚的生存,已有研究揭露了2015、2016、2018年涠洲岛珊瑚礁区海水、鱼类、浮游生物、珊瑚宿主组织和黏液中的OCPs的污染水平[9-11],但对于为珊瑚宿主生存提供大部分能量的珊瑚共生虫黄藻体内的OCPs含量水平以及富集特征尚不明确。本研究的结果将有助于了解涠洲岛珊瑚礁区代表性OCPs的污染水平、来源与生态风险,为涠洲岛珊瑚礁生态系统的保护与修复提供科学依据与理论基础。

1 材料与方法

1.1 样品采集

本研究于2021年9月根据《海洋监测规范》(GB17378—2007)在北部湾涠洲岛珊瑚礁区西北、西南和东边3个区域(图1)采集了3个海水样品、6个沉积物样品和10个珊瑚样品。3个采样区域都是涠洲岛珊瑚覆盖率较高区域,与涠洲岛陆地的最短距离几乎一致。其中,位于西南的S1区域靠近种植大量甘蔗和香蕉的村庄,农业活动可能是OCPs的排放源之一。位于西北的S2区域位于港口附近,频繁活动的船只可能是DDT的重要来源。位于东边的S3区域靠近多个旅游景区。除污染源外,水文特征和生物地球化学转化过程也会在污染物的空间分布中发挥重要作用。由于采样区域水深不足10 m,本研究仅采集表层水样,每个样品采集25 L海水,用玻璃纤维滤膜(Whatman, GF/F, 0.7 μm)过滤,滤液以1 L/min速度透过净化后的聚氨酯泡沫(PUF)对溶解态OCPs进行现场富集。珊瑚及沉积物样品通过水肺潜水采集,采集的样品用铝箔样品袋封口进行低温保存。全部样品密封冷藏后运回实验室,在−20 °C的冰箱保存等待后续分析 。

1.2 目标物标准品、化学试剂与药品

选取六氯苯(HCB)和6种DDTs为主要目标化合物,2,4,5,6-四氯-间二甲苯(TCMX)、2,4,6-三氯联苯(PCB30)、2,2',3,4,4',5,6,6'-八氯联苯(PCB204)为3种回收率指示剂,^{13}C标记2,2',3,4,4',5'-六氯联苯($^{13}C_{12}$-PCB138)为内标化合物,它们均购自美国Accustandard公司。二氯甲烷(色谱纯)、正己烷(色谱纯)和丙酮(色谱纯)均购自上海安谱公司。70~230目中性氧化铝购自德国Merck公司,在烤箱250 ℃烘烤12 h,马弗炉450 ℃灼烧6 h,冷却后按质量加入3%蒸馏水活化。无水硫酸钠购自上海安谱公司,于马弗炉450 ℃灼烧6 h。80~200目硅胶购自德国Merck公司,烤箱180 ℃烘烤12 h,马弗炉450 ℃灼烧6 h,冷却后加入占总质量一半的硫酸进行酸化。

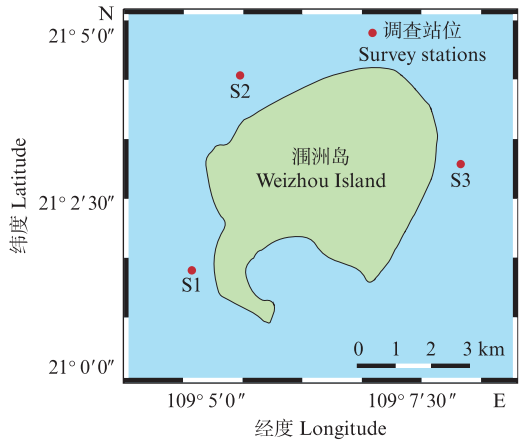


图1 涠洲岛珊瑚礁区采样点站位信息

Fig. 1 Station information of sampling points in the coral reef area of Weizhou Island

1.3 样品预处理

采用CAROSELLI等[12]的方法,使用高压水枪将珊瑚宿主组织与骨骼冲洗分离。冲洗液使用电动匀浆器以10 s/次机械破坏珊瑚宿主组织3次。匀浆液于4 ℃条件下5 000 r/min离心5 min,将共生虫黄藻从珊瑚宿主组织中分离,并收集离心管底部的共生虫黄藻,使用光学显微镜对收集到的虫黄藻进行形态学鉴定,确认收集到的是虫黄藻。上清液重复离心3次后,收集离心后的所有上清液和共生虫黄藻,其中上清液包含珊瑚宿主组织。将上清液和共生虫黄藻冷冻干燥以待OCPs的萃取。采用DING等[9]的方法,冷冻干燥后的珊瑚宿主组织和共生虫黄藻,在加入20 ng回收率指示剂(TCMX、PCB204、PCB30)后,使用体积比为1∶1的正己烷和丙酮混合溶剂在恒温水浴条件下索氏提取48 h。移取2 mL虫黄藻抽提液于4 mL规格的棕色瓶中,用温和的氮气吹扫浓缩提取液至刚刚盖住瓶底,加入丙酮以置换原混合溶剂(重复3次),使用Arnon法测定虫黄藻中叶绿素a(Chlorophyll a, *Chl*.a)的含量[13]。剩余抽提液使用旋转蒸发仪浓缩至约1 mL,加入3 mL正己烷继续浓缩以置换原溶剂,

重复3次。将提取液转移到4 mL棕色样品瓶中，使用温和的氮气将浓缩液吹扫至约1 mL。将浓缩液移入由上至下依次装有1 cm无水硫酸钠、3 cm酸性硅胶和3 cm中性氧化铝的玻璃层析柱进行分离和纯化。利用体积比为1∶1的正己烷和二氯甲烷混合溶剂洗脱玻璃层析柱，洗脱液装入15 mL规格的棕色样品瓶中。用温和的氮气将浓缩液吹扫至200 μL，加入100 ng $^{13}C_{12}$-PCB138作为内标，待仪器分析。

沉积物样品冷冻干燥，充分研磨过筛后混匀。准确称量10.00 g沉积物干样品，并用滤纸包裹置于抽提筒中以待OCPs的索氏抽提。另外再取2 g沉积物干样品于离心管中，加入1 mL 1 mol/L的盐酸溶液超声1.5 h，重复多次，直至去除全部无机碳。使用超纯水调节pH至中性后于烘箱中低温烘干，取100 mg干样品于元素分析仪上测定总有机碳百分数（TOC）。

富集海水样品的PUF冷冻干燥后放入抽提筒中等待抽提。沉积物和PUF，在加入20 ng回收率指示剂（TCMX、PCB204、PCB30）后，使用二氯甲烷在恒温水浴条件下索氏提取48 h。抽提液使用旋转蒸发仪浓缩至1 mL左右，加入约3 mL正己烷继续浓缩以置换原溶剂，重复3次后转移至4 mL棕色样品瓶中。后续处理方法与珊瑚和虫黄藻样品的处理方法一致。

1.4　仪器分析

使用安捷伦7890B气相色谱串联7000C三重四极杆质谱仪（GC-MS/MS）对样品进行分析。使用安捷伦公司生产的HP-5MS石英弹性毛细管柱（30 m×250 μm，0.25 μm）对OCPs进行分离。MS电离采用电子冲击（EI）源，在多反应监测（MRM）模式下进行数据采集[9]。7种目标OCPs、3种回收率指示剂和内标（ISTD）的GC-MS/MS参数见表1。

表1　目标OCPs、回收率指示剂及内标物的GC-MS/MS参数

Tab. 1　GC-MS/MS parameters of target OCPs, recovery indicators and internal standards

污染物 Contaminants	保留时间 Retention time/min	定量离子对 Quantitative ion pairs/(m/z)	定性离子对 Qualitative ion pairs/(m/z)	电离模式 Ionization mode
ISTD	23.4	371.9→301.9	299.9→229.9	+
HCB	10.6	283.8→213.9	283.8→248.8	+
o,p'-DDT	21.6	235.0→165.0	237.0→165.0	+
p,p'-DDT	23.3	235.0→165.0	237.0→165.0	+
o,p'-DDD	21.1	235.0→165.0	237.0→165.0	+
p,p'-DDD	22.6	235.0→165.0	237.0→165.0	+
o,p'-DDE	18.0	246.0→176.0	248.0→176.0	+
p,p'-DDE	21.1	246.0→176.0	316.0→246.0	+
TCMX	9.2	244.0→208.8	244.0→173.7	+
PCB204	25.9	429.8→359.8	427.8→357.8	+
PCB30	11.3	256.0→186.0	258.0→186.0	+

1.5　质量控制

整个实验过程严格按照相关标准，设置了实验室流程空白、野外空白、回收率指示剂、平行样和分析仪器检出限来进行质量控制。采用内标法定量分析目标OCPs含量。每批10个样品中加入实验室流程空白和对照样品来评估实验过程可能造成的污染，同时检测仪器的稳定性。回收率指示剂TCMX、PCB30和PCB204的回收率分别为（74±15）%、（85±13）%和（102±9）%。OCPs含量未经回收率指示剂校正。仪器的检出限（IDLs）定义为信噪比为3时的含量。

1.6　统计分析

采用Shapiro-Wilk检验数据的正态性。当数据服从正态分布时，分组数据之间的差异和相关性分别采用独立样本*t*检验和皮尔逊相关性检验（IBM SPSS Statistics 26.0），否则采用非参数检验和非参数秩相关性检验。$P<0.05$时为差异性或相关性显著，$P<0.01$为差异性或相关性极显著。

1.7　生态风险评估

使用生物的半数效应浓度（EC_{50}，ng/L）或半数致死浓度（LC_{50}，ng/L）计算海水或沉积物中OCPs的风险熵（RQ），由公式（1）和（2）计算：

$$PNEC = \frac{EC_{50}}{AF} 或 PNEC = \frac{LC_{50}}{AF} \quad (1)$$

$$RQ = \frac{MEC}{PNEC} \quad (2)$$

式中：MEC为海水或沉积物中OCPs的环境浓度或含量，ng/L或ng/g，如果未检出则使用1/2 MDLs代替计算；PNEC为OPEs的预测无效应浓度或含量，ng/L或ng/g；AF为评价因子，取1 000。当RQ≥1.0表示高风险，0.1≤RQ<1.0表示中风险，0.01≤RQ<0.1表示低风险[14]。

2 结果与讨论

2.1 涠洲岛珊瑚礁区海水和沉积物中有机氯农药的含量水平和组成特征

如表2的研究结果所示，OCPs在涠洲岛珊瑚礁区普遍存在，海水中7种目标OCPs检出率均达到100%，其含量之和（$\sum_7$OCPs）平均为（119±118）pg/L，其中$\sum_6$DDTs的含量为（84.1±82.3）pg/L，与2018年涠洲岛海水[$\sum_6$DDTs（55.9±12.0）pg/L]相比[11]，含量显著增加（P<0.01）。$\sum_6$DDTs浓度[(84.1±82.3) pg/L]低于中国海水水质标准（GB3097—1997）的最严格限值（<50 ng/L），满足一类水体要求。沉积物中7种目标OCPs的检出率相对海水较低，为17%~83%，$\sum_7$OCPs平均含量为（0.27±0.22）ng/g dw（干质量），与中国14个典型潮间带的OCPs平均含量（0.655~211.109 ng/g）相比[15]，处于较低水平。沉积物以珊瑚砂为主，珊瑚和贝壳碎片较多，无机碳酸盐在沉积物中的质量占比为69%~94%。因此，沉积物中TOC使用无机碳酸盐的质量进行了校准。沉积物中TOC范围为0.30%~2.59%，校准后TOC范围为0.09%~0.48%。沉积物中$\sum_7$OCPs与校准后的TOC具有显著相关性（P<0.05），表明TOC是影响该区域沉积物中OCPs水平的主要因素之一。如图2所示，不同的DDT在海水和沉积物中有不同的组成，在海水中p，p'-DDE占比最高，达到90%；沉积物中o，p'-DDD、p，p'-DDE和p，p'-DDD为主要成分，分别占38%、31%和18%。如图3所示，不同采样区域相比，位于港口附近的S2区域水体中$\sum_7$OCPs含量最高，并远远高于S1和S3区域，这可能与船舶防污漆中DDTs的释放相关。S1站点并没有预想中较高的OCPs含量，说明相比于港口，农业源残留的OCPs较低。

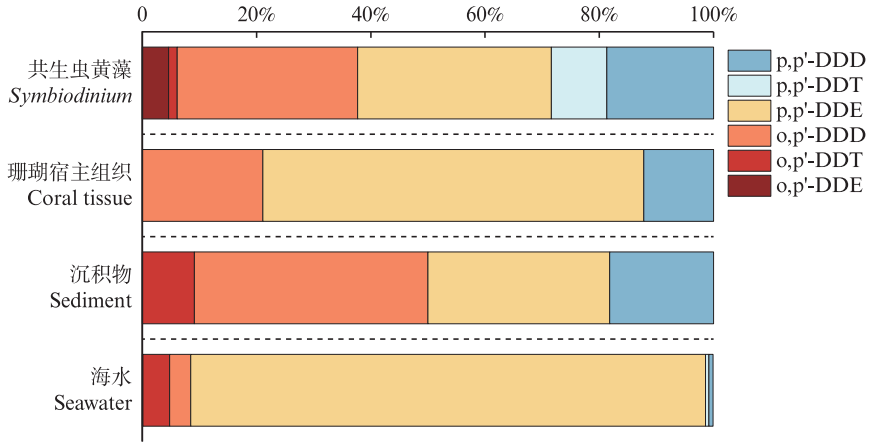


图2 涠洲岛珊瑚礁区海水、沉积物、珊瑚宿主组织和共生虫黄藻中DDTs的组成特征

Fig. 2 Composition of DDTs in seawater, sediment, coral tissues and *Symbiodinium* in the coral reef area of Weizhou Island

结果表明，在涠洲岛珊瑚礁区DDTs占检出OCPs中的较大部分，这与过去几十年中国大量生产和使用DDT有关。KANG等[11]对涠洲岛珊瑚礁区、DING等[9]对南海鱼类以及LYU等[15]对中国潮间带沉积物的研究结果也得出了类似的结论。在1983年禁止DDT在农业生产的使用之前，中国商业用途的DDTs生产总量超过43万t。直接使用技术性DDT和含DDT的三氯杀螨醇都可能使DDT进入环境。从1950年到2005年，中国平均每年利用250 t DDT来生产防污涂料[16]，研究表明，防污涂料是中国渔港DDT的重要来源。尽管在1983年斯德哥尔摩公约和2014年实施的相关政策已经禁止了技术性DDT和防污涂料中加入DDT，但是我国目前仍然存在4个

DDTs的来源，包括历史上使用DDTs造成过污染的土壤和海洋等、直接用于进行疾病防控（如疟疾等）的DDTs和含有DDTs的防污涂料以及三氯杀螨醇[15]。

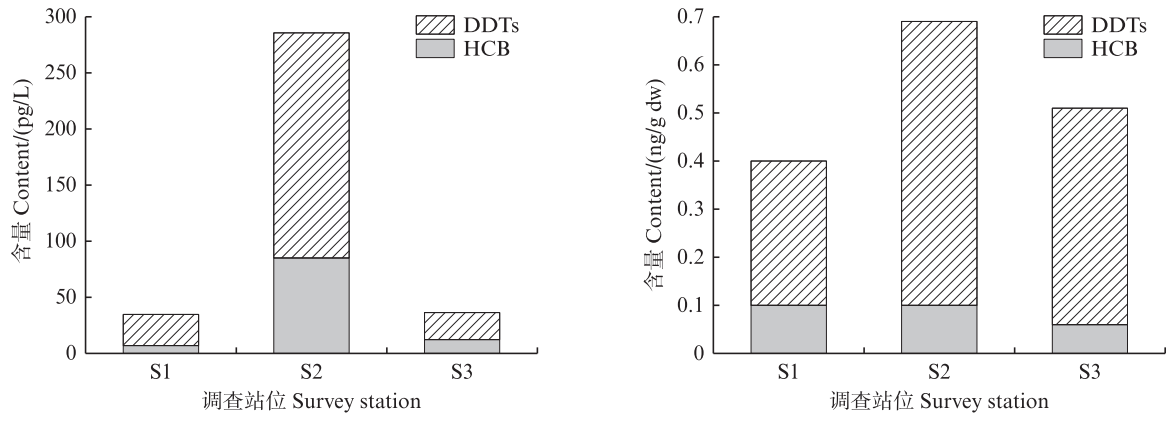
表2　涠洲岛珊瑚礁区海水和沉积物中OCPs检出率及含量水平

Tab. 2　Detection rates and concentrations of OCPs in seawater and sediments in the coral reef area of Weizhou Island

污染物 Contaminants	海水 Seawater/（pg/L）			沉积物 Sediment/（ng/g）		
	检出率 Detection rate	范围 Range	平均值±标准差 Mean±SD	检出率 Detection rate	范围 Range	平均值±标准差 Mean±SD
HCB	100%	6.93~85.18	34.82±35.57	83%	nd~0.10	0.04±0.03
o,p'-DDE	100%	0.04~0.20	0.10±0.07	50%	nd~0.01	nd
o,p'-DDT	100%	0.09~9.83	3.98±4.21	33%	nd~0.09	0.02±0.03
o,p'-DDD	100%	0.43~8.02	3.15±3.45	50%	nd~0.22	0.09±0.09
p,p'-DDE	100%	19.90~180.75	75.59±74.27	83%	nd~0.15	0.07±0.05
p,p'-DDT	100%	0.21~0.85	0.49±0.27	17%	nd~0.02	nd
p,p'-DDD	100%	0.38~0.88	0.57±0.02	67%	nd~0.12	0.04±0.04
∑DDTs		23.96~200.40	84.07±82.27		nd~0.59	0.22±0.19
$\sum_7$OCPs		34.79~285.57	118.89±117.86		nd~0.69	0.27±0.22

注：nd表示无检出。

Notes：nd means no detected.



(a) 海水 Seawater　　(b) 沉积物 Sediment

图3　涠洲岛3个不同站位的海水和沉积物中OCPs的含量

Fig. 3　Concentrations of OCPs in seawater and sediments at three different stations near Weizhou Island

2.2　珊瑚宿主组织和共生虫黄藻中有机氯农药的含量水平和组成特征

珊瑚共生虫黄藻中$\sum_7$OCPs含量[（17.70±7.29）ng/g dw]显著高于珊瑚宿主组织中$\sum_7$OCPs含量[（1.90±2.04）ng/g dw]（P<0.01），其中珊瑚共生虫黄藻中DDTs的含量显著高于珊瑚宿主组织中DDTs的含量（P<0.01），但HCB含量两者之间并无显著差异（P>0.05）。珊瑚宿主组织中$\sum_6$DDTs含量与南海沿岸珊瑚宿主组织中$\sum_6$DDTs含量[（22.00±15.10）ng/g dw]和南海近海珊瑚宿主组织中$\sum_6$DDTs含量[（3.23±5.06）ng/g dw][10]相比处于较低水平。与2018年涠洲岛珊瑚礁区珊瑚宿主组织中$\sum_6$DDTs含量[（1.05±1.02）ng/g dw]相比略微增大（图4）。

珊瑚共生虫黄藻富集OCPs的能力比珊瑚宿主组织更强，这可能会严重阻碍共生虫黄藻为珊瑚宿主提供能量的效率，进一步影响珊瑚的生长状态，破坏整个珊瑚礁生态系统的稳定。

2.3　涠洲岛珊瑚宿主组织和共生虫黄藻中有机氯农药的生物富集特征

图5展示了7种目标OCPs在涠洲岛珊瑚宿主组织和共生虫黄藻中的lgBAFs，珊瑚宿主组织

和共生虫黄藻中7种目标OCPs的lgBAFs的平均值为2.04~3.44和2.25~4.06，表明总体上虫黄藻比珊瑚宿主表现出更强的对OCPs的富集能力。化合物的辛醇-水分配系数（Kow）通常被认为是揭示化合物亲脂性能大小的指标。涠洲岛珊瑚礁区中7种目标OCPs的lgBAFs和lgKow在珊瑚宿主组织和共生虫黄藻中相关性均不显著（P=0.544>0.05、P>0.05）。这可能是因为样本数量较少，削弱了lgBAFs和lgKow之间的相关性，抑或是珊瑚表层黏液的存在影响了组织和虫黄藻对污染物的吸收。除此之外，在涠洲岛珊瑚礁区内7种目标OCPs在海水与珊瑚之间的平衡应当还存在其他不确定的影响因素，例如OCPs在海洋生物体内被吸收的速率可能较慢，并且经历了降解等过程。环境因素（如温度、溶解有机碳等）也可能潜在影响着OCPs的生物富集能力[9]。REN等[17]认为，摄食模式也是生物群落中OCPs生物富集潜力的重要因素。因此，影响珊瑚富集污染物的因素需要通过室内实验进一步探索和分析。除此之外，珊瑚宿主组织和共生虫黄藻对OCPs的富集也可能反过来影响OCPs在环境中的分布，使得珊瑚礁区作为OCPs的汇集，让生活在珊瑚礁生态系统中的生物富集更多的OCPs，这一点也需要进一步开展实验探究。

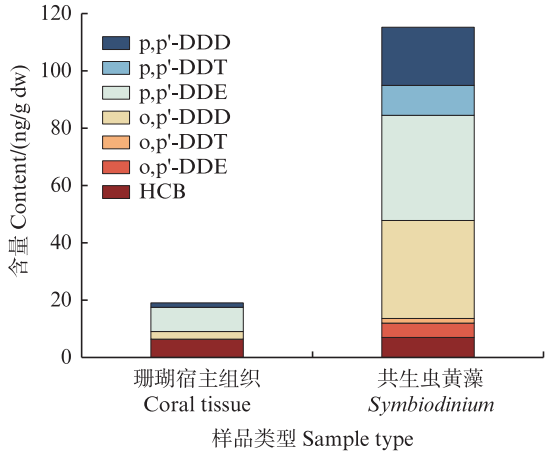


图4 涠洲岛珊瑚礁区珊瑚宿主组织和共生虫黄藻中OCPs的含量

Fig. 4 Concentrations of OCPs in coral tissues and *Symbiodinium* in the coral reef area of Weizhou Island

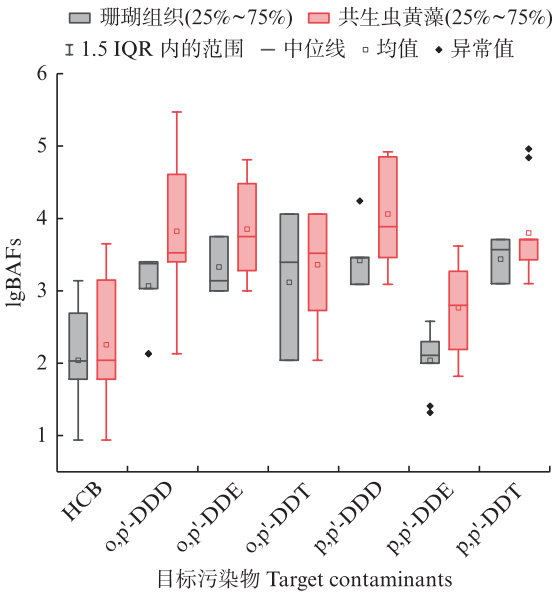


图5 涠洲岛珊瑚宿主组织和共生虫黄藻中OCPs的lgBAFs

Fig. 5 The lgBAFs of OCPs in the coral tissues and *Symbiodinium* of Weizhou Island

2.4 涠洲岛珊瑚礁区海水、沉积物与珊瑚中DDTs的来源解析

根据DDTs中DDT及其代谢产物DDE、DDD之间的不同组合比例可以指示DDTs的可能来源。根据图2可知海水中对DDTs贡献最大的是p,p' -DDE（90.1%），其次是o,p'-DDT（4.7%）、o,p'-DDD（3.7%）、p, p'-DDD（0.7%）、p, p'-DDT（0.6%）和o,p'-DDE（0.1%）；沉积物中贡献最大的是o,p'-DDD（40.9%）和p,p' -DDE（31.8%），其次是p,p'-DDD（18.2%）和o,p'-DDT（9.1%）。通常，DDT可以在好氧条件下生物降解为DDE，在厌氧条件下生物降解为DDD。表达式（DDE+DDD）/DDTs>0.5表明DDTs来自历史残留，而（DDE+DDD）/DDTs<0.5表示DDTs存在新的输入[18]。在本研究中，该比值为0.81~1.00，表明历史残留是涠洲岛珊瑚礁区DDTs的主要来源。o,p'-DDT与p,p'- DDT的比值可用于区分技术性DDT与三氯杀螨醇造成的DDT污染[19]。ZHOU等[21]的研究表明，技术性DDT的主要成分是p,p'-DDT（75%），o,p'-DDT（15%）和p,p'-DDE（5%），其他代谢产物的贡献<5%。o,p'-DDT /p,p'-DDT的值在技术性

DDT 中为 0.2 至 0.3，在三氯杀螨醇中为 1.3 至 9.3 或更高。本研究中 o，p'-DDT /p，p'-DDT 的数值为 0.44~15.67，表明该区域 DDTs 主要来源于三氯杀螨醇。

珊瑚宿主组织中存在多种 DDTs 低于检出限（o，p'-DDE、o，p'-DDT、p，p'-DDT），DDT 含量低于检测限可能是由于生物代谢转化过程的结果[20]，DDT 转化为 DDE、DDD、DDMS 和 DDMU 等高阶代谢产物。

2.5　涠洲岛珊瑚礁区海水、沉积物与珊瑚共生体中有机氯农药的生态风险评估

对比表 3 和表 4 的数据，根据公式 1 和 2 计算结果可知，涠洲岛珊瑚礁区沉积物和海水中 7 种目标 OCPs 的生态风险都处于较低水平。

当前关于 OCPs 对珊瑚礁无脊椎动物毒性的信息较少，无法评估 OCPs 对珊瑚礁共生体的慢性潜在影响。先前的一项实验室研究表明，千孔珊瑚（*Acropora millepora*）暴露在含低浓度（0.3~1.0 μg/L）硫丹的水环境中，会导致其沉降和变形减少 50%~100%[23]。结合 DING 等[24]之前的研究，涠洲岛珊瑚礁区生物体内多氯联苯（PCBs）和有机氯农药（OCPs）的部分化合物出现了随鱼类食物链持续积累的现象，结合食物链和食物网对有机氯农药的毒性研究是很有必要的。

表 3　涠洲岛珊瑚礁区表层沉积物中 OCPs 生态风险

Tab. 3　Ecological risks of OCPs in the surface sediments of the coral reef area of Weizhou Island

污染物名称 Name of pollutant	PNEC	WZ-01	WZ-02	WZ-03
HCB	3	3.47×10^{-2}	3.32×10^{-2}	1.89×10^{-2}
o,p'-DDD	37.9	5.69×10^{-4}	6.50×10^{-4}	5.74×10^{-4}
p,p'-DDD	9	2.59×10^{-3}	1.34×10^{-2}	1.03×10^{-2}
o,p'-DDT	30	3.33×10^{-4}	3.07×10^{-3}	9.61×10^{-4}
p,p'-DDT	9	1.11×10^{-3}	2.64×10^{-3}	1.11×10^{-3}
o,p'-DDE	15	5.69×10^{-4}	5.69×10^{-4}	5.69×10^{-4}
p,p'-DDE	53.5	2.33×10^{-3}	2.34×10^{-3}	3.14×10^{-3}

注：PNEC 数据来源于文献[21]。
Notes: The data are sourced from the literature [21].

表 4　涠洲岛珊瑚礁区海水中 OCPs 生态风险

Tab. 4　Ecological risks of OCPs in the seawater of the coral reef area of Weizhou Island

污染物名称 Name of pollutant	PNEC	WZ-01	WZ-02	WZ-03
DDTs	130	2.14×10^{-4}	1.5×10^{-3}	1.84×10^{-4}

注：PNEC 数据来源于文献，DDTs 表示 o，p'-DDD、p，p'-DDD、o，p'-DDT、p，p'-DDT、o，p'-DDE 和 p，p'-DDE 的总和[22]。
Notes: Data from the literature, DDTs represents the sum of o, p'-DDD, p, p'-DDD, o, p'-DDT, p, p'-DDT, o, p'-DDE and p, p'-DDE.

3　结论

2021 年 9 月涠洲岛周边珊瑚礁区海水中 7 种目标 OCPs 普遍存在，总含量为（119±118）pg/L，其中 $\sum_6$DDTs 达（84.1±82.3）pg/L，较 2018 年显著上升（P<0.01），表明海水 OCPs 污染加重，尤其是港口的人类活动会增加涠洲岛 OCPs 污染。沉积物中 7 种目标 OCPs 检出率为 17%~83%，$\sum_7$OCPs 含量为（0.27±0.22）ng/g dw，低于中国 14 个典型潮间带。共生虫黄藻中 $\sum_7$OCPs 含量[（17.7±7.29）ng/g dw]显著高于珊瑚宿主组织[（1.90±2.04）ng/g dw]（P<0.01），主要由 DDTs 贡献，HCB 在二者之间的差异不显著（P>0.05）。珊瑚宿主组织中 $\sum_6$DDTs 含量较 2018 年略增。珊瑚宿主组织与共生虫黄藻 7 种目标 OCPs 的 lgBAFs 均值分别为 2.04~3.44 和 2.25~4.06，虫黄藻比珊瑚宿主组织表现出更高的 OPCs 富集能力。来源解析表明，三氯杀螨醇相关产品是 DDTs 主要来源，且以历史残留为主。生态风险评估显示，当前该区域沉积物与水体中 7 种目标 OCPs 的生态风险均较低。

作者声明本文无利益冲突。

参考文献：

[1] 余克服. 珊瑚礁科学概论[M]. 北京：科学出版社，2018.
YU K F. Introduction to the science of coral reefs[M]. Beijing：China Science Publishing & Media Ltd.，2018.

[2] BELLWOOD D R，HUGHES T P，FOLKE C，et al. Confronting the coral reef crisis[J]. Nature，2004，429(6994)：827-833.

[3] BURKE L，SELIG E，SPALDING M. Reefs at risk in Southeast Asia[M]. World Resources Institute，2002.

[4] YU K F. Coral reefs in the South China Sea：their response to and records on past environmental changes[J]. Science China Earth Sciences，2012，55(8)：1217-1229.

[5] LEWIS S E，BRODIE J E，BAINBRIDGE Z T，et al. Herbicides：a new threat to the Great Barrier Reef[J]. Environmental Pollution，2009，157(8/9)：2470-2484.

[6] LOHMANN R，BREIVIK K，DACHS J，et al. Global fate of POPs：current and future research directions[J]. Environmental Pollution，2007，150(1)：150-165.

[7] WANG G，LU Y L，HAN J Y，et al. Hexachlorobenzene sources，levels and human exposure in the environment of China[J]. Environment International，2010，36(1)：122-130.

[8] SUN Y X，HU Y X，ZHANG Z W，et al. Halogenated organic pollutants in marine biota from the Xuande Atoll，South China Sea：levels，biomagnification and dietary exposure[J]. Marine Pollution Bulletin，2017，118(1/2)：413-419.

[9] DING Y，WU Z Q，ZHANG R J，et al. Organochlorines in fish from the coastal coral reefs of Weizhou Island，south China sea：levels，sources，and bioaccumulation[J]. Chemosphere，2019，232：1-8.

[10] KANG Y R，ZHANG R J，YU K F，et al. First report of organochlorine pesticides（OCPs）in coral tissues and the surrounding air-seawater system from the South China Sea：distribution，source，and environmental fate[J]. Chemosphere，2022，286：131711.

[11] KANG Y R，ZHANG R J，YU K F，et al. Organochlorine pesticides（OCPs）in corals and plankton from a coastal coral reef ecosystem，South China Sea[J]. Environmental Research，2022，214：114060.

[12] CAROSELLI E，FRAPICCINI E，FRANZELLITTI S，et al. Accumulation of PAHs in the tissues and algal symbionts of a common Mediterranean coral：skeletal storage relates to population age structure[J]. Science of the Total Environment，2020，743：140781.

[13] 段光明. 叶绿素含量测定中Arnon公式的推导[J]. 植物生理学通讯，1992，28(3)：221-222.
DUAN G M. Derivation of the Arnon formula in the determination of chlorophyll content[J]. Plant Physiology Communications，1992，28(3)：221-222.

[14] SONG W W，LIAO Z Y，WANG L F，et al. The distribution and ecological risks of antibiotics in the sediments from a diverging area of the bifurcated river：effects of hydrological properties[J]. Journal of Environmental Management，2022，320：115787.

[15] LYU M，LUAN X L，GUO X T，et al. A national-scale characterization of organochlorine pesticides（OCPs）in intertidal sediment of China：occurrence，fate and influential factors[J]. Environmental Pollution，2020，257：113634.

[16] YU H Y，SHEN R L，LIANG Y，et al. Inputs of antifouling paint-derived dichlorodiphenyltrichloroethanes（DDTs）to a typical mariculture zone（South China）：potential impact on aquafarming environment[J]. Environmental Pollution，2011，159(12)：3700-3705.

[17] REN J，WANG X P，WANG C F，et al. Biomagnification of persistent organic pollutants along a high-altitude aquatic food chain in the Tibetan Plateau：processes and mechanisms[J]. Environmental Pollution，2017，220：636-643.

[18] YU H Y，BAO L J，LIANG Y，et al. Field validation of anaerobic degradation pathways for dichloro diphenyl trichloroethane（DDT）and 13 metabolites in marine sediment cores from China[J]. Environmental Science & Technology，2011，45(12)：5245-5252.

[19] QIU X H，ZHU T，YAO B，et al. Contribution of dicofol to the current DDT pollution in China[J]. Environmental Science & Technology，2005，39(12)：4385-4390.

[20] CORSOLINI S，ANCORA S，BIANCHI N，et al. Organotropism of persistent organic pollutants and heavy metals in the Greenland shark *Somniosus microcephalus* in NE Greenland[J]. Marine Pollution Bulletin，2014，87(1/2)：381-387.

[21] 邹彬，张涵，王芝麟，等. 黄土高原北洛河表层沉积物中有机氯农药的分布、来源及生态风险评估[J]. 地球与环境，2023，51(6)：641-654
ZOU B，ZHANG H，WANG Z L，et al. Distribution，source and ecological risk assessment of organochlorine pesticides in surface sediments of the Beiluo River on the Loess Plateau[J]. Earth and Environment，2023，51(6)：641-654.

[22] 王意，刘静，久岚颖，等. 海水利用排放水中典型有机氯农药的环境安全性[J]. 环境监测管理与技术，2012，24(6)：35-38.
WANG Y，LIU J，JIU L Y，et al. Environmental safety on typical organochlorine pesticides in the drain of seawater utilization[J]. The Administration and Technique of Environmental Monitoring，2012，24(6)：35-38.

[23] MARKEY K L，BAIRD A H，HUMPHREY C，et al.

Insecticides and a fungicide affect multiple coral life stages［J］. Marine Ecology Progress Series，2007，330：127-137.

［24］ 丁洋. 涠洲岛珊瑚礁鱼类中OCPs、PCBs和OPEs生物积累的研究［D］. 南宁：广西大学，2019.
DING Y. Bioaccumulation of OCPs，PCBs and OPEs in coral reef fish from Weizhou Island［D］. Nanning：Guangxi University，2019.

Occurrence，sources and bioaccumulation of organochlorine pesticides in the Weizhou Island coral reef area

QIN Guibang[1,2,3]，ZHANG Ruijie[1,2,3]，WANG Yuxuan[1,2,3]，KANG Yaru[1,2,3]，SHI Jingwen[1,2,3]，WANG Chenyan[1,2,3]，HAN Minwei[1,2,3]，YU Kefu[1,2,3,4]

（1. *School of Marine Sciences*，*Guangxi University*，*Nanning* 530004，*Guangxi*，*China*；2. *Guangxi Laboratory on the Study of Coral Reefs in the South China Sea*，*Nanning* 530004，*Guangxi*，*China*；3. *Coral Reef Research Center of China*，*Guangxi Uhiversity*，*Nanning* 530004，*Guangxi*，*China*；4. *Southern Marine Science and Engineering Guangdong Laboratory*（*Guangzhou*），*Guangzhou* 511458，*Guangdong*，*China*）

Abstract: To explore the exposure situation of organochlorine pesticides（OCPs）in the coral reef area of Weizhou Island，Guangxi，gas chromatography-tandem triple quadrupole mass spectrometry（GC-MS/MS）was used to study the pollution levels，sources，and bioaccumulation characteristics of seven kinds of OCPs in seawater，sediments，coral host（i.e.，coral polyp hosts）tissues，and *Symbiodinium* in the coral reef areas in the northwest，southwest，and east directions around Weizhou Island. The results showed that OCPs were commonly present in the seawater of the coral reef area of Weizhou Island. DDTs were the main components among OCPs. The concentration of $\sum_7$OCPs in seawater was（119±118）pg/L，and the concentration of $\sum_6$DDTs was（84.1±82.3）pg/L. The concentrations of $\sum_7$OCPs in sediments，coral host tissues，and zooxanthellae were（0.27±0.22）ng/g dry weight，（1.90 ± 2.04）ng/g dry weight，and（17.7±7.29）ng/g dry weight，respectively. The average values of lg BAFs of the seven target OCPs in coral host tissues and *Symbiodinium* were 2.04−3.44 and 2.25−4.06，indicating that *Symbiodinium* had a stronger enrichment ability for OCPs than coral hosts. Whether this higher enrichment ability will bring higher ecological risks is worthy of in-depth study. The results of ecological risk assessment showed that the ecological risks of the seven target OCPs in the sediments and seawater of the coral reef area of Weizhou Island were currently at a relatively low level. The results of source apportionment showed that historical residues were the main sources of DDTs in the coral reef area of Weizhou Island，mainly dominated by dicofol products.

Key words: coral reef；organochlorine pesticides；source analysis；ecological risk assessment；bioaccumulation

DOI:10.19392/j.cnki.1671-7341.202509046

基于科教融合人才培养模式的“化学海洋学”教学改革与实践

裴继影[1*] 张樱元[2] 余克服[1] 余文峰[1] 张瑞杰[1] 王 瑞[1]

1.广西大学海洋学院 广西南宁 530004;2.广西大学资源环境与材料学院 广西南宁 530004

摘 要:“化学海洋学”课程作为海洋类专业的重要基础课之一,在培养创新型海洋人才中扮演着重要角色。本文以科教融合为主题,通过对“化学海洋学”课程教学现状的深入分析,提出了一系列新的教学改革思路。这些思路包括结合多种教学手段将科研融入课堂教学,以及优化教师与学生的评价体系。在实践中,科教融合的人才培养模式不仅取得了令人满意的成果,而且为提升海洋科学专业课程教学效果、强化科研育人功能提供了有益参考。

关键词:科教融合;化学海洋学;创新人才

一、概述

“化学海洋学”是海洋科学领域的一个重要分支,是海洋科学专业的核心课程之一[1]。它专注于研究海洋各部分的化学成分、物质分布和化学过程。在构建海洋强国的进程中,“化学海洋学”发挥着重要作用,为海洋资源的开发利用、环境保护、气候变化研究、能源开发以及药物研发等提供科学依据和技术支持[2]。作为理论与应用并重的基础课程,“化学海洋学”旨在培养学生掌握海水的基本性质,了解研究热点和发展方向,并提升学生对海洋化学重要性的认识。同时,它也致力于培养学生具备综合素质和扎实的海洋化学理论基础,使他们成为从事海洋化学研究与应用的高水平专业人才。这就要求教师在教学过程中不仅要引导学生学习基本理论知识,还应注重培养学生科学思维和解决问题的能力,运用科教融合的教学模式,鼓励学生运用所学知识来探索海洋科学领域的挑战和机遇。

科教融合是新时代高等院校落实现代化人才培养、提高一流人才培养质量的必然选择,目的是构建教学与科研协同发展、相互促进的人才培养体系,提高人才培养质量[3]。它将科研与教学深度结合,鼓励学生积极参与科研活动,并将最新科研成果引入教学过程。特别是在交叉学科如海洋化学中,科教融合为提供全面视角和方法、促进学科深度互动、培养学生跨学科思维和综合运用知识的能力发挥了积极作用。“化学海洋学”课程的科教融合,核心理念是促进学生跨学科思维,培养实践能力和环境保护意识,以解决海洋环境问题,推动可持续发展[4]。

本文在对“化学海洋学”课程教学中存在的问题进行分析的基础上,探讨了基于科教融合人才培养模式对该课程的目的与意义,并提出了相应的教学改革举措。为此,教师可以通过引入科研案例与成果、加强科研实践、优化评价体系等方式,在课程教学中培养学生的科学思维与科研创新意识,从而促进创新型海洋人才的培养。

二、高校“化学海洋学”教学中存在的问题

随着高校对科教融合人才培养模式的重视,化学海洋学作为一门重要的学科,在教学中面临着一系列挑战。首先,理论知识与科学研究之间存在脱节现象。在课程教学中,教师的科研内容与教学内容相对孤立,未能有效地将理论知识与实际海洋学问题相结合,导致学生难以理解和应用最新科研成果。同时,教材滞后且未能覆盖新兴科研技术,这限制了学生的学习深度和广度。其次,传统教学模式偏重理论而轻实践,无法激发学生的学习积极性和创新能力。由于海洋化学主要关注海水和海洋环境中化学物质的分布和运移,具有显著的地区性特征,实践教学的不完善导致学生科研思维受到限制,难以应用所学知识解决实际问题。尽管海洋院校积极通过专业实习来补充实践课程[5],但是海洋科学专业实习涉及海洋地质、海洋物理、海洋化学、海洋生物等各个方向,有限的实习经费使得化学海洋学方向实习质量难以达到预期目标。此外,传统的科教评价体系过于单一,主要侧重于对理论知识的考核[6],而忽视了学生的分析和应用能力,以及教师在科研与教学融合方面所做的贡献。缺乏对学生平时表现和综合能力的考核,以及对教师教学效果的全面评估,也会对教学质量和人才培养造成影响[7]。

三、基于科教融合人才培养模式的教学改革实践

在新时代教育理念的指导下,高等海洋院校专注于培养具备创新精神和实践能力的海洋人才。为解决海洋人才培养中传统教学模式所面临的课程内容与科学研究脱节的问题,我们在“化学海洋学”的教学中引入了科教融合的教学模式(图 1)。这一融合模式旨在提升学生的科学思维和实践创新能力,进而显著提升教学质量,实现教学相长[8]。

中国知网 https://www.cnki.net

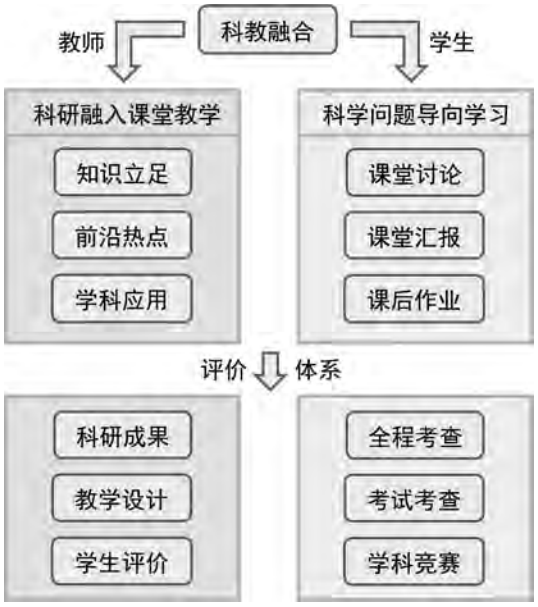


图 1“化学海洋学”科教融合教学改革模式设计

(一)科研融合教学,培养创新思维

在科教融合新模式下,教师通过将科研融入课堂教学,采用多种教学手段来帮助学生深入理解知识点。在课程设计中,设置与当前海洋化学研究前沿相关的内容,引导学生主动探索。同时,通过文献速递的方式介绍学科前沿问题,旨在唤起学生对科学研究的浓厚兴趣。以海水化学组成的恒定比为例,教师特别强调锶钙比在地球气候反演中的应用,从而引发学生对于实践应用的关注与思考。在教学过程中,积极引导学生思考科学研究与社会责任之间的紧密联系,激发学生对科研及社会责任的深刻思考。以海洋环境资源与利用为例,教师着重向学生介绍海洋环境保护、生态和平发展、可持续发展等理念,强调科学思维的重要性,鼓励学生从科学角度思考和解决现实世界中的挑战。此外,结合导师制培养模式,积极引导学生参与教师的科研项目[9]。学生根据兴趣选择科研课题,通过参与科研实践,不仅可以深化对课本知识的理解,而且能够运用所学知识解决科学问题。这一过程有助于提高学生的理论水平和科研能力,同时也能够激发学生的主动性,培养其创新思维,从而有效促进创新型人才的培养[10]。

(二)问题导向学习,激发学习兴趣

教师引导学生通过研究或实践等方式对特定问题或知识点进行探究,以增强学生的学习主动性并深化对知识的理解。这一方法强调课堂上的讨论,取代了传统的单向知识灌输,从而激发学生对学科内涵的深入思考。以海水和淡水结冰现象为例,教师通过实验、分析和讨论引导学生积极探索两者的差异,旨在加深他们对盐度、冰点、最大密度等概念的理解和应用。此外,将科学问题融入课后作业,通过资料查阅和实践,进一步激发学生对特定科学问题的深思。

采用多元化的教学方法有助于促进师生之间的积极互动。例如,结合线上与线下课程,引入学习通、雨课堂等多种信息化教学手段,及时了解学生对知识点的掌握情况。另外,通过课堂分组讨论和翻转课堂的策略,鼓励学生积极参与问题的解答和提出反向问题,从而提升对知识点的理解水平。这些方法能够激发学生的主动学习意识,使他们更深入地理解化学海洋学知识,培养其解决问题的能力和批判性思维。

(三)优化评价体系,推动人才培养

实现“化学海洋学”的科教融合人才培养模式的进一步优化,需要加强教师与学生的评价体系。针对教师评价体系的优化,可采取以下措施。首先,建立多维度评价体系,全面考察教师的科研成果、教学设计和学生指导能力,以实现对教师科教融合表现的全面客观评价。其次,定期对教师进行评价,并在评价结果反馈中协助教师改进实践。最后,引入学生参与评价,设立匿名评价专栏,鼓励学生评价教师的表现,以建立更加全面、科学的评价体系。

同时,对学生的学习效果评价体系也应进行优化。除了传统的考试外,应引入多元评价方式,如项目作业和口头报告,以全面评估学生在科教融合方面的学习成果。在评价过程中,需要结合校内外实践,着重评估学生的创新思维和问题解决能力。通过同时强调科研和教学的考核,推动学生评价体系的真正实施,促进“化学海洋学”科教融合人才培养模式的进一步发展。

四、科教融合教学模式的实施成效

(一)学生学习主动性与学习成绩稳步提升

经过 3 年多的“化学海洋学”课程教学改革,通过实施科教融合的教学模式,共有 231 名学生积极参与了课程学习。教学课堂的氛围逐年升温,学生的参与度不断攀升。为了深入了解学生对科研融合教学模式的接受情况,我们进行了问卷调查,结果显示,高达 80% 的学生积极肯定这种教学模式(图 2),认为它不仅拓宽了知识面,还深化了对知识点的理解。

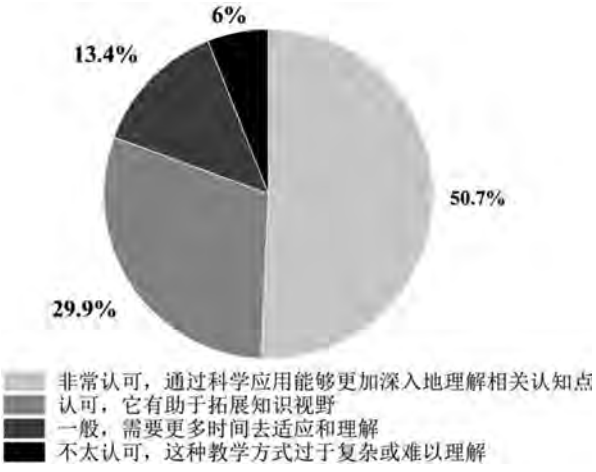


图 2 学生对科教融合教学模式的认可程度问卷调查结果

中国知网 https://www.cnki.net

对近 3 年学生的学习成绩进行综合分析，发现其呈现逐年增长的趋势。这一趋势清晰地证明了科教融合人才培养模式对教学水平的积极影响。这种增长不仅反映了学生对课程的更深入参与，同时也凸显了科研融合教学模式在激发学生学习兴趣、拓展认知层面的显著作用。

（二）科研创新成果持续涌现

在参与“化学海洋学”学习的本科生中，许多学生受到科教融合模式的影响，积极参与导师的科研项目。2021 级、2022 级和 2023 级本科生参与大创项目的覆盖率分别达到 100%、100%和 95%，并且有 35%、40%和 42%的学生参与并发表了学术论文。以裴继影教师和张瑞杰教师指导的本科生为例，他们将科教融合理念贯穿于实际操作中，积极参与导师指导的项目，在科研方面取得了显著的成绩。例如，他们先后共申请到 15 项大创项目，其中包括 1 项国家级、6 项省级和 6 项校级大创。此外，在大学生“挑战杯”比赛中，他们获得了 1 项省级二等奖、1 项校级一等奖和 1 项校级二等奖，并在科研过程中发表了多篇论文（图 3），这一系列数据明确表明了科教融合模式对本科生科研参与和人才培养的积极影响。

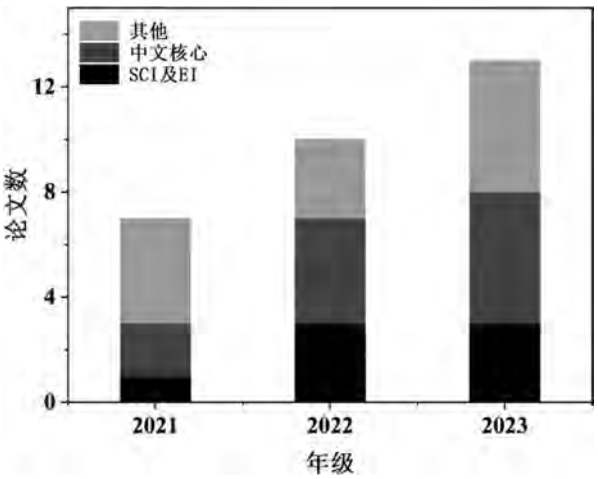


图 3 2021—2023 年大三学生发表论文情况

五、结论

“化学海洋学”课程的设立旨在培养研究型海洋化学领域的创新人才。经过对传统教学模式的分析，我们发现科教融合是突破教学瓶颈的有效途径。因此，我们通过多种教学手段的实施，强化科学研究在“化学海洋学”课程教学中的渗透，并通过优化教师与学生的评价体系等方式，探索基于科教融合人才培养模式的“化学海洋学”课程教学新模式。这一举措不仅推动了课程质量的提升，助力了课程目标的实现，还明显提升了教师的教学和科研能力。同时，这种基于科教融合的人才培养模式为海洋科学专业的教学提供了宝贵的经验和参考，为学院未来的教学改革与发展提供了指导方向。

参考文献：

[1]宋金明.奠基海洋化学研究，助推海洋科学发展：中国科学院海洋研究所海洋化学研究 70 年[J].海洋与湖沼，2020，51(04)：695-704.

[2]宋金明，王启栋，张润，等.70 年来中国化学海洋学研究的主要进展[J].海洋学报：中文版，2019，41(10)：65-80.

[3]胡军，于淦，陈雯，等.科教融合理念下理工科一流人才培养模式探索[J].高教学刊，2022，8(31)：139-142.

[4]李鸿莉，印春生.关于提高海洋化学课程建设的建议[J].教育教学论坛，2014(45)：211-213.

[5]宁志铭，方草，余克服，等.“海洋科学综合实验”（化学方向）教学的信息化应用探索[J].科技风，2023(04)：101-103.

[6]王晓跃.改革课程考试制度，提升应用型本科人才培养质量[J].江苏工程职业技术学院学报，2018，18(03)：78-82.

[7]谭珠珠，沈红.教研相长还是教研相抵：大学教师教学与科研时间分配对科研发表的影响[J].中国高校科技，2022(04)：61-66.

[8]陈永磊，付璐，付晓.论海洋类人才培养体系中的科教融合问题[J].大学，2020(35)：96-97.

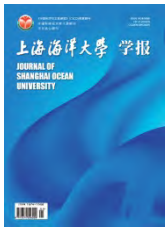
[9]林武辉，余克服，莫敏婷.基于科教融合、理工结合、校企联合的人才培养模式探索：以海洋科学专业为例[J].高教学刊，2023，9(04)：138-141.

[10]姜彦彬，王艳芳，樊文虎.基于科教融合的“工程地质”课程教学改革[J].新课程研究，2023(30)：10-12.

基金项目：国家自然科学基金——地区科学基金项目“基于非靶代谢组学及分子网络探究珊瑚对高温胁迫的代谢应答机制”（22264003）；广西自然科学基金面上项目“海洋环境中有机紫外吸收剂的常压质谱分析方法学研究与应用”（2023GXNSFAA026488）

*通信作者：裴继影（1989— ），女，汉族，安徽阜阳人，博士研究生，副教授，主要从事常压敞开式质谱离子化技术的开发及代谢组学分析。

中国知网 https://www.cnki.net



上海海洋大学学报
Journal of Shanghai Ocean University
ISSN 1674-5566,CN 31-2024/S

《上海海洋大学学报》网络首发论文

题目：广西北部湾典型水产品中有机磷酸酯的生物富集特征和食用风险评估
作者：康亚茹，张瑞杰，余克服，曾维斌，王瑞轩
收稿日期：2025-01-19
网络首发日期：2025-12-30
引用格式：康亚茹，张瑞杰，余克服，曾维斌，王瑞轩．广西北部湾典型水产品中有机磷酸酯的生物富集特征和食用风险评估[J/OL]．上海海洋大学学报．
https://link.cnki.net/urlid/31.2024.S.20251229.1909.004



网络首发：在编辑部工作流程中，稿件从录用到出版要经历录用定稿、排版定稿、整期汇编定稿等阶段。录用定稿指内容已经确定，且通过同行评议、主编终审同意刊用的稿件。排版定稿指录用定稿按照期刊特定版式（包括网络呈现版式）排版后的稿件，可暂不确定出版年、卷、期和页码。整期汇编定稿指出版年、卷、期、页码均已确定的印刷或数字出版的整期汇编稿件。录用定稿网络首发稿件内容必须符合《出版管理条例》和《期刊出版管理规定》的有关规定；学术研究成果具有创新性、科学性和先进性，符合编辑部对刊文的录用要求，不存在学术不端行为及其他侵权行为；稿件内容应基本符合国家有关书刊编辑、出版的技术标准，正确使用和统一规范语言文字、符号、数字、外文字母、法定计量单位及地图标注等。为确保录用定稿网络首发的严肃性，录用定稿一经发布，不得修改论文题目、作者、机构名称和学术内容，只可基于编辑规范进行少量文字的修改。

出版确认：纸质期刊编辑部通过与《中国学术期刊（光盘版）》电子杂志社有限公司签约，在《中国学术期刊（网络版）》出版传播平台上创办与纸质期刊内容一致的网络版，以单篇或整期出版形式，在印刷出版之前刊发论文的录用定稿、排版定稿、整期汇编定稿。因为《中国学术期刊（网络版）》是国家新闻出版广电总局批准的网络连续型出版物（ISSN 2096-4188，CN 11-6037/Z），所以签约期刊的网络版上网络首发论文视为正式出版。

网络首发时间：2025-12-30 13:36:31　网络首发地址：https://link.cnki.net/urlid/31.2024.S.20251229.1909.004

DOI:10.12024/jsou.20250104762

广西北部湾典型水产品中有机磷酸酯的生物富集特征和食用风险评估

康亚茹[1, 2, 3]，张瑞杰[1, 2, 3*]，余克服[1, 2, 3, 4]，曾维斌[1, 2, 3]，王瑞轩[1, 2, 3]

（1. 广西南海珊瑚礁研究重点实验室，广西 南宁 530004；2. 广西大学珊瑚礁研究中心，广西 南宁 530004；3. 广西大学海洋学院，广西 南宁 530004；4. 南方海洋科学与工程广东省实验室（广州），广东 广州 511458）

摘 要：为探究北部湾自然环境水产品中有机磷酸酯（OPEs）的富集特征和食用风险。本研究在夏季和冬季北部湾近岸和河口区共采集了 6 种 65 个典型水产品，采用气相色谱质谱联用仪测定了水产品中的 11 种常见 OPEs 的含量和组成特征。结果显示，11 种 OPEs 在冬季和夏季水产品中全部被检出，且在冬季水产品中的浓度[（127 ± 101）ng/g dw]显著高于夏季[（38.5 ± 28.6）ng/g dw]。不同季节鱼类中$\sum_{11}$OPEs 的污染水平低于底栖动物。水产品中 OPEs 的组成特征一致，其中磷酸三(2-氯丙基)酯（TCIPPs）和磷酸三(2-氯乙基)酯（TCEP）是其中主要检出物质。生物富集系数结果表明，整体上，北部湾水产品对氯代 OPEs（Cl-OPEs）的富集潜力高于烷基 OPEs（Alkyl-OPEs），且磷酸三(1,3-二氯异丙基)酯（TDCIPP）和磷酸三己酯（THP）在夏季和冬季部分水产品中具有明显富集性，其中生物的代谢能力、食性和栖息环境是其中的重要影响因素。食用风险评估显示，不同年龄和不同性别人群通过食用北部湾自然环境水产品而暴露于 OPEs 的健康风险熵值（Q_h）均低于阈值 1，表明食用风险较低。本研究不仅丰富了北部湾自然环境水产品中 OPEs 的污染现状，也为该区域的生态环境保护和食品安全管理提供了重要的科学依据。

关键词：有机磷酸酯；水产品；北部湾；生物富集；食用风险评估

新污染物是指在环境中新近被发现，尚未有相关管理规定和检测排放标准，但是其进入环境后对人体健康和生态环境存在较大风险隐患的污染物[1]。有机磷酸三酯(Organophosphate esters, OPEs)是近些年人们关注的新污染物之一，因其持久性、生物累积性和毒性也被称为持久且可传输的有机污染物（PMOCs）[2, 3]。OPEs 是一类有机磷阻燃剂（Organophosphate flame retardants, OPFRs）和增塑剂，作为溴系阻燃剂（Brominated flame

收稿日期：2025-01-19　　修回日期：2025-07-01
基金项目：国家自然科学基金（42090041）；广西科技基地和人才专项（编号：桂科 AD25069075）；广西研究生教育创新计划资助项目（YCBZ2023032）
作者简介：康亚茹（1995—），女，博士研究生，研究方向为新污染物的海洋环境地球化学行为。
E-mail: 2127402001@st.gxu.edu.cn
通信作者：张瑞杰，E-mail: rjzhang@gxu.edu.cn

retardants, BFRs）的主要替代品，广泛应用于塑料、纺织品、电子设备和建筑材料等领域[4]。近年来，OPEs 的产量和使用率快速增加[5]。据统计，2016 年至 2022 年间，全球 OPEs 生产工厂数量增加了 5.2%，反映出其市场需求和工业应用的快速扩展[6]。在中国，OPEs 的产量从 2007 年的 7 万 t 增加至 2020 年的 36.3 万 t[7]。OPEs 已被报道在大气、海水、河水、湖水、沉积物、雨水和水生生物等各种环境介质中广泛分布[8-16]。

海岸带是陆地与海洋交汇区域，蕴含着丰富的自然资源，具备重要的经济和生态价值，被誉为“黄金地带”。海岸带丰富的生物资源，包括鱼类、贝类、甲壳类和藻类等水产品是海岸带生态系统食物供给服务的重要组成部分[17]。据统计，鱼类、甲壳类和贝类是近岸海域水产品主要捕捞水产品，占比在 91%[18]。然而，随着人类对海岸带资源的不断开发和利用加剧，海洋污染和生态破坏等问题日益突出。近年来，水产品中 OPEs 污染及其健康风险评估受到国内外学者的普遍关注。研究表明，不同地区水产品中 OPEs 污染水平存在明显差异。例如，华南沿海地区软体动物中 8 种 OPEs 的平均污染水平为[295 ng/g 干重质量（dw）]，但三个年龄组（2 – 5 岁、6 – 18 岁和> 18 岁）男性和女性通过食用水产品暴露的非致癌和致癌风险均较低[19]。在渤海莱州湾，11 种 OPEs 在 39 种甲壳类、鱼类和软体动物中的总浓度为 2.04 – 28.6 ng/g dw，且八个年龄组人群（2 – 3 岁、3 – 4 岁、4 – 5 岁、5 – 6 岁、6 – 9 岁、9 – 12 岁、12 – 15 岁、15 – 18 岁和成年人）通过食用这些水产品的健康风险较低[15]。另外，在瑞典海岸蓝贻贝（*Mytilus edulis*）[16.23 ng/g 湿重质量（ww）][20]、西班牙北部海岸贻贝（*Mytilus edulis* 和 *Mytilus galloprovincialis*）（16.30 ng/g ww）[21]和美国旧金山湾的双壳类（*Mytilus californianus*）（0.80 ng/g ww）[22]等水产品中均发现 OPEs 广泛存在。然而，目前对于海岸带水产品中 OPEs 的研究仍然相对有限，一方面，研究区域和水产品种类覆盖有限；另一方面，针对摄食水产品而暴露于 OPEs 的食用风险评估研究较为匮乏。

北部湾位于南海西北部，是中国著名的半封闭海湾，被广东雷州半岛、海南岛、广西壮族自治区及越南三面环绕，面积为 1.3×10^5 km^2，接近于渤海面积的两倍，平均水深 38 m，海岸线长 2200 km。这里属于南亚热带海洋气候，适于各种生物繁殖生长，且陆上河流携带大量有机物及营养盐入海，使北部湾成为中国高生物量海区之一，也是我国著名四大渔场之一。周边居民主要从事海水养殖和海洋捕捞，金鲳鱼、鲈鱼、黄锡鲷、青蟹、对虾、牡蛎和带子螺等是重要的食用和经济水产品。然而，自 2008 年国家批准《广西北部湾经济区发展规划》后，工业化和城镇化的快速推进对北部湾海域带来了巨大的环境压力，海洋生态环境质量不容乐观[23]，水产品食用安全面临威胁。我们团队对北部湾近岸河流、海水、沉积物和养殖场对虾、螃蟹和牡蛎中 OPEs 的污染特征和环境行为等生物地球化学过程展开了调查和研究，结果表明 OPEs 在北部湾入海河流、近岸海域和养殖塘海水和沉积物中广泛分布，且养殖塘中虾、蟹和贝类体内 OPEs 的浓度与水体和沉积物相似，受人为活动干扰较大[11, 24, 25]。相较于养殖区，自然水域生物多样性丰富，在生物富集和生物放大的作用下，自然环境

水产品中的暴露浓度和风险可能增加[26]。然而，目前关于北部湾海岸带自然环境典型水产品中 OPEs 的富集特征研究较少，且对于食用这些典型水产品的风险未有相关报道。因此，本研究对北部湾近岸海域及河口典型水产品罗非鱼、青蟹、花蟹、对虾和牡蛎中的 OPEs 的富集特征进行了分析，并评估其食用风险。罗非鱼、青蟹、花蟹、对虾和牡蛎在北部湾近岸海域广泛分布，并且是主要的经济种类，资源丰富，人类食用量较高，是分析北部湾海岸带自然环境典型水产品中 OPEs 的富集特征以及食用风险的典型代表[27]。本研究为人体健康和生态环境保护提供科学依据，同时为海岸带生态环境保护和新污染物防控提供重要的指导意义。

1 材料与方法

1.1 样品采集

本研究于 2017 年 8 月（夏季）和 2017 年 12 月（冬季）在茅尾海和钦州湾近岸海域及河口区域共采集了 65 个样品，采样区域见图 1。夏季共采集了 5 种 43 个样品，包括罗非鱼、金鲳鱼、青蟹、对虾和牡蛎；冬季采集了 5 种 22 个样品，包括罗非鱼、青蟹、花蟹、对虾和牡蛎。采集后，对样品进行长度、宽度和重量等生物参数进行测定和记录，并进行物种鉴定。水产品样品详细信息见表 1。样品用锡箔纸包裹后密封于聚乙烯袋中，并置于–20℃冰柜中保存直至分析。

表 1 北部湾典型水产品的基本信息

Tab.1 Basic information of typical aquatic products from the Beibu Gulf

	物种名称 Species name	数量 Number	长度 Lengths (cm)	宽度 Width (cm)	含水率 Moisture content (%)	食性 Feeding habits
	夏季 Summer					
鱼类 Fish	尼罗罗非鱼 *Oreochromis niloticus*	5	26.5±4.65	11.0±1.47	74.8±7.39	杂食性，主要以浮游动物和草食性动物为主
	金鲳鱼 *Trachinotus ovatus*	5	26.8±1.3	11.4±0.82	71.3±1.52	肉食性，主要以小鱼、小虾和其他小型海洋生物为食
底栖生物 Benthic organisms	青蟹 *Portunus trituberculatus*	16	12.0±1.9	4.81±2.68	81.6±4.09	杂食性，以贝类、小鱼、虾蟹等为食
	对虾 *Penaeus vannamei*	6	10.2±2.72	3.86±0.74	81.5±4.58	
	牡蛎 *Crassostrea gigas*	11	14.5±1.88	5.45±0.92	83.0±2.43	滤食性，以浮游植物、浮游动物为食
	冬季 Winter					
鱼类 Fish	尼罗罗非鱼 *Oreochromis niloticus*	3	23.8±7.15	9.67±2.52	76.9±5.98	杂食性，主要以浮游动物和草食性动物为主
底栖生物 Benthic organisms	青蟹 *Portunus trituberculatus*	4	9.63±0.75	7.38±0.48	81.1±4.83	杂食性，以浮游生物、底栖生物为食，也会摄取一些植物性食物
	花蟹 *Portunus pelagicus*	6	12.1±1.46	6.60±0.94	75.5±5.71	
	对虾 *Penaeus vannamei*	4	10.2±2.32	1.45±0.44	80.5±8.11	
	牡蛎 *Crassostrea gigas*	5	11.8±5.40	7.49±3.89	82.8±10.3	滤食性，主要以浮游植物、浮游动物为食



图 1 北部湾典型水产品的采样区域

Fig.1 The sampling area of aquatic products in the Beibu Gulf

1.2 目标物标准品、化学试剂与药品

11 种目标 OPEs 根据其取代基的不同，主要分为 3 类。第一种为氯代有机磷酸酯（Cl-OPEs）,包括包括磷酸三（2-氯乙基）酯（TCEP）、磷酸三（2-氯异丙基）酯（TCIPPs，三种异构体的混合物）和磷酸三（1,3-二氯-2-异丙基）酯（TDCIPP）。第二种为烷基有机磷酸酯（Alkyl-OPEs），包括磷酸三异丁基（TiBP）、磷酸三正丁基（TnBP）、磷酸三（2-丁氧乙基）酯（TBOEP）、磷酸三戊酯（TPTP）、磷酸三己基酯（THP）、磷酸三异辛酯（TEHP）。第三种为芳香基有机磷酸酯（Aryl-OPEs），包括磷酸三苯酯（TPHP）和磷酸三甲苯酯（TMPPs，三种异构体的混合物）。各化合物的理化性质见表 2。回收率指示剂标样 TnBP-d27 和 TPHP-d15 以及内标六甲基苯（HMB，Hexamethylbenzene）购自 Accustandards (USA)公司。

表 2 11 种 OPEs 的理化性质

Tab.2 Physicochemical properties of 11 OPEs

化合物 Compounds	英文全称(简称) Full title in English (abbreviation)	CAS 号	分子式 Molecular formula	分子量 [a] Molecular weight/ (g/mol)	水溶性 [a] Water solubility/ (g/L)	Log K_{OW} [a]
磷酸三(2-氯乙基)酯	Tris(2-chloroethyl) Phosphate (TCEP)	115-96-8	$C_6H_{12}Cl_3O_4P$	285.49	7	1.44
磷酸三(2-氯丙基)酯	Tris(2-chloroisopropyl) Phosphate (TCIPPs)	13674-84-5	$C_9H_{18}Cl_3O_4P$	327.57	1.2	2.59
磷酸三(1,3-二氯异丙基)酯	Tri(1,3-dichloro-2-isopropyl) Phosphate (TDCIPP)	13674-87-8	$C_9H_{15}Cl_6O_4P$	430.91	7×10^{-3}	3.65
磷酸三异丁酯	Tri-iso-butyl phosphate (TiBP)	126-71-6	$C_{12}H_{27}O_4P$	266.31	6×10^{-4}	3.60
磷酸三正丁酯	Tri-n-butyl phosphate (TnBP)	126-73-8	$C_{12}H_{27}O_4P$	266.31	0.28	4.00
磷酸三戊酯	Tripentyl phosphate (TPTP)	2528-38-3	$C_{15}H_{33}O_4$	308.40	3.3×10^{-4}	5.29
磷酸三己酯	Trihexyl phosphate (THP)	2528-39-4	$C_{18}H_{39}O_4P$	350.48	1×10^{-5}	6.76
磷酸三(丁氧基乙基)酯	Tris(2-butoxyethyl) phosphate (TBOEP)	78-51-3	$C_{18}H_{39}O_7P$	398.48	1.1	3.75
磷酸三异辛酯	Tris(2-ethylhexyl) phosphate (TEHP)	78-42-2	$C_{24}H_{51}O_4P$	434.65	6×10^{-4}	9.49
磷酸三苯酯	Triphenyl phosphate (TPHP)	115-86-6	$C_{18}H_{15}O_4P$	285.49	1.9×10^{-3}	4.59
磷酸三甲苯酯	Tris(methylphenyl) phosphate (TMPPs)	1330-78-5	$C_{21}H_{21}O_4P$	368.36	3.6×10^{-4}	5.11

注：[a] 数据来自 US. EPA[28], K_{OW} 代表辛醇-水分配系数。

Notes: Data from US. EPA[29], K_{OW} means octanol-water partition coefficient.

本研究使用的有机溶剂均为色谱级（HPLC），包括甲醇、二氯甲烷、正己烷、乙酸乙酯和丙酮，均购自上海安谱实验室技术有限公司（CNW）。超纯水由 Milli-Q 水净化系统

（Millipore, Bedford, Massachusetts, USA）制备。固相萃取柱[Envi-Florisil 柱（500 mg，3 mL）]购自 SUPELCO。

1.3 样品预处理

所有生物样品在处理前先进行解冻，解冻后用超纯水冲洗样品表面以去除肉眼可见的杂质。利用解剖工具去除鱼类和底栖生物的皮和壳，获取肌肉样品。整个解剖过程在干净的锡箔纸上进行，以避免引入污染。所得肌肉样品冷冻干燥后研磨成粉末，并用锡箔纸包裹，储存于–20 ℃冰箱直至进一步处理和分析。

目标化合物的提取参考课题组既有方法[29]。具体步骤如下：每份生物组织样品精确称取 1.00 g，用滤纸包裹后放入索氏提取器中。取 120 mL [*V*(正己烷):*V*(丙酮)=1:1]的混合提取液，置于 150 mL 圆底烧瓶中，加入回收率指示剂 TnBP-d27 和 TPHP-d15 各 20 ng，在 65 ℃恒温水浴中抽提 48 h。萃取液经过旋转蒸发浓缩至近干，加入正己烷置换原溶剂，重复 3 次后浓缩并转移到 4 mL 棕色玻璃瓶中，氮吹浓缩至 1 mL。随后使用 Envi-Florisil 柱子（500 mg, 3 mL, SUPELCO）进一步纯化目标化合物。柱子在使用前分别用 6 mL 乙酸乙酯，6 mL [*V*(二氯甲烷):*V*(正己烷)=1:1]混合溶液和 6 mL 正己烷活化。为了分离其他持久性有机污染物（POPs）和目标 OPEs，先用约 15 mL [*V*(二氯甲烷):*V*(正己烷) =8:2]的混合溶液洗脱 SPE 柱，得到 POPs 组分，再用相同体积的乙酸乙酯进行洗脱，得到 OPEs 组分。将含有 OPEs 的第二组分液氮吹浓缩至 0.5 mL，最后加入 200 ng 六甲基苯（HMB）标准品，进行后续仪器分析。

1.4 仪器分析

采用电离离子源模式（Electron impact，EI）的安捷伦 7890B 气相色谱串联 7000C 三重四极杆质谱仪（GC-MS/MS）对样品中 OPEs 的含量进行测定和分析[30]。色谱柱为 HP-5MS 石英弹性毛细管柱（30 m × 250 μm，0.25 μm，Agilent Technologies Inc）。载气为氦气，流速为 1.5 mL/min。进样口温度设为 250 ℃，离子源温度为 230 ℃，进样体积为 1 μL，采用不分流进样模式。色谱升温程序如下：初始温度设定为 90 ℃并保持 1 min，以 16 ℃/min 的速度增加至 170 ℃；随后以 5 ℃/min 的速度升温至 200 ℃，再以 10 ℃/min 的速度升温至 250 ℃并保持 2 min；最后以 10 ℃/min 的速度升温至 300 ℃并保持 9 min。质谱采用多反应监测（MRM）模式进行数据采集。

1.5 质量控制与质量保证（QA/QC）

整个实验过程严格遵循 QA/QC 程序，设置了实验室流程空白、回收率指示剂、平行样和分析仪器检出限来进行质量控制。采用内标法定量分析目标 OPEs 浓度。标准曲线由七个点（1 – 200 ng/mL）构建，相关系数均大于 0.99。检测过程中，每 10 个样品中加入实验室流程空白和 20 ng/mL 标准溶液来检测本底干扰，确保仪器稳定性。回收率指示剂 TnBP-d27 和 TPHP-d15 的回收率分别为 89.5% ± 9.5%和 83.4% ± 8.1%。OPEs 的浓度未经回收率

指示剂校正，扣除空白平均浓度后作为样品最终浓度。方法检出限（MDL）和定量限（MQL）分别定义为 3 倍和 10 倍信噪比所对应的浓度。11 种 OPEs 的 MDL 和 MQL 浓度见表 3。此外，为去除背景污染，实验过程中使用到的玻璃器皿，如平底烧瓶、烧杯、索氏抽提器上的提取管、棕色样品瓶和滴管等，均提前用 RBS 洗液 20 ℃超声清洗，随后用自来水和超纯水依次冲洗、烘干，并在经 450 ℃下锻烧 6 h。所有样品和玻璃器皿使用前均用铝箔覆盖，以避免室内灰尘污染。另外，解剖工具（如解剖刀、刀片、镊子和剪刀等）均为不锈钢材质，使用前分别用丙酮、甲醇和正己烷依次超声萃取 5 min。用于包裹粉末状生物样品的滤纸，在使用前分别用甲醇和二氯甲烷索氏抽提 48 h，并在干燥器中干燥后恒温保存。

1.6 生物富集分析

生物富集因子（bioaccumulation factors（*BAFs*，L/Kg））用于分析 OPEs 在水生生物中的生物富集潜力，其计算公式如下[31]：

$$F_B = \frac{C_T}{C_W} \times 1000 \quad (1)$$

式中：F_B 代表生物富集因子 *BAFs*；C_T 代表生物中 OPEs 的浓度，单位 ng/g 湿重（ww）；C_W 代表海水中 OPEs 的浓度，单位 ng/L。本研究中，海水中 OPEs 的浓度取自本团队同时期在生物样本采样周围海域和河流中的数据[24]。OPEs 生物组织中 OPEs 的湿重浓度根据不同物种组织含水率转换而来（表 1）。根据欧洲化学品管理局的生物富集评估标准，$F_B \geq 5000$ L/kg（Log $F_B \geq 3.7$）表明化合物具有“生物富集性”，$3.3 < F_B < 5000$ L/kg（$3.3 \leq \text{Log } F_B < 3.7$）表示化合物具有“潜在生物富集性”[32]。

1.7 食用风险评估

本研究首先估算了 3 个不同年龄组（2 – 5、6 – 17 岁和> 18 岁）人群通过水产品摄入 OPEs 的每日摄入量（I_d）（ng/kg bw/day）[25, 33]，计算公式如下：

$$I_d = \sum_{i=1}^{n} C_i \times D_i / W_b \quad (2)$$

式中：C_i 是生物中 OPEs 的浓度，单位 ng/g ww，取夏季和冬季所有生物中 OPEs 的 95%水平浓度代表高风险浓度。D_i 是水产品的每日摄入量，单位 g/day，参考自华南沿海地区的膳食调查研究[34]。W_b 表示人体质量，单位 kg，成年男性和女性分别为 65.6 kg 和 56.5 kg，青年男性和女性分别为 41.7 kg 和 39.0 kg，男性儿童和女性儿童分别为 16.8 kg 和 16.0 kg[35]。

本研究根据美国环境保护署的评价标准[92]，采用风险熵值（Q_h）来评估水产品中 OPEs 的食用风险，计算公式如下：

$$Q_h = I_d / D_r \quad (3)$$

其中：D_r 为 OPEs 的口服参考计量单位 ng/kg bw/d，参考自其它文献[36-40]。当 $Q_h \geq 1$ 时，表示食用北部湾水产品暴露于 OPEs 的健康风险较高，反之，则表示不存在健康风险。将每种 OPEs 的 Q_h 相加即为 OPEs 的累积危险指数（I_h）[41]：

$$I_h = \sum Q_h \quad (4)$$

1.8 统计分析与图表绘制

首先采用 Shapiro-Wilk 检验数据的正态性。当数据服从正态分布时，分组数据之间的差异和相关性分别采用独立样本 T 检验和皮尔逊相关性检验，否则采用非参数检验和斯皮尔曼相关性检验。$P < 0.05$ 表示差异性或相关性显著，$P < 0.01$ 表示差异性或相关性极显著。数据分析和图表绘制主要在 Microsoft Office 2016（Washington, USA）、Origin 2024b（Origin Lab Corporation, Massachusetts, USA）和 Arcgis 10.2（Environmental Systems Research Institute, Inc）等软件进行处理。

2 结果与讨论

2.1 浓度水平

OPEs 在北部湾典型水产品中的浓度水平和组成特征详见表 3 和图 2。11 种 OPEs 在所有水产品中均有检出，检出率为 26% – 100%，表明 OPEs 在北部湾水产品中普遍存在。水产品中 11 种 OPEs 的总浓度（Σ_{11}OPEs）范围为 7.28 – 363 ng/g dw，平均值为 68.9 ± 74.9 ng/g dw，在全球范围内处于较低水平（表 4）。

表 3 北部湾典型水产品中 OPEs 的含量和检出限

Tab.3 Concentrations and detection limits of OPEs in typical aquatic products from the Beibu Gulf

OPEs	夏季 Summer			冬季 Winter			所有水产品 All aquatic products		MDL[a]	MQL[a]
	检出率 DFs (%)	范围 Range	平均值±标准差 Mean±SD	检出率 DFs (%)	范围 Range	平均值±标准差 Mean±SD	检出率 DFs (%)	平均值±标准差 Mean±SD	ng/g dw	
TCEP	100	1.21-38.2	8.86±9.30	100	0.95-156	24.9±36.2	100	14.2±23.3	1.12	3.73
TCIPPs	100	5.61-67.6	22.3±14.7	100	2.92-172	51.9±43.6	100	32.5±31.0	0.63	2.11
TDCIPP	98	nd [b]-13.0	1.74±2.74	100	0.08-301	27.6±65.2	99	10.7±39.4	0.61	2.03
TEHP	19	nd-3.25	0.22±0.65	100	0.19-3.45	1.44±0.83	49	0.69±0.96	0.10	0.35
TiBP	7	nd-0.78	0.02±0.12	87	nd-2.60	0.94±0.83	37	0.34±0.65	0.05	0.17
TnBP	63	nd-18.9	0.70±2.88	52	nd-2.88	0.57±0.86	59	0.64±2.34	0.24	0.81
TPTP	33	nd-17.0	1.22±3.58	17	nd-2.93	0.28±0.75	26	0.87±2.90	0.34	1.15
THP	100	0.02-13.9	0.82±2.07	100	0.05-180	8.03±37.39	100	3.24±21.8	0.11	0.37
TBOEP	63	nd-2.84	0.94±1.01	100	5.33-6.44	5.56±0.30	76	2.64±2.38	3.06	10.2
TPHP	7	nd-30.1	1.35±6.09	100	0.17-19.5	2.02±4.13	41	1.56±5.38	0.19	0.64
TMPPs	16	nd-5.31	0.27±1.11	100	0.05-33.6	4.00±6.88	47	1.57±4.41	2.42	8.06
Cl-OPEs		6.97-104	32.9±22.0		7.9-344	104±92.4		57.4±65.3		
Alkyl-OPEs		0.02-39.3	3.93±6.84		5.65-188	16.8±37.3		8.41±22.9		
Aryl-OPEs		nd-30.3	1.62±6.20		0.30-53.2	6.02±10.8		3.13±8.18		
$\sum_{11}$OPEs		7.28-149	38.5±28.6		13.9-363	127±101		68.9±74.9		

注：[a]MDL 和 MQL 分别代表方法检出限和方法定量限；[b]代表无检出，即低于方法检出限。

Notes: MDL and MQL represent the Method Detection Limit and Method Quantification Limit, respectively; b represents no detection, i.e., below the MDL.

OPEs 在夏季水产品中的检出率（7% – 100%）普遍低于冬季（17% – 100%）。冬季水产品中 Σ_{11}OPEs（127 ± 101 ng/g dw）显著高于夏季（38.5 ± 28.6 ng/g dw）（T 检验，$P < 0.05$），除了 TnBP 和 TPTP 外，其他 OPEs 的平均含量在冬季水产品中均高于夏季（表 3）。为排除物种组成差异的影响，对不同季节中相同物种进行了比较，结果同样发现$\sum_{11}$OPEs 在冬季高于夏季，如罗非鱼（冬季 50.7 ng/g dw >夏季 34.0 ng/g dw），青蟹（冬季 102 ng/g dw >夏季

39.9 ng/g dw），对虾（冬季 86.6 ng/g dw >夏季 47.9 ng/g dw），牡蛎（冬季 182 ng/g dw >夏季 40.8 ng/g dw）。这一季节分布特征与 Liu 等人在北部湾海岸带入海河流和海水中发现的规律不一致，但是与沉积物一致[11, 24]，可能是因为影响 OPEs 在生物介质和非生物介质中分布的因素不同所致[30]。

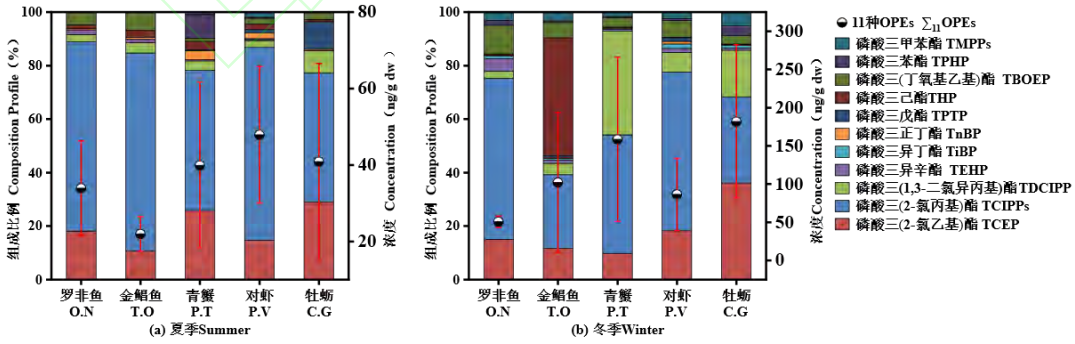
表 4 全球近岸海域水产品中 OPEs 污染水平比较

Tab.4 Global comparison of OPEs concentrations in aquatic products in nearshore aquatic products

研究区域 Research area	水产品(数量) Aquatic products (numbers)	OPEs 总浓度 ΣOPEs (ng/g)	主要检出化合物 Main detected compounds	参考文献 References
北部湾 Beibu Gulf	鱼 Fish (n=17) 虾 Shrimp (n=12) 蟹 Crab (n=27) 牡蛎 Oyster (n=13)	34.4[a], 8.62[b] 64.5[a], 35.0[b] 81.3[a], 34.5[b] 86.2[a], 34.2[b]	TCIPPs、TCEP 和 TDCIPP	本研究 This study
涠洲岛 Weizhou Island	牡蛎 Oyster (n=3) 蟹 Crab (n=2) 鱼 Fish (n=34)	309 [a] 225 [a] 58.2 [a]	TCIPPs 和 TBOEP	[42]
莱州湾 Laizhou Bay	鱼 Fish (n=6)	26.9 [a]	TEHP、TBOEP 和 TPHP	[43]
北部湾(海产养殖区) Beibu Gulf (Aquaculture area)	牡蛎 Oyster (n=4) 蟹 Crab (n=7) 虾 Shrimp (n=8)	8.9 [b] 20.4 [b] 12.5 [b]	TCIPPs 和 TCEP	[25]
红海湾 Red Bay	鱼 Fish (n=12)	55.8 [a]	TCEP、TBOEP、TCIPPs、TPHP 和 TnBP	[44]
越南沿海 Coastal areas of Vietnam	银鲳鱼 *Pampus argenteus* (n=172)	16.4 [a]	TEHP、TBOEP、TCEP 和 TDCIPP	[45]
朝鲜沿海 Coastal areas of North Korea	双壳贝类 Bivalve mollusks (n=50)	40.9 [a]	TCIPPs 和 TBOEP	[46]

注：[a] OPEs 浓度以单位干重质量表示，单位 ng/g dw；[b] OPEs 浓度以单位湿重质量表示，单位 ng/g ww。
Notes: [a] OPEs concentration is expressed in units of dry weight mass, ng/g dw; [b] OPEs concentration is expressed in units of wet weight mass, ng/g ww.

对于同一季节的不同物种，本研究鱼类中$\sum_{11}$OPEs 的污染水平通常低于底栖大型无脊椎动物（图 2）。在夏季鱼类中，$\sum_{11}$OPEs 的平均浓度依次为罗非鱼（34.0 ± 31.0 ng/g dw）> 金鲳鱼（22.0 ± 19.5 ng/g dw）（非参数检验，$P > 0.05$）。对于大型无脊椎动物，夏季样品中$\sum_{11}$OPEs 的浓度相近（39.4 – 47.9 ng/g dw），而冬季牡蛎中的浓度（182 ng/g dw）则明显高于对虾、青蟹、花蟹（86.6、102 和 159 ng/g dw）（ANOVA，$P > 0.05$）（图 2）。



O.N、T.O、P.T、P.V 和 C.G 分别代表罗非鱼、金鲳鱼、青蟹、对虾和牡蛎。
O.N, T.O, P.T, P.V, and C.G represent *Oreochromis niloticus*, *Trachinotus ovatus*, *Portunus trituberculatus*, *Penaeus vannamei*, and *Crassostrea gigas*, respectively.

图 2 北部湾夏季（a）和冬季（b）典型水产品中 OPEs 的组成特征及 Σ_{11}OPEs 的含量

Fig.2 Composition profiles of OPEs and concentration of Σ_{11}OPEs in aquatic products from the Beibu Gulf during summer (a) and winter (b)

2.2 组成特征

OPEs 的同系物组成模式显示，Cl-OPEs 是北部湾水产品中的主要检出同系物，其次为 Alkyl-OPEs 和 Aryl-OPEs，对 Σ_{11}OPEs 的贡献分别为 83.3%、12.2%和 4.54%（图 2）。对于单体 OPEs，Cl-OPEs 包括 TCIPPs（47.1%）、TCEP（20.7%）和 TDCIPP（15.5%）亦是水产品中的主要组成物质。北部湾自然环境水产品中 OPEs 组成特征与北部湾海水养殖区虾、蟹和牡蛎中的组成特征一致[25]。Cl-OPEs 在水产品中占主导地位的现象与其较高的生产量、历史使用量、较强的抗光解能力和降解能力密切相关[47]。Fu 等人指出，极地地区生物中 Cl-OPEs 在生物体内浓度较高，原因包括（1）周围环境中 Cl-OPEs 的高丰度；（2）Cl-OPEs 相比非氯代 OPEs 的生物转化率较低[47]。由于其较高的水溶性，Cl-OPEs 已被认为对水生生物构成长期威胁[4]。

尽管不同季节和物种 OPEs 总含量存在差异，但其组成特征整体相似。在夏季，TCIPPs 在所有水产品中的含量均明显高于其它 OPEs，且对$\sum_{11}$OPEs 的贡献为 24.8% – 85.8%（平均值：64.0% ± 18.5%）。在冬季，TCIPPs 在罗非鱼和对虾中的含量最高，其对$\sum_{11}$OPEs 的贡献达到 49.0% – 70.5%，平均为 59.9% ± 6.1%。然而，青蟹中 THP 的含量最高，其次为 TCIPPs，分别对$\sum_{11}$OPEs 的贡献为 44.1%和 27.5%。对虾中 TCEP 的含量则明显高于 TCIPPs，而牡蛎中 TCEP 略高于 TCIPPs。

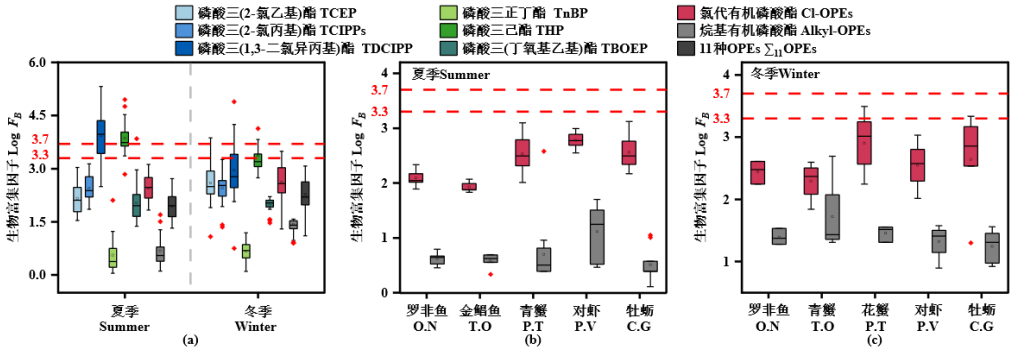
2.3 生物富集特征

探究 OPEs 在生物中的富集特征是评估其潜在生态风险的基础。本研究基于生物富集因子（F_B）来评估夏季和冬季检出率均超过 50%的 6 种 OPEs（TCEP、TCIPPs、TDCIPP、TnBP、THP、TBOEP）在北部湾典型水产品中的生物富集潜力，计算公式详见章节 1.6[31]。

如图 3 所示，单体 OPEs 在夏季和冬季水产品中的 Log F_B 值分别为 0.05 – 5.83 和 0.10 – 6.11。在夏季，33.2%的水产品中的 Log F_B 值大于 3.3，而在冬季，约 15.2%的水产品中的 Log F_B 值大于 3.3，表明北部湾大多数水产品对 OPEs 不具备生物富集性。如图 3a 所示，夏季 TDCIPP 和 THP 在水产品中的平均 Log F_B 值分别为 3.93 ± 0.66 和 3.86 ± 0.52，在 58.1%的样品中的 Log F_B 值大于 3.7，表现出明显的生物富集性。在冬季，仅有 THP 的平均 Log F_B 值大于 3.3，且 17.4%的水产品中 Log F_B 值大于 3.7，表明北部湾水产品在冬季对 THP 表现出明显的生物富集潜力。如图 3b 和 c 所示，同一季节，不同种类水产品对 Cl-OPEs 和 Alkyl-OPEs 表现出一致的富集趋势，且水产品对 Cl-OPEs 的富集潜力显著高于 Alkyl-OPEs（T 检验，$P < 0.01$）。

化合物的正辛醇-水分配系数（K_{OW}）是衡量有机污染物在水相和有机相（如生物组织和土壤有机质等）之间分配能力的关键参数。研究表明，K_{OW} 介于 1 – 7 之间的 OPEs 具有生物富集潜力[25, 48, 49]，而在珠江三角洲、五大湖、廉州湾和北部湾鱼类中，K_{OW} 与 F_B 之间并不存在显著相关性[26, 50, 51]，这表明生物代谢转化、食性、栖息地、生物参数（如含水率）

和生长状态等因素均可能在 OPEs 的生物积累过程中发挥重要作用[30, 52]。



O.N、T.O、P.T、P.V 和 C.G 分别代表罗非鱼、金鲳鱼、青蟹、对虾和牡蛎。
O.N, T.O, P.T, P.V, and C.G represent *Oreochromis niloticus*, *Trachinotus ovatus*, *Portunus trituberculatus*, *Penaeus vannamei*, and *Crassostrea gigas*, respectively.

图 3 OPEs 单体和同系物在北部湾夏季和冬季典型水产品中的生物富集因子（Log F_B）

Fig.3 The Log F_B of OPEs in the typical auqtic products from the Beibu Gulf

将各 OPEs 的 Log K_{OW} 值和 Log F_B 值进行相关性分析，显示夏季和冬季水产品中 OPEs 的 Log F_B 值与 Log K_{OW} 均呈不显著正相关关系（$P > 0.05$），说明 K_{OW} 值不是影响 OPEs 在北部湾水产品中富集的主要因素。值得注意的是，TnBP 在夏季水产品和冬季水产品中的 Log F_B 均较低（图 4），这可能与生物对化合物的降解代谢能力的差异性有关。研究指出，Cl-OPEs 在水产品中通常比 Alkyl-OPEs 更难转化[53, 54]，且 TnBP 在鱼肝微粒体中温育 140 min 后可被快速耗竭，内在清除率达到 3.1 μL/min/mg 蛋白质[55]，因此 TnBP 在生物中的快速降解可能是阻碍其在北部湾水产品中显著富集的重要因素。此外，本研究发现，底栖生物（虾、蟹和牡蛎）中 Σ_{11}OPEs 的 Log F_B 值在夏季和冬季均高于鱼类中的 Log F_B 值，且夏季呈显著差异（T 检验，$P < 0.05$），这可能与生物的食性和栖息环境有关[56, 57]。鱼类主要为肉食性，食性单一，而底栖动物食性则为杂食性，食物来源多样，可能在一定程度上增加其对 OPEs 的暴露。此外，鱼类主要栖息于中上层，而底栖生物栖息于底层，除暴露于水体中 OPEs 的风险外，还可能会增加其暴露于沉积物中 OPEs 的风险。

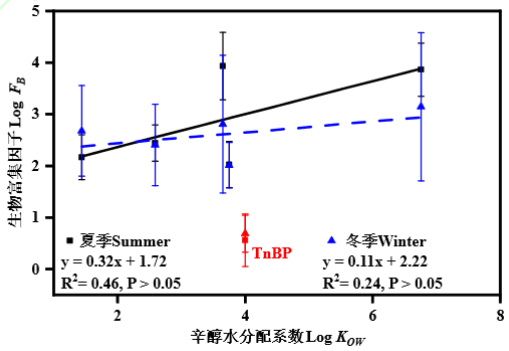


图 4 北部湾典型水产品中 OPEs 的 Log K_{OW} 与 Log F_B 之间的相关性

Fig.4 The relationships between Log K_{OW} and Log F_B of individual OPEs in typical aquatic products from the Beibu Gulf

2.4 食用风险评估

基于前述公式（章节 1.7），本研究对三个年龄组（2 – 5 岁，6 – 18 岁和>18 岁）男性和

女性因摄食北部湾水产品而暴露于 OPEs 的每日摄入量（I_d）进行了评估。三个年龄组的 $\sum_{11}$OPEs 的 I_d 值汇总于表 5，范围为 17.8 – 23.5 ng/g bw/day。其中，青年（6 – 18 岁）的 EDI 值最高，其次是儿童（2 – 5 岁）和成人（>18 岁）。在性别差异方面，男儿童和男青年的 I_d 值均高于女性，而成年男性的 I_d 值则略低于女性（表 5）。对于单体 OPEs，不同人群通过摄食水产品而摄入 OPEs 总量贡献无差异，总体上 TCIPPs 和 TCEP 的摄入量相对较高（图 5a），占 OPEs 总摄入量的 73.8%。对于不同种类水产品，鱼类和牡蛎对不同人群 I_d 值的贡献最高，二者之和占男性儿童、女性儿童、男性青年、女性青年、成年男子和成年女子 OPEs 总摄入量的比例分别为 80.1%、82.4%、78.7%、80.9%、84.2%和 83.7%（图 5b），总体而言，儿童和成年人群因摄食鱼类和牡蛎而对 OPEs 的 I_d 值高于青年。

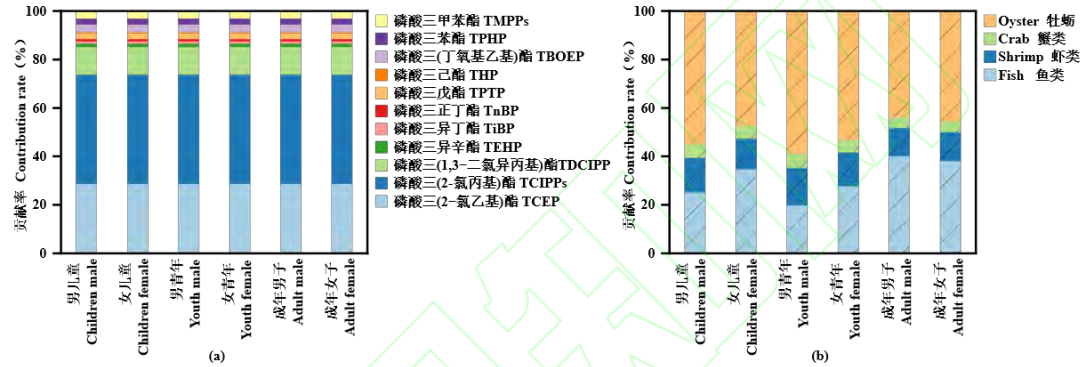


图 5 单体 OPEs（a）和不同种类生物（b）对不同年龄人群通过食用北部湾典型水产品对 OPEs 的每日摄入量的贡献率

Fig.5 Contribution rates of individual OPEs (a), and different species of aquatic products (b) to Estimated daily intake (I_d) by various age groups in different populations of the Beibu Gulf

表 5 北部湾不同年龄人群通过食用水产品对 OPEs 的每日摄入量（I_d）和口服参考计量（D_r）（ng/kg bw/d）

Tab.5 Estimated daily intake (ng/kg bw/day) (I_d) and oral reference dose (D_r) of OPEs from aquatic products across different age groups in the Beibu Gulf（ng/kg bw/d）

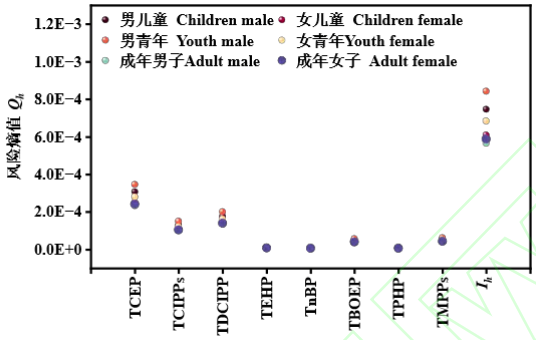
OPEs	儿童 Children (2~5 岁)		青年 Youth (6~18 岁)		成人 Adults (>18 岁)		参考计量 Reference dose [36-40]
	男 Male	女 Female	男 Male	女 Female	男 Male	女 Female	
TCEP	6.75	5.50	7.61	6.18	5.11	5.30	22000
TCIPPs	10.57	8.62	11.93	9.68	8.01	8.31	80000
TDCIPP	2.66	2.17	3.00	2.43	2.01	2.09	15000
TEHP	0.35	0.29	0.40	0.32	0.27	0.28	35000
TiBP	0.24	0.19	0.27	0.22	0.18	0.19	na
TnBP	0.18	0.14	0.20	0.16	0.13	0.14	24000
TPTP	0.55	0.44	0.62	0.50	0.41	0.43	na
THP	0.12	0.10	0.14	0.11	0.09	0.10	na
TBOEP	0.75	0.62	0.85	0.69	0.57	0.59	15000
TPHP	0.57	0.47	0.65	0.53	0.43	0.45	70000
TMPPs	0.71	0.58	0.81	0.65	0.54	0.56	13000
$\sum_{11}$OPEs	23.5	19.1	26.5	21.5	17.8	18.4	

注：na 表示没有查询到参考计量。

Notes: na indicates that no reference dose was found.

OPEs 的暴露风险指数如图 6 所示。因缺乏 D_r 值，TiBP、TPTP 和 THP 的风险熵值（Q_h）未作计算。北部湾水产品中 OPEs 对所有人群的 Q_h 值的范围为 5.60E-06 – 8.43E-04，其中 3 种 Cl-OPEs 的风险相对高于非氯代 OPEs，表明 Cl-OPEs 的食用风险较高。总体上，单体

OPEs 的 Q_h 值和 8 种 OPEs 的 I_h 值远远低于安全阈值 1.0，表明所有年龄段人群当前通过食用北部湾水产品而暴露于 OPEs 的风险很低。然而，随着 OPEs 使用量的持续增加，其在环境介质和水产品体残留水平可能呈现上升趋势。由于大多数 OPEs 具有较高的水溶性，且易于与蛋白质结合[58]，而北部湾水产品通常富含高蛋白，因此，未来需持续关注该区域水产品尤其是经济种类中 OPEs 的残留水平和其潜在的膳食暴露风险。



TCEP. 磷酸三(2-氯乙基)酯；TCIPPs. 磷酸三(2-氯丙基)酯；TDCIPP. 磷酸三(1,3-二氯异丙基)酯；TEHP. 磷酸三异辛酯；TnBP. 磷酸三正丁酯；TBOEP. 磷酸三(丁氧基乙基)酯；TPHP. 磷酸三苯酯；TMPPs. 磷酸三甲苯酯； I_h. 累积危险指数。
TCEP. Tris(2-chloroethyl)Phosphate; TCIPPs. Tris(2-chloroisopropyl)Phosphate; TDCIPP. Tri(1,3-dichloro-2-isopropyl)Phosphate (TDCIPP); TEHP. Tris(2-ethylhexyl) phosphate; TnBP. Tri-n-butyl phosphate; TBOEP. Tris(2-butoxyethyl) phosphate; TPHP. Triphenyl phosphate; TMPPs. Tris(methylphenyl) phosphate; I_h. Hazard index.

图 6 不同人群通过摄食北部湾典型水产品而暴露于 OPEs 的风险熵值（Q_h）

Fig.6 Hazard quotients (Q_h) for different populations exposed to OPEs through the ingestion of typical aquatic products from the Beibu Gulf

3 结论

（1）OPEs 在北部湾自然环境水产品中普遍存在，浓度处于全球较低水平。整体上，OPEs 在冬季水产品中的浓度显著高于夏季。在不同季节，两种鱼类中 OPEs 的浓度均普遍低于底栖水产品。Cl-OPEs 是水产品中的主要组成物质。

（2）Cl-OPEs 在水产品中的富集潜力普遍高于 Alkyl-OPEs。对于单体 OPEs，除了 TDCIPP 和 THP 之外，大部分 OPEs 在水产品中不具有生物富集性。水产品对 OPEs 的代谢能力、食性和栖息环境是影响 OPEs 在北部湾水产品中生物富集的重要因素。

（3）本研究调查时期，不同年龄和性别的人群通过食用北部湾典型水产品而暴露于 OPEs 的健康风险值较低，但随着 OPEs 污染的增加，未来仍需对北部湾水产品中 OPEs 的残留水平和食用风险进行持续关注。

（4）为保障水产品安全，建议政府等相关部门将 OPEs 纳入北部湾重点监测污染物清单，定期对不同水产品进行抽检。同时，通过可通过公众科普等方式引导消费者优化膳食结构，以预防潜在风险。

参考文献：

[1] 王亚韡, 张秋瑞, 于南洋, 等. 新污染物[J]. 化学进展, 2024, 36(11): 1607-1784.
WANG Y W, ZHANG Q R, YU N Y, et al. Emerging pollutants[J]. Progress in Chemistry, 2024, 36(11): 1607-1784.

[2] SAUVÉ S, DESROSIERS M. A review of what is an emerging contaminant[J]. Chemistry Central Journal, 2014, 8(1): 15.

[3] SÜHRING R, DIAMOND M L, BERNSTEIN S, et al. Organophosphate esters in the Canadian Arctic Ocean[J]. Environmental Science & Technology, 2021, 55(1): 304-312.

[4] VAN DER VEEN I, DE BOER J. Phosphorus flame retardants: properties, production, environmental occurrence, toxicity and analysis[J]. Chemosphere, 2012, 88(10): 1119-1153.

[5] BLUM A, BEHL M, BIRNBAUM L S, et al. Organophosphate ester flame retardants: are they a regrettable substitution for polybrominated diphenyl ethers?[J]. Environmental Science & Technology Letters, 2019, 6(11): 638-649.

[6] HUANG J N, YE L J, FANG M L, et al. Industrial production of organophosphate flame retardants (OPFRs): big knowledge gaps need to be filled?[J]. Bulletin of Environmental Contamination and Toxicology, 2022, 108(5): 809-818.

[7] 高蕴语, 董靖, 代然, 等. 洞庭湖水和沉积物中有机磷酸酯的分布特征及风险评估[J]. 环境科学, 2024, 45(7): 3919-3929.

GAO Y Y, DONG J, DAI R, et al. Distribution characteristics and risk assessment of organophosphates in water and sediment in Dongting Lake[J]. Environmental Science, 2024, 45(7): 3919-3929.

[8] ZHANG R J, XIE S L, LI J, et al. Occurrence, distribution, and sources of organophosphate esters (OPEs) in the air of the Indo-China Peninsula based on a passive air monitoring network[J]. Science of the Total Environment, 2024, 929: 172762.

[9] XIE C M, QIU N, XIE J L, et al. Organophosphate esters in seawater and sediments from the low-latitude tropical sea[J]. Science of the Total Environment, 2024, 907: 167930.

[10] ZHANG L, NI L F, WANG H, et al. Higher ecological risks and lower bioremediation potentials identified for emerging OPEs than legacy PCBs in the Beibu Gulf, China[J]. Environmental Research, 2023, 231: 116244.

[11] LIU F, ZHANG R J, LI H L, et al. Distribution and adsorption-desorption of organophosphate esters from land to sea in the sediments of the Beibu Gulf, South China Sea: impact of seagoing river input[J]. Science of the Total Environment, 2024, 917: 170359.

[12] XIE J Q, ZHANG G X, CHEN C C, et al. Tracing organophosphate ester pollutants in hadal trenches─distribution, possible origins, and transport mechanisms[J]. Environmental Science & Technology, 2024, 58(9): 4392-4403.

[13] ZHANG L, YAN C, MA J X, et al. Organophosphate esters in edible marine fish: tissue-specific distribution, species-specific bioaccumulation, and human exposure[J]. Environmental Pollution, 2024, 345: 123560.

[14] XIE Z H, ZHANG X Y, XIE Y Q, et al. Bioaccumulation and potential endocrine disruption risk of legacy and emerging organophosphate esters in Cetaceans from the Northern South China Sea[J]. Environmental Science & Technology, 2024, 58(9): 4368-4380.

[15] LIAN M S, WANG J, WANG Z X, et al. Occurrence, bioaccumulation and trophodynamics of organophosphate esters in the marine biota web of Laizhou Bay, Bohai Sea[J]. Journal of Hazardous Materials, 2024, 469: 134035.

[16] CASAS G, MARTINEZ-VARELA A, VILA-COSTA M, et al. Rain amplification of persistent organic pollutants[J]. Environmental Science & Technology, 2021, 55(19): 12961-12972.

[17] 刘玉斌. 中国海岸带典型生态系统服务价值评估研究[D]. 烟台: 中国科学院烟台海岸带研究所, 2021.

LIU Y B. Evaluation of typical ecosystem service value in China's coastal zone[D]. Yantai: Yantai Institute of Coastal Zone Research, Chinese Academy of Sciences, 2021.

[18] MI L J, XIE Z Y, ZHANG L L, et al. Organophosphate esters in air and seawater of the South China Sea: spatial distribution, transport, and air–sea exchange[J]. Environment & Health, 2023, 1(3): 191-202.

[19] WU H C, YU M L, HUANG J H, et al. Pollution characteristics and risk assessment of organophosphate esters in mollusks along the coast of South China[J]. Marine Pollution Bulletin, 2025, 210: 117317.

[20] SUNDKVIST A M, OLOFSSON U, HAGLUND P. Organophosphorus flame retardants and plasticizers in marine and fresh water biota and in human milk[J]. Journal of Environmental Monitoring, 2010, 12(4): 943-951.

[21] CASTRO V, MONTES R, QUINTANA J B, et al. Determination of 18 organophosphorus flame retardants/plasticizers in mussel samples by matrix solid-phase dispersion combined to liquid chromatography-tandem mass spectrometry[J]. Talanta, 2020, 208: 120470.

[22] SUTTON R, CHEN D, SUN J, et al. Characterization of brominated, chlorinated, and phosphate flame retardants in San Francisco Bay, an urban estuary[J]. Science of the Total Environment, 2019, 652: 212-223.

[23] 黄喜寿, 陈志明, 庞少静, 等. 广西北部湾近岸海域环境问题与对策[J]. 大众科技, 2018, 20(9): 29-32.

HUANG X S, CHEN Z M, PANG S J, et al. Environmental problems and countermeasures in the coastal waters of Beibu Gulf of Guangxi[J]. Popular Science & Technology, 2018, 20(9): 29-32.

[24] LIU F, WEI C S, ZHANG R J, et al. Occurrence, distribution, source identification, and risk assessment of organophosphate esters in the coastal waters of Beibu Gulf, South China Sea: impacts of riverine discharge and fishery[J]. Journal of Hazardous Materials, 2022, 436: 129214.

[25] ZHANG R J, YU K F, LI A, et al. Occurrence, phase distribution, and bioaccumulation of organophosphate esters (OPEs) in mariculture farms of the Beibu Gulf, China: A health risk assessment through seafood consumption [J]. Environmental Pollution, 2020, 263: 114426.

[26] ZHANG L, YANG X, LOW W V, et al. Fugacity- and biotransformation-based mechanistic insights into the trophic transfer of organophosphate flame retardants in a subtropical coastal food web from the Northern Beibu Gulf of China[J]. Water Research, 2024, 261: 122043.

[27] 陈德慰, 苏键, 颜栋美, 等. 广西北部湾常见水产品中甜菜碱含量测定及呈味效果评价[J]. 现代食品科技, 2011, 27(4): 468-472.

CHEN D W, SU J, YAN D M, et al. Determination and taste evaluation of betaine present in common aquatic products from Beibu Gulf in Guangxi[J]. Modern Food Science and Technology. 2011, 27(4): 468-472.

[28] BOLLMANN U E, MöLLER A, XIE Z Y, et al. Occurrence and fate of organophosphorus flame retardants and plasticizers in coastal and marine surface waters[J]. Water Research, 2012, 46(2): 531-538.

[29] 曾维斌. 北部湾海水养殖区有机磷酸酯污染特征及海产品食用风险[D]. 南宁: 广西大学, 2019.

ZENG W B. Occurrence of organophosphorusesters and risk assessment of seafood in mariculture areas of the Beibu Gulf[D]. Nanning: Guangxi University, 2019.

[30] KANG Y R, ZHANG R J, YU K F, et al. Organophosphate esters (OPEs) in a coral reef food web of the Xisha Islands, South China Sea: occurrence, trophodynamic, and exposure risk[J]. Chemosphere, 2023, 313: 137652.

[31] ZHANG R J, KANG Y R, YU K F, et al. Occurrence, distribution, and fate of polychlorinated biphenyls (PCBs) in multiple coral reef regions from the South China Sea: a case study in spring-summer[J]. Science of the Total Environment, 2021, 777: 146106.

[32] ARNOT J A, GOBAS F A P C. A review of bioconcentration factor (BCF) and bioaccumulation factor (BAF) assessments for organic chemicals in aquatic organisms[J]. Environmental Reviews, 2006, 14(4): 257-297.

[33] LABUNSKA I, ABDALLAH M A E, EULAERS I, et al. Human dietary intake of organohalogen contaminants at e-waste recycling sites in Eastern China[J]. Environment International, 2015, 74: 209-220.

[34] GUO J Y, WU F C, SHEN R L, et al. Dietary intake and potential health risk of DDTs and PBDEs via seafood consumption in South China[J]. Ecotoxicology and Environmental Safety, 2010, 73(7): 1812-1819.

[35] 杨晓光, 李艳平, 马冠生, 等. 中国2002年居民身高和体重水平及近10年变化趋势分析[J]. 中华流行病学杂志, 2005, 26(7): 489-493.

YANG X G, LI Y P, MA G S, et al. Study on weight and height of the Chinese people and the differences between 1992 and 2002[J]. Chinese Journal of Epidemiology, 2005, 26(7): 489-493.

[36] ALI N, VAN DEN EEDE N, DIRTU A C, et al. Assessment of human exposure to indoor

organic contaminants via dust ingestion in Pakistan[J]. Indoor Air, 2012, 22(3): 200-211.

[37] DING J J, SHEN X L, LIU W P, et al. Occurrence and risk assessment of organophosphate esters in drinking water from Eastern China[J]. Science of the Total Environment, 2015, 538: 959-965.

[38] HE C T, ZHENG J, QIAO L, et al. Occurrence of organophosphorus flame retardants in indoor dust in multiple microenvironments of southern China and implications for human exposure[J]. Chemosphere, 2015, 133: 47-52.

[39] LEE S, JEONG W, KANNAN K, et al. Occurrence and exposure assessment of organophosphate flame retardants (OPFRs) through the consumption of drinking water in Korea[J]. Water Research, 2016, 103: 182-188.

[40] TAJIMA S, ARAKI A, KAWAI T, et al. Detection and intake assessment of organophosphate flame retardants in house dust in Japanese dwellings[J]. Science of the Total Environment, 2014, 478: 190-199.

[41] DING J J, DENG T Q, XU M M, et al. Residuals of organophosphate esters in foodstuffs and implication for human exposure[J]. Environmental Pollution, 2018, 233: 986-991.

[42] DING Y, HAN M W, WU Z Q, et al. Bioaccumulation and trophic transfer of organophosphate esters in tropical marine food web, South China Sea[J]. Environment International, 2020, 143: 105919.

[43] BEKELE T G, ZHAO H X, WANG Q Z. Tissue distribution and bioaccumulation of organophosphate esters in wild marine fish from Laizhou Bay, North China: implications of human exposure via fish consumption[J]. Journal of Hazardous Materials, 2021, 401: 123410.

[44] 曾以梅, 刘奇, 柯常亮, 等. 红海湾海域水产品中有机磷酸酯(OPEs)类阻燃剂污染分析及健康风险评估[J]. 大连海洋大学学报, 2024, 39(1): 83-91.
ZENG Y M, LIU Q, KE C L, et al. Occurrence and health risk assessment of organophosphate ester flame retardants in fishery products from Honghai Bay[J]. Journal of Dalian Ocean University, 2024, 39(1): 83-91.

[45] TRAN-LAM T T, PHAM P T, BUI M Q, et al. Organophosphate esters and their metabolites in silver pomfret (*Pampus argenteus*) of the Vietnamese coastal areas: spatial-temporal distribution and exposure risk[J]. Chemosphere, 2024, 362: 142724.

[46] CHOI W, LEE S, LEE H K, et al. Organophosphate flame retardants and plasticizers in sediment and bivalves along the Korean coast: occurrence, geographical distribution, and a potential for bioaccumulation[J]. Marine Pollution Bulletin, 2020, 156: 111275.

[47] FU J, FU K H, CHEN Y, et al. Long-range transport, trophic transfer, and ecological risks of organophosphate esters in remote areas[J]. Environmental Science & Technology, 2021, 55(15): 10192-10209.

[48] BEKELE T G, ZHAO H X, WANG Y, et al. Measurement and prediction of bioconcentration

factors of organophosphate flame retardants in common carp (*Cyprinus carpio*)[J]. Ecotoxicology and Environmental Safety, 2018, 166: 270-276.

[49] TANG B, POMA G, BASTIAENSEN M, et al. Bioconcentration and biotransformation of organophosphorus flame retardants (PFRs) in common carp (*Cyprinus carpio*)[J]. Environment International, 2019, 126: 512-522.

[50] HUANG Q Y, HOU R, LIN L, et al. Bioaccumulation and trophic transfer of organophosphate flame retardants and their metabolites in the estuarine food web of the Pearl River, China[J]. Environmental Science & Technology, 2023, 57(9): 3549-3561.

[51] GUO J H, VENIER M, SALAMOVA A, et al. Bioaccumulation of Dechloranes, organophosphate esters, and other flame retardants in Great Lakes fish[J]. Science of the Total Environment, 2017, 583: 1-9.

[52] 姜菁秋, 许宜平, 赵高峰. 新污染物有机磷酸酯生物地球化学过程的研究进展[J]. 环境化学, 2023, 42(8): 2525-2538.

JIANG J Q, XU Y P, ZHAO G F. Research progress on biogeochemical process of emerging contaminants organophosphate esters[J]. Environmental Chemistry, 2023, 42(8): 2525-2538.

[53] LIU Q, WANG X L, ZHOU J, et al. Phosphorus deficiency promoted hydrolysis of organophosphate esters in plants: mechanisms and transformation Pathways[J]. Environmental Science & Technology, 2021, 55(14): 9895-9904.

[54] WAN W N, HUANG H L, LV J T, et al. Uptake, translocation, and biotransformation of organophosphorus esters in wheat (*Triticum aestivum* L.)[J]. Environmental Science & Technology, 2017, 51(23): 13649-13658.

[55] HOU R, HUANG C, RAO K F, et al. Characterized *in vitro* metabolism kinetics of Alkyl organophosphate esters in fish liver and intestinal microsomes[J]. Environmental Science & Technology, 2018, 52(5): 3202-3210.

[56] BOM F C, SÁ F. Concentration of microplastics in bivalves of the environment: a systematic review[J]. Environmental Monitoring and Assessment, 2021, 193(12): 846.

[57] XIE J L, PEI N C, SUN Y X, et al. Bioaccumulation and translocation of organophosphate esters in a Mangrove Nature Reserve from the Pearl River Estuary, South China[J]. Journal of Hazardous Materials, 2022, 427: 127909.

[58] WANG Z M, ZHANG W, HU X J, et al. Organophosphate esters inhibit enzymatic proteolysis through non-covalent interactions[J]. Environment International, 2025, 195: 109256.

Accumulation and dietary risk assessment of organophosphate esters in typical aquatic products of the Beibu Gulf

KANG Yaru [1, 2, 3], ZHANG Ruijie [1, 2, 3*], YU Kefu[1, 2, 3, 4], ZENG Weibin [1, 2, 3], WANG Ruixuan [1, 2, 3]

(1. *Guangxi Laboratory on the Study of Coral Reefs in the South China Sea*, *Guangxi Nanning 530004*, *China*; 2. *Coral Reef Research Center of China, Guangxi Nanning 530004*, *China*; 3. *School of Marine Sciences*, *Guangxi University*, *Guangxi Nanning 530004*, *China;* 4. *Southern Marine Science and Engineering Guangdong Laboratory (Guangzhou), Guangdong Guangzhou 511458, China*)

Abstract: This study aims to investigate the bioaccumulation characteristics and dietary risks of organophosphate esters (OPEs) in aquatic products from the natural environment of the Beibu Gulf. A total of 65 samples from six species were collected from nearshore and estuarine areas during summer and winter. The concentrations of OPEs were quantified using gas chromatography-tandem triple quadrupole mass spectrometry (GC-MS/MS). The results revealed the presence of 11 OPEs in aquatic products, with concentrations significantly higher in winter [(127 ± 101) ng/g dw] compared to summer [(38.5 ± 28.6) ng/g dw]. Fish exhibited lower concentration of OPEs than benthic organisms across both seasons. Seasonal compositional patterns were consistent, dominated by tris(2-chloroisopropyl) phosphates (TCIPPs) and tris(2-chloroethyl) phosphate (TCEP). Chlorinated OPEs (Cl-OPEs) exhibited higher bioaccumulation potential than Alkyl-OPEs, with tris(1,3-dichloroisopropyl) phosphate (TDCIPP) and trihexyl phosphate (THP) obviously bioaccumulated in all aquatic products. Key factors influencing bioaccumulation included metabolic capacity, feeding habits, and habitat conditions. Dietary risk assessment showed hazard quotients (Q_h) below 1 for all age and gender groups, indicating low dietary risk. This study advances the understanding of OPEs contamination in the Beibu Gulf aquatic products and provides a scientific basis for ecological protection and food safety management.

Keywords: organophosphate esters; aquatic products; Beibu Gulf; bioaccumulation; dietary risk assessment

remote sensing

MDPI

Article

Marine Heatwaves and Cold Spells in Global Coral Reef Regions (1982–2070): Characteristics, Drivers, and Impacts

Honglei Jiang [1], Tianfei Ren [1], Rongyong Huang [1] and Kefu Yu [1,2,*]

[1] Guangxi Laboratory on the Study of Coral Reefs in the South China Sea, School of Marine Sciences, Guangxi University, Nanning 530004, China; jianghonglei@gxu.edu.cn (H.J.); 2327301023@st.gxu.edu.cn (T.R.); 20150044@gxu.edu.cn (R.H.)
[2] Southern Marine Science and Engineering Guangdong Laboratory (Guangzhou), Guangzhou 511458, China
* Correspondence: kefuyu@scsio.ac.cn

Abstract

Extreme sea surface temperature (SST) events, such as marine heatwaves (MHWs) and marine cold spells (MCSs), severely affect warm water coral reefs. However, further study is required on their historical and future spatiotemporal patterns, driving mechanisms, and impacts in coral reef regions. This study analyzed the spatiotemporal patterns in MHWs/MCSs for the periods 1982–2022 and 2023–2070 using ten indices based on OISSTv2.1 and CMIP6 data, respectively, identified key MHW drivers via four machine learning methods (Random Forest, Extreme Gradient Boosting, Light Gradient Boosting Machine, and categorical boosting) and SHAP values (Shapley Additive Explanations), and then examined their relationship with coral coverage across ten global marine regions. Our results revealed that (1) MHWs are not only increasing in their average intensity but also becoming more extreme, while MCSs have declined. More MHW days are observed in regions like the Red Sea, the Persian Gulf, and the South Pacific Islands, with increases of up to 28 days per decade. (2) Higher-latitude coral reefs are experiencing more severe MHWs than equatorial regions, with up to 1.24 times more MHW days, emphasizing the urgent need to protect coral refuges. (3) MHWs are projected to occur nearly year-round by 2070 under scenario SSP5–8.5. The area ratio of MHWs to MCSs is expected to rise sharply from 2040 onward, reaching approximately 100-fold under the SSP2–4.5 scenario and 196-fold under the SSP5–8.5 scenario, particularly in the Marshall Islands and Caribbean Sea regions. (4) The coefficient of variation (CV) of annual temperature, annual ocean heat content, and monthly temperature were the top three factors driving MHW intensity. We emphasize that future MHW predictions should focus more on the CV of forecasting indicators rather than just the climate means. (5) Coral coverage exhibited post-mortality processes following MHWs, showing a strong negative correlation ($r = -0.54$, $p < 0.01$) with MHWs while demonstrating a significant positive correlation ($r = 0.6$, $p < 0.01$) with MCSs. Our research underscores the sustained efforts to protect and restore coral reefs amid escalating climate-induced stressors.

Keywords: marine heatwaves; marine cold spells; coral reef; machine learning

check for updates

Academic Editors: Yulong Yao and Wenjin Sun

Received: 6 July 2025
Revised: 10 August 2025
Accepted: 16 August 2025
Published: 19 August 2025

Citation: Jiang, H.; Ren, T.; Huang, R.; Yu, K. Marine Heatwaves and Cold Spells in Global Coral Reef Regions (1982–2070): Characteristics, Drivers, and Impacts. *Remote Sens.* **2025**, *17*, 2881. https://doi.org/10.3390/rs17162881

Copyright: © 2025 by the authors. Licensee MDPI, Basel, Switzerland. This article is an open access article distributed under the terms and conditions of the Creative Commons Attribution (CC BY) license (https://creativecommons.org/licenses/by/4.0/).

1. Introduction

A marine heatwave (MHW) or marine cold spell (MCS) is typically defined as a discrete and prolonged event characterized by high and low sea surface temperatures (SSTs), respectively [1]. They can have devastating impacts on marine ecosystems, particularly

coral reef ecosystems, which are among the most thoroughly documented [2–4]. Coral reef ecosystems are characterized by high primary productivity and rapid biogeochemical cycling, serving as critical habitats for a vast diversity of marine species [5]. Although coral reefs cover less than 2.5‰ of the global ocean area, they provide over 10% of the world's economically valuable fishery resources. However, due to their high sensitivity and vulnerability to climate change, coral reefs are predicted to be one of the first ecosystems to collapse under global warming [6,7]. For example, live coral cover in Australia's Great Barrier Reef declined from about 50% in 1960 to 20% in 2003, while coral cover in the Caribbean fell from 50% in 1977 to 10% by 2001 [8–10].

The effects of high temperatures on coral reef ecosystems are attracting increasing attention. Most research has mainly focused on low-latitude areas, such as the Great Barrier Reef [11,12], or isolated local sites, such as Weizhou Island in the Beibu Gulf [13]. As early as 1931, Yonge and Nicholls began investigating the impacts of thermal stress on coral reef ecosystems. The distinct spatial distribution of bleaching events on the Great Barrier Reef was closely related to the corresponding SST patterns [4]. MHWs in marginal seas are more pronounced than those in open oceans and exceed the global average in magnitude [14]. However, coral reefs are predominantly distributed in tropical marginal seas. As global warming continues, the interval between successive bleaching events may become too short for coral reefs to recover [4]. Given the uneven increase in the global SST and the scarcity of large-scale studies on MHWs in coral reef regions, accurately identifying MHW events, quantifying their trends (particularly the decadal and long-term trends), and investigating their primary regions and formation mechanisms require further efforts. Therefore, a more thorough quantification of the spatiotemporal patterns in MHWs in global coral reef regions over past and future decades is essential.

The formation mechanisms of MHWs are primarily driven by air–sea heat exchange and oceanic dynamic processes, including atmospheric circulation, advective transport, horizontal and vertical mixing, and entrainment at the bottom of the mixed layer [15–18]. Most current research focuses on low-frequency variability on seasonal or longer time scales. In general, these mechanisms can be categorized as detailed below.

Firstly, on a seasonal scale, MHWs are more frequent during summer and least frequent during winter. Moreover, the intensity of summer MHWs is typically higher than in winter, mainly due to a shallower mixed layer during summer [19,20]. Studies have shown that in the Beibu Gulf coral reef regions, lower sea level pressure in spring and autumn and stronger meridional (V component) winds in autumn and winter are associated with stronger average MHW intensity [21]. The temporal variation in MHWs also exhibits spatial heterogeneity, which is mainly attributed to local atmospheric forcing and oceanic dynamics [22]. Long-duration and higher-intensity MHWs occurred more frequently in tropical eastern waters and along western boundary currents [23].

Secondly, on an interannual scale, MHWs are primarily regulated by climate modes like the El Niño–Southern Oscillation (ENSO) and the Indian Ocean Dipole (IOD) [24,25]. ENSO exerts global impacts through both atmospheric and oceanic teleconnections. For example, ENSO can intensify the descending Walker circulation over the tropical western Indian Ocean, reduce cloud cover, enhance solar radiation, and weaken wind speed, thereby reducing latent heat flux cooling and promoting MHW development [26]. A positive IOD phase can induce thermocline shoaling and enhance the upwelling of cold water off of Sumatra and Java, thereby suppressing MHW formation [27,28].

Although The China Blue Book on Climate Change serves as an important scientific basis for China's marine economic development and policy decisions, it only began reporting MHW-related information in 2024 [21] and still only provides limited coverage on

MHWs in coral reef regions. MHWs have largely been overlooked, with MCSs receiving even less attention.

It is important to note that extreme low temperatures can also lead to coral bleaching, a phenomenon referred to as "cold bleaching" [29–32]. In July 2003, severe bleaching and even mortality were observed in Acropora species in the intertidal zone of Heron Island, Australia, due to extreme low temperatures (below 12 °C) [2]. Rich et al. [33] also observed cold-stress-induced coral bleaching on a reef flat in the central Red Sea, highlighting the necessity of long-term monitoring programs. Similarly, Yu et al. [34] reported widespread coral bleaching linked to significant cooling during the mid-Holocene. Therefore, while studying MHWs in coral reef regions is essential, MCSs should not be overlooked.

To address these research gaps, several key objectives were established to advance our understanding of MHWs/MCSs in relation to several critical aspects. (i) We utilized satellite observation data spanning from 1982 to 2022, along with ten indicators, to comparatively assess the spatial distribution and temporal variability of both MHWs and MCSs. This aspect, which has often been overlooked in prior studies, was a central focus of our investigation. (ii) Four machine learning models were applied to examine the influence of atmospheric, oceanic, and other environmental factors on the spatial heterogeneity of MHWs, with particular emphasis on coral reefs. (iii) We explored the relationship between MHWs/MCSs and coral coverage across ten global coral reef regions, as defined by the Marine Ecoregions of the World (MEOW). This study provides a crucial scientific foundation for coral reef conservation and ecological sustainability.

2. Materials and Methods

2.1. Data Sources

2.1.1. OISST V2.1 Dataset

The data used in the statistical analysis of MHW and MCS characteristics in coral reef regions can be derived from the OISST V2.1 dataset (https://psl.noaa.gov/data/gridded/data.noaa.oisst.v2.highres.html, accessed on 27 November 2023). The OISST V2 dataset is a sea surface temperature dataset obtained through optimal interpolation by the National Oceanic and Atmospheric Administration (NOAA). It has a daily temporal resolution, spanning from January 1982 to December 2022, with a spatial resolution of $0.25^\circ \times 0.25^\circ$.

2.1.2. CMIP6 Dataset

The future climate projections from the CMIP6 ocean model (2024–2070) were adopted to predict changes in MHWs and MCSs. The metrics were calculated separately for each model, and their multi-model ensemble mean was analyzed to assess the spatial patterns under the SSP2–4.5 and SSP5–8.5 scenarios. Because the areas of the coral reefs are scattered and small, high resolution enables a more accurate representation of SST and MHWs/MCSs in coral reef regions. Referring to previous studies [31,35,36], we selected the most recently released high-horizontal-resolution models (CMIP6), including AWI-CM-1-1-MR, GFDL-CM4, and MPI-ESM1-2-HR, under the "r1i1p1f1" scenario (extracted from https://cds.climate.copernicus.eu/datasets/projections-cmip6?tab=download (accessed on 27 November 2023), to predict future changes in MHWs and MCSs.

2.1.3. Climate Dataset

For the potential factors affecting MHWs, we selected six atmospheric, oceanic, and climatic variables, as they directly influence the onset, intensity, and persistence of MHWs (Table A1). Additionally, all independent variables were expanded into three indices, each incorporating the following components: "Mean" (multi-year average), "_a_cv" (multi-year coefficient of variation), "_m_cv" (monthly coefficient of variation), and "slp" (multi-year

trend). As a result, a total of 24 predictor features (independent variables) were obtained. Specifically, the data utilized in this study, including air temperature at 2 m in height (t2m), total cloud cover (tcc), 10 m wind field (si10m), surface latent heat net flux, surface sensible heat net flux, surface net long-wave radiation flux, surface net short-wave radiation flux, and 500 hPa geopotential height, were sourced from the ERA5 (ECMWF Reanalysis v5) dataset provided by the European Centre for Medium-Range Weather Forecasts (ECMWF). This dataset is accessible via the Climate Data Store at https://cds.climate.copernicus.eu (accessed on 27 November 2023). ERA5 integrates a wealth of historical observational data, including buoy and satellite observations. The dataset provides a temporal resolution of 1 h and a spatial resolution of 2.5° × 2.5°.

Wind speed (10 m) was derived as the square root of the sum of the squared u and v wind components. Net radiation (Q_net) was calculated by summing the four radiation components: surface net short-wave radiation flux, surface net long-wave radiation flux, surface latent heat net flux, and surface sensible heat net flux.

For the analysis, we processed these data by computing multi-year averages (mean), the coefficient of variation (a_CV), long-term trends (slp) (estimated using Theil–Sen's slope), and the coefficient of variation (m_CV) at a monthly scale. These metrics provide a robust foundation for assessing temporal variability and trends in the dataset.

2.1.4. The Hard Coral Coverage Dataset

The global coral reef regions were divided into 10 subregions, as shown in Figure 1. The hard coral coverage data came from the Global Coral Reef Monitoring Network (https://gcrmn.net, accessed on 27 November 2023), spanning from 1980 to 2019. We used data based on the 10 Marine Ecoregions of the World (MEOW) framework, rather than pixel-level data [37,38]. The data were collected at individual sites and assigned to 10 km × 10 km grid tiles by using a nearest-neighbor approach and Voronoi polygons for estimating the coral reef area. They were then aggregated hierarchically from the site level to MEOW Ecoregions, GCRMN subregions, and, ultimately, the global scale, with weighting based on coral reef area proportions. A pseudo-spatial hierarchy was applied, where the influence of neighboring data decreased incrementally, allowing data-poor areas to leverage patterns from data-rich areas within the same MEOW Ecoregion. Potential biases included sampling bias, spatial distribution bias, and unequal sample sizes. However, the above processing method effectively minimizes these biases. This is a widely used dataset for global coral cover.

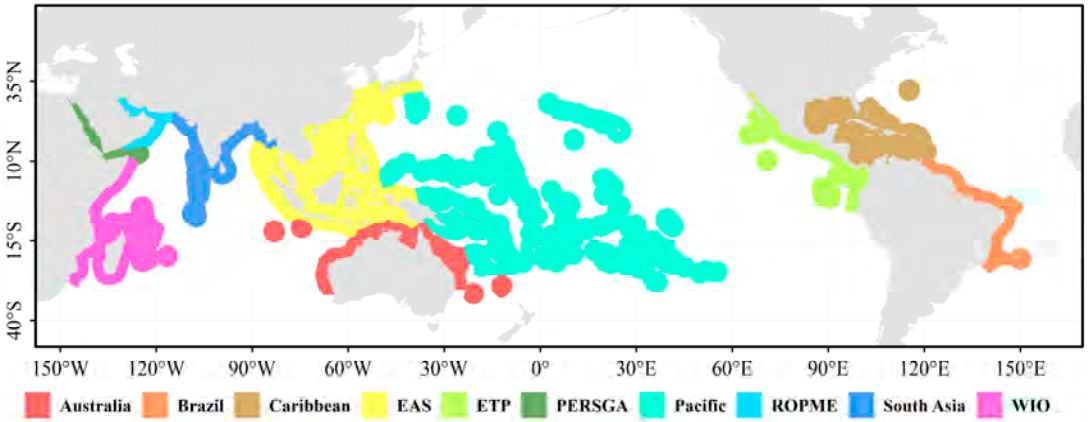


Figure 1. Overview of the global coral reef regions defined according to the Marine Ecoregions of the World (MEOW) framework. Notes: ETP refers to the Eastern Tropical Pacific, EAS refers to East Asia, ROPME refers to the Regional Organization for the Protection of the Marine Environment, PERSGA refers to the Persian Gulf and the Gulf of Oman, and WIO refers to the Western Indian Ocean.

2.2. Definition of MHWs and MCSs

Based on previous research, an MHW is defined as a discrete warm water event exceeding 5 days in duration, whereas an MCS is defined as an extremely cold water event [1]. The baseline climatology criteria for quantifying MHWs and MCSs are calculated using the OISST data for 1982–2022. There are two types of baseline calculations: those with a fixed baseline and those with a sliding baseline. A fixed baseline period was adopted for corals due to their slow thermal acclimation, as they are long-lived organisms. In contrast, sliding baselines are used for species that undergo rapid biological adaptation, such as phytoplankton and zooplankton, which have strong migratory abilities and shorter lifecycles [1,39,40]. In order to compare the spatiotemporal patterns of the past and the future, this baseline was used consistently for both historical analysis and future projections. Furthermore, 31-day smoothing was applied to previously calculated values to produce the final climatological mean SST (blue curve) and the 90th percentile threshold (green curve), shown in Figure 2. The use of a 31-day smoothing window is primarily to reduce short-term fluctuations in the data, preventing them from being influenced by occasional localized extreme short-term changes, while also filtering out noise caused by natural fluctuations or seasonal changes. This makes the baseline climate data smoother and more reliable, as demonstrated in previous studies [41–43]. The 90th percentile value serves as the threshold for an MHW, while the 10th percentile value serves as the threshold for an MCS [1,29,30].

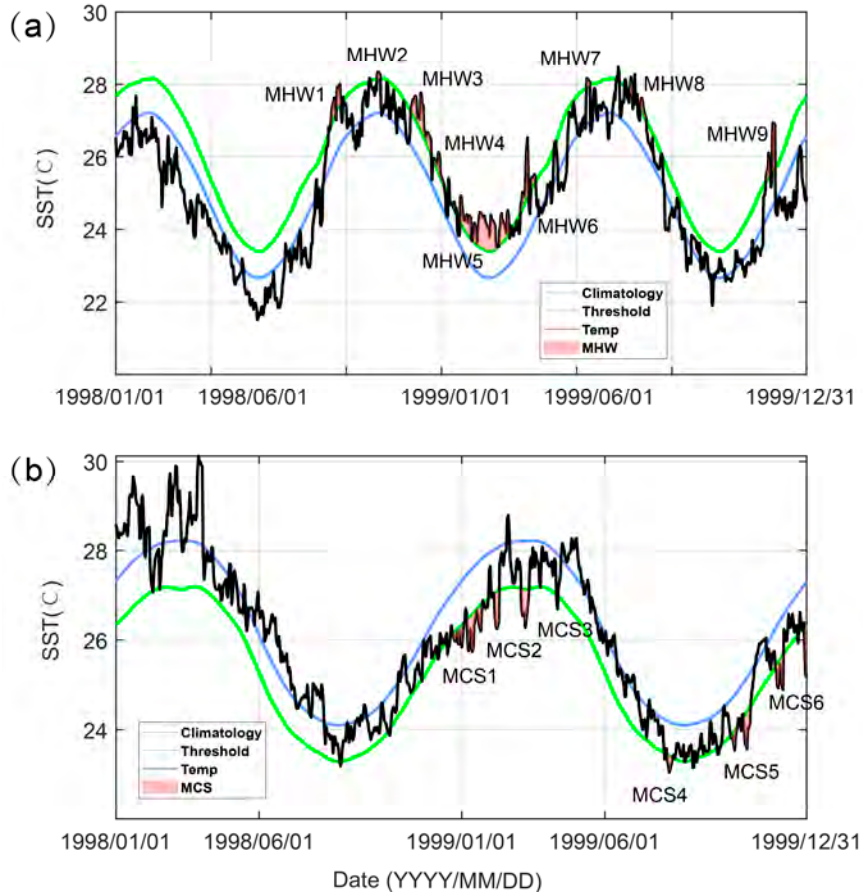


Figure 2. MHW and MCS cases from 1998 to 1999. (**a**) A case of an MHW occurring at an arbitrary point within the Great Barrier Reef, Australia. (**b**) A case of an MCS occurring at an arbitrary point in the vicinity of Mozambique. The blue line represents the climatological mean for the fixed climate baseline, the green line corresponds to the climatological 90th percentile for (**a**) and the 10th percentile for (**b**), the black line represents the observed SST, and the red shading highlights the occurrence of an MHW or an MCS.

To gain a comprehensive understanding of the spatiotemporal patterns in MHWs/MCSs, we used several indicators, including total days (the sum of all days of MHW/MCS events per year), average duration (the average duration of MHW/MCS events per year), frequency (the total counts of MHW/MCS events per year), average intensity (the average intensity of SST anomalies during MHW/MCS events per year), and maximum intensity (the maximum intensity of SST anomalies during MHW/MCS events per year) (Table 1).

Table 1. Definitions and calculation of MHWs/MCSs.

	Definition	Formula	Unit
Equation (1)	Yearly total count of MHW/MCS events	$No = N$	counts
Equation (2)	Yearly total days of MHW/MCS events	$TD = \sum_{i}^{n} D_i$	days
Equation (3)	Yearly average duration of all MHWs/MCSs	$DU = \sum_{i}^{n} (D_i)/N$	days/counts
Equation (4)	Yearly average intensity of SST anomalies during all MHWs/MCSs	$AI = \sum_{i}^{n} \sum_{j}^{Di} (mean(T_{ij}) - \widetilde{T}_{ij})$	°C/counts
Equation (5)	Yearly maximum intensity of SST anomalies during all MHWs/MCSs	$MI = \sum_{i}^{n} \sum_{j}^{Di} (max(T_{ij}) - \widetilde{T}_{ij})$	°C/counts

Notes: *No*, yearly total counts of MHW/MCS events. *N*, the number of MHW/MCS events counted during the year. *TD*, yearly total days of MHW/MCS events. D_i, the number of days associated with each MHW/MCS event. *DU*, yearly average duration of all MHWs/MCSs. *AI*, yearly average intensity of SST anomalies during all MHWs/MCSs. T_{ij}, the sea surface temperature of the *i*-th day of the *j*-th MHW/MCS event. $\widetilde{T}_{ij}$, mean SST anomalies for the corresponding MHW/MCS event. *MI*, yearly maximum intensity of SST anomalies during all MHWs/MCSs. *n* represents the total number of MHW/MCS events in all of the equations.

2.3. Analysis Methods

Random Forest (RF) is based on the Bagging framework. RF generates multiple decision trees through bootstrap sampling and incorporates random feature selection to reduce model variance. By constructing independent decision trees in parallel and aggregating results via voting or averaging, RF inherently adapts well to high-dimensional data. XGBoost (Extreme Gradient Boosting) is an optimized version of Gradient Boosting Decision Trees (GBDT) [44]. Innovations include block-structured feature storage for parallel computing and column subsampling to reduce computational overhead. Compared to traditional GBDT, XGBoost significantly improves both accuracy and efficiency, making it a mainstream algorithm in machine learning competitions. LightGbm (Light Gradient Boosting Machine) further optimizes XGBoost, with the following key improvements. It discretizes continuous features into histograms, reducing computation and memory usage; it prioritizes splitting leaf nodes with the highest gain, enhancing the model's efficiency; and it retains high-gradient samples while randomly sampling low-gradient ones, balancing data distribution and computational load. These optimizations make LightGbm significantly faster than XGBoost for large-scale datasets. CatBoost (categorical boosting) is renowned for handling categorical variables; it also optimizes the processing of continuous variables. Unlike traditional algorithms (e.g., decision trees requiring manual binning thresholds), CatBoost automatically optimizes split points for continuous features. While LightGBM generally achieves faster training speeds, CatBoost's key advantage lies in its automated feature processing (for continuous, categorical, and missing values), minimizing manual intervention while maintaining high predictive performance.

Recursive Feature Elimination (RFE) can efficiently control overfitting. It was implemented to select the most important predictors from the high-dimensional environmental variables. The algorithm iteratively removed the least important features, as determined by the feature importance scores, while optimizing the model's predictive performance through 10-fold cross-validation.

Regarding parameter optimization, we implemented diverse strategies to control overfitting. Table A2 lists the set of parameters for four machine learning models. Random Forest is configured with n_estimators = 500 and max_depth = 6, leveraging its inherent bootstrap sampling and leaf node constraint mechanisms to control overfitting. XGBoost comprehensively applies early stopping, feature subsampling (colsample_bytree = 0.8), and instance subsampling (subsample = 0.8) techniques to mitigate overfitting. CatBoost adopts an early stopping strategy (halting after 50 rounds without improvement) and L2 regularization (l2_leaf_reg = 3) to control model complexity. The LightGBM model utilizes RandomizedSearchCV for parameter tuning, with search ranges including n_estimators (200) and learning_rate (0.1), combined with 10-fold cross-validation to enhance generalization capability. All models employ an 80%/20% training/testing split strategy, ensuring reliability and effectiveness in model evaluation.

To interpret the four models' results, SHAP values (Shapley Additive Explanations) [45] were adopted to analyze the sensitivity of abrupt change probabilities to environmental factors. Based on game theory, SHAP values evaluate the impact of each predictor by assessing all possible combinations of predictors. For example, for the OHC feature, the approach evaluates model accuracy using all combinations of predictors, excluding OHC, and then tests how adding OHC improves the accuracy of each combination. SHAP values provide a consistent framework for quantifying the independent contribution of each environmental factor (i.e., feature) to MHWs while keeping other features constant, thus enhancing the model's transparency.

In addition, a combination of Theil–Sen and Mann–Kendall [46] trend analysis was adopted to identify the trend of spatiotemporal dynamics in MHWs/MCSs.

3. Results

3.1. Global Patterns in Mean MHW and MCS Metrics in Coral Reef Zones from 1982 to 2022

As illustrated in Figures 3 and 4, the spatiotemporal distribution patterns in MHWs and MCSs show significant spatial heterogeneity. In general, MHWs in higher-latitude coral reef zones are characterized by longer durations and higher intensity, with up to 1.24 times more MHW days than equatorial regions (Tables A3 and A4 and Figure A1). The spatial distribution of MCS frequency is similar to that of MHWs but features shorter durations and contrasting trends in average intensity.

Specifically, the total days of both MHWs and MCSs (the sum of all days of MHWs/MCSs per year) vary significantly across regions (Figures 3a and 4a). High figures for total days are observed in regions like the Red Sea, the Persian Gulf, the Hawaiian Islands, the Galapagos Islands, the South Pacific Islands, coastal Australia, and the southwestern coast of Sumatra, with MHWs reaching up to 32 days and MCSs reaching up to 31 days. In contrast, lower numbers of total days are observed in regions like eastern Africa, northern Madagascar, equatorial areas, and the Caribbean Sea.

The average duration of MHWs and MCSs (the average duration of MHW/MCS events per year) also varies across coral reef zones (Figures 3b and 4b). Most regions experience MHWs lasting fewer than 20 days/count and MCSs lasting fewer than 10 days/count. However, in some regions, the longest average duration of MHWs can extend up to 31 days/count, while MCSs can reach up to 20 days/count.

Regarding the frequency of MHWs and MCSs (the total counts of MHW/MCS events per year, Figures 3c and 4c), high-frequency MHWs primarily occur in East Asia, northern Australia, southern Madagascar, and the southern peninsula of Florida, where events occur several times per year on average. These regions, located near continents or at higher latitudes, experience multiple events per year on average. Similarly, high-frequency MCSs occur in western Madagascar, East Asia, northern Australia, and the Galapagos Islands,

with frequencies approaching three times per year. Conversely, low-frequency regions of both MHWs and MCSs are identified in the Pacific Ocean, the Red Sea, the Persian Gulf, and the Caribbean Sea.

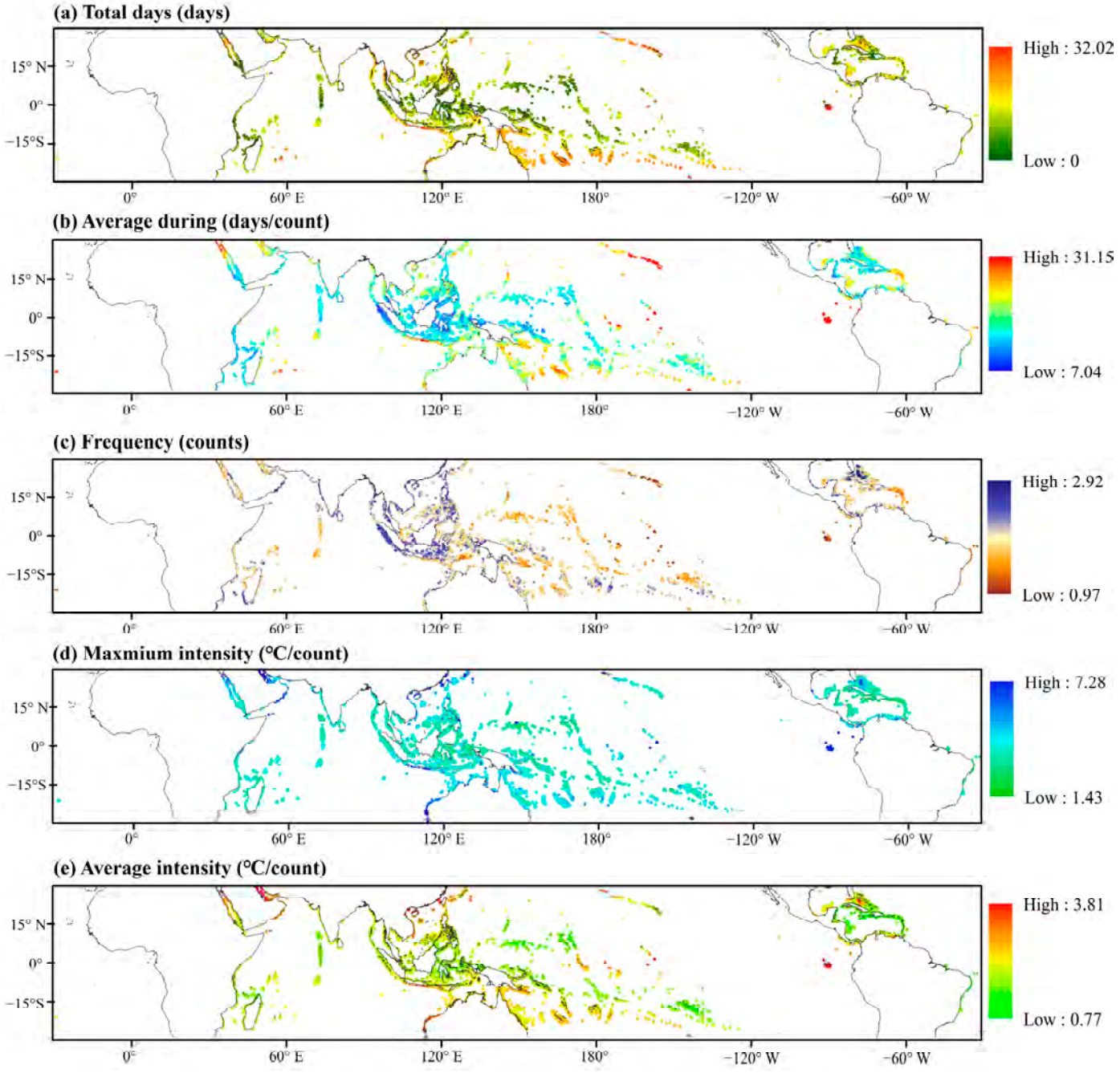


Figure 3. Spatial distribution of MHW metric means across global coral regions during the 41-year period (1982–2022). (**a**) Total days, (**b**) average duration, (**c**) frequency, (**d**) maximum intensity, and (**e**) average intensity.

Regions with a high maximum intensity of MHWs (the maximum intensity of SST anomalies during MHW/MCS events per year, Figures 3d and 4d) are typically located in high-latitude coral reef zones, whereas low-intensity areas are found in equatorial oceans. For MCS, most coral reef zones exhibit a high maximum intensity, with low-intensity areas mainly found in the Galapagos Islands, the South Pacific Islands, southwestern Sumatra, and northwestern Australia. The spatial distribution patterns of average intensity for both

MHWs and MCSs (the average intensity of SST anomalies during MHW/MCS events per year, Figures 3e and 4e) closely follow those of maximum intensity.

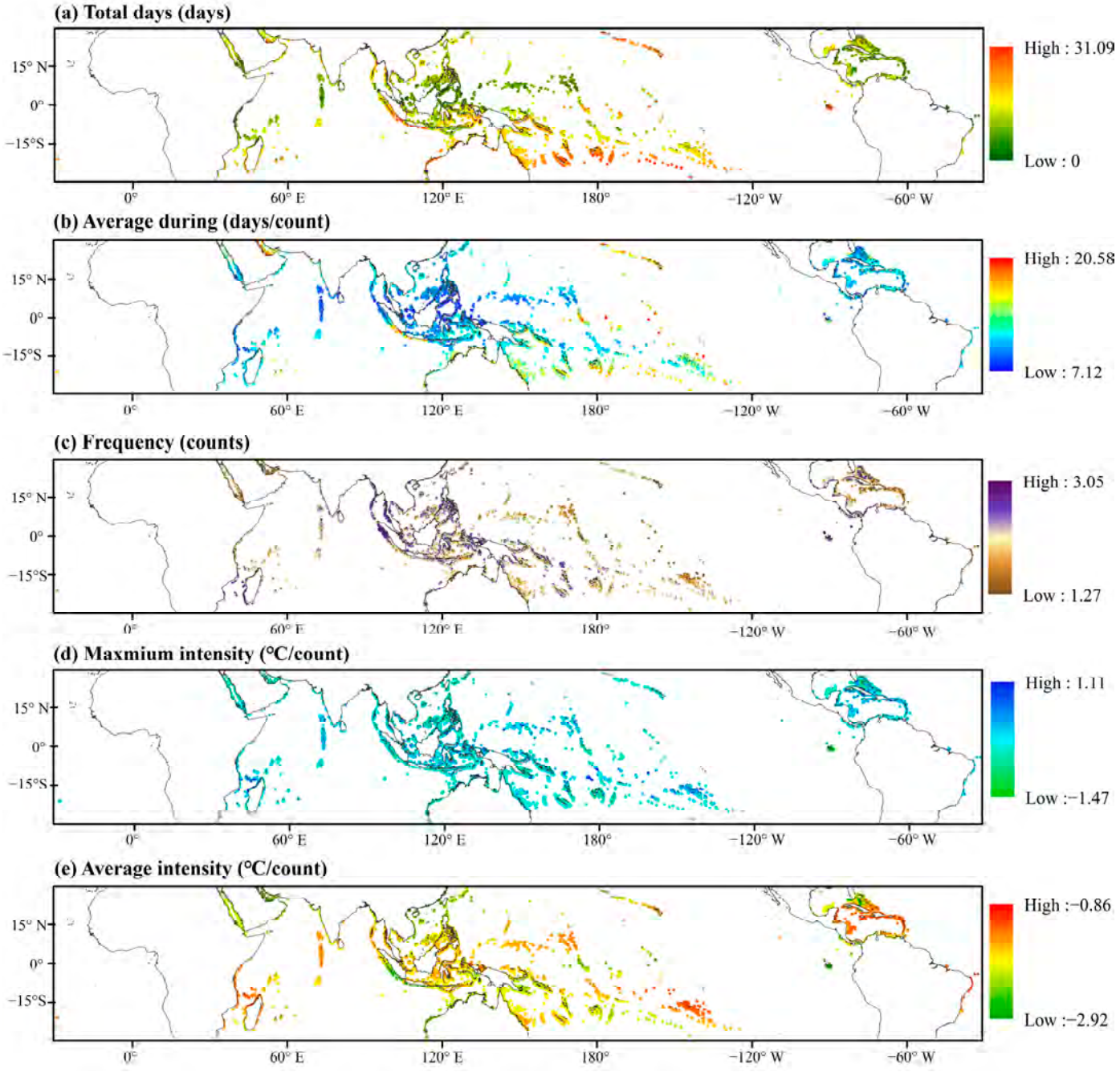


Figure 4. Spatial distribution of MCS metric means across global coral regions during the 41-year period (1982–2022). (**a**) Total days, (**b**) average duration, (**c**) frequency, (**d**) maximum intensity, and (**e**) average intensity.

3.2. Global Trends in Mean MHW and MCS Metrics in Coral Reef Zones from 1982 to 2022

From 1982 to 2022, MHW events have increased, while MCS events have decreased, exhibiting significant spatial heterogeneity across the entire coral reef regions, particularly in East Asia, the South Pacific, and the Caribbean (Figures 5 and 6). MHW total days have increased substantially in most regions, particularly in the Red Sea, the northern Persian Gulf, and the South Pacific islands, with rates of up to 28 days/decade. Additionally, the average duration of MHW events has increased by 1–2 days/event/decade, while the

frequency has increased by 1–1.9 events/decade, especially in the Red Sea, the Persian Gulf, eastern East Asia, and the South Pacific islands.

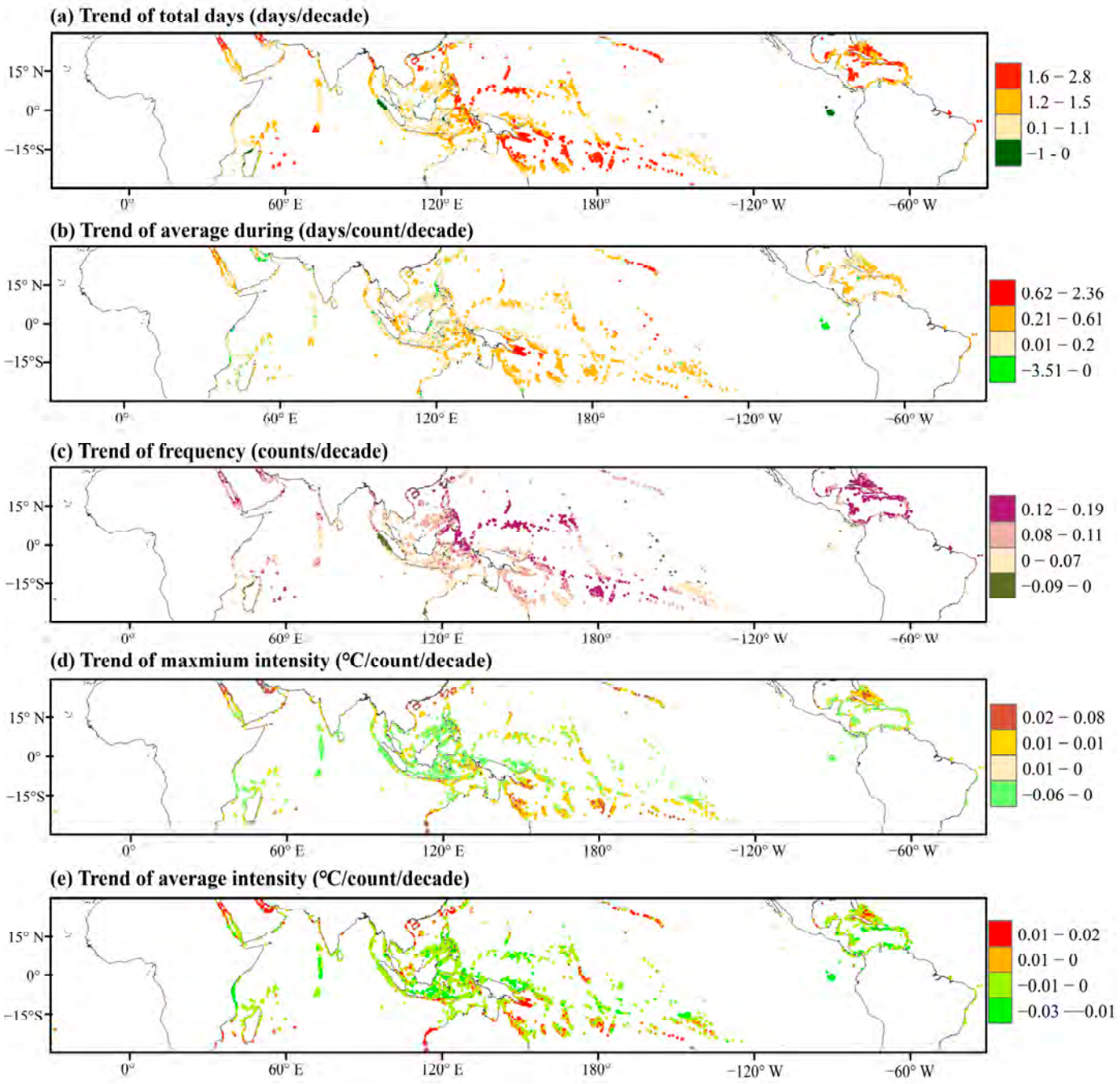


Figure 5. Spatial distribution of MHW metric trends across global coral regions during the 41-year period (1982–2022). (**a**) Trend of total days, (**b**) trend of average duration, (**c**) trend of frequency, (**d**) trend of maximum intensity, and (**e**) trend of average intensity. Note that red represents an increasing trend, while green indicates a decreasing trend.

MHW events in global coral reef regions have become more extreme over time (Figure 7g,i). Specifically, the average intensity of MHWs has decreased by 0.1 °C/count/decade, while the maximum intensity has increased by 0.1 °C/count/decade. Additionally, the average intensity tends to be higher during strong El Niño years.

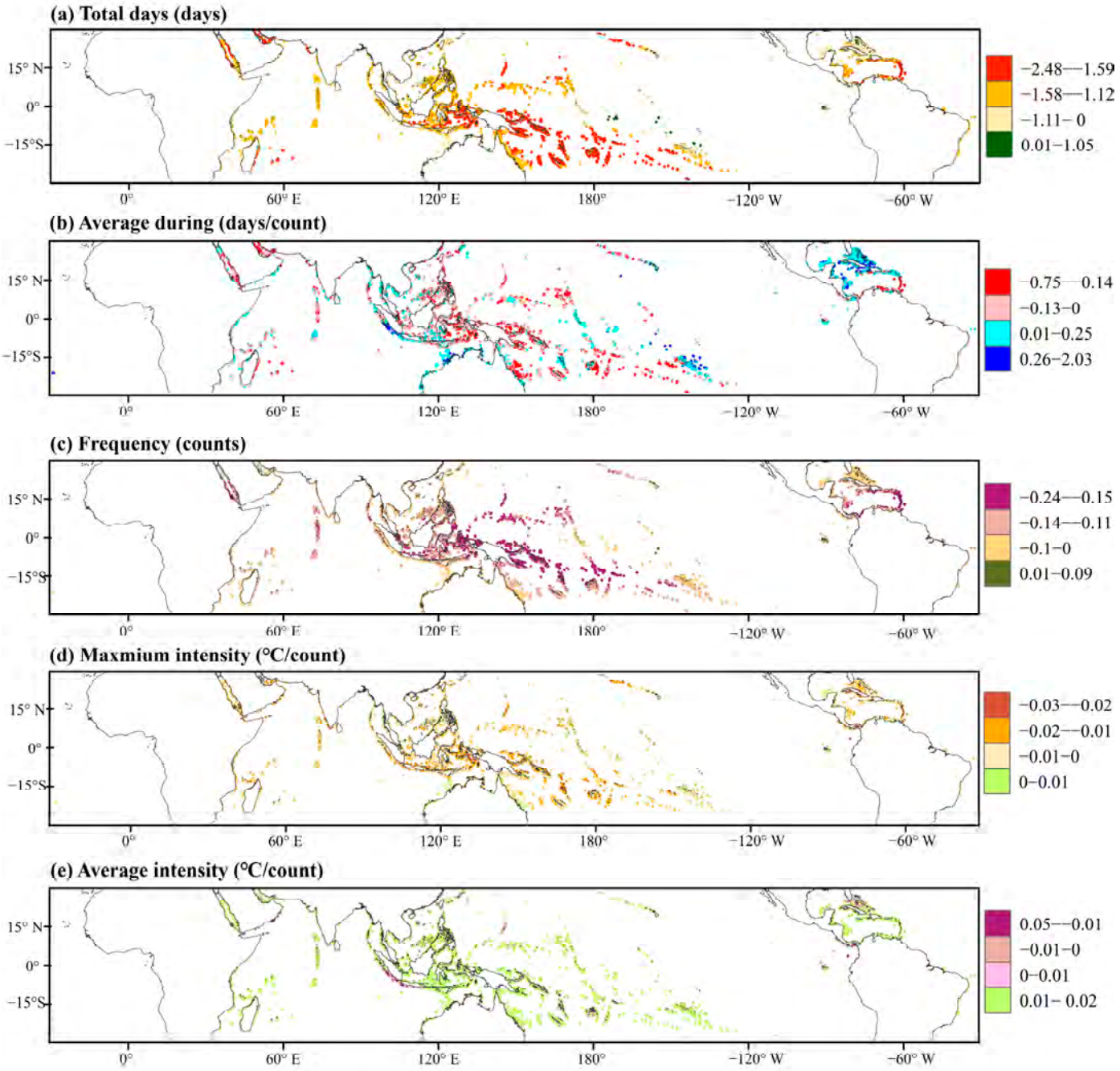


Figure 6. Spatial distribution of MCS metric trends across global coral regions during the 41-year period (1982–2022). (**a**) Trend of total days, (**b**) trend of average duration, (**c**) trend of frequency, (**d**) trend of maximum intensity, and (**e**) trend of average intensity. Note that red represents a decreasing trend, while green/blue indicates an increasing trend.

Conversely, as shown in Figure 7, the MCS total days have decreased by approximately 10.5 days/decade, with a similar reduction in average duration by 0–5 days/count/decade across most coral reef areas. The frequency of MCS events has also decreased by 0.9–2.4 counts/decade. However, the maximum intensity of MCSs has increased in coral reef regions between 15° and 30° latitude north and south at a rate of 0–0.1 °C/count/decade. Despite this overall decline, the maximum intensity of MCSs continues to show variability, as illustrated by the quadratic trend fitted to the MCS mean intensity variable (Figure 7j).

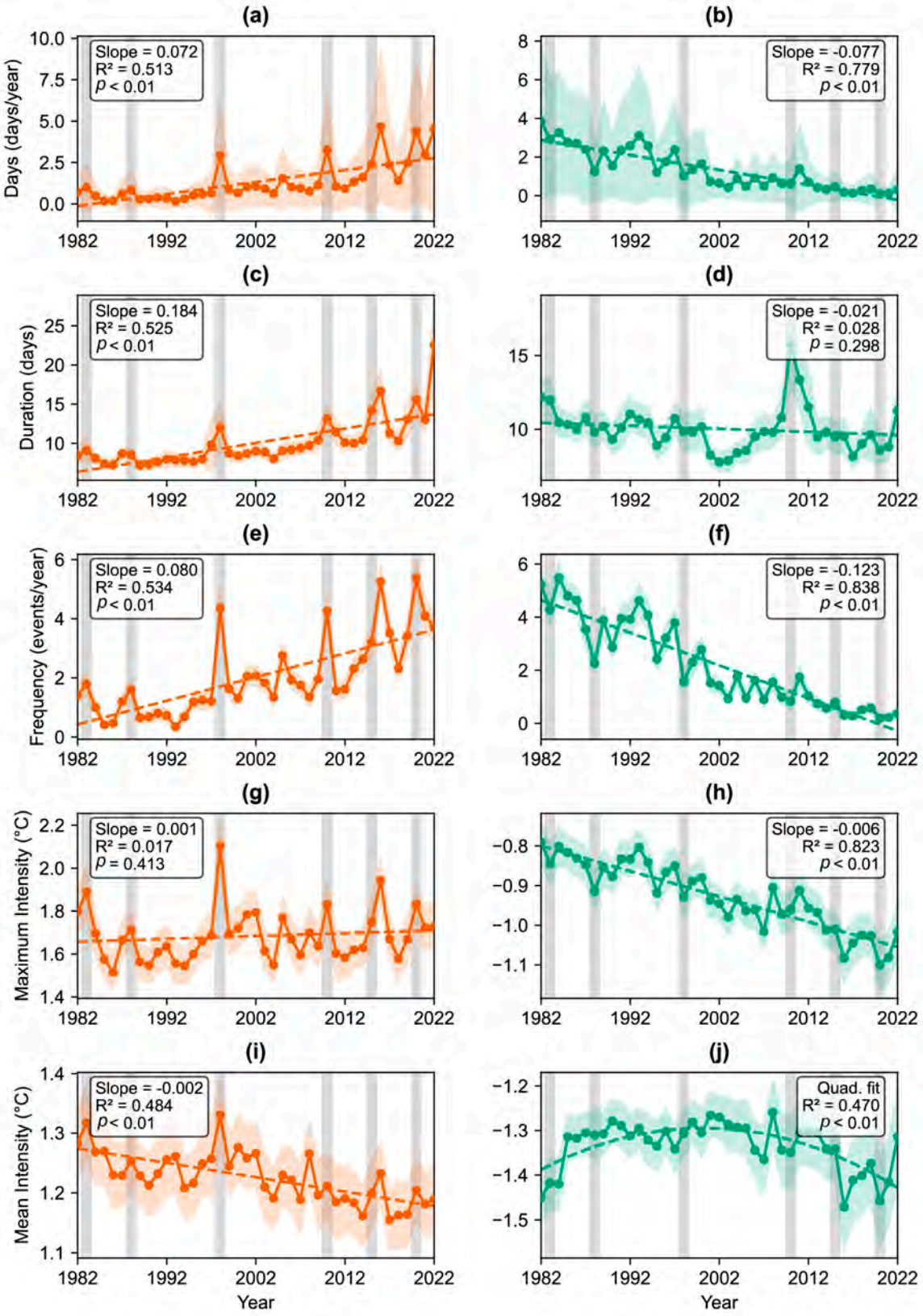


Figure 7. The temporal evolution from 1982 to 2022 of MHWs (**left panels**) and MCSs (**right panels**). Metrics displayed include annual occurrence days (**a**,**b**), event duration (**c**,**d**), annual frequency (**e**,**f**), and thermal intensity measures ((**g**,**h**) for maximum; (**i**,**j**) for mean). Highlighted bands mark major El Niño events (1983, 1988, 1998, 2010, 2015, 2020). The confidence intervals represent the spatial standard deviation across global coral reef areas. To avoid obscuring temporal trends, the confidence intervals were divided by 5 for visualization.

3.3. Global Trends in Mean MHW and MCS Metrics in Coral Reef Zones from 2023 to 2070

The projections suggest a significant increase in MHW duration, frequency, and intensity in the future, particularly under the SSP5–8.5 scenario in the Marshall Islands and the Caribbean Sea regions, while MCS events are expected to decrease in both frequency and intensity across most coral reef regions, particular in the South Pacific.

Under the SSP2–4.5 scenario, the results for MHWs showed that the total days of MHWs exceeded 150 days in most coral reef regions, with the eastern part of Indonesia, the Marshall Islands, and the Caribbean Sea approaching 300 days (Figure 8). The average annual duration of MHWs ranged from 14 to 170 days/count, with the aforementioned regions experiencing durations exceeding 120 days. The frequency of MHWs was particularly high in the Indo-Pacific and Caribbean regions, approaching eight counts per year. The average warming intensity of MHWs varied between 1 °C and 3 °C/count, with the maximum intensity reaching up to 8 °C, primarily observed in the Persian Gulf.

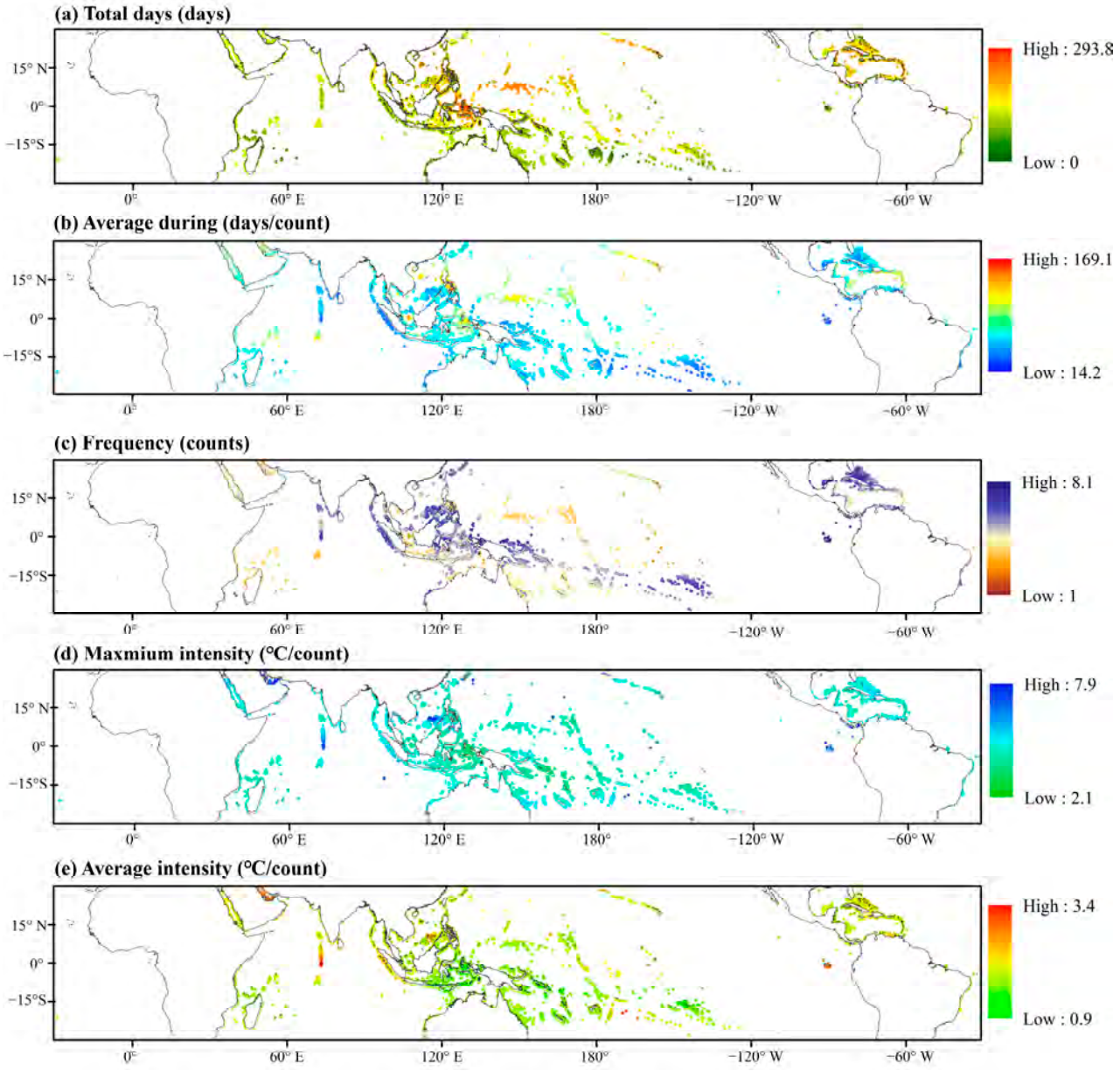


Figure 8. Spatial distribution of MHW metric means across global coral regions from 2023 to 2070 under SSP2–4.5. (**a**) Total days, (**b**) average duration, (**c**) frequency, (**d**) maximum intensity, and (**e**) average intensity.

When comparing the SSP5–8.5 scenario to the SSP2–4.5 scenario, all five MHW metrics showed an increasing trend under the SSP5–8.5 scenario (Figure 9). The main hotspot regions for MHWs under this scenario were the central–western Pacific and the Caribbean Sea, where both the total duration and intensity of MHW events were projected to intensify further. Furthermore, a summary of the total MHW days under the SSP5–8.5 scenario revealed that regions experiencing more than 200 MHW days per year would encompass over 70% of the area by 2070. As a result, MHWs are projected to become nearly year-round by 2070 under scenario SSP5–8.5.

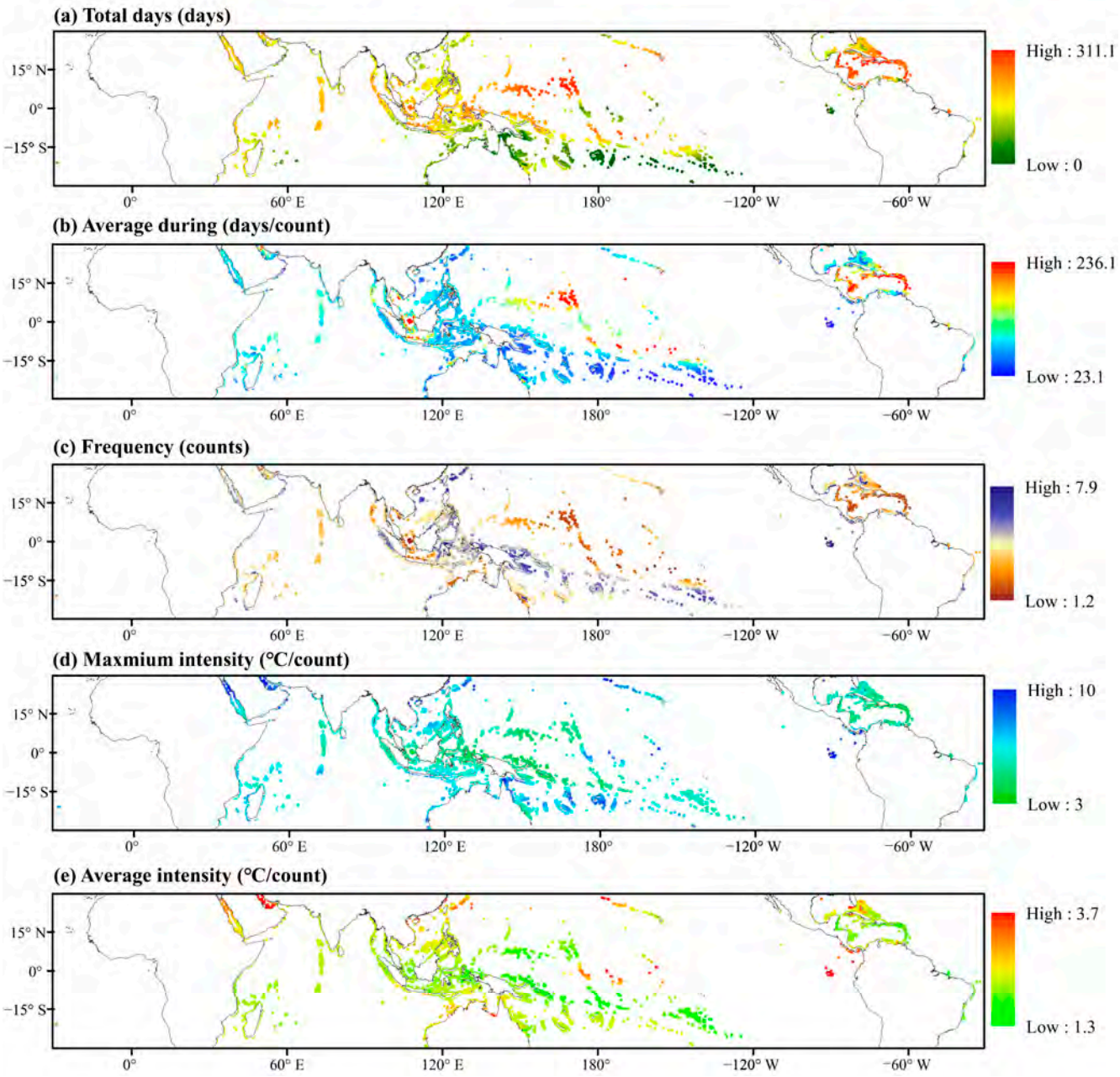


Figure 9. Spatial distribution of MHW metric means across global coral regions from 2023 to 2070 under SSP5–8.5. (**a**) Total days, (**b**) average duration, (**c**) frequency, (**d**) maximum intensity, and (**e**) average intensity.

Regarding MCS, under the SSP2–4.5 scenario, the total number of days of MCSs in most coral reef areas was less than 4 days, and the average duration of MCSs was typically less than 10 days/count. The frequency of MCS events was low, with the maximum

intensity of MCSs being weak, ranging from −3 °C to −1 °C/count, especially in the South Pacific region (Figure 10).

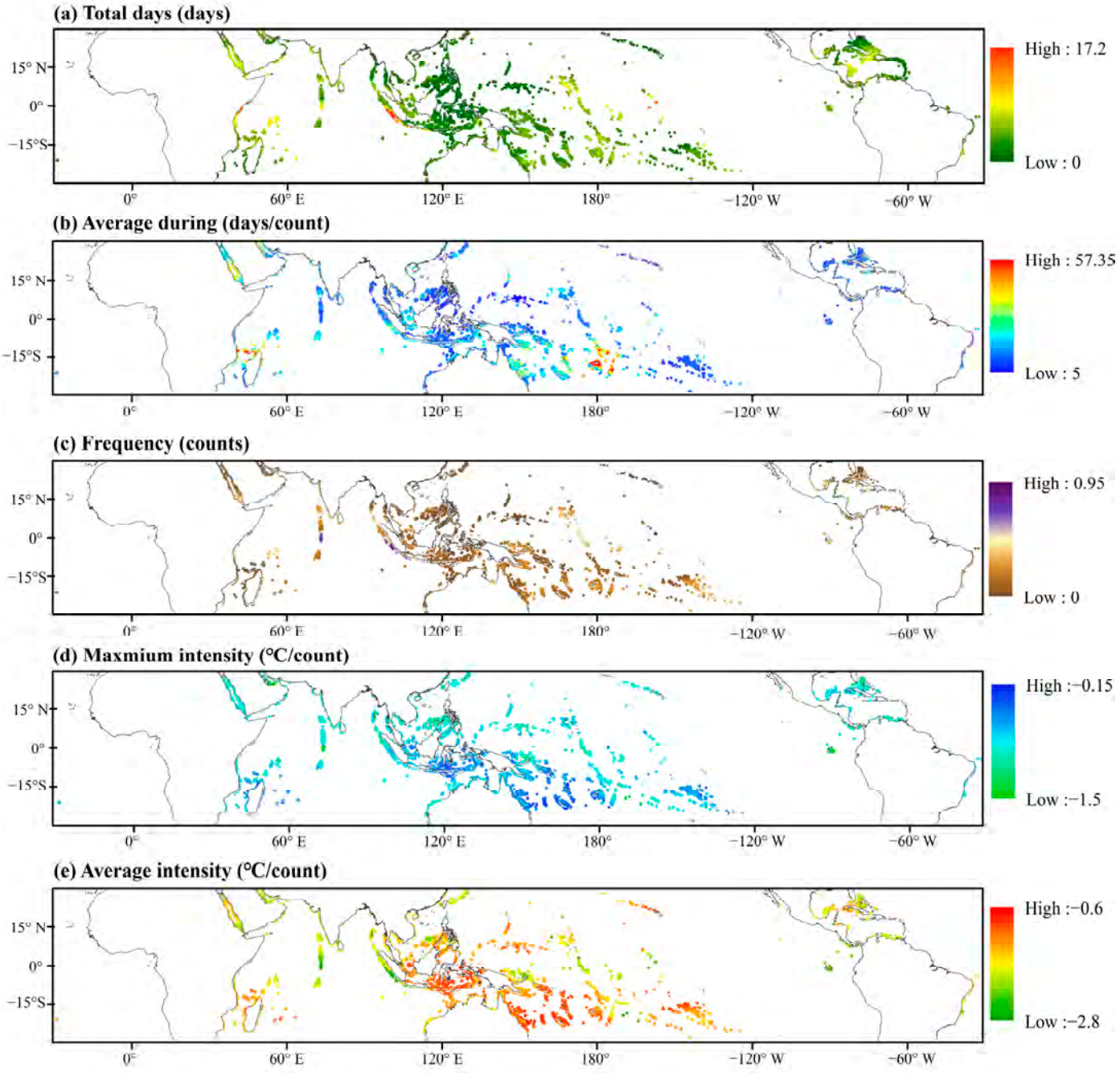


Figure 10. Spatial distribution of MCS metric means across global coral regions from 2023 to 2070 under SSP2–4.5. (**a**) Total days, (**b**) average duration, (**c**) frequency, (**d**) maximum intensity, and (**e**) average intensity.

Under the SSP5–8.5 scenario (Figure 11), the total number of days of MCS events was projected to decrease further, with even shorter average durations and lower frequencies. The intensity of MCS events also weakened under this scenario, particularly in the South Pacific, where the maximum intensity was significantly lower compared to other regions.

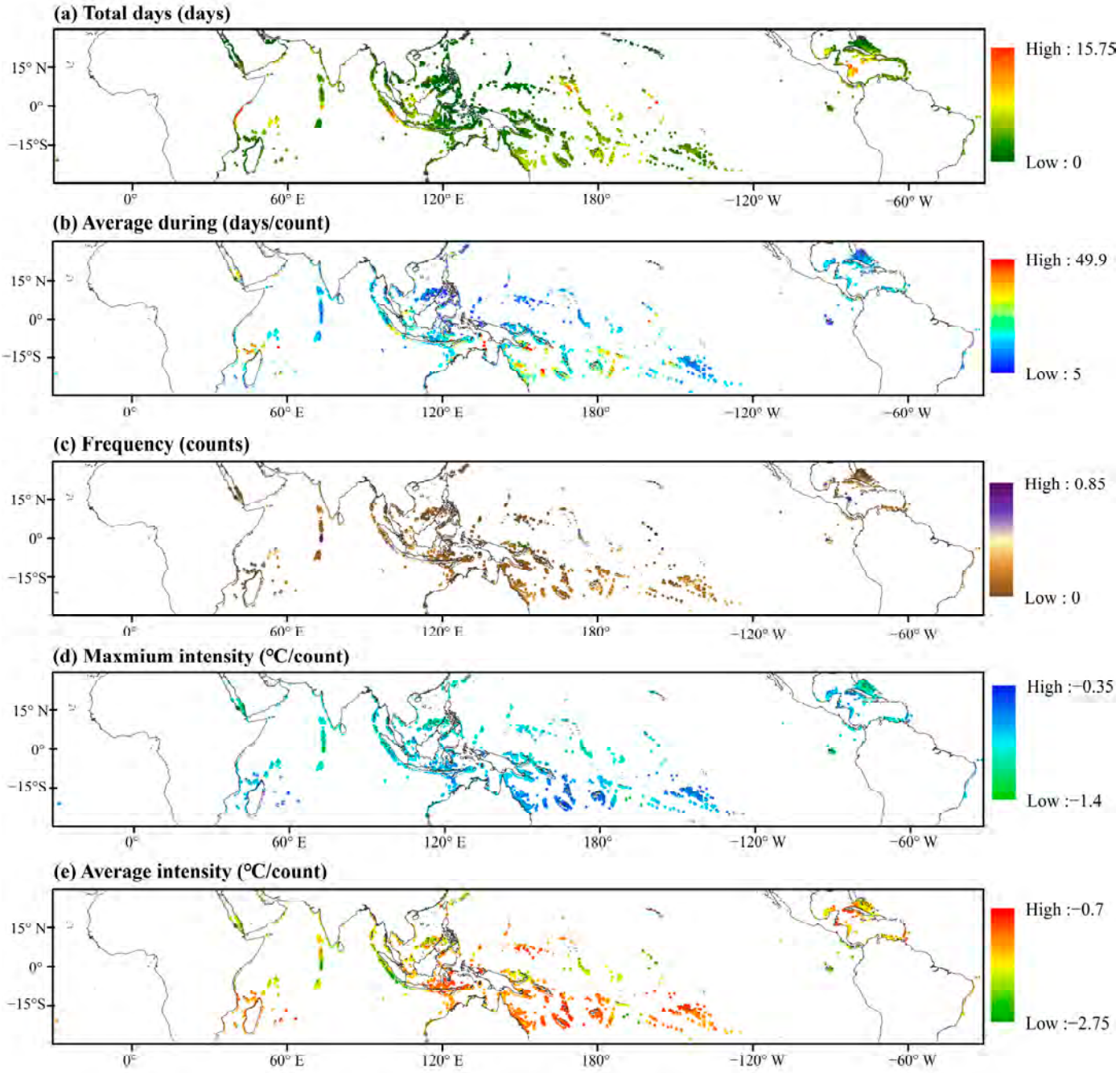


Figure 11. Spatial distribution of MCS metric means across global coral regions from 2023 to 2070 under SSP5–8.5. (**a**) Total days, (**b**) average duration, (**c**) frequency, (**d**) maximum intensity, and (**e**) average intensity.

Between 1982 and 2022, the area affected by MHWs was less than 20 times the size of the area impacted by MCSs. However, under future global warming scenarios, SSTs in coral reef zones are expected to increase at a rate of 0.2–0.3 °C per decade. In addition, the area ratio between MHWs and MCSs is projected to continue increasing significantly. By 2070, under the SSP2–4.5 scenario, this ratio is expected to reach a maximum of approximately 100 times, and under the more extreme SSP5–8.5 scenario, it could rise by as many as 196 times, especially after 2040 (Figure 12). As a result, MHWs are projected to dominate coral reef zones in the future, particularly under the SSP5–8.5 scenario.

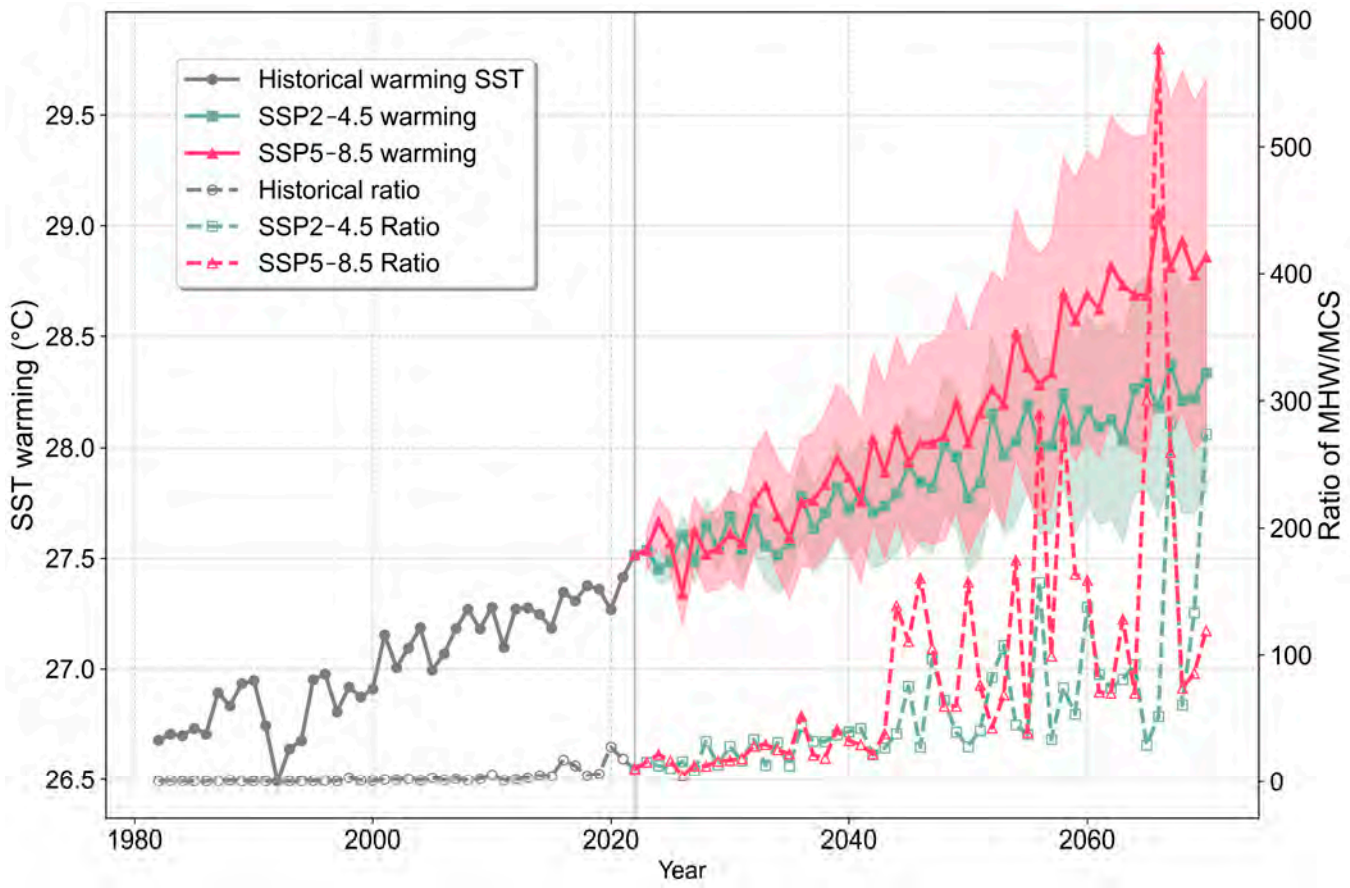


Figure 12. Temporal evolution of MHW/MCS ratio and corresponding SST trends through historical periods (1982–2022) to the future (2023–2070). Notes: The gray solid line with dots represents historical increases in the SST. The green solid line with squares represents SSP2–4.5 warming, and the green shading indicates the uncertainty range. The red solid line with triangles represents SSP5–8.5 warming, and the red shading indicates the uncertainty range. The gray dashed line with circles represents the historical ratio of MHW/MCS. The green dashed line with squares represents the SSP2–4.5 ratio of MHW/MCS. The red dashed line with triangles represents the SSP5–8.5 ratio of MHW/MCS.

3.4. The Underlying Factors Shaping the Spatial Heterogeneity of MHWs

Figure 13 shows that only 13 features were retained, effectively mitigating the risk of overfitting. The models performed well, with all R^2 values around 0.9 (Figure A2). While the importance ranking of features varied across the four models, a consistent trend emerged. In all models, t2m_a_cv (annual coefficient of variation of 2 m air temperature) was consistently ranked as the most important feature. The second and third most important features differed slightly across models. For the sake of simplicity and consistency, these features have been consolidated into the top three most influential factors, which are t2m_a_cv, OHC_a_cv (annual coefficient of variation in ocean heat content), and t2m_m_cv (monthly coefficient of variation of 2 m air temperature). As these factors increased, the number of MHW total days correspondingly rose. Furthermore, the coefficient of variation (CV) exerted a stronger influence than mean values, encompassing both interannual and intra-annual (month-to-month) CVs of temperature.

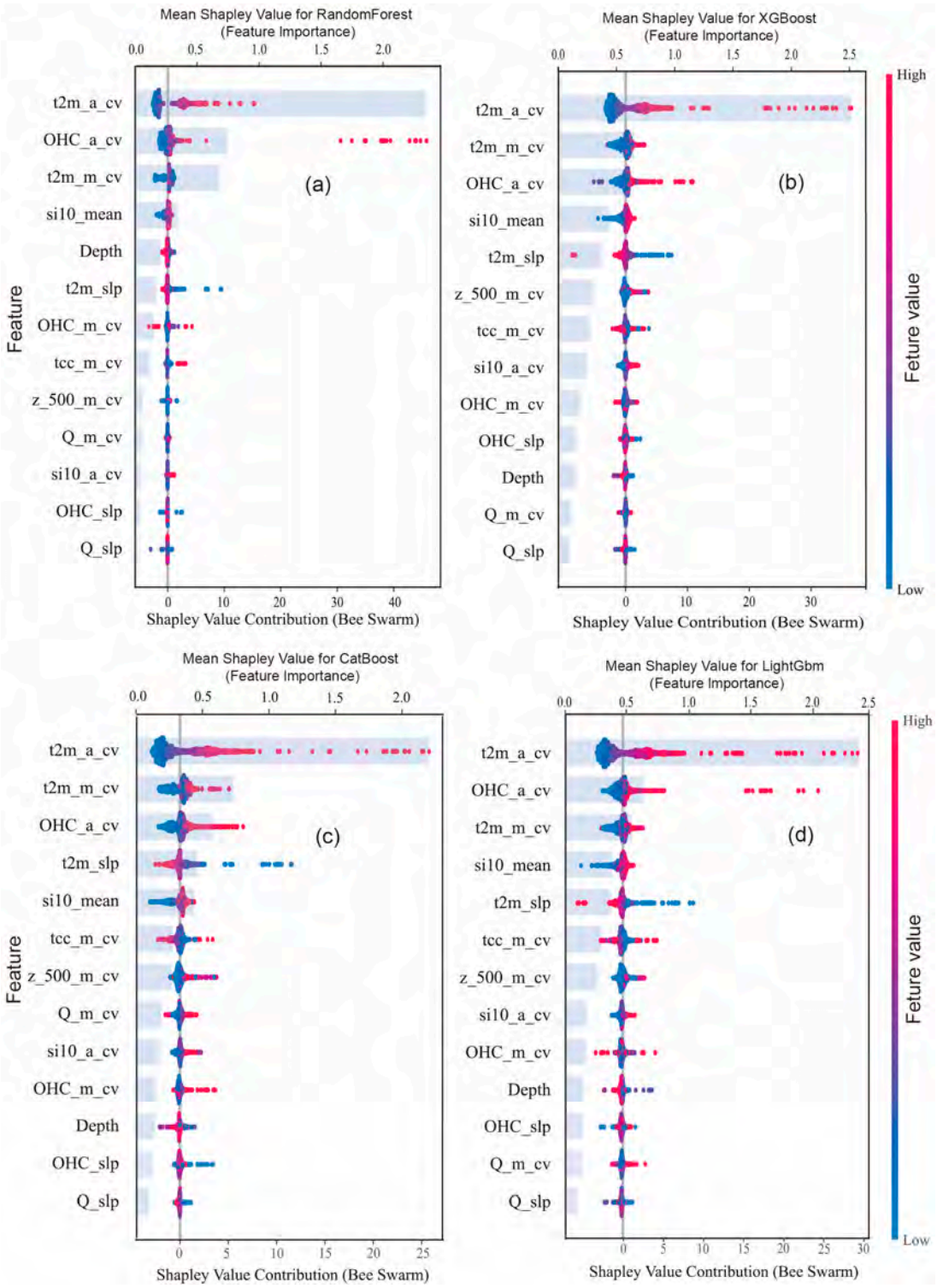


Figure 13. SHAP values of multiple models and the importance ranking plot of features. (**a**) SHAP values for Random Forest, (**b**) SHAP values for XGBoost, (**c**) SHAP values for CatBoost, (**d**) SHAP values for LightGbm. The higher feature eigenvalues are indicated by red dots, and lower eigenvalues are indicated by blue dots at the right of the plot. The importance ranking plot of features is indicated by bar plots. t2m refers to air temperature at 2 m height, si10 refers to wind speed at 10 m height, OHC stands for ocean heat content, z_500 represents geopotential height at 200 hPa, tcc denotes total cloud cover, and Q indicates net radiation. The suffix _a_cv refers to the multi-year coefficient of variation (CV), _m_cv refers to the monthly coefficient of variation (CV), "mean" denotes the multi-year average, and "slp" indicates the multi-year trend.

3.5. Relationship Between MHWs/MCSs and Coral Coverage

Figure 14 demonstrates an inverse relationship between coral coverage and MHWs ($c = -0.54$, $p < 0.01$) while showing a significant positive correlation with MCSs ($c = 0.6$, $p < 0.01$). Specifically, around 1998, 2010, and 2016, high MHW values corresponded to declining coral coverage. Despite a rapid decline in MHWs after 1998, coral coverage continued to decline, reaching 30% by 2001 and demonstrating post-mortality processes. Coral coverage continued to increase from 2001, until severe MHWs began in 2008. Due to the increasing frequency, intensity, and duration of MHWs, coral cover has exhibited a downward trend, with only a slight recovery observed in 2018.

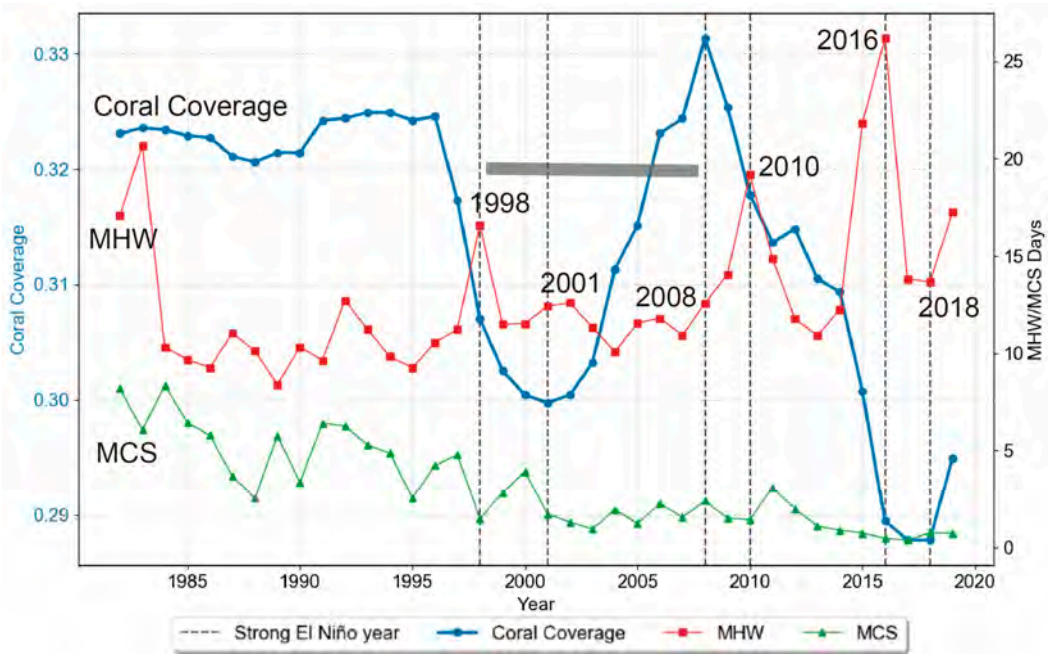


Figure 14. Changes in hard coral cover and the days of MHWs/MCSs from 1982 to 2019. Note: The blue line represents coral coverage. The red line represents MHW days. The green line represents MCS days.

From the perspective of different coral reef regions (Figure A3), the Pacific region shows the strongest negative correlation ($c = -0.87$, $p < 0.001$), followed by PERSGA ($c = -0.59$, $p < 0.001$), ROPME ($c = -0.54$, $p < 0.001$), and WIO ($c = -0.52$, $p < 0.001$). In contrast, MCSs and coral reef cover both exhibits decreasing trends, resulting in a positive correlation (Figure A4).

4. Discussion

4.1. Higher-Latitude Coral Reefs Are Experiencing More Severe MHWs than Equatorial Regions

Our findings reveal that MHW intensity is higher in lower-temperature regions. This implies that coral reefs at higher latitudes endure more intense MHWs compared to their equatorial counterparts (Tables A3 and A4 and Figure A1). Multiple factors may account for this warming asymmetry, as follows. (i) Greater seasonal SST variability (Figure 15a) and warming trends (Figure 15b) at higher latitudes may result in anomalies that more frequently exceed a fixed threshold. (ii) In higher-latitude coral reef areas, atmospheric conditions, such as high-pressure systems, may reduce cloud cover, thereby increasing solar radiation. This, in turn, enhances surface water temperature and stratification differences, promoting the development of MHWs [47]. (iii) Some physical oceanographic mechanisms could shape this pattern. For example, a study in the Northwestern South China Sea suggests that wind weakening and enhanced stratification can inhibit upwelling, which in

turn favors the development of MHWs [48]. (iv) The subtropical regions generally exhibit lower baseline temperatures relative to equatorial zones. This temperature gradient enables subtropical regions to absorb heat more efficiently. Coupled with elevated solar radiation, these conditions render subtropical regions especially vulnerable to MHW events [49].

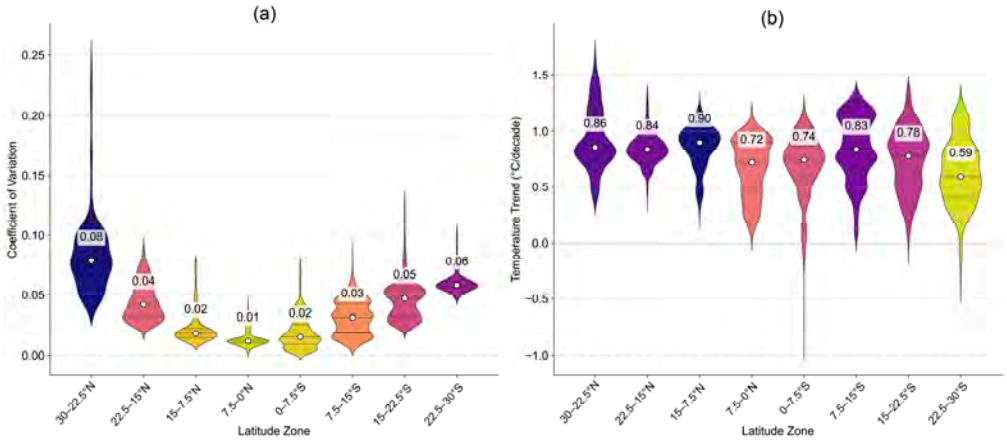


Figure 15. Seasonal SST variability (**a**) and warming trends (**b**) in global coral regions for different latitudinal bands. Note: White dots represent the position of the median, with the numerical labels above indicating the specific value.

Intense MHWs in higher-latitude regions threaten their potential as coral refuges—areas theorized to shelter coral species during global warming due to their naturally cooler temperatures [50]. What is worse, these regions are frequently subject to intense human activities, which may reduce live coral cover and degrade reef communities, thereby heightening the susceptibility of corals in higher-latitude waters to extreme climatic events [51].

4.2. Upper-Ocean Warming Is One of the Most Important Drivers of the Trends in MHWs and MCSs

Four machine learning approaches demonstrate that ocean heat content (OHC) is one of the primary drivers of MHWs. To elucidate spatial variations in OHC, we compared the multi-year linear trend of OHC at depths of 0–300 m with the spatial distribution of MHWs (Figure 16). The increase in OHC and SST corresponds to the areas where MHW days have increased. Specifically, SST shows an upward trend across the entire coral reef region, especially in the northern Indian Ocean, eastern East Asia, South Pacific islands, and the North Atlantic. In these regions, OHC is also increasing. This pattern aligns with the distribution of coral reefs, which are primarily located in regions with rising OHC.

Higher ocean heat content (0–300 m) can indicate a larger subsurface heat reservoir and increased stratification, which make the surface more susceptible to extremes [52,53]. Prior research has similarly established that SST warming predominantly drives increases in the duration and frequency of MHWs [16]. Additionally, high interannual variability suggests a greater likelihood of extreme deviations [54,55].

We also observed that strong El Niño years are associated with MHWs. The impact of ENSO is primarily evident in the tropical Pacific, the tropical Indian Ocean, and regions like the Great Barrier Reef in Australia [23]. SST anomalies in the tropical eastern Pacific can strengthen the downward branch of the tropical Walker circulation in the western Indian Ocean, leading to more frequent MHWs in areas where coral reefs are concentrated [56]. Furthermore, ENSO can increase the frequency and intensity of MHWs by stimulating warm atmospheric Rossby waves [26]. The influence of the Indian Ocean Dipole (IOD) on the interannual variation in MHWs is mainly observed in the tropical Indian Ocean and the tropical Pacific [23]. For example, negative IOD events cause the thermocline to

deepen, weakening the upwelling of cold waters along the coast and thereby promoting the occurrence of MHWs [57].

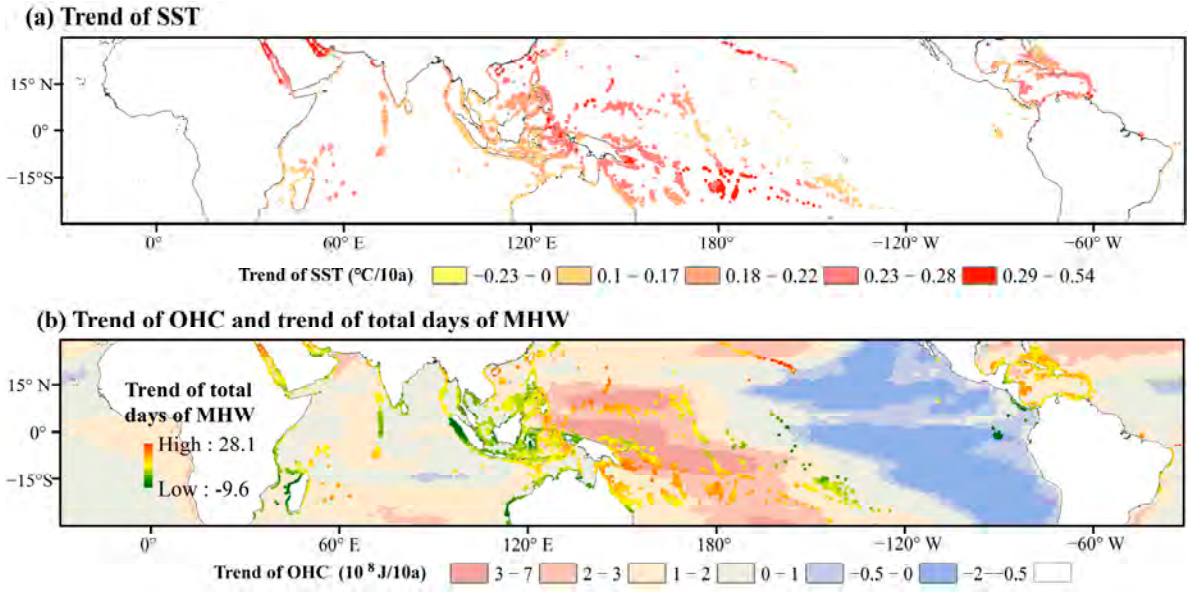


Figure 16. The spatial patterns of the trend in the multi-year average (**a**) sea temperature and (**b**) ocean heat content (OHC) changes at 0–300 m depth during the period from 1982 to 2022.

4.3. MHWs Are Projected to Continue Increasing in the Future

Under future warming, events are measured against present-day thresholds, resulting in the projection of nearly year-round MHWs by 2070. Oliver et al. [58] similarly noted that the frequency and duration of MHWs have risen, driving a 54% increase in global annual MHW days, with the most pronounced increases observed in the high-latitude North Atlantic. Under the SSP5–8.5 scenario, intensified global warming is projected to markedly increase the MHW-to-MCS area ratio, underscoring the pivotal role of warming magnitude in shaping future MHW and MCS dynamics. According to Hughes et al. [4], the extensive 2016 damage coupled with continuing temperature increases make the recovery of the northern Great Barrier Reef to its original status unlikely, with projections indicating that a fourth mass bleaching episode is probable within the next 10–20 years.

Forecasting MHWs is increasingly vital for safeguarding coral reef ecosystems. Our findings reveal that the coefficient of variation (CV), rather than the mean, exerts the strongest influence on MHW intensity. This stems primarily from MHW intensity reflecting the extent of SST deviation from its historical mean, with the CV of 2 m air temperature similarly capturing such variability. Consequently, the CV of air temperature and OHC has emerged as the most critical determinant. Accordingly, we underscore that future MHW predictions should prioritize the CV of predictive indicators over reliance on mean values alone. However, numerous studies have overlooked these factors [59–62].

4.4. Relationship Between MHWs/MCSs and Coral Coverage

MHWs have both direct and indirect effects that may lead to post-mortality processes in coral reefs. (i) Coral bleaching caused by symbiotic algae expulsion leads to coral mortality [63]. (ii) Phototrophic microbes lead to the rapid microbial bioerosion of coral skeletons, and this process is exacerbated by the nitrogen released from dead corals and high temperatures [64,65]. (iii) Competitive algae occupy the habitat, attracting excavating fish herbivores, further promoting bioerosion, and leading to coral larval recruitment failure [66,67], as well as suppressing algal competition [68]. Therefore, the destruction caused

by MHWs to both the biological community and physical structure reduces the ecosystem's structural complexity [69]. Coral death can still occur after severe MHW events.

The observed lag effects of recovery can be attributed to several interacting factors, including a limited larval supply [67,70,71], thermally tolerant symbionts reducing the growth of their coral hosts [66], shifts toward coral–algal dominance [72], and the cumulative impact of sequential disturbances, such as disease and ocean acidification [73,74].

We found that the decrease in MCS days and the reduction in coral coverage showed a significant positive relationship, which can be explained as follows. (i) The increase in MHWs is often accompanied by a decrease in MCSs, and the reduction in coral coverage is dominated by the positive correlation with MHW [20,75]. However, MCSs may still provide a window for coral to recover from heat stress [76]. (ii) Decreased cold spells may lead to reduced upwelling, thereby reducing nutrient supply and affecting coral health and recovery capacity [77]. Therefore, we emphasize that future research should focus not only on heatwaves but also on developing the study of cold spells.

4.5. Implications

In response to increasingly severe global warming, previous research has proposed various potential responses in coral reefs, including migration to refuges in high-latitude regions [78–80]. Our research asserts that high-latitude coral reefs are experiencing more intense MHWs and MCSs compared to equatorial regions, underscoring the need to prioritize the protection of coral refuges. Additionally, the coral reefs in the Pacific and Caribbean regions, where the intensity of MHWs is gradually increasing, should be given more attention.

Coral reef recovery exhibits a lag effect, meaning that even after a reduction in MHWs, recovery remains slow, showing a post-mortality process. This has emphasized the need for long-term protection and restoration efforts rather than reactive measures during extreme weather events. Integrating the establishment of protected areas and long-term strategies, such as ecological restoration, into climate change mitigation efforts is crucial for ensuring the sustained health of coral reef ecosystems.

4.6. Limitations and Prospects

Firstly, the selection of projection models primarily considers spatial resolution. Given that three models represent a relatively small ensemble, it is important to acknowledge that while they may provide an initial projection, they may not capture the full uncertainty range of CMIP6 outcomes. Further studies should utilize a larger ensemble of regionally downscaled data to reduce model uncertainty. Secondly, the baseline assumptions in the study are static, meaning that the research does not account for the adaptability of coral reefs. Corals are likely to experience conditions far outside of their historical norms in the next 50 years. The next step should involve considering multiple baseline scenarios to compare and analyze the spatial and temporal patterns of future marine heatwaves in coral reef areas, which could provide more robust results [81]. Thirdly, although the correlations between MHWs/MCSs and coral cover offer valuable insights into the relationship between these factors and coral dynamics, such relationships may not be easily captured through simple linear assumptions. Future studies should incorporate these indicators into lagged regression models or structural equation modeling to more effectively identify the key drivers of coral bleaching and mortality [82]. In addition, determining the top three factors in the four machine learning models, treated as equally important, should be further investigated. For example, Ensemble Learning techniques, such as Bagging, Boosting, or Stacking, could combine multiple learners (such as the four models we used)

to reduce variance and bias while improving prediction accuracy, ultimately yielding a unified result [83].

5. Conclusions

In this study, we utilized daily SST data from 1982 to 2070 to explicitly depict the spatiotemporal patterns and trends of MHWs and MCSs. Additionally, we applied four machine learning models to investigate the driving mechanisms of MHW intensity. At last, we explored the relationship between coral coverage and MHWs/MCSs. The conclusions and implications are as follows:

(1) Over the last four decades, MHWs have not only been increasing in average intensity but also becoming more extreme, while MCSs have declined. The Red Sea, the Persian Gulf, the Hawaiian Islands, the Galapagos Islands, the South Pacific Islands, coastal Australia, and southwestern Sumatra experience high numbers of total days of MHWs, reaching up to 32 days, and MCSs for up to 31 days. The average total days of MHWs are increasing at a rate of up to 28 days/decade.

(2) Higher-latitude coral reefs face more severe MHWs than their equatorial counterparts, with up to 1.24 times more MHW days, highlighting the need to prioritize the protection of coral refuges in these vulnerable regions.

(3) The coefficient of variation (CV) of annual temperature, the annual ocean heat content, and the monthly temperature were important factors driving MHW intensity. We emphasize the critical role of climate variability (CV) over mean climate as a major driver of MHW and further highlight that future MHW predictions should focus more on the CV of forecasting indicators rather than just the climate means to provide new insights for future projections.

(4) From 2023 to 2070, the SST in coral reef zones is projected to rise by 0.2–0.3 °C per decade. We highlight that MHWs are expected to occur nearly year-round under scenario SSP5–8.5, while MCSs are anticipated to decline sharply. The MHW-to-MCS area ratio is forecasted to surge after 2040, reaching approximately 100 times under SSP2–4.5 and 196 times under SSP5–8.5 by 2070, particularly in the Marshall Islands and the Caribbean Sea.

(5) Coral coverage shows a strong negative correlation with MHW intensity ($r = -0.54$, $p < 0.01$) and a significant positive correlation with MCSs ($r = 0.6$, $p < 0.01$). Coral coverage in the Pacific region demonstrates the highest sensitivity to MHWs. Globally, it shows a recovery lag and post-mortality processes following MHWs.

Author Contributions: Conceptualization, K.Y.; Methodology, H.J. and R.H.; Software, T.R. and R.H.; Formal analysis, H.J., T.R. and R.H.; Data curation, H.J.; Writing—original draft, H.J., T.R. and R.H.; Visualization, H.J., T.R. and R.H.; Project administration, K.Y.; Funding acquisition, K.Y. All authors have read and agreed to the published version of the manuscript.

Funding: This study was funded by the National Natural Science Foundation of China (No. 42030502), the Guangxi Science and Technology Program (No. AD25069075), The 2024 Guangxi Higher Education Institutions Young and Middle-Aged Teachers' Research Capacity Enhancement Program (2024KY0022), the Hainan Province Science and Technology Special Fund (ZDYF2024SHFZ086), and the First Batch of Inclusive Support Policies for Young Talent of Guangxi.

Data Availability Statement: The data presented in this study are available upon request from the corresponding author, as they are currently being used in an upcoming publication that is not yet released.

Acknowledgments: We give thanks to the Center of High-Performance Computing at Guangxi University. We would also like to thank the four anonymous reviewers for their constructive comments on this paper.

Conflicts of Interest: The authors declare no conflicts of interest.

Appendix A

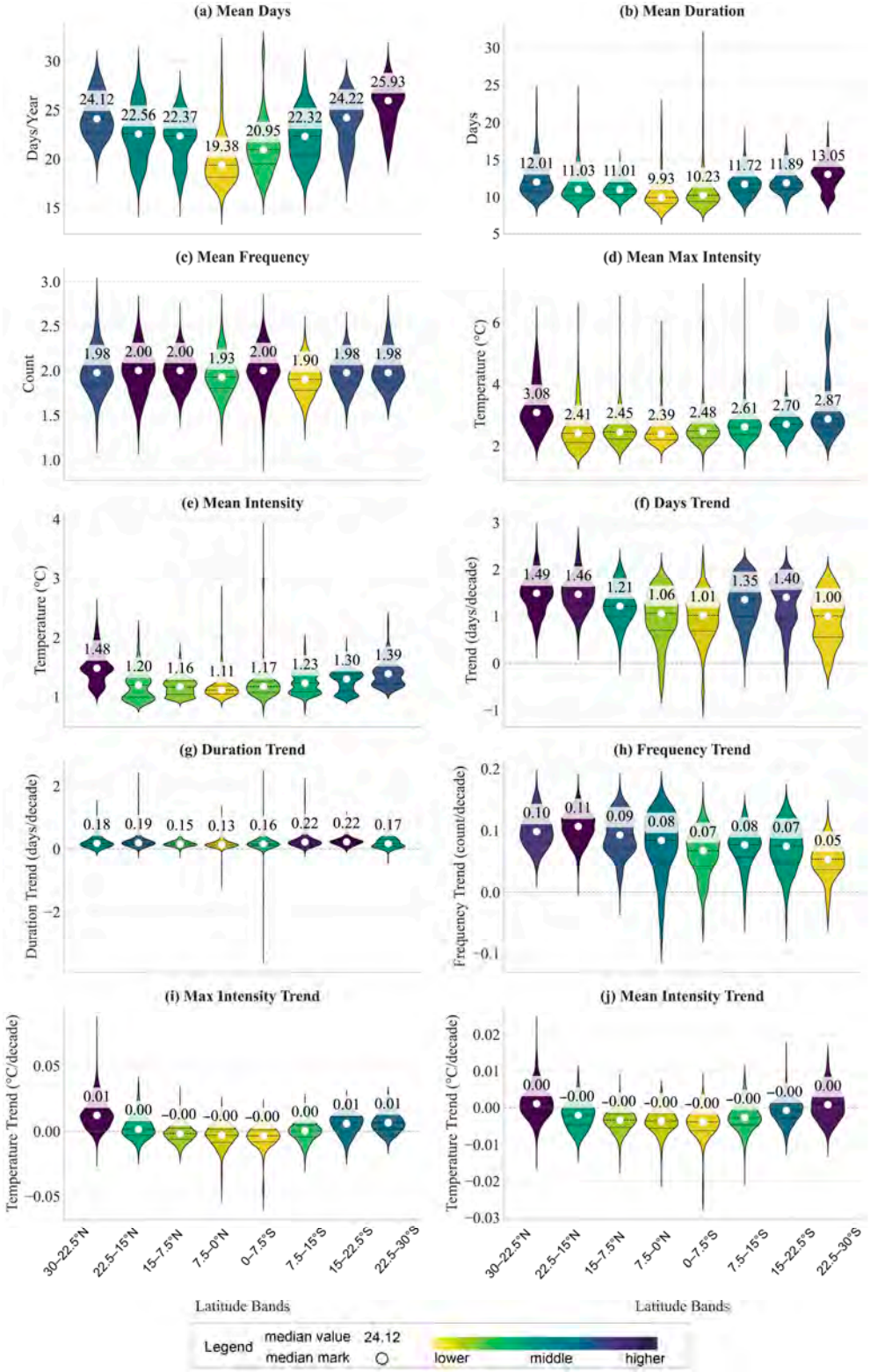


Figure A1. Spatial patterns of MHW metrics across different latitude bands. Note: White dots represent the position of the median, with the numerical labels above indicating the specific value. For example, for MHW days, the median at 22.5–30N is 24.12, while at 0–7.5N, it is 19.38, which is nearly 1.24 times higher, indicating that higher-latitude coral reefs face more severe MHWs than their equatorial counterparts.

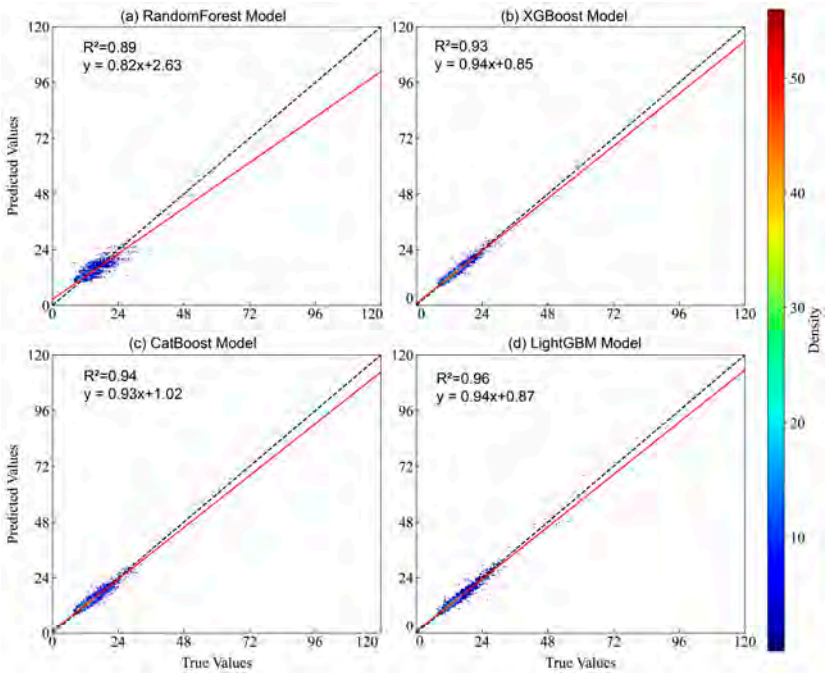


Figure A2. Validations for four machine learning models. Note: Dark blue indicates values with higher point density. The red solid line represents the fitted line, and the black dashed line represents the 1:1 line.

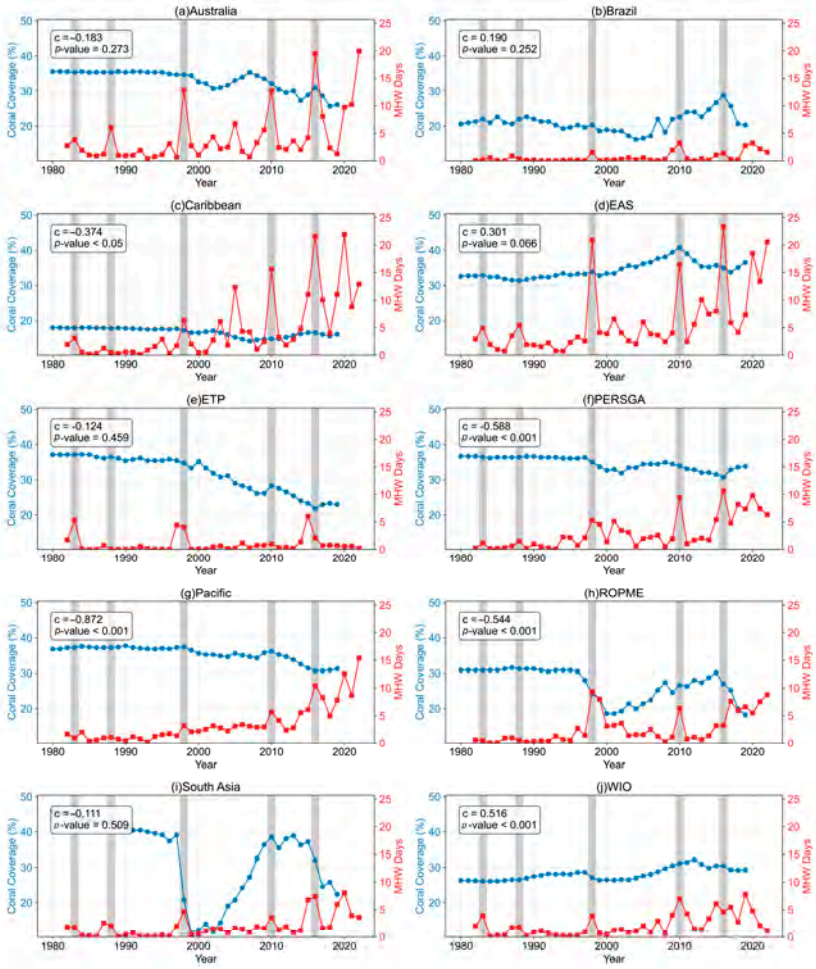


Figure A3. Interannual variation in marine heatwave days and annual changes in coral coverage. Shaded areas show strong El Niño years in 1983, 1988, 1998, 2010, 2016, and 2020.

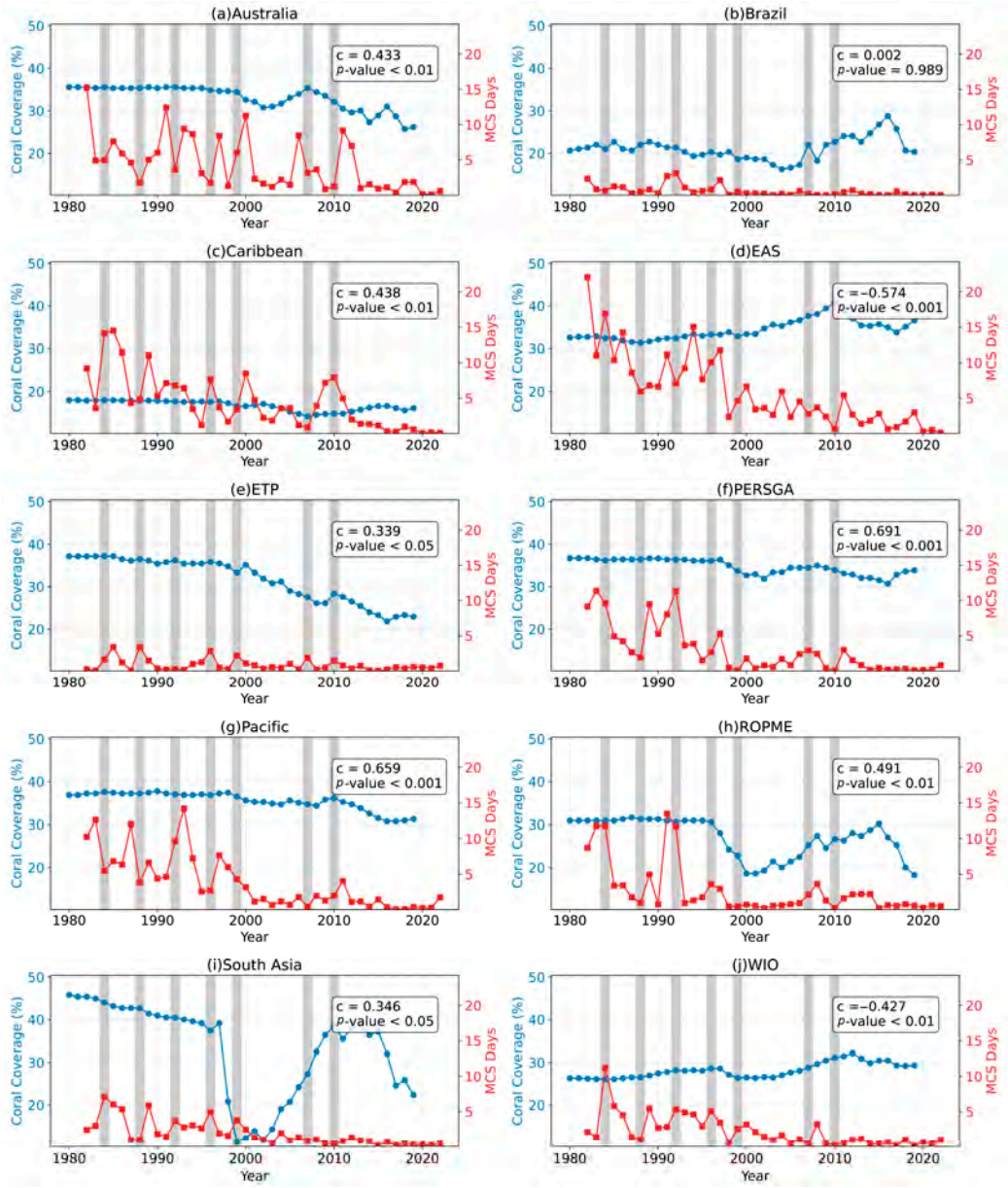


Figure A4. Interannual variation in MCS days and annual changes in coral coverage. Shaded areas show strong La Niña years in 1984, 1988, 1992, 1996, 1999, 2007, and 2010.

Table A1. Variables used in the four machine learning models.

Variable	Description	Unit	Reference
	Dependent variable.		
The total days of MHWs	The sum of all days of MHWs per year, which can directly reflect the severity of MHWs.	days	/
	Independent variables (features).		
Air temperature at 2 m (t2m)	Directly influences the surface ocean temperature, which is a key factor in the development of MHWs.	°C	[84]
Wind speed at 10 m (si10)	Influences ocean currents and mixing, affecting heat exchange between the ocean's surface and deeper layers. It impacts the distribution of heat in the ocean.	m/s	[58]
Ocean heat content (OHC)	Measures heat stored in the upper layers of the ocean. Higher OHC increases the likelihood of MHWs by providing more heat for surface transfer.	J/m^2	[85]

Table A1. *Cont.*

Variable	Description	Unit	Reference
Geopotential height at 200 hPa (z_500)	A key indicator of atmospheric circulation patterns that influence MHWs. High-pressure systems are associated with prolonged periods of warm temperatures.	m	[15]
Total cloud cover (tcc)	Affects the amount of solar radiation reaching the ocean's surface. Less cloud cover allows for more heat penetration, contributing to MHWs.	%	[86]
Net radiation (Q)	Governs the heat flux at the ocean's surface, impacting ocean temperature changes. Positive net radiation increases ocean heating and can lead to MHWs.	W/m^2	[1]

Notes: All of the independent variables were expanded into three indices, each incorporating the following components: "Mean" (multi-year average), "_a_cv" (multi-year coefficient of variation), "_m_cv" (monthly coefficient of variation), and "slp" (multi-year trend). "Mean" (multi-year average): This gives a baseline, providing context on how the features typically behave over the long term, which is important in understanding whether current conditions are anomalous. "_a_cv" (multi-year coefficient of variation) and "_m_cv" (monthly coefficient of variation): These suffixes represent the variability of the features over different time scales. MHWs are highly sensitive to variability in oceanic and atmospheric conditions. The multi-year CV captures long-term shifts in climate, while the monthly CV helps in identifying more transient, month-to-month changes that could indicate the onset of MHWs. "slp" (multi-year trend): This trend (slp) indicates the long-term direction of change in the variables, showing whether conditions are becoming more or less conducive to MHWs over time.

Table A2. The set of parameters for four machine learning models.

Random Forest	XGBoost	CatBoost	LightGBM
n_estimators: 500	objective: reg:squarederror	iterations: 500	n_estimators: 200
max_depth: 6	max_depth: 6	learning_rate: 0.05	learning_rate: 0.1
min_samples_split: 5	eta: 0.05	depth: 6	num_leaves: 123
min_samples_leaf: 2	subsample: 0.8	l2_leaf_reg: 3	objective: regression
random_state: 42	colsample_bytree: 0.8	random_seed: 42	
	gamma: 0.1	early_stopping_rounds: 50	

Table A3. Trend and significance of MHW indicators within latitude bands.

Total Days	30° N–15° N	15° N–0°	0° N–15° S	15° S–30° S
trend	1.309	1.051	1.135	1.241
p-value	0.000	0.000	0.000	0.000
Average Duration				
trend	0.196	0.148	0.193	0.213
p-value	0.000	0.000	0.000	0.000
Frequency				
trend	0.080	0.069	0.056	0.057
p-value	0.000	0.000	0.000	0.000
Max Intensity				
trend	0.006	−0.002	−0.002	0.006
p-value	0.000	0.444	0.347	0.002

Table A4. Trend and significance of MCS indicators within latitude bands.

Total Days	30° N–15° N	15° N–0°	0° N–15° S	15° S–30° S
trend	−0.929	−0.951	−1.038	−1.005
p-value	0.000	0.000	0.000	0.000
Average Duration				

Table A4. *Cont.*

Total Days	30° N–15° N	15° N–0°	0° N–15° S	15° S–30° S
trend	−0.031	−0.034	−0.012	−0.043
p-value	0.280	0.022	0.579	0.175
Frequency				
trend	−0.081	−0.096	−0.102	−0.077
p-value	0.000	0.000	0.000	0.000
Max Intensity				
trend	−0.009	−0.007	−0.006	−0.004
p-value	0.000	0.000	0.000	0.000

References

1. Hobday, A.J.; Alexander, L.V.; Perkins, S.E.; Smale, D.A.; Straub, S.C.; Oliver, E.C.; Benthuysen, J.A.; Burrows, M.T.; Donat, M.G.; Feng, M.; et al. A Hierarchical Approach to Defining Marine Heatwaves. *Prog. Oceanogr.* **2016**, *141*, 227–238. [CrossRef]
2. Hoegh-Guldberg, O.; Mumby, P.J.; Hooten, A.J.; Steneck, R.S.; Greenfield, P.; Gomez, E.; Harvell, C.D.; Sale, P.F.; Edwards, A.J.; Caldeira, K.; et al. Coral Reefs under Rapid Climate Change and Ocean Acidification. *Science* **2007**, *318*, 1737–1742. [CrossRef]
3. Pan, Y.; Sun, W.; Bao, S.; Xie, M.; Jiang, L.; Ji, J.; Yu, Y.; Dong, C. Global Variability and Future Projections of Marine Heatwave Onset and Decline Rates. *Remote Sens.* **2025**, *17*, 1362. [CrossRef]
4. Hughes, T.P.; Kerry, J.T.; Álvarez-Noriega, M.; Álvarez-Romero, J.G.; Anderson, K.D.; Baird, A.H.; Babcock, R.C.; Beger, M.; Bellwood, D.R.; Berkelmans, R.; et al. Global Warming and Recurrent Mass Bleaching of Corals. *Nature* **2017**, *543*, 373–377. [CrossRef]
5. Yao, Y.; Wang, J.; Yin, J.; Zou, X. Marine Heatwaves in China's Marginal Seas and Adjacent Offshore Waters: Past, Present, and Future. *J. Geophys. Res. Oceans* **2020**, *125*, e2019JC015801. [CrossRef]
6. Yu, X.; Yu, K.; Chen, B.; Liao, Z.; Liang, J.; Yao, Q.; Qin, Z.; Wang, H.; Yu, J. Different Responses of Scleractinian Coral *Acropora pruinosa* from Weizhou Island during Extreme High Temperature Events. *Coral Reefs* **2021**, *40*, 1697–1711. [CrossRef]
7. Pandolfi, J.M.; Connolly, S.R.; Marshall, D.J.; Cohen, A.L. Projecting Coral Reef Futures under Global Warming and Ocean Acidification. *Science* **2011**, *333*, 418–422. [CrossRef] [PubMed]
8. Gardner, T.A.; Côté, I.M.; Gill, J.A.; Grant, A.; Watkinson, A.R. Long-Term Region-Wide Declines in Caribbean Corals. *Science* **2003**, *301*, 958–960. [CrossRef] [PubMed]
9. Brodie, J.; Waterhouse, J. A Critical Review of Environmental Management of the 'Not so Great'Barrier Reef. *Estuar. Coast. Shelf Sci.* **2012**, *104*, 1–22. [CrossRef]
10. Birkeland, C. *Coral Reefs in the Anthropocene*; Springer: Berlin/Heidelberg, Germany, 2015.
11. Hughes, T.P.; Kerry, J.T.; Baird, A.H.; Connolly, S.R.; Dietzel, A.; Eakin, C.M.; Heron, S.F.; Hoey, A.S.; Hoogenboom, M.O.; Liu, G.; et al. Global Warming Transforms Coral Reef Assemblages. *Nature* **2018**, *556*, 492–496. [CrossRef] [PubMed]
12. Maynard, J.A.; Turner, P.J.; Anthony, K.R.; Baird, A.H.; Berkelmans, R.; Eakin, C.M.; Johnson, J.; Marshall, P.A.; Packer, G.R.; Rea, A.; et al. *ReefTemp*: An Interactive Monitoring System for Coral Bleaching Using High-Resolution SST and Improved Stress Predictors. *Geophys. Res. Lett.* **2008**, *35*. [CrossRef]
13. Feng, Y.; Bethel, B.J.; Dong, C.; Zhao, H.; Yao, Y.; Yu, Y. Marine Heatwave Events near Weizhou Island, Beibu Gulf in 2020 and Their Possible Relations to Coral Bleaching. *Sci. Total Environ.* **2022**, *823*, 153414. [CrossRef]
14. Van Woesik, R.; Houk, P.; Isechal, A.L.; Idechong, J.W.; Victor, S.; Golbuu, Y. Climate-Change Refugia in the Sheltered Bays of P Alau: Analogs of Future Reefs. *Ecol. Evol.* **2012**, *2*, 2474–2484. [CrossRef] [PubMed]
15. Schlegel, R.W.; Oliver, E.C.; Perkins-Kirkpatrick, S.; Kruger, A.; Smit, A.J. Predominant Atmospheric and Oceanic Patterns during Coastal Marine Heatwaves. *Front. Mar. Sci.* **2017**, *4*, 323. [CrossRef]
16. Oliver, E.C.; Donat, M.G.; Burrows, M.T.; Moore, P.J.; Smale, D.A.; Alexander, L.V.; Benthuysen, J.A.; Feng, M.; Sen Gupta, A.; Hobday, A.J.; et al. Longer and More Frequent Marine Heatwaves over the Past Century. *Nat. Commun.* **2018**, *9*, 1324. [CrossRef] [PubMed]
17. Tan, H.; Cai, R.; Yan, X.; Li, C. Amplification of Winter Sea Surface Temperature Response over East China Seas to Global Warming Acceleration and Slowdown. *Int. J. Climatol.* **2021**, *41*, 2082–2099. [CrossRef]
18. Ren, J.; Wang, C.; Yao, Y. Spatiotemporally Continuous Marine Heatwaves: A Novel Clustering Approach Reveals Increasing Frequency, Duration, Area, Intensity, and Movement Distance. *Geophys. Res. Lett.* **2025**, *52*, e2024GL113211. [CrossRef]
19. Amaya, D.J.; Miller, A.J.; Xie, S.-P.; Kosaka, Y. Physical Drivers of the Summer 2019 North Pacific Marine Heatwave. *Nat. Commun.* **2020**, *11*, 1903. [CrossRef]

20. Sun, W.; Wang, Y.; Yang, Y.; Yang, J.; Ji, J.; Dong, C. Marine Heatwaves/cold spells Associated with Mixed Layer Depth Variation Globally. *Geophys. Res. Lett.* **2024**, *51*, e2024GL112325. [CrossRef]
21. Zhang, W.; Zheng, Z.; Zhang, T.; Chen, T. Strengthened Marine Heatwaves over the Beibu Gulf Coral Reef Regions from 1960 to 2017. *Haiyang Xuebao* **2020**, *42*, 45–52.
22. Qiao, L.; Tang, H.; Huang, G. Drivers and Predictability of Summer Marine Heatwaves in the Northwest Pacific. *J. Geophys. Res. Atmospheres* **2025**, *130*, e2024JD042994. [CrossRef]
23. Holbrook, N.J.; Scannell, H.A.; Sen Gupta, A.; Benthuysen, J.A.; Feng, M.; Oliver, E.C.; Alexander, L.V.; Burrows, M.T.; Donat, M.G.; Hobday, A.J.; et al. A Global Assessment of Marine Heatwaves and Their Drivers. *Nat. Commun.* **2019**, *10*, 2624. [CrossRef]
24. Scannell, H.A.; Pershing, A.J.; Alexander, M.A.; Thomas, A.C.; Mills, K.E. Frequency of Marine Heatwaves in the North Atlantic and North Pacific since 1950. *Geophys. Res. Lett.* **2016**, *43*, 2069–2076. [CrossRef]
25. England, M.H.; Li, Z.; Huguenin, M.F.; Kiss, A.E.; Sen Gupta, A.; Holmes, R.M.; Rahmstorf, S. Drivers of the Extreme North Atlantic Marine Heatwave during 2023. *Nature* **2025**, *642*, 636–643. [CrossRef]
26. Di Lorenzo, E.; Mantua, N. Multi-Year Persistence of the 2014/15 North Pacific Marine Heatwave. *Nat. Clim. Change* **2016**, *6*, 1042–1047. [CrossRef]
27. Li, Z.; Holbrook, N.J.; Zhang, X.; Oliver, E.C.; Cougnon, E.A. Remote Forcing of Tasman Sea Marine Heatwaves. *J. Clim.* **2020**, *33*, 5337–5354. [CrossRef]
28. Zhang, Y.; Du, Y.; Feng, M.; Hu, S. Long-Lasting Marine Heatwaves Instigated by Ocean Planetary Waves in the Tropical Indian Ocean during 2015–2016 and 2019–2020. *Geophys. Res. Lett.* **2021**, *48*, e2021GL095350. [CrossRef]
29. Schlegel, R.W.; Oliver, E.C.; Wernberg, T.; Smit, A.J. Nearshore and Offshore Co-Occurrence of Marine Heatwaves and cold spells. *Prog. Oceanogr.* **2017**, *151*, 189–205. [CrossRef]
30. Schlegel, R.W.; Darmaraki, S.; Benthuysen, J.A.; Filbee-Dexter, K.; Oliver, E.C. Marine cold spells. *Prog. Oceanogr.* **2021**, *198*, 102684. [CrossRef]
31. Yao, Y.; Wang, C.; Fu, Y. Global Marine Heatwaves and cold spells in Present Climate to Future Projections. *Earths Future* **2022**, *10*, e2022EF002787. [CrossRef]
32. Li, C.; Sun, W.; Ji, J.; Zhu, Y. Historical Marine Cold Spells in the South China Sea: Characteristics and Trends. *Remote Sens.* **2024**, *16*, 1171. [CrossRef]
33. Rich, W.A.; Carvalho, S.; Berumen, M.L. Coral Bleaching Due to Cold Stress on a Central Red Sea Reef Flat. *Ecol. Evol.* **2022**, *12*, e9450. [CrossRef] [PubMed]
34. Yu, K.-F.; Zhao, J.-X.; Liu, T.-S.; Wei, G.-J.; Wang, P.-X.; Collerson, K.D. High-Frequency Winter Cooling and Reef Coral Mortality during the Holocene Climatic Optimum. *Earth Planet. Sci. Lett.* **2004**, *224*, 143–155. [CrossRef]
35. Dinesh, A.S.; Kumar, P.; Mishra, A.K.; Pandey, L.K.; Tewari, M.; Cabos, W.; Sein, D.V. Analyzing Future Marine Cold Spells in the Tropical Indian Ocean: Insights from a Regional Earth System Model. *Q. J. R. Meteorol. Soc.* **2024**, *150*, 1668–1685. [CrossRef]
36. Frölicher, T.L.; Fischer, E.M.; Gruber, N. Marine Heatwaves under Global Warming. *Nature* **2018**, *560*, 360–364. [CrossRef]
37. Souter, D.; Planes, S.; Wicquart, J.; Logan, M.; Obura, D.; Staub, F. Status of Coral Reefs of the World: 2020: Executive Summary. 2021. Available online: https://bvearmb.do/handle/123456789/3190 (accessed on 27 November 2023).
38. Souter, D.; Planes, S.; Wicquart, J.; Logan, M.; Obura, D.; Staub, F. Status of Coral Reefs of the World: 2020: Summary for Policymakers. 2021. Available online: https://bvearmb.do/handle/123456789/3191 (accessed on 27 November 2023).
39. Wang, Y.; Zhou, Y. Seasonal Dynamics of Global Marine Heatwaves over the Last Four Decades. *Front. Mar. Sci.* **2024**, *11*, 1406416. [CrossRef]
40. Oliver, E.C.; Benthuysen, J.A.; Darmaraki, S.; Donat, M.G.; Hobday, A.J.; Holbrook, N.J.; Schlegel, R.W.; Sen Gupta, A. Marine Heatwaves. *Annu. Rev. Mar. Sci.* **2021**, *13*, 313–342. [CrossRef]
41. Babcock, R.; Thomson, D.; Haywood, M.; Vanderklift, M.; Pillans, R.; Rochester, W.; Miller, M.; Speed, C.; Shedrawi, G.; Field, S.; et al. Recurrent Coral Bleaching in North-Western Australia and Associated Declines in Coral Cover. *Mar. Freshw. Res.* **2020**, *72*, 620–632. [CrossRef]
42. Li, Y.; Ren, G.; Wang, Q.; Mu, L. Changes in Marine Hot and Cold Extremes in the China Seas during 1982–2020. *Weather Clim. Extrem.* **2023**, *39*, 100553. [CrossRef]
43. Gupta, H.; Sil, S.; Gangopadhyay, A.; Gawarkiewicz, G. Observed Surface and Subsurface Marine Heat Waves in the Bay of Bengal from In-Situ and High-Resolution Satellite Data. *Clim. Dyn.* **2024**, *62*, 203–221. [CrossRef]
44. Chen, T.; Guestrin, C. Xgboost: A Scalable Tree Boosting System. In Proceedings of the 22nd ACM SIGKDD International Conference on Knowledge Discovery and Data Mining, San Francisco, CA, USA, 13–17 August 2016; pp. 785–794.
45. Futagami, K.; Fukazawa, Y.; Kapoor, N.; Kito, T. Pairwise Acquisition Prediction with SHAP Value Interpretation. *J. Financ. Data Sci.* **2021**, *7*, 22–44. [CrossRef]
46. Hirsch, R.M.; Slack, J.R. A Nonparametric Trend Test for Seasonal Data with Serial Dependence. *Water Resour. Res.* **1984**, *20*, 727–732. [CrossRef]
47. Zhang, Y.; Du, Y.; Feng, M.; Hobday, A.J. Vertical Structures of Marine Heatwaves. *Nat. Commun.* **2023**, *14*, 6483. [CrossRef]

48. Liu, S.; Lao, Q.; Zhou, X.; Jin, G.; Chen, C.; Chen, F. Impacts of Marine Heatwave Events on Three Distinct Upwelling Systems and Their Implications for Marine Ecosystems in the Northwestern South China Sea. *Remote Sens.* **2023**, *16*, 131. [CrossRef]
49. Mohamed, B.; Nilsen, F.; Skogseth, R. Marine Heatwaves Characteristics in the Barents Sea Based on High Resolution Satellite Data (1982–2020). *Front. Mar. Sci.* **2022**, *9*, 821646. [CrossRef]
50. Dimitrijević, D.; Santodomingo, N.; Kiessling, W. Reef Refugia in the Aftermath of Past Episodes of Global Warming. *Coral Reefs* **2024**, *43*, 1431–1442. [CrossRef]
51. Yu, W.; Wang, W.; Yu, K.; Wang, Y.; Huang, X.; Huang, R.; Liao, Z.; Xu, S.; Chen, X. Rapid Decline of a Relatively High Latitude Coral Assemblage at Weizhou Island, Northern South China Sea. *Biodivers. Conserv.* **2019**, *28*, 3925–3949. [CrossRef]
52. Storto, A.; Yang, C. Acceleration of the Ocean Warming from 1961 to 2022 Unveiled by Large-Ensemble Reanalyses. *Nat. Commun.* **2024**, *15*, 545. [CrossRef] [PubMed]
53. Cheng, L.; Abraham, J.; Trenberth, K.E.; Fasullo, J.; Boyer, T.; Locarnini, R.; Zhang, B.; Yu, F.; Wan, L.; Chen, X.; et al. Upper Ocean Temperatures Hit Record High in 2020. *Adv. Atmos. Sci.* **2021**, *38*, 523–530. [CrossRef]
54. Boer, G. Changes in Interannual Variability and Decadal Potential Predictability under Global Warming. *J. Clim.* **2009**, *22*, 3098–3109. [CrossRef]
55. Simon, A.; Pires, C.; Frölicher, T.L.; Russo, A. Long-Term Warming and Interannual Variability Contributions' to Marine Heatwaves in the Mediterranean. *Weather Clim. Extrem.* **2023**, *42*, 100619. [CrossRef]
56. Saranya, J.; Roxy, M.K.; Dasgupta, P.; Anand, A. Genesis and Trends in Marine Heatwaves over the Tropical Indian Ocean and Their Interaction with the Indian Summer Monsoon. *J. Geophys. Res. Oceans* **2022**, *127*, e2021JC017427. [CrossRef]
57. Han, W.; Zhang, L.; Meehl, G.; Kido, S.; Tozuka, T.; Li, Y.; McPhaden, M.; Hu, A.; Cazenave, A.; Rosenbloom, N.; et al. Climate-Driven Sea Level Extremes Compounded by Marine Heatwaves in Coastal Indonesia. *Res. Sq.* **2021**, *reprint*. [CrossRef]
58. Oliver, E.C.; Lago, V.; Hobday, A.J.; Holbrook, N.J.; Ling, S.D.; Mundy, C.N. Marine Heatwaves off Eastern Tasmania: Trends, Interannual Variability, and Predictability. *Prog. Oceanogr.* **2018**, *161*, 116–130. [CrossRef]
59. Giamalaki, K.; Beaulieu, C.; Prochaska, J.X. Assessing Predictability of Marine Heatwaves with Random Forests. *Geophys. Res. Lett.* **2022**, *49*, e2022GL099069. [CrossRef]
60. Prasad, A.; Sharma, S.; Agarwal, H. Forecasting Marine Heatwaves Using Machine Learning. 2022, *reprint*. [CrossRef]
61. Bonino, G.; Masina, S.; Galimberti, G.; Clementi, E. A Deep Machine Learning Approach to Predict Sea Surface Temperature and Marine Heatwaves Occurrences over the Mediterranean Sea. *Ocean Sci.* **2024**, *20*, 417–432. [CrossRef]
62. Mi, C.; Yi, A.; Xue, J.; Dong, C.; Shan, H. Forecasting Summer Marine Heatwaves in the South China Sea Using Explainable Machine Learning Models. *Deep Sea Res. Part Oceanogr. Res. Pap.* **2025**, *218*, 104457. [CrossRef]
63. Brown, B. Coral Bleaching: Causes and Consequences. *Coral Reefs* **1997**, *16*, S129–S138. [CrossRef]
64. Leggat, W.P.; Camp, E.F.; Suggett, D.J.; Heron, S.F.; Fordyce, A.J.; Gardner, S.; Deakin, L.; Turner, M.; Beeching, L.J.; Kuzhiumparambil, U.; et al. Rapid Coral Decay Is Associated with Marine Heatwave Mortality Events on Reefs. *Curr. Biol.* **2019**, *29*, 2723–2730. [CrossRef]
65. Bell, J.J.; Micaroni, V.; Strano, F.; Ryan, K.G.; Mitchell, K.; Mitchell, P.; Wilkinson, S.; Thomas, T.; Bachtiar, R.; Smith, R.O. Marine Heatwave-Driven Mass Mortality and Microbial Community Reorganisation in an Ecologically Important Temperate Sponge. *Glob. Change Biol.* **2024**, *30*, e17417. [CrossRef]
66. Idjadi, J.A.; Lee, S.C.; Bruno, J.F.; Precht, W.F.; Allen-Requa, L.; Edmunds, P.J. Rapid Phase-Shift Reversal on a Jamaican Coral Reef. *Coral Reefs* **2006**, *25*, 209–211. [CrossRef]
67. Gilmour, J.P.; Smith, L.D.; Heyward, A.J.; Baird, A.H.; Pratchett, M.S. Recovery of an Isolated Coral Reef System Following Severe Disturbance. *Science* **2013**, *340*, 69–71. [CrossRef]
68. Edmunds, P.J.; Carpenter, R.C. Recovery of Diadema Antillarum Reduces Macroalgal Cover and Increases Abundance of Juvenile Corals on a Caribbean Reef. *Proc. Natl. Acad. Sci. USA* **2001**, *98*, 5067–5071. [CrossRef]
69. Fordyce, A.J.; Ainsworth, T.D.; Heron, S.F.; Leggat, W. Marine Heatwave Hotspots in Coral Reef Environments: Physical Drivers, Ecophysiological Outcomes, and Impact upon Structural Complexity. *Front. Mar. Sci.* **2019**, *6*, 498. [CrossRef]
70. McManus, L.C.; Forrest, D.L.; Tekwa, E.W.; Schindler, D.E.; Colton, M.A.; Webster, M.M.; Essington, T.E.; Palumbi, S.R.; Mumby, P.J.; Pinsky, M.L. Evolution and Connectivity Influence the Persistence and Recovery of Coral Reefs under Climate Change in the Caribbean, Southwest Pacific, and Coral Triangle. *Glob. Change Biol.* **2021**, *27*, 4307–4321. [CrossRef] [PubMed]
71. Ortiz, J.-C.; Wolff, N.H.; Anthony, K.R.; Devlin, M.; Lewis, S.; Mumby, P.J. Impaired Recovery of the Great Barrier Reef under Cumulative Stress. *Sci. Adv.* **2018**, *4*, eaar6127. [CrossRef] [PubMed]
72. Roth, F.; Saalmann, F.; Thomson, T.; Coker, D.J.; Villalobos, R.; Jones, B.; Wild, C.; Carvalho, S. Coral Reef Degradation Affects the Potential for Reef Recovery after Disturbance. *Mar. Environ. Res.* **2018**, *142*, 48–58. [CrossRef]
73. Bourne, D.; Iida, Y.; Uthicke, S.; Smith-Keune, C. Changes in Coral-Associated Microbial Communities during a Bleaching Event. *ISME J.* **2008**, *2*, 350–363. [CrossRef] [PubMed]
74. Osborne, K.; Thompson, A.A.; Cheal, A.J.; Emslie, M.J.; Johns, K.A.; Jonker, M.J.; Logan, M.; Miller, I.R.; Sweatman, H.P. Delayed Coral Recovery in a Warming Ocean. *Glob. Change Biol.* **2017**, *23*, 3869–3881. [CrossRef]

75. Yao, Y.; Wang, C. Marine Heatwaves and cold spells in Global Coral Reef Zones. *Prog. Oceanogr.* **2022**, *209*, 102920. [CrossRef]
76. Napitupulu, G.; Nagi, A.; Nurdjaman, S.; Radjawane, I.M.; Rachmayani, R.; Ramadhan, M.R.; Nasution, M.I.; Habibullah, A.D.; Kelvin, F.M. Impact of Marine Heatwaves and Cold Spells on Coral Reef Ecosystem in a Tropical Region: A Case Study of Lombok Waters, Indonesia. *Mar. Syst. Ocean Technol.* **2025**, *20*, 16. [CrossRef]
77. Gravinese, P.M.; Toth, L.T.; Randall, C.J.; Aronson, R.B. How Do Upwelling and El Niño Impact Coral Reef Growth? A Guided, Inquiry-Based Lesson. *Oceanography* **2018**, *31*, 184–188. [CrossRef]
78. Ma, J.; Yu, K. Effects of Mass Bleaching Events on Coral Reef Ecosystems. *Chin. J. Ecol.* **2023**, *42*, 2227.
79. Mo, S.; Chen, T.; Chen, Z.; Zhang, W.; Li, S. Marine Heatwaves Impair the Thermal Refugia Potential of Marginal Reefs in the Northern South China Sea. *Sci. Total Environ.* **2022**, *825*, 154100. [CrossRef]
80. Soares, M.O.; Rossi, S.; Gurgel, A.R.; Lucas, C.C.; Tavares, T.C.L.; Diniz, B.; Feitosa, C.V.; Rabelo, E.F.; Pereira, P.H.C.; de Kikuchi, R.K.P.; et al. Impacts of a Changing Environment on Marginal Coral Reefs in the Tropical Southwestern Atlantic. *Ocean Coast. Manag.* **2021**, *210*, 105692. [CrossRef]
81. Rosselló, P.; Pascual, A.; Combes, V. Assessing Marine Heat Waves in the Mediterranean Sea: A Comparison of Fixed and Moving Baseline Methods. *Front. Mar. Sci.* **2023**, *10*, 1168368. [CrossRef]
82. Swaminathan, S.D.; Lafferty, K.D.; Knight, N.S.; Altieri, A.H. Stony Coral Tissue Loss Disease Indirectly Alters Reef Communities. *Sci. Adv.* **2024**, *10*, eadk6808. [CrossRef]
83. Brownlee, J. *Ensemble Learning Algorithms with Python: Make Better Predictions with Bagging, Boosting, and Stacking*; Machine Learning Mastery: Vermont, VIC, Australia, 2021.
84. Simpson, I.R.; Hitchcock, P.; Shepherd, T.G.; Scinocca, J.F. Southern annular mode dynamics in observations and models. Part I: The influence of climatological zonal wind biases in a comprehensive GCM. *J. Climate.* **2013**, *26*, 3953–3967. [CrossRef]
85. Vandemeulebrouck, J.; Roux, P.; Cros, E. The plumbing of Old Faithful Geyser revealed by hydrothermal tremor. *Geophys. Res. Lett.* **2013**, *40*, 1989–1993. [CrossRef]
86. Liu, Y.; Key, J.R.; Wang, X. The influence of changes in cloud cover on recent surface temperature trends in the Arctic. *J. Climate.* **2008**, *21*, 705–715. [CrossRef]

Disclaimer/Publisher's Note: The statements, opinions and data contained in all publications are solely those of the individual author(s) and contributor(s) and not of MDPI and/or the editor(s). MDPI and/or the editor(s) disclaim responsibility for any injury to people or property resulting from any ideas, methods, instructions or products referred to in the content.



International Journal of Digital Earth

ISSN: 1753-8947 (Print) 1753-8955 (Online) Journal homepage: www.tandfonline.com/journals/tjde20

A new remote sensing index of mildew for winter wheat disaster area extraction

Huade Li, Jinshui Zhang, Zhenghua Chen & Mingwei Zhang

To cite this article: Huade Li, Jinshui Zhang, Zhenghua Chen & Mingwei Zhang (2025) A new remote sensing index of mildew for winter wheat disaster area extraction, International Journal of Digital Earth, 18:2, 2553796, DOI: 10.1080/17538947.2025.2553796

To link to this article: https://doi.org/10.1080/17538947.2025.2553796

© 2025 The Author(s). Published by Informa UK Limited, trading as Taylor & Francis Group

Published online: 17 Oct 2025.

Submit your article to this journal

Article views: 245

View related articles

View Crossmark data

Full Terms & Conditions of access and use can be found at
https://www.tandfonline.com/action/journalInformation?journalCode=tjde20

INTERNATIONAL JOURNAL OF DIGITAL EARTH
2025, VOL. 18, NO. 2, 2553796
https://doi.org/10.1080/17538947.2025.2553796

OPEN ACCESS Check for updates

A new remote sensing index of mildew for winter wheat disaster area extraction

Huade Li[a,b,c], Jinshui Zhang[b,c], Zhenghua Chen[a] and Mingwei Zhang[d,e]

[a]School of Marine Sciences, Guangxi University, Nanning, People's Republic of China; [b]Faculty of Geographical Science, Beijing Normal University, Beijing, People's Republic of China; [c]State Key Laboratory of Remote Sensing Science, Beijing Normal University, Beijing, People's Republic of China; [d]Laboratory of Radiometric Calibration and Validation for Environmental Satellites, National Satellite Meteorological Center (National Center for Space Weather), China Meteorological Administration, Beijing, People's Republic of China; [e]Innovation Center for Feng Yun Meteorological Satellite (FYSIC), China Meteorological Administration, Beijing, People's Republic of China

ABSTRACT

Disasters caused by winter wheat mildew affect the quality and safety of grain. The purpose of this study was to construct a winter wheat mildew index based on multispectral remote sensing data combined with an automatic threshold segmentation algorithm to quickly extract the area affected by winter wheat mildew. Research has shown that the spectrum of winter wheat strongly absorbs after mildew. On the basis of this spectral feature difference, the 'area method' is used to construct the wheat mildew index to enhance the separability between normal wheat and mildewed wheat. Five threshold segmentation algorithms are used to automatically extract the mildewed wheat region, and the Otsu threshold segmentation algorithm and iterative threshold segmentation algorithm achieve the best performance. The results show that the overall accuracy of the wheat mildew index combined with the automatic threshold segmentation algorithm is similar to that of the random forest and support vector machine (SVM) classification methods, but the extraction process is greatly simplified. In addition, the extraction of mildewed wheat combined with an automatic threshold segmentation algorithm can effectively avoid the problem of unstable extraction accuracy caused by specific threshold segmentations.

ARTICLE HISTORY
Received 14 February 2025
Accepted 23 August 2025

KEYWORDS
Winter wheat; wheat mildew index; machine learning; automatic threshold segmentation algorithm; Gaofen-2

1. Introduction

At present, remote sensing disaster monitoring and recognition methods based on imaging technology include threshold segmentation, machine learning, and deep learning. These methods realize remote sensing monitoring and mapping of crop diseases by identifying features. The threshold segmentation method is simple and efficient. Using the normalized difference vegetation index (NDVI) to set the threshold to extract green vegetation is the simplest application of threshold segmentation. Some researchers have used the threshold segmentation method of the hue saturation intensity (HSI) color model to segment and extract the severity of soybean rust (Di Cui et al. 2010). The machine learning classification method realizes the classification prediction of the new dataset by learning the relationship between the characteristics and categories of the sample dataset. Scholars have estimated the severity of rice blast disease through a variety of machine learning methods, such as support vector machines and random forests (Mandal et al. 2023). Compared with the machine learning classification model, the deep learning model has stronger feature learning ability. Scholars have used deep convolutional neural networks (DCNNs) combined with image space and spectral information to monitor wheat yellow rust (X. Zhang et al. 2019) and classify wheat leaf diseases by integrating a variety of deep learning algorithms (Xu et al. 2023). Although the threshold segmentation method is simple to use, the selection of the segmentation threshold directly affects the final segmentation accuracy. In addition, the construction of segmented data and the selection of thresholds also have an impact on the segmentation results. Machine learning classification methods

CONTACT Zhenghua Chen chen.zhenghua@163.com School of Marine Sciences, Guangxi University, No.100,University East Road, 530004, People's Republic of China

© 2025 The Author(s). Published by Informa UK Limited, trading as Taylor & Francis Group
This is an Open Access article distributed under the terms of the Creative Commons Attribution-NonCommercial License (http://creativecommons.org/licenses/by-nc/4.0/), which permits unrestricted non-commercial use, distribution, and reproduction in any medium, provided the original work is properly cited. The terms on which this article has been published allow the posting of the Accepted Manuscript in a repository by the author(s) or with their consent.

such as support vector machines (SVMs) and random forests (RFs) are widely used in remote sensing classification. However, with the complexity and diversity of remote sensing data, machine learning classification algorithms face new challenges in high-dimensional small samples, high-dimensional data imbalance and feature engineering. The deep learning classification method has powerful deep feature learning ability, but with the deepening of the deep learning network, the selection of the classification neural network structure and parameters has become a problem that cannot be ignored. In addition, the interpretability of the neural network hidden layer is poor, which is not conducive to the interpretation of remote sensing classification physical features (Zhu et al. 2018).

The characteristics and spectral attributes of crop damage caused by disease stress constitute the basis of crop disease monitoring via remote sensing (Sindhuja Sankaran et al. 2010). When crops are stressed by diseases, pests or external environmental factors, external morphological changes are manifested mainly as pigment reduction, color changes in plant leaves, wilting and decay (Liu, Liu, Sun, et al. 2024). At the same time, the cells in the plant are damaged, leading to the inhibition of photosynthesis and respiration. The difference in the absorption and reflection of the electromagnetic spectrum in the leaves or canopy of crops under disease stress is called the spectral response characteristic. When crops are stressed by disease, the spectral and texture characteristics of remote sensing images change significantly (Liu, Liu, Liu, et al. 2024). The spectral response characteristics are affected by the external structure and internal physical and chemical properties of crops. Owing to differences in crop species, growth status and disease types, the spectral absorption and reflection characteristics of crops change under disease stress, and the spectral response characteristics of crops are diverse (Onisimo Mutanga and Andrew K. Skidmore 2007). When crops are stressed by external factors such as diseases, their absorption and reflection of sunlight change in the visible and near-infrared bands. The leaves of healthy vegetation have greater absorption and lower reflectivity in the visible light band, but the opposite is true in the near-infrared band (Knipling 1970). In addition, the near-infrared band and the near-infrared band are also spectral features related to plant growth, which are often used to characterize vegetation information, such as constructing the vegetation index formed by the red edge and near-infrared band for crop growth monitoring and yield estimation (Liu et al. 2025). Vegetation monitoring and agricultural research using remote sensing technology usually use a limited number of bands for vegetation monitoring (H. Zhang et al. 2025). When crops are subjected to stress, significant changes occur in the absorption and reflection characteristics of their leaves in the visible and near-infrared bands. Specifically, these changes are manifested as an increase in reflectance in the visible band, and a 'blue shift' phenomenon in which the position of the red edge shifts toward the shortwave direction between the near-infrared and shortwave infrared bands (Daniel A. Sims and John A. Gamon 2002). Satellite remote sensing technology utilizes such changes in spectral characteristics to extract ground object information, which also serves as the direct basis for remote sensing-based disease monitoring. When crops are exposed to external stress, the corresponding gray values in remote sensing images will exhibit corresponding variation characteristics (Daniel A. Sims and John A. Gamon 2002). Through remote sensing interpretation based on the variation characteristics of gray values in remote sensing images, it is further possible to realize remote sensing monitoring and assessment of crop diseases.

Currently, in the field of remote sensing monitoring for crop diseases and pests, various technical methods not only demonstrate unique advantages but also face their respective challenges. Threshold segmentation algorithm is simple and efficient, yet it is limited by the subjectivity in threshold selection. Machine learning plays a role in classification and prediction by virtue of its sample learning ability, but high-dimensional and complex data has emerged as a new challenge that it must confront. Although deep learning possesses powerful feature learning capabilities, its lack of interpretability and issues related to parameter selection still await breakthroughs. Furthermore, the application of these technologies is deeply dependent on the morphological and spectral changes exhibited by crops after being subjected to disease stress. Therefore, how to enhance the accuracy and universality of technical methods across diverse crop species, disease types, and growth environments remains a persistent problem that researchers need to continuously address. In this study, a remote sensing vegetation index capable of extracting the affected area of mildewed wheat is constructed based on multispectral remote sensing images. By exploring the mechanism of spectral changes in mildewed wheat, mathematical algebraic methods are employed to enhance the differences in spectral characteristics between normal wheat and mildewed wheat. Furthermore, combined with an automatic threshold segmentation algorithm, normal wheat

and mildewed wheat can be rapidly separated. This research provides a new solution for extracting the affected area of mildewed wheat.

2. Definition of the mildew index

2.1 Analysis of remote sensing spectral characteristics

Healthy crops have relatively stable remote sensing spectral reflectances. When crops suffer from diseases, their physical and chemical properties change, which is ultimately reflected in the abnormal absorption and reflection of a specific spectrum. Therefore, the reflectance of crops can be used as a comprehensive reflection of the physiological chemistry, structure and morphology of crops. This feature is closely related to the health status and growth environment of crops, which is also an important basis for remote sensing monitoring of crops.

The appearance of wheat mildew is characterized mainly by black mildew spots on leaves and stems. The main physiological change in wheat is the death of plant cells, and life processes such as water absorption, transportation and transformation are forced to change or stop. Regardless of whether the external shape or internal structure of the plant changes, it affects the absorption and reflection of the crop to the spectrum, thus affecting the spectral information in the remote sensing image. It can be clearly seen from the reflectance violin diagram of normal wheat and mildewed wheat in the multispectral image band (Figure 1) that the absorption and reflection of the spectrum of wheat changed after mildew. Taking the multispectral image as an example, the difference in reflectance between normal wheat and mildewed wheat in the four bands gradually increased with increasing wavelength from the blue band to the near-infrared band. In the blue wave band, the average reflectivity of normal wheat is between 0.06 and 0.08, whereas the average reflectivity of mildewed wheat is between 0.02 and 0.04. In the near-infrared band, the average reflectivity of normal wheat is between 0.15 and 0.20, whereas the average reflectivity of mildewed wheat is between 0.05 and 0.10. The spectral reflectance of normal wheat and mildewed wheat increases with increasing wavelength in the visible and near-infrared bands, and the difference in reflectance between them also increases. As shown in Figure 2, this change feature is also reflected in the scatter plot of the reflectances of normal wheat and mildewed wheat, and the influence of mildewed wheat on spectral absorption and reflection is more intuitively reflected in the scatter plot.

The scatter plot of the pixel reflectances of normal wheat and mildewed wheat (Figure 2) reveals that the spectral reflectances of normal wheat and mildewed wheat have different distribution characteristics in the visible and near-infrared bands. After wheat matures, the chlorophyll content decreases, and the absorption

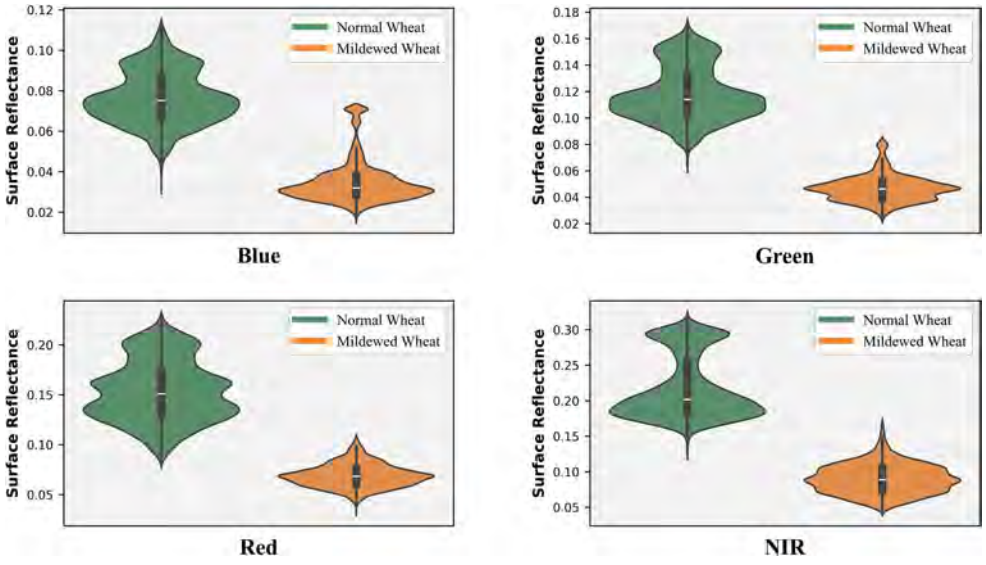


Figure 1. Violin diagram of the pixel reflectances of normal wheat and mildewed wheat.

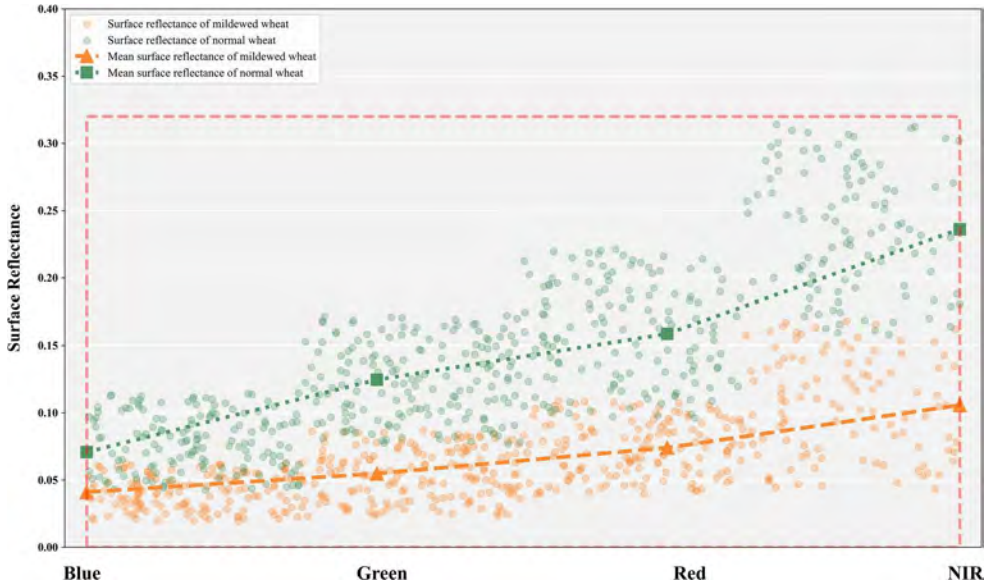


Figure 2. Scatter plot of the pixel reflectances of normal wheat and mildewed wheat.

of blue and red light decreases. There are no obvious absorption valleys in the blue or red bands (Figure 2), and mature wheat plants are golden yellow. However, the physiological and chemical processes of wheat plants are affected by the occurrence of mildew. The growth of mold on the plant surface presented black spots. At the same time, the leaves of the wheat plants gradually withered, the spectral energy reflection of each band decreased, and the absorption increased, which are the main characteristics of the spectral reflectance of mildew-susceptible wheat. Figure 2 clearly shows that with the large amount of growth and reproduction of mold on wheat plants, spectral differences between normal wheat and mildewed wheat appear, and relatively stable spectral characteristics appear. Compared with mildewed wheat, normal mature wheat has greater reflectance in all bands, and the difference in reflectance between the near-infrared band and blue band is large. In contrast, mildewed wheat has strong absorption in all bands due to the influence of mold, and even the near-infrared band with strong reflection from healthy vegetation is no exception, resulting in lower spectral reflectance and a smoother spectral reflection curve.

2.2 Wheat mildew index

The strong absorption effect of winter wheat after mildew on the spectra of various bands led to a great difference between the remote sensing reflectance spectra of mildewed wheat and normal wheat. As shown in Figure 2, the pixel values of normal wheat in each band are greater than those of mildewed wheat. Therefore, the area enclosed by the reflectance curve and abscissa axis of normal wheat should be larger than that enclosed by the reflectance curve and abscissa axis of mildewed wheat. The normalized wheat mildew index was constructed by selecting the area of the rectangle formed by the maximum reflectivity and the abscissa axis as the denominator. As shown in Figure 2, the wheat mildew index molecule is the area enclosed by the reflectivity curve of the pixel and the abscissa axis. The calculation of the area of the red rectangular box needs to find the maximum reflectivity of the pixel and the difference between the central wavelengths of the near-infrared band and the blue band. The molecule of the wheat mildew index is the area enclosed by the pixel reflectivity and the abscissa axis, which can be regarded as the sum of the areas of three right-angled trapezoids. The multiband image WMI constructed in this study is as follows:

$$\mathrm{WMI} = \frac{R_{blue} + R_{green} * \lambda_{green} - \lambda_{blue} + R_{green} + R_{red} * \lambda_{red} - \lambda_{green} + R_{red} + R_{nir} * \lambda_{nir} - \lambda_{red}}{2 * R_{max} * (\lambda_{nir} - \lambda_{blue})}$$

where R_{blue}, R_{green}, R_{red}, and R_{nir} represent the image bands, λ_{blue}, λ_{green}, λ_{red}, and λ_{nir} represent the central wavelength of the band, and R_{max} represents the maximum reflectivity of the image pixels.

According to the principle of constructing a normalized wheat mildew index, the theoretical maximum value of the wheat mildew index is 1, and the minimum value is 0. Because the reflectivity of mildewed wheat in each band is lower than that of normal wheat, the mildewed wheat is closer to 0 for the wheat mildew index, whereas the normal wheat has a stronger reflection on the spectrum and is closer to 1 for the wheat mildew index. Therefore, the closer the wheat mildew index is to 1, the lower the possibility of wheat mildew. In contrast, the closer the wheat mildew index is to 0, the greater the possibility of wheat mildew. This is characteristic of the wheat mildew index.

3. Experimental design

3.1 Research area and data

Henan Province is the largest granary in China and one of the main wheat-producing areas in China. The wheat planting area and yield rank first in China. In late May 2023, Henan Province experienced two rounds of continuous and obvious rainfall. From May 20–21, the recent rainfall event caused heavy rain or even torrential rain in some areas. In addition, from May 25 to 30, continuous rainy and scant sunshine weather, including rainstorms and local heavy rainstorms in the eastern, central and southern regions, occurred again in most areas of Henan Province. As shown in Figure 3, owing to the continuous cloudy and rainy weather, the winter wheat in the harvest period in Henan Province experienced local germination, mildew, lodging and other disasters. Wheat mildew is caused by the invasion of mold on the surface of wheat. Many molds grow and propagate on mature wheat plants, resulting in many black mold spots on the surface of the wheat plants. At this time, Henan winter wheat experienced typical rainy weather, which not only affected the harvest of wheat but also led to mildew and germination of some wheat.

The time at which the field survey data were obtained was approximately June 2, 2023. At this time, the winter wheat in Henan Province experienced continuous rainy weather, and wheat mildew disasters are very serious. The field survey data include the longitude and latitude information of the survey points. A total of 624 valid data points were obtained for the mildew of winter wheat at the survey points, including 306 mildew wheat data points and 318 normal wheat data points. At the same time, combined with the winter wheat planting distribution data in the experimental area, some sample points were selected to expand the sample dataset. As shown in Figure 4, a total of 230 normal wheat spots and 230 mildewed wheat spots were selected from the data as the wheat characteristic sample dataset and the validation dataset of the mildewed wheat extraction results.

3.2 Remote sensing image data and preprocessing

In this experiment, scenes of Gaofen-2 multispectral remote sensing image data on June 1st, 2023, and scenes of Gaofen-6 remote sensing image data on April 18th, 2023, were used. The multispectral remote sensing images of Gaofen-2 and Gaofen-6 are preprocessed via radiometric calibration, atmospheric correction and image registration. In Figure 5, the distribution information of wheat was extracted from the remote sensing images of Gaofen-2 and Gaofen-6 based on the normalized difference vegetation index (NDVI), which was used to extract mildewed wheat from cultivated land. The remote sensing images of



Figure 3. Mildewed wheat and normal wheat (mildewed wheat on the left and normal wheat on the right).

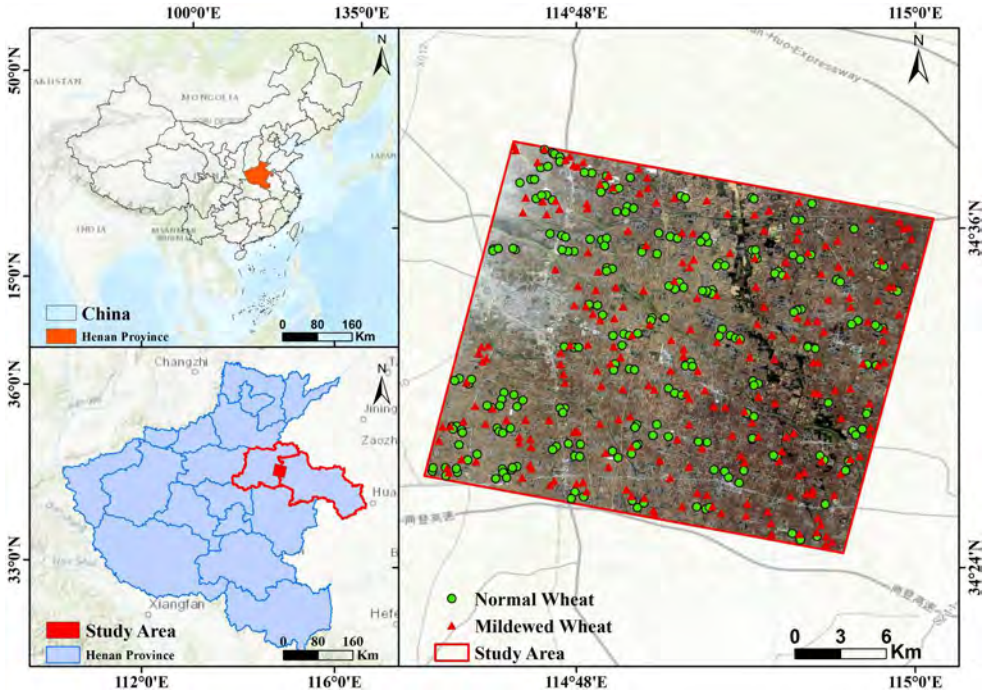


Figure 4. Study area and field survey data.

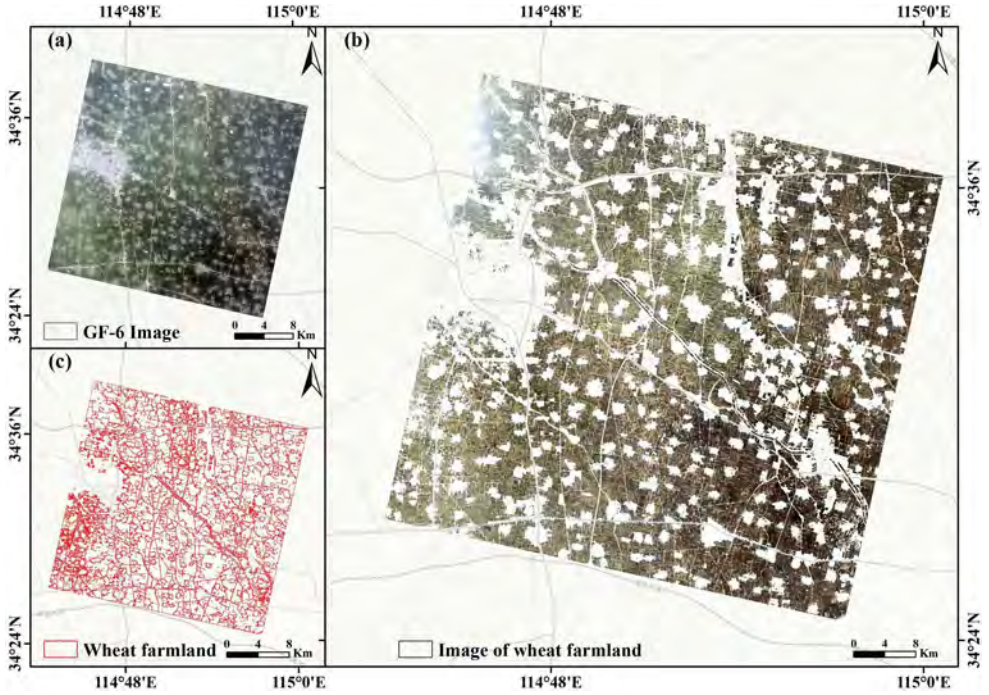


Figure 5. Cultivated land in the study area (a is the Gaofen-6 image; b is the wheat-cultivated land image; c is the scope of the wheat in the study area).

Sentinel-2 and landsat-9 on June 1st, 2023 were used in the wheat mildew index migration experiment. Sentinel 2 and landsat-9 multispectral remote sensing image data are derived from Google Earth engine (GEE), and the data has undergone radiometric calibration, image registration, atmospheric correction and other preprocessing operations.

3.3 Automatic threshold setting method

According to the construction principle of the wheat mildew index, the pixel value range of the wheat mildew index is 0–1, and the spectral reflectance of normal wheat is greater than that of mildewed wheat. In theory, two peaks are formed in the gray histogram of the WMI. The 'peak' close to 1 represents a normal wheat pixel, and the 'peak' close to 0 represents mildewed wheat. Therefore, finding a suitable threshold can separate normal wheat from mildewed wheat, and the automatic threshold segmentation algorithm meets the requirements of image segmentation. Image segmentation is an important part of pattern recognition and computer vision recognition. The automatic threshold segmentation method is widely used because of its simple algorithm and efficient segmentation efficiency (Dora et al. 2017; Mohamed H. Merzban and Mahmoud Elbayoumi 2018).

The difference between normal wheat and mildewed wheat was increased by the wheat mildew index, which further improved the distinguishability among different types of wheat. To avoid the influence of subjective factors on threshold selection, five segmentation algorithms, Otsu threshold segmentation, K-means clustering segmentation, iterative threshold segmentation, maximum entropy segmentation and triangle segmentation, were used in this study to perform automatic threshold segmentation of the wheat mildew index to obtain the range of mildewed wheat and explore the optimal threshold segmentation algorithm. The Otsu threshold segmentation method was first proposed by Japanese scholar Otsu (Otsu 1979). The algorithm is simple to calculate and is not affected by image brightness or contrast. Its principle is to find the corresponding gray level when the maximum variance between classes is the largest. This gray level makes the difference between the image foreground and background the largest, and the effect of distinguishing the foreground and background is the best. For the grayscale image f(x, y), the image is divided into a target and background when the threshold is T_0. At this time, the probability of occurrence of the foreground is P_0, and the average gray value of the foreground is R_0. The probability of occurrence of the background is P_1, the average gray value of the foreground is R_1, and the average gray value of the gray image f(x, y) is R_T; then, the interclass variance is:

$$\sigma^2 = P_0*(R_0 - R_T)^2 + P_1*(R_1 - R_T)^2$$

when σ^2 reaches the maximum value, the optimal segmentation threshold is obtained.

The K-means clustering segmentation algorithm (Likas, Vlassis, and J. Verbeek 2003; Sulaiman and Isa 2010; Tapas Kanungo et al. 2002) classifies the close data points into one class on the basis of the Euclidean distance, uses the distance mean as a new seed point, and repeatedly iterates to modify the clustering center until the objective function reaches the minimum value to obtain the optimal segmentation threshold. The K-means clustering segmentation algorithm needs to calculate the objective function E, which is the sum of the squares of the distances from the sample point to the cluster center of the category. When the objective function E is the smallest, the clustering segmentation of the image is completed.

$$E = \sum_{i=1}^{k} \sum_{j=1}^{N_i} (X_{ij} - C_i)^2$$

$$C_i = \frac{1}{N_i} \sum_{j=1}^{N_i} X_{ij} (i = 1, 2, 3, \ldots, k)$$

where k is the number of clusters; N_i is the number of samples of class i; X_{ij} is the j sample of class i; and C_i is the clustering center of i.

The basic principle of iterative threshold segmentation (Perez and Gonzalez 1987) is to obtain the segmentation threshold by iterating continuously and judging whether the average gray value of the foreground and background is equal to the threshold before iteration or iterating when the threshold change of the last two iterations is less than the set value. The iterative threshold segmentation method has high practicability and robustness and can effectively address image segmentation problems with complex and diverse backgrounds. The steps of the iterative threshold segmentation algorithm are as follows:

(1) Calculate the initial threshold $T_0 = \frac{R_{min}+R_{max}}{2}$. R_{min} and R_{max} are the minimum gray value and the maximum gray value of the image, respectively.
(2) The image is divided into two parts according to the T_0 threshold: the target and the background. The average gray value of the two parts is as follows:

$$T_{target} = \frac{\sum_{R(i,j)<T_k} R(i,j)*N(i,j)}{\sum_{R(i,j)<T_k} N(i,j)}$$

$$T_{background} = \frac{\sum_{R(i,j)>T_k} R(i,j)*N(i,j)}{\sum_{R(i,j)>T_k} N(i,j)}$$

In the formula, $R(i, j)$ is the gray value of (i, j) points on the gray image, $N(i, j)$ is the weight coefficient of (i, j) points, generally $N(i, j)$ is the number of $R(i, j)$ points, and t T_k is the threshold.

(1) After step 2), a new threshold $T_{k+1} = \frac{T_{target}+T_{background}}{2}$ is obtained.
(2) The cycle is performed from step 2) to step 4), and the optimal threshold is obtained when $T_k = T_{k+1}$ to end the cycle.

The maximum entropy segmentation algorithm (Kapur, Sahoo, and Wong 1980; Sahoo, Wilkins, and Yeager 1997) is similar to the Otsu threshold segmentation method. Otsu threshold segmentation is based on the maximum interclass variance of the image, whereas maximum entropy segmentation uses the information entropy of the image. When the information entropy of the foreground and background images is at a maximum, the gray value is used as the threshold of image segmentation. Suppose that the gray level t $0 \le t \le 255$ of the image divides the image into two parts: the target and the background. At this time, the information entropy of the target area is H_{target}, the information entropy of the background area is $H_{blackground}$, and the total information entropy of the image H is:

$$H = H_{target} + H_{blackground}$$

$$H_{target} = -\sum_{0\le i\le t} (P_i/P_t)\log_2(P_i/P_t)$$

$$H_{blackground} = -\sum_{t<i\le 255} [P_i/(1-P_t)]\log_2[P_i/(1-P_t)]$$

where P_i is the corresponding probability when the gray level is i and where P_t is the sum of the gray-level probabilities of the image target area. The optimal segmentation threshold is obtained when the total information entropy H_0 reaches the maximum.

The triangle segmentation algorithm (Zack, Rogers, and Latt 1977) uses the image gray histogram data to find the image segmentation threshold on the basis of geometry. Assuming that the image gray histogram has only one peak (single-peak histogram), at this time, it is only necessary to find the maximum vertical distance from the line where the highest point of the gray histogram and the leftmost point or rightmost point are located to each point on the histogram with respect to the line, and the gray value of this point is the segmentation threshold. The triangle threshold segmentation algorithm has a good segmentation effect on image types with obvious single peaks in the image gray histogram.

3.4 Accuracy evaluation method

The classification accuracy of the experimental results is verified through the confusion matrix, and the evaluation indices are the overall accuracy and kappa coefficient (Giles M. Foody 2002). Overall accuracy is the ratio of the number of all categories of classification results and classification samples to the number of all samples, which can directly reflect the overall accuracy of the classification results. The kappa coefficient is a classification accuracy evaluation index obtained via mutual operation between confusion matrices. It calculates the consistency between the classification prediction results and the real results by comparing the

actual value and the predicted value in the confusion matrix of the classification results. The closer the kappa coefficient is to 1, the better the consistency is (Ute Bradter et al. 2020). Compared with the overall accuracy, the kappa coefficient also considers the accuracy generated by random classification and removes the influence of this part from the overall accuracy.

$$P_{(OA)} = \frac{\sum_{i=1}^{n} X_i}{N}$$

$$Kappa = \frac{P_{(OA)} - \frac{\sum_{i=1}^{n} a_i * b_i}{N^2}}{1 - \frac{\sum_{i=1}^{n} a_i * b_i}{N^2}}$$

where $P_{(OA)}$ is the overall classification accuracy; X_i is the sum of correctly classified pixels in class n; a_i is the number of real sample pixels of class n; b_i is the number of pixels in the sample that are classified as class n; n is the total number of categories of classification results; and N is the total number of sample pixels. The dataset measured in this study includes 230 mildewed wheat spots and 230 normal wheat spots, 70% of which are used as the wheat characteristic sample dataset and 30% as the validation dataset of mildewed wheat extraction results.

In addition, to further study the difference between the threshold segmentation methods for the wheat mildew index and other methods, McNemar's test (McNEMAR 1947) was used for statistical testing. McNemar's test can be used to test the prediction accuracy and significance of two binary classification models(-Khan, Das, and Liu 2024). When McNemar's test is used, the results obtained by the two methods are sorted into the following 2*2 list:

	Method2	
Method1	TRUE	FALSE
TRUE	A	B
FALSE	C	D

In the list, A and D are the numbers of consistent results obtained by the two methods, and B and C are the numbers of inconsistent results obtained by the two methods. The test statistic of McNemar's test is as follows:

$$\chi^2 = \frac{(B-C)^2}{(B+C)} \quad (\mathrm{B}+\mathrm{C}) \geq 40$$

$$\chi^2 = \frac{(|B-C|-1)^2}{(B+C)} \quad (\mathrm{B}+\mathrm{C}) < 40$$

The original hypothesis of McNemar's test is H_0, and the alternative hypothesis is H_1. The original hypothesis H_0 shows that there is no significant difference in the prediction accuracy between the two methods, whereas the alternative hypothesis H_1 shows that there is a significant difference in the prediction accuracy between the two methods. In the experiment, the results of 1000 sample points in cultivated land were selected for McNemar's test, and the significance level was set as $\alpha = 0.05$.

4. Experimental results

4.1 Extraction results of the wheat mildew index based on different threshold segmentation algorithms

The wheat mildew index is a function of the spectral reflectance of pixels. Section 2.1 shows that the average reflectance of mildew wheat in each band of the multispectral image is lower than that of normal wheat. The numerator of the wheat mildew index is the area of the polygon surrounded by the reflectivity and the horizontal axis wavelength, and the denominator of the wheat mildew index is the rectangular area surrounded by the maximum reflectivity and the horizontal axis wavelength. The normal wheat has a relatively high

reflectance, and the mildew index value of wheat is relatively high, whereas the mildew wheat has a relatively high absorption spectrum, so the mildew index value of mildewed wheat is relatively low. In Figure 6, there are two peaks in the gray histogram of the WMI. The pixels near 1 on the right are normal wheat, whereas the pixels near 0 on the left are mildewed wheat. The index value of mildewed wheat was mainly concentrated in the range of 0.1–0.35, whereas the index value of normal wheat was mainly concentrated in the range of 0.35–0.8. After treatment, mildewed wheat and normal wheat had good separability. The pixel distribution of mildewed wheat (0.1–0.35) was more concentrated than that of normal wheat (0.35–0.8), indicating that the strong absorption of the spectrum after the wheat mildewed was an important remote sensing response feature after wheat mildew occurs. The normal wheat had a large peak range, indicating that the reflection and absorption of the spectrum of normal wheat were controlled by a variety of life activities of the wheat plants, showing diversification. Figure 6 shows that the pixel distributions of the wheat mildew indices of normal wheat and mildewed wheat were bimodal, which was consistent with the expected results. The pixels with a bimodal distribution had good separation. Normal wheat and mildewed wheat can be separated via the automatic threshold segmentation algorithm while avoiding the influence of human subjective factors in the selection of the threshold.

As shown in Figure 7, the Otsu, K-means, and Iterative Threshold segmentation algorithms have achieved good results in extracting mildewed wheat. This indicates that the wheat mildew index can enhance the distinction between normal and mildewed wheat in cultivated land by utilizing multispectral reflectance information. The pixel value of normal wheat tends to be 1, whereas the pixel value of mildewed wheat tends to be 0. Finally, normal wheat and mildewed wheat can be separated and extracted by selecting the optimal segmentation threshold through an automatic threshold segmentation algorithm. Table 1 shows that the selection of thresholds directly affects the extraction accuracy of the affected area of mildewed wheat. Too large a threshold setting (maximum entropy segmentation) or too small a threshold setting (triangular segmentation) will lead to poor extraction. The thresholds of the three segmentation methods with the best segmentation results are all approximately 0.35, which is very close to the best segmentation threshold in the pixel gray histogram of normal wheat and mildewed wheat in Figure 6. According to the segmentation results, the following experiments implemented the Otsu threshold segmentation method and the iterative threshold segmentation method with the best segmentation results.

As shown in Figure 8, to further analyze the performance differences among various algorithms, pixel-wise statistics were conducted on the results of different segmentation algorithms, thereby more accurately quantifying the performance gaps between these algorithms in distinguishing normal wheat from mildewed wheat. The results show that the segmentation results of normal wheat and mildewed wheat are different, but the difference is not obvious among the three algorithms with good segmentation effect, namely Otsu

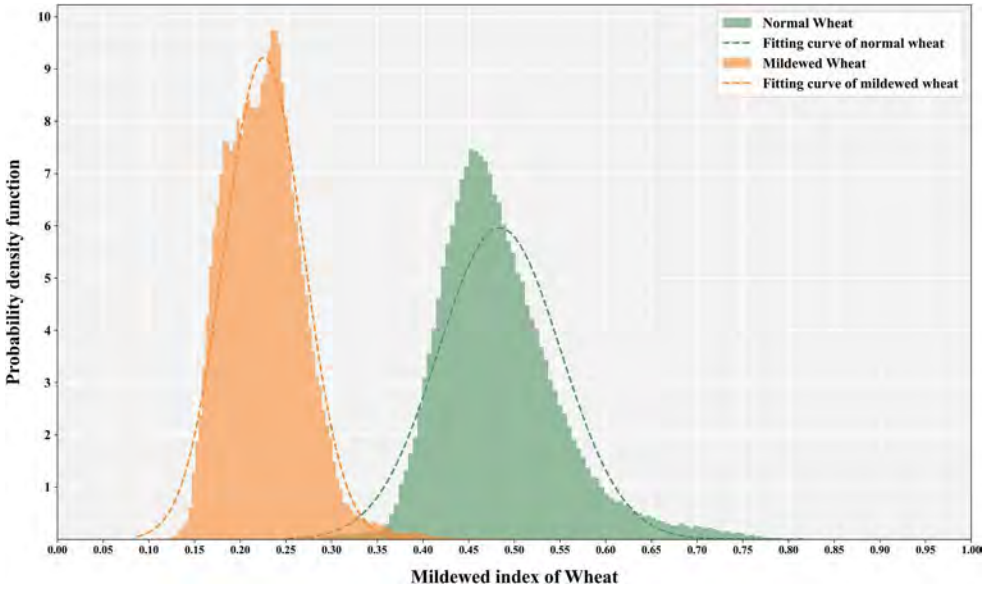


Figure 6. Histogram of the wheat mildew indices of normal wheat and mildewed wheat.

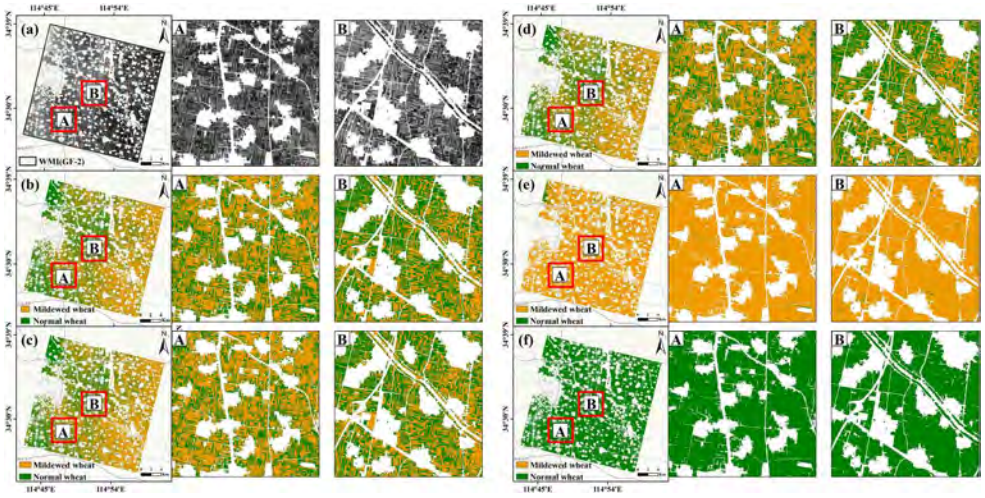


Figure 7. Automatic segmentation results of the wheat mildew index (a is the wheat mildew index in the study area; b is the Otsu threshold segmentation result; c is the K-means clustering segmentation result; d is the iterative threshold segmentation result; e is the maximum entropy segmentation result; and f is the triangle segmentation result).

Table 1. Accuracy evaluation of the automatic threshold segmentation results.

	Otsu	K-means	Iterative Threshold	Maximum Entropy	Triangle
Overall Accuracy	93.62%	93.05%	93.37%	66.53%	34.84%
Kappa	0.8570	0.8430	0.8509	0.0506	0.0
Threshold	0.3529	0.3608	0.3569	0.5686	0.0353

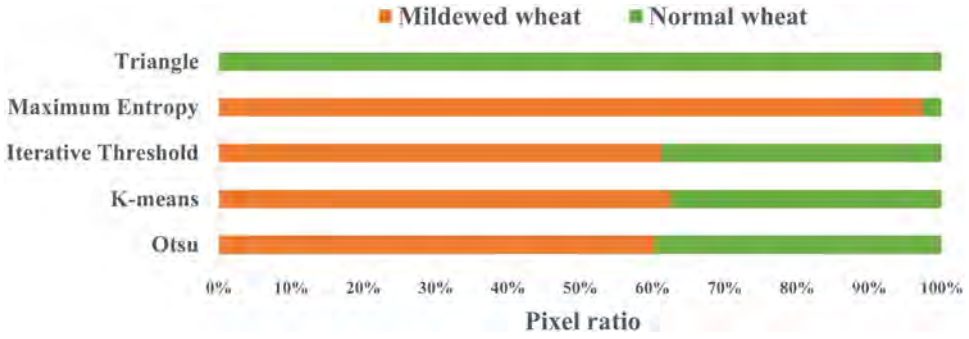


Figure 8. Percentage of normal wheat and mildewed wheat pixels in different segmentation algorithms.

threshold segmentation, K-means segmentation and iterative threshold segmentation. The specific data are as follows: in Otsu threshold segmentation, mildewed wheat accounted for 60.20%, and normal wheat accounted for 39.80%; In K-means segmentation, mildewed wheat accounted for 62.49%, and normal wheat accounted for 37.51%; In iterative threshold segmentation, mildewed wheat accounted for 61.32%, and normal wheat accounted for 38.68%. Taking the segmentation result of Otsu threshold with the best segmentation accuracy as a reference, the difference of K-means segmentation and iterative threshold segmentation for mildewed wheat was 3.80% and 1.87%, respectively, while the difference of segmentation results for normal wheat was −5.76% and −2.82%, respectively. The results of the other two segmentation algorithms are not ideal, so they are not used as the main segmentation algorithm of wheat mildew index, nor are they analyzed in depth. The main reason for the difference of segmentation results between normal wheat and mildewed wheat by different segmentation algorithms is that there are subtle differences in the selection of segmentation threshold by different algorithms. A threshold often corresponds to a different number of pixels. Whether these pixels are classified as normal wheat or mildewed wheat will affect the

segmentation accuracy of another category. In addition, in the process of image gray processing before segmentation, the number of different gray divisions of the image will also affect the selection of segmentation threshold. From the actual segmentation results, Otsu threshold segmentation, K-means segmentation and iterative threshold segmentation can find a better segmentation threshold.

4.2 Comparison with traditional machine learning results

In this study, two classical machine learning classification methods, random forest and support vector machine, were used to extract mildewed wheat from the study area, and the performance of mildewed wheat extraction was compared and analyzed with the proposed wheat mildew index. In the experiment, four original remote sensing image bands, 27 default index features in ENVI, and six remote sensing indices commonly used in wheat disease extraction in other references, including the greenness index (GI), triangular vegetation index (TVI), normalized chlorophyll ratio index (NPCI), structural insensitive vegetation index (SIPI), nitrogen reflectance index (NRI) and green chlorophyll index (GCI), were selected. There are 37 kinds of characteristics. To solve the redundancy of high-dimensional features and improve the correlation between classification features and categories. In the experiment, the relief F algorithm and mRMR algorithm (Hanchuan Peng, Fuhui Long, and Ding 2005; H. Zhang et al. 2024; Y. Zhang, Ding, and Li 2008) were combined to reduce the dimensions of 37 features and screen the optimal feature subset for the classification of mildewed wheat. After being processed by the relief F algorithm and mRMR algorithm, the first five features with the largest feature weights (Figure 9) are finally selected for random forest and support vector machine classification.

According to the results in Figure 10 and Table 2, the optimal feature subset based on the relief F and mRMR algorithms combined with random forest and support vector machine classification and extraction of mildewed wheat can achieve good classification results, with an overall accuracy of more than 92% and a kappa coefficient of more than 0.83. The range of mildewed wheat obtained by the machine learning method is very close to that extracted by the wheat mildew index combined with the automatic threshold segmentation method proposed in this study, which can extract the mildewed wheat in the study area well, but the result obtained by the index method is slightly better. The experimental results show that the wheat mildew index has reached a unified level with the traditional machine learning classification method in the extraction of mildewed wheat, but the wheat mildew index method does not involve the selection of features, the marking of training samples, or the parameter adjustment of the classification algorithm. Under the same conditions, the wheat mildew index is simpler and more efficient than the machine learning

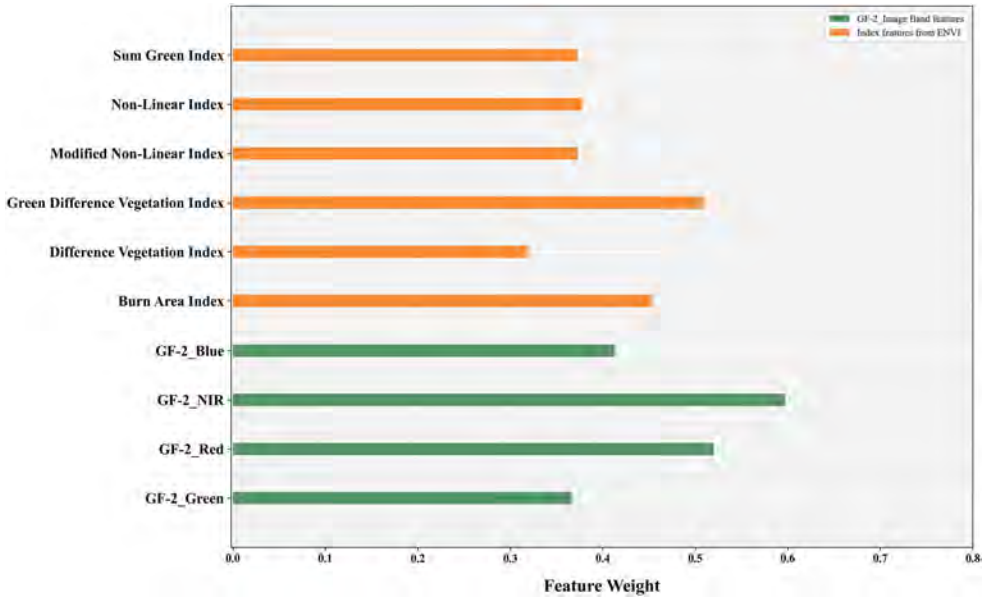


Figure 9. Relief F + m RMR feature selection results.

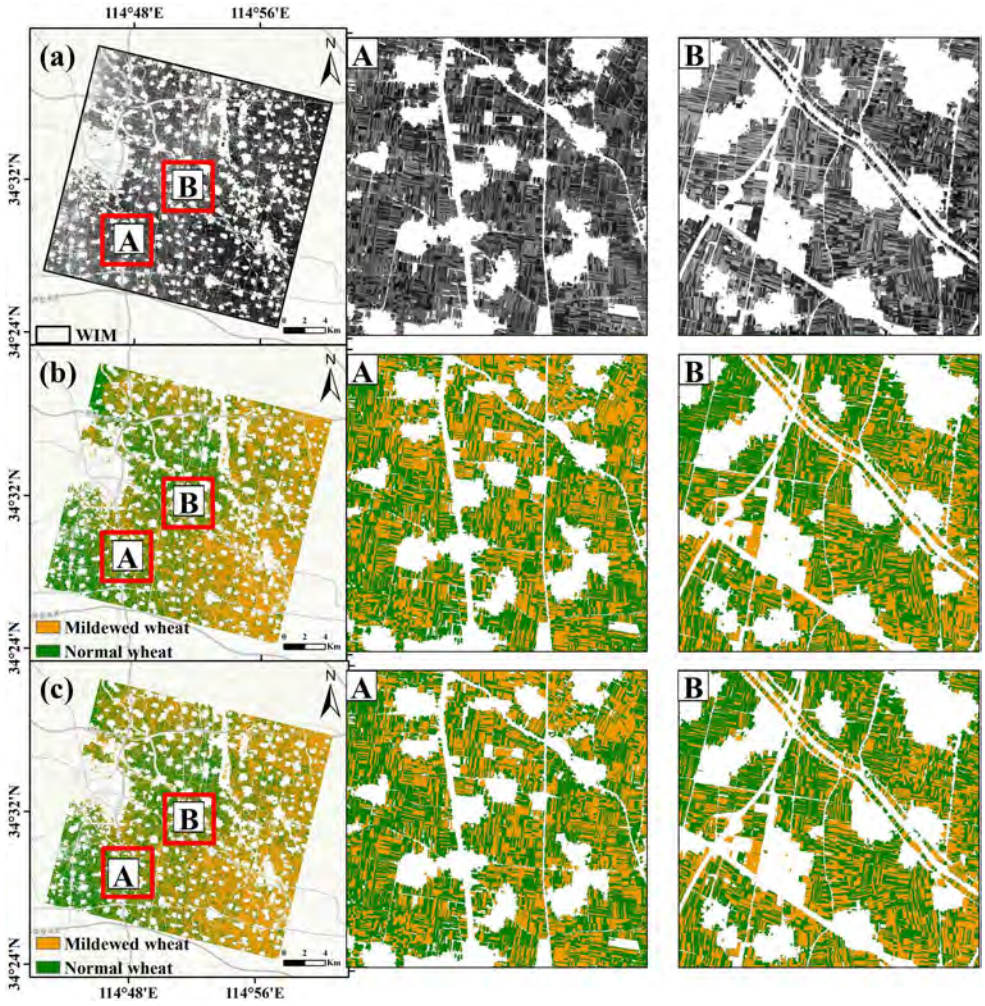


Figure 10. Classification results of machine learning (a is the mildew index of wheat in the study area; b is the result of random forest classification; and c is the result of the support vector machine classification).

Table 2. Accuracy evaluation of machine learning classification results with different quantitative characteristics.

	RF Classification	SVM Classification
Overall Accuracy	92.33%	92.78%
Kappa	0.8338	0.8430

classification method in practical applications. Notably, the Relief F + m RMR algorithm is used to screen out three original image band features among the five features used for machine learning classification. The spectral reflectance of wheat is very useful for distinguishing normal wheat from mildewed wheat. The wheat mildew index is constructed on the basis of the original spectral reflectance information of the image. The results show that the wheat mildew index constructed from spectral reflectance information is very effective in extracting the disaster area of wheat mildew. In addition, as shown in Table 3, although the p value of McNemar's test of the iterative threshold segmentation method and random forest

Table 3. McNemar's test results of the wheat mildew index threshold segmentation method and machine learning method.

Model	*p*-value	McNemar's Test (α = 0.05)
Otsu – RF	>0.05	no significant differences
Otsu – SVM	>0.05	no significant differences
Iterative Threshold – RF	<0.05	significant differences
Iterative Threshold – SVM	>0.05	no significant differences

classification method is less than the significance level of 0.05, the p value of the other methods is greater than the significance level of 0.05. In terms of statistics, this shows that the prediction accuracy of the iterative threshold segmentation method is better than that of the random forest classification method, whereas the prediction accuracy of the Otsu threshold segmentation method is not statistically significantly different from that of the random forest and SVM methods.

5. Discussion

5.1 Applicability of the wheat mildew index to different remote sensing data

To verify the effectiveness of the WMI proposed in this study in the application of different remote sensing sensor data sources, the same regional Sentinel-2 image and Landsat-9 image data from the same period were used to extract mildewed wheat. The Sentinel-2 and Landsat-9 multispectral images have resolutions of 10 and 30 meters, respectively, and have a high revisit period. They are ideal data sources for multitemporal and large-scale remote sensing monitoring (Sergii Skakun et al. 2019).

First, the wheat mildew index was calculated on the basis of Sentinel-2 images and Landsat-9 images, and then the mildewed wheat pixels were extracted via a threshold segmentation algorithm. In accordance with the experimental results of the Gaofen-2 image in Section 4.1, Otsu threshold segmentation and an iterative threshold segmentation algorithm are selected to segment and extract the range of mildewed wheat.

The experiment used Sentinel-2 and Landsat-9 remote sensing images to extract mildewed wheat via the WMI in the Gaofen-2 remote sensing image area. According to the results in Figure 11 and Table 4, when Sentinel-2 remote sensing images are used to extract mildewed wheat, the two threshold segmentation methods yield good results, and the overall accuracy is greater than 92%. The results of the Otsu threshold segmentation method are slightly better than those of iterative threshold segmentation. In this experiment, the extraction result of Sentinel-2 remote sensing images with a resolution of 10 m is slightly better than that of Landsat-9 remote sensing images with a resolution of 30 m, which may be due to the impact of pixel mixing caused by the resolution of remote sensing images on the extraction result of the wheat mildew index. The overall accuracy of the 10-meter resolution Sentinel-2 remote sensing image is similar to that of the 4-meter resolution Gaofen-2 image in Section 4.1. The Otsu threshold segmentation result based on the Sentinel-2 image is better than that of the Gaofen-2 image and iterative threshold segmentation, whereas the iterative threshold segmentation result based on the Sentinel-2 image is the opposite. The

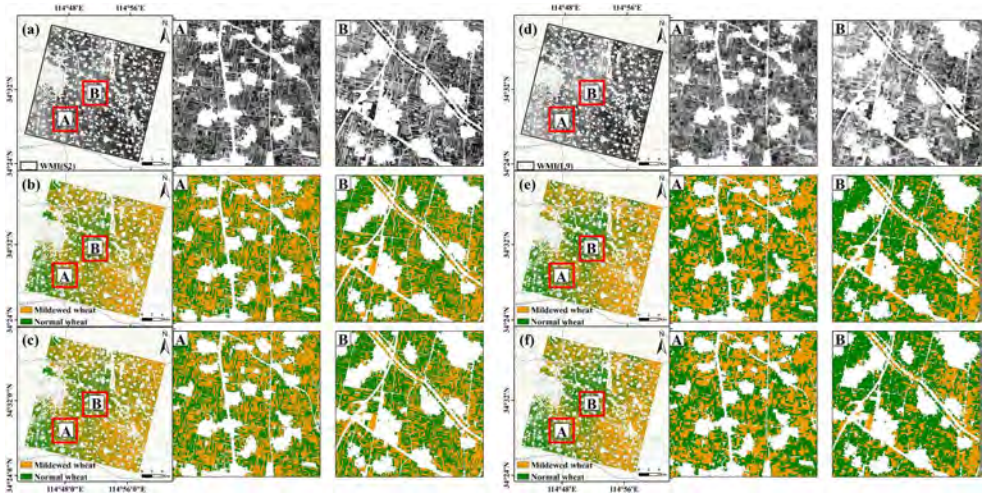


Figure 11. Segmentation results of the wheat mildew indices of different remote sensing datasets (a is the wheat mildew index of the Sentinel-2 image; b is the Otsu threshold segmentation result of the wheat mildew index of the Sentinel-2 image; c is the iterative threshold segmentation result of the wheat mildew index of the Sentinel-2 image; d is the wheat mildew index of the Landsat-9 remote sensing image; e is the Otsu threshold segmentation result of the wheat mildew index of the Landsat-9 remote sensing image; and f is the iterative threshold segmentation result of the wheat mildew index of the Landsat-9 remote sensing image).

Table 4. Accuracy evaluation of threshold segmentation results of the wheat mildew index from different remote sensing datasets.

Sentinel-2	Otsu	Iterative Threshold
Overall Accuracy	94.41%	92.94%
Kappa	0.8763	0.8461
Landsat-9		
Overall Accuracy	91.40%	91.14%
Kappa	0.8151	0.8102

extraction results of the Sentinel-2 image and Gaofen-2 image show that the wheat mildew index can obtain good results in remote sensing images with better spatial resolutions than 10 meters can achieve, and the results of higher-resolution images obtained via different threshold segmentation methods are more stable. The use of Sentinel-2 images and Landsat-9 images to extract the results of mildewed wheat based on the wheat mildew index also revealed that the difference in reflectivity between normal wheat and mildewed wheat is still well preserved in Sentinel-2 and Landsat-9 images and other medium- and high-resolution remote sensing images. The difference in spectral reflectance between normal wheat and mildewed wheat is not sensitive to remote sensing platforms or remote sensing sensors. The wheat mildew index constructed in this study still has good adaptability and generalizability in the face of different remote sensing image data sources, which greatly expands the application scenario of the wheat mildew index and can be used to monitor wheat mildew more frequently through the use of multiple-resolution remote sensing images.

5.2 Application analysis of the wheat mildew index in different regions

To explore the applicability of the extraction effect of the wheat mildew index in different regions, Gaofen-2 remote sensing images of different regions from the same period were used to monitor wheat mildew. This area is approximately 20 kilometers away from the experimental area discussed in Section 4.1, and wheat has a large range of mildew phenomena under the influence of continuous rainfall. The image acquisition time of the study area is June 1st, 2023, and the validation dataset is based on actual field data and supplemented appropriately. The wheat-cultivated land data were extracted from Gaofen-6 remote sensing images of the winter wheat growth period in April and from Gaofen-2 remote sensing images of the winter wheat harvest period in June on the basis of the NDVI vegetation index. In accordance with the extraction results of the different segmentation methods in Section 4.1, Otsu threshold segmentation and iterative threshold segmentation algorithms are used to extract mildewed wheat. This experiment aims to verify the applicability of the wheat mildew index proposed in this study and explore the extraction effect of the wheat mildew index in different regions. The experimental results are shown in Figure 12.

From the segmentation extraction results in Table 5, the extraction results of the wheat mildew index in different regions are better, the overall accuracy is greater than 91%, and the kappa coefficient is greater than 0.82, which is close to the extraction results in the experiment in Section 4.1. The results revealed that the difference in spectral reflectance between mildewed wheat and normal wheat was universal, and the difference could be captured by remote sensing sensors, which are less affected by regional factors. The wheat mildew index, which is based on spectral reflectance differences, has good applicability in different regions.

5.3 Simplified wheat mildew index

The wheat mildew index needs spectral reflectance and the central wavelength information of each band of the image, whereas the wheat mildew index is only a function of spectral reflectance. The wheat mildew index is constructed via the area method according to the difference in spectral reflectance between normal wheat and mildewed wheat (Figure 2). Its numerator is the area enclosed by the wheat pixel reflectance and the horizontal axis of the wavelength. The denominator uses the rectangular area enclosed by the maximum reflectivity of the wheat pixel and the horizontal axis of the wavelength, and the ratio of the two is used as the wheat mildew index. Since the wheat mildew index uses the central wavelength information of each band and the central wavelength is used as a scalar in the wheat mildew index, its function is to calculate the area

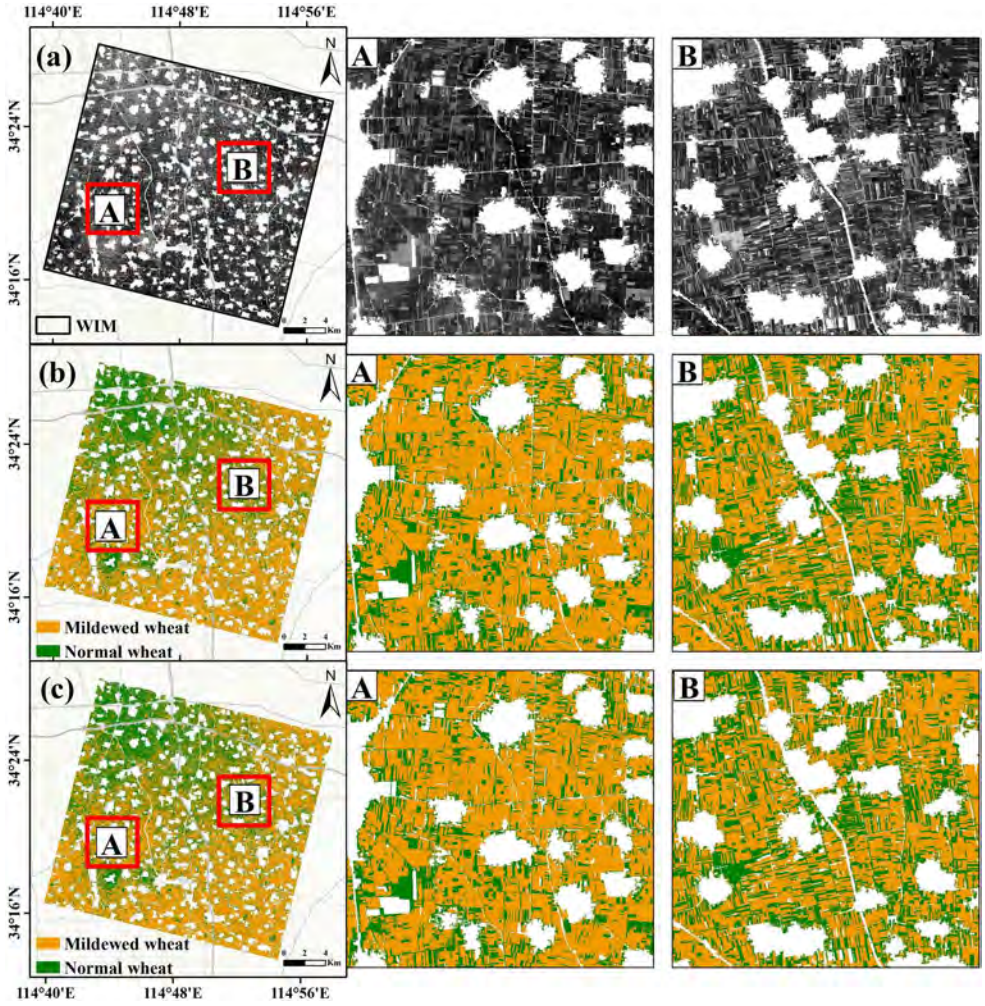


Figure 12. Segmentation results of the wheat mildew index in different regions (a is the wheat mildew index in the study area; b is the Otsu threshold segmentation result; and c is the iterative threshold segmentation result).

Table 5. Accuracy evaluation of threshold segmentation results of the wheat mildew index in different regions.

	Otsu Threshold Segmentation	Iterative Threshold Segmentation
Overall Accuracy	91.76%	91.91%
Kappa	0.8285	0.8320

enclosed by the crop reflectivity and the abscissa axis. The physical quantity that actually reflects whether wheat mildew occurs is still the spectral reflectance of wheat. In the actual use of the index, the actual use cost of the wheat mildew index is increased because of the difference in the central wavelength of each band of different remote sensing sensors. Therefore, the wheat mildew index can be simplified. Assuming that the interval between the central wavelengths of each band is equal, the central wavelength variable in the wheat mildew index can be eliminated. The simplified wheat mildew index does not require the central wavelength information of each band of the image, which is beneficial to the actual use of the index. The simplification of the wheat mildew index can also be explained as follows: each band of the multispectral remote sensing image has a specific wavelength range. When the wheat mildew index is constructed, a wavelength within the wavelength range of each band is selected to ensure that the frequency differences between adjacent bands are equal. The simplified wheat mildew index is as follows:

$$\mathrm{WMI} = \frac{R_{blue} + 2{*}R_{green} + 2{*}R_{red} + R_{nir}}{6{*}R_{max}}$$

where R_{blue}, R_{green}, R_{red}, *and* R_{nir} are image bands and where R_{max}. is the maximum pixel value of the image.

According to the results in Figure 13 and Table 6, the extraction accuracy of the simplified wheat mdew index shows little change, and the results of Otsu threshold segmentation and the iterative threshold segmentation algorithm are better. The overall extraction accuracy is approximately 1% different from the results without simplification, and the kappa coefficient is approximately 2%. The source of the difference can be attributed to two aspects. First, when the wheat mildew index is simplified, the difference between the central wavelengths of each band is approximately equal. Its essence is to approximate the original wheat mildew index, and the result has a certain degree of error. The second aspect is that the segmentation algorithm needs to stretch the threshold value to the range of 0–255 when segmenting the simplified image. The stretching process also involves approximating the wheat mildew index, which has a certain effect on the results. The experimental results show that the simplified wheat mildew index combined with the threshold segmentation algorithm can still yield good extraction results, and the accuracy of the extraction results is

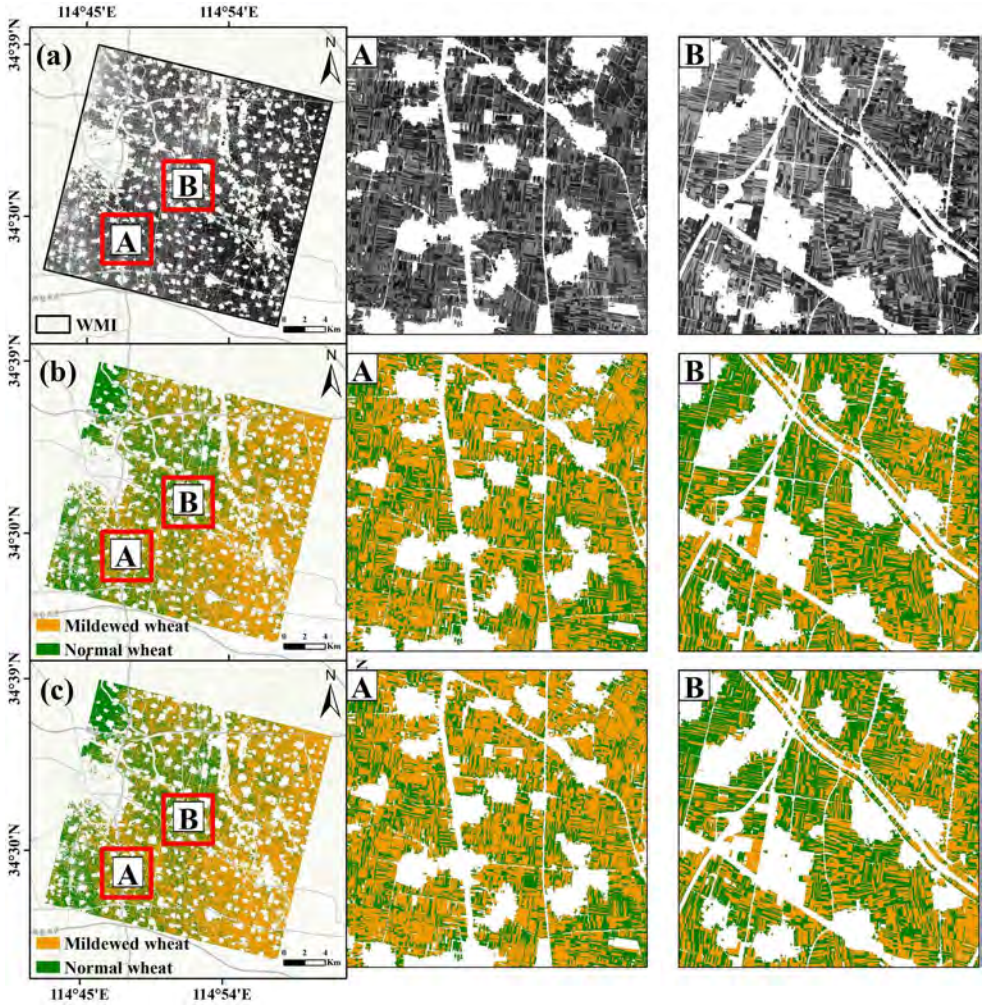


Figure 13. Automatic threshold segmentation results of the simplified wheat mildew index (a is the simplified wheat mildew index in the study area; b is the Otsu threshold segmentation result; and c is the iterative threshold segmentation result).

Table 6. Accuracy evaluation of simplified wheat mildew index segmentation results.

	Otsu	Iterative Threshold
Overall Accuracy	92.96% (0.66% ↓)	92.52% (0.86% ↓)
Kappa	0.841 (0.0160 ↓)	0.830 (0.0208 ↓)

Table 7. McNemar's test of different threshold segmentation methods before and after simplification of the wheat mildew index.

Model	*p*-value	McNemar's Test (α = 0.05)
WMI_{Otsu} − $Simplified_WMI_{Otsu}$	>0.05	no significant differences
$WMI_{Iterative\ Threshold}$ − $Simplified_WMI_{Iterative\ Threshold}$	>0.05	no significant differences

only slightly different from that of the original wheat mildew extraction results. The reason for this difference may be that the simplified wheat mildew index is similar to the original wheat mildew index, but the practicability and ease of use of the simplified wheat mildew index have improved. Moreover, as shown in Table 7, the *p* value of the simplified wheat mildew index using the same threshold segmentation method is greater than the significance level of 0.05, which shows that when the significance level is 0.05, the prediction performance of the simplified wheat mildew index based on the Otsu threshold and iterative threshold segmentation methods is not significantly different from that of the original threshold segmentation method. That is, the performance of the simplified wheat mildew index in extracting mildewed wheat is consistent with that of the original wheat mildew index. If high sensitivity exists to the minor errors caused by simplifying the wheat mildew index in practical applications, priority may be given to the use of remote sensing image data with equal or similar intervals between the central wavelengths of bands, or the issue can be mitigated by increasing the number of grayscale levels in grayscale images.

6. Conclusion

The wheat mildew index can capture the difference in spectral reflectance between normal wheat and mildewed wheat and enhance the difference in spectral reflectance characteristics via mathematical algebra so that normal wheat and mildewed wheat can be extracted quickly via an automatic threshold segmentation algorithm. The wheat mildew index combined with the Otsu threshold segmentation algorithm or iterative threshold segmentation algorithm can effectively extract the scope of mildewed wheat in the study area. Otsu threshold segmentation and iterative threshold segmentation are both full threshold segmentation algorithms, and their segmentation results are similar in accuracy, but the iterative threshold segmentation algorithm needs to obtain the final segmentation threshold through continuous iteration. When extracting large-scale mildewed wheat, this method requires a long iterative calculation time. The results of the wheat mildew index extraction method proposed in this study are similar to those of the machine learning method, but the process of wheat mildew index extraction is simpler without the feature selection and sample marking process of the machine learning classification process. In addition, the wheat mildew index is insensitive to different types of remote sensing sensor data. In the migration experiment presented in Section 5.1, multispectral remote sensing data from Sentinel-2 and Landsat-9 images were used. The findings show that the results of using Sentinel-2 and Landsat-9 remote sensing images as data sources to extract mildewed wheat based on the wheat mildew index are very close to those of the Gaofen-2 remote sensing image. Therefore, a variety of remote sensing data can be selected according to the actual situation when the wheat mildew index is used to monitor mildewed wheat. Finally, the simplified wheat mildew index approximates the original wheat mildew index. The physical meaning of the wheat mildew index indicates that the wheat mildew index is a function of spectral reflectance, and the extraction result of the simplified wheat mildew index is similar to that of the original wheat mildew index, which is proven by McNemar's test. The simplified wheat mildew index does not consider the central wavelength information of each band of remote sensing image data, which is simpler and more efficient in practical applications.

Wheat mildew index has excellent performance in the extraction of mildewed wheat, but it also has some limitations in practical use, such as the difficulty in obtaining optical remote sensing images during the wheat disaster period, and the lack of a large number of experimental verification on the universality of regions with different climate and soil conditions. The problem of remote sensing image data can be solved by combining multi-source remote sensing image data and UAV remote sensing image data, while the universality of wheat mildew index for different regions needs more data and experimental verification in the future. The method proposed in this paper based on wheat mildew index combined with automatic threshold segmentation algorithm to extract the affected area of mildewed wheat has great application value in the field of agriculture, and can be widely used in many aspects, such as wheat disaster loss

assessment, efficient dynamic monitoring of the affected area of wheat mildew, wheat mildew mechanism research, agricultural insurance and risk assessment. For example, in the wheat disaster loss assessment, by analyzing the scope and extent of the disaster, combined with historical data and crop growth models, we can accurately estimate the wheat yield loss caused by mildew, and provide a reliable basis for agricultural production planning and policy making; In terms of efficient dynamic monitoring of mildew affected areas, this method relies on the wheat mildew index, which can quickly and widely identify the location and range of mildewed wheat, without relying on time-consuming and labor-intensive manual field investigation, and can dynamically track the development status of mildew affected areas according to the re visit cycle of remote sensing images, so as to grasp the evolution trend of disasters in time.

CRediT authorship contribution statement

Huade Li: Writing – review & editing, Writing – original draft, Visualization, Validation, Methodology, Investigation, Formal analysis, Data curation, Conceptualization. **Jinshui Zhang**: Writing – review & editing, Validation, Supervision, Project administration, Funding acquisition, Formal analysis, **Zhenghua Chen**: Writing – review & editing, Validation, Supervision, Project administration, Conceptualization. **Mingwei Zhang**: Validation, Supervision, Project administration.

Geolocation information statement

The study area is located in the middle of Henan Province, China, spanning from 34°.25′N to 34°.39′N and 114°.43′E to 115°.1′E. Field data were collected was approximately June 2, 2023, including photos and GPS coordinates. Satellite imagery (Gaofen-2、Sentinel-2、Landsat-9) was obtained from China Centre for Resources Satellite Data and Application (https://data.cresda.cn) and Google Earth Engine (https://code.earthengine.google.com).

Disclosure statement

No potential conflict of interest was reported by the author(s).

Funding

This research was supported by the National Natural Science Foundation of China [grant number 42192580 and grant number 42192584].

Data availability statement (DAS)

The data that support the findings of this study are available from the corresponding author upon reasonable request.

References

Di Cui, Qin Zhang, Minzan Li, Glen L. Hartman, and Youfu Zhao. 2010. "Image Processing Methods for Quantitatively Detecting Soybean Rust from Multispectral Images." *Biosystems Engineering* 107 (3): 186–193. https://doi.org/10.1016/j.biosystemseng.2010.06.004.

Dora, Lingraj, Sanjay Agrawal, Rutuparna Panda, and Ajith Abraham. 2017. "State-of-the-Art Methods for Brain Tissue Segmentation: A Review." *IEEE Reviews in Biomedical Engineering* 10:235–249. https://doi.org/10.1109/RBME.2017.2715350.

Foody, Giles M. 2002 "Status of Land Cover Classification Accuracy Assessment." *Remote Sensing of Environment* 80 (1): 185–201. https://doi.org/10.1016/S0034-4257(01)00295-4.

Hanchuan, Peng, Fuhui Long, and C. Ding. 2005. "Feature Selection Based on Mutual Information Criteria of Max-Dependency, Max-Relevance, and Min-Redundancy." *IEEE Transactions on Pattern Analysis and Machine Intelligence* 27 (8): 1226–1238. https://doi.org/10.1109/TPAMI.2005.159.

Kapur, J. N., Prasanna Sahoo, and A. K. C. Wong. 1980. "A New Method for Gray-Level Picture Thresholding Using the Entropy of the Histogram." *Computer Vision, Graphics, and Image Processing* 29 (140): 273–285. https://doi.org/10.1016/0734-189X(85)90125-2.

Khan, Md Nasim, Subasish Das, and Jinli Liu. 2024. "Predicting Pedestrian-Involved Crash Severity Using Inception-v3 Deep Learning Model." *Accident Analysis & Prevention* 197 (March): 107457. https://doi.org/10.1016/j.aap.2024.107457.

Knipling, Edward B. 1970. "Physical and Physiological Basis for the Reflectance of Visible and Near-Infrared Radiation from Vegetation." *Remote Sensing of Environment* 1 (3): 155–159. https://doi.org/10.1016/S0034-4257(70)80021-9.

Likas, Aristidis, Nikos Vlassis, and Jakob J. Verbeek. 2003. "The Global *k*-Means Clustering Algorithm." *Pattern Recognition, Biometrics* 36 (2): 451–461. https://doi.org/10.1016/S0031-3203(02)00060-2.

Liu, Yang, Haikuan Feng, Yiguang Fan, Jibo Yue, Fuqin Yang, Jiejie Fan, Yanpeng Ma, Riqiang Chen, Mingbo Bian, and Guijun Yang. 2025. "Utilizing UAV-Based Hyperspectral Remote Sensing Combined with Various Agronomic Traits to Monitor Potato Growth and Estimate Yield." *Computers and Electronics in Agriculture* 231 (April): 109984. https://doi.org/10.1016/j.compag.2025.109984.

Liu, Yang, Guohui Liu, Hong Sun, Lulu An, Ruomei Zhao, Mingjia Liu, Weijie Tang, et al. 2024. "Exploring Multi-features in UAV Based Optical and Thermal Infrared Images to Estimate Disease Severity of Wheat Powdery Mildew." *Computers and Electronics in Agriculture* 225 (October): 109285. https://doi.org/10.1016/j.compag.2024.109285.

Liu, Yang, Mingjia Liu, Guohui Liu, Hong Sun, Lulu An, Ruomei Zhao, Weijie Tang, et al. 2024. "Estimating Canopy Chlorophyll Content of Powdery Mildew Stressed Winter Wheat by Different Spatial Resolutions of UAV-Imagery." *Computers and Electronics in Agriculture* 227 (December): 109621. https://doi.org/10.1016/j.compag.2024.109621.

Mandal, Nandita, Sujan Adak, Deb K. Das, Rabi N. Sahoo, Joydeep Mukherjee, Andy Kumar, Viswanathan Chinnusamy, et al. 2023. "Spectral Characterization and Severity Assessment of Rice Blast Disease Using Univariate and Multivariate Models." *Frontiers in Plant Science* 14:1067189. https://doi.org/10.3389/fpls.2023.1067189.

McNEMAR, Q. 1947. "Note on the Sampling Error of the Difference between Correlated Proportions or Percentages." *Psychometrika* 12 (2): 153–157. https://doi.org/10.1007/BF02295996.

Merzban, Mohamed H., and Mahmoud Elbayoumi. 2018 "Efficient Solution of Otsu Multilevel Image Thresholding: A Comparative Study." *Expert Systems with Applications* 116: 299–309. https://doi.org/10.1016/j.eswa.2018.09.008.

Onisimo, Mutanga, and Andrew K. Skidmore. 2007 "Red Edge Shift and Biochemical Content in Grass Canopies." *ISPRS Journal of Photogrammetry and Remote Sensing* 62 (1): 34–42. https://doi.org/10.1016/j.isprsjprs.2007.02.001.

Otsu, Nobuyuki. 1979. "A Threshold Selection Method from Gray-Level Histograms." *IEEE Transactions on Systems Man & Cybernetics* 9 (1): 62–66. https://doi.org/10.1109/TSMC.1979.4310076.

Perez, Arnulfo, and R. C. Gonzalez. 1987. "An Iterative Thresholding Algorithm for Image Segmentation." *IEEE Transactions on Pattern Analysis and Machine Intelligence9* 9 (6): 742–751. https://doi.org/10.1109/TPAMI.1987.4767981.

Sahoo, Prasanna, Carrye Wilkins, and Jerry Yeager. 1997. "Threshold Selection Using Renyi's Entropy." *Pattern Recognition* 30 (1): 71–84. https://doi.org/10.1016/S0031-3203(96)00065-9.

Sergii, Skakun, Eric Vermote, Belen Franch, Jean-Claude Roger, Nataliia Kussul, Junchang Ju, and Jeffrey Masek. 2019. "Winter Wheat Yield Assessment from Landsat 8 and Sentinel-2 Data: Incorporating Surface Reflectance, through Phenological Fitting, into Regression Yield Models." *Remote Sensing* 11 (15): 1768–1768. https://doi.org/10.3390/rs11151768.

Sims, Daniel A., and John A. Gamon. 2002 "Relationships between Leaf Pigment Content and Spectral Reflectance across a Wide Range of Species, Leaf Structures and Developmental Stages." *Remote Sensing of Environment* 81 (2): 337–354.

Sindhuja, Sankaran, Ashish Mishra, Reza Ehsani, and Cristina Davis. 2010. "A Review of Advanced Techniques for Detecting Plant Diseases." *Computers and Electronics in Agriculture* 72 (1): 1–13. https://doi.org/10.1016/j.compag.2010.02.007.

Sulaiman, S. N., and N. A. Mat Isa. 2010. "Adaptive Fuzzy-K-Means Clustering Algorithm for Image Segmentation." *IEEE Transactions on Consumer Electronics* 56 (4): 2661–2668. https://doi.org/10.1109/TCE.2010.5681154.

Tapas, Kanungo, David M. Mount, Nathan S. Netanyahu, Christine D. Piatko, Ruth Silverman, and Angela Y. Wu. 2002 "An Efficient K-Means Clustering Algorithm: Analysis and Implementation." *IEEE Trans. Pattern Anal. Mach. Intell* 24 (7): 881–892. https://doi.org/10.1109/TPAMI.2002.1017616.

Ute, Bradter, Jerome O'Connell, William E. Kunin, Caroline W. H. Boffey, Richard J. Ellis, and Tim G. Benton. 2020 "Classifying Grass-Dominated Habitats from Remotely Sensed Data: The Influence of Spectral Resolution, Acquisition Time and the Vegetation Classification System on Accuracy and Thematic Resolution." *Science of the Total Environment* 711: 134584. https://doi.org/10.1016/j.scitotenv.2019.134584.

Xu, Laixiang, Bingxu Cao, Fengjie Zhao, Shiyuan Ning, Peng Xu, Wenbo Zhang, and Xiangguan Hou. 2023. "Wheat Leaf Disease Identification Based on Deep Learning Algorithms." *Physiological and Molecular Plant Pathology* 123 (January): 101940. https://doi.org/10.1016/j.pmpp.2022.101940.

Zack, G. W., W. E. Rogers, and S. A. Latt. 1977. "Automatic Measurement of Sister Chromatid Exchange Frequency." *Journal of Histochemistry & Cytochemistry* 25 (7): 741–753. https://doi.org/10.1177/25.7.70454.

Zhang, Haiyang, Guolong Wang, Fanfan Song, Zhaoqi Wen, Wenwen Li, Ling Tong, and Shaozhong Kang. 2025. "Improving Chili Pepper LAI Prediction with TPE-2BVIs and UAV Hyperspectral Imagery." *Computers and Electronics in Agriculture* 235 (August): 110368. https://doi.org/10.1016/j.compag.2025.110368.

Zhang, Hongbo, Xiwen Qin, Xueliang Gao, Siqi Zhang, Yunsheng Tian, and Wei Zhang. 2024. "Improved Salp Swarm Algorithm Based on Newton Interpolation and Cosine Opposition-Based Learning for Feature Selection." *Mathematics and Computers in Simulation* 219 (May): 544–558. https://doi.org/10.1016/j.matcom.2023.12.037.

Zhang, Xin, Liangxiu Han, Yingying Dong, Yue Shi, Wenjiang Huang, Lianghao Han, Pablo González-Moreno, Huiqin Ma, Huichun Ye, and Tam Sobeih. 2019. "A Deep Learning-Based Approach for Automated Yellow Rust Disease Detection from High-Resolution Hyperspectral UAV Images." *Remote Sensing* 11 (13): 1554. https://doi.org/10.3390/rs11131554.

Zhang, Yi, Chris Ding, and Tao Li. 2008. "Gene Selection Algorithm by Combining ReliefF and mRMR." *BMC Genomics* 9 (S2): S27. https://doi.org/10.1186/1471-2164-9-S2-S27.

Zhu, X. X., D. Tuia, L. Mou, Xia Gui-Song, L. Zhang, F. Xu, and F. Fraundorfer. 2018. "Deep Learning in Remote Sensing: A Comprehensive Review and List of Resources." *IEEE Geoscience & Remote Sensing Magazine* 5 (4): 8–36. https://doi.org/10.1109/MGRS.2017.2762307

Journal of *Marine Science and Engineering*

MDPI

Article

Numerical Modeling of Wave Hydrodynamics Around Submerged Artificial Reefs on Fringing Reefs in Weizhou Island of Northern South China Sea

Zuodong Liang [1], Guangxian Huang [2], Wen Huang [1], Hailun Chen [1], Kefu Yu [1,3,*] and Dong-Sheng Jeng [4,5]

[1] Guangxi Laboratory on the Study of Coral Reefs in the South China Sea, Coral Reef Research Center of China, School of Marine Sciences, Guangxi University, Nanning 530004, China; liangzuodong@gxu.edu.cn (Z.L.)
[2] School of Resources, Environment and Materials, Guangxi University, Nanning 530004, China
[3] Southern Marine Science and Engineering Guangdong Laboratory (Guangzhou), Guangzhou 511458, China
[4] College of Civil Engineering, Qingdao University of Technology, Qingdao 266033, China; d.jeng@griffith.edu.au
[5] School of Engineering & Built Environment, Griffith University Gold Coast Campus, Southport, QLD 4222, Australia
* Correspondence: kefuyu@scsio.ac.cn

Abstract

This study numerically investigates wave transformation and setup processes across fringing reefs, focusing on artificial reef configuration effects under varying tidal conditions and incident wave parameters. The OpenFOAM-based waves2Foam model simulates hydrodynamic processes along reef profiles containing a fore-reef slope and reef flat. Following validation against laboratory data, the model simulates cross-shore wave height attenuation and setup within fringing reef systems. The results demonstrate that reef flat water depth substantially modulates wave dynamics: during low tide, intensified wave breaking elevates the maximum wave height and setup by up to 45.7% and 78.5%, respectively, compared to high-tide conditions. Furthermore, this water depth critically governs the reef configuration's influence on wave energy dissipation efficiency. Under high tide, additional reef rows increase the peak wave height by 5.2% while reducing wave setup by 10.5%. In contrast, expanded reef spacing reduces the peak wave height by 2.1% and decreases the peak wave setup by 2.4%. The temporal evolution of wave reflection (K_R) and transmission (K_T) coefficients reveals that shallow-water conditions amplify wave reflection while diminishing transmission capacity, as tidal variations directly regulate wave propagation mechanisms through water depth modulation. At the outer reef flat boundary, K_R and K_T values for existing artificial reefs exhibit variations below 5% across all tidal phases, row configurations, and spacing combinations. Consequently, current reef structures provide limited control over wave transmission in fringing reef terrains, indicating that structural modifications such as increasing reef elevation or deploying reefs on the fore-reef slope could enhance attenuation performance.

Keywords: fringing reef; wave dissipation; wave-induced setup; artificial reef; OpenFOAM

check for updates

Academic Editors: José Miguel Rodrigues and Decheng Wan

Received: 11 September 2025
Revised: 16 October 2025
Accepted: 21 October 2025
Published: 23 October 2025

Citation: Liang, Z.; Huang, G.; Huang, W.; Chen, H.; Yu, K.; Jeng, D.-S. Numerical Modeling of Wave Hydrodynamics Around Submerged Artificial Reefs on Fringing Reefs in Weizhou Island of Northern South China Sea. *J. Mar. Sci. Eng.* **2025**, *13*, 2031. https://doi.org/10.3390/jmse13112031

Copyright: © 2025 by the authors. Licensee MDPI, Basel, Switzerland. This article is an open access article distributed under the terms and conditions of the Creative Commons Attribution (CC BY) license (https://creativecommons.org/licenses/by/4.0/).

1. Introduction

Coral reefs represent highly complex underwater ecosystems that support more than 25% of all known marine species, and their morphological characteristics exhibit substantial variation depending on the geological setting. Fringing reefs function as effective natural

barriers that significantly dissipate wave energy, reducing nearshore hydrodynamic disturbance and protecting adjacent beaches [1]. Furthermore, waves breaking over complex reef topography generate flows that regulate sediment dynamics, nutrient fluxes, and benthic habitats on reef flats [2]. Consequently, site-specific hydrodynamic assessments are required to assess ecosystem stability.

Research on reef hydrodynamics has evolved since the late 20th century, employing diverse methodologies that include field observations, experimental studies, and numerical modeling. Early investigations extensively characterized wave and wave–current interactions through field campaigns [3–5] and wave flume experiments [6–10]. Later, numerical simulations of hydrodynamic processes in reef environments became established research approaches [11–16]. More recently, Yao et al. [17] examined the influences of tidal currents on the vertical structure of surf zone currents within coral reefs, including wave height, wave setup, turbulent kinetic energy, and Reynolds shear stress intensity. In contrast, Watanabe et al. [18] demonstrated that the structures of the reef slope at the micrometer scale enhance turbulence and the transport of nutrients driven by waves, yet they minimally affect wave energy density across reef flats or overall storm wave dissipation; these processes remain dominated by the slope, crest, and flat morphology of the macrometer scale of the reef. Wang et al. [19] further examined realistic topographical effects, quantifying how the height, position, and seaward slope gradient of a reef ledge affect secondary wave breaking and reflection during tsunami propagation.

Artificial coral reefs provide dual ecological restoration and coastal protection benefits by offering alternative habitats for degraded coral ecosystems. Fadli et al. [20] evaluated artificial reef modules' potential for habitat rehabilitation in degraded areas of Aceh, Indonesia, demonstrating effectiveness despite limited resilience to large-scale climatic disturbances such as anomalous warming. Corroborating this, Blakeway et al. [21] confirmed successful coral settlement and community development in nearshore artificial structures in high-turbidity environments of Dampier Harbour, Western Australia, through long-term monitoring. Further supporting evidence emerges from Tanaya et al. [22], whose 29-year observational dataset revealed significantly higher coral cover (predominantly *Acropora* spp.) on breakwaters versus adjacent natural reefs, establishing artificial structures as viable restoration tools. Knoester et al. [23] subsequently examined how the structural characteristics (e.g., material, orientation) of artificial reefs in southern Kenya influence the survival, recruitment, and recovery of coral fragments of associated fish and invertebrate communities. In addition, Reguero et al. [24] identified coral reef degradation as a primary driver of coastal erosion in Grenville Bay, proposing that engineered reef structures simultaneously attenuate wave energy, modify wave direction, and provide marine habitats. In summary, these investigations demonstrate that scientifically designed artificial reefs enhance biodiversity conservation and coastal resilience through the construction of three-dimensional habitats.

The hydrodynamic processes surrounding artificial reefs (ARs) exhibit strong dependencies on site selection, structural configuration, and ecological results. Webb and Allen [25] identified a significant negative correlation between the wave transmission coefficient and relative height for non-rock ARs, indicating limited attenuation capacity; conventional rubble mound formulae were shown to overestimate attenuation by neglecting porosity. Srineash and Murali [26] subsequently demonstrated that reef-induced wave breaking (RIB) constitutes the primary dissipation mechanism in modular porous ARs under varying crest widths, depths of submergence, and wave conditions. Consequently, the controlled adjustment of the relative depth of submergence can actively induce RIB for design optimization. In contrast, van Gent et al. [27] established that vertical impermeable screens in submerged ARs significantly reduce transmission by impeding orbital velocities, yielding a

unified hyperbolic tangent-based empirical formula for transmission coefficient (K_T) predictions across submerged and emergent structures. Complementarily, Ghiasian et al. [28] quantified the performance of a trapezoidal AR model, achieving larger than 35% incident wave height reduction and 63% energy dissipation; the incorporation of *Acropora cervicornis* skeletons further enhanced frictional resistance, providing additional reductions of 10% in wave height and 14% in energy. Huang et al. [29] differentiated dissipation mechanisms: solid ARs predominantly rely on wave breaking, while permeable designs utilize continuous internal drag forces, leading to a novel predictive formula based on effective water depth. Based on this, Huang et al. [30] developed a parameterized phase-averaged model that separately quantifies the dissipation of breaking, the dissipation of the reef drag, and the reflection processes. Their analysis revealed that reduced porosity or increased crest length substantially enhances drag-dominated attenuation efficiency, whereas wave reflection contributes minimally.

In summary, current artificial reef applications focus predominantly on fishery resource enhancement, while the hydrodynamic evaluation of wave attenuation efficacy for reefs in coral habitats remains critically insufficient. The new scientific contributions of the present work are outlined here:

1. The novel integration of in situ bathymetric measurements with submerged artificial reef data, thereby enabling the systematic quantification of morphology–hydrodynamic interactions.
2. A comprehensive analysis of wave hydrodynamics at fringing reef sites using field hydrological data, which evaluates the wave attenuation efficacy of deployed artificial reef configurations under diverse wave regimes.

In this study, a comprehensive numerical investigation of hydrodynamics at coral reef sites on Weizhou Island is conducted, focusing on wave transformation, breaking, and setup processes. The OpenFOAM-based waves2Foam model [31] is adopted in this study, which solves Reynolds-averaged Navier–Stokes equations to simulate complex flow dynamics over fringing reefs characterized by fore-reef slope and reef flat geometry. Before application, the model undergoes rigorous validation against laboratory experiments to ensure an accurate simulation of wave profiles at the reef front. Using the validated model, the cross-shore characteristics of the wave-induced setup and wave height attenuation under varying deep-water conditions are subsequently examined.

2. Field Investigation

Weizhou Island (21°00′–21°10′ N, 109°00′–109°15′ E; Figure 1a) hosts a relatively high-latitude coral reef system in the South China Sea. This system potentially functions as a thermal refuge under global warming [32], with well-developed reefs primarily distributed in shallow northern, southeastern, and southwestern coastal waters. These reefs are dominated by massive coral species, including *Porites* sp., *Favites abdita*, and *Goniopora stutchburyi* [33]. However, significant degradation has reduced average live coral cover to approximately 10.7% [34].

Hydrodynamic investigations focus on a 1.3 km fringing reef section along the southwestern coast of Weizhou Island (Figure 1b). During spring tides, underwater topography surveys employ an ultrasonic depth sounder (RISEN-SFCC; maximum range: 50 m; minimum detection depth: 0.8 m; sampling rate: 1 Hz), covering areas from nearshore shallows (depth $\geq$ 0.8 m) to deeper offshore zones. Simultaneously, beach profile measurements utilize a high-precision differential GNSS (Leica GS15; horizontal accuracy: 8 mm $\pm$ 1 ppm; vertical accuracy: 15 mm $\pm$ 1 ppm), extending from the vegetation line to water depths of $\geq$1 m. These integrated surveys produce the composite cross-sectional bathymetric profile shown in Figure 1c. The specific submerged artificial reef structures adopted in this study,

which are deployed in coral restoration initiatives on northern Weizhou Island, appear in Figure 1d.

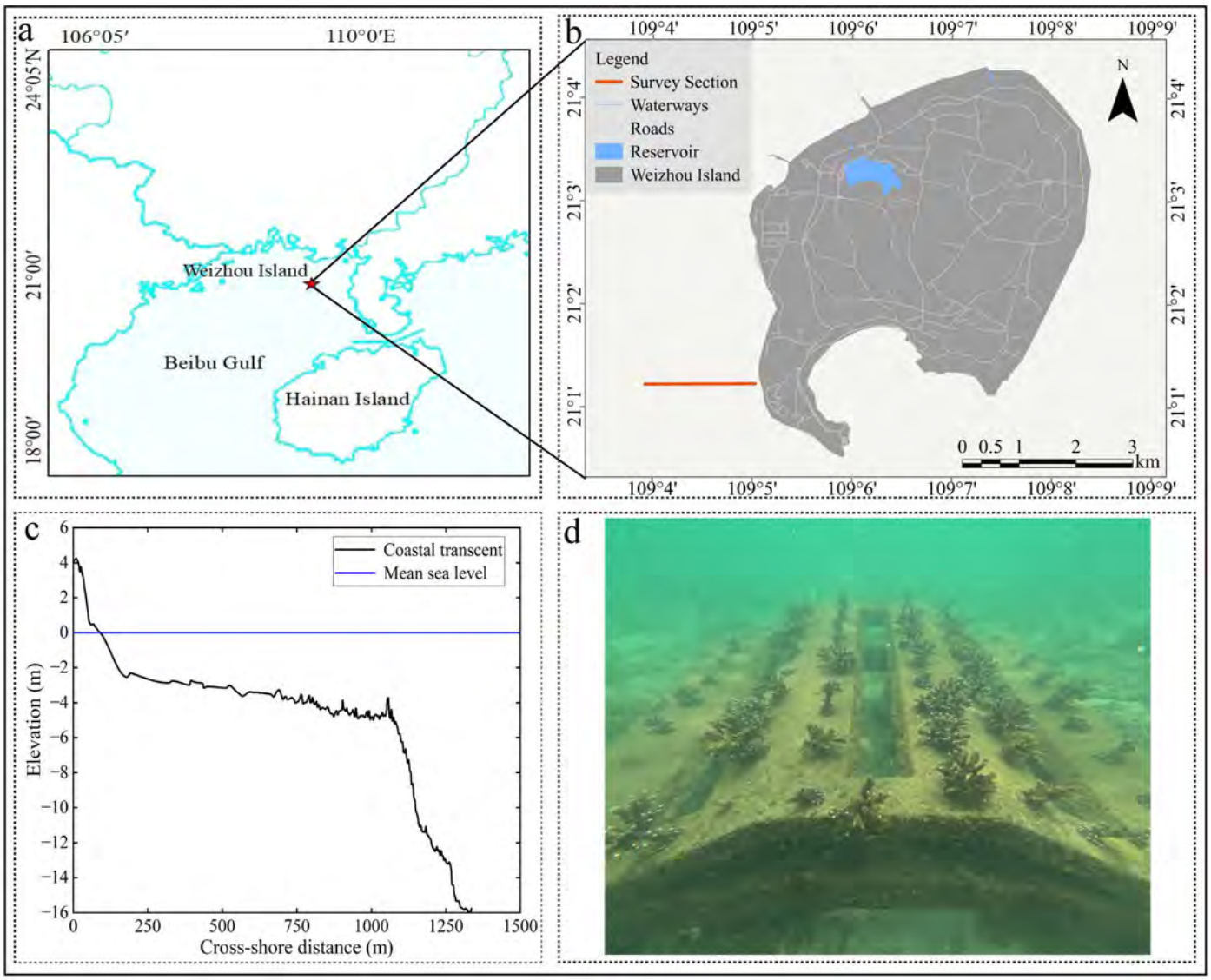


Figure 1. (**a**) Map showing location of study area. (**b**) Delineation of Weizhou Island's scope. (**c**) Cross-sectional profile of southwestern fringing reef. (**d**) Schematic of deployed submerged artificial reef.

There is a regular diurnal tidal regime with an annual mean range of 2.35 m in Weizhou Island [35]. An analysis of historical wave data (1973–1995) from the Weizhou Ocean Monitoring Station further identifies south–southwest (SSW) as the predominant wave direction [36]. Following the Code of Hydrology for Harbours and Waterways (JTS 145-2015) [37], wave heights and periods ($H_{1/3}$ and $T_{1/3}$) for 5-, 10-, 25-, and 50-year return periods are calculated, yielding respective values of 2.76 m and 7.82 s, 3.15 m and 8.4 s, 3.55 m and 8.97 s, and 3.86 m and 9.43 s. These offshore incident wave parameters, implemented as regular waves in the model simulations, are detailed in Table 1.

Table 1. Parameters for the present model.

Characteristics	Value	Unit
Wave and tide characteristics		
Wave height (H_0)	2.76, 3.15, 3.55, 3.86	[m]
Wave period (T_0)	7.82, 8.4, 8.97, 9.43	[s]
Deep water depth (d_0)	16	[m]
Tidal range (Δd)	0, 1.2, 2.35	[m]
Fringing reef characteristics		
Slope1 (S_1)	1:23	[-]
Slope2 (S_2)	1:23	[-]
Slope3 (S_3)	1:378	[-]
Length1 (L_1)	67.62	[m]
Length2 (L_2)	190.26	[m]
Length3 (L_3)	891.83	[m]
Reef flat water depth (h_r)	2.53, 3.68, 4.88	[m]
Artificial reef characteristics		
Porosity (n_{AR})	0.867	[-]
Reef top width (w_t)	0.614	[m]
Reef bottom width (w_b)	2	[m]
Reef height (h_{AR})	0.716	[m]
Submerged crest depth (h_c)	1.814, 2.964, 4.164	[m]
Effective crest depth ($h_{c,e}$)	2.435, 3.585, 4.785	[m]
Spacing (S_{AR})	0, 2, 5	[m]
Row (R_{AR})	1, 2, 3, 4	[-]

3. Numerical Model

3.1. Governing Equations

For an incompressible viscous fluid, the wave domain is governed by the Reynolds-averaged Navier–Stokes equations [31], which encompass both the continuity and momentum equations:

$$\nabla \cdot \boldsymbol{U} = 0\,, \tag{1}$$

$$\frac{\partial \rho \boldsymbol{U}}{\partial t} + \nabla \cdot (\rho \boldsymbol{U}\boldsymbol{U}^T) \;=\; -\nabla p^* - \boldsymbol{g} \cdot \boldsymbol{X} \nabla \rho + \nabla \cdot (\mu \nabla \boldsymbol{U} + \rho \boldsymbol{\tau}) + \sigma_T \kappa_{\alpha_1} \nabla \alpha_1\,, \tag{2}$$

in which $\boldsymbol{U}$ = the velocity vector; ρ = the density of the fluid; p^* = the pseudodynamic pressure; μ = the dynamic molecular viscosity; $\boldsymbol{X}$ = the position vector; $\boldsymbol{\tau}$ = the specific Reynolds stress tensor; σ_T = the surface tension coefficient; and κ_{α_1} = the curvature of the interface. The volume fraction index (α_1) is introduced to track the fluid surface (that is, α_1 is 0 for air and 1 for water); thus the distribution of α_1 is modeled by an advection equation.

$$\frac{\partial \alpha_1}{\partial t} + \nabla \cdot [\boldsymbol{U}\alpha_1] + \nabla \cdot [\boldsymbol{U_r}\alpha_1(1-\alpha_1)] \;=\; 0\,, \tag{3}$$

where $\boldsymbol{U_r}$ = the relative velocity, and the properties of the mixture are calculated as follows:

$$\Phi \;=\; \alpha_1 \Phi_w + (1-\alpha_1)\Phi_a, \tag{4}$$

in which Φ_w and Φ_a are any water and air properties, respectively. In addition, the $k-\epsilon$ model [38] is adopted to simulate the turbulence effect of breaking waves near the front reef slope.

3.2. Numerical Setup and Mesh Scheme

Specifically, Figure 2a illustrates the computational domain with a total length of 900 m, coinciding with the fore-reef slope toe. From this point, two onshore slopes (gradient 1:23) extend landward for 67.62 m and 190.26 m, respectively, transitioning to an approximately horizontal reef flat spanning 891.83 m (see Table 1). The boundary conditions consist of the following: (1) atmospheric pressure at the top boundary; (2) zero-gradient conditions at lateral boundaries; and (3) no-slip conditions at both the seabed and reef surfaces. It is noted that this study employs a two-dimensional approach. Wave generation employs second-order Stokes theory to produce monochromatic waves at the offshore (left) boundary. To suppress wave reflections, explicit relaxation absorption with weighting function $w_R \in [0, 1]$ adjusts the solution variables (Φ) within 100 m absorption zones at both domain ends, as indicated by the red lines. The artificial reef geometry, illustrated in Figure 2b,c, is imported as an STL file. Subsequently, the background mesh is generated using OpenFOAM's `surfaceFeatureExtract` and `snappyHexMesh` utilities, incorporating local refinement near the reef surface to resolve its geometric features accurately.

To balance computational accuracy and efficiency, the domain along the wave propagation direction is divided into three regions: a wave generation zone (0–150 m), a reef zone (150–800 m), and a wave absorption zone (800–900 m), with non-uniform gridding. Grid sizes in the X-direction are 0.8, 0.4, and 0.8 m, while the corresponding Z-direction dimensions are 0.1, 0.05, and 0.1 m. Finer resolution is employed near the free surface within the reef zone where significant wave deformation occurs.

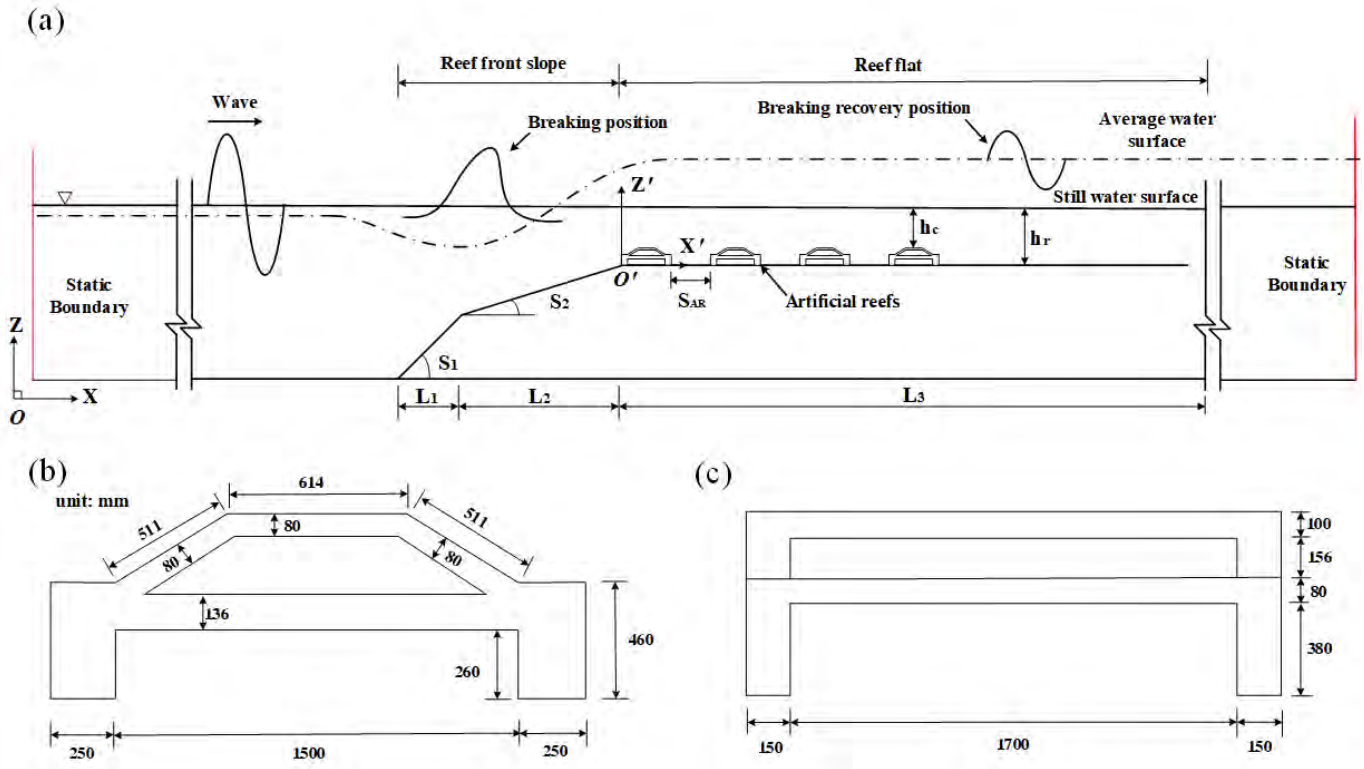


Figure 2. A schematic diagram of the model setup: (**a**) the computational domain, (**b**) the side view of the artificial reef structure, and (**c**) the corresponding front view.

3.3. Model Validation

To validate the numerical model, this study replicates three physical experiments simulating hydrodynamic processes induced by regular and solitary waves over varying coral reef topographies [10,19,39]. The key experimental parameters corresponding to the

validation cases are tabulated in Table 2. To quantitatively assess model performance, the *skill* value [40] is adopted, defined as follows:

$$\text{skill} = 1 - \frac{\sum \left| X_{model} - X_{obs} \right|^2}{\sum \left(\left| X_{model} - \overline{X_{obs}} \right| + \left| X_{obs} - \overline{X_{obs}} \right| \right)^2} \quad (5)$$

where X_{model} is the predicted value, X_{obs} is the measured value, and the overbar represents the average value. Then a skill value of 1 is assigned to a perfect model result and 0 to an obvious predictive error.

Table 2. Parameters for the validation cases (the data was from [10,19,39]).

Validation Case/Flow Characteristics	H [m]	T [s]	h_0 [m]	h_r [m]	U_c [m/s]
Yao et al. [10]	0.095	1.25	0.45	0.1	0
Wang et al. [19]	0.06	-	0.605/0.655	0/0.05	0
Chen et al. [39]	0.08	1	0.6	-	±0.2

3.3.1. Validation 1

The experiments of Yao et al. [10] are conducted in a custom flume (36.0 m long × 0.55 m wide × 0.6 m deep; see Figure 3a). A piston-type wave maker is installed at one end of the flume to generate the designed waves. Furthermore, two simplified fringing reef configurations are investigated: a steep reef slope with a 1:6 gradient and a 7 m flat section and a reef edge ridge represented by a rectangular box measuring 55 × 50 × 5 cm. Twelve wave gauges (G1–G12) are strategically positioned to quantify wave transformation across the reef topography. For model validation, the monochromatic wave scenario ($T = 1.25$ s, $H = 0.095$ m, and $h_r = 0.1$ m) is reproduced and compared with laboratory measurements. The temporal variation in free-surface elevation (see Figure 4) is strongly affected by the reef crest, which leads to reduced skill values at the reef flat (G9 and G11). However, the overall skill values remain above 0.7.

3.3.2. Validation 2

The experimental study of Wang et al. [19] is conducted in a wave flume measuring 45 m in length, 0.8 m in width, and 1 m in depth, which contains a geometrically scaled (1 : 40) reef model (see Figure 3b). A flap-type wave maker generates solitary waves for this study. The model topography comprises a fore-reef slope, a reef step, and a lagoon, interconnected by a 1 : 2.32 slope that links the outer and inner reef flats. The investigation considers four distinct water depths over the inner reef flat ($h_r = 0$, 0.025, 0.05, and 0.075 m) and five incident wave heights ($H_0 = 0.02$ to 0.1 m in 0.02 m increments). The temporal evolution of the free-surface elevation is measured by fifteen strategically placed wave gauges (G1–G15). For validation, experimental cases with $H_0 = 0.06$ m and water depths of $h_r = 0$ m and 0.05 m are reproduced. A comparison between simulated water levels and experimental data in Figure 5 demonstrates close agreement, with a minimum skill number exceeding 0.94.

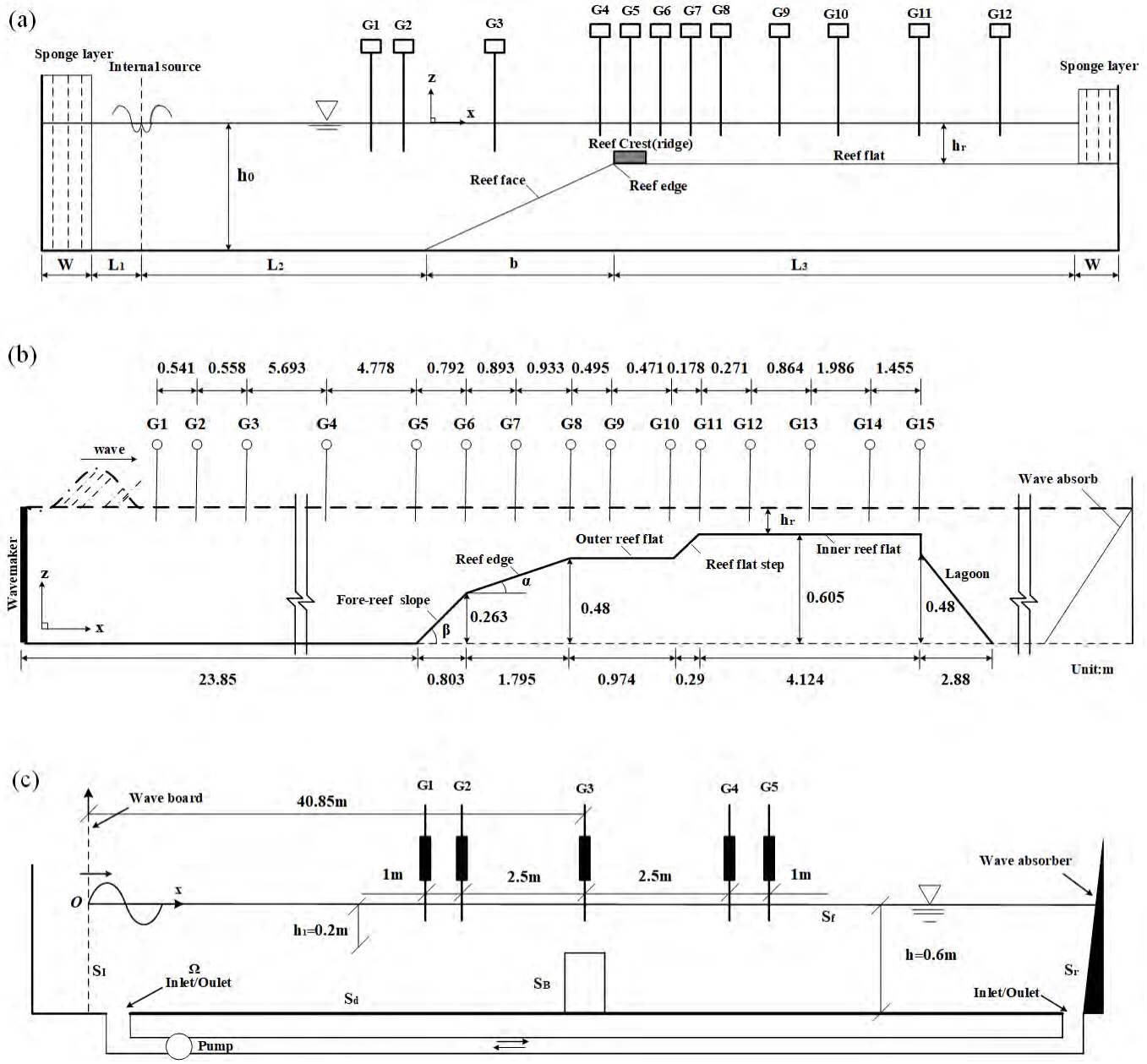


Figure 3. The experimental setup of previous wave flume tests [10,19,39] for the validation of the OpenFOAM-based model. (**a**) Yao et al. [10]'s experiment for wave-induced set-up over the horizontal reef with idealized ridge. (**b**) Wang et al. [19]'s experiment for tsunami-like wave over the uneven coral reef. (**c**) Chen et al. [39]'s experiment for the wave-current interaction with submerged rectangular breakwater.

3.3.3. Validation 3

The experimental setup of Chen et al. [39] utilizes a wave flume that measures 69 m in length, 2 m in width, and 1.8 m in height (see Figure 3c). Nonlinear regular waves are produced by a hydraulic piston-type wave generator, with uniform currents supplied through a bidirectional centrifugal pump. Wave propagation over a rectangular submerged breakwater (0.8 m long × 0.5 m wide × 0.4 m high) is investigated under the following and opposing current conditions. Free-surface elevations are recorded at multiple locations surrounding the structure. Figure 6 presents the time histories of free-surface elevations at wave gauges G1–G5 for the wave parameters of T = 2 s and H = 0.108 m. Experimental

measurements and numerical predictions are compared for co-current and counter-current scenarios at $U_c = 0.2$ m/s. These results demonstrate robust agreement in wave–current interaction dynamics, where all skill scores exceed 0.9.

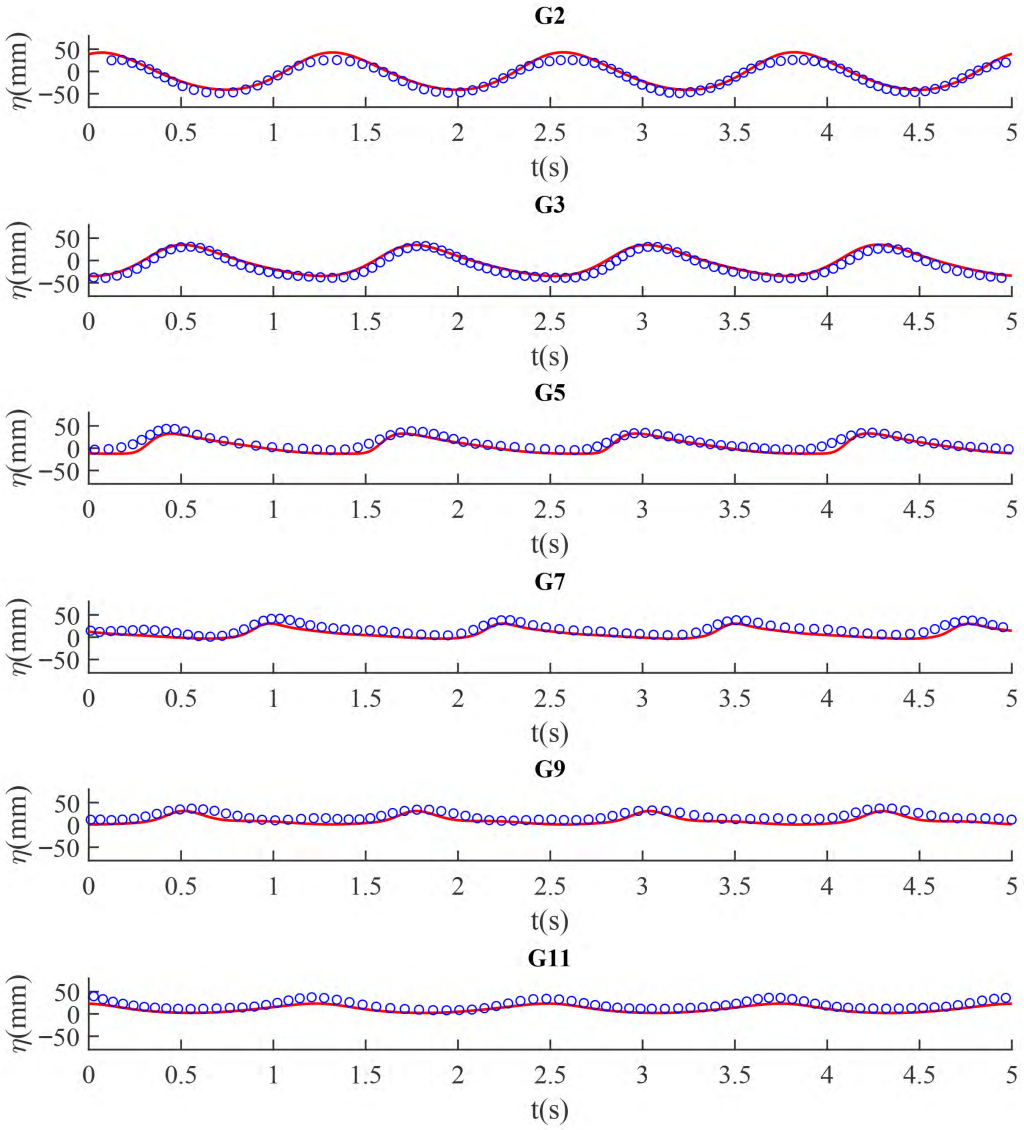


Figure 4. Time series of free-surface elevations at six gauge locations (G2, G3, G5, G7, G9, and G11). Note that laboratory measurements are indicated by circles and model predictions by solid lines. The respective skill scores for these gauges are 0.966, 0.967, 0.933, 0.84, 0.765, and 0.736.

3.4. Data Analysis

As mentioned previously, the numerical wave flume originates at the leftmost point (Point O, located at X = 0 m). The reef front slope spans from 172 m to 430 m, followed by a nearly horizontal reef flat section. Artificial reef units are deployed starting from the beginning of the reef flat at 430 m, where the first row is positioned; subsequent rows are arranged shoreward at fixed intervals. Additionally, a local coordinate system originates at 430 m (O'), where the negative X-direction extends seaward from the reef slope and the positive X-direction extends landward across the reef flat, thus facilitating a comparative analysis of the simulation results. Thereafter, each case is simulated for 400 s, and the data from the final 200 s of stable operation are extracted for post-processing analysis.

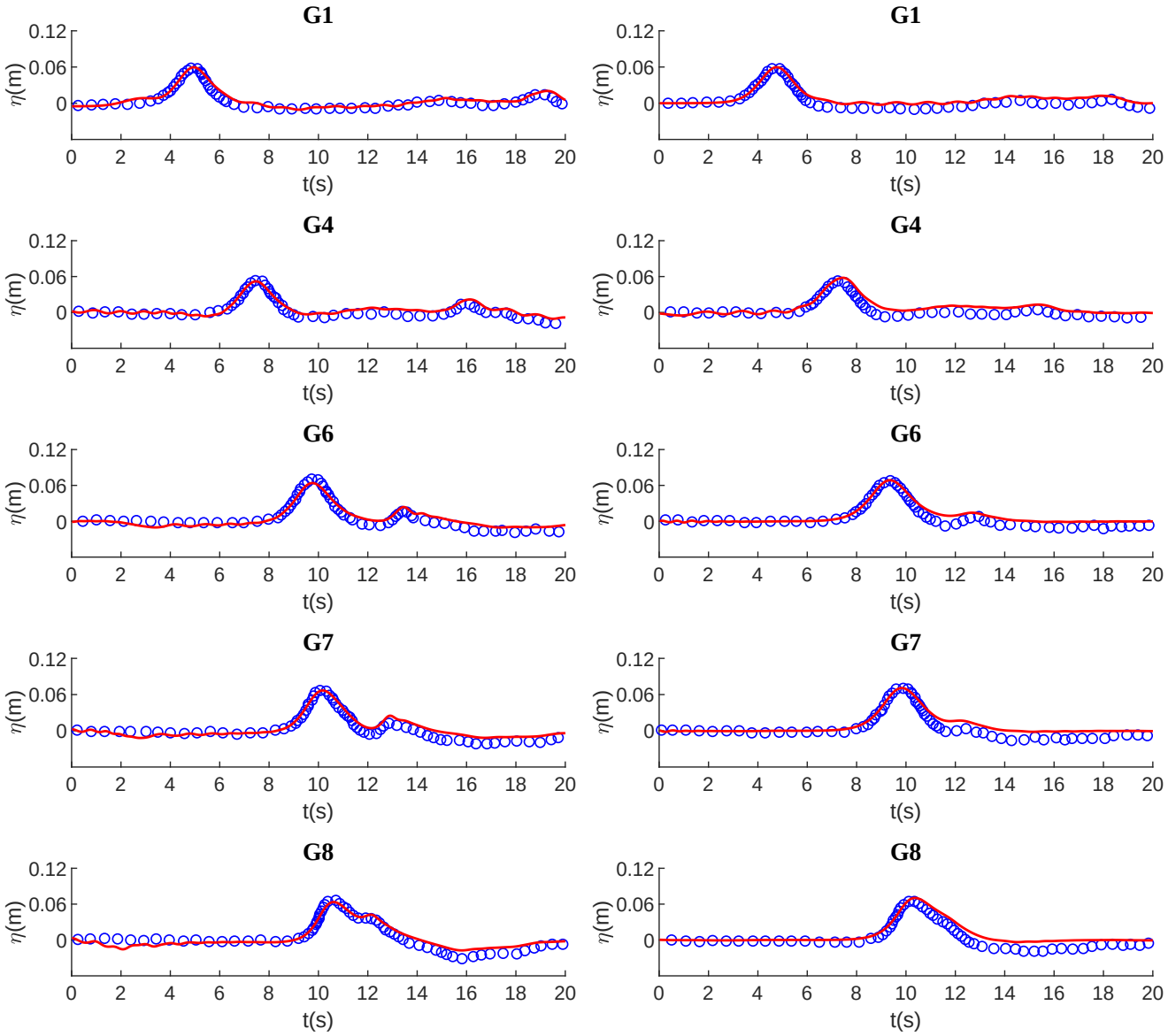


Figure 5. Time series of free-surface elevations at gauges G1, G4, G6, G7, and G8 under two submergence water depths (h_r). Circles: laboratory measurements; solid lines: predictions by the present model. The corresponding skill values for the gauges are 0.9823, 0.9552, 0.9489, 0.9546, and 0.9468 (h_r = 0 m, **left column**) and 0.9382, 0.917, 0.9587, 0.9457, and 0.9459 (h_r = 0.05 m, **right column**).

In all considered cases, the actual wavelength (L_w = 88–118 m) significantly exceeds the Bragg resonance wavelength corresponding to the artificial reef spacing (S_{AR} = 2–8 m). This substantial mismatch leads to an exceptionally weak Bragg reflection effect, which is considered negligible. Specifically, the ratio of $2S_{AR}/L_w$ remains much smaller than 1 across all scenarios. In short, this study employs a two-dimensional numerical model to quantitatively analyze the wave dissipation performance of existing artificial reefs under regular wave conditions.

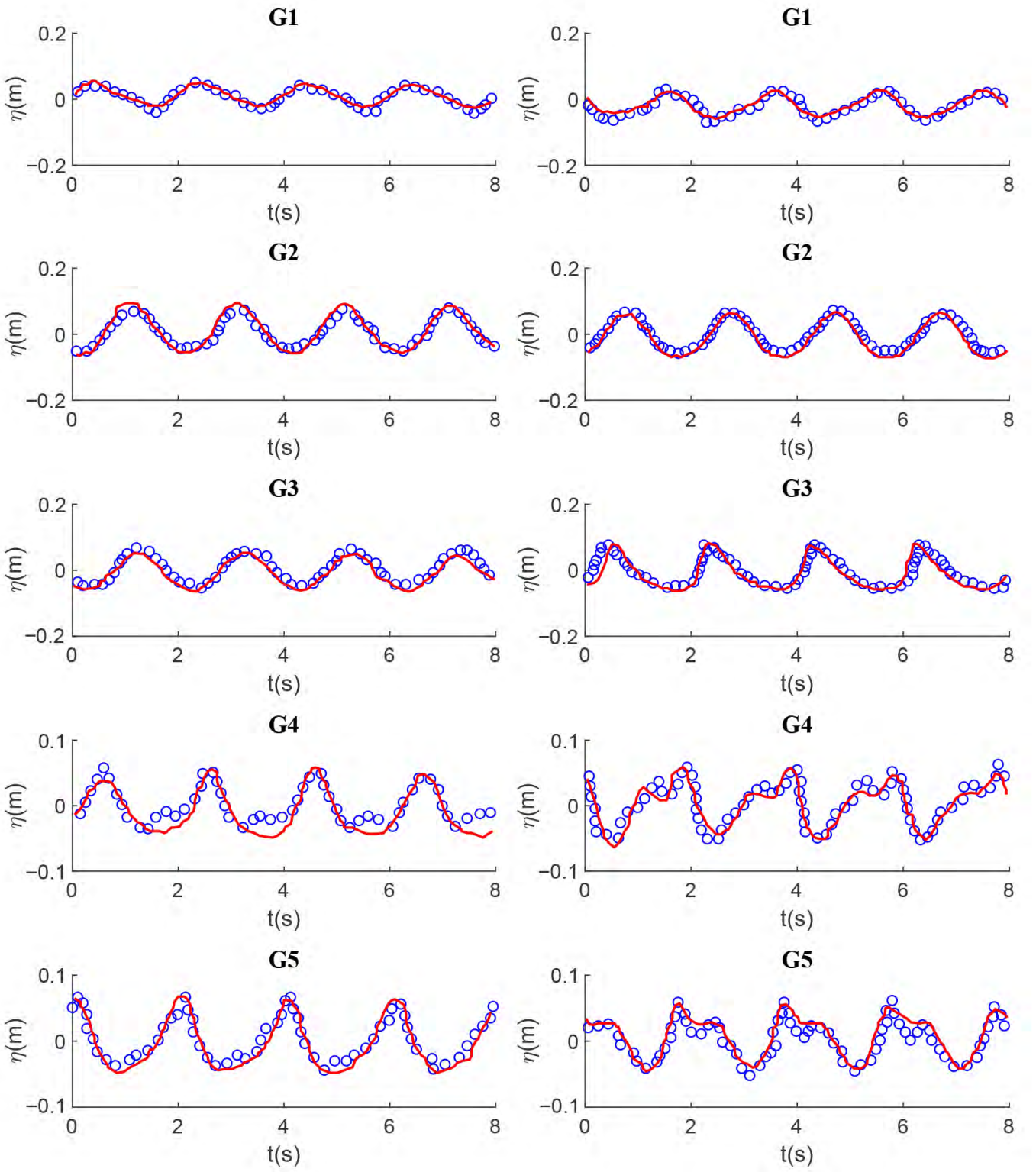


Figure 6. Time series of free-surface elevations at five gauge locations (G1 to G5). Circles: laboratory measurements; solid lines: predictions by the present model. The corresponding skill values for the gauges are 0.979, 0.9725, 0.9614, 0.9416, and 0.9749 (U_c = 0.2 m/s, **left column**) and 0.9582, 0.9744, 0.918, 0.955, and 0.9483 (U_c = −0.2 m/s, **right column**).

4. Results and Discussion

This section presents numerical examples demonstrating the engineering applications of the proposed model. Specifically, the variations in wave height (H_w) and setup (η) around both natural and artificial reef structures are analyzed to systematically investigate the effects of incident wave conditions (H_0 and T_0), reef flat water depth (h_r), tidal range (Δd), and structural parameters (R_{AR} and S_{AR}) on wave transformation processes. Furthermore, the wave dissipation capacity of artificial reefs within fringing reef systems is quantified using two metrics: the reflection coefficient (K_R) measured seaward of the reef front slope and the transmission coefficient (K_T) across the reef flat.

4.1. Spatial Variation in Wave Height and Setup Across the Reef Profile

4.1.1. Effect of Wave Conditions for Various Return Periods

This subsection simulates four wave conditions representing 5-, 10-, 25-, and 50-year return periods, characterized by offshore wave heights of 2.76 m, 3.15 m, 3.55 m, and 3.86 m with corresponding wave periods of 7.82 s, 8.4 s, 8.97 s, and 9.43 s, respectively. Figure 7a,b demonstrate that under high-tide conditions, the wave height amplification of onshore-propagating incident waves intensifies, with the maximum amplification consistently occurring on the fore-reef slope rather than the reef flat. For an incident wave height of 2.76 m and wave period of 7.82 s, a peak wave height of approximately 3.06 m emerges on the rear section of the fore-reef slope. The wave setup/set-down effects progressively strengthen shoreward, transitioning from set-down to setup near the reef edge ($X' = 0$ m), followed by the maximum setup developing on the outer reef flat, located within 250 m of the reef edge (O'). Quantitative analysis reveals that as the offshore wave height increases from 2.76 m to 3.86 m and the wave period extends from 7.82 s to 9.43 s, the maximum wave height on the fore-reef slope rises from 3.06 m to 4.29 m, while the peak setup increases from 0.09 m to 0.2 m, representing respective increases of approximately 40.3% and 123%.

Figure 7c,d demonstrate that enhanced wave shoaling and breaking under low-tide conditions generate pronounced cross-shore gradients in both wave height and setup/set-down distributions while inducing a seaward shift in the corresponding wave transformation zone relative to high-tide scenarios. The maximum wave height persistently concentrates on the fore-reef slope, with the setup/set-down transition point migrating shoreward to this region accompanied by significantly increased variation rates, where the extreme values occur within 100 m of the reef edge. Quantitative analysis reveals that as the offshore wave height increases from 2.76 m to 3.86 m and the wave period extends from 7.82 s to 9.43 s, the peak wave height on the fore-reef slope rises from 3.03 m to 4.42 m, whereas the maximum setup elevates from 0.19 m to 0.33 m, representing increases of 45.7% and 78.8%, respectively. The systematically amplified wave heights and setup magnitudes along the reef under low-tide conditions compared to high-tide conditions confirm the critical regulatory mechanism of the reef flat water level on wave transformation processes, where lower tidal stages enhance shoaling effects to augment wave heights and intensify breaking processes that subsequently steepen setup gradients.

4.1.2. The Effect of the Number of Rows

Figure 8a,b compare wave height distributions and setup characteristics for artificial reefs in single-row, double-row, and triple-row configurations ($R_{AR} = 1, 2, 3$) with constant spacing ($S_{AR} = 2$ m) under wave conditions corresponding to a 5-year return period. During high tide, wave heights demonstrate initial attenuation followed by local amplification along the fore-reef slope ($X = -130$ to 0 m) due to combined shoaling effects and reef interactions. The peak wave height for the single-row configuration occurs at $X = -30$ m on the landward portion of the fore-reef slope, reaching 3.07 m. This peak shifts shoreward to $X = -28$ m (3.10 m) for

double-row reefs and further to $X = -24$ m (3.26 m) for triple-row reefs. The maximum setup consistently develops within 250 m shoreward of the reef edge ($X > 250$ m), measuring 0.10 m for single-row structures but decreasing marginally to 0.09 m for multi-row configurations. Under low-tide conditions (Figure 8c,d), enhanced topographic forcing intensifies wave shoaling along the fore-reef slope, concentrating peak wave heights at $X = -74$ m where all configurations yield identical values of 3.15 m. The maximum setup emerges at $X = 125$ m on the reef flat, registering 0.21 m for single-row arrangements versus 0.22 m for multi-row systems with marginal differences. This reveals that increasing reef rows elevates peak wave heights by 5.2% during high tide, whereas this effect becomes negligible during low tide. Concurrently, additional reef rows reduce setup values by 10.5% under high-tidal conditions but merely 0.5% under low-tidal conditions, confirming that reef layouts significantly enhance wave energy dissipation efficiency during periods of high water levels.

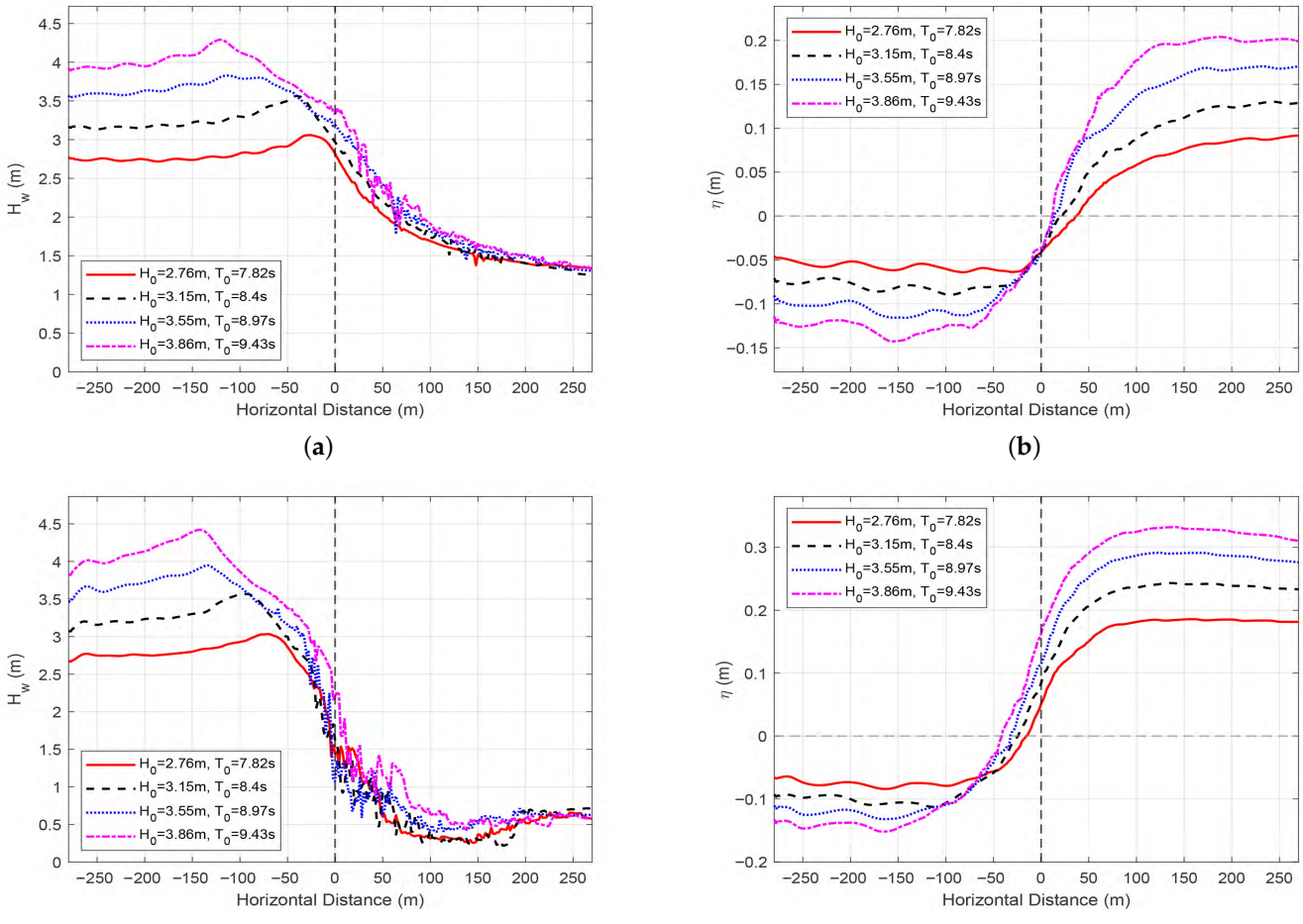


Figure 7. The variations in wave height (**left**) and wave-induced setup (**right**) across the reef profile are examined under different incident wave conditions (H_0 = 2.76, 3.15, 3.55, 3.86 m; T_0 = 7.82, 8.4, 8.97, 9.43 s) and reef flat water depths (h_r = 2.53, 4.88 m). Subfigures (**a**,**b**) and (**c**,**d**) illustrate the corresponding results for high-tide (h_r = 4.88 m, Δd = 0 m) and low-tide (h_r = 2.53 m, Δd = 2.35 m) scenarios, respectively.

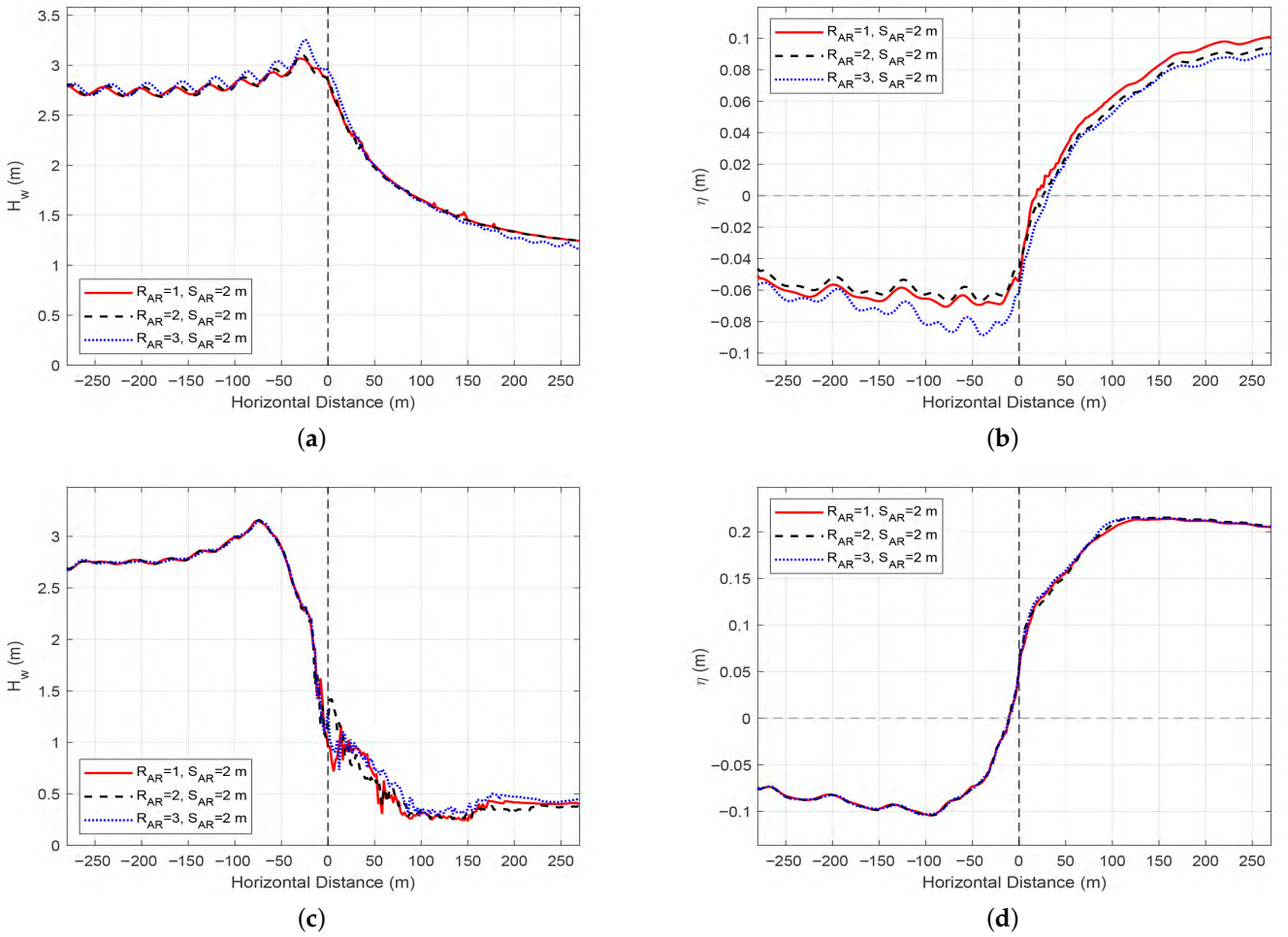


Figure 8. The variations in wave height (**left**) and wave-induced setup (**right**) across the reef profile are presented for configurations with different numbers of artificial reef rows (R_{AR} = 1, 2, 3), maintained at a constant spacing (S_{AR} = 2 m). These results are obtained under fixed incident wave conditions (H_0 = 2.76 m and T_0 = 7.82 s) and two reef flat water depths (h_r = 2.53, 4.88 m). Subfigures (**a**,**b**) and (**c**,**d**) correspond to the high-tide (h_r = 4.88 m, Δd = 0 m) and low-tide (h_r = 2.53 m, Δd = 2.35 m) conditions, respectively.

4.1.3. The Effect of the Spacing of Rows

Figure 9a,b illustrate the influence of artificial reef spacing (S_{AR} = 0 m, 2 m, 5 m) with fixed row (R_{AR} = 4) on wave height and setup distribution under high-tidal conditions using wave scenarios with a 5-year return period. Wave height peaks consistently occur at the fore-reef slope ($X = -26$ m), with the maximum value of approximately 3.12 m observed at the 0 m spacing, followed by 3.09 m at the 2 m spacing and 3.05 m at the 5 m spacing, indicating that the maximum wave height progressively decreases with increasing spacing. The peak setup emerges within the inner reef flat region ($X > 250$ m), reaching its highest magnitude of 0.09 m at the 2 m spacing, while both the 0 m and 5 m spacing configurations yield values around 0.10 m. Under low-tidal conditions (Figure 9c,d), wave height maxima concentrate along the fore-reef slope between $X = -74$ m and $X = -70$ m. The 0 m spacing configuration produces the highest peak of 3.20 m, whereas the 2 m and 5 m spacings generate peaks of 3.13 m and 3.18 m, respectively. The peak setup values manifest shoreward of the reef edge beyond X = 100 m, measuring approximately 0.23 m for both the 0 m and 5 m spacings, compared to 0.22 m for the 2 m spacing. Comprehensive analysis reveals that increasing reef spacing reduces the peak wave height across the reef profile under identical tidal stages, corresponding to reductions of 2.1% during high tide

and 0.8% during low tide. Concurrently, the peak setup decreases by 2.4% under high-tidal conditions but exhibits no significant variation during low tide. This trend parallels the influence of reef row arrangements, confirming that modifications in reef layout under high tidal levels substantially regulate wave energy dissipation efficiency.

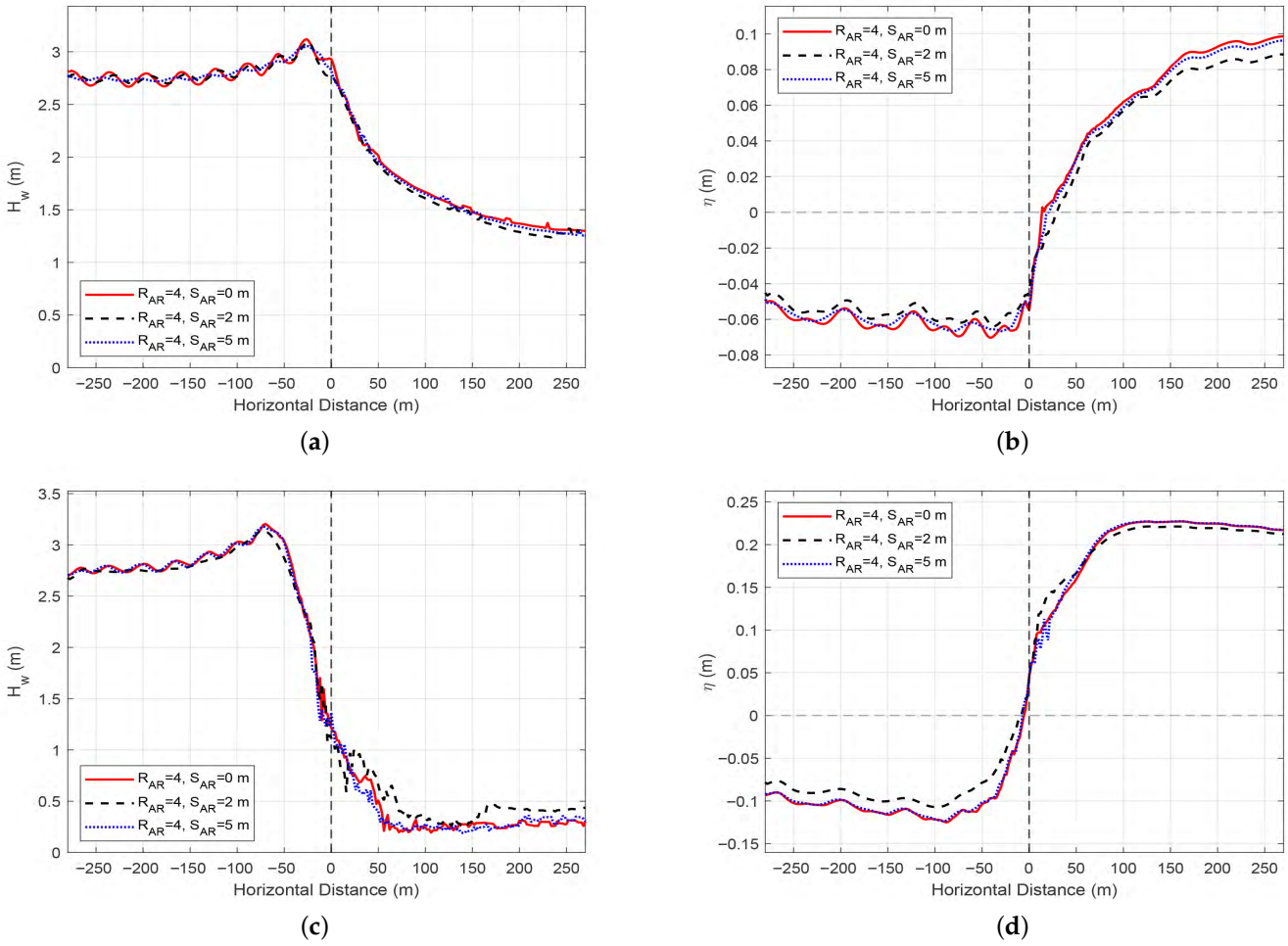


Figure 9. The variations in wave height (**left**) and wave-induced setup (**right**) across the reef profile are shown for different artificial reef spacings (S_{AR} = 0, 2, 5 m) with a constant number of reef rows (R_{AR} = 4). These results are obtained under fixed incident wave conditions (H_0 = 2.76 m and T_0 = 7.82 s) and two reef flat water depths (h_r = 2.53, 4.88 m). Subfigures (**a**,**b**) and (**c**,**d**) present the results for high-tide (h_r = 4.88 m, Δd = 0 m) and low-tide (h_r = 2.53 m, Δd = 2.35 m) conditions, respectively.

4.2. Characteristics of Wave Reflection and Transmission

Based on the variations in wave reflection and transmission coefficients, the following analysis examines how different reef configurations and hydrodynamic conditions influence wave dissipation, while the relationships among these factors are further elucidated to clarify their combined effects. For this purpose, the incident wave components are separated using the three-gauge method proposed by Mansard and Funke [41], applied immediately seaward of the reef slope. Subsequently, the reflection coefficient K_R for the fringing reef—either with or without an artificial reef—is defined as the ratio of the reflected wave height H_R to the incident wave height H_I, expressed as follows:

$$K_R = \frac{H_R}{H_I} \tag{6}$$

The transmission coefficient K_T for waves propagating across a coral reef flat is defined based on the ratio of transmitted to incident wave energy fluxes [42]. This definition accounts for two key factors: (i) the transmitted wave spectrum contains significantly higher-harmonic components in addition to the primary frequency, and (ii) water depths (and thus wave celerities) differ between the offshore and reef flat regions. Accordingly, K_T is expressed as follows:

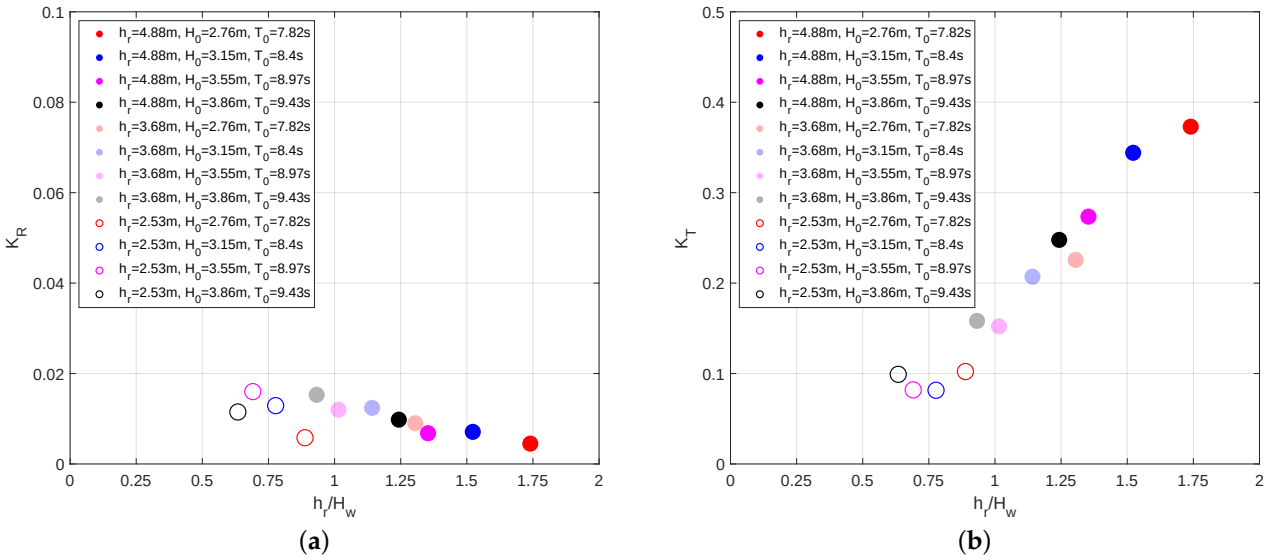
$$K_T = \sqrt{\frac{\sum_{i=1}^{5} E_T^i C_{g,T}^i}{E_I C_{g,I}}} \tag{7}$$

where E_T^i and E_I denote the energy densities of the i-th transmitted harmonic component (up to fifth order) over the reef flat and the incident wave in deep water, respectively, while $C_{g,T}^i$ and $C_{g,I}$ represent the corresponding wave group velocities. Specifically, the incident wave energy flux $E_I C_{g,I}$ can be converted from the deep-water wave energy flux $E_0 C_{g,0}$ using energy conservation principles. According to linear wave theory, the deep-water wave energy density is $E_0 = \rho g H_0^2/8$, where H_0 is derived from the incident wave height H_I. The deep-water group velocity is given by $C_{g,0} = gT/(4\pi)$. The total transmitted energy flux is obtained by analyzing the free-surface elevation time series recorded at a fixed location on the reef flat using Fast Fourier Transform (FFT). The energy spectrum derived from this analysis is used to compute the summation of $E_T^i C_{g,T}^i$ for each harmonic component ($i = 1$ to 5). The wave group velocity $C_{g,T}^i$ for each harmonic is determined by solving the dispersion relation.

Figure 10a,b first illustrate the influence of varying incident wave parameters and reef flat water depths on the wave reflection and transmission coefficients in the absence of an artificial reef. Under high-tide conditions (h_r = 4.88 m), the reflection coefficient K_R increases from approximately 0.005 to 0.009 as the wave height increases from 2.76 m to 3.86 m and the wave period increases from 7.82 s to 9.43 s. Meanwhile, the transmission coefficient K_T decreases from 0.373 to 0.248. This trend suggests that higher wave energy conditions enhance wave breaking and energy dissipation, leading to a reduction in transmission capacity, while the reflection coefficient exhibits only minor variations. Under low-tide conditions (h_r = 2.53 m), K_R values are significantly higher than those at high tide. For instance, under a specific wave condition with a height of 3.15 m and a period of 8.4 s, K_R reaches 0.013 during low tide compared to 0.007 during high tide, while under the same condition, K_T values are 0.082 and 0.344, respectively. These results indicate that shallow water conditions promote wave reflection and suppress wave transmission. Further comparison under identical wave parameters shows that K_R is markedly higher and K_T is significantly lower during low tide. Moreover, smaller incident wave heights generally lead to a decrease in K_R and an increase in K_T. It can thus be concluded that tidal variations directly modulate wave propagation mechanisms by altering the water depth over the reef flat.

Figure 11a,b analyze the influence of different tidal levels (Δd) and artificial reef rows (R_{AR}) on the wave reflection coefficient K_R and transmission coefficient K_T under fixed incident wave conditions and a reef spacing of 2 m. Under high-tide conditions (h_r = 4.88 m) with an incident wave height of 2.76 m and a period of 7.82 s, K_R exhibits an initial slight increase followed by a minor decrease as the number of reef rows increases, rising from approximately 0.011 for a single row to about 0.022 for three rows and then decreasing marginally to 0.016 for four rows. Meanwhile, K_T fluctuates within a narrow range of 0.366 to 0.395, showing no clear monotonic trend. The weak correlation between K_R and the reef row parameter S_{AR} indicates that the influence of reef rows on wave reflection behavior is inconsistent during high tide. Under low-tide conditions (h_r = 2.53 m) with the same wave parameters, K_R also displays a slight increasing trend with additional rows, with average

values across multiple-row configurations ranging between 0.002 and 0.006, whereas K_T remains relatively stable around 0.101. Altogether, significant differences are observed between high and low tidal levels across one to four rows of artificial reefs, with K_R and K_T varying by factors of up to 4.47 and 3.66, respectively.



(**a**) (**b**)

Figure 10. The variations in the reflection coefficient (K_R) and transmission coefficient (K_T) with three reef flat water depths under various incoming wave conditions. Note that three reef flat water depths h_r are set to 4.88 m, 3.68 m, and 2.53 m, represented by circles with fill levels of 100%, 50%, and 0%, respectively. Four wave conditions, characterized by wave height H_0 and wave period T_0 pairs of 2.76 m and 7.82 s, 3.15 m and 8.4 s, 3.55 m and 8.97 s, and 3.86 m and 9.43 s, are applied and denoted by the colors red, blue, magenta, and black, accordingly.

Figure 11c,d illustrate the influence of tidal level (Δd) and artificial reef spacing (S_{AR}) on the wave reflection coefficient K_R and transmission coefficient K_T under fixed incident wave conditions. Under high-tide conditions (h_r = 4.88 m) with an incident wave height of 2.76 m, a period of 7.82 s, and a reef configuration of four rows, K_R decreases significantly with increasing reef spacing, declining from approximately 0.021 at zero spacing to 0.016 at 2 m spacing and 0.005 at 5 m spacing, corresponding to reductions of 26.1% and 76.3%, respectively. In contrast, K_T shows only minor variations, with values of 0.362, 0.366, and 0.355, indicating that reef spacing has limited influence on wave transmission. Under low-tide conditions (h_r = 2.53 m) with identical wave parameters, K_R similarly decreases with greater spacing, falling from 0.009 at zero spacing to 0.004 at 2 m and 0.003 at 5 m, representing reductions of 55.9% and 72%, which demonstrates that reduced spacing consistently enhances wave reflection across tidal levels. Meanwhile, K_T remains stable around 0.1 under low-tide conditions regardless of spacing. Overall, substantial differences in K_R and K_T are observed between high and low tidal levels across reef spacings from 0 to 5 m, with corresponding factors of 2.61 and 3.87, respectively.

To enhance the wave attenuation performance of coral reefs in fringing reef environments, a systematic analysis of wave propagation characteristics with and without artificial reef units is essential. Figure 12a,b compare the ratios of reflection and transmission coefficients under high- and low-tidal conditions for existing artificial reef configurations deployed at the outer reef flat edge, incorporating varying row numbers and spacings, so as to evaluate their wave dissipation effectiveness. Here, K_R^0 and K_T^0 denote the wave reflection and transmission coefficients, respectively, in the absence of artificial reefs, whereas K_R^n and K_T^n represent the corresponding coefficients under identical incident wave and water depth conditions with artificial reefs present. Data points (K_R^n, K_R^0) and (K_T^n, K_T^0)

located below the red polyline in the figure indicate that the artificial reefs influence wave propagation. Points falling within the region bounded by two black dashed lines suggest that the differences in reflection and transmission coefficients induced by the reefs do not exceed 5%. The results show that under low-water-level conditions, the values of (K_R^n, K_R^0) remain below 0.01, indicating that the reefs enhance wave breaking, thereby reducing reflected wave energy to a very small fraction of the incident waves. In contrast, under high-water-level conditions, the distribution of (K_R^n, K_R^0) shifts rightward with different reef row numbers and spacing configurations, demonstrating the modulating effect of artificial reefs on wave reflection. By comparison, the distribution of (K_T^n, K_T^0) is relatively clustered, and reef-induced variations in transmission coefficients remain within 5% under both high and low water levels, indicating that the current reef structures provide limited control over wave transmission across the fringing reef profile. Therefore, modifications such as increasing reef height or deploying reefs on the fore-reef slope are required to improve overall wave attenuation capacity.

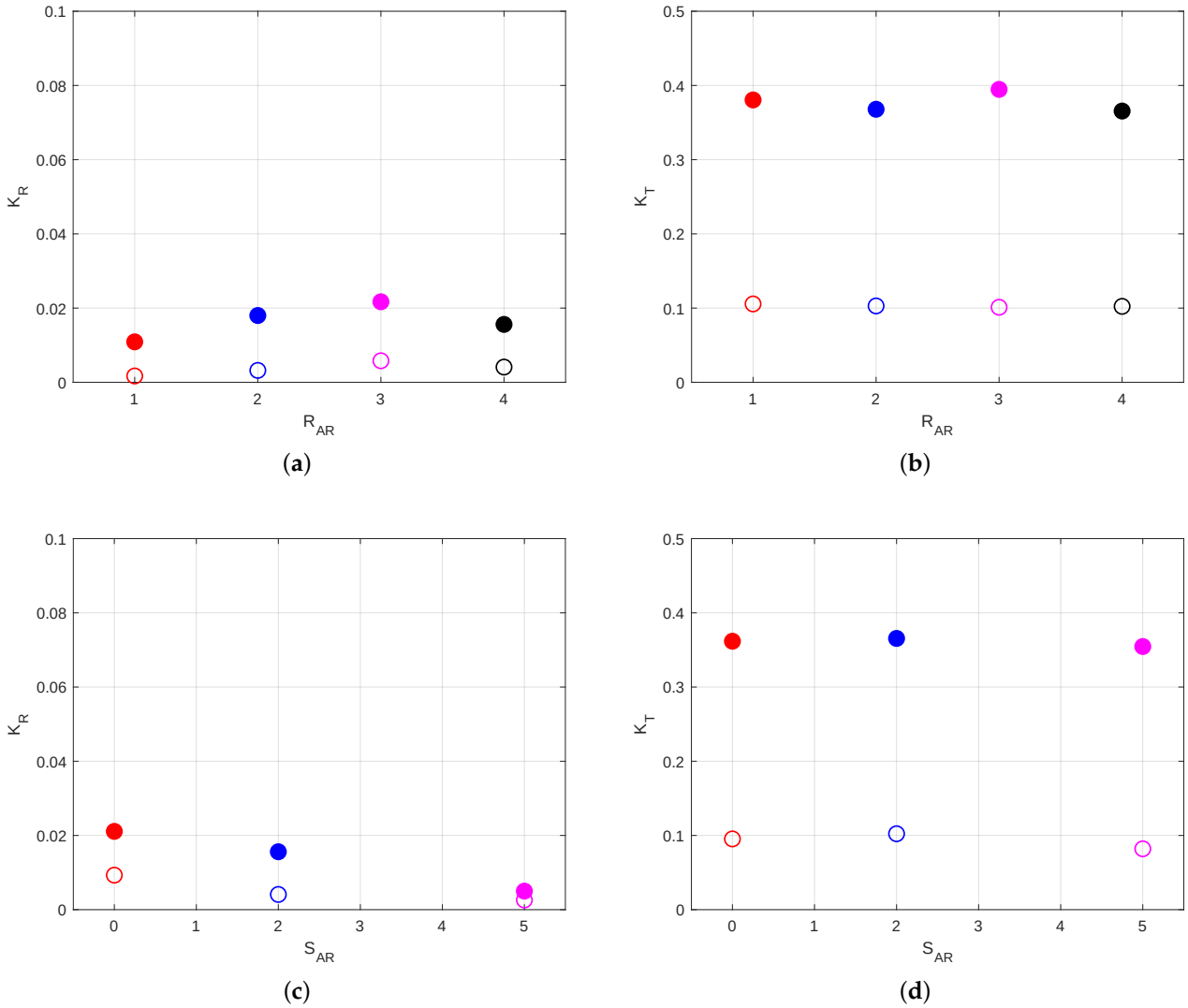


Figure 11. The variations in the wave reflection coefficient (K_R) and transmission coefficient (K_T) across different artificial reef configurations, including (**a**,**b**) various rows (R_{AR}) and (**c**,**d**) varying spacings (S_{AR}), under constant wave conditions with H_0 = 2.76 m, T_0 = 7.82 s, and d_0 = 16 m. Solid and hollow symbols correspond to high tide (h_r = 4.88 m; Δd = 0 m) and low tide (h_r = 2.53 m; Δd = 2.35 m), respectively.

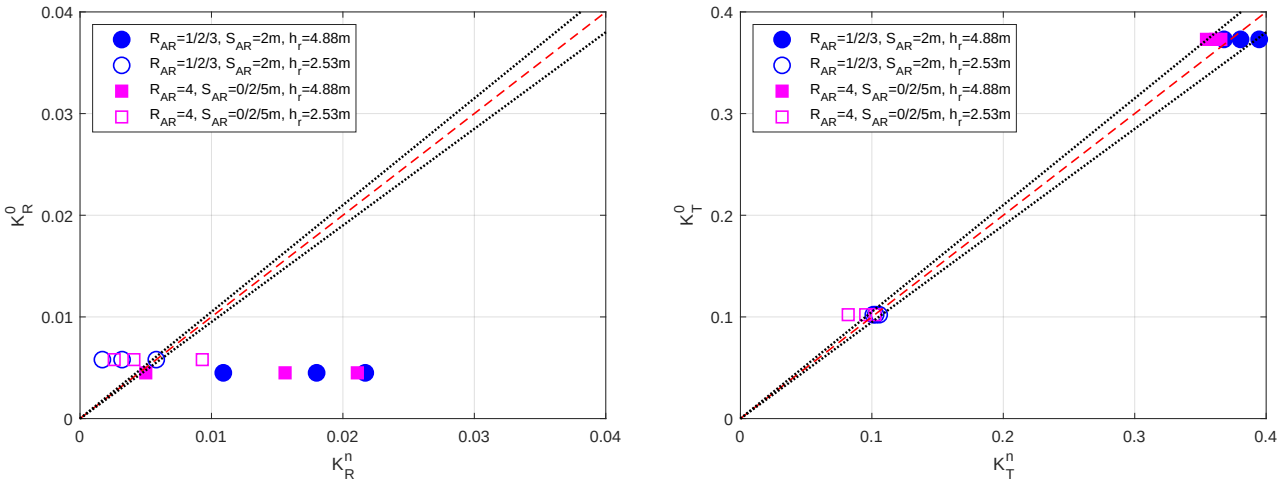


Figure 12. A comparison of the wave reflection coefficient (K_R) and transmission coefficient (K_T) under constant wave conditions (H_0 = 2.76 m; T_0 = 7.82 s; d_0 = 16 m). Note that R^0_{AR} and S^0_{AR} denote scenarios without artificial reefs, while R^n_{AR} and S^n_{AR} represent configurations with artificial reefs applied. Circle and square symbols correspond to variations in R_{AR} and S_{AR}, respectively, with solid and hollow markers indicating high-tide (h_r = 4.88 m; Δd = 0 m) and low-tide (h_r = 2.53 m; Δd = 2.35 m) conditions.

5. Conclusions

This study employs the OpenFOAM-based model to investigate hydrodynamic processes along the fringing reef of Weizhou Island under various conditions. Numerical analyses reveal key mechanisms governing wave transformation, with the following conclusions drawn:

(1) The transformation of wave energy across coral reef systems is modulated by reef flat water depth, where wave dissipation is enhanced on the gentle fore-reef slope. Under constant incident wave conditions, transmission coefficients (K_T) increase significantly as reflection coefficients (K_R) decrease with greater reef flat water depth, which demonstrates the critical control of depth-limited breaking on wave energy redistribution.

(2) Tidal conditions modulate how reef configuration influences wave transformation processes. The spacing of the reef significantly affects the reflection of the waves during low tide, while the number of rows of reefs exhibits limited influence. In contrast, the transmission coefficients show substantial variation during high tide, indicating that the tidal stage determines the relative importance of different structural parameters in the dissipation of wave energy.

(3) Existing reef design configurations markedly affect wave reflection, particularly during high-tide conditions. However, their impact on wave transmission remains minimal, with values of K_T varying less than 5% compared to scenarios without artificial reefs under identical hydrodynamic conditions. This limited effect suggests that structural modifications, such as increasing reef height or implementing fore-reef deployment, are necessary to achieve improved wave attenuation performance.

(4) This study quantitatively analyzes the wave dissipation performance of existing artificial reefs under regular wave conditions; however, certain limitations persist. Subsequent investigations will incorporate irregular wave regimes to examine distinct reef configurations, such as those transplanted with varying-sized *Acropora* coral canopies, thereby elucidating the impact mechanisms of reef structures on wave energy components, including short-crested waves and infragravity waves.

Author Contributions: Z.L.: Conceptualization, Methodology, Writing—original draft preparation; G.H.: Investigation, Validation; W.H.: Formal analysis, Visualization; H.C.: Software, Data curation; K.Y.: Conceptualization, Project administration, Writing—review and editing; D.-S.J.: Conceptualization, Writing—review and editing. All authors have read and agreed to the published version of the manuscript.

Funding: This research was funded by the Inclusive Support Policies for Young Talent of Guangxi (No. ZX02080031024002) and the Guangxi Science and Technology Program (No. AD25069075).

Data Availability Statement: The original contributions presented in this study are included in the article. Further inquiries can be directed to the corresponding author.

Acknowledgments: Special thanks go to the anonymous reviewers for their careful reading of the manuscript and valuable comments.

Conflicts of Interest: The authors declare no conflicts of interest.

References

1. Ferrario, F.; Beck, M.W.; Storlazzi, C.D.; Micheli, F.; Shepard, C.C.; Airoldi, L. The effectiveness of coral reefs for coastal hazard risk reduction and adaptation. *Nat. Commun.* **2014**, *5*, 3794. [CrossRef]
2. Monismith, S.G. Hydrodynamics of coral reefs. *Annu. Rev. Fluid Mech.* **2007**, *39*, 37–55. [CrossRef]
3. Young, I.R. Wave transformation over coral reefs. *J. Geophys. Res. Ocean.* **1989**, *94*, 9779–9789. [CrossRef]
4. Hardy, T.A.; Young, I.R. Field study of wave attenuation on an offshore coral reef. *J. Geophys. Res. Ocean.* **1996**, *101*, 14311–14326. [CrossRef]
5. Vetter, O.; Becker, J.M.; Merrifield, M.A.; Pequignet, A.C.; Aucan, J.; Boc, S.J.; Pollock, C.E. Wave setup over a Pacific Island fringing reef. *J. Geophys. Res. Ocean.* **2010**, *115*, C12066 [CrossRef]
6. Gourlay, M.R. Wave transformation on a coral reef. *Coast. Eng.* **1994**, *23*, 17–42. [CrossRef]
7. Gourlay, M.R. Wave set-up on coral reefs. 1. Set-up and wave-generated flow on an idealised two dimensional horizontal reef. *Coast. Eng.* **1996**, *27*, 161–193. [CrossRef]
8. Gourlay, M. Wave set-up on coral reefs. 2. Set-up on reefs with various profiles. *Coast. Eng.* **1996**, *28*, 17–55. [CrossRef]
9. Demirbilek, Z.; Nwogu, O.G.; Ward, D.L. *Laboratory Study of Wind Effect on Runup over Fringing Reefs. Report 1. Data Report*; Technical Report; U.S. Army Engineer Research and Development Center: Vicksburg, MS, USA, 2007.
10. Yao, Y.; Lo, E.Y.; Huang, Z.; Monismith, S.G. An experimental study of wave-induced set-up over a horizontal reef with an idealized ridge. In Proceedings of the International Conference on Offshore Mechanics and Arctic Engineering, Honolulu, HI, USA, 31 May–5 June 2009; Volume 43468, pp. 383–389.
11. Nwogu, O.; Demirbilek, Z. Infragravity wave motions and runup over shallow fringing reefs. *J. Waterw. Port Coastal Ocean. Eng.* **2010**, *136*, 295–305. [CrossRef]
12. Yao, Y.; Huang, Z.; Monismith, S.G.; Lo, E.Y. 1DH Boussinesq modeling of wave transformation over fringing reefs. *Ocean. Eng.* **2012**, *47*, 30–42. [CrossRef]
13. Ma, G.; Su, S.F.; Liu, S.; Chu, J.C. Numerical simulation of infragravity waves in fringing reefs using a shock-capturing non-hydrostatic model. *Ocean. Eng.* **2014**, *85*, 54–64. [CrossRef]
14. Shi, J.; Zhang, C.; Zheng, J.; Tong, C.; Wang, P.; Chen, S. Modelling wave breaking across coral reefs using a non-hydrostatic model. *J. Coast. Res.* **2018**, *85*, 501–505. [CrossRef]
15. Lowe, R.J.; Buckley, M.L.; Altomare, C.; Rijnsdorp, D.P.; Yao, Y.; Suzuki, T.; Bricker, J. Numerical simulations of surf zone wave dynamics using Smoothed Particle Hydrodynamics. *Ocean. Model.* **2019**, *144*, 101481. [CrossRef]
16. Liu, Y.; Li, S.; Liao, Z.; Liu, K. Physical and numerical modeling of random wave transformation and overtopping on reef topography. *Ocean. Eng.* **2021**, *220*, 108390. [CrossRef]
17. Yao, Y.; Li, Z.; Xu, C.; Jiang, C. A study of wave-driven flow characteristics across a reef under the effect of tidal current. *Appl. Ocean. Res.* **2023**, *130*, 103430. [CrossRef]
18. Watanabe, M.; Kan, H.; Toguchi, K.; Nakashima, Y.; Roeber, V.; Arikawa, T. Effect of the structural complexity of a coral reef on wave propagation: A case study from Komaka Island, Japan. *Ocean. Eng.* **2023**, *287*, 115632. [CrossRef]
19. Wang, C.; Qu, K.; Li, J.; Li, W. Physical and modelling analysis on hydrodynamic transforming processes of tsunami-like wave over an uneven coral reef. *Ocean. Eng.* **2025**, *320*, 120326. [CrossRef]
20. Fadli, N.; Campbell, S.J.; Ferguson, K.; Keyse, J.; Rudi, E.; Riedel, A.; Baird, A.H. The role of habitat creation in coral reef conservation: A case study from Aceh, Indonesia. *Oryx* **2012**, *46*, 501–507. [CrossRef]
21. Blakeway, D.; Byers, M.; Stoddart, J.; Rossendell, J. Coral colonisation of an artificial reef in a turbid nearshore environment, Dampier Harbour, western Australia. *PLoS ONE* **2013**, *8*, e75281. [CrossRef]

22. Tanaya, T.; Iwamura, S.; Okada, W.; Kuwae, T. Artificial structures can facilitate rapid coral recovery under climate change. *Sci. Rep.* **2025**, *15*, 9116. [CrossRef]
23. Knoester, E.; Rienstra, J.; Schürmann, Q.; Wolma, A.; Murk, A.; Osinga, R. Community-managed coral reef restoration in southern Kenya initiates reef recovery using various artificial reef designs. *Front. Mar. Sci.* **2023**, *10*, 1152106. [CrossRef]
24. Reguero, B.G.; Beck, M.W.; Agostini, V.N.; Kramer, P.; Hancock, B. Coral reefs for coastal protection: A new methodological approach and engineering case study in Grenada. *J. Environ. Manag.* **2018**, *210*, 146–161. [CrossRef] [PubMed]
25. Webb, B.M.; Allen, R. Wave transmission through artificial reef breakwaters. In *Coastal Structures and Solutions to Coastal Disasters Joint Conference 2015*; American Society of Civil Engineers: Reston, VA, USA, 2015; pp. 432–441.
26. Srineash, V.; Murali, K. Functional performance of modular porous reef breakwaters. *J.-Hydro-Environ. Res.* **2019**, *27*, 20–31. [CrossRef]
27. van Gent, M.R.; Buis, L.; van den Bos, J.P.; Wüthrich, D. Wave transmission at submerged coastal structures and artificial reefs. *Coast. Eng.* **2023**, *184*, 104344. [CrossRef]
28. Ghiasian, M.; Carrick, J.; Rhode-Barbarigos, L.; Haus, B.; Baker, A.C.; Lirman, D. Dissipation of wave energy by a hybrid artificial reef in a wave simulator: Implications for coastal resilience and shoreline protection. *Limnol. Oceanogr. Methods* **2021**, *19*, 1–7. [CrossRef]
29. Huang, J.; Lowe, R.J.; Ghisalberti, M.; Hansen, J.E. Wave transformation across impermeable and porous artificial reefs. *Coast. Eng.* **2024**, *189*, 104488. [CrossRef]
30. Huang, J.; Lowe, R.J.; Ghisalberti, M.; Hansen, J.E. Parametric modelling of wave transformation across porous artificial reefs. *Coast. Eng.* **2025**, *200*, 104754. [CrossRef]
31. Jacobsen, N.G.; Fuhrman, D.R.; J, F. A wave generation toolbox for the open-source CFD library: OpenFOAM. *Int. J. Numer. Methods Fluids* **2012**, *70*, 1073–1088. [CrossRef]
32. Yu, W.; Wang, W.; Yu, K.; Wang, Y.; Huang, X.; Huang, R.; Liao, Z.; Xu, S.; Chen, X. Rapid decline of a relatively high latitude coral assemblage at Weizhou Island, northern South China Sea. *Biodivers. Conserv.* **2019**, *28*, 3925–3949. [CrossRef]
33. Liang, W.; Zhou, H.; Wang, X.; Rongyong, H.; Kefu, Y. Studies on scleractinian coral community structure characteristics in the southwest seawaters of the Weizhou Island. *Haiyang Xuebao* **2021**, *43*, 123–135.
34. Yang, Z.; Zhang, J.; Lv, X.; Zheng, Y.; Jiang, G.; Shi, X.; Tao, W.; Li, X.; Lv, Y. The ecological succession of scleratinian coral communites and their environmental factors in Weizhou Island. *Acta Ecol. Sin.* **2021**, *41*, 7168–7179.
35. Li, G.; Liang, W.; Nong, H.; Liu, J. Preliminary Study on Conditions of Coral Reef Ecological Environment along the Coast of Weizhou Island. *Guangxi Sci.* **2004**, *11*, 379–384.
36. Huang, Z.; Zhang, C.; Shen, Y.; Jiang, S. Analysis of the climatic characteristics of wind and wave in Weizhou Island sea area. *Mar. Forecast.* **2021**, *38*, 62–68.
37. *Industry Standard JTS 145-2015*; Hydrological Code for Port and Waterway Engineering. China Communications Press: Beijing, China, 2015.
38. Launder, B.E.; Spalding, D.B. The numerical computation of turbulent flows. *Comput. Methods Appl. Mech. Eng.* **1974**, *3*, 269–289. [CrossRef]
39. Chen, L.F.; Ning, D.Z.; Teng, B.; Zhao, M. Numerical and Experimental Investigation of Nonlinear Wave-Current Propagation over a Submerged Breakwater. *J. Eng. Mech. ASCE* **2017**, *143*, 04017061. [CrossRef]
40. Willmott, C.J. On the validation of models. *Phys. Geogr.* **1981**, *2*, 184–194. [CrossRef]
41. Mansard, E.P.; Funke, E. The measurement of incident and reflected spectra using a least squares method. In *Coastal Engineering 1980*; American Society of Civil Engineers: Reston, VA, USA, 1980; pp. 154–172.
42. Yao, Y.; He, F.; Tang, Z.; Liu, Z. A study of tsunami-like solitary wave transformation and run-up over fringing reefs. *Ocean. Eng.* **2018**, *149*, 142–155. [CrossRef]

Disclaimer/Publisher's Note: The statements, opinions and data contained in all publications are solely those of the individual author(s) and contributor(s) and not of MDPI and/or the editor(s). MDPI and/or the editor(s) disclaim responsibility for any injury to people or property resulting from any ideas, methods, instructions or products referred to in the content.

Journal of Hazardous Materials 496 (2025) 139433

Contents lists available at ScienceDirect

Journal of Hazardous Materials

journal homepage: www.elsevier.com/locate/jhazmat

Metabolism of wildfire-derived methoxyphenol in *Acropora formosa*: Metabolite identification, toxicity prediction, and impact on coral health

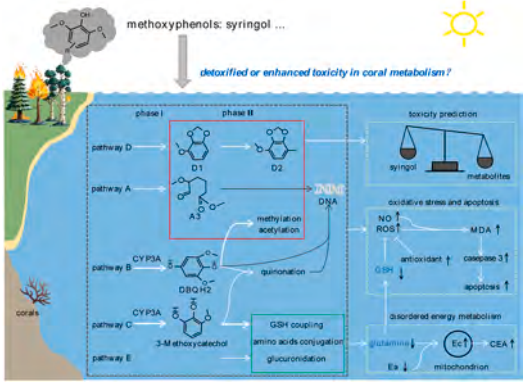
Yanliu Wu [a], Xiaoyan Chen [a,*], Yuhao Du [a], Zhenhua Chen [c], Zhaoqian Yan [a], Hongfei Su [a], Zhenjun Qin [a], Zhiming Ning [a], Yuxiao Li [a], Kefu Yu [a,b,**]

[a] *Guangxi Laboratory on the Study of Coral Reefs in the South China Sea; Coral Reef Research Center of China; School of Marine Sciences, Guangxi University, Nanning 530004, China*
[b] *Southern Marine Science and Engineering Guangdong Laboratory (Guangzhou), Guangzhou 511458, China*
[c] *Guangxi Laboratory of Marine Environmental Change and Disaster in Beibu Gulf, Qinzhou 535011, China*

HIGHLIGHTS

- A comprehensive inventory of wildfire pollutant metabolites in corals.
- Syringol metabolites show enhanced toxicity and bind multiple macromolecular targets.
- Metabolites deplete glutamine and GSH, causing oxidative stress and energy imbalance.
- CYP450-catalyzed syringol metabolism causes coral bleaching instead of detoxification.

GRAPHICAL ABSTRACT



ARTICLE INFO

Keywords:
Wildfire
Syringol
Metabolism
Apoptosis
Corals

ABSTRACT

The increasing frequency of extreme wildfires driven by climate warming threatens marine ecosystems. However, the mechanisms underlying coral responses to wildfire-derived organic pollutants remain poorly understood. This study analyzed the metabolism of syringol, a tracer of forest fires, in the coral *Acropora formosa* and identified its major transformation products. These metabolites are primarily produced through methylation, acetylation, amino acid conjugation, aromatic ring cleavage, and methylenedioxy bridge cyclization. The involvement of coral-associated microbial communities may further complicate the detoxification processes. *In-silico* analysis suggests that, except for amino acid conjugation, most syringol-derived metabolites exhibit enhanced toxicity compared to the parent compound. These metabolites may target multiple cellular macromolecules, disrupting coral photosynthesis and calcification. Cytochrome P450 family 3 subfamily A (CYP3A) enzymes catalyze the formation of bioactive metabolites through O-demethylation and hydroxylation, followed

* Corresponding author.
** Corresponding author at: Guangxi Laboratory on the Study of Coral Reefs in the South China Sea; Coral Reef Research Center of China; School of Marine Sciences, Guangxi University, Nanning 530004, China.
E-mail addresses: xychen@gxu.edu.cn (X. Chen), kefuyu@scsio.ac.cn (K. Yu).

https://doi.org/10.1016/j.jhazmat.2025.139433
Received 9 May 2025; Received in revised form 18 July 2025; Accepted 1 August 2025
Available online 5 August 2025
0304-3894/© 2025 Elsevier B.V. All rights are reserved, including those for text and data mining, AI training, and similar technologies.

by amino acid conjugation as part of the detoxification process. However, this conjugation process depletes intracellular glutamine and glutathione (GSH), triggering oxidative stress, apoptosis and coral bleaching within 24 h. Glutamine and GSH were identified as potential biomarkers of wildfire-induced stress in corals. This study improves our understanding of coral vulnerability to wildfire pollutants and offers novel insights for ecological risk assessment and coral reef conservation in wildfire-prone regions.

1. Introduction

Extreme wildfire events, intensified by climate warming [28], pose a substantial threat to coral reefs and their biodiversity. Although wildfire particles can enhance ocean primary productivity by delivering essential nutrients [47,63], they may concurrently harm corals and reef ecosystems, as evidenced by the 2023 Maui and 1997 Indonesian fires [1,67]. Recent studies indicate that wildfire particles inhibit heterotrophic plasticity and calcification [51], and cause tissue damage, likely due to the associated organic pollutants [39]. However, the mechanisms underlying coral responses to wildfire-derived organic pollutants remain unclear.

Metabolism is a primary defense mechanism against xenobiotics and play a crucial role in modulating chemical toxicity [21,29]. This process primarily involves Phase I reactions, mainly catalyzed by cytochrome P450 (CYP450) enzymes, followed by Phase II conjugation reactions that usually detoxify compounds to facilitate eventual excretion [19,6]. However, atypical metabolic pathways can generate metabolites that are more toxic than their parent chemicals. Recent studies have highlighted the role of CYP450 in converting phenolic compounds into more harmful conjugates [40,71,75]. Phase II metabolism, mediated by conjugating enzymes, leads to glucuronide-, GSH-, and sulfate-conjugated metabolites [25,6,71,75]. For example, CYP3A4-mediated reactions between phenolic pollutants and endogenous metabolites, such as vitamin E (VE) and estradiol, produce new lipophilic ether products [40]. Methylation can enhance the acute toxicity of diclofenac in aquatic invertebrates [21], while glucuronidation increases the phototoxicity of oxybenzone, a sunscreen chemical, to corals and sea anemones [69]. Further, xenobiotic metabolism can disrupt metabolic homeostasis, impairing biological functions [29,40,75]. Although conjugation of GSH with electrophilic compounds for detoxification [26], excessive GSH consumption can cause tissue damage [25,75]. For instance, bisphenol A binding to VE reduces VE levels and increases reactive oxygen species (ROS) production [40]. Hydroxylation and quinone metabolites derived from butylated hydroxyanisole and butylated hydroxytoluene can attack DNA, induce carcinogenicity, deplete GSH and adenine nucleoside triphosphate (ATP), and induce oxidative stress and apoptosis [71]. These dual detoxifying and toxification effects highlight the importance to explore coral metabolism of wildfire-derived chemicals and their resultant toxicities.

Globally, forest fires account for ~60 % of wildfire events [70], with methoxyphenols (MPs) recognized as reliable tracers of wood smoke emission [57]. Recent research on the metabolism and toxicological effects of specific phenols in humans and rats, emphasizes their potential adverse health impacts [40,6,75]. Syringol, a predominant MP in wildfire emissions, has been shown to cause cytotoxicity, embryotoxicity, and oxidative stress-related apoptosis in zebrafish models [49,7]. However, the metabolic pathways and toxicological profiles of syringol metabolites in organisms remain poorly understood. Wildfire aerosols can deposit into the ocean, posing threatens to ocean ecosystems [20]. Reef-building corals, especially branching species such as *Acropora* spp., are highly susceptible to environmental stressors, including eutrophication and certain organic pollutants [27,69]. Given their ecological importance in reef framework construction and documented sensitivity to wildfire particles [39,51], the potential impact of syringol on these corals raises serious concern. The capacity of corals to metabolize syringol may underlie their vulnerability to wildfire emissions, a hypothesis that requires experimental validation.

This study aimed to characterize the Phase I and Phase II metabolites of syringol in *Acropora formosa*, elucidate the associated metabolic pathways, and assess the toxicological implications of these transformations. Molecular docking and quantitative real-time polymerase chain reaction (RT-qPCR) analysis were explored to investigate the enzymatic mechanisms involved in syringol metabolism. *In-silico* modeling combined with protein-protein interaction (PPI) network analysis was used to predict the toxicity and biological effects of the metabolites. Meanwhile, assessments of coral physiological responses, including phenotypic changes, antioxidant status, and cellular energy allocation (CEA), provided an integrated understanding of the toxic effects during biotransformation.

2. Materials and methods

2.1. Syringol and coral collection

Weizhou Island (20°54′-21°10′N, 109°00′-109°15′E), located in the Beibu Gulf of China, lies downwind of several major wildfire hotspots, including the Indochinese Peninsula, East Asia, and Equatorial Asia (Fig. 1). The regional burning season typically occurs from March to April. To avoid potential contamination from wildfire pollutants, coral samples (*A. formosa*) were collected during the non-burning season (November 2023). Samples were collected by divers from a depth of 2–3 m around Weizhou Island. After collection, the corals were maintained in a 300 L aquarium with a recirculating natural seawater system for a 15-day acclimation. The coral colonies were then subdivided into 6 cm-long twigs and affixed to custom-made ceramic bases. These fragments underwent an additional 15-day acclimation under controlled laboratory conditions (26 ± 1℃; light intensity: 200 ± 20 μmol m^{-2} s^{-1}; 12 h dark: 12 h light cycle) prior to experimentation. The physicochemical parameters of the natural seawater, including nutrient concentrations, dissolved oxygen, and pH were measured and are provided in Supporting Information Table S1 to confirm the absence of wildfire-related contamination. Syringol (2,6-Dimethoxyphenol; purity ≥ 98 %) was purchased from Shanghai Aladdin Reagent Co., Ltd. (China).

In Fig. 1, fire point data were sourced from NASA's Fire Information for Resource Management System (https://firms.modaps.eosdis.nasa.gov/map/. Black Carbon Optical Depth (BCAOD) for 2023, serving as an indicator of fire aerosol loading, was derived from the CAMS Global Atmospheric Composition Forecasts and (https://ads.atmosphere.copernicus.eu/). Original aerosol data at 0.75° × 0.75° resolution were interpolated to 0.25° × 0.25° for regional visualization. Global coral reef distribution data were sourced from the UN Environment Programme World Conservation Monitoring Centre (https://resources.unepwcmc.org/products/0613604367334836863f5c0c10e452bf).

2.2. Experimental design

This experiment included four treatment groups, in which coral fragments were exposed to syringol at concentrations of 0 mg/L (control), 4 mg/L, 6 mg/L, and 8 mg/L, respectively. Each group comprised five biological replicates (n = 5), with coral twigs placed in individual tank (29 cm × 19 cm × 26 cm; 10 L natural seawater). The exposure concentrations were selected based on estimates of syringol input via wildfire particle deposition. During wildfire events, atmospheric concentrations of particulate matters with a diameters ≤ 2.5 μm ($PM_{2.5}$)

range from 1937 to 8357 μg/m^3 [23,52], accounting for 80 %–90 % of smoke particles [23]. MPs, including syringol, serve as tracers for forest fires, have been associated with adverse effects on human and ecological health (Supporting Information Text S1). Although ~75.1 % of syringol exist in the gas phase (Table S2) [55], particle-bound fractions still comprise 14.5–20.1 % of wildfire aerosols in coastal areas [56]. Given that wildfire plumes can reach the upper troposphere (17–20 km) and persist over extended periods [34], atmospheric deposition into the ocean may result in prolonged exposure [20]. Based on an 8-day cumulative deposition for a 2 m-depth coral reef region, the estimated syringol concentrations in seawater range from 1.4 to 8.2 mg/L, which justified the selected exposure levels in this study. Detailed calculations are provided in Supporting Information Text S2.

To prepare the exposure solutions, syringol was dissolved in ultrapure water, stored in amber glass bottles to avoid photodegradation, and added to the respective tanks to achieve the target concentrations. The control group received no syringol addition. The endpoint of the experiment was defined as the onset of visible coral decline, which was observed at 24 h post-exposure and manifested as bleaching. At this time point, all five coral twigs from each group were sampled for subsequent physiological and metabolites analyses. The determination of physiological parameters, including antioxidant capacity and cellular energy allocation, is detailed in Supporting Information Text S2.

2.3. Identification of syringol metabolites in coral tissues

Syringol metabolites were screened using a Thermo Scientific UPLC system coupled with a Q Exactive Orbitrap mass spectrometer (UPLC-QE, Thermo Fisher Company, USA) under both positive and negative electrospray ionization modes. Based on the significantly elevated superoxide dismutase (SOD), and catalase (CAT) activities observed in response to moderate injury and bleaching, a dose of 6 mg/L was selected for metabolite identification in coral tissues. A 4 cm coral twig was immersed in a methanol/acetonitrile solution (1:1, v/v) and extracted at 4 ℃ for 24 h. After extraction, the sample was sonicated for 20 min and then centrifuged at 5000 rpm for 10 min. The extraction procedure was repeated once, and the two extracts were combined. The combined extract was subjected to solid-phase extraction (SPE) using a C18 cartridge equilibrated with methanol. The solid phase was rinsed with methanol, and the eluent was evaporated to dryness and then stored at −80 ℃ until analysis.

To assess potential methylation of syringol during chemical analysis, a stock solution of syringol in methanol/acetonitrile mixture (1:1, v/v) was analyzed using ultra high performance liquid chromatography high resolution mass spectrometry (UPLC-HRMS). The chemical identities of potential metabolites were determined based on the *m/z* values and the patterns of MS^2 or MS fragments, with only those signals exceeding an intensity threshold of 1×10^5 being considered. Metabolites were identified through precursor ions scanning with a mass error threshold of less than 5 ppm. The relative intensity of each identified metabolite was determined by semi-quantitative analysis of peak area in the extracted ion chromatogram acquired under full scan ddMS^2 mode. Peak areas were normalized to the total ion intensity of syringol and its metabolites, which was set to 100 %. The operating parameters of the UPLC-HRMS are detailed in Supporting Information Text S2 and Table S3.

2.4. In-silico toxicity and functional target prediction

The Ecological Structure Activity Relationships (ECOSAR) program

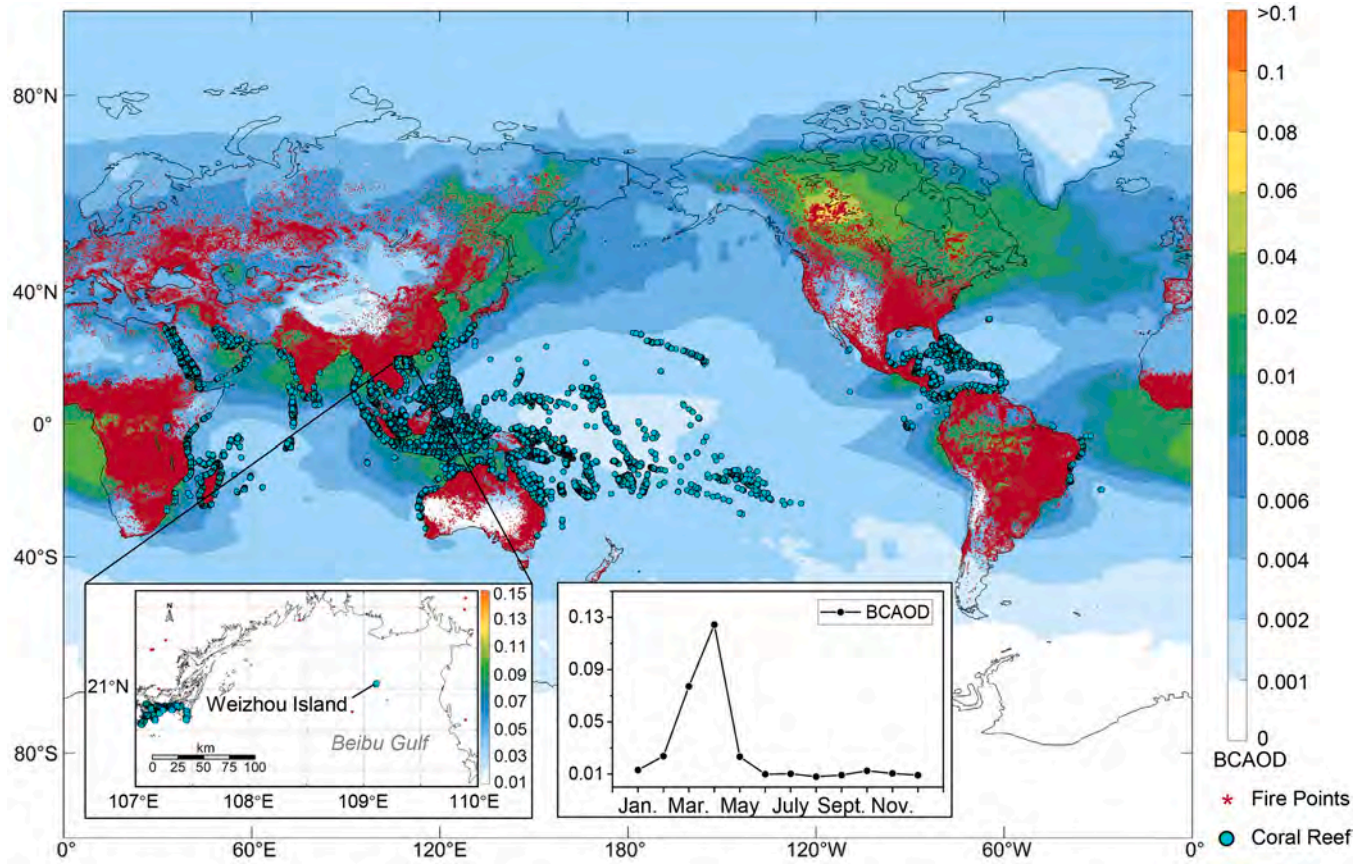


Fig. 1. Spatial distribution of global coral reefs, fire points, and black carbon aerosol optical depth (BCAOD) in 2023. The left inset shows BCAOD over the Weizhou Island region during the sampling period in the non-burning season (November 2023). The right inset illustrates monthly BCAOD variations over the same region during 2023.

was performed to predict the toxicity of syringol and its metabolites toward three non-target aquatic organisms: daphnia, fish, and green algae. Toxicity was evaluated based on lg LC_{50}/EC_{50} values and classified into four categories: very toxic (<0 mg/L), toxic (0–1 mg/L), harmful (1–2 mg/L), and not harmful (>2 mg/L) [10]. Acute and chronic toxicity values were predicted using the ECOSAR Class Program (version 2.2). The bioaccumulation factor, developmental toxicity and mutagenicity were further estimated using the Toxicity Estimation Software Tool.

The top 15 potential human macromolecular targets for each metabolite were identified using Swiss Target Prediction (http://www.swisstargetprediction.ch/) [12], and their disease associations were inferred from the GeneCards database (https://www.genecards.org). To investigate the biological processes and pathways regulated by these targets, Gene Ontology (GO) and Kyoto Encyclopedia of Genes and Genomes (KEGG) pathway enrichment analysis were conducted. Gene annotation was performed using the org.Hs.eg.db R package from Bioconductor (https://bioconductor.org/packages/release/data/annotation/html/org.Hs.eg.db. Html). To assess the functional connectivity among macromolecular targets, a PPI network analysis was constructed using STRING v11.5 database (https://string-db.org/) with a high-confidence interaction threshold (score > 0.7). The protein networks were visualized in Cytoscape (http://www.cytoscape.org/) and analyzed using the inbuilt MCODE package, with a maximum depth of 5 and a score cutoff of 0.2 to identify key functional modules.

2.5. Identification, expression validation, and molecular docking of Phase I/II enzymes

To identify candidate proteins involved in Phase I and II metabolism of syringol, we analyzed transcriptomic data from *A. formosa*, available in the NCBI Bioproject database (accession No. PRJNA992273; [39]). Key enzymes were identified through gene functional annotation using the NR databases and by assessing transcript abundance based on fragments per kilobase million (FPKM) values. The enzymes identified included cytochrome P450 3A24-like (CYP3A24-like), cytochrome P450 3A21-like (CYP3A21-like), UDP-glucuronosyltransferase 2B13-like (UGT2B13-like), glutathione S-transferase-like (GST-like) and N-acetyltransferase CML1 (NAT8).

The expression levels of genes encoding these five enzymes were further validated by RT-qPCR in *A. formosa* exposed to syringol. This validation was extended to compare with those exposed to wildfire-derived $PM_{2.5}$ [39], given that MPs serve as tracers of forest fires [57]. Genes showing a fold change (FC) > 1.5-fold and $p < 0.05$ were considered significantly differentially expressed. Statistical significance was indicated as $^{*}p < 0.05$, $^{**}p < 0.01$, and $^{***}p < 0.001$. RT-qPCR and FPKM data were visualized as $Log_2^{FC(Treated/Control)}$. Detailed methodologies for the identification and expression analysis of Phase I and II enzymes are provided in Supporting Information Text S2.

The potential for syringol and 2,6-Dimethoxyhydroquinone ($DBQH_2$) to be metabolized by the identified enzymes was further evaluated by molecular docking analysis. Three dimensional (3D) structures of the target proteins were predicted using the Alphafold3 server (https://golgi.sandbox.google.com/about) [2]. Molecular docking was performed using AutoDock Vina (version 1.5.6, Scripps Research Institute, La Jolla, CA, USA) to assess interactions between ligands (syringol, $DBQH_2$) with the proteins (CYP3A21-like, CYP3A24-like, UGT2B13-like, NAT8 and GST-like). Docking results, including 3D binding poses and the two-dimensional (2D) interaction maps, were visualized using Pymol and LigPlus, respectively. Hydrogen bonds and Vander Waals interactions were annealed at distances of 4.0 Å and 2.5 Å, respectively. Each docking simulation was run 50 times with default parameters.

2.6. Bacterial community structure analysis

Bacterial community structure was analyzed using coral samples exposed to 6 mg/L syringol (n = 5 per group). Total microbial genomic DNA was extracted using the E.Z.N.A.® soil DNA Kit (Omega Bio-tek, Norcross, GA, U.S.) following the manufacturer's instructions. The hypervariable region V3-V4 of the bacterial 16S rRNA gene were amplified with primer pairs 338 F and 806 R (Table S10) [38]. Amplicon sequencing was performed on an Illumina Nextseq2000 platform (Illumina, San Diego, USA) according to the standard protocols of Majorbio Bio-Pharm Technology Co. Ltd. (Shanghai, China). Raw sequencing data have been deposited in the NCBI Sequence Read Archive (SRA) database (Accession Number: PRJNA1290515). Details of sequence processing and downstream analysis, including intergroup differences of α-diversity, β-diversity, genus level and functional annotation of prokaryotic taxa (FAPROTAX), are provided in Supporting Information Text S2.

2.7. Statistical analyses

Differences in physiological parameters and RT-qPCR data between treatment and control groups were analyzed using Student's T-test, with significance levels indicated as $^{*}p < 0.05$, $^{**}p < 0.01$, and $^{***}p < 0.001$. Pearson correlation analysis was used to test the relationships between syringol concentrations and coral physiological parameters. Principal component analysis (PCA) based on physiological parameters was conducted to identify the primary factors contributing to oxidative damage and energy metabolism in corals. Linear regression analysis was conducted to examine the relationships between variables. PCA and linear regression analysis performed using origin 2022 with default settings.

3. Results and discussion

3.1. Syringol metabolism and microbial involvement in corals

3.1.1. Identification and semi-quantification of syringol metabolites

The specific mass spectral information for the metabolites is presented in Supporting Information Table S4 and illustrated in Figure S1. A total of 25 syringol metabolites were identified in the coral *A. formosa*, including 11 Phase I metabolites and 14 Phase II metabolites. Based on their structures and established transformation rules, a proposed metabolic pathway for syringol is presented in Fig. 2a. The 11 Phase I metabolites consist of aromatic ring cleavage metabolites (A1–3, B6), mono-hydroxylated metabolites [B1 (DBHQ2)], quinone metabolites (B2, C1), O-demethylated metabolites (C2–4), and a methylenedioxy bridged cyclization metabolite (D1). The 14 Phase II metabolites include glucuronidation metabolite (E2), GSH conjugates (C8 and E3), methylation products (B3, B4 and D2), acetylation product (B5), and amino acid conjugates (B7–9, C5–7 and E1). Hydroxylation, O-demethylation, quinonation, methylation, glucuronidation, and GSH conjugation are common transformations observed in phenolic compounds [60,71,75]. In addition, this study reported acetylation, amino acid conjugation, and methylenedioxy bridged cyclization metabolites, which are rarely documented in phenolic metabolism.

To estimate the relative contribution of each metabolite in corals, semiquantitative analysis based on signal intensities was conducted, revealing an overall syringol metabolic rate of 97.7 %. Major pathways, labeled A, B, and C, accounted for 10.3 %, 26.8 %, and 56.6 % of the total metabolism, respectively (Fig. 2b). Among these, glutamine conjugation (B9, C7, and E1) predominated at 56.4 %, followed by acetylation (B5) at 20.9 %, aromatic ring cleavage (A3) at 9.6 %, ornithine conjugation (C5) at 3.7 %, quinone formation (B2 and C1) at 2 %, GSH conjugation (C8 and E3) at 1.3 %, methylation (B2, B3, and D2) at 1.1 %, and glucuronidation at 0.9 % (Fig. 2c). Although 3-methoxycatechol was not directly detected, the presence of secondary conversion products (C1-C8) suggests active O-demethylation. Phase I metabolism was predominantly characterized by hydroxylation and O-demethylation, while Phase II mainly involved acetylation and amino acid conjugation. Similar metabolic transformations have been reported for

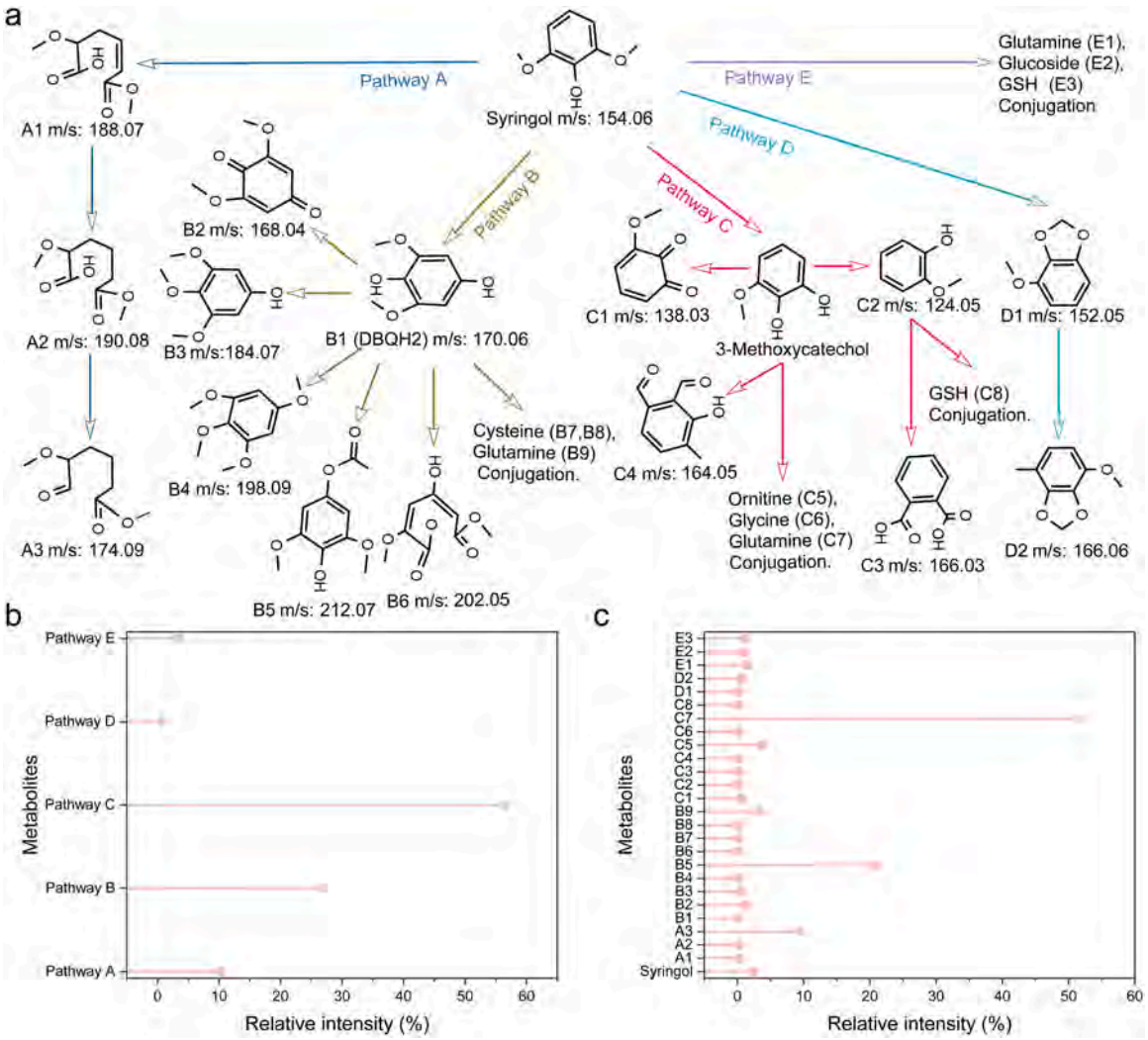


Fig. 2. Syringol metabolism in corals. (a) Metabolites of syringol identified by *in vivo* metabolism assay, and the proposed metabolic pathways. All the metabolites are displayed in the neutral forms. Relative intensity of the metabolic pathways (b) and syringol and its metabolites (c).

phenolic compounds like butylated hydroxyanisole and butylated hydroxytoluene [71], syringol underwent hydroxylation and O-demethylation. Amino acid conjugates, being more hydrophilic, are typically excreted more readily than their parent compounds [31]. In contrast, acetylated metabolites tend to be more lipophilic, potentially increase their bioaccumulation and toxicity risks [46]. However, aromatic ring cleavage and methylenedioxy bridged cyclization are distinctive Phase I reactions for syringol and are rarely observed in animal phenolic metabolism [40,71,75].

3.1.2. *Microbial mediation of syringol metabolism in corals*

Methylenedioxy bridged cyclization primarily occurs in plants during natural product synthesis [41] and in microbes during antibiotic biosynthesis [59]. The π-conjugated structure of aromatic rings confers high chemical stability, making their cleavage energetically challenging [24]. Animals generally possess limited metabolic capacity for aromatic substances, relying largely on microbial processes [22]. The presence of aromatic compound degradation genes in the genomes of coral-associated bacteria [68] may facilitate aromatic ring cleavage.

To investigate the potential involvement of coral-associated bacteria in syringol metabolism, we analyzed changes in microbial community. A total of 60 bacterial genera were shared, while 86 and 31 genera were unique to the control and syringol groups, respectively (Fig. 3b). The syringol-treated microbiome exhibited a lower Chao index (Fig. 3c), indicating reduced species richness and α-diversity. Additionally, significant differences in β-diversity were observed between groups ($p < 0.01$; Fig. 3d), reflecting shifts in microbial community composition. Importantly, *Acinetobacter* and *Acidovorax* remained abundant in both the control (6.5 %, 2.6 %) and syringol (5.0 %, 2.7 %) groups (Fig. 3a). They are keystone taxa in activated-sludge systems and pivotal for the catabolism of phenolic and aromatic pollutants [3]. The sustained presence of these aromatic-degrading bacteria, together with the detection of aromatic-ring cleavage metabolites (e.g., A1-A3 and B6; Fig. 2 and Figure S1) suggests their potential involvement in syringol ring degradation. Unfortunately, such cleavage processes may generate reactive electrophilic byproducts (e.g., aldehydes, carboxylic acids), which can covalently modify cellular macromolecules and cause damage [71]. These atypical metabolic pathways mediated by coral-associated microbes may complicate detoxification of wildfire emissions in corals and hinder their ability to mitigate toxic effects.

Predicted analysis through FAPROTAX revealed significant enrichment of microbial functions associated with methanol oxidation, methylotrophy and intracellular parasitism (all $p < 0.05$; Fig. 3e). Correspondingly, the relative abundances of methylotrophs (*Methylophaga*), dimethylsulfoniopropionate lyase bacteria (*Shimia*), and intracellular parasites (norank *Legionellaceae*, *Coxiella*, norank *Simkaniaceae*) significantly increased (all $p < 0.05$; Fig. 3f). In contrast, *Sphingomonadaceae* (putative aromatic degraders), *Tritoniibacter* (a

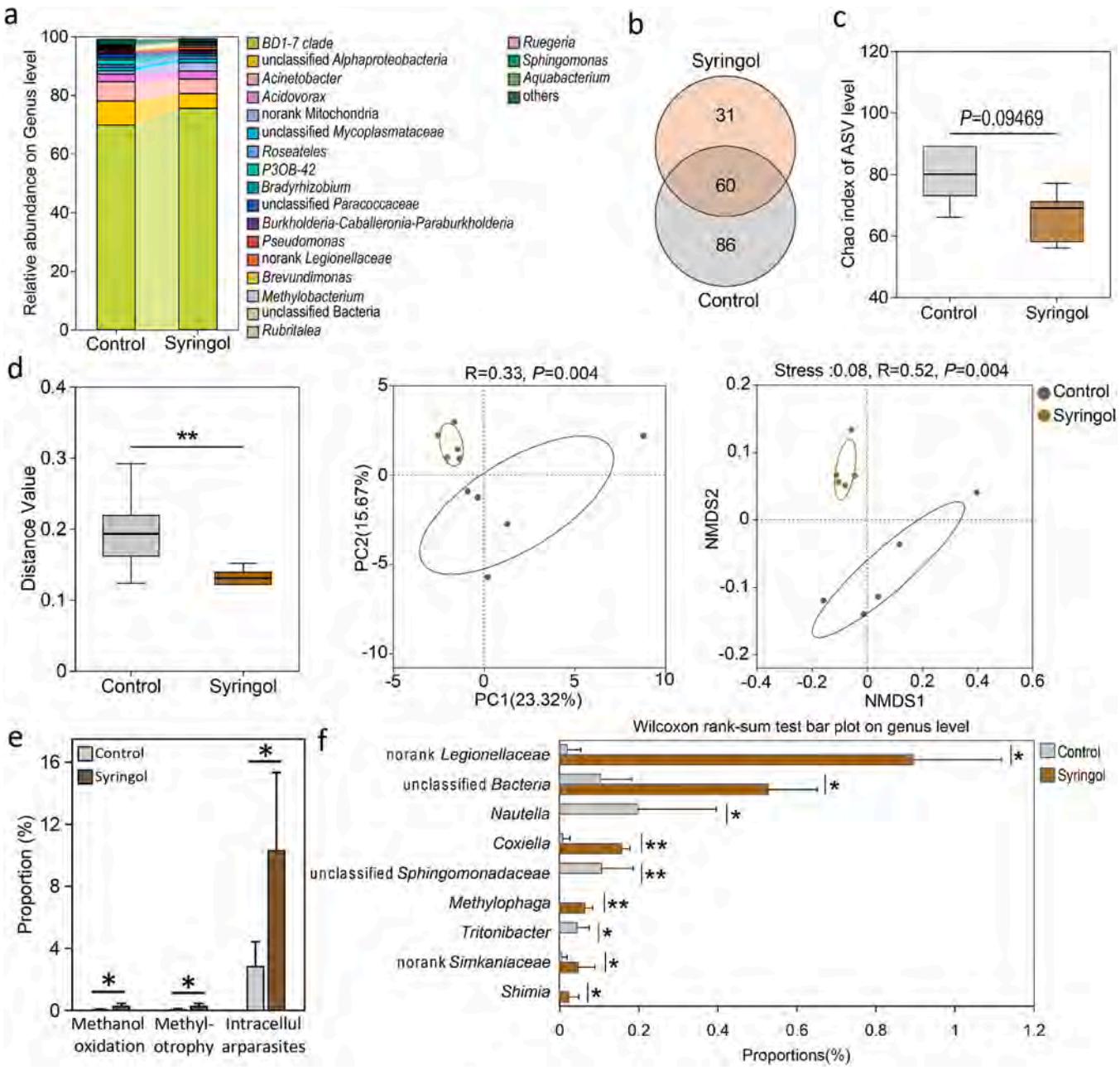


Fig. 3. Alterations in bacterial community composition structure under syringol exposure. (a) Genus-level differences in bacterial community composition. (b) Venn diagram showing shared core genera among the control and syringol groups. (c) Comparison of different α-diversity indicators Chao for control and syringol groups. (d) Principal coordinate analysis (PCoA), Non-metric multidimensional scaling (NMDS) and Bray-curtis analysis. (e) Functional bacterial community categories inferred by FAPROTAX function prediction. (f) Highlights differences in bacteria at the genus level.

producer of the antibacterial compound tropodithietic acid), and *Nautella* (an algal-bleaching pathogen) exhibited significant reductions (all $p < 0.05$; Fig. 3f). Syringol and its metabolites (e.g, 3-methoxycatechol, C1-C4; Figs. 2, 4 and 5) can undergo CYP-mediated O-demethylation, generating reactive one-carbon intermediates such as methanol or formaldehyde, which are cytotoxic to corals [15]. Methylotrophs may help mitigate these cytotoxic effects by rapidly oxidizing one-carbon compounds [43], thereby lowering their local concentrations and alleviating oxidative stress on the coral host. Moreover, the enrichment of *Simkaniaceae* under syringol exposure, along with their encoded catechol degradation genes [14], suggests a potential role for this taxon in the degradation of aromatic compound. Recently, *Simkaniaceae* were reported for the first time to infect dinoflagellate symbionts of cnidarians [42], raising concerns about their potential pathogenicity. But the impact of *Simkaniaceae*, *Coxiella*, and *Legionellaceae* on coral health remains largely unexplored. Together, these microbial shifts indicate a functional reorganization of the coral-associated microbiome under syringol stress, suggesting a trade-off between detoxification processes and susceptibility to infection.

3.2. Metabolic interactions between syringol and coral Phase I/II enzymes

3.2.1. Identification and evolutionary conservation of candidate enzymes

The biotransformation of syringol and its metabolites is likely mediated by multiple enzyme classes, including CYP3As, N-acetyltransferases (NATs), UDP-glucuronosyltransferases (UGTs), and glutathione S-transferases (GSTs). This inference is supported by prior studies indicating that CYP3A4 catalyzes the O-demethylation and

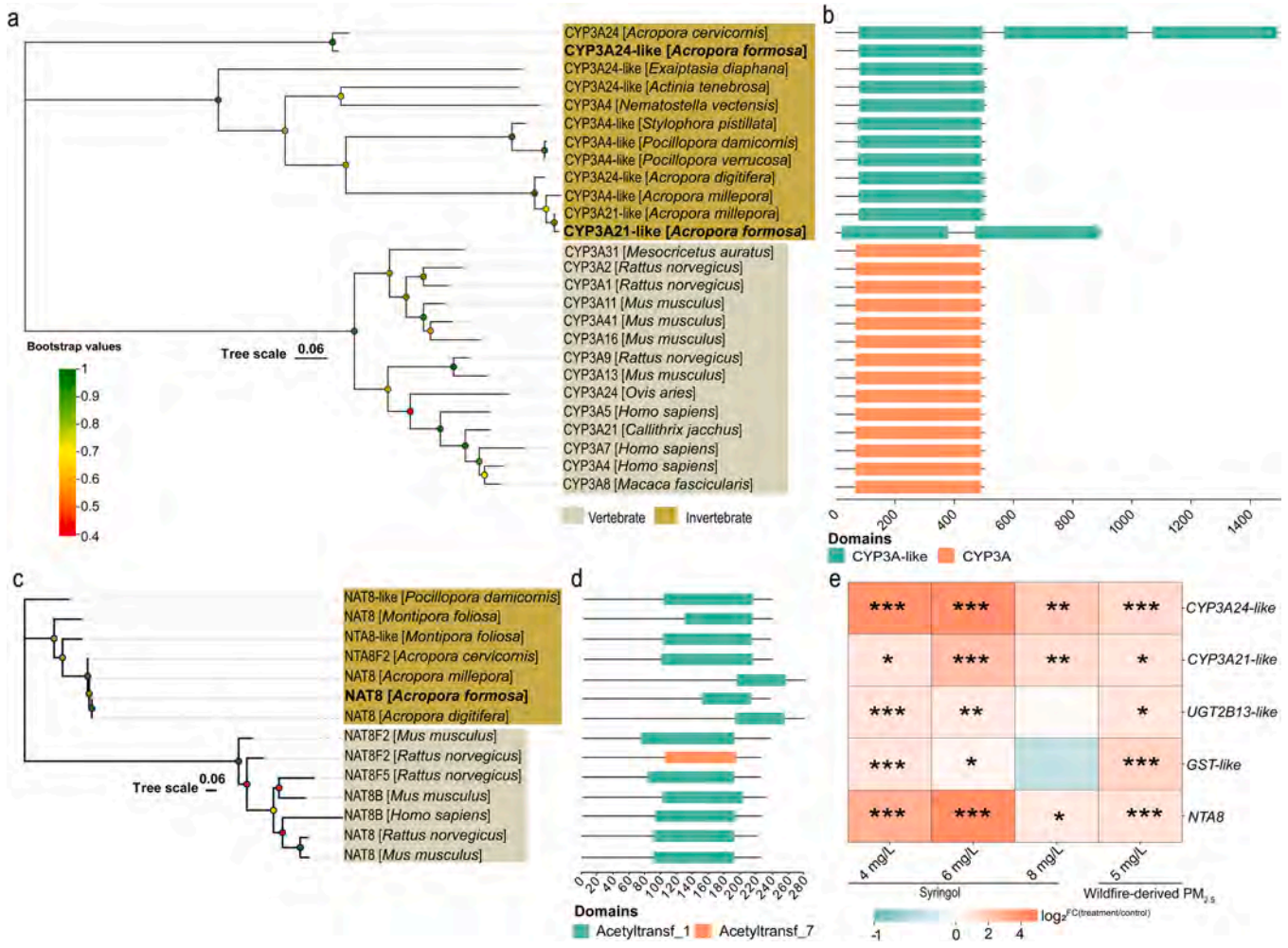


Fig. 4. (a) Phylogenetic tree of cytochrome P450 3A from invertebrates (marine anthozoans) and vertebrates. (b) Conservative domains in cytochrome P450 3A proteins. (c) Phylogenetic tree of N-acetyltransferase 8 proteins from invertebrates (coral) and vertebrates. (d) Conservative domains in N-acetyltransferase 8 proteins. Phylogenetic trees were constructed with full-length sequences with MEGA 11 software; protein lengths are indicated by the scale. Invertebrates are represented in yellow shade and vertebrates in yellow-green shade. (e) Gene expression pattern in *A. formosa* exposed to syringol or wildfire-derived $PM_{2.5}$. Syringol groups were assessed at 24 h post-treatment using RT-qPCR; wildfire -derived $PM_{2.5}$ group was analyzed at 9 days using transcript abundance analysis (FPKM) [39]. The statistical significance for RT-qPCR were determined by Student's T-test and FPKM were determined by DESeq2. * $p < 0.05$, ** $p < 0.01$, *** $p < 0.001$ and fold change (FC) > 1.5-fold.

hydroxylation of phenolic compounds, such as vanillin and butylated hydroxyanisole in mammals [71,75], and that CYP3A facilitates the hydroxylation of gramine [25]. NATs employs acetyl-coenzyme A (acetyl-CoA) as a cofactor to mediate N-acetylation (typically inactive) or O-acetylation (generally active) of aromatic and heterocyclic amines [17]. UGT and GST are also widely recognized for their essential roles in the conjugation and clearance of phenolic xenobiotics [25,6,71,75].

To identify candidate enzymes involved in syringol metabolism in corals, we performed phylogenetic and structural analyses of 78 proteins from both vertebrates (e.g., human, mice, rat) and invertebrate (marine anthozoans). These included 26 CYP3As, 19 UGTs, 14 N-acetyltransferase 8 proteins (NAT8s) and 19 GSTs (Table S5). Despite originating from divergent evolutionary lineages (Fig. 4a and c; Figure S2a and c), coral enzymes shared highly conserved domain structures and ligand-binding residues with their vertebrate homologs (Fig. 4b and d; Figure S2b and d; Figures S3–6). All of these are characteristics of intracellular proteins and are predicted to possess corresponding enzyme activities (Tables S6 and 7). For instance, the heme-binding domain of CYP3A is evolutionarily conserved across taxa (Fig. 4b; Figure S3). Proteins with homologous domain structures and conserved ligand-binding sites often retain analogous biological functions [37]. For example, the HSF1 protein from coral and its human homolog both facilitates thermal tolerance [11]. Likewise, the enzymatic activity of CYP3A-like proteins has been experimentally verified in crayfish [65], further supporting the functional conservation of this enzyme family across animal phyla. Nevertheless, functional data on CYP3A-like enzymes in corals and other invertebrates remains scarce.

3.2.2. *Structural mechanisms of syringol biotransformation by coral enzymes*

Enzyme-catalyzed reactions occur within biological microenvironments, where protein conformation and amino acid residue interactions can influence reaction kinetics [50]. To elucidate the molecular mechanisms underlying syringol metabolism in corals, we conducted homology modeling and molecular docking targeting key Phase I and II enzymes. Docking simulations revealed strong binding affinities between syringol and its metabolite DBHQ2 and candidate enzymes (Fig. 5a, b and c; Figure S7a and b). These interactions were stabilized by multiple hydrogen bonds and hydrophobic interactions Fig. 5a, b and c; Figure S7a and b), indicative of energetically favorable and specific binding. In CYP450 enzymes, catalytic efficiency depends on the distance between the substrate' reactive site and the heme-bound Fe (IV) = O center [61]. Our models showed syringol was located centrally in the active pocket (Fig. 5a-I and b-I), with its C_4 and C_6 atoms located

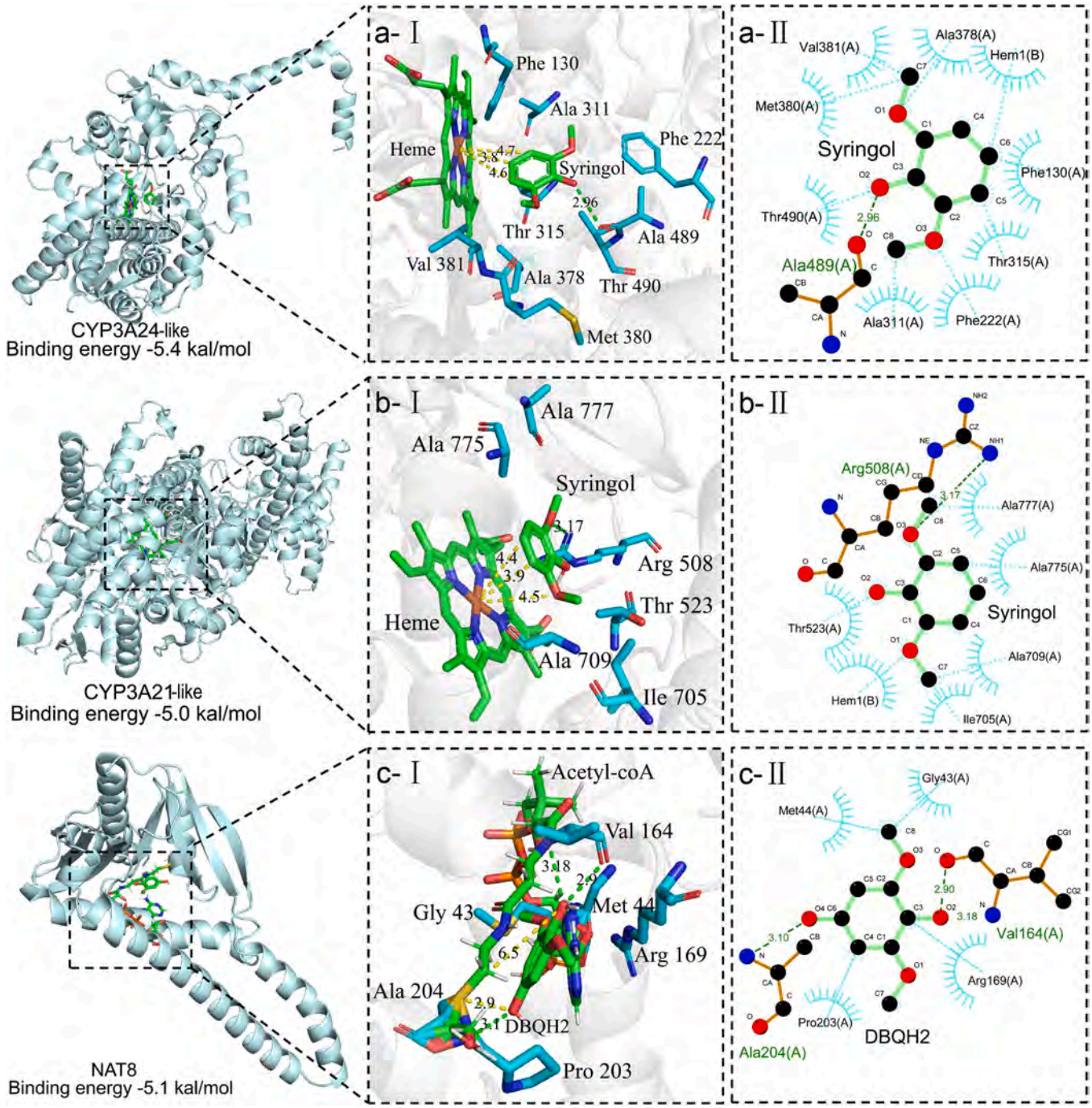


Fig. 5. Molecular docking simulation of CYP3A24-like, CYP3A21-like and NAT8 with their ligands (syringol or DBQH2). The active pockets of CYP3A24-like, CYP3A21-like and NAT8 are showed according to the spatial properties of the reaction centers and ligands, yellow dashes lines measure the distance between syringol and heme Fe, between DBQH2 and acetyl-CoA S, and analyzing hydrogen bonds (green dashes lines) (number in the parentheses, unit Å) (a-I, b-I and c-I). 2D structure showing the hydrophobic interaction and H-bonding between the ligands and the active site pockets of CYP3A24-like, CYP3A21-like and NAT8 (a-II, b-II and c-II). H-bonding and hydrophobic interaction are illustrated in olive green and cyan lines, respectively; atomic distances are expressed in angstroms and binding affinities in kcal/mol.

3.8 Å and 3.9 Å from the heme iron, respectively, suggesting accessibility for hydroxylation. Additionally, the methoxy group (-OCH_3) of syringol was situated 4.5 Å from the heme center in the CYP3A21-like enzyme, suggesting a favorable orientation for O-demethylation.

Among the Phase II enzymes, the UGT2B13-like and GST-like proteins exhibited relatively long distances between catalytic residues and the ligand's reactive centers (Figure S7a-I and b-I). Nonetheless, the formation of E2 and E3 metabolites suggests that these enzymes can undergo tautomeric acid-base catalysis or electrophilic substitutions reactions (Figure S1 and Figure S7a and b). In contrast, the NAT8-DBQH2 complex displayed close spatial alignment, with the O_4 atom of DBQH2 located only 2.9 Å from the acetyl donor (acetyl-CoA oxygen) (Fig. 5c–I), supporting the structurally feasibility of acetylation. Collectively, these structural findings indicate that CYP3A21-like, CYP3A24-like, NAT8, GST-like, and UGT2B13-like enzymes in corals possess the catalytic capacity to mediate syringol biotransformation, contributing to detoxification or the generation of potentially toxic metabolites.

3.2.3. Transcriptional response of coral detoxification enzymes to syringol and wildfire $PM_{2.5}$

To validate the vivo functional relevance of the identified metabolic enzymes, we examined their transcriptional response in *A. formosa* following exposure to syringol and wildfire $PM_{2.5}$. RT-qPCR analysis revealed a dose-dependent upregulation of *CYP3A24-like*, *CYP3A21-like*, *UGT2B13-like*, *NAT8* and *GST-like* genes in response to increasing syringol concentrations (Fig. 4e). A similar expression pattern was observed under wildfire $PM_{2.5}$ exposure (Fig. 4e). This suggests that comparable enzymatic pathways may be activated by MPs, which

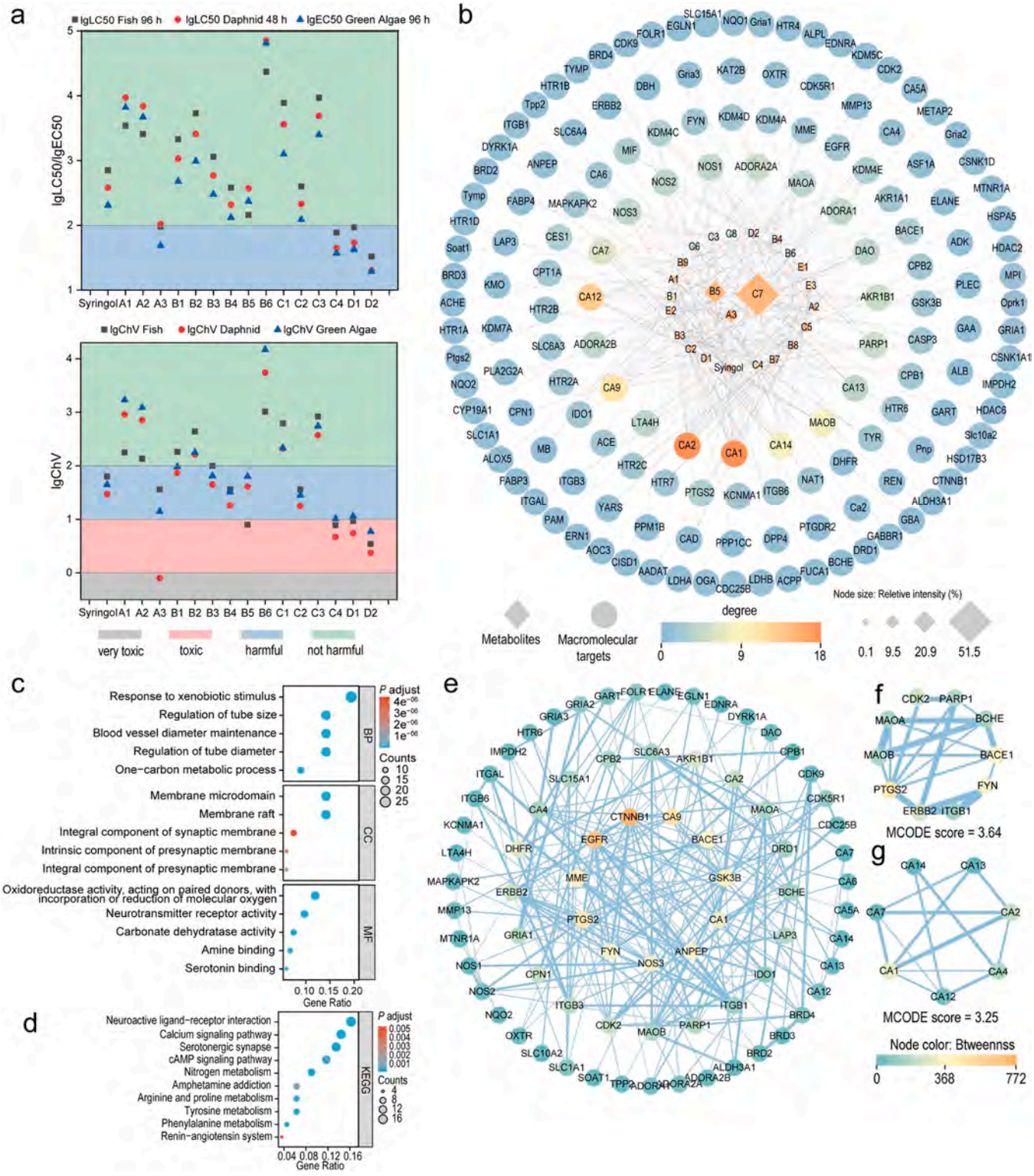


Fig. 6. Predicted toxicity and molecular targets of syringol and its metabolites in corals. (a) Estimated acute and chronic toxicity of syringol and its metabolites based on ECOSAR modeling. (b) Predicted interaction network between macromolecular targets and syringol/metabolites. (c-d) Gene Ontology (GO) and Kyoto Encyclopedia of Genes and Genomes (KEGG) enrichment analysis of the 146 macromolecular targets (BP: biological process; CC: cellular component; MF: molecular function); (e) Protein-protein interaction (PPI) network of the predicted targets. (f-g) Major PPI submodules identified using MCODE clustering.

account for 17∼44 % of the carbonaceous fraction in wildfire aerosols [55,57]. Interestingly, the mRNA levels of *GST-like* decreased at the high syringol concentration (8 mg/L). This suppression may reflect a feedback inhibition mechanism, likely due to electrophilic conjugation of syringol and its metabolite guaiacol (C2) with GSH to form GSH S-conjugates. Such reactions can deplete intracellular GSH and modulate GST gene expression [71,75].

The catalytic efficiency and transcriptional activity of detoxification enzymes may be influenced by environmental conditions. For instance, hypo-salinity has been shown to suppress CYP3A expression while upregulating GST in *Stylophora pistillata* [18]. In *Galaxea fascicularis*, GST activity increases at 30℃ and remains elevated under prolonged thermal stress, whereas *Acropora tenuis* fails to activate GST under comparable conditions, resulting in bleaching and eventual mortality [16]. These species-specific responses suggest the potential for environmental stressors, such as thermal anomalies, to interact with wildfire pollutants and disrupt detoxification pathways in stress-sensitive coral species.

3.3. Ecotoxicity and macromolecular target prediction of syringol and its metabolites

3.3.1. Ecotoxicological risks of syringol metabolites in corals

To assess the ecotoxicity of syringol and its metabolites, we employed *in-silico* models using ECOSAR program. The analysis included the parent compound and its major Phase I transformation products, as well as methylated, and acetylated metabolites (Table S8). Compared to syringol, several metabolites (B1, B3, B4, C2, D1 and D2) have higher bioaccumulation factors (Figure S8a), suggesting an increased potential for trophic transfer. Syringol itself has a developmental toxicity index of 0.64, classifying it as a developmental toxicant. Importantly, all tested metabolites except for C1 also displayed developmental toxicity (Figure S8b), raising concerns about their potential to impair coral growth, reproductive success, and disease resistance [49,7]. Moreover, all metabolites expect for syringol and C3 were predicted to enhance mutagenic potential (Figure S8c). The predicted acute toxicity values for syringol were LC_{50} (fish) = 716 mg/L, LC_{50} (daphnia) = 376 mg/L, and EC_{50} (green algae) = 203 mg/L, indicating ecological risks at environmentally relevant concentrations [49].

Compared to the parent compound, six metabolites (A3, B4, C2, C4, D1, and D2) showed higher acute and chronic toxicity across the three non-targeted aquatic taxa. B5 was specifically more toxic to fish (Fig. 6a). This is concerning, because A3 and B5 are among the major metabolites, comprising 9.6 % and 20.9 % of the total metabolite yield, respectively (Fig. 2c). The potential high bioaccumulation of B5 metabolites may further raises concerns about its magnification in the marine food web [46]. Structurally, the aldehyde groups of metabolites such as A3 and C4 exhibited electrophilic reactivity toward nucleic acids and thiol endogenous antioxidants, potentially inducing oxidative stress and cellular damage [71]. Although some of these metabolites occur at relatively low concentrations, their toxicological effects may be substantial. For instance, the methylated metabolite of diclofenac has been shown to exhibit a 430-fold increase in acute toxicity toward aquatic invertebrates compared to its parent compound [21]. These findings suggest that syringol metabolites, particularly those arising from methylation, acetylation, methylenedioxy-bridging, O-demethylation, and aromatic ring cleavage, exhibit greater ecotoxicity than the parent compound. This heightened toxicity, especially to corals, represent a significant ecological risk, given that coral reefs provide habitat for nearly one-quarter of all marine species [48].

Syringol and its hydroxylated metabolites (e.g., B1 and 3-methoxycatechol) underwent conjugation with amino acids and related molecules, including glutamine, ornithine, and GSH (Fig. 2; Figure S1). The relative abundance of these conjugates was 56.4 % for glutamine, 3.7 % for ornithine, and 1.28 % for GSH (Fig. 2c). While amino acid conjugation generally facilities detoxification by increasing hydrophilicity and promoting excretion [31], it also imposes a metabolic cost. Glutamine not only supports oxidative phosphorylation and ATP generation [66], but also serves as a precursor for GSH synthesis via the glutamate-glutamine cycle [73], which is essential for GST-mediated detoxification. Excessive depletion of glutamine and GSH for conjugation may compromise antioxidant defenses, elevate ROS levels, and compromise cellular homeostasis. Thus, glutamine and GSH levels may serve as sensitive biomarkers of syringol exposure, reflecting the coral's capacity to maintain redox balance and detoxification responses.

Several metabolites, particularly hydroxylated, quinone, and aldehyde derivatives, have electrophilic properties that allow them to form covalent adducts with nucleophilic sites on DNA, RNA and proteins. These adducts can initiate mutagenic or carcinogenic processes [71]. Metabolites such as A3, B1, B2, C2 and C4 are especially prone to such genotoxic effects. Collectively, these findings suggest that the transformation of syringol, primarily catalyzed by CYP3A21-like and CYP3A24-like enzymes, followed by Phase II reactions including methylation, acetylation, and amino acid conjugation, may generate toxic metabolites that impair coral physiology and amplify ecological risks.

3.3.2. Predicted biological effects of syringol mediated by macromolecular target interactions

To predict the potential biological macromolecular targets of syringol and its metabolites, we identified a total of 146 target proteins. These include multiple carbonic anhydrase (CA) isoforms (CA1, CA2, CA7, CA9, CA12, CA13, CA14), nitric-oxide synthase (NOS1, NOS2, NOS3), oxidoreductases (aldose reductase; AKR1B1), monoamine oxidases (MAOA, MAOB), and D-amino-acid oxidase (DAO), adenosine receptors (ADORA1, ADORA2A, ADORA2B), and signaling enzymes (cyclooxygenase-2; PTGS2), leukotriene A4 hydrolase (LTA4H), and poly [ADP-ribose] polymerase-1 (PARP1) (Fig. 6b; Table S9). These proteins are implicated in diverse physiological and pathological processes.

Phenolic compounds typically bind to zinc-bound water molecule at the active site of CA via their hydroxyl moieties, while their phenyl groups occupy the hydrophobic pocket, thereby hindering CO_2 access to the catalytic site and acting as CA inhibitors [44,7]. CA is essential for acid-base homeostasis and calcification process [9]. Inhibition of CA in cnidarian symbionts has been shown to reduce photosynthetic carbon assimilation by 56–85 % [13]. Under ocean warming, wildfire particles may serve as a heterotrophic nutrient source for corals, especially when autotrophic nutrient acquisition is compromised. However, despite temporarily promoting tissue biomass via the delivery of biogenic elements (e.g., N, P), wildfire particles can simultaneously inhibit coral calcification [51]. Our results suggest that syringol-containing particles tend to inhibit CA activity, thereby disrupting coral calcification and associated physiological processes.

The targeting of NOS suggests a potential modulation of NO signaling. Phenolic compounds have been shown to elevate NO production in endothelial cells via upregulation of endothelial NOS expression [5]. In addition, inhibition of AKR1B1 by phenolic compounds [64], may impair cellular redox homeostasis, thereby affecting GSH synthesis and antioxidant defenses [74]. Syringol metabolites may also modulate adenosine receptor signaling (ADORA1, ADORA2A, ADORA2B), potentially disrupting cyclic adenosine monophosphate (cAMP) pathways critical for coral energy metabolism, immune function, and calcification [35]. Moreover, pro-inflammatory pathways could be influenced through interactions with PTGS2 and LTA4H [33,58,62,72], with LTA4H activation previously reported in response to cigarette smoke [58]. The inhibition of monoamine oxidases (MAOA, MAOB) and DAO by phenolic compounds may disturb neurotransmitter metabolism and elevate oxidative stress [45,8] The suppression of PARP1, a DNA repair enzyme [54], by methoxyphenols may exacerbate DNA damage and promote apoptosis [30].

GO analysis of 146 predicted targets revealed enrichment in pathways related to response to xenobiotic stimulus, regulation of tube size,

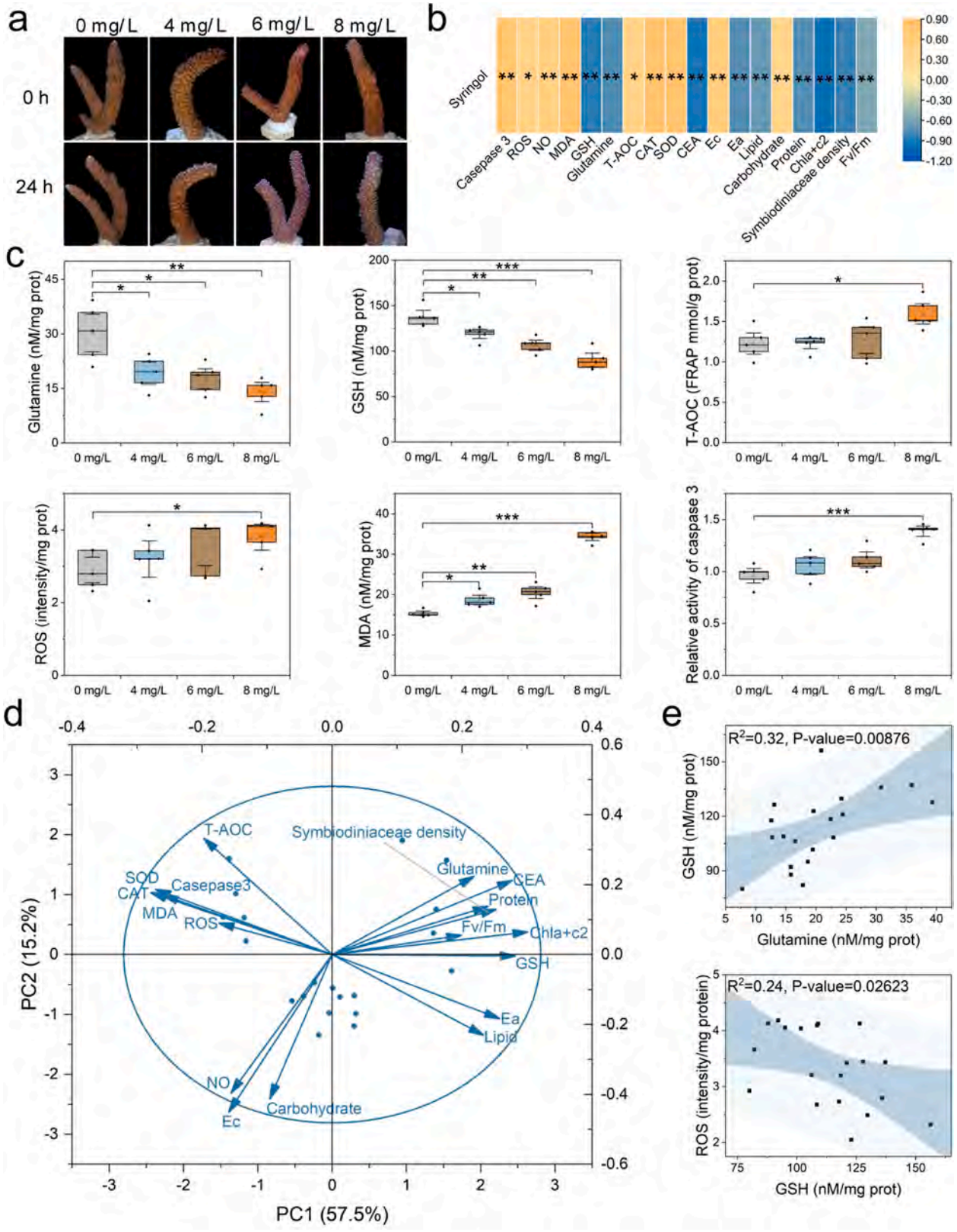


Fig. 7. Coral health status under syringol exposure. (a) Phenotypic changes in *A. formosa*. (b) Correlations between syringol concentration and physiological parameters. * $p < 0.05$, ** $p < 0.01$ and ***$p < 0.001$, as determined by Pearson correlation analysis. (c) Changes in the levels of glutamine, GSH, T-AOC, ROS, MDA, and caspase 3 activity. * $p < 0.05$, ** $p < 0.01$ and ***$p < 0.001$, as determined by Student's T-test. (d) Principal component analysis (PCA) of measured physiological parameters with 95 % confidence ellipse. (e) Regression analysis between glutamine and GSH, and between GSH and ROS with 95 % confidence intervals. The delicate blue shaded area is the confidence band, pale blue shaded area is the prediction band.

cell membrane components and oxidoreductase activity (Fig. 6c). KEGG pathway analysis identified the neuroactive ligand-receptor interaction and calcium signaling pathway as key enriched pathways (Fig. 6d). PPI network highlighted several hub genes based on the betweenness centrality metric, including PTGS2, CA1, CA9, EGFR, BACE1, GSK3B, NOS3, ANPEP, CTNNB1, FYN, and MME (Fig. 6e). Further modular clustering using MCODE identified two PPI submodules. Submodules 1 (score = 3.64) contains hub genes such as PTGS2, BACE1, ERBB2, CDK2, PARP1, BCHE, MAOA, MAOB, FYN, and ITGB1, which are mainly involved in oxidative stress response, energy metabolism, cell cycle regulation, DNA repair, and cell adhesion (Fig. 6f). Submodule 2 (score = 3.25) predominantly consists of seven CA isoforms (Fig. 6g), further emphasizing the potential for syringol metabolites to impair carbon transport and acid-base regulation, which are essential for coral calcification. In summary, syringol and its metabolites disrupt multiple key physiological processes in corals, particularly energy metabolism, redox homeostasis, signaling transduction pathways, and calcification.

3.4. Coral bleaching and physiological stress induced by syringol exposure

Exposure to syringol induced rapid tissue damage and visible bleaching in corals within 24 h (Fig. 7a), likely due to excessive oxidative stress. Significant positive correlations were observed between syringol levels and oxidative stress biomarkers, including ROS ($p < 0.05$) and nitric oxide (NO) ($p < 0.01$) (Fig. 7b and c; Figure S9). The concurrent increase in malondialdehyde (MDA) levels ($p < 0.01$) confirms enhanced lipid peroxidation. Caspase 3 activity also significantly increased ($p < 0.01$; Fig. 7b and c), suggesting activation of apoptotic pathways. Although antioxidant defenses were activated, as evidenced by the increased total antioxidant capacity (T-AOC) ($p < 0.05$), SOD ($p < 0.01$), and CAT ($p < 0.01$) (Fig. 7b and c; Figure S9), these responses were insufficient to restore redox balance under syringol exposure.

The failure to maintain redox homeostasis may be linked to energy metabolic disruption. Energy consumption (Ec) increased significantly with rising syringol levels ($p < 0.05$; Figure S10a), reflecting enhanced metabolic activity, likely associated with increased demands for antioxidant defenses and cellular repair [53]. Conversely, host energy available (Ea) declined significantly under increasing syringol exposure ($p < 0.05$; Figure S10b), indicating that energy demand exceeded supply. This energy deficit was compounded by the inhibition of photosynthetic energy input. Syringol exposure caused dose-dependent declines in maximum PSII quantum yield (Fv/Fm), symbiodiniaceae density, and chla+c2 content (Figure S10d, e and f). This photophysiological impairment may also result from the inhibition of CA, a key enzyme essential for photosynthetic function and calcification [13,9]. CA has been identified as a molecular target of MPs in other organisms [44,7] and is also may targeted by syringol and its metabolites in corals.

Healthy corals primarily depend on photosynthetic products to meet their energy demands [13], whereas bleached corals rely on catabolizing stored lipids, proteins and carbohydrates for survival and recovery [36]. Among these reserves, lipid content is widely recognized as a key indicator of coral stress resilience [4], as it supports metabolic activity, cell repair, and intracellular homeostasis [32]. However, exposure to increasing levels of syringol led to reductions in protein and lipid content (Figure S10g and h). PCA analysis identified lipid content as the primary factor influencing Ea (Fig. 7d). Consequently, the CEA ratio (Ea/Ec), a composite indicator of energy balance, decreased with syringol exposure, reflecting a shift toward energy deficiency (Figure S10c). Further PCA analysis illustrated 72.7 % variability of the factors influencing oxidative damage and energy metabolism (Fig. 7d). Specifically, glutamine had the primary impact on protein and GSH levels, while GSH was the primary regulator of ROS levels, which in turn affected MDA accumulation and caspase 3 activity. Linear regression analysis supported these associations, showing that glutamine accounted for 32 % of the variation in GSH levels (R^2=0.32; Fig. 7e), and GSH explained 24 % of the variation in ROS levels (R^2=0.24; Fig. 7e). These results suggest a close link between syringol metabolism and coral responses to oxidative and energy stress.

The depletion of glutamine and GSH with rising syringol concentrations (Fig. 7c) is likely driven by electrophilic conjugation between syringol (and its hydroxylated metabolites, such as B1 and 3-methoxycatechol) and intracellular nucleophiles, consistent with previously reported metabolic pathways [25,71,75]. As glutamine declines, corals appear to compensate by enhancing carbohydrate uptake and utilization (Fig. 7c; Figure S10i), presumably to maintain energy production. However, this compensatory mechanism may be insufficient, given that glutamine is crucial for mitochondrial function and ATP supply [66], while GSH plays a central role in ROS detoxification [73]. Additionally, syringol-derived hydroxylated metabolites (B1, B3 and C2), quinone metabolites (B2 and C1), and aldehyde metabolites (A3 and C4) may further contribute to ROS generation and DNA damage, consistent with similar findings in other biological systems [71]. Collectively, these findings suggest that syringol metabolism disrupts coral energy balance and induces rapid bleaching in branching *A. Formosa*, with no signs of recovery observed, by triggering oxidative stress and apoptotic pathways through depletion of glutamine and GSH. However, the resistance, tolerance and recovery of various coral species to syringol exposure remain largely unexplored, and further investigation into their resilience and adaptability under chronic, prolonged, or recurrent exposures across taxa is urgently needed.

Environmental implication

This study provides a comprehensive analysis of coral metabolic response to wildfire emissions, offering a detailed characterization of Phase I and Phase II metabolites of syringol, a marker compound indicative of forest fire exposure. Key metabolic transformations were identified, including methylation, acetylation, aromatic ring cleavage, and methylenedioxy bridge cyclization. Syringol is enzymatically converted into bioactive derivatives such as DBQH2 and 3-Methoxycatechol through host CYP3A21-like and CYP3A24-like enzymes. Coral-associated bacteria may facilitate atypical metabolic pathways that complicate detoxification processes. In particular, the genera *Acinetobacter, Acidovorax* and methylotrophs may serve as key taxa contributing to the aromatic degradation of syringol. The proliferation of intracellular parasites may exacerbate coral susceptibility to disease and bleaching. Further, the conjugation of syringol metabolites with intracellular amino acids and antioxidant molecules (e.g., GSH) intensifies oxidative stress and disrupts essential metabolic pathways in corals, ultimately leading to cellular dysfunction and apoptosis. Glutamine and GSH were identified as potential biomarkers for assessing coral health under syringol exposure. Importantly, many identified metabolites exhibit greater toxicity compared to the parent compound and demonstrate affinity for macromolecular targets involved in coral calcification and other critical physiological processes. These findings highlight serous ecological risks to the reef-building corals and the broader coral reef ecosystem. Overall, this study elucidates the biochemical mechanisms underlying coral biotransformation of methoxyphenols derived from wildfire emissions, providing essential information for understanding the detoxification capacity of corals to process environmental toxicants.

CRediT authorship contribution statement

Yuxiao Li: Methodology. **Zhiming Ning:** Methodology. **Zhenjun Qin:** Methodology. **Hongfei Su:** Methodology. **Kefu Yu:** Writing – review & editing, Resources, Funding acquisition. **Xiaoyan Chen:** Writing – review & editing, Methodology, Funding acquisition, Data curation, Conceptualization. **Zhaoqian Yan:** Methodology. **Zhenhua Chen:** Resources, Funding acquisition. **Yuhao Du:** Methodology. **Yanliu Wu:**

Writing – original draft, Methodology, Data curation, Conceptualization.

Declaration of Competing Interest

The authors declare that they have no known competing financial interests or personal relationships that could have appeared to influence the work reported in this paper.

Acknowledgements

This work was funded by the National Natural Science Foundation of China (No. 42090041), Guangxi Science and Technology Program (No. AD25069075), National Natural Science Foundation of China (No. 42076157 and 42030502). The authors wish to acknowledge Prof. Huiwang Gao for his constructive suggestions for the study on oceanic deposition of wildfire aerosols.

Appendix A. Supporting information

Supplementary data associated with this article can be found in the online version at doi:10.1016/j.jhazmat.2025.139433.

Data availability

Data will be made available on request.

References

[1] Abram, N.J., Gagan, M.K., McCulloch, M.T., Chappell, J., Hantoro, W.S., 2003. Coral reef death during the 1997 Indian Ocean dipole linked to Indonesian wildfires. Science 301, 952–955. https://doi.org/10.1126/science.1083841.
[2] Abramson, J., Adler, J., Dunger, J., Evans, R., Green, T., Pritzel, A., et al., 2024. Accurate structure prediction of biomolecular interactions with AlphaFold 3. Nature 630, 493–500. https://doi.org/10.1038/s41586-024-07487-w.
[3] Ailijiang, N., Chang, J., Liang, P., Zhang, X., Huang, X., 2021. Electrical stimulation on biodegradation of phenolics in a novel anaerobic–aerobic-coupled upflow bioelectrochemical reactor. Chem Eng J 421, 127840. https://doi.org/10.1016/j.cej.2020.127840.
[4] Anthony, K.R.N., 2006. Enhanced energy status of corals on coastal, high-turbidity reefs. Mar Ecol Prog Ser 0, 111–116. https://doi.org/10.3354/meps319111.
[5] Appeldoorn, M.M., Venema, D.P., Peters, T.H., Koenen, M.E., Arts, I.C., Vincken, J. P., et al., 2009. Some phenolic compounds increase the nitric oxide level in endothelial cells in vitro. J Agric Food Chem 57, 7693–7699. https://doi.org/10.1021/jf901381x.
[6] Ashrap, P., Zheng, G., Wan, Y., Li, T., Hu, W., Li, W., et al., 2017. Discovery of a widespread metabolic pathway within and among phenolic xenobiotics. Proc Natl Acad Sci 114, 6062–6067. https://doi.org/10.1073/pnas.1700558114.
[7] Babić, S., Čižmek, L., Maršavelski, A., Malev, O., Pflieger, M., Strunjak-Perović, I., et al., 2021. Utilization of the zebrafish model to unravel the harmful effects of biomass burning during amazonian wildfires, 2527-12 Sci Rep 11. https://doi.org/10.1038/s41598-021-81789-1.
[8] Bester, E., Petzer, A., Petzer, J.P., 2022. Coumarin derivatives as inhibitors of D-amino acid oxidase and monoamine oxidase. Bioorg Chem 123, 105791. https://doi.org/10.1016/j.bioorg.2022.105791.
[9] Chen, S., Gagnon, A.C., Adkins, J.F., 2018. Carbonic anhydrase, coral calcification and a new model of stable isotope vital effects. Geochim Et Cosmochim Acta 236, 179–197. https://doi.org/10.1016/j.gca.2018.02.032.
[10] Chu, Y., Zhang, C., Wang, R., Chen, X., Ren, N., Ho, S.H., 2022. Biotransformation of sulfamethoxazole by microalgae: removal efficiency, pathways, and mechanisms. Water Res 221, 118834. https://doi.org/10.1016/j.watres.2022.118834.
[11] Cleves, P.A., Tinoco, A.I., Bradford, J., Perrin, D., Bay, L.K., Pringle, J.R., 2020. Reduced thermal tolerance in a coral carrying CRISPR-induced mutations in the gene for a heat-shock transcription factor. Proc Natl Acad Sci USA 117, 28899–28905. https://doi.org/10.1073/pnas.1920779117.
[12] Daina, A., Michielin, O., Zoete, V., 2019. SwissTargetPrediction: updated data and new features for efficient prediction of protein targets of small molecules. Nucleic Acids Res 47, W357–W364. https://doi.org/10.1093/nar/gkz382.
[13] Davy, S.K., Allemand, D., Weis, V.M., 2012. Cell biology of cnidarian-dinoflagellate symbiosis. Microbiol Mol Biol Rev 76, 229–261. https://doi.org/10.1128/MMBR.05014-11.
[14] Dharamshi, J.E., Gaarslev, N., Steffen, K., Martin, T., Sipkema, D., Ettema, T., 2022. Genomic diversity and biosynthetic capabilities of sponge-associated chlamydiae. ISME J 16, 2725–2740. https://doi.org/10.1038/s41396-022-01305-9.
[15] Di Mauro, V., Kamyab, E., Kellermann, M.Y., Moeller, M., Nietzer, S., Luetjens, L. H., et al., 2023. Ecotoxicological effects of four commonly used organic solvents on the scleractinian coral *montipora digitata*. Toxics 11. https://doi.org/10.3390/toxics11040367.
[16] Dias, M., Ferreira, A., Gouveia, R., Madeira, C., Jogee, N., Cabral, H., et al., 2019. Long-term exposure to increasing temperatures on scleractinian coral fragments reveals oxidative stress. Mar Environ Res 150, 104758. https://doi.org/10.1016/j.marenvres.2019.104758.
[17] Doll, M.A., Zang, Y., Moeller, T., Hein, D.W., 2010. Codominant expression of N-acetylation and O-acetylation activities catalyzed by N-acetyltransferase 2 in human hepatocytes. J Pharm Exp Ther 334, 540–544. https://doi.org/10.1124/jpet.110.168567.
[18] Downs, C.A., Kramarsky-Winter, E., Woodley, C.M., Downs, A., Winters, G., Loya, Y., et al., 2009. Cellular pathology and histopathology of hypo-salinity exposure on the coral stylophora pistillata. Sci Total Environ 407, 4838–4851. https://doi.org/10.1016/j.scitotenv.2009.05.015.
[19] El-Haj, B.M., Ahmed, S., Garawi, M.A., Ali, H.S., 2018. Linking aromatic hydroxy metabolic functionalization of drug molecules to structure and pharmacologic activity. Molecules 23, 2119. https://doi.org/10.3390/molecules23092119.
[20] Feng, N., Yang, W., Zhao, X., Chen, M., Qiu, Y., Zheng, M., 2021. Semi-enclosed bays serve as hotspots for black carbon burial: a case study in jiaozhou bay, Western yellow sea. Sci Total Environ 797, 149100. https://doi.org/10.1016/j.scitotenv.2021.149100.
[21] Fu, Q., Fedrizzi, D., Kosfeld, V., Schlechtriem, C., Ganz, V., Derrer, S., et al., 2020. Biotransformation changes bioaccumulation and toxicity of diclofenac in aquatic organisms. Environ Sci Technol 54, 4400–4408. https://doi.org/10.1021/acs.est.9b07127.
[22] Fuchs, G., Boll, M., Heider, J., 2011. Microbial degradation of aromatic compounds - from one strategy to four. Nat Rev Microbiol 9, 803–816. https://doi.org/10.1038/nrmicro2652.
[23] Fujii, Y., Iriana, W., Oda, M., Puriwigati, A., Tohno, S., Lestari, P., et al., 2014. Characteristics of carbonaceous aerosols emitted from peatland fire in riau, sumatra, Indonesia. Atmos Environ 87, 164–169. https://doi.org/10.1016/j.atmosenv.2014.01.037.
[24] Furukawa, S., Fujita, M., Kanatomi, Y., Minoura, M., Hatanaka, M., Morokuma, K., et al., 2018. Double aromaticity arising from σ- and π-rings. Commun Chem 1. https://doi.org/10.1038/s42004-018-0057-4.
[25] Gao, X., Hu, Z., Wang, Y., Zhao, G., Shen, Y., Zhou, H., et al., 2024. Metabolic activation and cytotoxicity of gramine mediated by CYP3A in rats. J Agric Food Chem 72, 10897–10908. https://doi.org/10.1021/acs.jafc.4c00400.
[26] Georgiou-Siafis, S.K., Tsiftsoglou, A.S., 2023. The key role of GSH in keeping the redox balance in mammalian cells: mechanisms and significance of GSH in detoxification via formation of conjugates. Antioxid (Basel) 12, 1953. https://doi.org/10.3390/antiox12111953.
[27] Guan, Y., Hohn, S., Wild, C., Merico, A., 2020. Vulnerability of global coral reef habitat suitability to ocean warming, acidification and eutrophication. Glob Chang Biol 26, 5646–5660. https://doi.org/10.1111/gcb.15293.
[28] Gutierrez, A.A., Hantson, S., Langenbrunner, B., Chen, B., Jin, Y., Goulden, M.L., et al., 2021. Wildfire response to changing daily temperature extremes in california's Sierra Nevada. Sci Adv 7, eabe6417. https://doi.org/10.1126/sciadv.abe6417.
[29] Heindel, J.J., Blumberg, B., Cave, M., Machtinger, R., Mantovani, A., Mendez, M. A., et al., 2017. Metabolism disrupting chemicals and metabolic disorders. Reprod Toxicol 68, 3–33. https://doi.org/10.1016/j.reprotox.2016.10.001.
[30] Jaganathan, S.K., Supriyanto, E., 2012. Antiproliferative and molecular mechanism of eugenol-induced apoptosis in cancer cells. Molecules 17, 6290–6304. https://doi.org/10.3390/molecules17066290.
[31] Knights, Kathleen M., J.O.M, 2012. Amino acid conjugation: a novel route of xenobiotic carboxylic acid metabolism in man. Encycl Drug Metab Interact 0, 1–16. https://doi.org/10.1002/9780470921920.edm020.
[32] Keister, E.F., Gantt, S.E., Reich, H.G., Turnham, K.E., Bateman, T.G., LaJeunesse, T. C., et al., 2023. Similarities in biomass and energy reserves among coral colonies from contrasting reef environments. Sci Rep 13, 1355. https://doi.org/10.1038/s41598-023-28289-6.
[33] Kelm, M.A., Nair, M.G., Strasburg, G.M., DeWitt, D.L., 2000. Antioxidant and cyclooxygenase inhibitory phenolic compounds from *Ocimum sanctum* linn. Phytomedicine 7, 7–13. https://doi.org/10.1016/S0944-7113(00)80015-X.
[34] Kloss, C., Berthet, G., Sellitto, P., Ploeger, F., Bucci, S., Khaykin, S., et al., 2019. Transport of the 2017 Canadian wildfire plume to the tropics via the asian monsoon circulation. Atmos Chem Phys 19, 13547–13567. https://doi.org/10.5194/acp-19-13547-2019.
[35] Kowatschew, D., Korsching, S.I., 2021. An ancient adenosine receptor gains olfactory function in bony vertebrates. Genome Biol Evol 13. https://doi.org/10.1093/gbe/evab211.
[36] Lesser, M.P., 2013. Using energetic budgets to assess the effects of environmental stress on corals: are we measuring the right things? Coral reefs 32, 25–33. https://doi.org/10.1007/s00338-012-0993-x.
[37] Lichtarge, O., Bourne, H.R., Cohen, F.E., 1996. An evolutionary trace method defines binding surfaces common to protein families. J Mol Biol 257, 342–358. https://doi.org/10.1006/jmbi.1996.0167.
[38] Liu, C., Zhao, D., Ma, W., Guo, Y., Wang, A., Wang, Q., et al., 2016. Denitrifying sulfide removal process on high-salinity wastewaters in the presence of *halomonas* sp. Appl Microbiol Biotechnol 100, 1421–1426. https://doi.org/10.1007/s00253-015-7039-6.
[39] Liu, K., Qin, B., Hao, R., Chen, X., Zhou, Y., Zhang, W., et al., 2024. Genetic analyses reveal wildfire particulates as environmental pollutants rather than

nutrient sources for corals. J Hazard Mater 485, 136840. https://doi.org/10.1016/j.jhazmat.2024.136840.
[40] Liu, L., Cui, H., Huang, Y., Zhou, Y., Hu, J., Wan, Y., 2022. Enzyme-mediated reactions of phenolic pollutants and endogenous metabolites as an overlooked metabolic disruption pathway. Environ Sci Technol 56, 3634–3644. https://doi.org/10.1021/acs.est.1c08141.
[41] Liu, X., Jiao, X., Cheng, Y., Ma, Y., Bu, J., Jin, B., et al., 2023. Structure-function analysis of CYP719As involved in methylenedioxy bridge-formation in the biosynthesis of benzylisoquinoline alkaloids and its de novo production. Micro Cell Fact 22, 23. https://doi.org/10.1186/s12934-023-02024-2.
[42] Maire, J., Collingro, A., Tandon, K., Jameson, V.J., Judd, L.M., Horn, M., et al., 2024. Chlamydiae as symbionts of photosynthetic dinoflagellates. ISME J 18. https://doi.org/10.1093/ismejo/wrae139.
[43] Montgomery, A., Zhuang, G.C., Zhou, Z., Langwig, M.V., Millan-Motolinia, M., Choi, H., , 2025. Elevated Heterotrophic Activity in Guaymas Basin Hydrothermal Plumes Influences Deep-sea Carbon Cycling.
[44] Nair, S.K., Ludwig, P.A., Christianson, D.W., 1994. Two-site binding of phenol in the active site of human carbonic anhydrase II: structural implications for substrate association. J Am Chem Soc 116, 3659–3660. https://doi.org/10.1021/ja00087a086.
[45] Olennikov, D.N., Kashchenko, N.I., 2024. New acacetin glycosides and other phenolics from *agastache foeniculum* and their influence on monoamine oxidase a and b. Appl Biochem Microbiol 60, 663–675. https://doi.org/10.1134/S0003683824604402.
[46] Peng, H., Shahidi, F., 2024. Metabolic, toxicological, chemical, and commercial perspectives on esterification of dietary polyphenols: a review. Crit Rev Food Sci Nutr 64, 7465–7504. https://doi.org/10.1080/10408398.2023.2185589.
[47] Peng, R., Chen, X., Wu, Q., Yan, Z., Fu, Y., Qin, B., et al., 2024. Wildfire particulates enhance phytoplankton growth and alter communities in the South China Sea under wind-driven upwelling. J Geophys Res Biogeosciences 129, e2024JG008066. https://doi.org/10.1029/2024JG008066.
[48] Plaisance, L., Caley, M.J., Brainard, R.E., Knowlton, N., 2011. The Diversity of Coral Reefs: What Are We Missing?.
[49] Priya, P.S., Guru, A., Meenatchi, R., Haridevamuthu, B., Velayutham, M., Seenivasan, B., et al., 2023. Syringol, a wildfire residual methoxyphenol causes cytotoxicity and teratogenicity in zebrafish model. Sci Total Environ 864, 160968. https://doi.org/10.1016/j.scitotenv.2022.160968.
[50] Qi, X., Qin, J.Y., Ru, S., Xiong, J.Q., 2024. Functional characterization of a novel chlamydomonas reinhardtii hydrolase involved in biotransformation of chloramphenicol. Water Res 265, 122285. https://doi.org/10.1016/j.watres.2024.122285.
[51] Qin, B., Yu, K., Fu, Y., Zhou, Y., Wu, Y., Zhang, W., et al., 2024. Responses in reef-building corals to wildfire emissions: heterotrophic plasticity and calcification. Sci Total Environ 922, 171271. https://doi.org/10.1016/j.scitotenv.2024.171271.
[52] Robinson, M.S., Zhao, M., Zack, L., Brindley, C., Portz, L., Quarterman, M., et al., 2011. Characterization of $PM_{2.5}$ collected during broadcast and slash-pile prescribed burns of predominately ponderosa pine forests in Northern arizona. Atmos Environ 45, 2087–2094. https://doi.org/10.1016/j.atmosenv.2011.01.051.
[53] Rodrigues, L.J., Grottoli, A.G., 2007. Energy reserves and metabolism as indicators of coral recovery from bleaching. Limnol Oceanogr 52, 1874–1882. https://doi.org/10.4319/lo.2007.52.5.1874.
[54] Satoh, M.S., Lindahl, T., 1992. Role of Poly(ADP-ribose) formation in DNA repair. Nature 356, 356–358. https://doi.org/10.1038/356356a0.
[55] Schauer, J.J., Kleeman, M.J., Cass, G.R., Simoneit, B.R., 2001. Measurement of emissions from air pollution sources. 3. C1-C29 organic compounds from fireplace combustion of wood. Environ Sci Technol 35, 1716–1728. https://doi.org/10.1021/es001331e.
[56] Sheesley, R.J., Schauer, J.J., Chowdhury, Z., Cass, G.R., Simoneit, B.R.T., 2003. Characterization of organic aerosols emitted from the combustion of biomass indigenous to south Asia. J Geophys Res D Atmospheres 108. AAC8.1-n/a.
[57] Simpson, C.D., Paulsen, M., Dills, R.L., Liu, L.J., Kalman, D.A., 2005. Determination of methoxyphenols in ambient atmospheric particulate matter: tracers for wood combustion. Environ Sci Technol 39, 631–637. https://doi.org/10.1021/es0486871.
[58] Snelgrove, R.J., 2011. Leukotriene A4 hydrolase: an anti-inflammatory role for a proinflammatory enzyme. Thorax 66, 550–551. https://doi.org/10.1136/thoraxjnl-2011-200234.
[59] Sun, G., Hu, C., Mei, Q., Luo, M., Chen, X., Li, Z., et al., 2020. Uncovering the cytochrome P450-catalyzed methylenedioxy bridge formation in streptovaricins biosynthesis. Nat Commun 11, 4501–4512. https://doi.org/10.1038/s41467-020-18336-5.
[60] Suriguga, Li, X., Li, Y., Yu, C., Li, Y., Yi, Z., 2013. The role of catechol-O-methyltransferase in catechol-enhanced erythroid differentiation of K562 cells. Toxicol Appl Pharmacol 273, 635–643. https://doi.org/10.1016/j.taap.2013.10.009.
[61] Sykes, M.J., McKinnon, R.A., Miners, J.O., 2008. Prediction of metabolism by cytochrome P450 2C9: alignment and docking studies of a validated database of substrates. J Med Chem 51, 780–791. https://doi.org/10.1021/jm7009793.
[62] Talma, M., Mucha, A., 2020. P1′ residue-oriented virtual screening for potent and selective phosphinic (dehydro) dipeptide inhibitors of metallo-aminopeptidases. Biomolecules 10, 659. https://doi.org/10.3390/biom10040659.
[63] Tang, W., Llort, J., Weis, J., Perron, M., Basart, S., Li, Z., et al., 2021. Widespread phytoplankton blooms triggered by 2019-2020 Australian wildfires. Nature 597, 370–375. https://doi.org/10.1038/s41586-021-03805-8.
[64] Tang, Y., Zhang, Y., Chen, J., Zhao, C., Fan, J., Shao, J., 2023. Two new phenolic compounds from polygonatum cyrtonema flowers and their aldose reductase inhibitory activities. Chem Nat Compd 59, 56–58. https://doi.org/10.1007/s10600-023-03916-w.
[65] Thammatorn, W., Kouba, A., Novakova, P., Zlabek, V., Koubova, A., 2024. Effects of diphenhydramine on crayfish cytochrome P450 activity and antioxidant defence mechanisms: first evidence of CYP2C- and CYP3A-like activity in marbled crayfish. Ecotoxicol Environ Saf 285, 117035. https://doi.org/10.1016/j.ecoenv.2024.117035.
[66] Tohyama, S., Fujita, J., Hishiki, T., Matsuura, T., Hattori, F., Ohno, R., et al., 2016. Glutamine oxidation is indispensable for survival of human pluripotent stem cells. Cell Metab 23, 663–674. https://doi.org/10.1016/j.cmet.2016.03.001.
[67] Tollefson, J., 2023. Maui fires could taint the island's waters - scientists are investigating. Nature 621, 16–17. https://doi.org/10.1038/d41586-023-02707-1.
[68] Villela, H., Modolon, F., Schultz, J., Delgadillo-Ordonez, N., Carvalho, S., Soriano, A.U., et al., 2023. Genome analysis of a coral-associated bacterial consortium highlights complementary hydrocarbon degradation ability and other beneficial mechanisms for the host. Sci Rep 13, 12273. https://doi.org/10.1038/s41598-023-38512-z.
[69] Vuckovic, D., Tinoco, A.I., Ling, L., Renicke, C., Pringle, J.R., Mitch, W.A., 2022. Conversion of oxybenzone sunscreen to phototoxic glucoside conjugates by sea anemones and corals. Science 376, 644–648. https://doi.org/10.1126/science.abn2600.
[70] Xiang, M., Xiao, C., Feng, Z., Ma, Q., 2023. Global distribution, trends and types of active fire occurrences. Sci Total Environ 902, 166456. https://doi.org/10.1016/j.scitotenv.2023.166456.
[71] Xu, X., Liu, A., Hu, S., Ares, I., Martinez-Larranaga, M.R., Wang, X., et al., 2021. Synthetic phenolic antioxidants: metabolism, hazards and mechanism of action. Food Chem 353, 129488. https://doi.org/10.1016/j.foodchem.2021.129488.
[72] Zamuner, S.R., Warrier, N., Buret, A.G., MacNaughton, W.K., Wallace, J.L., 2003. Cyclooxygenase 2 mediates post-inflammatory colonic secretory and barrier dysfunction. Gut 52, 1714–1720. https://doi.org/10.1136/gut.52.12.1714.
[73] Zhang, H., Forman, H.J., 2012. Glutathione synthesis and its role in redox signaling. Semin Cell Dev Biol 23, 722–728. https://doi.org/10.1016/j.semcdb.2012.03.017.
[74] Zhang, K.R., Zhang, Y.F., Lei, H.M., Tang, Y.B., Ma, C.S., Lv, Q.M., et al., 2021. Targeting AKR1B1 inhibits glutathione de novo synthesis to overcome acquired resistance to EGFR-targeted therapy in lung cancer. eabg6428-eabg6428 Sci Transl Med 13. https://doi.org/10.1126/scitranslmed.abg6428.
[75] Zhao, Q., Hu, Z., Wang, A., Ding, Z., Zhao, G., Wang, X., et al., 2024. Correlation of vanillin-induced cytotoxicity with CYP3A-mediated metabolic activation. J Agric Food Chem 72, 20064–20076. https://doi.org/10.1021/acs.jafc.4c03060.

引 用 格 式:CHEN Zhenghua,LAN Sixiang,ZHANG Jinshui,*et al*.Reviews of remote sensing monitoring of urban black and odorous water[J].Remote Sensing Technology and Application,2025,40(4):909-922.[陈正华,兰思香,张锦水,等.城市黑臭水体遥感监测的研究现状与展望[J].遥感技术与应用,2025,40(4):909-922.]
DOI:10.11873/j.issn.1004-0323.2025.4.0909

城市黑臭水体遥感监测的研究现状与展望

陈正华[1],兰思香[1],张锦水[2],张 威[1],李华德[1],赵丽芳[3]
(1.广西大学 海洋学院,广西 南宁 530004;
2.北京师范大学 遥感科学国家重点实验室,北京 100875;
3.中国科学院空天信息创新研究院,北京 100094)

摘要:黑臭水体是一种极端的水污染现象,是许多城市普遍存在的问题,严重影响人居生活的幸福感、获得感。因此,解决城市黑臭水体问题迫在眉睫。科学监测水体黑臭情况是城市黑臭水体整治工作的第一步,为后续治理评估提供准确的整治对象。相对于传统的地面监测手段,遥感是一种更有效发现黑臭水体的方式,能更大范围、更快速连续地识别出水体黑臭区域并及时全面地展示黑臭水体时空演变过程。系统回顾了城市黑臭水体遥感监测的主要研究进展,首先,简要介绍了黑臭水体概况,总结了城市黑臭水体的遥感特征以及常用数据源。其次,详细探讨了城市黑臭水体遥感识别和分级的方法,并对比分析了各方法的适用性和优缺点。最后,总结了当前城市黑臭水体遥感研究现状以及不足之处,并展望了未来的发展方向。旨在为相关研究提供借鉴与思考,为黑臭水体长效治理提供更好的决策支持。

关 键 词:黑臭水体;遥感监测;识别分级;遥感特征;数据源
中图分类号:X832;TP79 **文献标志码**:A **文章编号**:1004-0323(2025)04-0909-14

1 引 言

黑臭水体整治是水污染防治的重要方向,《水污染防治行动计划》明确提出“到2030年,城市建成区黑臭水体总体得到消除”的工作目标[1]。为了实现这个目标,全国各个城市纷纷开展了黑臭水体整治环境保护专项行动。黑臭水体可以按监管区域类型分为城市黑臭水体和农村黑臭水体。城市黑臭水体的概念是在2015年9月住房城乡建设部颁布的《城市黑臭水体整治工作指南》(以下简称《指南》)中首次明确提出:它是指城市建成区内,呈现令人不悦的颜色和(或)散发令人不适气味的水体。这是从地理空间范围、颜色和气味三方面定性给出的定义,《指南》还从透明度(SD)、溶解氧(DO, Dissolved Oxygen)、氧化还原电位(ORP, Oxidation-reduction Potential)和氨氮(NH_3-N)4项水质指标上定量将黑臭水体细分为“轻度黑臭”和“重度黑臭”两个级别,具体如表1所示[2]。在城市黑臭水体概念提出之前,早期比较类似的研究主要是针对近岸海洋、内陆湖泊、河口中的“黑水团”或“湖泛”现象的遥感监测[3-6]。在此之前,我国对黑臭水体的监管与研究几乎处于空白状态,很多黑臭水体无历史监

表1 黑臭水体污染程度分级标准[2]

Table 1 Black and odorous water pollution degree classification standard

特征指标(单位)	轻度黑臭	重度黑臭
透明度/cm	25~10*	<10*
溶解氧/(mg/L)	0.2~2.0	<0.2
氧化还原电位/mV	-200~50	<-200
氨氮/(mg/L)	8.0~15	>15

收稿日期:2024-11-16;**修订日期**:2025-03-28
基金项目:国家重点研发计划(2021YFB3900505)资助。
作者简介:陈正华,副教授,主要从事环境遥感与海洋遥感研究。E-mail: chen.zhenghua@163.com

测资料。自此之后，研究界开始广泛关注黑臭水体，并对黑臭水体和“黑水团”进行区分，国内学者开始在各城市展开黑臭水体的实地调查，系统性研究黑臭水体的形成机理[7-8]、光学特性[9-11]、遥感识别算法[12-17]、遥感分级模型[18-19]等内容。随着城市黑臭水体的整治不断取得成效，生态环境部于2019年开始进一步推动农村黑臭水体治理工作，并在《农村黑臭水体治理工作指南(试行)》中定义了农村黑臭水体的概念。由于农村黑臭水体遥感监测刚刚起步[20-21]，已有研究多是以城市黑臭水体为对象来开展，因此本文主要是综述城市黑臭水体遥感监测相关研究。

黑臭水体成因复杂、影响因素众多，大多为细小沟渠，面积小且分布散的特点使其监测较为困难。传统的黑臭水体监测方式主要通过现场调查或问卷调查，识别定级方式通常是采取现场原位测定水质或实验室分析水样，传统方法的局限性和工作量大，往往需要耗费大量的人力、物力、财力和时间，还极易受到气候和水文条件的限制，且只能以点代面对部分河段的水质参数进行监测。遥感技术作为地面监测手段的重要补充，具有低成本、高效率、大范围、多时相、长时序、大面积同步观测的优点。因此，遥感技术在黑臭水体监测研究中极具优势，可以从宏观层面客观把握黑臭水体空间分布、污染状况、治理成效等，有利于快速全面地掌握黑臭水体时空演变过程、揭示污染源的迁移规律[22-23]。

目前，关于城市黑臭水体遥感监测的系统性综述还不够全面，已有综述只是单一总结了城市黑臭水体遥感监测急需解决的问题、关键技术或识别算法，而缺少对遥感特征、适用数据源的归纳分析，以及缺少对不同识别分级模型的优缺点和适用性的对比总结。因此，本研究在IEEE Xplore、Science Direct、Google Scholar、Web of Science、中国知网等数据库中，使用“黑臭水体”“遥感”“black and odorous water”“remote sensing”等关键词筛选了2017年以来的多篇文章形成本综述。从城市黑臭水体概念被提出后，各年文章发表情况总体呈增加趋势(图1)，研究的关键词主要为“黑臭水体”、“遥感识别”和“高分二号”等(图2)。

2 城市黑臭水体遥感特征

城市黑臭水体可以通过水体颜色、次生环境、

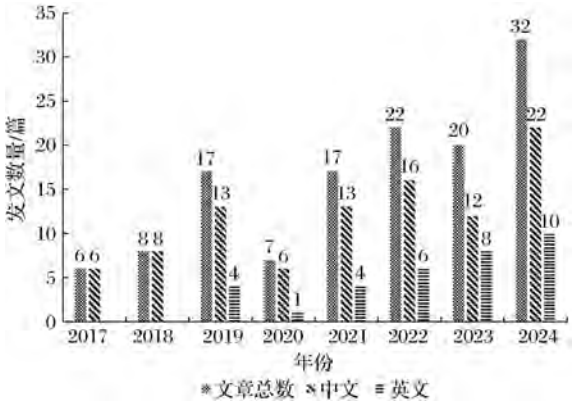


图1 相关研究文章发表情况

Fig.1 Publication of relevant research articles

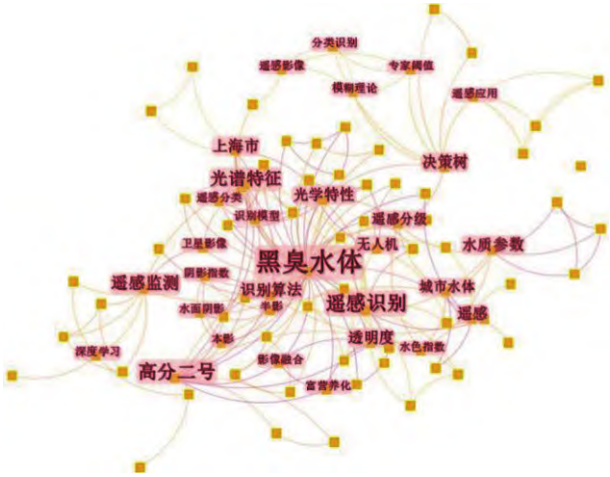


图2 主要关键词共现图

Fig.2 Main keyword co-occurrence map

河道淤塞、岸边垃圾堆放等解译标志结合光谱指数来共同识别[24]。其中，城市黑臭水体的水体颜色和遥感光谱是遥感解译黑臭水体的主要特征标志[12]。

2.1 颜色特征

水体颜色是最直观最有效的水体特征[25]，可通过目视初步解译。在真彩色影像中，正常水体多呈绿色、深绿色，而黑臭水体则呈黑色、灰黑色、灰绿色、褐色。图3为2016年10月和2020年4月南宁市水塘江与邕江交汇处的GF-2号影像，目视可清晰看出图3(a)中2016年水塘江水体颜色为浑浊暗淡的灰黑色，而邕江水体为绿色。经修整河道综合治理后，2020年水塘江水体有所改善呈淡绿色。水体色调差异可辅助在影像上定性识别出疑似黑臭水体，通过观察真彩色影像可以人工目视解译出颜色明显异常的黑臭水体[25]。

2.2 光谱特征

与颜色特征不同，水体的光学特性可以定量地表达和测算，包括表观光学特性和固有光学特性，



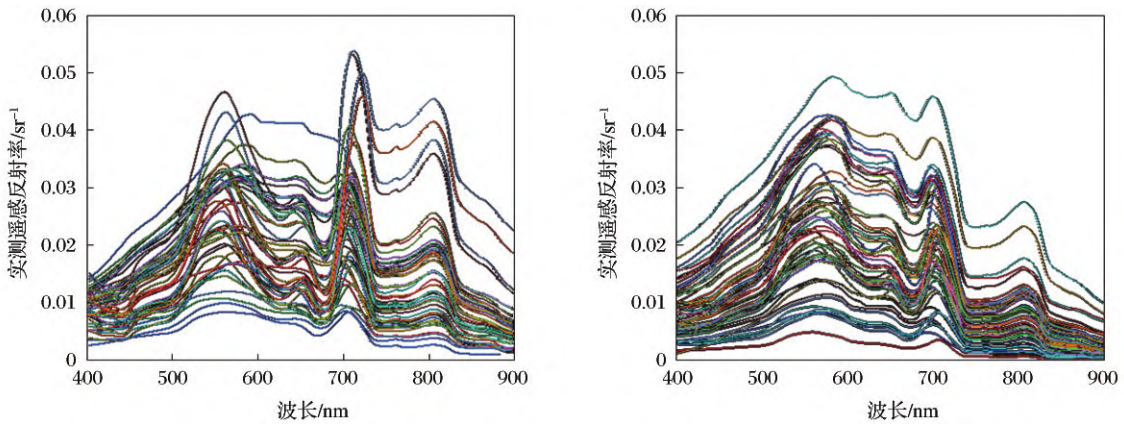
(a) 2016年黑臭水体　　(b) 2020年正常水体

图 3　GF-2影像的颜色特征

Fig.3　Color characteristics of GF-2 images of black and odorous water in 2016 and normal water in 2020

两种光学特性是光学遥感反演水质参数的研究基础[26],不同水体因其物质组分浓度的变化而呈现不同的光谱特征。水体固有光学量(包括吸收系数和后向散射系数)需要通过实验室分析获得,其特性不随入射光场的分布与强度的变化而变化[26-27]。水体表观光学量(包括遥感反射率)可以通过现场测量或者遥感手段获得,其特性随着外界光场的变化而变化[28-29]。固有光学量与叶绿素a(Chl-a)、总悬浮物(TSM, Total Suspended Matter)和有色可溶性有机物(CDOM, Chromophoric Dissolved Organic Matter)等水质参数存在半解析关系,而表观光学量与水质参数之间存在经验或半经验关系,因而固有光学量在表观光学量与水质参数之间起到关键变量作用[27-30]。城市黑臭水体的总颗粒物吸收系数、非色素颗粒物吸收系数和CDOM吸收系数总体上都高于正常水体[9,31]。例如,在特征波长440 nm处,黑臭水体的CDOM吸收系数的平均值比正常水体的高出1.7倍左右[9]。在一定条件下,可用以上几项水体指标来区分黑臭水体和正常水体,指标浓度高出特征值的被认为是黑臭水体。但该结论具有局限性,有研究发现有些叶绿素a浓度较低,但是水体悬浮泥沙含量很高的河段并不属于黑臭水体[32-33]。因此,针对在近红外波段同样具有高反射率但不属于黑臭水体的浑浊水体,这些指标能否正确反映黑臭水体特征有待商榷。

城市黑臭水体遥感识别可以通过分析黑臭水体与正常水体的实测遥感反射率或卫星遥感反射率的差异来构建模型,如图4为黑臭水体与正常水体的实测遥感反射率,将其经过归一化处理和波段拟合后可转换为等效的卫星遥感反射率[34-35],如图5所示。由卫星遥感反射率可知,大部分黑臭水体在蓝光波段到红光波段范围内的遥感反射率比正常水体更为平缓,在蓝光波段范围的黑臭水体反射率一般略低于正常水体,在绿光波段550 nm处正常水体反射率略高于大部分黑臭水体,且反射峰比黑臭水体的明显;红光波段和近红外波段范围的黑臭水



(a) 黑臭水体　　(b) 正常水体

图 4　实测遥感反射率[35]

Fig.4　Remote sensing reflectance of black and odorous water and normal water[35]

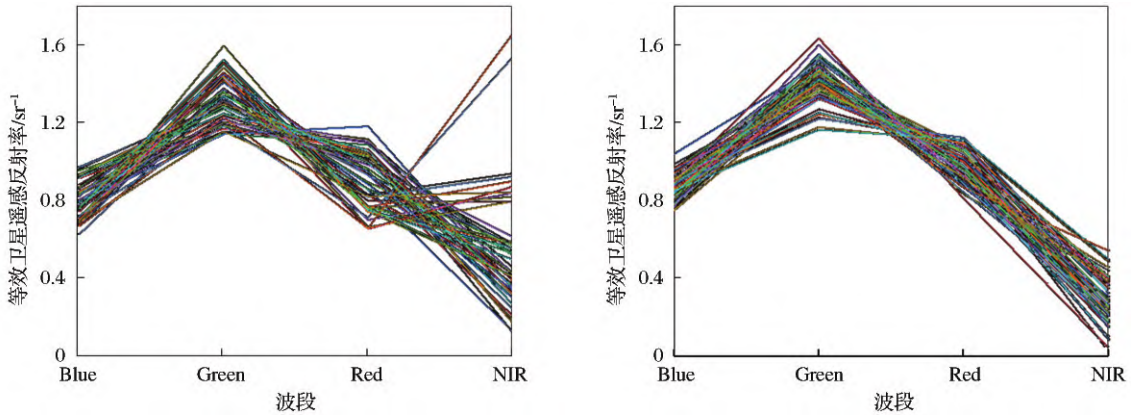


图 5 等效卫星遥感反射率[35]

Fig.5 Equivalent satellite remote sensing reflectance of black and odorous water and normal water[35]

体的反射率上升且明显高于正常水体。总体来看，不论是实测遥感反射率还是卫星遥感反射率，黑臭水体在可见光波段范围内的光谱曲线与正常水体均存在一定的差异，根据上述这些光谱特征可以有效识别出城市黑臭水体。但是由于影响黑臭水体光谱特征变化的总颗粒物、非色素颗粒物和CDOM浓度的不同，不同类别的黑臭水体呈现出的光谱特征也会有所差异，在进行黑臭水体遥感精细化监测时，不能将所有黑臭水体一概而论，需要进一步分类研究以及注意区分高浑浊水体。

3 城市黑臭水体遥感识别常用的数据源

高空间分辨率影像是研究黑臭水体最重要的数据源，为城市黑臭水体遥感监测提供了重要的数据支撑。国产GF系列和其他小型低轨卫星（如高景一号、吉林一号等）的快速发展为使用高分辨率影像监测黑臭水体提供了可能[36]。目前，城市黑臭水体遥感识别分级使用的数据源主要有GF-PMS系列、Planet Scope等，各卫星参数详见表2。其中，使用频率最高的是国产GF-2数据，其亚米级的空间分辨率能够更精细识别城市黑臭水体。Wei等[37-38]的研究证明了利用GF系列影像监测城市黑臭水体非常有效。王茹等[39]的研究中，基于GeoEye-1、WorldView-2、SuperView-1、GF-1、GF-2、GF-6、BJ-2（DMC3）影像识别黑臭水体的正确率均在89.5%以上，证明了多源高分辨率影像监测黑臭水

表 2 多源卫星影像参数对比表

Table 2 Multi-source satellite image parameter comparison table

序号	卫星类型	分辨率/m		幅宽	重访周	识别像元	光谱范围/μm					参考文献
		全色	多光谱	/km	期/天	尺度/个	蓝波段	绿波段	红波段	近红外	全色	
1	GF-2 PMS	1	4	45	5	≥5	0.45～0.52	0.52～0.59	0.63～0.69	0.77～0.89	0.45～0.9	[13,15,19,32,43-44]
2	GF-1 PMS	2	8	60	4	≥5	0.45～0.52	0.52～0.59	0.63～0.69	0.77～0.89	0.45～0.9	[12,45-46]
3	GF-6 PMS	2	8	≥90	4	≥5	0.45～0.52	0.52～0.6	0.63～0.69	0.76～0.89	0.45～0.9	[37,47-48]
4	BJ-2 DMC3	0.8	3.2	24	1	≥5	0.44～0.51	0.51～0.59	0.6～0.67	0.79～0.91	0.45～0.65	[39,49]
5	ZY-3	2.1	5.8	50	5	≥5	0.45～0.52	0.52～0.59	0.63～0.69	0.77～0.89	0.45～0.8	[49]
6	SuperView-1	0.2	2	12	2	≥5	0.45～0.52	0.52～0.59	0.63～0.69	0.77～0.89	0.45～0.89	[39,49]
7	GeoEye-1	0.41	1.65	15.2	≤3	≥5	0.45～0.51	0.51～0.58	0.655～0.69	0.78～0.92	0.45～0.8	[39]
8	WorldView-2	0.46	1.8	16.4	1.1	≥5	0.45～0.51	0.51～0.58	0.63～0.69	0.77～0.895	0.45～1.04	[39]
9	Planet Scope	/	3	24×16	1～2	≥5	0.455～0.515	0.5～0.59	0.59～0.67	0.78～0.86	/	[14,18]
10	Sentinel-2	/	10	290	5	≥5	0.458～0.523	0.543～0.578	0.65～0.68	0.785～0.90	/	[50-51]
11	Landsat-8	15	30	185	16	≥5	0.45～0.515	0.525～0.6	0.63～0.68	0.845～0.885	0.5～0.68	[52]

注：识别像元尺度是指不同数据源可识别黑臭水体的宽度范围。WorldView－2、Sentinel－2、Landsat－8只列出了可见光蓝绿红和近红外波段，完整波段请查询官网。WorldView－2（https://resources.maxar.com/data－sheets/worldview－2/）；Sentinel－2（https://scihub.copernicus.eu/）；Landsat－8（https://earthexplorer.usgs.gov/）

体有较好的适用性。随着无人机技术的发展,利用无人机影像来分析城市黑臭水体的研究逐渐增多,无人机影像也成为研究黑臭水体的重要数据源。买日阿巴等[40-42]通过无人机搭载多光谱或高光谱传感器获取高分辨率影像来识别城市黑臭水体,实现了无人机对城市黑臭水体的实时监管。

无论是来自卫星平台还是无人机载的影像,在城市黑臭水体遥感监测应用方面都取得了较好效果。目前,城市黑臭水体监测应用的影像多为光学多光谱或高光谱影像,极少应用雷达影像识别城市黑臭水体的研究,这与黑臭水体细小、纹理特征不明显,以及雷达影像分辨率不高、不能穿透水面,一般是获取水表粗糙度信息的特点相关。

4　城市黑臭水体遥感识别方法

目前,基于遥感的城市黑臭水体研究主要是利用城市黑臭水体的光谱特性和图像特征,大多研究集中于400~700 nm 的可见光波段。经总结分析,可以归纳为光谱指数法、水体色度法、水质参数法3种典型方法以及决策树、深度学习等综合方法。

4.1　基于特征波段的光谱指数法

基于特征波段的光谱指数法是利用城市黑臭水体不同组分的吸收特性或水体表观反射率的差异构建识别模型,即将黑臭水体和正常水体的反射率最强波段和最弱波段根据光谱值的特征规律进行线性组合,增强两者之间的区分度,在影像上使两者的亮度值有明显区别[45]。基于特征波段的光谱指数法是目前最常用的城市黑臭水体遥感识别方法,不少研究者提出了不同的算法模型。如温爽等[13]基于GF-2号影像构建的绿波段单波段阈值法、蓝绿波段差值指数DBWI(Difference Black-odorous Water Index)以及红绿波段比值的归一化黑臭水体指数NDBWI(Normalized Difference Black-odorous Water Index)有效识别了南京市主城区黑臭水体的空间分布,其中DBWI和NDBWI受到更多研究者的认可。经对比不同的算法模型,Yu等[53-54]认为NDBWI识别正确率更高更稳定,而胡国庆等[43,46]的研究则发现DBWI对深圳、芜湖的黑臭水体识别精度最高。在NDBWI的基础上,姚月等[15]引入了蓝波段的反射率构建BOI(Black and Odorous water Index)来识别沈阳市黑臭水体,同样取得较好的识别效果。韩文聪等[32]的研究也证明了BOI、NDBWI两种算法的识别结果均可靠。除了上述模型之外,纪纲[45]提出的HCI1和HCI2模型对城市黑臭水体的分类精度均达90%以上,黄祺宇等[48]经对比多种识别算法也发现HCI1在杭州市的适用性最好。姚焕玫等[14]基于Planet Scope影像提出的近红外单波段阈值法、HI、EHI、NDBWI在钦州市主城区黑臭水体识别中,NDBWI的正确率最高。李佳琦等[12]提出的水体清洁指数WCI(Water Cleanliness Index)在太原市黑臭水体的识别精度也高达92.86%。更多的研究模型详见表3,该表总结了当前研究中常见的城市黑臭水体光谱指数判别模型。若要将这些模型应用到其他城市,还需要根据不同研究区的环境情况对模型阈值进行修正,例如,蒋宇雯等[44]将NDBWI应用到南宁、高黎等[47]将BOI应用到广州时,均对阈值进行了重新验证,并取得了较好的结果,这也进一步验证了这两种指数的可靠性和适用性。

高分影像的分类极易受到阴影干扰,对于城市环境中黑臭水体也是如此。为了减少阴影对水体提取的影响,许佳峰等[55]利用无人机高光谱信息构建了城市黑臭水体的河面阴影指数(RSSI, River Surface Shadow Index),该阴影指数能突出显示阴影与水体的差异。黑臭水体相对正常水体而言更容易受阴影影响,对此,Wu等[56]提出了一种从复杂的城市环境中消除阴影效应提取城市黑臭水体的BOW检测模型,有效区分了黑臭水体、正常水体和阴影,这对城市黑臭水体监测的准确性提供了有力帮助。关于利用特征波段对城市黑臭水体识别的研究,不同地方的研究方法和效果不一,还没有一个绝对普适的方法,但是综合来看,DBWI、NDBWI、BOI 3种方法的使用频率最高、效果最好,对这些指数的阈值稳定性、结果正确性以及地区适用性,还需要进一步验证,以求获得一个更高效稳定的城市黑臭水体判别模型。

4.2　基于水体色度识别法

色度法是根据水体组分的差异而显示出不同颜色的特点,参照国际照明委员会(CIE, International Commission on Illumination)规定的CIE-XYZ标准颜色系统,分析城市黑臭水体颜色的主波长来定量表征城市黑臭水体。黑臭水体与正常水体的纯度具有一定的差异,通常黑臭水体的纯度小于正常水体,因此纯度可以作为识别黑臭水体的一项指标[36,60]。曹红业[27]是较早通过色度来识别城市黑臭水体的学者之一,其根据颜色指数与水质参数共变

表 3 黑臭水体光谱指数判别模型

Table 3 Discrimination model for spectral indices of black and odorous water

序号	指数	判别模型公式	阈值	正确率	实验影像	实验地点	参考文献
1	Green	$N_1 \leqslant R_{rs}(Green) \leqslant N_2$	N_1=0; N_2=0.019	50%	GF-2	南京	[13]
2	NIR	$N_1 \leqslant R_{rs}(NIR)$	N_1=0.12	35.71%	Planet Scope	钦州	[14]
3	DBWI	$N_1 \leqslant R_{rs}(Green) - R_{rs}(Blue) \leqslant N_2$	N_1=0; N_2=0.003 6	75%	GF-2	南京	[13]
4	HCI1	$N_1 \leqslant R_{rs}(Red) + R_{rs}(NIR) - R_{rs}(Blue)$	N_1=0.85	95.37%	GF-2/GF-1	北京	[45]
5	HCI2	$N_1 \leqslant R_{rs}(Red) + R_{rs}(NIR) - R_{rs}(Green)$	N_1=0.87	93.80%	GF-2/GF-1	北京	[45]
6	BOW	$(R_{rs}(Green) - R_{rs}(Blue)) \times (R_{rs}(Green) - R_{rs}(NIR)) \leqslant N_1$	N_1=0.1	85.7%	GF-2	南京	[56]
7	NDBWI	$N_1 \leqslant \frac{R_{rs}(Green) - R_{rs}(Red)}{R_{rs}(Green) + R_{rs}(Red)} \leqslant N_2$	N_1=0.06;N_2=0.115	100%	GF-2	南京	[13]
8	BOI	$N_1 \leqslant \frac{R_{rs}(Green) - R_{rs}(Red)}{R_{rs}(Blue) + R_{rs}(Green) + R_{rs}(Red)} \leqslant N_2$	N_1=0; N_2=0.065	100%	GF-2	沈阳	[15]
9	UBOW	$N_1 \leqslant \frac{R_{rs}(Green) - R_{rs}(Red)}{R_{rs}(Blue) + R_{rs}(Green) + R_{rs}(Red)} \leqslant N_2$	N_1=0.04; N_2=0.07	81%	GF-2	北京	[57]
10	HI	$\frac{R_{rs}(Green) - R_{rs}(Blue)}{R_{rs}(Green) + R_{rs}(Blue)} \leqslant N_1$	N_1=0.065	57.14%	Planet Scope	钦州	[14]
11	NDBWI	$\frac{R_{rs}(Blue) + R_{rs}(Green) + R_{rs}(Red) - R_{rs}(NIR)}{R_{rs}(Blue) + R_{rs}(Green) + R_{rs}(Red) + R_{rs}(NIR)} \leqslant N_1$	N_1=0.45	92.86%	Planet Scope	钦州	[14]
12	BOWI	$\frac{R_{rs}(Green)}{R_{rs}(Blue) + R_{rs}(Red)} \leqslant N_1$	N_1=0.65	100%	Sentinel-2	广州	[58]
13	HCI3	$N_1 \leqslant \frac{R_{rs}(Red) + R_{rs}(NIR) - R_{rs}(Blue)}{R_{rs}(Red) + R_{rs}(NIR) + R_{rs}(Blue)}$	N_1=0.4	89.05%	GF-2/GF-1	北京	[45]
14	HCI4	$N_1 \leqslant \frac{R_{rs}(Red) + R_{rs}(NIR) - R_{rs}(Green)}{R_{rs}(Red) + R_{rs}(NIR) + R_{rs}(Green)}$	N_1=0.45	85.42%	GF-2/GF-1	北京	[45]
15	WCI	$N_1 \leqslant \frac{\left\lvert \frac{(R_{rs}(Green) - R_{rs}(Blue))}{(\lambda_G - \lambda_B)} \right\rvert}{\left\lvert \frac{(R_{rs}(Red) - R_{rs}(Green))}{(\lambda_R - \lambda_G)} \right\rvert} \leqslant N_2$	N_1=0; N_2=1	92.86%	GF-1	太原	[12]
16	BOCI	$N_1 \leqslant \frac{R_{rs}(Green) - R'_{rs}(Green)}{R_{rs}(Red)} \leqslant N_2$ $R'_{rs}(Green) = R_{rs}(Blue) + \frac{(R_{rs}(Red) - R_{rs}(Blue)) \times (\lambda_G - \lambda_B)}{\lambda_R - \lambda_B}$	N_1=0.12; N_2=0.26	87.18%	GF-2/ZY-3 /BJ-2/SV-1	沈阳	[19]
17	BOIM	$N_1 \leqslant \frac{R_{rs}(Red) - R'_{rs}(Green)}{R_{rs}(Red) + R'_{rs}(Green)} \leqslant N_2$ $R'_{rs}(Green) = R_{rs}(Blue) + \frac{(R_{rs}(Red) - R_{rs}(Blue)) \times (\lambda_G - \lambda_B)}{\lambda_R - \lambda_B}$	N_1=0.014; N_2=0.122	87.88%	GF-2	哈尔滨	[59]

注：R_{rs}(Blue)、R_{rs}(Green)、R_{rs}(Red)、R_{rs}(NIR)分别表示蓝、绿、红和近红外波段的光谱反射率；N_1、N_2为阈值常数；λ 为中心波段，λ_B = 485 nm，λ_G = 555 nm，λ_R = 660 nm

规律，提出了一种基于实测遥感反射率的颜色饱和度算法，有效识别出了北京的黑臭水体和正常水体。

由于水体中物质组分的不同，水体呈现丰富的颜色，若没有对城市黑臭水体的水色进行细分，可能会导致色度法的分类效果不佳，例如温爽等[13-14]通过色度法来识别城市黑臭水体时分类精度不如基于特征波段的识别方法。为了准确区分黑臭水体与非黑臭水体的颜色，李玲玲等[18,61]构建了水体的色系图谱，将黑臭与非黑臭水体大致归为灰色系、绿色系和黄色系3类，并参照国际标准劳拉比色卡建立了水体色度分级表(图6)，其中黑色系代表黑臭水体、绿色系和黄色系代表非黑臭水体。Shen等[36]根据水体颜色和遥感反射率的差异将采集到的黑臭水体样本分为灰白色和灰黑色两组，基于GF-2影像计算水体颜色纯度和色度角，经对比基线高度法、红绿波段比值法发现色度法对此类黑臭水体识别效果最好。水体色度法对于颜色明显异

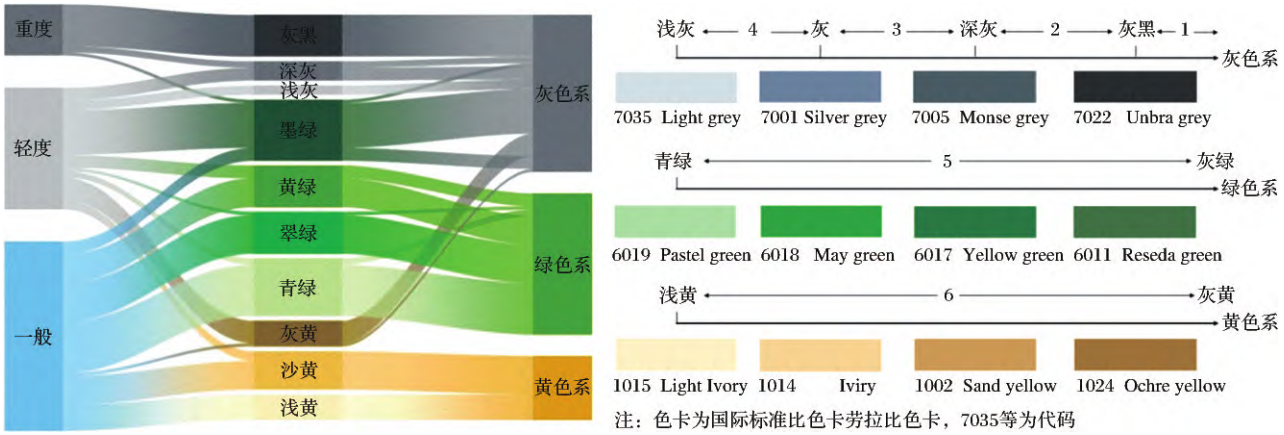


图 6　黑臭程度与水色的对应关系图[18,61]

Fig.6　The corresponding relationship between black odor degree and water color[18,61]

常的黑臭水体具有较好的识别效果,但是无法将一些呈现墨绿色或灰黄色的黑臭水体从正常水体中区分出来[60]。单靠色度一项指标难以应用到不同的研究场景中,需要结合其他指标来提高色度法的适用性和分类精度。有研究发现采用色度与透明度相结合的方法比仅根据色度或透明度来识别城市黑臭水体的效果更理想[31,60];还有研究证明了色度法结合饱和度法、角度法也可以提高城市黑臭水体的识别精度[34]。

4.3　基于典型水质参数识别法

基于典型水质参数识别法是通过分析水体的光学特性以及水体组分的反射和吸收光谱特性建立模型反演水质参数,探究典型水质参数或遥感影像波段组合与城市黑臭水体评价指标间的关系,进而构建城市黑臭水体识别模型。Zhou 等[62]根据《指南》的评估指标采用偏最小二乘法(PLS, Partial Least Squares)提出了一种连续黑臭水体指数 CBOWI (Continuous Black and Odorous Water Index)分类黑臭水体以及定量污染程度并在保定的应用中取得了较好效果。由于 DO、ORP、和 NH_3-N 属于不能直接作用于水体的吸收散射特性的化学水质指标,其与遥感影像的反演关系很难直接建立,因此除了《指南》中的 4 项指标以外,一些研究会增加其他水质指标辅助分析,例如叶绿素 a(Chl-a)[32,63]、总悬浮物(TSM, Total Suspended Matter)[32,63]、化学需氧量(COD, Chemical Oxygen Demand)[64,65]、总氮(TN, Total Nitrogen)、总磷(TP, Total Nitrogen)[65]、水温[41]、酸碱度(pH)、表观污染指数(SPI, Surface Pollution Index)[2]等,部分典型水质参数遥感反演模型如表 4 所示。

其中,城市黑臭水体研究中使用较多的典型水质参数是 Chl-a、TSM 和透明度(SD)等能够改变水体吸收、散射特征的光学水质指标。遥感定量反演出的悬浮物浓度、透明度和营养状态指数能够有效反映水体的黑臭程度[63]。韩文聪等[32]基于 GF-2 影像建立的 Chl-a 浓度、TSM 和透明度水体指标反演模型,有效提取了研究区的黑臭水体,但在透明度和 Chl-a 浓度低、悬浮泥沙含量高的河段容易被误判为黑臭水体,若是根据两种水质指标都高的结果来综合判断黑臭水体会更为合理。对于 DO、COD、和 NH_3-N 等化学水质指标,一般需要先将其与光学水质参数建立联系,再间接与水体遥感反射率建立联系,或者直接利用回归方程模拟生化性参数与遥感反射率建立联系[35]。例如,顾佳艳等[64]经分析多种水质指标与遥感反射率的相关性,发现 Chl-a 和 COD 可作为上海市黑臭水体反演的最佳特征指标。赵倩[65]基于水质实测数据与 GF-2 影像反演的 DO、

表 4　典型水质参数遥感反演模型

Table 4　Remote sensing inversion model of typical water quality parameters

水质参数	反演模型公式	参考文献
Chl-a	$4.089\times(b_4/b_3)^2-0.746\times(b_4/b_3)+29.733$	[63,66]
Chl-a	$208.39\times\left(\frac{b_4-b_3}{b_4+b_3}\right)^2+256.99\times\left(\frac{b_4-b_3}{b_4+b_3}\right)+95.477$	[35]
TSS	$119.62\times(b_3/b_2)^{6.0823}$	[63,66]
SD	$C_{SD}=284.15\times C_{TSS}^{-0.67}$	[63,66]
CODcr	$34.038\times\left(\frac{b_3-b_4}{b_3+b_4}\right)^2-64.448\times\left(\frac{b_3-b_4}{b_3+b_4}\right)+43.441$	[35]
COD	$(b_3/b_2-0.5777)/0.007$	[65]
DO	$15.73229-30.80257\times(b_2+b_3)$	[65]
NH_3-N	$(b_3/b_2-0.661)/0.07$	[65]

注:b_2、b_3、b_4分别为GF－2号影像的绿波段、红波段、近红外波段

NH_3-N、TP、COD等水质指标提出的一种城市黑臭水体评价模型B-OWQI(Black and Odorous Water Quality Index)在广州取得了较好结果。由此可见，SD、DO、ORP、NH_3-N、Chl-a、TSM、TP、水温等指标均可应用在城市黑臭水体监测的实际研究中。利用水质参数来识别城市黑臭水体是一种重要手段，且水质参数数值可以准确定量黑臭水体污染程度，这对城市黑臭水体分级具有重要意义。

4.4 决策树法

上述3种传统遥感方法操作容易、计算量小、实现简单，但是这些方法也存在不足。一方面，这些方法大多都需要实地采样并依赖于经验阈值做分类，极易受到人为主观因素的影响。因此，这些算法模型不能直接迁移到其他区域使用，往往需要结合实际重新判定阈值。另一方面，大部分方法只是利用影像的单一特征识别城市黑臭水体，尽管城市黑臭水体可以根据其光谱特征进行分类，但有些黑臭水体样本点的光谱特征与普通水体相似，阈值容易存在模糊区间，很难使用单一特征对其进行区分。针对上述问题，有研究融合多种特征指标来识别黑臭水体。例如，曹云等[67]基于GF-2影像分别计算影像的BOI和NDBWI值，采用面向对象的最优特征选择搜索算法确定黑臭水体与正常水体的4个分离特征，利用K-mean算法进行多特征聚类分析有效识别出城市黑臭水体。

除此之外，更多的研究是通过构建决策树模型融合多种特征来提取出城市黑臭水体。例如，Zhao等[50,68]基于Sentinel-2影像和CART(Classification and Regression Tree)模糊决策树算法来改进城市黑臭水体的遥感识别模型，利用多个典型黑臭水体指标(如BD、WCI、BOI和HI)构建多特征模糊决策树分类算法来识别廊坊市黑臭水体总体分布和局部聚集特征，实现了较高的准确率。此外，王晨[68]还对该决策树分类模型进行了迁移验证，在通州区获得了80%的识别准确率。除了CART决策树，ID3决策树也可以为建立多特征分类器提供可靠的方法。董旭鑫等[51,69]以蓝、绿、红波段之间的差和作为特征组合建立了ID3决策树，并通过计算模糊隶属度来确定分类结果，分类精度达84.78%。由于这些研究使用的Sentinel-2影像最高精度只有10 m，对于一些更为细小的黑臭水体难以区分，在未来应使用精度更高的影像进一步研究。不过这些研究仍然充分证明了决策树方法在城市黑臭水体的遥感识别方面具有较好的表现，其融合多特征的特性能够使城市黑臭水体识别更具科学性，但是如何选择稳定的识别特征也是决策树方法需要重点考虑的。

4.5 深度学习法

深度学习是近年新兴的研究领域，其目标是通过构建多层网络模型，利用复杂的网络参数将浅层特征转化为深层特征，从而实现对样本数据的自动学习和内在规律的解析[70]。在城市黑臭水体的遥感识别中，传统遥感识别方法在实际应用中流程繁琐、适用范围小、泛化性差。深度学习方法，特别是卷积神经网络，提供了一种可能解决这些问题的途径，它能够更好地利用原始数据本身的特征，挖掘出城市黑臭水体分类所需的条件。除了传统算法所用到的光谱特征，深度学习方法还能利用到城市黑臭水体的河道宽度、形态差异等特征[71]。胡国庆[71]基于GF-2影像分析了芜湖市黑臭水体的年际动态变化特征，在构建迁移模型中得到了最佳网络结构“Inception-V3_7a”，且在特征融合实验中，发现DBWI的加入对于帮助网络模型识别城市黑臭水体效果最佳，并得到了最佳特征融合数据集“RGB+DBWI”，其准确率和召回率分别是0.914 3、0.932 4。邵琥翔等[72]基于GF-2影像构建了PSPNet和U-Net深度学习模型来提取廊坊市的黑臭水体，其研究结果表明，选择“RGB+NIR+NDVI+NDBWI”的融合指标作为输入组合可以提供最丰富的特征信息并减少数据冗余，引入注意力机制的U-Net网络模型在城市黑臭水体提取方面表现最佳。此外，还有Huang等[73]基于U-Net构建的BDNet、Zheng等[74]基于FCN构建的FANet均对城市黑臭水体图像分割表现出优异性能。

深度学习方法虽然在城市黑臭水体遥感监测方面取得一定成效，但仍然有许多值得进一步探索和发展的领域，例如特征选择、网络构建等。通过不断优化和创新深度学习模型，结合多源数据和综合分析方法，引入更多的样本数据和丰富的特征表示，以使深度学习模型可以更好地捕捉到城市黑臭水体的复杂特征和变化模式，从而提高识别精度和可靠性。

4.6 城市黑臭水体遥感识别方法对比分析

上述5种类型的方法在城市黑臭水体监测中各有其适用的场景和优缺点，本研究从水体复杂情况、操作难易程度、效率高低、准确度等方面来进行对比分析(表5)。综合来看，光谱指数法和水体色

表 5　城市黑臭水体识别方法优缺点

Table 5　The advantages and disadvantages of urban black and odorous water identification methods

方法	适用性	优点	缺点
光谱指数法	适用于简单的水体类型分类	简单易行、计算量小;易于理解和应用;可以快速获取黑臭水体的大致位置和分布;成本较低。	依赖经验阈值,主观因素影响大;对于复杂的水体环境、混杂的光谱信息,识别精度较低。
水体色度法	适用于颜色变化较为显著的情况	颜色直观,可以快速判断色彩异常的水体,初步评估的水质情况。	受光照条件影响,难以处理光照变化较大的情况;只能对颜色明显变化的水体有效;不能准确判断黑臭程度和污染源。
水质参数法	适用于需要定量水体污染程度的情况	能够提供定量的水质信息和较准确的水质参数估计;更精确地全面评估水体污染程度。	部分水质参数的反演模型构建困难;需要实地采样和分析,耗时耗力;对数据要求较高。
决策树	可融合多种特征,适用于实现复杂水体的分类	适应能力强,可以处理多个特征之间的复杂关系;人为因素和噪声影响小,具有一定的自动化和可解释性。	需要事先建立训练数据集,对于复杂情况可能需要更多的训练样本;模型的构建依赖选择特征的质量,否则容易出现过拟合问题。
深度学习	适用于复杂情况下的黑臭水体分割和分类	可以从大量数据中学习复杂的特征表示;具有较高的自动化和预测准确性。	需要大量的标注数据进行训练,对计算资源要求较高。

度法适合快速初步判断,水质参数识别法可以提供定量的水质信息,决策树和深度学习则在更复杂情况下能够提供较高的分类精度。

5　城市黑臭水体遥感分级方法

《指南》上给出了判定城市黑臭水体级别的方法,判断某检测点的黑臭程度可以通过分析该点的4项水质指标(SD、DO、ORP和NH_3-N)来确定,其中1项指标有60%以上的检测数据或不少于2项指标有30%以上的检测数据达到“重度黑臭”级别的,该检测点认定为“重度黑臭”,否则可认定为“轻度黑臭”。连续3个以上检测点被认定为“重度黑臭”的,检测点之间的区域认定为“重度黑臭”;水体60%以上的检测点被认定为“重度黑臭”的,整个水体认定为“重度黑臭”[2]。《指南》定级城市黑臭水体的方法虽然较为精准,但是需要花费大量时间和人力。目前关于利用遥感直接对城市黑臭水体进行强度分级的研究较少,大多研究只停留在黑臭水体的识别层面,未能进一步对识别出的城市黑臭水体进行强度分级。

在已有的城市黑臭水体遥感分级研究中,七珂珂等[19,49]基于提出的黑臭水体遥感分级指数BOCI(Black and Odorous water Classification Index)具有更高的黑臭水体分级精度,何红术[75]将该模型分别应用到青岛的黑臭水体识别中时,识别结果与真实结果之间吻合程度均获得了较高的一致性。虽然BOCI模型在以上研究中取得了较好的识别效果,但由于引起水体黑臭的原因复杂多样,不同地区的黑臭水体类型存在差异性,因此该模型在其他城市应用的适用性、阈值稳定性以及识别精度有待进一步验证[19]。除了BOCI之外,还有Zhang等[57]提出的UBOW(Urban Black-Odor Water)模型,以及李玲玲等[18,61]基于水体色度构建的决策树模型均有效识别出了研究区的重度黑臭水体、轻度黑臭水体和非黑臭水体。

由于当前分级研究中采用的分级指标单一,且分级方法同识别方法一样,均存在需要人为确定阈值、同谱异物、自动化程度低、利用的遥感特征单一等问题。因此,分级时容易存在误判情况,将重度黑臭错分为轻度黑臭。为了更好地分级黑臭水体,未来的研究还需要同识别方法一起不断探索和引入新的模型和算法,不断改进以提高准确性和适用性。

6　结　语

城市黑臭水体已经成为许多城市普遍存在的环境污染问题,严重影响和损害群众健康和切身利益。因此,消除城市黑臭水体对提升人居环境质量具有重要意义。遥感技术凭其独特的优势,提供了一种更有效发现黑臭水体的方式,在城市黑臭水体的监测和治理中发挥着重要作用。针对城市黑臭水体遥感监测这一问题,本研究分析总结了当前城市黑臭水体遥感监测的识别特征、适用数据源、识别与分级方法及其优缺点和适用性等内容,旨在帮助相关研究者对该领域有更全面的了解。

总的来看,由于城市黑臭水体细小的特点,国产高分系列数据,特别是具有亚米级分辨率的GF-2数据是城市黑臭水体遥感监测研究中最适用的数

据源。在识别特征方面,城市黑臭水体在可见光波段具有特征光谱,在550~700 nm范围内的光谱曲线与正常水体存在明显差异,据此可以区分出大部分呈现灰黑色的黑臭水体,但是在近红外波段的光谱差异,黑臭水体易与悬浮泥沙含量高但不属于黑臭水体的浑浊水体混淆。由于水体的表观光学特性受到水体组分以及入射光场的影响,可能会使部分轻度黑臭水体与重度黑臭水体的光谱差异较小,从而影响到遥感识别分级的精度。

当前的城市黑臭水体遥感监测方法均具有一定的可行性,研究使用最多的是基于特征波段的光谱指数法,该方法简单有效,可以快速初步判断出黑臭水体区域。其中DBWI、NDBWI、BOI、BOCI等指数使用频率最高,并被验证在多个区域均具有良好的识别效果,决策树与深度学习方法也多基于这些较稳定的特征来进一步构建模型。光谱指数法、水体色度法和水质参数法这3种典型方法均涉及到阈值判定,深受人为主观影响,若将其迁移到其他地区或其他卫星影像应用时还需要进一步重新验证阈值,决策树与深度学习方法因其能融合多种特征实现对城市黑臭水体细微特征的自动学习和解析,可以更高效率识别分级复杂情况下的城市黑臭水体。

7 展 望

尽管城市黑臭水体遥感监测的研究已经取得不少成果,但是仍存在一些不足之处有待改进,本文从以下5个方面进行展望:

(1)精准分类及定义。黑臭水体种类多,成因复杂。从形成的时间尺度上看,既有短期突发性的水污染导致的,也有长期水体富营养化导致的。根据《指南》的定义,呈现令人不悦的颜色和(或)散发令人不适气味的水体都被视为黑臭水体。在遥感研究中,不同类型的水体呈现的不同颜色和光谱会对研究造成较大影响,甚至有些黑臭水体表面存在的浮萍、水华等覆盖物也会改变研究结果。因此,集合不同研究区更多类型的水体,建立黑臭水体样本数据库,精准细分黑臭水体种类,丰富黑臭水体光谱数据库,有利于研究更具针对性。

(2)多尺度挖掘遥感特征。目前关于城市黑臭水体遥感监测的研究主要使用光谱特征构建模型,缺少其他尺度的特征研究。未来研究需要解析基于变化检测的遥感敏感性特征与黑臭水体周边环境的相互关系,例如水体形态、次生环境等,融合多尺度像元级、结构级、对象级、场景级等敏感性特征指标进行黑臭水体遥感监测。

(3)光学/雷达协同监测。目前对城市黑臭水体的遥感研究主要为光学遥感,雷达遥感在该领域的应用还较为有限。雷达可以提供关于地表特征和物质构成的微观信息,对于监测水体表面存在垃圾、浮萍等辅助标志的黑臭水体具有一定潜力。随着对黑臭水体认识的深入和技术的发展,黑臭水体的研究除了使用多光谱影像和高光谱影像,还可以进一步探索雷达影像等其他数据源对具有不同表面特征的黑臭水体的监测潜力。

(4)多源光学卫星协同监测。由于黑臭水体细小的特点,在选择影像时往往采用高空间分辨率影像,而高空间分辨率卫星的幅宽一般很小,且容易受云雨和轨道回访周期的影响,单颗卫星的短时段内覆盖能力有限。因此,单一高空间分辨率卫星常常无法满足一定时段内的黑臭水体监测需求,需要多源光学卫星协同监测黑臭水体。

(5)天空地联合监测。黑臭水体监测的地面、无人机和卫星遥感方法各有其优缺点。现场原位测定方法能够获得更精确的结果,但其操作复杂且耗费时间和资源。相比之下,遥感方法更为高效,可以覆盖广阔的区域并提供大量数据,但卫星遥感的准确性和时效性可能受到天气等因素限制,可以将无人机遥感数据作为补充。因此,为了更精准高效地监测黑臭水体,更好地推进黑臭水体整治,需要充分将现场测定方法的精确性和无人机及卫星遥感方法的高效性结合起来,以获得更全面、准确和高效的数据,为黑臭水体环境整治提供更可靠的依据和决策支持。

参考文献(References):

[1] The State Council of the People's Republic of China. the Action Plan for the Prevention and Control of Water Pollution. [EB/OL]. 2015-04-02.[国务院.水污染防治行动计划[EB/OL]. 2015-04-02. https://www.gov.cn/zhengce/content/2015-04/16/content_9613.htm]

[2] Ministry of Housing and Urban-Rural Development of the People's Republic of China. Guidelines for the Remediation of Urban Black and Odorous Water Bodies[EB/OL].2015-08-28.[住房城乡建设部.城市黑臭水体整治工作指南[EB/OL]. 2015-08-28. https://www.mohurd.gov.cn/wjfb/201509/t20150911_224828.html]

[3] HU C M, HACKETT K E, CALLAHAN M K, *et al*. The 2002 ocean color anomaly in the Florida bight: A cause of local coral reef decline [J]. Geophysical Research Letters,

2003, 30(3):511-514. DOI: 10.1029/2002GL016479

[4] KUTSER T, PAAVEL B, VERPOORTER C, *et al*. Remote sensing of black lakes and using 810 nm reflectance peak for retrieving water quality parameters of optically complex waters[J]. Remote Sensing, 2016, 8(6): 497. DOI: 10.3390/rs8060497

[5] KUTSER T, TRANVIK L, PIERSON D C. Variations in colored dissolved organic matter between boreal lakes studied by satellite remote sensing[J]. Journal of Applied Remote Sensing, 2009, 3(1): 33538. DOI: 10.1117/1.3184437

[6] ZHAO J, HU C M, LAPOINTE B, *et al*. Satellite-observed black water events off southwest Florida: Implications for coral reef health in the Florida keys national marine sanctuary[J]. Remote Sensing, 2013, 5(1): 415-431. DOI: 10.3390/rs5010415

[7] FENG Qiang, YI Jing, LIU Shumin, *et al*. The pollution situation, treatment techniques and countermeasures of urban black and odors water in China[J]. Environmental Engineering, 2020, 38(8): 82-88.[冯强, 易境, 刘书敏, 等. 城市黑臭水体污染现状、治理技术与对策[J]. 环境工程, 2020, 38(8): 82-88.]

[8] WANG Xu, WANG Yonggang, SUN Changhong, *et al*. Formation mechanism and assessment method for urban black and odorous water body: A review[J]. Chinese Journal of Applied Ecology, 2016, 27(4): 1331-1340.[王旭, 王永刚, 孙长虹, 等. 城市黑臭水体形成机理与评价方法研究进展[J]. 应用生态学报, 2016, 27(4): 1331-1340.]

[9] DING Xiaolei, LI Yunmei, LÜ Heng , *et al*. Analysis of absorption characteristics of urban black-odor water[J]. Environmental Science, 2018, 39(10): 4519-4529.[丁潇蕾, 李云梅, 吕恒, 等. 城市黑臭水体的吸收特性分析[J]. 环境科学, 2018, 39(10): 4519-4529.]

[10] LÜ Chunjian, GAO Hongjie, LI Xiaojie, *et al*. DOM components and optical properties of black-odorous rivers in Shenyang city, China[J]. Chinese Journal of Environmental Engineering, 2019, 13(3): 559-568.[吕纯剑, 高红杰, 李晓洁, 等. 沈阳市黑臭水体溶解性有机物组分及其光学特征[J]. 环境工程学报, 2019, 13(3): 559-568.]

[11] ZHU Wenfei, LI Xiaojie, LIU Changfeng, *et al*. Analysis of DOM ultraviolet spectrum characteristics of surface water in black and odorous water body of Shenyang city, China[J]. Chinese Journal of Environmental Engineering, 2019, 13(3): 569-576.[朱文飞, 李晓洁, 刘长风, 等. 沈阳市黑臭水体表层水DOM紫外光谱特征分析[J]. 环境工程学报, 2019, 13(3): 569-576.]

[12] LI Jiaqi, LI Jiaguo, ZHU Li, *et al*. Remote sensing identification and validation of urban black and odorous water in Taiyuan city[J]. Journal of Remote Sensing, 2019, 23(4): 773-784.[李佳琦, 李家国, 朱利, 等. 太原市黑臭水体遥感识别与地面验证[J]. 遥感学报, 2019, 23(4): 773-784.]

[13] WEN Shuang, WANG Qiao, LI Yunmei, *et al*. Remote sensing identification of urban black-odor water bodies based on high-resolution images: A case study in Nanjing[J]. Environmental Science, 2018, 39(1): 57-67.[温爽, 王桥, 李云梅, 等. 基于高分影像的城市黑臭水体遥感识别: 以南京为例[J]. 环境科学, 2018, 39(1): 57-67.]

[14] YAO Huanmei, LU Yannan, GONG Zhuqing. Remote sensing identification of urban black and odorous water body based on PlanetScope images: A case study in Qinzhou, Guangxi[J]. Environmental Engineering, 2019, 37(10): 35-43.[姚焕玫, 卢燕南, 龚祝清. 基于PlanetScope影像的广西钦州市黑臭水体识别方法研究[J]. 环境工程, 2019, 37(10): 35-43.]

[15] YAO Yue, SHEN Qian, ZHU Li, *et al*. Remote sensing identification of urban black-odor water bodies in Shenyang city based on GF-2 image[J]. Journal of Remote Sensing, 2019, 23(2): 230-242.[姚月, 申茜, 朱利, 等. 高分二号的沈阳市黑臭水体遥感识别[J]. 遥感学报, 2019, 23(2): 230-242.]

[16] ZHANG Chun, GE Yi, REN Yue, *et al*. Semantic segmentation of rural black and odorous water body based on improved Deeplabv3+ network with remote sensing images[J]. Remote Sensing Technology and Application, 2023, 38(6): 1433-1444.[张淳, 葛毅, 任越, 等. 基于优化的DeeplabV^{3+}网络和高分影像分割浮萍型农村黑臭水体[J]. 遥感技术与应用, 2023, 38(6): 1433-1444.]

[17] LIU Bing, LI Tianhong. Research on remote sensing identification methods of urban black and odorous water bodies with Gaofen images[J]. Journal of Basic Science and Engineering, 2024, 32(2): 314-330.[刘冰, 李天宏. 基于高分影像的城市黑臭水体遥感识别方法研究[J]. 应用基础与工程科学学报, 2024, 32(2): 314-330.]

[18] LI Lingling, LI Yunmei, LÜ Heng , *et al*. Remote sensing classification of urban black-odor water based on decision tree[J]. Environmental Science, 2020, 41(11): 5060-5072.[李玲玲, 李云梅, 吕恒, 等. 基于决策树的城市黑臭水体遥感分级[J]. 环境科学, 2020, 41(11): 5060-5072.]

[19] QI Keke, SHEN Qian, LUO Xiaojun, *et al*. Remote sensing classification and recognition of black and odorous water in Shenyang based on GF-2 image[J]. Remote Sensing Technology and Application, 2020, 35(2): 424-434.[七珂珂, 申茜, 罗小军, 等. 基于GF-2影像的沈阳市黑臭水体遥感分级识别[J]. 遥感技术与应用, 2020, 35(2): 424-434.]

[20] FU Li, LIU Ge, SONG Kaishan, *et al*. Research on optical characterization and remote sensing identification of typical black and odorous water in rural areas[J]. Remote Sensing Technology and Application, 2024, 39(5): 1064-1074.[付丽, 刘阁, 宋开山, 等. 典型农村区域黑臭水体光学特性分析与遥感识别研究[J]. 遥感技术与应用, 2024, 39(5): 1064-1074.]

[21] ZHANG Baodong, WANG Biao, WU Yanlan, *et al*. Analysis and identification of characteristics of rural black and odorous water bodies in Anhui Province[J]. Ecology and Environmental Sciences, 2024, 33(8): 1257-1268.[张宝东, 王彪, 吴艳兰, 等. 安徽省农村黑臭水体特征分析及识别[J]. 生态环境学报, 2024, 33(8): 1257-1268.]

[22] WANG Qiao, ZHU Li. Urban black and odorous water monitoring technique and application using remote sensing[M]. Beijing: China Environmental Publishing Group, 2018.[王桥, 朱利. 城市黑臭水体遥感监测技术与应用示范[M]. 北京: 中国环境出版集团, 2018.]

[23] ZHANG Bing, LI Junsheng, SHEN Qian, *et al*. Recent research progress on long time series and large scale optical remote sensing of inland water[J]. National Remote Sensing Bulletin, 2021, 25(1): 37-52.[张兵, 李俊生, 申茜, 等. 长时序大范围内陆水体光学遥感研究进展[J]. 遥感学报, 2021, 25(1): 37-52.]

[24] SUN Yongbin, LU Huixiong, LI Qiliang, *et al*. A high-resolution remote sensing identification method for small, black and odorous water bodies coordinated by "algorithm-flag"[J]. Journal of Geo-Information Science, 2024, 26(12): 2788-2804.[孙永彬, 卢辉雄, 李启亮, 等. "算法-标志"协同的小微黑臭水体高分遥感识别方法[J]. 地球信息科学学报, 2024, 26(12): 2788-2804.]

[25] CAO Jianing.Research on remote sensing interpretation algorithm of black and odorous water based on fuzzy decision tree [D]. Langfang: North China Institute of Aerospace Engineering, 2021.[曹佳宁. 基于模糊决策树的黑臭水体遥感解译算法研究[D]. 廊坊: 北华航天工业学院, 2021.]

[26] LI Xiaojie. Pollutant characteristics and remote sensing identification of typical black and odorous water bodies in Shenyang [D]. Xi'an: Chang'an University, 2018.[李晓洁. 沈阳市典型黑臭水体污染物特征研究与遥感识别[D]. 西安: 长安大学, 2018.]

[27] CAO Hongye. Study on analysis of optical properties and remote sensing identifiable models of black and malodorous water in typical cities in China[D]. Chengdu: Southwest Jiao-Tong University, 2017.[曹红业. 中国典型城市黑臭水体光学特性分析及遥感识别模型研究[D]. 成都: 西南交通大学, 2017.]

[28] GORDON H R, WANG M. Retrieval of water-leaving radiance and aerosol optical thickness over the oceans with SeaWiFS: A preliminary algorithm[J]. Applied Optics, 1994, 33(3): 443-452. DOI: 10.1364/AO.33.000443

[29] MOBLEY C. Light and Water: Radiative transfer in natural waters [M]. New York: Academic Press, 1994.

[30] ZOU Lei. Measurement and application of inherent and polarized optical properties in inland water [D].Beijing: University of Chinese Academy of Sciences, 2013.[邹雷. 内陆水体固有光学特性及偏振特性的测量与应用[D]. 北京: 中国科学院大学, 2013.]

[31] FU Li, GUO Wenwen, SONG Kaishan, *et al*. Remote sensing identification of black and odorous water bodies in Changchun City in 2020[J]. Wetland Science, 2022, 20(4): 537-547.[付丽, 郭雯雯, 宋开山, 等. 2020年长春市黑臭水体遥感识别研究[J]. 湿地科学, 2022, 20(4): 537-547.]

[32] HAN Wencong, ZHANG Xiaoyu, CHEN Jiaxing, *et al*. Remote sensing monitoring of urban black and odorous water based on GF-2 image[J].Environmental Ecology,2021,3(1): 63-71.[韩文聪,张霄宇,陈嘉星,等. 基于高分二号影像的城镇黑臭水体遥感监测[J]. 环境生态学,2021,3(1):63-71.]

[33] WANG Xiaochen, YANG Xingzhong, LÜ Binbin , *et al*. Community structure of the phytoplankton and its relationship with environmental factors in lower reaches of the Yellow River[J]. Journal of Anhui Agricultural Sciences, 2012, 40(18): 9819-9821.[王晓臣, 杨兴中, 吕彬彬, 等. 黄河下游浮游植物群落结构及其与环境因子的关系[J]. 安徽农业科学, 2012, 40(18): 9819-9821.]

[34] GU Jiayan, HE Guofu, ZHAN Linghua, *et al*. Spectrum characteristics analysis of black and odorous waters in Shanghai and study of remote sensing recognition[J]. Research of Environmental Sciences, 2022, 35(1): 70-79.[顾佳艳, 何国富, 占玲骅, 等. 上海市黑臭水体光谱特征分析及遥感识别方法探究[J]. 环境科学研究, 2022, 35(1): 70-79.]

[35] ZHAN Linghua. Study on recognition models of urban black and odorous water bodies based on optical characteristics[D]. Shanghai: East China Normal University, 2019.[占玲骅. 基于光学特性的城市黑臭水体识别模型研究[D]. 上海: 华东师范大学, 2019.]

[36] SHEN Q, YAO Y, LI J S, *et al*. A CIE color purity algorithm to detect black and odorous water in urban rivers using high-resolution multispectral remote sensing images[J]. IEEE Transactions on Geoscience and Remote Sensing, 2019, 57(9): 6577-6590. DOI: 10.1109/TGRS.2019.2907283

[37] WEI C F, ZHENG Q Y, SHANG Y H, *et al*. Black and odorous water monitoring by using GF series remote sensing data[C]//Proceedings of the 9th International Conference on Agro-Geoinformatics (Agro-Geoinformatics). IEEE, 2021: 1-6. DOI: 10.1109/agro-geoinformatics50104.2021.9530312

[38] LI Jiaqi, DAI Huayang, LI Jiaguo, *et al*. Remote sensing identification of heavily polluted water in urban areas[J]. Bulletin of Surveying and Mapping, 2018(5): 54-58.[李佳琦, 戴华阳, 李家国, 等. 城区重度污染水体遥感识别研究[J]. 测绘通报, 2018(5): 54-58.]

[39] WANG Ru, SHEN Qian, PENG Hongchun, *et al*. Study on the applicability of multi-source high-resolution satellite images for monitoring black and odorous water body[J]. National Remote Sensing Bulletin, 2022, 26(1): 179-192.[王茹, 申茜, 彭红春, 等. 多源高分辨率卫星影像监测黑臭水体的适用性研究[J]. 遥感学报, 2022, 26(1): 179-192.]

[40] TURSUN Marhaba, LIU Zhenyu, ZHAO Wenjing, *et al*. Recognition of urban black and odorous water by UAV hyperspectral remote sensing[J]. Journal of South-Central Minzu University (Natural Science Edition), 2022, 41(6): 668-675.[买日阿巴·吐尔逊, 刘振宇, 赵文静, 等. 城市黑臭水体的无人机高光谱遥感识别[J]. 中南民族大学学报(自然科学版), 2022, 41(6): 668-675.]

[41] WEI L F, HUANG C, WANG Z X, *et al*. Monitoring of urban black-odor water based on nemerow index and gradient boosting decision tree regression using UAV-borne hyperspectral imagery [J]. Remote Sensing, 2019, 11(20): 2402. DOI: 10.3390/rs11202402

[42] CHENG Xin, XU Jie, LI Yunmei, *et al*. Discrimination method of unmanned aerial vehicle hyperspectral for the types of pollution sources of black-odor rivers in cities[J]. National Remote Sensing Bulletin, 2024, 28(8): 1914-1926.[成鑫, 徐杰, 李云梅, 等. 城市黑臭河流污染源类型的无人机高光谱判别[J]. 遥感学报, 2024, 28(8): 1914-1926.]

[43] HU Guoqing, CHEN Donghua, LIU Congfang, *et al*. Dynamic monitoring of urban black-odor water bodies based on GF-2 image [J]. Remote Sensing for Land & Resources, 2021, 33(1): 30-37.[胡国庆, 陈冬花, 刘聪芳, 等. 基于高分二号的城市黑臭水体动态监测[J]. 国土资源遥感, 2021, 33(1): 30-37.]

[44] JIANG Yuwen, ZHOU Ning, ZHOU Yanyan, *et al*. Research on remote sensing monitoring of urban black and odorous water[J]. Bulletin of Surveying and Mapping, 2019(S1): 98-104.[蒋宇雯, 周宁, 周艳艳, 等. 城市黑臭水体遥感动态监测方法研究[J]. 测绘通报, 2019(S1): 98-104.]

[45] JI Gang. Research and application on black and odorous water body by remote sensing [D]. Lanzhou: Lanzhou JiaoTong University, 2017.[纪刚. 基于遥感的黑臭水体识别方法研究及应用[D]. 兰州: 兰州交通大学, 2017.]

[46] ZHANG Xue, LAI Jibao, LI Jiaguo, *et al*. Remote sensing recognition of black-odor waterbodies in Shenzhen City based on GF-1 satellite[J]. Science Technology and Engineering, 2019, 19(4): 268-274.[张雪, 赖积保, 李家国, 等. 基于高分一号影像的深圳市黑臭水体遥感识别[J]. 科学技术与工程, 2019, 19(4): 268-274.]

[47] GAO Li, ZHANG Lulu, YE Mai, *et al*. Remote sensing recognition of black-odor waterbodies in Guangzhou City based on GF-6 image[J]. Environmental Ecology, 2021, 3(5): 13-18.[高黎, 张路路, 叶脉, 等. 基于GF-6影像的广州市建成区黑臭水体遥感识别[J]. 环境生态学, 2021, 3(5): 13-18.]

[48] HUANG Qiyu, XIAO Han, YU Zhifeng, *et al*. Remote sensing identification of black-odorous water in Hangzhou based on GF-6 images[J]. Journal of Hangzhou Normal University (Natural Science Edition), 2022, 21(5): 542-552.[黄祺宇, 肖晗, 于之锋, 等. 基于高分六号影像的杭州市黑臭水体遥感识别研究[J]. 杭州师范大学学报(自然科学版), 2022, 21(5): 542-552.]

[49] QI Keke. Remote sensing classification and recognition of urban black and odorous water based on multi-source high-resolution images[D]. Chengdu: Southwest JiaoTong University, 2019.[七珂珂. 基于多源高分影像的城市黑臭水体遥感分级识别[D]. 成都: 西南交通大学, 2019.]

[50] ZHAO Q C, DONG X X, LI G H, *et al*. Classification and regression tree models for remote recognition of black and odorous water bodies based on sensor networks[J]. Scientific Programming, 2022, 2022(1): 7390098. DOI: 10.1155/2022/7390098

[51] DONG Xuxin, ZHAO Qichao, LI Jiaguo, *et al*. Construction and application of CART model for remote sensing recognition of black and odorous water[J]. Remote Sensing Information, 2022, 37(5): 63-69.[董旭鑫, 赵起超, 李家国, 等. 黑臭水体遥感识别CART模型构建与应用[J]. 遥感信息, 2022, 37(5): 63-69.]

[52] CHEN Shuai. Remote sensing recognition of black and odorous water bodies based on Landsat-8 images[D]. Changsha: Changsha University of Science & Technology, 2021.[陈帅. 基于Landsat-8影像的黑臭水体遥感识别[D]. 长沙: 长沙理工大学, 2021.]

[53] YU Z F, HUANG Q Y, PENG X X, *et al*. Comparative study on recognition models of black-odorous water in Hangzhou based on GF-2 satellite data[J]. Sensors, 2022, 22(12): 4593. DOI: 10.3390/s22124593

[54] ZHANG Ling. Urban black and odorous water recognition principle and accuracy evaluation method based on remote sensing satellite image[J]. China-Arab States Science and Technology Forum, 2020(7): 151-153.[张玲. 基于遥感卫星影像技术的城市黑臭水体识别原理及精度评价方法[J]. 中阿科技论坛(中英阿文), 2020(7): 151-153.]

[55] XU Jiafeng, LI Yunmei, XU Jie, *et al*. Adaptive threshold for surface shadow detection of black and odor water[J]. Journal of Geo-Information Science, 2020, 22(10): 1959-1970.[许佳峰, 李云梅, 徐杰, 等. 黑臭水体水面阴影提取的自适应阈值算法研究[J]. 地球信息科学学报, 2020, 22(10): 1959-1970.]

[56] WU T X, LI M Y, WANG S D, *et al*. Urban black-odor water remote sensing mapping based on shadow removal: A case study in Nanjing[J]. IEEE Journal of Selected Topics in Applied Earth Observations and Remote Sensing, 2021, 14: 9584-9596.

[57] ZHANG Q, WANG B W, WANG S F, *et al*. Urban black-odor water body dynamic analysis with high-resolution remote sensing image[J]. IOP Conference Series: Earth and Environmental Science, 2019, 344(1): 012149. DOI: 10.1088/1755-1315/344/1/012149

[58] LI Wenqiang, HAN Liusheng. Remote sensing identification of black and odor water body in Guangzhou based on Sentinel-2A[J]. Science and Technology & Innovation, 2023(3): 44-48.[李文强, 韩留生. 基于Sentinel-2A的广州市黑臭水体遥感识别[J]. 科技与创新, 2023(3): 44-48.]

[59] ZHANG Ningning. Dynamic monitoring and evaluation of black and odorous water body in Harbin based on GF-2[D]. Harbin: Harbin Normal University, 2022.[张宁宁. 基于GF-2的哈尔滨市黑臭水体动态监测与评价[D]. 哈尔滨: 哈尔滨师范大学, 2022.]

[60] GUO Wenwen. Research on the optical characteristics and remote sensing recognition of black and odorous water bodies in Changchun city[D]. Liaocheng: Liaocheng University, 2021.[郭雯雯. 长春市黑臭水体光学特性与遥感识别研究[D]. 聊城: 聊城大学, 2021.]

[61] LI Lingling. Study on remote sensing classification method of urban black and odorous water based on water color classification[D]. Nanjing: Nanjing Normal University, 2021.[李玲玲. 基于水色分类的城市河流黑臭遥感分级方法研究[D]. 南京: 南京师范大学, 2021.]

[62] ZHOU X Y, HUANG Z Q, WAN Y C, *et al*. A new method for continuous monitoring of black and odorous water body using evaluation parameters: A case study in Baoding[J]. Remote Sensing, 2022, 14(2): 374. DOI: 10.3390/rs14020374

[63] JIN Haixia, PAN Jian. Urban black-odor water body remote sensing monitoring based on GF-2 satellite data fusion[J]. Scientific and Technological Management of Land and Resources, 2017, 34(4): 107-117.[靳海霞, 潘健. 基于高分二号卫星融合数据的城镇黑臭水体遥感监测研究[J]. 国土资源科技管理, 2017, 34(4): 107-117.]

[64] GU Jiayan, HE Guofu, ZHAN Linghua, *et al*. Construction of retrieval model for characteristic water quality indicators of black and odorous water in Shanghai based on hyperspectral remote sensing[J]. Environmental Pollution & Control, 2022, 44(8): 1030-1034.[顾佳艳, 何国富, 占玲骅, 等. 基于高光谱遥感的上海市黑臭水体特征水质指标反演模型构建[J]. 环境污染与防治, 2022, 44(8): 1030-1034.]

[65] ZHAO Qian. Evaluation model construction and pollution source traceability of black and odorous water body in Guangzhou[D]. Zibo: Shandong University of Technology, 2021.[赵倩. 广州市黑臭水体评价模型构建及污染溯源研究[D]. 淄博: 山东理工大学, 2021.]]

[66] ZHU Li, LI Yunmei, ZHAO Shaohua, *et al*. Remote sensing monitoring of Taihu Lake water quality by using GF-1 satellite WFV data[J]. Remote Sensing for Land & Resources, 2015, 27(1): 113-120.[朱利, 李云梅, 赵少华, 等. 基于GF-1号卫星WFV数据的太湖水质遥感监测[J]. 国土资源遥感, 2015, 27(1): 113-120.]

[67] CAO Yun, HANG Xin, GAO Yi, *et al*. Remote sensing monitoring of urban black and odorous water bodies using GF-2 images: Taking the main urban area of Nanjing as an exam-

ple[J]. Sichuan Environment, 2023, 42(1): 208-217.[曹云, 杭鑫, 高艺, 等. 利用高分二号影像对城市黑臭水体遥感监测——以南京市主城区为例[J]. 四川环境, 2023, 42(1): 208-217.]

[68] WANG Chen. Research on remote sensing image recognition of black and odorous water based on fuzzy decision tree algorithm [D]. Langfang: North China Institute of Aerospace Engineering, 2022.[王晨. 廊坊市黑臭水体光谱特征与时空分布分析[D]. 廊坊: 北华航天工业学院, 2022.]

[69] DONG Xuxin. Research on remote sensing image recognition of black and smelly water based on fuzzy decision tree algorithm [D]. Tianjin: Hebei University of Technology, 2022.[董旭鑫. 基于模糊决策树算法黑臭水体遥感影像识别研究[D]. 天津: 河北工业大学, 2022.]

[70] YASRAB R, ZHANG J C, SMYTH P, *et al*. Predicting plant growth from time-series data using deep learning[J]. Remote Sensing, 2021, 13(3): 331. DOI: 10.3390/rs13030331

[71] HU Guoqing. Research on remote sensing monitoring of black-odor water bodies based on deep learning[D]. Wuhu: Anhui Normal University, 2021.[胡国庆. 基于深度学习的黑臭水体遥感监测研究[D]. 芜湖: 安徽师范大学, 2021.]

[72] SHAO Huxiang, DING Feng, YANG Jian, *et al*. Model of extracting remotely-sensed information of black and odorous water based on deep learning[J]. Journal of Yangtze River Scientific Research Institute, 2022, 39(4): 156-162.[邵琥翔, 丁凤, 杨健, 等. 基于深度学习的黑臭水体遥感信息提取模型[J]. 长江科学院院报, 2022, 39(4): 156-162.]

[73] HUANG J J, XU J D, CHONG Q P, *et al*. Black and odorous water detection of remote sensing images based on improved deep learning[J]. Canadian Journal of Remote Sensing, 2023, 49(1): 1-14. DOI: 10.1080/07038992.2023.2237591

[74] ZHENG G Z, ZHAO Y Y, PAN Z X, *et al*. Fanet: A deep learning framework for black and odorous water extraction[J]. European Journal of Remote Sensing, 2023, 56 (1): 22340771-16. DOI: 10.1080/22797254.2023.2234077

[75] HE Hongshu. Urban black and odorous water body recognition based on improved U-Net network remote sensing semantic segmentation [D]. Beijing: Aerospace Information Research Institute, Chinese Academy of Sciences, 2020.[何红术. 基于改进U-Net网络遥感语义分割的城市黑臭水体识别——以青岛地区为例[D]. 北京: 中国科学院大学(中国科学院空天信息创新研究院), 2020.]

Reviews of Remote Sensing Monitoring of Urban Black and Odorous Water

CHEN Zhenghua[1], LAN Sixiang[1], ZHANG Jinshui[2], ZHANG Wei[1], LI Huade[1], ZHAO Lifang[3]

(1.*School of Marine Sciences*, *Guangxi University*, *Nanning* 530004, *China*;
2.*State Key Laboratory of Remote Sensing Science*, *Beijing Normal University*, *Beijing* 100875, *China*;
3.*Aerospace Information Research Institute*, *Chinese Academy of Sciences*, *Beijing* 100094, *China*)

Abstract: Black and odorous water is an extreme water pollution phenomenon that is a common problem in many cities, seriously affecting the well-being and satisfaction of residents. Therefore, addressing the issue of urban black and odorous water is urgent. Scientifically monitoring the urban black and odorous condition of water is the first step in the remediation of black and odorous water, providing accurate targets for subsequent assessment. Compared to traditional ground-based monitoring methods, remote sensing is a more effective way to discover black and odorous water, allowing for a wider and more rapid identification of black and odorous water areas and timely comprehensive representation of the spatiotemporal evolution of black and odorous water. This paper reviews the main research advances in remote sensing monitoring of urban black and odorous water. First, it briefly introduces the overview of black and odorous water, summarizes the remote sensing feature, and common data sources for urban black and odorous water. Second, it discusses in detail the methods for remote sensing identification and classification of urban black and odorous water and compares the applicability and advantages and disadvantages of each method. Finally, it summarizes the current status of remote sensing research on urban black and odorous water and its shortcomings and looks forward to future development directions. The aim is to provide reference and thinking for related research and better decision support for the long-term management of black and odorous water.

Key words: Black and odorous water; Remote sensing monitoring; Identification and classification; Remote sensing feature; Data sources

网络首发时间：2025-12-18 14:15:06　网络首发地址：https://link.cnki.net/urlid/11.5842.P.20251217.1032.008

中国科学：地球科学　SCIENTIA SINICA Terrae
论 文
《中国科学》杂志社
SCIENCE CHINA PRESS

相对高纬度珊瑚礁的有限弹性：气候变化和人类影响下的结构复杂度退化

滕君灿[1]，余克服[1,2]，左秀玲[1*]，李志文[1]，黄学勇[1]，段正贤[1]，蓝斐芳[1]

1. 广西大学海洋学院，广西南海珊瑚礁研究重点实验室，珊瑚礁研究中心，南宁 530004
2. 南方海洋科学与工程广东省实验室(广州)，广州 511458
* 通讯作者，E-mail：zuoxl@gxu.edu.cn

2025-06-07收稿，2025-10-10修回，2025-10-11接受，2025-12-16网络版发表
国家自然科学基金项目(42276182)、广西壮族自治区重大人才项目(GXR-2BGQ2525027)、广西大学自然科学与技术创新发展倍增计划项目(2023BZRC019)和广西自然科学基金项目(2022GXNSFAA035548)资助

摘要　珊瑚礁结构复杂度在维持生物多样性、海岸保护、渔业和旅游业等生态服务中发挥着重要作用。然而，由于缺乏结构复杂度的长期数据，珊瑚礁应对气候变化和人类干扰的弹性仍缺乏深入理解。基于2019–2024年在南海北部涠洲岛获取的实地调查数据，本研究首次探究了相对高纬度珊瑚礁中珊瑚群落与结构复杂度的响应轨迹及关键驱动因子。在2020年的珊瑚白化事件、2023年的两次气旋干扰后，活珊瑚覆盖度(LCC)先下降后恢复，珊瑚耐热性呈现增强的趋势。海洋保护区(MPA)内的珊瑚受影响程度低于非海洋保护区。然而，珊瑚礁结构复杂度却持续下降，从1.200降至1.076，并伴随珊瑚形态组成的简化。尽管持续下降，结构复杂度在MPA中仍与鱼密度显著正相关(R^2=0.91，p<0.05)。贝叶斯模型与广义线性模型分析结果表明，热胁迫、气旋及人类活动是导致结构复杂度下降的主要驱动因素。通过LCC与结构复杂度之间相反的变化轨迹，研究揭示了相对高纬度珊瑚礁在气候变化下的有限弹性，并进一步表明MPA在提升生态系统弹性方面发挥着关键作用。我们建议将结构复杂度纳入珊瑚礁长期监测与管理体系，以增强珊瑚礁生态系统应对气候变化的弹性。

关键词　活珊瑚覆盖度，结构复杂度，生态系统弹性，气候变化，海洋保护区

1　引言

全球气候变化下，热带珊瑚礁正面临前所未有的挑战。海洋热浪已引发大规模珊瑚白化和死亡，显著改变了珊瑚礁生态系统的群落组成(Hughes等，2017b，2018)。此外，热带气旋破坏了珊瑚礁生境的物理结构，摧毁了礁栖生物的生存地与庇护所(Cheal等，2017)。局部人为干扰(如破坏性捕捞、海洋污染及旅游等)也进一步加速了珊瑚礁的退化(Zaneveld等，2016；Spalding等，2017；Gove等，2023；Pinheiro等，2023)。以上因素不仅影响了珊瑚礁的物种多样性，而且削弱了珊瑚礁的关键生态服务功能。尽管海洋保护区(MPA)可以在一定程度上减轻局部压力，但随着海洋热浪发生频率以及热带气旋强度的增加，珊瑚礁面临着严峻的全球性威胁(van Hooidonk等，2014；Cheal等，2017)。因此，深入理解珊瑚礁应对多重干扰的弹性，对于评估其适应未来气候变化的能力至关重要。

珊瑚礁应对干扰的弹性具有多层含义，主要包括两方面。一方面是恢复力，即生态系统在干扰后恢复至原有结构和功能的能力(Knudby等，2013)。栖息地的结构复杂度在恢复过程中至关重要，可为珊瑚幼体提供附着基质，为礁栖生物提供庇护所，并维持生物多样性(Graham等，2015；González-Rivero等，2017；Yanovski和Abelson，2019)。即使活珊瑚覆盖度(LCC)因珊瑚白化

中文引用格式：滕君灿, 余克服, 左秀玲, 李志文, 黄学勇, 段正贤, 蓝斐芳. 2026. 相对高纬度珊瑚礁的有限弹性：气候变化和人类影响下的结构复杂度退化. 中国科学: 地球科学, doi: 10.1360/N072025-0276
英文引用格式：Teng J, Yu K, Zuo X, Li Z, Huang X, Duan Z, Lan F. 2026. Limited resilience of relatively high-latitude coral reefs: Structural complexity degradation under climate change and anthropogenic impacts. Science China Earth Sciences, https://doi.org/10.1007/s11430-025-1719-4

© 2025《中国科学》杂志社

或疾病下降，未破坏的礁体复杂结构仍可维持多年的生物多样性(Lindahl等，2001；Wilson等，2009；Graham等，2015)。然而，随着人类活动的加剧和极端气候事件的频发，全球珊瑚礁的结构复杂度正迅速下降(Alvarez-Filip等，2011b；Couch等，2017；Eakin等，2019)。另一方面是抵抗力，指生态系统面对干扰时仍能维持其结构和功能的能力(Knudby等，2013)。通过群落重组、遗传适应或生理驯化等机制，反复暴露于胁迫环境中的珊瑚可增强抵抗力(Lachs等，2023)。多项研究表明，温度频繁波动环境中的珊瑚群落在热胁迫中具有更强的抵抗力(Thompson和van Woesik，2009；Pratchett等，2013；McClanahan，2017；Hughes等，2019)。此外，由于区域环境差异，珊瑚礁的抵抗力具有显著的空间差异(Palumbi等，2014；Bay等，2017；Quigley等，2020)。例如，迎风区珊瑚的抗气旋破坏能力比背风区的珊瑚更强(Hansen等，2025)。温度频繁波动环境中的珊瑚白化严重性也通常低于温度稳定环境中的珊瑚(Guest等，2012；Safaie等，2018；Sully等，2019；Koester等，2020)。

相对高纬度珊瑚礁由热带、亚热带及温带物种组成，具有明显的季节性环境波动特点(Beger等，2014)。该区域的温度、光照及文石饱和度等比热带珊瑚礁波动更剧烈，珊瑚群落中小型且脆弱的物种被筛除，转而由更耐压的团块状珊瑚成为优势种(Guinotte等，2003；Beger等，2014；Comeau等，2014；Chong等，2023；Gonzalez等，2024)。由于热带珊瑚礁主要以敏感的分枝状珊瑚为主，理论上相对高纬度珊瑚礁对环境变化应具有更强的弹性(Mongin等，2016；Safaie等，2018)。耐压物种的选择过程还可能使珊瑚礁结构在面对干扰时更易维持，从而促进生态系统恢复。全球变暖背景下，相对高纬度珊瑚礁亦被视为热带珊瑚群落的气候避难所(Riegl和Piller，2003；Beger等，2014)。然而，尽管存在潜在优势，但前人基于群落的研究表明，相对高纬度珊瑚礁在经历气候干扰时具有较低的弹性，主要原因是珊瑚生长速率较慢、珊瑚幼体供应不足以及人类活动干扰等(Hoey等，2011；Jones等，2020；Ross等，2021)。因此，需要结合群落组成与结构复杂度的动态变化轨迹，在生态系统尺度上评估珊瑚礁应对气候变化的弹性，这对于综合验证“避难所假说”至关重要(Graham和Nash，2013；Burt等，2025)。

目前关于相对高纬度珊瑚礁的研究大多集中于群落尺度的分析(Polidoro和Carpenter，2013；MacNeil等，2019；Gove等，2023)或结构复杂度的定性研究(Robinson等，2019；Graham等，2020；Burt等，2025)，在珊瑚礁弹性评估方面仍不够完善。例如，即使LCC呈现恢复趋势，但珊瑚形态组成的简化，导致维持关键生态系统服务功能的结构复杂度在持续退化，这一现象通过视觉观测已被明确证实(Zawada等，2019；Bauman等，2022；Emslie等，2024)。由于结构复杂度在维持生态系统服务中具有重要作用(Alvarez-Filip等，2011a；Graham等，2011，2015；Guest等，2016；Darling等，2017；Magel等，2019)，定量分析其动态变化是评估生态系统弹性不可或缺的环节。然而，在具有潜在气候避难所功能的相对高纬度珊瑚礁中，相关研究仍显不足(Burns等，2019；Chen和Dai，2021；Wang Y等，2024；Wu等，2025)，从而凸显了开展长期、定量监测结构复杂度的迫切需求。

涠洲岛珊瑚礁位于中国南海北部的北部湾，是分布在相对高纬度区域的边缘珊瑚礁，被认为是未来全球变暖情景下可能的珊瑚避难所(Yu等，2019)。然而，过去十年海水表面温度(SST)快速升高，并在2020年引发了涠洲岛迄今最严重的大规模珊瑚白化事件，造成超过60%的珊瑚白化(Lyu等，2022；Zuo等，2023)。此外，涠洲岛珊瑚礁还受到热带气旋和局部人类活动的强烈干扰，进一步挑战了其作为未来气候避难所的能力(李邢凡等，2019；Yu等，2019)。

基于2019–2024年涠洲岛MPA和非海洋保护区(NPA)的珊瑚礁生态调查数据，本研究聚焦相对高纬度珊瑚礁生态系统的弹性机制，目的为：(1)探究相对高纬度珊瑚礁群落及结构复杂度在应对气候变化与人类干扰下的生态变化轨迹；(2)探究影响珊瑚礁恢复的主要因素；(3)综合评估珊瑚礁生态系统应对干扰的弹性。通过长期且定量的珊瑚群落与结构复杂度综合监测，本研究提出了相对高纬度珊瑚礁响应多重压力的新视角。研究结果不仅可加深人类世背景下对相对高纬度珊瑚礁生态弹性的理解，也可为未来珊瑚礁生态保护与管理提供重要参考。

2 方法

2.1 技术路线概述

本研究的技术路线如图1所示。首先，获取2019–2024年涠洲岛珊瑚礁实地调查的结构复杂度和生物数据(包括LCC、壳状珊瑚藻(CCA)、大型海藻、幼年珊瑚及海绵/海葵等)，并获取2024年鱼密度调查数据。其次，环境指标获取自公开数据集，如周热度(DHW)、490 nm波长下的光散射衰减系数(Kd490)、叶绿素a浓度(Chl a)及气旋频次。人类活动指标(如离岸距离、渔业产量及管理状态)则通过地理计算和政府记录获取。随后，基于实地生态调查数据开展时空变化分析，以探究生态变化轨

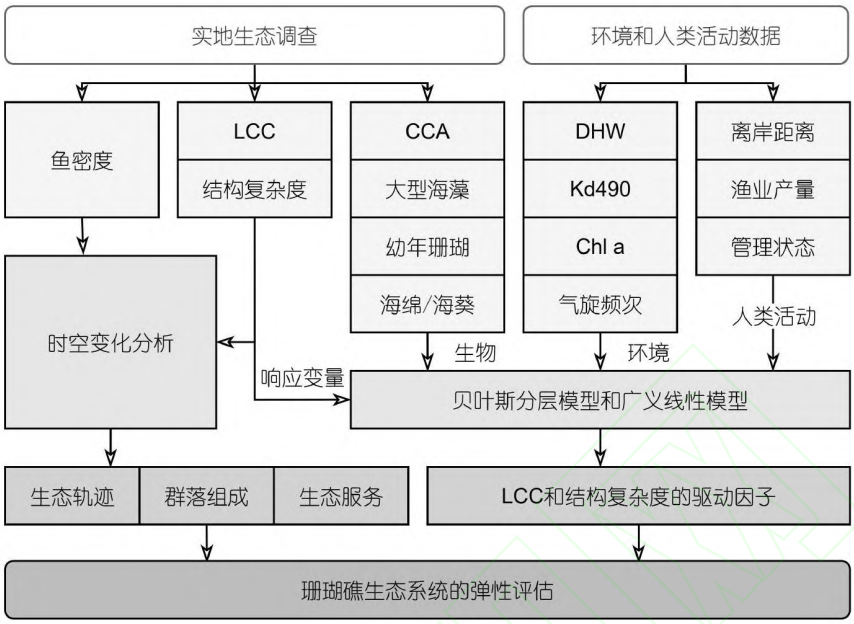


图1 技术路线图

迹、群落组成及生态系统服务。在此基础上，将生物、环境及人类活动指标纳入贝叶斯分层模型和广义线性模型(GLM)，探究LCC和结构复杂度的主要驱动因子。最后，基于分析结果，综合评估相对高纬度的涠洲岛珊瑚礁在气候变化和人类干扰下的生态系统弹性。

2.2 研究区

涠洲岛(21°00′–21°10′N，109°00′–109°15′E)位于南海北部的北部湾，总面积为26 km^2(图2A、2B)，具有明显的季节性环境波动特征。SST为15.3–28.9 ℃，pH为8.0–8.23，Chl a为1.58–3.08 mg/m^3(Yu等，2019；Zhang等，2024)。涠洲岛珊瑚礁属于岸礁，珊瑚沿着海岸不均匀分布。由于人类活动和气候变化的双重压力，涠洲岛LCC从1991年的70%锐减至2018年的17.6%，群落组成也由结构复杂的分枝、叶片状珊瑚转向以简单的团块状珊瑚为主(Yu等，2019；黄晖，2021)。2013年在涠洲岛东北部设立了MPA，面积为12.78 km^2(图2B)。MPA内禁止捕鱼及其他开发活动(Wang Y等，2024)。珊瑚群落及非生物基质方面，MPA主要为牡丹珊瑚(*Pavona* sp.)及碎枝；NPA主要为滨珊瑚(*Porites* sp.)及礁石(Wang Y等，2024)。

2020年涠洲岛珊瑚礁遭受了迄今最严重的热胁迫，月最大SST达到31.88 ℃，DHW高达18.27 ℃ 周，热胁迫持续时间超过90天。2021–2024年热胁迫时间仍每年高于50天(图2C)。此外，2023年涠洲岛还受到气旋“Sanba”和“Saola”的影响(图2A)。

2.3 实地调查和数据来源

2.3.1 实地生态调查

我们在2020、2022、2023和2024年共调查了41个站位，获取了涠洲岛MPA和NPA的底栖群落及结构复杂度数据。由于COVID-19疫情影响，2021年未能开展调查。2019年共22个站位数据，其中16个站位的LCC和结构复杂度数据获取自Wang Y等(2024)，6个站位的其他底栖群落数据获取自Lyu等(2022)。MPA数据来自涠洲岛政府(图2B)。由于MPA的生态影响可能大于其范围(Halpern，2003)，本研究将MPA外200 m缓冲区的站位也划分为MPA站位，其余则划分为NPA站位(网络版附表S1)。

底栖调查中，潜水员在各站位平行海岸线铺设一条50 m长的样带，以10–20 cm的高度、5 m/min的恒定速度连续录制样带底栖视频。随后样带视频被转化为连续不重叠的图像，每个视频平均247张，所有站位共计10115张图像。使用珊瑚点计数Excel扩展软件(Coral Point Count with Excel Extensions)在每张图像上生成10个随机点，通过随机点计数法计算底栖覆盖度(Kohler和Gill，2006)。依据涠洲岛的底质特征及法国国家珊瑚观测服务(Service National d’Observation CORAIL)的莫雷阿岛(Moorea Island)MPA调查方案(https://observatoire.criobe.pf/)，珊瑚礁底质共划分为六大类：活珊瑚、死珊瑚、大型海藻、海绵/海葵、CCA及非生物底质。活珊瑚进一步分为

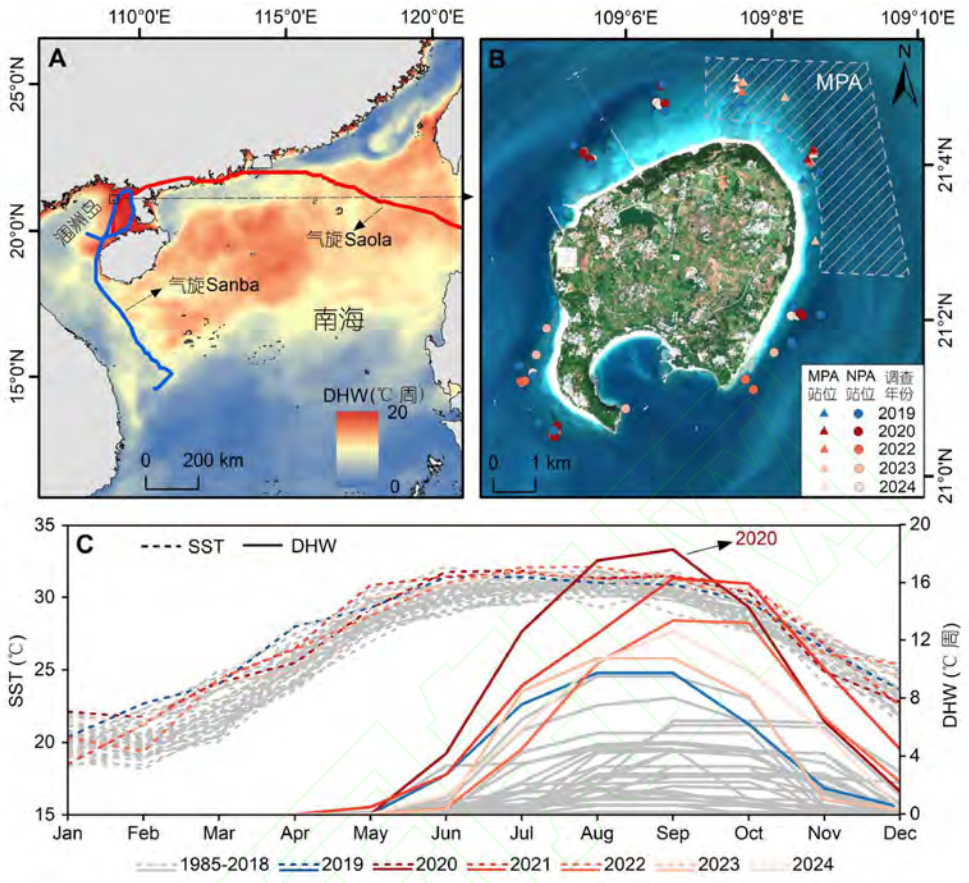


图 2 涠洲岛研究区与气候背景。(A) 地理位置与气候：地图展示了2020年9月的月最大周热度(DHW)，并叠加了气旋“Sanba”和“Saola”的路径；该图基于自然资源部标准地图服务网站GS(2016)1666号的标准地图制作，底图边界无修改；(B) Sentinel-2多光谱影像：为涠洲岛的真彩色影像，三角形和圆形分别为海洋保护区(MPA)与非海洋保护区(NPA)的调查站位，不同颜色表示不同调查年份；(C) 长期热胁迫趋势：1985–2024年的月最大海表温度(SST，虚线)和DHW(实线)时间序列数据；珊瑚严重白化或死亡的DHW预测阈值为8 °C 周

成年珊瑚、幼年珊瑚及白化珊瑚三类，并区分到团块状、叶状、板状及分枝状四种形态类型(网络版附表S2)。幼年珊瑚覆盖度为珊瑚补充的评价指标。珊瑚白化/死亡率为白化/死亡珊瑚占总珊瑚覆盖面积的比例。

2024年底栖调查中同步进行了鱼类调查。潜水员使用GoPro摄像机沿50 m长样带(两侧各2.5 m)拍摄鱼类视频，覆盖面积为5 m×50 m。由于其中一个站位水下能见度较差(<50 cm)而被剔除，最终获得了11个有效的鱼类数据。室内分析中，通过视频内观察到的鱼类个体数计算鱼密度(ind/m^2)。

2.3.2 结构复杂度的测量

珊瑚礁结构复杂度指栖息地物理三维结构的复杂程度，主要由造礁珊瑚及其他底质构成。底栖群落调查中，同步使用链条法沿50 m样带测量结构复杂度。参考Risk (1972)，结构复杂度(SC)为珊瑚礁表面轮廓长度(L)与样带水平距离(D)的比值。水平距离D固定为50 m。测量L时，将一条带刻度的金属链条(链宽0.8 cm，节长1.4 cm)沿珊瑚礁表面仔细铺设以贴合其轮廓，并在样带末端记录轮廓长度L(图3)。前人使用链条法测得的实地结构复杂度通常介于1.0–2.0之间(Alvarez-Filip等, 2011a；Graham和Nash，2013；Wang Y等，2024)，本研究将结构复杂度划分为低(1.0–1.2)、中(1.2–1.5)和高(>1.5)三个等级。

2.4 环境和人类活动数据

2.4.1 遥感数据

当SST超过多年平均最热温度1 ℃时，珊瑚会遭受热胁迫，12周内累积的热胁迫以DHW(℃ 周)进行量化(Zuo等，2023)。本研究将DHW作为珊瑚的热胁迫指标，数据来自美国国家海洋和大气管理局(NOAA)的珊瑚礁观察计划(Coral Reef Watch，www.coralreefwatch.noaa.gov/)。Chl a(mg/m^3)作为富营养化的指标(Guo等，

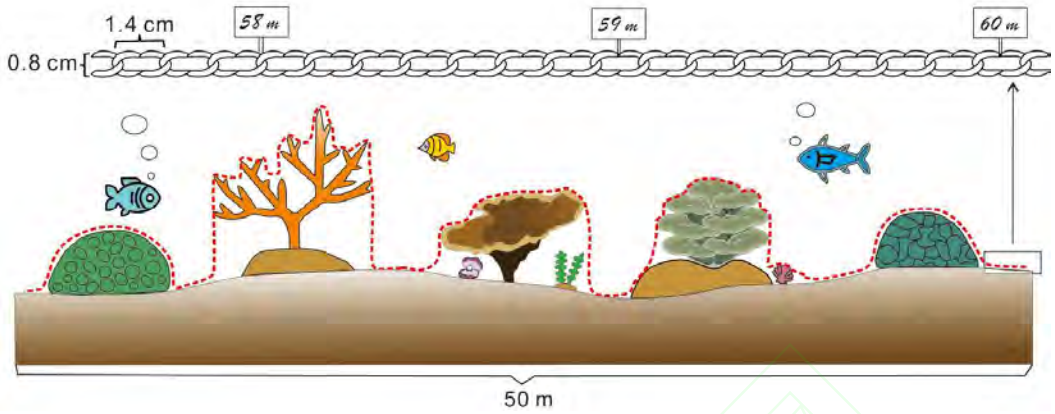


图3　实地调查结构复杂度测量示意图

2019)，Kd490(m^{-1})为水体浑浊度指标(Lucas等，2023)，均来自欧洲航天局的OceanColour-CCI项目(https://www.oceancolour.org/)。DHW、Chl a和Kd490数据的空间分辨率分别为5、4和4 km。

2.4.2　气旋频次

为了评估气旋对珊瑚礁的干扰程度，基于NOAA海岸服务中心(http://www.csc.noaa.gov)提供的气旋路径数据统计气旋频次。参考Gardner等(2005)，采用气旋等级和影响半径评估气旋是否对调查站位造成影响：1–2级气旋的影响半径为35 km，3级气旋为60 km，4–5级气旋为100 km。基于该标准获取了调查站位的气旋干扰频次。

2.4.3　离岸距离

靠近海岸的珊瑚礁更容易受到人类活动的干扰，因此将离岸距离作为人类干扰强度的指标(Asner等，2021)。本研究从欧洲航天局下载了2021-12-03的Sentinel-2 Level-2A影像(https://browser.dataspace.copernicus.eu)。由于近红外波段在水体中具有强烈的吸收特性，因此使用其0.03的反射率阈值在ArcMap 10.8软件中提取海岸线(Sun等，2012)。最后，根据各调查站位到海岸线的直线距离计算离岸距离。

2.4.4　渔业产量

破坏性捕捞活动会直接破坏珊瑚礁结构，如抛锚、拖网和炸鱼等，其通过减少食草性鱼类导致藻类过度生长并抑制珊瑚恢复，加剧了珊瑚礁生态退化(White等，2000；Zaneveld等，2016)。为量化涠洲岛捕捞活动相关的人为干扰，本研究从广西壮族自治区统计局(http://tjj.gxzf.gov.cn)下载了渔业产量数据。

2.5　统计分析

为了量化底栖覆盖度和结构复杂度的变化，使用以下公式计算其变化率：

$$C_r = \frac{(C_f - C_i)}{C_i} \times 100\% \quad (1)$$

$$SC_r = \frac{(SC_f - SC_i)}{(SC_i - 1)} \times 100\% \quad (2)$$

其中，C_r和SC_r分别表示底栖覆盖度和结构复杂度的相对变化率，C_f和SC_f表示终值，C_i和SC_i表示初始值。

为评估MPA与NPA的底栖覆盖度和结构复杂度差异，使用*rstatix*包进行Kruskal-Wallis检验(Kassambara，2023)。检验统计量H越大，组间基于秩的差异证据越强。通过*vegan*包中的PERMANOVA方法，评估MPA与NPA之间或不同年份之间的形态组成差异(Oksanen等，2025)。伪F统计量(F)越大，多变量空间中的组间分离程度就越大。通过决定系数(R^2)探究LCC和结构复杂度与鱼密度之间的关系，其值越接近1，表明协变量对鱼密度的解释力越强。在所有统计分析中，仅当假设概率(p)小于0.05时才认为结果具有统计显著性。

为了识别涠洲岛LCC和结构复杂度变化的驱动因子，本研究基于前人的发现选择了关键的生物、环境和人为因素的协变量(Hughes等，2017a；Yu等，2019；Gove等，2023)，并应用两种互补的统计方法——贝叶斯分层模型和GLM模型。贝叶斯模型具有分层结构并可纳入随机效应(例如调查年份)，能够灵活、稳健地分析基于站位的变化及复杂的生态交互关系(Clark，2005)。GLM模型不依赖先验知识，适用于小样本数据和估计年份尺度的固定效应(Knudby和Richardson，2023)。在站位尺度上，LCC/结构复杂度的贝叶斯模型固定协变量包括5个生物指标(CCA、大型海藻、海绵/海葵、幼年珊瑚、结

构复杂度/LCC)、2个环境指标(Chl a、Kd490)、离岸距离和管理状态([MPA, 1]或[NPA, 0])。调查年份作为随机效应，用于考虑时间变化(公式(S1)和(S2))。由于涠洲岛面积较小(约26 km^2)，调查站位间的气旋频次、渔业产量和DHW空间变化不明显，本研究将这些因子进行年平均，以探究其对LCC/结构复杂度的影响。因此，以气旋频次、渔业产量和DHW作为固定效应，构建了LCC/结构复杂度年份尺度的GLM模型(公式(S3)和(S4))。

参考Graham等(2020)，采用后验预测检验(Posterior Predictive Checks)、有效样本量(Effective Sample Size)、Gelman-Rubin收敛统计量(R-hat)以及赤池信息量准则(AIC)四项诊断指标对模型性能进行评估(网络版附表S3–S5)。所有协变量均被标准化为正态分布N(0,1)，以直接比较各协变量的效应。通过系数的95%置信区间判断驱动因子的统计显著性：若95%置信区间不包含零，则对应协变量被认为是显著驱动因子。贝叶斯模型通过*brms*包(Bürkner，2021)结合Stan(Stan Development Team，2020)运行。GLM模型则通过*glmmTMB*运行(McGillycuddy等，2025)。所有统计分析均在R 4.5.1软件中进行(R Core Team，2025)。

3 结果

3.1 活珊瑚覆盖度和结构复杂度的时间变化轨迹

涠洲岛LCC在2019–2024年间呈现出下降与恢复交替的波动趋势(图4A)。2019–2020年，平均LCC由14.84%下降至10.56%，下降率为28.84%。2020年大规模白化事件后，LCC出现一定程度的恢复，但又从2022年的12.78%下降至2023年的7.40%，下降率为42.10%。MPA的LCC在2024年恢复至13.31%，较2023年增长175%，几乎恢复至白化前水平。相比之下，NPA的LCC的增长率仅为4.40%。LCC在MPA与NPA之间的差异在所有年份均不显著(H=0.15–2.45，p>0.05)。

与LCC不同，结构复杂度在2019–2024年整体呈下降趋势(图4B)。平均结构复杂度由2019年的1.200下降至2020年的1.138，下降率为31.00%。随后又从2022年的1.147下降至2023年的1.079，下降率达46.26%。2024年，结构复杂度达到最低值1.076。除2019年(H=4.25，p<0.05)，其他年份MPA与NPA之间的结构复杂度差异均不显著(H=0.05–3.75，p>0.05)。调查期间(2019–2024年)，43个站位为低结构复杂度，其平均LCC为10.76%；14个站位为中等结构复杂度，平均LCC为15.47%；未发现高结构复杂度的站位。2024年，所有站位均为低结构复杂度。

3.2 其他底栖群落的时间变化轨迹

2020年11月，涠洲岛珊瑚白化率平均为6.39%(图5A)，其中MPA珊瑚白化率(0.66%)显著低于NPA(7.82%)(H=3.75，p<0.05)。2023年，MPA的珊瑚死亡率和大型海藻覆盖度(4.11%和2.97%)均显著低于NPA(18.01%和12.82%)(H=6.75，p<0.01；H=4.5，p<0.05；图5B、5D)。2023–2024年，MPA的幼年珊瑚覆盖度由0.13%上升至0.24%，而NPA则由0.35%下降至0.13%(图5C)。2020–2024年，MPA的海绵/海葵覆盖度从4.11%快速增加至31.95%，而NPA未见显著变化(图5F)。除2020年外(H=3.32，p<0.05)，调查期间MPA与NPA之间的CCA覆盖度差异均不显著(H=0.12–0.86，p>0.05；图5E)。

2020–2024年间，MPA(F=0.69，p>0.05；图6A)和NPA(F=1.10，p>0.05；图6B)珊瑚形态组成的年际变化均不显著。然而，块状珊瑚比例均有所增加，其他形态珊瑚则呈下降趋势，尤其是叶状和板状珊瑚。2020–2024年的平均数据表明，MPA与NPA的珊瑚形态组成存在显著差异(F=3.15，p<0.05；图6C)，其中MPA的叶状珊瑚比例更高，而块状珊瑚比例较低。

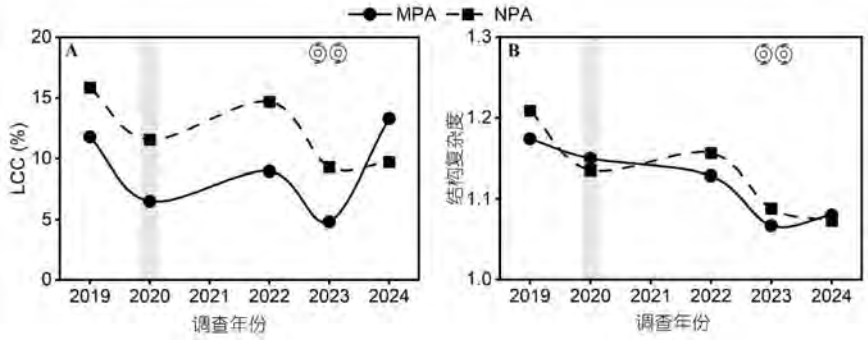


图4 2019–2024年涠洲岛(A)活珊瑚覆盖度(LCC)与(B)结构复杂度的时间变化轨迹。灰色阴影表示大规模白化事件，特殊符号表示气旋；实线与虚线分别代表海洋保护区(MPA)与非海洋保护区(NPA)的数据；2019年的数据来源于Wang Y等(2024)

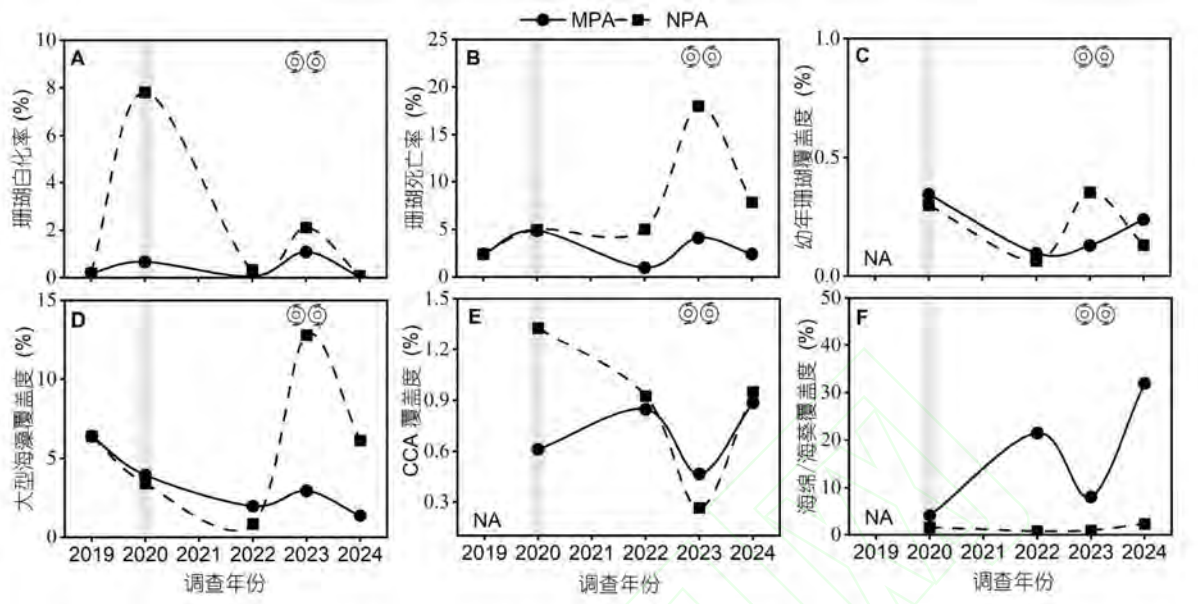


图5　2019–2024年其他底栖群落的时间变化轨迹。(A) 珊瑚白化率；(B) 珊瑚死亡率；(C) 幼年珊瑚覆盖度；(D) 大型海藻覆盖度；(E) 壳状珊瑚藻(CCA)覆盖度；(F) 海绵/海葵覆盖度；灰色阴影表示大规模白化事件，特殊符号表示气旋；实线与虚线分别代表海洋保护区(MPA)与非海洋保护区(NPA)的数据；2019年的数据来源于Lyu等(2022)

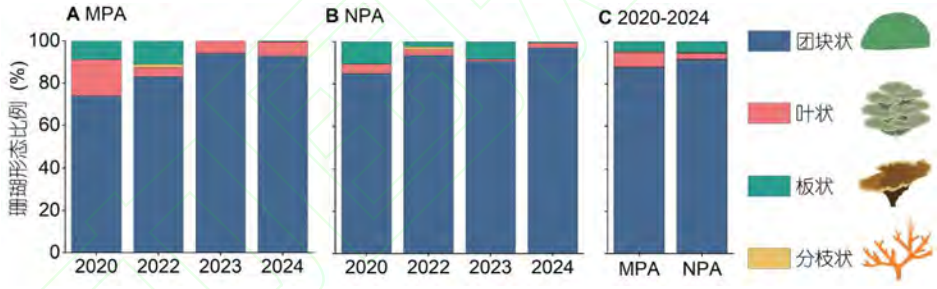


图6　珊瑚形态比例。(A) 2020–2024年海洋保护区(MPA)的时间序列数据；(B) 2020–2024年非海洋保护区(NPA)的时间序列数据；(C) MPA与NPA在2020–2024年的平均数据

3.3　活珊瑚覆盖度和结构复杂度的驱动因素

基于涠洲岛MPA和NPA的数据，发现协变量与珊瑚健康指标之间存在显著关系。结构复杂度和CCA是LCC的显著正影响因子，而离岸距离对LCC的影响较弱(图7A)。渔业产量、DHW、气旋频次、Chl a以及海绵/海葵则是LCC的显著负影响因子。LCC是结构复杂度的显著正影响因子，而气旋频次、DHW和渔业产量则对结构复杂度有显著负影响(图7B)。MPA/NPA管理状态对LCC和结构复杂度均未产生显著影响。

3.4　活珊瑚覆盖度和结构复杂度与鱼密度的关系

研究分析了2024年LCC/结构复杂度与鱼密度之间的关系。MPA的鱼密度与结构复杂度呈显著正相关(图8B)，但与LCC之间的关系不显著(图8A)。NPA的鱼密度与LCC(图8C)或结构复杂度(图8D)的关系均不显著。

4　讨论

4.1　活珊瑚覆盖度的关键驱动因素

与热带珊瑚礁的研究一致(Emslie等，2024；Anderson，2025)，本研究在涠洲岛也发现热胁迫、气旋与LCC显著负相关(图7A)。2020年的白化事件是关键转折点：2020年9月，LCC下降至8.70%，同时珊瑚白化率升高至60%(Lyu等，2022)。然而，珊瑚可以快速恢复：同年11月LCC恢复至10.56%(图4A)，珊瑚白化率和死亡率分别下降至6.39%和4.93%(图5A、5B)；2022年LCC恢复至12.78%，接近2019年白化前的14.84%。其恢复速度与其他相对高纬度珊瑚礁相近，如澳大利亚东南部的豪勋

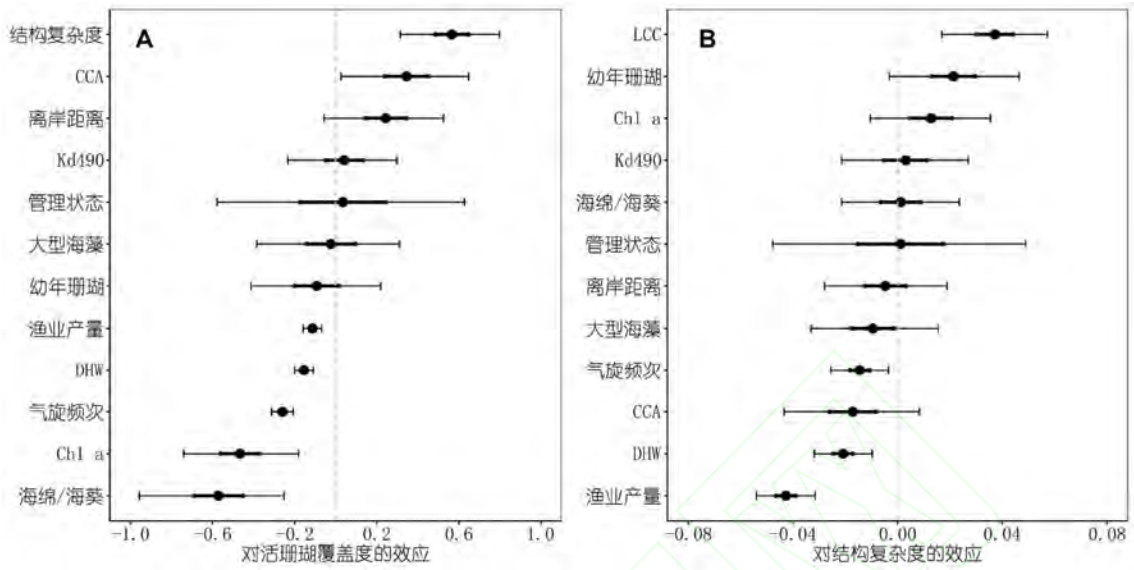


图 7 预测因子对(A)活珊瑚覆盖度(LCC)和(B)结构复杂度的效应。渔业产量、气旋频次和周热度(DHW)的效应通过广义线性模型评估，其余协变量通过贝叶斯分层模型评估；细线和粗线分别表示95%和50%的置信区间；仅当95%置信区间不与零重叠时，才认为预测因子具有统计显著性

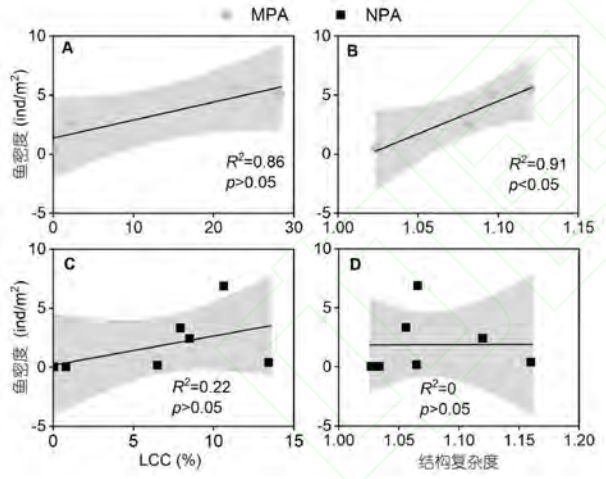


图 8 鱼密度与活珊瑚覆盖度(LCC)及结构复杂度的关系。(A) 海洋保护区(MPA)的鱼密度vs. LCC；(B)MPA的鱼密度vs.结构复杂度；(C)非海洋保护区(NPA)的鱼密度vs. LCC；(D) NPA的鱼密度vs.结构复杂度；阴影区域表示95%置信区间

爵岛(Lord Howe Island)LCC在干扰后3年恢复(Dalton等，2020)，日本西表岛(Iriomote Island)需要4年恢复(Nakamura等，2022)。恢复速度具有区域差异的影响因素包括珊瑚群落组成、初始覆盖度、干扰频率以及地方管理状态的差异等(Robinson等，2019)。

基因组模型、室内模拟实验和实地调查相结合的研究表明，珊瑚具有适应热胁迫的能力(Palumbi等，2014；Bay等，2017；Quigley等，2020)，其适应性受多种因素影响。首先，相对高纬度地区的SST存在季节性波动(Beger等，2014)，有助于增强珊瑚的耐热性(Wang X等，2024)。其次，涠洲岛的优势珊瑚为耐热性较强的团块状珊瑚(图6)。室内模拟实验表明，该区域团块状澄黄滨珊瑚(*Porites lutea*)优势种在热胁迫后的耐热性会增强(蒙林庆等，2022)。DHW记录显示2021–2024年涠洲岛珊瑚每年均受到严重热胁迫(图1C)，然而本研究实地调查与Lyu等(2022)的调查中，均未观察到大规模白化事件。这些分析综合表明，2020年的白化事件增强了涠洲岛珊瑚的耐热性，凸显了其在气候持续变化背景下的潜在弹性。

4.2 结构复杂度的驱动因素

气旋频次是结构复杂度的负影响因素(图7B)，会对珊瑚礁造成快速且严重的物理破坏(Alvarez-Filip等，2011b；Cheal等，2017)。2023年的两次气旋干扰造成涠洲岛珊瑚礁快速退化，其中LCC下降了42.10%(从12.78%降至7.40%)，结构复杂度下降了46.26%(从1.147降至1.079；图4)，珊瑚死亡率达到11.06%(图5B)。与此相类似，加勒比海频繁的气旋活动也导致结构复杂度持续下降(Alvarez-Filip等，2011b)。

除物理破坏外，热胁迫还通过生物机制间接加剧结构复杂度下降。虽然珊瑚热白化事件主要损伤珊瑚组织而非骨骼框架，但其会长期侵蚀珊瑚礁结构。例如，干扰后大型海藻和海绵/海葵的增加(图5D、5F)会抑制珊瑚生长且破坏珊瑚骨骼(Neumann，1966；Donovan等，2021)。此外，白化后未能恢复的珊瑚骨骼会被多种微生

物侵蚀，最终导致结构坍塌(Braz等，2022)。其他研究也表明热白化事件可引起结构复杂度的长期下降(Couch等，2017；Eakin等，2019；Bauman等，2022)。渔业产量、离岸距离与结构复杂度呈负相关关系(图7B)，表明人类活动进一步加剧了气候引起的结构复杂度下降。破坏性捕捞及陆源输入会通过降低生态系统弹性和破坏生态平衡加剧珊瑚礁退化。综上所述，本研究表明，气旋、热胁迫及人类活动的协同作用会持续侵蚀珊瑚礁结构，造成了涠洲岛的结构复杂度下降。

4.3 海洋保护区效应

研究发现，珊瑚白化率和死亡率在MPA显著低于NPA(图5A、5B)，且MPA的珊瑚恢复速度更快(图4A)。MPA比NPA的珊瑚表现出更强的抗干扰能力，可能与人为干扰有关。涠洲岛长期受到强烈的人为干扰，包括破坏性捕捞、陆源污染和旅游活动(Yu等，2019)。前人研究表明，水体富营养化和人类活动引起的海水污染会加剧海洋热浪后的珊瑚白化和死亡(Gove等，2023)。本研究也证明了富营养化(Chl a)及人类活动对珊瑚群落具有显著负面影响(图7A)。生长速度较快的叶片状珊瑚比例在MPA高于NPA(图6C)，可能是MPA珊瑚恢复较快的原因。然而，管理状态的影响相比其他因素较弱(图7)，原因在于气候因素的影响超过了管理效应。MPA管理可以有效减轻局部的人为干扰，但无法应对气候变化或大尺度环境变化(Johnson等，2022；Wang X等，2024)。尽管如此，本研究结果仍显示珊瑚礁的弹性在MPA强于NPA，表明减少局部的人为干扰对于提升生态系统弹性仍具有重要意义。

相对高纬度珊瑚礁的LCC与结构复杂度呈相反的变化趋势。虽然LCC在干扰后可快速恢复，但结构复杂度在MPA和NPA中均持续下降，未显示恢复迹象(图4)。这种相反的变化轨迹与珊瑚形态组成的简化相关，即复杂形态的珊瑚(如板状、叶片状和分枝状)向简单的团块状珊瑚转变(图6A、6B)。其他研究也认为，珊瑚礁的形态简化是珊瑚礁退化的主要表现(Couch等，2017；Bauman等，2022)。在涠洲岛，真叶珊瑚(*Echinophyllia* sp.)、牡丹珊瑚(*Pavona* sp.)和鹿角珊瑚(*Acropora* sp.)分别是板状、叶片状和分枝状珊瑚中覆盖度最高的属(网络版附表S2)。虽然这类珊瑚的热敏感性较低(Marshall和Baird，2000)，但其结构脆弱容易受到物理破坏。此外，幼年珊瑚覆盖度的增加可在一定程度上促进LCC的恢复，但由于体型较小(<5 cm)，对结构复杂度的贡献有限(图7B)。最主要的是，2020年大规模白化事件产生的滞后生物效应导致了结构复杂度的长期、持续下降，与前人研究一致(Neumann，1966；Graham等，2007；Donovan等，2021；Braz等，2022)。由于相对高纬度珊瑚的钙化速率比热带珊瑚慢(Howe和Marshall，2002)，且当前极端气候事件频繁出现，未来相对高纬度珊瑚结构复杂度的下降会比热带地区更加严重。

结构复杂度与生物多样性关系更强(Graham和Nash，2013；Darling等，2017)，是比LCC更稳健的珊瑚礁弹性指标。例如，MPA的鱼密度与结构复杂度呈显著正相关(图8B)，而与LCC的关系不显著(图8A)。NPA的鱼密度与结构复杂度之间没有显著关系(图8D)，可能是由于人为活动的干扰(Rees等，2018；Ford等，2020)。这些结果强调了结构复杂度在支持生态系统服务中的关键作用，并验证了其作为生态系统弹性指标的有效性。尽管MPA能够通过减轻局部人为干扰来增加生态系统弹性，但在气候压力与人类活动的双重干扰下，结构复杂度的持续下降总体上已降低了珊瑚礁的弹性。因此，虽然LCC在干扰后能快速恢复，我们仍亟需采取综合管理策略，以同时应对局部压力和全球气候变化下的结构复杂度持续下降。

4.4 结构复杂度的尺度效应

2020年我们测量的珊瑚礁结构复杂度明显低于2019年Wang Y等(2024)的数据(图4B)。虽然热胁迫会引起珊瑚白化和死亡，但短时间内不会破坏珊瑚礁结构(Lindahl等，2001；Wilson等，2009；Alvarez-Filip等，2011b)，因此2019–2020年结构复杂度的下降可能是测量方法差异引起的。Wang Y等(2024)在50 m的样带上每隔10 m测量1 m样线段的结构复杂度，实际上仅获得5 m的测量数据。本研究是沿整个50 m样带进行了连续测量，获取了完整断面的结构复杂度(图3)。由于结构复杂度值通常会随着测量尺度的增大而下降(Storlazzi等，2016)，Wang Y等(2024)测量的结构复杂度可能因采样尺度较小而偏高。因此，2019–2020年间结构复杂度的变化主要归因于测量方法差异，而非真实的生态变化。为进一步证实该推论，未来研究应关注不同测量方法引起的结构复杂度尺度效应。基于统一的调查方法将有助于提高研究结果之间的可比性，并使珊瑚礁结构复杂度的长期动态评估更加准确。

实际上，正是由于上述测量方法效率低，且不同方法的结果缺乏可比性，结构复杂度在珊瑚礁调查中常被忽视。因此，按生活史分类的珊瑚功能组通常作为珊瑚礁恢复的指标(Darling等，2012；Bierwagen等，2018；Chong等，2023)。近年来，技术的进步提供了高效且可广泛应用的多尺度结构复杂度调查方法，如水下摄影测

量、航空遥感以及卫星遥感(Storlazzi等，2016；Bachtiar等，2019；Asner等，2021)，不仅可提升不同结构复杂度结果的对比性，也可加深对生态弹性的理解。我们建议未来将结构复杂度与其他指标(如珊瑚功能组、幼年珊瑚)相结合，共同纳入珊瑚礁生态系统的弹性评估，以改进珊瑚礁弹性评估的长期监测体系。

4.5 局限性

由于数据的局限性，鱼密度与LCC、结构复杂度的关系仅开展了单年(2024年)的分析，可能会影响研究推论的稳健性。未来需要进一步开展长期的生态监测，以增强该部分研究结论的可信度，并进一步深入理解鱼类群落与栖息地特征的动态关系。

5 结论

长期以来，LCC一直是评估珊瑚礁健康状况的主要指标，但人们忽略了结构复杂度这一关键指标，无法全面理解珊瑚礁生态系统弹性。本研究对气候变化和人类活动双重干扰下的相对高纬度涠洲岛珊瑚礁开展研究，定量分析了2019–2024年珊瑚群落及结构复杂度的动态轨迹。结果表明，尽管LCC在干扰后两年内恢复，但结构复杂度的持续下降削弱了珊瑚礁的关键生态服务功能。MPA的珊瑚白化率和死亡率低于NPA，且恢复速度快于NPA。尽管持续下降，MPA的结构复杂度仍具有维持鱼类多样性的重要生态功能。将生物、环境及人为干扰指标纳入贝叶斯模型和GLM模型，研究结果表明气旋频次、DHW和渔业产量为结构复杂度下降的主要驱动因子。本研究揭示了相对高纬度珊瑚礁在气候变化和人类活动影响下的有限弹性，而构建MPA以减轻人为压力可作为增强生态系统弹性的重要措施，为珊瑚礁生态系统应对气候变化的综合弹性评估提供重要参考。鉴于结构复杂度的生态重要性及持续下降的趋势，我们建议将结构复杂度指标纳入珊瑚礁长期监测与管理体系。

补充材料 补充材料为作者提供的原始数据，作者对其学术质量和内容负责，详见网络版(http://earthcn.scichina.com)。

参考文献

黄晖. 2021. 中国珊瑚礁状况报告(2010–2019). 北京: 海洋出版社

李邢凡, 曹超, 蔡锋. 2019. 涠洲岛珊瑚礁系统特征及台风对其影响. 海洋开发与管理, 36: 49–52

蒙林庆, 黄雯, 阳恩广, 等. 2022. 高温白化事件可提高涠洲岛澄黄滨珊瑚(*Porites lutea*)的耐热性. 海洋学报, 44: 87–96

Alvarez-Filip L, Côté I M, Gill J A, et al. 2011a. Region-wide temporal and spatial variation in Caribbean reef architecture: Is coral cover the whole story? Glob Change Biol, 17: 2470–2477

Alvarez-Filip L, Gill J A, Dulvy N K, et al. 2011b. Drivers of region-wide declines in architectural complexity on Caribbean reefs. Coral Reefs, 30: 1051–1060

Anderson G D. 2025. Recovery of coral cover at Lizard Island Australia 6 years post-disturbance. Front Mar Sci, 11: 1509455

Asner G P, Vaughn N R, Foo S A, et al. 2021. Abiotic and human drivers of reef habitat complexity throughout the main Hawaiian Islands. Front Mar Sci, 8: 631842

Bachtiar I, Suharsono I, Damar A, et al. 2019. Practical resilience index for coral reef assessment. Ocean Sci J, 54: 117–127

Bauman A G, Januchowski-Hartley F A, Teo A, et al. 2022. Further flattening of a degraded, turbid reef system following a severe coral bleaching event. Front Mar Sci, 9: 910085

Bay R A, Rose N H, Logan C A, et al. 2017. Genomic models predict successful coral adaptation if future ocean warming rates are reduced. Sci Adv, 3: e1701413

Beger M, Sommer B, Harrison P L, et al. 2014. Conserving potential coral reef refuges at high latitudes. Divers Distrib, 20: 245–257

Bierwagen S L, Emslie M J, Heupel M R, et al. 2018. Reef-scale variability in fish and coral assemblages on the central Great Barrier Reef. Mar Biol, 165: 144

Braz G B, Lacerda C H F, Evangelista H, et al. 2022. Unprecedented erosion of *Mussismilia harttii*, a major reef-building species in the Southwestern Atlantic, after the 2019 bleaching event. Coral Reefs, 41: 1537–1548

Burns J H R, Fukunaga A, Pascoe K H, et al. 2019. 3D habitat complexity of coral reefs in the Northwestern Hawaiian Islands is driven by coral assemblage structure. Int Arch Photogramm Remote Sens Spatial Inf Sci, XLII-2/W10: 61–67

Burt A J, Koester A, Bunbury N, et al. 2025. Supporting resilience-based coral reef management using broadscale threshold approaches. Sci Rep, 15: 25836

Bürkner P C. 2021. Bayesian item response modeling in R with brms and Stan. J Stat Soft, 100: 1–54

Cheal A J, MacNeil M A, Emslie M J, et al. 2017. The threat to coral reefs from more intense cyclones under climate change. Glob Change Biol, 23: 1511–1524

Chen G K, Dai C F. 2021. Using 3D photogrammetry to quantify the subtle differences of coral reefs under the impacts of marine activities. Mar Pollut Bull, 173: 113032

Chong F, Sommer B, Stant G, et al. 2023. High-latitude marginal reefs support fewer but bigger corals than their tropical counterparts. Ecography, 2023: e06835

Clark J S. 2005. Why environmental scientists are becoming Bayesians. Ecol Lett, 8: 2–14

Comeau S, Carpenter R C, Nojiri Y, et al. 2014. Pacific-wide contrast highlights resistance of reef calcifiers to ocean acidification. Proc R Soc B, 281: 20141339

Couch C S, Burns J H R, Liu G, et al. 2017. Mass coral bleaching due to unprecedented marine heatwave in Papahānaumokuākea Marine National Monument (Northwestern Hawaiian Islands). PLoS One, 12: e0185121

Dalton S J, Carroll A G, Sampayo E, et al. 2020. Successive marine heatwaves cause disproportionate coral bleaching during a fast phase transition from El Niño to La Niña. Sci Total Environ, 715: 136951

Darling E S, Alvarez-Filip L, Oliver T A, et al. 2012. Evaluating life-history strategies of reef corals from species traits. Ecol Lett, 15: 1378–1386

Darling E S, Graham N A J, Januchowski-Hartley F A, et al. 2017. Relationships between structural complexity, coral traits, and reef fish assemblages. Coral Reefs, 36: 561–575

Donovan M K, Burkepile D E, Kratochwill C, et al. 2021. Local conditions magnify coral loss after marine heatwaves. Science, 372: 977–980

Eakin C M, Sweatman H P A, Brainard R E. 2019. The 2014–2017 global-

scale coral bleaching event: Insights and impacts. Coral Reefs, 38: 539–545
Emslie M J, Ceccarelli D M, Logan M, et al. 2024. Changing dynamics of Great Barrier Reef hard coral cover in the Anthropocene. Coral Reefs, 43: 747–762
Ford A K, Jouffray J B, Norström A V, et al. 2020. Local human impacts disrupt relationships between benthic reef assemblages and environmental predictors. Front Mar Sci, 7: 571115
Gardner T A, Côté I M, Gill J A, et al. 2005. Hurricanes and Caribbean coral reefs: Impacts, recovery patterns, and role in long-term decline. Ecology, 86: 174–184
Gonzalez K, Daraghmeh N, Lozano-Cortés D, et al. 2024. Differential spatio-temporal responses of Red Sea coral reef benthic communities to a mass bleaching event. Sci Rep, 14: 24229
González-Rivero M, Harborne A R, Herrera-Reveles A, et al. 2017. Linking fishes to multiple metrics of coral reef structural complexity using three-dimensional technology. Sci Rep, 7: 13965
Gove J M, Williams G J, Lecky J, et al. 2023. Coral reefs benefit from reduced land-sea impacts under ocean warming. Nature, 621: 536–542
Graham N A J, Wilson S K, Jennings S, et al. 2007. Lag effects in the impacts of mass coral bleaching on coral reef fish, fisheries, and ecosystems. Conserv Biol, 21: 1291–1300
Graham N A J, Nash K L, Kool J T. 2011. Coral reef recovery dynamics in a changing world. Coral Reefs, 30: 283–294
Graham N A J, Nash K L. 2013. The importance of structural complexity in coral reef ecosystems. Coral Reefs, 32: 315–326
Graham N A J, Jennings S, MacNeil M A, et al. 2015. Predicting climate-driven regime shifts versus rebound potential in coral reefs. Nature, 518: 94–97
Graham N A J, Robinson J P W, Smith S E, et al. 2020. Changing role of coral reef marine reserves in a warming climate. Nat Commun, 11: 2000
Guest J R, Baird A H, Maynard J A, et al. 2012. Contrasting patterns of coral bleaching susceptibility in 2010 suggest an adaptive response to thermal stress. PLoS One, 7: e33353
Guest J R, Tun K, Low J, et al. 2016. 27 years of benthic and coral community dynamics on turbid, highly urbanised reefs off Singapore. Sci Rep, 6: 36260
Guinotte J M, Buddemeier R W, Kleypas J A. 2003. Future coral reef habitat marginality: Temporal and spatial effects of climate change in the Pacific basin. Coral Reefs, 22: 551–558
Guo J, Yu K F, Wang Y H, et al. 2019. Potential impacts of anthropogenic nutrient enrichment on coral reefs in the South China Sea: Evidence from nutrient and chlorophyll a levels in seawater. Environ Sci-Processes Impacts, 21: 1745–1753
Halpern B S. 2003. The impact of marine reserves: Do reserves work and does reserve size matter? Ecol Appl, 13: 117–137
Hansen R L, Halford A, Maucieri D G, et al. 2025. Spatial variation in benthic community composition on a minimally disturbed coral reef in the years following a prolonged marine heatwave. bioRxiv: 636502
Hoey A S, Pratchett M S, Cvitanovic C, et al. 2011. High macroalgal cover and low coral recruitment undermines the potential resilience of the World's southernmost coral reef assemblages. PLoS One, 6: e25824
Howe S A, Marshall A T. 2002. Temperature effects on calcification rate and skeletal deposition in the temperate coral, *Plesiastrea versipora* (Lamarck). J Exp Mar Biol Ecol, 275: 63–81
Hughes T P, Barnes M L, Bellwood D R, et al. 2017a. Coral reefs in the Anthropocene. Nature, 546: 82–90
Hughes T P, Kerry J T, Álvarez-Noriega M, et al. 2017b. Global warming and recurrent mass bleaching of corals. Nature, 543: 373–377
Hughes T P, Kerry J T, Baird A H, et al. 2018. Global warming transforms coral reef assemblages. Nature, 556: 492–496
Hughes T P, Kerry J T, Baird A H, et al. 2019. Global warming impairs stock-recruitment dynamics of corals. Nature, 568: 387–390
Johnson J V, Dick J T A, Pincheira-Donoso D. 2022. Marine protected areas do not buffer corals from bleaching under global warming. BMC Ecol Evo, 22: 58
Jones N P, Figueiredo J, Gilliam D S. 2020. Thermal stress-related spatiotemporal variations in high-latitude coral reef benthic communities. Coral Reefs, 39: 1661–1673
Kassambara A. 2023. *rstatix*: Pipe-friendly framework for basic statistical tests. R package version 0.7.2
Knudby A, Jupiter S, Roelfsema C, et al. 2013. Mapping coral reef resilience indicators using field and remotely sensed data. Remote Sens, 5: 1311–1334
Knudby A, Richardson G. 2023. Incorporation of neighborhood information improves performance of SDB models. Remote Sens Appl-Soc Environ, 32: 101033
Koester A, Migani V, Bunbury N, et al. 2020. Early trajectories of benthic coral reef communities following the 2015/16 coral bleaching event at remote Aldabra Atoll, Seychelles. Sci Rep, 10: 17034
Kohler K E, Gill S M. 2006. Coral Point Count with Excel extensions (CPCe): A Visual Basic program for the determination of coral and substrate coverage using random point count methodology. Comput Geoscis, 32: 1259–1269
Lachs L, Donner S D, Mumby P J, et al. 2023. Emergent increase in coral thermal tolerance reduces mass bleaching under climate change. Nat Commun, 14: 4939
Lindahl U, Öhman M C, Schelten C K. 2001. The 1997/1998 mass mortality of corals: Effects on fish communities on a Tanzanian coral reef. Mar Pollut Bull, 42: 127–131
Lucas C C, Teixeira C E P, Braga M D A, et al. 2023. Heatwaves and a decrease in turbidity drive coral bleaching in Atlantic marginal equatorial reefs. Front Mar Sci, 10: 1061488
Lyu Y H, Zhou Z H, Zhang Y M, et al. 2022. The mass coral bleaching event of inshore corals form South China Sea witnessed in 2020: Insight into the causes, process and consequence. Coral Reefs, 41: 1351–1364
MacNeil M A, Mellin C, Matthews S, et al. 2019. Water quality mediates resilience on the Great Barrier Reef. Nat Ecol Evol, 3: 620–627
Magel J M T, Burns J H R, Gates R D, et al. 2019. Effects of bleaching-associated mass coral mortality on reef structural complexity across a gradient of local disturbance. Sci Rep, 9: 2512
Marshall P A, Baird A H. 2000. Bleaching of corals on the Great Barrier Reef: Differential susceptibilities among taxa. Coral Reefs, 19: 155–163
McClanahan T R. 2017. Changes in coral sensitivity to thermal anomalies. Mar Ecol Prog Ser, 570: 71–85
McGillycuddy M, Warton D I, Popovic G, et al. 2025. Parsimoniously fitting large multivariate random effects in glmmTMB. J Stat Soft, 112: 1–9
Mongin M, Baird M E, Tilbrook B, et al. 2016. The exposure of the Great Barrier Reef to ocean acidification. Nat Commun, 7: 10732
Nakamura M, Murakami T, Kohno H, et al. 2022. Rapid recovery of coral communities from a mass bleaching event in the summer of 2016, observed in Amitori Bay, Iriomote Island, Japan. Mar Biol, 169: 104
Neumann A C. 1966. Observations on coastal erosion in Bermuda and measurements of the boring rate of the sponge, *Cliona LAMPA* 1,2. Limnol Oceanogr, 11: 92–108
Oksanen J, Simpson G, Blanchet F, et al. 2025. *vegan*: Community ecology package. R package version 2.7-1
Palumbi S R, Barshis D J, Traylor-Knowles N, et al. 2014. Mechanisms of reef coral resistance to future climate change. Science, 344: 895–898
Pinheiro H T, MacDonald C, Santos R G, et al. 2023. Plastic pollution on the world's coral reefs. Nature, 619: 311–316
Polidoro B, Carpenter K. 2013. Dynamics of coral reef recovery. Science, 340: 34–35
Pratchett M S, McCowan D, Maynard J A, et al. 2013. Changes in bleaching

susceptibility among corals subject to ocean warming and recurrent bleaching in Moorea, French Polynesia. PLoS One, 8: e70443
Quigley K M, Bay L K, van Oppen M J H. 2020. Genome-wide SNP analysis reveals an increase in adaptive genetic variation through selective breeding of coral. Mol Ecol, 29: 2176–2188
R Core Team. 2025. R: A language and environment for statistical computing. Version 4.5.1
Rees M J, Knott N A, Neilson J, et al. 2018. Accounting for habitat structural complexity improves the assessment of performance in no-take marine reserves. Biol Conservation, 224: 100–110
Riegl B, Piller W E. 2003. Possible refugia for reefs in times of environmental stress. Int J Earth Sci, 92: 520–531
Risk M J. 1972. Fish diversity on a coral reef in the Virgin Islands. Atoll Res Bull, 153: 1–4
Robinson J P W, Wilson S K, Graham N A J. 2019. Abiotic and biotic controls on coral recovery 16 years after mass bleaching. Coral Reefs, 38: 1255–1265
Ross C L, French B, Lester E K, et al. 2021. Coral communities on marginal high-latitude reefs in West Australian Marine Parks. Diversity, 13: 554
Safaie A, Silbiger N J, McClanahan T R, et al. 2018. High frequency temperature variability reduces the risk of coral bleaching. Nat Commun, 9: 1671
Spalding M, Burke L, Wood S A, et al. 2017. Mapping the global value and distribution of coral reef tourism. Mar Policy, 82: 104–113
Stan Development Team. 2020. *RStan*: The R interface to Stan. R package version 2.18.2
Storlazzi C D, Dartnell P, Hatcher G A, et al. 2016. End of the chain? Rugosity and fine-scale bathymetry from existing underwater digital imagery using structure-from-motion (SfM) technology. Coral Reefs, 35: 889–894
Sully S, Burkepile D E, Donovan M K, et al. 2019. A global analysis of coral bleaching over the past two decades. Nat Commun, 10: 1264
Sun F D, Sun W X, Chen J, et al. 2012. Comparison and improvement of methods for identifying waterbodies in remotely sensed imagery. Int J Remote Sens, 33: 6854–6875
Thompson D M, van Woesik R. 2009. Corals escape bleaching in regions that recently and historically experienced frequent thermal stress. Proc R Soc B, 276: 2893–2901
van Hooidonk R, Maynard J A, Manzello D, et al. 2014. Opposite latitudinal gradients in projected ocean acidification and bleaching impacts on coral reefs. Glob Change Biol, 20: 103–112
Wang X, Li Y Q, Lin M Q, et al. 2024. Thermal bleaching in the northern South China Sea: Impact of abnormal environment and climate on high-latitude coral reefs. Environ Sci Pollut Res, 31: 1576–1588
Wang Y Z, Li Y X, Yu K F, et al. 2024. Evaluating coral reef restoration in marine protected areas using habitat structural complexity and coral communities. Environ Monit Assess, 196: 1242
White A T, Vogt H P, Arin T. 2000. Philippine coral reefs under threat: The economic losses caused by reef destruction. Mar Pollut Bull, 40: 598–605
Wilson S K, Dolman A M, Cheal A J, et al. 2009. Maintenance of fish diversity on disturbed coral reefs. Coral Reefs, 28: 3–14
Wu M H M, Ribas-Deulofeu L, Liu C H E, et al. 2025. Benthic drivers of structural complexity in coral reefs across a tropical-subtropical transition zone. Front Mar Sci, 12: 1513498
Yanovski R, Abelson A. 2019. Structural complexity enhancement as a potential coral-reef restoration tool. Ecol Eng, 132: 87–93
Yu W J, Wang W H, Yu K F, et al. 2019. Rapid decline of a relatively high latitude coral assemblage at Weizhou Island, northern South China Sea. Biodivers Conserv, 28: 3925–3949
Zaneveld J R, Burkepile D E, Shantz A A, et al. 2016. Overfishing and nutrient pollution interact with temperature to disrupt coral reefs down to microbial scales. Nat Commun, 7: 11833
Zawada K J A, Madin J S, Baird A H, et al. 2019. Morphological traits can track coral reef responses to the Anthropocene. Funct Ecol, 33: 962–975
Zhang W, Huang R Y, Deng S W, et al. 2024. Spatio-temporal distribution of sea surface chlorophyll-a in coral reefs of the South China Sea over the past decade based on Landsat-8 Operational Land Images. Sci Total Environ, 935: 173433
Zuo X L, Qin B N, Teng J C, et al. 2023. Optimized spatial and temporal pattern for coral bleaching heat stress alerts for China's coral reefs. Mar Environ Res, 191: 106152

（责任编委：张锐）

江蕾蕾, 黄达华, 赵佰玲, 等. 珊瑚骨骼荧光记录环境变化的研究进展[J]. 海洋学报, 2025, 47(x): 1–12, doi:
Jiang Leilei, Huang Dahua, Zhao Bailing, et al. Research progress on coral skeleton fluorescence as an indicator of environmental changes[J]. Haiyang Xuebao, 2025, 47(x): 1–12, doi:

珊瑚骨骼荧光记录环境变化的研究进展

江蕾蕾[1]，黄达华[1]，赵佰玲[1]，余克服[1, 2*]

(1. 广西大学 广西南海珊瑚礁研究重点实验室, 珊瑚礁研究中心, 海洋学院, 广西 南宁 530004; 2. 南方海洋科学与工程广东省实验室(广州), 广东 广州 511458)

摘要: 广泛分布于热带海域的块状滨珊瑚作为高分辨率环境变化记录的理想载体, 在古气候和古环境重建领域受到广泛关注。珊瑚骨骼在长波紫外线照射下发出的荧光因对陆地径流、污染物和气候事件的敏感性, 成为揭示与降雨和径流量等相关的多种环境变化信息的又一手段。本文综述了珊瑚骨骼荧光物质的形成机制、测量方法、在环境重建中的应用以及当前挑战和未来发展方向。总体而言, 珊瑚骨骼中的荧光信号主要来源于以富啡酸为主的陆源输入腐殖酸类物质, 以及共生藻类代谢产生的类腐殖质物质。珊瑚骨骼结构和矿物特性, 以及降雨、径流等环境因子的交互作用也会影响珊瑚骨骼荧光。通过高精度微取样技术与荧光分析方法的结合, 科学家们已成功重建了不同时间尺度的陆地径流、降雨、人类活动等环境变化历史。基于目前国际上的研究进展, 本文建议未来研究应探索新型分析技术, 结合多源数据建立更精确的荧光–水文定量模型, 并且加强与其他代用指标的交叉验证以建立高精度、高分辨率的全球珊瑚荧光数据库。

关键词: 珊瑚骨骼; 荧光条带; 陆源富啡酸; 陆地径流量; 降雨量

中图分类号:　　**文献标志码:** A　　**文章编号:** 0253−4193(2025)x−0001−12

1　引言

在热带浅海广泛分布的造礁珊瑚(主要是石珊瑚目)通过与虫黄藻共生构建碳酸钙骨骼。这一生物矿化过程使其成为记录环境变化的独特载体。块状滨珊瑚(*Porites*)因其清晰的年生长纹层(图 1a)、数百年连续生长能力、优异的物理稳定性以及文石骨骼的精确年代学特征, 被公认为重建热带海洋气候与环境历史的高分辨率档案[1–2]。其骨骼的多种地球化学指标和生长参数已广泛用于气候环境重建: 例如, 生长率[3]、Sr/Ca[4]、U/Ca[5]、Li/Mg[6]反映海表温度变化; Ba/Ca 是记录陆地径流的有效指标[7]; Cd/Ca 和稀土元素揭示季风变化[8–9]; Sr/Ca 与 $\delta^{18}O$ 结合得出的海水氧同位素($\delta^{18}O_{seawater}$)记录着海水表层盐度信息[10]; $\delta^{13}C$ 有助于示踪季风和野火变化[11–12]; $\delta^{11}B$ 则是重建古海水 pH 的有力工具[13]。这些指标不仅能够以月–年尺度记录环境变化, 更弥补了传统古气候重建方法在时间分辨率和空间覆盖上的不足[14–15]。

1984 年, Isdale[16]在澳大利亚大堡礁的块状滨珊瑚研究中首次发现, 骨骼切片在长波紫外线(320–400 nm)照射下会产生黄–绿荧光带(图 1b), 与背景蓝色荧光形成鲜明对比, 且荧光强度与河流径流量显著相关(图 1c)。后续研究证实, 这种由荧光(80%)和磷光(20%)组成的发光信号[17], 特别是黄白色、黄色、

收稿日期: 2025−06−23; **修订日期:** 2025−08−20。

基金项目: 广西自然科学基金青年项目(2024JJB150060); 国家重点研发计划(2023YFF0804801); 广西科技基地和人才专项(桂科AD25069075); 广西壮族自治区青苗人才资助科研项目(202401998); 广西壮族自治区教育厅 2024 年度广西高校中青年教师科研基础能力提升项目(2024KY0020)。

作者简介: 江蕾蕾(1995—), 女, 河南省新县人, 助理教授, 主要从事珊瑚礁地质和高分辨率环境记录研究。E-mail: jianglei@gxu.edu.cn

*** 通信作者:** 余克服, 教授, 主要从事珊瑚礁地质、生态与环境研究。E-mail: kefuyu@scsio.ac.cn

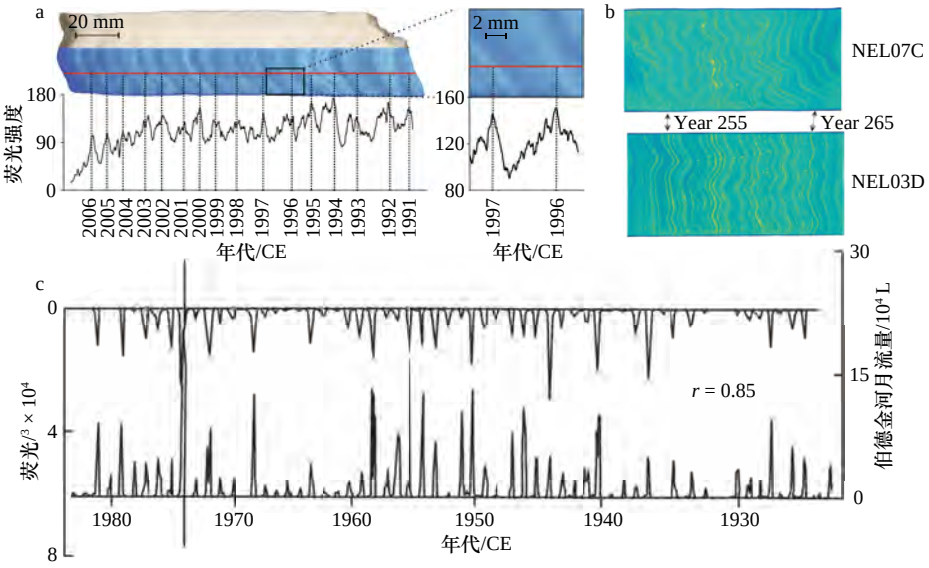


图 1 珊瑚骨骼荧光示意图

Fig. 1 Schematic diagram of coral skeleton fluorescence

(a) 可见光(上半部分)和紫外光(下半部分)扫描下的珊瑚岩芯剖面的数字图像示例。红色横截线代表测量绿色荧光强度的区域, 1991 年至 2006 年的峰值为原始数据的年周期。黑框显示的是 1996 年和 1997 年相对荧光强度的放大部分(右图)。在放大图像(红色)上创建了一个较小的单独横断面, 以确定强度的细微波动[22]。(b) 紫外光下珊瑚切片的数字增强照片表明荧光线的匹配模式[20]。(c) 伯德金河的月流量与对应的珊瑚骨骼的荧光强度[16]

(a) Example of digital images of a coral core section under visible light (upper panel) and UV light (lower panel). The red transect lines indicate the regions where green fluorescence intensity was measured, with peaks from 1991 to 2006 representing annual cycles in the raw data. The black box highlights a magnified view (right panel) of the relative luminescence intensity for 1996 and 1997. A smaller independent transect (red) was created on the zoomed-in image to resolve fine-scale intensity fluctuations[22]. (b) Digitally enhanced photograph of a coral slab under UV light, demonstrating the matching patterns of luminescent bands[20]. (c) Monthly discharge of the Burdekin River plotted against corresponding coral skeletal fluorescence intensity[16]

黄绿色或灰白色荧光带以及蓝色非荧光带, 能够非破坏性地记录降雨、径流等环境信息, 分辨率可达季节-年际尺度[18−19], 这为理解历史气候变异提供了独特视角。作为又一环境代用指标, 珊瑚骨骼荧光在记录与降雨、径流相关的古环境变化方面展现出显著优势: (1)相较于传统地球化学分析通常所需的复杂前处理、高成本精密仪器测试以及对样品的损耗, 荧光分析操作简便、成本低廉、耗时短且可以做到无损分析, 允许对同一样本重复测量或进行其他分析。(2)通过紫外光下目视判读或成像分析荧光, 可快速筛查珊瑚样品, 初步获取陆源输入等环境信息[19], 操作便捷性堪比测量生长率。(3)荧光信号主要反映珊瑚骨骼生长期间摄入并结合的陆源有机物质, 是一种可见的表面光学现象, 受珊瑚生长生理过程造成的骨骼结构扭曲影响远小于线性生长率、钙化率或密度等参数[18−19], 使其能更直接地反映环境驱动因子。(4)荧光信号对化石珊瑚中常见的、可能导致生长轴偏移或模糊的成岩作用相对不敏感, 使其在评估保存状况欠佳或生长轴难以精确定位的化石样品时具有独特价值。即使在整体方解石化程度高达 70% 的情况下, 其荧光信号仍能有效用于古环境重建[20]。这种稳定性主要源于珊瑚骨骼中腐殖酸异常的热稳定性(分解温度达 200℃), 使其经历数十万年成岩作用仍能保持现代珊瑚种 60%–80% 的含量[21]。

因此, 凭借其高效无损、操作便捷、抗生长变形干扰以及对化石样本适应性强等核心优势, 珊瑚骨骼荧光分析已成为古气候与古环境重建领域, 尤其是高分辨率水文气候研究中, 获取古降雨、径流信息的一种快速、可靠且不可替代的强有力工具。本文旨在系统阐述珊瑚荧光的形成机制、分析技术、环境指示意义及当前挑战, 以期推动珊瑚骨骼高分辨率环境记录研究, 并为全球变化研究提供新思路。

2 珊瑚骨骼荧光的形成机制

珊瑚骨骼荧光现象的形成机制涉及复杂的生物地球化学过程与多因素相互作用。珊瑚骨骼中的荧光信号主要来源于两类有机组分: 以富啡酸为主的陆源输入腐殖酸类物质, 以及共生藻类代谢产生的类腐殖质物质[22−23]。这些物质在紫外光或蓝光激发下会产生特征性荧光(440–480 nm), 其强度变化直接反映了环境中有机物输入的动态变化。此外, 海洋细菌产生的溶解有机物[24]、构成珊瑚骨骼碳酸盐矿物中的

微量元素、有机物质以及骨骼结构中的孔隙[25]均可能导致珊瑚骨骼发光(图 2)。本节将从荧光有机组分的来源、骨骼结构和矿物特性的调控, 以及环境因子与生物作用的交互影响三个层面系统阐述珊瑚骨骼荧光的形成机制。

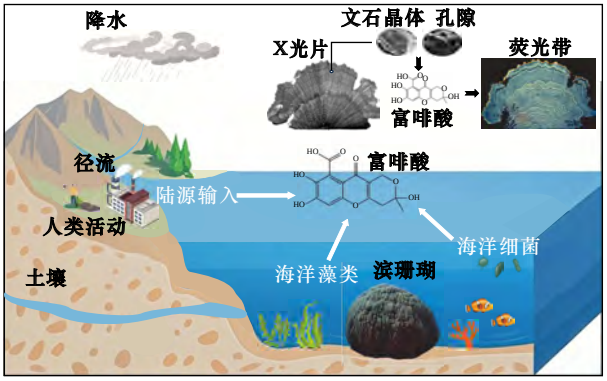


图 2　珊瑚荧光形成机制示意图

Fig. 2　Schematic diagram of the formation mechanism of coral fluorescence

滨珊瑚、X 光片和荧光带素材分别根据 http://heinzkrimmer.com 和 Lough[26] 改绘

Porites, positive print of X-ray of slice and bright luminescent lines are from http://heinzkrimmer.com and Lough[26]

2.1　荧光有机组分的来源

腐殖质是生物残体经微生物分解和化学作用形成的一类结构复杂、无特定化学组成的有机混合物统称, 外观呈黄色至棕色[27]。其分子量范围广(几百至数百万), 包含具有荧光特性的不饱和脂肪族和芳香族化合物等[28–29], 广泛存在于陆地和海洋生态系统。根据溶解性, 腐殖物质可分为三类: 不溶于碱但溶于乙酰溴的胡敏素、碱抽提液中可被无机酸沉淀的胡敏酸、以及酸处理后仍保留在溶液中的富啡酸。其中, 水溶性良好的胡敏酸和富啡酸合称腐殖酸, 是腐殖物质的主要成分。

早期研究明确了珊瑚荧光带的物质基础。Boto 和 Isdale[30] 发现珊瑚经稀盐酸或热碱(0.1M NaOH)处理后均呈现腐殖酸特有的宽荧光光谱, 并伴有 Fe^{3+} 诱导的荧光淬灭和红移现象; 结合离子交换实验, 证实其中 90% 的荧光物质为富啡酸。这些陆源腐殖酸主要经河流径流和地表侵蚀输入海洋, 并在迁移过程中呈现显著浓度梯度: 土壤含量(1 310–5 070 μg/g)比河水高 2–3 个数量级, 而河水又比海水高 2–10 倍[31]。珊瑚选择性吸收陆源腐殖酸[32], 导致骨骼中形成荧光带[24, 31, 33], 在紫外光激发下产生宽谱荧光并呈现黄绿色偏移[22, 23]。其中, 黄–绿色荧光带部位的腐殖酸含量比蓝色非荧光带部位高 1–3 倍, 直接导致了荧光特征的分异。因此, 这类荧光带强度随离岸距离呈指数衰减[34], 至大陆架外缘完全消失[30], 并与径流量变化同步消长[21, 35]。沿岸水体腐殖酸含量仅在河海混合界面显著增加, 结合富啡酸在水体中短半衰期(2–5 天)及随距离指数衰减的特性[30], 解释了黄–绿荧光带严格限于近岸珊瑚的现象。例如, 台湾南部珊瑚骨骼富啡酸的年分辨率荧光光谱分析明确证实了其陆源属性[36]。同样, 大堡礁大量珊瑚样本的系统研究也表明, 荧光强度能有效表征大陆物质输入对珊瑚礁的影响程度[37]。因此, 珊瑚荧光带可作为量化陆源物质输入及其对珊瑚礁生态系统潜在胁迫的关键指标。

然而, 传统上以陆源腐殖酸为主导的珊瑚荧光带形成理论面临挑战: Jones 等[38]在没有重大河流事件的情况下观测到异常荧光峰值; 同时, 远离陆源影响的珊瑚中也普遍记录着清晰的荧光条带[21, 31, 39–41]。这些现象推动了对荧光带形成机制的重新审视。研究表明, 珊瑚骨骼的蓝色荧光主要源于海洋内源性富啡酸[30–31, 42–43], 尤其在远洋或寡营养海域, 其荧光特性依赖于海洋内源有机物, 如共生藻类的代谢产物和海洋细菌分泌的溶解性有机物[24, 39]。尽管虫黄藻光合作用产生的类腐殖质物质的荧光光谱与陆源富啡酸相似(发射峰 420–450 nm), 但其更高的碳氮比(> 15)可通过三维荧光光谱区分[24]。此外, 内生蓝藻分泌的黄素类物质以及浮游植物降解产生的类蛋白成分也被认为可能贡献蓝色荧光[44]。Matthews 等[24]在泰国普吉岛的研究通过三维荧光光谱技术系统对比了珊瑚骨骼荧光带、非荧光带组分及周边海水溶解有机物, 发现三者荧光特征高度一致, 且均呈现典型的海洋溶解有机物光谱特征, 而非陆源腐殖酸信号。这表明珊瑚荧光带颜色的差异更可能源于腐殖酸浓度梯度、pH 波动以及色氨酸等小分子物质的能量转移-淬灭效应, 而非荧光物质种类的根本变化。

2.2　骨骼结构和矿物特性

珊瑚骨骼的物理结构特性对荧光现象的影响日益受到关注。研究表明, 在远离陆源的远洋环境中, 骨骼密度和孔隙结构的周期性变化可导致显著荧光差异[38, 41]。Barnes 和 Taylor[25]发现低密度带(孔隙率 > 30%)的荧光强度比高密度带(孔隙率< 15%)高 40%–60%, 这主要归因于大孔隙的多重反射效应和特定波长的优先吸收。基于此, 研究者提出了“荧光带”与“荧光线”的分类体系: 前者指与年生长周期相关的宽带弱荧光, 主要受骨骼孔隙结构调控; 后者则是与陆源径流密切相关的窄带强荧光, 可作为环境变化的精确指标。

珊瑚骨骼的晶体特性同样影响荧光表现。文石晶体的择优取向形成“光学波导”效应，可使光子传输效率提高 2–3 倍[45]。Prouty 等[46]在关岛的研究证实，晶体排列整齐区域的荧光强度比杂乱区域高出 50%。此外，晶体缺陷为荧光物质提供了高效吸附位点，导致荧光带内文石晶体表面的富啡酸覆盖率可达非荧光带的 3–4 倍[47]。然而，关于珊瑚微观结构主导荧光强度变化的观点仍存在争议：Ramseyer 等[48]认为珊瑚荧光与高孔隙度和低碳酸钙密度相关；Lough[26]发现滨珊瑚骨骼密度与荧光强度呈正相关；而 Tanzil 等[33]则指出荧光变化与盐度而非骨骼密度相关。Barnes 和 Taylor[47]通过粉末化实验进一步证明，除孔隙度外，碳酸盐矿物的粒度分布、固结程度和化学成分同样显著影响荧光特征。这些研究共同揭示了珊瑚荧光机制的复杂性，强调需要从物理-化学协同作用的角度进行更深入的理解。

2.3 环境因子与生物作用的交互影响

近海珊瑚骨骼荧光带作为量化陆源物质输入的关键指标，其形成受控于影响陆源输入的环境因子。一方面，强降雨事件通过增加陆源有机物输送显著增强荧光信号，导致珊瑚荧光强度与河流径流量高度正相关[16]。另一方面，强降雨引发的淡水输入通过改变盐度影响珊瑚荧光。Lough 等[37]研究表明，海水盐度仅需降低 1–2‰即可触发荧光响应，且荧光强度与盐度下降程度存在定量关系。然而，盐度对荧光强度的调控呈现非线性特征：大堡礁近岸珊瑚在盐度 25‰时，荧光强度较正常盐度（35‰）高出 80%[37]，而红海珊瑚在高盐（40‰）环境下的荧光强度则降至背景值的 50%[21]，这与富啡酸溶解–凝聚平衡的转变密切相关。

此外，大尺度气候模态通过遥相关作用调控珊瑚荧光特征。厄尔尼诺-南方涛动（El Niño-Southern Oscillation, ENSO）通过改变季风强度影响径流输入，导致大堡礁珊瑚荧光强度在拉尼娜年升高 25%，在厄尔尼诺年降低 18%[49−50]。太平洋年代际震荡（Pacific Decadal Oscillation, PDO）负相位期间（1947—1976 年），澳大利亚东北部珊瑚荧光呈现每 10 年上升 5% 的长期趋势[51]。需要注意的是，部分珊瑚荧光与河流径流量无显著关联[34]，且季节性洪水未必导致预期荧光带形成[46]。

珊瑚共生生物群落对荧光信号产生显著干扰。虫黄藻光合作用消耗溶解有机碳，减少富啡酸可利用量，导致虫黄藻密度与荧光强度呈负相关（$r=-0.65$）[52]。例如，虫黄藻密度较低的块状珊瑚（1×10^6 cells/cm^2）其荧光强度比密度较高的枝状珊瑚（2×10^5 cells/cm^2）高 30%–40%[1]。内生蓝藻分泌的类腐殖酸物质会产生光谱干扰，加勒比海珊瑚经抗生素处理后荧光强度下降 15%–20%[44]。这些生物效应随环境条件动态变化：水温从 25℃ 升至 30℃ 时，珊瑚对富啡酸的吸收率从 10 ng/(cm^2.d) 提升至 20 ng/(cm^2.d)，表明高温期富啡酸积累效率提高 50%[17]。

综上，珊瑚骨骼荧光的形成是“有机组分供给-结构物理调控-环境生物驱动”多过程耦合作用的结果。值得注意的是，不同海域珊瑚荧光信号的区域差异主要取决于当地主导的环境压力类型，这种特异性在利用荧光指标进行环境重建时需要特别关注。

3 荧光测量方法的技术演进

珊瑚骨骼荧光分析技术的发展历程展现了从单一到多元的技术演进路径。

早期研究阶段（1980s），Isdale[16]开创性地采用长波紫外灯（365 nm）照射珊瑚切片，通过分光荧光仪检测特征性宽谱荧光（激发峰 320–340 nm，发射峰 410–440 nm），首次建立了黄绿荧光带强度与伯德金河径流量的定量关系（图 1c）。Boto 和 Isdale[30]随后改进光源系统，采用 360 nm 带通滤波汞灯将空间分辨率提升至毫米级，这一技术突破使 Smith 等[53]成功重建了 1881—1986 年沙克河湾径流量变化，验证了早期紫外激发技术在水文重建中的可靠性。

技术革新阶段（1990s—2000s）见证了激光诱导荧光与色谱联用技术的突破性发展。Milne 和 Swart[43]开发的氮激光诱导系统（337 nm）实现了半月时间分辨率和 0.5 mm 空间分辨率，首次捕捉到腐殖酸脉冲与雨季的滞后响应关系。Nyberg[54]进一步开发三波长多通道检测系统，揭示了降雨驱动的陆源输入与风力对珊瑚荧光的双重调控机制。Peng 等[55]采用 266 nm 固态激光系统，建立了荧光强度与琼海年降雨量的定量关系模型，并成功重建了与 El Niño 事件相关的降雨序列。与此同时，色谱分析技术取得重要进展，Susic 和 Boto[56]建立的高效液相色谱-荧光检测法实现了纳克级腐殖酸检测。Barnes 等[57]的激光诱导击穿光谱-质谱联用技术实现了微区元素与分子同步成像。此外，Lough[58]采用四级强度分类法，基于主观视觉评估重建了 17 世纪以来的淡水流量和降雨量变化，并在此基础上提出采用年度荧光范围（夏季峰值与冬季最小值之差）作为降雨指标的新方法，显著提高了降雨重建的精确度。

现代技术整合阶段（2010s 至今）以三维荧光光谱

和多技术融合为特征。Grove 等[22]开发的快速光谱扫描技术通过蓝绿比(G/B)分离腐殖酸与背景信号,成功重建了 300 年径流序列[59]。Wagner 等[29]创新性地整合尺寸排阻色谱与多检测器联用,为分子量–荧光关联研究提供新思路。Kaushal 等[32]发展的溶液荧光法实现低于 4 mg 样品的精准定量,其建立的腐殖酸定量模型将技术应用拓展至陆地碳输入历史研究[60−61]。当前技术体系已形成“三波长校准协议”标准方法(激发波长 360 nm,发射波长 430 nm、490 nm 和 530 nm)[62],但仍需解决参数定义和数据处理的标准化问题以提升跨区域研究可比性。这一技术发展脉络不仅深化了对气候-水文机制的认识,也为环境变化研究提供了日益精确的分析工具。

4　珊瑚骨骼荧光在环境重建中的应用

4.1　珊瑚骨骼荧光在水文重建中的时空响应机制

珊瑚骨骼荧光作为重建古环境变化的重要指标,其形成机制与陆源有机质输入密切相关。当洪水发生时,河流携带大量泥沙和腐殖酸等有机物质进入海洋,被珊瑚吸收后能显著增强其荧光强度[16, 42];同时,洪水引发的盐度变化亦会改变荧光特征[53]。深入研究表明,洪水期河流携带的高浓度腐殖酸是珊瑚荧光信号的核心来源:珊瑚通过摄食和骨骼生长过程将荧光物质富集于骨骼孔隙结构中,而洪水期间 15%–20% 的骨骼孔隙率增幅进一步强化此过程[47]。这种机制使珊瑚荧光强度峰值与洪水规模、径流脉冲频率及陆源物质输入量呈显著正相关,成为重建历史洪水事件的可靠指标。例如,澳大利亚大堡礁 Pandora 礁的研究显示,1974 年的强洪水事件使珊瑚荧光强度骤升至年均值的 3 倍,荧光带厚度增加了 53%,直接记录了陆源有机质的脉冲式输入[16, 63]。中国海南岛的研究也证实,珊瑚荧光强度与降雨量($r = 0.78$)、河流流量($r = 0.74$)高度相关,据此重建的水文序列与实测数据的误差小于 8%[55]。这些共同验证了珊瑚骨骼荧光对极端水文事件的记录能力。

值得注意的是,珊瑚骨骼荧光的空间分布呈现出清晰的陆源影响梯度。巴布亚新几内亚 Motupore 地区的研究表明,距河口 2 km 范围内的滨珊瑚显示出典型的黄-绿荧光带,其强度与月降雨同步变化[40];大堡礁区域建立的荧光强度(FI, cps)与离岸距离(D, km)的指数模型($FI = 1\,020 \times e^{-0.04D}$)进一步量化了陆源影响的衰减规律[37]。这种空间特征同时受流域环境调制:热带雨林流域因植被覆盖度高,其对应的珊瑚荧光带通常呈现连续均匀的特征;而干旱半干旱流域因悬浮泥沙含量高,则导致珊瑚荧光强度波动更为显著[31, 37]。环境关联分析证实,荧光强度与河流排水量呈显著正相关、与盐度呈负相关[64],且水深因素影响有限[44],凸显其作为水文代用指标的系统性。

在时间维度上,珊瑚荧光不仅能记录瞬时洪水(如 1981—1982 年双峰降雨在台湾南部及海南岛珊瑚骨骼中均表现为双荧光带[36, 55, 65]),还可延伸至世纪尺度水文重建。澳大利亚大堡礁的荧光强度序列成功重建了长达 300 年的河流流量[66−67],揭示 20 世纪澳大利亚东北部降雨变率增强与全球变暖有关[50, 58]。中国南海北部的研究则证实了该方法在区域水文重建中的普适性[55, 65]。时空特征的统一性表现为:近岸强信号精确记录洪水脉冲事件,远岸弱信号则反映背景径流变化,二者共同构成完整的水文过程解码体系。

目前,珊瑚骨骼荧光强度已成功重建大堡礁伯德金河[16, 37, 51, 58, 68]、佛罗里达湾[53]和马达加斯加[23]等区域数十年至数百年尺度的历史降雨量和河流流量(图 3)。此外,由于陆源腐殖酸(陆源溶解有机碳的关键组分)比海洋来源的荧光有机物更容易结合到珊瑚文石骨骼中,使得珊瑚荧光成为陆源溶解有机碳的直接代用指标[32]。鉴于陆架海区的陆源溶解有机碳通常与盐度密切相关[69],珊瑚荧光强度进而具备间接指示盐度变化的能力[60]。这些研究通过时空耦合分析,不仅奠定了珊瑚荧光在古洪水重建中的科学基础,更持续推动其在气候-水文相互作用解析,历史水文重建和未来气候预测中的应用深化。

4.2　珊瑚骨骼荧光对区域降雨模式与全球气候模态的响应

珊瑚骨骼荧光特征为重建历史气候提供了独特视角,能有效反映降雨量在季节性、年际和年代际等多尺度上的变化[16, 37, 53, 58, 66−67]。季风环流的季节性切换直接控制着陆源有机碳输入,形成特征性珊瑚荧光信号。在海南岛近岸,夏季风期的珊瑚荧光强度较冬季显著提高 15%–20%[55],这与万泉河径流量 3–5 倍的季节性变化直接相关[47]。东南亚地区则呈现更复杂的季节性模式:马来西亚近岸珊瑚荧光 G/B 值在东北季风期升至 0.9;而 2019 年西南季风减弱导致苏门答腊泥炭地径流输入滞后 2—3 个月,同期 G/B 值较常年低 0.3,陆源腐殖酸占比下降[32, 60],反映了季风环流路径对陆源物质输送的决定性影响[61]。此外,加勒比海 Mona 岛的研究利用三维荧光光谱技术,建立了定量重建历史降雨量和风速的创新方法[54],成功揭示了 1760—1990 年间飓风活动频率的下降趋势[71]。这些

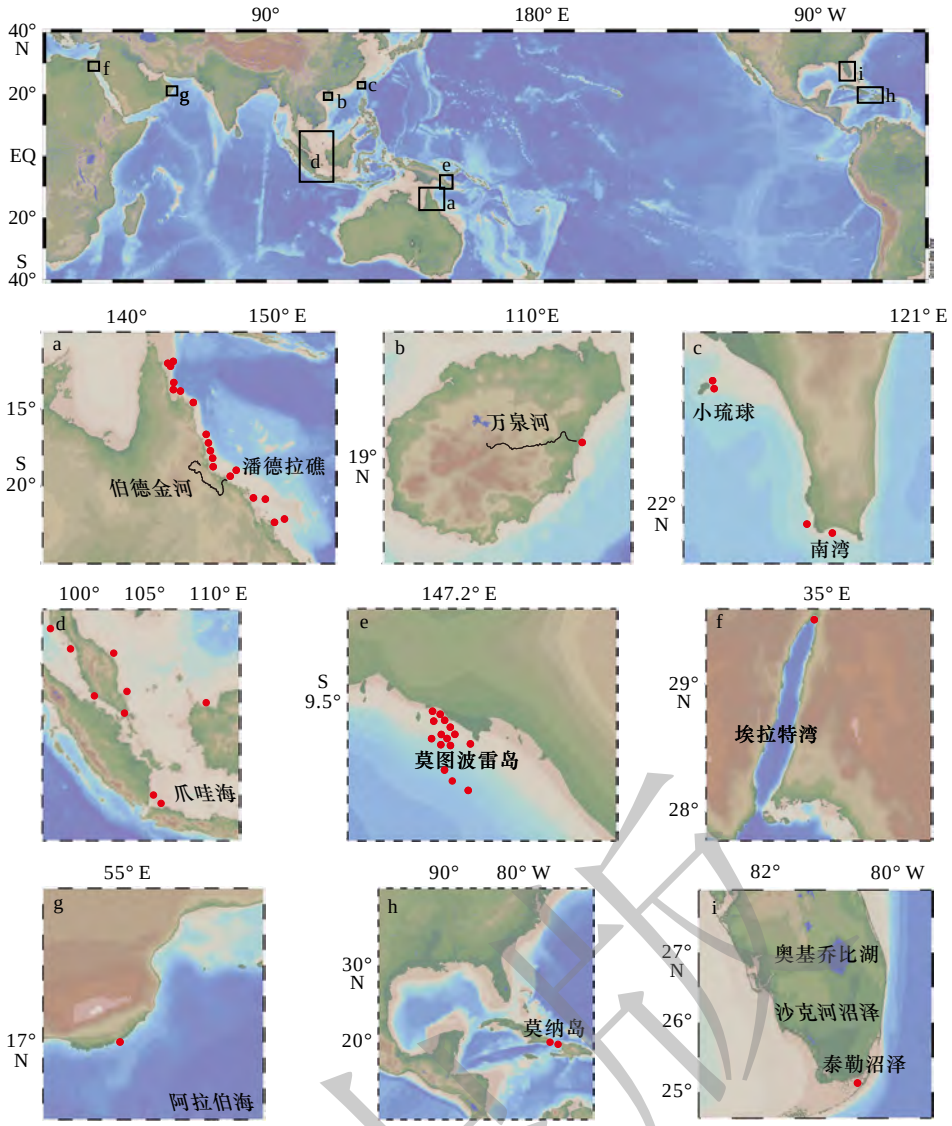


图 3 珊瑚骨骼荧光研究的主要区域

Fig. 3 Major coral sampling sites for paleoenvironmental studies using luminescent bands and their luminescent factors

(a) 大堡礁[19, 37, 51, 70]; (b) 海南岛[55]; (c) 台湾岛[36]; (d) 爪哇岛[40], 马来半岛[32−33, 61]和马来西亚 Sarawak[60]; (e) 新几内亚岛[40]; (f) 西奈半岛[21]; (g) 阿拉伯半岛[39]; (h) 莫纳岛[54, 57]; (i) 佛罗里达半岛[40]。红色的圆点表示珊瑚样品采集地

(a) Great Barrier Reef[19, 37, 51, 70]; (b) Hainan Island[55]; (c) Taiwan Island[36]; (d) Java Island[40], Malay Peninsula[32−33, 61], Sarawak in Malaysia[60]; (e) New Guinea Island[40]; (f) Sinai Peninsula[21]; (g) Arabian Peninsula[39]; (h) Mona Island[54, 57]; (i) Florida Peninsula[40]. The red dots indicate the collection sites of corals

研究为理解季风–气候–珊瑚系统的相互作用提供了重要依据。

作为全球年际气候变率的主导因子, ENSO 通过改变降雨格局和陆源物质输运显著影响珊瑚荧光特征。这一影响在澳大利亚伯德金河流域得到明确印证: 1931 年强 El Niño 事件导致降雨减少 30%, 伴随珊瑚荧光强度下降 18%; 而 1974 年强 La Niña 事件则使降雨增加 40%, 荧光强度骤升至年均值的 3 倍[16]。同样, Keppel 群岛珊瑚 G/B 比值揭示的河流流量峰值记录中, 75% 集中在 La Niña 事件期间[51](图 4)。重要的是, 这种荧光强度的变化与 ENSO 指数及实测河流流量严格同步, 有力证实了珊瑚荧光作为 ENSO 活动可靠指标的潜力[49, 63]。其灵敏度的优越性进一步在 Reed 等[72]的研究中得到凸显, 他们对大堡礁珊瑚进行月分辨率分析显示, 在捕捉区域水文信号对 ENSO 事件的响应方面, 珊瑚荧光比海表温度指标更灵敏, 这强化了其在重建气候模态方面的独特优势。

然而, 全球不同海域的珊瑚荧光对 ENSO 的响应存在显著的区域差异。1982—1997 年强 El Niño 事件期间, 海南岛东部降雨显著增加, 伴随珊瑚骨骼荧光强度升高[55]。然而在 2015—2016 年强 El Niño 事件期间, 澳大利亚大堡礁南部珊瑚骨骼荧光强度显著降低 25%, 这可能与增强的植被缓冲作用有关[50]。这些鲜明的对比揭示出区域环境特征对珊瑚荧光响应

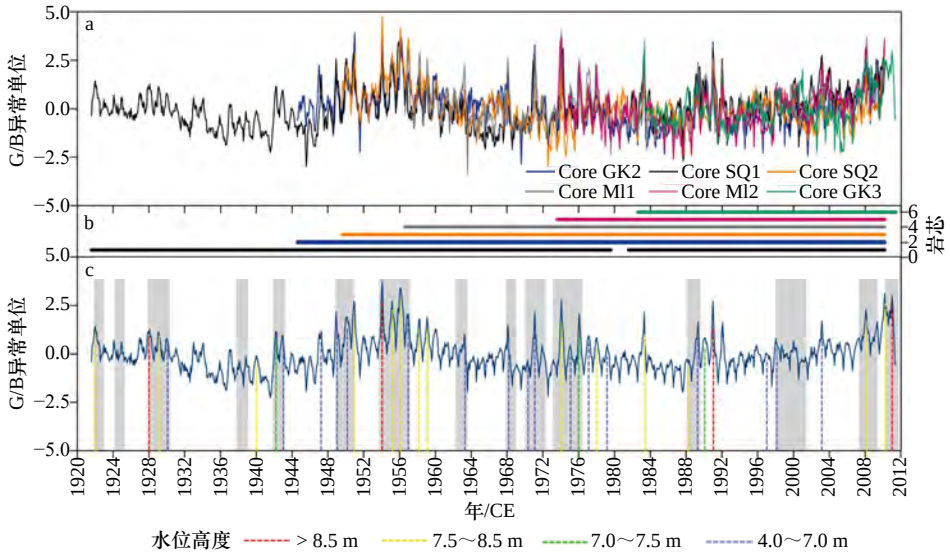


图 4　1921—2011 年期间大堡礁南部 keppel 群岛珊瑚 G/B 异常时间序列[51]

Fig. 4　Time series of G/B anomalies for the period 1921–2011 at Kappel Islands, southern Great Barrier Reef[51]

(a) 6 个珊瑚岩芯的月分辨率 G/B 异常。(b) 用于构建复合记录的岩芯数量。(c) 复合 G/B 记录和器测记录的重大洪水事件。彩色虚线代表在距离河口最近的水文站 Rockhampton 记录到的单次最高洪水事件。不同颜色对应水位高度 (单位: 米)。阴影区域对应 La Niña 时期

(a) Monthly G/B anomalies for all six cores. (b) Number of cores used to construct the composite record. (c) Long term G/B composite record, with major flood events registered by instrumental records. Color dashed lines under the profile denote the highest individual flood events registered at Rockhampton, the nearest gauging station to the river mouth. Colors refer to gauge height in m. Shaded areas correspond to La Niña periods

模式的调制作用。这种对区域差异的理解甚至延伸至更长时间尺度, 对大堡礁多个珊瑚荧光序列的综合分析揭示出, 6.0 ka BP 澳大利亚夏季风减弱可能与 ENSO 变率降低有关, 而 5.2–4.3 ka BP 期间 ENSO 变率呈现波动减弱趋势[19, 73]。

除年际变率外, 年代际气候模态如 PDO 和印度洋偶极子(Indian Ocean Dipole, IOD)也通过调控水汽输送对珊瑚荧光产生长期影响。大堡礁南部珊瑚荧光序列显示, 在 PDO 负相位期间(1970—1990 年), 荧光带厚度增至 1.8 mm, 与降雨量增加 12% 完全吻合[51]。交叉小波相干性分析证实了马达加斯加的珊瑚荧光记录与 PDO 代用记录之间存在关联[59]。印度洋-太平洋海域的研究表明, 当 1988 年 La Niña 事件与 IOD 正相位叠加时, 肯尼亚沿岸珊瑚荧光强度与降雨异常的相关系数达 0.62; 1996 年 IOD 正相位期间, 该区域珊瑚荧光强度较常年高 22%[74]。在东南亚, 2010 年 IOD 正相位与 La Niña 事件叠加期间, 马来西亚近岸珊瑚荧光 G/B 值达到 0.95 (近 30 年峰值), 直接对应于苏门答腊泥炭地径流输入激增 40%[32, 60]。这些发现证实珊瑚荧光是解析跨洋盆年代际气候联动的有效指标。

古环境重建的应用更延伸至地质历史时期。红海埃拉特海湾的研究表明, 距今 25—10 万年前的珊瑚荧光带指示当时西奈半岛气候远比现今湿润, 为晚第四纪古环境重建提供了关键证据[21]。综合来看, 珊瑚荧光带蕴含着丰富的气候环境信息, 能够有效揭示与入海径流量密切相关的多种古环境变化过程, 为理解区域乃至全球尺度的气候系统演变提供了独特视角。

4.3　人类活动在珊瑚骨骼荧光中的响应特征

珊瑚骨骼荧光特征不仅忠实地记录了自然气候变化, 还清晰地反映了人类活动对沿岸生态系统的深刻干扰。澳大利亚大堡礁地区的农业开发导致珊瑚骨骼磷含量增加 22%[68], 同时伴随荧光强度标准差从 80 cps 增长至 120 cps 及极端值频率上升 30%, 共同揭示了陆源物质输入的不稳定性加剧的态势[50]。这种人类活动对流域环境的影响具有历史延续性: 1648—2011 年伯德金河流量重建结果显示, 高流量事件频率的阶段性增加与 1851—1900 年欧洲殖民引发的土地利用方式转型的时间高度吻合[70, 75](图 5)。

工业化以来, 工程活动显著改变了流域侵蚀模式和水文节律, 在珊瑚荧光序列中留下了独特印记。例如, 中国台湾南湾 1975 年核电站建设导致土壤侵蚀模数激增 4 倍, 使珊瑚荧光强度与降雨量的相关性从 0.72 提升至 0.93, 同时信号地高频波动增加了 35%, 充分体现了流域土地利用变化对径流有机物组成的显著影响[36]。类似地, 佛罗里达海湾 1932 年人工排水工程则使珊瑚荧光年际波动幅度从±40% 收窄

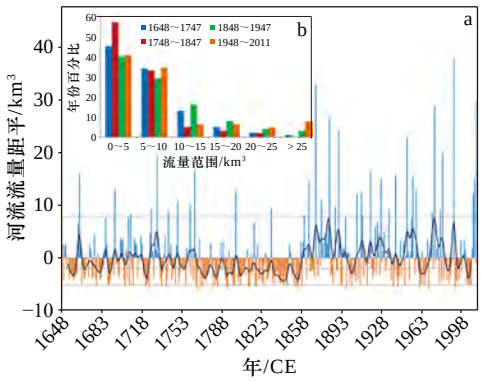


图 5 珊瑚骨骼荧光记录伯德金河流量变化[75]

Fig. 5 Coral skeletal luminescence records variations in Burdekin River discharge[75]

(a) 1648—2011 年重建的伯德金河流量，以 1648–2011 年平均值为基准的距平值。深蓝色线为 10 年高斯滤波曲线。灰色水平线分别代表相对于全记录期的第 90 百分位、中位数和第 10 百分位。(b)不同流量范围及连续子时段内重建的伯德金河流量的频率分布百分比

(a) Reconstructed Burdekin River flow as anomalies from 1648 to 2011 average, 1648–2011. Dark blue line is 10-year Gaussian filter. Horizontal grey lines are 90th percentile, median and 10th percentile relative to whole record length. (b) Percentage frequency distributions of reconstructed Burdekin. River flows for different flow ranges and successive subperiods

至±15%，导致自然径流周期特征完全消失[53]，有力证明了人类活动对水文系统的重塑作用。马来西亚近岸珊瑚的研究则发现，受泥炭地火灾影响的站点，其荧光 G/B 比值与陆源腐殖酸浓度显著相关($R^2 > 0.40$)，为定量追溯工业活动影响提供了新途径[32]。此外，新加坡和澳大利亚的研究表明，协同分析珊瑚 Ba/Ca 比值与荧光强度可有效区分自然与人为因素对径流的影响，凸显“荧光-元素”多指标模型在复杂环境下解耦环境信号的价值[7, 76−77]。

5 珊瑚骨骼荧光研究的挑战与未来方向

当前珊瑚骨骼荧光研究面临的核心挑战在于分析方法标准化不足，严重制约了数据可比性。不同研究团队在紫外波长选择、荧光强度定量等关键环节存在显著差异，导致跨研究数据难以直接对比。荧光带颜色表征缺乏统一标准，同一荧光带在不同文献中被描述为“黄绿色”[16]，“黄白色”[53]或“灰白色”[24]等。这种命名混乱源于观测者主观差异、光源类型变化以及样品保存状态不同等因素。更复杂的是非陆源荧光物质与陆源富啡酸的光谱重叠问题，如泰国普吉岛珊瑚研究中发现的“灰白色带”与“黄绿色带”虽均显示陆源富啡酸特征峰，但腐殖酸浓度差异显著[24]。此外，海洋浮游植物产生的类蛋白荧光也易与珊瑚荧光带混淆[32, 39]。这一发现凸显了荧光源区分的必要性。

在年代测定方法上，荧光带与密度带的关系仍存在争议。传统密度带定年法存在 3—8 年的误差[26]，而荧光带能更精确捕捉季节性径流脉冲[25]。值得注意的是，1982 年 El Niño 事件中珊瑚出现“双荧光带”但仅记录 1 个密度带周期，揭示了两者的本质差异。荧光带与密度带的空间对应关系也存在不同认识[16, 21, 40]。这种差异源于信息维度的不同：荧光带提供表面二维信息，密度带反映三维平均信息。为建立可靠年代学框架，亟需开发能量化骨骼表面孔隙率的专用设备。

样品制备方法的不统一也制约着研究进展。珊瑚骨骼内的内生藻类等有机物可显著影响荧光特征[78−79]，而不同预处理方法(如次氯酸钠漂白、氨水处理等)对荧光信号的保留程度差异显著[31, 34, 44, 80]。非破坏性分析技术如激光诱导击穿光谱为研究开辟了新途径[57]，但当前预处理方法的差异性严重影响了结果的可比性。

关于荧光物质来源的机制研究仍存在关键矛盾。珊瑚骨骼荧光光谱特征与海水化学常规认知不符[28, 81]，暗示可能存在选择性浓缩腐植酸的独特机制。虽然大量研究证实河流输入的陆源有机物对荧光光谱的重要影响[58, 64]，但非径流来源的腐殖酸类物质同样可能产生显著影响。例如，关岛近岸珊瑚的荧光带与褐藻代谢产物的光谱匹配度高达 89%，表明富啡酸可通过“藻类→浮游动物→珊瑚”的食物链途径进行传递[46]；而在东太平洋珊瑚荧光带中检测到的甲基菲等热解有机质，其荧光特征与典型陆源信号存在明显差异，这些物质很可能源自海底热液活动[39]。这些发现表明当前对海洋有机物融入珊瑚骨骼的具体机制、存在形式及其对荧光强度影响的认识仍不够全面。

未来研究需在以下方面取得突破：建立标准化的荧光分析流程和颜色表征体系；开发新型定年方法以协调荧光带和密度带的关系；制定统一的样品预处理规范；深入探究荧光物质的本体形成机制。这些工作的推进将显著提升珊瑚骨骼荧光在古环境重建中的应用价值，为理解气候变化提供更可靠的科学依据。

6 总结与展望

在全球气候变化背景下，珊瑚骨骼荧光研究为理解降雨变率提供了独特视角。作为高分辨率古气候记录载体，珊瑚荧光带不仅能重建年平均降雨量，还能捕捉极端水文事件，弥补了传统观测数据在时空覆

盖上的不足。研究表明, 珊瑚荧光强度与降雨量、径流量存在显著相关性, 其空间分布特征受离岸距离、水体交换速率等因素影响, 呈现出规律性梯度变化。例如, 马来西亚苏门答腊泥炭地研究显示, 当流速超过 0.5 m/s 时荧光信号衰减达 20%[60], 而台湾小琉球岛不同珊瑚种类对富啡酸的吸附能力差异可达 30%[36], 这些发现为采样策略优化提供了重要依据。

未来研究应重点关注三个方向: 首先, 需结合多源数据建立更精确的荧光-水文定量模型, 特别是针对不同珊瑚种类和环境条件的校正方法; 其次, 应加强珊瑚荧光与其他气候代用指标(如树轮、冰芯等)的交叉验证, 提升重建结果的可靠性; 最后, 需探索新型分析技术(如三维荧光光谱)在长时间尺度气候重建中的应用潜力。随着技术进步和方法完善, 珊瑚骨骼荧光研究将为预测全球变暖背景下的降雨变化、理解气候系统演变规律提供关键科学支撑。

参考文献:

[1] Yu Kefu. Coral reefs in the South China Sea: their response to and records on past environmental changes[J]. Science China Earth Sciences, 2012, 55(8): 1217−1229.

[2] 余克服. 珊瑚礁科学概论[M]. 北京: 科学出版社, 2018.
Yu Kefu. Introduction to the Science of Coral Reefs[M]. Beijing: Science Press, 2018.

[3] 陶士臣, 张会领, 余克服, 等. 近 500 年西沙群岛海面温度年际变化的珊瑚记录及其环境意义[J]. 第四纪研究, 2021, 41(2): 411−423.
Tao Shichen, Zhang Huiling, Yu Kefu, et al. Annual resolution sea surface temperature reconstructed quantitatively by *Porites* coral growth rate in the Xishaqundao Islands during the past five centuries and their environmental significance[J]. Quaternary Sciences, 2021, 41(2): 411−423.

[4] Jiang Leilei, Yu Kefu, Tao Shichen, et al. ENSO variability during the Medieval Climate Anomaly as recorded by *Porites* corals from the northern South China Sea[J]. Paleoceanography and Paleoclimatology, 2021, 36(4): e2020PA004173.

[5] Felis T, Suzuki A, Kuhnert H, et al. Subtropical coral reveals abrupt early-twentieth-century freshening in the western North Pacific Ocean[J]. Geology, 2009, 37(6): 527−530.

[6] Chen Xuefei, D'Olivo J P, Wei Gangjian, et al. Anthropogenic ocean warming and acidification recorded by Sr/Ca, Li/Mg, δ^{11}B and B/Ca in *Porites* coral from the Kimberley region of northwestern Australia[J]. Palaeogeography, Palaeoclimatology, Palaeoecology, 2019, 528: 50−59.

[7] Tanzil J T I, Goodkin N F, Sin T M, et al. Multi-colony coral skeletal Ba/Ca from Singapore's turbid urban reefs: relationship with contemporaneous in-situ seawater parameters[J]. Geochimica et Cosmochimica Acta, 2019, 250: 191−208.

[8] Sun Yinan, Jiang Wei, Yu Kefu, et al. High - resolution coral records of Cadmium in surface seawater: biogeochemical cycling and a novel proxy for winter monsoon[J]. Geochemistry, Geophysics, Geosystems, 2022, 23(11): e2022GC010600.

[9] Jiang Wei, Yu Kefu, Song Yinxian, et al. Annual REE signal of East Asian Winter monsoon in surface seawater in the northern South China Sea: evidence from a century - long *Porites* coral record[J]. Paleoceanography and Paleoclimatology, 2018, 33(2): 168−178.

[10] Jiang Leilei, Yu Kefu, Tao Shichen, et al. Modulation of East Asian monsoon strength by ENSO during the warm periods of the late Holocene: evidence from *Porites* corals in the northern South China Sea[J]. Global and Planetary Change, 2023, 225: 104136.

[11] Han Tao, Yu Kefu, Yan Hongqiang, et al. Links between the coral δ^{13}C record of primary productivity variations in the northern South China Sea and the East Asian Winter monsoon[J]. Geophysical Research Letters, 2019, 46(24): 14586−14594.

[12] Li Xiaohua, Wang Xiaowei, Liu Chuanyu, et al. Traces of the 1997 Indonesian wildfires in the marine environment from a network of coral δ^{13}C records[J]. Geophysical Research Letters, 2020, 47(22): e2020GL090383.

[13] Chen Xuefei, Deng Wenfeng, Kang Huiling, et al. A replication study on coral δ^{11}B and B/Ca and their variation in modern and fossil *Porites*: implications for coral calcifying fluid chemistry and seawater pH changes over the last millennium[J]. Paleoceanography and Paleoclimatology, 2021, 36(10): e2021PA004319.

[14] Cole J E, Fairbanks R G, Shen G T. Recent variability in the southern oscillation: isotopic results from a Tarawa Atoll coral[J]. Science, 1993, 260(5115): 1790−1793.

[15] Felis T, Pätzold J. Corals as climate archive[M]//Fischer H, Kumke T, Lohmann G, et al. The Climate in Historical Times. Berlin, Heidelberg: Springer, 2004: 91−108.

[16] Isdale P. Fluorescent bands in massive corals record centuries of coastal rainfall[J]. Nature, 1984, 310(5978): 578−579.

[17] Wild F J, Jones A C, Tudhope A W. Investigation of luminescent banding in solid coral: the contribution of phosphorescence[J]. Coral Reefs, 2000, 19(2): 132−140.

[18] Lough J M, Barnes D J. Intra-annual timing of density band formation of *Porites* coral from the central Great Barrier Reef[J]. Journal of Experimental Marine Biology and Ecology, 1990, 135(1): 35−57.

[19] Leonard N D, Welsh K J, Lough J M, et al. Evidence of reduced mid-Holocene ENSO variance on the Great Barrier Reef, Australia[J]. Paleoceanography, 2016, 31(9): 1248−1260.

[20] Lough J M, Llewellyn L E, Lewis S E, et al. Evidence for suppressed mid-Holocene northeastern Australian monsoon variability from coral luminescence[J]. Paleoceanography, 2014, 29(6): 581−594.

[21] Klein R, Loya Y, Gvirtzman G, et al. Seasonal rainfall in the Sinai Desert during the late Quaternary inferred from fluorescent bands in fossil corals[J]. Nature, 1990, 345(6271): 145−147.

[22] Grove C A, Nagtegaal R, Zinke J, et al. River runoff reconstructions from novel spectral luminescence scanning of massive coral skeletons[J]. Coral Reefs, 2010, 29(3): 579−591.

[23] Grove C A, Zinke J, Scheufen T, et al. Spatial linkages between coral proxies of terrestrial runoff across a large embayment in Madagascar[J]. Biogeosciences, 2012, 9(8): 3063−3081.

[24] Matthews B J H, Jones A C, Theodorou N K, et al. Excitation-emission-matrix fluorescence spectroscopy applied to humic acid bands in coral reefs[J]. Marine Chemistry, 1996, 55(3/4): 317−332.

[25] Barnes D J, Taylor R B. On the nature and causes of luminescent lines and bands in coral skeletons[J]. Coral Reefs, 2001, 19(3): 221−230.

[26] Lough J M. Climate records from corals[J]. WIREs Climate Change, 2010, 1(3): 318−331.

[27] Sharma A, Anthal R. Humic substances in aquatic ecosystems: a review[J]. International Journal of Innovative Research in Science, Engineering and Technology, 2016, 5(10): 18462−18470.

[28] Nagao S, Matsunaga T, Suzuki Y, et al. Characteristics of humic substances in the Kuji River waters as determined by high-performance size exclusion chromatography with fluorescence detection[J]. Water Research, 2003, 37(17): 4159−4170.

[29] Wagner M, Schmidt W, Imhof L, et al. Characterization and quantification of humic substances 2D-Fluorescence by usage of extended size exclusion chromatography[J]. Water Research, 2016, 93: 98−109.

[30] Boto K, Isdale P. Fluorescent bands in massive corals result from terrestrial fulvic acid inputs to nearshore zone[J]. Nature, 1985, 315(6018): 396−397.

[31] Susic M, Boto K, Isdale P. Fluorescent humic acid bands in coral skeletons originate from terrestrial runoff[J]. Marine Chemistry, 1991, 33(1/2): 91−104.

[32] Kaushal N, Yang Liudongqing, Tanzil J T I, et al. Sub-annual fluorescence measurements of coral skeleton: relationship between skeletal luminescence and terrestrial humic-like substances[J]. Coral Reefs, 2020, 39(5): 1257−1272.

[33] Tanzil J T I, Lee J N, Brown B E, et al. Luminescence and density banding patterns in massive *Porites corals* around the Thai-Malay Peninsula, Southeast Asia[J]. Limnology and Oceanography, 2016, 61(6): 2003−2026.

[34] 彭子成, 谢端, 何学贤, 等. 海南岛滨珊瑚的荧光强度与降雨量和径流量的相关性研究[J]. 自然科学进展, 2001, 11(8): 840−844.
Peng Zicheng, Xie Rui, He Xuexian, et al. A study on the correlation between fluorescence intensity of coastal corals in Hainan Island and rainfall and runoff[J]. Progress in Natural Science, 2001, 11(8): 840−844. **(查阅网上资料, 未找到对应的英文翻译, 请确认)**

[35] Llewellyn L E, Everingham Y L, Lough J M. Pharmacokinetic modelling of multi-decadal luminescence time series in coral skeletons[J]. Geochimica et Cosmochimica Acta, 2012, 83: 263−271.

[36] Fang L S, Chou Y C. Concentration of fulvic acid in the growth bands of hermatypic corals in relation to local precipitation[J]. Coral Reefs, 1992, 11(4): 187−191.

[37] Lough J, Barnes D, McAllister F. Luminescent lines in corals from the Great Barrier Reef provide spatial and temporal records of reefs affected by land runoff[J]. Coral Reefs, 2002, 21(4): 333−343.

[38] Jones P D, Briffa K R, Osborn T J, et al. High-resolution palaeoclimatology of the last millennium: a review of current status and future prospects[J]. The Holocene, 2009, 19(1): 3−49.

[39] Tudhope A W, Lea D W, Shimmield G B, et al. Monsoon climate and Arabian Sea coastal upwelling recorded in massive corals from southern Oman[J]. Palaios, 1996, 11(4): 347−361.

[40] Scoffin T P, Tudhope A W, Brown B E. Fluorescent and skeletal density banding in *Porites lutea* from Papua New Guinea and Indonesia[J]. Coral Reefs, 1989, 7(4): 169−178.

[41] Smithers S G, Woodroffe C D. Coral microatolls and 20th century sea level in the eastern Indian Ocean[J]. Earth and Planetary Science Letters, 2001, 191(1/2): 173−184.

[42] Willey J D. The effect of seawater magnesium on natural fluorescence during estuarine mixing, and implications for tracer applications[J]. Marine Chemistry, 1984, 15(1): 19−45.

[43] Milne P J, Swart P K. Fiber-optic-based sensing of banded luminescence in corals[J]. Applied Spectroscopy, 1994, 48(10): 1282−1284.

[44] Carricart-Ganivet J P, Lough J M, Barnes D J. Growth and luminescence characteristics in skeletons of massive *Porites* from a depth gradient in the central Great Barrier Reef[J]. Journal of Experimental Marine Biology and Ecology, 2007, 351(1/2): 27−36.

[45] MacRae C M, Wilson N C. Luminescence database I-Minerals and materials[J]. Microscopy and Microanalysis, 2008, 14(2): 184−204.

[46] Prouty N G, Storlazzi C D, McCutcheon A L, et al. Historic impact of watershed change and sedimentation to reefs along west-central Guam[J]. Coral Reefs, 2014, 33(3): 733−749.

[47] Barnes D J, Taylor R B. On the nature and causes of luminescent lines and bands in coral skeletons: II. Contribution of skeletal crystals[J]. Journal of Experimental Marine Biology and Ecology, 2005, 322(2): 135−142.

[48] Ramseyer K, Miano T M, D'Orazio V, et al. Nature and origin of organic matter in carbonates from speleothems, marine cements and coral skeletons[J]. Organic Geochemistry, 1997, 26(5/6): 361−378.

[49] Hendy E J, Gagan M K, Lough J M. Chronological control of coral records using luminescent lines and evidence for non-stationary EN-

SO teleconnections in northeast Australia[J]. The Holocene, 2003, 13(2): 187−199.

[50] Lough J M. Great Barrier Reef coral luminescence reveals rainfall variability over northeastern Australia since the 17th century[J]. Paleoceanography, 2011, 26(2): PA2201.

[51] Rodriguez-Ramirez A, Grove C A, Zinke J, et al. Coral luminescence identifies the Pacific Decadal Oscillation as a primary driver of river runoff variability impacting the southern Great Barrier Reef[J]. PLoS One, 2014, 9(1): e84305.

[52] 李淑, 余克服, 施祺, 等. 南海北部珊瑚共生虫黄藻密度的种间与空间差异及其对珊瑚礁白化的影响[J]. 科学通报, 2007, 52(22): 2655−2662.
Li Shu, Yu Kefu, Shi Qi, et al. Interspecies and spatial diversity in the symbiotic zooxanthellae density in corals from northern South China Sea and its relationship to coral reef bleaching[J]. Chinese Science Bulletin, 2008, 53(2): 295−303.

[53] Smith III T J, Hudson H J, Robblee M B, et al. Freshwater flow from the Everglades to Florida Bay: a historical reconstruction based on fluorescent banding in the coral *Solenastrea bournoni*[J]. Bulletin of Marine Science, 1989, 44(1): 274−282.

[54] Nyberg J. Luminescence intensity in coral skeletons from Mona Island in the Caribbean Sea and its Link to precipitation and wind speed[J]. Philosophical Transactions of the Royal Society A: Mathematical, Physical and Engineering Sciences, 2002, 360(1793): 749−766.

[55] Peng Zicheng, He Xuexian, Zhang Zhaofeng, et al. Correlation of coral fluorescence with nearshore rainfall and runoff in Hainan Island, South China Sea[J]. Progress in Natural Science, 2002, 12(1): 41−44.

[56] Susic M, Boto K G. High-performance liquid chromatographic determination of humic acid in environmental samples at the nanogram level using fluorescence detection[J]. Journal of Chromatography A, 1989, 482(1): 175−187.

[57] Barnes D J, Taylor R B, Lough J M. Measurement of luminescence in coral skeletons[J]. Journal of Experimental Marine Biology and Ecology, 2003, 295(1): 91−106.

[58] Lough J M. Tropical river flow and rainfall reconstructions from coral luminescence: Great Barrier Reef, Australia[J]. Paleoceanography, 2007, 22(2): PA2218.

[59] Grove C A, Zinke J, Peeters F, et al. Madagascar corals reveal a multidecadal signature of rainfall and river runoff since 1708[J]. Climate of the Past, 2013, 9(2): 641−656.

[60] Kaushal N, Sanwlani N, Tanzil J T I, et al. Coral skeletal luminescence records changes in terrestrial chromophoric dissolved organic matter in tropical coastal waters[J]. Geophysical Research Letters, 2021, 48(8): e2020GL092130.

[61] Kaushal N, Tanzil J T I, Zhou Yongli, et al. Environmental calibration of coral luminescence as a proxy for terrigenous dissolved organic carbon concentration in tropical coastal oceans[J]. Geochemistry, Geophysics, Geosystems, 2022, 23(10): e2022GC010529.

[62] Coble P G. Marine bacteria as a source of dissolved fluorescence in the ocean[D]. Cambridge: Massachusetts Institute of Technology, 1989.

[63] Sinclair D J, McCulloch M T. Corals record low mobile barium concentrations in the Burdekin River during the 1974 flood: evidence for limited Ba supply to rivers?[J] Palaeogeography, Palaeoclimatology, Palaeoecology, 2004, 214(1/2): 155−174.

[64] Jupiter S, Roff G, Marion G, et al. Linkages between coral assemblages and coral proxies of terrestrial exposure along a cross-shelf gradient on the southern Great Barrier Reef[J]. Coral Reefs, 2008, 27(4): 887−903.

[65] 贺剑峰, 彭子成, 何学贤, 等. 珊瑚荧光的古降水记录[J]. 海洋地质与第四纪地质, 2001, 21(2): 63−68.
He Jianfeng, Peng Zicheng, He Xuexian, et al. Paleo-precipitation records of fluorescent bands of coral[J]. Marine Geology & Quaternary Geology, 2001, 21(2): 63−68.

[66] Isdale P, Kotwicki V. Lake Eyre and the Great Barrier Reef: a paleohydrological ENSO (El Nino/ Southern Oscillation) connection[J]. South Australian Geographical Journal, 1987, 87: 44−55.

[67] Kotwicki V, Isdale P. Hydrology of lake Eyre, Australia: El Niño link[J]. Palaeogeography, Palaeoclimatology, Palaeoecology, 1991, 84(1/4): 87−98.

[68] Isdale P J, Stewart B J, Tickle K S, et al. Palaeohydrological variation in a tropical river catchment: a reconstruction using fluorescent bands in corals of the Great Barrier Reef, Australia[J]. The Holocene, 1998, 8(1): 1−8.

[69] Carr N, Davis C E, Blackbird S, et al. Seasonal and spatial variability in the optical characteristics of DOM in a temperate shelf sea[J]. Progress in Oceanography, 2019, 177: 101929.

[70] D'Olivo J P, McCulloch M. Impact of European settlement and land use changes on Great Barrier Reef river catchments reconstructed from long-term coral Ba/Ca records[J]. Science of the Total Environment, 2022, 830: 154461.

[71] Nyberg J, Malmgren B A, Winter A, et al. Low Atlantic hurricane activity in the 1970s and 1980s compared to the past 270 years[J]. Nature, 2007, 447(7145): 698−701.

[72] Reed E V, Cole J E, Lough J M, et al. Linking climate variability and growth in coral skeletal records from the Great Barrier Reef[J]. Coral Reefs, 2019, 38(1): 29−43.

[73] D'Arrigo R, Baker P, Palmer J, et al. Experimental reconstruction of monsoon drought variability for Australasia using tree rings and corals[J]. Geophysical Research Letters, 2008, 35(12): L12709.

[74] Kayanne H, Iijima H, Nakamura N, et al. Indian Ocean Dipole index recorded in Kenyan coral annual density bands[J]. Geophysical Research Letters, 2006, 33(19): L19709.

［75］ Lough J M, Lewis S E, Cantin N E. Freshwater impacts in the central Great Barrier Reef: 1648-2011[J]. Coral Reefs, 2015, 34(3): 739−751.
［76］ Tanzil J T I, Goodkin N F, Sin T M, et al. Multi-colony coral skeletal Ba/Ca from Singapore's turbid urban reefs: relationship with contemporaneous in-situ seawater parameters[J]. Geochimica et Cosmochimica Acta, 2019, 250: 191−208. **(查阅网上资料, 本条文献与第7条文献重复, 请确认)**
［77］ Lewis S E, Lough J M, Cantin N E, et al. A critical evaluation of coral Ba/Ca, Mn/Ca and Y/Ca ratios as indicators of terrestrial input: new data from the Great Barrier Reef, Australia[J]. Geochimica et Cosmochimica Acta, 2018, 237: 131−154.
［78］ DiSalvo L H. Isolation of bacteria from the corallum of *Porites lobata* (Vaughn) and its possible significance[J]. American Zoologist, 1969, 9(3): 735−740.
［79］ Bak R P M, Lanne R W P M. Annual black bands in skeletons of reef corals (Scleractinia)[J]. Marine Ecology Progress Series, 1987, 38: 169−175.
［80］ Nagtegaal R, Grove C A, Kasper S, et al. Spectral luminescence and geochemistry of coral aragonite: effects of whole-core treatment[J]. Chemical Geology, 2012, 318-319: 6-15.
［81］ Hudson N, Baker A, Reynolds D. Fluorescence analysis of dissolved organic matter in natural, waste and polluted waters-a review[J]. River Research and Applications, 2007, 23(6): 631−649.

Research progress on coral skeleton fluorescence as an indicator of environmental changes

Jiang Leilei[1], Huang Dahua[1], Zhao Bailing[1], Yu Kefu[1, 2]

(1. *Guangxi Laboratory on the Study of Coral Reefs in the South China Sea*, *Coral Reef Research Center of China*, *School of Marine Sciences*, *Guangxi University*, *Nanning* 530004, *China*; 2. *Southern Marine Science and Engineering Guangdong Laboratory*, *Guangzhou* 511458, *China*)

Abstract: Massive *Porites* corals, widely inhabiting in tropical oceans, are considered ideal archives for high-resolution environmental records and have garnered significant attention in the fields of paleoclimate and paleoenvironmental reconstruction. The fluorescence emitted by coral skeletons under long-wave ultraviolet (UV) light, due to its sensitivity to terrestrial runoff, pollutants, and climatic events, has emerged as an another tool for revealing various environmental changes related to rainfall, river discharge, and other factors. This review synthesizes the formation mechanisms of fluorescent substances in coral skeletons, measurement techniques, applications in environmental reconstruction, as well as current challenges and future research directions. Overall, the fluorescent signals in coral skeletons primarily originate from terrestrially derived organic matter dominated by fulvic acids and humic-like substances produced by symbiotic algal metabolism. Additionally, coral skeletal structure, mineral properties, and interactions with environmental factors such as rainfall and runoff influence fluorescence characteristics. By combining high-precision micro-sampling techniques with fluorescence analysis, scientists have successfully reconstructed environmental histories of terrestrial runoff, precipitation, and human activities across different timescales. Based on current international research progress, this paper suggests that future studies should explore novel analytical techniques, develop more accurate fluorescence-hydrological quantitative models by integrating multi-source data, and strengthen cross-validation with other proxy indicators to establish a high-precision, high-resolution global coral fluorescence database.

Key words: coral skeleton; fluorescent bands; terrestrial fulvic acid; runoff; precipitation

预出版

珊瑚礁领域研究生课程教学模式创新探索

左秀玲，梁甲元，余克服*，苏宏飞，梁作栋
（广西大学 海洋学院，广西 南宁 530004）

【摘要】该文旨在培养拥有深厚专业知识、独立研究能力、创新精神和爱国主义情怀综合素质的珊瑚礁领域高素质人才，率先在全国开设珊瑚礁领域研究生课程。通过探索交叉学科引领、深化前沿、科教融合、研究性教学模式等系列举措，深化研究生对珊瑚礁领域知识体系的理解，提升其分析及解决问题的能力。通过构建珊瑚礁理论与实践融合教学方法，弥补了课堂教学缺乏真实性与体验感的缺陷，培养其科学思维和思辨能力。通过实施爱国主义课程思政，牢筑研究生家国情怀，达到专业知识与爱国主义教育共同传授的育人效果。

【关键词】珊瑚礁；交叉学科；科教融合；研究性教学；爱国主义课程思政
中图分类号：G642 文献标识码：A

Innovative Exploration of Teaching Mode for Postgraduate Courses in the Field of Coral Reefs

Zuo Xiuling, Liang Jiayuan, Yu Kefu*, Su Hongfei, Liang Zuodong
(School of Marine Sciences, Guangxi University, Guangxi Nanning 530004, China)

【Abstract】This article aims to cultivate high-quality talents in the field of coral reefs who possess profound professional knowledge, independent research capabilities, innovative spirit, and a sense of patriotism. It has been the first program in the nation to offer graduate-level courses in the coral reef field. By implementing a series of measures such as interdisciplinary guidance, in-depth exploration of frontiers, integration of science and education, and research-based teaching models, it has deepened graduate students' understanding of the knowledge system in the coral reef field and enhanced their ability to analyze and solve problems. Through the construction of integrated teaching methods that combine coral reef theory with practice, it has compensated for the lack of reality and experientiality in classroom teaching, fostering students' scientific thinking and critical reasoning abilities. Through the implementation of patriotic ideological and political education in courses, it strengthens postgraduates' sense of national and family commitment, achieving the educational goal of concurrently imparting professional knowledge and patriotic education.

【Keywords】coral reefs; interdisciplinarity; integration of science and education; research-oriented teaching; patriotic ideological and political education in courses

引言

研究生教育肩负着高层次人才培养和创新创造的重要使命，是推动国家重点领域和紧缺人才培养、提升经济社会发展能力的关键环节。珊瑚礁是地球上生物多样性最丰富、资源最富集的生态系统之一。我国南海分布着 200 多座珊瑚礁，它们既是南海最重要的地质、地貌和生态特征之一，也是我国南海唯一的陆地国土类型。随着国家对珊瑚礁的重视程度的不断提升，依托广西南海珊瑚礁研究重点实验室，广西大学海洋学院于 2017 年在全国率先开设了具有“珊瑚礁”特色的研究生课程。该课程由长江学者特聘教授余克服领衔建设，是海洋科学专业研究生的一门专业必修课程，广西大学海洋学院则是目前国内唯一开设该类课程的学院，形成了独特的培养优势。

教学团队初期从科学研究的角度出发，着重构

1627
中国知网 https://www.cnki.net

建了系统的教学课件，以为国家开发、利用南海岛礁培养专业人才为核心目标。然而，单一科学研究角度构建的教学课件面临以下问题：一方面，课程内容存在前沿性和交叉性不足、科研与教学的融合不够紧密的问题，导致研究生难以灵活运用所学知识分析和解决珊瑚礁学科问题；另一方面，课程在思想政治教育方面关注不足，未能充分融入意识形态教育与引导，致使学生的家国情怀、生态环境保护意识以及南海主权意识融入不足，难以全面满足珊瑚礁领域高层次人才对思政素养的要求。因此，积极改革珊瑚礁领域研究生课程教学模式，提升学生探索解决珊瑚礁学科的科学思维、研究能力和创新能力等问题，培养研究生爱国情怀，以适应南海岛礁开发、利用的国家需求，对促进我国珊瑚礁领域紧缺高层次人才的培养具有重要意义。

针对当前珊瑚礁领域研究生培养中存在的“课程内容前沿性、交叉性不足”“科研与教学融合不够紧密”及“生态环境保护意识和南海主权意识及家国情怀薄弱”等问题，拟通过创新课程教学模式，系统推进以下改革措施。首先，通过构建交叉学科引领机制、系统引入前沿知识、深化科研与教学融合、创新研究性教学、强化理论与实践结合，全面提升研究生科学思维、研究能力和创新能力。其次，坚持把爱国主义精神贯穿于研究生课程教学全过程，通过强化生态环境保护意识、南海主权意识，培养学生的家国情怀和责任感。通过以上系统性改革措施，致力于培养既能满足科研与实际发展需求，又具有强烈家国情怀和社会责任感的高层次珊瑚礁领域人才。课程创新改革的具体内容包括交叉学科引领、深化前沿、科教融合、研究性教学模式、理论与实践融合、爱国主义课程思政六个方面（图1）。

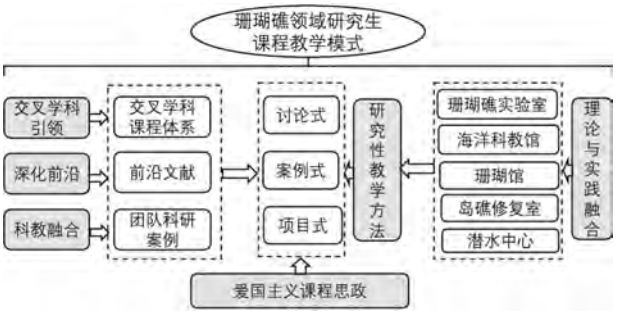


图 1　珊瑚礁领域研究生课程教学改革模式

一、多学科交叉与科教协同驱动的珊瑚礁课程体系重构

传统海洋科学知识传授中，普遍缺乏岛礁系统科学知识传授与研究，学生不具备探索解决珊瑚礁学科的科学思维、研究能力和创新能力。同时，珊瑚礁领域研究生课程内容存在前沿性和交叉性不足、教学方法单一的问题，也极大地阻碍了学生科研能力的培养与提升。基于当前现状，首先，需要积极开展珊瑚礁课程培养模式的改革与创新。其次，需要创新课程教学模式，提升课堂兴趣，激发研究生学习热情。再次，通过将科研案例库引入教学内容，实现基础理论和科研实践的相互衔接。最后，通过师生双主体教学模式，促进教研融合，实现“教学相长”的良性循环。

（一）交叉学科引领

本课程使用的教材是团队主编的《珊瑚礁科学概论》。该书汇集了珊瑚礁领域最新的科学研究成果，并系统融入了长江学者特聘教授余克服团队教师的科研成果，是我国迄今唯一的一部关于珊瑚礁的综合性教材。依据教材与学时安排，教学内容整合为 10 个专题：包括南海珊瑚礁对全球变化的响应与适应、珊瑚礁概述、珊瑚礁形成演化与地貌、珊瑚礁生态系统及其生物多样性、珊瑚礁保护管理、珊瑚礁区碳氮循环与海洋环境、珊瑚礁对海洋环境变化的记录、微环礁与全新世珊瑚礁环境记录、冷水珊瑚礁、珊瑚礁地下水、珊瑚礁监测技术。通过系统介绍珊瑚礁的基本科学原理与交叉学科最新研究成果，为研究生提供深入了解珊瑚礁生态系统及其变化的科学框架。

（二）深化前沿、科教融合

团队成员教学科研能力突出。近五年内，共主持科研项目（含 2 项国家自然科学基金重点项目）和省部级科研项目 17 项，累计科研经费 6370 万元；发表有关珊瑚礁的学术论文 197 篇，其中 SCI 论文 149 篇。依托上述项目成果，团队将取得的最新科研成果构建论文研究型和工程型教学案例库 23 个，并以理论和实践相结合的方式将相关案例贯穿于课程教学中，从而为探索更优化的珊瑚礁领域高层次人才教学模式提供有力支撑。比如，在“珊瑚的繁殖”一节，引入团队最新揭示的丛生盔形珊瑚 Galaxea fascicularis 从排卵、受精到形成幼体的全过程生活史；在“珊瑚礁白化”内容中，讲述团队基于遥感海水温度数据分析得到南海珊瑚热白化年及 El Niño 等驱动事件。在“珊瑚礁生态修复”内容中，融合南海不同纬度滨珊瑚对高温响应的差异性及其机制的研究成果，以及团队在广西涠洲岛珊瑚礁的生态修复效果，为珊瑚礁生态修复实践提供

中国知网　https://www.cnki.net

启示性指导。

（三）创新课程教学模式

综合运用讨论式、案例式、项目式等多种研究性教学方法，将教师的科研思维、方法、过程和成果有机融入授课内容，全面提升学生的科学思维和研究、创新能力。以讨论式教学为例，教师在课前精心设计问题，并在课堂上通过师生共同研讨和分析这些问题，科学地引导学生进行深入思考。比如，以小组形式在珊瑚礁生态系统课程上讨论珊瑚白化的成因与解决方案，每组围绕气候变化、人类活动、现有保护措施、创新性解决方案中的一个讨论问题进行深入探讨，每组选出代表向全班汇报讨论结果。基于讨论式教学方法，学生不仅能够深入理解珊瑚礁白化这一复杂问题，还能在讨论中培养科学思维和实践能力，为未来的科研和社会贡献打下坚实基础。该课程还鼓励学生组成跨学科的小组，来自环境科学、海洋科学、遥感等不同学科背景的研究生将互相合作，从多维度、多角度方面共同探讨和解决珊瑚礁领域问题。

二、做好实践教学

广西大学海洋学院已建成 5 个集教学、科研与社会服务于一体的校内人才培养平台：广西南海珊瑚礁研究重点实验室（省部级重点实验室）、广西大学海洋科教馆（广西海洋科普与意识教育基地）、涠洲岛珊瑚馆（首批广西海洋科普与意识教育基地）、海洋学院岛礁生态修复实验室、广西大学 SSI- 潜水中心。

依托这些平台和基地开展与课程内容相符合的实践活动，将理论与实践相结合，使学生能够在课内了解珊瑚礁科学考察实践与特色的实验，弥补课堂教学缺乏真实性与体验感的缺陷，培养学生的科学思维和思辨能力。比如，海洋学院岛礁生态修复实验室为 100 多平方米，建设 28 套珊瑚室内养殖系统，培育珊瑚 800 余株，并有 18 套珊瑚礁生态模拟实验缸，正在开展珊瑚对温度适应、营养盐、环境污染物胁迫的响应机制等方面的研究。在教学过程中安排学生至实验室考察，认识不同类别的珊瑚，掌握其肉眼鉴定特征，培养学生对于珊瑚的鉴定识别能力。同时，向研究生介绍珊瑚养殖实验室的研究性工作，激发学生的求知欲、探索欲和珊瑚礁保护意识。此外，基于课程实践教学，引导学生积极参与导师课题，研究实施方案，并参加潜水与珊瑚礁科学考察，做好学用并重、教研融合创新能力培养的教学改革。

三、推行爱国主义课程思政

南海星罗棋布的珊瑚礁事关我国海洋领土完整、主权行使与资源安全，故珊瑚礁课程思政尤为关键。深度挖掘我国开发南海珊瑚礁开发史、南海岛礁保卫史、南海岛礁建设史等典型案例，并融入相匹配的课程教学内容中，把价值理念贯穿在教育教学的全过程，以引领学生胸怀远大理想，厚植家国情怀，激发学习热情。具体实施方法如下。

（一）强化课程思政育人理念

在教学设计中，充分挖掘我国开发南海珊瑚礁的历史、南海岛礁保卫史、南海岛礁建设史等典型事件，形成课程思政教学案例库，以激发学生的爱国主义情怀。例如，珊瑚礁的自然地理证据表明，我国自汉代以来就对南海诸岛进行了不同程度的探测，这是我国拥有南海诸岛主权的重要证据。自 20 世纪 70 年代以来，为捍卫南海珊瑚岛礁主权，我国军民在南海进行了一系列艰苦卓绝的斗争，涌现出许多可歌可泣的英雄事迹，如 1974 年西沙群岛保卫战、1988 年南沙群岛赤瓜礁保卫战、2012 年的黄岩岛事件等。近年来，南海岛礁建设成效显著，英雄礁赤瓜礁已从曾经的海上高脚屋变成如今的战略岛礁，渚碧礁堡也变为小岛。这些课程思政案例不仅提升了课堂兴趣，而且有助于学生深入认识课程价值，并激发了学生投身于珊瑚礁事业的爱国情感。

（二）发挥课堂与实践的思政引领作用

授课教师通过明确任务目标，将教学内容划分为不同的任务点，然后根据不同任务点的特点，在线上和线下课堂中融入多项思想政治元素，实现专业知识与思想政治教育同向同行育。课后思政延伸部分以学生自主学习以及交流为主，教师引导为辅的原则，使学生在自主学习与交流过程中，自觉加强思想道德建设。实验室实践思政部分将思政蕴含在教学实践中，通过实验室的实践部分进一步提升研究生教学质量和培养学生爱国精神及勇于开拓创新的科研理想。

四、课程考核教学改革

本课程采用全过程、开放式、多样化的评价考核方式，注重学生综合素质的培养与能力的全面评估。成绩评定的核心在于知识与能力的综合评价，特别强调平时学习考核、小组讨论表现、课后思考题的独立思考和逻辑分析能力、自主学习能力等方

1629
中国知网 https://www.cnki.net

面。此外，课程期末采用撰写学位论文方式进行考核，要求基于各自的科研方向对教师给定主题进行深入探讨。学生需要综合运用所学的研究方法，从多角度分析研究问题，并基于分析得出合理观点。此外，课程鼓励学生将他们的研究成果投稿到国际期刊或者学术会议。通过这一形式，引导学生综合运用理论知识，提升其分析问题、解决问题的科研能力，培养其独立思考与学术研究的综合能力。

结语

针对珊瑚礁领域研究生课程教学存在“课程内容前沿性、交叉性不足”“科研与教学融合不够紧密”以及“生态环境保护意识、南海主权意识薄弱、家国情怀欠缺”等问题，本研究从创新研究生课程教学方式方法入手，打破理论与实践教学壁垒，开展系统性教学改革与创新。通过构建交叉学科引领机制、系统引入前沿知识、深化科研与教学融合、创新研究性教学模式等系列举措，深化研究生对珊瑚礁领域知识体系的理解，提升其分析及解决问题的能力。依托多平台实践教学，弥补课堂教学缺乏真实性与体验感的缺陷，进一步培养学生的科学思维和思辨能力。同时，将我国开发南海珊瑚礁的保卫与建设史等典型事件融入研究生课程理论与实践教学中，通过爱国主义课程思政，强化理想信念教育核心地位，牢筑研究生家国情怀与艰苦奋斗的精神。通过以上系统性改革举措，培养出了既能满足科研与实际发展需求，又具有强烈家国情怀和社会责任感的高层次珊瑚礁领域人才。

【参考文献】

[1] 教育部 . 关于加快新时代研究生教育改革发展的意见 [EB/OL]. (2020-09-23)[2025-04-20]. http://www.mof.gov.cn/zhengwuxinxi/caizhengxinwen/202009/t20200923_3593379.htm.

[2] 黄良民，林强，谭烨辉，等 . 热带海洋特色生态系统恢复重构与保护思考 [J]. 热带海洋学报，2024,43(6):1-12.

[3] 曲金良，秦立志，金永明 . “中国海洋强国建设的重要成就与启示”笔谈 [J]. 中国海洋大学学报 (社会科学版)，2024(4):1-10.DOI:10.16497/j.cnki.1672-335X.202404001.

[4] 余克服 . 珊瑚礁科学概论 [M]. 北京：科学出版社，2018.

[5] 李娟 . 青年教师在研究生培养过程中实践“教学相长”模式的探讨论 [J]. 广东化工，2017,44(18):240-243.

[6] 胡鑫，郭渊 .2015—2024 年南海疆域史研究评述——以国内文献为中心的考察 [J/OL]. 海南热带海洋学院学报，1-14[2025-05-20].

[7] 曾昭璇 . 中国珊瑚礁地貌研究 [M]. 广州：广东人民出版社，1997.

[8] 范双双，廖喜扬，汪慧，等 . 海洋强国背景下海洋技术课程思政教学探索与实践 [J]. 大学教育，2025(3):1-7+13.

【基金项目】2024 年广西研究生教育创新计划项目“《珊瑚与岛礁》研究生通识类教材建设的探索与实践”（项目编号：JGY2024002）；2025 年广西大学校级本科教学改革工程项目重点项目，项目名称：广西大学海洋科教馆“馆课一体”模式的探索与实践—以《走进海洋》课程为例（项目编号：JG2025ZDIAN038）。

【作者简介】左秀玲（1986—），女，汉族，山东济南人，博士，副教授，研究方向：珊瑚礁生态与遥感；梁甲元（1986—），男，汉族，广西桂平人，博士，副教授，研究方向：珊瑚礁生物；苏宏飞（1984—），男，壮族，广西南宁人，副教授，研究方向：珊瑚礁生物；梁作栋（1992—），男，汉族，广西灵山人，博士，讲师，研究方向：海洋和珊瑚礁工程

【通讯作者】余克服（1969—），男，汉族，湖北荆州人，博士，教授，研究方向：珊瑚礁系统科学

中国知网 https://www.cnki.net



广西南海珊瑚礁研究重点实验室
广西大学海洋学院、珊瑚礁研究中心

广西南宁市 - 西乡塘区大学东路100号
广西大学综合实验大楼
邮政编码：530004
联系电话：0771-3231358/3227855